SPRINGER
REFERENCE

VDI-Gesellschaft
Verfahrenstechnik und
Chemieingenieurwesen
Editor

VDI Heat Atlas

Second Edition

VDI

Springer

VDI Heat Atlas

Verein Deutscher Ingenieure
VDI-Gesellschaft Verfahrenstechnik und Chemieingenieurwesen (GVC)
Editor

VDI Heat Atlas

Second Edition

With 1011 Figures and 539 Tables

Springer

Editor
VDI e. V.
VDI-Gesellschaft Verfahrenstechnik und Chemieingenieurwesen
(VDI-GVC)
VDI-Platz 1
40468 Düsseldorf
Germany

1st edition published in 1993 by VDI-Verlag GmbH, Düsseldorf.

ISBN 978-3-540-77876-9 e-ISBN 978-3-540-77877-6
Print and electronic bundle ISBN 978-3-540-79999-3
DOI 10.1007/978-3-540-77877-6
Springer Heidelberg Dordrecht London New York

Library of Congress Control Number: 2010924812

Printed on acid-free paper

Springer is part of Springer Science+Business Media (www.springer.com)

Preface to the Second English Edition

The *VDI-Wärmeatlas* or *VDI Heat Atlas* has a long-lasting history and it can be considered as a standard book for heat exchanger and process engineering equipment design. It is not conceived as a textbook presenting an overall view of the theoretical or experimental findings in heat transfer sciences. The aim was and is to present and explain the state of the art of engineering methods to solve industrially relevant heat transfer problems for apparatus design and process modeling. The first German edition was published in 1963. The sixth German edition was translated into English to meet the demands of the more and more internationally acting industry. This first English edition was published in 1992. Since then, the German edition was regularly updated until the tenth edition published in 2006.

In view of today's globally acting industry, the editorial board felt the necessity to revise the English edition in order to account for the most recent state of our knowledge. Instead of only translating the latest German edition, we preferred restructuring it at the same time because this also enabled us to include new subjects and to update methods according to the recent state of the art. This new structure will also serve as a basis for the forthcoming German edition.

On behalf of the editorial board, I express my sincere thanks to the authors of the various sections for their contributions and kind cooperation. The editorial work was coordinated and assisted by Mrs. Sigrid Cuneus from Springer-Verlag, Berlin. We are indebted to her for the efficient work and pleasant collaboration. We are also grateful to Mrs. Tina Shelton from the Reference and Database Publishing group, Springer Reference Editorial, India, who handled the editorial workflow.

Professor Dr.-Ing. Peter Stephan, Editor-in-Chief
Darmstadt, May 2010

WE SUPPORT YOU

- → Heat Exchanger / Heat Transfer
- → Pressure Drop
- → Combustion
- → 2 Phase Flow
- → Properties of Gases and Fluids
- → Tube Bundle Vibration
- → Steam Generators for Chemical Plants / Power Plants


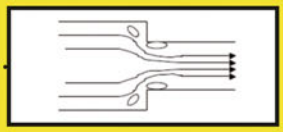

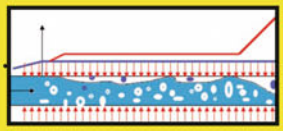
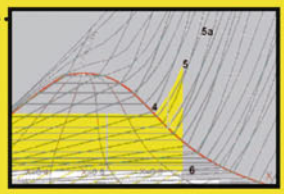

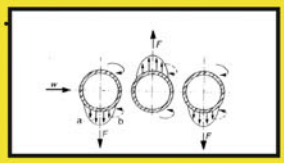
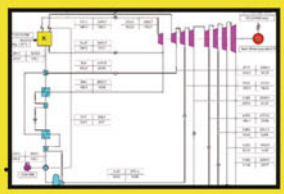

Contact us

KED GmbH
Talstr. 3
63517 Rodenbach
Germany

christian.voneichhain@ked.de
www.ked.de/heatatlas

Editorial Board to the Second English Edition

Prof. Dr.-Ing. Peter Stephan
Technische Universität Darmstadt
Fachbereich Maschinenbau
Institut für Technische Thermodynamik
Petersenstraße 30
64287 Darmstadt
Germany
pstephan@ttd.tu-darmstadt.de

Prof. Dr.-Ing. Stephan Kabelac
Helmut-Schmidt Universität
Universität der Bundeswehr Hamburg
Institut für Thermodynamik
Holstenhofweg 85
22043 Hamburg
Germany
Kabelac@hsu-hh.de

Prof. Dr.-Ing. Matthias Kind
Karlsruher Institut für Technologie (KIT)
Institut für Thermische Verfahrenstechnik
Kaiserstraße 12
76131 Karlsruhe
Germany
matthias.kind@kit.edu

Prof. Dr.-Ing. Holger Martin
Karlsruher Institut für Technologie (KIT)
Institut für Thermische Verfahrenstechnik
Kaiserstraße 12
76131 Karlsruhe
Germany
holger.martin@kit.edu

Prof. Dr.-Ing. Dr. h. c. Dieter Mewes
Leibniz Universität Hannover
Institut für Mehrphasenprozesse IMP
Callinstraße 36
30167 Hannover
Germany
mewes@imp.uni-hannover.de

Prof. Dr.-Ing. Karlheinz Schaber
Karlsruher Institut für Technologie (KIT)
Institut für Technische Thermodynamik und Kältetechnik ITTK
Engler-Bunte-Ring 21
76131 Karlsruhe
Germany
Karlheinz.schaber@kit.edu

Table of Contents

K Radiation

L Fluid Dynamics and Pressure Drop

Contributors

Klaus Anders, Dr.-Ing.[†]
Stuttgart
Germany

Hein Auracher, Prof. Dr.-Ing.
Stuttgart
Germany
heinaur@gmx.de

Wolfgang Bender, Dipl.-Ing.
VDEh-Betriebsforschungsinstitut GmbH
Düsseldorf
Germany

Thomas Bodmer, Dipl.-Ing.
Marl
Germany
thomas.bodmer@eon-energie.com

Hans-Gerd Brummel, Dr.-Ing.
Siemens Power Generation
Berlin
Germany
hans-gerd.brummel@siemens.com

Ulrich Busweiler, Prof. Dr.-Ing.
Sachverständigenbüro
Darmstadt
Germany
ulrich.busweiler@mmew.fh-giessen.de

Jogindar Mohan Chawla, Prof. Dr.-Ing.[†]
Ettlingen
Germany

Hans Detlef Dahl, Dr.-Ing.
Marl
Germany
h-dahl@versanet.de

Paul J. Erens, Dr.
Private Consulting Engineer
Stellenbosch
Republic of South Africa
paulerens@snowisp.com

Axel Eschner, Dr.
Osterode (Harz)
Germany
Axel.Eschner@t-online.de

Felix Flohr, Dipl.-Ing.
Solvay Fluor GmbH
Hannover
Germany
Felix.Flohr@solvay.com

Arnold Frohn, Prof. Dr.
Universität Stuttgart
Stuttgart
Germany
arnold.frohn@t-online.de

Edward S. Gaddis, Dr.-Ing.
Technische Universität Clausthal
Clausthal-Zellerfeld
Germany
Edward.Gaddis@t-online.de

Gerd Gaiser, Dr.-Ing.
Reutlingen
Germany
Gerd.Gaiser@eberspaecher.com

Bernhard Gampert, Prof. Dr.-Ing. habil.
Universität Duisburg-Essen
Essen
Germany
bfjg2008@gmx.de

Horst Gelbe, Prof. Dr.-Ing.
Technische Universität Berlin
Berlin
Germany
h.gelbe@gmx.de

Andreas Glück, Dr.
HTT Vertriebsbüro Süd GmbH
Ebersbach
Germany
a.glueck@htt.de

Volker Gnielinski, Prof. Dr.-Ing.
Karlsruher Institut für Technologie (KIT)
Karlsruhe
Germany
volker.gnielinski@tvt.uka.de

Dieter Gorenflo, Prof. Dr.-Ing.
Universität Paderborn
Paderborn
Germany
digo@thet.uni-paderborn.de

[†]Deceased

Klaus Görner, Prof. Dr.-Ing.
Universität Duisburg-Essen
Essen
Germany
luat@uni-due.de

Erich Hahne, Prof. Dr.-Ing.
Universität Stuttgart
Stuttgart
Germany
hahne@itw.uni-stuttgart.de

Helmuth Hausen, Dr.-Ing.†
Hannover
Germany

Wolfgang Heidemann, Dr.-Ing.
Universität Stuttgart
Stuttgart
Germany
heidemann@itw.uni-stuttgart.de

Oliver Herbst, Dr.
AREVA NP GmbH
Erlangen
Germany
Oliver.Herbst@areva.com

Ulrich Hochberg, Prof. Dr.-Ing.
Hochschule Offenburg
University of Applied Sciences
Offenburg
Germany
Ulrich.Hochberg@FH-Offenburg.de

Christof Hübner, Dr.-Ing.
Fraunhofer-Institut für Chemische Technologie (ICT)
Pfinztal
Germany
christof.huebner@ict.fraunhofer.de

Dietmar Hunold, Dr.-Ing.
HTT Energy Systems GmbH
Herford
Germany
d.hunold@htt.de

Ralph Joh, Dr. rer. nat.
Siemens AG
Frankfurt
Germany
ralph.joh@siemens.com

Stephan Kabelac, Prof. Dr.-Ing.
Helmut-Schmidt-Universität
Universität der Bundeswehr Hamburg
Hamburg
Germany
Kabelac@hsu-hh.de

Günther Kasparek, Dr.-Ing.
Munich
Germany
guenther.kasparek@t-online.de

Werner Kast, Prof. Dr.-Ing.
Technische Universität Darmstadt
Darmstadt
Germany

Anastassios Katsaounis, Prof. Dipl.-Ing.
Beuth Hochschule für Technik Berlin
Berlin
Germany
akatsaounis@arcor.de

Paul Bernd Kempa, Dr.
Fraunhofer-Institut für Chemische Technologie (ICT)
Pfinztal
Germany
paul-bernd.kempa@ict.fraunhofer.de

David Kenning, Prof. Dr.
Brunel and Oxford Universities
UK
David.Kenning@brunel.ac.uk

Matthias Kind, Prof. Dr.-Ing.
Karlsruher Institut für Technologie (KIT)
Karlsruhe
Germany
matthias.kind@kit.edu

Günther Kirchner, Dipl.-Ing.
BASF SE, Ludwigshafen
Germany
guenther.kirchner@basf.com

Herbert Klan, Dr.-Ing.
Technische Universität Darmstadt
Darmstadt
Germany

Michael Kleiber, Dr.-Ing.
Uhde GmbH
Bad Soden
Germany
michael.kleiber@thyssenkrupp.com

Gernot Krakat
FRAGOL Schmierstoffe GmbH & Co.
Mülheim (Ruhr), Germany
g.krakat@fragol.de

Rolf Krauss, Dipl.-Ing.
Universität Stuttgart
Stuttgart
Germany
krauss@itt.uni-stuttgart.de

Hans-Joachim Kretzschmar, Prof. Dr.-Ing. habil.
Hochschule Zittau/Görlitz
University of Applied Sciences
Zittau
Germany
HJ.Kretzschmar@hs-zigr.de

Alfred Leipertz, Prof. Dr.-Ing.
Friedrich-Alexander-Universität Erlangen-Nürnberg
Erlangen
Germany
sek@ltt.uni-erlangen.de

Xing Luo, Prof. Dr.-Ing.
Helmut-Schmidt-Universität
Universität der Bundeswehr Hamburg
Hamburg
Germany
luoxing1122@hotmail.com

Holger Martin, Prof. Dr.-Ing.
Karlsruher Institut für Technologie (KIT)
Karlsruhe
Germany
holger.martin@kit.edu

Alfons Mersmann, Prof. Dr.-Ing.
Technische Universität München
Munich
Germany
alfons.mersmann@online.de

Dieter Mewes, Prof. Dr.-Ing. Dr. h. c.
Leibniz Universität Hannover
Hannover
Germany
mewes@imp.uni-hannover.de

Nimai-Kumar Mitra, Prof. Dr.-Ing†
Bochum
Germany

Jürgen Müller, Dr.-Ing.
BASF AG Ludwigshafen
Germany
juergen.mueller@basf-ag.de

Hans Müller-Steinhagen, Prof. D. Eng. Dr.-Ing.
Universität Stuttgart
Stuttgart
Germany
Hans.Mueller-Steinhagen@dlr.de

Sebastian Muschelknautz, Dr.-Ing.
Linde AG, Pullach
Germany
sebastian.muschelknautz@linde-le.com

Ulrich Muschelknautz, Prof. Dr.-Ing.
MK Engineering
Innsbruck
Austria
um@mkengineering.de

Matthias Neubronner, Dr.-Ing.
EON Energie
Munich
Germany
matthias.neubronner@eon-energie.com

Hermann Nirschl, Prof. Dr.-Ing. habil.
Karlsruher Institut für Technologie (KIT)
Karlsruhe
Germany
hermann.nirschl@kit.edu

Reiner Numrich, Prof. Dr.-Ing.
Paderborn
Germany
r.numrich@numrich-gev.de

Fabian Ochs, Dipl.-Ing.
Universität Stuttgart
Stuttgart
Germany
fabian.ochs@gmx.net

Andreas Pfennig, Prof. Dr.-Ing.
RWTH Aachen
Aachen
Germany
andreas.pfennig@avt.rwth-aachen.de

Ewald Preisegger, Dipl.-Ing.
Solvay Fluor GmbH
Hannover
Germany
familie.preisegger@gmx.de

Norbert Räbiger, Prof. Dr.-Ing.
Universität Bremen
Bremen
Germany
nraebiger@iuv.de

Harald Reiss, Prof. Dr. rer. nat.
Julius-Maximilians-Universität Würzburg
Würzburg
Germany

Wolfgang Richter, Dr.-Ing.†
Essen
Germany

Wilfried Roetzel, Prof. Dr.-Ing.
Helmut-Schmidt-Universität
Universität der Bundeswehr Hamburg
Hamburg
Germany
Wilfried.Roetzel@hsu-hh.de

Norbert Roth, Dr.-Ing.
Universität Stuttgart
Stuttgart
Germany
norbert.roth@itlr.uni-stuttgart.de

Yasushi Saito, Dr. Eng.
Kyoto University
Osaka
Japan
ysaito@rri.kyoto-u.ac.jp

Wilhelm Schabel, Prof. Dr.-Ing.
Karlsruher Institut für Technologie (KIT)
Karlsruhe
Germany
wilhelm.schabel@kit.edu

Karlheinz Schaber, Prof. Dr.-Ing.
Karlsruher Institut für Technologie (KIT)
Karlsruhe
Germany
Karlheinz.Schaber@KIT.edu

Ernst-Ulrich Schlünder, Prof. Dr.-Ing. Dr. h. c.
Karlsruher Institut für Technologie (KIT)
Karlsruhe
Germany

Michael Schlüter, Prof. Dr.-Ing.
Technische Universität Hamburg-Harburg
Hamburg
Germany
michael.schlueter@tu-harburg.de

Florian Schmidt, Dr.-Ing.
Bayer Technology Services GmbH
Krefeld
Germany
florian.schmidt@bayertechnology.com

Holger Schmidt, Dr.-Ing.
Areva NP GmbH
Erlangen
Germany
Holger.Schmidt@areva.com

Jürgen Schmidt, Prof. Dr.-Ing.
BASF SE
Ludwigshafen
Germany
juergen.schmidt@onlinehome.de

Klaus Gerhard Schmidt, Prof. Dr.-Ing.
Institut für Energie- und Umwelttechnik (IUTA) e.V.
Duisburg
Germany
k.schmidt@iuta.de

Günter Schnabel, Dr.-Ing.
BIDECO GmbH
Biberach (Riss)
Germany
guenter.schnabel@bideco.de

Günter H. Schnerr, Prof. Dr.-Ing. habil.
Technische Universität München
Garching
Germany
Schnerr@flm.mw.tu – muenchen.de

Jens-Jürgen Schröder, Dr.-Ing.[†]
Hannover
Germany

Martin Sommerfeld, Prof. Dr.-Ing. habil.
Martin-Luther-Universität Halle-Wittenberg
Halle (Saale)
Germany
martin.sommerfeld@iw.uni-halle.de

Roland Span, Prof. Dr.-Ing.
Ruhr-Universität Bochum
Bochum
Germany
roland.span@thermo.rub.de

Bernhard Spang, Dr.-Ing.
BUCO Wärmeaustauscher International GmbH
Geesthacht
Germany
bernhard@spang-hh.de

Martin H. Spitzner, Dr.-Ing.
FIW München
Gräfelfing
Germany

Dieter Steiner, Prof. Dr.-Ing.[†]
Karlsruhe
Germany

Karl Stephan, Prof. Dr.-Ing.
Universität Stuttgart
Stuttgart
Germany
stephan.karl1@gmx.de

Peter Stephan, Prof. Dr.-Ing.
Technische Universität Darmstadt
Darmstadt
Germany
pstephan@ttd.tu-darmstadt.de

Johann Stichlmair, Prof. Dr.-Ing.
Technische Universität München
Garching
Germany
Johann.Stichlmair@apt.mw.tum.de

André Thess, Prof. Dr.-Ing.
Technische Universität Ilmenau
Ilmenau
Germany
tthess@tu-ilmenau.de

Evangelos Tsotsas, Prof. Dr.-Ing.
Otto-von-Guericke-Universität Magdeburg
Magdeburg
Germany
evangelos.tsotsas@vst.uni-magdeburg.de

Dieter Vortmeyer, Prof. Dr.
Munich
Germany

Manfred H. Wagner, Prof. Dr.-Ing.
Technische Universität Berlin
Berlin
Germany
manfred.wagner@tu-berlin.de

Wolfgang Wagner, Prof. Dr.-Ing.
Ruhr-Universität Bochum
Bochum
Germany
wagner@thermo.rub.de

Bernhard Weigand, Prof. Dr.-Ing.
Universität Stuttgart
Stuttgart
Germany
itlr@itlr.uni-stuttgart.de

Anton Wellenhofer, Dipl.-Ing.
Linde AG, Pullach
Germany
anton.wellenhofer@linde-le.com

Hans Werner, Prof. Dr.-Ing.
Hochschule für Angewandte Wissenschaften (FH)
München
Germany
dr.hans.werner@t-online.de

Karl-Ernst Wirth, Prof. Dr.-Ing.
Friedrich-Alexander-Universität Erlangen-Nürnberg
Erlangen
Germany
k.e.wirth@lfg.uni-erlangen.de

Hartwig Wolf, Dr.-Ing.
Alstom Switzerland Ltd.
Baden
Switzerland
hartwig.wolf@power.alstom.com

Manfred Zeller, Prof. Dr.-Ing.
RWTH Aachen
Aachen
Germany
manfred.zeller@rwth-aachen.de

Samir Ziada, Prof. Dr.-Ing.
McMaster University
Hamilton, ON
Canada
ziadas@mcmaster.ca

Symbols, Units and Dimensionless Numbers

A1 Symbols and Units

Matthias Kind · Holger Martin
Karlsruher Institut für Technologie (KIT), Karlsruhe, Germany

1 Introduction: Legal Units

"The International Committee for Weights and Measures" (BIPM, Paris) publishes the "SI Brochure" [1]. Most of the base and derived units used in this VDI-Heat Atlas are SI units and are assorted below. The SI units are the units that are recognized globally in order to establish a worldwide dialog and can be seen in the further reading. Although there are a variety of non-SI units for the same quantity in the literature, only some of them can be found below due to the fact that not all of them are widely used [2, 3].

As of October 2007, there are 51 Member States of the Metre Convention and 25 Associate States and Economies of the General Conference.

2 SI Base Units of Base Quantities

Quantity	Symbol of the quantity	Unit	Symbol of the unit
Length	$L, x, y, z, r, \ldots$	Meter	m
Mass	M, m	Kilogram	kg
Time	t	Second	s
Electric current	I, i	Ampere	A
Thermodynamic temperature	T	Kelvin	K
Amount of substance	N	Mol	mol
Luminous intensity	I_v	Candela	cd

3 SI Derived Units with Special Names and Symbols

Quantity	Symbol of the quantity	SI coherent derived unit[a]			
		Unit	Symbol of the unit	Expressed in terms of other SI units	Expressed in terms of SI base units
Plane angle	$\alpha, \beta, \gamma, \ldots$	Radian[b]	rad	1[b]	m/m
Solid angle	$\alpha, \beta, \gamma, \ldots$	Steradian[b]	sr[c]	1[b]	m^2/m^2
Frequency	f	Hertz[c]	Hz		s^{-1}
Force	F	Newton	N		m kg s^{-2}
Pressure, stress	p, P, σ, τ	Pascal	Pa	N/m^2	m^{-1} kg s^{-2}
Energy, work, amount of heat	E, W, Q	Joule	J	N m	m^2 kg s^{-2}
Power, heat flow	$P, \dot{Q}$	Watt	W	J/s	m^2 kg s^{-3}
Electric charge, amount of electricity	Q	Coulomb	C		s A

VDI-GVC (ed.), *VDI Heat Atlas*, DOI 10.1007/978-3-540-77877-6_1,

Quantity	Symbol of the quantity	SI coherent derived unit[a]			
		Unit	Symbol of the unit	Expressed in terms of other SI units	Expressed in terms of SI base units
Electric potential	U	Volt	V	W/A	$m^2\ kg\ s^{-3}\ A^{-1}$
Capacitance	C	Farad	F	C/V	$m^{-2}\ kg^{-1}\ s^4\ A^2$
Electric resistance	R	Ohm	Ω	V/A	$m^2\ kg\ s^{-3}\ A^{-2}$
Electric conductance	G	Siemens	S	A/V	$m^{-2}\ kg^{-1}\ s^3\ A^2$
Magnetic flux	Φ	Weber	Wb	V s	$m^2\ kg\ s^{-2}\ A^{-1}$
Magnetic flux density	B	Tesla	T	Wb/m^2	$kg\ s^{-2}\ A^{-1}$
Inductance	L	Henry	H	Wb/A	$m^2\ kg\ s^{-2}\ A^{-2}$
Celsius temperature	ϑ	Degree Celsius[d]	°C		K
Luminous flux	I	Lumen	lm	cd sr[e]	cd
Illuminance	E	Lux	lx	lm/m^2	m^{-2} cd
Activity referred to a radionuclide[f]		Becquerel[c]	Bq		s^{-1}
Absorbed dose, specific energy (imparted), kerma		Gray	Gy	J/kg	$m^2\ s^{-2}$
Dose equivalent, ambient dose equivalent, directional dose equivalent, personal dose equivalent		Sievert[g]	Sv	J/kg	$m^2\ s^{-2}$
Catalytic activity		Katal	kat		s^{-1} mol

[a]The SI prefixes (see Sect. 7) may be used with any of the special names and symbols, but when this is done, the resulting unit will no longer be coherent.
[b]Radian and steradian are special names for the number 1 that may be used to convey information about the quantity concerned. In practice, the symbols rad and sr are used where appropriate, but the symbol for the derived unit 1 is generally omitted in specifying the values of dimensionless quantities.
[c]Hertz is used only for periodic phenomena, and Becquerel is used only for stochastic processes in activity referred to a radionuclide.
[d]Degree Celsius is the special name for Kelvin, which is used to express Celsius temperatures. Degree Celsius and the Kelvin are equal in size, so that the numerical value of a temperature difference or temperature interval is the same when expressed in either degree Celsius or Kelvin.
[e]In photometry, the name steradian and the symbol sr are usually retained in expression for units.
[f]Activity referred to a radionuclide is sometimes incorrectly called radioactivity.
[g]See http://www.bipm.org/en/CIPM/db/2002/2/ on the use of the sievert.

4 Quantities and Symbols

The following alphabetically listed symbols are generally used in the Heat Atlas. Other more specific notations and symbols, which may differ from the ones listed here are defined within the special sections if needed.

4.1 Quantities

Quantity	Symbol of the quantity	Symbol of the unit
Acceleration of gravity	g	$m\ s^{-2}$
Amount of substance	N	mol
Coefficient of thermal expansion	β	K^{-1}
Coordinate in flow direction	x	m
Coordinate perpendicular to flow direction	y	m
Coordinate perpendicular to flow direction	z	m
Cross-sectional area	A, S	m^2
Density	ρ	$kg\ m^{-3}$
Diameter	D	m
Diffusion coefficient	D_{ij}, δ_{ij}	$m^2\ s^{-1}$
Dynamic viscosity	η	Pa s
Emissivity	ε	1
Energy	E	J
Enthalpy	H	J
Enthalpy stream	$\dot{H}$	W
Entropy	S	$J\ K^{-1}$
Gibbs enthalpy	G	J
Heat	Q	J
Heat flow	$\dot{Q}$	W
Heat flux	$\dot{q}$	$W\ m^{-2}$
Heat transfer coefficient	α	$W\ m^{-2}\ K^{-1}$
Hydraulic diameter $d_h = 4 \times$ cross-sectional area/circumference	d_h	m
Individual gas constant	R	$J\ kg^{-1}\ K^{-1}$
Internal energy	U	J
Kinematic viscosity	ν	$m^2\ s^{-1}$
Length	L, l	m
Mass	M, m	kg
Mass flow rate	$\dot{M}$	$kg\ s^{-1}$

Quantity	Symbol of the quantity	Symbol of the unit
Mass flux	$\dot{m}$	kg m^{-2} s^{-1}
Mass fraction of component j in the liquid or vapor phase, respectively	x_j, y_j	kg kg^{-1}
Mass loading of component j in the liquid or vapor phase, respectively	X_j, Y_j	kg kg^{-1}
Mass transfer coefficient of a component *i*	β_i	m s^{-1}
Molar density	n	mol m^{-3}
Molar enthalpy	$\tilde{h}$	J mol^{-1}
Molar entropy	$\tilde{s}$	J mol^{-1} K^{-1}
Molar flow	$\dot{N}$	mol s^{-1}
Molar flux	$\dot{n}$	mol m^{-2} s^{-1}
Molar Gibbs enthalpy	$\tilde{g}$	J mol^{-1}
Molar heat capacity at constant pressure or volume respectively	$\tilde{c}_p$, $\tilde{c}_v$	J mol^{-1} K^{-1}
Molar internal energy	$\tilde{u}$	J mol^{-1}
Molar mass	$\tilde{M}$	kg kmol^{-1}
Molar loading of component j in the liquid or vapor phase, respectively	$\tilde{X}_j$, $\tilde{Y}_j$	mol mol^{-1}
Molar volume	$\tilde{v}$	m^3 mol^{-1}
Mole fraction of component j in the liquid or vapor phase, respectively	$\tilde{x}_j$, $\tilde{y}_j$	mol mol^{-1}
Overall heat transfer coefficient	k	W m^{-2} K^{-1}
Overall mass transfer coefficient	k'	m s^{-1}
Partial pressure of component *j*	p_j	Pa; bar
Power	P	W
Radiation coefficient	C	W m^{-2} K^{-4}
Radius	r	M
Specific enthalpy	h	J kg^{-1}
Specific entropy	s	J kg^{-1} K^{-1}
Specific Gibbs enthalpy	g	J kg^{-1}
Specific heat capacity at constant pressure or volume, respectively	c_p, c_v	J kg^{-1} K^{-1}
Specific internal energy	u	J kg^{-1}
Specific volume	v	m^3 kg^{-1}
Surface, phase interphase	A	m^2
Surface tension	σ	N m^{-1}
Temperature difference (or centigrade temperature)	θ	K
Thermal conductivity	λ	W m^{-1} K^{-1}
Thermal diffusivity	κ	m^2 s^{-1}
Thermodynamic temperature	T	K
Time	t	s
Total pressure	p	Pa; bar
Universal gas constant	$\tilde{R}$	J mol^{-1} K^{-1}
Vapor quality (ratio of vapor mass flow/total mass flow)	$\dot{x}$	1
Vapor pressure of component *j*	p_{0j}	Pa; bar
Velocity in *x*-direction	u	m s^{-1}
Velocity in *y*-direction	v	m s^{-1}
Velocity in *z*-direction	w	m s^{-1}
Velocity of sound	c	m s^{-1}
Volumetric flow rate	$\dot{V}$	m^3 s^{-1}
Voidage, gas volume fraction	ψ	1
Volume	V	m^3
Wall thickness	s	m
Work	W	J

4.2 Symbols

Latin letters

Symbol of the quantity	Unit	Quantity
A	m^2	Surface, phase interphase
A, S	m^2	Cross-sectional area
a	ms^{-1}	Velocity of sound
C	W m^{-2} K^{-4}	Radiation coefficient
c_p, c_v	J kg^{-1} K^{-1}	Specific heat capacity at constant pressure or volume respectively
$\tilde{c}_p$, $\tilde{c}_v$	J mol^{-1} K^{-1}	Molar heat capacity at constant pressure or volume respectively
D_{ij}	m^2 s^{-1}	Diffusion coefficient
D	M	Diameter
d_h	m	Hydraulic diameter $d_h = 4 \times$ cross-sectional area/circumference
E	J	Energy
G	J	Gibbs enthalpy
g	J kg^{-1}	Specific Gibbs enthalpy
$\tilde{g}$	J mol^{-1}	Molar Gibbs enthalpy
g	m s^{-2}	Acceleration of gravity
H	J	Enthalpy
$\dot{H}$	W	Enthalpy stream
h	J kg^{-1}	Specific enthalpy
$\tilde{h}$	J mol^{-1}	Molar enthalpy
k	W m^{-2} K^{-1}	Overall heat transfer coefficient
k'	m s^{-1}	Overall mass transfer coefficient
W	J	Work
$\dot{W}$	W	Power
L, l	m	Length
M	kg	Mass
$\tilde{M}$	kg kmol^{-1}	Molar mass
$\dot{M}$	kg s^{-1}	Mass flow rate
$\dot{m}$	kg m^{-2} s^{-1}	Mass flux
N	mol	Amount of substance
$\dot{N}$	mol s^{-1}	Molar flow
n	mol m^{-3}	Molar density
$\dot{n}$	mol m^{-2} s^{-1}	Molar flux
p	Pa; bar	Total pressure
p_j	Pa; bar	Partial pressure of component *j*
p_{0j}	Pa; bar	Vapor pressure of component *j*

Symbol of the quantity	Unit	Quantity
Q	J	Heat
$\dot{Q}$	W	Heat flow
$\dot{q}$	W m^{-2}	Heat flux
R	J kg^{-1} K^{-1}	Individual gas constant
$\widetilde{R}$	J mol^{-1} K^{-1}	Universal gas constant
r	m	Radius
S	J K^{-1}	Entropy
s	J kg^{-1} K^{-1}	Specific entropy
$\widetilde{s}$	J mol^{-1} K^{-1}	Molar entropy
s	m	Wall thickness
T	K	Thermodynamic temperature
t	s	Time
U	J	Internal energy
u	J kg^{-1}	Specific internal energy
$\widetilde{u}$	J mol^{-1}	Molar internal energy
u	m s^{-1}	Velocity in x-direction
V	m^3	Volume
$\dot{V}$	m^3 s^{-1}	Volumetric flow rate
v	M^3 kg^{-1}	Specific volume
$\widetilde{v}$	m^3 mol^{-1}	Molar volume
v	m s^{-1}	Velocity in y-direction
w	m s^{-1}	Velocity in z-direction
X_j, Y_j	kg kg^{-1}	Mass loading in the liquid or vapor phase
$\widetilde{X}_j$, $\widetilde{Y}_j$	mol mol^{-1}	Molar mass loading in the liquid or vapor phase of component j, respectively
x_j, y_j	kg kg^{-1}	Mass fraction in the liquid or vapor phase of component j, respectively
$\widetilde{x}_j$, $\widetilde{y}_j$	mol mol^{-1}	Mole fraction in the liquid or vapor phase
$\dot{x}$	1	Vapor quality (ratio of vapor mass flow/total mass flow)
x	m	Coordinate in flow direction
y	m	Coordinate perpendicular to flow direction
z	m	Coordinate perpendicular to flow direction

Greek letters

Symbol of the quantity	Unit	Quantity
α	W m^{-2} K^{-1}	Heat transfer coefficient
β_i	m s^{-1}	Mass transfer coefficient of a component i
β	K^{-1}	Coefficient of thermal expansion
δ_{ij}	m^2 s^{-1}	Diffusion coefficient
ε	1	Emissivity
η	Pa s	Dynamic viscosity
θ	K	Temperature difference (or centigrade temperature)
κ	m^2 s^{-1}	Thermal diffusivity
λ	W $m^{-1}K^{-1}$	Thermal conductivity
ν	m^2 s^{-1}	Kinematic viscosity
ρ	kg m^{-3}	Density
σ	N m^{-1}	Surface tension
ψ	1	Voidage, gas volume fraction

Subscripts to denote

Phase

F	Fluid phase
G	Gas phase
L	Liquid phase
S	Solid phase

Time

I	Initial value
t	Instantaneous value
F	Final value

Position

o	Outside
out	At the exit
in	At the inlet
i	Inside
loc	Local value
s	At the surface
w	At the wall

State

c	At the critical point
p	At constant pressure
r	Relative (related to the corresponding value at the critical point)
v	At constant volume
′, ″,	(Superscripts) at the phase boundaries

Process

lam	In laminar flow
turb	In turbulent flow
rev	Reversible

Others

tot	Total
LM	Logarithmic mean
m	Mean
G0	Total mass flow as gas
L0	Total mass flow as liquid

5 Non-SI Units Accepted for Use with the SI, and Units Based on Fundamental Constants

Quantity	Symbol of the quantity	Name of the unit	Symbol of the unit	Value in SI unit
Time	t	Minute	min	1 min = 60 s
		Hour[a]	h	1 h = 60 min = 3,600 s
		day	d	1 d = 24 h = 86,400 s
Plane angle	α, β, γ,. . .	Degree[b,c]	°	1° = (π/180) rad
		Minute	′	1′ = (1/60)° = (π/10,800) rad
		Second[d]	″	1″ = (1/60)′ = (π/648,000) rad
Area	A, S	Hectare[e]	ha	1 ha = 1 hm^2 = 10^4 m^2
Volume	V	Liter[f]	L, l	1 L = 1 l = 1 dm^3 = 10^3 cm^3 = 10^{-3} m^3
Mass	M, m	Ton[g]	t	1 t = 10^3 kg

[a]The symbol of this unit is included in "Resolution 7" of the 9th CGPM (1948).
[b]ISO 31 recommends that the degree be divided decimally rather than using minute and second. For navigation and surveying, however, minute has the advantage that one minute of latitude on the surface of the Earth corresponds (approximately) to one nautical mile.
[c]Gon (or grad(e), where grad is an alternative name for the gon) is an alternative unit of plane angle to the degree, defined as (π/200) rad. Thus, there are 100 gon in a right angle. The potential value of gon in navigation is that because the distance from the pole to the equator of the Earth is approximately 10,000 km, 1 km on the surface of the Earth subtends an angle of one centigon at the center of the Earth. However, gon is rarely used.
[d]For applications in astronomy, small angles are measured in arcseconds (i.e., seconds of plane angle), denoted as "milliarcseconds, microarcseconds, and picoarcseconds, denoted as mas, μas, and pas," respectively, where arcsecond is an alternative name for second of plane angle.
[e]The unit hectare and its symbol ha were adopted by the CIPM in 1879 (PV, 1879, 41). Hectare is used to express land area.
[f]Liter and the symbol lower case l were adopted by the CIPM in 1879 (PV, 1879, 41). The alternative symbol, capital L, was adopted by the 16th CPGM (1979, "Resolution 6") in order to avoid the risk of confusion between the letter l (el) and the numeral 1 (one).
[g]Ton and its symbol t were adopted by the CIPM in 1879 (PV, 1879, 41). In English-speaking countries, this unit is usually called "metric ton."

6 Other Non-SI Units Not Recommended for Use

Values in **boldface** are exact

Acceleration

Foot per second squared, 1 ft/s^2	**= 3.048 · 10^{-1}**	m/s^2
Inch per second squared, 1 in/s^2	**= 2.54 · 10^{-2}**	m/s^2

Angle

1 Mil	**= 5.625 · 10^{-2}**	°
1 Revolution®	= 6.283 185	rad

Area and second moment of area

Square foot, 1 ft^2	**= 9.290 304 · 10^{-2}**	m^2
Square inch, 1 in^2	= **6.451 6 · 10^{-4}**	m^2
Square mile, 1 mi^2	= 2.589 988 · 10^{-4}	m^2

Capacity, see volume

Density, see mass divided by volume

Electricity and magnetism

Biot, 1 Bi	**= 1.0 · 10^1**	A
Franklin, 1 Fr	= 3.335 641 · 10^{-10}	C
Gamma, 1 γ	= **1.0 · 10^{-9}**	T

Energy (includes work)

Calorie (15°C), 1 cal_{15}	= 4.185 80	J
Calorie (20°C), 1 cal_{20}	= 4.181 90	J
Electronvolt, 1 eV	= 1.602 177 · 10^{-19}	J
Erg, 1 erg	= **1.0 · 10^{-7}**	J

Energy divided by area time

Erg per square centimeter second, 1 $erg/(cm^2 \cdot s)$	= **1.0 · 10^{-3}**	W/m^2

Flow, see mass divided by time, or see volume divided by time

Force

Dyne, 1 dyn	**= 1.0 · 10^{-5}**	N
Kilogram-force, 1 kgf	= **9.806 65**	N

Force divided by area, see pressure

Force divided by length

Pound-force per foot, 1 lbf/ft	= 1.459 390 · 10^1	N/m

Heat, available energy

British thermal $unit_{IT}$ per cubic foot, 1 Btu_{IT}/ft^3	= 3.725 895 · 10^4	J/m^3

British thermal $unit_{th}$ per cubic foot, 1 Btu_{th}/ft^3	$= 3.723\,403 \cdot 10^4$	J/m^3

Heat, coefficient of heat transfer

British thermal $unit_{th}$ per second square foot degree Fahrenheit, 1 $Btu_{th}/(s \cdot ft^2 \cdot °F)$	$= 2.042\,808 \cdot 10^4$	$W/(m^2 \cdot K)$

Heat, density of heat

$Calorie_{th}$ per square centimeter, 1 cal_{th}/cm^2	$\mathbf{= 4.184 \cdot 10^4}$	J/m^2

Heat, density of heat flow rate

$Calorie_{th}$ per square centimeter minute, 1 $cal_{th}/(cm^2 \cdot min)$	$= 6.973\,333 \cdot 10^2$	W/m^2

Heat, fuel consumption

Gallon (US) per horsepower hour, 1 $gal/(hp \cdot h)$	$= 1.141\,089 \cdot 10^{-9}$	m^3/J

Heat, heat capacity and entropy

British thermal $unit_{IT}$ per degree Fahrenheit, 1 $Btu_{IT}/°F$	$= 1.899\,101 \cdot 10^3$	J/K
British thermal $unit_{th}$ per degree Fahrenheit, 1 $Btu_{th}/°F$	$= 1.897\,830 \cdot 10^3$	J/K

Heat, heat flow rate

$Calorie_{th}$ per minute, 1 cal_{th}/min	$= 6.973\,333 \cdot 10^{-2}$	W

Heat, specific heat capacity and specific entropy

$Calorie_{IT}$ per gram kelvin, 1 $cal_{IT}/(g \cdot K)$	$\mathbf{= 4.186\,8 \cdot 10^3}$	$J/(kg \cdot K)$
$Calorie_{th}$ per gram kelvin, 1 $cal_{th}/(g \cdot K)$	$= \mathbf{4.184 \cdot 10^3}$	$J/(kg \cdot K)$

Heat, thermal conductivity

$Calorie_{th}$ per centimeter second degree Celsius, 1 $cal_{th}/(cm \cdot s \cdot °C)$	$= \mathbf{4.184 \cdot 10^2}$	$W/(m \cdot K)$

Heat, thermal diffusivity

Square foot per hour, 1 ft^2/h	$= \mathbf{2.580\,64 \cdot 10^{-5}}$	m^2/s

Heat, thermal insulance

Clo, 1 clo	$= 1.55 \cdot 10^{-1}$	$m^2 \cdot K/W$
Degree Fahrenheit hour square foot per British thermal $unit_{IT}$, 1 $°F \cdot h \cdot ft^2/Btu_{IT}$	$= 1.761\,102 \cdot 10^{-1}$	$m^2 \cdot K/W$
Degree Fahrenheit hour square foot per British thermal $unit_{th}$, 1 $°F \cdot h \cdot ft^2/Btu_{th}$	$= 1.762\,280 \cdot 10^{-1}$	$m^2 \cdot K/W$

Heat, thermal resistance

Degree Fahrenheit second per British thermal $unit_{IT}$, 1 $°F \cdot s/Btu_{IT}$	$= 5.265\,651 \cdot 10^{-4}$	K/W
Degree Fahrenheit second per British thermal $unit_{th}$ 1 $°F \cdot s/Btu_{th}$	$= 5.269\,175 \cdot 10^{-4}$	K/W

Heat, thermal resistivity

Degree Fahrenheit hour square foot per British thermal $unit_{IT}$ inch $[°F \cdot h \cdot ft^2/(Btu_{IT} \cdot in)]$	= 6.933 472	$m \cdot K/W$

Length

Angström, 1 Å	$\mathbf{= 1.0 \cdot 10^{-10}}$	m
Micron, 1 µm	$= \mathbf{1.0 \cdot 10^{-6}}$	m
Mil (0.001 in), 1 mil	$= \mathbf{2.54 \cdot 10^{-5}}$	m
Mile, 1 mi	$= \mathbf{1.609\,344 \cdot 10^3}$	m
Yard, 1 yd	$= \mathbf{9.144 \cdot 10^{-1}}$	m

Light

Candela per square inch, 1 cd/in^2	$= 1.550\,003 \cdot 10^3$	cd/m^2
Lumen per square foot, 1 lm/ft^2	$= 1.076\,391 \cdot 10^1$	lx

Mass and moment of inertia

Grain, 1 gr	$= \mathbf{6.479\,891 \cdot 10^{-5}}$	kg
Ounce (avoirdupois), 1 oz	$= 2.834\,952 \cdot 10^{-2}$	kg
Ounce (troy or apothecary), 1 oz	$= 3.110\,348 \cdot 10^{-2}$	kg
Pound (avoirdupois) (*1), 1 lb	$= 4.535\,924 \cdot 10^{-1}$	kg
Pound (troy or apothecary), 1 lb	$= 3.732\,417 \cdot 10^{-1}$	kg
Ton, assay, 1 AT	$= 2.916\,667 \cdot 10^{-2}$	kg
Ton, metric, 1 t	$= \mathbf{1.0 \cdot 10^3}$	kg

Mass density see mass divided by volume

Mass divided by area

Ounce (avoirdupois) per square foot, 1 oz/ft^2	$= 3.051\,517 \cdot 10^{-1}$	kg/m^2
Ounce (avoirdupois) per square inch, 1 oz/in^2	$= 4.394\,185 \cdot 10^1$	kg/m^2
Pound per square foot, 1 lb/ft^2	= 4.882 428	kg/m^2

Mass divided by capacity see mass divided by volume

Mass divided by length

Denier, 1 denier	$= 1.111\,111 \cdot 10^{-7}$	kg/m

Mass divided by time (includes flow)

Pound per hour, 1 lb/h	$= 1.259\,979 \cdot 10^{-4}$	kg/s

Mass divided by volume (includes mass density and mass concentration)

Grain per gallon (U.S.), 1 gr/gal	= 1.711 806 · 10^{-2}	kg/m^3
Pound per cubic foot, 1 lb/ft^3	= 1.601 846 · 10^{1}	kg/m^3

Moment of force or torque

Dyne centimeter, 1 dyn · cm	= **1.0 · 10^{-7}**	N · m
Kilogram-force meter, 1 kgf · m	= **9.806 65**	N · m

Moment of force or torque divided by length

Pound-force foot per inch, 1 lbf · ft/in	= 5.337 866 · 10^{1}	N · m/m
Pound-force inch per inch, 1 lbf · in/in	= 4.448 222	N · m/m

Permeability

Darcy (*2), 1 darcy	= 9.869 233 · 10^{-13}	m^2

Power

Erg per second, 1 erg/s	**= 1.0 · 10^{-7}**	W
Foot pound-force per hour, 1 ft · lbf/h	= 3.766 161 · 10^{-4}	W
Horsepower (metric), 1 hp	= 7.354 988 · 10^{2}	W
Horsepower (U.K.), 1 hp	= 7.457 0 · 10^{2}	W
Horsepower (electric), 1 hp	= 7.460 43 · 10^{2}	W
Horsepower (boiler), 1 hp	= 9.809 50 · 10^{3}	W

Pressure or stress (force divided by area)

Atmosphere, standard, 1 atm	**= 1.013 25 · 10^{5}**	Pa
Atmosphere, technical (*3), 1 at	= **9.806 65 · 10^{4}**	Pa
Bar, 1 bar	= **1.0 · 10^{5}**	Pa
Millimeter of mercury, conventional (*4), 1 mmHg	= 1.333 224 · 10^{2}	Pa
Millimeter of water, conventional (*4), 1 mmH_2O	= **9.806 65**	Pa
Pound-force per square inch (psi), lbf/in^2), 1 psi	= 6.894 757 · 10^{3}	Pa
Torr, 1 Torr	= 1.333 224 · 10^{2}	Pa

Radiology

Curie, 1 Ci	= **3.7 · 10^{10}**	Bq
Rad (absorbed dose), 1 rad	= **1.0 · 10^{-2}**	Gy
Rem, 1 rem	= **1.0 · 10^{-2}**	Sv
Roentgen, 1 R	= **2.58 · 10^{-4}**	C/kg

Speed see **velocity**

Stress see **pressure**

Temperature

Degree Celsius, 1°C	T/K = t/°C + **273.15**	K
Degree centigrade(*5), 1 degree centigrade	t/°C ≈ t/deg. cent.	°C
Degree Fahrenheit, 1°F	t/°C = (t/°F − **32**)/**1.8**	°C
Degree Fahrenheit, 1°F	T/K = t/°F + **459.67**)/**1.8**	K
Degree Rankine, 1°R	T/K = (T/°R)/**1.8**	K

Temperature Interval

Degree Celsius, 1°C	**= 1.0**	K
Degree centigrade(*5), 1 degree centigrade	= 1.0	°C
Degree Fahrenheit, 1°F	= 5.555 556 · 10^{-1}	°C
Degree Fahrenheit, 1°F	= 5.555 556 · 10^{-1}	K
Degree Rankine, 1°R	= 5.555 556 · 10^{-1}	K

Time

Day, 1 d	= **8.64 · 10^{4}**	s
Year (365 days), 1 year	= **3.153 6 · 10^{7}**	s

Torque, see **moment of force**

Velocity (includes speed)

Foot per hour, 1 ft/h	= 8.466 667 · 10^{-5}	m/s
Mile per hour, 1 mi/h	= **4.470 4 · 10^{-1}**	m/s

Viscosity, dynamic

Centipoise, 1 cP	= **1.0 · 10^{-3}**	Pa · s
Poise, 1 P	= **1.0 · 10^{-1}**	Pa · s

Viscosity, kinematic

Centistokes, 1 cSt	= **1.0 · 10^{-6}**	m^2/s
Stokes, 1 St	= **1.0 · 10^{-4}**	m^2/s
Square foot per second, 1 ft^2/s	= **9.290 304 · 10^{-2}**	m^2/s

Volume (includes capacity)

Cubic foot, 1 ft^3	= 2.831 685 · 10^{-2}	m^3
Liter (*6), 1 L	= **1.0 · 10^{-3}**	m^3
Gallon (US), 1 gal	= 3.785 412 · 10^{-3}	m^3

Volume divided by time

Cubic foot per minute, 1 ft^3/min	= 4.719 474 · 10^{-4}	m^3/s
Cubic foot per minute, 1 ft^3/min	= 4.719 474 · 10^{-1}	L/s
Cubic inch per minute, in^3/min	= 2.731 177 · 10^{-7}	m^3/s
Cubic yard per minute, 1 yd^3/min	= 1.274 258 · 10^{-2}	m^3/s
Gallon (U.S.) per minute (gpm), 1 gal/min	= 6.309 020 · 10^{-5}	m^3/s

Work see **energy**

(*1) The exact conversion factor is $4.535\ 923\ 700 \cdot 10^{-1}$. All units that contain pound refer to the avoirdupois pound.
(*2) Darcy is a unit for expressing the permeability of porous solids, not area.
(*3) One technical atmosphere equals one kilogram-force per square centimeter (1 at = 1 kgf/cm^2).
(*4) Conversion factors for mercury manometer pressure units are calculated using the standard value for the acceleration of gravity and the density of mercury at the stated temperature. Additional digits are not justified because the definitions of the units do not take into account the compressibility of mercury or the change in density caused by the revised practical temperature scale, ITS-90. Similar comments also apply to water manometer pressure units.
(*5) The centigrade temperature scale is obsolete; the degree centigrade is only approximately equal to degree Celsius
(*6) In 1964, the General Conference on Weights and Measures reestablished the name "liter or litre" as a special name for the cubic decimeter. Between 1901 and 1964, liter was slightly larger (1.000 028 dm^3); when one uses high-accuracy volume data of that time, this fact must be kept in mind.

7 SI Prefixes

Decimal multipliers and parts of units can be described by means of prefixes that are written before the names of the units.

Factor	Prefix	Abbreviation
10^{24}	Yotta	Y
10^{21}	Zetta	Z
10^{18}	Exa	E
10^{15}	Peta	P
10^{12}	Tera	T
10^{9}	Giga	G
10^{6}	Mega	M
10^{3}	Kilo	k
10^{2}	Hecto	h
10^{1}	Deca	da
10^{-1}	Deci	d
10^{-2}	Centi	c
10^{-3}	Milli	m
10^{-6}	Micro	μ
10^{-9}	Nano	n
10^{-12}	Pico	p
10^{-15}	Femto	f
10^{-18}	Atto	a
10^{-21}	Zepto	z
10^{-24}	Yocto	y

8 Bibliography

1. SI Brochure, 8th ed. The International Committee for Weights and Measures, 2006
2. http://www.bipm.org/
3. http://www.bipm.org/en/si/si_brochure/

Fundamentals of Heat Transfer

B1 Fundamentals of Heat Transfer

Peter Stephan
Technische Universität Darmstadt, Darmstadt, Germany

1 Introduction

The term *heat* is defined by the first law of thermodynamics as the energy that is transported across the boundary of a thermodynamic system due to a temperature difference between the system and its surroundings. The first law of thermodynamics in a general form can be written as follows:

$$\Delta E = W + Q + E_{\mathrm{M}}. \tag{1}$$

The right hand side of this equation summarizes the three different forms of energy that can be transported across the system boundary: heat Q, work W, and energy E_{M} that is tied to a mass transport. As a result of such energy transfer across the system boundary the energy inside the system changes by ΔE, written on the left hand side of the equation. The transport process related to the transfer of heat is called *heat transfer*. Applying the second law of thermodynamics, one can derive that heat is always transferred in the direction of decreasing temperature. But thermodynamics does not tell us how the amount of heat transferred depends on this driving temperature difference or temperature gradient. Nor does it tell us how it depends on the geometry of a heat exchanger, or on material or process properties, including the duration of the process. Before these dependencies can be described in detail some general relations and definitions must be given.

The heat transferred per unit of time is referred to as the *heat flow rate* $\dot{Q}$ (SI-unit W),

$$\dot{Q} = \frac{\mathrm{d}Q}{\mathrm{d}t}. \tag{2}$$

The *heat flux* $\dot{q}$ (SI-unit W/m^2) is defined by

$$\dot{q} = \frac{\mathrm{d}\dot{Q}}{\mathrm{d}A} \tag{3}$$

and describes the heat transferred per unit of time and per unit area perpendicular to the heat flow. Generally, three modes of heat transfer are distinguished:

- *Conduction*,
- *Convection*, and
- *Radiation*.

The detailed description of calculation procedures for heat transfer related to all these modes in general and for many specific technical applications is subject of the *VDI Heat Atlas*

VDI-GVC (ed.), *VDI Heat Atlas*, DOI 10.1007/978-3-540-77877-6_3,

(Parts E–N). Additionally, fundamental heat exchanger design and construction methods as well as information on material properties are presented (Parts C, D, and O). In the following Chapters of Part B, the fundamentals of the three heat transfer modes and primary rules of calculation procedures are presented and applied in an exemplary manner to some basic configurations. For further details, the reader is referred to the specific parts of the *VDI Heat Atlas*.

2 Heat Transfer Modes and Basic Principles of Their Description

2.1 Heat Conduction

Conduction is the transfer of energy due to molecular interactions between neighbouring molecules caused by their random motion. Thus, heat conduction can take place in solids, liquids, or gases, but it does not require any macroscopic motion or flow of the substance. With increasing temperature the random motion of molecules is intensified, and with this the kinetic energy on the molecular level. Collisions between neighboring molecules cause a transfer of energy from those with higher kinetic energy to those with lower kinetic energy. In metals, the energy transported by free electrons additionally contributes to heat conduction.

Fortunately, we do not need to look closely into the details and statistics of these molecular processes to derive calculation procedures for heat conduction. It is sufficient to know a single material property together with the local driving temperature gradient. Considering a temperature gradient $\partial T/\partial x$ in direction of a coordinate x, the heat flux $\dot{q}$ depends only on the single material property called *thermal conductivity* λ. The relation

$$\dot{q} = -\lambda \frac{\partial T}{\partial x} \tag{4}$$

is well-known as Fourier's law, named after Jean Baptiste Joseph Fourier, who expressed this relation first in 1822 [1]. The minus sign results from the fact that positive heat transfer is directed toward decreasing temperature. For isotropic materials, i.e., materials with equal thermal conductivities in any direction, Fourier's law can be written in vector form as

$$\vec{\dot{q}} = -\lambda \operatorname{grad} T. \tag{5}$$

The thermal conductivity λ [SI-unit W/(K m)] is typically highest for solids, followed by liquids and gases.

For *gases* under normal conditions λ is approximately in the range

$$0.015\,\mathrm{W/(K\,m)} \le \lambda_{\mathrm{gas}} \le 0.15\,\mathrm{W/(K\,m)}$$

with, e.g., hydrogen at the upper end and carbon dioxide at the lower end of the range. The thermal conductivity of air at atmospheric conditions is, e.g., $\lambda_{\mathrm{air}} \approx 0.0246\,\mathrm{W/(K\,m)}$.

For *liquids* (except liquid metals) under normal conditions λ is approximately in the range

$$0.1\,\mathrm{W/(K\,m)} \le \lambda_{\mathrm{liquid}} \le 0.65\,\mathrm{W/(K\,m)}$$

with, e.g., water at the upper end and carbon dioxide or some organic liquids at the lower end of the range. The thermal conductivity of liquid water at atmospheric conditions is, e.g., $\lambda_{\mathrm{water,liq.}} \approx 0.6\,\mathrm{W/(K\,m)}$.

For *solids* under normal conditions λ is approximately in the range

$$1\,\mathrm{W/(K\,m)} \le \lambda_{\mathrm{solid}} \le 450\,\mathrm{W/(K\,m)}$$

with, e.g., metallic materials such as silver and copper at the upper end and nonmetallic materials such as coal, glass, or ice at the lower end of the range. The thermal conductivity of ice (solid water) at 0°C is, e.g., $\lambda_{\mathrm{water,ice}} \approx 2.2\,\mathrm{W/(K\,m)}$, values for some metallic materials are $\lambda_{\mathrm{copper}} \approx 395\,\mathrm{W/(K\,m)}$, $\lambda_{\mathrm{aluminum}} \approx 220\,\mathrm{W/(K\,m)}$, or $\lambda_{\mathrm{st.steel,18Cr8Ni}} \approx 21\,\mathrm{W/(K\,m)}$.

Further data and details such as dependency on temperature or pressure can be found in Part D.

2.2 Convective Heat Transfer

Convection refers to the heat transport mode in a macroscopically flowing fluid. It is a superposition of conductive heat transport in the fluid and the energy transport due to the macroscopic movement of the fluid, which includes the transport of enthalpy and kinetic energy. Thus, convective heat flux depends not only on material properties, but also on process properties, such as, e. g., fluid velocity.

For the design of technical devices the descriptions of convective heat transfer from a moving bulk fluid to the solid fluid boundary (wall) or vice versa are of special interest. A situation with a bulk fluid temperature T_{F}, a bulk fluid velocity w_{F} parallel to the wall, and a wall temperature T_{W}, will result in a velocity and a temperature profile in the fluid near the wall as shown in Fig. 1 where y is the direction normal to the wall. The near wall region with high velocity gradients and high temperature gradients are known as *velocity boundary layer* and *temperature boundary layer*. The underlying *boundary layer theory* was formulated first by Prandtl [2].

The convective heat transport normal to the wall in this boundary layer is directed towards the lower temperature, thus for $T_{\mathrm{F}} > T_{\mathrm{W}}$ the wall is heated by the fluid, for $T_{\mathrm{F}} < T_{\mathrm{W}}$ the wall is cooled by the fluid. The heat flux $\dot{q}$ depends on the temperature difference but also on the temperature and velocity profiles in the boundary layer, which can be very complex and even nonstationary, e.g., for turbulent boundary layer flows. However, the simple relation

$$\dot{q} = \alpha(T_{\mathrm{W}} - T_{\mathrm{F}}) \tag{6}$$

allows to calculate the heat flux. Herein, α is the *heat transfer coefficient* [SI-unit $\mathrm{W/(m^2K)}$]. This quantity depends on the relevant fluid and process properties as well as geometrical configurations of the wall or surface roughness, etc.

The thickness of the thermal boundary layer δ_{T} can be approximated as the thickness of a fictitious nonmoving fluid layer adjacent to the wall that results in the same heat flux as the convective one given by Eq. (6). Figure 2 demonstrates this relationship. The temperature profile caused by convective heat transfer is approximated by a linear temperature drop $T_{\mathrm{W}} - T_{\mathrm{F}}$ in the fictitious nonmoving fluid layer and a constant

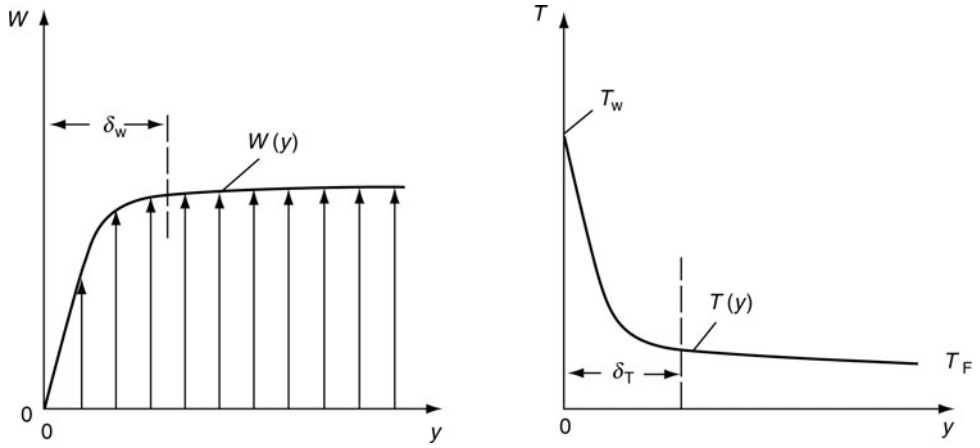

B1. Fig. 1. Boundary layers (left: velocity, right: temperature).

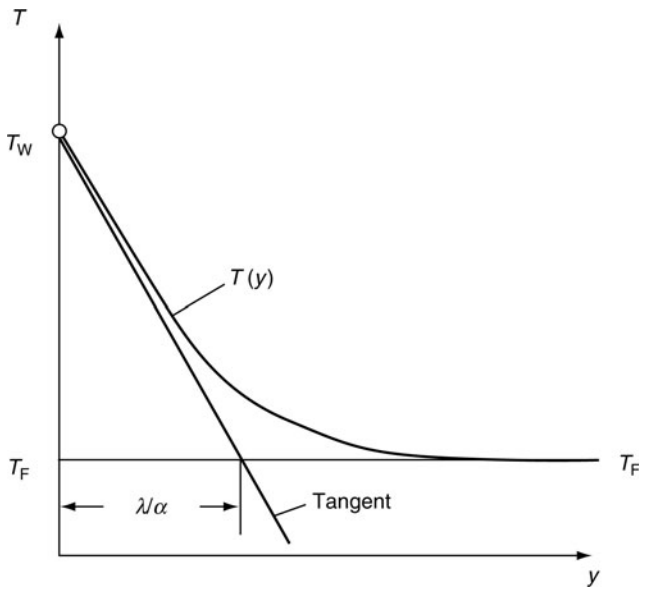

B1. Fig. 2. Thickness $\delta_T \approx \lambda/\alpha$ of the thermal boundary layer.

fluid temperature T_F outside. As the fluid is definitely at rest at the wall surface ($y = 0$) due to the nonslip condition Fourier's law for conduction [Eq. (4)] delivers the relation between heat flux and temperature gradient at the wall surface:

$$\dot{q} = -\lambda \left.\frac{\partial T}{\partial y}\right|_{y=0} . \tag{7}$$

Comparing Eqs. (6) and (7) the thickness of the fictitious nonmoving fluid layer adjacent to the wall follows as λ/α, where λ is the thermal conductivity of the fluid. With this the heat transfer coefficient can also be interpreted as

$$\alpha = -\lambda \frac{\left.\frac{\partial T}{\partial y}\right|_{y=0}}{T_W - T_F} \tag{8}$$

and the thermal boundary layer thickness can be approximated by $\delta_T \approx \lambda / \alpha$.

Based on this theoretical approach the heat transfer coefficient α can be determined for some special cases. However, in general it is determined experimentally and correlations for many technical configurations were derived from such experiments. The basis for the description of the heat transfer coefficient is the use of *similarity methods*.

These descriptions allow the considerable reduction of the number of influencing parameters and for the expression of the general heat transfer laws for geometrically similar bodies and different substances. For this purpose a dimensionless heat transfer coefficient, called *Nusselt number* named after Wilhelm Nusselt, who first formulated dimensionless numbers in this context [3], is defined by

$$\mathrm{Nu} = \frac{\alpha L}{\lambda}, \tag{9}$$

where L is a characteristic length of the system and λ the thermal conductivity of the fluid. To derive correlations for the Nusselt number two situations have to be distinguished: *forced convection* and *natural convection*.

In forced convection, the fluid motion is caused by outer forces, e.g., by the pressure increase in a pump. In natural convection, the fluid motion is caused by density differences in the fluid and the corresponding buoyancy effects in a gravitational field. These density differences usually arise due to temperature differences, rarely due to pressure differences. In mixtures, density differences are also caused by concentration differences.

The flow characteristics in forced convection are generally described by the *Reynolds number*

$$\mathrm{Re} = \frac{w L}{\nu}, \tag{10}$$

where w is the bulk fluid velocity and ν the kinematic viscosity of the fluid.

The flow characteristics in natural convection are generally described by the *Grashof number*

$$\mathrm{Gr} = \frac{L^3 g \beta \Delta T}{\nu^2}, \tag{11}$$

where g is the gravitational acceleration, β the thermal volume expansion coefficient at a reference temperature [typically, $(T_W + T_F)/2$], and $\Delta T = T_W - T_F$ the difference between wall and bulk fluid temperature.

Further some fluid properties can be summarized in the dimensionless form of a *Prandtl number*

$$\mathrm{Pr} = \frac{v}{a}, \tag{12}$$

where $a = \lambda/(\rho\, c_\mathrm{p})$ is the thermal diffusivity, ρ the density, and c_p the constant pressure specific heat.

Based on these dimensionless numbers the heat transfer coefficient α can be expressed by correlations in the following form:

$$\mathrm{Nu} = f_1(\mathrm{Re}, \mathrm{Pr}) \tag{13}$$

for forced convection and

$$\mathrm{Nu} = f_2(\mathrm{Gr}, \mathrm{Pr}) \tag{14}$$

for natural convection.

Typical values of α for different situations are:

2–25	W/m^{2}K	For free convection in gases
10–1,000	W/m^{2}K	For free convection in liquids
25–250	W/m^{2}K	For forced convection in gases
50–20,000	W/m^{2}K	For forced convection in liquids
2,500–100,000	W/m^{2}K	For boiling and condensing fluids

2.3 Thermal Radiation

The energy emitted by any matter to its surroundings in the form of electromagnetic waves is called *radiation*. Unlike conduction or convection the energy transport from a location A to a location B by radiation is not bounded to any interlinking transport medium because electromagnetic waves can travel through a vacuum.

Every matter or body emits radiation corresponding to its surface temperature (To be more precise one should write "Every matter or body with $T > 0$ K emits ...," but as known from thermodynamics other bodies do not exist.). The maximum radiation possible for a given temperature is emitted by a *black body*. A black body can be experimentally approximated by a blackened surface (e.g., with soot) or by a hollow space, whose walls have the same temperature everywhere, that has a small opening to let radiation out. The total radiation emitted by a black body per unit area is

$$\dot{e}_\mathrm{b} = \sigma\, T^4, \tag{15}$$

where $\dot{e}_\mathrm{b}$ is the energy emitted per unit surface area of the black radiator (SI-unit W/m^2), simply called the *emission*, and $\sigma = 5.67 \times 10^{-8}$ W/(m^{2}K^4) is the *radiation coefficient*, also called the *Stefan–Boltzmann constant*. The above relation is called the *Stefan–Boltzmann law*. It was found 1879 by Josef Stefan as a result of many experiments and later in 1884 derived theoretically by his scholar Ludwig Boltzmann [4].

The emission $\dot{e}_\mathrm{b}$ is an energy flux and thus the related heat flux emitted by a black body follows as

$$\dot{q}_\mathrm{b} = \dot{e}_\mathrm{b} = \mathrm{d}\dot{Q}_\mathrm{b}/\mathrm{d}A. \tag{16}$$

The radiation emitted by *real surfaces* is less than the radiation emitted by a black body at the same temperature. The reduced radiative energy or heat flux of a real body $\dot{e}$ compared to a black body is expressed by

$$\dot{e} = \varepsilon \cdot \dot{e}_\mathrm{b} = \varepsilon \cdot \sigma\, T^4, \tag{17}$$

where ε is the *emissivity* of the real surface with $0 \le \varepsilon \le 1$. The emissivity is generally a function of the surface material. It can also be a function of the surface morphology, its temperature, the direction of the radiation, and the wave length of the radiation. However, many surfaces can be treated in good approximation as *grey bodies*, which are defined by $\varepsilon = \text{const}$. Typical values for the emissivity are: $\varepsilon \approx 0.96$ for dead oxidized steel, $\varepsilon \approx 0.3$ for polished steel, $\varepsilon \approx 0.04$ for polished aluminium. Further values are given in Part K.

3 Heat Conduction and Overall Heat Resistances

3.1 One-Dimensional, Steady State Heat Conduction Through a Wall

The heat conduction through a wall under steady state conditions can be analyzed on the basis of Fourier's law [see Eqs. (4) or (5)]. For simple geometries, such as a plane wall or a tube wall, and one-dimensional heat transfer analytical solutions can be derived.

3.1.1 Conduction Through a Plane Wall

If different temperatures T_1 and T_2 are prescribed on two surfaces of a plane wall with the thickness δ, according to Fourier's law the heat

$$Q = \lambda A \frac{T_1 - T_2}{\delta}\, t \tag{18}$$

flows through the area A in the time t. The heat flow rate follows as

$$\dot{Q} = \lambda A \frac{T_1 - T_2}{\delta} \tag{19}$$

and the heat flux as

$$\dot{q} = \lambda \frac{T_1 - T_2}{\delta}. \tag{20}$$

Similar to electric conduction, where a current I flows only when a voltage U exists to overcome the resistance R_el, heat flows only when a temperature difference $\Delta T = T_1 - T_2$ exists:

$$\dot{Q} = \frac{\lambda A}{\delta} \Delta T. \tag{21}$$

Ohm's law for an electrical current flow says $I = U/R_\mathrm{el}$. Analogous to the electrical resistance R_el one can define a *thermal resistance* or *heat resistance*, which is defined by

$$R = \frac{\Delta T}{\dot{Q}} \tag{22}$$

in general (SI-unit K/W). In the case considered above, conduction through the plane wall, the *conductive heat resistance* follows as

$$R_{\text{cond}} = \frac{\delta}{\lambda A}. \tag{23}$$

3.1.2 Conduction Through a Tube Wall

According to Fourier's law, the heat flow rate through a cylindrical area of radius r and length L is

$$\dot{Q} = -\lambda 2\pi r L \frac{\mathrm{d}T}{\mathrm{d}r}. \tag{24}$$

Under steady state conditions, the heat flow rate is the same for all radii and thus $\dot{Q} = \text{const}$. It is therefore possible to separate the variables T and r and to integrate from the inner surface of the cylinder, $r = r_\text{i}$ with $T = T_\text{i}$, to an arbitrary location r with temperature T. The temperature profile in a tube wall of thickness $r - r_\text{i}$ becomes

$$T_\text{i} - T = \frac{\dot{Q}}{\lambda 2\pi L} \ln \frac{r}{r_\text{i}}. \tag{25}$$

With temperature T_o at the outer surface at radius r_o, the heat flow rate through a tube of thickness $r_\text{o} - r_\text{i}$ and length L becomes

$$\dot{Q} = \lambda\, 2\pi\, L \frac{T_\text{i} - T_\text{o}}{\ln(r_\text{o}/r_\text{i})}. \tag{26}$$

In order to get formal agreement with Eq. (19), it is also possible to write

$$\dot{Q} = \lambda A_\text{m} \frac{T_\text{i} - T_\text{o}}{\delta} \tag{27}$$

where $\delta = r_\text{o} - r_\text{i}$ and $A_\text{m} = \frac{A_\text{o} - A_\text{i}}{\ln(A_\text{o}/A_\text{i})}$, if $A_\text{o} = 2\pi r_\text{o} L$ is the outer and $A_\text{i} = 2\pi r_\text{i} L$ is the inner surface of the tube. A_m is the logarithmic mean between outer and inner tube surface.

With this the thermal resistance of the tube can be derived as $R_{\text{cond}} = \delta/(\lambda A_\text{m})$ or

$$R_{\text{cond}} = \frac{\ln(r_\text{o}/r_\text{i})}{\lambda\, 2\pi L}. \tag{28}$$

3.2 Heat Transmission, Overall Heat Resistances, and Overall Heat Transfer Coefficients

Heat transmission through a plane wall

If heat is transferred from a fluid at bulk temperature T_{F1} to a wall by convection, conducted through the wall to the other side, and then transferred to a second fluid at bulk temperature T_{F2}, this process is called *heat transmission* through a wall. The related temperature profile for the case of a plane wall is plotted in Fig. 3.

In case of one-dimensional heat transfer perpendicular to the wall, as assumed above in Sect. 3.1, the two convective heat

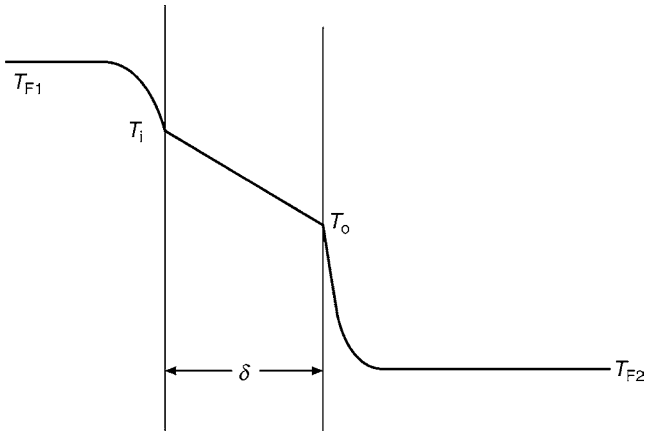

B1. Fig. 3. Heat transmission through a plane wall.

transfer processes and the heat conduction process are connected in series. Thus, analogous to electrical resistances, one can add the individual thermal resistances and thereby write an equation for an *overall heat resistance* as

$$R = \frac{1}{\alpha_\text{i} A} + \frac{\delta}{\lambda A} + \frac{1}{\alpha_\text{o} A} \tag{29}$$

with the two *convective heat resistances* defined by

$$R_{\text{conv}} = \frac{1}{\alpha A}. \tag{30}$$

The heat flow passing through the plane wall then can be written as

$$\dot{Q} = \frac{T_{\text{F1}} - T_{\text{F2}}}{R} \tag{31}$$

or

$$\dot{Q} = k A (T_{\text{F1}} - T_{\text{F2}}) \tag{32}$$

with the quantity k called the *overall heat transfer coefficient* or *heat transmission coefficient* [SI-unit W/(m^{2}K)]. It follows

$$R = \frac{1}{k A}. \tag{33}$$

If the wall consists of several homogeneous layers with thicknesses $\delta_1, \delta_2, \ldots$ and thermal conductivities $\lambda_1, \lambda_2, \ldots$, Eq. (29) holds likewise with the overall heat resistance

$$R = \frac{1}{k A} = \frac{1}{\alpha_\text{i} A} + \sum_j \frac{\delta_j}{\lambda_j A} + \frac{1}{\alpha_\text{o} A}. \tag{34}$$

Of course this analogy to electrical resistances is not restricted to serial circuits but hold also for parallel circuits. In case of parallel heat conduction resistances under the assumption of one-dimensional heat transfer, e.g., the overall heat conduction resistance yields

$$\frac{1}{R} = \frac{1}{\sum_j R_j} = \frac{1}{\sum_j \frac{\delta_j}{\lambda_j A_j}}. \tag{35}$$

Example:

The wall of a cold store consists of a 5 cm thick internal concrete layer [λ = 1 W/(K m)], a 10 cm thick cork stone insolation [λ = 0.04 W/(K m)], and a 50 cm thick external brick wall. The

inner heat transfer coefficient is $\alpha_i = 7\,\mathrm{W/(m^2K)}$ and the outer one $\alpha_o = 20\,\mathrm{W/(m^2K)}$. What is the heat flow rate through 1 $\mathrm{m^2}$ of the wall if the temperatures inside and outside are –5°C and 25°C, respectively?

According to Eq. (34) the overall heat resistance is

$$\frac{1}{kA} = \left(\frac{1}{7\cdot 1} + \frac{0.05}{1\cdot 1} + \frac{0.1}{0.04\cdot 1} + \frac{0.5}{0.75\cdot 1} + \frac{1}{20\cdot 1}\right)\mathrm{K/W} = 3.41\,\mathrm{K/W}$$

The heat flow is $\dot{Q} = \frac{1}{3.41}(-5-25)\,\mathrm{W}$, $|\dot{Q}| = 8.8\,\mathrm{W}$.

3.2.1 Heat Transmission Through a Tube Wall

For one-dimensional heat transmission through tubes, Eqs. (31) and (32) again hold, where the heat resistance is the sum of the individual resistances

$$R = \frac{1}{kA} = \frac{1}{\alpha_i A_i} + \frac{\delta}{\lambda A_m} + \frac{1}{\alpha_o A_o}, \tag{36}$$

where $\delta = r_o - r_i$ and $A_m = \frac{A_o - A_i}{\ln(A_o/A_i)}$ with the outer and inner tube surfaces A_o and A_i, respectively. It becomes obvious that the overall heat transfer coefficient k must be related to a single surface A. This is usually the outer tube surface $A = A_o$, which is often easier to determine.

If the tube consists of several homogeneous layers with thicknesses δ_1, δ_2, ... and thermal conductivities λ_1, λ_2, ... Eq. (34) holds likewise with the overall heat resistance

$$R = \frac{1}{kA} = \frac{1}{\alpha_i A_i} + \sum_j \frac{\delta_j}{\lambda_j A_{mj}} + \frac{1}{\alpha_o A_o}. \tag{37}$$

With the mean logarithmic areas $A_{mj} = (A_{oj} - A_{ij})/\ln(A_{oj}/A_{ij})$.

3.3 Transient Heat Conduction

During transient heat conduction, the temperatures vary with respect to time. Assuming constant thermal conductivity (isotropy) Fourier's heat conduction equation follows as

$$\frac{\partial T}{\partial t} = a\,\nabla^2 T + \dot{q}_s \tag{38}$$

with the volumetric heat source term $\dot{q}_s$ (SI-unit $\mathrm{W/m^3}$) and the quantity a which is a material property and defined as *thermal diffusivity* $a = \lambda/(\rho c)$ (SI-unit $\mathrm{m^2/s}$).

The Laplace operator yields

$$\nabla^2 T = \frac{\partial^2 T}{\partial x^2} + \frac{\partial^2 T}{\partial y^2} + \frac{\partial^2 T}{\partial z^2}$$

for Cartesian coordinates,

$$\nabla^2 T = \frac{1}{r}\frac{\partial}{\partial r}\left(r\frac{\partial T}{\partial r}\right) + \frac{1}{r^2}\frac{\partial^2 T}{\partial \varphi^2} + \frac{\partial^2 T}{\partial z^2}$$

for cylindrical coordinates, and

$$\nabla^2 T = \frac{1}{r^2}\frac{\partial}{\partial r}\left(r^2\frac{\partial T}{\partial r}\right) + \frac{1}{r^2\sin^2\Theta}\frac{\partial^2 T}{\partial \varphi^2} + \frac{1}{r^2\sin\Theta}\frac{\partial}{\partial \Theta}\left(\sin\Theta\frac{\partial T}{\partial \Theta}\right)$$

for polar coordinates.

For plane walls with heat flow in the direction of the x-axis and no heat source, Eq. (38) reduces to

$$\frac{\partial T}{\partial t} = a\,\frac{\partial^2 T}{\partial x^2}. \tag{39}$$

Thus, in a plane wall with prescribed surface temperatures, the temperature profile is no longer linear as the heat transfer into the wall differs from the heat transfer out. The difference between heat transfer in and out increases (or decreases) the internal energy of the wall and thus, its temperature as a function of time.

For the solution of Fourier's equation, it is suitable to introduce – as in other heat transfer problems – dimensionless quantities, which reduce the number of variables. Equation (39) is considered in order to demonstrate the basic procedure. The dimensionless temperature is set to $\Theta = (T - T_c)/(T_0 - T_c)$, where T_c is a characteristic constant temperature and T_0 the initial temperature. If the cooling of a plate with an initial temperature T_0 in a cold environment is considered, T_c could be, for example, the ambient temperature T_{env}. All lengths are related to a characteristic length X, e.g., half of the plate thickness. Furthermore, it is suitable to introduce the dimensionless time, which is called *Fourier number*, as $\mathrm{Fo} = at/X^2$. The solution of the heat conduction equation then has the dimensionless form

$$\Theta = f(x/X, \mathrm{Fo}). \tag{40}$$

In many problems, the heat conducted internally to the surface of a solid body is transferred by convection to the surrounding fluid of temperature T_{env}. The energy balance then holds at the surface (index w = wall)

$$-\lambda\left(\frac{\partial T}{\partial x}\right)_w = \alpha\,(T_w - T_{env}) \tag{41}$$

or

$$\frac{1}{\Theta_w}\left(\frac{\partial \Theta}{\partial \xi}\right)_w = -\frac{\alpha X}{\lambda}, \tag{42}$$

where $\xi = x/X$, $\Theta = (T - T_{env})/(T_0 - T_{env})$ and $\Theta_w = (T_w - T_{env})/(T_0 - T_{env})$. The solution is also a function of the dimensionless quantity $\alpha X/\lambda$, which is defined as the *Biot number* Bi, where the thermal conductivity λ of the solid body is assumed to be constant, and α is the heat transfer coefficient between the body and surrounding fluid. Solutions of Eq. (39) considering the Biot number have the form

$$\Theta = f(x/X, \mathrm{Fo}, \mathrm{Bi}). \tag{43}$$

3.3.1 Semi-Infinite Body

Temperature changes may also take place in a region that is thin in comparison to the overall dimensions of the body. Such a body is called semi-infinite. In this case, a semi-infinite plane wall (Fig. 4) with a constant initial temperature T_0 is considered. At time $t = 0$, the surface temperature of the wall is reduced to $T(x = 0) = T_{env}$ and then remains constant. The temperature

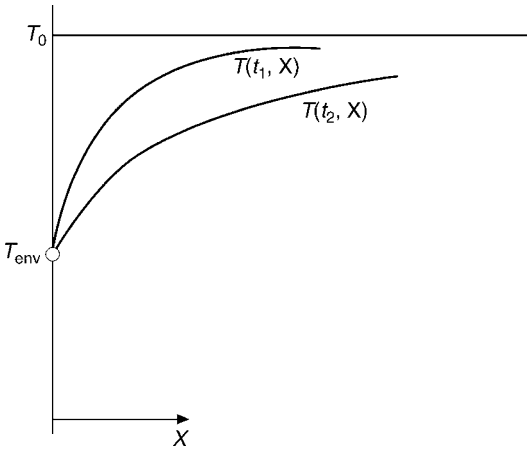

B1. Fig. 4. Semi-infinite body.

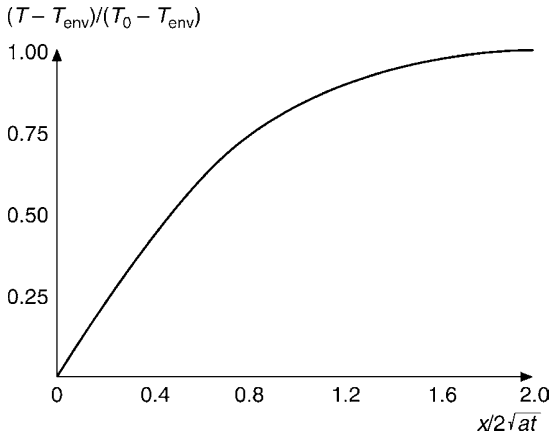

B1. Fig. 5. Temperature profile in a semi-infinite body.

profiles normal to the surface at different times t_1, t_2. ... are given by:

$$\frac{T - T_{env}}{T_0 - T_{env}} = f\left(\frac{x}{2\sqrt{a\,t}}\right) \tag{44}$$

with the Gaussian error function $f\left(x/\left(2\sqrt{a\,t}\right)\right)$, see Fig. 5. The heat flux at the surface results from the differentiation $\dot{q} = -\lambda(\partial T/\partial x)_{x=0}$ which yields

$$\dot{q} = \frac{b}{\sqrt{\pi\,t}}\,(T_{env} - T_0). \tag{45}$$

The heat penetration coefficient $b = \sqrt{\lambda\rho c}$ [SI-unit W $s^{1/2}$/(m^2K)], is a measure for the heat transfer that has penetrated into the body at a given time if the surface temperature was suddenly changed by the amount $T_{env} - T_0$ as compared to the initial temperature T_0. Some typical values for b are: approximately 36,000 W $s^{1/2}$/(m^2K) for copper, 1,600 W $s^{1/2}$/(m^2K) for concrete, 1,400 W $s^{1/2}$/(m^2K) for water, or 6 W $s^{1/2}$/(m^2K) for gases. For details see Part D.

Example:

A sudden change in weather causes the temperature at the earth's surface to drop from +5 to –5°C. How much does the temperature decrease at a depth of 1 m after 20 days? The thermal diffusivity of the soil is $a = 6.94 \times 10^{-7}$ m/s. According to Eq. (44), the decrease is:

$$\frac{T - (-5)}{5 - (-5)} = f\left(\frac{1}{2(6.94 \times 10^{-7} \cdot 20 \cdot 24 \cdot 3{,}600)^{1/2}}\right) = f(0.456)$$

Figure 5 gives $f(0.456) = 0.48$, thus, $T = -0.2$°C.

3.3.2 Finite Heat Transfer at the Surface

Let us assume, heat transfer is by convection from the surface of a body to the fluidic environment. At the surface, the relation $\dot{q} = -\lambda(\partial T/\partial x) = \alpha(T_w - T_{env})$ holds, with the ambient temperature T_{env} and the time dependent variable wall temperature $T_w = T(x = 0)$. In this case, Eqs. (44) and (45) no longer hold. Instead, the heat flux is given by

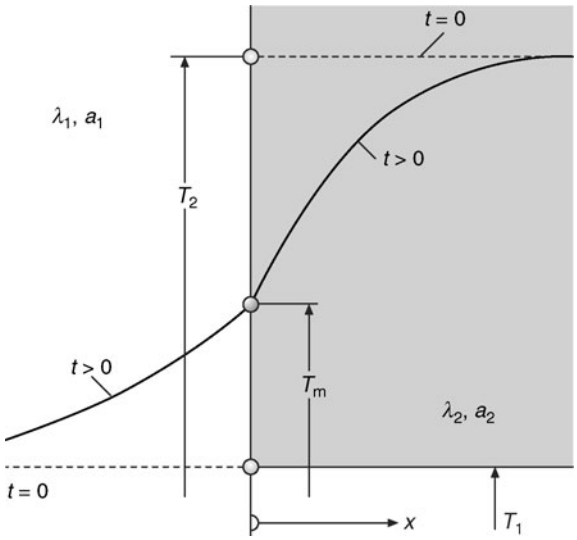

B1. Fig. 6. Contact temperature T_m between two semi-infinite bodies.

$$\dot{q} = \frac{b}{\sqrt{\pi\,t}}\,(T_{env} - T_0)\,\Phi(z), \tag{46}$$

where

$$\Phi(z) = 1 - \frac{1}{2z^2} + \frac{1 \cdot 3}{2^2 z^4} - \cdots + (-1)^{n-1}\frac{1 \cdot 3 \ldots (2n-3)}{2^{n-1} z^{2n-2}}$$

and $z = \alpha\sqrt{a\,t}/\lambda$.

3.3.3 Two Semi-Infinite Bodies in Thermal Contact

Two semi-infinite bodies of different, but initially constant, temperatures T_1 and T_2 with the thermal properties λ_1, a_1 and λ_2, a_2 are suddenly brought into contact at time $t = 0$ (Fig. 6). After a very short time at both sides of the contact area, a temperature T_m is present and remains constant. This temperature is given by:

$$\frac{T_m - T_1}{T_2 - T_1} = \frac{b_2}{b_1 + b_2}. \quad (47)$$

The contact temperature T_m is closer to the temperature of the body with the higher heat penetration coefficient b. One of the values b can be determined by measuring T_m, if the other value is known.

3.3.4 Temperature Equalization in Simple Bodies

A simple body such as a plate, a cylinder, or a sphere may have a uniform temperature T_0 at time $t = 0$. Afterwards, however, it is cooled or heated due to heat transfer between the body and a surrounding fluid of temperature T_{env} given by the boundary condition $-\lambda(\partial T/\partial n)_w = \alpha(T_w - T_{env})$, where n is the coordinate perpendicular to the body surface.

3.3.5 Plane Plate

The temperature profile shown in Fig. 7 is described by an infinite series. However, for Fourier numbers (or dimensionless times) $at/X^2 \geq 0.24$, the following relation provides a good approximation

$$\frac{T - T_{env}}{T_0 - T_{env}} = C \exp\left(-\delta^2 \frac{at}{X^2}\right) \cos\left(\delta \frac{x}{X}\right) \quad (48)$$

with less than a 1% error in temperature. The constants C and δ depend, according to Table 1, on the Biot number $Bi = \alpha X/\lambda$. Where $x = X$, Eq. (48) leads to the surface temperature T_w at the wall, and x = 0 leads to the temperature in the center of the wall. The heat transfer rate follows from $\dot{Q} = -\lambda A(\partial T/\partial x)_{x=X}$.

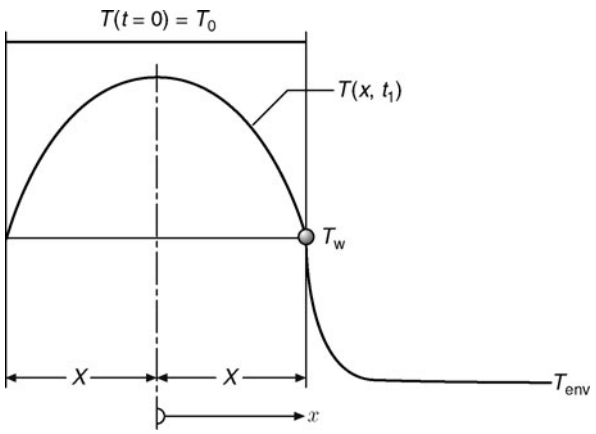

B1. Fig. 7. Cooling of a plane plate.

3.3.6 Cylinder

The radial coordinate r replaces coordinate x in Fig. 7, and the radius of the cylinder is R. Again, the temperature profile is described by an infinite series, which can be approximated for Fourier numbers $at/R^2 \geq 0.21$ by

$$\frac{T - T_{env}}{T_0 - T_{env}} = C \exp\left(-\delta^2 \frac{at}{R^2}\right) I_0\left(\delta \frac{r}{R}\right) \quad (49)$$

with less than 1% error. The term I_0 is a Bessel function of zeroth order. Its values are presented in tables in many textbooks for mathematics, e.g., in [5]. The constants C and δ depend, according to Table 2, on the Biot number. When $r = R$, the surface temperature at the cylinder results from Eq. (49), and for r = 0 the temperature in the center of the cylinder. The heat transfer rate results from $\dot{Q} = -\lambda A(\partial T/\partial r)_{r=R}$, where the first derivative of the Bessel function $I_0' = I_1$ appears. The Bessel function of first order I_1 is also given in [5].

3.3.7 Sphere

The cooling or heating of a sphere of radius R is also described by an infinite series. For Fourier numbers $a\,t/R^2 \geq 0.18$, temperature profile can be approximated by:

$$\frac{T - T_{env}}{T_0 - T_{env}} = C \exp\left(-\delta^2 \frac{at}{R^2}\right) \frac{\sin\left(\delta \frac{r}{R}\right)}{\delta \frac{r}{R}} \quad (50)$$

with less than 2% error. The constants C and δ depend, according to Table 3, on the Biot number.

4 Convective Heat Transfer and Nusselt Numbers

The desired convective heat transfer coefficient α in $\dot{q} = \alpha\Delta T$ is obtained from the Nusselt number [Eq. (9)] by $\alpha = Nu\lambda/L$ with Eq. (13)

$$Nu = f_1(Re, Pr)$$

for forced convection and Eq. (14)

$$Nu = f_2(Gr, Pr)$$

for natural convection. As stated above in Sect. 2.2, the heat transfer coefficient α and also the functions f_1 and f_2 can be determined theoretically only for special cases. In general, they must be determined through experimentation and depend on the shape of the cooling or heating areas (even, vaulted, smooth, rough, or finned), the flow structure, and usually to a minor extent, on the direction of the heat transfer (heating or cooling).

B1. Table 1. Constants C and δ in Eq. (48)

Bi	∞	10	5	2	1	0.5	0.2	0.1	0.01
C	1.2732	1.2620	1.2402	1.1784	1.1191	1.0701	1.0311	1.0161	1.0017
δ	1.5708	1.4289	1.3138	1.0769	0.8603	0.6533	0.4328	0.3111	0.0998

B1. Table 2. Constants C and δ in Eq. (49)

Bi	∞	10	5	2	1	0.5	0.2	0.1	0.01
C	1.6020	1.5678	1.5029	1.3386	1.2068	1.1141	1.0482	1.0245	1.0025
δ	2.4048	2.1795	1.9898	1.5994	1.2558	0.9408	0.6170	0.4417	0.1412

B1. Table 3. Constants C and δ in Eq. (50)

Bi	∞	10	5	2	1	0.5	0.2	0.1	0.01
C	2.0000	1.9294	1.7870	1.4793	1.2732	1.1441	1.0592	1.0298	1.0030
δ	3.1416	2.8363	2.5704	2.0288	1.5708	1.1656	0.7593	0.5423	0.1730

In the following some frequently encountered configurations are presented in an *exemplary manner*. Further details, configurations and related Nusselt correlations including references are given in Parts F–J.

4.1 Single Phase Forced Convection

4.1.1 Laminar Flow Along a Flat Plate

According to Pohlhausen, for the mean Nusselt number of a plate of length L, the following relation holds

$$\mathrm{Nu} = 0.664\,\mathrm{Re}^{1/2}\,\mathrm{Pr}^{1/3}, \tag{51}$$

where $\mathrm{Nu} = \alpha L/\lambda$, $\mathrm{Re} = wL/\nu < 10^5$, and $0.6 \le \mathrm{Pr} \le 2{,}000$. The material properties must be evaluated at the mean fluid temperature $T_\mathrm{m} = (T_\mathrm{w} - T_\infty)/2$, where T_w is the wall temperature and T_∞ the free-stream temperature far beyond the wall surface.

4.1.2 Turbulent Flow Along a Flat Plate

From about $\mathrm{Re} = 5 \times 10^5$ the boundary layer becomes turbulent. The mean Nusselt number of a plate of length L in this case is

$$\mathrm{Nu} = \frac{0.037\,\mathrm{Re}^{0.8}\,\mathrm{Pr}}{1 + 2.443\,\mathrm{Re}^{-0.1}\left(\mathrm{Pr}^{2/3} - 1\right)}, \tag{52}$$

where $\mathrm{Nu} = \alpha L/\lambda$, $\mathrm{Re} = wL/\nu$, $5 \times 10^5 < \mathrm{Re} < 10^7$ and $0.6 \le \mathrm{Pr} \le 2{,}000$. The material properties must be evaluated at the mean fluid temperature $T_\mathrm{m} = (T_\mathrm{w} + T_\infty)/2$. T_w is the wall temperature and T_∞, the free-stream temperature far beyond the wall surface.

4.1.3 Flow Through Pipes in General

Below a Reynolds number of Re = 2,300 ($\mathrm{Re} = wd/\nu$, where w is the mean cross-sectional velocity and d is the pipe diameter), the flow is laminar, while above $\mathrm{Re} = 10^4$, the flow is turbulent. In the range $2{,}300 < \mathrm{Re} < 10^4$, whether the flow is laminar or turbulent depends on the roughness of the pipe, the means of inflow, and the shape of the pipe in the inflow section. The mean heat transfer coefficient α over the pipe length L is defined by $\dot{q} = \alpha \Delta T_\mathrm{m}$, with the mean logarithmic temperature difference described by

$$\Delta T_\mathrm{m} = \frac{(T_\mathrm{w} - T_\mathrm{in}) - (T_\mathrm{w} - T_\mathrm{out})}{\ln \frac{T_\mathrm{w} - T_\mathrm{in}}{T_\mathrm{w} - T_\mathrm{out}}}, \tag{53}$$

where T_w is the wall temperature, T_in is the temperature at the inlet, and T_out is the temperature at the outlet cross section.

4.1.4 Laminar Flow Through Pipes

A flow is termed hydrodynamically developed if the velocity profile no longer changes in flow direction. In a laminar flow of a highly viscous fluid, the velocity profile adopts the shape of a Poiseuillean parabola after only a short distance from the inlet. The mean Nusselt number at constant wall temperature can be calculated exactly via an infinite series (Graetz solution), which, however, converges poorly. According to Baehr and Stephan [4], as an approximate solution for the hydrodynamically developed laminar flow, the following equation holds

$$\mathrm{Nu}_0 = \frac{3.657}{\tanh(2.264X^{1/3} + 1.7X^{2/3})} + \frac{0.0499}{X}\tanh X, \tag{54}$$

where $\mathrm{Nu}_0 = \alpha_0 d/\lambda$, $X = L/(d\,\mathrm{Re}\,\mathrm{Pr})$, $\mathrm{Re} = wd/\nu$, and $\mathrm{Pr} = \nu/a$. This equation is valid for laminar flow ($\mathrm{Re} \le 2{,}300$) in the entire range $0 \le X \le \infty$ and the maximum deviation from the exact values of the Nusselt number is 1%. The fluid properties must be evaluated at the mean fluid temperature $T_\mathrm{m} = (T_\mathrm{w} + T_\mathrm{B})/2$ where $T_\mathrm{B} = (T_\mathrm{in} + T_\mathrm{out})/2$.

If a fluid enters a pipe at an approximately constant velocity, the velocity profile changes along the flow path until it reaches the Poiseuillean parabola after a distance L_entry described by the equation $L_\mathrm{entry}/(d\,\mathrm{Re}) = 5.75 \times 10^{-2}$. According to [4], for this case, that of a hydrodynamically developed laminar flow, the following equation holds for the range $0.1 \le \mathrm{Pr} \le \infty$

$$\frac{\mathrm{Nu}}{\mathrm{Nu}_0} = \frac{1}{\tanh\left(2.43\,\mathrm{Pr}^{1/6}\,X^6\right)}, \tag{55}$$

where $\mathrm{Nu} = \alpha d/\lambda$ and the quantities are defined as above. The error is less than 5% for $1 \le \mathrm{Pr} \le \infty$ but is up to 10% for $0.1 \le \mathrm{Pr} \le 1$. The fluid properties must be evaluated at the mean fluid temperature $T_\mathrm{m} = (T_\mathrm{w} + T_\mathrm{B})/2$ where $T_\mathrm{B} = (T_\mathrm{in} + T_\mathrm{out})/2$.

4.1.5 Turbulent Flow Through Pipes

For a hydrodynamically developed flow ($L/d \geq 60$) the following equation holds in the range $10^4 \leq \mathrm{Re} \leq 10^5$ and $0.5 \leq \mathrm{Pr} \leq 100$,

$$\mathrm{Nu} = 0.024\,\mathrm{Re}^{0.8}\,\mathrm{Pr}^{1/3}\,. \tag{56}$$

The fluid properties have to be evaluated at the mean fluid temperature $T_\mathrm{m} = (T_\mathrm{w} + T_\mathrm{B})/2$ where $T_\mathrm{B} = (T_\mathrm{in} + T_\mathrm{out})/2$.

For hydrodynamically undeveloped flow and for developed flow, Petukhov's equation (modified by Gnielinski) holds in the range $10^4 \leq \mathrm{Re} \leq 10^6$ and $0.6 \leq \mathrm{Pr} \leq 1{,}000$,

$$\mathrm{Nu} = \frac{\mathrm{Re}\,\mathrm{Pr}\,\zeta/8}{1 + 12.7\sqrt{\zeta/8}\,(\mathrm{Pr}^{2/3} - 1)}\left[1 + \left(\frac{d}{L}\right)^{2/3}\right], \tag{57}$$

where the friction factor $\zeta = (0.78\ln\mathrm{Re} - 1.5)^{-2}$, $\mathrm{Nu} = \alpha d/\lambda$, and $\mathrm{Re} = wd/\nu$. The fluid properties must be evaluated at the mean temperature $T_\mathrm{m} = (T_\mathrm{w} + T_\mathrm{B})/2$. Under otherwise similar conditions, the heat transfer coefficients are larger in pipe bends than in straight pipes with the same cross section. For a pipe bend with a bend diameter D, he following equation holds, according to Hausen, for turbulent flow

$$\alpha = \alpha_\mathrm{straight}\left[1 + \left(21\,\mathrm{Re}^{0.14}\right)(d/D)\right]. \tag{58}$$

4.1.6 Single Pipe Placed Transversely in a Flow

The heat transfer coefficient for a pipe placed transversely in a flow can be determined from Gnielinski's equation

$$\mathrm{Nu} = 0.3 + \left(\mathrm{Nu}_\mathrm{lam}^2 + \mathrm{Nu}_\mathrm{turb}^2\right)^{1/2}, \tag{59}$$

where the Nusselt number Nu_lam of the laminar plate flow is described according to Eq. (51), $\mathrm{Nu}_\mathrm{turb}$ of the turbulent plate flow is described according to Eq. (52), and $\mathrm{Nu} = \alpha L/\lambda$, $1 < \mathrm{Re} = wL/\nu < 10^7$, and $0.6 < \mathrm{Pr} < 1{,}000$. For length L, the overflowed length $L = d\pi/2$ must be inserted. The fluid properties must be evaluated at the mean temperature $T_\mathrm{m} = (T_\mathrm{in} + T_\mathrm{out})/2$. This equation holds for mean turbulence intensities of 6–10%, which can be expected in technical applications.

4.1.7 Row of Pipes Placed Transversely in a Flow

Mean heat transfer coefficients for a single row of pipes placed transversely in a flow (Fig. 8) can also be determined using Eq. (59). Now, however, the Reynolds number must be calculated with the mean velocity w_m in the pipe row placed transversely in the flow. The Reynolds number is described by the equation: $\mathrm{Re} = w_\mathrm{m}L/\nu$ where $w_\mathrm{m} = w\psi$, w is the far field velocity, and $\psi = 1 - \pi/(4a)$ is the void space fraction, where $a = s_1/d$ (Fig. 8).

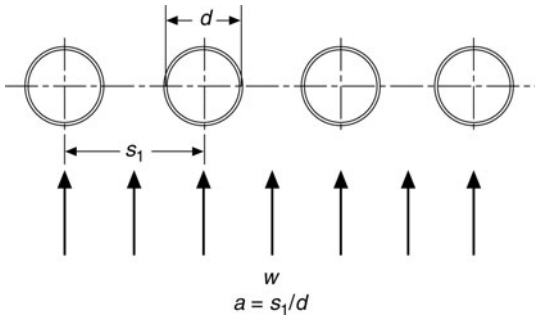

B1. Fig. 8. A row of pipes placed transversely in a flow.

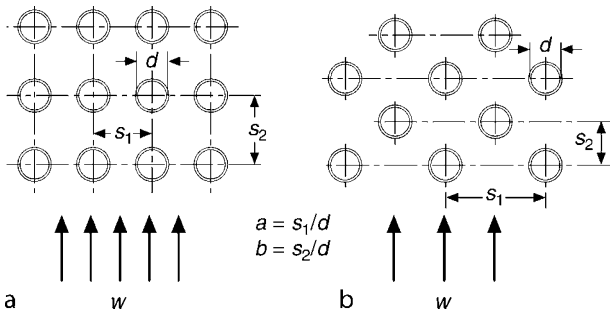

B1. Fig. 9. Arrangement of pipes in pipe bundles: (**a**) in straight lines and (**b**) staggered.

4.1.8 Pipe Bundle

If the pipes are placed in straight lines (Fig. 9a), the axes of all pipes are consecutively in the flow direction. If the arrangement is staggered (Fig. 9b), the axes of a pipe row are shifted in comparison to the axes of the row in front. The heat transfer depends additionally on the crosswise and longwise division of the pipes, $a = s_1/d$ and $b = s_2/d$. The determination of the heat transfer coefficient starts with the calculation of the Nusselt number for a single pipe placed transversely in the flow, according to Eq. (59), in which the Reynolds number contains the mean velocity w_m in the pipe bundle: $\mathrm{Re} = w_\mathrm{m}L/\nu$, where $w_\mathrm{m} = w/\psi$, w is the far field velocity of the pipe row, ψ is the void space fraction $\psi = 1 - \pi/(4a)$ for $b > 1$, and $\psi = 1 - \pi/(4ab)$ for $b < 1$. The characteristic length is $L = d\pi/2$. The Nusselt number determined in this way must be multiplied with an arrangement factor f_A. This leads to the Nusselt number $\mathrm{Nu}_\mathrm{B} = \alpha_\mathrm{B}L/\lambda$ of the bundle:

$$\mathrm{Nu}_\mathrm{B} = f_\mathrm{A}\,\mathrm{Nu}. \tag{60}$$

For a straight arrangement

$$f_\mathrm{A} = 1 + 0.7\,\frac{b/a - 0.3}{\psi^{3/2}\,(b/a + 0.7)^2} \tag{61}$$

and for a staggered arrangement

$$f_\mathrm{A} = 1 + 2/(3b). \tag{62}$$

The heat flux is $\dot{q} = \alpha\Delta T_\mathrm{m}$ with ΔT_m according to Eq. (53). Equations (61) and (62) hold for pipe bundles consisting of 10 or more pipe rows. For heat exchangers with fewer pipe rows, the heat transfer coefficient (Eq. 60) must be multiplied by a factor $(1 + (n-1)f_\mathrm{A}/n)$, where n is the number of pipe rows.

4.2 Single Phase Natural Convection

The heat transfer coefficient for natural convection at a vertical wall can be calculated with the equation of Churchill and Chu

$$\mathrm{Nu} = \left(\frac{0.825 + 0.387\,\mathrm{Ra}^{1/6}}{\left[1 + (0.492/\mathrm{Pr})^{9/16}\right]^{8/27}} \right)^2, \tag{63}$$

in which the mean Nusselt number $\mathrm{Nu} = \alpha L/\lambda$ is formed with the wall height L, and the *Rayleigh number* is defined as

$$\mathrm{Ra} = \mathrm{Gr}\,\mathrm{Pr}, \tag{64}$$

where the Grashof number is defined by

$$\mathrm{Gr} = \frac{gL^3}{\nu^2} \frac{\rho_\infty - \rho_\mathrm{w}}{\rho_\mathrm{w}}.$$

If natural convection is caused solely by temperature differences, the Grashof number can be written according to Eq. (11) as

$$\mathrm{Gr} = \frac{gL^3}{\nu^2} \beta (T_\mathrm{w} - T_\infty),$$

where the volume expansion coefficient is denoted by β, where $\beta = 1/T_\mathrm{w}$ holds for ideal gases. Equation (63) holds in the range $0 < \mathrm{Pr} < \infty$ and $0 < \mathrm{Ra} < 10^{12}$. The fluid properties must be evaluated at the mean temperature $T_\mathrm{m} = (T_\mathrm{w} - T_\infty)/2$. A similar equation holds according to Churchill and Chu also for natural convection in a horizontal cylinder

$$\mathrm{Nu} = \left(\frac{0.60 + 0.387\,\mathrm{Ra}^{1/6}}{\left[1 + (0.559/\mathrm{Pr})^{9/16}\right]^{8/27}} \right)^2. \tag{65}$$

The same definitions used in Eq. (65) hold over the range of validity is $0 < \mathrm{Pr} < \infty$ and $10^{-5} \le \mathrm{Ra} \le 10^{12}$, and the characteristic length is the diameter d. For horizontal rectangular plates, the following holds for $0 < \mathrm{Pr} < \infty$:

$$\mathrm{Nu} = 0.766\,(\mathrm{Ra}\,f_2)^{1/5} \quad \text{if } \mathrm{Ra}\,f_2 < 7 \times 10^4 \tag{66}$$

and

$$\mathrm{Nu} = 0.15\,(\mathrm{Ra}\,f_2)^{1/3} \quad \text{if } \mathrm{Ra}\,f_2 > 7 \times 10^4, \tag{67}$$

where

$$f_2 = \left[1 + (0.322/\mathrm{Pr})^{11/20}\right]^{-20/11},$$

where $\mathrm{Nu} = \alpha L/\lambda$, if L is the shorter side of the rectangle.

4.3 Heat Transfer in Condensation and Boiling

4.3.1 Condensation

If the temperature of a wall surface is lower than the saturation temperature of adjacent vapor, the vapor is condensed at the wall surface. Depending on the wetting characteristics, the condensate forms drops or a continuous liquid film. The heat transfer coefficients are usually larger for *dropwise condensation* than for *film condensation*. However, in order to maintain dropwise condensation for a certain amount of time, particular measures such as the application of dewetting agents are necessary. Dropwise condensation therefore appears rather seldom in technical applications. Calculation methods are presented in Part J3.

If the condensate flows as a laminar film on a vertical wall of height L, the mean heat transfer coefficient α is according to Nusselt's film condensation theory [4]

$$\alpha = 0.943 \left[\frac{\rho_\mathrm{l}(\rho_\mathrm{l} - \rho_\mathrm{v})\, g\, \Delta h_\mathrm{v} \lambda_\mathrm{l}^3}{4\,\eta_\mathrm{l}\,(T_\mathrm{s} - T_\mathrm{w})} \frac{1}{L} \right]^{1/4}, \tag{68}$$

where g is the gravitational acceleration, ρ the densities of the liquid (index l) and the vapor (index v) phase, respectively, Δh_v the latent heat of vaporization, η_l the dynamic viscosity of the liquid, λ_l its thermal conductivity, and T_s and T_w the saturation temperature and the wall temperature, respectively.

For condensation on horizontal single pipes with an outer diameter d, the following relation holds:

$$\alpha = 0.728 \left[\frac{\rho_\mathrm{l}(\rho_\mathrm{l} - \rho_\mathrm{v})\, g\, \Delta h_\mathrm{v} \lambda_\mathrm{l}^3}{\eta_\mathrm{l}\,(T_\mathrm{s} - T_\mathrm{w})} \frac{1}{d} \right]^{1/4}. \tag{69}$$

The equations require that no noticeable shear stress is exerted by the vapor on the condensate film.

At Reynolds number $\mathrm{Re}_\delta = w_\mathrm{m}\delta/\nu$ (where w_m is the velocity of the condensate, δ the film thickness, and ν the kinematic viscosity) between 75 and 1,200 the transition to turbulent flow in the condensate film gradually takes place. In the transition range

$$\alpha = 0.22\,\lambda_\mathrm{l} \left(\nu_\mathrm{l}^2/g\right)^{1/3}, \tag{70}$$

whereas for turbulent film flow ($\mathrm{Re}_\delta > 1{,}200$), the following relation according to Grigull holds

$$\alpha = 0.003 \left[\frac{\lambda_\mathrm{l}^3\, g\,(T_\mathrm{s} - T_\mathrm{w})}{\rho_\mathrm{l} \nu_\mathrm{l}^3\, \Delta h_\mathrm{v}} L \right]^{1/2}. \tag{71}$$

Equations (70) and (71) are valid also for vertical pipes and plates but not for horizontal pipes.

4.3.2 Boiling

If a liquid in a container is heated, evaporation starts after the saturation temperature T_s is exceeded. For small excess wall temperatures $T_\mathrm{w} - T_\mathrm{s}$ the liquid evaporates only on its free surface (*silent boiling*). Heat is transported by conduction and the buoyancy flow from the heating surface to the free surface of the liquid. For higher, excess wall temperatures vapor bubbles are formed at the heating surface (*nucleate boiling*) and rise. They increase the movement of the liquid and thus the heat transfer. With increasing excess wall temperature, the bubbles merge more and more into a continuous vapor film, whereby the heat transfer is decreased (*transition boiling*). Figure 10 shows the different heat transfer ranges for such *pool boiling* situations. The heat transfer coefficient α is defined as

$$\alpha = \dot{q}/(T_\mathrm{w} - T_\mathrm{s}) \tag{72}$$

where the heat flux is $\dot{q}$ in W/m^2.

Industrial evaporators work in the range of silent boiling or, more often, in the nucleate boiling range. In the silent boiling range the laws for heat transfer in natural convection hold (see Sect. 4.2. and Part F).

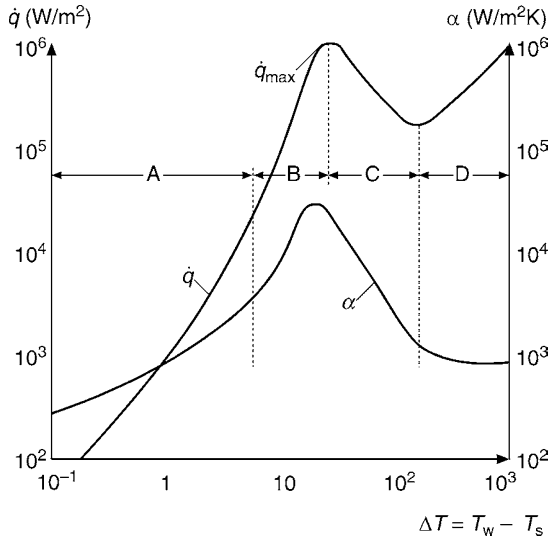

B1. Fig. 10. Boiling ranges for water of 1 bar. A – natural convection (silent boiling), B – nucleate boiling, C – transition boiling, D – film boiling.

In the nucleate boiling region, the general relation $\alpha = c\dot{q}^n F(p)$ with $0.5 < n < 0.8$ holds.

For water at boiling pressures between 0.5 and 20 bar, according to Fritz, the following relation holds:

$$\alpha = 1.95\, \dot{q}^{0.72}\, p^{0.24} \tag{73}$$

with α in W/(m²K), $\dot{q}$ in W/m², and p in bar. According to Stephan and Preußer, for arbitrary liquids the following relation is valid for nucleate boiling close to ambient pressure

$$\mathrm{Nu} = 0.0871 \left(\frac{\dot{q}\, d}{\lambda_l\, T_s}\right)^{0.674} \left(\frac{\rho_v}{\rho_l}\right)^{0.156} \left(\frac{\Delta h_v d^2}{a_l^2}\right)^{0.371} \left(\frac{a_l^2 \rho_l}{\sigma\, d}\right)^{0.350} \mathrm{Pr}_l^{-0.162}\,. \tag{74}$$

Properties of the liquid and vapor are taken at saturation conditions. $\mathrm{Nu} = \alpha d/\lambda_l$ is formed with the detachment diameter of the vapor bubbles $d = 0.851\beta_0[2\sigma/g(\rho_l - \rho_v)]^{1/2}$, where the contact angle is $\beta_0 = 45°$ for water, 1° for low boiling and 35° for other liquids. The equations above are not valid for boiling in forced flow. Detailed calculation procedures for *pool boiling* are given in Chap. H2.

If boiling occurs in a forced flow, e.g. in a pipe heated externally, both, boiling heat transfer and forced convective heat transfer are driving the transport process. *Flow boiling* calculation procedures are presented in Chap. H3.

5 Thermal Radiation and Radiative Heat Exchange

5.1 Emission, Absorption, and Transmission

As stated in Sect. 2.3. real bodies emit less than black radiators, where the energy emitted from real surfaces is, according to Eq. (17),

$$\dot{e} = \varepsilon \cdot \dot{e}_b = \varepsilon \cdot \sigma\, T^4.$$

In limited temperature ranges, many engineering surfaces (with the exception of shiny metal) can be interpreted as grey radiators. The energy radiated by them is distributed over the wave lengths in the same way as it is for black radiators. However, it is reduced by a factor $\varepsilon < 1$. Strictly speaking, $\varepsilon = \varepsilon(T)$ holds true for grey radiators. For small temperature ranges, however, it is admissible to assume ε as constant.

Assuming a body emits the energy flow per unit area $\dot{e}$, and this energy flux strikes another body, this second body absorbs the energy flow or rather the heat flow

$$\mathrm{d}\dot{Q}_a = a\, \mathrm{d}\dot{Q} = a\, \dot{e}\, \mathrm{d}A. \tag{75}$$

The *absorptivity* a defined by this equation depends on the temperature T of the origin of the incident radiation and on the temperature T' of the receiving surface. For black bodies, this value is $a = 1$, as all radiation striking the surface is absorbed. For surfaces which are not black, this value is $a < 1$. For grey radiators, the absorptivity is $a = \varepsilon$. According to *Kirchhoff's law*, the emissivity is equal to the absorptivity, $\varepsilon = a$, for each surface which is in thermal equilibrium with its environment so that the temperature of the surface does not change in time.

The remaining fractions of $\mathrm{d}\dot{Q}$ are reflected at the surface, $\mathrm{d}\dot{Q}_r = r\, \mathrm{d}\dot{Q}$, or transmitted through the body, $\mathrm{d}\dot{Q}_d = d\, \mathrm{d}\dot{Q}$. It follows

$$r + d + a = 1. \tag{76}$$

A body that reflects radiation completely ($r = 1$, $d = a = 0$) is called an ideal mirror, a body that absorbs radiation completely ($a = 1$, $r = d = 0$) is called a black body. A body is called diathermal ($d = 1$, $r = a = 0$) if radiation passes completely through. Examples for this are gases such as O_2, N_2, and others.

5.2 Heat Exchange Between Two Bodies

If two bodies emit radiation to each other the heat transfer between the bodies is equal to the net result of the radiation balance. Assuming, e.g., two parallel black surfaces of temperatures T_1 and T_2, and area A, which is very large in comparison to their distance, the net heat flow rate

$$\dot{Q}_{12} = \sigma A \left(T_1^4 - T_2^4\right) \tag{77}$$

is transferred by radiation. Between two such grey surfaces with the emissivities ε_1 and ε_2, the heat flow rate is

$$\dot{Q}_{12} = C_{12} A \left(T_1^4 - T_2^4\right) \tag{78}$$

with the *radiation exchange number*

$$C_{12} = \frac{\sigma}{\frac{1}{\varepsilon 1} + \frac{1}{\varepsilon_2} - 1}. \tag{79}$$

Between an internal pipe with the outer surface A_1 and an external pipe with the inner surface A_2, which are both grey radiators with emissivities ε_1 and ε_2, a heat flow rate is given according to Eq. (78), however, with:

$$C_{12} = \frac{\sigma}{\frac{1}{\varepsilon_1} + \frac{A_1}{A_2}\left(\frac{1}{\varepsilon_2} - 1\right)}. \tag{80}$$

If $A_1 << A_2$, e.g., for a pipe in a large room, the equation holds that $C_{12} = \sigma\varepsilon_1$.

For a number of more complex geometrical configurations with two bodies, specific radiation exchange numbers are given in Chap. K1.

More general relationships for the radiative heat transfer between two grey surfaces, which are arbitrarily arranged in space, make use of the definition of so-called *view factors* φ that depend on the geometric arrangement of the surfaces. A view factor φ_{ij} is defined as the fraction of the radiative energy leaving body *i* that strikes body *j*. Details for such arrangements as well as for enclosed spaces with multiple surfaces involved in radiative heat exchange are given in Chap. K2.

5.3 Gas Radiation

Most gases are transparent to thermal radiation and neither emit nor absorb radiation. Exceptions are some gases such as carbon dioxide, carbon monoxide, hydrocarbons, water vapor, sulfur dioxide, ammonia, hydrochloric acid, and alcohols. They emit and absorb radiation only in certain wave length regions. Emissivity and absorptivity of these gases depend not only on temperature, but also on the geometric shape of the gas body. Details are given in Chap. K3.

6 Bibliography

1. Fourier JBJ (1822) Théorie Analytique de la Chaleur, see reprint (2009): Cambridge University Press, 1st edn
2. Prandtl L (1904) Über Flüssigkeitsbewegungen bei sehr kleiner Reibung. Internationaler Mathematischer Kongress, Heidelberg; see also: Oertel H, Bolle M, Efling D (2004): Prandtl's Essentials of Fluid Mechanics, Springer
3. Nusselt W (1915) Das Grundgesetz des Wärmeübergangs. Gesundheits-Ingenieur 38, pp. 477–482
4. Baehr HD, Stephan K (2006) Heat and mass transfer, 2nd edn. Springer
5. Bronstein IN, Semendjajew KA, Musiol G, Muehlig H (2007) Handbook of mathematics, 5th edn. Springer

A2 Dimensionless Numbers

Holger Martin
Karlsruher Institut für Technologie (KIT), Karlsruhe, Germany

1 Introduction

The equations in the VDI-Heat Atlas are often given in dimensionless forms. The dimensionless numbers used in these equations are presented below in tabular form with notation, name, and definition, and by a numerical example for each of these numbers.

2 Dimensionless Numbers

Notation	Name	Definition
Ar	Archimedes number	$gl^3\Delta\rho/(\rho\nu^2)$
Bi	Biot number	$\alpha_a l/\lambda_i$
Fo	Fourier number	$\kappa t/l^2$
Fr	Froude number	$w^2/(gl)$
Ga	Galilei number	$g\,l^3/\nu^2$
Gr	Grashof number	$g\beta\Delta T\,l^3/\nu^2$
Gz	Graetz number	$l^2/(\kappa\,t_r)$
Hg	Hagen number	$(\Delta p/\Delta L)\,l^3/(\rho\nu^2)$
Ka	Kapitza number	$g\eta^4/(\rho\sigma^3)$
Le	Lewis number	κ/δ_{ij}
Nu	Nusselt number	$\alpha l/\lambda$
Pe	Péclet number	$w\,l/\kappa$
Pr	Prandtl number	ν/κ
Ra	Rayleigh number	$g\beta\Delta T\,l^3/(\nu\kappa)$
Re	Reynolds number	$\rho w l/\eta$
Sh	Sherwood number	$\beta\,l/\delta_{ij}$
Sc	Schmidt number	ν/δ_{ij}
St	Stanton number	$\alpha/(\rho c_p w)$
We	Weber number	$w^2 l\rho/\sigma$

3 Examples of Usage

The **Archimedes number**, Ar, is often used in equations describing the motion of particles (solid particles, drops, or bubbles) in gases or liquids (as in Chaps. L3.2 and M5). Usually, it appears in these equations together with the Reynolds number, Re. The number $\mathrm{Ar}/\mathrm{Re}^2$ can be interpreted as the ratio of weight minus buoyancy and the inertial force:

$$\mathrm{Ar}/\mathrm{Re}^2 = (\Delta\rho/\rho)/\mathrm{Fr} = gl^3\Delta\rho/(\rho w^2 l^2)$$

The diameter of the particles, drops, or bubbles is usually chosen as the characteristic length l.

Example
Quartz sand, with an average size $d = 500$ µm and a solid density $\rho_S = 2{,}610$ kg/m^3, is to be fluidized in air at a pressure of $p = 1$ bar und $T = 300$ K. With the gas density $\rho = 0.6072$ kg/m^3 and the kinematic viscosity of $\nu = 48.09 \cdot 10^{-6}$ m^2/s (Chap. D2) from the definition of Ar, with $l = 500 \cdot 10^{-6}$ m, $\rho = 0.6072$ kg/m^3, $\nu = 48.09 \cdot 10^{-6}$ m^2/s, and $\Delta\rho = (2{,}610 - 0.6)$ kg/m^3 = 2,609 kg/m^3, the result is Ar = 2,278.

The **Biot number**, Bi, may be seen as a ratio of two heat transfer resistances in series: $(l/\lambda_i)/(1/\alpha_a)$. It is often very useful in calculations of transient heating or cooling processes of solid bodies in liquid, or gas flows (Chap. E2).

Example
Spherical PVC particles with a heat conductivity $\lambda_i = 0.15$ W/m K and a radius of $R = 2$ cm shall be cooled in an airstream. The heat transfer coefficient (surface-to-ambient air) was determined to be $\alpha_a = 60$ W/m^2 K.

With $l = R = 2 \cdot 10^{-2}$ m, the Biot number becomes Bi = 8.00, which means that the internal conductive resistance is eight times the outer heat transfer resistance in this case. The transient conduction inside the particles is rate-controlling.

The **Fourier number**, Fo, as a dimensionless time is commonly used in transient conduction problems (see Sect. B and Chap. E2).

Example
A steel ball with the thermal diffusivity $\kappa = 7.0 \cdot 10^{-6}$ m^2/s and the radius $R = 1$ cm is cooled in water for 1 min.

Using $t = 1$ min $= 60$ s and $l = R = 10^{-2}$ m, the Fourier number turns out to be Fo = 4.2.

The **Froude number**, Fr, which can be seen as a ratio of inertial force and gravity, appears in problems of forced motion when gravity has some additional influence, for example, with free liquid (or granular solid) surfaces and in other multiphase flow problems.

Example
A water–steam mixture flows through a horizontal tube of internal diameter $d_i = 25$ mm with an average liquid-phase velocity of $w_L = 5$ m/s. With the characteristic length $l = d_i = 25 \cdot 10^{-3}$ m, the Froude number for the liquid phase is Fr = 102.

VDI-GVC (ed.), *VDI Heat Atlas*, DOI 10.1007/978-3-540-77877-6_2,

The **Galilei number**, Ga, may be written in terms of the Reynolds and Froude numbers: $Ga = Re^2/Fr$. It is also a factor in Ar and Gr: $Ar = Ga\ \Delta\rho/\rho$; $Gr = Ga\ \beta\ \Delta T$

Example
In the example for the Archimedes number, Ga = 0.5302 und $\Delta\rho/\rho$ = 4,297.

The **Grashof number**, Gr, is formed similarly to the Archimedes number, Ar. The term $\Delta\rho/\rho$, being the relative difference of densities of two different phases, such as solid–gas, for Ar, is replaced by the term $\beta\ \Delta T$ in the Grashof number (where β is the thermal expansion coefficient, and ΔT a characteristic spatial temperature difference). It is a relative difference of densities within one phase only (liquid or gaseous), which occurs because of a spatial temperature difference ΔT. For an ideal gas, $\beta = 1/T$. The Grashof number is important in describing heat transfer in natural convection flow problems (Sects. B and F).

Example
A flat, vertically mounted heater of a height l = 60 cm in a room at a temperature T_∞ = 20°C has a surface temperature of T_s = 60°C. At a reference temperature of $T_m = (T_s + T_\infty)/2$ = 40°C, the relevant physical properties, β, the thermal expansion coefficient, and ν, the kinematic viscosity are found to be

$$\beta_{40°C} = 1/313.15\,\mathrm{K} = 3.1 \cdot 10^{-3}\mathrm{K}^{-1},$$

$\nu_{40°C} = 16.92 \cdot 10^{-6}$ m²/s, and the Grashof number becomes Gr = $9.47{\cdot}10^8$.

The **Graetz number**, Gz, is the reciprocal of a Fourier number, Fo. It is mainly used in calculations for steady flow, in which the time t_r (the residence time of the fluid in a heated or cooled portion of a channel) is usually expressed via the length L and the mean flow velocity w. The characteristic length l in this case is the diameter, d, of the flow channel:

$$Gz = d^2/(\kappa t_r) = wd^2/(\kappa L) = Pe_d\, d/L = Re_d Pr\, d/L$$

Example
Waster at an average temperature of 30°C flows with a velocity of w = 1.5 m/s through a tube with the internal diameter of d_i = 18 mm. The tube is heated over a length of L = 3.0 m. With $\kappa_{30°C} = 0.148 \cdot 10^{-6}$ m²/s, $t_r = L/w$ = 2 s and $l = d_i = 18 \cdot 10^{-3}$ m the result is Gz = 1,095.

The **Hagen number**, Hg, though not as widely used in the relevant literature so far, has proven to be a very useful generalization of the two similarly built Archimedes and Grashof numbers. It works for both the forced convection and the natural convection flow problems. It can be seen as a dimensionless pressure gradient, $(\Delta p/\Delta L)/(\rho\nu^2/l^3)$. In case of natural convection flows, $\Delta p/\Delta L$ is the static pressure gradient $g\,\Delta\rho$ or $g\,\rho\,\beta\,\Delta T$ in a gravity field, and the Hagen number becomes an Archimedes number or a Grashof number. The linear Hagen-Poiseuille law of fully developed forced laminar tube flow (Re ≤ 2,300) simply reads as Hg = 32 Re, if the internal tube diameter is used as the characteristic length l.

Example
In a tube of the internal diameter d = 0.022 m a pressure drop of Δp = 103 Pa was measured over the length of ΔL = 10 m. Water at 20°C is flowing inside: ρ = 998.21 kg/m³, $\nu = 1.004 \cdot 10^{-6}$ m²/s. With the internal diameter, d, as the characteristic length, l, a Hagen number of Hg = 1 058 227 is obtained. With such a high value of Hg, a turbulent tube flow can be expected, because the critical Hagen number for the transition of laminar to turbulent flow is Hg_{crit} = 73,600 (Hg = 32 · Re, corresponding to a critical Reynolds number of Re_{crit} = 2,300).

The **Kapitza number**, Ka, contains only the physical properties, viscosity, density, and surface tension, apart from the acceleration of gravity, g. It plays a certain role in liquid film flows, as for example in film condensation. Ka can be written in terms of Weber, Froude, and Reynolds numbers, We, Fr, and Re, respectively as: $Ka = We^3/(Fr\ Re^4)$.

Example
With the data for water at 20°C and 1 bar from Chap. D2, the result is $Ka = 2.57{\cdot}10^{-11}$.

The **Lewis number**, Le, is the ratio of two physical properties, that is the quotient of thermal diffusivity and the (mass) diffusion coefficient. It occurs in problems of coupled heat and mass transfer, as for example, in drying or in evaporative cooling. The Lewis number can also be written in terms of Prandtl and Schmidt numbers: Le = Sc/Pr.

Example
For the evaporation of water in (dry) air at a total pressure of p = 1 bar and a temperature of T = 273.15 K with a diffusivity of $\delta_{water-air} = 22.6 \cdot 10^{-6}$ m²/s and a thermal diffusivity of $\kappa = 19.1 \cdot 10^{-6}$ m²/s, a Lewis number of Le = 0.845.

The **Nusselt number**, Nu, is a dimensionless heat transfer coefficient. For steady-state conduction through a stagnant plane layer of thickness l and conductivity λ the heat transfer coefficient, defined as $\alpha = \dot{q}/\Delta T$, is simply $\alpha = \lambda/l$. The Nusselt number $\alpha l/\lambda$, in this case, by definition, has a value of Nu = 1.

As the characteristic length l, the internal diameter of a flow channel (as in Chap. G1), the length (in flow direction) of a plate in parallel flow (in Chap. G4), or the quantity $(\nu^2/g)^{1/3}$, having the dimension of a length can be chosen (see Sect. B and Chap. J1). In any case, the definition of α, the choice of the characteristic length l, and the reference temperature for the physical properties must be specified.

Example
For a cylinder with an outer diameter of d = 25 mm in a crossflow of air, from Chap. G6, a Nusselt number Nu_l = 126.3 has been calculated. The reference temperature turns out to be T_m = 100°C, so that $\lambda = 31.81 \cdot 10^{-3}$ W/m K. The characteristic length for (long) cylinders in crossflow, following Chap. G6, is $l = (\pi/2)\ d = 39.27 \cdot 10^{-3}$ m. So, to get the heat transfer coefficient, $\alpha = (\lambda/l) \cdot Nu_l = 102.3$ W/(m² K) needs to be calculated.

The **Péclet number**, Pe, can be written as the product of Re and Pr: Pe = Re Pr. It does not contain the viscosity, as this property is found in Pr in the numerator, and in Re in the denominator. The Péclet number is found in forced convection flow problems with heat transfer (see also the numbers Gz, Re, and Pr). It can be seen as a ratio of convective

enthalpy transport (with the flow) to heat transfer (by conduction) to the fluid.

Example
At a Reynolds number of Re = 1,400, the Péclet number for air at 0°C (Pr = 0.7) has a value of Pe = 1,400 · 0.7 = 980; for water at 0°C (Pr = 13.0) one gets Pe = 1,400 · 13.0 = 18,200.

The **Prandtl number**, Pr, like Le and Sc, is a ratio of physical properties; with $\nu = \eta/\rho$ und $\kappa = \lambda/(\rho c_p)$ it can also be written in the form $Pr = \eta c_p/\lambda$.

Example
Liquid benzene at 50°C has the physical properties $\eta = 43.6 \cdot 10^{-5}$ Pas, $c_p = 1.821 \cdot 103$ J/kg K, and $\lambda = 0.134$ W/(m K). One obtains a Prandtl number of Pr = 5.93.

The product Gr Pr is also known as the **Rayleigh number**, Ra.

The **Reynolds number**, Re, can be seen as a ratio of inertial forces to frictional forces. The numerical value of Re is the crucial criterium to decide whether a flow remains in a stable laminar mode, or it may undergo a transition to turbulent flow: For the fluid flow in a circular tube, the critical Reynolds number is $Re_{cr} = 2{,}300$. For $Re < Re_{cr}$ the flow is laminar, for $Re > Re_{cr}$ it may become turbulent. The characteristic length l in this case is usually taken as the inner diameter of the tube (Chap. G1). For parallel flow over a flat plate (see Chap. G4), the characteristic length l is the length x in flow direction, measured from the leading edge. The critical Reynolds number for this flow is about $Re_{x,crit} = 5 \cdot 10^5$. In liquid film flow, the stability does not depend on Re alone, but also from a number that contains the surface tension, such as Ka or We.

Example
Water, at a mass flow rate of $\dot{M} = 8{,}000$ kg/h passes a tube with the internal diameter $d_i = 52$ mm. The temperature is 10°C, so that the density is $\rho = 999.8$ kg/m^3. The flow velocity is

$$w = \dot{M}/\left(\rho d^2 \pi/4\right) = 1.05\, m/s,\ l = d_i = 52 \cdot 10^{-3}\ \mathrm{m},$$
$$\nu = 1.300 \cdot 10^{-6}\ \mathrm{m^2}/s,$$
$$\mathrm{Re} = 41\,900.$$

The **Sherwood number**, Sh – corresponding to the Nusselt number – is formed as a dimensionless mass transfer coefficient. The equations in the form Nu = Nu (Re, Pr, ...) used to calculate the heat transfer coefficient α can also be applied to predict the mass transfer coefficient β: Just replace Nu by Sh and Pr by Sc (this is called the "analogy between heat and mass transfer").

Example
The diffusivity of steam (subscript "1") in air (subscript "2") at 1 bar and 25°C is $\delta_{12} = 26.5 \cdot 10^{-6}$ m^2/s. With $\nu = 15.6 \cdot 10^{-6}$ m^2/s one arrives at a Schmidt number of Sc = 0.589. Using this value, in place of Pr, in Eq. (5) of Chap. G4 with $Re_1 = 104$, one gets (in place of Nu) the value $Sh_l = 73.8$. The mass transfer coefficient β is obtained from this with $l = 10$ cm (the flow velocity of air ought to be $w = 1.56$ m/s to make $Re_1 = 104$) as $\beta = (\delta_{12}/l) \cdot Sh_l = 19.6$ mm/s.

The **Schmidt number**, Sc, is the mass transfer analog of the Prandtl number, Pr. For its use and calculation see the example at the Sherwood number, Sh. The Schmidt number can also be obtained from Sc = Le Pr.

The ratio $Nu/Pe = \alpha/(\rho c_p w)$ is also known as the **Stanton number**, St.

The **Weber number**, We, as the Kapitza number, Ka, contains the surface tension σ. So it plays a role for flow problems with free surfaces, for drop formation, and for the atomization of liquids. It can be expressed in terms of Ka, Fr, and Re: $We = (Ka\ Fr\ Re^4)^{1/3}$.

Example
A drop of water with a diameter of $d = 5$ mm is falling in stagnant air (20°C, 1 bar) with a velocity of $w = 11$ m/s. The Weber number, with $\rho_G = 1.188$ kg/m^3, the characteristic length $l = d = 5 \cdot 10^{-3}$ m, and with $\sigma_{20°C} = 72.78 \cdot 10^{-3}$ N/m, is We = 9.88.

Part C

Fundamentals of Heat Exchanger Design

C1 Thermal Design of Heat Exchangers

Wilfried Roetzel[1] · *Bernhard Spang*[2]
[1]Helmut-Schmidt-Universität, Universität der Bundeswehr Hamburg, Hamburg, Germany
[2]BUCO Wärmeaustauscher International GmbH, Geesthacht, Germany

1 Introduction

Widely different tasks are involved in designing heat exchangers. They range from thermal rating or dimensioning through mechanical analysis and costing, to the optimization of heat exchangers and systems. This chapter is restricted to steady state thermal design of heat exchangers in which two fluids are separated by fixed walls [1].

2 Nomenclature, Definitions, and Basic Equations

A schematic diagram of a heat exchanger showing the main parameters is presented in Fig. 1.

The local heat flux $\dot{q}$ at the heat transfer surface can be expressed in terms of the local temperature difference $(\vartheta_1 - \vartheta_2)$ between the two fluids and the local overall heat transfer coefficient k_{loc}, i.e.,

$$\dot{q} = k_{\mathrm{loc}}(\vartheta_1 - \vartheta_2) \tag{1}$$

The total heat flow rate $\dot{Q}$ is obtained by integrating the local heat flux over the entire area of the heat transfer surface, i.e.,

$$\dot{Q} = \int_A \dot{q}\,\mathrm{d}A \tag{2}$$

With the introduction of a mean overall heat transfer coefficient k and a mean temperature difference $\Delta\vartheta_{\mathrm{m}}$ Eqs. (1) and (2) can be replaced by

$$\dot{Q} = kA\Delta\vartheta_{\mathrm{m}} \tag{3}$$

One of these two mean values must be defined separately. The following definition of the mean temperature difference is chosen:

$$\Delta\vartheta_{\mathrm{m}} = \frac{1}{A}\int_A (\vartheta_1 - \vartheta_2)^*\,\mathrm{d}A \tag{4}$$

in which $(\vartheta_1 - \vartheta_2)^*$ is the hypothetical local temperature difference if the heat capacities and the mean value k are constant. The mean value k is then defined by Eq. (3). Its determination is dealt with in ➲ Chap. C2. In the special case of constant local overall heat transfer coefficient k_{loc} and of constant heat capacities over the entire heat transfer surface area, it is $k = k_{\mathrm{loc}}$.

Both the heat flow rate $\dot{Q}$ and the mean temperature difference are considered to be positive if heat is transferred from fluid 1 to fluid 2, i.e., if $\vartheta_1' > \vartheta_2'$. The mean temperature difference depends on the flow arrangement of the heat exchanger and on the degree and direction of mixing within the two fluid streams. Its (implicit or explicit) determination allows for a simple method of calculating the heat flow rate transferred over a given area or the area required to transfer a given heat flow rate.

Using the energy balance equations for the two fluids in the heat exchanger, the heat flow rate transferred in steady state operation can be expressed in terms of the changes in enthalpy within the two streams. Thus,

$$\dot{Q} = \dot{M}_1\left(h_1' - h_1''\right) = -\dot{M}_2\left(h_2' - h_2''\right) \tag{5}$$

VDI-GVC (ed.), *VDI Heat Atlas*, DOI 10.1007/978-3-540-77877-6_4,

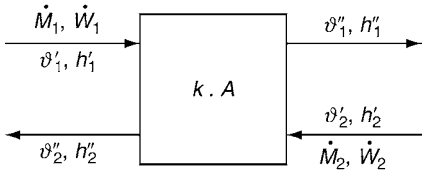

C1. Fig. 1. Schematic diagram of a heat exchanger.
$\dot{M}_1$, $\dot{M}_2$ = mass flow rates
$\dot{W}_1$, $\dot{W}_2$ = heat capacity rates
h_1, h_2 = specific enthalpies
ϑ_1, ϑ_2 = temperatures

In Eq. (5), heat flow to the surroundings, kinetic and potential energies, and all energy transferred into the system from the outside (e.g., energy dissipated by an agitator) are ignored. It is valid for temperature changes in single-phase systems, changes in phase, and chemical reactions. In single-phase systems, the change in enthalpy can be expressed as a change in temperature by introducing the heat capacity rate $\dot{W}$:

$$\dot{W}_i = \frac{\dot{M}_i\left(h'_i - h''_i\right)}{\vartheta'_i - \vartheta''_i} = \dot{M}_i c_{pm,i} \quad (i = 1, 2) \tag{6}$$

If the enthalpy is independent of pressure (e.g., as in an ideal gas) or if the pressure drop in flow direction can be neglected (isobaric change of state), $c_{pm,i}$ is the mean specific heat capacity at constant pressure between the inlet and the outlet temperatures. If a phase change occurs in a system that consists of only one pure substance (and the pressure remains constant), the heat capacity flow rate becomes infinite. Equations (3), (5), and (6) can then be combined to

$$\dot{Q} = kA\Delta\vartheta_m = \dot{W}_1\left(\vartheta'_1 - \vartheta''_1\right) = \dot{W}_2\left(\vartheta''_2 - \vartheta'_2\right) \tag{7}$$

The following dimensionless numbers are useful in the design of heat exchangers. They are obtained by dividing Eq. (7) by the absolutely largest temperature difference $\left(\vartheta'_1 - \vartheta'_2\right)$ in the heat exchanger and by the heat capacity flow rate $\dot{W}_1$ or $\dot{W}_2$.

(a) Dimensionless mean temperature difference

$$\Theta = \frac{\Delta\vartheta_m}{\vartheta'_1 - \vartheta'_2} \tag{8}$$

where $0 \leq \Theta \leq 1$.

(b) Dimensionless temperature changes in the two streams 1 and 2

$$P_1 = \frac{\vartheta'_1 - \vartheta''_1}{\vartheta'_1 - \vartheta'_2} \tag{9}$$

$$P_2 = \frac{\vartheta''_2 - \vartheta'_2}{\vartheta'_1 - \vartheta'_2} \tag{10}$$

where $0 \leq P_i \leq 1$ $(i = 1,2)$.

(c) Number of transfer units in streams 1 and 2

$$NTU_1 = \frac{kA}{\dot{W}_1} \tag{11}$$

$$NTU_2 = \frac{kA}{\dot{W}_2} \tag{12}$$

where $0 \leq NTU_i \leq \infty$ $(i = 1,2)$.

(d) Heat capacity rate ratios

$$R_1 = \frac{\dot{W}_1}{\dot{W}_2} \tag{13}$$

$$R_2 = \frac{\dot{W}_2}{\dot{W}_1} = \frac{1}{R_1} \tag{14}$$

where $0 \leq R_i \leq \infty$ $(i = 1,2)$.

The following relationships between the dimensionless numbers can be derived from Eq. (7):

$$\frac{P_1}{P_2} = \frac{NTU_1}{NTU_2} = \frac{1}{R_1} = R_2 \tag{15}$$

$$\Theta = \frac{P_1}{NTU_1} = \frac{P_2}{NTU_2} \tag{16}$$

3 Design Concepts

There are many methods for designing heat exchangers. They differ from one another in their field of application, physical and mathematical complexity, and accuracy. The most accurate but also most involved are the numerical finite difference or step-by-step methods. At the outset, not only the temperature field but also the flow field may be unknown. In this case, the equation of continuity and the momentum balance equations as well as the energy balance equation have to be solved numerically. The results depend greatly on the quality of the equations and mathematical models adopted for the calculation (turbulence models, equations for the flow resistance of fittings, etc.). In view of the tremendous expenditure and the uncertainty involved, the use of such methods in the design of heat exchangers is only rarely justified. Those methods are not discussed in this chapter. A much easier method has been developed by Gaddis and Schlünder [2, 3] for rating baffled shell-and-tube heat exchangers.

3.1 Cell Method

The method consists of subdividing the heat transfer area into a finite number of area elements over which the two fluid streams or their branches successively flow in the same or in a different sequence. By this, the entire heat exchanger is represented by a system of interconnected but nonoverlapping modules or cells with individual flow arrangements.

If the inlet temperatures for any one cell are given and the corresponding value of kA is known, the outlet temperatures can be determined from the equations for the appropriate flow arrangement (see Sect. 4). If the two streams pass through all the cells in series or in parallel, two equations can be derived for the relationship between the inlet and outlet temperatures of both streams in each cell. The temperature of each stream at the inlet to the respective first cell is known. If there are n cells, a total of $2n$ equations can be drawn up to determine the $2n$ unknown outlet temperatures for both streams. The system of equations can then be solved to yield all unknown temperatures including the outlet temperatures of the complete heat exchanger.

By means of the intermediate temperatures between the cells, individual values of the thermophysical properties and hence for the heat transfer coefficients in each cell may be determined, making the cell method more sophisticated. Differences in the correlations for the heat transfer coefficients, the heat transfer areas, and the flow arrangement in each cell can thus be embraced.

To illustrate this method, an example is given. Consider a shell-and-tube heat exchanger with n tube-side and one shell-side passes and with z baffles on the shell side. In the model shown in Fig. 2, it is $n = 2$ and $z = 2$. For simplification, it is assumed that each cell has the same number of transfer units (NTU). Let the number of transfer units in the entire heat exchanger be $\mathrm{NTU}_{1\mathrm{tot}}$ and $\mathrm{NTU}_{2\mathrm{tot}} = R_1\mathrm{NTU}_{1\mathrm{tot}}$. Then, the following applies for the individual cells:

$$\mathrm{NTU}_i = \frac{\mathrm{NTU}_{i,\mathrm{tot}}}{n(z+1)} \quad i = 1, 2 \tag{17}$$

The dimensionless temperature changes P_1 and P_2 in the cells can then be obtained from the individual flow arrangement (e.g., cross-flow with lateral mixing on the shell-side and no mixing on the tube-side, see Sect. 4) and from NTU_1 and $R_1 = \mathrm{NTU}_2/\mathrm{NTU}_1$.

The dimensionless temperatures for the streams are

$$T_1 = \frac{\vartheta_1 - \vartheta_2'}{\vartheta_1' - \vartheta_2'} \text{ and } T_2 = \frac{\vartheta_2 - \vartheta_2'}{\vartheta_1' - \vartheta_2'} \tag{18}$$

Hence the following applies for the cell j in Fig. 3:

$$(1 - P_1)T_{1\mathrm{p}}'' - T_{1\mathrm{j}}'' + P_1 T_{2\mathrm{q}}'' = 0 \tag{19}$$

and

$$P_2 T_{1\mathrm{p}}'' - T_{2\mathrm{j}}'' + (1 - P_2)T_{2\mathrm{q}}'' = 0 \tag{20}$$

If the entire flow arrangement is fixed, cell j can be uniquely tied in with the adjacent cells p and q. If j is the cell in which the streams 1 and/or 2 enter into the complete heat exchanger, it is

$$T_{1\mathrm{p}}'' = 1 \text{ and } T_{2\mathrm{q}}'' = 0 \tag{21}$$

If Eqs. (19) and (20) are written for all $n(z+1)$ cells, a system of linear equations is obtained for the $2n(z+1)$ unknown cell outlet temperatures which can be solved by known methods. If stream 1 leaves the entire heat exchanger from cell m, the relevant dimensionless temperature change is given by

$$P_{1\mathrm{tot}} = 1 - T_{1\mathrm{m}}'' \tag{22}$$

The cell method can be recommended for the thermal design of flow arrangements for which none of the analytical solutions described below can be applied. It is also recommended for studying effects for which no allowance can be made in the analytical solutions, e.g., small number of baffles in shell-and-tube heat exchangers (see Sect. 4.3). It is to observe that the results obtained from the cell method are of no higher accuracy than the heat transfer coefficients used, even if the exchanger is subdivided into a large number of cells. An example is presented in Sect. 6.1 to illustrate the application of the cell method in rating an existing heat exchanger.

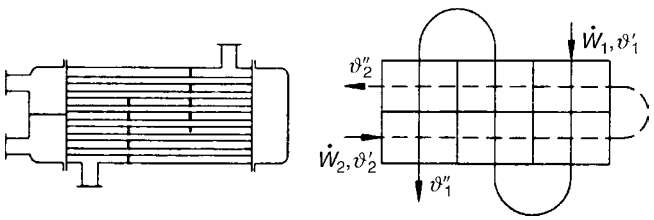

C1. Fig. 2. Shell-and-tube heat exchanger with one shell-side and two tube-side passes and two shell-side baffles; longitudinal section and cell model.

3.2 Mean Temperature Difference Concept

Usually, simple mathematical methods based on the mean temperature difference concept for the complete heat exchanger yield results with sufficient accuracy for the design. The charts and equations involved are easy to use.

The equations are derived by integrating the local energy balances as given by Eqs. (1)–(4) for a given flow arrangement. The flow arrangements are characterized by idealizing assumptions concerning the flow direction and the degree of lateral and axial mixing. The real flow pattern can greatly deviate from the ideal flow, as occurs, e.g., in baffled shell-and-tube heat exchangers. Nevertheless, the design equations derived for the ideal flow arrangements are usually sufficiently accurate. Only under extreme conditions, such as high NTUs or small number of baffles, more complex calculation models, such as the cell method [2, 3] (Sect. 3.1) or the axial dispersion model [4, 5] are recommended.

In addition to the idealizations of the flow arrangements, the following simplifying assumptions are made.

- The heat exchanger is operated in steady state.
- The only parameter that changes the enthalpy of the streams is the heat flux that is transferred, that is, heat losses to the surroundings and kinetic and potential energies are ignored.

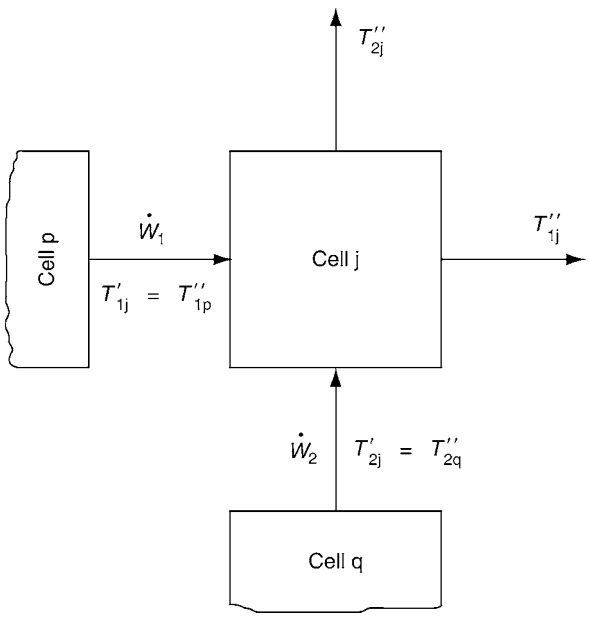

C1. Fig. 3. Cell j in the heat exchanger.

– If no phase change occurs, the specific heat capacities, and thus their rates, are constant. Allowance for the change in heat capacity with temperature is discussed in Chap. C2.
– If a change in phase does occur, the local heat capacity flow rate is assumed to be constant as well, which implies a linear relationship between enthalpy flow rate and temperature. The analysis of heat exchangers in which superheating or subcooling occurs as well as a change in phase is explained in Sect. 5.3.
– The effects of conduction and mixing in the direction of flow are ignored, except in the case of a stirred tank (Sect. 4.1).

Another assumption that must be made in determining the temperature fields in the equipment is that the overall heat transfer coefficient is constant. It is unnecessary for the calculation of outlet temperatures if the mean coefficient as defined by Eqs. (3) and (4) is taken (Chap. C2).

Equations for common flow arrangements are presented in Sect. 4. Since the dimensionless temperature change P_1 is expressed as a function of NTU_1 and R_1, the equations can be applied directly to the rating of existing heat exchangers. Only in some cases these equations can be solved for NTU_1. Hence heat exchanger design usually involves iterative solution of the equation $P_1 = f(NTU_1, R_1)$. If the flow arrangement is symmetric, the subscript 1 of P, NTU, and R may be replaced by the subscript 2. In the equations for these flow arrangements, the subscript attached to the dimensionless numbers is i, where $i = 1$ or $i = 2$.

Most of the 31 design charts presented in Figs. 15–45 were plotted from the equations listed in the tables of Sect. 4. A few were plotted from the results of analytical or numerical methods due to the lack of closed-form solutions; the same assumptions as those listed above were made in their determination.

3.3 Key to the Design Charts

The design charts can be explained with Fig. 4 [6]. The flow arrangements involved, together with the geometrically defined streams 1 and 2, are sketched alongside the respective charts. The coordinate axes represent the dimensionless temperature changes P_1 and P_2 of the two streams. If the flow arrangements are symmetric, the charts will also be symmetrical about the $P_1 = P_2$ axis. In this case, P_1 and P_2 can be interchanged, as is indicated in the diagrams by the subscripts 1,2 and 2,1, the first or second digit of which is respectively valid for the particular case in question.

The scale at the top of each chart represents the heat capacity rate ratio R_1 ($0 \le R_1 \le 1$); and that on the right-hand margin, the heat capacity rate ratio $R_2 = 1/R_1$ ($0 \le R_2 \le 1$). The straight line connecting the scale on the margin to the origin is the geometric location of the respective heat capacity rate ratio marked on the scale.

Two different sets of curves are plotted in the charts. The full-line curves apply for NTU_1 = const. above the diagonal, and for NTU_2 = const. below the diagonal. As is evident from Eq. (15), the curves intersect on the diagonal at $NTU_1 = NTU_2$.

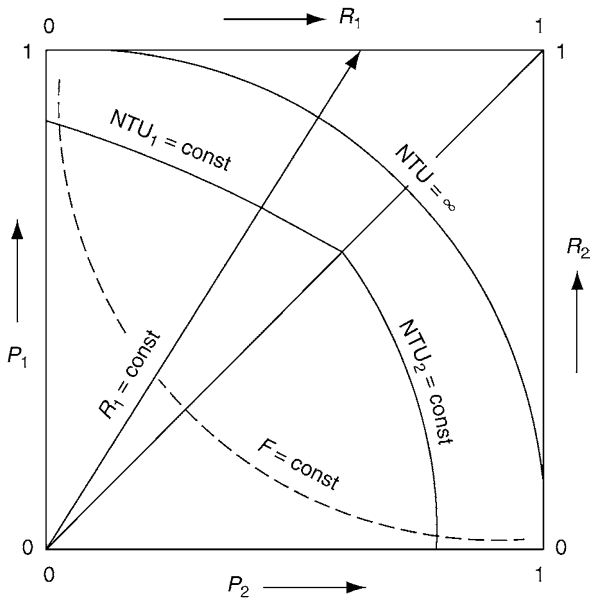

C1. Fig. 4. Schematic diagram of the design charts.

The only curve with a smooth transition at the diagonal is that for the limiting curve $NTU = \infty$, which is valid for infinitely large heat transfer areas. Temperature changes beyond this curve are usually impossible. Only a few special flow arrangements, e.g., the mixed–mixed cross-flow (Fig. 32), can attain higher temperature changes with two finite values of NTU. In these cases, the locus of the maximum possible dimensionless temperature changes has been designated as P_{max} and included in the chart. No operating points are possible above the limiting curve $NTU = \infty$ or the P_{max} curve. The limiting curve $NTU = \infty$ for some flow arrangements, e.g., pure countercurrent flow (Fig. 17), coincides with the right-hand and upper margins, i.e., $P_1 = 1$ and $P_2 = 1$.

The second set of curves, which are shown as dashed lines in the charts, are those for constant values of the correction factor F for the logarithmic mean temperature difference. The factor F is defined by

$$F = \frac{\Theta}{\Theta_C} = \frac{NTU_{iC}}{NTU_i} (i = 1, 2) \qquad (23)$$

where Θ_C is the dimensionless temperature difference and NTU_C is the number of transfer units in a pure countercurrent heat exchanger in which the dimensionless temperature changes P_1 and P_2 are the same as that attained for Θ and NTU_i in the flow arrangement investigated. If flow is purely countercurrent, the relationship $F = 1$ applies over the entire range of the chart. For all other flow arrangements, the limiting curve $NTU = \infty$ coincides with the $F = 0$ curve.

3.4 General Approximation Equation for the Estimation of *F*

For flow arrangements in which axial mixing or dispersion does not occur, the following generally valid approximation equation with individual empirical coefficients for each flow arrangement

can be recommended for the estimation of the logarithmic mean temperature difference correction factor [7]:

$$F = \frac{1}{\left(1 + aR_1^{db}\mathrm{NTU}_1^{b}\right)^{c}} \tag{24}$$

The coefficients *a*, *b*, *c*, *d* were determined through least square fits for numerous flow arrangements [7], based on the data calculated for the design charts. The values of *a*, *b*, *c*, *d* are given in Table 1. For symmetric flow arrangements, $d = ½$. Coefficients for additional flow arrangements can be found in the works by B. Spang and W. Roetzel [7].

With the correction factor *F*, the dimensionless temperature changes can be calculated using the known formula for counterflow.

C1. Table 1. Values of the coefficients *a*, *b*, *c*, and *d* for Eq. (24)

Flow arrangement	*a*	*b*	*c*	*d*
Pure cocurrent flow	0.671	2.11	0.534	0.500
Shell-and-tube heat exchanger with one shell-side and two tube-side passes; $\varepsilon = 1/2$	0.317	2.09	0.543	0.500
Shell-and-tube heat exchanger with one shell-side and four tube-side passes	0.274	2.08	0.624	0.508
Shell-and-tube heat exchanger with one shell-side and six tube-side passes	0.262	2.07	0.650	0.509
Shell-and-tube heat exchanger with one shell-side and eight tube-side passes	0.258	2.07	0.661	0.509
Shell-and-tube heat exchanger with one shell-side and three tube-side passes, two of it in countercurrent flow; $\varepsilon = 1/3$	0.431	2.33	0.371	0.450
Shell-and-tube heat exchanger with one shell-side and two countercurrent tube-side passes	0.168	2.18	0.490	0.395
Shell-and-tube heat exchanger; divided flow with one shell-side and one tube-side pass	0.272	1.86	0.529	0.329
Shell-and-tube heat exchanger; divided flow with one shell-side and two tube-side passes	0.230	2.03	0.733	0.531
Shell-and-tube heat exchanger; split flow with longitudinal baffle and two shell-side and two tube-side passes	0.0763	2.05	0.536	0.344
Shell-and-tube heat exchanger; double split flow with two longitudinal baffles and two shell-side passes on each side; two tube-side passes	0.0749	2.00	0.544	0.337
Pure cross-flow	0.433	1.60	0.267	0.500
Cross-flow with one tube row; laterally mixed on one side	0.234	1.91	0.597	0.668
Cross-flow, laterally mixed on both sides	0.251	2.06	0.677	0.500
Cross-flow with two tube rows and one pass	0.158	1.53	0.705	0.617
Cross-flow with three tube rows and one pass	0.150	1.38	0.722	0.596
Cross-flow with four tube rows and one pass	0.167	1.34	0.648	0.583
Cross-flow with five tube rows and one pass	0.195	1.35	0.560	0.569
Cross-flow with six tube rows and one pass	0.226	1.37	0.486	0.559
Cross-flow with ten tube rows and one pass	0.333	1.50	0.338	0.535
Counterdirected countercurrent cross-flow with two tube rows and two passes	0.0737	1.97	0.553	0.640
Counterdirected countercurrent cross-flow with three tube rows and three passes	0.0332	2.01	0.540	0.640
Counterdirected countercurrent cross-flow with four tube rows and four passes	0.0188	2.01	0.540	0.650
Counterdirected countercurrent cross-flow with six tube rows and six passes	0.00820	2.03	0.537	0.659
Counterdirected countercurrent cross-flow with four tube rows and two passes	0.0649	1.63	0.625	0.608
Codirected countercurrent cross-flow with two tube rows and two passes	0.0537	1.88	0.621	0.651
Codirected countercurrent cross-flow with three tube rows and three passes	0.0227	1.88	0.632	0.657
Counterdirected countercurrent cross-flow with two passes; stream 2 unmixed, stream 1 mixed only between passes	0.149	1.76	0.264	0.497
Counterdirected countercurrent cross-flow with three passes; stream 2 unmixed, stream 1 mixed only between passes	0.0711	1.85	0.253	0.422
Counterdirected countercurrent cross-flow with four passes; stream 2 unmixed, stream 1 mixed only between passes	0.0419	1.89	0.246	0.399
Plate heat exchanger with one pass for stream 1 and two passes for stream 2	0.272	1.86	0.529	0.322
Plate heat exchanger with one pass for stream 1 and three passes for stream 2, two of them in countercurrent flow	0.211	1.85	0.582	0.292
Plate heat exchanger with one pass for stream 1 and four passes for stream 2	0.244	1.90	0.577	0.323
Plate heat exchanger with two passes for stream 1 and four passes for stream 2 in overall countercurrent flow arrangement	0.0748	1.87	0.525	0.317

For $R_i \neq 1$

$$P_i = \frac{1 - \exp[(R_i - 1)\mathrm{NTU}_i F]}{1 - R_i \exp[(R_i - 1)\mathrm{NTU}_i F]} \tag{25}$$

and for $R_i = 1$, $\mathrm{NTU}_1 = \mathrm{NTU}_2 = \mathrm{NTU}$

$$P_1 = P_2 = \frac{\mathrm{NTU}F}{1 + \mathrm{NTU}F} \tag{26}$$

For the m,$2m$ shell-and-tube heat exchanger with $m \geq 2$ (Figs. 28 and 29), the correction factor could also be calculated using the formula for $m = 1$ (1,2-shell-and-tube heat exchanger). One has to merely divide the total NTU by m:

$$F_{m,2m} = F_{1,2}\left(\frac{\mathrm{NTU}_i}{m}; R_i\right) \tag{27}$$

The presented coefficients are valid for $1 \geq \mathrm{F} \geq 0.25$ and $0 \leq R_i \leq \infty$. The maximum relative error in F falls below 5% and in P below 3%. In the generally recommended range $1 \geq \mathrm{F} \geq 0.7$ below 1% and 2%, respectively.

The general approximation Eqs. (24–27) are mainly suitable for rating purposes. For the design from given temperature changes iterations are required: first the required NTU_{1C} for pure countercurrent flow is calculated, then the required $\mathrm{NTU}_1 = \mathrm{NTU}_{1C}/F$ can be introduced in the approximation Eqs. (24–27) with a guessed value of F, yielding an improved value of F, etc.

4 Analytical Design Formulae for Common Flow Arrangements

4.1 Stirred Tank

The stirred tank is the only heat exchanger in which mixing and heat conduction are assumed to take place in the direction of flow. In one-sided tanks (Fig. 16), stream 2 is completely mixed in both the flow and transverse directions, but stream 1 is mixed only in the transverse direction. In two-sided tanks (Fig. 15), both streams are completely mixed in all directions. The flow arrangement is symmetric in two-sided tanks, but not in one-sided.

The NTU_j = const. curves for the stream j that is completely mixed in the flow direction merge into the coordinate axis at points given by

$$P_j = \frac{\mathrm{NTU}_j}{1 + \mathrm{NTU}_j} \tag{28}$$

The curves for the stream i that is not mixed in the flow direction merge into the coordinate axis at points given by

$$P_i = 1 - \mathrm{e}^{\mathrm{NTU}_i} \tag{29}$$

The end points described by Eq. (29) apply to all the flow arrangements that are dealt with below, because all of them are analyzed under the idealized assumption that mixing and heat conduction do not occur in the direction of flow.

Mixing in the flow direction reduces the performance of a heat exchanger. Hence, if it is anticipated, the heat exchanger concerned should be designed as a stirred tank in order to obtain results on the safe side. Schematic flow diagrams and design charts for the two types of stirred tanks are presented in Figs. 15 and 16, and the design formulae are summarized in Table 2.

4.2 Countercurrent and Cocurrent Flow

The best-known flow arrangements are those for countercurrent and cocurrent flow. Both are symmetrical. If the NTU is given, countercurrent flow reaches the highest values of P; and if P is given the smallest required NTUs. The thermal efficiency of cocurrent flow is very poor, only the two types of stirred tanks have a lower efficiency.

The mean temperature difference, as defined by Eq. (4), is both in cocurrent and countercurrent flow the logarithmic mean of the local temperature differences $\Delta\vartheta_a$ and $\Delta\vartheta_b$ at both ends of the heat exchanger, i.e.,

$$\Delta\vartheta_m = \frac{\Delta\vartheta_a - \Delta\vartheta_b}{\ln\frac{\Delta\vartheta_a}{\Delta\vartheta_b}} \tag{30}$$

In the limiting case of $\Delta\vartheta_a \to \Delta\vartheta_b$, which arises for $R_1 \to 1$ in countercurrent flow and for $\mathrm{NTU} \to 0$ in cocurrent flow, the logarithmic approaches the arithmetic mean:

$$\Delta\vartheta_m = \frac{1}{2}(\Delta\vartheta_a + \Delta\vartheta_b) \tag{31}$$

The equations in dimensionless notation that correspond to Eqs. (30) and (31) are listed in Table 3, and the charts for the two flow arrangements are shown in Figs. 17 and 18.

4.3 Multipass Shell-and-Tube Heat Exchangers

For asymmetric flow arrangements, subscript 1 is allotted to the shell-side stream and subscript 2 to the tube-side stream.

The simplest case with one shell-side and one tube-side pass and a sufficiently large number of baffles on the shell side, or none at all, is the countercurrent or cocurrent flow according to Sect. 4.2.

Charts for multipass flow arrangements are shown in Figs. 19–29. That for the shell-and-tube heat exchanger with one shell-side and five tube-side passes (1,5-HEX, cf. Fig. 23)

C1. Table 2. Equations for stirred tanks

Flow arrangement	$P = f(\mathrm{NTU}, R)$	$\mathrm{NTU} = f(P, R)$	Limiting curve
Two-sided stirred tank; $i = 1, 2$	$P_i = \frac{\mathrm{NTU}_i}{1 + \mathrm{NTU}_i(1 + R_i)}$	$\mathrm{NTU}_i = \frac{P_i}{1 - P_i(1 + R_i)}$	$P_{i\infty} = \frac{1}{1 + R_i}$
One-sided stirred tank, stream 2 mixed	$\frac{1}{P_1} = R_1 + \frac{1}{1 - \mathrm{e}^{-\mathrm{NTU}_1}}$	$\mathrm{NTU}_1 = -\ln\left(1 - \frac{P_1}{1 - R_1 P_1}\right)$	$P_{1\infty} = \frac{1}{1 + R_1}$

C1. Table 3. Equations for countercurrent and cocurrent flow

Flow arrangement	$P = f(\mathrm{NTU}, R)$	$\mathrm{NTU} = f(P, R)$	$\Theta = f(P_1, P_2)$	Limiting curve
Pure counter current flow i = 1, 2	$P_i = \frac{1-\exp[(R_i-1)\mathrm{NTU}_i]}{1-R_i\exp[(R_i-1)\mathrm{NTU}_i]}$ for $R_i \neq 1$ $P_i = \frac{\mathrm{NTU}}{1+\mathrm{NTU}}$ for $R_i \neq 1$	$\mathrm{NTU}_i = \frac{1}{1-R_i}\ln\frac{1-R_iP_i}{1-P_i}$ $\mathrm{NTU} = \frac{P}{1-P}$	$\Theta = \frac{P_1-P_2}{\ln\frac{1-P_2}{1-P_1}}$ $\Theta = 1-P$	$P_{i\infty} = \begin{cases} 1; & R_i \leq 1 \\ \frac{1}{R_i}; & R_i > 1 \end{cases}$
Pure cocurrent flow i = 1, 2	$P_i = \frac{1-\exp[-\mathrm{NTU}_i(1+R_i)]}{1+R_i}$	$\mathrm{NTU}_i = -\frac{\ln[1-P_i(1+R_i)]}{1+R_i}$	$\Theta = \frac{-(P_1+P_2)}{\ln[1-(P_1+P_2)]}$	$P_{i\infty} = \frac{1}{1+R_i}$

was obtained by an analytical design method [8, 9]; and that in Fig. 27 for double split flow by a closed-form equation [10]. The equations for the other flow arrangements are listed in Table 4.

The NTU-ratio ε that occurs in the equations for the 1,2- and 1,3-HEX is defined by

$$\varepsilon = \frac{(kA)_{\mathrm{cocurr.pass}}}{(kA)_{\mathrm{tot}}} \tag{32}$$

The ratio ε allows for differences in the heat transfer area and in the heat transfer coefficient for the various passes (with the restriction that the product kA is the same in each of the two counterflow passes in the 1,3-HEX).

The heat transfer coefficient on the tube side depends on temperature. In the 1,2-HEX, this can be allowed for by determining separate heat transfer coefficients for each pass. The reference temperature in this case is the arithmetic mean of the inlet and outlet temperatures in the pass concerned. The intermediate temperature ϑ_{2z}, i.e., at the outlet of the first pass and at the inlet to the second, is required for its determination. Concerning the flow direction in the tube-side passes, two layouts I and II are possible. In layout I, the first pass is countercurrent to the shell-side stream, in layout II cocurrent. The equations for the determination of the temperatures ϑ^{I}_{2z} and ϑ^{II}_{2z} are given in Table 4.

The 1,2-HEX can be adopted as an approximate model for a 1,n-HEX with $n = 2m$ tube-side passes (m = 1, 2, 3, ...) of roughly the same area [8, 9]. The areas of the countercurrent and the cocurrent passes in the 1,2-model must be the same as those in the actual 1,2m-HEX. In the normal case the areas are the same in all the passes and a constant mean heat transfer coefficient can be adopted for the complete heat exchanger. Under these circumstances, a ratio of ε = ½ can be taken for the 1,2-HEX, and of ε = 1/3 for the 1,3-HEX. The charts in Figs. 19 and 21 are also calculated with these values.

The flow arrangement obtained with one shell-side pass and an infinite number of equal tube-side passes (1,n-HEX with $n \rightarrow \infty$) corresponds to that of mixed–mixed cross-flow (cf. Sect. 4.4) [17]. It can also serve as an approximation for a large even number of tube-side passes (1,2m-system with m = 2, 3, ...). The results from this approximation are more on the safe side than those obtained from the approximation with the equations for the 1,2-system. An upper limit for the error of the approximation can be derived from a comparison with the chart (Fig. 20) or the equation (Table 4) for the 1,4-HEX.

Shell-and-tube heat exchangers with an odd number of tube-side passes can be approximately described by the equations for the 1,3-system with two countercurrent passes of the same area if the NTU-ratio ε is formed from the sum of the areas of all the cocurrent passes; for instance, ε = 3/7 for a total of seven passes of the same area, four of which are countercurrent.

As has already been mentioned, the first of a number of tube-side passes may flow countercurrent (layout I) or cocurrent (layout II) to the shell-side stream. If the number is odd, layout I is always the more advantageous, because the countercurrent passes predominate. If there is an even number of tube-side passes of the same area and if the calculation is based on constant values for the heat transfer coefficient, the same results are obtained for both layouts. However, a more accurate calculation with varying heat transfer coefficients reveals that the more favorable layout is that in which the coefficients for the countercurrent passes are higher than those for the cocurrent [8, 9]. Hence, the following rule can be derived for an even number of equal tube-side passes.

If a liquid is to be heated in the tubes, the first tube-side pass should be cocurrent to the shell-side stream (layout II); if it is to be cooled, countercurrent (layout I). The opposite applies if a gas flows in the tubes.

A number m of identical 1,n-HEXs can be connected in series {m,(m×n)-HEXs} in order to achieve higher temperature changes. The equations that apply in this case are those given in Sect. 5.1 for the countercurrent coupling of identical individual heat exchangers. Charts for n = 2 and m = 2 and 4 are shown in Figs. 28 and 29. Also the Eq. (27) can be applied for the m,2m-HEX.

Strictly speaking, the equations and charts presented in this section are valid only if there is an infinite number of baffles on the shell side, or none at all. The equations and charts allow a good approximation if the number of baffles is sufficiently large, i.e., at least ten for countercurrent flow and at least five for 1,2-HEXs (according to Gardner and Taborek [18]). If the number of baffles is small, allowance must be made for the fact that both streams are in cross-flow between two baffles. This can be done by subdividing the system into cells, as described in Sect. 3.1. The equations to be adopted in the calculations for each cell are those for cross-flow with one tube row (Sect. 4.4) and laterally mixed stream 1 on the shell side (which corresponds to stream 1 on the tube-side as conventionally designated in cross-flow heat exchangers).

For a finite number of baffles, there are two layouts A and B with different positions of the inlet and outlet relative to one another (Fig. 5). In both layouts they are adjacent. In layout A they exert a certain cocurrent effect, in layout B a

C1. Table 4. Equations for shell-and-tube heat exchangers, stream 1 on shell side, stream 2 inside the tubes

Flow arrangement	Equation	Limiting curve
One shell-side and two tube-side passes [8, 9] $i = 1, 2$	$\frac{1}{P_i} = \frac{1}{2}\left(1 + R_i + S\coth\left(\frac{1}{2}S\mathrm{NTU}_i\right)\right)$ or $\mathrm{NTU}_i = \frac{2}{S}\operatorname{arcoth}\left(\frac{2-P_i(1+R_i)}{SP_i}\right)$ where $S = \sqrt{1 + R_i^2 + 2R_i(2\varepsilon - 1)}$ NTU-ratio ε from Eq. (32) Temperature ϑ_{2z} of tube-side stream between passes Layout I: $\frac{\vartheta'_{2z} - \vartheta'_2}{\vartheta'_1 - \vartheta'_2} = 1 - \frac{SP_1 \exp\left[\frac{\mathrm{NTU}_1}{2}(1 + R_1(2\varepsilon - 1))\right]}{2\sinh\left(\frac{\mathrm{NTU}_1}{2}S\right)}$ Layout II: $\frac{\vartheta''_{2z} - \vartheta'_2}{\vartheta'_1 - \vartheta'_2} = 1 - P_1 - \frac{SP_1 \exp\left[-\frac{\mathrm{NTU}_1}{2}(1 + R_1(2\varepsilon - 1))\right]}{2\sinh\left(\frac{\mathrm{NTU}_1}{2}S\right)}$	$P_{i\infty} = \frac{2}{1 + R_i + S}$
One shell-side and $2m$ tube-side passes, $m = 1, 2, \ldots, \infty$ [1, 11]	$\frac{1}{P_1} = \frac{\sqrt{1 + (R_1/m)^2}}{1 - \exp\left(-\mathrm{NTU}_1\sqrt{1 + (R_1/m)^2}\right)} + \frac{R_1}{1 - e^{-R_1\mathrm{NTU}_1}} - \frac{R_1/m}{1 - e^{-R_1\mathrm{NTU}_1/m}}$ $+ \frac{1}{2}\left(1 + \frac{R_1}{m} - \sqrt{1 + \left(\frac{R_1}{m}\right)^2}\right)$	$P_{1\infty} = \frac{2}{1 + 2R_1 - R_1/m + \sqrt{1 + (R_1/m)^2}}$
One shell-side and three tube-side passes, two countercurrent [12]	$P_1 = \frac{S_1\left(e^{S_1} + e^{S_3}\right)\left(e^{S_2} - 1\right) + S_2\left(e^{S_2} + e^{S_3}\right)\left(1 - e^{S_1}\right) + \ldots}{S_1\left(e^{S_1} + e^{S_3}\right)\left(R_1 e^{S_2} - 1\right) + S_2\left(e^{S_2} + e^{S_3}\right)\left(1 - R_1 e^{S_1}\right) + \ldots}$ $\frac{\ldots + \mathrm{NTU}_1(1 - R_1)\left(e^{S_2} - e^{S_1}\right)\left(1 + e^{S_3}\right)}{\ldots + \mathrm{NTU}_1(1 - R_1)\left(e^{S_2} - e^{S_1}\right)\left(1 + R_1 e^{S_3}\right)}$ $S_{1/2} = \frac{p}{2} \pm \sqrt{\frac{p^2}{4} - q}$ $S_3 = \frac{1}{2}R_1\mathrm{NTU}_1(1 - \varepsilon)$ $p = \mathrm{NTU}_1\left(1 - \frac{1}{2}R_1(1 - 3\varepsilon)\right)$ $q = \frac{1}{2}\varepsilon(1 - \varepsilon)\mathrm{NTU}_1^2 R_1(1 - R_1)$ NTU-ratio ε from Eq. (32) $\frac{P}{1-P} = \mathrm{NTU}\frac{\varepsilon(1-\varepsilon)}{1+3\varepsilon} - 2\left(\frac{1+\varepsilon}{1+3\varepsilon}\right)^2\left[\left(e^{-0.5\mathrm{NTU}(1+3\varepsilon)} - 1\right)^{-1} + \left(e^{0.5\mathrm{NTU}(1-\varepsilon)} + 1\right)^{-1}\right]^{-1}$ for $R_1 = 1$	$P_{1\infty} = \begin{cases} 1; & R_1 \le 1 \\ \frac{1}{R_1}; & R_1 > 1 \end{cases}$
One shell-side and two tube-side passes, both countercurrent [12]	$P_1 = \frac{\left(e^{\mathrm{NTU}_1(0.5R_1 - 1)} - 1\right)\left(e^{0.5R_1\mathrm{NTU}_1} + 1\right)}{(0.5R_1 - 1)\left(e^{\mathrm{NTU}_1(0.5R_1-1)} + e^{0.5R_1\mathrm{NTU}_1}\right) + (R_1 e^{0.5R_1\mathrm{NTU}_1} + 1)\left(e^{\mathrm{NTU}_1(0.5R_1-1)} - 1\right)}$ for $R_1 \neq 2$ $\frac{1}{P_1} = 1 + \frac{1}{\mathrm{NTU}_1} + \frac{1}{1 + \exp(-\mathrm{NTU}_1)}$ for $R_1 = 2$	$P_{1\infty} = \begin{cases} 2/(2 + R_1); R_1 \le 2 \\ 1/R_1; & R_1 > 2 \end{cases}$
Divided flow with one shell-side and one tube-side pass [13]	$P_1 = \frac{1}{R_1} - \frac{(2 - R_1)(2 + R_1\exp[-\mathrm{NTU}_1(1 + R_1/2)])}{R_1(2 + R_1)(2 - R_1\exp[-\mathrm{NTU}_1(1 - R_1/2)])}$ for $R_1 \neq 2$ $P_1 = \frac{1}{2} - \frac{1 + \exp(-2\mathrm{NTU}_1)}{4(1 + \mathrm{NTU}_1)}$ for $R_1 = 2$	$P_{1\infty} = \begin{cases} 2/(2 + R_1); R_1 \le 2 \\ 1/R_1; R_1 > 2 \end{cases}$
Divided flow with one shell-side and two tube-side passes [14]	$\frac{1}{P_1} = 1 + \frac{R_1}{2} + \kappa\frac{e^{\kappa\mathrm{NTU}_1} + 1}{e^{\kappa\mathrm{NTU}_1} - 1} - \frac{2\kappa e^{0.5\,\mathrm{NTU}_1(1+\kappa)} + 1}{\kappa - 1 + (\kappa + 1)e^{\kappa\mathrm{NTU}_1}}\left(1 - \frac{\kappa e^{0.5\,\mathrm{NTU}_1(\kappa-1)}}{1 - e^{\kappa\mathrm{NTU}_1}}\right)$ $\kappa = 0.5\sqrt{R_1^2 + 4}$	$\frac{1}{P_{1\infty}} = 1 + \frac{R_1}{2} + \kappa$
Split flow with longitudinal baffle and two shell-side and two tube-side passes (tube-side outlet and shell-side inlet at the same side) [15, 16]	$P_1 = \frac{1}{R_1} - \frac{(1 - \beta)^2(1 - \gamma)}{R_1 - 2\beta^2(1 - \gamma)}$ for $R_1 \neq 2$ $\beta = \frac{1 - \exp[-\mathrm{NTU}_1(2 + R_1)/4]}{1 + 2/R_1}$ $\gamma = \frac{1 - \exp[-\mathrm{NTU}_1(2 - R_1)/2]}{2/R_1 - \exp[-\mathrm{NTU}_1(2 - R_1)/2]}$ $P_1 = \frac{(1 + 2\mathrm{NTU}_1)e^{\mathrm{NTU}_1} - e^{-\mathrm{NTU}_1}}{2 + (3 + 4\mathrm{NTU}_1)e^{\mathrm{NTU}_1} - e^{-\mathrm{NTU}_1}}$ for $R_1 = 2$	$P_{1\infty} = \begin{cases} \frac{2+R_1}{2+R_1+R_1^2}; & R_1 \le 2 \\ 1/R_1; & R_1 > 2 \end{cases}$

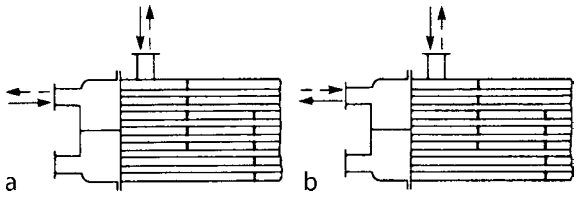

C1. Fig. 5. Layouts of shell-and-tube heat exchangers with one shell-side and two tube-side passes and with baffles on the shell side. Layout A: the adjacent nozzles for stream 1 and 2 are either both inlets or both outlets. Layout B: one of the adjacent nozzles for stream 1 and 2 is an inlet, the other one is an outlet.

countercurrent one. Analysis by the cell method [2, 3] shows that layout B is fundamentally superior to layout A and should therefore be preferred, although the differences are not very pronounced.

4.4 Cross-flow Heat Exchangers

If the flow arrangement is asymmetric, subscript 1 is allotted to the stream inside the tubes and subscript 2 to that outside the tubes. In Sect. 4.3, complete lateral mixing in each pass for all shell-and-tube flow arrangements was assumed. In cross-flow heat exchangers, however, even the limiting case of no lateral mixing is of significance. Thus, there are three fundamental cross-flow arrangements, each with one pass on both sides, as indicated below.

- Both streams are unmixed in the lateral direction (pure cross-flow or unmixed–unmixed cross-flow; Fig. 30).
- Stream 1 (inside the tubes) is laterally mixed, and stream 2 (outside the tubes) is not (cross-flow with one tube row or mixed–unmixed cross-flow; Fig. 31).
- Both streams are laterally mixed (mixed–mixed cross-flow; Fig. 32).

The analytical solutions for these flow arrangements are given in Table 5. Since the thermal efficiency is reduced by lateral mixing, the calculation for the case of complete mixing yields results on the safe side.

The degree of lateral mixing of stream 1 and the thermal efficiency achieved in cross-flow arrangements with n tube rows ($n = 2, 3, \ldots$) in one pass lie between the figures obtained for cross-flow with one tube row and those for pure cross-flow (Figs. 33–35, and the equations in Table 5).

In multipass cross-flow heat exchangers, the thermal efficiency depends not only on the degree of lateral mixing in each pass but also on the overall flow arrangement, i.e., on whether the flow is overall countercurrent or cocurrent, and on the degree of mixing between passes. If the outer stream is not laterally mixed, the thermal efficiency also depends on whether the flow on the tube side is in alternate directions in successive passes (counterdirected countercurrent cross-flow) or in the same direction in each pass (codirected countercurrent cross-flow). Many flow arrangements are feasible, but only a few are of practical significance. If the two streams are adequately mixed between each pass, the coupling equations given in Sect. 5.1 for overall cocurrent or countercurrent flow should be used.

The counterdirected countercurrent cross-flow with stream 2 unmixed is easy to realize in tube bundles of rectangular cross-section. The relevant design charts are shown in Figs. 36–41. Equations are presented in Table 5 for flow arrangements with four or less passes and with stream 1 completely mixed in the lateral direction (one tube row for each pass; Figs. 36–38) and for flow arrangements with two passes and two tube rows in each pass (Fig. 39).

Counterdirected cross-flow heat exchangers with four or more passes and one tube row per pass can be designed with the aid of the following approximate equation [24]:

$$F = \frac{n}{\mathrm{NTU}_1\sqrt{R_1}} \frac{3\sinh\left(\frac{\mathrm{NTU}_1}{n}\sqrt{R_1}\right)}{1 + 2\cosh\left(\frac{\mathrm{NTU}_1}{n}\sqrt{R_1}\right)} \qquad (33)$$

where n is the number of passes. The dimensionless temperature change P_i ($i = 1, 2$) can then be obtained from Eq. (25) or (26). The error in P is at the most 1% for $n \geq 4$.

The charts for flow arrangements in which the number of tube rows in each pass is very large (each pass as in pure cross-flow; Figs. 40 and 41) were calculated numerically. For the numerical calculation each pass was subdivided into 40 × 40 cells. In addition to the given charts and coefficients for Eq. (24), a most powerful approximation [24] can be recommended which is valid for any number of counterdirected pure cross-flow passes.

The codirected countercurrent cross-flow arrangement in which the flow is in the same direction in each pass is the more effective one. It is realized in helical coil heat exchangers (Fig. 6), in which each turn corresponds to one pass with one row of tubes. In Table 5 design equations are given for arbitrary values of n. Alternatively, if mixing between passes or counterdirected pass flow is assumed for the design calculation, the exchanger surface will be overestimated and one is on the safe side.

Countercurrent cross-flow transforms into pure countercurrent flow as the number of passes increases. However, if the NTU is high, i.e., NTU > 5, the equations for countercurrent flow do not apply unless the number of passes is about 20 or more.

4.5 Plate Heat Exchangers

The following is restricted to the thermal analysis of heat exchangers with a large number of plates, i.e., those in which thermal end effects can be ignored (heat is transferred on only one side of the channels at the ends). According to Kandlikar and Shah [25], this end effect can generally be neglected if there are more than 40 plates in the complete heat exchanger. Solutions that have been determined numerically or analytically for equipment with a smaller number of plates and for various flow arrangements can be found in the literature [25, 26].

Plate heat exchangers can be classified regarding the number of passes for the two streams. Subscript 1 is allotted to the stream with the smaller number of passes. Flow arrangements with the same number of passes on each side are symmetrical. Several flow arrangements are feasible with a given number of passes on each side. They are partly identical regarding the

C1. Table 5. Equations for cross-flow heat exchangers, stream 1 inside tubes

Flow arrangement	Equation	Limiting curve
Pure cross-flow [19, 20] $i = 1, 2$	$P_i = \frac{1}{R_i \mathrm{NTU}_i} \sum_{m=0}^{\infty} \left\{ \left[1 - e^{-\mathrm{NTU}_i} \sum_{j=0}^{m} \frac{1}{j!} \mathrm{NTU}_i^j \right] \left[1 - e^{-R_i \mathrm{NTU}_i} \sum_{j=0}^{m} \frac{1}{j!} (R_i \mathrm{NTU}_i)^j \right] \right\}$	$P_{i\infty} = \begin{cases} 1; R_i \le 1 \\ 1/R_i; R_i > 1 \end{cases}$
Cross-flow with one tube row, laterally mixed on one side [21]	$P_1 = 1 - \exp\left[\left(e^{-R_1 \mathrm{NTU}_1} - 1 \right) / R_1 \right]$ or $\mathrm{NTU}_1 = -\frac{1}{R_1} \ln[1 + R_1 \ln(1 - P_1)]$	$P_{1\infty} = 1 - e^{-1/R_1}$
Cross-flow, laterally mixed on both sides [21] $i = 1, 2$	$\frac{1}{P_i} = \frac{1}{1 - e^{-\mathrm{NTU}_i}} + \frac{R_i}{1 - e^{-R_i \mathrm{NTU}_i}} - \frac{1}{\mathrm{NTU}_i}$	$P_{i\infty} = \frac{1}{1 + R_i}$
Cross-flow with n tube rows and one pass[a]	$P_1 = 1 - e^{-nB} \sum_{j=0}^{n-1} \left(1 - \frac{j}{n} \right) (v_j - a v_{j-1})$ where $\nu_{-1} = 0$; $\nu_0 = 1$ $v_{j+1} = \frac{1}{j+1} \left[(nR_1B^2 + 2ja + a) v_j - ja^2 v_{j-1} \right]$; $j = 0, 1, 2, \ldots$ $a = e^{-R_1 \mathrm{NTU}_1 / n}$; $B = (1 - a)/R_1$	$P_{1\infty} = 1 - e^{-n/R_1} \sum_{j=0}^{n-1} \frac{1}{j!} \left(1 - \frac{j}{n} \right) \left(\frac{n}{R_1} \right)^j$
Counterdirected countercurrent cross-flow with two tube rows and two passes [22]	$\frac{1}{1 - P_1} = \frac{\delta}{2} + \left(1 - \frac{\delta}{2} \right) e^{2\delta/R_1}$ where $\delta = 1 - e^{-R_1 \mathrm{NTU}_1 / 2}$	$P_{1\infty} = 1 - \frac{2}{1 + e^{2/R_1}}$
Counterdirected countercurrent cross-flow with three tube rows and three passes [22]	$\frac{1}{1 - P_1} = \left(1 - \frac{\delta}{2} \right)^2 e^{3\delta/R_1} + \left[\delta \left(1 - \frac{\delta}{4} \right) - \frac{\delta^2}{R_1} \left(1 - \frac{\delta}{2} \right) \right] e^{\delta/R_1}$ where $\delta = 1 - e^{-R_1 \mathrm{NTU}_1 / 3}$	$P_{1\infty} = 1 - \frac{4}{\left(3 - \frac{2}{R_1} \right) e^{1/R_1} + e^{3/R_1}}$
Counterdirected countercurrent cross-flow with four tube rows and four passes [23]	$\frac{1}{1 - P_1} = \frac{\delta}{2} \left(1 - \frac{\delta}{2} + \frac{\delta^2}{4} \right) + \delta \left(1 - \frac{\delta}{2} \right) \left[1 - \frac{2\delta}{R_1} \left(1 - \frac{\delta}{2} \right) \right] e^{2\delta/R_1} + \left(1 - \frac{\delta}{2} \right)^3 e^{4\delta/R_1}$ where $\delta = 1 - e^{-R_1 \mathrm{NTU}_1 / 4}$	$\frac{8}{1 - P_{1\infty}} = 3 + 4 \left(1 - \frac{1}{R_1} \right) e^{2/R_1} + e^{4/R_1}$
Counterdirected countercurrent cross-flow with four tube rows and two passes [23]	$\frac{1}{1 - P_1} = \frac{\frac{1}{2R_1} \delta^3 \left(4 - \delta + \frac{2\delta^2}{R_1} \right) + \delta \left(1 - \frac{\delta}{2} + \frac{\delta^2}{8} \right) \left(1 - e^{4\delta/R_1} \right) + e^{4\delta/R_1}}{\left(1 + \frac{\delta^2}{R_1} \right)^2}$ where $\delta = 1 - e^{-R_1 \mathrm{NTU}_1 / 4}$	$\frac{1}{1 - P_{1\infty}} = \frac{\frac{1}{2R_1} \left(3 + \frac{2}{R_1} \right) + \frac{5}{8} \left(1 - e^{4/R_1} \right) + e^{4/R_1}}{\left(1 + \frac{1}{R_1} \right)^2}$
Codirected countercurrent cross-flow with n tube rows and n passes[a]	$\frac{1}{1 - P_1} = e^B \prod_{j=0}^{n-1} \delta_j$ where $\delta_0 = 1$; $\delta_1 = e^B - R_1 B^2$ $\delta_i = \delta_1 - \sum_{j=2}^{i} \frac{\mu_j - a\mu_{j-1}}{\prod_{k=i-j+1}^{i-1} \delta_k}$; $i = 2, 3, 4, \ldots$ $\mu_{-1} = 0$; $\mu_0 = 1$ $\mu_{j+1} = \frac{1}{j+1} \left[(R_1 B^2 + 2ja + a) \mu_j - ja^2 \mu_{j-1} \right]$; $j = 0, 1, 2, \ldots$ $a = e^{-R_1 \mathrm{NTU}_1 / n}$; $B = (1 - a)/R_1$	$\frac{1}{1 - P_{1\infty}} = e^{1/R_1} \prod_{j=0}^{n-1} \delta_{j\infty}$ where $\delta_{0\infty} = 1$; $\delta_{1\infty} = e^{1/R_1} - 1/R_1$ $\delta_{i\infty} = \delta_{1\infty} - \sum_{j=2}^{i} \frac{1}{j! R_1^j \prod_{k=i-j+1}^{i-1} \delta_{k\infty}}$ $i = 2, 3, 4, \ldots$

[a]These equations have been derived by Th. Bes, Institute of Thermodynamics, Helmut Schmidt University/University of the Federal Armed Forces Hamburg, 1993

thermal performance. A method of determining the thermal efficiency is to break down the flow arrangement into a system of cocurrent and countercurrent units connected in series and parallel and to apply the coupling equations (Sect. 5.1).

Design charts showing the most favorable flow configurations in four different arrangements of passes are presented in Figs. 42–45. The equations used for their determination are listed in Table 6. The most advantageous flow arrangement with the same number of passes on both sides is pure countercurrent flow.

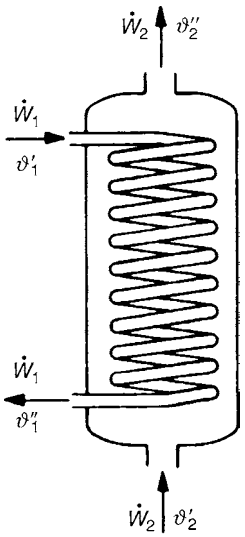

C1. Fig. 6. Schematic diagram of a helical coil heat exchanger with $n = 10$ turns (or passes).

4.6 Spiral Heat Exchangers

In spiral heat exchangers with a finite number of turns, the two streams flow in countercurrent, but the thermal efficiency is poorer than that in pure countercurrent flow. A schematic diagram of the flow arrangement is shown in Fig. 7. The stream that enters on the inside is allotted the subscript 1. The following approximation equation [28] applies to the logarithmic mean temperature difference correction factor:

$$F = \frac{1}{\mathrm{NTU}^2} \ln \frac{1 + \mathrm{NTU}^2}{1 + \left(\frac{\mathrm{NTU} r_1}{r_1 + nb}\right)^2} \tag{34}$$

where

$$\mathrm{NTU} = \frac{k\pi d_o H}{\sqrt{\dot{W}_1 \dot{W}_2}} \tag{35}$$

is formed with the geometric mean of both heat capacity flow rates, and with the outside shell surface of diameter d_o and height H. The number of turns is denoted with n, r_i is the radius of the central tube and b the width of the flow channels.

The temperature change P_i ($i = 1, 2$) can be determined from the correction factor F by means of Eqs. (25) or (26) (Sect. 3.4). If $n \geq 4$ and $F > 0.8$, the relative error for P is less than 1%. The approximation equation yields symmetrical results, although the flow arrangement is slightly asymmetric.

Equations (34) and (35) are valid for a constant overall heat transfer coefficient. In a special method [29] the effect of changing radius of channel curvature on the transfer coefficients can also be taken into account.

C1. Table 6. Equations for plate heat exchangers [27]. P_{1c} dimensionless temperature change for pure countercurrent flow (Table 3). P_{1p} dimensionless temperature change for pure cocurrent flow (Table 3)

Flow arrangement	Equation	Limiting curve
One pass for stream 1 and two passes for stream 2	$P_1 = \frac{1}{2}\left(P_{1c} + P_{1p} - \frac{1}{2}R_1 P_{1c} P_{1p}\right)$ where $P_{1c} = P_{1c}(\mathrm{NTU}_1, R_1/2)$ and $P_{1p} = P_{1p}(\mathrm{NTU}_1, R_1/2)$	$P_{1\infty} = \begin{cases} 2/(2+R_1); & R_1 \leq 2 \\ 1/R_1; & R_1 > 2 \end{cases}$
One pass for stream 1 and three passes for stream 2, two in countercurrent	$P_1 = \frac{1}{3}\left(P_{1p} + P_{1c}\left(1 - \frac{1}{3}R_1 P_{1p}\right)\left(2 - \frac{1}{3}R_1 P_{1c}\right)\right)$ where $P_{1c} = P_{1c}(\mathrm{NTU}_1, R_1/3)$ and $P_{1p} = P_{1p}(\mathrm{NTU}_1, R_1/3)$	$P_{1\infty} = \begin{cases} (9-R_1)/(9+3R_1); & R_1 \leq 3 \\ 1/R_1; & R_1 > 3 \end{cases}$
One pass for stream 1 and four passes for stream 2	$P_1 = \delta\left(1 - \frac{1}{4}R_1\delta\right)$ $\delta = \frac{1}{2}\left(P_{1c} + P_{1p} - \frac{1}{4}R_1 P_{1c} P_{1p}\right)$ where $P_{1c} = P_{1c}(\mathrm{NTU}_1, R_1/4)$ and $P_{1p} = P_{1p}(\mathrm{NTU}_1, R_1/4)$	$P_{1\infty} = \begin{cases} (4/(4+R_1))^2; & R_1 \leq 4 \\ 1/R_1; & R_1 > 4 \end{cases}$
Two passes for stream 1 and four passes for stream 2 in overall counterflow	$P_1 = \delta + \frac{\delta(1-\delta)(1-\delta R_1)}{1-\delta^2 R_1}$ $\delta = \frac{1}{2}\left(P_{1c} + P_{1p} - \frac{1}{2}R_1 P_{1c} P_{1p}\right)$ where $P_{1c} = P_{1c}(\mathrm{NTU}_1, R_1/2)$ and $P_{1p} = P_{1p}(\mathrm{NTU}_1, R_1/2)$	$P_{1\infty} = \begin{cases} 4/\left(4+R_1^2\right); & R_1 \leq 2 \\ 1/R_1; & R_1 > 2 \end{cases}$

4.7 Plug-in Double-Pipe Heat Exchangers

The dimensionless temperature change P that occurs within a heating or cooling medium that flows in a double-pipe heat exchanger with closed ends (Fig. 8) can be obtained from the following equation [1]:

$$P = 2\frac{1 - e^{-\mu NTU}}{1 + \mu + (\mu - 1)e^{-\mu NTU}} \qquad (36)$$

where

$$P = \frac{\vartheta' - \vartheta''}{\vartheta' - \vartheta_s},$$

$$NTU = \frac{(kA)_o}{\dot{W}},$$

$$\mu = \sqrt{1 + 4\frac{(kA)_i}{(kA)_o}},$$

ϑ_s is the temperature of the ambient medium to be heated or cooled and is assumed to be constant (complete mixing or phase change),

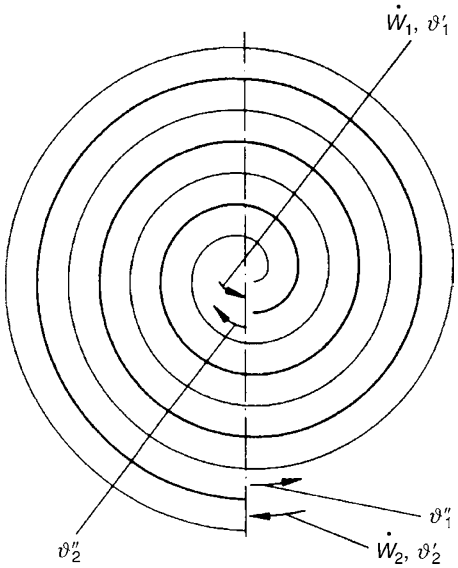

C1. Fig. 7. Schematic diagram of a spiral heat exchanger with $n = 3$ turns in the double spiral.

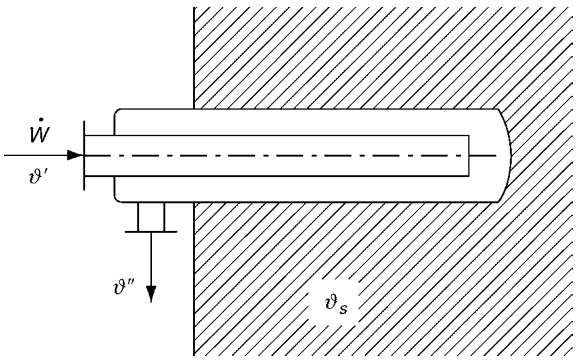

C1. Fig. 8. Inserted double-pipe heat exchanger for heating or cooling a medium at a constant temperature.

$\dot{W}$ is the heat capacity flow rate of the heating or cooling medium,

$(kA)_o$ is the product of the overall heat transfer coefficient and the area of the outer pipe,

and

$(kA)_i$ is the corresponding product for the inner pipe.

Equation (36) is valid regardless of whether the heating or cooling medium enters the inner or outer pipe.

5 Heat Exchanger Systems

5.1 Coupled Heat Exchangers

A number of heat exchangers of the same or different types may be connected together. The temperature changes that can be achieved by the coupled system depend on the nature of the connections, the behavior of the individual units, and the degree of mixing of the streams between the units.

It is assumed here that the streams between the individual exchangers are completely mixed and that the heat capacity rates in the entire system are constant. Exchangers can be connected in series with overall cocurrent (Fig. 9) or countercurrent (Fig. 10) flow, and stream 2 can be readily divided into a number of parallel substreams (Fig. 11). The individual flow arrangements are unaffected by the nature of the series or parallel connections, and the equations and design charts in Sect. 4 still apply.

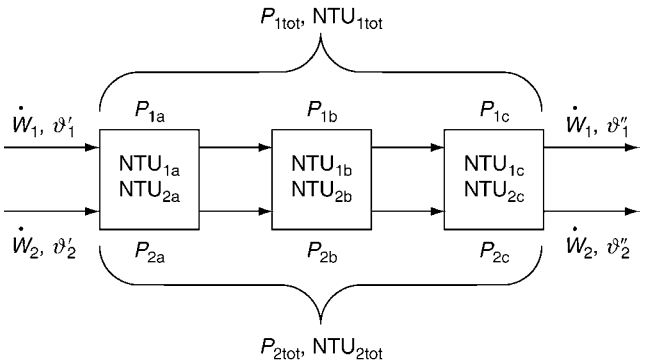

C1. Fig. 9. Schematic diagram of three heat exchangers in series connection with overall cocurrent flow.

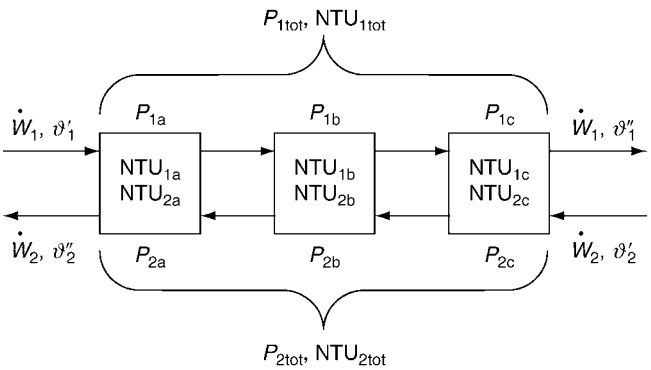

C1. Fig. 10. Schematic diagram of three heat exchangers in series connection with overall countercurrent flow.

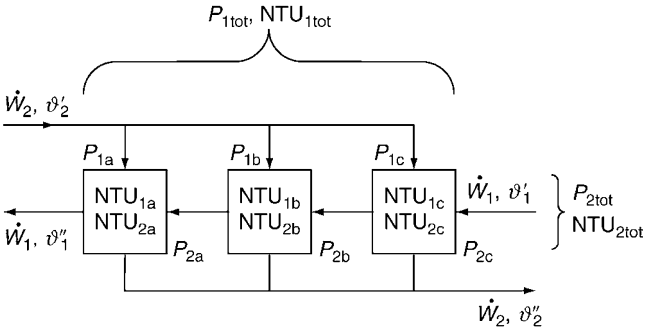

C1. Fig. 11. Schematic diagram of three heat exchangers in parallel connection, stream 2 divided into three substreams.

The number of transfer units NTU_{1tot} and the heat transfer area A_{tot} in a coupled system are the sums of the corresponding values NTU_{1i} and A_i for the individual exchangers, regardless of the type of connection. Thus,

$$NTU_{1tot} = \sum_{i=1}^{n} NTU_{1i} \tag{37}$$

If $NTU_{1a} = NTU_{1b} = \ldots = NTU_1$,

$$NTU_{1tot} = nNTU_1 \tag{38}$$

If the exchangers are connected in series (Figs. 9 and 10), the heat capacity rate ratios R_1 and R_2 in each of them are equal and identical to the corresponding ratios for the entire system. If they are connected in parallel (Fig. 11), the following applies:

$$\frac{1}{R_{1tot}} = \sum_{i=1}^{n} \frac{1}{R_{1i}} \tag{39}$$

If $R_{1a} = R_{1b} = \ldots = R_1$,

$$\frac{1}{R_{1tot}} = \frac{n}{R_1} \tag{40}$$

The relationship between the dimensionless temperature change in each of the exchangers P_{1i} and that in the entire system P_{1tot} differs for the types of connection.

(a) Series connection with overall cocurrent flow

The following equation applies [30]:

$$1 - P_{1tot}(1 + R_1) = \prod_{i=1}^{n} [1 - P_{1i}(1 + R_1)] \tag{41}$$

Groups of exchangers within a system may be considered as single units. The total effect is independent of the sequence in which the individual elements are connected.

In the special case that the dimensionless temperature change is the same in each exchanger, i.e., $P_{1a} = P_{1b} = \ldots = P_1$, Eq. (41) can be simplified to give

$$1 - P_{1tot}(1 + R_1) = [1 - P_1(1 + R_1)]^n \tag{42}$$

It could be closely approximated if, for example, the individual exchangers are all identical.

A possible adverse effect of the series connection in overall cocurrent flow should be mentioned: If in the first exchanger the temperatures cross, i.e., if $P_{11}(1 + R_1) > 1$, the following exchangers will partially or totally reduce the overall temperature changes P_{1tot} and P_{2tot}. This effect is particularly pronounced for two exchangers with crossing temperatures. If, for example, for $n = 2$ identical exchangers $R_1 = 1$ and $P_1 = 1$ (counterflow, $NTU_1 = NTU_2 = \infty$), the total temperature change $P_{1tot} = 0$, according to Eq. (42).

Similar effects may also occur in single heat exchangers, e.g., in multipass shell-and-tube exchangers (Fig. 5, layout A) or in the mixed–mixed cross-flow.

(b) Series connection with overall countercurrent flow

In principle, series connections with overall countercurrent flow are more effective than those in cocurrent flow [30]. The equation that applies in this case is

$$\frac{1 - P_{1tot}}{1 - R_1 P_{1tot}} = \prod_{i=1}^{n} \left(\frac{1 - P_{1i}}{1 - R_1 P_{1i}} \right) \text{for } R_1 \neq 1 \tag{43}$$

$$\text{or } \frac{P_{tot}}{1 - P_{tot}} = \sum_{i=1}^{n} \frac{P_i}{1 - P_i} \tag{44}$$

for $R_1 = 1$ ($P_i = P_{1i} = P_{2i}$ and $P_{tot} = P_{1tot} = P_{2tot}$).

From Eq. (43) one can derive for the correction factor

$$F_{tot} NTU_{1tot} = F_{tot} \sum_{i=1}^{n} NTU_{1i} = \sum_{i=1}^{n} F_i NTU_i \tag{45}$$

In the special case of equal dimensionless temperature changes, i.e., $P_i = P$, Eqs. (43) and (44) become

$$\frac{1 - P_{1tot}}{1 - R_1 P_{1tot}} = \left(\frac{1 - P_1}{1 - R_1 P_1} \right)^n \quad \text{for } R_1 \neq 1 \tag{46}$$

$$\text{and } \frac{P_{tot}}{1 - P_{tot}} = \frac{nP}{1 - P} \quad \text{for } R_1 = 1 \tag{47}$$

In this particular case, $F_{tot} = F_i = F$, where F_i is the correction factor for the individual exchanger and F_{tot} is the value for the whole system.

(c) Stream 2 split up into parallel substreams

The equation that applies in this case is [31]

$$1 - P_{1tot} = \prod_{i=1}^{n} (1 - P_{1i}) \tag{48}$$

For the special case in which the dimensionless temperature change is the same in each exchanger, i.e., $P_{1i} = P_1$, Eq. (48) can be simplified to give

$$1 - P_{1tot} = (1 - P_1)^n \tag{49}$$

Many types of connections other than those dealt with above are feasible. They are described and discussed in detail in Chap. C5. In the cell method, as described in Sect. 2, a single exchanger is regarded as a system of individual elements.

5.2 Two Heat Exchangers Coupled by a Circulating Thermal Fluid

For heat transfer between two gases, space considerations or safety aspects sometimes require systems that consist of two

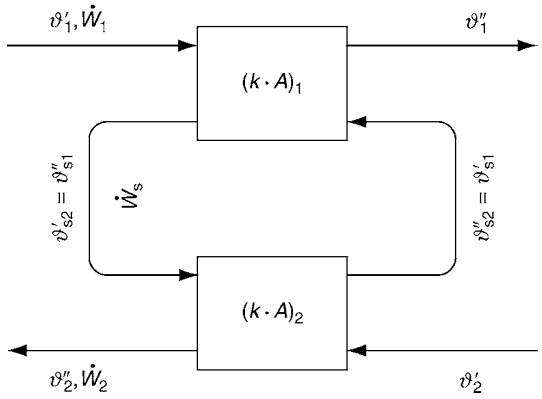

C1. Fig. 12. Schematic diagram of a system of two heat exchangers coupled by a circulating stream.

single heat exchangers coupled by a circulating thermal fluid. Such a system is shown in Fig. 12.

The following equations apply to the individual exchangers. When the subscripts consist of two digits, the first refers to the fluid, and the second to the exchanger.

Heat exchanger 1 Heat exchanger 2

$$\mathrm{NTU}_{11} = \frac{(kA)_1}{\dot{W}_1} \qquad \mathrm{NTU}_{22} = \frac{(kA)_2}{\dot{W}_2}$$

$$R_{11} = \frac{\dot{W}_1}{\dot{W}_s} \qquad R_{22} = \frac{\dot{W}_2}{\dot{W}_s}$$

$$P_{11} = \frac{\vartheta'_1 - \vartheta''_1}{\vartheta'_1 - \vartheta'_{s1}} \qquad P_{22} = \frac{\vartheta''_2 - \vartheta'_2}{\vartheta'_{s2} - \vartheta'_2}$$

The following apply to the entire system.

$$P_{1\mathrm{tot}} = \frac{\vartheta'_1 - \vartheta''_1}{\vartheta'_1 - \vartheta'_2}$$

$$R_{1\mathrm{tot}} = \frac{\dot{W}_1}{\dot{W}_2} = \frac{1}{R_{2\mathrm{tot}}}$$

$$\mathrm{NTU}_{1\mathrm{tot}} = \frac{(kA)_{\mathrm{eff}}}{\dot{W}_1}$$

The first step in rating a system is to determine the dimensionless temperature changes $P_{11}(\mathrm{NTU}_{11}; R_{11})$ and $P_{22}(\mathrm{NTU}_{22}; R_{22})$ for the individual exchangers and their flow arrangements using the equations and design charts in Sect. 4. The dimensionless temperature change within the whole system can then be determined from the following equation [1, 32]:

$$\frac{1}{P_{1\mathrm{tot}}} = \frac{1}{P_{11}} + \frac{1}{P_{22}} R_{1\mathrm{tot}} - R_{11} \tag{50}$$

Concerning the total temperature change $P_{1\mathrm{tot}}$, there exists an optimum value of the circulating heat capacity flow rate $\dot{W}_{s,\mathrm{opt}}$ [1] if the overall heat transfer coefficients do not depend on the circulating flow rate. For two counterflow heat exchangers [33]

$$\frac{1}{\dot{W}_{s,\mathrm{opt}}} = \frac{\kappa_1}{\dot{W}_1} + \frac{\kappa_2}{\dot{W}_2} \tag{51}$$

with

$$\kappa_1 = \frac{(kA)_1}{(kA)_1 + (kA)_2} \text{ and } \kappa_2 = \frac{(kA)_2}{(kA)_1 + (kA)_2} \tag{52}$$

Under this optimum condition, the exchanger system can be regarded as one single counterflow heat exchanger with the effective overall heat transfer resistance

$$\frac{1}{(kA)_{\mathrm{eff}}} = \frac{1}{(kA)_1} + \frac{1}{(kA)_2} \tag{53}$$

The required value of $(kA)_{\mathrm{eff}}$ is determined from the given data $(P_{1\mathrm{tot}}, \dot{W}_1, \dot{W}_2)$ in the known manner for the hypothetical single counterflow heat exchanger.

The individual values of the real counterflow exchangers $(kA)_1$ and $(kA)_2$ have to be designed such that Eq. (53) is fulfilled. For individual flow arrangements other than counterflow one can, as an approximation, simply replace in Eqs. (52) and (53) $(kA)_1$ and $(kA)_2$ by $(kA)_1 F_1$ and $(kA)_2 F_2$, respectively.

Many designs are possible which fulfill Eq. (53). The economically optimal values of both heat transfer surface areas A_1 and A_2 depend on the ratio of the prices per unit area π_1/π_2 as well as the ratios of both the overall heat transfer coefficients k_1/k_2 and the correction factors F_1/F_2 [33]. The optimum surfaces can be estimated as follows [33].

With guessed values of the above-mentioned ratios one can first calculate optimal values of κ_1 and κ_2 according to

$$\frac{1}{\kappa_1} = 1 + \sqrt{\frac{k_2 F_2 \pi_1}{k_1 F_1 \pi_2}}; \quad \kappa_2 = 1 - \kappa_1 \tag{54}$$

and the optimum flow rate $\dot{W}_{s,\mathrm{opt}}$ from Eq. (51). Then, the unknown inlet and outlet temperatures of the circulating flow stream can be determined from

$$\begin{aligned} \vartheta''_{s1} &= \vartheta'_{s2} = \kappa_1 \vartheta'_1 + \kappa_2 \vartheta''_2 \\ \vartheta'_{s1} &= \vartheta''_{s2} = \kappa_1 \vartheta''_1 + \kappa_2 \vartheta'_2 \end{aligned} \tag{55}$$

Using the charts or equations for the individual flow arrangements one can determine for both exchangers the required values of $(kA)_1$ and $(kA)_2$ as well as F_1 and F_2.

The heat transfer calculations yield κ_1 and κ_2, and the guessed values in Eq. (54) can be improved. This way the required heat transfer surfaces A_1 and A_2 can iteratively be determined.

A detailed investigation of the thermal behavior of such systems was carried out by NaRanong [34, 35]. In his work, various individual flow arrangements are considered and the effect of transfer coefficients varying with the circulating flow rate are taken into account. Not only the steady state but also the transient behaviour is investigated.

The coupled system can also be regarded as a heat exchanger network (see Chap. C5).

5.3 Phase Change with Superheating and Subcooling

Normally, heat exchangers in which superheated vapor is cooled and completely condensed and the condensate is subcooled are also regarded as coupled systems. The same applies to the reverse case of evaporation. The three unit operations are designed as if they were to take place in separate exchangers and the individual areas are added together to obtain the area of the entire system.

In Fig. 13, the average temperatures over the cross-sections have been plotted against the heat flow rate $\dot{Q}$ transferred from the vapor in the heat exchanger (on the assumption of constant specific heat capacities and constant pressure during condensation). Since it is unknown how the entire heat transfer area has to be divided over the three unit operations, assumptions must be made on the flow arrangement in the desuperheating section *a* and the subcooling section *c*. These assumptions must be checked in the light of the results obtained, and the calculation must then be repeated when necessary.

If the inlet and outlet temperatures for the complete heat exchanger and the boiling point ϑ_{bp} are known, the temperatures ϑ_{2ab} and ϑ_{2bc} can be derived from the energy balances for the desuperheating and subcooling sections. The dimensionless temperature changes P_{1j} and P_{2j} (j = *a*, *b*, *c*) can thus be determined for the three parts of the exchanger. The values obtained for P_{1j} and P_{2j} can then be taken to calculate the number of transfer units NTU_{2j} (j = *a*, *b*, *c*) for the flow arrangements in each part. The method to be adopted is that described in Sect. 4. Regardless of the flow arrangement, Eq. (29) with $i = 2$ always applies for the condensation section *b*. The mean overall heat transfer coefficient in the condensation section can be calculated by the three-point method described in Chap. C2, Sect. 6. The single-phase coefficients at the ends *ab* and *bc* may be used for this purpose. The values for $(kA)_j$ and A_j (j = *a*, *b*, *c*) can be obtained directly from NTU_{2j}, and the partial areas can be added to the total area.

This simple mathematical treatment actually applies only to evaporation and condensation in the tubes of a countercurrent heat exchanger. In other cases, the results must be regarded merely as a rough guide. More accurate results can be obtained only by step-by-step numerical calculations [36].

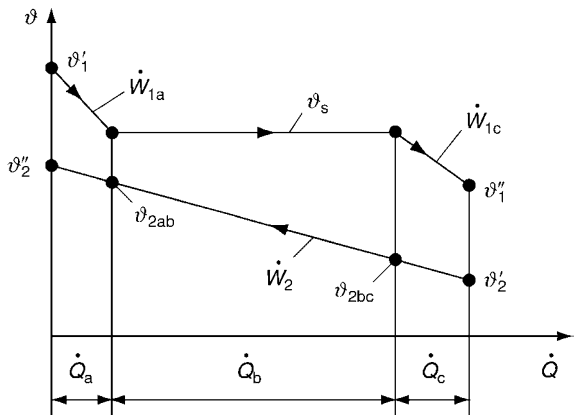

C1. Fig. 13. Temperature as a function of the heat transferred in a countercurrent condenser with vapor desuperheating and condensate subcooling.

6 Examples of Application

The two principal aims in heat exchanger design are

- Rating existing designs
- Designing or dimensioning heat exchangers from scratch

Each aim requires different means of applying the equations and charts given above. This is demonstrated with some characteristic examples.

6.1 Rating of Existing Designs

For this problem the design of the heat exchanger, the mass flow rates (and hence the heat capacity rates $\dot{W}_1$ and $\dot{W}_2$), and the inlet temperatures ϑ'_1 and ϑ'_2 are known. The aim is to determine the outlet temperatures ϑ''_1 and ϑ''_2 and the transferred heat flow rate $\dot{Q}$. The product (kA) can be obtained from the design data, the mass flow rates, and by means of estimated reference temperatures for the thermophysical properties (Chap. C2). The estimated values of the reference temperatures must be checked with the results and the calculation must be repeated with improved estimates if necessary.

Example 1

Ambient air (volumetric flow rate at the inlet 2 m^3/s, inlet temperature ϑ'_2 = 20°C, pressure 1 bar) shall be heated in an existing heat exchanger using hot water (mass flow rate 1 kg/s, inlet temperature ϑ'_1= 120°C, pressure 10 bar). The heat exchanger consists of a rectangular tube bundle with 120 finned tubes (material aluminium) in staggered arrangement. The tubes are arranged in six tube rows and six counterdirected passes. The air on the outside flows perpendicular to the tubes, the water inside the tubes. The dimensions of the finned tubes are as follows:

Outside tube diameter = 16 mm
Inside tube diameter = 12 mm
Tube length = 1 m
Circular fins with outside diameter = 42 mm
Fin pitch = 400 fins/m
Fin thickness = 0.4 mm
Tube pitch in the bundle = 45 mm

The outlet temperatures and the thermal performance shall be calculated. Additional heat transfer resistances due to fouling are to be neglected.

Solution

In this case, the usual mean value of the overall heat transfer coefficient shall approximately be used: $k \approx \bar{k}$ (cf. Chap. C2). In Example 2 of Chap. C2, it is shown that in this case the

usual mean value is a very good approximation for the true mean overall heat transfer coefficient.

The reference temperatures (arithmetic mean of inlet and outlet temperatures) must be estimated: tube side $\vartheta_1 = 100°C$, on the outside $\vartheta_2 = 60°C$. At these reference temperatures the properties of water and air, respectively, are determined (Chap. D2). For the tube-side heat transfer, the correlations from Chap. G1 yield

$Re_1 = 1.88 \cdot 10^4$ and $\alpha_1 = 4{,}625$ W/m^2 K,

where the correction for temperature-dependent properties has been neglected. For the outside heat transfer, the correlations from Chap. M1 yield

$Re_2 = 3.78 \cdot 10^3$ and $\alpha_2 = 48.7$ W/m^2 K.

Following Chap. C2 it is

$k \cdot A = 4{,}495$ W/K.

With the heat capacity flow rates

$\dot{W}_1 = 4{,}220$ W/K and $\dot{W}_2 = 2{,}404$ W/K

the dimensionless parameters NTU_2 and R_2 can be determined:

$NTU_2 = 1.87$ ($NTU_1 = 1.06$)

$R_2 = 0.57$ ($R_1 = 1.76$).

From the chart Fig. 38, for counterdirected countercurrent cross-flow with six tube rows and six passes one obtains

$P_1 = 0.42$ ($P_2 = 0.74$).

The outlet temperatures can then be calculated from Eqs. (9) and (10):

$\vartheta_1'' = 78°C$ and $\vartheta_2'' = 94°C$.

From Eq. (7) the transferred heat flow rate is

$\dot{Q} = 177$ kW.

Note

From the chart Fig. 38, one can see that in this case the correction factor F exceeds 0.99. Generally, for small NTU-values the flow arrangement has little impact on the thermal performance. The equations for pure countercurrent flow (or the chart Fig. 17) yield nearly the same results. However, there is no general limit where the impact of the flow arrangement can be neglected (see for example the flow arrangement "two-sided stirred tank" in Fig. 15 with the NTU-values and heat capacity rate ratios of this example). It is recommended to use always the equations or the chart for the flow arrangement under consideration because this requires no significant additional work.

Example 2

In this example, the cell method (Sect. 3.1) is applied.

The design data of a shell-and-tube heat exchanger are given. The flow arrangement consists of two tube-side and one shell-side pass with one shell-side baffle.

Heat transfer: $k \cdot A = 4{,}749$ W/K

Stream 1 on the shell side: $\dot{W}_1 = 3{,}500$ W/K, $\vartheta_1' = 100°C$

Stream 2 inside the tubes: $\dot{W}_2 = 3{,}500$ W/K, $\vartheta_2' = 20°C$

The outlet temperatures ϑ_1'' and ϑ_2'' shall be determined. The (unrealistic) assumption of only one shell-side baffle has been made in order to facilitate the calculation required to follow this numerical example.

Solution

The heat exchanger is considered to be a system of four single and identical units (Fig. 14).

It is assumed that stream 2 (inside the tubes) is not laterally mixed in the individual units and that stream 1 (on the shell side) is completely laterally mixed. Thus the flow arrangement selected for each unit is mixed–unmixed cross-flow or cross-flow with one tube row (Fig. 31, equation in Table 5).

For the whole exchanger, Eqs. (11) and (12) yield

$$NTU_{1tot} = NTU_{2tot} = 1.357 (R_1 = R_2 = 1).$$

For the individual cells, Eq. (17) yields

$$NTU_{1,2} = \frac{1}{4} NTU_{1,2tot} = 0.3392$$

The equation for cross-flow with one tube row or mixed–unmixed cross-flow, stream 1 mixed (Table 5) yields

$$P_1 = P_2 = 0.25$$

Dimensionless temperatures according to Eq. (18) are introduced to simplify the further calculations.

At the inlet $T_1' = 1$ and $T_2' = 0$. The unknown outlet temperatures in the individual units are designated as T_{1a}, T_{1b}, T_{1c}, and $T_{1d} = 1 - P_{1tot}$ as well as T_{2a}, T_{2b}, T_{2c}, and $T_{2d} = P_{2tot}$ (see Fig. 14). If the dimensionless temperature changes in each unit are expressed as defined in Eqs. (9) and (10), eight equations are obtained for these eight unknown temperatures. Following stream 2 through the units, one gets

$$P_{2a} = \frac{T_{2a} - 0}{T_{1b} - 0}, \quad P_{2b} = \frac{T_{2b} - T_{2a}}{T_{1c} - T_{2a}},$$
$$P_{2c} = \frac{T_{2c} - T_{2b}}{1 - T_{2b}}, \quad P_{2d} = \frac{T_{2d} - T_{2c}}{T_{1a} - T_{2c}}.$$

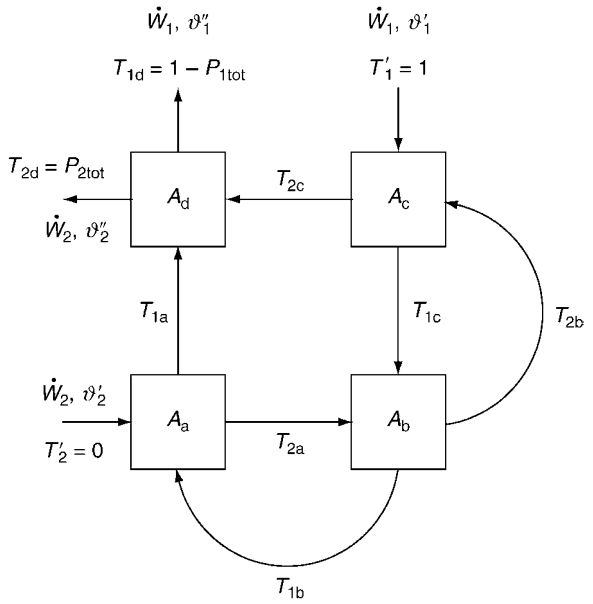

C1. Fig. 14. System of four coupled heat exchangers as a model for a shell-and-tube design with two tube-side passes and one shell-side pass with one shell-side baffle in layout A (Example 2).

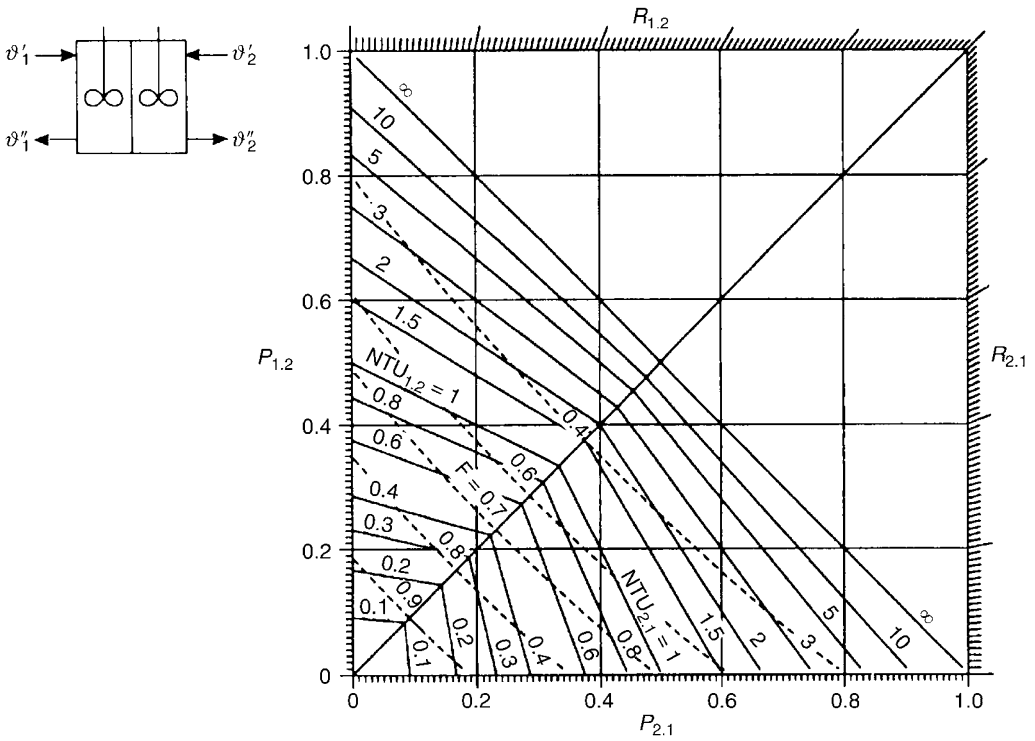

C1. Fig. 15. Two-sided stirred tank.

C1. Table 7. Results for the calculation of the dimensionless outlet temperatures of the individual units with $P_1 = P_2 = 0.25$

T_{2a}	T_{2b}	T_{2c}	T_{2d}	T_{1c}	T_{1b}	T_{1a}	T_{1d}
0.167	0.333	0.5	0.5	0.833	0.667	0.5	0.5

With identical individual units it is $P_{2a} = P_{2b} = P_{2c} = P_{2d} = P_2$. Following stream 1 through the units yields

$$P_{1c} = \frac{1 - T_{1c}}{1 - T_{2b}},\ P_{1b} = \frac{T_{1c} - T_{1b}}{T_{1c} - T_{2a}},$$

$$P_{1a} = \frac{T_{1b} - T_{1a}}{T_{1b} - 0},\ P_{1d} = \frac{T_{1a} - T_{1d}}{T_{1a} - T_{2c}}.$$

In this case, too, $P_{1a} = P_{1b} = P_{1c} = P_{1d} = P_1$.

This system of linear equations can be solved iteratively by known numerical methods. The results are listed in Table 7.

The dimensionless temperature changes for the complete heat exchanger are obtained from the dimensionless outlet temperatures T_{1d} and T_{2d}, i.e.,

$$P_{1tot} = P_{2tot} = 0.5$$

and the real outlet temperatures from Eqs. (9) and (10), i.e.,

$$\vartheta''_1 = \vartheta''_2 = 60^\circ\mathrm{C}$$

6.2 Design and Dimensioning of Heat Exchangers

In this case a heat exchanger has to be designed to solve a given heat transfer problem. Designing and dimensioning of a heat exchanger is much more difficult than rating an existing exchanger and requires a lot of experience. The procedure depends on the problem to be solved, and in particular, on the specified heat transfer conditions.

Example 3

The following heat capacity flow rates and inlet temperatures are given:

$$\dot{W}_1 = 8{,}500\,\mathrm{W/K},\ \dot{W}_2 = 7{,}000\,\mathrm{W/K},$$
$$\vartheta'_1 = 300^\circ\mathrm{C},\ \vartheta'_2 = 100^\circ\mathrm{C}.$$

For stream 1 an outlet temperature of $\vartheta''_1 = 160^\circ\mathrm{C}$ is prescribed. The outlet temperature for stream 2 follows from the energy balance for the complete exchanger according to Eq. (7) as $\vartheta''_2 = 270^\circ\mathrm{C}$.

A shell-and-tube heat exchanger with several shell-side passes and two tube-side passes per shell-side pass shall be used. How many shell-side passes and which heat transfer area are required?

Solution

The flow arrangement corresponds to the coupling of several identical shell-and-tube heat exchangers, each with one

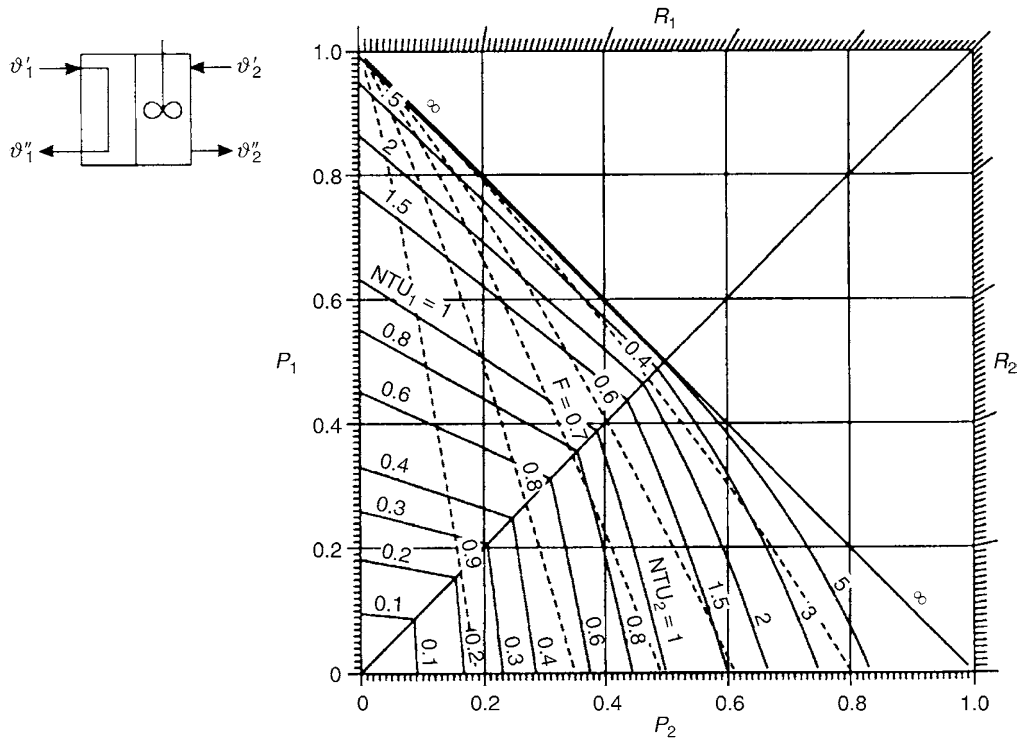

C1. Fig. 16. One-sided stirred tank.

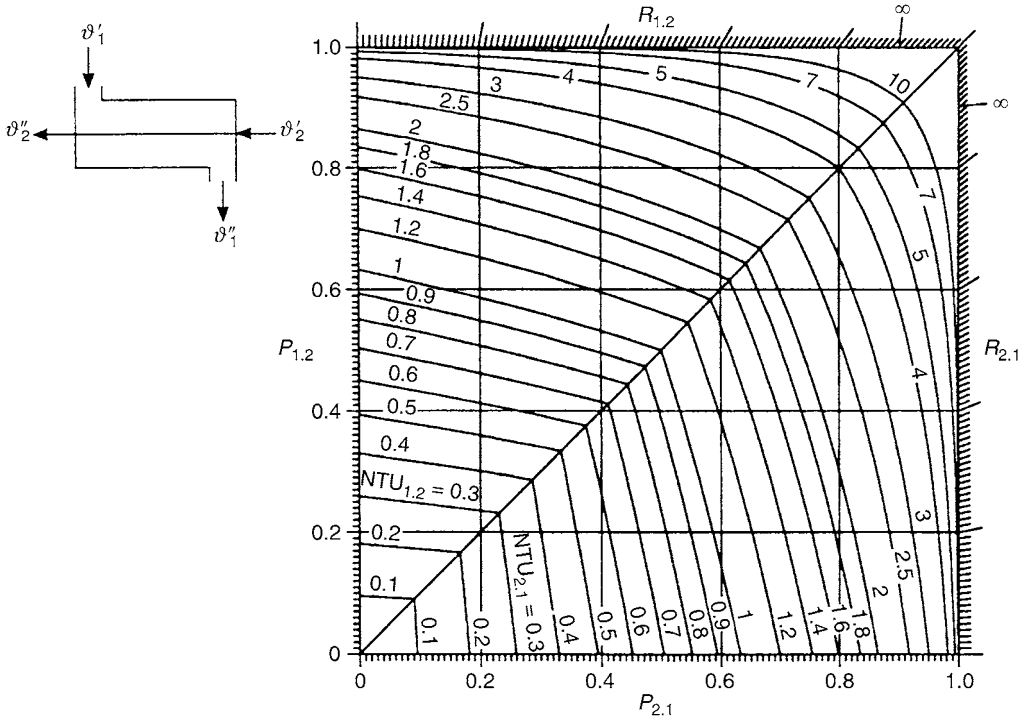

C1. Fig. 17. Pure countercurrent flow.

shell-side and two tube-side passes in overall countercurrent flow. The dimensionless temperature changes for the complete heat exchanger are

$$P_{1\text{tot}} = \frac{300 - 160}{300 - 100} = 0.7 \text{ and } P_{2\text{tot}} = \frac{270 - 100}{300 - 100} = 0.85.$$

The heat capacity rate ratio is

$$R_1 = \frac{8{,}500}{7{,}000} = 1.214 \ (R_2 = 0.8235).$$

From Eq. (46) for the countercurrent series connection of identical individual exchangers together with the equation

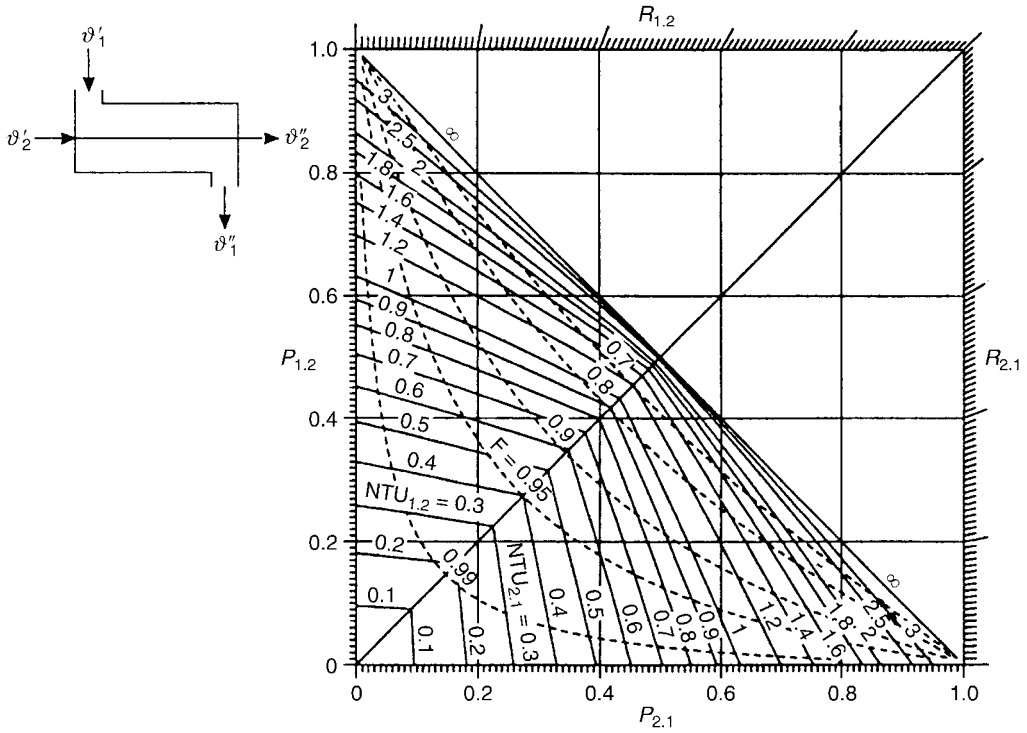

C1. Fig. 18. Pure cocurrent flow.

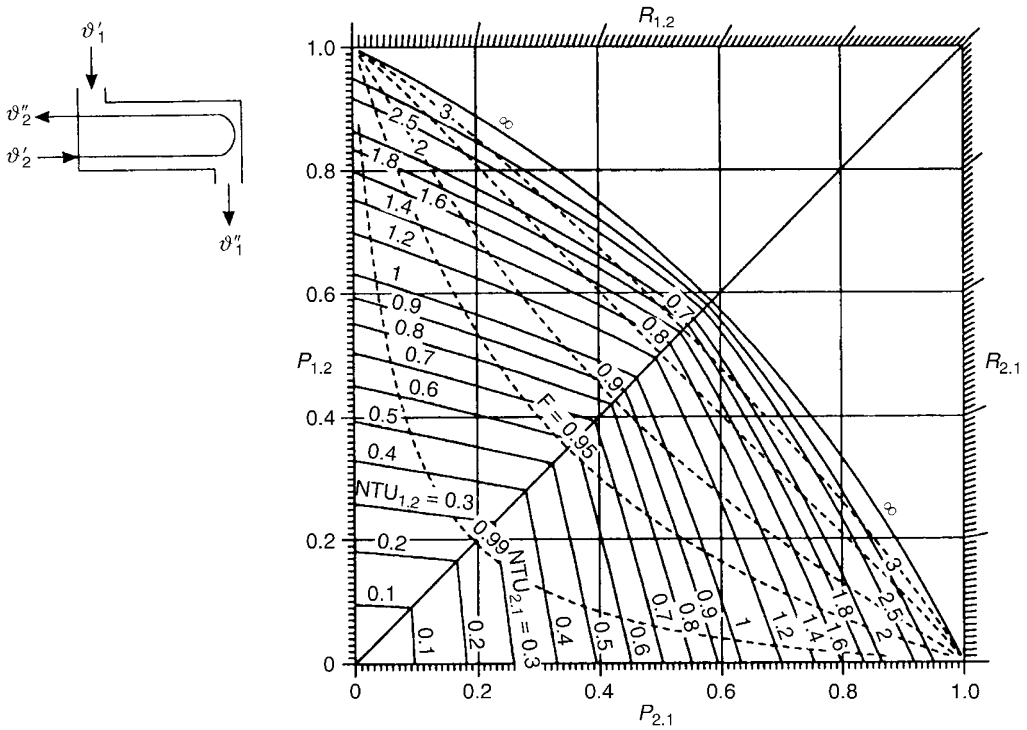

C1. Fig. 19. Shell-and-tube heat exchanger with one shell-side and two tube-side passes; $\varepsilon = 1/2$.

for the shell-and-tube exchanger with one shell-side and two tube-side passes (Table 4) it can be calculated that at least three shell-side passes for the complete exchanger are necessary to reach the required thermal performance. For three shell-side passes the logarithmic mean temperature difference correction factor F is marginally smaller than 0.7. A rule of thumb in heat exchanger design says that the correction factor should be $F > 0.7 - 0.8$ (see also [37]). For smaller

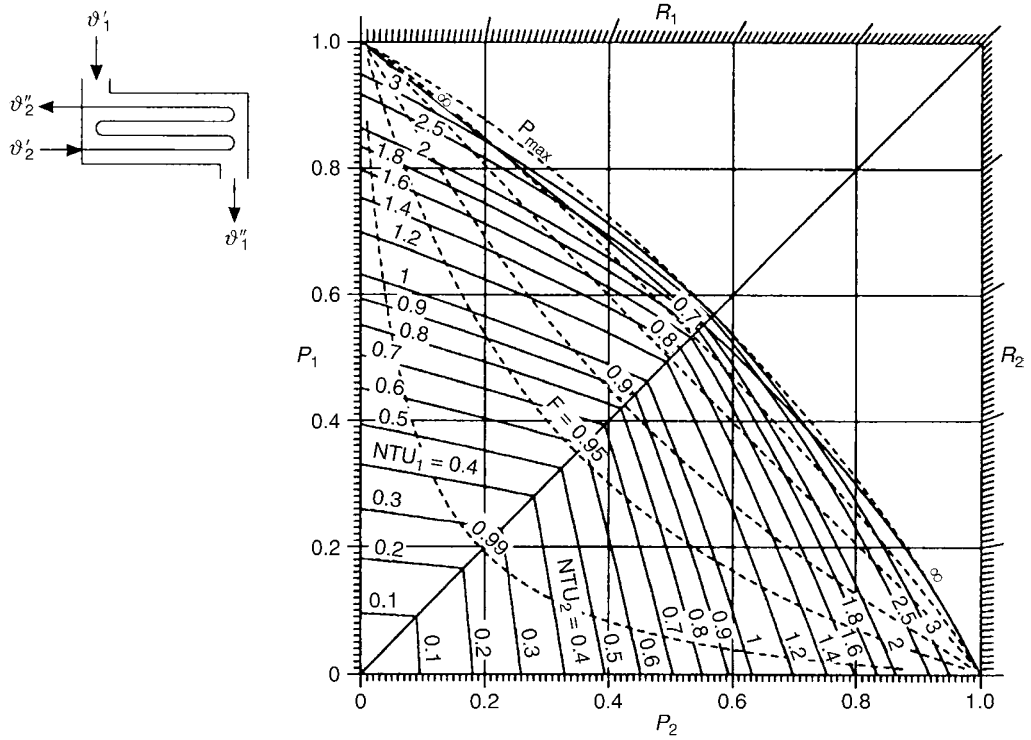

C1. Fig. 20. Shell-and-tube heat exchanger with one shell-side and four tube-side passes.

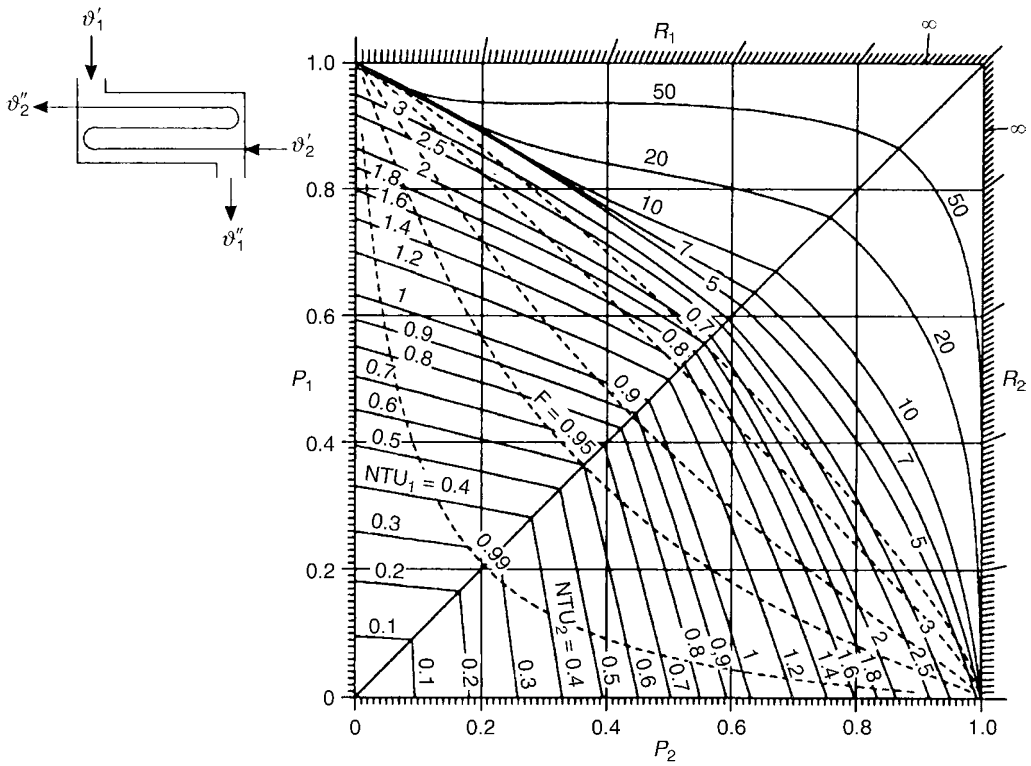

C1. Fig. 21. Shell-and-tube heat exchanger with one shell-side and three tube-side passes, two of it in countercurrent flow; $\varepsilon = 1/3$.

values of F the operating point falls within a range where small changes in P cause pronounced changes in F, with the result that the thermal performance is very sensitive to fluctuations. Therefore, in practice at least four shell-side passes are necessary to reach the required temperature changes. For four shell-side passes it is $P_1 = 0.426$, $NTU_1 = 0.95$ and $NTU_{1tot} = 4 \cdot 0.95 = 3.8$.

As the design details are not yet fixed, resort must be taken to typical values of the overall heat transfer coefficient (Chap. C3) for estimating the heat transfer area. With

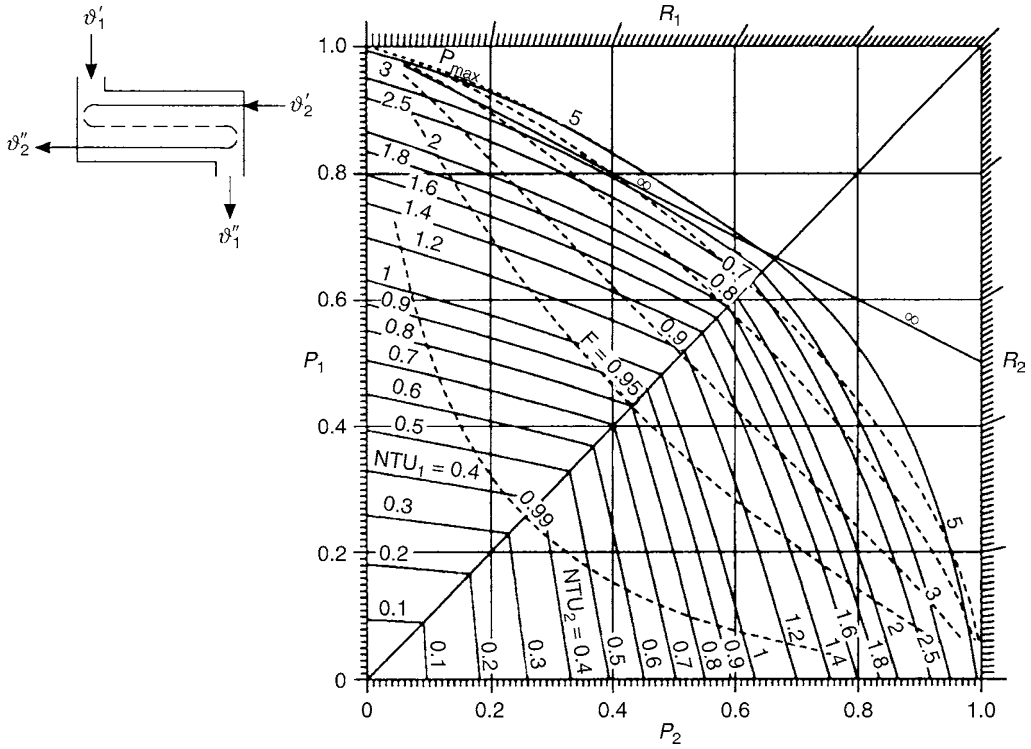

C1. Fig. 22. Shell-and-tube heat exchanger with one shell-side and two countercurrent tube-side passes.

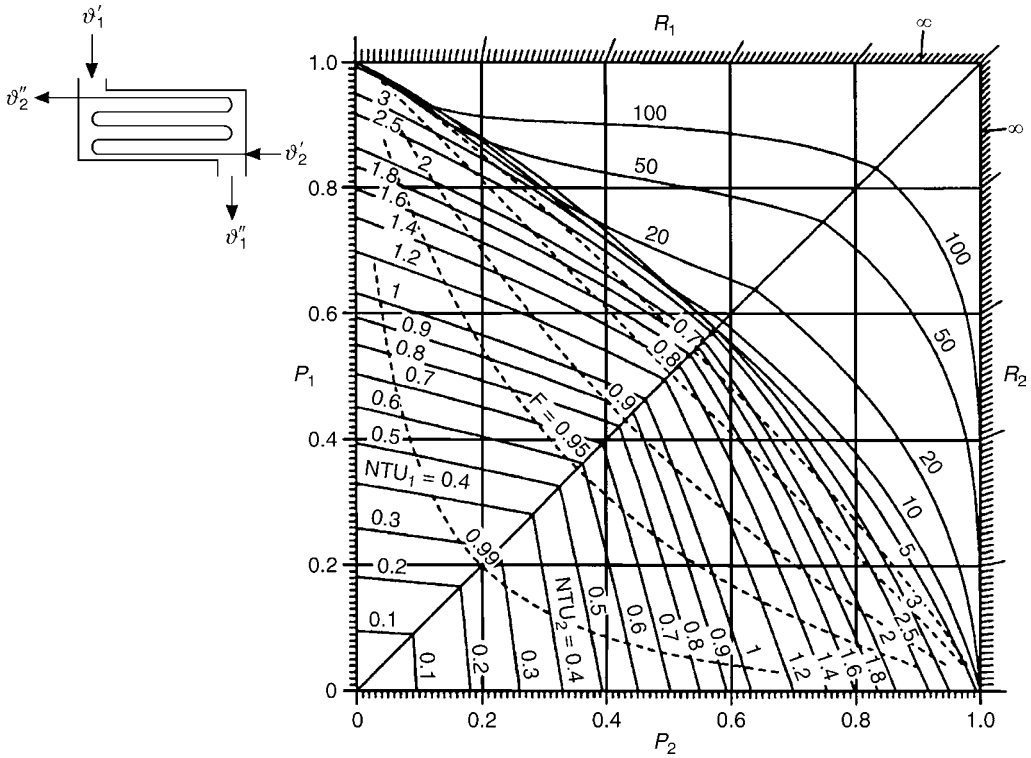

C1. Fig. 23. Shell-and-tube heat exchanger with one shell-side and five tube-side passes, three of it in countercurrent flow.

k = 500 W/m^2 K (liquid inside and outside the tubes) the required total area is

$$(A_{tot})_{req} = \frac{R_1 NTU_{1tot} \dot{W}_2}{k} \approx 65\,m^2$$

After the design details have been fixed, the overall heat transfer coefficient can be determined and it can be checked by rating (Sect. 6.1), whether the required thermal performance is actually attained.

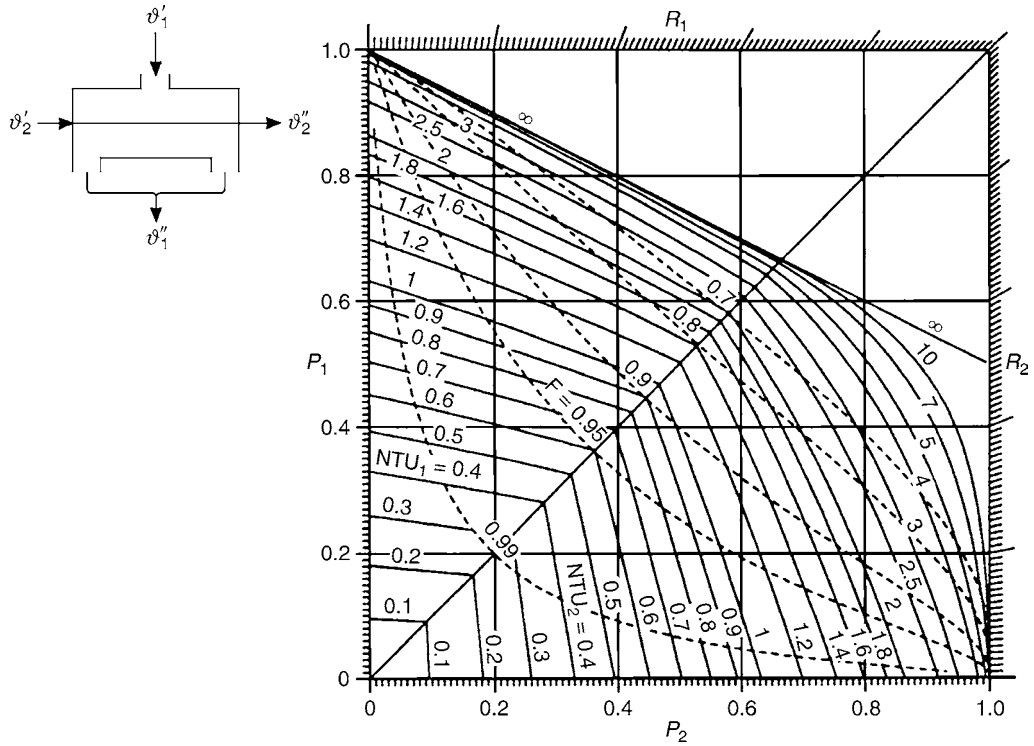

C1. Fig. 24. Shell-and-tube heat exchanger; divided flow with one shell-side and one tube-side pass.

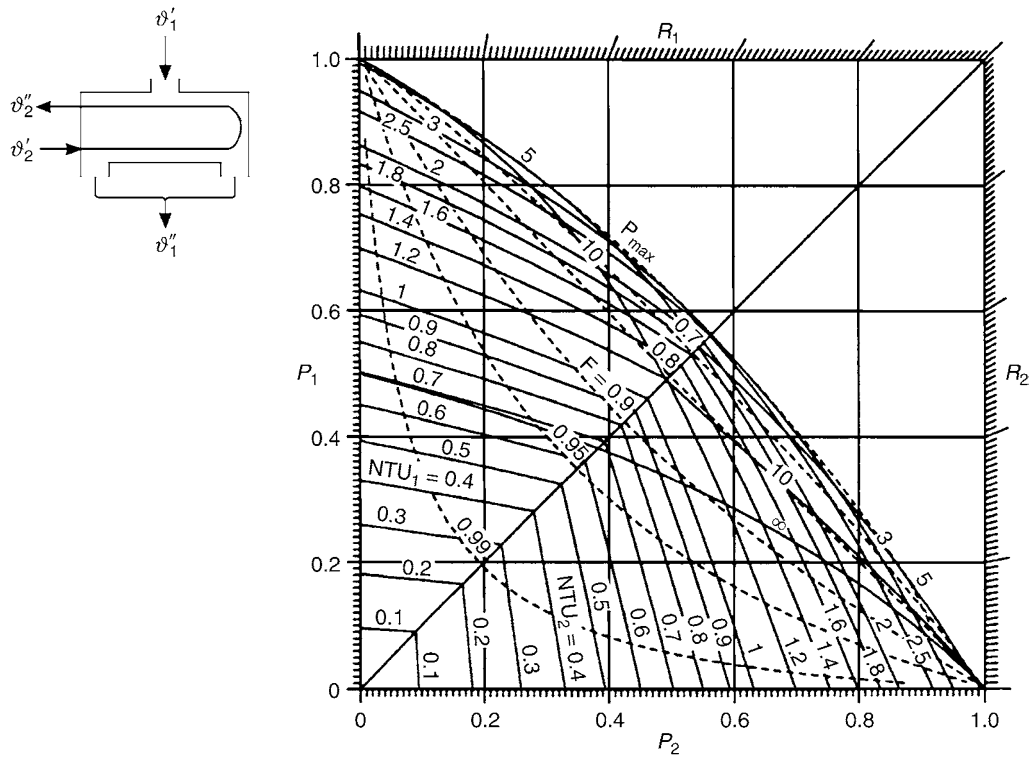

C1. Fig. 25. Shell-and-tube heat exchanger; divided flow with one shell-side and two tube-side passes.

In this case the NTU-value of the individual exchanger could be calculated from an explicit equation NTU = $f(P, R)$. For most flow arrangements this is not possible, and the equation $P = f(\text{NTU}, R)$ must be solved iteratively for NTU if P and R are given.

Example 4

For air-cooled cross-flow heat exchangers usually the inlet and outlet temperature and the heat capacity rate of the process stream 1 are given, whereas for the air (stream 2) only the

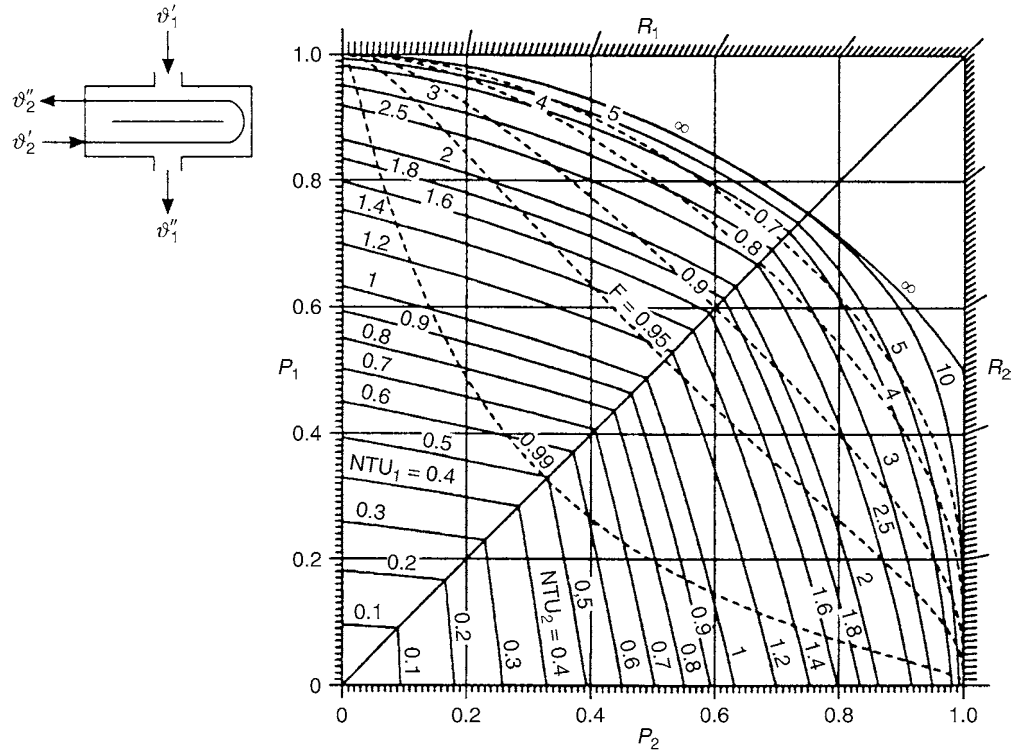

C1. Fig. 26. Shell-and-tube heat exchanger; split flow with longitudinal baffle and two shell-side and two tube-side passes.

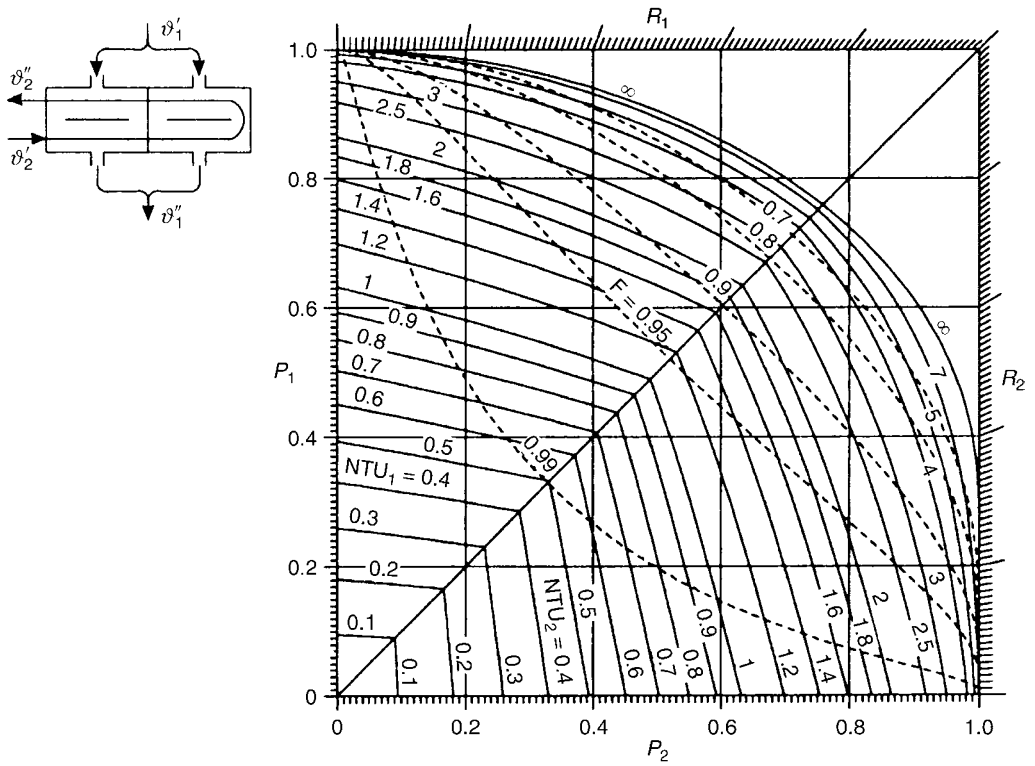

C1. Fig. 27. Shell-and-tube heat exchanger; double split flow with two longitudinal baffles and two shell-side passes on each side; two tube-side passes.

inlet temperature is known. However, empirical values for preferred approach velocities w_2 in certain finned tube bundles are also known. With these values the overall heat transfer coefficient and the number of transfer units NTU_2 can be estimated. For this purpose, only the ratio of total heat transfer area A and the cross-sectional area f for the air flow has to be known, but not their individual values, as shown by the following relationship:

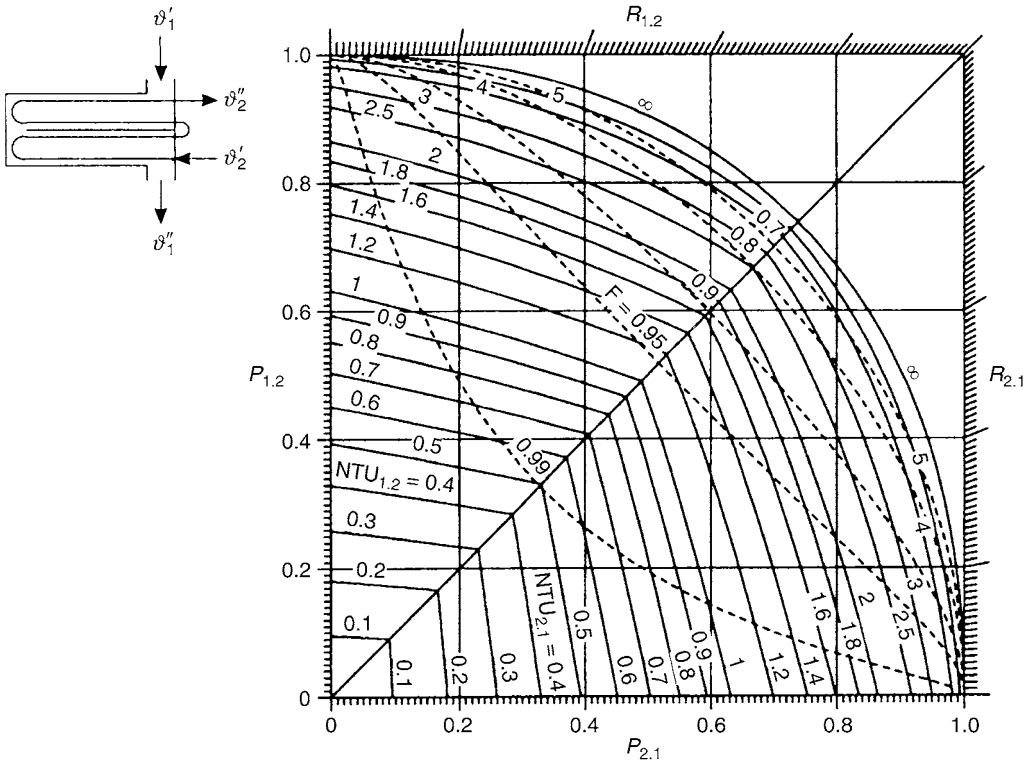

C1. Fig. 28. Shell-and-tube heat exchanger with two shell-side and four tube-side passes.

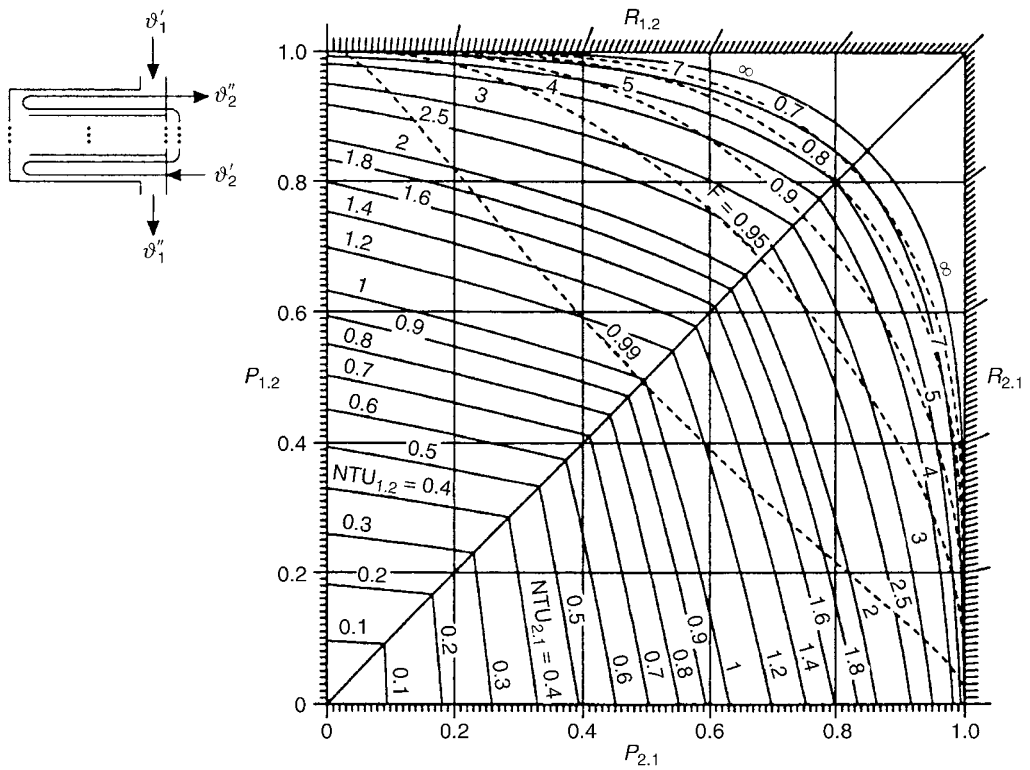

C1. Fig. 29. Shell-and-tube heat exchanger with four shell-side and eight tube-side passes.

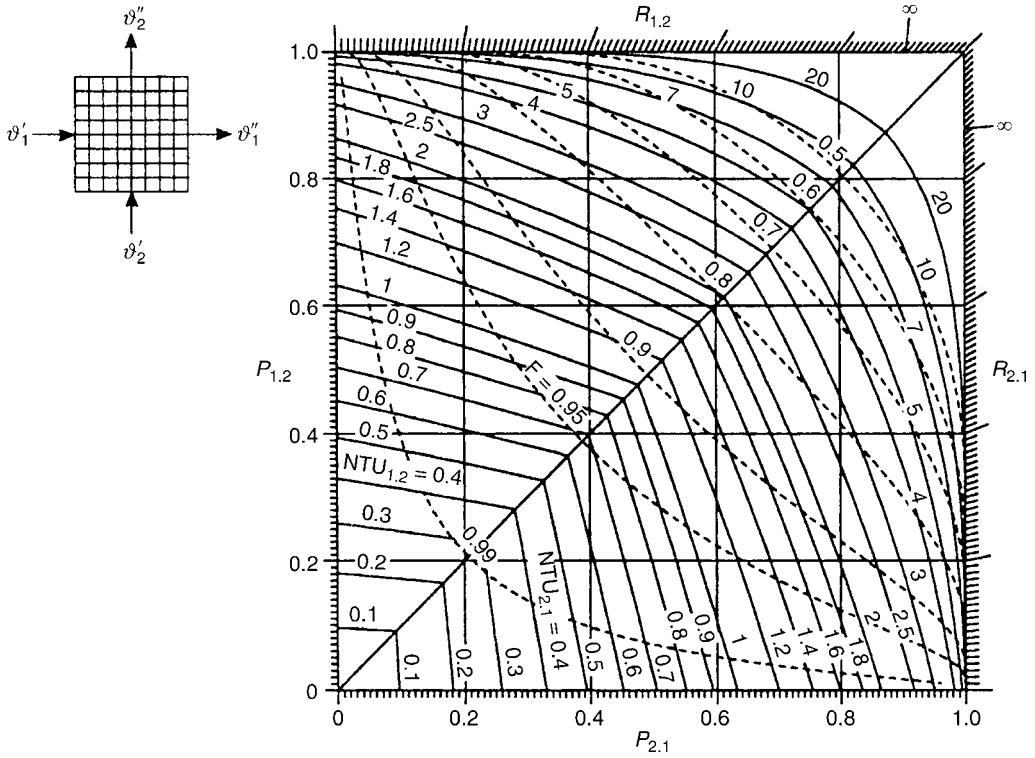

C1. Fig. 30. Pure cross-flow.

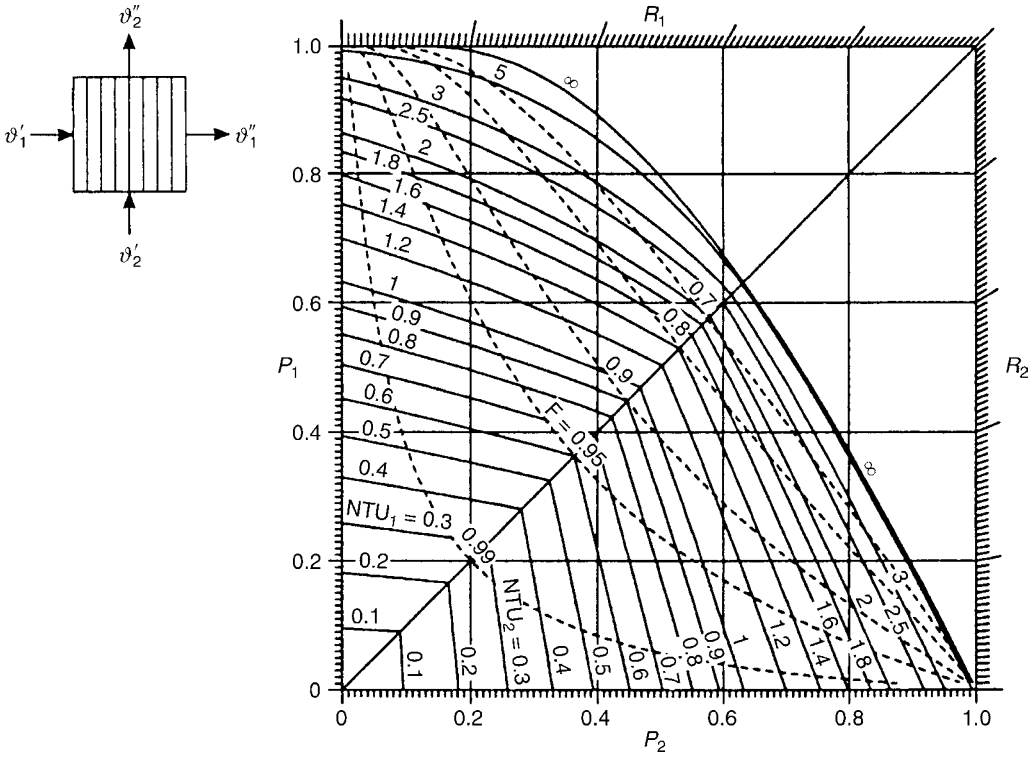

C1. Fig. 31. Cross-flow with one tube row; laterally mixed on one side.

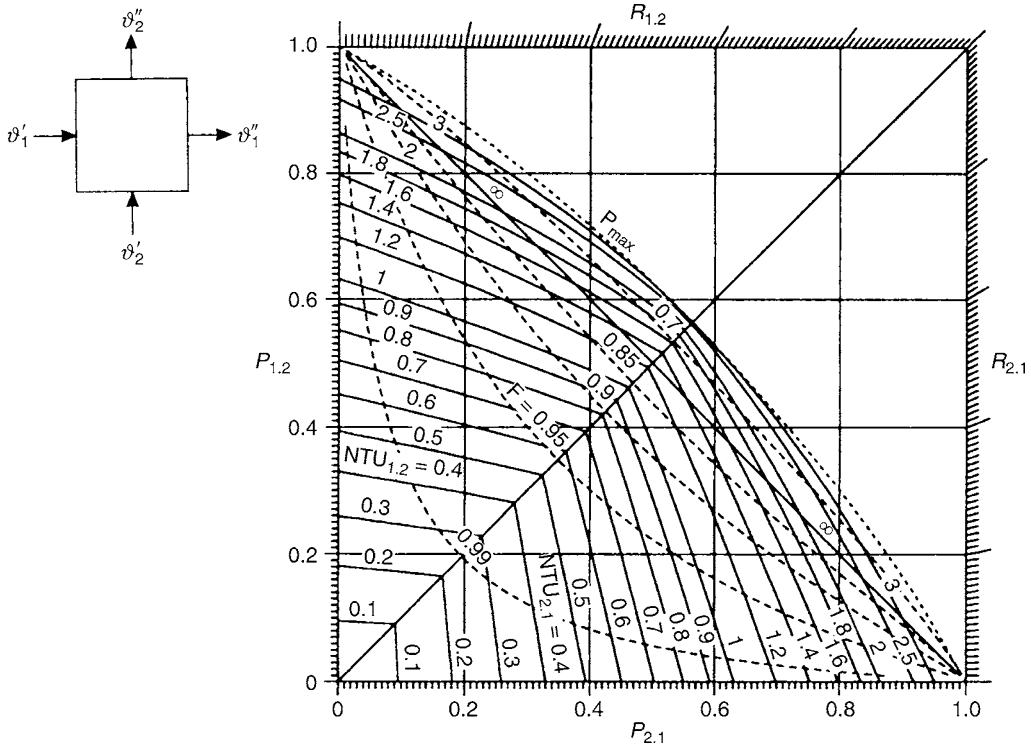

C1. Fig. 32. Cross-flow, laterally mixed on both sides.

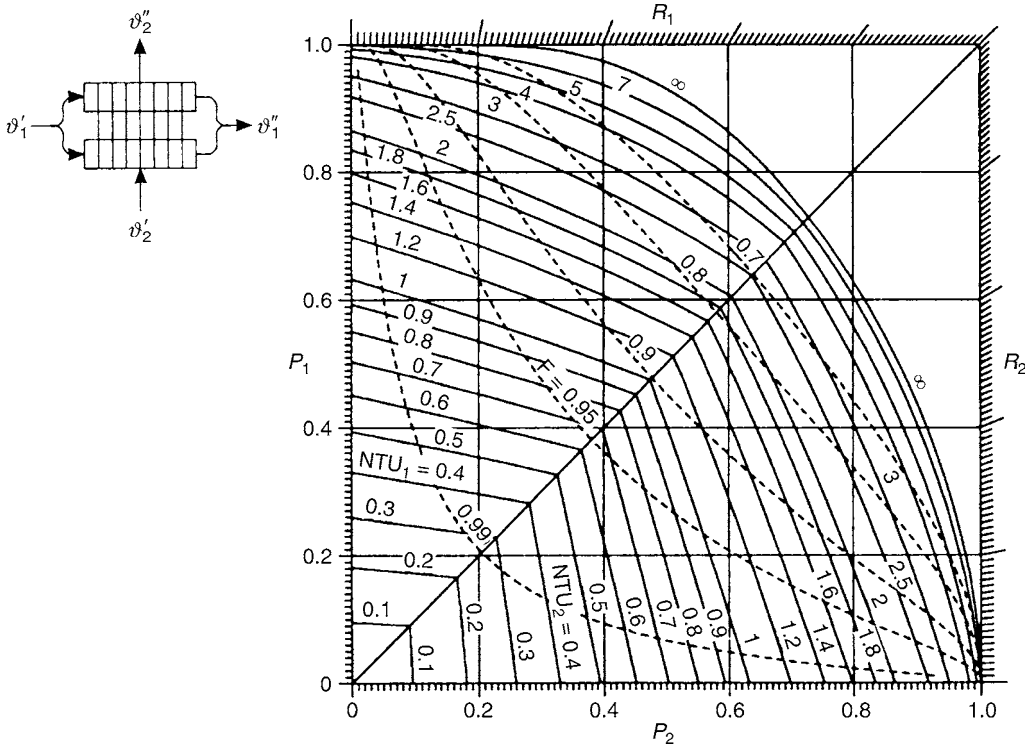

C1. Fig. 33. Cross-flow with two tube rows and one pass.

$$\mathrm{NTU}_2 = \frac{kA}{w_2 f \rho_2 c_{p2}} \tag{56}$$

One can also introduce the overall heat transfer coefficient relating to the cross-sectional area f

$$k_f = \frac{(kA)_{req}}{f} \tag{57}$$

which subsequently allows the immediate calculation of the required cross-sectional area

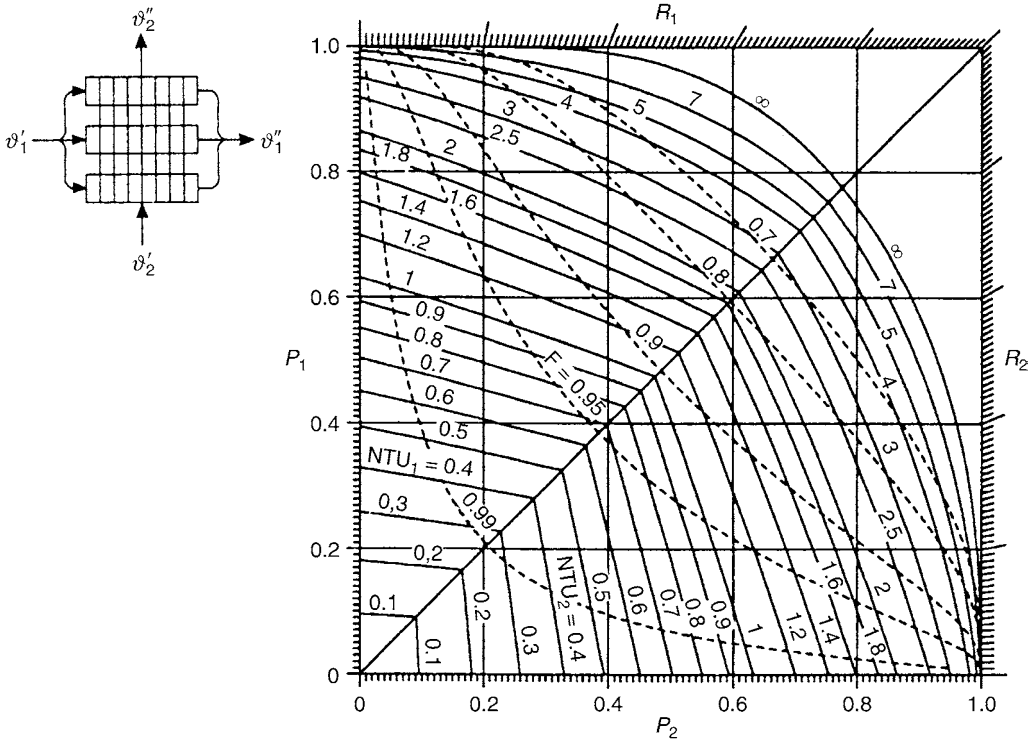

C1. Fig. 34. Cross-flow with three tube rows and one pass.

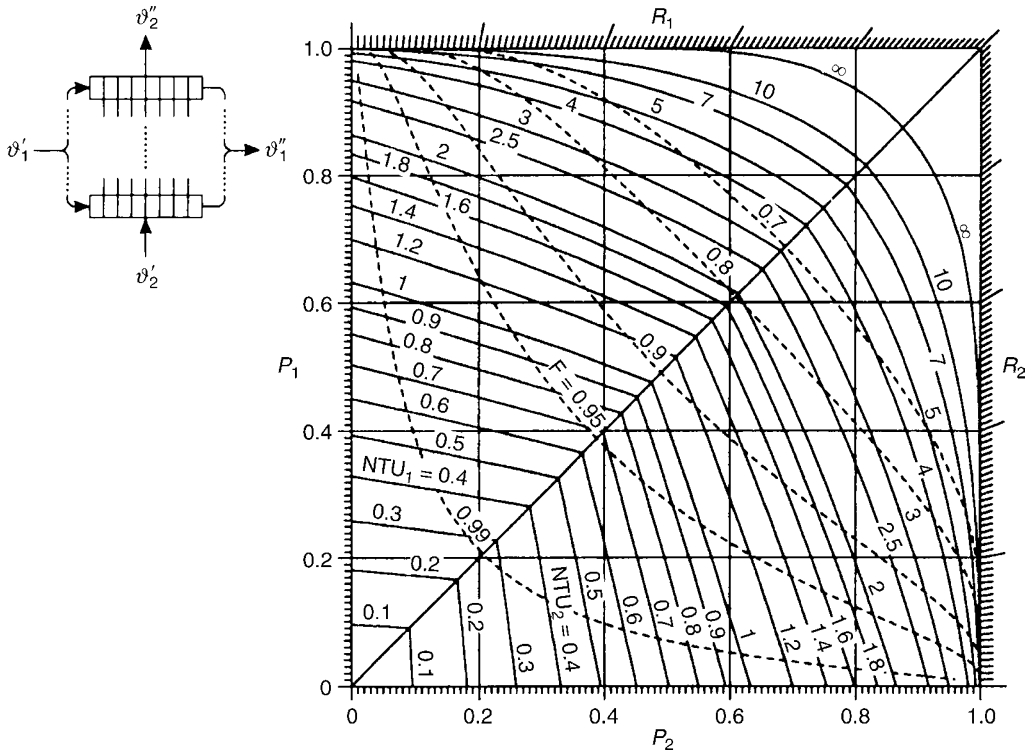

C1. Fig. 35. Cross-flow with ten tube rows and one pass.

$$f_{\text{req}} = \frac{(kA)_{\text{req}}}{k_{\text{f}}} \tag{58}$$

In the following the flow arrangement and the heat transfer data from Example 1 are taken. Thus, the flow arrangement is a counterdirected countercurrent cross-flow with six tube rows and six passes and the design data of the finned tube bundle from Example 1 except for the tube length. The process stream (water, $\dot{W}_1$ = 4,220 W/K) is to be cooled from ϑ_1' = 120°C to

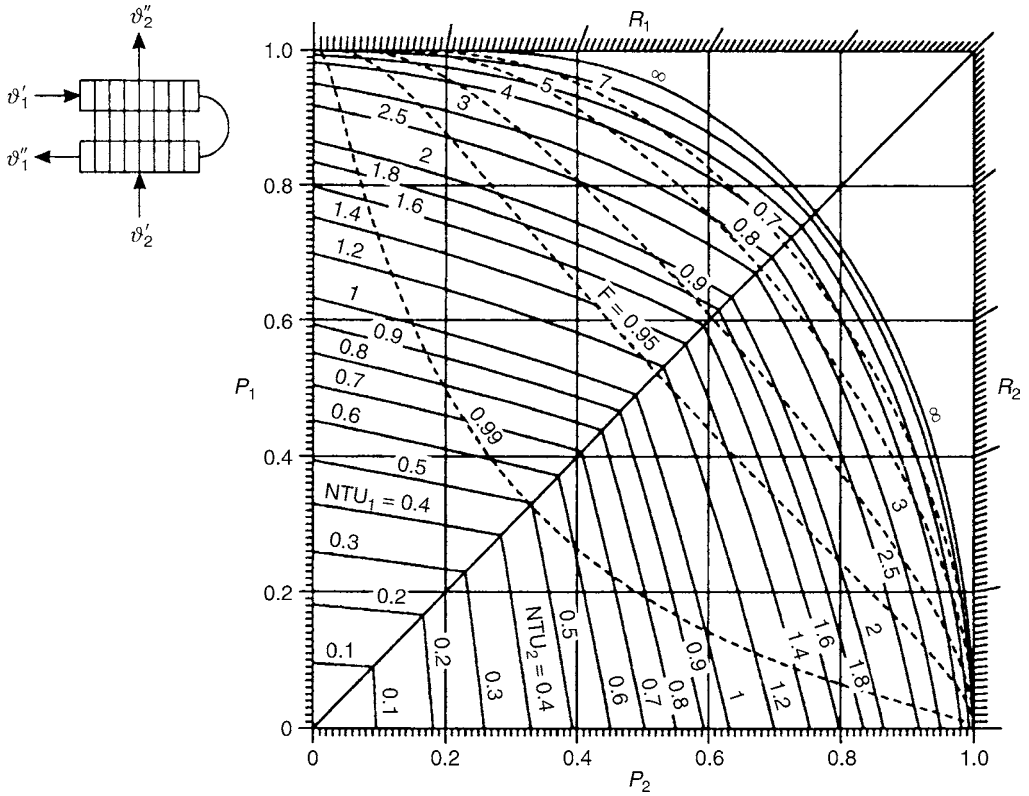

C1. Fig. 36. Counterdirected countercurrent cross-flow with two tube rows and two passes.

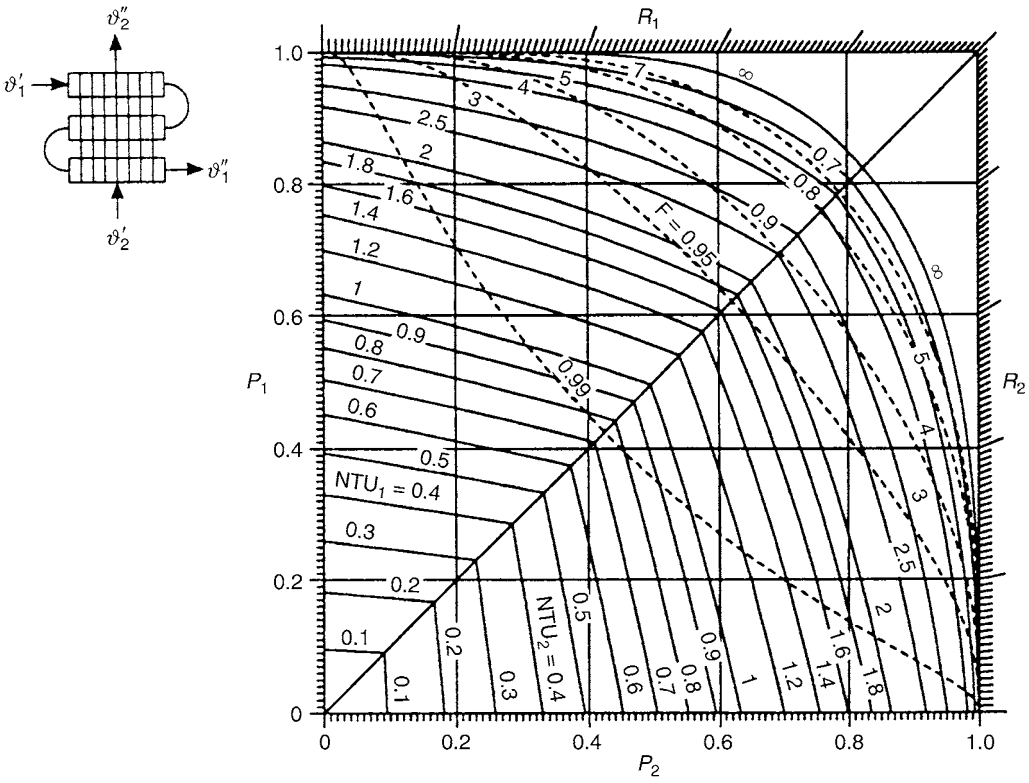

C1. Fig. 37. Counterdirected countercurrent cross-flow with three tube rows and three passes.

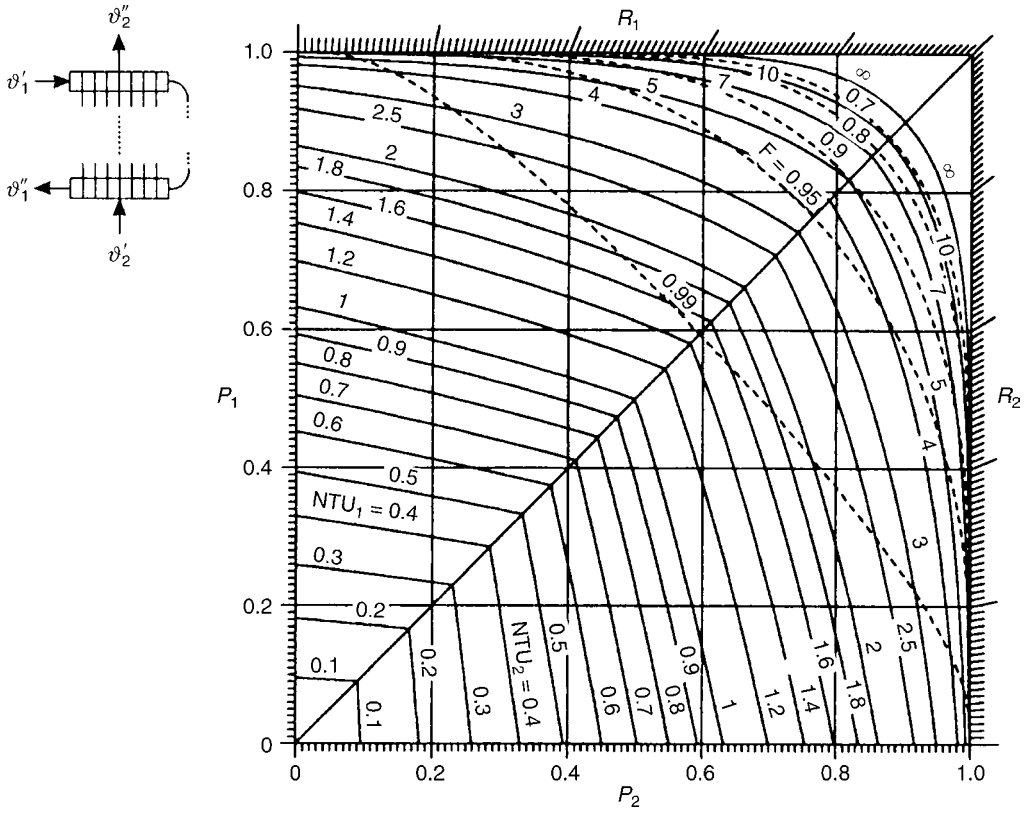

C1. Fig. 38. Counterdirected countercurrent cross-flow with six tube rows and six passes.

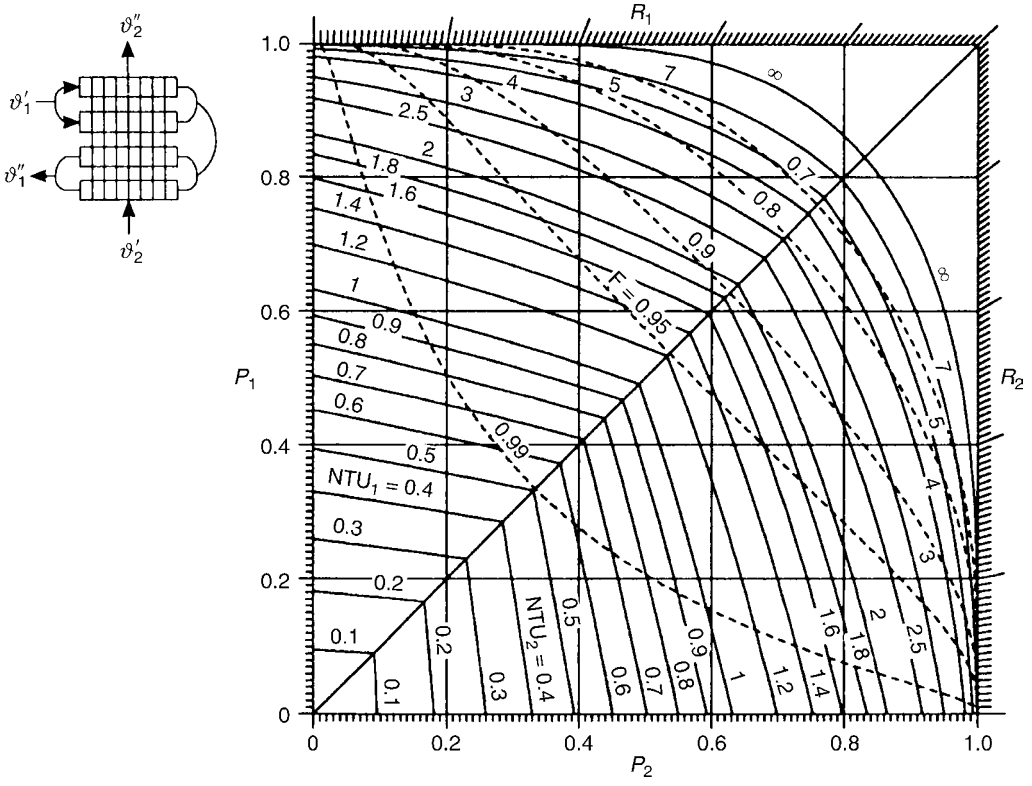

C1. Fig. 39. Counterdirected countercurrent cross-flow with four tube rows and two passes.

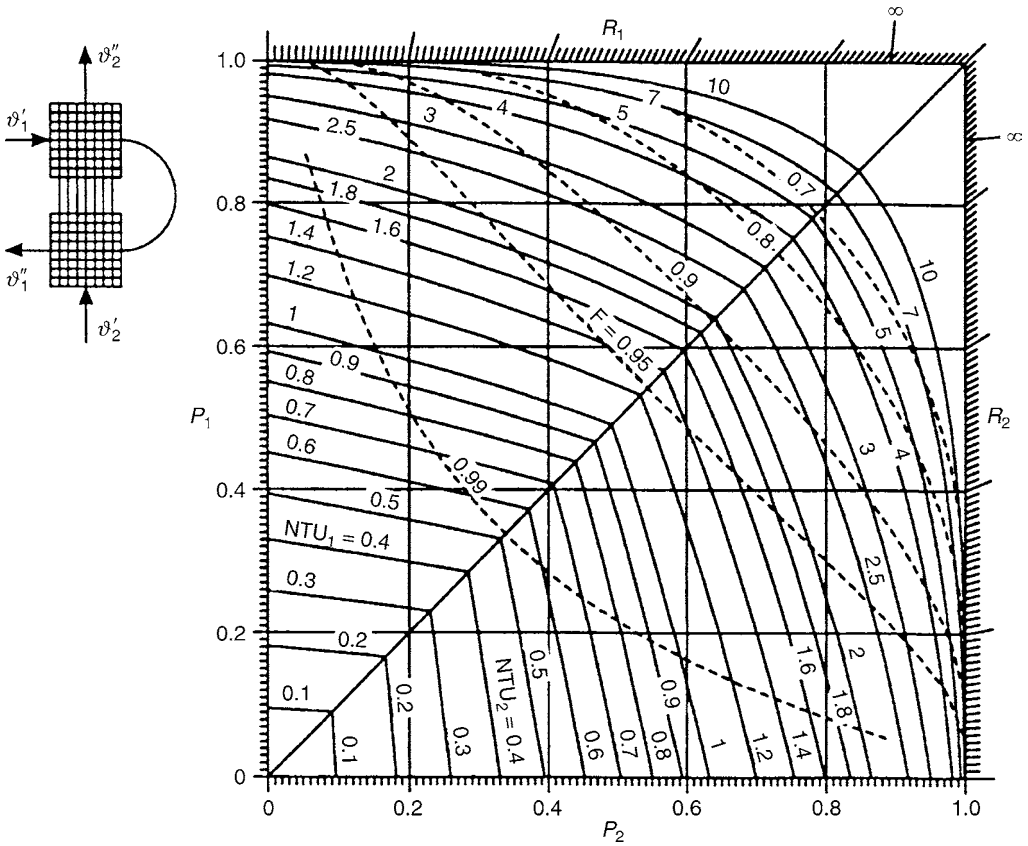

C1. Fig. 40. Counterdirected countercurrent cross-flow with two passes; stream 2 unmixed, stream 1 mixed only between passes.

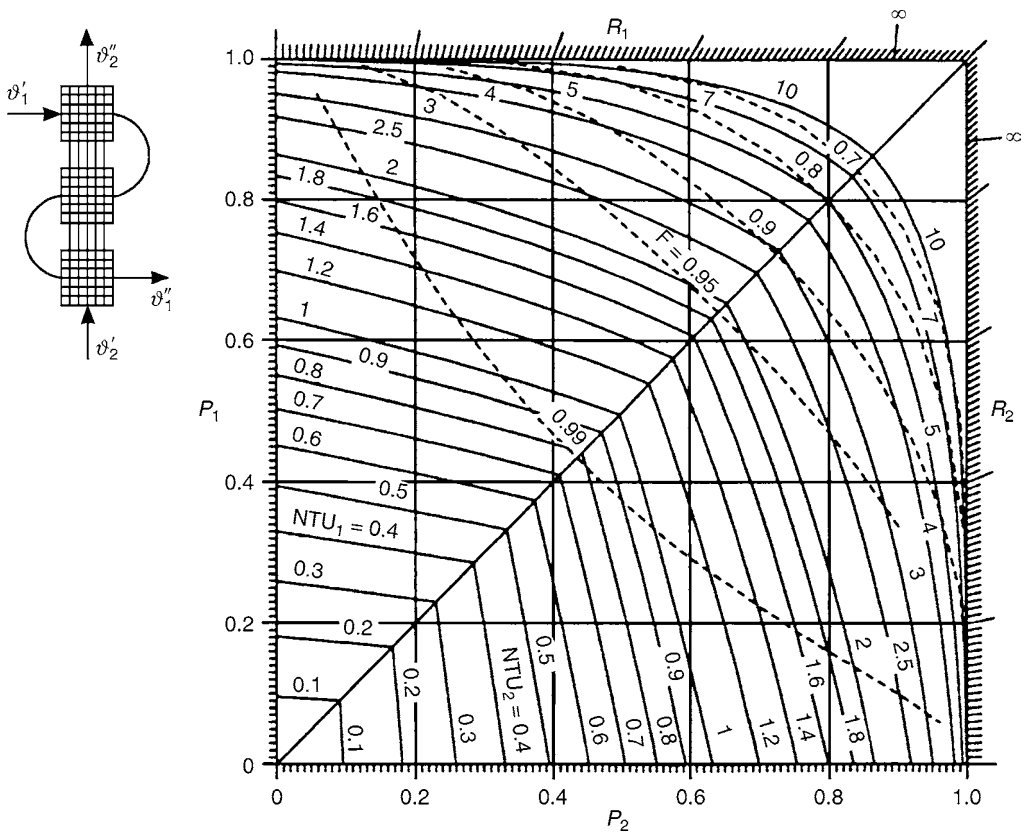

C1. Fig. 41. Counterdirected countercurrent cross-flow with three passes; stream 2 unmixed, stream 1 mixed only between passes.

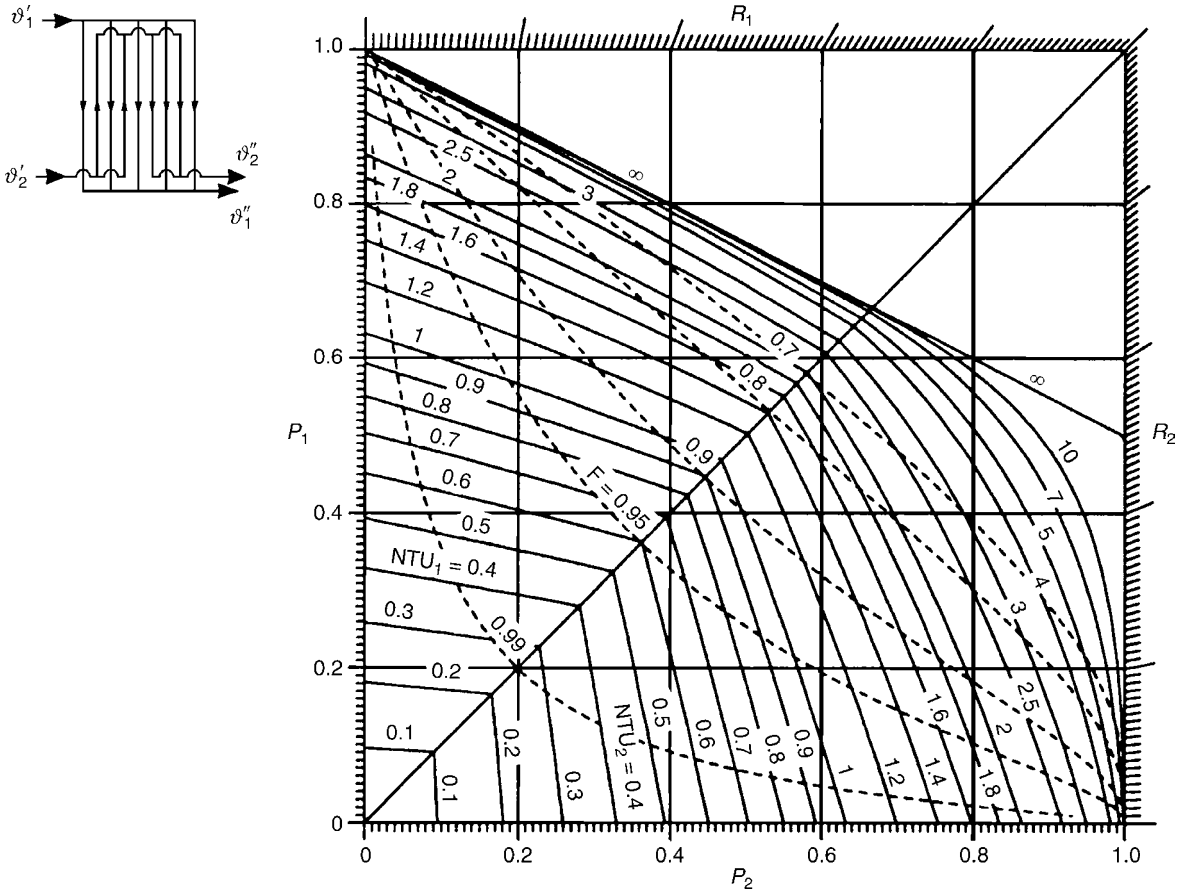

C1. Fig. 42. Plate heat exchanger with one pass for stream 1 and two passes for stream 2.

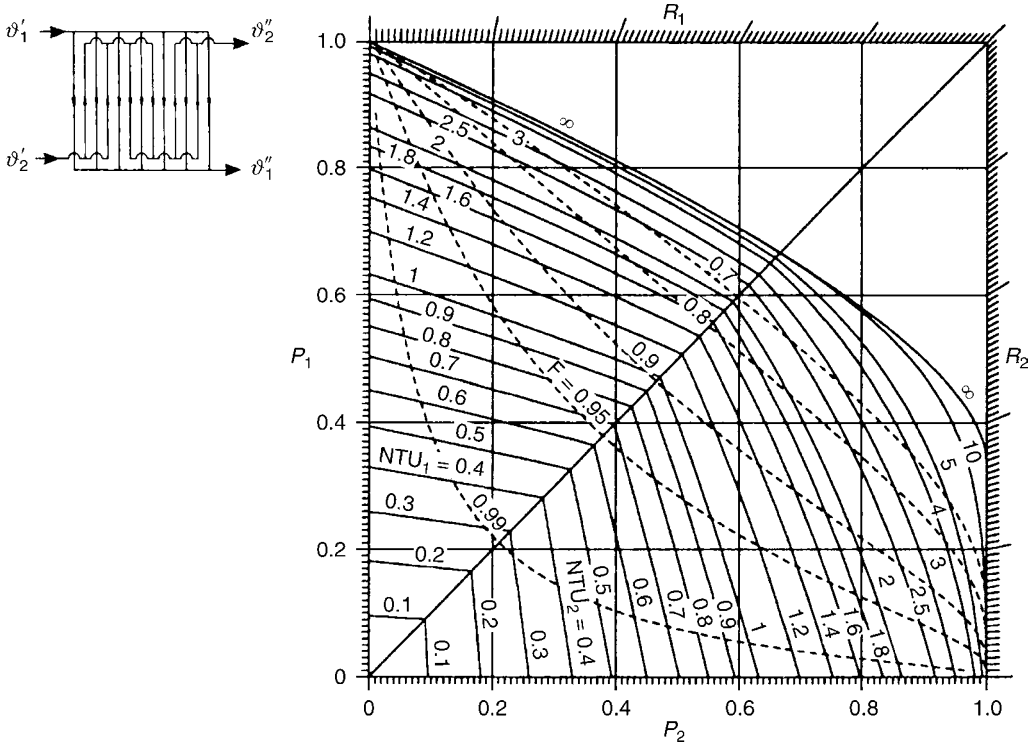

C1. Fig. 43. Plate heat exchanger with one pass for stream 1 and three passes for stream 2, two of it in countercurrent flow.

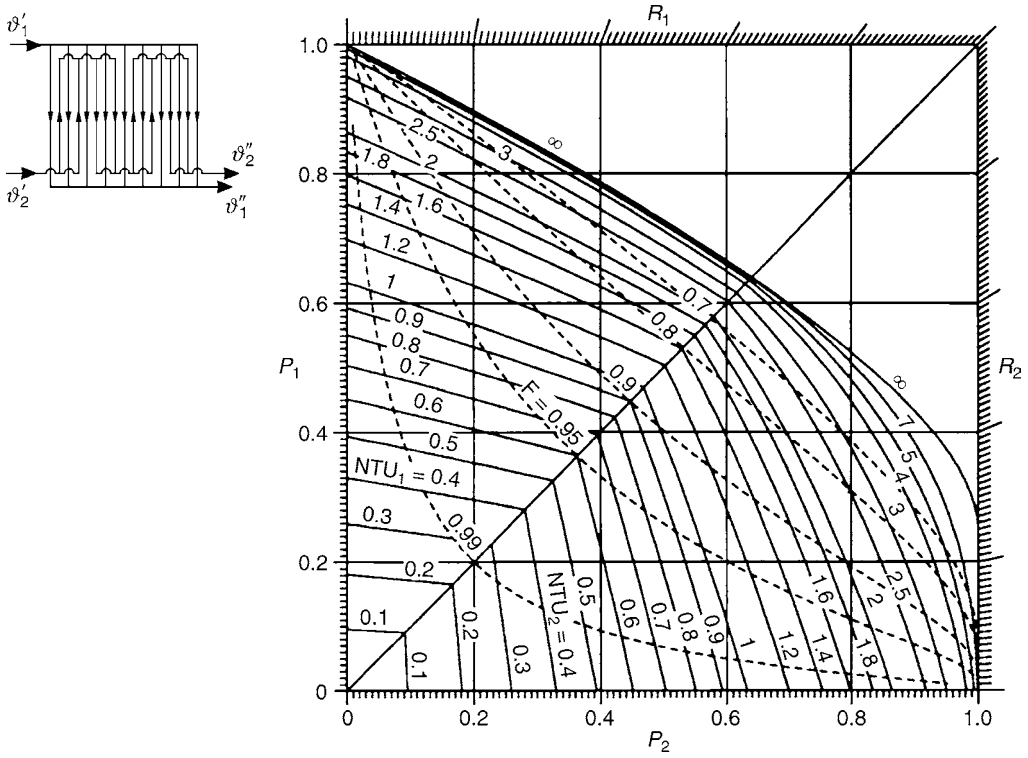

C1. Fig. 44. Plate heat exchanger with one pass for stream 1 and four passes for stream 2.

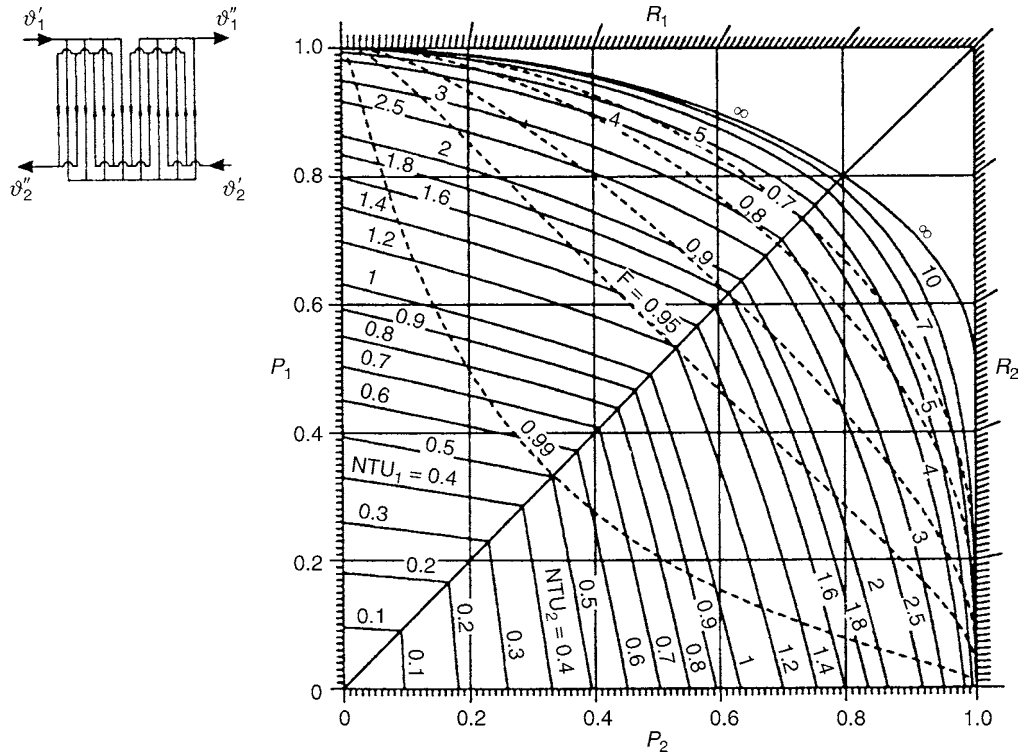

C1. Fig. 45. Plate heat exchanger with two passes for stream 1 and four passes for stream 2 in overall countercurrent flow arrangement.

$\vartheta_1'' = 70°C$. The inlet temperature of the air is $\vartheta_2' = 20°C$. The required cross-sectional area of the tube bundle and the tube length shall be calculated.

Solution

The ratio of the heat transfer area A and the cross-sectional area f follows from the design data of the finned tube bundle:

$$\frac{A}{f} = 132.$$

In Chap. C3 typical values of the overall heat transfer coefficient (related to the outside surface area) for gas heaters with finned tubes of 12–50 W/m^2 K are given. With $k = 20$ W/m^2 K

$$k_f = 2,640 \text{ W/m}^2 \text{ K}.$$

The air approach velocities are usually in the range of 2–5 m/s. With $w_2 = 2$ m/s Eq. (56) yields $\text{NTU}_2 = 1.25$.

From Eq. (9) it follows $P_1 = 0.5$

From the chart in Fig. 38 it is $P_2 = 0.57$ and $R_2 = 0.88$. It follows

$$\text{NTU}_1 = R_2\text{NTU}_2 = 1.10 \text{ and}$$
$$(kA)_{\text{req}} = 4,640 \text{ W/K}$$

Equation (58) yields $f_{\text{req}} = 1.76$ m^2. With the design data of the tube bundle the required tube length is 1.96 m $\approx$ 2 m.

7 Additional Symbols

Symbol	Description	Unit
F	Logarithmic mean temperature difference correction factor (Eq. (23))	–
m	Number of shell-side passes	–
n	Number of tube-side passes, tube rows, turns, or items of equipment	–
NTU	Number of transfer units (Eqs. (11), (12))	–
P	Dimensionless temperature change (Eqs. (9) and (10))	–
R	Heat capacity rate ratio (Eqs. (13) and (14))	–
T	Dimensionless temperature (Eq. (18))	–
$\dot{W}$	Heat capacity flow rate (Eq. (6))	W/K
z	Number of baffles	–
ε	NTU-ratio for cocurrent pass (Eq. (32))	–
Θ	Dimensionless mean temperature difference (Eq. (8))	–
ϑ	Temperature	K
Subscripts		
1, 2	Stream 1 or 2 in the heat exchanger	
a, b	Ends of the heat exchanger	
C	Pure countercurrent flow	
w	Wall	
z	Intermediate value	
Superscripts		
$'$	At the inlet	
$''$	At the outlet	
*	Hypothetical value	

8 Bibliography

1. Martin H (1992) Heat exchangers. Hemisphere Publ. Co, Washington, Philadelphia/London
2. Gaddis ES, Schlünder EU (1975) Temperaturverlauf und übertragbare Wärmemenge in Röhrenkesselapparaten mit Umlenkblechen. Verfahrenstechnik 9(12):617–621
3. Gaddis ES (1978) Über die Berechnung des Austauscherwirkungsgrades und der mittleren Temperaturdifferenz in mehrgängigen Rohrbündelwärmeaustauschern mit Umlenkblechen. Verfahrenstechnik 12(3):144–149
4. Spang B (1991) Über das thermische Verhalten von Rohrbündelwärmeübertragern mit Segmentumlenkblechen. Fortschr.-Ber. VDI, Reihe 19, No. 48, Düsseldorf: VDI-Verlag
5. Roetzel W, Na Ranong Ch (2000) Axial dispersion models for heat exchangers. Heat and Technology - Calore e Tecnologia, 18:7–17
6. Roetzel W, Spang B (1990) Verbessertes Diagramm zur Berechnung von Wärmeübertragern. Wärme- und Stoffübertragung 25:259–264
7. Spang B, Roetzel W (1995) Neue Näherungsgleichung zur einheitlichen Berechnung von Wärmeübertragern. Heat Mass Transfer 30:417–422
8. Roetzel W, Spang B (1987) Analytisches Verfahren zur thermischen Berechnung mehrgängiger Rohrbündelwärmeübertrager. Fortschr.-Ber. VDI, Reihe 19, No. 18, Düsseldorf: VDI-Verlag
9. Roetzel W, Spang B (1989) Thermal calculation of multipass shell and tube heat exchangers. Chem Eng Res Des 67:115–120
10. Ishihara K, Palen JW (1986) Mean temperature difference correction factor for the TEMA "H" shell. Heat Transfer Eng 7(3–4):27–34
11. Underwood AJV (1934) The calculation of the mean temperature difference in multi-pass heat exchangers. J Inst Petroleum Technologists 20:145–158
12. Roetzel W (1988) Thermische Berechnung von dreigängigen Rohrbündelwärmeübertragern mit zwei Gegenstromdurchgängen gleicher Größe. Wärme- und Stoffübertragung 22:3–11
13. Gardner KA (1941) Mean temperature difference in multipass exchangers – correction factors with shell fluid unmixed. Ind Eng Chem 33:1495–1500
14. Jaw L (1964) Temperature relations in shell and tube exchangers having one-pass split-flow shells. J Heat Transfer 86:408–416
15. Schindler DL, Bates HT (1960) True temperature difference in a 1–2 divided flow heat exchanger. Chem Eng Progr Symp Ser No 30 56:203–206
16. Martin H (1992) Compact new formulae for mean temperature difference and efficiency of heat exchanger. In: Roetzel W, Heggs PJ, Butterworth D (eds) Design and Operation of Heat Exchangers, Proc. Eurotherm Seminar No. 18, Hamburg, Feb. 27–March 1, 1991. Springer: Berlin/Heidelberg/New York, pp 19–29
17. Bowman RA (1936) Mean temperature difference correction in multipass exchangers. Ind Eng Chem 28:541–544
18. Gardner KA, Taborek J (1977) Mean temperature difference: a reappraisal. AIChE J 23:777–786
19. Nusselt W (1930) Eine neue Formel für den Wärmeübergang im Kreuzstrom. Tech Mech U Therm 1:417–422
20. Mason JL (1955) Heat transfer in cross-flow. Proc 2nd US Natl Congr Appl Mech ASME:801–803
21. Smith DM (1934) Mean temperature difference in cross flow. Engineering 138:479–481; 606–607
22. Stevens RA, Fernandez J, Woolf JR (1957) Mean temperature difference in one, two and three-pass crossflow heat exchangers. Trans ASME 79:287–297
23. Nicole FJL (1972) Mean temperature difference in cross-flow heat exchange, applied to multipass air-cooled fin-tube units with a finite number of rows. MSc (Engineering) Thesis, University of Pretoria, CSIR Special Report CHEM 223
24. Spang B, Roetzel W (1992) Approximate equations for the design of cross-flow heat exchangers. In: Roetzel W, Heggs PJ, Butterworth D (eds) Design and Operation of Heat Exchangers, Proc. Eurotherm Seminar No. 18,

Hamburg, Feb. 27–March 1, 1991. Springer, Berlin/Heidelberg/New York, pp 125–134
25. Kandlikar SG, Shah RK (1989) Multipass plate heat exchangers – effectiveness-NTU results and guidelines for selecting pass arrangements. J Heat Transfer 111:300–313
26. Bassiouny MK (1985) Experimentelle und theoretische Untersuchungen über Mengenstromverteilung, Druckverlust und Wärmeübergang in Plattenwärmeaustauschern. Fortschr.-Ber. VDI, Reihe 6, No. 181, Düsseldorf: VDI-Verlag
27. Kandlikar SG, Shah RK (1989) Asymptotic effectiveness-NTU formulas for multipass plate heat exchangers. J Heat Transfer 111:314–321
28. Bes Th (2001) Thermal design of spiral heat exchanger. Int J Heat Exchangers 2:59–96
29. Bes Th, Roetzel W (1998) Effectiveness of spiral heat exchanger with variable overall heat transfer coefficient. In: Heat Transfer and Renewable Energy Sources, Proc. VII Int. Symp. Heat Transfer and Renewable Energy Sources, Szczecin-Swinoujscie, Sept. 7–9, pp 415–424
30. Bošnjaković F, Vilićić M, Slipćević B (1951) Einheitliche Berechnung von Rekuperatoren. VDI-Forschungsheft 432, Düsseldorf: VDI-Verlag
31. Domingos JD (1969) Analysis of complex assemblies of heat exchangers. Int J Heat Mass Transfer 12:537–548
32. Kays WM, London AL (1964) Compact Heat Exchangers, 2nd edn. McGraw Hill, New York
33. Roetzel W (1990) Thermische Auslegung von Wärmeübertragersystemen mit umlaufendem Wärmeträger. BWK 42(5):254–258
34. Na Ranong Ch (2001) Stationäres und instationäres Verhalten von zwei gekoppelten Wärmeübertragern mit umlaufenden Fluidstrom. Ph.D. thesis, Department of Mechanical Engineering, University of the Federal Armed Forces Hamburg, Hamburg
35. Na Ranong Ch, Roetzel W (2002) Steady-state and transient behaviour of two heat exchangers coupled by a circulating flowstream. Int J Therm Sci 41:1029–1043
36. Butterworth D (1975) A calculation method for shell and tube heat exchangers in which the overall coefficient varies along the length. NEL Report No. 590, pp. 56–71, National Engineering Laboratory East Kilbride, Glasgow
37. Taborek J (1979) Evolution of heat exchanger design techniques. Heat Transfer Eng 1(1):15–29

C2 Overall Heat Transfer

Wilfried Roetzel[1] · *Bernhard Spang*[2]
[1]Helmut-Schmidt-Universität, Universität der Bundeswehr Hamburg, Hamburg, Germany
[2]BUCO Wärmeaustauscher International GmbH, Geesthacht, Germany

1 Introduction

In a heat exchanger hot and cold fluids are separated by a wall of one or more layers. The process of steady state heat transport from the hot fluid to the cold fluid through the separating wall is denoted with overall heat transfer and characterized by the overall heat transfer coefficient. This overall coefficient varies together with the two local heat transfer coefficients, and suitable mean values have to be introduced for the thermal design and rating of heat exchangers.

2 Local and Mean Heat Transfer Coefficient

If heat transfer is convective, the local heat transfer coefficient at a surface is directly related to the length of the flow path x, the local temperature of the fluid ϑ, and the temperature of the wall surface ϑ_w over which the fluid flows. In other words, it is given by

$$\alpha_{loc} = \alpha_{loc}(x, \vartheta, \vartheta_w).$$

The direct dependence of heat transfer on the length of the flow path is caused by the development of the velocity and temperature profiles, and is referred to as the flow length effect. The relationship to temperature is brought about by the temperature-dependent properties of the fluid or by radiation, and is referred to as the temperature effect.

The mean coefficient of heat transfer at a surface is obtained directly from the correlation for convective heat transfer (cf. Part G). Thus

$$\alpha = \frac{1}{L}\int_{x=0}^{L} \alpha_{loc}\, dx = \frac{1}{A}\int_{A} \alpha_{loc}\, dA \qquad (1)$$

is valid for constant temperatures ϑ and ϑ_w (or for constant fluid properties) and is averaged over the length of flow path or area of contact.

The average applies only for the length effect and depends on the local temperatures ϑ and ϑ_w, i.e.,

$$\alpha = \alpha(\vartheta, \vartheta_w).$$

3 Local Overall Heat Transfer Coefficient

The local overall heat transfer coefficient is the reciprocal of the total heat transfer resistance, consisting of the two heat transfer resistances at surfaces A_1 and A_2, and the conductive wall resistance R_w:

$$\frac{1}{k_{loc}A} = \frac{1}{\alpha_{1,loc}A_1} + R_w + \frac{1}{\alpha_{2,loc}A_2}. \qquad (2)$$

The left-hand side of Eq. (2) applies to an area A of any given size.

The resistance offered by the wall is calculated from its thickness δ and the material's thermal conductivity λ, i.e.,

$$R_w = \frac{\delta}{\lambda A_m}, \qquad (3)$$

where A_m is the mean area that governs the thermal conductivity.

VDI-GVC (ed.), *VDI Heat Atlas*, DOI 10.1007/978-3-540-77877-6_5,

For a cylindrical tube of circular cross-section,

$$A_m = \frac{A_1 - A_2}{\ln \frac{A_1}{A_2}} = \frac{d_1 - d_2}{\ln \frac{d_1}{d_2}} \pi L. \quad (4)$$

For a spherical shell,

$$A_m = \sqrt{A_1 A_2} = d_1 d_2 \pi. \quad (5)$$

The local temperatures at the surfaces ϑ_{w1} and ϑ_{w2} on which heat is transferred are obtained from the following equation:

$$\alpha_{1,\mathrm{loc}} A_1 (\vartheta_1 - \vartheta_{w1}) = \alpha_{2,\mathrm{loc}} A_2 (\vartheta_{w2} - \vartheta_2) = k_{\mathrm{loc}} A (\vartheta_1 - \vartheta_2). \quad (6)$$

If the wall consists of n layers, its total resistance to heat transfer is the sum of those offered by the individual layers, i.e.,

$$R_w = \sum_{j=1}^{n} R_{wj} = \sum_{j=1}^{n} \left(\frac{\delta}{\lambda A_m} \right)_j. \quad (7)$$

The intermediate temperature $\vartheta_{z,p}$ behind the pth layer, as counted from the temperature ϑ_{w1}, can be derived from the equation

$$(\vartheta_{w1} - \vartheta_{z,p}) \sum_{j=1}^{n} R_{wj} = (\vartheta_{w1} - \vartheta_{w2}) \sum_{j=1}^{p} R_{wj}. \quad (8)$$

The local overall heat transfer coefficient, as defined by Eq. (2), depends on the temperatures of the two fluids, the two wall surface temperatures, and the lengths of both flow paths, i.e.,

$$k_{\mathrm{loc}} = k_{\mathrm{loc}}(\vartheta_1, \vartheta_2, \vartheta_{w1}, \vartheta_{w2}, x_1, x_2).$$

4 Mean Overall Heat Transfer Coefficient

The local overall heat transfer coefficient k_{loc} varies with the length of the flow path and the local fluid and wall temperatures over the area available for heat transfer. A mean value k must be found that can be used in the equations and charts given in Chap. C1. A figure that is frequently taken for this purpose is the value $\tilde{k}$ obtained by substituting the mean for the local heat transfer coefficients in Eqs. (2) and (6), i.e.,

$$\frac{1}{\tilde{k}A} = \frac{1}{\alpha_1 A_1} + R_w + \frac{1}{\alpha_2 A_2}. \quad (9)$$

This value depends only on the local fluid and wall temperatures, i.e.,

$$\tilde{k} = \tilde{k}(\vartheta_1, \vartheta_2, \vartheta_{w1}, \vartheta_{w2}).$$

As a rule, iteration must be resorted to for determining either the overall coefficient from Eq. (9) or the wall temperatures, because they are interdependent. Of practical importance are a few cases where the heat transfer coefficient can be calculated without iteration [1]. The mean value $\tilde{k}$ determined from Eq. (9) is merely an approximation for the true mean value of the overall heat transfer coefficient k.

The true mean value can be derived as follows from Eqs. (1)–(4) in Chap. C1, but only if the temperature difference remains unchanged over the entire heat transfer area ($\triangle\vartheta = \vartheta_1 - \vartheta_2 = \mathrm{const.}$):

$$k = k_A = \frac{1}{A} \int_A k_{loc} dA. \quad (10)$$

In this case, the local overall heat transfer coefficient may be an arbitrary function of location and temperature. In addition, it can be demonstrated that the area-average overall coefficient, as defined by Eq. (10), is the true mean value in cocurrent and countercurrent flow without restrictions if the heat capacity rates are constant.

Equation (10) does not apply in most other cases. However, the better the P_1,P_2-chart in the operating range agrees with that for pure countercurrent or pure cocurrent flow, the less the difference between k_A and k, provided the heat capacity rates are constant.

The difference is particularly small for arrangements in countercurrent cross-flow and in countercurrent coupling of individual units, because they closely agree with pure countercurrent flow. Likewise, cocurrent cross-flow, cocurrent coupling of individual units, and cross-flow with lateral mixing on both sides agree well with pure cocurrent flow, and again very small differences are obtained. Larger differences may arise in pure cross-flow and in cross-flow equipment with few passes [2].

Reservations must also be made for mixed flow arrangements in which so-called true cocurrent and countercurrent passes occur. Examples are multipass plate (true cocurrent and countercurrent flow) and shell-and-tube heat exchangers. In these cases, the (area-average) overall heat transfer coefficient must be determined separately for each pass in order to ensure accuracy, because the sizes of the countercurrent and cocurrent passes relative to one another, i.e., the NTUs, affect the quality of the flow arrangement. A simplifiation can be made by determining a common mean coefficient for all the cocurrent passes and another one for all the countercurrent passes [3].

If the overall heat transfer coefficient depends on temperature and the flow differs greatly from pure countercurrent or cocurrent flow arrangement, an approximate value for k can be obtained by correcting the reference temperatures in the methods described below [2]. If the specific heat capacity varies with temperature, an apparent mean value must be taken [4] that differs from the mean value k, as determined from Eq. (10), even in pure cocurrent and countercurrent flow.

For the determination of the mean value k the temperature and the flow length effect have to be taken into account. This can be done separately as shown in the following.

5 Allowance for the Flow Length Effect

The frequently adopted mean value $\tilde{k}$ that is obtained from Eq. (9) makes only a rough allowance for the flow length effect, because it is determined from heat transfer coefficients that have already been integrated. However, in analogy to Eq. (1), which corresponds to Eq. (10), the values for k_{loc} ought to be integrated over the whole area at constant temperatures (or properties).

Therefore, a distinction is drawn between $\tilde{k}$ and a mean value $\bar{k}$ that makes due allowance for the flow length effect. In common with the usual approximation $\tilde{k}$, $\bar{k}$ still depends on the local fluid and wall temperatures, i.e.,

$$\bar{k} = \bar{k}(\vartheta_1, \vartheta_2, \vartheta_{w1}, \vartheta_{w2}).$$

In most cases of practical importance, e.g., turbulent flow on both sides, the flow length effect is so slight that the normal, simplified approach according to Eq. (9) yields sufficient accuracy ($\tilde{k} \approx \bar{k}$ [5]).

However, if flow is laminar, unacceptable errors on the unsafe side with an uncertainty of more than 10% may occur ($\tilde{k} > \bar{k}$). In such cases, the approximate value must be corrected by a factor $V \leq 1$, i.e.,

$$\bar{k} = \tilde{k}V. \tag{11}$$

Equations for the determination of V in various cases are given below [6, 7].

5.1 Flow Length Effect on One Side Only

It is assumed that the flow length effect of one stream can be expressed as

$$\alpha_{L,loc} = \alpha_L \left(1 - \frac{1}{p}\right) \left(\frac{x}{L}\right)^{-1/p} \tag{12}$$

with integer values $p \geq 2$. For laminar flow in channels of uniform cross-section $p = 3$ [5, 6]. The heat transfer coefficient of the other stream does not directly depend on the flow length $0 \leq x/L \leq 1$ (no length effect). The correction factor is

$$V = (1+u)(p-1)\left[\left(-u\frac{p-1}{p}\right)^{p-1} \ln\left(1 + \frac{p}{u(p-1)}\right) + \sum_{j=0}^{p-2} \frac{\left(-u\frac{p-1}{p}\right)^j}{p-1-j}\right] \tag{13}$$

with $u = \dfrac{\alpha_L A_L}{\tilde{k}A} - 1$.

The coefficient α_L is the mean heat transfer coefficient determined from the correlation under consideration and A_L is the corresponing surface area. Although Eq. (13) is valid for all integer values $p \geq 2$ and arbitrary values of u, the numerical evaluation becomes difficult for $p > 5$ and $u > 1$. In such cases the following equation is recommended which has been found by a series development:

$$V = (1+u)(p-1)\sum_{j=1}^{\infty} \frac{1}{\left(-u\frac{p-1}{p}\right)^j (1-p-j)}. \tag{14}$$

The equation is valid for $u(p–1)/p > 1$ and arbitrary values of p. The truncation error of the sum is smaller than the following summand.

Equations (13) and (14) can be applied to all flow arrangements in which no axial dispersion takes place.

5.2 Laminar Flow in Both Streams

For both laminar streams the flow length effect is expressed by Eq. (12) with $p = 3$. Regarding the mean value α_L for laminar flow (Part G), one should keep in mind that the boundary conditions for heat transfer depend on the flow arrangement. For countercurrent flow and $R \approx 1$ the boundary condition "uniform heat flux, $\dot{q}$ = const." is more appropriate than the condition "uniform wall temperature, ϑ_w = const." The reverse is valid for cocurrent flow.

Using the abbreviations

$$a_1 = \alpha_{L1} A_1;\ a_2 = \alpha_{L2} A_2 \tag{15}$$

V is given by the following equations:

For countercurrent flow

$$V = 1 + \frac{0.65 + 0.23R_w(a_1 + a_2)}{4.1 + \frac{a_1}{a_2} + \frac{a_2}{a_1} + 3R_w(a_1 + a_2) + 2R_w^2 a_1 a_2}. \tag{16}$$

For cross-flow

$$V = 1 + \frac{0.44 + 0.23R_w(a_1 + a_2)}{4.1 + \frac{a_1}{a_2} + \frac{a_2}{a_1} + 3R_w(a_1 + a_2) + 2R_w^2 a_1 a_2}. \tag{17}$$

If both fluids are transversally mixed at the inlets to each pass, Eq. (17) is valid for all kinds of cross-flow.

For cocurrent flow, with the simplifying abbreviation

$$Z = \frac{R_w}{\frac{1}{a_1} + \frac{1}{a_2}} \tag{18}$$

V is given by [6, 7]

$$V = (1+Z)\left[1 - \frac{4}{3}Z + \frac{8}{9}Z^2 \ln\left(1 + \frac{3}{2Z}\right)\right] \tag{19}$$

The correction equations, Eqs. (13)–(19), are valid for laminar flow in channels of constant cross-section.

An additional effect of the flow path length that occurs in spiral heat exchangers is that the heat transfer coefficients depend on the radius of curvature of the channel wall, which varies with the length of the flow path. The relationship is linear for an Archimedes' spiral. The normal methods of calculation with mean heat transfer coefficients allow quite accurately for this effect, because the coefficients on both sides of the curved wall change in the same manner. The allowance for laminar length effects is as discussed above.

Other definite relationships between local heat transfer coefficients and the flow length exist for flow channels of changing cross-section, e.g., in conical tubes. In these cases, the mean value $\bar{k}$ is calculated from Eq. (10) by determining the values of k_{loc} with constant temperature at several points and integrating these values over the surface A. In the case of conical tubes, it is advisable to integrate the product $k_{loc}d$ over the length of the channels.

6 Allowance for the Temperature Effect

6.1 Usual Method

The simplest method of allowing for the temperature effect is to determine the temperature-dependent mean coefficient $\bar{k}$ at one reference temperature for each fluid – usually the arithmetic mean of the temperatures at the inlet and outlet, i.e.,

$$\vartheta_i = \frac{1}{2}(\vartheta_i' + \vartheta_i'')$$

where $i = 1, 2$.

The same simple method is usually adopted for the calculation of pressure drop (cf. Chap. L1). It can give rise to unacceptable errors if the fluid properties depend strongly on temperature or if heat is transferred by radiation or free convection. If this is the case, a more accurate method of calculating the overall heat transfer coefficients at several points in the heat exchanger is recommended [5, 8]. The pressure drop can also be determined more accurately by a similar procedure [9].

6.2 Multi-Point Method

This method applies to cocurrent and countercurrent flow, including the limiting cases of $\dot{W}_1 = \infty$ or $\dot{W}_2 = \infty$ for any given flow arrangement with the exception of the stirred tank. It allows for the temperature dependence of heat transfer coefficients and heat capacities.

If the effects of length and temperature are pronounced and occur simultaneously, it is assumed that the local overall heat transfer coefficient k_{loc} can be approximated (in the same way as a heat transfer coefficient) by the product of a pure flow length function and a pure temperature function in the range considered [5].

The desired mean value k can be determined from the equation

$$\frac{1}{k} = \frac{\dfrac{1}{\dot{M}_1 c_{pm1}} \pm \dfrac{1}{\dot{M}_2 c_{pm2}}}{\ln \dfrac{\Delta\vartheta_b}{\Delta\vartheta_a}} \int_{\ln\Delta\vartheta_a}^{\ln\Delta\vartheta_b} \frac{d(\ln\Delta\vartheta)}{\bar{k}\left(\dfrac{1}{\dot{M}_1 c_{p1}} \pm \dfrac{1}{\dot{M}_2 c_{p2}}\right)}, \qquad (20)$$

where the indices "a" and "b" designate the ends of the exchanger. The positive sign is valid for parallel flow and the negative sign for counterflow. The integral is approximated according to Gauss [5, 8] or Simpson [8, 11] using $n = 2$ or $n = 3$ (or more) reference points j at which the mean (with respect to laminar length effect) overall heat transfer coefficient $\bar{k}_j$ has to be determined. First two simple special cases are considered.

6.2.1 One Constant Fluid Temperature

The fluid temperature ϑ_k remains constant if the heat capacity rate ratio $R_i = \dot{M}_i c_{pmi} / \dot{M}_k c_{pmk} = 0$ ($i = 1, 2$; $k = 2, 1$). The Gauss or Simpson integration yields

$$\frac{1}{k} = \frac{1}{c_{pmi}} \sum_{j=1}^{n} a_j \frac{c_{pi,j}}{\bar{k}_j} \qquad (21)$$

with the local values $\bar{k}_j(\vartheta_{i,j}, \vartheta_k, \vartheta_{w,i,j}, \vartheta_{w,k,j}, R_w)$ and $c_{pi,j}(\vartheta_{i,j})$, determined for the reference temperatures

$$\vartheta_{i,j} = \vartheta_k + \Delta\vartheta_b \left(\frac{\Delta\vartheta_a}{\Delta\vartheta_b}\right)^{s_j}. \qquad (22)$$

The coefficients a_j and s_j are given in Table 1.

6.2.2 Constant Heat Capacities

In the special case of constant heat capacities, which often can be assumed as an approximation, the mean overall heat transfer coefficient

$$\frac{1}{k} = \sum_{j=1}^{n} a_j \frac{1}{\bar{k}_j} \qquad (23)$$

and the reference temperatures

$$\vartheta_{i,j} = \vartheta_{i,b} + (\vartheta_{i,a} - \vartheta_{i,b}) \frac{\left(\frac{\Delta\vartheta_a}{\Delta\vartheta_b}\right)^{s_j} - 1}{\frac{\Delta\vartheta_a}{\Delta\vartheta_b} - 1} \qquad (24)$$

for the calculation of $\bar{k}_j(\vartheta_{1,j}, \vartheta_{2,j}, \vartheta_{w1,j}, \vartheta_{w2,j}, R_w)$.

In the limiting case $\Delta\vartheta_a = \Delta\vartheta_b$ which occurs in a balanced counterflow exchanger, the fraction on the right hand side in Eq. (24) turns to the value s_j.

6.2.3 Temperature-Dependent Heat Capacities

In the general case of temperature-dependent heat transfer coefficients and heat capacities the integral in Eq. (20) cannot be calculated directly [5, 8]. For the simple integration as in the case of constant heat capacities the hypothetical temperatures have been introduced which are linear functions of the related enthalpies and coincide with the true fluid temperatures at the inlets and outlets of the exchanger [4, 8]. If the heat capacities are constant, the hypothetical temperatures and the true temperatures are identical. The concept of hypothetical temperatures leads to the following equations, in which the hypothetical

C2. Table 1. Coefficients for Gauss and Simpson integration with n points

	n	j	a_j	s_j
Gauss	2	1	$\frac{1}{2}$	$\frac{1}{2}+\frac{1}{6}\sqrt{3}$
		2	$\frac{1}{2}$	$\frac{1}{2}-\frac{1}{6}\sqrt{3}$
	3	1	$\frac{5}{18}$	$\frac{1}{2}+\frac{1}{2}\sqrt{\frac{3}{5}}$
		2	$\frac{4}{9}$	$\frac{1}{2}$
		3	$\frac{5}{18}$	$\frac{1}{2}-\frac{1}{2}\sqrt{\frac{3}{5}}$
Simpson	3	1 = a	$\frac{1}{6}$	1
		2	$\frac{2}{3}$	$\frac{1}{2}$
		3 = b	$\frac{1}{6}$	0

temperatures are eliminated. All temperatures are true fluid temperatures.

With the factor

$$\Psi_j = \frac{\Delta\vartheta_b}{\Delta\vartheta_j}\left(\frac{\Delta\vartheta_a}{\Delta\vartheta_b}\right)^{s_j}$$

it is

$$\frac{1}{k} = \sum_{j=1}^{n} a_j \frac{1}{\bar{k}_j}\Psi_j. \tag{25}$$

The factor Ψ_j represents a correction for variable heat capacities. For the determination of the local temperatures $\vartheta_{i,j}$ and their difference $\Delta\vartheta_j = \vartheta_{1,j} - \vartheta_{2,j}$ the local specific enthalpies $h_{i,j}$ have to be calculated from

$$h_{i,j} = h_{i,b} + \left(h_{i,a} - h_{i,b}\right)\frac{\left(\frac{\Delta\vartheta_a}{\Delta\vartheta_b}\right)^{s_j} - 1}{\frac{\Delta\vartheta_a}{\Delta\vartheta_b} - 1}. \tag{26}$$

The local temperatures $\vartheta_{i,j}\left(h_{i,j}\right)$ are then determined from the enthalpies $h_{i,j}$ with the help of equations of state, tables or diagrams. With the temperatures $\vartheta_{i,j}$ the local mean coefficient $\bar{k}_j\left(\vartheta_{1,j}, \vartheta_{2,j}, \vartheta_{w1,j}, \vartheta_{w2,j}, R_w\right)$ and $\Delta\vartheta_j$ can be calculated.

If the heat capacities are constant $h = c_p\vartheta + h_0$ and Eq. (26) turns to Eq. (24). With the temperatures from Eq. (24) the correction factor in Eq. (25) $\Psi_j = 1$. So for $c_{pi} = \text{const}(i = 1, 2)$ all three methods described in 6.2.1, 6.2.2, and 6.2.3 are identical.

For variable heat capacities and one constant fluid temperature the Eqs. (25) and (26) and the Eqs. (21) and (22) do not yield identical results, but their accuracy is about the same. The Eqs. (21) and (22) are more convenient for the special case of one constant fluid temperature.

Concerning the appropriate integration method: Basically the Gauss integrations achieve the highest accuracy for a given number of reference points. With two points a polynomial of third degree is exactly integrated, a polynomial of fifth degree requires three points. In normal cases of industrial application the two-point-Gauss method is sufficiently accurate. However, extreme cases may arise in which the three-point-Gauss integration is required [10, 8]. This may occur when high viscous oils are heated up by condensing steam or when a transition takes place between laminar and turbulent flow. However, the main problem in such extreme cases is not the proper integration but the accurate prediction of the local heat transfer coefficients.

The Simpson method is nearly as accurate as the two-point-Gauss integration, although three reference points are used. The method has been recommended [11] because the Reynolds numbers are frequently determined anyhow at the inlet and outlet in order to check whether or not the flow is turbulent or laminar throughout the exchanger. Another advantage is that at the terminal reference points $j = 1 = a$ and $j = 3 = b$ the reference temperatures are the given inlet and outlet temperatures and the correction factors in Eq. (25) $\Psi_1 = \Psi_a = \Psi_3 = \Psi_b = 1$. So, only at the central reference point $j = 2$ the enthalpies are needed for the determination of the reference temperatures if the heat capacities vary with temperature.

If the heat capacities vary, this mean value of k must be regarded as an apparent coefficient that differs from the area-average value obtained from Eq. (10) and even from a value that remains unchanged over the heat transfer area, i.e., $\bar{k} = \bar{k}_j$. In other words, $k \neq \bar{k}$.

Unsuitable cases may arise if the specific heat capacities depend considerably on temperature or if other pronounced nonlinear relationships exist between enthalpy and temperature, e.g., in the $h(\vartheta)$ condensing curve for mixtures. Thus, in countercurrent flow with high values of $\text{NTU}_1 \approx \text{NTU}_2$, the temperature curves for both fluids may theoretically intersect at a point ($\vartheta_1 = \vartheta_2$). This would entail that the process concerned would be impracticable. A case of this nature would occur if the values for $\Delta\vartheta_a$ and $\Delta\vartheta_b$ were positive and a temperature difference $\Delta\vartheta_j$ were negative or zero.

Example 1

An example given by Colburn [12] is calculated with the three-point-Simpson method.

Aniline ($\dot{W}_1 = 5.4\text{kW/K}$) is to be cooled down from $\vartheta_1' = 125°\text{C}$ to $\vartheta_1'' = 25°\text{C}$ in a countercurrent heat exchanger. The coolant is water ($\dot{W}_2 = 12\text{kW/K}$) at an inlet temperature of $\vartheta_2' = 20°\text{C}$. From the energy balance it follows $\vartheta_2'' = 65°\text{C}$. The wall resistance is $1.76 \times 10^{-4}\ \text{m}^2\,\text{K/W}$. It can be assumed as a close approximation that the heat capacities in this case (two liquids) are constant. Since flow is turbulent on both sides, there are no length effects to be taken into account.

For the data used by Colburn the temperature dependence of the heat transfer coefficients can be expressed by the following numerical equations [12] (converted into SI units):

$$\alpha_1 = 829 + 8.3\vartheta_1 + 0.0834\vartheta_1^2,$$

$$\alpha_2 = 6,092(1 + 0.0127\vartheta_2),$$

ϑ in °C, α in $\text{W/(m}^2\,\text{K)}$.

The usual method (calculation of the heat transfer coefficients at the arithmetic mean fluid temperatures $\vartheta_{1m} = 75°\text{C}$ and $\vartheta_{2m} = 42.5°\text{C}$, respectively) yields with $A_1 = A_2 = A$ the approximate value $k = 1{,}245\ \text{W/(m}^2\,\text{K)}$.

For the three-point-Simpson method the mean overall heat transfer coefficients $\bar{k}_a$ and $\bar{k}_b$ at both ends ($j = 1, 3$) must be calculated. They are

$$\bar{k}_a(\vartheta_1 = 125°\text{C}, \vartheta_2 = 65°\text{C}) = 1,720\,\text{W/(m}^2\,\text{K)},$$
$$\bar{k}_b(\vartheta_1 = 25°\text{C}, \vartheta_2 = 20°\text{C}) = 816\,\text{W/(m}^2\,\text{K)}.$$

According to Eq. (24) the fluid temperatures at the central reference point $j = 2$ are

$$\vartheta_{1,2} = 47.4°\,\text{C} \text{ and } \vartheta_{2,2} = 30.1°\,\text{C}$$

and hence the central mean overall heat transfer coefficient

$$\bar{k}_2 = 996\,\text{W/(m}^2\text{K)}$$

From Eq. (23) the approximation for the desired mean value is $k = 1{,}030\ \text{W/(m}^2\,\text{K)}$. A numerical finite-difference calculation yields the exact value $k = 1{,}034\ \text{W/(m}^2\,\text{K)}$.

The two-point-Gauss method yields $k = 1{,}037\ \text{W/(m}^2\,\text{K)}$ and the three-point-Gauss method the exact value $k = 1{,}034\ \text{W/(m}^2\,\text{K)}$.

6.2.4 Averaging the Resistances to Heat Transfer

Since the resistances to heat transfer in Eqs. (9) and (20) are additive, Eqs. (20)–(25) can also be applied separately to $1/\alpha_1$, R_w and $1/\alpha_2$ by substituting α and $1/R_w$ for k in Eqs. (21), (23), and (25). The triple application then yields the proper (for variable heat capacities) apparent mean values (with respect to temperature effects) of both heat transfer coefficients and the wall resistance.

Subsequently the mean value $\tilde{k}$ with respect to temperature effects according to Eq. (9) and, if flow is laminar, the desired mean value $k = \tilde{k}V$ using the correction equations Eqs. (11)–(19) can be determined.

6.2.5 Other Flow Arrangements

Although, strictly speaking, the multi-point method is valid only for pure cocurrent or countercurrent flow, it can be applied as an approximation to other flow arrangements in which the thermal behaviour is similar.

Similarity to countercurrent flow can be found in countercurrent spiral heat exchangers, all counter-crossflow configurations, and systems coupled in overall countercurrent flow. For a system of identical heat exchangers, a combined mean overall heat transfer coefficient common to all individual units can be determined analogous to that for a single countercurrent flow exchanger. Thus the total effect is correctly described but intermediate temperatures cannot be correctly calculated with the common mean coefficient. If the arrangement deviates more from pure countercurrent flow, an additional correction to the reference temperatures for calculating the true overall coefficient is recommended [7]. The logarithmic mean temperature difference correction factor F is used to express the degree of deviation from pure countercurrent flow. No correction is needed if $F = 1$.

The correction equations for $i = 1, 2$ and the reference point j are

$$\vartheta_{i,j,corr} = \vartheta_{i,j} + (-1)^i \left(\vartheta_{1,j} - \vartheta_{2,j}\right) \frac{1 - F}{1 + R_i^{2/3}}. \qquad (27)$$

The two corrected reference temperatures are used solely for calculating the true heat transfer coefficients at the reference point. The remaining equations for countercurrent flow are unaffected.

If the three-point-Simpson method is used, for simplicity the correction is only applied to the central reference point ($j = 2$), but has to be weighted with the factor 3/2 in front of $(-1)^i$ for compensation [2].

Considerations corresponing to those for countercurrent flow apply to cocurrent spiral exchangers, all cocurrent cross-flow configurations, and systems coupled in overall cocurrent flow. For the purpose of calculating the common mean coefficient k, the cocurrent system can be regarded as one single cocurrent heat exchanger, provided that $P_{1tot} + P_{2tot} < 1$.

A comparison of the P_1, P_2-charts for other flow arrangements with those for cocurrent or countercurrent flow allows an estimation on whether the flow arrangement concerned conforms more to the one or to the other. For instance, pure crossflow corresponds more to countercurrent flow, mixed-mixed cross-flow more to cocurrent flow.

As mentioned above the cocurrent method can only be used as a model for the calculation of the mean overall heat transfer coefficient $\tilde{k}$ if $P_1 + P_2 < 1$. However, the mixed-mixed crossflow can reach values $P_1 + P_2 > 1$. In such cases either the general method, i.e., counterflow with correction Eq. (27) or preferably a special method [8], derived for mixed-mixed crossflow ($\alpha(\vartheta)$ and $c_p(\vartheta)$), has to be applied. This method [8] is also applicable to multipass shell-and-tube heat exchangers with one shell-side and a high even number of tube-side passes (1,2m-HEX; $m \geq 2$; see Chap. C1).

For other types of multipass 1,n-HEX the most general analytical method [3] can be used, in which for each pass an individual tubeside heat transfer coefficient is calculated, using the arithmetic mean of the terminal pass temperatures as reference temperature. One mean shellside coefficient (for all passes) could be determined as discussed before, e.g., as for the counterflow with correction Eq. (27).

For the mixed-unmixed cross-flow (one tube row) a special method ($\alpha(\vartheta)$ and $c_p(\vartheta)$) can be recommended for the calculation of $\tilde{k}$ [8].

Example 2

It shall be checked with the three-point-Simpson method if the usual mean value of the overall heat transfer coefficient used in the calculation of Example 1 in Chap. C1 is sufficiently accurate.

Solution

As the flow on both sides is turbulent, only the temperature effect has to be taken into account: $\bar{k} = \tilde{k}$. The heat capacities of water and air at the present temperatures and pressures are nearly constant, so that Eqs. (23) and (24) can be applied.

At first the outlet temperatures have to be estimated. The outlet temperatures calculated in Example 1 of Chap. C1 are taken. Hence the temperatures at both ends of the heat exchanger are

$$\vartheta_{1,a} = \vartheta_1' = 120°C,\ \vartheta_{2,a} = \vartheta_2'' = 94°C \text{ and}$$

$$\vartheta_{1,b} = \vartheta_1'' = 78°C,\ \vartheta_{2,b} = \vartheta_2' = 20°C$$

The fluid temperatures at the point $j = 2$ follow from Eq. (24) (constant heat capacities) $\vartheta_{1,2} = 103°C$, $\vartheta_{2,2} = 64°C$. The correction from Eq. (27) is negligible because the correction factor F is greater than 0.99 (Chap. C1, Example 1).

The fluid property values of water at a pressure of 10 bar and of air at 1 bar can be taken from the tables in Chap. D2 at the fluid temperatures at both ends and at the central reference point "2". With these property values the tubeside heat transfer coefficients follow from correlations given in Chap. G1:

at point a: $\alpha_{1,a} = 4{,}912$ W/(m^2 K),
at point b: $\alpha_{1,b} = 4{,}129$ W/(m^2 K),
at point "2": $\alpha_{1,2} = 4{,}668$ W/(m^2 K).

On the shellside it follows from Chap. M1:

at point a: $\alpha_{2,a} = 50.3$ W/(m^2 K),

at point b: $\alpha_{2,b} = 46.8$ W/(m^2 K),
at point "2": $\alpha_{2,2} = 49.0$ W/(m^2 K).

Equation (9) yields the mean overall heat transfer coefficient $\bar{k} = \tilde{k}$:

at point a: $\bar{k}_a A = 4,679$ W/K,
at point b: $\bar{k}_b A = 4,253$ W/K,
at point "2": $\bar{k}_2 A = 4,528$ W/K

where area A is arbitrary. From Eq. (23) the desired mean value is kA = 4,504 W/K. In this case the usual mean value kA = 4,495 W/K deviates only slightly from the actual mean value.

7 Reduction in Heat Transfer Caused by Protective Layers and Fouling

Heat transfer surfaces often have to be coated to provide protection against corrosion. Other coats, e.g., oxides, may also be formed if the heat transfer surfaces react with the flowing substance; or deposits that are difficult to remove may accumulate on the heating and cooling surfaces.

All these layers impede the heat flow through the wall of an exchanger. Their effect depends on their thickness and thermal conductivity and, in particular, on the heat flow through the wall. While, for example, a lead coating on the heat transfer surface of a gas cooler would have practically no effect on overall heat transfer, the same lead layer may considerably reduce the thermal performance of an evaporator with its usually very high heat flux.

The reduction of overall heat transfer can be expressed by a correction factor φ, i.e.,

$$k = \varphi\, k_0, \tag{28}$$

where k_0 is the overall heat transfer coefficient if no layers were present and k is the actual heat transfer coefficient. With the thickness δ_j of layer j and its thermal conductivity λ_j it is

$$\frac{1}{\varphi} = 1 + k_0 A \sum_{j=1}^{n} \left(\frac{\delta}{\lambda A_m} \right)_j . \tag{29}$$

The thermal conductivities of some protective coatings and fouling layers are listed in Table 2. The corresponding figures for materials of construction and insulation are presented in Chap. D6, and for various forms of fouling in Chap. C4.

C2. Table 2. Thermal conductivity in W/m K at room temperature

Protective coatings		Fouling
Tin 65	Oppanol (polyisobutylene) 0.2–0.35	Scale, high-gypsum 0.6–2.3
Lead 35		Scale, high-silicate 0.08–0.18
Glass 0.76–0.84	Acid-resistant bricks ≈ 1.2	Soot, dry 0.035–0.07
Vitreous silica 1.34		Coal dust, dry 0.11
Enamel 0.9–1.2	Carbon bricks 1.6–4.7	Ice 1.75–2.3
Rubber 0.15–0.17	Porcelain 1.7–3.5	Slime from cooling water ≈ 0.35
Asphalt 0.76	Salting ≈ 0.6	
Igelit (PVC film) 0.16		Slime from brine ≈ 0.46

8 Symbols

Symbol	Description	Unit
F	logarithmic mean temperature difference correction factor (C1 Eq. (23))	-
n	number of layers or of reference points	-
NTU	number of transfer units (C1 Eqs. (11) and (12))	-
P	dimensionless temperature change (C1 Eqs. (9) and (10))	-
R	heat capacity rate ratio (C1 Eqs. (13) and (14))	-
R_w	wall resistance	m^2 K/W
$\dot{W}$	heat capacity flow rate (C1 Eq. (6))	W/K
δ	thickness	m
ϑ	temperature	K
Subscripts		
1, 2	stream 1 or 2 in the heat exchanger or j = 1, 2, 3 for reference points	
a, b	ends of the heat exchanger	
L	on the laminar flow or length effect side	
w	wall	
z	intermediate value	
Superscripts		
$'$	at the inlet	
$''$	at the outlet	

9 Bibliography

1. Roetzel W (1977) Iteration-free calculation of heat transfer coefficients in heat exchangers. Chem Eng J 13(3):233–237.
2. Spang B, Roetzel W (1992) Test of a thermal design method considering variable transfer coefficients and heat capacities for cross-flow arrangements. Heat Transfer, 3rd UK Natnl. Conf. Incorp. 1st Europ. Conf. Thermal Sciences, IChemE Symp. Ser. No. 129, Vol. 1, pp. 435–442
3. Roetzel W, Spang B (1987) Analytisches Verfahren zur thermischen Berechnung mehrgängiger Rohrbündelwärmeübertrager. Fortschr.-Ber. VDI, Reihe 19, No. 18, VDI-Verlag, Düsseldorf
4. Roetzel W (1988) Analytische Berechnung von Wärmeübertragern mit nachträglicher Berücksichtigung temperaturabhängiger Wärmekapazitäten. Wärme- und Stoffübertragung 23:175–177
5. Roetzel W (1969) Berücksichtigung veränderlicher Wärmeübergangskoeffizienten und Wärmekapazitäten bei der Bemessung von Wärmeaustauschern. Wärme- und Stoffübertragung 2:163–170
6. Peters DL (1970) Heat exchanger design with transfer coefficients varying with temperature or length of flow path. Wärme- und Stoffübertragung 3:222–226
7. Roetzel W (1974) Heat exchanger design with variable transfer coefficients for cross-flow and mixed flow arrangements. Int. J. Heat Mass Transfer 17:1037–1049

8. Roetzel W, Luo X (2008) Mean overall heat transfer coefficient in heat exchangers allowing for temperature dependent fluid properties. Paper RW1 in: Proc. 6th Int. Conf. On Heat Transfer, Fluid Mechanics and Thermodynamics, HEFAT 2008, Pretoria, South Africa, 30 June–2 July 2008, CD ROM, ISBN 978–1–86854–691–6. An extended and revised version is accepted for publication in Heat Transfer Engineering.
9. Roetzel W (1973) Calculation of single phase pressure drop in heat exchangers considering the change of fluid properties along the flow path. Wärme- und Stoffübertragung 6:3–13
10. Shah RK, Sekulic DP (1998) Nonuniform heat transfer coefficients in conventional heat exchanger design theory. ASME J Heat Transfer 119:520–525
11. VDI-Wärmeatlas, 10. Auflage, Springer-Verlag, Berlin Heidelberg, 2006
12. Colburn AP (1933) Mean temperature difference and heat transfer coefficient in liquid heat exchangers. Ind Eng Chem 25:873–877

C3 Typical Values of Overall Heat Transfer Coefficients

Wilfried Roetzel[1] · *Bernhard Spang*[2]
[1]Helmut-Schmidt-Universität, Universität der Bundeswehr Hamburg, Hamburg, Germany
[2]BUCO Wärmeaustauscher International GmbH, Geesthacht, Germany

1 Introduction

The empirical values listed below are intended for the preliminary design of heat exchangers. The lower values apply to comparatively adverse conditions, e.g., low flow velocities, viscous liquids, free convection, and fouling. The higher values are valid for particularly favorable conditions, e.g., high flow velocities, thin fluid layers, optimum mass flow ratios, and clean surfaces. In special cases, values may fall below or exceed the given range. Therefore, the figures must be regarded critically and with the necessary caution. The given k values do not take additional heat conduction resistances of insulation and protective coatings into account.

Type of exchanger	Conditions of heat transfer	Typical k value (W/m^2 K)
Shell-and-tube heat exchanger 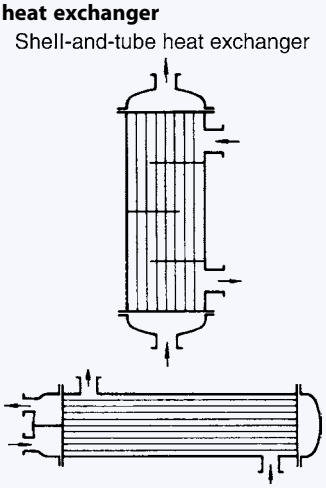	Gas (≈1 bar) on tube side and gas (≈1 bar) on shell side	5–35
	High-pressure gas (200–300 bar) on shell side and high-pressure gas (200–300 bar) on tube side	150–500
	Liquid on shell side (tube side) and gas (≈1 bar) on tube side (shell side)	15–70
	High-pressure gas (200–300 bar) on tube side and liquid on shell side	200–400
	Liquid on shell and tube sides	150–1,200
	Heating steam on shell side and liquid on tube side	300–1,200
	See below for use as evaporator or condenser	
Evaporator 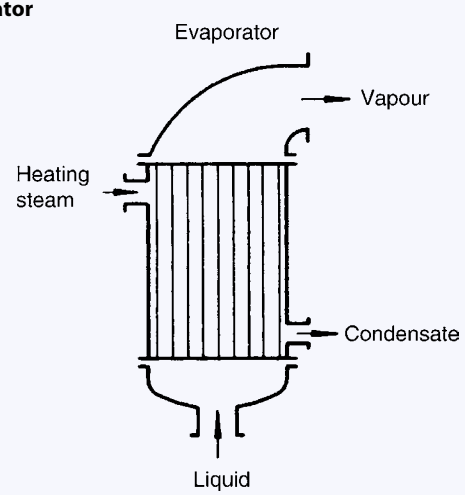	Heating steam outside the tubes	
	1. With natural circulation	
	(a) Viscous liquids	300–900
	(b) Low viscosity liquids	600–1,700
	2. With forced circulation	900–3,000
	Brine-heated ammonia evaporator	200–800

continued

VDI-GVC (ed.), *VDI Heat Atlas*, DOI 10.1007/978-3-540-77877-6_6,

Type of exchanger	Conditions of heat transfer	Typical k value (W/m^2 K)
Condenser 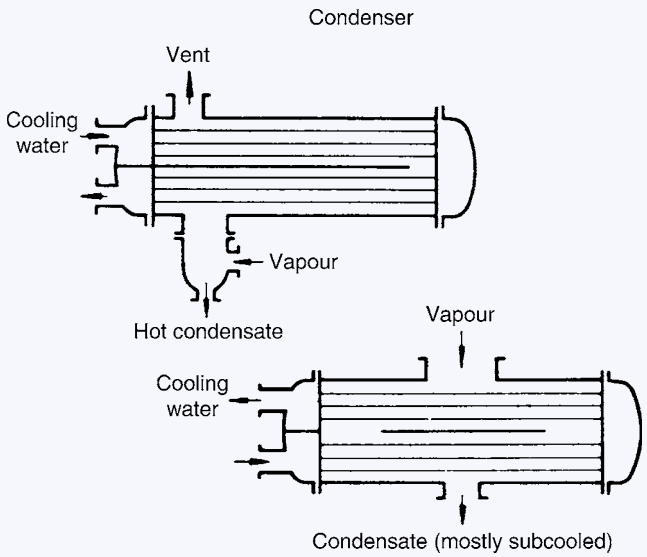	Cooling water on tube side and organic vapors or ammonia on shell side	300–1,200
	Steam-turbine condenser (pure steam; thin brass tubes) k decreases with an increase in the inert gas fraction	1,500–4,000
Waste-heat boiler 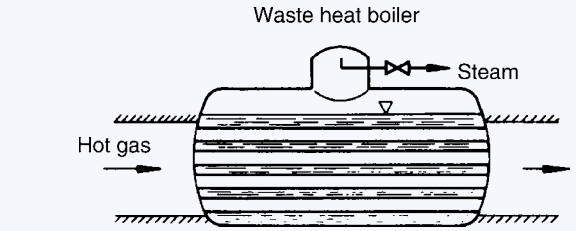	Hot gas on tube side and boiling water on shell side	15–50
Gas heater 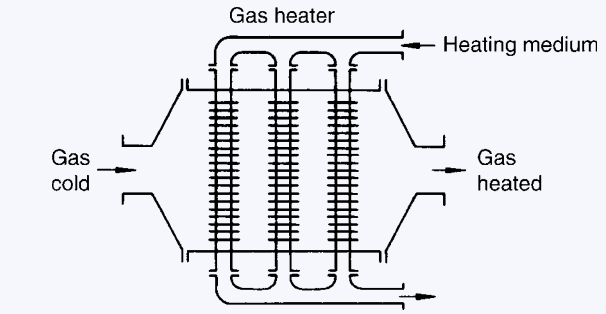	Steam or hot water on (finned) tube side and gas outside finned tubes	
	(a) Free convection (heater)	5–12
	(b) Forced flow	12–50
Double-pipe heat exchanger 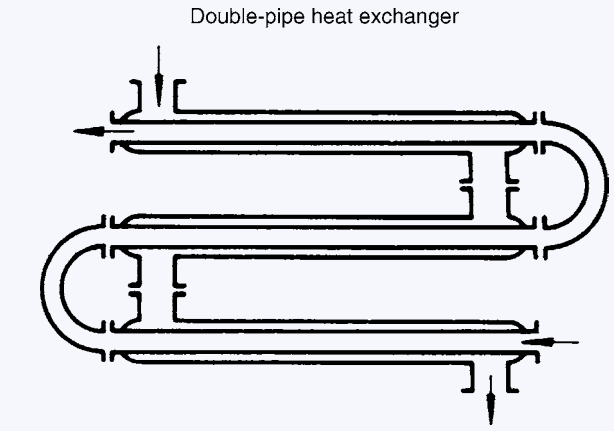	Gas (≈1 bar) on tube side and gas (≈1 bar) on shell side	10–35
	High-pressure gas (200–300 bar) on tube side and gas (≈1 bar) on shell side	20–60
	High-pressure gas (200–300 bar) on tube side and high-pressure gas (200–300 bar) on shell side	150–500
	High-pressure gas (200–300 bar) on tube side and liquid on shell side	200–600
	Liquid on shell and tube sides	300–1,400

continued

Type of exchanger	Conditions of heat transfer	Typical k value (W/m^2 K)
Falling-film cooler 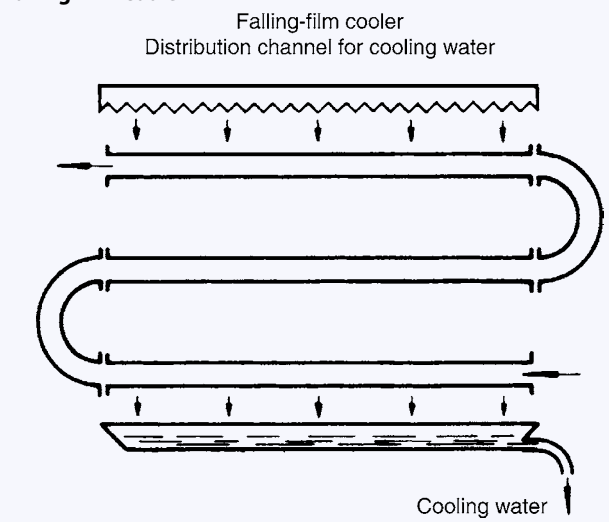 	Cooling water on shell side and gas (≈1 bar) on tube side	20–60
	Cooling water on shell side and high-pressure gas (200–300 bar) on tube side	150–350
	Cooling water on shell side and liquid on tube side	300–900
	Falling-film condenser, e.g., for refrigerants: cooling water outside and condensing vapor inside tubes	300–1,200
Helical coil heat exchanger 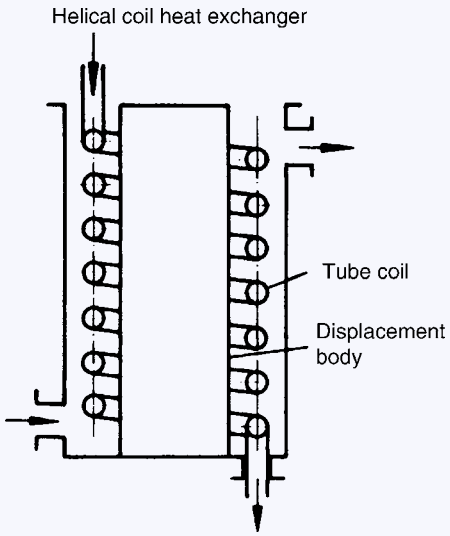 	Cooling water or brine outside and gas (≈1 bar) inside the coils	20–60
	Cooling water outside and high-pressure gas (200–300 bar) inside the coils	150–500
	Cooling water or brine outside and liquid inside the coils	200–700
	Cooling water or brine outside and condensing vapor inside the coils	350–900
Plate heat exchanger 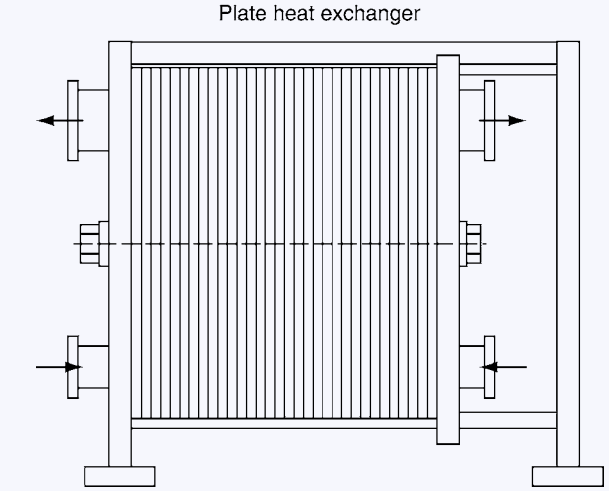 	Flat channels, gas to water	20–60
	Flat channels, liquid to water	350–1,200
	Corrugated plates, liquid to liquid	1,000–4,000

continued

Type of exchanger	Conditions of heat transfer	Typical k value (W/m^2 K)
Compartmental heat exchanger Compartmental heat exchanger 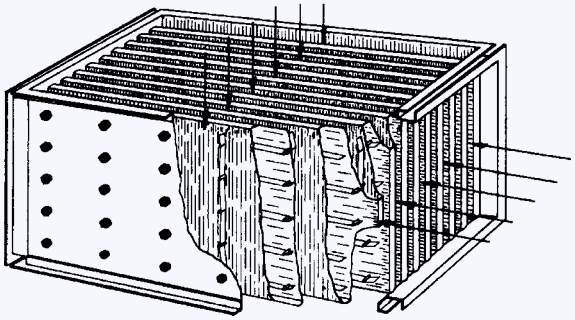	Gas to gas (≈1 bar)	10–35
	Gas to liquid	20–60
Spiral plate heat exchanger Spiral heat exchanger 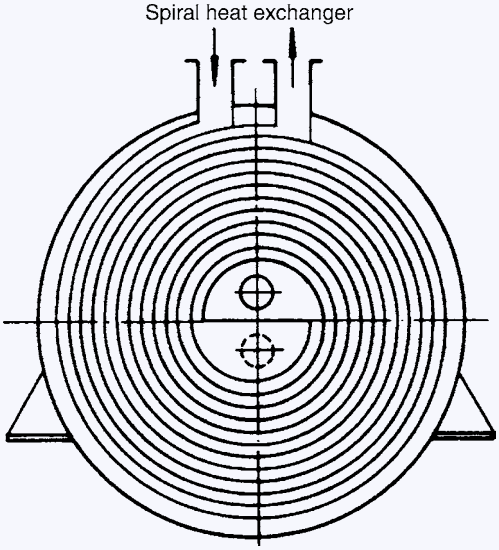	Liquid to liquid	700–2,500
	Condensing vapor to liquid	900–3,500
Stirred tank 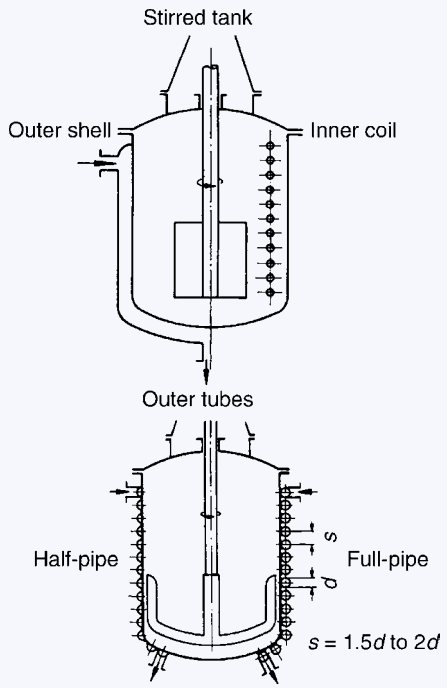	(A) Outer shell	
	Condensing vapor outside and liquid inside the tank	500–1,500
	Condensing vapor outside and boiling liquid inside the tank	700–1,700
	Cooling water or brine outside and liquid inside the tank	150–350
	(B) Inner coil	
	Condensing vapor inside the coils and liquid inside the tank	700–2,500
	Condensing vapor inside the coils and boiling liquid inside the tank	1,200–3,500
	Cooling water or brine inside the coils and liquid inside the tank	500–1,200
	(C) Outer tube welded onto shell	
	Condensing vapor inside the heating channels and liquid inside the tank	500–1,700
	Condensing vapor inside the heating channels and boiling liquid inside the tank	700–2,300
	Cooling water or brine inside the cooling channels and liquid inside the tank	350–900

C4 Fouling of Heat Exchanger Surfaces

Hans Müller-Steinhagen
Universität Stuttgart, Stuttgart, Germany

1 Introduction

In most industrial processes, heat exchanging fluids contain certain amounts of dissolved or suspended material or provide conditions favorable for the growth of biological organisms. Design and operation of heat exchangers are still to a major extent determined by the process-related formation of deposits on the heat transfer surfaces, i.e., fouling. Since the thermal conductivity of such deposits is low, see Table 1, their resistance to heat transfer may well exceed that of the clean fluids, resulting in significantly reduced heat exchanger performance.

As a result, substantial safety margins in the design, pretreatment of hot/cold fluids and regular cleaning of equipment may be required.

VDI-GVC (ed.), *VDI Heat Atlas*, DOI 10.1007/978-3-540-77877-6_7,

C4. Table 1. Thermal conductivity of various deposits

Sodium aluminum silicate	0.2–0.4 W/mK
Milk components	0.5–0.7 W/mK
Hematite (boiler deposit)	0.6 W/mK
Biofilm	0.7 W/mK
Calcium sulfate (boiler)	0.8–2.2 W/mK
Calcite (boiler deposit)	0.9 W/mK
Serpentine (boiler deposit)	1.0 W/mK
Gypsum (boiler deposit)	1.3 W/mK
Calcium sulfate	2.3 W/mK
Magnesium phosphate	2.3 W/mK
Calcium phosphate	2.6 W/mK
Calcium carbonate	2.9 W/mK
Magnetite iron oxide	2.9 W/mK

Surveys [1–3] have indicated that more than 90% of heat exchangers suffer from fouling problems. Table 2 identifies the kind and typical extent of fouling for fluids from various industries [39]. More information about research and industrial fouling problems may be found under www.heatexchanger-fouling.com.

1.1 The Fouling Resistance

The possibility of deposition on heat transfer surfaces is generally considered in the design of heat exchangers by using the so-called fouling resistances in the calculation of the overall heat transfer coefficient k.

$$\frac{1}{k} = \left(\frac{1}{\alpha_1} + R_{f,1}\right)\frac{A_2}{A_1} + R_{wall} + \frac{1}{\alpha_2} + R_{f,2} \qquad (1)$$

In Eq. (1), α, A, and R_f are the heat transfer coefficients, the heat transfer areas and the fouling resistances, respectively, for the two heat exchanging fluids; R_{wall} is the thermal resistance of the separating wall. It is obvious that the frequently used expression "fouling factor" is incorrect, as the effect of fouling is to create an additional thermal resistance. The fouling resistance reduces the overall heat transfer coefficient k, and hence leads to the reduction of heat duty of an existing heat exchanger or to additional surface requirement in the design of new heat exchangers.

In the utility industry, it is common to use the cleanliness factor CF

$$CF = \frac{k_f}{k_c} \qquad (2)$$

instead of the fouling resistance R_f, where CF is a function of tube material, flow velocity, and fouling propensity of the cooling water. Typically, cleanliness factors are adding less excess surface and are, hence, more realistic than fouling resistances. However, this purely empirical ratio of overall heat transfer coefficients for fouled and dirty conditions does not provide any access to the understanding of the mechanisms of deposit formation and hence the potential effects of operating conditions.

The main source of publicly available fouling resistances are the approximately 100 values suggested by the Tubular Exchanger Manufacturers Association (TEMA) [4], which are reproduced in Tables 3–5. Although the TEMA tables were originally considered to be only a rough guideline for shell-and-tube heat exchanger design, they are unfortunately often treated as accurate values. This may cause considerable errors because

1. The values were developed in 1949 and were based on hand calculation procedures for heat exchanger design in use at the time. Even though calculation methods have evolved, the values presented by TEMA have not been altered since its publication.
2. Fouling resistances are included for a number of fluids that are known not to foul, such as refrigerants, demineralized water, liquefied natural gas (LNG) and non-polymerizing (diolefin-free) condensing gases, or any other streams which do not foul within the operating conditions of the heat exchanger.
3. R_f values in the tables tend to be used without adequate engineering, resulting in exchangers that are much larger

C4. Table 2. Fouling of heat exchangers in various industries [3]

Industry group	Type of fouling	Extent of problem
Food and kindred products	Chemical reaction	Major
	Crystallization	Major
	Biological	Medium
	Particulate	Minor/Major
	Corrosion	Minor
Textile mill products	Particulate	
	Biological	
Wood and paper products	Crystallization	Major
	Particulate	Minor
	Biological	Minor
	Chemical reaction	Minor
	Corrosion	Medium
Chemical and allied industries	Crystallization	Medium
	Particulate	Minor/Medium
	Biological	Medium
	Chemical reaction	Minor/Major
	Corrosion	Medium
Petroleum refineries	Chemical reaction	Major
	Crystallization	Medium
	Particulate	Minor/Medium
	Biological	Medium
	Corrosion	Medium
Tone, glass, concrete	Particulate	Minor/Major
Electricity generation	Biological	Major
	Crystallization	Medium
	Particulate	Major
	Freezing	Major
	Corrosion	Minor

C4. Table 3. TEMA fouling resistances for water (m^2K/kW) [4]

Temperature of heating medium	Up to 115 °C		115–200 °C	
Temperature of water	50 °C		Over 50 °C	
	Water velocity m/s		Water velocity m/s	
	1.0 and less	Over 1.0	1.0 and less	Over 1.0
Cooling tower and artificial spray pond				
Treated make up	0.088	0.088	0.17	0.17
Untreated	0.35	0.17	0.53	0.35
City or well water	0.17	0.17	0.35	0.35
River water				
Minimum	0.35	0.17	0.53	0.35
Average	0.53	0.35	0.70	0.53
Muddy or silty	0.53	0.35	0.70	0.53
Hard (over 250 ppm)	0.53	0.53	0.88	0.88
Engine jacket	0.17	0.17	0.17	0.17
Distilled or closed cycle				
Condensate	0.088	0.088	0.088	0.088
Treated boiler feedwater	0.17	0.088	0.17	0.17
Boiler blowdown	0.35	0.35	0.35	0.35
Seawater	0.09	0.09	0.18	0.18
Brakish water	0.35	0.18	0.54	0.35

than required. For example, Fig. 1 includes a summary of the percent overdesign of all cases submitted to HTRI in 2006. As can be seen from the figure, most exchangers are 50–500% too large, based primarily on the assumed fouling resistances. This results in unnecessary capital expense and exchangers that foul due to poor design.

4. R_f values are only available for a limited number of process fluids and process conditions.
5. Tabulated R_f values provide only limited information about the influence of process parameters such as flow velocity, fluid, and wall temperature on the fouling resistance. These parameters have a considerable influence on the deposition of foulants matter onto the heat transfer surface.
6. Using constant fouling resistances, the transient character of the fouling process is ignored. Conditions in the initially overdesigned heat exchanger often promote deposition, thus making fouling a self-fulfilling prophecy.
7. The TEMA values do not apply for heat exchanger types other than conventional shell and tube heat exchangers, e.g., plate heat exchangers, compact heat exchangers or finned tubes. Some fouling resistances for other heat exchanger types are given in Tables 6–8.

To demonstrate the significance of the selected fouling resistance on the sizing of heat exchangers, Table 9 shows the excess heat transfer surface required for several heat exchanger types, if a typical TEMA fouling resistance of 0.18 m^2K/kW is used for each of the two heat exchanging fluids. As shown in the following

C4. Table 4. TEMA fouling resistances for oil refinery streams in shell-and-tube exchangers, (m^2K/kW) [4]

Crude and vacuum unit gases and vapors						
Atmospheric tower overhead vapors	0.18					
Light naphthas	0.18					
Vacuum overhead vapors	0.35					
Crude and vacuum liquids						
Crude oil						
	0–120 °C			120–175 °C		
	Velocity (m/s)			Velocity (m/s)		
	<0.6	0.6–1.2	>1.2	<0.6	0.6–1.2	>1.2
Dry	0.53	0.35	0.35	0.53	0.35	0.35
Salt[a]	0.53	0.35	0.35	0.88	0.70	0.70
	175–230°C			230°C and over		
	Velocity (m/s)			Velocity (m/s)		
	<0.6	0.6–1.2	>1.2	<0.6	0.6–1.2	>1.2
Dry	0.70	0.53	0.53	0.88	0.70	0.70
Salt[a]	1.1	0.88	0.88	1.2	1.1	1.1
[a]Assumes desalting at approximately 120°C						
Gasoline	0.35					
Naphtha and light distillates	0.35–0.53					
Kerosene	0.35–0.53					
Light gas oil	0.35–0.53					
Heavy gas oil	0.53–0.88					
Heavy fuel oils	0.88–1.2					
Asphalt and residuum						
Vacuum tower bottoms	1.8					
Atmosphere tower bottoms	1.2					

equation, the percentage excess surface area for a fixed heat duty increases with increasing clean heat transfer coefficient.

$$\frac{A_f}{A_c} = 1 + k_c R_f \tag{3}$$

Obviously, the impact of the fouling resistance is more severe for heat exchangers with high overall heat transfer coefficients.

To account for unreliable design procedures and operational problems, heat exchangers are typically overdesigned by 70–80%, from which 30–50% is attributed to fouling [8]. While the installation of excess heat transfer surface may extend the operation time of heat exchangers, it provides no remedy against the deposition of dirt. Fluid pretreatment, antifouling installations, and regular cleaning will still be required in most cases. Industrial practice and state of the art of such fouling mitigation and of heat exchanger cleaning are outlined in this chapter.

1.2 Mechanisms of Heat Exchanger Fouling

Because of the great variety of fouling mechanisms it is useful to divide fouling according to the key physical/chemical processes into five major categories:

1. Crystallization Fouling
   - Precipitation and deposition of dissolved salts, which at process conditions become supersaturated at the heat

C4. Table 5. Fouling resistances for various processing streams in shell-and-tube exchangers, (m^2K/kW)

Hydrocarbons	Fuel oil no.2	0.35
	Fuel oil no.6	0.88
	Transformer oil	0.18
	Lube oil	0.18
	Hydraulic oil	0.18
	Quench oil	0.7
	Pitch	0.8
	Tar	0.9
	Vegetable oil	0.53
Gases and vapors	Steam (oil free)	0.0
	Steam (oil contaminated)	0.18
	Refrigerant vapor (oil contaminated)	0.35 0.0
	Alcohol vapor	0.09
	Organic vapor	0.18
	Ammonia	0.35
	Carbon dioxide	0.18
	Combustion gas (coal)	0.18–0.35
	Combustion gas (natural gas)	1.8
	Diesel exhaust gas	1.8
	Synthesis gas	0.18–0.35
	Compressed air	0.18
	Natural gas	0.18–0.35
	Nitrogen	0.18–0.35
	Stabil column overhead product	
Liquids	Refrigerant	0.10–0.18
	Organic heat transfer liquid	0.18–0.35
	Ammonia (oil free)	0.18
	Ammonia (oil contaminated)	0.53
	Methanol solution	0.35
	Ethanol solution	0.35
	Glycol solution	0.35
	LPG, LNG	0.18–0.35
	MEA- and DEA solution	0.35
	DEG- and TEG solution	0.35
	Stable column side stream	0.18–0.35
	Stable column bottom stream	0.18–0.35
	Caustic solutions	0.35
	Black liquor	0.7–1.4

transfer surface. Supersaturation may be caused by the following processes:

(a) Evaporation of solvent
(b) Cooling below solubility limit for solution with normal solubility, e.g., increasing solubility with increasing temperature
(c) Heating above the solubility limit for solutions with inverse solubility such as $CaCO_3$, $CaSO_4$, $Ca_3(PO_4)_2$, $CaSiO_3$, $Ca(OH)_2$, $Mg(OH)_2$, $MgSiO_3$, Na_2SO_4, Li_2SO_4, and Li_2CO_3 in water
(d) Mixing of streams with different composition
(e) Variation of pH which affects the solubility of CO_2 in water
(f) Solidification fouling due to cooling below the solidification temperature of a dissolved component (e.g., solidification of wax from crude oil streams)

2. Particulate Fouling
   - Deposition of small suspended particles such as clay, silt, or iron oxide on heat transfer surfaces of any orientation
   - Gravitational settling of relatively large particles onto horizontal surfaces
3. Chemical Reaction Fouling

   Deposit formation at the heat transfer surface by a chemical reaction in which the surface material itself does not participate (polymerization, food processing).
4. Corrosion Fouling

   The thermal resistance of corrosion layers is usually low because of the relatively high thermal conductivity of oxides. However, the increased surface roughness may promote fouling due to other fouling mechanisms.
5. Biological Fouling

   Biological fouling refers to the development and deposition of organic films consisting of microorganisms and their products such as bacteria (microbial or micro-biofouling) and the attachment and growth of macro-organisms such as mussels, algae, etc. (macro-biofouling) on the heat transfer surfaces. Microbial fouling always precedes fouling by macro-organisms, with the microorganisms acting as the nutrient source for the macro-organisms. Suspensions of seaweed and other organic fibres often cause fouling. Many types of bacteria will deposit slime on the heat transfer surfaces and other types of foulants can adhere to these deposits. Larger growth restricts the fluid flow and often causes pitting of the metal. This type of fouling is common in untreated water such as sea, river, or lake water. Microbiological fouling is a particularly serious problem as the microbes may be introduced into the water cycle not only by the fluid, but also from the ambient air in the cooling tower. Temperatures between 15°C and 50°C in cooling towers are ideal for microbial growth. Both dead and alive microorganisms adhere to the heat transfer surfaces and form a layer of slime with a thermal conductivity similar to that of water. As a consequence of the filtering effect of biological layers, more suspended particles amass in the deposit.
6. Mixed Fouling

   Fouling mechanisms within each category may be described with similar models. Generally, several fouling mechanisms occur at the same time, nearly always being mutually reinforcing. Exceptions are the combination of crystallization and particulate fouling, where particles of the crystallizing matter accelerate fouling, whereas particles from other material may lead to reduced fouling due to a weakening of the deposit structure [9].

Figures 2 and 3 show typical effects of surface temperature and flow velocity on most of the above fouling mechanisms.

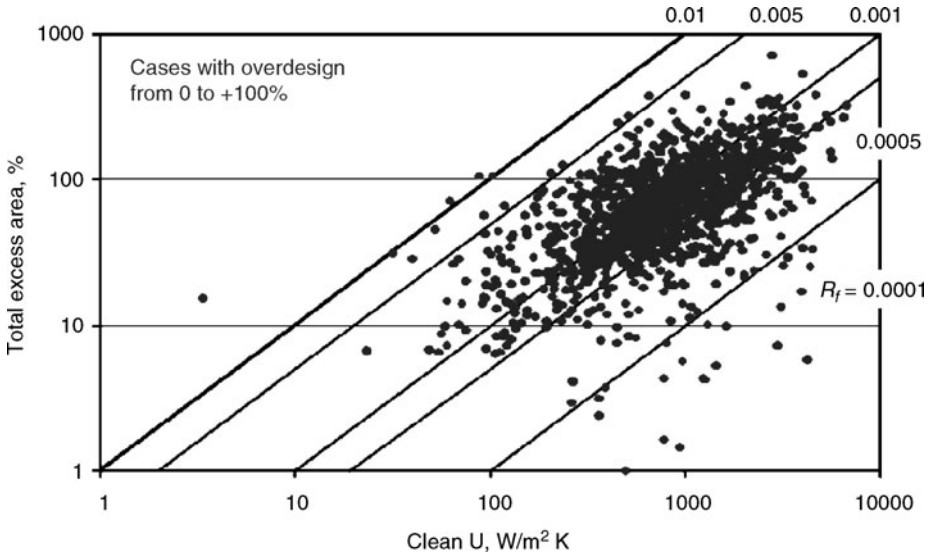

C4. Fig. 1. Impact of fouling resistance on 2000 shell and tube heat exchangers designed from 2003–2008

1.3 Sequential Events of Fouling

The above fouling mechanisms generally occur in five consecutive steps:

(i) *Initiation Period or Delay Period*

When the new or cleaned heat exchanger has been taken into operation, the initially high heat transfer coefficients may remain unchanged for a certain time. During this time, nuclei for crystallization are formed or nutrients for biological growth are deposited. This delay period may last anytime from few seconds to several days. According to [10], no delay period occurs for particulate fouling. For crystallization fouling and for chemical reaction fouling, the initiation period decreases with increasing surface temperature, as supersaturation and/or reaction rate increase [11]. Generally, it is reported that the delay time, before deposition starts, decreases with increasing roughness of the heat transfer surface.

(ii) *Mass Transport*

To form a deposit at the heat transfer surface it is necessary that at least one key component is transported from the fluid bulk to the heat transfer surface. In most cases, this occurs by diffusion. For the transport of particles to the wall, inertia effects and thermophoretic forces have to be considered, as well.

(iii) *Formation of Deposit*

After the foulant has been transported to the heat transfer surface, it must stick to the surface (for particulate fouling) or react to the deposit forming substance (e.g., $CaCO_3$).

(iv) *Removal or Auto-Retardation*

Depending on the strength of the deposit, erosion occurs immediately after the first deposit has been laid down. Furthermore, several mechanisms exist, which cause auto-retardation of the deposition process. For the thermal boundary condition of constant temperature difference between heated and cooled fluid, the growth of deposit causes a reduction of the driving temperature difference between heat transfer surface and fluid.

C4. Table 6. Fouling resistances in plate and frame heat exchangers, (m^2K/W) [5]

Fluid	Fouling resistance (m^2K/kW)
Water	
Demineralized or distilled	0.009
Soft	0.017
Hard	0.043
Treated cooling tower water	0.034
Coastal sea water	0.043
Ocean sea water	0.026
River water	0.043
Engine jacket	0.052
Lube oil	0.017–0.043
Vegetable oil	0.017–0.052
Organic solvents	0.009–0.026
Steam	0.009
General process fluids	0.009–0.052

(v) *Aging*

Every deposit is subjected to aging. Aging may increase the strength of the deposit by polymerization, recrystallization, dehydration, etc. Biological deposits get poisoned by metal ions and may be washed away by the bulk flow. Aging is the least investigated and understood step and is usually ignored in modelling attempts.

Depending on the process parameters and the dominant fouling mechanism, the fouling rate can be either constant or decreasing with time (see Fig. 4).

For hard, adherent deposits such as silicates and some polymerization products, steps iv and v may be ignored and the growth rate of deposits is constant or continuously decreasing with time. For weaker deposits (e.g., particles >1 μm), the fouling resistance approaches a constant (or asymptotic) value which may or may not allow acceptable operation of the process.

C4. Table 7. Fouling resistances for combustion gases on finned surfaces (m^2K/W) [6]

Fuel	Fouling resistance (m^2K/kW)	Flow velocity m/s
Natural gas	0.09–0.53	30–40
Propane	0.18–0.53	25–30
Butane	0.18–0.53	18–24
Clean turbine gas	0.18	15–21
Moderately clean turbine gas	0.27–0.5	
Light oil	0.36–0.7	
Diesel oil	0.53	
Heavy oil	0.53–1.24	
Crude oil	0.7–2.7	
Coal	0.89–8.85	

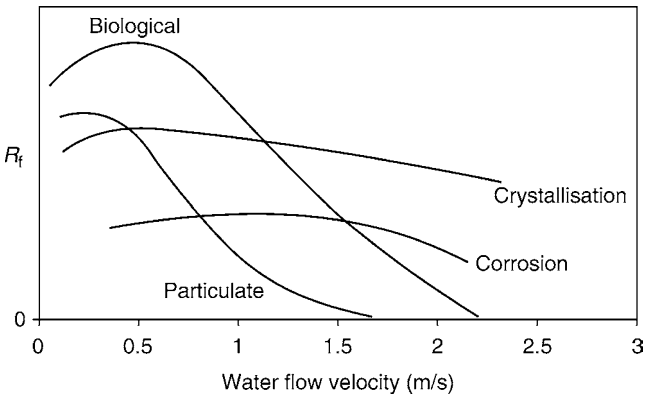

C4. Fig. 2. Effect of flow velocity on the fouling resistance for flow of water

C4. Table 8. Fouling resistances in evaporators, (m^2K/W) [7]

	Fouling resistance (m^2K/kW)
Boiling medium	
Hydrocarbon C_1–C_4	0–0.18
Higher hydrocarbons	0.18–0.5
Olefins and polymerizing hydrocarbons	0.5–0.9
Heating medium	
Condensing steam	0–0.09
Condensing organic vapor	0.09–0.18
Organic liquid	0.09–0.052

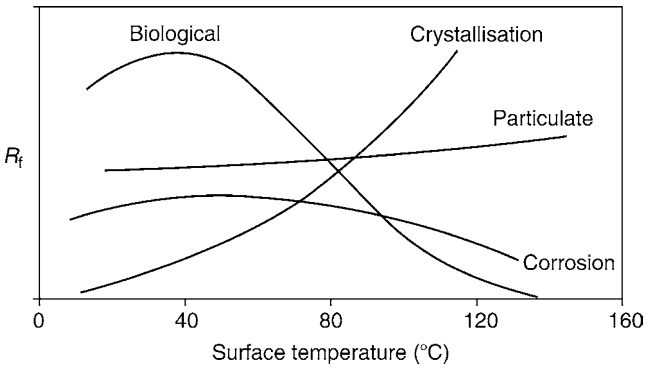

C4. Fig. 3. Effect of surface temperature on the fouling resistance for flow of water

C4. Table 9. Excess surface area for various heat exchanger applications, R_f = 0.36 m^2K/kW

Application	Clean overall coefficient	Excess area
Gas/gas shell & tube heat exchanger	50 W/m^2K	1.8%
Liquid/gas shell & tube heat exchanger	150 W/m^2K	5.4%
Liquid/liquid shell & tube heat exchanger	1000 W/m^2K	36%
Liquid/liquid plate & frame heat exchanger	3000 W/m^2K	108%
Water-cooled shell & tube steam condenser	4500 W/m^2K	162%

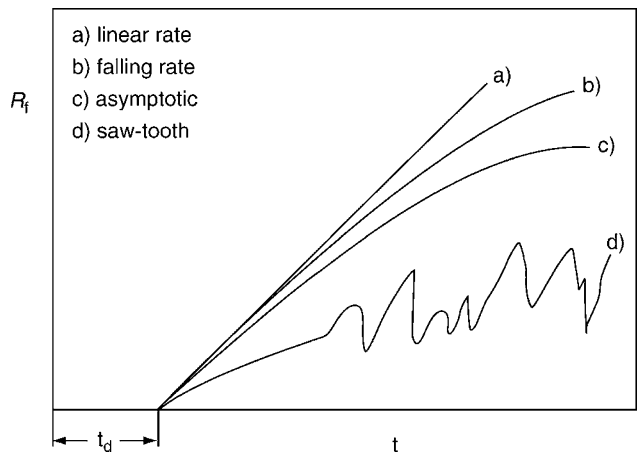

C4. Fig. 4. Possible fouling resistance versus time curves

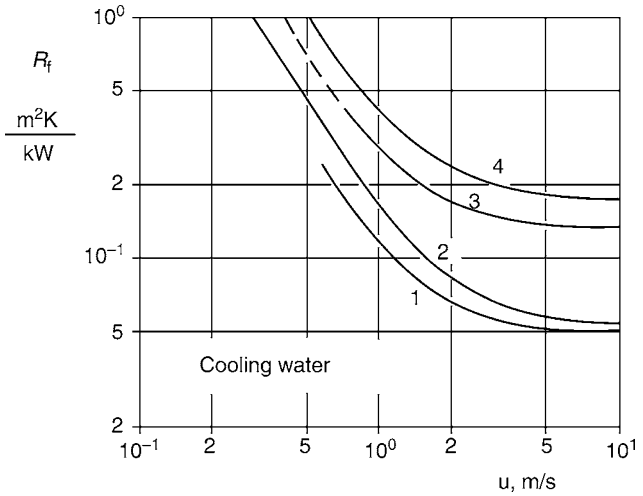

C4. Fig. 5. Fouling resistance in shell and tube heat exchangers as a function of flow velocity and water quality [13]. Water quality decreasing from 1 to 4

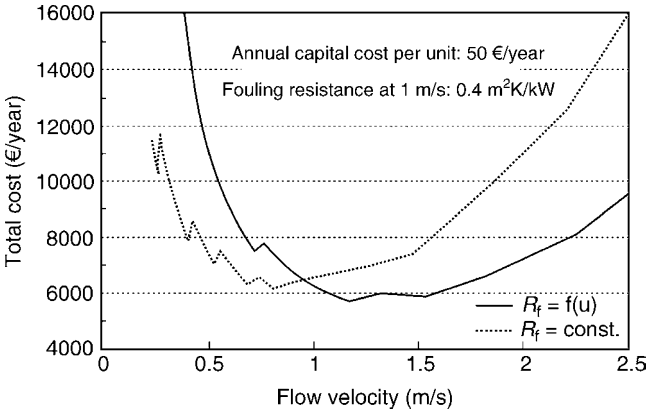

C4. Fig. 6. Total annual costs of a double pipe heat exchanger arrangement as a function of the flow velocity

1.4 Approximate Influence of Operating Conditions on Fouling in Industrial Heat Exchangers

Many correlations have been recommended for the prediction of individual fouling mechanisms [12]. However, these correlations are generally not applicable to industrial conditions where a combination of fouling mechanisms and foulants occurs. Comparing fouling data from a range of industries, the following approximate influence of process parameters on industrial fouling has been found:

(a) Fouling usually increases linearly with increasing foulant concentration in the fluid bulk.
(b) The fouling resistance nearly always decreases with increasing wall shear stress due to increased removal forces. As an average, it was found that the fouling resistance is proportional to the flow velocity to the power of −1.5. Figure 5 shows the effect of dirt content and of flow velocity on the fouling resistance for cooling water [13].
(c) For many fouling mechanisms, the fouling resistance increases with increasing surface temperature (see e.g., Fig. 3). For crystallization and chemical reaction fouling, this trend frequently follows an Arrhenius relationship

$$\frac{dR_f}{dt} = Ke^{-E/RT_S} \quad (4)$$

For biological fouling, a maximum is observed for temperatures around 35°C.
(d) Fouling was found to increase with increasing roughness of the heat transfer surface.

To date, not even these simple rules are considered in the design of heat exchangers, even though they could significantly improve some heat exchanger optimization procedures. This is demonstrated in Fig. 6, which shows the sum of annual operating and capital service costs of an arrangement of multiple double pipe heat exchangers as a function of the flow velocity in the pipes. One curve has been calculated according to Martin [14] for a constant fouling resistance, the second is for the case where the fouling resistance is velocity dependent as suggested above. The optimum flow velocity shifts from 0.8 to about 1.3 m/s and the total annual costs are reduced by 10% despite the higher friction losses.

1.5 Costs due to Heat Exchanger Fouling

Despite the enormous costs associated with heat exchanger fouling, only very limited research has been done to determine accurately the economic penalties due to fouling and to attribute these costs to the various aspects of heat exchanger design and operation. However, reliable knowledge of fouling economics is desirable to evaluate the cost-efficiency of various mitigation strategies. The total fouling related costs consist of

1.5.1 Capital Expenditure

According to Thackery [15], total capital cost due to fouling in England added up to £100 million in 1978, which corresponds to US$190 million. For the United States, Garrett-Price et al. found that capital costs excluding costs for antifouling equipment were US$960–280 million in 1982 [3].

(a) Excess Heat Transfer Surface Area

Thackery [15] found that design excess surface area for fouling varies between 10–500%, with an average around 30%. This result was confirmed by Garrett-Price et al. [3], who obtained a similar value for the USA and by Steinhagen et al. for New Zealand [2]. Investigations by Heat Transfer Research Inc. and TEMA among the major North American heat exchanger manufacturers showed excess surface areas between 11% and 67% [8].

Excess area of 30–40% may correspond to 25% additional capital cost. To estimate the absolute costs of excess heat transfer area in the United Kingdom, Pritchard [16] took the value of

the process plant built in the UK. As much as 6.5% of the process plant hardware consisted of heat exchangers. If each heat exchanger has 30–40% extra surface area to allow for fouling, he concluded that additional costs were £5 million in 1968 and £20 million in 1977. The corresponding American figure is $US320 million per year for 1982 [3].

(b) Transport and Installation Costs

As a result of additional surface area, heat exchangers become bigger and heavier. Therefore costs for stronger foundations, provisions for extra space, increased transport and installation costs must be considered. Woods et al. [17] assume that installation costs tend to increase with the size of the heat exchanger and are usually 2–3 times the delivered costs. Adding these extra costs to the costs for excess heat transfer surface may increase the costs for oversized equipment to $640–960 million per year [3].

(c) Capital Costs for Antifouling Equipment

These costs include expenses for online and off-line cleaning equipment, extra cost for providing non-fouling heat exchangers such as scraped surface or fluidized bed heat exchangers, pretreatment plants, cleaning-in-place equipment, dosing pumps and tanks for antifouling chemicals.

1.5.2 Fuel Costs

Costs for extra fuel only occur if fouling leads to extra fuel burning in furnaces or boilers or if more secondary energy such as electricity or process steam is needed to overcome the effects of fouling. Thackery [15] estimated additional UK fuel costs in 1978 as £100–200 million ($US290–480 million). Garrett-Price et al. [3] calculate that 1–5% of the energy consumed by the industrial sector is used to overcome fouling. The result leads to fouling related fuel costs between $US700 and $US3,500 million.

1.5.3 Maintenance Costs

Maintenance costs are costs for removing fouling deposits and costs for chemicals or other operating costs of antifouling devices. According to Pritchard [16] and Thackery [15], about 15% of the maintenance costs of process plant could be attributed to heat exchangers and boilers and of that 50% was probably due to fouling. Garrett-Price et al. [3] quote a figure of $US2,000 million for annual sales of companies supplying heat exchanger online and off-line cleaning equipment, chemicals, and cleaning services in the USA for 1982.

1.5.4 Costs due to Production Loss

Because of planned and unplanned plant shutdowns due to fouling in heat exchangers, large production losses are possible. These costs are often considered to be the main cost of fouling. For example: Sart and Eimer [18] state that the loss of production for 1 day shutdown of a 1300 MW power plant is about $US500,000; Taborek [13] estimates that shutdown losses of a large oil refinery are about $US1.5 million per day. In addition to production losses during plant shutdown and start-up, penalties for not keeping to a deadline and the loss of customers must be considered. Garrett-Price et al. [3] suggested that an upper limit for loss of production costs may be estimated by assuming that the loss of production has to be less than the cost of providing redundant exchangers. For the US in 1984, this would be $US200 million. According to Thackery, [15] 1978 costs due to production losses in the UK are about £100 million ($US190 million).

The above fouling-related costs will have to be inflated to current prizes. For crude oil heat exchangers, more recent information is available in [19].

2 Consideration of Fouling in the Design of Heat Exchangers

2.1 Preliminary Remarks

Not all heat exchangers have serious problems with fouling; many of them operate satisfactorily for long periods of time without being cleaned. If fouling is anticipated, however, some allowance must be provided in the design of a heat exchanger. Regardless of the approach, the selection of appropriate values still relies more on engineering judgement from past experience than on the application of results from experimental and theoretical research. It is important to keep in mind that heat exchanger fouling can be effectively mitigated at the design stage of the heat exchanger. To design for reliable operation,

(i) Select a suitable heat exchanger type
(ii) Try to avoid operating conditions which promote fouling
(iii) Attempt an optimum design with adequate velocities in the heat exchanger and which avoids hot spots, bypass flow or dead zones
(iv) Design for easy cleaning

Additional guidance is included in Sect. 3. Due to their frequent occurrence and economic importance, detailed best practice guidelines have been prepared by ESDU [19–21] for fouling in crude oil preheat exchangers, and for seawater and fresh water as

C4. Table 10. Reboiler selection guide [8]

Anticipated fouling	Kettle or internal boiler	Horizontal shell-side thermosyphon	Vertical tube-side thermosyphon	Forced flow
No fouling	Good	Good	Good	Expensive
Moderate	Risky	Good	Best	Expensive
Heavy	Poor	Risky	Best	Good
Very heavy	Poor	Poor	Risky	Best

cooling media. These reports present the state-of-the-art of fundamental aspects and industrial practice.

2.2 Selection of Heat Exchanger Type

If fouling will be significant, it may well control the selection of the type of heat exchanger and its size. This is very clearly demonstrated in Table 10, which recommends different reboiler types depending on the severity of fouling [7]. Other examples are:

- Shell and tube heat exchangers are not particularly suitable for fouling conditions; however, good design practices [22–26] and special baffle and tube design may be applied to reduce fouling.
- Plate and frame heat exchangers may be attractive as they can be disassembled for cleaning and sterilizing.
- Since there are no local low velocity regions in spiral plate heat exchangers, these heat exchangers perform well for fluids with a high concentration of suspended solids.
- Scraped heat exchangers improve the heat transfer by continuously removing deposit from the heat transfer surfaces with rotating blades.
- Fluidized bed heat exchangers can be used where the fluidized particles remove deposit from the embedded tubes.
- Direct contact heat transfer may be a suitable alternative.
- Highly compact heat exchangers are normally avoided for severe fouling conditions, as they are difficult to clean.

2.3 Material Selection

The second most important point is the proper selection of the heat exchanger material, as already minor corrosion may considerably increase other fouling mechanisms. In addition, the pipe material itself can also have an effect on fouling. For example, biofouling is reduced in brass tubing, as shown in Fig. 7 for seawater fouling [27], and crude oil fouling can be minimized by careful material selection [26].

Surface roughness increases the contact surface area such that the true contact area is much larger than the apparent surface area. As a result of this difference, stronger adhesion should occur on rough surfaces. This is confirmed by measurements with Kraft black liquor in electropolished tubes shown in Fig. 8 [28].

Surface coatings for reducing the adhesion of deposits on heat transfer surfaces have attracted increased interest in recent years. For example, organic materials such as PTFE and Säkaphen have indeed been shown to reduce fouling from various fluids, for example during seawater evaporation and heat transfer to Kraft black liquor. The main reason why such materials/coatings are not more widely used is that they are poor heat conductors and form an additional resistance to heat transfer which is comparable to the TEMA fouling resistance for cooling water. If very thin coatings were used, the resistance against erosion or other mechanical stress would be greatly diminished. These problems may be avoided with several novel coating methods, such as Ion Beam Implantation, Magnetron Sputtering, Multi-Arc Ion Plating, Filtered Cathodic Vacuum Arc Plating or electroless Ni-P-PTFE plating which have been investigated in recent years [29–33]. These thin and stable coatings have been found to reduce scale formation during convective and boiling heat transfer as well as the adhesion of bacteria.

2.4 Shell and Tube Heat Exchangers

Experience has shown that higher flow velocities and lower tube surface temperatures generally tend to reduce fouling. Therefore, arrangements that eliminate stagnant or low velocity regions have less overall fouling. As a general rule, the more fouling and more corroding fluid should be placed on the tube-side. The inside of tubes can be cleaned much easier than the outside and the tubes can be made from exotic alloys at lower cost than the shell.

The orientation of a heat exchanger influences the ease by which it can be cleaned and can effect particulate fouling. If particulate fouling is anticipated, a vertical down-flow orientation will permit the solids to move through the exchanger. If a horizontal orientation is unavoidable, place the slurry on the

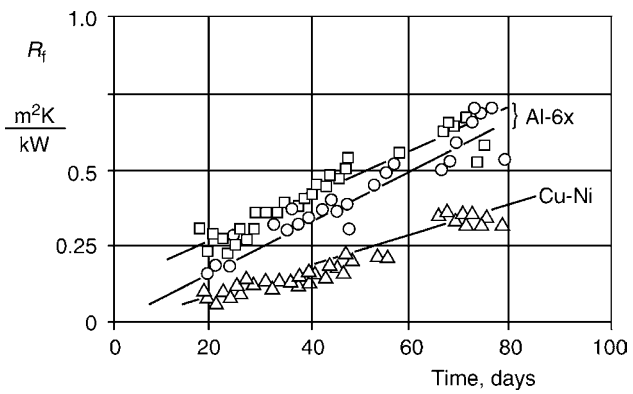

C4. Fig. 7. Influence of pipe material on biofouling [27]

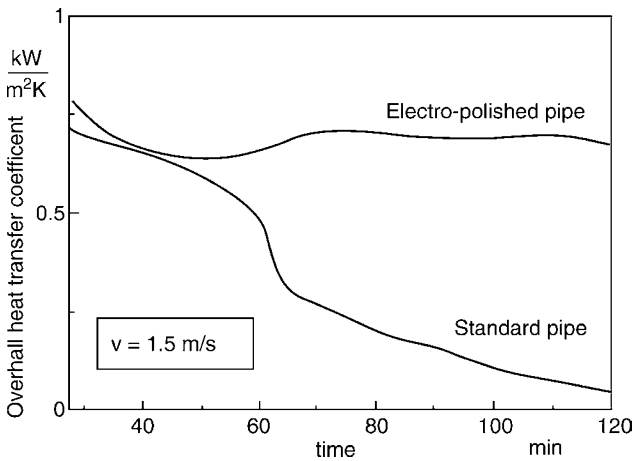

C4. Fig. 8. Reduction of heat transfer coefficient during the evaporation of Kraft black liquor in pulp mills [28]

C4. Table 11. Cooling water flow velocities in condensers [29]

Pipe material	Recommended velocity	Minimum velocity
Arsenical copper	<1.5 m/s	1.0 m/s
Admiralty	1.4–2.0 m/s	1.0 m/s
Aluminum brass	1.8–2.2 m/s	1.0 m/s
9010 cupro-nickel	1.8–2.5 m/s	1.5 m/s
90/30 cupro/nickel	2.4–3.5 m/s	1.8 m/s
Cu	1.5–2.0 m/s	1.0 m/s
Steel	2.0–4.0 m/s	1.0 m/s

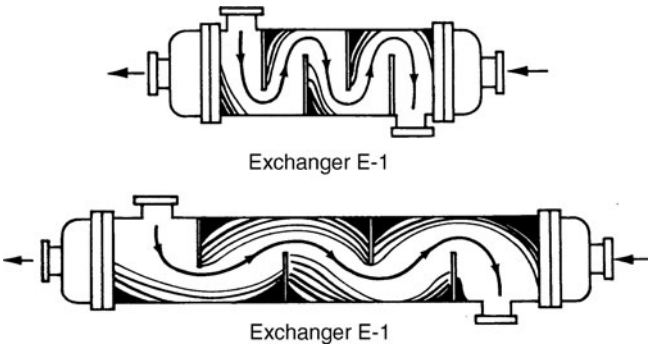

C4. Fig. 9. Sketch of heat exchanger geometry and observed deposit formation [8]

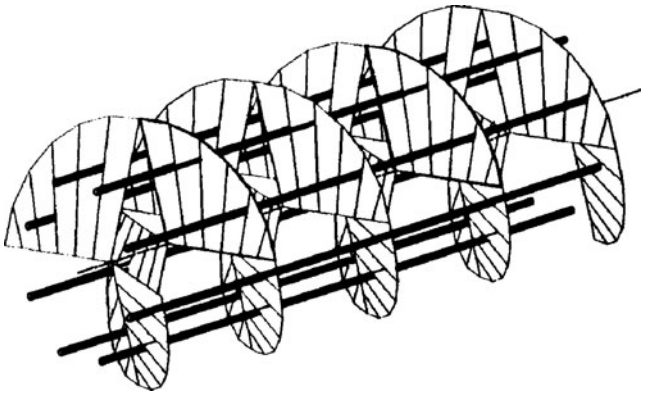

C4. Fig. 10. Helixchanger Baffles (courtesy ABB Lummus)

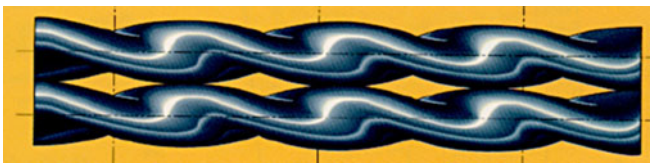

C4. Fig. 11. Twisted Tubes (courtesy Brown Fintube Company)

tube-side and ensure down-flow for multiple tube pass designs. While placing a slurry on the shell-side of a horizontal heat exchanger is not recommended, some success has been reported for vertical-cut double-segmental baffles because they allow the sediment to travel through the exchanger.

While heat exchangers used to be designed for tube-side flow velocities around 1 m/s, modern design velocities are about 2.0 m/s. Table 11 shows optimum and minimum cooling water velocities for condensers of various pipe materials [34].

Based on 20 years of experience in the design of heat exchangers, Gilmour [35] states that "for most applications, only negligible fouling occurs if the heat exchanger is well designed. It is obvious that the majority of poorly performing shell and tube heat exchangers were caused by mistakes in the design of the shell-side flow path." He especially emphasizes that zones with low flow velocity and bypass flows should be avoided under any circumstances. If half-moon baffles are used, the baffle cut should not exceed 20% of the shell inside diameter. Vertical baffles should only be used for condensation or evaporation duties but not for sensible heat transfer situations, because they allow a stratification of flow and hence a sedimentation of suspended particles. Figure 9 [8] shows qualitatively the deposit formation in two shell and tube heat exchangers for identical heat duty. The smaller heat exchanger is designed with appropriate baffle spacing and baffle cut, and hence has higher heat transfer coefficients and less fouling.

Helical flow baffles, as shown in Fig. 10, have been used successfully because they avoid both, flow stratification and stagnant flow zones [36]. Reduced fouling has also been reported for the EM-baffle design developed by Shell Global Solutions [37].

Successful installations of heat exchangers with twisted tubes (Fig. 11) have been reported which may reduce deposit formation both, on the shell and on the tube-side [38].

It is often assumed that finned tubes tend more to fouling because of low flow velocity zones at the base of the fins. While these problems may occur for fouling mechanisms which depend strongly on the flow velocity (such as biological fouling and particulate fouling), there are a number of applications where fouling was even reduced by the use of finned tubes. This effect is explained by the nonuniform thermal expansion of finned tubes due do the temperature profile along the fins, which may reduce the strength of hard and adherent deposits. In [39] numerous investigations on fouling on finned tubes are compared with respect to the effects of fin geometry on deposit formation. When selecting finned tubes for fouling duties it should always be considered that mechanical cleaning of finned surfaces may be difficult or even impossible.

A fairly recent solution for heat transfer involving severely fouling liquids is the fluid bed heat exchanger, which has been described by Klaren [40]. Small solid particles (glass, ceramic, metal) are fluidized inside parallel tubes by the upward flow of liquid. The solid particles regularly break through the viscous boundary layer, so that good heat transfer is achieved in spite of relatively low flow velocities. More importantly, the solid particles have a slightly abrasive effect on the wall of the heat exchanger tubes, thus removing most deposits at an early stage. Fluid bed heat exchangers have been installed in water

treatment plants, paper mills, food and dairy plants, geothermal plants and in various chemical plants. In all cases, a substantial reduction in fouling has been achieved.

2.5 Other Heat Exchanger Types

The widespread installation of compact heat exchangers has been hindered by the perception that the small passages are stronger affected by the formation of deposits. Obviously, compact heat exchangers are unsuitable for fluids containing large particulate material or debris. However, several investigations demonstrated that the high shear forces, low wall superheat and homogeneous flow distribution typical for compact heat exchangers reduce the formation and adhesion of deposits on the heat transfer surfaces. The use of more corrosion resistant materials with smoother heat transfer surfaces further reduces the formation of deposits. Most compact heat exchangers have to be cleaned chemically. Unfortunately, there is very little published information about fouling and cleaning of compact heat exchanger types.

As indicated by Eq. (3), the excess heat transfer surface area increases with increasing clean heat transfer coefficient for a constant heat duty. This places a heavy penalty on compact heat exchanger types, such as plate and frame heat exchangers, if, because of ignorance or because of cautiousness, the TEMA fouling resistances for shell and tube heat exchangers are used. Typical clean overall heat transfer coefficients for plate and frame heat exchangers are about 3000 W/m^{2}K, for shell and tube heat exchangers about 1000 W/m^{2}K. A design fouling resistances of 0.3 m^{2}K/kW then corresponds to 30% overdesign for a shell and tube heat exchanger and to 90% overdesign for a plate and frame heat exchanger.

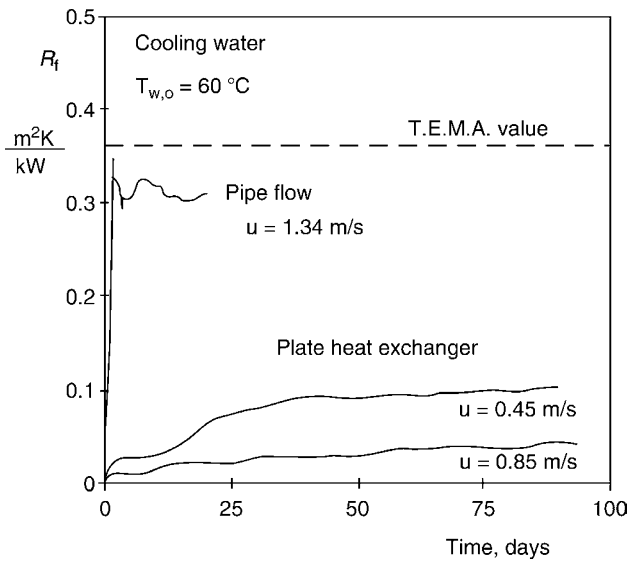

C4. Fig. 12. Comparison of fouling in plate and frame, and in shell and tube heat exchangers [41]

2.5.1 Plate and Frame Heat Exchangers

The application of plate heat exchangers in the chemical process industry is increasing rapidly, where they begin to replace tubular heat exchangers in several traditional applications. Cooper [36] investigated cooling water fouling using an APV model R405 plate heat exchanger. The water was chemically treated before entering the heat exchangers. As shown in Fig. 12, the fouling resistance in the plate and frame heat exchanger is significantly lower than in the shell and tube heat exchanger, despite the typically lower flow velocities. If the flow velocity is increased, the fouling resistance decreases similarly as it is found for shell and tube heat exchangers. Novak [42] studied the fouling behavior of Rhine River water near Mannheim (Germany), and of Öresund seawater in Sweden. For both waters, mainly biological fouling was observed. The fouling resistances increased almost linearly over the observed period of time. Table 12 summarizes the measured effect of flow velocity on the fouling rate.

Typical values for fouling resistances in plate heat exchangers are given in Table 6. Most manufacturers of plate and frame heat exchangers recommend that the excess surface should not exceed 25% of the heat transfer surface area calculated for the clean duty. Due to the nonuniformity of flow distribution and deposit formation, measured pressure drop increases are significantly higher than values predicted using an average deposit thickness calculated from the fouling resistance.

The actual plate geometry (angle, amplitude, and wavelength of corrugations) affects the formation of deposits [43]. Delplace et al. found that deposition from whey protein solutions on chevron plates is only half of that of straight corrugations, for otherwise identical conditions [44].

2.5.2 Plate-Fin Heat Exchangers

Plate-fin heat exchangers are brazed/welded compact heat exchangers with a heat transfer surface density of about ten times that of tubular heat exchangers. Typical applications are cryogenic, chemical/petrochemical, and hydrocarbon offshore installations. Molecular sieves and 100 µm filters are used in cryogenic installations to remove particulate matter or components that may freeze-out on the heat transfer surfaces. Systematic investigations have been performed on particulate fouling [45] and on river water fouling [46].

C4. Table 12. Fouling rates of Rhine river water for a surface temperature of 25°C [33]

Type	u, m/s	τ, Pa	dR_f/dt, 10^4 m^{2}K/kWh
Plate heat exchanger	0.13	6.7	7.4
Plate heat exchanger	0.19	14.5	4.3
Plate heat exchanger	0.77	190.0	0.6
Spiral plate exchanger	0.43	7.5	5.0

For 3 µm ferric oxide particles suspended in water, no blockage of plain fin or wavy fin channels was observed. Wavy fin channels fouled more than plain fin channels. All experiments showed asymptotic behavior. Higher deposition rates were obtained for non isothermal conditions and at higher bulk temperatures. Maximum deposition occurred at a Reynolds number of about 1500 [45].

Fibrous and biological material partially block the inlet of the aluminum plate-fin test sections when used with river water, which was filtered through a 1 mm mesh. Some deposition was found at locations where corrosion of the aluminum had occurred. In the wavy fin test section, a thin, uniform deposit of fine mud was observed. Pressure drop for the plain finning increased linearly with time, whereas asymptotic behavior was found for the wavy finning. The initial slope of the relative pressure drop vs. time curves was $5.8{\cdot}10^{-8}s^{-1}$ for the plain fins and $1.71{\cdot}10^{-7}s^{-1}$ for the wavy fins. For the latter, an initial deposition rate of $4.8{\cdot}10^{-12}$ s m^2K/W and an asymptotic – fouling resistance of $6{\cdot}10^{-6}m^2K/W$ was measured [46].

2.5.3 Printed Circuit Heat Exchanger

The passages in Printed Circuit Heat Exchangers (PCHEs) are typically between 0.3 mm and 1.5 mm deep. The specific design leads to volumetric heat transfer areas of 500–2,500 m^2/m^3, which is an order of magnitude higher than shell and tube heat exchangers. Experiments are described in [47] to compare the fouling related drop in performance of a PCHE and of a double pipe heat exchanger (DPHE). The cooling water treated against corrosion, scale formation and biofouling, and a 0.5/1.0 mm strainers was installed to reduce particulate fouling. For operating times of 500–660 h, no change in thermal effectiveness was observed for the PCHE, but the pressure drop increased by up to 55% due to the deposition of particulate material. The addition of a stainless steel mesh insert for the removal of fibrous material significantly reduced the increase in pressure drop. No deposition was observed in the parallel DPHE.

PCHEs have been used for gas cooling using seawater [47]. 200 µm strainers have been installed upstream of the heat exchanger and chlorine was added to counter biofouling. No operational problems have been reported. Another application involved the heating of tail gas in a nitric acid plant using condensing steam. After 18 months of operation, no indication of channel blockage could be detected.

2.5.4 Polymer Compact Heat Exchangers

Polymer heat exchangers are used for low pressure operations involving corrosive gases or liquids. The low surface energy and the smooth surface of their construction materials (polypropylene, fluoropolymer etc.) reduce the stickability of most deposits. Since clean heat transfer coefficients are already low (150–250 W/m^2K), these heat exchangers react less sensitively to an additional fouling resistance than metallic heat exchangers.

2.6 Effect of Fouling on Pressure Drop

The formation of deposits on the heat transfer surfaces causes an increase of the frictional pressure drop due to increased surface roughness and restricted cross-sectional flow area. According to Chenoweth [8], more heat exchangers are taken out of service because of excessive pressure drop than because of reduced heat transfer.

2.6.1 Tube-Side Pressure Drop

A rough estimate of the tube-side pressure drop can be made if it is assumed that the deposit is distributed evenly at the tube inside. The frictional pressure drop in cylindrical tubes is calculated from Eq. (5):

$$\frac{\Delta p}{\Delta L} = \xi \frac{\rho\, u^2}{2 d_i} \tag{5}$$

the friction factor for smooth tubes

$$\xi = 0.0056 + 0.5\ \mathrm{Re}^{-0,32} \tag{6}$$

and for rough tubes

$$\xi = 0.014 + 1.056\ \mathrm{Re}^{-0,42} \tag{7}$$

If the fouling resistance and the thermal conductivity of the deposit are known, the inside diameter of the fouled pipe can be determined by Eqs. (8) and (9):

$$R_f = \frac{d_i}{2\lambda_d} \ln\left(\frac{d_i}{d_f}\right) \tag{8}$$

$$d_f = d_i \exp\left(\frac{-2\lambda_d R_f}{d_i}\right) \tag{9}$$

The pressure drop for the fouled tube is obtained by using Eq. (5) in conjunction with Eqs. (7) and (9). It is generally found that the above equations under-predict the effect of fouling on pressure drop, since they assume a uniform distribution of deposit over the total heat transfer surface.

C4. Table 13. Ratio of fouled to clean shell-side pressure drop [48]

Deposit heat transfer coefficient	Shell diameter/baffle spacing		
	1.0	2.0	5.0
Laminar flow			
$1/R_f = 6000$ W/m^{2}K	1.06	1.20	1.28
$1/R_f = 2000$ W/m^{2}K	1.19	1.44	1.55
$1/R_f < 1000$ W/m^{2}K	1.32	1.99	2.38
Turbulent flow			
$1/R_f = 6000$ W/m^{2}K	1.12	1.38	1.55
$1/R_f = 2000$ W/m^{2}K	1.37	2.31	2.96
$1/R_f < 1000$ W/m^{2}K	1.64	3.44	4.77

2.6.2 Shell-Side Pressure Drop

The effect of fouling on the shell-side pressure drop can be estimated using Table 13 from Coulson et al. [48].

3 HTRI Fouling Mitigation by Design Method

Based on almost 50 years of experience as some of the world's leading heat exchanger design experts, Heat Transfer Research Incorporated (HTRI) [22–26] have developed a design methodology that yields smaller, more cost-effective shell and tube heat exchangers with extended run times between cleanings. While this methodology has, so far, only been validated for crude oil processing, its rigorous approach can be taken as an example for other fluids and heat exchangers types. These techniques were developed by HTRI with help from industry through the HTRI Exchanger Design Margin Task Force (EDMTF). The goal of the EDMTF is to develop the design philosophy for adding margins to heat exchangers to allow for process uncertainties and fouling.

Experience has shown that fouling may be mitigated for many services through proper heat exchanger design and operation. For the experienced designer, fouling resistances are not used when operating data for identical or similar services are available. In these cases, designing with the proper attention to velocity (or shear stress) and wall temperature can prevent significant fouling whereas "the mere use of a high fouling resistance will generally engender a high degree of fouling."

A small design margin may be added to the design to address design uncertainties. Rarely is this margin in excess of 30%. More than 30% excess margin calls for a root cause analysis of the problem followed by a fouling (or design) mitigation strategy. Except for rare cases of intentional high variability in throughput, more than 30% excess margin in a heat exchanger design indicates the presence of unresolved engineering issues and can often be a significant source of hidden cost to the owner.

It is good practice to design for an allowable pressure drop derived by reducing the maximum available pressure drop in the clean condition by the amount of excess margin anticipated. This permits any excess margin to be applied in such a way that design shear rates and wall temperatures are not reduced. The maximum available pressure drop in the clean condition is estimated as the maximum available pressure drop divided by the fractional pressure drop increase when the exchanger is operated in the fouled condition.

3.1 Crude Oil Best Practice Operating Conditions

The fluid scope for this design methodology is:

- Medium-to-high boiling point liquid hydrocarbon mixture with API gravity less than 45
- Heavy particulate matter (e.g., catalyst fines) absent
- Reasonable salt content (no desalter malfunctions)

a) Minimum Liquid Velocity

- Tube-side velocity of 2 m/s. This velocity limit is applicable for tubes with outside diameters of 19.05 mm and 25.4 mm. Increase velocity to 2.2 m/s for tube diameters of 31.75 mm and 38.1 mm to maintain shear stress.
- Shell-side cross flow stream should be at least 0.6 m/s. If the shell-side flow is fully longitudinal, the minimum shell-side velocity should be 1.2 m/s. For longitudinal flow bundles, tubes removed for entrance/exit considerations at the shell nozzles should be replaced in the bundle proper with plugged dummy tubes or rods of the same diameter to maintain a uniform flow field and minimize bypass streams. The bundle-to-shell diameter ratio is to be made as close to 1.0 as practical under TEMA [4] clearance rules.

b) Maximum Temperature

- The maximum tube wall temperature should be 300°C. Shell-side design with cross-flow baffles
- The B-stream fraction according to TEMA nomenclature [4] should be at least 0.65.
- Single-segmental baffles should be selected. If the shell-side pressure drop is prohibitively high, double-segmental, helical, EMbaffle, rod baffle, squared, or no-tube-in-window (NTIW) baffle configurations may be considered.
- Baffle cut orientation should normally be horizontal for TEMA type E and J shells. Baffle cut orientation for TEMA type F and G shells should be vertical. If slurry must be placed on the shell-side of a horizontal heat exchanger, consider vertical cut double-segmental baffles to allow the sediment to exit the shell.
- Baffle cut for single-segmental designs should be 20–25% of the shell inside diameter, where 20% is preferred. It may be increased up to 25% to reduce leakage streams.
- The ratio of window velocity to cross-flow velocity (including leakage streams) should be less than 2.0 for designs with tubes in the window (1.0–1.5 is preferred). For no tubes in window designs, the ratio of window velocity to cross flow velocity should be less than 3.0 (1.5–2.0 is preferred). Refinement of this guideline is an area of research.

3.2 Cooling Tower Water Best Practice Operating Conditions

For the case of those cooling water streams which are closely regulated in the plant for velocity control and are kept reasonably clean with a water maintenance program, fouling mitigation strategies apply. The cooling water temperatures should be designed and operated to not exceed a maximum bulk temperature of 50°C or a maximum wall temperature of 60°C.

In addition, there must be sufficient velocity to maintain any particulate in suspension as well as to produce enough wall shear to stabilize any fouling which does occur. There are many

sources for information on minimum cooling water velocities for design, such as those given in Table 11. In reality, the exact minimum value for any cooling water system is so dependent upon the contaminants dissolved in the water that one single value for this purpose can only be regarded as an approximation. In the final analysis, the judgment as to minimum design water velocities while adhering to prudent water temperature limitations must be made by those knowledgeable about the water used.

3.3 Excess Surface/Coefficient Adjustments

- If both fluids are within the scope outlined above, approximately 20–25% excess surface should be provided instead of applying fouling resistances. This design margin may be reduced when the designer has confidence in the fluid properties, predictive methods, and successful mitigation of fouling (usually based on prior experience for a similar service).
- If only one fluid is operating under the best practice conditions, a fouling resistance should be selected for the fluid outside scope. For non-fouling fluids outside scope, a fouling resistance of 0.000088 m^2K/W is recommended to compensate for heat transfer surface changes during start-up. For the fluid within scope, the heat transfer coefficient is multiplied by 0.83 and no fouling resistance is used. As above, the design margin may be reduced based upon operating experience.

3.4 Design Recommendations

3.4.1 Shell-Side Bundle Geometry Exit/Entrance Constraints

- Where impingement protection is required, use impingement rods. One row of rods is acceptable for 90° tube layouts, two rows for staggered pitch. Impingement plates should be avoided.
- Large baffle end spaces and correspondingly low local velocity sometimes occur due to geometry constraints. When the end baffle space is greater than or equal to 1.5 times the space between baffles, the area back from the first baffle to 1.5 times the baffle spacing is to be considered 65% effective regardless of baffle type or orientation. All remaining area to the tube-sheet is to be considered ineffective for heat transfer. Additional area should be provided in the bundle proper as compensation. An annular distributor may be considered if the affected surface area is large.

3.4.2 Allowable Pressure Drop

Pressure drop should be provided as required to meet the minimum critical velocities noted in Sect. 3.1. If the pressure drop (and hence the flow velocity) is too low, fouling may become inevitable and fouling mitigation impractical.

3.4.3 Longitudinal Baffles

If a longitudinal baffle is used in heavy fouling service where shell-side pressure drop in one shell exceeds 35 kPa (70 kPa with a "kempchen" style of seal), the baffle shall be welded to the shell. Note that welding the longitudinal baffle to the shell requires a shell inside diameter of at least 0.7 m and, for the bundle to be removable, U-tubes must be used with the U-bends in the horizontal plane (normally two or more tube passes per shell pass). The designer should investigate differential thermal stresses across the shell. In general, a welded longitudinal baffle is probably acceptable where the shell-side temperature difference across one shell does not exceed 90°C. For leaf seal construction, shell-side operating temperature differentials of 195°C across one shell have been accommodated with proper mechanical design. These rules are for 6.7 m straight-length tube bundles and will vary with bundle length. Bundle slide rails in both top and bottom portions of the bundle need to be provided.

The following segmental-baffle construction features may be considered to improve shell-side performance:

- American Petroleum Institute Standard 660 requires that a seal device (dummy tubes, rods, or strips) be implemented from 25–75 mm from the baffle tips, and for every 5–7 tube pitches thereafter. The number of seals may have to be increased to limit the bundle and pass lane leak streams.
- Where the tube-to-baffle diametral tolerance (as specified by TEMA [4]) is 0.8 mm, the tolerance may be reduced to 0.4 mm if required to reduce the leak stream between the tube and baffle hole.
- The TEMA [4] baffle-to-shell diametral clearance may be reduced to limit the baffle-to-shell leakage stream. A clearance of 0.0035–0.004 times the shell diameter is achievable for shells rolled from plate, but use this extra tight clearance only if necessary, as it is difficult to guarantee compliance. Extra tight clearance is not recommended for shells made from pipe (typically NPS 24 and smaller).
- Baffled TEMA [4] F and G shells may be considered to increase shell-side velocity, reduce the number of shells in series, and/or improve the baffle-spacing-to-shell-diameter aspect ratio.

3.5 Example for Fouling Mitigation by Design

To demonstrate the potential savings of the design methods outlined in this section, the following example will be used. This example is for the last shell-and-tube heat exchanger in the crude oil preheat train prior to the fired heater. Selection of material is important, and stainless steel or high chrome steel should be selected for the design. The process conditions are summarized in Table 14a.

3.5.1 Original Design

The original heat exchanger is a TEMA type AES consisting of two shells. The design and performance parameters for the exchanger unit are given in Table 14b.

3.5.2 Operation History with Original Design

This service was a consistent high fouling problem and would lose about 57% of its performance capacity within the first 6 months after cleaning, resulting in excess energy (fired heater fuel) and related costs of about €62.000 per month averaged over a 2 year turnaround cycle.

3.5.3 Root Cause Analysis of Performance

At the next turnaround, the bundles were pulled for cleaning. Prior to cleaning, visual bundle inspection revealed a "fuzzy" looking coating on the outside of the tubes consisting of oil and coking fines from the vacuum unit. The coating was slightly sticky but did not solidly adhere to the surface and could be easily wiped away. The tube-side fouling appeared to be slight. In addition, analyzing the fouling performance monitor over the course of the 2-year turnaround cycle indicated a performance plateau at about 6 months after which the fouling seemed to stabilize for the next 1.5 years. These data strongly indicated shear rate controlled fouling at the shell-side.

From the above data, it was estimated that a shell-side velocity slightly greater than 1.5 m/s should keep the fouling from adhering to the outside of the tubes and allow it to be carried through the exchanger without deposition. However, to do this required an appropriate redesign of the heat exchanger.

3.5.4 New Design

Using the procedures outlined in this section, a replacement heat exchanger was designed for this service as given in Table 14c.

The new design consists of a horizontal welded long baffle on the shell-side, shell nozzles located at the rear of the shell beyond the bundle U-bends so that there are no erosion concerns, and horizontal U-bends with a vertical channel pass partition to produce a removable, two tube pass bundle in a welded long baffle F-shell. Both the original and new designs employed segmental baffles on the shell-side.

3.5.5 Final Outcome

The new design used no preset fouling resistances but instead used the allowable pressure drop to produce the higher shear rate necessary to inhibit deposition. A minimum of 15% excess surface was thought prudent to handle design uncertainties in the new configuration. The new exchanger performed at or above expected design over the 2-year turnaround cycle producing an average €68.000 per month cost savings over the original heat exchanger.

C4. Table 14a. Process conditions for design example

Stream	Fluid	Flow rate	Temperature in	Temperature out	Allowable ΔP
Location	Designation	kg/s	°C	°C	kPa
Shell-side	Heavy Vacuum Gas Oil	71	366	338	100
Tube-side	Crude Preheat	88	289	311	70

C4. Table 14b. Original heat exchanger design

Number of shells	TEMA	Number of passes		Fouling resistance		Velocity m/s		ΔP design kPa		U_c/U_f
Size	Type	Shell	Tube	Shell	Tube	Shell	Tube	Shell	Tube	
2	AES	1	2	0.00123	0.0007	0.37	1.22	8.5	32	1.95
1016 mm × 6.1 m										

C4. Table 14c. Improved heat exchanger design

Number of shells	TEMA	Number of passes		Fouling resistance		Velocity m/s		ΔP design kPa		U_c/U_f
Size	Type	Shell	Tube	Shell	Tube	Shell	Tube	Shell	Tube	
1	AFU	2	2	–	–	1.85	2.38	91	58	1.16
610 mm × 6.1 m										

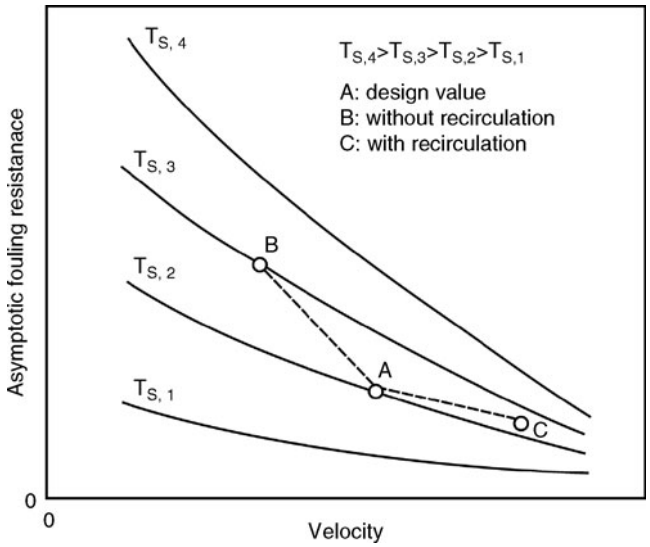

C4. Fig. 13. Fouling resistance as a function of flow velocity and surface temperature during start-up of a new or cleaned heat exchanger

4 Online Mitigation Methods

The following section provides an overview of the broad categories of mitigation methods, and describes some general approaches. For more detailed information see [49].

4.1 Start-Up Procedures

The use of constant fouling resistances in the design of heat exchangers leads to initially oversized equipment. Heat duties in new or cleaned heat exchangers can, therefore, be considerably higher than the design specifications. In most chemical processes, however, product inlet and outlet temperatures, product flow rate and cooling water inlet temperature are specified. If this is the case, the heat exchanger is usually controlled via the flow rate of the cooling water. To reduce the heat duty, the water flow velocity must be reduced. Figure 13 shows that this procedure may cause a considerable increase of fouling as compared to fouling under design operating conditions.

Point "A" refers to the design values of flow velocity and heat transfer surface temperature. As the heat exchanger is initially overdesigned, the cooling water flow velocity is throttled which also causes an increase of the heat transfer surface temperature, see point "B." However, fouling at "B" is considerably worse and deposits created during this part of the operation may not be removed completely, even if the flow velocity is increased, later. Therefore, by specifying high fouling resistances, fouling may become a self-fulfilling prophecy. If part of the cooling water is recirculated, as shown in Fig. 14, the flow velocity and the cooling water inlet temperature can be increased to meet the required heat duty. The anticipated fouling ("C") will be similar to the design value ("A"), but a price is to be paid to provide the higher flow velocity.

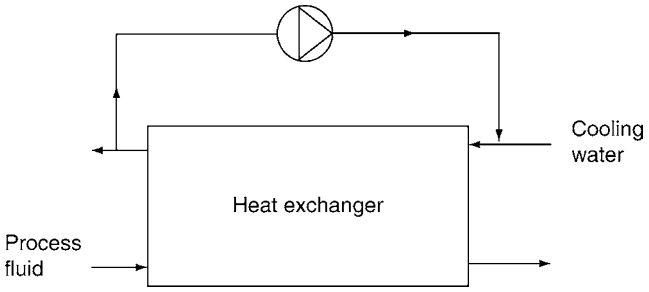

C4. Fig. 14. Recirculation of cooling water

4.2 Chemical Fouling Mitigation Methods

Since about 1920, a number of companies have specialized in the mitigation of fouling and corrosion, mainly for the flow of cooling water and hydrocarbons. These companies have gained considerable expertise and have developed a wide range of additives and equipment. Services include the supply of chemicals as well as the analysis of cooling water, the evaluation of potential fouling and corrosion problems, and complete treatment programs including continuous monitoring of the system. In what follows in this subsection, only a small selection of methods to reduce fouling by chemical means is discussed. For the final selection of the treatment as well as for the dosage of treatment chemicals, specialists should be consulted. More details may be found in [49] provided by industrial fouling mitigation companies.

Commercial antifoulants usually contain a number of components. These polyfunctional antifoulants are more versatile and effective since they can be designed to combat various types of fouling that can be present in any given system. Antifoulants are designed to prevent equipment surfaces from fouling, but they are not designed to clean up existing deposits. Therefore, antifoulant addition should be started immediately after equipment is cleaned.

4.2.1 Scale Formation

In general, there are three alternatives available to mitigate or to prevent scale deposition due to high concentration of scale-forming ions in aqueous solutions:

Removal of Scaling Species

Scaling species may be removed by ion exchange and by chemical treatment. In the latter treatment, carbonic acid, and calcium hardness are removed by the addition of chemicals. If the lime treatment is used:

$$Ca(HCO_3)_2 + Ca(OH)_2 \rightarrow 2\,CaCO_3 + 2H_2O \qquad (10)$$

$$CO_2 + Ca(OH)_2 \rightarrow CaCO_3 + H_2O \qquad (11)$$

During slow decarbonization (1–3 h reactor residence time), the calcium carbonate precipitates as silt, during fast decarbonization (5–10 min reactor residence time) it precipitates in the form of particles. With the exception of installations with high

calcium hardness or large throughput, chemical removal of scaling species is not used anymore.

Instead, ion exchangers are used in which the "harmful" scaling species in the fluid are replaced by "harmless" ions (for example Ca^{++} or Mg^{++} by Na^{+}). Ion exchangers are usually manufactured from styrene based polymers. The so-called cationic exchangers contain weak and strong acids; the anionic exchangers contain weak and strong alkaline groups. With these two variations, all cations and anions can be removed from the fluid. Ion exchangers have to be regenerated regularly with the appropriate salt solution. According to [50], chemical decarbonization leaves a residual hardness of 17–30 ppm as $CaCO_3$, ion exchange can reduce the hardness down to 2 ppm as $CaCO_3$. Both methods of fluid treatment have high capital and operating costs.

In the oil industry, desalters are installed at the beginning of the crude oil heat exchanger train to replace salty water, which may otherwise cause scale formation at higher temperatures.

pH Control

The solubility of scale-forming constituents increases with decreasing pH. Many treatment programs, therefore, involve the addition of acid (usually H_2SO_4) to the system to maintain a pH in the region of 6.5–7.5. If the system contains corrosion-resistant materials, a pH may be selected at which no scaling will occur. The Langelier Saturation Index or the Ryznar Stability Index [51] are commonly used to determine the value of pH to be adjusted.

Scale Inhibitors

Growth of crystals or the nucleation of crystals can be inhibited by the addition of scale inhibitors. Many proprietary compounds are available for scale control.

Chelating agents (for example EDTA) complex strongly with the scaling cations and hence inhibit their deposition at the heat transfer surface. Inhibitor and scalant must be available in stoichiometric ratios.

Processes, which are based on physical rather than on chemical reactions are those that stabilize supersaturated solutions by adsorption at the crystal nuclei (for example polyphosphates) or that modify or weaken the crystalline structure (for example polycarboxylic acid). Table 15, which has been adopted from Harris and Marshall [52], shows the ability of additives to maintain $CaCO_3$ in solution. Lists of additives to reduce crystallization from hard waters have been compiled by Harris and Marshall [52] and by Krisher [53].

C4. Table 15. Ability of various additives to maintain $CaCO_3$ in solution [52]

Additive	% Inhibition at dose level			
	2.5 ppm	5.0 ppm	7.5 ppm	10 ppm
Polyphosphate	98%	98%	99%	100%
Aminophosphonic acid	97%	96%	95%	94%
Acetodiphosphonic acid	83%	82%	83%	90%
Polyacrylate	30%	65%	84%	93%
Polymaleic acid	26%	35%	44%	56%
EDTA	15%	20%	20%	20%

4.2.2 Particulate Fouling

Particulate fouling is usually mitigated by the addition of surfactants or dispersants. If the surface tension is reduced, large particle agglomerates can break down into smaller particles, which tend less to sedimentation. Dispersants impart like charges to both the heat transfer surface and the particles and reduce deposition. For cooling water applications polyacrylates or polysulfonates are used with molecular weights between 2000 and 3000 g/mol. According to [53], the addition of polyphosphates to reduce scaling may cause a slight reduction of the dispersion of particulates.

4.2.3 Chemical Reaction Fouling

Chemical reaction fouling increases exponentially with increasing heat transfer surface temperature according to an Arrhenius term, see Eq. (4). As activation energies E are fairly high for chemical processes, even a modest reduction of the heat transfer surface temperature due to process or design modifications may already cause a considerable reduction of fouling. Particles suspended in the fluid (e.g., from upstream corrosion) can act as catalysts. Reaction fouling may be mitigated by removing these particles.

Especially for oil refining processes a number of chemical additives to reduce reaction fouling have been developed. Most antifoulants have several functions. Generally they are oxygen scavengers, metal deactivators and dispersants [54]. For autoxidation-induced fouling, antioxidants can be added to consume oxygen or react with oxidation products in a way as to prevent the chain reaction of the autoxidation process, or metal deactivators are added to chelate metal ions thereby preventing their catalytic effect on the autoxidation process. Once insolubles form by either autoxidation or thermal decomposition, dispersants can be added to minimize agglomeration of small insoluble polymeric or coke-like particles into larger particles or deposit, or sticking of particles to the tube wall [55].

Antioxidants

Even very small amounts of oxygen can cause or accelerate polymerization. Accordingly, antioxidant type antifoulants have been developed to prevent oxygen from initiating polymerization. Antioxidants act as chain-stoppers by forming inert molecules with the oxidized free radical hydrocarbons.

Metal Deactivators

Traces of metals are invariably present in hydrocarbon streams, which may catalyze polymerization reactions. For example transition metal ions, such as Cu, Fe, Zn, and Mn are powerful hydroperoxide decomposers and provide a steady source of free

radicals for oxidation chain initiation. By complexing the metal ion, it can be prevented from participating. Thus chelating compounds are used as metal deactivators [55].

Dispersants

Dispersants or stabilizers prevent insoluble polymers, coke, and other particulate matter from agglomerating into large particles which can settle out of the process stream and adhere to the metal surfaces of process equipment. They also modify the particle surface so that polymerization cannot readily take place. Dispersants generally play an important role in antifoulant programs. The feedstock or hydrocarbon stream may already contain polymerized materials which, if allowed to agglomerate, would deposit. In most applications it is not possible to fully eliminate oxygen- or metal-induced reactions and dispersants are necessary to prevent the polymerized materials from agglomerating and depositing on heat transfer surfaces [54, 56]. Dispersants are believed to function by absorbing on the surface of materials which are insoluble in the organic fluid and converting them to stable colloidal suspensions. They generally contain polar groups which absorb on the particle surface and nonpolar hydrocarbon-soluble groups to affect dispersion by their solubilization. Mayo et al. [57–62] argue that it is the solubilizing properties of dispersants which are most important in reducing deposit formation.

Figure 15 shows the performance of the feed/effluent heat exchanger in an oil refinery with and without chemical treatment.

4.2.4 Biofouling

The environment in cooling towers and cooling systems is particularly conducive to the growth of microorganisms in water and on surfaces of the system. Microorganisms attach and grow on surfaces, and produce polysaccharides, which increase the stickability of suspended matter and hence promote further deposition. Biological growth is usually controlled by addition of biocides. In recent years, chlorine has most widely been used, which reacts with water to hydrochloric and hypochlorous acid:

$$Cl_2 + H_2O \rightarrow HCl + HOCl \qquad (12)$$

Hypochlorous acid is an extremely powerful oxidant that easily diffuses through the cellular walls of microorganisms. It is assumed [64–66] that HClO oxidizes the active sites of certain enzyme sulfhydryl groups, which constitute intermediate steps in the production of adenosine triphosphate (ATP). The system ATP-ADP allows conversion of carbohydrates and hence the energy supply for living organisms. Contrariwise to other, nonoxidizing biocides, chlorination also weakens the biofilm matrix allowing the removal of biofilms from the heat transfer surface by fluid shear forces. Continuous application of chlorine at concentrations between 0.1 and 0.5 ppm has shown to be a reliable but costly method to avoid deposition. Cheaper but less effective is a dosage of 1–10 ppm for 15 min in intervals of 4 h. However, it was found that biofilm growth is accelerated after a shock chlorination, see Fig. 16.

Biological fouling control with chlorination has the disadvantage that chlorine has to be added continuously, since it does not only react with microbes but also with process contaminants such as H_2S or NH_3. Chlorine concentration in water exceeding 0.5 ppm may give rise to corrosion problems, especially for stainless steel equipment. Due to the biocidal action of chlorine, there are increasing restrictions on the effluent chlorine concentration. For these reasons, chlorine is increasingly replaced by other chemicals such as methylene-thiocyanate or chlorophenoles, see Waite and Fagan [68].

Even though the addition of hypochlorous acid provides an effective method against the growth of a wide range of bacteria and algae, there are a number of species that can only be controlled by excessively high HOCl concentrations (>30 ppm). Since this may cause operational problems, compounds have been developed to eliminate these species, which can be added to the chlorinated water. Grade and Thomas [69] discuss treatment programs, which are effective against bacteria and algae. Generally, it is recommended to

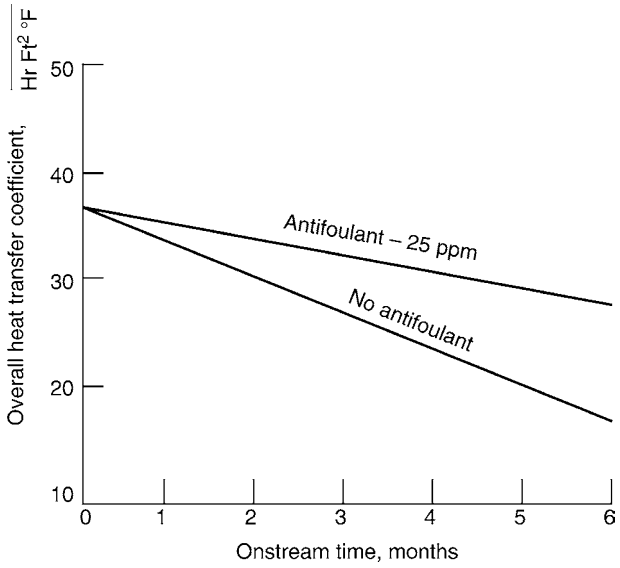

C4. Fig. 15. Reformer feed/effluent exchanger performance [63]

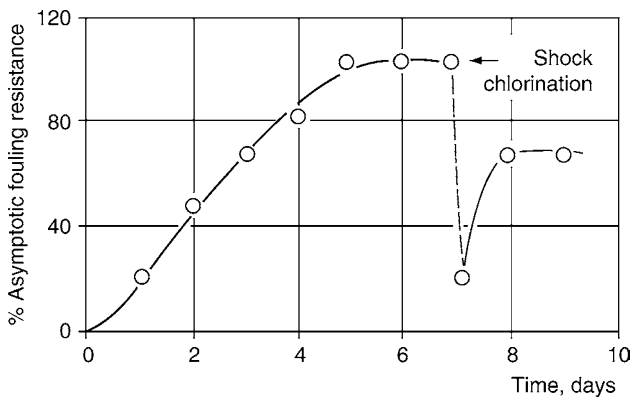

C4. Fig. 16. Effect of shock chlorination on the growth of biological matter at heat transfer surfaces [67]

vary biocide treatment regularly to avoid immunization of microorganisms.

Because of the toxic effect of copper ions on biological matter, another method to reduce bacterial growth is the use of piping with a copper content above 60% or the addition of copper sulfate to the water. For potable water, the copper concentration must be below 1 ppm.

4.2.5 Corrosion Fouling

Generally, it is desirable to have a thin, passivating oxide layer on the heat transfer pipes. Epstein [11] mentions that this oxide layer is removed if the flow velocity exceeds 30 m/s. Excessive corrosion can be controlled by the addition of corrosion inhibitors (chromate or polyphosphate based) or by control of the pH. Chromate is a highly efficient and cost effective inhibitor. However, the toxicity of chromates in the environment has restricted their use. This also holds for zinc based inhibitors. Under some circumstances, corrosion inhibitors (such as phosphates) themselves can be the source of fouling in heat exchangers as they increase the total salt content of the water. However, this can be mitigated by careful control of parameters such as inhibitor concentration, flow velocity and surface temperature [70].

4.2.6 Gas-Side Fouling [3]

Removal of contaminants which promote fouling, such as sodium, sulfur, or vanadium, from fuels prior to combustion and contaminant removal from combustion gases are two approaches to mitigate gas-side fouling. Water washing has helped to overcome some of the fouling problems experienced with residual oils in marine applications by removing sodium and sediment. Inorganic sulfur can be removed from coal by gravity settling or by froth floatation if the mineral particles are well above micron size.

Electrostatic precipitators, mechanical collectors, fabric filters or wet scrubbers can be used to remove particles from combustion gas streams. Removal of gaseous constituents, which is considerably more difficult than particle removal, may involve limestone addition, wet scrubbing without sulfur recovery, MgO systems with sulfur recovery or use of dry sorbent systems.

Under certain conditions, chemical fuel additives or chemical flue gas additives can mitigate the effects of gas-side fouling and corrosion. Many proprietary additives have been marketed, with varying degrees of success in mitigating fouling. Fuel additives to improve combustion efficiency in boilers and to keep gas-side heat transfer surfaces clean by reducing soot and slag formation have been developed by companies such as Betz [71], Dearborn, Drew [72], and Nalco [73]. Additives that have been used to control gas-side fouling in boilers include aluminum oxide, ammonium bicarbonate, magnesium oxide, magnesium carbonate, silica, and zinc. For coal-fired boilers, additives are used for fly ash conditioning for electrostatic precipitation, convective tube fouling and coal-ash slag. Magnesium oxide can minimize fouling of coal-fired boilers by acting as a catalytic inhibitor to retard the formation of SO_3 and reacting to $MgSO_4$ which is inert and has a high melting point. Often, the amount of MgO required, 0.4–3% of the fuel burned, makes the practice uneconomical. However, using fine, particle-size magnesia dispersions at rates of 0.005–0.015% (weight) of the fuel has reportedly reduced fouling.

For oil-fired boilers, additives are used to control SO_3 related problems, high temperature fouling, high temperature corrosion.

4.3 Mechanical Fouling Mitigation Methods

A number of mechanical mitigation techniques have been developed which generally are based on one of the following mechanisms:

(a) Short-time overheating of the heat transfer surfaces. The different thermal expansion of tubes and tube deposits may cause cracking of the deposit
(b) Mechanical vibration of heat transfer surfaces
(c) Acoustical vibration of heat transfer surfaces
(d) Increased shear stress at fluid deposit interface.
(e) Reduced adhesion of deposits

4.3.1 Liquid Flow

Most of the commonly used fouling mitigation techniques have been developed for the tube-side liquid in shell and tube heat exchangers. Even though attempts have been made to develop mechanical online mitigation devices for non-tubular heat exchangers, their installation has not penetrated the market.

Reversal of Flow Direction

Regular reversal of the flow direction in conjunction with a short-time increase of the flow velocity is sometimes used as a method to mitigate the formation of weak deposits. Figure 17 shows that this procedure reduces the fouling resistance, but

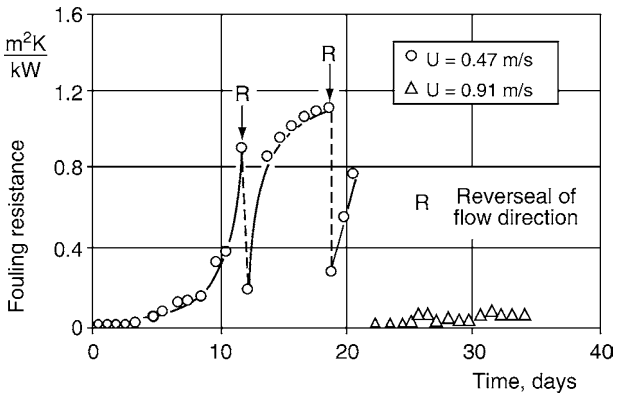

C4. Fig. 17. Continuous cleaning by reversal of flow direction [74]

only for a short period of time. A much better performance could be achieved by operating at a higher flow velocity.

Gas Rumbling

Deposits with moderate stickability to the heat transfer surfaces (e.g., particulate, and some biological deposits) can be dislocated and washed out by increasing the fluid shear forces for a short time, in regular time intervals. This can be achieved by increasing the flow velocity, if enough pump capacity is available. More effective is, however, to introduce compressed air or nitrogen into the liquid system. The resulting highly turbulent gas-liquid two-phase flow can provide shear forces and pressure fluctuations, which are substantially higher than for single-phase flow. Gas rumbling is commonly used in cooling water applications.

Ultrasound

On the laboratory scale, some success has been achieved in removing/inhibiting deposits by ultrasonic vibrations. So far, however, technical limitations have prevented the extrapolation of these results into industrial practice.

Tube Inserts

Tube corrugations and tube inserts can increase the plain tube heat transfer coefficient by a factor of 2–15 [49]. This is achieved by reducing the average thermal boundary layer thickness. As deposition rates for most fouling mechanisms are inversely dependent on fluid wall shear stress and heat transfer surface temperature, reduction of the viscous and thermal sublayer thickness may also considerably reduce fouling. It must be considered that, for constant mass flux, the increased thermal efficiency is always accompanied by an increased pressure drop per unit length; therefore, these inserts work best for flow in the laminar or transitional flow regime. In combination with further reduction of flow velocity (i.e., tube passes) design variations may be possible where significant improvements of heat transfer can be achieved with no or little increase in pressure drop. Typical inserts are twisted tapes, coils (Fig. 18) and wire matrix inserts (Fig. 19). The potential of some of these inserts with respect to reducing deposit formation is reported in [49]. Figure 20 shows the effectiveness of the TURBOTAL system in reducing fouling in a crude oil preheater [77].

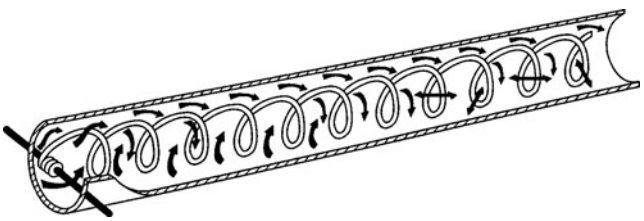

C4. Fig. 18. Spiral insert (SPIRELF system) [75]

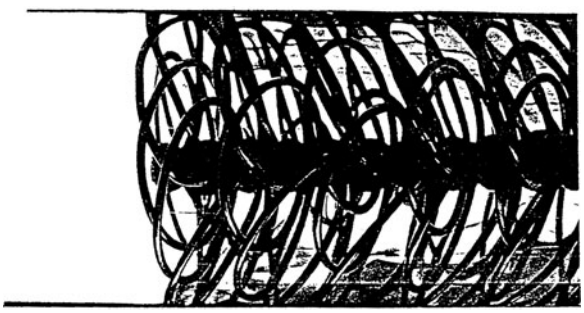

C4. Fig. 19. Cal-Gavin wire insert to increase heat transfer for flow in pipes [76]

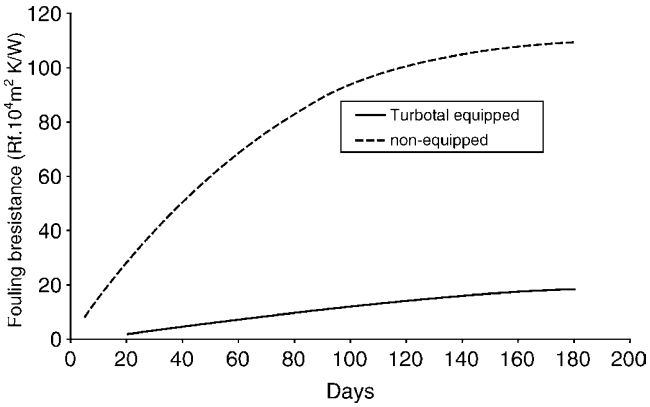

C4. Fig. 20. Crude oil fouling mitigation with Turbotal inserts [77]

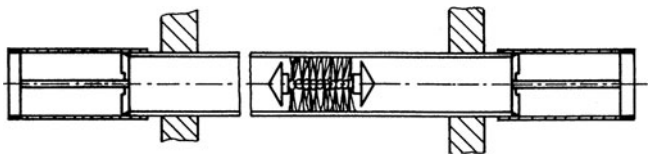

C4. Fig. 21. Continuous cleaning with wire brush system

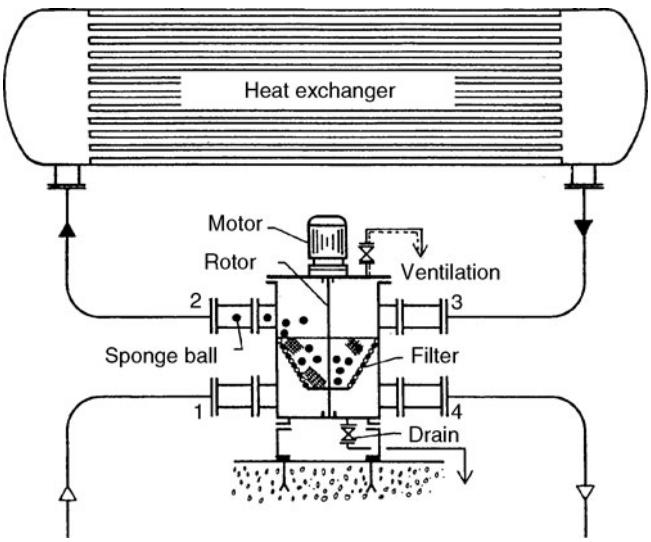

C4. Fig. 22. Typical layout of sponge ball cleaning system [79]

Continuous Transport of Cleaning Devices Through Tubes

These methods require major modifications of the flow system and are, therefore, best implemented in the design stage. However, they have the advantage that exchangers may be kept clean over long periods of time. All systems work best if applied to an initially clean heat exchanger.

A number of companies (MAN, Water Services of America, KALVO [78], ATCS) have developed continuous tube cleaning systems using small nylon brushes which are inserted into each tube, see Fig. 21. These brushes are pushed through the tubes by the fluid flow. For continuous operation and optimum cleaning efficiency, the flow direction has to be reversed about every 8 h. Life expectancy of the brushes is about 5 years. It is claimed that the time for amortization is between 8 and 16 months.

There are many examples for the successful application of the brush tube cleaning system. However, their most effective installation is in smaller, water-cooled heat exchangers, for example, for the central air-conditioning systems of office buildings, hotels, or hospitals.

For large installations, more consistent results were obtained with a system where sponge balls with a rough surface are circulated through the heat exchanger, see Fig. 22. The diameter of the sponge balls is slightly larger than the inside diameter of the tubes and the system is designed such that each tube sees a sponge ball every 5–10 minutes. Since the diameter of the sponge balls decreases with time and because of inevitable ball losses through the screening system, the sponge balls have to be replaced regularly. For hard and adherent deposits, carborundum coated sponge balls can be used. According to the manufacturers, application of sponge ball systems may reduce the fouling resistance to close to 0 m^2K/kW. The application of sponge ball systems is limited to temperatures below 120°C. Several companies, for example, TAPROGGE or CQM supply sponge ball systems and complete maintenance packages with different levels of complexity, size, and cost.

Online cleaning systems are not effective against stones, clamshells, etc. and need upstream devices to remove debris and macroscopic organic matter from the incoming water.

4.3.2 Gas Flow

Online mechanical techniques vary greatly, but soot blowers are the most popular for gas-side use [80]. Some of other techniques such as scrapers, rappers, and chains work well in special applications but are not as readily available. Two common types of soot blowers are jet soot blowers and sonic soot blowers.

- The jet type of soot blower operates by emitting pulses of steam, air or water at programmed intervals directed at the tubes and/or down tube lanes to dislodge the deposits and re-entrain them in the gas stream. These soot blowers work best if used frequently, thus avoiding the build-up of material. When build-up occurs, it insulates the surface from the coolant, allowing a temperature rise that can produce a glassy deposit. Glassy deposits are much harder to dislodge and frequently require shutdown for their removal. Jet soot blowers come in two types: (i) The fixed position rotating type is installed inside the heat exchanger and (ii) the retractable type periodically passes an externally mounted nozzle through the heat exchanger. The fixed position soot blowers require little additional floor space, but they can usually not be used if the temperature exceeds 1000°C. As more than 100 soot blowers may be installed in large fired boilers, steam, and pressurized air consumption may cause considerable costs.
- According to the manufacturers, installation, and operation costs of sonic soot blowers are only 10% of those of jet soot blowers. Sonic soot blowers perform best in the cooler regions of furnaces or in other apparatus where glassy phases of deposits are not encountered. They operate by emitting sound pressure waves that loosen the particulates and allow them to be carried away with the gas stream. Under normal operations, sonic horns need only sound for 15–30 s every 10–30 min. Horns are constructed of materials that can withstand temperatures up to 1000°C. Sonic soot blowers may not, however, be able to loosen the harder deposits that can be removed by the high velocity steam, air or water jets. Sonic soot blowers are available at sonic or infrasonic range.

For very sticky deposits or if jet soot blowing may cause the temperature to drop below the acid dew point, 5 mm diameter cast iron spheres may be poured over the pipe arrangement. For extremely severe gas-side fouling problems, fluidized bed technology should be considered as an alternative.

The control of operating conditions is a very important consideration in the prevention of gas-side fouling. Some of the most important controls are:

- Maintain surface temperature above acid dew-point temperature
- Control amount of excess air, which governs the conversion of SO_2 to SO_3 and hence the amount of H_2SO_4 formed
- Control combustion parameters such as fuel injection pattern, fuel injection schedule and fuel viscosity
- Use fuel/air premixing to eliminate soot production
- Quench hot flue gases to solidify molten and soft particles to prevent attachment at cooler heat transfer surfaces

The control of combustion conditions is a difficult task due to the great variability in the quality of fuel supplies. Variability of fuel characteristics is a particular problem for those industries that burn waste products.

4.3.3 Other Devices for Fouling Mitigation

When it comes to commercial mitigation of scale formation, one of the most frequently and emotionally discussed topics are devices, which claim to reduce scaling by magnetic, electronic, or catalytic means. To-date, no conclusive scientific proof or theory for the mechanisms, which may be responsible for the beneficial effects of such technologies, has been found. A considerable number of investigations have been reported in the literature; many of them claim some sort of success with the

applied technology. Most of the research-related literature originates from the former Soviet Union, the UK and the USA, while several systematic investigations have been performed by public and private organizations in Austria, Germany, and Switzerland. German Industry Standards (DIN) have been formulated for performance evaluation of physical water conditioners. Pilot plant and laboratory scale investigations have provided contradicting results. For example, [81, 82] report that the installation of magnets considerably reduced cooling water fouling, whereas [83, 84] found no effect of the water conditioner. Even the mechanisms of scale inhibition are highly disputed. There are claims that clatherate formation or impact on the nuclear spin of dissolved ions will reduce the chemical reaction on the surface; or that very high frequency current favors bulk precipitation of scale-forming materials and hence weakly adhering particulate deposit rather than a strong crystalline layer. Other investigators believe that minute changes in local pH may affect the $CaCO_3$ equilibrium in the solution. More recently, claims have been made that the key mechanism is the release of iron ions or iron oxide into the water, which has an adverse effect on the growth behavior of crystals. Another plausible explanation is that the electrical field, together with dissolved impurities, changes the crystal form of $CaCO_3$ from Calcite to Aragonite. Some agreement exists that magnetic or electromagnetic fields are effective for a relatively narrow range of flow velocities only [85].

Manufacturers of such equipment have impressive reference lists of successful installations, where the formation of crystalline deposits has been substantially reduced or even avoided. However, it is also fair to say that there have been numerous cases where no improvement has been achieved. Until the applications and limitations of these installations have been clearly established, no general statement can be made about their economic evaluation with respect to other available scale prevention methods. While most suppliers of physical water treatment facilities recommend installation of their devices at a relatively short distance upstream of the heat exchanger which is to be protected, others claim "memory effects" in the fluid of up to 6 months.

5 Cleaning of Heat Exchangers

Periodical cleaning of heat exchangers will be necessary, even if the heat exchanger is well-designed and the fluid treatment is effective. Additionally, conditions in the heat exchanger may deviate from the design conditions due to changes in flow rates and temperatures, plant failures, ingress of air and bacteria, changes in the fluid composition or upstream corrosion, which all may promote fouling. If a heat exchanger or pipeline suffers from deposit formation, this can be the start of a whole series of problems. Corrosion processes may take place under the deposit, fouling rates may be increased due to the surface roughness of the deposit or irregular behavior of the exchanger may be observed due to build-up and removal of deposits. It is, therefore, advantageous to remove non-protective deposits soon after the onset of their formation. Heat exchangers may be cleaned by chemical or mechanical methods or by a combination of both.

5.1 Chemical Cleaning Methods

Chemical cleaning methods have a number of advantages over mechanical methods, namely:

(a) They are relatively quick.
(b) Surfaces do not experience mechanical damage.
(c) Chemical solutions reach normally inaccessible areas.
(d) They are less labor intensive than mechanical cleaning.
(e) Cleaning can be performed in situ.

5.1.1 The Basic Process

Most chemical cleans consist of five distinct processes, each being monitored for results before proceeding to the next. The five stages are:

1. The alkaline clean primarily aims to remove the organic portion of the deposit (oil, fat) in order to render the inorganic surface hydrophilic. This is necessary to make the following acid cleaning effective.
2. Before and after each chemical step, high flow water flushes are required to physically remove loose or softened material.
3. Once the surface is hydrophilic, the deposit is softened and/or dissolved by application of the appropriate acid blend. This blend usually contains an inhibitor, which prevents corrosion of the base metal by the acid. The analysis of the spent acid strength and the concentration of dissolved scale species indicate whether the acid clean is completed.
4. After the acid stage, water rinsing is required to remove loose debris, sludge, and residual acid. Water rinsing may be accompanied by inert gas purging and sequestrant addition, depending on the cleaning technique and the plant configuration.
5. After the acid and rinse stages, the base metal which has been exposed as a result of the cleaning operation is in a very active state. If left and exposed to the atmosphere, the surface would rapidly reoxidize in an uncontrolled fashion. A passivation process is performed to form a tightly adherent, protective oxide film on the base metal.

Particular applications may require modifications of the above sequence. The selection of the cleaning agent and the cleaning procedure strongly depend on the type of deposit, the material and configuration of the installation and on economical and environmental considerations.

5.1.2 Cleaning Procedure

Among the many possible choices available for cleaning procedures are ambient temperature treatments, high temperature treatments, fill-and-soak techniques, circulating techniques, on-stream techniques, vapor phase techniques, foam techniques and emulsion techniques. Soaking treatments are effective in many instances. Their application generally reduces equipment costs while increasing chemical costs and downtime costs.

Obviously, it is advantageous to circulate the cleaning agent in order to improve evenly mixing of the chemicals and to reduce concentration profiles near the fouled surfaces. Circulation also increases physical disintegration of the deposit by mechanical scouring. As chemical reaction rates increase exponentially with temperature, the cleaning process may be improved if the cleaning agent is heated. Foaming reduces the cleaning agent requirements and increases the effectiveness of cleaning. Also, the foaming treatment may be faster in some cases. It allows for good contact in large shell and tube heat exchanger.

Research on the mechanisms of chemical cleaning of heat transfer surfaces is far less developed than research of fouling mechanisms. Nevertheless, some first modelling has been attempted, assuming that the cleaning process is an inverse fouling process.

5.1.3 Cleaning Agents

Table 16 shows typical deposits that can be removed chemically [86]. Deposits that can not be removed are given in Table 17.

Table 18 lists a number of chemicals used for cleaning. Sulfuric acid and hydrochloric acid are the most widely used chemical cleaning agents. When used properly, they are safe, relatively low-cost materials. However, these mineral acids are highly ionized and strong, which may cause rapid corrosion if the solution is insufficiently inhibited. Therefore, weaker organic acids and chelating agents are coming into wider use.

Generally, a mixture of several chemicals is used to attack complex deposits. Dispersants are added to disperse oils or fats and to allow better penetration of the deposit. Sometimes, the addition of small quantities of a second cleaning agent (e.g., the addition of 0.25% ammonium bifluoride or 0.5% sodium bromate to citric solutions) may considerably increase the effectiveness of the cleanup [87].

The type of cleaning agent to be chosen has a major effect on the economics of the cleaning job. The selection of cleaning chemicals is not only depending on the type of deposit, but also on the exchanger material and the cleaning conditions. In many cases, chemical cleaning of heat exchangers involves the use of acids. Although some metal loss is inevitable, the addition of inhibitors greatly reduces corrosion. It must be emphasized that inhibitors are only suitable for specific metal under specific conditions. Personal danger and disposal problems have to be

C4. Table 16. Typical deposits removed by chemical cleaning [86]

Organic
Oil, grease, fat, waxes, soft carbon, tars, silt, vegetation, biological matter, polymers, resins, paints
Inorganic
Rust, magnetite, calcium carbonate, calcium sulfate, magnesium hydroxide, calcium phosphate, silica, magnesium silicate, copper, copper oxides, alumina, nickel oxides

C4. Table 17. Intractable deposits [86]

Glasses, ceramics, hard carbon, inert plastics, vulcanized rubber, rubber latex

C4. Table 18. Common types of chemicals utilized for in-situ chemical cleaning [87]

Acids	Alkalis	Complexing agents
Hydrochloric	Caustic Soda	EDTA
Nitric	Ammonia	Gluconates
Sulfuric	Trisodium phosphate	
Hydrofluoric	Sodium metasilicate	
Citric	Soda ash	
Formic		
Sulphamic		
Oxidants	**Solvents**	**Others**
Potassium permangangate	Aromatic	Biocides
Sodium bromate	Aliphatic	Surfactants
Sodium nitrite	Chlorinated	Inhibitors
Sodium hypochlorite	Emulsifiers	Antifoams
Ammonium persulfate	Dewatering formulations	Dispersants
		Hydrazine bifluoride

C4. Table 19. Scale and deposit removal [87]

Deposit	Cleaning method
Calcium sulfate	Boil with Na_2CO_3 solution, treat with inhibited acid
Calcium carbonate	Inhibited acid
Magnesium hydroxide	Inhibited acid
Calcium phosphate sludge	Inhibited acid
Magnesium silicate	Inhibited acid + small % of HF
Sodium aluminum silicate	Hydrofluoric acid
Ferric oxide (Fe_2O_3)	Inhibited acid or ammoniated citric acid
Ferrous oxide (Fe_3O_4)	Inhibited acid or ammoniated citric acid. Add 0.25–0.5% stannous chloride for protection against ferric ion attack. Ammoniated EDTA
Copper	Ammoniated bromate, ammoniated EDTA
Organic material	High velocity liquids or circulate 20% chromic acid heated to 95°C. Hot alkaline solutions useful for removing light oils, grease, or other sludge materials

considered, too. Table 19 shows some deposits and scales with the recommended cleaning agents [87].

For plants in operation, the timing of cleaning operations is of economical importance. Energy losses, production losses and safety aspects have to be compared with cleaning costs and losses due to shutdown. Table 20 shows typical application of some of the most common cleaning agents.

C4. Table 20. Chemical cleaning agents [87]

Agent	Application
Hydrochloric acid	General removal of rust and scale for non-stainless steel piping
Inhibited HCL	Same as above
Sulfuric acid	General usage for stainless steel for removal of rust and scale. H_2SO_4 is dangerous to personnel and must be used with caution
Inhibited H_2SO_4	Same as above
Hydroxyacetic acid	General acidizing. Safer than H_2SO_4
Formic acid	Often used as 1% formic, 2% hydroxy-acetic acid solution for cleaning of supercritical "once-through" boilers where stainless steel is the prevalent material of construction and chloride ions must be avoided. Also used for non-ferrous metals as a 1–2% solution. Must be heated to 95°C. Safter than mineral acids
Citric acid	Used as 0.01 solution to chelate iron. Used at ambient temperature or slightly warm
Ammoniated citric acid	Very safe (corrosion and handling) cleaning agent. By changing pH and adding sodium nitrite, the same solution. may be used for passivation. pH is adjusted by adding NH_3 and resulting solution is effective for copper removal
Hydrofluoric acid	Used for new piping and for stainless steel where chloride ions are critical as a 3–5% solution. Also used for silica deposit removal. Dangerous!
Sulphamic acid	Fairly safe. Used at a 5–10% solution for removal of iron oxides. Must be maintained below 60°C or decomposes to ammonium bisulfate
Ammoniated bromate	Use for removal of copper. Does not attack scale or iron oxides. For each kg of copper use
	0.9 kg $NaBrO_3$
	1.4 kg $(NH_4)_2CO_3$
	4.5 l NH_4OH 30%
Phosphoric acid	Less aggressive than sulfuric acid and more aggressive than sulphamic acid. Use for general removal of oxides and scales, particularly for stainless steel
Ammoniated EDTA	Use for removal of iron oxides or copper, as a 5–10% solution. Safe material!
Sodium salt	Use for removal of water hardness scales as a 5–10% solution

5.1.4 OnStream Chemical Cleaning

In most cases, chemical cleaning is done while the heat exchanger is off-line. However, there have been several attempts to develop chemicals that can be used for onstream cleaning to avoid expensive plant shutdown. Examples for these chemicals are complexing agents which can be added during operation of boilers.

Shock dosage of chlorine (>15 ppm) is often used to remove bio-deposits while the exchanger is onstream. However, it was found that biofilms regrow at an accelerated rate after the chlorine dosage. As chlorination has come under increasing regulatory control, methods to use chlorine more efficiently and to minimize the amount of chlorine discharged to the water ways become increasingly important.

5.1.5 Problems Associated with Chemical Cleaning

Problems associated with chemical cleaning of heat exchangers are due to the danger of handling (burn, toxic), due to elevated application temperatures, due to the costs of cleaning agents, due to the chemical attack on the heat exchanger material (overcleaning, uneven cleaning, corrosion) and due to disposal problems. Acids and alkalis must be neutralized, organic materials may be burned and fluorides must be reacted to inactive solid residues. Some of the organic acids, such as citric acid and gluconic acid are biodegradable.

5.2 Mechanical Cleaning Methods

For the following cleaning methods, heat exchangers have to be taken off-line and dismantled. Some of the deposits may then be removed manually, for example from the water box. Steam-blasting and hydro-blasting with pressures up to 1500 bar are probably the most common mechanical cleaning methods, see [49]. They can be performed completely manually or semiautomatically in cleaning stations. If deposits are very tenacious, sand can be added to the pressurized water to increase the cleaning efficiency. Both, steam- and hydro-blasting are labor intensive and keep the exchanger off-line for a considerable time. Blasting may not completely eliminate all deposits and some significant roughness can remain. The shell-side of tube bundles can only be cleaned completely if the tubes are arranged in-line. The particular geometry of twisted tubes provides flow lanes for pressurized water or steam which facilitates cleaning. Experienced maintenance crews are required and strict safety regulations must be obeyed due to the danger of handling equipment at very high pressures.

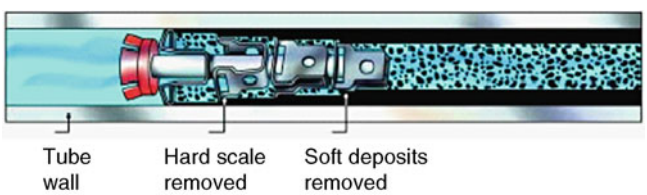

C4. Fig. 23. CONCO cleaning device [89]

While blasting is the only available alternative for the shell-side of the tube bundle, several cleaning methods can be used for the inside of straight tubes. The continuous cleaning sponge ball system described in detail in Sect. 4.3 can also be used as a transportable, off-line cleaning system, particularly if used with corundum-coated sponge balls. Very dirty and plugged tubes can be cleaned with drills equipped with drill bits, brushes, or bit-brush combinations.

To avoid damage of the heat transfer surfaces, cleaning must be done carefully, thus increasing costs for labor and downtime.

Using air- or hydropressure, rubber plugs or metal scrapers can be shot through the tubes. These techniques are considerably faster than the above methods, cleaning up to 15,000 tubes in 24 h. Rubber plugs fail for hard deposits. Shooting metal scrapers through the tubes at a water pressure of 35 bar and a scraper velocity of 3–6 m/s results in the removal of most deposits [88]. An example of those scrapers is shown in Fig. 23. In general, water pressure systems are safer than air pressure systems, due to the compressibility and subsequent rapid expansion of gases.

Most mechanical cleaning methods remove not only the deposit but also the protective oxide layer. Under certain circumstances, this may create a corrosion problem. On the other hand, regular cleaning removes deposit and avoids flow conditions, which promote corrosion due to chemical reaction or stagnant flow. For very severe fouling problems, a combination of chemical and mechanical cleaning may be recommended.

6 Symbols

CF	Cleanliness factor
E	Activation energy (J/mol)
K	Constant
R	Universal Gas Constant, 8.314 J/(mol K)
Re	Reynolds Number
R_f	Fouling resistance (m^2K/W)
s	Deposit thickness (m)
u	Flow velocity (m/s)
τ_w	Wall shear stress (N/m^2)
ξ	Friction factor
1,2	Fluid 1, fluid 2

Subscript/Superscripts

c	Clean
d	Deposit
f	Fouled

7 Bibliography

1. Steinhagen R, Müller-Steinhagen HM, Maani K (1993) Fouling problems and fouling costs in New Zealand industries. Heat Transfer Eng 14(1):19–30
2. Steinhagen R, Müller-Steinhagen HM, MaaniK (1990) Heat exchanger applications, fouling problems and fouling costs in New Zealand Industries. Ministry of Commerce Report RD8829 1–116
3. Garrett-Price BA, et al. (1985) Fouling of heat exchangers – characteristics, costs, prevention, control and removal. Noyes Publications, Park Ridge, New Jersey
4. TEMA (1978) Standards of the Tubular Exchanger Manufacturers Association, 6th edn., New York
5. Marriott J (1971) Where and how to use Plate Heat Exchangers. Chem Eng 78(8):127–134
6. Weierman RC (1982) Design of heat transfer equipment for gas-side fouling service. In: Marner WJ, Webb RL (eds) Workshop on an assesment of Gas-Side Fouling in Fossil Fuel Exhaust Environments. Publication 82–67, Jet Propulsion Laboratory, California Institute of Technology, Pasadena, California
7. Palen JW (1983) Shell and tube re-boiler. Sect. 3.7.8, Heat Exchanger Design Handbook. Hemisphere Publ. Corp
8. Chenoweth JM (1987) General design of heat exchangers for fouling conditions. In the NATO Advanced Study Institute on Advances in Fouling Science and Technology, Alvor, Portugal
9. Bansal B, Chen XD, Müller-Steinhagen H (1997) Effect of suspended particles on calcium sulphate fouling in plate heat exchangers. ASME J Heat Transfer 119:568–574
10. Blöchl R, Müller-Steinhagen HM (1990) Influence of particle size and particle/liquid combination on particulate fouling in heat exchangers. Can J Chem Eng 68(4):585–591
11. Epstein N (1983) Fouling in heat exchangers. In: Taborek J, Hewitt G (eds) Heat exchanger theory and practice, McGraw-Hill, New York
12. Müller-Steinhagen H (2000) Modellierung der Ablagerungsbildung in Wärmeübertragern – *Vom Laborversuch zur Produktionsanlage* – Berichte zur Energie- und Verfahrenstechnik Vol 20.1, ISBN 3-931901-14-9
13. Taborek J (1987) Private communications
14. Martin H (1988) Wärmeübertrager. Georg Thieme, Verlag Stuttgart
15. Thackery PA (1980) The cost of fouling in heat exchanger plant. Effluent and Water Treatment J 20(3):112–115
16. Pritchard AM (1987) The economics of fouling. In: Melo LF, Bott TR, Bernardo CA (eds) Fouling science and technology, NATO ASI Series E, vol. 145. Kluwer, Amsterdam
17. Woods DR, Anderson SJ, Norman SL (1976) Evaluation of capital-cost data – heat-exchangers. Can J Chem Eng 54(6):469–488
18. Sart P, Eimer K (1979) Control of scaling or fouling effects in cooling water system for improvement of heat exchanger efficiency, Paper presented at international meeting on industrial heat exchangers and heat recovery, Liege, Belgium
19. Hewitt G, Müller-Steinhagen H (2000) Heat exchanger fouling in crude oil distillation units. ESDU Data Item 00016:1–80
20. Hewitt G, Müller-Steinhagen, H (2003) Fouling in cooling water systems using seawater. ESDU Data Item 03004, pp 1–100, International Ltd., London
21. Hewitt G, Müller-Steinhagen H (2007) Fouling in cooling systems using fresh water. ESDU Data Item 08002, International Ltd., London, pp 1–172
22. Bennett CA, Kistler RS, Lestina TG, et al. (2007) Improving heat exchanger designs. CEP 103(4):40–45
23. Aguirre FJ (2006) Reviewing the use of fouling factors in heat exchanger design. http://www.ChemicalProcessing.com. Cited 15 February 2000
24. Bennett CA (2005) Using a non-traditional approach to account for crude oil fouling in heat exchangers. http://www.ChemicalProcessing.com. Cited 30 September 2005
25. Nesta JM, Bennett CA (2005) Fouling mitigation by design. The 6th international conference on petroleum phase behavior and fouling, Amsterdam, The Netherlands
26. Nesta J, Bennett CA (2004) Reduce fouling in shell-and-tube heat exchangers. Hydrocarb Process 83(7):77–82
27. Knudsen JG (1983) Fouling in heat exchangers. Heat Exchanger Design Handbook Hemisphere Publications Corporation, Washington, DC
28. TUBEC Tubes. AST, Avesta Sandvik Tube AB, Helmond, Holland
29. Bornhorst A, Zhao Q, Müller-Steinhagen H (1999) Reduction of scale formation by Ion implantation and magnetron sputtering on heat transfer surfaces. Heat Transfer Eng 20(2):6–14
30. Müller-Steinhagen H, Zhao Q, Helalizadeh A, et al. (2000) The effect of surface properties on $CaSO_4$ scale formation during convective heat transfer and subcooled flow boiling. Can J Chem Eng 78:12–20
31. Förster M, Augustin W, Bohnet M (1999) Influence of the adhesion force crystal/heat exchanger surface on fouling mitigation. Chem Eng Process 38:449–461

32. Zhao Q, Müller-Steinhagen H (2001) Intermolecular and adhesion forces of deposits on modified heat transfer surfaces. In Proceedings of UEFC on heat exchanger fouling (Session II), Davos, Switzerland
33. Zhao Q, Liu Y, Müller-Steinhagen H, Liu G (2002) Graded Ni-P-PTFE coatings and their potential applications. Surface and Coatings Technology 155:279–284
34. Paikert P (1983) Verschmutzung von Kondensatoren und Kühltürmen. GVC Weihnachtstagung 371–390
35. Gilmour CH (1965) No fooling – no fouling. Chem Eng Prog 61(7):49–54
36. Kral D, Stehlik P, van der Ploeg HJ, et al. (1996) Helical baffles in shell and tube heat exchangers, Part I: Experimental verification. Heat Transfer Eng 17 (1):93–101
37. http://www.embaffle.com/
38. Butterworth D, Guy AR, Welkey JJ (1998) Design and application of twisted-tube exchangers. Brown Fintube, London
39. Müller-Steinhagen H (2001) Numerical investigation on plate heat exchanger design. UEF Conference on Compact Heat Exchangers, Davos, Switzerland
40. Klaren DG (1987) Fluid bed heat exchanger. CPP Edition, Europe
41. Cooper A, Suitor JW, Usher JD (1980) Cooling water fouling in plate heat exchangers. Heat Transfer Eng 1(3):50–55
42. Novak L (1982) Comparison of the Rhine river and the Öresund sea water fouling and its removal by chlorination. J Heat Transfer 104:663–670
43. Zettler HU, Weiss M, Zhao Q, et al. (2005) Influence of surface properties/ characteristics on fouling in plate heat exchangers. Heat Transfer Eng 26:3–17
44. Delplace F, Leuliet JC, Bott TR (1997) Influence of plate geometry on fouling of plate heat exchangers by whey protein solutions. In: Panchal CB, Bott TR, Somerscales, FC, et al. (eds) Fouling mitigation of industrial heat-exchange equipment. Begell House, Redding, pp 565–576
45. Masri MA, Cliffe KR (1997) Investigation into the fouling of a plate and frame heat exchanger. In: Panchal CB, Bott TR, Somerscales FC, et al. (eds) Fouling mitigation of industrial heat-exchange equipment. Begell House, Redding, pp 549–561
46. Pritchard AM, Clarke RH, de Block MX (1992) Fouling of small passages in compact heat exchangers. In: Bott et al. (eds) Fouling mechanisms: Theoretical and practical aspects. Eurotherm Semin 23:47–56
47. Kew P (1991) An investigation into fouling of a printed circuit heat exchanger. Future Practice Report 13, Energy Efficiency Enquiries Bureau, Harwell, London
48. Coulson JM, Richardson JF, Sinnott RK (1985) Chemical Engineering, Volume 6. Pergamon Press
49. Müller-Steinhagen H (2000) Heat exchanger fouling – mitigation and cleaning technologies. Publico Publications, ISBN 0 85295 436(0):1–382
50. DUBBEL (1974) Taschenbuch für den Maschinenbau, vol. 2, 13th edn., pp 87–94
51. Müller-Steinhagen H (1999) Cooling water fouling in heat exchangers. Adv Heat Transfer 33:415–496
52. Harris A, Marshall A (1981) The evaluation of scale control additives. Conference on progress in the prevention of fouling in industrial plant, University of Nottingham, Nottingham
53. Krisher AS (1978) Raw water treatment in the CPI. Chem Eng 79–98
54. Haluska JL (1976) Process fouling control by effective antifoulant selection. Paper No. 153 presented at Corrosion/76, Houston
55. Watkinson AP (1988) Critical review of organic fluid fouling: Final Report No. ANL/CNSV-TM-208 Argonne National Laboratory, III
56. Gillies WV (1979) Fouling and its control by chemical additives in hydrocarbon streams. Proceedings of the Institute of Corrosion Science and Technology, and Institute of Chemical Engineering Fouling Conference, University of Surrey, Guildford, London
57. Mayo FR, Miller AA (1856) The oxidation of unsaturated compounds. The oxidation of styrene. J Am Chem Soc 78:1017–1022
58. Mayo FR, Miller AA (1956) The oxidation of unsaturated compounds. Reaction of styrene peroxide. J Am Chem Soc 78:1023–1034
59. Mayo FR, Miller AA, Russel GA (1958) The oxidation of unsaturated compounds. J Am Chem Soc 80:2500–2507
60. Mayo FR (1958) The oxidation of unsaturated compounds. The effect of oxygen pressure on the oxidation of styrene. J Am Chem Soc 80:2465–2480
61. Mayo FR (1986) Gum and deposit formation from jet turbine and diesel fuels at 130°C. Ind Eng Chem Prod Res Dev 25:333–348
62. Mayo FR, Stavinoha LL, Lee GH (1988) Source of jet fuel thermal oxidation tester deposits from an oxidized JP-8 fuel. Ind Eng Chem Res 27(2):362–363
63. Dugan CP, Van Nostrand WL, Jr. Haluska JL (1978) How antifoulants reduce the energy consumption of refineries. Chem Eng Prog 74:53–57
64. Novak L (1982) Comparison of the Rhine river and the Öresund sea water fouling and its removal by chlorination. J Heat Transfer 104:663–670
65. Miller PC, Bott TR (1979) The removal of biological films using sodium hypochloride. Internaional Chemical Engineering Conference on Fouling Science or Art? Surrey University, Guildford, England
66. Birchall GA (1981) Achieving microbiolocal control in open recirculating cooling systems. Conference on progress in the prevention of fouling in industrial plant. University of Nottingham, Nottingham
67. Grier JC, Christensen RJ (1975) Microbiological control in alkaline cooling water systems. Paper presented at the national association of corrosion engineers annual meeting, Toronto, Canada
68. Waite TD, Fagan JR (1980) Summary of biofouling control alternatives. Condenser Biofouling Control, Publisher J. Garey, Ann Arbor Science
69. Grade R, Thomas BM (1979) The influence and control of algae in industrial cooling systems. International Chemical Engineering Conference on Fouling Science or Art? Surrey University, Guildford, England
70. Knudsen J (1991) Conquer cooling-water fouling. Chem Eng Prog 87(4):42–48
71. Betz Laboratories (1976) Handbook of industrial water conditioning, 7th edn Trevose, PA, pp 24–29
72. Drew Chemical Corporation (1977) Principles of industrial water treatment, 1st edn Boonton, NJ, pp 99–103
73. Nalco Chemical Comp (1979) Nalco Water Handbook, 1st edn. McGraw-Hill, New York
74. Knudsen JG, Jou HY, Herman KW (1985) Heat transfer characteristics of an electrically heated annular test section for determining fouling resistances. DREW Ind. Div., Report CWI-TP-18
75. SPIRELF System (1987) American European consulting company. Houston, TX
76. HEATEX Radial Mixing Element: A patented system developed by CAL GAVIN LTD., Birmingham, England
77. Haquet I (1994) TURBOTAL-system for reduced fouling in crude oil heat exchangers. Proceedings engineering foundation conference on heat exchanger fouling, Snells Beach, California
78. KALVO VOGLER GMBH: Automatisches Reinigungssystem für Kondensatoren und Röhrenwärmeaustauscher
79. TAPROGGE Report 84–15 (1984) Test of TAPROGGE condenser tube cleaning system to prevent silica and calcium carbonate scaling. TAPROGGE GmbH
80. Simon S, Zachay R (2000) Clyde Bergemann cleaning technology for heat exchangers In: heat exchanger fouling – mitigation and cleaning technologies Publico Publications, ISBN 0 85295 436 0:1–382
81. Parkinson G, Price W (1984) Getting the most out of cooling water. Chem Eng 91(1):22–25
82. Donaldson J, Grimes S (1988) Lifting the scale from our pipes. New Sci 18:43–46
83. Hasson D, Bramson D (1985) Effectiveness of magnetic water treatment in suppressing $CaCO_3$ scale deposition. Ind Eng Chem Process Des Dev 24:588–592
84. Söhnel O, Mullin J (1988) Some comments on the influence of a magnetic field on crystalline scale formation. Chem Ind 6:356–358
85. Cho YI, Lee SH, Kim W, et al. (2003) Physical water treatment for the mitigation of mineral fouling in cooling-tower water applications. In: Watkinson AP, Müller-Steinhagen H, Reza Malayeri M (eds) Heat exchanger fouling and cleaning: Fundamentals and applications, ECI Symposium Series, volume RP1. http://services.bepress.com/eci/heatexchanger/4
86. French MA (1981) Chemical cleaning in practice. Conference on progress in the prevention of fouling in industrial plant. Universität Nottingham, Nottingham
87. Roebuck AH, Bennett CA (1977) Heat transfer payback is a key to chemical cleaning choice. Oil Gas J 9:93–96
88. Hovland AW (1978) Effective condenser cleaning improves system heat rate. Pow Eng 82:49–50
89. Conco Systems, Inc., 135 Sylvan St., Verona, PA 15147

C5 Heat Exchanger Networks

Xing Luo · Wilfried Roetzel
Helmut-Schmidt-Universität, Universität der Bundeswehr Hamburg, Hamburg, Germany

1 Introduction

Many process industries are energy-intensive. A large amount of heat energy applied to process streams is normally dissipated through cooling utilities. It is possible to reuse the heat energy of hot process streams for heating cold process streams by means of additional heat exchangers. Such a system is called heat recovery system. The heat recovery system consists of a set of heat exchangers including heaters, coolers, condensers, reboilers, or other equipment and attachments for heat transfer between process streams. It can be treated as a heat exchanger network with different kinds of exchangers in which hot process streams can be cooled by the cold streams to be heated, and vice versa. In this way, the heating and cooling loads from external sources (hot and cold utilities) can be dramatically reduced. However, the reduction in utility costs is often accompanied by the increase in investment costs. Therefore, a balance between utility costs and investment costs should be established.

The optimal design of a heat exchanger network is to structure a system capable of performing the prescribed tasks at the minimum total annual costs, which is the sum of the utility costs and investment costs [1]. Because of its structural characteristics, it is also named the synthesis of heat exchanger networks. A further extension of the network synthesis is the optimal retrofit design of existing networks. Principally, the methodologies of optimal design of heat exchanger networks do not focus on the determination of detailed parameters of heat exchangers of a network. It takes the network as a system and determines the network configuration and heat loads of the exchangers used in the network for the further detailed unit design. The well-known synthesis methodologies are the Pinch design method [2], mathematical programming [3], and stochastic or heuristic algorithms such as genetic algorithm [4], simulated annealing algorithm [5] and Tabu search procedure [6]. The genetic algorithm was also combined with simulated annealing algorithm for the synthesis of multistream heat exchanger networks [7, 8]. This chapter introduces only the fundamental theories of the design of heat exchanger networks.

2 Temperature Calculation of Heat Exchanger Networks

2.1 Temperature Calculation of a Single Heat Exchanger

For a single heat exchanger, the heat load can be determined by

$$\dot{Q} = (\dot{M}c_p)_h(\vartheta'_h - \vartheta''_h) = (\dot{M}c_p)_c(\vartheta''_c - \vartheta'_c) = FkA\Delta\vartheta_{LM} \quad (1)$$

where the subscripts "h" and "c" denote hot stream and cold stream, ϑ' and ϑ'' are inlet and outlet temperatures, k is the overall heat transfer coefficient, A the heat transfer area, $\dot{M}$ the mass flow rate, and c_p the specific heat capacity at constant pressure. The product term $(\dot{M}c_p)$ is also named heat capacity flow rate. The correction factor F is the ratio of the real mean temperature difference to the logarithmic mean temperature difference of the counterflow heat exchanger $\Delta\vartheta_{LM}$ (see also Chap. C1),

$$\Delta\vartheta_{LM} = \frac{(\vartheta'_h - \vartheta''_c) - (\vartheta''_h - \vartheta'_c)}{\ln[(\vartheta'_h - \vartheta''_c)/(\vartheta''_h - \vartheta'_c)]} \quad (2)$$

If $(\vartheta'_h - \vartheta''_c) \approx (\vartheta''_h - \vartheta'_c)$, the arithmetic mean can be used,

$$\Delta\vartheta_{LM} \approx \frac{1}{2}[(\vartheta'_h - \vartheta''_c) + (\vartheta''_h - \vartheta'_c)] \quad (3)$$

Equation (1) is used to determine the exchanger size according to known stream temperatures. In Chap. C1 the two flow streams are denoted with indexes "1" and "2," as defined for the channels of each flow arrangement. For heat exchanger networks the notations "h" and "c" is more appropriate.

VDI-GVC (ed.), *VDI Heat Atlas*, DOI 10.1007/978-3-540-77877-6_8,

For an existing heat exchanger, the outlet stream temperatures are given by

$$\begin{bmatrix} \vartheta''_h \\ \vartheta''_c \end{bmatrix} = \begin{bmatrix} v_{hh} & v_{hc} \\ v_{ch} & v_{cc} \end{bmatrix} \begin{bmatrix} \vartheta'_h \\ \vartheta'_c \end{bmatrix} \tag{4}$$

or in the matrix form

$$\Theta'' = \mathbf{V}\Theta' \tag{5}$$

in which Θ' and Θ'' are the inlet and outlet temperature vectors of the exchanger, respectively, and

$$\mathbf{V} = \begin{bmatrix} v_{hh} & v_{hc} \\ v_{ch} & v_{cc} \end{bmatrix} = \begin{bmatrix} \frac{(1-R_h)e^{-NTU_h^*(1-R_h)}}{1-R_h e^{-NTU_h^*(1-R_h)}} & \frac{1-e^{-NTU_h^*(1-R_h)}}{1-R_h e^{-NTU_h^*(1-R_h)}} \\ \frac{R_h[1-e^{-NTU_h^*(1-R_h)}]}{1-R_h e^{-NTU_h^*(1-R_h)}} & \frac{1-R_h}{1-R_h e^{-NTU_h^*(1-R_h)}} \end{bmatrix} \tag{6}$$

$$R_h = 1/R_c = (\dot{M}c_p)_h/(\dot{M}c_p)_c \tag{7}$$

$$NTU_h^* = R_c NTU_c^* = FkA/(\dot{M}c_p)_h \tag{8}$$

Special cases:

$$R_h \to 0 : \mathbf{V} = \begin{bmatrix} e^{-NTU_h^*} & 1-e^{-NTU_h^*} \\ 0 & 1 \end{bmatrix} \tag{9}$$

$$R_h \to \infty : \mathbf{V} = \begin{bmatrix} 1 & 0 \\ 1-e^{-NTU_c^*} & e^{-NTU_c^*} \end{bmatrix} \tag{10}$$

$$(FkA) \to 0 : \mathbf{V} = \begin{bmatrix} 1 & 0 \\ 0 & 1 \end{bmatrix} \tag{11}$$

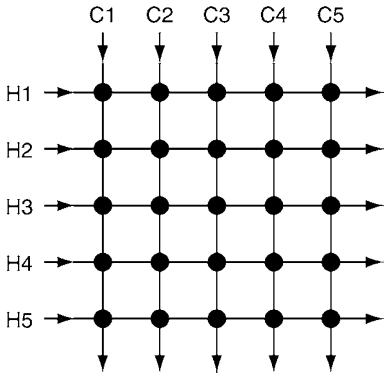

C5. Fig. 1. Heat exchanger network with sequential flow arrangement.

If the parameters appearing in the above equations depend on temperature, they can be modified with newly calculated outlet stream temperatures. The procedure will be repeated until the iteration deviation is less than the required accuracy.

2.2 Temperature Calculation of Heat Exchanger Networks with Sequential Flow Arrangements

For sequential flow arrangements the stream temperatures can be calculated from their entry positions. One of such arrangements is shown in Fig. 1, in which each cross-point of hot and cold streams indicates a possible heat exchanger. Hot streams are to be cooled down and cold streams are to be heated up. The hot and cold streams Hi and Ci ($i = 1, 2, 3, \cdots$) are arranged according to the network structure to be calculated. Usually they are arranged in the order of their supply temperatures, beginning with the highest temperatures. The calculation begins from the upper left exchanger and the calculated outlet stream temperatures of an exchanger become the inlet stream temperatures of the following exchangers. Thus, Eq. (4) can be applied to the exchangers sequentially, and the exit stream temperatures of the network can be finally obtained.

Example 1

This example was taken from the network design given by Ravagnani et al. [9]. The original problem data is listed in Table 1. The network design given by Ravagnani et al. [9] is shown in Fig. 2, where the data in brackets are the heat capacity flow rates in the branches. Its sequential relation is illustrated in Fig. 3.

The calculation begins from EX4.

$$\text{EX4: } R_h = (\dot{M}c_p)_h/(\dot{M}c_p)_c = 33.33/20 = 1.6665$$

$$k = (1/\alpha_h + 1/\alpha_c)^{-1} = (1/1.333 + 1/0.917)^{-1} = 0.54327\ \text{kW/m}^2\text{K}$$

$$NTU_h^* = FkA/(\dot{M}c_p)_h = 1 \times 0.54327 \times 202.23/33.33 = 3.2963$$

$$v_{hh} = \frac{(1-R_h)e^{-NTU_h^*(1-R_h)}}{1-R_h e^{-NTU_h^*(1-R_h)}} = \frac{(1-1.6665)\times e^{-3.2963\times(1-1.6665)}}{1-1.6665\times e^{-3.2963\times(1-1.6665)}} = 0.42852$$

$$v_{hc} = 1 - v_{hh} = 1 - 0.42852 = 0.57148$$

$$v_{cc} = \frac{1-R_h}{1-R_h e^{-NTU_h^*(1-R_h)}} = \frac{1-1.6665}{1-1.6665\times e^{-3.2963\times(1-1.6665)}} = 0.04762$$

$$v_{ch} = 1 - v_{cc} = 1 - 0.04762 = 0.95238$$

C5. Table 1. Problem data [9]

Stream	ϑ'(°C)	ϑ''(°C)	$\dot{M}_{c_p}$ (kW/K)	α(kW/m²K)	Cost ($/kW year)
H1	175	45	10	2.615	–
H2	125	65	40	1.333	–
C1	20	155	20	0.917	–
C2	40	112	15	0.166	–
Steam	180	179	–	5.000	110
Cooling water	15	25	–	2.500	10

Heat exchanger cost = 1,200 $A^{0.57}$ $/year ($A$ in m²). Correction factor $F = 1$ for all heat exchangers including heaters and coolers.

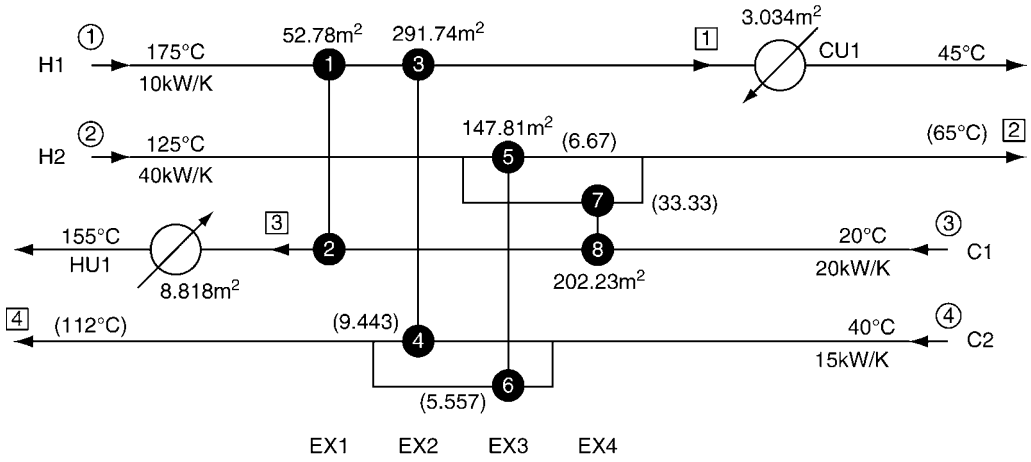

C5. Fig. 2. A network design given by Ravagnani et al. [9], 117,069 $/year.

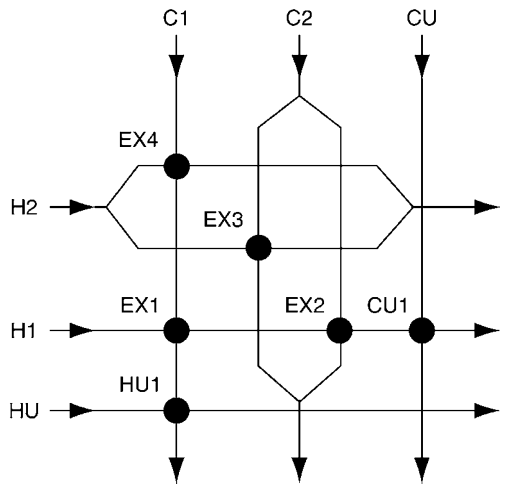

C5. Fig. 3. Heat exchanger network with the sequential flow arrangement.

$$\begin{bmatrix}\vartheta''_h\\ \vartheta''_c\end{bmatrix}=\begin{bmatrix}0.42852 & 0.57148\\ 0.95238 & 0.04762\end{bmatrix}\begin{bmatrix}125\\ 20\end{bmatrix}=\begin{bmatrix}64.99\\ 120.0\end{bmatrix}$$

The outlet stream temperatures of other exchangers can be obtained with the same method and the results are listed in Table 2. The heating and cooling loads and heat transfer areas of the heater HU1 and cooler CU1 are calculated by Eq. (1).

$$\text{CU1: } \dot{Q}=(\dot{M}c_p)_h(\vartheta'_h-\vartheta''_h)=10\times(57.02-45)=120.2\,\text{kW}$$

$$\Delta\vartheta_{LM}=\frac{(\vartheta'_h-\vartheta''_c)-(\vartheta''_h-\vartheta'_c)}{\ln[(\vartheta'_h-\vartheta''_c)/(\vartheta''_h-\vartheta'_c)]}=\frac{(57.02-25)-(45-15)}{\ln[(57.02-25)/(45-15)]}$$

$$=31.00^\circ\text{C}$$

$$k=(1/\alpha_h+1/\alpha_c)^{-1}=(1/2.615+1/2.5)^{-1}=1.2781\,\text{kW/m}^2\text{K}$$

$$A=\dot{Q}/(kF\Delta\vartheta_{LM})=120.2/(1.2781\times1\times31.00)=3.034\,\text{m}^2$$

$$\text{HU1: }\dot{Q}=(\dot{M}c_p)_c(\vartheta''_c-\vartheta'_c)=20\times(155-145)=200\,\text{kW}$$

$$\Delta\vartheta_{LM}=\frac{(180-155)-(179-145)}{\ln[(180-155)/(179-145)]}=29.27^\circ\text{C}$$

$$k=(1/5+1/0.917)^{-1}=0.7749\,\text{kW/m}^2\text{K}$$

$$A=200/(0.7749\times1\times29.27)=8.818\,\text{m}^2$$

2.3 Temperature Calculation of General Heat Exchanger Networks

In general cases the heat exchanger networks might have loops and the inlet stream temperatures of some exchangers might be unknown. An easy way is the use of iteration method. However, for complex networks the convergence of the iteration method might not be ensured. An alternative solution is the matrix method [10, 11].

Consider a heat exchanger network with N' stream entrances, N'' stream exits and N_{EX} heat exchangers. Each exchanger has two channels: the hot stream channel and the cold stream channel; therefore, the number of channels $N=2N_{EX}$. The channel indexes are related to the exchanger indexes, i.e., the index of the hot stream in the ith exchanger is $2i-1$, and that of the cold stream is $2i$. The indexes of the network entrances and network exits can be arbitrarily labeled.

Extending Eq. (5) to the whole network yields,

$$\Theta''_{EX}=\mathbf{V}\Theta'_{EX} \tag{12}$$

in which,

$$\mathbf{V}=\begin{bmatrix}\mathbf{V}_1 & & \mathbf{0}\\ & \ddots & \\ \mathbf{0} & & \mathbf{V}_{N_{EX}}\end{bmatrix} \tag{13}$$

$$\mathbf{V}_i=\begin{bmatrix}v_{hh,i} & v_{hc,i}\\ v_{ch,i} & v_{cc,i}\end{bmatrix}=\begin{bmatrix}\frac{(1-R_i)e^{-\text{NTU}_i^*(1-R_i)}}{1-R_ie^{-\text{NTU}_i^*(1-R_i)}} & \frac{1-e^{-\text{NTU}_i^*(1-R_i)}}{1-R_ie^{-\text{NTU}_i^*(1-R_i)}}\\ \frac{R_i[1-e^{-\text{NTU}_i^*(1-R_i)}]}{1-R_ie^{-\text{NTU}_i^*(1-R_i)}} & \frac{1-R_i}{1-R_ie^{-\text{NTU}_i^*(1-R_i)}}\end{bmatrix}$$

$$(i=1,2,\cdots,N_{EX}) \tag{14}$$

$$R_i=\frac{(\dot{M}c_p)_{h,i}}{(\dot{M}c_p)_{c,i}},\text{NTU}_i^*=\frac{(FkA)_i}{(\dot{M}c_p)_{h,i}}\quad(i=1,2,\cdots,N_{EX}) \tag{15}$$

Θ'_{EX} and Θ''_{EX} are the temperature vectors containing the inlet and outlet stream temperatures of N_{EX} exchangers, respectively,

$$\Theta'_{EX}=\left[\vartheta'_{h,1},\vartheta'_{c,1},\vartheta'_{h,2},\vartheta'_{c,2},\cdots,\vartheta'_{h,N_{EX}},\vartheta'_{c,N_{EX}}\right]^T \tag{16}$$

$$\Theta''_{EX} = \left[\vartheta''_{h,1}, \vartheta''_{c,1}, \vartheta''_{h,2}, \vartheta''_{c,2}, \cdots, \vartheta''_{h,N_{EX}}, \vartheta''_{c,N_{EX}}\right]^T \quad (17)$$

To illustrate the interconnections among the streams, the following four matching matrices need to be introduced [12]:

Interconnection matrix **G**: $N \times N$ matrix whose elements g_{ij} are defined as the ratio of the heat capacity flow rate flowing from channel j into channel i to that flowing through channel i.

Entrance matching matrix $\mathbf{G}'$: $N \times N'$ matrix whose elements g'_{ik} are defined as the ratio of the heat capacity flow rate flowing from the entrance k to channel i to that flowing through channel i.

Exit matching matrix $\mathbf{G}''$: $N'' \times N$ matrix whose elements g''_{li} are defined as the ratio of the heat capacity flow rate flowing from channel i to the exit l to that flowing out of exit l.

Bypass matrix $\mathbf{G}'''$: $N'' \times N'$ matrix whose elements g'''_{lk} are defined as the ratio of the heat capacity flow rate flowing from entrance k to exit l to that flowing out of exit l.

In a heat exchanger network, there might be such a knot at which the streams mix and split again, which can be defined as a mixer. If there is a mixer before channel i or exit l, then, in the above definitions of the matrices, the denominator should be the heat capacity flow rate flowing through the mixer.

By the use of the aforementioned matrices, the stream temperatures in the network can be obtained by

$$\Theta'_{EX} = (\mathbf{I} - \mathbf{GV})^{-1}\mathbf{G}'\Theta'_N \quad (18)$$

$$\Theta''_{EX} = \mathbf{V}\Theta'_{EX} = \mathbf{V}(\mathbf{I} - \mathbf{GV})^{-1}\mathbf{G}'\Theta'_N \quad (19)$$

$$\Theta''_N = \mathbf{G}'''\Theta'_N + \mathbf{G}''\Theta''_{EX} = [\mathbf{G}''' + \mathbf{G}''\mathbf{V}(\mathbf{I} - \mathbf{GV})^{-1}\mathbf{G}']\Theta'_N \quad (20)$$

in which $\mathbf{I}$ is the unit matrix, Θ'_N and Θ''_N are two vectors containing the stream temperatures at the network entrances and exits before entering the external heaters and coolers.

A more complicated problem is the temperature calculation of multistream heat exchangers and their networks. For general cases a numerical procedure should be adopted. However, if the stream arrangement in a multistream heat exchanger is one-dimensional, e.g., parallel flow and counterflow, an analytical solution of the stream temperatures can be obtained [13].

Example 2

The network shown in Fig. 4 is the optimal solution of the design problem given by Table 1. The indexes of channels, entrances, and exits are labeled in Fig. 4.

The entrance temperature vector is $\Theta'_N = [175\ \ 125\ \ 20\ \ 40]^T$. For EX1,

$$\text{EX1: } R_1 = \frac{(\dot{M}c_p)_{H1}}{(\dot{M}c_p)_{C1}} = \frac{10}{20} = 0.5$$

$$k_1 = (1/\alpha_{H1} + 1/\alpha_{C1})^{-1} = (1/2.615 + 1/0.917)^{-1} = 0.6789\,\text{kW/m}^2\text{K}$$

$$\text{NTU}_1^* = \frac{(FkA)_1}{(\dot{M}c_p)_{H1}} = \frac{1 \times 0.6789 \times 51.65}{10} = 3.5066$$

$$\nu_{hh,1} = \frac{(1 - R_1)e^{-\text{NTU}_1^*(1-R_1)}}{1 - R_1 e^{-\text{NTU}_1^*(1-R_1)}} = \frac{(1 - 0.5) \times \exp[-3.5066 \times (1 - 0.5)]}{1 - 0.5 \times \exp[-3.5066 \times (1 - 0.5)]} = 0.09481$$

$$\nu_{hc,1} = 1 - \nu_{hh,1} = 1 - 0.09481 = 0.90519$$

C5. Table 2. Calculation results of example 1

	ϑ'_h (°C)	ϑ'_c (°C)	A (m²)	R_h	NTU^*_h	ϑ''_h (°C)	ϑ''_c (°C)
EX4	125	20	202.23	1.6665	3.2963	64.99	120.00
EX3	125	40	147.81	1.2003	3.2713	65.00	112.02
EX1	175	120.00	52.78	0.5000	3.5834	125.00	145.00
EX2	125.00	40	291.74	1.0590	4.5538	57.02	111.99
	ϑ'_h (°C)	ϑ''_h (°C)	ϑ'_c (°C)	ϑ''_c (°C)	$\dot{Q}$ (kW)	$\Delta\vartheta_{LM}$ (°C)	A (m²)
CU1	57.02	45	15	25	120.2	31.00	3.034
HU1	180	179	145	155	200	29.27	8.818

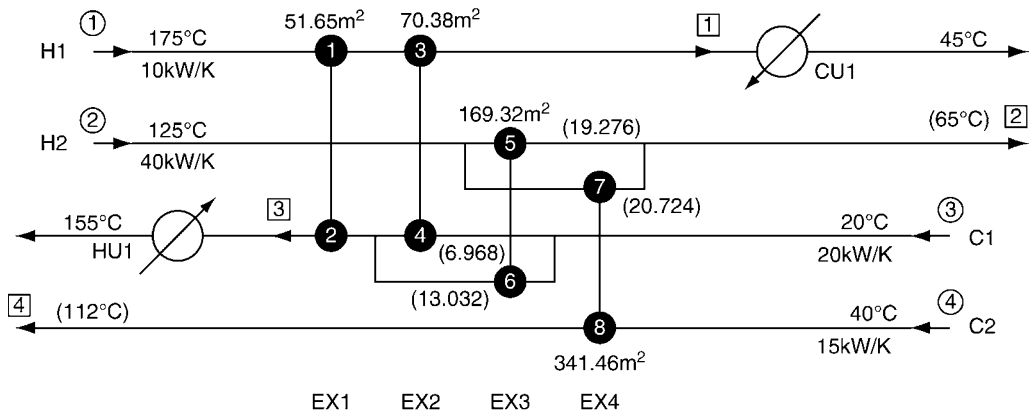

C5. Fig. 4. Optimal design of heat exchanger network, 108,072 $/year.

$$v_{cc,1}=\frac{1-R_1}{1-R_1 e^{-\mathrm{NTU}_1^*(1-R_1)}}=\frac{1-0.5}{1-0.5\times\exp[-3.5066\times(1-0.5)]}=0.54740$$

$$v_{ch,1}=1-v_{cc,1}=1-0.54740=0.45260$$

The calculations for EX2, EX3, and EX4 are similar, which yields,

$$\mathbf{v}=\begin{bmatrix}0.09481 & 0.90519 & 0 & 0 & 0 & 0 & 0 & 0\\ 0.45260 & 0.54740 & 0 & 0 & 0 & 0 & 0 & 0\\ 0 & 0 & 0.33214 & 0.66786 & 0 & 0 & 0 & 0\\ 0 & 0 & 0.95847 & 0.04153 & 0 & 0 & 0 & 0\\ 0 & 0 & 0 & 0 & 0.34782 & 0.65218 & 0 & 0\\ 0 & 0 & 0 & 0 & 0.96465 & 0.03535 & 0 & 0\\ 0 & 0 & 0 & 0 & 0 & 0 & 0.38690 & 0.61310\\ 0 & 0 & 0 & 0 & 0 & 0 & 0.84706 & 0.15294\end{bmatrix}$$

According to the stream arrangement and channel indexes shown in Fig. 4, the matching matrices are

$$\mathbf{G}=\begin{bmatrix}0 & 0 & 0 & 0 & 0 & 0 & 0 & 0\\ 0 & 0 & 0 & 6.968/20 & 0 & 13.032/20 & 0 & 0\\ 1 & 0 & 0 & 0 & 0 & 0 & 0 & 0\\ 0 & 0 & 0 & 0 & 0 & 0 & 0 & 0\\ 0 & 0 & 0 & 0 & 0 & 0 & 0 & 0\\ 0 & 0 & 0 & 0 & 0 & 0 & 0 & 0\\ 0 & 0 & 0 & 0 & 0 & 0 & 0 & 0\\ 0 & 0 & 0 & 0 & 0 & 0 & 0 & 0\end{bmatrix}$$

$$\mathbf{G}'=\begin{bmatrix}1 & 0 & 0 & 0\\ 0 & 0 & 0 & 0\\ 0 & 0 & 0 & 0\\ 0 & 0 & 1 & 0\\ 0 & 1 & 0 & 0\\ 0 & 0 & 1 & 0\\ 0 & 1 & 0 & 0\\ 0 & 0 & 0 & 1\end{bmatrix}$$

$$\mathbf{G}''=\begin{bmatrix}0 & 0 & 1 & 0 & 0 & 0 & 0 & 0\\ 0 & 0 & 0 & 0 & 19.276/40 & 0 & 20.724/40 & 0\\ 0 & 1 & 0 & 0 & 0 & 0 & 0 & 0\\ 0 & 0 & 0 & 0 & 0 & 0 & 0 & 1\end{bmatrix}$$

$$\mathbf{G}'''=\mathbf{0}$$

The calculation of Eqs. (18–20) yields,

$$\Theta'_{EX}=\begin{bmatrix}175.00\\ 121.63\\ 126.69\\ 20.00\\ 125.00\\ 20.00\\ 125.00\\ 40.00\end{bmatrix},\ \Theta''_{EX}=\begin{bmatrix}126.69\\ 145.78\\ 55.43\\ 122.26\\ 56.52\\ 121.29\\ 72.89\\ 112.00\end{bmatrix},\ \Theta''_{N}=\begin{bmatrix}55.43\\ 65.00\\ 145.78\\ 112.00\end{bmatrix}$$

The matrix calculation can also be performed with Microsoft Excel© by the use of matrix multiplication function MMULT and matrix inverse function MINVERSE.

The calculation of hot and cold utilities depends on the calculated exit stream temperatures of the network Θ''_N and their target values Θ''_{N^*}. In this network, streams H1 and C1 should be further cooled and heated, respectively:

CU1: $\dot{Q}=(\dot{M}c_p)_h(\vartheta'_h-\vartheta''_h)=10\times(55.43-45)=104.34\,\mathrm{kW}$

$$\Delta\vartheta_{LM}=\frac{(\vartheta'_h-\vartheta''_c)-(\vartheta''_h-\vartheta'_c)}{\ln[(\vartheta'_h-\vartheta''_c)/(\vartheta''_h-\vartheta'_c)]}=\frac{(55.43-25)-(45-15)}{\ln[(55.43-25)/(45-15)]}=30.22^\circ\mathrm{C}$$

$$k=(1/\alpha_h+1/\alpha_c)^{-1}=(1/2.615+1/2.5)^{-1}=1.2781\,\mathrm{kW/m^2K}$$

$$A=\dot{Q}/(kF\Delta\vartheta_{LM})=104.34/(1.278\times1\times30.22)=2.702\,\mathrm{m^2}$$

HU1: $\dot{Q}=(\dot{M}c_p)_c(\vartheta''_c-\vartheta'_c)=20\times(155-145.78)=184.35\,\mathrm{kW}$

$$\Delta\vartheta_{LM}=\frac{(180-155)-(179-145.78)}{\ln[(180-155)/(179-145.78)]}=28.91^\circ\mathrm{C}$$

$$k=(1/5+1/0.917)^{-1}=0.7749\,\mathrm{kW/m^2K}$$

$$A=184.35/(0.7749\times1\times28.91)=8.228\,\mathrm{m^2}$$

3 Synthesis of Heat Exchanger Networks with the Pinch Design Method

The parameters of a heat exchanger network can be classified into three sets: (1) Design parameters, e.g., flowsheet of the network, heat exchanger type, heat transfer area, and other structural parameters. (2) Operation parameters, e.g., supply stream temperatures and flow rates. Their values might be disturbed or passively changed but cannot be regulated. (3) Control parameters, e.g., bypass flow rates and flow rates in stream split branches. Their values can be manually or automatically regulated by controlling units. A fundamental synthesis problem can be stated as: For given operation parameters of a heat recovery system, find the design parameters and control parameters of the heat exchanger network in their feasible regions so that the target temperatures of the process streams and other additional constraints (e.g., pressure drop, flow rate, and size limitations) can be fulfilled; meanwhile the sum of investment and operation costs reaches the minimum.

In a typical synthesis task, the supply temperatures, heat capacity flow rates (or mass flow rates) and target temperatures of the process streams, and the temperature levels of the available hot and cold utilities are given as the operation parameters. The heat transfer coefficients of the process streams and utility mediums as well as the equipment and utility costs are previously specified. The design and control parameters to be optimized include: (1) the flowsheet of the heat exchanger network, (2) the area of each heat exchanger in the network, and (3) the heat capacity flow rates of hot and cold streams in each heat exchanger. As the number of possible flowsheets could be astronomical figures, traditional optimization solvers are not suitable for such a task. In the past 3 decades, many synthesis methodologies have been developed. As a practical procedure, the Pinch design method is introduced in this section in detail.

3.1 The Problem Table

The problem table proposed by Linnhoff and Flower [14] is used to find the position of the Pinch and the minimum hot and cold utility duties. For a given synthesis task dealing with N_h hot streams and N_c cold streams, Let

$$\Theta'_{\mathrm{h}} = \begin{bmatrix} \vartheta'_{\mathrm{h},1} \\ \vartheta'_{\mathrm{h},2} \\ \vdots \\ \vartheta'_{\mathrm{h},N_{\mathrm{h}}} \end{bmatrix}, \Theta''_{\mathrm{h}} = \begin{bmatrix} \vartheta''_{\mathrm{h},1} \\ \vartheta''_{\mathrm{h},2} \\ \vdots \\ \vartheta''_{\mathrm{h},N_{\mathrm{h}}} \end{bmatrix},$$

$$\Theta'_{\mathrm{c}^*} = \begin{bmatrix} \vartheta'_{\mathrm{c}^*,1} \\ \vartheta'_{\mathrm{c}^*,2} \\ \vdots \\ \vartheta'_{\mathrm{c}^*,N_{\mathrm{c}}} \end{bmatrix} = \begin{bmatrix} \vartheta'_{\mathrm{c},1} + \Delta\vartheta_{\min} \\ \vartheta'_{\mathrm{c},2} + \Delta\vartheta_{\min} \\ \vdots \\ \vartheta'_{\mathrm{c},N_{\mathrm{c}}} + \Delta\vartheta_{\min} \end{bmatrix},$$

$$\Theta''_{\mathrm{c}^*} = \begin{bmatrix} \vartheta''_{\mathrm{c}^*,1} \\ \vartheta''_{\mathrm{c}^*,2} \\ \vdots \\ \vartheta''_{\mathrm{c}^*,N_{\mathrm{c}}} \end{bmatrix} = \begin{bmatrix} \vartheta''_{\mathrm{c},1} + \Delta\vartheta_{\min} \\ \vartheta''_{\mathrm{c},2} + \Delta\vartheta_{\min} \\ \vdots \\ \vartheta''_{\mathrm{c},N_{\mathrm{c}}} + \Delta\vartheta_{\min} \end{bmatrix} \tag{21}$$

in which $\Delta\vartheta_{\min}$ is the minimum temperature difference in the network. Let the set

$$\begin{aligned} \mathrm{S_T} = &\{\vartheta'_{\mathrm{h},1}, \vartheta'_{\mathrm{h},2}, \cdots, \vartheta'_{\mathrm{h},N_{\mathrm{h}}}\} \cup \{\vartheta''_{\mathrm{h},1}, \vartheta''_{\mathrm{h},2}, \cdots, \vartheta''_{\mathrm{h},N_{\mathrm{h}}}\} \\ &\cup \{\vartheta'_{\mathrm{c}^*,1}, \vartheta'_{\mathrm{c}^*,2}, \cdots, \vartheta'_{\mathrm{c}^*,N_{\mathrm{c}}}\} \cup \{\vartheta''_{\mathrm{c}^*,1}, \vartheta''_{\mathrm{c}^*,2}, \cdots, \vartheta''_{\mathrm{c}^*,N_{\mathrm{c}}}\} \end{aligned} \tag{22}$$

then define a temperature level vector

$$\Theta = [\vartheta_1 \quad \vartheta_2 \quad \cdots \quad \vartheta_{N_{\mathrm{SN}}+1}]^{\mathrm{T}} \tag{23}$$

in which the temperature levels $\vartheta_i \in \mathrm{S_T} (i = 1, 2, \cdots, N_{\mathrm{SN}} + 1)$ and $\vartheta_1 > \vartheta_2 > \cdots > \vartheta_{N_{\mathrm{SN}}+1}$. The streams in each temperature interval $[\vartheta_i, \vartheta_{i+1}]$ constitute a subnetwork SN_i $(i = 1, 2, \cdots, N_{\mathrm{SN}})$. The heat transport difference between the heat input I_i and heat output O_i in SN_i can be calculated by means of Eq. (24),

$$D_i = I_i - O_i = \Delta\dot{H}_{\mathrm{c},i} - \Delta\dot{H}_{\mathrm{h},i} \tag{24}$$

in which

$$\Delta\dot{H}_{\mathrm{h},i} = (\vartheta_i - \vartheta_{i+1}) \sum_{j=1}^{N_{\mathrm{h}}} \dot{C}_{\mathrm{h},ij} \tag{25}$$

$$\Delta\dot{H}_{\mathrm{c},i} = (\vartheta_i - \vartheta_{i+1}) \sum_{j=1}^{N_{\mathrm{c}}} \dot{C}_{\mathrm{c},ij} \tag{26}$$

$$\dot{C}_{\mathrm{h},ij} = \begin{cases} (\dot{M}c_{\mathrm{p}})_{\mathrm{h},j}, & \vartheta''_{\mathrm{h},j} \le \vartheta_{i+1} \text{ and } \vartheta_i \le \vartheta'_{\mathrm{h},j} \\ 0, & \text{others} \end{cases} \tag{27}$$

$$\dot{C}_{\mathrm{c},ij} = \begin{cases} (\dot{M}c_{\mathrm{p}})_{\mathrm{c},j}, & \vartheta'_{\mathrm{c}^*,j} \le \vartheta_{i+1} \text{ and } \vartheta_i \le \vartheta''_{\mathrm{c}^*,j} \\ 0, & \text{others} \end{cases} \tag{28}$$

At first, assume a zero heat input to SN_1, that is, $I_1 = 0$. If there is no additional connection between SN_{i+1} and heat utility, the heat input of SN_{i+1} should be equal to the heat output of SN_i,

$$I_{i+1} = O_i \tag{29}$$

The assumption $I_1 = 0$ might yield negative values of heat inputs and heat outputs of the sub-networks. This is not allowed because the heat cannot flow from a lower temperature region to a higher temperature region. The modification is performed by subtracting the minimum value of heat inputs/outputs to I_1,

$$I_1 = -\dot{Q}_{\min} = -\min\{I_i, O_i | i = 1, 2, \cdots, N_{\mathrm{SN}}\} \tag{30}$$

and repeating the calculation. This can also be done by subtracting $\dot{Q}_{\min}$ from all heat inputs and outputs. After the modification, the minimum hot utility duty $\dot{Q}_{\mathrm{HU,min}} = I_1$ and the minimum cold utility duty $\dot{Q}_{\mathrm{CU,min}} = O_{\mathrm{SN}}$ is obtained. The position where the heat input is zero is called the Pinch.

3.2 The Composite Curves

Let j_1 and j_2 indicate the maximum and minimum temperature levels of the hot streams, respectively; k_1 and k_2 indicate those of the cold streams, so that

$$\vartheta_{j_1} = \max\{\vartheta'_{\mathrm{h},1}, \vartheta'_{\mathrm{h},2}, \cdots, \vartheta'_{\mathrm{h},N_{\mathrm{h}}}, \vartheta''_{\mathrm{h},1}, \vartheta''_{\mathrm{h},2}, \cdots, \vartheta''_{\mathrm{h},N_{\mathrm{h}}}\} \tag{31}$$

$$\vartheta_{j_2} = \min\{\vartheta'_{\mathrm{h},1}, \vartheta'_{\mathrm{h},2}, \cdots, \vartheta'_{\mathrm{h},N_{\mathrm{h}}}, \vartheta''_{\mathrm{h},1}, \vartheta''_{\mathrm{h},2}, \cdots, \vartheta''_{\mathrm{h},N_{\mathrm{h}}}\} \tag{32}$$

$$\vartheta_{k_1} = \max\{\vartheta'_{\mathrm{c},1}, \vartheta'_{\mathrm{c},2}, \cdots, \vartheta'_{\mathrm{c},N_{\mathrm{c}}}, \vartheta''_{\mathrm{c},1}, \vartheta''_{\mathrm{c},2}, \cdots, \vartheta''_{\mathrm{c},N_{\mathrm{c}}}\} \tag{33}$$

$$\vartheta_{k_2} = \min\{\vartheta'_{\mathrm{c},1}, \vartheta'_{\mathrm{c},2}, \cdots, \vartheta'_{\mathrm{c},N_{\mathrm{c}}}, \vartheta''_{\mathrm{c},1}, \vartheta''_{\mathrm{c},2}, \cdots, \vartheta''_{\mathrm{c},N_{\mathrm{c}}}\} \tag{34}$$

The points for the composite curve of hot and cold streams are $(\vartheta_j, \dot{H}_{\mathrm{h},j})$ $(j = j_1, j_1 + 1, \cdots, j_2)$ and $(\vartheta_k, \dot{H}_{\mathrm{c},k})$ $(k = k_1, k_1 + 1, \cdots, k_2)$, respectively, in which $\dot{H}_{\mathrm{h},j}$ and $\dot{H}_{\mathrm{c},k}$ are enthalpy flow rates of the hot and cold streams in the jth (or kth) subnetwork,

$$\dot{H}_{\mathrm{h},j} = \sum_{i=j}^{j_2-1} \Delta\dot{H}_{\mathrm{h},i} \tag{35}$$

$$\dot{H}_{\mathrm{c},k} = \sum_{i=k}^{k_2-1} \Delta\dot{H}_{\mathrm{c},i} + O_{\mathrm{SN}} \tag{36}$$

3.3 Pinch Design Method

Because any network design that transfers heat across the Pinch will cause both heating and cooling duties larger than their minimum, there are three principles:

1. Do not use cold utilities above the Pinch
2. Do not use hot utilities below the Pinch
3. Do not transfer heat across the Pinch

Therefore, for the network design there are three consequences:

1. Divide the network at the Pinch into two parts
2. Design each part separately
3. Avoid the use of coolers in the part above the Pinch (hot end part); avoid the use of heaters in the part below the Pinch (cold end part)

For the matching of streams there are the following two rules:

1. In the part above the Pinch, the number of the hot streams (including their branches) should be less than or equal to that of the cold streams (including their branches), that is,

$$N_{\mathrm{h}} \le N_{\mathrm{c}} \text{ (above the Pinch)} \tag{37}$$

otherwise, the stream splitting is necessary to ensure that Eq. (37) is fulfilled. Similarly, in the part below the Pinch, the inequality is inversed,

$$N_h \geq N_c \text{ (below the Pinch)} \tag{38}$$

2. For a match in the part above the Pinch, the heat capacity flow rate of the hot stream (or the branch of a hot stream) should be less than or equal to that of the cold stream (or the branch of a cold stream) to be matched, that is,

$$(\dot{M}c_p)_h \leq (\dot{M}c_p)_c \text{ (above the Pinch)} \tag{39}$$

otherwise, the stream splitting is necessary. For a match in the part below the Pinch, the inequality is inversed,

$$(\dot{M}c_p)_h \geq (\dot{M}c_p)_c \text{ (below the Pinch)} \tag{40}$$

In the Pinch design method $\Delta\vartheta_{min}$ is an important parameter for the balance between the investment costs and utility costs. A large value of $\Delta\vartheta_{min}$ would decrease the investment costs but increase the utility costs, and vice versa. Further more, the Pinch position could also change with $\Delta\vartheta_{min}$. The value of $\Delta\vartheta_{min}$ can be optimized by taking the total costs of the network as the objective function.

The Pinch design method focuses on the matches of streams near the Pinch because at that point the temperature difference is the minimum. For the matches away from the Pinch, the above rules must not be fulfilled. In some cases there might be multiple Pinches or no Pinch. A detailed description of the Pinch design method can be found in [15].

Example 3

We use the problem data in Table 1 to illustrate the calculation of problem table and composite curves and let $\Delta\vartheta_{min} = 5K$. The temperature intervals are formed according to the following temperatures,

$$\Theta'_h = \begin{bmatrix} 175 \\ 125 \end{bmatrix}, \Theta''_h = \begin{bmatrix} 45 \\ 65 \end{bmatrix}, \Theta'_{c^*} = \begin{bmatrix} 20+5 \\ 40+5 \end{bmatrix} = \begin{bmatrix} 25 \\ 45 \end{bmatrix},$$
$$\Theta''_{c^*} = \begin{bmatrix} 155+5 \\ 112+5 \end{bmatrix} = \begin{bmatrix} 160 \\ 117 \end{bmatrix}$$

Put the above temperatures into Eq. (23) and arrange them according to their magnitude; six subnetworks are obtained, $N_{SN} = 6$, and the temperature levels are,

$$\Theta = [175 \quad 160 \quad 125 \quad 117 \quad 65 \quad 45 \quad 25]^T$$

Equations (24–29) are applied to the following calculations.

$$SN_1 : \vartheta_1 = 175, \vartheta_2 = 160$$
$$\Delta\dot{H}_{c,1} = 0$$
$$\Delta\dot{H}_{h,1} = (\vartheta_1 - \vartheta_2)(\dot{M}c_p)_{h,1} = (175 - 160) \times 10 = 150$$
$$I_1 = 0$$
$$D_1 = \Delta\dot{H}_{c,1} - \Delta\dot{H}_{h,1} = 0 - 150 = -150$$
$$O_1 = I_1 - D_1 = 0 - (-150) = 150$$
$$SN_2 : \vartheta_2 = 160, \vartheta_3 = 125$$
$$\Delta\dot{H}_{c,2} = (\vartheta_2 - \vartheta_3)(\dot{M}c_p)_{c,1} = (160 - 125) \times 20 = 700$$
$$\Delta\dot{H}_{h,2} = (\vartheta_2 - \vartheta_3)(\dot{M}c_p)_{h,1} = (160 - 125) \times 10 = 350$$
$$I_2 = O_1 = 150$$
$$D_2 = \Delta\dot{H}_{c,2} - \Delta\dot{H}_{h,2} = 700 - 350 = 350$$
$$O_2 = I_2 - D_2 = 150 - 350 = -200$$

The calculation results are provided in Table 3, where the modified heat input and output are denoted with "*". At the temperature level $\vartheta_3 = 125°C$, the heat input $I_3^* = 0$, that means that there is no heat flowing through this interface. This position is the pinch at which the temperature difference reaches the given minimum value, $\Delta\vartheta_{min} = 5°C$. The corresponding minimum heating duty is 200 kW, and the minimum cooling duty is 120 kW. The composite curves are shown in Fig. 5. The point data of the curves are also provided in Table 3.

To design the network, the problem is divided into two parts at the Pinch as is shown in Fig. 6. In the part above the Pinch (the left part in Fig. 6), there is only one match: H1C1, i.e., $N_h = N_c = 1$, therefore, Eq. (37) is fulfilled. Since $(\dot{M}c_p)_{H1} = 10$ kW/K and $(\dot{M}c_p)_{C1} = 20$ kW/K, Eq. (39) is also valid and no splitting is necessary.

In the part below the Pinch (the right part in Fig. 6), $N_h = N_c = 2$, which meets Eq. (38). The matches H1C1 and H2C2 can be considered due to their temperature intervals. Since $(\dot{M}c_p)_{H1} = 10$kW/K and $(\dot{M}c_p)_{C1} = 20$ kW/K, according to Eq. (40), a splitting in C1 is necessary, $(\dot{M}c_p)_{C1(H1C1)} \leq 10$ kW/K, and a new match H2C1 should be added with $(\dot{M}c_p)_{C1(H2C1)} = (\dot{M}c_p)_{C1} - (\dot{M}c_p)_{C1(H1C1)} \geq 10\,kW/K$, which yield a splitting in stream H2 with $(\dot{M}c_p)_{H2(H2C1)} \geq (\dot{M}c_p)_{C1(H2C1)} \geq 10\,kW/K$.

For the match H2C2, since $(\dot{M}c_p)_{C2} = 15\,kW/K$, then, Eq. (40) indicates

$$15\,kW/K \leq (\dot{M}c_p)_{H2(H2C2)} = (\dot{M}c_p)_{H2} - (\dot{M}c_p)_{H2(H2C1)} \leq 30\,kW/K$$

This design step yields a network structure shown in Fig. 7. At first it is assumed that the branches are isothermally mixed, i.e., the split-flows of a stream at the branch outlets have the

C5. Table 3. The problem table, $\Delta\vartheta_{min} = 5K$

SN	ϑ, ϑ_h (°C)	$\Delta\dot{H}_c$ (kW)	$\Delta\dot{H}_h$ (kW)	D (kW)	I (kW)	O (kW)	I^* (kW)	O^* (kW)	$\dot{H}_h$ (kW)	ϑ_c (°C)	$\dot{H}_c$ (kW)
1	175	0	150	−150	0	150	200	350	3700		
2	160	700	350	350	150	−200	350	0	3550	155	3900
3	125	160	400	−240	−200	40	0	240	3200	120	3200
4	117	1820	2600	−780	40	820	240	1020	2800	112	3040
5	65	700	200	500	820	320	1,020	520	200	60	1220
6	45	400	0	400	320	−80	520	120	0	40	520
7	25									20	120

same temperature before they are mixed. Further more, as has been analyzed in the aforementioned problem table, the minimum cooling duty is 120 kW for stream H1; therefore, a cooler is added to stream H1. The detailed calculations for EX1 and EX4 are given as follows:

$$\text{EX1}: \dot{Q} = (\dot{M}c_p)_{H1}(\vartheta'_{H1} - \vartheta_{h,Pinch}) = 10 \times (175 - 125) = 500\ \text{kW}$$

$$\vartheta''_{C1} = \vartheta_{c,Pinch} + \dot{Q}/(\dot{M}c_p)_{C1} = 120 + 500/20 = 145^\circ\text{C}$$

$$\Delta\vartheta_{LM} = \frac{(\vartheta'_{H1} - \vartheta''_{C1}) - (\vartheta_{h,Pinch} - \vartheta_{c,Pinch})}{\ln[(\vartheta'_{H1} - \vartheta''_{C1})/(\vartheta_{h,Pinch} - \vartheta_{c,Pinch})]}$$

$$= \frac{(175 - 145) - (125 - 120)}{\ln[(175 - 145)/(125 - 120)]} = 13.95^\circ\text{C}$$

$$k = (1/\alpha_{H1} + 1/\alpha_{C1})^{-1} = (1/2.615 + 1/0.917)^{-1}$$

$$= 0.6789\ \text{kW/m}^2\text{K}$$

$$A = \dot{Q}/(kF\Delta\vartheta_{LM}) = 500/(0.6789 \times 1 \times 13.95) = 52.78\ \text{M}^2$$

$$\text{EX4}: \dot{Q} = (\dot{M}c_p)_{C2}(\vartheta''_{C2} - \vartheta'_{C2}) = 15 \times (112 - 40) = 1{,}080\ \text{kW}$$

$$(\dot{M}c_p)_{H2(H2C2)} = \dot{Q}/(\vartheta'_{H2} - \vartheta''_{H2}) = 1080/(125 - 65) = 18\ \text{kW/K}$$

$$\Delta\vartheta_{LM} = \frac{(\vartheta'_{H2} - \vartheta''_{C2}) - (\vartheta''_{H2} - \vartheta'_{C2})}{\ln[(\vartheta'_{H2} - \vartheta''_{C2})/(\vartheta''_{H2} - \vartheta'_{C2})]}$$

$$= \frac{(125 - 112) - (65 - 40)}{\ln[(125 - 112)/(65 - 40)]} = 18.35^\circ\text{C}$$

$$k = (1/\alpha_{H2} + 1/\alpha_{C2})^{-1} = (1/1.333 + 1/0.166)^{-1}$$

$$= 0.1476\ \text{kW/m}^2\text{K}$$

$$A = \dot{Q}/(kF\Delta\vartheta_{LM}) = 1080/(0.1476 \times 1 \times 18.35) = 398.69\ \text{m}^2$$

More calculation results can be found in Fig. 7. The investment costs and utility costs can then be calculated according to the cost data in Table 1:

$$\text{EX1: } C_{EX,1} = 1{,}200A^{0.57} = 1{,}200 \times 52.78^{0.57} = 11{,}508\,\$/\text{year}$$

$$\text{EX2: } C_{EX,2} = 1{,}200 \times 62.65^{0.57} = 12{,}688\,\$/\text{year}$$

$$\text{EX3: } C_{EX,3} = 1{,}200 \times 133.47^{0.57} = 19{,}527\,\$/\text{year}$$

$$\text{EX4: } C_{EX,4} = 1{,}200 \times 398.69^{0.57} = 36{,}437\,\$/\text{year}$$

$$\text{CU1: } C_{U,1} = 1{,}200A^{0.57} + 10(\dot{M}c_p)_{H1}(\vartheta''_{N,H1} - \vartheta''_{N*,H1})\,\$/\text{year}$$

$$= 1{,}200 \times 3.03^{0.57} + 10 \times 10 \times (57 - 45)$$

$$= 3{,}457\,\$/\text{year}$$

$$\text{HU1: } C_{U,2} = 1{,}200 \times 8.82^{0.57} + 110 \times 20 \times (155 - 145)$$

$$= 26{,}150\,\$/\text{year}$$

The total annual cost of the network is the sum of the above costs,

$$C_{tot} = \sum_{n=1}^{4} C_{EX,n} + \sum_{n=1}^{2} C_{U,n} = 109{,}768\,\$/\text{year}$$

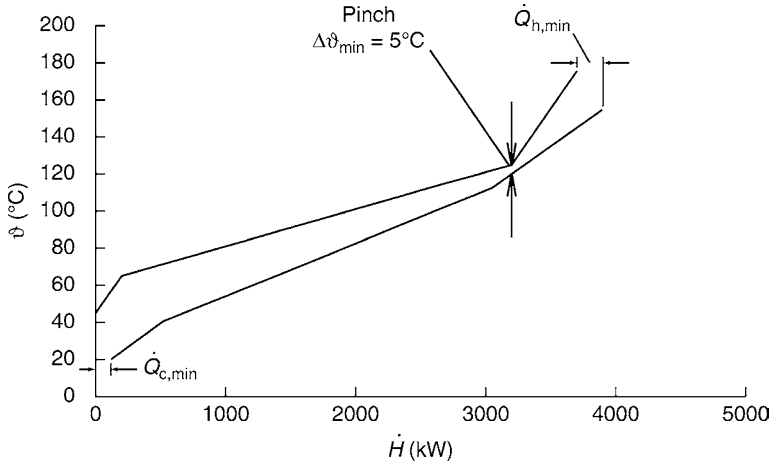

C5. Fig. 5. Composite curves of Example 3.

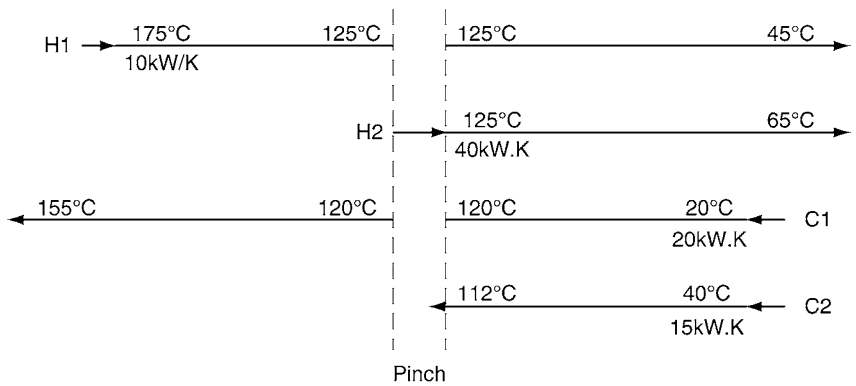

C5. Fig. 6. The Pinch decomposition.

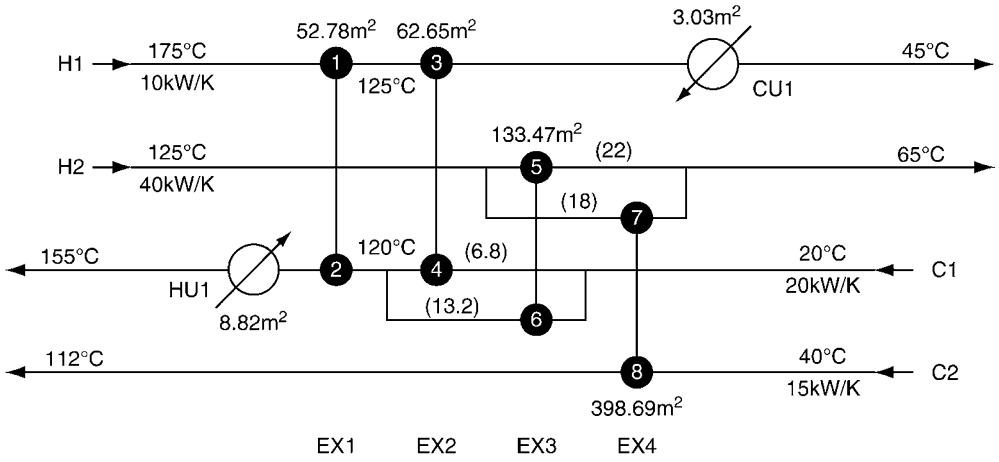

C5. Fig. 7. The structure design of the heat exchanger network, 109,768 $/year.

As has been mentioned, the isothermal mixing is assumed in the above calculation, and $\Delta t_{\min}$ is also an empirical value. Therefore, it is possible to optimize the solution. Let $x_1 = \dot{Q}_{CU1}$, $x_2 = \dot{Q}_{EX2}$, $x_3 = (\dot{M}c_p)_{EX2,c}$, and $x_4 = (\dot{M}c_p)_{EX3,h}$, and take them as the controlling variables to be optimized. The optimal design can be obtained by means of the iteration procedure of the Newton method,

$$x_i = x_i^* - \frac{\frac{\partial C_{tot}}{\partial x_i}}{\frac{\partial^2 C_{tot}}{\partial x_i^2}} \approx x_i^* - \frac{\Delta x}{2}\frac{C_{tot}(x_i+\Delta x) - C_{tot}(x_i-\Delta x)}{C_{tot}(x_i+\Delta x) + C_{tot}(x_i-\Delta x) - 2C_{tot}(x_i)} \quad (i=1,2,3,4) \tag{41}$$

which yields the optimal network design with the total annual cost of 108,072 $/year, as is shown in Fig. 4. This procedure is simple, but might not converge in some cases. For such cases other optimization solvers can be used.

Example 3 deals with only four process streams; therefore, it is suitable to use the Pinch design method. For more complicated synthesis problems, e.g., the synthesis of large-scale heat exchanger networks, the stochastic algorithms such as the hybrid genetic algorithm [16] and monogenetic algorithm [17] are recommended to solve the optimization problem.

4 Symbols

C	annual cost (monetary unit/year)
F	correction factor of logarithmic mean temperature difference
$\dot{H}$	enthalpy flow rate (kW)
N	number of stream channels
N'	number of stream entrances of network
N''	number of stream exits of network
N_{EX}	number of heat exchangers
NTU^*	modified number of transfer units defined by Eq. (8)
R	ratio of heat capacity flow rates
Θ	temperature vector (°C)
ϑ	temperature (°C)
$\Delta\vartheta_{LM}$	logarithmic mean temperature difference (K)

Superscripts

T	transpose
$'$	inlet
$''$	outlet

Subscripts

c	cold stream
EX	heat exchanger
h	hot stream
N	heat exchanger network excluding heaters and coolers
N*	heat exchanger network including heaters and coolers
U	utility

5 Bibliography

1. Masso AH, Rudd DF (1969) The synthesis of system designs - II. Heuristic structuring. AIChE J. 15:10–17
2. Linnhoff B, Mason DR, Wardle I (1979) Understanding heat exchanger networks. Comp Chem Eng 3:295–302
3. Grossmann IE, Sargent RWH (1978) Optimum design of heat exchanger networks. Comp Chem Eng 2:1–7
4. Lewin DR (1998) A generalized method for HEN synthesis using stochastic optimization - II. The synthesis of cost-optimal networks. Comp Chem Eng 22:1387–1405
5. Dolan WB, Cummings PT, LeVan MD (1989) Process optimization via simulated annealing: application to network design. AIChE J 35:725–736
6. Lin B, Miller DC (2004) Solving heat exchanger network synthesis problems with Tabu Search. Comp Chem Eng 28:1451–1464
7. Wei G-F, Yao P-J, Luo X, Roetzel W (2004) Study on multi-stream heat exchanger network synthesis with parallel genetic/simulated annealing algorithm. Chinese J Chem Eng 12:66–77
8. Xiao W, Dong H-G, Li X-Q, Yao P-J, Luo X, Roetzel W (2006) Synthesis of large-scale multistream heat exchanger networks based on stream pseudo temperature. Chinese J Chem Eng 14:574–583
9. Ravagnani MASS, Silva AP, Arroyo PA, Constantino AA (2005) Heat exchanger network synthesis and optimisation using genetic algorithm. Appl Therm Eng 25:1003–1017
10. Strelow O (2000) A general calculation method for plate heat exchangers. Int J Therm Sci 39:645–658
11. Chen D-Z, Yang S-S, Luo X, Wen Q-Y, Ma H-G (2007) An explicit solution for thermal calculation and synthesis of superstructure heat exchanger networks. Chinese J Chem Eng 15:296–301

12. Roetzel W, Luo X (2005) Thermal analysis of heat exchanger networks. Archives Thermodynamics 26:5–16
13. Luo X, Li M-L, Roetzel W (2002) A general solution for one-dimensional multistream heat exchangers and their networks. Int J Heat Mass Transfer 45:2695–2705
14. Linnhoff B, Flower JR (1978) Synthesis of heat exchanger networks: I. Systematic generation of energy optimal networks. AIChE J 24: 633–642
15. Linnhoff B, Townsend DW, Boland D, Hewitt GF, Thomas BEA, Guy AR, Marsland RH. (1982) User guide on process integration for the efficient use of energy. Oxford: Institution of Chemical
16. Luo X, Wen Q-Y, Fieg G (2009) A hybrid genetic algorithm for synthesis of heat exchanger networks. Comp Chem Eng 33:1169–1181
17. Fieg G, Luo X, Jezowski J (2009) A monogenetic algorithm for optimal design of large-scale heat exchanger networks. Chem Eng Proc, 48:1506–1516

C6 Costs and Economy of Heat Exchangers

Bernhard Spang[1] · *Wilfried Roetzel*[2]
[1]BUCO Wärmeaustauscher International GmbH, Geesthacht, Germany
[2]Helmut-Schmidt-Universität, Universität der Bundeswehr Hamburg, Hamburg, Germany

1 Introduction

Heat exchangers are essential components in process technology. Therefore, the economic selection and design of heat exchangers plays an important role for the profitability of a process.

In this connection profitability means the ratio of income to costs. Income and costs are value quantities (monetary units per unit time) which are linked to the physical variables used in engineering by cost coefficients. Applying the notion of profitability to heat exchangers allows either to compare marginal cost and marginal utility of a transferred heat flow or to consider the amount of heat transferred during a period of time as an externally specified quantity. The definition of marginal values in economics is given by W. H. Bartzsch [1].

In the former case the increase in income (usually in the form of lower energy costs) must be compared to the additional cost for the higher amount of transferred heat or for heat integration (Chap. C5). The additional costs for increasing the heat transfer surface area of an exchanger for heat recovery entail lower energy costs. However, the heat flow rate per unit surface area decreases with increasing surface area (Chap. C1). Consequently, a plot of the net amount of saved annual costs (saved energy costs less operating expenses including depreciation) versus the investment costs for the heat exchanger shows a maximum [2]. The actual heat exchanger should be smaller than at this maximum because the marginal return of the invested capital becomes just zero at this point. The optimal surface area of the heat exchanger for a requested return on investment can graphically be determined from the chart at the point where the gradient of the curve equals this return on investment.

The following considerations are limited to the case where the amount of heat to be transferred is an externally specified quantity, given, for example, by the requirements for the proper functioning of the whole process. In this case the income is fixed, albeit usually not explicitly but only as an inseparable part of the income of the whole plant, and a cost-effectiveness study is limited to the minimization of costs by comparative cost methods.

2 Costs

The total costs C_{tot} (monetary units/year) can be subdivided into costs of capital C_{CA} composed of the annual depreciation or amortization, the (imputed) interest, and the operating expenses for energy and supplies C_E as well as the other operating expenses C_S (for maintenance, repair, staff, and replacement of heat transfer fluids):

$$C_{tot} = C_{CA} + C_E + C_S. \quad (1)$$

2.1 Costs of Capital

The annual costs of capital depend on the capital requirements for the heat exchanger I_{EX} (price or acquisition value), for pumps or compressors I_{P1} plus I_{P2} to convey the fluids through both channels of the exchanger, the number n of years of the recovery period, and the interest rate z:

$$C_{CA} = \left(\frac{1}{n} + \frac{z}{2}\right)(I_{EX} + I_{P1} + I_{P2}) = a(I_{EX} + I_{P1} + I_{P2}) \quad (2)$$

where linear depreciation and a declining balance of zero are assumed. Equation (2) takes into account the fact that over the whole recovery period on average only half the capital employed is tied up.

The value of the payback coefficient a falls usually between 0.1/year and 0.25/year (recovery period 5–20 years, interest rate 5–15%). While the recovery period and the interest rate are externally given, the capital requirements for the heat exchanger and pumps or compressors depend on the design of the exchanger. For the precise determination of I quotations from different manufacturers should be solicited. Several publications [2–5] give numerous methods and data for the estimation of acquisition costs of heat exchangers. However, these are associated with a high degree of uncertainity and are also not transferable offhand to other regions of the world.

In order to estimate costs previously carried out projects or quotations for "similar" heat exchangers of different size or

VDI-GVC (ed.), *VDI Heat Atlas*, DOI 10.1007/978-3-540-77877-6_9,

materials may be taken. The effect of the size on the equipment price I_{EX} may be taken into account using the surface area A:

$$I_{EX} = I_{EX0}\left(\frac{A}{A_0}\right)^{m_{EX}}, \tag{3}$$

where I_{EX0} is the reference price of an exchanger with surface area A_0. The value of the exponent m_{EX} is usually less than 1 and is called degression exponent. Following the so-called 6/10-rule [6] a value of $m = 0.6$ can be used for rough estimates. For shell-and-tube heat exchangers with surface areas between 2 and 2,000 m^2 a value of $m_{EX} = 0.59$ is recommended [7].

Accordingly, the pumping power $\dot{L}$ may be used as a reference variable for pumps or compressors:

$$I_P = I_{P0}\left(\frac{\dot{L}}{\dot{L}_0}\right)^{m_P}. \tag{4}$$

Values of $m_P = 0.30$ for small centrifugal pumps (0.35–30 kW), $m_P = 0.67$ for large centrifugal pumps (30–300 kW), and $m_P = 0.84$ for compressors (0.75–1,500 kW) are recommended by F. A. Holland and J. K. Wilkinson [7].

Different materials may be taken into account by correction coefficients for the price of the construction using a reference material. Values of such material correction coefficients for a shell-and-tube heat exchanger with a surface area of 140 m^2 are given in Table 1 [2]. Both values for the tubes and for the whole heat exchanger are specified. Carbon steel is used as the reference material. For smaller heat exchangers the correction coefficients tend to be smaller and vice versa.

Prices of the past have to be corrected by means of price indexes:

$$I_{j2} = I_{j1}\frac{j_2}{j_1} \tag{5}$$

with I_{j1} and j_1 as the price and the price index at a particular time in the past and I_{j2} and j_2 as the current price and the current price index. A common index is the Chemical Engineering Plant Cost Index (CEPCI) which is published periodically in the magazine *Chemical Engineering* [8] or is available online [9]. The CEPCI contains subindexes for heat exchangers and tanks as well as for pumps and compressors.

C6. Table 1. Material correction coefficients for a shell-and-tube heat exchanger [2]

Material	Tubes	Heat exchanger
Unalloyed carbon steel	1.0	1.0
Stainless steel 304L, welded	2.2	1.6
Stainless steel Cu/Ni-90/30, welded	2.4	1.6
Stainless steel Cu/Ni-70/30, seamless	2.9	1.8
Stainless steel 316L, welded	3.2	1.8
Titanium, 20 BWG, welded	3.6	1.9
E-Brite 26-1, welded	5.2	2.4
Titanium, welded	6.8	2.8
Monel 400, welded	7.5	3.0
Incoloy 825, welded	7.6	3.0
Carpenter 20/CB3, welded	8.6	3.3
Inconel 625, welded	15.1	5.0
Zirconium 20 BWG, seamless	15.8	5.2
Hastelloy C276, welded	18.2	5.9
Zirconium, seamless	25.1	7.7

2.2 Energy Costs and Other Operating Expenses

The total costs for energy and supplies C_E are composed of the pumping costs on both sides, of the additional energy costs $C_{\Delta T}$ for increasing the temperature difference in the heat exchanger and of the costs of supplies C_M. They are proportional to the annual operating time τ (hours/year):

$$C_E = c_{el}\tau\left(\frac{\dot{M}_1\Delta p_1}{\rho_1\eta_{P1}} + \frac{\dot{M}_2\Delta p_2}{\rho_2\eta_{P2}}\right) + C_{\Delta T} + C_M \tag{6}$$

with the price of electrical energy c_{el} (monetary units/kWh) and the mass flow rate $\dot{M}_i$, the absolute pressure drop Δp_i, the mean fluid density ρ_i, and the pump efficiencies η_{Pi} on both sides ($i = 1$ or 2). The additional energy costs $C_{\Delta T}$ for increasing the temperature difference in the exchanger result from the costs for combustibles, steam, or electrical energy.

In many cases Eq. (6) may be simplified. While pumping costs always arise at least on one side, additional energy costs $C_{\Delta T}$ for increasing the temperature difference do not occur for heat transfer between two process fluids or for cooling with fluids at ambient temperature. Moreover, for cooling with water there may be costs. Costs of supplies do not occur for heat transfer between process fluids or for cooling with air.

The other operating expenses primarily include maintenance and cleaning costs. Although they are at least partially proportional to the annual operating time like the energy costs, it is usual practice to assume them to be proportional to the equipment price like the capital costs [10]:

$$C_s = sI_{EX}. \tag{7}$$

For cost estimation purposes with the objective of economic design this is justified as well because operating time-dependent or constant parts of the maintenance costs do not depend on the construction of the heat exchanger. Rough values for the coefficient s are given by Schnell [10]:

s = 0.01 to 0.02 for low maintenance requirements (no danger of fouling and corrosion),

s = 0.02 to 0.05 for medium maintenance requirements (planned maintenance and cleaning intervals),

s = 0.05 to 0.10 for high maintenance requirements (rapid fouling, high corrosion).

Maintenance costs for the pumps may be taken into account accordingly.

3 Economic Design

In general the following parameters are specified for the design of a heat exchanger:

- Mass flow rate of one of both streams (process fluid)
- Inlet and outlet temperature of the process fluid

In many cases the inlet temperature of the fluid on the other side is also defined (supplies like air or water for cooling) or restricted to a few discrete values (heating steam).

The objective of the economic design is the selection of a heat exchanger (type, heat transfer surface area, design details) and the specification of operating conditions (mass flow rate and inlet temperatures of supplies where necessary) in order both to meet above specifications and to minimize the annual total costs according to Eq. (1).

Generally the total costs depend on many factors, some of them having only discrete values. The formal way for determining the minimum of the cost function Eq. (1) by means of analytical or numerical partial derivation with respect to all relevant variables would require either simple analytical relations or an extensive data base. This formal way is rarely justified because of the high costs for collection of the required data.

In the special case of heat transfer between two process fluids mass flow rates and terminal temperatures of both streams are specified. Additional energy costs for increasing the temperature difference do not occur. The cost function is reduced to

$$C_{\mathrm{tot}} = (a+s) I_{\mathrm{EX0}} \left(\frac{A}{A_0}\right)^{m_{\mathrm{EX}}} + c_{\mathrm{el}} \tau \left(\frac{\dot{M}_1 \Delta p_1}{\rho_1 \eta_{\mathrm{P1}}} + \frac{\dot{M}_2 \Delta p_2}{\rho_2 \eta_{\mathrm{P2}}}\right) \tag{8}$$

where costs of capital and maintenance for the pumps are neglected. According to Chap. C1, Eq. (3), the required surface area A depends on the mean overall heat transfer coefficient k and the mean temperature difference $\Delta\vartheta_{\mathrm{m}}$. The overall heat transfer coefficient k, in turn, depends on the geometry of the flow channels and the mean flow velocities (Chap. C2 and Part G), and the mean temperature difference $\Delta\vartheta_{\mathrm{m}}$depends on the flow arrangement (Chap. C1). Pressure drops Δp_1 and Δp_2 depend on the mean flow velocities and the geometries of the flow paths, especially on their lengths (Part L).

Minimization of the cost function Eq. (8) may be considerably simplified by using an analogy between heat transfer and pressure drop. Martin [11] has shown that an analogy following the generalized Lévêque equation may be used for the economic design of plate heat exchangers, tube bundles, packed beds, and other types of compact heat exchangers.

4 Thermodynamic Analysis

The economic valuation on the basis of costs is expensive and unreliable. On the other hand, a thermodynamic analysis for minimization of the entropy production or of the exergy loss by means of entropy or exergy balances may be carried out easily and quickly. There is no general relation between entropy production or exergy loss on the one hand and total costs on the other hand. However, in cases where energy costs preponderate the thermodynamic analysis may provide indications for the most economic solution (see Chap. C5 about the optimization of heat exchanger networks).

An exergy balance for an adiabatic heat exchanger with two streams in steady-state operation according to Chap. C1, Fig. 1, yields the exergy loss $\dot{E}_{\mathrm{V}}$:

$$\dot{E}_{\mathrm{V}} = T_u \left[\dot{M}_1 \left(s_1'' - s_1'\right) + \dot{M}_2 \left(s_2'' - s_2'\right)\right] \tag{9}$$

where T_{u} is the ambient thermodynamic temperature and $\dot{M}_1$ and $\dot{M}_2$ are the mass flow rates of both streams. By heat losses to the surroundings an additional exergy loss is generated. This additional exergy loss, however, is usually small and may be neglected in most cases, especially if the heat exchanger is properly insulated.

Evaluation of Eq. (9) for single-phase systems requires inlet and outlet temperatures and pressures of both streams in order to determine the specific entropies s_1', s_1'', s_2', and s_2''. For wet vapor of a pure fluid, temperature or pressure and vapor quality at the inlet and outlet must be known; for mixtures, additionally the compositions of vapor and liquid must be known.

For the single-phase model fluids "perfect gas" and "incompressible fluid," which are good approximations for real gases at low pressures and liquids, respectively, the following simple equations for the calculation of the exergy loss may be used. They have been derived for constant heat capacities [12].

The exergy loss is composed of three parts:

$$\dot{E}_{\mathrm{V}} = \dot{E}_{\mathrm{V,Q}} + \dot{E}_{\mathrm{V},\Delta\mathrm{p},1} + \dot{E}_{\mathrm{V},\Delta\mathrm{p},2}. \tag{10}$$

The first term $\dot{E}_{V,Q}$ represents the main exergy loss due to heat transfer at finite temperature difference. Included is a small fraction which is caused by the mixing of fluid parts of different temperatures at the outlet.

For gases and liquids the exergy loss $\dot{E}_{\mathrm{V,Q}}$ is calculated according to

$$\dot{E}_{\mathrm{V,Q}} = \dot{Q}_{12} T_{\mathrm{u}} \left(\frac{1}{T_{\mathrm{M},2}} - \frac{1}{T_{\mathrm{M},1}}\right) \geq 0. \tag{11}$$

In Eq. (11) $\dot{Q}_{12}$ means the heat flow rate transferred from stream 1 to stream 2 and $T_{\mathrm{M,i}}$ means the logarithmic mean values of the thermodynamic inlet and outlet temperatures of stream $i = 1$ and 2:

$$T_{\mathrm{Mi}} = \frac{T_{\mathrm{i}}' - T_{\mathrm{i}}''}{\ln \frac{T_{\mathrm{i}}'}{T_{\mathrm{i}}''}}. \tag{12}$$

If stream 1 is the hot stream, $\dot{Q}_{12} > 0$ and $T_{\mathrm{M1}} > T_{\mathrm{M2}}$. If stream 1 is the cold stream, $\dot{Q}_{12} < 0$ and $T_{\mathrm{M1}} < T_{\mathrm{M2}}$.

The second and third term in Eq. (10) represent the exergy loss due to frictional pressure drop of stream $i = 1$ and 2, respectively. For gases this exergy loss is calculated according to

$$\dot{E}_{\mathrm{V},\Delta\mathrm{p,i}} = \dot{M}_{\mathrm{i}} R_{\mathrm{i}} \ln \frac{p_{\mathrm{i}}'}{p_{\mathrm{i}}''} \tag{13}$$

where R_{i} is the specific gas constant and p_{i}' and p_{i}'' are the gas pressures at the inlet and outlet of the heat exchanger. The following equation applies to liquids:

$$\dot{E}_{\mathrm{V},\Delta\mathrm{p,i}} = \frac{\dot{M}_{\mathrm{i}} \Delta p_{\mathrm{i}}}{\rho_{\mathrm{i}} T_{\mathrm{M,i}}} \tag{14}$$

with $\dot{M}_{\mathrm{i}}$ as the mass flow rate, ρ_{i} the density, $\Delta p_{\mathrm{i}} = p_{\mathrm{i}}' - p_{\mathrm{i}}''$ the absolute value of the pressure drop, and $T_{\mathrm{M,i}}$ the logarithmic mean value of the temperature according to Eq. (12).

Equating Eqs. (13) and (14) reveals that Eq. (14) can also be applied to gases provided the mean density is determined for the mean temperature according to Eq. (12) and the mean pressure

$$p_M = \frac{p' - p''}{\ln \frac{p'}{p''}}.$$

The considerations refer also to Eqs. (6) and (8).

Unlike the general exergy balance Eq. (9), Eqs. (10–14) allow the separate evaluation of exergy losses caused by heat transfer with finite temperature difference and those caused by frictional pressure drop on both sides. This becomes important if they are covered by exergy sources which are energetically unequal (e.g., fuel oil for the exergy loss caused by finite temperature differences and electrical energy for the exergy loss caused by pressure drop). This is not so important if all exergy losses are eventually covered by the same source as in heat exchangers of thermal power plants.

5 Symbols

a payback coefficient (1/year)
$\dot{E}_V$ exergy loss (W)
j price index
I price (monetary units)
C costs (monetary units/year)
m degression exponent
n number of periods (year)
z annual interest rate (1/year)

6 Bibliography

1. Bartzsch WH (1997) Betriebswirtschaft für Ingenieure, 6th edn. VDE-Verlag, Berlin/Offenbach
2. Peters MS,Timmerhaus KD (1991) Plant design and economics for chemical engineers, 4th edn. McGraw-Hill, New York
3. Chisholm D et al. (1983) Costing of heat exchangers. Chap. 4.8 in: Heat Exchanger Design Handbook. Hemisphere Publishing Corporation, Washington
4. Purohit GP (1987) Heat exchangers, cost of double-pipe and multitube units. In: Encyclopedia of chemical processing and design, vol 25. Marcel Dekker, New York, pp 310–324
5. Vatavuk WM (1995) A potpourri of equipment prices. Chem Eng 102 (August): 68–73
6. Williams R (1947) 'Six-tenths factor' aids in approximating costs. Chem Eng 54:124–125
7. Holland FA, Wilkinson JK (1997) Process economics. Section 9 in: Perry's chemical engineers' handbook, 7th edn. McGraw-Hill, New York
8. Chemical Engineering. Access Intelligence LLC Inc., New York
9. Chemical Engineering Online Plant Cost Index, http://www.che.com/pcitrial/
10. Schnell H (1991) Technisch-wirtschaftliche Optimierung von Wärmeaustauschern. In: Wärmeaustauscher, Energieeinsparung durch Optimierung von Wärmeprozessen, 1st edn, Vulkan-Verlag, Essen, pp 348–353
11. Martin H (1998) Prediction of heat transfer from pressure drop in heat exchangers – a better tool for thermohydraulic and economic design. Proc Int Conf Heat Exchangers for Sustainable Development, Lisbon, Portugal, June 15–18, pp 249–256
12. Roetzel W (1983–2001) Lecture "Prozesse und Apparate der Enegietechnik"., Helmut Schmidt University, University of the Federal Armed Forces Hamburg. See also Roetzel W (1985) Comments on the paper of A. L. London and R. K. Shah, Costs of irreversibilities in heat exchanger design. Heat Transfer Eng 5(3–4):5–17 and 6(2):73

Thermophysical Properties

D1 Calculation Methods for Thermophysical Properties

Michael Kleiber[1] · *Ralph Joh*[2]
[1]Uhde GmbH, Bad Soden, Germany
[2]Siemens AG, Frankfurt, Germany

1 Introduction

For the description of the heat transfer, the knowledge of thermophysical properties is essential. They occur as parameters in particular equations and have usually a significant influence on the results. For example, the thermal conductivity, the dynamic viscosity, the density, and the specific heat capacity are important for the calculation of heat transfer in a single-phase forced convection.

In case of natural convection, the movement of the fluid is caused by temperature differences in the gravitational field. Therefore, the temperature-dependence of the density is important to know. If a phase change happens (condensation or evaporation), the vapor pressure curve is necessary to determine the temperature at the interface between the two phases. The enthalpy of vaporization then determines the heat flux, whereas the surface tension is an important parameter to describe the formation of such an interface, for example, the bubble formation in a vessel containing a boiling liquid. In fluid mixtures, the heat transfer is always connected with a simultaneous mass transfer, where the particular diffusion coefficients are decisive for the evaluation.

All these thermophysical properties depend on the thermodynamic state, which is characterized by two coordinates in the single-phase region. Normally, it is convenient to use temperature and pressure. The temperature-dependence is usually strong, whereas the dependence on the pressure is not negligible, but comparably weak. Only the density of gases is an exception. For mixtures, the dependence on the concentration has to be taken into account.

Values for thermophysical properties should, if possible, always be based on reliable experimental data. Extensive measurements have been performed for various technically important pure substances. These data have been collected in tables in Chap. D2, for example, for water, carbon dioxide, nitrogen, or air, which is often treated like a pure substance. High-precision equations of state have been developed and published for these substances, which ensure the reproduction of all thermodynamic quantities with extraordinary accuracy [1]. The structure of these equations is not based on physical relationships but on the numerical optimization of the terms contributing to the equation. For a large number of other substances, values and correlations are listed in Subchap. D3.1.

However, the heat transfer must often be determined in fluids for which no measured data are available. For multicomponent mixtures, this is even the normal case. Therefore,

VDI-GVC (ed.), *VDI Heat Atlas*, DOI 10.1007/978-3-540-77877-6_10,

methods for the estimation of physical properties are required. In the following sections, a collection of simple correlation and estimation methods for the calculation of thermophysical properties of fluids is compiled.

2 Systematics of Calculation Methods

Physical properties are determined by the internal structure of the molecules and the intermolecular forces between them. Therefore, most of the practical calculation methods are based on considerations in the molecular scale. Nevertheless, the step from the molecular scale to measurable thermophysical properties is extremely difficult. An independent calculation of properties without using experimental data points will not be possible in the near future. Instead, the molecular theories deliver the structure of the calculation methods, and parameters of the particular methods are adjusted to experimental data. The calculation methods, which are established today, are a combination of a theoretically founded structure and parameters determined by experimental data.

It must be distinguished between correlation and estimation methods. The target of correlations is to reproduce a certain number of data points as exactly as possible, to interpolate between the data points safely and to extrapolate beyond the range covered by the data points in a reasonable way. Certainly, care must be taken for the latter case. Many correlations are so well established that the quality of the parameter adjustment can be taken as a consistency test, that is, data points are only accepted if the correlation can reproduce them within their experimental uncertainty.

In contrast, estimation methods shall predict thermophysical properties with or without a few experimental information available. Accuracy is not the main focus of estimation methods; it is more important that unacceptably high deviations from the true values are avoided.

In this chapter, only those estimation methods are listed, which can be recommended to a non-specialized user as a useful compromise between general applicability, accuracy in the sense mentioned above, and simplicity. The use of commercial programs is not necessary. All the calculation methods introduced are mainly founded on two basic elements, that is, the description of the structure of the molecules by group contribution methods and the calculation of molecular interactions by means of the principle of corresponding states.

Group contributions are contributions of the particular functional groups of a molecule to a thermophysical property. It is usually assumed that the contributions of the structural groups are independent of the kind of structural groups in the neighborhood. Then, comparably few structural groups can describe a huge number of chemical substances. The success of the group contribution methods demonstrates that the assumption mentioned above is reasonably justified.

The 3-parameter corresponding states principle is based on the assumption that intermolecular forces can be described by a generalized function, where the substance itself is characterized by few constant parameters. If a calculation function depending on these constants has been derived for a thermophysical property by adjustment to experimental data, this function can be applied to substances where the particular property is unknown. The use of the corresponding states principle is, in most cases, easier to perform than the use of group contributions.

For mixtures, the composition must be introduced into the calculation equations. Essentially, there are two ways to do that. If the pure component data are reliable, so-called mixing rules can be used to evaluate the mixture data from the pure component values. These mixing rules are different for each property, and there are also different forms for different thermodynamic states. Less frequently, mixing rules are applied to the characteristic property constants of the components involved. In this way, a pseudo-pure component is generated with property constants that depend on the concentration of the mixture. The properties of the mixture are then determined with the corresponding pure component methods.

Altogether, the combination of group contribution methods, the 3-parameter corresponding states principle and the mixing rules form a powerful but not perfect system of calculation methods for thermophysical properties of fluid substances.

For all generalized calculation methods, the structural formula is sufficient for the characterization of a substance. Especially, it allows the group assignment of a molecule with structural groups.

3 Characteristic Property Constants

Physical property estimation methods based on the 3-parameter corresponding states principle revert to the characteristic property constants critical temperature (T_c), critical pressure (p_c), and acentric factor (ω). These constants are mainly the basis of the cubic equations of state, which are valuable tools for the description of density and enthalpy of real gases. As the results of an estimation method mainly depend on the quality of the input data, it is worth to determine them carefully.

However, the evaluation of critical data is related with a huge experimental effort, not to mention the fact that many substances already decompose before the critical point can be reached. In these cases, estimation methods are necessary.

In the following section, a number of estimation methods for T_c, p_c, and ω are introduced. Other scalar properties such as normal boiling point (T_{NBP}), critical volume (v_c), melting point (T_m) and enthalpy of fusion (q_m), standard enthalpy of formation (Δh^{0f}), and standard Gibbs energy of formation (Δg^{0f}) as well as the dipole moment (μ), which are used in property estimation methods and process simulations, are also considered. In combination with the correlation and estimation methods for temperature-dependent properties, a system is formed where the optimal calculation method can be found to determine unknown properties with an arbitrary set of known data points for a substance. The extreme case would be to determine all the data required just on the basis of the structural formula as the only ensured information. This case occurs in practical applications; however, it should of course not be aspired, as uncertainties and error propagation might yield in bad results. The standard strategy should be to gain as much information as possible from databanks or experiments and to estimate only the missing information.

3.1 Critical Data

Critical temperature, critical pressure, and critical volume can be quite well-determined with group contribution methods. The methods of Joback [2] and Constantinou/Gani [3] are well-established in this area. A more complicated but accurate method has been developed by Rarey et al. [4].

The Joback method uses only the structural formula as input information. For the estimation of the critical temperature, the normal boiling point is additionally needed; if it is not known, it can be estimated from the structural formula as well (Sect. 3.3). The calculation equations are:

$$\frac{T_c}{K} = \frac{T_{NBP}}{K}\left[0.584 + 0.965\sum\Delta_T - \left(\sum\Delta_T\right)^2\right]^{-1} \quad (1)$$

$$\frac{p_c}{\text{bar}} = \left(0.113 + 0.0032\ n_A - \sum\Delta_p\right)^{-2} \quad (2)$$

$$\frac{v_c}{\text{cm}^3/\text{mol}} = 17.5 + \sum\Delta_v \quad (3)$$

The group contributions for Δ_T, Δ_p, and Δ_v can be taken from Table 1. n_A is the number of atoms in the molecule. The group assignment of the Joback method is simple, as the increments are directly listed. It is only distinguished between chain and ring increments; there is no difference between aromatic and aliphatic rings. It is worth mentioning that there are two kinds of OH groups for alcohols and phenols.

The Constantinou/Gani method uses only the structural formula for all quantities as input information. The authors have introduced the so-called second-order groups, where special configurations of structural groups are assigned with their own group contributions which can simply be added to the normal "first-order" groups. However, acceptable results can also be obtained using only the first-order groups; the improvement achieved with the second-order groups turned out to be relatively small in tests.

The calculation equations for the Constantinou/Gani method are:

$$\exp\frac{T_c}{181.128\ K} = \sum_i \Delta_{T,i} + \sum_j \Delta_{T,j} \quad (4)$$

$$\left(\frac{p_c}{\text{bar}} - 1.3705\right)^{-0.5} = 0.10022 + \sum_i \Delta_{p,i} + \sum_j \Delta_{p,j} \quad (5)$$

$$\frac{v_c}{\text{m}^3/\text{kmol}} = \sum_i \Delta_{v,i} + \sum_j \Delta_{v,j} - 0.00435 \quad (6)$$

where the indices i and j represent the first-order and the second-order groups, respectively. The group contributions for Δ_T, Δ_p, and Δ_v are listed in Tables 2 and 3. The first-order groups are molecular segments which can easily be assigned. Consistently, it is distinguished between aromatic (AC) and aliphatic carbon atoms. As mentioned above, the second-order groups are additive contributions to the first-order groups; they do not replace them.

The quality of the estimation is usually very good for the critical temperature; in most of the cases, the true value is met within a few *K*. Poling et al. [2] indicate an average error of 1.1% of the absolute temperature for the Joback method, if the normal boiling point is known. Only 1% of the test substances have an average error larger than 5%. The average error for the Constantinou/Gani method is reported to be somewhat higher (2.3%) due to the fact that the normal boiling point is not used as input information. Approximately, 11% of the tested substances had an average error larger than 5%. However, the Constantinou/Gani method is superior if the normal boiling point has to be estimated itself.

For the critical pressure, the average errors are reported according to Poling et al. [2] to be 4.6% (Joback) and 5.5% (Constantinou/Gani). As the case may be, these errors can be transferred to the estimation of the vapor pressure (Sect. 5) or to the accuracy of cubic equations of state (Sect. 4.2).

The critical volume is of less importance. It has an influence on the estimation of the density with the COSTALD method (Sect. 4.1), if no reference value is available. The average errors are reported to be 3.1% (Joback) and 3.7% (Constantinou/Gani).

The numbers reported for the average errors refer in all cases to molecules with more than three carbon atoms, since for substances with less carbon atoms property estimations do not make much sense, as usually experimental data are available.

As for the Constantinou/Gani method only the structural formula is used as input, it is also possible to take similar substances with known critical data as reference and to exchange or add only the differing structural groups. Often, but not in every case, this procedure results in an improvement. The target of this procedure is in fact to reduce the probability of a large error. An example is shown below.

If values for T_c, p_c, and v_c are available, it is strongly recommended to check the consistency of the values by calculating the critical compressibility factor

$$Z_c = \frac{p_c v_c}{\tilde{R} T_c} \quad (7)$$

Z_c is usually in the range $0.21 < Z_c < 0.29$.

Example 1:
Estimate the critical properties of m-xylene (Fig. 1). The normal boiling point is T_{NBP} = 412.25 K.

(a) Joback's method

The group assignment of m-xylene is given by:

4 x = CH– (ring)
2 x = C < (ring)
2 x –CH_3

The group contributions are:

$$\sum\Delta_T = 4\cdot(0.0082) + 2\cdot(0.0143) + 2\cdot(0.0141) = 0.0896$$

$$\sum\Delta_p = 4\cdot(0.0011) + 2\cdot(0.0008) + 2\cdot(-0.0012) = 0.0036$$

$$\sum\Delta_v = 4\cdot(41) + 2\cdot(32) + 2\cdot(65) = 358$$

Thus, the critical data can be calculated to be:

$$T_c = 412.25\,\text{K}/(0.584 + 0.965\cdot 0.0896 - 0.0896^2) = 622.32\,\text{K}$$

$$p_c = (0.113 + 0.0032\cdot 18 - 0.0036)^{-2}\text{bar} = 35.86\,\text{bar}$$

$$v_c = (17.5 + 358)\,\text{cm}^3/\text{mol} = 0.3755\,\text{m}^3/\text{kmol}$$

D1. Table 1. Group contributions of the Joback method

Structural group	Δ_T	Δ_p	Δ_v	Δ_{NBP}	Δ_M	Δ_H	Δ_G
$-CH_3$	0.0141	−0.0012	65	23.58	−5.10	−76.45	−43.96
$>CH_2$	0.0189	0.0000	56	22.88	11.27	−20.64	8.42
>CH–	0.0164	0.0020	41	21.74	12.64	29.89	58.36
>C<	0.0067	0.0043	27	18.25	46.43	82.23	116.02
$=CH_2$	0.0113	−0.0028	56	18.18	−4.32	−9.63	3.77
=CH–	0.0129	−0.0006	46	24.96	8.73	37.97	48.53
=C<	0.0117	0.0011	38	24.14	11.14	83.99	92.36
=C=	0.0026	0.0028	36	26.15	17.78	142.14	136.70
≡CH	0.0027	−0.0008	46	9.20	−11.18	79.30	77.71
≡C–	0.0020	0.0016	37	27.38	64.32	115.51	109.82
$-CH_2$–(ring)	0.0100	0.0025	48	27.15	7.75	−26.80	−3.68
>CH– (ring)	0.0122	0.0004	38	21.78	19.88	8.67	40.99
>C< (ring)	0.0042	0.0061	27	21.32	60.15	79.72	87.88
=CH– (ring)	0.0082	0.0011	41	26.73	8.13	2.09	11.30
=C< (ring)	0.0143	0.0008	32	31.01	37.02	46.43	54.05
–F	0.0111	−0.0057	27	−0.03	−15.78	−251.92	−247.19
–Cl	0.0105	−0.0049	58	38.13	13.55	−71.55	−64.31
–Br	0.0133	0.0057	71	66.86	43.43	−29.48	−38.06
–I	0.0068	−0.0034	97	93.84	41.69	21.06	5.74
–OH (alcohols)	0.0741	0.0112	28	92.88	44.45	−208.04	−189.20
–OH (phenols)	0.0240	0.0184	−25	76.34	82.83	−221.65	−197.37
–O–	0.0168	0.0015	18	22.42	22.23	−132.22	−105.00
–O– (ring)	0.0098	0.0048	13	31.22	23.05	−138.16	−98.22
>C=O	0.0380	0.0031	62	76.75	61.20	−133.22	−120.50
>C=O (ring)	0.0284	0.0028	55	94.97	75.97	−164.50	−126.27
–CH=O	0.0379	0.0030	82	72.24	36.90	−162.03	−143.48
–COOH	0.0791	0.0077	89	169.09	155.50	−426.72	−387.87
–COO–	0.0481	0.0005	82	81.10	53.60	−337.92	−301.95
=O	0.0143	0.0101	36	−10.50	2.08	−247.61	−250.83
$-NH_2$	0.0243	0.0109	38	73.23	66.89	−22.02	14.07
>NH	0.0295	0.0077	35	50.17	52.66	53.47	89.39
>NH (ring)	0.0130	0.0114	29	52.82	101.51	31.65	75.61
>N–	0.0169	0.0074	9	11.74	48.84	123.34	163.16
–N=	0.0255	−0.0099		74.60		23.61	
–N= (ring)	0.0085	0.0076	34	57.55	68.40	55.52	79.93
=NH						93.70	119.66
–CN	0.0496	−0.0101	91	125.66	59.89	88.43	89.22
$-NO_2$	0.0437	0.0064	91	152.54	127.24	−66.57	−16.83
–SH	0.0031	0.0084	63	63.56	20.09	−17.33	−22.99
–S–	0.0119	0.0049	54	68.78	34.40	41.87	33.12
–S– (ring)	0.0019	0.0051	38	52.10	79.93	39.10	27.76

(b) Method of Constantinou/Gani

The group assignment of m-xylene is:

4 × ACH

2 × $ACCH_3$

Second-Order-Groups cannot be assigned.

The results for the group contributions are:

$$\sum \Delta_T = 4 \cdot (3.7337) + 2 \cdot (8.213) = 31.3608$$

$$\sum \Delta_p = 4 \cdot (0.007542) + 2 \cdot (0.01936) = 0.068888$$

$$\sum \Delta_v = 4 \cdot (0.04215) + 2 \cdot (0.10364) = 0.37588$$

D1. Table 2. Constantinou / Gani group contributions for first-order groups

Structural group	Δ_T	Δ_p	Δ_v	Δ_{NBP}	Δ_H	Δ_G
CH_3	1.6781	0.019904	0.07504	0.8894	−45.947	−8.030
CH_2	3.4920	0.010558	0.05576	0.9225	−20.763	8.231
CH	4.0330	0.001315	0.03153	0.6033	−3.766	19.848
C	4.8823	−0.010404	−0.00034	0.2878	17.119	37.977
CH_2=CH	5.0146	0.025014	0.11648	1.7827	53.712	84.926
CH=CH	7.3691	0.017865	0.09541	1.8433	69.939	92.900
CH_2=C	6.5081	0.022319	0.09183	1.7117	64.145	88.402
CH=C	8.9582	0.012590	0.07327	1.7957	82.528	93.745
C=C	11.3764	0.002044	0.07618	1.8881	104.293	116.613
CH_2=C=CH	9.9318	0.031270	0.14831	3.1243	197.322	221.308
ACH	3.7337	0.007542	0.04215	0.9297	11.189	22.533
AC	14.6409	0.002136	0.03985	1.6254	27.016	30.485
$ACCH_3$	8.2130	0.019360	0.10364	1.9669	−19.243	22.505
$ACCH_2$	10.3239	0.012200	0.10099	1.9478	9.404	41.228
ACCH	10.4664	0.002769	0.07120	1.7444	27.671	52.948
OH	9.7292	0.005148	0.03897	3.2152	−181.422	−158.589
ACOH	25.9145	−0.007444	0.03162	4.4014	−164.609	−132.097
CH_3CO	13.2896	0.025073	0.13396	3.5668	−182.329	−131.366
CH_2CO	14.6273	0.017841	0.11195	3.8967	−164.410	−132.386
CHO	10.1986	0.014091	0.08635	2.8526	−129.158	−107.858
CH_3COO	12.5965	0.029020	0.15890	3.6360	−389.737	−318.616
CH_2COO	3.8116	0.021836	0.13649	3.3953	−359.258	−291.188
HCOO	11.6057	0.013797	0.10565	3.1459	−332.822	−288.902
CH_3O	6.4737	0.020440	0.08746	2.2536	−163.569	−105.767
CH_2O	6.0723	0.015135	0.07286	1.6249	−151.143	−101.563
CH-O	5.0663	0.009857	0.05865	1.1557	−129.488	−92.099
CH_2O (cyclic)	9.5059	0.009011	0.06858	2.5892	−140.313	−90.883
CH_2NH_2	12.1726	0.012558	0.13128	3.1656	−15.505	58.085
$CHNH_2$	10.2075	0.010694	0.07527	2.5983	3.320	63.051
CH_3NH	9.8544	0.012589	0.12152	3.1376	5.432	82.471
CH_2NH	10.4677	0.010390	0.09956	2.6127	23.101	95.888
CHNH	7.2121	−0.000462	0.09165	1.5780	26.718	85.001
CH_3N	7.6924	0.015874	0.12598	2.1647	54.929	128.602
CH_2N	5.5172	0.004917	0.06705	1.2171	69.885	132.756
$ACNH_2$	28.7570	0.001120	0.06358	5.4736	20.079	68.861
C_5H_4N	29.1528	0.029565	0.24831	6.2800	134.062	199.958
C_5H_3N	27.9464	0.025653	0.17027	5.9234	139.758	199.288
CH_2CN	20.3781	0.036133	0.15831	5.0525	88.298	121.544
COOH	23.7593	0.011507	0.10188	5.8337	−396.242	−349.439
CH_2Cl	11.0752	0.019789	0.11564	2.9637	−73.568	−33.373
CHCl	10.8632	0.011360	0.10350	2.6948	−63.795	−31.502
CCl	11.3959	0.003086	0.07922	2.2073	−57.795	−25.261
$CHCl_2$	16.3945	0.026808	0.16951	3.9300	−82.921	−35.814
CCl_2				3.5600		
CCl_3	18.5875	0.034935	0.21031	4.5797	−107.188	−53.332
ACCl	14.1565	0.013135	0.10158	2.6293	−16.752	−0.596
CH_2NO_2	24.7369	0.020974	0.16531	5.7619	−66.138	17.963
$CHNO_2$	23.2050	0.012241	0.14227	5.0767	−59.142	18.088
$ACNO_2$	34.5870	0.015050	0.14258	6.0837	−7.365	60.161

D1. Table 2. (continued)

Structural group	Δ_T	Δ_p	Δ_v	Δ_{NBP}	Δ_H	Δ_G
CH_2SH	13.8058	0.013572	0.10252	3.2914	−8.253	16.731
I	17.3947	0.002753	0.10814	3.6650	57.546	46.945
Br	10.5371	−0.001771	0.08281	2.6495	1.834	−1.721
CH≡C	7.5433	0.014827	0.09331	2.3678	220.803	217.003
C≡C	11.4501	0.004115	0.07627	2.5645	227.368	216.328
Cl- (attached to >C=C<)	5.4334	0.016004	0.05687	1.7824	−36.097	−28.148
ACF	2.8977	0.013027	0.05672	0.9442	−161.740	−144.549
$HCON(CH_2)_2$				7.2644		
CF_3	2.4778	0.044232	0.11480	1.2880	−679.195	−626.580
CF_2	1.7399	0.012884	0.09519	0.6115		
CF	3.5192	0.004673		1.1739		
COO	12.1084	0.011294	0.08588	2.6446	−313.545	−281.495
CCl_2F	9.8408	0.035446	0.18212	2.8881	−258.960	−209.337
HCClF				2.3086		
$CClF_2$	4.8923	0.039004	0.14753	1.9163	−446.835	−392.975
F	1.5974	0.014434	0.03783	1.0081	−223.398	−212.718
$CONH_2$	65.1053	0.004266	0.14431	10.3428	-203.188	−136.742
$CONHCH_3$					−67.778	
$CONHCH_2$					−182.096	
$CON(CH_3)_2$	36.1403	0.040149	0.25031	7.6904	−189.888	−65.642
$CONCH_3CH_2$					−46.562	
$CON(CH_2)_2$				6.7822		
$C_2H_5O_2$	17.9668	0.025435	0.16754	5.5566	−344.125	−241.373
$C_2H_4O_2$				5.4248		
CH_3S	14.3969	0.016048	0.13021	3.6796	−2.084	30.222
CH_2S	17.7916	0.011105	0.11650	3.6763	18.022	38.346
CHS				2.6812		
C_4H_3S				5.7093		
C_4H_2S				5.8260		

The critical data can be calculated to be:

$$T_c = 181.128\,\text{K} \cdot \ln 31.3608 = 624.09\,\text{K}$$
$$p_c = [(0.10022 + 0.068888)^{-2} + 1.3705]\,\text{bar} = 36.34\,\text{bar}$$
$$v_c = (0.37588 - 0.00435)\,\text{m}^3/\text{kmol} = 0.37153\ \text{m}^3/\text{kmol}$$

(c) Method of Constantinou/Gani with toluene as reference substance

The critical data of toluene are:

$$T_c = 591.75\,\text{K},\ p_c = 41.1\,\text{bar},\ v_c = 0.3156\,\text{m}^3/\text{kmol}$$

A backwards calculation to obtain the group contributions of toluene (Fig. 2) yields:

$$\sum \Delta_{T,\text{toluene}} = \exp(591.75/181.128) = 26.233$$
$$\sum \Delta_{p,\text{toluene}} = (41.1 - 1.3705)^{-0.5} - 0.10022 = 0.05843$$
$$\sum \Delta_{v,\text{toluene}} = 0.3156 - 0.00435 = 0.31125$$

The difference in the structural formulas of toluene and m-xylene is that one ACH group has to be replaced by an $ACCH_3$ group. Thus, the group contributions for m-xylene can be determined to be:

$$\sum \Delta_T = 26.233 - (3.7337) + (8.213) = 30.7123$$
$$\sum \Delta_p = 0.05843 - (0.007542) + (0.01936) = 0.070248$$
$$\sum \Delta_v = 0.31125 - (0.04215) + (0.10364) = 0.37274$$

Therefore, the critical data can be estimated:

$$T_c = 181.128\,\text{K} \cdot \ln 30.7123 = 620.3\,\text{K}$$
$$p_c = [(0.10022 + 0.070248)^{-2} + 1.3705]\,\text{bar} = 35.78\,\text{bar}$$
$$v_c = (0.37274 - 0.00435)\,\text{m}^3/\text{kmol} = 0.36839\ \text{m}^3/\text{kmol}$$

The experimental values for m-xylene are:

$$T_c = 617.05\,\text{K}$$
$$p_c = 35.4\,\text{bar}$$
$$v_c = 0.37516\,\text{m}^3/\text{kmol}$$

For all the three calculation options, the agreement between estimated and experimental values is remarkably good. The check of the critical compressibility factor yields

D1. Table 3. Constantinou/Gani group contributions for second-order groups

Structural group	Δ_T	Δ_p	Δ_v	Δ_{NBP}	Δ_H	Δ_G	Values for k,l,m,n,p
$(CH_3)_2$–CH	–0.5334	0.000488	0.00400	–0.1157	–0.860	0.297	
$(CH_3)_3$–C	–0.5143	0.001410	0.00572	–0.0489	–1.338	–0.399	
$CH(CH_3)CH(CH_3)$	1.0699	–0.001849	–0.00398	0.1798	6.771	6.342	
$CH(CH_3)C(CH_3)_2$	1.9886	–0.005198	–0.01081	0.3189	7.205	7.466	
$C(CH_3)_2$–$C(CH_3)_2$	5.8254	–0.013230	–0.02300	0.7273	14.271	16.224	
3-membered ring	–2.3305	0.003714	–0.00014	0.4745	104.800	94.564	
4-membered ring	–1.2978	0.001171	–0.00851	0.3563	99.455	92.573	
5-membered ring	–0.6785	0.000424	–0.00866	0.1919	13.782	5.733	
6-membered ring	0.8479	0.002257	0.01636	0.1957	–9.660	–8.180	
7-membered ring	3.6714	–0.009799	–0.02700	0.3489	15.465	20.597	
CH_n=CH_m–CH_p=CH_k	0.4402	0.004186	–0.00781	0.1589	–8.392	–5.505	0,1,2
CH_3–CH_m=CH_n	0.0167	–0.000183	–0.00098	0.0668	0.474	0.950	0,1,2
CH_2–CH_m=CH_n	–0.5231	0.003538	0.00281	–0.1406	1.472	0.699	0,1,2
CH–CH_m=CH_n or C–CH_m=CH_n	–0.3850	0.005675	0.00826	–0.0900	4.504	1.013	0,1,2
C_{cyclic} – C_m (C-chain attached to ring)	2.1160	–0.002546	–0.01755	0.0511	1.252	1.041	m>1
CH_3CH_3	2.0427	0.005175	0.00227	0.6884	–2.792	–1.062	
CHCHO or CCHO	–1.5826	0.003659	–0.00664	–0.1074	–2.092	–1.359	
CH_3COCH_2	0.2996	0.001474	–0.00510	0.0224	0.975	0.075	
CH_3COCH or CH_3COC	0.5018	–0.002303	–0.00122	0.0920	4.753		
C_{cyclic}(=O)	2.9571	0.003818	–0.01966	0.5580	14.145	23.539	
ACCHO	1.1696	–0.002481	0.00664	0.0735	–3.173	–2.602	
CHCOOH or CCOOH	–1.7493	0.004920	0.00559	0.1552	1.279	2.149	
ACCOOH	6.1279	0.000344	–0.00415	0.7801	12.245	10.715	
CH_3COOCH or CH_3COOC	–1.3406	0.000659	–0.00293	–0.2383	–7.807	–6.208	
$COCH_2COO$, COCHCOO or COCCOO	2.5413	0.001067	–0.00591	0.4456	37.462	29.181	
CO–O–CO	–2.7617	–0.004877	–0.00144	–0.1977	–16.097	–11.809	
ACCOO	–3.4235	–0.000541	0.02605	0.0835	–9.874	–7.415	
CHOH	–2.8035	–0.004393	–0.00777	–0.5385	–3.887	–6.770	
COH	–3.5442	0.000178	0.01511	–0.6331	–24.125	–20.770	
CH_m(OH)CH_n(OH)	5.4941	0.005052	0.00397	1.4108	0.366	3.805	0,1,2
CH_m(cyclic)–OH	0.3233	0.006917	–0.02297	–0.0690	–16.333	–5.487	0,1
CH_m(OH)–CH_n(NH_p)	5.4864	0.001408	0.00433	1.0682	–2.992	–1.600	0,1,2,3
CH_m(NH_2)–CH_n(NH_2)	2.0699	0.002148	0.00580	0.4247	2.855	1.858	0,1,2
CH_m(cyclic)–NH_p–CH_n(cyclic)	2.1345	–0.005947	–0.01380	0.2499	0.351	8.846	0,1,2
CH_m–O–CH_n=CH_p	1.0159	–0.000878	0.00297	0.1134	–8.644	–13.167	0,1,2
AC–O–CH_m	–5.3307	–0.002249	–0.00045	–0.2596	1.532	–0.654	0,1,2,3
CH_m(cyclic)–S–CH_n(cyclic)	4.4847			0.4408	–0.329	–2.091	0,1,2
CH_m=CH_n–F	–0.4996	0.000319	–0.00596	–0.1168			0,1,2
CH_m=CH_n–Br	–1.9334	–0.004305	0.00507	–0.3201	11.989	12.373	0,1,2
CH_m=CH_n–I				–0.4453			0,1,2
ACBr	–2.2974	0.009027	–0.00832	–0.6776	12.285	14.161	
ACI	2.8907	0.008247	–0.00341	–0.3678	11.207	12.530	
CH_m(NH_2)–COOH					11.740		0,1,2

$$Z_c = \frac{35.4 \cdot 10^5 \cdot 0.37516 \cdot 10^{-3}}{8.3143 \cdot 617.05} = 0.259$$

which is a reasonable value between 0.21 and 0.29.

3.2 Acentric Factor

The simple 2-parameter principle of corresponding states says that it is possible to set up a generalized equation of state valid

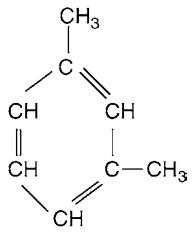

D1. Fig. 1. Structural formula of m-xylene.

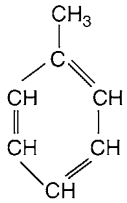

D1. Fig. 2. Structural formula of toluene.

for all substances with only two specific parameters, for example, T_c and p_c. The success of this approach was limited to simple, spherical molecules like Ar, Kr, Xe, or CH_4, where vapor pressure and compressibility factor could be adequately reproduced. For other molecules, the 2-parameter principle of corresponding states yielded results with considerable deviations. Therefore, it was replaced by the extended 3-parameter principle of corresponding states, where a third parameter has been introduced, which gives additional information about the vapor pressure line. The most popular parameter of this kind is the acentric factor ω, which is defined as

$$\omega = -1 - \log_{10}\left(\frac{p_s}{p_c}\right)_{T/T_c=0.7} \tag{8}$$

Physically, ω takes into account the influence of the intermolecular forces depending on the orientation of the molecules. The parameter is used in many correlations for the estimation of thermophysical properties. Especially, ω is decisive for the application of cubic equations of state (Sect. 4.2). The definition given in Eq. (8) makes sense, as the vapor pressure is a quantity with high significance and accessibility. The reference temperature $T = 0.7\ T_c$ has been chosen because it is often in the neighborhood of the normal boiling point. An estimation of ω is therefore equivalent to an estimation of the vapor pressure curve or, respectively, the normal boiling point.

Although estimation methods for the acentric factor are available (e.g., group contribution method of Constantinou/Gani [5]), this concept is not recommended in this transaction, as it is, as mentioned above, a redundancy to the estimation of the normal boiling point. To avoid inconsistencies, it is instead recommended to evaluate ω directly via the definition Eq. (8) from the vapor pressure equation. If a vapor pressure equation is not available at all, it is still possible to estimate the normal boiling point (Sect. 3.3) and the critical point (Sect. 3.1) and to determine the vapor pressure curve as described in Sect. 5.

The acentric factor increases with the size of the molecule. Only in single cases, values $\omega > 1$ occur. Helium ($\omega = -0.39$) and hydrogen ($\omega = -0.216$), the so-called quantum gases, have negative acentric factors. Methane and the noble gases argon, krypton, xenon, and neon have values that are near zero. In other cases, $\omega \leq 0$ can strictly be excluded. If a value like this is evaluated, the conclusion must be that the vapor pressure curve or the critical point or both of them are wrong.

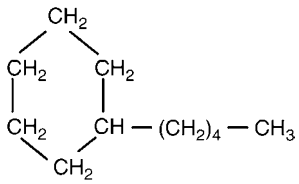

D1. Fig. 3. Structural formula of pentyl cyclohexane.

3.3 Normal Boiling Point

The normal boiling point is an easily accessible property and well known for a wide variety of substances. Even values from chemical catalogues, safety datasheets, or from the Internet (e.g., www.nist.gov) can give reasonable values, although high-precision data should not be expected.

In case no information is available, the normal boiling point (NBP) can be estimated using the methods of Joback [2] or Constantinou/Gani [3], analogously to the estimation of the critical temperature. The corresponding relationships are:

Joback:

$$T_{NBP}/\mathrm{K} = 198 + \sum \Delta_{NBP} \tag{9}$$

Constantinou/Gani:

$$\exp\frac{T_{NBP}}{204.359\ \mathrm{K}} = \sum_i \Delta_{NBP,i} + \sum_j \Delta_{NBP,j} \tag{10}$$

The corresponding group contributions can again be taken from Tables 1, 2 and 3. In both cases, the accuracy is much lower than for the estimation of the critical data.

As for the critical data, the possibility of taking a reference substance with a similar structure can be made use of. Because of the high uncertainties of the normal boiling point estimation, this procedure is strongly recommended if possible to avoid large errors.

Example 2:
Estimate the normal boiling point of pentyl cyclohexane (Fig. 3).

(a) Joback method

The group assignment of pentyl cyclohexane is:
- 5 × CH_2 (ring)
- 1 × CH (ring)
- 1 × CH_3
- 4 × CH_2

The group contribution can be added up to:

$$\sum \Delta_{NBP} = 5 \cdot (27.15) + 1 \cdot (21.78) + 1 \cdot (23.58) + 4 \cdot (22.88) = 272.63$$

Thus, the normal boiling point is calculated to be:

$$T_{NBP} = (198 + 272.63)\,K = 470.63\,K$$

(b) Method of Constantinou/Gani

The group assignment of pentyl cyclohexane is:

$9 \times CH_2$
$1 \times CH_3$
$1 \times CH$

As second-order groups can be assigned:

$1 \times$ 6 membered ring
$1 \times$ C-chain attached to ring

The sum of the group contributions is:

$$\sum \Delta_{NBP} = 9 \cdot (0.9225) + 1 \cdot (0.8894) + 1 \cdot (0.6033) + 1 \cdot (0.1957) + 1 \cdot (0.0511) = 10.042$$

The normal boiling point is determined to be:

$$T_{NBP} = 204.359\,K \cdot \ln 10.042 = 471.41\,K$$

(c) Joback method with methyl cyclohexane as reference substance

The normal boiling point of methyl cyclohexane (Fig. 4) is:

$$T_{NBP} = 373.95\,K.$$

To evaluate the sum of group contributions for methyl cyclohexane, a backward calculation yields:

$$\sum \Delta_{NBP,Methylcyclohexan} = 373.95 - 198 = 175.95$$

The difference in the structural formulas of pentyl cyclohexane and methyl cyclohexane is that four aliphatic CH_2-groups have been added. In this way, the sum of group contributions for pentyl cyclohexane can be determined to be:

$$\sum \Delta_{NBP} = 175.95 + 4 \cdot (22.88) = 267.47$$

Thus, what is obtained for the normal boiling point is:

$$T_{NBP} = (198 + 267.47)\,K = 465.47\,K$$

(d) Methode of Constantinou/Gani with methyl cyclohexane as reference substance

The normal boiling point of methyl cyclohexane is:

$$T_{NBP} = 373.95\ K.$$

For the group contributions of methyl cyclohexane, a backward calculation yields:

$$\sum \Delta_{NBP,Methylcyclohexan} = \exp(373.95/204.359) = 6.233$$

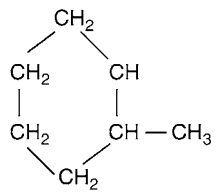

D1. Fig. 4. Structural formula of methyl cyclohexane.

The difference in the structural formulas of pentyl cyclohexane and methyl cyclohexane is that four aliphatic CH_2-groups have been added. Moreover, the contribution of the second-order group "C-chain attached to ring", which is only valid for $m > 1$, has to be supplemented. In this way, the sum of group contributions for pentyl cyclohexane can be evaluated to be:

$$\sum \Delta_{NBP} = 6.233 + 4 \cdot (0.9225) + 0.0511 = 9.9741$$

Thus, the result for the normal boiling point is:

$$T_{NBP} = 204.359\,K \cdot \ln 9.9741 = 470.02\,K$$

The experimental value for pentyl cyclohexane is: $T_{NBP} = 476.75$ K. All the methods shown above yield a reasonable result. Again, the use of a reference substance does not necessarily guarantee a better result, but it lowers the probability of a large error.

A new recommendable method for the estimation of the normal boiling point has been developed by Rarey et al. [6]. However, its group assignment is somewhat more complicated.

3.4 Melting Point and Enthalpy of Fusion

Besides normal boiling point and liquid density at 20°C, the melting point is the thermophysical property which can be found most frequently and is often found in chemical catalogues and handbooks. The estimation of melting points is a very complex task, as is determined both by the enthalpy of fusion, which depends on intermolecular forces, and by the entropy of fusion, which is a function of the symmetry of the molecule. Therefore, the applicability of group contribution methods is limited, as information about the molecular symmetry is lost if a group contribution concept is applied. Joback [2] lists, in fact, group contributions for the melting point; however, the average error is expected to be more than 20 K even for simple molecules, which is not acceptable for practical applications.

The enthalpy of fusion itself depends partly on the crystalline form that is transformed into a liquid, which can hardly be expressed in terms of mathematics for complex substances. In principle, the Clausius-Clapeyron equation can be applied, but information on the pressure dependence of the melting point is also usually missing. For aromatic compounds like benzene and naphthalene derivatives, the Walden rule [6, 7] can be applied:

$$\widetilde{M}\,\Delta h_m(T_m)/T_m \approx 13\ \text{cal}\cdot\text{K}^{-1}\cdot\text{mol}^{-1} = 54.4\ \text{J}\cdot\text{mol}^{-1}\cdot\text{K}^{-1} \quad (11)$$

3.5 Standard Enthalpy of Formation and Gibbs Energy of Formation

The enthalpy of formation Δh^{0f} and the Gibbs energy of formation Δg^{0f} are decisive for the calculation of enthalpies of reaction and chemical equilibria. For heat exchange calculations of chemical reactors, they are relevant as well, as these quantities determine the maximum possible product temperature or the heat to be removed. The reference state for Δh^{0f} and Δg^{0f} is $T_0 = 298.15$ K and $p_0 = 1$ atm in the ideal gas state.

In process simulation, the enthalpy of formation is also taken as the reference state for the calculation of enthalpies

(Sect. 6.4), so that these enthalpies are then consistent if chemical reactions are considered.

Further explanations, especially for the switch to liquid and solid phases, can be found in the textbook of J. Gmehling and B. Kolbe [8]. In both cases, the problem of the difference of large numbers has to be taken into account. Small relative deviations of Δh^{0f} or Δg^{0f} can cause severe errors when differences are calculated. Therefore, estimation methods for these quantities must be taken as rough numbers for orientation.

Analogously to the estimation of the critical data, the methods of Joback and Constantinou/Gani are recommended. The equations for calculation are:

Joback [2]:

$$\frac{\Delta h^{0f}}{\mathrm{kJ/mol}} = 68.29 + \sum \Delta_H \tag{12}$$

$$\frac{\Delta g^{0f}}{\mathrm{kJ/mol}} = 53.88 + \sum \Delta_G \tag{13}$$

Constantinou/Gani [3]:

$$\frac{\Delta h^{0f}}{\mathrm{kJ/mol}} = \sum_i \Delta_{H,i} + \sum_j \Delta_{H,j} + 10.835 \tag{14}$$

$$\frac{\Delta g^{0f}}{\mathrm{kJ/mol}} = \sum_i \Delta_{G,i} + \sum_j \Delta_{G,j} - 14.828 \tag{15}$$

where the second-order group concept is again applied. The group contributions for both methods can be found in Tables 1, 2 and 3.

Example 3:

Determine the enthalpy of formation and the Gibbs energy of formation for ethyl acetate with the Joback method (structural formula in Fig. 7).The group assignment of ethyl acetate is

2 × CH_3
1 × CH_2
1 × COO

Thus, one gets for the group contributions:

$$\sum \Delta_H = 2 \cdot (-76.45) + 1 \cdot (-20.64) + 1 \cdot (-337.92) = -511.46$$

$$\sum \Delta_G = 2 \cdot (-43.96) + 1 \cdot (8.42) + 1 \cdot (-301.95) = -381.45$$

The values finally obtained are:

$$\frac{\Delta h^{0f}}{\mathrm{kJ/mol}} = 68.29 - 511.46 = -443.17$$

$$\frac{\Delta g^{0f}}{\mathrm{kJ/mol}} = 53.88 - 381.45 = -327.57$$

The values obtained from databanks are $\Delta h^{0f} = -444.5$ kJ/mol and $\Delta g^{0f} = -328$ kJ/mol. The excellent agreement can be explained by the fact that ethyl acetate is very well known from esterification reactions.

3.6 Dipole Moment

For polyatomic molecules containing atoms with different electronegativity, the charge distribution can be asymmetric according to the geometry of the molecule. In the simplest case, this can be described as an electric dipole, which consists of two charges q of the same magnitude but with opposite sign, where the distance between them is r. The product of charge q and distance r is called dipole moment μ:

$$\mu = rq \tag{16}$$

As the charges are smaller than the elementary charge, that is, approximately 10^{-20} C, and the distances like an atom, that is, 10^{-10} m, the order of magnitude of dipole moments is 10^{-30} m. Usually, the unit debye is used:
1 debye = $3.3356 \cdot 10^{-30}$ Cm. Some values are given in Table 4.

For complex molecules, higher electrical moments may occur, for example, the quadrupolar moment, which consists of two pairs of charges with opposite sign. Dipole moments can be determined by measurement of the electric capacity or by molecular simulations.

D1. Table 4. Some numbers for the dipole moment

Substance	Formula	Dipole moment ($\mu/10^{-30}$ Cm)	Debye
Hydrogen chloride	HCl	3.44	1.03
Carbon monoxide	CO	0.40	0.12
Carbon dioxide	CO_2	0.00	0.00
Water	H_2O	6.00	1.80
Ammonia	NH_3	4.97	1.49
Methane	CH_4	0.00	0.00
Ethanol	C_2H_6O	5.67	1.70
Benzene	C_6H_6	0.00	0.00
Chlorobenzene	C_6H_5Cl	5.90	1.77
Nitrobenzene	$C_6H_5NO_2$	13.40	4.02

4 Density

4.1 Density of Liquids

The density of liquids is one of the most important quantities for equipment design. There are considerable demands on the accuracy. Simple equations of state do usually not fulfill these requirements; therefore, direct correlations for the liquid density on the saturation line are used. The most popular one is the Rackett equation

$$\frac{\rho_{liq}}{\mathrm{kg/m^3}} = \frac{A}{B^{1+\left(1-\frac{T/K}{C}\right)^D}} \tag{17}$$

Currently, the PPDS equation

$$\frac{\rho_{liq}}{\mathrm{kg/m^3}} = \frac{\rho_c}{\mathrm{kg/m^3}} + \left[A\left(1-\frac{T}{T_c}\right)^{0.35} + B\left(1-\frac{T}{T_c}\right)^{2/3} + C\left(1-\frac{T}{T_c}\right) + D\left(1-\frac{T}{T_c}\right)^{4/3}\right] \tag{17a}$$

is considered to be the most precise one. For this correlation, coefficients for approximately 270 substances are given in Subchap. D3.1.

For the estimation of liquid densities or, respectively, specific liquid volumes on the saturation line, the COSTALD equation [9] has been widely applied:

$$v_s = \tilde{\rho}^{-1} = v^* v_R^{(0)} \left[1 - \omega\, v_R^{(\delta)}\right] \tag{18}$$

$$v_R^{(0)} = 1 + a(1 - T_r)^{1/3} + b(1 - T_r)^{2/3} + c(1 - T_r) + d(1 - T_r)^{4/3};\ 0.25 < T_r < 0.95 \tag{19}$$

$$v_R^{(\delta)} = \left(e + fT_r + gT_r^2 + hT_r^3\right)/(T_r - 1.00001);\ 0.25 < T_r < 1.0 \tag{20}$$

$$T_r = T/T_c \tag{21}$$

where

$a = -1.52816$; $b = 1.43907$; $c = -0.81446$;
$d = 0.190454$; $e = -0.296123$; $f = 0.386914$;
$g = -0.0427458$; $h = -0.0480645$

The characteristic volume v^* is an adjustable parameter which can be fitted to one or more experimental data points. If no information is available, it is useful to replace it by the critical volume v_c, which often yields reasonable results.

Example 4:
Estimate the liquid density of n-hexane at $T = 293.15$ K with the COSTALD method:

The given data are:
$T_c = 507.5$ K
$v^* = v_c = 370$ cm^3/mol
$\omega = 0.299$
$M = 86.18$ g/mol
Using Eqs. (18)–(21), one can obtain:

$$v_R^{(0)} = 0.3799$$
$$v_R^{(\delta)} = 0.2277$$
$$v_s = 130.99\ \text{cm}^3/\text{mol} \Rightarrow \rho_{liq} = 657.9\ \text{kg/m}^3$$

The value given in the literature is 659 kg/m^3.

For a first approximation, liquids can be regarded as incompressible. If the pressure dependence plays a major role, the application of high-precision equations of state [1] would be desirable. If such an equation is not available, some equations for estimation are given in [2].

The evaluation of the density of liquid mixtures should be performed via the linear mixing rule for the specific volume:

$$v_{mix} = \sum_i \tilde{x}_i v_i \tag{22}$$

or, respectively:

$$\rho_{liq}^{mix} = \left(\sum_i x_i \rho_{liq,i}^{-1}\right)^{-1} \tag{23}$$

Equation (22) is not exact, as the mixture influence, the so-called excess volume, is neglected. However, the error of Eq. (22) can hardly be larger than 2–3%.

4.2 Density of Gases

At moderate pressures up to approximately 5 bar, the ideal gas law

$$pv = \tilde{R}T \tag{24}$$

can be used for the calculation of gas phase densities of non-associating compounds with sufficient accuracy.

At higher pressures, the cubic equations of state like Peng-Robinson [10] (PR) and Soave-Redlich-Kwong [11] (SRK) are well-suited for nonassociating compounds, as they are sufficiently accurate and comparably easy to apply. The equations are derived from the van der Waals equation and can be written as follows:

Peng-Robinson:

$$p = \frac{\tilde{R}T}{v - b} - \frac{a(T)}{v^2 + 2bv - b^2} \tag{25}$$

Soave-Redlich-Kwong:

$$p = \frac{\tilde{R}T}{v - b} - \frac{a(T)}{v^2 + bv} \tag{26}$$

It can be shown by mathematical rearrangement that these equations can be reduced to the search for the roots of a cubic function of the specific volume. In the subcritical region, they can deliver three real solutions for a given temperature and pressure, where the smallest solution describes the liquid phase and the largest solution represents the vapor phase. Nevertheless, the cubic equations are not suitable for the calculation of liquid densities, as long as no additional terms have been introduced into the equation [12]. The middle solution has no physical meaning. Above the critical point and at pressures far below saturation one gets one real and two complex solutions, where the real solution describes the fluid phase. The particular solutions can be obtained by application of the Cardanic formula [13] or by iteration.

To evaluate gas densities with the PR or the SRK equation, critical temperature, critical pressure and acentric factor have to be known. Using the reduced temperature $T_r = T/T_c$, the following relationships can be set up:

Peng-Robinson:

$$a(T) = a_c \alpha(T)$$
$$\alpha(T) = \left[1 + \left(0.37464 + 1.54226\omega - 0.26992\omega^2\right)\left(1 - T_r^{0.5}\right)\right]^2$$
$$a_c = 0.45724 \frac{\tilde{R}^2 T_c^2}{p_c} \tag{25a}$$
$$b = 0.0778 \frac{\tilde{R}T_c}{p_c}$$

Soave-Redlich-Kwong:

$$a(T) = a_c \alpha(T)$$
$$\alpha(T) = \left[1 + \left(0.48 + 1.574\omega - 0.176\omega^2\right)\left(1 - T_r^{0.5}\right)\right]^2$$
$$a_c = 0.42748 \frac{\tilde{R}^2 T_c^2}{p_c} \tag{26a}$$
$$b = 0.08664 \frac{\tilde{R}T_c}{p_c}$$

If these equations are applied to mixtures, the parameters can be calculated via the mixing rules

$$a_{\mathrm{mix}} = \sum_i \sum_j \tilde{y}_i \tilde{y}_j \left(a_{ii} a_{jj}\right)^{0.5} (1 - k_{ij}) \tag{27}$$

$$b_{\mathrm{mix}} = \sum_i \tilde{y}_i b_i \tag{28}$$

The binary parameters k_{ij} can be set to zero as long as phase equilibria are not involved (Part D). For the calculation of vapor densities, their influence is negligible.

Example 5:

Determine the vapor density of R22 (chlorodifluoromethane) at $T = 301.15$ K, $p = 11.308$ bar using the Peng-Robinson equation.

The following input data are given:

$T_c = 369.28$ K

$p_c = 49.88$ bar

$\omega = 0.221$

$\tilde{M} = 86.47$ g/mol

Thus, one gets the following coefficients:

$$\alpha(301.15\,\mathrm{K}) = \left[1 + \left(0.37464 + 1.54226 \cdot 0.221 - 0.26992 \cdot 0.221^2\right)\left(1 - (301.15/369.28)^{0.5}\right)\right]^2 = 1.1408$$

$$a_c = 0.45724 \frac{8.3143^2 \cdot 369.28^2}{49.88 \cdot 10^5} \frac{\mathrm{Pa \cdot m^6}}{\mathrm{mol^2}} = 0.864133 \frac{\mathrm{Pa \cdot m^6}}{\mathrm{mol^2}}$$

$$b = 0.0778 \frac{8.3143 \cdot 369.28}{49.88 \cdot 10^5} \frac{\mathrm{m^3}}{\mathrm{mol}} = 4.789 \cdot 10^{-5} \frac{m^3}{\mathrm{mol}}$$

$$a(301.15\,K) = a\alpha(301.15\,\mathrm{K}) = 0.98581 \frac{\mathrm{Pa \cdot m^6}}{\mathrm{mol^2}}$$

The Peng-Robinson equation can be rearranged to

$$f(Z) = Z^3 + Z^2\left(\frac{bp}{\tilde{R}T} - 1\right) + Z\left(\frac{ap}{\tilde{R}^2T^2} - 3\frac{p^2b^2}{\tilde{R}^2T^2} - 2\frac{pb}{\tilde{R}T}\right) + \frac{p^3b^3}{\tilde{R}^3T^3} + \frac{p^2b^2}{\tilde{R}^2T^2} - \frac{abp^2}{\tilde{R}^3T^3} = 0 \tag{29}$$

with Z as the compressibility factor $Z = pv/(RT)$. For this example, one gets:

$$f(Z) = Z^3 - 0.978372\ Z^2 + 0.133153\ Z - 0.003368 = 0$$

with the derivation

$$f'(Z) = 3\ Z^2 - 1.956744\ Z + 0.133153$$

The compressibility factor can then iteratively be determined either with the Cardanic formula or iteratively with Newton's method, where f and f' are evaluated with an estimated value for Z. As long as the results for Z and the estimated value do not sufficiently agree, the calculation is repeated with a new estimated value

$$Z_{n+1} = Z_n - \frac{f(Z)}{f'(Z)}$$

In this example, the calculation procedure is as follows, starting with an estimated value of $Z_0 = 1$ (ideal gas):

$Z_0 = 1$	$f(Z_0) = 0.15141$	$f'(Z_0) = 1.17641$	$Z_1 = 0.87129$
$Z_1 = 0.87129$	$f(Z_1) = 0.03136$	$f'(Z_1) = 0.70571$	$Z_2 = 0.82686$
$Z_2 = 0.82686$	$f(Z_2) = 0.00314$	$f'(Z_2) = 0.56629$	$Z_3 = 0.82123$
$Z_3 = 0.82131$	$f(Z_3) = 4.606.10^{-5}$	$f'(Z_3) = 0.54971$	$Z_4 = 0.82123$
$Z_4 = 0.82123$	$f(Z_3) = 1.043.10^{-8}$	$f'(Z_3) = 0.54946$	$Z_4 = 0.82123$ o.k.

The final result $Z = 0.82123$ corresponds to a specific volume $v = 0.0018184$ m³/mol and a density $\rho = 47.55$ kg/m³. The value obtained from a high precision equation of state is $\rho = 48.02$ kg/m³, corresponding to $v = 0.001801$ m³/mol and $Z = 0.81326$.

Strongly polar and associating substances show large deviations from the ideal gas behavior even at low pressures, which is not in line with the cubic equations of state. The reason for this deviation is the formation of dimers or higher associates in the vapor phase. In these cases, the chemical theory [8] is a good tool for the description of the vapor phase nonidealities. Its main assumption is that the association is comparable to a chemical reaction. Normally, it is sufficient to regard only the formation of dimers, as it is the case for carboxylic acids. An exception is hydrogen fluoride, where hexamers are formed. Besides the overall mole fraction $\tilde{y}$, a true mole fraction $\tilde{z}$ is defined, which considers the particular associates as own species.

For the formation of dimers (D) from monomers (M) the following reaction can be defined:

$$2M_i \leftrightarrows D_{ii}$$

The equilibrium of this reaction can be described with the law of mass actions:

$$K_D = \frac{f_D/f_D^0}{\left(f_M/f_M^0\right)^2} \tag{30}$$

using the standard fugacity

$$f_D^0 = f_M^0 = f^0 = 1\,\mathrm{bar} \tag{31}$$

The fugacity of a component i can be expressed with the fugacity coefficient φ_i, the true mole fraction $\tilde{z}_i$ and the pressure p:

$$f_i = \tilde{z}_i \varphi_i p \tag{32}$$

Thus, the equilibrium constant is given by:

$$K_D = \frac{\tilde{z}_D \varphi_D f^0}{\tilde{z}_M^2 \varphi_M^2 p} \tag{33}$$

Values for K_D can be obtained by the measurement of vapor densities and vapor heat capacities. K_D depends on the temperature and can be correlated by

$$\ln K_D = \left(A - \frac{B}{T}\right)\frac{f^0}{\mathrm{bar}} \tag{34}$$

In Table 5, some constants A and B for carboxylic acids are listed.

Furthermore, for the calculation of the true mole fractions of monomers and dimers the fugacity coefficients are necessary. At low pressures, the behavior of the particular species can be

D1. Table 5. Equilibrium constants for vapor phase association

Substance	Formula	A / bar^{-1}	B/K bar^{-1}
Formic acid	HCOOH	–18.117	–7099
Acetic acid	CH_3COOH	–17.374	–7290
Propionic acid	$CH_3–CH_2–COOH$	–18.347	–7635
Butanoic acid	$CH_3–CH_2–CH_2–COOH$	–16.636	–7000

considered to be ideal, that is, $\varphi_M = \varphi_D = 1$. With this assumption, one gets:

$$K_D^* = \frac{K_D p}{f^0} = \frac{\tilde{z}_D}{\tilde{z}_M^2} \tag{35}$$

As the sum of the true mole fractions must be 1

$$\tilde{z}_D + \tilde{z}_M = 1 \tag{36}$$

one gets for given temperature and pressure

$$\tilde{z}_M^2 K_D^* = 1 - \tilde{z}_M \tag{37}$$

or, respectively,

$$\tilde{z}_M = \frac{\sqrt{1 + 4K_D^*} - 1}{2K_D^*} \tag{38}$$

The specific volume can then be determined by

$$v = \frac{\tilde{M}}{\rho} = \frac{\tilde{R}T}{p} \frac{1}{\tilde{z}_M + 2\tilde{z}_D} \tag{39}$$

Example 6:
Calculate the vapor density of acetic acid (AA) at the normal boiling point (T_{NBP} = 391.35 K).

Given data:
Association constants: A = −17.374 bar^{-1}, B = −7290 K bar^{-1}
Standard fugacity f^0 = 1bar
$\tilde{M}_{AA}$ = 60.05 g/mol
The results are:
K_D = 3.504
K_D* = 3.55
$\tilde{z}_M$ = 0.408
$\tilde{z}_D$ = 0.592
and finally, for the specific volume:

$$v = \frac{\tilde{M}}{\rho} = \frac{8.3143 \cdot 391.35}{101325} \frac{1}{0.408 + 2 \cdot 0.592} \text{m}^3/\text{mol}$$
$$= 0.0202\,\text{m}^3/\text{mol} \Rightarrow \rho = 2.977\,\text{kg/m}^3$$

This result is in line with experimental values and exceeds the result obtained with the ideal gas equation by approximately 60%.

4.3 Coefficient of Thermal Expansion

The coefficient of thermal expansion β is defined as

$$\beta = \frac{1}{v} \frac{\Delta v}{\Delta T} \tag{40}$$

At standard conditions (273.15 K, 1.01325 bar), the coefficient of thermal expansion for ideal gases is

$$\beta = 1/273.15\text{K}^{-1}.$$

Example 7:
At p = 1.013 bar and T = 273.15 K, the specific volume of helium is 0.02242 m^3/mol. To which extent will the specific volume increase, if the gas is heated up by ΔT = 100 K?

$$\Delta v = v \cdot \frac{1}{273.15\ \text{K}} \cdot \Delta T = 0.008207\text{m}^3/\text{mol}$$

5 Vapor Pressure

For many process calculations, the vapor pressure is the most important quantity. It is decisive for the determination of the number of separation stages of distillation columns and for the evaluation of temperature profiles in general. Therefore, data should be carefully searched, measured and correlated. Additionally, a good vapor pressure curve is helpful for the estimation of other thermophysical properties, especially of the enthalpy of vaporization (Sect. 6.1).

Good data points for the vapor pressure should be correlated with deviations considerably less than 1%, the average deviation of a good data set should be by far less than 0.5%. Values with deviations greater than 1% should be regarded as outliers and removed from the database, as long as enough other data points are available.

Exceptions are values below approximately 1 mbar, as their accuracy is much lower. It is recommended to set their weighting factor in the regression to 0 but keep an eye on the correct order of magnitude, when the vapor pressure curve is extrapolated to low temperatures.

Vapor pressure curves are strictly monotonically increasing. They exist between triple point and critical point of a particular substance, where a vapor–liquid equilibrium is possible.

For the description of vapor pressures several equations are available. The most frequently used one is the Antoine equation with three adjustable parameters

$$\ln \frac{p_s}{\text{Pa}} = A + \frac{B}{T + C} \tag{41}$$

It is appropriate for the reproduction of data sets within a certain temperature range. For thermodynamic reasons, both B and C must have a negative sign. There are many different notations in the literature, which has always to be taken into account.

The Antoine equation (41) is well-known for its bad extrapolation behavior. The temperature range from the triple point to the critical point cannot be covered with sufficient accuracy. Often two equations are given for vapor pressures below and above 1 atm; however, such an approach usually implies a discontinuity in the junction point. There is a singularity at $T = -C$, and in the vicinity of this point the application of the Antoine equation does not make sense.

The Wagner equation [14]

$$\ln \frac{p_s}{p_c} = \frac{1}{T_r} \left[A(1 - T_r) + B(1 - T_r)^{1.5} + C(1 - T_r)^3 + D(1 - T_r)^6 \right] \tag{42}$$

with

$$T_r = T/T_c \tag{42a}$$

can describe the whole temperature range from the triple point to the critical point and should be applied for the precise adjustment of good data in sufficient quantity. The correct reproduction of the critical point is ensured by the mathematical form of Eq. (42). The only weakness of the equation is the extrapolation to low temperatures. In most cases, the ranges of the coefficients are

$$A = -9 \ldots -5$$
$$B = -10 \ldots 10$$
$$C = -10 \ldots 10$$
$$C = -20 \ldots 20$$

If these conditions are not fulfilled, a critical check of the data should take place, especially for the critical point used. Further constraints and many good parameter sets have been set up by McGarry [15].

In the recent years, the so-called 3-6-form (Eq. (42); the numbers refer to the exponents of the last two terms) has mostly been replaced by the 2.5-5-form, which is considered to be slightly more accurate:

$$\ln\frac{p_s}{p_c} = \frac{1}{T_r}\left[A(1-T_r) + B(1-T_r)^{1.5} + C(1-T_r)^{2.5} + D(1-T_r)^5\right] \quad (42c)$$

The reasonable ranges for the coefficients stay the same. For Eq. (42c), coefficients for 275 substances are given in Subchap. D3.1.

The estimation of vapor pressures is one of the most difficult problems in thermodynamics. There are several methods based on the 3-parameter principle of corresponding states or group contributions [16–18]. A new method developed by Rarey et al. [19] yields good results but is difficult to apply.

One of the most reliable methods is the application of the vapor pressure curve of Hoffmann-Florin [20], which has only two adjustable parameters:

$$\ln\frac{p_s}{\mathrm{Pa}} = A + Bf(T) \quad (43)$$

with

$$f(T) = \frac{1}{T/\mathrm{K}} - 7.9151\cdot 10^{-3} + 2.6726\cdot 10^{-3}\log_{10}\frac{T}{\mathrm{K}} - 0.8625\cdot 10^{-6}\frac{T}{\mathrm{K}} \quad (43a)$$

The equation can be fitted to two or more experimental data points. As a correlation equation it is not very accurate, but its extrapolation behavior is supposed to be quite good. Especially, it is superior to the widely used simplified Antoine equation with $C = 0$ in Eq. (41). If only one or, in the extreme case, no data point is available, normal boiling point and/or critical point can be estimated, and the parameters A and B can be adjusted to these artificial data. It should be emphasized that the two points for adjustment must be far away from each other to obtain significant coefficients.

For two arbitrarily given data points of the vapor pressure curve (T_1,p_{s1}), (T_2,p_{s2}), the coefficients of the Hoffmann-Florin equation can be determined to be

$$A = \ln\frac{p_{s1}}{\mathrm{Pa}} - \ln\frac{p_{s1}}{p_{s2}}\cdot\frac{f(T_1)}{f(T_1)-f(T_2)} \quad (44)$$

$$B = \frac{\ln(p_{s1}/p_{s2})}{f(T_1)-f(T_2)} \quad (45)$$

Because of the exponential relationship between vapor pressure and temperature, a high accuracy in the estimation of vapor pressures should not be expected. Deviations of 5% have to be regarded as excellent. For the assessment of a vapor pressure estimation method, the number of substances where the method yields completely unusable results is decisive. In this context, especially, the method described above has considerable advantages in comparison with several group contribution methods.

Example 8:
Estimate the vapor pressure of chloroform at $t = -41.7°C$, $t = 4.5°C$, and $t = 120.1°C$. Using the Joback method, the estimated values for normal boiling point and critical point are:
$T_{NBP} = 334.13$ K (true value: 334.26 K)
$T_c = 532.11$ K (true value: 536.45 K)
$p_c = 49.8$ bar (true value: 55.54 bar)
With
$T_1 = 334.13$ K
$p_{s1} = 1.01325$ bar
$T_2 = 532.11$ K
$p_{s2} = 49.8$ bar
we get
$A = 19.5596$
$B = -5233.61$
The results are:
$p_s(-41.7°C) = 5.69$ mbar
$p_s(4.5°C) = 99.94$ mbar
$p_s(120.1°C) = 5.18$ bar
The values calculated with the Wagner equation (Subchap. D3.1) are $p_s = 5.04$ mbar ($t = -41.7°C$), $p_s = 100$ mbar ($t = 4.5°C$), and $p_s = 5.01$ bar ($t = 120.1°C$). As in this case, the quality of the normal boiling point or another reference value is usually decisive. The relatively large error in the critical pressure does not have a large influence in this example.

The estimation of vapor pressures of mixtures does not make sense physically, as the concentrations of the vapor and liquid are different. Moreover, boiling point and dew point of a mixture are not identical. Azeotropic mixtures are often treated as a pure substance, but even this is only valid within a certain temperature range, as the azeotropic composition is temperature-dependent. The vapor–liquid equilibria of mixtures are explained in Subchap. D5.1.

6 Enthalpy Determination

Enthalpies are the key quantity for heat transfer problems, as the difference of the enthalpies of the particular streams determines the energy balance of the process and therefore the state of the outlet streams. Enthalpy changes can be caused:

- By a phase change. The most important one is the vapor–liquid transition, which is determined by the enthalpy of vaporization.
- By heating or cooling of a homogeneous phase. In this case, the most important quantity is the heat capacity of the particular phase.

- By pressure change of a phase, which is, however, only relevant for gases.
- By mixing or separating mixture components.
- By chemical reaction.

All of these processes can run in parallel, for example, in a heat exchanger with high pressure drop. Therefore, a thermodynamically consistent enthalpy description, which connects the vapor and the liquid region, is needed. This enthalpy is then calculated using the standard enthalpy of formation as the starting point to make the enthalpy consistent with respect to chemical reactions, the specific heat capacities of liquid and ideal gas, the enthalpy of vaporization, and the real gas correction. The difficulty is that the two heat capacities are not independent from each other and can be calculated in different ways. The consequences are explained in Sect. 6.5.

6.1 Enthalpy of Vaporization

In Fig. 5, typical curvatures of the enthalpy of vaporization as a function of temperature are given. It is a strictly monotonic decreasing function, at low temperatures with a small slope, at high temperatures with an increasing slope. At the critical point, vapor and liquid become identical, and the enthalpy of vaporization approaches zero. A different curvature is shown by substances with association in the vapor phase, where a more or less well-defined maximum occurs (e.g., formic acid in Fig. 5).

Enthalpies of vaporization can be very well correlated with the extended Watson equation

$$\frac{\Delta h_v}{\mathrm{J/kg}} = A\,(1 - T_r)^{B+CT_r+DT_r^2+ET_r^3} \tag{46}$$

with

$$T_r = T/T_c \tag{46a}$$

The order of magnitude of their deviation should be approximately 0.5%; at temperatures in the vicinity of the critical point, where the values are low and the slopes are large, higher deviations can be accepted. The parameters C, D, and E are needed only for a good data situation; otherwise, they could be set to zero. If $C = D = E = 0$, $B = 0.38$ is often a good first guess.

For high precision data, the PPDS equation

$$\Delta h_v = RT_c(A\tau^{1/3} + B\tau^{2/3} + C\tau + D\tau^2 + E\tau^6) \tag{46b}$$

with

$$\tau = 1 - T/T_c \tag{46c}$$

is a very useful correlation tool. In Subchap. D3.1, this equation has been fitted to approximately 275 substances.

There is a peculiarity for the estimation of the enthalpy of vaporization. The Clausius-Clapeyron equation

$$\Delta h_v = T\,(v'' - v')\,\frac{\mathrm{d}p_s}{\mathrm{d}T} \tag{47}$$

is an exact thermodynamic relationship, using the easily available quantities vapor pressure curve, bubble point volume, and dew point volume. In fact, most of the data points available have been evaluated this way and not by direct measurement.

However, there are some restrictions for the application of the Clausius-Clapeyron equation in practical applications. It is important to check that only the temperature range is considered where the vapor pressure curve is validated. The most important vapor pressure equations Wagner (Eqs. (42) and (42c)) and Antoine (Eq. (41)) extrapolate badly to low temperatures. Even if data points are available, the relative errors, which of course have an influence on the slope, are often still quite large. As a rule of thumb, it is recommended not to apply the Clausius-Clapeyron equation for vapor pressures $p_s < 1$ mbar.

The term $(v'' - v')$ is decisive for the accuracy. v' is negligible in comparison with v'' with the exception of the region just below the critical point. Moreover, in this region the quality of the correlations for the liquid density is low. If v'' is determined with the ideal gas equation, the error can be tolerated in the low pressure region, but the curve has a concave curvature instead of a convex one, which becomes less and less acceptable when the saturation pressure increases.

Therefore, v'' is usually calculated with a cubic equation of state (Sect. 4.2). From test calculations, it can be concluded that

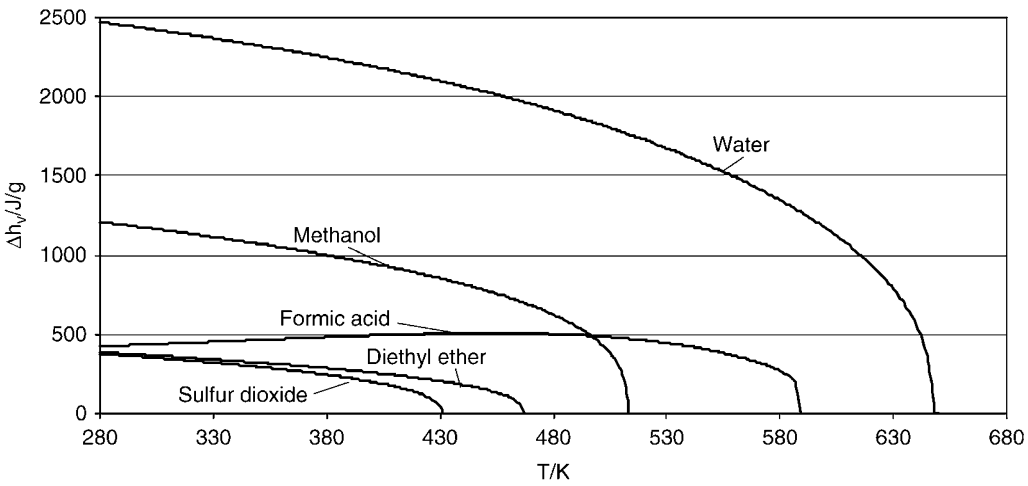

D1. Fig. 5. Curvature of the enthalpy of vaporization as a function of temperature.

an error of 1%...2% might occur. In the region just below the critical point, the deviations are larger. As both v'' and v' are much less accurate in the vicinity of the critical point and the term $(v''–v')$ behaves as a difference of large numbers, the application of the Clausius-Clapeyron equation should be excluded in this area. As a rule of thumb, the application should be restricted to $T < T_c - 30$ K.

Values outside the application range of the Clausius-Clapeyron equation can be estimated by correlating values generated with the Clausius-Clapeyron equation in the valid range with Eq. (46) or (46b) and extrapolate this equation towards the critical point. For associating substances, it should be taken into account that the chemical theory (Sect. 4.2) is not valid for high pressures.

In case no information is available, one can estimate the normal boiling point (Sect. 3.3) and critical point (Sect. 3.1). Then, a vapor pressure curve could be estimated with the Hoffmann-Florin equation. The acentric factor can also be determined by its definition (Eq. 8). Thus, all information for the application of the Clausius-Clapeyron equation is available.

Example 9:
Estimate the enthalpy of vaporization of acetone at $t = 0°C$. The following values are given:

$\rho_{liq} = 812.9$ kg/m^3, $T_c = 508.1$ K, $p_c = 46.924$ bar, $\omega = 0.3064$, $M = 58.08$ g/mol

Wagner-coefficients $A = -7.67033$, $B = 1.96469$, $C = -2.4438$, $D = -2.90162$ (Eq. (42c))

The vapor pressure at $t = 0°C$ can be determined with the Wagner equation to be $p_s = 0.093$ bar. The specific volumes are:

$v' = 7.145 \cdot 10^{-5}$ m^3/mol

$v'' = 0.2431$ m^3/mol (from Peng-Robinson equation)

The derivative of the modified Wagner Equation (42c) is:

$$\frac{dp_s}{dT} = -\frac{p_s}{T}\left[\ln\frac{p_s}{p_c} + A + 1.5\,B\,(1-T_r)^{0.5} + 2.5\,C\,(1-T_r)^{1.5} + 5\,D\,(1-T_r)^4\right] \quad (48)$$

At $t = 0°C$, the result is $dp_s/dT = 492.84$ Pa/K. Thus, one gets:

$$\Delta h_v = 273.15\,\text{K} \cdot (0.2453 - 7.145 \cdot 10^{-5})\,\text{m}^3/\text{mol} \cdot 492.84\,\text{Pa/K} = 32721\ \text{J/mol} = 563.4\ \text{J/g}$$

The value listed in Subchap. D3.1 is 558.9 J/g. The deviation is 0.8%.

For mixtures, an enthalpy of vaporization is not a useful quantity, as during the vaporization temperatures, the compositions of both vapor and liquid vary. For reasonable calculations, it is recommended that the calculation of the energy balance be performed by determining the exact enthalpy differences according to Sect. 6.4.

For an isothermal evaporation, a linear mixing rule can be applied as an approximation:

$$\Delta h_{v,Gem} = \sum_i \tilde{x}_i\,\Delta h_{vi} \quad (49)$$

For the isobaric evaporation, Eq. (49) is not appropriate at all, as the enthalpies of vaporization would then have to be evaluated at their particular boiling temperatures, and the temperature increase of the liquid is not taken into account.

6.2 Specific Heat Capacity of Ideal Gases

The specific heat capacity of ideal gases is a measure of the capability of a molecule to store energy. c_p^{id} is defined as the heat a molecule must be exposed to at constant pressure to achieve a certain change in temperature. It must be strongly distinguished between the isobaric specific heat capacity c_p^{id} at constant pressure and the isochoric specific heat capacity c_v^{id} at constant volume. Both quantities are related by

$$c_v^{id} = c_p^{id} - R \quad (50)$$

The following considerations are focusing on the specific isobaric heat capacity. It depends only on temperature and increases in a strictly monotonic way.

In general, there are two contributions to c_p^{id}: the temperature-independent one describing the kinetic energy and the rotational energy of the molecules, and a vibration contribution, which is only activated at high temperatures and that causes the temperature-dependence of the molecule [21, 22]. If a molecule consists only of 1 atom (He, Ne, Ar, Kr, Xe), the vibration and the rotational contributions are zero, and c_p^{id} is constant.

Typical curvatures of c_p^{id} as a function of temperature are depicted in Fig. 6. On the left hand side, only the constant contributions for the kinetic and for the rotational contributions are active. Then, the function increases monotonically until all the vibration options in the molecules are fully active. Then, the function becomes constant again.

The curvature can be well represented with the Aly-Lee equation [23], which is based on statistical thermodynamics:

$$\tilde{c}_p^{id} = A + B\left(\frac{C/T}{\sinh(C/T)}\right)^2 + D\left(\frac{E/T}{\cosh(E/T)}\right)^2 \quad (51)$$

During the recent years, a PPDS equation

$$\frac{c_p^{id}}{R} = B + (C-B)\left(\frac{T}{A+T}\right)^2 \left[1 - \frac{A}{A+T}\left(D + E\frac{T}{A+T} + F\left(\frac{T}{A+T}\right)^2 + G\left(\frac{T}{A+T}\right)^3\right)\right] \quad (51a)$$

has been widely applied and proved to yield good results. Its disadvantage is the increased number of adjustable parameters. Equation (51a) has been used in Subchap. D3.1 for 275 substances.

Acceptable results can also be obtained with a simpler equation like

$$\frac{c_p^{id}}{\text{J/kg K}} = A + B\frac{T}{K} + C\left(\frac{T}{K}\right)^2 + D\left(\frac{T}{K}\right)^3 + \frac{E}{(T/K)^2} \quad (52)$$

although the extrapolation capability is weak, especially toward low temperatures. However, for most of the process engineering applications the quality of Eq. (52) should be sufficient. The last term is often omitted, leaving a polynomial of degree 3.

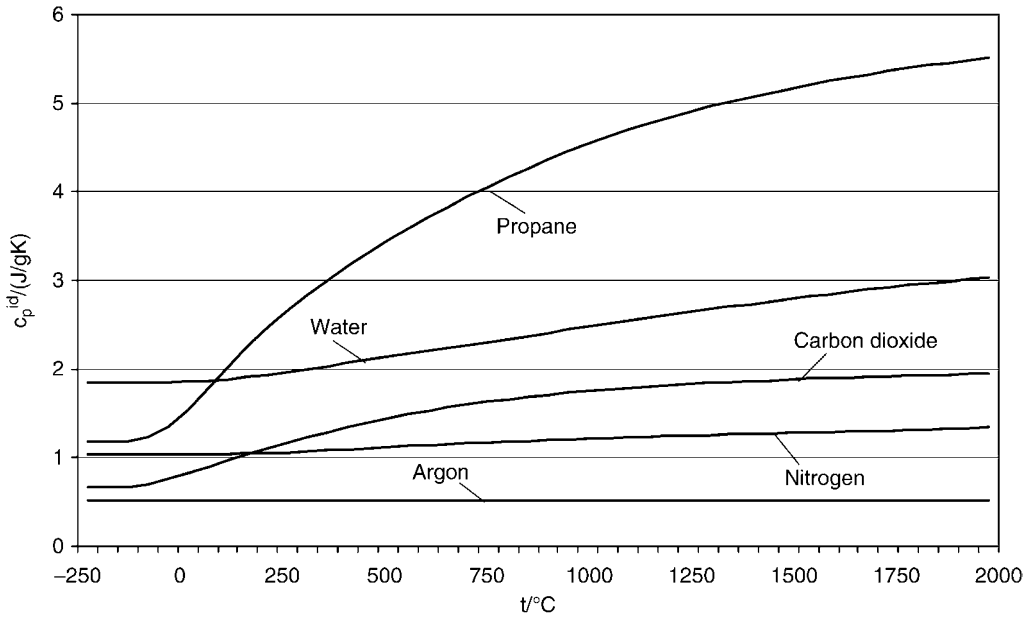

D1. Fig. 6. Typical curvatures of the specific isobaric heat capacity of ideal gases.

$$CH_3–COO–CH_2–CH_3$$

D1. Fig. 7. Structural formula of ethyl acetate.

The estimation of the specific isobaric heat capacity of ideal gases can be performed with Joback's group contribution method. The particular group contributions form the coefficients of a 3rd degree polynomial:

$$\frac{\tilde{c}_p^{id}}{\mathrm{J/mol\,K}} = \left(\sum \Delta_A - 37.93\right) + \left(\sum \Delta_B + 0.21\right) \cdot (T/K) + \left(\sum \Delta_C - 3.91 \cdot 10^{-4}\right) \cdot (T/K)^2 + \left(\sum \Delta_D + 2.06 \cdot 10^{-7}\right) \cdot (T/K)^3 \quad (53)$$

The corresponding coefficients for the group contributions are listed in Table 6. Relatively small deviation of approximately 1%. . .2% can be expected. The deviations become larger with increasing complexity of the molecule.

Example 10:
Determine the specific isobaric heat capacity of ethyl acetate in the ideal gas state at $t = 25°C$.
The molecular weight of ethyl acetate is $M = 88.11$ g/mol.
The group assignment of ethyl acetate is:
$2 \times CH_3$
$1 \times CH_2$
$1 \times COO$
The group contributions are:

$$\sum \Delta_A = 2 \cdot (19.5) + 1 \cdot (-0.909) + 1 \cdot (24.5) = 62.591$$

$$\sum \Delta_B = 2 \cdot (-8.08 \cdot 10^{-3}) + 1 \cdot (9.5 \cdot 10^{-2}) + 1 \cdot (4.02 \cdot 10^{-2}) = 0.11904$$

$$\sum \Delta_C = 2 \cdot (1.53 \cdot 10^{-4}) + 1 \cdot (-5.44 \cdot 10^{-5}) + 1 \cdot (4.02 \cdot 10^{-5}) = 2.918 \cdot 10^{-4}$$

$$\sum \Delta_D = 2 \cdot (-9.67 \cdot 10^{-8}) + 1 \cdot (1.19 \cdot 10^{-8}) + 1 \cdot (-4.52 \cdot 10^{-8}) = -2.267 \cdot 10^{-7}$$

The result for c_p^{id} is

$$\frac{\tilde{c}_p^{id}}{\mathrm{J/mol\,K}} = (62.591 - 37.93) + (0.11904 + 0.21) \cdot (298.15) + \left(2.918 \cdot 10^{-4} - 3.91 \cdot 10^{-4}\right) \cdot (298.15)^2 + \left(-2.267 \cdot 10^{-7} + 2.06 \cdot 10^{-7}\right) \cdot (298.15)^3 = 113.397$$

or $c_p^{id} = 1.287$ J/gK, respectively. The true value is considered to be 1.290 J/gK.

The thermodynamically exact mixing rule for mixtures of ideal gases is

$$\tilde{c}_{p,mix}^{id} = \sum_i \tilde{x}_i \tilde{c}_{p,i}^{id} \quad (54)$$

6.3 Real Gas Corrections

With increasing pressure, intermolecular forces play a more and more important role in the calculation of the enthalpy of gases. Usually, these forces are attractive so that energy is needed to increase the distance between the molecules. If this energy is not supplied, the substance cools down during the expansion. A famous example is the liquefaction of air by adiabatic throttling. To take these effects into account, the ideal gas heat capacity on its own is not sufficient.

The difference of enthalpies between the ideal gas state at $p = 0$ and a state at an arbitrary pressure is called the residual part of the enthalpy. It can be evaluated for nonassociating

D1. Table 6. Group contribution for c_p^{id} according to Joback

Structural group	Δ_A	Δ_B x 10^2	Δ_C x 10^4	Δ_D x 10^8
$-CH_3$	19.500	−0.808	1.5300	−9.670
$>CH_2$	−0.909	9.500	−0.5440	1.190
>CH–	−23.000	20.400	−2.6500	12.000
>C<	−66.200	42.700	−6.4100	30.100
$=CH_2$	23.600	−3.810	1.7200	−10.300
=CH–	−8.000	10.500	−0.9630	3.560
=C<	−28.100	20.800	−3.0600	14.600
=C=	27.400	−5.570	1.0100	−5.020
≡CH	24.500	−2.710	1.1100	−6.780
≡C–	7.870	2.010	−0.0833	0.139
$-CH_2-$ (ring)	−6.030	8.540	−0.0800	−1.800
>CH– (ring)	−20.500	16.200	−1.6000	6.240
>C< (ring)	−90.900	55.700	−9.0000	46.900
=CH– (ring)	−2.140	5.740	−0.0164	−1.590
=C< (ring)	−8.250	10.100	−1.4200	6.780
–F	26.500	−9.130	1.9100	−10.300
–Cl	33.300	−9.630	1.8700	−9.960
–Br	28.600	−6.490	1.3600	−7.450
–I	32.100	−6.410	1.2600	−6.870
–OH (alcohols)	25.700	−6.910	1.7700	−9.880
–OH (phenols)	−2.810	11.100	−1.1600	4.940
–O–	25.500	−6.320	1.1100	−5.480
–O– (ring)	12.200	−1.260	0.6030	−3.860
>C=O	6.450	6.700	−0.3570	0.286
>C=O (ring)	30.400	−8.290	2.3600	−13.100
–CH=O	30.900	−3.360	1.6000	−9.880
–COOH	24.100	4.270	0.8040	−6.870
–COO–	24.500	4.020	0.4020	−4.520
=O	6.820	1.960	0.1270	−1.780
$-NH_2$	26.900	−4.120	1.6400	−9.760
>NH	−1.210	7.620	−0.4860	1.050
>NH (ring)	11.800	−2.300	1.0700	−6.280
>N–	−31.100	22.700	−3.2000	14.600
–N=				
–N= (ring)	8.830	−0.384	0.4350	−2.600
=NH	5.690	−0.412	1.2800	−8.880
–CN	36.500	−7.330	1.8400	−10.300
$-NO_2$	25.900	−0.374	1.2900	−8.880
–SH	35.300	−7.580	1.8500	−10.300
–S–	19.600	−0.561	0.4020	−2.760
–S– (ring)	16.700	0.481	0.2770	−2.110

substances by cubic equations of state. The corresponding expressions are:

Peng-Robinson equation:

$$\Delta h_{\text{Gas}}^{\text{real}} = \widetilde{h}(T,p) - \widetilde{h}(T,p=0) = \widetilde{R}T(Z-1) - \frac{1}{\sqrt{8}b}\left(a - T\frac{\partial a}{\partial T}\right)\ln\left(\frac{v+(1+\sqrt{2})b}{v+(1-\sqrt{2})b}\right) \tag{55}$$

Soave-Redlich-Kwong equation:

$$\Delta h_{\text{Gas}}^{\text{real}} = \widetilde{h}(T,p) - \widetilde{h}(T,p=0) = \widetilde{R}T(Z-1) - \frac{1}{b}\left(a - T\frac{\partial a}{\partial T}\right)\ln\left(\frac{v+b}{v}\right) \tag{56}$$

The residual part of the specific heat capacity of gases can be calculated by the derivatives of Eqs. (55) and (56):

$$\Delta c_{\text{p,Gas}}^{\text{real}} = \left(\frac{\partial \Delta h_{\text{Gas}}^{\text{real}}}{\partial T}\right)_{\text{p}} \tag{57}$$

As it yields a very complicated expression, it is recommended to perform the differentiation in Eq. (57) numerically.

Taking into account the residual part of the enthalpy is important especially for associating substances. Considering only the dimerization of molecules of the same kind, the residual part can be evaluated with the association model described in Sect. 4.2:

$$\Delta h_{\text{Gas,Ass.}}^{\text{real}} = \frac{\widetilde{z}_{\text{D}}\Delta h_{\text{D}}}{\widetilde{z}_{\text{M}} + 2\,\widetilde{z}_{\text{D}}} \tag{58}$$

with

$$\Delta h_{\text{D}} = \widetilde{R} f^0 B \tag{59}$$

where B is the coefficient in Eq. (34). This calculation is quite complicated, as first the true concentrations must be evaluated via Eqs. (36) and (38). The residual part of the specific heat capacity must again be determined by numerical differentiation. For illustration, Fig. 8 shows the specific isobaric heat capacities of acetic acid vapor with and without consideration of the residual part.

6.4 Specific Heat Capacity of Liquids

The specific isobaric heat capacity of liquids ($c_{\text{p}}^{\text{liq}}$) is a function of temperature. The pressure dependence is usually negligible. Isobaric and isochoric heat capacity differ significantly, as in the isobaric case work has to be spent to increase the distance between the molecules. At low temperatures (approximately up to the normal boiling point), $c_{\text{p}}^{\text{liq}}$ is an almost linear function of temperature. At higher temperatures, the slope increases. In many cases, a flat minimum is formed (Fig. 9). At the critical point, the specific heat capacity of a liquid becomes infinity.

For a boiling liquid, as it often occurs in process engineering, the specific isobaric heat capacity is not a useful quantity, as the heating at constant pressure would result in evaporation and not in temperature increase. For practical applications, a "specific heat capacity along the saturation line" (c_σ) is used, without distinguishing these quantities in the colloquial language. The relationship is

$$\widetilde{c}_\sigma = \widetilde{c}_{\text{p}} + \left[v - T\left(\frac{\partial v}{\partial T}\right)_{\text{p}}\right]\frac{\text{d}p_s}{\text{d}T} \tag{60}$$

The difference between both heat capacities is only relevant for high temperatures. As a rule of thumb, it can be neglected

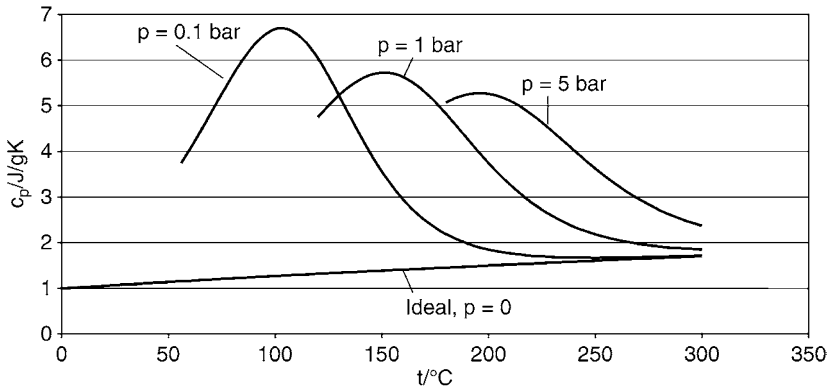

D1. Fig. 8. Specific isobaric heat capacity of acetic acid vapor at various pressures.

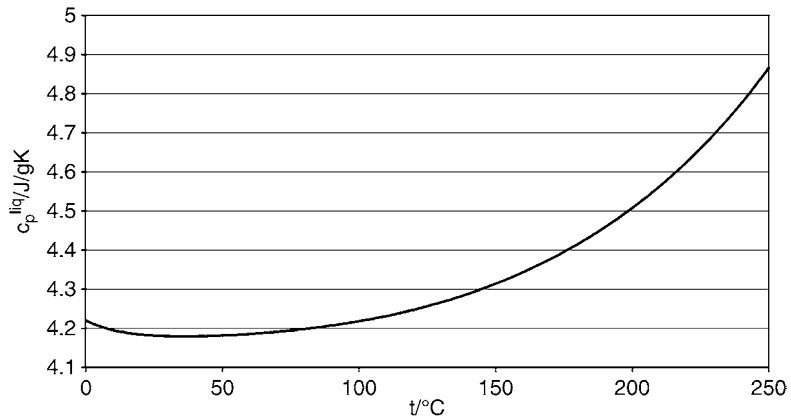

D1. Fig. 9. Specific heat capacity of liquid water as a function of temperature.

for $T < 0.8\ T_c$. The difference can be estimated with the equation

$$\tilde{c}_\sigma = \tilde{c}_p^{liq} - \tilde{R}\ \exp(20.1\ T_r - 17.9) \tag{61}$$

The liquid heat capacity can be correlated with an extended polynomial

$$\frac{c_p^{liq}}{J/kgK} = A + B\frac{T}{K} + C\left(\frac{T}{K}\right)^2 + D\left(\frac{T}{K}\right)^3 + \frac{E}{(T/K)^2} \tag{62}$$

For more precise calculations, the PPDS equation can be used

$$c_p^{liq} = R\left(\frac{A}{\tau} + B + C\tau + D\tau^2 + E\tau^3 + F\tau^4\right) \tag{62a}$$

with

$$\tau = 1 - \frac{T}{T_c} \tag{62b}$$

Eq. (62a) is used in Subchap. D3.1 for the correlation of heat capacities of approximately 275 substances.

There are few substances where all coefficients have to be fitted. In most cases, a quadratic temperature-dependence is sufficient; in case Eq. (62a) is used, the coefficients B, C and D are active. The extrapolation towards the critical point is often not considered to be important, as the quantity becomes more and more difficult to handle due to the increasing difference between c_p and c_σ. For many substances, no data exist above the normal boiling point. Often only a linear temperature-dependence is justified, which leads to an underestimation of c_p when it is extrapolated to high temperatures. To overcome this difficulty, artificial data points can be generated with an estimation method and fitted together with the data available.

For the estimation of c_p^{liq} the method of Rowlinson-Bondi can be used, which is based on the specific heat capacity of ideal gases and the 3-parameter principle of corresponding states:

$$\tilde{c}_p^{fl} = \tilde{c}_p^{id} + 1.45\,\tilde{R} + 0.45\,\tilde{R}\,(1 - T_r)^{-1} + 0.25\,\omega\,\tilde{R}\left[17.11 + 25.2\,(1 - T_r)^{1/3}\,T_r^{-1} + 1.742\,(1 - T_r)^{-1}\right] \tag{63}$$

The deviation to be expected should be approximately 5%.

Example 11:

Estimate the specific heat capacity of liquid methyl ethyl ketone at t = 100°C. The given data are: c_p^{id} (100°C) = 1.655 J/gK, T_c = 535.55 K, ω = 0.323, $\tilde{M}$ = 72.11 g/mol.

From c_p^{id} (100°C) = 120.496 J/molK and T_r = 0.697 it can be calculated

$$\frac{\tilde{c}_p^{liq}}{J/molK} = 119.342 + 1.45 \cdot 8.3143 + 0.45 \cdot 8.3143\,(1-0.697)^{-1} + 0.25 \cdot 0.323 \cdot 8.3143 \left[17.11 + 25.2\,(1-0.697)^{1/3} 0.697^{-1} + 1.742\,(1-0.697)^{-1}\right] = 175.4$$

$$\Rightarrow c_p^{liq} = 2.432\ J/gK$$

The value given in Subchap. D3.1 is 2.430 J/gK.

For mixtures, the specific heat capacity of liquids can be calculated with a linear mixing rule

$$c_{p,mix}^{liq} = \sum_i x_i\, c_{p,i}^{liq} \tag{64}$$

neglecting the influence of the excess enthalpy.

6.5 Routes for Enthalpy Calculation

For process simulation it is necessary that the enthalpy is continuously described in the vapor as well as in the two-phase and in the liquid region. The problem occurs that the particular quantities contributing to the enthalpy are not independent from each other. Depending on the way the enthalpy is calculated (route), there is always one quantity that results from the summation of the other contributions. The most often used routes are described in the following section.

A. Route: Vapor as starting phase

I. **Enthalpy of a vapor**

1. Set the reference point to the standard condition ($T_0 = 298.15$ K, $p_0 = 0$, $h_{0i} = \Delta h_i^{0f}$) for all components.

$$\tilde{h}_i^{id}(T_0, p=0) = \Delta h_i^{0f} \tag{65}$$

Therefore, the enthalpy is consistent regarding chemical reactions.

2. Calculation of the enthalpy of the ideal gas at $p = 0$ for the system temperature T, using c_{pi}^{id} for all components:

$$\tilde{h}_i^{id}(T, p=0) = \Delta h_i^{0f} + \int_{T_0}^{T} \tilde{c}_{pi}^{id}\, dT \tag{66}$$

3. Transition to the mixture at $p = 0$ in the ideal gas state, that is, without an excess enthalpy

$$\tilde{h}_{mix}^{id}(T, p=0, x_i) = \sum \tilde{x}_i \tilde{h}_i^{id}(T, p=0) \tag{67}$$

4. Addition of the residual part in the vapor phase Δh_{Gas}^{real}

$$\Delta h_{Gas}^{real}(T, p, \tilde{x}_i) = \tilde{h}(T, p, \tilde{x}_i) - \tilde{h}^{id}(T, p=0, \tilde{x}_i) \tag{68}$$

until the required state in the vapor phase is obtained:

$$\tilde{h}_{mix}^{real}(T, p, \tilde{x}_i) = h_{mix}^{id}(T, p=0, \tilde{x}_i) + \Delta h_{Gas}^{real}(T, p, \tilde{x}_i) \tag{69}$$

II. **Enthalpy of a liquid**

If the enthalpy of a liquid is calculated (Fig. 10), the steps 1 and 2 are identical to the calculation of a vapor phase enthalpy. The transition to the mixture takes place in the liquid phase. In step 3, the residual part is determined for the pure components to reach the dew point curve at $p = p_{si}$.

3. Calculation of the dew point curve state

$$\tilde{h}_i''(T) = \Delta h_i^{0f} + \int_{T_0}^{T} \tilde{c}_{pi}^{id}\, dT + \Delta h_{Gas,i}^{real}(T, p_{si}) \tag{70}$$

4. Subtraction of the enthalpy of vaporization at the system temperature T to reach the bubble point curve

$$\tilde{h}_i^{liq}(T) = \Delta h_i^{0f} + \int_{T_0}^{T} \tilde{c}_{pi}^{id}\, dT + \Delta h_{Gas,i}^{real}(T, p_{si}) - \Delta h_{vi}(T) \tag{71}$$

In process simulation, liquids are in general treated as if they are at their bubble point at the system temperature. Enthalpy changes by compression of the liquid are neglected, which is at least at low pressures an acceptable approximation.

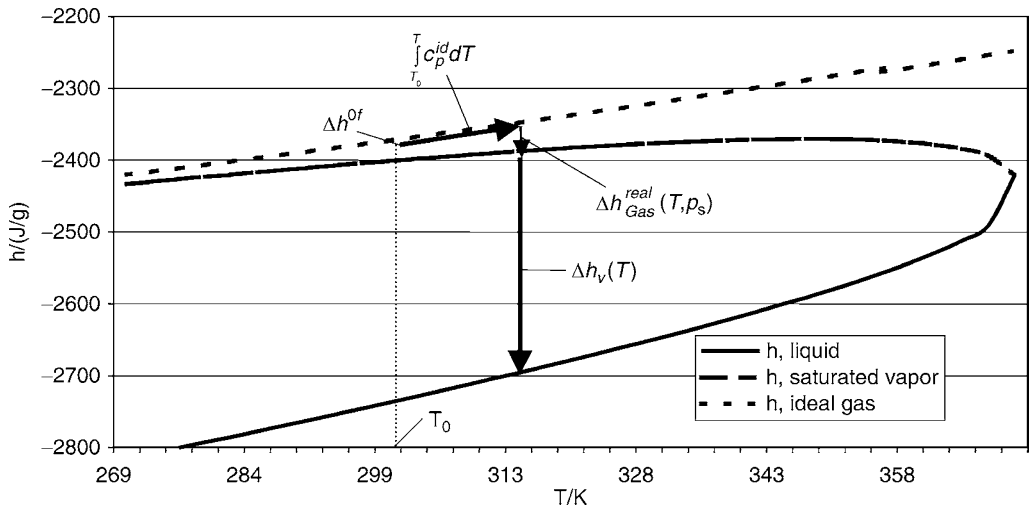

D1. Fig. 10. Calculation of the enthalpy of a liquid with the route "vapor as starting phase".

5. Integration of the excess enthalpy

The transition to the mixture takes place in the liquid phase via

$$\widetilde{h}^{\mathrm{liq}}_{\mathrm{mix}}(T,\widetilde{x}_i) = \sum_i \widetilde{x}_i \widetilde{h}^{\mathrm{liq}}_i(T) + \widetilde{h}^{E}(T,\widetilde{x}_i) \qquad (72)$$

The calculation of the excess enthalpy h^{E} itself is explained in Subchap. D5.1.

The main disadvantage of this method is the error in the determination of the liquid heat capacity, which is calculated by deriving the enthalpy with respect to temperature. Even for well-known substances like water or methanol the deviations for $c^{\mathrm{liq}}_{\mathrm{p}}$ are considerable [24], which can hardly be accepted if, for example, liquid–liquid heat exchangers are designed. A procedure has been developed [24] where $c^{\mathrm{liq}}_{\mathrm{p}}$ can be reproduced using "vapor as starting phase."

B. Route: Liquid as starting phase

I. **Enthalpy of a liquid**

1. Enthalpy of a pure liquid

Starting from a reference state in the liquid phase $h_{\mathrm{ref,i}}(T_{\mathrm{ref,i}})$ the enthalpy of the liquid is evaluated by integration of the specific heat capacity of the liquid:

$$\widetilde{h}^{\mathrm{liq}}_i(T) = \int_{T_{\mathrm{ref},i}}^{T} \widetilde{c}^{\mathrm{liq}}_{pi}\mathrm{d}T + \widetilde{h}_{\mathrm{ref},i}(T_{\mathrm{ref},i}) \qquad (73)$$

2. Transition to the mixture

$$\widetilde{h}^{\mathrm{liq}}_{\mathrm{mix}}(T,\widetilde{x}_i) = \sum_i \widetilde{x}_i \widetilde{h}^{\mathrm{liq}}_i(T) + h^{E}(T,\widetilde{x}_i) \qquad (74)$$

analogous to Eq. (72).

II. **Enthalpy of a vapor**

1. Integration of the specific heat capacity to the transition temperature T_{LG}.

$$\widetilde{h}^{\mathrm{liq}}_i(T_{\mathrm{LG},i}) = \int_{T_{\mathrm{ref},i}}^{T_{\mathrm{LG},i}} \widetilde{c}^{\mathrm{liq}}_{\mathrm{pi}}\mathrm{d}T + \widetilde{h}_{\mathrm{ref},i}(T_{\mathrm{ref},i}) \qquad (75)$$

A useful choice for $T_{\mathrm{LG},i}$ is the normal boiling point.

2. Transition to the vapor phase to reach the dew point curve:

$$\widetilde{h}_i{}''(T_{\mathrm{LG},i}) = \widetilde{h}^{\mathrm{liq}}_i(T_{\mathrm{LG},i}) + \Delta h_{\mathrm{v}}(T_{\mathrm{LG},i}) \qquad (76)$$

3. Transition to the ideal gas state

$$\widetilde{h}^{\mathrm{id}}_i(T_{\mathrm{LG},i}, p=0) = \widetilde{h}_i{}''(T_{\mathrm{LG},i}) - \Delta h^{\mathrm{real}}_{\mathrm{Gas},i}(T_{\mathrm{LG},i}, p_{\mathrm{si}}(T_{\mathrm{LG},i})) \qquad (77)$$

4. Integration to the system temperature

$$\widetilde{h}^{\mathrm{id}}_i(T,p=0) = \widetilde{h}^{\mathrm{id}}_i(T_{\mathrm{LG},i},p=0) + \int_{T_{\mathrm{LG},i}}^{T} \widetilde{c}^{\mathrm{id}}_{\mathrm{pi}}\mathrm{d}T \qquad (78)$$

5. Transition to the mixture at $p = 0$ in the ideal gas state, that is, without an excess enthalpy

$$\widetilde{h}^{\mathrm{id}}_{\mathrm{mix}}(T,p=0,\widetilde{x}_i) = \sum_i \widetilde{x}_i \widetilde{h}^{\mathrm{id}}_i(T,p=0) \qquad (79)$$

6. Addition of the residual part to reach the required state in the vapor phase analogously to Eq. (69)

$$\widetilde{h}^{\mathrm{real}}_{\mathrm{mix}}(T,p,\widetilde{x}_i) = \widetilde{h}^{\mathrm{id}}_{\mathrm{mix}}(T,p=0,\widetilde{x}_i) + \Delta h^{\mathrm{real}}_{\mathrm{Gas}}(T,p,\widetilde{x}_i) \qquad (80)$$

$h_{\mathrm{ref},i}(T_{\mathrm{ref},i})$ has to be chosen for each component in a way that the enthalpy for the standard state ($t = 25°\mathrm{C}$, ideal gas state) results in the standard enthalpy of formation $\Delta^{0\mathrm{f}}_{h_i}$. A useful choice for $T_{\mathrm{ref},i}$ is the melting point. The method is illustrated in Fig. 11.

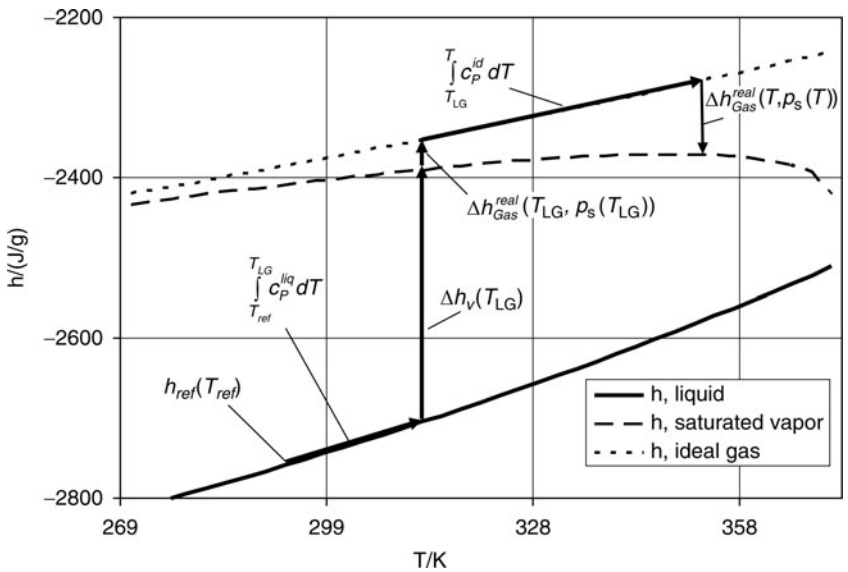

D1. Fig. 11. Calculation of the enthalpy of a saturated vapor with the route "liquid as starting phase".

The specific heat capacity of a liquid is reproduced with this route; nevertheless, it has also its disadvantages. The calculation of the enthalpy of vaporization is indirect and therefore not exact; it does not equal 0 at the critical point. The correlation for c_p^{liq} is often only verified in the temperature region below the normal boiling point and extrapolates poorly, giving large errors in the high-pressure region. Many arrangements (T_{ref}, h_{ref}, T_{LG} for each component) have to be set up.

7 Viscosity

The viscosity is a measure of the momentum transfer in a fluid perpendicular to the flow direction. It is needed especially for the calculation of pressure drops. Furthermore, it is a factor in the Reynolds and in the Grashof number for the determination of the heat transfer coefficient.

It is distinguished between the dynamic viscosity η and the kinematic viscosity ν. They are related via

$$\eta = \nu\,\rho \tag{81}$$

In the following section, only the dynamic viscosity is regarded.

7.1 Dynamic Viscosity of Liquids

Fig. 12 shows the typical curvature of the dynamic viscosity of liquids. In the temperature region above the melting point, it decreases with a large slope. The slope decreases with increasing temperatures, but remains negative. The dynamic viscosity can be roughly correlated with the simple approach

$$\ln\frac{\eta}{\text{Pas}} = A + \frac{B}{T} \tag{82}$$

This equation is appropriate to reproduce the curvature qualitatively. For a precise reproduction, further terms have to be added to Eq. (82), for example,

$$\ln\frac{\eta}{\text{Pas}} = A + \frac{B}{T/K} + C\frac{T}{K} + D\left(\frac{T}{K}\right)^2 + E\left(\frac{T}{K}\right)^3 \tag{83}$$

All of these equations have difficulties when they are extrapolated to high temperatures. It is necessary to check the equation in the temperature range of interest before it is applied. During the recent years, the PPDS equation

$$\frac{\eta}{\text{Pas}} = E\cdot\exp\left[A\left(\frac{C-T}{T-D}\right)^{1/3} + B\left(\frac{C-T}{T-D}\right)^{4/3}\right] \tag{84}$$

has been widely applied. Currently, this equation seems to be the most accurate correlation for liquid viscosities. Furthermore, it seems to extrapolate quite well. When it is programmed, it must be taken care that the term in brackets $(C - T)/(T - D)$ sometimes turns out to be negative, so that it makes sense to write in these cases

$$\left(\frac{C-T}{T-D}\right)^{1/3} = -\left(\frac{T-C}{T-D}\right)^{1/3} \text{ and}$$

$$\left(\frac{C-T}{T-D}\right)^{4/3} = -\left(\frac{T-C}{T-D}\right)^{1/3}\left(\frac{C-T}{T-D}\right)$$

One of the simplest options to estimate the dynamic viscosity of liquids is the group contribution method of Orrick/Erbar [2]. The calculation equation is

$$\ln\frac{\eta}{\text{mPas}} = \ln\left(\frac{\rho(20^\circ C)}{\text{g/cm}^3}\frac{\tilde{M}}{\text{g/mol}}\right) + \left(\sum\Delta_A + \frac{\sum\Delta_B}{T/K}\right) \tag{85}$$

For substances that are not liquid at $t = 20°C$, the liquid density at the melting point has to be inserted. The group contributions for Δ_A and Δ_B can be taken from Table 7. Partially, the group contributions do not refer to molecular segments but to structural units. First, the molecule has to be checked for aromatic and nonaromatic 5-membered and 6-membered rings. Then, the remaining groups can be assigned. For carbon atoms not recorded so far, a contribution according to the first line in Table 7 is added. Finally, additional corrections for double bonds and the particular kinds of substitution on aromatic rings

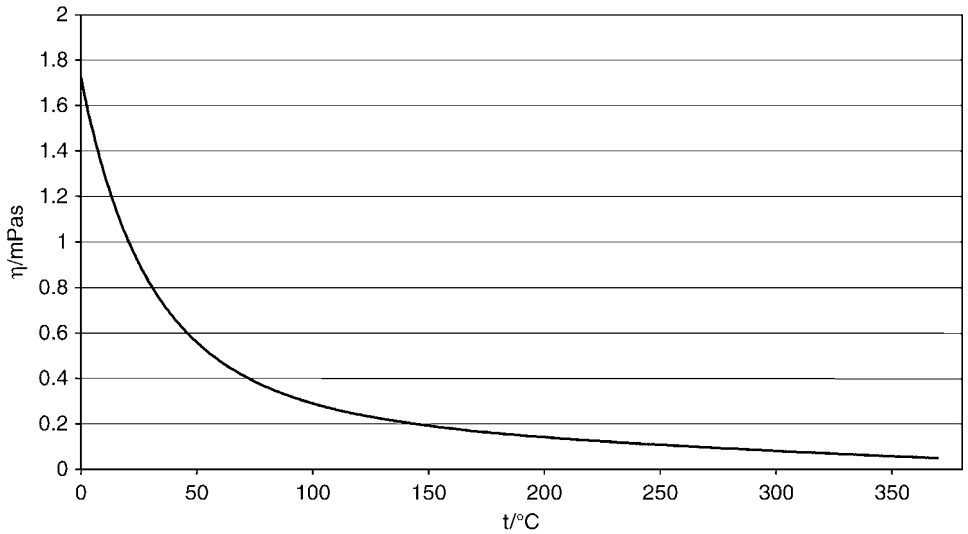

D1. Fig. 12. Dynamic viscosity of liquid water as a function of temperature.

D1. Table 7. Group contributions of the Orrick/Erbar method for the calculation of the dynamic viscosity of liquids

Structural groups	Δ_A	Δ_B
Carbon atoms	–6.95 – 0.21n	275 + 99n
–CH with 3 radicals	–0.15	35
C with 4 radicals	–1.20	400
Double bond	0.24	–90
5-membered ring	0.10	32
6-membered ring	–0.45	250
Aromatic ring	0.00	20
Ortho substitution	–0.12	100
Meta substitution	0.05	–34
Para substitution	–0.01	–5
–Cl	–0.61	220
–Br	–1.25	365
–I	–1.75	400
–OH	–3.00	1,600
–COO	–1.00	420
–O–	–0.38	140
>C=O	–0.50	350
–COOH	–0.90	770

n: number of carbon atoms not belonging to the groups shown above

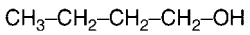

D1. Fig. 13. Structural formula of n-butanol.

(ortho: neighbor C-atoms, para: opposite C-atoms, meta: C-atoms, where one non-substituted C-atom in the ring is between) are made. Components containing nitrogen or sulfur cannot be treated. Deviations of 15% and more should be expected. Better results can be obtained with the group contribution methods of Sastri/Rao [25, 26], van Velzen [27], and, especially, Nannoolal/Rarey [28], where, however, the explanation of the complicated increments would be beyond the scope of this chapter.

Example 12:
Estimate the dynamic viscosity of n-butanol ($C_4H_{10}O$) at $t = 50°C$.

$\rho(20°C) = 810.6$ kg/m^3, $\tilde{M} = 74.12$ g/mol.

The group assignment of n-butanol (Fig. 13) is:

1 OH

4 carbon atoms

The analysis of Table 7 yields the group contributions:

$$\sum \Delta_A = 1 \cdot (-3) + (-6.95 - 0.21 \cdot 4) = -10.79$$
$$\sum \Delta_B = 1 \cdot (1{,}600) + (275 + 99 \cdot 4) = 2{,}271$$

giving a dynamic viscosity of

$$\ln \frac{\eta}{\text{mPas}} = \ln(0.8106 \cdot 74.12) + \left(-10.79 + \frac{2271}{323.15}\right)$$
$$= 0.3334 \Rightarrow \eta = 1.3957 \text{ mPas}$$

The value listed in Subchap. D3.1 is $\eta = 1.418$ mPas.

For $T > 0.7\ T_c$ Sastri [26] recommends the equation

$$\ln \frac{\eta}{\text{mPas}} = \left[\frac{\ln \eta(T_{NBP})}{\ln[\alpha\eta(T_{NBP})]}\right]^{\frac{1 - T/T_c}{1 - T_{NBP}/T_c}} \ln\left(\frac{\alpha\eta(T_{NBP})}{\text{mPas}}\right) \quad (85a)$$

For alcohols, $\alpha = 0.1175$, for other components, $\alpha = 0.248$. Deviations of approximately 10% can be expected.

Example 13:
Determine the dynamic viscosity of n-butane on the saturation line at $t = 100°C$.

$T_{NBP} = 272.65$ K, $T_c = 425.13$ K, $\eta_{NBP} = 0.202$ mPas.

$$\ln \frac{\eta}{\text{mPas}} = \left[\frac{\ln 0.202}{\ln[0.248 \cdot 0.202]}\right]^{\frac{1 - 373.15/425.13}{1 - 272.65/425.13}} \ln(0.248 \cdot 0.202)$$
$$= -2.4177 \Rightarrow \eta = 0.089 \text{ mPas}$$

The actual value is 0.077 mPas.

The liquid viscosity increases with increasing pressure. According to Lucas [29], the effect can be estimated via

$$\eta(T, p) = \eta(T, p_s(T)) \frac{1 + D(\Delta p_r / 2.118)^A}{1 + C\omega\Delta p_r} \quad (86)$$

with

$$\Delta p_r = \frac{p - p_s(T)}{p_c}$$
$$A = 0.9991 - \frac{4.674 \cdot 10^{-4}}{1.0523\ T_r^{-0.03877} - 1.0513}$$
$$D = \frac{0.3257}{\left(1.0039 - T_r^{2.573}\right)^{0.2906}} - 0.2086$$
$$C = -0.07921 + 2.1616\ T_r - 13.404\ T_r^2 + 44.1706\ T_r^3 - 84.8291\ T_r^4 + 96.1209\ T_r^5 - 59.8127\ T_r^6 + 15.6719\ T_r^7 \quad (86a)$$

Errors of approximately 10% should be expected.

Example 14:
Determine the dynamic viscosity of methyl cyclohexane at $T = 300$ K and $p = 500$ bar.

η (300 K, Siedelinie) = 0.661 mPas

p_s (300 K) = 67.56 mbar

$p_c = 34.71$ bar

$T_c = 572.15$ K

$\omega = 0.235$

The results for the particular terms are:

$T_r = 0.5243$

$\Delta p_r = 14.403$

$A = 0.98221$

$D = 0.13717$

$C = 0.06191$

Thus, one gets:

$$\eta(300\,\text{K}, 500\,\text{bar}) = 0.661\ \text{mPas} \frac{1 + 0.13717 \cdot (14.403/2.118)^{0.98221}}{1 + 0.06191 \cdot 0.235 \cdot 14.403}$$
$$= 1.04\,\text{mPas}$$

The experimental value is reported to be 1.09 mPas.

For mixtures, the viscosity can be estimated via

$$\ln\frac{\eta}{\text{Pas}} = \sum_i \widetilde{x}_i \ln\frac{\eta_i}{\text{Pas}} \tag{87}$$

In fact, the prediction of the viscosity of a mixture is much more difficult and Eq. (87) is not very reliable. It can be expected to meet the correct order of magnitude, but hardly more. With the help of an experimental value or the application of group contribution methods, significant improvements can be achieved, however, with a high effort. A detailed compilation of methods of this kind can be found in [2].

Example 15:
Determine the dynamic viscosity of a methanol/water mixture at $t = 40°C$ for $\widetilde{x}_{\text{Methanol}} = 0.5164$.

$$\eta_{\text{Water}} = 0.6652 \text{ mPas}, \quad \eta_{\text{Methanol}} = 0.4421 \text{ mPas}.$$
$$\ln\frac{\eta}{\text{mPas}} = 0.5164 \ln 0.4421 + 0.4836 \ln 0.6652$$
$$= -0.6186 \Rightarrow \eta = 0.5387 \text{ mPas}$$

The actual value is $\eta = 0.9345$ mPas. It is higher than both pure component values, which cannot be reproduced with the mathematical structure of Eq. (87).

7.2 Dynamic Viscosity of Gases

According to the kinetic gas theory, the viscosity of an ideal gas does not depend on the density [22]. This can be explained as follows: There are fewer particles available for the momentum transfer at low densities, but on the other hand they have a larger mean free path so that more momentum can be transferred across the flow direction. Both effects compensate for the ideal gas. For the real gas the viscosity slightly increases with density. There is a strong dependence on temperature, as the mean kinetic energy of the molecules increases with temperature, giving more momentum to be transferred in a collision.

The dynamic viscosity of gases at low pressures can be estimated according to Lucas [30]:

$$\frac{\eta^{\text{id}}}{10^{-7}\text{Pas}} = \frac{F_P^{\text{id}}}{\xi}\left[0.807\ T_r^{0.618} - 0.357\ \exp(-0.449\ T_r) + 0.34\ \exp(-4.058\ T_r) + 0.018\right] \tag{88}$$

where the correction factor F_P^{id} takes into account the influence of the polarity, which is characterized by the reduced dipole moment μ_r

$$\mu_r = 52.46\left(\frac{\mu}{\text{debye}}\right)^2 \frac{p_c}{\text{bar}}\left(\frac{T_c}{\text{K}}\right)^{-2} \tag{89}$$

For a given μ_r, F_P^{id} can be evaluated by

$$\begin{aligned} F_P^{\text{id}} &= 1 && \text{for } 0 \le \mu_r \le 0.022 \\ F_P^{\text{id}} &= 1 + 30.55\,(0.292 - Z_c)^{1.72} && \text{for } 0.022 \le \mu_r \le 0.075 \\ F_P^{\text{id}} &= 1 + 30.55\,(0.292 - Z_c)^{1.72}\,|0.96 + 0.1\,(T_r - 0.7)| && \text{for } \mu_r \ge 0.075 \end{aligned} \tag{90}$$

ξ is the reduced inverse viscosity and can be determined by

$$\xi = 0.176\left(\frac{T_c}{\text{K}}\right)^{1/6}\left(\frac{\widetilde{M}}{\text{g/mol}}\right)^{-1/2}\left(\frac{p_c}{\text{bar}}\right)^{-2/3} \tag{91}$$

For the so-called quantum gases H_2, D_2, and He, there is another correction factor [2]. The average error of the method is reported to be 1%...4% [2]; therefore, this quantity is usually not measured.

The typical curvature of the dynamic viscosity of gases is depicted in Fig. 14. For process simulation, it is sufficient to reproduce it by a simple polynomial

$$\frac{\eta^{\text{id}}}{\text{Pas}} = A + B\frac{T}{\text{K}} + C\left(\frac{T}{\text{K}}\right)^2 + D\left(\frac{T}{\text{K}}\right)^3 + E\left(\frac{T}{\text{K}}\right)^4 \tag{92}$$

Coefficients for Eq. (92) are given in Subchap. D3.1.

The DIPPR equation

$$\eta^{\text{id}} = \frac{AT^B}{1 + CT^{-1} + DT^{-2}} \tag{92a}$$

shows a better extrapolation behavior but is less flexible.

Example 16:
Estimate the dynamic viscosity of ammonia at $t = 300°C$ and $p = 1$ bar.

The following data are given:
$T_c = 405.5$ K
$p_c = 113.59$ bar

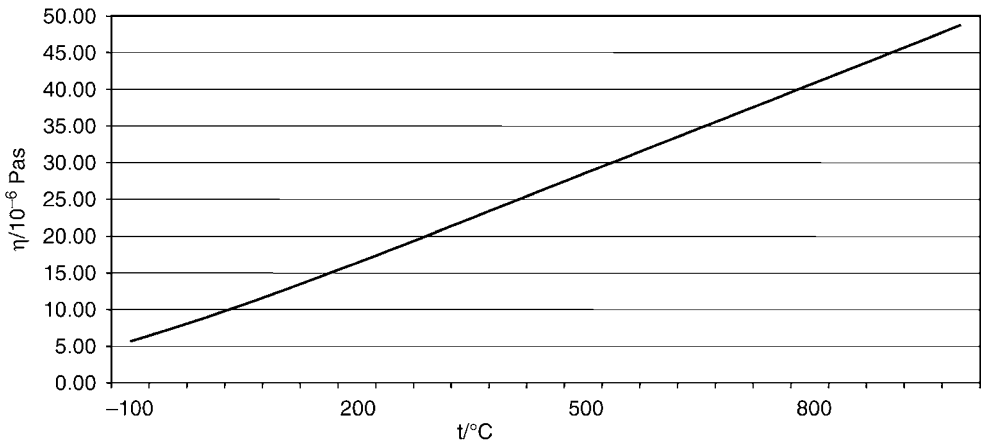

D1. Fig. 14. Dynamic viscosity of gaseous water as a function of temperature at low pressures.

$Z_c = 0.255$
$\mu = 1.5$ debye
$\widetilde{M} = 17.03$ g/mol
We obtain:

$$T_r = 573.15/405.5 = 1.4134$$
$$\mu_r = 52.46 \cdot 1.5^2 \cdot 113.59 \cdot 405.5^{-2} = 0.0815$$
$$\xi = 0.176\ (405.5)^{1/6}\ (17.03)^{-1/2}\ (113.59)^{-2/3} = 0.004947$$
$$F_p^{id} = 1 + 30.55\ (0.292 - 0.255)^{1.72}\ |0.96 + 0.1\ (1.4134 - 0.7)|$$
$$= 1.1086$$

Thus, the viscosity is:

$$\frac{\eta^{id}}{10^{-7}\text{Pas}} = \frac{1.1086}{0.004947}[0.807 \cdot 1.4134^{0.618} - 0.357\ \exp(-0.449 \cdot 1.4134) + 0.34\ \exp(-4.058 \cdot 1.4134) + 0.018]$$
$$= 185.83 \Rightarrow \eta^{id} = 18.58\,\mu\text{Pas}$$

The value from Subchap. D3.1 is η^{id} = 20.1 µPas.

The pressure-dependence of the viscosity of gases can be determined according to Lucas [30] for $1 \le T_r \le 40$ and $0 \le p_r \le 100$:

$$\eta = \eta^{id} Z_2\ F_p \tag{93}$$

with η^{id} from Eq. (88) or (92) and Z_2 via

$$Z_2 = 1 + \frac{A\ p_r^E}{B\ p_r^F + (1 + C p_r^D)^{-1}} \tag{94}$$

with

$$A = \frac{0.001245}{T_r}\exp(5.1726\ T_r^{-0.3286})$$
$$B = A\ (1.6553\ T_r - 1.2723)$$
$$C = \frac{0.4489}{T_r}\exp(3.0578\ T_r^{-37.7332})$$
$$D = \frac{1.7368}{T_r}\exp(2.231\ T_r^{-7.6351}) \tag{94a}$$
$$E = 1.3088$$
$$F = 0.9425\ \exp(-0.1853\ T_r^{0.4489})$$

The correction factor F_p is

$$F_p = \frac{1 + (F_p^{id} - 1)\ Z_2^{-3}}{F_p^{id}} \tag{95}$$

For $T_r < 1$ and $p < p_s(T_r)$ Lucas [30] gives the function

$$\frac{\eta}{10^{-7}\ \text{Pas}} = Z_2 \frac{F_p}{\xi} \tag{96}$$

with

$$Z_2 = 0.6 + 0.76\ p_r^A + (6.99\ p_r^B - 0.6)(1 - T_r)$$
$$A = 3.262 + 14.98\ p_r^{5.508} \tag{96a}$$
$$B = 1.39 + 5.746\ p_r$$

and the correction factor

$$F_p = \frac{1 + (F_p^{id} - 1)\ [Z_2/(\xi \eta^{id}/10^{-7}\ \text{Pas})]^{-3}}{F_p^{id}} \tag{97}$$

As a rule of thumb, an error of approximately 10% should be expected [30] except for the quantum gases, where again additional correction factors are necessary.

Example 17:
Determine the dynamic viscosity of ammonia at T = 420 K and p = 300 bar.
The following data are given:
$T_c = 405.5$ K
$p_c = 113.59$ bar
$Z_c = 0.255$
$\mu = 1.5$ debye
$\widetilde{M} = 17.03$g/mol
η^{id} (420 K, 1 bar) = 14.57 µPas
$\xi = 0.004947$
$\mu_r = 0.0815$
With $T_r = 1.0358$ and $p_r = 2.6411$ one gets:
$A = 0.1998$
$B = 0.08834$
$C = 0.9764$
$D = 9.2349$
$E = 1.3088$
$F = 0.7808$
and

$$Z_2 = 1 + \frac{A\ p_r^E}{B\ p_r^F + (1 + C p_r^D)^{-1}} = 4.77398$$

Furthermore, one obtains:

$$F_p^{id} = 1 + 30.55\ (0.292 - 0.255)^{1.72}\ |0.96 + 0.1\ (1.0358 - 0.7)|$$
$$= 1.1046$$
$$F_p = \frac{1 + (1.1046 - 1)\ \cdot 4.77398^{-3}}{1.1046} = 0.9062$$

The result for the dynamic viscosity is:

$$\eta = 14.57\ \mu Pas \cdot 4.77398 \cdot 0.9062 = 63.03\ \mu Pas$$

The reference value [31] is η = 56.6 µPas.

For the calculation of the viscosity of gas mixtures the Wilke mixing rule [32] can be applied at low pressures:

$$\eta^{Gem} = \sum_i \frac{\widetilde{y}_i \eta_i}{\sum_j \widetilde{y}_i F_{ij}} \tag{98}$$

with

$$F_{ij} = \frac{\left[1 + (\eta_i/\eta_j)^{1/2}\ (\widetilde{M}_j/\widetilde{M}_i)^{1/4}\right]^2}{\sqrt{8\ (1 + \widetilde{M}_i/\widetilde{M}_j)}} \tag{98a}$$

At high pressures, mixing rules based on the corresponding-states principle are available [2].

8 Thermal Conductivity

The thermal conductivity is often the decisive quantity in heat transfer processes. Its order of magnitude is λ = 0.1... 0.2 W/Km for most liquids. Exceptions are water ($\lambda \approx$ 0.6... 0.7 W/Km) and some oligoethers. For gases, an order of magnitude of $\lambda \approx$ 0.01... 0.03 W/Km can be expected. The quantum gases hydrogen ($\lambda \approx$ 0.2 W/Km) and helium ($\lambda \approx$ 0.14 W/Km) behave differently.

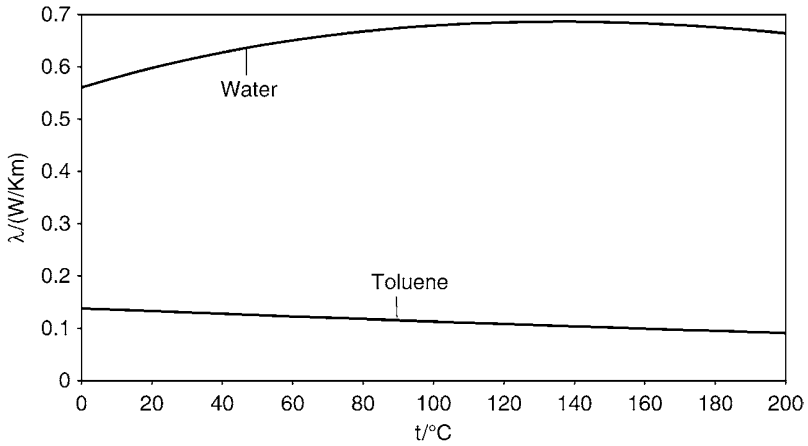

D1. Fig. 15. Curvatures of the liquid thermal conductivity as a function of temperature for water and toluene.

8.1 Thermal Conductivity of Liquids

The thermal conductivity of liquids can be described with a 4th degree polynomial

$$\frac{\lambda_{\mathrm{fl}}}{\mathrm{W/Km}} = A + B\frac{T}{\mathrm{K}} + C\left(\frac{T}{\mathrm{K}}\right)^2 + D\left(\frac{T}{\mathrm{K}}\right)^3 + E\left(\frac{T}{\mathrm{K}}\right)^4 \qquad (99)$$

or with the Jamieson [33] equation

$$\lambda_{\mathrm{L}} = A\,(1 + B\tau^{1/3} + C\tau^{2/3} + D\tau) \qquad (99a)$$

with

$$\tau = 1 - \frac{T}{T_{\mathrm{c}}} \qquad (99b)$$

Values for the coefficients of Eq. (99) are given in Subchap. D3.1. The thermal conductivity decreases almost linearly with the temperature over a wide range, so that a polynomial of the 1st degree is often sufficient, especially if only data below the normal boiling point are available. The other coefficients are also necessary, if either data at higher temperatures are given or if a maximum has to be described, as is the case for water. The curvatures for the liquid thermal conductivity for water and toluene as a typical organic substance are depicted in Fig. 15.

As the thermal conductivities are in the same order of magnitude for most substances, the estimation is comparably simple. The method of Sato-Riedel [34] is well established:

$$\frac{\lambda_{\mathrm{fl}}}{\mathrm{W/Km}} = 1.11\left(\frac{\widetilde{M}}{\mathrm{g/mol}}\right)^{-1/2} \frac{3 + 20\,(1 - T_{\mathrm{r}})^{2/3}}{3 + 20\,\left(1 - T_{\mathrm{NBP,r}}\right)^{2/3}} \qquad (100)$$

Example 18:
Determine the thermal conductivity of liquid acetone at $t = -50°\mathrm{C}$.
The given values are:
$t_{\mathrm{c}} = 234.95°\mathrm{C}$
$t_{\mathrm{NBP}} = 56.08°\mathrm{C}$
$\widetilde{M} = 58.08\,\mathrm{g/mol}$

$$\frac{\lambda_{fl}}{\mathrm{W/Km}} = 1.11(58.08)^{-1/2}\,\frac{3+20\,(1-223.15/508.1)^{2/3}}{3+20\,(1-329.23/508.1)^{2/3}} = 0.1864$$

The value given in Subchap. D3.1 is $\lambda = 0.193$ W/Km.

D1. Table 8. Values for Q in Eq. (101)

T_{r}	p_{r}					
	1	5	10	50	100	200
0.8	0.036	0.038	0.038	0.038	0.038	0.038
0.7	0.018	0.025	0.027	0.031	0.032	0.032
0.6	0.015	0.02	0.022	0.024	0.025	0.025
0.5	0.012	0.0165	0.017	0.019	0.02	0.02

The pressure dependence of thermal conductivity for liquids is almost negligible. At very high pressures, it has a certain influence, which can be estimated with the Missenard method

$$\frac{\lambda(p_{\mathrm{r}}, T)}{\lambda(p_{\mathrm{s}}, T)} = 1 + Q\,p_{\mathrm{r}}^{0.7} \qquad (101)$$

Values for Q are listed in Table 8.

Example 19:
Determine the thermal conductivity of toluene at $T = 304$ K and $p = 6{,}330$ bar.
The given values are:
λ (304 K, 1 bar) = 0.1309 W/Km
$p_{\mathrm{c}} = 41.26$ bar
$T_{\mathrm{c}} = 591.75$ K
With $T_{\mathrm{r}} = 0.5137$ and $p_{\mathrm{r}} = 153.42$ one gets $Q = 0.0207$ from Table 8 by interpolation. Thus, it is

$$\lambda(p_{\mathrm{r}}, T) = \lambda(p_{\mathrm{s}}, T) \cdot \left(1 + Q\,p_{\mathrm{r}}^{0.7}\right) = 0.1309\,\mathrm{W/Km}.$$
$$\left(1 + 0.0207 \cdot 153.42^{0.7}\right) = 0.2227\,\mathrm{W/Km}$$

The experimental value [2] is 0.228 W/Km.

As a mixing rule for the thermal conductivity of liquids, the method of Li [35] is appropriate, as it can also be extended to multicomponent mixtures:

$$\lambda_{\mathrm{mix}} = \sum_{i=1}^{n}\sum_{j=1}^{n} \frac{2\Phi_i\Phi_j}{\lambda_i^{-1} + \lambda_j^{-1}} \qquad (102)$$

with

$$\Phi_i = \frac{\widetilde{x}_i v_{\mathrm{liq},i}}{\sum_{j=1}^{n} \widetilde{x}_j v_{\mathrm{liq},j}} \qquad (102a)$$

Example 20:
Determine the thermal conductivity of a liquid mixture of benzene and methanol with $x_{benzene} = 0.381$ at $T = 273$ K.
The following data at $T = 273$ K are given:
$\lambda_{benzene} = 0.151$ W/Km (extrapolated below melting point)
$\lambda_{methanol} = 0.207$ W/Km

$\widetilde{M}_{benzene} = 78.11$g/mol
$\widetilde{M}_{methanol} = 32.04$g/mol

$\rho_{benzene} = 897.6$ kg/m^3 => $\nu_{benzene} = 8.702 \cdot 10^{-5}$ m^3/mol (extrapolated below melting point)
$\rho_{methanol} = 810.7$ kg/m^3 => $\nu_{methanol} = 3.952 \cdot 10^{-5}$ m^3/mol

$$\Phi_{benzene} = \frac{0.381 \cdot 8.702 \cdot 10^{-5}}{0.381 \cdot 8.702 \cdot 10^{-5} + 0.619 \cdot 3.952 \cdot 10^{-5}} = 0.5754$$

$$\Phi_{methanol} = 1 - \Phi_{benzene} = 0.4246$$

$$\frac{\lambda_{mix}}{\mathrm{W/Km}} = \frac{2 \cdot 0.5754^2}{2 \cdot 0.151^{-1}} + 2 \cdot \frac{2 \cdot 0.5754 \cdot 0.4246}{0.151^{-1} + 0.207^{-1}} + \frac{2 \cdot 0.4246^2}{2 \cdot 0.207^{-1}} = 0.1726$$

The experimental value [2] is $\lambda = 0.17$ W/Km.

8.2 Thermal Conductivity of Gases

The thermal conductivity of gases can be derived from the kinetic gas theory analogously to the viscosity. Instead of the momentum transfer, the transfer of kinetic energy has to be regarded [22]. Similar to viscosity, the thermal conductivity increases with increasing temperature. At low to moderate pressures (approximately 0.1...10 bar), it does not depend on the pressure. The thermal conductivity of gases can be correlated with a 4th degree polynomial:

$$\frac{\lambda^{id}}{\mathrm{W/Km}} = A + B\frac{T}{\mathrm{K}} + C\left(\frac{T}{\mathrm{K}}\right)^2 + D\left(\frac{T}{\mathrm{K}}\right)^3 + E\left(\frac{T}{\mathrm{K}}\right)^4 \quad (103)$$

The typical, almost linear curvature is depicted in Fig. 16.

The thermal conductivity of gases at low pressures can be estimated according to Chung [36] via

$$\lambda = \frac{3.75 \Psi \eta \widetilde{R}}{\widetilde{M}} \quad (104)$$

with

$$\Psi = 1 + \alpha \frac{0.215 + 0.28288\,\alpha - 1.061\,\beta + 0.26665\,\gamma}{0.6366 + \beta\gamma + 1.061\,\alpha\beta} \quad (104a)$$

and

$$\alpha = \widetilde{c}_p/\widetilde{R} - 2.5$$
$$\beta = 0.7862 - 0.7109\,\omega + 1.3168\,\omega^2 \quad (104b)$$
$$\gamma = 2 + 10.5\,T_r^2$$

For nonpolar substances, deviations of about 5%...10% might be expected. For polar compounds, the error is often higher. In these cases, the group contribution method of Roy/Thodos [2] is recommended.

Example 21:
Determine the thermal conductivity of 2-methylpentane at $t = 100°C$ and 1 bar.
The given data are:
$\widetilde{M} = 86.16$ g/mol
$\omega = 0.280$
$T_c = 497.7$ K
$c_p = 2.008$ J/gK
$\eta = 8.2$ µPas
One gets:

$$\alpha = \frac{2.016 \cdot 86.16}{8.3143} - 2.5 = 18.308$$
$$\beta = 0.7862 - 0.7109 \cdot 0.280 + 1.3168 \cdot 0.280^2 = 0.6904$$
$$\gamma = 2 + 10.5 \cdot (373.15/497.7)^2 = 7.9023$$
$$\Psi = 1 + \alpha \frac{0.215 + 0.28288\,\alpha - 1.061\,\beta + 0.26665\,\gamma}{0.6366 + \beta\gamma + 1.061\,\alpha\beta} = 7.3538$$
$$\lambda = \frac{3.75 \cdot 7.3538 \cdot 8.2 \cdot 10^{-6} \cdot 8.3143}{86.16 \cdot 10^{-3}} \frac{\mathrm{W}}{\mathrm{Km}} = 0.0218\,\mathrm{W/Km}$$

The value listed in Subchap. D3.1 is 0.0206 W/Km.

The thermal conductivity of gases depends on the pressure in an unusual way. At very low pressures ($p < 10^{-3}$ mbar), when the mean free path is large in comparison with the vessel dimensions, the thermal conductivity is proportional to the pressure and to the distance d between the limiting walls in the direction of the heat flux:

$$\lambda = \frac{3}{8} p d \sqrt{\frac{3\widetilde{R}}{\widetilde{M}T}} \quad (105)$$

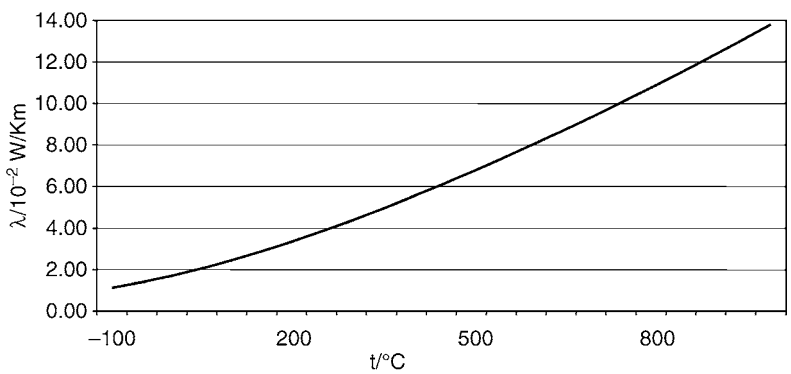

D1. Fig. 16. Thermal conductivity of gaseous water as a function of temperature.

At normal pressures (p = 0.001 bar ... 10 bar), it is almost independent of the pressure. At high pressures, the thermal conductivity can be estimated according to Stiel and Thodos [37]:

$$\begin{aligned}
\lambda &= \lambda^{id} + 0.0122\,\Gamma^{-1}Z_c^{-5}\times \\
&\quad [\exp(0.535\,\rho/\rho_c) - 1] \qquad \text{for} \quad \rho/\rho_c < 0.5 \\
\lambda &= \lambda^{id} + 0.0114\,\Gamma^{-1}Z_c^{-5}\times \\
&\quad [\exp(0.67\,\rho/\rho_c) - 1.069] \qquad \text{for} \quad 0.5 < \rho/\rho_c < 2 \\
\lambda &= \lambda^{id} + 0.0026\,\Gamma^{-1}Z_c^{-5}\times \\
&\quad [\exp(1.155\,\rho/\rho_c) + 2.016] \qquad \text{for} \quad 2 < \rho/\rho_c < 2.8
\end{aligned} \tag{106}$$

Γ is given by

$$\frac{\Gamma}{(\mathrm{W/Km})^{-1}} = 210\left(\frac{T_c}{\mathrm{K}}\right)^{1/6}\left(\frac{\widetilde{M}}{\mathrm{g/mol}}\right)^{1/2}\left(\frac{p_c}{\mathrm{bar}}\right)^{-2/3} \tag{107}$$

The method is not considered to be very accurate, deviations of 10%. . .20% are usual. For polar compounds, this method is not appropriate. There are other, more difficult methods available [2], which are more accurate. However, none of them can really handle polar compounds.

Example 22:
Determine the thermal conductivity of nitrous oxide at t = 105°C and p = 138 bar.
The given values are:

λ^{id} = 0.02375 W/Km
p_c = 72.45 bar
T_c = 309.52 K
ρ_c = 454 kg/m^3
ρ (105°C, 138 bar) = 303.978 kg/m^3
$\widetilde{M}$ = 44.01g/mol
For Γ, one gets:

$$\frac{\Gamma}{(\mathrm{W/Km})^{-1}} = 210 \cdot 309.52^{1/6} \cdot 44.01^{1/2} \cdot 72.45^{-2/3} = 208.49$$

$$\rho/\rho_c = 0.66956$$

$$Z_c = \frac{72.45 \cdot 10^5 \cdot 44.01 \cdot 10^{-3}}{454 \cdot 8.3143 \cdot 309.52} = 0.2729$$

which yields

$$\frac{\lambda}{\mathrm{W/Km}} = 0.02375 + 0.0114 \cdot 208.49^{-1} \cdot 0.2729^{-5}$$
$$[\exp(0.67 \cdot 0.66956) - 1.069] = 0.0417$$

The experimental value is 0.039 W/Km.

For the calculation of the thermal conductivity of gaseous mixtures, the mixing rule of Wassiljeva, Mason, and Saxena [2] can be applied analogously to the mixing rule of Wilke for viscosity:

$$\lambda^{mix} = \sum_i \frac{\widetilde{y}_i \lambda_i}{\sum_j y_j F_{ij}} \tag{108}$$

with

$$F_{ij} = \frac{\left[1 + (\eta_i/\eta_j)^{1/2}\,(\widetilde{M}_j/\widetilde{M}_i)^{1/4}\right]^2}{\sqrt{8\,(1 + \widetilde{M}_i/\widetilde{M}_j)}} \tag{108a}$$

Example 23:
Determine the thermal conductivity of a gaseous mixture consisting of 25 mol% benzene and 75 mol% argon at t = 100.6°C and p = 1 bar.
The following values are given:
$\widetilde{M}_{benzene}$ = 78.11 g/mol
$\widetilde{M}_{argon}$ = 39.95 g/mol
$\eta_{benzene}$ = 9.465 µPas
η_{argon} = 27.05 µPas
$\lambda_{benzene}$ = 0.01694 W/Km
λ_{argon} = 0.02089 W/Km
We get:

$$F_{12} = \frac{\left[1 + (9.465/27.05)^{1/2}\,(39.95/78.11)^{1/4}\right]^2}{\sqrt{8\,(1 + 78.11/39.95)}} = 0.4629$$

$$F_{21} = \frac{\left[1 + (27.05/9.465)^{1/2}\,(78.11/39.95)^{1/4}\right]^2}{\sqrt{8\,(1 + 39.95/78.11)}} = 2.58655$$

$$F_{11} = F_{22} = 1$$

The thermal conductivity of the mixture is calculated to be:

$$\frac{\lambda^{mix}}{\mathrm{W/Km}} = \frac{0.25 \cdot 0.01694}{0.25 \cdot 1 + 0.75 \cdot 0.4629} + \frac{0.75 \cdot 0.02089}{0.25 \cdot 2.58655 + 0.75 \cdot 1}$$
$$= 0.0183$$

The experimental value is λ = 0.0192 W/Km.

9 Surface Tension

The surface tension is a quantity which decides whether a liquid is prone to form droplets or not. For pure substances, it decreases with increasing temperature and becomes 0 at the critical point (Fig. 17), where vapor and liquid are identical. It is essentially determined by intermolecular forces, especially by the differences of the attractive forces acting on the molecules located in the surface, one from the vapor side and one from the liquid side. The surface tension can be correlated by

$$\frac{\sigma}{\mathrm{N/m}} = A\,(1 - T_r)^{B + CT_r + DT_r^2 + ET_r^3} \tag{109}$$

where the coefficients C, D, and E can either be set to 0 or be fitted according to demand. Coefficients for Eq. (109) are given in Subchap. D3.1.

The surface tension can be estimated according to Brock/Bird/Miller [2], based on the 3-parameter corresponding states principle:

$$\frac{\sigma}{\mathrm{mN/m}} = \left(\frac{p_c}{\mathrm{bar}}\right)^{2/3}\left(\frac{T_c}{\mathrm{K}}\right)^{1/3} Q(1 - T_r)^{11/9} \tag{110}$$

with

$$Q = 0.1196\left[1 + \frac{\frac{T_{NBP}}{T_c}\ln\frac{p_c}{1.01325\,\mathrm{bar}}}{1 - T_{NBP}/T_c}\right] - 0.279 \tag{110a}$$

For substances which are not strongly polar, the deviations are usually less than 5%.

Example 24:
Estimate the surface tension of bromobenzene at t = 50°C.
The given data are:
T_{NBP} = 429.15 K

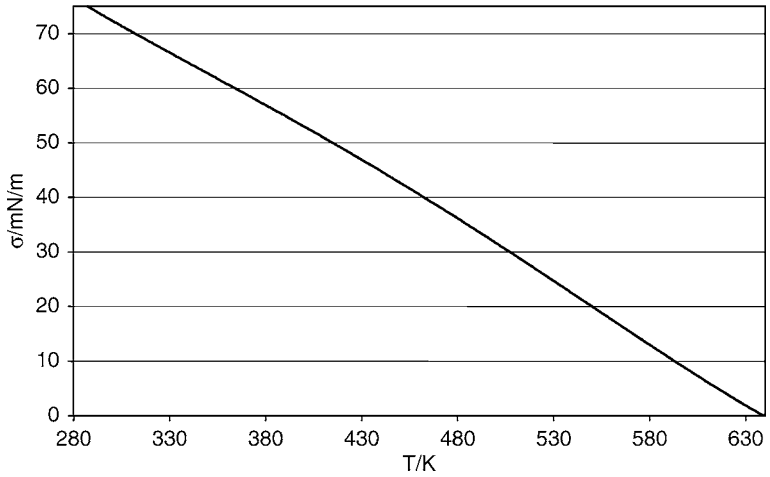

D1. Fig. 17. Surface tension of water as a function of temperature.

$T_c = 670.20$ K
$p_c = 45.19$ bar
With

$$Q = 0.1196\left[1 + \frac{\frac{429.15}{670.20}\ln\frac{45.19}{1.01325}}{1 - 429.15/670.20}\right] - 0.279 = 0.6492$$

we get

$$\frac{\sigma}{\text{mN/m}} = 45.19^{2/3} \cdot 670.20^{1/3} \cdot 0.6492 \cdot (1 - 323.15/670.2)^{11/9} = 32.25$$

The value listed in Subchap. D3.1 is 33 mN/m.

As a mixing rule, the equation

$$\frac{\sigma_{\text{mix}}}{\text{mN/m}} = \left(P^{\text{liq}}_{\text{mix}} \frac{\widetilde{\rho}^{\text{mix}}_{liq}}{\text{mol/cm}^3} - P^{\text{vap}}_{\text{mix}} \frac{\widetilde{\rho}^{\text{mix}}_{\text{vap}}}{\text{mol/cm}^3}\right)^4 \qquad (111)$$

is suggested, where the terms for the gas phase can be neglected at low pressures. P is the parachor

$$P = \left(\frac{\widetilde{\rho}}{\text{mol/cm}^3}\right)^{-1}\left(\frac{\sigma}{\text{mN/m}}\right)^{1/4} \qquad (112)$$

which can be averaged via

$$P_{mix} = \sum_i \sum_j \widetilde{x}_i \widetilde{x}_j \frac{P_i + P_j}{2} \qquad (113)$$

More accurate methods, especially for aqueous systems, are listed in Poling/Prausnitz/O'Connell [2].

Example 25:
Estimate the surface tension of a mixture of diethyl ether (1) and benzene (2) with a mole fraction $x_1 = 0.423$ at $T = 298$ K. The influence of the vapor in Eq. (107) can be neglected due to the low pressure.
The given data are:
$\widetilde{M}_1 = 74.12$g/mol
$\widetilde{M}_2 = 78.11$g/mol
$\sigma_1 = 16.429$ mN/m
$\sigma_2 = 28.214$ mN/m
$\rho_1 = 707.8$ kg/m^3 = 0.009549 mol/cm^3
$\rho_2 = 872.80$ kg/m^3 = 0.011174 mol/cm^3
One gets:

$$P_1 = 0.009549^{-1} \cdot 16.429^{1/4} = 210.84$$
$$P_2 = 0.011174^{-1} \cdot 28.214^{1/4} = 206.26$$
$$P_{\text{mix}} = 0.423^2 \cdot 210.84 + 2 \cdot 0.423 \cdot 0.577 \frac{210.84 + 206.26}{2} + 0.577^2 \cdot 206.26 = 208.20$$
$$\rho^{\text{mix}}_{\text{liq}} = \left(\widetilde{x}_1 \widetilde{\rho}^{-1}_{\text{liq},1} + \widetilde{x}_2 \widetilde{\rho}^{-1}_{\text{liq},2}\right)^{-1} = \left(\frac{0.423}{0.009549} + \frac{0.577}{0.011174}\right)^{-1} \frac{\text{mol}}{\text{cm}^3} = 0.0104237 \text{ mol/cm}^3$$
$$\sigma_{\text{mix}} = (208.20 \cdot 0.0104237)^4 \text{ mN/m} = 22.18 \text{ mN/m}$$

The experimental value [34] is 21.81 mN/m.

10 Diffusion Coefficient

The binary diffusion coefficient D_{12} is needed for all calculations where mass transfer is involved. In this chapter, it is defined as

$$j_{12} = -\rho_{\text{mix}} D_{12}\left(\frac{dx}{dz}\right) \qquad (114)$$

with j_{12} as mass flux density and z as coordinate direction. The diffusion coefficient is symmetric, that is, $D_{12} = D_{21}$. It is essentially determined by intermolecular forces. For its evaluation, experimental values are difficult to measure and hardly available. In almost all cases, it has to be relied on estimation methods.

10.1 Diffusion Coefficients in Gases

In addition for its role in viscosity and thermal conductivity, the kinetic gas theory [22] is the basis for the estimation methods for diffusion coefficients in the gas phase. It depends not only on temperature but also on pressure. At pressures up to $p = 10$ bar,

it is inversely proportional to the pressure. It is almost independent from the concentration. At low pressures, the binary diffusion coefficient for gases can be estimated according to Fuller [38] with a remarkable accuracy. The calculation equation is given by:

$$\frac{D_{12}}{\mathrm{cm^2/s}} = \frac{0.00143\left(\frac{T}{\mathrm{K}}\right)^{1.75}\left[\left(\frac{\widetilde{M}_1}{\mathrm{g/mol}}\right)^{-1} + \left(\frac{\widetilde{M}_2}{\mathrm{g/mol}}\right)^{-1}\right]^{1/2}}{\frac{p}{\mathrm{bar}}\sqrt{2}\left[\left(\sum \Delta_{v_1}\right)^{1/3} + \left(\sum \Delta_{v_2}\right)^{1/3}\right]^2} \quad (115)$$

Δ_v is the so-called diffusion volume, which can be determined with the group contributions from Table 9. The accuracy of the Fuller method is approximately 4% [2].

Example 26:

Determine the binary diffusion coefficient of a mixture of ammonia (NH_3) and diethyl ether ($C_4H_{10}O$) at $T = 288$ K and $p = 2$ bar. The molecular weights are $M_{NH3} = 17.03$ g/mol and $M_{C4H10O} = 74.12$ g/mol.

The diffusion volumes for both components can be evaluated as:

$$\left(\sum \Delta_{v_1}\right) = 20.7$$

$$\left(\sum \Delta_{v_2}\right) = 4 \cdot 15.9 + 10 \cdot 2.31 + 6.11 = 92.81$$

After inserting the diffusion volumes into Eq. (115), one gets:

$$D_{12} = \frac{0.00143(288)^{1.75}\left[(17.03)^{-1} + (74.12)^{-1}\right]^{1/2}}{2\sqrt{2}\left[(20.7)^{1/3} + (92.81)^{1/3}\right]^2}\,\mathrm{cm^2/s}$$

$$= 0.0517\,\mathrm{cm^2/s}$$

The value taken from the literature [2] is $D_{12} = 0.0505$ cm^2/s.

D1. Table 9. Group contributions for the diffusion volumes in the Fuller method

Atom and structure contributions			
C	15.9	Br	21.9
H	2.31	I	29.8
O	6.11	S	22.9
N	4.54	Aromatic ring	–18.3
F	14.7	Heterocyclic ring	–18.3
Cl	21		
Simple molecules			
He	2.67	CO	18.0
Ne	5.98	CO_2	26.9
Ar	16.2	N_2O	35.9
Kr	24.5	NH_3	20.7
Xe	32.7	H2O	13.1
H_2	6.12	SF_6	71.3
D_2	6.84	Cl_2	38.4
N_2	18.5	Br_2	69.0
O_2	16.3	SO_2	41.8
Air	19.7		

The influence of the pressure can be evaluated with the equation of Riazi and Whitson [2]:

$$\frac{(\rho D_{12})}{(\rho D_{12})^{\mathrm{id}}} = 1.07\left(\frac{\eta}{\eta^{\mathrm{id}}}\right)^{B + C\,p/p_c} \quad (116)$$

with

$$B = -0.27 - 0.38\,\omega \quad (116a)$$

and

$$C = -0.05 + 0.1\,\omega \quad (116b)$$

For mixtures, ω and p_c can be calculated with a linear mixing rule:

$$\omega = \sum_i \widetilde{y}_i \omega_i \quad (117)$$

$$p_c = \sum_i \widetilde{y}_i p_{ci} \quad (118)$$

The disadvantage of this relationship is that it requires the dynamic viscosity of the vapor mixture, which has to be estimated itself. Therefore, approximately 15% deviation for the estimation of vapor diffusion coefficients at high pressures should be expected.

10.2 Diffusion Coefficients in Liquids

The binary diffusion coefficient in liquid mixtures is a complicated function of the concentration and furthermore depends on temperature and pressure. A reliable estimation method is not available. For most of the related engineering problems it is sufficient to meet the correct order of magnitude. It is distinguished between the limiting case of the ideally diluted solution and the case with arbitrary concentrations.

For the limiting case of infinite dilution of the solute A in the solvent B the diffusion coefficient can be estimated using several methods [2]. They are all characterized by individual rules for special components, limited ranges of applicability, or input parameters which are difficult to access. A reasonable compromise between accuracy and applicability is the simplified version of the method of Tyn/Calus [2]:

$$\frac{D_{AB}^{\infty}}{\mathrm{cm^2/s}} = 8.93 \cdot 10^{-8}\left(\frac{v_B(T_{NBP})}{\mathrm{cm^3/mol}}\right)^{-1/3}\left(\frac{v_A(T_{NBP})}{\mathrm{cm^3/mol}}\right)^{1/6}\left(\frac{P_B}{P_A}\right)^{0.6}\frac{T}{K}\left(\frac{\eta_B}{\mathrm{mPas}}\right)^{-1} \quad (119)$$

with P as the parachor, which can be estimated to be

$$P_i = \frac{v_i(T)}{\mathrm{cm^3/mol}}\left(\frac{\sigma_i}{\mathrm{mN/m}}\right)^{0.25} \quad (120)$$

There is also a group contribution method available [2], which, however, only covers a small part of all possible applications.

The special rules of the Tyn/Calus equation are:

- The dynamic viscosity of the solvent should be less than 20...30 mPas.
- If the solute is water, v_A and P_A should be set to $v_A = 37.4$ cm^3/mol and $P_A = 105.2$.

- If the solute is an organic acid, the values for v_A and P_A should be doubled. Exceptions are made if the solvent is water, methanol, or n-butanol.
- If the solvent is an alcohol and the solute is nonpolar, the values for v_A and P_A should be multiplied with a factor corresponding to $8\eta_B$/mPas.

The deviations of the Tyn/Calus equation that should be expected are approximately 10%.

The temperature dependence of Eq. (119) is only an approximation. The actual functional relationship is not finally clarified. Moreover, the pressure dependence is not well defined. It is only known that the liquid diffusion coefficient decreases with increasing pressure at very high pressures.

The model of the ideally diluted solution is applicable if the concentration of the solute does not exceed 5%. . .10%. For the transition of the ideally diluted solution to the general case with arbitrary concentrations the Vignes correlation can be used:

$$D_{AB} = (D_{AB}^{\infty})^{\widetilde{x}_B}(D_{BA}^{\infty})^{\widetilde{x}_A}\left(\frac{\partial \ln(\widetilde{x}_A\gamma_A)}{\partial \ln \widetilde{x}_A}\right)_{T,p} \qquad (121)$$

where γ is the activity coefficient (see Subchap. D5.1). Because of the validity of the Gibbs-Duhem equation it does not matter which component is used for the differential quotient.

Example 27:
Determine the binary diffusion coefficient in a liquid mixture of benzene (A) and toluene (B) at T = 298 K for x_A = 0.4. Approximately, it is an ideal mixture so that the activity coefficients can be regarded to be unity.

The given values are:
$v_A(T_{NBP})$ = 95.84 cm^3/mol
$v_B(T_{NBP})$ = 118.31 cm^3/mol
v_A(T) = 89.49 cm^3/mol
v_B(T) = 106.79 cm^3/mol
σ_A(T) = 28.21 mN/m
σ_B(T) = 27.94 mN/m
η_A(T) = 0.601 mPas
η_B(T) = 0.553 mPas
The parachors can be determined to be:
P_A = 206.24
P_B = 245.52
Thus, the diffusion coefficients in the ideally diluted state are:

$$D_{AB}^{\infty} = 8.93 \cdot 10^{-8}(118.31)^{-1/3}(95.84)^{1/6}\left(\frac{245.52}{206.24}\right)^{0.6} \cdot 298 \cdot (0.553)^{-1}\,\mathrm{cm^2/s} = 2.33 \cdot 10^{-5}\,\mathrm{cm^2/s}$$

$$D_{BA}^{\infty} = 8.93 \cdot 10^{-8}(95.84)^{-1/3}(118.31)^{1/6}\left(\frac{206.24}{245.52}\right)^{0.6} \cdot 298 \cdot (0.601)^{-1}\,\mathrm{cm^2/s} = 1.93 \cdot 10^{-5}\,\mathrm{cm^2/s}$$

There is only one experimental value available [2] (D_{BA}^{∞} = 1.85·10^{-5} cm^2/s), which is met very well.

For the actual concentration, the diffusion coefficient is determined with the Vignes correlation

$$D_{AB} = (2.33 \cdot 10^{-5})^{0.6}(1.93 \cdot 10^{-5})^{0.4}\,\mathrm{cm^2/s} = 2.16 \cdot 10^{-5}\,\mathrm{cm^2/s}$$

10.3 Diffusion in Multicomponent Mixtures

In multicomponent mixtures, the diffusion flow depends not only on its own but also on the interaction of all concentration gradients. In extreme cases, a component can even diffuse in the opposite direction of its own concentration gradient [39]. The calculation of such processes is very complex and beyond the scope of this chapter.

11 Symbols

a	parameter in RKS and PR equation of state (Pa m^6 mol^{-2})
b	parameter in RKS and PR equation of state (m^3 mol^{-1})
A, B, C, D, E, F	coefficients
c_σ	specific heat capacity along the saturation line (J kg^{-1} K^{-1})
D	diffusion coefficient (m^2 s^{-1})
f	fugacity (Pa)
F_{ij}	weighting factor
F_P	factor for pressure correction
j	mole flux density (mol m^{-2} s^{-1})
k_{ij}	interaction parameter in cubic equations of state
K	equilibrium constant (Pa^{-1})
n	degree of association
n_A	number of atoms in a molecule
P	parachor
q	electric charge (C)
r	distance (m)
t	Celsius temperature (°C)
v	specific volume (m^3 mol^{-1})
z	coordinate (m)
$\widetilde{z}$	true concentration (association) (mol mol^{-1})
Z	compressibility factor
Z_2	correction factor
α	coefficient
γ	activity coefficient
Δ_G	group contribution for standard Gibbs energy of formation
Δ_H	group contribution for standard enthalpy of formation
Δ_T	group contribution for critical temperature
Δ_p	group contribution for critical pressure
Δ_{NBP}	group contribution for normal boiling point
Δ_v	group contribution for critical volume
Δg^{0f}	standard Gibbs energy of formation (J mol^{-1})
Δh^{0f}	standard enthalpy of formation (J mol^{-1})
Δh_{Gas}^{real}	residual part of vapor enthalpy (J mol^{-1})
Δh_{in}	enthalpy of association (J mol^{-1}) (component i, degree of association n)
Δh_m	enthalpy of fusion (J mol^{-1})
Δh_v	enthalpy of vaporization (J mol^{-1})
μ	dipole moment (debye)
ν	kinematic viscosity (m^{2}s^{-1})
ξ	reduced inverse viscosity

$\Sigma\Delta_v$	diffusion volume
φ	fugacity coefficient
Φ	parameter in thermal conductivity mixing rule
ω	acentric factor

Indices

D	dimer
E	excess quantity
Gas	Gas
id	ideal gas
LG	transition liquid–gas
liq	liquid
m	melting point
M	monomer
mix	mixture
NBP	normal boiling point
ref	reference state
s	saturation state
SRK	Soave-Redlich-Kwong
$'$	boiling liquid
$''$	saturated vapor
∞	state of infinite dilution

12 Bibliography

1. Span R, Wagner W (2003) Equations of state for technical applications. Int J Thermophys 24(1):1–162
2. Poling BE, Prausnitz JM, O'Connell JP (2001) The properties of gases and liquids, 5th ed. McGraw-Hill, New York
3. Constantinou L, Gani R (1994) New group contribution method for estimating properties of pure compounds. AIChE J 40(10):1697–1710
4. Nannoolal Y, Rarey J, Ramjugernath D (2007) Estimation of Pure Component Properties, Part 2: Estimation of Critical Property Data by Group Contribution. Fluid Phase Equilibria 252:1–27
5. Constantinou L, Gani R, O'Connell JP (1995) Estimation of the acentric factor and the liquid molar volume at 298K using a new group contribution method. Fluid Phase Equilibria 103:11–22
6. Nannoolal Y, Rarey J, Ramjugernath D, Cordes W (2004) Estimation of pure component properties. Part 1: Estimation of the normal boiling point of non-electrolyte organic compounds via group contributions and group interactions. Fluid Phase Equilibria 226:45–63
7. Jakob A (1995) Thermodynamische Grundlagen der Kristallisation und ihre Anwendung in der Modellentwicklung. Dissertation Universität Oldenburg
8. Gmehling J, Kolbe B (1988) Thermodynamik. Georg Thieme Verlag, Stuttgart
9. Hankinson RW, Thomson GH (1979) A new correlation for saturated densities of liquids and their mixtures. AIChE J 25:653–663
10. Peng D-Y, Robinson DB (1976) A new two constant equation of state. Ind Eng Chem Fundam 15(1):59–64
11. Soave G (1972) Equilibrium constants from a modified Redlich-Kwong equation of state. Chem Eng Sci 27:1197–1203
12. Ahlers J, Gmehling J (2001) Development of a universal group contribution equation of state: 1. Prediction of fluid densities for pure compounds with a volume translated Peng-Robinson equation of state. Fluid Phase Equilibria 191:177–188
13. Bronstein IN, Semendjajew KA (2000) Taschenbuch der Mathematik. Verlag Harri Deutsch, Leipzig
14. Wagner W (1973) New vapour pressure measurements for argon and nitrogen and a new method of establishing rational vapour pressure equations. Cryogenics. August 470–482
15. McGarry J (1983) Correlation and prediction of vapor pressures of pure liquids over large pressure ranges. Ind Eng Chem Proc Des Dev 22:313–322
16. Li P, Ma P-S, Yi S-Z, Zhao Z-G, Cong L-Z (1994) A new Corresponding-States Group-Contribution method (CSGC) for estimating vapor pressures of pure compounds. Fluid Phase Equilibria 101:101–119
17. Riedel L (1957) Die Berechnung unbekannter thermischer Daten mit Hilfe des erweiterten Korrespondenzprinzips. Kältetechnik 9(5):127–134
18. Vetere A (1991) Predicting the vapor pressures of pure compounds by using the Wagner equation. Fluid Phase Equilibria 62:1–10
19. Nannoolal Y, Rarey J, Ramjugernath D (2008) Estimation of Pure Component Properties, Part 3: Estimation of the Vapor Pressure of Non-Electrolyte Organic Compounds via Group Contributions and Group Interactions. Fluid Phase Equilibria 269(1–2):117–133
20. Hoffmann W, Florin F (1943) Zweckmäßige Darstellung von Dampfdruckkurven. Verfahrenstechnik, Z. VDI-Beiheft Nr. 2
21. Löffler HJ (1969) Thermodynamik. Grundlagen und Anwendung auf reine Stoffe. Springer-Verlag, Berlin/Heidelberg/New York
22. Moore WJ, Hummel DO (1986) Physikalische Chemie. Verlag Walter de Gruyter, Berlin
23. Aly FA, Lee LL (1981) Self consistent equations for calculating the ideal gas heat capacity, enthalpy and entropy. Fluid Phase Equilibria 6:169–179
24. Kleiber M (2003) The trouble with c_p^{liq}. Ind. Eng. Chem. Res. 42:2007–2014
25. Sastri SRS, Rao KK (1992) A new group contribution method for predicting viscosity of organic liquids. Chem Eng J 50:9
26. Sastri SRS, Rao KK (2000) A new method for predicting saturated liquid viscosity at temperatures above the normal boiling point. Fluid Phase Equilibria 175:311–323
27. van Velzen D, Lopes Cardozo R, Langenkamp H (1972) A Liquid Viscosity – Temperature - Chemical Constitution Relation for Organic Compunds. Ind Eng Chem Fundam 11(1):20–25
28. Nannoolal Y (2006) Development and Critical Evaluation of Group Contribution Methods for the Estimation of Critical Properties, Liquid Vapor Pressure and Liquid Viscosity of Organic Compounds. Thesis, University of Kwazulu-Natal, December
29. Lucas K (1981) Die Druckabhängigkeit der Viskosität von Flüssigkeiten - eine einfache Abschätzung. Chem.-Ing.-Tech. 53:959–960
30. Lucas K, Luckas M (2002) VDI-Wärmeatlas, 9. Auflage Abschnitt D. Springer Verlag, Berlin/Heidelberg/New York
31. Wagner W (2005) FLUIDCAL. Software Package, Ruhr-Universität Bochum
32. Wilke CR (1950) A viscosity equation for gas mixtures. J Chem Phys 18:517
33. Jamieson DT (1979) Thermal conductivity of liquids. J. Chem. Eng. Data 24:244
34. Reid RC, Prausnitz JM, Poling BE (1987) The properties of gases and liquids. McGraw-Hill,New York
35. Li CC (1976) Thermal conductivity of liquid mixtures. AIChE J 22:927–930
36. Chung T-H, Ajlan M, Lee LL, Starling KE (1988) Generalized Multiparameter Correlation for Nonpolar and Polar Fluid Transport Properties. Ind Eng Chem Res 27:671
37. Stiel LI, Thodos G (1964) The Thermal Conductivity of Nonpolar Substances in the Dense Gaseous and Liquid Regions. AIChE J 10:26
38. Fuller EN, Ensley K, Giddings JC (1969) Diffusion of halogenated hydrocarbons in helium. J Phys Chem 73:3679
39. Duncan JB, Toor HL (1962) An experimental study of three component gas diffusion. AIChE J 8(1):38–41

D2.1 Properties of Water and Steam

Wolfgang Wagner[1] · *Hans-Joachim Kretzschmar*[2]
[1]Ruhr-Universität Bochum, Bochum, Germany
[2]Hochschule Zittau/Görlitz, University of Applied Sciences, Zittau, Germany

1 Introduction

The International Association for the Properties of Water and Steam (IAPWS) adopted two international standards for the thermodynamic properties of water substance.

The scientific equation of state was adopted in 1995 and is called "The IAPWS Formulation 1995 for the Thermodynamic Properties of Ordinary Water Substance for General and Scientific Use" [1] or just IAPWS-95 for short. The formulation is valid in the entire stable fluid region of H_2O from the melting curve to 1,000°C at pressures up to 10,000 bar; the lowest temperature on the melting curve is $t = -21.985$°C (at 2099 bar). In this entire region, IAPWS-95 represents the most accurate experimental data within their uncertainties. This formulation can be reasonably extrapolated far beyond its range of validity. A comprehensive article [2] describes all details about this formulation.

The industrial standard for the thermodynamic properties of water and steam was adopted in 1997 and is called "IAPWS Industrial Formulation 1997 for the Thermodynamic Properties of Water and Steam" [3] or "IAPWS-IF97" for short. IAPWS-IF97 consists of a set of equations for different regions that covers the following range of validity:

$$0°C \le t \le 800°C \qquad p \le 1000 \text{ bar}$$
$$800°C < t \le 2000°C \qquad p \le 500 \text{ bar}$$

This industrial standard has been coupled to the scientific standard IAPWS-95 by fitting the basic equations of IAPWS-IF97 to values of several thermodynamic properties calculated from IAPWS-95. The Industrial Formulation IAPWS-IF97 is comprehensively described in the book "International Steam Tables" [4].

2 Tables of Thermophysical Properties

The values of the thermophysical properties listed in the following tables were calculated from the Industrial Formulation IAPWS-IF97 [3, 4], except for the temperature range $t < 0$°C of Table 1. The tabulated values of the transport properties were calculated from the current IAPWS equations for the thermal conductivity [5] and the dynamic viscosity [6], each in the version for industrial use. These equations are also given in the latest International Steam Tables [4]. Apart from the basic equations of IAPWS-IF97, this book contains all backward equations that have been developed in the past years. These backward equations allow quick calculations of properties for input values other than (p,T), for example, (p,h), (p,s), and (h,s) without iterations. The book also contains the representation of 25 properties in pressure-temperature diagrams. The property values in Tables 1–14 were calculated with the CD providing the interactive program "IAPWS-IF97 Electronic Steam Tables" that accompanies the International Steam Tables [4]. This software allows the calculation of "personal" steam tables for arbitrary values of pressure and temperature.

Tables 1–14 cover the following properties:

t – Celsius temperature	α_v – Isobaric cubic expansion coefficient, $\alpha_v = (1/v)(\partial v/\partial T)_p$
T – Thermodynamic temperature	
p – Pressure	λ – Thermal conductivity
ρ – Density	η – Dynamic viscosity
v – Specific volume	ν – Kinematic viscosity, $\nu = \eta/\rho$
Z – Compression factor, $Z = p/(\rho RT)$	a – Thermal diffusivity, $a = \lambda/(c_p\,\rho)$
h – Specific enthalpy	Pr – Prandtl number, $\Pr = \eta\, c_p/\lambda$
s – Specific entropy	σ – Surface tension
c_p – Specific isobaric heat capacity	b – Laplace coefficient, $b = \{\sigma/[g(\rho' - \rho'')]\}^{0.5}$, where g is the acceleration of gravity, $g = 9.80655$ m s^{-2}

Further properties are tabulated in the International Steam Tables [4].

The characteristic properties of water are:

Molar mass $\tilde{M} = 18.015\,275$ g mol^{-1}	Triple point: $T_t = 273.16$ K or $t_t = 0.01$°C $p_t = 6.116\,57$ mbar
Specific gas constant $R = 0.461\,526$ kJ kg^{-1} K^{-1}	
Critical point: $T_c = 647.096$ K or $t_c = 373.946$°C $p_c = 220.64$ bar $\rho_c = 322$ kg m^{-3}	Normal boiling point ($p = 1.013\,25$ bar): $T_b = 373.124$ K or $t_b = 99.974$°C

(Continued on page 171)

VDI-GVC (ed.), *VDI Heat Atlas*, DOI 10.1007/978-3-540-77877-6_11,

D2.1. Table 1. Properties of water at the pressure p = 1 bar[a]

t °C	ρ kg m^{-3}	h kJ kg^{-1}	s kJ kg^{-1} K^{-1}	c_p kJ kg^{-1} K^{-1}	α_v 10^{-3} K^{-1}	λ 10^{-3} W m^{-1} K^{-1}	η 10^{-6} Pa s	ν 10^{-6} m^2 s^{-1}	a 10^{-6} m^2 s^{-1}	Pr –
−20	993.57	−85.624	−0.32600	4.401	−0.6604		4392.1	4.421		
−15	996.30	−63.836	−0.24076	4.321	−0.4488		3348.5	3.361		
−14	996.73	−59.521	−0.22408	4.309	−0.4137		3186.5	3.197		
−13	997.13	−55.217	−0.20751	4.299	−0.3806		3036.6	3.045		
−12	997.49	−50.924	−0.19103	4.289	−0.3492		2897.4	2.905		
−11	997.82	−46.639	−0.17466	4.280	−0.3194		2768.1	2.774		
−10	998.13	−42.363	−0.15838	4.272	−0.2911		2647.7	2.653		
−9	998.40	−38.095	−0.14219	4.265	−0.2641		2535.3	2.539		
−8	998.66	−33.833	−0.12609	4.258	−0.2384		2430.4	2.434		
−7	998.88	−29.579	−0.11007	4.252	−0.2139		2332.1	2.335		
−6	999.08	−25.330	−0.09414	4.246	−0.1904		2240.1	2.242		
−5	999.26	−21.087	−0.07828	4.241	−0.1679		2153.7	2.155		
−4	999.42	−16.849	−0.06251	4.236	−0.1463		2072.4	2.074		
−3	999.55	−12.616	−0.04681	4.231	−0.1255		1996.0	1.997		
−2	999.67	−8.3865	−0.03118	4.227	−0.1055		1924.0	1.925		
−1	999.77	−4.1616	−0.01563	4.223	−0.0863		1856.0	1.856		
0	999.84	0.05966	−0.00015	4.219	−0.0677	562.0	1791.8	1.792	0.1332	13.45
1	999.90	4.2774	0.01526	4.216	−0.0497	564.1	1731.0	1.731	0.1338	12.94
2	999.94	8.4918	0.03061	4.213	−0.0324	566.2	1673.5	1.674	0.1344	12.45
3	999.97	12.703	0.04589	4.210	−0.0156	568.3	1619.0	1.619	0.1350	11.99
4	999.97	16.912	0.06110	4.207	0.0006	570.3	1567.3	1.567	0.1356	11.56
5	999.97	21.118	0.07625	4.205	0.0163	572.3	1518.2	1.518	0.1361	11.15
6	999.94	25.322	0.09134	4.203	0.0315	574.3	1471.5	1.472	0.1367	10.77
7	999.90	29.524	0.10636	4.201	0.0463	576.3	1427.0	1.427	0.1372	10.40
8	999.85	33.723	0.12133	4.199	0.0606	578.2	1384.7	1.385	0.1377	10.06
9	999.78	37.921	0.13623	4.197	0.0746	580.1	1344.4	1.345	0.1382	9.727
10	999.70	42.117	0.15108	4.195	0.0881	582.0	1305.9	1.306	0.1388	9.414
11	999.61	46.312	0.16586	4.194	0.1013	583.8	1269.2	1.270	0.1393	9.117
12	999.50	50.505	0.18060	4.193	0.1142	585.7	1234.0	1.235	0.1398	8.834
13	999.38	54.697	0.19527	4.191	0.1267	587.5	1200.5	1.201	0.1403	8.565
14	999.25	58.888	0.20989	4.190	0.1389	589.3	1168.3	1.169	0.1407	8.308
15	999.10	63.078	0.22446	4.189	0.1509	591.0	1137.6	1.139	0.1412	8.063
20	998.21	84.012	0.29648	4.185	0.2066	599.5	1001.6	1.003	0.1435	6.991
25	997.05	104.93	0.36723	4.182	0.2569	607.5	890.0	0.893	0.1457	6.127
30	995.65	125.83	0.43676	4.180	0.3029	615.0	797.2	0.801	0.1478	5.419
35	994.04	146.73	0.50513	4.179	0.3453	622.0	719.1	0.723	0.1497	4.831
40	992.22	167.62	0.57239	4.179	0.3849	628.6	652.7	0.658	0.1516	4.339
45	990.22	188.52	0.63859	4.179	0.4222	634.8	595.8	0.602	0.1534	3.922
50	988.05	209.41	0.70375	4.180	0.4574	640.5	546.5	0.553	0.1551	3.566
55	985.71	230.31	0.76794	4.181	0.4910	645.8	503.6	0.511	0.1567	3.260
60	983.21	251.22	0.83117	4.183	0.5231	650.8	466.0	0.474	0.1582	2.995
65	980.57	272.14	0.89350	4.185	0.5541	655.4	432.9	0.441	0.1597	2.764
70	977.78	293.07	0.95495	4.188	0.5841	659.6	403.6	0.413	0.1611	2.562
75	974.86	314.02	1.0156	4.192	0.6132	663.5	377.4	0.387	0.1624	2.384
80	971.80	334.99	1.0754	4.196	0.6417	667.0	354.1	0.364	0.1636	2.227
85	968.62	355.98	1.1344	4.200	0.6695	670.2	333.1	0.344	0.1647	2.087

D2.1. Table 1. (continued)

t °C	ρ kg m^{-3}	h kJ kg^{-1}	s kJ kg^{-1} K^{-1}	c_p kJ kg^{-1} K^{-1}	α_v 10^{-3} K^{-1}	λ 10^{-3} W m^{-1} K^{-1}	η 10^{-6} Pa s	ν 10^{-6} m^2 s^{-1}	a 10^{-6} m^2 s^{-1}	Pr –
90	965.32	376.99	1.1926	4.205	0.6970	673.0	314.2	0.325	0.1658	1.963
95	961.89	398.03	1.2502	4.211	0.7241	675.5	297.1	0.309	0.1668	1.852
99.606[b]	958.64	417.44	1.3026	4.216	0.7489	677.6	282.7	0.295	0.1676	1.759

[a]The values for the properties at $t \leq 0°C$ and $p = 1$ bar correspond to the (metastable) subcooled liquid; in the stable state at these t-p values, water is in the solid phase (ice). The values were calculated with the scientific standard equation of state IAPWS-95 [1, 2] that can be extrapolated up to these for $t < 0°C$ temperatures. The equation for λ [4, 5] cannot be extrapolated to temperatures $t < 0°C$; thus, the properties a and Pr cannot be calculated, either.
[b]Temperature at the saturated-liquid line.
t, Temperature; ρ, Density; h, Specific enthalpy; s, Specific entropy; c_p, Specific isobaric heat capacity; α_v, Isobaric cubic expansion coefficient; λ, Thermal conductivity; η, Dynamic viscosity; ν, Kinematic viscosity; a, Thermal diffusivity; Pr, Prandtl number.

D2.1. Table 2. Thermodynamic properties of water in the saturation state from the triple point to the critical point

t	p_s	ρ'	ρ''	h'	h''	s'	s''	c_p'	c_p''	α_v'	α_v''
°C	bar	kg m^{-3}		kJ kg^{-1}		kJ kg^{-1} K^{-1}		kJ kg^{-1} K^{-1}		10^{-3} K^{-1}	
0.00[a]	0.006112	999.79	0.004851	−0.041588	2500.9	−0.000155	9.1558	4.220	1.888	−0.06807	3.681
0.01[b]	0.006117	999.79	0.004854	0.000612	2500.9	0.000000	9.1555	4.220	1.888	−0.06789	3.681
5.00	0.008726	999.92	0.006802	21.019	2510.1	0.076252	9.0249	4.205	1.892	0.01599	3.618
10.00	0.012282	999.65	0.009407	42.021	2519.2	0.15109	8.8998	4.196	1.896	0.08789	3.559
15.00	0.017057	999.05	0.01284	62.984	2528.4	0.22447	8.7804	4.189	1.900	0.1507	3.501
20.00	0.023392	998.16	0.01731	83.920	2537.5	0.29650	8.6661	4.185	1.906	0.2065	3.447
25.00	0.031697	997.00	0.02307	104.84	2546.5	0.36726	8.5568	4.182	1.912	0.2568	3.395
30.00	0.042467	995.61	0.03041	125.75	2555.6	0.43679	8.4521	4.180	1.918	0.3028	3.346
35.00	0.056286	994.00	0.03967	146.64	2564.6	0.50517	8.3518	4.179	1.925	0.3453	3.298
40.00	0.073844	992.18	0.05124	167.54	2573.5	0.57243	8.2557	4.179	1.932	0.3849	3.254
45.00	0.095944	990.18	0.06556	188.44	2582.5	0.63862	8.1634	4.179	1.940	0.4222	3.211
50.00	0.12351	988.01	0.08314	209.34	2591.3	0.70379	8.0749	4.180	1.948	0.4574	3.171
55.00	0.15761	985.67	0.10455	230.24	2600.1	0.76798	7.9899	4.181	1.957	0.4910	3.133
60.00	0.19946	983.18	0.13042	251.15	2608.8	0.83122	7.9082	4.183	1.966	0.5232	3.098
65.00	0.25041	980.53	0.16145	272.08	2617.5	0.89354	7.8296	4.185	1.976	0.5542	3.064
70.00	0.31201	977.75	0.19842	293.02	2626.1	0.95499	7.7540	4.188	1.987	0.5841	3.033
75.00	0.38595	974.83	0.24218	313.97	2634.6	1.0156	7.6812	4.192	1.999	0.6133	3.005
80.00	0.47415	971.78	0.29366	334.95	2643.0	1.0754	7.6110	4.196	2.012	0.6417	2.979
85.00	0.57867	968.60	0.35387	355.95	2651.3	1.1344	7.5434	4.200	2.026	0.6696	2.955
90.00	0.70182	965.30	0.42388	376.97	2659.5	1.1927	7.4781	4.205	2.042	0.6970	2.934
95.00	0.84609	961.89	0.50489	398.02	2667.6	1.2502	7.4150	4.211	2.059	0.7241	2.916
100.00	1.0142	958.35	0.59814	419.10	2675.6	1.3070	7.3541	4.217	2.077	0.7510	2.901
110.00	1.4338	950.95	0.82686	461.36	2691.1	1.4187	7.2380	4.230	2.121	0.8044	2.880
120.00	1.9867	943.11	1.1220	503.78	2705.9	1.5278	7.1291	4.246	2.174	0.8580	2.871
130.00	2.7026	934.83	1.4968	546.39	2720.1	1.6346	7.0264	4.265	2.237	0.9124	2.876
140.00	3.6150	926.13	1.9665	589.20	2733.4	1.7393	6.9293	4.286	2.311	0.9683	2.894
150.00	4.7610	917.01	2.5478	632.25	2745.9	1.8420	6.8370	4.310	2.396	1.026	2.927
160.00	6.1814	907.45	3.2593	675.57	2757.4	1.9428	6.7491	4.338	2.492	1.087	2.975
170.00	7.9205	897.45	4.1217	719.21	2767.9	2.0419	6.6649	4.369	2.599	1.152	3.038
180.00	10.026	887.01	5.1583	763.19	2777.2	2.1395	6.5841	4.406	2.716	1.222	3.117
190.00	12.550	876.08	6.3948	807.57	2785.3	2.2358	6.5060	4.447	2.846	1.297	3.214
200.00	15.547	864.67	7.8603	852.39	2792.1	2.3308	6.4303	4.494	2.990	1.379	3.332
210.00	19.074	852.73	9.5875	897.73	2797.4	2.4248	6.3565	4.548	3.150	1.469	3.474

D2.1. Table 2. (continued)

t °C	p_s bar	ρ' kg m^{-3}	ρ'' kg m^{-3}	h' kJ kg^{-1}	h'' kJ kg^{-1}	s' kJ kg^{-1} K^{-1}	s'' kJ kg^{-1} K^{-1}	c_p' kJ kg^{-1} K^{-1}	c_p'' kJ kg^{-1} K^{-1}	α_v' 10^{-3} K^{-1}	α_v'' 10^{-3} K^{-1}
220.00	23.193	840.23	11.614	943.64	2801.1	2.5178	6.2842	4.611	3.328	1.570	3.643
230.00	27.968	827.12	13.984	990.21	2803.0	2.6102	6.2131	4.683	3.528	1.683	3.845
240.00	33.467	813.36	16.748	1037.5	2803.1	2.7019	6.1425	4.767	3.755	1.811	4.085
250.00	39.759	798.89	19.965	1085.7	2801.0	2.7934	6.0722	4.865	4.012	1.958	4.372
260.00	46.921	783.62	23.710	1134.8	2796.6	2.8847	6.0017	4.981	4.308	2.130	4.717
270.00	55.028	767.46	28.072	1185.1	2789.7	2.9762	5.9304	5.119	4.655	2.334	5.137
280.00	64.165	750.27	33.163	1236.7	2779.8	3.0681	5.8578	5.286	5.070	2.580	5.658
290.00	74.416	731.91	39.128	1289.8	2766.6	3.1608	5.7832	5.492	5.581	2.886	6.316
300.00	85.877	712.14	46.162	1344.8	2749.6	3.2547	5.7058	5.752	6.223	3.274	7.167
310.00	98.647	690.67	54.529	1402.0	2727.9	3.3506	5.6243	6.088	7.051	3.785	8.297
320.00	112.84	667.08	64.616	1462.1	2700.7	3.4491	5.5373	6.541	8.157	4.483	9.858
330.00	128.58	640.78	77.018	1525.7	2666.2	3.5516	5.4425	7.189	9.738	5.504	12.16
340.00	146.00	610.68	92.731	1594.4	2622.1	3.6599	5.3359	8.217	12.24	7.186	15.89
350.00	165.29	574.69	113.62	1670.9	2563.6	3.7783	5.2109	10.10	16.64	10.36	22.66
360.00	186.66	527.84	143.99	1761.5	2481.0	3.9164	5.0527	14.87	27.57	18.81	39.74
370.00	210.43	450.03	202.18	1892.6	2333.5	4.1142	4.7996	47.10	93.40	79.65	148.0
373.00	218.13	395.81	248.68	1974.1	2227.6	4.2377	4.6299	231.91	401.13	435.72	679.1
373.946[c]	220.64	322.00		2087.5		4.4120		∞[d]		∞[d]	

[a]The values at $t = 0°C$ were determined by extrapolating the saturation curves from $t = 0.01°C$ (triple-point temperature) to $t = 0°C$.
[b]Triple-point temperature.
[c]Critical temperature.
[d]At the critical point, IAPWS-IF97 does not yield accurate values for c_p and α_v.
t, Temperature; p_s, Saturation pressure; ρ, Density; h, Specific enthalpy; s, Specific entropy; c_p, Specific isobaric heat capacity; α_v, Isobaric cubic expansion coefficient; ′, Saturated liquid; ″, Saturated vapor.

D2.1. Table 3. Transport properties of water in the saturation state from the triple point to the critical point

t °C	p_s bar	λ' 10^{-3} W m^{-1} K^{-1}	λ'' 10^{-3} W m^{-1} K^{-1}	η' 10^{-6} Pa s	η'' 10^{-6} Pa s	ν' 10^{-6} m^2 s^{-1}	ν'' 10^{-6} m^2 s^{-1}	Pr′ –	Pr″ –	σ 10^{-3} N m^{-1}	b 10^{-3} m
0.00[a]	0.006112	562.0	16.49	1792.0	8.945	1.792	1844.0	13.46	1.024	75.65	2.778
0.01[b]	0.006117	562.0	16.49	1791.4	8.946	1.792	1842.8	13.45	1.024	75.65	2.778
5.00	0.008726	572.3	16.85	1518.3	9.090	1.518	1336.4	11.16	1.020	74.94	2.765
10.00	0.012282	581.9	17.21	1306.0	9.238	1.306	982.1	9.417	1.017	74.22	2.752
15.00	0.017057	591.0	17.58	1137.6	9.390	1.139	731.3	8.065	1.015	73.49	2.739
20.00	0.023392	599.5	17.95	1001.6	9.544	1.003	551.3	6.993	1.013	72.74	2.726
25.00	0.031697	607.5	18.33	890.0	9.701	0.8927	420.5	6.128	1.012	71.97	2.713
30.00	0.042467	615.0	18.71	797.2	9.860	0.8007	324.2	5.419	1.011	71.19	2.700
35.00	0.056286	622.0	19.09	719.1	10.02	0.7235	252.6	4.832	1.010	70.40	2.688
40.00	0.073844	628.6	19.48	652.7	10.18	0.6579	198.8	4.339	1.010	69.60	2.675
45.00	0.095944	634.7	19.88	595.8	10.35	0.6017	157.9	3.922	1.010	68.78	2.661
50.00	0.12351	640.5	20.28	546.5	10.52	0.5531	126.5	3.567	1.010	67.94	2.648
55.00	0.15761	645.8	20.69	503.6	10.68	0.5109	102.2	3.260	1.011	67.10	2.635
60.00	0.19946	650.8	21.10	466.0	10.85	0.4740	83.22	2.995	1.011	66.24	2.621
65.00	0.25041	655.3	21.53	432.9	11.02	0.4415	68.28	2.765	1.012	65.37	2.607
70.00	0.31201	659.6	21.96	403.5	11.19	0.4127	56.42	2.562	1.013	64.48	2.593
75.00	0.38595	663.4	22.41	377.4	11.37	0.3872	46.93	2.385	1.014	63.58	2.579
80.00	0.47415	667.0	22.86	354.0	11.54	0.3643	39.29	2.227	1.016	62.67	2.565
85.00	0.57867	670.1	23.32	333.1	11.71	0.3439	33.10	2.087	1.017	61.75	2.550
90.00	0.70182	673.0	23.80	314.2	11.89	0.3255	28.04	1.963	1.019	60.82	2.535

D2.1. Table 3. (continued)

t °C	p_s bar	λ' 10^{-3} W m^{-1} K^{-1}	λ'' 10^{-3} W m^{-1} K^{-1}	η' 10^{-6} Pa s	η'' 10^{-6} Pa s	ν' 10^{-6} m^2 s^{-1}	ν'' 10^{-6} m^2 s^{-1}	Pr′ –	Pr″ –	σ 10^{-3} N m^{-1}	b 10^{-3} m
95.00	0.84609	675.5	24.29	297.1	12.06	0.3089	23.88	1.852	1.022	59.87	2.520
100.00	1.0142	677.8	24.79	281.6	12.23	0.2938	20.45	1.752	1.025	58.91	2.504
110.00	1.4338	681.3	25.85	254.6	12.58	0.2677	15.21	1.581	1.032	56.96	2.473
120.00	1.9867	683.6	26.96	232.0	12.93	0.2460	11.52	1.441	1.042	54.97	2.439
130.00	2.7026	684.8	28.15	212.9	13.27	0.2278	8.867	1.326	1.055	52.93	2.405
140.00	3.6150	684.9	29.42	196.6	13.62	0.2123	6.925	1.231	1.070	50.86	2.369
150.00	4.7610	683.9	30.77	182.6	13.96	0.1991	5.480	1.151	1.087	48.74	2.331
160.00	6.1814	681.8	32.22	170.4	14.30	0.1878	4.389	1.084	1.106	46.59	2.292
170.00	7.9205	678.7	33.77	159.8	14.64	0.1780	3.553	1.029	1.127	44.41	2.251
180.00	10.026	674.6	35.42	150.4	14.99	0.1695	2.905	0.9821	1.149	42.19	2.209
190.00	12.550	669.5	37.19	142.0	15.33	0.1621	2.397	0.9435	1.173	39.95	2.164
200.00	15.547	663.4	39.10	134.6	15.67	0.1557	1.993	0.9118	1.198	37.67	2.117
210.00	19.074	656.3	41.14	127.9	16.01	0.1500	1.670	0.8862	1.226	35.38	2.069
220.00	23.193	648.2	43.34	121.8	16.35	0.1449	1.408	0.8662	1.256	33.07	2.017
230.00	27.968	639.1	45.72	116.2	16.70	0.1405	1.195	0.8514	1.289	30.74	1.963
240.00	33.467	629.0	48.32	111.1	17.06	0.1365	1.019	0.8417	1.326	28.39	1.906
250.00	39.759	617.8	51.16	106.3	17.43	0.1330	0.8730	0.8369	1.367	26.04	1.846
260.00	46.921	605.6	54.30	101.8	17.81	0.1299	0.7511	0.8374	1.413	23.69	1.783
270.00	55.028	592.2	57.81	97.58	18.21	0.1272	0.6486	0.8434	1.466	21.34	1.715
280.00	64.165	577.7	61.79	93.55	18.63	0.1247	0.5618	0.8559	1.529	18.99	1.643
290.00	74.416	562.0	66.37	89.66	19.08	0.1225	0.4877	0.8761	1.605	16.66	1.566
300.00	85.877	545.0	71.75	85.86	19.58	0.1206	0.4242	0.9061	1.698	14.36	1.483
310.00	98.647	526.5	78.24	82.09	20.13	0.1189	0.3693	0.9493	1.815	12.09	1.392
320.00	112.84	506.5	86.35	78.31	20.77	0.1174	0.3215	1.011	1.962	9.864	1.292
330.00	128.58	484.8	96.96	74.43	21.53	0.1162	0.2796	1.104	2.163	7.703	1.180
340.00	146.00	461.4	111.7	70.33	22.48	0.1152	0.2424	1.252	2.462	5.625	1.052
350.00	165.29	436.5	134.5	65.80	23.74	0.1145	0.2089	1.523	2.936	3.665	0.9004
360.00	186.66	411.9	176.6	60.32	25.64	0.1143	0.1781	2.178	4.002	1.877	0.7062
370.00	210.43	418.1	309.5	51.90	29.60	0.1153	0.1464	5.846	8.933	0.3882	0.3997
373.00	218.13	535.0	507.0	46.38	33.11	0.1172	0.1331	20.11	26.19	0.0648	0.2118
373.946[c]	220.64	–[d]		39.33		0.1221		∞[e]		0	0

[a]The values at $t = 0°C$ were determined by extrapolating the saturation curves from $t = 0.01°C$ (triple-point temperature) to $t = 0°C$.
[b]Triple-point temperature.
[c]Critical temperature.
[d]The industrial equations for λ [4, 5] and η [4, 6] do not represent the critical enhancement in the near-critical region. If more accurate values are needed in this region, the scientific equations for λ [5] and η [6] should be used.
[e]In the near-critical region, the use of IAPWS-IF97 for c_p and the use of the industrial equations for λ [4, 5] and η [4, 6] do not yield accurate values for Pr.
t, Temperature; p_s; Saturation pressure; λ, Thermal conductivity; η, Dynamic viscosity; ν, Kinematic viscosity; Pr, Prandtl number; σ, Surface tension; b, Laplace coefficient; ′, Saturated liquid; ″, Saturated vapor.

D2.1. Table 4. Density ρ/(kg m^{-3}) of water for given values of pressure and temperature[a]

Pressure p bar	Temperature t / °C									
	0	25	50	75	100	125	150	200	250	300
1	999.84[b]	997.05	988.05	974.86	0.5896	0.5503	0.5163	0.4603	0.4156	0.3790
5	1000.0	997.23	988.22	975.03	958.54	939.16	917.02	2.3528	2.1078	1.9135
10	1000.3	997.45	988.44	975.25	958.77	939.41	917.30	4.8543	4.2967	3.8763
20	1000.8	997.90	988.87	975.70	959.24	939.92	917.87	865.01	8.9699	7.9681
30	1001.3	998.35	989.30	976.14	959.71	940.43	918.43	865.77	14.160	12.319
40	1001.8	998.80	989.74	976.58	960.17	940.93	919.00	866.52	798.92	16.987

D2.1. Table 4. (continued)

Pressure p bar	Temperature t / °C									
	0	25	50	75	100	125	150	200	250	300
50	1002.3	999.24	990.17	977.02	960.64	941.43	919.56	867.27	800.08	22.052
60	1002.8	999.69	990.60	977.45	961.10	941.93	920.11	868.02	801.23	27.631
70	1003.3	1000.1	991.03	977.89	961.56	942.43	920.67	868.75	802.37	33.905
80	1003.8	1000.6	991.46	978.33	962.02	942.93	921.22	869.49	803.49	41.186
90	1004.3	1001.0	991.88	978.76	962.47	943.43	921.77	870.22	804.60	713.07
100	1004.8	1001.5	992.31	979.19	962.93	943.92	922.32	870.95	805.70	715.29
150	1007.3	1003.7	994.43	981.35	965.20	946.37	925.03	874.51	811.02	725.55
200	1009.7	1005.8	996.53	983.48	967.43	948.78	927.69	877.97	816.09	734.71
250	1012.2	1008.0	998.60	985.58	969.64	951.16	930.30	881.34	820.92	743.01
300	1014.5	1010.1	1000.7	987.66	971.82	953.50	932.86	884.62	825.55	750.64
350	1016.9	1012.2	1002.7	989.72	973.97	955.80	935.38	887.82	830.00	757.72
400	1019.2	1014.3	1004.7	991.76	976.10	958.07	937.86	890.94	834.28	764.34
450	1021.5	1016.4	1006.7	993.77	978.19	960.31	940.30	893.99	838.41	770.57
500	1023.8	1018.4	1008.7	995.77	980.27	962.52	942.70	896.98	842.40	776.46
600	1028.3	1022.5	1012.6	999.69	984.34	966.85	947.39	902.75	850.02	787.38
700	1032.7	1026.4	1016.4	1003.5	988.32	971.07	951.94	908.29	857.20	797.36
800	1037.0	1030.3	1020.1	1007.3	992.22	975.18	956.36	913.62	864.00	806.58
900	1041.2	1034.1	1023.8	1011.0	996.02	979.19	960.66	918.77	870.47	815.15
1000	1045.3	1037.9	1027.4	1014.6	999.75	983.12	964.85	923.74	876.65	823.18

Pressure p bar	Temperature t / °C									
	350	400	450	500	550	600	650	700	750	800
1	0.3483	0.3223	0.2999	0.2805	0.2634	0.2483	0.2348	0.2227	0.2118	0.2019
5	1.7540	1.6200	1.5056	1.4066	1.3200	1.2436	1.1757	1.1149	1.0601	1.0104
10	3.5399	3.2616	3.0263	2.8240	2.6479	2.4931	2.3557	2.2330	2.1226	2.0227
20	7.2153	6.6134	6.1148	5.6922	5.3278	5.0097	4.7289	4.4791	4.2551	4.0529
30	11.043	10.063	9.2692	8.6064	8.0407	7.5503	7.1199	6.7384	6.3975	6.0905
40	15.043	13.618	12.493	11.569	10.788	10.116	9.5290	9.0112	8.5499	8.1357
50	19.241	17.289	15.792	14.581	13.570	12.706	11.956	11.298	10.712	10.188
60	23.667	21.087	19.169	17.646	16.388	15.322	14.403	13.598	12.885	12.249
70	28.357	25.024	22.630	20.765	19.243	17.965	16.868	15.912	15.068	14.317
80	33.358	29.114	26.180	23.941	22.138	20.634	19.352	18.240	17.261	16.392
90	38.732	33.374	29.826	27.177	25.071	23.332	21.857	20.582	19.465	18.475
100	44.559	37.822	33.574	30.476	28.046	26.057	24.381	22.939	21.679	20.566
150	87.103	63.812	54.118	48.011	43.582	40.127	37.309	34.941	32.909	31.135
200	600.65	100.51	78.615	67.600	60.348	54.992	50.776	47.320	44.405	41.896
250	625.47	166.53	108.99	89.750	78.522	70.723	64.810	60.084	56.171	52.847
300	643.95	357.60	148.41	115.07	98.285	87.380	79.430	73.238	68.203	63.984
350	659.00	474.92	201.66	144.23	119.79	105.01	94.645	86.778	80.495	75.300
400	671.86	523.37	270.80	177.78	143.16	123.62	110.45	100.69	93.037	86.784
450	683.16	554.46	343.02	215.78	168.40	143.21	126.83	114.97	105.81	98.424
500	693.27	577.74	402.02	257.11	195.37	163.70	143.73	129.57	118.80	110.20
600	710.89	612.39	479.69	338.80	252.86	206.89	178.86	159.61	145.31	134.11
700	726.04	638.41	528.52	406.02	310.25	251.58	215.13	190.41	172.31	158.31
800	739.40	659.49	563.73	457.03	362.31	295.54	251.57	221.43	199.47	182.61
900	751.40	677.35	591.36	496.46	406.89	336.75	287.17	252.12	226.46	206.78
1000	762.33	692.92	614.19	528.20	444.48	374.22	321.08	282.00	252.96	230.65

[a]The bold horizontal lines in the columns indicate the transition from the liquid phase to the gas phase.

[b]The values for the properties at $t = 0$°C and $p = 1$ bar correspond to the (metastable) subcooled liquid; in the stable state at these t-p values, water is in the solid phase (ice).

D2.1. Table 5. Compression factor Z of water for given values of pressure and temperature[a]

Pressure p bar	Temperature t / °C									
	0	25	50	75	100	125	150	200	250	300
1	0.000793[b]	0.000729	0.000679	0.000638	0.9848	0.9890	0.9917	0.9949	0.9966	0.9976
5	0.003966	0.003644	0.003392	0.003191	0.003029	0.002897	0.002792	0.9732	0.9825	0.9878
10	0.007930	0.007286	0.006783	0.006381	0.006056	0.005793	0.005582	0.9434	0.9639	0.9753
20	0.01585	0.01457	0.01356	0.01276	0.01211	0.01158	0.01116	0.01059	0.9235	0.9489
30	0.02377	0.02184	0.02033	0.01913	0.01815	0.01736	0.01673	0.01587	0.8775	0.9206
40	0.03167	0.02910	0.02710	0.02549	0.02419	0.02313	0.02229	0.02114	0.02074	0.8902
50	0.03957	0.03636	0.03386	0.03185	0.03022	0.02890	0.02784	0.02640	0.02588	0.8571
60	0.04746	0.04362	0.04061	0.03820	0.03625	0.03466	0.03339	0.03165	0.03101	0.8209
70	0.05534	0.05086	0.04736	0.04455	0.04227	0.04042	0.03893	0.03690	0.03613	0.7805
80	0.06322	0.05810	0.05410	0.05089	0.04829	0.04617	0.04447	0.04213	0.04124	0.7343
90	0.07108	0.06534	0.06084	0.05723	0.05430	0.05191	0.05000	0.04736	0.04633	0.04771
100	0.07894	0.07257	0.06757	0.06356	0.06030	0.05765	0.05552	0.05258	0.05140	0.05285
150	0.1181	0.1086	0.1011	0.09513	0.09024	0.08626	0.08303	0.07855	0.07660	0.07816
200	0.1571	0.1445	0.1346	0.1266	0.1200	0.1147	0.1104	0.1043	0.1015	0.1029
250	0.1959	0.1802	0.1679	0.1579	0.1497	0.1430	0.1376	0.1299	0.1261	0.1272
300	0.2346	0.2158	0.2010	0.1890	0.1792	0.1712	0.1647	0.1553	0.1505	0.1511
350	0.2730	0.2513	0.2340	0.2201	0.2087	0.1993	0.1916	0.1805	0.1746	0.1746
400	0.3113	0.2866	0.2669	0.2510	0.2380	0.2272	0.2184	0.2056	0.1986	0.1978
450	0.3494	0.3218	0.2997	0.2818	0.2671	0.2550	0.2451	0.2305	0.2223	0.2208
500	0.3874	0.3568	0.3324	0.3125	0.2962	0.2827	0.2716	0.2553	0.2458	0.2434
600	0.4628	0.4264	0.3973	0.3735	0.3539	0.3377	0.3243	0.3044	0.2923	0.2881
700	0.5377	0.4956	0.4618	0.4341	0.4113	0.3923	0.3765	0.3529	0.3382	0.3319
800	0.6120	0.5643	0.5258	0.4943	0.4682	0.4464	0.4283	0.4010	0.3835	0.3750
900	0.6857	0.6325	0.5894	0.5540	0.5247	0.5002	0.4797	0.4486	0.4282	0.4174
1000	0.7589	0.7002	0.6526	0.6134	0.5808	0.5535	0.5307	0.4957	0.4724	0.4592

Pressure p bar	Temperature t / °C									
	350	400	450	500	550	600	650	700	750	800
1	0.9983	0.9987	0.9990	0.9992	0.9994	0.9995	0.9996	0.9997	0.9998	0.9998
5	0.9912	0.9935	0.9951	0.9962	0.9970	0.9977	0.9982	0.9985	0.9988	0.9991
10	0.9822	0.9869	0.9901	0.9924	0.9941	0.9954	0.9963	0.9971	0.9977	0.9982
20	0.9638	0.9734	0.9800	0.9847	0.9881	0.9907	0.9927	0.9942	0.9954	0.9963
30	0.9446	0.9596	0.9697	0.9769	0.9821	0.9860	0.9890	0.9913	0.9931	0.9945
40	0.9245	0.9454	0.9593	0.9690	0.9760	0.9813	0.9852	0.9883	0.9908	0.9927
50	0.9035	0.9309	0.9487	0.9610	0.9699	0.9765	0.9815	0.9854	0.9884	0.9909
60	0.8815	0.9159	0.9379	0.9529	0.9637	0.9717	0.9778	0.9824	0.9861	0.9890
70	0.8583	0.9004	0.9268	0.9447	0.9575	0.9669	0.9740	0.9795	0.9838	0.9872
80	0.8339	0.8845	0.9156	0.9365	0.9512	0.9621	0.9703	0.9765	0.9815	0.9854
90	0.8079	0.8680	0.9041	0.9281	0.9449	0.9572	0.9665	0.9736	0.9791	0.9836
100	0.7803	0.8510	0.8924	0.9196	0.9385	0.9523	0.9627	0.9706	0.9768	0.9817
150	0.5988	0.7566	0.8305	0.8756	0.9060	0.9276	0.9436	0.9558	0.9653	0.9727
200	0.1158	0.6405	0.7623	0.8291	0.8724	0.9025	0.9245	0.9410	0.9538	0.9638
250	0.1390	0.4832	0.6873	0.7806	0.8381	0.8772	0.9054	0.9264	0.9425	0.9551
300	0.1620	0.2700	0.6057	0.7306	0.8035	0.8520	0.8865	0.9120	0.9315	0.9467
350	0.1847	0.2372	0.5200	0.6801	0.7691	0.8271	0.8680	0.8980	0.9208	0.9385
400	0.2070	0.2460	0.4426	0.6305	0.7355	0.8029	0.8500	0.8845	0.9105	0.9306
450	0.2290	0.2612	0.3931	0.5844	0.7034	0.7798	0.8328	0.8715	0.9006	0.9231
500	0.2508	0.2786	0.3726	0.5450	0.6737	0.7579	0.8165	0.8592	0.8913	0.9160
600	0.2935	0.3154	0.3748	0.4963	0.6246	0.7197	0.7873	0.8370	0.8744	0.9033

D2.1. Table 5. (continued)

Pressure p bar	Temperature t / °C									
	350	400	450	500	550	600	650	700	750	800
700	0.3352	0.3529	0.3968	0.4832	0.5939	0.6905	0.7637	0.8185	0.8603	0.8928
800	0.3762	0.3905	0.4252	0.4905	0.5812	0.6717	0.7464	0.8044	0.8493	0.8845
900	0.4165	0.4277	0.4560	0.5080	0.5822	0.6632	0.7356	0.7948	0.8416	0.8788
1000	0.4561	0.4645	0.4878	0.5306	0.5922	0.6631	0.7310	0.7896	0.8372	0.8754

[a]The bold horizontal lines in the columns indicate the transition from the liquid phase to the gas phase.
[b]The values for the properties at $t = 0$°C and $p = 1$ bar correspond to the (metastable) subcooled liquid; in the stable state at these t-p values, water is in the solid phase (ice).

D2.1. Table 6. Specific enthalpy h/(kJ kg^{-1}) of water for given values of pressure and temperature[a]

Pressure p bar	Temperature t / °C									
	0	25	50	75	100	125	150	200	250	300
1	0.05966[b]	104.93	209.41	314.02	2675.8	2726.7	2776.6	2875.5	2974.5	3074.5
5	0.46700	105.30	209.76	314.35	419.40	525.25	632.27	2855.9	2961.1	3064.6
10	0.97582	105.76	210.19	314.75	419.77	525.59	632.57	2828.3	2943.2	3051.7
20	1.9923	106.69	211.05	315.56	420.53	526.28	633.19	852.57	2903.2	3024.3
30	3.0072	107.61	211.91	316.36	421.28	526.97	633.81	852.98	2856.5	2994.3
40	4.0206	108.53	212.77	317.17	422.03	527.67	634.43	853.39	1085.7	2961.7
50	5.0325	109.46	213.63	317.98	422.78	528.36	635.06	853.80	1085.7	2925.6
60	6.0429	110.38	214.49	318.78	423.53	529.05	635.68	854.22	1085.7	2885.5
70	7.0517	111.30	215.36	319.59	424.29	529.75	636.30	854.64	1085.6	2839.8
80	8.0591	112.22	216.22	320.40	425.04	530.44	636.93	855.06	1085.7	2786.4
90	9.0649	113.14	217.07	321.20	425.79	531.14	637.56	855.49	1085.7	1344.3
100	10.069	114.06	217.93	322.01	426.55	531.83	638.18	855.92	1085.7	1343.1
150	15.069	118.64	222.23	326.04	430.32	535.32	641.34	858.12	1086.0	1338.1
200	20.034	123.21	226.51	330.07	434.10	538.82	644.52	860.39	1086.6	1334.1
250	24.964	127.76	230.78	334.10	437.88	542.34	647.73	862.73	1087.3	1331.1
300	29.860	132.29	235.05	338.13	441.67	545.87	650.96	865.14	1088.3	1328.7
350	34.724	136.81	239.31	342.16	445.47	549.42	654.22	867.61	1089.4	1326.8
400	39.556	141.30	243.56	346.18	449.27	552.97	657.49	870.12	1090.6	1325.4
450	44.357	145.78	247.80	350.20	453.07	556.53	660.78	872.69	1092.0	1324.4
500	49.129	150.25	252.03	354.22	456.87	560.11	664.10	875.31	1093.4	1323.7
600	58.586	159.14	260.47	362.25	464.49	567.28	670.77	880.67	1096.7	1323.3
700	67.935	167.96	268.88	370.28	472.12	574.49	677.50	886.19	1100.4	1323.7
800	77.180	176.73	277.26	378.28	479.75	581.72	684.29	891.85	1104.3	1324.9
900	86.329	185.44	285.60	386.28	487.39	588.98	691.13	897.63	1108.6	1326.6
1000	95.386	194.10	293.92	394.26	495.04	596.27	698.01	903.51	1113.0	1328.9

Pressure p bar	Temperature t / °C									
	350	400	450	500	550	600	650	700	750	800
1	3175.8	3278.5	3382.8	3488.7	3596.3	3705.6	3816.6	3929.4	4043.9	4160.2
5	3168.1	3272.3	3377.7	3484.4	3592.6	3702.5	3813.9	3927.0	4041.9	4158.4
10	3158.2	3264.4	3371.2	3479.0	3588.1	3698.6	3810.5	3924.1	4039.3	4156.1
20	3137.6	3248.2	3358.1	3468.1	3578.9	3690.7	3803.8	3918.2	4034.2	4151.6
30	3116.1	3231.6	3344.7	3457.0	3569.6	3682.8	3797.0	3912.3	4029.0	4147.0
40	3093.3	3214.4	3331.0	3445.8	3560.2	3674.8	3790.2	3906.4	4023.8	4142.5
50	3069.3	3196.6	3317.0	3434.5	3550.8	3666.8	3783.3	3900.5	4018.6	4137.9

D2.1. Table 6. (continued)

Pressure p bar	Temperature t / °C									
	350	400	450	500	550	600	650	700	750	800
60	3043.9	3178.2	3302.8	3422.9	3541.2	3658.8	3776.4	3894.5	4013.4	4133.3
70	3016.8	3159.1	3288.2	3411.3	3531.5	3650.6	3769.4	3888.5	4008.1	4128.7
80	2988.1	3139.3	3273.2	3399.4	3521.8	3642.4	3762.4	3882.4	4002.9	4124.0
90	2957.2	3118.8	3257.9	3387.3	3511.9	3634.2	3755.4	3876.4	3997.6	4119.4
100	2924.0	3097.4	3242.3	3375.1	3501.9	3625.8	3748.3	3870.3	3992.3	4114.7
150	2693.0	2975.5	3157.8	3310.8	3450.5	3583.3	3712.4	3839.5	3965.6	4091.3
200	1646.0	2816.8	3061.5	3241.2	3396.2	3539.2	3675.6	3808.2	3938.5	4067.7
250	1623.9	2578.6	2950.4	3165.9	3339.3	3493.7	3638.0	3776.4	3911.2	4044.0
300	1608.8	2152.4	2820.9	3084.8	3279.8	3446.9	3599.7	3744.2	3883.8	4020.2
350	1597.5	1988.4	2671.0	2998.0	3218.1	3399.0	3560.9	3711.9	3856.3	3996.5
400	1588.7	1931.1	2511.8	2906.7	3154.6	3350.4	3521.8	3679.4	3828.8	3972.8
450	1581.7	1897.6	2377.3	2813.4	3090.2	3301.5	3482.5	3647.0	3801.3	3949.3
500	1576.0	1874.3	2284.4	2722.5	3025.7	3252.6	3443.5	3614.8	3774.1	3926.0
600	1567.4	1843.1	2179.8	2570.4	2902.1	3157.0	3366.8	3551.4	3720.6	3880.2
700	1561.6	1822.9	2123.4	2466.2	2795.0	3067.5	3293.6	3490.5	3669.0	3835.8
800	1557.7	1808.8	2087.6	2397.6	2709.9	2988.1	3225.7	3432.9	3619.7	3793.3
900	1555.2	1798.6	2062.7	2350.3	2645.2	2920.8	3164.4	3379.5	3573.5	3753.0
1000	1553.9	1791.1	2044.5	2316.2	2596.1	2865.1	3110.6	3330.8	3530.7	3715.2

[a]The bold horizontal lines in the columns indicate the transition from the liquid phase to the gas phase.
[b]The values for the properties at $t = 0$°C and $p = 1$ bar correspond to the (metastable) subcooled liquid; in the stable state at these t-p values, water is in the solid phase (ice).

D2.1. Table 7. Specific entropy s/(kJ kg^{-1} K^{-1}) of water for given values of pressure and temperature[a]

Pressure p bar	Temperature t / °C									
	0	25	50	75	100	125	150	200	250	300
1	−0.00015[b]	0.36723	0.70375	1.0156	7.3610	7.4931	7.6147	7.8356	8.0346	8.2171
5	−0.00012	0.36713	0.70357	1.0153	1.3067	1.5813	1.8419	7.0611	7.2726	7.4614
10	−0.00009	0.36700	0.70334	1.0150	1.3063	1.5808	1.8414	6.6955	6.9266	7.1247
20	−0.00003	0.36674	0.70287	1.0144	1.3055	1.5798	1.8403	2.3301	6.5474	6.7685
30	0.00003	0.36648	0.70241	1.0137	1.3048	1.5789	1.8391	2.3285	6.2893	6.5412
40	0.00009	0.36622	0.70195	1.0131	1.3040	1.5780	1.8380	2.3269	2.7933	6.3638
50	0.00014	0.36596	0.70149	1.0125	1.3032	1.5770	1.8369	2.3254	2.7909	6.2109
60	0.00019	0.36569	0.70103	1.0119	1.3024	1.5761	1.8358	2.3238	2.7885	6.0702
70	0.00023	0.36543	0.70057	1.0112	1.3017	1.5752	1.8347	2.3223	2.7861	5.9335
80	0.00027	0.36516	0.70011	1.0106	1.3009	1.5743	1.8337	2.3207	2.7837	5.7935
90	0.00031	0.36490	0.69965	1.0100	1.3001	1.5734	1.8326	2.3192	2.7814	3.2529
100	0.00034	0.36463	0.69919	1.0094	1.2994	1.5724	1.8315	2.3177	2.7791	3.2484
150	0.00045	0.36328	0.69689	1.0063	1.2956	1.5679	1.8262	2.3102	2.7679	3.2275
200	0.00047	0.36190	0.69460	1.0033	1.2918	1.5635	1.8209	2.3030	2.7572	3.2087
250	0.00041	0.36051	0.69232	1.0003	1.2881	1.5591	1.8158	2.2959	2.7469	3.1915
300	0.00028	0.35908	0.69004	0.99729	1.2845	1.5548	1.8107	2.2890	2.7371	3.1756
350	0.00006	0.35764	0.68777	0.99433	1.2809	1.5505	1.8058	2.2823	2.7276	3.1608
400	−0.00023	0.35618	0.68551	0.99139	1.2773	1.5463	1.8009	2.2758	2.7185	3.1469
450	−0.00059	0.35469	0.68325	0.98848	1.2738	1.5422	1.7961	2.2693	2.7097	3.1338
500	−0.00102	0.35319	0.68099	0.98558	1.2703	1.5381	1.7914	2.2631	2.7012	3.1214
600	−0.00208	0.35012	0.67649	0.97987	1.2634	1.5301	1.7822	2.2509	2.6848	3.0982

D2.1. Table 7. (continued)

Pressure p / bar	Temperature t / °C									
	0	25	50	75	100	125	150	200	250	300
700	−0.00338	0.34698	0.67201	0.97423	1.2567	1.5223	1.7732	2.2392	2.6694	3.0769
800	−0.00491	0.34377	0.66754	0.96866	1.2501	1.5146	1.7645	2.2280	2.6548	3.0572
900	−0.00665	0.34049	0.66309	0.96317	1.2436	1.5071	1.7560	2.2171	2.6408	3.0388
1000	−0.00858	0.33716	0.65864	0.95774	1.2373	1.4998	1.7477	2.2066	2.6275	3.0215
Pressure p / bar	Temperature t / °C									
	350	400	450	500	550	600	650	700	750	800
1	8.3865	8.5451	8.6945	8.8361	8.9709	9.0998	9.2234	9.3424	9.4571	9.5681
5	7.6345	7.7954	7.9464	8.0891	8.2247	8.3543	8.4784	8.5977	8.7128	8.8240
10	7.3028	7.4668	7.6198	7.7640	7.9007	8.0309	8.1557	8.2755	8.3909	8.5024
20	6.9582	7.1290	7.2863	7.4335	7.5723	7.7042	7.8301	7.9509	8.0670	8.1791
30	6.7449	6.9233	7.0853	7.2356	7.3767	7.5102	7.6373	7.7590	7.8759	7.9885
40	6.5843	6.7712	6.9383	7.0919	7.2353	7.3704	7.4989	7.6215	7.7391	7.8523
50	6.4515	6.6481	6.8208	6.9778	7.1235	7.2604	7.3901	7.5137	7.6321	7.7459
60	6.3356	6.5431	6.7216	6.8824	7.0306	7.1692	7.3002	7.4248	7.5439	7.6583
70	6.2303	6.4501	6.6351	6.7997	6.9505	7.0909	7.2232	7.3488	7.4687	7.5837
80	6.1319	6.3657	6.5577	6.7264	6.8798	7.0221	7.1557	7.2823	7.4030	7.5186
90	6.0378	6.2875	6.4871	6.6601	6.8163	6.9605	7.0955	7.2231	7.3446	7.4608
100	5.9458	6.2139	6.4217	6.5993	6.7584	6.9045	7.0409	7.1696	7.2918	7.4087
150	5.4435	5.8817	6.1433	6.3479	6.5230	6.6797	6.8235	6.9576	7.0839	7.2039
200	3.7288	5.5525	5.9041	6.1445	6.3390	6.5077	6.6596	6.7994	6.9301	7.0534
250	3.6803	5.1399	5.6755	5.9642	6.1816	6.3638	6.5246	6.6706	6.8057	6.9324
300	3.6435	4.4750	5.4419	5.7956	6.0403	6.2374	6.4077	6.5602	6.7000	6.8303
350	3.6131	4.2140	5.1945	5.6331	5.9093	6.1229	6.3032	6.4625	6.6072	6.7411
400	3.5870	4.1141	4.9447	5.4746	5.7859	6.0170	6.2079	6.3743	6.5239	6.6614
450	3.5638	4.0505	4.7362	5.3209	5.6685	5.9179	6.1197	6.2932	6.4479	6.5891
500	3.5430	4.0028	4.5892	5.1759	5.5566	5.8245	6.0372	6.2180	6.3777	6.5226
600	3.5064	3.9316	4.4134	4.9356	5.3519	5.6528	5.8867	6.0815	6.2512	6.4034
700	3.4747	3.8778	4.3080	4.7662	5.1786	5.5003	5.7522	5.9600	6.1390	6.2982
800	3.4465	3.8339	4.2331	4.6474	5.0391	5.3674	5.6321	5.8509	6.0382	6.2039
900	3.4211	3.7965	4.1747	4.5593	4.9288	5.2540	5.5255	5.7526	5.9470	6.1184
1000	3.3978	3.7638	4.1267	4.4899	4.8407	5.1580	5.4316	5.6640	5.8644	6.0405

[a]The bold horizontal lines in the columns indicate the transition from the liquid phase to the gas phase.
[b]The values for the properties at $t = 0$°C and $p = 1$ bar correspond to the (metastable) subcooled liquid; in the stable state at these t-p values, water is in the solid phase (ice).

D2.1. Table 8. Specific isobaric heat capacity c_p/(kJ kg^{-1} K^{-1}) of water for given values of pressure and temperature[a]

Pressure p / bar	Temperature t / °C									
	0	25	50	75	100	125	150	200	250	300
1	4.219[b]	4.182	4.180	4.192	2.074	2.011	1.986	1.976	1.989	2.012
5	4.217	4.181	4.179	4.191	4.216	4.255	4.310	2.145	2.078	2.066
10	4.215	4.179	4.177	4.190	4.215	4.253	4.309	2.429	2.212	2.141
20	4.210	4.176	4.175	4.187	4.212	4.251	4.305	4.491	2.560	2.320
30	4.205	4.174	4.173	4.185	4.210	4.248	4.302	4.486	3.077	2.543
40	4.200	4.171	4.171	4.183	4.208	4.245	4.299	4.480	4.865	2.820
50	4.196	4.168	4.168	4.181	4.206	4.243	4.296	4.474	4.851	3.171
60	4.191	4.165	4.166	4.179	4.203	4.240	4.293	4.469	4.838	3.638

D2.1. Table 8. (continued)

Pressure p bar	Temperature t / °C									
	0	25	50	75	100	125	150	200	250	300
70	4.186	4.162	4.164	4.177	4.201	4.238	4.290	4.463	4.825	4.292
80	4.181	4.160	4.162	4.175	4.199	4.235	4.287	4.458	4.812	5.287
90	4.177	4.157	4.159	4.173	4.197	4.233	4.284	4.452	4.800	5.730
100	4.172	4.154	4.157	4.170	4.194	4.230	4.281	4.447	4.788	5.682
150	4.150	4.141	4.147	4.160	4.184	4.218	4.266	4.422	4.732	5.476
200	4.129	4.128	4.136	4.150	4.173	4.206	4.252	4.398	4.682	5.317
250	4.109	4.116	4.126	4.141	4.163	4.195	4.238	4.376	4.637	5.188
300	4.090	4.104	4.116	4.131	4.153	4.184	4.225	4.355	4.596	5.081
350	4.072	4.093	4.107	4.122	4.144	4.173	4.213	4.335	4.558	4.991
400	4.054	4.082	4.097	4.113	4.135	4.163	4.200	4.316	4.523	4.912
450	4.038	4.072	4.088	4.105	4.126	4.153	4.189	4.298	4.491	4.843
500	4.022	4.061	4.080	4.096	4.117	4.143	4.177	4.281	4.461	4.782
600	3.994	4.042	4.063	4.080	4.100	4.125	4.156	4.249	4.407	4.677
700	3.968	4.024	4.047	4.064	4.084	4.107	4.136	4.219	4.360	4.591
800	3.945	4.008	4.032	4.050	4.068	4.090	4.116	4.192	4.317	4.518
900	3.924	3.992	4.018	4.036	4.054	4.074	4.098	4.167	4.279	4.455
1000	3.906	3.978	4.005	4.023	4.040	4.059	4.081	4.144	4.245	4.400

Pressure p bar	Temperature t / °C									
	350	400	450	500	550	600	650	700	750	800
1	2.040	2.070	2.101	2.135	2.169	2.203	2.238	2.273	2.308	2.343
5	2.075	2.095	2.121	2.149	2.180	2.213	2.246	2.280	2.314	2.348
10	2.123	2.128	2.145	2.168	2.195	2.224	2.255	2.287	2.320	2.353
20	2.230	2.200	2.196	2.207	2.225	2.249	2.275	2.303	2.333	2.364
30	2.354	2.278	2.251	2.247	2.256	2.273	2.295	2.320	2.347	2.375
40	2.497	2.364	2.309	2.289	2.288	2.298	2.315	2.336	2.360	2.387
50	2.661	2.459	2.371	2.333	2.321	2.324	2.335	2.353	2.374	2.398
60	2.850	2.563	2.436	2.379	2.355	2.350	2.356	2.369	2.387	2.409
70	3.070	2.678	2.507	2.426	2.390	2.377	2.377	2.386	2.401	2.421
80	3.329	2.804	2.582	2.476	2.426	2.404	2.398	2.403	2.415	2.432
90	3.637	2.943	2.662	2.529	2.463	2.432	2.420	2.421	2.429	2.444
100	4.012	3.096	2.747	2.583	2.501	2.460	2.442	2.438	2.443	2.456
150	8.789	4.178	3.269	2.896	2.711	2.612	2.557	2.529	2.517	2.515
200	8.106	6.360	4.007	3.284	2.955	2.781	2.682	2.625	2.593	2.578
250	6.980	13.00	5.086	3.766	3.235	2.968	2.817	2.727	2.673	2.642
300	6.393	25.80	6.691	4.360	3.553	3.171	2.960	2.833	2.755	2.707
350	6.015	11.65	8.976	5.071	3.907	3.389	3.110	2.944	2.840	2.774
400	5.742	8.701	10.95	5.875	4.294	3.619	3.267	3.057	2.926	2.843
450	5.534	7.472	10.86	6.688	4.700	3.857	3.426	3.172	3.013	2.912
500	5.370	6.778	9.567	7.309	5.103	4.097	3.587	3.288	3.101	2.981
600	5.124	5.997	7.540	7.522	5.753	4.556	3.901	3.515	3.273	3.119
700	4.946	5.555	6.510	6.969	6.037	4.923	4.182	3.727	3.436	3.253
800	4.808	5.262	5.918	6.375	5.982	5.137	4.408	3.914	3.583	3.377
900	4.697	5.052	5.532	5.916	5.778	5.206	4.558	4.069	3.713	3.486
1000	4.605	4.892	5.258	5.576	5.549	5.171	4.628	4.191	3.823	3.576

[a]The bold horizontal lines in the columns indicate the transition from the liquid phase to the gas phase.

[b]The values for the properties at $t = 0$°C and $p = 1$ bar correspond to the (metastable) subcooled liquid; in the stable state at these t-p values, water is in the solid phase (ice).

D2.1. Table 9. Isobaric cubic expansion coefficient $\alpha_v/(10^{-3}\ K^{-1})$ of water for given values of pressure and temperature[a]

Pressure p / bar	Temperature t / °C									
	0	25	50	75	100	125	150	200	250	300
1	−0.06769[b]	0.2569	0.4574	0.6132	2.897	2.646	2.452	2.159	1.937	1.761
5	−0.06617	0.2574	0.4574	0.6128	0.7503	0.8843	1.026	2.370	2.051	1.829
10	−0.06427	0.2579	0.4573	0.6123	0.7494	0.8830	1.024	2.720	2.217	1.923
20	−0.06049	0.2591	0.4572	0.6113	0.7477	0.8805	1.021	1.375	2.649	2.143
30	−0.05674	0.2602	0.4570	0.6104	0.7460	0.8779	1.017	1.368	3.289	2.416
40	−0.05300	0.2614	0.4569	0.6094	0.7443	0.8754	1.014	1.360	1.958	2.760
50	−0.04930	0.2625	0.4568	0.6085	0.7426	0.8729	1.010	1.353	1.939	3.203
60	−0.04561	0.2637	0.4567	0.6075	0.7409	0.8705	1.007	1.346	1.921	3.800
70	−0.04195	0.2648	0.4566	0.6066	0.7393	0.8680	1.003	1.339	1.903	4.647
80	−0.03831	0.2659	0.4565	0.6056	0.7376	0.8656	0.9999	1.332	1.885	5.953
90	−0.03469	0.2670	0.4564	0.6047	0.7360	0.8632	0.9965	1.325	1.869	3.243
100	−0.03110	0.2681	0.4563	0.6038	0.7344	0.8609	0.9932	1.318	1.852	3.170
150	−0.01348	0.2736	0.4559	0.5994	0.7265	0.8493	0.9771	1.286	1.776	2.865
200	0.00358	0.2790	0.4555	0.5952	0.7190	0.8383	0.9618	1.256	1.708	2.633
250	0.02009	0.2842	0.4552	0.5912	0.7118	0.8278	0.9473	1.229	1.647	2.449
300	0.03606	0.2893	0.4550	0.5874	0.7049	0.8177	0.9334	1.203	1.592	2.298
350	0.05152	0.2943	0.4548	0.5837	0.6983	0.8081	0.9202	1.178	1.542	2.170
400	0.06647	0.2992	0.4547	0.5802	0.6919	0.7988	0.9075	1.155	1.496	2.062
450	0.08092	0.3040	0.4546	0.5769	0.6858	0.7899	0.8954	1.133	1.455	1.967
500	0.09491	0.3086	0.4546	0.5736	0.6799	0.7814	0.8839	1.113	1.416	1.884
600	0.1215	0.3176	0.4547	0.5676	0.6688	0.7652	0.8621	1.075	1.347	1.744
700	0.1464	0.3261	0.4549	0.5621	0.6585	0.7502	0.8419	1.040	1.287	1.630
800	0.1697	0.3341	0.4551	0.5569	0.6488	0.7363	0.8233	1.009	1.234	1.535
900	0.1916	0.3418	0.4555	0.5521	0.6398	0.7232	0.8060	0.9807	1.187	1.454
1000	0.2122	0.3490	0.4559	0.5477	0.6313	0.7109	0.7897	0.9545	1.144	1.384

Pressure p / bar	Temperature t / °C									
	350	400	450	500	550	600	650	700	750	800
1	1.615	1.493	1.388	1.297	1.218	1.147	1.085	1.029	0.9784	0.9327
5	1.660	1.523	1.410	1.313	1.229	1.156	1.092	1.034	0.9827	0.9361
10	1.719	1.563	1.437	1.333	1.244	1.168	1.100	1.041	0.9880	0.9404
20	1.848	1.647	1.495	1.374	1.275	1.190	1.118	1.055	0.9988	0.9490
30	1.997	1.738	1.556	1.417	1.306	1.214	1.136	1.069	1.010	0.9578
40	2.169	1.839	1.621	1.462	1.338	1.238	1.154	1.083	1.021	0.9666
50	2.368	1.950	1.691	1.509	1.372	1.262	1.173	1.097	1.032	0.9755
60	2.600	2.072	1.765	1.558	1.406	1.288	1.191	1.111	1.043	0.9844
70	2.873	2.208	1.845	1.610	1.442	1.313	1.211	1.126	1.055	0.9935
80	3.198	2.358	1.930	1.664	1.479	1.340	1.230	1.141	1.066	1.003
90	3.593	2.525	2.021	1.721	1.517	1.367	1.250	1.156	1.078	1.012
100	4.080	2.711	2.119	1.780	1.556	1.394	1.270	1.171	1.090	1.021
150	10.85	4.079	2.729	2.124	1.774	1.543	1.377	1.251	1.150	1.068
200	6.982	7.052	3.626	2.559	2.030	1.710	1.493	1.335	1.213	1.117
250	5.171	17.05	4.992	3.109	2.327	1.894	1.617	1.422	1.278	1.166
300	4.260	37.84	7.117	3.795	2.664	2.094	1.747	1.513	1.344	1.215
350	3.694	12.91	10.24	4.627	3.039	2.306	1.883	1.606	1.411	1.265
400	3.293	7.963	12.82	5.566	3.444	2.528	2.021	1.699	1.477	1.314
450	2.990	5.984	12.13	6.487	3.861	2.752	2.160	1.792	1.543	1.362
500	2.754	4.899	9.692	7.108	4.257	2.971	2.295	1.883	1.606	1.408

D2.1. Table 9. (continued)

Pressure p bar	Temperature t / °C									
	350	400	450	500	550	600	650	700	750	800
600	2.408	3.717	6.227	6.878	4.809	3.355	2.542	2.050	1.726	1.496
700	2.161	3.069	4.579	5.685	4.843	3.594	2.734	2.190	1.829	1.573
800	1.973	2.652	3.676	4.611	4.481	3.632	2.848	2.292	1.909	1.637
900	1.825	2.357	3.106	3.840	3.988	3.510	2.875	2.352	1.964	1.685
1000	1.704	2.136	2.712	3.294	3.526	3.295	2.821	2.373	1.992	1.716

[a]The bold horizontal lines in the columns indicate the transition from the liquid phase to the gas phase.
[b]The values for the properties at $t = 0$°C and $p = 1$ bar correspond to the (metastable) subcooled liquid; in the stable state at these t-p values, water is in the solid phase (ice).

D2.1. Table 10. Thermal conductivity $\lambda/(10^{-3}\ \mathrm{W\ m^{-1}\ K^{-1}})$ of water for given values of pressure and temperature[a,c]

Pressure p bar	Temperature t / °C									
	0	25	50	75	100	125	150	200	250	300
1	562.0[b]	607.5	640.5	663.5	24.78	26.69	28.80	33.37	38.28	43.49
5	562.3	607.7	640.7	663.7	678.0	684.5	683.9	34.24	38.81	43.90
10	562.6	608.0	641.0	663.9	678.3	684.8	684.2	36.06	39.70	44.49
20	563.2	608.5	641.5	664.5	678.8	685.4	684.9	663.8	42.22	45.95
30	563.7	609.1	642.0	665.0	679.4	686.0	685.6	664.7	45.95	47.81
40	564.3	609.6	642.5	665.5	679.9	686.6	686.2	665.5	617.8	50.14
50	564.9	610.1	643.0	666.0	680.5	687.2	686.9	666.4	619.1	53.03
60	565.5	610.6	643.5	666.6	681.0	687.8	687.5	667.3	620.4	56.65
70	566.1	611.2	644.1	667.1	681.6	688.4	688.2	668.1	621.7	61.24
80	566.7	611.7	644.6	667.6	682.1	689.0	688.8	669.0	623.0	67.24
90	567.3	612.2	645.1	668.1	682.7	689.6	689.5	669.8	624.2	545.9
100	567.8	612.7	645.6	668.6	683.2	690.2	690.2	670.7	625.5	548.1
150	570.8	615.4	648.1	671.2	685.9	693.1	693.4	674.9	631.5	558.7
200	573.6	617.9	650.6	673.8	688.6	696.0	696.5	678.9	637.2	568.3
250	576.5	620.5	653.1	676.3	691.2	698.8	699.6	682.9	642.7	577.2
300	579.3	623.1	655.6	678.8	693.8	701.6	702.7	686.7	648.0	585.5
350	582.1	625.6	658.0	681.3	696.4	704.4	705.7	690.5	653.2	593.2
400	584.9	628.1	660.4	683.7	699.0	707.1	708.6	694.2	658.1	600.5
450	587.6	630.6	662.8	686.1	701.5	709.8	711.6	697.8	662.9	607.4
500	590.3	633.0	665.2	688.5	704.0	712.4	714.4	701.3	667.5	614.0
600	595.7	637.9	669.9	693.2	708.9	717.6	720.0	708.1	676.4	626.3
700	600.9	642.6	674.5	697.9	713.7	722.7	725.5	714.7	684.8	637.7
800	606.1	647.3	679.0	702.4	718.4	727.6	730.8	721.1	692.8	648.2
900	611.1	651.9	683.5	706.9	723.0	732.5	736.0	727.2	700.4	658.1
1000	616.0	656.4	687.8	711.3	727.5	737.2	741.0	733.2	707.7	667.4

Pressure p bar	Temperature t / °C									
	350	400	450	500	550	600	650	700	750	800
1	48.97	54.71	60.69	66.90	73.30	79.90	86.66	93.57	100.6	107.7
5	49.32	55.03	60.98	67.16	73.55	80.13	86.88	93.78	100.8	107.9
10	49.80	55.44	61.35	67.51	73.87	80.43	87.16	94.04	101.0	108.2
20	50.87	56.32	62.13	68.22	74.53	81.05	87.74	94.59	101.6	108.6
30	52.11	57.30	62.97	68.97	75.22	81.68	88.33	95.15	102.1	109.1
40	53.55	58.36	63.86	69.75	75.93	82.34	88.95	95.72	102.6	109.7
50	55.22	59.53	64.81	70.58	76.67	83.02	89.58	96.31	103.2	110.2

D2.1. Table 10. (continued)

Pressure p bar	Temperature t / °C									
	350	400	450	500	550	600	650	700	750	800
60	57.14	60.80	65.82	71.44	77.44	83.72	90.22	96.91	103.8	110.7
70	59.36	62.20	66.90	72.35	78.24	84.44	90.89	97.53	104.3	111.3
80	61.95	63.72	68.04	73.30	79.07	85.19	91.57	98.16	104.9	111.8
90	64.97	65.40	69.26	74.29	79.93	85.96	92.27	98.81	105.5	112.4
100	68.55	67.25	70.56	75.34	80.83	86.76	93.00	99.47	106.1	113.0
150	104.1	79.94	78.50	81.38	85.85	91.13	96.91	103.0	109.4	116.0
200	454.1	103.4	89.76	89.10	91.91	96.22	101.4	107.0	113.0	119.3
250	474.1	160.0	106.3	99.02	99.22	102.1	106.4	111.5	117.0	123.0
300	490.6	328.1	131.5	111.9	108.0	109.0	112.1	116.4	121.4	126.9
350	504.7	373.0	170.8	128.5	118.6	116.9	118.5	121.8	126.2	131.2
400	517.3	398.5	225.0	149.7	131.2	125.9	125.7	127.8	131.4	135.8
450	528.7	419.9	277.9	175.7	145.9	136.2	133.6	134.3	136.9	140.7
500	539.1	438.3	315.7	205.5	162.9	147.7	142.3	141.4	143.0	145.9
600	557.7	468.8	365.2	264.6	201.8	174.1	162.1	157.2	156.2	157.4
700	574.0	493.7	401.3	311.7	242.7	203.8	184.4	175.0	171.0	170.0
800	588.7	514.9	430.9	348.2	280.2	234.6	208.5	194.3	187.0	183.7
900	602.0	533.5	456.0	378.5	312.7	264.2	233.1	214.5	203.9	198.2
1000	614.3	550.0	477.9	404.8	341.0	291.7	257.3	235.0	221.3	213.2

[a]The bold horizontal lines in the columns indicate the transition from the liquid phase to the gas phase.
[b]The values for the properties at $t = 0$°C and $p = 1$ bar correspond to the (metastable) subcooled liquid; in the stable state at these t-p values, water is in the solid phase (ice).
[c]The λ values below the dashed lines are beyond the range of validity of the λ equation for industrial use [4, 5]; for details of this extrapolation, see [4]. If more accurate λ values are needed in this range, the λ equation for scientific use [5] should be used.

D2.1. Table 11. Dynamic viscosity $\eta/(10^{-6}$ Pa s) of water for given values of pressure and temperature[a]

Pressure p bar	Temperature t / °C									
	0	25	50	75	100	125	150	200	250	300
1	1791.8[b]	890.0	546.5	377.4	12.23	13.21	14.19	16.20	18.25	20.31
5	1790.9	890.0	546.6	377.5	281.7	222.2	182.6	16.06	18.16	20.26
10	1789.7	889.9	546.7	377.7	281.8	222.3	182.7	15.88	18.06	20.21
20	1787.5	889.8	546.9	377.9	282.1	222.6	183.0	134.7	17.85	20.09
30	1785.3	889.6	547.1	378.2	282.4	222.8	183.3	135.0	17.64	19.98
40	1783.2	889.5	547.3	378.5	282.6	223.1	183.5	135.2	106.3	19.89
50	1781.0	889.4	547.5	378.7	282.9	223.3	183.8	135.5	106.6	19.79
60	1778.9	889.3	547.7	379.0	283.2	223.6	184.0	135.7	106.9	19.71
70	1776.8	889.1	547.9	379.2	283.4	223.9	184.3	136.0	107.1	19.65
80	1774.7	889.0	548.1	379.5	283.7	224.1	184.5	136.2	107.4	19.60
90	1772.6	888.9	548.3	379.8	284.0	224.4	184.8	136.5	107.7	86.03
100	1770.6	888.8	548.5	380.0	284.2	224.6	185.0	136.7	108.0	86.43
150	1760.7	888.3	549.6	381.4	285.6	225.9	186.3	137.9	109.3	88.35
200	1751.2	887.9	550.6	382.7	286.9	227.2	187.5	139.1	110.7	90.10
250	1742.3	887.6	551.7	384.0	288.2	228.5	188.7	140.3	111.9	91.72
300	1733.9	887.4	552.8	385.3	289.6	229.8	189.9	141.5	113.2	93.25
350	1725.9	887.2	553.9	386.7	290.9	231.0	191.1	142.6	114.4	94.70
400	1718.4	887.1	555.1	388.0	292.2	232.3	192.3	143.8	115.5	96.08
450	1711.3	887.1	556.2	389.3	293.5	233.5	193.5	144.9	116.7	97.40
500	1704.7	887.2	557.4	390.7	294.8	234.8	194.7	146.0	117.8	98.67

D2.1. Table 11. (continued)

Pressure p bar	Temperature t / °C									
	0	25	50	75	100	125	150	200	250	300
600	1692.8	887.6	559.8	393.3	297.4	237.2	197.0	148.2	120.0	101.1
700	1682.5	888.4	562.2	396.0	300.0	239.7	199.4	150.3	122.1	103.4
800	1673.7	889.4	564.8	398.7	302.6	242.1	201.6	152.4	124.2	105.5
900	1666.4	890.7	567.4	401.4	305.1	244.5	203.9	154.5	126.2	107.6
1000	1660.6	892.4	570.1	404.1	307.7	246.9	206.2	156.5	128.1	109.6

Pressure p bar	Temperature t / °C									
	350	400	450	500	550	600	650	700	750	800
1	22.38	24.45	26.51	28.56	30.60	32.61	34.60	36.57	38.51	40.43
5	22.36	24.44	26.52	28.57	30.61	32.62	34.62	36.59	38.53	40.45
10	22.33	24.43	26.52	28.58	30.62	32.64	34.64	36.61	38.55	40.47
20	22.28	24.42	26.53	28.60	30.66	32.68	34.68	36.65	38.60	40.52
30	22.23	24.41	26.54	28.63	30.69	32.73	34.73	36.70	38.65	40.57
40	22.19	24.40	26.56	28.67	30.74	32.77	34.78	36.75	38.70	40.62
50	22.16	24.41	26.58	28.70	30.78	32.82	34.83	36.80	38.75	40.67
60	22.14	24.42	26.61	28.75	30.83	32.87	34.88	36.86	38.80	40.72
70	22.12	24.44	26.65	28.79	30.88	32.93	34.94	36.92	38.86	40.78
80	22.13	24.46	26.69	28.84	30.94	32.99	35.00	36.97	38.92	40.83
90	22.14	24.50	26.74	28.90	31.00	33.05	35.06	37.04	38.98	40.89
100	22.18	24.55	26.80	28.97	31.07	33.12	35.13	37.10	39.04	40.95
150	22.91	25.02	27.23	29.38	31.46	33.50	35.49	37.45	39.37	41.26
200	69.27	26.14	27.95	29.97	31.99	33.97	35.93	37.85	39.74	41.61
250	72.74	29.29	29.14	30.80	32.66	34.55	36.44	38.31	40.16	41.99
300	75.44	44.20	31.09	31.92	33.49	35.24	37.03	38.83	40.63	42.41
350	77.72	56.08	34.35	33.43	34.52	36.04	37.69	39.40	41.13	42.86
400	79.73	61.50	39.44	35.41	35.76	36.96	38.44	40.03	41.68	43.34
450	81.55	65.18	45.54	37.92	37.23	38.01	39.26	40.72	42.26	43.85
500	83.22	68.07	50.97	40.92	38.92	39.18	40.17	41.45	42.88	44.39
600	86.24	72.61	58.74	47.51	42.91	41.88	42.19	43.07	44.23	45.54
700	88.95	76.24	64.07	53.48	47.29	44.92	44.45	44.85	45.69	46.77
800	91.43	79.35	68.20	58.36	51.56	48.12	46.86	46.75	47.24	48.07
900	93.74	82.11	71.64	62.39	55.44	51.30	49.35	48.71	48.84	49.41
1000	95.92	84.62	74.64	65.83	58.91	54.34	51.83	50.71	50.48	50.78

[a]The bold horizontal lines in the columns indicate the transition from the liquid phase to the gas phase.
[b]The values for the properties at $t = 0$°C and $p = 1$ bar correspond to the (metastable) subcooled liquid; in the stable state at these t-p values, water is in the solid phase (ice).

D2.1. Table 12. Kinematic viscosity ν / (10^{-6} m^2 s^{-1}) of water for given values of pressure and temperature[a]

Pressure p bar	Temperature t / °C									
	0	25	50	75	100	125	150	200	250	300
1	1.792[b]	0.8927	0.5531	0.3872	20.75	24.00	27.49	35.20	43.91	53.60
5	1.791	0.8924	0.5531	0.3872	0.2939	0.2366	0.1991	6.826	8.618	10.59
10	1.789	0.8922	0.5531	0.3872	0.2939	0.2366	0.1992	3.271	4.203	5.213
20	1.786	0.8916	0.5531	0.3873	0.2941	0.2368	0.1994	0.1557	1.990	2.522
30	1.783	0.8911	0.5530	0.3874	0.2942	0.2369	0.1995	0.1559	1.246	1.622
40	1.780	0.8906	0.5530	0.3875	0.2944	0.2371	0.1997	0.1560	0.1330	1.171
50	1.777	0.8901	0.5529	0.3876	0.2945	0.2372	0.1998	0.1562	0.1332	0.8976

D2.1. Table 12. (continued)

Pressure p bar	Temperature t / °C									
	0	25	50	75	100	125	150	200	250	300
60	1.774	0.8895	0.5529	0.3877	0.2946	0.2374	0.2000	0.1563	0.1334	0.7134
70	1.771	0.8890	0.5529	0.3878	0.2948	0.2375	0.2001	0.1565	0.1335	0.5794
80	1.768	0.8885	0.5529	0.3879	0.2949	0.2377	0.2003	0.1567	0.1337	0.4758
90	1.765	0.8880	0.5528	0.3880	0.2951	0.2378	0.2005	0.1568	0.1339	0.1206
100	1.762	0.8875	0.5528	0.3881	0.2952	0.2380	0.2006	0.1570	0.1340	0.1208
150	1.748	0.8851	0.5527	0.3886	0.2959	0.2387	0.2014	0.1577	0.1348	0.1218
200	1.734	0.8828	0.5526	0.3891	0.2966	0.2395	0.2021	0.1585	0.1356	0.1226
250	1.721	0.8806	0.5525	0.3896	0.2973	0.2402	0.2029	0.1592	0.1363	0.1234
300	1.709	0.8785	0.5524	0.3901	0.2980	0.2410	0.2036	0.1599	0.1371	0.1242
350	1.697	0.8765	0.5524	0.3907	0.2986	0.2417	0.2044	0.1607	0.1378	0.1250
400	1.686	0.8746	0.5525	0.3912	0.2993	0.2424	0.2051	0.1614	0.1385	0.1257
450	1.675	0.8728	0.5525	0.3918	0.3000	0.2432	0.2058	0.1621	0.1392	0.1264
500	1.665	0.8711	0.5526	0.3923	0.3007	0.2439	0.2065	0.1628	0.1399	0.1271
600	1.646	0.8681	0.5528	0.3934	0.3021	0.2454	0.2080	0.1641	0.1412	0.1284
700	1.629	0.8655	0.5532	0.3946	0.3035	0.2468	0.2094	0.1655	0.1425	0.1296
800	1.614	0.8632	0.5536	0.3958	0.3049	0.2483	0.2108	0.1668	0.1437	0.1308
900	1.601	0.8613	0.5542	0.3970	0.3064	0.2497	0.2123	0.1681	0.1449	0.1320
1000	1.589	0.8598	0.5548	0.3983	0.3078	0.2511	0.2137	0.1694	0.1461	0.1332

Pressure p bar	Temperature t / °C									
	350	400	450	500	550	600	650	700	750	800
1	64.26	75.87	88.41	101.8	116.2	131.3	147.4	164.2	181.8	200.2
5	12.75	15.09	17.61	20.31	23.19	26.23	29.44	32.82	36.35	40.03
10	6.308	7.491	8.762	10.12	11.56	13.09	14.70	16.39	18.16	20.01
20	3.087	3.692	4.338	5.025	5.754	6.524	7.334	8.183	9.072	10.00
30	2.013	2.425	2.863	3.327	3.817	4.334	4.878	5.447	6.041	6.661
40	1.475	1.792	2.126	2.478	2.849	3.240	3.650	4.078	4.526	4.993
50	1.152	1.412	1.683	1.969	2.268	2.583	2.913	3.258	3.617	3.992
60	0.9353	1.158	1.388	1.629	1.881	2.145	2.422	2.711	3.012	3.325
70	0.7802	0.9765	1.178	1.387	1.605	1.833	2.071	2.320	2.579	2.848
80	0.6633	0.8403	1.020	1.205	1.398	1.599	1.809	2.027	2.255	2.491
90	0.5717	0.7342	0.8967	1.063	1.237	1.417	1.604	1.799	2.002	2.213
100	0.4977	0.6492	0.7983	0.950	1.108	1.271	1.441	1.617	1.801	1.991
150	0.2630	0.3921	0.5031	0.6119	0.7219	0.8348	0.951	1.072	1.196	1.325
200	0.1153	0.2601	0.3556	0.4434	0.5301	0.6178	0.7076	0.7999	0.8950	0.9932
250	0.1163	0.1759	0.2674	0.3431	0.4159	0.4885	0.5622	0.6376	0.7150	0.7946
300	0.1172	0.1236	0.2095	0.2774	0.3408	0.4032	0.4662	0.5302	0.5957	0.6629
350	0.1179	0.1181	0.1704	0.2318	0.2882	0.3432	0.3983	0.4541	0.5110	0.5692
400	0.1187	0.1175	0.1457	0.1992	0.2498	0.2990	0.3480	0.3976	0.4480	0.4994
450	0.1194	0.1176	0.1327	0.1757	0.2211	0.2654	0.3096	0.3541	0.3994	0.4456
500	0.1200	0.1178	0.1268	0.1592	0.1992	0.2394	0.2795	0.3199	0.3610	0.4028
600	0.1213	0.1186	0.1225	0.1402	0.1697	0.2024	0.2359	0.2698	0.3044	0.3396
700	0.1225	0.1194	0.1212	0.1317	0.1524	0.1785	0.2066	0.2355	0.2652	0.2955
800	0.1237	0.1203	0.1210	0.1277	0.1423	0.1628	0.1863	0.2111	0.2368	0.2632
900	0.1248	0.1212	0.1211	0.1257	0.1363	0.1523	0.1718	0.1932	0.2157	0.2390
1000	0.1258	0.1221	0.1215	0.1246	0.1325	0.1452	0.1614	0.1798	0.1995	0.2202

[a] The bold horizontal lines in the columns indicate the transition from the liquid phase to the gas phase.

[b] The values for the properties at $t = 0$ °C and $p = 1$ bar correspond to the (metastable) subcooled liquid; in the stable state at these t-p values, water is in the solid phase (ice).

D2.1. Table 13. Thermal diffusivity a / (10^{-6} m^2 s^{-1}) of water for given values of pressure and temperature[a,c]

Pressure p / bar	Temperature t / °C									
	0	25	50	75	100	125	150	200	250	300
1	0.1332[b]	0.1457	0.1551	0.1624	20.26	24.12	28.09	36.69	46.31	57.04
5	0.1333	0.1458	0.1552	0.1624	0.1678	0.1713	0.1730	6.786	8.860	11.11
10	0.1334	0.1458	0.1552	0.1625	0.1679	0.1714	0.1731	3.058	4.177	5.361
20	0.1337	0.1460	0.1554	0.1626	0.1680	0.1716	0.1733	0.1709	1.839	2.486
30	0.1339	0.1462	0.1555	0.1628	0.1681	0.1717	0.1735	0.1711	1.054	1.526
40	0.1341	0.1463	0.1557	0.1629	0.1683	0.1719	0.1737	0.1714	0.1590	1.047
50	0.1343	0.1465	0.1558	0.1631	0.1684	0.1720	0.1739	0.1717	0.1595	0.7583
60	0.1346	0.1467	0.1559	0.1632	0.1686	0.1722	0.1741	0.1720	0.1601	0.5636
70	0.1348	0.1468	0.1561	0.1633	0.1687	0.1724	0.1743	0.1723	0.1606	0.4208
80	0.1350	0.1470	0.1562	0.1635	0.1689	0.1725	0.1744	0.1726	0.1611	0.3088
90	0.1352	0.1471	0.1564	0.1636	0.1690	0.1727	0.1746	0.1729	0.1616	0.1336
100	0.1354	0.1473	0.1565	0.1637	0.1692	0.1728	0.1748	0.1732	0.1621	0.1349
150	0.1365	0.1481	0.1572	0.1644	0.1699	0.1736	0.1757	0.1745	0.1645	0.1406
200	0.1376	0.1488	0.1579	0.1651	0.1706	0.1744	0.1766	0.1758	0.1668	0.1455
250	0.1386	0.1496	0.1585	0.1657	0.1712	0.1751	0.1774	0.1771	0.1688	0.1497
300	0.1396	0.1503	0.1592	0.1664	0.1719	0.1759	0.1783	0.1783	0.1708	0.1535
350	0.1406	0.1510	0.1598	0.1670	0.1726	0.1766	0.1791	0.1794	0.1726	0.1569
400	0.1415	0.1517	0.1604	0.1676	0.1732	0.1773	0.1799	0.1805	0.1744	0.1599
450	0.1425	0.1524	0.1610	0.1682	0.1738	0.1780	0.1807	0.1816	0.1760	0.1628
500	0.1433	0.1530	0.1617	0.1688	0.1745	0.1786	0.1814	0.1826	0.1776	0.1654
600	0.1451	0.1543	0.1628	0.1700	0.1757	0.1800	0.1829	0.1846	0.1805	0.1701
700	0.1467	0.1556	0.1640	0.1711	0.1768	0.1812	0.1843	0.1865	0.1832	0.1742
800	0.1482	0.1568	0.1651	0.1722	0.1780	0.1824	0.1856	0.1883	0.1857	0.1779
900	0.1496	0.1579	0.1661	0.1732	0.1791	0.1836	0.1869	0.1899	0.1880	0.1812
1000	0.1509	0.1590	0.1672	0.1743	0.1801	0.1847	0.1882	0.1915	0.1902	0.1843

Pressure p / bar	Temperature t / °C									
	350	400	450	500	550	600	650	700	750	800
1	68.94	82.02	96.29	111.7	128.3	146.1	164.9	184.8	205.7	227.6
5	13.55	16.21	19.10	22.22	25.56	29.12	32.91	36.90	41.10	45.49
10	6.626	7.986	9.451	11.02	12.71	14.50	16.40	18.41	20.52	22.72
20	3.161	3.872	4.626	5.430	6.286	7.195	8.156	9.168	10.23	11.34
30	2.005	2.499	3.018	3.566	4.146	4.759	5.406	6.087	6.800	7.545
40	1.426	1.813	2.214	2.634	3.076	3.542	4.032	4.547	5.086	5.648
50	1.078	1.400	1.731	2.075	2.434	2.812	3.208	3.624	4.058	4.510
60	0.8470	1.125	1.409	1.702	2.007	2.325	2.659	3.008	3.373	3.752
70	0.6818	0.9282	1.179	1.436	1.701	1.978	2.267	2.569	2.883	3.210
80	0.5579	0.7807	1.007	1.236	1.472	1.718	1.973	2.239	2.517	2.805
90	0.4612	0.6660	0.8724	1.081	1.295	1.515	1.745	1.983	2.232	2.489
100	0.3834	0.5743	0.7651	0.9569	1.152	1.353	1.562	1.779	2.004	2.237
150	0.1359	0.2999	0.4438	0.5853	0.7266	0.8694	1.016	1.166	1.321	1.481
200	0.0933	0.1617	0.2849	0.4013	0.5154	0.6291	0.7442	0.8615	0.9818	1.105
250	0.1086	0.0739	0.1917	0.2929	0.3906	0.4866	0.5829	0.6804	0.7796	0.8810
300	0.1192	0.0356	0.1325	0.2230	0.3094	0.3933	0.4769	0.5609	0.6462	0.7327
350	0.1273	0.0674	0.0943	0.1756	0.2534	0.3285	0.4026	0.4770	0.5520	0.6279
400	0.1341	0.0875	0.0759	0.1433	0.2134	0.2815	0.3483	0.4152	0.4825	0.5503
450	0.1398	0.1014	0.0746	0.1218	0.1844	0.2466	0.3074	0.3683	0.4295	0.4909
500	0.1448	0.1119	0.0821	0.1093	0.1634	0.2202	0.2760	0.3320	0.3881	0.4442

D2.1. Table 13. (continued)

Pressure p bar	Temperature t / °C									
	350	400	450	500	550	600	650	700	750	800
600	0.1531	0.1276	0.1010	0.1038	0.1387	0.1847	0.2323	0.2803	0.3284	0.3762
700	0.1599	0.1392	0.1167	0.1101	0.1296	0.1645	0.2050	0.2467	0.2888	0.3302
800	0.1656	0.1484	0.1291	0.1195	0.1293	0.1545	0.1880	0.2242	0.2616	0.2979
900	0.1706	0.1559	0.1394	0.1289	0.1330	0.1507	0.1781	0.2091	0.2425	0.2749
1000	0.1750	0.1623	0.1480	0.1375	0.1383	0.1508	0.1732	0.1988	0.2288	0.2585

[a]The bold horizontal lines in the columns indicate the transition from the liquid phase to the gas phase.
[b]The values for the properties at $t = 0$°C and $p = 1$ bar correspond to the (metastable) subcooled liquid; in the stable state at these t-p values, water is in the solid phase (ice).
[c]The a values below the dashed lines were calculated with λ values from the λ equation for industrial use [4, 5] beyond its range of validity; for details of this extrapolation, see [4]. If more accurate a values are needed in this range, the λ equation for scientific use [5] should be used.

D2.1. Table 14. Prandtl number Pr of water for given values of pressure and temperature[a,c]

Pressure p bar	Temperature t / °C									
	0	25	50	75	100	125	150	200	250	300
1	13.45[b]	6.127	3.566	2.384	1.024	0.9947	0.9785	0.9594	0.9482	0.9398
5	13.43	6.122	3.565	2.384	1.752	1.381	1.151	1.0059	0.9727	0.9536
10	13.41	6.117	3.563	2.383	1.751	1.381	1.151	1.069	1.0061	0.9723
20	13.36	6.107	3.560	2.382	1.751	1.380	1.150	0.9114	1.082	1.0144
30	13.32	6.096	3.556	2.380	1.750	1.380	1.150	0.9108	1.181	1.063
40	13.27	6.086	3.553	2.379	1.749	1.379	1.150	0.9101	0.8369	1.118
50	13.23	6.076	3.549	2.377	1.748	1.379	1.149	0.9095	0.8351	1.184
60	13.18	6.066	3.546	2.376	1.748	1.379	1.149	0.9089	0.8333	1.266
70	13.14	6.056	3.542	2.375	1.747	1.378	1.149	0.9083	0.8316	1.377
80	13.10	6.046	3.539	2.373	1.746	1.378	1.148	0.9077	0.8299	1.541
90	13.05	6.036	3.536	2.372	1.746	1.377	1.148	0.9071	0.8283	0.9030
100	13.01	6.026	3.532	2.370	1.745	1.377	1.148	0.9065	0.8267	0.8959
150	12.80	5.978	3.516	2.364	1.742	1.375	1.146	0.9038	0.8195	0.8659
200	12.61	5.932	3.501	2.357	1.739	1.373	1.145	0.9014	0.8131	0.8429
250	12.42	5.888	3.485	2.351	1.736	1.372	1.143	0.8992	0.8075	0.8245
300	12.24	5.845	3.471	2.345	1.733	1.370	1.142	0.8972	0.8025	0.8094
350	12.07	5.805	3.457	2.340	1.731	1.369	1.141	0.8954	0.7981	0.7967
400	11.91	5.766	3.444	2.334	1.728	1.368	1.140	0.8939	0.7942	0.7859
450	11.76	5.728	3.431	2.329	1.726	1.366	1.139	0.8924	0.7906	0.7766
500	11.62	5.692	3.418	2.324	1.724	1.365	1.139	0.8912	0.7874	0.7685
600	11.35	5.625	3.395	2.315	1.720	1.363	1.137	0.8890	0.7820	0.7550
700	11.11	5.563	3.373	2.306	1.716	1.362	1.136	0.8873	0.7775	0.7443
800	10.89	5.506	3.354	2.299	1.713	1.361	1.136	0.8861	0.7739	0.7356
900	10.70	5.454	3.336	2.292	1.711	1.360	1.135	0.8852	0.7709	0.7285
1000	10.53	5.407	3.319	2.286	1.709	1.359	1.135	0.8846	0.7685	0.7226

Pressure p bar	Temperature t / °C									
	350	400	450	500	550	600	650	700	750	800
1	0.9322	0.9250	0.9181	0.9114	0.9051	0.8991	0.8936	0.8884	0.8837	0.8795
5	0.9408	0.9307	0.9221	0.9143	0.9073	0.9008	0.8948	0.8893	0.8844	0.8800
10	0.9520	0.9381	0.9272	0.9180	0.9100	0.9028	0.8963	0.8904	0.8852	0.8806
20	0.9766	0.9536	0.9376	0.9254	0.9154	0.9067	0.8992	0.8926	0.8868	0.8817
30	1.0040	0.9704	0.9486	0.9330	0.9208	0.9107	0.9022	0.8948	0.8884	0.8829

D2.1. Table 14. (continued)

Pressure p bar	Temperature t / °C									
	350	400	450	500	550	600	650	700	750	800
40	1.034	0.9886	0.9601	0.9408	0.9263	0.9147	0.9051	0.8969	0.8899	0.8840
50	1.068	1.0082	0.9723	0.9488	0.9319	0.9187	0.9080	0.8990	0.8914	0.8851
60	1.104	1.029	0.9851	0.9571	0.9376	0.9227	0.9109	0.9011	0.8929	0.8861
70	1.144	1.052	0.9986	0.9657	0.9433	0.9268	0.9138	0.9032	0.8944	0.8871
80	1.189	1.076	1.013	0.9746	0.9492	0.9308	0.9166	0.9052	0.8959	0.8882
90	1.240	1.102	1.028	0.9838	0.9552	0.9349	0.9195	0.9072	0.8973	0.8892
100	1.298	1.130	1.043	0.9932	0.9613	0.9390	0.9224	0.9093	0.8987	0.8901
150	1.935	1.308	1.134	1.045	0.9936	0.9602	0.9367	0.9191	0.9054	0.8947
200	1.236	1.608	1.248	1.105	1.029	0.9820	0.9508	0.9285	0.9116	0.8987
250	1.071	2.381	1.394	1.171	1.065	1.0039	0.9646	0.9372	0.9171	0.9020
300	0.9832	3.475	1.581	1.244	1.102	1.025	0.9776	0.9451	0.9218	0.9046
350	0.9262	1.751	1.806	1.320	1.137	1.045	0.9893	0.9520	0.9256	0.9065
400	0.8850	1.343	1.920	1.390	1.171	1.062	0.9992	0.9575	0.9284	0.9075
450	0.8536	1.160	1.781	1.443	1.199	1.076	1.0070	0.9614	0.9299	0.9076
500	0.8290	1.053	1.544	1.456	1.220	1.087	1.0124	0.9637	0.9302	0.9069
600	0.7924	0.9289	1.213	1.351	1.223	1.096	1.0154	0.9627	0.9268	0.9027
700	0.7664	0.8578	1.039	1.196	1.176	1.085	1.0080	0.9549	0.9182	0.8949
800	0.7467	0.8109	0.9367	1.069	1.101	1.054	0.9909	0.9415	0.9054	0.8837
900	0.7313	0.7775	0.8691	0.9753	1.024	1.011	0.9651	0.9242	0.8895	0.8693
1000	0.7190	0.7525	0.8211	0.9067	0.9586	0.9632	0.9322	0.9045	0.8722	0.8517

[a]The bold horizontal lines in the columns indicate the transition from the liquid phase to the gas phase.
[b]The values for the properties at $t = 0°C$ and $p = 1$ bar correspond to the (metastable) subcooled liquid; in the stable state at these t-p values, water is in the solid phase (ice).
[c]The Pr values below the dashed lines were calculated with λ values from the λ equation for industrial use [4, 5] beyond its range of validity; for details of this extrapolation, see [4]. If more accurate Pr values are needed in this range, the λ equation for scientific use [5] should be used.

As usual for water, the reference state for the caloric properties was set by choosing the specific internal energy and the specific entropy of the saturated liquid to be zero at the triple point, i.e., $u_t'(T_t) = 0$ and $s_t'(T_t) = 0$. As a consequence of this zero-point setting, the specific enthalpy of the saturated liquid at the triple point is given by $h_t'(T_t) = 0.000\,611\,783$ kJ kg^{-1}.

3 Bibliography

1. IAPWS Revised Release on the *IAPWS Formulation 1995 for the Thermodynamic Properties of Ordinary Water Substance for General and Scientific Use* (September 2009). Available at http://www.iapws.org
2. Wagner W, Pruß A (2002) The IAPWS Formulation 1995 for the Thermodynamic Properties of Ordinary Water Substance for General and Scientific Use. J Phys Chem Ref Data 31, 387–535
3. IAPWS Revised Release on the *IAPWS Industrial Formulation 1997 for the Thermodynamic Properties of Water and Steam* (August 2009). Available at http://www.iapws.org
4. Wagner W, Kretzschmar H-J (2008) International steam tables – Properties of water and steam based on the industrial formulation IAPWS-IF97. Springer-Verlag, Berlin
5. IAPWS Revised Release on the *IAPS Formulation 1985 for the Thermal Conductivity of Ordinary Water Substance* (September 2008). Available at http://www.iapws.org
6. IAPWS Release on the *IAPWS Formulation 2008 for the Viscosity of Ordinary Water Substance* (September 2008). Available at http://www.iapws.org

D2.2 Properties of Dry Air

Roland Span
Ruhr-Universität Bochum, Bochum, Germany

1 Composition of Dry Air

Substance	Mole fraction	Molecular mass g/mol	Mass fraction
N_2	0.7812	28.013	0.75570
Ar	0.0092	39.948	0.01269
O_2	0.2096	31.999	0.23161

Molecular mass of the mixture: $\widetilde{M}$ = 28.9583 g/mol

Specific gas constant of the mixture: R = 0.28712 kJ/(kg K)

Deviations caused by neglecting the CO_2 fraction in air always remain smaller than the uncertainty of the equations used to calculate the tabulated properties. The impact of all other trace components is smaller than the impact of CO_2. Humidity has to be considered separately.

To calculate the properties tabulated in the following pages, the "pseudo pure-component" equations from the cited references were used. According to the authors, these equations are slightly more accurate than the mixture models published in the same articles.

Z	Compression factor $Z = p/(\rho RT)$	β	Isobaric expansion coefficient in 10^{-3}/K $\beta = v^{-1}\,(\partial_v/\partial T)_p$
Pr	Prandtl number Pr = $\eta\, c_p/\lambda$	c_p	Specific isobaric heat capacity in kJ/(kg K)
		w_s	Isentropic speed of sound in m/s

p	Pressure in bar	v	Specific volume in m^3/kg
ρ	Density in kg/m^3	λ	Thermal conductivity in mW/(m K)
ϑ	Temperature in °C	ν	Kinematic viscosity ν in 10^{-7} m^2/s
h	Specific enthalpy in kJ/kg	η	Dynamic viscosity in 10^{-6} Pa·s
s	Specific entropy in kJ/(kg K)	a	Thermal diffusivity in 10^{-7} m^2/s

2 Critical Parameters of Dry Air

	Temperatures	Pressures	Densities
Critical	132.531 K	3.7860 MPa	11.8308 mol/dm^3
	−140.619 °C	37.860 bar	342.599 kg/m^3
Maxcondentherm	132.631 K	3.7850 MPa	10.4477 mol/dm^3
	−140.519 °C	37.850 bar	302.547 kg/m^3
Maxcondenbar	132.604 K	3.7891 MPa	11.0948 mol/dm^3
	−140.547 °C	37.891 bar	321.286 kg/m^3

2.1 Reference States of Enthalpy and Entropy

h = 0 kJ/kg, s = 0 kJ/(kg K) at T = 298.15 K (ϑ) = 25°C), p = 1.01325 bar for the pure components

D2.2. Table 1. Properties of dry air at $p = 1$ bar

ϑ °C	ρ kg/m³	h kJ/kg	s kJ/(kg K)	c_p kJ/(kg K)	β 10^{-3}/K	λ mW/(m K)	η μ Pa*s	ν 10^{-7} m²/s	a 10^{-7} m²/s	Pr –	w_s m/s
−200	900.81	−435.60	−4.0270	1.9145	4.8833	149.590	206.790	2.296	0.867	2.6466	917.9
−194.36	875.52	−424.76	−3.8842	1.9329	5.2331	140.180	167.360	1.912	0.828	2.3076	866.7
−191.54	4.4419	−219.76	−1.3183	1.0891	13.8730	7.673	5.811	13.08	15.86	0.8248	177.1
−190	4.3492	−218.09	−1.2980	1.0818	13.5040	7.824	5.921	13.62	16.63	0.8187	179.0
−180	3.8383	−207.44	−1.1770	1.0517	11.6120	8.803	6.630	17.28	21.81	0.7921	190.8
−170	3.4418	−197.01	−1.0707	1.0359	10.2600	9.774	7.323	21.28	27.41	0.7762	201.6
−160	3.1230	−186.70	−0.9753	1.0266	9.2236	10.733	8.001	25.62	33.48	0.7653	211.7
−150	2.8600	−176.47	−0.8886	1.0206	8.3947	11.679	8.664	30.29	40.01	0.7571	221.3
−140	2.6390	−166.28	−0.8091	1.0165	7.7122	12.611	9.313	35.29	47.01	0.7507	230.4
−130	2.4503	−156.13	−0.7356	1.0137	7.1381	13.529	9.948	40.60	54.47	0.7454	239.2
−120	2.2873	−146.01	−0.6672	1.0116	6.6471	14.434	10.571	46.22	62.38	0.7409	247.6
−110	2.1448	−135.90	−0.6033	1.0101	6.2217	15.326	11.182	52.13	70.74	0.7370	255.7
−100	2.0193	−125.80	−0.5432	1.0090	5.8490	16.205	11.780	58.34	79.54	0.7335	263.5
−90	1.9078	−115.72	−0.4866	1.0081	5.5196	17.071	12.368	64.83	88.76	0.7304	271.1
−80	1.8080	−105.64	−0.4330	1.0074	5.2260	17.924	12.944	71.59	98.41	0.7275	278.5
−70	1.7183	−95.57	−0.3822	1.0068	4.9627	18.766	13.511	78.63	108.5	0.7249	285.7
−60	1.6371	−85.51	−0.3338	1.0064	4.7250	19.596	14.067	85.93	118.9	0.7224	292.7
−50	1.5632	−75.44	−0.2877	1.0061	4.5094	20.416	14.614	93.49	129.8	0.7202	299.5
−40	1.4958	−65.38	−0.2436	1.0059	4.3128	21.224	15.152	101.3	141.1	0.7181	306.2
−30	1.4340	−55.33	−0.2013	1.0058	4.1329	22.023	15.680	109.4	152.7	0.7161	312.7
−20	1.3771	−45.27	−0.1608	1.0057	3.9675	22.811	16.201	117.7	164.7	0.7143	319.1
−10	1.3245	−35.21	−0.1218	1.0058	3.8149	23.590	16.714	126.2	177.1	0.7126	325.4
0	1.2758	−25.15	−0.0843	1.0059	3.6738	24.360	17.218	135.0	189.8	0.7110	331.5
10	1.2306	−15.09	−0.0481	1.0061	3.5428	25.121	17.715	144.0	202.9	0.7095	337.5
20	1.1885	−5.03	−0.0132	1.0064	3.4209	25.873	18.205	153.2	216.3	0.7081	343.4
30	1.1492	5.04	0.0205	1.0067	3.3071	26.618	18.689	162.6	230.1	0.7068	349.2
40	1.1124	15.11	0.0532	1.0071	3.2007	27.354	19.165	172.3	244.2	0.7056	354.9
50	1.0779	25.18	0.0849	1.0077	3.1010	28.082	19.635	182.2	258.5	0.7045	360.5
60	1.0455	35.26	0.1156	1.0082	3.0073	28.804	20.099	192.2	273.2	0.7035	365.9
70	1.0150	45.34	0.1454	1.0089	2.9192	29.518	20.557	202.5	288.2	0.7026	371.3
80	0.9862	55.44	0.1744	1.0097	2.8361	30.225	21.009	213.0	303.5	0.7018	376.7
90	0.9590	65.54	0.2026	1.0105	2.7576	30.925	21.455	223.7	319.1	0.7011	381.9
100	0.9333	75.65	0.2301	1.0115	2.6833	31.620	21.896	234.6	335.0	0.7004	387.0
120	0.8858	95.90	0.2830	1.0136	2.5463	32.989	22.763	257.0	367.5	0.6994	397.1
140	0.8428	116.19	0.3333	1.0160	2.4225	34.336	23.610	280.1	401.0	0.6986	406.9
160	0.8039	136.54	0.3814	1.0188	2.3103	35.660	24.439	304.0	435.4	0.6982	416.4
180	0.7684	156.95	0.4275	1.0218	2.2081	36.964	25.251	328.6	470.8	0.6980	425.7
200	0.7359	177.42	0.4717	1.0252	2.1145	38.248	26.046	353.9	507.0	0.6981	434.7
250	0.6655	228.91	0.5751	1.0347	1.9120	41.382	27.970	420.3	601.0	0.6993	456.2
300	0.6075	280.90	0.6700	1.0454	1.7450	44.417	29.811	490.7	699.5	0.7016	476.6
350	0.5587	333.46	0.7579	1.0568	1.6048	47.367	31.579	565.2	802.2	0.7046	495.9
400	0.5172	386.60	0.8399	1.0688	1.4855	50.240	33.284	643.5	908.9	0.7081	514.3
450	0.4815	440.33	0.9170	1.0808	1.3827	53.047	34.932	725.6	1019.5	0.7117	532.0
500	0.4503	494.67	0.9896	1.0927	1.2932	55.795	36.530	811.2	1133.9	0.7154	549.0
550	0.4230	549.60	1.0584	1.1043	1.2147	58.490	38.084	900.4	1252.3	0.7190	565.4
600	0.3988	605.09	1.1239	1.1154	1.1451	61.139	39.597	993.0	1374.6	0.7224	581.3
650	0.3772	661.13	1.1863	1.1260	1.0830	63.745	41.073	1089.0	1501.0	0.7255	596.7

D2.2. Table 1. (continued)

ϑ °C	ρ kg/m³	h kJ/kg	s kJ/(kg K)	c_p kJ/(kg K)	β 10^{-3}/K	λ mW/(m K)	η μ Pa*s	ν 10^{-7} m²/s	a 10^{-7} m²/s	Pr –	w_s m/s
700	0.3578	717.68	1.2459	1.1361	1.0274	66.312	42.517	1188.3	1631.4	0.7284	611.7
750	0.3403	774.72	1.3031	1.1455	0.9772	68.846	43.931	1290.9	1766.0	0.7310	626.3
800	0.3245	832.22	1.3580	1.1544	0.9317	71.348	45.317	1396.7	1904.9	0.7333	640.6
850	0.3100	890.16	1.4107	1.1628	0.8902	73.822	46.679	1505.7	2047.9	0.7352	654.6
900	0.2968	948.49	1.4615	1.1706	0.8522	76.271	48.018	1617.8	2195.3	0.7370	668.3
950	0.2847	1007.20	1.5106	1.1778	0.8174	78.695	49.336	1733.1	2347.0	0.7384	681.7
1000	0.2735	1066.30	1.5579	1.1846	0.7853	81.099	50.635	1851.4	2503.1	0.7396	694.8

D2.2. Table 2. Properties of the saturated liquid

ϑ °C	p' bar	ρ' kg/m³	h' kJ/kg	s' kJ/(kg K)	c_p' kJ/(kg K)	β' 10^{-3}/K	λ' mW/(m K)	η' μ Pa*s	ν' 10^{-7} m²/s	a' 10^{-7} m²/s	Pr′	Z'	w' m/s	σ' N/m
−212	0.070027	951.78	−458.54	−4.3679	1.9013	4.3568	169.16	351.22	3.6902	0.93477	3.9477	0.000419	1019.0	13.81
−210	0.10276	943.46	−454.73	−4.3067	1.9017	4.4305	165.92	318.80	3.3791	0.92475	3.6541	0.000601	1002.8	13.32
−208	0.14697	935.07	−450.92	−4.2474	1.9027	4.5093	162.66	290.38	3.1055	0.91425	3.3968	0.000840	986.2	12.83
−206	0.20536	926.60	−447.11	−4.1899	1.9045	4.5936	159.40	265.40	2.8642	0.90325	3.1710	0.001150	969.5	12.34
−204	0.28095	918.06	−443.30	−4.1340	1.9071	4.6842	156.13	243.38	2.6510	0.89174	2.9728	0.001541	952.4	11.86
−202	0.37705	909.43	−439.47	−4.0797	1.9105	4.7817	152.84	223.90	2.4620	0.87968	2.7987	0.002030	935.1	11.39
−200	0.49727	900.71	−435.64	−4.0267	1.9149	4.8870	149.55	206.63	2.2941	0.86707	2.6458	0.002629	917.6	10.91
−198	0.64543	891.88	−431.79	−3.9751	1.9202	5.0008	146.24	191.26	2.1444	0.85388	2.5114	0.003354	899.8	10.45
−196	0.82562	882.94	−427.93	−3.9246	1.9267	5.1242	142.91	177.53	2.0107	0.84010	2.3934	0.004221	881.7	9.983
−194	1.0421	873.87	−424.06	−3.8754	1.9344	5.2583	139.58	165.23	1.8908	0.82570	2.2899	0.005248	863.3	9.525
−192	1.2993	864.67	−420.16	−3.8271	1.9434	5.4044	136.22	154.17	1.7830	0.81068	2.1993	0.006449	844.7	9.071
−190	1.6019	855.32	−416.25	−3.7799	1.9538	5.5640	132.86	144.18	1.6857	0.79501	2.1204	0.007845	825.8	8.622
−188	1.9545	845.81	−412.31	−3.7336	1.9659	5.7389	129.53	135.14	1.5977	0.77902	2.0509	0.009452	806.5	8.179
−186	2.3620	836.12	−408.34	−3.688	1.9798	5.9310	126.19	126.90	1.5178	0.76228	1.9911	0.011290	787.0	7.741
−184	2.8295	826.24	−404.33	−3.6433	1.9957	6.1428	122.82	119.39	1.4449	0.74482	1.9399	0.013379	767.1	7.308
−182	3.3619	816.15	−400.30	−3.5992	2.0139	6.3772	119.44	112.49	1.3783	0.72666	1.8967	0.015740	746.9	6.880
−180	3.9644	805.83	−396.22	−3.5558	2.0347	6.6374	116.05	106.13	1.3170	0.70779	1.8608	0.018394	726.4	6.458
−178	4.6422	795.25	−392.10	−3.5129	2.0584	6.9277	112.65	100.25	1.2606	0.6882	1.8317	0.021367	705.5	6.043
−176	5.4006	784.39	−387.92	−3.4705	2.0854	7.2530	109.25	94.782	1.2084	0.66789	1.8092	0.024683	684.2	5.633
−174	6.2450	773.22	−383.69	−3.4285	2.1164	7.6195	105.85	89.677	1.1598	0.64686	1.7930	0.028371	662.6	5.230
−172	7.1809	761.70	−379.40	−3.3868	2.1518	8.0348	102.45	84.887	1.1144	0.62508	1.7829	0.032462	640.6	4.833
−170	8.2139	749.80	−375.03	−3.3454	2.1927	8.5085	99.062	80.373	1.0719	0.60255	1.7790	0.036989	618.2	4.444
−168	9.3494	737.47	−370.59	−3.3042	2.2398	9.0531	95.680	76.099	1.0319	0.57924	1.7815	0.041992	595.3	4.062
−166	10.593	724.66	−366.05	−3.2631	2.2947	9.6846	92.313	72.033	0.99402	0.55514	1.7906	0.047516	572.1	3.687
−164	11.951	711.31	−361.42	−3.2220	2.3590	10.4250	88.966	68.146	0.95804	0.53019	1.8070	0.053613	548.4	3.321
−162	13.429	697.34	−356.67	−3.1808	2.4352	11.3020	85.644	64.413	0.92369	0.50433	1.8315	0.060343	524.3	2.963
−160	15.032	682.66	−351.79	−3.1393	2.5266	12.3600	82.353	60.809	0.89076	0.47745	1.8656	0.067781	499.6	2.615
−158	16.767	667.17	−346.75	−3.0974	2.6382	13.6570	79.097	57.312	0.85903	0.44939	1.9116	0.076017	474.4	2.276
−156	18.640	650.70	−341.53	−3.0550	2.7773	15.2870	75.879	53.898	0.82831	0.41987	1.9728	0.085165	448.5	1.949
−154	20.656	633.06	−336.10	−3.0116	2.9560	17.4020	72.701	50.544	0.79840	0.38850	2.0551	0.095377	421.9	1.632
−152	22.821	613.97	−330.40	−2.9671	3.1948	20.2620	69.564	47.220	0.76910	0.35464	2.1687	0.10686	394.2	1.329
−150	25.140	592.99	−324.35	−2.9207	3.5324	24.3640	66.469	43.890	0.74016	0.31733	2.3325	0.11990	365.2	1.040
−148	27.618	569.39	−317.83	−2.8716	4.0503	30.7800	63.433	40.496	0.71123	0.27506	2.5857	0.13499	334.3	0.768
−146	30.259	541.83	−310.60	−2.8181	4.9562	42.2910	60.546	36.939	0.68176	0.22546	3.0238	0.15298	300.6	0.516
−144	33.060	507.16	−302.13	−2.7562	6.9740	68.8600	58.297	32.997	0.65062	0.16482	3.9474	0.17580	262.3	0.289
−142	35.992	454.16	−290.48	−2.6714	15.256	184.2900	60.168	27.911	0.61458	0.08684	7.0773	0.21046	215.0	0.097

D2.2. Table 3. Properties of the saturated vapor

ϑ °C	p'' bar	ρ'' kg/m³	h'' kJ/kg	s'' kJ/(kg K)	c_p'' kJ/(kg K)	β'' 10^{-3}/K	λ'' mW/(m K)	η'' μ Pa*s	ν'' 10^{-7} m²/s	a'' 10^{-7} m²/s	Pr″ –	Z″ –	w_s m/s
−212	0.033892	0.19366	−237.64	−0.61444	1.0106	16.529	5.4401	4.3230	223.230	277.95	0.80310	0.9968	156.57
−210	0.052874	0.29293	−235.71	−0.71069	1.0137	16.072	5.6497	4.4701	152.600	190.26	0.80202	0.9955	158.99
−208	0.079916	0.42988	−233.82	−0.79906	1.0175	15.661	5.8602	4.6167	107.400	133.98	0.80156	0.99384	161.33
−206	0.11739	0.61391	−231.95	−0.88042	1.0221	15.294	6.0718	4.7628	77.581	96.766	0.80174	0.99178	163.59
−204	0.16804	0.85556	−230.11	−0.95552	1.0276	14.970	6.2848	4.9085	57.372	71.483	0.80260	0.98927	165.76
−202	0.23499	1.1663	−228.32	−1.0250	1.0342	14.688	6.4997	5.0538	43.330	53.883	0.80415	0.98625	167.85
−200	0.32171	1.5587	−226.57	−1.0895	1.0419	14.447	6.7169	5.1987	33.352	41.358	0.80642	0.98269	169.83
−198	0.43200	2.0461	−224.86	−1.1496	1.0508	14.246	6.9368	5.3434	26.115	32.263	0.80945	0.97854	171.72
−196	0.56999	2.6425	−223.22	−1.2057	1.0611	14.086	7.1600	5.4879	20.768	25.537	0.81327	0.97378	173.50
−194	0.74008	3.3630	−221.63	−1.2581	1.0727	13.966	7.3872	5.6325	16.749	20.478	0.81789	0.96838	175.17
−192	0.9469	4.2233	−220.10	−1.3074	1.0859	13.886	7.6190	5.7773	13.680	16.614	0.82337	0.9623	176.73
−190	1.1953	5.2399	−218.65	−1.3539	1.1007	13.847	7.8564	5.9225	11.303	13.622	0.82974	0.95552	178.17
−188	1.4904	6.4304	−217.27	−1.3977	1.1173	13.850	8.1002	6.0684	9.4371	11.274	0.83704	0.94803	179.50
−186	1.8374	7.8132	−215.97	−1.4394	1.1359	13.897	8.3516	6.2153	7.9549	9.4103	0.84533	0.93980	180.70
−184	2.2415	9.4081	−214.75	−1.4790	1.1566	13.989	8.6118	6.3636	6.7640	7.9140	0.85468	0.93082	181.77
−182	2.7085	11.236	−213.63	−1.5168	1.1798	14.130	8.8823	6.5137	5.7971	6.7006	0.86516	0.92107	182.72
−180	3.2438	13.320	−212.60	−1.5531	1.2056	14.323	9.165	6.6662	5.0045	5.7072	0.87688	0.91053	183.53
−178	3.8531	15.686	−211.67	−1.5880	1.2344	14.574	9.4618	6.8216	4.3490	4.8866	0.88997	0.89918	184.21
−176	4.5424	18.359	−210.86	−1.6217	1.2668	14.888	9.7755	6.9806	3.8022	4.2032	0.90460	0.88700	184.76
−174	5.3174	21.372	−210.16	−1.6544	1.3031	15.274	10.109	7.1442	3.3427	3.6296	0.92096	0.87396	185.17
−172	6.1843	24.760	−209.60	−1.6864	1.3443	15.743	10.466	7.3132	2.9537	3.1444	0.93934	0.86004	185.43
−170	7.1491	28.560	−209.17	−1.7177	1.3911	16.309	10.851	7.4889	2.6221	2.7311	0.96008	0.84520	185.56
−168	8.2181	32.821	−208.89	−1.7485	1.4448	16.989	11.269	7.6727	2.3378	2.3766	0.98364	0.82938	185.54
−166	9.3976	37.594	−208.78	−1.7791	1.5069	17.809	11.729	7.8663	2.0924	2.0704	1.01060	0.81254	185.36
−164	10.694	42.945	−208.84	−1.8095	1.5796	18.800	12.238	8.0719	1.8796	1.8041	1.04180	0.79460	185.04
−162	12.115	48.952	−209.11	−1.8401	1.6659	20.007	12.809	8.2920	1.6939	1.5708	1.07840	0.77548	184.55
−160	13.666	55.710	−209.61	−1.8710	1.7698	21.495	13.458	8.5299	1.5311	1.3649	1.12180	0.75506	183.91
−158	15.354	63.341	−210.37	−1.9025	1.8975	23.354	14.205	8.7900	1.3877	1.1818	1.17420	0.73320	183.10
−156	17.188	72.001	−211.42	−1.9350	2.0581	25.723	15.079	9.0779	1.2608	1.0176	1.23900	0.70971	182.13
−154	19.175	81.902	−212.83	−1.9688	2.2658	28.819	16.124	9.4012	1.1479	0.8689	1.32110	0.68435	180.98
−152	21.323	93.336	−214.67	−2.0045	2.5446	33.001	17.404	9.7708	1.0468	0.7328	1.42860	0.65677	179.67
−150	23.642	106.73	−217.04	−2.0429	2.9374	38.912	19.021	10.203	0.9560	0.6067	1.57570	0.62649	178.19
−148	26.144	122.75	−220.10	−2.0852	3.5294	47.822	21.152	10.724	0.8737	0.4883	1.78940	0.59274	176.55
−146	28.843	142.55	−224.14	−2.1334	4.5166	62.639	24.144	11.380	0.7983	0.3750	2.12880	0.55424	174.77
−144	31.764	168.49	−229.71	−2.1916	6.4725	91.847	28.812	12.270	0.7282	0.2642	2.75650	0.50839	172.82
−142	34.964	207.50	−238.43	−2.2718	12.181	176.500	38.048	13.697	0.6601	0.1505	4.38490	0.44749	170.61

D2.2. Table 4. Density ρ of dry air in kg/m^3

Pressure in bar	Temperature in °C										
	−150	−125	−100	−75	−50	−25	0	25	50	75	100
1	2.860	2.366	2.019	1.762	1.5632	1.4049	1.2758	1.1685	1.0779	1.0004	0.93328
5	15.007	12.146	10.257	8.897	7.8645	7.0518	6.3940	5.8500	5.3923	5.0017	4.6643
10	32.203	25.162	20.931	18.013	15.8490	14.1700	12.8230	11.7170	10.7900	10.0020	9.3227
20	79.159	54.508	43.667	36.923	32.1730	28.5940	25.7770	23.4920	21.5950	19.9920	18.617
30	605.220	90.103	68.511	56.770	48.9570	43.2480	38.8400	35.3080	32.4010	29.9600	27.876
40	624.490	135.840	95.798	77.577	66.1780	58.1070	51.9910	47.1490	43.1960	39.8960	37.091
50	639.390	199.180	125.820	99.339	83.8040	73.1430	65.2070	58.9970	53.9680	49.7920	46.257
60	651.750	288.200	158.700	122.000	101.790	88.320	78.4660	70.8380	64.7050	59.6390	55.367
70	662.390	377.410	194.180	145.440	120.060	103.600	91.7420	82.6540	75.3960	69.4300	64.415
80	671.790	437.030	231.440	169.460	138.540	118.940	105.010	94.428	86.0300	79.1560	73.397
90	680.240	476.340	269.090	193.810	157.130	134.280	118.240	106.140	96.5960	88.8100	82.307
100	687.940	504.790	305.450	218.180	175.710	149.590	131.400	117.780	107.080	98.386	91.140
150	719.020	585.850	439.950	330.190	264.770	223.640	195.260	174.280	157.980	144.850	134.010
200	742.640	631.230	515.070	413.950	340.680	290.050	253.850	226.720	205.550	188.490	174.390
250	761.990	663.570	564.110	473.840	401.340	346.750	305.730	274.170	249.190	228.890	212.020
300	778.530	688.990	600.320	518.690	449.580	394.320	350.890	316.490	288.750	265.940	246.830
350	793.060	710.100	629.070	554.080	488.720	434.340	390.060	354.030	324.420	299.750	278.900
400	806.080	728.230	652.980	583.170	521.280	468.410	424.160	387.340	356.560	330.570	308.400
450	817.910	744.200	673.490	607.850	549.020	497.830	454.110	417.050	385.580	358.700	335.540
500	828.790	758.500	691.500	629.280	573.110	523.590	480.640	443.680	411.880	384.420	360.560
600	848.280	783.400	722.120	665.230	613.390	566.930	525.770	489.550	457.750	429.790	405.110
700	865.480	804.700	747.670	694.770	646.320	602.450	563.060	527.880	496.530	468.580	443.610
800	880.920	823.410	769.700	719.920	674.180	632.490	594.720	560.630	529.920	502.250	477.290
900	894.990	840.150	789.120	741.870	698.360	658.520	622.190	589.150	559.150	531.890	507.120
1000	907.950	855.340	806.540	761.380	719.740	681.480	646.430	614.380	585.080	558.310	533.810

Pressure in bar	Temperature in °C										
	125	150	200	300	400	500	600	700	800	900	1000
1	0.87461	0.8229	0.7359	0.6075	0.5172	0.4503	0.3988	0.3578	0.3245	0.2968	0.2735
5	4.3698	4.1106	3.6749	3.0329	2.5823	2.2484	1.9911	1.7867	1.6203	1.4824	1.3660
10	8.7310	8.2109	7.3382	6.0547	5.1550	4.4888	3.9755	3.5677	3.2359	2.9606	2.7285
20	17.424	16.378	14.629	12.065	10.272	8.9456	7.9241	7.1127	6.4525	5.9047	5.4428
30	26.073	24.497	21.868	18.028	15.350	13.370	11.846	10.635	9.6500	8.8324	8.1428
40	34.673	32.564	29.055	23.945	20.388	17.762	15.741	14.135	12.828	11.744	10.829
50	43.218	40.574	36.186	29.814	25.388	22.122	19.609	17.612	15.987	14.639	13.500
60	51.705	48.525	43.260	35.635	30.348	26.449	23.450	21.067	19.128	17.517	16.158
70	60.129	56.413	50.275	41.408	35.268	30.744	27.264	24.500	22.249	20.380	18.802
80	68.486	64.237	57.230	47.131	40.149	35.007	31.052	27.910	25.351	23.226	21.431
90	76.772	71.992	64.123	52.805	44.990	39.237	34.813	31.298	28.435	26.056	24.047
100	84.986	79.678	70.954	58.429	49.791	43.435	38.547	34.663	31.499	28.870	26.649
150	124.850	116.990	104.140	85.802	73.207	63.950	56.828	51.165	46.547	42.704	39.454
200	162.500	152.300	135.640	111.930	95.653	83.686	74.471	67.135	61.143	56.152	51.925
250	197.750	185.500	165.440	136.830	117.160	102.670	91.499	82.591	75.305	69.227	64.073
300	230.580	216.560	193.540	160.530	137.750	120.930	107.940	97.554	89.049	81.943	75.909
350	261.040	245.560	219.990	183.080	157.470	138.500	123.810	112.050	102.390	94.313	87.444
400	289.260	272.580	244.850	204.520	176.360	155.410	139.140	126.080	115.350	106.350	98.689
450	315.410	297.760	268.240	224.920	194.450	171.690	153.950	139.690	127.940	118.070	109.660

D2.2. Table 4. (continued)

Temperature in °C											
Pressure in bar	125	150	200	300	400	500	600	700	800	900	1000
500	339.670	321.250	290.230	244.330	211.790	187.370	168.270	152.880	140.170	129.480	120.350
600	383.230	363.730	330.480	280.410	244.370	217.040	195.530	178.090	163.630	151.430	140.980
700	421.230	401.090	366.390	313.240	274.400	244.660	221.070	201.850	185.850	172.300	160.660
800	454.720	434.260	398.620	343.240	302.170	270.420	245.060	224.290	206.920	192.160	179.450
900	484.550	463.950	427.770	370.770	327.940	294.520	267.650	245.520	226.950	211.110	197.420
1000	511.360	490.750	454.290	396.150	351.940	317.140	288.970	265.660	246.010	229.200	214.630

D2.2. Table 5. Compression factor Z of dry air

Temperature in °C											
Pressure in bar	−150	−125	−100	−75	−50	−25	0	25	50	75	100
1	0.9889	0.9937	0.9961	0.9976	0.9984	0.9990	0.9994	0.9997	0.9999	1.0000	1.0001
5	0.9423	0.9678	0.9806	0.9879	0.9923	0.9952	0.9971	0.9984	0.9994	1.0001	1.0006
10	0.8782	0.9343	0.9610	0.9758	0.9848	0.9905	0.9944	0.9970	0.9989	1.0002	1.0012
20	0.7146	0.8626	0.9213	0.9521	0.9702	0.9817	0.9893	0.9945	0.9982	1.0008	1.0027
30	0.1402	0.7827	0.8808	0.9289	0.9564	0.9736	0.9849	0.9926	0.9979	1.0017	1.0045
40	0.1812	0.6923	0.8399	0.9063	0.9434	0.9662	0.9810	0.9911	0.9980	1.0030	1.0066
50	0.2212	0.5902	0.7993	0.8847	0.9312	0.9595	0.9777	0.9900	0.9986	1.0046	1.0089
60	0.2604	0.4894	0.7605	0.8645	0.9200	0.9535	0.9750	0.9894	0.9994	1.0065	1.0115
70	0.2989	0.4360	0.7251	0.8460	0.9100	0.9483	0.9729	0.9893	1.0007	1.0086	1.0143
80	0.3368	0.4304	0.6953	0.8298	0.9013	0.9441	0.9714	0.9897	1.0022	1.0111	1.0173
90	0.3742	0.4442	0.6728	0.8162	0.8940	0.9407	0.9706	0.9905	1.0042	1.0138	1.0206
100	0.4111	0.4657	0.6585	0.8056	0.8883	0.9383	0.9704	0.9918	1.0065	1.0168	1.0241
150	0.5900	0.6019	0.6858	0.7985	0.8842	0.9414	0.9795	1.0054	1.0234	1.0359	1.0448
200	0.7617	0.7449	0.7811	0.8492	0.9163	0.9678	1.0046	1.0305	1.0487	1.0615	1.0705
250	0.9279	0.8857	0.8914	0.9274	0.9722	1.0119	1.0427	1.0652	1.0813	1.0927	1.1006
300	1.0898	1.0236	1.0052	1.0166	1.0415	1.0678	1.0902	1.1073	1.1198	1.1285	1.1344
350	1.2482	1.1588	1.1192	1.1103	1.1178	1.1310	1.1441	1.1549	1.1628	1.1681	1.1713
400	1.4034	1.2913	1.2322	1.2056	1.1977	1.1986	1.2024	1.2063	1.2091	1.2105	1.2106
450	1.5560	1.4215	1.3440	1.3013	1.2793	1.2687	1.2635	1.2605	1.2579	1.2550	1.2518
500	1.7062	1.5497	1.4544	1.3966	1.3617	1.3403	1.3264	1.3165	1.3084	1.3012	1.2943
600	2.0004	1.8006	1.6713	1.5854	1.5267	1.4854	1.4551	1.4317	1.4127	1.3966	1.3824
700	2.2874	2.0450	1.8832	1.7709	1.6904	1.6308	1.5852	1.5491	1.5195	1.4945	1.4728
800	2.5684	2.2841	2.0907	1.9532	1.8521	1.7753	1.7152	1.6669	1.6271	1.5935	1.5645
900	2.8440	2.5184	2.2941	2.1324	2.0114	1.9182	1.8444	1.7845	1.7348	1.6927	1.6565
1000	3.1149	2.7485	2.4940	2.3086	2.1685	2.0595	1.9725	1.9014	1.8421	1.7919	1.7485
Temperature in °C											
Pressure in bar	125	150	200	300	400	500	600	700	800	900	1000
1	1.0002	1.0002	1.0003	1.0004	1.0004	1.0004	1.0003	1.0003	1.0003	1.0003	1.0003
5	1.0009	1.0012	1.0015	1.0018	1.0018	1.0018	1.0017	1.0016	1.0015	1.0014	1.0013
10	1.0019	1.0024	1.0031	1.0036	1.0037	1.0036	1.0034	1.0032	1.0030	1.0028	1.0026
20	1.0041	1.0051	1.0064	1.0074	1.0074	1.0072	1.0068	1.0064	1.0060	1.0056	1.0052
30	1.0065	1.0080	1.0098	1.0112	1.0112	1.0108	1.0102	1.0096	1.0090	1.0084	1.0079

D2.2. Table 5. (continued)

Pressure in bar	Temperature in °C										
	125	150	200	300	400	500	600	700	800	900	1000
40	1.0092	1.0111	1.0134	1.0151	1.0151	1.0145	1.0137	1.0128	1.0120	1.0112	1.0105
50	1.0120	1.0143	1.0171	1.0191	1.0190	1.0182	1.0171	1.0160	1.0150	1.0141	1.0132
60	1.0151	1.0177	1.0210	1.0232	1.0230	1.0219	1.0206	1.0193	1.0181	1.0169	1.0158
70	1.0184	1.0213	1.0249	1.0273	1.0269	1.0257	1.0241	1.0226	1.0211	1.0197	1.0185
80	1.0218	1.0251	1.0290	1.0315	1.0310	1.0295	1.0277	1.0259	1.0242	1.0226	1.0212
90	1.0255	1.0290	1.0332	1.0357	1.0350	1.0333	1.0312	1.0292	1.0273	1.0255	1.0239
100	1.0293	1.0330	1.0374	1.0400	1.0392	1.0371	1.0348	1.0325	1.0303	1.0283	1.0265
150	1.0510	1.0554	1.0603	1.0624	1.0602	1.0566	1.0529	1.0492	1.0459	1.0428	1.0401
200	1.0767	1.0809	1.0853	1.0858	1.0818	1.0766	1.0713	1.0662	1.0616	1.0574	1.0537
250	1.1059	1.1093	1.1123	1.1103	1.1041	1.0969	1.0899	1.0833	1.0774	1.0721	1.0674
300	1.1381	1.1402	1.1410	1.1356	1.1268	1.1175	1.1087	1.1006	1.0934	1.0869	1.0812
350	1.1729	1.1732	1.1712	1.1617	1.1500	1.1384	1.1276	1.1180	1.1094	1.1018	1.0950
400	1.2097	1.2079	1.2025	1.1885	1.1735	1.1594	1.1467	1.1354	1.1255	1.1166	1.1088
450	1.2480	1.2439	1.2349	1.2158	1.1974	1.1807	1.1659	1.1530	1.1416	1.1315	1.1227
500	1.2877	1.2811	1.2681	1.2436	1.2215	1.2021	1.1852	1.1705	1.1577	1.1464	1.1365
600	1.3696	1.3578	1.3364	1.3003	1.2704	1.2453	1.2241	1.2058	1.1900	1.1763	1.1642
700	1.4537	1.4365	1.4064	1.3580	1.3199	1.2889	1.2631	1.2412	1.2224	1.2062	1.1919
800	1.5390	1.5163	1.4773	1.4164	1.3698	1.3327	1.3022	1.2766	1.2548	1.2360	1.2196
900	1.6248	1.5967	1.5487	1.4751	1.4200	1.3766	1.3413	1.3119	1.2871	1.2657	1.2471
1000	1.7107	1.6772	1.6204	1.5339	1.4702	1.4205	1.3804	1.3472	1.3193	1.2953	1.2746

D2.2. Table 6. Specific enthalpy h of dry air in kJ/kg

Pressure in bar	Temperature in °C										
	−150	−125	−100	−75	−50	−25	0	25	50	75	100
1	−176.47	−151.07	−125.80	−100.61	−75.44	−50.30	−25.15	0.00	25.18	50.39	75.65
5	−181.40	−154.48	−128.36	−102.60	−77.05	−51.61	−26.24	−0.91	24.41	49.74	75.10
10	−188.29	−158.97	−131.63	−105.13	−79.07	−53.26	−27.60	−2.04	23.46	48.94	74.43
20	−206.60	−168.83	−138.45	−110.27	−83.11	−56.52	−30.29	−4.28	21.60	47.38	73.12
30	−325.76	−180.29	−145.68	−115.52	−87.17	−59.77	−32.94	−6.46	19.78	45.86	71.85
40	−327.72	−194.14	−153.34	−120.88	−91.24	−62.99	−35.54	−8.60	18.00	44.38	70.62
50	−328.98	−211.58	−161.41	−126.32	−95.30	−66.17	−38.10	−10.70	16.27	42.95	69.43
60	−329.85	−232.79	−169.80	−131.80	−99.33	−69.31	−40.62	−12.75	14.59	41.56	68.28
70	−330.44	−250.57	−178.33	−137.25	−103.32	−72.39	−43.07	−14.74	12.95	40.21	67.17
80	−330.84	−260.81	−186.72	−142.62	−107.22	−75.40	−45.47	−16.69	11.36	38.90	66.09
90	−331.09	−266.84	−194.64	−147.83	−111.02	−78.33	−47.80	−18.57	9.82	37.63	65.06
100	−331.22	−270.78	−201.79	−152.81	−114.69	−81.17	−50.06	−20.40	8.32	36.41	64.06
150	−330.72	−279.19	−223.68	−172.79	−130.43	−93.64	−60.09	−28.55	1.67	30.98	59.64
200	−329.08	−281.28	−231.98	−184.26	−141.29	−102.92	−67.82	−34.94	−3.58	26.69	56.18
250	−326.82	−281.17	−235.10	−190.09	−147.95	−109.21	−73.34	−39.62	−7.46	23.53	53.67
300	−324.15	−279.92	−235.84	−192.74	−151.65	−113.12	−76.97	−42.79	−10.12	21.39	52.02
350	−321.20	−277.98	−235.25	−193.51	−153.37	−115.24	−79.10	−44.69	−11.71	20.16	51.33
400	−318.05	−275.60	−233.84	−193.09	−153.73	−116.04	−80.04	−45.57	−12.41	19.69	50.92
450	−314.75	−272.89	−231.87	−191.88	−153.16	−115.88	−80.07	−45.63	−12.38	19.87	51.29
500	−311.34	−269.94	−229.49	−190.10	−151.90	−114.99	−79.39	−45.02	−11.74	20.59	52.14

D2.2. Table 6. (continued)

Temperature in °C											
Pressure in bar	−150	−125	−100	−75	−50	−25	0	25	50	75	100
600	−304.24	−263.54	−223.93	−185.40	−147.97	−111.67	−76.46	−42.29	−9.05	23.35	55.05
700	−296.89	−256.68	−217.64	−179.70	−142.81	−106.95	−72.07	−38.11	−4.97	27.43	59.19
800	−289.38	−249.52	−210.88	−173.35	−136.86	−101.34	−66.72	−32.93	0.10	32.46	64.23
900	−281.74	−242.14	−203.80	−166.58	−130.38	−95.11	−60.69	−27.06	5.88	38.19	69.95
1000	−274.03	−234.62	−196.49	−159.50	−123.51	−88.44	−54.18	−20.67	12.18	44.45	76.19

Temperature in °C											
Pressure in bar	125	150	200	300	400	500	600	700	800	900	1000
1	100.97	126.36	177.42	280.90	386.60	494.67	605.09	717.68	832.22	948.49	1066.30
5	100.51	125.98	177.16	280.82	386.63	494.78	605.26	717.90	832.48	948.77	1066.60
10	99.95	125.51	176.84	280.72	386.67	494.93	605.48	718.17	832.80	949.13	1067.00
20	98.85	124.60	176.23	280.53	386.76	495.22	605.92	718.73	833.44	949.84	1067.70
30	97.79	123.72	175.65	280.37	386.88	495.53	606.37	719.29	834.08	950.55	1068.50
40	96.77	122.88	175.10	280.23	387.01	495.85	606.83	719.86	834.74	951.27	1069.30
50	95.79	122.07	174.58	280.11	387.15	496.18	607.31	720.43	835.40	952.00	1070.00
60	94.84	121.30	174.09	280.01	387.31	496.53	607.78	721.02	836.06	952.73	1070.80
70	93.93	120.55	173.62	279.92	387.48	496.88	608.27	721.61	836.73	953.46	1071.60
80	93.05	119.84	173.18	279.86	387.67	497.24	608.77	722.20	837.41	954.20	1072.40
90	92.20	119.16	172.76	279.81	387.87	497.62	609.27	722.81	838.09	954.94	1073.20
100	91.39	118.51	172.37	279.78	388.08	498.00	609.78	723.41	838.77	955.69	1074.00
150	87.83	115.68	170.74	279.85	389.29	500.04	612.43	726.53	842.27	959.48	1078.00
200	85.09	113.57	169.68	280.29	390.77	502.26	615.23	729.77	845.85	963.35	1082.10
250	83.15	112.15	169.14	281.07	392.48	504.66	618.15	733.11	849.52	967.28	1086.30
300	81.95	111.37	169.08	282.16	394.40	507.21	621.18	736.53	853.25	971.27	1090.50
350	81.42	111.16	169.48	283.53	396.51	509.90	624.32	740.03	857.05	975.31	1094.70
400	81.47	111.48	170.29	285.17	398.81	512.71	627.56	743.61	860.90	979.40	1099.00
450	82.04	112.25	171.45	287.05	401.28	515.65	630.88	747.24	864.80	983.52	1103.30
500	83.04	113.41	172.95	289.16	403.90	518.70	634.29	750.94	868.75	987.67	1107.60
600	86.14	116.74	176.76	293.95	409.56	525.10	641.32	758.51	876.77	996.08	1116.40
700	90.39	121.12	181.47	299.39	415.69	531.86	648.61	766.27	884.93	1004.60	1125.20
800	95.48	126.30	186.88	305.36	422.23	538.91	656.13	774.20	893.22	1013.20	1134.10
900	101.23	132.10	192.85	311.75	429.09	546.22	663.84	782.27	901.61	1021.90	1143.00
1000	107.49	138.39	199.25	318.50	436.22	553.73	671.71	790.46	910.10	1030.60	1152.00

D2.2. Table 7. Specific entropy *s* of dry air in kJ/(kg K)

Temperature in °C											
Pressure in bar	−150	−125	−100	−75	−50	−25	0	25	50	75	100
1	−0.8886	−0.7008	−0.5432	−0.4073	−0.2877	−0.1809	−0.0843	0.0038	0.0849	0.1600	0.2301
5	−1.3777	−1.1786	−1.0156	−0.8767	−0.7552	−0.6471	−0.5497	−0.4610	−0.3794	−0.3039	−0.2336
10	−1.6157	−1.3985	−1.2279	−1.0849	−0.9610	−0.8514	−0.7529	−0.6634	−0.5812	−0.5053	−0.4346
20	−1.9258	−1.6448	−1.4551	−1.3030	−1.1739	−1.0609	−0.9602	−0.8690	−0.7857	−0.7089	−0.6375
30	−2.9387	−1.8184	−1.6019	−1.4391	−1.3042	−1.1878	−1.0848	−0.9921	−0.9075	−0.8298	−0.7577
40	−2.9678	−1.9730	−1.7173	−1.5419	−1.4010	−1.2809	−1.1755	−1.0812	−0.9955	−0.9168	−0.8440
50	−2.9910	−2.1320	−1.8164	−1.6268	−1.4792	−1.3554	−1.2477	−1.1516	−1.0648	−0.9852	−0.9118

D2.2. Table 7. (continued)

Temperature in °C											
Pressure in bar	−150	−125	−100	−75	−50	−25	0	25	50	75	100
60	−3.0106	−2.3034	−1.9057	−1.7002	−1.5458	−1.4181	−1.3080	−1.2103	−1.1223	−1.0419	−0.9677
70	−3.0277	−2.4437	−1.9879	−1.7656	−1.6041	−1.4726	−1.3601	−1.2608	−1.1716	−1.0903	−1.0156
80	−3.0431	−2.5293	−2.0636	−1.8248	−1.6563	−1.5211	−1.4061	−1.3053	−1.2149	−1.1328	−1.0574
90	−3.0572	−2.5848	−2.1325	−1.8789	−1.7037	−1.5647	−1.4475	−1.3451	−1.2536	−1.1707	−1.0946
100	−3.0701	−2.6251	−2.1938	−1.9286	−1.7471	−1.6046	−1.4851	−1.3812	−1.2886	−1.2049	−1.1282
150	−3.1237	−2.7433	−2.3972	−2.1221	−1.9204	−1.7640	−1.6351	−1.5246	−1.4272	−1.3399	−1.2604
200	−3.1659	−2.8128	−2.5053	−2.2477	−2.0432	−1.8801	−1.7452	−1.6300	−1.5290	−1.4387	−1.3569
250	−3.2015	−2.8641	−2.5768	−2.3338	−2.1334	−1.9687	−1.8309	−1.7127	−1.6091	−1.5167	−1.4331
300	−3.2325	−2.9055	−2.6306	−2.3979	−2.2026	−2.0388	−1.8999	−1.7801	−1.6749	−1.5810	−1.4960
350	−3.2603	−2.9407	−2.6741	−2.4488	−2.2580	−2.0959	−1.9571	−1.8366	−1.7303	−1.6353	−1.5494
400	−3.2855	−2.9715	−2.7110	−2.4911	−2.3040	−2.1438	−2.0055	−1.8847	−1.7779	−1.6822	−1.5956
450	−3.3087	−2.9991	−2.7431	−2.5273	−2.3432	−2.1848	−2.0473	−1.9266	−1.8195	−1.7234	−1.6362
500	−3.3302	−3.0241	−2.7717	−2.5591	−2.3775	−2.2207	−2.0840	−1.9635	−1.8563	−1.7599	−1.6724
600	−3.3694	−3.0684	−2.8213	−2.6133	−2.4354	−2.2811	−2.1459	−2.0262	−1.9191	−1.8225	−1.7346
700	−3.4045	−3.1071	−2.8635	−2.6587	−2.4834	−2.3310	−2.1971	−2.0781	−1.9713	−1.8747	−1.7866
800	−3.4365	−3.1416	−2.9006	−2.6980	−2.5246	−2.3736	−2.2407	−2.1223	−2.0159	−1.9194	−1.8313
900	−3.4659	−3.1730	−2.9337	−2.7329	−2.5608	−2.4109	−2.2788	−2.1609	−2.0548	−1.9585	−1.8704
1000	−3.4933	−3.2018	−2.9639	−2.7643	−2.5932	−2.4442	−2.3126	−2.1952	−2.0894	−1.9932	−1.9052
Temperature in °C											
Pressure in bar	125	150	200	300	400	500	600	700	800	900	1000
1	0.2958	0.3576	0.4717	0.6700	0.8399	0.9896	1.1239	1.2459	1.3580	1.4615	1.5579
5	−0.1677	−0.1057	0.0087	0.2074	0.3775	0.5272	0.6616	0.7837	0.8958	0.9994	1.0957
10	−0.3684	−0.3061	−0.1915	0.0076	0.1780	0.3279	0.4623	0.5845	0.6966	0.8003	0.8966
20	−0.5707	−0.5080	−0.3927	−0.1927	−0.0219	0.1282	0.2629	0.3852	0.4974	0.6010	0.6975
30	−0.6904	−0.6272	−0.5112	−0.3105	−0.1393	0.0112	0.1460	0.2684	0.3807	0.4844	0.5809
40	−0.7762	−0.7126	−0.5960	−0.3944	−0.2228	−0.0720	0.0629	0.1855	0.2978	0.4016	0.4982
50	−0.8434	−0.7794	−0.6621	−0.4598	−0.2877	−0.1367	−0.0016	0.1211	0.2335	0.3374	0.4339
60	−0.8989	−0.8344	−0.7165	−0.5134	−0.3409	−0.1897	−0.0544	0.0684	0.1809	0.2849	0.3815
70	−0.9461	−0.8813	−0.7627	−0.5589	−0.3860	−0.2345	−0.0990	0.0238	0.1364	0.2404	0.3371
80	−0.9875	−0.9222	−0.8030	−0.5985	−0.4252	−0.2734	−0.1378	−0.0148	0.0978	0.2019	0.2986
90	−1.0242	−0.9585	−0.8388	−0.6336	−0.4598	−0.3078	−0.1720	−0.0490	0.0638	0.1679	0.2646
100	−1.0573	−0.9913	−0.8710	−0.6650	−0.4909	−0.3387	−0.2027	−0.0795	0.0333	0.1375	0.2342
150	−1.1872	−1.1194	−0.9964	−0.7872	−0.6112	−0.4578	−0.3211	−0.1974	−0.0842	0.0202	0.1172
200	−1.2819	−1.2125	−1.0872	−0.8751	−0.6974	−0.5430	−0.4056	−0.2814	−0.1679	−0.0632	0.0339
250	−1.3566	−1.2860	−1.1587	−0.9440	−0.7649	−0.6095	−0.4715	−0.3468	−0.2330	−0.1281	−0.0307
300	−1.4183	−1.3467	−1.2177	−1.0009	−0.8204	−0.6641	−0.5255	−0.4005	−0.2863	−0.1812	−0.0836
350	−1.4708	−1.3983	−1.2680	−1.0493	−0.8676	−0.7106	−0.5714	−0.4460	−0.3315	−0.2261	−0.1285
400	−1.5163	−1.4432	−1.3118	−1.0915	−0.9087	−0.7510	−0.6113	−0.4855	−0.3707	−0.2652	−0.1674
450	−1.5564	−1.4828	−1.3506	−1.1288	−0.9451	−0.7867	−0.6466	−0.5204	−0.4054	−0.2997	−0.2017
500	−1.5922	−1.5183	−1.3852	−1.1624	−0.9778	−0.8188	−0.6782	−0.5518	−0.4365	−0.3306	−0.2325
600	−1.6539	−1.5794	−1.4453	−1.2205	−1.0346	−0.8746	−0.7332	−0.6062	−0.4905	−0.3842	−0.2858
700	−1.7057	−1.6308	−1.4960	−1.2698	−1.0828	−0.9219	−0.7799	−0.6523	−0.5362	−0.4296	−0.3310
800	−1.7502	−1.6752	−1.5398	−1.3126	−1.1246	−0.9630	−0.8204	−0.6924	−0.5760	−0.4691	−0.3702
900	−1.7892	−1.7140	−1.5783	−1.3503	−1.1616	−0.9993	−0.8563	−0.7279	−0.6111	−0.5040	−0.4049
1000	−1.8240	−1.7487	−1.6127	−1.3840	−1.1947	−1.0319	−0.8884	−0.7597	−0.6426	−0.5353	−0.4360

D2.2. Table 8. Specific isobaric heat capacity c_p of dry air in kJ/kg (kg K)

Temperature in °C											
Pressure in bar	−150	−125	−100	−75	−50	−25	0	25	50	75	100
1	1.0206	1.0126	1.0090	1.0071	1.0061	1.0058	1.0059	1.0065	1.0077	1.0093	1.0115
5	1.1049	1.0565	1.0360	1.0254	1.0194	1.0159	1.0139	1.0129	1.0129	1.0137	1.0152
10	1.2512	1.1206	1.0729	1.0496	1.0366	1.0288	1.0239	1.0210	1.0196	1.0193	1.0199
20	1.9732	1.2939	1.1589	1.1025	1.0729	1.0553	1.0443	1.0372	1.0328	1.0302	1.0292
30	3.1906	1.5720	1.2651	1.1617	1.1115	1.0829	1.0651	1.0536	1.0460	1.0412	1.0384
40	2.8042	2.0715	1.3956	1.2273	1.1524	1.1113	1.0862	1.0700	1.0591	1.0520	1.0475
50	2.5864	3.0575	1.5531	1.2989	1.1951	1.1403	1.1075	1.0863	1.0722	1.0627	1.0564
60	2.4418	4.4725	1.7355	1.3751	1.2391	1.1697	1.1288	1.1026	1.0851	1.0733	1.0652
70	2.3367	4.3335	1.9317	1.4537	1.2836	1.1991	1.1499	1.1187	1.0979	1.0836	1.0739
80	2.2560	3.5940	2.1197	1.5319	1.3278	1.2281	1.1708	1.1346	1.1104	1.0939	1.0824
90	2.1915	3.0994	2.2702	1.6064	1.3706	1.2565	1.1912	1.1501	1.1227	1.1038	1.0907
100	2.1384	2.7881	2.3592	1.6741	1.4113	1.2837	1.2109	1.1652	1.1347	1.1136	1.0988
150	1.9679	2.1643	2.2000	1.8506	1.5625	1.3960	1.2960	1.2318	1.1883	1.1578	1.1360
200	1.8729	1.9514	1.9704	1.8228	1.6184	1.4609	1.3540	1.2812	1.2302	1.1936	1.1668
250	1.8114	1.8398	1.8350	1.7521	1.6161	1.4873	1.3875	1.3143	1.2606	1.2209	1.1912
300	1.7679	1.7697	1.7507	1.6898	1.5932	1.4911	1.4035	1.3345	1.2815	1.2410	1.2100
350	1.7355	1.7213	1.6938	1.6415	1.5666	1.4843	1.4087	1.3457	1.2952	1.2554	1.2242
400	1.7105	1.6857	1.6528	1.6045	1.5420	1.4733	1.4079	1.3510	1.3037	1.2654	1.2347
450	1.6907	1.6585	1.6219	1.5757	1.5206	1.4614	1.4040	1.3525	1.3086	1.2722	1.2425
500	1.6747	1.6371	1.5979	1.5529	1.5026	1.4499	1.3987	1.3519	1.3112	1.2767	1.2481
600	1.6504	1.6058	1.5631	1.5194	1.4746	1.4300	1.3870	1.3474	1.3120	1.2813	1.2551
700	1.6334	1.5843	1.5395	1.4964	1.4546	1.4143	1.3764	1.3415	1.3101	1.2824	1.2585
800	1.6209	1.5690	1.5227	1.4800	1.4399	1.4024	1.3676	1.3359	1.3073	1.2820	1.2599
900	1.6117	1.5577	1.5105	1.4679	1.4289	1.3931	1.3605	1.3309	1.3044	1.2809	1.2604
1000	1.6048	1.5494	1.5015	1.4589	1.4207	1.3861	1.3548	1.3268	1.3018	1.2797	1.2603

Temperature in °C											
Pressure in bar	125	150	200	300	400	500	600	700	800	900	1000
1	1.0142	1.0174	1.0252	1.0454	1.0688	1.0927	1.1154	1.1361	1.1544	1.1706	1.1846
5	1.0174	1.0202	1.0274	1.0467	1.0697	1.0934	1.1159	1.1365	1.1547	1.1708	1.1849
10	1.0214	1.0237	1.0301	1.0485	1.0709	1.0942	1.1166	1.1370	1.1551	1.1711	1.1851
20	1.0294	1.0305	1.0354	1.0519	1.0732	1.0959	1.1178	1.1379	1.1559	1.1717	1.1856
30	1.0372	1.0373	1.0405	1.0552	1.0755	1.0976	1.1191	1.1389	1.1567	1.1724	1.1861
40	1.0449	1.0440	1.0456	1.0584	1.0778	1.0992	1.1203	1.1398	1.1574	1.1730	1.1866
50	1.0525	1.0505	1.0507	1.0616	1.0800	1.1008	1.1215	1.1408	1.1581	1.1735	1.1871
60	1.0600	1.0569	1.0556	1.0648	1.0821	1.1024	1.1227	1.1417	1.1589	1.1741	1.1876
70	1.0673	1.0633	1.0604	1.0678	1.0843	1.1039	1.1238	1.1426	1.1596	1.1747	1.1880
80	1.0745	1.0694	1.0651	1.0709	1.0863	1.1054	1.1250	1.1435	1.1603	1.1753	1.1885
90	1.0816	1.0755	1.0697	1.0738	1.0884	1.1069	1.1261	1.1444	1.1610	1.1758	1.1889
100	1.0885	1.0814	1.0743	1.0767	1.0904	1.1084	1.1272	1.1452	1.1617	1.1764	1.1894
150	1.1202	1.1088	1.0954	1.0904	1.1000	1.1154	1.1326	1.1494	1.1650	1.1791	1.1916
200	1.1470	1.1323	1.1138	1.1027	1.1087	1.1219	1.1375	1.1533	1.1681	1.1816	1.1937
250	1.1688	1.1519	1.1297	1.1136	1.1166	1.1279	1.1422	1.1570	1.1711	1.1840	1.1957
300	1.1861	1.1678	1.1431	1.1232	1.1238	1.1334	1.1465	1.1604	1.1739	1.1864	1.1976
350	1.1997	1.1806	1.1543	1.1317	1.1303	1.1384	1.1505	1.1637	1.1766	1.1886	1.1995
400	1.2103	1.1909	1.1637	1.1391	1.1361	1.1431	1.1542	1.1667	1.1791	1.1907	1.2012

D2.2. Table 8. (continued)

Pressure in bar	Temperature in °C										
	125	150	200	300	400	500	600	700	800	900	1000
450	1.2184	1.1990	1.1714	1.1456	1.1413	1.1473	1.1577	1.1696	1.1815	1.1927	1.2029
500	1.2246	1.2056	1.1779	1.1512	1.1460	1.1512	1.1610	1.1723	1.1837	1.1946	1.2046
600	1.2331	1.2149	1.1879	1.1605	1.1541	1.1580	1.1667	1.1772	1.1879	1.1982	1.2076
700	1.2381	1.2209	1.1950	1.1678	1.1607	1.1638	1.1718	1.1815	1.1917	1.2014	1.2105
800	1.2410	1.2248	1.2001	1.1735	1.1661	1.1687	1.1761	1.1854	1.1951	1.2044	1.2131
900	1.2426	1.2274	1.2039	1.1782	1.1707	1.1730	1.1800	1.1888	1.1981	1.2071	1.2155
1000	1.2435	1.2291	1.2068	1.1820	1.1746	1.1767	1.1833	1.1919	1.2009	1.2096	1.2177

D2.2. Table 9. Thermal conductivity λ of dry air in mW/(mK)

Pressure in bar	Temperature in °C										
	−150	−125	−100	−75	−50	−25	0	25	50	75	100
1	11.679	13.984	16.205	18.347	20.416	22.418	24.360	26.247	28.082	29.872	31.620
5	12.088	14.293	16.456	18.558	20.599	22.579	24.504	26.376	28.201	29.981	31.720
10	12.809	14.765	16.817	18.854	20.849	22.797	24.696	26.549	28.357	30.124	31.852
20	15.903	16.074	17.714	19.550	21.422	23.284	25.118	26.925	28.696	30.432	32.134
30	68.194	18.097	18.865	20.386	22.086	23.836	25.589	27.340	29.067	30.767	32.439
40	71.300	21.364	20.305	21.360	22.835	24.447	26.102	27.789	29.466	31.126	32.765
50	74.010	26.955	22.064	22.469	23.663	25.111	26.653	28.269	29.892	31.508	33.111
60	76.460	35.540	24.166	23.708	24.564	25.823	27.238	28.777	30.340	31.909	33.473
70	78.718	42.807	26.611	25.071	25.530	26.577	27.853	29.309	30.808	32.327	33.851
80	80.829	47.734	29.356	26.547	26.557	27.370	28.495	29.862	31.295	32.761	34.243
90	82.820	51.522	32.298	28.127	27.639	28.198	29.160	30.435	31.798	33.209	34.646
100	84.710	54.641	35.290	29.795	28.770	29.056	29.846	31.024	32.314	33.669	35.061
150	93.066	65.987	47.908	38.623	34.939	33.716	33.534	34.170	35.065	36.115	37.263
200	100.160	74.556	56.916	46.559	41.223	38.672	37.508	37.550	38.011	38.731	39.617
250	106.410	81.886	64.314	53.295	46.985	43.506	41.545	41.025	41.059	41.445	42.064
300	112.030	88.410	70.883	59.302	52.228	48.044	45.469	44.465	44.115	44.190	44.552
350	117.150	94.330	76.900	64.864	57.126	52.319	49.228	47.800	47.112	46.908	47.037
400	121.850	99.765	82.487	70.108	61.798	56.414	52.848	51.020	50.021	49.566	49.484
450	126.170	104.800	87.712	75.092	66.302	60.392	56.371	54.149	52.848	52.154	51.876
500	130.300	109.480	92.621	79.846	70.664	64.285	59.831	57.219	55.613	54.682	54.213
600	137.810	117.990	101.630	88.733	78.994	71.852	66.630	63.266	61.041	59.618	58.761
700	144.540	125.530	109.720	96.878	86.815	79.127	73.285	69.251	66.424	64.496	63.226
800	150.640	132.430	117.060	104.370	94.144	86.084	79.767	75.169	71.796	69.375	67.683
900	156.220	138.710	123.710	111.270	101.010	92.706	86.039	80.986	77.140	74.267	72.164
1000	161.380	144.490	129.930	117.660	107.430	98.991	92.074	86.664	82.423	79.149	76.665

Pressure in bar	Temperature in °C										
	125	150	200	300	400	500	600	700	800	900	1000
1	33.328	35.000	38.248	44.417	50.240	55.795	61.139	66.312	71.348	76.271	81.099
5	33.421	35.088	38.325	44.479	50.292	55.839	61.177	66.347	71.379	76.298	81.124
10	33.543	35.201	38.425	44.559	50.358	55.896	61.227	66.390	71.418	76.334	81.157
20	33.803	35.442	38.635	44.726	50.496	56.014	61.329	66.480	71.499	76.406	81.223
30	34.084	35.701	38.860	44.903	50.641	56.136	61.435	66.574	71.582	76.481	81.291

D2.2. Table 9. (continued)

Pressure in bar	Temperature in °C										
	125	150	200	300	400	500	600	700	800	900	1000
40	34.382	35.977	39.097	45.088	50.793	56.264	61.545	66.670	71.667	76.558	81.361
50	34.698	36.267	39.347	45.282	50.951	56.396	61.659	66.770	71.756	76.638	81.433
60	35.028	36.570	39.607	45.484	51.114	56.533	61.776	66.872	71.847	76.719	81.506
70	35.372	36.886	39.877	45.692	51.283	56.674	61.897	66.978	71.940	76.803	81.582
80	35.729	37.212	40.156	45.907	51.457	56.819	62.021	67.086	72.035	76.888	81.659
90	36.096	37.549	40.444	46.129	51.635	56.968	62.148	67.196	72.133	76.975	81.737
100	36.473	37.894	40.739	46.356	51.818	57.121	62.278	67.309	72.233	77.064	81.818
150	38.475	39.728	42.307	47.562	52.791	57.931	62.969	67.909	72.761	77.535	82.241
200	40.615	41.690	43.987	48.860	53.840	58.806	63.715	68.556	73.331	78.042	82.698
250	42.843	43.735	45.742	50.222	54.946	59.730	64.505	69.243	73.936	78.581	83.183
300	45.117	45.828	47.546	51.629	56.093	60.693	65.330	69.962	74.570	79.147	83.692
350	47.402	47.941	49.378	53.069	57.271	61.685	66.183	70.707	75.228	79.735	84.221
400	49.667	50.047	51.220	54.530	58.474	62.701	67.059	71.473	75.907	80.342	84.769
450	51.893	52.127	53.055	56.002	59.693	63.736	67.953	72.257	76.603	80.966	85.333
500	54.072	54.171	54.872	57.477	60.924	64.785	68.863	73.057	77.314	81.604	85.910
600	58.306	58.144	58.424	60.407	63.397	66.909	70.714	74.691	78.772	82.915	87.098
700	62.437	62.004	61.868	63.281	65.858	69.047	72.592	76.358	80.265	84.263	88.324
800	66.542	65.816	65.238	66.087	68.284	71.176	74.479	78.044	81.782	85.638	89.577
900	70.664	69.632	68.580	68.836	70.666	73.282	76.360	79.735	83.312	87.031	90.851
1000	74.817	73.478	71.928	71.551	73.007	75.359	78.226	81.424	84.848	88.434	92.139

D2.2. Table 10. Dynamic viscosity η of dry air in 10^{-6} Pa·s

Pressure in bar	Temperature in °C										
	−150	−125	−100	−75	−50	−25	0	25	50	75	100
1	8.664	10.261	11.780	13.229	14.614	15.942	17.218	18.448	19.635	20.783	21.896
5	8.750	10.344	11.859	13.303	14.684	16.008	17.280	18.506	19.690	20.836	21.946
10	8.918	10.480	11.977	13.409	14.780	16.097	17.363	18.583	19.762	20.904	22.010
20	9.631	10.884	12.285	13.666	15.004	16.296	17.544	18.749	19.916	21.047	22.144
30	45.850	11.539	12.701	13.984	15.267	16.523	17.745	18.931	20.082	21.200	22.286
40	49.163	12.617	13.247	14.369	15.571	16.778	17.966	19.127	20.259	21.361	22.435
50	51.933	14.525	13.947	14.823	15.916	17.059	18.205	19.337	20.447	21.532	22.591
60	54.379	18.094	14.829	15.350	16.300	17.366	18.463	19.560	20.644	21.709	22.753
70	56.603	23.028	15.918	15.952	16.725	17.698	18.737	19.795	20.851	21.894	22.921
80	58.665	27.373	17.223	16.629	17.187	18.053	19.028	20.042	21.066	22.086	23.094
90	60.602	30.839	18.729	17.379	17.687	18.430	19.333	20.300	21.290	22.284	23.272
100	62.438	33.705	20.388	18.197	18.221	18.829	19.653	20.568	21.521	22.488	23.455
150	70.614	43.949	28.901	23.009	21.323	21.090	21.431	22.036	22.774	23.583	24.429
200	77.771	51.399	36.003	28.162	24.859	23.671	23.437	23.671	24.154	24.776	25.480
250	84.346	57.676	41.945	33.032	28.507	26.419	25.590	25.423	25.624	26.041	26.590
300	90.546	63.288	47.165	37.524	32.095	29.230	27.828	27.254	27.162	27.362	27.746
350	96.486	68.468	51.906	41.691	35.561	32.038	30.109	29.138	28.751	28.727	28.939
400	102.240	73.345	56.308	45.596	38.893	34.810	32.405	31.057	30.377	30.129	30.164
450	107.860	77.997	60.458	49.291	42.099	37.532	34.697	32.994	32.032	31.559	31.417
500	113.370	82.479	64.412	52.816	45.191	40.197	36.974	34.940	33.706	33.013	32.694

D2.2. Table 10. (continued)

Pressure in bar	Temperature in °C										
	−150	−125	−100	−75	−50	−25	0	25	50	75	100
600	124.190	91.067	71.885	59.472	51.086	45.358	41.457	38.827	37.087	35.973	35.306
700	134.830	99.307	78.939	65.731	56.669	50.315	45.833	42.681	40.483	38.977	37.976
800	145.380	107.310	85.697	71.699	62.009	55.095	50.102	46.484	43.872	42.001	40.684
900	155.890	115.160	92.242	77.446	67.156	59.727	54.270	50.232	47.240	45.032	43.417
1000	166.410	122.910	98.627	83.021	72.146	64.233	58.348	53.922	50.581	48.058	46.163

Pressure in bar	Temperature in °C										
	125	150	200	300	400	500	600	700	800	900	1000
1	22.977	24.027	26.046	29.811	33.284	36.530	39.597	42.517	45.317	48.018	50.635
5	23.024	24.072	26.087	29.845	33.314	36.557	39.621	42.538	45.337	48.036	50.651
10	23.085	24.129	26.139	29.890	33.352	36.591	39.650	42.565	45.361	48.058	50.672
20	23.211	24.249	26.247	29.980	33.429	36.658	39.710	42.619	45.410	48.103	50.713
30	23.344	24.374	26.358	30.071	33.508	36.726	39.771	42.674	45.459	48.148	50.754
40	23.482	24.503	26.473	30.165	33.587	36.796	39.832	42.728	45.509	48.193	50.796
50	23.626	24.637	26.591	30.261	33.668	36.865	39.893	42.783	45.558	48.238	50.837
60	23.775	24.775	26.712	30.358	33.750	36.936	39.955	42.838	45.608	48.284	50.879
70	23.929	24.917	26.836	30.457	33.832	37.007	40.018	42.894	45.658	48.329	50.921
80	24.087	25.063	26.962	30.557	33.915	37.078	40.080	42.950	45.709	48.375	50.963
90	24.249	25.212	27.090	30.658	33.999	37.150	40.143	43.006	45.759	48.421	51.005
100	24.415	25.364	27.221	30.761	34.084	37.223	40.207	43.062	45.810	48.467	51.047
150	25.293	26.164	27.902	31.290	34.518	37.591	40.527	43.346	46.065	48.698	51.259
200	26.234	27.016	28.620	31.838	34.964	37.967	40.853	43.634	46.322	48.931	51.472
250	27.222	27.907	29.366	32.402	35.419	38.349	41.183	43.924	46.581	49.165	51.685
300	28.248	28.830	30.133	32.978	35.881	38.736	41.515	44.216	46.842	49.401	51.900
350	29.306	29.779	30.920	33.564	36.348	39.126	41.850	44.509	47.103	49.636	52.114
400	30.392	30.752	31.724	34.159	36.821	39.519	42.186	44.804	47.365	49.872	52.329
450	31.502	31.747	32.544	34.764	37.300	39.915	42.525	45.099	47.627	50.108	52.543
500	32.635	32.762	33.380	35.377	37.783	40.314	42.865	45.396	47.890	50.344	52.758
600	34.960	34.847	35.098	36.633	38.767	41.122	43.551	45.992	48.418	50.818	53.188
700	37.348	36.997	36.874	37.926	39.775	41.946	44.247	46.595	48.950	51.294	53.618
800	39.784	39.199	38.701	39.259	40.810	42.787	44.954	47.205	49.486	51.772	54.050
900	42.255	41.443	40.574	40.630	41.873	43.648	45.675	47.824	50.029	52.255	54.486
1000	44.752	43.720	42.487	42.038	42.964	44.529	46.411	48.454	50.579	52.744	54.925

D2.2. Table 11. Kinematic viscosity ν of dry air in 10^{-7} m^2/s

Pressure in bar	Temperature in °C										
	−150	−125	−100	−75	−50	−25	0	25	50	75	100
1	30.293	43.371	58.338	75.078	93.485	113.470	134.960	157.870	182.150	207.750	234.620
5	5.8303	8.5168	11.5630	14.9530	18.6710	22.7000	27.0260	31.6350	36.5160	41.6570	47.0510
10	2.7694	4.1651	5.7224	7.4443	9.3256	11.3600	13.5400	15.8600	18.3150	20.9000	23.6090
20	1.2166	1.9969	2.8133	3.7011	4.6634	5.6991	6.8059	7.9812	9.2226	10.5280	11.8950
30	0.7576	1.2806	1.8539	2.4633	3.1185	3.8206	4.5687	5.3616	6.1979	7.0761	7.9949
40	0.7873	0.9288	1.3828	1.8522	2.3529	2.8874	3.4556	4.0568	4.6900	5.3543	6.0487

D2.2. Table 11. (continued)

Temperature in °C											
Pressure in bar	−150	−125	−100	−75	−50	−25	0	25	50	75	100
50	0.8122	0.7293	1.1085	1.4922	1.8991	2.3323	2.7919	3.2776	3.7886	4.3243	4.8839
60	0.8344	0.6278	0.9344	1.2582	1.6014	1.9662	2.3530	2.7612	3.1905	3.6401	4.1096
70	0.8545	0.6102	0.8198	1.0968	1.3930	1.7083	2.0424	2.3950	2.7655	3.1535	3.5583
80	0.8733	0.6263	0.7442	0.9813	1.2406	1.5178	1.8120	2.1225	2.4487	2.7902	3.1465
90	0.8909	0.6474	0.6960	0.8967	1.1257	1.3725	1.6351	1.9125	2.2040	2.5092	2.8275
100	0.9076	0.6677	0.6675	0.8340	1.0370	1.2587	1.4956	1.7462	2.0098	2.2857	2.5735
150	0.9821	0.7502	0.6569	0.6968	0.8053	0.9430	1.0976	1.2644	1.4416	1.6280	1.8230
200	1.0472	0.8143	0.6990	0.6803	0.7297	0.8161	0.9233	1.0441	1.1751	1.3144	1.4611
250	1.1069	0.8692	0.7436	0.6971	0.7103	0.7619	0.8370	0.9273	1.0283	1.1377	1.2541
300	1.1630	0.9186	0.7857	0.7234	0.7139	0.7413	0.7931	0.8611	0.9407	1.0289	1.1241
350	1.2166	0.9642	0.8251	0.7525	0.7276	0.7376	0.7719	0.8231	0.8862	0.9584	1.0376
400	1.2684	1.0072	0.8623	0.7819	0.7461	0.7432	0.7640	0.8018	0.8520	0.9114	0.9781
450	1.3187	1.0481	0.8977	0.8109	0.7668	0.7539	0.7641	0.7911	0.8307	0.8798	0.9363
500	1.3680	1.0874	0.9315	0.8393	0.7885	0.7677	0.7693	0.7875	0.8183	0.8588	0.9068
600	1.4640	1.1625	0.9955	0.8940	0.8328	0.8001	0.7885	0.7931	0.8102	0.8370	0.8715
700	1.5579	1.2341	1.0558	0.9461	0.8768	0.8352	0.8140	0.8085	0.8153	0.8318	0.8561
800	1.6503	1.3033	1.1134	0.9959	0.9198	0.8711	0.8425	0.8292	0.8279	0.8363	0.8524
900	1.7419	1.3708	1.1689	1.0439	0.9616	0.9070	0.8723	0.8526	0.8449	0.8466	0.8562
1000	1.8328	1.4369	1.2228	1.0904	1.0024	0.9426	0.9026	0.8777	0.8645	0.8608	0.8648

Temperature in °C											
Pressure in bar	125	150	200	300	400	500	600	700	800	900	1000
1	262.700	291.980	353.940	490.740	643.520	811.210	993.010	1188.300	1396.700	1617.800	1851.400
5	52.6880	58.5610	70.9870	98.4060	129.0100	162.5900	198.9900	238.0900	279.8000	324.0500	370.7900
10	26.4400	29.3870	35.6210	49.3660	64.6980	81.5150	99.7370	119.3100	140.1800	162.3300	185.7100
20	13.3210	14.8060	17.9420	24.8490	32.5450	40.9790	50.1130	59.9200	70.3760	81.4650	93.1750
30	8.9531	9.9495	12.0530	16.6800	21.8300	27.4690	33.5740	40.1250	47.1080	54.5130	62.3300
40	6.7725	7.5246	9.1115	12.5980	16.4740	20.7160	25.3050	30.2290	35.4750	41.0370	46.9090
50	5.4667	6.0721	7.3485	10.1500	13.2610	16.6650	20.3450	24.2920	28.4960	32.9530	37.6560
60	4.5982	5.1056	6.1748	8.5191	11.1210	13.9650	17.0390	20.3340	23.8440	27.5640	31.4880
70	3.9796	4.4169	5.3378	7.3553	9.5928	12.0370	14.6780	17.5080	20.5220	23.7150	27.0830
80	3.5171	3.9016	4.7111	6.4834	8.4475	10.5920	12.9080	15.3890	18.0300	20.8280	23.7800
90	3.1586	3.5020	4.2247	5.8060	7.5572	9.4681	11.5310	13.7410	16.0930	18.5830	21.2100
100	2.8728	3.1833	3.8364	5.2647	6.8455	8.5697	10.4310	12.4230	14.5430	16.7880	19.1550
150	2.0259	2.2364	2.6794	3.6467	4.7151	5.8782	7.1316	8.4718	9.8965	11.4040	12.9920
200	1.6144	1.7739	2.1099	2.8445	3.6553	4.5369	5.4858	6.4994	7.5760	8.7141	9.9126
250	1.3766	1.5045	1.7750	2.3681	3.0232	3.7352	4.5009	5.3182	6.1857	7.1021	8.0666
300	1.2251	1.3312	1.5569	2.0543	2.6047	3.2031	3.8463	4.5324	5.2602	6.0287	6.8371
350	1.1227	1.2127	1.4055	1.8333	2.3082	2.8249	3.3802	3.9724	4.6003	5.2629	5.9597
400	1.0507	1.1282	1.2956	1.6702	2.0879	2.5428	3.0320	3.5535	4.1063	4.6894	5.3024
450	0.9988	1.0662	1.2133	1.5456	1.9182	2.3248	2.7622	3.2286	3.7228	4.2440	4.7917
500	0.9608	1.0198	1.1501	1.4479	1.7840	2.1516	2.5473	2.9694	3.4166	3.8882	4.3836
600	0.9122	0.9581	1.0620	1.3064	1.5864	1.8947	2.2274	2.5826	2.9590	3.3558	3.7726
700	0.8866	0.9224	1.0064	1.2108	1.4496	1.7145	2.0015	2.3084	2.6338	2.9770	3.3374
800	0.8749	0.9027	0.9709	1.1438	1.3506	1.5822	1.8344	2.1046	2.3915	2.6942	3.0120
900	0.8721	0.8933	0.9485	1.0958	1.2768	1.4820	1.7065	1.9478	2.2044	2.4753	2.7599
1000	0.8752	0.8909	0.9352	1.0612	1.2208	1.4041	1.6061	1.8239	2.0560	2.3012	2.5591

D2.2. Table 12. Thermal diffusivity a of dry air in 10^{-7} m^2/s

Pressure in bar	Temperature in °C										
	−150	−125	−100	−75	−50	−25	0	25	50	75	100
1	40.011	58.368	79.536	103.390	129.810	158.660	189.810	223.150	258.540	295.850	334.960
5	7.291	11.138	15.487	20.343	25.693	31.519	37.800	44.512	51.630	59.130	66.986
10	3.179	5.236	7.489	9.972	12.690	15.639	18.809	22.193	25.777	29.550	33.499
20	1.018	2.279	3.500	4.803	6.206	7.716	9.331	11.050	12.866	14.775	16.771
30	0.3532	1.2776	2.1767	3.0911	4.0587	5.0894	6.1854	7.3495	8.5764	9.8633	11.2070
40	0.4072	0.7592	1.5188	2.2434	2.9942	3.7857	4.6220	5.5086	6.4405	7.4163	8.4335
50	0.4475	0.4426	1.1290	1.7414	2.3626	3.0106	3.6908	4.4108	5.1657	5.9546	6.7759
60	0.4805	0.2757	0.8774	1.4132	1.9475	2.4996	3.0753	3.6843	4.3210	4.9851	5.6756
70	0.5086	0.2617	0.7095	1.1858	1.6566	2.1395	2.6402	3.1697	3.7218	4.2967	4.8936
80	0.5333	0.3039	0.5984	1.0226	1.4437	1.8738	2.3177	2.7873	3.2759	3.7837	4.3104
90	0.5556	0.3490	0.5287	0.9034	1.2834	1.6713	2.0704	2.4931	2.9321	3.3876	3.8594
100	0.5758	0.3882	0.4897	0.8157	1.1602	1.5131	1.8757	2.2606	2.6596	3.0731	3.5010
150	0.6577	0.5204	0.4950	0.6321	0.8446	1.0800	1.3251	1.5917	1.8678	2.1533	2.4478
200	0.7201	0.6053	0.5608	0.6170	0.7477	0.9127	1.0913	1.2927	1.5031	1.7215	1.9470
250	0.7710	0.6708	0.6213	0.6420	0.7244	0.8436	0.9794	1.1385	1.3070	1.4830	1.6654
300	0.8140	0.7251	0.6745	0.6766	0.7292	0.8171	0.9233	1.0528	1.1922	1.3389	1.4917
350	0.8511	0.7718	0.7217	0.7132	0.7461	0.8116	0.8959	1.0033	1.1212	1.2465	1.3777
400	0.8837	0.8127	0.7643	0.7493	0.7688	0.8175	0.8849	0.9750	1.0761	1.1849	1.2995
450	0.9124	0.8490	0.8030	0.7840	0.7942	0.8301	0.8842	0.9600	1.0474	1.1429	1.2443
500	0.9388	0.8817	0.8383	0.8171	0.8206	0.8468	0.8900	0.9540	1.0298	1.1141	1.2047
600	0.9843	0.9379	0.9004	0.8779	0.8733	0.8863	0.9137	0.9591	1.0164	1.0826	1.1557
700	1.0225	0.9846	0.9533	0.9318	0.9235	0.9286	0.9456	0.9779	1.0211	1.0733	1.1325
800	1.0550	1.0251	0.9987	0.9795	0.9698	0.9705	0.9807	1.0037	1.0364	1.0774	1.1255
900	1.0830	1.0599	1.0379	1.0218	1.0122	1.0105	1.0164	1.0328	1.0576	1.0900	1.1290
1000	1.1075	1.0902	1.0729	1.0593	1.0506	1.0480	1.0513	1.0632	1.0821	1.1078	1.1395

Pressure in bar	Temperature in °C										
	125	150	200	300	400	500	600	700	800	900	1000
1	375.740	418.070	506.98	699.48	908.87	1133.90	1374.60	1631.40	1904.90	2195.30	2503.10
5	75.175	83.672	101.510	140.110	182.060	227.140	275.340	326.750	381.480	439.620	501.210
10	37.613	41.881	50.835	70.192	91.220	113.800	137.930	163.670	191.070	220.160	250.980
20	18.847	20.999	25.509	35.245	45.806	57.136	69.238	82.137	95.862	110.430	125.870
30	12.6030	14.0500	17.0770	23.6040	30.6750	38.2540	46.3440	54.9640	64.1310	73.8620	84.1670
40	9.4899	10.5830	12.8690	17.7900	23.1150	28.8170	34.9010	41.3800	4.2690	55.5790	63.3200
50	7.6278	8.5086	10.3490	14.3060	18.5830	23.1590	28.0380	33.2330	38.7540	44.6110	50.8130
60	6.3912	7.1303	8.6737	11.9870	15.5640	19.3890	23.4660	27.8030	32.4120	37.3010	42.4760
70	5.5116	6.1495	7.4802	10.3340	13.4110	16.6990	20.2010	23.9270	27.8840	32.0810	36.5230
80	4.8551	5.4169	6.5878	9.0959	11.7980	14.6830	17.7540	21.0210	24.4900	28.1680	32.0600
90	4.3470	4.8496	5.8961	8.1352	10.5450	13.1160	15.8530	18.7620	21.8500	25.1250	28.5890
100	3.9428	4.3979	5.3448	7.3684	9.5443	11.8650	14.3330	16.9560	19.7400	22.6910	25.8130
150	2.7511	3.0626	3.7090	5.0838	6.5559	8.1215	9.7836	11.5470	13.4180	15.3990	17.4930
200	2.1792	2.4175	2.9114	3.9588	5.0770	6.2635	7.5213	8.8545	10.2670	11.7620	13.3420
250	1.8536	2.0469	2.4474	3.2960	4.2002	5.1581	6.1723	7.2464	8.3838	9.5869	10.8580
300	1.6496	1.8121	2.1491	2.8633	3.6235	4.4281	5.2793	6.1801	7.1335	8.1416	9.2060
350	1.5136	1.6537	1.9445	2.5613	3.2178	3.9121	4.6463	5.4230	6.2446	7.1131	8.0298
400	1.4187	1.5418	1.7977	2.3406	2.9185	3.5296	4.1755	4.8587	5.5812	6.3448	7.1506

D2.2. Table 12. (continued)

Temperature in °C											
Pressure in bar	125	150	200	300	400	500	600	700	800	900	1000
450	1.3503	1.4601	1.6885	2.1735	2.6897	3.2356	3.8126	4.4227	5.0679	5.7497	6.4691
500	1.2999	1.3987	1.6050	2.0435	2.5101	3.0035	3.5250	4.0764	4.6596	5.2758	5.9259
600	1.2338	1.3158	1.4882	1.8562	2.2480	2.6621	3.0998	3.5627	4.0524	4.5698	5.1157
700	1.1972	1.2661	1.4130	1.7299	2.0679	2.4250	2.8024	3.2017	3.6241	4.0706	4.5417
800	1.1792	1.2374	1.3637	1.6407	1.9379	2.2520	2.5841	2.9354	3.3072	3.7002	4.1150
900	1.1736	1.2228	1.3317	1.5758	1.8406	2.1212	2.4179	2.7318	3.0640	3.4153	3.7861
1000	1.1766	1.2181	1.3120	1.5281	1.7661	2.0195	2.2876	2.5715	2.8720	3.1899	3.5254

D2.2. Table 13. Prandtl number Pr of dry air

Temperature in °C											
Pressure in bar	−150	−125	−100	−75	−50	−25	0	25	50	75	100
1	0.7571	0.7431	0.7335	0.7262	0.7202	0.7152	0.7110	0.7075	0.7045	0.7022	0.7004
5	0.7997	0.7646	0.7466	0.7351	0.7267	0.7202	0.7150	0.7107	0.7073	0.7045	0.7024
10	0.8711	0.7954	0.7641	0.7465	0.7349	0.7264	0.7199	0.7147	0.7105	0.7073	0.7048
20	1.1950	0.8761	0.8038	0.7707	0.7514	0.7386	0.7294	0.7223	0.7168	0.7125	0.7093
30	2.1452	1.0023	0.8517	0.7969	0.7684	0.7507	0.7386	0.7295	0.7227	0.7174	0.7134
40	1.9336	1.2234	0.9105	0.8256	0.7858	0.7627	0.7476	0.7365	0.7282	0.7220	0.7172
50	1.8149	1.6476	0.9818	0.8569	0.8038	0.7747	0.7565	0.7431	0.7334	0.7262	0.7208
60	1.7366	2.2770	1.0650	0.8903	0.8223	0.7866	0.7651	0.7495	0.7384	0.7302	0.7241
70	1.6802	2.3312	1.1555	0.9250	0.8409	0.7985	0.7736	0.7556	0.7431	0.7339	0.7271
80	1.6374	2.0609	1.2436	0.9596	0.8593	0.8100	0.7818	0.7615	0.7475	0.7374	0.7300
90	1.6036	1.8552	1.3164	0.9926	0.8771	0.8212	0.7898	0.7671	0.7517	0.7407	0.7326
100	1.5762	1.7198	1.3629	1.0224	0.8939	0.8319	0.7974	0.7725	0.7557	0.7438	0.7351
150	1.4931	1.4415	1.3272	1.1025	0.9535	0.8732	0.8283	0.7944	0.7718	0.7561	0.7447
200	1.4542	1.3453	1.2464	1.1026	0.9759	0.8942	0.8461	0.8077	0.7817	0.7636	0.7505
250	1.4358	1.2958	1.1968	1.0859	0.9805	0.9032	0.8546	0.8144	0.7867	0.7672	0.7530
300	1.4289	1.2668	1.1649	1.0693	0.9790	0.9072	0.8590	0.8179	0.7890	0.7684	0.7536
350	1.4295	1.2494	1.1432	1.0551	0.9752	0.9089	0.8616	0.8203	0.7904	0.7688	0.7532
400	1.4352	1.2393	1.1282	1.0435	0.9705	0.9091	0.8633	0.8224	0.7917	0.7692	0.7527
450	1.4453	1.2344	1.1179	1.0343	0.9656	0.9082	0.8642	0.8241	0.7932	0.7698	0.7525
500	1.4572	1.2333	1.1112	1.0272	0.9609	0.9066	0.8643	0.8255	0.7947	0.7708	0.7527
600	1.4873	1.2394	1.1056	1.0184	0.9537	0.9027	0.8630	0.8269	0.7971	0.7731	0.7541
700	1.5237	1.2533	1.1076	1.0153	0.9495	0.8994	0.8608	0.8268	0.7985	0.7750	0.7559
800	1.5644	1.2714	1.1148	1.0168	0.9484	0.8975	0.8590	0.8261	0.7989	0.7762	0.7574
900	1.6083	1.2933	1.1263	1.0217	0.9501	0.8976	0.8582	0.8255	0.7988	0.7767	0.7583
1000	1.6549	1.3180	1.1397	1.0294	0.9541	0.8994	0.8586	0.8255	0.7989	0.7770	0.7589
Temperature in °C											
Pressure in bar	125	150	200	300	400	500	600	700	800	900	1000
1	0.6992	0.6984	0.6981	0.7016	0.7081	0.7154	0.7224	0.7284	0.7333	0.7370	0.7396
5	0.7009	0.6999	0.6993	0.7024	0.7086	0.7158	0.7227	0.7286	0.7335	0.7371	0.7398
10	0.7029	0.7017	0.7007	0.7033	0.7093	0.7163	0.7231	0.7289	0.7337	0.7373	0.7399
20	0.7068	0.7051	0.7034	0.7051	0.7105	0.7172	0.7238	0.7295	0.7341	0.7377	0.7403

D2.2. Table 13. (continued)

Pressure in bar	Temperature in °C										
	125	150	200	300	400	500	600	700	800	900	1000
30	0.7104	0.7082	0.7058	0.7067	0.7116	0.7181	0.7245	0.7300	0.7346	0.7380	0.7406
40	0.7137	0.7110	0.7080	0.7081	0.7127	0.7189	0.7251	0.7305	0.7350	0.7384	0.7408
50	0.7167	0.7136	0.7101	0.7095	0.7136	0.7196	0.7256	0.7310	0.7353	0.7387	0.7411
60	0.7195	0.7161	0.7119	0.7107	0.7145	0.7202	0.7261	0.7314	0.7357	0.7390	0.7413
70	0.7220	0.7183	0.7136	0.7118	0.7153	0.7208	0.7266	0.7317	0.7360	0.7392	0.7415
80	0.7244	0.7203	0.7151	0.7128	0.7160	0.7214	0.7270	0.7321	0.7362	0.7394	0.7417
90	0.7266	0.7221	0.7165	0.7137	0.7167	0.7219	0.7274	0.7324	0.7365	0.7397	0.7419
100	0.7286	0.7238	0.7178	0.7145	0.7172	0.7223	0.7277	0.7327	0.7367	0.7399	0.7421
150	0.7364	0.7302	0.7224	0.7173	0.7192	0.7238	0.7289	0.7337	0.7376	0.7406	0.7427
200	0.7409	0.7338	0.7247	0.7185	0.7200	0.7243	0.7294	0.7340	0.7379	0.7409	0.7430
250	0.7427	0.7350	0.7253	0.7185	0.7198	0.7241	0.7292	0.7339	0.7378	0.7408	0.7429
300	0.7427	0.7346	0.7245	0.7175	0.7188	0.7234	0.7286	0.7334	0.7374	0.7405	0.7427
350	0.7417	0.7333	0.7228	0.7158	0.7173	0.7221	0.7275	0.7325	0.7367	0.7399	0.7422
400	0.7406	0.7317	0.7207	0.7136	0.7154	0.7204	0.7261	0.7314	0.7357	0.7391	0.7415
450	0.7396	0.7302	0.7186	0.7111	0.7132	0.7185	0.7245	0.7300	0.7346	0.7381	0.7407
500	0.7391	0.7291	0.7166	0.7086	0.7107	0.7164	0.7227	0.7284	0.7332	0.7370	0.7397
600	0.7394	0.7282	0.7137	0.7038	0.7057	0.7117	0.7186	0.7249	0.7302	0.7343	0.7375
700	0.7406	0.7285	0.7122	0.6999	0.7010	0.7070	0.7142	0.7210	0.7268	0.7313	0.7348
800	0.7419	0.7295	0.7119	0.6972	0.6969	0.7026	0.7099	0.7170	0.7231	0.7281	0.7320
900	0.7431	0.7305	0.7123	0.6954	0.6937	0.6986	0.7058	0.7130	0.7195	0.7248	0.7290
1000	0.7438	0.7314	0.7128	0.6944	0.6912	0.6953	0.7021	0.7093	0.7159	0.7214	0.7259

D2.2. Table 14. Isobaric expansion coefficient β of dry air in 10^{-3}/K

Pressure in bar	Temperature in °C										
	−150	−125	−100	−75	−50	−25	0	25	50	75	100
1	8.3947	6.8834	5.8490	5.0909	4.5094	4.0485	3.6738	3.3630	3.1010	2.8770	2.6833
5	9.6919	7.4647	6.1576	5.2720	4.6231	4.1233	3.7248	3.3987	3.1264	2.8954	2.6968
10	11.9870	8.3180	6.5768	5.5083	4.7678	4.2171	3.7880	3.4426	3.1576	2.9179	2.7132
20	23.4830	10.6350	7.5455	6.0152	5.0658	4.4052	3.9127	3.5281	3.2177	2.9608	2.7442
30	20.3790	14.3470	8.7203	6.5682	5.3735	4.5933	4.0346	3.6103	3.2747	3.0012	2.7732
40	15.9500	20.8880	10.1310	7.1628	5.6876	4.7795	4.1530	3.6891	3.3288	3.0391	2.8001
50	13.4970	33.1700	11.7720	7.7866	6.0026	4.9616	4.2669	3.7640	3.3797	3.0745	2.8250
60	11.8890	48.2830	13.5650	8.4182	6.3114	5.1369	4.3751	3.8345	3.4272	3.1073	2.8479
70	10.7310	41.2590	15.3220	9.0276	6.6055	5.3023	4.4766	3.9002	3.4713	3.1374	2.8688
80	9.8472	29.2540	16.7560	9.5802	6.8759	5.4548	4.5701	3.9605	3.5115	3.1648	2.8876
90	9.1449	22.0780	17.5530	10.0420	7.1142	5.5915	4.6544	4.0150	3.5479	3.1895	2.9045
100	8.5696	17.8280	17.5460	10.3870	7.3134	5.7100	4.7286	4.0634	3.5801	3.2113	2.9193
150	6.7302	9.8964	12.3270	10.1820	7.6376	5.9945	4.9334	4.2052	3.6771	3.2768	2.9626
200	5.7054	7.3535	8.7385	8.4420	7.0936	5.8302	4.8844	4.1920	3.6736	3.2742	2.9581
250	5.0330	6.0436	6.8646	6.9330	6.2757	5.4248	4.6713	4.0684	3.5942	3.2182	2.9150
300	4.5500	5.2236	5.7483	5.8604	5.5196	4.9577	4.3848	3.8842	3.4683	3.1268	2.8451
350	4.1821	4.6530	5.0060	5.0985	4.9004	4.5179	4.0845	3.6764	3.3194	3.0158	2.7590
400	3.8903	4.2285	4.4733	4.5382	4.4066	4.1332	3.8002	3.4676	3.1635	2.8962	2.6647

D2.2. Table 14. (continued)

Temperature in °C											
Pressure in bar	−150	−125	−100	−75	−50	−25	0	25	50	75	100
450	3.6517	3.8981	4.0698	4.1105	4.0115	3.8050	3.5429	3.2694	3.0101	2.7755	2.5678
500	3.4520	3.6320	3.7521	3.7733	3.6911	3.5269	3.3147	3.0868	2.8643	2.6581	2.4719
600	3.1346	3.2271	3.2805	3.2740	3.2060	3.0882	2.9375	2.7713	2.6030	2.4414	2.2908
700	2.8914	2.9305	2.9443	2.9200	2.8568	2.7617	2.6447	2.5156	2.3830	2.2529	2.1290
800	2.6976	2.7021	2.6904	2.6543	2.5930	2.5106	2.4135	2.3078	2.1990	2.0912	1.9873
900	2.5385	2.5195	2.4908	2.4466	2.3860	2.3115	2.2271	2.1370	2.0446	1.9529	1.8638
1000	2.4048	2.3694	2.3289	2.2791	2.2188	2.1495	2.0739	1.9945	1.9139	1.8340	1.7561

Temperature in °C											
Pressure in bar	125	150	200	300	400	500	600	700	800	900	1000
1	2.5142	2.3651	2.1145	1.7450	1.4855	1.2932	1.1451	1.0274	0.9317	0.8522	0.7853
5	2.5241	2.3724	2.1185	1.7458	1.4852	1.2926	1.1443	1.0266	0.9309	0.8515	0.7846
10	2.5361	2.3813	2.1232	1.7468	1.4849	1.2917	1.1433	1.0256	0.9299	0.8506	0.7838
20	2.5587	2.3978	2.1318	1.7484	1.4839	1.2899	1.1412	1.0235	0.9280	0.8488	0.7822
30	2.5796	2.4129	2.1395	1.7495	1.4828	1.2880	1.1391	1.0214	0.9260	0.8470	0.7805
40	2.5988	2.4266	2.1463	1.7502	1.4814	1.2859	1.1369	1.0193	0.9240	0.8452	0.7789
50	2.6165	2.4391	2.1523	1.7505	1.4798	1.2838	1.1346	1.0171	0.9220	0.8433	0.7772
60	2.6325	2.4503	2.1575	1.7505	1.4781	1.2815	1.1323	1.0149	0.9199	0.8415	0.7755
70	2.6470	2.4603	2.1619	1.7501	1.4762	1.2792	1.1299	1.0127	0.9179	0.8396	0.7738
80	2.6600	2.4691	2.1655	1.7494	1.4741	1.2767	1.1275	1.0104	0.9158	0.8377	0.7721
90	2.6715	2.4768	2.1685	1.7484	1.4719	1.2742	1.1251	1.0081	0.9137	0.8359	0.7704
100	2.6814	2.4833	2.1708	1.7471	1.4696	1.2717	1.1226	1.0058	0.9117	0.8340	0.7687
150	2.7089	2.4994	2.1724	1.7368	1.4561	1.2581	1.1098	0.9941	0.9011	0.8245	0.7602
200	2.7018	2.4899	2.1593	1.7208	1.4402	1.2433	1.0965	0.9822	0.8905	0.8150	0.7518
250	2.6664	2.4592	2.1339	1.7001	1.4223	1.2277	1.0828	0.9702	0.8799	0.8056	0.7434
300	2.6104	2.4127	2.0988	1.6756	1.4029	1.2114	1.0689	0.9581	0.8693	0.7963	0.7351
350	2.5414	2.3556	2.0569	1.6482	1.3822	1.1947	1.0548	0.9461	0.8589	0.7871	0.7270
400	2.4650	2.2922	2.0106	1.6187	1.3606	1.1776	1.0407	0.9341	0.8485	0.7780	0.7189
450	2.3856	2.2259	1.9618	1.5880	1.3384	1.1604	1.0266	0.9222	0.8383	0.7691	0.7110
500	2.3060	2.1587	1.9120	1.5565	1.3160	1.1430	1.0125	0.9104	0.8282	0.7603	0.7033
600	2.1530	2.0280	1.8132	1.4934	1.2709	1.1085	0.9847	0.8873	0.8084	0.7432	0.6882
700	2.0134	1.9067	1.7193	1.4319	1.2268	1.0747	0.9576	0.8648	0.7893	0.7267	0.6738
800	1.8888	1.7968	1.6324	1.3736	1.1845	1.0421	0.9315	0.8432	0.7710	0.7108	0.6598
900	1.7787	1.6983	1.5529	1.3188	1.1442	1.0109	0.9064	0.8224	0.7533	0.6955	0.6465
1000	1.6814	1.6104	1.4806	1.2679	1.1063	0.9813	0.8825	0.8025	0.7364	0.6809	0.6337

D2.2. Table 15. Isentropic speed of sound w_s in dry air in m/s

Temperature in °C											
Pressure in bar	−150	−125	−100	−75	−50	−25	0	25	50	75	100
1	221.3	243.4	263.5	282.1	299.5	315.9	331.5	346.3	360.5	374.0	387.0
5	215.8	240.4	261.9	281.3	299.2	316.0	331.8	346.7	361.0	374.7	387.8
10	208.3	236.7	259.9	280.3	298.9	316.1	332.2	347.4	361.8	375.6	388.8
20	188.9	229.0	256.3	278.8	298.6	316.6	333.2	348.8	363.5	377.5	390.8

D2.2. Table 15. (continued)

Temperature in °C											
Pressure in bar	−150	−125	−100	−75	−50	−25	0	25	50	75	100
30	389.0	221.4	253.2	277.7	298.7	317.4	334.5	350.5	365.4	379.6	393.0
40	427.5	214.7	250.9	277.3	299.3	318.6	336.1	352.3	367.5	381.8	395.3
50	458.1	211.3	249.9	277.6	300.3	320.2	338.0	354.5	369.8	384.2	397.8
60	484.1	219.0	250.7	278.8	302.0	322.1	340.2	356.8	372.2	386.7	400.4
70	506.9	248.8	253.9	281.0	304.2	324.5	342.7	359.4	374.8	389.3	403.0
80	527.5	287.9	260.0	284.4	307.1	327.3	345.4	362.1	377.6	392.1	405.8
90	546.2	324.1	269.3	289.0	310.6	330.5	348.5	365.1	380.6	395.1	408.7
100	563.5	355.6	281.8	294.9	314.9	334.1	351.9	368.3	383.7	398.1	411.7
150	635.2	468.7	366.3	340.3	345.5	358.4	372.9	387.5	401.6	415.2	428.2
200	691.6	546.1	445.8	399.0	387.3	390.8	399.9	411.1	423.0	435.0	446.8
250	738.8	607.0	511.5	456.5	433.1	427.5	430.6	437.8	446.9	456.9	467.2
300	779.8	658.0	567.0	509.0	478.3	465.7	463.2	466.4	472.5	480.2	488.7
350	816.2	702.2	615.2	556.3	521.3	503.3	496.2	495.6	498.8	504.3	511.0
400	849.2	741.6	658.0	599.1	561.4	539.7	528.8	525.0	525.5	528.8	533.7
450	879.4	777.1	696.6	638.2	598.9	574.4	560.5	553.9	552.0	553.2	556.5
500	907.3	809.7	731.9	674.1	633.8	607.3	591.1	582.1	578.1	577.5	579.3
600	957.9	867.8	794.7	738.6	697.4	668.4	648.7	636.1	628.7	625.0	623.9
700	1002.9	918.9	849.8	795.4	754.1	723.7	701.9	686.7	676.7	670.5	667.1
800	1043.8	964.7	899.0	846.3	805.3	774.1	750.9	734.0	722.0	713.8	708.5
900	1081.3	1006.4	943.7	892.7	852.2	820.6	796.4	778.2	764.7	754.9	748.1
1000	1116.2	1044.9	984.8	935.3	895.4	863.7	838.9	819.7	805.0	794.0	785.9

Temperature in °C											
Pressure in bar	125	150	200	300	400	500	600	700	800	900	1000
1	399.6	411.7	434.7	476.6	514.3	549.0	581.3	611.7	640.6	668.3	694.8
5	400.4	412.5	435.6	477.5	515.2	549.9	582.1	612.5	641.4	669.0	695.6
10	401.4	413.6	436.7	478.7	516.4	551.0	583.2	613.6	642.4	670.0	696.5
20	403.6	415.8	439.0	481.1	518.7	553.3	585.4	615.7	644.5	672.0	698.4
30	405.9	418.2	441.4	483.5	521.1	555.6	587.6	617.8	646.5	674.0	700.3
40	408.3	420.6	443.9	486.0	523.5	557.9	589.9	620.0	648.6	676.0	702.2
50	410.8	423.2	446.5	488.5	526.0	560.2	592.1	622.1	650.7	677.9	704.1
60	413.4	425.8	449.1	491.0	528.4	562.6	594.4	624.3	652.8	679.9	706.1
70	416.1	428.5	451.8	493.6	530.9	565.0	596.7	626.5	654.8	682.0	708.0
80	418.8	431.2	454.5	496.3	533.4	567.4	598.9	628.7	656.9	684.0	709.9
90	421.7	434.1	457.3	498.9	536.0	569.8	601.2	630.9	659.0	686.0	711.9
100	424.7	437.0	460.1	501.6	538.5	572.2	603.6	633.1	661.2	688.0	713.8
150	440.6	452.5	475.0	515.4	551.5	584.5	615.2	644.2	671.8	698.2	723.6
200	458.3	469.5	490.9	529.8	564.8	597.0	627.0	655.4	682.5	708.5	733.5
250	477.5	487.7	507.6	544.6	578.4	609.7	639.0	666.7	693.3	718.8	743.4
300	497.7	506.8	525.0	559.8	592.2	622.4	651.0	678.1	704.1	729.1	753.3
350	518.5	526.4	542.8	575.3	606.2	635.3	663.0	689.5	714.9	739.5	763.2
400	539.8	546.5	561.0	590.9	620.2	648.2	675.1	700.9	725.7	749.8	773.1
450	561.2	566.7	579.3	606.7	634.3	661.2	687.2	712.3	736.6	760.1	783.0
500	582.6	586.9	597.7	622.5	648.5	674.2	699.3	723.6	747.3	770.4	792.9

D2.2. Table 15. (continued)

Temperature in °C											
Pressure in bar	125	150	200	300	400	500	600	700	800	900	1000
600	624.8	627.1	634.3	654.2	676.8	700.1	723.3	746.3	768.8	790.9	812.5
700	665.9	666.2	670.3	685.5	704.9	725.8	747.2	768.7	790.1	811.2	832.0
800	705.5	704.2	705.4	716.3	732.6	751.2	770.9	791.0	811.2	831.3	851.3
900	743.6	740.9	739.5	746.4	759.8	776.3	794.2	812.9	832.0	851.2	870.3
1000	780.2	776.2	772.6	775.9	786.6	800.9	817.2	834.6	852.5	870.8	889.1

3 Bibliography

1. Lemmon EW, Jacobsen RT, Penoncello SG, Friend DG (2000) Thermodynamic properties of air and mixtures of nitrogen, argon, and oxygen from 60 to 2000 K at pressures to 2000 MPa. J Phys Chem Ref Data 29(3):331–385
2. Lemmon EW, Jacobsen RT (2004) Viscosity and thermal conductivity equations for nitrogen, oxygen, argon, and air. Int J Thermophys 25 (1):21–69

D2.3 Properties of Nitrogen

Roland Span[1] · *Rolf Krauss*[2]
[1]Ruhr-Universität Bochum, Bochum, Germany
[2]Universität Stuttgart, Stuttgart, Germany

1 Properties of Nitrogen

Tables with thermodynamic properties of nitrogen were calculated with the reference equation of state established by Span et al. [1], see also Span et al. [2].

The thermal conductivity and viscosity of nitrogen were calculated with the corresponding equations by Stephan and Krauss [3]. The densities required as input for the equations by Stephan and Krauss were calculated using the equation by Span et al.

p	Pressure in bar	v	Specific volume in m^3/kg
ρ	Density in kg/m^3	λ	Thermal conductivity in mW/(m K)
ϑ	Temperature in °C	ν	Kinematic viscosity ν in $10^{-7} m^2/s$
h	Specific enthalpy in kJ/kg	η	Dynamic viscosity in 10^{-6} Pa·s
s	Specific entropy in kJ/(kg K)	a	Thermal diffusivity in 10^{-7} m^2/s
Z	Compression factor $Z = p/(\rho RT)$	β	Isobaric expansion coefficient in 10^{-3}/K $\beta = v^{-1}\cdot(\partial v/\partial T)_p$
Pr	Prandtl number $Pr = \eta\, c_p/\lambda$	c_p	Specific isobaric heat capacity in kJ/(kg K)
w_s	Isentropic speed of sound in m/s	c_v	Specific isochoric heat capacity in kJ/(kg K)

2 Characteristic Quantities

Molecular mass $\widetilde{M}$ = 28.01348 g/mol, specific gas constant R = 296.8039 J/(kg K)

3 Critical Point [1]

p_c = 33.958 bar, T_c = 126.192 K (ϑ_c = −146.958°C), ρ_c = 313.3 kg/m^3

4 Triple Point [1]

T_t = 63.151 K (ϑ_t = −209.999°C)

5 Reference States of Enthalpy and Entropy [1]

h = 309.494 kJ/kg, s = 6.8360 kJ/(kg K) at T = 298.15 K (ϑ = 25°C), p = 1.01325 bar corresponding to h = 0 kJ/kg, s = 0 kJ/(kg K) for a perfect crystal at T = 0 K

D2.3. Table 1. Properties of nitrogen at $p = 1$ bar

ϑ °C	ρ kg/m³	h kJ/kg	s kJ/(kg K)	c_p kJ/(kg K)	c_v kJ/(kg K)	β 10^{-3}/K	w_s m/s	λ mW/(m K)	η 10^{-6} Pa·s	ν 10^{-7} m²/s	a 10^{-7} m²/s	Pr –
−210	867.38	−150.7	2.425	2.000	1.177	4.727	995.8	176.1	215.9	2.489	1.015	2.451
−200	824.94	−130.6	2.721	2.024	1.110	5.339	894.3	155.7	159.1	1.929	0.9327	2.068
−190	4.1949	83.64	5.494	1.102	0.7627	13.32	182.3	8.061	5.470	13.04	17.44	0.7477
−180	3.7067	94.54	5.617	1.080	0.7546	11.53	194.1	9.108	6.201	16.73	22.74	0.7355
−170	3.3259	105.3	5.727	1.068	0.7503	10.22	205.0	10.13	6.912	20.78	28.52	0.7288
−160	3.0187	115.9	5.825	1.061	0.7478	9.200	215.3	11.13	7.603	25.19	34.75	0.7248
−150	2.7651	126.5	5.915	1.056	0.7462	8.380	225.0	12.10	8.276	29.93	41.44	0.7222
−140	2.5517	137.0	5.997	1.052	0.7452	7.703	234.2	13.04	8.931	35.00	48.57	0.7205
−130	2.3695	147.5	6.073	1.050	0.7445	7.132	243.1	13.96	9.568	40.38	56.13	0.7193
−120	2.2119	158.0	6.144	1.048	0.7440	6.643	251.7	14.86	10.19	46.06	64.11	0.7185
−110	2.0742	168.5	6.210	1.047	0.7437	6.218	259.9	15.74	10.79	52.04	72.49	0.7179
−100	1.9529	179.0	6.273	1.045	0.7434	5.847	267.9	16.59	11.38	58.30	81.27	0.7174
−90	1.8451	189.4	6.331	1.045	0.7432	5.518	275.6	17.43	11.96	64.83	90.42	0.7170
−80	1.7486	199.9	6.387	1.044	0.7431	5.224	283.1	18.24	12.53	71.63	99.95	0.7167
−70	1.6619	210.3	6.439	1.043	0.7430	4.961	290.4	19.04	13.08	78.70	109.8	0.7165
−60	1.5833	220.7	6.490	1.043	0.7429	4.724	297.5	19.83	13.62	86.01	120.1	0.7163
−50	1.5119	231.1	6.537	1.042	0.7429	4.508	304.4	20.59	14.15	93.58	130.7	0.7162
−40	1.4467	241.6	6.583	1.042	0.7428	4.312	311.2	21.35	14.67	101.4	141.6	0.7161
−30	1.3869	252.0	6.627	1.042	0.7428	4.132	317.9	22.09	15.18	109.4	152.8	0.7160
−20	1.3319	262.4	6.669	1.042	0.7428	3.967	324.4	22.81	15.68	117.7	164.4	0.7159
−10	1.2811	272.8	6.709	1.042	0.7428	3.814	330.7	23.53	16.17	126.2	176.3	0.7158
0	1.2340	283.2	6.748	1.041	0.7429	3.673	337.0	24.23	16.65	134.9	188.5	0.7158
10	1.1903	293.7	6.785	1.041	0.7430	3.542	343.1	24.92	17.13	143.9	201.0	0.7158
20	1.1496	304.1	6.822	1.041	0.7431	3.420	349.1	25.60	17.60	153.1	213.8	0.7157
30	1.1116	314.5	6.857	1.041	0.7432	3.307	355.0	26.27	18.06	162.4	226.9	0.7157
40	1.0760	324.9	6.890	1.041	0.7434	3.200	360.8	26.93	18.51	172.0	240.3	0.7157
50	1.0426	335.3	6.923	1.042	0.7436	3.101	366.5	27.59	18.96	181.8	254.0	0.7158
60	1.0113	345.7	6.955	1.042	0.7439	3.007	372.1	28.23	19.40	191.8	268.0	0.7158
70	0.98177	356.1	6.986	1.042	0.7443	2.919	377.7	28.87	19.83	202.0	282.2	0.7158
80	0.95392	366.6	7.016	1.042	0.7447	2.836	383.1	29.50	20.26	212.4	296.7	0.7159
90	0.92762	377.0	7.045	1.043	0.7451	2.757	388.5	30.13	20.69	223.0	311.5	0.7160
100	0.90273	387.4	7.073	1.043	0.7457	2.683	393.7	30.75	21.10	233.8	326.5	0.7160
110	0.87914	397.9	7.101	1.044	0.7463	2.613	398.9	31.36	21.52	244.8	341.8	0.7161
120	0.85676	408.3	7.128	1.044	0.7469	2.546	404.0	31.97	21.93	255.9	357.3	0.7163
130	0.83549	418.7	7.154	1.045	0.7477	2.483	409.1	32.58	22.33	267.3	373.1	0.7164
140	0.81525	429.2	7.179	1.046	0.7485	2.422	414.1	33.18	22.73	278.8	389.1	0.7165
150	0.79597	439.7	7.204	1.047	0.7495	2.365	419.0	33.78	23.13	290.5	405.4	0.7167
160	0.77758	450.1	7.229	1.048	0.7505	2.310	423.8	34.37	23.52	302.4	421.9	0.7169
170	0.76003	460.6	7.253	1.049	0.7515	2.258	428.6	34.96	23.90	314.5	438.6	0.7171
180	0.74325	471.1	7.276	1.050	0.7527	2.208	433.3	35.55	24.29	326.8	455.6	0.7173
190	0.72719	481.6	7.299	1.051	0.7539	2.160	438.0	36.14	24.67	339.2	472.7	0.7175
200	0.71181	492.1	7.322	1.053	0.7553	2.114	442.6	36.72	25.04	351.8	490.2	0.7177
250	0.64376	545.0	7.428	1.060	0.7630	1.912	464.7	39.61	26.87	417.4	580.4	0.7191
300	0.58760	598.2	7.525	1.070	0.7725	1.745	485.5	42.47	28.62	487.1	675.8	0.7208
350	0.54045	651.9	7.615	1.080	0.7831	1.605	505.3	45.30	30.31	560.8	776.0	0.7227
400	0.50031	706.2	7.699	1.092	0.7947	1.485	524.1	48.12	31.94	638.4	881.0	0.7247
450	0.46572	761.1	7.777	1.104	0.8067	1.383	542.1	50.91	33.52	719.8	990.4	0.7267

D2.3. Table 1. (continued)

ϑ °C	ρ kg/m³	h kJ/kg	s kJ/(kg K)	c_p kJ/(kg K)	c_v kJ/(kg K)	β 10^{-3}/K	w_s m/s	λ mW/(m K)	η 10^{-6} Pa·s	ν 10^{-7} m²/s	a 10^{-7} m²/s	Pr –
500	0.43561	816.6	7.851	1.116	0.8189	1.293	559.4	53.68	35.06	804.8	1,104	0.7288
550	0.40915	872.7	7.922	1.128	0.8309	1.215	576.1	56.42	36.56	893.5	1,223	0.7308
600	0.38573	929.4	7.989	1.140	0.8427	1.145	592.2	59.13	38.02	985.6	1,345	0.7327
700	0.34610	1,044	8.113	1.162	0.8649	1.027	623.1	64.45	40.85	1,180	1,603	0.7363
800	0.31385	1,162	8.228	1.182	0.8850	0.9316	652.4	69.63	43.57	1,388	1,877	0.7394
900	0.28711	1,281	8.334	1.200	0.9028	0.8522	680.4	74.67	46.19	1,609	2,168	0.7422
1,000	0.26456	1,402	8.433	1.215	0.9184	0.7853	707.3	79.57	48.74	1,842	2,475	0.7445

D2.3. Table 2. Properties of the saturated liquid

ϑ °C	p bar	ρ' kg/m³	h' kJ/kg	s' kJ/(kg K)	c_p' kJ/(kg K)	c_v' kJ/(kg K)	β' 10^{-3}/K	w_s' m/s	λ' mW/(m K)	η' 10^{-6} Pa·s	ν' 10^{-7} m²/s	a' 10^{-7} m²/s	Pr′ –
−210	0.12517	867.23	−150.7	2.426	2.000	1.176	4.733	995.3	176.1	215.6	2.486	1.015	2.450
−208	0.17860	858.97	−146.7	2.488	2.004	1.162	4.840	974.8	171.9	202.6	2.359	0.9989	2.361
−206	0.24894	850.62	−142.7	2.549	2.008	1.149	4.953	954.5	167.8	190.5	2.240	0.9827	2.279
−204	0.33973	842.15	−138.7	2.608	2.012	1.135	5.075	934.3	163.7	179.3	2.129	0.9662	2.203
−202	0.45484	833.56	−134.6	2.665	2.018	1.122	5.204	914.1	159.7	168.8	2.025	0.9495	2.133
−200	0.59842	824.85	−130.6	2.721	2.024	1.109	5.343	894.0	155.7	159.0	1.928	0.9324	2.068
−198	0.77491	816.00	−126.5	2.775	2.032	1.097	5.492	873.8	151.7	149.9	1.837	0.9150	2.008
−196	0.98899	807.01	−122.4	2.829	2.041	1.085	5.653	853.5	147.7	141.4	1.752	0.8972	1.952
−194	1.2456	797.87	−118.3	2.881	2.051	1.074	5.828	833.1	143.8	133.4	1.671	0.8789	1.902
−192	1.5497	788.56	−114.2	2.932	2.063	1.063	6.018	812.5	139.9	125.8	1.596	0.8602	1.855
−190	1.9067	779.08	−110.0	2.982	2.076	1.052	6.225	791.8	136.0	118.8	1.525	0.8409	1.813
−188	2.3219	769.40	−105.8	3.031	2.092	1.042	6.453	770.9	132.2	112.1	1.457	0.8211	1.775
−186	2.8009	759.51	−101.6	3.080	2.110	1.033	6.705	749.7	128.3	105.9	1.394	0.8006	1.741
−184	3.3492	749.40	−97.34	3.127	2.131	1.023	6.984	728.2	124.5	99.96	1.334	0.7795	1.711
−182	3.9725	739.03	−93.03	3.174	2.155	1.015	7.296	706.4	120.7	94.36	1.277	0.7576	1.685
−180	4.6767	728.38	−88.66	3.221	2.183	1.007	7.647	684.3	116.8	89.07	1.223	0.7349	1.664
−178	5.4677	717.43	−84.24	3.266	2.215	0.9990	8.044	661.8	113.0	84.05	1.172	0.7112	1.647
−176	6.3514	706.13	−79.74	3.312	2.253	0.9920	8.498	638.8	109.2	79.28	1.123	0.6866	1.635
−174	7.3338	694.45	−75.18	3.357	2.297	0.9857	9.022	615.4	105.4	74.74	1.076	0.6608	1.629
−172	8.4212	682.33	−70.52	3.402	2.349	0.9800	9.631	591.3	101.6	70.41	1.032	0.6338	1.628
−170	9.6198	669.70	−65.77	3.447	2.411	0.9751	10.35	566.7	97.72	66.28	0.9896	0.6053	1.635
−168	10.936	656.50	−60.90	3.492	2.485	0.9712	11.21	541.4	93.84	62.31	0.9492	0.5752	1.650
−166	12.377	642.63	−55.89	3.537	2.575	0.9684	12.26	515.2	89.91	58.50	0.9104	0.5433	1.676
−164	13.949	627.97	−50.73	3.582	2.687	0.9669	13.56	488.2	85.92	54.83	0.8731	0.5092	1.715
−162	15.659	612.34	−45.38	3.628	2.829	0.9671	15.21	460.2	81.86	51.27	0.8373	0.4726	1.772
−160	17.516	595.55	−39.80	3.675	3.013	0.9694	17.39	431.0	77.69	47.81	0.8027	0.4330	1.854
−158	19.527	577.27	−33.94	3.723	3.262	0.9747	20.37	400.3	73.39	44.41	0.7693	0.3897	1.974
−156	21.702	557.07	−27.70	3.774	3.617	0.9842	24.70	367.9	68.89	41.04	0.7368	0.3419	2.155
−154	24.051	534.19	−20.95	3.827	4.168	1.000	31.59	333.1	64.13	37.66	0.7049	0.2880	2.447
−152	26.588	507.27	−13.44	3.886	5.147	1.029	44.25	294.6	58.93	34.16	0.6734	0.2257	2.983
−150	29.329	473.20	−4.608	3.954	7.421	1.089	75.00	249.6					
−148	32.300	420.66	7.586	4.046	19.01	1.262	243.2	190.0					
−147	33.889	347.58	22.34	4.160	632.7	1.725		139.7					

D2.3. Table 3. Properties of the saturated vapor

ϑ °C	p bar	ρ'' kg/m³	h'' kJ/kg	s'' kJ/(kg K)	c_p'' kJ/(kg K)	c_v'' kJ/(kg K)	β'' 10^{-3}/K	w_s'' m/s	λ'' mW/(m K)	η'' 10^{-6} Pa·s	ν'' 10^{-7} m²/s	a'' 10^{-7} m²/s	Pr –
−210	0.12517	0.67416	64.78	5.838	1.058	0.7499	16.30	161.1	5.680	3.898	57.82	79.62	0.7263
−208	0.17860	0.93502	66.68	5.764	1.064	0.7519	15.93	163.4	5.919	4.057	43.39	59.50	0.7292
−206	0.24894	1.2688	68.53	5.695	1.070	0.7542	15.61	165.5	6.160	4.217	33.23	45.36	0.7327
−204	0.33973	1.6884	70.34	5.630	1.078	0.7568	15.35	167.6	6.403	4.377	25.92	35.18	0.7368
−202	0.45484	2.2074	72.10	5.571	1.087	0.7598	15.13	169.5	6.651	4.537	20.55	27.72	0.7415
−200	0.59842	2.8403	73.80	5.515	1.097	0.7631	14.95	171.4	6.902	4.698	16.54	22.15	0.7468
−198	0.77491	3.6025	75.44	5.463	1.109	0.7668	14.83	173.1	7.158	4.860	13.49	17.92	0.7529
−196	0.98899	4.5102	77.00	5.414	1.122	0.7708	14.75	174.7	7.419	5.023	11.14	14.65	0.7599
−194	1.2456	5.5807	78.49	5.368	1.138	0.7753	14.72	176.1	7.686	5.187	9.294	12.10	0.7678
−192	1.5497	6.8322	79.90	5.324	1.155	0.7802	14.74	177.5	7.961	5.352	7.834	10.09	0.7767
−190	1.9067	8.2843	81.22	5.282	1.175	0.7856	14.81	178.7	8.243	5.520	6.663	8.468	0.7869
−188	2.3219	9.9578	82.44	5.243	1.197	0.7914	14.94	179.8	8.534	5.690	5.714	7.156	0.7984
−186	2.8009	11.875	83.56	5.204	1.223	0.7978	15.14	180.7	8.834	5.862	4.936	6.083	0.8116
−184	3.3492	14.062	84.57	5.168	1.252	0.8047	15.39	181.5	9.146	6.038	4.294	5.195	0.8265
−182	3.9725	16.544	85.47	5.133	1.285	0.8123	15.73	182.1	9.470	6.218	3.758	4.454	0.8437
−180	4.6767	19.353	86.24	5.098	1.323	0.8205	16.14	182.7	9.808	6.401	3.308	3.831	0.8634
−178	5.4677	22.523	86.87	5.065	1.366	0.8295	16.66	183.0	10.16	6.591	2.926	3.302	0.8862
−176	6.3514	26.093	87.36	5.032	1.416	0.8393	17.28	183.2	10.53	6.786	2.601	2.850	0.9127
−174	7.3338	30.107	87.68	5.000	1.475	0.8500	18.04	183.3	10.92	6.990	2.322	2.460	0.9438
−172	8.4212	34.621	87.83	4.967	1.543	0.8617	18.97	183.2	11.34	7.202	2.080	2.121	0.9806
−170	9.6198	39.696	87.79	4.935	1.625	0.8745	20.09	182.9	11.77	7.425	1.871	1.826	1.024
−168	10.936	45.412	87.53	4.903	1.722	0.8885	21.48	182.5	12.24	7.662	1.687	1.566	1.077
−166	12.377	51.863	87.03	4.870	1.840	0.9038	23.19	181.9	12.75	7.915	1.526	1.336	1.142
−164	13.949	59.174	86.26	4.837	1.987	0.9205	25.36	181.1	13.30	8.189	1.384	1.131	1.224
−162	15.659	67.505	85.16	4.803	2.177	0.9398	28.17	180.2	13.90	8.489	1.257	0.9456	1.330
−160	17.516	77.074	83.69	4.766	2.429	0.9630	31.93	179.1	14.56	8.822	1.145	0.7777	1.472
−158	19.527	88.191	81.75	4.728	2.780	0.9920	37.14	177.6	15.31	9.201	1.043	0.6245	1.671
−156	21.702	101.32	79.22	4.687	3.295	1.028	44.77	175.9	16.17	9.641	0.9516	0.4844	1.964
−154	24.051	117.20	75.90	4.640	4.116	1.075	56.92	173.7	17.20	10.17	0.8680	0.3566	2.434
−152	26.588	137.23	71.43	4.586	5.613	1.136	79.04	170.9	18.50	10.85	0.7908	0.2401	3.293
−150	29.329	164.48	65.01	4.519	9.169	1.229	131.3	167.1					
−148	32.300	210.05	53.83	4.416	27.29	1.427	394.7	159.3					
−147	33.889	278.92	36.95	4.276	832.3	1.831		141.9					

D2.3. Table 4. Density ρ of nitrogen in kg/m³

	Temperature in °C											
Pressure in bar	−200	−175	−150	−125	−100	−75	−50	−25	0	25	50	75
1	824.9	3.505	2.765	2.288	1.953	1.704	1.512	1.359	1.234	1.130	1.043	0.9676
5	825.8	19.36	14.47	11.73	9.908	8.597	7.601	6.816	6.181	5.656	5.213	4.836
10	827.0	702.2	30.90	24.24	20.19	17.39	15.30	13.69	12.39	11.32	10.43	9.665
20	829.2	707.7	74.04	52.15	41.97	35.55	31.01	27.57	24.87	22.67	20.84	19.30
30	831.3	712.8	479.8	85.18	65.53	54.50	47.09	41.64	37.42	34.03	31.24	28.90
40	833.4	717.6	527.6	125.6	91.03	74.22	63.50	55.85	50.02	45.39	41.61	38.45
50	835.5	722.2	552.0	176.6	118.6	94.66	80.21	70.17	62.65	56.73	51.93	47.94

D2.3. Table 4. (continued)

Pressure in bar	Temperature in °C											
	−200	−175	−150	−125	−100	−75	−50	−25	0	25	50	75
60	837.5	726.5	569.6	239.7	148.1	115.7	97.16	84.57	75.27	68.04	62.20	57.37
70	839.5	730.6	583.6	306.5	179.2	137.3	114.3	99.00	87.87	79.29	72.40	66.72
80	841.5	734.6	595.3	362.1	211.3	159.2	131.4	113.4	100.4	90.47	82.52	76.00
90	843.4	738.3	605.6	403.3	243.3	181.1	148.6	127.8	112.9	101.6	92.56	85.19
100	845.3	742.0	614.6	434.2	274.1	203.0	165.7	142.0	125.2	112.5	102.5	94.29
150	854.2	758.3	649.6	522.1	393.3	302.3	246.5	210.3	184.7	165.5	150.4	138.2
200	862.4	772.3	675.1	569.7	464.7	377.7	315.0	270.8	238.6	214.1	194.8	179.1
250	870.1	784.7	695.4	603.0	512.3	432.9	370.1	322.4	286.2	257.9	235.2	216.7
300	877.3	795.8	712.6	628.8	547.7	475.0	414.4	365.9	327.5	296.8	271.8	251.1
350	884.1	806.0	727.5	650.0	575.8	508.5	450.6	402.7	363.5	331.3	304.7	282.4
400	890.6	815.3	740.8	668.1	599.1	536.1	481.0	434.1	394.9	362.0	334.4	310.9
450	896.7	824.1	752.8	684.0	619.1	559.7	507.0	461.4	422.5	389.4	361.1	336.9
500	902.5	832.2	763.7	698.2	636.7	580.2	529.7	485.4	447.1	414.0	385.4	360.7
600	913.5	847.1	783.2	722.8	666.4	614.6	567.7	525.9	489.0	456.5	427.9	402.6
700	923.6	860.6	800.3	743.7	691.2	642.9	598.9	559.3	523.8	492.1	463.8	438.6
800	933.1	872.8	815.6	762.0	712.5	666.9	625.3	587.6	553.4	522.6	494.9	469.9
900	942.0	884.1	829.4	778.4	731.3	688.0	648.3	612.1	579.2	549.3	522.1	497.5
1,000	950.3	894.6	842.0	793.2	748.1	706.6	668.6	633.8	602.0	572.9	546.4	522.1

Pressure in bar	Temperature in °C											
	100	125	150	200	300	400	500	600	700	800	900	1,000
1	0.9027	0.8460	0.7960	0.7118	0.5876	0.5003	0.4356	0.3857	0.3461	0.3139	0.2871	0.2646
5	4.510	4.225	3.975	3.554	2.933	2.497	2.175	1.926	1.728	1.567	1.434	1.321
10	9.010	8.439	7.936	7.094	5.854	4.984	4.340	3.844	3.450	3.129	2.863	2.639
20	17.98	16.83	15.82	14.13	11.66	9.927	8.646	7.660	6.876	6.238	5.709	5.262
30	26.89	25.16	23.64	21.11	17.41	14.83	12.92	11.45	10.28	9.326	8.537	7.871
40	35.75	33.43	31.40	28.03	23.11	19.69	17.15	15.20	13.66	12.39	11.35	10.46
50	44.55	41.64	39.10	34.89	28.76	24.50	21.36	18.93	17.01	15.44	14.14	13.04
60	53.28	49.78	46.73	41.68	34.36	29.28	25.53	22.64	20.34	18.47	16.92	15.61
70	61.94	57.85	54.29	48.42	39.91	34.01	29.66	26.31	23.65	21.48	19.68	18.16
80	70.52	65.84	61.78	55.08	45.41	38.70	33.76	29.96	26.93	24.47	22.42	20.69
90	79.02	73.75	69.20	61.68	50.85	43.35	37.83	33.58	30.19	27.44	25.15	23.21
100	87.43	81.58	76.53	68.22	56.24	47.96	41.86	37.17	33.43	30.39	27.86	25.72
150	128.0	119.4	112.0	99.85	82.42	70.40	61.54	54.72	49.29	44.86	41.17	38.04
200	166.0	154.9	145.4	129.7	107.3	91.84	80.43	71.63	64.61	58.87	54.09	50.03
250	201.2	188.0	176.6	157.9	131.0	112.3	98.56	87.92	79.41	72.45	66.63	61.69
300	233.6	218.7	205.7	184.3	153.4	131.9	116.0	103.6	93.72	85.60	78.81	73.04
350	263.4	247.0	232.8	209.1	174.7	150.6	132.7	118.7	107.6	98.36	90.66	84.10
400	290.7	273.3	257.9	232.4	194.9	168.5	148.7	133.3	120.9	110.7	102.2	94.86
450	315.9	297.5	281.4	254.2	214.1	185.6	164.2	147.4	133.9	122.8	113.4	105.4
500	339.0	320.0	303.2	274.7	232.3	201.9	179.0	161.0	146.5	134.4	124.3	115.6
600	380.3	360.4	342.7	312.3	266.1	232.6	207.1	186.9	170.4	156.8	145.2	135.3
700	416.0	395.7	377.4	345.7	296.8	260.8	233.1	211.0	193.0	177.9	165.1	154.1
800	447.3	426.8	408.2	375.7	324.8	286.9	257.4	233.7	214.2	197.9	184.0	172.0
900	475.0	454.5	435.8	402.8	350.5	311.0	280.0	255.0	234.3	216.9	202.0	189.1
1,000	499.9	479.5	460.7	427.5	374.2	333.5	301.3	275.1	253.4	235.0	219.2	205.5

D2.3. Table 5. Compression factor *Z* of nitrogen

Temperature in °C												
Pressure in bar	−200	−175	−150	−125	−100	−75	−50	−25	0	25	50	75
1	0.006	0.979	0.989	0.994	0.996	0.998	0.999	0.999	1.000	1.000	1.000	1.000
5	0.028	0.886	0.945	0.970	0.982	0.989	0.993	0.996	0.998	0.999	1.000	1.001
10	0.056	0.049	0.885	0.938	0.964	0.978	0.987	0.992	0.996	0.998	1.000	1.001
20	0.111	0.097	0.739	0.872	0.927	0.957	0.974	0.985	0.992	0.997	1.000	1.003
30	0.166	0.144	0.171	0.801	0.891	0.936	0.962	0.978	0.989	0.996	1.001	1.005
40	0.221	0.191	0.207	0.724	0.855	0.916	0.951	0.972	0.986	0.996	1.002	1.007
50	0.276	0.238	0.248	0.644	0.820	0.898	0.941	0.967	0.984	0.996	1.004	1.009
60	0.330	0.283	0.288	0.569	0.788	0.882	0.932	0.963	0.983	0.997	1.006	1.012
70	0.384	0.329	0.328	0.519	0.760	0.867	0.925	0.960	0.983	0.998	1.008	1.015
80	0.438	0.374	0.368	0.502	0.737	0.855	0.919	0.958	0.983	0.999	1.011	1.019
90	0.492	0.418	0.407	0.507	0.720	0.845	0.914	0.956	0.983	1.001	1.014	1.022
100	0.545	0.463	0.445	0.524	0.710	0.838	0.911	0.956	0.985	1.004	1.017	1.026
150	0.809	0.679	0.632	0.653	0.742	0.844	0.919	0.969	1.002	1.024	1.040	1.050
200	1.068	0.889	0.811	0.798	0.837	0.900	0.959	1.003	1.034	1.056	1.071	1.081
250	1.323	1.094	0.984	0.943	0.950	0.982	1.020	1.053	1.078	1.096	1.108	1.116
300	1.575	1.294	1.152	1.085	1.066	1.074	1.093	1.113	1.130	1.142	1.151	1.156
350	1.823	1.491	1.316	1.225	1.183	1.170	1.173	1.180	1.188	1.194	1.198	1.200
400	2.069	1.684	1.477	1.362	1.299	1.269	1.256	1.251	1.250	1.249	1.247	1.245
450	2.311	1.875	1.635	1.496	1.414	1.367	1.340	1.324	1.314	1.306	1.299	1.293
500	2.552	2.062	1.791	1.629	1.528	1.465	1.425	1.399	1.380	1.365	1.353	1.342
600	3.025	2.431	2.096	1.888	1.752	1.660	1.596	1.549	1.513	1.485	1.462	1.442
700	3.491	2.792	2.393	2.140	1.971	1.851	1.765	1.699	1.648	1.607	1.573	1.545
800	3.949	3.146	2.684	2.387	2.185	2.040	1.932	1.849	1.783	1.730	1.685	1.648
900	4.401	3.494	2.969	2.630	2.395	2.224	2.096	1.996	1.917	1.852	1.797	1.751
1,000	4.847	3.837	3.249	2.867	2.601	2.406	2.258	2.142	2.049	1.972	1.908	1.854
Temperature in °C												
Pressure in bar	100	125	150	200	300	400	500	600	700	800	900	1,000
1	1.000	1.000	1.000	1.000	1.000	1.000	1.000	1.000	1.000	1.000	1.000	1.000
5	1.001	1.001	1.002	1.002	1.002	1.002	1.002	1.002	1.002	1.002	1.002	1.001
10	1.002	1.003	1.003	1.004	1.004	1.004	1.004	1.004	1.004	1.003	1.003	1.003
20	1.005	1.006	1.007	1.008	1.009	1.008	1.008	1.008	1.007	1.007	1.006	1.006
30	1.007	1.009	1.010	1.012	1.013	1.013	1.012	1.011	1.011	1.010	1.009	1.009
40	1.010	1.012	1.014	1.016	1.017	1.017	1.016	1.015	1.014	1.013	1.012	1.012
50	1.013	1.016	1.018	1.021	1.022	1.021	1.020	1.019	1.018	1.017	1.015	1.014
60	1.017	1.020	1.022	1.025	1.026	1.026	1.024	1.023	1.021	1.020	1.019	1.017
70	1.020	1.024	1.027	1.030	1.031	1.030	1.028	1.027	1.025	1.023	1.022	1.020
80	1.024	1.028	1.031	1.034	1.036	1.035	1.033	1.030	1.028	1.026	1.025	1.023
90	1.028	1.033	1.036	1.039	1.040	1.039	1.037	1.034	1.032	1.030	1.028	1.026
100	1.033	1.037	1.040	1.044	1.045	1.044	1.041	1.038	1.036	1.033	1.031	1.029
150	1.058	1.063	1.066	1.070	1.070	1.066	1.062	1.058	1.054	1.050	1.046	1.043
200	1.088	1.092	1.095	1.098	1.096	1.090	1.084	1.077	1.072	1.067	1.062	1.058
250	1.122	1.125	1.127	1.128	1.122	1.114	1.105	1.097	1.090	1.083	1.078	1.072
300	1.160	1.161	1.161	1.159	1.150	1.138	1.127	1.117	1.108	1.100	1.093	1.087
350	1.200	1.199	1.197	1.192	1.178	1.163	1.150	1.137	1.127	1.117	1.109	1.101
400	1.242	1.239	1.235	1.226	1.207	1.188	1.172	1.158	1.145	1.134	1.124	1.116

D2.3. Table 5. (continued)

Pressure in bar	Temperature in °C											
	100	125	150	200	300	400	500	600	700	800	900	1,000
450	1.286	1.280	1.273	1.260	1.236	1.214	1.195	1.178	1.163	1.151	1.140	1.130
500	1.332	1.322	1.313	1.296	1.265	1.239	1.217	1.198	1.182	1.168	1.156	1.145
600	1.424	1.409	1.394	1.368	1.326	1.291	1.263	1.239	1.219	1.202	1.187	1.174
700	1.519	1.497	1.477	1.442	1.386	1.343	1.309	1.280	1.256	1.235	1.218	1.202
800	1.615	1.586	1.551	1.516	1.448	1.396	1.355	1.321	1.293	1.269	1.249	1.231
900	1.711	1.676	1.644	1.591	1.509	1.448	1.400	1.362	1.330	1.303	1.280	1.260
1,000	1.806	1.765	1.728	1.666	1.571	1.501	1.446	1.403	1.367	1.336	1.310	1.288

D2.3. Table 6. Specific enthalpy *h* of nitrogen in kJ/kg

Pressure in bar	Temperature in °C											
	−200	−175	−150	−125	−100	−75	−50	−25	0	25	50	75
1	−130.6	99.92	126.5	152.8	179.0	205.1	231.1	257.2	283.2	309.3	335.3	361.4
5	−130.3	91.95	121.7	149.4	176.4	203.1	229.5	255.9	282.2	308.4	334.6	360.7
10	−129.9	−77.40	115.0	145.0	173.2	200.6	227.5	254.3	280.8	307.3	333.6	360.0
20	−129.1	−77.15	97.97	135.4	166.4	195.5	223.5	251.0	278.2	305.1	331.8	358.5
30	−128.4	−76.84	−5.654	124.5	159.4	190.3	219.6	247.9	275.6	303.0	330.1	357.0
40	−127.6	−76.48	−12.73	112.0	152.1	185.1	215.6	244.7	273.1	300.9	328.4	355.6
50	−126.9	−76.08	−15.80	97.49	144.6	179.9	211.7	241.6	270.6	298.9	326.7	354.3
60	−126.1	−75.64	−17.67	81.40	136.8	174.8	207.8	238.6	268.2	296.9	325.1	352.9
70	−125.3	−75.18	−18.92	66.46	129.2	169.7	204.0	235.7	265.8	295.0	323.6	351.7
80	−124.6	−74.68	−19.78	55.50	121.7	164.7	200.4	232.9	263.6	293.2	322.1	350.5
90	−123.8	−74.17	−20.36	48.20	114.7	159.9	196.8	230.1	261.4	291.4	320.6	349.3
100	−123.0	−73.63	−20.75	43.25	108.3	155.3	193.4	227.5	259.3	289.7	319.3	348.2
150	−119.0	−70.67	−20.92	32.52	87.93	137.2	179.1	216.0	250.1	282.3	313.3	343.3
200	−115.0	−67.38	−19.49	29.74	79.60	126.8	169.3	207.8	243.2	276.7	308.7	339.7
250	−110.8	−63.88	−17.23	29.67	76.44	121.5	163.5	202.3	238.5	272.8	305.5	337.2
300	−106.7	−60.22	−14.47	30.92	75.77	119.2	160.4	199.1	235.6	270.3	303.6	335.7
350	−102.5	−56.44	−11.37	32.97	76.49	118.7	159.2	197.6	234.1	269.0	302.6	335.1
400	−98.30	−52.56	−8.032	35.52	78.10	119.4	159.2	197.3	233.8	268.8	302.5	335.2
450	−94.06	−48.61	−4.515	38.44	80.31	121.0	160.2	198.0	234.3	269.3	303.1	336.0
500	−89.80	−44.61	−0.8618	41.62	82.93	123.0	161.8	199.3	235.4	270.4	304.3	337.3
600	−81.23	−36.45	6.745	48.53	89.05	128.3	166.5	203.4	239.3	274.1	308.0	341.0
700	−72.61	−28.16	14.63	55.94	95.92	134.7	172.3	208.9	244.5	279.1	313.0	346.1
800	−63.96	−19.78	22.71	63.68	103.3	141.7	179.0	215.3	250.6	285.1	318.9	352.0
900	−55.29	−11.33	30.93	71.64	111.0	149.1	186.1	222.2	257.4	291.8	325.5	358.6
1,000	−46.61	−2.841	39.24	79.76	118.9	156.8	193.7	229.6	264.7	299.0	332.6	365.7

Pressure in bar	Temperature in °C											
	100	125	150	200	300	400	500	600	700	800	900	1,000
1	387.4	413.5	439.7	492.1	598.2	706.2	816.6	929.4	1,044	1,162	1,281	1,402
5	386.9	413.1	439.3	491.9	598.1	706.3	816.8	929.6	1,045	1,162	1,281	1,402
10	386.3	412.6	438.9	491.7	598.1	706.4	817.0	929.9	1,045	1,162	1,281	1,402
20	385.0	411.6	438.1	491.1	598.0	706.6	817.4	930.4	1,046	1,163	1,282	1,403
30	383.8	410.6	437.3	490.6	597.9	706.8	817.8	931.0	1,046	1,164	1,283	1,404

D2.3. Table 6. (continued)

Temperature in °C												
Pressure in bar	100	125	150	200	300	400	500	600	700	800	900	1,000
40	382.7	409.6	436.5	490.2	597.9	707.0	818.2	931.6	1,047	1,165	1,284	1,405
50	381.6	408.7	435.8	489.7	597.9	707.3	818.6	932.1	1,048	1,165	1,285	1,406
60	380.5	407.9	435.1	489.3	597.9	707.5	819.1	932.7	1,048	1,166	1,286	1,407
70	379.5	407.0	434.4	488.9	597.9	707.8	819.5	933.3	1,049	1,167	1,287	1,408
80	378.5	406.2	433.8	488.6	597.9	708.1	820.0	933.9	1,050	1,168	1,287	1,409
90	377.5	405.5	433.2	488.3	597.9	708.4	820.5	934.5	1,051	1,169	1,288	1,410
100	376.6	404.8	432.6	488.0	598.0	708.7	821.0	935.1	1,051	1,169	1,289	1,410
150	372.8	401.7	430.3	486.8	598.5	710.4	823.5	938.3	1,055	1,173	1,293	1,415
200	369.9	399.6	428.8	486.3	599.5	712.4	826.2	941.6	1,059	1,178	1,298	1,420
250	368.0	398.2	427.9	486.3	600.8	714.6	829.1	945.0	1,063	1,182	1,302	1,424
300	367.0	397.6	427.7	486.8	602.4	717.0	832.2	948.6	1,066	1,186	1,307	1,429
350	366.8	397.7	428.1	487.8	604.3	719.7	835.4	952.2	1,071	1,190	1,311	1,434
400	367.1	398.4	429.0	489.1	606.5	722.5	838.7	956.0	1,075	1,195	1,316	1,439
450	368.1	399.5	430.4	490.9	608.9	725.5	842.2	959.8	1,079	1,199	1,321	1,443
500	369.5	401.0	432.1	492.9	611.6	728.7	845.8	963.8	1,083	1,204	1,325	1,448
600	373.4	405.2	436.5	497.8	617.4	735.4	853.2	971.9	1,092	1,213	1,335	1,458
700	378.5	410.4	441.8	503.5	623.9	742.6	861.0	980.2	1,100	1,222	1,344	1,468
800	384.5	416.5	448.0	509.9	630.9	750.1	869.1	988.7	1,109	1,231	1,354	1,478
900	391.1	423.1	454.7	516.8	638.3	758.0	877.4	997.5	1,118	1,240	1,364	1,488
1,000	398.2	430.2	461.9	524.1	646.0	766.1	886.0	1,006	1,128	1,250	1,373	1,498

D2.3. Table 7. Specific entropy *s* of nitrogen in kJ/(kg K)

Temperature in °C												
Pressure in bar	−200	−175	−150	−125	−100	−75	−50	−25	0	25	50	75
1	2.721	5.674	5.915	6.109	6.273	6.413	6.537	6.648	6.748	6.839	6.923	7.001
5	2.718	5.141	5.411	5.616	5.785	5.928	6.054	6.166	6.267	6.359	6.443	6.521
10	2.715	3.331	5.167	5.389	5.565	5.713	5.841	5.955	6.057	6.150	6.235	6.313
20	2.709	3.319	4.860	5.138	5.332	5.488	5.622	5.739	5.843	5.937	6.023	6.103
30	2.702	3.308	3.944	4.963	5.182	5.348	5.487	5.608	5.714	5.810	5.897	5.978
40	2.696	3.297	3.870	4.814	5.065	5.243	5.388	5.512	5.621	5.718	5.807	5.888
50	2.690	3.287	3.830	4.670	4.966	5.157	5.308	5.435	5.546	5.645	5.735	5.817
60	2.685	3.277	3.801	4.529	4.877	5.082	5.240	5.371	5.484	5.585	5.676	5.759
70	2.679	3.268	3.777	4.403	4.798	5.017	5.180	5.315	5.431	5.533	5.625	5.709
80	2.673	3.259	3.756	4.309	4.725	4.957	5.127	5.265	5.383	5.487	5.580	5.665
90	2.668	3.251	3.738	4.242	4.659	4.904	5.079	5.221	5.341	5.446	5.540	5.626
100	2.662	3.242	3.721	4.192	4.600	4.854	5.036	5.180	5.302	5.409	5.504	5.591
150	2.636	3.205	3.656	4.050	4.396	4.663	4.862	5.019	5.150	5.262	5.362	5.452
200	2.612	3.171	3.606	3.970	4.281	4.536	4.738	4.901	5.038	5.155	5.258	5.350
250	2.589	3.142	3.565	3.912	4.204	4.447	4.647	4.812	4.951	5.071	5.176	5.271
300	2.568	3.114	3.530	3.865	4.145	4.380	4.576	4.740	4.880	5.002	5.109	5.205
350	2.547	3.089	3.499	3.826	4.098	4.326	4.518	4.682	4.822	4.944	5.052	5.149
400	2.528	3.066	3.470	3.793	4.058	4.281	4.471	4.632	4.772	4.895	5.004	5.101
450	2.509	3.044	3.445	3.762	4.024	4.243	4.430	4.590	4.729	4.852	4.961	5.059

D2.3. Table 7. **(continued)**

Temperature in °C												
Pressure in bar	−200	−175	−150	−125	−100	−75	−50	−25	0	25	50	75
500	2.492	3.024	3.421	3.735	3.993	4.209	4.394	4.553	4.692	4.814	4.923	5.022
600	2.458	2.985	3.378	3.687	3.939	4.152	4.333	4.490	4.627	4.749	4.859	4.957
700	2.427	2.950	3.339	3.645	3.894	4.103	4.282	4.438	4.574	4.696	4.805	4.903
800	2.398	2.918	3.304	3.607	3.854	4.062	4.239	4.393	4.529	4.650	4.759	4.857
900	2.371	2.888	3.272	3.573	3.819	4.025	4.201	4.354	4.489	4.610	4.718	4.817
1,000	2.345	2.860	3.243	3.542	3.787	3.991	4.166	4.319	4.454	4.574	4.682	4.781
Temperature in °C												
Pressure in bar	100	125	150	200	300	400	500	600	700	800	900	1,000
1	7.073	7.141	7.204	7.322	7.525	7.699	7.851	7.989	8.113	8.228	8.334	8.433
5	6.594	6.662	6.726	6.843	7.047	7.221	7.373	7.511	7.636	7.750	7.856	7.955
10	6.386	6.454	6.518	6.636	6.840	7.014	7.167	7.305	7.430	7.544	7.650	7.749
20	6.176	6.245	6.310	6.428	6.633	6.808	6.961	7.099	7.224	7.338	7.445	7.543
30	6.052	6.121	6.186	6.306	6.511	6.686	6.840	6.978	7.103	7.218	7.324	7.423
40	5.963	6.033	6.098	6.218	6.425	6.600	6.754	6.892	7.017	7.132	7.238	7.337
50	5.893	5.963	6.029	6.150	6.357	6.533	6.687	6.825	6.951	7.066	7.172	7.271
60	5.835	5.906	5.972	6.093	6.302	6.478	6.632	6.771	6.896	7.011	7.118	7.217
70	5.786	5.857	5.924	6.046	6.255	6.431	6.586	6.724	6.850	6.965	7.072	7.171
80	5.742	5.814	5.882	6.004	6.214	6.391	6.546	6.684	6.810	6.925	7.032	7.131
90	5.704	5.777	5.844	5.967	6.177	6.355	6.510	6.649	6.775	6.890	6.997	7.096
100	5.669	5.742	5.810	5.934	6.145	6.323	6.478	6.617	6.743	6.859	6.965	7.065
150	5.533	5.609	5.678	5.804	6.019	6.199	6.355	6.495	6.621	6.737	6.844	6.944
200	5.434	5.511	5.582	5.711	5.928	6.109	6.267	6.407	6.534	6.651	6.758	6.857
250	5.356	5.434	5.507	5.637	5.857	6.040	6.198	6.339	6.467	6.583	6.691	6.791
300	5.292	5.371	5.445	5.576	5.798	5.983	6.142	6.284	6.411	6.528	6.636	6.736
350	5.237	5.317	5.392	5.525	5.748	5.934	6.094	6.236	6.364	6.482	6.589	6.690
400	5.190	5.271	5.345	5.480	5.705	5.891	6.052	6.195	6.324	6.441	6.549	6.649
450	5.148	5.230	5.305	5.440	5.666	5.854	6.016	6.159	6.288	6.405	6.514	6.614
500	5.111	5.193	5.268	5.404	5.632	5.820	5.982	6.126	6.255	6.373	6.482	6.582
600	5.047	5.129	5.206	5.343	5.572	5.762	5.925	6.069	6.199	6.317	6.426	6.527
700	4.993	5.076	5.153	5.290	5.521	5.712	5.876	6.021	6.152	6.270	6.379	6.481
800	4.947	5.030	5.107	5.245	5.477	5.669	5.834	5.980	6.110	6.229	6.339	6.440
900	4.907	4.990	5.067	5.206	5.439	5.631	5.797	5.943	6.074	6.193	6.303	6.404
1,000	4.871	4.954	5.031	5.170	5.404	5.597	5.763	5.910	6.041	6.161	6.271	6.372

D2.3. Table 8. Specific isobaric heat capacity c_p of nitrogen in kJ/(kg K)

Temperature in °C												
Pressure in bar	−200	−175	−150	−125	−100	−75	−50	−25	0	25	50	75
1	2.024	1.073	1.056	1.049	1.045	1.044	1.042	1.042	1.041	1.041	1.042	1.042
5	2.020	1.278	1.134	1.091	1.072	1.062	1.056	1.052	1.050	1.048	1.047	1.047
10	2.016	2.258	1.269	1.153	1.108	1.086	1.073	1.065	1.060	1.056	1.054	1.052
20	2.008	2.214	1.847	1.315	1.191	1.138	1.109	1.092	1.080	1.073	1.067	1.064
30	2.000	2.176	6.534	1.557	1.291	1.195	1.147	1.119	1.101	1.089	1.081	1.075
40	1.993	2.144	3.649	1.940	1.408	1.257	1.187	1.147	1.122	1.105	1.094	1.086

D2.3. Table 8. (continued)

Temperature in °C												
Pressure in bar	−200	−175	−150	−125	−100	−75	−50	−25	0	25	50	75
50	1.986	2.115	3.047	2.544	1.545	1.323	1.227	1.175	1.143	1.122	1.107	1.096
60	1.979	2.090	2.752	3.294	1.696	1.391	1.268	1.203	1.164	1.138	1.120	1.107
70	1.973	2.068	2.568	3.644	1.853	1.461	1.309	1.231	1.184	1.153	1.132	1.117
80	1.966	2.047	2.440	3.436	1.999	1.529	1.349	1.258	1.204	1.168	1.144	1.127
90	1.961	2.029	2.345	3.110	2.115	1.594	1.388	1.284	1.223	1.183	1.156	1.137
100	1.955	2.012	2.270	2.843	2.190	1.652	1.424	1.309	1.241	1.198	1.168	1.146
150	1.931	1.947	2.050	2.222	2.139	1.806	1.559	1.412	1.320	1.260	1.218	1.189
200	1.911	1.901	1.938	1.998	1.965	1.797	1.611	1.471	1.374	1.306	1.258	1.223
250	1.895	1.868	1.869	1.881	1.849	1.746	1.614	1.496	1.405	1.337	1.287	1.248
300	1.880	1.841	1.822	1.809	1.773	1.696	1.598	1.502	1.421	1.356	1.306	1.268
350	1.868	1.820	1.787	1.759	1.719	1.656	1.577	1.498	1.427	1.368	1.320	1.282
400	1.857	1.803	1.761	1.724	1.681	1.624	1.558	1.490	1.427	1.373	1.328	1.291
450	1.848	1.789	1.740	1.697	1.651	1.599	1.540	1.481	1.425	1.376	1.334	1.298
500	1.840	1.777	1.724	1.676	1.629	1.579	1.525	1.472	1.421	1.376	1.337	1.303
600	1.825	1.758	1.699	1.645	1.596	1.548	1.501	1.455	1.412	1.373	1.339	1.308
700	1.814	1.744	1.681	1.625	1.574	1.528	1.484	1.443	1.404	1.369	1.338	1.310
800	1.803	1.733	1.668	1.610	1.559	1.513	1.471	1.433	1.397	1.365	1.337	1.311
900	1.795	1.723	1.658	1.600	1.548	1.502	1.462	1.425	1.392	1.362	1.335	1.311
1,000	1.787	1.716	1.651	1.592	1.540	1.495	1.455	1.419	1.387	1.359	1.333	1.311

Temperature in °C												
Pressure in bar	100	125	150	200	300	400	500	600	700	800	900	1,000
1	1.043	1.045	1.047	1.053	1.070	1.092	1.116	1.140	1.162	1.182	1.200	1.215
5	1.047	1.048	1.050	1.055	1.071	1.093	1.117	1.140	1.162	1.182	1.200	1.215
10	1.052	1.052	1.053	1.058	1.073	1.094	1.117	1.141	1.163	1.183	1.200	1.216
20	1.061	1.060	1.060	1.063	1.076	1.096	1.119	1.142	1.164	1.183	1.201	1.216
30	1.071	1.068	1.067	1.068	1.080	1.099	1.121	1.143	1.165	1.184	1.202	1.217
40	1.080	1.076	1.074	1.073	1.083	1.101	1.123	1.145	1.166	1.185	1.202	1.217
50	1.089	1.084	1.081	1.079	1.086	1.103	1.124	1.146	1.167	1.186	1.203	1.218
60	1.098	1.091	1.087	1.084	1.089	1.105	1.126	1.147	1.168	1.186	1.203	1.218
70	1.106	1.099	1.093	1.088	1.093	1.108	1.127	1.148	1.169	1.187	1.204	1.219
80	1.115	1.106	1.100	1.093	1.096	1.110	1.129	1.150	1.170	1.188	1.205	1.219
90	1.123	1.113	1.106	1.098	1.099	1.112	1.130	1.151	1.170	1.189	1.205	1.220
100	1.131	1.120	1.112	1.102	1.102	1.114	1.132	1.152	1.171	1.189	1.206	1.220
150	1.167	1.150	1.138	1.123	1.115	1.124	1.139	1.157	1.176	1.193	1.209	1.223
200	1.196	1.176	1.161	1.141	1.127	1.132	1.146	1.162	1.180	1.196	1.211	1.225
250	1.219	1.197	1.180	1.156	1.138	1.140	1.152	1.167	1.183	1.199	1.214	1.227
300	1.237	1.214	1.195	1.169	1.148	1.147	1.157	1.171	1.187	1.202	1.216	1.229
350	1.251	1.227	1.207	1.180	1.156	1.154	1.162	1.175	1.190	1.205	1.218	1.231
400	1.261	1.237	1.217	1.189	1.163	1.159	1.167	1.179	1.193	1.207	1.220	1.232
450	1.269	1.245	1.226	1.197	1.169	1.164	1.171	1.182	1.196	1.210	1.222	1.234
500	1.275	1.251	1.232	1.204	1.175	1.169	1.175	1.186	1.199	1.212	1.224	1.236
600	1.282	1.260	1.242	1.214	1.184	1.177	1.181	1.191	1.203	1.216	1.228	1.239
700	1.286	1.266	1.248	1.221	1.192	1.184	1.187	1.196	1.208	1.220	1.231	1.242
800	1.289	1.269	1.252	1.226	1.198	1.189	1.192	1.201	1.211	1.223	1.234	1.244
900	1.290	1.271	1.256	1.231	1.203	1.194	1.197	1.205	1.215	1.226	1.236	1.246
1,000	1.291	1.273	1.258	1.234	1.207	1.198	1.200	1.208	1.218	1.229	1.239	1.249

D2.3. Table 9. Specific isochoric heat capacity c_v of nitrogen in kJ/(kg K)

Pressure in bar	Temperature in °C											
	−200	−175	−150	−125	−100	−75	−50	−25	0	25	50	75
1	1.110	0.7522	0.7462	0.7443	0.7434	0.7430	0.7429	0.7428	0.7429	0.7431	0.7436	0.7445
5	1.111	0.8058	0.7642	0.7529	0.7484	0.7462	0.7451	0.7444	0.7441	0.7441	0.7445	0.7452
10	1.112	0.9891	0.7914	0.7644	0.7547	0.7502	0.7478	0.7465	0.7457	0.7454	0.7455	0.7460
20	1.114	0.9905	0.8760	0.7905	0.7678	0.7582	0.7533	0.7504	0.7488	0.7478	0.7475	0.7477
30	1.117	0.9922	1.064	0.8210	0.7815	0.7662	0.7586	0.7543	0.7517	0.7502	0.7495	0.7494
40	1.120	0.9941	0.9711	0.8560	0.7954	0.7741	0.7638	0.7581	0.7546	0.7525	0.7514	0.7510
50	1.122	0.9961	0.9503	0.8935	0.8092	0.7817	0.7688	0.7617	0.7574	0.7548	0.7533	0.7526
60	1.125	0.9982	0.9412	0.9234	0.8223	0.7891	0.7737	0.7652	0.7602	0.7570	0.7551	0.7542
70	1.127	1.000	0.9367	0.9310	0.8338	0.7960	0.7783	0.7686	0.7628	0.7591	0.7569	0.7557
80	1.129	1.002	0.9346	0.9228	0.8432	0.8023	0.7826	0.7718	0.7653	0.7612	0.7586	0.7572
90	1.132	1.005	0.9337	0.9128	0.8501	0.8079	0.7867	0.7749	0.7678	0.7632	0.7603	0.7587
100	1.134	1.007	0.9338	0.9054	0.8547	0.8129	0.7905	0.7778	0.7701	0.7652	0.7620	0.7601
150	1.146	1.018	0.9393	0.8943	0.8607	0.8287	0.8054	0.7903	0.7805	0.7740	0.7696	0.7668
200	1.156	1.028	0.9477	0.8977	0.8637	0.8365	0.8152	0.7998	0.7891	0.7816	0.7764	0.7728
250	1.167	1.038	0.9567	0.9043	0.8689	0.8428	0.8226	0.8075	0.7963	0.7882	0.7824	0.7784
300	1.176	1.048	0.9656	0.9119	0.8754	0.8490	0.8292	0.8141	0.8027	0.7943	0.7880	0.7835
350	1.186	1.057	0.9743	0.9197	0.8823	0.8554	0.8354	0.8202	0.8086	0.7998	0.7932	0.7883
400	1.194	1.065	0.9826	0.9275	0.8893	0.8619	0.8415	0.8261	0.8142	0.8050	0.7981	0.7929
450	1.203	1.074	0.9906	0.9350	0.8962	0.8683	0.8475	0.8317	0.8195	0.8100	0.8028	0.7973
500	1.211	1.081	0.9983	0.9423	0.9030	0.8746	0.8533	0.8372	0.8246	0.8149	0.8073	0.8015
600	1.226	1.096	1.013	0.9562	0.9161	0.8867	0.8646	0.8477	0.8345	0.8241	0.8159	0.8096
700	1.240	1.110	1.026	0.9692	0.9283	0.8982	0.8754	0.8577	0.8438	0.8328	0.8241	0.8173
800	1.253	1.123	1.039	0.9813	0.9399	0.9091	0.8856	0.8673	0.8528	0.8412	0.8320	0.8247
900	1.264	1.135	1.051	0.9928	0.9509	0.9194	0.8953	0.8764	0.8613	0.8492	0.8395	0.8317
1,000	1.275	1.146	1.062	1.004	0.9612	0.9293	0.9046	0.8851	0.8695	0.8569	0.8467	0.8385

Pressure in bar	Temperature in °C											
	100	125	150	200	300	400	500	600	700	800	900	1,000
1	0.7457	0.7473	0.7495	0.7553	0.7725	0.7947	0.8189	0.8427	0.8649	0.8850	0.9028	0.9184
5	0.7463	0.7478	0.7499	0.7556	0.7727	0.7949	0.8190	0.8428	0.8650	0.8851	0.9029	0.9185
10	0.7470	0.7485	0.7505	0.7561	0.7731	0.7952	0.8192	0.8430	0.8652	0.8852	0.9030	0.9187
20	0.7485	0.7498	0.7516	0.7570	0.7737	0.7957	0.8197	0.8434	0.8655	0.8855	0.9033	0.9189
30	0.7499	0.7510	0.7528	0.7580	0.7744	0.7962	0.8201	0.8437	0.8658	0.8858	0.9035	0.9191
40	0.7513	0.7523	0.7539	0.7589	0.7751	0.7967	0.8205	0.8441	0.8661	0.8861	0.9038	0.9193
50	0.7527	0.7535	0.7550	0.7597	0.7757	0.7972	0.8209	0.8445	0.8665	0.8864	0.9040	0.9196
60	0.7541	0.7547	0.7560	0.7606	0.7764	0.7977	0.8214	0.8448	0.8668	0.8866	0.9043	0.9198
70	0.7554	0.7559	0.7571	0.7615	0.7770	0.7983	0.8218	0.8452	0.8671	0.8869	0.9045	0.9200
80	0.7567	0.7570	0.7581	0.7624	0.7776	0.7988	0.8222	0.8455	0.8674	0.8872	0.9048	0.9202
90	0.7580	0.7582	0.7592	0.7632	0.7783	0.7993	0.8226	0.8459	0.8677	0.8875	0.9050	0.9205
100	0.7593	0.7593	0.7602	0.7641	0.7789	0.7998	0.8230	0.8463	0.8680	0.8877	0.9053	0.9207
150	0.7652	0.7647	0.7650	0.7682	0.7820	0.8023	0.8251	0.8480	0.8696	0.8891	0.9065	0.9218
200	0.7707	0.7696	0.7696	0.7720	0.7850	0.8047	0.8271	0.8498	0.8711	0.8905	0.9077	0.9229
250	0.7757	0.7743	0.7739	0.7757	0.7879	0.8070	0.8291	0.8515	0.8726	0.8918	0.9089	0.9240
300	0.7805	0.7787	0.7779	0.7793	0.7907	0.8093	0.8311	0.8532	0.8741	0.8931	0.9101	0.9251
350	0.7849	0.7828	0.7818	0.7827	0.7934	0.8116	0.8330	0.8548	0.8755	0.8944	0.9113	0.9262
400	0.7892	0.7868	0.7856	0.7860	0.7961	0.8138	0.8349	0.8565	0.8770	0.8957	0.9125	0.9272

D2.3. Table 9. (continued)

Pressure in bar	Temperature in °C											
	100	125	150	200	300	400	500	600	700	800	900	1,000
450	0.7933	0.7907	0.7892	0.7892	0.7987	0.8160	0.8367	0.8581	0.8784	0.8970	0.9136	0.9283
500	0.7973	0.7944	0.7927	0.7923	0.8012	0.8181	0.8386	0.8597	0.8798	0.8983	0.9148	0.9293
600	0.8049	0.8015	0.7994	0.7983	0.8061	0.8222	0.8421	0.8628	0.8826	0.9008	0.9170	0.9314
700	0.8121	0.8083	0.8058	0.8041	0.8108	0.8262	0.8456	0.8658	0.8853	0.9032	0.9192	0.9334
800	0.8190	0.8149	0.8120	0.8096	0.8154	0.8301	0.8489	0.8688	0.8879	0.9056	0.9214	0.9354
900	0.8257	0.8212	0.8179	0.8150	0.8199	0.8339	0.8522	0.8717	0.8905	0.9079	0.9235	0.9373
1,000	0.8321	0.8272	0.8237	0.8202	0.8242	0.8376	0.8554	0.8745	0.8931	0.9102	0.9256	0.9393

D2.3. Table 10. Isobaric expansion coefficient β of nitrogen in 10^{-3}/K

Pressure in bar	Temperature in °C											
	−200	−175	−150	−125	−100	−75	−50	−25	0	25	50	75
1	5.339	10.83	8.380	6.878	5.847	5.089	4.508	4.048	3.673	3.362	3.101	2.877
5	5.300	14.62	9.599	7.433	6.143	5.264	4.617	4.119	3.722	3.396	3.124	2.894
10	5.253	8.589	11.70	8.236	6.542	5.489	4.756	4.209	3.782	3.437	3.153	2.914
20	5.162	8.133	20.73	10.33	7.441	5.965	5.037	4.386	3.899	3.518	3.209	2.954
30	5.076	7.744	62.97	13.42	8.489	6.470	5.321	4.561	4.012	3.594	3.262	2.991
40	4.993	7.407	25.73	18.17	9.689	6.996	5.604	4.730	4.120	3.666	3.311	3.025
50	4.915	7.111	18.52	25.26	11.02	7.530	5.880	4.892	4.222	3.733	3.356	3.056
60	4.840	6.849	15.08	32.90	12.39	8.054	6.144	5.044	4.317	3.794	3.398	3.085
70	4.768	6.614	12.98	33.96	13.67	8.544	6.388	5.183	4.403	3.850	3.435	3.110
80	4.699	6.402	11.55	28.50	14.66	8.976	6.607	5.309	4.480	3.901	3.469	3.133
90	4.634	6.209	10.48	22.90	15.18	9.326	6.795	5.418	4.548	3.944	3.498	3.152
100	4.570	6.033	9.656	18.83	15.19	9.574	6.948	5.510	4.606	3.982	3.523	3.169
150	4.288	5.334	7.241	10.36	11.55	9.302	7.135	5.698	4.744	4.076	3.585	3.208
200	4.050	4.832	6.013	7.574	8.492	7.882	6.623	5.507	4.663	4.034	3.557	3.185
250	3.846	4.449	5.244	6.166	6.758	6.592	5.907	5.126	4.446	3.900	3.465	3.117
300	3.669	4.144	4.706	5.298	5.684	5.639	5.240	4.701	4.174	3.717	3.336	3.020
350	3.512	3.894	4.303	4.702	4.957	4.944	4.686	4.303	3.895	3.518	3.189	2.908
400	3.373	3.683	3.987	4.263	4.432	4.422	4.238	3.952	3.632	3.321	3.039	2.791
450	3.248	3.503	3.730	3.923	4.033	4.017	3.876	3.653	3.395	3.136	2.893	2.674
500	3.135	3.346	3.517	3.651	3.719	3.695	3.578	3.397	3.184	2.965	2.755	2.561
600	2.937	3.086	3.181	3.238	3.253	3.214	3.122	2.990	2.834	2.670	2.508	2.355
700	2.769	2.876	2.924	2.937	2.920	2.871	2.790	2.683	2.561	2.431	2.301	2.176
800	2.624	2.703	2.720	2.706	2.669	2.613	2.537	2.445	2.343	2.236	2.128	2.023
900	2.497	2.556	2.553	2.520	2.472	2.410	2.337	2.255	2.166	2.074	1.982	1.892
1,000	2.384	2.430	2.412	2.368	2.312	2.247	2.176	2.100	2.020	1.939	1.858	1.779
Pressure in bar	Temperature in °C											
	100	125	150	200	300	400	500	600	700	800	900	1,000
1	2.683	2.514	2.365	2.114	1.745	1.485	1.293	1.145	1.027	0.9316	0.8522	0.7853
5	2.695	2.523	2.371	2.118	1.745	1.485	1.292	1.144	1.026	0.9307	0.8514	0.7845
10	2.710	2.534	2.379	2.122	1.746	1.484	1.291	1.143	1.025	0.9296	0.8504	0.7836
20	2.739	2.554	2.394	2.129	1.746	1.482	1.289	1.140	1.023	0.9274	0.8483	0.7817

D2.3. Table 10. (continued)

Pressure in bar	Temperature in °C											
	100	125	150	200	300	400	500	600	700	800	900	1,000
30	2.765	2.572	2.407	2.135	1.746	1.481	1.286	1.138	1.020	0.9251	0.8463	0.7799
40	2.789	2.589	2.419	2.140	1.746	1.479	1.284	1.135	1.018	0.9229	0.8442	0.7780
50	2.810	2.604	2.429	2.145	1.746	1.476	1.281	1.133	1.015	0.9206	0.8422	0.7762
60	2.830	2.618	2.438	2.148	1.745	1.474	1.279	1.130	1.013	0.9184	0.8401	0.7743
70	2.847	2.630	2.446	2.151	1.744	1.472	1.276	1.127	1.010	0.9161	0.8381	0.7725
80	2.863	2.640	2.452	2.153	1.742	1.469	1.273	1.125	1.008	0.9138	0.8360	0.7707
90	2.876	2.648	2.458	2.155	1.740	1.466	1.270	1.122	1.005	0.9115	0.8340	0.7688
100	2.886	2.655	2.462	2.156	1.738	1.463	1.267	1.119	1.003	0.9092	0.8319	0.7670
150	2.909	2.667	2.465	2.149	1.723	1.447	1.251	1.105	0.9901	0.8978	0.8217	0.7578
200	2.888	2.646	2.444	2.127	1.703	1.428	1.235	1.090	0.9771	0.8863	0.8115	0.7488
250	2.834	2.601	2.405	2.095	1.678	1.408	1.217	1.075	0.9641	0.8749	0.8015	0.7398
300	2.758	2.538	2.352	2.055	1.650	1.386	1.199	1.060	0.9510	0.8635	0.7915	0.7310
350	2.670	2.466	2.292	2.009	1.619	1.363	1.181	1.044	0.9380	0.8523	0.7817	0.7224
400	2.575	2.389	2.226	1.961	1.587	1.339	1.162	1.029	0.9251	0.8412	0.7720	0.7139
450	2.480	2.309	2.159	1.910	1.555	1.316	1.144	1.014	0.9123	0.8303	0.7625	0.7055
500	2.387	2.231	2.093	1.860	1.522	1.292	1.125	0.9989	0.8997	0.8195	0.7532	0.6973
600	2.212	2.082	1.964	1.761	1.457	1.245	1.089	0.9695	0.8751	0.7985	0.7350	0.6814
700	2.058	1.948	1.846	1.669	1.395	1.200	1.054	0.9411	0.8515	0.7784	0.7176	0.6661
800	1.923	1.828	1.740	1.584	1.337	1.157	1.020	0.9139	0.8288	0.7591	0.7009	0.6514
900	1.805	1.723	1.646	1.507	1.283	1.116	0.9884	0.8880	0.8072	0.7406	0.6849	0.6374
1,000	1.703	1.630	1.562	1.437	1.233	1.078	0.9584	0.8635	0.7866	0.7231	0.6696	0.6240

D2.3. Table 11. Isentropic speed of sound w_s in nitrogen in m/s

Pressure in bar	Temperature in °C											
	−200	−175	−150	−125	−100	−75	−50	−25	0	25	50	75
1	894	199	225	247	267	286.8	304.4	321.1	337.0	352.1	366.5	380.4
5	897	189	219	244	266	286.1	304.3	321.3	337.4	352.7	367.3	381.2
10	901	632	213	241	264	285.4	304.2	321.7	338.0	353.5	368.2	382.3
20	908	649	196	234	261	284.4	304.4	322.6	339.5	355.3	370.3	384.6
30	915	664	262	228	259	284.0	305.0	323.9	341.2	357.4	372.6	387.0
40	922	678	351	224	258	284.3	306.2	325.6	343.3	359.7	375.1	389.6
50	929	692	399	223	258	285.4	307.9	327.7	345.6	362.2	377.7	392.4
60	936	704	434	229	260	287.4	310.2	330.2	348.3	365.0	380.6	395.3
70	943	716	464	249	264	290.5	313.1	333.1	351.3	368.0	383.6	398.3
80	949	728	489	278	271	294.6	316.6	336.5	354.5	371.2	386.8	401.5
90	956	739	511	310	280	299.9	320.8	340.2	358.1	374.7	390.2	404.8
100	962	750	531	340	292	306.3	325.7	344.4	362.0	378.4	393.7	408.2
150	992	798	612	455	370	352.4	358.5	371.1	385.3	399.7	413.7	427.2
200	1,020	839	674	536	447	409.5	400.9	404.9	414.0	425.1	436.9	448.8
250	1,045	876	725	600	513	466.1	446.6	442.5	446.0	453.2	462.3	472.1
300	1,069	909	769	653	569	518.3	491.8	481.0	479.4	482.8	489.0	496.6
350	1,092	940	808	700	619	565.8	534.7	519.0	513.0	512.9	516.3	521.8
400	1,113	968	844	741	663	609.0	575.1	555.7	546.1	542.9	543.7	547.2
450	1,133	995	876	778	702	648.7	612.8	590.7	578.3	572.4	571.0	572.4

D2.3. Table 11. (continued)

Pressure in bar	Temperature in °C											
	−200	−175	−150	−125	−100	−75	−50	−25	0	25	50	75
500	1,153	1,020	906	812	739	685.4	648.2	624.0	609.3	601.2	597.7	597.4
600	1,190	1,066	960	873	804	751.4	712.8	685.8	667.7	656.2	649.4	646.1
700	1,223	1,108	1,009	927	861	809.7	770.6	742.0	721.6	707.5	698.2	692.5
800	1,255	1,146	1,053	975	912	862.0	823.0	793.4	771.4	755.5	744.3	736.7
900	1,285	1,181	1,093	1,020	958	909.6	870.9	840.8	817.7	800.5	787.7	778.6
1,000	1,313	1,214	1,131	1,060	1,001	953.5	915.1	884.7	861.0	842.7	828.7	818.3

Pressure in bar	Temperature in °C											
	100	125	150	200	300	400	500	600	700	800	900	1,000
1	393.7	406.6	419.0	442.6	485.5	524.1	559.4	592.2	623.1	652.4	680.4	707.3
5	394.6	407.5	420.0	443.6	486.6	525.2	560.4	593.2	624.0	653.3	681.3	708.2
10	395.8	408.8	421.2	444.9	487.9	526.5	561.7	594.4	625.2	654.5	682.4	709.2
20	398.2	411.3	423.8	447.6	490.6	529.1	564.2	596.9	627.6	656.7	684.6	711.3
30	400.8	413.9	426.5	450.3	493.4	531.8	566.8	599.4	629.9	659.0	686.8	713.4
40	403.4	416.6	429.3	453.1	496.1	534.5	569.4	601.8	632.3	661.3	689.0	715.5
50	406.3	419.5	432.1	456.0	498.9	537.2	572.0	604.3	634.7	663.6	691.1	717.6
60	409.2	422.4	435.1	458.9	501.8	539.9	574.6	606.8	637.1	665.8	693.3	719.7
70	412.2	425.5	438.1	461.9	504.6	542.6	577.2	609.3	639.5	668.1	695.5	721.9
80	415.4	428.6	441.2	464.9	507.5	545.4	579.8	611.8	641.8	670.4	697.7	724.0
90	418.6	431.8	444.4	468.0	510.5	548.1	582.4	614.3	644.2	672.7	699.9	726.1
100	422.0	435.1	447.6	471.1	513.4	550.9	585.1	616.8	646.6	675.0	702.1	728.2
150	440.3	452.8	464.8	487.5	528.5	565.0	598.4	629.4	658.6	686.4	713.1	738.7
200	460.6	472.1	483.3	504.8	544.1	579.4	611.8	642.0	670.6	697.9	724.0	749.2
250	482.3	492.6	502.9	522.8	560.0	594.0	625.3	654.7	682.6	709.3	734.9	759.7
300	505.1	514.1	523.2	541.3	576.3	608.7	639.0	667.5	694.6	720.7	745.8	770.1
350	528.5	536.0	543.9	560.3	592.7	623.5	652.6	680.2	706.7	732.1	756.7	780.5
400	552.2	558.2	565.0	579.4	609.3	638.4	666.3	693.0	718.6	743.4	767.5	790.8
450	575.8	580.5	586.1	598.6	625.9	653.3	679.9	705.7	730.6	754.7	778.3	801.1
500	599.3	602.7	607.1	617.8	642.5	668.2	693.6	718.3	742.5	766.0	789.0	811.4
600	645.3	646.3	648.6	655.9	675.6	697.9	720.7	743.5	766.1	788.4	810.3	831.7
700	689.5	688.5	689.0	693.1	708.2	727.2	747.6	768.5	789.5	810.5	831.3	851.9
800	731.8	729.1	728.0	729.4	740.1	756.0	774.0	793.1	812.6	832.4	852.1	871.8
900	772.2	768.0	765.6	764.5	771.3	784.3	800.1	817.3	835.4	854.0	872.7	891.4
1,000	810.7	805.3	801.7	798.4	801.7	811.9	825.6	841.2	857.9	875.2	892.9	910.8

D2.3. Table 12. Thermal conductivity λ of nitrogen in mW/(m K)

Pressure in bar	Temperature in °C											
	−200	−175	−150	−125	−100	−75	−50	−25	0	25	50	75
1	155.7	9.623	12.10	14.41	16.59	18.65	20.59	22.45	24.23	25.94	27.59	29.19
5	156.2	10.33	12.62	14.83	16.95	18.95	20.86	22.69	24.45	26.14	27.77	29.36
10	156.7	108.0	13.36	15.40	17.41	19.35	21.21	23.00	24.72	26.39	28.00	29.58
20	157.8	109.9	15.39	16.68	18.40	20.17	21.92	23.63	25.29	26.90	28.47	30.01
30	158.8	111.7	54.09	18.28	19.51	21.05	22.66	24.27	25.86	27.42	28.94	30.44
40	159.9	113.4	63.15	20.38	20.77	22.00	23.44	24.94	26.44	27.94	29.42	30.88

D2.3. Table 12. (continued)

Pressure in bar	Temperature in °C											
	−200	−175	−150	−125	−100	−75	−50	−25	0	25	50	75
50	160.9	115.1	68.36	23.36	22.20	23.01	24.25	25.62	27.04	28.47	29.90	31.32
60	161.9	116.7	72.35	27.75	23.84	24.11	25.10	26.33	27.65	29.01	30.39	31.76
70	162.9	118.2	75.70	33.50	25.72	25.29	25.99	27.06	28.27	29.56	30.88	32.21
80	163.8	119.7	78.62	39.42	27.86	26.56	26.92	27.81	28.91	30.12	31.38	32.66
90	164.8	121.1	81.25	44.61	30.21	27.91	27.89	28.58	29.56	30.68	31.88	33.11
100	165.8	122.5	83.65	49.02	32.74	29.35	28.91	29.38	30.23	31.26	32.39	33.57
150	170.3	129.0	93.55	64.37	45.47	37.35	34.49	33.67	33.74	34.25	35.01	35.92
200	174.6	134.7	101.4	74.73	56.03	45.55	40.54	38.34	37.52	37.44	37.77	38.36
250	178.7	140.0	108.1	82.91	64.63	53.08	46.58	43.16	41.47	40.76	40.63	40.88
300	182.7	144.9	114.1	89.87	71.93	59.84	52.35	47.95	45.46	44.15	43.58	43.47
350	186.4	149.5	119.6	96.00	78.35	65.95	57.77	52.60	49.44	47.58	46.56	46.10
400	190.0	153.9	124.6	101.6	84.12	71.52	62.85	57.08	53.34	50.98	49.55	48.76
450	193.5	158.0	129.3	106.7	89.40	76.67	67.62	61.38	57.15	54.35	52.53	51.42
500	196.9	161.9	133.7	111.4	94.29	81.47	72.13	65.49	60.85	57.65	55.49	54.09
600	203.4	169.4	141.9	120.1	103.2	90.24	80.47	73.23	67.92	64.07	61.30	59.35
700	209.5	176.3	149.4	128.1	111.2	98.16	88.08	80.40	74.58	70.20	66.93	64.52
800	215.4	182.9	156.5	135.3	118.6	105.4	95.13	87.09	80.87	76.06	72.37	69.55
900	221.0	189.1	163.1	142.2	125.5	112.2	101.7	93.40	86.83	81.67	77.61	74.45
1,000	226.4	195.0	169.3	148.6	131.9	118.6	107.9	99.37	92.52	87.05	82.68	79.21

Pressure in bar	Temperature in °C											
	100	125	150	200	300	400	500	600	700	800	900	1,000
1	30.75	32.28	33.78	36.72	42.47	48.12	53.68	59.13	64.45	69.63	74.67	79.57
5	30.91	32.43	33.92	36.85	42.58	48.21	53.75	59.20	64.51	69.69	74.72	79.61
10	31.11	32.62	34.10	37.01	42.71	48.32	53.85	59.28	64.59	69.76	74.78	79.67
20	31.51	32.99	34.45	37.32	42.96	48.54	54.04	59.45	64.74	69.89	74.91	79.79
30	31.92	33.37	34.80	37.64	43.22	48.76	54.23	59.62	64.89	70.03	75.04	79.90
40	32.32	33.74	35.15	37.95	43.48	48.97	54.42	59.79	65.04	70.17	75.16	80.02
50	32.73	34.12	35.51	38.26	43.74	49.19	54.61	59.96	65.19	70.31	75.29	80.14
60	33.13	34.50	35.86	38.58	43.99	49.41	54.80	60.12	65.34	70.44	75.41	80.25
70	33.54	34.88	36.22	38.89	44.25	49.63	54.99	60.29	65.49	70.58	75.54	80.37
80	33.96	35.26	36.57	39.20	44.50	49.84	55.18	60.46	65.64	70.71	75.66	80.48
90	34.37	35.64	36.93	39.51	44.76	50.06	55.36	60.62	65.79	70.85	75.78	80.59
100	34.79	36.03	37.28	39.83	45.01	50.27	55.55	60.79	65.94	70.98	75.91	80.71
150	36.92	37.98	39.09	41.40	46.28	51.34	56.47	61.60	66.67	71.65	76.52	81.27
200	39.11	39.98	40.92	42.99	47.54	52.40	57.39	62.41	67.40	72.31	77.12	81.83
250	41.37	42.02	42.80	44.60	48.81	53.45	58.30	63.21	68.12	72.96	77.72	82.38
300	43.68	44.11	44.71	46.24	50.09	54.51	59.21	64.01	68.83	73.61	78.31	82.93
350	46.03	46.24	46.65	47.89	51.38	55.58	60.12	64.81	69.54	74.25	78.90	83.47
400	48.42	48.40	48.62	49.57	52.68	56.65	61.03	65.61	70.25	74.89	79.49	84.01
450	50.82	50.58	50.61	51.27	53.99	57.72	61.94	66.41	70.97	75.54	80.07	84.55
500	53.22	52.77	52.62	52.98	55.32	58.80	62.86	67.21	71.68	76.18	80.66	85.09
600	58.02	57.15	56.65	56.44	58.00	60.99	64.72	68.82	73.10	77.46	81.83	86.16
700	62.76	61.52	60.69	59.93	60.71	63.21	66.59	70.44	74.54	78.75	83.00	87.24
800	67.42	65.84	64.71	63.43	63.46	65.45	68.49	72.09	75.99	80.05	84.18	88.32
900	71.99	70.10	68.69	66.92	66.23	67.72	70.41	73.75	77.46	81.37	85.37	89.41
1,000	76.46	74.29	72.62	70.40	69.00	70.02	72.35	75.43	78.94	82.69	86.57	90.50

D2.3. Table 13. Dynamic viscosity η of nitrogen in 10^{-6} Pa · s

Pressure in bar	Temperature in °C											
	−200	−175	−150	−125	−100	−75	−50	−25	0	25	50	75
1		6.559	8.276	9.880	11.38	12.80	14.15	15.43	16.65	17.83	18.96	20.05
5		6.762	8.422	9.996	11.48	12.89	14.22	15.49	16.71	17.88	19.01	20.09
10		77.72	8.656	10.17	11.62	13.00	14.32	15.58	16.79	17.95	19.07	20.15
20		80.00	9.434	10.62	11.95	13.27	14.54	15.77	16.96	18.10	19.21	20.28
30		82.21	31.06	11.28	12.38	13.59	14.81	16.00	17.15	18.27	19.36	20.42
40		84.35	36.98	12.27	12.92	13.98	15.11	16.25	17.37	18.46	19.53	20.57
50		86.46	40.63	13.81	13.60	14.43	15.45	16.52	17.60	18.66	19.71	20.73
60		88.52	43.57	16.18	14.42	14.94	15.83	16.83	17.85	18.88	19.90	20.90
70		90.54	46.13	19.35	15.41	15.53	16.25	17.16	18.13	19.11	20.10	21.08
80		92.53	48.44	22.65	16.55	16.18	16.71	17.51	18.42	19.36	20.32	21.27
90		94.50	50.59	25.60	17.84	16.89	17.20	17.89	18.72	19.62	20.54	21.47
100		96.44	52.60	28.17	19.23	17.66	17.73	18.29	19.05	19.89	20.77	21.67
50		105.9	61.54	37.84	26.34	22.06	20.75	20.57	20.87	21.41	22.07	22.81
200		115.0	69.42	45.20	32.58	26.63	24.09	23.12	22.92	23.11	23.53	24.08
250		124.0	76.78	51.64	38.05	30.98	27.46	25.78	25.09	24.93	25.09	25.44
300		133.0	83.84	57.59	43.07	35.08	30.75	28.46	27.30	26.80	26.70	26.85
350		141.9	90.74	63.25	47.80	38.98	33.96	31.11	29.52	28.70	28.35	28.30
400		150.9	97.54	68.75	52.34	42.75	37.08	33.72	31.73	30.60	30.01	29.77
450		160.0	104.3	74.14	56.76	46.42	40.14	36.30	33.93	32.50	31.67	31.25
500		169.2	111.1	79.47	61.11	50.03	43.17	38.85	36.13	34.40	33.35	32.74
600			124.7	90.08	69.70	57.13	49.13	43.92	40.49	38.21	36.70	35.73
700			138.6	100.7	78.27	64.20	55.06	48.98	44.85	42.02	40.08	38.74
800			152.9	111.6	86.91	71.30	61.02	54.06	49.25	45.87	43.48	41.79
900			167.7	122.7	95.71	78.50	67.05	59.20	53.70	49.77	46.94	44.88
1,000				134.1	104.7	85.83	73.18	64.43	58.22	53.73	50.45	48.02

Pressure in bar	Temperature in °C											
	100	125	150	200	300	400	500	600	700	800	900	1,000
1	21.10	22.13	23.13	25.04	28.62	31.94	35.06	38.02	40.85	43.57	46.19	48.74
5	21.15	22.17	23.16	25.07	28.65	31.96	35.08	38.04	40.86	43.58	46.21	48.76
10	21.20	22.22	23.21	25.12	28.68	31.99	35.10	38.06	40.88	43.60	46.22	48.77
20	21.32	22.33	23.31	25.21	28.76	32.05	35.16	38.10	40.92	43.64	46.26	48.80
30	21.45	22.45	23.42	25.30	28.83	32.12	35.21	38.15	40.97	43.67	46.29	48.83
40	21.58	22.57	23.54	25.40	28.91	32.18	35.27	38.20	41.01	43.71	46.33	48.87
50	21.73	22.70	23.66	25.51	28.99	32.25	35.33	38.25	41.05	43.75	46.36	48.90
60	21.88	22.84	23.79	25.62	29.08	32.32	35.39	38.30	41.10	43.79	46.40	48.93
70	22.04	22.99	23.92	25.73	29.17	32.40	35.45	38.36	41.15	43.84	46.44	48.97
80	22.21	23.14	24.06	25.85	29.26	32.47	35.51	38.41	41.20	43.88	46.48	49.00
90	22.39	23.30	24.21	25.98	29.36	32.55	35.58	38.47	41.24	43.92	46.52	49.04
100	22.57	23.47	24.36	26.10	29.46	32.63	35.64	38.52	41.29	43.97	46.56	49.07
150	23.58	24.37	25.18	26.80	29.98	33.05	36.00	38.83	41.56	44.20	46.77	49.27
200	24.70	25.38	26.09	27.57	30.56	33.51	36.38	39.15	41.84	44.45	46.99	49.47
250	25.91	26.46	27.07	28.39	31.18	34.01	36.79	39.50	42.15	44.72	47.23	49.68
300	27.17	27.59	28.10	29.25	31.83	34.53	37.22	39.87	42.46	45.00	47.48	49.91
350	28.46	28.76	29.15	30.14	32.51	35.07	37.67	40.25	42.80	45.29	47.74	50.14
400	29.77	29.94	30.23	31.06	33.20	35.62	38.13	40.65	43.14	45.60	48.01	50.39
450	31.10	31.14	31.33	31.99	33.91	36.20	38.61	41.05	43.49	45.91	48.29	50.64

D2.3. Table 13. (continued)

Pressure in bar	Temperature in °C											
	100	125	150	200	300	400	500	600	700	800	900	1,000
500	32.44	32.36	32.44	32.93	34.63	36.78	39.09	41.47	43.85	46.23	48.58	50.90
600	35.13	34.80	34.68	34.84	36.10	37.97	40.09	42.32	44.60	46.88	49.16	51.43
700	37.85	37.28	36.94	36.78	37.60	39.18	41.11	43.20	45.36	47.56	49.77	51.98
800	40.60	39.78	39.24	38.74	39.12	40.42	42.15	44.09	46.15	48.26	50.40	52.54
900	43.39	42.32	41.57	40.73	40.66	41.67	43.20	45.00	46.95	48.97	51.04	53.12
1,000	46.23	44.90	43.93	42.76	42.23	42.95	44.27	45.93	47.76	49.69	51.69	53.71

D2.3. Table 14. Kinematic viscosity ν of nitrogen in 10^{-7} m^2/s

Pressure in bar	Temperature in °C											
	−200	−175	−150	−125	−100	−75	−50	−25	0	25	50	75
1		18.71	29.93	43.18	58.30	75.13	93.58	113.5	134.9	157.7	181.8	207.2
5		3.492	5.820	8.524	11.59	14.99	18.71	22.73	27.04	31.61	36.46	41.55
10		1.107	2.801	4.194	5.754	7.478	9.357	11.38	13.55	15.86	18.29	20.85
20		1.130	1.274	2.036	2.848	3.732	4.691	5.721	6.820	7.986	9.216	10.51
30		1.153	0.6474	1.325	1.889	2.494	3.145	3.842	4.584	5.370	6.197	7.066
40		1.175	0.7010	0.9772	1.420	1.883	2.379	2.909	3.472	4.067	4.693	5.350
50		1.197	0.7360	0.7821	1.147	1.524	1.926	2.355	2.809	3.290	3.795	4.324
60		1.218	0.7649	0.6750	0.9737	1.291	1.630	1.990	2.372	2.775	3.199	3.643
70		1.239	0.7904	0.6313	0.8596	1.131	1.422	1.733	2.063	2.411	2.776	3.159
80		1.260	0.8137	0.6254	0.7835	1.016	1.271	1.544	1.834	2.140	2.462	2.798
90		1.280	0.8354	0.6347	0.7333	0.9326	1.158	1.400	1.659	1.932	2.219	2.520
100		1.300	0.8559	0.6487	0.7015	0.8704	1.070	1.288	1.521	1.767	2.027	2.298
150		1.396	0.9473	0.7247	0.6698	0.7297	0.8416	0.9781	1.130	1.294	1.467	1.650
200		1.490	1.028	0.7934	0.7011	0.7052	0.7647	0.8538	0.9605	1.079	1.208	1.344
250		1.581	1.104	0.8564	0.7428	0.7157	0.7419	0.7997	0.8767	0.9667	1.066	1.174
300		1.671	1.177	0.9159	0.7864	0.7385	0.7422	0.7777	0.8335	0.9030	0.9823	1.069
350		1.761	1.247	0.9732	0.8301	0.7667	0.7536	0.7725	0.8122	0.8661	0.9302	1.002
400		1.851	1.317	1.029	0.8736	0.7973	0.7709	0.7767	0.8037	0.8453	0.8974	0.9576
450		1.942	1.386	1.084	0.9169	0.8294	0.7918	0.7867	0.8032	0.8347	0.8771	0.9276
500		2.033	1.454	1.138	0.9599	0.8622	0.8149	0.8005	0.8081	0.8311	0.8652	0.9076
600			1.592	1.246	1.046	0.9296	0.8654	0.8352	0.8280	0.8370	0.8578	0.8873
700			1.732	1.355	1.132	0.9986	0.9194	0.8757	0.8563	0.8540	0.8640	0.8833
800			1.875	1.464	1.220	1.069	0.9758	0.9201	0.8899	0.8777	0.8786	0.8894
900			2.021	1.576	1.309	1.141	1.034	0.9672	0.9271	0.9061	0.8989	0.9022
1,000				1.691	1.400	1.215	1.095	1.017	0.9671	0.9378	0.9233	0.9198

Pressure in bar	Temperature in °C											
	100	125	150	200	300	400	500	600	700	800	900	1,000
1	233.8	261.6	290.5	351.8	487.1	638.4	804.8	985.6	1,180	1,388	1,609	1,842
5	46.89	52.47	58.27	70.56	97.68	128.0	161.3	197.5	236.5	278.1	322.3	369.0
10	23.53	26.33	29.25	35.41	49.00	64.10	80.88	99.00	118.5	139.3	161.4	184.8
20	11.86	13.27	14.74	17.84	24.67	32.29	40.66	49.75	59.52	69.95	81.03	92.74

D2.3. Table 14. (continued)

Pressure in bar	Temperature in °C											
	100	125	150	200	300	400	500	600	700	800	900	1,000
30	7.975	8.922	9.906	11.99	16.56	21.66	27.26	33.33	39.86	46.83	54.23	62.04
40	6.036	6.751	7.494	9.062	12.51	16.35	20.56	25.12	30.03	35.27	40.83	46.70
50	4.877	5.452	6.050	7.311	10.08	13.16	16.54	20.20	24.14	28.33	32.79	37.49
60	4.107	4.589	5.090	6.146	8.463	11.04	13.86	16.92	20.21	23.71	27.43	31.35
70	3.559	3.974	4.406	5.315	7.309	9.525	11.95	14.58	17.40	20.41	23.60	26.97
80	3.150	3.515	3.895	4.693	6.445	8.390	10.52	12.82	15.30	17.93	20.73	23.68
90	2.833	3.160	3.498	4.211	5.774	7.508	9.404	11.46	13.66	16.01	18.50	21.12
100	2.582	2.877	3.183	3.827	5.237	6.803	8.514	10.37	12.35	14.47	16.71	19.08
150	1.842	2.041	2.248	2.684	3.638	4.695	5.849	7.095	8.431	9.854	11.36	12.95
200	1.488	1.638	1.795	2.125	2.848	3.649	4.523	5.466	6.476	7.551	8.689	9.888
250	1.288	1.408	1.533	1.798	2.381	3.027	3.733	4.493	5.307	6.173	7.089	8.053
300	1.163	1.262	1.366	1.587	2.075	2.618	3.210	3.848	4.531	5.257	6.025	6.833
350	1.081	1.164	1.253	1.441	1.861	2.328	2.839	3.390	3.979	4.605	5.266	5.963
400	1.024	1.096	1.172	1.336	1.704	2.115	2.564	3.048	3.567	4.117	4.699	5.312
450	0.9845	1.047	1.113	1.258	1.584	1.951	2.352	2.785	3.248	3.740	4.260	4.807
500	0.9567	1.011	1.070	1.198	1.491	1.821	2.184	2.575	2.994	3.439	3.909	4.404
600	0.9237	0.9656	1.012	1.116	1.357	1.632	1.936	2.265	2.617	2.991	3.386	3.801
700	0.9099	0.9421	0.9790	1.064	1.267	1.502	1.763	2.047	2.351	2.674	3.015	3.374
800	0.9078	0.9321	0.9614	1.031	1.204	1.409	1.638	1.887	2.154	2.439	2.739	3.055
900	0.9135	0.9311	0.9539	1.011	1.160	1.340	1.543	1.765	2.003	2.258	2.527	2.810
1,000	0.9248	0.9365	0.9536	1.000	1.128	1.288	1.469	1.669	1.885	2.115	2.358	2.614

D2.3. Table 15. Thermal diffusivity a of nitrogen in 10^{-7} m^2/s

Pressure in bar	Temperature in °C											
	−200	−175	−150	−125	−100	−75	−50	−25	0	25	50	75
1	0.9327	25.57	41.44	60.07	81.27	104.8	130.7	158.6	188.5	220.4	254.0	289.4
5	0.9360	4.174	7.690	11.59	15.95	20.76	26.00	31.64	37.69	44.10	50.88	58.00
10	0.9399	0.6808	3.409	5.511	7.779	10.24	12.91	15.78	18.83	22.07	25.49	29.08
20	0.9477	0.7012	1.126	2.434	3.680	4.985	6.372	7.847	9.411	11.06	12.80	14.62
30	0.9553	0.7199	0.1725	1.378	2.307	3.232	4.195	5.208	6.275	7.397	8.573	9.803
40	0.9626	0.7372	0.3280	0.8365	1.620	2.358	3.110	3.893	4.711	5.568	6.464	7.399
50	0.9698	0.7533	0.4063	0.5202	1.212	1.838	2.464	3.107	3.777	4.475	5.202	5.959
60	0.9767	0.7683	0.4616	0.3514	0.9490	1.497	2.037	2.588	3.157	3.749	4.364	5.002
70	0.9835	0.7825	0.5051	0.2999	0.7745	1.261	1.738	2.221	2.718	3.233	3.767	4.321
80	0.9901	0.7958	0.5412	0.3168	0.6597	1.091	1.518	1.949	2.392	2.849	3.323	3.813
90	0.9966	0.8085	0.5723	0.3557	0.5873	0.9668	1.352	1.742	2.142	2.553	2.979	3.419
100	1.003	0.8205	0.5996	0.3971	0.5454	0.8755	1.225	1.580	1.944	2.319	2.706	3.106
150	1.033	0.8735	0.7025	0.5550	0.5406	0.6843	0.8972	1.134	1.384	1.643	1.910	2.186
200	1.060	0.9175	0.7752	0.6566	0.6137	0.6710	0.7989	0.9625	1.145	1.339	1.541	1.752
250	1.084	0.9555	0.8320	0.7311	0.6823	0.7023	0.7798	0.8946	1.031	1.182	1.343	1.511
300	1.107	0.9889	0.8791	0.7903	0.7410	0.7427	0.7906	0.8724	0.9770	1.097	1.227	1.366
350	1.129	1.019	0.9195	0.8395	0.7914	0.7831	0.8127	0.8721	0.9533	1.050	1.158	1.274
400	1.149	1.046	0.9550	0.8818	0.8354	0.8213	0.8388	0.8826	0.9465	1.025	1.116	1.215

D2.3. Table 15. (continued)

Pressure in bar	Temperature in °C											
	−200	−175	−150	−125	−100	−75	−50	−25	0	25	50	75
450	1.168	1.072	0.9868	0.9191	0.8743	0.8567	0.8660	0.8984	0.9493	1.015	1.091	1.176
500	1.186	1.095	1.016	0.9524	0.9094	0.8895	0.8929	0.9169	0.9578	1.012	1.077	1.151
600	1.220	1.137	1.067	1.010	0.9703	0.9483	0.9442	0.9566	0.9834	1.022	1.070	1.127
700	1.251	1.175	1.111	1.060	1.022	0.9995	0.9912	0.9965	1.014	1.042	1.078	1.123
800	1.280	1.209	1.150	1.103	1.068	1.045	1.034	1.035	1.046	1.066	1.094	1.129
900	1.307	1.241	1.186	1.142	1.108	1.086	1.073	1.071	1.077	1.092	1.114	1.142
1,000	1.333	1.270	1.218	1.177	1.145	1.123	1.110	1.105	1.108	1.118	1.135	1.158

Pressure in bar	Temperature in °C											
	100	125	150	200	300	400	500	600	700	800	900	1,000
1	326.5	365.2	405.4	490.2	675.8	881.0	1,104	1,345	1,603	1,877	2,168	2,475
5	65.45	73.22	81.30	98.31	135.5	176.7	221.4	269.6	321.2	376.1	434.3	495.7
10	32.83	36.73	40.79	49.33	68.01	88.62	111.0	135.2	161.0	188.5	217.6	248.3
20	16.52	18.49	20.54	24.85	34.25	44.60	55.85	67.96	80.91	94.68	109.3	124.7
30	11.08	12.41	13.79	16.69	22.99	29.93	37.46	45.55	54.21	63.41	73.15	83.43
40	8.370	9.379	10.42	12.61	17.37	22.60	28.26	34.35	40.86	47.78	55.10	62.82
50	6.746	7.560	8.403	10.17	14.00	18.20	22.75	27.63	32.85	38.40	44.26	50.45
60	5.665	6.350	7.059	8.541	11.75	15.27	19.07	23.15	27.51	32.14	37.04	42.20
70	4.895	5.488	6.100	7.380	10.15	13.17	16.44	19.95	23.70	27.68	31.88	36.31
80	4.319	4.843	5.383	6.510	8.945	11.60	14.48	17.56	20.84	24.33	28.01	31.90
90	3.874	4.343	4.826	5.835	8.011	10.38	12.95	15.69	18.62	21.72	25.00	28.46
100	3.519	3.944	4.383	5.297	7.265	9.410	11.72	14.20	16.84	19.64	22.60	25.71
150	2.471	2.764	3.065	3.692	5.034	6.490	8.055	9.727	11.51	13.39	15.38	17.47
200	1.970	2.194	2.424	2.904	3.929	5.038	6.228	7.496	8.843	10.27	11.77	13.35
250	1.686	1.867	2.054	2.443	3.275	4.174	5.136	6.161	7.249	8.398	9.610	10.88
300	1.511	1.662	1.819	2.145	2.846	3.603	4.412	5.274	6.188	7.154	8.171	9.239
350	1.397	1.526	1.660	1.940	2.545	3.199	3.899	4.644	5.433	6.266	7.144	8.065
400	1.320	1.432	1.548	1.793	2.324	2.900	3.517	4.173	4.868	5.602	6.375	7.185
450	1.268	1.365	1.468	1.685	2.157	2.671	3.223	3.809	4.431	5.088	5.778	6.503
500	1.231	1.318	1.408	1.602	2.027	2.491	2.989	3.520	4.083	4.677	5.302	5.957
600	1.190	1.258	1.331	1.489	1.840	2.228	2.645	3.091	3.565	4.064	4.590	5.141
700	1.173	1.228	1.289	1.420	1.717	2.047	2.406	2.790	3.199	3.630	4.084	4.561
800	1.170	1.216	1.266	1.377	1.631	1.918	2.232	2.569	2.928	3.308	3.708	4.128
900	1.175	1.213	1.255	1.350	1.571	1.824	2.101	2.401	2.721	3.060	3.418	3.794
1,000	1.185	1.217	1.253	1.334	1.528	1.752	2.000	2.270	2.558	2.865	3.188	3.528

D2.3. Table 16. Prandtl number Pr of nitrogen

Pressure in bar	Temperature in °C											
	−200	−175	−150	−125	−100	−75	−50	−25	0	25	50	75
1		0.7317	0.7222	0.7189	0.7174	0.7166	0.7162	0.7159	0.7158	0.7157	0.7158	0.7159
5		0.8367	0.7568	0.7352	0.7264	0.7221	0.7197	0.7183	0.7174	0.7168	0.7165	0.7164
10		1.626	0.8218	0.7611	0.7398	0.7299	0.7246	0.7215	0.7196	0.7184	0.7176	0.7171
20		1.612	1.132	0.8368	0.7738	0.7487	0.7361	0.7290	0.7247	0.7219	0.7200	0.7188

D2.3. Table 16. (continued)

Temperature in °C												
Pressure in bar	−200	−175	−150	−125	−100	−75	−50	−25	0	25	50	75
30		1.602	3.753	0.9612	0.8190	0.7717	0.7497	0.7377	0.7305	0.7259	0.7229	0.7208
40		1.595	2.137	1.168	0.8764	0.7986	0.7650	0.7473	0.7369	0.7304	0.7260	0.7231
50		1.589	1.811	1.504	0.9462	0.8291	0.7819	0.7578	0.7439	0.7352	0.7295	0.7256
60		1.586	1.657	1.921	1.026	0.8623	0.7999	0.7689	0.7513	0.7403	0.7331	0.7283
70		1.584	1.565	2.105	1.110	0.8970	0.8186	0.7804	0.7589	0.7456	0.7370	0.7311
80		1.583	1.503	1.974	1.188	0.9316	0.8375	0.7921	0.7667	0.7511	0.7409	0.7340
90		1.583	1.460	1.784	1.249	0.9646	0.8560	0.8037	0.7745	0.7566	0.7449	0.7370
100		1.584	1.428	1.634	1.286	0.9942	0.8738	0.8151	0.7822	0.7621	0.7490	0.7400
150		1.599	1.348	1.306	1.239	1.066	0.9380	0.8621	0.8165	0.7875	0.7682	0.7548
200		1.624	1.327	1.208	1.142	1.051	0.9571	0.8870	0.8391	0.8064	0.7837	0.7674
250		1.655	1.327	1.171	1.089	1.019	0.9514	0.8939	0.8501	0.8179	0.7943	0.7768
300		1.690	1.338	1.159	1.061	0.9944	0.9388	0.8915	0.8531	0.8234	0.8005	0.7831
350		1.728	1.356	1.159	1.049	0.9790	0.9272	0.8857	0.8520	0.8249	0.8035	0.7867
400		1.769	1.379	1.167	1.046	0.9708	0.9190	0.8800	0.8491	0.8243	0.8044	0.7884
450		1.812	1.404	1.179	1.049	0.9681	0.9143	0.8756	0.8461	0.8227	0.8040	0.7889
500		1.857	1.432	1.195	1.056	0.9693	0.9127	0.8730	0.8437	0.8211	0.8031	0.7886
600			1.493	1.234	1.078	0.9804	0.9165	0.8730	0.8420	0.8190	0.8014	0.7875
700			1.559	1.278	1.108	0.9991	0.9276	0.8789	0.8446	0.8197	0.8012	0.7869
800			1.630	1.328	1.142	1.023	0.9437	0.8893	0.8510	0.8235	0.8031	0.7878
900			1.705	1.381	1.181	1.051	0.9636	0.9033	0.8606	0.8299	0.8073	0.7903
1,000				1.437	1.222	1.082	0.9864	0.9201	0.8729	0.8387	0.8135	0.7946

Temperature in °C												
Pressure in bar	100	125	150	200	300	400	500	600	700	800	900	1,000
1	0.7160	0.7163	0.7167	0.7177	0.7208	0.7247	0.7288	0.7327	0.7363	0.7394	0.7422	0.7445
5	0.7164	0.7165	0.7168	0.7177	0.7206	0.7245	0.7286	0.7326	0.7362	0.7393	0.7420	0.7444
10	0.7169	0.7169	0.7170	0.7177	0.7205	0.7243	0.7284	0.7324	0.7360	0.7391	0.7419	0.7442
20	0.7181	0.7177	0.7175	0.7179	0.7203	0.7240	0.7281	0.7320	0.7356	0.7388	0.7416	0.7439
30	0.7195	0.7187	0.7182	0.7181	0.7202	0.7237	0.7277	0.7317	0.7353	0.7385	0.7413	0.7436
40	0.7212	0.7199	0.7191	0.7185	0.7201	0.7235	0.7274	0.7314	0.7350	0.7382	0.7410	0.7434
50	0.7230	0.7212	0.7200	0.7190	0.7201	0.7233	0.7272	0.7311	0.7347	0.7379	0.7407	0.7431
60	0.7249	0.7226	0.7211	0.7196	0.7202	0.7231	0.7269	0.7308	0.7344	0.7376	0.7405	0.7429
70	0.7270	0.7242	0.7223	0.7202	0.7203	0.7230	0.7267	0.7306	0.7342	0.7374	0.7402	0.7426
80	0.7292	0.7259	0.7235	0.7209	0.7205	0.7230	0.7266	0.7304	0.7339	0.7372	0.7400	0.7424
90	0.7315	0.7276	0.7248	0.7217	0.7207	0.7229	0.7264	0.7302	0.7337	0.7369	0.7398	0.7422
100	0.7338	0.7293	0.7262	0.7225	0.7209	0.7229	0.7263	0.7300	0.7335	0.7367	0.7396	0.7420
150	0.7453	0.7384	0.7333	0.7270	0.7226	0.7233	0.7261	0.7294	0.7328	0.7359	0.7387	0.7411
200	0.7556	0.7468	0.7403	0.7317	0.7248	0.7242	0.7263	0.7292	0.7324	0.7353	0.7381	0.7405
250	0.7637	0.7538	0.7463	0.7361	0.7270	0.7254	0.7267	0.7293	0.7322	0.7350	0.7376	0.7400
300	0.7696	0.7592	0.7511	0.7398	0.7293	0.7266	0.7274	0.7296	0.7322	0.7348	0.7373	0.7396
350	0.7734	0.7629	0.7546	0.7429	0.7313	0.7279	0.7281	0.7300	0.7323	0.7348	0.7372	0.7394
400	0.7756	0.7653	0.7571	0.7452	0.7330	0.7291	0.7289	0.7304	0.7326	0.7349	0.7372	0.7392
450	0.7766	0.7667	0.7587	0.7469	0.7345	0.7302	0.7297	0.7310	0.7329	0.7351	0.7372	0.7392
500	0.7769	0.7673	0.7596	0.7480	0.7357	0.7312	0.7305	0.7315	0.7333	0.7353	0.7373	0.7392
600	0.7764	0.7674	0.7600	0.7491	0.7373	0.7327	0.7318	0.7326	0.7341	0.7359	0.7377	0.7394

D2.3. Table 16. (continued)

Temperature in °C												
Pressure in bar	100	125	150	200	300	400	500	600	700	800	900	1,000
700	0.7758	0.7669	0.7598	0.7493	0.7381	0.7338	0.7329	0.7336	0.7349	0.7365	0.7382	0.7397
800	0.7760	0.7668	0.7596	0.7492	0.7384	0.7344	0.7337	0.7344	0.7357	0.7372	0.7387	0.7401
900	0.7775	0.7676	0.7599	0.7491	0.7384	0.7348	0.7342	0.7350	0.7363	0.7378	0.7392	0.7406
1,000	0.7803	0.7694	0.7610	0.7495	0.7384	0.7349	0.7346	0.7355	0.7369	0.7383	0.7397	0.7410

6 Bibliography

1. Span R, Lemmon EW, Wagner W, Jacobsen RT (1998) A reference quality equation of state for nitrogen. Int J Thermophys 19:1121–1132
2. Span R, Lemmon EW, Jacobsen RT, Wagner W, Yokozeki A (2000) A reference equation of state for the thermodynamic properties of nitrogen for temperatures from 63.151 K to 1000 K and pressures to 2200 MPa. J Phys Chem Ref Data 29:1361–1433
3. Stephan K, Krauss R (1987) Viscosity and thermal conductivity of nitrogen for a wide range of fluid states. J Phys Chem Ref Data 16:993–1023

D2.4 Properties of Carbon Dioxide

Roland Span[1] · *Rolf Krauss*[2]
[1]Ruhr-Universität Bochum, Bochum, Germany
[2]Universität Stuttgart, Stuttgart, Germany

1 Properties of Carbon Dioxide

Tables with thermodynamic properties of carbon dioxide were calculated with the reference equation of state established by Span and Wagner [1].

The thermal conductivity and viscosity of carbon dioxide were calculated with the corresponding equations by Vesovic et al. [2]. The densities required as input to the equations by Vesovic et al. were calculated using the equation by Span and Wagner. The critical enhancement was considered for the thermal conductivity, where it significantly affects a rather large region around the critical point.

p	Pressure in bar	ν	Specific volume in m^3/kg
ρ	Density in kg/m^3	λ	Thermal conductivity in mW/(m K)
ϑ	Temperature in °C	ν	Kinematic viscosity ν in $10^{-7} m^2/s$
h	Specific enthalpy in kJ/kg	η	Dynamic viscosity in 10^{-6} Pa·s
s	Specific entropy in kJ/(kg K)	a	Thermal diffusivity in 10^{-7} m^2/s
Z	Compression factor $Z = p/(\rho RT)$	β	Isobaric expansion coefficient in 10^{-3}/K $\beta = \nu^{-1}\cdot(\partial\nu/\partial T)_p$
Pr	Prandtl number $Pr = \eta\, c_p/\lambda$	c_p	Specific isobaric heat capacity in kJ/(kg K)
w_s	Isentropic speed of sound in m/s	c_v	Specific isochoric heat capacity in kJ/(kg K)

2 Characteristic Quantities

Molecular mass $\tilde{M}$ = 44.0098 g/mol, specific gas constant R = 188.9241 J/(kg K).

3 Critical Point [1]

p_c = 73.773 bar, T_c = 304.1282 K (ϑ_c = 30.9782°C), ρ_c = 467.6 kg/m^3.

4 Triple Point [1]

p_t = 5.1795 bar, T_t =216.592 K (ϑ_t = −56.558°C).

5 Reference States of Enthalpy and Entropy

h = 506.78 kJ/kg, s = 2.739 kJ/(kg K) at T = 298.15 K (ϑ = 25°C), p = 1.01325 bar corresponding to h' = 200 kJ/kg, s' = 1 kJ/(kg K) for saturated liquid at ϑ = 0°C.

D2.4. Table 1. Properties of carbon dioxide at $p = 1$ bar

ϑ °C	kg/m³	h kJ/kg	s kJ/(kg K)	c_p kJ/(kg K)	c_v kJ/(kg K)	β 10^{-3}/K	w_s m/s	λ mW/(m K)	η 10^{-6}Pa·s	ν 10^{-7} m²/s	a 10^{-7} m²/s	Pr –
−55	2.461	440.8	2.486	0.7790	0.5771	4.808	232.5	10.78	10.97	44.57	56.24	0.7925
−50	2.403	444.7	2.504	0.7825	0.5816	4.682	235.0	11.10	11.22	46.69	59.05	0.7907
−40	2.296	452.6	2.538	0.7903	0.5912	4.453	239.9	11.77	11.72	51.05	64.85	0.7873
−30	2.198	460.5	2.571	0.7988	0.6011	4.248	244.6	12.45	12.22	55.60	70.92	0.7839
−20	2.109	468.5	2.604	0.8078	0.6113	4.063	249.2	13.17	12.72	60.32	77.28	0.7805
−10	2.027	476.7	2.635	0.8172	0.6216	3.896	253.7	13.90	13.22	65.21	83.94	0.7769
0	1.951	484.9	2.666	0.8267	0.6319	3.742	258.1	14.66	13.71	70.28	90.89	0.7732
10	1.880	493.2	2.696	0.8363	0.6422	3.601	262.4	15.43	14.20	75.51	98.13	0.7695
20	1.815	501.6	2.725	0.8459	0.6524	3.471	266.6	16.22	14.69	80.92	105.7	0.7659
30	1.754	510.1	2.754	0.8555	0.6624	3.351	270.7	17.03	15.17	86.49	113.5	0.7623
40	1.697	518.7	2.781	0.8650	0.6724	3.239	274.7	17.84	15.65	92.22	121.5	0.7589
50	1.644	527.4	2.809	0.8744	0.6821	3.134	278.7	18.67	16.13	98.12	129.8	0.7557
60	1.594	536.2	2.836	0.8837	0.6917	3.037	282.6	19.50	16.61	104.2	138.4	0.7526
70	1.547	545.1	2.862	0.8929	0.7011	2.945	286.4	20.34	17.08	110.4	147.2	0.7498
80	1.503	554.1	2.888	0.9018	0.7103	2.859	290.2	21.18	17.55	116.8	156.3	0.7471
90	1.461	563.1	2.913	0.9107	0.7193	2.778	294.0	22.03	18.01	123.3	165.5	0.7447
100	1.422	572.3	2.938	0.9193	0.7282	2.702	297.6	22.87	18.47	129.9	175.0	0.7425
110	1.384	581.5	2.962	0.9278	0.7368	2.630	301.3	23.72	18.93	136.8	184.7	0.7404
120	1.349	590.8	2.986	0.9361	0.7453	2.561	304.9	24.57	19.39	143.7	194.6	0.7386
130	1.315	600.2	3.010	0.9443	0.7536	2.497	308.4	25.42	19.84	150.8	204.7	0.7369
140	1.283	609.7	3.033	0.9523	0.7617	2.435	311.9	26.27	20.28	158.1	215.0	0.7353
150	1.253	619.3	3.056	0.9601	0.7696	2.377	315.3	27.12	20.73	165.5	225.4	0.7339
160	1.224	628.9	3.078	0.9678	0.7774	2.321	318.8	27.96	21.17	173.0	236.1	0.7327
170	1.196	638.6	3.101	0.9753	0.7850	2.268	322.1	28.80	21.60	180.6	246.9	0.7316
180	1.169	648.4	3.122	0.9827	0.7925	2.217	325.5	29.64	22.04	188.4	257.9	0.7306
190	1.144	658.3	3.144	0.9900	0.7998	2.168	328.8	30.48	22.47	196.4	269.1	0.7297
200	1.120	668.2	3.165	0.9971	0.8070	2.122	332.0	31.31	22.89	204.4	280.5	0.7289
220	1.074	688.3	3.207	1.011	0.8209	2.035	338.5	32.97	23.73	220.9	303.7	0.7276
240	1.032	708.7	3.247	1.024	0.8342	1.955	344.8	34.62	24.56	237.9	327.5	0.7265
260	0.9933	729.3	3.287	1.037	0.8471	1.881	350.9	36.25	25.37	255.4	351.9	0.7258
280	0.9573	750.1	3.325	1.049	0.8595	1.812	357.0	37.87	26.17	273.4	377.0	0.7252
300	0.9238	771.2	3.363	1.061	0.8714	1.749	363.0	39.47	26.96	291.8	402.6	0.7248
320	0.8926	792.6	3.399	1.072	0.8829	1.689	368.8	41.05	27.74	310.7	428.9	0.7245
340	0.8634	814.1	3.435	1.083	0.8939	1.634	374.6	42.63	28.50	330.1	455.7	0.7243
360	0.8361	835.9	3.470	1.094	0.9046	1.582	380.3	44.18	29.25	349.8	483.0	0.7242
380	0.8105	857.9	3.504	1.104	0.9149	1.533	385.9	45.73	29.99	370.0	510.9	0.7242
400	0.7864	880.1	3.537	1.114	0.9248	1.488	391.4	47.26	30.72	390.6	539.4	0.7242
425	0.7582	908.1	3.578	1.126	0.9367	1.434	398.2	49.15	31.61	416.9	575.7	0.7242
450	0.7319	936.4	3.618	1.137	0.9480	1.384	404.9	51.02	32.49	443.9	612.9	0.7242
475	0.7075	964.9	3.657	1.148	0.9589	1.338	411.4	52.87	33.35	471.4	650.9	0.7242
500	0.6846	993.8	3.695	1.159	0.9693	1.294	417.9	54.70	34.20	499.5	689.7	0.7242
550	0.6430	1,052	3.768	1.178	0.9888	1.216	430.5	58.31	35.84	557.5	769.8	0.7242
600	0.6061	1,112	3.838	1.196	1.007	1.146	442.7	61.84	37.44	617.7	853.2	0.7239
650	0.5733	1,172	3.905	1.212	1.023	1.084	454.7	65.30	38.98	680.0	939.8	0.7235
700	0.5438	1,233	3.969	1.227	1.038	1.028	466.3	68.69	40.48	744.3	1,030	0.7229
750	0.5172	1,294	4.031	1.240	1.051	0.9776	477.7	72.03	41.93	810.6	1,123	0.7221
800	0.4931	1,357	4.091	1.253	1.064	0.9320	488.8	75.30	43.34	878.9	1,219	0.7212
850	0.4712	1,420	4.148	1.264	1.075	0.8905	499.6	78.52	44.72	949.0	1,318	0.7201
900	0.4511	1,483	4.203	1.275	1.086	0.8525	510.2	81.69	46.06	1,021	1,420	0.7189

D2.4. Table 2. Properties of the saturated liquid

ϑ °C	p bar	ρ' kg/m³	h' kJ/kg	s' kJ/(kg K)	c_p' kJ/(kg K)	c_v' kJ/(kg K)	β' 10^{-3}/K	w_s' m/s	λ' mW/(m K)	η' 10^{-6} Pa·s	ν' 10^{-7} m²/s	a' 10^{-7} m²/s	Pr′ –
−56	5.306	1,177	81.04	0.5259	1.971	0.9851	3.100	972.3	180.1	256.1	2.176	0.7765	2.803
−54	5.780	1,169	85.00	0.5439	1.973	0.9801	3.153	958.0	177.4	247.5	2.117	0.7689	2.753
−52	6.286	1,162	88.96	0.5617	1.976	0.9754	3.209	943.6	174.7	239.3	2.060	0.7610	2.706
−50	6.824	1,155	92.93	0.5793	1.980	0.9711	3.267	929.1	172.1	231.5	2.005	0.7529	2.663
−48	7.395	1,147	96.91	0.5968	1.985	0.9671	3.330	914.7	169.5	224.1	1.954	0.7446	2.624
−46	8.002	1,140	100.9	0.6142	1.990	0.9634	3.395	900.2	166.9	217.0	1.904	0.7360	2.587
−44	8.645	1,132	104.9	0.6315	1.997	0.9600	3.465	885.6	164.4	210.2	1.857	0.7272	2.553
−42	9.325	1,124	108.9	0.6487	2.005	0.9568	3.539	871.0	161.9	203.6	1.811	0.7181	2.522
−40	10.05	1,116	112.9	0.6658	2.013	0.9539	3.617	856.4	159.4	197.3	1.768	0.7089	2.494
−38	10.81	1,109	117.0	0.6828	2.023	0.9512	3.699	841.7	156.9	191.3	1.726	0.6994	2.467
−36	11.61	1,101	121.1	0.6997	2.034	0.9487	3.787	826.9	154.4	185.5	1.685	0.6898	2.443
−34	12.45	1,092	125.1	0.7165	2.045	0.9464	3.881	812.0	151.9	179.8	1.646	0.6799	2.421
−32	13.34	1,084	129.2	0.7333	2.058	0.9444	3.980	797.1	149.5	174.4	1.609	0.6699	2.401
−30	14.28	1,076	133.4	0.7500	2.072	0.9425	4.087	782.1	147.0	169.1	1.572	0.6596	2.384
−28	15.26	1,067	137.5	0.7666	2.087	0.9407	4.201	767.0	144.6	164.0	1.537	0.6491	2.368
−26	16.29	1,059	141.7	0.7832	2.104	0.9392	4.323	751.7	142.2	159.1	1.503	0.6384	2.354
−24	17.37	1,050	145.9	0.7998	2.122	0.9379	4.454	736.4	139.8	154.3	1.470	0.6274	2.343
−22	18.51	1,041	150.2	0.8164	2.142	0.9367	4.595	721.0	137.4	149.6	1.438	0.6162	2.333
−20	19.70	1,032	154.5	0.8329	2.164	0.9357	4.747	705.4	135.0	145.1	1.406	0.6048	2.325
−18	20.94	1,022	158.8	0.8495	2.187	0.9349	4.913	689.7	132.6	140.7	1.376	0.5930	2.320
−16	22.24	1,013	163.2	0.8660	2.213	0.9342	5.092	673.9	130.2	136.3	1.346	0.5810	2.317
−14	23.59	1,003	167.6	0.8825	2.241	0.9338	5.288	657.9	127.8	132.1	1.317	0.5687	2.316
−12	25.01	993.1	172.0	0.8991	2.272	0.9335	5.503	641.7	125.4	128.0	1.289	0.5560	2.318
−10	26.49	982.9	176.5	0.9157	2.306	0.9335	5.740	625.3	123.0	123.9	1.261	0.5429	2.323
−8	28.03	972.4	181.1	0.9324	2.343	0.9337	6.001	608.7	120.7	120.0	1.234	0.5294	2.330
−6	29.63	961.7	185.7	0.9492	2.385	0.9343	6.292	591.8	118.3	116.1	1.207	0.5156	2.341
−4	31.30	950.6	190.4	0.9660	2.432	0.9353	6.617	574.5	115.9	112.2	1.181	0.5012	2.356
−2	33.04	939.2	195.2	0.9829	2.484	0.9368	6.983	556.9	113.5	108.5	1.155	0.4864	2.374
0	34.85	927.4	200.0	1.000	2.542	0.9390	7.397	538.9	111.0	104.7	1.129	0.4710	2.398
2	36.73	915.2	204.9	1.017	2.608	0.9420	7.869	520.4	108.6	101.0	1.104	0.4550	2.427
4	38.69	902.5	209.9	1.035	2.684	0.9459	8.412	501.6	106.2	97.38	1.079	0.4383	2.462
6	40.72	889.3	215.1	1.052	2.772	0.9509	9.042	482.3	103.7	93.75	1.054	0.4209	2.505
8	42.83	875.5	220.3	1.070	2.874	0.9569	9.783	462.6	101.3	90.14	1.030	0.4026	2.558
10	45.02	861.0	225.7	1.088	2.996	0.9639	10.67	442.7	98.86	86.54	1.005	0.3832	2.622
12	47.30	845.8	231.3	1.107	3.143	0.9720	11.75	422.4	96.42	82.93	0.9804	0.3627	2.703
14	49.66	829.6	237.0	1.126	3.325	0.9809	13.09	401.8	94.00	79.30	0.9558	0.3408	2.805
16	52.11	812.4	243.0	1.146	3.555	0.9908	14.81	380.8	91.61	75.63	0.9309	0.3172	2.935
18	54.65	793.8	249.2	1.166	3.856	1.002	17.09	359.4	89.28	71.89	0.9057	0.2917	3.105
20	57.29	773.4	255.8	1.188	4.266	1.015	20.26	337.1	87.07	68.07	0.8801	0.2639	3.335
22	60.03	750.8	262.9	1.210	4.855	1.030	24.90	313.8	85.06	64.09	0.8536	0.2333	3.659
24	62.88	725.0	270.6	1.235	5.778	1.052	32.35	289.0	83.39	59.87	0.8259	0.1991	4.149
26	65.84	694.4	279.3	1.263	7.448	1.085	46.22	261.5	82.37	55.26	0.7958	0.1593	4.997
28	68.92	655.3	289.6	1.296	11.50	1.148	81.20	228.7	83.06	50.05	0.7637	0.1102	6.932
30	72.14	593.3	304.6	1.343	35.11	1.354	297.2	180.8	94.73	43.73	0.7371	0.04548	16.21

D2.4. Table 3. Properties of the saturated vapor

ϑ °C	p bar	ρ'' kg/m³	h'' kJ/kg	s'' kJ/(kg K)	c_p'' kJ/(kg K)	c_v'' kJ/(kg K)	β'' 10^{-3}/K	w_s'' m/s	λ'' mW/(m K)	η'' 10^{-6} Pa·s	ν'' 10^{-7} m²/s	a'' 10^{-7} m²/s	Pr″ –
−56	5.306	14.08	430.6	2.136	0.9176	0.6346	6.162	222.8	11.11	10.97	7.793	8.597	0.9065
−54	5.780	15.28	431.4	2.124	0.9308	0.6407	6.219	223.0	11.28	11.08	7.251	7.932	0.9142
−52	6.286	16.56	432.0	2.113	0.9447	0.6469	6.283	223.2	11.46	11.19	6.756	7.327	0.9221
−50	6.824	17.93	432.7	2.102	0.9592	0.6533	6.353	223.3	11.65	11.30	6.303	6.775	0.9304
−48	7.395	19.37	433.3	2.091	0.9744	0.6599	6.429	223.4	11.84	11.41	5.889	6.272	0.9389
−46	8.002	20.91	433.9	2.080	0.9903	0.6665	6.513	223.4	12.04	11.52	5.508	5.812	0.9477
−44	8.645	22.55	434.4	2.069	1.007	0.6734	6.605	223.5	12.24	11.63	5.158	5.391	0.9568
−42	9.325	24.28	434.9	2.059	1.025	0.6803	6.705	223.4	12.45	11.74	4.836	5.005	0.9663
−40	10.05	26.12	435.3	2.048	1.043	0.6875	6.813	223.4	12.67	11.86	4.539	4.650	0.9762
−38	10.81	28.07	435.7	2.038	1.063	0.6947	6.931	223.2	12.90	11.97	4.265	4.324	0.9864
−36	11.61	30.14	436.1	2.028	1.083	0.7022	7.059	223.1	13.14	12.09	4.011	4.023	0.9970
−34	12.45	32.33	436.4	2.018	1.105	0.7098	7.199	222.9	13.38	12.21	3.776	3.746	1.008
−32	13.34	34.65	436.6	2.008	1.128	0.7175	7.350	222.6	13.64	12.33	3.558	3.490	1.020
−30	14.28	37.10	436.8	1.998	1.153	0.7255	7.514	222.4	13.91	12.45	3.355	3.253	1.032
−28	15.26	39.70	436.9	1.988	1.179	0.7336	7.692	222.0	14.19	12.57	3.167	3.033	1.044
−26	16.29	42.45	437.0	1.978	1.206	0.7418	7.886	221.6	14.49	12.70	2.992	2.829	1.057
−24	17.37	45.36	437.0	1.968	1.236	0.7503	8.097	221.2	14.80	12.83	2.828	2.640	1.071
−22	18.51	48.44	437.0	1.958	1.267	0.7589	8.328	220.7	15.12	12.96	2.675	2.464	1.086
−20	19.70	51.70	436.9	1.949	1.301	0.7677	8.580	220.2	15.47	13.09	2.533	2.300	1.101
−18	20.94	55.16	436.7	1.939	1.337	0.7767	8.856	219.6	15.83	13.23	2.399	2.146	1.118
−16	22.24	58.82	436.4	1.929	1.377	0.7861	9.160	219.0	16.22	13.38	2.274	2.003	1.136
−14	23.59	62.70	436.1	1.919	1.420	0.7958	9.495	218.4	16.63	13.52	2.157	1.868	1.155
−12	25.01	66.82	435.7	1.909	1.467	0.8059	9.864	217.6	17.07	13.68	2.047	1.741	1.175
−10	26.49	71.19	435.1	1.898	1.519	0.8166	10.27	216.8	17.54	13.83	1.943	1.622	1.198
−8	28.03	75.83	434.5	1.888	1.576	0.8277	10.73	216.0	18.04	14.00	1.846	1.510	1.223
−6	29.63	80.77	433.8	1.878	1.639	0.8394	11.24	215.1	18.58	14.17	1.755	1.403	1.250
−4	31.30	86.04	432.9	1.867	1.710	0.8517	11.82	214.1	19.16	14.35	1.668	1.303	1.280
−2	33.04	91.65	432.0	1.856	1.789	0.8647	12.46	213.0	19.80	14.55	1.587	1.208	1.314
0	34.85	97.65	430.9	1.845	1.878	0.8783	13.20	211.9	20.49	14.75	1.510	1.117	1.352
2	36.73	104.1	429.6	1.834	1.979	0.8927	14.04	210.7	21.24	14.96	1.438	1.031	1.395
4	38.69	111.0	428.2	1.822	2.096	0.9078	15.02	209.4	22.07	15.20	1.369	0.9488	1.443
6	40.72	118.4	426.7	1.810	2.230	0.9238	16.15	208.1	22.98	15.45	1.304	0.8702	1.499
8	42.83	126.4	424.9	1.798	2.388	0.9408	17.50	206.7	24.00	15.72	1.243	0.7947	1.564
10	45.02	135.2	422.9	1.785	2.577	0.9590	19.10	205.1	25.15	16.01	1.185	0.7220	1.641
12	47.30	144.7	420.6	1.771	2.805	0.9786	21.06	203.5	26.44	16.34	1.130	0.6515	1.734
14	49.66	155.1	418.0	1.756	3.088	0.9999	23.48	201.8	27.92	16.71	1.077	0.5830	1.848
16	52.11	166.7	415.1	1.741	3.448	1.023	26.58	199.9	29.65	17.12	1.028	0.5159	1.992
18	54.65	179.6	411.8	1.724	3.922	1.050	30.67	197.9	31.68	17.60	0.9802	0.4499	2.178
20	57.29	194.2	407.9	1.706	4.574	1.080	36.30	195.7	34.16	18.16	0.9351	0.3846	2.431
22	60.03	211.0	403.3	1.686	5.531	1.117	44.54	193.2	37.27	18.83	0.8920	0.3193	2.794
24	62.88	231.0	397.8	1.663	7.065	1.162	57.73	190.4	41.39	19.66	0.8509	0.2536	3.356
26	65.84	255.8	390.8	1.635	9.918	1.224	82.17	186.8	47.35	20.76	0.8114	0.1866	4.348
28	68.92	289.1	381.2	1.600	16.96	1.321	142.2	181.6	57.59	22.37	0.7737	0.1174	6.589
30	72.14	345.3	365.0	1.543	57.48	1.550	485.1	170.5	93.37	25.67	0.7434	0.04705	15.80

D2.4. Table 4. Density ρ of carbon dioxide in kg/m^3

Pressure in bar	Temperature in °C											
	−55	−50	−40	−30	−20	−10	0	10	20	30	40	50
1	2.461	2.403	2.296	2.198	2.109	2.027	1.951	1.880	1.815	1.754	1.697	1.644
5	13.12	12.74	12.06	11.47	10.94	10.46	10.03	9.637	9.276	8.944	8.636	8.350
10	1,174	1,155	25.99	24.38	23.03	21.86	20.84	19.92	19.10	18.35	17.67	17.04
20	1,176	1,158	1,119	1,078	1,032	48.76	45.61	43.00	40.77	38.84	37.13	35.60
30	1,178	1,160	1,122	1,081	1,036	985.1	77.33	71.01	66.16	62.21	58.89	56.03
40	1,180	1,162	1,125	1,085	1,041	991.1	932.1	108.4	97.49	89.76	83.76	78.86
50	1,182	1,164	1,127	1,088	1,045	996.7	940.5	868.5	140.6	124.0	113.0	104.8
60	1,184	1,167	1,130	1,091	1,049	1,002	948.2	881.7	782.7	171.5	149.3	135.2
70	1,186	1,169	1,133	1,094	1,053	1,007	955.3	893.1	808.6	266.5	198.0	172.0
80	1,188	1,171	1,135	1,097	1,057	1,012	962.0	903.1	827.7	701.7	277.9	219.2
90	1,190	1,173	1,138	1,100	1,060	1,017	968.2	912.2	843.2	744.3	485.6	285.0
100	1,192	1,175	1,140	1,103	1,064	1,021	974.1	920.5	856.3	771.5	628.7	384.4
150	1,201	1,185	1,151	1,117	1,080	1,041	999.6	954.3	904.0	847.0	780.3	699.8
200	1,209	1,194	1,162	1,129	1,094	1,058	1,021	980.3	937.2	890.6	839.9	784.4
250	1,217	1,202	1,172	1,140	1,107	1,074	1,038	1,002	963.1	922.5	879.6	834.4
300	1,225	1,210	1,181	1,150	1,119	1,087	1,054	1,020	984.7	948.1	910.0	870.6
350	1,232	1,218	1,189	1,160	1,130	1,100	1,068	1,036	1,003	969.6	934.9	899.4
400	1,239	1,225	1,197	1,169	1,140	1,111	1,081	1,051	1,020	988.3	956.1	923.4
450	1,246	1,232	1,205	1,178	1,150	1,122	1,093	1,064	1,035	1,005	974.6	944.1
500	1,252	1,239	1,213	1,186	1,159	1,132	1,104	1,076	1,048	1,020	991.2	962.4
600	1,264	1,252	1,226	1,201	1,176	1,150	1,124	1,098	1,072	1,046	1,020	993.7
700	1,275	1,263	1,239	1,215	1,191	1,166	1,142	1,117	1,093	1,069	1,044	1,020
800	1,286	1,274	1,251	1,228	1,204	1,181	1,158	1,135	1,112	1,089	1,066	1,043
900	1,296	1,284	1,262	1,240	1,217	1,195	1,173	1,150	1,128	1,107	1,085	1,063
1,000	1,305	1,294	1,272	1,251	1,229	1,208	1,186	1,165	1,144	1,123	1,102	1,082
2,000	1,380	1,371	1,354	1,336	1,319	1,302	1,286	1,269	1,253	1,237	1,222	1,207

Pressure in bar	Temperature in °C											
	60	80	100	150	200	300	400	500	600	700	800	900
1	1.594	1.503	1.422	1.253	1.120	0.9238	0.7864	0.6846	0.6061	0.5438	0.4931	0.4511
5	8.084	7.602	7.176	6.300	5.619	4.626	3.933	3.422	3.029	2.717	2.463	2.253
10	16.46	15.43	14.52	12.69	11.29	9.267	7.868	6.841	6.052	5.428	4.921	4.501
20	34.22	31.81	29.77	25.77	22.79	18.59	15.75	13.67	12.09	10.83	9.821	8.982
30	53.52	49.29	45.82	39.24	34.50	27.98	23.63	20.49	18.10	16.22	14.70	13.44
40	74.73	68.03	62.75	53.13	46.42	37.42	31.52	27.29	24.09	21.58	19.55	17.88
50	98.30	88.24	80.66	67.43	58.55	46.92	39.41	34.08	30.06	26.92	24.39	22.30
60	124.9	110.1	99.64	82.18	70.89	56.46	47.30	40.85	36.01	32.24	29.20	26.69
70	155.5	134.1	119.8	97.37	83.43	66.04	55.19	47.60	41.94	37.53	33.99	31.07
80	191.6	160.3	141.3	113.0	96.16	75.67	63.08	54.34	47.85	42.80	38.76	35.43
90	235.4	189.4	164.2	129.1	109.1	85.32	70.96	61.06	53.73	48.05	43.50	39.76
100	290.0	221.6	188.6	145.6	122.2	95.00	78.82	67.76	59.59	53.28	48.22	44.08
150	603.9	426.8	332.2	234.0	189.8	143.6	117.9	100.9	88.51	79.03	71.50	65.34
200	723.8	594.1	480.4	327.1	259.0	192.0	156.3	133.3	116.7	104.2	94.19	86.08

D2.4. Table 4. (continued)

Pressure in bar	Temperature in °C											
	60	80	100	150	200	300	400	500	600	700	800	900
250	786.8	686.6	589.0	415.1	326.6	239.2	193.8	164.8	144.2	128.6	116.3	106.3
300	830.0	746.0	662.3	492.2	389.6	284.7	230.0	195.3	170.8	152.3	137.8	126.0
350	863.2	789.4	715.7	555.8	446.7	327.8	264.7	224.7	196.5	175.3	158.6	145.1
400	890.3	823.5	757.1	607.4	497.4	368.3	297.9	253.0	221.4	197.6	178.9	163.7
450	913.4	851.7	790.7	650.4	541.8	406.0	329.4	280.1	245.3	219.1	198.5	181.7
500	933.5	875.8	819.0	687.0	580.5	441.0	359.4	306.1	268.3	239.9	217.5	199.3
600	967.6	915.8	865.0	746.3	645.3	503.2	414.4	354.7	311.9	279.3	253.7	232.8
700	996.0	948.3	901.8	792.9	697.7	556.3	463.5	399.2	352.1	316.2	287.7	264.4
800	1,020	975.9	932.6	831.1	741.3	602.2	507.2	439.7	389.4	350.6	319.6	294.2
900	1,042	1,000	959.1	863.5	778.4	642.4	546.4	476.7	423.9	382.7	349.6	322.4
1,000	1,061	1,021	982.6	891.7	810.5	678.1	581.7	510.6	456.0	412.9	378.0	349.1
2,000	1,192	1,162	1,134	1,067	1,007	901.3	814.9	743.5	684.1	634.1	591.6	554.9

D2.4. Table 5. Compression factor Z of carbon dioxide

Pressure in bar	Temperature in °C											
	−55	−50	−40	−30	−20	−10	0	10	20	30	40	50
1	0.9859	0.9870	0.9888	0.9902	0.9915	0.9925	0.9934	0.9941	0.9948	0.9953	0.9958	0.9962
5	0.9250	0.9310	0.9411	0.9493	0.9559	0.9614	0.9660	0.9699	0.9733	0.9761	0.9786	0.9808
10	0.02067	0.02053	0.8737	0.8928	0.9079	0.9200	0.9300	0.9384	0.9454	0.9515	0.9566	0.9611
20	0.04127	0.04098	0.04057	0.04040	0.04053	0.8250	0.8498	0.8695	0.8857	0.8992	0.9105	0.9203
30	0.06179	0.06135	0.06070	0.06040	0.06053	0.06126	0.7518	0.7898	0.8188	0.8420	0.8611	0.8770
40	0.08224	0.08164	0.08074	0.08028	0.08037	0.08118	0.08316	0.6898	0.7409	0.7781	0.8072	0.8309
50	0.1026	0.1019	0.1007	0.1001	0.1001	0.1009	0.1030	0.1076	0.6419	0.7040	0.7476	0.7812
60	0.1229	0.1220	0.1205	0.1197	0.1196	0.1204	0.1226	0.1272	0.1384	0.6110	0.6795	0.7269
70	0.1432	0.1421	0.1403	0.1393	0.1390	0.1398	0.1420	0.1465	0.1563	0.4586	0.5975	0.6666
80	0.1534	0.1621	0.1600	0.1587	0.1583	0.1590	0.1612	0.1656	0.1745	0.1991	0.4866	0.5978
90	0.1835	0.1820	0.1796	0.1781	0.1775	0.1781	0.1801	0.1844	0.1927	0.2111	0.3133	0.5173
100	0.2036	0.2019	0.1992	0.1974	0.1966	0.1970	0.1989	0.2031	0.2109	0.2263	0.2689	0.4262
150	0.3031	0.3004	0.2958	0.2924	0.2904	0.2898	0.2908	0.2938	0.2996	0.3092	0.3250	0.3511
200	0.4013	0.3974	0.3908	0.3857	0.3821	0.3801	0.3798	0.3814	0.3853	0.3921	0.4025	0.4176
250	0.4983	0.4932	0.4845	0.4774	0.4720	0.4684	0.4665	0.4666	0.4687	0.4732	0.4804	0.4908
300	0.5943	0.5879	0.5768	0.5677	0.5604	0.5550	0.5514	0.5498	0.5501	0.5525	0.5572	0.5644
350	0.6892	0.6816	0.6681	0.6568	0.6475	0.6402	0.6348	0.6313	0.6298	0.6303	0.6328	0.6374
400	0.7833	0.7743	0.7584	0.7448	0.7334	0.7241	0.7168	0.7115	0.7082	0.7067	0.7072	0.7096
450	0.8765	0.8662	0.8477	0.8318	0.8182	0.8069	0.7977	0.7905	0.7853	0.7819	0.7805	0.7808
500	0.9690	0.9573	0.9362	0.9178	0.9021	0.8887	0.8775	0.8684	0.8613	0.8561	0.8527	0.8510
600	1.152	1.137	1.111	1.088	1.067	1.050	1.034	1.021	1.010	1.002	0.9944	0.9890
700	1.332	1.314	1.283	1.254	1.229	1.207	1.188	1.171	1.156	1.144	1.133	1.124
800	1.510	1.489	1.452	1.419	1.389	1.362	1.339	1.318	1.299	1.283	1.269	1.256
900	1.685	1.662	1.619	1.581	1.546	1.515	1.487	1.462	1.440	1.420	1.402	1.386
1,000	1.859	1.833	1.784	1.741	1.701	1.666	1.634	1.605	1.579	1.555	1.534	1.514
2,000	3.516	3.459	3.354	3.258	3.170	3.089	3.014	2.945	2.882	2.822	2.767	2.715

D2.4. Table 5. (continued)

Pressure in bar	Temperature in °C											
	60	80	100	150	200	300	400	500	600	700	800	900
1	0.9966	0.9972	0.9977	0.9986	0.9991	0.9997	1.000	1.000	1.000	1.000	1.000	1.000
5	0.9827	0.9859	0.9884	0.9927	0.9954	0.9983	0.9997	1.000	1.001	1.001	1.001	1.001
10	0.9651	0.9716	0.9767	0.9854	0.9908	0.9966	0.9994	1.001	1.002	1.002	1.002	1.002
20	0.9287	0.9423	0.9529	0.9709	0.9817	0.9933	0.9988	1.002	1.003	1.004	1.005	1.005
30	0.8905	0.9122	0.9288	0.9563	0.9727	0.9902	0.9984	1.003	1.005	1.006	1.007	1.007
40	0.8505	0.8813	0.9042	0.9419	0.9639	0.9871	0.9980	1.004	1.007	1.008	1.009	1.009
50	0.8082	0.8493	0.8794	0.9275	0.9553	0.9842	0.9977	1.005	1.008	1.010	1.011	1.012
60	0.7632	0.8165	0.8542	0.9133	0.9469	0.9815	0.9974	1.006	1.010	1.012	1.014	1.014
70	0.7151	0.7826	0.8288	0.8993	0.9387	0.9789	0.9973	1.007	1.012	1.014	1.016	1.017
80	0.6633	0.7479	0.8032	0.8856	0.9307	0.9764	0.9973	1.008	1.014	1.017	1.018	1.019
90	0.6075	0.7124	0.7776	0.8721	0.9231	0.9742	0.9974	1.009	1.015	1.019	1.020	1.021
100	0.5479	0.6764	0.7522	0.8591	0.9157	0.9721	0.9976	1.010	1.017	1.021	1.023	1.024
150	0.3946	0.5268	0.6405	0.8017	0.8843	0.9646	1.000	1.018	1.027	1.032	1.035	1.036
200	0.4390	0.5046	0.5906	0.7648	0.8639	0.9622	1.006	1.027	1.039	1.045	1.047	1.048
250	0.5048	0.5458	0.6021	0.7533	0.8563	0.9652	1.014	1.039	1.051	1.058	1.060	1.061
300	0.5743	0.6027	0.6426	0.7624	0.8614	0.9732	1.026	1.052	1.065	1.071	1.074	1.075
350	0.6442	0.6646	0.6937	0.7877	0.8766	0.9860	1.040	1.066	1.080	1.086	1.088	1.088
400	0.7138	0.7280	0.7495	0.8237	0.8997	1.003	1.056	1.082	1.095	1.101	1.103	1.103
450	0.7828	0.7919	0.8073	0.8655	0.9292	1.024	1.074	1.100	1.112	1.117	1.118	1.117
500	0.8510	0.8557	0.8660	0.9105	0.9635	1.047	1.094	1.118	1.130	1.134	1.134	1.132
600	0.9853	0.9820	0.9839	1.006	1.040	1.101	1.138	1.158	1.166	1.168	1.167	1.163
700	1.117	1.106	1.101	1.104	1.122	1.162	1.188	1.201	1.205	1.204	1.200	1.194
800	1.246	1.229	1.217	1.204	1.207	1.227	1.240	1.246	1.245	1.241	1.235	1.227
900	1.372	1.349	1.331	1.304	1.293	1.294	1.295	1.293	1.287	1.279	1.270	1.259
1,000	1.497	1.468	1.444	1.403	1.380	1.362	1.352	1.341	1.329	1.317	1.305	1.292
2,000	2.667	2.579	2.502	2.344	2.223	2.049	1.930	1.842	1.772	1.715	1.667	1.626

D2.4. Table 6. Specific enthalpy *h* of carbon dioxide in kJ/kg

Pressure in bar	Temperature in °C											
	−55	−50	−40	−30	−20	−10	0	10	20	30	40	50
1	440.8	444.7	452.6	460.5	468.5	476.7	484.9	493.2	501.6	510.1	518.7	527.4
5	432.3	436.7	445.6	454.3	462.9	471.6	480.2	488.9	497.7	506.5	515.3	524.3
10	83.14	93.01	435.4	445.5	455.2	464.7	474.0	483.3	492.5	501.7	510.9	520.2
20	83.42	93.25	113.1	133.4	154.5	448.6	460.0	470.8	481.3	491.5	501.6	511.6
30	83.71	93.50	113.2	133.4	154.3	176.4	442.2	456.0	468.5	480.2	491.4	502.4
40	84.00	93.75	113.4	133.5	154.2	175.9	199.5	436.6	453.0	467.1	480.1	492.3
50	84.29	94.02	113.6	133.5	154.0	175.5	198.5	224.6	432.4	451.4	467.1	481.1
60	84.59	94.29	113.8	133.6	154.0	175.2	197.7	222.8	254.3	430.7	451.7	468.5
70	84.90	94.57	114.0	133.7	153.9	174.9	197.1	221.3	249.9	392.7	432.1	453.9
80	85.21	94.85	114.2	133.8	153.9	174.7	196.5	220.0	246.9	284.1	402.8	436.3
90	85.53	95.14	114.4	134.0	153.9	174.5	196.0	219.0	244.6	276.3	343.7	413.8

D2.4. Table 6. (continued)

Pressure in bar	Temperature in °C											
	−55	−50	−40	−30	−20	−10	0	10	20	30	40	50
100	85.85	95.44	114.7	134.1	153.9	174.3	195.5	218.0	242.7	271.6	313.0	384.0
150	87.53	97.00	115.9	135.0	154.3	173.9	194.1	215.0	236.8	260.1	285.5	313.9
200	89.31	98.67	117.4	136.1	155.0	174.1	193.5	213.4	233.9	255.0	277.0	300.1
250	91.18	100.4	118.9	137.4	156.0	174.7	193.6	212.8	232.3	252.2	272.6	293.5
300	93.11	102.3	120.6	138.9	157.1	175.5	194.0	212.7	231.6	250.8	270.2	289.8
350	95.11	104.2	122.4	140.4	158.5	176.6	194.8	213.1	231.5	250.1	268.8	287.7
400	97.17	106.2	124.2	142.1	160.0	177.9	195.8	213.8	231.8	250.0	268.2	286.5
450	99.28	108.3	126.2	143.9	161.6	179.3	197.0	214.7	232.5	250.3	268.1	286.0
500	101.4	110.4	128.2	145.8	163.3	180.8	198.3	215.8	233.3	250.9	268.4	285.9
600	105.8	114.7	132.3	149.7	167.0	184.3	201.4	218.6	235.7	252.8	269.9	286.9
700	110.4	119.2	136.6	153.9	171.0	188.0	204.9	221.8	238.6	255.4	272.1	288.8
800	115.0	123.8	141.1	158.2	175.1	192.0	208.7	225.4	242.0	258.5	275.0	291.4
900	119.8	128.5	145.7	162.6	179.4	196.1	212.7	229.2	245.7	262.0	278.3	294.5
1,000	124.6	133.3	150.3	167.2	183.9	200.5	216.9	233.3	249.6	265.8	281.9	297.9
2,000	175.3	183.7	200.2	216.5	232.7	248.7	264.6	280.3	296.0	311.5	327.0	342.3

Pressure in bar	Temperature in °C											
	60	80	100	150	200	300	400	500	600	700	800	900
1	536.2	554.1	572.3	619.3	668.2	771.2	880.1	993.8	1,112	1,233	1,357	1,483
5	533.2	551.4	569.9	617.5	666.8	770.3	879.4	993.3	1,111	1,232	1,357	1,483
10	529.4	548.1	567.0	615.2	665.0	769.1	878.6	992.7	1,111	1,232	1,356	1,483
20	521.5	541.2	560.9	610.6	661.4	766.7	876.9	991.6	1,110	1,232	1,356	1,483
30	513.1	534.0	554.7	606.0	657.8	764.3	875.3	990.4	1,109	1,231	1,356	1,483
40	504.0	526.5	548.2	601.3	654.1	761.9	873.6	989.3	1,108	1,231	1,355	1,483
50	494.2	518.5	541.5	596.5	650.5	759.6	872.0	988.1	1,108	1,230	1,355	1,482
60	483.4	510.1	534.5	591.7	646.8	757.3	870.5	987.0	1,107	1,230	1,355	1,482
70	471.5	501.2	527.3	586.8	643.2	755.0	868.9	985.9	1,106	1,229	1,354	1,482
80	458.1	491.7	519.9	581.9	639.5	752.7	867.3	984.9	1,105	1,229	1,354	1,482
90	442.7	481.6	512.1	576.9	635.9	750.4	865.8	983.8	1,105	1,228	1,354	1,482
100	425.0	470.9	504.1	571.9	632.2	748.1	864.3	982.8	1,104	1,228	1,354	1,482
150	346.5	412.8	462.1	546.8	614.4	737.3	857.0	977.8	1,101	1,225	1,352	1,481
200	324.4	376.1	426.2	523.3	597.6	727.2	850.4	973.3	1,098	1,223	1,351	1,481
250	315.0	359.5	404.3	503.7	582.7	718.0	844.3	969.2	1,095	1,222	1,350	1,480
300	309.8	350.5	391.7	488.3	570.2	709.8	838.9	965.6	1,092	1,220	1,350	1,480
350	306.7	345.2	383.9	477.1	559.9	702.7	834.0	962.4	1,090	1,219	1,349	1,481
400	304.9	341.8	378.9	469.1	551.6	696.5	829.8	959.6	1,089	1,218	1,349	1,481
450	303.9	339.7	375.5	463.4	545.1	691.3	826.1	957.2	1,087	1,218	1,349	1,481
500	303.5	338.5	373.4	459.1	540.1	687.0	823.0	955.1	1,086	1,217	1,349	1,482
600	303.9	337.7	371.4	454.0	533.5	680.6	818.2	952.1	1,085	1,217	1,350	1,484
700	305.4	338.5	371.2	451.7	529.8	676.7	815.2	950.2	1,084	1,217	1,351	1,486
800	307.7	340.2	372.4	451.3	528.1	674.6	813.6	949.4	1,084	1,218	1,353	1,488
900	310.6	342.6	374.3	452.1	527.9	673.8	813.2	949.5	1,085	1,220	1,355	1,491
1,000	313.9	345.5	376.9	453.8	528.9	674.1	813.7	950.4	1,086	1,222	1,358	1,494
2,000	357.5	387.7	417.6	491.1	563.2	704.6	843.9	982.3	1,121	1,259	1,398	1,537

D2.4. Table 7. Specific entropy *s* of carbon dioxide in kJ/(kg K)

Temperature in °C												
Pressure in bar	−55	−50	−40	−30	−20	−10	0	10	20	30	40	50
1	2.486	2.504	2.538	2.571	2.604	2.635	2.666	2.696	2.725	2.754	2.781	2.809
5	2.154	2.174	2.213	2.249	2.284	2.318	2.350	2.381	2.411	2.441	2.470	2.498
10	0.5337	0.5784	2.050	2.092	2.131	2.168	2.203	2.236	2.268	2.299	2.329	2.358
20	0.5311	0.5756	0.6626	0.7478	0.8328	1.992	2.034	2.073	2.109	2.144	2.176	2.208
30	0.5285	0.5729	0.6594	0.7441	0.8283	0.9137	1.907	1.957	2.000	2.039	2.076	2.110
40	0.5259	0.5702	0.6564	0.7405	0.8239	0.9081	0.9960	1.848	1.905	1.952	1.994	2.033
50	0.5234	0.5675	0.6533	0.7370	0.8197	0.9028	0.9887	1.082	1.805	1.869	1.920	1.964
60	0.5209	0.5649	0.6504	0.7336	0.8156	0.8978	0.9819	1.072	1.181	1.778	1.846	1.899
70	0.5185	0.5623	0.6474	0.7302	0.8117	0.8929	0.9756	1.063	1.162	1.637	1.765	1.834
80	0.5160	0.5597	0.6446	0.7269	0.8078	0.8882	0.9696	1.054	1.148	1.272	1.658	1.763
90	0.5136	0.5572	0.6417	0.7237	0.8041	0.8837	0.9639	1.047	1.136	1.242	1.460	1.681
100	0.5113	0.5547	0.6390	0.7206	0.8004	0.8794	0.9586	1.040	1.125	1.222	1.356	1.579
150	0.4998	0.5427	0.6257	0.7057	0.7834	0.8596	0.9348	1.010	1.086	1.164	1.246	1.335
200	0.4889	0.5314	0.6133	0.6919	0.7680	0.8421	0.9147	0.9862	1.057	1.128	1.199	1.272
250	0.4786	0.5206	0.6016	0.6792	0.7540	0.8265	0.8970	0.9660	1.034	1.101	1.167	1.233
300	0.4687	0.5104	0.5906	0.6672	0.7409	0.8121	0.8812	0.9484	1.014	1.078	1.141	1.203
350	0.4592	0.5006	0.5801	0.6560	0.7288	0.7989	0.8667	0.9325	0.9964	1.059	1.120	1.179
400	0.4501	0.4912	0.5701	0.6453	0.7173	0.7865	0.8533	0.9180	0.9806	1.041	1.101	1.158
450	0.4413	0.4822	0.5605	0.6351	0.7064	0.7749	0.8409	0.9046	0.9662	1.026	1.084	1.140
500	0.4328	0.4734	0.5513	0.6254	0.6961	0.7639	0.8292	0.8921	0.9529	1.012	1.069	1.124
600	0.4166	0.4569	0.5339	0.6071	0.6768	0.7436	0.8077	0.8693	0.9287	0.9861	1.041	1.095
700	0.4014	0.4413	0.5177	0.5901	0.6590	0.7249	0.7881	0.8488	0.9072	0.9635	1.018	1.070
800	0.3869	0.4266	0.5024	0.5741	0.6424	0.7077	0.7701	0.8301	0.8877	0.9432	0.9966	1.048
900	0.3732	0.4126	0.4879	0.5591	0.6269	0.6916	0.7535	0.8128	0.8698	0.9246	0.9774	1.028
1,000	0.3600	0.3992	0.4741	0.5449	0.6122	0.6764	0.7378	0.7967	0.8532	0.9075	0.9597	1.010
2,000	0.2515	0.2894	0.3619	0.4305	0.4956	0.5576	0.6168	0.6735	0.7278	0.7799	0.8300	0.8782

Temperature in °C												
Pressure in bar	60	80	100	150	200	300	400	500	600	700	800	900
1	2.836	2.888	2.938	3.056	3.165	3.363	3.537	3.695	3.838	3.969	4.091	4.203
5	2.525	2.578	2.629	2.749	2.859	3.057	3.232	3.390	3.533	3.665	3.786	3.899
10	2.386	2.441	2.493	2.614	2.725	2.924	3.100	3.258	3.402	3.534	3.655	3.768
20	2.238	2.296	2.350	2.475	2.588	2.790	2.967	3.126	3.270	3.402	3.523	3.636
30	2.143	2.204	2.261	2.390	2.506	2.710	2.888	3.047	3.192	3.324	3.446	3.559
40	2.068	2.134	2.194	2.327	2.445	2.652	2.831	2.991	3.136	3.269	3.391	3.504
50	2.004	2.075	2.138	2.276	2.397	2.606	2.787	2.948	3.093	3.226	3.348	3.461
60	1.944	2.022	2.090	2.233	2.357	2.568	2.750	2.912	3.057	3.190	3.313	3.426
70	1.887	1.974	2.046	2.195	2.321	2.536	2.719	2.881	3.027	3.160	3.283	3.397
80	1.829	1.927	2.005	2.161	2.290	2.507	2.691	2.854	3.001	3.134	3.257	3.371
90	1.769	1.883	1.967	2.130	2.262	2.481	2.667	2.830	2.977	3.111	3.234	3.348
100	1.704	1.838	1.930	2.101	2.236	2.458	2.645	2.809	2.956	3.090	3.214	3.328
150	1.435	1.628	1.764	1.978	2.129	2.365	2.558	2.725	2.874	3.009	3.134	3.248
200	1.346	1.497	1.635	1.880	2.046	2.295	2.493	2.663	2.814	2.951	3.076	3.191
250	1.298	1.428	1.551	1.802	1.979	2.238	2.442	2.615	2.767	2.905	3.031	3.147

D2.4. Table 7. (continued)

Pressure in bar	Temperature in °C											
	60	80	100	150	200	300	400	500	600	700	800	900
300	1.264	1.383	1.496	1.739	1.922	2.191	2.398	2.574	2.728	2.867	2.993	3.110
350	1.237	1.349	1.456	1.690	1.875	2.150	2.361	2.539	2.695	2.834	2.962	3.078
400	1.214	1.322	1.424	1.651	1.835	2.114	2.328	2.508	2.665	2.806	2.934	3.051
450	1.195	1.299	1.398	1.619	1.801	2.082	2.299	2.481	2.639	2.781	2.909	3.027
500	1.177	1.279	1.375	1.591	1.772	2.054	2.273	2.456	2.615	2.758	2.887	3.005
600	1.147	1.245	1.338	1.546	1.724	2.006	2.228	2.413	2.574	2.718	2.848	2.967
700	1.121	1.217	1.307	1.510	1.684	1.966	2.189	2.376	2.539	2.684	2.815	2.934
800	1.098	1.193	1.281	1.480	1.651	1.933	2.156	2.344	2.508	2.654	2.786	2.906
900	1.077	1.171	1.258	1.454	1.623	1.903	2.127	2.316	2.481	2.627	2.760	2.881
1,000	1.059	1.151	1.237	1.431	1.599	1.877	2.102	2.291	2.456	2.604	2.737	2.858
2,000	0.9246	1.013	1.095	1.280	1.441	1.712	1.936	2.128	2.296	2.446	2.582	2.706

D2.4. Table 8. Specific isobaric heat capacity c_p of carbon dioxide in kJ/(kg K)

Pressure in bar	Temperature in °C											
	−55	−50	−40	−30	−20	−10	0	10	20	30	40	50
1	0.7790	0.7825	0.7903	0.7988	0.8078	0.8172	0.8267	0.8363	0.8459	0.8555	0.8650	0.8744
5	0.9013	0.8890	0.8743	0.8673	0.8648	0.8653	0.8679	0.8719	0.8769	0.8828	0.8891	0.8959
10	1.969	1.977	1.041	0.9864	0.9567	0.9393	0.9291	0.9234	0.9210	0.9208	0.9224	0.9252
20	1.962	1.969	2.002	2.063	2.163	1.180	1.107	1.063	1.034	1.015	1.002	0.9936
30	1.956	1.962	1.992	2.047	2.137	2.289	1.473	1.298	1.204	1.146	1.107	1.080
40	1.950	1.955	1.981	2.032	2.113	2.247	2.495	1.833	1.501	1.344	1.252	1.192
50	1.944	1.948	1.972	2.018	2.092	2.210	2.417	2.879	2.210	1.690	1.469	1.346
60	1.938	1.941	1.963	2.005	2.072	2.177	2.353	2.703	3.945	2.490	1.834	1.567
70	1.933	1.935	1.954	1.992	2.054	2.148	2.299	2.577	3.299	7.929	2.582	1.913
80	1.927	1.929	1.946	1.981	2.037	2.121	2.253	2.480	2.974	5.229	4.946	2.515
90	1.922	1.923	1.938	1.970	2.021	2.097	2.213	2.403	2.768	3.802	12.87	3.701
100	1.917	1.917	1.930	1.959	2.006	2.075	2.178	2.339	2.623	3.260	5.660	5.813
150	1.895	1.891	1.897	1.915	1.945	1.989	2.049	2.132	2.248	2.417	2.672	3.044
200	1.875	1.870	1.869	1.879	1.899	1.927	1.965	2.014	2.075	2.153	2.251	2.369
250	1.859	1.851	1.846	1.850	1.862	1.881	1.905	1.935	1.972	2.015	2.064	2.118
300	1.844	1.835	1.826	1.826	1.832	1.844	1.859	1.879	1.902	1.927	1.954	1.983
350	1.831	1.821	1.809	1.805	1.807	1.814	1.824	1.836	1.850	1.865	1.880	1.896
400	1.819	1.808	1.794	1.787	1.786	1.789	1.794	1.801	1.810	1.818	1.827	1.835
450	1.809	1.797	1.780	1.772	1.768	1.768	1.770	1.773	1.778	1.782	1.786	1.790
500	1.800	1.786	1.768	1.758	1.752	1.750	1.749	1.750	1.751	1.753	1.754	1.754
600	1.783	1.769	1.748	1.735	1.726	1.720	1.716	1.713	1.711	1.708	1.705	1.702
700	1.769	1.754	1.732	1.717	1.706	1.697	1.691	1.685	1.680	1.675	1.670	1.665
800	1.757	1.741	1.718	1.701	1.689	1.679	1.671	1.663	1.657	1.650	1.644	1.637
900	1.747	1.731	1.706	1.688	1.675	1.664	1.655	1.646	1.638	1.631	1.623	1.616
1,000	1.738	1.721	1.696	1.678	1.663	1.652	1.641	1.632	1.623	1.615	1.607	1.599
2,000	1.685	1.668	1.642	1.623	1.608	1.594	1.582	1.570	1.559	1.548	1.538	1.528

D2.4. Table 8. (continued)

Pressure in bar	Temperature in °C											
	60	80	100	150	200	300	400	500	600	700	800	900
1	0.8837	0.9018	0.9193	0.9601	0.9971	1.061	1.114	1.159	1.196	1.227	1.253	1.275
5	0.9030	0.9175	0.9323	0.9688	1.003	1.065	1.117	1.160	1.197	1.228	1.254	1.276
10	0.9289	0.9383	0.9494	0.9800	1.011	1.069	1.119	1.162	1.198	1.229	1.255	1.276
20	0.9885	0.9847	0.9865	1.003	1.027	1.078	1.125	1.166	1.202	1.231	1.256	1.278
30	1.061	1.038	1.028	1.028	1.044	1.088	1.131	1.170	1.205	1.234	1.258	1.279
40	1.152	1.102	1.075	1.055	1.062	1.097	1.137	1.175	1.207	1.236	1.260	1.281
50	1.267	1.176	1.128	1.083	1.080	1.106	1.143	1.179	1.210	1.238	1.262	1.282
60	1.421	1.266	1.189	1.114	1.098	1.116	1.149	1.183	1.213	1.240	1.264	1.284
70	1.631	1.374	1.257	1.145	1.117	1.125	1.155	1.187	1.216	1.243	1.265	1.285
80	1.931	1.505	1.334	1.179	1.137	1.135	1.160	1.190	1.219	1.245	1.267	1.286
90	2.376	1.666	1.422	1.215	1.157	1.144	1.166	1.194	1.222	1.247	1.269	1.288
100	3.032	1.859	1.521	1.252	1.178	1.154	1.172	1.198	1.225	1.249	1.270	1.289
150	3.433	2.920	2.103	1.452	1.283	1.201	1.200	1.217	1.238	1.259	1.279	1.296
200	2.497	2.603	2.367	1.632	1.383	1.246	1.226	1.234	1.251	1.269	1.286	1.302
250	2.175	2.259	2.197	1.744	1.463	1.286	1.250	1.251	1.263	1.278	1.293	1.308
300	2.011	2.057	2.050	1.790	1.515	1.321	1.272	1.266	1.274	1.286	1.300	1.313
350	1.911	1.933	1.934	1.765	1.551	1.348	1.291	1.279	1.284	1.294	1.306	1.318
400	1.842	1.851	1.849	1.733	1.568	1.369	1.308	1.292	1.293	1.301	1.312	1.323
450	1.792	1.792	1.787	1.705	1.568	1.385	1.322	1.303	1.302	1.308	1.318	1.327
500	1.753	1.749	1.739	1.678	1.561	1.397	1.334	1.313	1.310	1.315	1.323	1.332
600	1.698	1.687	1.673	1.627	1.548	1.411	1.351	1.329	1.324	1.326	1.332	1.340
700	1.659	1.646	1.630	1.588	1.532	1.416	1.362	1.341	1.335	1.336	1.341	1.347
800	1.631	1.616	1.600	1.558	1.514	1.419	1.369	1.350	1.344	1.345	1.348	1.353
900	1.608	1.593	1.577	1.536	1.498	1.420	1.373	1.356	1.351	1.352	1.355	1.359
1,000	1.591	1.575	1.559	1.519	1.484	1.421	1.377	1.361	1.357	1.358	1.361	1.365
2,000	1.519	1.501	1.486	1.455	1.431	1.401	1.387	1.383	1.382	1.385	1.389	1.393

D2.4. Table 9. Specific isochoric heat capacity c_v of carbon dioxide in kJ/(kg K)

Pressure in bar	Temperature in °C											
	−55	−50	−40	−30	−20	−10	0	10	20	30	40	50
1	0.5771	0.5816	0.5912	0.6011	0.6113	0.6216	0.6319	0.6422	0.6524	0.6624	0.6724	0.6821
5	0.6282	0.6254	0.6248	0.6279	0.6331	0.6396	0.6470	0.6549	0.6632	0.6717	0.6804	0.6891
10	0.9832	0.9715	0.6867	0.6704	0.6651	0.6650	0.6677	0.6720	0.6776	0.6839	0.6908	0.6981
20	0.9846	0.9727	0.9549	0.9428	0.9357	0.7353	0.7194	0.7125	0.7103	0.7111	0.7137	0.7176
30	0.9859	0.9740	0.9558	0.9435	0.9358	0.9332	0.8037	0.7678	0.7512	0.7431	0.7397	0.7392
40	0.9873	0.9752	0.9568	0.9441	0.9360	0.9325	0.9372	0.8621	0.8075	0.7829	0.7701	0.7635
50	0.9886	0.9764	0.9577	0.9448	0.9363	0.9320	0.9344	0.9568	0.9014	0.8363	0.8071	0.7915
60	0.9899	0.9776	0.9587	0.9455	0.9366	0.9317	0.9324	0.9465	1.003	0.9196	0.8544	0.8242
70	0.9912	0.9787	0.9596	0.9462	0.9369	0.9315	0.9308	0.9397	0.9717	1.141	0.9208	0.8637
80	0.9925	0.9799	0.9606	0.9469	0.9373	0.9314	0.9297	0.9351	0.9541	1.031	1.032	0.9128
90	0.9937	0.9810	0.9615	0.9476	0.9378	0.9314	0.9288	0.9319	0.9437	0.9792	1.147	0.9745
100	0.9950	0.9821	0.9624	0.9483	0.9382	0.9315	0.9282	0.9295	0.9370	0.9569	1.025	1.035

D2.4. Table 9. (continued)

Temperature in °C												
Pressure in bar	−55	−50	−40	−30	−20	−10	0	10	20	30	40	50
150	1.001	0.9875	0.9669	0.9519	0.9407	0.9326	0.9270	0.9239	0.9233	0.9254	0.9313	0.9423
200	1.007	0.9926	0.9711	0.9554	0.9435	0.9345	0.9276	0.9227	0.9196	0.9181	0.9183	0.9201
250	1.012	0.9975	0.9752	0.9589	0.9464	0.9367	0.9291	0.9232	0.9188	0.9157	0.9138	0.9131
300	1.017	1.002	0.9791	0.9622	0.9493	0.9392	0.9310	0.9245	0.9193	0.9153	0.9124	0.9104
350	1.022	1.006	0.9828	0.9655	0.9522	0.9417	0.9332	0.9262	0.9206	0.9160	0.9124	0.9097
400	1.026	1.010	0.9864	0.9687	0.9551	0.9443	0.9355	0.9283	0.9223	0.9173	0.9133	0.9102
450	1.030	1.014	0.9898	0.9718	0.9580	0.9470	0.9380	0.9305	0.9243	0.9190	0.9147	0.9113
500	1.034	1.018	0.9932	0.9748	0.9608	0.9496	0.9405	0.9328	0.9264	0.9210	0.9165	0.9128
600	1.042	1.025	0.9994	0.9806	0.9662	0.9549	0.9455	0.9377	0.9311	0.9255	0.9207	0.9167
700	1.049	1.032	1.005	0.9861	0.9715	0.9600	0.9506	0.9427	0.9360	0.9303	0.9254	0.9213
800	1.056	1.038	1.011	0.9914	0.9767	0.9651	0.9556	0.9478	0.9410	0.9353	0.9304	0.9262
900	1.062	1.044	1.016	0.9964	0.9816	0.9700	0.9606	0.9528	0.9461	0.9404	0.9355	0.9312
1,000	1.067	1.049	1.021	1.001	0.9864	0.9748	0.9655	0.9578	0.9512	0.9455	0.9406	0.9364
2,000	1.108	1.089	1.060	1.041	1.028	1.018	1.010	1.004	0.9985	0.9940	0.9900	0.9864

Temperature in °C												
Pressure in bar	60	80	100	150	200	300	400	500	600	700	800	900
1	0.6917	0.7103	0.7282	0.7696	0.8070	0.8714	0.9248	0.9693	1.007	1.038	1.064	1.086
5	0.6978	0.7150	0.7319	0.7719	0.8085	0.8721	0.9252	0.9696	1.007	1.038	1.064	1.086
10	0.7056	0.7211	0.7367	0.7747	0.8103	0.8731	0.9258	0.9700	1.007	1.038	1.064	1.086
20	0.7224	0.7338	0.7466	0.7805	0.8140	0.8750	0.9269	0.9708	1.008	1.039	1.065	1.087
30	0.7406	0.7472	0.7568	0.7864	0.8177	0.8768	0.9281	0.9715	1.008	1.039	1.065	1.087
40	0.7607	0.7615	0.7676	0.7923	0.8215	0.8787	0.9292	0.9723	1.009	1.039	1.065	1.087
50	0.7828	0.7768	0.7787	0.7983	0.8252	0.8805	0.9303	0.9730	1.009	1.040	1.066	1.087
60	0.8076	0.7929	0.7903	0.8043	0.8289	0.8823	0.9313	0.9738	1.010	1.040	1.066	1.088
70	0.8356	0.8101	0.8022	0.8104	0.8325	0.8841	0.9324	0.9745	1.010	1.041	1.066	1.088
80	0.8671	0.8282	0.8144	0.8164	0.8362	0.8858	0.9335	0.9752	1.011	1.041	1.067	1.088
90	0.9024	0.8470	0.8268	0.8224	0.8397	0.8875	0.9345	0.9759	1.011	1.042	1.067	1.089
100	0.9393	0.8662	0.8393	0.8284	0.8432	0.8892	0.9355	0.9766	1.012	1.042	1.067	1.089
150	0.9521	0.9300	0.8935	0.8558	0.8595	0.8971	0.9403	0.9800	1.014	1.044	1.069	1.090
200	0.9234	0.9255	0.9152	0.8768	0.8729	0.9040	0.9447	0.9830	1.017	1.046	1.070	1.091
250	0.9133	0.9151	0.9133	0.8912	0.8831	0.9099	0.9486	0.9859	1.019	1.048	1.072	1.093
300	0.9093	0.9089	0.9085	0.8988	0.8906	0.9147	0.9520	0.9885	1.021	1.049	1.073	1.094
350	0.9078	0.9060	0.9053	0.9008	0.8960	0.9187	0.9551	0.9909	1.023	1.051	1.075	1.095
400	0.9078	0.9049	0.9038	0.9013	0.8999	0.9220	0.9578	0.9931	1.025	1.052	1.076	1.096
450	0.9085	0.9050	0.9034	0.9020	0.9028	0.9247	0.9602	0.9951	1.026	1.054	1.077	1.097
500	0.9098	0.9058	0.9038	0.9030	0.9052	0.9272	0.9624	0.9970	1.028	1.055	1.078	1.098
600	0.9135	0.9088	0.9062	0.9057	0.9097	0.9318	0.9662	1.000	1.031	1.058	1.081	1.100
700	0.9178	0.9128	0.9098	0.9091	0.9141	0.9364	0.9697	1.003	1.034	1.060	1.083	1.102
800	0.9226	0.9173	0.9141	0.9131	0.9184	0.9409	0.9731	1.006	1.036	1.062	1.085	1.104
900	0.9277	0.9222	0.9188	0.9174	0.9229	0.9453	0.9765	1.009	1.039	1.064	1.087	1.106
1,000	0.9328	0.9273	0.9237	0.9220	0.9273	0.9495	0.9799	1.012	1.041	1.066	1.088	1.107
2,000	0.9832	0.9780	0.9740	0.9694	0.9711	0.9872	1.011	1.037	1.062	1.084	1.104	1.121

D2.4. Table 10. Isobaric expansion coefficient β of carbon dioxide in 10^{-3}/K

Pressure in bar	Temperature in °C											
	−55	−50	−40	−30	−20	−10	0	10	20	30	40	50
1	4.808	4.682	4.453	4.248	4.063	3.896	3.742	3.601	3.471	3.351	3.239	3.134
5	5.979	5.701	5.247	4.883	4.580	4.323	4.100	3.904	3.729	3.573	3.431	3.302
10	3.108	3.253	6.794	5.997	5.429	4.993	4.641	4.348	4.100	3.886	3.698	3.531
20	3.070	3.208	3.553	4.032	4.743	7.199	6.244	5.575	5.070	4.671	4.346	4.074
30	3.034	3.166	3.493	3.941	4.592	5.641	9.564	7.684	6.556	5.782	5.209	4.764
40	2.998	3.124	3.436	3.856	4.455	5.387	7.095	12.50	9.185	7.489	6.421	5.673
50	2.964	3.085	3.381	3.777	4.330	5.165	6.603	9.863	15.50	10.50	8.249	6.920
60	2.931	3.047	3.329	3.702	4.215	4.969	6.203	8.681	17.85	17.49	11.34	8.728
70	2.899	3.010	3.280	3.632	4.109	4.794	5.869	7.844	13.12	64.86	17.68	11.55
80	2.868	2.975	3.232	3.566	4.011	4.637	5.584	7.210	10.81	28.61	37.61	16.45
90	2.838	2.941	3.187	3.503	3.920	4.494	5.338	6.708	9.383	17.36	99.50	25.95
100	2.809	2.908	3.144	3.443	3.834	4.364	5.121	6.297	8.393	13.27	33.46	41.90
150	2.677	2.759	2.951	3.187	3.480	3.851	4.333	4.981	5.890	7.237	9.345	12.64
200	2.562	2.632	2.791	2.981	3.209	3.486	3.824	4.244	4.772	5.445	6.310	7.404
250	2.461	2.520	2.654	2.811	2.994	3.209	3.461	3.758	4.108	4.521	5.006	5.566
300	2.371	2.422	2.537	2.668	2.818	2.989	3.185	3.407	3.658	3.940	4.255	4.598
350	2.291	2.335	2.433	2.545	2.670	2.810	2.966	3.138	3.328	3.534	3.755	3.988
400	2.218	2.257	2.342	2.437	2.543	2.659	2.786	2.924	3.073	3.230	3.394	3.563
450	2.152	2.186	2.261	2.343	2.433	2.531	2.636	2.749	2.868	2.991	3.118	3.246
500	2.091	2.122	2.187	2.259	2.336	2.419	2.508	2.601	2.698	2.798	2.899	2.999
600	1.984	2.009	2.060	2.115	2.173	2.235	2.299	2.365	2.433	2.501	2.568	2.633
700	1.893	1.912	1.953	1.996	2.041	2.087	2.135	2.184	2.232	2.281	2.328	2.373
800	1.813	1.829	1.862	1.896	1.930	1.966	2.002	2.038	2.074	2.109	2.143	2.175
900	1.742	1.755	1.782	1.809	1.836	1.864	1.891	1.918	1.945	1.971	1.995	2.018
1,000	1.679	1.691	1.713	1.734	1.755	1.776	1.797	1.817	1.837	1.856	1.874	1.890
2,000	1.289	1.292	1.294	1.294	1.292	1.288	1.284	1.278	1.273	1.267	1.261	1.255

Pressure in bar	Temperature in °C											
	60	80	100	150	200	300	400	500	600	700	800	900
1	3.037	2.859	2.702	2.377	2.122	1.749	1.488	1.294	1.146	1.028	0.9320	0.8525
5	3.183	2.974	2.793	2.430	2.156	1.764	1.495	1.299	1.148	1.029	0.9326	0.8528
10	3.382	3.126	2.912	2.500	2.199	1.783	1.505	1.304	1.151	1.031	0.9334	0.8531
20	3.842	3.466	3.171	2.644	2.288	1.822	1.524	1.314	1.156	1.034	0.9349	0.8537
30	4.406	3.861	3.461	2.797	2.378	1.860	1.543	1.324	1.162	1.036	0.9364	0.8543
40	5.115	4.326	3.788	2.959	2.471	1.899	1.561	1.333	1.167	1.039	0.9377	0.8549
50	6.025	4.875	4.155	3.129	2.565	1.936	1.579	1.343	1.172	1.042	0.9390	0.8554
60	7.231	5.532	4.569	3.307	2.661	1.973	1.597	1.352	1.177	1.044	0.9403	0.8559
70	8.882	6.320	5.035	3.493	2.758	2.010	1.614	1.360	1.181	1.047	0.9414	0.8563
80	11.23	7.272	5.558	3.687	2.856	2.046	1.630	1.368	1.186	1.049	0.9425	0.8567
90	14.66	8.416	6.140	3.887	2.954	2.081	1.646	1.376	1.190	1.051	0.9435	0.8570
100	19.59	9.772	6.781	4.092	3.051	2.116	1.661	1.384	1.194	1.053	0.9444	0.8573
150	16.72	15.53	10.05	5.099	3.512	2.271	1.729	1.417	1.210	1.061	0.9476	0.8578
200	8.693	10.69	10.15	5.733	3.858	2.391	1.781	1.442	1.222	1.066	0.9488	0.8569

D2.4. Table 10. (continued)

Pressure in bar	Temperature in °C											
	60	80	100	150	200	300	400	500	600	700	800	900
250	6.187	7.387	7.758	5.787	4.012	2.470	1.817	1.458	1.229	1.068	0.9481	0.8547
300	4.964	5.687	6.140	5.451	3.985	2.507	1.836	1.466	1.231	1.067	0.9456	0.8514
350	4.229	4.702	5.062	4.825	3.864	2.505	1.842	1.467	1.229	1.064	0.9416	0.8470
400	3.733	4.061	4.330	4.289	3.663	2.471	1.835	1.463	1.224	1.059	0.9363	0.8417
450	3.372	3.611	3.810	3.872	3.411	2.415	1.818	1.454	1.217	1.052	0.9299	0.8358
500	3.096	3.275	3.424	3.523	3.174	2.347	1.792	1.441	1.208	1.044	0.9228	0.8292
600	2.695	2.804	2.892	2.979	2.793	2.189	1.723	1.406	1.184	1.025	0.9068	0.8151
700	2.414	2.486	2.539	2.591	2.492	2.029	1.642	1.361	1.156	1.005	0.8897	0.8002
800	2.204	2.252	2.286	2.309	2.245	1.890	1.559	1.312	1.125	0.9822	0.8719	0.7851
900	2.039	2.072	2.093	2.097	2.044	1.770	1.480	1.261	1.092	0.9587	0.8538	0.7701
1,000	1.905	1.928	1.941	1.932	1.881	1.664	1.409	1.210	1.057	0.9344	0.8354	0.7552
2,000	1.249	1.238	1.226	1.193	1.153	1.056	0.9612	0.8738	0.7939	0.7244	0.6658	0.6164

D2.4. Table 11. Isentropic speed of sound w_s in carbon dioxide in m/s

Pressure in bar	Temperature in °C											
	−55	−50	−40	−30	−20	−10	0	10	20	30	40	50
1	232.5	235.0	239.9	244.6	249.2	253.7	258.1	262.4	266.6	270.7	274.7	278.7
5	224.2	227.3	233.2	238.8	244.1	249.2	254.0	258.7	263.3	267.7	272.1	276.3
10	967.7	931.1	223.5	230.6	237.1	243.1	248.7	254.0	259.1	264.0	268.7	273.3
20	973.4	937.3	863.8	787.2	705.7	228.8	236.6	243.6	250.0	256.0	261.7	267.0
30	978.9	943.4	871.0	796.0	716.7	630.4	221.5	231.5	240.0	247.4	254.2	260.5
40	984.4	949.3	878.1	804.5	727.3	644.1	549.1	216.1	228.3	238.0	246.3	253.8
50	989.8	955.2	885.0	812.8	737.4	657.0	567.4	458.1	213.4	227.2	237.8	246.8
60	995.2	961.0	891.8	820.9	747.2	669.3	584.0	484.9	351.9	214.1	228.6	239.6
70	1,000	966.7	898.5	828.8	756.6	680.9	599.4	507.7	395.8	192.3	218.2	232.1
80	1,006	972.3	905.0	836.4	765.8	692.1	613.7	527.7	428.7	293.0	205.8	224.7
90	1,011	977.8	911.4	843.9	774.7	702.8	627.1	545.7	455.4	346.5	205.9	218.2
100	1,016	983.3	917.7	851.2	783.3	713.1	639.8	562.1	478.1	383.3	270.2	217.5
150	1,040	1,009	947.7	885.7	823.1	759.7	695.3	629.8	563.0	495.3	427.3	362.7
200	1,063	1,034	975.5	917.1	858.6	800.2	741.7	683.3	625.2	567.8	511.9	458.9
250	1,085	1,057	1,001	946.1	890.9	836.2	782.1	728.6	676.0	624.7	575.2	528.4
300	1,106	1,079	1,026	973.1	920.7	869.0	818.2	768.3	719.7	672.6	627.4	584.6
350	1,126	1,100	1,049	998.5	948.5	899.2	851.0	804.0	758.3	714.3	672.2	632.3
400	1,145	1,120	1,071	1,023	974.5	927.3	881.3	836.5	793.2	751.6	711.9	674.2
450	1,163	1,140	1,092	1,045	999.0	953.7	909.4	866.6	825.2	785.5	747.6	711.8
500	1,181	1,158	1,112	1,067	1,022	978.5	935.9	894.5	854.8	816.6	780.3	745.9
600	1,215	1,194	1,151	1,108	1,066	1,024	984.4	945.6	908.3	872.6	838.7	806.5
700	1,247	1,227	1,186	1,146	1,106	1,066	1,028	991.6	956.2	922.3	890.1	859.5
800	1,277	1,258	1,219	1,181	1,143	1,105	1,069	1,034	999.6	967.2	936.3	907.0
900	1,305	1,287	1,251	1,214	1,177	1,141	1,106	1,072	1,040	1,008	978.5	950.1
1,000	1,332	1,315	1,280	1,245	1,210	1,175	1,141	1,108	1,077	1,046	1,017	989.9
2,000	1,554	1,543	1,519	1,493	1,466	1,438	1,411	1,384	1,358	1,332	1,308	1,284

D2.4. Table 11. (continued)

Pressure in bar	Temperature in °C											
	60	80	100	150	200	300	400	500	600	700	800	900
1	282.6	290.2	297.6	315.3	332.0	363.0	391.4	417.9	442.7	466.3	488.8	510.2
5	280.4	288.4	296.2	314.5	331.5	362.9	391.6	418.2	443.2	466.8	489.3	510.8
10	277.7	286.2	294.3	313.4	330.9	362.9	391.9	418.7	443.8	467.5	490.0	511.5
20	272.1	281.7	290.7	311.2	329.8	362.9	392.5	419.6	444.9	468.8	491.4	512.9
30	266.4	277.2	287.2	309.2	328.7	363.0	393.1	420.6	446.1	470.1	492.7	514.4
40	260.6	272.8	283.7	307.4	327.8	363.1	393.8	421.6	447.3	471.4	494.1	515.8
50	254.7	268.5	280.4	305.7	327.0	363.3	394.6	422.6	448.5	472.7	495.5	517.2
60	248.8	264.3	277.3	304.2	326.4	363.6	395.4	423.7	449.7	474.0	496.9	518.7
70	243.0	260.3	274.4	302.8	325.9	364.0	396.2	424.8	451.0	475.4	498.3	520.1
80	237.5	256.7	271.9	301.8	325.6	364.5	397.1	426.0	452.3	476.7	499.7	521.6
90	232.7	253.6	269.8	300.9	325.5	365.1	398.1	427.2	453.6	478.1	501.2	523.0
100	229.9	251.4	268.2	300.4	325.5	365.9	399.1	428.4	454.9	479.5	502.6	524.5
150	310.0	270.8	274.9	303.3	329.1	371.1	405.4	435.2	462.1	486.9	510.1	531.9
200	411.2	341.9	312.7	317.9	338.9	379.2	413.3	443.1	470.0	494.8	517.9	539.7
250	485.3	415.0	370.7	343.2	355.0	390.0	422.8	452.1	478.7	503.2	526.2	547.8
300	544.8	476.9	427.8	375.6	376.2	403.3	433.8	462.1	488.1	512.2	534.8	556.2
350	595.1	529.9	479.5	414.7	400.6	418.7	446.0	472.9	498.1	521.7	543.9	564.9
400	639.0	576.4	525.9	453.2	428.3	435.7	459.3	484.4	508.7	531.6	553.2	573.9
450	678.1	617.9	567.9	489.3	458.0	454.0	473.3	496.5	519.6	541.7	562.9	583.1
500	713.6	655.3	606.2	523.7	487.4	473.2	487.9	508.9	530.8	552.2	572.7	592.5
600	776.2	721.2	673.9	587.8	542.2	513.7	518.7	534.7	553.9	573.5	592.8	611.6
700	830.7	778.2	732.5	645.7	593.5	554.5	550.8	561.5	577.5	595.2	613.2	631.0
800	879.2	828.7	784.3	698.1	641.8	593.5	583.4	588.8	601.4	617.0	633.6	650.4
900	923.3	874.2	830.9	745.7	687.3	630.6	615.4	616.4	625.6	638.9	654.0	669.7
1,000	963.8	915.8	873.5	789.2	729.7	666.2	646.4	643.8	649.8	660.8	674.3	688.8
2,000	1,261	1,219	1,180	1,100	1,039	958.2	910.3	883.0	870.3	866.2	867.1	870.9

D2.4. Table 12. Thermal conductivity λ of carbon dioxide in mW/(m K)

Pressure in bar	Temperature in °C											
	−55	−50	−40	−30	−20	−10	0	10	20	30	40	50
1	10.78	11.10	11.77	12.45	13.17	13.90	14.66	15.43	16.22	17.03	17.84	18.67
5	11.13	11.44	12.07	12.73	13.42	14.14	14.88	15.64	16.42	17.22	18.03	18.84
10	179.1	172.4	12.67	13.24	13.86	14.53	15.24	15.97	16.72	17.50	18.29	19.09
20	179.9	173.2	160.3	147.6	135.0	15.86	16.34	16.91	17.55	18.24	18.96	19.71
30	180.7	174.1	161.2	148.7	136.3	123.6	18.48	18.53	18.86	19.33	19.91	20.54
40	181.5	174.9	162.1	149.7	137.5	125.0	112.0	21.74	21.04	21.00	21.25	21.67
50	182.3	175.7	163.0	150.8	138.6	126.5	113.8	100.1	25.36	23.70	23.23	23.23
60	183.1	176.6	163.9	151.7	139.8	127.8	115.5	102.5	87.89	28.76	26.28	25.42
70	183.9	177.4	164.8	152.7	140.9	129.1	117.1	104.6	90.88	46.34	31.43	28.58
80	184.6	178.2	165.7	153.7	142.0	130.4	118.7	106.5	93.59	80.14	42.57	33.34
90	185.4	179.0	166.5	154.6	143.0	131.6	120.1	108.4	96.03	82.96	70.37	41.03

D2.4. Table 12. (continued)

Temperature in °C												
Pressure in bar	−55	−50	−40	−30	−20	−10	0	10	20	30	40	50
100	186.2	179.7	167.4	155.6	144.1	132.8	121.5	110.1	98.25	85.85	73.49	53.06
150	189.9	183.6	171.5	160.0	149.0	138.3	127.8	117.5	107.3	97.08	86.92	76.97
200	193.4	187.2	175.4	164.2	153.5	143.2	133.3	123.7	114.3	105.2	96.33	87.81
250	196.9	190.7	179.1	168.1	157.7	147.7	138.2	129.0	120.2	111.8	103.7	95.91
300	200.2	194.2	182.7	171.9	161.7	152.0	142.7	133.9	125.5	117.4	109.8	102.5
350	203.5	197.5	186.1	175.5	165.4	155.9	146.9	138.4	130.2	122.5	115.2	108.3
400	206.7	200.7	189.4	178.9	169.0	159.7	150.9	142.5	134.6	127.1	120.0	113.4
450	209.8	203.8	192.7	182.3	172.5	163.3	154.7	146.5	138.7	131.4	124.5	118.0
500	212.8	206.9	195.8	185.5	175.9	166.8	158.2	150.2	142.6	135.4	128.6	122.3
600	218.6	212.8	201.9	191.7	182.2	173.4	165.0	157.1	149.7	142.8	136.2	130.1
700	224.3	218.5	207.7	197.6	188.3	179.5	171.3	163.6	156.4	149.5	143.1	137.1
800	229.7	224.0	213.2	203.3	194.0	185.4	177.3	169.7	162.5	155.8	149.5	143.6
900	235.0	229.3	218.6	208.7	199.5	190.9	182.9	175.4	168.3	161.7	155.5	149.6
1,000	240.1	234.4	223.7	213.9	204.8	196.3	188.3	180.8	173.8	167.3	161.1	155.3

Temperature in °C												
Pressure in bar	60	80	100	150	200	300	400	500	600	700	800	900
1	19.50	21.18	22.87	27.12	31.31	39.47	47.26	54.70	61.84	68.69	75.30	81.69
5	19.67	21.34	23.02	27.24	31.43	39.56	47.34	54.77	61.90	68.75	75.35	81.73
10	19.90	21.55	23.22	27.41	31.57	39.68	47.44	54.86	61.97	68.81	75.41	81.79
20	20.48	22.06	23.67	27.78	31.89	39.93	47.65	55.04	62.13	68.95	75.54	81.90
30	21.22	22.68	24.21	28.19	32.23	40.20	47.86	55.22	62.29	69.10	75.67	82.02
40	22.20	23.45	24.85	28.66	32.60	40.48	48.09	55.42	62.46	69.25	75.80	82.14
50	23.48	24.39	25.60	29.17	33.01	40.78	48.33	55.62	62.63	69.40	75.94	82.26
60	25.18	25.56	26.49	29.74	33.44	41.09	48.58	55.83	62.81	69.56	76.08	82.39
70	27.46	27.00	27.54	30.37	33.90	41.42	48.84	56.04	63.00	69.72	76.22	82.52
80	30.53	28.77	28.76	31.06	34.39	41.77	49.11	56.26	63.18	69.88	76.36	82.65
90	34.71	30.93	30.19	31.81	34.92	42.13	49.39	56.49	63.38	70.05	76.51	82.78
100	40.35	33.53	31.82	32.63	35.48	42.50	49.68	56.72	63.58	70.22	76.66	82.92
150	67.48	51.61	43.04	37.75	38.72	44.59	51.24	57.98	64.63	71.13	77.46	83.63
200	79.73	65.70	55.48	44.25	42.66	46.98	52.98	59.36	65.77	72.10	78.31	84.38
250	88.61	75.67	65.45	51.27	47.10	49.62	54.88	60.84	66.99	73.14	79.22	85.19
300	95.73	83.56	73.58	58.02	51.79	52.42	56.88	62.40	68.28	74.23	80.16	86.02
350	101.8	90.15	80.44	64.23	56.49	55.33	58.96	64.03	69.61	75.36	81.14	86.89
400	107.1	95.88	86.40	69.86	61.07	58.28	61.10	65.70	70.98	76.52	82.15	87.78
450	111.9	101.0	91.69	74.99	65.46	61.23	63.26	67.40	72.38	77.71	83.18	88.68
500	116.4	105.6	96.49	79.71	69.64	64.16	65.44	69.12	73.80	78.92	84.23	89.61
600	124.3	114.0	105.0	88.15	77.36	69.84	69.76	72.58	76.67	81.37	86.36	91.50
700	131.5	121.3	112.5	95.59	84.34	75.26	74.00	76.01	79.54	83.84	88.53	93.42
800	138.0	128.0	119.3	102.3	90.73	80.40	78.11	79.40	82.40	86.31	90.70	95.35
900	144.1	134.2	125.5	108.5	96.63	85.29	82.10	82.71	85.23	88.76	92.86	97.29
1,000	149.8	140.0	131.3	114.2	102.1	89.93	85.95	85.95	88.01	91.19	95.01	99.22

D2.4. Table 13. Dynamic viscosity η of carbon dioxide in 10^{-6} Pa·s

Temperature in °C												
Pressure in bar	−55	−50	−40	−30	−20	−10	0	10	20	30	40	50
1	10.97	11.22	11.72	12.22	12.72	13.22	13.71	14.20	14.69	15.17	15.65	16.13
5	11.02	11.27	11.77	12.27	12.76	13.25	13.75	14.23	14.72	15.20	15.69	16.16
10	252.7	232.2	11.86	12.35	12.83	13.32	13.81	14.29	14.78	15.26	15.73	16.21
20	254.8	234.2	199.3	170.2	145.1	13.56	14.02	14.48	14.95	15.42	15.88	16.35
30	257.0	236.3	201.2	172.1	147.1	124.7	14.42	14.81	15.24	15.67	16.11	16.56
40	259.1	238.3	203.1	174.0	149.0	126.8	106.1	15.44	15.72	16.07	16.46	16.86
50	261.3	240.4	205.0	175.8	150.9	128.9	108.5	88.26	16.63	16.73	16.98	17.30
60	263.4	242.4	206.9	177.7	152.8	130.9	110.8	91.39	69.72	17.92	17.80	17.93
70	265.6	244.4	208.8	179.5	154.6	132.8	113.0	94.20	74.54	21.40	19.21	18.89
80	267.7	246.5	210.6	181.2	156.4	134.7	115.1	96.76	78.33	55.98	22.30	20.40
90	269.9	248.5	212.5	183.0	158.1	136.5	117.1	99.14	81.56	61.94	34.93	23.06
100	272.0	250.5	214.3	184.8	159.9	138.3	119.1	101.4	84.42	66.16	47.84	28.34
150	282.8	260.6	223.4	193.3	168.2	146.7	127.9	111.1	95.73	79.98	67.79	56.54
200	293.6	270.6	232.4	201.7	176.2	154.5	135.8	119.3	104.6	89.63	78.58	68.93
250	304.5	280.7	241.3	209.8	183.8	161.9	143.1	126.7	112.2	97.65	87.06	77.95
300	315.5	290.9	250.2	217.9	191.3	169.0	150.0	133.5	119.0	104.7	94.39	85.50
350	326.6	301.1	259.1	225.8	198.6	175.9	156.6	139.9	125.4	111.3	101.0	92.20
400	338.0	311.4	268.0	233.7	205.9	182.7	163.0	146.1	131.4	117.4	107.2	98.36
450	349.5	321.9	277.0	241.7	213.0	189.3	169.2	152.0	137.1	123.2	113.0	104.1
500	361.2	332.6	286.0	249.6	220.1	195.8	175.3	157.8	142.6	128.7	118.6	109.6
600	385.4	354.4	304.3	265.5	234.3	208.7	187.2	168.9	153.2	139.3	129.1	120.0
700	410.7	377.1	323.1	281.6	248.5	221.5	198.9	179.8	163.3	149.4	139.1	129.7
800	437.3	400.7	342.5	298.0	262.9	234.3	210.5	190.4	173.2	159.2	148.8	139.1
900	465.3	425.4	362.5	314.8	277.4	247.1	222.1	201.0	183.0	168.7	158.1	148.2
1,000	495.0	451.4	383.2	332.1	292.2	260.1	233.7	211.5	192.6	178.0	167.2	157.0
Temperature in °C												
Pressure in bar	60	80	100	150	200	300	400	500	600	700	800	900
1	16.61	17.55	18.47	20.73	22.89	26.96	30.72	34.20	37.44	40.48	43.34	46.06
5	16.64	17.57	18.50	20.75	22.91	26.98	30.73	34.21	37.45	40.48	43.35	46.06
10	16.68	17.62	18.54	20.78	22.94	27.00	30.75	34.22	37.46	40.50	43.36	46.07
20	16.81	17.73	18.64	20.86	23.01	27.05	30.79	34.26	37.49	40.52	43.38	46.09
30	17.00	17.90	18.79	20.98	23.10	27.12	30.84	34.30	37.53	40.55	43.41	46.12
40	17.28	18.12	18.98	21.12	23.21	27.19	30.90	34.35	37.57	40.59	43.44	46.14
50	17.65	18.42	19.23	21.30	23.35	27.29	30.97	34.40	37.61	40.62	43.47	46.17
60	18.18	18.82	19.55	21.51	23.51	27.39	31.05	34.46	37.66	40.67	43.51	46.20
70	18.91	19.32	19.94	21.76	23.69	27.51	31.13	34.53	37.71	40.71	43.55	46.24
80	19.95	19.98	20.42	22.05	23.90	27.65	31.23	34.60	37.77	40.76	43.59	46.27
90	21.46	20.82	21.01	22.39	24.14	27.79	31.33	34.68	37.84	40.82	43.63	46.31
100	23.74	21.89	21.72	22.78	24.41	27.95	31.45	34.77	37.91	40.87	43.68	46.35
150	46.09	32.39	27.67	25.53	26.18	28.97	32.14	35.29	38.32	41.21	43.97	46.60
200	60.19	45.98	37.09	29.66	28.68	30.32	33.05	35.96	38.84	41.63	44.32	46.90

D2.4. Table 13. (continued)

Pressure in bar	Temperature in °C											
	60	80	100	150	200	300	400	500	600	700	800	900
250	69.78	56.19	46.35	34.78	31.80	31.96	34.13	36.75	39.46	42.13	44.74	47.25
300	77.55	64.26	54.17	40.21	35.34	33.86	35.38	37.66	40.16	42.70	45.21	47.65
350	84.33	71.11	60.88	45.49	39.06	35.95	36.76	38.67	40.94	43.33	45.73	48.10
400	90.48	77.22	66.84	50.46	42.80	38.16	38.24	39.76	41.79	44.02	46.30	48.58
450	96.21	82.82	72.26	55.10	46.47	40.45	39.81	40.92	42.70	44.75	46.91	49.10
500	101.6	88.07	77.31	59.47	50.03	42.77	41.43	42.13	43.65	45.53	47.56	49.65
600	111.8	97.81	86.61	67.53	56.78	47.41	44.78	44.68	45.67	47.18	48.94	50.84
700	121.3	106.9	95.20	74.95	63.10	51.97	48.18	47.32	47.79	48.93	50.43	52.11
800	130.4	115.5	103.3	81.93	69.08	56.40	51.57	50.00	49.98	50.76	51.98	53.45
900	139.2	123.8	111.1	88.60	74.79	60.69	54.91	52.70	52.20	52.63	53.58	54.84
1,000	147.8	131.8	118.7	95.04	80.31	64.86	58.20	55.37	54.44	54.53	55.22	56.28

D2.4. Table 14. Kinematic viscosity ν of carbon dioxide in 10^{-7} m^2/s

Pressure in bar	Temperature in °C											
	−55	−50	−40	−30	−20	−10	0	10	20	30	40	50
1	44.57	46.69	51.05	55.60	60.32	65.21	70.28	75.51	80.92	86.49	92.22	98.12
5	8.401	8.846	9.756	10.70	11.67	12.67	13.70	14.77	15.87	17.00	18.16	19.36
10	2.153	2.010	4.563	5.063	5.573	6.093	6.627	7.175	7.737	8.314	8.905	9.512
20	2.167	2.023	1.780	1.579	1.407	2.780	3.074	3.368	3.666	3.969	4.278	4.592
30	2.181	2.037	1.793	1.592	1.420	1.266	1.864	2.086	2.303	2.519	2.736	2.955
40	2.196	2.051	1.806	1.604	1.432	1.280	1.138	1.424	1.613	1.791	1.965	2.138
50	2.210	2.064	1.818	1.616	1.445	1.293	1.154	1.016	1.182	1.349	1.502	1.650
60	2.225	2.078	1.831	1.628	1.457	1.306	1.169	1.037	0.8907	1.045	1.192	1.327
70	2.239	2.092	1.843	1.640	1.468	1.319	1.183	1.055	0.9218	0.8029	0.9698	1.098
80	2.254	2.105	1.856	1.652	1.480	1.331	1.197	1.071	0.9464	0.7979	0.8023	0.9305
90	2.268	2.119	1.868	1.664	1.492	1.343	1.210	1.087	0.9673	0.8321	0.7194	0.8090
100	2.282	2.132	1.880	1.675	1.503	1.354	1.222	1.101	0.9858	0.8575	0.7610	0.7374
150	2.355	2.200	1.941	1.732	1.558	1.409	1.280	1.164	1.059	0.9443	0.8688	0.8080
200	2.428	2.267	2.000	1.787	1.610	1.460	1.331	1.217	1.116	1.006	0.9355	0.8788
250	2.501	2.335	2.060	1.840	1.660	1.508	1.378	1.265	1.165	1.058	0.9897	0.9342
300	2.575	2.403	2.119	1.894	1.709	1.555	1.423	1.309	1.209	1.105	1.037	0.9820
350	2.651	2.472	2.179	1.947	1.758	1.600	1.466	1.350	1.249	1.147	1.081	1.025
400	2.727	2.542	2.238	1.999	1.805	1.644	1.507	1.390	1.288	1.188	1.121	1.065
450	2.805	2.612	2.298	2.052	1.852	1.687	1.548	1.428	1.325	1.226	1.159	1.103
500	2.885	2.684	2.359	2.104	1.900	1.730	1.588	1.466	1.360	1.262	1.196	1.139
600	3.049	2.832	2.482	2.211	1.993	1.815	1.666	1.538	1.429	1.332	1.266	1.207
700	3.221	2.985	2.608	2.318	2.088	1.899	1.742	1.609	1.494	1.398	1.332	1.272
800	3.401	3.145	2.738	2.428	2.183	1.983	1.818	1.678	1.558	1.462	1.396	1.334
900	3.591	3.312	2.872	2.540	2.279	2.068	1.894	1.747	1.622	1.524	1.457	1.394
1,000	3.793	3.488	3.012	2.656	2.378	2.154	1.970	1.816	1.684	1.585	1.517	1.452

D2.4. Table 14. (continued)

Pressure in bar	Temperature in °C											
	60	80	100	150	200	300	400	500	600	700	800	900
1	104.2	116.8	129.9	165.5	204.4	291.8	390.6	499.5	617.7	744.3	878.9	1,021
5	20.58	23.12	25.78	32.93	40.77	58.32	78.13	99.97	123.6	149.0	176.0	204.4
10	10.13	11.42	12.76	16.37	20.31	29.13	39.08	50.03	61.89	74.60	88.10	102.4
20	4.913	5.574	6.261	8.097	10.09	14.55	19.55	25.06	31.02	37.40	44.17	51.32
30	3.177	3.631	4.100	5.345	6.695	9.690	13.05	16.74	20.73	25.00	29.53	34.31
40	2.312	2.664	3.025	3.975	5.000	7.267	9.804	12.59	15.59	18.81	22.21	25.81
50	1.796	2.088	2.384	3.158	3.987	5.816	7.858	10.09	12.51	15.09	17.83	20.71
60	1.455	1.708	1.962	2.617	3.316	4.852	6.563	8.436	10.46	12.61	14.90	17.31
70	1.216	1.441	1.664	2.235	2.840	4.166	5.641	7.253	8.992	10.85	12.81	14.88
80	1.041	1.246	1.445	1.952	2.486	3.654	4.951	6.368	7.894	9.523	11.25	13.06
90	0.9116	1.099	1.280	1.735	2.213	3.257	4.416	5.680	7.042	8.494	10.03	11.65
100	0.8187	0.9879	1.152	1.565	1.998	2.942	3.990	5.132	6.361	7.672	9.058	10.52
150	0.7631	0.7589	0.8328	1.091	1.379	2.017	2.726	3.499	4.330	5.214	6.149	7.132
200	0.8316	0.7740	0.7721	0.9067	1.107	1.579	2.114	2.698	3.328	3.998	4.705	5.449
250	0.8869	0.8184	0.7871	0.8378	0.9737	1.336	1.761	2.230	2.737	3.277	3.847	4.446
300	0.9343	0.8613	0.8180	0.8169	0.9069	1.189	1.538	1.929	2.352	2.804	3.281	3.784
350	0.9769	0.9009	0.8507	0.8184	0.8744	1.096	1.388	1.721	2.083	2.472	2.883	3.315
400	1.016	0.9377	0.8828	0.8307	0.8605	1.036	1.284	1.571	1.888	2.228	2.589	2.968
450	1.053	0.9724	0.9139	0.8472	0.8578	0.9961	1.208	1.461	1.741	2.043	2.364	2.702
500	1.089	1.006	0.9439	0.8656	0.8618	0.9698	1.153	1.376	1.627	1.898	2.187	2.492
600	1.155	1.068	1.001	0.9049	0.8800	0.9422	1.081	1.259	1.464	1.689	1.929	2.184
700	1.218	1.127	1.056	0.9453	0.9044	0.9342	1.040	1.185	1.357	1.548	1.753	1.971
800	1.278	1.183	1.108	0.9858	0.9318	0.9365	1.017	1.137	1.284	1.448	1.626	1.817
900	1.336	1.238	1.158	1.026	0.9609	0.9447	1.005	1.105	1.231	1.375	1.533	1.701
1,000	1.393	1.291	1.208	1.066	0.9909	0.9566	1.001	1.085	1.194	1.321	1.461	1.612

D2.4. Table 15. Thermal diffusivity a of carbon dioxide in 10^{-7} m^2/s

Pressure in bar	Temperature in °C											
	−55	−50	−40	−30	−20	−10	0	10	20	30	40	50
1	56.24	59.05	64.85	70.92	77.28	83.94	90.89	98.13	105.7	113.5	121.5	129.8
5	9.419	10.10	11.44	12.80	14.19	15.62	17.09	18.62	20.19	21.81	23.47	25.19
10	0.7749	0.7546	4.681	5.504	6.292	7.076	7.870	8.680	9.507	10.35	11.22	12.11
20	0.7797	0.7598	0.7153	0.6642	0.6051	2.756	3.236	3.701	4.163	4.628	5.097	5.572
30	0.7843	0.7650	0.7215	0.6720	0.6154	0.5479	1.623	2.010	2.368	2.713	3.054	3.395
40	0.7889	0.7700	0.7276	0.6795	0.6251	0.5615	0.4818	1.094	1.438	1.741	2.027	2.305
50	0.7934	0.7749	0.7334	0.6868	0.6344	0.5741	0.5008	0.4005	0.8159	1.131	1.399	1.646
60	0.7978	0.7797	0.7392	0.6938	0.6432	0.5858	0.5178	0.4298	0.2847	0.6736	0.9599	1.200
70	0.8022	0.7844	0.7448	0.7006	0.6517	0.5968	0.5332	0.4544	0.3407	0.2192	0.6147	0.8685
80	0.8064	0.7890	0.7503	0.7071	0.6598	0.6073	0.5474	0.4756	0.3802	0.2185	0.3097	0.6049
90	0.8106	0.7935	0.7556	0.7135	0.6676	0.6171	0.5605	0.4944	0.4114	0.2931	0.1126	0.3889

D2.4. Table 15. (continued)

Temperature in °C												
Pressure in bar	−55	−50	−40	−30	−20	−10	0	10	20	30	40	50
100	0.8148	0.7980	0.7608	0.7197	0.6751	0.6265	0.5727	0.5113	0.4374	0.3413	0.2065	0.2375
150	0.8345	0.8192	0.7853	0.7484	0.7091	0.6677	0.6240	0.5777	0.5279	0.4743	0.4169	0.3613
200	0.8529	0.8388	0.8076	0.7739	0.7385	0.7020	0.6646	0.6264	0.5876	0.5485	0.5096	0.4725
250	0.8701	0.8571	0.8282	0.7970	0.7646	0.7317	0.6986	0.6656	0.6330	0.6014	0.5709	0.5427
300	0.8864	0.8743	0.8473	0.8182	0.7882	0.7580	0.7280	0.6986	0.6701	0.6429	0.6174	0.5941
350	0.9019	0.8905	0.8651	0.8378	0.8098	0.7817	0.7541	0.7273	0.7017	0.6775	0.6552	0.6349
400	0.9167	0.9060	0.8820	0.8562	0.8298	0.8034	0.7777	0.7529	0.7293	0.7074	0.6872	0.6690
450	0.9308	0.9207	0.8980	0.8734	0.8484	0.8235	0.7993	0.7760	0.7541	0.7337	0.7151	0.6984
500	0.9443	0.9348	0.9132	0.8897	0.8658	0.8422	0.8192	0.7973	0.7766	0.7575	0.7400	0.7245
600	0.9700	0.9614	0.9416	0.9200	0.8980	0.8762	0.8552	0.8353	0.8165	0.7992	0.7834	0.7693
700	0.9940	0.9862	0.9678	0.9477	0.9271	0.9068	0.8873	0.8687	0.8513	0.8352	0.8205	0.8074
800	1.017	1.009	0.9922	0.9732	0.9538	0.9347	0.9162	0.8988	0.8824	0.8672	0.8533	0.8408
900	1.038	1.031	1.015	0.9971	0.9786	0.9603	0.9428	0.9261	0.9106	0.8961	0.8828	0.8707
1,000	1.058	1.052	1.037	1.019	1.002	0.9842	0.9673	0.9514	0.9364	0.9225	0.9096	0.8980
Temperature in °C												
Pressure in bar	60	80	100	150	200	300	400	500	600	700	800	900
1	138.4	156.3	175.0	225.4	280.5	402.6	539.4	689.7	853.2	1,030	1,219	1,420
5	26.95	30.59	34.41	44.63	55.74	80.33	107.8	138.0	170.7	206.1	244.0	284.3
10	13.02	14.89	16.84	22.03	27.65	40.05	53.86	69.00	85.44	103.2	122.1	142.4
20	6.054	7.041	8.060	10.74	13.62	19.91	26.89	34.52	42.79	51.69	61.22	71.36
30	3.737	4.430	5.139	6.986	8.946	13.21	17.91	23.03	28.57	34.54	40.91	47.70
40	2.580	3.129	3.683	5.112	6.615	9.861	13.42	17.29	21.47	25.96	30.76	35.87
50	1.885	2.350	2.813	3.993	5.221	7.857	10.73	13.85	17.21	20.82	24.68	28.77
60	1.419	1.834	2.237	3.250	4.295	6.524	8.941	11.56	14.37	17.40	20.62	24.04
70	1.083	1.466	1.829	2.723	3.637	5.574	7.665	9.922	12.35	14.95	17.72	20.67
80	0.8251	1.192	1.526	2.331	3.146	4.865	6.710	8.697	10.83	13.12	15.55	18.14
90	0.6206	0.9807	1.293	2.029	2.767	4.315	5.969	7.746	9.653	11.69	13.86	16.17
100	0.4589	0.8136	1.110	1.791	2.466	3.878	5.378	6.987	8.711	10.55	12.51	14.59
150	0.3255	0.4142	0.6161	1.111	1.590	2.585	3.622	4.723	5.897	7.147	8.474	9.879
200	0.4411	0.4248	0.487	0.8289	1.191	1.965	2.764	3.609	4.505	5.456	6.465	7.531
250	0.5178	0.4878	0.5059	0.7081	0.9861	1.613	2.265	2.952	3.680	4.451	5.268	6.130
300	0.5735	0.5445	0.5420	0.6587	0.8771	1.394	1.945	2.525	3.139	3.789	4.476	5.201
350	0.6172	0.5907	0.5810	0.6546	0.8155	1.252	1.725	2.227	2.759	3.322	3.916	4.543
400	0.6531	0.6290	0.6171	0.6637	0.7831	1.156	1.568	2.011	2.480	2.976	3.501	4.054
450	0.6839	0.6615	0.6490	0.6761	0.7707	1.089	1.453	1.847	2.267	2.711	3.181	3.676
500	0.7109	0.6899	0.6774	0.6914	0.7682	1.042	1.365	1.720	2.100	2.503	2.928	3.377
600	0.7569	0.7377	0.7254	0.7258	0.7746	0.9840	1.246	1.539	1.857	2.196	2.555	2.934
700	0.7958	0.7774	0.7653	0.7595	0.7892	0.9552	1.172	1.420	1.692	1.985	2.295	2.623
800	0.8297	0.8118	0.7996	0.7903	0.8082	0.9410	1.125	1.338	1.574	1.831	2.105	2.394
900	0.8600	0.8423	0.8299	0.8180	0.8287	0.9347	1.094	1.279	1.488	1.715	1.960	2.220
1,000	0.8874	0.8700	0.8572	0.8432	0.8491	0.9337	1.073	1.237	1.422	1.627	1.847	2.082

D2.4. Table 16. Prandtl number Pr of carbon dioxide

Temperature in °C												
Pressure in bar	−55	−50	−40	−30	−20	−10	0	10	20	30	40	50
1	0.7925	0.7907	0.7873	0.7839	0.7805	0.7769	0.7732	0.7695	0.7659	0.7623	0.7589	0.7557
5	0.8920	0.8758	0.8525	0.8356	0.8223	0.8112	0.8017	0.7934	0.7861	0.7795	0.7737	0.7684
10	2.778	2.663	0.9747	0.9199	0.8857	0.8612	0.8421	0.8267	0.8138	0.8029	0.7936	0.7855
20	2.779	2.663	2.489	2.378	2.325	1.009	0.9499	0.9100	0.8806	0.8577	0.8393	0.8242
30	2.781	2.663	2.485	2.369	2.307	2.310	1.149	1.038	0.9728	0.9285	0.8958	0.8704
40	2.783	2.663	2.482	2.361	2.291	2.279	2.362	1.302	1.121	1.029	0.9695	0.9277
50	2.786	2.664	2.479	2.353	2.277	2.253	2.304	2.538	1.449	1.193	1.074	1.002
60	2.789	2.665	2.477	2.347	2.265	2.230	2.258	2.412	3.129	1.552	1.242	1.106
70	2.791	2.666	2.475	2.341	2.253	2.209	2.219	2.321	2.706	3.662	1.578	1.264
80	2.795	2.668	2.473	2.336	2.243	2.192	2.186	2.253	2.489	3.652	2.590	1.538
90	2.798	2.670	2.472	2.331	2.234	2.176	2.158	2.198	2.351	2.839	6.388	2.080
100	2.801	2.672	2.471	2.327	2.226	2.162	2.134	2.154	2.254	2.512	3.684	3.105
150	2.822	2.685	2.471	2.314	2.197	2.111	2.051	2.015	2.006	1.991	2.084	2.237
200	2.846	2.703	2.477	2.309	2.180	2.080	2.002	1.943	1.899	1.835	1.836	1.860
250	2.874	2.724	2.487	2.309	2.171	2.061	1.973	1.900	1.840	1.760	1.733	1.721
300	2.905	2.749	2.501	2.315	2.169	2.051	1.955	1.873	1.804	1.718	1.680	1.653
350	2.939	2.776	2.518	2.323	2.170	2.047	1.944	1.857	1.781	1.694	1.649	1.615
400	2.975	2.806	2.538	2.335	2.176	2.046	1.938	1.846	1.766	1.679	1.631	1.592
450	3.014	2.837	2.559	2.349	2.184	2.049	1.937	1.841	1.757	1.670	1.621	1.579
500	3.055	2.871	2.583	2.365	2.194	2.054	1.938	1.838	1.752	1.666	1.616	1.572
600	3.143	2.945	2.636	2.403	2.220	2.071	1.947	1.842	1.750	1.667	1.616	1.569
700	3.240	3.027	2.695	2.446	2.252	2.094	1.963	1.852	1.755	1.674	1.624	1.575
800	3.345	3.115	2.759	2.495	2.288	2.122	1.984	1.867	1.766	1.686	1.636	1.586
900	3.460	3.211	2.829	2.548	2.329	2.154	2.009	1.886	1.781	1.701	1.651	1.601
1,000	3.583	3.315	2.905	2.605	2.374	2.189	2.036	1.908	1.798	1.718	1.668	1.617
Temperature in °C												
Pressure in bar	60	80	100	150	200	300	400	500	600	700	800	900
1	0.7526	0.7471	0.7425	0.7339	0.7289	0.7248	0.7242	0.7242	0.7239	0.7229	0.7212	0.7189
5	0.7637	0.7557	0.7492	0.7379	0.7314	0.7260	0.7248	0.7246	0.7242	0.7231	0.7213	0.7189
10	0.7785	0.7669	0.7579	0.7429	0.7346	0.7274	0.7256	0.7251	0.7244	0.7232	0.7214	0.7190
20	0.8115	0.7916	0.7769	0.7536	0.7412	0.7305	0.7272	0.7260	0.7250	0.7236	0.7216	0.7191
30	0.8501	0.8195	0.7979	0.7652	0.7483	0.7336	0.7289	0.7270	0.7256	0.7240	0.7218	0.7193
40	0.8962	0.8515	0.8213	0.7776	0.7558	0.7369	0.7306	0.7279	0.7262	0.7243	0.7221	0.7195
50	0.9530	0.8884	0.8474	0.7910	0.7637	0.7402	0.7323	0.7290	0.7268	0.7247	0.7224	0.7196
60	1.026	0.9316	0.8768	0.8053	0.7720	0.7437	0.7341	0.7300	0.7275	0.7252	0.7226	0.7198
70	1.123	0.9830	0.9100	0.8208	0.7809	0.7473	0.7359	0.7311	0.7281	0.7256	0.7229	0.7200
80	1.262	1.045	0.9474	0.8373	0.7902	0.7510	0.7378	0.7322	0.7288	0.7260	0.7232	0.7202
90	1.469	1.121	0.9899	0.8550	0.7999	0.7549	0.7398	0.7333	0.7295	0.7265	0.7235	0.7204
100	1.784	1.214	1.038	0.8737	0.8102	0.7588	0.7418	0.7345	0.7303	0.7270	0.7239	0.7207
150	2.345	1.832	1.352	0.9820	0.8674	0.7802	0.7526	0.7407	0.7342	0.7296	0.7257	0.7220
200	1.885	1.822	1.582	1.094	0.9299	0.8039	0.7645	0.7478	0.7387	0.7327	0.7278	0.7235

D2.4. Table 16. (continued)

Temperature in °C												
Pressure in bar	60	80	100	150	200	300	400	500	600	700	800	900
250	1.713	1.678	1.556	1.183	0.9875	0.8286	0.7775	0.7555	0.7437	0.7361	0.7303	0.7253
300	1.629	1.582	1.509	1.240	1.034	0.8531	0.7910	0.7638	0.7492	0.7400	0.7331	0.7274
350	1.583	1.525	1.464	1.250	1.072	0.8760	0.8048	0.7725	0.7551	0.7441	0.7362	0.7297
400	1.556	1.491	1.431	1.252	1.099	0.8965	0.8186	0.7816	0.7614	0.7486	0.7395	0.7322
450	1.540	1.470	1.408	1.253	1.113	0.9148	0.8319	0.7909	0.7679	0.7534	0.7431	0.7350
500	1.531	1.458	1.393	1.252	1.122	0.9310	0.8445	0.8002	0.7747	0.7584	0.7468	0.7379
600	1.526	1.448	1.380	1.247	1.136	0.9576	0.8672	0.8182	0.7885	0.7689	0.7550	0.7443
700	1.531	1.450	1.379	1.245	1.146	0.9780	0.8867	0.8350	0.8022	0.7799	0.7637	0.7513
800	1.540	1.458	1.386	1.247	1.153	0.9953	0.9036	0.8503	0.8154	0.7909	0.7727	0.7587
900	1.554	1.469	1.396	1.254	1.159	1.011	0.9187	0.8640	0.8278	0.8016	0.7819	0.7664
1,000	1.569	1.484	1.409	1.264	1.167	1.024	0.9326	0.8767	0.8393	0.8120	0.7909	0.7741

6 Bibliography

1. Span R, Wagner W (1996) A new equation of state for carbon dioxide covering the fluid region from the triple point temperature to 1100 K at pressures up to 800 MPa. J Phys Chem Ref Data 25:1509/1596
2. Vesovic V, Wakeham WA, Olchowy GA, Sengers JV, Watson JTR, Millat J (1990) The transport properties of carbon dioxide. J Phys Chem Ref Data 19:763/808

D2.5 Properties of Oxygen

Roland Span[1] · *Rolf Krauss*[2]
[1]Ruhr-Universität Bochum, Bochum, Germany
[2]Universität Stuttgart, Stuttgart, Germany

The tables with thermodynamic properties of oxygen were calculated using the fundamental equation of state by Schmidt and Wagner [1], see also Wagner and de Reuck [2]. This equation formally is valid for temperatures up to 300 K (26.85°C). However, it allows for reasonable extrapolation to much higher temperatures [2], even far beyond the limit of 100°C chosen for the tables in this section.

p	Pressure in bar	β	Isobaric expansion coefficient in 10^{-3}/K $\beta = v^{-1}\cdot(\partial v/\partial T)_p$
ρ	Density in kg/m^3	w_s	Isentropic speed of sound in m/s
ϑ	Temperature in °C	λ	Thermal conductivity in mW/(m K)
Z	Compression factor $Z = p/(\rho RT)$	η	Dynamic viscosity in 10^{-6} Pa·s
h	Specific enthalpy in kJ/kg	ν	Kinematic viscosity ν in 10^{-7} m^2/s
s	Specific entropy in kJ/(kg K)	a	Thermal diffusivity in 10^{-7} m^2/s
c_p	Specific isobaric heat capacity in kJ/(kg K)	Pr	Prandtl number Pr = $\eta\, c_p/\lambda$
c_v	Specific isochoric heat capacity in kJ/(kg K)	v	Specific volume in m^3/kg

The correlations by Laesecke et al. [3] were used to calculate the thermal conductivity and viscosities. The required densities were calculated using the fundamental equation [1, 2].

1 Characteristic Quantities

Molecular mass $\tilde{M}$ = 31.9988 g/mol, specific gas constant R = 259.832869 J/(kg K).

2 Critical Point [1]

p_c = 50.460 bar, T_c = 154.599 K (ϑ_c = −118.551°C), ρ_c = 417 kg/m^3.

3 Triple Point [1]

p_t = 0.0014633 bar, T_t = 54.361 K (ϑ_t = −218.789°C).

4 Reference States of Enthalpy and Entropy

h = 0 kJ/kg, s = 0 kJ/(kg K) at T = 298.15 K (ϑ = 25°C), p = 1 bar for the ideal gas.

D2.5. Table 1. Properties of oxygen at $p = 1$ bar

ϑ °C	ρ kg/m³	h kJ/kg	s kJ/(kg K)	c_p kJ/(kg K)	c_v kJ/(kg K)	β 10^{-3}/K	w_s m/s	λ mW/(m K)	η 10^{-6} Pa·s	ν 10^{-7} m²/s	a 10^{-7} m²/s	Pr –
−215	1290.2	−458.5	−4.207	1.671	1.113	3.36	1132	–	–	–	–	–
−210	1268.1	−450.1	−4.069	1.676	1.059	3.53	1113	–	–	–	–	–
−200	1222.6	−433.3	−3.822	1.678	1.001	3.78	1042	176.6	311.6	2.55	0.861	2.96
−190	1175.6	−416.5	−3.607	1.685	0.9566	4.08	962.1	162.5	224.8	1.91	0.820	2.33
−180	4.2538	−188.7	−1.072	0.9473	0.6587	11.7	181.1	8.611	6.810	16.0	21.4	0.749
−170	3.8130	−179.3	−0.9768	0.9338	0.6531	10.3	191.5	9.633	7.640	20.0	27.1	0.741
−160	3.4584	−170.0	−0.8906	0.9305	0.6543	9.26	201.1	10.64	8.452	24.4	33.1	0.739
−150	3.1660	−160.7	−0.8119	0.9269	0.6542	8.43	210.2	11.62	9.244	29.2	39.6	0.737
−140	2.9205	−151.5	−0.7397	0.9237	0.6535	7.74	218.9	12.58	10.02	34.3	46.6	0.735
−130	2.7111	−142.2	−0.6729	0.9211	0.6528	7.16	227.2	13.52	10.77	39.7	54.1	0.734
−120	2.5302	−133.0	−0.6108	0.9191	0.6522	6.66	235.2	14.44	11.51	45.5	62.1	0.733
−110	2.3723	−123.9	−0.5527	0.9175	0.6518	6.23	242.9	15.33	12.23	51.5	70.5	0.732
−100	2.2332	−114.7	−0.4982	0.9164	0.6515	5.86	250.4	16.21	12.93	57.9	79.2	0.731
−90	2.1097	−105.5	−0.4467	0.9155	0.6513	5.53	257.6	17.07	13.62	64.6	88.4	0.730
−80	1.9992	−96.38	−0.3981	0.9149	0.6512	5.23	264.6	17.92	14.29	71.5	98.0	0.730
−70	1.8999	−87.24	−0.3519	0.9145	0.6513	4.97	271.5	18.74	14.95	78.7	108	0.730
−60	1.8100	−78.09	−0.3080	0.9143	0.6514	4.73	278.1	19.55	15.60	86.2	118	0.729
−50	1.7283	−68.95	−0.2661	0.9142	0.6517	4.51	284.6	20.35	16.23	93.9	129	0.729
−40	1.6536	−59.81	−0.2260	0.9144	0.6521	4.32	290.9	21.14	16.86	102	140	0.729
−30	1.5852	−50.66	−0.1876	0.9147	0.6527	4.14	297.1	21.91	17.47	110	151	0.729
−20	1.5223	−41.52	−0.1507	0.9152	0.6534	3.97	303.1	22.68	18.07	119	163	0.729
−10	1.4642	−32.36	−0.1152	0.9158	0.6542	3.82	309.0	23.43	18.66	127	175	0.729
0	1.4103	−23.20	−0.0811	0.9167	0.6552	3.68	314.8	24.18	19.24	136	187	0.729
10	1.3603	−14.03	−0.0481	0.9177	0.6564	3.54	320.5	24.92	19.81	146	200	0.729
20	1.3138	−4.843	−0.0162	0.9189	0.6577	3.42	326.0	25.66	20.37	155	213	0.730
25	1.2917	−0.2470	−0.0007	0.9196	0.6584	3.36	328.7	26.02	20.65	160	219	0.730
30	1.2703	4.353	0.0146	0.9203	0.6592	3.31	331.4	26.38	20.92	165	226	0.730
40	1.2296	13.56	0.0445	0.9219	0.6609	3.20	336.7	27.11	21.47	175	239	0.730
50	1.1915	22.79	0.0735	0.9236	0.6627	3.10	341.9	27.83	22.00	815	253	0.730
60	1.1556	32.04	0.1017	0.9255	0.6647	3.01	347.1	28.54	22.53	195	267	0.731
70	1.1219	41.30	0.1291	0.9276	0.6668	2.92	352.1	29.25	23.06	206	281	0.731
80	1.0900	50.59	0.1558	0.9298	0.6690	2.84	357.0	29.96	23.57	216	296	0.732
90	1.0600	59.90	0.1818	0.9321	0.6714	2.76	361.9	30.67	24.08	227	310	0.732
100	1.0315	69.23	0.2071	0.9345	0.6739	2.68	366.6	31.37	24.58	238	325	0.732
110	1.0045	78.59	0.2319	0.9371	0.6765	2.61	371.3	32.07	25.08	250	341	0.733
120	0.97896	87.97	0.2561	0.9398	0.6792	2.55	375.9	32.77	25.57	261	356	0.733
130	0.95465	97.38	0.2797	0.9425	0.6820	2.48	380.5	33.46	26.06	273	372	0.734
140	0.93151	106.8	0.3028	0.9454	0.6849	2.42	384.9	34.16	26.54	285	388	0.734
150	0.90947	116.3	0.3255	0.9483	0.6879	2.37	389.3	34.85	27.01	297	404	0.735
160	0.88846	125.8	0.3477	0.9513	0.6909	2.31	393.7	35.54	27.48	309	421	0.736
170	0.86839	135.3	0.3694	0.9543	0.6940	2.26	398.0	36.23	27.95	322	437	0.736
180	0.84921	144.9	0.3907	0.9574	0.6971	2.21	402.2	36.92	28.41	334	454	0.737
190	0.83086	154.5	0.4117	0.9605	0.7002	2.16	406.4	37.60	28.86	347	471	0.737
200	0.81329	164.1	0.4322	0.9636	0.7034	2.11	410.5	38.28	29.31	360	488	0.738
250	0.73551	212.7	0.5298	0.9795	0.7193	1.91	430.3	41.66	31.50	428	578	0.741
300	0.67133	262.0	0.6199	0.9951	0.7350	1.75	449.1	44.98	33.60	501	673	0.743
350	0.61745	312.2	0.7038	1.010	0.7500	1.61	467.1	48.23	35.63	577	773	0.746
400	0.57158	363.0	0.7823	1.024	0.7640	1.49	484.3	51.41	37.58	657	878	0.748
450	0.53206	414.5	0.8561	1.037	0.7769	1.38	500.9	54.52	39.47	742	988	0.751
500	0.49765	466.7	0.9258	1.049	0.7887	1.29	517.0	57.56	41.30	830	1103	0.752

D2.5. Table 1. (continued)

ϑ °C	ρ kg/m³	h kJ/kg	s kJ/(kg K)	c_p kJ/(kg K)	c_v kJ/(kg K)	β 10^{-3}/K	w_s m/s	λ mW/(m K)	η 10^{-6} Pa·s	ν 10^{-7} m²/s	a 10^{-7} m²/s	Pr –
550	0.46742	519.4	0.9919	1.059	0.7994	1.21	532.5	60.52	43.09	922	1222	0.754
600	0.44066	572.6	1.055	1.069	0.8091	1.15	547.6	63.42	44.83	1017	1346	0.756
650	0.41679	626.3	1.114	1.078	0.8180	1.08	562.4	66.25	46.53	1116	1475	0.757
700	0.39538	680.4	1.171	1.086	0.8261	1.03	576.7	69.02	48.20	1219	1607	0.758

D2.5. Table 2. Properties of the saturated liquid

ϑ °C	p bar	ρ' kg/m³	h' kJ/kg	s' kJ/(kg K)	c_p' kJ/(kg K)	c_v' kJ/(kg K)	β' 10^{-3}/K	w_s' m/s	λ' mW/(m K)	η' 10^{-6} Pa·s	ν' 10^{-7} m²/s	a' 10^{-7} m²/s	Pr′ –
−218	0.00187	1302.8	−463.6	−4.295	1.671	1.173	3.18	1128	–	–	–	–	–
−216	0.00337	1294.4	−460.2	−4.236	1.671	1.129	3.31	1132	–	–	–	–	–
−214	0.00582	1285.7	−456.9	−4.178	1.673	1.099	3.40	1130	–	–	–	–	–
−212	0.00967	1276.9	−453.5	−4.122	1.675	1.077	3.47	1123	–	–	–	–	–
−210	0.01552	1268.0	−450.2	−4.068	1.676	1.059	3.53	1113	–	–	–	–	–
−208	0.02411	1259.0	−446.8	−4.016	1.677	1.045	3.59	1101	–	–	–	–	–
−206	0.03640	1250.0	−443.5	−3.965	1.678	1.032	3.63	1087	–	–	–	–	–
−204	0.05354	1240.8	−440.1	−3.916	1.678	1.021	3.68	1073	–	–	–	–	–
−202	0.07690	1231.7	−436.7	−3.868	1.678	1.011	3.73	1058	179.3	335.8	2.73	0.868	3.14
−200	0.10808	1222.5	−433.4	−3.822	1.678	1.001	3.78	1042	176.5	311.2	2.55	0.860	2.96
−198	0.14892	1213.2	−430.0	−3.777	1.679	0.9914	3.84	1026	173.7	289.6	2.39	0.853	2.80
−196	0.20148	1203.9	−426.7	−3.732	1.680	0.9822	3.89	1010	170.9	270.6	2.25	0.845	2.66
−194	0.26807	1194.5	−423.3	−3.690	1.681	0.9734	3.95	994.3	168.1	253.6	2.12	0.837	2.54
−192	0.35123	1185.0	−419.9	−3.648	1.683	0.9648	4.02	978.1	165.3	238.4	2.01	0.829	2.43
−190	0.45372	1175.5	−416.6	−3.607	1.685	0.9565	4.08	961.9	162.5	224.6	1.91	0.820	2.33
−188	0.57851	1165.8	−413.2	−3.567	1.688	0.9483	4.16	945.6	159.7	212.2	1.82	0.811	2.24
−186	0.72876	1156.1	−409.8	−3.527	1.692	0.9404	4.24	929.3	156.9	200.8	1.74	0.802	2.17
−184	0.90782	1146.3	−406.4	−3.489	1.697	0.9328	4.32	912.9	154.0	190.4	1.66	0.792	2.10
−182	1.1192	1136.4	−403.0	−3.451	1.702	0.9253	4.42	896.4	151.2	180.8	1.59	0.782	2.03
−180	1.3666	1126.3	−399.6	−3.414	1.708	0.9181	4.52	879.8	148.4	172.0	1.53	0.771	1.98
−178	1.6538	1116.2	−396.1	−3.378	1.716	0.9110	4.62	863.1	145.7	163.7	1.47	0.761	1.93
−176	1.9848	1105.8	−392.7	−3.343	1.724	0.9042	4.74	846.3	143.0	156.1	1.41	0.750	1.88
−174	2.3636	1095.4	−389.2	−3.308	1.733	0.8976	4.86	829.4	140.2	149.0	1.36	0.739	1.84
−172	2.7943	1084.8	−385.7	−3.273	1.744	0.8913	5.00	812.4	137.5	142.3	1.31	0.727	1.81
−170	3.2812	1074.0	−382.2	−3.239	1.755	0.8851	5.14	795.1	134.7	136.1	1.27	0.714	1.77
−168	3.8286	1063.0	−378.6	−3.205	1.769	0.8792	5.30	777.8	131.9	130.2	1.22	0.702	1.74
−166	4.4408	1051.8	−375.1	−3.172	1.783	0.8735	5.48	760.2	129.1	124.6	1.18	0.689	1.72
−164	5.1223	1040.4	−371.4	−3.140	1.799	0.8680	5.67	742.4	126.4	119.3	1.15	0.675	1.70
−162	5.8776	1028.8	−367.8	−3.107	1.817	0.8628	5.87	724.4	123.6	114.3	1.11	0.661	1.68
−160	6.7111	1016.9	−364.1	−3.075	1.838	0.8578	6.10	706.1	120.8	109.6	1.08	0.646	1.67
−158	7.6276	1004.7	−360.4	−3.043	1.860	0.8532	6.35	687.6	118.0	105.0	1.05	0.631	1.66
−156	8.6316	992.21	−356.6	−3.012	1.886	0.8488	6.63	668.8	115.2	100.7	1.02	0.616	1.65
−154	9.7278	979.40	−352.8	−2.980	1.914	0.8447	6.94	649.7	112.3	96.57	0.986	0.599	1.65
−152	10.921	966.24	−348.9	−2.949	1.946	0.8409	7.29	630.3	109.5	92.59	0.958	0.582	1.65
−150	12.216	952.67	−345.0	−2.918	1.982	0.8375	7.68	610.5	106.7	88.75	0.932	0.565	1.65
−148	13.618	938.65	−341.0	−2.887	2.024	0.8346	8.13	590.3	103.8	85.05	0.906	0.547	1.66
−146	15.131	924.14	−336.9	−2.856	2.072	0.8320	8.65	569.7	101.0	81.46	0.882	0.527	1.67
−144	16.761	909.07	−332.7	−2.824	2.127	0.8300	9.25	548.6	98.10	77.98	0.858	0.507	1.69
−142	18.513	893.36	−328.5	−2.793	2.192	0.8285	9.95	527.0	95.21	74.59	0.835	0.486	1.72

D2.5. Table 2. (continued)

ϑ °C	p bar	ρ' kg/m³	h' kJ/kg	s' kJ/(kg K)	c_p' kJ/(kg K)	c_v' kJ/(kg K)	β' 10^{-3}/K	w_s' m/s	λ' mW/(m K)	η' 10^{-6} Pa·s	ν' 10^{-7} m²/s	a' 10^{-7} m²/s	Pr′ –
−140	20.393	876.93	−324.1	−2.762	2.269	0.8277	10.8	504.8	92.31	71.27	0.813	0.464	1.75
−138	22.406	859.66	−319.6	−2.730	2.362	0.8277	11.8	481.9	89.38	68.01	0.791	0.440	1.80
−136	24.558	841.39	−314.9	−2.697	2.475	0.8287	13.1	458.3	86.44	64.80	0.770	0.415	1.86
−134	26.856	821.93	−310.1	−2.664	2.618	0.8309	14.7	433.8	83.48	61.60	0.749	0.388	1.93
−132	29.305	801.01	−305.0	−2.630	2.803	0.8348	16.8	408.3	80.52	58.41	0.729	0.359	2.03
−130	31.915	778.27	−299.7	−2.595	3.050	0.8410	19.6	381.4	77.59	55.18	0.709	0.327	2.17
−128	34.692	753.15	−294.0	−2.559	3.399	0.8506	23.7	353.0	74.76	51.88	0.689	0.292	2.36
−126	37.646	724.78	−287.9	−2.519	3.930	0.8657	30.1	322.5	72.23	48.45	0.668	0.254	2.64
−124	40.789	691.67	−281.1	−2.477	4.840	0.8903	41.5	289.2	70.63	44.78	0.647	0.211	3.07
−122	44.137	650.56	−273.2	−2.427	6.805	0.9344	66.9	251.3	72.09	40.68	0.625	0.163	3.84
−120	47.710	590.99	−262.7	−2.362	14.65	1.031	174	204.4	86.69	35.45	0.600	0.100	5.99

D2.5. Table 3. Properties of the saturated vapor

ϑ °C	p bar	ρ'' kg/m³	h'' kJ/kg	s'' kJ/(kg K)	c_p'' kJ/(kg K)	c_v'' kJ/(kg K)	β'' 10^{-3}/K	w_s'' m/s	λ'' mW/(m K)	η'' 10^{-6} Pa·s	ν'' 10^{-7} m²/s	a'' 10^{-7} m²/s	Pr″ –
−218	0.00187	0.01305	−221.4	0.0951	0.9286	0.6660	18.2	141.3	–	–	–	–	–
−216	0.00337	0.02272	−219.6	−0.0259	0.9359	0.6721	17.6	143.7	–	–	–	–	–
−214	0.00582	0.03792	−217.8	−0.1368	0.9440	0.6788	17.1	146.1	–	–	–	–	–
−212	0.00967	0.06095	−216.0	−0.2387	0.9523	0.6857	16.6	148.3	–	–	–	–	–
−210	0.01552	0.0947	−214.3	−0.3326	0.9602	0.6921	16.1	150.6	–	–	–	–	–
−208	0.02411	0.14271	−212.5	−0.4191	0.9672	0.6976	15.7	152.8	–	–	–	–	–
−206	0.03640	0.20920	−210.7	−0.4990	0.9728	0.7018	15.3	155.0	–	–	–	–	–
−204	0.05354	0.29909	−208.9	−0.5729	0.9768	0.7045	14.9	157.2	–	–	–	–	–
−202	0.07690	0.41798	−207.2	−0.6415	0.9791	0.7056	14.5	159.3	6.111	4.878	117	149	0.782
−200	0.10808	0.57218	−205.4	−0.7052	0.9798	0.7052	14.2	161.4	6.335	5.056	88.4	113	0.782
−198	0.14892	0.76864	−203.7	−0.7646	0.9792	0.7034	13.8	163.5	6.561	5.233	68.1	87.2	0.781
−196	0.20148	1.0150	−202.0	−0.8199	0.9776	0.7005	13.5	165.5	6.878	5.409	53.3	68.4	0.779
−194	0.26807	1.3194	−200.3	−0.8717	0.9753	0.6967	13.2	167.5	7.015	5.586	42.3	54.5	0.777
−192	0.35123	1.6906	−198.6	−0.9203	0.9729	0.6925	13.0	169.5	7.244	5.763	34.1	44.0	0.774
−190	0.45372	2.1381	−197.0	−0.9659	0.9708	0.6882	12.8	171.4	7.475	5.939	27.8	36.0	0.771
−188	0.57851	2.6715	−195.4	−1.009	0.9693	0.6840	12.6	173.2	7.708	6.115	22.9	29.8	0.769
−186	0.72876	3.3014	−193.8	−1.049	0.9688	0.6801	12.4	174.9	7.944	6.292	19.1	24.8	0.767
−184	0.90782	4.0386	−192.3	−1.088	0.9696	0.6769	12.3	176.6	8.184	6.469	16.0	20.9	0.766
−182	1.1192	4.8944	−190.9	−1.124	0.9721	0.6745	12.2	178.2	8.427	6.646	13.6	17.7	0.767
−180	1.3666	5.8808	−189.5	−1.159	0.9763	0.6729	12.1	179.7	8.675	6.823	11.6	15.1	0.768
−178	1.6538	7.0102	−188.1	−1.192	0.9824	0.6724	12.1	181.1	8.928	7.001	9.99	13.0	0.770
−176	1.9848	8.2958	−186.8	−1.224	0.9907	0.6728	12.0	182.4	9.188	7.180	8.65	11.2	0.774
−174	2.3636	9.7513	−185.6	−1.254	1.001	0.6743	12.1	183.6	9.455	7.359	7.55	9.68	0.779
−172	2.7943	11.391	−184.4	−1.283	1.014	0.6767	12.1	184.7	9.730	7.540	6.62	8.42	0.786
−170	3.2812	13.231	−183.4	−1.312	1.029	0.6802	12.2	185.6	10.01	7.722	5.84	7.35	0.794
−168	3.8286	15.287	−182.3	−1.339	1.047	0.6846	12.3	186.5	10.31	7.905	5.17	6.44	0.803
−166	4.4408	17.577	−181.4	−1.365	1.068	0.6899	12.5	187.3	10.62	8.091	4.60	5.66	0.813
−164	5.1223	20.119	−180.5	−1.391	1.091	0.6960	12.7	187.9	10.94	8.278	4.11	4.99	0.825
−162	5.8776	22.935	−179.8	−1.415	1.117	0.7029	12.9	188.4	11.28	8.468	3.69	4.40	0.838
−160	6.7111	26.046	−179.1	−1.440	1.146	0.7105	13.2	188.8	11.64	8.662	3.33	3.90	0.853
−158	7.6276	29.479	−178.5	−1.464	1.179	0.7187	13.5	189.1	12.02	8.858	3.00	3.46	0.869
−156	8.6316	33.259	−178.0	−1.487	1.216	0.7277	13.9	189.3	12.43	9.059	2.72	3.07	0.886
−154	9.7278	37.417	−177.6	−1.510	1.257	0.7372	14.4	189.4	12.87	9.265	2.48	2.73	0.905
−152	10.921	41.990	−177.4	−1.533	1.304	0.7474	14.9	189.4	13.34	9.477	2.26	2.44	0.926
−150	12.216	47.016	−177.2	−1.556	1.356	0.7582	15.6	189.2	13.85	9.696	2.06	2.17	0.949

D2.5. Table 3. (continued)

ϑ °C	p bar	ρ'' kg/m³	h'' kJ/kg	s'' kJ/(kg K)	c_p'' kJ/(kg K)	c_v'' kJ/(kg K)	β'' 10^{-3}/K	w_s'' m/s	λ'' mW/(m K)	η'' 10^{-6} Pa·s	ν'' 10^{-7} m²/s	a'' 10^{-7} m²/s	Pr″ –
−148	13.618	52.542	−177.2	−1.578	1.416	0.7696	16.3	188.9	14.41	9.923	1.89	1.94	0.975
−146	15.131	58.621	−177.3	−1.601	1.484	0.7816	17.2	188.5	15.02	10.16	1.73	1.73	1.00
−144	16.761	65.318	−177.6	−1.624	1.563	0.7945	18.2	188.0	15.70	10.41	1.59	1.54	1.04
−142	18.513	72.708	−178.1	−1.647	1.655	0.8081	19.4	187.4	16.46	10.67	1.47	1.37	1.07
−140	20.393	80.886	−178.7	−1.670	1.765	0.8228	20.9	186.6	17.32	10.95	1.35	1.21	1.12
−138	22.406	89.968	−179.6	−1.694	1.897	0.8386	22.7	185.7	18.29	11.25	1.25	1.07	1.17
−136	24.558	100.10	−180.7	−1.719	2.060	0.8558	24.9	184.6	19.41	11.58	1.16	0.941	1.23
−134	26.856	111.48	−182.1	−1.745	2.265	0.8747	27.7	183.4	20.70	11.94	1.07	0.820	1.31
−132	29.305	124.37	−183.8	−1.772	2.533	0.8960	31.5	182.0	22.23	12.34	0.992	0.706	1.41
−130	31.915	139.13	−186.0	−1.801	2.896	0.9202	36.5	180.4	24.06	12.80	0.920	0.597	1.54
−128	34.692	156.30	−188.7	−1.833	3.416	0.9484	43.8	178.6	26.30	13.34	0.853	0.493	1.73
−126	37.646	176.76	−192.0	−1.868	4.223	0.9827	55.1	176.6	29.15	13.98	0.791	0.390	2.03
−124	40.789	202.04	−196.4	−1.909	5.640	1.026	74.9	174.1	32.97	14.81	0.733	0.289	2.53
−122	44.137	235.45	−202.4	−1.959	8.750	1.087	118	170.9	38.68	15.96	0.678	0.188	3.61
−120	47.710	287.30	−212.1	−2.031	20.74	1.185	285	165.9	50.23	17.89	0.623	0.084	7.39

D2.5. Table 4. Density ρ of oxygen in kg/m³

	Temperature in °C											
Pressure in bar	−200	−180	−160	−140	−120	−100	−90	−80	−70	−60	−50	−40
1	1223	4.254	3.458	2.920	2.530	2.233	2.110	1.999	1.900	1.810	1.728	1.654
5	1223	1127	18.66	15.27	13.02	11.38	10.72	10.13	9.609	9.139	8.714	8.327
10	1224	1128	1018	32.57	27.06	23.36	21.90	20.62	19.50	18.51	17.61	16.80
20	1226	1131	1022	78.50	59.30	49.38	45.80	42.79	40.21	37.97	35.99	34.22
30	1227	1133	1026	886.7	100.3	78.90	72.17	66.76	62.28	58.47	55.17	52.28
40	1229	1135	1030	895.8	161.3	113.2	101.6	92.83	85.85	80.08	75.20	70.98
50	1230	1138	1034	904.2	632.9	154.3	134.9	121.4	111.1	102.9	96.11	90.36
60	1231	1140	1038	911.9	696.9	205.8	173.0	152.7	138.2	127.0	117.9	110.4
70	1233	1142	1041	919.0	729.6	273.3	217.3	187.3	167.2	152.3	140.6	131.1
80	1234	1144	1045	925.7	753.0	360.9	268.6	225.3	198.2	178.9	164.2	152.4
90	1236	1146	1148	932.0	771.5	453.7	326.5	266.6	231.1	206.8	188.6	174.2
100	1237	1148	1051	938.0	787.0	525.4	387.1	310.4	265.6	235.6	213.6	196.5
120	1240	1152	1058	949.1	812.4	613.3	493.6	399.1	336.9	295.1	265.0	242.0
140	1243	1156	1064	959.3	832.9	666.3	568.0	476.7	405.8	354.4	316.7	287.9
160	1245	1160	1070	968.7	850.3	703.9	620.2	537.9	466.5	410.1	366.6	332.8
180	1248	1164	1075	977.4	865.5	733.0	659.4	585.5	517.6	459.9	413.1	375.6
200	1251	1168	1080	985.6	879.1	757.0	690.6	623.5	559.9	503.3	455.3	415.4
225	1254	1172	1087	995.2	894.3	782.0	722.2	661.8	603.3	549.4	501.7	460.6
250	1257	1176	1093	1004	908.0	803.2	748.3	693.0	638.9	588.0	541.7	500.5
275	1260	1181	1099	1013	920.5	821.8	770.6	719.3	668.9	620.8	576.2	535.8
300	1263	1185	1105	1021	931.9	838.3	790.2	742.0	694.7	649.2	606.4	567.0
325	1266	1189	1110	1028	942.6	853.1	807.6	762.1	717.3	674.0	633.0	594.7
350	1269	1193	1115	1035	952.5	866.7	823.3	780.0	737.4	696.1	656.7	619.6
375	1272	1197	1120	1042	961.9	879.2	837.6	796.2	755.5	715.9	678.0	642.1
400	1275	1200	1125	1049	970.7	890.9	850.8	811.1	772.0	733.9	697.3	662.5
450	1281	1208	1135	1061	987.0	911.9	874.5	837.5	801.1	765.6	731.3	698.5
500	1286	1215	1144	1073	1002	930.6	895.3	860.5	826.3	792.9	760.5	729.4

D2.5. Table 4. (continued)

Pressure in bar	Temperature in °C											
	−30	−20	−10	0	10	20	30	40	50	60	80	100
1	1.585	1.522	1.464	1.410	1.360	1.314	1.270	1.230	1.191	1.156	1.090	1.032
5	7.975	7.651	7.354	7.079	6.824	6.587	6.366	6.160	5.967	5.786	5.455	5.160
10	16.07	15.40	14.79	14.22	13.70	13.22	12.77	12.36	11.96	11.59	10.92	10.33
20	32.64	31.21	29.91	28.72	27.62	26.61	25.68	24.81	24.01	23.25	21.88	20.67
30	49.71	47.42	45.35	43.47	41.75	40.18	38.73	37.38	36.14	34.98	32.88	31.03
40	67.30	64.03	61.10	58.47	56.08	53.90	51.90	50.05	48.34	46.76	43.90	41.39
50	85.39	81.03	77.17	73.71	70.60	67.77	65.18	62.80	60.61	58.59	54.95	51.76
60	104.0	98.41	93.52	89.18	85.28	81.76	78.56	75.63	72.94	70.45	66.00	62.13
70	123.0	116.1	110.1	104.8	100.1	95.88	92.03	88.52	85.31	82.35	77.06	72.48
80	142.5	134.2	127.0	120.7	115.1	110.1	105.6	101.5	97.70	94.25	88.12	82.82
90	162.4	152.5	144.1	136.7	130.2	124.4	119.2	114.4	110.1	106.2	99.17	93.13
100	182.6	171.1	161.3	152.8	145.3	138.7	132.8	127.4	122.5	118.1	110.2	103.4
120	223.7	208.7	196.1	185.2	175.8	167.4	160.0	153.4	147.3	141.8	132.1	123.9
140	265.1	246.5	230.9	217.7	206.2	196.1	187.2	179.2	172.0	165.4	153.9	144.1
160	305.8	283.8	265.4	249.8	236.3	224.5	214.0	204.7	196.3	188.7	175.4	164.1
180	345.2	320.1	299.1	281.3	265.8	252.4	240.5	229.8	220.3	211.7	196.6	183.8
200	382.4	354.9	331.7	311.8	294.6	279.6	266.3	254.5	243.8	234.2	217.4	203.2
225	425.6	395.8	370.3	348.4	329.3	312.5	297.6	284.4	272.4	261.6	242.8	226.9
250	464.6	433.4	406.4	382.8	362.1	343.9	327.7	313.1	300.0	288.2	267.5	250.0
275	499.7	467.8	439.8	415.0	393.1	373.7	356.3	340.7	326.6	313.8	291.3	272.3
300	531.2	499.1	470.5	445.0	422.2	401.8	383.5	366.9	352.0	338.3	314.3	294.0
325	559.6	527.6	498.8	472.8	449.4	428.3	409.2	391.9	376.2	361.8	336.5	314.9
350	585.2	553.6	524.8	498.5	474.7	453.1	433.5	415.6	399.3	384.3	357.8	335.1
375	608.5	577.3	548.7	522.4	498.4	476.5	456.4	438.0	431.2	405.7	378.2	354.5
400	629.7	599.1	570.8	544.6	520.5	498.4	478.0	459.3	442.0	426.1	397.8	373.3
450	667.3	637.9	610.3	584.5	560.5	538.3	517.6	498.4	480.7	464.1	434.4	408.6
500	699.6	671.3	644.6	619.4	595.8	573.6	553.0	533.6	515.6	498.7	468.1	441.2

D2.5. Table 5. Compression factor Z of oxygen

Pressure in bar	Temperature in °C											
	−200	−180	−160	−140	−120	−100	−90	−80	−70	−60	−50	−40
1	0.004	0.971	0.984	0.990	0.993	0.995	0.996	0.997	0.997	0.998	0.998	0.998
5	0.022	0.018	0.911	0.947	0.965	0.976	0.980	0.983	0.986	0.988	0.990	0.991
10	0.043	0.037	0.033	0.887	0.929	0.952	0.960	0.966	0.971	0.976	0.979	0.982
20	0.086	0.073	0.067	0.736	0.848	0.900	0.918	0.931	0.942	0.951	0.959	0.965
30	0.129	0.109	0.099	0.098	0.751	0.845	0.874	0.895	0.913	0.926	0.938	0.947
40	0.171	0.146	0.132	0.129	0.623	0.785	0.827	0.859	0.883	0.902	0.917	0.930
50	0.214	0.182	0.164	0.160	0.199	0.720	0.779	0.821	0.853	0.877	0.897	0.913
60	0.256	0.218	0.197	0.190	0.216	0.648	0.729	0.783	0.823	0.853	0.878	0.897
70	0.299	0.253	0.229	0.220	0.241	0.569	0.677	0.745	0.793	0.830	0.858	0.882
80	0.341	0.289	0.260	0.250	0.267	0.493	0.626	0.708	0.765	0.807	0.840	0.867
90	0.383	0.324	0.292	0.279	0.293	0.441	0.579	0.673	0.738	0.786	0.823	0.853
100	0.425	0.360	0.324	0.308	0.319	0.423	0.543	0.642	0.713	0.766	0.807	0.840

D2.5. Table 5. (continued)

Temperature in °C												
Pressure in bar	−200	−180	−160	−140	−120	−100	−90	−80	−70	−60	−50	−40
120	0.509	0.430	0.386	0.365	0.371	0.435	0.511	0.599	0.675	0.734	0.781	0.818
140	0.583	0.500	0.448	0.422	0.422	0.467	0.518	0.585	0.654	0.713	0.762	0.803
160	0.676	0.570	0.509	0.477	0.473	0.505	0.542	0.593	0.650	0.704	0.753	0.794
180	0.759	0.639	0.570	0.532	0.523	0.546	0.574	0.613	0.659	0.707	0.751	0.791
200	0.841	0.708	0.630	0.587	0.572	0.587	0.609	0.639	0.677	0.717	0.758	0.795
225	0.944	0.793	0.704	0.653	0.632	0.640	0.655	0.677	0.707	0.739	0.774	0.806
250	1.046	0.878	0.778	0.720	0.692	0.692	0.702	0.719	0.741	0.768	0.796	0.824
275	1.148	0.962	0.851	0.785	0.751	0.744	0.750	0.762	0.779	0.800	0.823	0.847
300	1.249	1.046	0.924	0.850	0.809	0.795	0.798	0.806	0.818	0.834	0.853	0.873
325	1.350	1.130	0.996	0.914	0.866	0.847	0.846	0.850	0.858	0.871	0.886	0.902
350	1.451	1.212	1.067	0.977	0.923	0.898	0.893	0.894	0.899	0.908	0.919	0.932
375	1.551	1.295	1.138	1.040	0.980	0.948	0.941	0.938	0.940	0.946	0.954	0.964
400	1.650	1.377	1.209	1.102	1.036	0.998	0.988	0.983	0.982	0.984	0.989	0.997
450	1.849	1.540	1.349	1.225	1.146	1.097	1.081	1.071	1.064	1.061	1.061	1.063
500	2.045	1.701	1.487	1.347	1.254	1.194	1.174	1.158	1.146	1.139	1.134	1.132

Temperature in °C												
Pressure in bar	−30	−20	−10	0	10	20	30	40	50	60	80	100
1	0.998	0.999	0.999	0.999	0.999	0.999	0.999	1.000	1.000	1.000	1.000	1.000
5	0.992	0.994	0.994	0.995	0.996	0.997	0.997	0.998	0.998	0.998	0.999	0.999
10	0.985	0.987	0.989	0.991	0.992	0.993	0.994	0.995	0.996	0.997	0.998	0.999
20	0.970	0.974	0.978	0.981	0.984	0.987	0.989	0.991	0.992	0.994	0.996	0.998
30	0.955	0.962	0.968	0.972	0.977	0.980	0.983	0.986	0.989	0.991	0.994	0.997
40	0.941	0.950	0.957	0.964	0.969	0.974	0.979	0.982	0.985	0.988	0.993	0.997
50	0.927	0.938	0.948	0.956	0.963	0.969	0.974	0.978	0.982	0.986	0.992	0.996
60	0.913	0.927	0.938	0.948	0.956	0.963	0.970	0.975	0.980	0.984	0.991	0.996
70	0.901	0.916	0.929	0.941	0.950	0.959	0.966	0.972	0.977	0.982	0.990	0.996
80	0.888	0.906	0.921	0.934	0.945	0.954	0.962	0.969	0.975	0.981	0.989	0.996
90	0.877	0.897	0.914	0.928	0.940	0.950	0.959	0.967	0.973	0.979	0.989	0.997
100	0.867	0.888	0.907	0.922	0.935	0.946	0.956	0.965	0.972	0.978	0.989	0.997
120	0.849	0.874	0.895	0.913	0.928	0.941	0.952	0.962	0.970	0.977	0.990	0.999
140	0.836	0.864	0.887	0.906	0.923	0.937	0.950	0.960	0.970	0.978	0.991	1.002
160	0.828	0.857	0.882	0.903	0.920	0.936	0.949	0.961	0.971	0.979	0.994	1.005
180	0.825	0.855	0.880	0.902	0.920	0.936	0.950	0.962	0.973	0.982	0.998	1.010
200	0.828	0.857	0.882	0.904	0.923	0.939	0.953	0.966	0.977	0.987	1.003	1.015
225	0.837	0.864	0.889	0.910	0.929	0.945	0.960	0.972	0.984	0.993	1.010	1.023
250	0.852	0.877	0.900	0.920	0.938	0.954	0.969	0.981	0.992	1.002	1.019	1.032
275	0.871	0.894	0.915	0.934	0.951	0.966	0.980	0.992	1.003	1.013	1.029	1.041
300	0.894	0.914	0.933	0.950	0.966	0.980	0.993	1.005	1.015	1.024	1.040	1.052
325	0.919	0.936	0.953	0.969	0.983	0.996	1.008	1.019	1.029	1.038	1.053	1.064
350	0.947	0.961	0.975	0.989	1.002	1.014	1.025	1.035	1.044	1.052	1.066	1.077
375	0.975	0.987	1.000	1.011	1.023	1.033	1.043	1.052	1.060	1.068	1.081	1.091
400	1.005	1.015	1.025	1.035	1.045	1.054	1.062	1.070	1.078	1.084	1.096	1.105
450	10.67	1.073	1.078	1.085	1.091	1.098	1.104	1.110	1.115	1.120	1.129	1.136
500	1.131	1.132	1.134	1.137	1.141	1.144	1.148	1.152	1.155	1.158	1.164	1.169

D2.5. Table 6. Specific enthalpy h of oxygen in kJ/kg

Pressure in bar	Temperature in °C											
	−200	−180	−160	−140	−120	−100	−90	−80	−70	−60	−50	−40
1	−433.3	−188.7	−170.0	−151.5	−133.0	−114.7	−105.5	−96.38	−87.24	−78.09	−68.95	−59.81
5	−433.1	−399.4	−176.1	−155.8	−136.4	−117.3	−107.9	−98.55	−89.22	−79.91	−70.63	−61.36
10	−432.8	−399.1	−364.0	−161.8	−140.7	−120.7	−111.0	−101.3	−91.73	−82.21	−72.74	−63.31
20	−432.2	−398.6	−363.7	−177.9	−150.6	−128.0	−117.4	−107.1	−96.92	−86.93	−77.05	−67.27
30	−431.6	−398.1	−363.4	−324.5	−162.8	−136.1	−124.3	−113.1	−102.3	−91.78	−81.46	−71.29
40	−431.0	−397.5	−363.0	−324.8	−180.0	−145.1	−131.8	−119.5	−107.9	−96.78	−85.95	−75.37
50	−430.4	−397.0	−362.6	−325.0	−268.0	−155.4	−139.9	−126.3	−113.8	−101.9	−90.54	−79.50
60	−429.8	−396.5	−362.3	−325.1	−275.6	−167.6	−148.9	−133.5	−119.8	−107.2	−95.19	−83.67
70	−429.2	−395.9	−361.9	−325.2	−279.1	−182.2	−158.7	−141.1	−126.1	−112.6	−99.91	−87.87
80	−428.6	−395.4	−361.5	−325.2	−281.3	−199.1	−169.3	−149.1	−132.6	−118.0	−104.7	−92.07
90	−428.0	−394.9	−361.1	−325.1	−282.9	−214.6	−180.4	−157.3	−139.2	−123.5	−109.4	−96.26
100	−427.4	−394.3	−360.7	−325.0	−284.1	−225.3	−191.0	−165.5	−145.7	−129.0	−114.2	−100.4
120	−426.2	−393.2	−359.8	−324.7	−285.7	−236.7	−207.5	−180.5	−158.4	−139.7	−123.4	−108.5
140	−425.0	−392.1	−358.9	−324.3	−286.7	−242.6	−217.4	−192.2	−169.4	−149.5	−132.0	−116.2
160	−423.8	−391.0	−358.0	−323.8	−287.3	−246.2	−223.5	−200.3	−178.1	−157.9	−139.7	−123.2
180	−422.6	−389.9	−357.0	−323.3	−287.6	−248.5	−227.5	−206.0	−184.8	−164.8	−146.4	−129.4
200	−421.4	−388.7	−356.1	−322.6	−287.6	−250.1	−230.2	−209.9	−189.7	−170.3	−151.9	−134.8
225	−419.9	−387.3	−354.8	−321.8	−287.5	−251.4	−232.6	−213.4	−194.2	−175.5	−157.5	−140.4
250	−418.4	−385.9	−353.6	−320.8	−287.2	−252.1	−234.0	−215.7	−197.4	−179.3	−161.7	−144.8
275	−416.8	−384.4	−352.3	−319.8	−286.7	−252.5	−235.0	−217.3	−199.6	−182.1	−165.0	−148.4
300	−415.3	−383.0	−351.0	−318.8	−286.1	−252.6	−235.5	−218.4	−201.2	−184.2	−167.4	−151.1
325	−413.8	−381.5	−349.7	−317.7	−285.3	−252.4	−235.8	−219.0	−202.3	−185.7	−169.3	−153.2
350	−412.2	−380.1	−348.3	−316.6	−284.5	−252.1	−235.8	−219.4	−203.0	−186.7	−170.6	−154.8
375	−410.7	−378.6	−347.0	−315.4	−283.7	−251.7	−235.6	−219.5	−203.4	−187.4	−171.6	−156.0
400	−409.2	−377.1	−345.6	−314.2	−282.7	−251.1	−235.2	−219.4	−203.6	−187.8	−172.3	−156.9
450	−406.1	−374.1	−342.8	−311.7	−280.7	−249.7	−234.2	−218.7	−203.3	−188.0	−172.8	−157.8
500	−403.0	−371.2	−340.0	−309.2	−278.5	−248.0	−232.8	−217.6	−202.5	−187.5	−172.7	−158.0

Pressure in bar	Temperature in °C											
	−30	−20	−10	0	10	20	30	40	50	60	80	100
1	−50.66	−41.52	−32.36	−23.20	−14.03	−4.843	−4.353	13.56	22.79	32.04	50.59	69.23
5	−52.10	−42.85	−33.61	−24.36	−15.12	−5.863	−3.397	12.67	21.95	31.24	49.89	68.63
10	−53.91	−44.53	−35.17	−25.82	−16.48	−7.137	−2.203	11.55	20.90	30.25	49.01	67.83
20	−57.56	−47.91	−38.31	−28.74	−19.20	−9.680	−0.1772	9.316	18.80	28.29	47.27	66.29
30	−61.25	−51.31	−41.46	−31.66	−21.92	−12.21	−2.545	7.101	16.73	24.34	45.56	64.77
40	−64.98	−54.74	−44.61	−34.58	−24.63	−14.74	−4.896	4.904	14.67	24.42	42.86	63.28
50	−68.73	−58.17	−47.76	−37.49	−27.32	−17.24	−7.228	2.729	12.64	22.52	42.19	61.80
60	−72.50	−61.60	−50.91	−40.39	−30.00	−19.72	−9.536	0.5786	10.63	20.64	40.54	60.35
70	−76.28	−65.03	−54.04	−43.27	−32.66	−22.18	−11.82	−1.544	8.654	18.79	38.92	58.93
80	−80.05	−68.44	−57.15	−46.11	−35.28	−24.61	−14.07	−3.636	6.705	16.97	37.33	57.53
90	−83.79	−71.82	−60.23	−48.93	−37.87	−27.00	−16.28	−5.693	4.789	15.18	35.77	56.16
100	−87.50	−75.16	−63.26	−51.70	−40.42	−29.35	−18.46	−7.713	2.909	13.43	34.24	54.82
120	−94.72	−81.66	−69.16	−57.09	−45.36	−33.91	−22.68	−11.63	−0.7338	10.04	31.28	52.23
140	−101.6	−87.35	−74.78	−62.23	−50.08	−38.26	−26.71	−15.37	−4.207	6.801	28.46	49.76
160	−107.9	−93.62	−80.05	−67.07	−54.53	−42.37	−30.51	−18.90	−7.497	3.736	25.79	47.42
180	−113.7	−98.91	−84.93	−71.56	−58.69	−46.22	−34.09	−22.22	−10.59	0.8499	23.27	45.21
200	−118.8	−103.7	−89.36	−75.68	−62.52	−49.79	−37.41	−25.32	−13.48	−1.850	20.91	43.15
225	−124.2	−108.9	−94.28	−80.30	−66.85	−53.84	−41.20	−28.87	−16.80	−4.959	18.18	40.75
250	−128.7	−113.3	−98.50	−84.33	−70.67	−57.44	−44.59	−32.06	−19.80	−7.772	15.70	35.58
275	−132.3	−116.9	−102.1	−87.79	−73.99	−60.60	−47.59	−34.89	−22.47	−12.53	13.47	34.85
300	−135.2	−119.9	−105.1	−90.73	−76.84	−63.35	−50.21	−37.39	−24.84	−12.53	11.48	34.85

D2.5. Table 6. (continued)

Pressure in bar	Temperature in °C											
	−30	−20	−10	0	10	20	30	40	50	60	80	100
325	−137.5	−122.3	−107.5	−93.19	−79.26	−65.70	−52.48	−39.56	−26.91	−14.50	9.718	33.29
350	−139.4	−124.3	−109.5	−95.23	−81.29	−67.69	−54.42	−41.44	−28.71	−16.22	8.173	31.91
375	−140.7	−125.8	−111.2	−96.90	−82.97	−69.37	−56.06	−43.03	−30.25	−17.69	6.835	30.72
400	−141.8	−127.0	−112.4	−98.24	−84.35	−70.75	−57.43	−44.37	−31.55	−18.95	5.690	29.69
450	−143.0	−128.5	−114.2	−100.1	−86.30	−72.76	−59.45	−46.38	−33.52	−20.86	3.931	28.12
500	−143.5	−129.1	−115.0	−101.1	−87.40	−73.93	−60.67	−47.62	−34.75	−22.07	2.798	27.10

D2.5. Table 7. Specific entropy *s* of oxygen in kJ/(kg K)

Pressure in bar	−200	−180	−160	−140	−120	−100	−90	−80	−70	−60	−50	−40
1	−3.822	−1.072	−0.8906	−0.7397	−0.6108	−0.4982	−0.4467	−0.3981	−0.3519	−0.3080	−0.2661	−0.2260
5	−3.823	−3.416	−1.345	−1.180	−1.043	−0.9266	−0.8738	−0.8240	−0.7769	−0.7322	−0.6896	−0.6490
10	−3.825	−3.418	−3.077	−1.391	−1.243	−1.120	−1.065	−1.014	−0.9657	−0.9199	−0.8765	−0.8351
20	−3.828	−3.422	−3.083	−1.660	−1.468	−1.330	−1.270	−1.215	−1.164	−1.116	−1.071	−1.028
30	−3.831	−3.426	−3.088	−2.773	−1.633	−1.468	−1.402	−1.343	−1.288	−1.238	−1.190	−1.146
40	−3.834	−3.430	−3.094	−2.784	−1.797	−1.581	−1.507	−1.442	−1.383	−1.329	−1.280	−1.233
50	−3.837	−3.433	−3.099	−2.793	−2.399	−1.685	−1.598	−1.525	−1.462	−1.405	−1.353	−1.305
60	−3.840	−3.437	−3.105	−2.803	−2.458	−1.787	−1.682	−1.601	−1.532	−1.471	−1.416	−1.365
70	−3.843	−3.441	−3.110	−2.811	−2.490	−1.896	−1.764	−1.671	−1.595	−1.530	−1.472	−1.419
80	−3.846	−3.444	−3.115	−2.819	−2.514	−2.012	−1.845	−1.737	−1.654	−1.584	−1.522	−1.467
90	−3.849	−3.448	−3.119	−2.827	−2.533	−2.116	−1.924	−1.801	−1.709	−1.634	−1.569	−1.512
100	−3.851	−3.451	−3.124	−2.834	−2.549	−2.190	−1.997	−1.861	−1.761	−1.681	−1.613	−1.553
120	−3.857	−3.458	−3.133	−2.848	−2.576	−2.276	−2.112	−1.968	−1.856	−1.767	−1.692	−1.627
140	−3.863	−3.465	−3.142	−2.861	−2.598	−2.328	−2.187	−2.052	−1.937	−1.842	−1.761	−1.692
160	−3.868	−3.471	−3.150	−2.873	−2.617	−2.366	−2.238	−2.115	−2.003	−1.906	−1.822	−1.750
180	−3.873	−3.478	−3.159	−2.884	−2.634	−2.395	−2.277	−2.162	−2.056	−1.960	−1.875	−1.801
200	−3.879	−3.484	−3.166	−2.895	−2.650	−2.420	−2.308	−2.200	−2.098	−2.005	−1.921	−1.845
225	−3.885	−3.492	−3.176	−2.907	−2.667	−2.446	−2.340	−2.238	−2.141	−2.051	−1.969	−1.894
250	−3.892	−3.499	−3.185	−2.919	−2.683	−2.468	−2.367	−2.269	−2.177	−2.090	−2.009	−1.935
275	−3.898	−3.507	−3.194	−2.930	−2.698	−2.488	−2.390	−2.296	−2.207	−2.123	−2.044	−1.971
300	−3.904	−3.514	−3.202	−2.940	−2.711	−2.506	−2.410	−2.319	−2.233	−2.151	−2.074	−2.002
325	−3.910	−3.521	−3.211	−2.951	−2.724	−2.522	−2.429	−2.340	−2.255	−2.175	−2.100	−2.030
350	−3.916	−3.527	−3.219	−2.960	−2.736	−2.537	−2.445	−2.358	−2.276	−2.197	−2.124	−2.054
375	−3.922	−3.534	−3.226	−2.970	−2.748	−2.551	−2.461	−2.375	−2.294	−2.217	−2.145	−2.077
400	−3.928	−3.541	−3.234	−2.979	−2.758	−2.564	−2.475	−2.391	−2.311	−2.235	−2.164	−2.097
450	−3.940	−3.553	−3.248	−2.995	−2.778	−2.588	−2.501	−2.419	−2.341	−2.268	−2.198	−2.132
500	−3.951	−3.566	−3.262	−3.011	−2.797	−2.609	−2.524	−2.443	−2.367	−2.295	−2.227	−2.163
Pressure in bar	Temperature in °C											
	−30	−20	−10	0	10	20	30	40	50	60	80	100
1	−0.1876	−0.1507	−0.1152	−0.0811	−0.0481	−0.0162	0.0146	0.0445	0.0735	0.1017	0.1558	0.2071
5	−0.6101	−0.5728	−0.5370	−0.5025	−0.4693	−0.4372	−0.4061	−0.3760	−0.3468	−0.3185	−0.2642	−0.2126
10	−0.7957	−0.7579	−0.7216	−0.6857	−0.6531	−0.6207	−0.5894	−0.5591	−0.5297	−0.5011	−0.4465	−0.3946
20	−0.9869	−0.9480	−0.9108	−0.8751	−0.8408	−0.8077	−0.7759	−0.7450	−0.7152	−0.6863	−0.6310	−0.5786

D2.5. Table 7. **(continued)**

Pressure in bar	Temperature in °C											
	−30	−20	−10	0	10	20	30	40	50	60	80	100
30	−0.104	−1.063	−1.025	−0.9887	−0.9537	−0.9200	−0.8876	−0.8563	−0.8260	−0.7967	−0.7407	−0.6878
40	−1.190	−1.148	−1.109	−1.072	−1.036	−1.002	−0.9687	−0.9369	−0.9061	−0.8764	−0.8198	−0.7663
50	−1.259	−1.217	−1.176	−1.138	−1.102	−1.067	−1.033	−1.001	−0.9695	−0.9394	−0.8820	−0.8280
60	−1.318	−1.274	−1.233	−1.194	−1.156	−1.121	−1.087	−1.054	−1.022	−0.9917	−0.9337	−0.8791
70	−1.370	−1.325	−1.282	−1.242	−1.204	−1.168	−1.133	−1.100	−1.067	−1.037	−0.9779	−0.9228
80	−1.417	−1.370	−1.326	−1.285	−1.246	−1.209	−1.174	−1.140	−1.107	−1.076	−1.017	−0.9611
90	−1.459	−1.411	−1.366	−1.324	−1.284	−1.246	−1.210	−1.176	−1.143	−1.111	−1.051	−0.9953
100	−1.498	−1.449	−1.402	−1.359	−1.319	−1.280	−1.244	−1.209	−1.176	−1.144	−1.083	−1.026
120	−1.569	−1.516	−1.468	−1.423	−1.380	−1.341	−1.303	−1.267	−1.233	−1.200	−1.138	−1.080
140	−1.631	−1.575	−1.525	−1.478	−1.434	−1.393	−1.354	−1.318	−1.282	−1.249	−1.186	−1.127
160	−1.686	−1.628	−1.575	−1.527	−1.482	−1.440	−1.400	−1.362	−1.326	−1.292	−1.228	−1.168
180	−1.734	−1.675	−1.621	−1.571	−1.525	−1.481	−1.441	−1.402	−1.366	−1.331	−1.265	−1.205
200	−1.778	−1.717	−1.662	−1.611	−1.563	−1.519	−1.478	−1.438	−1.401	−1.366	−1.299	−1.238
225	−1.826	−1.764	−1.708	−1.655	−1.607	−1.562	−1.519	−1.479	−1.441	−1.405	−1.338	−1.276
250	−1.867	−1.805	−1.748	−1.695	−1.646	−1.600	−1.557	−1.516	−1.478	−1.441	−1.373	−1.310
275	−1.904	−1.842	−1.784	−1.731	−1.681	−1.635	−1.591	−1.550	−1.511	−1.474	−1.404	−1.341
300	−1.936	−1.874	−1.816	−1.763	−1.713	−1.666	−1.622	−1.580	−1.541	−1.503	−1.433	−1.369
325	−1.964	−1.903	−1.845	−1.792	−1.742	−1.695	−1.650	−1.608	−1.569	−1.531	−1.460	−1.395
350	−1.989	−1.928	−1.871	−1.818	−1.768	−1.721	−1.676	−1.634	−1.594	−1.556	−1.485	−1.420
375	−2.012	−1.952	−1.895	−1.842	−1.792	−1.745	−1.700	−1.658	−1.618	−1.579	−1.508	−1.442
400	−2.033	−1.973	−1.917	−1.864	−1.814	−1.767	−1.722	−1.680	−1.640	−1.601	−1.529	−1.463
450	−2.070	−2.011	−1.956	−1.903	−1.854	−1.807	−1.762	−1.720	−1.679	−1.641	−1.568	−1.502
500	−2.102	−2.044	−1.989	−1.937	−1.888	−1.841	−1.797	−1.755	−1.714	−1.676	−1.603	−1.536

D2.5. Table 8. Specific isobaric heat capacity c_p of oxygen in kJ/(kg K)

Pressure in bar	Temperature in °C											
	−200	−180	−160	−140	−120	−100	−90	−80	−70	−60	−50	−40
1	1.678	0.9473	0.9305	0.9237	0.9191	0.9164	0.9155	0.9149	0.9145	0.9143	0.9142	0.9144
5	1.677	1.706	1.047	0.9885	0.9599	0.9440	0.9348	0.9317	0.9293	0.9275	0.9262	0.9253
10	1.676	1.703	1.832	1.100	1.021	0.9829	0.9709	0.9618	0.9547	0.9492	0.9449	0.9415
20	1.674	1.698	1.815	1.706	1.198	1.079	1.047	1.023	1.006	0.9928	0.9824	0.9742
30	1.672	1.692	1.799	2.182	1.535	1.210	1.143	1.098	1.066	1.042	1.024	1.010
40	1.669	1.687	1.785	2.110	2.531	1.400	1.268	1.188	1.135	1.097	1.069	1.048
50	1.667	1.682	1.771	2.052	6.755	1.690	1.434	1.299	1.216	1.159	1.119	1.089
60	1.665	1.677	1.759	2.004	3.640	2.167	1.657	1.435	1.309	1.229	1.173	1.133
70	1.663	1.673	1.748	1.963	2.974	2.964	1.956	1.599	1.416	1.305	1.232	1.179
80	1.661	1.669	1.737	1.928	2.648	3.974	2.329	1.790	1.535	1.388	1.293	1.228
90	1.660	1.664	1.727	1.897	2.447	4.194	2.718	1.998	1.663	1.476	1.358	1.278
100	1.658	1.660	1.717	1.870	2.308	3.658	2.984	2.199	1.793	1.565	1.423	1.328
120	1.654	1.653	1.700	1.823	2.124	2.838	2.904	2.448	2.015	1.732	1.550	1.427

D2.5. Table 8. (continued)

Temperature in °C												
Pressure in bar	−200	−180	−160	−140	−120	−100	−90	−80	−70	−60	−50	−40
140	1.651	1.646	1.684	1.785	2.005	2.434	2.571	2.430	2.127	1.855	1.657	1.515
160	1.648	1.639	1.670	1.754	1.920	2.204	2.317	2.293	2.128	1.916	1.730	1.585
180	1.645	1.633	1.658	1.726	1.856	2.056	2.141	2.153	2.068	1.921	1.766	1.631
200	1.642	1.627	1.646	1.703	1.806	1.952	2.016	2.036	1.992	1.894	1.774	1.656
225	1.639	1.621	1.633	1.678	1.756	1.859	1.903	1.922	1.902	1.842	1.757	1.663
250	1.636	1.614	1.621	1.656	1.715	1.790	1.822	1.837	1.826	1.787	1.726	1.653
275	1.633	1.609	1.611	1.637	1.683	1.737	1.759	1.770	1.763	1.736	1.691	1.634
300	1.630	1.603	1.601	1.621	1.655	1.695	1.710	1.717	1.712	1.691	1.657	1.611
325	1.628	1.599	1.593	1.606	1.631	1.660	1.671	1.675	1.669	1.653	1.625	1.588
350	1.626	1.594	1.585	1.593	1.611	1.631	1.638	1.639	1.634	1.619	1.596	1.565
375	1.623	1.590	1.577	1.581	1.593	1.607	1.610	1.610	1.604	1.591	1.570	1.544
400	1.621	1.586	1.570	1.570	1.578	1.585	1.587	1.584	1.578	1.565	1.548	1.525
450	1.618	1.579	1.558	1.552	1.551	1.551	1.548	1.544	1.536	1.524	1.509	1.490
500	1.614	1.572	1.548	1.536	1.530	1.523	1.518	1.512	1.503	1.492	1.478	1.462

Temperature in °C												
Pressure in bar	−30	−20	−10	0	10	20	30	40	50	60	80	100
1	0.9147	0.9152	0.9158	0.9167	0.9177	0.9189	0.9203	0.9219	0.9236	0.9255	0.9298	0.9345
5	0.9253	0.9247	0.9245	0.9246	0.9249	0.9255	0.9264	0.9275	0.9288	0.9304	0.9340	0.9382
10	0.9389	0.9370	0.9355	0.9346	0.9341	0.9339	0.9341	0.9346	0.9354	0.9364	0.9392	0.9428
20	0.9677	0.9626	0.9585	0.9553	0.9528	0.9510	0.9497	0.9490	0.9487	0.9487	0.9498	0.9521
30	0.9985	0.9896	0.9824	0.9767	0.9721	0.9685	0.9657	0.9636	0.9621	0.9611	0.9605	0.9613
40	1.031	1.018	1.007	0.9989	0.9920	0.9864	0.9819	0.9784	0.9756	0.9735	0.9711	0.9706
50	1.066	1.048	1.033	1.022	1.012	1.005	0.9983	0.9933	0.9892	0.9860	0.9818	0.9798
60	1.102	1.079	1.060	1.045	1.033	1.023	1.015	1.008	1.003	0.9985	0.9924	0.9889
70	1.140	1.111	1.087	1.069	1.054	1.042	1.032	1.023	1.017	1.011	1.003	0.9980
80	1.180	1.143	1.115	1.093	1.075	1.060	1.048	1.038	1.030	1.023	1.013	1.007
90	1.220	1.177	1.143	1.117	1.096	1.079	1.065	1.053	1.044	1.036	1.024	1.016
100	1.260	1.210	1.171	1.141	1.117	1.097	1.081	1.068	1.057	1.048	1.034	1.024
120	1.340	1.276	1.227	1.188	1.158	1.134	1.113	1.097	1.083	1.072	1.054	1.041
140	1.413	1.337	1.279	1.233	1.197	1.168	1.144	1.124	1.108	1.094	1.073	1.058
160	1.474	1.390	1.325	1.274	1.233	1.200	1.173	1.150	1.131	1.116	1.091	1.073
180	1.521	1.434	1.365	1.310	1.266	1.229	1.199	1.174	1.153	1.135	1.108	1.088
200	1.553	1.467	1.397	1.340	1.293	1.255	1.223	1.196	1.173	1.154	1.124	1.101
225	1.574	1.494	1.427	1.370	1.322	1.282	1.248	1.219	1.195	1.174	1.141	1.117
250	1.578	1.508	1.445	1.390	1.343	1.303	1.268	1.239	1.214	1.192	1.157	1.131
275	1.572	1.512	1.455	1.404	1.358	1.319	1.285	1.255	1.229	1.207	1.171	1.144
300	1.561	1.508	1.458	1.411	1.368	1.330	1.297	1.268	1.242	1.220	1.183	1.155
325	1.546	1.501	1.456	1.413	1.374	1.338	1.306	1.278	1.253	1.230	1.193	1.165
350	1.529	1.490	1.451	1.413	1.376	1.343	1.312	1.285	1.260	1.239	1.202	1.173
375	1.513	1.479	1.444	1.409	1.376	1.345	1.316	1.290	1.266	1.245	1.209	1.180
400	1.497	1.467	1.436	1.405	1.374	1.345	1.318	1.294	1.271	1.250	1.215	1.186
450	1.469	1.444	1.419	1.393	1.367	1.342	1.319	1.296	1.276	1.257	1.223	1.196
500	1.444	1.423	1.402	1.380	1.358	1.336	1.315	1.296	1.277	1.259	1.229	1.203

D2.5. Table 9. Specific isochoric heat capacity c_v of oxygen in kJ/(kg K)

Pressure in bar	Temperature in °C											
	−200	−180	−160	−140	−120	−100	−90	−80	−70	−60	−50	−40
1	1.001	0.6587	0.6543	0.6535	0.6522	0.6515	0.6513	0.6512	0.6513	0.6514	0.6517	0.6521
5	1.002	0.9188	0.6798	0.6690	0.6617	0.6574	0.6560	0.6551	0.6545	0.6542	0.6540	0.6541
10	1.003	0.9198	0.8584	0.6922	0.6748	0.6652	0.6622	0.6601	0.6586	0.6576	0.6570	0.6567
20	1.005	0.9218	0.8601	0.8111	0.7064	0.6825	0.6756	0.6707	0.6672	0.6647	0.6630	0.6618
30	1.006	0.9238	0.8619	0.8264	0.7513	0.7023	0.6904	0.6821	0.6762	0.6720	0.6691	0.6670
40	1.008	0.9258	0.8637	0.8258	0.8400	0.7255	0.7067	0.6942	0.6856	0.6796	0.6753	0.6722
50	1.010	0.9277	0.8655	0.8257	0.9324	0.7527	0.7247	0.7072	0.6954	0.6873	0.6815	0.6774
60	1.012	0.9297	0.8673	0.8260	0.8515	0.7846	0.7441	0.7207	0.7055	0.6951	0.6878	0.6826
70	1.013	0.9316	0.8691	0.8266	0.8301	0.8193	0.7644	0.7345	0.7156	0.7029	0.6940	0.6877
80	1.015	0.9334	0.8709	0.8275	0.8196	0.8449	0.7835	0.7480	0.7255	0.7105	0.7001	0.6927
90	1.017	0.9353	0.8727	0.8285	0.8136	0.8436	0.7981	0.7601	0.7349	0.7178	0.7060	0.6976
100	1.018	0.9371	0.8745	0.8296	0.8099	0.8286	0.8052	0.7699	0.7432	0.7246	0.7115	0.7022
120	1.022	0.9407	0.8780	0.8322	0.8063	0.8066	0.8009	0.7796	0.7555	0.7359	0.7213	0.7105
140	1.025	0.9442	0.8815	0.8350	0.8054	0.7954	0.7912	0.7793	0.7612	0.7434	0.7288	0.7175
160	1.028	0.9477	0.8849	0.8379	0.8060	0.7897	0.7841	0.7755	0.7624	0.7475	0.7340	0.7229
180	1.031	0.9510	0.8883	0.8409	0.8074	0.7871	0.7799	0.7720	0.7616	0.7494	0.7374	0.7269
200	1.034	0.9543	0.8916	0.8440	0.8093	0.7864	0.7779	0.7697	0.7606	0.7502	0.7396	0.7299
225	1.038	0.9582	0.8956	0.8478	0.8121	0.7870	0.7773	0.7685	0.7598	0.7507	0.7415	0.7327
250	1.041	0.9621	0.8995	0.8515	0.8151	0.7885	0.7780	0.7687	0.7599	0.7514	0.7429	0.7349
275	1.045	0.9658	0.9032	0.8552	0.8183	0.7907	0.7796	0.7698	0.7608	0.7524	0.7444	0.7369
300	1.048	0.9694	0.9069	0.8588	0.8216	0.7932	0.7816	0.7714	0.7623	0.7538	0.7460	0.7388
325	1.052	0.9730	0.9104	0.8622	0.8248	0.7959	0.7840	0.7735	0.7641	0.7556	0.7478	0.7407
350	1.055	0.9764	0.9138	0.8657	0.8280	0.7986	0.7865	0.7757	0.7661	0.7575	0.7497	0.7426
375	1.058	0.9797	0.9172	0.8690	0.8312	0.8015	0.7891	0.7781	0.7683	0.7596	0.7517	0.7446
400	1.061	0.9829	0.9204	0.8722	0.8342	0.8043	0.7917	0.7806	0.7706	0.7617	0.7538	0.7467
450	1.067	0.9891	0.9266	0.8783	0.8402	0.8098	0.7970	0.7855	0.7753	0.7662	0.7580	0.7508
500	1.072	0.9950	0.9325	0.8841	0.8458	0.8151	0.8020	0.7904	0.7800	0.7706	0.7623	0.7548

Pressure in bar	Temperature in °C											
	−30	−20	−10	0	10	20	30	40	50	60	80	100
1	0.6527	0.6534	0.6542	0.6552	0.6564	0.6577	0.6592	0.6609	0.6627	0.6647	0.6690	0.6739
5	0.6544	0.6549	0.6556	0.6565	0.6575	0.6587	0.6602	0.6617	0.6635	0.6654	0.6697	0.6745
10	0.6566	0.6569	0.6573	0.6580	0.6589	0.6600	0.6613	0.6628	0.6645	0.6663	0.6705	0.6752
20	0.6611	0.6608	0.6608	0.6611	0.6617	0.6626	0.6637	0.6650	0.6665	0.6682	0.6721	0.6766
30	0.6655	0.6647	0.6642	0.6642	0.6645	0.6651	0.6660	0.6671	0.6684	0.6700	0.6737	0.6780
40	0.6700	0.6685	0.6677	0.6672	0.6672	0.6676	0.6682	0.6692	0.6703	0.6718	0.6752	0.6793
50	0.6744	0.6724	0.6710	0.6702	0.6699	0.6700	0.6704	0.6712	0.6722	0.6735	0.6767	0.6807
60	0.6788	0.6762	0.6744	0.6732	0.6726	0.6724	0.6726	0.6732	0.6741	0.6752	0.6782	0.6820
70	0.6832	0.6799	0.6776	0.6761	0.6751	0.6747	0.6748	0.6751	0.6759	0.6769	0.6796	0.6833
80	0.6874	0.6835	0.6808	0.6789	0.6777	0.6770	0.6768	0.6771	0.6776	0.6785	0.6811	0.6845
90	0.6915	0.6870	0.6839	0.6816	0.6801	0.6792	0.6789	0.6789	0.6793	0.6801	0.6824	0.6857
100	0.6854	0.6904	0.6868	0.6843	0.6825	0.6814	0.6808	0.6807	0.6810	0.6816	0.6838	0.6869
120	0.7026	0.6968	0.6924	0.6893	0.6870	0.6855	0.6846	0.6842	0.6842	0.6846	0.6864	0.6892
140	0.7089	0.7024	0.6975	0.6938	0.6912	0.6893	0.6881	0.6874	0.6872	0.6874	0.6889	0.6914
160	0.7141	0.7072	0.7020	0.6980	0.6950	0.6928	0.6914	0.6905	0.6901	0.6901	0.6912	0.6935
180	0.7183	0.7113	0.7059	0.7017	0.6984	0.6960	0.6944	0.6933	0.6927	0.6926	0.6934	0.6954

D2.5. Table 9. (continued)

Pressure in bar	Temperature in °C											
	−30	−20	−10	0	10	20	30	40	50	60	80	100
200	0.7217	0.7148	0.7093	0.7049	0.7016	0.6992	0.6972	0.6959	0.6952	0.6949	0.6955	0.6973
225	0.7250	0.7184	0.7129	0.7085	0.7050	0.7023	0.7003	0.6989	0.6980	0.6986	0.6979	0.6995
250	0.7277	0.7214	0.7161	0.7117	0.7081	0.7053	0.7032	0.7017	0.7007	0.7001	0.7002	0.7016
275	0.7300	0.7240	0.7188	0.7144	0.7109	0.7080	0.7058	0.7042	0.7031	0.7025	0.7023	0.7035
300	0.7322	0.7263	0.7212	0.7169	0.7134	0.7105	0.7082	0.7065	0.7054	0.7046	0.7043	0.7053
325	0.7342	0.7285	0.7235	0.7193	0.7157	0.7128	0.7105	0.7087	0.7075	0.7066	0.7062	0.7070
350	0.7363	0.7306	0.7257	0.7214	0.7179	0.7149	0.7126	0.7107	0.7094	0.7085	0.7079	0.7086
375	0.7383	0.7327	0.7277	0.7235	0.7199	0.7169	0.7145	0.7127	0.7113	0.7103	0.7096	0.7102
400	0.7403	0.7347	0.7297	0.7255	0.7219	0.7189	0.7164	0.7145	0.7130	0.7120	0.7111	0.7116
450	0.7443	0.7386	0.7336	0.7293	0.7256	0.7225	0.7199	0.7179	0.7163	0.7152	0.7141	0.7143
500	0.7482	0.7424	0.7373	0.7328	0.7290	0.7258	0.7231	0.7210	0.7193	0.7181	0.7167	0.7168

D2.5. Table 10. Isobaric expansion coefficient β of oxygen in 10^{-3}/K

Pressure in bar	Temperature in °C											
	−200	−180	−160	−140	−120	−100	−90	−80	−70	−60	−50	−40
1	3.78	11.7	9.26	7.74	6.66	5.86	5.53	5.23	4.97	4.73	4.51	4.32
5	3.77	4.49	11.6	8.81	7.25	6.21	5.81	5.46	5.16	4.89	4.65	4.43
10	3.75	4.46	6.04	10.7	8.14	6.71	6.20	5.78	5.41	5.09	4.82	4.57
20	3.72	4.40	5.87	20.0	10.7	7.95	7.12	6.48	5.97	5.54	5.18	4.87
30	3.70	4.35	5.72	9.90	15.6	7.64	8.29	7.33	6.61	6.04	5.58	5.20
40	3.67	4.29	5.58	9.17	30.0	12.1	9.78	8.35	7.34	6.60	6.01	5.54
50	3.64	4.24	5.45	8.58	66.8	15.7	11.7	9.57	8.18	7.20	6.47	5.90
60	3.61	4.19	5.33	8.10	27.3	21.6	14.3	11.0	9.13	7.87	6.96	6.27
70	3.59	4.14	5.21	7.68	19.4	31.0	17.6	12.7	10.2	8.57	7.47	6.65
80	3.56	4.09	5.10	7.33	15.6	41.5	21.5	14.6	11.3	9.31	7.98	7.04
90	3.54	4.04	5.00	7.02	13.4	40.4	25.1	16.6	12.4	10.0	8.50	7.41
100	3.51	4.00	4.91	6.74	11.9	31.2	26.7	18.2	13.5	10.7	8.99	7.77
120	3.47	3.92	4.73	6.28	9.85	19.6	22.7	19.2	14.9	11.8	9.82	8.40
140	3.42	3.84	4.57	5.90	8.57	14.4	17.3	17.2	14.8	12.3	10.3	8.83
160	3.38	3.76	4.43	5.58	7.68	11.5	13.7	14.5	13.7	12.0	10.4	9.02
180	3.34	3.69	4.30	5.30	7.00	9.79	11.3	12.3	12.2	11.3	10.1	8.96
200	3.30	3.62	4.18	5.07	6.48	8.59	9.75	10.6	10.8	10.4	9.61	8.71
225	3.25	3.54	4.04	4.81	5.95	7.53	8.37	9.05	9.37	9.28	8.85	8.24
250	3.20	3.47	3.92	4.59	5.53	6.76	7.40	7.94	8.26	8.30	8.08	7.69
275	3.16	3.40	3.81	4.39	5.19	6.17	6.67	7.10	7.39	7.49	7.39	7.14
300	3.11	3.33	3.70	4.22	4.90	5.70	6.11	6.46	6.71	6.82	6.79	6.63
325	3.07	3.27	3.61	4.07	4.65	5.32	5.65	5.94	6.16	6.27	6.27	6.18
350	3.03	3.21	3.52	3.93	4.44	5.00	5.28	5.52	5.70	5.81	5.83	5.77
375	2.99	3.16	3.43	3.80	4.25	4.73	4.96	5.17	5.32	5.42	5.45	5.42
400	2.96	3.11	3.36	3.69	4.08	4.50	4.70	4.87	5.00	5.09	5.13	5.11
450	2.89	3.01	3.21	3.49	3.80	4.11	4.26	4.39	4.49	4.56	4.59	4.59
500	2.82	2.92	3.09	3.31	3.56	3.81	3.92	4.02	4.10	4.15	4.18	4.18

D2.5. Table 10. (continued)

Pressure in bar	Temperature in °C											
	−30	−20	−10	0	10	20	30	40	50	60	80	100
1	4.14	3.97	3.82	3.68	3.54	3.42	3.31	3.20	3.10	3.01	2.84	2.68
5	4.23	4.05	3.89	3.74	3.60	3.47	3.35	3.24	3.13	3.04	2.86	2.70
10	4.35	4.15	3.98	3.81	3.66	3.53	3.40	3.28	3.17	3.07	2.89	2.72
20	4.61	4.37	4.16	3.97	3.80	3.64	3.50	3.37	3.25	3.14	2.94	2.76
30	4.87	4.59	4.34	4.13	3.93	3.76	3.60	3.46	3.33	3.20	2.99	2.81
40	5.15	4.82	4.53	4.29	4.07	3.87	3.70	3.54	3.40	3.27	3.04	2.84
50	5.43	5.05	4.72	4.45	4.20	3.99	3.80	3.63	3.47	3.33	3.09	2.88
60	5.73	5.28	4.92	4.60	4.33	4.10	3.89	3.71	3.54	3.40	3.14	2.92
70	6.02	5.52	5.11	4.76	4.47	4.21	3.99	3.79	3.61	3.46	3.18	2.95
80	6.32	5.75	5.29	4.91	4.59	4.32	4.08	3.87	3.68	3.51	3.23	2.99
90	6.60	5.98	5.47	5.06	4.71	4.42	4.16	3.94	3.74	3.57	3.27	3.02
100	6.88	6.19	5.64	5.20	4.83	4.51	4.24	4.01	3.80	3.62	3.30	3.05
120	7.36	6.57	5.95	5.45	5.03	4.69	4.39	4.13	3.91	3.71	3.37	3.10
140	7.72	6.87	6.19	5.65	5.20	4.83	4.51	4.23	3.99	3.78	3.43	3.14
160	7.92	7.06	6.36	5.80	5.33	4.94	4.60	4.31	4.06	3.84	3.48	3.18
180	7.96	7.13	6.45	5.88	5.41	5.01	4.67	4.37	4.11	3.89	3.51	3.21
200	7.86	7.10	6.46	5.91	5.44	5.04	4.70	4.41	4.15	3.92	3.53	3.22
225	7.57	6.94	6.37	5.87	5.43	5.04	4.71	4.42	4.16	3.93	3.55	3.24
250	7.20	6.69	6.20	5.76	5.35	5.00	4.68	4.40	4.15	3.92	3.54	3.23
275	6.79	6.39	5.99	5.60	5.24	4.91	4.62	4.35	4.11	3.90	3.53	3.22
300	6.38	6.07	5.74	5.41	5.10	4.80	4.53	4.29	4.06	3.86	3.50	3.20
325	5.99	5.76	5.49	5.21	4.94	4.68	4.43	4.20	3.99	3.80	3.46	3.18
350	5.64	5.46	5.24	5.01	4.77	4.54	4.32	4.11	3.92	3.74	3.41	3.14
375	5.32	5.18	5.00	4.81	4.60	4.40	4.20	4.01	3.83	3.67	3.36	3.10
400	5.03	4.92	4.78	4.61	4.44	4.26	4.08	3.91	3.75	3.59	3.31	3.06
450	4.55	4.47	4.37	4.25	4.12	3.98	3.84	3.70	3.56	3.43	3.18	2.96
500	4.15	4.10	4.03	3.94	3.84	3.73	3.62	3.50	3.39	3.27	3.06	2.86

D2.5. Table 11. Isentropic speed of sound w_s in oxygen in m/s

Pressure in bar	Temperature in °C											
	−200	−180	−160	−140	−120	−100	−90	−80	−70	−60	−50	−40
1	1042	181.1	201.1	218.9	235.2	250.4	257.6	264.6	271.5	278.1	284.6	290.9
5	1044	881.7	193.1	213.8	231.8	248.1	255.7	263.1	270.2	277.1	283.8	290.3
10	1045	884.3	709.2	206.7	227.4	245.2	253.4	261.2	268.7	275.8	282.8	289.5
20	1048	889.4	718.2	187.7	217.8	239.3	248.7	257.4	265.7	273.5	281.0	288.1
30	1052	894.5	726.8	523.8	206.7	233.4	244.1	253.9	263.0	271.4	279.4	287.0
40	1055	899.4	735.1	541.5	192.4	227.5	239.8	250.7	260.6	269.7	278.1	286.1
50	1058	904.2	743.1	557.6	248.5	222.0	236.0	248.0	258.6	268.3	277.3	285.6
60	1061	909.0	750.8	572.4	323.5	217.5	233.1	246.0	257.3	267.5	276.8	285.5
70	1064	913.6	758.2	586.0	365.3	216.0	231.6	245.0	256.7	267.3	276.9	285.8
80	1067	918.2	765.4	598.8	396.9	222.1	232.7	245.4	257.2	267.8	277.6	286.6
90	1070	922.8	772.5	610.8	423.0	242.5	237.9	247.9	258.8	269.2	278.9	288.0

D2.5. Table 11. (continued)

Temperature in °C												
Pressure in bar	−200	−180	−160	−140	−120	−100	−90	−80	−70	−60	−50	−40
100	1073	927.2	779.3	622.2	445.5	271.9	248.6	252.9	262.0	271.7	281.1	290.0
120	1079	936.0	792.4	643.2	483.4	328.3	284.3	271.7	273.6	280.1	287.8	295.8
140	1085	944.5	804.9	662.4	514.9	374.8	325.5	300.0	292.3	293.4	298.2	304.4
160	1091	952.7	816.8	680.1	542.2	413.6	364.0	331.9	316.0	311.1	311.9	315.6
180	1097	960.8	828.2	696.5	566.4	446.8	398.5	363.4	342.1	331.7	328.4	329.2
200	1102	968.8	839.2	712.0	588.3	475.8	429.3	393.1	368.4	353.9	346.8	344.5
225	1110	978.4	852.4	730.1	613.0	507.7	463.3	427.1	400.2	382.0	371.1	365.4
250	1116	987.8	865.1	747.1	635.6	536.0	493.6	457.9	429.9	409.4	395.7	387.2
275	1123	997.1	877.3	763.2	656.3	561.4	520.7	485.9	457.5	435.7	419.9	409.2
300	1130	1006	889.1	778.4	675.6	584.7	545.5	511.5	483.1	460.4	443.3	430.9
325	1137	1015	900.5	793.0	693.7	606.2	568.3	535.1	506.9	483.8	465.7	452.0
350	1144	1024	911.6	806.9	710.8	626.3	589.5	557.1	529.2	505.9	487.1	472.5
375	1150	1032	922.4	820.2	727.0	645.1	609.4	577.7	550.1	526.8	507.6	492.2
400	1157	1040	932.8	833.1	742.4	662.9	628.1	597.0	569.8	546.5	527.1	511.1
450	1170	1057	953.0	857.6	771.3	695.8	662.7	632.8	606.3	583.3	563.5	546.9
500	1183	1073	972.3	880.6	798.1	726.0	694.2	665.4	639.6	616.9	597.1	580.2

Temperature in °C												
Pressure in bar	−30	−20	−10	0	10	20	30	40	50	60	80	100
1	297.1	303.1	309.0	314.8	320.5	326.0	331.4	336.7	341.9	347.1	357.0	366.6
5	296.6	302.8	308.8	314.7	320.4	326.0	331.5	336.9	342.2	347.3	357.4	367.0
10	296.0	302.4	308.5	314.5	320.4	326.1	331.6	337.1	342.4	347.7	357.8	367.6
20	295.0	301.7	308.1	314.3	320.4	326.3	332.0	337.6	343.1	348.4	358.8	368.7
30	294.2	301.2	307.9	314.4	320.6	326.7	332.6	338.3	343.9	349.3	359.8	369.9
40	293.7	301.0	307.9	314.6	321.0	327.3	333.3	339.1	344.8	350.4	361.0	371.2
50	293.5	301.0	308.2	315.1	321.7	328.0	334.2	340.1	345.9	351.5	362.3	372.6
60	293.7	304.4	308.7	315.8	322.5	329.0	335.2	341.3	347.1	352.8	363.7	374.1
70	294.2	302.1	309.6	316.7	323.6	330.1	336.5	342.6	348.5	354.2	365.3	375.7
80	395.1	303.1	310.7	317.9	324.9	331.5	337.9	344.1	350.0	355.8	366.9	377.4
90	296.5	304.6	312.2	319.5	326.4	333.1	339.5	345.7	351.7	357.5	368.7	379.2
100	298.4	306.4	314.0	321.3	328.2	334.9	341.4	347.6	353.6	359.4	370.6	381.1
120	303.7	311.3	318.7	325.8	332.6	339.3	345.6	351.8	357.8	363.6	374.7	385.3
140	311.1	318.0	324.8	331.6	338.1	344.5	350.7	356.8	362.7	368.4	379.3	389.8
160	320.7	326.4	332.5	338.6	344.7	350.7	356.7	362.5	368.2	373.7	384.4	394.7
180	332.2	336.5	341.4	346.7	352.2	357.8	363.3	368.8	374.3	379.6	390.0	400.0
200	345.3	347.9	351.6	356.0	360.7	365.7	370.7	375.9	381.0	386.0	396.0	405.7
225	363.4	363.8	365.8	368.8	372.5	376.6	380.9	385.4	390.1	374.7	404.0	413.2
250	382.7	380.9	381.2	382.7	385.2	388.4	392.0	395.8	399.9	404.1	412.6	421.2
275	402.5	398.8	397.4	397.5	398.8	401.0	403.7	406.9	410.3	414.0	421.7	429.7
300	422.4	417.0	414.1	412.9	413.0	414.2	416.1	418.5	421.3	424.4	431.2	438.5
325	442.1	435.3	431.0	428.5	427.6	427.8	428.8	430.5	432.7	435.2	441.1	447.7
350	461.4	453.4	447.9	444.3	442.4	441.6	441.8	442.8	444.3	446.3	451.3	457.1
375	480.2	471.2	464.7	460.1	457.2	455.6	455.1	455.3	456.2	457.7	461.7	466.7
400	498.5	488.6	481.2	475.8	472.1	469.7	468.4	468.0	468.3	469.2	472.3	476.5
450	533.2	522.2	513.4	506.5	501.4	497.6	495.0	493.4	492.6	492.5	493.8	496.5
500	565.8	553.9	544.1	536.2	529.9	525.0	521.4	518.7	517.0	515.9	515.5	516.9

D2.5. Table 12. Thermal conductivity λ of oxygen in mW/(m K)

Pressure in bar	Temperature in °C											
	−200	−180	−160	−140	−120	−100	−90	−80	−70	−60	−50	−40
1	176.6	8.611	10.64	12.58	14.44	16.21	17.07	17.92	18.74	19.55	20.35	21.14
5	176.8	148.7	11.25	13.00	14.76	16.48	17.32	18.15	18.96	19.76	20.55	21.32
10	177.0	149.1	121.1	13.77	15.28	16.88	17.68	18.48	19.27	20.05	20.81	21.58
20	177.5	149.8	122.2	17.09	16.90	17.96	18.62	19.30	20.01	20.72	21.44	22.15
30	178.0	150.5	123.2	94.09	19.81	19.52	19.88	20.37	20.94	21.55	22.18	22.83
40	178.5	151.1	124.2	95.82	26.00	21.76	21.57	21.74	22.08	22.53	23.05	23.62
50	179.0	151.8	125.1	97.43	70.65	24.96	23.80	23.44	23.46	23.70	24.06	24.50
60	179.5	152.5	126.1	98.95	68.91	29.58	26.69	25.53	25.09	25.04	25.20	25.50
70	180.0	153.1	127.0	100.4	71.67	36.10	30.33	28.03	26.99	26.56	26.48	26.60
80	180.4	153.8	127.9	101.8	74.29	44.05	34.69	30.93	29.14	28.27	27.88	27.80
90	180.9	154.4	128.7	103.1	76.66	50.60	39.44	34.14	31.51	30.12	29.41	29.09
100	181.4	155.1	129.6	104.3	78.80	54.46	43.96	37.49	34.02	32.10	31.03	30.45
120	182.3	156.3	131.3	106.7	82.59	60.02	50.88	43.84	39.17	36.26	34.47	33.36
140	183.3	157.5	132.9	109.0	85.91	64.73	56.00	49.09	43.96	40.39	37.99	36.40
160	184.2	158.7	134.5	111.1	88.88	68.79	60.36	53.49	48.20	44.26	41.43	39.42
180	185.1	159.9	136.0	113.1	91.60	72.36	64.20	57.38	51.97	47.81	44.68	42.36
200	185.9	161.0	137.4	115.0	94.11	75.55	67.63	60.88	55.40	51.07	47.72	45.16
225	187.0	162.4	139.2	117.3	97.03	79.15	71.47	64.83	59.30	54.82	51.27	48.47
250	188.1	163.8	140.9	119.5	99.75	82.42	74.94	68.40	62.85	58.27	54.56	51.58
275	189.2	165.2	142.6	121.6	102.3	85.42	78.11	71.67	66.13	61.48	57.64	54.51
300	190.2	166.5	144.2	123.6	104.7	88.22	81.06	74.70	69.17	64.47	60.54	57.28
325	191.2	167.8	145.7	125.5	107.0	90.84	83.80	77.52	72.02	67.29	63.28	59.92
350	192.2	169.0	147.2	127.3	109.2	93.33	86.39	80.18	74.70	69.95	65.88	62.43
375	193.2	170.3	148.8	129.1	111.3	95.68	88.84	82.69	77.24	72.47	68.35	64.83
400	194.2	171.5	150.2	130.9	113.3	97.93	91.18	85.09	79.66	74.88	70.72	67.14
450	196.1	173.8	153.1	134.2	117.1	102.2	95.55	89.56	84.17	79.39	75.17	71.49
500	198.0	176.1	155.8	137.3	120.7	106.1	99.60	93.69	88.35	83.56	79.31	75.56

Pressure in bar	Temperature in °C											
	−30	−20	−10	0	10	20	30	40	50	60	80	100
1	21.91	22.68	23.43	24.18	24.92	25.66	26.38	27.11	27.83	28.54	29.96	31.37
5	22.09	22.85	23.59	24.34	25.07	25.80	26.52	27.24	27.95	28.66	30.08	31.48
10	22.33	23.07	23.81	24.54	25.27	25.99	26.70	27.41	28.12	28.83	30.23	31.62
20	22.87	23.58	24.29	25.00	25.70	26.40	27.10	27.79	28.48	29.18	30.55	31.93
30	23.49	24.16	24.83	25.50	26.18	26.85	27.53	28.20	28.87	29.55	30.90	32.25
40	24.21	24.81	25.44	26.07	26.71	27.35	27.99	28.63	29.29	29.95	31.28	32.60
50	25.00	25.54	26.10	26.68	27.28	27.88	28.49	29.10	29.74	30.38	31.67	32.96
60	25.89	26.34	26.83	27.35	27.89	28.45	29.03	29.60	30.21	30.83	32.08	33.34
70	26.85	27.20	27.61	28.06	28.55	29.06	29.59	30.12	30.71	31.30	32.51	33.74
80	27.90	28.13	28.44	28.82	29.24	29.70	30.18	30.66	31.22	31.79	32.96	34.15
90	29.02	29.11	29.32	29.62	29.97	30.37	30.80	31.23	31.76	32.30	33.42	34.58
100	30.20	30.15	30.25	30.45	30.73	31.07	31.44	31.81	32.31	32.83	33.90	35.01
120	32.71	32.36	32.21	32.22	32.34	32.53	32.78	33.04	33.46	33.92	34.89	35.92
140	35.35	34.68	34.29	34.09	34.03	34.08	34.19	34.31	34.67	35.06	35.92	36.86
160	38.02	37.06	36.42	36.01	35.78	35.67	35.64	35.63	35.91	36.23	36.98	37.83
180	40.66	39.44	38.57	37.96	37.55	37.30	37.13	36.98	37.18	37.44	38.06	38.82
200	43.23	41.78	40.70	39.91	39.34	38.94	38.64	38.35	38.47	38.65	39.16	39.82

D2.5. Table 12. (continued)

Pressure in bar	Temperature in °C											
	−30	−20	−10	0	10	20	30	40	50	60	80	100
225	46.30	44.61	43.31	42.32	41.56	40.99	40.52	40.07	40.09	40.19	40.55	41.09
250	49.21	47.33	45.84	44.67	43.75	43.02	42.40	41.79	41.72	41.73	41.95	42.36
275	51.97	49.93	48.28	46.95	45.88	45.01	44.26	43.51	43.34	43.27	43.34	43.64
300	54.61	52.42	50.63	49.16	47.96	46.97	46.09	45.21	44.95	44.79	44.72	44.91
325	57.12	54.81	52.89	51.31	49.99	48.88	47.89	46.89	46.54	46.30	46.10	46.17
350	59.53	57.11	55.08	53.38	51.96	50.74	49.66	48.55	48.11	47.80	47.46	47.42
375	61.85	59.32	57.19	55.40	53.88	52.57	51.39	50.18	49.67	49.28	48.81	48.66
400	64.07	61.46	59.24	57.36	55.74	54.35	53.08	51.79	51.20	50.74	50.15	49.89
450	68.30	65.54	63.17	61.12	59.35	57.80	56.38	54.94	54.20	53.61	52.77	52.31
500	72.27	69.39	66.88	64.70	62.79	61.10	59.56	58.00	57.12	56.40	55.34	54.69

D2.5. Table 13. Dynamic viscosity η of oxygen in 10^{-6} Pa·s

Pressure in bar	Temperature in °C											
	−200	−180	−160	−140	−120	−100	−90	−80	−70	−60	−50	−40
1	311.6	6.810	8.452	10.02	11.51	12.93	13.62	14.29	14.95	15.60	16.23	16.86
5	313.1	172.7	8.587	10.12	11.60	13.01	13.69	14.36	15.02	15.66	16.29	16.91
10	315.1	173.7	110.1	10.30	11.74	13.12	13.80	14.46	15.11	15.75	16.37	16.99
20	319.0	175.8	111.8	10.91	12.13	13.42	14.07	14.70	15.33	15.95	16.57	17.17
30	323.0	177.9	113.5	73.31	12.77	13.84	14.43	15.02	15.62	16.21	16.80	17.39
40	327.1	180.0	115.2	75.29	14.04	14.43	14.91	15.43	15.98	16.53	17.09	17.65
50	331.2	182.1	116.8	77.16	39.15	15.30	15.56	15.96	16.42	16.92	17.43	17.95
60	335.4	184.2	118.4	78.95	45.66	16.64	16.45	16.63	16.97	17.38	17.83	18.31
70	339.6	186.3	120.1	80.67	49.48	18.81	17.66	17.49	17.64	17.93	18.30	18.72
80	343.9	188.4	121.7	82.33	52.45	22.39	19.33	18.58	18.45	18.58	18.85	19.19
90	348.3	190.6	123.3	83.93	54.96	27.24	21.56	19.93	19.42	19.34	19.47	19.72
100	352.7	192.7	124.9	85.50	57.18	31.86	24.33	21.58	20.56	20.21	20.17	20.30
120	361.7	197.1	128.1	88.53	61.08	38.80	30.36	25.61	23.35	22.29	21.82	21.67
140	371.1	201.5	131.2	91.44	64.50	43.83	35.71	29.99	26.61	24.77	23.78	23.27
160	380.7	205.9	134.4	94.26	67.60	47.87	40.10	34.11	30.03	27.49	25.96	25.07
180	390.7	210.4	137.5	97.02	70.49	51.32	43.82	37.79	33.34	30.28	28.28	27.01
200	401.0	215.0	140.6	99.71	73.22	54.40	47.07	41.07	36.42	33.02	30.64	29.03
225	414.3	220.8	144.6	103.0	76.45	57.88	50.69	44.73	39.95	36.27	33.54	31.58
250	428.3	226.8	148.5	106.3	79.54	61.06	53.95	48.01	43.16	39.31	36.33	34.09
275	442.9	232.8	152.5	109.5	82.51	64.04	56.95	51.02	46.11	42.14	38.98	36.53
300	458.2	239.0	156.5	112.7	85.40	66.86	59.77	53.81	48.86	44.79	41.49	38.87
325	474.2	245.4	160.5	115.9	88.22	69.55	62.43	56.45	51.44	47.29	43.88	41.12
350	491.1	251.9	164.6	119.0	90.98	72.15	64.98	58.95	53.89	49.66	46.16	43.28
375	508.8	258.5	168.7	122.1	93.70	74.67	67.44	61.35	56.23	51.93	48.34	45.36
400	527.5	265.3	172.8	125.3	96.38	77.12	69.81	63.66	58.48	54.11	50.44	47.37
450	568.0	279.5	181.3	131.6	101.7	81.88	74.39	68.08	62.76	58.24	54.42	51.19
500	613.4	294.5	190.0	137.9	106.9	86.49	78.79	72.30	66.81	62.15	58.18	54.80

D2.5. Table 13. (continued)

Pressure in bar	Temperature in °C											
	−30	−20	−10	0	10	20	30	40	50	60	80	100
1	17.47	18.07	18.66	19.24	19.81	20.37	20.92	21.47	22.00	22.53	23.57	24.58
5	17.52	18.12	18.71	19.28	19.85	20.41	20.96	21.51	22.04	22.57	23.61	24.62
10	17.59	18.19	18.77	19.35	19.91	20.47	21.02	21.56	22.10	22.62	23.66	24.66
20	17.76	18.35	18.92	19.49	20.05	20.60	21.15	21.68	22.21	22.73	23.76	24.76
30	17.97	18.54	19.10	19.66	20.21	20.75	21.29	21.82	22.34	22.86	23.87	24.87
40	18.21	18.76	19.31	19.85	20.39	20.92	21.45	21.97	22.49	23.00	24.00	24.99
50	18.48	19.01	19.54	20.07	20.60	21.12	21.63	22.14	22.65	23.15	24.14	25.11
60	18.80	19.30	19.81	20.32	20.82	21.33	21.83	22.33	22.83	23.32	24.30	25.25
70	19.17	19.63	20.11	20.59	21.08	21.56	22.05	22.54	23.02	23.51	24.46	25.40
80	19.58	20.00	20.44	20.89	21.35	21.82	22.29	22.76	23.23	23.70	24.64	25.56
90	20.04	20.40	20.80	21.22	21.66	22.10	22.55	23.00	23.46	23.91	24.83	25.73
100	20.54	20.85	21.20	21.58	21.98	22.40	22.83	23.26	23.70	24.14	25.03	25.92
120	21.71	21.86	22.09	22.38	22.71	23.06	23.44	23.83	24.23	24.63	25.46	26.31
140	23.06	23.03	23.12	23.29	23.53	23.81	24.12	24.46	24.81	25.18	25.94	26.74
160	24.57	24.33	24.26	24.31	24.44	24.63	24.87	25.15	25.45	25.77	26.47	27.20
180	26.22	25.75	25.50	25.41	25.43	25.53	25.69	25.90	26.14	26.42	27.03	27.70
200	27.95	27.26	26.83	26.58	26.48	26.48	26.56	26.70	26.88	27.10	27.63	28.23
225	30.19	29.22	28.56	28.13	27.87	27.74	27.71	27.75	27.86	28.01	28.42	28.93
250	32.43	31.22	30.35	29.74	29.33	29.07	28.92	28.87	28.89	28.96	29.25	29.66
275	34.65	33.23	32.17	31.39	30.83	30.44	30.18	30.03	29.96	29.96	30.12	30.44
300	36.81	35.21	33.98	33.05	32.34	31.83	31.46	31.22	31.06	30.99	31.02	31.24
325	38.91	37.16	35.78	34.70	33.87	33.24	32.77	32.43	32.19	32.04	31.95	32.06
350	40.94	39.05	37.54	36.34	35.39	34.65	34.08	33.65	33.33	33.11	32.90	32.90
375	42.91	40.91	39.28	37.96	36.90	36.06	35.40	34.88	34.49	34.20	33.86	33.76
400	44.82	42.71	40.97	39.55	38.40	37.46	36.71	36.11	35.65	35.29	34.83	34.63
450	48.46	46.18	44.26	42.66	41.32	40.22	39.31	38.57	37.96	37.47	36.79	36.40
500	51.92	49.48	47.40	45.65	44.16	42.91	41.86	40.99	40.25	39.65	38.75	38.18

D2.5. Table 14. Kinematic viscosity v of oxygen in 10^{-7} m^2/s

Pressure in bar	Temperature in °C											
	−200	−180	−160	−140	−120	−100	−90	−80	−70	−60	−50	−40
1	2.55	16.0	24.4	34.3	45.5	57.9	64.6	71.5	78.7	86.2	93.9	102
5	2.56	1.53	4.60	6.63	8.91	11.4	12.8	14.2	15.6	17.1	18.7	20.3
10	2.57	1.54	1.08	3.16	4.34	5.62	6.30	7.01	7.75	8.51	9.30	10.1
20	2.60	1.55	1.09	1.39	2.04	2.72	3.07	3.44	3.81	4.20	4.60	5.02
30	2.63	1.57	1.11	0.827	1.27	1.75	2.00	2.25	2.51	2.77	3.05	3.33
40	2.66	1.59	1.12	0.840	0.971	1.28	1.47	1.66	1.86	2.06	2.27	2.49
50	2.69	1.60	1.13	0.853	0.619	0.992	1.15	1.31	1.48	1.64	1.81	1.99
60	2.72	1.62	1.14	0.866	0.655	0.808	0.950	1.09	1.23	1.37	1.51	1.66
70	2.75	1.63	1.15	0.878	0.678	0.688	0.813	0.934	1.05	1.18	1.30	1.43
80	2.79	1.65	1.16	0.889	0.697	0.620	0.720	0.825	0.931	1.04	1.15	1.26
90	2.82	1.66	1.18	0.901	0.712	0.600	0.661	0.748	0.840	0.935	1.03	1.13

D2.5. Table 14. (continued)

Temperature in °C												
Pressure in bar	−200	−180	−160	−140	−120	−100	−90	−80	−70	−60	−50	−40
100	2.85	1.68	1.19	0.911	0.727	0.606	0.629	0.695	0.774	0.858	0.944	1.03
120	2.92	1.71	1.21	0.933	0.752	0.633	0.616	0.642	0.693	0.755	0.823	0.895
140	2.99	1.74	1.23	0.953	0.774	0.658	0.629	0.629	0.656	0.699	0.751	0.808
160	3.06	1.77	1.26	0.973	0.795	0.680	0.647	0.634	0.644	0.670	0.708	0.753
180	3.13	1.81	1.28	0.993	0.814	0.700	0.664	0.645	0.644	0.658	0.685	0.719
200	3.21	1.84	1.30	1.01	0.833	0.719	0.682	0.659	0.650	0.656	0.673	0.699
225	3.30	1.88	1.33	1.04	0.855	0.740	0.702	0.676	0.662	0.660	0.669	0.686
250	3.41	1.93	1.36	1.06	0.876	0.760	0.721	0.693	0.675	0.668	0.671	0.681
275	3.51	1.97	1.39	1.08	0.896	0.779	0.739	0.709	0.689	0.679	0.676	0.682
300	3.63	2.02	1.42	1.10	0.916	0.798	0.756	0.725	0.703	0.690	0.684	0.686
325	3.74	2.06	1.45	1.13	0.936	0.815	0.773	0.741	0.717	0.702	0.693	0.691
350	3.87	2.11	1.48	1.15	0.955	0.832	0.789	0.756	0.731	0.713	0.703	0.699
375	4.00	2.16	1.51	1.17	0.974	0.849	0.805	0.771	0.744	0.725	0.713	0.707
400	4.14	2.21	1.54	1.19	0.993	0.866	0.821	0.785	0.757	0.737	0.723	0.715
450	4.43	2.31	1.60	1.24	1.03	0.898	0.851	0.813	0.783	0.761	0.744	0.733
500	4.77	2.42	1.66	1.29	1.07	0.929	0.880	0.840	0.809	0.784	0.765	0.751

Temperature in °C												
Pressure in bar	−30	−20	−10	0	10	20	30	40	50	60	80	100
1	110	119	127	136	146	155	165	175	185	195	216	238
5	22.0	23.7	25.4	27.2	29.1	31.0	32.9	34.9	36.9	39.0	43.3	47.7
10	10.9	11.8	12.7	13.6	14.5	15.5	16.5	17.5	18.5	19.5	21.7	23.9
20	5.44	5.88	6.33	6.79	7.26	7.74	8.23	8.74	9.25	9.78	10.9	12.0
30	3.61	3.91	4.21	4.52	4.84	5.17	5.50	5.84	6.18	6.54	7.26	8.01
40	2.71	2.93	3.16	3.40	3.64	3.88	4.13	4.39	4.65	4.92	5.47	6.04
50	2.16	2.35	2.53	2.72	2.92	3.12	3.32	3.53	3.74	3.95	4.39	4.85
60	1.81	1.96	2.12	2.28	2.44	2.61	2.78	2.95	3.13	3.31	3.68	4.06
70	1.56	1.69	1.83	1.96	2.11	2.25	2.40	2.55	2.70	2.85	3.17	3.50
80	1.37	1.49	1.61	1.73	1.86	1.98	2.11	2.24	2.38	2.51	2.80	3.09
90	1.23	1.34	1.44	1.55	1.66	1.78	1.89	2.01	2.13	2.25	2.50	2.76
100	1.12	1.22	1.31	1.41	1.51	1.61	1.72	1.83	1.93	2.04	2.27	2.51
120	0.970	1.05	1.13	1.21	1.29	1.38	1.46	1.55	1.64	1.74	1.93	2.12
140	0.870	0.934	1.00	1.07	1.14	1.21	1.29	1.36	1.44	1.52	1.69	1.85
160	0.804	0.857	0.914	0.973	1.03	1.10	1.16	1.23	1.30	1.37	1.51	1.66
180	0.760	0.804	0.853	0.903	0.956	1.01	1.07	1.13	1.19	1.25	1.37	1.51
200	0.731	0.768	0.809	0.853	0.899	0.947	0.997	1.05	1.10	1.16	1.27	1.39
225	0.709	0.738	0.771	0.808	0.847	0.888	0.931	0.976	1.02	1.07	1.17	1.27
250	0.698	0.720	0.747	0.777	0.810	0.845	0.883	0.922	0.963	1.01	1.09	1.19
275	0.693	0.710	0.731	0.756	0.784	0.814	0.847	0.881	0.917	0.955	1.03	1.12
300	0.693	0.705	0.722	0.743	0.766	0.792	0.820	0.851	0.883	0.916	0.987	1.06
325	0.695	0.704	0.717	0.734	0.754	0.776	0.801	0.827	0.856	0.886	0.950	1.02
350	0.700	0.705	0.715	0.729	0.746	0.765	0.786	0.810	0.835	0.862	0.919	0.982
375	0.705	0.709	0.716	0.727	0.740	0.757	0.776	0.796	0.819	0.843	0.895	0.952
400	0.712	0.713	0.718	0.726	0.738	0.752	0.768	0.786	0.806	0.828	0.876	0.928
450	0.726	0.724	0.725	0.730	0.737	0.747	0.759	0.774	0.790	0.807	0.847	0.891
500	0.742	0.737	0.735	0.737	0.741	0.748	0.757	0.768	0.781	0.795	0.828	0.865

D2.5. Table 15. Thermal diffusivity a of oxygen in 10^{-7} m^2/s

Pressure in bar	Temperature in °C											
	−200	−180	−160	−140	−120	−100	−90	−80	−70	−60	−50	−40
1	0.861	21.4	33.1	46.6	62.1	79.2	88.4	98.0	108	118	129	140
5	0.862	0.773	5.76	8.61	11.8	15.3	17.2	19.2	21.2	23.3	25.4	27.6
10	0.863	0.776	0.649	3.84	5.53	7.36	8.32	9.32	10.3	11.4	12.5	13.6
20	0.865	0.780	0.658	1.28	2.38	3.37	3.88	4.41	4.95	5.50	6.06	6.64
30	0.868	0.785	0.667	0.486	1.29	2.04	2.41	2.78	3.15	3.54	3.93	4.33
40	0.870	0.789	0.675	0.507	0.637	1.37	1.67	1.97	2.27	2.56	2.87	3.17
50	0.873	0.793	0.683	0.525	0.165	0.957	1.23	1.49	1.74	1.99	2.24	2.49
60	0.875	0.798	0.691	0.541	0.272	0.663	0.930	1.16	1.39	1.60	1.82	2.04
70	0.878	0.802	0.698	0.556	0.330	0.446	0.714	0.936	1.14	1.34	1.53	1.72
80	0.880	0.806	0.705	0.570	0.373	0.307	0.554	0.767	0.958	1.14	1.31	1.49
90	0.882	0.810	0.711	0.583	0.406	0.266	0.444	0.641	0.820	0.987	1.15	1.31
100	0.884	0.813	0.718	0.595	0.434	0.283	0.381	0.549	0.715	0.871	1.02	1.17
120	0.889	0.821	0.730	0.617	0.479	0.345	0.355	0.449	0.577	0.709	0.839	0.966
140	0.893	0.828	0.742	0.636	0.514	0.399	0.383	0.424	0.509	0.614	0.724	0.834
160	0.897	0.835	0.753	0.654	0.544	0.443	0.420	0.434	0.486	0.563	0.653	0.748
180	0.901	0.841	0.763	0.670	0.570	0.480	0.455	0.455	0.486	0.541	0.612	0.691
200	0.905	0.848	0.773	0.685	0.593	0.511	0.486	0.480	0.497	0.536	0.591	0.657
225	0.910	0.855	0.784	0.703	0.618	0.544	0.520	0.510	0.517	0.542	0.582	0.633
250	0.915	0.863	0.795	0.718	0.640	0.573	0.550	0.537	0.539	0.555	0.584	0.623
275	0.919	0.870	0.806	0.733	0.661	0.598	0.576	0.563	0.561	0.570	0.592	0.623
300	0.923	0.876	0.815	0.747	0.679	0.621	0.600	0.586	0.582	0.587	0.603	0.627
325	0.927	0.883	0.824	0.760	0.696	0.641	0.621	0.607	0.601	0.604	0.615	0.634
350	0.932	0.889	0.833	0.772	0.711	0.660	0.641	0.627	0.620	0.621	0.629	0.644
375	0.935	0.895	0.842	0.784	0.726	0.677	0.659	0.645	0.648	0.636	0.642	0.654
400	0.939	0.901	0.850	0.794	0.740	0.693	0.675	0.662	0.654	0.652	0.655	0.665
450	0.947	0.912	0.866	0.815	0.765	0.722	0.706	0.693	0.684	0.680	0.681	0.687
500	0.953	0.922	0.880	0.833	0.787	0.748	0.733	0.720	0.711	0.706	0.705	0.709

Pressure in bar	Temperature in °C											
	−30	−20	−10	0	10	20	30	40	50	60	80	100
1	151	163	175	187	200	213	226	239	253	267	296	325
5	29.9	32.3	34.7	37.2	39.7	42.3	45.0	47.7	50.4	53.3	59.0	65.0
10	14.8	16.0	17.2	18.5	19.7	21.1	22.4	23.8	25.1	26.6	29.5	32.5
20	7.24	7.85	8.47	9.11	9.76	10.4	11.1	11.8	12.5	13.2	14.7	16.2
30	4.73	5.15	5.57	6.01	6.45	6.90	7.36	7.83	8.30	8.79	9.79	10.8
40	3.49	3.81	4.13	4.46	4.80	5.14	5.49	5.85	6.21	6.58	7.34	8.11
50	2.75	3.01	3.27	3.54	3.82	4.10	4.38	4.67	4.96	5.26	5.87	6.50
60	2.26	2.48	2.71	2.93	3.17	3.40	3.64	3.88	4.13	4.38	4.90	5.43
70	1.91	2.11	2.31	2.50	2.71	2.91	3.12	3.32	3.54	3.76	4.21	4.66
80	1.66	1.83	2.01	2.18	2.36	2.54	2.73	2.91	3.10	3.30	3.69	4.10
90	1.46	1.62	1.78	1.94	2.10	2.26	2.43	2.59	2.76	2.94	3.29	3.65
100	1.31	1.46	1.60	1.75	1.89	2.04	2.19	2.34	2.49	2.65	2.98	3.30
120	1.09	1.22	1.34	1.46	1.59	1.71	1.84	1.96	2.10	2.23	2.51	2.78
140	0.944	1.05	1.16	1.27	1.38	1.49	1.60	1.70	1.82	1.94	2.18	2.42
160	0.843	0.939	1.04	1.13	1.23	1.32	1.42	1.51	1.62	1.72	1.93	2.15
180	0.774	0.859	0.944	1.03	1.12	1.20	1.29	1.37	1.46	1.56	1.75	1.94

D2.5. Table 15. (continued)

Pressure in bar	Temperature in °C											
	−30	−20	−10	0	10	20	30	40	50	60	80	100
200	0.728	0.802	0.878	0.955	1.03	1.11	1.19	1.26	1.35	1.43	1.60	1.78
225	0.691	0.754	0.820	0.887	0.955	1.02	1.09	1.16	1.23	1.31	1.46	1.62
250	0.671	0.724	0.781	0.839	0.899	0.960	1.02	1.08	1.15	1.21	1.36	1.50
275	0.661	0.706	0.755	0.806	0.859	0.913	0.967	1.02	1.08	1.14	1.27	1.40
300	0.659	0.696	0.738	0.783	0.830	0.879	0.927	0.972	1.03	1.09	1.20	1.32
325	0.660	0.692	0.728	0.768	0.810	0.853	0.896	0.936	0.988	1.04	1.15	1.26
350	0.665	0.692	0.723	0.758	0.795	0.834	0.873	0.909	0.956	1.00	1.10	1.21
375	0.672	0.695	0.722	0.752	0.785	0.820	0.855	0.888	0.931	0.976	1.07	1.16
400	0.679	0.699	0.723	0.750	0.779	0.811	0.842	0.872	0.911	0.952	1.04	1.13
450	0.697	0.711	0.729	0.751	0.774	0.800	0.826	0.850	0.884	0.919	0.993	1.07
500	0.716	0.726	0.740	0.757	0.776	0.797	0.819	0.839	0.868	0.898	0.962	1.03

D2.5. Table 16. Prandtl number Pr of oxygen

Pressure in bar	Temperature in °C											
	−200	−180	−160	−140	−120	−100	−90	−80	−70	−60	−50	−40
1	2.96	0.749	0.739	0.735	0.733	0.731	0.730	0.730	0.730	0.729	0.729	0.729
5	2.97	1.98	0.800	0.770	0.754	0.745	0.742	0.740	0.738	0.737	0.735	0.735
10	2.98	1.99	1.67	0.823	0.784	0.764	0.758	0.753	0.749	0.746	0.743	0.741
20	3.01	1.99	1.66	1.09	0.860	0.806	0.791	0.780	0.771	0.764	0.759	0.755
30	3.03	2.00	1.66	1.70	0.989	0.858	0.829	0.809	0.795	0.784	0.776	0.769
40	3.06	2.01	1.66	1.66	1.37	0.929	0.876	0.844	0.821	0.805	0.793	0.783
50	3.08	2.02	1.65	1.63	3.74	1.04	0.938	0.885	0.851	0.828	0.811	0.798
60	3.11	2.03	1.65	1.60	2.41	1.22	1.02	0.935	0.885	0.853	0.830	0.813
70	3.14	2.04	1.65	1.58	2.05	1.54	1.14	0.998	0.925	0.881	0.851	0.830
80	3.17	2.04	1.65	1.56	1.87	2.02	1.30	1.08	0.972	0.912	0.874	0.847
90	3.19	2.05	1.65	1.54	1.75	2.26	1.49	1.17	1.02	0.947	0.899	0.866
100	3.22	2.06	1.65	1.53	1.67	2.14	1.65	1.27	1.08	0.985	0.925	0.886
120	3.28	2.08	1.66	1.51	1.57	1.83	1.73	1.43	1.20	1.06	0.981	0.927
140	3.34	2.10	1.66	1.50	1.51	1.65	1.64	1.49	1.29	1.14	1.04	0.969
160	3.41	2.13	1.67	1.49	1.46	1.53	1.54	1.46	1.33	1.19	1.08	1.01
180	3.47	2.15	1.68	1.48	1.43	1.46	1.46	1.42	1.33	1.22	1.12	1.04
200	3.54	2.17	1.68	1.48	1.40	1.41	1.40	1.37	1.31	1.22	1.14	1.06
225	3.63	2.20	1.70	1.47	1.38	1.36	1.35	1.33	1.28	1.22	1.15	1.08
250	3.72	2.23	1.71	1.47	1.37	1.33	1.31	1.29	1.25	1.21	1.15	1.09
275	3.82	2.27	1.72	1.47	1.36	1.30	1.28	1.26	1.23	1.19	1.14	1.10
300	3.93	2.30	1.74	1.48	1.35	1.28	1.26	1.24	1.21	1.17	1.14	1.09
325	4.04	2.34	1.75	1.48	1.35	1.27	1.24	1.22	1.19	1.16	1.13	1.09
350	4.15	2.38	1.77	1.49	1.34	1.26	1.23	1.21	1.18	1.15	1.12	1.09
375	4.27	2.41	1.79	1.50	1.34	1.25	1.22	1.19	1.17	1.14	1.11	1.08
400	4.40	2.45	1.81	1.50	1.34	1.25	1.21	1.19	1.16	1.13	1.10	1.08
450	4.68	2.54	1.85	1.52	1.35	1.24	1.21	1.17	1.14	1.12	1.09	1.07
500	5.00	2.63	1.89	1.54	1.36	1.24	1.20	1.17	1.14	1.11	1.08	1.06

D2.5. Table 16. (continued)

Pressure in bar	Temperature in °C											
	−30	−20	−10	0	10	20	30	40	50	60	80	100
1	0.729	0.729	0.729	0.729	0.729	0.730	0.730	0.730	0.730	0.731	0.732	0.732
5	0.734	0.733	0.733	0.733	0.732	0.732	0.732	0.732	0.732	0.733	0.733	0.734
10	0.740	0.739	0.738	0.737	0.736	0.736	0.735	0.735	0.735	0.735	0.735	0.735
20	0.752	0.749	0.747	0.745	0.743	0.742	0.741	0.740	0.740	0.739	0.739	0.738
30	0.764	0.759	0.756	0.753	0.750	0.748	0.747	0.746	0.744	0.743	0.742	0.741
40	0.776	0.770	0.765	0.761	0.757	0.755	0.752	0.751	0.749	0.748	0.745	0.744
50	0.788	0.780	0.774	0.769	0.764	0.761	0.758	0.756	0.753	0.751	0.749	0.746
60	0.801	0.791	0.783	0.776	0.771	0.767	0.763	0.761	0.758	0.755	0.752	0.749
70	0.814	0.802	0.792	0.784	0.778	0.773	0.769	0.766	0.762	0.759	0.755	0.751
80	0.828	0.813	0.801	0.792	0.785	0.779	0.774	0.771	0.767	0.763	0.758	0.754
90	0.842	0.825	0.811	0.800	0.792	0.785	0.780	0.776	0.771	0.767	0.760	0.756
100	0.857	0.837	0.821	0.809	0.799	0.791	0.785	0.781	0.775	0.771	0.763	0.758
120	0.889	0.862	0.841	0.826	0.813	0.804	0.796	0.791	0.784	0.778	0.769	0.763
140	0.922	0.888	0.862	0.843	0.828	0.816	0.807	0.801	0.793	0.786	0.775	0.767
160	0.953	0.913	0.883	0.860	0.842	0.829	0.818	0.812	0.802	0.794	0.781	0.772
180	0.981	0.937	0.903	0.877	0.857	0.841	0.830	0.822	0.811	0.801	0.787	0.776
200	1.00	0.957	0.921	0.893	0.871	0.853	0.840	0.832	0.820	0.809	0.793	0.781
225	1.03	0.979	0.941	0.911	0.886	0.867	0.853	0.845	0.830	0.818	0.800	0.786
250	1.04	0.995	0.957	0.926	0.901	0.880	0.865	0.856	0.840	0.827	0.807	0.792
275	1.05	1.01	0.969	0.938	0.913	0.892	0.876	0.866	0.850	0.836	0.814	0.798
300	1.05	1.01	0.978	0.948	0.923	0.902	0.885	0.875	0.859	0.844	0.821	0.803
325	1.05	1.02	0.985	0.956	0.931	0.910	0.894	0.884	0.866	0.851	0.827	0.809
350	1.05	1.02	0.989	0.962	0.937	0.917	0.901	0.891	0.873	0.858	0.833	0.814
375	1.05	1.02	0.992	0.966	0.943	0.923	0.907	0.897	0.879	0.864	0.839	0.819
400	1.05	1.02	0.993	0.969	0.947	0.927	0.912	0.902	0.885	0.869	0.844	0.824
450	1.04	1.02	0.994	0.972	0.952	0.934	0.919	0.910	0.893	0.878	0.853	0.832
500	1.04	1.01	0.994	0.974	0.955	0.938	0.925	0.916	0.900	0.885	0.860	0.840

5 Bibliography

1. Schmidt R, Wagner W (1985) A new form of equation of state for pure substances and its application to oxygen. Fluid Phase Equilibria 19:175–200
2. Wagner W, de Reuck M (1987) International thermodynamic tables of the fluid state – 9, oxygen. Blackwell Science Publications, Oxford
3. Laesecke A, Krauss R, Stephan K, Wagner W (1990) Transport properties of fluid oxygen. J Phys Chem Ref Data 19:1089–1122

D2.6 Properties of Ammonia

Roland Span[1] · *Rolf Krauss*[2]
[1]Ruhr-Universität Bochum, Bochum, Germany
[2]Universität Stuttgart, Stuttgart, Germany

Tables with thermodynamic properties of ammonia were calculated using the reference equation of state established by Tillner-Roth et al. [1, 2].

Tabulated thermal conductivities were calculated using the equation by Tufeu et al. [3]. Viscosities were calculated using the equation by Fenghour et al. [4]. The densities required as input to these correlations were calculated using the reference equation of state.

p	Pressure in bar	v	Specific volume in m^3/kg
ρ	Density in kg/m^3	β	Isobaric expansion coefficient in $10^{-3}/K$ $\beta = v^{-1}\cdot(\partial v/\partial T)_p$
ϑ	Temperature in °C	w_s	Isentropic speed of sound in m/s
Z	Compression factor $Z = p/(\rho RT)$	λ	Thermal conductivity in mW/(m K)
h	Specific enthalpy in kJ/kg	η	Dynamic viscosity in 10^{-6} Pa·s
s	Specific entropy in kJ/(kg K)	ν	Kinematic viscosity ν in 10^{-7} m^2/s
c_p	Specific isobaric heat capacity in kJ/(kg K)	a	Thermal diffusivity in 10^{-7} m^2/s
c_v	Specific isochoric heat capacity in kJ/(kg K)	Pr	Prandtl number $Pr = \eta\, c_p/\lambda$

1 Characteristic Quantities

Molecular mass $\tilde{M}$ = 17.0305 g/mol, specific gas constant R = 488.2175 J/(kg K).

2 Critical Point [2]

p_c = 113.39 bar, T_c = 405.4 K (ϑ_c = 132.25 °C), ρ_c = 225 kg/m^3.

3 Triple Point [2]

T_t = 195.5 K (ϑ_t = −77.65 °C).

4 Reference States of Enthalpy and Entropy

h' = 200 kJ/kg and s' = 1 kJ/(kg K) for saturated liquid at ϑ = 0 °C.

D2.6. Table 1. Properties of ammonia at $p = 1$ bar

ϑ °C	ρ kg/m³	h kJ/kg	s kJ/(kg K)	c_p kJ/(kg K)	c_v kJ/(kg K)	β 10^{-3}/K	w_s m/s	λ mW/(m K)	η 10^{-6} Pa·s	ν 10^{-7} m²/s	a 10^{-7} m²/s	Pr –
−75	730.13	−131.9	−0.4150	4.216	2.930	1.46	2098	809.7	527.9	7.23	2.63	2.75
−70	724.75	−110.7	−0.3096	4.245	2.921	1.50	2051	792.2	475.1	6.56	2.57	2.55
−65	719.25	−89.43	−0.2060	4.274	2.911	1.54	2.008	774.6	430.1	5.98	2.52	2.37
−60	713.65	−67.99	−0.1042	4.303	2.902	1.59	1967	757.1	391.4	5.48	2.47	2.22
−55	707.93	−46.40	−0.0041	4.332	2.893	1.63	1928	739.7	358.0	5.06	2.41	2.10
−50	702.11	−24.67	0.0944	4.360	2.884	1.67	1890	722.4	328.9	4.68	2.36	1.99
−45	696.19	−2.808	0.1913	4.387	2.875	1.72	1853	705.2	303.5	4.36	2.31	1.89
−40	690.16	19.19	0.2867	4.414	2.866	1.76	1816	688.1	281.3	4.08	2.26	1.80
−35	684.04	41.33	0.3806	4.439	2.858	1.80	1780	671.3	261.5	3.82	2.21	1.73
−30	0.86	1426	6.161	2.273	1.690	4.61	389.3	21.12	8.165	94.5	108	0.879
−25	0.84	1437	6.207	2.247	1.676	4.46	393.7	21.37	8.332	98.6	113	0.876
−20	0.83	1449	6.251	2.226	1.664	4.33	398.0	21.64	8.501	103	118	0.875
−15	0.81	1460	6.295	2.210	1.655	4.21	402.2	21.93	8.671	107	123	0.874
−10	0.79	1471	6.337	2.196	1.649	4.10	406.4	22.24	8.844	112	128	0.873
−5	0.78	1482	6.378	2.186	1.644	3.99	410.4	22.57	9.018	116	133	0.873
0	0.76	1492	6.418	2.178	1.641	3.90	414.3	22.91	9.194	121	138	0.874
5	0.75	1503	6.458	2.172	1.640	3.81	418.2	23.28	9.371	125	144	0.874
10	0.73	1514	6.497	2.168	1.639	3.72	422.0	23.67	9.549	130	149	0.875
15	0.72	1525	6.534	2.165	1.640	3.64	425.8	24.07	9.729	135	155	0.875
20	0.71	1536	6.572	2.164	1.642	3.57	429.4	24.49	9.911	140	160	0.875
25	0.69	1547	6.608	2.164	1.644	3.50	433.1	24.93	10.09	145	166	0.876
30	0.68	1558	6.644	2.164	1.647	3.43	436.6	25.39	10.28	151	172	0.876
35	0.67	1568	6.680	2.166	1.651	3.36	440.2	25.86	10.46	156	178	0.876
40	0.66	1579	6.715	2.169	1.656	3.30	443.6	26.36	10.65	161	184	0.876
45	0.65	1590	6.749	2.172	1.661	3.24	447.1	26.86	10.83	167	191	0.876
50	0.64	1601	6.783	2.176	1.666	3.19	450.4	27.39	11.02	173	197	0.875
55	0.63	1612	6.816	2.180	1.672	3.13	453.8	27.93	11.21	178	204	0.875
60	0.62	1623	6.849	2.185	1.678	3.08	457.1	28.48	11.40	184	211	0.874
65	0.61	1634	6.882	2.191	1.685	3.03	460.3	29.05	11.59	190	218	0.874
70	0.60	1645	6.914	2.196	1.692	2.98	463.6	29.64	11.78	196	225	0.873
75	0.59	1656	6.946	2.203	1.699	2.93	466.7	30.24	11.97	202	232	0.872
80	0.58	1667	6.977	2.209	1.706	2.89	469.9	30.85	12.16	209	239	0.871
85	0.57	1678	7.008	2.216	1.714	2.85	473.0	31.48	12.35	215	247	0.869
90	0.57	1689	7.039	2.223	1.722	2.80	476.1	32.12	12.54	221	255	0.868
95	0.56	1700	7.070	2.231	1.730	2.76	479.1	32.78	12.74	228	263	0.867
100	0.55	1711	7.100	2.238	1.738	2.72	482.2	33.44	12.93	235	271	0.865
110	0.54	1734	7.159	2.254	1.756	2.65	488.1	34.81	13.32	248	288	0.862
120	0.52	1756	7.218	2.271	1.774	2.58	494.0	36.22	13.70	262	305	0.859
130	0.51	1779	7.275	2.289	1.792	2.51	499.7	37.68	14.09	276	323	0.856
140	0.50	1802	7.331	2.307	1.811	2.45	505.4	39.17	14.48	291	341	0.853
150	0.49	1825	7.386	2.326	1.830	2.39	510.9	40.69	14.87	306	360	0.850
160	0.47	1848	7.441	2.345	1.850	2.33	516.4	42.25	15.26	322	380	0.847
170	0.46	1872	7.495	2.365	1.870	2.28	521.8	43.83	15.65	338	400	0.844
180	0.45	1896	7.548	2.385	1.891	2.22	527.1	45.44	16.04	354	421	0.842
190	0.44	1920	7.600	2.405	1.912	2.18	532.3	47.06	16.43	371	442	0.840
200	0.43	1944	7.652	2.426	1.933	2.13	537.5	48.69	16.82	388	463	0.838
210	0.42	1968	7.703	2.447	1.954	2.08	542.5	50.34	17.21	405	484	0.836
220	0.42	1993	7.753	2.468	1.975	2.04	547.6	51.99	17.60	423	506	0.835
230	0.41	2018	7.803	2.489	1.997	2.00	552.5	53.64	17.98	441	529	0.835
240	0.40	2043	7.852	2.511	2.019	1.96	557.4	55.28	18.37	460	551	0.834
250	0.39	2068	7.901	2.533	2.041	1.92	562.2	56.92	18.76	478	573	0.835
260	0.38	2093	7.949	2.555	2.064	1.88	567.0	58.54	19.14	498	596	0.835

D2.6. Table 1. (continued)

ϑ °C	ρ kg/m³	h kJ/kg	s kJ/(kg K)	c_p kJ/(kg K)	c_v kJ/(kg K)	β 10^{-3}/K	w_s m/s	λ mW/(m K)	η 10^{-6} Pa·s	ν 10^{-7} m²/s	a 10^{-7} m²/s	Pr –
270	0.38	2119	7.996	2.577	2.086	1.85	571.8	60.14	19.52	517	618	0.837
280	0.37	2145	8.044	2.600	2.109	1.82	576.4	61.72	19.91	537	640	0.838
290	0.36	2171	8.090	2.622	2.131	1.78	581.1	63.28	20.29	557	663	0.841
300	0.36	2197	8.137	2.645	2.154	1.75	585.6	64.77	20.67	578	685	0.844

D2.6. Table 2. Properties of the saturated liquid

ϑ °C	p bar	ρ' kg/m³	h' kJ/kg	s' kJ/(kg K)	c_p' kJ/(kg K)	c_v' kJ/(kg K)	β' 10^{-3}/K	w_s' m/s	λ' mW/(m K)	η' 10^{-6} Pa·s	ν' 10^{-7} m²/s	a' 10^{-7} m²/s	Pr' –
−75	0.07507	730.10	−132.0	−0.4148	4.217	2.930	1.46	2098	809.6	527.8	7.23	2.63	2.75
−70	0.10941	724.72	−110.8	−0.3094	4.245	2.921	1.50	2051	792.1	475.0	6.55	2.57	2.55
−65	0.15624	719.22	−89.51	−0.2058	4.274	2.911	1.54	2008	774.5	429.9	5.98	2.52	2.37
−60	0.21893	713.62	−68.06	−0.1040	4.303	2.902	1.59	1967	757.0	391.2	5.48	2.47	2.22
−55	0.30145	707.90	−46.47	−0.004	4.332	2.893	1.63	1928	739.6	357.8	5.06	2.41	2.10
−50	0.40836	702.09	−24.73	0.095	4.360	2.884	1.67	1890	722.3	328.8	4.68	2.36	1.99
−45	0.54489	696.17	−2.847	0.1914	4.387	2.875	1.72	1853	705.1	303.5	4.36	2.31	1.89
−40	0.71692	690.15	19.17	0.2867	4.414	2.866	1.76	1816	688.1	281.2	4.07	2.26	1.80
−35	0.93098	684.04	41.32	0.3806	4.439	2.858	1.80	1780	671.3	261.5	3.82	2.21	1.73
−30	1.1943	677.83	63.60	0.4730	4.465	2.849	1.85	1744	654.6	244.1	3.60	2.16	1.66
−25	1.5147	671.53	86.01	0.5641	4.489	2.841	1.90	1709	638.2	228.4	3.40	2.12	1.61
−20	1.9008	665.14	108.6	0.6538	4.514	2.833	1.94	1673	622.0	214.4	3.22	2.07	1.56
−15	2.3617	658.65	131.2	0.7421	4.538	2.824	1.99	1638	605.9	201.7	3.06	2.03	1.51
−10	2.9071	652.06	154.0	0.8293	4.564	2.816	2.05	1602	590.1	190.2	2.92	1.98	1.47
−5	3.5476	645.37	176.9	0.9152	4.589	2.808	2.10	1566	574.6	179.7	2.78	1.94	1.44
0	4.2938	638.57	200.0	1.000	4.617	2.800	2.16	1531	559.2	170.1	2.66	1.90	1.40
5	5.1575	631.66	223.2	1.084	4.645	2.793	2.23	1494	544.1	161.2	2.55	1.85	1.38
10	6.1505	624.64	246.6	1.166	4.676	2.785	2.30	1458	529.1	153.0	2.45	1.81	1.35
15	7.2852	617.49	270.1	1.248	4.709	2.778	2.37	1421	514.4	145.4	2.35	1.77	1.33
20	8.5748	610.20	293.8	1.329	4.745	2.771	2.45	1384	499.9	138.3	2.27	1.73	1.31
25	10.032	602.76	317.7	1.409	4.784	2.765	2.54	1347	485.5	131.7	2.18	1.68	1.30
30	11.672	595.17	341.8	1.488	4.828	2.759	2.64	1309	471.4	125.4	2.11	1.64	1.29
35	13.508	587.40	366.1	1.567	4.877	2.753	2.75	1271	457.4	119.6	2.04	1.60	1.28
40	15.554	579.44	390.6	1.645	4.932	2.748	2.87	1232	443.5	114.0	1.97	1.55	1.27
45	17.827	571.27	415.5	1.722	4.994	2.744	3.01	1193	429.9	108.8	1.90	1.51	1.26
50	20.340	562.86	440.6	1.799	5.064	2.741	3.16	1153	416.3	103.8	1.84	1.46	1.26
55	23.111	554.20	466.1	1.876	5.143	2.739	3.34	1112	402.9	99.03	1.79	1.41	1.26
60	26.156	545.24	492.0	1.952	5.235	2.738	3.54	1070	389.6	94.48	1.73	1.36	1.27
65	29.491	535.96	518.3	2.029	5.341	2.738	3.77	1028	376.4	90.12	1.68	1.31	1.28
70	33.135	526.31	545.0	2.105	5.465	2.740	4.04	984.4	363.2	85.93	1.63	1.26	1.29
75	37.105	516.23	572.4	2.182	5.610	2.744	4.36	940.0	350.2	81.89	1.59	1.21	1.31
80	41.420	505.67	600.3	2.260	5.784	2.750	4.75	894.7	337.1	77.98	1.54	1.15	1.34
85	46.100	494.54	629.0	2.338	5.993	2.759	5.22	848.1	324.1	74.18	1.50	1.09	1.37
90	51.167	482.75	658.6	2.417	6.250	2.772	5.81	800.4	311.0	70.47	1.46	1.03	1.42
95	56.643	470.17	689.2	2.497	6.573	2.789	6.55	751.3	297.9	66.83	1.42	0.964	1.47
100	62.553	456.63	721.0	2.580	6.991	2.811	7.53	700.7	284.8	63.23	1.38	0.892	1.55
105	68.923	441.90	754.4	2.665	7.555	2.840	8.88	648.5	271.5	59.64	1.35	0.813	1.66
110	75.783	425.61	789.7	2.753	8.362	2.879	10.8	594.4	258.1	56.03	1.32	0.725	1.82
115	83.170	407.18	827.7	2.847	9.628	2.931	14.0	537.7	244.6	52.30	1.28	0.624	2.06
120	91.125	385.49	869.9	2.950	11.940	3.004	19.9	477.4	231.2	48.34	1.25	0.502	2.50
125	99.702	357.80	919.7	3.070	17.658	3.116	35.0	411.4	219.1	43.80	1.22	0.347	3.53
130	108.98	312.29	992.0	3.244	54.210	3.345	136	333.6	221.9	37.29	1.19	0.131	9.11

D2.6. Table 3. Properties of the saturated vapour

ϑ °C	p bar	ρ'' kg/m³	h'' kJ/kg	s'' kJ/(kg K)	c_p'' kJ/(kg K)	c_v'' kJ/(kg K)	β'' 10^{-3}/K	w_s'' m/s	λ'' mW/(m K)	η'' 10^{-6} Pa·s	ν'' 10^{-7} m²/s	a'' 10^{-7} m²/s	Pr″ –
−75	0.07507	0.08	1346	7.045	2.070	1.561	5.18	356.4	19.66	6.905	886	1218	0.727
−70	0.10941	0.11	1356	6.909	2.086	1.572	5.08	360.5	19.73	7.032	633	852	0.743
−65	0.15624	0.15	1365	6.781	2.104	1.584	5.00	364.5	19.82	7.162	462	608	0.760
−60	0.21893	0.21	1374	6.660	2.125	1.597	4.93	368.4	19.93	7.296	343	441	0.778
−55	0.30145	0.29	1383	6.547	2.150	1.613	4.87	372.1	20.07	7.433	259	326	0.796
−50	0.40836	0.38	1391	6.440	2.178	1.631	4.82	375.6	20.24	7.573	199	244	0.815
−45	0.54489	0.50	1400	6.338	2.209	1.651	4.78	379.0	20.43	7.715	155	186	0.834
−40	0.71692	0.64	1408	6.243	2.244	1.672	4.75	382.2	20.64	7.859	122	143	0.854
−35	0.93098	0.82	1416	6.152	2.283	1.696	4.73	385.2	20.88	8.004	97.4	111	0.875
−30	1.1943	1.04	1423	6.065	2.326	1.722	4.72	388.1	21.15	8.152	78.6	87.7	0.896
−25	1.5147	1.30	1431	5.983	2.373	1.750	4.72	390.7	21.44	8.300	64.0	69.7	0.918
−20	1.9008	1.60	1438	5.904	2.425	1.779	4.74	393.2	21.77	8.449	52.7	56.0	0.941
−15	2.3617	1.97	1444	5.829	2.481	1.811	4.77	395.4	22.12	8.600	43.7	45.4	0.964
−10	2.9071	2.39	1451	5.757	2.542	1.845	4.81	397.5	22.50	8.751	36.6	37.0	0.988
−5	3.5476	2.88	1457	5.688	2.608	1.880	4.86	399.3	22.92	8.903	30.9	30.5	1.01
0	4.2938	3.46	1462	5.621	2.680	1.918	4.93	400.8	23.37	9.056	26.2	25.2	1.04
5	5.1575	4.11	1467	5.557	2.758	1.957	5.01	402.2	23.85	9.209	22.4	21.0	1.06
10	6.1505	4.87	1472	5.495	2.841	1.998	5.10	403.2	24.37	9.364	19.2	17.6	1.09
15	7.2852	5.73	1476	5.434	2.932	2.041	5.22	404.1	24.92	9.519	16.6	14.8	1.12
20	8.5748	6.70	1480	5.376	3.030	2.085	5.35	404.6	25.52	9.676	14.4	12.6	1.15
25	10.032	7.81	1483	5.319	3.135	2.131	5.50	404.9	26.16	9.835	12.6	10.7	1.18
30	11.672	9.05	1486	5.263	3.250	2.178	5.67	404.9	26.85	9.995	11.0	9.12	1.21
35	13.508	10.46	1488	5.209	3.375	2.227	5.87	404.6	27.58	10.16	9.71	7.82	1.24
40	15.554	12.03	1490	5.155	3.510	2.278	6.10	404.0	28.38	10.33	8.58	6.72	1.28
45	17.827	13.80	1491	5.102	3.659	2.329	6.36	403.1	29.23	10.50	7.60	5.79	1.31
50	20.340	15.79	1491	5.050	3.823	2.383	6.65	401.9	30.16	10.67	6.76	5.00	1.35
55	23.111	18.01	1491	4.998	4.005	2.438	7.00	400.3	31.16	10.86	6.03	4.32	1.40
60	26.156	20.49	1489	4.946	4.208	2.494	7.40	398.3	32.26	11.05	5.39	3.74	1.44
65	29.491	23.28	1487	4.894	4.438	2.552	7.86	396.0	33.47	11.25	4.83	3.24	1.49
70	33.135	26.41	1484	4.842	4.699	2.613	8.41	393.3	34.80	11.47	4.34	2.80	1.55
75	37.105	29.92	1480	4.788	5.001	2.675	9.06	390.1	36.30	11.70	3.91	2.43	1.61
80	41.420	33.89	1474	4.734	5.355	2.739	9.84	386.5	38.00	11.95	3.53	2.09	1.68
85	46.100	38.38	1468	4.679	5.777	2.807	10.8	382.5	39.95	12.23	3.19	1.80	1.77
90	51.167	43.48	1459	4.621	6.291	2.877	12.0	377.9	42.24	12.55	2.89	1.54	1.87
95	56.643	49.34	1449	4.561	6.933	2.951	13.5	372.7	44.99	12.91	2.62	1.32	1.99
100	62.533	56.12	1437	4.497	7.762	3.030	15.5	367.0	48.36	13.32	2.37	1.11	2.14
105	68.923	64.06	1422	4.429	8.877	3.114	18.3	360.5	52.65	13.82	2.16	0.926	2.33
110	75.783	73.55	1403	4.354	10.463	3.205	22.3	353.3	58.33	14.42	1.96	0.758	2.59
115	83.170	85.18	1380	4.270	12.909	3.305	28.5	345.0	66.28	15.19	1.78	0.603	2.96
120	91.125	100.07	1350	4.172	17.212	3.416	39.6	335.4	78.40	16.21	1.62	0.455	3.56
125	99.702	120.73	1309	4.048	26.996	3.545	65.5	323.6	100.01	17.73	1.47	0.307	4.79
130	108.98	156.77	1239	3.857	76.490	3.701	199	306.6	160.39	20.63	1.32	0.134	9.84

D2.6. Table 4. Density ρ of ammonia in kg/m³

Pressure in bar	Temperature in °C											
	−50	−40	−30	−20	−10	0	10	20	30	40	50	60
1	702.1	690.2	0.8641	0.8263	0.7923	0.7612	0.7328	0.7066	0.6823	0.6597	0.6387	0.6190
5	702.3	690.4	678.0	665.3	652.2	638.6	3.883	3.711	3.559	3.422	3.298	3.184
10	702.5	690.6	678.3	665.6	652.5	639.0	624.9	610.3	7.574	7.212	6.898	6.621
15	702.7	690.8	678.5	665.9	652.8	639.3	625.3	610.8	595.5	11.52	10.90	10.38

D2.6. Table 4. (continued)

Pressure in bar	Temperature in °C											
	−50	−40	−30	−20	−10	0	10	20	30	40	50	60
20	702.9	691.0	678.8	666.2	653.1	639.7	625.7	611.2	596.0	580.0	15.45	14.54
25	703.1	691.3	679.0	666.4	653.4	640.0	626.1	611.7	596.5	580.5	563.5	19.29
30	703.3	691.5	679.3	666.7	653.8	640.4	626.5	612.1	597.0	581.1	564.2	545.9
35	703.5	691.7	679.6	667.0	654.1	640.7	626.9	612.5	597.5	581.7	564.9	546.7
40	703.7	692.0	679.8	667.3	654.4	641.0	627.3	613.0	598.0	582.3	565.5	547.5
50	704.2	692.4	680.3	667.8	655.0	641.7	628.0	613.8	599.0	583.4	566.9	549.1
60	704.6	692.9	680.8	668.4	655.6	642.4	628.8	614.7	599.9	584.5	568.1	550.6
70	705.0	693.3	681.3	668.9	656.2	643.1	629.5	615.5	600.9	585.6	569.4	552.1
80	705.4	693.8	681.8	669.5	656.8	643.7	630.3	616.3	601.8	586.7	570.7	553.6
90	705.8	694.2	682.3	670.0	657.4	644.4	631.0	617.1	602.7	587.7	571.9	555.1
100	706.2	694.7	682.8	670.5	658.0	645.0	631.7	617.9	603.7	588.7	573.1	556.5
110	706.6	695.1	683.3	671.1	658.6	645.7	632.4	618.7	604.6	589.8	574.2	557.8
120	707.0	695.6	683.8	671.6	659.1	646.3	633.1	619.5	605.4	590.8	575.4	559.2
130	707.4	696.0	684.2	672.1	659.7	647.0	633.8	620.3	606.3	591.8	576.5	560.5
140	707.8	696.4	684.7	672.7	660.3	647.6	634.5	621.1	607.2	592.8	577.7	561.8
150	708.2	696.9	685.2	673.2	660.9	648.2	635.2	621.9	608.1	593.7	578.8	563.1
160	708.6	697.3	685.7	673.7	661.4	648.9	635.9	622.6	608.9	594.7	579.9	564.3
180	709.4	698.2	686.6	674.7	662.6	650.1	637.3	624.1	610.6	596.6	582.0	566.7
200	710.2	699.0	687.5	675.7	663.7	651.3	638.6	625.6	612.2	598.4	584.0	569.1
250	712.1	701.1	689.8	678.2	666.4	654.3	641.9	629.2	616.2	602.8	589.0	574.6
300	714.0	703.2	692.1	680.7	669.0	657.1	645.0	642.6	619.9	606.9	593.6	579.8
400	717.7	707.2	696.4	685.4	674.1	662.6	651.0	639.1	627.0	614.7	602.1	589.2
500	721.3	711.1	700.5	689.8	678.9	667.8	656.6	645.2	633.6	621.8	609.9	597.7

Pressure in bar	Temperature in °C											
	70	80	90	100	110	120	140	160	180	200	250	300
1	0.6005	0.5832	0.5668	0.5513	0.5367	0.5229	0.4973	0.4741	0.4530	0.4337	0.3920	0.3577
5	3.079	2.982	2.892	2.807	2.728	2.654	2.517	2.395	2.285	2.185	1.970	1.795
10	6.372	6.147	5.941	5.751	5.575	5.412	5.116	4.855	4.622	4.412	3.966	3.606
15	9.924	9.527	9.171	8.849	8.555	8.285	7.803	7.383	7.013	6.682	5.988	5.434
20	13.80	13.17	12.61	12.12	11.68	11.29	10.59	9.985	9.461	8.998	8.038	7.279
25	18.09	17.13	16.31	15.61	14.98	14.43	13.47	12.66	11.97	11.36	10.11	9.140
30	22.96	21.49	20.32	19.33	18.48	17.73	16.47	15.43	14.54	13.78	12.22	11.02
35	526.7	26.40	24.71	23.34	22.20	21.22	19.60	18.28	17.18	16.24	14.36	12.92
40	527.7	32.08	29.60	27.71	26.19	24.92	22.86	21.24	19.90	18.76	16.52	14.83
50	529.7	507.9	41.74	37.93	35.21	33.08	29.87	27.47	25.56	23.98	20.94	18.71
60	531.6	510.3	485.8	51.59	46.26	42.63	37.65	34.20	31.56	29.45	25.50	22.67
70	533.4	512.7	489.0	460.2	61.13	54.31	46.43	41.52	37.96	35.19	30.18	26.71
80	535.2	514.9	492.0	464.7	428.9	69.83	56.58	49.56	44.81	41.24	35.02	30.82
90	536.9	517.1	494.8	468.7	435.8	95.43	68.66	58.49	52.17	47.63	40.00	35.01
100	538.6	519.2	497.5	472.5	441.8	398.1	83.79	68.55	60.14	54.39	45.13	39.28
110	540.3	521.2	500.1	475.9	447.0	408.5	104.4	80.06	68.80	61.56	50.43	43.63
120	541.9	523.1	502.5	479.2	451.7	416.8	138.9	93.51	78.28	69.20	55.90	48.07
130	543.4	525.0	504.9	482.3	456.0	423.7	242.3	109.7	88.74	77.34	61.55	52.58
140	544.9	526.8	507.1	485.2	460.0	429.7	317.0	129.8	100.3	86.04	67.37	57.18
150	546.4	528.6	509.3	487.9	463.7	435.1	344.2	155.9	113.3	95.35	73.38	61.87
160	547.9	530.3	511.4	490.6	467.1	440.0	360.8	189.7	127.9	105.3	79.59	66.64
180	550.7	533.7	515.4	495.5	473.5	448.5	382.9	262.1	162.8	127.5	92.56	76.42
200	553.4	536.8	519.1	500.1	479.2	456.0	398.3	308.9	204.0	152.8	106.3	86.52
250	559.7	544.1	527.7	510.2	491.5	471.3	424.8	365.9	291.7	223.4	143.7	113.0
300	565.6	550.7	535.3	519.0	501.9	483.7	443.3	396.2	341.0	282.4	183.6	140.8
400	576.0	562.4	548.4	533.9	518.9	503.3	470.0	433.7	394.3	352.5	256.7	196.5
500	585.3	572.7	559.7	546.4	532.8	518.9	489.7	458.9	426.4	392.8	310.5	246.4

D2.6. Table 5. Compression factor Z of ammonia

Pressure in bar	Temperature in °C											
	−50	−40	−30	−20	−10	0	10	20	30	40	50	60
1	0.001	0.001	0.975	0.979	0.982	0.985	0.987	0.989	0.990	0.991	0.992	0.993
5	0.007	0.006	0.006	0.006	0.006	0.006	0.932	0.941	0.949	0.956	0.961	0.965
10	0.013	0.013	0.012	0.012	0.012	0.012	0.012	0.011	0.892	0.907	0.919	0.929
15	0.020	0.019	0.019	0.018	0.018	0.018	0.017	0.017	0.017	0.852	0.873	0.889
20	0.026	0.025	0.025	0.024	0.024	0.023	0.023	0.023	0.023	0.023	0.821	0.845
25	0.033	0.032	0.031	0.030	0.030	0.029	0.029	0.029	0.028	0.028	0.028	0.797
30	0.039	0.038	0.037	0.026	0.036	0.035	0.035	0.034	0.034	0.034	0.034	0.034
35	0.046	0.044	0.043	0.042	0.042	0.041	0.040	0.040	0.040	0.039	0.039	0.039
40	0.052	0.051	0.050	0.049	0.048	0.047	0.046	0.046	0.045	0.045	0.045	0.045
50	0.065	0.063	0.062	0.061	0.059	0.058	0.058	0.057	0.056	0.056	0.056	0.056
60	0.078	0.076	0.074	0.073	0.071	0.070	0.069	0.068	0.068	0.067	0.067	0.067
70	0.091	0.089	0.087	0.085	0.083	0.082	0.080	0.079	0.079	0.078	0.078	0.078
80	0.104	0.101	0.099	0.097	0.095	0.093	0.092	0.091	0.090	0.089	0.089	0.089
90	0.117	0.114	0.111	0.109	0.107	0.105	0.103	0.102	0.101	0.100	0.100	0.100
100	0.130	0.126	0.123	0.121	0.118	0.116	0.115	0.113	0.112	0.111	0.111	0.110
110	0.143	0.139	0.136	0.133	0.130	0.128	0.126	0.124	0.123	0.122	0.121	0.121
120	0.156	0.152	0.148	0.145	0.142	0.139	0.137	0.135	0.134	0.133	0.132	0.132
130	0.169	0.164	0.160	0.156	0.153	0.151	0.148	0.146	0.145	0.144	0.143	0.143
140	0.182	0.177	0.172	0.168	0.165	0.162	0.160	0.157	0.156	0.154	0.154	0.153
150	0.194	0.189	0.184	0.180	0.177	0.174	0.171	0.169	0.167	0.165	0.164	0.164
160	0.207	0.202	0.197	0.192	0.188	0.185	0.182	0.180	0.178	0.176	0.175	0.174
180	0.233	0.226	0.221	0.216	0.211	0.208	0.204	0.202	0.199	0.197	0.196	0.195
200	0.258	0.251	0.245	0.239	0.235	0.230	0.227	0.223	0.221	0.219	0.217	0.216
250	0.322	0.313	0.305	0.298	0.292	0.287	0.282	0.278	0.274	0.271	0.269	0.267
300	0.386	0.375	0.365	0.357	0.349	0.342	0.336	0.331	0.327	0.323	0.320	0.318
400	0.512	0.497	0.484	0.472	0.462	0.453	0.444	0.437	0.431	0.426	0.421	0.417
500	0.636	0.618	0.601	0.586	0.573	0.561	0.551	0.541	0.533	0.526	0.520	0.514
Pressure in bar	Temperature in °C											
	70	80	90	100	110	120	140	160	180	200	250	300
1	0.994	0.995	0.995	0.996	0.996	0.996	0.997	0.997	0.998	0.998	0.999	0.999
5	0.969	0.972	0.975	0.978	0.980	0.982	0.985	0.987	0.989	0.991	0.994	0.995
10	0.937	0.944	0.949	0.954	0.959	0.963	0.969	0.974	0.978	0.981	0.987	0.991
15	0.902	0.913	0.923	0.930	0.937	0.943	0.953	0.961	0.967	0.972	0.981	0.986
20	0.865	0.881	0.894	0.905	0.915	0.923	0.937	0.947	0.956	0.962	0.974	0.982
25	0.825	0.847	0.865	0.879	0.892	0.903	0.920	0.933	0.944	0.953	0.968	0.977
30	0.780	0.810	0.833	0.852	0.868	0.881	0.903	0.919	0.932	0.943	0.961	0.973
35	0.040	0.769	0.799	0.823	0.843	0.859	0.885	0.905	0.921	0.933	0.955	0.968
40	0.045	0.723	0.762	0.792	0.816	0.836	0.867	0.891	0.909	0.923	0.948	0.964
50	0.056	0.057	0.676	0.724	0.759	0.787	0.830	0.861	0.884	0.903	0.935	0.955
60	0.067	0.068	0.070	0.638	0.693	0.733	0.790	0.830	0.859	0.882	0.921	0.946
70	0.078	0.079	0.081	0.083	0.612	0.671	0.747	0.797	0.833	0.861	0.908	0.937
80	0.089	0.090	0.092	0.095	0.100	0.597	0.701	0.763	0.807	0.840	0.895	0.928
90	0.100	0.101	0.103	0.105	0.110	0.491	0.650	0.728	0.780	0.818	0.881	0.919
100	0.111	0.112	0.113	0.116	0.121	0.131	0.592	0.690	0.752	0.796	0.867	0.910
110	0.122	0.122	0.124	0.127	0.132	0.140	0.522	0.650	0.723	0.773	0.854	0.901
120	0.132	0.133	0.135	0.137	0.142	0.150	0.428	0.607	0.693	0.751	0.840	0.892
130	0.143	0.144	0.145	0.148	0.152	0.160	0.266	0.560	0.662	0.728	0.827	0.884
140	0.153	0.154	0.156	0.158	0.163	0.170	0.219	0.510	0.631	0.704	0.814	0.875

D2.6. Table 5. (continued)

Pressure in bar	Temperature in °C											
	70	80	90	100	110	120	140	160	180	200	250	300
150	0.164	0.165	0.166	0.169	0.173	0.180	0.216	0.455	0.598	0.681	0.800	0.866
160	0.174	0.175	0.176	0.179	0.183	0.189	0.220	0.399	0.565	0.658	0.787	0.858
180	0.195	0.196	0.197	0.199	0.203	0.209	0.233	0.325	0.500	0.611	0.761	0.842
200	0.216	0.216	0.217	0.220	0.223	0.229	0.249	0.306	0.443	0.566	0.737	0.826
250	0.267	0.266	0.267	0.269	0.272	0.276	0.292	0.323	0.387	0.484	0.681	0.791
300	0.317	0.316	0.316	0.317	0.320	0.323	0.335	0.358	0.398	0.460	0.640	0.762
400	0.414	0.412	0.411	0.411	0.412	0.414	0.422	0.436	0.459	0.491	0.610	0.727
500	0.510	0.506	0.504	0.502	0.502	0.502	0.506	0.515	0.530	0.551	0.630	0.725

D2.6. Table 6. Specific enthalpy *h* of ammonia in kJ/kg

Pressure in bar	Temperature in °C											
	−50	−40	−30	−20	−10	0	10	20	30	40	50	60
1	−24.67	19.19	1426	1449	1471	1492	1514	1536	1558	1579	1601	1623
5	−24.32	19.54	63.91	108.8	154.2	200.0	1482	1508	1533	1558	1582	1605
10	−23.87	19.96	64.32	109.2	154.5	200.4	246.8	293.8	1499	1528	1556	1582
15	−23.42	20.39	64.73	109.6	154.9	200.7	247.1	294.1	341.9	1494	1527	1557
20	−22.98	20.82	65.13	109.9	155.2	201.0	247.3	294.3	342.0	390.7	1494	1529
25	−22.53	21.25	65.54	110.3	155.6	201.3	247.6	294.6	342.2	390.8	440.6	1497
30	−22.08	21.68	65.95	110.7	155.9	201.7	247.9	294.8	342.4	390.9	440.6	491.8
35	−21.63	22.11	66.36	111.1	156.3	202.0	248.2	295.0	342.6	391.0	440.6	491.7
40	−21.18	22.54	66.77	111.5	156.7	202.3	248.5	295.3	342.8	391.1	440.6	491.6
50	−20.28	23.40	67.59	112.3	157.4	203.0	249.1	295.8	343.1	391.4	440.6	491.3
60	−19.38	24.27	68.42	113.0	158.1	203.7	249.7	296.3	343.5	391.6	440.7	491.1
70	−18.48	25.14	69.25	113.8	158.8	204.3	250.3	296.8	343.9	391.9	440.8	490.9
80	−17.57	26.01	70.08	114.6	159.6	205.0	250.9	297.3	344.4	392.1	440.9	490.8
90	−16.67	26.88	70.91	115.4	160.3	205.7	251.5	297.8	344.8	392.4	441.0	490.7
100	−15.76	27.75	71.74	116.2	161.1	206.4	252.1	298.4	345.2	392.8	441.2	490.7
110	−14.85	28.62	72.58	117.0	161.8	207.1	252.8	298.9	345.7	393.1	441.3	490.6
120	−13.94	29.50	73.42	117.8	162.6	207.8	253.4	299.5	346.1	393.4	441.5	490.6
130	−13.03	30.38	74.26	118.6	163.3	208.5	254.0	300.0	346.6	393.8	441.7	490.6
140	−12.12	31.26	75.10	119.4	164.1	209.2	254.7	300.6	347.1	394.1	442.0	490.7
150	−11.20	32.14	75.95	120.2	164.8	209.9	255.3	301.2	347.6	394.5	442.2	490.7
160	−10.29	33.02	76.79	121.0	165.6	210.6	256.0	301.8	348.1	394.9	442.5	490.8
180	−8.452	34.79	78.49	122.6	167.1	212.0	257.3	303.0	349.1	395.7	443.0	491.1
200	−6.611	36.57	80.20	124.2	168.7	213.5	258.6	304.2	350.1	396.6	443.6	491.4
250	−1.988	41.03	84.50	128.4	172.6	217.2	262.1	307.3	352.9	398.9	445.4	492.5
300	2.666	45.54	88.85	132.5	176.6	220.9	265.6	310.5	355.8	401.5	447.5	494.1
400	12.05	54.64	97.65	141.0	184.7	228.7	272.9	317.4	362.1	407.1	452.4	498.0
500	21.54	63.87	106.6	149.7	193.1	236.7	280.6	324.6	368.9	413.3	458.0	502.9

Pressure in bar	Temperature in °C											
	70	80	90	100	110	120	140	160	180	200	250	300
1	1645	1667	1689	1711	1734	1756	1802	1848	1896	1944	2068	2197
5	1629	1652	1676	1699	1722	1746	1793	1841	1889	1938	2063	2193
10	1608	1634	1659	1683	1708	1733	1781	1830	1880	1930	2057	2188
15	1586	1614	1641	1667	1693	1719	1770	1820	1871	1921	2050	2183
20	1562	1593	1622	1650	1678	1705	1757	1810	1861	1913	2044	2178

D2.6. Table 6. (continued)

Pressure in bar	Temperature in °C											
	70	80	90	100	110	120	140	160	180	200	250	300
25	1535	1570	1602	1632	1661	1690	1745	1799	1852	1905	2038	2173
30	1505	1544	1580	1613	1644	1674	1732	1788	1842	1897	2031	2168
35	544.9	1516	1557	1593	1627	1658	1719	1777	1833	1888	2025	2163
40	544.6	1484	1531	1571	1608	1642	1705	1765	1823	1879	2018	2158
50	543.9	599.2	1468	1521	1566	1606	1677	1741	1803	1862	2005	2148
60	543.3	598.1	656.7	1457	1516	1565	1646	1716	1781	1843	1992	2137
70	542.8	597.0	654.7	718.2	1453	1516	1612	1690	1759	1825	1978	2127
80	542.3	596.1	652.9	714.9	786.7	1456	1574	1661	1736	1805	1964	2116
90	541.9	595.2	651.3	712.0	780.7	1366	1532	1631	1713	1785	1951	2106
100	541.6	594.4	649.9	709.4	775.7	857.3	1481	1598	1687	1765	1936	2095
110	541.3	593.7	648.6	707.1	771.4	847.2	1418	1562	1661	1744	1922	2084
120	541.0	593.0	647.4	705.0	767.6	839.5	1326	1523	1633	1722	1907	2073
130	540.7	592.4	646.3	703.1	764.4	833.2	1127	1478	1604	1699	1893	2063
140	540.5	591.9	645.3	701.4	761.4	827.9	1028	1427	1572	1675	1878	2052
150	540.4	591.4	644.4	699.8	758.8	823.3	996.3	1367	1539	1651	1863	2041
160	540.3	591.0	643.5	698.4	756.4	819.3	977.7	1299	1504	1626	1847	2030
180	540.1	590.3	642.1	695.9	752.3	812.6	954.3	1181	1428	1574	1817	2008
200	540.1	589.8	640.9	693.7	748.9	807.2	939.0	1118	1350	1520	1785	1986
250	540.4	589.0	638.8	689.8	742.5	797.2	915.2	1052	1218	1392	1708	1931
300	541.2	589.0	637.7	687.3	738.2	790.5	900.9	1022	1157	1306	1635	1879
400	544.0	590.5	637.6	685.3	733.7	783.0	884.6	991.2	1104	1222	1523	1786
500	548.1	593.6	639.5	685.8	732.6	780.0	876.6	976.1	1079	1185	1457	1717

D2.6. Table 7. Specific entropy *s* of ammonia in kJ/(kg K)

Pressure in bar	Temperature in °C											
	−50	−40	−30	−20	−10	0	10	20	30	40	50	60
1	0.0944	0.2867	6.1607	6.2513	6.3369	6.4184	6.4965	6.5717	6.6443	6.7146	6.7829	6.8493
5	0.0934	0.2856	0.4720	0.6529	0.8286	0.9998	5.6241	5.7143	5.7983	5.8776	5.9530	6.0252
10	0.0922	0.2844	0.4706	0.6514	0.8271	0.9981	1.1650	1.3283	5.3721	5.4667	5.5536	5.6348
15	0.0910	0.2831	0.4693	0.6499	0.8255	0.9964	1.1631	1.3263	1.4866	5.1832	5.2862	5.3789
20	0.0898	0.2818	0.4679	0.6485	0.8239	0.9947	1.1613	1.3243	1.4844	1.6424	5.0641	5.1729
25	0.0887	0.2806	0.4666	0.6471	0.8224	0.9930	1.1595	1.3223	1.4822	1.6399	1.7964	4.9876
30	0.0875	0.2793	0.4652	0.6456	0.8209	0.9914	1.1577	1.3204	1.4800	1.6375	1.7936	1.9498
35	0.0863	0.2781	0.4639	0.6442	0.8193	0.9897	1.1559	1.3184	1.4779	1.6351	1.7909	1.9466
40	0.0851	0.2768	0.4626	0.6428	0.8178	0.9881	1.1541	1.3165	1.4757	1.6327	1.7882	1.9435
50	0.0828	0.2743	0.4599	0.6399	0.8147	0.9848	1.1506	1.3126	1.4715	1.6279	1.7828	1.9373
60	0.0805	0.2718	0.4572	0.6371	0.8117	0.9815	1.1470	1.3088	1.4673	1.6232	1.7775	1.9312
70	0.0782	0.2694	0.4546	0.6343	0.8087	0.9783	1.1436	1.3050	1.4631	1.6186	1.7724	1.9253
80	0.0759	0.2669	0.4520	0.6315	0.8057	0.9751	1.1401	1.3012	1.4590	1.6141	1.7673	1.9194
90	0.0736	0.2645	0.4494	0.6287	0.8027	0.9719	1.1367	1.2975	1.4549	1.6096	1.7622	1.9137
100	0.0713	0.2620	0.4468	0.6259	0.7998	0.9687	1.1333	1.2938	1.4509	1.6052	1.7573	1.9081
110	0.0690	0.2596	0.4442	0.6232	0.7968	0.9656	1.1299	1.2901	1.4469	1.6008	1.7524	1.9026
120	0.0668	0.2572	0.4416	0.6204	0.7939	0.9625	1.1265	1.2865	1.4430	1.5965	1.7476	1.8972
130	0.0645	0.2548	0.4391	0.6177	0.7910	0.9594	1.1232	1.2829	1.4391	1.5922	1.7429	1.8919
140	0.0623	0.2524	0.4365	0.6150	0.7881	0.9563	1.1199	1.2794	1.4352	1.5880	1.7382	1.8867

D2.6. Table 7. (continued)

Pressure in bar	Temperature in °C											
	−50	−40	−30	−20	−10	0	10	20	30	40	50	60
150	0.0600	0.2500	0.4340	0.6123	0.7853	0.9532	1.1166	1.2758	1.4314	1.5838	1.7336	1.8816
160	0.0578	0.2477	0.4315	0.6096	0.7824	0.9502	1.1134	1.2723	1.4276	1.5797	1.7291	1.8765
180	0.0534	0.2430	0.4265	0.6043	0.7768	0.9442	1.1069	1.2654	1.4202	1.5716	1.7202	1.8667
200	0.0490	0.2383	0.4215	0.5991	0.7712	0.9382	1.1006	1.2586	1.4128	1.5636	1.7115	1.8571
250	0.0382	0.2268	0.4094	0.5862	0.7575	0.9237	1.0851	1.2421	1.3951	1.5444	1.6907	1.8342
300	0.0277	0.2156	0.3975	0.5736	0.7442	0.9096	1.0701	1.2262	1.3780	1.5262	1.6709	1.8128
400	0.0071	0.1938	0.3745	0.5493	0.7186	0.8826	1.0416	1.1959	1.3459	1.4919	1.6342	1.7733
500	−0.0126	0.1729	0.3524	0.5261	0.6941	0.8569	1.0146	1.1675	1.3159	1.4601	1.6005	1.7374
Pressure in bar	Temperature in °C											
	70	80	90	100	110	120	140	160	180	200	250	300
1	6.9141	6.9774	7.0392	7.0998	7.1592	7.2175	7.3311	7.4410	7.5478	7.6516	7.9006	8.1368
5	6.0948	6.1619	6.2271	6.2905	6.3523	6.4126	6.5295	6.6420	6.7507	6.8561	7.1079	7.3459
10	5.7113	5.7842	5.8540	5.9213	5.9863	6.0494	6.1707	6.2865	6.3979	6.5054	6.7607	7.0010
15	5.4642	5.5439	5.6192	5.6908	5.7595	5.8257	5.9518	6.0712	6.1852	6.2949	6.5539	6.7965
20	5.2695	5.3576	5.4393	5.5160	5.5888	5.6584	5.7897	5.9129	6.0298	6.1417	6.4046	6.6495
25	5.0996	5.1983	5.2879	5.3706	5.4480	5.5214	5.6583	5.7856	5.9056	6.0198	6.2866	6.5340
30	4.9405	5.0534	5.1526	5.2424	5.3253	5.4029	5.5462	5.6778	5.8010	5.9176	6.1885	6.4384
35	2.1040	4.9146	5.0265	5.1250	5.2142	5.2967	5.4469	5.5832	5.7098	5.8290	6.1041	6.3564
40	2.1002	4.7752	4.9044	5.0139	5.1107	5.1988	5.3567	5.4982	5.6283	5.7502	6.0296	6.2845
50	2.0928	2.2517	4.6531	4.7974	4.9156	5.0181	5.1947	5.3477	5.4857	5.6133	5.9019	6.1620
60	2.0856	2.2428	2.4065	4.5651	4.7216	4.8461	5.0475	5.2144	5.3615	5.4954	5.7937	6.0593
70	2.0786	2.2343	2.3954	2.5678	4.5072	4.6709	4.9076	5.0918	5.2492	5.3901	5.6989	5.9702
80	2.0718	2.2261	2.3849	2.5532	2.7430	4.4759	4.7694	4.9755	5.1451	5.2939	5.6138	5.8911
90	2.0652	2.2181	2.3749	2.5396	2.7212	4.2137	4.6272	4.8625	5.0465	5.2040	5.5360	5.8195
100	2.0587	2.2104	2.3654	2.5270	2.7021	2.9123	4.4735	4.7503	4.9516	5.1190	5.4639	5.7538
110	2.0524	2.2030	2.3562	2.5151	2.6851	2.8804	4.2946	4.6363	4.8590	5.0376	5.3964	5.6929
120	2.0462	2.1957	2.3474	2.5039	2.6696	2.8546	4.0508	4.5180	4.7674	4.9588	5.3326	5.6359
130	2.0401	2.1886	2.3389	2.4932	2.6553	2.8326	3.5567	4.3921	4.6759	4.8820	5.2718	5.5823
140	2.0342	2.1818	2.3308	2.4831	2.6419	2.8131	3.3083	4.2544	4.5835	4.8065	5.2136	5.5314
150	2.0284	2.1751	2.3228	2.4734	2.6294	2.7956	3.2238	4.1000	4.4896	4.7319	5.1576	5.4830
160	2.0227	2.1685	2.3151	2.4641	2.6176	2.7796	3.1719	3.9295	4.3935	4.6579	5.1035	5.4367
180	2.0116	2.1559	2.3004	2.4465	2.5958	2.7511	3.1023	3.6370	4.1950	4.5111	5.0001	5.3494
200	2.0009	2.1438	2.2865	2.4300	2.5759	2.7260	3.0529	3.4758	3.9996	4.3660	4.9020	5.2681
250	1.9757	2.1155	2.2544	2.3930	2.5323	2.6732	2.9659	3.2889	3.6630	4.0387	4.6764	5.0849
300	1.9522	2.0895	2.2254	2.3603	2.4948	2.6296	2.9033	3.1890	3.4951	3.8147	4.4783	4.9244
400	1.9094	2.0430	2.1743	2.3039	2.4319	2.5589	2.8110	3.0628	3.3167	3.5727	4.1779	4.6588
500	1.8710	2.0018	2.1299	2.2557	2.3795	2.5015	2.7411	2.9763	3.2082	3.4370	3.9842	4.4582

D2.6. Table 8. Specific isobaric heat capacity c_p of ammonia in kJ/(kg K)

Pressure in bar	Temperature in °C											
	−50	−40	−30	−20	−10	0	10	20	30	40	50	60
1	4.360	4.414	2.273	2.226	2.196	2.178	2.168	2.164	2.164	2.169	2.176	2.185
5	4.358	4.412	4.463	4.512	4.562	4.616	2.656	2.546	2.470	2.418	2.382	2.358
10	4.356	4.410	4.461	4.510	4.559	4.612	4.672	4.743	3.009	2.830	2.707	2.621
15	4.355	4.408	4.458	4.507	4.556	4.609	4.668	4.738	4.823	3.427	3.143	2.954
20	4.353	4.406	4.456	4.504	4.553	4.605	4.663	4.732	4.816	4.923	3.770	3.397

D2.6. Table 8. (continued)

Pressure in bar	Temperature in °C											
	−50	−40	−30	−20	−10	0	10	20	30	40	50	60
25	4.351	4.404	4.454	4.502	4.550	4.602	4.659	4.727	4.809	4.914	5.051	4.023
30	4.349	4.402	4.452	4.499	4.547	4.598	4.655	4.721	4.802	4.905	5.039	5.221
35	4.348	4.400	4.450	4.497	4.544	4.595	4.650	4.716	4.795	4.896	5.027	5.203
40	4.346	4.398	4.447	4.495	4.542	4.591	4.646	4.711	4.789	4.887	5.015	5.186
50	4.342	4.394	4.443	4.490	4.536	4.584	4.638	4.700	4.776	4.870	4.991	5.153
60	4.339	4.391	4.439	4.485	4.530	4.578	4.630	4.690	4.763	4.854	4.969	5.122
70	4.335	4.387	4.435	4.480	4.525	4.571	4.622	4.681	4.751	4.838	4.948	5.093
80	4.332	4.383	4.431	4.475	4.519	4.565	4.614	4.671	4.739	4.822	4.928	5.065
90	4.329	4.379	4.427	4.471	4.514	4.559	4.607	4.662	4.728	4.808	4.909	5.039
100	4.325	4.376	4.423	4.466	4.509	4.553	4.600	4.653	4.716	4.794	4.890	5.014
110	4.322	4.372	4.419	4.462	4.504	4.546	4.592	4.644	4.706	4.780	4.872	4.990
120	4.319	4.369	4.415	4.457	4.499	4.541	4.585	4.636	4.695	4.767	4.855	4.968
130	4.315	4.365	4.411	4.453	4.494	4.535	4.579	4.628	4.685	4.754	4.839	4.946
140	4.312	4.362	4.407	4.449	4.489	4.529	4.572	4.619	4.675	4.741	4.823	4.925
150	4.309	4.358	4.403	4.445	4.484	4.524	4.565	4.612	4.665	4.729	4.808	4.905
160	4.306	4.355	4.399	4.440	4.479	4.518	4.559	4.604	4.656	4.717	4.793	4.886
180	4.299	4.348	4.392	4.432	4.470	4.507	4.546	4.589	4.638	4.695	4.765	4.850
200	4.293	4.341	4.385	4.424	4.461	4.497	4.534	4.574	4.620	4.674	4.739	4.817
250	4.278	4.325	4.368	4.405	4.440	4.473	4.506	4.541	4.581	4.626	4.680	4.744
300	4.263	4.310	4.351	4.387	4.420	4.450	4.480	4.511	4.545	4.584	4.629	4.682
400	4.235	4.281	4.321	4.354	4.384	4.410	4.434	4.459	4.485	4.513	4.545	4.582
500	4.209	4.254	4.293	4.325	4.352	4.375	4.395	4.415	4.434	4.455	4.478	4.505

Pressure in bar	Temperature in °C											
	70	80	90	100	110	120	140	160	180	200	250	300
1	2.196	2.209	2.223	2.238	2.254	2.271	2.307	2.345	2.385	2.426	2.533	2.645
5	2.344	2.336	2.333	2.334	2.339	2.346	2.366	2.393	2.425	2.459	2.556	2.661
10	2.560	2.517	2.486	2.466	2.453	2.446	2.445	2.457	2.477	2.503	2.585	2.682
15	2.823	2.730	2.663	2.615	2.581	2.556	2.530	2.524	2.531	2.548	2.615	2.704
20	3.154	2.988	2.870	2.785	2.723	2.677	2.621	2.595	2.588	2.595	2.646	2.725
25	3.586	3.306	3.115	2.981	2.883	2.811	2.719	2.670	2.648	2.644	2.678	2.747
30	4.183	3.713	3.414	3.210	3.066	2.961	2.826	2.750	2.711	2.694	2.710	2.770
35	5.455	4.261	3.787	3.484	3.277	3.130	2.941	2.836	2.777	2.747	2.743	2.792
40	5.428	5.055	4.274	3.819	3.525	3.322	3.068	2.927	2.846	2.802	2.777	2.816
50	5.378	5.713	5.966	4.801	4.183	3.802	3.363	3.130	2.997	2.918	2.847	2.863
60	5.332	5.638	6.126	6.805	5.246	4.485	3.731	3.367	3.165	3.045	2.921	2.912
70	5.290	5.570	6.004	6.786	7.409	5.567	4.206	3.647	3.354	3.184	2.998	2.962
80	5.250	5.509	5.898	6.560	8.061	7.662	4.850	3.985	3.570	3.337	3.080	3.014
90	5.212	5.452	5.804	6.376	7.525	14.83	5.785	4.400	3.816	3.504	3.165	3.067
100	5.177	5.400	5.720	6.221	7.143	9.794	7.292	4.923	4.100	3.689	3.255	3.121
110	5.144	5.352	5.645	6.088	6.852	8.633	10.22	5.602	4.432	3.894	3.349	3.178
120	5.113	5.307	5.577	5.973	6.621	7.938	19.01	6.518	4.820	4.121	3.447	3.235
130	5.084	5.266	5.514	5.871	6.430	7.462	49.44	7.807	5.280	4.373	3.550	3.294
140	5.056	5.227	5.457	5.781	6.270	7.110	18.48	9.704	5.829	4.653	3.657	3.354
150	5.029	5.190	5.404	5.700	6.133	6.835	12.50	12.49	6.483	4.963	3.769	3.416
160	5.004	5.156	5.355	5.627	6.014	6.613	10.26	15.63	7.256	5.304	3.885	3.478
180	4.957	5.093	5.268	5.499	5.815	6.271	8.304	14.68	9.084	6.082	4.129	3.606
200	4.915	5.036	5.191	5.391	5.655	6.018	7.375	11.05	10.44	6.933	4.386	3.738

D2.6. Table 8. (continued)

Pressure in bar	Temperature in °C											
	70	80	90	100	110	120	140	160	180	200	250	300
250	4.822	4.917	5.034	5.179	5.360	5.590	6.277	7.517	8.893	8.129	5.039	4.069
300	4.745	4.821	4.913	5.023	5.155	5.316	5.747	6.384	7.179	7.464	5.556	4.380
400	4.625	4.676	4.735	4.804	4.883	4.975	5.196	5.471	5.784	6.052	5.740	4.814
500	4.535	4.569	4.609	4.655	4.707	4.765	4.899	5.055	5.220	5.373	5.411	4.927

D2.6. Table 9. Specific isochoric heat capacity c_v of ammonia in kJ/(kg K)

Pressure in bar	Temperature in °C											
	−50	−40	−30	−20	−10	0	10	20	30	40	50	60
1	2.884	2.866	1.690	1.664	1.649	1.641	1.639	1.642	1.647	1.656	1.666	1.678
5	2.885	2.867	2.850	2.833	2.816	2.800	1.904	1.848	1.811	1.787	1.773	1.767
10	2.886	2.868	2.851	2.834	2.817	2.801	2.786	2.771	2.071	1.987	1.930	1.893
15	2.887	2.869	2.852	2.835	2.818	2.802	2.786	2.772	2.759	2.244	2.122	2.041
20	2.888	2.870	2.852	2.835	2.819	2.802	2.787	2.772	2.759	2.748	2.364	2.217
25	2.889	2.871	2.853	2.836	2.819	2.803	2.787	2.773	2.759	2.748	2.741	2.436
30	2.890	2.872	2.854	2.837	2.820	2.804	2.788	2.773	2.760	2.748	2.741	2.737
35	2.891	2.873	2.855	2.838	2.821	2.804	2.788	2.773	2.760	2.749	2.740	2.736
40	2.892	2.874	2.856	2.838	2.821	2.805	2.789	2.774	2.760	2.749	2.740	2.736
50	2.894	2.875	2.858	2.840	2.823	2.806	2.790	2.775	2.761	2.749	2.740	2.734
60	2.896	2.877	2.859	2.842	2.824	2.807	2.791	2.776	2.762	2.749	2.739	2.733
70	2.898	2.879	2.861	2.843	2.826	2.809	2.792	2.777	2.762	2.750	2.739	2.732
80	2.900	2.881	2.863	2.845	2.827	2.810	2.794	2.778	2.763	2.750	2.739	2.732
90	2.902	2.883	2.864	2.846	2.829	2.811	2.795	2.779	2.764	2.751	2.739	2.731
100	2.904	2.884	2.866	2.848	2.830	2.813	2.796	2.780	2.765	2.751	2.740	2.731
110	2.906	2.886	2.867	2.849	2.831	2.814	2.797	2.781	2.766	2.752	2.740	2.731
120	2.908	2.888	2.869	2.851	2.833	2.815	2.798	2.782	2.767	2.753	2.740	2.730
130	2.910	2.890	2.871	2.852	2.834	2.817	2.800	2.783	2.768	2.753	2.741	2.730
140	2.912	2.891	2.872	2.854	2.836	2.818	2.801	2.784	2.769	2.754	2.741	2.730
150	2.913	2.893	2.874	2.855	2.837	2.819	2.802	2.785	2.770	2.755	2.742	2.731
160	2.915	2.895	2.875	2.857	2.838	2.821	2.803	2.787	2.771	2.756	2.742	2.731
180	2.919	2.898	2.878	2.860	2.841	2.823	2.806	2.789	2.773	2.757	2.744	2.732
200	2.922	2.901	2.881	2.862	2.844	2.826	2.808	2.791	2.775	2.759	2.745	2.733
250	2.931	2.909	2.889	2.869	2.851	2.833	2.815	2.797	2.780	2.764	2.749	2.736
300	2.939	2.916	2.896	2.876	2.857	2.839	2.821	2.803	2.786	2.770	2.754	2.740
400	2.953	2.930	2.909	2.889	2.870	2.852	2.833	2.816	2.798	2.781	2.765	2.750
500	2.966	2.942	2.921	2.901	2.882	2.864	2.845	2.828	2.810	2.793	2.777	2.762
Pressure in bar	Temperature in °C											
	70	80	90	100	110	120	140	160	180	200	250	300
1	1.692	1.706	1.722	1.738	1.756	1.774	1.811	1.850	1.891	1.933	2.041	2.154
5	1.766	1.769	1.775	1.784	1.795	1.808	1.837	1.871	1.908	1.946	2.050	2.160
10	1.868	1.854	1.846	1.844	1.847	1.852	1.871	1.898	1.929	1.964	2.061	2.168
15	1.985	1.948	1.924	1.909	1.901	1.899	1.906	1.925	1.951	1.981	2.073	2.175
20	2.120	2.054	2.009	1.979	1.959	1.948	1.943	1.953	1.972	1.999	2.084	2.183
25	2.278	2.174	2.103	2.054	2.021	2.000	1.980	1.981	1.995	2.017	2.095	2.191
30	2.469	2.312	2.208	2.136	2.087	2.054	2.019	2.010	2.017	2.035	2.106	2.198
35	2.740	2.475	2.326	2.227	2.159	2.112	2.059	2.040	2.040	2.053	2.117	2.206

D2.6. Table 9. (continued)

Pressure in bar	Temperature in °C											
	70	80	90	100	110	120	140	160	180	200	250	300
40	2.738	2.674	2.463	2.327	2.236	2.173	2.101	2.070	2.063	2.071	2.129	2.214
50	2.735	2.745	2.823	2.571	2.414	2.310	2.190	2.133	2.111	2.108	2.151	2.229
60	2.732	2.740	2.763	2.913	2.638	2.472	2.287	2.199	2.159	2.146	2.174	2.244
70	2.730	2.736	2.754	2.796	2.946	2.670	2.395	2.270	2.210	2.184	2.196	2.259
80	2.728	2.732	2.746	2.780	2.862	2.931	2.518	2.345	2.262	2.223	2.219	2.274
90	2.727	2.729	2.740	2.767	2.829	3.345	2.658	2.425	2.315	2.263	2.242	2.289
100	2.726	2.726	2.734	2.756	2.805	2.927	2.825	2.510	2.371	2.303	2.264	2.304
110	2.725	2.723	2.729	2.747	2.786	2.873	3.031	2.603	2.428	2.343	2.286	2.319
120	2.724	2.721	2.725	2.739	2.770	2.836	3.305	2.702	2.487	2.384	2.308	2.333
130	2.723	2.720	2.722	2.733	2.758	2.808	3.456	2.809	2.547	2.425	2.330	2.348
140	2.722	2.718	2.710	2.727	2.747	2.787	3.111	2.919	2.607	2.465	2.352	2.362
150	2.722	2.717	2.716	2.723	2.738	2.770	2.975	3.023	2.668	2.506	2.373	2.376
160	2.722	2.716	2.714	2.718	2.731	2.757	2.902	3.092	2.726	2.545	2.394	2.389
180	2.722	2.714	2.711	2.712	2.719	2.736	2.820	3.024	2.824	2.619	2.434	2.416
200	2.722	2.714	2.708	2.707	2.711	2.721	2.774	2.898	2.870	2.681	2.471	2.442
250	2.724	2.714	2.706	2.700	2.698	2.700	2.717	2.756	2.794	2.745	2.550	2.499
300	2.727	2.716	2.706	2.698	2.693	2.690	2.693	2.707	2.724	2.720	2.604	2.548
400	2.736	2.723	2.712	2.702	2.693	2.687	2.678	2.675	2.675	2.675	2.647	2.615
500	2.747	2.734	2.721	2.710	2.700	2.692	2.679	2.670	2.666	2.664	2.658	2.652

D2.6. Table 10. Isobaric expansion coefficient β of ammonia in 10^{-3}/K

Pressure in bar	Temperature in °C											
	−50	−40	−30	−20	−10	0	10	20	30	40	50	60
1	1.67	1.76	4.61	4.33	4.10	3.90	3.72	3.57	3.43	3.30	3.19	3.08
5	1.67	1.76	1.85	1.94	2.04	2.16	4.72	4.34	4.05	3.80	3.60	3.43
10	1.67	1.75	1.84	1.94	2.04	2.15	2.29	2.45	5.16	4.65	4.26	3.96
15	1.66	1.75	1.84	1.93	2.03	2.15	2.28	2.44	2.63	5.92	5.18	4.65
20	1.66	1.75	1.83	1.93	2.03	2.14	2.27	2.43	2.62	2.85	6.54	5.60
25	1.66	1.74	1.83	1.92	2.02	2.13	2.26	2.42	2.60	2.83	3.14	6.98
30	1.65	1.74	1.82	1.92	2.01	2.13	2.25	2.40	2.59	2.82	3.11	3.51
35	1.65	1.73	1.82	1.91	2.01	2.12	2.25	2.39	2.57	2.80	3.09	3.47
40	1.65	1.73	1.82	1.91	2.00	2.11	2.24	2.38	2.56	2.78	3.06	3.44
50	1.64	1.72	1.81	1.90	1.99	2.10	2.22	2.36	2.53	2.75	3.01	3.37
60	1.63	1.72	1.80	1.89	1.98	2.09	2.20	2.34	2.51	2.71	2.97	3.31
70	1.63	1.71	1.79	1.88	1.97	2.07	2.19	2.32	2.48	2.68	2.93	3.25
80	1.62	1.70	1.78	1.87	1.96	2.06	2.17	2.30	2.46	2.65	2.89	3.19
90	1.61	1.69	1.77	1.86	1.95	2.05	2.16	2.29	2.44	2.62	2.85	3.14
100	1.61	1.69	1.77	1.85	1.94	2.03	2.14	2.27	2.42	2.59	2.81	3.09
110	1.60	1.68	1.76	1.84	1.93	2.02	2.13	2.25	2.39	2.56	2.77	3.04
120	1.60	1.67	1.75	1.83	1.92	2.01	2.11	2.23	2.37	2.54	2.74	2.99
130	1.59	1.67	1.74	1.82	1.91	2.00	2.10	2.22	2.35	2.51	2.71	2.95
140	1.58	1.66	1.74	1.81	1.90	1.99	2.09	2.20	2.33	2.49	2.68	2.91
150	1.58	1.65	1.73	1.81	1.89	1.98	2.07	2.18	2.31	2.46	2.64	2.87
160	1.57	1.65	1.72	1.80	1.88	1.96	2.06	2.17	2.29	2.44	2.61	2.83
180	1.56	1.63	1.71	1.78	1.86	1.94	2.03	2.14	2.26	2.39	2.56	2.76

D2.6. Table 10. (continued)

Pressure in bar	Temperature in °C											
	−50	−40	−30	−20	−10	0	10	20	30	40	50	60
200	1.55	1.62	1.69	1.77	1.84	1.92	2.01	2.11	2.22	2.35	2.51	2.69
250	1.52	1.59	1.66	1.73	1.80	1.87	1.95	2.04	2.14	2.26	2.39	2.54
300	1.49	1.56	1.63	1.69	1.76	1.83	1.90	1.98	2.07	2.17	2.28	2.42
400	1.44	1.51	1.57	1.63	1.69	1.74	1.81	1.87	1.95	2.02	2.11	2.21
500	1.40	1.46	1.52	1.57	1.62	1.67	1.73	1.78	1.84	1.91	1.98	2.05
Pressure in bar	**Temperature in °C**											
	70	**80**	**90**	**100**	**110**	**120**	**140**	**160**	**180**	**200**	**250**	**300**
1	2.98	2.89	2.80	2.72	2.65	2.58	2.45	2.33	2.22	2.13	1.92	1.75
5	3.27	3.14	3.02	2.91	2.81	2.72	2.56	2.42	2.30	2.19	1.96	1.78
10	3.71	3.50	3.32	3.17	3.04	2.92	2.71	2.54	2.39	2.26	2.01	1.81
15	4.25	3.94	3.68	3.47	3.29	3.13	2.87	2.66	2.49	2.34	2.06	1.84
20	4.95	4.48	4.11	3.82	3.58	3.37	3.05	2.80	2.60	2.43	2.11	1.87
25	5.89	5.16	4.63	4.23	3.91	3.65	3.24	2.94	2.71	2.52	2.16	1.91
30	7.22	6.05	5.27	4.71	4.29	3.96	3.46	3.10	2.83	2.61	2.21	1.94
35	4.02	7.28	6.10	5.31	4.74	4.31	3.69	3.27	2.95	2.70	2.27	1.97
40	3.97	9.13	7.20	6.05	5.28	4.72	3.95	3.45	3.08	2.80	2.32	2.01
50	3.86	4.60	11.2	8.30	6.75	5.77	4.57	3.86	3.38	3.02	2.44	2.08
60	3.77	4.44	5.53	13.1	9.22	7.31	5.36	4.35	3.71	3.26	2.57	2.16
70	3.68	4.29	5.26	7.06	14.5	9.85	6.42	4.94	4.09	3.53	2.70	2.23
80	3.59	4.16	5.03	6.54	10.1	15.0	7.88	5.66	4.53	3.82	2.84	2.31
90	3.52	4.04	4.83	6.12	8.83	33.4	10.1	6.56	5.03	4.15	2.99	2.40
100	3.45	3.94	4.65	5.78	7.93	14.4	13.7	7.72	5.63	4.52	3.14	2.48
110	3.38	3.84	4.48	5.48	7.25	11.6	20.9	9.26	6.33	4.92	3.31	2.57
120	3.31	3.74	4.34	5.23	6.72	9.86	43.5	11.4	7.16	5.38	3.48	2.65
130	3.25	3.66	4.21	5.01	6.29	8.73	125	14.4	8.15	5.89	3.66	2.74
140	3.20	3.58	4.09	4.81	5.93	7.90	37.6	18.9	9.33	6.45	3.84	2.84
150	3.14	3.50	3.97	4.64	5.62	7.26	21.6	25.5	10.8	7.08	4.04	2.93
160	3.09	3.43	3.87	4.48	5.36	6.75	15.8	32.9	12.4	7.77	4.24	3.02
180	3.00	3.30	3.69	4.21	4.92	5.97	10.9	28.6	16.3	9.32	4.65	3.21
200	2.91	3.18	3.53	3.98	4.58	5.41	8.64	18.3	18.8	11.0	5.08	3.40
250	2.72	2.94	3.21	3.54	3.95	4.47	6.09	9.17	13.2	12.5	6.10	3.86
300	2.57	2.75	2.96	3.21	3.52	3.88	4.90	6.45	8.60	9.91	6.72	4.24
400	2.32	2.45	2.60	2.76	2.95	3.17	3.69	4.37	5.18	6.00	6.13	4.54
500	2.14	2.23	2.34	2.46	2.59	2.73	3.06	3.45	3.89	4.33	4.87	4.25

D2.6. Table 11. Isentropic speed of sound w_s in ammonia in m/s

Pressure in bar	Temperature in °C											
	−50	−40	−30	−20	−10	0	10	20	30	40	50	60
1	1890	1816	389.3	398.0	406.4	414.3	422.0	429.4	436.6	443.6	450.4	457.1
5	1891	1818	1746	1675	1603	1531	407.8	417.2	426.0	434.2	442.1	449.6
10	1892	1819	1748	1677	1605	1534	1460	1385	410.7	421.1	430.7	439.6
15	1894	1821	1749	1679	1608	1536	1463	1389	1312	405.9	417.8	428.5
20	1895	1822	1751	1681	1610	1539	1466	1392	1316	1236	403.0	416.2
25	1896	1824	1753	1683	1612	1541	1469	1395	1319	1240	1157	402.0
30	1898	1825	1755	1685	1615	1544	1472	1399	1323	1245	1162	1075
35	1899	1827	1757	1687	1617	1546	1475	1402	1327	1249	1167	1081

D2.6. Table 11. (continued)

Pressure in bar	Temperature in °C											
	−50	−40	−30	−20	−10	0	10	20	30	40	50	60
40	1900	1828	1758	1689	1619	1549	1478	1405	1330	1253	1172	1086
50	1903	1831	1762	1693	1624	1554	1483	1412	1338	1261	1182	1098
60	1905	1835	1765	1697	1628	1559	1489	1418	1345	1269	1192	1109
70	1908	1838	1769	1701	1632	1564	1495	1424	1352	1277	1200	1119
80	1911	1841	1772	1704	1637	1569	1500	1430	1359	1285	1209	1130
90	1913	1844	1776	1708	1641	1574	1505	1436	1365	1293	1218	1140
100	1916	1846	1779	1712	1645	1578	1511	1442	1372	1300	1226	1150
110	1918	1849	1782	1716	1650	1583	1516	1448	1378	1308	1235	1159
120	1921	1852	1786	1720	1654	1588	1521	1454	1385	1315	1243	1168
130	1923	1855	1789	1723	1658	1592	1526	1459	1391	1322	1251	1177
140	1926	1858	1792	1727	1662	1597	1531	1465	1397	1329	1259	1186
150	1928	1861	1796	1731	1666	1601	1536	1470	1404	1336	1266	1195
160	1931	1864	1799	1734	1670	1606	1541	1476	1410	1342	1274	1203
180	1935	1870	1805	1742	1678	1615	1551	1486	1421	1355	1288	1220
200	1940	1875	1812	1749	1686	1623	1560	1497	1433	1368	1302	1236
250	1952	1889	1827	1766	1705	1644	1583	1522	1461	1399	1336	1273
300	1964	1903	1842	1783	1724	1664	1605	1546	1487	1427	1367	1307
400	1987	1929	1872	1815	1759	1703	1647	1591	1535	1479	1423	1368
500	2010	1954	1900	1846	1792	1738	1685	1632	1579	1526	1474	1422

Pressure in bar	Temperature in °C											
	70	80	90	100	110	120	140	160	180	200	250	300
1	463.6	469.9	476.1	482.2	488.1	494.0	505.4	516.4	527.1	537.5	562.2	585.6
5	456.9	463.9	470.6	477.2	483.6	489.8	501.8	513.4	524.5	535.2	560.7	584.5
10	448.0	455.9	463.5	470.7	477.7	484.4	497.3	509.6	521.2	532.4	558.7	583.1
15	438.3	447.4	455.9	463.9	471.6	478.9	492.7	505.7	517.9	529.6	556.7	581.7
20	427.8	438.2	447.8	456.8	465.2	473.1	488.0	501.7	514.6	526.7	554.8	580.4
25	416.0	428.3	439.2	449.2	458.5	467.2	483.1	497.7	511.2	523.8	552.8	579.0
30	402.7	417.3	430.0	441.2	451.5	461.0	478.1	493.6	507.7	520.9	550.8	577.6
35	987.1	405.1	419.9	432.7	444.1	454.5	473.0	489.4	504.3	518.0	548.9	576.3
40	994.1	391.0	408.7	423.5	436.3	447.7	467.7	485.2	500.8	515.1	547.0	575.0
50	1008	909.5	381.7	402.5	419.1	433.2	456.7	476.4	493.7	509.2	543.1	572.4
60	1021	925.9	819.4	375.6	398.8	416.8	445.0	467.4	486.5	503.3	539.3	569.8
70	1034	941.4	839.5	721.7	373.2	397.9	432.4	458.0	479.1	497.4	535.6	567.4
80	1046	956.3	858.3	747.4	611.2	374.6	418.7	448.3	471.7	491.5	531.9	565.0
90	1058	970.5	876.0	770.8	646.6	340.9	403.7	438.3	464.2	485.6	528.4	562.7
100	1069	984.1	892.7	792.4	677.3	529.5	386.7	427.8	456.6	479.8	524.9	560.5
110	1080	997.2	908.6	812.4	704.6	574.3	366.6	416.9	449.1	474.0	521.6	558.5
120	1091	1010	923.7	831.2	729.2	611.0	340.3	405.7	441.6	468.4	518.4	556.5
130	1101	1022	938.2	848.9	751.8	642.5	319.8	394.1	434.2	463.1	515.4	554.7
140	1111	1034	952.1	865.6	772.8	670.5	395.5	382.5	427.1	458.0	512.7	553.1
150	1121	1045	965.4	881.5	792.3	695.7	456.6	372.3	420.5	453.2	510.1	551.5
160	1131	1056	978.2	896.7	810.7	718.7	503.2	367.9	414.6	448.9	507.7	550.2
180	1150	1077	1003	925.1	844.4	759.9	574.4	400.0	407.7	442.2	503.9	548.0
200	1167	1097	1025	951.3	875.0	796.2	629.5	462.6	414.3	439.6	501.3	546.5
250	1208	1143	1077	1010	941.4	872.4	733.1	597.2	494.9	464.7	502.2	546.5
300	1246	1184	1122	1060	997.6	935.0	811.3	693.4	592.0	529.2	516.6	552.6
400	1312	1257	1201	1146	1091	1037	930.9	831.8	743.1	670.2	584.0	584.9
500	1370	1319	1268	1218	1168	1119	1024	935.3	854.9	785.3	672.2	638.8

D2.6. Table 12. Thermal conductivity λ of ammonia in mW/(m K)

Pressure in bar	Temperature in °C											
	−50	−40	−30	−20	−10	0	10	20	30	40	50	60
1	722.4	688.1	21.12	21.64	22.24	22.91	23.67	24.49	25.39	26.36	27.39	28.48
5	722.9	688.7	655.2	622.4	590.5	559.3	24.20	25.00	25.87	26.82	27.83	28.91
10	723.5	689.3	655.8	623.1	591.2	560.1	529.8	500.1	26.58	27.48	28.46	29.52
15	724.1	690.0	656.5	623.9	592.0	560.9	530.6	501.0	472.0	28.28	29.20	30.21
20	724.7	690.6	657.2	624.6	592.7	561.7	531.5	501.9	473.0	444.5	30.09	31.02
25	725.4	691.3	657.9	625.3	593.5	562.5	532.3	502.8	473.9	445.5	417.4	32.00
30	726.0	691.9	658.6	626.0	594.2	563.3	533.1	503.7	474.9	446.5	418.5	390.6
35	726.6	692.6	659.3	626.7	595.0	564.1	534.0	504.6	475.8	447.6	419.6	391.8
40	727.2	693.3	660.0	627.4	595.7	564.9	534.8	505.5	476.8	448.6	420.8	393.1
50	728.5	694.6	661.3	628.9	597.2	566.4	536.5	507.2	478.6	450.6	423.0	395.5
60	729.7	695.9	662.7	630.3	598.7	568.0	538.1	509.0	480.5	452.6	425.1	397.9
70	730.9	697.1	664.0	631.7	600.2	569.5	539.7	510.7	482.3	454.6	427.3	400.3
80	732.2	698.4	665.4	633.1	601.7	571.1	541.3	512.4	484.1	456.5	429.4	402.6
90	733.4	699.7	666.7	634.5	603.1	572.6	543.0	514.1	486.0	458.5	431.5	404.9
100	734.6	701.0	668.1	635.9	604.6	574.1	544.6	515.8	487.7	460.4	433.6	407.2
110	735.8	702.3	669.4	637.3	606.0	575.7	546.2	517.5	489.5	462.3	435.6	409.4
120	737.1	703.6	670.7	638.7	607.5	577.2	547.7	519.1	491.3	464.1	437.6	411.6
130	738.3	704.8	672.0	640.1	608.9	578.7	549.3	520.8	493.0	466.0	439.6	413.7
140	739.5	706.1	673.4	641.4	610.4	580.2	550.9	522.4	494.8	467.8	441.6	415.8
150	740.7	707.4	674.7	642.8	611.8	581.7	552.4	524.1	496.5	469.7	443.5	417.9
160	741.9	708.6	676.0	644.2	613.2	583.1	554.0	525.7	498.2	471.5	445.4	420.0
180	744.3	711.1	678.6	646.9	616.0	586.1	557.0	528.9	501.6	475.0	449.2	424.1
200	746.7	713.6	681.2	649.6	618.8	589.0	560.1	532.1	504.9	478.5	452.9	428.0
250	752.7	719.8	687.6	656.3	625.8	596.2	567.6	539.8	513.0	487.1	461.9	437.6
300	758.5	725.9	694.0	662.8	632.6	603.2	574.9	547.4	520.9	495.3	470.6	446.6
350	764.4	732.0	700.2	669.3	639.2	610.1	582.0	554.8	528.6	503.3	478.9	455.3
400	770.1	737.9	706.4	675.7	645.8	616.9	589.0	562.1	536.1	511.0	486.9	463.7
500	781.5	749.7	718.5	688.2	658.7	630.2	602.6	576.1	550.5	525.9	502.3	479.7

Pressure in bar	Temperature in °C											
	70	80	90	100	110	120	140	160	180	200	250	300
1	29.64	30.85	32.12	33.44	34.81	36.22	39.17	42.25	45.44	48.69	56.92	64.77
5	30.05	31.26	32.51	33.82	35.18	36.59	39.52	42.57	45.74	48.99	57.18	65.01
10	30.63	31.81	33.05	34.35	35.70	37.10	40.00	43.02	46.15	49.37	57.52	65.31
15	31.29	32.45	33.66	34.94	36.28	37.67	40.55	43.50	46.59	49.78	57.87	65.63
20	32.05	33.16	34.35	35.61	36.93	38.32	41.17	44.03	47.07	50.21	58.24	65.96
25	32.94	33.99	35.13	36.36	37.66	39.05	41.87	44.61	47.58	50.67	58.62	66.29
30	34.01	34.96	36.03	37.21	38.49	39.88	42.65	45.24	48.12	51.16	59.02	66.64
35	363.8	36.11	37.08	38.19	39.44	40.82	43.52	45.93	48.71	51.67	59.43	67.00
40	365.2	37.53	38.32	39.33	40.51	41.88	44.50	46.68	49.34	52.22	59.86	67.38
50	368.0	340.0	41.72	42.26	43.20	44.48	46.83	48.40	50.74	53.40	60.78	68.16
60	370.8	343.2	314.5	46.74	46.96	47.97	49.78	50.45	52.35	54.74	61.76	68.98
70	373.4	346.3	318.3	288.5	52.79	52.86	53.56	52.91	54.20	56.22	62.83	69.86
80	376.0	349.3	321.9	293.2	261.1	60.40	58.51	55.88	56.34	57.89	63.97	70.79
90	378.6	352.2	325.4	297.6	267.4	75.36	65.21	59.50	58.81	59.76	65.20	71.77
100	381.1	355.0	348.7	301.7	272.9	240.1	74.80	63.97	61.68	61.86	66.52	72.81
110	383.5	357.8	331.9	305.5	278.0	248.0	90.02	69.59	65.04	64.21	67.94	73.90
120	385.9	360.5	335.0	309.2	282.6	254.5	120.9	76.83	68.98	66.86	69.45	75.05

D2.6. Table 12. (continued)

Pressure in bar	Temperature in °C											
	70	80	90	100	110	120	140	160	180	200	250	300
130	388.3	363.1	338.0	312.7	286.9	260.3	215.1	86.46	73.65	69.84	71.08	76.26
140	390.6	365.7	340.9	316.1	291.0	265.5	209.5	99.84	79.21	73.19	72.81	77.53
150	392.9	368.2	343.7	319.3	294.9	270.3	216.8	117.8	85.89	76.98	74.67	78.86
160	395.1	370.6	346.5	322.5	298.5	274.7	224.0	141.6	93.96	81.26	76.64	80.25
180	399.5	375.4	351.8	328.4	305.4	282.8	236.2	177.9	113.7	91.55	80.98	83.22
200	403.7	380.0	356.8	334.1	311.8	290.1	246.3	193.2	137.4	103.9	85.86	86.45
250	413.9	391.0	368.7	347.0	326.1	306.1	266.6	221.9	178.7	139.8	100.5	95.62
300	423.5	401.2	379.6	358.7	338.7	319.8	282.9	242.7	204.2	169.2	117.8	106.3
350	432.7	410.8	389.8	369.6	350.2	332.0	296.8	259.4	224.2	191.7	136.3	118.0
400	441.4	419.9	399.4	379.7	360.9	343.2	309.3	273.7	240.7	210.1	154.2	130.4
500	457.9	437.1	417.2	398.3	380.3	363.4	331.1	298.0	267.6	239.7	185.3	155.3

D2.6. Table 13. Dynamic viscosity η of ammonia in 10^{-6} Pa·s

Pressure in bar	Temperature in °C											
	−50	−40	−30	−20	−10	0	10	20	30	40	50	60
1	328.9	281.3	8.165	8.501	8.844	9.194	9.549	9.911	10.28	10.65	11.02	11.40
5	329.5	281.8	244.5	214.7	190.4	170.1	9.407	9.789	10.17	10.56	10.94	11.33
10	330.3	282.4	245.1	215.3	190.9	170.6	153.4	138.4	10.04	10.45	10.85	11.25
15	331.0	283.1	245.7	215.8	191.4	171.1	153.8	138.8	125.7	10.34	10.76	11.18
20	331.7	283.8	246.3	216.3	191.9	171.5	154.2	139.3	126.1	114.4	10.68	11.12
25	332.5	284.4	246.9	216.9	192.4	172.0	154.7	139.7	126.5	114.8	104.2	11.06
30	333.2	285.1	247.4	217.4	192.9	172.4	155.1	140.1	126.9	115.2	104.6	94.79
35	333.9	285.7	248.0	217.9	193.4	172.9	155.5	140.5	127.3	115.6	104.9	95.20
40	334.7	286.4	248.6	218.5	193.8	173.3	155.9	140.9	127.7	116.0	105.3	95.61
50	336.2	287.7	249.8	219.5	194.8	174.2	156.8	141.7	128.5	116.7	106.1	96.40
60	337.6	289.0	251.0	220.6	195.8	175.1	157.6	142.5	129.3	117.5	106.9	97.18
70	339.1	290.3	252.1	221.6	196.8	176.0	158.5	143.3	130.0	118.2	107.6	97.95
80	340.5	291.6	253.3	222.7	197.7	176.9	159.3	144.1	130.8	119.0	108.4	98.71
90	342.0	292.9	254.4	223.7	198.7	177.8	160.1	144.9	131.6	119.7	109.1	99.46
100	343.5	294.2	255.6	224.8	199.6	178.7	161.0	145.7	132.3	120.5	109.8	100.2
110	344.9	295.4	256.8	225.8	200.6	179.6	161.8	146.5	133.1	121.2	110.6	100.9
120	346.4	296.7	257.9	226.9	201.5	180.5	162.6	147.3	133.8	121.9	111.3	101.6
130	347.8	298.0	259.0	227.9	202.5	181.3	163.4	148.0	134.6	122.7	112.0	102.3
140	349.3	299.3	260.2	228.9	203.4	182.2	164.3	148.8	135.3	123.4	112.7	103.0
150	350.7	300.6	261.3	230.0	204.4	183.1	165.1	149.6	136.0	124.1	113.4	103.7
160	352.2	301.9	262.5	231.0	205.3	184.0	165.9	150.3	136.8	124.8	114.1	104.4
180	355.0	304.4	264.7	233.0	207.2	185.7	167.5	151.8	138.2	126.2	115.4	105.8
200	357.9	306.9	267.0	235.1	209.0	187.4	169.1	153.3	139.6	127.5	116.8	107.1
250	365.0	313.2	272.6	240.1	213.6	191.6	173.0	157.0	143.1	130.9	120.0	110.2
300	372.1	319.5	278.2	245.1	218.2	195.8	176.8	160.6	146.5	134.1	123.1	113.3
400	386.1	331.8	289.1	255.0	227.1	203.9	184.4	167.6	153.1	140.4	129.1	119.1
500	400.0	344.0	299.9	264.6	235.8	211.8	191.7	174.4	159.4	146.4	134.8	124.5

D2.6. Table 13. (continued)

Pressure in bar	Temperature in °C											
	70	80	90	100	110	120	140	160	180	200	250	300
1	11.78	12.16	12.54	12.93	13.32	13.70	14.48	15.26	16.04	16.82	18.76	20.67
5	11.72	12.11	12.50	12.89	13.29	13.68	14.47	15.25	16.04	16.82	18.76	20.68
10	11.65	12.06	12.46	12.86	13.26	13.65	14.45	15.25	16.04	16.83	18.78	20.70
15	11.60	12.01	12.42	12.82	13.23	13.63	14.44	15.24	16.04	16.83	18.79	20.72
20	11.54	11.97	12.38	12.80	13.21	13.62	14.44	15.24	16.05	16.84	18.81	20.74
25	11.50	11.94	12.36	12.78	13.20	13.62	14.44	15.25	16.06	16.86	18.83	20.76
30	11.47	11.92	12.35	12.78	13.20	13.62	14.45	15.27	16.08	16.88	18.86	20.79
35	86.09	11.92	12.36	12.79	13.21	13.63	14.47	15.29	16.20	16.90	18.88	20.82
40	86.52	11.94	12.38	12.81	13.24	13.66	14.49	15.31	16.13	16.93	18.91	20.85
50	87.37	78.78	12.52	12.93	13.34	13.75	14.58	15.39	16.20	17.01	18.98	20.92
60	88.19	79.68	71.40	13.20	13.55	13.93	14.71	15.51	16.31	17.10	19.07	21.00
70	88.99	80.56	72.41	64.18	13.96	14.23	14.92	15.67	16.45	17.23	19.17	21.08
80	89.78	81.41	73.37	65.37	56.76	14.76	15.22	15.89	16.62	17.38	19.28	21.18
90	90.56	82.23	74.29	66.48	58.32	15.96	15.66	16.18	16.85	17.56	19.41	21.29
100	91.31	83.04	75.18	67.52	59.70	50.67	16.33	16.57	17.12	17.78	19.56	21.40
110	92.06	83.82	76.04	68.51	60.95	52.68	17.45	17.08	17.46	18.04	19.73	21.53
120	92.79	84.59	76.87	69.45	62.10	54.34	19.74	17.76	17.88	18.34	19.92	21.67
130	93.51	85.34	77.67	70.35	63.17	55.78	29.22	18.69	18.39	18.70	20.13	21.82
140	94.22	86.07	78.45	71.21	64.18	57.07	38.28	20.01	19.02	19.12	20.36	21.98
150	94.92	86.79	79.22	72.05	65.13	58.25	42.13	21.96	19.80	19.60	20.61	22.16
160	95.60	87.50	79.96	72.85	66.04	59.34	44.67	24.83	20.75	20.17	20.89	22.34
180	96.95	88.88	81.40	74.40	67.75	61.32	48.27	32.15	23.34	21.56	21.52	22.75
200	98.27	90.21	82.78	75.85	69.33	63.10	50.97	37.77	26.90	23.36	22.26	23.21
250	101.4	93.39	86.02	79.22	72.89	66.97	56.00	45.73	36.10	29.40	24.60	24.58
300	104.4	96.37	89.03	82.28	76.06	70.29	59.87	50.61	42.32	35.47	27.54	26.24
400	110.1	101.9	94.53	87.79	81.63	75.98	65.99	57.46	50.16	44.00	33.91	30.14
500	115.3	107.0	99.54	92.73	86.54	80.88	70.97	62.64	55.63	49.75	39.37	34.18

D2.6. Table 14. Kinematic viscosity ν of ammonia in 10^{-7} m^2/s

Pressure in bar	Temperature in °C											
	−50	−40	−30	−20	−10	0	10	20	30	40	50	60
1	4.68	4.08	94.5	103	112	121	130	140	151	161	173	184
5	4.69	4.08	3.61	3.23	2.92	2.66	24.2	26.4	28.6	30.9	33.2	35.6
10	4.70	4.09	3.61	3.23	2.93	2.67	2.45	2.27	13.3	14.5	15.7	17.0
15	4.71	4.10	3.62	3.24	2.93	2.68	2.46	2.27	2.11	8.98	9.88	10.8
20	4.72	4.11	3.63	3.25	2.94	2.68	2.46	2.28	2.12	1.97	6.91	7.64
25	4.73	4.11	3.64	3.25	2.94	2.69	2.47	2.28	2.12	1.98	1.85	5.73
30	4.74	4.12	3.64	3.26	2.95	2.69	2.48	2.29	2.13	1.98	1.85	1.74
35	4.75	4.13	3.65	3.27	2.96	2.70	2.48	2.29	2.13	1.99	1.86	1.74
40	4.76	4.14	3.66	3.27	2.96	2.70	2.49	2.30	2.14	1.99	1.86	1.75
50	4.77	4.15	3.67	3.29	2.97	2.72	2.50	2.31	2.15	2.00	1.87	1.76
60	4.79	4.17	3.69	3.30	2.99	2.73	2.51	2.32	2.15	2.01	1.88	1.76

D2.6. Table 14. (continued)

Pressure in bar	Temperature in °C											
	−50	−40	−30	−20	−10	0	10	20	30	40	50	60
70	4.81	4.19	3.70	3.31	3.00	2.74	2.52	2.33	2.16	2.02	1.89	1.77
80	4.83	4.20	3.71	3.33	3.01	2.75	2.53	2.34	2.17	2.03	1.90	1.78
90	4.85	4.22	3.73	3.34	3.02	2.76	2.54	2.35	2.18	2.04	1.91	1.79
100	4.86	4.23	3.74	3.35	3.03	2.77	2.55	2.36	2.19	2.05	1.92	1.80
110	4.88	4.25	3.76	3.37	3.05	2.78	2.56	2.37	2.20	2.06	1.93	1.81
120	4.90	4.27	3.77	3.38	3.06	2.79	2.57	2.38	2.21	2.06	1.93	1.82
130	4.92	4.28	3.79	3.39	3.07	2.80	2.58	2.39	2.22	2.07	1.94	1.83
140	4.93	4.30	3.80	3.40	3.08	2.81	2.59	2.40	2.23	2.08	1.95	1.83
150	4.95	4.31	3.81	3.42	3.09	2.82	2.60	2.40	2.24	2.09	1.96	1.84
160	4.97	4.33	3.83	3.43	3.10	2.84	2.61	2.41	2.25	2.10	1.97	1.85
180	5.00	4.36	3.86	3.45	3.13	2.86	2.63	2.43	2.26	2.11	1.98	1.87
200	5.04	4.39	3.88	3.48	3.15	2.88	2.65	2.45	2.28	2.13	2.00	1.88
250	5.13	4.47	3.95	3.54	3.21	2.93	2.70	2.50	2.32	2.17	2.04	1.92
300	5.21	4.54	4.02	3.60	3.26	2.98	2.74	2.54	2.36	2.21	2.07	1.95
400	5.38	4.69	4.15	3.72	3.37	3.08	2.83	2.62	2.44	2.28	2.14	2.02
500	5.55	4.84	4.28	3.84	3.47	3.17	2.92	2.70	2.52	2.35	2.21	2.08

Pressure in bar	Temperature in °C											
	70	80	90	100	110	120	140	160	180	200	250	300
1	196	209	221	235	248	262	291	322	354	388	478	578
5	38.1	40.6	43.2	45.9	48.7	51.5	57.5	63.7	70.2	77.0	95.2	115
10	18.3	19.6	21.0	22.4	23.8	25.2	28.2	31.4	34.7	38.1	47.3	57.4
15	11.7	12.6	13.5	14.5	15.5	16.5	18.5	20.6	22.9	25.2	31.4	38.1
20	8.36	9.09	9.82	10.6	11.3	12.1	13.6	15.3	17.0	18.7	23.4	28.5
25	6.36	6.97	7.58	8.19	8.81	9.44	10.7	12.0	13.4	14.8	18.6	22.7
30	5.00	5.54	6.08	6.61	7.14	7.68	8.77	9.89	11.1	12.3	15.4	18.9
35	1.63	4.51	5.00	5.48	5.95	6.42	7.38	8.36	9.37	10.4	13.2	16.1
40	1.64	3.72	4.18	4.62	5.05	5.48	6.34	7.21	8.11	9.02	11.4	14.1
50	1.65	1.55	3.00	3.41	3.79	4.16	4.88	5.60	6.34	7.09	9.06	11.2
60	1.66	1.56	1.47	2.56	2.93	3.27	3.91	4.54	5.17	5.81	7.48	9.26
70	1.67	1.57	1.48	1.39	2.28	2.62	3.21	3.78	4.33	4.90	6.35	7.89
80	1.68	1.58	1.49	1.41	1.32	2.11	2.69	3.21	3.71	4.21	5.51	6.87
90	1.69	1.59	1.50	1.42	1.34	1.67	2.28	2.77	3.23	3.69	4.85	6.08
100	1.70	1.60	1.51	1.43	1.35	1.27	1.95	2.42	2.85	3.27	4.33	5.45
110	1.70	1.61	1.52	1.44	1.36	1.29	1.67	2.13	2.54	29.93	3.91	4.94
120	1.71	1.62	1.53	1.45	1.37	1.30	1.42	1.90	2.28	2.65	3.56	4.51
130	1.72	1.63	1.54	1.46	1.39	1.32	1.21	1.70	2.07	2.42	3.27	4.15
140	1.73	1.63	1.55	1.47	1.40	1.33	1.21	1.54	1.90	2.22	3.02	3.84
150	1.74	1.64	1.56	1.48	1.40	1.34	1.22	1.41	1.75	2.06	2.81	3.58
160	1.75	1.65	1.56	1.49	1.41	1.35	1.24	1.31	1.62	1.91	2.62	3.35
180	1.76	1.67	1.58	1.50	1.43	1.37	1.26	1.23	1.43	1.69	2.32	2.98
200	1.78	1.68	1.59	1.52	1.45	1.38	1.28	1.22	1.32	1.53	2.09	2.68
250	1.81	1.72	1.63	1.55	1.48	1.42	1.32	1.25	1.24	1.32	1.71	2.18
300	1.85	1.75	1.66	1.59	1.52	1.45	1.35	1.28	1.24	1.26	1.50	1.86
400	1.91	1.81	1.72	1.64	1.57	1.51	1.40	1.32	1.27	1.25	1.32	1.53
500	1.97	1.87	1.78	1.70	1.62	1.56	1.45	1.37	1.30	1.27	1.27	1.39

D2.6. Table 15. Thermal diffusivity a of ammonia in 10^{-7} m^2/s

Pressure in bar	Temperature in °C											
	−50	−40	−30	−20	−10	0	10	20	30	40	50	60
1	2.36	2.26	108	118	128	138	149	160	172	184	197	211
5	2.36	2.26	2.17	2.07	1.98	1.90	23.5	26.5	29.4	32.4	35.4	38.5
10	2.36	2.26	2.17	2.08	1.99	1.90	1.81	1.73	11.7	13.5	15.2	17.0
15	2.37	2.27	2.17	2.08	1.99	1.90	1.82	1.73	1.64	7.17	8.53	9.86
20	2.37	2.27	2.17	2.08	1.99	1.91	1.82	1.74	1.65	1.56	5.17	6.28
25	2.37	2.27	2.18	2.08	2.00	1.91	1.82	1.74	1.65	1.56	1.47	4.12
30	2.37	2.27	2.18	2.09	2.00	1.91	1.83	1.74	1.66	1.57	1.47	1.37
35	2.38	2.28	2.18	2.09	2.00	1.92	1.83	1.75	1.66	1.57	1.48	1.38
40	2.38	2.28	2.18	2.09	2.00	1.92	1.83	1.75	1.66	1.58	1.48	1.38
50	2.38	2.28	2.19	2.10	2.01	1.93	1.84	1.76	1.67	1.59	1.49	1.40
60	2.39	2.29	2.19	2.10	2.02	1.93	1.85	1.77	1.68	1.60	1.51	1.41
70	2.39	2.29	2.20	2.11	2.02	1.94	1.85	1.77	1.69	1.60	1.52	1.42
80	2.40	2.30	2.20	2.11	2.03	1.94	1.86	1.78	1.70	1.61	1.53	1.44
90	2.40	2.30	2.21	2.12	2.03	1.95	1.87	1.79	1.71	1.62	1.54	1.45
100	2.41	2.31	2.21	2.12	2.04	1.96	1.87	1.79	1.71	1.63	1.55	1.46
110	2.41	2.31	2.22	2.13	2.04	1.96	1.88	1.80	1.72	1.64	1.56	1.47
120	2.41	2.32	2.22	2.13	2.05	1.97	1.89	1.81	1.73	1.65	1.57	1.48
130	2.42	2.32	2.23	2.14	2.05	1.97	1.89	1.81	1.74	1.66	1.58	1.49
140	2.42	2.32	2.23	2.14	2.06	1.98	1.90	1.82	1.74	1.66	1.58	1.50
150	2.43	2.33	2.24	2.15	2.06	1.98	1.90	1.83	1.75	1.67	1.59	1.51
160	2.43	2.33	2.24	2.15	2.07	1.99	1.91	1.83	1.76	1.68	1.60	1.52
180	2.44	2.34	2.25	2.16	2.08	2.00	1.92	1.85	1.77	1.70	1.62	1.54
200	2.45	2.35	2.26	2.17	2.09	2.01	1.93	1.86	1.78	1.71	1.64	1.56
250	2.47	2.37	2.28	2.20	2.12	2.04	1.96	1.89	1.82	1.75	1.68	1.61
300	2.49	2.40	2.30	2.22	2.14	2.06	1.99	1.92	1.85	1.78	1.71	1.65
350	2.51	2.42	2.33	2.24	2.16	2.09	2.02	1.95	1.88	1.81	1.75	1.68
400	2.53	2.44	2.35	2.26	2.19	2.11	2.04	1.97	1.91	1.84	1.78	1.72
500	2.57	2.48	2.39	2.31	2.23	2.16	2.09	2.02	1.96	1.90	1.84	1.78

Pressure in bar	Temperature in °C											
	70	80	90	100	110	120	140	160	180	200	250	300
1	225	239	255	271	288	305	341	380	421	463	573	685
5	41.6	44.9	48.2	51.6	55.1	58.8	66.3	74.3	82.6	91.2	114	136
10	18.8	20.6	22.4	24.2	26.1	28.0	32.0	36.1	40.3	44.7	56.1	67.5
15	11.2	12.5	13.8	15.1	16.4	17.8	20.5	23.3	26.2	29.2	36.9	44.7
20	7.36	8.43	9.49	10.5	11.6	12.7	14.8	17.0	19.2	21.5	27.4	33.2
25	5.08	6.00	6.91	7.82	8.72	9.63	11.4	13.2	15.0	16.9	21.6	26.4
30	3.54	4.38	5.20	6.00	6.79	7.59	9.16	10.7	12.2	13.8	17.8	21.8
35	1.27	3.21	3.96	4.70	5.42	6.15	7.55	8.86	10.2	11.6	15.1	18.6
40	1.27	2.31	3.03	3.72	4.39	5.06	6.34	7.51	8.71	9.93	13.0	16.1
50	1.29	1.17	1.67	2.32	2.93	3.54	4.66	5.63	6.62	7.63	10.2	12.7
60	1.31	1.19	1.06	1.33	1.93	2.51	3.54	4.38	5.24	6.10	8.29	10.5
70	1.32	1.21	1.08	0.92	1.17	1.75	2.74	3.49	4.26	5.02	6.94	8.83
80	1.34	1.23	1.11	0.96	0.76	1.13	2.13	2.83	3.52	4.21	5.93	7.62
90	1.35	1.25	1.13	1.00	0.82	0.53	1.64	2.31	2.95	3.58	5.15	6.69
100	1.37	1.27	1.16	1.03	0.86	0.62	1.22	1.90	2.50	3.08	4.53	5.94

D2.6. Table 15. **(continued)**

Pressure in bar	Temperature in °C											
	70	80	90	100	110	120	140	160	180	200	250	300
110	1.38	1.28	1.18	1.05	0.91	0.70	0.84	1.55	2.13	2.68	4.02	5.33
120	1.39	1.30	1.20	1.08	0.94	0.77	0.46	1.26	1.83	2.34	3.60	4.83
130	1.41	1.31	1.21	1.10	0.98	0.82	0.18	1.01	1.57	2.06	3.25	4.40
140	1.42	1.33	1.23	1.13	1.01	0.87	0.36	0.79	1.35	1.83	2.96	4.04
150	1.43	1.34	1.25	1.15	1.04	0.91	0.50	0.60	1.17	1.63	2.70	3.73
160	1.44	1.36	1.27	1.17	1.06	0.94	0.61	0.48	1.01	1.45	2.48	3.46
180	1.46	1.38	1.30	1.21	1.11	1.01	0.74	0.46	0.77	1.18	2.12	3.02
200	1.48	1.41	1.32	1.24	1.15	1.06	0.84	0.57	0.65	0.98	1.84	2.67
250	1.53	1.46	1.39	1.31	1.24	1.16	1.00	0.81	0.69	0.77	1.39	2.08
300	1.58	1.51	1.44	1.38	1.31	1.24	1.11	0.96	0.83	0.80	1.15	1.72
350	1.62	1.56	1.49	1.43	1.37	1.31	1.20	1.07	0.96	0.89	1.06	1.51
400	1.66	1.60	1.54	1.48	1.42	1.37	1.27	1.15	1.06	0.99	1.05	1.38
500	1.73	1.67	1.62	1.57	1.52	1.47	1.38	1.28	1.20	1.14	1.10	1.28

D2.6. Table 16. Prandtl number Pr of ammonia

Pressure in bar	Temperature in °C											
	−50	−40	−30	−20	−10	0	10	20	30	40	50	60
1	1.99	1.80	0.879	0.875	0.873	0.874	0.875	0.875	0.876	0.876	0.875	0.874
5	1.99	1.81	1.67	1.56	1.47	1.40	1.03	1.00	0.971	0.952	0.937	0.924
10	1.99	1.81	1.67	1.56	1.47	1.40	1.35	1.31	1.14	1.08	1.03	1.00
15	1.99	1.81	1.67	1.56	1.47	1.41	1.35	1.31	1.28	1.25	1.16	1.09
20	1.99	1.81	1.67	1.56	1.47	1.41	1.35	1.31	1.28	1.27	1.34	1.22
25	1.99	1.81	1.67	1.56	1.48	1.41	1.35	1.31	1.28	1.27	1.26	1.39
30	2.00	1.81	1.67	1.56	1.48	1.41	1.35	1.31	1.28	1.27	1.26	1.27
35	2.00	1.82	1.67	1.56	1.48	1.41	1.35	1.31	1.28	1.26	1.26	1.26
40	2.00	1.82	1.68	1.57	1.48	1.41	1.35	1.31	1.28	1.26	1.26	1.26
50	2.00	1.82	1.68	1.57	1.48	1.41	1.36	1.31	1.28	1.26	1.25	1.26
60	2.01	1.82	1.68	1.57	1.48	1.41	1.36	1.31	1.28	1.26	1.25	1.25
70	2.01	1.83	1.68	1.57	1.48	1.41	1.36	1.31	1.28	1.26	1.25	1.25
80	2.02	1.83	1.69	1.57	1.49	1.41	1.36	1.31	1.28	1.26	1.24	1.24
90	2.02	1.83	1.69	1.58	1.49	1.42	1.36	1.31	1.28	1.26	1.24	1.24
100	2.02	1.84	1.69	1.58	1.49	1.42	1.36	1.31	1.28	1.25	1.24	1.23
110	2.03	1.84	1.69	1.58	1.49	1.42	1.36	1.31	1.28	1.25	1.24	1.23
120	2.03	1.84	1.70	1.58	1.49	1.42	1.36	1.32	1.28	1.25	1.23	1.23
130	2.03	1.85	1.70	1.59	1.49	1.42	1.36	1.32	1.28	1.25	1.23	1.22
140	2.04	1.85	1.70	1.59	1.50	1.42	1.36	1.32	1.28	1.25	1.23	1.22
150	2.04	1.85	1.71	1.59	1.50	1.42	1.36	1.32	1.28	1.25	1.23	1.22
160	2.04	1.86	1.71	1.59	1.50	1.43	1.37	1.32	1.28	1.25	1.23	1.21
180	2.05	1.86	1.71	1.60	1.50	1.43	1.37	1.32	1.28	1.25	1.22	1.21
200	2.06	1.87	1.72	1.60	1.51	1.43	1.37	1.32	1.28	1.25	1.22	1.21
250	2.08	1.88	1.73	1.61	1.52	1.44	1.37	1.32	1.28	1.24	1.22	1.20
300	2.09	1.90	1.74	1.62	1.52	1.44	1.38	1.32	1.28	1.24	1.21	1.19
350	2.11	1.91	1.76	1.63	1.53	1.45	1.38	1.33	1.28	1.24	1.21	1.18
400	2.12	1.93	1.77	1.64	1.54	1.46	1.39	1.33	1.28	1.24	1.21	1.18
500	2.15	1.95	1.79	1.66	1.56	1.47	1.40	1.34	1.28	1.24	1.20	1.17

D2.6. Table 16. (continued)

Pressure in bar	Temperature in °C											
	70	80	90	100	110	120	140	160	180	200	250	300
1	0.873	0.871	0.868	0.865	0.862	0.859	0.853	0.847	0.842	0.838	0.835	0.844
5	0.914	0.905	0.897	0.890	0.883	0.877	0.866	0.857	0.850	0.845	0.839	0.847
10	0.974	0.954	0.937	0.923	0.911	0.900	0.883	0.871	0.861	0.853	0.844	0.850
15	1.05	1.01	0.982	0.960	0.941	0.925	0.901	0.884	0.871	0.862	0.849	0.853
20	1.14	1.08	1.03	1.00	0.974	0.952	0.919	0.898	0.883	0.871	0.855	0.857
25	1.25	1.16	1.10	1.05	1.01	0.980	0.938	0.913	0.894	0.880	0.860	0.861
30	1.41	1.27	1.17	1.10	1.05	1.01	0.957	0.928	0.906	0.889	0.866	0.864
35	1.29	1.41	1.26	1.17	1.10	1.05	0.978	0.944	0.918	0.899	0.871	0.868
40	1.29	1.61	1.38	1.24	1.15	1.08	1.00	0.960	0.930	0.909	0.877	0.871
50	1.28	1.32	1.79	1.47	1.29	1.18	1.05	1.00	0.957	0.929	0.889	0.879
60	1.27	1.31	1.39	1.92	1.51	1.30	1.10	1.04	0.986	0.952	0.902	0.886
70	1.26	1.30	1.37	1.51	1.96	1.50	1.17	1.08	1.02	0.976	0.915	0.894
80	1.25	1.28	1.34	1.46	1.75	1.87	1.26	1.13	1.05	1.00	0.928	0.902
90	1.25	1.27	1.33	1.42	1.64	3.14	1.39	1.20	1.09	1.03	0.942	0.910
100	1.24	1.26	1.31	1.39	1.56	2.07	1.59	1.27	1.14	1.06	0.957	0.918
110	1.23	1.25	1.29	1.37	1.50	1.83	1.98	1.37	1.19	1.09	0.973	0.926
120	1.23	1.25	1.28	1.34	1.45	1.69	3.11	1.51	1.25	1.13	0.989	0.934
130	1.22	1.24	1.27	1.32	1.42	1.60	6.72	1.69	1.32	1.17	1.01	0.943
140	1.22	1.23	1.26	1.30	1.38	1.53	3.38	1.95	1.40	1.22	1.02	0.951
150	1.22	1.22	1.25	1.29	1.35	1.47	2.43	2.33	1.49	1.26	1.04	0.960
160	1.21	1.22	1.24	1.27	1.33	1.43	2.05	2.74	1.60	1.32	1.06	0.969
180	1.20	1.21	1.22	1.25	1.29	1.36	1.70	2.65	1.86	1.43	1.10	0.986
200	1.20	1.20	1.20	1.22	1.26	1.31	1.53	2.16	2.04	1.56	1.14	1.00
250	1.18	1.17	1.17	1.18	1.20	1.22	1.32	1.55	1.80	1.71	1.23	1.05
300	1.17	1.16	1.15	1.15	1.16	1.17	1.22	1.33	1.49	1.56	1.30	1.08
350	1.16	1.15	1.13	1.13	1.13	1.13	1.15	1.22	1.31	1.39	1.30	1.11
400	1.15	1.13	1.12	1.11	1.10	1.10	1.11	1.15	1.21	1.27	1.26	1.11
500	1.14	1.12	1.10	1.08	1.07	1.06	1.05	1.06	1.09	1.11	1.15	1.08

5 Bibliography

1. Tillner-Roth R, Harms-Watzenberg F, Baehr HD (1993) Eine neue Fundamentalgleichung für Ammoniak, DKV-Tagungsbericht (20), Nürnberg, Band II/1, 167/181
2. Baehr HD, Tillner-Roth R (1995) Thermodynamische Eigenschaften umweltverträglicher Kältemittel. Springer, Berlin
3. Tufeu R, Ivanov DY, Garrabos Y, Le Neindre B (1984) Thermal conductivity of ammonia in a large temperature and pressure range including the critical region. Ber Bunsenges Phys Chem 88:422–427
4. Fenghour A, Wakeham WA, Vesovic V, Watson JTR, Millat J, Vogal E (1995) The viscosity of ammonia. J Phys Chem Ref Data 24:1649–1667

D2.7 Properties of R134a (1,1,1,2-tetrafluoromethane)

Roland Span[1] · *Rolf Krauss*[2]
[1]Ruhr-Universität Bochum, Bochum, Germany
[2]Universität Stuttgart, Stuttgart, Germany

Tables with thermodynamic properties of R134a (1,1,1,2-Tetrafluoroethan) were calculated with the reference equation of state established by Tillner-Roth and Baehr [1, 2].

The thermal conductivity and viscosity of R134a were calculated with the corresponding equations by Krauss et al. [3]. The densities required as input to these equations were calculated using the equation by Tillner-Roth and Baehr.

p	Pressure in bar	β	Isobaric expansion coefficient in 10^{-3}/K $\beta = v^{-1}\,(\partial v/\partial T)_p$
ρ	Density in kg/m^3	w_s	Isentropic speed of sound in m/s
ϑ	Temperature in °C	λ	Thermal conductivity in mW/m K
Z	Compression factor $Z = p/(\rho RT)$	η	Dynamic viscosity in 10^{-6} Pa·s
h	Specific enthalpy in kJ/kg	ν	Kinematic viscosity ν in 10^{-7} m^2/s
s	Specific entropy in kJ/(kg K)	a	Thermal diffusivity in 10^{-7} m^2/s
c_p	Specific isobaric heat capacity in kJ/(kg K)	Pr	Prandtl number Pr = $\eta\, c_p/\lambda$
c_v	Specific isochoric heat capacity in kJ/(kg K)	v	Specific volume in m^3/kg

1 Characteristic Quantities

Molecular mass $\widetilde{M}$ = 102.032 g/mol, specific gas constant R = 81.488856 J/(kg K).

2 Critical Point [1]

p_c = 40.56 bar, T_c = 374.18 K (ϑ_c = 101.03°C), ρ_c = 508 kg/m^3.

3 Triple Point [1]

p_t = 0.00391 bar, T_t = 169.85 K (ϑ_t = −103.3°C), ρ'_t = 1591kg/m^3.

4 Reference States of Enthalpy and Entropy

h' = 200 kJ/kg and s' = 1 kJ/(kg K) for saturated liquid at ϑ = 0 °C.

D2.7. Table 1. Properties of R134a at p = 1 bar

ϑ °C	ρ kg/m³	h kJ/kg	s kJ/(kg K)	c_p kJ/(kg K)	c_v kJ/(kg K)	β 10^{-3}/K	w_s m/s	λ mW/(m K)	η 10^{-6} Pa·s	ν 10^{-7} m²/s	a 10^{-7} m²/s	Pr –
−90	1556.0	87.27	0.5019	1.189	0.7921	1.71	1053	–	–	–	–	–
−85	1542.6	93.22	0.5340	1.193	0.7941	1.74	1027	–	–	–	–	–
−80	1529.2	99.20	0.5653	1.198	0.7968	1.76	1002	–	–	–	–	–
−75	1515.6	105.2	0.5960	1.203	0.8002	1.79	977.2	–	–	–	–	–
−70	1502.0	111.2	0.6261	1.209	0.8040	1.82	952.4	–	–	–	–	–
−65	1488.3	117.3	0.6556	1.216	0.8083	1.85	927.8	–	–	–	–	–
−60	1474.5	123.4	0.6845	1.223	0.8128	1.88	903.4	–	–	–	–	–
−55	1460.5	129.5	0.7130	1.230	0.8175	1.92	879.2	–	–	–	–	–
−50	1446.5	135.7	0.7409	1.238	0.8225	1.96	855.1	–	–	–	–	–
−45	1432.2	141.9	0.7684	1.246	0.8276	2.00	831.2	–	–	–	–	–
−40	1417.8	148.2	0.7955	1.255	0.8328	2.04	807.5	–	–	–	–	–
−35	1403.2	154.5	0.8223	1.263	0.8382	2.09	783.9	108.9	405.8	2.89	0.614	4.71
−30	1388.4	160.8	0.8486	1.273	0.8438	2.15	760.4	106.8	381.2	2.75	0.604	4.54
−25	5.1594	383.7	1.752	0.7932	0.6886	4.77	146.1	9.576	9.930	19.2	23.4	0.823
−20	5.0401	387.6	1.768	0.7951	0.6932	4.60	147.8	10.01	10.14	20.1	25.0	0.806
−15	4.9275	391.6	1.783	0.7987	0.6990	4.44	149.5	10.43	10.35	21.0	26.5	0.792
−10	4.8208	395.6	1.799	0.8035	0.7056	4.31	151.1	10.86	10.56	21.9	28.0	0.781
−5	4.7196	399.7	1.814	0.8092	0.7128	4.19	152.7	11.28	10.76	22.8	29.5	0.772
0	4.6232	403.7	1.829	0.8154	0.7203	4.07	154.2	11.69	10.97	23.7	31.0	0.765
5	4.5312	407.8	1.844	0.8221	0.7280	3.97	155.7	12.10	11.17	24.7	32.5	0.759
10	4.4433	412.0	1.858	0.8290	0.7359	3.87	157.2	12.51	11.38	25.6	34.0	0.754
15	4.3591	416.1	1.873	0.8362	0.7440	3.78	158.7	12.91	11.58	26.6	35.4	0.750
20	4.2784	420.3	1.887	0.8435	0.7521	3.69	160.1	13.31	11.78	27.5	36.9	0.746
25	4.2010	424.5	1.902	0.8510	0.7602	3.61	161.5	13.71	11.98	28.5	38.3	0.744
30	4.1265	428.8	1.916	0.8586	0.7684	3.54	162.9	14.10	12.18	29.5	39.8	0.742
35	4.0549	433.1	1.930	0.8662	0.7767	3.46	164.3	14.49	12.38	30.5	41.3	0.740
40	3.9860	437.5	1.944	0.8740	0.7849	3.40	165.7	14.88	12.58	31.6	42.7	0.739
45	3.9195	441.9	1.958	0.8817	0.7931	3.33	167.1	15.26	12.77	32.6	44.1	0.738
50	3.8554	446.3	1.972	0.8895	0.8014	3.27	168.4	15.63	12.97	33.6	45.6	0.738
55	3.7935	450.8	1.985	0.8974	0.8096	3.21	169.7	16.01	13.16	34.7	47.0	0.738
60	3.7336	455.3	1.999	0.9052	0.8178	3.15	171.0	16.38	13.36	35.8	48.5	0.738
65	3.6758	459.8	2.013	0.9131	0.8260	3.10	172.3	16.74	13.55	36.9	49.9	0.739
70	3.6198	464.4	2.026	0.9209	0.8341	3.04	173.6	17.10	13.74	38.0	51.3	0.740
75	3.5655	469.0	2.040	0.9288	0.8423	2.99	174.8	17.46	13.93	39.1	52.7	0.741
80	3.5130	473.7	2.053	0.9367	0.8504	2.95	176.1	17.82	14.12	40.2	54.1	0.742
85	3.4621	478.4	2.066	0.9445	0.8585	2.90	177.3	18.17	14.31	41.3	55.6	0.744
90	3.4126	483.1	2.079	0.9524	0.8666	2.85	178.6	18.51	14.50	42.5	57.0	0.746
95	3.3647	487.9	2.092	0.9602	0.8747	2.81	179.8	18.86	14.68	43.6	58.4	0.748
100	3.3181	492.7	2.105	0.9681	0.8827	2.77	181.0	19.20	14.87	44.8	59.8	0.750
105	3.2728	497.6	2.118	0.9759	0.8907	2.73	182.2	19.53	15.05	46.0	61.2	0.752
110	3.2288	502.5	2.131	0.9837	0.8987	2.69	183.4	19.86	15.24	47.2	62.5	0.755
115	3.1860	507.4	2.144	0.9915	0.9066	2.65	184.6	20.19	15.42	48.4	63.9	0.757
120	3.1444	512.4	2.157	0.9992	0.9145	2.61	185.7	20.51	15.60	49.6	65.3	0.760
125	3.1038	517.4	2.169	1.007	0.9224	2.58	186.9	20.83	15.79	50.9	66.7	0.763
130	3.0644	522.5	2.182	1.015	0.9303	2.54	188.0	21.15	15.97	52.1	68.0	0.766
135	3.0259	527.6	2.194	1.022	0.9381	2.51	189.2	21.46	16.15	53.4	69.4	0.769
140	2.9885	532.7	2.207	1.030	0.9459	2.48	190.3	21.77	16.33	54.6	70.7	0.773
145	2.9519	537.9	2.219	1.038	0.9537	2.44	191.4	22.08	16.51	55.9	72.1	0.776
150	2.9163	543.1	2.232	1.045	0.9614	2.41	192.6	22.38	16.68	57.2	73.4	0.779
155	2.8476	553.6	2.256	1.061	0.9768	2.35	194.8	–	–	–	–	–

D2.7. Table 1. (continued)

ϑ °C	ρ kg/m³	h kJ/kg	s kJ/(kg K)	c_p kJ/(kg K)	c_v kJ/(kg K)	β 10^{-3}/K	w_s m/s	λ mW/(m K)	η 10^{-6} Pa·s	ν 10^{-7} m²/s	a 10^{-7} m²/s	Pr –
160	2.8476	553.6	2.256	1.061	0.9768	2.35	194.8	–	–	–	–	–
165	2.8145	558.9	2.269	1.068	0.9845	2.32	195.9	–	–	–	–	–
170	2.7822	564.3	2.281	1.076	0.9921	2.30	197.0	–	–	–	–	–
175	2.7506	569.7	2.293	1.083	0.9997	2.27	198.0	–	–	–	–	–
180	2.7198	575.1	2.305	1.091	1.007	2.24	199.1	–	–	–	–	–

D2.7. Table 2. Properties of the saturated liquid

ϑ °C	p bar	ρ' kg/m³	h' kJ/kg	s' kJ/(kg K)	c_p' kJ/(kg K)	c_v' kJ/(kg K)	β' 10^{-3}/K	w_s' m/s	λ' mW/(m K)	η' 10^{-6} Pa·s	ν' 10^{-7} m²/s	a' 10^{-7} m²/s	Pr′ –
−90	0.01524	1555.8	87.23	0.5020	1.189	0.7920	1.71	1052	–	–	–	–	–
−85	0.02399	1542.5	93.18	0.5341	1.193	0.7940	1.74	1027	–	–	–	–	–
−80	0.03672	1529.0	99.16	0.5654	1.198	0.7968	1.76	1002	–	–	–	–	–
−75	0.05478	1515.5	105.2	0.5961	1.204	0.8002	1.79	976.8	–	–	–	–	–
−70	0.07981	1501.9	111.2	0.6262	1.210	0.8040	1.82	952.0	–	–	–	–	–
−65	0.11380	1488.2	117.3	0.6557	1.216	0.8082	1.85	927.4	–	–	–	–	–
−60	0.15906	1474.3	123.4	0.6846	1.223	0.8127	1.88	903.0	–	–	–	–	–
−55	0.21828	1460.4	129.5	0.7131	1.230	0.8175	1.92	878.8	–	–	–	–	–
−50	0.29451	1446.3	135.7	0.7410	1.238	0.8224	1.96	854.7	–	–	–	–	–
−45	0.39117	1432.1	141.9	0.7685	1.246	0.8276	2.00	830.9	–	–	–	–	–
−40	0.51209	1417.7	148.1	0.7956	1.255	0.8328	2.05	807.2	–	–	–	–	–
−35	0.66144	1403.1	154.4	0.8223	1.264	0.8382	2.09	783.7	108.9	405.6	2.89	0.614	4.71
−30	0.84378	1388.4	160.8	0.8486	1.273	0.8438	2.15	760.3	106.8	381.1	2.75	0.604	4.54
−25	1.0640	1373.4	167.2	0.8746	1.283	0.8494	2.20	737.0	104.6	358.4	2.61	0.594	4.39
−20	1.3273	1358.3	173.6	0.9002	1.293	0.8551	2.27	713.8	102.4	337.2	2.48	0.583	4.26
−15	1.6394	1342.8	180.1	0.9256	1.304	0.8609	2.33	690.7	100.2	317.4	2.36	0.572	4.13
−10	2.0060	1327.1	186.7	0.9506	1.316	0.8669	2.41	667.6	98.06	298.9	2.25	0.562	4.01
−5	2.4334	1311.1	193.3	0.9754	1.328	0.8729	2.49	644.6	95.87	281.6	2.15	0.551	3.90
0	2.9280	1294.8	200.0	1.000	1.341	0.8791	2.58	621.6	93.67	265.3	2.05	0.539	3.80
5	3.4966	1278.1	206.8	1.024	1.355	0.8854	2.69	598.7	91.46	249.9	1.96	0.528	3.70
10	4.1461	1261.0	213.6	1.048	1.370	0.8918	2.80	575.7	89.25	235.4	1.87	0.516	3.61
15	4.8837	1243.4	220.5	1.072	1.387	0.8983	2.93	552.7	87.02	221.7	1.78	0.505	3.53
20	5.7171	1225.3	227.5	1.096	1.405	0.9050	3.07	529.6	84.78	208.7	1.70	0.493	3.46
25	6.6538	1206.7	234.5	1.120	1.425	0.9119	3.24	506.5	82.53	196.3	1.63	0.480	3.39
30	7.7020	1187.5	241.7	1.144	1.446	0.9189	3.43	483.2	80.27	184.6	1.55	0.467	3.33
35	8.8698	1167.5	249.0	1.167	1.471	0.9262	3.64	359.9	77.98	173.4	1.49	0.454	3.27
40	10.166	1146.7	256.4	1.190	1.498	0.9336	3.90	436.4	75.69	162.7	1.42	0.440	3.22
45	11.599	1125.1	263.9	1.214	1.530	0.9414	4.20	412.8	73.37	152.5	1.36	0.426	3.18
50	13.179	1102.3	271.6	1.237	1.566	0.9494	4.56	389.0	71.05	142.7	1.29	0.412	3.14
55	14.915	1078.3	279.5	1.261	1.609	0.9579	5.00	364.9	68.71	133.2	1.24	0.396	3.12
60	16.818	1052.9	287.5	1.285	1.660	0.9668	5.55	340.5	66.36	124.1	1.18	0.380	3.10
65	18.898	1025.6	295.8	1.309	1.723	0.9764	6.25	315.7	64.02	115.2	1.12	0.362	3.10
70	21.168	996.25	304.3	1.333	1.804	0.9869	7.19	290.3	61.69	106.6	1.07	0.343	3.12
75	23.641	964.09	313.1	1.358	1.911	0.9988	8.48	264.1	59.39	98.13	1.02	0.322	3.16
80	26.332	928.24	322.4	1.384	2.065	1.013	10.4	236.6	57.15	89.69	0.966	0.298	3.24
85	29.258	887.16	332.2	1.410	2.306	1.031	13.6	207.4	54.99	81.15	0.915	0.269	3.40
90	32.442	837.83	342.9	1.439	2.756	1.056	19.9	175.9	52.93	72.22	0.862	0.229	3.76
95	35.912	772.70	355.2	1.472	3.938	1.094	37.4	141.2	51.21	62.34	0.807	0.168	4.79
100	39.724	651.18	373.3	1.519	17.59	1.174	254	101.0	55.59	48.63	0.747	0.049	15.4

D2.7. Table 3. Properties of the saturated vapor

ϑ °C	p bar	ρ'' kg/m³	h'' kJ/kg	s'' kJ/(kg K)	c_p'' kJ/(kg K)	c_v'' kJ/(kg K)	β'' 10^{-3}/K	w_s'' m/s	λ'' mW/(m K)	η'' 10^{-6} Pa·s	ν'' 10^{-7} m²/s	a'' 10^{-7} m²/s	Pr″ –
−90	0.01524	0.10236	342.8	1.897	0.6173	0.5341	5.53	131.0	–	–	–	–	–
−85	0.02399	0.15697	345.8	1.877	0.6294	0.5457	5.40	132.6	–	–	–	–	–
−80	0.03672	0.23429	348.8	1.858	0.6417	0.5573	5.29	134.0	–	–	–	–	–
−75	0.05478	0.34116	351.9	1.841	0.6540	0.5689	5.19	135.5	–	–	–	–	–
−70	0.07981	0.48568	355.0	1.826	0.6665	0.5806	5.09	136.8	–	–	–	–	–
−65	0.11380	0.67728	358.2	1.813	0.6793	0.5923	5.01	138.2	–	–	–	–	–
−60	0.15906	0.92676	361.3	1.801	0.6924	0.6040	4.94	139.4	–	–	–	–	–
−55	0.21828	1.2463	364.5	1.790	0.7058	0.6159	4.89	140.6	–	–	–	–	–
−50	0.29451	1.6496	367.7	1.781	0.7197	0.6280	4.84	141.7	–	–	–	–	–
−45	0.39117	2.1518	370.8	1.772	0.7341	0.6402	4.81	142.7	–	–	–	–	–
−40	0.51209	2.7695	374.0	1.764	0.7490	0.6526	4.80	143.6	–	–	–	–	–
−35	0.66144	3.5209	377.2	1.758	0.7646	0.6652	4.79	144.5	8.704	9.507	27.0	32.3	0.835
−30	0.84378	4.4259	380.3	1.751	0.7809	0.6781	4.81	145.2	9.142	9.719	22.0	26.5	0.830
−25	1.0640	5.5059	383.4	1.746	0.7979	0.6912	4.83	145.8	9.656	9.946	18.1	22.0	0.822
−20	1.3273	6.7845	386.6	1.741	0.8158	0.7046	4.87	146.3	10.11	10.16	15.0	18.3	0.820
−15	1.6394	8.2870	389.6	1.737	0.8346	0.7183	4.93	146.6	10.57	10.38	12.5	15.3	0.819
−10	2.0060	10.041	392.7	1.733	0.8544	0.7322	5.01	146.9	11.03	10.59	10.5	12.9	0.821
−5	2.4334	12.077	395.7	1.730	0.8752	0.7464	5.11	147.0	11.49	10.81	8.95	10.9	0.823
0	2.9280	14.428	398.6	1.727	0.8972	0.7608	5.22	146.9	11.96	11.02	7.64	9.24	0.827
5	3.4966	17.131	401.5	1.724	0.9206	0.7755	5.36	146.7	12.43	11.24	6.56	7.88	0.832
10	4.1461	20.226	404.3	1.722	0.9455	0.7904	5.53	146.4	12.92	11.46	5.67	6.76	0.839
15	4.8837	23.758	407.1	1.720	0.9721	0.8056	5.72	145.9	13.42	11.68	4.92	5.81	0.846
20	5.7171	27.780	409.7	1.718	1.001	0.8210	5.95	145.1	13.93	11.91	4.29	5.01	0.856
25	6.6538	32.350	412.3	1.716	1.032	0.8367	6.22	144.3	14.46	12.14	3.75	4.33	0.867
30	7.7020	37.535	414.8	1.714	1.065	0.8527	6.54	143.2	15.01	12.38	3.30	3.75	0.879
35	8.8698	43.416	417.2	1.713	1.103	0.8691	6.92	141.9	15.58	12.63	2.91	3.25	0.894
40	10.166	50.085	419.4	1.711	1.145	0.8858	7.36	140.3	16.19	12.89	2.57	2.82	0.911
45	11.599	57.657	421.5	1.709	1.192	0.9029	7.90	138.6	16.84	13.17	2.28	2.45	0.932
50	13.179	66.272	423.4	1.707	1.246	0.9205	8.55	136.6	17.54	13.47	2.03	2.12	0.957
55	14.915	76.104	425.2	1.705	1.310	0.9387	9.36	134.3	18.30	13.79	1.81	1.84	0.987
60	16.818	87.379	426.6	1.702	1.387	0.9577	10.4	131.7	19.14	14.15	1.62	1.58	1.03
65	18.898	100.40	427.8	1.699	1.482	0.9775	11.7	128.7	20.09	14.56	1.45	1.35	1.07
70	21.168	115.57	428.6	1.696	1.605	0.9986	13.4	125.5	21.17	15.04	1.30	1.14	1.14
75	23.641	133.49	429.0	1.691	1.771	1.021	15.9	121.8	22.44	15.60	1.17	0.949	1.23
80	26.332	155.08	428.8	1.685	2.012	1.046	19.5	117.7	24.00	16.31	1.05	0.769	1.37
85	29.258	181.85	427.8	1.677	2.397	1.074	25.4	113.1	26.01	17.23	0.947	0.597	1.59
90	32.442	216.76	425.4	1.666	3.121	1.107	36.6	107.9	28.88	18.53	0.855	0.427	2.00
95	35.912	267.14	420.7	1.649	5.019	1.149	66.5	101.9	36.49	20.70	0.775	0.272	2.85
100	39.724	373.01	407.7	1.611	25.35	1.218	390	93.95	58.45	26.26	0.704	0.062	11.4

D2.7. Table 4. Density ρ of R134a in kg/m³

Temperature in °C												
Pressure in bar	−70	−60	−50	−40	−30	−20	−10	0	10	20	30	40
1	1502	1474	1446	1418	1388	5.040	4.821	4.623	4.443	4.278	4.127	3.986
5	1503	1475	1447	1419	1389	1359	1328	1296	1261	23.74	22.55	21.53
10	1504	1476	1448	1420	1391	1361	1330	1298	1264	1228	1189	49.00
15	1504	1477	1449	1421	1392	1362	1331	1299	1266	1230	1192	1151
20	1505	1478	1450	1422	1393	1364	1333	1301	1268	1233	1195	1155

D2.7. Table 4. (continued)

Temperature in °C												
Pressure in bar	−70	−60	−50	−40	−30	−20	−10	0	10	20	30	40
25	1506	1479	1451	1423	1395	1365	1335	1303	1270	1236	1199	1159
30	1507	1480	1452	1424	1396	1367	1336	1305	1272	1238	1202	1162
35	1508	1481	1453	1425	1397	1368	1338	1307	1274	1241	1205	1166
40	1508	1482	1454	1427	1398	1369	1339	1309	1277	1243	1207	1169
45	1509	1482	1455	1428	1399	1371	1351	1310	1279	1245	1210	1173
50	1510	1483	1456	1429	1401	1372	1343	1312	1281	1248	1213	1176
60	1512	1485	1458	1431	1403	1375	1346	1316	1284	1252	1218	1182
70	1513	1487	1460	1433	1405	1377	1348	1319	1288	1257	1223	1188
80	1515	1488	1462	1435	1408	1380	1351	1322	1292	1261	1228	1194
90	1516	1490	1464	1437	1410	1382	1354	1325	1296	1265	1233	1200
100	1518	1492	1466	1439	1412	1385	1357	1328	1299	1269	1238	1205
110	1519	1493	1467	1441	1414	1387	1360	1331	1302	1273	1242	1210
120	1521	1495	1469	1443	1417	1390	1362	1334	1306	1276	1246	1215
140	1524	1498	1473	1447	1421	1394	1367	1340	1312	1284	1254	1224
160	1526	1501	1476	1451	1425	1399	1372	1346	1318	1291	1262	1233
180	1529	1504	1479	1454	1429	1403	1377	1351	1324	1297	1269	1241
200	1532	1507	1483	1458	1433	1408	1382	1356	1330	1303	1276	1249
220	1535	1510	1486	1461	1437	1412	1387	1361	1335	1309	1283	1256
240	1537	1513	1489	1465	1440	1416	1391	1366	1341	1315	1289	1263
260	1540	1516	1492	1468	1444	1420	1395	1371	1346	1321	1296	1270
280	1543	1519	1495	1471	1448	1424	1400	1375	1351	1326	1301	1276
300	1545	1522	1498	1475	1451	1427	1404	1380	1356	1331	1307	1283

Temperature in °C												
Pressure in bar	50	60	70	80	90	100	110	120	130	140	160	180
1	3.855	3.734	3.620	3.513	3.413	3.318	3.229	3.144	3.064	2.988	2.848	2.720
5	20.62	19.81	19.07	18.41	17.79	17.23	16.70	16.21	15.75	15.32	14.54	13.84
10	45.88	43.35	41.22	39.37	37.75	36.29	34.98	33.79	32.70	31.69	29.89	28.31
15	1104	73.45	68.19	64.07	60.67	57.78	55.27	53.05	51.07	49.28	46.15	43.48
20	1109	1057	104.5	94.89	88.00	82.61	78.18	74.43	71.17	68.30	63.44	59.42
25	1114	1064	1004	138.5	122.8	112.4	104.7	98.53	93.42	89.05	81.90	76.19
30	1119	1071	1014	940.6	173.9	150.6	136.5	126.3	118.4	111.9	101.7	93.88
35	1124	1077	1022	954.9	856.4	206.8	176.9	159.3	146.9	137.3	123.0	112.6
40	1128	1082	1030	967.2	882.8	677.8	234.0	200.3	180.2	166.0	146.2	132.4
45	1132	1088	1037	978.2	902.5	782.9	341.9	254.7	220.2	198.8	171.3	153.4
50	1136	1093	1044	988.0	918.7	822.1	607.8	335.3	270.0	236.8	198.7	175.7
60	1144	1103	1057	1005	944.7	869.5	764.6	591.2	415.9	334.3	261.6	224.4
70	1151	1112	1068	1020	965.5	901.3	821.9	717.3	582.4	460.5	336.0	278.7
80	1158	1120	1078	1033	983.0	925.8	859.1	779.0	682.4	576.8	418.6	337.9
90	1165	1128	1088	1045	998.2	946.1	887.3	820.0	742.8	657.5	499.7	399.5
100	1171	1135	1097	1056	1012	963.4	910.2	850.9	785.1	713.5	569.7	460.1
110	1177	1142	1105	1066	1024	978.6	929.5	876.0	817.7	755.2	626.3	516.0
120	1182	1148	1113	1075	1035	992.2	946.4	897.1	844.3	788.2	671.9	565.5
140	1193	1161	1127	1092	1055	1016	974.8	931.6	886.2	838.7	740.5	645.4
160	1203	1172	1140	1107	1072	1036	998.4	959.4	918.8	876.9	790.8	705.7
180	1212	1182	1152	1120	1087	1054	1019	982.7	945.7	907.7	830.1	753.0
200	1221	1192	1162	1132	1101	1069	1036	1003	968.6	933.6	862.3	791.4

D2.7. Table 4. (continued)

Temperature in °C												
Pressure in bar	50	60	70	80	90	100	110	120	130	140	160	180
220	1229	1201	1173	1143	1114	1083	1052	1021	988.6	955.9	889.6	823.7
240	1237	1210	1182	1154	1125	1096	1067	1037	1006	975.5	913.3	851.4
260	1244	1218	1191	1164	1136	1108	1080	1051	1022	993.1	934.2	875.7
280	1251	1225	1199	1173	1146	1120	1092	1065	1037	1009	952.9	897.3
300	1258	1233	1207	1182	1156	1130	1104	1077	1050	1024	969.9	916.7

D2.7. Table 5. Compression factor *Z* of R 134a

Temperature in °C												
Pressure in bar	−70	−60	−50	−40	−30	−20	−10	0	10	20	30	40
1	0.004	0.004	0.004	0.004	0.004	0.962	0.967	0.972	0.975	0.978	0.981	0.983
5	0.020	0.020	0.019	0.019	0.018	0.018	0.018	0.017	0.017	0.882	0.897	0.910
10	0.040	0.039	0.038	0.037	0.036	0.036	0.035	0.035	0.034	0.034	0.034	0.800
15	0.060	0.058	0.057	0.056	0.054	0.053	0.053	0.052	0.051	0.051	0.051	0.051
20	0.080	0.078	0.076	0.074	0.072	0.071	0.070	0.069	0.068	0.068	0.068	0.068
25	0.100	0.097	0.095	0.092	0.090	0.089	0.087	0.086	0.085	0.085	0.084	0.085
30	0.120	0.117	0.114	0.111	0.108	0.106	0.105	0.103	0.102	0.101	0.101	0.101
35	0.140	0.136	0.132	0.129	0.126	0.124	0.122	0.120	0.119	0.118	0.118	0.118
40	0.160	0.155	0.151	0.148	0.144	0.142	0.139	0.137	0.136	0.135	0.134	0.134
45	0.180	0.175	0.170	0.166	0.162	0.159	0.156	0.154	0.153	0.151	0.151	0.150
50	0.200	0.194	0.189	0.184	0.180	0.177	0.174	0.171	0.169	0.168	0.167	0.167
60	0.240	0.233	0.226	0.221	0.216	0.212	0.208	0.205	0.202	0.201	0.199	0.199
70	0.279	0.271	0.264	0.257	0.251	0.246	0.242	0.238	0.235	0.233	0.232	0.231
80	0.319	0.309	0.301	0.293	0.287	0.281	0.276	0.272	0.268	0.266	0.264	0.263
90	0.359	0.348	0.338	0.330	0.322	0.316	0.310	0.305	0.301	0.298	0.295	0.294
100	0.398	0.386	0.375	0.366	0.357	0.350	0.344	0.338	0.334	0.330	0.327	0.325
110	0.437	0.424	0.412	0.402	0.393	0.384	0.377	0.371	0.366	0.362	0.359	0.356
120	0.477	0.462	0.449	0.438	0.428	0.419	0.411	0.404	0.398	0.394	0.390	0.387
140	0.555	0.538	0.523	0.509	0.497	0.487	0.477	0.469	0.462	0.457	0.452	0.448
160	0.633	0.614	0.596	0.581	0.567	0.554	0.544	0.534	0.526	0.519	0.513	0.509
180	0.711	0.689	0.669	0.651	0.636	0.622	0.609	0.599	0.589	0.581	0.574	0.568
200	0.789	0.764	0.742	0.722	0.704	0.689	0.675	0.663	0.652	0.642	0.634	0.628
220	0.866	0.839	0.814	0.792	0.773	0.755	0.740	0.726	0.714	0.703	0.694	0.686
240	0.943	0.913	0.886	0.862	0.841	0.822	0.805	0.789	0.776	0.764	0.753	0.745
260	1.020	0.987	0.958	0.932	0.909	0.888	0.869	0.852	0.837	0.824	0.812	0.802
280	1.096	1.061	1.030	1.002	0.976	0.953	0.933	0.915	0.898	0.884	0.871	0.860
300	1.173	1.135	1.101	1.071	1.043	1.019	0.997	0.977	0.959	0.943	0.929	0.917
Temperature in °C												
Pressure in bar	50	60	70	80	90	100	110	120	130	140	160	180
1	0.985	0.987	0.988	0.989	0.990	0.991	0.992	0.993	0.993	0.994	0.995	0.996
5	0.921	0.930	0.937	0.944	0.950	0.955	0.959	0.963	0.966	0.969	0.974	0.978
10	0.828	0.850	0.868	0.883	0.895	0.906	0.915	0.924	0.931	0.937	0.948	0.956
15	0.052	0.752	0.787	0.814	0.835	0.854	0.869	0.883	0.894	0.904	0.921	0.934

D2.7. Table 5. (continued)

Pressure in bar	Temperature in °C											
	50	60	70	80	90	100	110	120	130	140	160	180
20	0.068	0.070	0.685	0.732	0.768	0.796	0.819	0.839	0.855	0.870	0.893	0.912
25	0.085	0.087	0.089	0.627	0.688	0.731	0.765	0.792	0.815	0.834	0.865	0.889
30	0.102	0.103	0.106	0.111	0.583	0.655	0.704	0.741	0.771	0.796	0.836	0.865
35	0.118	0.120	0.122	0.127	0.138	0.557	0.634	0.686	0.725	0.757	0.806	0.842
40	0.135	0.136	0.139	0.144	0.153	0.194	0.547	0.623	0.676	0.716	0.775	0.818
45	0.151	0.152	0.155	0.160	0.168	0.189	0.422	0.551	0.622	0.672	0.744	0.795
50	0.167	0.169	0.171	0.176	0.184	0.200	0.263	0.465	0.564	0.627	0.713	0.771
60	0.199	0.200	0.203	0.207	0.215	0.227	0.251	0.317	0.439	0.533	0.650	0.724
70	0.231	0.232	0.234	0.238	0.245	0.255	0.273	0.305	0.366	0.451	0.590	0.680
80	0.262	0.263	0.265	0.269	0.275	0.284	0.298	0.321	0.357	0.412	0.541	0.641
90	0.293	0.294	0.296	0.299	0.305	0.313	0.325	0.343	0.369	0.407	0.510	0.610
100	0.324	0.325	0.326	0.329	0.334	0.341	0.352	0.367	0.388	0.416	0.497	0.589
110	0.355	0.355	0.356	0.359	0.363	0.370	0.379	0.392	0.409	0.433	0.498	0.577
120	0.385	0.385	0.386	0.388	0.392	0.398	0.406	0.418	0.433	0.452	0.506	0.575
140	0.446	0.444	0.444	0.446	0.449	0.453	0.460	0.469	0.481	0.496	0.536	0.587
160	0.505	0.503	0.502	0.502	0.504	0.508	0.513	0.521	0.530	0.542	0.573	0.614
180	0.564	0.561	0.559	0.559	0.559	0.562	0.566	0.572	0.579	0.589	0.614	0.647
200	0.622	0.618	0.615	0.614	0.614	0.615	0.618	0.622	0.629	0.636	0.657	0.684
220	0.680	0.675	0.671	0.669	0.667	0.668	0.670	0.673	0.677	0.684	0.701	0.723
240	0.737	0.731	0.726	0.723	0.721	0.720	0.721	0.723	0.726	0.731	0.745	0.763
260	0.794	0.787	0.781	0.776	0.773	0.771	0.771	0.772	0.774	0.778	0.788	0.804
280	0.850	0.842	0.835	0.829	0.825	0.823	0.821	0.821	0.822	0.824	0.832	0.845
300	0.906	0.896	0.889	0.882	0.877	0.873	0.871	0.869	0.869	0.871	0.876	0.886

D2.7. Table 6. Specific enthalpy *h* of R134 a in kJ/kg

Pressure in bar	Temperature in °C											
	−70	−60	−50	−40	−30	−20	−10	0	10	20	30	40
1	111.2	123.4	135.7	148.2	160.8	387.6	395.6	403.7	412.0	420.3	428.8	437.5
5	111.4	123.6	135.9	148.3	160.9	173.8	186.8	200.0	213.6	411.6	421.2	430.6
10	111.6	123.8	136.1	148.5	161.1	173.9	186.9	200.2	213.7	227.5	241.7	419.9
15	111.8	124.0	136.2	148.7	161.3	174.1	187.1	200.3	213.8	227.6	241.7	256.3
20	112.0	124.2	136.4	148.9	161.5	174.2	187.2	200.4	213.9	227.6	241.7	256.2
25	112.2	124.4	136.6	149.1	161.6	174.4	187.4	200.5	214.0	227.7	241.7	256.2
30	112.5	124.6	136.8	149.2	161.8	174.6	187.5	200.7	214.1	227.7	241.7	256.1
35	112.7	124.8	137.0	149.4	162.0	174.7	187.6	200.8	214.2	227.8	241.8	256.1
40	112.9	125.0	137.2	149.6	162.2	174.9	187.8	200.9	214.3	227.9	241.8	256.1
45	113.1	125.2	137.4	149.8	162.4	175.1	187.9	201.0	214.4	227.9	241.8	256.0
50	113.3	125.4	137.6	150.0	162.5	175.2	188.1	201.2	214.5	228.0	241.9	256.0
60	113.7	125.8	138.0	150.4	162.9	175.6	188.4	201.5	214.7	228.2	242.0	256.0
70	114.2	126.2	138.4	150.8	163.3	175.9	188.7	201.7	214.9	228.4	242.1	256.1
80	114.6	126.7	138.8	151.2	163.6	176.3	189.1	202.0	215.2	228.6	242.2	256.1

D2.7. Table 6. (continued)

Temperature in °C												
Pressure in bar	−70	−60	−50	−40	−30	−20	−10	0	10	20	30	40
90	115.0	127.1	139.2	151.6	164.0	176.6	189.4	202.3	215.5	228.8	242.4	256.2
100	115.5	127.5	139.7	152.0	164.4	177.0	189.7	202.6	215.7	229.0	242.5	256.3
110	115.9	127.9	140.1	152.3	164.8	177.3	190.0	202.9	216.0	229.3	242.7	256.4
120	116.3	128.3	140.5	152.7	165.1	177.7	190.4	203.2	216.3	229.5	242.9	256.6
140	117.2	129.2	141.3	153.5	165.9	178.4	191.1	203.9	216.9	230.0	243.4	256.9
160	118.1	130.0	142.1	254.4	166.7	179.2	191.8	204.6	217.5	230.6	243.8	257.3
180	118.9	130.9	143.0	155.2	167.5	179.9	192.5	205.2	218.1	231.1	244.3	257.7
200	119.8	131.8	143.8	156.0	168.3	180.7	193.2	205.9	218.8	231.7	244.9	258.2
220	120.7	132.6	144.7	156.8	169.1	181.5	194.0	206.6	219.4	232.3	245.4	258.7
240	121.6	133.5	145.5	157.7	169.9	182.3	194.7	207.4	220.1	233.0	246.0	259.2
260	122.5	134.4	146.4	158.5	170.7	183.1	195.5	208.1	220.8	233.6	246.6	259.8
280	123.4	135.3	147.2	159.3	171.5	183.9	196.3	208.8	221.5	234.3	247.3	260.3
300	124.3	136.1	148.1	160.2	172.4	184.7	197.1	209.6	222.2	235.0	247.9	260.9

Temperature in °C												
Pressure in bar	50	60	70	80	90	100	110	120	130	140	160	180
1	446.3	455.3	464.4	473.7	483.1	492.7	502.5	512.4	522.5	532.7	553.6	575.1
5	440.1	449.6	459.2	468.9	478.8	488.7	498.7	508.9	519.2	529.6	550.9	572.7
10	430.9	441.5	452.0	462.4	472.8	483.2	493.7	504.2	514.8	525.6	547.3	569.5
15	271.5	431.3	443.4	454.9	466.1	477.2	488.2	499.2	510.2	521.3	543.6	566.2
20	271.4	287.3	432.1	445.8	458.4	470.4	482.2	493.8	505.3	516.8	539.7	562.9
25	271.2	286.9	303.8	433.4	448.9	462.6	475.5	487.9	500.0	512.0	535.7	559.4
30	271.0	286.6	303.1	321.4	435.8	453.1	467.8	481.3	494.3	506.9	531.5	555.8
35	270.9	286.3	302.6	320.3	341.3	440.0	458.5	473.9	487.9	501.3	527.1	552.1
40	270.8	286.1	302.2	319.5	339.1	370.7	446.3	465.1	480.9	495.4	522.4	548.3
45	270.7	285.9	301.8	318.7	337.4	360.8	426.2	454.3	472.9	488.9	517.6	544.4
50	270.6	285.7	301.4	318.0	336.2	357.2	391.0	440.1	463.7	481.7	512.4	540.3
60	270.5	285.4	300.8	317.0	334.2	353.1	375.4	405.9	440.5	465.2	501.4	531.9
70	270.4	285.1	300.3	316.1	332.8	350.6	370.1	392.7	419.7	447.2	489.7	523.1
80	270.3	284.9	299.9	315.5	331.7	348.7	367.0	386.9	409.1	433.1	478.0	514.2
90	270.3	284.8	299.6	314.9	330.8	347.3	364.7	383.3	403.2	424.4	467.6	505.7
100	270.3	284.7	299.4	314.5	330.1	346.2	363.0	380.7	399.3	418.9	459.5	498.0
110	270.4	284.6	299.2	314.1	329.5	345.3	361.7	378.7	396.5	415.0	453.4	491.3
120	270.5	284.6	299.1	313.8	329.0	344.6	360.6	377.2	394.3	412.1	448.8	485.7
140	270.7	284.6	298.9	313.4	328.3	343.4	359.0	374.9	391.2	408.0	442.4	477.5
160	270.9	284.8	298.9	313.2	327.8	342.7	357.9	373.3	389.1	405.2	438.2	471.9
180	271.2	285.0	298.9	313.1	327.5	342.2	357.1	372.2	387.6	403.3	435.3	467.9
200	271.6	285.3	299.1	313.2	327.4	341.9	356.5	371.4	386.5	401.9	433.1	465.0
220	272.1	285.6	299.4	313.3	327.4	341.7	356.2	370.9	385.8	400.8	431.5	462.8
240	272.5	286.0	299.7	313.5	327.5	341.6	356.0	370.5	385.2	400.1	430.3	461.1
260	273.0	286.4	300.0	313.7	327.6	341.7	355.9	370.3	384.8	399.6	429.4	459.8
280	273.5	286.9	300.4	314.1	327.9	341.8	355.9	370.2	384.6	399.2	428.7	458.8
300	274.1	287.4	300.8	314.4	328.2	342.0	356.0	370.2	384.5	399.0	428.3	458.0

D2.7. Table 7. Specific entropy s of R134a in kJ/(kg K)

Pressure in bar	Temperature in °C											
	−70	−60	−50	−40	−30	−20	−10	0	10	20	30	40
1	0.6261	0.6845	0.7409	0.7955	0.8486	1.768	1.799	1.829	1.858	1.887	1.916	1.944
5	0.6256	0.6840	0.7404	0.7950	0.8480	0.8996	0.9501	0.9996	1.048	1.734	1.766	1.797
10	0.6250	0.6834	0.7397	0.7942	0.8472	0.8988	0.9492	0.9986	1.047	1.095	1.143	1.713
15	0.6244	0.6827	0.7390	0.7935	0.8465	0.8980	0.9483	0.9976	1.046	1.094	1.141	1.189
20	0.6238	0.6821	0.7384	0.7928	0.8457	0.8972	0.9474	0.9967	1.045	1.093	1.140	1.187
25	0.6232	0.6815	0.7377	0.7921	0.8450	0.8964	0.9466	0.9957	1.044	1.092	1.139	1.186
30	0.6226	0.6809	0.7371	0.7914	0.8442	0.8956	0.9457	0.9948	1.043	1.090	1.137	1.184
35	0.6220	0.6802	0.7364	0.7907	0.8435	0.8948	0.9448	0.9938	1.042	1.089	1.136	1.183
40	0.6214	0.6796	0.7357	0.7901	0.8427	0.8940	0.9440	0.9929	1.041	1.088	1.135	1.181
45	0.6208	0.6790	0.7351	0.7894	0.8420	0.8932	0.9432	0.9920	1.040	1.087	1.134	1.180
50	0.6203	0.6784	0.7345	0.7887	0.8413	0.8924	0.9423	0.9911	1.039	1.086	1.132	1.178
60	0.6191	0.6772	0.7332	0.7873	0.8398	0.8909	0.9407	0.9893	1.037	1.084	1.130	1.176
70	0.6180	0.6760	0.7319	0.7860	0.8384	0.8894	0.9391	0.9876	1.035	1.082	1.128	1.173
80	0.6168	0.6748	0.7307	0.7847	0.8370	0.8879	0.9375	0.9859	1.033	1.080	1.125	1.171
90	0.6157	0.6736	0.7294	0.7834	0.8356	0.8864	0.9359	0.9842	1.031	1.078	1.123	1.168
100	0.6146	0.6724	0.7282	0.7821	0.8343	0.8850	0.9344	0.9825	1.030	1.076	1.121	1.166
110	0.6134	0.6713	0.7270	0.7808	0.8329	0.8836	0.9328	0.9809	1.028	1.074	1.119	1.164
120	0.6123	0.6701	0.7258	0.7795	0.8316	0.8822	0.9313	0.9793	1.026	1.072	1.117	1.161
140	0.6101	0.6678	0.7234	0.7770	0.8290	0.8794	0.9284	0.9762	1.023	1.068	1.113	1.157
160	0.6080	0.6656	0.7210	0.7746	0.8264	0.8767	0.9255	0.9732	1.020	1.065	1.110	1.153
180	0.6058	0.6634	0.7187	0.7722	0.8239	0.8740	0.9228	0.9702	1.016	1.062	1.106	1.149
200	0.6037	0.6612	0.7164	0.7698	0.8214	0.8714	0.9200	0.9673	1.013	1.059	1.103	1.146
220	0.6017	0.6590	0.7142	0.7675	0.8190	0.8689	0.9174	0.9646	1.011	1.055	1.099	1.142
240	0.5996	0.6569	0.7120	0.7652	0.8166	0.8664	0.9148	0.9618	1.008	1.052	1.096	1.139
260	0.5976	0.6548	0.7098	0.7629	0.8143	0.8640	0.9122	0.9592	1.005	1.049	1.093	1.136
280	0.5956	0.6527	0.7077	0.7607	0.8120	0.8616	0.9098	0.9566	1.002	1.047	1.090	1.132
300	0.5936	0.6507	0.7056	0.7585	0.8097	0.8592	0.9073	0.9540	0.9995	1.044	1.087	1.129

Pressure in bar	Temperature in °C											
	50	60	70	80	90	100	110	120	130	140	160	180
1	1.972	1.999	2.026	2.053	2.079	2.105	2.131	2.157	2.182	2.207	2.256	2.305
5	1.826	1.856	1.884	1.912	1.939	1.966	1.993	2.019	2.045	2.070	2.121	2.170
10	1.748	1.781	1.812	1.841	1.870	1.899	1.926	1.954	1.980	2.007	2.058	2.108
15	1.237	1.723	1.759	1.792	1.823	1.853	1.883	1.911	1.939	1.966	2.018	2.070
20	1.235	1.283	1.709	1.748	1.783	1.816	1.847	1.877	1.906	1.934	1.988	2.041
25	1.233	1.281	1.331	1.700	1.744	1.781	1.815	1.847	1.878	1.907	1.963	2.017
30	1.231	1.278	1.327	1.380	1.698	1.745	1.784	1.819	1.852	1.882	1.941	1.996
35	1.229	1.276	1.324	1.375	1.434	1.702	1.751	1.791	1.826	1.859	1.920	1.977
40	1.227	1.274	1.322	1.371	1.426	1.512	1.713	1.762	1.801	1.837	1.901	1.959
45	1.226	1.272	1.319	1.368	1.420	1.483	1.656	1.729	1.775	1.814	1.882	1.943
50	1.224	1.270	1.317	1.364	1.415	1.472	1.561	1.688	1.747	1.791	1.864	1.927
60	1.221	1.266	1.312	1.358	1.407	1.458	1.517	1.595	1.682	1.743	1.829	1.897
70	1.218	1.263	1.308	1.353	1.400	1.448	1.500	1.558	1.626	1.693	1.794	1.869
80	1.215	1.260	1.304	1.349	1.394	1.440	1.488	1.540	1.595	1.654	1.760	1.842
90	1.213	1.257	1.300	1.344	1.389	1.434	1.480	1.527	1.577	1.629	1.732	1.818
100	1.210	1.254	1.297	1.340	1.384	1.428	1.472	1.518	1.565	1.612	1.709	1.795
110	1.207	1.251	1.294	1.337	1.380	1.423	1.466	1.510	1.554	1.600	1.691	1.776

D2.7. Table 7. (continued)

Temperature in °C												
Pressure in bar	50	60	70	80	90	100	110	120	130	140	160	180
120	1.205	1.248	1.291	1.333	1.376	1.418	1.460	1.503	1.546	1.590	1.676	1.760
140	1.200	1.243	1.285	1.327	1.368	1.410	1.451	1.492	1.533	1.574	1.655	1.734
160	1.196	1.238	1.280	1.321	1.362	1.402	1.442	1.482	1.522	1.561	1.639	1.715
180	1.192	1.234	1.275	1.316	1.356	1.396	1.435	1.474	1.513	1.551	1.627	1.701
200	1.188	1.230	1.271	1.311	1.351	1.390	1.429	1.467	1.505	1.543	1.617	1.688
220	1.184	1.226	1.266	1.306	1.346	1.384	1.423	1.461	1.498	1.535	1.608	1.678
240	1.181	1.222	1.262	1.302	1.341	1.379	1.417	1.455	1.492	1.528	1.600	1.669
260	1.177	1.218	1.258	1.298	1.337	1.375	1.412	1.449	1.486	1.522	1.593	1.661
280	1.174	1.215	1.255	1.294	1.332	1.370	1.408	1.444	1.481	1.516	1.586	1.654
300	1.171	1.211	1.251	1.290	1.328	1.366	1.403	1.440	1.476	1.511	1.580	1.647

D2.7. Table 8. Specific isobaric heat capacity c_p of R134a in kJ/(kg K)

Temperature in °C												
Pressure in bar	−70	−60	−50	−40	−30	−20	−10	0	10	20	30	40
1	1.209	1.223	1.238	1.255	1.273	0.7951	0.8035	0.8154	0.8290	0.8435	0.8586	0.8740
5	1.209	1.222	1.237	1.254	1.272	1.292	1.314	1.340	1.370	0.9635	0.9494	0.9468
10	1.208	1.222	1.236	1.253	1.270	1.290	1.312	1.337	1.366	1.401	1.443	1.134
15	1.208	1.221	1.235	1.252	1.269	1.289	1.310	1.335	1.363	1.396	1.437	1.489
20	1.207	1.220	1.235	1.250	1.268	1.287	1.308	1.332	1.359	1.391	1.430	1.479
25	1.207	1.219	1.234	1.249	1.267	1.285	1.306	1.330	1.356	1.387	1.424	1.471
30	1.206	1.219	1.233	1.248	1.265	1.284	1.304	1.327	1.353	1.383	1.419	1.463
35	1.205	1.218	1.232	1.247	1.264	1.282	1.303	1.325	1.350	1.379	1.414	1.455
40	1.205	1.217	1.231	1.246	1.263	1.281	1.301	1.323	1.347	1.376	1.409	1.448
45	1.204	1.217	1.230	1.246	1.262	1.280	1.299	1.321	1.345	1.372	1.404	1.442
50	1.204	1.216	1.230	1.245	1.261	1.278	1.297	1.318	1.342	1.369	1.399	1.436
60	1.203	1.215	1.228	1.243	1.259	1.276	1.294	1.314	1.337	1.362	1.391	1.425
70	1.202	1.214	1.227	1.241	1.256	1.273	1.291	1.311	1.332	1.356	1.383	1.414
80	1.201	1.212	1.225	1.239	1.254	1.271	1.288	1.307	1.328	1.351	1.376	1.405
90	1.200	1.211	1.224	1.238	1.253	1.268	1.285	1.304	1.324	1.346	1.370	1.397
100	1.199	1.210	1.223	1.236	1.251	1.266	1.283	1.300	1.320	1.341	1.364	1.389
110	1.198	1.209	1.221	1.235	1.249	1.264	1.280	1.297	1.316	1.336	1.358	1.382
120	1.197	1.208	1.220	1.233	1.247	1.262	1.278	1.295	1.313	1.332	1.353	1.376
140	1.195	1.206	1.218	1.230	1.244	1.258	1.273	1.289	1.306	1.324	1.344	1.365
160	1.193	1.204	1.215	1.228	1.241	1.254	1.269	1.284	1.300	1.317	1.335	1.355
180	1.192	1.202	1.213	1.225	1.238	1.251	1.265	1.280	1.295	1.311	1.328	1.346
200	1.190	1.200	1.211	1.223	1.235	1.248	1.261	1.275	1.290	1.305	1.321	1.338
220	1.189	1.198	1.209	1.221	1.233	1.245	1.258	1.272	1.286	1.300	1.315	1.331
240	1.187	1.197	1.207	1.219	1.230	1.242	1.255	1.268	1.281	1.295	1.310	1.325
260	1.186	1.195	1.206	1.217	1.228	1.240	1.252	1.265	1.278	1.291	1.305	1.319
280	1.185	1.194	1.204	1.215	1.226	1.237	1.249	1.262	1.274	1.287	1.300	1.314
300	1.183	1.192	1.202	1.213	1.224	1.235	1.247	1.259	1.271	1.283	1.296	1.310

D2.7. Table 8. (continued)

Pressure in bar	Temperature in °C											
	50	60	70	80	90	100	110	120	130	140	160	180
1	0.8895	0.9052	0.9209	0.9367	0.9524	0.9681	0.9837	0.9992	1.015	1.030	1.061	1.091
5	0.9500	0.9565	0.9651	0.9751	0.9862	0.9979	1.010	1.023	1.036	1.049	1.077	1.104
10	1.079	1.054	1.042	1.039	1.040	1.044	1.050	1.058	1.067	1.077	1.099	1.122
15	1.560	1.248	1.172	1.134	1.114	1.104	1.100	1.100	1.103	1.109	1.123	1.142
20	1.545	1.643	1.465	1.302	1.228	1.188	1.166	1.154	1.148	1.146	1.152	1.164
25	1.532	1.619	1.764	1.731	1.436	1.319	1.258	1.224	1.203	1.192	1.184	1.189
30	1.520	1.599	1.722	1.970	2.003	1.556	1.398	1.319	1.274	1.247	1.221	1.216
35	1.509	1.580	1.687	1.880	2.455	2.175	1.642	1.459	1.369	1.316	1.265	1.246
40	1.498	1.564	1.659	1.815	2.168	9.404	2.187	1.684	1.499	1.405	1.315	1.280
45	1.489	1.550	1.634	1.764	2.016	2.912	4.459	2.096	1.689	1.520	1.374	1.317
50	1.480	1.537	1.613	1.724	1.917	2.382	5.675	2.976	1.979	1.672	1.443	1.359
60	1.465	1.514	1.577	1.663	1.792	2.015	2.510	3.641	2.933	2.123	1.615	1.454
70	1.451	1.495	1.549	1.619	1.714	1.854	2.082	2.473	2.848	2.546	1.820	1.562
80	1.439	1.478	1.525	1.584	1.659	1.759	1.899	2.097	2.334	2.433	1.997	1.672
90	1.428	1.464	1.505	1.556	1.617	1.694	1.793	1.918	2.063	2.179	2.059	1.764
100	1.418	1.451	1.488	1.532	1.584	1.647	1.722	1.811	1.910	2.000	2.015	1.818
110	1.409	1.440	1.474	1.513	1.558	1.610	1.670	1.739	1.812	1.882	1.937	1.830
120	1.401	1.429	1.461	1.496	1.536	1.580	1.631	1.686	1.744	1.799	1.861	1.814
140	1.387	1.412	1.439	1.468	1.500	1.535	1.573	1.613	1.653	1.692	1.747	1.751
160	1.375	1.397	1.421	1.446	1.474	1.502	1.533	1.564	1.595	1.624	1.672	1.690
180	1.365	1.385	1.406	1.429	1.452	1.477	1.502	1.528	1.554	1.578	1.619	1.641
200	1.356	1.374	1.394	1.414	1.435	1.457	1.479	1.501	1.523	1.544	1.580	1.603
220	1.348	1.365	1.383	1.401	1.420	1.440	1.460	1.479	1.499	1.517	1.550	1.573
240	1.341	1.357	1.373	1.391	1.408	1.426	1.444	1.462	1.479	1.496	1.526	1.549
260	1.334	1.349	1.365	1.381	1.397	1.414	1.430	1.447	1.463	1.478	1.507	1.530
280	1.328	1.343	1.358	1.373	1.388	1.404	1.419	1.434	1.449	1.464	1.491	1.513
300	1.323	1.337	1.351	1.365	1.380	1.395	1.409	1.424	1.438	1.451	1.477	1.499

D2.7. Table 9. Specific isochoric heat capacity c_v of R134a in kJ/(kg K)

Pressure in bar	Temperature in °C											
	−70	−60	−50	−40	−30	−20	−10	0	10	20	30	40
1	0.8040	0.8128	0.8225	0.8328	0.8438	0.6932	0.7056	0.7203	0.7359	0.7521	0.7684	0.7849
5	0.8042	0.8129	0.8225	0.8329	0.8438	0.8551	0.8669	0.8790	0.8917	0.8052	0.8074	0.8155
10	0.8043	0.8130	0.8226	0.8330	0.8438	0.8551	0.8668	0.8790	0.8916	0.9047	0.9187	0.8824
15	0.8044	0.8131	0.8228	0.8331	0.8439	0.8552	0.8668	0.8789	0.8914	0.9045	0.9182	0.9329
20	0.8046	0.8132	0.8229	0.8332	0.8440	0.8552	0.8668	0.8788	0.8912	0.9042	0.9178	0.9323
25	0.8047	0.8134	0.8230	0.8333	0.8440	0.8552	0.8668	0.8787	0.8911	0.9040	0.9174	0.9317
30	0.8048	0.8135	0.8231	0.8334	0.8441	0.8553	0.8668	0.8787	0.8910	0.9037	0.9171	0.9311
35	0.8050	0.8136	0.8232	0.8334	0.8442	0.8553	0.8668	0.8786	0.8909	0.9035	0.9167	0.9306
40	0.8051	0.8137	0.8233	0.8335	0.8443	0.8553	0.8668	0.8786	0.8908	0.9034	0.9164	0.9301
45	0.8053	0.8139	0.8234	0.8336	0.8443	0.8554	0.8668	0.8786	0.8907	0.9032	0.9162	0.9297
50	0.8054	0.8140	0.8236	0.8337	0.8444	0.8555	0.8668	0.8785	0.8906	0.9030	0.9159	0.9293

D2.7. Table 9. (continued)

Temperature in °C												
Pressure in bar	−70	−60	−50	−40	−30	−20	−10	0	10	20	30	40
60	0.8057	0.8143	0.8238	0.8340	0.8446	0.8556	0.8669	0.8785	0.8905	0.9028	0.9155	0.9286
70	0.8060	0.8146	0.8241	0.8342	0.8448	0.8557	0.8670	0.8785	0.8904	0.9026	0.9151	0.9281
80	0.8063	0.8148	0.8243	0.8344	0.8450	0.8559	0.8671	0.8785	0.8903	0.9024	0.9148	0.9276
90	0.8066	0.8151	0.8246	0.8346	0.8452	0.8560	0.8672	0.8786	0.8903	0.9023	0.9145	0.9271
100	0.8069	0.8154	0.8248	0.8349	0.8454	0.8562	0.8673	0.8787	0.8903	0.9022	0.9143	0.9268
110	0.8072	0.8157	0.8251	0.8351	0.8456	0.8564	0.8674	0.8787	0.8903	0.9021	0.9142	0.9265
120	0.8075	0.8160	0.8254	0.8354	0.8458	0.8566	0.8676	0.8788	0.8903	0.9021	0.9140	0.9263
140	0.8082	0.8166	0.8260	0.8359	0.8463	0.8570	0.8679	0.8791	0.8905	0.9021	0.9139	0.9259
160	0.8088	0.8172	0.8265	0.8365	0.8468	0.8574	0.8683	0.8794	0.8906	0.9021	0.9138	0.9257
180	0.8095	0.8179	0.8271	0.8370	0.8473	0.8579	0.8687	0.8797	0.8909	0.9023	0.9139	0.9256
200	0.8101	0.8185	0.8278	0.8376	0.8478	0.8583	0.8691	0.8800	0.8912	0.9025	0.9140	0.9256
220	0.8108	0.8191	0.8284	0.8382	0.8484	0.8588	0.8695	0.8804	0.8915	0.9027	0.9141	0.9257
240	0.8115	0.8198	0.8290	0.8388	0.8489	0.8594	0.8700	0.8809	0.8919	0.9030	0.9144	0.9258
260	0.8122	0.8205	0.8296	0.8394	0.8495	0.8599	0.8705	0.8813	0.8923	0.9034	0.9146	0.9260
280	0.8129	0.8211	0.8303	0.8400	0.8501	0.8604	0.8710	0.8818	0.8927	0.9037	0.9149	0.9263
300	0.8135	0.8218	0.8309	0.8406	0.8506	0.8610	0.8715	0.8822	0.8931	0.9041	0.9153	0.9266
Temperature in °C												
Pressure in bar	50	60	70	80	90	100	110	120	130	140	160	180
1	0.8014	0.8178	0.8341	0.8504	0.8666	0.8827	0.8987	0.9145	0.9303	0.9459	0.9768	1.007
5	0.8265	0.8389	0.8522	0.8660	0.8802	0.8946	0.9091	0.9238	0.9385	0.9532	0.9827	1.012
10	0.8717	0.8727	0.8791	0.8883	0.8990	0.9107	0.9232	0.9361	0.9493	0.9628	0.9903	1.018
15	0.9490	0.9266	0.9158	0.9158	0.9209	0.9289	0.9385	0.9492	0.9607	0.9728	0.9981	1.024
20	0.9479	0.9657	0.9765	0.9537	0.9481	0.9499	0.9556	0.9635	0.9729	0.9833	1.006	1.031
25	0.9470	0.9640	0.9844	1.018	0.9852	0.9756	0.9751	0.9792	0.9860	0.9944	1.015	1.037
30	0.9461	0.9626	0.9816	1.007	1.047	1.010	0.9985	0.9969	1.000	1.006	1.023	1.044
35	0.9453	0.9613	0.9794	1.002	1.043	1.063	1.028	1.017	1.016	1.019	1.032	1.051
40	0.9446	0.9602	0.9775	0.9981	1.029	1.151	1.070	1.041	1.033	1.032	1.041	1.057
45	0.9440	0.9592	0.9759	0.9951	1.020	1.070	1.139	1.071	1.052	1.046	1.050	1.064
50	0.9434	0.9583	0.9745	0.9926	1.015	1.049	1.139	1.108	1.073	1.061	1.059	1.071
60	0.9424	0.9568	0.9721	0.9888	1.008	1.031	1.064	1.114	1.111	1.090	1.077	1.083
70	0.9415	0.9555	0.9702	0.9859	1.003	1.022	1.045	1.074	1.101	1.105	1.092	1.095
80	0.9408	0.9544	0.9687	0.9837	0.9995	1.017	1.036	1.057	1.080	1.097	1.102	1.104
90	0.9401	0.9535	0.9674	0.9819	0.9970	1.013	1.030	1.048	1.067	1.084	1.103	1.110
100	0.9396	0.9528	0.9663	0.9804	0.9949	1.010	1.026	1.042	1.059	1.075	1.100	1.113
110	0.9392	0.9521	0.9654	0.9791	0.9933	1.008	1.023	1.038	1.054	1.069	1.096	1.113
120	0.9388	0.9516	0.9647	0.9781	0.9919	1.006	1.020	1.035	1.050	1.065	1.091	1.112
140	0.9382	0.9507	0.9635	0.9765	0.9897	1.003	1.017	1.031	1.045	1.058	1.085	1.108
160	0.9378	0.9501	0.9626	0.9753	0.9882	1.001	1.014	1.028	1.041	1.054	1.080	1.104
180	0.9376	0.9497	0.9620	0.9744	0.9871	0.9998	1.013	1.026	1.039	1.052	1.077	1.101
200	0.9374	0.9494	0.9615	0.9738	0.9862	0.9988	1.011	1.024	1.037	1.050	1.075	1.099
220	0.9374	0.9493	0.9613	0.9734	0.9856	0.9980	1.010	1.023	1.035	1.048	1.073	1.097
240	0.9375	0.9492	0.9611	0.9731	0.9852	0.9974	1.010	1.022	1.034	1.047	1.072	1.096
260	0.9376	0.9492	0.9610	0.9729	0.9849	0.9970	1.009	1.021	1.034	1.046	1.071	1.095
280	0.9377	0.9493	0.9610	0.9729	0.9848	0.9968	1.009	1.021	1.033	1.045	1.070	1.094
300	0.9380	0.9495	0.9611	0.9729	0.9847	0.9966	1.009	1.021	1.033	1.045	1.069	1.093

D2.7. Table 10. Isobaric expansion coefficient β of R134a in 10^{-3}/K

Pressure in bar	Temperature in °C											
	−70	−60	−50	−40	−30	−20	−10	0	10	20	30	40
1	1.82	1.88	1.96	2.04	2.15	4.60	4.31	4.07	3.87	3.69	3.54	3.40
5	1.81	1.88	1.95	2.04	2.13	2.25	2.40	2.57	2.79	5.44	4.88	4.47
10	1.81	1.87	1.94	2.02	2.12	2.24	2.38	2.55	2.76	3.03	3.39	7.21
15	1.80	1.86	1.93	2.01	2.11	2.22	2.36	2.52	2.72	2.98	3.32	3.80
20	1.79	1.85	1.92	2.00	2.10	2.20	2.34	2.49	2.69	2.94	3.26	3.70
25	1.79	1.85	1.91	1.99	2.08	2.19	2.32	2.47	2.66	2.89	3.20	3.61
30	1.78	1.84	1.91	1.98	2.07	2.17	2.30	2.45	2.63	2.85	3.14	3.53
35	1.78	1.83	1.90	1.97	2.06	2.16	2.28	2.42	2.60	2.81	3.09	3.45
40	1.77	1.82	1.89	1.96	2.05	2.15	2.26	2.40	2.57	2.78	3.04	3.38
45	1.76	1.82	1.88	1.95	2.03	2.13	2.24	2.38	2.54	2.74	2.99	3.31
50	1.76	1.81	1.87	1.94	2.02	2.12	2.23	2.36	2.51	2.71	2.94	3.24
60	1.74	1.80	1.86	1.92	2.00	2.09	2.19	2.32	2.46	2.64	2.86	3.13
70	1.73	1.78	1.84	1.91	1.98	2.06	2.16	2.28	2.42	2.58	2.78	3.02
80	1.72	1.77	1.83	1.89	1.96	2.04	2.13	2.24	2.37	2.52	2.71	2.93
90	1.71	1.76	1.81	1.87	1.94	2.02	2.11	2.21	2.33	2.47	2.64	2.84
100	1.70	1.75	1.80	1.85	1.92	1.99	2.08	2.18	2.29	2.42	2.58	2.76
110	1.69	1.73	1.78	1.84	1.90	1.97	2.05	2.14	2.25	2.38	2.52	2.69
120	1.68	1.72	1.77	1.82	1.88	1.95	2.03	2.12	2.22	2.33	2.47	2.62
140	1.66	1.70	1.74	1.79	1.85	1.91	1.98	2.06	2.15	2.25	2.37	2.51
160	1.64	1.68	1.72	1.76	1.81	1.87	1.94	2.01	2.09	2.18	2.28	2.40
180	1.62	1.65	1.69	1.74	1.78	1.84	1.90	1.96	2.03	2.12	2.21	2.31
200	1.60	1.63	1.67	1.71	1.75	1.80	1.86	1.92	1.98	2.06	2.14	2.23
220	1.58	1.61	1.65	1.69	1.73	1.77	1.82	1.88	1.94	2.00	2.08	2.16
240	1.57	1.60	1.63	1.66	1.70	1.74	1.79	1.84	1.89	1.95	2.02	2.09
260	1.55	1.58	1.61	1.64	1.67	1.71	1.76	1.80	1.85	1.91	1.97	2.03
280	1.53	1.56	1.59	1.62	1.65	1.69	1.73	1.77	1.81	1.86	1.92	1.98
300	1.52	1.54	1.57	1.60	1.63	1.66	1.70	1.74	1.78	1.82	1.87	1.93

Pressure in bar	Temperature in °C											
	50	60	70	80	90	100	110	120	130	140	160	180
1	3.27	3.15	3.04	2.95	2.85	2.77	2.69	2.61	2.54	2.48	2.35	2.24
5	4.15	3.89	3.67	3.48	3.31	3.16	3.03	2.92	2.81	2.71	2.54	2.40
10	6.06	5.32	4.79	4.39	4.06	3.79	3.57	3.37	3.21	3.06	2.81	2.61
15	4.50	8.26	6.74	5.79	5.14	4.64	4.26	3.94	3.69	3.47	3.11	2.84
20	4.34	5.36	11.2	8.36	6.84	5.87	5.19	4.68	4.28	3.96	3.46	3.10
25	4.19	5.09	6.72	15.0	10.0	7.81	6.52	5.66	5.03	4.55	3.87	3.39
30	4.06	4.86	6.22	9.22	18.9	11.4	8.58	7.02	6.01	5.29	4.34	3.71
35	3.94	4.66	5.83	8.10	15.7	21.0	12.2	9.05	7.33	6.23	4.88	4.07
40	3.83	4.49	5.50	7.31	11.8	123	20.4	12.3	9.16	7.43	5.52	4.47
45	3.73	4.33	5.21	6.71	9.85	22.5	55.0	18.3	11.8	8.99	6.27	4.92
50	3.64	4.18	4.97	6.23	8.59	14.9	67.4	31.0	15.9	11.0	7.13	5.40
60	3.47	3.94	4.57	5.52	7.04	9.91	17.0	36.0	28.4	16.9	9.23	6.49
70	3.33	3.73	4.26	5.00	6.09	7.83	10.9	16.9	24.0	21.3	11.6	7.67
80	3.20	3.55	4.00	4.60	5.43	6.63	8.46	11.3	15.2	17.8	13.2	8.74
90	3.09	3.39	3.78	4.28	4.94	5.83	7.07	8.80	11.0	13.2	13.0	9.44
100	2.99	3.26	3.60	4.02	4.56	5.25	6.16	7.34	8.79	10.3	11.5	9.56
110	2.89	3.14	3.43	3.80	4.25	4.81	5.51	6.38	7.40	8.50	9.91	9.14

D2.7. Table 10. (continued)

Pressure in bar	Temperature in °C											
	50	60	70	80	90	100	110	120	130	140	160	180
120	2.81	3.03	3.29	3.61	3.99	4.46	5.02	5.69	6.46	7.28	8.54	8.45
140	2.66	2.84	3.06	3.30	3.59	3.93	4.32	4.76	5.25	5.75	6.64	6.99
160	2.54	2.69	2.86	3.06	3.29	3.55	3.83	4.15	4.49	4.84	5.48	5.85
180	2.43	2.56	2.70	2.87	3.05	3.25	3.48	3.72	3.97	4.22	4.70	5.02
200	2.33	2.44	2.57	2.71	2.86	3.02	3.20	3.39	3.58	3.78	4.15	4.41
220	2.25	2.34	2.45	2.57	2.70	2.83	2.98	3.13	3.29	3.44	3.73	3.95
240	2.17	2.26	2.35	2.45	2.56	2.67	2.79	2.92	3.05	3.17	3.41	3.60
260	2.10	2.18	2.26	2.35	2.44	2.54	2.64	2.75	2.85	2.96	3.15	3.31
280	2.04	2.11	2.18	2.26	2.34	2.42	2.51	2.60	2.69	2.78	2.94	3.07
300	1.98	2.04	2.11	2.17	2.24	2.32	2.39	2.47	2.55	2.62	2.76	2.88

D2.7. Table 11. Isentropic speed of sound w_s in R134a in m/s

Pressure in bar	Temperature in °C											
	−70	−60	−50	−40	−30	−20	−10	0	10	20	30	40
1	952.4	903.4	855.1	807.5	760.4	147.8	151.1	154.2	157.2	160.1	162.9	165.7
5	954.3	905.4	857.3	809.8	762.9	716.4	669.9	623.4	576.5	147.8	152.1	156.1
10	956.6	907.9	859.9	812.7	766.1	719.8	673.7	627.6	581.3	534.2	486.1	140.9
15	958.8	910.3	862.6	815.6	769.2	723.2	677.5	631.8	585.9	539.5	492.1	443.3
20	961.1	912.8	865.2	818.4	772.3	726.6	681.2	635.9	590.5	544.6	498.0	450.1
25	963.4	915.2	867.8	821.3	775.4	729.9	684.9	640.0	595.0	549.7	503.8	456.8
30	965.6	917.6	870.4	824.1	778.4	733.3	688.5	643.9	599.4	554.6	509.4	463.2
35	967.8	920.0	873.0	826.9	781.4	736.5	692.1	647.9	603.8	559.5	514.8	469.5
40	970.0	922.3	875.6	829.6	784.4	739.8	695.6	651.8	608.0	564.3	520.2	475.6
45	972.2	924.7	878.1	832.3	787.3	743.0	699.1	655.6	612.3	568.9	525.4	481.5
50	974.4	927.1	880.6	835.1	790.3	746.2	702.6	659.4	616.4	573.5	530.6	487.3
60	978.8	931.7	885.6	840.4	796.1	752.4	709.4	666.8	624.5	582.5	540.5	498.4
70	983.1	936.3	890.5	845.7	801.8	758.6	716.0	674.0	632.4	591.2	550.1	509.1
80	987.3	940.8	895.4	850.9	807.3	764.6	722.5	681.1	640.1	599.6	559.3	519.3
90	991.5	945.3	900.2	856.0	812.9	770.5	728.9	688.0	647.6	607.7	568.3	529.1
100	995.6	949.7	904.9	861.1	818.3	776.3	735.2	694.8	655.0	615.7	576.9	538.6
110	999.7	954.1	909.6	866.1	823.6	782.1	741.3	701.4	662.1	623.4	585.3	547.7
120	1004	958.4	914.2	871.0	828.9	787.7	747.4	707.9	669.1	631.0	593.5	556.5
140	1012	966.9	923.2	880.7	839.2	798.7	759.1	720.5	682.6	645.5	609.1	573.4
160	1020	975.3	932.1	890.1	849.2	809.4	770.5	732.6	695.6	659.4	624.0	589.4
180	1027	983.4	940.7	899.3	858.9	819.7	781.5	744.3	708.1	672.7	638.2	604.5
200	1035	991.4	949.2	908.2	868.4	829.8	792.2	755.7	720.1	685.5	651.7	618.9
220	1042	999.3	957.5	917.0	877.7	839.6	802.6	766.7	731.7	697.8	664.8	632.7
240	1050	1007	965.6	925.6	886.8	849.2	812.7	777.3	743.0	709.7	677.3	646.0
260	1057	1015	973.6	934.0	895.6	858.5	822.6	787.7	753.9	721.2	689.4	658.7
280	1064	1022	981.4	942.2	904.3	867.6	832.1	797.8	764.5	732.3	701.1	671.0
300	1071	1029	989.1	950.3	912.8	876.6	841.5	807.6	774.8	743.1	712.4	682.8

D2.7. Table 11. (continued)

Pressure in bar	Temperature in °C											
	50	60	70	80	90	100	110	120	130	140	160	180
1	168.4	171.0	173.6	176.1	178.6	181.0	183.4	185.7	188.0	190.3	194.8	199.1
5	159.8	163.2	166.6	169.7	172.8	175.7	178.5	181.3	183.9	186.5	191.5	196.4
10	146.9	152.0	156.7	160.9	164.9	168.6	172.1	175.4	178.6	181.7	187.5	192.9
15	392.1	138.0	145.0	150.9	156.1	160.9	165.2	169.3	173.0	176.6	183.3	189.4
20	400.3	347.1	129.9	138.9	146.2	152.3	157.8	162.7	167.2	171.4	179.1	185.9
25	408.2	356.8	300.4	123.2	134.3	142.7	149.7	155.8	161.2	166.1	174.8	182.4
30	415.7	366.1	312.5	250.4	118.9	131.6	140.8	148.3	154.8	160.5	170.5	179.0
35	423.0	374.8	323.6	266.5	192.7	117.7	130.9	140.4	148.2	154.9	166.2	175.6
40	430.1	383.1	333.9	280.5	217.3	108.9	119.4	132.0	141.5	149.3	162.0	172.3
45	436.9	391.1	343.6	293.0	236.2	163.2	106.0	123.2	134.7	143.7	157.9	169.2
50	443.5	398.8	352.7	304.5	252.1	191.1	113.9	115.1	128.3	138.4	154.1	166.3
60	456.1	413.2	369.7	325.0	278.5	229.0	175.1	127.3	121.6	130.7	147.8	161.3
70	468.0	426.8	385.2	343.2	300.5	256.9	212.3	169.3	139.5	133.0	144.7	158.2
80	479.4	439.5	399.6	359.7	319.8	279.8	240.2	202.3	170.1	150.5	147.0	157.6
90	490.2	451.6	413.1	374.9	337.1	299.7	263.3	228.7	198.0	174.4	156.1	160.4
100	500.6	463.0	425.8	389.1	352.9	317.6	283.4	251.1	221.9	197.7	170.3	166.8
110	510.6	473.9	437.8	402.3	367.6	333.8	301.4	270.8	242.9	218.9	186.9	176.4
120	520.2	484.4	449.3	414.9	381.3	348.8	317.7	288.5	261.7	238.2	203.9	188.1
140	538.4	504.2	470.7	438.0	406.4	376.0	347.0	319.7	294.6	272.0	236.2	214.2
160	555.5	522.5	490.4	459.2	429.1	400.2	372.8	346.9	323.0	301.3	265.4	240.5
180	571.7	539.8	508.8	478.8	449.9	422.3	396.0	371.3	348.4	327.3	291.7	265.4
200	587.0	556.0	526.1	497.1	469.3	442.6	417.4	393.5	371.3	350.9	315.8	288.6
220	601.6	571.5	542.3	514.3	487.3	461.5	437.1	414.0	392.5	372.6	337.9	310.4
240	615.6	586.2	557.8	530.5	504.3	479.3	455.5	433.1	412.1	392.6	358.4	330.7
260	628.9	600.2	572.5	545.9	520.4	496.0	472.9	451.0	430.5	411.4	377.6	349.9
280	641.8	613.7	586.6	560.6	535.6	511.9	489.3	467.9	447.8	429.1	395.7	368.0
300	654.2	626.6	600.1	574.6	550.2	526.9	504.8	483.9	464.2	445.8	412.8	385.1

D2.7. Table 12. Thermal conductivity λ of R134a in mW/(m K)

Pressure in bar	Temperature in °C											
	−35	−30	−25	−20	−15	−10	−5	0	5	10	20	30
1	108.9	106.8	9.576	10.01	10.43	10.86	11.28	11.69	12.10	12.51	13.31	14.10
5	109.1	107.0	104.8	102.6	100.4	98.22	96.02	93.80	91.56	89.31	13.80	14.53
10	109.3	107.2	105.0	102.9	100.7	98.50	96.31	94.10	91.89	89.65	85.12	80.47
15	109.5	107.4	105.3	103.1	100.9	98.77	96.59	94.40	92.20	89.99	85.50	80.91
20	109.7	107.6	105.5	103.3	101.2	99.04	96.87	94.70	92.52	90.32	85.88	81.34
25	109.9	107.8	105.7	103.6	101.4	99.30	97.15	95.00	92.83	90.65	86.25	81.76
30	110.1	108.1	105.9	103.8	101.7	99.56	97.43	95.29	93.14	90.97	86.61	82.18
35	110.3	108.3	106.2	104.1	101.9	99.83	97.70	95.57	93.44	91.29	86.97	82.58
40	110.5	108.5	106.4	104.3	102.2	100.1	97.97	95.86	93.74	91.61	87.32	82.98
45	110.7	108.7	106.6	104.5	102.4	100.3	98.24	96.14	94.03	91.92	87.67	83.37
50	110.9	108.9	106.8	104.8	102.7	100.6	98.51	96.42	94.33	92.23	88.01	83.75
60	111.3	109.3	107.3	105.2	103.2	101.1	99.03	96.97	94.90	92.83	88.68	84.50

D2.7. Table 12. (continued)

Temperature in °C												
Pressure in bar	−35	−30	−25	−20	−15	−10	−5	0	5	10	20	30
70	111.8	109.6	107.7	105.7	103.6	101.6	99.54	97.51	95.47	93.42	89.33	85.22
80	112.2	110.1	108.1	106.1	104.1	102.1	100.0	98.03	96.02	94.00	89.97	85.92
90	112.6	110.5	108.5	106.5	104.5	102.5	100.5	98.55	96.56	94.57	90.59	86.60
100	113.0	110.9	108.9	107.0	105.0	103.0	101.0	99.06	97.09	95.12	91.19	87.26
110	113.4	111.3	109.2	107.4	105.4	103.5	101.5	99.56	97.61	95.66	91.78	87.91
120	113.8	111.7	109.7	107.8	105.9	103.9	102.0	100.0	98.12	96.19	92.36	88.54
140	114.5	112.5	110.5	108.6	106.7	104.8	102.9	101.0	99.11	97.23	93.48	89.75
160	115.3	113.3	111.3	109.3	107.5	105.7	103.8	101.9	100.1	98.22	94.55	90.91
180	116.0	114.1	112.1	110.1	108.3	106.5	104.6	102.8	101.0	99.19	95.59	92.03
200	116.8	114.8	112.9	110.9	109.0	107.3	105.5	103.7	101.9	100.1	96.59	93.10
220	117.5	115.5	113.6	111.7	109.8	108.0	106.3	104.5	102.8	101.0	97.56	94.13
240	118.2	116.3	114.4	112.5	110.6	108.8	107.1	105.3	103.6	101.9	98.49	95.13
260	118.9	117.0	115.1	113.2	111.4	109.6	107.8	106.1	104.4	102.8	99.40	96.10
280	119.5	117.7	115.8	114.0	112.1	110.3	108.5	106.9	105.2	103.6	100.3	97.03
300	120.2	118.3	116.5	114.7	112.9	111.1	109.3	107.6	106.0	104.4	101.1	97.94

Temperature in °C												
Pressure in bar	40	50	60	70	80	90	100	110	120	130	140	150
1	14.88	15.63	16.38	17.10	17.82	18.51	19.20	19.86	20.51	21.15	21.77	22.38
5	15.24	15.95	16.65	17.34	18.02	18.69	19.34	19.99	20.62	21.24	21.85	22.44
10	16.15	16.72	17.32	17.92	18.53	19.14	19.74	20.33	20.92	21.50	22.07	22.63
15	76.18	71.27	18.48	18.87	19.33	19.83	20.34	20.86	21.38	21.90	22.42	22.93
20	76.68	71.86	66.82	20.55	20.59	20.84	21.19	21.59	22.01	22.45	22.90	23.35
25	77.17	72.44	67.51	62.34	22.90	22.39	22.38	22.56	22.83	23.16	23.51	23.88
30	77.64	72.99	68.17	63.15	57.89	25.35	24.18	23.89	23.90	24.04	24.26	24.53
35	78.11	73.53	68.81	63.92	58.83	53.53	27.49	25.82	25.30	25.16	25.18	25.31
40	78.56	74.05	69.42	64.65	59.72	54.64	51.74	29.01	27.22	26.56	26.30	26.23
45	79.00	74.56	70.01	65.35	60.55	55.65	50.56	36.40	30.04	28.36	27.65	27.31
50	79.43	75.05	70.58	66.01	61.34	56.59	51.74	46.99	34.39	30.79	29.29	28.58
60	80.27	76.00	71.67	67.27	62.81	58.31	53.84	49.34	44.31	37.45	33.64	31.83
70	81.08	76.91	72.70	68.45	64.16	59.86	55.61	51.43	47.42	43.08	38.63	35.55
80	81.86	77.78	73.68	69.55	65.41	61.28	57.20	53.26	49.47	45.94	42.41	39.19
90	82.61	78.61	74.61	70.59	66.58	62.59	58.66	54.86	51.26	47.90	44.85	41.99
100	83.34	79.42	75.50	71.58	67.68	63.82	60.01	56.33	52.83	49.58	46.65	44.05
110	84.05	80.20	76.35	72.53	68.73	64.97	61.28	57.69	54.28	51.11	48.21	45.67
120	84.74	80.95	77.18	73.43	69.72	66.05	62.46	58.97	55.64	52.52	49.65	47.08
140	86.05	82.38	78.74	75.14	71.57	68.07	64.64	61.31	58.12	55.10	52.29	49.72
160	87.31	83.74	80.21	76.72	73.29	69.92	66.62	63.43	60.35	57.42	54.67	52.12
180	88.51	85.03	81.59	78.21	74.88	71.62	68.44	65.36	62.38	59.54	56.84	54.33
200	89.65	86.25	82.91	79.61	76.38	73.22	70.14	67.14	64.25	61.49	58.85	56.37
220	90.76	87.43	84.16	80.94	77.80	74.72	71.72	68.81	66.00	63.30	60.72	58.28
240	91.82	88.56	85.36	82.21	79.14	76.14	73.21	70.37	67.63	64.99	62.47	60.07
260	92.84	89.64	86.51	83.43	80.42	77.48	74.63	71.85	69.17	66.59	64.11	61.75
280	93.83	90.69	87.61	84.59	81.65	78.77	75.97	73.26	70.63	68.10	65.66	63.34
300	94.79	91.70	88.68	85.72	82.82	80.00	77.26	74.59	72.02	69.53	67.14	64.85

D2.7. Table 13. Dynamic viscosity η of R134a in 10^{-6} Pa·s

Pressure in bar	Temperature in °C											
	15	20	25	30	35	40	45	50	55	60	65	70
1	11.58	11.78	11.98	12.18	12.38	12.58	12.77	12.97	13.16	13.36	13.55	13.74
5	221.7	11.88	12.08	12.28	12.47	12.67	12.86	13.05	13.24	13.44	13.63	13.82
10	223.6	210.3	197.6	185.5	173.9	12.88	13.06	13.25	13.43	13.61	13.79	13.97
15	225.5	212.2	199.6	187.5	175.9	164.7	154.0	143.5	133.3	13.95	14.11	14.27
20	227.4	214.1	201.5	189.4	177.9	166.8	156.1	145.7	135.7	125.7	115.9	14.83
25	229.3	216.0	203.4	191.4	179.8	168.8	158.2	147.9	138.0	128.2	118.6	108.9
30	231.1	217.9	205.3	193.2	181.8	170.8	160.2	150.0	140.2	130.6	121.1	111.8
35	232.9	219.7	207.1	195.1	183.7	172.7	162.2	152.1	142.3	132.9	123.6	114.4
40	234.8	221.5	208.9	197.0	185.6	174.7	164.2	154.1	144.4	135.1	125.9	117.0
45	236.6	223.3	210.8	198.8	187.4	176.5	166.1	156.1	146.5	137.2	128.2	119.4
50	238.4	225.1	212.6	200.6	189.2	178.4	168.0	158.1	148.5	139.3	130.4	121.7
60	241.9	228.7	216.1	204.2	192.8	182.0	171.7	161.8	152.4	143.3	134.5	126.0
70	245.4	232.2	219.6	207.7	196.4	185.6	175.3	165.5	156.1	147.1	138.5	130.1
80	248.9	235.6	223.1	211.1	199.8	189.1	178.8	169.1	159.7	150.8	142.2	134.0
90	252.4	239.1	226.5	214.5	203.2	192.5	182.3	172.5	163.2	154.3	145.8	137.7
100	255.8	242.5	229.8	217.9	206.6	195.8	185.6	175.9	166.6	157.8	149.3	141.3
110	259.2	245.8	233.2	221.2	209.9	199.1	188.9	179.2	170.0	161.1	152.7	144.7
120	262.5	249.1	236.5	224.5	213.1	202.4	192.2	182.5	173.2	164.4	156.0	148.0
140	269.2	255.7	243.0	230.9	219.5	208.7	198.5	188.8	179.5	170.8	162.4	154.4
160	275.8	262.2	249.3	237.2	225.8	214.9	204.7	194.9	185.7	176.9	168.5	160.5
180	282.3	268.6	255.6	243.4	231.9	221.0	210.7	200.9	191.6	182.8	174.4	166.4
200	288.7	274.9	261.9	249.6	238.0	227.0	216.6	206.7	197.4	188.5	180.1	172.1
220	295.1	281.1	268.0	255.6	243.9	232.9	222.4	212.5	203.1	194.1	185.7	177.6
240	301.4	287.4	274.1	261.6	249.8	238.7	228.1	218.1	208.6	199.7	191.1	183.0
260	307.7	293.5	280.2	267.5	255.6	244.4	233.7	223.7	214.1	205.1	196.5	188.3
280	314.0	299.7	286.2	273.4	261.4	250.1	239.3	229.2	219.5	210.4	201.7	193.5
300	320.2	305.8	292.1	279.3	267.1	255.7	244.8	234.6	224.9	215.7	206.9	198.6
Pressure in bar	Temperature in °C											
	75	80	90	95	100	105	110	115	120	130	140	150
1	13.93	14.12	14.50	14.68	14.87	15.05	15.24	15.42	15.60	15.97	16.33	16.68
5	14.00	14.19	14.57	14.75	14.94	15.12	15.30	15.48	15.67	16.03	16.38	16.74
10	14.16	14.34	14.70	14.88	15.06	15.24	15.42	15.60	15.78	16.13	16.48	16.83
15	14.43	14.59	14.93	15.10	15.27	15.44	15.61	15.78	15.95	16.30	16.64	16.98
20	14.92	15.04	15.31	15.45	15.60	15.75	15.90	16.06	16.21	16.53	16.86	17.18
25	99.08	15.91	15.94	16.01	16.11	16.21	16.33	16.46	16.59	16.86	17.15	17.45
30	102.3	92.58	17.19	17.01	16.94	16.94	16.98	17.04	17.12	17.32	17.55	17.81
35	105.3	96.08	75.48	19.50	18.55	18.18	18.00	17.92	17.89	17.95	18.08	18.27
40	108.1	99.23	80.49	69.46	51.23	20.95	19.87	19.33	19.06	18.82	18.79	18.86
45	110.7	102.1	84.55	75.04	64.06	46.14	24.51	22.02	20.99	20.06	19.73	19.62
50	113.2	104.8	88.06	79.38	70.05	59.30	44.07	28.78	24.56	21.96	21.00	20.60
60	117.8	109.8	94.08	86.27	78.35	70.24	61.74	52.48	42.53	29.42	25.24	23.53
70	122.1	114.3	99.25	91.95	84.73	77.52	70.30	63.13	55.89	41.99	32.69	28.24
80	126.1	118.4	103.9	96.90	90.08	83.39	76.81	70.29	64.04	52.07	41.79	34.76
90	129.9	122.4	108.1	101.4	94.80	88.43	82.22	76.18	70.32	59.37	49.64	41.76
100	133.5	126.1	112.1	105.5	99.09	92.92	86.96	81.20	75.64	65.19	55.97	48.07

D2.7. Table 13. (continued)

Temperature in °C												
Pressure in bar	75	80	90	95	100	105	110	115	120	130	140	150
110	137.0	129.7	115.8	109.3	103.1	97.04	91.24	85.66	80.29	70.24	61.23	53.52
120	140.4	133.1	119.4	112.9	106.8	100.9	95.18	89.73	84.50	74.72	65.92	58.22
140	146.8	139.6	126.0	119.7	113.7	107.9	102.3	97.04	91.97	82.53	73.99	66.41
160	152.9	145.7	132.3	126.0	120.0	114.3	108.8	103.6	98.61	89.33	80.93	73.41
180	158.8	151.6	138.1	131.9	125.9	120.2	114.8	109.6	104.7	95.48	87.14	79.64
200	164.5	157.2	143.8	137.5	131.5	125.9	120.4	115.3	110.3	101.2	92.83	85.32
220	170.0	162.7	149.2	142.9	136.9	131.2	125.8	120.6	115.7	106.5	98.14	90.60
240	175.3	168.0	154.4	148.1	142.1	136.4	130.9	125.7	120.8	111.5	103.2	95.56
260	180.6	173.2	159.5	153.2	147.1	141.4	135.9	130.7	125.7	116.4	107.9	100.3
280	185.7	178.3	164.5	158.1	152.0	146.2	140.7	135.4	130.4	121.0	112.5	104.8
300	190.8	183.3	169.4	162.9	156.8	150.9	145.4	140.1	135.0	125.6	117.0	109.2

D2.7. Table 14. Kinematic viscosity ν of R134a in 10^{-7} m^2/s

Temperature in °C												
Pressure in bar	15	20	25	30	35	40	45	50	55	60	65	70
1	26.6	27.5	28.5	29.5	30.5	31.6	32.6	33.6	34.7	35.8	36.9	38.0
5	1.78	5.01	5.22	5.44	5.66	5.88	6.11	6.33	6.56	6.78	7.01	7.24
10	1.79	1.71	1.64	1.56	1.49	2.63	2.76	2.89	3.01	3.14	3.26	3.39
15	1.81	1.72	1.65	1.57	1.50	1.43	1.36	1.30	1.24	1.90	2.00	2.09
20	1.82	1.74	1.66	1.58	1.51	1.44	1.38	1.31	1.25	1.19	1.13	1.42
25	1.83	1.75	1.67	1.60	1.53	1.46	1.39	1.33	1.27	1.20	1.14	1.08
30	1.84	1.76	1.68	1.61	1.54	1.47	1.40	1.34	1.28	1.22	1.16	1.10
35	1.85	1.77	1.69	1.62	1.55	1.48	1.42	1.35	1.29	1.23	1.18	1.12
40	1.86	1.78	1.71	1.63	1.56	1.49	1.43	1.37	1.31	1.25	1.19	1.14
45	1.87	1.79	1.72	1.64	1.57	1.51	1.44	1.38	1.32	1.26	1.21	1.15
50	1.89	1.80	1.73	1.65	1.58	1.52	1.45	1.39	1.33	1.27	1.22	1.17
60	1.91	1.83	1.75	1.68	1.61	1.54	1.48	1.41	1.36	1.30	1.25	1.19
70	1.93	1.85	1.77	1.70	1.63	1.56	1.50	1.44	1.38	1.32	1.27	1.22
80	1.95	1.87	1.79	1.72	1.65	1.58	1.52	1.46	1.40	1.35	1.29	1.24
90	1.97	1.89	1.81	1.74	1.67	1.60	1.54	1.48	1.42	1.37	1.32	1.27
100	1.99	1.91	1.83	1.76	1.69	1.63	1.56	1.50	1.45	1.39	1.34	1.29
110	2.01	1.93	1.85	1.78	1.71	1.65	1.58	1.52	1.47	1.41	1.36	1.31
120	2.03	1.95	1.87	1.80	1.73	1.67	1.60	1.54	1.49	1.43	1.38	1.33
140	2.07	1.99	1.91	1.84	1.77	1.71	1.64	1.58	1.53	1.47	1.42	1.37
160	2.11	2.03	1.95	1.88	1.81	1.74	1.68	1.62	1.56	1.51	1.46	1.41
180	2.15	2.07	1.99	1.92	1.85	1.78	1.72	1.66	1.60	1.55	1.49	1.45
200	2.19	2.11	2.03	1.96	1.88	1.82	1.75	1.69	1.64	1.58	1.53	1.48
220	2.23	2.15	2.07	1.99	1.92	1.85	1.79	1.73	1.67	1.62	1.56	1.51
240	2.27	2.18	2.10	2.03	1.96	1.89	1.82	1.76	1.71	1.65	1.60	1.55
260	2.31	2.22	2.14	2.07	1.99	1.92	1.86	1.80	1.74	1.68	1.63	1.58
280	2.35	2.26	2.18	2.10	2.03	1.96	1.89	1.83	1.77	1.72	1.66	1.61
300	2.38	2.30	2.21	2.14	2.06	1.99	1.93	1.87	1.81	1.75	1.70	1.65

D2.7. Table 14. (continued)

Pressure in bar	Temperature in °C											
	75	80	90	95	100	105	110	115	120	130	140	150
1	39.1	40.2	42.5	43.6	44.8	46.0	47.2	48.4	49.6	52.1	54.6	57.2
5	7.48	7.71	8.19	8.43	8.67	8.92	9.16	9.41	9.66	10.2	10.7	11.2
10	3.52	3.64	3.89	4.02	4.15	4.28	4.41	4.54	4.67	4.93	5.20	5.47
15	2.19	2.28	2.46	2.55	2.64	2.73	2.82	2.92	3.01	3.19	3.38	3.56
20	1.50	1.59	1.74	1.81	1.89	1.96	2.03	2.11	2.18	2.32	2.47	2.61
25	1.02	1.15	1.30	1.37	1.43	1.50	1.56	1.62	1.68	1.81	1.93	2.05
30	1.04	0.984	0.988	1.06	1.13	1.19	1.24	1.30	1.36	1.46	1.57	1.67
35	1.06	1.01	0.881	0.820	0.897	0.960	1.02	1.07	1.12	1.22	1.32	1.41
40	1.08	1.03	0.912	0.847	0.756	0.786	0.849	0.902	0.951	1.04	1.13	1.22
45	1.10	1.04	0.937	0.880	0.818	0.736	0.717	0.775	0.824	0.911	0.992	1.07
50	1.11	1.06	0.959	0.907	0.852	0.794	0.725	0.693	0.733	0.813	0.887	0.959
60	1.14	1.09	0.996	0.949	0.901	0.854	0.808	0.761	0.719	0.707	0.755	0.810
70	1.17	1.12	1.03	0.984	0.940	0.897	0.855	0.816	0.779	0.721	0.710	0.736
80	1.19	1.15	1.06	1.01	0.973	0.933	0.894	0.856	0.822	0.763	0.725	0.717
90	1.22	1.17	1.08	1.04	1.00	0.964	0.927	0.891	0.858	0.799	0.755	0.729
100	1.24	1.19	1.11	1.07	1.03	0.991	0.955	0.921	0.889	0.830	0.784	0.752
110	1.26	1.22	1.13	1.09	1.05	1.02	0.982	0.948	0.917	0.859	0.811	0.775
120	1.28	1.24	1.15	1.11	1.08	1.04	1.01	0.973	0.942	0.885	0.836	0.797
140	1.32	1.28	1.19	1.16	1.12	1.08	1.05	1.02	0.987	0.931	0.882	0.841
160	1.36	1.32	1.23	1.20	1.16	1.12	1.09	1.06	1.03	0.972	0.923	0.880
180	1.40	1.35	1.27	1.23	1.20	1.16	1.13	1.10	1.07	1.01	0.960	0.916
200	1.43	1.39	1.31	1.27	1.23	1.20	1.16	1.13	1.10	1.04	0.994	0.950
220	1.47	1.42	1.34	1.30	1.26	1.23	1.20	1.16	1.13	1.08	1.03	0.982
240	1.50	1.46	1.37	1.33	1.30	1.26	1.23	1.20	1.16	1.11	1.06	1.01
260	1.53	1.49	1.40	1.36	1.33	1.29	1.26	1.23	1.20	1.14	1.09	1.04
280	1.57	1.52	1.43	1.40	1.36	1.32	1.29	1.26	1.22	1.17	1.12	1.07
300	1.60	1.55	1.47	1.43	1.39	1.35	1.32	1.28	1.25	1.20	1.14	1.10

D2.7. Table 15. Thermal diffusivity a of R134a in 10^{-7} m^2/s

Pressure in bar	Temperature in °C											
	−35	−30	−25	−20	−15	−10	−5	0	5	10	20	30
1	0.614	0.604	23.4	25.0	26.5	28.0	29.5	31.0	32.5	34.0	36.9	39.8
5	0.615	0.605	0.595	0.584	0.574	0.563	0.552	0.540	0.529	0.517	6.03	6.78
10	0.617	0.607	0.596	0.586	0.575	0.564	0.554	0.542	0.531	0.519	0.495	0.469
15	0.618	0.608	0.598	0.587	0.577	0.566	0.555	0.544	0.533	0.522	0.498	0.472
20	0.619	0.609	0.599	0.589	0.578	0.568	0.557	0.546	0.535	0.524	0.501	0.476
25	0.620	0.610	0.600	0.590	0.580	0.570	0.559	0.548	0.537	0.526	0.503	0.479
30	0.621	0.612	0.602	0.592	0.582	0.571	0.561	0.550	0.539	0.528	0.506	0.482
35	0.622	0.613	0.603	0.593	0.583	0.573	0.562	0.552	0.541	0.531	0.508	0.485
40	0.624	0.614	0.604	0.595	0.585	0.574	0.564	0.554	0.543	0.533	0.511	0.488
45	0.625	0.615	0.606	0.596	0.586	0.576	0.566	0.556	0.545	0.535	0.513	0.491
50	0.626	0.617	0.607	0.597	0.587	0.578	0.567	0.557	0.547	0.537	0.515	0.493

D2.7. Table 15. (continued)

Temperature in °C												
Pressure in bar	−35	−30	−25	−20	−15	−10	−5	0	5	10	20	30
60	0.628	0.619	0.610	0.600	0.590	0.581	0.571	0.561	0.551	0.541	0.520	0.499
70	0.631	0.621	0.612	0.603	0.593	0.583	0.574	0.564	0.554	0.544	0.524	0.504
80	0.633	0.623	0.614	0.605	0.596	0.586	0.577	0.567	0.558	0.548	0.528	0.508
90	0.635	0.626	0.617	0.608	0.598	0.589	0.580	0.570	0.561	0.551	0.532	0.513
100	0.637	0.628	0.619	0.610	0.601	0.592	0.583	0.573	0.564	0.555	0.536	0.517
110	0.640	0.630	0.621	0.612	0.603	0.594	0.585	0.576	0.567	0.558	0.540	0.521
120	0.642	0.632	0.623	0.615	0.606	0.597	0.588	0.579	0.570	0.561	0.543	0.525
140	0.646	0.637	0.628	0.619	0.611	0.602	0.593	0.585	0.576	0.567	0.550	0.533
160	0.650	0.641	0.632	0.623	0.615	0.607	0.598	0.590	0.581	0.573	0.556	0.539
180	0.654	0.645	0.636	0.627	0.619	0.611	0.603	0.595	0.587	0.578	0.562	0.546
200	0.657	0.649	0.640	0.631	0.623	0.615	0.607	0.599	0.591	0.584	0.568	0.552
220	0.661	0.652	0.644	0.636	0.627	0.619	0.612	0.604	0.596	0.588	0.573	0.558
240	0.664	0.656	0.648	0.639	0.631	0.623	0.616	0.608	0.601	0.593	0.578	0.563
260	0.668	0.660	0.651	0.643	0.635	0.627	0.619	0.612	0.605	0.598	0.583	0.568
280	0.671	0.663	0.655	0.647	0.639	0.631	0.623	0.616	0.609	0.602	0.587	0.573
300	0.674	0.666	0.658	0.650	0.643	0.635	0.627	0.620	0.613	0.606	0.592	0.578
Temperature in °C												
Pressure in bar	40	50	60	70	80	90	100	110	120	130	140	150
1	42.7	45.6	48.5	51.3	54.1	57.0	59.8	62.5	65.3	68.0	70.7	73.4
5	7.48	8.14	8.79	9.42	10.0	10.7	11.3	11.8	12.4	13.0	13.6	14.2
10	2.91	3.38	3.79	4.17	4.53	4.88	5.21	5.53	5.85	6.16	6.47	6.76
15	0.445	0.414	2.02	2.36	2.66	2.93	3.19	3.43	3.66	3.89	4.10	4.31
20	0.449	0.419	0.385	1.34	1.67	1.93	2.16	2.37	2.56	2.75	2.92	3.09
25	0.453	0.424	0.392	0.352	0.955	1.27	1.51	1.71	1.89	2.06	2.22	2.36
30	0.457	0.429	0.398	0.362	0.312	0.728	1.03	1.25	1.43	1.59	1.74	1.87
35	0.460	0.434	0.404	0.371	0.328	0.255	0.611	0.889	1.09	1.25	1.39	1.52
40	0.464	0.438	0.410	0.378	0.340	0.286	0.081	0.567	0.807	0.983	1.13	1.25
45	0.467	0.442	0.415	0.385	0.351	0.306	0.222	0.239	0.563	0.762	0.915	1.04
50	0.470	0.446	0.420	0.392	0.360	0.321	0.264	0.136	0.345	0.576	0.740	0.871
60	0.477	0.454	0.429	0.404	0.376	0.344	0.307	0.257	0.206	0.307	0.474	0.614
70	0.482	0.460	0.438	0.414	0.389	0.362	0.333	0.301	0.267	0.260	0.330	0.442
80	0.488	0.467	0.445	0.423	0.400	0.376	0.351	0.326	0.303	0.288	0.302	0.359
90	0.493	0.473	0.452	0.431	0.410	0.388	0.366	0.345	0.326	0.313	0.313	0.336
100	0.498	0.478	0.459	0.438	0.418	0.398	0.378	0.359	0.343	0.331	0.327	0.337
110	0.502	0.484	0.465	0.445	0.426	0.407	0.389	0.372	0.356	0.345	0.339	0.343
120	0.507	0.489	0.470	0.452	0.434	0.416	0.398	0.382	0.368	0.357	0.350	0.350
140	0.515	0.498	0.481	0.463	0.447	0.430	0.414	0.400	0.387	0.376	0.369	0.365
160	0.523	0.506	0.490	0.474	0.458	0.443	0.428	0.414	0.402	0.392	0.384	0.379
180	0.530	0.514	0.498	0.483	0.468	0.454	0.440	0.427	0.415	0.405	0.397	0.391
200	0.537	0.521	0.506	0.491	0.477	0.463	0.450	0.438	0.427	0.417	0.408	0.402
220	0.543	0.528	0.513	0.499	0.486	0.472	0.460	0.448	0.437	0.427	0.419	0.412
240	0.549	0.534	0.520	0.506	0.493	0.480	0.468	0.457	0.446	0.437	0.428	0.421
260	0.554	0.540	0.526	0.513	0.500	0.488	0.476	0.465	0.455	0.445	0.437	0.429
280	0.559	0.546	0.532	0.520	0.507	0.495	0.483	0.473	0.462	0.453	0.445	0.437
300	0.564	0.551	0.538	0.525	0.513	0.502	0.490	0.480	0.470	0.460	0.452	0.444

D2.7. Table 16. Prandtl number Pr of R 134a

Pressure in bar	Temperature in °C											
	15	20	25	30	35	40	45	50	55	60	65	70
1	0.750	0.746	0.744	0.742	0.740	0.739	0.738	0.738	0.738	0.738	0.739	0.740
5	3.53	0.830	0.814	0.802	0.794	0.787	0.781	0.777	0.774	0.772	0.770	0.769
10	3.54	3.46	3.39	3.33	3.27	0.905	0.875	0.854	0.839	0.828	0.819	0.813
15	3.54	3.47	3.39	3.33	3.27	3.22	3.18	3.14	3.12	0.942	0.909	0.886
20	3.55	3.47	3.40	3.33	3.27	3.22	3.17	3.13	3.11	3.09	3.10	1.06
25	3.55	3.47	3.40	3.33	3.27	3.22	3.17	3.13	3.10	3.07	3.07	3.08
30	3.56	3.48	3.41	3.34	3.27	3.22	3.17	3.12	3.09	3.06	3.05	3.05
35	3.56	3.48	3.41	3.34	3.28	3.22	3.17	3.12	3.08	3.05	3.03	3.02
40	3.57	3.49	3.41	3.34	3.28	3.22	3.17	3.12	3.08	3.04	3.02	3.00
45	3.58	3.50	3.42	3.35	3.28	3.22	3.17	3.12	3.07	3.04	3.01	2.98
50	3.58	3.50	3.42	3.35	3.29	3.22	3.17	3.12	3.07	3.03	3.00	2.97
60	3.60	3.51	3.43	3.36	3.29	3.23	3.17	3.12	3.07	3.03	2.99	2.95
70	3.61	3.52	3.45	3.37	3.30	3.24	3.18	3.12	3.07	3.02	2.98	2.94
80	3.62	3.54	3.46	3.38	3.31	3.25	3.18	3.13	3.07	3.02	2.98	2.94
90	3.64	3.55	3.47	3.39	3.32	3.25	3.19	3.13	3.08	3.03	2.98	2.94
100	3.65	3.56	3.48	3.41	3.33	3.26	3.20	3.14	3.08	3.03	2.98	2.94
110	3.67	3.58	3.50	3.42	3.34	3.28	3.21	3.15	3.09	3.04	2.99	2.94
120	3.68	3.59	3.51	3.43	3.36	3.29	3.22	3.16	3.10	3.05	2.99	2.94
140	3.71	3.62	3.54	3.46	3.38	3.31	3.24	3.18	3.12	3.06	3.01	2.96
160	3.74	3.65	3.57	3.48	3.41	3.33	3.27	3.20	3.14	3.08	3.03	2.97
180	3.78	3.68	3.60	3.51	3.43	3.36	3.29	3.22	3.16	3.10	3.05	2.99
200	3.81	3.71	3.63	3.54	3.46	3.39	3.32	3.25	3.19	3.12	3.07	3.01
220	3.84	3.75	3.66	3.57	3.49	3.42	3.34	3.28	3.21	3.15	3.09	3.03
240	3.88	3.78	3.69	3.60	3.52	3.44	3.37	3.30	3.24	3.17	3.11	3.06
260	3.91	3.81	3.72	3.63	3.55	3.47	3.40	3.33	3.26	3.20	3.14	3.08
280	3.94	3.85	3.75	3.66	3.58	3.50	3.43	3.36	3.29	3.22	3.16	3.11
300	3.98	3.88	3.79	3.70	3.61	3.53	3.46	3.38	3.32	3.25	3.19	3.13
Pressure in bar	Temperature in °C											
	75	80	90	95	100	105	110	115	120	130	140	150
1	0.741	0.742	0.746	0.748	0.750	0.752	0.755	0.757	0.760	0.766	0.773	0.779
5	0.768	0.768	0.769	0.769	0.771	0.772	0.773	0.775	0.777	0.782	0.787	0.793
10	0.807	0.804	0.799	0.797	0.797	0.796	0.796	0.797	0.798	0.801	0.804	0.809
15	0.869	0.856	0.839	0.833	0.829	0.826	0.823	0.822	0.821	0.821	0.823	0.826
20	0.993	0.951	0.902	0.886	0.875	0.866	0.859	0.854	0.850	0.845	0.844	0.845
25	3.14	1.20	1.02	0.979	0.949	0.927	0.911	0.898	0.889	0.876	0.870	0.867
30	3.07	3.15	1.36	1.18	1.09	1.03	0.993	0.966	0.945	0.918	0.902	0.894
35	3.03	3.07	3.46	2.11	1.47	1.25	1.14	1.08	1.03	0.976	0.945	0.927
40	3.00	3.02	3.19	3.58	9.31	2.03	1.50	1.29	1.18	1.06	1.00	0.970
45	2.97	2.98	3.06	3.22	3.69	7.68	3.00	1.82	1.46	1.20	1.08	1.03
50	2.95	2.95	2.98	3.05	3.23	3.70	5.32	3.57	2.13	1.41	1.20	1.10
60	2.93	2.91	2.89	2.90	2.93	3.00	3.14	3.38	3.49	2.30	1.59	1.32
70	2.91	2.88	2.84	2.83	2.82	2.83	2.85	2.88	2.91	2.78	2.15	1.66
80	2.90	2.87	2.81	2.79	2.77	2.75	2.74	2.73	2.71	2.65	2.40	2.00
90	2.90	2.86	2.79	2.76	2.74	2.71	2.69	2.66	2.63	2.56	2.41	2.17
100	2.89	2.85	2.78	2.75	2.72	2.69	2.66	2.63	2.59	2.51	2.40	2.23

D2.7. Table 16. (continued)

Temperature in °C												
Pressure in bar	75	80	90	95	100	105	110	115	120	130	140	150
110	2.90	2.85	2.78	2.74	2.71	2.67	2.64	2.61	2.57	2.49	2.39	2.26
120	2.90	2.86	2.78	2.74	2.70	2.67	2.63	2.60	2.56	2.48	2.39	2.28
140	2.91	2.86	2.78	2.74	2.70	2.66	2.63	2.59	2.55	2.48	2.39	2.30
160	2.92	2.88	2.79	2.75	2.71	2.67	2.63	2.59	2.56	2.48	2.41	2.33
180	2.94	2.89	2.80	2.76	2.72	2.68	2.64	2.60	2.56	2.49	2.42	2.35
200	2.96	2.91	2.82	2.77	2.73	2.69	2.65	2.61	2.58	2.51	2.44	2.37
220	2.98	2.93	2.84	2.79	2.75	2.71	2.67	2.63	2.59	2.52	2.45	2.39
240	3.00	2.95	2.86	2.81	2.77	2.73	2.69	2.65	2.61	2.54	2.47	2.41
260	3.03	2.97	2.88	2.83	2.79	2.75	2.71	2.67	2.63	2.56	2.49	2.42
280	3.05	3.00	2.90	2.85	2.81	2.77	2.73	2.69	2.65	2.58	2.51	2.45
300	3.07	3.02	2.92	2.87	2.83	2.79	2.75	2.71	2.67	2.60	2.53	2.47

5 Bibliography

1. Tillner-Roth R, Baehr HD (1994) An international standard formulation of the thermodynamic properties of 1,1,1,2-tetrafluoroethane (HFC-134a). J Phys Chem Ref Data 23:657–729
2. Baehr HD, Tillner-Roth R (1995) Thermodynamische Eigenschaften umweltverträglicher Kältemittel. Springer, Berlin
3. Krauss RJ, Luettmer-Strathmann J, Sengers JV, Stephan K (1993) Transport properties of 1,1,1,2-tetrafluoroethane (R134a). Int J Thermophys 14:951–988

D3.1 Liquids and Gases

Michael Kleiber[1] · *Ralph Joh*[2]
[1]Uhde GmbH, Bad Soden, Germany
[2]Siemens AG, Frankfurt, Germany

In the previous edition, this section containing thermophysical data of 275 compounds had been supplemented by correlations for temperature-dependent properties in order to give a better opportunity for interpolation and, with the appropriate caution, extrapolation. With the help of these correlations, the user can make use of the data in process simulation programs.

Most of the data points given in the tables have been obtained by regression of experimental data from the literature or the relevant databanks. During this regression, a careful evaluation of the data has been performed, and outliers have been removed from the database. The equations listed below have been used for this regression. The final correlations are at least valid in the temperature range where data points are given in the tables. Although the correlations are usually suitable for extrapolation, one should be careful to go beyond this range. Especially when polynoms are used, a plausible curvature should be maintained (see Chap. D1).

In comparison to the previous German edition of the VDI Heat Atlas, for the liquid density, the liquid viscosity, the enthalpy of vaporization and the specific heat capacities of liquids and ideal gases the new PPDS equations have been used. Currently, these equations seem to be the most accurate ones and show a reasonable extrapolation behavior. For the vapor pressure, the 2.5-5-form of the Wagner equation is used, which performs slightly better than the well established 3-6-form.

Whenever it was possible, high-precision equations of state have been used to obtain artificial data points as the basis for the regression. On the other hand, many values for transport properties, especially for gases, have been obtained by the estimation methods described in Chap. D1.

In general, all the values and correlations are not the absolutely correct ones but refer to the best possible data according to the knowledge of the authors. Like all data collections, also this one cannot claim completeness or absolute reliability. The authors are grateful for hints on mistakes and general improvements of this chapter.

The correlation equations for the temperature-dependent properties are:

Liquid density

$$\frac{\rho_{\mathrm{liq}}}{\mathrm{kg/m^3}} = \frac{\rho_c}{\mathrm{kg/m^3}} + A\left(1-\frac{T}{T_c}\right)^{0.35} + B\left(1-\frac{T}{T_c}\right)^{2/3} + C\left(1-\frac{T}{T_c}\right) + D\left(1-\frac{T}{T_c}\right)^{4/3} \tag{1}$$

Dynamic viscosity of liquids

$$\frac{\eta}{\mathrm{Pa\,s}} = E\cdot\exp\left[A\left(\frac{C-T}{T-D}\right)^{1/3} + B\left(\frac{C-T}{T-D}\right)^{4/3}\right] \tag{2}$$

When Eq. (2) is programmed, it must be taken care that the term in brackets $(C-T)/(T-D)$ sometimes turns out to be negative, so that it makes sense to write in these cases

$$\left(\frac{C-T}{T-D}\right)^{1/3} = -\left(\frac{T-C}{T-D}\right)^{1/3}$$

and

$$\left(\frac{C-T}{T-D}\right)^{4/3} = -\left(\frac{T-C}{T-D}\right)^{1/3}\left(\frac{C-T}{T-D}\right) \tag{2a}$$

Dynamic viscosity of gases

$$\frac{\eta}{\mathrm{Pa\,s}} = A + B\frac{T}{K} + C\left(\frac{T}{K}\right)^2 + D\left(\frac{T}{K}\right)^3 + E\left(\frac{T}{K}\right)^4 \tag{3}$$

Thermal conductivity of liquids

$$\frac{\lambda}{\mathrm{W/mK}} = A + B\frac{T}{K} + C\left(\frac{T}{K}\right)^2 + D\left(\frac{T}{K}\right)^3 + E\left(\frac{T}{K}\right)^4 \tag{4}$$

Thermal conductivity of gases

$$\frac{\lambda}{\mathrm{W/mK}} = A + B\frac{T}{K} + C\left(\frac{T}{K}\right)^2 + D\left(\frac{T}{K}\right)^3 + E\left(\frac{T}{K}\right)^4 \tag{5}$$

Surface tension

$$\frac{\sigma}{\mathrm{N/m}} = A\left(1-\frac{T}{T_c}\right)^{B+C(T/T_c)+D(T/T_c)^2+E(T/T_c)^3} \tag{6}$$

Vapor pressure

$$\ln\frac{p_s}{p_c} = \frac{T_c}{T}\left[A\left(1-\frac{T}{T_c}\right) + B\left(1-\frac{T}{T_c}\right)^{1.5} + C\left(1-\frac{T}{T_c}\right)^{2.5} + D\left(1-\frac{T}{T_c}\right)^{5}\right] \tag{7}$$

Specific heat capacity of liquids

$$c_p^{\mathrm{liq}} = R\left(\frac{A}{1-\frac{T}{T_c}} + B + C\left(1-\frac{T}{T_c}\right) + D\left(1-\frac{T}{T_c}\right)^2 + E\left(1-\frac{T}{T_c}\right)^3 + F\left(1-\frac{T}{T_c}\right)^4\right) \tag{8}$$

VDI-GVC (ed.), *VDI Heat Atlas*, DOI 10.1007/978-3-540-77877-6_12,

Equation (8) reduces to a polynomial if the first parameter A is set to 0. For many substances, only few data points are known so that it is not justified to fit all the parameters.
In these cases, extrapolation beyond the range of validity should be avoided.

Enthalpy of vaporization

$$\Delta h_v = RT_c\left[A\left(1-\frac{T}{T_c}\right)^{1/3}+B\left(1-\frac{T}{T_c}\right)^{2/3}+C\left(1-\frac{T}{T_c}\right)+D\left(1-\frac{T}{T_c}\right)^{2}+E\left(1-\frac{T}{T_c}\right)^{6}\right] \quad (9)$$

Specific heat capacity of ideal gases

$$\frac{c_p^{id}}{R} = B+(C-B)\left(\frac{T}{A+T}\right)^2\left[1-\frac{A}{A+T}\left(D+E\frac{T}{A+T}+F\left(\frac{T}{A+T}\right)^2+G\left(\frac{T}{A+T}\right)^3\right)\right] \quad (10)$$

The symbols are explained in Chap. D1. If the data points are recalculated from the parameters, small deviations due to approximation errors of the parameters might occur.

D3.1. Table 1. Caloric and critical data

Substance	Formula	Molecular weight g/mol	Melting temperature °C	Enthalpy of fusion J/g	Boiling point at 1.013 bar °C	Enthalpy of vaporization at 1.013 bar J/g	Critical temperature K	Critical pressure bar	Critical density kg/m³	Acentric factor
Elements										
Xenon	Xe	131.29	−111.9	17.5	−108.1	95.6	289.73	58.42	1103	0.004
Krypton	Kr	83.80	−157.4	19.6	−153.4	107.1	209.48	55.25	910	−0.001
Argon	Ar	39.95	−189.4	29.6	−185.9	161.1	150.69	48.63	536	−0.002
Neon	Ne	20.18	−248.6	16.3	−246.1	85.8	44.49	26.79	482	−0.039
Helium	He	4.00	−271.4	12.5	−268.9	20.8	5.20	2.27	70	−0.384
Air		28.96	−210.1	25.7	−194.2	191.9	132.53	37.86	343	0.038
Hydrogen	H_2	2.02	−259.3	58.1	−252.8	459.2	33.19	13.15	30	−0.219
Nitrogen	N_2	28.01	−210.1	25.7	−195.8	199.2	126.19	33.96	313	0.037
Oxygen	O_2	32.00	−218.8	13.9	−183.0	213.1	154.60	50.46	427	0.022
Sulfur	S	32.06	115.3	53.9	444.2	277.4	1312.95	182.08	203	0.246
Fluorine	F_2	38.00	−219.7	13.4	−188.1	174.3	144.41	52.40	593	0.051
Chlorine	Cl_2	70.91	−101.0	90.3	−34.0	288.0	416.96	79.91	577	0.087
Bromine	Br_2	159.82	−7.3	66.1	58.7	186.5	584.15	103.00	1183	0.129
Iodine	I_2	253.80	113.7	61.1	184.4	165.3	819.15	116.54	1637	0.112
Anorganic compounds										
Hydrogen fluoride	HF	20.01	−83.4	228.9	19.5	380.5	461.15	64.80	290	0.381
Hydrogen chloride	HCl	36.46	−114.3	54.9	−85.1	448.3	324.65	83.10	450	0.131
Hydrogen bromide	HBr	80.92	−86.9	29.7	−66.6	220.3	363.15	85.52	809	0.073
Hydrogen iodide	HI	127.91	−50.9	22.5	−35.4	158.4	423.85	83.10	1049	0.038
Hydrogen cyanide	HCN	27.02	−13.3	311.0	25.7	998.6	456.65	53.90	194	0.410
Water	H_2O	18.02	0.0	333.1	100.0	2256.6	647.10	220.64	322	0.344
Hydrogen sulfide	H_2S	34.08	−85.5	69.7	−60.3	546.5	373.10	89.99	349	0.100
Ammonia	NH_3	17.03	−77.8	332.2	−33.3	1369.2	405.50	113.59	225	0.256
Nitric oxide	NO	30.01	−161.0	76.7	−151.8	452.6	180.15	64.80	517	0.583
Nitrogen dioxide	NO_2	46.01	−11.3	318.4	21.2	720.5	431.15	101.32	558	0.851
Nitrous oxide	N_2O	44.01	−90.9	148.6	−88.5	374.4	309.52	72.45	454	0.162
Dinitrogentetroxide	N_2O_4	92.01	−11.3	159.2	21.3	358.4	431.10	101.32	1115	0.853
Cyanogen	C_2N_2	52.04	−27.9	155.8	−21.1	448.8	400.15	59.78	267	0.279
Phosphorus trichloride	PCl_3	137.33	−92.0	51.6	75.0	216.9	563.15	56.70	528	0.220
Cyanogen chloride	ClCN	61.47	−6.5	185.3	12.8	435.1	449.05	59.90	377	0.323
Silane	SiH_4	32.12	−184.7	20.8	−112.0	374.5	269.75	48.40	242	0.093
Tetrachlorosilane	$SiCl_4$	169.90	−68.8	45.1	57.2	165.4	507.05	35.90	521	0.232

D3.1. Table 1. (continued)

Substance	Formula	Molecular weight g/mol	Melting temperature °C	Enthalpy of fusion J/g	Boiling point at 1.013 bar °C	Enthalpy of vaporization at 1.013 bar J/g	Critical temperature K	Critical pressure bar	Critical density kg/m³	Acentric factor
Carbon monoxide	CO	28.01	−205.0	30.0	−191.5	214.7	132.86	34.98	304	0.050
Carbon dioxide	CO_2	44.01	−56.6	204.9			304.13	73.77	468	0.224
Carbon suboxide	C_3O_2	68.03	−112.2	79.4	6.4	363.8	427.58	69.44	383	0.522
Carbonyl sulfide	COS	60.07	−138.9	78.7	−50.2	309.0	378.77	63.69	447	0.098
Phosgene	CCl_2O	98.92	−127.9	58.0	7.7	249.3	455.05	56.74	521	0.201
Carbon disulfide	CS_2	76.14	−111.6	57.7	46.2	353.3	552.05	79.00	476	0.121
Sulfur dioxide	SO_2	64.06	−73.2	115.5	−10.0	389.1	430.64	78.76	525	0.255
Sulfur trioxide	SO_3	80.06	16.8	94.1	44.5	509.0	490.85	82.10	631	0.424
Sulfuryl chloride	Cl_2SO_2	134.97	−54.1		69.4	222.1	545.05	46.10	577	0.176
Sulfur hexafluoride	SF_6	146.05	−50.8	34.4			318.88	37.66	742	0.215
Organic compounds containing sulfur										
Methyl mercaptan	CH_4S	48.11	−123.0	122.7	6.0	511.0	469.95	72.30	332	0.158
Ethyl mercaptan	C_2H_6S	62.13	−147.9	80.1	35.0	432.5	499.15	54.90	300	0.188
Dimethyl sulfide	C_2H_6S	62.13	−98.0		37.4	437.1	503.00	55.30	309	0.195
Diethyl sulfide	$C_4H_{10}S$	90.19	−103.9	132.0	92.2	352.4	557.15	39.60	284	0.290
Thiophene	C_4H_4S	84.14	−38.3	60.4	84.2	375.8	579.35	56.90	384	0.197
Halogenated hydrocarbons										
Fluoromethane (R41)	CH_3F	34.03	−141.9	145.4	−78.4	487.8	317.28	59.06	319	0.200
Difluoromethane (R32)	CH_2F_2	52.02	−136.1	99.2	−51.7	382.0	351.26	57.83	424	0.277
Trifluoromethane (R23)	CHF_3	70.01	−155.2	58.0	−82.1	238.7	299.75	48.69	526	0.258
Tetrafluoromethane (R14)	CF_4	88.00	−183.7	8.1	−128.1	133.6	227.55	37.40	629	0.178
Methyl chloride	CH_3Cl	50.49	−97.8	129.7	−24.1	428.1	416.25	66.80	353	0.154
Methylene chloride	CH_2Cl_2	84.93	−95.1	54.2	39.8	333.9	510.05	60.80	459	0.198
Chloroform	$CHCl_3$	119.38	−63.5	79.9	61.1	247.5	536.45	55.54	508	0.229
Carbon tetrachloride	CCl_4	153.82	−22.9	16.5	76.7	194.2	556.35	45.60	557	0.193
Bromomethane	CH_3Br	94.94	−93.6	63.0	3.6	255.2	467.05	80.00	609	0.191
Dibromomethane	CH_2Br_2	173.85	−52.5	43.2	97.0	194.4	611.05	71.70	779	0.209
Tribromomethane	$CHBr_3$	252.75	8.2	45.9	149.2	149.3	696.05	60.90	883	0.156
Tetrabromomethane	CBr_4	331.65	92.0		189.3	120.6	724.80	96.31	1009	0.584
Chlorodifluoromethane (R22)	$CHClF_2$	86.47	−157.4	47.7	−40.8	234.0	369.28	49.88	520	0.221
Dichlorofluoromethane (R21)	$CHCl_2F$	102.92	−135.0	51.0	8.8	242.2	451.55	51.84	525	0.205
Chlorotrifluoromethane (R13)	$CClF_3$	104.46	−181.0	33.5	−81.4	150.0	302.05	38.70	579	0.172
Dichlorodifluoromethane (R12)	CCl_2F_2	120.91	−158.0	34.2	−29.8	166.2	385.12	41.36	565	0.179
Trichlorofluoromethane (R11)	CCl_3F	137.37	−111.1	50.2	23.6	181.8	471.06	43.94	565	0.188
Ethyl fluoride (R161)	C_2H_5F	48.06	−143.3	124.8	−37.7	418.3	375.30	50.28	293	0.220
Ethyl chloride	C_2H_5Cl	64.52	−136.4	69.0	12.3	383.0	460.35	52.70	323	0.192
Ethyl bromide	C_2H_5Br	108.97	−118.6	53.8	38.4	249.6	503.75	62.30	507	0.252
1,1-Dichloroethane	$C_2H_4Cl_2$	98.96	−97.0	79.5	57.1	296.7	523.05	50.70	412	0.233
1,2-Dichloroethane	$C_2H_4Cl_2$	98.96	−35.7	89.2	83.6	323.7	561.60	53.70	450	0.285
1,2-Dibromoethane	$C_2H_4Br_2$	187.87	9.8	58.3	131.5	191.3	650.20	54.77	718	0.207
1,1,1-Trifluoroethane (R143a)	$C_2H_3F_3$	84.04	−111.4	73.7	−47.2	226.7	345.86	37.62	431	0.262
1,1,1-Trichloroethane	$C_2H_3Cl_3$	133.41	−30.0	17.6	74.1	223.0	545.05	43.00	475	0.217
1,1,2,2-Tetrachloroethane	$C_2H_2Cl_4$	167.85	−43.9	54.6	145.9	225.5	645.05	40.90	517	0.253
Pentachloroethane	C_2HCl_5	202.29	−29.0	56.1	160.4	191.5	646.00	34.80	548	0.337
Hexachloroethane	C_2Cl_6	236.74	186.8	41.2			695.05	33.40	575	0.238

D3.1. Table 1. (continued)

Substance	Formula	Molecular weight g/mol	Melting temperature °C	Enthalpy of fusion J/g	Boiling point at 1.013 bar °C	Enthalpy of vaporization at 1.013 bar J/g	Critical temperature K	Critical pressure bar	Critical density kg/m³	Acentric factor
1,1,2,2-Tetrachlorodifluoroethane	$C_2Cl_4F_2$	203.83	24.9	18.2	93.0	156.8	551.05	34.34	581	0.290
1,1,2-Trichlorotrifluoroethane	$C_2Cl_3F_3$	187.38	−36.3	13.2	47.6	144.3	487.21	33.92	560	0.253
1,2-Dichlorotetrafluoroethane	$C_2Cl_2F_4$	170.92	−92.5	8.8	3.6	135.7	418.85	32.60	581	0.252
1-Chloropropane	C_3H_7Cl	78.54	−122.9	70.6	46.5	354.7	503.15	45.80	318	0.227
1-Chlorobutane	C_4H_9Cl	92.57	−123.1	89.0	78.7	327.7	542.00	36.80	309	0.226
1-Chloropentane	$C_5H_{11}Cl$	106.60	−99.0		108.5	314.3	568.05	33.50	303	0.318
Chlorotrifluoroethene	C_2ClF_3	116.47	−158.1	47.7	−28.8	224.2	379.15	40.53	549	0.242
Vinyl chloride	C_2H_3Cl	62.50	−153.9	75.9	−13.8	353.5	432.05	56.70	349	0.100
1,1-Dichloroethene	$C_2H_2Cl_2$	96.94	−122.6	67.2	31.7	269.6	482.05	51.90	433	0.272
Trichloroethene	C_2HCl_3	131.39	−84.9		86.2	242.4	571.05	49.10	513	0.210
Tetrachloroethene	C_2Cl_4	165.83	−22.4	63.1	121.0	210.5	620.05	44.90	669	0.214
Fluorobenzene	C_6H_5F	96.10	−42.3	117.6	85.2	329.4	560.05	45.51	357	0.248
Chlorobenzene	C_6H_5Cl	112.56	−45.3	84.9	131.9	316.4	632.35	45.19	366	0.250
Bromobenzene	C_6H_5Br	157.01	−30.8	67.7	156.0	239.4	670.20	45.19	485	0.251
Iodobenzene	C_6H_5I	204.01	−31.4	47.8	188.3	200.4	721.20	45.19	581	0.247
m-Chlorotoluene	C_7H_7Cl	126.59	−48.0		162.8	312.1	660.75	39.54	347	0.307
Benzyl chloride	C_7H_7Cl	126.59	−39.0		179.5	324.1	686.05	39.10	352	0.314
***n*-Alkanes**										
Methane	CH_4	16.04	−182.5	58.7	−161.5	510.8	190.56	45.99	163	0.011
Ethane	C_2H_6	30.07	−182.9	95.1	−88.6	489.5	305.32	48.72	206	0.100
Propane	C_3H_8	44.10	−187.7	79.9	−42.1	426.1	369.82	42.48	221	0.152
n-Butane	C_4H_{10}	58.12	−138.4	80.2	−0.5	385.9	425.13	37.96	228	0.201
n-Pentane	C_5H_{12}	72.15	−129.8	116.4	36.1	357.7	469.66	33.69	235	0.252
n-Hexane	C_6H_{14}	86.18	−95.4	151.8	68.7	334.9	507.79	30.42	223	0.300
n-Heptane	C_7H_{16}	100.21	−90.6	140.2	98.4	316.7	541.23	27.74	225	0.346
n-Octane	C_8H_{18}	114.23	−56.9	181.6	125.6	302.1	569.57	25.07	228	0.394
n-Nonane	C_9H_{20}	128.26	−53.5	120.6	150.8	288.5	594.55	22.82	234	0.444
n-Decane	$C_{10}H_{22}$	142.29	−29.6	201.8	174.1	276.3	617.70	21.01	234	0.488
n-Undecane	$C_{11}H_{24}$	156.31	−25.6	141.9	195.9	270.2	639.05	19.50	237	0.530
n-Dodecane	$C_{12}H_{26}$	170.34	−9.5	216.3	216.3	256.2	658.10	18.18	238	0.574
n-Tridecane	$C_{13}H_{28}$	184.37	−5.3	154.6	235.4	252.0	675.05	16.80	238	0.618
n-Tetradecane	$C_{14}H_{30}$	198.39	6.0	227.2	253.5	242.5	693.05	15.70	239	0.643
n-Pentadecane	$C_{15}H_{32}$	212.42	10.0	162.8	270.6	237.7	708.05	14.80	239	0.685
n-Hexadecane	$C_{16}H_{34}$	226.45	18.3	235.6	286.7	231.6	723.05	14.00	240	0.717
n-Heptadecane	$C_{17}H_{36}$	240.47	22.0	167.0	302.4	228.9	736.05	13.40	241	0.769
n-Octadecane	$C_{18}H_{38}$	254.50	28.3	242.5	316.2	219.5	747.05	12.70	240	0.811
n-Nonadecane	$C_{19}H_{40}$	268.53	32.0	170.6	330.1	214.2	758.05	12.10	240	0.852
n-Eicosane	$C_{20}H_{42}$	282.56	36.5	247.3	343.7	204.8	769.63	11.28	234	0.875
Isoalkanes										
Isobutane	C_4H_{10}	58.12	−159.6	78.1	−11.7	365.4	407.81	36.29	226	0.184
2-Methyl butane	C_5H_{12}	72.15	−159.9	71.4	27.8	343.6	460.35	33.78	237	0.228
2,2-Dimethyl propane	C_5H_{12}	72.15	−16.6	43.6	9.5	315.5	433.74	31.96	238	0.196
2-Methyl pentane	C_6H_{14}	86.18	−153.6	72.7	60.2	323.0	497.70	30.43	236	0.280
3-Methyl pentane	C_6H_{14}	86.18	−162.9	61.5	63.3	326.6	504.65	31.20	234	0.270
2,2-Dimethyl butane	C_6H_{14}	86.18	−98.9	6.7	49.7	307.5	489.00	31.00	241	0.234
2,3-Dimethyl butane	C_6H_{14}	86.18	−128.0	9.3	57.9	317.6	500.00	31.51	240	0.248

D3.1. Table 1. (continued)

Substance	Formula	Molecular weight g/mol	Melting temperature °C	Enthalpy of fusion J/g	Boiling point at 1.013 bar °C	Enthalpy of vaporization at 1.013 bar J/g	Critical temperature K	Critical pressure bar	Critical density kg/m³	Acentric factor
Olefins										
Ethylene	C_2H_4	28.05	−169.1	119.4	−103.8	482.7	282.35	50.42	214	0.087
Propylene	C_3H_6	42.08	−85.4	71.4	−47.7	439.5	365.57	46.65	223	0.141
1-Butene	C_4H_8	56.11	−185.4	68.6	−6.3	392.2	419.29	40.06	238	0.192
1-Pentene	C_5H_{10}	70.14	−165.1	84.7	30.0	362.2	464.75	35.60	235	0.237
1-Hexene	C_6H_{12}	84.16	−139.9	111.1	63.5	339.1	504.05	31.40	238	0.280
1-Heptene	C_7H_{14}	98.19	−118.9		93.7	319.5	537.40	29.20	244	0.344
1-Octene	C_8H_{16}	112.22	−101.8	136.4	121.3	306.4	567.05	26.80	240	0.392
Propadiene	C_3H_4	40.06	−136.4		−34.4	489.5	393.15	50.90	243	0.132
1,2-Butadiene	C_4H_6	54.09	−136.3	128.7	10.9	440.5	452.00	43.60	246	0.166
1,3-Butadiene	C_4H_6	54.09	−108.9	147.6	−4.5	416.3	425.15	42.77	245	0.190
1,2-Pentadiene	C_5H_8	68.12	−137.4	111.0	44.8	398.6	500.05	38.00	247	0.154
trans-1,3-Pentadiene	C_5H_8	68.12	−87.4	104.9	42.0	392.2	500.05	37.40	247	0.116
1,4-Pentadiene	C_5H_8	68.12	−148.3	89.2	26.0	359.5	479.00	37.40	225	0.084
2,3-Pentadiene	C_5H_8	68.12	−125.7	95.8	48.3	407.4	497.00	38.00	231	0.218
Acetylene and derivatives										
Acetylene	C_2H_2	26.04	−80.9	144.8			308.35	61.39	230	0.190
Propyne	C_3H_4	40.06	−102.8	133.5	−23.1	554.9	402.40	56.30	244	0.211
2-Butyne	C_4H_6	54.09	−32.3	170.7	27.0	492.0	473.20	48.70	245	0.238
1-Butyne	C_4H_6	54.09	−125.8	111.5	8.1	459.8	440.00	46.00	260	0.247
Naphthenes										
Cyclopropane	C_3H_6	42.08	−127.6	129.3	−32.8	473.4	397.95	54.95	259	0.133
Cyclobutane	C_4H_8	56.11	−90.7	19.4	12.5	427.8	459.90	49.80	267	0.185
Cyclopentane	C_5H_{10}	70.14	−93.9	8.7	49.2	387.3	511.70	45.25	270	0.196
Methyl cyclopentane	C_6H_{12}	84.16	−142.4	82.3	71.8	347.6	532.75	37.90	264	0.231
Ethyl cyclopentane	C_7H_{14}	98.19	−138.5	70.0	103.4	326.6	569.50	34.00	262	0.270
Propyl cyclopentane	C_8H_{16}	112.22	−117.4	89.4	131.0	310.9	596.00	30.20	262	0.327
Butyl cyclopentane	C_9H_{18}	126.24	−108.0	89.6	156.4	286.7	621.00	27.20	261	0.372
Pentyl cyclopentane	$C_{10}H_{20}$	140.27	−83.0		180.5	278.1	656.20	24.67	257	0.329
Hexyl cyclopentane	$C_{11}H_{22}$	154.30	−73.0		203.1	273.0	660.10	21.38	259	0.476
Cyclohexane	C_6H_{12}	84.16	6.5	32.6	80.7	356.1	553.60	40.75	273	0.209
Methyl cyclohexane	C_7H_{14}	98.19	−126.6	68.8	100.9	320.1	572.15	34.71	267	0.235
Ethyl cyclohexane	C_8H_{16}	112.22	−111.4	74.3	131.9	305.6	609.15	30.40	261	0.246
Propyl cyclohexane	C_9H_{18}	126.24	−94.9	82.1	156.7	288.7	639.20	28.07	265	0.260
Butyl cyclohexane	$C_{10}H_{20}$	140.27	−74.8	100.9	181.0	278.2	667.00	25.70	263	0.274
Pentyl cyclohexane	$C_{11}H_{22}$	154.30	−72.9		203.7	275.8	667.85	22.04	264	0.430
Hexyl cyclohexane	$C_{12}H_{24}$	168.32	−45.3		224.7	270.6	693.60	22.60	249	0.468
Cyclopentene	C_5H_8	68.12	−135.1	49.4	44.3	396.6	507.00	48.00	278	0.196
Cyclohexene	C_6H_{10}	82.15	−103.5	40.1	83.0	371.3	560.45	43.50	282	0.211
Aromatic compounds										
Benzene	C_6H_6	78.11	5.5	126.3	80.1	393.7	562.01	49.01	306	0.210
Toluene	C_7H_8	92.14	−95.0	72.0	110.6	360.8	591.75	41.26	292	0.266
Ethyl benzene	C_8H_{10}	106.17	−94.9	86.5	136.2	336.8	617.05	36.13	283	0.304
Propyl benzene	C_9H_{12}	120.19	−99.6	77.1	159.2	313.1	638.35	31.96	274	0.344
Butyl benzene	$C_{10}H_{14}$	134.22	−87.9	83.6	183.3	301.5	660.50	28.90	270	0.394
Pentyl benzene	$C_{11}H_{16}$	148.25	−75.1	102.8	205.6	286.5	679.90	26.04	270	0.438
Hexyl benzene	$C_{12}H_{18}$	162.28	−61.2	113.4	226.2	274.4	698.00	23.80	274	0.479
o-Xylene	C_8H_{10}	106.17	−25.3	128.1	144.4	347.6	630.25	37.32	287	0.312
m-Xylene	C_8H_{10}	106.17	−47.9	109.0	139.1	342.3	617.05	35.41	283	0.327

D3.1. Table 1. (continued)

Substance	Formula	Molecular weight g/mol	Melting temperature °C	Enthalpy of fusion J/g	Boiling point at 1.013 bar °C	Enthalpy of vaporization at 1.013 bar J/g	Critical temperature K	Critical pressure bar	Critical density kg/m³	Acentric factor
p-Xylene	C_8H_{10}	106.17	13.3	161.2	138.4	339.8	616.25	35.11	281	0.322
1,2,3-Trimethyl benzene	C_9H_{12}	120.19	−25.4	68.1	176.2	335.4	664.50	34.54	290	0.367
1,2,4-Trimethyl benzene	C_9H_{12}	120.19	−43.9	109.7	169.4	328.2	649.05	32.32	280	0.378
1,3,5-Trimethyl benzene	C_9H_{12}	120.19	−44.8	79.2	164.7	326.1	637.30	31.27	278	0.399
1,2,3,4-Tetramethyl benzene	$C_{10}H_{14}$	134.22	−6.3	83.7	205.1	321.1	693.00	31.10	283	0.417
1,2,3,5-Tetramethyl benzene	$C_{10}H_{14}$	134.22	−23.7	79.9	198.1	317.4	679.00	29.70	279	0.424
1,2,4,5-Tetramethyl benzene	$C_{10}H_{14}$	134.22	79.3	156.5	196.7	317.9	676.00	29.00	279	0.422
Pentamethyl benzene	$C_{11}H_{16}$	148.25	54.4	83.2	231.5	312.7	719.20	28.70	276	0.464
Hexamethyl benzene	$C_{12}H_{18}$	162.28	165.5	127.2	263.5	311.5	758.00	27.70	274	0.496
Styrene	C_8H_8	104.15	−30.6	105.1	145.4	355.7	636.05	38.40	296	0.295
Isopropyl benzene	C_9H_{12}	120.19	−96.0	61.0	152.4	310.7	631.05	32.09	277	0.327
Biphenyl	$C_{12}H_{10}$	154.21	69.2	120.5	255.3	315.5	789.00	38.50	310	0.365
Diphenyl methane	$C_{13}H_{12}$	168.24	25.3	108.2	264.6	292.7	760.00	27.10	299	0.482
Triphenyl methane	$C_{19}H_{16}$	244.34	92.2	90.0	359.5	245.5	865.00	22.00	325	0.574
Tetraphenyl methane	$C_{25}H_{20}$	320.43	288.1		469.7	221.6	983.00	17.90	332	0.679
Naphthalene	$C_{10}H_8$	128.17	80.3	148.1	218.0	338.5	748.45	40.50	315	0.304
1-Methylnaphthalene	$C_{11}H_{10}$	142.20	−30.5	48.8	244.5	327.3	772.00	36.00	306	0.342
2-Methylnaphthalene	$C_{11}H_{10}$	142.20	34.6	85.2	241.6	325.1	761.00	35.00	306	0.378
1-Ethylnaphthalene	$C_{12}H_{12}$	156.23	−13.9	104.3	258.2	312.1	776.00	33.20	300	0.407
2-Ethylnaphthalene	$C_{12}H_{12}$	156.23	−7.3	94.1	258.4	307.3	771.00	31.70	300	0.421
Alcohols										
Methanol	CH_4O	32.04	−97.7	100.3	64.5	1102.0	513.38	82.16	282	0.563
Ethanol	C_2H_6O	46.07	−114.1	107.0	78.3	850.1	513.90	61.48	276	0.644
1-Propanol	C_3H_8O	60.10	−126.3	89.4	97.2	696.9	536.75	51.75	274	0.621
1-Butanol	$C_4H_{10}O$	74.12	−89.4	126.4	117.8	585.3	563.05	44.23	270	0.591
1-Pentanol	$C_5H_{12}O$	88.15	−77.6	111.1	137.9	500.4	586.15	38.80	270	0.591
1-Hexanol	$C_6H_{14}O$	102.18	−44.6	150.7	157.7	448.7	611.35	35.10	268	0.578
1-Heptanol	$C_7H_{16}O$	116.20	−34.1	156.4	176.6	401.2	632.60	30.58	267	0.567
1-Octanol	$C_8H_{18}O$	130.23	−15.6	172.8	195.3	368.5	652.55	28.60	266	0.593
Isopropanol	C_3H_8O	60.10	−87.9	90.0	82.2	677.2	508.25	47.62	273	0.663
2-Methyl-1-propanol	$C_4H_{10}O$	74.12	−108.0	85.3	107.9	564.0	547.75	43.00	272	0.590
3-Methyl-1-butanol	$C_5H_{12}O$	88.15	−117.3	75.0	131.3	500.5	577.25	39.30	270	0.595
Ethylene glycol	$C_2H_6O_2$	62.07	−13.1	160.4	197.1	867.5	719.15	82.00	325	0.513
1,3-Propylene glycol	$C_3H_8O_2$	76.09	−26.8	93.3	214.1	733.7	724.05	95.00	351	0.738
Glycerol	$C_3H_8O_3$	92.09	18.3	198.5	287.7	718.6	850.05	75.00	349	0.512
Cyclohexanol	$C_6H_{12}O$	100.16	23.5	17.8	160.9	451.7	650.05	42.60	311	0.370
Benzyl alcohol	C_7H_8O	108.14	−15.3	83.0	204.5	454.3	720.15	45.01	323	0.362
Phenols										
o-Cresol	C_7H_8O	108.14	31.0	146.3	190.8	423.1	697.55	50.10	383	0.433
m-Cresol	C_7H_8O	108.14	12.3	99.0	202.2	445.2	705.85	45.60	347	0.448
p-Cresol	C_7H_8O	108.14	34.8	117.5	202.0	445.3	704.65	51.50	391	0.509
Phenol	C_6H_6O	94.11	41.0	122.3	181.9	489.5	694.25	61.30	411	0.442
Carboxylic acids										
Formic acid	CH_2O_2	46.02	8.5	275.9	100.6	480.7	588.05	58.10	368	0.316
Acetic acid	$C_2H_4O_2$	60.05	16.8	195.3	117.9	397.9	591.95	57.86	334	0.463
Propionic acid	$C_3H_6O_2$	74.08	−20.8	143.9	141.2	419.4	600.85	46.17	318	0.576
Butyric acid	$C_4H_8O_2$	88.11	−5.3	131.5	163.7	402.6	615.75	40.64	302	0.681
Valeric acid	$C_5H_{10}O_2$	102.13	−29.4	71.7	175.6	395.3	634.05	38.90	304	0.647

D3.1. Table 1. (continued)

Substance	Formula	Molecular weight g/mol	Melting temperature °C	Enthalpy of fusion J/g	Boiling point at 1.013 bar °C	Enthalpy of vaporization at 1.013 bar J/g	Critical temperature K	Critical pressure bar	Critical density kg/m³	Acentric factor
Caproic acid	$C_6H_{12}O_2$	116.16	−3.8	132.6	204.5	394.0	660.20	33.08	281	0.730
Acetic anhydride	$C_4H_6O_3$	102.09	−73.0	102.8	139.5	394.5	606.05	40.00	352	0.454
Propionic anhydride	$C_6H_{10}O_3$	130.14	−45.1		167.0	326.9	623.00	32.70	329	0.560
Chloroacetic acid	$C_2H_3ClO_2$	94.50	60.0	130.2	189.0	523.8	686.05	57.80	428	0.546
Dichloroacetic acid	$C_2H_2Cl_2O_2$	128.94	13.5	95.7	193.9	379.5	686.05	51.70	487	0.555
Trichloroacetic acid	$C_2HCl_3O_2$	163.39	57.0	36.0	197.7	302.7	688.05	48.10	529	0.549
Ketones										
Ketene	C_2H_2O	42.04	−151.1		−49.7	461.0	370.05	58.10	292	0.125
Acetone	C_3H_6O	58.08	−94.8	99.4	56.1	501.7	508.10	46.92	274	0.306
Methyl ethyl ketone	C_4H_8O	72.11	−86.8	116.3	79.6	441.2	535.55	41.50	270	0.323
Diethyl ketone	$C_5H_{10}O$	86.13	−39.0	134.6	101.9	393.3	561.00	37.40	256	0.345
Dipropyl ketone	$C_7H_{14}O$	114.19	−32.6	162.9	144.2	327.8	602.00	29.20	263	0.412
Acetophenone	C_8H_8O	120.15	19.7	85.7	202.4	367.4	709.50	38.40	311	0.364
Benzophenone	$C_{13}H_{10}O$	182.22	48.3	92.8	305.6	301.0	830.05	33.52	321	0.500
Ethers										
Dimethyl ether	C_2H_6O	46.07	−141.5	107.2	−24.8	470.5	400.30	53.41	277	0.188
Diethyl ether	$C_4H_{10}O$	74.12	−116.4	97.0	34.5	357.7	466.63	36.51	264	0.283
Dipropyl ether	$C_6H_{14}O$	102.18	−123.3	105.4	90.0	310.4	530.60	30.28	268	0.369
Methyl propyl ether	$C_4H_{10}O$	74.12	−139.2	103.5	38.9	363.5	476.30	38.01	269	0.277
Ethyl propyl ether	$C_5H_{12}O$	88.15	−127.6	95.2	63.8	312.9	500.20	33.70	260	0.347
Ethylene oxide	C_2H_4O	44.05	−112.5	117.4	10.5	587.1	469.15	71.90	314	0.197
Furane	C_4H_4O	68.08	−85.6	55.9	31.4	400.2	490.15	55.00	312	0.203
1,4-Dioxane	$C_4H_8O_2$	88.11	11.8	145.7	101.4	389.5	587.05	52.08	370	0.279
Aldehydes										
Formaldehyde	CH_2O	30.03	−92.0	234.8	−19.1	769.2	408.05	65.90	261	0.281
Acetaldehyde	C_2H_4O	44.05	−123.0	73.1	20.3	595.7	466.05	55.50	286	0.262
Paraldehyde	$C_6H_{12}O_3$	132.16	12.7	104.8	124.2	285.1	579.05	35.00	362	0.437
Furfural	$C_5H_4O_2$	96.08	−36.6	149.9	161.4	436.1	670.20	56.60	381	0.368
Benzaldehyde	C_7H_6O	106.12	−57.1	87.8	178.9	387.0	695.05	46.50	328	0.322
Salicylaldehyde	$C_7H_6O_2$	122.12	1.7	87.6	196.3	373.4	680.00	49.90	357	0.619
Esters										
Methyl formate	$C_2H_4O_2$	60.05	−99.0	125.4	31.8	470.6	487.25	60.00	349	0.255
Ethyl formate	$C_3H_6O_2$	74.08	−79.6	124.3	54.0	405.6	508.45	47.40	324	0.276
Propyl formate	$C_4H_8O_2$	88.11	−92.9	149.8	81.1	366.1	538.00	40.20	309	0.309
Methyl acetate	$C_3H_6O_2$	74.08	−98.0	107.6	56.9	411.8	506.55	47.50	325	0.331
Ethyl acetate	$C_4H_8O_2$	88.11	−83.5	118.9	77.1	366.2	523.20	38.30	308	0.361
Propyl acetate	$C_5H_{10}O_2$	102.13	−95.0	109.7	101.5	336.1	549.75	33.60	296	0.390
Methyl propionate	$C_4H_8O_2$	88.11	−87.6	114.6	79.5	368.4	530.60	40.04	312	0.347
Ethyl propionate	$C_5H_{10}O_2$	102.13	−73.9	120.4	99.0	333.8	546.05	33.62	296	0.389
Propyl propionate	$C_6H_{12}O_2$	116.16	−75.9	129.1	122.5	315.1	568.60	30.60	299	0.449
Methyl butyrate	$C_5H_{10}O_2$	102.13	−85.8	112.6	102.7	336.5	554.50	34.73	300	0.378
Ethyl butyrate	$C_6H_{12}O_2$	116.16	−98.1	107.6	121.4	310.9	571.00	29.50	288	0.401
Methyl benzoate	C_8H_8O2	136.15	−12.4	71.5	199.4	323.5	693.05	35.90	312	0.415
Ethyl benzoate	$C_9H_{10}O_2$	150.18	−34.8	94.6	213.3	300.3	698.00	31.80	307	0.477
Methyl salicylate	$C_8H_8O_3$	152.15	−8.0	117.0	220.6	313.7	709.00	40.90	371	0.581
Amines										
Methyl amine	CH_5N	31.06	−93.5	197.5	−6.4	843.4	430.05	74.60	202	0.282
Ethyl amine	C_2H_7N	45.09	−81.0	207.4	16.8	608.8	456.15	56.20	218	0.285
Propyl amine	C_3H_9N	59.11	−83.0	256.4	47.6	510.4	496.95	47.40	227	0.280
n-Butyl amine	$C_6H_{15}N$	73.14	−49.1	202.4	77.5	442.0	531.95	42.00	236	0.329
Dimethyl amine	C_2H_7N	45.09	−92.3	131.8	7.0	590.0	437.25	53.40	250	0.298

D3.1. Table 1. (continued)

Substance	Formula	Molecular weight g/mol	Melting temperature °C	Enthalpy of fusion J/g	Boiling point at 1.013 bar °C	Enthalpy of vaporization at 1.013 bar J/g	Critical temperature K	Critical pressure bar	Critical density kg/m³	Acentric factor
Trimethyl amine	C_3H_9N	59.11	−117.1	110.7	3.1	391.1	433.25	41.02	233	0.206
Diethyl amine	$C_6H_{15}N$	73.14	−49.9	155.9	55.6	397.2	496.65	37.10	243	0.301
Triethyl amine	C6H15N	101.19	−114.8	84.2	88.8	304.8	535.15	30.40	260	0.318
Piperidine	$C_5H_{11}N$	85.15	−10.6	134.1	106.4	394.0	594.00	46.51	277	0.243
Pyridine	C_6H_7N	79.10	−41.7	104.7	115.2	447.6	620.00	56.30	311	0.239
Aniline	C6H7N	93.13	−6.0	113.2	183.9	479.5	699.05	53.10	345	0.378
N-methyl aniline	C_7H_9N	107.16	−57.1	88.8	195.6	423.2	701.50	52.00	287	0.475
N,N-dimethyl aniline	$C_8H_{11}N$	121.18	2.5	95.4	193.4	352.4	687.20	36.30	261	0.402
N,N-diethyl aniline	$C_{10}H_{15}N$	149.24	−38.1	56.9	216.1	304.4	702.00	28.50	268	0.426
Phenylhydrazine	$C_6H_8N_2$	108.14	19.3	151.9	244.0	486.5	761.00	49.10	259	0.535
Diphenyl amine	$C_{12}H_{11}N$	169.23	53.0	110.5	302.4	323.7	817.00	31.80	314	0.530
Nitriles										
Acetonitrile	C_2H_3N	41.05	−43.9	198.9	81.4	778.7	545.55	48.30	237	0.334
Propionitrile	C_3H_5N	55.08	−92.9	91.3	97.7	572.2	564.40	41.80	241	0.324
Butyronitrile	C_4H_7N	69.11	−111.9	72.7	117.4	500.0	582.30	37.90	249	0.371
Benzonitrile	C_7H_5N	103.12	−12.8	105.5	190.8	403.6	699.35	42.15	329	0.367
Amides										
Formamide	CH_3NO	45.04	2.6	177.2	219.6	1136.0	771.00	78.00	276	0.412
Nitroderivates										
Nitromethane	CH_3NO_2	61.04	−28.6	159.0	101.2	571.4	588.20	63.10	353	0.347
Nitrobenzene	$C_6H_5NO_2$	123.11	5.8	94.2	210.7	359.7	719.05	44.00	353	0.443
o-Nitrotoluene	$C_7H_7NO_2$	137.14	−3.3	83.7	221.5	338.0	720.05	38.00	311	0.480
m-Nitrotoluene	$C_7H_7NO_2$	137.14	16.2	102.5	232.7	343.1	734.05	38.00	311	0.495
p-Nitrotoluene	$C_7H_7NO_2$	137.14	51.7	121.6	238.7	339.9	743.05	32.07	311	0.420

D3.1. Table 2. Density of saturated liquids in kg/m^3

Substance	Formula	Temperature (°C)									Equation (1)			
		−50	−25	0	20	50	100	150	200	250	*A*	*B*	*C*	*D*
Elements														
Xenon	Xe	2503.6	2256.2	1906.9							2097.8096	−117.2877	962.2241	−217.6634
Krypton	Kr										1612.0090	342.4370	130.7723	178.6945
Argon	Ar										895.4345	297.7907	−15.9601	119.8686
Air											410.6099	777.4610	−841.3265	495.5129
Nitrogen	N_2										470.9224	493.2507	−560.4689	389.6108
Oxygen	O_2										748.3728	396.2376	−416.2389	372.6904
Sulfur	S							1777.7	1752.9	1727.1	3728.2432	−5258.9909	5203.2088	−1927.9722
Fluorine	F_2										677.5368	1399.1215	−1526.3565	870.3285
Chlorine	Cl_2	1605.5	1537.6	1467.0	1407.8	1311.9	1113.0				908.9019	948.0463	−1353.2681	1093.5278
Bromine	Br_2			3187.2	3119.8	3015.5	2831.1	2628.5	2397.7	2113.1	1672.7965	449.5091	676.7593	15.3973
Iodine	I_2							3874.9	3729.9	3576.4	1995.2359	589.1905	627.3536	65.6236
Anorganic compounds														
Hydrogen fluoride	HF	1124.3	1063.6	1002.2	952.4	875.9	739.5	574.6			232.8396	1347.9901	−1296.9204	1091.0626
Hydrogen chloride	HCl	1090.6	1009.6	916.3	825.2						640.0181	462.1796	−180.0873	273.3275
Hydrogen bromide	HBr	2115.2	2006.9	1887.2	1779.5	1584.0					1716.6784	−697.6208	1545.2372	−534.0575
Hydrogen iodide	HI	2857.0	2752.5	2640.9	2545.3	2387.8	2061.5				2159.6727	−837.4455	1907.8899	−675.9615
Hydrogen cyanide	HCN			716.3	687.2	640.7	552.8	436.3			576.9982	−153.5039	576.1976	−153.0246
Water	H_2O			1000.0	998.0	988.0	958.0	917.0	865.0	799.0	1094.0233	−1813.2295	3863.9557	−2479.8130
Hydrogen sulfide	H_2S	931.0	884.3	833.0	787.4	706.2					454.1590	757.2956	−698.1045	404.4247
Ammonia	NH_3	701.9	671.5	638.7	610.4	562.8	456.7				531.7253	−31.5027	257.0928	−63.9457
Nitric oxide	NO										1496.5803	−1584.2431	2252.1437	−1031.3210
Nitrogen dioxide	NO_2			1496.5	1450.1	1372.9	1211.1	901.6			1690.6809	−1592.7803	2233.6217	−968.0655
Nitrous oxide	N_2O	1109.7	1018.2	907.0	785.1						954.7062	−399.5870	1000.6634	−350.0132
Dinitrogentetroxide	N_2O_4			1472.7	1443.5						276.2115	−44.5981	604.1720	−135.9384
Cyanogen	C_2N_2		958.2	915.2	876.9	810.7	653.2				1378.7351	−1668.4751	2299.1821	−1052.1005
Phosphorus trichloride	PCl_3	1702.5	1658.5	1613.1	1575.8	1517.7	1414.0	1298.3	1162.5	982.2	1077.6858	−98.8936	665.5992	−117.8757
Cyanogen chloride	ClCN			1221.9	1182.2	1117.0	987.0	794.2			1387.6330	−1242.5960	1899.5222	−814.8977
Silane	SiH_4	453.5	384.5								202.1021	310.6035	−45.2615	142.0821
Tetrachlorosilane	$SiCl_4$	1611.8	1566.7	1519.7	1480.4	1418.3	1303.4	1165.8	974.6		1212.2339	−448.0911	977.9054	−307.7212
Carbon monoxide	CO										571.9328	−67.0956	387.1443	−121.7294
Carbon dioxide	CO_2	1154.5	1054.3	927.4	773.5						897.8727	170.0410	169.0516	37.9218
Carbon suboxide	C_3O_2	1195.8	1148.1	1097.1	1053.6	982.4	839.4				1139.6512	−1261.4775	2221.6476	−959.2381

D3.1. Table 2. (continued)

Substance	Formula	Temperature (°C)									Equation (1)			
		−50	−25	0	20	50	100	150	200	250	*A*	*B*	*C*	*D*
Carbonyl sulfide	COS	1174.3	1118.4	1057.7	1004.2	910.3					614.6483	835.4859	−850.8364	540.4800
Phosgene	CCl_2O	1521.4	1471.5	1418.9	1374.4	1302.7	1163.2	967.3			1175.3830	−403.6009	832.6348	−231.8645
Carbon disulfide	CS_2	1366.5	1330.7	1293.9	1263.5	1216.4	1132.1	1037.7	925.7	770.0	731.6284	105.4039	368.2583	−27.6945
Sulfur dioxide	SO_2	1559.8	1499.3	1435.6	1381.6	1293.7	1115.8				1026.6061	287.4616	−59.1497	243.0818
Sulfur trioxide	SO_3				1925.6	1782.4	1536.2	1269.4	931.1		441.4331	1592.9448	−778.3064	1407.6855
Sulfuryl chloride	Cl_2SO_2	1806.7	1758.8	1709.4	1668.5	1604.5	1489.4	1358.8	1200.5	966.1	1181.0337	−220.5274	868.5840	−221.9166
Sulfur hexafluoride	SF_6	1851.6	1716.1	1558.5	1395.0						1159.8382	1894.1251	−3293.5522	2428.5215
Organic compounds containing sulfur														
Methyl mercaptan	CH_4S	956.4	926.3	894.6	868.1	825.6	744.9	639.9			704.5697	−263.8878	591.8503	−181.3799
Ethyl mercaptan	C_2H_6S	915.7	889.3	861.9	838.9	802.6	735.2	653.5	534.8		691.9049	−266.2214	555.0990	−164.0295
Dimethyl sulfide	C_2H_6S	921.0	896.3	870.3	848.5	813.8	749.3	671.2	559.9		761.5375	−501.7612	869.4948	−333.3843
Diethyl sulfide	$C_4H_{10}S$	899.9	878.1	855.5	836.7	807.4	754.6	694.7	623.0	523.6	681.7218	−323.6418	640.5198	−212.6743
Thiophene	C_4H_4S		1115.5	1087.6	1064.7	1029.1	965.9	896.1	815.7	714.2	669.4387	34.8407	278.2567	−4.5806
Halogenated hydrocarbons														
Fluoromethane (R41)	CH_3F	818.4	755.0	678.8	599.2						579.2311	238.0353	7.7800	65.3812
Difluoromethane (R32)	CH_2F_2	1208.7	1135.8	1054.9	980.9	839.4					895.2753	224.1922	−50.9228	229.6600
Trifluoromethane (R23)	CHF_3	1307.4	1188.8	1031.1	808.2						640.3526	2164.8814	−3066.7802	1825.7135
Tetrafluoromethane (R14)	CF_4	930.7									1095.6241	429.5476	−317.3820	397.1853
Methyl chloride	CH_3Cl	1051.8	1008.6	962.6	923.3	858.4	722.0				811.5515	−235.2020	591.6820	−153.4405
Methylene chloride	CH_2Cl_2	1451.9	1408.7	1363.9	1326.8	1268.6	1162.4	1037.2	867.4		937.7851	96.8605	196.4483	106.8482
Chloroform	$CHCl_3$	1613.5	1571.7	1528.2	1492.2	1435.6	1332.8	1214.1	1065.8	819.4	1175.1441	−347.5847	842.3866	−239.1385
Carbon tetrachloride	CCl_4			1629.5	1593.3	1536.9	1435.9	1322.4	1186.8	997.6	1168.4410	−175.3077	535.7568	−28.0071
Bromomethane	CH_3Br	1857.1	1795.2	1730.5	1676.2	1589.8	1425.3	1208.8			1295.9529	−43.9173	439.6850	35.7205
Dibromomethane	CH_2Br_2	2663.5	2604.8	2544.3	2494.6	2417.6	2281.2	2131.8	1963.3	1762.6	1922.8847	−620.7007	1443.7506	−392.2980
Tribromomethane	$CHBr_3$				2889.3	2811.7	2677.1	2534.4	2381.4	2213.8	1813.5394	−117.4543	1179.3409	−192.4309
Tetrabromomethane	CBr_4						2966.4	2821.7	2668.8	2504.7	1925.6988	207.2291	370.8863	404.8231
Chlorodifluoromethane (R22)	$CHClF_2$	1435.3	1361.3	1281.2	1210.1	1083.1					904.1321	874.1686	−1176.1342	881.0060
Dichlorofluoromethane (R21)	$CHCl_2F$	1536.1	1483.2	1427.5	1380.5	1304.7	1157.1	946.9			1070.5872	−98.6131	523.2526	−85.7030
Chlorotrifluoromethane (R13)	$CClF_3$	1393.0	1271.2	1116.7	922.9						1180.7265	−216.9828	745.9367	−183.8510
Dichlorodifluoromethane (R12)	CCl_2F_2	1544.9	1472.7	1395.4	1328.3	1213.0	903.1				914.8406	994.9276	−1324.3128	961.0344
Trichlorofluoromethane (R11)	CCl_3F	1646.4	1591.1	1534.3	1487.3	1413.4	1275.1	1095.0			851.6332	1187.6894	−1625.7708	1135.7392
Ethyl fluoride (R161)	C_2H_5F	835.4	798.6	757.8	721.4	656.3	420.3				871.5416	−639.9577	872.5932	−320.7747
Ethyl chloride	C_2H_5Cl	992.5	959.8	925.3	896.1	849.3	759.2	637.4			856.3593	−570.9783	973.9418	−348.5034

Ethyl bromide	C_2H_5Br	1598.9	1550.4	1500.0	1458.1	1392.2	1271.2	1127.1	926.4		1073.9100	−116.4739	607.8587	−92.9976
1,1-Dichloroethane	$C_2H_4Cl_2$	1277.7	1242.6	1206.2	1175.9	1128.4	1041.7	940.7	810.5		885.9945	−205.7961	614.0614	−155.3254
1,2-Dichloroethane	$C_2H_4Cl_2$		1317.1	1282.4	1253.7	1209.0	1129.1	1039.6	934.1	793.0	822.5207	−75.2915	548.0378	−126.6480
1,2-Dibromoethane	$C_2H_4Br_2$				2175.0	2115.7	2011.9	1900.3	1777.7	1638.1	1450.4550	59.2274	351.5599	106.9717
1,1,1-Trifluoroethane (R143a)	$C_2H_3F_3$	1174.5	1103.5	1023.8	950.2	803.5					889.8086	159.4135	−27.5628	218.1093
1,1,1-Trichloroethane	$C_2H_3Cl_3$		1408.1	1369.8	1338.1	1288.4	1198.9	1096.9	972.9	787.9	966.6160	−230.0350	721.5753	−197.3209
1,1,2,2-Tetrachloroethane	$C_2H_2Cl_4$		1662.9	1626.3	1596.2	1549.9	1468.8	1381.5	1285.7	1176.8	1072.7673	−212.8525	808.8989	−195.6070
Pentachloroethane	C_2HCl_5		1742.5	1709.4	1681.8	1638.7	1561.9	1478.1	1386.3	1284.0	2495.1281	−4923.0789	6727.3035	−2845.4099
Hexachloroethane	C_2Cl_6								1619.7	1506.3	1430.9034	−692.7360	1783.3601	−734.5438
1,1,2,2-Tetrachlorodifluoroethane	$C_2Cl_4F_2$					1595.1	1487.3	1364.7	1216.7	1004.3	1175.4506	−180.3605	754.7753	−196.5778
1,1,2-Trichlorotrifluoroethan	$C_2Cl_3F_3$		1677.7	1622.0	1575.8	1503.1	1368.5	1201.9	924.6		1218.9337	135.4996	−143.7455	397.6751
1,2-Dichlorotetrafluoroethane	$C_2Cl_2F_4$	1661.5	1597.8	1529.4	1470.5	1373.1	1168.4				1357.5613	−783.4204	1599.8675	−650.4350
1-Chloropropane	C_3H_7Cl	971.9	944.1	915.1	890.9	852.7	782.1	697.4	577.9		731.5526	−294.7994	610.0420	−179.1843
1-Chlorobutane	C_4H_9Cl	960.0	934.4	908.1	886.4	852.4	791.0	720.2	631.7		364.8430	899.0805	−876.2568	472.1917
1-Chloropentane	$C_5H_{11}Cl$	946.7	924.3	901.2	882.2	852.5	799.4	740.0	669.8	576.5	655.9881	−103.0953	303.1006	−33.1451
Chlorotrifluoroethene	C_2ClF_3	1539.5	1459.1	1372.2	1296.3	1166.0					1045.3953	−51.8354	734.1349	−161.2374
Vinyl chloride	C_2H_3Cl	1020.4	983.8	944.8	911.5	857.0	746.4				845.5168	−410.8391	753.8048	−252.5094
1,1-Dichloroethene	$C_2H_2Cl_2$	1332.2	1292.3	1250.5	1215.4	1159.3	1053.3	919.2			1069.3566	−480.9307	903.7241	−294.1212
Trichloroethene	C_2HCl_3	1573.0	1535.3	1496.3	1464.1	1413.9	1324.2	1223.9	1106.9	955.9	1044.2371	−345.2637	975.1438	−317.8707
Tetrachloroethene	C_2Cl_4			1652.0	1621.0	1573.4	1489.9	1399.9	1300.4	1185.7	706.7100	340.6747	313.2121	−0.4034
Fluorobenzene	C_6H_5F		1077.0	1048.5	1025.2	989.1	925.2	854.0	769.7	653.4	714.7826	136.3923	−139.1048	267.2267
Chlorobenzene	C_6H_5Cl		1150.6	1125.8	1105.6	1074.3	1019.6	960.3	894.7	818.5	780.6202	−22.5318	178.8073	71.8433
Bromobenzene	C_6H_5Br		1548.7	1518.4	1493.6	1455.3	1388.3	1316.2	1237.3	1148.7	1089.0319	−346.8409	823.6222	−233.4489
Iodobenzene	C_6H_5I		1892.9	1858.3	1830.2	1787.1	1712.5	1633.7	1549.3	1457.4	1226.0761	−102.2072	516.6255	−13.8056
m-Chlorotoluene	C_7H_7Cl			1091.3	1072.2	1042.9	992.1	938.0	879.3	813.5	768.5321	−122.6643	283.8313	52.6685
Benzyl chloride	C_7H_7Cl		1142.6	1119.9	1101.3	1072.8	1023.1	970.1	912.7	849.0	691.0301	23.2005	325.7146	−44.8929
***n*-Alkanes**														
Methane	CH_4										267.8594	129.3958	−73.6070	69.9714
Ethane	C_2H_6	491.5	451.3	400.5							339.4205	278.1378	−326.5550	246.5842
Propane	C_3H_8	589.8	560.3	528.3	500.0	449.2					373.2481	324.1771	−431.6048	327.5258
n-Butane	C_4H_{10}	652.0	626.9	600.6	578.4	542.1	467.3				418.6986	246.8434	−317.6272	274.8875
n-Pentane	C_5H_{12}	691.0	668.3	644.9	625.6	595.0	537.4	460.4			331.1104	681.0817	−965.3279	602.3613
n-Hexane	C_6H_{14}	721.8	699.9	677.6	659.4	631.1	580.3	520.8	437.7		537.3940	87.8728	−283.3888	344.5049
n-Heptane	C_7H_{16}	742.1	721.4	700.6	683.7	657.9	612.5	561.2	496.3		308.4582	1071.6860	−1664.6321	990.2540
n-Octane	C_8H_{18}	758.0	738.2	718.3	702.3	677.8	635.3	588.6	533.4	457.1	314.7545	1031.5341	−1576.7740	940.0026
n-Nonane	C_9H_{20}	772.4	753.2	733.9	718.2	694.4	653.4	609.5	560.1	499.2	438.9742	485.2660	−813.4139	597.9116

D3.1. Table 2. (continued)

Substance	Formula	Temperature (°C)									Equation (1)			
		−50	−25	0	20	50	100	150	200	250	*A*	*B*	*C*	*D*
n-Decane	$C_{10}H_{22}$		764.9	745.8	730.4	707.1	667.4	625.4	579.1	524.3	309.6055	987.2944	−1482.3904	909.4231
n-Undecane	$C_{11}H_{24}$		771.4	754.3	740.2	718.6	680.6	639.6	594.4	542.6	507.1171	−85.9952	339.0114	−73.5121
n-Dodecane	$C_{12}H_{26}$			761.9	748.3	727.4	690.9	651.7	608.6	560.0	444.4040	138.4886	69.0787	37.5477
n-Tridecane	$C_{13}H_{28}$			771.2	757.2	735.7	698.4	658.7	615.8	568.4	448.8395	22.4550	270.4767	−35.9422
n-Tetradecane	$C_{14}H_{30}$				762.8	742.3	706.6	668.9	628.4	584.0	463.1763	−2.7765	279.4555	−36.6553
n-Pentadecane	$C_{15}H_{32}$				767.9	747.8	712.9	676.0	636.7	593.8	455.5302	11.7043	271.6956	−32.9927
n-Hexadecane	$C_{16}H_{34}$				772.6	753.0	719.0	683.2	645.0	603.6	452.8468	−20.7559	361.8764	−90.6718
n-Heptadecane	$C_{17}H_{36}$					757.2	723.9	688.9	651.8	611.9	447.6449	26.3796	258.9645	−26.2511
n-Octadecane	$C_{18}H_{38}$					759.4	727.5	693.7	657.8	619.0	463.0348	−70.7347	461.9766	−157.7468
n-Nonadecane	$C_{19}H_{40}$					765.4	732.9	698.8	662.9	624.5	444.3944	16.7270	294.2676	−43.2837
n-Eicosane	$C_{20}H_{42}$					768.7	736.3	702.6	667.2	629.6	432.7631	133.9129	81.0102	76.9690
Isoalkanes														
Isobutane	C_4H_{10}	634.5	608.3	580.5	556.7	517.3	429.8				383.6237	363.6942	−483.9167	353.6428
2-Methyl butane	C_5H_{12}	686.9	663.6	639.5	619.6	588.0	527.8	444.4			361.5111	560.1453	−819.7357	546.2874
2,2-Dimethyl propane	C_5H_{12}			611.1	590.0	555.4	484.3	360.6			399.8287	153.5783	29.4362	2.5978
2-Methyl pentane	C_6H_{14}	715.3	693.4	671.1	652.8	624.5	573.0	510.5			341.4133	769.6707	−1184.6190	747.5074
3-Methyl pentane	C_6H_{14}	722.8	703.0	682.3	665.1	637.7	586.9	525.5	438.2		573.2071	−229.0097	414.0510	−118.6548
2,2-Dimethyl butane	C_6H_{14}	710.4	689.3	667.3	648.9	619.8	565.2	497.6			486.0676	−45.2379	223.2189	−32.0169
2,3-Dimethyl butane	C_6H_{14}	721.0	699.8	678.3	660.6	633.1	582.6	520.3	422.9		254.1215	1135.4205	−1652.2629	932.1970
Olefins														
Ethylene	C_2H_4	480.6	426.7								364.3614	211.7762	−203.5475	188.4411
Propylene	C_3H_6	611.6	579.2	544.1	512.9	456.3					369.7127	440.5724	−608.9598	438.0705
1-Butene	C_4H_8	673.9	646.3	617.7	593.7	554.8	473.7				375.1257	531.6721	−821.5718	584.8143
1-Pentene	C_5H_{10}	711.9	687.8	662.5	641.4	607.7	543.6	459.0			498.6016	−53.1963	229.8900	−12.1005
1-Hexene	C_6H_{12}	737.9	716.0	693.1	674.1	644.2	589.1	523.4	432.1		510.1814	−116.4131	367.6914	−90.9801
1-Heptene	C_7H_{14}	755.9	736.1	715.7	698.7	672.1	623.8	568.4	499.8	388.8	532.8059	−176.2433	442.2244	−133.5518
1-Octene	C_8H_{16}	767.8	749.6	730.8	715.2	690.8	647.0	597.8	540.3	464.9	657.1207	−575.9768	946.0894	−359.8622
Propadiene	C_3H_4	683.0	651.2	617.0	587.3	537.2	419.7				502.0141	−158.5711	487.7855	−166.4310
1,2-Butadiene	C_4H_6	731.3	704.1	675.6	651.6	613.2	539.6	438.3			470.2546	−43.2316	338.1675	−71.5782
1,3-Butadiene	C_4H_6	701.7	674.9	646.4	621.9	581.9	499.5				516.9714	−153.0729	432.6257	−146.9736
1,2-Pentadiene	C_5H_8	758.1	735.6	712.2	692.6	661.8	604.8	536.3	438.0		526.0862	−102.9607	338.7486	−76.0606
trans-1,3-Pentadiene	C_5H_8	741.6	719.1	695.6	676.0	645.0	587.6	518.8			459.5187	−71.6617	434.8700	−156.7892

1,4-Pentadiene	C_5H_8	746.1	716.2	685.4	660.0	620.2	547.7	460.8			372.0249	140.8959	213.7531	36.0847
2,3-Pentadiene	C_5H_8	761.7	738.8	715.0	695.1	663.5	604.9	533.7	428.2		601.3221	−231.5055	468.4758	−132.5235
Acetylene and derivatives														
Acetylene	C_2H_2	567.0	521.0	464.7	401.2						522.9178	−240.7307	475.3756	−144.5991
Propyne	C_3H_4	704.7	674.5	642.2	614.2	567.4	462.0				534.1335	−75.2467	252.8497	−31.8209
2-Butyne	C_4H_6		737.9	712.4	691.0	657.0	592.5	509.1	268.3		586.6064	−155.7016	326.9444	−53.3841
1-Butyne	C_4H_6	732.3	705.7	677.7	654.0	615.6	539.8	422.6			503.9674	−90.2536	337.8005	−80.7264
Naphthenes														
Cyclopropane	C_3H_6	700.7	670.3	637.7	609.4	561.9	453.1				509.4024	−123.2450	381.1163	−107.6052
Cyclobutane	C_4H_8	757.3	735.9	713.3	694.0	662.8	601.4	514.7			710.5761	−476.8125	625.0484	−214.8659
Cyclopentane	C_5H_{10}	810.3	787.9	765.2	746.5	717.6	665.2	602.6	513.3		450.0150	692.7447	−1131.7809	724.4630
Methyl cyclopentane	C_6H_{12}	810.6	789.4	767.4	749.2	720.5	668.5	608.5	533.1		586.1851	−206.8126	465.6426	−133.2315
Ethyl cyclopentane	C_7H_{14}	821.9	802.8	783.0	766.7	741.3	695.7	644.5	584.1	504.2	591.7101	−161.9096	367.1965	−85.7409
Propyl cyclopentane	C_8H_{16}	829.4	811.2	792.5	777.0	753.0	710.2	662.9	608.9	542.7	599.4701	−246.4926	524.2674	−166.6909
Butyl cyclopentane	C_9H_{18}	836.4	818.5	800.2	785.2	761.9	721.0	676.4	626.5	568.1	549.8797	−94.1561	328.1468	−64.8716
Pentyl cyclopentane	$C_{10}H_{20}$		825.6	806.5	791.1	767.5	726.7	683.3	635.8	581.5	21.3865	1705.0458	−1919.0378	944.3151
Hexyl cyclopentane	$C_{11}H_{22}$			811.3	796.4	773.8	734.6	693.2	648.4	598.5	496.4226	118.3606	−44.5909	170.4166
Cyclohexane	C_6H_{12}				778.8	749.9	699.5	643.8	577.0	478.9	373.9221	848.7461	−1261.1653	815.8631
Methyl cyclohexane	C_7H_{14}	827.2	807.2	786.7	769.8	743.5	696.6	644.4	583.6	504.8	541.8145	−87.5463	328.4257	−63.2825
Ethyl cyclohexane	C_8H_{16}	840.1	821.9	803.3	788.0	764.3	722.3	676.4	624.5	562.4	577.6869	−104.1979	295.7576	−43.8897
Propyl cyclohexane	C_9H_{18}	845.3	827.3	809.0	794.0	770.9	730.4	686.9	638.9	584.1	496.0892	31.4274	199.9535	−0.0783
Butyl cyclohexane	$C_{10}H_{20}$	848.1	831.1	813.7	799.5	777.6	739.4	698.5	654.2	604.6	506.3817	−49.6664	336.9189	−68.8765
Pentyl cyclohexane	$C_{11}H_{22}$			811.2	796.5	773.8	734.8	693.4	648.6	598.5	279.5792	762.8400	−746.6601	440.9901
Hexyl cyclohexane	$C_{12}H_{24}$			821.2	807.1	785.6	748.3	708.8	666.4	620.1	593.6577	−303.4227	620.1121	−164.7850
Cyclopentene	C_5H_8	842.1	818.4	793.6	772.9	739.9	679.0	606.7	509.5		725.9817	−741.6349	1302.8902	−550.8221
Cyclohexene	C_6H_{10}	873.1	851.8	829.8	811.7	783.3	732.4	675.1	606.9	514.2	599.5856	−158.4142	433.0116	−115.8632
Aromatic compounds														
Benzene	C_6H_6				877.7	847.1	792.9	732.4	660.4	560.5	502.4341	531.5980	−663.9865	469.5949
Toluene	C_7H_8	931.9	909.1	886.0	867.4	839.0	789.7	736.5	676.0	600.3	439.5835	839.1558	−1234.8445	797.8741
Ethyl benzene	C_8H_{10}	927.5	906.1	884.6	867.2	840.7	795.0	746.4	692.8	629.6	570.2499	385.5562	−683.9919	559.6340
Propyl benzene	C_9H_{12}	920.6	899.9	879.3	862.8	838.0	796.2	752.6	705.4	650.5	374.7765	1406.9407	−2323.0960	1383.0818
Butyl benzene	$C_{10}H_{14}$	915.2	896.3	876.9	861.1	836.8	794.3	748.9	699.4	643.8	567.3503	−44.2239	325.9459	−48.9536
Pentyl benzene	$C_{11}H_{16}$	907.1	890.1	872.6	858.3	836.3	797.9	756.7	711.8	661.8	625.0808	−192.5173	472.6577	−129.2587
Hexyl benzene	$C_{12}H_{18}$	906.9	889.8	872.4	858.2	836.4	798.6	758.3	714.9	667.2	560.4851	−87.4540	385.4265	−85.5450
o-Xylene	C_8H_{10}		915.6	896.0	879.8	854.7	810.5	762.3	708.5	646.1	676.6371	−299.1691	624.5571	−201.7643
m-Xylene	C_8H_{10}		900.8	880.6	864.0	838.3	792.9	743.3	687.6	622.0	670.0403	−300.7884	613.6168	−189.3359

D3.1. Table 2. (continued)

Substance	Formula	Temperature (°C)									Equation (1)			
		−50	−25	0	20	50	100	150	200	250	*A*	*B*	*C*	*D*
p-Xylene	C_8H_{10}				860.6	835.0	789.6	739.9	684.0	618.1	660.6795	−279.7896	602.8083	−192.6478
1,2,3-Trimethyl benzene	C_9H_{12}		925.3	908.3	894.3	872.6	834.4	792.9	747.1	695.1	754.5071	−413.8427	666.3695	−223.9630
1,2,4-Trimethyl benzene	C_9H_{12}		911.6	892.2	876.4	852.0	809.4	763.6	713.1	655.6	578.6385	85.6763	66.0157	76.6911
1,3,5-Trimethyl benzene	C_9H_{12}		900.5	881.3	865.5	841.0	798.0	751.4	699.7	640.0	640.9570	−176.3320	437.2828	−109.0875
1,2,3,4-Tetramethyl benzene	$C_{10}H_{14}$			919.6	905.0	882.5	843.0	800.5	754.3	703.0	673.8483	−377.2864	846.4842	−333.8113
1,2,3,5-Tetramethyl benzene	$C_{10}H_{14}$			905.7	890.5	867.1	826.3	782.7	735.3	682.6	608.7104	−85.1256	355.8065	−66.4080
1,2,4,5-Tetramethyl benzene	$C_{10}H_{14}$						823.0	781.8	736.6	685.8	716.4977	−373.2590	668.4023	−225.6822
Pentamethyl benzene	$C_{11}H_{16}$				917.1	894.2	854.5	812.5	767.5	718.4	613.3655	−145.7886	514.0054	−142.3577
Hexamethyl benzene	$C_{12}H_{18}$								803.3	763.8	856.0941	−710.6638	1125.6113	−483.2720
Styrene	C_8H_8		944.7	923.2	905.5	878.3	830.6	779.2	722.7	658.1	596.1525	−108.0248	457.6070	−104.3199
Isopropyl benzene	C_9H_{12}	918.8	899.2	879.1	862.6	837.3	792.8	744.8	691.7	630.2	612.6486	−67.4355	255.7468	2.0865
Biphenyl	$C_{12}H_{10}$						969.4	929.7	888.7	845.5	−144.5769	3294.2798	−4370.6493	2181.5445
Diphenyl methane	$C_{13}H_{12}$					983.6	945.6	905.4	862.5	816.1	721.9528	−259.8678	651.0631	−218.7731
Triphenyl methane	$C_{19}H_{16}$						1011.7	976.3	939.4	900.7	658.1058	−42.5371	332.2151	−26.7722
Tetraphenyl methane	$C_{25}H_{20}$										858.8627	−205.4402	780.2431	−214.3411
Naphthalene	$C_{10}H_8$						963.6	922.0	877.5	829.2	827.8845	−650.9380	1177.1336	−454.2853
1-Methylnaphthalene	$C_{11}H_{10}$		1052.3	1034.7	1020.4	998.4	960.5	920.7	878.6	833.4	731.0545	−216.5763	499.7559	−106.6647
2-Methylnaphthalene	$C_{11}H_{10}$			1018.5	1004.1	982.2	944.5	905.1	863.4	818.8	812.2186	−440.4793	644.4363	−123.2879
1-Ethylnaphthalene	$C_{12}H_{12}$			1021.1	1007.7	987.3	952.0	914.9	875.4	833.0	768.0808	−208.0320	385.7996	−59.6192
2-Ethylnaphthalene	$C_{12}H_{12}$			1005.5	992.4	972.1	937.1	900.1	860.8	818.4	762.4014	−281.5464	517.9806	−131.1086
Alcohols														
Methanol	CH_4O	857.7	834.1	810.5	791.5	762.4	710.1	646.4	549.4		164.7611	2257.7678	−3545.6923	1929.7376
Ethanol	C_2H_6O	842.2	824.9	806.2	790.2	763.9	712.9	648.1	554.9		748.6170	−412.3622	776.4394	−436.6757
1-Propanol	C_3H_8O	860.7	841.5	821.3	804.5	777.9	729.1	671.6	597.9		816.2709	−549.2099	696.9841	−232.0820
1-Butanol	$C_4H_{10}O$	862.9	844.4	825.2	809.3	784.3	738.9	687.1	624.4	536.7	777.2534	−446.8420	578.8813	−172.9538
1-Pentanol	$C_5H_{12}O$	866.9	849.3	831.0	815.9	792.2	749.5	701.4	644.9	572.7	751.4379	−445.8311	657.1566	−231.1445
1-Hexanol	$C_6H_{14}O$		850.4	833.5	819.5	797.6	758.4	714.9	665.1	604.5	779.5145	−533.7565	743.6153	−264.3245
1-Heptanol	$C_7H_{16}O$		855.8	837.8	823.1	800.3	760.0	716.0	667.0	609.9	637.2821	−224.8073	464.7011	−131.7231
1-Octanol	$C_8H_{18}O$			841.1	826.8	804.6	765.4	722.9	676.0	622.6	635.0506	−325.7666	688.5827	−254.0193
Isopropanol	C_3H_8O	845.4	825.4	804.3	786.5	758.0	704.4	638.5	544.2		865.9165	−744.0943	975.9052	−381.1278
2-Methyl-1-propanol	$C_4H_{10}O$	854.8	836.9	817.9	801.9	776.4	729.1	673.7	605.3	503.1	934.7519	−1180.1957	1728.8821	−777.3781
3-Methyl-1-butanol	$C_5H_{12}O$	858.5	842.2	825.2	811.0	788.7	748.1	701.7	646.1	572.0	879.1766	−733.0487	895.9805	−330.6835
Ethylene glycol	$C_2H_6O_2$			1127.2	1113.5	1092.3	1054.7	1013.9	969.1	919.0	1305.5931	−1374.2561	1691.0501	−665.0358

1,3-Propylene glycol	$C_3H_8O_2$		1079.0	1064.4	1052.4	1033.9	1001.5	966.7	928.8	886.6	1122.4836	−875.9683	844.9680	−234.3532
Glycerol	$C_3H_8O_3$				1261.0	1241.6	1208.0	1172.3	1134.3	1093.5	1341.5932	−1168.2050	1429.7634	−527.7710
Cyclohexanol	$C_6H_{12}O$					925.4	880.1	831.0	776.9	715.2	691.7418	−231.6456	571.5227	−175.7843
Benzyl alcohol	C_7H_8O			1061.0	1046.0	1022.8	982.4	939.3	892.7	841.5	850.4338	−421.4897	717.9510	−227.4262
Phenols														
o-Cresol	C_7H_8O					1021.9	979.2	933.9	885.2	831.7	632.5598	−17.3349	263.1021	0.0173
m-Cresol	C_7H_8O				1033.7	1011.1	971.7	929.5	883.7	832.9	789.9775	−285.5601	515.7326	−142.1040
p-Cresol	C_7H_8O					1011.3	971.7	929.7	884.5	834.9	622.7984	36.9513	126.9550	56.8974
Phenol	C_6H_6O					1050.1	1005.6	958.3	907.3	851.1	572.3325	39.7056	345.4050	−72.2556
Carboxylic acids														
Formic acid	CH_2O_2				1220.1	1182.6	1115.5	1040.4	953.0	842.3	1181.5822	−735.7666	1040.1334	−334.6213
Acetic acid	$C_2H_4O_2$				1048.0	1016.2	959.9	897.7	826.2	736.6	925.3897	−312.7993	340.0633	29.7204
Propionic acid	$C_3H_6O_2$			1012.2	992.6	962.4	908.6	849.3	781.6	699.1	797.1701	−247.0129	471.4726	−96.1474
Butyric acid	$C_4H_8O_2$			974.4	956.9	929.8	882.2	830.4	772.3	702.9	863.4643	−339.3183	323.8065	40.4813
Valeric acid	$C_5H_{10}O_2$		969.7	949.7	933.3	907.6	862.0	812.2	756.4	691.7	783.8282	−574.7117	1043.4452	−417.5824
Caproic acid	$C_6H_{12}O_2$			937.3	922.8	900.1	860.0	816.3	767.6	712.0	864.3467	−628.7969	947.6116	−358.8242
Acetic anhydride	$C_4H_6O_3$	1162.4	1134.3	1105.4	1081.7	1045.1	980.4	910.0	831.3	738.6	682.0673	−119.7326	679.5899	−205.8780
Propionic anhydride	$C_6H_{10}O_3$		1058.0	1032.3	1011.1	978.5	921.3	859.4	791.0	712.3	634.5554	−111.1548	605.3432	−170.7870
Chloroacetic acid	$C_2H_3ClO_2$						1320.5	1250.1	1174.0	1089.7	997.2610	−242.9622	764.1551	−197.3080
Dichloroacetic acid	$C_2H_2Cl_2O_2$				1561.4	1515.8	1436.9	1353.7	1264.6	1167.5	835.2438	125.7524	573.8920	−58.3985
Trichloroacetic acid	$C_2HCl_3O_2$						1542.5	1461.3	1374.0	1277.8	1051.8830	−25.9784	525.2987	−32.4824
Ketones														
Ketene	C_2H_2O	793.4	753.2	709.1	669.9	600.5					622.1840	−165.9732	442.6230	−119.5770
Acetone	C_3H_6O	865.8	839.7	812.9	790.8	756.2	693.3	619.0	516.3		547.3820	208.7420	−203.7599	253.9936
Methyl ethyl ketone	C_4H_8O	877.4	852.5	826.7	805.3	771.9	711.7	643.1	558.8		560.7857	−90.7312	454.3929	−120.5211
Diethyl ketone	$C_5H_{10}O$		857.3	833.8	814.5	784.3	730.1	669.3	597.3	500.2	631.4702	−197.4050	514.5685	−146.1064
Dipropyl ketone	$C_7H_{14}O$		855.2	833.9	816.4	789.4	741.8	689.7	631.1	560.9	550.0551	−47.0791	332.7349	−55.1781
Acetophenone	C_8H_8O				1027.7	1002.3	958.2	911.4	860.9	805.7	729.4145	−204.6406	556.0093	−145.9565
Benzophenone	$C_{13}H_{10}O$					1083.3	1045.9	1007.0	966.4	923.5	782.3121	−159.9513	358.9665	−0.1287
Ethers														
Dimethyl ether	C_2H_6O	764.6	731.2	695.4	664.4	612.4	494.3				493.6395	92.1379	137.7856	5.8434
Diethyl ether	$C_4H_{10}O$	794.9	766.5	737.5	713.7	676.5	607.7	518.6			521.2805	257.7528	−489.2726	486.7458
Dipropyl ether	$C_6H_{14}O$	806.5	785.9	764.5	746.8	718.9	668.1	609.1	533.7		560.6008	−66.0979	231.3743	−25.4168
Methyl propyl ether	$C_4H_{10}O$	804.4	777.7	749.8	726.5	689.5	620.3	533.2			519.3865	−39.7274	321.5971	−58.9568
Ethyl propyl ether	$C_5H_{12}O$	798.7	774.9	750.0	729.3	696.7	636.5	564.3	461.2		556.9149	−128.7853	384.7507	−88.7772
Ethylene oxide	C_2H_4O	963.3	932.8	900.7	873.6	830.3	747.5	638.5			757.9994	−286.5638	583.1649	−177.0206
Furane	C_4H_4O	1027.4	996.9	964.9	938.1	895.4	815.3	715.8	557.5		874.7486	−463.4642	800.9808	−268.1611

D3.1. Table 2. (continued)

Substance	Formula	Temperature (°C)									Equation (1)			
		−50	−25	0	20	50	100	150	200	250	*A*	*B*	*C*	*D*
1,4-dioxane	$C_4H_8O_2$				1033.2	999.8	940.4	874.6	799.1	705.7	678.8964	−120.4207	544.3169	−167.1524
Aldehydes														
Formaldehyde	CH_2O	865.3	823.7	779.8	742.3	680.8	549.5				625.7638	5.7090	245.3425	43.9601
Acetaldehyde	C_2H_4O	866.9	837.4	806.5	780.6	739.4	661.2	558.6			588.8420	−39.6103	285.7658	−26.6228
Paraldehyde	$C_6H_{12}O_3$				993.9	959.1	898.2	831.9	756.5	662.3	560.5579	264.0982	−148.6559	262.2179
Furfural	$C_5H_4O_2$		1204.7	1179.9	1159.7	1128.5	1074.1	1016.0	952.7	882.1	747.7699	−99.6602	513.8809	−116.7313
Benzaldehyde	C_7H_6O	1103.7	1083.1	1062.1	1045.0	1018.7	973.0	924.3	871.7	813.7	696.5787	−30.8195	301.9063	−22.2959
Salicylaldehyde	$C_7H_6O_2$				1153.1	1127.9	1083.2	1034.6	980.7	919.5	1156.0689	−926.0141	1233.5363	−464.4392
Esters														
Methyl formate	$C_2H_4O_2$	1069.3	1036.8	1002.8	974.3	929.2	844.6	739.7			775.1812	−197.0272	529.3064	−138.9492
Ethyl formate	$C_3H_6O_2$	1005.1	976.6	946.8	922.1	882.9	810.8	725.0	607.9		765.9448	−360.7128	737.2408	−242.8289
Propyl formate	$C_4H_8O_2$	979.3	953.8	927.3	905.4	871.0	808.7	737.0	648.0		695.5638	−166.9122	452.1853	−110.8676
Methyl acetate	$C_3H_6O_2$	1019.0	989.7	959.4	934.1	894.2	820.7	732.9	610.5		735.8282	−133.1048	374.1594	−55.0194
Ethyl acetate	$C_4H_8O_2$	977.3	950.7	923.1	900.1	864.1	798.2	720.9			660.3752	8.8513	207.1680	1.5101
Propyl acetate	$C_5H_{10}O_2$	958.5	934.1	908.7	887.8	855.1	796.1	729.2	648.0	530.1	682.4676	−162.2018	432.6427	−97.3592
Methyl propionate	$C_4H_8O_2$	990.9	964.5	937.1	914.4	878.8	814.0	738.9	643.7		708.5713	−154.0179	420.6243	−90.1472
Ethyl propionate	$C_5H_{10}O_2$	960.6	935.8	910.1	888.8	855.5	795.4	726.9	643.4	518.9	693.9231	−209.9952	516.2012	−141.1864
Propyl propionate	$C_6H_{12}O_2$	948.9	925.7	901.7	881.9	851.1	796.1	734.7	662.7	568.3	632.5301	−108.1101	391.7953	−80.5204
Methyl butyrate	$C_5H_{10}O_2$	965.2	942.0	918.0	898.1	866.9	810.6	746.4	668.7	558.1	752.8912	−322.2388	595.9627	−181.6941
Ethyl butyrate	$C_6H_{12}O_2$	944.4	921.6	898.2	878.8	848.7	794.7	734.3	663.5	571.0	676.2305	−183.8280	454.1518	−110.2246
Methyl benzoate	$C_8H_8O_2$			1105.3	1087.7	1060.6	1012.8	961.5	905.6	843.4	884.1769	−486.5499	965.3906	−361.7121
Ethyl benzoate	$C_9H_{10}O_2$		1086.5	1064.6	1046.8	1019.4	971.8	921.2	866.7	806.8	733.0282	−164.2079	529.3259	−121.7958
Methyl salicylate	$C_8H_8O_3$			1198.6	1180.9	1153.7	1106.2	1055.5	1000.6	940.2	905.2883	−355.4925	695.0348	−203.3611
Amines														
Methyl amine	CH_5N	743.6	715.9	686.4	661.1	619.5	533.7				803.3522	−545.1488	695.6625	−211.9019
Ethyl amine	C_2H_7N	760.9	734.5	706.6	683.1	645.1	571.2	466.7			633.5210	−127.7781	267.0804	−30.4806
Propyl amine	C_3H_9N	784.1	761.9	738.6	719.1	687.9	629.5	557.5	448.6		743.8388	−508.9910	757.8672	−271.2439

n-Butyl amine	$C_6H_{15}N$		778.5	756.8	738.8	710.3	657.9	596.3	516.8		536.8539	99.8023	86.4297	−0.0872
Dimethyl amine	C_2H_7N	727.2	703.3	677.7	655.9	620.0	547.1	425.2			669.2053	−452.4323	686.3039	−257.5126
Trimethyl amine	C_3H_9N	712.5	686.2	658.3	634.5	595.7	517.1				595.8605	−277.4351	522.6859	−170.4614
Diethyl amine	$C_6H_{15}N$		750.1	726.5	706.9	675.7	617.5	546.4	440.0		587.2056	−154.6153	354.6121	−84.9548
Triethyl amine	$C_6H_{15}N$	787.9	767.4	746.1	728.4	700.8	650.6	592.9	520.8		527.4070	−73.2089	292.3398	−56.6226
Piperidine	$C_5H_{11}N$			879.5	862.2	835.2	787.0	733.4	671.8	596.1	715.9263	−375.9305	715.6680	−252.9803
Pyridine	C_6H_7N	1051.2	1027.6	1003.3	983.4	952.5	898.1	838.9	773.0	696.0	690.1939	−203.6045	639.6026	−197.2534
Aniline	C_6H_7N			1036.0	1020.1	995.7	953.4	908.4	859.9	806.4	658.6221	−14.6944	242.0930	0.7157
N-methyl aniline	C_7H_9N	1037.2	1019.4	1001.2	986.3	963.3	923.0	879.7	832.7	780.5	864.2138	−497.9953	785.4701	−259.5471
N,*N*-dimethyl aniline	$C_8H_{11}N$				954.9	932.4	892.6	849.7	802.5	749.4	947.8512	−688.2637	967.8765	−348.1476
N,*N*-diethyl aniline	$C_{10}H_{15}N$		967.5	949.2	934.3	911.4	871.5	829.0	783.2	732.6	741.1539	−219.0978	404.9792	−62.8648
Phenylhydrazine	$C_6H_8N_2$				1096.2	1072.3	1030.5	985.7	937.4	884.7	1059.0386	−909.0434	1516.7029	−633.0667
Diphenyl amine	$C_{12}H_{11}N$						1023.9	984.5	942.9	898.8	741.2921	−188.1027	546.9112	−136.8931
Nitriles														
Acetonitrile	C_2H_3N		828.1	802.7	781.8	749.2	690.9	625.2	546.2	430.3	565.3431	−36.8917	312.7935	−27.5047
Propionitrile	C_3H_5N	846.0	823.8	801.0	782.2	752.9	700.5	641.9	573.1	481.8	593.9656	−143.8921	437.8666	−106.4610
Butyronitrile	C_4H_7N	851.5	830.4	808.7	790.8	763.1	713.8	659.4	596.8	518.5	574.0426	−109.8505	395.2330	−87.6033
Benzonitrile	C_7H_5N			1021.7	1005.0	979.3	934.8	887.7	837.1	781.6	609.1142	−3.9828	337.9801	−43.7599
Amides														
Formamide	CH_3NO				1132.8	1107.4	1063.3	1016.7	967.1	913.7	965.0375	−531.0847	957.2988	−315.4745
Nitroderivates														
Nitromethane	CH_3NO_2		1191.9	1159.8	1133.4	1092.8	1021.5	943.5	854.9	745.7	675.9080	381.0708	−203.4493	278.9247
Nitrobenzene	$C_6H_5NO_2$				1203.2	1173.7	1122.4	1067.9	1009.5	945.7	902.6390	−421.4692	914.1481	−291.7604
o-Nitrotoluene	$C_7H_7NO_2$			1180.4	1162.6	1134.9	1085.5	1031.6	972.6	907.3	1144.0002	−1639.6486	2962.1530	−1405.4992
m-Nitrotoluene	$C_7H_7NO_2$				1158.1	1130.8	1083.5	1033.5	980.2	922.2	921.6086	−241.0428	446.4670	−40.2498
p-Nitrotoluene	$C_7H_7NO_2$						1080.0	1031.0	978.7	922.1	878.9128	−151.3942	353.3063	−0.4124

D3.1. Table 3. Boiling temperatures at different pressures in °C

Substance	Formula	Vapor pressure in mbar										Equation (7)			
		5	10	50	100	250	500	1,000	2,000	5,000	10,000	*A*	*B*	*C*	*D*
Elements															
xenon	Xe							−108.3	−95.3	−74.2	−54.5	−6.00659	1.37325	−0.77703	−1.22529
Krypton	Kr							−153.6	−144.0	−128.5	−114.0	−5.98396	1.34334	−0.66521	−1.30012
Argon	Ar							−186.0	−178.9	−167.4	−156.6	−5.92801	1.21982	−0.53967	−1.52312
Neon	Ne						−248.2	−246.1	−243.6	−239.5	−235.6	−5.74238	1.08860	−0.05896	−1.19851
Helium	He			−271.0	−270.7	−270.1	−269.6	−268.9	−268.1			−4.06856	1.04379	1.11594	0.08835
Air						−204.8	−200.0	−194.4	−187.8	−177.0	−167.0	−5.35069	−0.21537	0.93623	−3.02641
Hydrogen	H_2				−258.5	−256.6	−254.9	−252.8	−250.3	−246.0	−241.8	−4.83622	0.94200	0.76650	−0.47071
Nitrogen	N_2					−206.0	−201.3	−195.9	−189.5	−179.2	−169.4	−6.12498	1.26499	−0.76765	−1.78173
Oxygen	O_2	−214.6	−211.9	−204.4	−200.5	−194.5	−189.2	−183.1	−175.9	−164.3	−153.5	−6.05148	1.23506	−0.62883	−1.61288
Sulfur	S	211.7	232.1	287.9	316.6	360.3	398.8	443.3	495.5	579.7	657.9	−15.68872	19.60608	−12.56687	1.67046
Fluorine	F_2	−217.2	−214.7	−207.8	−204.2	−198.7	−193.8	−188.2	−181.7	−171.2	−161.4	−6.27045	1.53939	−1.25605	−1.27235
Chlorine	Cl_2			−85.8	−76.2	−61.7	−48.9	−34.3	−17.4	9.6	34.5	−6.43911	1.48278	−1.21184	−2.02926
Bromine	Br_2				2.4	21.9	38.9	58.3	80.8	116.5	149.1	−6.76024	1.50339	−0.64097	−3.62166
Iodine	I_2					134.5	157.5	183.8	214.3	262.8	307.5	−6.98158	2.33987	−1.48090	−3.73441
Anorganic compounds															
Hydrogen fluoride	HF		−75.2	−48.4	−35.2	−15.7	0.8	19.2	39.7	71.0	98.3	−9.73172	5.07747	−2.98832	5.51671
Hydrogen chloride	HCl					−106.5	−96.6	−85.3	−72.1	−51.2	−32.1	−6.63222	1.06066	0.05415	−4.45907
Hydrogen bromide	HBr						−79.4	−66.8	−52.4	−29.6	−8.7	−5.92115	0.77533	−1.67956	1.00212
Hydrogen iodide	HI						−50.5	−35.7	−18.6	8.8	34.0	−5.92123	0.95693	−1.04474	−1.03336
Hydrogen cyanide	HCN					−7.4	8.0	25.3	45.1	75.7	103.0	−9.77338	5.29679	−4.36059	1.58018
Water	H_2O		7.0	32.9	45.8	65.0	81.3	99.6	120.2	151.8	179.9	−7.86975	1.90561	−2.30891	−2.06472
Hydrogen sulfide	H_2S					−84.4	−73.3	−60.6	−45.9	−22.5	−1.1	−6.50342	1.52011	−1.36969	−1.96704
Ammonia	NH_3				−71.2	−58.0	−46.5	−33.6	−18.8	4.1	24.9	−7.30274	1.64638	−2.01606	−1.96884
Nitric oxide	NO						−157.6	−151.9	−145.4	−135.3	−126.2	−8.38772	0.85755	−3.11447	−8.98765
Nitrogen dioxide	NO_2					−6.2	6.8	20.9	36.4	59.3	78.7	−11.33898	2.37620	0.67820	−2.53997
Nitrous oxide	N_2O							−88.7	−76.2	−56.4	−38.2	−6.79599	1.59751	−1.85163	−2.29494
Dinitrogentetroxide	N_2O_4					−6.1	6.8	21.0	36.6	59.6	79.1	−11.71738	3.10196	0.59704	−5.33648
Cyanogen	C_2N_2							−21.4	−5.1	20.7	44.3	−7.51492	1.94916	−2.36750	−4.23472
Phosphorus trichloride	PCl_3	−35.6	−25.9	0.7	14.4	35.2	53.5	74.6	99.2	138.4	174.6	−8.83133	5.61883	−4.80318	−1.25347
Cyanogen chloride	ClCN						−3.9	12.5	30.9	59.3	84.9	−7.49333	1.78753	−4.04253	8.50574
Silane	SiH_4	−167.8	−163.1	−150.2	−143.4	−132.8	−123.3	−112.3	−99.2	−78.2	−58.9	−7.30552	2.71060	−0.09783	−4.71464
Tetrachlorosilane	$SiCl_4$	−47.9	−38.7	−13.3	−0.3	19.5	36.8	56.8	79.9	116.8	151.0	−6.60174	0.34409	−1.09066	−3.15050

Carbon monoxide	CO					−202.1	−197.2	−191.6	−185.0	−174.3	−164.2	−6.19574	1.32502	−0.95226	−1.98513
Carbon dioxide	CO_2										−40.1	−7.02916	1.53937	−2.28330	−2.34853
Carbon suboxide	C_3O_2	−82.8	−74.8	−53.1	−41.9	−25.1	−10.5	6.0	24.9	53.8	78.8	−13.34201	11.51312	−6.91741	−0.29406
Carbonyl sulfide	COS	−123.0	−116.6	−99.1	−90.1	−76.4	−64.3	−50.5	−34.3	−8.6	15.3	−6.51272	1.55373	−1.33074	−2.08761
Phosgene	CCl_2O	−80.1	−72.4	−51.3	−40.4	−23.9	−9.3	7.4	26.7	57.5	85.7	−6.82435	0.89402	−0.50281	−4.67598
Carbon disulfide	CS_2	−57.9	−48.8	−23.8	−10.9	8.7	26.0	45.8	68.8	105.2	138.5	−6.58802	1.03676	0.15875	−3.44094
Sulfur dioxide	SO_2			−61.9	−52.1	−37.5	−24.8	−10.3	6.3	32.5	56.3	−7.27858	1.72871	−2.37473	−2.70464
Sulfur trioxide	SO_3					19.6	31.1	44.2	59.5	84.1	107.3	−8.74717	6.32513	−13.93665	−9.67972
Sulfuryl chloride	Cl_2SO_2	−36.5	−27.0	−1.3	11.9	31.7	49.1	69.0	92.1	129.2	163.9	−6.32835	0.89929	−2.88437	−1.24330
Sulfur hexafluoride	SF_6									−29.8	−8.0	−7.08034	1.65103	−1.96365	−0.25060
Organic compounds containing sulfur															
Methyl mercaptan	CH_4S	−81.6	−73.8	−52.6	−41.8	−25.3	−10.9	5.7	24.9	55.7	84.3	−8.04229	4.64898	−4.38751	−1.03684
Ethyl mercaptan	C_2H_6S	−62.2	−53.6	−30.1	−18.0	0.3	16.3	34.7	55.9	89.7	120.8	−6.85400	1.41434	−1.74027	−2.40242
Dimethyl sulfide	C_2H_6S	−59.7	−51.2	−27.9	−15.9	2.4	18.5	37.0	58.5	92.9	124.6	−7.20168	1.99080	−1.67979	−3.99499
Diethyl sulfide	$C_4H_{10}S$	−23.6	−13.1	15.4	29.8	51.5	70.3	91.7	116.3	155.0	190.5	−6.90446	0.48320	−1.77018	−0.12336
Thiophene	C_4H_4S	−26.0	−16.3	10.2	23.8	44.6	62.8	83.8	108.1	147.0	182.8	−7.01021	1.63774	−1.66720	−4.21813
Halogenated hydrocarbons															
Fluoromethane (R41)	CH_3F	−140.5	−135.0	−120.0	−112.2	−100.5	−90.3	−78.6	−65.1	−43.7	−24.0	−7.21927	1.95643	−1.73271	−2.07627
Difluoromethane (R32)	CH_2F_2	−119.6	−113.5	−96.9	−88.5	−75.7	−64.6	−51.9	−37.3	−14.3	6.6	−7.47027	1.75595	−2.01429	−2.62147
Trifluoromethane (R23)	CHF_3	−141.6	−136.3	−121.8	−114.4	−103.2	−93.4	−82.3	−69.4	−49.1	−30.3	−7.38216	1.96234	−2.68392	−1.43178
Tetrafluoromethane (R14)	CF_4	−175.8	−171.6	−160.3	−154.4	−145.4	−137.4	−128.3	−117.6	−100.4	−84.6	−6.92188	1.54525	−1.41276	−2.87791
Methyl chloride	CH_3Cl		−96.2	−77.1	−67.3	−52.5	−39.4	−24.5	−7.1	20.4	45.7	−6.71862	1.27727	−0.96338	−3.14698
Methylene chloride	CH_2Cl_2	−56.3	−47.8	−24.5	−12.6	5.5	21.3	39.4	60.5	94.2	125.5	−7.57368	3.17104	−3.53296	−2.27696
Chloroform	$CHCl_3$	−41.8	−32.9	−8.2	4.5	23.9	41.0	60.7	83.6	120.0	153.4	−7.32485	1.69599	−0.93627	−5.89590
Carbon tetrachloride	CCl_4			2.1	15.8	36.7	55.1	76.3	101.0	140.5	177.1	−7.11728	1.96174	−2.05900	−3.26771
Bromomethane	CH_3Br	−84.4	−76.6	−55.3	−44.4	−27.8	−13.3	3.3	22.4	52.7	80.2	−7.65380	2.84555	−1.71564	−2.54232
Dibromomethane	CH_2Br_2	−16.0	−6.0	21.3	35.4	56.6	75.2	96.5	121.2	160.3	196.1	−7.25658	1.92921	−1.61527	−4.04404
Tribromomethane	$CHBr_3$	18.8	30.4	62.0	78.2	102.7	124.1	148.7	177.2	223.0	265.7	−7.16326	2.92794	−3.91279	−1.16341
Tetrabromomethane	CBr_4			95.2	111.8	137.8	161.3	188.8	220.6	269.5	310.6	−13.48480	9.03531	1.84773	−22.26830
Chlorodifluoromethane (R22)	$CHClF_2$	−113.5	−107.0	−89.5	−80.4	−66.8	−54.8	−41.1	−25.2	0.1	23.4	−7.09210	1.61905	−2.01221	−2.73123
Dichlorofluoromethane (R21)	$CHCl_2F$	−78.7	−70.9	−49.8	−39.0	−22.5	−8.1	8.5	27.7	58.3	86.7	−6.95944	1.53177	−1.97969	−3.25683
Chlorotrifluoromethane (R13)	$CClF_3$	−144.2	−138.7	−123.7	−115.9	−104.1	−93.7	−81.7	−67.7	−45.2	−24.4	−6.82801	1.52677	−1.75147	−2.23841
Dichlorodifluoromethane (R12)	CCl_2F_2	−108.7	−101.8	−82.9	−73.1	−58.3	−45.2	−30.1	−12.5	15.7	41.7	−6.92085	1.62615	−1.73939	−2.58282
Trichlorofluoromethane (R11)	CCl_3F	−71.6	−63.3	−40.4	−28.6	−10.7	5.1	23.3	44.4	78.2	109.4	−6.91946	1.52457	−1.66128	−2.85320
Ethyl fluoride (R161)	C_2H_5F	−113.2	−106.5	−88.2	−78.8	−64.6	−52.1	−38.0	−21.6	4.4	28.1	−7.07032	1.42577	−1.49199	−1.92623
Ethyl chloride	C_2H_5Cl	−78.2	−70.2	−48.3	−37.1	−20.1	−5.2	11.9	31.7	63.4	92.7	−7.36967	2.69543	−3.02790	−1.39375
Ethyl bromide	C_2H_5Br	−62.1	−53.0	−28.2	−15.7	3.1	19.5	38.1	59.5	93.7	125.1	−9.71666	7.74488	−7.76676	3.99427

D3.1. Table 3. (continued)

Substance	Formula	Vapor pressure in mbar										Equation (7)			
		5	10	50	100	250	500	1,000	2,000	5,000	10,000	*A*	*B*	*C*	*D*
1,1-Dichloroethane	$C_2H_4C_2H_4Cl_2$	−45.7	−36.5	−11.5	1.3	20.6	37.4	56.7	78.9	114.0	146.3	−6.63204	0.36053	−1.04822	−2.87286
1,2-Dichloroethane	$C_2H_4Cl_2$	−26.2	−16.4	10.2	23.8	44.4	62.5	83.2	107.2	145.1	179.8	−8.26850	3.49184	−3.19752	−2.97053
1,2-Dibromoethane	$C_2H_4Br_2$		17.5	47.9	63.4	86.8	107.4	131.0	158.4	202.3	243.1	−7.96068	4.07852	−4.74206	−0.88410
1,1,1-Trifluoroethane (R143a)	$C_2H_3F_3$			−95.2	−86.4	−72.9	−61.1	−47.5	−31.8	−6.7	16.3	−7.35995	1.71203	−2.01879	−2.98413
1,1,1-Trichloroethane	$C_2H_3Cl_3$		−25.9	0.4	14.0	34.6	52.8	73.7	98.0	136.9	172.8	−7.21356	1.90482	−2.08892	−3.31006
1,1,2,2-Tetrachloroethane	$C_2H_2Cl_4$	18.0	29.5	60.9	76.9	100.9	121.7	145.4	172.7	215.9	256.0	−5.60385	−1.82148	−0.70234	−1.88475
Pentachloroethane	C_2HCl_5	27.3	39.2	71.5	88.1	113.1	134.9	159.9	188.7	234.6	276.7	−7.59524	1.63691	−2.82337	−2.34305
Hexachloroethane	C_2Cl_6								215.1	265.9	313.7	−6.84574	1.14406	−2.27578	−7.15228
1,1,2,2-Tetrachlorodifluoroethane	$C_2Cl_4F_2$				31.2	52.5	71.1	92.6	117.5	157.4	194.5	−7.71309	2.64672	−3.98878	−1.66517
1,1,2-Trichlorotrifluoroethan	$C_2Cl_3F_3$			−20.7	−8.1	11.0	27.8	47.2	69.8	105.9	139.3	−7.24399	1.63003	−2.12928	−3.49922
1,2-Dichlorotetrafluoroethane	$C_2Cl_2F_4$	−84.9	−77.0	−55.6	−44.7	−28.1	−13.5	3.3	22.8	54.1	83.3	−7.64719	2.95529	−4.23671	0.15959
1-Chloropropane	C_3H_7Cl	−53.5	−44.7	−20.6	−8.2	10.7	27.2	46.1	68.2	103.3	135.7	−7.23105	1.89946	−2.29641	−2.86891
1-Chlorobutane	C_4H_9Cl	−30.6	−21.1	4.9	18.4	39.0	57.2	78.3	102.8	142.2	178.8	−6.77199	0.79529	−1.25773	−5.53709
1-Chloropentane	$C_5H_{11}Cl$	−11.5	−1.0	27.7	42.5	65.1	85.0	108.0	134.8	177.6	216.6	−9.45097	5.86945	−5.57003	−2.09598
Chlorotrifluoroethene	C_2ClF_3	−117.7	−108.5	−85.3	−74.1	−57.9	−44.3	−29.1	−11.8	15.5	40.7	−8.22217	4.87114	−7.47925	13.31070
Vinyl chloride	C_2H_3Cl	−96.2	−89.0	−69.2	−59.0	−43.5	−29.9	−14.1	4.3	33.8	61.3	−6.32153	1.11198	−1.35813	−3.25332
1,1-Dichloroethene	$C_2H_2Cl_2$	−63.4	−55.1	−32.4	−20.7	−2.8	13.0	31.3	52.8	87.5	119.4	−10.49400	9.03819	−7.79814	−1.10724
Trichloroethene	C_2HCl_3	−26.8	−16.6	11.2	25.3	46.4	64.8	85.7	109.9	148.4	184.2	−6.86463	1.75400	−3.57287	0.95588
Tetrachloroethene	C_2Cl_4	−2.1	8.9	39.0	54.3	77.4	97.6	120.6	147.1	189.5	228.8	−6.50488	0.75823	−2.53992	−0.58809
Fluorobenzene	C_6H_5F	−26.8	−16.8	10.5	24.4	45.4	63.8	84.8	109.1	147.8	183.5	−7.42663	2.30457	−3.23481	−1.05236
Chlorobenzene	C_6H_5Cl	5.6	16.8	47.5	63.2	86.9	107.7	131.4	159.0	202.8	243.2	−7.41321	2.18452	−2.95675	−1.66197
Bromobenzene	C_6H_5Br	22.9	34.6	66.7	83.2	108.2	130.2	155.5	184.9	232.0	275.6	−8.10313	3.78791	−4.14347	−2.11742
Iodobenzene	C_6H_5I	45.4	58.1	92.8	110.5	137.4	160.8	187.8	219.0	268.9	315.1	−7.47909	2.53825	−3.54320	−1.50458
m-Chlorotoluene	C_7H_7Cl	24.5	37.3	71.6	88.8	114.6	137.0	162.3	191.3	237.3	279.7	−7.90360	2.90903	−4.76707	3.62554
Benzyl chloride	C_7H_7Cl	42.9	55.4	89.2	106.2	131.8	153.9	179.0	207.9	253.8	296.4	−6.24204	−0.59859	−2.50951	0.21300
***n*-Alkanes**															
Methane	CH_4					−176.1	−169.4	−161.6	−152.5	−137.8	−124.0	−6.02388	1.26813	−0.56948	−1.37648
Ethane	C_2H_6	−150.6	−145.2	−130.4	−122.7	−111.0	−100.7	−88.8	−75.0	−52.7	−32.1	−6.46252	1.35760	−1.04922	−2.03789
Propane	C_3H_8	−118.1	−111.5	−93.3	−83.9	−69.6	−57.0	−42.4	−25.5	1.7	26.9	−6.71480	1.38388	−1.30695	−2.56827
n-Butane	C_4H_{10}	−89.0	−81.3	−60.0	−49.1	−32.4	−17.7	−0.8	18.8	50.3	79.5	−7.08562	1.79335	−2.00003	−2.31975
n-Pentane	C_5H_{12}	−62.8	−54.1	−30.4	−18.1	0.5	16.9	35.7	57.6	92.6	124.9	−7.36401	1.94358	−2.47191	−2.34757
n-Hexane	C_6H_{14}	−38.9	−29.5	−3.6	9.8	30.0	47.8	68.3	92.1	130.1	165.1	−7.61075	2.00527	−2.74158	−2.82824

n-Heptane	C_7H_{16}	−16.7	−6.6	21.1	35.4	57.0	76.1	98.0	123.4	163.9	201.1	−7.75469	1.84795	−2.80333	−3.62418
n-Octane	C_8H_{18}	3.9	14.6	43.9	59.0	81.9	102.0	125.2	152.0	194.8	234.1	−8.01133	1.98859	−3.26507	−3.99439
n-Nonane	C_9H_{20}	22.7	34.0	64.9	80.7	104.8	126.0	150.3	178.5	223.3	264.4	−8.45145	2.57850	−4.17533	−3.66755
n-Decane	$C_{10}H_{22}$	40.4	52.2	84.5	101.1	126.3	148.3	173.6	202.9	249.5	292.0	−8.62717	2.55890	−4.50221	−3.63420
n-Undecane	$C_{11}H_{24}$	57.3	69.6	103.1	120.3	146.3	169.2	195.3	225.7	273.8	317.7	−8.73044	2.35716	−4.52576	−4.46648
n-Dodecane	$C_{12}H_{26}$	73.2	85.9	120.4	138.2	165.1	188.7	215.7	247.1	296.6	341.4	−8.97902	2.40530	−4.55315	−5.99492
n-Tridecane	$C_{13}H_{28}$	88.4	101.4	136.9	155.2	182.9	207.1	234.9	266.9	317.3	363.0	−8.71245	1.11086	−3.15308	−8.81599
n-Tetradecane	$C_{14}H_{30}$	102.1	115.6	152.4	171.2	199.6	224.5	252.9	285.8	338.0	385.4	−8.99672	1.98553	−5.38986	−4.09226
n-Pentadecane	$C_{15}H_{32}$	115.8	129.5	167.1	186.3	215.4	240.9	270.0	303.5	356.4	404.4	−8.86498	0.89612	−3.70098	−8.72916
n-Hexadecane	$C_{16}H_{34}$	128.5	142.6	181.0	200.7	230.5	256.5	286.1	320.4	374.3	423.4	−8.96067	0.85195	−4.04080	−8.42218
n-Heptadecane	$C_{17}H_{36}$	141.2	155.7	195.1	215.2	245.4	271.7	301.8	336.4	390.9	440.2	−9.43782	1.65057	−5.70751	−4.71679
n-Octadecane	$C_{18}H_{38}$	152.6	167.3	207.3	227.7	258.4	285.1	315.6	350.8	406.1	455.6	−9.87775	2.42883	−7.03772	−3.36978
n-Nonadecane	$C_{19}H_{40}$	163.9	178.8	219.3	240.0	271.2	298.5	329.5	365.1	420.8	470.3	−9.91003	1.64273	−5.20678	−10.43208
n-Eicosane	$C_{20}H_{42}$	174.7	189.8	231.1	252.2	284.0	311.7	343.1	379.0	435.2	486.5	−8.99815	−1.30230	−1.45511	−16.74038
Isoalkanes															
Isobutane	C_4H_{10}	−97.2	−89.8	−69.4	−58.8	−42.7	−28.5	−12.1	7.0	37.7	66.2	−6.90675	1.57740	−1.80160	−2.42893
2-Methyl butane	C_5H_{12}	−69.3	−60.9	−37.6	−25.6	−7.3	8.9	27.5	49.1	83.7	115.8	−7.18224	1.72845	−2.05353	−2.71274
2,2-Dimethyl propane	C_5H_{12}						−8.6	9.1	29.9	63.3	94.4	−6.98355	1.67850	−2.08470	−2.42800
2-Methyl pentane	C_6H_{14}	−45.6	−36.3	−10.9	2.2	22.1	39.6	59.8	83.3	120.8	155.5	−7.49311	1.93828	−2.57247	−2.85203
3-Methyl pentane	C_6H_{14}	−43.8	−34.4	−8.7	4.6	24.7	42.4	62.8	86.6	124.7	160.0	−7.76049	2.81104	−3.61863	−1.53175
2,2-Dimethyl butane	C_6H_{14}	−54.7	−45.7	−20.7	−7.8	11.9	29.3	49.3	72.7	110.0	144.4	−6.84403	0.74239	−0.92872	−4.01577
2,3-Dimethyl butane	C_6H_{14}	−48.7	−39.3	−13.7	−0.5	19.6	37.2	57.5	81.1	118.8	153.8	−7.23412	1.74312	−2.49507	−1.81829
Olefins															
Ethylene	C_2H_4	−160.5	−155.5	−142.0	−135.0	−124.3	−114.9	−104.0	−91.3	−70.9	−51.8	−6.41327	1.45469	−1.24183	−1.99446
Propylene	C_3H_6	−121.5	−115.1	−97.4	−88.3	−74.4	−62.1	−48.0	−31.5	−5.2	19.2	−6.66599	1.43430	−1.39324	−2.46883
1-Butene	C_4H_8	−92.5	−84.9	−64.3	−53.7	−37.4	−23.1	−6.7	12.6	43.3	71.8	−7.07897	1.87819	−2.02256	−2.64845
1-Pentene	C_5H_{10}	−67.1	−58.7	−35.4	−23.4	−5.1	11.0	29.6	51.2	85.6	117.4	−7.23957	1.68881	−1.87158	−3.19856
1-Hexene	C_6H_{12}	−42.7	−33.4	−8.0	5.2	25.2	42.8	63.1	86.7	124.4	159.2	−7.47396	1.85450	−2.38903	−3.50639
1-Heptene	C_7H_{14}	−20.6	−10.6	16.9	31.0	52.5	71.4	93.2	118.7	159.2	196.4	−8.62839	3.98397	−4.58652	−2.45443
1-Octene	C_8H_{16}	0.0	10.6	39.8	54.8	77.7	97.8	120.8	147.5	189.7	228.1	−7.93750	1.47392	−1.85509	−5.72867
Propadiene	C_3H_4	−109.8	−103.4	−85.8	−76.6	−62.4	−49.6	−34.7	−17.1	11.8	38.9	−8.00232	4.45942	−2.87994	−5.85178
1,2-Butadiene	C_4H_6	−80.9	−72.7	−50.4	−38.9	−21.7	−6.7	10.5	30.4	62.1	91.5	−6.07102	0.12159	−1.55692	−0.53215
1,3-Butadiene	C_4H_6	−90.8	−83.3	−62.6	−52.0	−35.7	−21.4	−4.8	14.4	45.1	73.5	−6.79824	1.08553	−0.96279	−3.84778
1,2-Pentadiene	C_5H_8	−55.0	−46.2	−22.1	−9.7	9.0	25.5	44.4	66.6	102.3	136.1	−5.94252	0.26690	−2.35857	−1.73048
trans-1,3-Pentadiene	C_5H_8	−57.9	−49.1	−25.0	−12.6	6.2	22.6	41.6	63.8	99.7	133.9	−5.50529	−0.22313	−2.15448	−1.34395
1,4-Pentadiene	C_5H_8	−69.3	−60.9	−38.0	−26.2	−8.3	7.4	25.6	46.9	81.5	114.7	−5.36609	−0.09618	−2.39750	−1.13323
2,3-Pentadiene	C_5H_8	−51.8	−43.0	−18.7	−6.3	12.5	29.0	47.9	69.9	105.2	138.2	−6.57492	0.82240	−2.46643	−2.03177

D3.1. Table 3. (continued)

Substance	Formula	Vapor pressure in mbar										Equation (7)			
		5	10	50	100	250	500	1,000	2,000	5,000	10,000	*A*	*B*	*C*	*D*
Acetylene and derivatives															
Acetylene	C_2H_2								−72.1	−51.7	−32.9	−6.99241	1.57338	−1.33202	−5.21884
Propyne	C_3H_4	−100.9	−93.9	−75.0	−65.3	−50.7	−38.0	−23.4	−6.6	20.2	44.8	−7.11026	1.86493	−2.56109	−1.65671
2-Butyne	C_4H_6				−23.9	−6.3	9.1	26.6	46.9	79.1	108.6	−6.85375	0.83418	−1.42544	−2.91847
1-Butyne	C_4H_6	−79.1	−71.3	−50.2	−39.4	−23.0	−8.7	7.8	26.8	57.1	85.0	−7.17126	1.56844	−2.22263	−2.83839
Naphthenes															
Cyclopropane	C_3H_6	−111.2	−104.3	−85.4	−75.7	−61.0	−48.1	−33.1	−15.7	12.6	39.0	−8.18446	5.40338	−5.26106	0.29975
Cyclobutane	C_4H_8	−80.0	−71.9	−49.6	−38.1	−20.7	−5.4	12.2	32.6	65.0	94.8	−7.11287	1.86338	−1.59855	−2.35844
Cyclopentane	C_5H_{10}	−53.7	−44.7	−19.9	−7.1	12.3	29.3	48.8	71.5	107.8	141.3	−7.00184	1.67430	−1.95254	−2.43833
Methyl cyclopentane	C_6H_{12}	−37.7	−28.1	−1.8	11.8	32.4	50.5	71.4	95.7	134.5	170.5	−7.22687	1.83847	−2.26044	−2.89788
Ethyl cyclopentane	C_7H_{14}	−15.1	−4.7	23.7	38.4	60.7	80.3	102.9	129.2	171.2	209.9	−7.33383	1.58750	−2.00285	−3.84956
Propyl cyclopentane	C_8H_{16}	5.5	16.5	46.6	62.1	85.8	106.6	130.5	158.3	202.5	243.0	−7.56400	1.41441	−1.85483	−4.86488
Butyl cyclopentane	C_9H_{18}	24.6	36.3	68.2	84.5	109.2	130.9	155.9	185.0	231.7	274.9	−8.82045	4.56618	−6.39502	0.04910
Pentyl cyclopentane	$C_{10}H_{20}$	42.1	54.5	87.9	105.0	130.9	153.6	179.9	210.8	261.3	309.1	−8.34838	4.60920	−8.05957	2.47945
Hexyl cyclopentane	$C_{11}H_{22}$	60.4	72.9	107.3	125.0	151.9	175.5	202.6	233.9	283.6	328.9	−8.25942	1.53284	−2.79124	−6.47404
Cyclohexane	C_6H_{12}				19.2	40.3	58.9	80.3	105.2	145.1	182.0	−7.00979	1.57475	−1.96820	−3.26095
Methyl cyclohexane	C_7H_{14}	−17.9	−7.7	20.7	35.4	57.8	77.6	100.5	127.1	169.6	208.9	−6.99290	1.02989	−1.06613	−4.84894
Ethyl cyclohexane	C_8H_{16}	4.7	15.7	46.2	61.9	85.9	107.0	131.4	159.8	205.4	247.9	−6.62098	0.32843	−1.34736	−4.41951
Propyl cyclohexane	C_9H_{18}	23.2	34.9	67.0	83.5	108.6	130.7	156.2	186.0	233.9	279.1	−6.58910	0.42832	−2.35856	−3.12499
Butyl cyclohexane	$C_{10}H_{20}$	41.8	54.0	87.5	104.7	130.9	153.9	180.4	211.5	261.7	309.3	−6.34269	−0.12784	−2.48780	−3.28017
Pentyl cyclohexane	$C_{11}H_{22}$	58.7	71.5	106.5	124.4	151.6	175.5	203.1	235.4	287.2	334.7	−9.46392	5.58832	−7.94937	0.81254
Hexyl cyclohexane	$C_{12}H_{24}$	75.6	88.9	125.0	143.4	171.3	195.9	224.1	257.0	309.7	357.8	−9.74155	5.86346	−8.50766	1.30484
Cyclopentene	C_5H_8	−57.1	−48.1	−23.7	−11.1	8.0	24.7	43.9	66.2	101.7	134.5	−7.05071	1.79116	−2.02594	−2.17803
Cyclohexene	C_6H_{10}	−29.4	−19.6	7.4	21.3	42.5	61.1	82.5	107.5	147.3	184.3	−7.19079	1.97175	−2.26256	−3.04106
Aromatic compounds															
Benzene	C_6H_6			6.3	20.0	40.6	58.8	79.7	103.9	142.6	178.4	−7.11451	1.83981	−2.25158	−3.15179
Toluene	C_7H_8	−9.0	1.5	30.4	45.3	67.8	87.5	110.2	136.4	178.3	216.8	−7.50051	2.08939	−2.56368	−2.85042
Ethyl benzene	C_8H_{10}	9.6	20.8	51.3	67.0	90.8	111.7	135.7	163.5	207.7	248.4	−7.64476	2.01616	−2.69311	−3.25571
Propyl benzene	C_9H_{12}	26.2	38.0	70.1	86.6	111.6	133.5	158.7	187.9	234.3	276.9	−7.90921	2.25623	−3.18277	−3.03789
Butyl benzene	$C_{10}H_{14}$	44.8	57.0	90.4	107.5	133.6	156.5	182.8	213.2	261.3	305.3	−7.91469	1.51273	−2.16430	−5.64758
Pentyl benzene	$C_{11}H_{16}$	61.6	74.3	108.9	126.7	153.7	177.5	205.0	237.1	288.3	334.8	−9.80886	6.07290	−7.50612	−1.56859
Hexyl benzene	$C_{12}H_{18}$	77.4	90.5	126.4	144.8	172.7	197.3	225.6	258.5	311.0	358.4	−9.64511	5.19130	−6.86455	−2.47938
o-Xylene	C_8H_{10}	15.6	27.0	58.1	74.1	98.4	119.6	143.9	172.1	216.8	257.9	−7.60791	1.79921	−2.42215	−3.36892
m-Xylene	C_8H_{10}	12.1	23.3	54.0	69.8	93.7	114.6	138.6	166.4	210.5	250.9	−7.63902	1.65289	−2.19801	−3.94677

p-Xylene	C_8H_{10}		22.2	53.0	68.8	92.8	113.8	137.9	165.8	210.0	250.6	−7.67395	1.81953	−2.39673	−3.44627
1,2,3-Trimethyl benzene	C_9H_{12}	38.5	50.8	84.4	101.5	127.4	149.9	175.7	205.3	252.0	294.7	−7.62987	1.23706	−2.24536	−2.65979
1,2,4-Trimethyl benzene	C_9H_{12}	34.2	46.2	79.0	95.8	121.2	143.5	168.9	198.3	244.8	287.2	−8.03805	2.10078	−2.99671	−3.00299
1,3,5-Trimethyl benzene	C_9H_{12}	31.3	43.2	75.7	92.3	117.3	139.2	164.2	193.0	238.4	279.7	−7.82434	1.27065	−2.17890	−3.60299
1,2,3,4-Tetramethyl benzene	$C_{10}H_{14}$	61.0	73.9	108.8	126.7	153.7	177.4	204.6	236.2	286.5	332.6	−9.61420	5.81425	−7.22553	−0.17754
1,2,3,5-Tetramethyl benzene	$C_{10}H_{14}$	56.4	69.1	103.5	121.1	147.7	170.9	197.6	228.3	277.2	321.9	−8.71211	3.45458	−5.00258	−1.61174
1,2,4,5-Tetramethyl benzene	$C_{10}H_{14}$			102.2	119.9	146.5	169.7	196.2	226.8	275.0	319.1	−7.76585	0.96770	−2.26413	−3.93132
Pentamethyl benzene	$C_{11}H_{16}$	80.3	93.9	131.0	149.8	178.2	202.9	230.9	263.1	313.7	359.8	−8.00728	1.10336	−2.69076	−2.48217
Hexamethyl benzene	$C_{12}H_{18}$				179.3	208.4	233.8	262.9	296.5	349.7	398.5	−8.54789	2.39022	−4.64673	−4.09546
Styrene	C_8H_8	17.1	28.4	59.4	75.2	99.4	120.5	144.9	173.3	218.7	260.6	−8.15126	3.51813	−4.34082	−2.42333
Isopropyl benzene	C_9H_{12}	21.7	33.2	64.6	80.8	105.5	127.1	151.9	180.7	226.6	268.8	−7.53496	1.50829	−2.32928	−4.31012
Biphenyl	$C_{12}H_{10}$	97.0	111.1	149.7	169.4	199.2	225.1	254.7	288.9	342.9	392.4	−7.75945	1.70606	−2.96632	−3.06189
Diphenyl methane	$C_{13}H_{12}$	105.4	119.5	158.1	177.9	207.8	234.0	264.0	298.6	353.1	402.4	−8.53233	2.00873	−2.93179	−6.03029
Triphenyl methane	$C_{19}H_{16}$	178.3	194.6	238.8	261.3	295.3	324.9	358.8	397.9	459.9	516.6	−8.84156	2.41421	−5.56532	−2.75668
Tetraphenyl methane	$C_{25}H_{20}$			330.3	356.3	395.6	429.8	468.9	514.0	585.3	649.7	−9.59635	3.13229	−6.82319	−2.76211
Naphthalene	$C_{10}H_8$		80.6	117.1	135.8	164.1	188.9	217.4	250.4	303.0	351.4	−7.97682	2.86601	−3.50249	−2.67778
1-Methylnaphthalene	$C_{11}H_{10}$	86.8	100.9	139.4	159.0	188.7	214.5	243.9	277.8	331.2	380.1	−6.84372	−0.39471	−0.79459	−3.92723
2-Methylnaphthalene	$C_{11}H_{10}$	85.6	99.2	136.6	155.8	185.1	211.0	241.0	276.1	332.4	383.7	−10.50759	8.20742	−8.41116	−1.58015
1-Ethylnaphthalene	$C_{12}H_{12}$	99.8	113.9	152.3	171.9	201.6	227.7	257.6	292.3	347.6	398.3	−9.12884	4.70431	−6.05976	−1.87388
2-Ethylnaphthalene	$C_{12}H_{12}$	96.8	111.0	150.0	170.1	200.5	227.2	257.8	293.0	348.3	398.1	−8.42943	2.12066	−1.95832	−6.02831
Alcohols															
Methanol	CH_4O	−29.3	−20.4	3.4	15.2	32.7	47.5	64.1	82.8	111.4	136.6	−8.72963	1.45860	−2.78449	−0.70669
Ethanol	C_2H_6O	−15.7	−6.7	17.2	29.0	46.5	61.4	77.9	96.6	125.2	150.7	−8.33803	0.08720	−3.30575	−0.26001
1-Propanol	C_3H_8O	0.7	9.9	34.3	46.4	64.3	79.6	96.8	116.3	146.8	174.5	−8.60671	2.17353	−8.04678	3.69194
1-Butanol	$C_4H_{10}O$	16.8	26.3	51.5	64.1	82.9	99.1	117.4	138.3	171.4	201.9	−8.33120	2.05530	−8.17754	0.19316
1-Pentanol	$C_5H_{12}O$	30.6	40.4	66.8	80.1	100.2	117.6	137.5	160.3	196.4	229.6	−8.62225	2.10135	−6.29175	−6.79293
1-Hexanol	$C_6H_{14}O$	44.9	55.2	83.0	97.0	118.1	136.4	157.3	181.5	220.1	256.1	−9.17319	4.30846	−10.11890	−0.93221
1-Heptanol	$C_7H_{16}O$	59.9	70.3	98.4	112.8	134.7	153.9	176.1	202.0	243.7	282.4	−8.85687	3.21033	−7.48606	−12.12938
1-Octanol	$C_8H_{18}O$	72.5	83.4	113.0	128.2	151.2	171.4	194.8	222.1	266.4	307.4	−10.26829	6.70186	−11.65601	−6.37873
Isopropanol	C_3H_8O	−8.9	−0.3	22.7	34.1	51.1	65.6	81.9	100.4	129.3	155.6	−8.44737	1.17402	−6.97876	0.69248
2-Methyl-1-propanol	$C_4H_{10}O$	11.8	20.5	44.2	56.2	74.2	89.7	107.5	127.9	160.2	190.0	−7.82960	0.44510	−5.32308	−10.00835
3-Methyl-1-butanol	$C_5H_{12}O$	27.6	36.9	62.3	75.2	94.6	111.5	130.9	153.1	188.4	220.8	−8.27417	1.16334	−5.04768	−11.64372
Ethylene glycol	$C_2H_6O_2$	75.1	86.6	117.3	132.7	155.4	174.8	196.6	221.3	259.7	294.2	−7.85575	1.06762	−5.14271	−1.65660
1,3-Propylene glycol	$C_3H_8O_2$	85.6	97.8	130.2	146.4	170.4	190.9	213.7	239.1	277.7	311.2	−10.42988	2.74631	−2.20347	−6.30476
Glycerol	$C_3H_8O_3$	147.5	160.8	196.2	213.9	239.9	262.2	287.2	315.6	359.8	400.1	−6.94758	−0.33345	−5.98569	−1.33011
Cyclohexanol	$C_6H_{12}O$	47.1	57.3	84.8	98.8	120.2	138.9	160.4	185.6	226.3	264.7	−6.96569	0.93439	−5.00403	−10.29700
Benzyl alcohol	C_7H_8O	74.9	86.7	118.5	134.6	158.8	179.9	204.0	232.0	276.9	319.2	−7.38172	2.18313	−6.78536	−2.57851

D3.1. Table 3. (continued)

Substance	Formula	Vapor pressure in mbar										Equation (7)			
		5	10	50	100	250	500	1,000	2,000	5,000	10,000	*A*	*B*	*C*	*D*
Phenols															
o-Cresol	C_7H_8O	60.1	71.8	103.6	119.9	144.4	165.8	190.3	218.6	263.2	303.8	−8.83275	3.46650	−4.36291	−6.10327
m-Cresol	C_7H_8O	70.8	82.7	114.9	131.2	155.8	177.2	201.7	229.9	274.8	316.1	−8.84466	4.00993	−6.76021	−3.02124
p-Cresol	C_7H_8O	72.0	83.6	115.2	131.3	155.6	177.0	201.5	229.9	275.0	316.2	−11.38986	9.13086	−10.26796	−3.81158
Phenol	C_6H_6O	55.5	67.0	98.0	113.8	137.4	158.0	181.4	208.5	251.5	290.9	−10.48951	7.87328	−9.54201	−0.49292
Carboxylic acids															
Formic acid	CH_2O_2			22.3	37.0	59.2	78.4	100.2	125.0	163.7	198.4	−7.48216	0.88805	−0.32253	−2.58053
Acetic acid	$C_2H_4O_2$			41.2	55.7	77.5	96.3	117.5	141.6	179.1	212.5	−9.34304	3.77735	−3.59092	−1.57006
Propionic acid	$C_3H_6O_2$	23.7	34.8	64.3	79.0	100.9	119.7	140.8	164.7	201.7	234.9	−9.05245	2.46694	−4.73604	1.29659
Butyric acid	$C_4H_8O_2$	46.8	57.6	86.8	101.4	123.2	142.0	163.2	187.4	225.0	258.8	−9.92279	3.73064	−6.94231	−1.65235
Valeric acid	$C_5H_{10}O_2$	54.9	66.0	96.0	111.1	133.6	153.1	175.1	200.2	239.3	274.5	−9.07960	1.91018	−4.75458	−4.73450
Caproic acid	$C_6H_{12}O_2$	82.1	93.5	123.9	139.2	162.0	181.7	204.0	229.7	270.3	307.8	−9.90505	4.66763	−11.56156	2.59120
Acetic anhydride	$C_4H_6O_3$	20.7	31.5	60.7	75.5	97.8	117.1	139.1	164.3	204.0	240.2	−8.15436	1.80785	−3.76039	−3.04616
Propionic anhydride	$C_6H_{10}O_3$	37.5	50.2	83.5	99.8	123.8	144.0	166.5	191.9	231.3	267.1	−6.66964	−2.70670	−1.76623	7.54170
Chloroacetic acid	$C_2H_3Cl\ O_2$	67.3	78.4	108.4	123.5	146.3	166.0	188.6	214.5	255.6	293.3	−10.72534	7.62232	−10.44634	−2.56382
Dichloroacetic acid	$C_2H_2Cl_2O_2$	69.5	80.7	111.0	126.5	149.8	170.2	193.5	220.3	262.7	301.1	−10.38040	6.03907	−7.42780	−7.72727
Trichloroacetic acid	$C_2HCl_3O_2$	70.5	82.3	114.1	130.0	153.7	174.1	197.2	223.6	265.1	302.8	−8.80390	2.91469	−6.75915	−0.26065
Ketones															
Ketene	C_2H_2O	−121.4	−114.9	−97.4	−88.5	−75.0	−63.3	−50.0	−34.6	−10.1	12.6	−5.93228	0.34819	−1.82981	−0.11750
Acetone	C_3H_6O	−44.6	−35.7	−11.2	1.4	20.3	36.8	55.7	77.5	111.9	143.3	−7.67033	1.96469	−2.44380	−2.90162
Methyl ethyl ketone	C_4H_8O	−28.9	−19.2	7.4	20.9	41.2	59.0	79.2	102.5	139.4	173.2	−7.89149	2.46953	−3.52510	−0.92713
Diethyl ketone	$C_5H_{10}O$	−11.4	−1.3	26.2	40.3	61.6	80.2	101.4	125.9	164.7	200.2	−7.27265	0.63120	−1.64177	−4.36962
Dipropyl ketone	$C_7H_{14}O$	18.2	29.3	59.9	75.5	99.2	120.0	143.7	171.1	214.5	254.0	−7.98923	1.58266	−2.61251	−4.38408
Acetophenone	C_8H_8O	60.3	73.0	107.7	125.4	152.1	175.4	201.9	232.4	280.4	324.2	−6.96667	−0.37241	−0.80507	−4.88404
Benzophenone	$C_{13}H_{10}O$	138.2	153.2	194.0	214.8	246.2	273.6	305.0	341.3	398.8	450.9	−10.03049	5.92909	−7.69343	−1.20468
Ethers															
Dimethyl ether	C_2H_6O	−103.8	−96.7	−77.5	−67.6	−52.8	−39.9	−25.1	−8.0	19.3	44.5	−7.33288	2.67700	−3.40250	−0.11957
Diethyl ether	$C_4H_{10}O$	−61.3	−52.8	−29.7	−17.8	0.2	16.0	34.1	55.1	88.7	119.7	−7.55709	2.15613	−3.02766	−2.37858
Dipropyl ether	$C_6H_{14}O$	−21.9	−12.0	15.0	28.8	49.9	68.3	89.6	114.2	153.4	189.1	−8.55629	3.49469	−4.22192	−2.61530
Methyl propyl ether	$C_4H_{10}O$	−57.9	−49.4	−26.1	−14.1	4.1	20.1	38.5	60.1	94.8	127.1	−8.76101	5.30514	−6.07025	−0.78235
Ethyl propyl ether	$C_5H_{12}O$	−39.8	−30.9	−6.3	6.4	25.9	43.2	63.4	87.1	125.2	160.0	−10.68465	8.88906	−8.58949	−2.06505
Ethylene oxide	C_2H_4O	−76.9	−69.1	−47.9	−37.1	−20.6	−6.2	10.2	29.1	58.9	86.0	−6.39656	−0.13545	0.30047	−4.54866

Furane	C_4H_4O	−64.6	−55.8	−32.1	−20.1	−2.2	13.3	31.0	51.4	84.1	114.6	−7.98347	4.71720	−6.64737	3.77132
1,4-Dioxane	$C_4H_8O_2$			24.8	39.3	61.0	79.7	101.0	125.4	163.9	199.3	−7.40401	2.12025	−3.88819	1.69876
Aldehydes															
Formaldehyde	CH_2O		−90.5	−71.5	−61.7	−47.0	−34.1	−19.4	−2.6	23.8	47.7	−7.46907	1.28290	−0.50464	−4.29089
Acetaldehyde	C_2H_4O	−71.0	−62.8	−40.7	−29.3	−12.2	2.8	19.9	39.6	70.8	99.2	−7.48323	1.89754	−1.87991	−2.74165
Paraldehyde	$C_6H_{12}O_3$		18.9	47.2	61.6	83.3	102.2	123.8	148.7	188.1	224.3	−8.39247	2.66850	−4.68103	−2.64044
Furfural	$C_5H_4O_2$	32.9	44.7	76.4	92.5	116.6	137.4	160.9	187.8	229.7	267.6	−7.19466	0.15098	−1.29504	−2.81404
Benzaldehyde	C_7H_6O	42.3	54.5	87.6	104.6	130.2	152.7	178.3	208.0	254.8	297.6	−7.62714	1.75696	−2.27084	−3.91930
Salicylaldehyde	$C_7H_6O_2$	55.1	68.2	103.5	121.3	147.8	170.5	195.8	224.1	267.0	304.2	−10.08822	2.82918	−0.83177	−3.21642
Esters															
Methyl formate	$C_2H_4O_2$	−60.4	−52.1	−29.6	−18.1	−0.8	14.2	31.4	51.2	82.5	111.3	−7.09661	1.33571	−2.14672	−2.79247
Ethyl formate	$C_3H_6O_2$	−43.7	−35.0	−11.4	0.7	19.0	35.1	53.6	75.0	109.1	140.5	−7.17811	1.31054	−2.17904	−4.85150
Propyl formate	$C_4H_8O_2$	−25.1	−15.7	10.0	23.1	43.1	60.6	80.6	103.9	141.1	175.4	−7.55263	1.95726	−3.16613	−3.81792
Methyl acetate	$C_3H_6O_2$	−42.1	−33.2	−9.0	3.3	21.9	38.1	56.6	78.0	112.0	143.2	−8.57584	4.22791	−5.37346	−0.82045
Ethyl acetate	$C_4H_8O_2$	−27.4	−18.0	7.4	20.4	40.0	57.1	76.7	99.4	135.4	168.4	−7.89734	2.16798	−3.52390	−3.10641
Propyl acetate	$C_5H_{10}O_2$	−9.7	0.2	27.0	40.8	61.8	80.1	101.1	125.4	164.0	199.3	−7.89781	1.68898	−2.74051	−5.47967
Methyl propionate	$C_4H_8O_2$	−25.7	−16.2	9.4	22.5	42.2	59.4	79.1	102.0	138.4	172.0	−8.30872	3.53745	−5.20774	−1.27089
Ethyl propionate	$C_5H_{10}O_2$	−11.5	−1.7	25.1	38.8	59.6	77.7	98.5	122.7	161.4	197.0	−8.75519	4.14793	−5.89411	−1.78473
Propyl propionate	$C_6H_{12}O_2$	3.7	14.5	43.6	58.5	80.7	100.1	122.0	147.2	186.8	222.9	−7.79443	0.71065	−2.20915	−2.58752
Methyl butyrate	$C_5H_{10}O_2$	−9.5	0.6	27.9	41.8	62.8	81.2	102.3	126.6	165.6	201.5	−8.52321	3.78350	−5.74769	−0.69681
Ethyl butyrate	$C_6H_{12}O_2$	0.3	11.1	40.6	55.7	78.4	98.3	120.9	147.1	188.5	226.2	−8.18197	2.21896	−3.32406	−2.03342
Methyl benzoate	C_8H_8O2	60.0	72.3	105.8	123.1	149.3	172.4	198.9	229.7	278.6	323.1	−9.52872	5.22508	−5.67192	−4.59960
Ethyl benzoate	$C_9H_{10}O_2$	70.8	83.0	117.0	134.6	161.5	185.3	212.8	244.5	294.5	339.0	−9.49777	3.93518	−3.00984	−10.93022
Methyl salicylate	$C_8H_8O_3$	78.0	89.2	121.0	138.2	165.4	190.4	220.0	254.6	307.4	350.7	−14.30891	11.86128	−2.67256	−30.85630
Amines															
Methyl amine	CH_5N	−83.8	−76.8	−57.7	−48.1	−33.5	−21.0	−6.7	9.7	35.4	58.9	−6.93594	0.77016	−2.12846	−3.11687
Ethyl amine	C_2H_7N	−69.1	−61.3	−40.4	−29.7	−13.6	0.5	16.5	34.9	64.1	90.9	−7.14146	1.24486	−2.55143	−3.09059
Propyl amine	C_3H_9N	−48.5	−39.7	−16.1	−4.2	13.8	29.5	47.2	67.6	99.9	129.7	−6.32807	−0.41527	−1.86755	−1.82733
n-butyl amine	$C_6H_{15}N$	−27.3	−17.9	7.6	20.7	40.3	57.5	77.1	99.8	135.9	169.2	−7.88889	2.67770	−4.27421	−1.85122
Dimethyl amine	C_2H_7N	−74.4	−67.1	−47.3	−37.2	−22.0	−8.7	6.6	24.4	52.9	79.4	−8.48833	4.67224	−6.24955	−1.96675
Trimethyl amine	C_3H_9N	−84.8	−77.3	−56.4	−45.5	−28.9	−14.2	2.8	22.6	54.4	83.7	−7.30365	1.94801	−1.34682	−5.07582
Diethyl amine	$C_6H_{15}N$	−46.1	−36.9	−12.0	0.7	19.7	36.3	55.2	77.1	111.9	144.1	−7.36200	1.77888	−3.69788	0.28823
Triethyl amine	$C_6H_{15}N$	−24.6	−14.5	13.0	27.1	48.4	67.0	88.4	113.1	152.6	189.2	−7.73549	2.33990	−3.77932	−0.63259
Piperidine	$C_5H_{11}N$		−0.7	28.1	42.7	64.8	84.0	105.9	131.2	171.2	208.3	−6.79875	1.00957	−2.60941	−0.67208
Pyridine	C_6H_7N	−2.9	7.6	36.3	51.0	73.2	92.6	114.8	140.4	181.1	218.6	−7.07868	1.45189	−2.11714	−3.20359
Aniline	C_6H_7N	51.2	63.3	96.0	112.6	137.4	159.0	183.4	211.5	255.6	295.9	−7.86006	1.96206	−3.65571	−2.00622
N-methyl aniline	C_7H_9N	57.4	69.9	104.0	121.2	147.2	169.7	195.1	224.0	269.0	309.0	−8.99983	2.75304	−2.46251	−3.78980

D3.1. Table 3. (continued)

Substance	Formula	Vapor pressure in mbar										Equation (7)			
		5	10	50	100	250	500	1,000	2,000	5,000	10,000	*A*	*B*	*C*	*D*
N,*N*-dimethyl aniline	$C_8H_{11}N$	52.0	65.0	100.0	117.7	144.2	167.1	192.9	222.4	268.6	310.8	−6.91926	−0.79562	−1.01346	−1.30692
N,*N*-diethyl aniline	$C_{10}H_{15}N$	73.6	86.6	121.6	139.3	166.0	189.1	215.5	246.0	294.7	340.1	−7.13341	0.21353	−3.88149	−0.98901
Phenylhydrazine	$C_6H_8N_2$	93.8	107.0	143.4	162.1	190.4	215.2	243.4	275.7	325.9	370.0	−10.65944	5.59074	−3.56952	−8.23026
Diphenyl amine	$C_{12}H_{11}N$	134.0	149.3	190.7	211.7	243.3	270.7	301.8	337.3	392.8	442.8	−8.75985	2.00629	−3.23950	−3.32510
Nitriles															
Acetonitrile	C_2H_3N	−31.0	−20.6	7.3	21.4	42.3	60.5	81.0	104.6	141.9	175.9	−9.22263	5.68045	−6.67111	4.51306
Propionitrile	C_3H_5N	−17.9	−7.7	20.4	34.7	56.5	75.5	97.3	122.3	161.8	197.6	−7.82826	1.87534	−1.74704	−3.40003
Butyronitrile	C_4H_7N	−2.0	8.6	37.6	52.4	74.8	94.4	117.0	143.0	184.4	222.0	−9.07674	4.63491	−4.96526	−1.94727
Benzonitrile	C_7H_5N	51.3	63.4	96.8	114.1	140.4	163.6	190.3	221.2	270.1	314.2	−8.76503	3.46762	−2.58071	−7.03902
Amides															
Formamide	CH_3NO	82.2	94.8	129.0	146.2	171.9	194.0	219.1	247.6	292.1	332.3	−8.05102	1.89555	−3.34638	−3.18188
Nitroderivates															
Nitromethane	CH_3NO_2	−11.8	−1.7	26.0	40.1	61.3	79.8	100.8	124.9	162.6	196.7	−8.40409	2.96310	−2.55125	−3.12626
Nitrobenzene	$C_6H_5NO_2$	65.8	78.5	113.5	131.4	158.7	182.6	210.2	242.1	292.6	337.8	−11.42180	9.08136	−8.03968	−2.40144
o-Nitrotoluene	$C_7H_7NO_2$	75.0	88.0	123.6	141.8	169.4	193.5	220.9	252.4	301.5	345.5	−9.20649	3.25360	−2.90528	−5.87732
m-Nitrotoluene	$C_7H_7NO_2$	81.8	95.3	132.1	150.9	179.3	204.0	232.1	264.4	314.8	359.8	−9.97904	5.05231	−4.85807	−3.04363
p-Nitrotoluene	$C_7H_7NO_2$	85.1	98.9	136.2	155.3	184.1	209.3	238.1	271.5	324.6	373.0	−9.14840	4.60236	−6.10485	−0.71761

D3.1. Table 4. Enthalpies of vaporization at different temperatures in J/g

Substance	Formula	Temperature (°C)								Equation (9)				
		−50	−25	0	20	50	100	150	200	*A*	*B*	*C*	*D*	*E*
Elements														
Xenon	Xe	77.9	65.5	45.8						4.69619	6.10287	−3.768319	−1.078236	0.917114
Krypton	Kr									4.53207	6.22827	−3.542952	−1.700226	4.022385
Argon	Ar									4.84261	5.03919	−2.218775	−2.402365	7.051085
Air										0.28652	11.97235	−1.145111	−8.064787	14.645081
Nitrogen	N_2									5.07184	5.47148	−2.581923	−2.026983	5.480425
Oxygen	O_2									4.97014	5.30204	−2.421192	−2.154911	3.472270
Sulfur	S	355.5	352.0	348.6	345.8	341.5	334.3	326.8	319.1	0.83391	0.29462	0.000023		
Fluorine	F_2									4.47837	8.72648	−6.584538	0.389714	0.579951
Chlorine	Cl_2	296.6	282.9	267.4	253.2	228.0	168.2			5.11396	5.49446	−1.638879	−2.194771	4.360453
Bromine	Br_2			200.9	196.2	188.8	175.1	159.1	139.5	7.49419	0.92568	−0.113163	−0.025698	−0.197360
Iodine	I_2							171.4	162.4	6.56592	2.00206	0.000206		
Anorganic compounds														
Hydrogen fluoride	HF	287.7	313.4	347.1	381.4	444.2	555.8	561.6		−5.18098	64.63309	−88.769460	38.475692	−19.213870
Hydrogen chloride	HCl	405.1	367.6	320.4	269.9					7.67088	0.20254	0.928667	−1.253068	4.544424
Hydrogen bromide	HBr	214.4	201.8	184.2	165.7	128.0				3.64108	7.03187	1.546295	−8.296772	2.449759
Hydrogen iodide	HI	162.9	155.0	146.3	138.8	126.0				6.52572	1.44631	−0.100655	−0.009376	−0.219261
Hydrogen cyanide	HCN			1024	1005	969.0	881.6	710.4		14.93438	−6.80314	−0.045868	−0.065004	−0.145955
Water	H_2O				2454	2380	2257	2115	1940	6.85307	7.43804	−2.937595	−3.282093	8.397378
Hydrogen sulfide	H_2S	534.2	501.3	462.7	425.9	355.0				4.03399	11.42509	−8.776318	1.195807	0.952448
Ammonia	NH_3	1416	1345	1263	1187	1051	715.6			5.74477	7.28288	−2.428744	−2.261942	2.909378
Nitric oxide	NO									9.22523	6.92520	−0.413269	−5.159373	97.203137
Nitrogen dioxide	NO_2									10.54674	37.16610	−51.619512	10.653997	68.680656
Nitrous oxide	N_2O	326.0	285.9	232.7	170.0					6.47229	3.13505	0.829428	−2.961623	12.969986
Dinitrogentetroxide	N_2O_4									17.10093	9.30852	−21.253959	−1.535179	102.679020
Cyanogen	C_2N_2		452.7	426.3	401.4	356.0	241.4			9.34416	−2.91283	7.147434	−6.240980	9.063880
Phosphorus trichloride	PCl_3				236.3	226.1				5.00588	9.40431	−6.091275	0.740321	0.097910
Cyanogen chloride	ClCN			446.3	428.6	398.9	336.7	234.8		9.94103	0.20022	−0.085934	−0.000108	−0.000005
Silane	SiH_4	302.2	250.0							12.04169	−12.66485	9.554284	−3.383685	18.437953
Tetrachlorosilane	$SiCl_4$	197.0	188.7	181.6	176.2	167.6	150.0	124.9		5.69074	7.26313	−0.726791	−5.904069	18.531250
Carbon monoxide	CO									5.36544	4.61398	−1.500151	−2.362494	7.223824
Carbon dioxide	CO_2	339.7	293.3	230.9						6.29356	5.58825	−1.150946	−2.168773	31.513859
Carbon suboxide	C_3O_2	388.8	379.9	367.7						3.85706	12.51979	−1.466541	−12.059981	18.935744

D3.1. Table 4. (continued)

Substance	Formula	Temperature (°C)								Equation (9)				
		−50	−25	0	20	50	100	150	200	*A*	*B*	*C*	*D*	*E*
Carbonyl sulfide	COS	308.9	291.1	270.3	250.5	213.0				5.26390	6.82633	−4.049718	−0.902566	4.719170
Phosgene	CCl_2O	277.4	265.4	253.2	243.0	226.1	190.2	128.3		1.27695	26.84919	−25.323901	7.711919	0.246138
Carbon disulfide	CS_2		388.1	374.0	364.6	351.7	329.5	300.1	255.6	5.11988	10.62906	−9.288902	−0.698735	15.386540
Sulfur dioxide	SO_2	423.2	402.2	380.0	360.8	328.2	256.5			6.43046	6.41093	−2.662978	−0.896060	6.489831
Sulfur trioxide	SO_3				548.3	499.8	409.0	299.5	140.3	1.55618	23.48861	−9.147534	3.259366	−11.225329
Sulfuryl chloride	Cl_2SO_2	270.8	261.6	252.0	243.9	231.0	207.0	178.7	142.6	4.81312	9.37570	−4.943116	1.064302	−0.564284
Sulfur hexafluoride	SF_6	109.0	98.4	83.4	66.6					6.26231	6.40501	−2.747029	−2.003031	−72.803197
Organic compounds containing sulfur														
Methyl mercaptan	CH_4S	562.7	540.6	516.9	496.6	463.2	396.4	301.9		6.55525	4.23299	−2.363875	0.468305	−0.180912
Ethyl mercaptan	C_2H_6S	493.3	476.5	459.0	444.2	420.1	372.1	308.0	205.0	6.80697	4.46965	−1.818387	−0.923775	2.612589
Dimethyl sulfide	C_2H_6S	503.5	486.0	467.4	451.6	426.0	376.8	313.7	216.4	6.69172	5.20665	−3.208643	0.819280	−0.480074
Diethyl sulfide	$C_4H_{10}S$	435.0	422.4	409.1	397.9	380.1	346.9	307.5	257.5	7.32192	5.56252	−3.142609	0.674413	−0.388006
Thiophene	C_4H_4S		438.8	425.7	414.7	397.2	365.1	327.9	282.4	6.26860	6.29557	−3.767889	0.917693	−0.585746
Halogenated hydrocarbons														
Fluoromethane (R41)	CH_3F	444.4	396.3	333.0	261.4					5.34432	8.19605	−4.716205	−0.915983	4.082077
Difluoromethane (R32)	CH_2F_2	380.3	350.7	315.3	280.6	209.7				6.31467	6.57339	−2.449336	−1.596805	4.969907
Trifluoromethane (R23)	CHF_3	208.4	178.1	136.1						5.33728	10.11434	−6.515737	0.912341	−0.142635
Tetrafluoromethane (R14)	CF_4	45.8								6.90451	4.53442	−2.632334	−0.511569	3.574074
Methyl chloride	CH_3Cl	449.6	428.9	406.1	385.7	350.1	266.4			7.52784	1.79702	−0.314797	−1.088274	3.513993
Methylene chloride	CH_2Cl_2	389.5	375.2	360.1	347.3	326.8	287.7	238.9	168.1	5.48913	8.05864	−4.482770	0.992992	−0.431660
Chloroform	$CHCl_3$	289.8	281.5	272.5	264.8	252.4	229.2	201.2	163.6	7.16193	6.32194	−5.851382	2.576553	−2.746384
Carbon tetrachloride	CCl_4			219.0	212.8	203.3	185.8	165.0	138.1	6.79262	4.74990	−2.315979	−0.172679	3.053272
Bromomethane	CH_3Br	276.0	266.2	256.6	248.6	235.6	208.3	164.5		7.76803	5.56727	−7.230582	2.085873	4.403709
Dibromomethane	CH_2Br_2	236.4	229.5	222.5	216.9	208.3	193.5	177.3	158.7	5.90217	10.54835	−10.131479	4.169979	−0.342291
Tribromomethane	$CHBr_3$				174.1	169.2	159.8	149.2	137.0	10.34541	−11.68591	15.407923	−5.463728	0.309434
Tetrabromomethane	CBr_4						148.5	131.0		2.94192	12.07940	−3.508842	−3.779087	76.220152
Chlorodifluoromethane (R22)	$CHClF_2$	239.7	223.5	204.9	187.4	154.1				5.95795	7.77266	−4.647429	0.074274	4.096136
Dichlorofluoromethane (R21)	$CHCl_2F$	272.7	260.3	247.1	235.8	217.3	179.1	118.6		4.64484	12.93588	−10.395393	3.264061	−0.819565
Chlorotrifluoromethane (R13)	$CClF_3$	132.9	115.4	91.3						6.92913	3.46700	−0.923899	−1.124899	1.918255
Dichlorodifluoromethane (R12)	CCl_2F_2	174.3	164.2	152.8	142.2	122.5				5.66938	8.02998	−5.154107	−0.177208	4.608970
Trichlorofluoromethane (R11)	CCl_3F	206.6	198.6	190.2	183.1	171.4	147.0	111.1		5.41567	8.96541	−5.714602	−0.216220	4.647955
Ethyl fluoride (R161)	C_2H_5F	429.8	405.7	378.1	352.6	304.6				9.51720	−1.16297	0.541747	−0.037504	−0.041491
Ethyl chloride	C_2H_5Cl	428.4	411.1	392.6	376.7	350.5	296.6	215.3		6.30209	7.06337	−5.249715	1.249095	0.126838

Ethyl bromide	C_2H_5Br	258.9	264.4	262.0	256.5	244.7	220.7	193.8	155.2	14.52139	−12.89817	4.869861	7.100285	−46.731533
1,1-Dichloroethane	$C_2H_4Cl_2$	345.8	334.6	323.8	314.9	300.4	271.3	232.9	178.4	8.70837	−2.71451	7.371502	−6.147699	8.485117
1,2-Dichloroethane	$C_2H_4Cl_2$		379.1	366.5	356.6	341.5	314.6	283.3	243.5	8.56126	3.70808	−3.680483	1.403329	2.953142
1,2-Dibromoethane	$C_2H_4Br_2$				222.6	214.9	201.0	185.1	166.7	7.20165	−0.00816	5.018803	−3.197728	1.855801
1,1,1-Trifluoroethane (R143a)	$C_2H_3F_3$	228.6	210.2	187.8	165.6	118.5				6.71900	5.01141	−0.763635	−2.672683	10.182873
1,1,1-Trichloroethane	$C_2H_3Cl_3$		260.4	251.2	243.9	232.6	211.9	186.7	153.1	6.56423	6.65046	−4.263724	0.292419	3.965763
1,1,2,2-Tetrachloroethane	$C_2H_2Cl_4$		279.9	272.3	266.5	257.7	242.1	223.8	201.6	8.22713	−3.08321	10.707890	−7.956865	7.682273
Pentachloroethane	C_2HCl_5				228.2	220.8	208.5	194.7	178.1	7.04290	8.50532	−4.661553	−1.636031	7.068760
Hexachloroethane	C_2Cl_6								162.3	4.61352	12.12143	−7.667006	2.877370	−12.587588
1,1,2,2-Tetrachlorodifluoroethane	$C_2Cl_4F_2$					169.9	154.4	135.8	111.6	6.68635	7.51370	−3.993648	0.369246	−0.772752
1,1,2-Trichlorotrifluoroethan	$C_2Cl_3F_3$		166.1	158.7	152.8	143.6	125.4	100.5	55.8	6.97858	5.20404	−1.607386	−1.851544	12.696545
1,2-Dichlorotetrafluoroethane	$C_2Cl_2F_4$	152.3	145.1	137.0	129.7	117.3	89.1			7.99294	2.61639	−0.316162	−0.688124	−0.357781
1-Chloropropane	C_3H_7Cl	417.2	401.1	385.3	372.5	352.2	313.2	262.1	181.2	6.90066	6.18780	−4.021580	0.188325	5.019332
1-Chlorobutane	C_4H_9Cl	402.1	391.1	377.8	366.1	347.0	312.5	272.7	220.3	1.98680	26.31367	−26.025459	11.315390	−11.713944
1-Chloropentane	$C_5H_{11}Cl$	414.2	392.0	373.5	360.8	343.9	318.5	292.6		11.98674	0.04158	−5.045087	4.124543	14.191365
Chlorotrifluoroethene	C_2ClF_3		223.1	212.5	199.8					8.69389	10.04815	−6.152915	−4.930659	−53.084616
Vinyl chloride	C_2H_3Cl	382.9	362.7	341.8	324.0	293.7	224.9			−0.22946	25.94228	−21.553912	5.266260	3.943125
1,1-Dichloroethene	$C_2H_2Cl_2$	311.2	299.5	286.9	276.2	258.7	224.1	177.3		6.71423	5.31563	−2.937984	0.470263	−0.042603
Trichloroethene	C_2HCl_3	302.7	288.5	276.7	268.3	256.5	236.7	213.4	182.8	6.16853	7.47248	−3.556057	−2.178505	14.713520
Tetrachloroethene	C_2Cl_4			245.5	239.6	231.3	217.1	200.2	178.4	4.18516	10.62968	−2.623837	−5.374835	12.451366
Fluorobenzene	C_6H_5F		377.3	369.0	361.3	347.9	320.7	286.2	241.5	8.94237	−1.76739	4.988190	−3.559387	−1.628015
Chlorobenzene	C_6H_5Cl		380.9	371.5	364.0	352.4	331.4	307.2	278.1	8.17299	1.26513	1.758153	−2.434400	3.109045
Bromobenzene	C_6H_5Br		299.8	292.9	286.9	277.3	260.2	241.7	221.8	11.61418	−7.64685	6.214276	0.960149	−2.936095
Iodobenzene	C_6H_5I		256.4	248.7	243.1	235.3	223.0	210.6	197.1	6.50840	7.27177	−3.890897	−0.822891	6.073514
m-Chlorotoluene	C_7H_7Cl				332.5	329.7	324.2	315.3		8.03813	9.13193	−6.497782	−5.826589	9.843847
Benzyl chloride	C_7H_7Cl		406.8	396.6	389.1	378.1	359.4	338.3	313.3	9.17816	−2.64989	8.362278	−6.724665	7.266772
***n*-Alkanes**														
Methane	CH_4									4.99314	5.01992	−2.261379	−2.477646	4.425783
Ethane	C_2H_6	429.7	376.8							5.22295	7.28006	−4.737913	−0.589830	2.231339
Propane	C_3H_8	434.3	406.9	374.7	344.1	284.9				5.52801	7.88661	−5.323736	0.088186	2.147194
n-Butane	C_4H_{10}	426.3	406.7	385.4	366.5	333.7	258.3			5.90836	7.81092	−4.959362	−0.194761	3.830824
n-Pentane	C_5H_{12}	419.5	402.5	385.0	370.3	346.0	296.2	222.9		5.75681	9.95286	−6.871727	0.521979	4.474608
n-Hexane	C_6H_{14}	412.6	397.1	381.6	368.8	348.5	309.6			5.82255	11.20578	−8.077144	1.351285	3.455363
n-Heptane	C_7H_{16}	412.6	396.3	380.7	368.2	349.4	315.6	275.2	220.2	3.33801	21.88936	−18.680507	5.467222	2.994395
n-Octane	C_8H_{18}	411.5	395.1	379.6	367.6	349.8	319.1	284.5	241.5	4.48143	19.69699	−16.729253	5.297036	4.040976
n-Nonane	C_9H_{20}	408.2	392.1	377.0	365.4	348.5	319.9	289.0	252.6	6.04659	15.52925	−12.556768	4.153161	5.008624

D3.1. Table 4. (continued)

Substance	Formula	Temperature (°C)								Equation (9)				
		−50	−25	0	20	50	100	150	200	*A*	*B*	*C*	*D*	*E*
n-Decane	$C_{10}H_{22}$		389.9	375.1	363.8	347.3	320.0	291.4	258.8	4.95196	20.62050	−17.243223	5.887415	4.332104
n-Undecane	$C_{11}H_{24}$		394.9	377.0	364.5	347.7	322.3	296.7	267.6	7.78079	10.07916	−4.141098	−1.829586	18.468668
n-Dodecane	$C_{12}H_{26}$			377.1	364.3	346.9	320.5	294.5	266.3	7.96676	8.96561	−2.426306	−1.278554	16.571637
n-Tridecane	$C_{13}H_{28}$			365.5	358.2	346.4	324.8	300.7	273.6	7.10363	14.69528	−8.501852	2.345396	−3.139495
n-Tetradecane	$C_{14}H_{30}$				369.4	348.1	320.4	296.9	272.7	7.96599	7.28007	4.698876	−9.566327	41.044420
n-Tentadecane	$C_{15}H_{32}$				372.1	348.6	318.6	294.6	272.3	10.21651	9.06799	−4.682578	−0.826136	38.409983
n-Hexadecane	$C_{16}H_{34}$				369.6	347.8	318.3	294.0	271.8	11.99309	8.12193	−8.228896	5.197405	26.068465
n-Heptadecane	$C_{17}H_{36}$					342.4	316.8	293.9	272.5	15.94792	2.03335	−8.589551	11.148766	7.322380
n-Octadecane	$C_{18}H_{38}$					337.4	312.5	291.8	272.4	9.51541	13.40476	−6.317356	−2.039126	29.956901
n-Nonadecane	$C_{19}H_{40}$					373.1	326.0	294.9	271.7	10.54728	11.87652	−5.153424	−3.744106	87.493331
n-Eicosane	$C_{20}H_{42}$					322.6	306.7	289.2	270.1	12.81896	4.66635	−0.617286	2.595100	−5.396590
Isoalkanes														
Isobutane	C_4H_{10}	397.1	377.0	354.5	334.3	298.5	211.2			5.98835	6.85491	−3.938590	−0.367091	2.965412
2-Methyl butane	C_5H_{12}	397.4	381.1	364.2	349.6	325.3	274.3	196.8		6.35592	6.65305	−3.411011	−0.779434	4.472309
2,2-Dimethyl propane	C_5H_{12}			322.7	307.4	281.5	223.1	111.8		6.46867	4.15130	0.521940	−4.307291	26.542963
2-Methyl pentane	C_6H_{14}	394.5	378.9	363.4	350.6	330.4	291.0	238.5	150.9	4.81796	14.28905	−11.187698	2.386775	3.472905
3-Methyl pentane	C_6H_{14}	398.1	384.5	369.7	357.0	336.4	296.9	246.8	171.4	7.07983	5.84423	−3.391733	1.111535	−2.171129
2,2-Dimethyl butane	C_6H_{14}	365.9	351.5	337.4	325.9	307.4	270.0	218.2		7.18105	4.13376	−0.743441	−2.296211	8.667922
2,3-Dimethyl butane	C_6H_{14}	377.5	365.0	351.9	340.8	322.7	286.5	236.5	151.9	3.71503	17.70893	−14.535304	2.757326	1.283650
Olefines														
Ethylene	C_2H_4	383.5	311.1							5.15017	6.90546	−4.236236	−0.597914	3.214310
Propylene	C_3H_6	442.1	412.4	377.4	343.9	278.6				4.87035	9.25307	−6.242188	0.360560	1.336162
1-Butene	C_4H_8	431.3	409.5	386.1	365.6	330.3	249.3			5.50512	9.20052	−6.866370	1.422830	2.320790
1-Pentene	C_5H_{10}	418.8	401.4	384.3	369.8	345.6	293.9	216.4		7.66871	1.15392	3.415900	−4.960346	12.898598
1-Hexene	C_6H_{12}	413.3	397.1	381.4	368.8	348.8	309.9	258.5	178.6	7.38311	5.02928	−1.646030	−1.616197	7.915952
1-Heptene	C_7H_{14}	405.3	391.6	377.4	365.7	347.5	315.3	278.5	231.1	10.68425	−0.03078	−1.897634	3.500746	−2.348299
1-Octene	C_8H_{16}	430.0	401.9	379.9	365.3	346.7	318.7	288.3	249.0	8.37599	7.64620	−5.811718	−0.575961	28.208226
Propadiene	C_3H_4	514.9	475.2	439.7	413.3	374.1				10.85574	−2.93460	−5.277903	10.932970	2.693704
1,2-Butadiene	C_4H_6	497.7	475.4	451.5	430.8	396.7	326.7	219.6		5.98729	6.05637	−3.164536	0.585024	−0.256915
1,3-Butadiene	C_4H_6	457.1	435.4	411.9	391.1	355.6	275.8			6.12668	7.20781	−4.977657	0.788958	0.983749
1,2-Pentadiene	C_5H_8	476.1	457.9	438.3	421.4	393.6	338.5	268.3	168.3	6.21662	0.23633	7.289616	−5.206911	3.359798
trans-1,3-Pentadiene	C_5H_8	461.1	445.0	427.3	411.5	384.5	328.3	253.6		3.99567	3.66631	7.516396	−8.228076	5.648565

1,4-Pentadiene	C_5H_8	427.4	406.3	384.0	365.3	335.1	277.2	202.5		2.62969	11.50101	−4.967289	0.927654	−0.260803
2,3-Pentadiene	C_5H_8	491.7	472.2	451.5	434.0	405.8	351.7	282.7	175.4	5.27437	9.08302	−4.723587	0.949364	−0.314331
Acetylene and derivatives														
Acetylene	C_2H_2	569.0	501.5	413.0						7.01232	5.82528	−5.445163	3.417345	−34.680940
Propyne	C_3H_4	588.0	557.3	522.7	491.2	435.4	296.5			6.48101	6.32478	−3.509968	−0.188971	0.363183
2-Butyne	C_4H_6		537.5	516.3	498.6	468.4	402.0	302.0		6.53927	3.54709	3.287518	−7.257675	17.508732
1-Butyne	C_4H_6	517.4	494.0	468.6	446.3	408.6	327.6	188.7		6.40166	6.42355	−2.507973	−0.883718	2.487889
Naphthenes														
Cyclopropane	C_3H_6	492.1	464.5	434.6	408.8	364.0	243.8			4.10398	16.22930	−17.831464	8.643670	−10.417706
Cyclobutane	C_4H_8	473.6	456.1	437.6	421.7	395.0	338.0	245.6		5.02909	12.58788	−11.443639	2.642137	1.339011
Cyclopentane	C_5H_{10}	455.0	438.5	421.9	408.3	386.8	345.8	292.4	208.8	3.48031	17.33664	−15.181137	4.136664	1.169032
Methyl cyclopentane	C_6H_{12}	420.4	406.4	392.2	380.4	362.0	327.5	284.9	225.7	5.36513	11.93058	−9.827485	2.605197	0.886476
Ethyl cyclopentane	C_7H_{14}	407.5	396.1	384.1	374.1	358.2	328.8	294.3	251.2	7.41293	5.09188	−2.727834	0.483221	−0.097023
Propyl cyclopentane	C_8H_{16}	401.4	390.9	379.8	370.6	356.0	329.3	298.7	262.0	7.51798	6.17117	−3.334058	0.617716	−0.142182
Butyl cyclopentane	C_9H_{18}	399.4	387.8	375.8	365.8	350.2	322.2	290.9	255.0	4.61191	12.28173	−5.906447	1.146999	−0.354122
Pentyl cyclopentane	$C_{10}H_{20}$		386.0	374.9	365.7	351.3	325.7	297.3	264.8	−2.36442	34.80637	−24.840574	5.444180	−1.296219
Hexyl cyclopentane	$C_{11}H_{22}$						326.9	300.9	274.7	6.01832	12.39627	−3.910071	−6.188255	57.277450
Cyclohexane	C_6H_{12}				394.9	376.7	341.9	299.0	242.8	3.43321	14.08811	−8.768835	0.700818	−0.075958
Methyl cyclohexane	C_7H_{14}	401.9	388.2	375.2	364.8	349.1	320.7	287.2	244.8	5.86225	8.38591	−4.688241	−0.234104	4.663049
Ethyl cyclohexane	C_8H_{16}	402.0	387.3	374.1	364.0	349.3	323.6	294.4	258.8	6.06462	5.99669	0.021058	−3.147369	8.089475
Propyl cyclohexane	C_9H_{18}	390.6	380.1	369.2	360.2	346.0	320.8	292.8	260.8	4.77281	11.27564	−5.859548	1.220392	−0.393610
Butyl cyclohexane	$C_{10}H_{20}$	387.0	375.9	365.1	356.7	343.8	321.2	295.9	266.5	3.11699	13.76670	−3.940294	−2.637072	4.182641
Pentyl cyclohexane	$C_{11}H_{22}$			369.2	354.9	338.2	317.8	299.5	277.7	1.09595	27.77240	−16.042648	−6.665319	37.301542
Hexyl cyclohexane	$C_{12}H_{24}$			372.8	357.4	339.3	317.3	299.6	281.1	7.39273	11.52195	−5.039922	−6.350955	35.495677
Cyclopentene	C_5H_8	457.4	442.4	426.7	413.6	392.4	350.6	294.7	205.3	4.47191	13.66093	−11.313902	2.320078	1.098033
Cyclohexene	C_6H_{10}	446.8	434.3	421.1	410.1	392.5	359.4	319.8	269.2	6.95475	4.47360	−1.826880	−0.308833	0.588157
Aromatic compounds														
Benzene	C_6H_6				436.6	415.4	378.6	335.9	281.5	5.01506	10.64512	−7.248132	1.081122	7.042247
Toluene	C_7H_8	459.2	443.0	427.7	415.9	398.3	367.7	333.0	290.6	4.60584	13.97224	−10.592315	2.120205	4.277128
Ethyl benzene	C_8H_{10}	439.8	424.7	410.7	400.0	384.3	357.6	328.3	293.8	7.02317	7.61074	−4.976695	0.602265	5.080508
Propyl benzene	C_9H_{12}	425.8	410.9	396.9	386.1	370.5	344.8	318.3	288.6	3.62566	22.73230	−21.222047	7.252477	2.271518
Butyl benzene	$C_{10}H_{14}$	473.3	439.2	412.0	394.1	372.1	343.3	318.4	292.5	5.14898	17.70384	−14.168239	1.589433	27.482771
Pentyl benzene	$C_{11}H_{16}$	402.7	393.4	383.8	375.8	363.4	341.3	317.0	289.8	6.66503	10.39716	−5.545843	1.118460	−0.335753
Hexyl benzene	$C_{12}H_{18}$	399.1	389.9	380.5	372.7	360.5	338.9	315.4	289.4	6.28846	11.79255	−5.802187	1.043274	−0.288998
o-Xylene	C_8H_{10}		443.6	426.5	414.3	397.7	371.7	344.4	312.8	8.11493	5.01374	−2.818447	−0.894619	11.408042
m-Xylene	C_8H_{10}		425.1	413.4	404.1	389.8	364.4	335.6	301.1	7.31900	7.77601	−5.382762	0.652283	2.134955

D3.1. Table 4. (continued)

Substance	Formula	Temperature (°C)								Equation (9)				
		−50	−25	0	20	50	100	150	200	*A*	*B*	*C*	*D*	*E*
p-Xylene	C_8H_{10}				400.3	385.9	361.0	332.9	298.9	7.27992	7.34567	−4.422644	−0.568151	5.980841
1,2,3-Trimethyl benzene	C_9H_{12}		428.5	414.6	404.9	391.8	371.1	348.8	322.0	10.39204	−4.42696	9.379954	−7.666363	13.273177
1,2,4-Trimethyl benzene	C_9H_{12}		404.7	399.6	394.2	384.4	363.9	339.0	309.8	14.14613	−14.31772	14.977031	−4.290274	−4.728401
1,3,5-Trimethyl benzene	C_9H_{12}		414.1	404.4	396.3	383.6	360.5	334.5	304.2	9.36093	3.70265	−2.284621	0.510869	−0.170751
1,2,3,4-Tetramethyl benzene	$C_{10}H_{14}$		443.5	436.9	429.5	415.6	387.8	356.8	324.5	14.72574	−13.04599	9.651435	5.333190	−15.111565
1,2,3,5-Tetramethyl benzene	$C_{10}H_{14}$		415.7	406.7	399.2	387.4	366.2	342.8	316.3	8.84089	5.68826	−3.500096	0.827094	−0.386192
1,2,4,5-Tetramethyl benzene	$C_{10}H_{14}$						361.5	340.7	316.1	8.26210	3.55266	3.825610	−8.200753	20.230350
Pentamethyl benzene	$C_{11}H_{16}$						364.8	347.4	327.3	8.55594	8.30926	−5.296077	−1.074775	2.719078
Hexamethyl benzene	$C_{12}H_{18}$								344.6	9.10299	5.01384	−0.785047	0.133023	−10.509367
Styrene	C_8H_8		451.8	438.8	428.3	412.1	383.8	352.7	317.1	5.47731	11.91525	−8.564188	2.365441	0.547993
Isopropyl benzene	C_9H_{12}	417.3	402.4	388.8	378.5	363.6	338.8	312.1	281.2	6.66408	9.33907	−6.038411	0.676301	5.975822
Biphenyl	$C_{12}H_{10}$						382.4	362.8	341.6	1.70054	25.15686	−18.899436	4.251738	−0.855146
Diphenyl methane	$C_{13}H_{12}$					394.0	366.0	342.8	321.4	9.00675	7.69856	−5.652358	0.748699	18.859222
Triphenyl methane	$C_{19}H_{16}$						348.0	320.9	301.0	11.04977	−4.00253	14.380095	−13.942709	51.676539
Tetraphenyl methane	$C_{25}H_{20}$									13.46819	−9.33186	20.483970	−18.580654	98.978472
Naphthalene	$C_{10}H_8$						395.7	373.8	348.6	6.77024	−1.52986	11.675602	−8.848106	6.693238
1-Methylnaphthalene	$C_{11}H_{10}$		419.6	413.2	407.7	398.9	383.1	365.6	346.3	9.25713	3.48065	−2.766466	1.004761	−1.145790
2-Methylnaphthalene	$C_{11}H_{10}$					406.5	381.7	361.6	342.4	3.25417	22.06250	−16.524312	−0.013957	18.711257
1-Ethylnaphthalene	$C_{12}H_{12}$		423.9	415.9	409.2	398.9	380.7	361.1	339.8	7.36124	8.46271	−4.662002	0.982685	−0.388774
2-Ethylnaphthalene	$C_{12}H_{12}$		417.8	407.3	399.5	388.5	370.9	353.0	333.5	9.05108	0.98067	4.290927	−4.442335	6.238904
Alcohols														
Methanol	CH_4O	1264	1236	1206	1178	1130	1020	860.5		5.87513	13.91543	−5.817880	−5.692542	6.867206
Ethanol	C_2H_6O	978.3	961.7	943.4	925.9	892.3	810.5	687.4	503.8	14.68765	−15.27120	26.062308	−20.049654	15.816504
1-Propanol	C_3H_8O	866.3	850.5	829.0	807.9	770.4	691.9	590.2	453.5	7.09691	11.44183	−0.591839	−4.892172	−6.194349
1-Butanol	$C_4H_{10}O$	785.7	763.0	738.2	716.6	681.3	612.9	529.8	425.3	4.03015	18.33568	−4.805636	−3.203926	0.121902
1-Pentanol	$C_5H_{12}O$	723.0	699.6	673.4	650.8	615.0	551.5	483.4	408.1	8.13707	10.66862	−5.837508	6.657004	−9.699874
1-Hexanol	$C_6H_{14}O$		644.3	621.1	601.7	571.3	517.3	458.4	392.0	2.44435	25.74538	−15.196810	5.362395	−3.664521
1-Heptanol	$C_7H_{16}O$		617.1	598.1	580.7	551.6	496.5	435.4	370.4	23.75612	−56.83212	67.088469	−16.584142	−7.134212
1-Octanol	$C_8H_{18}O$			593.8	565.8	528.4	473.0	419.6	362.9	1.58827	18.29196	1.067691	−4.809578	30.814714
Isopropanol	C_3H_8O	809.6	804.0	788.6	769.8	731.4	641.6	518.6	351.1	14.13231	−18.02015	33.713095	−20.808299	−7.959708
2-Methyl-1-propanol	$C_4H_{10}O$	789.9	758.2	725.5	698.3	655.5	577.3	486.9	376.0	4.97368	15.12048	−3.192398	−0.405800	1.018629
3-Methyl-1-butanol	$C_5H_{12}O$	715.4	690.6	664.3	642.2	607.4	544.0	472.4	388.0	3.88255	20.24928	−8.853088	2.052090	−2.258462
Ethylene glycol	$C_2H_6O_2$			1086	1067	1037	986.1	929.3	863.3	8.13928	4.42093	5.642486	−7.124221	6.367364

1,3-Propylene glycol	$C_3H_8O_2$	1045	988.0	941.2	909.5	869.8	818.5	778.6	743.5	14.64626	9.65793	−19.564276	9.124923	16.992097
Glycerol	$C_3H_8O_3$				928.1	922.0	898.2	861.7	815.9	4.73387	16.62968	−6.646488	2.052518	−13.771300
Cyclohexanol	$C_6H_{12}O$					591.4	531.0	466.3	396.9	−2.55487	29.64441	−14.287549	6.116097	−7.186767
Benzyl alcohol	C_7H_8O						546.2	506.6	458.9	3.34913	13.24673	−1.996925	1.494200	−22.898760
Phenols														
o-Cresol	C_7H_8O					537.4	493.3	453.9	416.3	10.08581	4.98638	−6.884921	6.896322	9.981746
m-Cresol	C_7H_8O				585.7	563.9	527.1	488.6	447.1	4.82038	16.25429	−9.515663	2.639245	1.427210
p-Cresol	C_7H_8O					584.7	538.6	493.8	447.2	3.01380	18.92231	−9.261038	1.816957	9.840609
Phenol	C_6H_6O					603.1	564.5	519.4	472.4	16.25689	−15.34588	9.259460	8.211334	−23.563509
Carboxylic acids														
Formic acid	CH_2O_2				432.3	447.4	480.2	504.1	503.2	9.14069	4.41867	−8.928896	−8.183706	34.855085
Acetic acid	$C_2H_4O_2$				390.6	390.7	396.1	398.9	389.6	6.68664	15.01449	−22.086618	3.077691	17.355072
Propionic acid	$C_3H_6O_2$			416.5	416.4	418.1	421.0	418.3	403.5	11.77484	2.45068	−8.403845	−2.905673	13.942673
Butyric acid	$C_4H_8O_2$			463.6	457.3	448.3	432.0	410.2	377.7	0.50559	36.57824	−33.991377	4.980803	6.390699
Valeric acid	$C_5H_{10}O_2$					449.3	432.5	410.4	377.7	2.90159	24.06047	−14.773870	−6.523610	19.2954
Caproic acid	$C_6H_{12}O_2$			554.6	540.5	519.0	481.7	441.9	398.1	4.25370	23.26701	−17.198935	5.834191	−1.078919
Acetic anhydride	$C_4H_6O_3$	540.1	513.8	491.9	476.5	455.7	422.6	386.4	342.1	7.67997	8.28034	−2.531167	−3.283667	18.320222
Propionic anhydride	$C_6H_{10}O_3$		419.3	409.4	401.1	388.1	364.3	337.1	305.1	11.45713	2.15584	−1.286751	0.295048	−0.165848
Chloroacetic acid	$C_2H_3ClO_2$						487.6	535.0	516.2	7.80889	14.48961	−14.106871	13.335034	−317.4308
Dichloroacetic acid	$C_2H_2Cl_2O_2$						403.7	398.1	376.2	9.84708	2.73482	4.148698	−6.722742	−63.020357
Trichloroacetic acid	$C_2HCl_3O_2$						351.0	327.6	301.4	8.28156	10.25534	−5.999703	1.470064	−1.111776
Ketones														
Ketene	C_2H_2O	461.4	431.4	395.2	360.6	296.1				8.36565	−5.55025	10.724366	−7.158805	6.288894
Acetone	C_3H_6O	605.9	582.5	558.9	539.4	508.3	448.7	372.3	258.2	5.74063	9.13074	−4.880084	0.019915	3.765513
Methyl ethyl ketone	C_4H_8O	518.1	506.6	494.0	482.7	463.4	423.7	370.6	295.2	7.14228	6.74892	−2.395885	−2.807929	1.610334
Diethyl ketone	$C_5H_{10}O$		479.9	463.3	450.5	431.0	394.8	350.0	291.2	7.24751	4.39650	1.992158	−4.861266	10.588261
Dipropyl ketone	$C_7H_{14}O$		418.0	406.8	397.3	382.4	355.2	323.9	286.6	8.54054	6.18280	−3.862185	0.981831	−0.611406
Acetophenone	C_8H_8O				452.6	439.4	417.4	394.4	368.7	−0.98031	38.40600	−33.357359	7.603605	1.866879
Benzophenone	$C_{13}H_{10}O$					394.5	381.6	365.5	346.9	7.76821	10.29210	−7.292775	3.327307	−7.132167
Ethers														
Dimethyl ether	C_2H_6O	493.8	470.7	442.6	415.8	366.9	242.6			6.61358	3.90987	0.389855	−3.265474	−1.047992
Diethyl ether	$C_4H_{10}O$	423.6	405.3	386.3	370.1	343.4	289.2	211.0		5.72696	9.12303	−4.705274	−0.175016	3.557340
Dipropyl ether	$C_6H_{14}O$	388.1	376.1	363.5	352.8	335.7	303.5	263.9	209.8	8.43477	5.37680	−3.634751	1.020844	−0.445512
Methyl propyl ether	$C_4H_{10}O$	438.5	418.7	397.9	380.5	353.1	302.4	240.0	104.8	12.29808	−12.22318	12.791077	−1.853721	−0.396068
Ethyl propyl ether	$C_5H_{12}O$	431.2	407.2	382.2	361.4	328.6	268.8	198.6	105.3	0.63409	15.10518	−3.156607	0.612196	−0.252355
Ethylene oxide	C_2H_4O	647.3	623.5	598.4	576.4	538.8	459.1	344.8		8.52547	−3.93731	8.784981	−6.457998	7.902455

D3.1. Table 4. (continued)

Substance	Formula	Temperature (°C)								Equation (9)				
		−50	−25	0	20	50	100	150	200	*A*	*B*	*C*	*D*	*E*
Furane	C_4H_4O	461.7	443.4	424.9	409.4	384.2	334.4	267.3	153.4	6.01449	6.38875	−2.231449	−1.256419	4.886085
1,4-Dioxane	$C_4H_8O_2$				422.1	413.0	390.3	357.2	311.3	8.80566	−2.87837	9.443275	−9.170193	0.833694
Aldehydes														
Formaldehyde	CH_2O	808.8	777.1	741.8	709.1	649.3	496.4			12.06808	−7.97155	7.710808	−4.856937	11.036836
Acetaldehyde	C_2H_4O	666.4	641.3	616.7	595.9	561.2	486.2			7.20109	6.63553	−4.441975	−1.480320	10.024175
Paraldehyde	$C_6H_{12}O_3$				338.9	325.6	299.4	268.4	230.8	9.33129	3.24299	−0.057958	0.120535	−6.743412
Furfural	$C_5H_4O_2$		532.3	518.8	508.6	494.0	469.5	442.8	411.0	0.70876	32.70269	−28.222034	5.205805	4.040472
Benzaldehyde	C_7H_6O	497.2	487.0	476.8	468.6	455.8	432.4	405.1	372.5	3.54711	12.53164	−3.340287	−3.677402	3.016282
Salicylaldehyde	$C_7H_6O_2$				416.6	410.3	399.5	387.2	372.2	26.90848	−41.82693	31.807059	−8.848384	5.540309
Esters														
Methyl formate	$C_2H_4O_2$	539.3	519.5	499.0	481.5	452.8	395.3	316.7		6.89413	6.01843	−2.694377	−0.840353	3.110258
Ethyl formate	$C_3H_6O_2$	488.5	470.3	451.1	434.9	409.2	360.8	300.0	208.3	4.47415	15.95005	−13.035900	4.462419	−2.281851
Propyl formate	$C_4H_8O_2$	455.6	440.3	424.4	411.1	390.0	350.2	302.3	239.8	7.59455	3.76681	0.594088	−1.239979	1.558213
Methyl acetate	$C_3H_6O_2$	488.2	474.0	457.2	442.2	417.8	371.3	313.0	222.2	6.24651	13.81319	−13.592686	6.280357	−9.776838
Ethyl acetate	$C_4H_8O_2$	450.9	436.3	420.9	407.9	387.0	347.0	297.2	228.4	8.65545	3.30110	−0.160488	−0.850538	1.010147
Propyl acetate	$C_5H_{10}O_2$	429.9	416.4	402.4	390.7	372.2	337.3	295.0	240.0	6.63509	9.44227	−4.350780	−0.398819	1.849160
Methyl propionate	$C_4H_8O_2$	460.0	444.3	427.8	414.0	391.9	350.8	301.6	236.5	8.24495	3.87501	−0.829044	0.344109	−0.413604
Ethyl propionate	$C_5H_{10}O_2$	386.5	395.1	393.0	386.0	369.5	333.0	290.7	241.3	10.48291	1.90991	−4.415043	9.017366	−46.620420
Propyl propionate	$C_6H_{12}O_2$			373.3	365.0	352.2	328.0	296.7	253.0	3.40390	24.73760	−19.159863	0.929405	7.696521
Methyl butyrate	$C_5H_{10}O_2$	429.7	416.6	402.8	391.2	372.7	338.5	298.1	246.7	7.22592	8.50382	−5.024452	1.195632	−0.550681
Ethyl butyrate	$C_6H_{12}O_2$	402.4	391.1	379.3	369.4	353.7	324.7	290.7	248.6	8.41156	6.59984	−3.794374	0.802575	−0.278759
Methyl benzoate	$C_8H_8O_2$						375.3	344.9		11.25328	1.94206	−1.556784	−5.351100	89.919764
Ethyl benzoate	$C_9H_{10}O_2$		386.0	378.7	372.7	363.2	346.3	327.6	306.5	11.62555	−0.15927	0.128177	−0.053452	0.079776
Methyl salicylate	$C_8H_8O_3$			410.3	403.1	391.8	371.6	349.4	324.8	8.98498	7.09493	−4.043975	0.869200	−0.378981
Amines														
Methyl amine	CH_5N	923.1	878.6	830.6	788.2	714.8	552.2			6.68704	5.59469	−0.071556	−3.085246	7.431487

Ethyl amine	C_2H_7N	693.4	662.8	631.4	604.3	558.9	463.2	319.4		7.77766	1.82614	3.635806	−4.492103	9.842348
Propyl amine	C_3H_9N	586.4	570.3	552.7	536.6	507.8	443.2	348.7	197.7	3.39340	12.71924	−1.316011	−8.140440	9.108951
n-Butyl amine	$C_6H_{15}N$		525.8	507.5	492.0	467.0	419.5	361.0	282.1	6.90260	7.60459	−3.614348	0.074152	0.044303
Dimethyl amine	C_2H_7N	672.1	637.9	600.9	568.9	515.8	404.9	214.3		5.68174	10.17800	−5.691902	1.408236	−1.170463
Trimethyl amine	C_3H_9N	433.5	414.5	393.8	375.6	345.0	278.5			7.62398	3.76969	−2.925155	0.979043	−1.193023
Diethyl amine	$C_6H_{15}N$		469.6	448.8	431.2	402.8	348.5	279.3	171.7	5.33934	10.56571	−5.837037	1.428051	−1.122078
Triethyl amine	$C_6H_{15}N$	378.0	366.9	354.9	344.7	328.3	297.5	259.9	209.2	7.74933	6.41111	−4.878480	1.631371	−1.542623
Piperidine	$C_5H_{11}N$			461.8	450.3	432.0	398.6	360.3	314.4	6.48159	6.79118	−3.820956	0.886131	−0.635871
Pyridine	C_6H_7N		539.1	522.9	510.4	491.5	458.4	421.0	376.2	6.78808	5.19130	−1.422034	−1.391907	4.491260
Aniline	C_6H_7N			585.0	574.7	559.3	532.4	502.5	467.7	7.07225	8.70667	−3.991451	−1.656520	3.263408
N-Methyl aniline	C_7H_9N	527.4	518.8	509.9	502.5	490.9	470.2	447.0	420.8	13.26061	−5.02657	3.272891	−0.737961	0.244629
N,N-dimethyl aniline	$C_8H_{11}N$				418.6	408.8	391.3	371.7	349.3	13.47310	−6.35431	4.138973	−0.981377	0.533077
N,N-diethyl aniline	$C_{10}H_{15}N$		421.6	411.5	403.1	390.1	367.0	341.9	314.0	6.19042	11.73523	−5.842622	1.090567	−0.337465
Phenylhydrazine	$C_6H_8N_2$				564.3	555.4	540.2	523.8	505.3	21.89034	−26.13478	18.999009	−5.040744	2.813373
Diphenyl amine	$C_{12}H_{11}N$						397.0	381.4	364.4	11.96840	0.31904	−0.177413	0.024112	0.020506
Nitriles														
Acetonitrile	C_2H_3N					805.5	755.2	679.3	589.8	12.63773	−0.41956	−9.636566	15.912158	−123.3607
Propionitrile	C_3H_5N	725.9	703.1	679.2	659.2	627.6	569.4	501.7	417.9	5.39746	9.28762	−5.079418	1.116363	−0.448885
Butyronitrile	C_4H_7N	640.6	621.3	601.2	584.7	559.3	515.6	469.6	418.6	15.18066	−13.56898	8.892253	1.838158	−2.367991
Benzonitrile	C_7H_5N			508.3	497.9	482.2	455.3	427.4	398.0	9.80839	3.44990	−5.365836	4.172565	−1.195374
Amides														
Formamide	CH_3NO				1378	1346	1291	1230	1164	9.70079	3.52359	−2.149747	0.503265	−0.248567
Nitroderivates														
Nitromethane	CH_3NO_2		669.9	649.6	634.0	611.1	572.4	529.3	476.6	10.84612	0.90457	−3.763319	2.190125	3.811262
Nitrobenzene	$C_6H_5NO_2$				448.3	434.7	413.5	391.3	365.8	13.98596	−19.90491	26.349415	−13.211884	12.803755
o-Nitrotoluene	$C_7H_7NO_2$			434.5	425.5	412.4	391.3	370.1	348.1	11.62596	2.43803	−5.209765	3.612648	1.807934
m-Nitrotoluene	$C_7H_7NO_2$				417.8	411.8	397.4	379.1	358.1	12.46410	−0.06534	−3.559221	4.246115	−10.130675
p-Nitrotoluene	$C_7H_7NO_2$						401.2	382.3	359.6	9.68851	4.92278	−5.325247	4.020553	−13.754145

D3.1. Table 5. Specific heat capacity c_P of liquids at constant pressure in J/g K

Substance	Formula	Temperature (°C)								Equation (8)					
		−25	0	20	50	100	150	200	250	*A*	*B*	*C*	*D*	*E*	*F*
Elements															
Xenon	Xe	0.470	0.770							0.4536	4.0921	3.9528	−29.0063	75.8030	−62.9962
Krypton	Kr									0.4540	4.3618	−0.8361	−2.7617	12.9684	−9.9919
Argon	Ar									0.4509	4.5477	−4.1814	18.3045	−39.5634	38.7660
Air										0.4764	5.5446	1.1919	−13.3371	37.8579	−29.7212
Nitrogen	N_2									0.4786	5.6086	−1.1144	2.1294	5.8166	−8.5275
Oxygen	O_2									0.4842	5.1121	2.1237	−12.2421	29.7659	−21.3778
Sulfur	S						1.439				−11.2815	24.8360			
Fluorine	F_2									0.5138	5.1344	3.5766	−14.2066	29.8332	−21.5485
Chlorine	Cl_2	0.948	0.979	1.003	1.041	1.272				0.3453	9.6564	−36.4320	201.1762	−460.0757	367.6988
Bromine	Br_2		0.484	0.477							7.2677	3.8178			
Iodine	I_2						0.318	0.318	0.318		9.7011				
Anorganic compounds															
Hydrogen fluoride	HF	2.297	2.428	2.562						1.0347	2.8797	4.1022	−9.5518	0.6808	10.6306
Hydrogen chloride	HCl									1.1345	−5.2809	71.8140	−174.0520	135.2957	12.3158
Hydrogen bromide	HBr										7.3745	−0.4312			
Hydrogen iodide	HI	0.455									5.2636	4.1993			
Hydrogen cyanide	HCN		2.607	2.621							8.9009	−1.0655			
Water	H_2O		4.212	4.188	4.180	4.217	4.313	4.499	4.869	0.2399	12.8647	−33.6392	104.7686	−155.4709	92.3726
Hydrogen sulfide	H_2S	2.021	2.095	2.208	2.565					0.5378	6.1881	4.7466	−25.8471	62.3782	−43.2404
Ammonia	NH_3	4.488	4.616	4.746	5.064					0.5616	7.2382	2.7201	−7.7814	22.6538	−30.8592
Nitric oxide	NO									2.9046	28.5404	−169.6540	120.0529	913.7753	−1501.0300
Nitrogen dioxide	NO_2		3.006	3.079	3.189	3.371					19.8275	−8.7134			
Nitrous oxide	N_2O	1.941	2.273	3.199						0.4454	8.8255	−6.7522	17.5923	−23.641	22.0174
Dinitrogentetroxide	N_2O_4		1.503	1.539	1.594	1.686					19.8244	−8.7114			
Cyanogen	C_2N_2	2.016	2.567	3.846						12.4311	−1.4598	−91.6976	13.6141	−159.9473	1104.1285
Phosphorus trichloride	PCl_3	0.837	0.841	0.844	0.848						14.5988	−1.3758			
Cyanogen chloride	ClCN		1.478	1.504	1.542						12.6072	−4.2927			
Silane	SiH_4										7.8085	−0.8564			
Tetrachlorosilane	$SiCl_4$		0.814	0.821	0.831						18.2610	−3.5363			
Carbon monoxide	CO									0.4361	6.7941	−7.2244	22.9749	−33.6968	27.3780
Carbon dioxide	CO_2	2.115	2.542							0.4826	9.4642	−12.2772	62.6197	−153.1172	174.3140
Carbon suboxide	C_3O_2	1.500									18.1002	−22.2303	19.8732		
Carbonyl sulfide	COS	1.218	1.277	1.347	1.535	5.383				0.4434	9.1623	−11.2214	33.1793	−58.3488	47.4275
Phosgene	CCl_2O	1.011	1.018							−0.1917	12.3376	5.7238	−11.6654	−15.9746	33.2033
Carbon disulfide	CS_2	0.988	0.994	1.001	1.019	1.072	1.165	1.316	1.546	−0.000602	15.8105	−34.7870	67.8378	−61.7414	23.2452

Sulfur dioxide	SO_2	1.360	1.370	1.389	1.444	1.689	4.946			0.49318	9.838616	−5.2162	10.4498	−2.538	0.2025
Sulfur trioxide	SO_3			3.224							31.0397				
Sulfuryl chloride	Cl_2SO_2														
Sulfur hexafluoride	SF_6	0.904	1.027	1.225						0.4919	17.0151	−22.8856	17.9435	344.1647	−1202.8247
Organic compounds containing sulfur															
Methyl mercaptan	CH_4S	1.812	1.838	1.872						1.2188	5.9008	6.5471	−5.9594	−2.3710	9.8656
Ethyl mercaptan	C_2H_6S	1.826	1.856	1.887						−0.2394	18.8932	−8.8336	−15.0253	33.0373	−11.4703
Dimethyl sulfide	C_2H_6S	1.847	1.867	1.884							15.3628	−3.0859			
Diethyl sulfide	$C_4H_{10}S$	1.816	1.854	1.885							24.8907	−9.3678			
Thiophene	C_4H_4S	1.372	1.423	1.463	1.528	1.660	1.818			−1.3455	36.7609	−57.0029	0.3735	132.9958	−120.8312
Halogenated hydrocarbons															
Fluoromethane (R41)	CH_3F	2.254	2.555	3.237						0.4573	7.35738	−1.7868	2.5438	3.9312	−0.887
Difluoromethane (R32)	CH_2F_2	1.645								0.4827	9.7395	−7.7860	19.1934	−23.1056	16.5271
Trifluoromethane (R23)	CHF_3	1.462	1.847							0.5822	8.8835	2.9305	−24.8820	62.5446	−50.3571
Tetrafluoromethane (R14)	CF_4									−0.5912	21.4346	−54.6356	103.9865	−99.3261	44.1957
Methyl chloride	CH_3Cl	1.502	1.545	1.593	1.690	1.918				0.00097	13.2684	−17.7900	20.1696	−3.7396	−0.2871
Methylene chloride	CH_2Cl_2	1.158	1.175	1.188							13.6156	−3.4804			
Chloroform	$CHCl_3$	0.920	0.939	0.954	0.977						16.3925	−5.9310			
Carbon tetrachloride	CCl_4		0.857	0.856	0.866	0.982				9.0974	−11.8485	−31.2549	116.6462	64.4058	−193.2563
Bromomethane	CH_3Br	0.820	0.823								9.6167	−0.5387			
Dibromomethane	CH_2Br_2	0.602	0.598	0.602	0.619					3.5496	4.5450	1.9519	−1.4975	−13.8676	34.9504
Tribromomethane	$CHBr_3$				0.528						22.2716	−11.6166			
Tetrabromomethane	CBr_4					0.410	0.421				19.4442	−6.3606			
Chlorodifluoromethane (R22)	$CHClF_2$	1.123	1.175	1.239	1.42					0.5093	11.1754	−3.9432	−0.5057	9.8669	−4.5687
Dichlorofluoromethane (R21)	$CHCl_2F$	1.014	1.033	1.049	1.073						14.5385	−4.4214			
Chlorotrifluoromethane (R13)	$CClF_3$	1.040								0.1045	14.5341	−11.4812	−6.1931	37.4740	−16.4165
Dichlorodifluoromethane (R12)	CCl_2F_2	0.894	0.934	0.976	1.071	1.996				0.4707	14.3575	−16.6484	52.1728	−101.8845	76.6065
Trichlorofluoromethane (R11)	CCl_3F	0.847	0.866	0.883	0.912	0.986	1.164			0.4914	14.93805	−5.8469	5.5124	−4.9302	1.4427
Ethyl fluoride (R161)	C_2H_5F	1.881								0.3964	10.9715	−2.7972	−5.3547	7.6366	−0.0810
Ethyl chloride	C_2H_5Cl	1.528	1.579	1.633	1.734					0.3496	15.7297	−11.0908	−10.4450	33.5779	−12.9713
Ethyl bromide	C_2H_5Br	0.875	0.898	0.917							14.5606	−6.0873			
1,1-Dichloroethane	$C_2H_4Cl_2$	1.245	1.262	1.276	1.296						17.0357	−4.2085			
1,2-Dichloroethane	$C_2H_4Cl_2$	1.273	1.285	1.301	1.330					0.1540	23.8336	−61.2569	203.4469	−341.8857	219.5230
1,2-Dibromoethane	$C_2H_4Br_2$			0.715	0.738	0.776					22.2955	−11.1806			
1,1,1-Trifluoroethane (R143a)	$C_2H_3F_3$	1.392	1.495	1.624	2.118					0.4659	15.4281	−20.4118	60.4809	−117.8952	92.7296
1,1,1-Trichloroethane	$C_2H_3Cl_3$	1.044	1.064	1.079	1.102						20.4451	−6.7692			
1,1,2,2-Tetrachloroethane	$C_2H_2Cl_4$	0.971	0.986	1.000	1.027	1.085	1.159	1.251			34.1473	−40.8553	27.9921		
Pentachloroethane	C_2HCl_5				1.010	1.023	1.065	1.133		0.8082	28.8553	−13.4334	−25.1521	56.4550	0.9020
Hexachloroethane	C_2Cl_6							0.995			36.1662	−24.5603			

D3.1. Table 5. (continued)

Substance	Formula	Temperature (°C)								Equation (8)					
		−25	0	20	50	100	150	200	250	*A*	*B*	*C*	*D*	*E*	*F*
1,1,2,2-Tetrachlorodifluoroethane	$C_2Cl_4F_2$				0.950						27.4571	−10.0780			
1,1,2-Trichlorotrifluoroethan	$C_2Cl_3F_3$	0.878	0.896	0.913	0.943	1.006	1.117	1.786		0.51793	22.73059	−15.7371	45.2567	−105.0239	90.1894
1,2-Dichlorotetrafluoroethane	$C_2Cl_2F_4$	0.973	1.000	1.021	1.053	1.106					23.7241	−9.1099			
1-Chloropropane	C_3H_7Cl	1.614	1.641	1.662							17.8270	−5.0952			
1-Chlorobutane	C_4H_9Cl	1.653	1.696	1.738	1.812					1.8076	17.3296	−0.7740	−11.4579	4.5232	9.2855
1-Chloropentane	$C_5H_{11}Cl$	1.618	1.704	1.773	1.875	2.047					34.8116	−24.9739			
Chlorotrifluoroethene	C_2ClF_3	1.058									19.4091	−18.1599	14.1834		
Vinyl chloride	C_2H_3Cl	1.117	1.246	1.349	1.504	1.762					15.5355	−16.7781			
1,1-Dichloroethene	$C_2H_2Cl_2$	1.081	1.110	1.140						1.5539	8.3161	5.0683	−5.9131	−6.4196	13.4921
Trichloroethene	C_2HCl_3	0.936	0.952	0.965	0.984						18.0501	−5.7665			
Tetrachloroethene	C_2Cl_4		0.839	0.851	0.870	0.902					21.0779	−7.7665			
Fluorobenzene	C_6H_5F	1.455	1.492	1.522							22.1914	−9.6517			
Chlorobenzene	C_6H_5Cl	1.288	1.322	1.331	1.376					51.1281	−92.3533	−306.5358	812.1606	−43.2394	−574.0475
Bromobenzene	C_6H_5Br			0.940	0.992	1.077	1.163	1.249			29.9725	−21.7182			
Iodobenzene	C_6H_5I		0.770	0.777	0.789						23.0925	−6.7777			
m-Chlorotoluene	C_7H_7Cl					1.609	1.803	1.997			41.4660	−38.9736			
Benzyl chloride	C_7H_7Cl	1.342	1.393	1.433	1.494	1.596	1.697				33.9739	−21.2148			
***n*-Alkanes**															
Methane	CH_4									0.4708	5.7207	−0.6552	−0.4530	5.0199	−5.0556
Ethane	C_2H_6	2.961	3.621	5.682						0.4281	10.4584	−18.1757	51.6811	−75.8320	44.4690
Propane	C_3H_8	2.340	2.503	2.676	3.094					0.5219	13.0156	−3.9111	−21.2164	49.1038	−30.2438
n-Butane	C_4H_{10}	2.206	2.311	2.412	2.599	3.102				0.4943	19.1915	−11.5900	−13.3471	38.1134	−18.8852
n-Pentane	C_5H_{12}	2.123	2.210	2.292	2.437	2.749	3.283			0.4935	25.3941	−18.4831	−8.8055	27.9787	−5.5481
n-Hexane	C_6H_{14}	2.066	2.153	2.231	2.362	2.616	2.934	3.565		0.5687	29.2523	−5.2270	−66.7829	110.6460	−52.8290
n-Heptane	C_7H_{16}	2.079	2.153	2.222	2.340	2.565	2.828	3.184	4.544	0.6767	34.8802	−9.4333	−51.0547	57.7955	−1.9863
n-Octane	C_8H_{18}	2.074	2.144	2.209	2.321	2.531	2.766	3.040	3.500	0.6399	42.0897	−21.4435	−14.6527	−19.5539	54.7506
n-Nonane	C_9H_{20}	2.047	2.121	2.189	2.302	2.509	2.730	2.968	3.271	0.52876	50.2959	−37.7839	31.5903	−103.5592	105.4389
n-Decane	$C_{10}H_{22}$	2.025	2.104	2.174	2.288	2.493	2.706	2.929	3.180	0.5805	55.8884	−34.0842	6.4319	−67.7489	81.0979
n-Undecane	$C_{11}H_{24}$	2.051	2.137	2.206	2.309	2.481	2.653	2.825	2.997		63.8410	−41.3410			
n-Dodecane	$C_{12}H_{26}$		2.137	2.197	2.298	2.487	2.688	2.895	3.112	0.4831	71.9423	−57.3220	54.8202	−156.5306	146.1074
n-Tridecane	$C_{13}H_{28}$		2.150	2.200	2.283	2.444	2.633	2.847	3.091	1.0540	74.7978	−31.5528	−117.6551	208.0928	−98.0633
n-Tetradecane	$C_{14}H_{30}$			2.174	2.281	2.461	2.640	2.820	2.999		86.1144	−59.3516			
n-Pentadecane	$C_{15}H_{32}$			2.181	2.287	2.465	2.642	2.819	2.997		93.3129	−64.1464			
n-Hexadecane	$C_{16}H_{34}$			2.168	2.275	2.453	2.631	2.809	2.986		100.7177	−70.0879			
n-Heptadecane	$C_{17}H_{36}$				2.277	2.452	2.628	2.803	2.978		107.7204	−74.6158			
n-Octadecane	$C_{18}H_{38}$				2.271	2.445	2.618	2.792	2.965		114.5685	−79.3947			

n-Nonadecane	$C_{19}H_{40}$				2.267	2.443	2.619	2.795	2.971		122.6402	−86.1313			
n-Eicosane	$C_{20}H_{42}$				2.244	2.421	2.598	2.774	2.951		129.9485	−92.5652			
Isoalkanes															
Isobutane	C_4H_{10}	2.159	2.283	2.398	2.615	3.347				0.5019	18.6631	−13.6773	−3.2077	23.7670	−18.2744
2-Methyl butane	C_5H_{12}	2.036	2.151	2.250	2.412	2.746	3.390			0.4261	26.6688	−36.0009	67.0523	−114.4751	80.5553
2,2-Dimethyl propane	C_5H_{12}		2.166	2.280	2.468	2.899	4.955			0.4460	25.4168	−28.8264	36.1755	−53.5413	32.3813
2-Methyl pentane	C_6H_{14}	2.012	2.120	2.213	2.360	2.632	2.988	3.904		0.4974	31.9938	−35.1230	55.9259	−112.2866	88.1404
3-Methyl pentane	C_6H_{14}	2.016	2.109	2.190	2.321					0.2478	31.9772	−22.6839	−13.5507	32.0412	−11.1087
2,2-Dimethyl butane	C_6H_{14}	1.997	2.092	2.168							30.1997	−19.2861			
2,3-Dimethyl butane	C_6H_{14}	1.961	2.067	2.161	2.317	2.611	2.984	3.917		0.6360	29.6520	−15.3827	−23.3590	13.2590	21.6627
Olefines															
Ethylene	C_2H_4	3.290	6.565							0.4832	7.3899	−1.8990	−6.9588	33.3709	−27.4230
Propylene	C_3H_6	2.282	2.440	2.617	3.078					0.5432	10.8992	4.9726	−56.4635	124.9919	−89.5562
1-Butene	C_4H_8	2.098	2.192	2.284	2.457	2.991				0.4539	17.8592	−18.9490	26.8206	−31.7310	21.9467
1-Pentene	C_5H_{10}	2.054	2.138	2.213	2.333	2.550	2.900			0.4317	18.9109	14.8383	−83.2734	100.4051	−31.8309
1-Hexene	C_6H_{12}	2.014	2.092	2.161	2.275	2.488	2.734			0.2126	29.3722	−17.2174	−13.0392	18.2316	4.7262
1-Heptene	C_7H_{14}	1.940	2.042	2.128	2.262	2.485	2.715	3.083	5.879	1.1623	25.0569	22.4762	−75.7051	8.8914	49.3886
1-Octene	C_8H_{16}	1.997	2.069	2.135	2.245	2.443	2.656			0.8558	35.5492	−2.5332	−37.7196	−15.1334	59.2556
Propadiene	C_3H_4	2.262									12.6130	−4.6505			
1,2-Butadiene	C_4H_6	2.132	2.207							1.8310	7.9190	8.7781	−10.9833	−5.3964	16.0089
1,3-Butadiene	C_4H_6	2.064	2.163	2.259	2.431					0.1214	19.4545	−17.4079	−8.0930	41.2556	−21.3766
1,2-Pentadiene	C_5H_8	1.904	2.003	2.082	2.201						23.7833	−16.2516			
trans-1,3-Pentadiene	C_5H_8	2.037	2.108	2.164							22.4904	−11.5084			
1,4-Pentadiene	C_5H_8	1.990	2.064	2.138						2.2223	11.2795	5.5371	−13.7108	3.0954	10.8000
2,3-Pentadiene	C_5H_8	2.101	2.161	2.219						1.5604	16.3736	−7.4995	13.7603	−27.7122	23.9452
Acetylene and derivatives															
Acetylene	C_2H_2	3.310									11.2882	−4.7196			
Propyne	C_3H_4	2.546									13.9264	−4.3314			
2-Butyne	C_4H_6	2.199	2.257	2.303							17.6692	−7.0682			
1-Butyne	C_4H_6	2.316	2.418	2.509						−0.0061	24.8755	−47.5092	107.1645	−157.0534	98.7463
Naphthenes															
Cyclopropane	C_3H_6	1.933	2.017	2.100						0.4150	9.4185	2.0685	−19.3393	25.3390	−6.3267
Cyclobutane	C_4H_8	1.766	1.845	1.909							16.4351	−9.8045			
Cyclopentane	C_5H_{10}	1.581	1.670	1.755	1.901	2.185	2.540	3.239		0.5911	20.2987	−8.6195	−31.5870	25.6255	17.1836
Methyl cyclopentane	C_6H_{12}	1.691	1.782	1.864	2.001					0.2323	30.2852	−24.7645	−17.6496	30.2720	0.5545
Ethyl cyclopentane	C_7H_{14}	1.705	1.793	1.874						5.7711	7.7296	16.3179	−15.4401	−38.2401	46.8886
Propyl cyclopentane	C_8H_{16}	1.741	1.830	1.908	2.031	2.241				−0.8267	43.7797	−15.1467	−53.0231	21.3862	32.6773
Butyl cyclopentane	C_9H_{18}	1.771	1.849	1.920	2.038	2.269	2.544			1.7801	45.8700	−36.6364	−26.1177	49.3700	−9.4185
Pentyl cyclopentane	$C_{10}H_{20}$		1.821	1.911	2.047	2.272	2.498	2.724	2.949		59.8890	−49.9621			

D3.1. Table 5. (continued)

Substance	Formula	Temperature (°C)								Equation (8)					
		−25	0	20	50	100	150	200	250	*A*	*B*	*C*	*D*	*E*	*F*
Hexyl cyclopentane	$C_{11}H_{22}$		1.841	1.915	2.029	2.226	2.432	2.651	2.886	0.1807	65.9848	−74.1315	62.1031	−74.2454	41.8551
Cyclohexane	C_6H_{12}			1.773	1.979	2.248	2.511	2.848	3.574	0.4835	28.0569	−6.7431	−118.2361	355.2759	−383.5819
Methyl cyclohexane	C_7H_{14}	1.688	1.779	1.860						5.5654	8.9219	1.2715	−7.0391	−36.0234	35.0283
Ethyl cyclohexane	C_8H_{16}	1.696	1.788	1.866	1.992	2.223				2.3215	32.3872	−15.4092	−20.3689	6.6446	12.0597
Propyl cyclohexane	C_9H_{18}	1.728	1.818	1.896	2.021	2.252	2.514			1.8529	44.6977	−28.2578	−36.0078	45.5607	−8.2807
Butyl cyclohexane	$C_{10}H_{20}$	1.746	1.832	1.908	2.032	2.269	2.543	2.856	3.206	0.0000	74.2074	−102.7589	37.7432	32.4584	−20.2443
Pentyl cyclohexane	$C_{11}H_{22}$		1.841	1.915	2.029	2.225	2.432	2.651	2.887	0.2992	64.8603	−62.1122	17.0306	−0.3030	−3.1476
Hexyl cyclohexane	$C_{12}H_{24}$		1.815	1.893	2.012	2.215	2.426	2.648	2.880	0.4211	70.2456	−45.4883	−67.7512	128.0094	−75.8804
Cyclopentene	C_5H_8	1.600	1.690	1.777						1.7041	15.4605	−7.8794	−23.6606	37.9550	−8.0892
Cyclohexene	C_6H_{10}	1.617	1.707	1.787	1.919						34.7359	−48.6391	26.8882		
Aromatic compounds															
Benzene	C_6H_6			1.710	1.802	1.980	2.189	2.460	3.037	0.4928	22.5398	−16.8877	10.0243	−39.3837	49.5380
Toluene	C_7H_8	1.561	1.625	1.685	1.783	1.964	2.158	2.380	2.697	0.4806	28.5306	−7.4267	39.8253	−98.5476	85.5686
Ethyl benzene	C_8H_{10}	1.587	1.653	1.714	1.814	1.997	2.189	2.392	2.636	0.4534	35.2674	−36.6767	62.8911	−149.3270	122.1201
Propyl benzene	C_9H_{12}	1.645	1.713	1.771	1.866	2.034	2.211	2.395	2.598	0.7061	36.1020	−5.9477	−47.3163	24.7981	15.5593
Butyl benzene	$C_{10}H_{14}$	1.668	1.737	1.796	1.893	2.076				6.0249	17.9699	20.0300	−33.0605	−27.6367	42.2093
Pentyl benzene	$C_{11}H_{16}$	1.693	1.754	1.808	1.900	2.079	2.292	2.538		0.5085	62.6754	−60.6823	−34.3506	104.3206	−46.7914
Hexyl benzene	$C_{12}H_{18}$		1.777	1.826	1.912	2.086	2.298	2.549		1.9918	62.0635	−52.3332	−40.5346	82.4337	−17.2071
o-Xylene	C_8H_{10}	1.622	1.689	1.742	1.822	1.955					33.6972	−21.4077			
m-Xylene	C_8H_{10}	1.583	1.649	1.706	1.799	1.974	2.174	2.398	2.646	0.1118	38.6021	−35.2435	−15.7768	55.5289	−29.2411
p-Xylene	C_8H_{10}			1.675	1.770	1.955	2.145	2.341	2.580	−0.2990	48.9714	−144.5391	451.2798	−811.3867	551.2969
1,2,3-Trimethyl benzene	C_9H_{12}	1.664	1.731	1.785	1.866	2.001	2.136				40.3021	−25.9359			
1,2,4-Trimethyl benzene	C_9H_{12}	1.650	1.723	1.782	1.870						40.9035	−27.6128			
1,3,5-Trimethyl benzene	C_9H_{12}	1.590	1.669	1.732	1.826						40.6495	−28.9186			
1,2,3,4-Tetramethyl benzene	$C_{10}H_{14}$		1.732	1.779	1.862	2.026	2.216	2.437		4.2848	23.9196	24.7840	−53.0483	−47.5743	89.1333
1,2,3,5-Tetramethyl benzene	$C_{10}H_{14}$		1.717	1.787	1.940	2.320	2.851			10.5141	41.7201	−50.9341	−52.6964	14.5810	114.1617
1,2,4,5-Tetramethyl benzene	$C_{10}H_{14}$					2.020	2.144	2.267			44.6614	−26.8893			
Pentamethyl benzene	$C_{11}H_{16}$					2.036	2.197	2.357				−41.1902			
Hexamethyl benzene	$C_{12}H_{18}$							2.456	2.678		72.5988	−65.6444			
Styrene	C_8H_8	1.599	1.679	1.744	1.841	2.002					35.6852	−25.6714			
Isopropyl benzene	C_9H_{12}	1.540	1.643	1.725	1.845	2.042	2.232	2.416	2.594		42.7501	−29.5504	−6.9534		
Biphenyl	$C_{12}H_{10}$					1.828	1.968	2.107	2.246		55.3863	−40.7411			
Diphenyl methane	$C_{13}H_{12}$				1.632	1.750					53.9814	−36.4781			
Triphenyl methane	$C_{19}H_{16}$					1.849	2.017	2.186	2.354		103.0521	−85.6927			
Tetraphenyl methane	$C_{25}H_{20}$										124.7397	−98.4474			
Naphthalene	$C_{10}H_8$					1.770	1.968	2.156		2.4359	66.8590	−230.4433	405.3486	−105.5278	−276.8274

1-Methylnaphthalene	$C_{11}H_{10}$	1.430	1.507	1.568	1.660	1.813					51.8774	−40.4029			
2-Methylnaphthalene	$C_{11}H_{10}$				1.645	1.791	1.938	2.084			50.0618	−38.1222			
1-Ethylnaphthalene	$C_{12}H_{12}$		1.454	1.552	1.692	1.903	2.085	2.238	2.365	1.1098	40.9009	20.6195	−46.8963	−59.6600	41.2343
2-Ethylnaphthalene	$C_{12}H_{12}$				1.717	1.887	2.057	2.226	2.396		60.8250	−49.1561			
Alcohols															
Methanol	CH_4O	2.305	2.403	2.508	2.709	3.168	3.843	5.271		0.5687	14.1100	−11.9505	−23.4782	57.5551	−25.6027
Ethanol	C_2H_6O	2.005	2.273	2.512	2.871	3.408	3.901	4.811		0.4637	23.4689	−46.2095	199.4259	−540.6041	448.4512
1-Propanol	C_3H_8O	2.037	2.200	2.360	2.649	3.260				0.6912	38.2179	−58.7413	−12.0901	85.0842	−35.0164
1-Butanol	$C_4H_{10}O$	2.045	2.204	2.359	2.635	3.221				3.3654	31.6732	−30.7096	−46.5224	71.5993	−2.6518
1-Pentanol	$C_5H_{12}O$	2.038	2.191	2.336	2.590	3.117				5.7640	26.6380	−15.5749	−36.3870	3.5382	48.5789
1-Hexanol	$C_6H_{14}O$	2.189	2.228	2.267	2.338	2.488	2.677			0.9947	35.4470	−10.7701	−46.3435	73.1515	−22.5061
1-Heptanol	$C_7H_{16}O$	2.053	2.200	2.359	2.629	3.057				−2.9491	33.7457	165.4492	−191.4845	−590.5931	751.6760
1-Octanol	$C_8H_{18}O$		2.177	2.284	2.444	2.710	2.977				65.7798	−54.4787			
Isopropanol	C_3H_8O	2.079	2.326	2.556	2.927	3.538	4.078			0.0754	34.1737	−31.0153	31.5827	−23.8811	267.0049
2-Methyl-1-propanol	$C_4H_{10}O$	2.022	2.214	2.402	2.737	3.421				−1.1541	67.1054	−109.6802	−30.0361	184.3930	−91.2685
3-Methyl-1-butanol	$C_5H_{12}O$		2.177	2.348	2.632	3.108				−7.5978	91.8057	−67.9468	−196.7676	270.8408	−45.4001
Ethylene glycol	$C_2H_6O_2$		2.285	2.382	2.527	2.769	3.010	3.252			33.1585	−25.9580			
1,3-Propylene glycol	$C_3H_8O_2$	2.096	2.223	2.324	2.475	2.728	2.980	3.233			41.1843	−33.4694			
Glycerol	$C_3H_8O_3$				2.539	2.800	3.061	3.322	3.583		58.5772	−49.1381			
Cyclohexanol	$C_6H_{12}O$				2.353	2.778	3.204				61.8783	−66.6885			
Benzyl alcohol	C_7H_8O		1.852	1.977	2.164						60.3553	−58.4291			
Phenols															
o-Cresol	C_7H_8O				2.196	2.288					37.4785	−16.6030			
m-Cresol	C_7H_8O			2.072	2.160	2.307					42.7196	−26.9635			
p-Cresol	C_7H_8O				2.158	2.314					43.5313	−28.5582			
Phenol	C_6H_6O				2.171	2.340	2.509				38.7496	−26.5137			
Formic acid	CH_2O_2			2.152	2.198	2.276					14.4461	−5.0581			
Acetic acid	$C_2H_4O_2$			2.028	2.172	2.412					24.9984	−20.5089			
Propionic acid	$C_3H_6O_2$		1.963	2.028	2.158	2.466					47.2236	−94.2476	72.8580		
Butyric acid	$C_4H_8O_2$		1.937	2.000	2.127	2.425	2.829				57.1427	−113.8183	86.2909		
Valeric acid	$C_5H_{10}O_2$	1.730	1.849	1.945	2.088	2.324	2.561	2.809	3.085	−0.0598	49.0702	−80.7494	137.7914	−190.2687	96.7981
Caproic acid	$C_6H_{12}O_2$		1.956	2.030							47.2637	−34.0079			
Acetic anhydride	$C_4H_6O_3$		1.726	1.826	1.976						41.6471	−37.2452			
Propionic anhydride	$C_6H_{10}O_3$	1.713	1.746	1.778	1.835	1.952	2.098			0.8390	38.3509	−23.8366	−16.1349	38.9280	−9.3758
Chloroacetic acid	$C_2H_3ClO_2$					1.705	1.878	2.051			31.6919	−26.9876			
Dichloroacetic acid	$C_2H_2Cl_2O_2$			1.425	1.436	1.455	1.474				24.4101	−4.0323			
Trichloroacetic acid	$C_2HCl_3O_2$				1.496						29.4068				
Ketones															
Ketene	C_2H_2O	2.356	2.605							1.0168	9.3536	8.0381	−38.4052	19.0861	26.1846
Acetone	C_3H_6O	2.048	2.089	2.131	2.210	2.390	2.667	3.351		0.4401	17.6746	−9.0149	−10.9833	32.7183	−16.4221

D3.1. Table 5. (continued)

Substance	Formula	Temperature (°C)								Equation (8)					
		−25	0	20	50	100	150	200	250	*A*	*B*	*C*	*D*	*E*	*F*
Methyl ethyl ketone	C_4H_8O	2.120	2.154	2.190	2.260	2.430	2.671			0.0258	29.5239	−34.9573	9.5140	57.6739	−49.1627
Diethyl ketone	$C_5H_{10}O$	2.130	2.178	2.217	2.276	2.373					28.3672	−11.3035			
Dipropyl ketone	$C_7H_{14}O$	2.095	2.128	2.164	2.232	2.387	2.590	2.843		0.4867	44.1126	−28.1477	−54.4215	133.7556	−66.9157
Acetophenone	C_8H_8O				1.813	2.071	2.330	2.588	2.846		55.0435	−52.9669			
Benzophenone	$C_{13}H_{10}O$				1.663	1.787	1.912	2.037	2.162		64.1483	−45.3702			
Ethers															
Dimethyl ether	C_2H_6O	2.235									15.6505	−12.3916	9.9810		
Diethyl ether	$C_4H_{10}O$	2.167	2.228	2.287	2.394	2.644	3.120			0.4579	24.2072	−12.4384	−23.6768	75.2867	−53.6772
Dipropyl ether	$C_6H_{14}O$	2.036	2.100	2.157	2.252					0.8489	32.9852	−19.0684	−6.6259	17.1316	−1.3498
Methyl propyl ether	$C_4H_{10}O$	2.102	2.154	2.196							22.9736	−8.8446			
Ethyl propyl ether	$C_5H_{12}O$	2.122	2.178	2.223							28.5216	−11.9588			
Ethylene oxide	C_2H_4O	1.898	1.948							0.5144	9.1319	5.0866	−14.4010	−5.0022	23.4152
Furane	C_4H_4O	1.564	1.616	1.657							16.8854	−8.2558			
1,4-Dioxane	$C_4H_8O_2$			1.737	1.861	2.504				14.9556	−8.2892	−15.2032	−10.6474	−95.5742	303.9206
Aldehydes															
Formaldehyde	CH_2O	2.260	2.252	2.245							7.9630	0.5129			
Acetaldehyde	C_2H_4O		2.172	2.187	2.237	2.366	2.529			0.0301	13.5502	−4.3471	−10.5345	10.1945	26.1676
Paraldehyde	$C_6H_{12}O_3$			1.932	2.023						44.4541	−27.8338			
Furfural	$C_5H_4O_2$		1.588	1.633	1.700	1.812	1.925				28.6613	−17.4104			
Benzaldehyde	C_7H_6O	1.514	1.573	1.619	1.690	1.807	1.924				32.6724	−20.7589			
Salicylaldehyde	$C_7H_6O_2$			1.806	1.924	2.090	2.216			−0.1761	35.6500	3.4142	−9.9814	−57.1498	28.5470
Esters															
Methyl formate	$C_2H_4O_2$	1.773	1.870	1.966						2.4323	8.5529	2.6949	−10.5378	−6.8571	22.7822
Ethyl formate	$C_3H_6O_2$		1.904	1.965	2.055	2.206					23.2978	−13.6769			
Propyl formate	$C_4H_8O_2$				2.055	2.240					30.2098	−21.1066			
Methyl acetate	$C_3H_6O_2$			1.899	2.009	2.191					23.8692	−16.4962			
Ethyl acetate	$C_4H_8O_2$	1.837	1.878	1.925	2.020					2.7113	14.3161	4.2455	−12.3726	−9.7711	34.0380
Propyl acetate	$C_5H_{10}O_2$			1.919	2.032	2.220					35.4286	−25.3978			
Methyl propionate	$C_4H_8O_2$				2.038	2.228					29.9676	−21.4123			
Ethyl propionate	$C_5H_{10}O_2$				2.013	2.209					35.4565	−26.2732			
Propyl propionate	$C_6H_{12}O_2$			1.922	2.091	2.373	2.655				48.5529	−44.7961			
Methyl butyrate	$C_5H_{10}O_2$			1.900	2.064	2.337					40.8805	−37.2237			
Ethyl butyrate	$C_6H_{12}O2$			1.928	2.075	2.321	2.567				46.0171	−39.2174			

Methyl benzoate	C_8H_8O2		1.468	1.511	1.576	1.684	1.792				38.8848	−24.5138			
Ethyl benzoate	$C_9H_{10}O_2$	1.441	1.503	1.552	1.627	1.750	1.873	1.997			46.0903	−31.1162			
Methyl salicylate	C_8H_8O3				1.740	1.968	2.196	2.423	2.651		63.9845	−59.0472			
Amines															
Methyl amine	CH_5N	3.278									13.0650	−1.9359			
Ethyl amine	C_2H_7N	2.914	2.936								16.7792	−2.1398			
Propyl amine	C_3H_9N	2.688	2.721	2.747	2.787						21.4447	−4.6636			
n-Butyl amine	$C_6H_{15}N$	2.546	2.590	2.625	2.678						26.7711	−8.1938			
Dimethyl amine	C_2H_7N	2.992	3.023	3.047						0.0978	23.0471	−48.3890	105.8461	−43.5416	−68.4601
Trimethyl amine	C_3H_9N	2.129	2.187								18.2045	−7.1891			
Diethyl amine	$C_6H_{15}N$			2.418	2.525						27.6677	−15.6070			
Triethyl amine	$C_6H_{15}N$	2.004	2.095	2.168	2.277						37.1018	−23.6946			
Piperidine	$C_5H_{11}N$		2.080	2.116	2.170	2.260					27.2105	−10.9318			
Pyridine	C_6H_7N	1.556	1.622	1.675	1.754	1.885					24.1188	−15.5308			
Aniline	C_6H_7N		2.021	2.058	2.113	2.205	2.297				31.4110	−14.3919			
N-methyl aniline	C_7H_9N				1.982	2.165	2.348				43.4050	−33.1095			
N,N-dimethyl aniline	$C_8H_{11}N$			1.677	1.799	2.001	2.204				47.6961	−40.5442			
N,N-diethyl aniline	$C_{10}H_{15}N$				1.847	2.047	2.246	2.445			60.2696	−50.2392			
Phenylhydrazine	$C_6H_8N_2$						1.899	2.059	2.218		38.7215	−31.5745			
Diphenyl amine	$C_{12}H_{11}N$					1.806	1.964	2.122	2.280		65.2766	−52.4820			
Nitriles															
Acetonitrile	C_2H_3N	2.146	2.193	2.230	2.285						13.3227	−5.0019			
Propionitrile	C_3H_5N	2.071	2.117	2.159	2.233					1.5599	10.2610	6.6484	−9.8995	−9.1685	16.9766
Butyronitrile	C_4H_7N	2.130	2.193	2.243	2.318	2.444					24.6958	−12.1876			
Benzonitrile	C_7H_5N		1.548	1.595	1.666	1.783	1.901				31.6340	−20.4009			
Amides															
Formamide	CH_3NO			2.388	2.488	2.655	2.822	2.989			21.5877	−13.9625			
Nitroderivates															
Nitromethane	CH_3NO_2	1.703	1.721	1.741	1.779	1.865	1.979	2.122		0.1694	16.3236	−5.5744	−21.9064	46.8488	−23.4828
Nitrobenzene	$C_6H_5NO_2$			1.477	1.518	1.629	1.812	2.077		4.9788	21.6842	−2.7282	−59.2234	47.0123	34.6561
o-Nitrotoluene	$C_7H_7NO_2$		1.469	1.495	1.548	1.670	1.835			5.4736	20.8001	−1.6916	−20.7020	−12.8946	45.2649
M-Nitrotoluene	$C_7H_7NO_2$			1.465	1.546	1.683	1.819				43.9773	−32.9937			
p-Nitrotoluene	$C_7H_7NO_2$					1.680	1.834				46.5037	−37.7369			

D3.1. Table 6. Specific heat capacity c_P of ideal gases at constant pressure in J/g K

Substance	Formula	Temperature (°C)								Equation (10)						
		−50	0	25	100	200	300	400	500	*A*	*B*	*C*	*D*	*E*	*F*	*G*
Elements																
Xenon	Xe	0.158	0.158	0.158	0.158	0.158	0.158	0.158	0.158	0.0000	2.5000	2.5000	0.0000	0.0000	0.0000	0.0000
Krypton	Kr	0.248	0.248	0.248	0.248	0.248	0.248	0.248	0.248	0.0000	2.5000	2.5000	0.0000	0.0000	0.0000	0.0000
Argon	Ar	0.520	0.520	0.520	0.520	0.520	0.520	0.520	0.520	0.0000	2.5000	2.5000	0.0000	0.0000	0.0000	0.0000
Neon	Ne	1.030	1.030	1.030	1.030	1.030	1.030	1.030	1.030	0.0000	2.5000	2.5000	0.0000	0.0000	0.0000	0.0000
Helium	He	5.193	5.193	5.193	5.193	5.193	5.193	5.193	5.193	0.0000	2.5000	2.5000	0.0000	0.0000	0.0000	0.0000
Air		1.003	1.004	1.006	1.013	1.027	1.047	1.068	1.091	2548.9320	3.5248	−0.6366	−3.4281	49.8238	−120.3466	98.8658
Hydrogen	H_2	13.81	14.24	14.36	14.49	14.46	14.45	14.54	14.69	392.8422	2.4906	−3.6262	−1.9624	35.6197	−81.3691	62.6668
Nitrogen	N_2	1.039	1.039	1.039	1.042	1.053	1.070	1.092	1.115	432.2027	3.5160	2.8021	−4.1924	42.0153	−114.2500	111.1019
Oxygen	O_2	0.910	0.915	0.919	0.935	0.963	0.992	1.021	1.047	2122.2098	3.5302	−7.1076	−1.4542	30.6057	−83.6696	79.4375
Sulfur	S			0.738												
Fluorine	F_2	0.791	0.812	0.824	0.856	0.893	0.921	0.940	0.954	774.7434	3.5724	1.1782	−7.8357	66.9134	−126.3602	84.8592
Chlorine	Cl_2	0.456	0.472	0.479	0.494	0.506	0.513	0.518	0.521	443.2316	3.4079	0.3974	−2.9833	39.3781	−76.8680	54.8748
Bromine	Br_2	0.219	0.224	0.226	0.229	0.232	0.233	0.234	0.235	397.2602	3.4138	1.5597	2.2676	36.9159	−95.8106	76.6528
Iodine	I_2	0.143	0.145	0.146	0.147	0.147	0.148	0.148	0.149	366.5747	3.6859	2.5951	6.9245	30.7878	−102.6339	89.1827
Anorganic compounds																
Hydrogen fluoride	HF	1.457	1.456	1.456	1.456	1.456	1.459	1.465	1.475	3438.3914	3.5031	2.9592	9.0174	−168.6398	1068.5062	−1578.0575
Hydrogen chloride	HCl	0.799	0.799	0.799	0.799	0.803	0.810	0.820	0.833	1638.3959	3.5004	2.9346	8.4727	−98.1948	399.2317	−384.8918
Hydrogen bromide	HBr	0.361	0.361	0.361	0.361	0.363	0.367	0.373	0.380	1203.5373	3.4970	2.7948	10.7652	−91.1043	274.9226	−208.0079
Hydrogen iodide	HI	0.228	0.228	0.228	0.229	0.232	0.236	0.241	0.247	441.4535	3.4542	3.0037	6.5208	−1.2264	−62.0818	106.0830
Hydrogen cyanide	HCN	1.212	1.288	1.325	1.422	1.523	1.602	1.670	1.733	515.6639	4.2813	−4.7794	−8.9029	56.8035	−102.7379	71.0228
Water	H_2O	1.884	1.868	1.869	1.890	1.940	2.000	2.064	2.131	706.3032	5.1703	−6.0865	−6.6011	36.2723	−63.0965	46.2085
Hydrogen sulfide	H_2S	0.982	0.994	1.001	1.030	1.078	1.131	1.185	1.238	1132.4648	4.0398	2.7018	−8.5655	67.3144	−72.9692	42.8369
Ammonia	NH_3	2.016	2.057	2.090	2.219	2.422	2.623	2.809	2.977	931.6298	4.8468	−7.1757	−7.6727	51.3877	−93.4217	67.9515
Nitric oxide	NO				0.994	1.006	1.030	1.058	1.085	287.2527	2.8998	2.6046	85.3765	−134.9868	−124.2972	275.4122
Nitrogen dioxide	NO_2	0.759	0.788	0.804	0.855	0.922	0.981	1.031	1.071	1102.7744	4.0267	−1.3131	−3.5919	52.4358	−106.3789	75.9808
Nitrous oxide	N_2O	0.791	0.849	0.875	0.947	1.025	1.087	1.137	1.179	617.4643	3.1103	1.2306	6.1055	46.3864	−110.8822	97.5602
Dinitrogentetroxide	N_2O_4	0.766	0.849	0.884	0.968	1.051	1.115	1.167	1.210	337.3088	5.7078	−0.9773	−19.6801	135.9757	−243.3166	160.1653
Cyanogen	C_2N_2	0.978	1.060	1.092	1.167	1.236	1.292	1.342	1.388	376.7870	4.4648	−3.8440	−9.8745	79.1176	−152.6285	105.8138
Phosphorus trichloride	PCl_3	0.477	0.511	0.523	0.549	0.567	0.577	0.584	0.589	398.1926	4.3525	−0.1531	1.1615	71.8056	−167.9929	123.8929
Cyanogen chloride	ClCN	0.669	0.719	0.738	0.781	0.819	0.849	0.875	0.899	398.4260	3.3356	−3.3611	−4.8745	57.6110	−119.3350	87.3449
Silane	SiH_4	1.154	1.270	1.334	1.530	1.780	2.000	2.188	2.349	629.0517	4.5596	−2.1197	−12.7035	79.0943	−122.6738	80.9687
Tetrachlorosilane	$SiCl_4$	0.481	0.518	0.532	0.563	0.586	0.600	0.609	0.615	419.0276	5.0010	1.9959	14.9372	72.1162	−207.0673	166.0017
Carbon monoxide	CO	1.039	1.039	1.040	1.045	1.059	1.080	1.105	1.131	407.9796	3.5028	2.8524	−2.3018	32.9055	−100.1815	106.1141

Carbon dioxide	CO_2	0.761	0.817	0.844	0.916	0.996	1.060	1.113	1.158	514.5073	3.4923	−0.9306	−6.0861	54.1586	−97.5157	70.9687
Carbon suboxide	C_3O_2		0.928	0.964	1.061	1.161	1.237	1.296	1.344	631.7238	4.7475	2.2252	5.2648	98.7873	−230.0819	182.8060
Carbonyl sulfide	COS	0.616	0.667	0.690	0.747	0.803	0.843	0.875	0.901	543.0047	3.1567	−0.5532	−0.4687	52.1727	−114.4401	89.2277
Phosgene	CCl_2O	0.513	0.562	0.583	0.633	0.679	0.711	0.734	0.753	443.0941	4.0648	−1.2498	−6.3664	77.7307	−151.8155	106.2799
Carbon disulfide	CS_2	0.541	0.582	0.599	0.641	0.681	0.709	0.732	0.750	436.2681	3.2047	−0.1319	0.2557	53.8613	−119.4039	93.1550
Sulfur dioxide	SO_2	0.580	0.608	0.622	0.665	0.715	0.755	0.787	0.811	848.4734	4.1379	−0.0601	−4.0449	56.0276	−109.3350	76.8400
Sulfur trioxide	SO_3	0.553	0.607	0.633	0.700	0.772	0.827	0.869	0.901	648.4989	3.5687	1.2040	8.5348	57.7911	−128.2153	100.3963
Sulfuryl chloride	Cl_2SO_2	0.503	0.553	0.573	0.621	0.663	0.693	0.715	0.733	408.3318	3.3807	−0.1149	10.6613	66.5305	−176.9697	146.1224
Sulfur hexafluoride	SF_6	0.525	0.621	0.664	0.768	0.861	0.920	0.958	0.984	524.1686	3.5677	−1.3539	−10.7270	196.7052	−395.4602	263.8890
Organic compounds containing sulfur																
Methyl mercaptan	CH_4S	0.933	1.003	1.043	1.174	1.348	1.503	1.630	1.733	1407.0543	5.1177	−17.2008	−4.5149	69.3978	−185.7461	168.6903
Ethyl mercaptan	C_2H_6S	1.002	1.103	1.161	1.348	1.590	1.787	1.945	2.105	2728.1680	6.8872	−201.1551	−1.9961	74.6970	−408.9731	728.6239
Dimethyl sulfide	C_2H_6S	1.043	1.138	1.193	1.363	1.578	1.770	1.939	2.089	472.3136	11.9843	1.2309	−32.3455	145.0474	−221.3676	136.0872
Diethyl sulfide	$C_4H_{10}S$	1.102	1.225	1.296	1.522	1.815	2.072	2.289	2.469	764.7944	12.8974	7.4937	−68.3733	426.8748	−709.5073	437.1287
Thiophene	C_4H_4S	0.637	0.775	0.850	1.073	1.322	1.496	1.626	1.767	1585.4574	5.5875	14.0271	85.1905	−1221.8570	4559.8896	−5488.4600
Halogenated hydrocarbons																
Fluoromethane (R41)	CH_3F	0.986	0.988	0.990	0.993	0.997	1.001	1.005	1.009	1176.9659	4.0143	3.8936	7.5362	27.9098	−97.9809	137.9880
Difluoromethane (R32)	CH_2F_2		0.791	0.827	0.944	1.100	1.243	1.365	1.467	962.8984	4.3711	−5.4665	−7.5447	71.6125	−131.6434	90.6773
Trifluoromethane (R23)	CHF_3	0.620	0.693	0.729	0.836	0.960	1.060	1.139	1.201	809.8615	3.9766	−1.6866	−4.3891	84.4263	−165.5706	115.7209
Tetrafluoromethane (R14)	CF_4	0.580	0.658	0.694	0.791	0.893	0.968	1.024	1.066	666.5894	3.2199	0.9296	19.5008	69.7537	−169.5636	132.1724
Methyl chloride	CH_3Cl	0.715	0.771	0.806	0.916	1.059	1.184	1.293	1.388	563.6035	6.6853	−8.5011	−13.6955	69.5041	−111.0175	71.4223
Methylene chloride	CH_2Cl_2	0.517	0.574	0.602	0.678	0.762	0.831	0.890	0.939	444.2757	5.5626	−2.8582	−16.0285	90.2509	−150.0431	98.4722
Chloroform	$CHCl_3$	0.477	0.528	0.550	0.606	0.661	0.703	0.735	0.762	432.3855	4.0882	0.0186	−4.9929	91.3991	−181.0173	132.7780
Carbon tetrachloride	CCl_4		0.526	0.544	0.586	0.620	0.642	0.657	0.668	404.6502	3.9042	1.4383	10.3685	120.5467	−291.2140	219.4177
Bromomethane	CH_3Br	0.392	0.429	0.448	0.507	0.580	0.643	0.699	0.748	582.5462	4.7518	−3.2915	−11.6866	71.7139	−119.4291	82.6436
Dibromomethane	CH_2Br_2	0.278	0.306	0.319	0.354	0.392	0.423	0.449	0.471	441.4487	5.5801	−1.4537	−16.0331	96.3766	−164.1834	108.8416
Tribromomethane	$CHBr_3$	0.253	0.273	0.281	0.304	0.326	0.344	0.357	0.368	444.2945	5.0879	3.2074	4.1568	101.0388	−218.2270	173.4973
Tetrabromomethane	CBr_4			0.275	0.288	0.300	0.308	0.312	0.315	708.6138	9.1392	6.7159	−4.8212	132.6970	−300.7419	213.9957
Chlorodifluoromethane (R22)	$CHClF_2$	0.557	0.62	0.65	0.733	0.827	0.902	0.960	1.006	923.7514	3.6501	1.0809	26.3036	33.6589	−138.0860	130.3725
Dichlorofluoromethane (R21)	$CHCl_2F$	0.511	0.568	0.594	0.661	0.731	0.785	0.828	0.863	448.3265	4.2561	0.0709	−8.4348	93.5761	−171.5023	122.5675
Chlorotrifluoromethane (R13)	$CClF_3$	0.542	0.611	0.642	0.720	0.798	0.852	0.892	0.921	530.6755	3.5003	0.9604	6.6125	106.4268	−228.0132	168.3566
Dichlorodifluoromethane (R12)	CCl_2F_2	0.517	0.578	0.604	0.668	0.729	0.770	0.799	0.821	546.7956	3.4416	1.5333	31.2296	71.5046	−234.2425	204.0779
Trichlorofluoromethane (R11)	CCl_3F	0.501	0.553	0.576	0.629	0.678	0.710	0.732	0.749	497.5032	4.6223	1.5688	3.0209	115.7598	−261.4310	192.6300
Ethyl fluoride (R161)	C_2H_5F	1.034	1.152	1.221	1.444	1.738	1.994	2.201	2.365	1291.3906	5.7586	−60.6316	−2.6539	39.8753	−99.0265	86.9333
Ethyl chloride	C_2H_5Cl		0.911	0.969	1.143	1.354	1.532	1.683	1.811	613.2333	6.9421	−3.7386	−19.7168	117.1200	−194.1976	126.2574
Ethyl bromide	C_2H_5Br		0.555	0.591	0.695	0.815	0.917	1.004	1.079	559.9347	4.6195	−1.4702	−13.3648	114.1759	−202.0764	146.4189
1,1-Dichloroethane	C_2H_4 $C_2H_4Cl_2$	0.647	0.729	0.771	0.887	1.019	1.125	1.211	1.284	544.1036	7.3477	−0.0939	−23.5320	146.8019	−247.1889	160.4226

D3.1. Table 6. (continued)

Substance	Formula	Temperature (°C)								Equation (10)						
		−50	0	25	100	200	300	400	500	*A*	*B*	*C*	*D*	*E*	*F*	*G*
1,2-Dichloroethane	$C_2H_4Cl_2$	0.693	0.749	0.783	0.890	1.023	1.134	1.226	1.301	405.3433	15.1092	20.1123	78.6790	−267.3812	327.7670	−148.4968
1,2-Dibromoethane	$C_2H_4Br_2$		0.437	0.454	0.510	0.580	0.637	0.684	0.724	520.5231	17.6437	4.0296	−44.3921	193.3612	−293.1946	165.7688
1,1,1-Trifluoroethane (R143a)	$C_2H_3F_3$		0.875	0.929	1.076	1.239	1.370	1.475	1.561	787.7535	4.0477	1.6043	27.4029	120.4143	−334.2206	293.7670
1,1,1-Trichloroethane	$C_2H_3Cl_3$	0.588	0.658	0.691	0.780	0.874	0.945	1.001	1.047	502.9630	7.5393	1.5858	−21.3038	156.9331	−273.6844	179.7290
1,1,2,2-Tetrachloroethane	$C_2H_2Cl_4$			0.589	0.667	0.748	0.807	0.852	0.886	593.3413	6.6303	1.6959	−10.3067	157.6395	−309.7356	215.3104
Pentachloroethane	C_2HCl_5	0.510	0.564	0.587	0.643	0.697	0.739	0.771	0.797	359.0845	5.8297	2.0795	−6.1565	163.1966	−336.2104	248.4292
Hexachloroethane	C_2Cl_6		0.569	0.590	0.637	0.676	0.701	0.720	0.734	388.1012	6.1294	1.8568	5.6538	139.7052	−321.6115	237.9069
1,1,2,2-Tetrachlorodifluoroethane	$C_2Cl_4F_2$			0.648	0.717	0.776	0.807	0.822	0.828	812.9972	8.3770	0.5771	9.2512	111.7561	−351.8827	296.9848
1,1,2-Trichlorotrifluoroethan	$C_2Cl_3F_3$	0.557	0.619	0.647	0.720	0.791	0.841	0.876	0.902	554.3205	8.6962	2.2845	−10.0887	136.8359	−264.2738	178.3853
1,2-Dichlorotetrafluoroethane	$C_2Cl_2F_4$		0.654	0.686	0.770	0.853	0.910	0.948	0.973	618.1865	9.1614	2.9195	−16.9605	175.4260	−328.2318	208.3301
1-Chloropropane	C_3H_7Cl	0.890	1.012	1.080	1.287	1.533	1.739	1.912	2.062	450.2002	17.8443	0.8004	−41.5155	178.9604	−268.0433	153.8763
1-Chlorobutane	C_4H_9Cl	0.953	1.089	1.164	1.387	1.655	1.881	2.073	2.237	499.3815	16.9613	−1.4125	−35.0788	166.1639	−258.1227	155.7875
1-Chloropentane	$C_5H_{11}Cl$		1.136	1.222	1.465	1.748	1.988	2.193	2.369	634.3626	5.5185	−0.3864	4.5387	128.3503	−260.6794	221.9824
Chlorotrifluoroethene	C_2ClF_3				0.792	0.868	0.924	0.965	0.997	554.9252	6.3699	1.6592	−7.1911	107.4319	−205.1290	141.6516
Vinyl chloride	C_2H_3Cl	0.736	0.813	0.858	0.995	1.156	1.285	1.390	1.477	491.7027	10.6121	−5.5113	−24.6400	112.4196	−171.9770	100.5379
1,1-Dichloroethene	$C_2H_2Cl_2$	0.605	0.661	0.692	0.782	0.879	0.953	1.009	1.055	483.9491	12.1716	−4.7585	−25.0224	116.3062	−180.1138	104.3240
Trichloroethene	C_2HCl_3	0.529	0.584	0.609	0.676	0.741	0.788	0.823	0.851	451.8908	8.9582	−1.6449	−21.3433	117.8717	−193.6722	118.0824
Tetrachloroethene	C_2Cl_4	0.513	0.559	0.578	0.623	0.665	0.695	0.718	0.736	358.9475	4.8891	1.7481	4.5515	104.8901	−235.9012	182.2698
Fluorobenzene	C_6H_5F		0.900	0.985	1.227	1.503	1.727	1.906	2.051	646.6513	4.7333	−2.1501	−19.1687	195.8215	−342.9686	228.1173
Chlorobenzene	C_6H_5Cl		0.820	0.873	1.055	1.291	1.485	1.637	1.755	676.0917	20.3111	−6.9381	−36.9151	185.3827	−302.0124	178.2699
Bromobenzene	C_6H_5Br		0.584	0.627	0.764	0.928	1.062	1.168	1.253	508.8340	20.2369	2.7854	−48.4022	210.5292	−306.5724	167.8627
Iodobenzene	C_6H_5I		0.459	0.494	0.601	0.727	0.827	0.907	0.971	513.7413	18.0569	2.9747	−49.8646	225.0068	−333.4845	185.4410
m-Chlorotoluene	C_7H_7Cl			0.955	1.166	1.420	1.627	1.792	1.926	789.7233	11.4264	−17.9541	−15.6452	119.6219	−226.4380	155.1910
Benzyl chloride	C_7H_7Cl	0.586	0.709	0.773	0.954	1.159	1.321	1.451	1.556	522.1899	10.7951	−1.5160	−38.6145	205.2761	−324.2009	194.5097
***n*-Alkanes**																
Methane	CH_4			2.237	2.445	2.790	3.164	3.535	3.882	1530.8043	4.2038	−16.6150	−3.5668	43.0563	−86.5507	65.5986
Ethane	C_2H_6		1.651	1.748	2.059	2.481	2.873	3.220	3.520	1402.8537	4.3393	−13.6034	−2.2216	71.8248	−184.4821	162.4948
Propane	C_3H_8	1.358	1.566	1.676	2.009	2.437	2.822	3.158	3.447	1089.3798	4.7246	−1.1767	3.7776	129.3687	−281.4223	216.9425
n-Butane	C_4H_{10}	1.391	1.591	1.698	2.028	2.449	2.823	3.144	3.418	852.6025	7.9657	−2.6234	−13.9200	143.1800	−262.3816	183.6957
n-Pentane	C_5H_{12}		1.562	1.667	1.995	2.422	2.803	3.131	3.411	789.3078	10.6168	0.9888	−24.2821	191.4972	−315.5929	203.9787
n-Hexane	C_6H_{14}		1.551	1.657	1.988	2.413	2.788	3.108	3.377	752.9844	13.4279	1.5402	−29.6772	208.3733	−342.0902	217.4263
n-Heptane	C_7H_{16}		1.545	1.652	1.983	2.408	2.780	3.095	3.358	785.9090	14.6277	−1.8476	−21.5324	168.6597	−283.0262	181.4694
n-Octane	C_8H_{18}		1.538	1.645	1.979	2.405	2.774	3.083	3.339	662.4091	20.7046	4.6878	−40.7644	232.4401	−359.1133	215.4126
n-Nonane	C_9H_{20}		1.532	1.641	1.977	2.401	2.768	3.073	3.324	828.9112	18.2983	−7.0327	−19.5401	163.6825	−294.9747	195.6096
n-Decane	$C_{10}H_{22}$		1.528	1.638	1.976	2.400	2.764	3.066	3.315	807.8718	20.1071	−3.9883	−22.5527	184.3994	−327.2729	214.1176

n-Undecane	$C_{11}H_{24}$		1.543	1.647	1.975	2.389	2.746	3.047	3.303	527.8639	45.4181	14.2637	−55.4188	248.2431	−370.4082	213.9896
n-Dodecane	$C_{12}H_{26}$		1.523	1.634	1.974	2.397	2.760	3.059	3.303	844.1850	21.6766	2.1683	−25.2676	244.7925	−447.8236	295.3902
n-Tridecane	$C_{13}H_{28}$		1.520	1.634	1.981	2.399	2.749	3.042	3.293	474.4332	59.5849	22.6875	−66.2783	286.5523	−426.4025	241.9263
n-Tetradecane	$C_{14}H_{30}$		1.528	1.640	1.977	2.389	2.741	3.038	3.291	544.0586	42.6709	4.2513	−40.5758	203.7442	−317.2459	194.1666
n-Pentadecane	$C_{15}H_{32}$		1.518	1.632	1.981	2.400	2.748	3.038	3.285	499.0399	65.1836	8.3493	−48.4514	218.6957	−332.8050	192.8519
n-Hexadecane	$C_{16}H_{34}$		1.519	1.638	1.980	2.387	2.734	3.030	3.283	668.1744	18.2523	2.5022	−4.1518	177.7261	−329.3481	256.6324
n-Heptadecane	$C_{17}H_{36}$		1.527	1.638	1.974	2.385	2.735	3.031	3.282	578.0195	45.7412	5.8301	−39.9872	215.2157	−341.8782	213.0248
n-Octadecane	$C_{18}H_{38}$		1.526	1.637	1.974	2.384	2.733	3.027	3.279	536.1229	55.9070	9.8791	−44.9358	222.4113	−345.4429	210.0998
n-Nonadecane	$C_{19}H_{40}$		1.528	1.638	1.972	2.381	2.731	3.026	3.277	582.1373	49.4869	10.0892	−42.4034	230.8885	−366.4691	228.9834
n-Eicosane	$C_{20}H_{42}$	1.323	1.527	1.637	1.972	2.380	2.729	3.024	3.274	566.8372	54.1062	12.4032	−44.8725	237.4861	−374.5789	232.4371
Isoalkanes																
Isobutane	C_4H_{10}	1.326	1.551	1.667	2.016	2.453	2.838	3.166	3.442	1301.6129	5.3582	−3.2872	14.9841	121.8152	−370.6200	338.4127
2-Methyl butane	C_5H_{12}	1.287	1.532	1.653	2.002	2.428	2.807	3.142	3.436	796.3567	4.0740	1.8753	88.8118	−8.9551	−19.1416	144.6959
2,2-Dimethyl propane	C_5H_{12}	1.296	1.548	1.674	2.038	2.483	2.877	3.225	3.534	788.3550	5.1118	0.2138	14.9499	142.6273	−312.3498	289.4580
2-Methyl pentane	C_6H_{14}	1.286	1.529	1.651	2.008	2.442	2.819	3.142	3.418	1104.3653	6.0050	−0.6741	40.9931	79.5055	−276.2953	271.7875
3-Methyl pentane	C_6H_{14}	1.252	1.495	1.621	1.986	2.422	2.795	3.115	3.393	521.3512	13.5283	2.8620	−47.9590	267.2919	−436.4879	284.5608
2,2-Dimethyl butane	C_6H_{14}	1.274	1.509	1.635	2.007	2.456	2.844	3.180	3.477	516.5015	18.4334	3.0526	−50.8916	257.3425	−416.1133	262.7746
2,3-Dimethyl butane	C_6H_{14}	1.213	1.485	1.616	1.983	2.421	2.806	3.142	3.434	544.9676	20.1015	−0.2858	−34.4718	167.8659	−253.4422	152.8084
Olefins																
Ethylene	C_2H_4	1.308	1.449	1.530	1.792	2.137	2.443	2.707	2.934	765.3491	4.9341	−7.9136	−11.0137	74.3661	−127.7199	86.5313
Propylene	C_3H_6	1.267	1.441	1.532	1.810	2.168	2.490	2.768	3.005	1453.8112	4.3426	−6.0609	7.4494	78.9678	−249.5605	239.4544
1-Butene	C_4H_8	1.235	1.424	1.520	1.814	2.194	2.540	2.842	3.097	479.7773	4.3256	3.2718	58.5093	−95.3387	274.4396	26.8526
1-Pentene	C_5H_{10}	1.247	1.437	1.542	1.861	2.247	2.575	2.852	3.089	502.0995	16.7161	0.9681	−40.6210	189.9928	−289.8708	173.3031
1-Hexene	C_6H_{12}		1.454	1.569	1.890	2.268	2.594	2.876	3.118	518.3938	4.6055	−0.3015	3.6653	130.7511	−256.1823	235.6529
1-Heptene	C_7H_{14}		1.478	1.576	1.886	2.280	2.618	2.903	3.145	576.1412	24.8325	−1.5064	−36.2342	175.2815	−271.1906	162.1852
1-Octene	C_8H_{16}		1.460	1.569	1.900	2.301	2.635	2.911	3.142	498.9280	28.4670	10.9147	−62.5606	280.9159	−414.8178	236.4554
Propadiene	C_3H_4	1.221	1.384	1.472	1.723	2.008	2.241	2.437	2.607	465.8339	10.5594	−7.2102	−23.6194	112.3287	−177.9108	107.9555
1,2-Butadiene	C_4H_6	1.226	1.381	1.466	1.725	2.046	2.319	2.548	2.742	831.1926	7.9556	−123.6259	−1.1003	16.8009	−32.1157	26.9538
1,3-Butadiene	C_4H_6	1.144	1.357	1.470	1.800	2.172	2.465	2.696	2.885	504.8693	12.3472	−3.1700	−35.7105	172.8337	−267.9782	156.3704
1,2-Pentadiene	C_5H_8	1.206	1.383	1.479	1.766	2.112	2.404	2.652	2.865	502.0836	13.9603	5.1488	−56.7015	270.6766	−417.5797	251.6702
trans-1,3-Pentadiene	C_5H_8	1.169	1.355	1.454	1.745	2.092	2.385	2.634	2.850	472.2185	14.6639	0.2031	−38.6990	182.6697	−283.2016	172.1526
1,4-Pentadiene	C_5H_8	1.187	1.400	1.511	1.832	2.189	2.460	2.664	2.822	612.0521	11.1024	−0.1201	−42.4491	249.5228	−421.3161	255.7897
2,3-Pentadiene	C_5H_8	1.265	1.455	1.548	1.809	2.112	2.376	2.611	2.821	395.7408	14.3200	2.2651	−43.4952	207.7465	−335.7468	210.2750
Acetylene and derivatives																
Acetylene	C_2H_2		1.611	1.689	1.883	2.065	2.196	2.304	2.404	484.7405	5.5806	−12.0091	−11.2823	67.5455	−119.9447	79.3902
Propyne	C_3H_4	1.281	1.424	1.500	1.728	2.002	2.230	2.420	2.583	727.9002	6.1061	3.7308	−66.5183	462.2200	−863.7855	588.4012
2-Butyne	C_4H_6		1.363	1.435	1.670	1.969	2.232	2.462	2.664	435.9800	20.0593	3.1224	−42.6319	171.2131	−248.9928	140.1474
1-Butyne	C_4H_6	1.236	1.406	1.496	1.758	2.068	2.328	2.546	2.734	594.1889	8.2395	5.6383	−93.5136	553.0655	−936.2200	602.0223
Naphthenes																
Cyclopropane	C_3H_6		1.208	1.324	1.679	2.120	2.493	2.800	3.055	713.7107	5.4496	−10.9497	−15.5049	104.0811	−178.3456	116.5964

D3.1. Table 6. (continued)

Substance	Formula	Temperature (°C)								Equation (10)						
		−50	0	25	100	200	300	400	500	*A*	*B*	*C*	*D*	*E*	*F*	*G*
Cyclobutane	C_4H_8	0.951	1.140	1.248	1.598	2.057	2.459	2.792	3.062	930.8483	6.6039	2.5778	−89.4518	677.7646	−1285.7835	851.3535
Cyclopentane	C_5H_{10}		1.064	1.183	1.553	2.019	2.426	2.772	3.063	473.9844	12.2517	0.5415	−45.2376	197.8917	−275.7756	164.1954
Methyl cyclopentane	C_6H_{12}	0.983	1.188	1.302	1.662	2.122	2.519	2.851	3.125	791.7216	10.3687	−14.9347	−19.6640	139.2833	−244.4440	160.0311
Ethyl cyclopentane	C_7H_{14}	1.032	1.236	1.350	1.711	2.172	2.568	2.893	3.159	852.6188	12.3264	7.3838	−124.4888	900.0820	−1660.7870	1083.7922
Propyl cyclopentane	C_8H_{16}	1.095	1.289	1.399	1.748	2.198	2.588	2.910	3.173	879.8969	14.9509	7.5889	−92.9435	686.4537	−1278.7989	840.7984
Butyl cyclopentane	C_9H_{18}	1.055	1.285	1.409	1.776	2.212	2.580	2.891	3.157	510.2287	24.5355	−6.6885	−36.8382	182.9135	−287.1827	176.4629
Pentyl cyclopentane	$C_{10}H_{20}$		1.356	1.470	1.816	2.243	2.613	2.924	3.186	744.0656	15.0124	−2.5387	−23.5233	200.6802	−346.2344	230.7800
Hexyl cyclopentane	$C_{11}H_{22}$		1.384	1.494	1.833	2.259	2.625	2.933	3.192	651.5098	24.8279	4.4206	−45.1909	260.9829	−418.0936	259.0299
Cyclohexane	C_6H_{12}		1.132	1.262	1.651	2.138	2.568	2.936	3.245	1034.0205	2.2661	−9.7253	12.5999	83.1032	−176.0842	129.9521
Methyl cyclohexane	C_7H_{14}		1.261	1.380	1.755	2.232	2.648	2.997	3.287	700.0371	13.0168	−3.3396	−33.5298	208.2013	−329.5953	202.0251
Ethyl cyclohexane	C_8H_{16}		1.300	1.417	1.793	2.266	2.669	3.006	3.288	494.0977	37.1700	−3.2420	−40.6508	172.9927	−249.9383	140.6195
Propyl cyclohexane	C_9H_{18}		1.353	1.463	1.825	2.290	2.687	3.015	3.288	552.0598	40.0743	−1.2145	−43.5560	193.6083	−286.0221	161.3476
Butyl cyclohexane	$C_{10}H_{20}$			1.485	1.836	2.292	2.687	3.015	3.287	676.3415	28.9482	−2.9127	−39.5752	211.5104	−334.3413	199.5951
Pentyl cyclohexane	$C_{11}H_{22}$		1.377	1.496	1.855	2.301	2.687	3.013	3.285	813.5232	13.5351	−1.2542	−15.0986	213.1065	−381.0515	259.5647
Hexyl cyclohexane	$C_{12}H_{24}$		1.398	1.515	1.869	2.309	2.692	3.015	3.285	851.9134	15.6834	−6.0321	−11.2562	167.7792	−308.2092	211.9792
Cyclopentene	C_5H_8	0.875	1.079	1.192	1.533	1.943	2.286	2.571	2.810	524.2790	12.7122	−6.6494	−32.6534	158.5544	−243.7381	146.0656
Cyclohexene	C_6H_{10}	0.898	1.115	1.233	1.586	2.010	2.365	2.663	2.914	481.0918	16.5468	1.9341	−54.6373	249.2469	−373.4469	218.8272
Aromatic compounds																
Benzene	C_6H_6		0.956	1.055	1.349	1.703	1.991	2.212	2.373	809.7723	3.7727	−3.6189	−9.0633	149.9616	−223.5093	99.7303
Toluene	C_7H_8	0.839	1.029	1.127	1.417	1.767	2.061	2.302	2.499	841.2618	5.3563	−8.1268	−8.4229	132.4066	−258.0367	181.8666
Ethyl benzene	C_8H_{10}		1.102	1.201	1.498	1.859	2.160	2.405	2.604	908.5227	7.9010	−9.1146	−12.9499	165.9928	−343.4212	248.2148
Propyl benzene	C_9H_{12}		1.161	1.264	1.565	1.926	2.229	2.475	2.674	1950.0270	5.3147	−37.4089	24.6757	−9.7945	−173.2279	305.2206
Butyl benzene	$C_{10}H_{14}$		1.193	1.295	1.604	1.975	2.285	2.543	2.759	485.2103	29.2013	7.1705	−55.8817	250.3890	−371.2898	213.7531
Pentyl benzene	$C_{11}H_{16}$	1.037	1.220	1.323	1.636	2.016	2.329	2.584	2.796	753.8201	23.4443	−425.7090	−1.9835	20.1155	−37.1862	29.4457
Hexyl benzene	$C_{12}H_{18}$		1.257	1.357	1.662	2.038	2.357	2.621	2.839	775.6700	16.7476	7.0631	−47.8570	404.9666	−713.9274	462.9704
o-Xylene	C_8H_{10}		1.151	1.249	1.529	1.857	2.137	2.375	2.579	609.8388	5.3273	−0.3832	−3.6723	168.1564	−306.0474	244.1396
m-Xylene	C_8H_{10}	0.899	1.086	1.185	1.479	1.829	2.122	2.366	2.572	524.8743	14.4547	2.1723	−49.8936	255.6358	−395.9105	241.3380
p-Xylene	C_8H_{10}	0.895	1.083	1.182	1.475	1.826	2.121	2.366	2.573	554.5575	12.5185	1.7380	−47.3879	260.5644	−409.1711	253.7921
1,2,3-Trimethyl benzene	C_9H_{12}	1.056	1.232	1.324	1.597	1.929	2.215	2.458	2.666	552.6305	14.7160	6.4505	−50.8017	292.8565	−458.6487	296.1082
1,2,4-Trimethyl benzene	C_9H_{12}	1.017	1.193	1.284	1.554	1.884	2.170	2.417	2.630	531.4374	13.9593	−1.2014	−26.5814	156.1717	−248.3199	167.1423
1,3,5-Trimethyl benzene	C_9H_{12}	0.957	1.139	1.236	1.528	1.878	2.168	2.410	2.615	759.3563	14.4362	−307.7057	−1.3812	17.7781	−33.6487	27.8002
1,2,3,4-Tetramethyl benzene	$C_{10}H_{14}$	1.126	1.305	1.397	1.668	1.996	2.278	2.519	2.726	569.2235	15.7579	5.5793	−36.6740	237.6957	−384.0478	257.8036
1,2,3,5-Tetramethyl benzene	$C_{10}H_{14}$	1.075	1.252	1.346	1.623	1.955	2.240	2.486	2.699	425.1269	29.6833	10.6318	−59.1867	258.9429	−389.8433	231.4145
1,2,4,5-Tetramethyl benzene	$C_{10}H_{14}$	1.107	1.275	1.364	1.633	1.962	2.248	2.494	2.706	496.9808	21.4489	10.2592	−59.7259	294.1429	−449.9035	282.1546
Pentamethyl benzene	$C_{11}H_{16}$	1.174	1.358	1.453	1.730	2.062	2.345	2.587	2.793	518.4634	20.1576	9.4405	−50.8594	287.9065	−455.8520	296.4273
Hexamethyl benzene	$C_{12}H_{18}$	1.221	1.414	1.512	1.793	2.125	2.406	2.645	2.850	503.3786	22.0085	5.6201	−36.1051	211.8811	−343.8426	227.8486
Styrene	C_8H_8		1.091	1.178	1.445	1.767	2.033	2.250	2.427	614.9612	14.2195	1.6222	−45.1906	248.7041	−395.9648	237.9188

Isopropyl benzene	C_9H_{12}		1.162	1.258	1.557	1.926	2.231	2.479	2.683	541.8872	28.4457	5.2895	−54.7513	249.1932	−373.2738	210.7473
Biphenyl	$C_{12}H_{10}$	0.783	0.928	1.021	1.323	1.695	1.984	2.197	2.357	839.2611	29.0956	−840.9403	−1.7659	18.1764	−34.5202	27.6537
diphenyl methane	$C_{13}H_{12}$	0.763	0.980	1.083	1.373	1.704	1.975	2.195	2.376	912.0247	0.3789	−7.3276	68.9251	−6.9247	−117.1357	156.2244
Triphenyl methane	$C_{19}H_{16}$				1.322	1.648	1.917	2.136	2.315	693.7541	12.2683	−1.5320	−26.8670	285.6544	−503.9054	335.7974
Tetraphenyl methane	$C_{25}H_{20}$				1.317	1.645	1.913	2.129	2.306	704.0798	11.6368	−13.1994	−10.6609	180.0007	−329.3314	227.2214
Naphthalene	$C_{10}H_8$	0.741	0.933	1.030	1.310	1.633	1.896	2.107	2.278	810.0175	5.4557	−126.8803	−0.3906	20.9245	−42.2188	34.6214
1-Methylnaphthalene	$C_{11}H_{10}$	0.824	1.006	1.103	1.394	1.734	2.000	2.198	2.346	737.4298	13.6993	4.6727	−76.5654	524.0127	−924.2788	562.5966
2-Methylnaphthalene	$C_{11}H_{10}$			1.122	1.397	1.719	1.984	2.200	2.378	692.3897	7.8093	−0.1056	−21.8522	268.0494	−481.6940	328.2843
1-Ethylnaphthalene	$C_{12}H_{12}$			1.178	1.464	1.797	2.069	2.291	2.472	688.2104	9.5394	−3.1238	−18.5037	207.2486	−373.2825	253.7499
2-Ethylnaphthalene	$C_{12}H_{12}$			1.180	1.460	1.787	2.057	2.278	2.460	701.0440	9.2404	−1.2002	−16.7838	224.0503	−407.6486	281.3767
Alcohols																
Methanol	CH_4O		1.328	1.376	1.545	1.795	2.035	2.253	2.445	846.6321	5.7309	−4.8842	−12.8501	78.9997	−127.3725	82.7107
Ethanol	C_2H_6O		1.524	1.599	1.827	2.115	2.372	2.596	2.791	615.0622	7.4449	10.6424	39.8445	−229.0321	358.5449	−228.5963
1-Propanol	C_3H_8O	1.169	1.338	1.431	1.708	2.045	2.336	2.586	2.804	506.0032	12.1539	0.0041	−36.1389	175.9466	−276.1927	171.3886
1-Butanol	$C_4H_{10}O$	1.167	1.354	1.456	1.765	2.133	2.440	2.699	2.920	492.3989	18.1172	0.2036	−41.5543	192.4340	−295.5686	175.0644
1-Pentanol	$C_5H_{12}O$	1.186	1.375	1.481	1.799	2.175	2.486	2.746	2.967	456.0466	26.3377	5.3197	−51.8114	223.3194	−331.4368	188.1740
1-Hexanol	$C_6H_{14}O$		1.413	1.515	1.816	2.179	2.492	2.760	2.989	539.7646	13.6357	−2.5712	−21.6173	133.0466	−212.0847	143.2168
1-Heptanol	$C_7H_{16}O$		1.406	1.514	1.839	2.227	2.547	2.810	3.031	472.7577	32.1074	12.4362	−65.6487	284.9801	−418.5724	235.1440
1-Octanol	$C_8H_{18}O$		1.434	1.539	1.847	2.220	2.541	2.814	3.046	473.5372	21.6301	3.8006	−36.3164	182.8327	−277.2652	176.9866
Isopropanol	C_3H_8O	1.186	1.389	1.492	1.783	2.114	2.389	2.624	2.826	418.8801	14.1696	−1.4167	−36.6301	168.5334	−261.1031	156.5725
2-Methyl-1-propanol	$C_4H_{10}O$				1.766	2.118	2.427	2.690	2.913	798.5957	9.0864	1.3782	−21.1202	195.9087	−342.6424	230.5518
3-Methyl-1-butanol	$C_5H_{12}O$			1.483	1.794	2.155	2.464	2.729	2.957	551.4814	3.6966	−0.0476	15.9099	144.3529	−303.3896	290.0544
Ethylene glycol	$C_2H_6O_2$				1.454	1.705	1.924	2.111	2.271	710.7946	6.0109	1.5905	−11.3311	139.2296	−234.0852	165.8867
1,3-Propylene glycol	$C_3H_8O_2$				1.539	1.835	2.084	2.284	2.446	764.0921	18.9126	−9.9306	−31.5200	172.4209	−303.9785	193.8688
Glycerol	$C_3H_8O_3$			1.251	1.450	1.705	1.917	2.087	2.226	830.0781	16.2564	−11.1044	−25.4696	162.1117	−309.8217	212.4448
Cyclohexanol	$C_6H_{12}O$			1.325	1.633	2.036	2.401	2.711	2.964	335.6044	3.1522	−2.1230	29.3992	−48.7158	11.4720	130.4559
Benzyl alcohol	C_7H_8O			1.033	1.303	1.630	1.900	2.118	2.296	806.5585	9.1764	−22.3177	−13.5166	111.0271	−211.6739	146.7900
Phenols																
o-Cresol	C_7H_8O		1.084	1.180	1.442	1.736	1.977	2.176	2.341	781.3184	1.5589	−4.2264	52.1150	−23.7416	−39.2506	93.9738
m-Cresol	C_7H_8O		1.050	1.154	1.432	1.734	1.976	2.173	2.337	711.0546	−1.1668	−7.9357	48.3832	−20.0224	−58.0273	111.3934
p-Cresol	C_7H_8O		1.054	1.151	1.418	1.717	1.961	2.162	2.332	493.7805	6.6781	−4.1148	−23.5492	172.1028	−293.9660	200.9190
Phenol	C_6H_6O	0.817	1.015	1.108	1.359	1.637	1.867	2.060	2.222	344.0544	12.3852	−3.4905	−38.7742	183.2357	−287.4124	175.9400
Carboxylic acids																
Formic acid	CH_2O_2	0.859	0.947	0.992	1.132	1.314	1.479	1.621	1.741	1422.9543	3.5792	−2.8439	8.3366	48.7114	−138.2338	113.0764
Acetic acid	$C_2H_4O_2$	0.858	0.987	1.054	1.254	1.501	1.716	1.899	2.054	608.8356	5.1040	0.3115	−18.4327	135.3287	−205.9415	138.0387
Propionic acid	$C_3H_6O_2$			1.211	1.446	1.699	1.904	2.079	2.231	457.0683	5.1709	−3.4822	−24.0638	172.4621	−312.7397	215.4305
Butyric acid	$C_4H_8O_2$			1.312	1.541	1.812	2.043	2.237	2.398	459.6913	5.9009	4.0620	3.9149	181.7266	−291.7462	291.5314
Valeric acid	$C_5H_{10}O_2$			1.349	1.599	1.888	2.134	2.342	2.521	514.8584	6.6566	2.2909	−9.1907	194.6026	−358.7199	290.3090
Caproic acid	$C_6H_{12}O_2$			1.386	1.647	1.946	2.200	2.416	2.602	451.7423	7.1043	−2.0512	−11.4873	139.7141	−261.2768	206.1596
Acetic anhydride	$C_4H_6O_3$		0.908	0.977	1.189	1.446	1.659	1.831	1.973	539.2754	16.7548	−0.7395	−39.4099	184.3347	−277.7276	159.5938

D3.1. Table 6. (continued)

Substance	Formula	Temperature (°C)								Equation (10)						
		−50	0	25	100	200	300	400	500	*A*	*B*	*C*	*D*	*E*	*F*	*G*
Propionic anhydride	$C_6H_{10}O_3$			1.161	1.409	1.677	1.898	2.085	2.244	532.8036	−3.1593	−10.1506	49.8107	−27.4669	−59.7251	135.5787
Chloroacetic acid	$C_2H_3ClO_2$			0.823	0.952	1.093	1.205	1.296	1.371	513.1194	5.0317	0.1128	−13.7464	135.2842	−240.6474	169.3052
Dichloroacetic acid	$C_2H_2Cl_2O_2$				0.792	0.876	0.947	1.005	1.051	817.0589	10.0416	4.6688	−22.0572	170.5135	−302.1516	192.3847
Trichloroacetic acid	$C_2HCl_3O_2$				0.737	0.810	0.863	0.904	0.935	576.9782	8.1143	3.1010	−8.6521	139.2451	−275.8220	193.3559
Ketones																
Ketene	C_2H_2O	0.993	1.097	1.149	1.297	1.462	1.596	1.711	1.811	468.8498	6.9008	−5.6398	−17.1500	88.2773	−144.6588	91.7470
Acetone	C_3H_6O	1.092	1.216	1.286	1.505	1.792	2.049	2.270	2.458	705.8948	7.7263	0.4677	−23.3910	148.3440	−229.3625	144.1393
Methyl ethyl ketone	C_4H_8O	1.210	1.344	1.420	1.655	1.950	2.210	2.436	2.632	482.3897	15.6860	4.3811	−42.2777	189.9671	−285.2067	172.9528
Diethyl ketone	$C_5H_{10}O$	1.286	1.434	1.509	1.737	2.030	2.296	2.532	2.735	1765.2345	9.0644	−1.5515	40.2552	−22.0621	−74.5494	104.5099
Dipropyl ketone	$C_7H_{14}O$	1.288	1.449	1.534	1.792	2.118	2.406	2.651	2.857	735.3618	14.3567	9.4665	−32.5304	310.8597	−478.7656	302.7430
Acetophenone	C_8H_8O			0.940	1.174	1.472	1.731	1.946	2.121	763.6426	10.1937	−2.3585	−29.5326	204.0248	−329.8159	198.9534
Benzophenone	$C_{13}H_{10}O$				1.232	1.528	1.774	1.976	2.140	733.7134	6.6859	−0.9461	−4.1615	224.2713	−394.9366	268.1667
Ethers																
Dimethyl ether	C_2H_6O	1.221	1.353	1.426	1.656	1.950	2.217	2.459	2.675	465.9073	10.4329	−2.4883	−24.9240	115.5549	−180.8060	116.0588
Diethyl ether	$C_4H_{10}O$	1.391	1.523	1.598	1.841	2.172	2.464	2.701	2.894	2983.3712	10.7009	−42.8010	−5.8344	309.3391	−1779.9754	3121.8402
Dipropyl ether	$C_6H_{14}O$		1.466	1.553	1.825	2.179	2.497	2.771	3.004	705.4836	15.9106	6.9763	−38.3882	243.6142	−372.7539	231.0957
Methyl propyl ether	$C_4H_{10}O$			1.519	1.771	2.102	2.404	2.668	2.896	882.1014	9.7244	0.6484	−12.9184	142.8094	−245.9753	166.8905
Ethyl propyl ether	$C_5H_{12}O$			1.535	1.803	2.151	2.465	2.739	2.973	1138.2872	9.6137	1.3570	5.9532	147.9699	−323.5530	242.4878
Ethylene oxide	C_2H_4O	0.872	1.012	1.091	1.334	1.637	1.896	2.113	2.294	634.8610	5.7870	−8.5443	−15.4287	89.6330	−144.6410	92.4648
Furane	C_4H_4O		0.871	0.960	1.222	1.518	1.749	1.931	2.079	486.3671	12.0372	−4.5658	−36.8218	170.9486	−259.5831	148.5210
1,4-Dioxane	$C_4H_8O_2$		0.953	1.046	1.326	1.667	1.956	2.198	2.403	484.0338	15.6011	−0.2760	−44.0774	198.9436	−295.1276	172.8842
Aldehydes																
Formaldehyde	CH_2O	1.119	1.157	1.182	1.272	1.415	1.565	1.708	1.835	1636.6439	4.0763	−17.0910	−2.4580	38.3216	−87.5064	71.7045
Acetaldehyde	C_2H_4O	1.094	1.195	1.253	1.435	1.676	1.895	2.088	2.256	586.5086	6.5867	0.0587	−20.9195	110.1906	−164.8871	107.6335
Paraldehyde	$C_6H_{12}O_3$				1.415	1.792	2.085	2.296	2.450	773.1687	27.7745	−44.6451	−25.3175	148.3349	−268.2676	171.6125
Furfural	$C_5H_4O_2$	0.791	0.949	1.026	1.238	1.475	1.668	1.824	1.951	413.7560	7.7545	1.2143	−39.4944	214.9979	−331.8139	211.2817
Benzaldehyde	C_7H_6O		0.971	1.054	1.298	1.584	1.817	2.004	2.154	671.1861	8.3938	−1.9508	−26.9338	201.7159	−344.2504	219.1408
Salicylaldehyde	$C_7H_6O_2$				1.328	1.607	1.836	2.020	2.168	669.6069	5.1161	0.0212	3.1101	172.7490	−303.1054	213.6292
Esters																
Methyl formate	$C_2H_4O_2$		1.039	1.105	1.295	1.521	1.710	1.867	1.999	650.0705	5.0360	−0.4487	−13.5453	126.9502	−219.5695	151.4586
Ethyl formate	$C_3H_6O_2$	0.998	1.137	1.204	1.396	1.638	1.861	2.064	2.242	404.9129	3.7636	0.9389	10.0507	93.3832	−253.2640	280.9690
Propyl formate	$C_4H_8O_2$			1.249	1.498	1.793	2.035	2.232	2.395	648.4015	11.8633	−2.9629	−29.6799	181.7404	−312.5326	200.3552
Methyl acetate	$C_3H_6O_2$			1.147	1.342	1.591	1.817	2.014	2.183	1067.5571	5.8357	3.3580	24.4866	171.0516	−317.8321	204.6031
Ethyl acetate	$C_4H_8O_2$		1.238	1.290	1.485	1.763	2.012	2.219	2.386	750.2984	19.6540	−1.2186	−36.4137	186.0861	−297.5340	174.1510
Propyl acetate	$C_5H_{10}O_2$			1.330	1.565	1.849	2.099	2.313	2.496	468.6307	6.3075	4.6248	25.2463	171.5921	−323.6548	393.4110

Methyl propionate	$C_4H_8O_2$				1.534	1.817	2.037	2.218	2.374	511.6446	8.3735	−3.5348	−32.5843	210.7834	−374.4899	246.1545
Ethyl propionate	$C_5H_{10}O_2$				1.579	1.887	2.134	2.335	2.503	573.7088	7.7317	−1.7971	−24.4531	206.2430	−371.7278	254.3115
Propyl propionate	$C_6H_{12}O_2$			1.335	1.627	1.948	2.202	2.411	2.588	578.4427	8.0466	−10.2830	−14.6931	135.7510	−254.7277	179.9220
Methyl butyrate	$C_5H_{10}O_2$			1.318	1.592	1.889	2.127	2.327	2.499	481.5596	7.2303	−4.7969	−24.3266	182.1370	−329.2853	227.0399
Ethyl butyrate	$C_6H_{12}O_2$			1.341	1.624	1.942	2.199	2.411	2.590	611.9893	8.3737	−6.7042	−12.5524	135.5255	−253.6930	181.7482
Methyl benzoate	$C_8H_8O_2$				1.143	1.433	1.675	1.867	2.020	777.6575	19.3345	−21.9744	−26.0082	154.6223	−274.4153	175.8682
Ethyl benzoate	$C_9H_{10}O_2$				1.215	1.520	1.771	1.972	2.136	746.8498	13.3061	−3.6685	−38.3335	264.3178	−475.3466	308.6488
Methyl salicylate	$C_8H_8O_3$				1.173	1.435	1.648	1.818	1.954	731.4071	11.4812	−1.4487	−32.3335	247.6723	−444.5874	288.4964
Amines																
Methyl amine	CH_5N	1.450	1.618	1.710	1.988	2.317	2.596	2.834	3.043	526.2987	8.1347	−6.7634	−19.4168	99.1609	−161.5452	102.4923
Ethyl amine	C_2H_7N		1.530	1.615	1.895	2.258	2.577	2.851	3.087	536.5039	13.9460	−0.9874	−33.9284	152.3293	−230.0192	135.6922
Propyl amine	C_3H_9N		1.529	1.621	1.916	2.288	2.610	2.884	3.121	485.4942	20.2338	1.8071	−40.8876	174.7357	−258.6134	148.6605
n-Butyl amine	$C_6H_{15}N$		1.524	1.616	1.913	2.294	2.623	2.904	3.144	521.8162	22.5154	3.3114	−43.2202	190.4295	−283.4029	163.9525
Dimethyl amine	C_2H_7N		1.480	1.572	1.869	2.248	2.579	2.862	3.104	517.1446	13.7294	−1.4905	−33.7718	150.1642	−224.7214	131.9666
Trimethyl amine	C_3H_9N		1.448	1.556	1.880	2.281	2.628	2.923	3.173	556.5448	8.8001	1.0661	−31.1281	176.1563	−265.6208	170.2390
Diethyl amine	$C_4H_{11}N$		1.489	1.584	1.889	2.279	2.618	2.907	3.154	481.9254	24.4069	7.0965	−51.6239	214.2465	−308.3217	173.5640
Triethyl amine	$C_6H_{15}N$		1.488	1.584	1.902	2.307	2.654	2.945	3.191	471.8903	40.9534	6.6919	−46.2079	186.7660	−265.4862	145.4154
Piperidine	$C_5H_{11}N$				1.843	2.279	2.641	2.921	3.132	789.5315	14.3328	−7.2974	−28.8283	185.2647	−313.8948	186.7509
Pyridine	C_6H_7N		0.895	0.992	1.261	1.567	1.816	2.020	2.187	931.3885	−0.2894	−4.7426	61.0122	−41.5212	−31.1320	87.8622
Aniline	C_6H_7N	0.906	1.096	1.192	1.467	1.779	2.027	2.226	2.389	553.0789	10.0504	−2.1951	−33.8931	200.8168	−328.5051	204.3701
N-methyl aniline	C_7H_9N				1.468	1.808	2.080	2.300	2.479	617.5389	4.7482	−4.0307	−16.4466	192.1456	−342.6990	234.9554
N,*N*-dimethyl aniline	$C_8H_{11}N$				1.454	1.820	2.120	2.366	2.565	588.2014	2.5877	−2.6448	−3.1347	202.5766	−325.4600	235.2223
N,*N*-diethyl aniline	$C_{10}H_{15}N$				1.542	1.922	2.233	2.486	2.693	695.7592	8.7586	−8.2134	−16.8824	178.2587	−319.5727	215.8269
Phenylhydrazine	$C_6H_8N_2$				1.417	1.724	1.968	2.163	2.321	596.7362	3.9280	−2.2980	−14.6956	225.7757	−416.3451	292.5245
Diphenyl amine	$C_{12}H_{11}N$				1.334	1.666	1.932	2.144	2.315	705.0600	5.5301	−7.3743	−12.6309	204.7976	−387.7767	268.3223
Nitriles																
Acetonitrile	C_2H_3N	1.119	1.218	1.271	1.435	1.642	1.827	1.989	2.132	575.7440	5.8067	−0.7216	−15.8722	92.6961	−149.0017	101.9069
Propionitrile	C_3H_5N	1.115	1.260	1.337	1.562	1.827	2.051	2.244	2.413	467.1284	11.0885	−1.3805	−31.1335	148.5534	−234.2472	144.0482
Butyronitrile	C_4H_7N	1.168	1.336	1.423	1.677	1.973	2.221	2.431	2.610	495.5976	11.9010	4.4644	−53.0329	268.1488	−426.2804	263.2369
Benzonitrile	C_7H_5N	0.832	0.977	1.056	1.288	1.556	1.770	1.942	2.081	486.6942	17.2633	2.8971	−49.4846	226.3075	−336.3367	190.1459
Amides																
Formamide	CH_3NO			1.020	1.187	1.412	1.612	1.781	1.922	771.4776	6.0800	−8.0917	−13.8793	84.4610	−140.6239	89.9474
Nitroderivates																
Nitromethane	CH_3NO_2	0.788	0.877	0.927	1.086	1.292	1.468	1.612	1.726	1055.4685	5.3794	−10.9553	−8.2607	88.4218	−187.4973	138.2815
Nitrobenzene	$C_6H_5NO_2$			1.044	1.201	1.424	1.620	1.777	1.901	766.3016	22.4706	0.2908	−41.1361	213.1554	−347.2088	202.9334
o-Nitrotoluene	$C_7H_7NO_2$			1.096	1.268	1.510	1.724	1.899	2.039	815.1681	23.1378	1.0993	−41.1763	228.3301	−381.3986	227.7271
m-Nitrotoluene	$C_7H_7NO_2$			1.096	1.268	1.510	1.724	1.899	2.039	815.1681	23.1378	1.0993	−41.1763	228.3301	−381.3986	227.7271
p-Nitrotoluene	$C_7H_7NO_2$			1.096	1.268	1.510	1.724	1.899	2.039	815.1681	23.1378	1.0993	−41.1763	228.3301	−381.3986	227.7271

D3.1. Table 7. Dynamic viscosity of saturated liquids in mPa s

Substance	Formula	Temperature (°C)								Equation (2)				
		−50	−25	0	20	50	100	150	200	*A*	*B*	*C*	*D*	*E*
Elements														
Xenon	Xe	0.23	0.16	0.11						0.55314	−37.82854	164.800	−1106.936	0.00050739
Krypton	Kr									1.20479	0.60580	216.325	2.278	0.00008756
Argon	Ar									2.92010	3.51821	151.048	−164.493	0.00002311
Air										2.22755	0.49596	132.897	4.000	0.00001638
Nitrogen	N_2									2.23392	0.01273	127.145	36.807	0.00001343
Oxygen	O_2									2.14927	0.00116	157.423	36.005	0.00001839
Fluorine	F_2									3.79391	2.18842	331.029	−177.692	0.00000080
Chlorine	Cl_2	0.56	0.46	0.39	0.34	0.30	0.24			0.48281	1.35353	439.327	−110.083	0.00017187
Bromine	Br_2			1.25	1.02	0.77				3.19074	1.61660	499.481	−209.817	0.00005839
Iodine	I_2							1.78	1.28	3.26629	2.09143	793.019	−407.779	0.00007227
Anorganic compounds														
Hydrogen fluoride	HF	0.56	0.36	0.26						0.52901	0.61638	475.848	81.999	0.00007721
Hydrogen chloride	HCl		0.14	0.11	0.08					6.63052	−0.88397	445.763	72.787	0.00000041
Hydrogen bromide	HBr	0.55	0.39	0.28	0.21	0.14				4.16618	0.00407	382.714	11.651	0.00001234
Hydrogen iodide	HI	1.46	1.08	0.81	0.64	0.45	0.23	0.09		5.17952	−0.00350	446.147	−81.737	0.00001373
Hydrogen cyanide	HCN			0.24	0.19					0.59249	1.74862	394.903	−1.249	0.00008283
Water	H_2O				1.01	0.56	0.28	0.18	0.13	0.45047	1.39753	613.181	63.697	0.00006896
Hydrogen sulfide	H_2S	0.37	0.25	0.17	0.12	0.07				5.74095	−0.46553	425.493	98.235	0.00000105
Ammonia	NH_3	0.33	0.23	0.17	0.14	0.10	0.06			0.76099	6.53802	373.726	−304.733	0.00005863
Nitric oxide	NO									7.22569	−0.17859	202.500	−106.123	0.00000172
Nitrogen Dioxide	NO_2			0.53	0.43	0.30	0.14			6.86768	−0.14884	423.463	−446.706	0.00000919
Nitrous oxide	N_2O	0.17	0.12	0.09						3.47166	2.50311	379.730	−222.126	0.00000792
Dinitrogentetroxide	N_2O_4			0.53	0.43					−0.03739	0.96651	615.987	11.286	0.00013891
Cyanogen	C_2N_2		19.29	3.09	0.91					1.47085	5.11957	729.566	−34.528	0.00000010
Phosphorus trichloride	PCl_3	1.22	0.87	0.66	0.55	0.44				0.41897	0.69273	676.023	−10.272	0.00013570
Cyanogen chloride	ClCN			0.78						0.85260	1.26974	632.123	−38.108	0.00006912
Silane	SiH_4	0.07								0.61446	0.39805	505.030	−16.673	0.00002342
Tetrachlorosilane	$SiCl_4$			0.56	0.47	0.37	0.25	0.17		2.64937	4.43604	883.209	−795.200	0.00000763
Carbon monoxide	CO									1.12644	1.20497	177.745	−40.077	0.00002545
Carbon dioxide	CO_2	0.23	0.15	0.10	0.07					2.68801	4.19607	305.198	−186.836	0.00002914
Carbon suboxide	C_3O_2	2.00	1.18	0.76	0.57	0.39	0.24	0.17		1.36451	1.23603	651.929	−33.959	0.00003443
Carbonyl sulfide	COS	0.33								1.09689	1.29173	344.677	−34.000	0.00008662

Phosgene	CCl_2O			0.59						2.05445	0.57499	405.660	−78.105	0.00011430
Carbon disulfide	CS_2	0.96	0.60	0.44	0.36					−1.21697	2.07022	423.015	16.676	0.00044103
Sulfur dioxide	SO_2		0.53	0.38	0.29	0.19	0.10			11.30591	4.76771	588.187	−978.880	0.00000014
Sulfur trioxide	SO_3				2.19					1.05142	1.92462	680.960	61.410	0.00001373
Sulfuryl chloride	Cl_2SO_2			0.91	0.73	0.55				0.89331	0.87316	742.201	−42.953	0.00007532
Sulfur hexafluoride	SF_6	0.54	0.42	0.34	0.29					1.61414	2.05898	451.978	−219.147	0.00006271
Organic compounds containing sulfur														
Methyl mercaptan	CH_4S	0.50	0.38	0.30						0.95210	0.76506	550.522	−25.991	0.00005879
Ethyl mercaptan	C_2H_6S	0.67	0.48	0.36	0.30					−0.01119	1.88058	472.369	−65.473	0.00014524
Dimethyl sulfide	C_2H_6S		0.48	0.36	0.29					0.72488	0.86931	589.869	−12.293	0.00006185
Diethyl sulfide	$C_4H_{10}S$		0.78	0.56	0.45	0.33				1.53683	1.21439	583.673	−63.530	0.00004208
Thiophene	C_4H_4S			0.87	0.66	0.47	0.30			0.41152	1.31563	668.146	−36.622	0.00009023
Halogenated hydrocarbons														
Fluoromethane (R41)	CH_3F	0.21								−1.76244	6.54755	277.164	−206.901	0.00033288
Difluoromethane (R32)	CH_2F_2	0.37	0.26	0.19						2.02991	0.63260	324.135	42.295	0.00005219
Trifluoromethane (R23)	CHF_3	0.21	0.16							0.72088	2.00276	267.675	−32.095	0.00011482
Tetrafluoromethane (R14)	CF_4	0.16								1.28783	0.76244	405.676	−14.981	0.00002872
Methyl chloride	CH_3Cl	0.46	0.31	0.22	0.18	0.14	0.09			0.67544	2.38486	379.438	−35.279	0.00007741
Methylene chloride	CH_2Cl_2	1.07	0.73	0.53	0.43	0.33	0.24			0.85505	0.90417	608.752	−18.795	0.00007319
Chloroform	$CHCl_3$	1.50	0.99	0.71	0.57	0.43				0.61822	0.98765	660.257	−29.324	0.00009188
Carbon tetrachloride	CCl_4			1.31	0.96	0.64	0.38	0.26		0.83033	2.29078	562.119	−73.328	0.00009929
Bromomethane	CH_3Br	0.65	0.49	0.38						0.58164	1.14346	527.197	−56.840	0.00010019
Dibromomethane	CH_2Br_2		1.93	1.33	1.04	0.77				2.55875	−0.00001	884.158	142.141	0.00001849
Tribromomethane	$CHBr_3$				1.99	1.39	0.88			1.18800	0.70521	870.903	−15.622	0.00009053
Tetrabromomethane	CBr_4						0.25	0.13	0.08	0.71298	1.97356	549.836	121.421	0.00003942
Chlorodifluoromethane (R22)	$CHClF_2$	0.32	0.25	0.20	0.16	0.12				2.50542	0.00079	369.199	56.279	0.00002948
Dichlorofluoromethane (R21)	$CHCl_2F$	0.72	0.52	0.40	0.33	0.26	0.19	0.13		1.10954	1.04245	429.188	−2.978	0.00009772
Chlorotrifluoromethane (R13)	$CClF_3$	0.22	0.17							0.76360	1.63878	278.217	−10.329	0.00010624
Dichlorodifluoromethane (R12)	CCl_2F_2	0.43	0.32	0.24	0.19	0.14				2.23435	96.51808	363.171	−3940.344	0.00007311
Trichlorofluoromethane (R11)	CCl_3F	0.98	0.72	0.53	0.42	0.31	0.18			1.85826	74.83744	443.154	−3365.675	0.00007753
Ethyl fluoride (R161)	C_2H_5F	0.24								−2.84655	2.06943	550.110	−106.565	0.00052565
Ethyl chloride	C_2H_5Cl	0.58	0.42	0.32	0.26	0.20				2.32681	0.36985	448.229	35.146	0.00003041
Ethyl bromide	C_2H_5Br	0.97	0.66	0.48	0.39					0.83478	2.99446	335.850	−59.764	0.00021716
1,1-Dichloroethane	$C_2H_4Cl_2$	1.35	0.88	0.62	0.49	0.36				1.37295	1.23179	556.460	−39.335	0.00005608
1,2-Dichloroethane	$C_2H_4Cl_2$		1.56	1.09	0.84	0.58	0.33	0.21	0.14	−0.45273	17.42862	610.982	−1044.345	0.00008499
1,2-Dibromoethane	$C_2H_4Br_2$				1.73	1.14	0.67			1.30990	0.80947	895.720	−17.882	0.00004775
1,1,1-Trifluoroethane (R143a)	$C_2H_3F_3$	0.31	0.22	0.16	0.13	0.09				4.61506	1.76477	546.015	−252.896	0.00000187

D3.1. Table 7. (continued)

Substance	Formula	Temperature (°C)								Equation (2)				
		−50	−25	0	20	50	100	150	200	*A*	*B*	*C*	*D*	*E*
1,1,1-Trichloroethane	$C_2H_3Cl_3$		1.86	1.13	0.82	0.56	0.35			0.61256	2.57080	431.477	−5.988	0.00020394
1,1,2,2-Tetrachloroethane	$C_2H_2Cl_4$		4.65	2.60	1.77	1.11	0.63	0.43		−1.87216	3.09287	643.532	−79.592	0.00064250
Pentachloroethane	C_2HCl_5		6.15	3.46	2.35	1.45	0.78	0.47		1.19161	3.53080	457.262	−59.526	0.00026156
Hexachloroethane	C_2Cl_6								0.38	0.93763	1.54402	933.967	−95.372	0.00004948
1,1,2,2-Tetrachlorodifluoroethane	$C_2Cl_4F_2$					0.89				2.43919	1.98108	589.547	−55.108	0.00002928
1,1,2-Trichlorotrifluoroethan	$C_2Cl_3F_3$		1.47	0.94	0.70	0.49	0.30			0.82677	1.39278	641.776	−33.411	0.00006607
1,2-Dichlorotetrafluoroethane	$C_2Cl_2F_4$	1.07	0.69	0.48	0.37	0.27	0.17			1.87065	0.72922	852.495	−53.946	0.00001040
1-Chloropropane	C_3H_7Cl	0.89	0.61	0.44	0.36	0.27	0.18	0.11		1.92904	0.84928	457.628	5.103	0.00004817
1-Chlorobutane	C_4H_9Cl	1.28	0.82	0.57	0.45	0.33	0.22	0.16		1.52415	0.59496	866.798	−26.351	0.00001925
1-Chloropentane	$C_5H_{11}Cl$	1.86	1.14	0.77	0.59	0.42	0.27			0.62392	1.37795	655.392	−49.534	0.00007030
Chlorotrifluoroethene	C_2ClF_3	2.80								2.44328	0.87633	677.365	−14.748	0.00001698
Vinyl chloride	C_2H_3Cl	0.39	0.29	0.22	0.18	0.14	0.10	0.07		3.40346	0.04475	1554.962	−9.904	0.00000057
1,1-Dichloroethene	$C_2H_2Cl_2$	1.21	0.79	0.54	0.42					1.81449	1.43005	596.573	−79.313	0.00002607
Trichloroethene	C_2HCl_3		0.97	0.70	0.57	0.44				0.09853	0.87464	646.099	−1.547	0.00016897
Tetrachloroethene	C_2Cl_4			1.12	0.89	0.67	0.45	0.33	0.25	1.65634	0.78790	633.414	−20.306	0.00006745
Fluorobenzene	C_6H_5F		1.17	0.76	0.58	0.42	0.27	0.18		2.04963	0.38729	532.926	91.376	0.00004074
Chlorobenzene	C_6H_5Cl			1.06	0.80	0.57	0.37	0.26	0.19	2.62728	−0.00003	685.399	159.643	0.00001868
Bromobenzene	C_6H_5Br		2.47	1.55	1.14	0.78	0.48	0.34		2.12889	0.10412	1705.036	59.324	0.00000753
Iodobenzene	C_6H_5I		4.05	2.38	1.69	1.11	0.65	0.43		2.37813	0.16293	1304.037	67.555	0.00001003
m-Chlorotoluene	C_7H_7Cl		2.08	1.30	0.95	0.65	0.41	0.29		0.66570	2.57537	448.320	−26.587	0.00021128
Benzyl chloride	C_7H_7Cl		2.67	1.67	1.20	0.79	0.44	0.28		1.98218	1.93498	643.943	−99.094	0.00003369
***n*-Alkanes**														
Methane	CH_4									2.31365	0.66803	200.211	−19.178	0.00001039
Ethane	C_2H_6	0.10	0.08	0.06						2.43591	0.09710	309.734	33.467	0.00001554
Propane	C_3H_8	0.22	0.16	0.13	0.10	0.07				2.56344	0.16137	372.533	38.033	0.00001751
n-Butane	C_4H_{10}	0.36	0.26	0.20	0.17	0.13	0.08			2.62924	0.23703	428.069	37.093	0.00001801
n-Pentane	C_5H_{12}	0.51	0.37	0.28	0.23	0.18	0.11			2.80331	0.25074	474.455	32.856	0.00001653
n-Hexane	C_6H_{14}	0.75	0.51	0.38	0.31	0.24				0.69508	0.53665	704.295	16.747	0.00005657
n-Heptane	C_7H_{16}	1.17	0.76	0.53	0.42	0.30	0.19			2.96002	0.24715	553.942	62.172	0.00001424
n-Octane	C_8H_{18}	1.63	1.03	0.71	0.55	0.39	0.24			2.87088	0.35483	577.534	48.983	0.00001722
n-Nonane	C_9H_{20}	2.48	1.45	0.94	0.70	0.48	0.29	0.19		2.91497	0.49850	609.361	38.982	0.00001562
n-Decane	$C_{10}H_{22}$		2.01	1.28	0.94	0.64	0.38	0.24		2.76810	0.64646	621.362	24.170	0.00002107
n-Undecane	$C_{11}H_{24}$		2.95	1.71	1.19	0.76	0.43	0.28		1.42789	1.36923	615.194	−0.597	0.00005825

n-Dodecane	$C_{12}H_{26}$			2.25	1.50	0.92	0.51	0.33	0.23	1.87106	0.59429	757.672	63.871	0.00003070
n-Tridecane	$C_{13}H_{28}$			2.78	1.87	1.14	0.60	0.37	0.26	1.05863	1.73484	695.337	−39.851	0.00006504
n-Tetradecane	$C_{14}H_{30}$				2.29	1.34	0.69	0.42	0.29	1.70345	1.10500	696.658	26.022	0.00004770
n-Pentadecane	$C_{15}H_{32}$				2.75	1.60	0.80	0.47	0.32	1.32056	1.61496	714.996	−23.879	0.00006051
n-Hexadecane	$C_{16}H_{34}$				3.30	1.87	0.91	0.53	0.35	1.75863	0.59899	1140.067	17.721	0.00001758
n-Heptadecane	$C_{17}H_{36}$					2.16	1.03	0.59	0.39	0.25719	1.55014	986.952	−71.139	0.00007134
n-Octadecane	$C_{18}H_{38}$					2.44	1.13	0.64	0.42	1.77701	0.56471	1241.303	18.268	0.00001609
n-Nonadecane	$C_{19}H_{40}$					2.79	1.29	0.72	0.46	0.56468	1.52936	1020.103	−76.599	0.00005702
n-Eicosane	$C_{20}H_{42}$					3.20	1.44	0.79	0.49	0.77549	2.16016	789.785	−65.277	0.00008902
Isoalkanes														
Isobutane	C_4H_{10}	0.38	0.27	0.20	0.16					2.79529	0.37315	419.630	28.072	0.00001567
2-Methyl butane	C_5H_{12}	0.55	0.38	0.28	0.22					1.34155	1.33584	426.654	−16.753	0.00005280
2,2-Dimethyl propane	C_5H_{12}			0.33	0.24	0.18	0.12			0.20382	2.65306	366.672	40.292	0.00012836
2-Methyl pentane	C_6H_{14}	0.75	0.50	0.36	0.29	0.22				1.25443	1.20225	495.370	−20.972	0.00005066
3-Methyl pentane	C_6H_{14}	0.73	0.51	0.38	0.30	0.23				−1.65266	4.71153	545.792	−273.697	0.00021598
2,2-Dimethyl butane	C_6H_{14}	1.10	0.69	0.48	0.37					0.78335	1.79719	521.065	−50.880	0.00006606
2,3-Dimethyl butane	C_6H_{14}	1.04	0.70	0.49	0.38	0.27				2.40720	2.47024	483.731	−163.832	0.00002948
Olefins														
Ethylene	C_2H_4	0.09	0.07							2.09844	0.09095	281.469	47.654	0.00002107
Propylene	C_3H_6	0.18	0.14	0.11	0.10					1.41868	0.31808	772.733	−16.157	0.00001059
1-Butene	C_4H_8	0.30	0.22							1.12328	1.46382	431.592	−78.509	0.00004504
1-Pentene	C_5H_{10}	0.43	0.31	0.24	0.20					1.23863	0.83928	552.930	−31.663	0.00003416
1-Hexene	C_6H_{12}	0.63	0.43	0.32	0.26	0.20				0.78658	1.77502	489.925	−75.082	0.00006364
1-Heptene	C_7H_{14}	0.87	0.59	0.44	0.35	0.27	0.19	0.15	0.12	0.86573	0.25317	1520.715	−26.413	0.00001982
1-Octene	C_8H_{16}	1.36	0.88	0.61	0.48	0.35	0.23			1.29101	1.29302	586.319	−48.960	0.00004920
Propadiene	C_3H_4	0.22	0.19	0.16	0.14					0.89336	0.66484	424.315	−49.755	0.00006299
1,2-Butadiene	C_4H_6	0.28	0.23	0.19						0.67336	0.50405	612.623	−27.742	0.00005206
1,3-Butadiene	C_4H_6			0.19	0.15	0.10	0.06			0.88238	101.98307	384.667	−3372.077	0.00005430
1,2-Pentadiene	C_5H_8	0.39	0.30	0.24	0.20					0.90990	0.49699	702.284	−22.926	0.00003729
trans-1,3-Pentadiene	C_5H_8	0.39	0.30	0.24	0.20					0.67882	1.19675	469.034	−52.560	0.00007247
1,4-Pentadiene	C_5H_8	0.39	0.30	0.24	0.20					0.95705	0.89154	474.141	−25.365	0.00006023
2,3-Pentadiene	C_5H_8	0.39	0.30	0.24	0.20					0.87673	0.76868	537.821	−27.161	0.00005318
Acetylene and derivatives														
Acetylene	C_2H_2	0.15	0.12	0.10						2.52365	1.17810	426.582	−212.035	0.00001364
Propyne	C_3H_4	0.29	0.22	0.17	0.15	0.12	0.09			1.51137	0.90164	554.417	−83.957	0.00002240
2-Butyne	C_4H_6		0.35	0.27	0.22	0.17				1.18604	2.76132	469.413	−204.254	0.00004722
1-Butyne	C_4H_6	0.40	0.31	0.25	0.21	0.17	0.13			1.63188	0.65707	586.283	−56.906	0.00002696

D3.1. Table 7. (continued)

Substance	Formula	Temperature (°C)								Equation (2)				
		−50	−25	0	20	50	100	150	200	*A*	*B*	*C*	*D*	*E*
Naphthenes														
Cyclopropane	C_3H_6	0.31	0.24	0.19						1.54429	0.85237	493.205	−65.344	0.00003113
Cyclobutane	C_4H_8	0.54	0.41	0.32	0.27	0.22				1.32593	0.96765	615.982	−101.863	0.00003774
Cyclopentane	C_5H_{10}		0.79	0.56	0.43					0.87341	38.24451	488.485	−1832.850	0.00005995
Methyl cyclopentane	C_6H_{12}		0.93	0.65	0.50	0.36				2.03241	1.34658	511.445	−48.471	0.00004178
Ethyl cyclopentane	C_7H_{14}			0.72	0.57	0.41	0.27			1.26432	1.29189	649.180	−71.893	0.00004633
Propyl cyclopentane	C_8H_{16}	2.32	1.36	0.89	0.68	0.49	0.33			−0.10699	1.30324	655.283	−17.596	0.00015405
Butyl cyclopentane	C_9H_{18}	3.26	1.88	1.20	0.89	0.61	0.37	0.25		1.34628	1.62686	558.215	−34.525	0.00007450
Pentyl cyclopentane	$C_{10}H_{20}$			1.59	1.14	0.76	0.45	0.31	0.24	−1.11498	1.19528	983.833	−53.542	0.00023152
Hexyl cyclopentane	$C_{11}H_{22}$			2.10	1.47	0.94	0.53	0.35	0.26	−1.13172	1.69976	925.702	−92.482	0.00020910
Cyclohexane	C_6H_{12}				0.97	0.61	0.33	0.21	0.14	0.75690	2.02779	787.882	−117.742	0.00003221
Methyl cyclohexane	C_7H_{14}	2.83	1.59	0.99	0.73	0.50	0.33			−0.74619	6.01059	429.985	−152.623	0.00034647
Ethyl cyclohexane	C_8H_{16}	3.18	1.78	1.13	0.84	0.58	0.36			1.52910	0.51211	842.298	28.257	0.00003076
Propyl cyclohexane	C_9H_{18}	4.60	2.35	1.40	1.00	0.67	0.42	0.30		−0.55711	1.64220	646.674	−10.660	0.00024150
Butyl cyclohexane	$C_{10}H_{20}$			1.88	1.30	0.84	0.50	0.37		−0.87038	1.86712	617.939	2.177	0.00036852
Pentyl cyclohexane	$C_{11}H_{22}$	6.63	3.52	2.09	1.47	0.94	0.53	0.35	0.26	−2.02019	1.03757	1391.703	−90.787	0.00038189
Hexyl cyclohexane	$C_{12}H_{24}$			3.55	2.18	1.26	0.69	0.47	0.36	0.39759	0.73957	722.436	94.236	0.00016567
Cyclopentene	C_5H_8	0.88	0.60	0.44	0.35	0.26	0.18			3.03864	0.13240	1265.791	−1.551	0.00000199
Cyclohexene	C_6H_{10}	2.22	1.33	0.87	0.66	0.46	0.29			1.32523	1.09890	682.520	−31.539	0.00003971
Aromatic compounds														
Benzene	C_6H_6				0.64	0.44	0.26	0.17	0.11	2.35743	2.43122	760.674	−267.449	0.00001031
Toluene	C_7H_8	2.12	1.20	0.78	0.59	0.42	0.26			2.95480	0.00003	1048.107	137.144	0.00000397
Ethyl benzene	C_8H_{10}	2.24	1.35	0.90	0.68	0.48	0.30			1.62469	0.79236	745.185	−16.276	0.00002899
Propyl benzene	C_9H_{12}	3.40	1.89	1.18	0.86	0.58	0.36	0.25		0.57949	1.41702	663.889	−28.020	0.00008430
Butyl benzene	$C_{10}H_{14}$	4.71	2.44	1.46	1.04	0.69	0.41	0.28		1.15033	1.50259	547.276	7.044	0.00009568
Pentyl benzene	$C_{11}H_{16}$			2.03	1.35	0.86	0.50	0.31	0.18	2.25142	0.05803	500.962	195.336	0.00006352
Hexyl benzene	$C_{12}H_{18}$			2.69	1.69	1.01	0.58	0.35	0.28	0.63147	1.93122	423.312	91.152	0.00033398
o-Xylene	C_8H_{10}		1.73	1.10	0.81	0.56	0.34			1.88479	0.23639	1377.129	22.892	0.00000903
m-Xylene	C_8H_{10}		1.19	0.80	0.62	0.44	0.29			0.83592	1.33199	637.761	−46.156	0.00006847
p-Xylene	C_8H_{10}				0.65	0.46	0.29			0.80720	1.37688	638.213	−40.858	0.00006787
1,2,3-Trimethyl benzene	C_9H_{12}		2.47	1.43	0.98	0.61	0.33	0.20		1.30935	2.05880	633.423	−61.927	0.00003863
1,2,4-Trimethyl benzene	C_9H_{12}		2.22	1.35	0.96	0.62	0.35	0.22		1.53346	1.54307	674.260	−51.363	0.00003357

1,3,5-Trimethyl benzene	C_9H_{12}		1.91	1.14	0.81	0.53	0.31	0.21		0.66691	1.78474	611.651	−30.201	0.00007216
1,2,3,4-Tetramethyl benzene	$C_{10}H_{14}$			2.71	1.73	0.97	0.46	0.26	0.16	1.36952	2.99462	598.830	−76.944	0.00004700
1,2,3,5-Tetramethyl benzene	$C_{10}H_{14}$			2.06	1.35	0.79	0.39	0.23		1.37525	2.47071	620.301	−64.925	0.00003980
1,2,4,5-Tetramethyl benzene	$C_{10}H_{14}$						0.40	0.25		0.99413	2.50337	681.125	−109.874	0.00004350
Pentamethyl benzene	$C_{11}H_{16}$						0.58	0.28	0.16	1.45987	4.29539	616.285	−107.695	0.00003215
Hexamethyl benzene	$C_{12}H_{18}$								0.17	1.22472	10.29732	584.012	−288.554	0.00004085
Styrene	C_8H_8		1.61	1.02	0.76	0.52	0.32			2.52817	0.19295	1189.840	44.635	0.00000538
Isopropyl benzene	C_9H_{12}	3.11	1.72	1.08	0.80	0.55	0.34			1.59020	0.52734	825.677	29.696	0.00002771
Biphenyl	$C_{12}H_{10}$		9.77	5.16	3.36	1.95	0.96	0.56	0.37	1.44526	0.96526	1040.250	−32.003	0.00002670
Diphenyl methane	$C_{13}H_{12}$		8.74	4.64	3.04	1.79	0.91	0.55	0.37	0.73771	1.12625	964.267	−30.528	0.00006040
Triphenyl methane	$C_{19}H_{16}$		71.70	31.26	17.65	8.47	3.20	1.51	0.84	1.19279	2.16005	961.714	−90.134	0.00004502
Tetraphenyl methane	$C_{25}H_{20}$									1.13557	4.22608	895.853	−201.703	0.00010734
Naphthalene	$C_{10}H_8$						0.77	0.53	0.38	2.91719	−0.00009	725.690	152.240	0.00002552
1-Methylnaphthalene	$C_{11}H_{10}$		16.26	6.06	3.34	1.73	0.88	0.63	0.56	−4.70967	2.73910	679.956	24.202	0.00797964
2-Methylnaphthalene	$C_{11}H_{10}$					1.40	0.72	0.48	0.37	−0.95968	1.92015	645.748	28.287	0.00043145
1-Ethylnaphthalene	$C_{12}H_{12}$			8.07	4.11	1.97	0.94	0.64	0.55	−3.11745	2.51548	622.592	56.635	0.00267011
2-Ethylnaphthalene	$C_{12}H_{12}$			5.06	2.92	1.57	0.79	0.53	0.42	−2.15924	2.20844	659.680	28.821	0.00106785
Alcohols														
Methanol	CH_4O	2.22	1.26	0.80	0.58	0.39				3.79226	0.17755	546.563	87.845	0.00000791
Ethanol	C_2H_6O	6.27	3.13	1.76	1.17	0.69	0.32	0.17		6.16832	−0.00125	740.323	90.778	0.00000038
1-Propanol	C_3H_8O	21.41	8.01	3.70	2.20	1.12				4.91749	0.83615	482.980	73.079	0.00001026
1-Butanol	$C_4H_{10}O$	35.76	12.17	5.16	2.91	1.42	0.55			4.35655	1.01095	742.263	26.911	0.00000214
1-Pentanol	$C_5H_{12}O$			7.63	4.03	1.81	0.65			1.29984	2.31754	793.256	−36.745	0.00001600
1-Hexanol	$C_6H_{14}O$			10.78	5.30	2.25	0.78	0.36		2.38169	2.01882	628.673	36.282	0.00002196
1-Heptanol	$C_7H_{16}O$		55.91	15.68	6.98	2.68	0.88	0.44		−0.90610	4.79159	549.369	−1.348	0.00030998
1-Octanol	$C_8H_{18}O$				8.70	3.25	0.97	0.43		−3.01414	4.51847	742.731	−58.271	0.00043189
Isopropanol	C_3H_8O	35.98	11.48	4.46	2.33	1.02				3.07172	3.84587	580.414	−62.691	0.00000742
2-Methyl-1-propanol	$C_4H_{10}O$	103.71	25.05	8.23	3.97	1.63	0.54	0.24	0.13	1.75100	4.27573	508.236	−6.909	0.00005339
3-Methyl-1-butanol	$C_5H_{12}O$			8.57	4.28	1.82	0.62			2.37997	2.49622	630.920	5.329	0.00001584
Ethylene glycol	$C_2H_6O_2$			55.27	21.23	6.98	1.99	0.93	0.61	−2.46697	5.00103	587.004	10.679	0.00132759
1,3-Propylene glycol	$C_3H_8O_2$					15.57	3.72	1.37		4.54401	0.75893	711.876	132.080	0.00000695
Glycerol	$C_3H_8O_3$				1433	151.4	14.49	3.93	2.02	−3.91153	6.54946	582.480	73.885	0.00799640
Cyclohexanol	$C_6H_{12}O$					12.72	1.99	0.70		0.02813	3.61442	534.094	121.724	0.00026465
Benzyl alcohol	C_7H_8O			13.88	5.93	2.50	1.05	0.63	0.44	0.44585	0.08077	2571.495	151.699	0.00007198
Phenols														
o-Cresol	C_7H_8O					2.95	1.00	0.50		−1.89618	3.60949	631.884	15.554	0.00052426

D3.1. Table 7. (continued)

Substance	Formula	Temperature (°C)								Equation (2)				
		−50	−25	0	20	50	100	150	200	*A*	*B*	*C*	*D*	*E*
m-Cresol	C_7H_8O					4.20	1.19	0.58	0.32	1.25683	1.54210	482.684	175.193	0.00021035
p-Cresol	C_7H_8O					4.60	1.29	0.61	0.36	1.06826	2.00817	491.556	150.679	0.00022764
Phenol	C_6H_6O					3.46	1.10	0.58	0.43	−0.58868	3.54041	505.278	86.084	0.00049135
Carboxylic acids														
Formic acid	CH_2O_2				1.78	1.04	0.53			1.06486	0.68065	1102.891	11.307	0.00002427
Acetic acid	$C_2H_4O_2$				1.22	0.79	0.45			1.74793	1.33728	482.347	41.780	0.00009963
Propionic acid	$C_3H_6O_2$			1.53	1.10	0.74	0.45			1.40324	1.23452	507.512	36.027	0.00011180
Butyric acid	$C_4H_8O_2$			2.31	1.61	1.01	0.55	0.35		−0.59438	3.25801	702.490	−155.864	0.00016068
Valeric acid	$C_5H_{10}O_2$		6.19	3.37	2.23	1.31	0.64	0.36		4.18858	0.59968	696.703	32.858	0.00000596
Caproic acid	$C_6H_{12}O_2$			5.23	3.17	1.75	0.87	0.55	0.41	−0.09052	2.89549	536.223	1.885	0.00035472
Acetic anhydride	$C_4H_6O_3$	3.41	1.93	1.22	0.90	0.61	0.38			0.83036	2.94744	443.462	−55.683	0.00018360
Propionic anhydride	$C_6H_{10}O_3$			1.59	1.13	0.74	0.43	0.28		0.91350	1.53689	664.075	−33.692	0.00007064
Chloroacetic acid	$C_2H_3ClO_2$					3.30	1.29			1.55021	0.00012	475.704	291.063	0.00024327
Dichloroacetic acid	$C_2H_2Cl_2O_2$				7.29	3.17	0.68			11.44422	0.73703	438.241	−120.582	0.00000190
Trichloroacetic acid	$C_2HCl_3O_2$						1.10	0.19		0.89511	−51.82878	337.101	−405.316	0.00359585
Ketones														
Ketene	C_2H_2O	0.52								1.31545	1.31192	334.574	−25.576	0.00012225
Acetone	C_3H_6O	0.80	0.54	0.40	0.32	0.24				1.65496	0.57330	610.687	11.477	0.00002915
Methyl ethyl ketone	C_4H_8O	1.08	0.73	0.53	0.42	0.31	0.20	0.14	0.10	3.36887	0.15106	994.604	10.710	0.00000262
Diethyl ketone	$C_5H_{10}O$		0.83	0.59	0.47	0.34	0.23			1.78235	1.27121	589.709	−76.509	0.00003465
Dipropyl ketone	$C_7H_{14}O$		1.74	1.06	0.76	0.51	0.30			0.53899	1.60566	636.434	−28.275	0.00007612
Acetophenone	C_8H_8O				1.81	1.10				1.33990	0.72070	519.145	125.271	0.00014141
Benzophenone	$C_{13}H_{10}O$						1.74	0.75		−1.02889	2.62407	887.912	−31.349	0.00014250
Ethers														
Dimethyl ether	C_2H_6O	0.18	0.15							−24.14991	826.18026	333.839	−9717.889	0.00504502
Diethyl ether	$C_4H_{10}O$	0.53	0.39	0.29	0.24	0.18	0.11			2.19245	3.83507	520.594	−370.873	0.00002040
Dipropyl ether	$C_6H_{14}O$	1.24	0.79	0.54	0.42	0.30				1.70133	1.11633	592.026	−34.625	0.00003012
Methyl propyl ether	$C_4H_{10}O$	0.59	0.41	0.31	0.25					1.23830	1.16190	484.926	−27.978	0.00004941
Ethyl propyl ether	$C_5H_{12}O$	0.78	0.54	0.40	0.32	0.24				1.88361	1.70057	486.071	−102.106	0.00003744
Ethylene oxide	C_2H_4O	0.57	0.41	0.32						2.03182	0.24658	923.371	−4.439	0.00000986
Furane	C_4H_4O	0.99	0.66	0.48	0.38					0.99383	1.26306	558.327	−41.885	0.00006015
1,4-Dioxane	$C_4H_8O_2$				1.30	0.81	0.46			−0.88995	5.54776	466.802	−109.574	0.00041685

Aldehydes														
Formaldehyde	CH_2O	0.33	0.24							0.69796	1.14046	549.921	−44.110	0.00003565
Acetaldehyde	C_2H_4O	0.58	0.39	0.28	0.22					1.93622	1.28342	451.995	−34.901	0.00003002
Paraldehyde	$C_6H_{12}O_3$				1.19	0.68	0.37			2.30632	0.16500	580.288	180.024	0.00002892
Furfural	$C_5H_4O_2$		5.01	2.55	1.72	1.13	0.75	0.65		−1.74070	2.22317	510.261	48.654	0.00137465
Benzaldehyde	C_7H_6O	6.53	3.47	2.09	1.49	0.97	0.57	0.38		0.68640	1.42033	705.459	−31.539	0.00010016
Salicylaldehyde	$C_7H_6O_2$				2.69	1.57	0.80	0.49		−1.05492	3.11770	694.096	−97.628	0.00030993
Esters														
Methyl formate	$C_2H_4O_2$			0.44	0.35					−0.91668	1.04562	600.645	30.794	0.00025227
Ethyl formate	$C_3H_6O_2$	1.09	0.71	0.50	0.40	0.30				0.70107	1.29587	586.673	−38.736	0.00006727
Propyl formate	$C_4H_8O_2$	1.62	1.00	0.68	0.52	0.37				3.44810	0.00004	653.964	118.712	0.00000644
Methyl acetate	$C_3H_6O_2$			0.47	0.38	0.28	0.18	0.12		2.35777	1.57824	508.322	−127.221	0.00002998
Ethyl acetate	$C_4H_8O_2$	1.08	0.78	0.57	0.45	0.33	0.20	0.13	0.09	2.87505	3.82999	701.624	−475.816	0.00000853
Propyl acetate	$C_5H_{10}O_2$			0.75	0.59	0.42	0.25	0.16	0.10	2.51468	7.47712	600.279	−667.720	0.00002056
Methyl propionate	$C_4H_8O_2$			0.58	0.46	0.34				1.95117	0.93694	615.575	−40.012	0.00002716
Ethyl propionate	$C_5H_{10}O_2$			0.69	0.53	0.38				1.13267	1.39120	636.287	−63.713	0.00004664
Propyl propionate	$C_6H_{12}O_2$	2.60	1.47	0.93	0.69	0.47	0.29			0.97927	1.56323	602.941	−33.934	0.00006131
Methyl butyrate	$C_5H_{10}O_2$	1.88	1.14	0.76	0.58	0.41	0.26			1.19242	1.14545	659.315	−32.416	0.00004368
Ethyl butyrate	$C_6H_{12}O_2$			0.89	0.67	0.47	0.30			0.69721	1.44466	631.106	−37.809	0.00007509
Methyl benzoate	C_8H_8O2				2.03	1.14	0.55	0.32		1.09205	2.23998	629.397	−30.878	0.00006372
Ethyl benzoate	$C_9H_{10}O_2$			3.46	2.19	1.27	0.67	0.44	0.33	−0.52423	2.21075	621.267	−1.514	0.00029435
Methyl salicylate	$C_8H_8O_3$			4.50	2.83	1.61	0.81	0.50	0.35	0.78116	2.21500	566.049	2.932	0.00017111
Amines														
Methyl amine	CH_5N	0.46	0.31	0.23						0.67474	1.15788	540.516	−19.923	0.00004244
Ethyl amine	C_2H_7N	0.82	0.48	0.30						4.57723	3.23212	461.592	−187.220	0.00000375
Propyl amine	C_3H_9N	1.27	0.78	0.53	0.40					1.43759	1.38853	576.592	−41.604	0.00003388
n-Butyl amine	$C_6H_{15}N$			0.83	0.62	0.41				4.93315	5.56240	539.687	−504.926	0.00000690
Dimethyl amine	C_2H_7N	0.41	0.31	0.23	0.19	0.14				2.36300	0.00009	401.423	108.715	0.00002662
Trimethyl amine	C_3H_9N	0.39	0.29	0.23	0.19	0.14				2.49364	3.31500	473.868	−357.809	0.00001998
Diethyl amine	$C_6H_{15}N$		0.70	0.46	0.35	0.24				2.23041	0.67794	410.269	75.910	0.00004206
Triethyl amine	$C_6H_{15}N$			0.46	0.37	0.27				1.14057	1.76812	540.640	−101.165	0.00005323
Piperidine	$C_5H_{11}N$				1.50	0.93	0.47			2.87595	2.15313	604.743	−97.645	0.00002125
Pyridine	C_6H_7N		2.45	1.37	0.96	0.63	0.40			−1.07330	2.28184	531.855	9.899	0.00042903
Aniline	C_6H_7N			10.34	4.54	1.95	0.83	0.49		0.85750	1.71069	462.011	136.981	0.00028187
N-methyl aniline	C_7H_9N			3.95	2.26	1.19	0.57	0.37		−1.58729	2.74662	611.361	10.495	0.00047319
N,*N*-dimethyl aniline	$C_8H_{11}N$				1.40	0.90	0.52	0.35		2.17192	0.33015	782.598	90.952	0.00002587

D3.1. Table 7. (continued)

Substance	Formula	Temperature (°C)								Equation (2)				
		−50	−25	0	20	50	100	150	200	*A*	*B*	*C*	*D*	*E*
N,*N*-diethyl aniline	$C_{10}H_{15}N$			3.55	2.18	1.22	0.61	0.39	0.29	−2.17946	2.59836	712.387	−32.879	0.00061721
Phenylhydrazine	$C_6H_8N_2$				16.49	4.57	0.85			4.03637	4.11517	716.323	−44.624	0.00000082
Diphenyl amine	$C_{12}H_{11}N$						1.69	0.80	0.50	−1.88236	2.76806	703.956	42.025	0.00069814
Nitriles														
Acetonitrile	C_2H_3N				0.37	0.28				−0.08444	3.22207	685.539	−331.224	0.00006935
Propionitrile	C_3H_5N			0.54	0.43	0.32				0.15621	2.63370	600.424	−178.151	0.00008475
Butyronitrile	C_4H_7N	1.75	1.09	0.75	0.57	0.41	0.27			1.43860	0.97107	678.200	−30.941	0.00003687
Benzonitrile	C_7H_5N			1.92	1.33	0.87	0.52	0.36		1.74964	0.45048	621.897	104.361	0.00006329
Amides														
Formamide	CH_3NO				3.85	1.89	0.84	0.50	0.36	−0.82268	2.80139	592.004	19.366	0.00038574
Nitroderivates														
Nitromethane	CH_3NO_2		1.27	0.86	0.67	0.48	0.30			2.74060	0.08984	536.681	119.119	0.00002704
Nitrobenzene	$C_6H_5NO_2$				2.05	1.26	0.71	0.48	0.35	1.75794	0.36655	679.009	124.816	0.00006683
o-Nitrotoluene	$C_7H_7NO_2$			3.82	2.37	1.38	0.76	0.54	0.46	−1.52541	2.37156	581.717	24.432	0.00083353
m-Nitrotoluene	$C_7H_7NO_2$				2.33	1.36	0.76	0.54	0.45	−1.89318	2.22744	626.017	17.125	0.00099984
p-Nitrotoluene	$C_7H_7NO_2$						0.75	0.54	0.45	0.00118	1.22450	513.379	128.908	0.00041885

D3.1. Table 8. Dynamic viscosity of gases in μPa s at low pressures

Substance	Formula	Temperature (°C)								Equation (3)				
		−50	0	25	100	200	300	400	500	10^5 *A*	10^7 *B*	10^{10} *C*	10^{12} *D*	10^{15} *E*
Elements														
Xenon	Xe	17.4	21.3	23.2	28.6	35.3	41.5	47.3	52.7	−0.23692	0.98454	−0.48314	0.01953	−0.00342
Krypton	Kr	19.6	23.5	25.4	30.8	37.5	43.5	49.1	54.2	−0.07920	1.02624	−0.55428	0.02187	−0.00369
Argon	Ar		21.1	22.6	27.0	32.5	37.5	42.2	46.5	0.16196	0.81279	−0.41263	0.01668	−0.00276
Neon	Ne	25.4	29.6	31.5	37.1	43.7	49.6	54.9	59.9	0.23014	1.22527	−0.97141	0.05386	−0.01103
Helium	He	16.2	18.6	19.8	23.2	27.4	31.3	35.1	38.6	0.39223	0.61300	−0.31007	0.01479	−0.00284
Air		14.6	17.2	18.5	21.9	26.1	29.8	33.2	36.5	−0.01702	0.79965	−0.72183	0.04960	−0.01388
Hydrogen	H_2	7.3	8.3	8.9	10.4	12.2	14.0	15.6	17.1	0.18024	0.27174	−0.13395	0.00585	−0.00104
Nitrogen	N_2	14.0	16.5	17.8	21.1	25.2	28.7	32.0	35.0	−0.01020	0.74785	−0.59037	0.03230	−0.00673
Oxygen	O_2	16.2	19.2	20.7	24.7	29.5	33.8	37.7	41.4	−0.10257	0.92625	−0.80657	0.05113	−0.01295
Sulfur	S					6.9	8.3	9.7	11.1	0.09670	0.11835	0.01588		
Fluorine	F_2	18.1	21.5	23.2	27.8	33.6	38.9	43.9	48.7	−0.11373	1.03844	−0.96327	0.08073	−0.02846
Chlorine	Cl_2	10.0	12.3	13.4	16.6	20.8	24.8	28.6	32.2	−0.06348	0.49801	−0.09451		
Bromine	Br_2		14.3	15.4	19.0	23.8	28.7			0.19483	0.43743	0.05031		
Iodine	I_2					21.8	26.0	30.2	34.3	0.06758	0.46358	−0.03714		
Anorganic compounds														
Hydrogen fluoride	HF			11.3	16.0					−7.08883	4.18933	−1.19859	−1.98523	2.59754
Hydrogen chloride	HCl	10.8	13.4	14.6	18.3	22.9	27.3	31.5	35.4	−0.12146	0.56696	−0.12126		
Hydrogen bromide	HBr	13.8	16.6	18.1	22.2	27.7	33.1	38.5	43.7	0.09163	0.58825	−0.04531		
Hydrogen iodide	HI		17.4	19.0	23.5	29.4	35.1			−0.01823	0.67176	−0.09695		
Hydrogen cyanide	HCN				3.6					−0.06954	0.08177	0.09107		
Water	H_2O		9.1	9.9	12.4	16.2	20.3	24.5	28.6	0.64966	−0.15102	1.15935	0.10080	0.03100
Hydrogen sulfide	H_2S		11.7	12.6	15.7	20.6				0.54442	0.10851	0.44565		
Ammonia	NH_3	7.4	9.2	10.1	12.9	16.5	20.1	23.7	27.4	−0.07883	0.36749	−0.00451		
Nitric oxide	NO	14.9	17.8	19.1	22.9	27.3	31.2	34.8	38.0	−0.09105	0.84998	−0.71473	0.04240	−0.01020
Nitrogen dioxide	NO_2				18.7	24.6	29.4	33.6	37.4	−2.28505	1.75834	−2.29768	0.17134	−0.04920
Nitrous oxide	N_2O	11.0	13.4	14.6	18.1	22.4	26.4	30.0	33.4	−0.09569	0.57181	−0.16548		
Dinitrogentetroxide	N_2O_4	13.5	16.6	18.1	22.5	28.2	33.6	38.7	43.6	−0.08683	0.67450	−0.12834		
Cyanogen	C_2N_2		9.3	10.1	12.7	16.0	19.3			−0.00521	0.34573	−0.01265		
Phosphorus trichloride	PCl_3	7.8	9.6	10.5	13.2	16.6	19.8	22.9	26.0	−0.11382	0.42969	−0.14926	0.00744	−0.00177
Cyanogen chloride	ClCN	6.2	7.6	8.4	10.4	13.1	15.6	18.0	20.2	−0.07162	0.32567	−0.07104		
Silane	SiH_4	8.9	10.7	11.6	14.2	17.8	21.3	24.8	28.4	0.10189	0.35395			
Tetrachlorosilane	$SiCl_4$	7.5	9.3	10.2	12.8	16.1	19.2	22.2	25.1	−0.13422	0.42941	−0.15995	0.00734	−0.00161
Carbon monoxide	CO	14.0	16.5	17.7	20.9	24.9	28.4	31.5	34.5	0.01384	0.74306	−0.62996	0.03948	−0.01032
Carbon dioxide	CO_2	11.2	13.8	15.0	18.4	22.6	26.5	30.0	33.3	−0.18024	0.65989	−0.37108	0.01586	−0.00300
Carbon suboxide	C_3O_2	9.1	11.2	12.2	15.2	19.0	22.6	26.1	29.4	−0.05865	0.45539	−0.08739		
Carbonyl sulfide	COS	9.5	11.7	12.8	16.0	20.2	24.1	27.8	31.4	−0.10565	0.49410	−0.09608		
Phosgene	CCl_2O			9.3	11.6	14.6	17.3	20.0	22.5	−0.06483	0.35637	−0.07409		
Carbon disulfide	CS_2	7.3	9.0	9.9	12.5	16.0	19.4	22.7	26.0	−0.07840	0.36608	−0.02490		
Sulfur dioxide	SO_2	9.5	11.8	12.9	16.1	20.3	24.2	27.9	31.3	−0.13559	0.51230	−0.11626		
Sulfur trioxide	SO_3			13.6	16.8	20.9	24.7	28.1		−0.12683	0.54605	−0.16261		
Sulfuryl chloride	Cl_2SO_2	8.1	10.1	11.1	14.1	17.9	21.6	25.2	28.6	−0.12421	0.43363	−0.06167		
Sulfur hexafluoride	SF_6	10.8	13.6	15.0	18.7	23.2	27.3	30.9	34.3	−0.41132	0.77468	−0.51939	0.02409	−0.00438
Organic compounds containing sulfur														
Methyl mercaptan	CH_4S	7.0	8.6	9.5	11.9	15.0	18.0	20.9	23.6	−0.08906	0.36632	−0.06330		
Ethyl mercaptan	C_2H_6S	6.5	8.0	8.7	10.9	13.8	16.5	19.2	21.8	−0.05276	0.32400	−0.04604		
Dimethyl sulfide	C_2H_6S	6.1	7.7	8.5	10.9	13.9	16.8	19.5	22.1	−0.14799	0.35516	−0.06417		
Diethyl sulfide	$C_4H_{10}S$	5.5	6.8	7.4	9.3	11.8	14.2	16.6	18.8	−0.05015	0.27483	−0.03176		
Thiophene	C_4H_4S		7.3	8.1	10.6	13.8	16.9	20.0	22.9	−0.21336	0.35715	−0.04267		
Halogenated hydrocarbons														
Fluoromethane (R41)	CH_3F	9.7	11.8	12.9	15.9	19.6	23.1	26.3	29.2	−0.06024	0.49305	−0.13889		
Difluoromethane (R32)	CH_2F_2	10.5	12.9	14.0	17.4	21.6	25.5	29.2	32.5	−0.09600	0.54630	−0.14683		

D3.1. Table 8. (continued)

Substance	Formula	Temperature (°C)								Equation (3)				
		−50	0	25	100	200	300	400	500	10^5 *A*	10^7 *B*	10^{10} *C*	10^{12} *D*	10^{15} *E*
Trifluoromethane (R23)	CHF_3	10.8	13.1	14.3	17.7	21.9	25.9	29.5	32.8	−0.07808	0.55122	−0.15092		
Tetrafluoromethane (R14)	CF_4	13.3	15.9	17.2	20.8	25.3	29.5	33.2	36.5	0.04703	0.61890	−0.19722		
Methyl chloride	CH_3Cl		10.0	10.9	13.6	17.1	20.4	23.7		−0.02001	0.38917	−0.05170		
Methylene chloride	CH_2Cl_2	7.7	9.5	10.5	13.2	16.6	19.9	22.9	25.8	−0.13776	0.42638	−0.09660		
Chloroform	$CHCl_3$	7.6	9.4	10.2	12.8	16.1	19.2	22.3	25.2	−0.06453	0.38402	−0.06457		
Carbon tetrachloride	CCl_4		9.2	10.0	12.4	15.4	18.2	20.8	23.2	−0.07132	0.39021	−0.10535		
Bromomethane	CH_3Br	10.1	12.4	13.5	16.9	21.1	25.2	29.0	32.6	−0.08606	0.51383	−0.10426		
Dibromomethane	CH_2Br_2				15.5	19.6	23.6	27.4	31.1	−0.10912	0.47247	−0.07256		
Tribromomethane	$CHBr_3$		7.3	8.1	10.5	13.6				−0.17201	0.34298	−0.04096		
Tetrabromomethane	CBr_4	14.0	16.7	18.1	22.5	28.5	34.6	40.6	46.4	0.43125	0.31175	0.68684	−0.06508	0.01952
Chlorodifluoromethane (R22)	$CHClF_2$		11.8	12.9	15.9	19.9	23.7	27.2	30.6	−0.04130	0.47290	−0.09230		
Dichlorofluoromethane (R21)	$CHCl_2F$			11.5	14.3	17.8	21.3	24.6	27.8	0.01328	0.39826	−0.05196		
Chlorotrifluoromethane (R13)	$CClF_3$	10.9	13.3	14.4	17.8	21.9	25.8	29.3	32.5	−0.05012	0.54778	−0.15645		
Dichlorodifluoromethane (R12)	CCl_2F_2		11.6	12.5	15.3	18.9	22.5			0.13920	0.37652	−0.01344		
Trichlorofluoromethane (R11)	CCl_3F	8.6	10.6	11.6	14.5	18.3	22.0	25.6	29.2	−0.03449	0.40992	−0.03558		
Ethyl fluoride (R161)	C_2H_5F	7.7	9.5	10.4	13.0	16.2	19.1	21.9	24.5	−0.09973	0.41549	−0.11166		
Ethyl chloride	C_2H_5Cl	7.2	8.9	9.7	12.1	15.1	17.9	20.6	23.0	−0.07591	0.37662	−0.08906		
Ethyl bromide	C_2H_5Br	8.0	10.0	11.0	13.9	17.5	21.0	24.3	27.4	−0.14674	0.44584	−0.09301		
1,1-Dichloroethane	$C_2H_4Cl_2$	7.1	8.7	9.6	11.9	15.0	17.9	20.7	23.3	−0.06882	0.36469	−0.07069		
1,2-Dichloroethane	$C_2H_4Cl_2$		8.3	9.1	11.4	14.3	17.2	19.9	22.5	−0.10944	0.37538	−0.13037	0.00629	−0.00146
1,2-Dibromoethane	$C_2H_4Br_2$			11.0	14.0	17.8	21.6	25.4	29.0	−0.12583	0.42355	−0.04178		
1,1,1-Trifluoroethane (R143a)	$C_2H_3F_3$	9.2	11.3	12.3	15.3	19.0	22.5	25.6	28.5	−0.09470	0.48575	−0.13494		
1,1,1-Trichloroethane	$C_2H_3Cl_3$		8.1	9.0	11.4	14.5	17.5	20.3	23.0	−0.15006	0.37287	−0.07221		
1,1,2,2-Tetrachloroethane	$C_2H_2Cl_4$		7.9	8.6	10.8	13.7	16.4	19.1	21.7	−0.06039	0.32246	−0.04471		
Pentachloroethane	C_2HCl_5		7.6	8.4	10.5	13.3	16.0	18.6	21.1	−0.05940	0.31301	−0.04155		
Hexachloroethane	C_2Cl_6					12.9	15.5	18.1	20.6	−0.08639	0.31029	−0.04215		
1,1,2,2-Tetrachlorodifluoroethane	$C_2Cl_4F_2$				11.7	14.7	17.7	20.5	23.2	−0.08776	0.36025	−0.06342		
1,1,2-Trichlorotrifluoroethan	$C_2Cl_3F_3$		9.6	10.6	13.4	17.0	20.4	23.6	26.6	−0.14690	0.43026	−0.08626		
1,2-Dichlorotetrafluoroethane	$C_2Cl_2F_4$		10.6	11.5	14.1	17.4	20.7	23.9	27.1	0.09820	0.36272	−0.03272		
1-Chloropropane	C_3H_7Cl	6.0	7.5	8.3	10.4	13.1	15.7	18.2	20.5	−0.10368	0.33313	−0.07059		
1-Chlorobutane	C_4H_9Cl	5.4	6.8	7.5	9.4	11.9	14.3	16.6	18.7	−0.09753	0.30131	−0.06077		
1-Chloropentane	$C_5H_{11}Cl$					11.0	13.2	15.3	17.3	−0.07931	0.27190	−0.04930		
Chlorotrifluoroethene	C_2ClF_3		11.1	12.1	14.9	18.6	22.0	25.2	28.2	−0.06719	0.46061	−0.11357		
Vinyl chloride	C_2H_3Cl	7.8	9.5	10.3	12.8	15.9	18.9	21.8	24.5	−0.03375	0.37915	−0.07484		
1,1-Dichloroethene	$C_2H_2Cl_2$	7.3	9.1	10.0	12.6	15.8	18.9	21.8	24.5	−0.12601	0.40415	−0.09104		
Trichloroethene	C_2HCl_3	6.9	8.5	9.3	11.6	14.6	17.6	20.3	23.0	−0.07353	0.35321	−0.05952		
Tetrachloroethene	C_2Cl_4		7.9	8.8	11.1	14.2	17.1	19.9	22.5	−0.15830	0.36902	−0.07459		
Fluorobenzene	C_6H_5F				9.9	12.5	15.0	17.3	19.6	−0.05724	0.29935	−0.04944		
Chlorobenzene	C_6H_5Cl		6.8	7.4	9.3	11.8	14.2	16.5	18.7	−0.05654	0.28115	−0.04142		
Bromobenzene	C_6H_5Br					13.1	15.8	18.4	20.9	−0.09017	0.31781	−0.04670		
Iodobenzene	C_6H_5I		7.7	8.5	11.1	14.4	17.6	20.7	23.7	−0.19399	0.36436	−0.04213		
m-Chlorotoluene	C_7H_7Cl		6.4	7.1	9.2	11.8	14.4	17.0	19.4	−0.14194	0.29743	−0.03641		
Benzyl chloride	C_7H_7Cl					10.8	13.1	15.3	17.4	−0.09774	0.26922	−0.04092		
***n*-Alkanes**														
Methane	CH_4	8.7	10.4	11.2	13.5	16.3	18.8	21.2	23.4	−0.07759	0.50484	−0.43101	0.03118	−0.00981
Ethane	C_2H_6	7.0	8.5	9.3	11.5	14.2	16.7	19.1	21.2	−0.04537	0.35537	−0.09658		
Propane	C_3H_8	6.2	7.5	8.2	10.2	12.8	15.2	17.5	19.6	0.07353	0.20874	0.24208	−0.03914	0.01784
n-Butane	C_4H_{10}	5.8	7.0	7.6	9.3	11.6	13.9	16.1	18.3	0.02688	0.25130	−0.02326		
n-Pentane	C_5H_{12}	5.2	6.4	6.9	8.6	10.8	12.9	14.9	16.9	−0.01656	0.24855	−0.03565		
n-Hexane	C_6H_{14}	4.7	5.9	6.4	8.1	10.3	12.3	14.3	16.1	−0.07450	0.25522	−0.04815		
n-Heptane	C_7H_{16}	4.3	5.3	5.8	7.3	9.3	11.2	13.1	14.9	−0.05425	0.22117	−0.02853		
n-Octane	C_8H_{18}	3.8	4.8	5.2	6.7	8.5	10.4	12.2	14.1	−0.05272	0.19657	−0.01009		

D3.1. Table 8. (continued)

Substance	Formula	Temperature (°C)								Equation (3)				
		−50	0	25	100	200	300	400	500	10^5 *A*	10^7 *B*	10^{10} *C*	10^{12} *D*	10^{15} *E*
n-Nonane	C_9H_{20}	3.4	4.4	4.9	6.3	8.2	10.1	12.0	13.7	−0.11361	0.20732	−0.01914		
n-Decane	$C_{10}H_{22}$		4.3	4.7	6.1	7.9	9.7	11.5	13.3	−0.07177	0.18465	−0.00450		
n-Undecane	$C_{11}H_{24}$		4.0	4.4	5.7	7.5	9.3	11.0	12.7	−0.09673	0.18199	−0.00624		
n-Dodecane	$C_{12}H_{26}$		3.7	4.1	5.4	7.1	8.9	10.5	12.2	−0.11853	0.18014	−0.00876		
n-Tridecane	$C_{13}H_{28}$		3.4	3.8	5.1	6.7	8.3	9.9	11.5	−0.10665	0.16513	−0.00257		
n-Tetradecane	$C_{14}H_{30}$			3.7	4.8	6.4	8.0	9.6	11.1	−0.10594	0.15831	−0.00071		
n-Pentadecane	$C_{15}H_{32}$			3.5	4.7	6.2	7.8	9.3	10.9	−0.11473	0.15678	−0.00150		
n-Hexadecane	$C_{16}H_{34}$			3.4	4.5	6.1	7.6	9.2	10.7	−0.13795	0.16148	−0.00748		
n-Heptadecane	$C_{17}H_{36}$			3.3	4.4	5.9	7.5	9.0	10.5	−0.12993	0.15482	−0.00366		
n-Octadecane	$C_{18}H_{38}$				4.3	5.8	7.3	8.7	10.2	−0.12837	0.15164	−0.00385		
n-Nonadecane	$C_{19}H_{40}$				4.2	5.7	7.1	8.5	10.0	−0.12631	0.14796	−0.00355		
n-Eicosane	$C_{20}H_{42}$				4.1	5.5	6.9	8.3	9.7	−0.12507	0.14488	−0.00364		
Isoalkanes														
Isobutane	C_4H_{10}	5.6	6.9	7.5	9.3	11.7	13.9	16.0	18.0	−0.03056	0.27695	−0.05120		
2-Methyl butane	C_5H_{12}	5.4	6.6	7.2	8.9	11.0	13.0	14.8	16.5	−0.04174	0.27672	−0.07472		
2,2-Dimethyl propane	C_5H_{12}		6.5	7.1	9.0	11.3	13.5	15.6	17.6	−0.08799	0.28748	−0.06331		
2-Methyl pentane	C_6H_{14}	4.8	6.0	6.5	8.2	10.2	12.1	13.8	15.4	−0.06762	0.26309	−0.07101		
3-Methyl pentane	C_6H_{14}	4.9	6.0	6.6	8.3	10.3	12.3	14.1	15.8	−0.07196	0.26542	−0.06661		
2,2-Dimethyl butane	C_6H_{14}	5.3	6.4	7.0	8.6	10.7	12.6	14.4	16.1	−0.01151	0.25664	−0.06103		
2,3-Dimethyl butane	C_6H_{14}	5.2	6.4	7.0	8.8	11.0	13.0	14.9	16.7	−0.07160	0.28230	−0.07453		
Olefins														
Ethylene	C_2H_4	7.6	9.3	10.1	12.5	15.5	18.2	20.6	22.9	−0.06216	0.39695	−0.12059		
Propylene	C_3H_6	6.3	7.8	8.6	10.7	13.4	15.9	18.2	20.4	−0.08571	0.34209	−0.08730		
1-Butene	C_4H_8	5.7	7.1	7.7	9.7	12.1	14.4	16.6	18.5	−0.08782	0.31254	−0.07958		
1-Pentene	C_5H_{10}	5.3	6.5	7.1	8.9	11.2	13.3	15.3	17.1	−0.07462	0.28548	−0.07046		
1-Hexene	C_6H_{12}	4.8	6.0	6.5	8.1	10.2	12.0	13.8	15.4	−0.06612	0.26302	−0.07209		
1-Heptene	C_7H_{14}	4.7	5.8	6.4	8.0	10.0	11.9	13.8	15.6	−0.05798	0.25536	−0.08534	0.00392	−0.00072
1-Octene	C_8H_{16}	4.4	5.4	5.9	7.3	9.1	10.7	12.3	13.7	−0.05166	0.23337	−0.06468		
Propadiene	C_3H_4	6.2	7.5	8.2	10.0	12.3	14.4	16.2	17.9	−0.01925	0.30937	−0.09700		
1,2-Butadiene	C_4H_6	5.6	6.8	7.4	9.1	11.2	13.1	14.9	16.5	−0.03543	0.28468	−0.08701		
1,3-Butadiene	C_4H_6	6.3	7.8	8.5	10.5	13.1	15.6	17.9	20.0	−0.05408	0.32462	−0.07543		
1,2-Pentadiene	C_5H_8	5.1	6.2	6.7	8.3	10.3	12.1	13.7	15.2	−0.04030	0.26299	−0.07884		
trans-1,3-Pentadiene	C_5H_8				8.2	10.1	11.8	13.4	14.9	0.03342	0.23396	−0.05955		
1,4-Pentadiene	C_5H_8				8.8	11.1	13.2	15.2	17.1	−0.08176	0.28139	−0.06431		
2,3-Pentadiene	C_5H_8	5.1	6.3	6.8	8.5	10.6	12.6	14.4	16.1	−0.04668	0.26365	−0.06320		
Acetylene and Derivatives														
Acetylene	C_2H_2	7.6	9.4	10.2	12.7	15.7	18.5			−0.11075	0.42019	−0.13611		
Propyne	C_3H_4	6.4	7.9	8.6	10.7	13.3	15.7	17.9	19.9	−0.08716	0.34947	−0.10490		
2-Butyne	C_4H_6		6.9	7.5	9.4	11.8	14.0	16.1	18.0	−0.08278	0.30252	−0.07563		
1-Butyne	C_4H_6	5.4	6.8	7.4	9.3	11.8	14.1	16.3	18.4	−0.09787	0.30050	−0.06407		
Naphthenes														
Cyclopropane	C_3H_6	6.6	8.1	8.9	11.0	13.6	16.1	18.3	20.4	−0.07419	0.35270	−0.10321		
Cyclobutane	C_4H_8	6.0	7.4	8.1	10.1	12.6	14.9	17.1	19.1	−0.07904	0.32310	−0.08579		
Cyclopentane	C_5H_{10}	5.6	6.9	7.5	9.3	11.6	13.8	15.9	17.8	−0.04981	0.28692	−0.06427		
Methyl cyclopentane	C_6H_{12}	5.1	6.3	6.9	8.7	10.9	13.0	15.0	16.8	−0.08377	0.28117	−0.06915		
Ethyl cyclopentane	C_7H_{14}	4.8	5.9	6.5	8.1	10.2	12.2	14.0	15.7	−0.07561	0.26139	−0.06289		
Propyl cyclopentane	C_8H_{16}	4.7	5.8	6.3	7.8	9.8	11.6	13.3	14.8	−0.06188	0.25185	−0.06740		
Butyl cyclopentane	C_9H_{18}	4.4	5.4	5.9	7.4	9.2	10.9	12.4	13.9	−0.05389	0.23625	−0.06461		
Pentyl cyclopentane	$C_{10}H_{20}$	4.1	5.0	5.4	6.7	8.5	10.3	12.1	13.8	0.10176	0.10630	0.18840	−0.01918	0.00597
Hexyl cyclopentane	$C_{11}H_{22}$	3.9	4.6	5.0	6.3	8.0	9.6	11.3	12.9	0.09880	0.09722	0.17809	−0.01789	0.00553
Cyclohexane	C_6H_{12}			7.1	8.7	10.9	12.9	14.9	16.9	0.02184	0.24010	−0.03187		
Methyl cyclohexane	C_7H_{14}	4.8	5.9	6.5	8.2	10.3	12.2	14.1	15.8	−0.07951	0.26416	−0.06422		

D3.1. Table 8. (continued)

Substance	Formula	Temperature (°C)								Equation (3)				
		−50	0	25	100	200	300	400	500	10^5 *A*	10^7 *B*	10^{10} *C*	10^{12} *D*	10^{15} *E*
Ethyl cyclohexane	C_8H_{16}	4.4	5.5	6.0	7.5	9.3	11.1	12.7	14.2	−0.05710	0.23787	−0.06047		
Propyl cyclohexane	C_9H_{18}	4.2	5.2	5.7	7.1	8.8	10.5	12.0	13.4	−0.06014	0.22794	−0.05991		
Butyl cyclohexane	$C_{10}H_{20}$	4.0	4.9	5.4	6.7	8.3	9.9	11.3	12.6	−0.04605	0.21223	−0.05550		
Pentyl cyclohexane	$C_{11}H_{22}$	3.9	4.7	5.1	6.3	8.0	9.7	11.4	13.0	0.10143	0.09711	0.17962	−0.01790	0.00551
Hexyl cyclohexane	$C_{12}H_{24}$	4.0	4.8	5.2	6.4	8.1	9.9	11.6	13.2	0.11242	0.09394	0.18952	−0.01844	0.00561
Cyclopentene	C_5H_8	5.8	7.2	7.8	9.8	12.3	14.6	16.8	18.8	−0.07481	0.30921	−0.07262		
Cyclohexene	C_6H_{10}	5.2	6.5	7.1	8.9	11.2	13.4	15.4	17.3	−0.09348	0.28961	−0.06919		
Aromatic compounds														
Benzene	C_6H_6			7.6	9.4	11.9	14.4	16.9	19.3	0.00177	0.25542	−0.00711		
Toluene	C_7H_8	5.1	6.4	7.0	8.7	10.8	12.9	14.8	16.5	−0.07109	0.27885	−0.07300		
Ethyl benzene	C_8H_{10}	4.7	5.9	6.4	8.0	10.1	12.0	13.8	15.5	−0.06862	0.25645	−0.06139		
Propyl benzene	C_9H_{12}	4.5	5.5	6.1	7.6	9.5	11.4	13.1	14.7	−0.06657	0.24175	−0.05492		
Butyl benzene	$C_{10}H_{14}$	4.2	5.3	5.8	7.2	9.1	10.8	12.5	14.0	−0.06561	0.23072	−0.05302		
Pentyl benzene	$C_{11}H_{16}$	4.0	5.0	5.4	6.8	8.5	10.1	11.6	13.0	−0.05520	0.21706	−0.05321		
Hexyl benzene	$C_{12}H_{18}$	3.9	4.8	5.2	6.5	8.1	9.6	11.0	12.2	−0.04233	0.20516	−0.05370		
o-Xylene	C_8H_{10}		5.8	6.4	8.0	10.0	12.0	13.8	15.5	−0.07549	0.25676	−0.06047		
m-Xylene	C_8H_{10}		5.8	6.4	8.0	10.1	12.0	13.8	15.5	−0.07474	0.25782	−0.06128		
p-Xylene	C_8H_{10}			6.3	7.9	9.9	11.7	13.5	15.1	−0.05863	0.24914	−0.06026		
1,2,3-Trimethyl benzene	C_9H_{12}		5.5	6.1	7.6	9.6	11.4	13.1	14.7	−0.07172	0.24462	−0.05774		
1,2,4-Trimethyl benzene	C_9H_{12}		5.5	6.0	7.5	9.4	11.2	12.9	14.4	−0.06620	0.23995	−0.05812		
1,3,5-Trimethyl benzene	C_9H_{12}		5.3	5.8	7.3	9.2	11.0	12.6	14.2	−0.05772	0.23072	−0.05097		
1,2,3,4-Tetramethyl benzene	$C_{10}H_{14}$		5.2	5.7	7.2	9.1	10.9	12.8	14.5	−0.03426	0.20863	−0.02088		
1,2,3,5-Tetramethyl benzene	$C_{10}H_{14}$		5.2	5.7	7.1	8.9	10.6	12.2	13.6	−0.05896	0.22610	−0.05454		
1,2,4,5-Tetramethyl benzene	$C_{10}H_{14}$				7.0	8.7	10.4	11.9	13.3	−0.02841	0.21491	−0.05071		
Pentamethyl benzene	$C_{11}H_{16}$				6.8	8.6	10.3	11.9	13.3	−0.07246	0.22029	−0.04972		
Hexamethyl benzene	$C_{12}H_{18}$					8.3	9.9	11.5	13.0	−0.07149	0.21074	−0.04305		
Styrene	C_8H_8		5.9	6.4	8.0	10.0	11.9	13.6	15.3	−0.05863	0.25269	−0.06181		
Isopropyl benzene	C_9H_{12}	4.5	5.6	6.1	7.7	9.7	11.5	13.3	14.9	−0.06816	0.24574	−0.05656		
Biphenyl	$C_{12}H_{10}$				6.8	8.8	10.6	12.4	14.1	−0.11853	0.22925	−0.04067		
Diphenyl methane	$C_{13}H_{12}$				7.0	8.7	10.4	12.1	13.8	0.03209	0.18126	−0.00911		
Triphenyl methane	$C_{19}H_{16}$				5.9	7.5	9.0	10.6	12.1	−0.02175	0.16673	−0.00881		
Tetraphenyl methane	$C_{25}H_{20}$						7.8	9.1	10.5	−0.05425	0.15092	−0.01080		
Naphthalene	$C_{10}H_8$				7.6	9.6	11.6	13.5	15.3	−0.10205	0.24744	−0.04743		
1-Methylnaphthalene	$C_{11}H_{10}$		5.2	5.7	7.2	9.2	11.0	12.8	14.4	−0.08065	0.23138	−0.04407		
2-Methylnaphthalene	$C_{11}H_{10}$				7.1	9.0	10.8	12.5	14.0	−0.07835	0.23048	−0.04996		
1-Ethylnaphthalene	$C_{12}H_{12}$		4.8	5.3	6.6	8.2	9.8	11.3	12.6	−0.04469	0.20718	−0.04940		
2-Ethylnaphthalene	$C_{12}H_{12}$		5.0	5.5	6.9	8.8	10.5	12.2	13.7	−0.08142	0.22516	−0.04792		
Alcohols														
Methanol	CH_4O		8.7	9.6	12.2	15.6	18.8	22.0	24.9	−0.15159	0.39270	−0.06541		
Ethanol	C_2H_6O	6.7	8.2	8.9	11.0	13.7	16.3	18.8	21.2	−0.06394	0.36445	−0.17984	0.01280	−0.00413
1-Propanol	C_3H_8O	5.4	6.9	7.6	9.7	12.4	15.0	17.5	19.9	−0.14675	0.32078	−0.05720		
1-Butanol	$C_4H_{10}O$	5.0	6.3	6.9	8.8	11.2	13.5	15.7	17.8	−0.11787	0.28940	−0.05708		
1-Pentanol	$C_5H_{12}O$					10.5	12.6	14.6	16.5	−0.05553	0.25174	−0.03963		
1-Hexanol	$C_6H_{14}O$		5.6	6.1	7.7	9.8	11.8	13.7	15.6	−0.07635	0.24326	−0.04168		
1-Heptanol	$C_7H_{16}O$		5.2	5.7	7.2	9.2	11.2	13.0	14.7	−0.09367	0.23519	−0.04239		
1-Octanol	$C_8H_{18}O$		4.9	5.4	6.9	8.8	10.6	12.3	14.0	−0.08403	0.22020	−0.03669		
Isopropanol	C_3H_8O	5.5	7.0	7.7	9.8	12.5	15.0	17.5	19.9	−0.11534	0.31142	−0.05033		
2-Methyl-1-propanol	$C_4H_{10}O$	5.3	6.6	7.3	9.2	11.7	14.0	16.2	18.4	−0.10257	0.29598	−0.05854		
3-Methyl-1-butanol	$C_5H_{12}O$	5.1	6.3	6.9	8.6	10.8	12.9	15.0	17.0	−0.04325	0.25708	−0.04134		
Ethylene glycol	$C_2H_6O_2$		7.5	8.3	10.4	13.1	15.8	18.4	21.0	−0.05600	0.30619	−0.03555		
1,3-Propylene glycol	$C_3H_8O_2$		6.8	7.4	9.4	12.0	14.5	17.1	19.6	−0.03782	0.26432	−0.00784		
Glycerol	$C_3H_8O_3$			6.8	8.5	10.8	13.1	15.4	17.7	−0.00146	0.22666	0.00328		

D3.1. Table 8. (continued)

Substance	Formula	Temperature (°C)								Equation (3)				
		−50	0	25	100	200	300	400	500	10^5 *A*	10^7 *B*	10^{10} *C*	10^{12} *D*	10^{15} *E*
Cyclohexanol	$C_6H_{12}O$			7.0	8.9	11.3	13.7	16.1	18.4	−0.08693	0.27102	−0.02804		
Benzyl alcohol	C_7H_8O		6.0	6.6	8.3	10.5	12.7	14.8	16.8	−0.04461	0.24537	−0.02845		
Phenols														
o-Cresol	C_7H_8O				8.3	10.5	12.6	14.7	16.7	−0.05130	0.24653	−0.03094		
m-Cresol	C_7H_8O			6.4	8.2	10.4	12.6	14.7	16.7	−0.09147	0.25736	−0.03778		
p-Cresol	C_7H_8O				8.3	10.5	12.7	14.8	16.8	−0.08575	0.25847	−0.03823		
Phenol	C_6H_6O				9.0	11.4	13.7	15.9	18.1	−0.05584	0.26838	−0.03487		
Carboxylic acids														
Formic acid	CH_2O_2			9.3	11.8	14.9	18.0	20.9	23.7	−0.11464	0.37037	−0.06416		
Acetic acid	$C_2H_4O_2$			8.6	10.8	13.8	16.8	19.8	22.8	−0.02958	0.29595	0.00377		
Propionic acid	$C_3H_6O_2$		6.7	7.3	9.3	11.9	14.4	16.7	19.0	−0.10200	0.29386	−0.04443		
Butyric acid	$C_4H_8O_2$		6.3	6.9	8.7	11.0	13.3	15.4	17.6	−0.04956	0.25868	−0.03263		
Valeric acid	$C_5H_{10}O_2$		6.1	6.7	8.4	10.6	12.7	14.8	16.8	−0.05626	0.25433	−0.03911		
Caproic acid	$C_6H_{12}O_2$		5.6	6.1	7.6	9.7	11.6	13.5	15.4	−0.04646	0.22877	−0.03110		
Acetic anhydride	$C_4H_6O_3$	5.9	7.3	8.0	10.1	12.9	15.5	18.0	20.4	−0.07992	0.31028	−0.04599		
Propionic anhydride	$C_6H_{10}O_3$		5.4	5.9	7.4	9.3	11.2	13.0	14.8	−0.03616	0.21856	−0.02950		
Chloroacetic acid	$C_2H_3ClO_2$				10.5	13.3	16.0	18.6	21.2	−0.07379	0.31522	−0.04103		
Dichloroacetic acid	$C_2H_2Cl_2O_2$			8.3	10.4	13.2	15.9	18.5	21.0	−0.06382	0.31055	−0.03966		
Trichloroacetic acid	$C_2HCl_3O_2$				10.3	13.0	15.6	18.2	20.7	−0.04675	0.30091	−0.03513		
Ketones														
Ketene	C_2H_2O	7.6	9.4	10.4	13.0	16.4	19.5	22.5	25.2	−0.12721	0.41928	−0.09870		
Acetone	C_3H_6O	5.5	6.8	7.5	9.5	12.1	14.7	17.3	19.9	−0.04063	0.26639	−0.00533		
Methyl ethyl ketone	C_4H_8O	5.5	6.6	7.2	9.0	11.3	13.7	16.1	18.5	0.03088	0.22920	0.00704		
Diethyl ketone	$C_5H_{10}O$		6.0	6.5	8.2	10.3	12.4	14.3	16.2	−0.04632	0.24695	−0.04071		
Dipropyl ketone	$C_7H_{14}O$		5.3	5.8	7.3	9.2	11.0	12.7	14.4	−0.04379	0.21864	−0.03379		
Acetophenone	C_8H_8O			6.5	8.2	10.5	12.8	15.0	17.2	−0.05627	0.24178	−0.01586		
Benzophenone	$C_{13}H_{10}O$				6.3	8.2	10.0	11.7	13.4	−0.12330	0.21440	−0.03233		
Ethers														
Dimethyl ether	C_2H_6O	6.8	8.4	9.2	11.6	14.5	17.3	19.9	22.3	−0.10763	0.37311	−0.09094		
Diethyl ether	$C_4H_{10}O$	5.6	6.9	7.6	9.5	11.9	14.1	16.2	18.2	−0.08933	0.30626	−0.07705		
Dipropyl ether	$C_6H_{14}O$	5.2	6.2	6.7	8.2	10.1	12.1	13.9	15.8	0.04652	0.21533	−0.02252		
Methyl propyl ether	$C_4H_{10}O$	5.7	6.9	7.6	9.4	11.8	14.0	16.2	18.2	−0.02933	0.27827	−0.04984		
Ethyl propyl ether	$C_5H_{12}O$	5.0	6.2	6.8	8.6	10.9	13.0	15.0	16.9	−0.09340	0.27850	−0.06111		
Ethylene oxide	C_2H_4O	7.0	8.7	9.5	11.9	15.0	18.1	21.0	23.9	−0.07074	0.35618	−0.04906		
Furane	C_2H_4O	6.2	7.8	8.6	11.0	14.0	16.9	19.6	22.2	−0.14789	0.36008	−0.06896		
1,4-Dioxane	$C_4H_8O_2$			12.9	16.1	20.3	24.4	28.3	32.0	−0.09914	0.48891	−0.08042		
Aldehydes														
Formaldehyde	CH_2O	8.8	10.8	11.8	14.7	18.3	21.7	25.0	28.0	−0.08285	0.45568	−0.10791		
Acetaldehyde	C_2H_4O	6.4	7.8	8.6	10.7	13.4	16.0	18.5	20.9	−0.04826	0.32014	−0.05638		
Paraldehyde	$C_6H_{12}O_3$			7.7	9.8	12.7	15.4	18.0	20.5	−0.16710	0.32863	−0.05351		
Furfural	$C_5H_4O_2$		7.3	8.0	10.1	12.9	15.6	18.3	21.0	−0.05317	0.29341	−0.02009		
Benzaldehyde	C_7H_6O	4.7	5.9	6.5	8.2	10.5	12.6	14.8	16.8	−0.07865	0.25494	−0.03580		
Salicylaldehyde	$C_7H_6O_2$			6.3	8.0	10.1	12.1	14.1	16.0	−0.04767	0.23738	−0.03080		
Esters														
Methyl formate	$C_2H_4O_2$	6.8	8.6	9.4	12.0	15.3	18.4	21.4	24.3	−0.13632	0.38184	−0.06475		
Ethyl formate	$C_3H_6O_2$	6.0	7.6	8.4	10.8	13.8	16.6	19.4	22.0	−0.15589	0.35441	−0.06412		
Propyl formate	$C_4H_8O_2$	5.5	7.0	7.7	9.9	12.6	15.3	17.9	20.3	−0.14742	0.32392	−0.05416		
Methyl acetate	$C_3H_6O_2$		7.2	8.0	10.2	13.0	15.7	18.2	20.6	−0.15412	0.33832	−0.06684		
Ethyl acetate	$C_4H_8O_2$	5.6	6.9	7.6	9.6	12.0	14.4	16.5	18.6	−0.09641	0.30876	−0.07229		
Propyl acetate	$C_5H_{10}O_2$	4.9	6.2	6.8	8.6	10.8	13.0	15.1	17.0	−0.08641	0.27161	−0.05164		
Methyl propionate	$C_4H_8O_2$	5.4	6.7	7.4	9.3	11.8	14.1	16.4	18.5	−0.10184	0.29907	−0.06099		
Ethyl propionate	$C_5H_{10}O_2$	6.6	8.3	9.1	11.5	14.6	17.6	20.4	23.0	−0.13863	0.37449	−0.07577		

D3.1. Table 8. (continued)

Substance	Formula	Temperature (°C)								Equation (3)				
		−50	0	25	100	200	300	400	500	10^5 *A*	10^7 *B*	10^{10} *C*	10^{12} *D*	10^{15} *E*
Propyl propionate	$C_6H_{12}O_2$	4.6	5.7	6.3	8.0	10.1	12.2	14.1	16.0	−0.08710	0.25499	−0.04799		
Methyl butyrate	$C_5H_{10}O_2$	4.9	6.2	6.8	8.6	10.9	13.0	15.1	17.1	−0.09985	0.27719	−0.05607		
Ethyl butyrate	$C_6H_{12}O_2$	4.5	5.7	6.3	8.0	10.1	12.2	14.1	16.0	−0.09654	0.25850	−0.05101		
Methyl benzoate	$C_8H_8O_2$					10.1	12.1	14.1	16.1	−0.03621	0.23330	−0.02657		
Ethyl benzoate	$C_9H_{10}O_2$		5.5	6.0	7.5	9.5	11.4	13.3	15.2	−0.03954	0.22199	−0.02695		
Methyl salicylate	$C_8H_8O_3$		5.6	6.1	7.7	9.7	11.7	13.6	15.5	−0.04401	0.22727	−0.02759		
Amines														
Methyl amine	CH_5N	6.6	8.2	8.9	11.2	14.0	16.7	19.2	21.5	−0.09272	0.35586	−0.08531		
Ethyl amine	C_2H_7N	5.9	7.3	8.0	10.0	12.6	15.0	17.3	19.4	−0.09010	0.31981	−0.07363		
Propyl amine	C_3H_9N	5.5	6.7	7.4	9.2	11.5	13.8	15.9	17.9	−0.05315	0.28073	−0.05425		
n-butyl amine	$C_4H_{11}N$		6.2	6.8	8.5	10.7	12.8	14.8	16.7	−0.05588	0.26084	−0.04835		
Dimethyl amine	C_2H_7N	7.0	8.6	9.3	11.6	14.5	17.3	19.9	22.3	−0.06089	0.35730	−0.07854		
Trimethyl amine	C_3H_9N	5.7	7.1	7.8	9.9	12.5	15.0	17.4	19.6	−0.11661	0.32114	−0.06794		
Diethyl amine	$C_4H_{11}N$		6.7	7.3	9.2	11.7	14.0	16.1	18.2	−0.09105	0.29587	−0.06378		
Triethyl amine	$C_6H_{15}N$	4.9	6.2	6.8	8.7	11.1	13.4	15.6	17.8	−0.11188	0.27992	−0.04612		
Piperidine	$C_5H_{11}N$					11.3	13.7	16.0	18.3	−0.14811	0.29184	−0.04677		
Pyridine	C_5H_5N		6.7	7.3	9.3	11.9	14.4	16.9	19.4	−0.07020	0.27549	−0.02026		
Aniline	C_6H_7N		6.0	6.7	8.5	10.8	13.0	15.2	17.3	−0.09488	0.26669	−0.03931		
N-Methyl aniline	C_7H_9N	5.1	6.3	6.9	8.6	10.8	13.1	15.2	17.3	−0.03068	0.24766	−0.02540		
N,N-dimethyl aniline	$C_8H_{11}N$			5.9	7.4	9.5	11.5	13.5	15.5	−0.05089	0.21904	−0.01598		
N,N-diethyl aniline	$C_{10}H_{15}N$		5.1	5.6	7.0	8.9	10.7	12.5	14.2	−0.01689	0.19904	−0.01628		
Phenylhydrazine	$C_6H_8N_2$			6.2	7.8	9.9	11.9	14.0	15.9	−0.02900	0.22291	−0.01672		
Diphenyl amine	$C_{12}H_{11}N$				7.0	9.0	10.8	12.7	14.5	−0.06505	0.21491	−0.02526		
Nitriles														
Acetonitrile	C_2H_3N		6.5	7.1	8.9	11.2	13.5	15.7	17.9	−0.01722	0.25237	−0.02396		
Propionitrile	C_3H_5N	5.0	6.1	6.7	8.3	10.5	12.6	14.6	16.5	−0.04528	0.25157	−0.04200		
Butyronitrile	C_4H_7N	4.7	5.8	6.3	7.9	9.9	11.9	13.7	15.6	−0.03917	0.23503	−0.03726		
Benzonitrile	C_7H_5N		6.4	7.0	8.9	11.3	13.7	16.1	18.4	−0.04813	0.25611	−0.01517		
Amides														
Formamide	CH_3NO			8.6	10.7	13.6	16.4	19.1	21.8	−0.04372	0.31013	−0.02858		
Nitroderivates														
Nitromethane	CH_3NO_2		6.6	7.3	9.6	12.4	15.2	18.0	20.6	−0.18903	0.32181	−0.04020		
Nitrobenzene	$C_6H_5NO_2$			6.8	8.9	11.6	14.2	16.8	19.4	−0.16371	0.29108	−0.02490		
o-Nitrotoluene	$C_7H_7NO_2$		5.8	6.3	8.0	10.2	12.4	14.5	16.7	−0.04061	0.22985	−0.01161		
m-Nitrotoluene	$C_7H_7NO_2$			6.3	7.9	10.1	12.3	14.4	16.5	−0.04500	0.22850	−0.01162		
p-Nitrotoluene	$C_7H_7NO_2$				7.8	10.0	12.2	14.3	16.4	−0.05845	0.23080	−0.01379		

D3.1. Table 9. Thermal conductivity of saturated liquids in W/mK

Substance	Formula	Temperature (°C)								Equation (4)				
		−50	−25	0	20	50	100	150	200	*A*	10^2 *B*	10^4 *C*	10^7 *D*	10^{10} *E*
Elements														
Xenon	Xe	0.049	0.039							0.1372	−0.03997	0.00074	−0.00377	0.00562
Krypton	Kr									0.1728	−0.06558	−0.00193	−0.00094	0.01428
Argon	Ar									0.1821	−0.03726	−0.02781	−0.11115	0.30999
Air										−0.0006	0.95952	−1.70225	11.14335	−26.70110
Nitrogen	N_2									0.2621	−0.15793	−0.00737	−0.01546	0.23198
Oxygen	O_2									0.2716	−0.12812	−0.01371	0.08022	−0.16812
Sulfur	S							0.138	0.152	−0.0986	0.06958	0.00029	−0.01067	0.00553
Fluorine	F_2									0.2755	−0.16169	−0.00200	0.01254	−0.02573
Chlorine	Cl_2	0.171	0.160	0.148	0.138	0.122	0.091			0.2265	−0.00950	−0.00608	−0.00441	0.00391
Bromine	Br_2			0.129	0.125	0.117	0.105	0.093	0.081	−0.1426	0.34711	−0.15092	0.26902	−0.17744
Iodine	I_2							0.112	0.105	0.1156	0.00461	0.00003	−0.00384	0.00158
Anorganic compounds														
Hydrogen fluoride	HF	0.509	0.482	0.455	0.433	0.400	0.346			0.7335	−0.08293	−0.01349	0.03071	−0.02573
Hydrogen chloride	HCl			0.230	0.188	0.125				0.6690	−0.09277	−0.02690	−0.01103	0.06800
Hydrogen bromide	HBr	0.131	0.119	0.107						0.2371	−0.04914	0.00020	0.00372	−0.00821
Hydrogen iodide	HI		0.049	0.046	0.043	0.039	0.030			0.1510	−0.06435	0.00443	0.03809	−0.07231
Hydrogen cyanide	HCN			0.243	0.229					0.4031	−0.04529	−0.00361	−0.01167	0.02592
Water	H_2O			0.555	0.598	0.643	0.680	0.682	0.661	−2.4149	2.45165	−0.73121	0.99492	−0.53730
Hydrogen sulfide	H_2S	0.220	0.190	0.161						0.4588	−0.08190	−0.01903	0.04211	−0.03272
Ammonia	NH_3	0.602	0.563	0.518	0.478	0.416	0.298			−0.5047	1.74960	−0.92075	1.97003	−1.61999
Nitric oxide	NO									0.2268	0.01517	−0.02647	−0.19936	0.14484
Nitrogen dioxide	NO_2			0.157						0.3147	−0.05645	−0.00064	0.00262	−0.00698
Nitrous oxide	N_2O									0.1011				
Dinitrogentetroxide	N_2O_4					0.131				0.1864	0.01841	−0.01083	−0.00544	0.01509
Cyanogen	C_2N_2		0.254							0.3376	−0.01640	0.00048	−0.00449	−0.10407
Phosphorus trichloride	PCl_3	0.146	0.140	0.134	0.129	0.121	0.109			0.2008	−0.02466			
Cyanogen chloride	ClCN			0.175						0.2788	−0.03245	−0.00008	−0.00364	−0.01280
Silane	SiH_4	0.056	0.032							0.2764	−0.09858			
Tetrachlorosilane	$SiCl_4$			0.103	0.100	0.096				0.1371	−0.01265			
Carbon monoxide	CO									0.2845	−0.17440	−0.00543	0.02657	−0.02637
Carbon dioxide	CO_2	0.169	0.139	0.108	0.084					0.3881	−0.06561	−0.01769	0.00700	0.03031
Carbon suboxide	C_3O_2	0.159	0.149	0.138	0.128	0.113	0.084			0.2203	0.00745	−0.02962	0.08522	−0.10022

D3.1. Table 9. (continued)

Substance	Formula	Temperature (°C)								Equation (4)				
		−50	−25	0	20	50	100	150	200	A	$10^2\ B$	$10^4\ C$	$10^7\ D$	$10^{10}\ E$
Carbonyl sulfide	COS									0.2620	−0.05256	0.00567	−0.02701	0.04524
Phosgene	CCl_2O	0.150	0.144	0.138						0.2004	−0.01457	−0.00721	0.02243	−0.02587
Carbon disulfide	CS_2	0.172	0.165	0.158	0.153					0.2301	−0.02261	−0.00269	0.00630	−0.00523
Sulfur dioxide	SO_2	0.243	0.227	0.211	0.199	0.180	0.149			0.3833	−0.06393	0.00065	−0.00130	0.00096
Sulfur trioxide	SO_3				0.254	0.211	0.150	0.102	0.067	0.8854	−0.26459	0.01050	0.02624	−0.01586
Sulfuryl chloride	Cl_2SO_2	0.148	0.141	0.135	0.129	0.121				0.2029	−0.02307	−0.00003	−0.00468	0.00811
Sulfur hexafluoride	SF_6	0.107	0.091	0.074	0.061					0.2444	−0.05733	−0.00157	−0.00339	0.00914
Organic compounds containing sulfur														
Methyl mercaptan	CH_4S	0.176	0.166	0.156						0.2492	−0.01542	−0.01615	0.04983	−0.05680
Ethyl mercaptan	C_2H_6S	0.162	0.154	0.146	0.140					0.2336	−0.03104	−0.00100	0.00389	−0.00522
Dimethyl sulfide	C_2H_6S	0.166	0.157	0.149	0.142					0.2365	−0.02907	−0.00203	0.00431	−0.00321
Diethyl sulfide	$C_4H_{10}S$	0.152	0.146	0.139	0.134	0.126				0.2119	−0.02688	−0.00039	0.00280	−0.00416
Thiophene	C_4H_4S		0.156	0.151	0.147	0.141				0.2031	−0.01367	−0.00462	0.01347	−0.01388
Halogenated hydrocarbons														
Fluoromethane (R41)	CH_3F	0.217	0.191	0.166						0.4469	−0.10555	0.00200	−0.00503	0.00417
Difluoromethane (R32)	CH_2F_2	0.188	0.167	0.147	0.131					0.3594	−0.06623	−0.01007	0.03153	−0.03617
Trifluoromethane (R23)	CHF_3	0.109								0.2216	−0.02927	−0.02195	0.07958	−0.10654
Tetrafluoromethane (R14)	CF_4									0.2200	−0.09284	−0.00627	0.09634	−0.17838
Methyl chloride	CH_3Cl	0.221	0.200	0.179	0.162	0.137				0.4125	−0.08698	0.00096	−0.00171	0.00103
Methylene chloride	CH_2Cl_2	0.164	0.156	0.147	0.141	0.131				0.2449	−0.04325	0.00563	−0.01401	0.01288
Chloroform	$CHCl_3$	0.133	0.128	0.123	0.118	0.112	0.102			0.1773	−0.01965	−0.00020	0.00020	0.00005
Carbon tetrachloride	CCl_4			0.105	0.101	0.095				0.1509	−0.01298	−0.00156	−0.00071	0.00398
Bromomethane	CH_3Br	0.124	0.117	0.109	0.104	0.095				0.1885	−0.02596	−0.00217	0.00518	−0.00456
Dibromomethane	CH_2Br_2	0.125	0.120	0.114	0.110	0.103				0.1724	−0.01869	−0.00166	0.00309	−0.00203
Tribromomethane	$CHBr_3$				0.100	0.095	0.088			0.1476	−0.01496	−0.00122	0.00389	−0.00383
Tetrabromomethane	CBr_4						0.083	0.077	0.071	0.1310	−0.01303	−0.00001	−0.00003	0.00041
Chlorodifluoromethane (R22)	$CHClF_2$	0.12	0.109	0.097	0.088	0.075				0.2211	−0.04472	−0.00061	0.00210	−0.00241
Dichlorofluoromethane (R21)	$CHCl_2F$	0.128	0.119	0.110	0.102	0.091	0.073			0.2104	−0.03641	−0.00024	0.00024	0.00015
Chlorotrifluoromethane (R13)	$CClF_3$	0.082	0.069	0.056	0.046					0.1950	−0.05177	0.00095	−0.00340	0.00432
Dichlorodifluoromethane (R12)	CCl_2F_2	0.103	0.092	0.081	0.073	0.059				0.2016	−0.04522	0.00090	−0.00227	0.00212
Trichlorofluoromethane (R11)	CCl_3F	0.115	0.106	0.098	0.092	0.082	0.066			0.1863	−0.03138	−0.00054	0.00107	−0.00077
Ethyl fluoride (R161)	C_2H_5F	0.148	0.135	0.123						0.2590	−0.04949	−0.00012	−0.00053	0.00161
Ethyl chloride	C_2H_5Cl	0.150	0.140	0.129	0.121	0.108	0.087			0.2416	−0.03815	−0.00223	0.00563	−0.00509

Ethyl bromide	C_2H_5Br	0.121	0.115	0.108	0.103	0.095	0.082			0.1780	−0.02343	−0.00143	0.00321	−0.00262
1,1-Dichloroethane	$C_2H_4Cl_2$	0.131	0.124	0.118	0.112	0.105	0.092			0.1888	−0.02598	−0.00015	0.00055	−0.00058
1,2-Dichloroethane	$C_2H_4Cl_2$			0.141	0.136	0.128				0.2140	−0.02654	−0.00002		
1,2-Dibromoethane	$C_2H_4Br_2$				0.102	0.098	0.092			0.1313	−0.00855	−0.00025	−0.00182	0.00300
1,1,1-Trifluoroethane (R143a)	$C_2H_3F_3$	0.104	0.093	0.082						0.1742	−0.02303	−0.00300	−0.00627	0.01123
1,1,1-Trichloroethane	$C_2H_3Cl_3$		0.111	0.106	0.102	0.096	0.086	0.076	0.066	0.1593	−0.01887	−0.00027	0.00014	0.00014
1,1,2,2-Tetrachloroethane	$C_2H_2Cl_4$				0.114	0.108	0.099			0.1622	−0.01468	−0.00061	−0.00061	0.00162
Pentachloroethane	C_2HCl_5		0.102	0.098	0.095	0.090	0.083	0.075	0.067	0.1379	−0.01362	−0.00063	0.00108	−0.00067
Hexachloroethane	C_2Cl_6								0.066	0.0559	0.02715	−0.00627	0.00044	0.00350
1,1,2,2-Tetrachlorodifluoroethane	$C_2Cl_4F_2$					0.077	0.070	0.062	0.054	0.1263	−0.01442	−0.00058	0.00147	−0.00122
1,1,2-Trichlorotrifluoroethan	$C_2Cl_3F_3$		0.085	0.079	0.075	0.069	0.058	0.048		0.1404	−0.02415	0.00098	−0.00131	0.00053
1,2-Dichlorotetrafluoroethane	$C_2Cl_2F_4$	0.083	0.076	0.070	0.065	0.058	0.046			0.1382	−0.02496	0.00001	0.00019	−0.00030
1-Chloropropane	C_3H_7Cl	0.137	0.130	0.122	0.117	0.108	0.094			0.2004	−0.02756	−0.00062	0.00111	−0.00064
1-Chlorobutane	C_4H_9Cl	0.139	0.132	0.125	0.120	0.112	0.099			0.1985	−0.02671	−0.00008	0.00030	−0.00038
1-Chloropentane	$C_5H_{11}Cl$	0.134	0.128	0.122	0.117	0.110	0.098	0.086		0.1870	−0.02372	−0.00005	0.00010	−0.00008
Chlorotrifluoroethene	C_2ClF_3	0.096	0.088	0.080	0.074	0.064	0.048			0.1671	−0.03202	0.00003	0.00010	−0.00027
Vinyl chloride	C_2H_3Cl	0.146	0.136	0.126	0.118	0.107				0.2326	−0.03792	−0.00091	0.00274	−0.00303
1,1-Dichloroethene	$C_2H_2Cl_2$	0.127	0.119	0.112	0.107	0.098	0.084			0.1900	−0.02748	−0.00079	0.00219	−0.00220
Trichloroethene	C_2HCl_3	0.137	0.130	0.122	0.116	0.108				0.2069	−0.03658	0.00406	−0.00961	0.00841
Tetrachloroethene	C_2Cl_4			0.116	0.111	0.104	0.091			0.1862	−0.02656	0.00059	−0.00111	0.00079
Fluorobenzene	C_6H_5F		0.140	0.133	0.127	0.119				0.1968	−0.01565	−0.00363	0.00207	0.00333
Chlorobenzene	C_6H_5Cl		0.137	0.132	0.128	0.122	0.113			0.1831	−0.01817	−0.00034	0.00045	−0.00016
Bromobenzene	C_6H_5Br		0.121	0.116	0.112	0.106	0.096	0.086		0.1677	−0.01823	−0.00023	−0.00051	0.00107
Iodobenzene	C_6H_5I		0.105	0.102	0.100	0.097	0.092	0.087		0.1313	−0.01133	0.00049	−0.00093	0.00066
m-chlorotoluene	C_7H_7Cl		0.136	0.131	0.127	0.121	0.111	0.101		0.1860	−0.02044	0.00012	−0.00004	−0.00015
Benzyl chloride	C_7H_7Cl		0.145	0.140	0.136	0.130	0.121	0.111	0.101	0.1923	−0.01925		0.00002	−0.00003
***n*-Alkanes**														
Methane	CH_4									0.4011	−0.19773	−0.01440	0.22814	−0.38138
Ethane	C_2H_6	0.133	0.111	0.091	0.075					0.3505	−0.09878	−0.00627	0.04136	−0.04929
Propane	C_3H_8	0.133	0.120	0.107	0.097	0.082				0.2661	−0.06336	0.00057	0.00655	−0.00701
n-Butane	C_4H_{10}	0.140	0.128	0.117	0.109	0.097	0.079			0.2699	−0.06508	0.00136	0.00992	−0.00933
n-Pentane	C_5H_{12}	0.142	0.132	0.122	0.114	0.103	0.087	0.072		0.2529	−0.05640	0.00284	0.00123	−0.00089
n-Hexane	C_6H_{14}	0.146	0.137	0.128	0.121	0.111				0.2331	−0.04813	0.00735	−0.01833	0.01680
n-Heptane	C_7H_{16}	0.147	0.140	0.132	0.126	0.117				0.2149	−0.02998	−0.00030	0.00103	−0.00120
n-Octane	C_8H_{18}	0.150	0.142	0.135	0.129	0.120	0.106			0.2150	−0.02839	−0.00072	0.00203	−0.00206
n-Nonane	C_9H_{20}	0.150	0.143	0.137	0.132	0.124	0.110	0.097		0.2096	−0.02727	0.00046	−0.00109	0.00095

D3.1. Table 9. (continued)

Substance	Formula	Temperature (°C)								Equation (4)				
		−50	−25	0	20	50	100	150	200	A	$10^2\,B$	$10^4\,C$	$10^7\,D$	$10^{10}\,E$
n-Decane	$C_{10}H_{22}$		0.144	0.138	0.133	0.126	0.113	0.101		0.2084	−0.02784	0.00139	−0.00298	0.00234
n-Undecane	$C_{11}H_{24}$		0.146	0.140	0.135	0.128	0.116	0.104		0.2053	−0.02477	0.00062	−0.00165	0.00147
n-Dodecane	$C_{12}H_{26}$			0.141	0.137	0.130	0.118	0.106	0.095	0.1994	−0.01715	−0.00259	0.00480	−0.00330
n-Tridecane	$C_{13}H_{28}$			0.143	0.138	0.131	0.120	0.109	0.097	0.2043	−0.02259	0.00008	−0.00031	0.00030
n-Tetradecane	$C_{14}H_{30}$				0.139	0.132	0.122	0.111	0.100	0.2023	−0.02148	0.00001	−0.00025	0.00029
n-Pentadecane	$C_{15}H_{32}$				0.142	0.136	0.125	0.114	0.103	0.2098	−0.02412	0.00040	0.00002	−0.00041
n-Hexadecane	$C_{16}H_{34}$				0.143	0.137	0.126	0.115	0.104	0.2106	−0.02430	0.00060	−0.00059	0.00017
n-Heptadecane	$C_{17}H_{36}$					0.138	0.127	0.116	0.104	0.2074	−0.02019	−0.00075	0.00127	−0.00078
n-Octadecane	$C_{18}H_{38}$					0.141	0.130	0.118	0.107	0.2078	−0.01754	−0.00153	0.00204	−0.00099
n-Nonadecane	$C_{19}H_{40}$					0.141	0.130	0.119	0.108	0.2078	−0.01771	−0.00152	0.00234	−0.00133
n-Eicosane	$C_{20}H_{42}$					0.146	0.134	0.123	0.112	0.2178	−0.02203	−0.00020	0.00043	−0.00030
Isoalkanes														
Isobutane	C_4H_{10}	0.123	0.114	0.105	0.097	0.086	0.068			0.2042	−0.03609	−0.00027	0.00057	−0.00042
2-Methyl butane	C_5H_{12}	0.133	0.125	0.118	0.111	0.102				0.2031	−0.02924	−0.00163	0.00417	−0.00379
2,2-Dimethyl propane	C_5H_{12}			0.105	0.097	0.087	0.071	0.055		0.2663	−0.08142	0.00768	0.00622	−0.01599
2-Methyl pentane	C_6H_{14}	0.131	0.124	0.117	0.111	0.103	0.089			0.1932	−0.02786	−0.00004	−0.00010	0.00028
3-Methyl pentane	C_6H_{14}	0.133	0.126	0.119	0.113	0.105	0.091			0.1950	−0.02734	−0.00055	0.00169	−0.00182
2,2-Dimethyl butane	C_6H_{14}	0.121	0.115	0.108	0.103					0.1797	−0.02584	0.00012	−0.00186	0.00334
2,3-Dimethyl butane	C_6H_{14}	0.123	0.117	0.111	0.106	0.099				0.1770	−0.02372	−0.00046	0.00156	−0.00197
Olefins														
Ethylene	C_2H_4	0.129	0.105	0.082						0.4145	−0.14789	0.00393	0.03157	−0.03936
Propylene	C_3H_6	0.131	0.121	0.111	0.102	0.090				0.2229	−0.04006	−0.00097	0.00325	−0.00390
1-Butene	C_4H_8	0.135	0.127							0.2141	−0.03645	0.00124	−0.00451	0.00593
1-Pentene	C_5H_{10}	0.139	0.131	0.124	0.117					0.2079	−0.03131	0.00028	−0.00052	0.00023
1-Hexene	C_6H_{12}	0.146	0.138	0.129	0.122	0.112				0.2227	−0.03417	−0.00015	0.00069	−0.00101
1-Heptene	C_7H_{14}	0.148	0.141	0.133	0.126	0.116	0.099	0.082	0.064	0.1390	0.05288	−0.03202	0.05190	−0.03149
1-Octene	C_8H_{16}	0.144	0.138	0.132	0.128	0.121	0.110			0.1934	−0.02199	−0.00014	−0.00009	0.00041
Propadiene	C_3H_4	0.140								0.2303	−0.04051	0.00039	−0.00356	0.00770
1,2-Butadiene	C_4H_6	0.143	0.134	0.126						0.2168	−0.02879	−0.00406	0.01300	−0.01536
1,3-Butadiene	C_4H_6	0.141	0.131							0.2111	−0.01862	−0.01043	0.02551	−0.02178
1,2-Pentadiene	C_5H_8	0.147	0.139	0.132	0.126					0.2110	−0.02792	−0.00072	0.00163	−0.00126
trans-1,3-Pentadiene	C_5H_8	0.144	0.136	0.129	0.123					0.2116	−0.03216	0.00080	0.00067	−0.00361

1,4-Pentadiene	C_5H_8	0.142	0.134	0.127	0.121					0.2084	−0.03030	0.00054	−0.00241	0.00371
2,3-Pentadiene	C_5H_8	0.148	0.140	0.133	0.127					0.2147	−0.03021	−0.00001	0.00055	−0.00114
Acetylene and derivatives														
Acetylene	C_2H_2	0.147	0.126							0.3031	−0.05158	−0.00609	−0.02848	0.08429
Propyne	C_3H_4	0.144	0.133							0.2345	−0.04068	0.00133	−0.01037	0.01914
2-Butyne	C_4H_6		0.141	0.133	0.126					0.2147	−0.02341	−0.00179	−0.00702	0.01726
1-Butyne	C_4H_6	0.145	0.136	0.127						0.2167	−0.02247	−0.00888	0.02718	−0.03070
Naphthenes														
Cyclopropane	C_3H_6	0.148								0.2399	−0.03803	−0.00119	−0.00420	0.01611
Cyclobutane	C_4H_8	0.147	0.138	0.130						0.2169	−0.02128	−0.01016	0.03434	−0.04204
Cyclopentane	C_5H_{10}	0.146	0.140	0.133	0.128					0.2060	−0.02668	0.00020	−0.00149	0.00235
Methyl cyclopentane	C_6H_{12}	0.137	0.131	0.125	0.120	0.112				0.1927	−0.02441	−0.00045	0.00165	−0.00210
Ethyl cyclopentane	C_7H_{14}	0.134	0.128	0.122	0.118	0.111	0.100			0.1812	−0.01850	−0.00234	0.00616	−0.00587
Propyl cyclopentane	C_8H_{16}	0.130	0.125	0.120	0.116	0.110	0.099			0.1763	−0.02054	−0.00007	0.00017	−0.00013
Butyl cyclopentane	C_9H_{18}	0.127	0.123	0.118	0.114	0.108	0.099	0.089		0.1705	−0.01968	0.00034	−0.00099	0.00099
Pentyl cyclopentane	$C_{10}H_{20}$			0.129	0.122	0.113	0.100	0.089	0.079	0.2731	−0.06961	0.00448	0.00963	−0.01333
Hexyl cyclopentane	$C_{11}H_{22}$			0.129	0.122	0.113	0.100	0.089	0.080	0.2744	−0.07215	0.00619	0.00514	−0.00925
Cyclohexane	C_6H_{12}				0.125	0.117				0.1771	−0.01050	−0.00114	−0.00967	0.01707
Methyl cyclohexane	C_7H_{14}			0.116	0.112	0.105	0.094			0.1656	−0.01293	−0.00155	−0.00297	0.00681
Ethyl cyclohexane	C_8H_{16}	0.132	0.127	0.122	0.118	0.112	0.101			0.1761	−0.01964	−0.00013	−0.00006	0.00034
Propyl cyclohexane	C_9H_{18}	0.128	0.124	0.119	0.115	0.110	0.101	0.091		0.1691	−0.01769	−0.00041	0.00082	−0.00057
Butyl cyclohexane	$C_{10}H_{20}$	0.126	0.121	0.117	0.114	0.108	0.100	0.091		0.1652	−0.01888	0.00085	−0.00187	0.00149
Pentyl cyclohexane	$C_{11}H_{22}$			0.129	0.122	0.113	0.100	0.089	0.080	0.2744	−0.07215	0.00619	0.00514	−0.00925
Hexyl cyclohexane	$C_{12}H_{24}$			0.132	0.125	0.117	0.104	0.093	0.084	0.2636	−0.06258	0.00398	0.00716	−0.00970
Cyclopentene	C_5H_8	0.156	0.149	0.142	0.136	0.128				0.2182	−0.02857	0.00046	−0.00108	0.00087
Cyclohexene	C_6H_{10}	0.151	0.145	0.138	0.133	0.125				0.2104	−0.02785	0.00105	−0.00259	0.00231
Aromatic compounds														
Benzene	C_6H_6				0.145	0.136	0.120			0.2318	−0.03081	0.00151	−0.00546	0.00564
Toluene	C_7H_8	0.151	0.144	0.138	0.134	0.126	0.114	0.102	0.090	0.2038	−0.02353	−0.00019	0.00010	0.00013
Ethyl benzene	C_8H_{10}	0.147	0.141	0.135	0.130	0.123	0.111			0.1996	−0.02319	−0.00039	0.00102	−0.00094
Propyl benzene	C_9H_{12}	0.143	0.138	0.133	0.129	0.123	0.113	0.103	0.093	0.1873	−0.02008	0.00008	−0.00010	0.00003
Butyl benzene	$C_{10}H_{14}$	0.142	0.137	0.132	0.128	0.122	0.112	0.102	0.092	0.1866	−0.01959	−0.00010	−0.00004	0.00020
Pentyl benzene	$C_{11}H_{16}$	0.142	0.137	0.133	0.129	0.124	0.114	0.105	0.096	0.1835	−0.01867	0.00010	−0.00022	0.00018
Hexyl benzene	$C_{12}H_{18}$	0.143	0.138	0.133	0.130	0.124	0.115	0.106	0.097	0.1851	−0.02027	0.00087	−0.00170	0.00121
o-Xylene	C_8H_{10}		0.143	0.137	0.133	0.126	0.114			0.1990	−0.02186	−0.00052	0.00107	−0.00085
m-Xylene	C_8H_{10}		0.142	0.136	0.131	0.124	0.113			0.1992	−0.02211	−0.00057	0.00095	−0.00053

D3.1. Table 9. (continued)

Substance	Formula	Temperature (°C)								Equation (4)				
		−50	−25	0	20	50	100	150	200	A	$10^2\ B$	$10^4\ C$	$10^7\ D$	$10^{10}\ E$
p-Xylene	C_8H_{10}				0.131	0.124	0.112			0.2036	−0.03045	0.00408	−0.00977	0.00825
1,2,3-Trimethyl benzene	C_9H_{12}		0.140	0.135	0.131	0.125	0.115	0.105		0.1888	−0.02000	0.00017	−0.00028	0.00011
1,2,4-Trimethyl benzene	C_9H_{12}		0.140	0.135	0.130	0.124	0.114	0.103		0.1917	−0.02076	−0.00001	−0.00022	0.00033
1,3,5-Trimethyl benzene	C_9H_{12}		0.146	0.141	0.136	0.130	0.119	0.107		0.2023	−0.02354	0.00053	−0.00077	0.00036
1,2,3,4-Tetramethyl benzene	$C_{10}H_{14}$			0.134	0.130	0.125	0.115	0.105	0.096	0.1856	−0.01764	−0.00071	0.00132	−0.00092
1,2,3,5-Tetramethyl benzene	$C_{10}H_{14}$			0.132	0.128	0.122	0.113	0.103		0.1814	−0.01489	−0.00202	0.00392	−0.00282
1,2,4,5-Tetramethyl benzene	$C_{10}H_{14}$						0.123	0.114	0.105	0.1925	−0.02008	0.00040	0.00003	−0.00030
Pentamethyl benzene	$C_{11}H_{16}$						0.119	0.114	0.109	0.1494	−0.00447	−0.00139	0.00113	−0.00004
Hexamethyl benzene	$C_{12}H_{18}$								0.107	0.1125	−0.00097	−0.00005	−0.00001	0.00004
Styrene	C_8H_8		0.148	0.142	0.138	0.131	0.120			0.2002	−0.02031	−0.00044	0.00017	0.00043
Isopropyl benzene	C_9H_{12}	0.139	0.134	0.128	0.124	0.118	0.108			0.1856	−0.02089	−0.00008	0.00023	−0.00015
Biphenyl	$C_{12}H_{10}$						0.134	0.126	0.119	0.1919	−0.01611	0.00024	−0.00026	0.00010
Diphenyl methane	$C_{13}H_{12}$					0.133	0.127	0.120	0.114	0.1751	−0.01287	0.00004	−0.00023	0.00023
Triphenyl methane	$C_{19}H_{16}$						0.124	0.116	0.108	0.1855	−0.01942	0.00126	−0.00164	0.00079
Tetraphenyl methane	$C_{25}H_{20}$									0.1758	−0.00352	−0.00044	−0.00217	0.00184
Naphthalene	$C_{10}H_8$						0.133	0.128	0.123	0.1684	−0.00779	−0.00075	0.00110	−0.00059
1-Methylnaphthalene	$C_{11}H_{10}$		0.153	0.149	0.145	0.140	0.131	0.122	0.113	0.1962	−0.01643	−0.00061	0.00105	−0.00067
2-Methylnaphthalene	$C_{11}H_{10}$					0.137	0.127	0.118	0.109	0.1958	−0.01847	0.00016	−0.00046	0.00040
1-Ethylnaphthalene	$C_{12}H_{12}$			0.144	0.140	0.135	0.126	0.118	0.109	0.1905	−0.01568	−0.00093	0.00191	−0.00136
2-Ethylnaphthalene	$C_{12}H_{12}$			0.142	0.138	0.133	0.124	0.116	0.107	0.1903	−0.01802	0.00014	−0.00010	−0.00002
Alcohols														
Methanol	CH_4O	0.221	0.214	0.207	0.201	0.193				0.2803	−0.02234	−0.00359	0.00975	−0.00974
Ethanol	C_2H_6O	0.188	0.181	0.175	0.169	0.162				0.2467	−0.02636			
1-Propanol	C_3H_8O	0.172	0.167	0.161	0.157	0.151				0.2219	−0.02331	0.00067	−0.00097	0.00039
1-Butanol	$C_4H_{10}O$	0.168	0.163	0.158	0.154	0.148	0.138			0.2139	−0.02011	−0.00044	0.00178	−0.00215
1-Pentanol	$C_5H_{12}O$			0.157	0.154	0.149				0.1967	−0.01311	−0.00042	−0.00120	0.00264
1-Hexanol	$C_6H_{14}O$		0.165	0.159	0.155	0.148	0.137	0.126	0.115	0.2200	−0.02279	0.00031	−0.00052	0.00032
1-Heptanol	$C_7H_{16}O$		0.168	0.162	0.158	0.151	0.140	0.128	0.117	0.2241	−0.02268	−0.00001	0.00008	−0.00008
1-Octanol	$C_8H_{18}O$			0.166	0.161	0.154	0.142	0.130	0.118	0.2332	−0.02571	0.00060	−0.00096	0.00056
Isopropanol	C_3H_8O	0.152	0.146	0.141	0.136	0.129	0.118			0.2028	−0.02238	−0.00031	0.00083	−0.00069
2-Methyl-1-propanol	$C_4H_{10}O$	0.145	0.141	0.136	0.133	0.127	0.118			0.1845	−0.01726	−0.00022	0.00028	−0.00004
3-Methyl-1-butanol	$C_5H_{12}O$	0.161	0.154	0.148	0.142	0.134	0.12	0.106		0.2225	−0.02752	0.00005	−0.00014	0.00013

Ethylene glycol	$C_2H_6O_2$			0.249	0.253	0.257	0.259	0.254		0.1125	0.06626	−0.00088	−0.02300	0.01597
1,3-Propylene glycol	$C_3H_8O_2$		0.212	0.218	0.222	0.226	0.227	0.222	0.210	0.0867	0.06667	−0.00281	−0.01797	0.01228
Glycerol	$C_3H_8O_3$				0.291	0.295	0.300	0.306	0.312	0.2562	0.01190	0.00023	−0.00105	0.00102
Cyclohexanol	$C_6H_{12}O$					0.131	0.125	0.118	0.112	0.1708	−0.01180	−0.00028	0.00044	−0.00026
Benzyl alcohol	C_7H_8O			0.162	0.161	0.159	0.155	0.152	0.149	0.1798	−0.00640	−0.00004	−0.00007	0.00014
Phenols														
o-Cresol	C_7H_8O					0.150	0.143	0.137		0.1969	−0.01634	0.00043	0.00088	−0.00164
m-Cresol	C_7H_8O				0.150	0.147	0.141	0.135	0.130	0.1813	−0.01047	−0.00004	−0.00027	0.00038
p-Cresol	C_7H_8O					0.141	0.135	0.129	0.123	0.1914	−0.02103	0.00224	−0.00167	−0.00031
Phenol	C_6H_6O					0.156	0.151	0.146		0.1828	−0.00700	−0.00007	−0.00181	0.00243
Carboxylic acids														
Formic acid	CH_2O_2				0.270	0.267	0.262			0.2971	−0.00743	−0.00030	−0.00196	0.00347
Acetic acid	$C_2H_4O_2$				0.160	0.155	0.146			0.1726	0.01538	−0.00818	0.00287	0.00746
Propionic acid	$C_3H_6O_2$			0.151	0.147	0.142	0.134	0.126	0.118	0.1954	−0.01641			
Butyric acid	$C_4H_8O_2$			0.151	0.147	0.142	0.134	0.126	0.117	0.1967	−0.01681			
Valeric acid	$C_5H_{10}O_2$		0.145	0.139	0.134	0.126	0.114	0.102		0.2114	−0.02925	0.00156	−0.00236	0.00120
Caproic acid	$C_6H_{12}O_2$			0.146	0.143	0.138	0.131	0.124	0.116	0.1906	−0.01948	0.00172	−0.00261	0.00146
Acetic anhydride	$C_4H_6O_3$	0.182	0.176	0.170	0.165	0.158	0.146			0.2363	−0.02436	0.00013	−0.00047	0.00054
Propionic anhydride	$C_6H_{10}O_3$		0.156	0.150	0.145	0.137	0.125	0.112		0.2206	−0.02771	0.00099	−0.00141	0.00058
Chloroacetic acid	$C_2H_3ClO_2$						0.159	0.146		0.2322	−0.01111	−0.00091	−0.00730	0.00999
Dichloroacetic acid	$C_2H_2Cl_2O_2$				0.188	0.180	0.166	0.151		0.2727	−0.02907	0.00011	−0.00001	−0.00009
Trichloroacetic acid	$C_2HCl_3O_2$						0.181	0.165		0.2848	−0.02372	−0.00046	−0.00339	0.00463
Ketones														
Ketene	C_2H_2O	0.228								0.3761	−0.03390	−0.03604	0.14382	−0.21167
Acetone	C_3H_6O	0.193	0.182	0.171	0.163	0.150				0.2871	−0.04233	0.00019	−0.00148	0.00228
Methyl ethyl ketone	C_4H_8O	0.164	0.158	0.151	0.146	0.139				0.2215	−0.02706	0.00061	−0.00008	−0.00132
Diethyl ketone	$C_5H_{10}O$		0.156	0.150	0.145	0.138	0.126			0.2044	−0.01212	−0.00441	0.00636	−0.00254
Dipropyl ketone	$C_7H_{14}O$		0.150	0.144	0.140	0.133	0.121	0.110	0.098	0.2075	−0.02376	0.00032	−0.00052	0.00030
Acetophenone	C_8H_8O				0.148	0.143	0.134	0.126	0.117	0.1965	−0.01643	0.00018	−0.00114	0.00127
Benzophenone	$C_{13}H_{10}O$					0.186	0.175	0.163	0.152	0.2610	−0.02455	0.00066	−0.00093	0.00049
Ethers														
Dimethyl ether	C_2H_6O	0.186	0.172	0.158	0.146					0.3129	−0.05870	0.00170	−0.00532	0.00607
Diethyl ether	$C_4H_{10}O$	0.159	0.149	0.138	0.130	0.118	0.098	0.077		0.2499	−0.04131	0.00036	−0.00086	0.00073
Dipropyl ether	$C_6H_{14}O$	0.149	0.141	0.134	0.128	0.119	0.105			0.2131	−0.02833	−0.00043	0.00088	−0.00065
Methyl propyl ether	$C_4H_{10}O$	0.164	0.155	0.145	0.138	0.126				0.2475	−0.03664	−0.00060	0.00132	−0.00100
Ethyl propyl ether	$C_5H_{12}O$	0.154	0.145	0.137	0.131	0.121	0.104			0.2276	−0.03363	0.00036	−0.00079	0.00060

D3.1. Table 9. (continued)

Substance	Formula	Temperature (°C)								Equation (4)				
		−50	−25	0	20	50	100	150	200	A	$10^2\ B$	$10^4\ C$	$10^7\ D$	$10^{10}\ E$
Ethylene oxide	C_2H_4O	0.181	0.171	0.161						0.2529	−0.00990	−0.01984	0.05755	−0.06175
Furane	C_4H_4O	0.150	0.142	0.134	0.128					0.2058	−0.01538	−0.00537	0.00236	0.00981
1,4-Dioxane	$C_4H_8O_2$				0.161	0.147	0.123			0.2815	−0.03069	−0.00435	0.00160	0.00401
Aldehydes														
Formaldehyde	CH_2O	0.228								0.3834	−0.07422	0.00084	0.01156	−0.02638
Acetaldehyde	C_2H_4O	0.214	0.203	0.192	0.183					0.2979	−0.01871	−0.01741	0.05316	−0.05982
Paraldehyde	$C_6H_{12}O_3$					0.142	0.135			0.1820	−0.00949	−0.00080	−0.00103	0.00253
Furfural	$C_5H_4O_2$				0.173	0.167	0.157			0.1911	0.00303	−0.00101	−0.01267	0.01783
Benzaldehyde	C_7H_6O	0.166	0.162	0.157	0.153	0.148	0.139	0.130	0.121	0.2080	−0.01952	0.00048	−0.00069	0.00035
Salicylaldehyde	$C_7H_6O_2$				0.168	0.160	0.147	0.134		0.2425	−0.02472	−0.00062	0.00149	−0.00122
Esters														
Methyl formate	$C_2H_4O_2$	0.220	0.208	0.197	0.187	0.173	0.150			0.3250	−0.04714	0.00001	0.00041	−0.00076
Ethyl formate	$C_3H_6O_2$	0.185	0.177	0.169	0.162	0.152	0.136	0.119		0.2619	−0.03750	0.00233	−0.00521	0.00426
Propyl formate	$C_4H_8O_2$	0.166	0.159	0.153	0.147	0.139	0.126	0.113	0.100	0.2246	−0.02626	−0.00010	0.00026	−0.00023
Methyl acetate	$C_3H_6O_2$	0.185	0.174	0.164	0.155	0.143	0.122			0.2795	−0.04392	0.00097	−0.00169	0.00097
Ethyl acetate	$C_4H_8O_2$	0.171	0.162	0.153	0.146	0.135				0.2487	−0.03472	0.00014	−0.00183	0.00289
Propyl acetate	$C_5H_{10}O_2$	0.164	0.156	0.149	0.142	0.133	0.118	0.102		0.2323	−0.03003	−0.00030	0.00028	0.00007
Methyl propionate	$C_4H_8O_2$	0.165	0.159	0.152	0.147	0.139	0.125	0.112	0.098	0.2242	−0.02552	−0.00054	0.00096	−0.00060
Ethyl propionate	$C_5H_{10}O_2$	0.158	0.151	0.145	0.140	0.132	0.120	0.107	0.095	0.2140	−0.02537	0.00005	0.00001	−0.00008
Propyl propionate	$C_6H_{12}O_2$	0.157	0.150	0.143	0.138	0.129	0.115	0.101		0.2208	−0.02909	0.00039	−0.00048	0.00011
Methyl butyrate	$C_5H_{10}O_2$	0.160	0.153	0.147	0.142	0.134	0.121	0.108	0.095	0.2173	−0.02580	0.0	−0.00012	0.00017
Ethyl butyrate	$C_6H_{12}O_2$	0.155	0.149	0.142	0.137	0.130	0.117	0.105		0.2097	−0.02404	−0.00036	0.00064	−0.00039
Methyl benzoate	$C_8H_8O_2$			0.160	0.155	0.149	0.137	0.125	0.114	0.2246	−0.02449	0.00055	−0.00106	0.00074
Ethyl benzoate	$C_9H_{10}O_2$		0.155	0.150	0.145	0.139	0.128	0.118	0.107	0.2074	−0.02103	−0.00005	0.00001	0.00004
Methyl salicylate	$C_8H_8O_3$			0.149	0.145	0.138	0.128	0.118	0.107	0.1937	−0.00824	−0.00491	0.00838	−0.00525

Amines														
Methyl amine	CH_5N	0.224	0.217	0.210						0.3130	−0.03506	−0.00970	0.04159	−0.03482
Ethyl amine	C_2H_7N	0.204	0.197	0.191	0.187					0.2923	−0.04639	0.00066	0.01270	−0.00936
Propyl amine	C_3H_9N	0.188	0.182	0.177	0.173	0.168				0.2597	−0.03808	0.00174	0.00537	−0.00462
n-butyl amine	$C_4H_{11}N$		0.171	0.166	0.162	0.157				0.2685	−0.04797	0.00062	0.01465	−0.01150
Dimethyl amine	C_2H_7N	0.170	0.162	0.153	0.146	0.136	0.119			0.2444	−0.03272	−0.00039	0.00057	−0.00027
Trimethyl amine	C_3H_9N	0.152	0.143	0.133						0.2257	−0.01529	−0.01592	0.04807	−0.05383
Diethyl amine	$C_6H_{15}N$		0.150	0.142	0.136	0.127	0.115	0.104		0.2496	−0.04387	−0.00016	0.00792	−0.00526
Triethyl amine	$C_6H_{15}N$	0.137	0.131	0.125	0.120	0.113	0.100	0.088	0.076	0.1914	−0.02402	−0.00020	0.00032	−0.00016
Piperidine	$C_5H_{11}N$			0.187	0.181	0.171	0.154			0.2913	−0.05011	0.00823	−0.01803	0.01475
Pyridine	C_6H_7N		0.177	0.169	0.164	0.155	0.141	0.127	0.112	0.2477	−0.02862	0.00001	−0.00003	0.00003
Aniline	C_6H_7N			0.178	0.173	0.167	0.156	0.145	0.135	0.2365	−0.02199	0.00023	−0.00036	0.00021
N-methyl aniline	C_7H_9N	0.172	0.167	0.162	0.159	0.153	0.144	0.135	0.125	0.2137	−0.01923	0.00025	−0.00040	0.00024
N,N-dimethyl aniline	$C_8H_{11}N$				0.143	0.138	0.129	0.121		0.1921	−0.01666	−0.00006	−0.00004	0.00012
N,N-diethyl aniline	$C_{10}H_{15}N$		0.151	0.146	0.142	0.136	0.126	0.116	0.105	0.2028	−0.02163	0.00050	−0.00087	0.00057
Phenylhydrazine	$C_6H_8N_2N_2$				0.141	0.135	0.126	0.117	0.108	0.1942	−0.01858	0.00016	−0.00028	0.00020
Diphenyl amine	$C_{12}H_{11}N$						0.127	0.119	0.110	0.1832	−0.01130	−0.00178	0.00261	−0.00142
Nitriles														
Acetonitrile	C_2H_3N		0.208	0.198	0.190	0.178				0.3109	−0.04357	0.00094	−0.00022	−0.00134
Propionitrile	C_3H_5N	0.192	0.184	0.176	0.169	0.159				0.2660	−0.03337	0.00048	−0.00181	0.00209
Butyronitrile	C_4H_7N	0.191	0.183	0.175	0.169	0.160	0.144			0.2602	−0.03188	0.00057	−0.00161	0.00164
Benzonitrile	C_7H_5N			0.154	0.150	0.143	0.132	0.121		0.2152	−0.02440	0.00126	−0.00244	0.00175
Amides														
Formamide	CH_3NO				0.353	0.350	0.345	0.340	0.334	0.3852	−0.01102	0.00005	0.00008	−0.00017
Nitroderivates														
Nitromethane	CH_3NO_2		0.227	0.217	0.209	0.197	0.176			0.3307	−0.04243	−0.00006	0.00219	−0.00330
Nitrobenzene	$C_6H_5NO_2$				0.149	0.145	0.138			0.1793	−0.00759	−0.00088	−0.00120	0.00295
o-Nitrotoluene	$C_7H_7NO_2$			0.146	0.142	0.136	0.126	0.116	0.106	0.2013	−0.02041	0.00018	−0.00043	0.00032
m-Nitrotoluene	$C_7H_7NO_2$				0.141	0.135	0.125	0.116	0.106	0.1961	−0.01788	−0.00049	0.00064	−0.00030
p-Nitrotoluene	$C_7H_7NO_2$						0.126	0.117	0.107	0.1968	−0.01682	−0.00101	0.00159	−0.00093

D3.1. Table 10. Thermal conductivity of gases in W/mK at low pressures

Substance	Formula	Temperature (°C)								Equation (5)				
		−50	0	25	100	200	300	400	500	10^3 *A*	10^3 *B*	10^6 *C*	10^9 *D*	10^{12} *E*
Elements														
Xenon	Xe	0.0043	0.0052	0.0056	0.0069	0.0086	0.0102	0.0117	0.0132	−0.006	0.020	−0.003680		
Krypton	Kr	0.0073	0.0088	0.0095	0.0115	0.0140	0.0163	0.0184	0.0204	−0.389	0.039	−0.021190	0.008780	−0.001520
Argon	Ar		0.0166	0.0177	0.0209	0.0249	0.0288	0.0326	0.0362	4.303	0.047	−0.007780		
Neon	Ne	0.0393	0.0459	0.0490	0.0578	0.0682	0.0774	0.0858	0.0936	2.778	0.194	−0.155500	0.086380	−0.017700
Helium	He	0.1263	0.1446	0.1536	0.1793	0.2116	0.2420	0.2708	0.2983	34.000	0.457	−0.214890	0.100710	−0.019140
Air		0.0204	0.0244	0.0263	0.0317	0.0383	0.0444	0.0502	0.0557	−0.908	0.112	−0.084333	0.056964	−0.015631
Hydrogen	H_2	0.1429	0.1685	0.1807	0.2149	0.2566	0.2952	0.3319	0.3678	0.651	0.767	−0.687050	0.506510	−0.138540
Nitrogen	N_2	0.0198	0.0237	0.0256	0.0309	0.0375	0.0437	0.0495	0.0551	−0.133	0.101	−0.060650	0.033610	−0.007100
Oxygen	O_2	0.0201	0.0244	0.0264	0.0324	0.0398	0.0468	0.0534	0.0597	−1.285	0.107	−0.052630	0.025680	−0.005040
Sulfur	S								0.0145	1.596	0.016	0.001450		
Fluorine	F_2	0.0195	0.0237	0.0258	0.0318	0.0395	0.0469	0.0539	0.0605	−0.246	0.093	−0.018470		
Chlorine	Cl_2	0.0063	0.0081	0.0089	0.0115	0.0147	0.0179	0.0210	0.0239	−1.867	0.038	−0.006090		
Bromine	Br_2				0.0061	0.0089				5.455	−0.018	0.054230		
Iodine	I_2					0.0052	0.0063	0.0074	0.0085	−0.014	0.011	0.000020		
Anorganic compounds														
Hydrogen fluoride	HF	0.0167	0.0198	0.0214	0.0263	0.0329	0.0396	0.0464	0.0534	2.921	0.060	0.006940		
Hydrogen chloride	HCl	0.0112	0.0134	0.0146	0.0179	0.0224	0.0269	0.0314	0.0359	1.233	0.045	0.000370		
Hydrogen bromide	HBr	0.0061	0.0077	0.0086	0.0110	0.0142	0.0173			−1.740	0.036	−0.004870		
Hydrogen iodide	HI		0.0056	0.0061	0.0077	0.0098	0.0118	0.0138	0.0157	−0.308	0.022	−0.001840		
Hydrogen cyanide	HCN		0.0098	0.0118	0.0178	0.0259	0.0338	0.0418		−12.121	0.080	−0.000500		
Water	H_2O			0.0185	0.0239	0.0329	0.0433	0.0547	0.0669	13.918	−0.047	0.258066	−0.183149	0.055092
Hydrogen sulfide	H_2S	0.0083	0.0126	0.0144	0.0190	0.0247	0.0308			−37.786	0.366	−0.980220	1.341110	−0.662840
Ammonia	NH_3		0.0221	0.0251	0.0344	0.0476	0.0618	0.0770	0.0931	−6.678	0.092	0.047670		
Nitric oxide	NO	0.0196	0.0236	0.0255	0.0312	0.0383	0.0449	0.0509		0.144	0.093	−0.02601		
Nitrogen dioxide	NO_2				0.0280					66.085	−0.479	1.011240		
Nitrous oxide	N_2O	0.0119	0.0157	0.0176	0.0234	0.0310	0.0388	0.0465	0.0543	−5.049	0.076	0.001460		
Dinitrogentetroxide	N_2O_4													
Cyanogen	C_2N_2		0.0144	0.0160	0.0211	0.0280	0.0351	0.0424	0.0499	−2.939	0.061	0.009930		
Phosphorus trichloride	PCl_3	0.0053	0.0068	0.0075	0.0098	0.0127	0.0156	0.0183	0.0209	−1.274	0.028	0.008226	−0.013677	0.005121
Cyanogen chloride	ClCN			0.0094	0.0122	0.0160	0.0196	0.0231	0.0265	−2.531	0.042	−0.005290		
Silane	SiH_4	0.0157	0.0204	0.0228	0.0305	0.0416	0.0534	0.0659	0.0788	−1.601	0.062	0.074888	−0.029302	0.003487
Tetrachlorosilane	$SiCl_4$	0.0043	0.0057	0.0065	0.0086	0.0115	0.0144	0.0173	0.0202	−2.173	0.029			

Carbon monoxide	CO	0.0193	0.0231	0.0249	0.0302	0.0366	0.0426	0.0481	0.0534	−0.783	0.103	−0.067590	0.039450	−0.009470
Carbon dioxide	CO_2		0.0145	0.0165	0.0225	0.0306	0.0386	0.0463	0.0536	−3.882	0.053	0.071460	−0.070310	0.018090
Carbon suboxide	C_3O_2	0.0077	0.0110	0.0127	0.0183	0.0260	0.0335	0.0405	0.0472	1.362	−0.017	0.267780	−0.322540	0.133290
Carbonyl sulfide	COS	0.0095	0.0125	0.0140	0.0184	0.0242	0.0300	0.0356	0.0412	−4.089	0.062	−0.004270		
Phosgene	CCl_2O		0.0076	0.0088	0.0125	0.0179	0.0238	0.0301	0.0368	−3.777	0.036	0.021900		
Carbon disulfide	CS_2		0.0077	0.0087	0.0118	0.0159	0.0200	0.0241	0.0282	−3.468	0.041	0.000210		
Sulfur dioxide	SO_2		0.0084	0.0095	0.0131	0.0183	0.0238	0.0292	0.0343	0.358	0.013	0.069520	−0.032070	−0.008300
Sulfur trioxide	SO_3				0.0172	0.0231	0.0287	0.0340	0.0391	−7.361	0.071	−0.014220		
Sulfuryl chloride	Cl_2SO_2				0.0119	0.0159	0.0199	0.0238	0.0276	−3.541	0.043	−0.002860		
Sulfur hexafluoride	SF_6		0.0118	0.0135	0.0184	0.0243	0.0296	0.0343	0.0384	−9.510	0.087	−0.031860		
Organic compounds containing sulfur														
Methyl mercaptan	CH_4S		0.0116	0.0137	0.0199	0.0284	0.0371	0.0461	0.0554	−9.622	0.074	0.012580		
Ethyl mercaptan	C_2H_6S				0.0202	0.0289	0.0381	0.0478	0.0579	−8.457	0.068	0.022700		
Dimethyl sulfide	C_2H_6S				0.0204	0.0293	0.0386	0.0484	0.0587	−8.509	0.069	0.023630		
Diethyl sulfide	$C_4H_{10}S$				0.0180	0.0270	0.0365	0.0463	0.0566	−12.116	0.073	0.020380		
Thiophene	C_4H_4S				0.0163	0.0239	0.0320	0.0406	0.0496	−8.013	0.057	0.023220		
Halogenated hydrocarbons														
Fluoromethane (R41)	CH_3F	0.0099	0.0129	0.0144	0.0190	0.0250	0.0310	0.0369	0.0429	−3.680	0.061	−0.001100		
Difluoromethane (R32)	CH_2F_2	0.0073	0.0098	0.0111	0.0148	0.0199	0.0251	0.0304	0.0358	−3.440	0.047	0.004350		
Trifluoromethane (R23)	CHF_3	0.0088	0.0120	0.0136	0.0189	0.0263	0.0337	0.0408	0.0475	−0.732	0.018	0.136890	−0.135880	0.041920
Tetrafluoromethane (R14)	CF_4	0.0099	0.0138	0.0158	0.0219	0.0302	0.0382	0.0456	0.0524	−2.200	0.026	0.167240	−0.199700	0.074660
Methyl chloride	CH_3Cl	0.0064	0.0092	0.0107	0.0159	0.0241	0.0338	0.0450		−1.448	0.018	0.075410		
Methylene chloride	CH_2Cl_2			0.0072	0.0108	0.0159	0.0214	0.0274	0.0337	−4.536	0.033	0.021050		
Chloroform	$CHCl_3$		0.0060	0.0066	0.0083	0.0106	0.0130	0.0153	0.0177	−0.216	0.022	0.001040		
Carbon tetrachloride	CCl_4		0.0059	0.0067	0.0088	0.0118	0.0147	0.0175	0.0204	−2.101	0.030	−0.000530		
Bromomethane	CH_3Br		0.0066	0.0077	0.0108	0.0152	0.0198	0.0247	0.0297	−3.766	0.035	0.010400		
Dibromomethane	CH_2Br_2				0.0069	0.0104	0.0142	0.0182	0.0226	−3.217	0.021	0.015550		
Tribromomethane	$CHBr_3$					0.0083	0.0114	0.0149	0.0187	−1.531	0.012	0.017770		
Tetrabromomethane	CBr_4	0.0081	0.0097	0.0105	0.0132	0.0168	0.0205	0.0240	0.0273	2.432	0.018	0.041190	−0.032120	0.004000
Chlorodifluoromethane (R22)	$CHClF_2$		0.0094	0.0109	0.0154	0.0212	0.0269	0.0324	0.0377	−8.104	0.066	−0.009410		
Dichlorofluoromethane (R21)	$CHCl_2F$			0.0086	0.0125	0.0177	0.0227	0.0275	0.0323	−7.857	0.057	−0.006660		
Chlorotrifluoromethane (R13)	$CClF_3$	0.0076	0.0106	0.0121	0.0169	0.0232	0.0293	0.0348	0.0397	−1.734	0.020	0.132510	−0.160810	0.059510
Dichlorodifluoromethane (R12)	CCl_2F_2		0.0085	0.0097	0.0135	0.0193	0.0257	0.0328		−1.873	0.029	0.034090		
Trichlorofluoromethane (R11)	CCl_3F		0.0069	0.0079	0.0108	0.0150				−2.430	0.031	0.012940		
Ethyl fluoride (R161)	C_2H_5F		0.0121	0.0140	0.0196	0.0275	0.0359	0.0446	0.0538	−6.157	0.061	0.021240		
Ethyl chloride	C_2H_5Cl		0.0095	0.0112	0.0167	0.0247	0.0335	0.0431	0.0535	−6.153	0.046	0.039790		
Ethyl bromide	C_2H_5Br				0.0135	0.0192	0.0252	0.0314	0.0379	−5.547	0.046	0.012890		

D3.1. Table 10. (continued)

Substance	Formula	Temperature (°C)								Equation (5)				
		−50	0	25	100	200	300	400	500	10^3 *A*	10^3 *B*	10^6 *C*	10^9 *D*	10^{12} *E*
1,1-Dichloroethane	$C_2H_4Cl_2$				0.0141	0.0212	0.0290	0.0376	0.0470	−6.137	0.041	0.036390		
1,2-Dichloroethane	$C_2H_4Cl_2$				0.0127	0.0192	0.0266	0.0346	0.0433	0.513	−0.004	0.125349	−0.085225	0.028133
1,2-Dibromoethane	$C_2H_4Br_2$					0.0136	0.0178	0.0222	0.0267	−4.774	0.036	0.006440		
1,1,1-Trifluoroethane (R143a)	$C_2H_3F_3$		0.0112	0.0128	0.0181	0.0260	0.0346	0.0435	0.0524	0.069	0.014	0.111220	−0.053330	−0.001330
1,1,1-Trichloroethane	$C_2H_3Cl_3$				0.0125	0.0191	0.0265	0.0345	0.0433	−5.829	0.035	0.036400		
1,1,2,2-Tetrachloroethane	$C_2H_2Cl_4$					0.0144	0.0200	0.0264	0.0334	−2.397	0.019	0.035930		
Pentachloroethane	C_2HCl_5					0.0134	0.0188	0.0248	0.0316	−2.200	0.016	0.035390		
Hexachloroethane	C_2Cl_6					0.0122	0.0172	0.0228	0.0290	−2.033	0.014	0.033490		
1,1,2,2-Tetrachlorodifluoroethane	$C_2Cl_4F_2$				0.0096	0.0149	0.0207	0.0271	0.0341	−4.773	0.028	0.029320		
1,1,2-Trichlorotrifluoroethan	$C_2Cl_3F_3$		0.0076	0.0089	0.0125	0.0171	0.0216	0.0259	0.0300	−6.397	0.054	−0.008760		
1,2-Dichlorotetrafluoroethane	$C_2Cl_2F_4$			0.0103	0.0143	0.0196	0.0247	0.0296	0.0343	−6.889	0.060	−0.008890		
1-Chloropropane	C_3H_7Cl				0.0162	0.0244	0.0334	0.0433	0.0540	−7.089	0.047	0.041460		
1-Chlorobutane	C_4H_9Cl		0.0084	0.0100	0.0153	0.0232	0.0322	0.0421	0.0530	−5.369	0.037	0.050150		
1-Chloropentane	$C_5H_{11}Cl$				0.0150	0.0232	0.0324	0.0427	0.0541	−5.738	0.035	0.054510		
Chlorotrifluoroethene	C_2ClF_3		0.0102	0.0117	0.0170	0.0250	0.0338	0.0432	0.0528	0.014	0.009	0.116740	−0.051520	−0.000700
Vinyl chloride	C_2H_3Cl		0.0104	0.0121	0.0173	0.0252	0.0341	0.0440	0.0549	−3.095	0.036	0.050930		
1,1-Dichloroethene	$C_2H_2Cl_2$		0.0068	0.0079	0.0117	0.0171	0.0232	0.0299	0.0371	−3.531	0.030	0.029680		
Trichloroethene	C_2HCl_3			0.0079	0.0107	0.0144	0.0180	0.0217	0.0254	−3.226	0.037	−0.000650		
Tetrachloroethene	C_2Cl_4					0.0122	0.0152	0.0182	0.0211	−2.838	0.033	−0.002620		
Fluorobenzene	C_6H_5F				0.0167	0.0256	0.0358			−5.050	0.034	0.065160		
Chlorobenzene	C_6H_5Cl					0.0217	0.0307	0.0407	0.0516	−8.355	0.041	0.046620		
Bromobenzene	C_6H_5Br					0.0154	0.0210	0.0266	0.0323	−10.831	0.055	0.000840		
Iodobenzene	C_6H_5I					0.0132	0.0182	0.0233	0.0284	−9.845	0.047	0.002660		
m-Chlorotoluene	C_7H_7Cl					0.0124	0.0171	0.0224	0.0283	−2.219	0.017	0.028710		
Benzyl chloride	C_7H_7Cl					0.0159	0.0217	0.0275	0.0333	−11.207	0.057	0.001190		
***n*-Alkanes**														
Methane	CH_4	0.0241	0.0305	0.0340	0.0453	0.0619	0.0797	0.0985	0.1184	8.154	0.008	0.351530	−0.338650	0.140920
Ethane	C_2H_6	0.0127	0.0184	0.0215	0.0320	0.0481	0.0661	0.0857	0.1066	−0.907	0.009	0.267380	−0.165560	0.048330
Propane	C_3H_8		0.0154	0.0181	0.0272	0.0411	0.0571	0.0750	0.0950	−6.656	0.053	0.101810		
n-Butane	C_4H_{10}		0.0134	0.0162	0.0253	0.0389	0.0543	0.0715	0.0905	−9.954	0.061	0.088710		
n-Pentane	C_5H_{12}		0.0128	0.0150	0.0224	0.0340	0.0475	0.0630	0.0806	−3.267	0.032	0.099040		
n-Hexane	C_6H_{14}				0.0203	0.0311	0.0439	0.0587	0.0753	−3.277	0.027	0.096500		
n-Heptane	C_7H_{16}				0.0190	0.0297	0.0422	0.0564	0.0724	−5.442	0.033	0.088020		

n-Octane	C_8H_{18}				0.0179	0.0278	0.0396	0.0532	0.0687	−2.456	0.020	0.093390		
n-Nonane	C_9H_{20}					0.0262	0.0374	0.0505	0.0653	−2.317	0.017	0.090970		
n-Decane	$C_{10}H_{22}$					0.0242	0.0351	0.0479	0.0625	−1.409	0.009	0.095140		
n-Undecane	$C_{11}H_{24}$					0.0229	0.0338	0.0462	0.0603	−6.240	0.023	0.081070		
n-Dodecane	$C_{12}H_{26}$						0.0323	0.0441	0.0575	−7.217	0.027	0.073790		
n-Tridecane	$C_{13}H_{28}$						0.0308	0.0422	0.0551	−7.043	0.025	0.071680		
n-Tetradecane	$C_{14}H_{30}$						0.0296	0.0403	0.0526	−1.684	0.010	0.077940		
n-Pentadecane	$C_{15}H_{32}$						0.0281	0.0388	0.0508	−6.608	0.022	0.068200		
n-Hexadecane	$C_{16}H_{34}$						0.0269	0.0373	0.0490	−6.286	0.019	0.067930		
n-Heptadecane	$C_{17}H_{36}$							0.0339	0.0451	1.219	−0.007	0.081760		
n-Octadecane	$C_{18}H_{38}$							0.0327	0.0435	1.394	−0.007	0.079670		
n-Nonadecane	$C_{19}H_{40}$							0.0315	0.0421	−1.657	0.000	0.072870		
n-Eicosane	$C_{20}H_{42}$							0.0307	0.0409	1.519	−0.008	0.075880		
Isoalkanes														
Isobutane	C_4H_{10}		0.0139	0.0164	0.0251	0.0383	0.0528	0.0679	0.0832	1.433	−0.022	0.305790	−0.226490	0.058610
2-Methyl butane	C_5H_{12}		0.0120	0.0144	0.0227	0.0353	0.0491	0.0635	0.0782	0.912	−0.029	0.319870	−0.259160	0.079360
2,2-Dimethyl propane	C_5H_{12}		0.0120	0.0149	0.0241	0.0372	0.0512	0.0660	0.0817	−16.839	0.093	0.044110		
2-Methyl pentane	C_6H_{14}				0.0206	0.0329	0.0455	0.0585	0.0719	−22.140	0.108	0.017500		
3-Methyl pentane	C_6H_{14}				0.0205	0.0328	0.0455	0.0586	0.0721	−22.148	0.107	0.019360		
2,2-Dimethyl butane	C_6H_{14}				0.0216	0.0342	0.0474	0.0610	0.0752	−20.993	0.105	0.025680		
2,3-Dimethyl butane	C_6H_{14}				0.0207	0.0332	0.0462	0.0595	0.0733	−22.295	0.107	0.020880		
Olefins														
Ethylene	C_2H_4	0.0130	0.0180	0.0208	0.0303	0.0454	0.0628	0.0823	0.1036	3.246	−0.010	0.271040	−0.156820	0.050860
Propylene	C_3H_6		0.0151	0.0178	0.0263	0.0389	0.0529	0.0685	0.0855	−7.786	0.064	0.073320		
1-Butene	C_4H_8		0.0130	0.0152	0.0225	0.0341	0.0478	0.0636	0.0815	−2.290	0.027	0.104930		
1-Pentene	C_5H_{10}				0.0208	0.0319	0.0449	0.0599	0.0768	−2.635	0.026	0.099680		
1-Hexene	C_6H_{12}				0.0203	0.0315	0.0441	0.0581	0.0735	−8.882	0.052	0.070750		
1-Heptene	C_7H_{14}	0.0052	0.0097	0.0120	0.0192	0.0296	0.0412	0.0542	0.0687	−15.924	0.106	−0.085770	0.168444	−0.067405
1-Octene	C_8H_{16}					0.0279	0.0395	0.0525	0.0669	−7.408	0.041	0.071630		
Propadiene	C_3H_4		0.0130	0.0155	0.0234	0.0340	0.0450	0.0562	0.0677	−14.020	0.095	0.013700		
1,2-Butadiene	C_4H_6			0.0129	0.0205	0.0309	0.0417	0.0529	0.0644	−15.212	0.089	0.017970		
1,3-Butadiene	C_4H_6		0.0132	0.0157	0.0244	0.0388	0.0565	0.0774	0.1015	−0.789	0.007	0.162080		
1,2-Pentadiene	C_5H_8				0.0189	0.0294	0.0401	0.0511	0.0624	−17.311	0.092	0.014980		
trans-1,3-Pentadiene	C_5H_8				0.0190	0.0297	0.0404	0.0513	0.0624	−19.350	0.100	0.007280		
1,4-Pentadiene	C_5H_8				0.0203	0.0312	0.0422	0.0535	0.0650	−18.130	0.099	0.011060		
2,3-Pentadiene	C_5H_8				0.0192	0.0294	0.0400	0.0509	0.0621	−15.702	0.087	0.017770		

D3.1. Table 10. (continued)

Substance	Formula	Temperature (°C)								Equation (5)				
		−50	0	25	100	200	300	400	500	10^3 *A*	10^3 *B*	10^6 *C*	10^9 *D*	10^{12} *E*
Acetylene and derivatives														
Acetylene	C_2H_2	0.0140	0.0188	0.0213	0.0295	0.0418	0.0555			−3.020	0.059	0.074580		
Propyne	C_3H_4		0.0138	0.0164	0.0244	0.0354	0.0466	0.0582	0.0700	−13.853	0.097	0.014860		
2-Butyne	C_4H_6				0.0201	0.0306	0.0416	0.0530	0.0648	−15.509	0.088	0.021160		
1-Butyne	C_4H_6			0.0143	0.0225	0.0337	0.0452	0.0569	0.0689	−16.681	0.100	0.014050		
Naphthenes														
Cyclopropane	C_3H_6		0.0135	0.0160	0.0245	0.0383	0.0551	0.0747	0.0972	−1.614	0.016	0.144720		
Cyclobutane	C_4H_8			0.0147	0.0235	0.0373	0.0537	0.0725	0.0938	−6.078	0.033	0.125010		
Cyclopentane	C_5H_{10}				0.0208	0.0338	0.0495	0.0677	0.0885	−5.091	0.021	0.129630		
Methyl cyclopentane	C_6H_{12}				0.0188	0.0304	0.0434	0.0571	0.0711	4.354	−0.058	0.346100	−0.262790	0.072170
Ethyl cyclopentane	C_7H_{14}					0.0291	0.0411	0.0535	0.0665	−20.576	0.093	0.025380		
Propyl cyclopentane	C_8H_{16}					0.0287	0.0392	0.0506	0.0627	−10.781	0.065	0.039010		
Butyl cyclopentane	C_9H_{18}					0.0259	0.0370	0.0484	0.0601	−23.525	0.098	0.012600		
Pentyl cyclopentane	$C_{10}H_{20}$	0.0057	0.0087	0.0105	0.0165	0.0261	0.0369	0.0486	0.0607	1.460	−0.023	0.215370	−0.134660	0.028890
Hexyl cyclopentane	$C_{11}H_{22}$	0.0052	0.0078	0.0093	0.0146	0.0230	0.0324	0.0425	0.0531	1.294	−0.018	0.184080	−0.113900	0.024090
Cyclohexane	C_6H_{12}				0.0187	0.0310	0.0462	0.0642	0.0850	−2.616	0.005	0.140460		
Methyl cyclohexane	C_7H_{14}					0.0311	0.0428	0.0556	0.0694	−10.624	0.064	0.051310		
Ethyl cyclohexane	C_8H_{16}					0.0286	0.0394	0.0511	0.0637	−10.644	0.062	0.044020		
Propyl cyclohexane	C_9H_{18}					0.0272	0.0371	0.0480	0.0601	−5.219	0.043	0.053230		
Butyl cyclohexane	$C_{10}H_{20}$					0.0261	0.0359	0.0465	0.0578	−10.937	0.061	0.035720		
Pentyl cyclohexane	$C_{11}H_{22}$	0.0049	0.0077	0.0093	0.0149	0.0238	0.0339	0.0447	0.0560	1.206	−0.023	0.200870	−0.121290	0.023210
Hexyl cyclohexane	$C_{12}H_{24}$	0.0044	0.0070	0.0084	0.0135	0.0216	0.0308	0.0407	0.0510	1.058	−0.020	0.179090	−0.105400	0.019300
Cyclopentene	C_5H_8				0.0193	0.0310	0.0439	0.0575	0.0711	3.598	−0.055	0.354970	−0.285390	0.083400
Cyclohexene	C_6H_{10}				0.0207	0.0312	0.0426	0.0550	0.0682	−10.302	0.066	0.046170		
Aromatic compounds														
Benzene	C_6H_6				0.0169	0.0263	0.0369	0.0488	0.0618	−7.339	0.042	0.061410		
Toluene	C_7H_8					0.0280	0.0392	0.0517	0.0653	−9.260	0.051	0.059090		
Ethyl benzene	C_8H_{10}					0.0264	0.0375	0.0498	0.0634	−8.932	0.045	0.063110		
Propyl benzene	C_9H_{12}					0.0238	0.0334	0.0433	0.0534	−17.869	0.082	0.013230		
Butyl benzene	$C_{10}H_{14}$					0.0229	0.0323	0.0420	0.0519	−18.506	0.082	0.011860		
Pentyl benzene	$C_{11}H_{16}$						0.0317	0.0408	0.0504	−10.248	0.058	0.025960		
Hexyl benzene	$C_{12}H_{18}$						0.0302	0.0394	0.0488	−18.297	0.079	0.010450		

o-Xylene	C_8H_{10}				0.0200	0.0294	0.0390	0.0486	0.0583	−14.739	0.092	0.003690		
m-Xylene	C_8H_{10}				0.0149	0.0265	0.0382	0.0503	0.0633	−30.341	0.123	0.009470	−0.060540	0.058390
p-Xylene	C_8H_{10}				0.0158	0.0267	0.0380	0.0495	0.0615	−21.818	0.095	0.016980		
1,2,3-Trimethyl benzene	C_9H_{12}					0.0244	0.0334	0.0429	0.0531	−10.155	0.059	0.029520		
1,2,4-Trimethyl benzene	C_9H_{12}					0.0235	0.0322	0.0415	0.0514	−9.642	0.056	0.029870		
1,3,5-Trimethyl benzene	C_9H_{12}					0.0227	0.0321	0.0417	0.0517	−16.563	0.075	0.017570		
1,2,3,4-Tetramethyl benzene	$C_{10}H_{14}$						0.0322	0.0414	0.0512	−10.379	0.059	0.026580		
1,2,3,5-Tetramethyl benzene	$C_{10}H_{14}$					0.0229	0.0315	0.0406	0.0503	−10.012	0.056	0.028030		
1,2,4,5-Tetramethyl benzene	$C_{10}H_{14}$					0.0230	0.0316	0.0407	0.0503	−9.990	0.057	0.027510		
Pentamethyl benzene	$C_{11}H_{16}$						0.0309	0.0401	0.0497	−10.473	0.056	0.028030		
Hexamethyl benzene	$C_{12}H_{18}$						0.0304	0.0394	0.0489	−10.820	0.057	0.026460		
Styrene	C_8H_8					0.0231	0.0322	0.0416	0.0510	−17.470	0.081	0.009440		
Isopropyl benzene	C_9H_{12}					0.0247	0.0348	0.0453	0.0560	−19.870	0.088	0.013230		
Biphenyl	$C_{12}H_{10}$				0.0111	0.0195	0.0279	0.0362	0.0446	−20.015	0.083	0.000330		
Diphenyl methane	$C_{13}H_{12}$						0.0258	0.0332	0.0410	−9.251	0.050	0.019680		
Triphenyl methane	$C_{19}H_{16}$							0.0292	0.0362	−9.366	0.047	0.016050		
Tetraphenyl methane	$C_{25}H_{20}$								0.0311	−14.302	0.056	0.004050		
Naphthalene	$C_{10}H_8$						0.0288	0.0371	0.0458	−9.546	0.053	0.023490		
1-Methylnaphthalene	$C_{11}H_{10}$						0.0278	0.0362	0.0448	−15.377	0.068	0.013020		
2-Methylnaphthalene	$C_{11}H_{10}$						0.0280	0.0360	0.0445	−9.656	0.053	0.022100		
1-Ethylnaphthalene	$C_{12}H_{12}$						0.0271	0.0349	0.0430	−9.589	0.052	0.020140		
2-Ethylnaphthalene	$C_{12}H_{12}$						0.0281	0.0362	0.0447	−9.941	0.054	0.021040		
Alcohols														
Methanol	CH_4O		0.0137	0.0157	0.0227	0.0344	0.0487	0.0656	0.0852	2.362	0.005	0.131510		
Ethanol	C_2H_6O			0.0152	0.0227	0.0348	0.0490	0.0653	0.0839	−2.398	0.024	0.118133	−0.009986	0.003912
1-Propanol	C_3H_8O				0.0216	0.0331	0.0467	0.0623		−3.174	0.028	0.102720		
1-Butanol	$C_4H_{10}O$				0.0225	0.0314	0.0439	0.0599	0.0796	20.932	−0.063	0.178900		
1-Pentanol	$C_5H_{12}O$					0.0273	0.0392	0.0532	0.0692	−2.061	0.014	0.100590		
1-Hexanol	$C_6H_{14}O$					0.0266	0.0382	0.0519	0.0676	−0.248	0.008	0.103440		
1-Heptanol	$C_7H_{16}O$					0.0259	0.0372	0.0504	0.0655	−1.443	0.012	0.096390		
1-Octanol	$C_8H_{18}O$					0.0243	0.0350	0.0477	0.0624	−0.202	0.006	0.097410		
Isopropanol	C_3H_8O				0.0231	0.0348	0.0489	0.0656	0.0848	1.447	0.011	0.124550		
2-Methyl-1-propanol	$C_4H_{10}O$					0.0275	0.0394	0.0531	0.0688	−2.405	0.018	0.096240		
3-Methyl-1-butanol	$C_5H_{12}O$					0.0286	0.0412	0.0559	0.0728	−2.114	0.015	0.106160		
Ethylene glycol	$C_2H_6O_2$					0.0254	0.0357	0.0477	0.0615	−0.375	0.014	0.085000		
1,3-Propylene glycol	$C_3H_8O_2$						0.0401	0.0540	0.0698	−3.521	0.023	0.093530		
Glycerol	$C_3H_8O_3$						0.0313	0.0397	0.0485	−9.158	0.059	0.020260		

D3.1. Table 10. (continued)

Substance	Formula	Temperature (°C)								Equation (5)				
		−50	0	25	100	200	300	400	500	10^3 *A*	10^3 *B*	10^6 *C*	10^9 *D*	10^{12} *E*
Cyclohexanol	$C_6H_{12}O$					0.0283	0.0402	0.0525	0.0653	−21.830	0.095	0.022340		
Benzyl alcohol	C_7H_8O						0.0296	0.0382	0.0468	−18.135	0.082	0.003140		
Phenols														
o-Cresol	C_7H_8O					0.0229	0.0307	0.0388	0.0472	−9.427	0.061	0.016190		
m-Cresol	C_7H_8O						0.0307	0.0388	0.0471	−9.645	0.062	0.015310		
p-Cresol	C_7H_8O						0.0308	0.0389	0.0474	−9.696	0.062	0.015840		
Phenol	C_6H_6O					0.0233	0.0320	0.0407	0.0495	−16.864	0.083	0.003190		
Carboxylic acids														
Formic acid	CH_2O_2					0.0284	0.0372	0.0462	0.0555	−9.344	0.073	0.013480		
Acetic acid	$C_2H_4O_2$			0.0107	0.0160	0.0251	0.0366	0.0504		2.600	−0.008	0.116860		
Propionic acid	$C_3H_6O_2$						0.0418	0.0537		82.837	−0.233	0.282310		
Butyric acid	$C_4H_8O_2$						0.0405	0.0513		118.594	−0.344	0.362900		
Valeric acid	$C_5H_{10}O_2$					0.0251	0.0334	0.0420	0.0509	−9.912	0.066	0.015740		
Caproic acid	$C_6H_{12}O_2$						0.0312	0.0394	0.0479	−9.851	0.063	0.015240		
Acetic anhydride	$C_4H_6O_3$					0.0236	0.0321	0.0407	0.0495	−14.506	0.077	0.007670		
Propionic anhydride	$C_6H_{10}O_3$					0.0191	0.0263	0.0333	0.0402	−16.900	0.080	−0.007700		
Chloroacetic acid	$C_2H_3ClO_2$					0.0192	0.0250	0.0310	0.0370	−7.014	0.053	0.005220		
Dichloroacetic acid	$C_2H_2Cl_2O_2$					0.0151	0.0194	0.0237	0.0280	−5.032	0.042	0.000710		
Trichloroacetic acid	$C_2HCl_3O_2$					0.0135	0.0171	0.0208	0.0244	−4.036	0.038	−0.001120		
Ketones														
Ketene	C_2H_2O		0.0156	0.0180	0.0252	0.0348	0.0442	0.0536	0.0630	−10.895	0.098	−0.003100		
Acetone	C_3H_6O				0.0173	0.0272	0.0392	0.0533	0.0695	−1.474	0.012	0.103580		
Methyl ethyl ketone	C_4H_8O				0.0172	0.0270	0.0392	0.0536	0.0704	0.990	0.000	0.115870		
Diethyl ketone	$C_5H_{10}O$		0.0090	0.0107	0.0168	0.0270	0.0396	0.0547	0.0722	0.018	0.000	0.120990		
Dipropyl ketone	$C_7H_{14}O$					0.0251	0.0371	0.0514	0.0681	0.722	−0.005	0.118740		
Acetophenone	C_8H_8O						0.0273	0.0356	0.0442	−16.048	0.069	0.010920		
Benzophenone	$C_{13}H_{10}O$							0.0278	0.0340	−8.154	0.045	0.011700		
Ethers														
Dimethyl ether	C_2H_6O		0.0138	0.0164	0.0251	0.0384	0.0532	0.0689	0.0851	−0.250	−0.009	0.263410	−0.171130	0.038110
Diethyl ether	$C_4H_{10}O$	0.0092	0.0129	0.0150	0.0222	0.0337	0.0476			−0.513	0.018	0.115680		
Dipropyl ether	$C_6H_{14}O$				0.0184	0.0273	0.0367	0.0465	0.0568	−10.871	0.070	0.022340		
Methyl propyl ether	$C_4H_{10}O$				0.0221	0.0320	0.0424	0.0532	0.0644	−10.912	0.080	0.022060		
Ethyl propyl ether	$C_5H_{12}O$		0.0114	0.0138	0.0208	0.0299				−16.155	0.106	−0.018180		

Ethylene oxide	C_2H_4O		0.0102	0.0121	0.0195	0.0333	0.0514	0.0738	0.1006	6.735	−0.047	0.217600		
Furane	C_4H_4O				0.0208	0.0334	0.0482	0.0654	0.0848	−5.580	0.028	0.115470		
1,4-Dioxane	$C_4H_8O_2$					0.0252	0.0349	0.0466	0.0602	5.404	−0.004	0.097250		
Aldehydes														
Formaldehyde	CH_2O		0.0140	0.0159	0.0222	0.0323	0.0443	0.0581	0.0737	0.887	0.023	0.092560		
Acetaldehyde	C_2H_4O		0.0103	0.0119	0.0174	0.0263	0.0371	0.0496	0.0639	0.076	0.013	0.090020		
Paraldehyde	$C_6H_{12}O_3$					0.0279	0.0389	0.0496	0.0601	−26.540	0.120	−0.010130		
Furfural	$C_5H_4O_2$					0.0246	0.0328	0.0414	0.0503	−9.590	0.064	0.017620		
Benzaldehyde	C_7H_6O					0.0208	0.0285	0.0362	0.0441	−14.819	0.074	0.003070		
Salicylaldehyde	$C_7H_6O_2$					0.0199	0.0275	0.0350	0.0425	−16.830	0.079	−0.003160		
Esters														
Methyl formate	$C_2H_4O_2$				0.0204	0.0316	0.0453	0.0614	0.0799	0.081	0.009	0.122170		
Ethyl formate	$C_3H_6O_2$				0.0183	0.0287	0.0413	0.0561	0.0730	−1.656	0.013	0.107800		
Propyl formate	$C_4H_8O_2$				0.0156	0.0249	0.0363	0.0499	0.0656	−0.466	0.003	0.106020		
Methyl acetate	$C_3H_6O_2$				0.0178	0.0278	0.0401	0.0546	0.0715	0.813	0.003	0.114990		
Ethyl acetate	$C_4H_8O_2$		0.0092	0.0107	0.0159	0.0248	0.0361	0.0496	0.0654	2.735	−0.007	0.114350		
Propyl acetate	$C_5H_{10}O_2$					0.0242	0.0356	0.0491	0.0647	0.005	0.000	0.108330		
Methyl propionate	$C_4H_8O_2$				0.0159	0.0250	0.0363	0.0497	0.0653	0.707	0.001	0.107360		
Ethyl propionate	$C_5H_{10}O_2$				0.0142	0.0217	0.0314	0.0430	0.0567	3.777	−0.010	0.101720		
Propyl propionate	$C_6H_{12}O_2$					0.0246	0.0361	0.0499	0.0660	1.430	−0.006	0.115150		
Methyl butyrate	$C_5H_{10}O_2$					0.0237	0.0347	0.0478	0.0631	−0.099	0.001	0.104930		
Ethyl butyrate	$C_6H_{12}O_2$					0.0228	0.0336	0.0465	0.0614	0.286	−0.002	0.104790		
Methyl benzoate	$C_8H_8O_2$					0.0178	0.0249	0.0321	0.0393	−14.909	0.068	0.003120		
Ethyl benzoate	$C_9H_{10}O_2$						0.0246	0.0317	0.0389	−15.024	0.068	0.002650		
Methyl salicylate	$C_8H_8O_3$						0.0236	0.0298	0.0362	−7.619	0.048	0.011280		
Amines														
Methyl amine	CH_5N		0.0132	0.0158	0.0252	0.0411	0.0611			0.998	−0.010	0.200200		
Ethyl amine	C_2H_7N			0.0169	0.0254	0.0372	0.0494	0.0622	0.0754	−14.418	0.098	0.023590		
Propyl amine	C_3H_9N				0.0225	0.0336	0.0454	0.0576	0.0704	−14.582	0.089	0.026680		
n-Butyl amine	$C_6H_{15}N$		0.0125	0.0145	0.0209	0.0306	0.0413	0.0526	0.0642	−0.321	0.012	0.150360	−0.086020	0.014280
Dimethyl amine	C_2H_7N			0.0204	0.0300	0.0433	0.0573	0.0719	0.0871	−14.266	0.107	0.031230		
Trimethyl amine	C_3H_9N		0.0128	0.0154	0.0239	0.0365	0.0499	0.0634	0.0770	−2.224	−0.008	0.294620	−0.263930	0.086550
Diethyl amine	$C_6H_{15}N$		0.0113	0.0140	0.0222	0.0335	0.0451	0.0571	0.0695	−16.698	0.098	0.017830		
Triethyl amine	$C_6H_{15}N$		0.0102	0.0124	0.0198	0.0310	0.0431	0.0555	0.0681	−0.268	−0.025	0.295400	−0.257610	0.084340
Piperidine	$C_5H_{11}N$					0.0319	0.0444	0.0569	0.0691	−29.974	0.135	−0.008300		
Pyridine	C_6H_7N					0.0240	0.0354	0.0487	0.0639	−3.523	0.012	0.096720		
Aniline	C_6H_7N					0.0246	0.0328	0.0414	0.0503	−9.960	0.065	0.016230		

D3.1. Table 10. (continued)

Substance	Formula	Temperature (°C)								Equation (5)				
		−50	0	25	100	200	300	400	500	10^3 *A*	10^3 *B*	10^6 *C*	10^9 *D*	10^{12} *E*
N-methyl aniline	C_7H_9N					0.0242	0.0334	0.0427	0.0521	−18.314	0.088	0.003880		
N,*N*-dimethyl aniline	$C_8H_{11}N$					0.0210	0.0298	0.0387	0.0477	−18.759	0.081	0.006300		
N,*N*-diethyl aniline	$C_{10}H_{15}N$						0.0288	0.0369	0.0453	−9.478	0.055	0.020120		
Phenylhydrazine	$C_6H_8N_2$						0.0290	0.0368	0.0448	−9.778	0.059	0.014480		
Diphenyl amine	$C_{12}H_{11}N$							0.0325	0.0397	−9.441	0.054	0.012730		
Nitriles														
Acetonitrile	C_2H_3N				0.0141	0.0218	0.0320	0.0447	0.0600	7.632	−0.030	0.125860		
Propionitrile	C_3H_5N		0.0076	0.0090	0.0140	0.0226	0.0336	0.0472	0.0640	0.189	0.001	0.100180	−0.018130	0.033270
Butyronitrile	C_4H_7N		0.0070	0.0092	0.0159	0.0251	0.0344	0.0439	0.0536	−16.453	0.083	0.009510		
Benzonitrile	C_7H_5N					0.0224	0.0302	0.0383	0.0467	−9.406	0.059	0.017860		
Amides														
Formamide	CH_3NO						0.0367	0.0462	0.0562	−11.800	0.075	0.016570		
Nitroderivates														
Nitromethane	CH_3NO_2					0.0216	0.0297	0.0380	0.0464	−15.934	0.077	0.004770		
Nitrobenzene	$C_6H_5NO_2$						0.0287	0.0364	0.0446	−9.275	0.056	0.017100		
o-Nitrotoluene	$C_7H_7NO_2$						0.0263	0.0334	0.0408	−8.654	0.052	0.015100		
m-Nitrotoluene	$C_7H_7NO_2$						0.0260	0.0331	0.0404	−8.730	0.052	0.014750		
p-Nitrotoluene	$C_7H_7NO_2$						0.0259	0.0329	0.0402	−8.747	0.052	0.014500		

D3.1. Table 11. Surface tensions in mN/m

Substance	Formula	Temperature (°C)								Equation (6)				
		−50	−25	0	20	50	100	150	200	*A*	*B*	*C*	*D*	*E*
Elements														
Xenon	Xe	8.2	4.5	1.4						0.05435	1.28359			
Krypton	Kr									0.04405	1.22807			
Argon	Ar									0.03813	1.29069			
Air										0.02919	1.15656	0.06889	0.17918	−0.14564
Nitrogen	N_2									0.02921	1.25537			
Oxygen	O_2									0.03797	1.21036			
Sulfur	S							58.3	55.0	0.08603	1.00082			
Fluorine	F_2									0.04004	1.22411			
Chlorine	Cl_2	29.4	25.3	21.3	18.1	13.4	5.9			0.06760	1.08562			
Bromine	Br_2			45.2	41.8	36.8	28.8	21.0	13.6	0.09404	1.16321			
Iodine	I_2							44.3		0.23475	2.29332			
Anorganic compounds														
Hydrogen fluoride	HF	14.3	12.3	10.3	8.8	6.6	3.5	1.1		0.03648	1.41220			
Hydrogen chloride	HCl	18.9	13.1	7.8	4.1					0.08517	1.29670			
Hydrogen bromide	HBr	23.5	18.5	13.7	10.1	5.1				0.07541	1.22318			
Hydrogen iodide	HI	28.6	24.7	21.0	18.0	13.6	6.5			0.06376	1.07475			
Hydrogen cyanide	HCN			20.6	18.3	14.9	9.2	3.6		0.05231	1.02047			
Water	H_2O			77.8	73.8	67.9	58.2	48.3	37.7	0.15488	1.64129	−0.75986	−0.85291	1.14113
Hydrogen sulfide	H_2S	22.8	18.0	13.5	10.1	5.5				0.07436	1.30090			
Ammonia	NH_3	38.5	32.2	26.1	21.4	14.6	4.7			0.10175	1.21703			
Nitric oxide	NO									0.12062	1.54592			
Nitrogen dioxide	NO_2			31.1	27.3	21.6	11.9			0.08109	0.95509			
Nitrous oxide	N_2O	15.3	10.1	5.4	2.1					0.07134	1.20607			
Dinitrogentetroxide	N_2O_4			49.4	41.9	31.1	14.5	1.3		0.16856	1.22183			
Cyanogen	C_2N_2		22.9	18.5	15.0	10.1	2.9			0.07339	1.20282			
Phosphorus trichloride	PCl_3	38.3	34.9	31.5	28.9	25.0	18.8	12.9	7.5	0.07098	1.22441			
Cyanogen chloride	ClCN			26.1	22.6	17.5	9.6	2.7		0.07941	1.18902			
Silane	SiH_4	5.1	2.0							0.04274	1.21421			
Tetrachlorosilane	$SiCl_4$	26.6	24.0	21.3	19.3	16.2	11.3	6.6	2.4	0.05154	1.14006			
Carbon monoxide	CO									0.02792	1.13266			
Carbon dioxide	CO_2	15.2	9.5	4.5	1.2					0.08167	1.27339			
Carbon suboxide	C_3O_2	40.9	34.9	29.1	24.6	18.1	8.2	0.4		0.10041	1.21621			

D3.1. Table 11. (continued)

Substance	Formula	Temperature (°C)								Equation (6)				
		−50	−25	0	20	50	100	150	200	*A*	*B*	*C*	*D*	*E*
Carbonyl sulfide	COS	20.6	16.0	11.7	8.6	4.6				0.07598	1.46595			
Phosgene	CCl_2O	29.8	26.1	22.5	19.7	15.5	8.9	3.0		0.06520	1.16027			
Carbon disulfide	CS_2	43.5	39.5	35.5	32.4	27.8	20.6	13.7	7.5	0.08219	1.22945			
Sulfur dioxide	SO_2	36.8	31.7	26.6	22.7	16.9	8.1			0.08730	1.18191			
Sulfur trioxide	SO_3				34.1	27.9	18.1	9.2	1.8	0.10346	1.21917			
Sulfuryl chloride	Cl_2SO_2	46.0	41.5	37.1	33.6	28.6	20.6	13.3	6.8	0.09002	1.27637			
Sulfur hexafluoride	SF_6	11.6	8.6							0.03785	0.98021			
Organic compounds containing sulfur														
Methyl mercaptan	CH_4S	37.2	32.6	28.2	24.7	19.7	11.8	4.8		0.08186	1.22601			
Ethyl mercaptan	C_2H_6S	32.0	28.9	25.8	23.4	19.8	13.9	8.1	2.6	0.06002	1.06332			
Dimethyl sulfide	C_2H_6S	34.6	31.1	27.6	24.8	20.8	14.3	8.2	2.6	0.06790	1.15009			
Diethyl sulfide	$C_4H_{10}S$	33.6	30.5	27.6	25.2	21.8	16.3	11.1	6.3	0.06254	1.21632			
Thiophene	C_4H_4S		39.0	35.1	32.1	27.7	20.7	14.3	8.5	0.08229	1.33643			
Halogenated hydrocarbons														
Fluoromethane (R41)	CH_3F	14.2	9.6	5.5	2.5					0.06598	1.26598			
Difluoromethane (R32)	CH_2F_2	21.0	15.9	11.1	7.6	3.0				0.07647	1.28512			
Trifluoromethane (R23)	CHF_3	10.8	6.6	2.9						0.05858	1.23456			
Tetrafluoromethane (R14)	CF_4	0.4								0.05626	1.23364			
Methyl chloride	CH_3Cl	28.5	23.8	19.4	16.0	11.2	4.2			0.07623	1.28255			
Methylene chloride	CH_2Cl_2	40.2	35.8	31.4	28.1	23.2	15.5	8.6	2.9	0.08432	1.28714			
Chloroform	$CHCl_3$	36.8	33.4	30.0	27.3	23.4	17.1	11.1	5.6	0.06931	1.17639			
Carbon tetrachloride	CCl_4			29.4	26.9	23.2	17.3	11.8	6.7	0.06666	1.21285			
Bromomethane	CH_3Br	34.4	29.9	25.5	22.1	17.3	9.9	3.7		0.08027	1.30463			
Dibromomethane	CH_2Br_2	53.1	48.7	44.4	41.0	36.0	28.0	20.6	13.8	0.09615	1.30603			
Tribromomethane	$CHBr_3$				45.5	41.6	35.1	28.8	22.7	0.08674	1.17862			
Tetrabromomethane	CBr_4						62.6	51.9	41.6	0.15153	1.22270			
Chlorodifluoromethane (R22)	$CHClF_2$	19.8	15.7	11.8	8.8	4.7				0.06238	1.23996			
Dichlorofluoromethane (R21)	$CHCl_2F$	29.5	25.5	21.6	18.6	14.3	7.7			0.06925	1.25278			
Chlorotrifluoromethane (R13)	$CClF_3$	10.1	6.3	2.9						0.05415	1.25006			
Dichlorodifluoromethane (R12)	CCl_2F_2		15.5	12.0	9.3	5.6	0.7			0.05898	1.28862			
Trichlorofluoromethane (R11)	CCl_3F	28.4	24.8	21.3	18.6	14.7	8.7	3.5		0.06409	1.27077			
Ethyl fluoride (R161)	C_2H_5F	19.7	16.2	12.6	9.9	6.0				0.05419	1.11840			

Ethyl chloride	C_2H_5Cl	29.1	25.3	21.7	18.9	14.8	8.5	3.0		0.06597	1.23494			
Ethyl bromide	C_2H_5Br	35.2	31.1	27.2	24.1	19.7	12.9	6.8	1.9	0.07599	1.31627			
1,1-Dichloroethane	$C_2H_4Cl_2$	35.5	31.9	28.3	25.5	21.4	15.0	9.0	3.8	0.07110	1.24746			
1,2-Dichloroethane	$C_2H_4Cl_2$		39.1	35.3	32.3	27.8	20.8	14.2	8.1	0.08099	1.24885	0.00096	−0.01186	0.00695
1,2-Dibromoethane	$C_2H_4Br_2$				38.8	34.9	28.4	22.3	16.4	0.08093	1.22574			
1,1,1-Trifluoroethane (R143a)	$C_2H_3F_3$	15.9	12.3	8.9	6.2	2.5				0.05023	1.11401			
1,1,1-Trichloroethane	$C_2H_3Cl_3$		31.4	28.2	25.7	22.0	16.1	10.6	5.6	0.06587	1.22121			
1,1,2,2-Tetrachloroethane	$C_2H_2Cl_4$		41.9	38.6	36.1	32.3	26.2	20.4	14.9	0.07626	1.23498			
Pentachloroethane	C_2HCl_5		40	37.1	34.8	31.4	25.9	20.5	15.3	0.07017	1.15768			
Hexachloroethane	C_2Cl_6								31.9	0.14133	1.30430			
1,1,2,2-Tetrachlorodifluoroethane	$C_2Cl_4F_2$					20.5	14.9	9.7	5.1	0.06418	1.29363			
1,1,2-Trichlorotrifluoroethan	$C_2Cl_3F_3$		22.9	20	17.7	14.4	9.2	4.5	0.7	0.05521	1.23559			
1,2-Dichlorotetrafluoroethane	$C_2Cl_2F_4$	20.1	16.9	13.9	11.5	8.2	3.3			0.05178	1.24664			
1-Chloropropane	C_3H_7Cl	31.7	28.1	24.6	21.9	18	11.9	6.4	1.8	0.06684	1.27458			
1-Chlorobutane	C_4H_9Cl	31.8	28.8	26	23.7	20.4	15	9.8	4.9	0.06373	1.36371	0.17790	−1.11469	0.86417
1-Chloropentane	$C_5H_{11}Cl$	33.4	30.5	27.7	25.5	22.2	16.9	11.9		0.06031	1.18716			
Chlorotrifluoroethene	C_2ClF_3	25.9	20.6	15.6	11.8	6.7				0.08373	1.31939			
Vinyl chloride	C_2H_3Cl	27.9	23.7	19.7	16.6	12.2	5.6			0.07032	1.27270			
1,1-Dichloroethene	$C_2H_2Cl_2$	36.4	32.2	28.1	24.9	20.2	12.8	6.1		0.07702	1.20663			
Trichloroethene	C_2HCl_3	39.7	36	32.5	29.7	25.7	19.2	13.2	7.8	0.07498	1.28458			
Tetrachloroethene	C_2Cl_4			34.7	32.2	28.6	22.8	17.3	12.1	0.07067	1.22671			
Fluorobenzene	C_6H_5F		33.7	30.2	27.5	23.5	17.3	11.5	6.4	0.07216	1.30234			
Chlorobenzene	C_6H_5Cl		39.1	36	33.5	29.9	24	18.4	13.1	0.07269	1.24185			
Bromobenzene	C_6H_5Br		41.9	38.9	36.5	33	27.2	21.7	16.4	0.07406	1.23020			
Iodobenzene	C_6H_5I		44.7	41.8	39.5	36	30.4	25	19.9	0.07595	1.25538			
m-Chlorotoluene	C_7H_7Cl		38.8	35.8	33.4	30	24.6	19.5	14.6	0.07978	1.77729	−0.55705	−0.51952	0.63993
Benzyl chloride	C_7H_7Cl		43.4	40.1	37.5	33.7	27.7	21.9	16.5	0.07908	1.33849			
***n*-Alkanes**														
Methane	CH_4									0.03640	1.14306			
Ethane	C_2H_6	10.1	6.5	3.3	1.0					0.04863	1.19828			
Propane	C_3H_8	16.5	13.1	9.9	7.5	4.1				0.05094	1.22051			
n-Butane	C_4H_{10}	21.0	17.9	14.8	12.5	9.1	4.0			0.05203	1.21961			
n-Pentane	C_5H_{12}	23.9	21.0	18.2	16.0	12.8	7.7	3.2		0.05202	1.20435			
n-Hexane	C_6H_{14}	26.4	23.5	20.7	18.5	15.2	10.2	5.7		0.05500	1.26769			
n-Heptane	C_7H_{16}	27.8	25.1	22.4	20.3	17.3	12.5	8.0	4.0	0.05422	1.25287			
n-Octane	C_8H_{18}	28.6	26.0	23.6	21.6	18.8	14.2	9.8	5.9	0.05277	1.23210			

D3.1. Table 11. (continued)

Substance	Formula	Temperature (°C)								Equation (6)				
		−50	−25	0	20	50	100	150	200	*A*	*B*	*C*	*D*	*E*
n-Nonane	C_9H_{20}	30.0	27.4	24.9	22.9	20.0	15.4	11.1	7.1	0.05496	1.28917			
n-Decane	$C_{10}H_{22}$		28.3	25.8	23.9	21.0	16.5	12.2	8.3	0.05540	1.30900			
n-Undecane	$C_{11}H_{24}$		29.0	26.6	24.7	21.9	17.5	13.3	9.4	0.05555	1.32037			
n-Dodecane	$C_{12}H_{26}$			27.2	25.4	22.7	18.3	14.2	10.3	0.05549	1.32644			
n-Tridecane	$C_{13}H_{28}$			27.8	26.0	23.3	19.0	15.0	11.2	0.05539	1.32719			
n-Tetradecane	$C_{14}H_{30}$				26.6	23.9	19.6	15.6	11.8	0.05634	1.36445			
n-Pentadecane	$C_{15}H_{32}$				27.2	24.5	20.2	16.2	12.5	0.05644	1.36901			
n-Hexadecane	$C_{16}H_{34}$				27.6	24.9	20.7	16.6	12.9	0.05742	1.40834			
n-Heptadecane	$C_{17}H_{36}$					25.3	21.1	17.2	13.4	0.05701	1.40336			
n-Octadecane	$C_{18}H_{38}$					25.8	21.6	17.6	13.9	0.05782	1.42315			
n-Nonadecane	$C_{19}H_{40}$					26.1	21.9	17.9	14.2	0.05806	1.44010			
n-Eicosane	$C_{20}H_{42}$					26.5	22.3	18.3	14.5	0.05887	1.46686			
Isoalkanes														
Isobutane	C_4H_{10}	19.0	15.9	12.8	10.5	7.2	2.3			0.05132	1.25196			
2-Methyl butane	C_5H_{12}	22.9	20.0	17.2	15.0	11.8	6.8	2.4		0.05095	1.20843			
2,2-Dimethyl propane	C_5H_{12}			13.4	11.4	8.4	4.0	0.4		0.04660	1.25255			
2-Methyl pentane	C_6H_{14}	24.7	22.0	19.4	17.4	14.4	9.6	5.2	1.4	0.05005	1.18920			
3-Methyl pentane	C_6H_{14}	25.8	23.0	20.3	18.1	15.0	10.0	5.5	1.7	0.05324	1.24020			
2,2-Dimethyl butane	C_6H_{14}	23.3	20.7	18.2	16.3	13.4	8.8	4.6		0.04744	1.16905			
2,3-Dimethyl butane	C_6H_{14}	24.7	22.0	19.4	17.4	14.4	9.7	5.3	1.5	0.05015	1.20133			
Olefins														
Ethylene	C_2H_4	7.2	3.6							0.05296	1.27846			
Propylene	C_3H_6	17.1	13.6	10.2	7.6	4.0				0.05312	1.19763			
1-Butene	C_4H_8	22.0	18.6	15.3	12.7	9.1	3.7			0.05607	1.23722			
1-Pentene	C_5H_{10}	23.8	21.0	18.2	16.0	12.8	7.7	3.1		0.05072	1.15769			
1-Hexene	C_6H_{12}	25.9	23.2	20.5	18.4	15.3	10.4	5.9	1.9	0.05216	1.19509			
1-Heptene	C_7H_{14}	28.3	25.4	22.6	20.4	17.2	12.2	7.6	3.6	0.05697	1.33692	−0.12198	0.13265	−0.05353
1-Octene	C_8H_{16}	28.9	26.3	23.8	21.8	18.9	14.2	9.8	5.7	0.05394	1.24599			
Propadiene	C_3H_4	19.8	16.2	12.7	10.0	6.4	1.3			0.05813	1.28260			
1,2-Butadiene	C_4H_6	25.4	21.8	18.3	15.6	11.8	6.1	1.6		0.06322	1.33841			
1,3-Butadiene	C_4H_6	22.2	18.8	15.6	13.1	9.5	4.1			0.05629	1.24878			
1,2-Pentadiene	C_5H_8	27.8	24.6	21.5	19.1	15.6	10.2	5.3	1.4	0.05944	1.28818			
trans-1,3-Pentadiene	C_5H_8	25.4	22.4	19.5	17.3	14.1	9.1	4.7		0.05506	1.31227			

1,4-Pentadiene	C_5H_8	26.9	22.9	19.1	16.2	12.3	6.6	2.4		0.07299	1.58928			
2,3-Pentadiene	C_5H_8	27.5	24.3	21.2	18.9	15.4	10.0	5.2	1.2	0.05870	1.27433			
Acetylene and derivatives														
Acetylene	C_2H_2	13.2	8.9	4.8	1.9					0.05698	1.13545			
Propyne	C_3H_4	24.9	21.0	17.2	14.2	9.8	3.2			0.06252	1.13872			
2-Butyne	C_4H_6		28.8	24.9	21.8	17.4	10.5	4.4		0.07283	1.24690			
1-Butyne	C_4H_6	26.0	22.7	19.4	16.8	13.0	7.0	1.5		0.05729	1.11793			
Naphthenes														
Cyclopropane	C_3H_6	23.5	19.4	15.4	12.4	8.1	2.0			0.06588	1.25086			
Cyclobutane	C_4H_8	31.3	27.2	23.3	20.2	15.7	8.9	3.0		0.07176	1.25065			
Cyclopentane	C_5H_{10}	33.2	29.3	25.4	22.5	18.3	11.9	6.3		0.07418	1.40256			
Methyl cyclopentane	C_6H_{12}	30.8	27.7	24.6	22.2	18.8	13.3	8.2	3.8	0.06138	1.27048			
Ethyl cyclopentane	C_7H_{14}	31.3	28.6	25.9	23.8	20.8	15.8	11.1	6.7	0.05675	1.19902			
Propyl cyclopentane	C_8H_{16}	32.0	29.4	26.9	24.9	22.0	17.2	12.7	8.4	0.05638	1.20639			
Butyl cyclopentane	C_9H_{18}	32.8	30.3	27.8	25.9	23.0	18.3	13.9	9.7	0.05690	1.23479			
Pentyl cyclopentane	$C_{10}H_{20}$			29.9	27.0	23.0	16.9	11.7		0.08233	1.88316			
Hexyl cyclopentane	$C_{11}H_{22}$			30.4	27.6	23.6	17.6	12.4		0.08116	1.83729			
Cyclohexane	C_6H_{12}			27.7	25.3	21.6	15.9	10.5	5.7	0.06560	1.26601			
Methyl cyclohexane	C_7H_{14}	32.3	29.2	26.2	23.9	20.5	15.1	10.2	5.9	0.06306	1.35225			
Ethyl cyclohexane	C_8H_{16}	33.2	30.4	27.7	25.6	22.5	17.5	12.8	8.5	0.06008	1.30159			
Propyl cyclohexane	C_9H_{18}	33.2	30.8	28.4	26.5	23.8	19.3	15.0	10.9	0.05586	1.21290			
Butyl cyclohexane	$C_{10}H_{20}$	34.0	31.5	29.0	27.0	24.1	19.5	15.2	11.1	0.05898	1.35018			
Pentyl cyclohexane	$C_{11}H_{22}$			30.4	27.6	23.6	17.5	12.4		0.08212	1.88661			
Hexyl cyclohexane	$C_{12}H_{24}$			29.8	28.0	25.3	21.0	16.8	12.9	0.05687	1.29305			
Cyclopentene	C_5H_8	32.6	29.0	25.5	22.8	18.8	12.6	7.0	2.2	0.06801	1.26679			
Cyclohexene	C_6H_{10}	35.7	32.4	29.2	26.6	22.9	17.0	11.5	6.5	0.06763	1.25801			
Aromatic compounds														
Benzene	C_6H_6				28.9	24.9	18.7	12.8	7.3	0.07178	1.23593			
Toluene	C_7H_8	37.1	34.0	30.9	28.5	25.0	19.3	14.0	9.0	0.06676	1.24386			
Ethyl benzene	C_8H_{10}	37.3	34.3	31.4	29.1	25.8	20.4	15.2	10.5	0.06576	1.26285			
Propyl benzene	C_9H_{12}	36.7	33.9	31.2	29.0	25.9	20.8	15.9	11.4	0.06332	1.26870			
Butyl benzene	$C_{10}H_{14}$	36.8	34.0	31.3	29.2	26.0	21.0	16.3	11.9	0.06364	1.32979			
Pentyl benzene	$C_{11}H_{16}$	36.5	34.0	31.5	29.6	26.7	22.1	17.6	13.4	0.06026	1.26163			
Hexyl benzene	$C_{12}H_{18}$	37.2	34.7	32.3	30.4	27.5	22.9	18.5	14.3	0.06098	1.28086			
o-Xylene	C_8H_{10}		35.2	32.3	30.1	26.8	21.5	16.4	11.7	0.06547	1.24184			
m-Xylene	C_8H_{10}		34.0	31.1	28.8	25.5	20.1	15.0	10.3	0.06539	1.27146			

D3.1. Table 11. (continued)

Substance	Formula	Temperature (°C)								Equation (6)				
		−50	−25	0	20	50	100	150	200	*A*	*B*	*C*	*D*	*E*
p-Xylene	C_8H_{10}				28.5	25.1	19.8	14.8	10.1	0.06456	1.26881			
1,2,3-Trimethyl benzene	C_9H_{12}		36.1	33.4	31.3	28.1	23.1	18.2	13.6	0.06489	1.25491			
1,2,4-Trimethyl benzene	C_9H_{12}		34.5	31.8	29.7	26.6	21.6	16.8	12.3	0.06319	1.25600			
1,3,5-Trimethyl benzene	C_9H_{12}		32.9	30.4	28.5	25.5	20.8	16.2	11.8	0.05903	1.18447			
1,2,3,4-Tetramethyl benzene	$C_{10}H_{14}$			38.8	36.5	33.1	27.6	22.4	17.3	0.07244	1.24623			
1,2,3,5-Tetramethyl benzene	$C_{10}H_{14}$			36.2	34.0	30.8	25.5	20.5	15.7	0.06826	1.23312			
1,2,4,5-Tetramethyl benzene	$C_{10}H_{14}$						22.9	18.5	14.3	0.05884	1.17748			
Pentamethyl benzene	$C_{11}H_{16}$						29.8	24.4	19.2	0.07615	1.28379			
Hexamethyl benzene	$C_{12}H_{18}$								23.5	0.07106	1.12978			
Styrene	C_8H_8		38.5	35.1	32.5	28.8	23.0	17.5	12.2	0.09046	2.08018	−0.54300	−1.54530	1.58212
Isopropyl benzene	C_9H_{12}	36.1	33.2	30.4	28.2	25.0	19.9	15.0	10.5	0.06364	1.30197			
Biphenyl	$C_{12}H_{10}$						32.2	27.2	22.5	0.09827	2.35540	−1.14035	−0.87565	1.17200
Diphenyl methane	$C_{13}H_{12}$					35.7	30.7	25.9	21.2	0.07086	1.23688			
Triphenyl methane	$C_{19}H_{16}$						34.4	30.0	25.6	0.07159	1.29713			
Tetraphenyl methane	$C_{25}H_{20}$									0.15512	1.30899			
Naphthalene	$C_{10}H_8$						31.8	26.1	20.7	0.08245	1.37955			
1-Methylnaphthalene	$C_{11}H_{10}$		45.7	42.9	40.7	37.4	32.1	27.0	22.1	0.07538	1.29250			
2-Methylnaphthalene	$C_{11}H_{10}$					35.1	30.1	25.3	20.7	0.07043	1.25945			
1-Ethylnaphthalene	$C_{12}H_{12}$			40.5	38.4	35.4	30.4	25.6	21.0	0.07116	1.29758			
2-Ethylnaphthalene	$C_{12}H_{12}$			39.1	37.0	34.0	29.1	24.4	19.9	0.06961	1.31923			
Alcohols														
Methanol	CH_4O			24.2	22.6	20.1	15.6	10.4		0.04372	0.86460	−0.07327	−0.51872	0.66269
Ethanol	C_2H_6O			24.1	22.5	19.9	15.3	10.2	4.5	0.06165	2.37635	−3.15086	1.98424	−0.15806
1-Propanol	C_3H_8O				23.8	21.4				0.04419	0.78485			
1-Butanol	$C_4H_{10}O$			26.4	24.8	22.3	18.0			0.04839	0.91063			
1-Pentanol	$C_5H_{12}O$				25.7	23.1	18.8			0.05084	0.98216			
1-Hexanol	$C_6H_{14}O$		30.1	28.0	26.3	23.8	19.6	15.5	11.3	0.05089	1.01000			
1-Heptanol	$C_7H_{16}O$		31.1	28.9	27.2	24.5	20.2	16.0	11.8	0.05380	1.09810			
1-Octanol	$C_8H_{18}O$			29.1	27.5	25.1	21.1	17.2	13.3	0.05146	1.04985			
Isopropanol	C_3H_8O			22.9	21.4	19.0				0.04172	0.77686			
2-Methyl-1-propanol	$C_4H_{10}O$				22.9	20.6	16.5			0.04451	0.86556			
3-Methyl-1-butanol	$C_5H_{12}O$	30.4	28.2	26.0	24.3	21.7	17.3	13.0	8.7	0.05018	1.02349			
Ethylene glycol	$C_2H_6O_2$			50.0	48.4	45.8	41.4	36.9		0.07130	0.74162			

1,3-Propylene glycol	$C_3H_8O_2$				46.0	43.2	38.5			0.07242	0.87291			
Glycerol	$C_3H_8O_3$				64.1	61.3	56.6	51.7		0.09019	0.80707			
Cyclohexanol	$C_6H_{12}O$					30.8	25.5	20.4	15.4	0.06671	1.12611			
Benzyl alcohol	C_7H_8O			42.0	39.8	36.5	31.2	25.9	20.9	0.07347	1.17511			
Phenols														
o-Cresol	C_7H_8O					34.9	29.6	24.5	19.4	0.07124	1.14543			
m-Cresol	C_7H_8O				37.0	34.1	29.2	24.5	19.8	0.06621	1.08611			
p-Cresol	C_7H_8O					33.9	29.4	24.9	20.4	0.06352	1.02226			
Phenol	C_6H_6O					37.9	32.5	27.1	21.7	0.07444	1.07602			
Carboxylic acids														
Formic acid	CH_2O_2				37.7	34.4	28.9			0.06684	0.83158			
Acetic acid	$C_2H_4O_2$				27.5	24.6	19.7	14.9	10.2	0.05749	1.07671			
Propionic acid	$C_3H_6O_2$			28.7	26.7	23.7	18.8	14.1	9.6	0.05827	1.16546			
Butyric acid	$C_4H_8O_2$			28.6	26.6	23.8	19.1	14.6	10.3	0.05651	1.16381			
Valeric acid	$C_5H_{10}O_2$		29.5	27.2	25.5	22.9	18.6	14.5	10.6	0.05273	1.17141			
Caproic acid	$C_6H_{12}O_2$			29.6	27.9	25.4	21.2	17.1	13.1	0.05396	1.12272			
Acetic anhydride	$C_4H_6O_3$	43.7	39.7	35.7	32.7	28.3	21.4	15.2	9.6	0.08435	1.43282			
Propionic anhydride	$C_6H_{10}O_3$		35.9	32.8	30.4	26.9	21.3	16.0	11.0	0.06895	1.28546			
Chloroacetic acid	$C_2H_3ClO_2$						31.8	25.8	20.1	0.08078	1.18886			
Dichloroacetic acid	$C_2H_2Cl_2O_2$				35.7	32.9	28.3	23.7	19.1	0.06283	1.01553			
Trichloroacetic acid	$C_2HCl_3O_2$					31.0	26.5	22.0	17.6	0.06108	1.07076			
Ketones														
Ketene	C_2H_2O	16.4	12.9	9.6	7.1	3.8				0.05360	1.28253			
Acetone	C_3H_6O	32.5	29.3	26.1	23.7	20.0	14.0	8.3	3.1	0.06223	1.12463			
Methyl ethyl ketone	C_4H_8O	32.6	29.7	26.8	24.5	21.2	15.7	10.4	5.4	0.05945	1.11696			
Diethyl ketone	$C_5H_{10}O$		30.3	27.5	25.3	22.0	16.7	11.6	6.9	0.06000	1.17040			
Dipropyl ketone	$C_7H_{14}O$		30.6	28.0	25.9	22.8	17.9	13.2	8.8	0.05888	1.23032			
Acetophenone	C_8H_8O				39.5	36.1	30.6	25.2	20.0	0.07479	1.19785			
Benzophenone	$C_{13}H_{10}O$					40.9	35.7	30.8	26.0	0.07725	1.29069			
Ethers														
Dimethyl ether	C_2H_6O	22.4	18.6	14.9	12.0	8.0	2.2			0.06105	1.23032			
Diethyl ether	$C_4H_{10}O$	25.9	22.7	19.5	17.0	13.5	7.9	3.1		0.05804	1.23997			
Dipropyl ether	$C_6H_{14}O$	28.2	25.4	22.7	20.5	17.4	12.4	7.8	3.6	0.05497	1.22576			
Methyl propyl ether	$C_4H_{10}O$	27.7	24.1	20.7	18.1	14.3	8.5	3.6		0.06336	1.31065			
Ethyl propyl ether	$C_5H_{12}O$	27.4	24.6	21.9	19.8	16.6	11.5	6.6	2.1	0.05275	1.11029			
Ethylene oxide	C_2H_4O	35.8	31.7	27.6	24.4	19.7	12.2	5.3		0.07469	1.14048			

D3.1. Table 11. (continued)

Substance	Formula	Temperature (°C)								Equation (6)				
		−50	−25	0	20	50	100	150	200	*A*	*B*	*C*	*D*	*E*
Furane	C_4H_4O	33.9	30.3	26.8	24.1	20.0	13.4	7.2	1.5	0.06708	1.12451			
1,4-Dioxane	$C_4H_8O_2$				33.7	29.3	22.3	15.8	9.9	0.08221	1.29052			
Aldehydes														
Formaldehyde	CH_2O	54.6	45.0	35.9	29.0	19.4	6.0			0.15579	1.32552			
Acetaldehyde	C_2H_4O	32.7	28.6	24.6	21.5	17.0	10.0	3.9		0.07272	1.22767			
Paraldehyde	$C_6H_{12}O_3$				26.2	22.8	17.4	12.3	7.6	0.06289	1.24144			
Furfural	$C_5H_4O_2$		49.6	46.3	43.6	39.6	33.1	26.8	20.6	0.08451	1.15138			
Benzaldehyde	C_7H_6O	47.7	44.6	41.6	39.2	35.7	29.9	24.4	19.0	0.07643	1.21837			
Salicylaldehyde	$C_7H_6O_2$				42.8	39.0	33.0	27.0	21.2	0.08057	1.12359			
Esters														
Methyl formate	$C_2H_4O_2$	37.1	32.7	28.4	25.1	20.2	12.7	6.1		0.08104	1.27510			
Ethyl formate	$C_3H_6O_2$	32.3	29.2	26.1	23.7	20.1	14.2	8.6	3.2	0.06099	1.10043			
Propyl formate	$C_4H_8O_2$	32.5	29.6	26.8	24.5	21.2	15.7	10.5	5.5	0.05942	1.12521			
Methyl acetate	$C_3H_6O_2$	33.8	30.7	27.6	25.1	21.5	15.4	9.4	3.6	0.06212	1.04624			
Ethyl acetate	$C_4H_8O_2$	32.1	29.1	26.1	23.8	20.4	14.8	9.4	4.3	0.05977	1.11993			
Propyl acetate	$C_5H_{10}O_2$	32.9	29.8	26.8	24.4	21.0	15.5	10.3	5.5	0.06223	1.22645			
Methyl propionate	$C_4H_8O_2$	34.1	30.8	27.5	25.0	21.2	15.3	9.6	4.5	0.06560	1.20059			
Ethyl propionate	$C_5H_{10}O_2$	32.9	29.8	26.7	24.3	20.8	15.2	10.0	5.2	0.06295	1.23411			
Propyl propionate	$C_6H_{12}O_2$	32.5	29.7	26.9	24.7	21.5	16.4	11.5	6.9	0.05922	1.20436			
Methyl butyrate	$C_5H_{10}O_2$	33.7	30.6	27.5	25.1	21.7	16.1	10.8	6.0	0.06334	1.22797			
Ethyl butyrate	$C_6H_{12}O_2$	32.1	29.3	26.6	24.5	21.3	16.3	11.5	7.0	0.05815	1.20103			
Methyl benzoate	$C_8H_8O_2$			40.3	37.9	34.3	28.5	22.9	17.6	0.07654	1.27952			
Ethyl benzoate	$C_9H_{10}O_2$		40.0	37.3	35.2	32.1	27.0	22.1	17.4	0.06785	1.20294			
Methyl salicylate	$C_8H_8O_3$			43.1	40.7	37.0	31.1	25.4	20.0	0.07943	1.25423			
Amines														
Methyl amine	CH_5N	34.2	29.1	24.1	20.3	14.9	6.8			0.08559	1.25562			

Ethyl amine	C_2H_7N	31.5	27.2	23.1	19.9	15.4	8.4	2.6		0.07421	1.27662			
Propyl amine	C_3H_9N	31.7	28.2	24.8	22.0	18.1	11.9	6.3	1.6	0.06625	1.23432			
n-Butyl amine	$C_6H_{15}N$		29.7	26.6	24.2	20.7	15.0	9.6	4.6	0.06231	1.17982			
Dimethyl amine	C_2H_7N	26.8	23.3	19.9	17.1	13.2	6.9	1.2		0.06007	1.12956			
Trimethyl amine	C_3H_9N	23.0	19.6	16.4	13.9	10.3	4.8			0.05664	1.24654			
Diethyl amine	$C_6H_{15}N$		25.3	22.5	20.3	17.0	11.7	6.6	1.9	0.05398	1.09669			
Triethyl amine	$C_6H_{15}N$	28.2	25.5	22.8	20.8	17.7	12.8	8.2	4.0	0.05414	1.20778			
Piperidine	$C_5H_{11}N$			31.9	29.5	26.0	20.3	14.9	9.8	0.06712	1.20830			
Pyridine	C_6H_7N		43.7	40.2	37.4	33.3	26.6	20.2	14.1	0.08141	1.21501			
Aniline	C_6H_7N			45.3	43.0	39.5	33.9	28.3	22.8	0.07730	1.08060			
N-methyl aniline	C_7H_9N	47.7	44.9	42.0	39.8	36.5	31.0	25.7	20.5	0.07391	1.14353			
N,N-dimethyl aniline	$C_8H_{11}N$				36.4	33.1	27.7	22.5	17.5	0.07084	1.19971			
N,N-diethyl aniline	$C_{10}H_{15}N$		39.0	36.4	34.3	31.2	26.1	21.3	16.6	0.06723	1.24697			
Phenylhydrazine	$C_6H_8N_2$				45.5	41.7	35.6	29.7	24.1	0.08574	1.30394			
Diphenyl amine	$C_{12}H_{11}N$						35.2	30.0	25.1	0.07841	1.31441			
Nitriles														
Acetonitrile	C_2H_3N		35.1	31.9	29.3	25.5	19.3	13.2	7.4	0.06835	1.09864			
Propionitrile	C_3H_5N	35.3	32.4	29.5	27.2	23.8	18.3	13.0	7.9	0.06264	1.13719			
Butyronitrile	C_4H_7N	34.9	32.2	29.6	27.5	24.3	19.2	14.2	9.4	0.05959	1.10579			
Benzonitrile	C_7H_5N			41.4	39.1	35.7	30.1	24.7	19.5	0.07466	1.19036			
Amides														
Formamide	CH_3NO				58.2	55.5	50.8			0.08328	0.74835			
Nitroderivates														
Nitromethane	CH_3NO_2		43.9	40.1	37.1	32.6	25.4	18.5	12.0	0.08458	1.19508			
Nitrobenzene	$C_6H_5NO_2$				43.8	40.3	34.6	29.0	23.5	0.07946	1.13667			
o-Nitrotoluene	$C_7H_7NO_2$			43.7	41.4	38.0	32.4	27.0	21.7	0.07678	1.17965			
m-Nitrotoluene	$C_7H_7NO_2$				41.1	37.7	32.2	26.9	21.7	0.07641	1.21693			
p-Nitrotoluene	$C_7H_7NO_2$						32.3	27.2	22.3	0.07341	1.17727			

D3.2 Properties at Saturation

Roland Span
Ruhr-Universität Bochum, Bochum, Germany

The tables in this chapter contain values of thermal, caloric, and transport properties of the saturated liquid and vapor of the corresponding fluids. Originally, these tables were adapted from the Heat Exchanger Design Handbook (*R. N. Maddox*, Hemisphere Publishing Corporation, 1983). However, most tables were recalculated by now. References are included to enable access to more detailed information. An alphabetic list of references is given at the end of Subchap. D3.2.

At a given temperature, properties of the saturated vapor (except for the saturated vapor density) can be used for the homogeneous gas region as a first-order approximation. In the same sense, data for the saturated liquid can be used for the homogeneous liquid at a given temperature. However, when approaching the critical temperature this approximation results in an increasing systematic error. Wherever possible, the cited equations of state should be used to directly calculate properties at homogeneous states.

Since critical parameters are required for many relations used to calculate properties on the phase boundary and since they are important parameters of the correlations used to calculate the given tables, values of the critical temperature, T_c, the critical pressure, p_c, and the critical density, ρ_c, are given for each of the fluids. The values given in this chapter are parameters of the used correlations and are as such independent of the values reported in Chap. D1.

The following properties are reported in the tables of this section:

T_s	Saturation temperature in K
p_s	Vapor pressure in kPa
h	Specific enthalpy in kJ/kg
Δh_v	Specific enthalpy of evaporation in kJ/kg
c_p	Specific isobaric heat capacity in kJ/(kg K)
η	Dynamic viscosity in kg/(m s)
λ	Thermal conductivity in W/(m K)
Pr	Prandtl number
σ	Surface tension in N/m
β'	volumetric expansion coefficient of the liquid in K^{-1} with $\beta' = \frac{(v_2 - v_1)}{v_1(T_2 - T_1)}$

Properties marked with $'$ denote saturated liquid states. Properties marked with $''$ denote saturated vapor states.

In most cases, "typical" uncertainties exist for properties of the saturated liquid or of the saturated vapor at temperatures ranging from the normal-boiling temperature to about 90% of the critical temperature. In most cases, the uncertainty of all properties except for the vapor pressure significantly increases at temperatures above 90% of the critical temperature. Between triple-point temperature and normal-boiling temperature particularly, relative uncertainties of vapor pressure and saturated vapor density increase. However, depending on the data situation the uncertainty of properties may very well vary significantly with temperature even in the range where by principle no problems would be expected. Thus, reducing a discussion of uncertainties to a single value always is a critical simplification. On the other hand, information on the uncertainty of properties is essential for the user. Therefore, it has been tried to characterize the "typical" relative uncertainty of the data presented in the tables by classifying them into groups a to f:

a	$\Delta y/y \leq \pm 0.2\%$
b	$\Delta y/y \leq \pm 0.5\%$
c	$\Delta y/y \leq \pm 1\%$
d	$\Delta y/y \leq \pm 2\%$
e	$\Delta y/y \leq \pm 5\%$
f	$\Delta y/y \leq \pm 10\%$
g	$\Delta y/y > \pm 10\%$
h	Insufficient information for classification

Typically, the category h is found where data were adapted from other compilations.

Interpolation between the values given in the tables is permitted. However, due to large temperature steps in the tables simple linear interpolation may result in errors up to 10% even at moderate temperatures sufficiently far away from the critical temperature. The magnitude of the error caused by interpolation strongly depends on the algorithm used for interpolation and on characteristics of the property. Based on the general formula for interpolation,

$$y = y_1 + \frac{\tau - \tau_1}{\tau_2 - \tau_1}\,(y_2 - y_1),$$

we recommend the following algorithms.

Linear interpolation over temperature ($\tau = T$) for enthalpies of the saturated liquid ($y = h'$) and the saturated vapor ($y = h''$) and for the thermal conductivity of the saturated liquid ($y = \lambda'$).

Linear interpolation in the logarithmic distance to the critical temperature ($\tau = \ln(T_c - T)$) for the dynamic viscosity ($y = \eta''$) and the thermal conductivity ($y = \lambda''$) of the saturated vapor.

Tables are given for the following fluids:

Logarithmic interpolation in the logarithmic distance to the critical temperature ($\tau = \ln(T_c - T)$) for the saturated liquid density ($y = \ln(\rho')$), the enthalpy of evaporation ($y = \ln(\Delta h_v)$), the isobaric heat capacity of the saturated liquid ($y = \ln(c_p')$) and the saturated vapor ($y = \ln(c_p'')$), the Prandtl number of the saturated liquid ($y = \ln(\mathrm{Pr}')$) and of the saturated vapor ($y = \ln(\mathrm{Pr}'')$), the surface tension ($y = \ln(\sigma)$) and the volumetric expansion coefficient of the liquid ($y = \ln(\beta')$).

Linear interpolation in the inverse temperature ($\tau = T^{-1}$) for the dynamic viscosity of the saturated liquid ($y = \eta'$).

Logarithmic interpolation in the inverse temperature ($\tau = T^{-1}$) for the vapor pressure ($y = \ln(p_s)$) and the saturated vapor density ($y = \ln(\rho'')$).

Even when these algorithms are used, additional uncertainties between ±0.2% and ±1% have to be considered for interpolated values. This becomes particularly relevant for properties with the uncertainty class a or b – the "typical" uncertainties given in the tables do not include errors due to interpolation. Interpolation errors up to ±3% occur for the Prandtl number of the saturated vapor. Interpolation between the last two columns of the table (for temperatures close to the critical temperature) may result in significantly larger errors.

Normal Hydrogen H_2 (T_c = 33.15 K, p_c = 1.296 MPa, ρ_c = 31.26 kg/m^3)

T_s, K	p_s, kPa	ρ', kg/m^3	ρ'', kg/m^3	h', kJ/kg	h'', kJ/kg	Δh_v, kJ/kg	$c_{p'}$, kJ/(kg K)	$c_{p''}$, kJ/(kg K)	η', 10^{-6} kg/(m s)	η'', 10^{-6} kg/(m s)	λ', 10^{-3} W/(m K)	λ'', 10^{-3} W/(m K)	Pr$'$	Pr$''$	σ, 10^{-3} N/m	β, 10^{-3}/K
20.37	101.33	70.85	1.332	0.00	448.7	448.70	9.772	12.036	12.7	1.1	119	16.3	1.04	0.83	1.92	16.68
21	121.5	70.12	1.570	6.47	451.97	445.50	10.137	12.311	12.0	1.2	121	16.9	1.01	0.85	1.81	17.61
23	204.38	67.59	2.533	28.72	459.87	431.15	11.489	13.471	10.5	1.3	126	19.2	0.96	0.91	1.47	21.24
25	321.00	64.70	3.894	54.16	463.36	409.20	13.297	15.289	9.1	1.4	127	22	0.95	0.99	1.13	26.57
27	477.89	61.31	5.806	83.72	461.17	377.45	15.987	18.357	7.8	1.6	122	25	1.03	1.15	0.796	35.35
29	682.05	57.12	8.560	119.19	450.91	331.71	20.807	24.444	6.8	1.7	112	29	1.26	1.47	0.483	52.82
30	804.32	54.54	10.44	140.29	441.18	300.88	25.284	30.424	6.3	1.9	106	31	1.50	1.83	0.333	70.28
31	941.65	51.38	12.91	165.07	426.40	261.33	33.758	42.068	5.7	2.0	100	35	1.91	2.40	0.207	105.2
32	1095.7	47.09	16.50	196.72	402.29	205.56	57.285	74.634	5.0	2.2	91	40	3.15	4.09	0.106	208.3
33.15	1296.4	31.26	31.26	298.15	298.15				3.4	3.4	60	60				
Uncertainty	a[1]	a[1]	b[1]	c[1]	c[1]	c[1]	d[1]	d[1]	h[1]	h[1]	h[2]	h[2]	h[3]	h[3]	h[1]	d[1]

[1]Ref. [51]; [2]Ref. [117]; [3]Calc. from other properties.

Argon Ar (T_c = 150.69 K, p_c = 4.863 MPa, ρ_c = 535.6 kg/m^3)

T_s, K	p_s, kPa	ρ', kg/m^3	ρ'', kg/m^3	h$'$, kJ/kg	h'', kJ/kg	Δh_v, kJ/kg	$c_{p'}$, kJ/(kg K)	$c_{p''}$, kJ/(kg K)	η', 10^{-6} kg/(m s)	η'', 10^{-6} kg/(m s)	λ', 10^{-3} W/(m K)	λ'', 10^{-3} W/(m K)	Pr$'$	Pr$''$	σ, 10^{-3} N/m	β, 10^{-3}/K
83.81	68.89	1416.8	4.055	−121.44	42.28	163.72	1.116	0.555	290.2	6.86	133.63	5.36	2.42	0.71	13.42	4.294
87.3	101.33	1395.4	5.774	−117.52	43.62	161.14	1.117	0.566	260.3	7.17	128.46	5.62	2.26	0.721	12.53	4.443
90	133.51	1378.6	7.436	−114.49	44.57	159.06	1.121	0.576	240	7.41	124.51	5.83	2.16	0.731	11.85	4.575
100	323.77	1313.7	16.86	−103.06	47.4	150.46	1.154	0.627	181.3	8.35	110.22	6.69	1.9	0.782	9.42	5.222
110	665.26	1242.8	33.29	−91.13	48.84	139.97	1.218	0.712	140.4	9.37	96.41	7.73	1.77	0.863	7.11	6.219
120	1213	1162.8	60.14	−78.35	48.41	126.77	1.332	0.863	110.2	10.54	83.13	9.15	1.77	0.993	4.96	7.886
130	2025.5	1068.1	103.56	−64.16	45.3	109.46	1.564	1.172	85.9	12.03	70.43	11.45	1.91	1.23	3	11.2
140	3168.2	943.7	178.86	−47.16	37.47	84.63	2.225	2.104	63.6	14.32	58.06	16.39	2.44	1.84	1.29	21.01
145	3889.6	854.3	244.44	−36.19	29.76	65.95	3.399	3.896	52.1	16.27	52.01	22.53	3.4	2.81	0.58	39.75
150.69	4863	535.6	535.6	−4.33	−4.33											
Uncertainty	a[1]	a[1]	a[1]	b[1]	b[1]	b[1]	b[1]	b[1]	c[2]	c[2]	d[2]	d[2]	d[3]	d[3]	d[4]	b[1]

[1]Ref. [111]; [2]Ref. [54]; [3]Calc. from other properties; [4]Ref. [57].

Neon Ne (T_c = 44.49 K, p_c = 2.679 MPa, ρ_c = 481.9 kg/m^3)

T_s, K	p_s, kPa	ρ', kg/m^3	ρ'', kg/m^3	h', kJ/kg	h'', kJ/kg	Δh_v, kJ/kg	$c_{p'}$, kJ/(kg K)	$c_{p''}$, kJ/(kg K)	η', 10^{-6} kg/(m s)	η'', 10^{-6} kg/(m s)	λ', 10^{-3} W/(m K)	λ'', 10^{-3} W/(m K)	Pr$'$	Pr$''$	σ, 10^{-3} N/m	β, 10^{-3}/K
27.11	101.34	1206.95	9.579	0	85.75	85.75	1.862	1.415	127	4.6	113	7.7	2.09	0.85	4.78	14.56
29	172.87	1172.99	15.647	3.63	86.96	83.32	1.948	1.306	105	5	110	8.5	1.86	0.77	4.15	16.129
31	283.24	1134.02	24.803	7.7	87.79	80.09	2.079	1.347	92.5	5.4	108	9.3	1.78	0.79	3.5	18.499
33	437.82	1091.23	37.584	12.05	88.18	76.13	2.22	1.469	77.9	5.8	102	10.2	1.7	0.84	1.87	21.425
35	645.43	1044.24	55.106	16.69	88.04	71.35	2.384	1.669	65.9	6.1	96.5	11.1	1.63	0.92	2.26	25.243
37	915.4	992.03	79.087	21.67	87.22	65.55	2.625	1.994	56.6	6.8	88.6	12.4	1.68	1.1	1.69	30.959
39	1258.1	932	112.575	27.18	85.48	58.3	3.059	2.584	47.3	7.4	78.9	13.9	1.83	1.38	1.15	41.31
41	1685.5	857.03	162.165	33.62	82.25	48.63	4.089	3.916	38.6	8.5	67.3	16	2.35	2.07	0.65	66.81
43	2212.1	739.37	248.26	42.54	75.96	33.42	8.761	9.132	27.8	11.9	50.3	22.8	4.84	4.77	0.2	195.49
44.49	2678.6	481.91	481.91	59.46	59.46				16.7	16.7	33	33				
Uncertainty	a[1]	a[1]	b[1]	c[1]	c[1]	c[1]	d[1]	d[1]	h[1,2]	h[2]	h[3]	h[3]	h[5]	h[5]	h[1,4]	d[1]

[1]Ref. [44]; [2]Ref. [121]; [3]Ref. [118]; [4]Ref. [73]; [5]Calc. from other properties.

Chlorine Cl (T_c = 416.92 K, p_c = 7.9914 MPa, ρ_c = 576.8 kg/m^3)

T_s, K	P_s, kPa	ρ', kg/m^3	ρ'', kg/m^3	h', kJ/kg	h'', kJ/kg	Δh_v, kJ/kg	c_p', kJ/(kg K)	c_p'', kJ/(kg K)	η', 10^{-6} kg/(m s)	η'', 10^{-6} kg/(m s)	λ', 10^{-3} W/(m K)	λ'', 10^{-3} W/(m K)	Pr′	Pr″	σ, 10^{-3} N/m	β, 10^{-3}/K
172.18	1.39	1743.2	0.07	−380.8	−57.9	322.9	1.03	0.44	1256	7.9	196.8	4.3	6.57	0.82	39.9	
195	8.73	1677.6	0.38	−358.5	−47.9	310.6	0.94	0.44	788.5	9	186.9	5	3.97	0.79	35	1.59
217	34.07	1620.3	1.35	−338	−38.4	299.6	0.93	0.45	552.1	10	176.7	5.7	2.91	0.79	30.6	1.59
139.17	101.33	1562.5	3.7	−317.4	−29.3	288.1	0.94	0.46	411.9	11.1	165.7	6.5	2.34	0.78	26.3	1.7
267	299.85	1486.3	10.1	−290.9	−19.1	271.8	0.97	0.49	305.5	12.4	151.1	7.7	1.96	0.75	21.2	1.92
296	733.88	1400.2	23.5	−262	−10.8	251.2	1	0.53	232.4	13.9	134.9	9.1	1.72	0.81	16.3	2.25
324	1482.8	1308.6	46.7	−233.2	−6.1	227.1	1.04	0.6	181	15.5	118.1	10.7	1.59	0.87	11.9	2.73
352	2675.9	1204.8	86.3	−203.1	−6	197.1	1.12	0.75	141.4	17.4	100.4	12.7	1.58	1.03	8	3.59
380	4447.6	1077.2	156.2	−170.2	−13.2	157	1.36	1.12	108	20.4	81.7	15.6	1.8	1.46	4.3	5.79
408.6	7040.5	858.4	322.3	−124.9	−39.5	85.4	3.62	3.97	71.8	28.8	61.5	51.9	4.22	5.12	0.9	23.97
Uncertainty	c[1]	c[1]	e[1]	e[1]	e[1]	e[1]	e[1]	e[1]	g[2,6]	f[2,6]	g[3,6]	g[4,6]	g[7]	g[7]	g[5,6]	e[1]

[1]Ref. [2]; [2]Ref. [14]; [3]Ref. [68]; [4]Ref. [108]; [5]Ref. [41]; [6]Estimated values; [7]Calc. from other properties.

Fluorine F2 (T_c = 144.41 K, p_c = 5.172 MPa, ρ_c = 592.9 kg/m^3)

T_s, K	p_s, kPa	ρ', kg/m^3	ρ'', kg/m^3	h', kJ/kg	h'', kJ/kg	Δh_v, kJ/kg	c_p', kJ/(kg K)	c_p'', kJ/(kg K)	η', 10^{-6} kg/(m s)	η'', 10^{-6} kg/(m s)	λ', 10^{-3} W/(m K)	λ'', 10^{-3} W/(m K)	Pr′	Pr″	σ, 10^{-3} N/m	β, 10^{-3}/K
53.49	0.24	1706.7	0.02	−46.79	152.27	199.06	1.525	0.767	854.8	4.4	205.7	4.1	6.34	0.82	22.7	3.887
64	3.74	1640.3	0.268	−31.36	160.19	191.55	1.475	0.771	499.6	5.2	192.4	5	3.83	0.8	20	3.831
74	23.22	1576.4	1.452	−16.55	167.35	183.9	1.485	0.787	332.4	6.1	178.8	6	2.76	0.8	16.6	4.151
85.04	101.32	1501.8	5.641	0	174.37	174.37	1.511	0.825	231.7	7	162.8	7.1	2.15	0.81	13.6	4.691
92	210.8	1451.6	11.1	10.65	178.11	167.45	1.539	0.864	190.2	7.6	151.8	7.9	1.93	0.83	11.7	5.158
102	500.9	1373.8	24.96	26.41	182.29	155.88	1.6	0.946	147.7	8.5	135.4	9.3	1.75	0.86	9.2	6.081
112	1012.9	1286.9	49.27	42.99	184.73	141.73	1.705	1.076	116.5	9.6	118	10.9	1.68	0.95	6.8	7.549
122	1824.4	1185.5	90.14	60.92	184.6	123.69	1.914	1.328	91.4	10.9	99.7	13	1.75	1.11	4.5	10.384
132	3023	1054.7	162	81.51	179.9	98.39	2.483	2.061	68.8	13.1	80.3	16.1	2.13	1.68	2.4	18.31
144.41	5172.4	592.9	592.9	133.13	133.13				45.6	17.8	61.2	22.5			0.55	
Uncertainty	a[1]	a[1]	b[1]	c[1]	c[1]	c[1]	d[1]	d[1]	e[2]	f[3,8]	g[4,8]	g[5,8]	h[9]	h[9]	g[6,7,8]	d[1]

[1]Ref. [90]; [2]Ref. [34]; [3]Ref. [14]; [4]Ref. [68]; [5]Ref. [108]; [6]Ref. [19]; [7]Ref. [38]; [8]Estimated values; [9]Calc. from other properties.

Mercury Hg (T_c = 1763.2 K, p_c = 151.00 MPa, ρ_c = 5500 kg/m^3)

T_s, K	p_s, kPa	ρ', kg/m^3	ρ'', kg/m^3	h', kJ/kg	h'', kJ/kg	Δh_v, kJ/kg	c_p' kJ/(kg K)	c_p'', kJ/(kg K)	η', 10^{-6} kg/(m s)	η'', 10^{-6} kg/(m s)	λ', 10^{-3} W/(m K)	λ'', 10^{-3} W/(m K)	Pr′	Pr″	σ, 10^{-3} N/m	β, 10^{-3}/K
630.1	101.3	12737	3.91	91.8	386.7	294.9	0.136	0.104	884	61.7	121.9	10.4	0.987	0.617		0.194
650	145	12688	5.37	94.5	388.7	294.2	0.136	0.104	870	63.5	123.6	10.8	0.957	0.612		0.192
700	316	12567	10.9	101.3	393.6	292.3	0.137	0.105	841	68.6	128	11.7	0.9	0.616		0.192
750	620	12444	20.1	108.2	398.4	290.2	0.138	0.106	816	73.5	131.9	12.6	0.854	0.618		0.198
800	1120	12318	34.2	115.2	403	287.8	0.14	0.107	794	78.4	135.1	13.5	0.823	0.621		0.205
850	1880	12190	54.6	122.3	407.4	285.1	0.142	0.108	776	83.5	137.8	14.4	0.8	0.626		0.212
900	2990	12059	82.7	129.5	411.6	282.1	0.144	0.109	760	88.4	141.8	15.3	0.772	0.63		0.218
950	4530	11927	119.9	136.9	415.5	278.6	0.146	0.111	746	93.2	144.5	16.2	0.754	0.637		0.226
1000	6580	11791	167.7	144.4	419.1	274.7	0.149	0.113	736	98	146.9	17.2	0.744	0.644		0.234
1050	9230	11650	227.3	153.8	423	269.2	0.153	0.116	723	103	147.9	18.1	0.748	0.66		0.246
Uncertainty	h[1]	h[1]	h[1]	h[1]	h[1]	h[1]	h[1]	h[1]	h[1]	h[1]	h[1,2]	h[1]	h[4]	h[4]		h[3]

[1]Ref. [125]; [2]Ref. [119]; [3]Estimated values; [4]Calc. from other properties.

Hydrogen fluoride HF (T_c = 461.15 K, p_c = 6.485 MPa, ρ_c = 290 kg/m^3)

T_s, K	p_s, kPa	ρ', kg/m^3	ρ'', kg/m^3	h', kJ/kg	h'', kJ/kg	Δh_v, kJ/kg	$c_{p'}$, kJ/(kg K)	$c_{p''}$, kJ/(kg K)	η', 10^{-6} kg/(m s)	η'', 10^{-6} kg/(m s)	λ', 10^{-3} W/(m K)	λ'', 10^{-3} W/(m K)	Pr$'$	Pr$''$	σ, 10^{-3} N/m	β, 10^{-3}/K
292.69	101.3	968	2	0	330	330	3.04	1.46	215	10.9	402	21	1.63	0.76	8.65	1.93
305	152	945	3.5	37.9	407.9	370	3.12	1.46	191	12.2	387	21.8	1.54	0.82	7.85	2.08
325	285	905	5	101.6	536.6	435	3.26	1.46	161	13.5	362	23	1.45	0.85	6.75	2.29
345	500	862	10	168	653	485	3.44	1.46	139	14.5	335	24.3	1.43	0.87	5.6	2.59
365	820	816	14	239	769	530	3.68	1.46	121	15.4	310	25.6	1.44	0.88	4.6	2.91
385	1320	765	20	316	896	580	4	1.46	106	16.3	283	26.9	1.5	0.88	3.5	3.48
405	2100	710	28	400	1010	610	4.41	1.46	93	17.2	255	28.3	1.61	0.88	2.5	4.46
425	3150	640	45	493	1068	574	4.92	1.46	81.6	18.1	227	29.6	1.77	0.89	1.6	6.6
445	4800	545	88	598	993	395	5.56	1.46	71.2	18.9	199	30.9	1.99	0.89	0.7	15.54
461.15	6490	290	290						39.8	39.8		32	2.22			
Uncertainty	h[1]	h[1]	h[1]	h[11]	h[11]	h[2]	h[3]	h[4]	h[8,1]	h[9,1]	h[5,1]	h[6,1]	h[11]	h[11]	h[7]	h[10]

[1]Ref. [37]; [2]Ref. [29]; [3]Ref. [67]; [4]Ref. [6]; [5]Ref. [68]; [6]Ref. [69]; [7]Ref. [73]; [8]Ref. [71]; [9]Ref. [70]; [10]Estimated values; [11]Calc. from other properties.

Hydrogen chloride HCl (T_c = 324.6 K, p_c = 8.309 MPa, ρ_c = 450 kg/m^3)

T_s, K	p_s, kPa	ρ', kg/m^3	ρ'', kg/m^3	h', kJ/kg	h'', kJ/kg	Δh_v, kJ/kg	$c_{p'}$, kJ/(kg K)	$c_{p''}$, kJ/(kg K)	η', 10^{-6} kg/(m s)	η'', 10^{-6} kg/(m s)	λ', 10^{-3} W/(m K)	λ'', 10^{-3} W/(m K)	Pr$'$	Pr$''$	σ, 10^{-3} N/m	β, 10^{-3}/K
188.05	101.3	1190	2.5	0	442	442	1.61	0.85	407	9	337	8.6	1.94	0.89	23.2	2.31
200	180	1155	5	20	452	432	1.66	0.87	332	9.6	323	9.3	1.71	0.9	21	2.42
215	370	1115	10	45	461	416	1.74	0.91	259	10.4	305	10.5	1.48	0.9	18.3	2.55
230	670	1070	15	71	467	396	1.84	0.96	204	11.2	285	12	1.32	0.9	15.5	2.97
245	1100	1020	25	99	473	374	1.95	1.04	160	12.1	264	13.5	1.18	0.93	12.9	3.27
260	1800	970	40	130	478	348	2.15	1.16	126	13	242	15.6	1.12	0.97	10.2	3.26
275	2700	925	55	164	480	316	2.34	1.36	101	14.1	219	17.8	1.08	1.06	7.7	4.59
290	3800	845	90	203	478	275	2.67	1.74	77	15.1	195	21.6	1.05	1.22	5.2	6.78
305	5500	755	140	247	465	218	3.28	2.74	60	16.8	169	26.9	1.16	1.71	2.8	19.38
324.6	8309	450	450						34	34	61	61				
Uncertainty	h[1]	h[1]	h[1]	h[11]	h[12]	h[2]	h[3,4]	h[5,6]	h[11,1]	h[12,1,7]	h[8,1]	h[9,13]	h[15]	h[15]	h[10]	h[14]

[1]Ref. [37]; [2]Ref. [29]; [3]Ref. [67]; [4]Ref. [63]; [5]Ref. [6]; [6]Ref. [52]; [7]Ref. [107]; [8]Ref. [68]; [9]Ref. [69]; [10]Ref. [73]; [11]Ref. [71]; [12]Ref. [70]; [13]Ref. [108]; [14]Estimated values; [15]Calc. from other properties.

Hydrogen sulfide H_2S (T_c = 373.15 K, p_c = 8.937 MPa, ρ_c = 346 kg/m^3)

T_s, K	p_s, kPa	ρ', kg/m^3	ρ'', kg/m^3	h', kJ/kg	h'', kJ/kg	Δh_v, kJ/kg	$c_{p'}$, kJ/(kg K)	$c_{p''}$, kJ/(kg K)	η', 10^{-6} kg/(m s)	η'', 10^{-6} kg/(m s)	λ', 10^{-3} W/(m K)	λ'', 10^{-3} W/(m K)	Pr$'$	Pr$''$	σ, 10^{-3} N/m	β, 10^{-3}/K
212.8	101.3	965	2	−356	199	555	1.83	1.02	423	9.2	233	9.1	3.32	1.03	29	1.86
220	140	955	2.6	−341	204	545	1.85	1.03	378	9.6	224	9.6	3.12	1.03	27.5	1.96
240	325	915	5.5	−301	219	520	1.91	1.08	272	10.5	199	11.1	2.61	1.02	23.5	2.19
260	680	875	11	−256	230	485	2	1.16	205	11.4	175	12.9	2.34	1.03	19.6	2.44
280	1200	830	21	−207	239	445	2.13	1.28	162	12.4	153	14.7	2.26	1.08	16	2.87
300	2000	780	35	−161	244	405	2.35	1.45	130	13.5	131	17	2.33	1.15	12.5	3.56
320	3250	720	55	−104	241	345	2.64	1.77	110	14.8	107	19.8	2.71	1.32	9.2	4.55
340	4890	650	95	−42	228	270	3.1	2.48	87	16.5	85	24.1	3.17	1.7	5.5	6.06
360	7050	565	160	45	190	145	4.38	6.45	66	19.2	62	30.5	4.66	4.06	2.2	18.66
373.15	8937	346	346	68	68				40.5	40.5	49.5	49.5				
Uncertainty	h[1]	h[2]	h[1]	h[9]	h[3,4]	h[1]	h[5]	h[1,3,4]	h[1,6]	h[1,7]	h[1,8]	h[1,8]	h[10]	h[10]	h[1]	h[9]

[1]Refs. [121]; [2]Ref. [37]; [3]Ref. [115]; [4]Ref. [52]; [5]Ref. [63]; [6]Ref. [59]; [7]Ref. [107]; [8]Ref. [108]; [9]Estimated values; [10]Calc. from other properties.

Ammonia NH_3 (T_c = 405.5 K, p_c = 11.353 MPa, ρ_c = 234.7 kg/m^3)

T_s, K	p_s, kPa	ρ', kg/m^3	ρ'', kg/m^3	h,′ kJ/kg	h'', kJ/kg	Δh_v, kJ/kg	$c_{p'}$, kJ/(kg K)	c_{p}'', kJ/(kg K)	η', 10^{-6} kg/(m s)	η'', 10^{-6} kg/(m s)	λ', 10^{-3} W/(m K)	λ'', 10^{-3} W/(m K)	Pr′	Pr″	σ, 10^{-3} N/m	β, 10^{-3}/K
195.5	60.9	732.9	0.064	−143.1	1341.2	1484.3	4.202	2.063	559	6.84					43.9	
239.75	101	682.1	0.886	48.4	1418.2	1369.8	4.448	2.296	256.4	8.05	613.7	17.53	1.86	1.05	33.9	1.76
270	381	642.9	3.087	185.45	1458.8	1273.4	4.599	2.634	176.1	8.96	544.3	21.34	1.49	1.11	26.9	2.17
290	774	614.8	6.074	278.8	1477.8	1199	4.722	2.967	142.7	9.58	499.6	24.78	1.35	1.15	22.4	2.63
310	1424	584.5	11.019	375.1	1489	1112.9	4.897	3.423	117.5	10.22	454.9	28.67	1.26	1.22	18	3.11
330	2421	550.9	18.983	475.6	1490.2	1014.6	5.176	4.078	97.32	10.93	409.8	33.19	1.23	1.34	13.7	4.03
350	3866	512.4	31.334	582.6	1477.9	895.3	5.671	5.125	80.43	11.79	364.3	39.14	1.25	1.54	9.6	5.36
370	5878	465.3	51.729	700.8	1444.7	743.9	6.715	7.214	65.49	13.05	318.7	48.2	1.38	1.95	5.74	8.3
390	8605	399.6	90.224	842.75	1369.9	527.15	10.305	14.192	50.88	15.53	273.4	64.74	1.92	3.4	2.21	17.63
400	10305	344.6	131.09	941.86	1288.8	346.94	22.728	34.924	42.02	18.45	251.2	81.52	3.8	7.9	0.68	41.72
Uncertainty	a[1]	a[1]	b[1]	b[1]	b[1]	b[1]	c[1]	c[1]	c[2]	c[2]	e[3,4,5,6]	e[7]	f[11]	f[11]	d[8,9]	h[10]

[1]Ref. [112]; [2]Ref. [131]; [3]Ref. [124]; [4]Ref. [121]; [5]Ref. [76]; [6]Ref. [95]; [7]Ref. [1]; [8]Ref. [104]; [9]Ref. [72]; [10]Estimated values; [11]Calc. from other properties.

Carbon monoxide CO (T_c = 132.86 K, p_c = 3.494 MPa, ρ_c = 303.9 kg/m^3)

T_s, K	p_s, kPa	ρ', kg/m^3	ρ'', kg/m^3	h', kJ/kg	h'', kJ/kg	Δh_v, kJ/kg	$c_{p'}$, kJ/(kg K)	c_{p}'', kJ/(kg K)	η', 10^{-6} kg/(m s)	η'', 10^{-6} kg/(m s)	λ', 10^{-3} W/(m K)	λ'', 10^{-3} W/(m K)	Pr′	Pr″	σ, 10^{-3} N/m	β, 10^{-3}/K
81.66	101.58	793.12	4.371	0.05	214.7	214.65	2.146	1.132	154	7.1	141	6.9	2.34	1.16	9.47	5.544
90	238.52	755.35	9.66	18.18	220.39	202.22	2.188	1.216	120	7.5	125	8.2	2.1	1.11	7.73	6.33
95	368.6	731.15	14.568	29.3	223.03	193.73	2.236	1.29	105	7.8	116	8.9	2.02	1.13	6.71	6.978
100	544.38	705.41	21.204	40.71	224.95	184.24	2.306	1.389	93.5	8.1	107	9.7	2.02	1.16	5.71	7.828
105	774.17	677.71	30.038	52.52	226	173.47	2.408	1.526	83.9	8.4	98.2	10.5	2.06	1.23	4.73	8.984
110	1066.6	647.44	41.743	64.89	225.97	161.09	2.558	1.725	75.9	8.8	89.3	11.5	2.17	1.32	3.78	10.642
115	1430.7	613.63	57.368	78.02	224.56	146.54	2.793	2.039	69.1	9.2	80.3	12.6	2.4	1.49	2.86	13.21
120	1876.5	574.58	78.772	92.3	221.2	128.9	3.202	2.601	63.3	9.8	71.4	14	2.84	1.82	1.97	17.76
125	2415.7	526.53	109.99	108.5	214.7	106.21	4.1	3.898	58.3	11.7	62.5	18.4	3.82	2.48	1.13	28.14
132.86	3494	303.91	303.91	164.71	164.71											
Uncertainty	a[1]	a[1]	b[1]	c[1]	c[1]	c[1]	d[1]	d[1]	h[2]	h[3,4]	h[5]	h[5,6]	h[8]	h[8]	h[7]	d[1]

[1]Ref. [58]; [2]Ref. [71]; [3]Ref. [70]; [4]Ref. [107]; [5]Ref. [118]; [6]Ref. [108]; [7]Ref. [73]; [8]Calc. from other properties.

R22 $CHClF_2$ (T_c = 369.3 K, p_c = 4.990 MPa, ρ_c = 523.8 kg/m^3)

T_s, K	p_s, kPa	ρ', kg/m^3	ρ'', kg/m^3	h', kJ/kg	h'', kJ/kg	Δh_v, kJ/kg	$c_{p'}$, kJ/(kg K)	c_{p}'', kJ/(kg K)	η', 10^{-6} kg/(m s)	η'', 10^{-6} kg/(m s)	λ', 10^{-3} W/(m K)	λ'', 10^{-3} W/(m K)	Pr′	Pr″	σ, 10^{-3} N/m	β, 10^{-3}/K
115.73	0.000379	1721.3	0.000034	29.6	332.71	303.11	1.075	0.425	13435.3	4.88	177.01	2.59	81.61	0.8	38.56	1.53
200	16.67	1499.7	0.875	119.22	372.15	252.93	1.064	0.539	544	8.37	129.11	5.54	4.48	0.814	23.46	1.809
225	70.91	1430.3	3.371	146.03	384.3	238.27	1.081	0.589	379.4	9.4	116.85	6.68	3.51	0.828	19.27	2.001
232.34	101.33	1409.2	4.704	154	387.75	233.75	1.09	0.606	345.4	9.7	113.37	7.05	3.32	0.834	18.08	2.074
250	216.9	1356.3	9.605	173.51	395.71	222.2	1.117	0.655	279.6	10.41	105.22	7.99	2.97	0.854	15.25	2.292
275	528.65	1275.2	22.5	202.17	405.72	203.55	1.174	0.747	211.7	11.44	93.91	9.53	2.65	0.897	11.42	2.742
300	1097	1183.4	46.54	232.62	413.5	180.88	1.265	0.885	161	12.61	82.64	11.51	2.47	0.97	7.82	3.51
325	2026.4	1073.2	90.19	265.84	417.55	151.71	1.438	1.139	120.1	14.21	71.01	14.52	2.43	1.11	4.51	5.155
350	3442.7	920.1	177.54	304.7	413.7	109	1.996	1.956	83.1	17.33	58.3	21.29	2.85	1.59	1.62	11.35
369.3	4990	523.8	523.8	366.9	366.9											
Uncertainty	a[1]	a[1]	b[1]	c[1]	c[1]	c[1]	d[1]	d[1]	e[2]	e[2]	e[3]	e[3]	e[4]	e[4]	f[5]	b[1]

[1]Ref. [43]; [2]Ref. [45]; [3]Ref. [66]; [4]Calc. from other properties; [5]Ref. [79].

R123 $C_2HCl_2F_3$ (T_c = 456,83 K, p_c = 3.662 MPa, ρ_c = 550 kg/m^3)

T_s, K	p_s, kPa	ρ', kg/m^3	ρ'', kg/m^3	h', kJ/kg	h'', kJ/kg	Δh_v, kJ/kg	$c_{p'}$, kJ/(kg K)	$c_{p''}$, kJ/(kg K)	η', 10^{-6} kg/(m s)	η'', 10^{-6} kg/(m s)	λ', 10^{-3} W/(m K)	λ'', 10^{-3} W/(m K)	Pr$'$	Pr$''$	σ, 10^{-3} N/m	β, 10^{-3}/K
166	0	1771	0.0005	98.811	322.5	223.69	0.929	0.474	7170	5.57	113.83	4.99	58.52	0.53	32.07	
210	0.62	1672.1	0.054	139.52	344.95	205.42	0.93	0.548	1690.6	7.39	101.92	6.61	15.43	0.61	26.19	1.333
255	13.27	1569.4	0.967	182.21	370.61	188.41	0.97	0.62	729.19	9.17	89.73	8.42	7.88	0.68	20.43	1.495
301	101.3	1456.6	6.471	228.03	398.22	170.19	1.023	0.701	405.78	10.89	77.05	10.5	5.38	0.72	14.84	1.771
325	224.8	1392.7	13.752	253.01	412.6	159.59	1.054	0.749	313.9	11.65	70.36	11.74	4.7	0.74	12.07	1.989
350	451.5	1320.8	26.977	279.89	427.12	147.23	1.094	0.808	244.14	12.58	63.41	13.19	4.21	0.77	9.31	2.322
375	818.5	1240.6	49.027	307.89	440.74	132.85	1.148	0.885	190.27	13.73	56.46	14.89	3.87	0.82	6.7	2.866
400	1372	1146.8	85.321	337.45	452.74	115.3	1.237	1.004	145.85	15.33	49.51	16.96	3.64	0.91	4.27	3.907
425	2167	1026.4	148.41	369.63	461.53	91.897	1.438	1.273	106.17	17.96	42.56	19.71	3.59	1.16	2.08	6.604
447	3126	857.44	265.82	403.31	461.79	58.478	2.34	2.55	71.78	23.28	36.44	23.06	4.61	2.57	0.49	19.644
Uncertainty	a[1]	a[1]	d[1]	d[1]	d[1]	d[1]	d[1]	d[1]	f[2]	f[3]	f[4,5]	f[6]	g[8]	g[8]	e[7]	c[1]

[1]Ref. [136]; [2]Ref. [80]; [3]Ref. [75]; [4]Ref. [31]; [5]Ref. [123]; [6]Ref. [133]; [7]Ref. [77]; [8]Calc. from other properties.

R125 C_2HF_5 (T_c = 339.17 K, p_c = 3.618 MPa, ρ_c = 573.6 kg/m^3)

T_s, K	p_s, kPa	ρ', kg/m^3	ρ'', kg/m^3	h', kJ/kg	h'', kJ/kg	Δh_v, kJ/kg	$c_{p'}$, kJ/(kg K)	$c_{p''}$, kJ/(kg K)	η', 10^{-6} kg/(m s)	η'', 10^{-6} kg/(m s)	λ', 10^{-3} W/(m K)	λ'', 10^{-3} W/(m K)	Pr$'$	Pr$''$	σ, 10^{-3} N/m	β, 10^{-3}/K
172.52	2.914	1690.7	0.2446	87.13	277.39	190.26	1.035	0.569	1152.4	7.43	116.02	5.23	10.28	0.81	21.79	1.906
200	24.6	1600.5	1.804	115.98	293.01	177.02	1.069	0.631	631	8.63	103.06	7.04	6.54	0.774	17.43	2.101
225.06	101.32	1513.6	6.79	143.34	307.44	164.1	1.115	0.697	411.1	9.71	91.3	8.75	5.02	0.774	13.63	2.391
240	200.04	1458.2	12.918	160.26	315.87	155.6	1.149	0.744	327.4	10.35	84.44	9.81	4.45	0.785	11.45	2.643
260	432.5	1378	27.179	183.82	326.63	142.8	1.205	0.819	245.4	11.25	75.52	11.36	3.92	0.811	8.66	3.14
280	827.82	1287.2	52.22	208.69	336.3	127.6	1.286	0.919	184.7	12.27	66.94	13.17	3.55	0.856	6.04	3.991
300	1446.3	1178.2	95.71	235.45	343.83	108.38	1.425	1.104	136.9	13.64	58.67	15.68	3.32	0.961	3.62	5.741
320	2360	1031.3	177.36	265.53	347.03	81.5	1.783	1.643	95.6	16.1	50.53	20.57	3.37	1.29	1.49	11.184
330	2957.9	921.1	255.28	283.42	344.56	61.13	2.468	2.736	74.6	18.77	46.66	26.61	3.95	1.93	0.6	23.14
339.17	3617.7	573.6	573.6	318.06	318.06											
Uncertainty	a[1]	a[1]	b[1]	c[1]	c[1]	c[1]	c[1]	c[1]	e[2]	e[2]	e[3]	e[3]	e[4]	e[4]	f[5]	b[1]

[1]Ref. [55]; [2]Ref. [39], [3] Ref. [85]; [4]Calc. from other properties; [5]Ref. [78].

R134a $C_2H_2F_4$ (T_c = 374.18 K, p_c = 4.056 MPa, ρ_c = 508 kg/m^3)

T_s, K	p_s, kPa	ρ', kg/m^3	ρ'', kg/m^3	h', kJ/kg	h'', kJ/kg	Δh_v, kJ/kg	$c_{p'}$, kJ/(kg K)	$c_{p''}$, kJ/(kg K)	η', 10^{-6} kg/(m s)	η'', 10^{-6} kg/(m s)	λ', 10^{-3} W/(m K)	λ'', 10^{-3} W/(m K)	Pr$'$	Pr$''$	σ, 10^{-3} N/m	β, 10^{-3}/K
169.85	0.39	1591.1	0.0282	71.45	334.94	263.49	1.18	0.585	1152	6.5	141	2.34	9.65	1.63	28.07	
195	4.27	1524	0.27	101.38	349.96	248.58	1.2	0.646	749	7.63	129	4.76	6.95	1.03	23.79	1.77
220	24.43	1455.2	1.39	131.78	365.65	233.87	1.23	0.711	521	8.73	118	7.08	5.47	0.876	19.69	1.93
246.78	100	1377.6	5.19	165.43	382.59	217.16	1.28	0.793	368	9.89	105	9.49	4.47	0.827	15.48	2.18
265	215.67	1321.2	10.76	189.14	393.78	204.64	1.32	0.862	294	10.67	97.3	11.2	3.99	0.821	12.75	2.43
285	440.83	1254.5	21.48	216.12	405.35	189.23	1.38	0.955	231	11.54	88.4	13.1	3.59	0.841	9.88	2.83
305	811.97	1180.2	39.63	244.4	415.71	171.31	1.46	1.08	181	12.47	79.4	15.22	3.31	0.885	7.17	3.47
325	1380.3	1093.6	69.76	274.51	424.1	149.59	1.58	1.27	139	13.59	70.2	17.82	3.14	0.967	4.67	4.65
345	2205.9	984.7	121.84	307.51	428.85	121.34	1.84	1.66	104	15.23	60.8	21.62	3.13	1.17	2.42	7.43
365	3369.1	816.3	232.9	347.23	424.04	76.81	3.04	3.58	68.7	19.21	52.2	31.02	4	2.22	0.565	21.55
Uncertainty	a[1]	a[1]	d[1]	d[1]	d[1]	d[1]	c[1]	c[1]	f[2]	f[2]	e[2]	f[2]	f[4]	f[4]	e[3]	c[4]

[1]Ref. [114]; [2]Ref. [47]; [3]Ref. [77]; [4]Calc. from other properties.

R152a $C_2H_4F_2$ (T_c = 386.41 K, p_c = 4.517 MPa, ρ_c = 368 kg/m^3)

T_s, K	p_s, kPa	ρ', kg/m^3	ρ'', kg/m^3	h', kJ/kg	h'', kJ/kg	Δh_v, kJ/kg	$c_{p'}$, kJ/(kg K)	$c_{p''}$, kJ/(kg K)	η', 10^{-6} kg/(ms)	η'', 10^{-6} kg/(m s)	λ', 10^{-3} W/(m K)	λ'', 10^{-3} W/(m K)	Pr$'$	Pr$''$	σ, 10^{-3} N/m	β, 10^{-3}/K
154.56	0.07	1190.3	0.003	14.26	417.09	402.83	1.472	0.727	1935.2	9.02	171.33	2.62	16.63	2.51	31.65	
190	2.78	1125.8	0.117	66.99	443.85	376.86	1.511	0.805	746.5	9.78	155.02	5.5	7.28	1.43	25.85	
220	22.82	1069.2	0.837	113.13	467.32	354.2	1.567	0.902	430.43	10.43	141.21	7.94	4.78	1.18	21.11	1.809
249.13	101.3	1010.8	3.38	159.78	489.53	329.74	1.636	1.046	305.24	11.06	127.8	10.34	3.91	1.12	16.69	2.06
270	235.51	965.9	7.51	194.62	504.5	309.88	1.699	1.173	226.77	11.51	118.2	12.05	3.26	1.12	13.65	2.321
290	465.43	919.43	14.499	229.39	517.72	288.34	1.774	1.312	179.43	11.94	108.99	13.86	2.92	1.13	10.84	2.679
310	835.96	868.14	26.018	265.86	529.29	263.43	1.875	1.483	144.1	12.37	99.78	16.44	2.71	1.12	8.16	3.231
330	1393.7	809.51	44.602	304.64	538.31	233.67	2.028	1.728	114.48	12.8	90.58	19.8	2.56	1.12	5.64	4.181
350	2192.4	738.36	75.333	346.87	542.95	196.08	2.31	2.182	88.18	13.24	81.37	23.91	2.5	1.21	3.3	6.175
378	3850.9	580.1	176.16	419.75	529.48	109.73	4.519	6.02	56.44	16.72	68.48	30.98	3.72	3.25	0.55	23.59
Uncertainty	a[1]	a[1]	d[1]	d[1]	d[1]	d[1]	d[1]	d[1]	f[2,3]	f[2,4]	f[5]	f[5]	f[7]	f[7]	e[6]	c[1]

[1]Ref. [113]; [2]Ref. [32]; [3]Ref. [49]; [4]Ref. [109]; [5]Ref. [31]; [6]Ref. [78]; [7]Calc. from other properties.

Methane CH_4 (T_c = 190.564 K, p_c = 4.5992 MPa, ρ_c = 162.66 kg/m^3)

T_s, K	p_s, kPa	ρ', kg/m^3	ρ'', kg/m^3	h', kJ/kg	h'', kJ/kg	Δh_v, kJ/kg	$c_{p'}$, kJ/(kg K)	$c_{p''}$, kJ/(kg K)	η', 10^{-6} kg/(m s)	η'', 10^{-6} kg/(m s)	λ', 10^{-3} W/(m K)	λ'', 10^{-3} W/(m K)	Pr$'$	Pr$''$	σ, 10^{-3} N/m	β, 10^{-3}/K
111.67	101.3	422.36	1.8165	−910.9	−397.9	513	3.481	2.162	106.5	4.49	193	12.1	1.88	0.77	13.5	3.473
120	191.4	409.9	3.2619	−881.5	−386.9	494.6	3.549	2.293	86.05	4.84	178	12.9	1.7	0.79	11.5	3.776
130	367.3	394.04	5.9804	−845.3	−373.3	472	3.658	2.421	71.65	5.28	163	16.4	1.6	0.71	9.28	4.254
140	641.2	376.87	10.152	−807.7	−362.6	445.1	3.813	2.611	61.26	5.74	148	19.6	1.56	0.68	7.22	4.928
150	1040	357.9	16.328	−768.3	−355.7	412.6	4.047	2.908	52.24	6.27	133	23	1.55	0.69	5.31	5.942
160	1592.1	336.31	25.382	−726.1	−353.9	372.3	4.435	3.419	44.54	6.89	118	27.6	1.56	0.72	3.58	7.633
170	2328.3	310.5	38.974	−679.7	−359.4	320.3	5.187	4.459	37.69	7.69	103	33.7	1.89	0.83	2.06	11.01
180	3285.2	276.23	61.375	−625.0	−378.1	246.9	7.292	7.574	30.98	8.89	88	39.9	2.62	1.33	0.81	21.07
185	3861.7	251.36	80.435	−590.4	−398.5	191.9	11.109	13.527	26.92	9.84	80	45.3	3.8	1.38	0.33	40.71
190	4518.6	200.78	125.18	−532.7	−451.9	80.8	94.01	140.81	19.34	12.96	73	62	18.8	58.01	0.01	523.3
Uncertainty	a[1]	a[1]	a[1]	a[1]	a[1]	a[1]	c[1]	c[1]	h[2]	h[2]	h[3]	h[4]	h[6]	h[6]	h[5]	c[1]

[1]Ref. [96]; [2]Ref. [125]; [3]Ref. [118]; [4]Ref. [60]; [5]Ref. [73]; [6]Calc. from other properties.

Methanol CH_3OH (T_c = 512.6 K, p_c = 8.1035 MPa, ρ_c = 275.6 kg/m^3)

T_s, K	p_s, kPa	ρ', kg/m^3	ρ'', kg/m^3	h', kJ/kg	h'', kJ/kg	Δh_v, kJ/kg	$c_{p'}$, kJ/(kg K)	$c_{p''}$, kJ/(kg K)	η', 10^{-6} kg/(m s)	η'', 10^{-6} kg/(m s)	λ', 10^{-3} W/(m K)	λ'', 10^{-3} W/(m K)	Pr$'$	Pr$''$	σ, 10^{-3} N/m	β, 10^{-3}/K
175.61	0.0002	904.56	4.10^{-6}	−1471.8	−157.33	1314.5	2.2	1.26			243		108.5			
230	0.1511	850.76	0.0025	−1350.9	−92.77	1258.2	2.26	1.9	1890		224		19.05			1.1
280	6.177	803.22	0.0864	−1234.2	−38.60	1195.6	2.43	3.17	713		207		8.38		23.8	1.17
337.63	101.33	748.35	1.221	−1083.5	17.52	1101.1	2.83	4.44	329	11.1	188	18.3	4.95	2.69	18.9	1.28
360	229.92	725.36	2.668	−1018.0	35.91	1053.9	3.03	4.86	248	11.8	183	21.4	4.11	2.68	16.9	1.48
385	507.17	697.22	5.744	−938.7	51.43	990.15	3.31	5.44	187	12.7	178	24.9	3.47	2.78	14.5	1.73
410	1006.4	665.22	11.401	−852.0	58.35	910.35	3.63	6.36	141	13.6	173	29.1	2.96	2.97	11.8	2.04
435	1834.9	627.36	21.486	−756.2	53.26	809.48	4.06	7.71	107	14.6	170	34.2	2.56	3.29	9.08	2.28
460	3121.6	580.14	38.821	−648.6	41.38	689.97	4.71	8.2	82	15.9	165	41.6	2.34	3.13	6.08	3.94
500	6525	451.53	109.88	−426.5	−35.42	391.06	9.97	19.04	54	20.4		66.4		5.85	1.26	12.2
Uncertainty	a[1]	a[1]	d[1]	d[1]	d[1]	d[1]	c[1]	d[1]	f[2]	f[2]	f[2]	f[3,5]	f[6]	f[6]	e[4]	c[1]

[1]Ref. [91]; [2]Ref. [35]; [3]Ref. [120]; [4]Ref. [125]; [5]Estimated values; [6]Calc. from other properties.

Ethane C_2H_6 (T_c = 305.32 K, p_c = 4.872 MPa, ρ_c = 206.2 kg/m^3)

T_s, K	p_s, kPa	ρ', kg/m^3	ρ'', kg/m^3	h', kJ/kg	h'', kJ/kg	Δh_v, kJ/kg	$c_{p'}$, kJ/(kg K)	$c_{p''}$, kJ/(kg K)	η', 10^{-6} kg/(m s)	η'', 10^{-6} kg/(m s)	λ', 10^{-3} W/(m K)	λ'', 10^{-3} W/(m K)	Pr′	Pr″	σ, 10^{-3} N/m	β, 10^{-3}/K
90.37	0.001142	651.5	0.000046	−219.19	375.58	594.77	2.326	1.168	1280.8	3.04	255.62	2.91	11.65	1.22	31.67	1.692
150	9.64	585.2	0.234	−82.41	448	530.41	2.333	1.312	269.6	4.8	200.71	6.67	3.13	0.944	21.67	1.968
175	58.59	555.6	1.239	−23.21	478.35	501.56	2.403	1.387	187.9	5.58	176.17	8.64	2.56	0.896	17.58	2.196
184.57	101.33	543.8	2.05	0	489.4	489.4	2.439	1.433	166.4	5.89	166.97	9.49	2.43	0.888	16.03	2.313
200	217.2	524	4.17	38.3	506.19	467.89	2.512	1.537	138.3	6.39	152.56	11.01	2.28	0.892	13.59	2.55
225	589.4	488.9	10.72	103.4	529.76	426.36	2.687	1.775	104	7.28	130.24	13.97	2.15	0.924	9.76	3.14
250	1300.8	448	23.59	174.18	546.53	372.35	2.994	2.16	78.2	8.34	109.29	17.93	2.14	1.01	6.16	4.28
275	2495.2	395.8	48.64	254.92	550.55	295.63	3.702	3.11	56.9	9.92	89.37	24.32	2.36	1.27	2.91	7.37
300	4357.3	303.5	114.5	364.39	514.1	149.7	10.022	13.299	35	14.02	71.49	47.46	4.9	3.93	0.33	43.3
305.32	4872.2	206.2	206.2	438.99	438.99											
Uncertainty	a[1]	a[1]	a[1]	b[1]	b[1]	b[1]	c[1]	c[1]	d[2]	d[2]	d[2]	d[2]	d[3]	d[3]	e[4]	b[1]

[1]Refs. [8]; [2]Ref. [21]; [3]Calc. from other properties; [4]Ref. [53].

Ethylene C_2H_4 (T_c = 282.35 K, p_c = 5.042 MPa, ρ_c = 214.2 kg/m^3)

T_s, K	p_s, kPa	ρ', kg/m^3	ρ'', kg/m^3	h', kJ/kg	h'', kJ/kg	Δh_v, kJ/kg	$c_{p'}$, kJ/(kg K)	$c_{p''}$, kJ/(kg K)	η', 10^{-6} kg/(m s)	η'', 10^{-6} kg/(m s)	λ', 10^{-3} W/(m K)	λ'', 10^{-3} W/(m K)	Pr′	Pr″	σ, 10^{-3} N/m	β, 10^{-3}/K
103.99	0.122	654.6	0.00396	−158.10	409.42	567.52	2.429	1.187	685.7	0.77	270.65	6.8	6.16	0.135	28.14	1.93
125	2.53	627.7	0.068	−107.04	434.12	541.17	2.422	1.195	378.7	3.83	242.07	7.01	3.79	0.652	24.03	2.067
150	27.38	594.6	0.624	−46.74	462.39	509.13	2.404	1.232	233.4	5.31	209.67	8.51	2.68	0.769	19.32	2.284
169.38	101.33	567.7	2.09	0	482.41	482.41	2.418	1.295	175.5	6.03	186.47	9.68	2.28	0.807	15.83	2.529
175	139.4	559.5	2.81	13.66	487.76	474.1	2.428	1.32	163	6.23	180.09	10.04	2.2	0.819	14.84	2.618
200	455.5	521.2	8.49	75.68	508.13	432.45	2.529	1.492	120.5	7.13	153.73	11.86	1.98	0.897	10.63	3.177
225	1127.6	477.2	20.59	141.72	520.8	379.08	2.764	1.826	90.2	8.26	129.81	14.61	1.92	1.03	6.74	4.253
250	2329.5	422	44.97	216.09	520.38	304.3	3.363	2.661	65.4	9.93	106.84	19.56	2.06	1.35	3.27	7.052
275	4275.2	330.8	106.46	314.62	484.31	169.7	7.588	9.293	40.4	13.76	81.58	39.17	3.76	3.27	0.51	30.78
282.35	5041.8	214.2	214.2	399.43	399.43											
Uncertainty	a[1]	a[1]	a[1]	b[1]	b[1]	b[1]	c[1]	c[1]	e[2]	f[2]	e[2]	f[2]	e[3]	f[3]	f[4]	b[1]

[1]Ref. [98]; [2]Ref. [36]; [3]Calc. from other properties; [4]Ref. [99].

Ethine C_2H_2 (T_c = 308.7 K, p_c = 6.240 MPa, ρ_c = 230 kg/m^3)

T_s, K	p_s, kPa	ρ', kg/m^3	ρ'', kg/m^3	h', kJ/kg	h'', kJ/kg	Δh_v, kJ/kg	$c_{p'}$, kJ/(kg K)	$c_{p''}$, kJ/(kg K)	η', 10^{-6} kg/(m s)	η'', 10^{-6} kg/(m s)	λ', 10^{-3} W/(m K)	λ'', 10^{-3} W/(m K)	Pr′	Pr″	σ, 10^{-3} N/m	β, 10^{-3}/K
192.2	128	617	2.16	−369.5	214.8	584.3	3.09	1.47	169	7.35	55.9	11.2	9.34	0.96	19.1	2.2
200	189	606	3.11	−351.8	222.9	574.7	3.12	1.51	156	7.67	54.3	12	8.96	0.97	17.6	2.4
210	304	590	4.86	−331.6	230.9	562.5	3.15	1.59	146	8.1	51.9	13.1	8.86	0.98	15.6	2.66
230	689	556	10.8	−271.6	248.6	520.2	3.27	1.8	127	8.68	48	15.4	8.65	1.01	11.8	3.2
240	986	538	15.6	−236.1	254.4	490.5	3.35	1.93	116	9.03	48.3	16.9	8.39	1.03	9.92	3.49
250	1370	519	22.1	−202.0	257.6	459.6	3.46	2.14	99.6	9.44	44.9	18.5	7.68	1.09	8.12	3.87
270	2450	473	41	−136.2	257	393.2	3.87	2.64	79.9	10.5	43	22.6	7.19	1.23	4.64	5.56
280	3190	445	54	−100.5	252.8	363.3	4.25	2.93	66.9	11.2	42.2	25	6.75	1.31	3.11	6.45
290	4080	411	73.2	−66.2	238.8	305	5.14	3.39	56.9	12.1	41.5	28.3	7.04	1.45	1.73	10.36
308.7	6240	231	231	104.7	104.7											
Uncertainty	h[1]	h[1]	h[1]	h[1]	h[1]	h[1]	h[2,3]	h[1]	h[2,4]	h[5,6]	h[7]	h[8,9]	h[12]	h[12]	h[10]	h[11]

[1]Ref. [60]; [2]Ref. [89]; [3]Ref. [137]; [4]Ref. [59]; [5]Ref. [106]; [6]Ref. [42]; [7]Ref. [93]; [8]Ref. [117]; [9]Ref. [108]; [10]Ref. [40]; [11]Estimated values; [12]Calc. from other properties.

Ethanol C_2H_6O, CH_3CH_2OH (T_c = 513.90 K, p_c = 6.148 MPa, ρ_c = 276.0 kg/m^3)

T_s, K	p_s, kPa	ρ', kg/m^3	ρ'', kg/m^3	h', kJ/kg	h'', kJ/kg	Δh_v, kJ/kg	$c_{p'}$, kJ/(kg K)	$c_{p''}$, kJ/(kg K)	η', 10^{-6} kg/(m s)	η'', 10^{-6} kg/(m s)	λ', 10^{-3} W/(m K)	λ'', 10^{-3} W/(m K)	Pr$'$	Pr$''$	σ, 10^{-3} N/m	β, 10^{-3}/K
300	8.84	783.82	0.164	265.2	1185	919.7	2.597	1.605	1043	8.6	175.1	15.1	15.47	0.91	21.95	1.083
320	25.46	766.38	0.446	319.6	1216.1	896.4	2.838	1.673	736.3	9.2	171.4	16.8	12.19	0.92	20.25	1.174
340	63.54	747.74	1.058	378.7	1247.0	868.3	3.064	1.753	534	9.8	167.6	18.7	9.76	0.92	18.45	1.3
351.39	101.33	736.44	1.647	414.3	1264.3	849.9	3.185	1.806	448.7	10.2	165.4	19.9	8.64	0.93	17.38	1.388
375	239.88	711.05	3.75	492.4	1298.5	806.0	3.423	1.944	319	11	160.9	22.6	6.79	0.94	15.09	1.619
400	524.46	680.64	8.009	581.2	1331.2	750.0	3.665	2.148	226.4	11.8	155.7	25.3	5.33	1	12.53	1.959
425	1029.28	645.46	15.701	676.0	1358.3	682.2	3.923	2.444	163	12.6	149.6	28.2	4.27	1.09	9.85	2.472
450	1850.55	603.51	29.001	777.7	1377.2	599.5	4.261	2.916	118.5	13.6	141.2	31.6	3.58	1.25	7.08	3.36
475	3096.32	550.1	51.995	888.7	1383.7	495	4.877	3.823	86.7	14.8	127.2	35.7	3.32	1.58	4.25	5.36
513.9	6148	276	276	1191.8	1191.8				63.7	16.9	100.1	42.5			1.43	
Uncertainty	a[1]	a[1]	b[1]	c[1]	c[1]	c[1]	d[1]	d[1]	f[1]	e[2]	f[1]	h[3,4]	h[5]	h[5]	e[1]	d[1]

[1]Ref. [16]; [2]Ref. [125]; [3]Ref. [118]; [4]Ref. [108]; [5]Calc. from other properties.

Ethylenoxide C_2H_4O, $(CH_2)_2O$ (T_c = 469 K, p_c = 7.194 MPa, ρ_c = 315 kg/m^3)

T_s, K	p_s, kPa	ρ', kg/m^3	ρ'', kg/m^3	h', kJ/kg	h'', kJ/kg	Δh_v, kJ/kg	$c_{p'}$, kJ/(kg K)	$c_{p''}$, kJ/(kg K)	η', 10^{-6} kg/(m s)	η'', 10^{-6} kg/(m s)	λ', 10^{-3} W/(m K)	λ'', 10^{-3} W/(m K)	Pr$'$	Pr$''$	σ, 10^{-3} N/m	β, 10^{-3}/K
283.5	101.3	889	1.94	−440	129	569	1.96	1.09	284	9	158	11.5	3.52	0.85	25.87	1.6
300	186	866	3.44	−409	144	553	2.01	1.17	245	9.6	152	13.6	3.24	0.83	23.24	1.71
320	359	835	6.33	−367	161	528	2.09	1.28	210	10.3	144	16.3	3.04	0.81	20.1	1.86
340	621	804	10.8	−333	178	511	2.19	1.4	182	11	135	19.3	2.93	0.8	17.03	2.08
360	1030	760	17.5	−289	193	482	2.32	1.55	160	11.7	127	22.5	2.92	0.81	14.03	2.32
380	1660	721	27.2	−238	206	444	2.48	1.73	142	12.5	119	25.1	2.97	0.86	11.11	2.68
400	2480	691	41.1	−183	215	398	2.68	1.99	128	13.4	110	29.9	3.12	0.89	8.29	3.26
420	3450	682	61.6	−129	219	348	2.92	2.47	116	14.4	102	34.5	3.34	1.01	5.5	4.42
440	4830	584	93.9	−65	211	276	3.21	3.4	105	15.9	93	40.4	3.63	1.34	3.05	6.08
469	7194	315	315	66	66				47	47	69	69				
Uncertainty	h[1]	h[2]	h[3]	h[11]	h[4,3]	h[1]	h[5]	h[3,4]	h[6,1]	h[1,7]	h[8,1]	h[9,1]	h[12]	h[12]	h[10]	h[11]

[1]Ref. [22]; [2]Ref. [97]; [3]Ref. [52]; [4]Ref. [6]; [5]Ref. [67]; [6]Ref. [71]; [7]Ref. [107]; [8]Ref. [68]; [9]Ref. [69]; [10]Ref. [48]; [11]Estimated values; [12]Calc. from other properties.

Acetic acid $C_2H_4O_2$ (T_c = 594.75 K, p_c = 5.790 MPa, ρ_c = 350.6 kg/m^3)

T_s, K	p_s, kPa	ρ', kg/m^3	ρ'', kg/m^3	h', kJ/kg	h'', kJ/kg	Δh_v, kJ/kg	$c_{p'}$, kJ/(kg K)	$c_{p''}$, kJ/(kg K)	η', 10^{-6} kg/(m s)	η'', 10^{-6} kg/(m s)	λ', 10^{-3} W/(m K)	λ'', 10^{-3} W/(m K)	Pr$'$	Pr$''$	σ, 10^{-3} N/m	β, 10^{-3}/K
391.15	101.3	939	1.93	260	642	382	2.42	1.39	372	10.4	158	20.7	5.7	0.7	18.1	1.4
420	230	900	4.53	326	703	377	2.55	1.49	276	11.4	150	23.8	4.69	0.71	15.3	1.46
440	382	874	7.56	372	740	368	2.66	1.58	232	11.9	143	26.3	4.32	0.71	13.5	1.52
460	427	846	12	420	775	355	2.76	1.69	194	12.4	137	29	3.91	0.72	11.6	1.68
480	898	815	18.4	473	807	334	2.91	1.82	166	13	131	32.2	3.69	0.73	9.7	1.94
500	1320	782	27.3	524	834	310	3.04	1.99	138	13.7	125	35.9	3.36	0.76	7.9	2.29
520	1890	743	39.9	580	850	270	3.21	2.24	115	14.4	118	40.3	3.13	0.8	6	2.86
540	2630	697	57.8	643	874	231	3.43	2.66	95	15.3	112	45.9	2.91	0.89	4.28	3.82
560	3590	642	85	710	882	172	3.82	3.59	76	16.5	105	53.6	2.76	1.11	2.47	5.47
594.75	5790	350.6	350.6	854	854						93	93				
Uncertainty	h[1]	h[1]	h[2]	h[3]	h[3]	h[13]	h[4]	h[5,2]	h[6,7]	h[6,8]	h[9,10,11]	h[10,12]	h[14]	h[14]	h[1]	h[13]

[1]Ref. [125]; [2]Ref. [52]; [3]Ref. [12]; [4]Ref. [63]; [5]Ref. [115]; [6]Ref. [87]; [7]Ref. [59]; [8]Ref. [107]; [9]Ref. [94]; [10]Ref. [89]; [11]Ref. [88]; [12]Ref. [108]; [13]Estimated values; [14]Calc. from other properties.

Propane C_3H_8 (T_c = 369.89 K, p_c = 4.251 MPa, ρ_c = 220.5 kg/m^3)

T_s, K	p_s, kPa	ρ', kg/m^3	ρ'', kg/m^3	h', kJ/kg	h'', kJ/kg	Δh_v, kJ/kg	$c_{p'}$, kJ/(kg K)	$c_{p''}$, kJ/(kg K)	η', 10^{-6} kg/(m s)	η'', 10^{-6} kg/(m s)	λ', 10^{-3} W/(m K)	λ'', 10^{-3} W/(m K)	Pr$'$	Pr$''$	σ, 10^{-3} N/m	β, 10^{-3}/K
85.53	1.7×10^{-7}	733.1	1×10^{-8}	−196.63	366.26	562.9	1.916	0.879	10779	2.64	207.92	1.71	99.32	1.36	37.71	1.425
200	20.19	615.4	0.542	32.53	488.63	456.1	2.127	1.287	288	5.51	147.84	8.97	4.14	0.791	20.27	1.752
225	77.02	587.8	1.873	86.86	518.7	431.85	2.219	1.407	211.4	6.15	132.73	11.04	3.53	0.784	16.68	1.94
231.04	101.33	580.9	2.416	100.36	525.95	425.59	2.246	1.44	197.2	6.31	129.18	11.57	3.43	0.786	15.83	1.997
250	217.96	558.3	4.94	143.93	548.45	404.52	2.343	1.558	160	6.8	118.37	13.32	3.17	0.796	13.21	2.218
275	501.8	526.1	10.93	204.64	576.9	372.26	2.507	1.756	123.2	7.5	105.02	15.95	2.94	0.826	9.89	2.652
300	997.7	489.4	21.63	270.15	602.6	332.45	2.74	2.041	95.3	8.34	92.86	19.24	2.81	0.885	6.76	3.409
325	1783.3	445.2	40.43	342.46	622.87	280.41	3.128	2.552	72.5	9.51	81.81	23.89	2.77	1.02	3.89	5.031
350	2951.4	383.8	77.03	426.7	629.95	203.26	4.208	4.16	51.6	11.63	71.48	32.73	3.03	1.48	1.4	10.95
369.89	4251.2	220.5	220.5	555.24	555.24											
Uncertainty	a[1]	a[1]	a[1]	b[1]	b[1]	b[1]	c[1]	c[1]	d[2]	d[2]	d[3]	d[3]	d[4]	d[4]	e[5]	b[1]

[1]Ref. [56]; [2]Ref. [128]; [3]Ref. [65]; [4]Calc. from other properties; [5]Ref. [4].

Propylene C_3H_6, $CH_3CH{=}CH_2$ (T_c = 364.21 K, p_c = 4.555 MPa, ρ_c = 230.1 kg/m^3)

T_s, K	p_s, kPa	ρ', kg/m^3	ρ'', kg/m^3	h', kJ/kg	h'', kJ/kg	Δh_v, kJ/kg	$c_{p'}$, kJ/(kg K)	$c_{p''}$, kJ/(kg K)	η', 10^{-6} kg/(m s)	η'', 10^{-6} kg/(m s)	λ', 10^{-3} W/(m K)	λ'', 10^{-3} W/(m K)	Pr$'$	Pr$''$	σ, 10^{-3} N/m	β, 10^{-3}/K
225.53	101.33	610.1	2.358	90.12	529.08	438.96	2.193	1.332	151	6.6	119	9.5	2.78	0.93	16.5	2.039
240	187.15	591.8	4.178	122.32	544.59	422.27	2.25	1.413	132	7.1	111	11.2	2.68	0.9	14.7	2.2
255	325.97	571.9	7.044	156.71	560.08	403.37	2.324	1.512	108	7.5	104	13	2.41	0.88	12.6	2.417
270	531.03	550.8	11.239	192.34	574.7	382.36	2.414	1.632	101	8	98.6	14.9	2.47	0.88	10.5	2.706
285	819.2	528	17.2	229.48	588.12	358.64	2.53	1.782	99.2	8.7	93.6	17.1	2.68	0.91	8.7	3.109
300	1208.6	503.1	25.57	268.52	599.85	331.32	2.684	1.976	90.3	9.3	90.9	19.4	2.67	0.94	6.5	3.706
315	1718.6	474.9	37.35	310.03	609.01	298.98	2.906	2.279	80.9	10.1	88	22.2	2.67	1.04	5.1	4.68
330	2370.8	441.7	54.41	355.01	614.32	259.32	3.279	2.802	78.7	11.4	83.3	25.4	3.1	1.26	3.4	6.52
345	3191.3	398.9	81.3	405.8	612.16	206.36	4.143	4.102	61.1	12.7	76.1	29.6	3.33	1.76	2	11.39
364.21	4555	230.1	230.1	529.62	529.62				32	32	49.3	49.3				
Uncertainty	a[1]	a[1]	a[1]	b[1]	b[1]	b[1]	c[1]	c[1]	h[2]	h[2]	h[3]	h[4,5]	h[6]	h[6]	h[2]	b[1]

[1]Ref. [81]; [2]Ref. [22]; [3]Ref. [93]; [4]Ref. [74]; [5]Ref. [108]; [6]Calc. from other properties.

1-Propanol C_3H_8O, $CH_3CH_2CH_2OH$ (T_c = 536.85 K, p_c = 5.050 MPa, ρ_c = 273 kg/m^3)

T_s, K	p_s, kPa	ρ', kg/m^3	ρ'', kg/m^3	h$'$, kJ/kg	h'', kJ/kg	Δh_v, kJ/kg	$c_{p'}$, kJ/(kg K)	$c_{p''}$, kJ/(kg K)	η', 10^{-6} kg/(m s)	η'', 10^{-6} kg/(m s)	λ', 10^{-3} W/(m K)	λ'', 10^{-3} W/(m K)	Pr$'$	Pr$''$	σ, 10^{-3} N/m	β, 10^{-3}/K
373.2	109.4	732.5	2.26	0	687	687	3.21	1.65	447	9.61	142.4	20.9	10.1	0.76	17.6	1.33
393.2	218.5	711	4.43	65	710	645	3.47	1.82	337	10.3	139.2	23	8.4	0.82	16.15	1.52
413.2	399.2	687.5	8.05	139	733	594	3.86	1.93	250	10.9	138.4	26.2	6.97	0.8	14.42	1.79
433.2	683.6	660	13.8	222	766	544	4.36	2.05	188	11.5	133.5	28.9	5.14	0.82	12.7	2.19
453.2	1089	628.5	22.5	315	802	486	5.02	2.2	148	12.2	127.9	31.4	5.81	0.85	10.77	2.7
473.2	1662	592	35.3	433	860	427	5.9	2.36	119	12.9	120.7	34.7	5.82	0.88	8.85	3.35
493.2	2426	548.5	55.6	548	904	356	6.78	2.97	90.6	14.2	111.8	38	5.5	1.11	6.35	4.36
513.2	3402	492	90.4	691	955	264	7.79	3.94	70	15.7	100.6	43.9	5.42	1.41	4.04	6.17
523.2	3998	452.5	118			209			61.4	17	94.1	47.5			2.6	8.4
533.1	4689	390.5	161			138			53.9	19.3	89.3	53.5		0.96		
Uncertainty	h[1]	h[1]	h[1]	h[9]	h[9]	h[1]	h[2]	h[3,4]	h[1,5]	h[5,6]	h[2]	h[5,7]	h[9]	h[9]	h[2]	h[8]

[1]Ref. [125]; [2]Ref. [73]; [3]Ref. [67]; [4]Ref. [18]; [5]Ref. [68]; [6]Ref. [107]; [7]Ref. [108]; [8]Estimated values; [9]Calc. from other properties.

Propylene oxide C_3H_6O, $CH_3(CHCH_2)O$ (T_c = 482.2 K, p_c = 4.920 MPa, ρ_c = 312 kg/m^3)

T_s, K	p_s, kPa	ρ', kg/m^3	ρ'', kg/m^3	h', kJ/kg	h'', kJ/kg	Δh_v, kJ/kg	$c_{p'}$, kJ/(kg K)	$c_{p''}$, kJ/(kg K)	η', 10^{-6} kg/(m s)	η'', 10^{-6} kg/(m s)	λ', 10^{-3} W/(m K)	λ'', 10^{-3} W/(m K)	Pr$'$	Pr$''$	σ, 10^{-3} N/m	β, 10^{-3}/K
307.5	101.3	812	2.38	−293	184	477	2.06	1.32	278	9.1	147	12.1	3.9	0.9	19.9	1.59
320	159	796	3.57	−271	198	469	2.1	1.39	251	9.5	143	13.3	3.69	0.99	18.2	1.68
340	297	769	6.39	−220	220	440	2.18	1.49	217	10.2	135	15.5	3.49	0.98	15.5	1.8
360	496	740	10.7	−177	242	419	2.29	1.62	191	10.8	128	17.8	3.41	0.98	12.9	2.04
380	814	709	17.2	−135	263	39	2.42	1.76	171	11.5	120	20.5	3.44	0.99	10.4	2.31
400	1230	675	26.6	−86	282	368	2.6	1.94	155	12.3	113	23.5	3.57	1.02	8	2.72
420	1790	636	40.5	−37	298	335	2.81	2.19	143	13.1	105	26.9	3.84	1.07	5.7	3.34
440	2480	591	61.1	33	309	276	3.07	2.63	133	14.1	96	31.3	4.23	1.18	3.5	3.76
460	3450	531	95.9	106	307	201	3.38	3.83	125	15.5	88	47.4	4.79	1.25	1.6	12.69
482.2	4920	312	312	200	200				48	48	71	71				
Uncertainty	h[1]	h[2]	h[3]	h[13]	h[3,4]	h[1]	h[5]	h[3,4]	h[1,6]	h[1,7,8]	h[9,1]	h[10,1]	h[13]	h[13]	h[11]	h[12]

[1]Ref. [22]; [2]Ref. [97]; [3]Ref. [52]; [4]Ref. [6]; [5]Ref. [67]; [6]Ref. [71]; [7]Ref. [70]; [8]Ref. [107]; [9]Ref. [68]; [10]Ref. [69]; [11]Ref. [48]; [12]Estimated values; [13]Calc. from other properties.

Isopropylalcohol C_3H_8O, $(CH_3)_2CHOH$ (T_c = 508.75 K, p_c = 5.370 MPa, r_c = 274 kg/m^3)

T_s, K	p_s, kPa	ρ', kg/m^3	ρ'', kg/m^3	h', kJ/kg	h'', kJ/kg	Δh_v, kJ/kg	$c_{p'}$, kJ/(kg K)	$c_{p''}$, kJ/(kg K)	η', 10^{-6} kg/(m s)	η'', 10^{-6} kg/(m s)	λ', 10^{-3} W/(m K)	λ'', 10^{-3} W/(m K)	Pr$'$	Pr$''$	σ, 10^{-3} N/m	β, 10^{-3}/K
355.65	101.3	732.3	2.06	0	677.8	677.8	3.37	1.63	502	9.08	131.1	19.8	12.9	0.75	18.6	1.41
373	200	712.7	4.15	60.1	688	627.9	3.55	1.71	376	9.8	127.5	22.2	10.5	0.75	17.2	1.76
390	380	683	7.73	121.8	736.8	615	3.71	1.8	295	10.3	124.3	24.6	8.81	0.75	14.2	2.12
408	580	660	14.3	190.2	767.9	577.7	3.88	1.94	230	10.9	122.8	27.1	7.27	0.78	11.84	2.39
425	925	630.1	21	257.6	796.1	538.5	4.04	2.15	184	11.4	120.1	29.3	6.19	0.84	9.4	2.75
443	1425	597.4	32.78	331.8	822.9	491.1	4.2	2.37	147	11.9	117.3	31.8	5.27	0.89	6.9	3.22
459	2025	566	46.4	400.1	841.7	441.6	4.34	2.83	122	12.5	115.8	34.9	4.57	1.01	4.97	3.94
478	3039	514.8	72.3	484	851.5	367.5	4.49	3.97	93.5	13.7	113.2	38.9	3.71	1.4	2.6	5.46
498	4052	460.5	108.4			284.5			72.5	15.2	110.7	42.3		1.05	23.46	
508	5369	288	252			82.5				28.2	107.7	47.1			0	
Uncertainty	h[1,2]	h[1,2]	h[1,2]	h[9]	h[9]	h[1,3]	h[2]	h[4,5]	h[1]	h[1,6]	h[1]	h[1,7]	h[9]	h[9]	h[1]	h[8]

[1]Ref. [125]; [2]Ref. [116]; [3]Ref. [132]; [4]Ref. [42]; [5]Ref. [18]; [6]Ref. [107]; [7]Ref. [108]; [8]Estimated values; [9]Calc. from other properties.

Acetone C_3H_6O, CH_3COCH_3 (T_c = 508.10 K, p_c = 4.700 MPa, ρ_c = 273 kg/m^3)

T_s, K	p_s, kPa	ρ', kg/m^3	ρ'', kg/m^3	h', kJ/kg	h'', kJ/kg	Δh_v, kJ/kg	$c_{p'}$, kJ/(kg K)	$c_{p''}$, kJ/(kg K)	η', 10^{-6} kg/(m s)	η'', 10^{-6} kg/(m s)	λ', 10^{-3} W/(m K)	λ'', 10^{-3} W/(m K)	Pr$'$	Pr$''$	σ, 10^{-3} N/m	β, 10^{-3}/K
329.23	101.33	748.95	2.268	0	501.43	501.43	2.229	1.567	235	9.4	142	12.7	3.69	1.16	18.4	1.587
340	144.5	736.03	3.173	24.23	513.55	489.32	2.264	1.635	213	9.8	137	14.1	3.52	1.14	17	1.659
360	261.88	711.08	5.597	70.28	535.79	465.51	2.336	1.77	188	10.4	129	16.1	3.4	1.14	14.5	1.824
380	442.4	684.55	9.313	117.89	557.43	439.54	2.42	1.921	165	11.1	121	18.5	3.3	1.15	12.1	2.043
400	705.59	655.92	14.83	167.3	578.03	410.74	2.519	2.099	141	11.8	112	21.2	3.17	1.17	9.6	2.346
420	1073.31	624.5	22.895	218.84	596.98	378.14	2.643	2.322	119	12.6	104	24.2	3.02	1.21	7.1	2.789
440	1570.25	589.14	34.72	272.98	613.25	340.28	2.81	2.634	99	13.5	96	27.2	2.9	1.31	4.6	3.49
460	2224.94	547.85	52.555	330.55	625.11	294.57	3.067	3.156	80	14.4	87	31	2.82	1.47	3.1	4.76
480	3072.5	496.13	81.608	393.32	628.82	235.5	3.597	4.338	64	15.8	77	36	2.99	1.9	1.6	7.84
508.1	4700	272.97	272.97	544.34	544.34				49	49	58	58				
Uncertainty	a[1]	a[1]	b[1]	c[1]	c[1]	c[1]	d[1]	d[1]	h[2,3,4]	h[5,6]	h[7,8,9]	h[8,9]	h[11]	h[11]	h[10]	d[1]

[1]Ref. [58]; [2]Ref. [89]; [3]Ref. [82]; [4]Ref. [59]; [5]Ref. [106]; [6]Ref. [107]; [7]Ref. [93]; [8]Ref. [127]; [9]Ref. [108]; [10]Ref. [61]; [11]Calc. from other properties.

Methyl acetate $C_3H_6O_2$ (T_c = 506.8 K, p_c = 4.687 MPa, ρ_c = 325 kg/m^3)

T_s, K	p_s, kPa	ρ', kg/m^3	ρ'', kg/m^3	h′, kJ/kg	h'', kJ/kg	Δh_v, kJ/kg	$c_{p'}$, kJ/(kg K)	$c_{p''}$, kJ/(kg K)	η', 10^{-6} kg/(m s)	η'', 10^{-6} kg/(m s)	λ', 10^{-3} W/(m K)	λ'', 10^{-3} W/(m K)	Pr′	Pr″	σ, 10^{-3} N/m	β, 10^{-3}/K
331	101.3	875	2.83	−173.4	228.5	401.9	1.92	1.19	260	8.9	157	14.2	3.18	0.75	19.4	1.64
350	200	850	5.16	−136.1	249.1	385.2	1.99	1.25	225	9.5	146	15.7	3.07	0.76	17	1.79
370	359	820	8.87	−96.5	269.8	366.3	2.08	1.35	192	10.1	133	17.5	3	0.78	14.7	1.98
390	537	780	14.5	−57.7	289.8	347.5	2.18	1.45	168	10.7	122	19.5	3	0.8	12	2.19
410	854	750	22.7	−17.8	308.8	326.6	2.32	1.57	145	11.4	110	21.7	3.04	0.82	9.4	2.53
430	1344	715	34.6	26.7	326	297.3	2.46	1.72	121	12.1	98	24.1	3.05	0.86	6.9	3
450	1930	680	52.2	76.4	340.2	263.8	2.65	1.95	99	13.1	86	27	3.06	0.95	4.6	3.78
470	2688	620	79.3	126.7	348.6	221.9	2.94	2.38	80	14.1	74	30.4	3.18	1.1	2.4	5.12
490	3723	540	127.8	196.4	342.9	146.5	3.58	3.86	62	16.1	61	35.3	3.64	1.76	1.1	8.89
506.8	4687	325	325	254.6	254.6				56	56	50.3	50.3				
Uncertainty	h[1]	h[1]	h[2]	h[10]	h[3,2]	h[1]	h[4]	h[1,2]	h[1,5]	h[1,6]	h[1,7]	h[1,7]	h[10]	h[10]	h[1,8]	h[9]

[1]Ref. [22]; [2]Ref. [52]; [3]Ref. [115]; [4]Ref. [63]; [5]Ref. [126]; [6]Ref. [107]; [7]Ref. [108]; [8]Ref. [89]; [9]Estimated values; [10]Calc. from other properties.

n-Butane C_4H_{10} (T_c = 425.13 K, p_c = 3.796 MPa, ρ_c = 228 kg/m^3)

T_s, K	p_s, kPa	ρ', kg/m^3	ρ'', kg/m^3	h', kJ/kg	h'', kJ/kg	Δh_v, kJ/kg	$c_{p'}$, kJ/(kg K)	$c_{p''}$, kJ/(kg K)	η', 10^{-6} kg/(m s)	η'', 10^{-6} kg/(m s)	λ', 10^{-3} W/(m K)	λ'', 10^{-3} W/(m K)	Pr′	Pr″	σ, 10^{-3} N/m	β, 10^{-3}/K
134.9	0.000666	735	0.000034	−89.82	406.11	495.93	1.973	1.106	2304.3	3.32	176.56	4.85	25.75	0.757	33.49	1.271
225	10.57	649.9	0.331	93.36	518.07	424.71	2.127	1.412	349.8	5.6	137.5	10.25	5.41	0.771	20.97	1.506
250	39.15	625	1.118	147.6	552.57	404.97	2.213	1.523	259.3	6.21	125.77	12.2	4.56	0.775	17.72	1.635
272.66	101.33	601.3	2.71	198.87	584.58	385.71	2.31	1.641	203.5	6.76	115.53	14.14	4.07	0.784	14.88	1.795
300	257.6	570.7	6.52	264	623.58	359.58	2.451	1.811	155.6	7.44	103.93	16.78	3.67	0.802	11.6	2.073
325	520.1	539.9	12.83	327.34	658.9	331.56	2.612	2.002	123.3	8.12	94.24	19.6	3.42	0.83	8.76	2.467
350	944.2	505.2	23.39	395.14	692.84	297.7	2.82	2.25	97.6	8.96	85.5	23.06	3.22	0.875	6.1	3.13
375	1581.6	463.7	41.01	468.72	723.35	254.63	3.132	2.637	75.9	10.11	77.68	27.66	3.06	0.964	3.66	4.45
400	2495.4	408.5	73.08	551.22	745.21	193.99	3.838	3.623	56	12.03	70.6	35.03	3.04	1.24	1.53	8.52
425.13	3796	228	228	693.91	693.91											
Uncertainty	a[1]	a[1]	a[1]	b[1]	b[1]	b[1]	c[1]	c[1]	d[2]	d[2]	d[3]	d[3]	d[4]	d[4]	e[5]	b[1]

[1]Refs. [9]; [2]Ref. [130]; [3]Ref. [86]; [4]Calc. from other properties; [5]Ref. [10].

Isobutane C_4H_{10} (T_c = 407.81 K, p_c = 3.629 MPa, ρ_c = 225.5 kg/m^3)

T_s, K	p_s, kPa	ρ', kg/m^3	ρ'', kg/m^3	h', kJ/kg	h'', kJ/kg	Δh_v, kJ/kg	$c_{p'}$, kJ/(kg K)	$c_{p''}$, kJ/(kg K)	η', 10^{-6} kg/(m s)	η'', 10^{-6} kg/(m s)	λ', 10^{-3} W/(m K)	λ'', 10^{-3} W/(m K)	Pr′	Pr″	σ, 10^{-3} N/m	β, 10^{-3}/K
113.73	0.000023	740.3	0.000001	−112.38	368.32	480.7	1.689	0.88	8767.2	2.85	157.92	2.27	93.76	1.1	33.23	1.276
225	18.62	632.5	0.586	95.57	490.85	395.28	2.061	1.353	367.5	5.7	118.44	10.03	6.39	0.769	18.92	1.623
250	63.35	606.3	1.825	148.44	523.43	374.99	2.168	1.481	262	6.3	107.94	12.17	5.26	0.767	15.83	1.784
261.4	101.33	593.8	2.83	173.49	538.6	365.1	2.222	1.547	227.8	6.58	103.29	13.2	4.9	0.771	14.44	1.877
275	167.51	578.4	4.53	204.24	556.82	352.58	2.293	1.631	194.4	6.91	97.91	14.48	4.55	0.778	12.81	2.01
300	370	548.3	9.61	263.5	590.37	326.87	2.442	1.81	148.2	7.55	88.6	17.02	4.09	0.802	9.89	2.349
325	716.6	514.7	18.42	326.92	623.2	296.28	2.631	2.036	114.7	8.28	80.17	20.02	3.76	0.842	7.11	2.9
350	1258.7	475.5	33.23	395.61	653.77	258.16	2.898	2.355	88.6	9.24	72.68	23.93	3.53	0.91	4.52	3.95
375	2055.7	425.3	59.24	471.92	678.4	206.48	3.404	3.031	66.2	10.81	66.12	30.04	3.41	1.09	2.2	6.69
407.81	3629	225.5	225.5	633.94	633.94											
Uncertainty	a[1]	a[1]	a[1]	b[1]	b[1]	b[1]	c[1]	c[1]	d[2]	d[2]	d[3]	d[3]	d[4]	d[4]	e[5]	b[1]

[1] Refs. [9]; [2]Ref. [130]; [3]Ref. [84]; [4]Calc. from other properties; [5]Ref. [4].

1,2-Butadiene C_4H_6, $CH_3CH{=}C{=}CH_2$ (T_c = 443.7 K, p_c = 4.500 MPa, ρ_c = 246.8 kg/m^3)

T_s, K	p_s, kPa	ρ', kg/m^3	ρ'', kg/m^3	h', kJ/kg	h'', kJ/kg	Δh_v, kJ/kg	$c_{p'}$, kJ/(kg K)	$c_{p''}$, kJ/(kg K)	η', 10^{-6} kg/(m s)	η'', 10^{-6} kg/(m s)	λ', 10^{-3} W/(m K)	λ'', 10^{-3} W/(m K)	Pr′	Pr″	σ, 10^{-3} N/m	β, 10^{-3}/K
284	101.3	651	2.32	−197	237	434	2.2	1.48	200	7.4	126	12.5	3.62	0.88	18	1.71
300	189	643	4.04	−166	257	423	2.24	1.56	185	7.78	119	14.1	3.48	0.86	15.7	1.87
315	265	625	6.43	−131	275	406	2.3	1.65	170	8.27	113	15.8	3.46	0.86	13.9	2.02
330	445	605	9.8	−94	293	387	2.41	1.75	150	8.76	107	17.5	3.38	0.88	12.1	2.18
345	661	585	14.4	−57	311	368	2.49	1.87	134	9.26	102	19.3	3.27	0.9	10.4	2.39
360	945	563	20.7	−19	327	346	2.6	2.01	116	9.77	98	21.2	3.08	0.93	8.65	3.26
375	1310	537	29.2	79	341	322	2.72	2.18	100	10.4	93	23.3	2.92	0.97	7	3.39
390	1770	507	40.7	61	354	293	2.87	2.43	85	11	88	25.6	2.77	1.04	5.3	3.78
400	2140	485	50.8	88	359	271	3.01	2.68	76	11.5	82	27.3	2.79	1.13	4.1	4.28
443.7	4500	246.8	246.8	255	255				43	43	49	49				
Uncertainty	h[1,2]	h[1]	h[3]	h[10]	h[1,3]	h[1]	h[1]	h[1,3]	h[1,4]	h[1,5]	h[6]	h[7,8]	h[10]	h[10]	h[1]	h[9]

[1]Ref. [22]; [2]Ref. [27]; [3]Ref. [52]; [4]Ref. [59]; [5]Ref. [42]; [6]Ref. [93]; [7]Ref. [74]; [8]Ref. [108]; [9]Estimated values; [10]Calc. from other properties.

1,3-Butadiene C_4H_6, $CH_2{=}CHCH{=}CH_2$ (T_c = 425.15 K, p_c = 4.330 MPa, ρ_c = 245 kg/m^3)

T_s, K	p_s, kPa	ρ', kg/m^3	ρ'', kg/m^3	h', kJ/kg	h'', kJ/kg	Δh_v, kJ/kg	$c_{p'}$, kJ/(kg K)	$c_{p''}$, kJ/(kg K)	η', 10^{-6} kg/(m s)	η'', 10^{-6} kg/(m s)	λ', 10^{-3} W/(m K)	λ'', 10^{-3} W/(m K)	Pr′	Pr″	σ, 10^{-3} N/m	β, 10^{-3}/K
268.69	101.3	650	2.53	493.3	908.7	415.4	2.14	1.42	200	7.57	126	9.54	3.4	1.13	16.6	1.79
285	184	631	4.41	529	928.4	399.4	2.22	1.53	164	8.43	117	12.3	3.11	1.05	14.5	1.92
300	298	612	6.97	563	946.4	383.4	2.29	1.63	138	8.91	110	14.7	2.87	0.99	12.7	2.07
315	458	593	10.5	598.4	964.4	366	2.37	1.74	117	9.41	103	17.3	2.169	0.95	10.9	2.24
330	676	572	15.5	635	981.7	346.7	2.47	1.87	99.5	9.94	95.6	19.9	2.57	0.93	9.12	2.5
350	1080	541	26.7	686.5	1003.8	317.3	2.63	2.07	84.3	10.7	86.6	23.7	2.56	0.93	6.86	2.97
370	1630	507	38.7	741.5	1023.2	281.7	2.81	2.35	71.3	11.6	78	27.5	2.57	1.02	4.73	3.81
390	2370	464	53.5	800.1	1038.3	238.2	3.03	2.92	61.7	12.6	69.8	31.6	2.68	1.16	2.75	5.45
410	3350	405	101	867.5	1041.4	173.9	3.28	4.54	53.4	15	62	37.8	2.83	1.3	1	12.46
425.15	4330	245	245								53.7	53.7				
Uncertainty	h[1]	h[1]	h[1]	h[1]	h[1]	h[1]	h[1,2]	h[3,4]	h[1,5]	h[6,7]	h[8]	h[9,10]	h[13]	h[13]	h[11]	h[12]

[1]Ref. [125]; [2]Ref. [67]; [3]Ref. [6]; [4]Ref. [18]; [5]Ref. [71]; [6]Ref. [70]; [7]Ref. [42]; [8]Ref. [68]; [9]Ref. [69]; [10]Ref. [108]; [11]Ref. [73]; [12]Estimated values; [13]Calc. from other properties.

n-Butanol $C_4H_{10}O$, $C_2H_5CH_2CH_2OH$ (T_c = 561.15 K, p_c = 4.960 MPa, ρ_c = 270.5 kg/m^3)

T_s, K	p_s, kPa	ρ', kg/m^3	ρ'', kg/m^3	h', kJ/kg	h'', kJ/kg	Δh_v, kJ/kg	$c_{p'}$, kJ/(kg K)	$c_{p''}$, kJ/(kg K)	η', 10^{-6} kg/(m s)	η'', 10^{-6} kg/(m s)	λ', 10^{-3} W/(m K)	λ'', 10^{-3} W/(m K)	Pr′	Pr″	σ, 10^{-3} N/m	β, 10^{-3}/K
390.65	101.3	712	2.3	0	591.3	591.3	3.2	1.87	422.9	9.29	122.9	21.7	11.01	0.81	17.1	1.69
410.2	182	688	4.1	64.8	629.8	565	3.54	1.95	317.3	10.3	117.9	24.2	9.53	0.83	15.6	1.86
429.2	327	664	7.9	135	672.3	537.3	3.95	2.03	245	10.7	113.1	26.7	8.58	0.81	13.9	2.04
446.5	482	640	12.5	206.8	716.5	509.7	4.42	2.14	196.4	11.4	108.7	28.2	7.97	0.86	12.3	2.11
469.5	759	606	23.8	315.3	784.1	468.8	5.15	2.24	149	12.1	102.9	31.3	7.46	0.87	10.2	2.54
485.2	1190	581	27.8	399.6	836.8	437.2	5.74	2.37	124	12.7	99	33.1	7.22	0.91	7.5	2.84
508.3	1830	538	48.2	541.9	924.4	382.5	6.76	2.69	96.8	13.9	93.2	36.9	7.02	1.01	6.44	3.7
530.2	2530	487	74	700.2	1015.3	315.1	7.9	3.05	76.9	15.4	87.7	40.2	6.93	1.17	4.23	5.78
545.5	3210	440	102.3			248.4	3.97	65.8	17.1	74	43.6		1.56	2.11	9.08	
558.9	4030	364	240.2			143			57.6	28.3	62.8	51.5			0.96	
Uncertainty	h[1]	h[2]	h[1]	h[10]	h[10]	h[3]	h[2]	h[4,5]	h[6]	h[6,7]	h[2]	h[6,8]	h[10]	h[10]	h[2]	h[9]

[1]Ref. [73]; [2]Ref. [116]; [3]Ref. [132]; [4]Ref. [67]; [5]Ref. [18]; [6]Ref. [68]; [7]Ref. [107]; [8]Ref. [108]; [9]Estimated values; [10]Calc. from other properties.

Tert.-butanol $C_4H_{10}O$, $(CH_3)_3COH$ (T_c = 506.2 K, p_c = 3.970 MPa, ρ_c = 270 kg/m^3)

T_s, K	p_s, kPa	ρ', kg/m^3	ρ'', kg/m^3	h', kJ/kg	h'', kJ/kg	Δh_v, kJ/kg	$c_{p'}$, kJ/(kg K)	$c_{p''}$, kJ/(kg K)	h', 10^{-6} kg/(m s)	h'', 10^{-6} kg/(m s)	λ', 10^{-3} W/(m K)	λ'', 10^{-3} W/(m K)	Pr$'$	Pr$''$	σ, 10^{-3} N/m	β, 10^{-3}/K
355.6	101.3	710	2.64	−182.0	324.6	506.6	2.9	1.81	531	9.4	109	17.9	14.1	0.95	14.5	1.84
375	207	688	5.12	−130.7	355	485.7	3.06	1.92	312	10	104	19.8	9.18	0.97	13	2.03
390	322	670	8.11	−78.4	378	456.4	3.19	2.02	235	10.4	100	21.4	7.5	0.98	11.5	2.19
405	483	647	12.4	−35.2	400.2	435.4	3.34	2.13	180	11	96	23.1	6.26	1.01	10	2.98
420	779	621	18.5	15	421.1	406.1	3.47	2.26	142	11.5	92	24.9	5.36	1.04	8.6	3.04
435	1010	596	27.1	63.3	440.1	376.8	3.62	2.42	118	12.1	88	26.9	4.85	1.09	7.1	3.23
450	1516	567	39.1	117.4	456.5	339.1	3.79	2.64	98	12.8	83	29.1	4.47	1.16	5.5	3.65
465	1896	533	56.4	171.2	468.5	297.3	4.01	3	84	13.6	77	31.6	4.37	1.29	3.8	4.49
480	2619	487	82.3	238.1	472.6	234.5	4.38	3.73	66	14.8	70	34.5	4.13	1.59	2.2	6.26
506.2	3970	270	270	351.6	351.6				65	65	53	53				
Uncertainty	h[1]	h[1]	h[2]	h[12]	h[2,3]	h[1]	h[4]	h[1,2]	h[5,6]	h[1,7]	h[1,8]	h[1,9]	h[12]	h[12]	h[1,10]	h[11]

[1]Ref. [22]; [2]Ref. [52]; [3]Ref. [115]; [4]Ref. [63]; [5]Ref. [126]; [6]Ref. [59]; [7]Ref. [107]; [8]Ref. [93]; [9]Ref. [108]; [10]Ref. [89]; [11]Estimated values; [12]Calc. from other properties.

Ethyl ether $C_4H_{10}O$, $(CH_3CH_2)_2O$ (T_c = 467 K, p_c = 3.610 MPa, ρ_c = 265 kg/m^3)

T_s, K	p_s, kPa	ρ', kg/m^3	ρ'', kg/m^3	h', kJ/kg	h'', kJ/kg	Δh_v, kJ/kg	$c_{p'}$, kJ/(kg K)	$c_{p''}$, kJ/(kg K)	h', 10^{-6} kg/(m s)	h'', 10^{-6} kg/(m s)	λ', 10^{-3} W/(m K)	λ'', 10^{-3} W/(m K)	Pr$'$	Pr$''$	σ, 10^{-3} N/m	β, 10^{-3}/K
307.75	101.3	696.2	3.16	0	349.9	349.9	2.37	1.4	210	7.86	126	15.8	3.95	0.7	15.25	1.93
323	170	676.4	5.08	36.6	373.6	337	2.43	1.96	177	8.28	120	17.4	3.58	0.93	13.5	1.75
343	307	653.2	8.92	85.9	404.1	318.2	2.51	2.05	148	8.86	112	19.5	3.32	0.93	11.3	1.88
363	511	625	14.77	137	434.3	297.3	2.61	2.14	127	9.45	104	22.4	3.19	0.9	9.1	2.23
383	811	594.2	23.49	190.3	464.5	274.2	2.72	2.26	109	10.1	95.6	24.2	3.1	0.94	7	2.79
403	1220	558	36.38	248.6	497.7	249.1	2.86	2.43	95	10.9	87.5	27	3.11	0.98	4.9	3.51
423	1770	517.9	55.51	305	520.6	215.6	3.01	2.75	84	11.7	79.9	30.2	3.16	1.07	3.1	4.54
443	2490	465.8	87.31	367.1	532.5	165.4	3.2	3.44	77	13.1	71.4	34.2	3.45	1.32	1.5	5.9
458	3150	401.8	132	416.1	523.9	107.8	3.75	4.15	70	15	65.3	38.6	4.02	1.61	0.5	14.89
463	3490	366.3	162	433	524.6	81.6	4.07	4.5	67	16.4	63.3	41.5	4.31	1.78	0.2	24.04
Uncertainty	h[1]	h[1]	h[1]	h[9]	h[9]	h[1]	h[1]	h[2,3]	h[1,8]	h[4,5]	h[6]	h[6,7]	h[9]	h[9]	h[1]	h[8]

[1]Ref. [125]; [2]Ref. [6]; [3]Ref. [18]; [4]Refs. [122]; [5]Ref. [107]; [6]Ref. [118]; [7]Ref. [108]; [8]Estimated values; [9]Calc. from other properties.

Ethylacetate $C_4H_8O_2$, $CH_3CO_2C_2H_5$ (T_c = 523.25 K, p_c = 3.832 MPa, ρ_c = 307.7 kg/m^3)

T_s, K	p_s, kPa	ρ', kg/m^3	ρ'', kg/m^3	h', kJ/kg	h'', kJ/kg	Δh_v, kJ/kg	$c_{p'}$, kJ/(kg K)	$c_{p''}$, kJ/(kg K)	η', 10^{-6} kg/(m s)	η'', 10^{-6} kg/(m s)	λ', 10^{-3} W/(m K)	λ'', 10^{-3} W/(m K)	Pr$'$	Pr$''$	σ, 10^{-3} N/m	β, 10^{-3}/K
350.25	101.3	830	3.2	−89.7	274.6	364.3	2.1	1.46	255	8.9	125	15.8	4.28	0.82	17.4	1.65
370	193	800	5.63	−47.3	300.2	347.5	2.17	1.54	221	9.5	118	17.4	4.08	0.84	15	1.79
390	310	770	9.45	− 6.7	326.2	332.9	2.28	1.63	193	10.1	111	19.3	3.96	0.85	12.6	1.99
410	510	740	15.1	35.7	351.8	316.1	2.36	1.73	158	10.7	104	21.5	3.59	0.86	10	2.23
430	792	705	23.4	81.3	376.5	295.2	2.5	1.85	134	11.4	98	23.5	3.42	0.9	7.8	2.57
450	1172	670	35.5	131.7	399.6	267.9	2.64	2	111	12.2	92	25.8	3.19	0.95	5.8	3.06
470	1655	625	54.2	182	420.6	238.6	2.82	2.25	90	13	85	28.5	2.99	1.03	3.9	3.89
490	2275	570	81.3	241.7	434.3	192.6	3.09	2.68	72	14.3	77	32	2.89	1.2	2.3	5.36
510	3172	475	134.5	315.8	433	117.2	3.76	4.52	56	16.4	66	36.5	3.19	2.03	0.74	9.46
523.2	3832	307.7	307.7	362.8	362.8				57	57	48.2	48.2				
Uncertainty	h[1]	h[1]	h[2]	h[11]	h[3,2]	h[1]	h[1,4]	h[3,2]	h[5,6]	h[1,7]	h[8,9]	h[1,9]	h[11]	h[11]	h[11]	h[10]

[1]Ref. [22]; [2]Ref. [52]; [3]Ref. [115]; [4]Ref. [63]; [5]Ref. [126]; [6]Ref. [59]; [7]Ref. [42]; [8]Ref. [93]; [9]Ref. [108]; [10]Estimated values; [11]Calc. from other properties.

n-Pentane C_5H_{12} (T_c = 469.70 K, p_c = 3.370 MPa, ρ_c = 232.0 kg/m^3)

T_s, K	p_s, kPa	ρ', kg/m^3	ρ'', kg/m^3	h', kJ/kg	h'', kJ/kg	Δh_v, kJ/kg	c_p', kJ/(kg K)	c_p'', kJ/(kg K)	η', 10^{-6} kg/(m s)	η'', 10^{-6} kg/(m s)	λ', 10^{-3} W/(m K)	λ'', 10^{-3} W/(m K)	Pr′	Pr″	σ, 10^{-3} N/m	β, 10^{-3}/K
300	73.17	619	2.194	−21.63	343.22	364.86	2.324	1.714	218.6	6.7	106.6	14.9	4.77	0.77	15.26	1.609
309.21	101.33	609.7	2.975	0	357.58	357.58	2.368	1.764	201.3	7	102.7	15.7	4.64	0.78	14.26	1.672
320	144.35	598.6	4.15	25.86	374.55	348.69	2.422	1.826	183.2	7.2	98.9	16.7	4.49	0.79	13.11	1.758
340	260.16	577	7.261	75.45	406.37	330.92	2.532	1.951	154.5	7.8	92.4	18.7	4.23	0.81	11	1.957
360	436.1	553.9	11.98	127.38	438.38	311.01	2.656	2.092	130.7	8.4	86.8	21	4	0.83	8.96	2.234
380	689.2	528.4	18.93	181.94	470.15	288.21	2.801	2.258	110.7	9	81.5	23.6	3.8	0.86	6.99	2.641
400	1038.4	499.7	29.12	239.57	500.99	261.41	2.981	2.471	93.7	9.7	76.6	26.4	3.65	0.91	5.12	3.29
420	1505	466	44.32	300.97	529.66	228.69	3.233	2.789	78.9	10.7	71.6	29.8	3.56	1	3.37	4.46
440	2114.7	423.5	68.6	367.61	553.52	185.91	3.689	3.441	66.1	12.3	66.5	34.9	3.67	1.22	1.77	7.23
469.7	3370	232	232	520.48	520.48				54.9	14.2	61.5	45.8			0.44	
Uncertainty	a[1]	a[1]	c[1]	c[1]	c[1]	c[1]	d[1]	d[1]	f[5]	f[2]	f[3]	f[3]	h[6]	h[6]	e[4]	d[1]

[1]Ref. [102]; [2]Ref. [25]; [3]Ref. [11]; [4]Ref. [100]; [5]Ref. [50]; [6]Calc. from other properties.

Cyclopentane C_5H_{10} (T_c = 511.8 K, p_c = 4.508 MPa, ρ_c = 272 kg/m^3)

T_s, K	p_s, kPa	ρ', kg/m^3	ρ'', kg/m^3	h', kJ/kg	h'', kJ/kg	Δh_v, kJ/kg	c_p', kJ/(kg K)	c_p'', kJ/(kg K)	η', 10^{-6} kg/(m s)	η'', 10^{-6} kg/(m s)	λ', 10^{-3} W/(m K)	λ'', 10^{-3} W/(m K)	Pr′	Pr″	σ, 10^{-3} N/m	β, 10^{-3}/K
322.4	101.3	706	10.8	−288.7	104.9	393.6	1.92	1.34	320	7.9	125	16.3	4.92	0.65	18.6	1.49
350	239	680	20	−217.3	138.6	355.9	2.05	1.47	255	8.9	117	18.5	4.47	0.71	15.1	1.69
370	406	656	36.3	−179.4	163.9	343.3	2.12	1.61	200	9.7	111	20.8	3.82	0.75	13	1.85
390	642	635	52.1	−155.3	189.6	334.9	2.22	1.79	160	10.5	105	23.2	3.38	0.81	11.1	2.07
410	948	607	69.2	−92.8	215.4	318.2	2.37	1.93	128	11.2	98	25.7	3.1	0.84	8.7	2.35
430	1309	577	97.5	−44.2	240.5	284.7	2.53	2.11	109	11.9	91	28.4	3.03	0.88	6.6	2.75
450	1861	547	117	−3.8	264.1	267.9	2.73	2.4	92	12.8	85	31.3	2.95	0.98	4.7	3.38
470	2742	505	141	62.2	284.1	221.9	3.04	2.81	76	13.9	79	34.8	2.92	1.12	2.9	4.45
490	3562	455	176	127.4	294.9	167.5	3.78	3.91	58	15.9	68	39	3.22	1.59	1.3	7.12
511.8	4508	272	272	227.1	227.1				43	43	51.1	51.1				
Uncertainty	h[1]	h[1]	h[11]	h[11]	h[2,3]	h[1]	h[1,4]	h[1,3]	h[1,5]	h[1,6]	h[7]	h[1,8]	h[11]	h[11]	h[1,9]	h[10]

[1]Ref. [22]; [2]Ref. [115]; [3]Ref. [52]; [4]Ref. [126]; [5]Ref. [59]; [6]Ref. [42]; [7]Ref. [68]; [8]Ref. [108]; [9]Ref. [89]; [10]Estimated values; [11]Calc. from other properties.

Isopentane, 2-Methyl Butane C_5H_{12}, $(CH_3)_2C(CH_3)_2$ (T_c = 460.4 K, p_c = 3.380 MPa, ρ_c = 236 kg/m^3)

T_s, K	p_s, kPa	ρ', kg/m^3	ρ'', kg/m^3	h', kJ/kg	h'', kJ/kg	Δh_v, kJ/kg	c_p', kJ/(kg K)	c_p'', kJ/(kg K)	η', 10^{-6} kg/(m s)	η'', 10^{-6} kg/(m s)	λ', 10^{-3} W/(m K)	λ'', 10^{-3} W/(m K)	Pr′	Pr″	σ, 10^{-3} N/m	β, 10^{-3}/K
301	101.3	613	3.07	290.8	632.7	341.9	2.29	1.72	201	7.4	103	14.7	4.47	0.87	14	1.73
325	217	586	6.3	348.9	669.9	321	2.43	1.86	163	8	95	17.4	4.17	0.86	11.5	1.94
340	328	569	9.41	383.8	693.1	309.3	2.53	1.96	146	8.5	91	19.3	4.06	0.86	9.9	2.11
355	476	552	13.5	423.3	716.4	293.1	2.62	2.08	126	9	87	21.5	3.79	0.87	8.4	2.32
370	667	532	18.9	465.2	739.7	274.5	2.71	2.2	111	9.5	84	23.4	3.58	0.89	7	2.59
385	915	511	26.2	504.7	765.3	260.6	2.8	2.34	97	9.9	80	25	3.4	0.93	5.6	2.95
400	1222	488	36	546.6	783.9	237.3	2.91	2.54	84	10.5	75	27.6	3.22	0.97	4.3	3.47
415	1603	461	49.3	588.5	807.1	218.6	3.05	2.81	71	11.2	70	29.4	3.05	1.07	3	4.26
430	2070	428	68.3	639.7	825.7	186	3.24	3.28	60	12.2	63	33.4	2.99	1.2	1.9	5.66
460.4	3380	236	236	790.8	790.8						48.3	48.3				
Uncertainty	h[1]	h[1]	h[1]	h[2]	h[2]	h[2]	h[11,3]	h[1,4]	h[5,6]	h[2,7]	h[8,9]	h[2,10,9]	h[12]	h[12]	h[3]	h[11]

[1]Ref. [125]; [2]Ref. [110]; [3]Ref. [89]; [4]Ref. [52]; [5]Ref. [126]; [6]Ref. [59]; [7]Ref. [42]; [8]Ref. [93]; [9]Ref. [108]; [10]Ref. [22]; [11]Estimated values; [12]Calc. from other properties.

Neopentane, 2,2-Dimethylpropane C_5H_{12}, $C(CH_3)_4$ (T_c = 433.78 K, p_c = 3.196 MPa, ρ_c = 238 kg/m³)

T_s, K	P_s, kPa	ρ', kg/m³	ρ'', kg/m³	h', kJ/kg	h'', kJ/kg	Δh_v, kJ/kg	c_p', kJ/(kg K)	c_p'', kJ/(kg K)	η', 10^{-6} kg/(m s)	η'', 10^{-6} kg/(m s)	λ', 10^{-3} W/(m K)	λ'', 10^{-3} W/(m K)	Pr′	Pr″	σ, 10^{-3} N/m	β, 10^{-3}/K
282.65	101.3	603	3.28	−111	204	315	2.14	1.65	280	6.89	90	13.2	6.66	0.86	12.9	1.8
305	215	575	6.38	−50	237	297	2.27	1.8	211	7.44	84	15	5.7	0.89	10.6	2.01
320	362	558	9.91	−25	260	284	2.37	1.91	169	7.88	80	16.3	5.01	0.92	9.11	2.2
335	482	543	14.5	13	282	269	2.48	2.03	140	8.27	76	18	4.57	0.03	7.67	2.44
350	676	519	20.7	51	305	254	2.63	2.16	112	8.73	72	19.8	4.09	0.95	6.27	2.75
365	945	497	29	91	327	236	2.77	2.32	94	9.25	67	21.6	3.89	0.99	4.93	3.16
380	1280	472	40.2	128	347	219	2.96	2.53	82	9.87	63	24.2	3.85	1.03	3.65	3.76
395	1700	443	55.8	175	366	191	3.2	2.85	69	10.3	58	26.6	3.81	1.1	2.45	4.75
410	2200	407	79.1	221	379	158	3.59	3.51	61	11.8	54	30.8	4.06	1.34	1.34	6.74
433.78	3196	238	238	329	329				36	36	42	42				
Uncertainty	h[1]	h[1]	h[1,2]	h[13]	h[3,2]	h[1]	h[4]	h[3,2]	h[5,6]	h[7,1,8]	h[9,1,10]	h[1,10]	h[13]	h[13]	h[11]	h[12]

[1]Ref. [30]; [2]Ref. [52]; [3]Ref. [115]; [4]Ref. [63]; [5]Ref. [126]; [6]Ref. [59]; [7]Ref. [60]; [8]Ref. [42]; [9]Ref. [93]; [10]Ref. [108]; [11]Ref. [7]; [12]Estimated values; [13]Calc. from other properties.

Methyl-tert-butylether $C_5H_{12}O$, $CH_3OC_4H_9$ (T_c = 503.4 K, p_c = 3.411 MPa, ρ_c = 275 kg/m³)

T_s, K	p_s, kPa	ρ', kg/m³	ρ'', kg/m³	h', kJ/kg	h'', kJ/kg	Δh_v, kJ/kg	c_p', kJ/(kg K)	c_p'', kJ/(kg K)	η', 10^{-6} kg/(m s)	η'', 10^{-6} kg/(m s)	λ', 10^{-3} W/(m K)	λ'', 10^{-3} W/(m K)	Pr′	Pr″	σ, 10^{-3} N/m	β, 10^{-3}/K
331.2	101.3	706	3.4	−22.2	292.2	314.4	2.3	1.78	231	8.5	108	15.4	4.9	0.98	14.7	1.56
340	133	697	4.39	−1.7	306.6	308.3	2.35	1.83	214	8.76	106	16.2	4.76	0.99	13.8	1.62
360	234	673	7.51	46.5	339.8	293.3	2.46	1.95	184	9.38	100	18.2	4.53	1.01	11.7	1.76
380	386	649	12.2	96.6	373.7	277.1	2.57	2.08	151	10	94	20.3	4.12	1.02	9.8	1.96
400	602	623	18.9	143.7	407.8	259.1	2.69	2.23	129	10.7	89	22.5	3.92	1.06	7.9	2.17
420	897	591	28.5	203.1	441.8	238.7	2.83	2.39	109	11.5	83	24.9	3.73	1.1	6.1	2.55
440	1290	556	42.3	259.8	474.9	215.1	3.01	2.61	91	12.3	78	27.6	3.52	1.16	4.3	3.22
460	1800	517	62.7	319.2	505.4	186.3	3.27	2.95	74	13.3	71	30.7	3.36	1.28	2.7	4.12
480	2440	467	96.2	382	529.3	147.3	3.83	3.76	59	14.9	62	34.4	3.53	1.63	1.3	6.68
503.4	3411	275	275	488.1	488.1				44	44	47	47				
Uncertainty	h[1]	h[2]	h[3]	h[16]	h[3,4]	h[5,6]	h[7]	h[3,4]	h[8,9]	h[10,11]	h[12]	h[13,14]	h[16]	h[16]	h[13]	h[15]

[1]Ref. [26]; [2]Ref. [33]; [3]Ref. [52]; [4]Ref. [92]; [5]Ref. [13]; [6]Ref. [132]; [7]Ref. [5]; [8]Ref. [126]; [9]Ref. [62]; [10]Ref. [106]; [11]Ref. [107]; [12]Ref. [93]; [13]Ref. [89]; [14]Ref. [108]; [15]Estimated values; [16]Calc. from other properties.

n-Hexane C_6H_{14} (T_c = 507.82 K, p_c = 3.034 MPa, ρ_c = 233.2 kg/m³)

T_s, K	P_s, kPa	ρ', kg/m³	ρ'', kg/m³	h', kJ/kg	h'', kJ/kg	Δh_v, kJ/kg	c_p', kJ/(kg K)	c_p'', kJ/(kg K)	η', 10^{-6} kg/(m s)	η'', 10^{-6} kg/(m s)	λ', 10^{-3} W/(m K)	λ'', 10^{-3} W/(m K)	Pr′	Pr″	σ, 10^{-3} N/m	β, 10^{-3}/K
300	21.87	653	0.768	−98.60	265.66	364.26	2.26	1.682	294.8	6.4	117.8	12.8	5.66	0.84	17.73	1.413
325	57.77	629.5	1.906	−40.70	306.52	347.22	2.371	1.809	235.2	6.9	109	15.1	5.12	0.83	15.05	1.53
341.86	101.33	613	3.231	0	334.93	334.93	2.452	1.901	203.7	7.3	103.5	16.8	4.83	0.82	13.3	1.631
350	129.92	604.8	4.086	20.14	348.84	328.71	2.493	1.948	190.4	7.5	101	17.7	4.7	0.82	12.48	1.689
375	258.2	578.6	7.87	84.18	392.27	308.09	2.626	2.101	155.6	8.1	93.6	20.4	4.37	0.83	10.01	1.911
400	466.1	550.1	14.05	151.72	436.28	284.56	2.774	2.275	127.8	8.8	87	23.2	4.08	0.87	7.68	2.238
425	780.3	518.2	23.81	223.16	480.06	256.9	2.948	2.485	105	9.8	81.1	26.3	3.82	0.93	5.49	2.76
450	1231.3	481.1	39.36	299.18	522.12	222.94	3.18	2.785	86	11.2	76	29.5	3.6	1.06	3.48	3.75
475	1856.7	433.6	66.1	381.51	559.07	177.57	3.606	3.4	69.9	13.2	71.5	32.9	3.52	1.37	1.7	6.34
507.82	3034	233.2	233.2	543.34	543.34				56.1	17.5	68	36			0.27	
Uncertainty	a[1]	a[1]	c[1]	c[1]	c[1]	c[1]	d[1]	d[1]	f[3]	e[4]	e[5]	e[6]	h[7]	h[7]	d[2]	d[1]

[1]Ref. [102]; [2]Ref. [101]; [3]Ref. [50]; [4]Ref. [25]; [5]Ref. [20]; [6]Ref. [15]; [7]Calc. from other properties.

Cyclohexane C_6H_{12} (T_c = 553.64 K, p_c = 4.075 MPa, ρ_c = 273.0 kg/m³)

T_s, K	p_s, kPa	ρ', kg/m³	ρ'', kg/m³	h', kJ/kg	h'', kJ/kg	Δh_v, kJ/kg	c_p', kJ/(kg K)	c_p'', kJ/(kg K)	η', 10^{-6} kg/(m s)	η'', 10^{-6} kg/(m s)	λ', 10^{-3} W/(m K)	λ'', 10^{-3} W/(m K)	Pr′	Pr″	σ, 10^{-3} N/m	β, 10^{-3}/K
353.89	101.33	719.5	3.013	0	355.99	355.99	2.149	1.586	400	8.6	102	16.5	8.43	0.83	18	1.409
360	121.31	713.3	3.567	13.25	364.83	351.58	2.18	1.623	370	8.7	100	17.4	8.07	0.81	17.2	1.437
385	236.5	687.2	6.7	69.43	401.95	332.52	2.308	1.787	280	9.4	92.6	20.1	6.98	0.84	13	1.577
410	420.5	659.5	11.66	128.84	440.26	311.42	2.439	1.972	230	10.2	86.5	22.9	6.49	0.88	11	1.773
435	695.1	629.5	19.23	191.64	479.15	287.51	2.581	2.189	190	10.7	77.9	26	6.3	0.9	8.1	2.062
460	1084.5	596.1	30.6	258.14	517.81	259.67	2.745	2.465	160	11.6	69.2	30.4	6.35	0.94	5.2	2.52
485	1614.7	557.5	47.84	328.91	555.1	226.19	2.954	2.856	135	12.3	60.6	36.1	6.58	0.98	2	3.32
510	2315	510.5	75.19	404.95	589.18	184.23	3.267	3.509	115	13.6	56.5	39.4	6.65	1.21	1.5	4.96
535	3223.2	444.4	126	489.85	615.4	125.54	4.287	5.038	95	17.7	48.3	46	8.43	1.94	0.5	12.06
553.64	4075	273	273	596.89	596.89				54	54	57.9	57.9				
Uncertainty	a[1]	a[1]	c[1]	c[1]	c[1]	c[1]	d[1]	d[1]	h[2,3]	h[4]	h[5,6]	h[7]	h[9]	h[9]	h[8]	d[1]

[1]Ref. [83]; [2]Ref. [17]; [3]Ref. [23]; [4]Ref. [105]; [5]Ref. [93]; [6]Ref. [71]; [7]Ref. [127]; [8]Ref. [12]; [9]Calc. from other properties.

Benzene C_6H_6 (T_c = 562.05 K, p_c = 4.895 MPa, ρ_c = 305.0 kg/m³)

T_s, K	p_s, kPa	ρ', kg/m³	ρ'', kg/m³	h', kJ/kg	h'', kJ/kg	Δh_v, kJ/kg	c_p', kJ/(kg K)	c_p'', kJ/(kg K)	η', 10^{-6} kg/(m s)	η'', 10^{-6} kg/(m s)	λ', 10^{-3} W/(m K)	λ'', 10^{-3} W/(m K)	Pr′	Pr″	σ, 10^{-3} N/m	β, 10^{-3}/K
278.7	4.79	896.5	0.16	0	447.3	447.3	1.69		815						30.8	
300	13.81	872.2	0.44	36.7	469.9	433.2	1.75		587	7.83	140.5		7.3		28	1.17
325	38.81	844.3	1.14	81.3	495.5	414.2	1.82		428	8.49	132.3		5.9		24.7	1.26
353.3	101.5	812.9	2.79	134.3	528.2	393.9	1.92	1.29	321	9.26	122.9	14.8	5.02	0.81	21.1	1.36
400	352.3	759.2	9.02	228.5	585.4	356.9	2.1	1.53	205	10.7	119	19.8	3.62	0.83	15.5	1.66
450	971.6	694.3	24.4	339.3	648.2	308.9	2.3	1.81	138	12.5	106	26.7	2.99	0.85	9.88	2.37
475	1481.9	656	37.9	398.9	678.6	279.7	2.46	2.01	116	13.7	100	31	2.85	0.89	7.25	3.03
500	2166.4	610.9	57.9	461.9	706.7	244.8	2.66	2.32	97.6	15	93.5	35.7	2.78	0.97	4.79	4.19
525	3060.9	553.8	89.4	530	729.9	199.8	3.05	2.73	80.7	16.8	87.1	41.1	2.83	1.12	2.54	6.68
550	4215.5	465.5	151.1	609.6	738.7	129.1	4.26		59.6	19.1	77.4	50.2	3.28		0.63	16.48
Uncertainty	b[1]	b[1]	c[1]	c[1]	c[1]	c[1]	d[1]	d[2,3]	c[4,5]	d[5,6]	e[7,8]	e[8,9]	h[13]	h[13]	d[10, 11]	h[12]

[1]Ref. [28]; [2]Ref. [122]; [3]Ref. [18]; [4]Ref. [46]; [5]Ref. [125]; [6]Ref. [24]; [7]Ref. [3]; [8]Ref. [121]; [9]Ref. [108]; [10]Ref. [40]; [11]Refs. [100]; [12]Estimated values; [13]Calc. from other properties.

Phenol C_6H_6O (T_c = 693.2 K, p_c = 6.130 MPa, ρ_c = 435.7 kg/m³)

T_s, K	p_s, kPa	ρ', kg/m³	ρ'', kg/m³	h', kJ/kg	h'', kJ/kg	Δh_v, kJ/kg	c_p', kJ/(kg K)	c_p'', kJ/(kg K)	η', 10^{-6} kg/(m s)	η'', 10^{-6} kg/(m s)	λ', 10^{-3} W/(m K)	λ'', 10^{-3} W/(m K)	Pr′	Pr″	σ, 10^{-3} N/m	β, 10^{-3}/K
455	101.3	955	2.6	−153	336	351	12.8	175	28.9	489	2.55	1.63	5.11	0.72	24.5	0.91
480	216	932	5.36	−93	374	256	13.5	170	31.6	467	2.61	1.74	3.93	0.74	20.9	1.02
505	404	905	9.88	−41	411	219	14.3	166	34.8	452	2.66	1.85	3.51	0.76	18.2	1.2
530	693	877	16.9	20	447	166	15.2	162	38.4	427	2.76	1.95	2.83	0.77	14.6	1.23
555	1100	851	27.2	80	482	137	16.2	157	42.4	402	2.85	2.06	2.59	0.79	12.4	1.63
580	1650	809	41.9	147	515	113	17.3	154	46.8	368	3.01	2.22	2.21	0.82	10.02	2.04
605	2360	772	62.9	206	545	90.1	18.6	149	51.4	339	3.1	2.44	1.87	0.88	7.6	2.63
635	3410	713	101	290	575	75.2	20.2	141	56.2	285	3.43	2.94	1.57	1.07	5.3	3.52
665	4720	636	170	399	587	65.3	23.4	130	64.3	188	3.77	5.1	1.89	1.86	2.7	10.39
693.15	6129	436	436	514	514				45.3	45.3	92	92				
Uncertainty	h[1]	h[2]	h[3]	h[16]	h[3,4]	h[5]	h[6]	h[3,7]	h[8]	h[9,10]	h[11]	h[12,13]	h[16]	h[16]	h[14]	h[15]

[1]Ref. [26]; [2]Ref. [127]; [3]Ref. [52]; [4]Ref. [48]; [5]Ref. [29]; [6]Ref. [67]; [7]Ref. [6]; [8]Ref. [71]; [9]Ref. [70]; [10]Ref. [107]; [11]Ref. [68]; [12]Ref. [69]; [13]Ref. [108]; [14]Ref. [73]; [15]Estimated values; [16]Calc. from other properties.

Aniline $C_6H_5NH_2$ (T_c = 699 K, p_c = 5.301 MPa, ρ_c = 340 kg/m^3)

T_s, K	p_s, kPa	ρ', kg/m^3	ρ'', kg/m^3	h', kJ/kg	h'', kJ/kg	Δh_v, kJ/kg	c_p', kJ/(kg K)	c_p'', kJ/(kg K)	η', 10^{-6} kg/(m s)	η'', 10^{-6} kg/(m s)	λ', 10^{-3} W/(m K)	λ'', 10^{-3} W/(m K)	Pr$'$	Pr$''$	σ, 10^{-3} N/m	β, 10^{-3}/K
457.5	101.3	875	2.56	−114	357	471	2.37	1.74	303	11.8	154	23.5	4.66	0.87	25.2	1.17
500	276	828	6.62	−10	427	437	2.52	1.89	213	13.1	146	28.1	3.68	0.88	19.9	1.34
525	456	800	10.7	53	468	415	2.61	1.99	178	13.9	141	30.9	3.29	0.89	16.9	1.48
550	716	769	16.7	137	509	372	2.71	2.09	152	14.7	136	33.8	3.03	0.91	14	1.65
575	1080	736	25.3	184	549	365	2.84	2.2	132	15.6	131	36.8	2.86	0.93	11.2	1.88
600	1560	699	37.5	154	589	335	2.97	2.35	117	16.5	126	40.1	2.76	0.97	8.5	2.21
625	2200	658	55.1	323	623	300	3.13	2.55	104	17.6	121	43.6	2.69	1.03	5.9	2.72
650	3010	608	81.7	396	653	257	3.36	2.9	94	19	116	47.8	2.72	1.5	3.6	3.65
675	4050	541	128	473	669	196	3.84	3.95	86	21.1	111	53.1	2.98	1.57	1.5	6.07
699	5300	340	340	584	584				71	71	70	70				
Uncertainty	h[1]	h[2]	h[3]	h[14]	h[3,4]	h[2]	h[5]	h[3,4]	h[6]	h[7,8]	h[9]	h[10,11]	h[14]	h[14]	h[12]	h[13]

[1]Ref. [125]; [2]Ref. [22]; [3]Ref. [52]; [4]Ref. [115]; [5]Ref. [63]; [6]Ref. [71]; [7]Ref. [70]; [8]Ref. [107]; [9]Ref. [68]; [10]Ref. [69]; [11]Ref. [108]; [12]Ref. [89]; [13]Estimated values; [14]Calc. from other properties.

n-Heptane C_7H_{16} (T_c = 540.13 K, p_c = 2.736 MPa, ρ_c = 232.0 kg/m^3)

T_s, K	p_s, kPa	ρ', kg/m^3	ρ'', kg/m^3	h', kJ/kg	h'', kJ/kg	Δh_v, kJ/kg	c_p', kJ/(kg K)	c_p'', kJ/(kg K)	η', 10^{-6} kg/(m s)	η'', 10^{-6} kg/(m s)	λ', 10^{-3} W/(m K)	λ'', 10^{-3} W/(m K)	Pr$'$	Pr$''$	σ, 10^{-3} N/m	β, 10^{-3}/K
371.53	101.33	614.2	3.471	0	316.89	316.89	2.558	2.028	201	7.3	98	18	5.25	0.82	12.5	1.559
380	129.1	606.1	4.369	21.85	332.52	310.67	2.599	2.076	186	7.7	95.5	18.4	5.06	0.87	11.8	1.617
400	218.25	586	7.228	74.89	369.98	295.09	2.701	2.193	159	8.3	88.8	20.1	4.84	0.91	10	1.785
420	348.5	564.6	11.424	130.03	407.99	277.96	2.81	2.32	135	9	82.9	22.6	4.58	0.92	8.3	2.013
440	530.7	541.3	17.46	187.43	446.19	258.76	2.93	2.462	115	9.7	76.1	24.9	4.43	0.96	6.6	2.34
460	777	515.3	26.08	247.33	484.07	236.74	3.072	2.632	97	10.7	69.9	27.7	4.26	1.02	5.1	2.841
480	1101.1	485.3	38.6	310.15	520.77	210.62	3.255	2.863	82	12.1	61.1	29.9	4.37	1.16	3.6	3.71
500	1519.1	448.2	57.74	376.79	554.66	177.87	3.549	3.257	67	14	52	33	4.57	1.38	2.2	5.56
520	2052.4	395.8	91.1	449.77	581.67	131.9	4.312	4.338	54	17.6	41.8	36	5.57	2.12	0.8	11.91
540.13	2736	232	232	562.23	562.23				41	41						
Uncertainty	a[1]	a[1]	c[1]	c[1]	c[1]	c[1]	d[1]	d[1]	h[1]	h[1]	h[2,3]	h[2]	h[4]	h[4]	h[1]	d[1]

[1]Ref. [102]; [2]Ref. [22]; [3]Ref. [89]; [4]Calc. from other properties.

n-Octane C_8H_{18} (T_c = 569.32 K, p_c = 2.497 MPa, ρ_c = 234.9 kg/m^3)

T_s, K	P_s, kPa	ρ', kg/m^3	ρ'', kg/m^3	h', kJ/kg	H'', kJ/kg	Δh_v, kJ/kg	c_p', kJ/(kg K)	c_p'', kJ/(kg K)	η', 10^{-6} kg/(m s)	η'', 10^{-6} kg/(m s)	λ', 10^{-3} W/(m K)	λ'', 10^{-3} W/(m K)	Pr$'$	Pr$''$	σ, 10^{-3} N/m	β, 10^{-3}/K
398.77	101.33	612.2	3.696	0	302.19	302.19	2.649	2.143	203	7.4	98	18.4	5.49	0.86	11.9	1.535
415	155.82	596.7	5.576	43.63	334.31	290.67	2.726	2.232	174	7.9	93	20.3	5.1	0.87	10.5	1.652
435	251.55	576.6	8.869	99.18	374.56	275.38	2.826	2.347	149	8.5	88	22.5	4.78	0.89	8.9	1.84
455	386.97	554.8	13.596	156.77	415.29	258.52	2.933	2.471	126	9.2	83	24.3	4.45	0.94	7.3	2.098
475	571.7	531	20.29	216.57	456.14	239.57	3.052	2.612	107	10	78	26.7	4.19	0.98	5.8	2.475
495	816.3	504	29.79	278.83	496.55	217.72	3.195	2.785	91	11.1	73	29.1	3.98	1.06	4.4	3.073
515	1133	472.3	43.61	344.02	535.57	191.55	3.39	3.031	75	12.5	68	31.6	3.74	1.2	2.9	4.16
535	1536.6	432	65.14	413.22	571.24	158.01	3.732	3.5	61	14.7	62	34.4	3.67	1.5	1.8	6.69
555	2047.6	370.7	105.7	489.95	597.73	107.78	4.905	5.241	48	19.4	56	38.6	4.2	2.63	0.6	18.07
569.32	2497	234.9	234.9	575.52	575.52						47.7	47.7				
Uncertainty	a[1]	a[1]	c[1]	c[1]	c[1]	c[1]	d[1]	d[1]	h[1]	h[1,4]	h[2,3]	h[2,3,5]	h[6]	h[6]	h[1]	d[1]

[1]Ref. [102]; [2]Ref. [110]; [3]Ref. [22]; [4]Ref. [42]; [5]Ref. [108]; [6]Calc. from other properties.

n-Nonane C_9H_{20} (T_c = 594.63 K, p_c = 2.289 MPa, ρ_c = 234 kg/m^3)

T_s, K	p_s, kPa	ρ', kg/m^3	ρ'', kg/m^3	h', kJ/kg	h'', kJ/kg	Δh_v, kJ/kg	c_p', kJ/(kg K)	c_p'', kJ/(kg K)	η', 10^{-6} kg/(m s)	η'', 10^{-6} kg/(m s)	λ', 10^{-3} W/(m K)	λ'', 10^{-3} W/(m K)	Pr′	Pr″	σ, 10^{-3} N/m	β, 10^{-3}/K
423.97	101.3	614	3.94	195	490	295	2.72	2.24	213	7.4	95	20.8	6.1	0.8	11.3	1.6
435	134	602	5.18	226	513	287	2.77	2.3	177	7.6	92	22	5.33	0.79	10.4	1.68
455	214	581	8.22	282	555	273	2.87	2.4	153	7.9	87	24.1	5.04	0.79	8.86	1.84
475	338	560	12.6	340	598	258	2.97	2.51	132	8.3	82	26.4	4.78	0.79	7.33	2.07
495	496	535	18.7	402	640	238	3.1	2.63	112	8.7	77	28.7	4.51	0.8	5.86	2.35
515	717	510	27.3	464	683	219	3.23	2.77	94	9.1	72	31.2	4.22	0.81	4.46	2.77
535	965	479	39.6	529	724	195	3.38	2.95	78	9.7	66	33.8	3.99	0.85	3.13	3.9
555	1320	444	58	594	762	168	3.59	3.25	63	10.6	60	36.6	3.77	0.94	1.9	4.56
575	1750	394	89.8	664	792	128	4	4.05	50	12.2	55	40	3.64	1.24	1.81	7.51
594.63	2289	234	234	754	754						49	49				
Uncertainty	h[1,2]	h[2]	h[3]	h[15]	h[3,4]	h[2]	h[5]	h[3,4]	h[6,7]	h[8,9]	h[10,11,12]	h[11,12]	h[15]	h[15]	h[13]	h[14]

[1]Ref. [27]; [2]Ref. [110]; [3]Ref. [52]; [4]Ref. [115]; [5]Ref. [63]; [6]Ref. [125]; [7]Ref. [126]; [8]Ref. [42]; [9]Ref. [93]; [10]Ref. [74]; [11]Ref. [108]; [12]Ref. [7]; [13]Estimated values; [14]Calc. from other properties.

n-Decane $C_{10}H_{22}$ (T_c = 617.6 K, p_c = 2.096 MPa, ρ_c = 235.9 kg/m^3)

T_s, K	p_s, kPa	ρ', kg/m^3	ρ'', kg/m^3	h', kJ/kg	h'', kJ/kg	Δh_v, kJ/kg	c_p', kJ/(kg K)	c_p'', kJ/(kg K)	η', 10^{-6} kg/(m s)	η'', 10^{-6} kg/(m s)	λ', 10^{-3} W/(m K)	λ'', 10^{-3} W/(m K)	Pr′	Pr″	σ, 10^{-3} N/m	β, 10^{-3}/K
447.31	101.3	621	4.13	265	542	277	2.79	2.33	205	8.1	91	21.8	6.29	0.87	10.64	1.61
460	141	608	5.6	299	569	270	2.85	2.39	180	8.3	88	23.1	5.83	0.86	9.68	1.66
480	227	588	8.73	357	613	256	2.94	2.49	149	8.7	83	25.3	5.28	0.86	8.2	1.88
500	329	564	13.2	416	658	242	3.06	2.59	127	9.1	78	27.5	4.98	0.86	6.77	2.09
520	479	538	19.4	476	702	226	3.16	2.71	108	9.6	73	29.8	4.68	0.87	5.39	2.35
540	675	513	28.1	538	746	208	3.29	2.85	91	10.1	68	32.1	4.4	0.9	4.07	2.81
560	927	479	40.7	603	789	186	3.44	3.03	75	10.7	63	34.7	4.1	0.93	2.83	3.53
580	1250	445	59.6	673	829	156	3.65	3.33	61	11.6	58	37.5	3.84	1.03	1.68	4.73
600	1650	392	93.1	743	859	116	4.06	4.2	48	13.3	54	40.9	3.61	1.37	0.67	8.08
617.6	2096	235.9	235.9	824	824						49	49				
Uncertainty	h[1,2]	h[2]	h[3]	h[15]	h[3,4]	h[2]	h[5]	h[3,4]	h[6,7]	h[8,9]	h[10,11,12]	h[11,12]	h[15]	h[15]	h[13]	h[14]

[1]Ref. [27]; [2]Ref. [110]; [3]Ref. [52]; [4]Ref. [115]; [5]Ref. [63]; [6]Ref. [126]; [7]Ref. [59]; [8]Ref. [135]; [9]Ref. [42]; [10]Ref. [93]; [11]Ref. [74]; [12]Ref. [108]; [12]Ref. [7]; [13]Estimated values; [14]Calc. from other properties.

Ethylbenzene C_8H_{10}, C_6H_5–CH_2CH_3 (T_c = 617.1 K, p_c = 3.610 MPa, ρ_c = 284 kg/m^3)

T_s, K	p_s, kPa	ρ', kg/m^3	ρ'', kg/m^3	h', kJ/kg	h'', kJ/kg	Δh_v, kJ/kg	c_p', kJ/(kg K)	c_p'', kJ/(kg K)	η', 10^{-6} kg/(m s)	η'', 10^{-6} kg/(m s)	λ', 10^{-3} W/(m K)	λ'', 10^{-3} W/(m K)	Pr′	Pr″	σ, 10^{-3} N/m	β, 10^{-3}/K
409.3	101.3	751	3.26	−42.8	298.8	341.6	1.98	1.67	230	9	99	16.9	4.6	0.87	16.6	1.35
433	189	727	5.76	9	335.6	326.6	2.04	1.77	197	9.6	95	19.4	4.31	0.88	14.5	1.47
453	297	705	8.88	53.3	367.3	314	2.11	1.86	176	10.3	90	21.5	4.13	0.89	12.5	1.6
473	447	682	13.2	101.6	399.3	297.7	2.19	1.95	158	11	85	23.6	4.07	0.91	10.5	1.75
493	645	657	29	159.3	431.4	272.1	2.28	2.05	142	11.7	80	25.9	4.05	0.93	8.8	1.95
513	903	630	26.9	207.9	463.3	255.4	2.38	2.16	129	12.4	75	28.2	4.09	0.95	7.1	2.21
553	1640	568	52.1	306.7	524.4	217.7	2.63	2.48	108	13.7	65	33.2	4.37	1.02	3.9	3.13
573	2150	529	72.9	368.2	550.8	192.6	2.85	2.78	99	14.8	60	36.1	4.7	1.14	2.5	4.09
593	2770	478	106	427.8	570.2	142.4	3.22	3.52	91	16.6	55	39.5	5.32	1.48	1.2	6.29
613	3450	388	189	481.6	557	75.4	4.2	17.5	84	22.6	50	45.8	7.02	8.64	0.23	
Uncertainty	h[1]	h[1]	h[2]	h[14]	h[3,2]	h[4]	h[5]	h[3,2]	h[6]	h[7,8]	h[9]	h[10,11]	h[14]	h[14]	h[12]	h[13]

[1]Ref. [110]; [2]Ref. [52]; [3]Ref. [115]; [4]Ref. [29]; [5]Ref. [67]; [6]Ref. [71]; [7]Ref. [70]; [8]Ref. [42]; [9]Ref. [68]; [10]Ref. [74]; [11]Ref. [108]; [12]Ref. [73]; [13]Estimated values; [14]Calc. from other properties.

Toluene C_7H_8, $C_6H_5CH_3$ (T_c = 591.75 K, p_c = 4.126 MPa, ρ_c = 292.0 kg/m^3)

T_s, K	p_s, kPa	ρ', kg/m^3	ρ'', kg/m^3	h', kJ/kg	h'', kJ/kg	Δh_v, kJ/kg	c_p', kJ/(kg K)	c_p'', kJ/(kg K)	η', 10^{-6} kg/(m s)	η'', 10^{-6} kg/(m s)	λ', 10^{-3} W/(m K)	λ'', 10^{-3} W/(m K)	Pr′	Pr″	σ, 10^{-3} N/m	β, 10^{-3}/K
320	10.73	841.66	0.374	−120.29	279.68	399.96	1.773	1.221	434.4	7.6	123	7.1	6.26	1.31	25.44	1.124
350	34.82	812.87	1.124	−65.51	316.49	382	1.878	1.348	327.4	8.3	115	8.9	5.35	1.26	22.06	1.202
383.75	101.33	779.14	3.05	0	360.7	360.7	2.003	1.496	247.7	9.1	106.8	11.1	4.65	1.23	18.38	1.323
410	202.14	751.46	5.847	53.98	396.7	342.72	2.105	1.616	203.2	9.7	101.1	13	4.23	1.2	15.6	1.455
440	396.98	717.63	11.17	119.04	438.98	319.94	2.228	1.762	164.3	10.4	95	15.2	3.85	1.2	12.54	1.666
470	709.05	680.44	19.83	187.96	481.72	293.75	2.365	1.926	134.2	11.5	89.4	17.4	3.55	1.27	9.6	1.99
500	1176.62	638.14	33.64	261.19	523.74	262.55	2.529	2.132	110.5	11.7	84.3	19.8	3.31	1.26	6.83	2.54
530	1844.36	587.26	56.18	339.64	562.96	223.32	2.762	2.453	91.5	12.4	79.5	22.3	3.18	1.37	4.24	3.65
560	2769.1	519.05	96.97	425.67	594.41	168.74	3.259	3.269	76.1	13.1	75.1	25.4	3.3	1.68	1.93	6.99
591.75	4126.3	291.99	291.99	565.77	565.77				63.5	13.8	71	34.1			0.11	
Uncertainty	a[1]	a[1]	b[1]	c[1]	c[1]	c[1]	d[1]	d[1]	e[2]	f[3]	e[4]	h[5,6]	h[8]	h[8]	d[7]	d[1]

[1]Ref. [58]; [2]Ref. [103]; [3]Ref. [15]; [4]Ref. [64]; [5]Ref. [135]; [6]Ref. [108]; [7]Ref. [134]; [8]Calc. from other properties.

m-Xylol C_8H_{10}, $C_6H_4(CH_3)_2$ (T_c = 617 K, p_c = 3.543 MPa, ρ_c = 283 kg/m^3)

T_s, K	P_s, kPa	ρ', kg/m^3	ρ'', kg/m^3	H', kJ/kg	h'', kJ/kg	Δh_v, kJ/kg	c_p', kJ/(kg K)	c_p'', kJ/(kg K)	η', 10^{-6} kg/(m s)	η'', 10^{-6} kg/(m s)	λ', 10^{-3} W/(m K)	λ'', 10^{-3} W/(m K)	Pr′	Pr″	σ, 10^{-3} N/m	β, 10^{-3}/K
412	101.3	752	3.22	−34.6	310.8	345.4	2.13	1.66	232	9.1	92	16.9	5.38	0.89	16.7	1.38
430	162	731	4.98	−1.2	337.9	339.1	2.19	1.73	207	9.5	88	19.4	5.18	0.85	14.8	1.46
455	281	700	8.69	50.2	376.8	326.6	2.29	1.84	182	10	82	22.1	5.08	0.83	12.5	1.61
480	472	673	14.3	114.7	416.1	301.4	2.4	1.95	158	10.7	77	24.6	4.92	0.85	10.2	1.83
505	741	642	22.6	172.6	455.2	282.6	2.54	2.08	135	11.4	72	27.2	4.76	0.87	8	2.11
530	1121	604	34.6	233.9	493.5	259.6	2.69	2.24	112	12.2	67	29.9	4.54	0.91	5.9	2.52
555	1601	570	52.6	299.2	529.5	230.3	2.87	2.47	90	13.2	62	33.1	4.17	0.99	3.9	3.25
580	2264	505	81.3	371.4	559.8	188.4	3.16	2.91	71	14.6	57	37.1	3.94	1.15	2.1	4.59
605	3052	396	140	460.6	571.1	100.5	3.86	5.27	55	18.3	52	42.2	4.08	2.29	0.5	9.48
617	3543	283	283	516.7	516.7				54	54	50	50				
Uncertainty	h[1,2]	h[3]	h[4]	h[14]	h[4,5]	h[3]	h[6]	h[4,5]	h[3,7]	h[3,8]	h[3,9]	h[3,10]	h[13]	h[13]	h[3,11]	h[12]

[1]Ref. [125]; [2]Ref. [110]; [3]Ref. [22]; [4]Ref. [52]; [5]Ref. [115]; [6]Ref. [63]; [7]Ref. [59]; [8]Ref. [42]; [9]Ref. [93]; [10]Ref. [108]; [11]Ref. [89]; [12]Estimated values; [13]Calc. from other properties.

o-Xylol C_8H_{10}, $C_6H_4(CH_3)_2$ (T_c = 630.4 K, p_c = 3.729 MPa, ρ_c = 288 kg/m^3)

T_s, K	p_s, kPa	ρ', kg/m^3	ρ'', kg/m^3	h', kJ/kg	h'', kJ/kg	Δh_v, kJ/kg	c_p', kJ/(kg K)	c_p'', kJ/(kg K)	η', 10^{-6} kg/(m s)	η'', 10^{-6} kg/(m s)	λ', 10^{-3} W/(m K)	λ'', 10^{-3} W/(m K)	Pr′	Pr″	σ, 10^{-3} N/m	β, 10^{-3}/K
417.56	101.3	764	3.17	6.5	349.9	343.4	2.16	1.71	253	9.2	99	18.4	5.51	0.86	17.9	1.31
430	142	751	4.31	30.4	369.5	339.1	2.2	1.76	231	9.5	96	19.3	5.28	0.87	16.4	1.37
455	249	725	7.54	83.2	409.8	326.6	2.3	1.86	197	10.2	91	21.9	5	0.87	14.1	1.51
480	422	696	12.5	145	450.5	305.5	2.4	1.97	171	10.8	85	24.4	4.83	0.88	11.4	1.69
505	655	666	19.6	201.7	491.4	289.7	2.52	2.08	147	11.5	80	27	4.65	0.89	9.2	1.92
530	995	632	30	263.7	531.7	268	2.65	2.22	124	12.2	74	29.9	4.43	0.91	7	2.24
555	1420	594	45.1	331	570.5	239.5	2.81	2.4	102	13.1	69	33	4.14	0.95	4.9	2.75
580	2040	549	67.8	400.6	605.8	205.2	3.02	2.7	82	14.3	63	36.5	3.92	1.06	3	3.67
605	2750	489	107	476.9	631.8	154.9	3.44	3.49	65	16.3	58	40.6	3.87	1.4	1.3	5.99
630.4	3729	288	288	581.2	581.2				55	55	52	52				
Uncertainty	h[1,2]	h[3]	h[4]	h[14]	h[4,5]	h[3]	h[6]	h[4,7]	h[3,8]	h[3,9]	h[3,10]	h[3,11]	h[14]	h[14]	h[3,12]	h[13]

[1]Ref. [125]; [2]Ref. [110]; [3]Ref. [22]; [4]Ref. [52]; [5]Ref. [29]; [6]Ref. [63]; [7]Ref. [115]; [8]Ref. [59]; [9]Ref. [42]; [10]Ref. [93]; [11]Ref. [108]; [12]Ref. [89]; [13]Estimated values; [14]Calc. from other properties.

p-Xylol C_8H_{10}, $CH_4(CH_3)_2$ (T_c = 616.3 K, p_c = 3.510 MPa, ρ_c = 280 kg/m^3)

T_s, K	p_s, kPa	ρ', kg/m^3	ρ'', kg/m^3	h', kJ/kg	h'', kJ/kg	Δh_v, kJ/kg	c_p', kJ/(kg K)	c_p'', kJ/(kg K)	η', 10^{-6} kg/(m s)	η'', 10^{-6} kg/(m s)	λ', 10^{-3} W/(m K)	λ'', 10^{-3} W/(m K)	Pr′	Pr″	σ, 10^{-3} N/m	β, 10^{-3}/K
412	101.3	753	3.23	−35.7	309.7	354.4	2.11	1.64	232	8.8	98	17.1	5	0.84	16	1.57
430	161	734	5.08	−2.4	337.7	339.1	2.18	1.72	205	9.5	93	19.7	4.81	1.83	14.2	1.69
455	287	706	8.83	49.7	376.3	326.6	2.27	1.83	176	1.01	87	22.1	4.59	0.84	11.8	1.72
480	476	676	14.5	113.8	415.2	301.4	2.39	1.94	155	10.7	81	24.6	4.57	0.84	10	1.77
505	752	643	22.8	171.4	454	282.6	2.52	2.07	132	11.4	75	27.2	4.44	0.87	7.8	2.24
530	1120	607	34.9	232.3	491.9	259.6	2.67	2.23	109	12.2	69	30	4.22	0.91	5.7	2.44
555	1590	565	52.9	297.2	527.5	230.3	2.86	2.46	89	13.1	63	33	4.04	0.98	3.8	3.65
580	2270	513	81.8	368.9	557.3	188.4	3.15	2.92	70	14.6	57	37.1	3.87	1.15	2	8.38
605	3100	432	142	466.7	567.2	100.5	3.88	5.51	54	18	52	42.3	4.03	2.34	0.5	24.5
616.3	3510	280	280	514	514				53	53	49	49				
Uncertainty	h[1]	h[2]	h[3]	h[13]	h[3,4]	h[2]	h[2,5]	h[3,4]	h[2,6]	h[2,7]	h[2,8]	h[2,9]	h[12]	h[12]	h[2,10]	h[11]

[1]Refs. [22, 125]; [2]Ref. [52]; [3]Ref. [115]; [4]Ref. [63]; [5]Ref. [59]; [6]Ref. [42]; [7]Ref. [93]; [8]Ref. [108]; [9]Ref. [89]; [10]Estimated values; [11]Calc. from other properties.

1 Bibliography

1. Ahrendts J, Baehr HD (1979) Die thermodynamischen Eigenschaften von Ammoniak. VDI-Forschungsheft 596. VDI-Verlag, Düsseldorf
2. Angus S, Armstrong B, De Reuck KM (1985) Chlorine – tentative tables. IUPAC Chemical Data Series, No. 31. Pergamon Press, Oxford
3. Assael MJ, Ramires MLV, Nietro de Castro CA, Wakeham WA (1990) Benzene: A further liquid thermal conductivity standard. J Phys Chem Ref Data 19:113–117
4. Baidakov VG, Sulla II (1985) Surface tension of propane and isobutane at near-critical temperatures. Russ J Phys Chem 59:551–554
5. Bondi A (1966) Estimation of the heat capacity of liquids. Ind Eng Chem Fundam 5:442–449
6. Borreson RW, Schorr GR, Yaws CL (1976) Correlation constants for chemical compounds – heat capacities of gases. Chem Eng 16:79–81
7. Brock JR, Bird RB (1955) Surface tension and the principle of corresponding states. AIChE J 1:174–177
8. Bücker D, Wagner W (2006) A reference equation of state for the thermodynamic properties of ethane for temperatures from the melting line to 675 K and pressures up to 900 MPa. J Phys Chem Ref Data 35: 205–266
9. Bücker D, Wagner W (2006) Reference equations of state for the thermodynamic properties of fluid phase n-butane and isobutane. J Phys Chem Ref Data 35:929–1019
10. Calado JCG, McLure IA, Soares VAM (1978) Surface tension for octafluorocyclobutane, n-butane and their mixtures from 233 K to 254 K, and vapour pressure, excess gibbs function and excess volume for the mixture at 233 K. Fluid Phase Equilibria 2:199–213
11. Carmichael LT, Jacobs J, Sage BH (1969) Thermal conductivity of fluid *n*-pentane. J Chem Eng Data 14:31–37
12. Chase JD (1979) Persönliche Mitteilung
13. Chen NH (1965) Generalized correlation for latent heat of vaporization. J Chem Eng Data 10:207–210
14. Chung TH, Ajlan M, Lee LL, Starling KE (1984) Ind Eng Chem Fundam 23:8
15. Daubert TE, Danner RP (1985) Data compilation tables of properties of pure components. American Institute of Chemical Engineers, New York
16. Dillon HE, Penoncello SG (2004) A fundamental equation for calculation of the thermodynamic properties of ethanol. Int J Thermophys 25: 321–335
17. Dixon JA, Schiesser RW (1954) Viscosities of benzene-d6 and cyclohexane-d12. J Phys Chem 58:430–432
18. Edminster WC (1961) Applied hydrocarbon thermodynamics, vol. 56. Gulf Publishing Co., Houston, TX
19. Elverum GW, Doescher RN (1952) Physical properties of liquid fluorine. J Chem Phys 20:1834–1836
20. Fillipov LP, Nefedov SN, Kolykalova EA (1980) An experimental investigation into the complex of thermophysical properties of liquids. Inzherno-Fizicheskii Zhurnal 38:644–650
21. Friend DG, Ingham H, Ely JF (1991) Thermophysical properties of ethane. J Phys Chem Ref Data 20:275–347
22. Gallant RW (1970) Physical properties of hydrocarbons, vols. 1 and 2. Gulf Publishing Co., Houston, TX
23. Geist JM, Cannon MR (1946) Viscosities of pure hydrocarbons, Ind Eng Chem Anal Ed 18:611–613
24. Golubev IF (1959) Viscosity of gases and gas mixtures. Fizmat Press, Moscow
25. Golubev IF, Agaev NA (1964) Viscosity of limiting hydrocarbons. Azerbaydzhan State Press, Baku
26. Gomez-Nieto M, Thodos G (1977) Generalized treatment for the vapour pressure behaviour of polar and hydrogen-bonding compounds. Can J Chem Eng 55:445–449
27. Gomez-Nieto M, Thodos G (1978) Generalized vapour pressure equation for nonpolar substances. Ind Eng Chem Fundam 17:45–51
28. Goodwin RD (1988) Benzene thermophysical properties from 279 to 900 k at pressures to 1000 bar. J Phys Chem Ref Data 17:1541–1635
29. Gorin CE, Yaws CL (1976) correlation constants for chemical compounds – heat of vaporization, Chem Eng 83:85–87
30. GPSA Engineering Data Book (1977) Gas processors suppliers association. Tulsa, Oklahoma
31. Gross U, Song YW, Hahne E (1992) Thermal conductivity of the new refrigerants R134a, R152a and R123 measured by the transient hot-wire method. Int J Thermophys 13:957–983
32. Van der Gulik PS (1993) The viscosity of the refrigerant 1,1-difluoroethane along the saturation line. Int J Thermophys 12:105–117
33. Gunn RD, Yamada TA (1971) Corresponding states correlation of saturated liquid volumes. AIChE J 17:1341–1345
34. Haynes WM (1974) Measurements of the viscosity of compressed gaseous and liquid fluorine. Physica 76:1–20
35. Ho CY (1988) Data series on material properties, vol. 5: properties of inorganic and organic fluids
36. Holland PM, Eaton BE, Hanley HJM (1983) A correlation of the viscosity and thermal conductivity data of gaseous and liquid ethylene. J Phys Chem Ref Data 12:917–932
37. Horvath AL (1975) Physical properties of inorganic compounds Sl units. Crane, Russak & Company, New York
38. Hu J-H, Johnston HL, White D (1954) The density and surface tension of liquid fluorine between 66 and 80 K. J Am Soc 76:2584–2586
39. Huber ML, Laesecke A (2006) Correlation for the viscosity of pentafluoroethane (R125) from the triple point to 500 K at pressures up to 60 MPa. Ind Eng Chem Res 45:4447–4453
40. Jasper JJ (1972) The surface tension of pure liquid compounds. J Phys Chem Ref Data 1:841–1009

41. Johnson FMJ, McIntosh D (1909) Liquid chlorine. J Am Chem Soc 31: 1138–1144
42. Jossi JA, Stiel LI, Thodos G (1962) The viscosity of pure substances in the dense gaseous and liquid phases. AIChE J 8:59–63
43. Kamei A, Beyerlein SW, Jacobsen RT (1995) Application of nonlinear regression in the development of a wide range formulation for HCFC-22. Int J Thermophys 16:1155–1164
44. Katti RS, Jacobsen RT, Stewart RB, Jahangiri M (1986) Thermodynamic properties for neon for temperatures from the triple point to 700 K at pressures to 700 MPa. Adv Cryo Eng 31:1189–1197
45. Klein SA, McLinden MO, Laesecke A (1997) An improved extended corresponding states method for estimation of viscosity of pure refrigerants and mixtures. Int J Refrig 20:208–217
46. Knappstad B, Skjolsvik PA, Oye HA (1989) Viscosity of pure hydrocarbons. J Chem Eng Data 34:37–43
47. Kraus R, Luettmer-Strahtmann J, Sengers J, Stephan K (1993) Transport properties of 1,1,1,2-tetrafluorethane (R134a). Int J Thermophys 14: 951–988
48. Kudchadker AP, Alani GH, Zwolinski BJ (1968) Critical constants of organic substances. Chem Rev 68:729–735
49. Kumagi A, Takahashi S (1991) Viscosity of saturated liquid fluorocarbon refrigerants from 273 to 353 K. Int J Thermophys 12:105–117
50. Latini G, Laurenti L, Marcotullio F, Pierpaoli P (1990) Liquid dynamic viscosity: A general method with application to refrigerant and refrigerant mixtures. Int J Refrig 13:248–255
51. Leachman JW, Jacobsen RT, Penoncello SG, Lemmon EW (2009) Fundamental equations of state for parahydrogen, normal hydrogen, and orthohydrogen. J Phys Chem Ref Data 38:721
52. Lee BI, Kesler MG (1975) A generalized thermodynamic correlation based on three- parameter corresponding states. AIChE J 21:510–527
53. Lemmon EW (2009) The surface tension of ethane. Private Communication, NIST, Boulder
54. Lemmon EW, Jacobsen RT (2004) Viscosity and thermal conductivity equations for nitrogen, oxygen, argon, and air. Int J Thermophys 25:21–69
55. Lemmon EW, Jacobsen RT (2005) A new functional form and new fitting techniques for equations of state with application to pentafluoroethane (HFC-125). J Phys Chem Ref Data 34:69–108
56. Lemmon EW, McLinden MO, Wagner W (2009) Thermodynamic properties of propane. III. A reference equation of state for temperatures from the melting line to 650 K and Pressures up to 1000 MPa. J Chem Eng Data 54: 3141–3180
57. Lemmon EW, Penoncello SG (1994) The surface tension of air and air component mixtures. Adv Cryo Eng 39:1927–1934
58. Lemmon EW, Span R (2006) Short fundamental equations of state for 20 industrial fluids. J Chem Eng Data 51:785–850
59. Letsou A, Stiel LI (1973) Viscosities of saturated nonpolar liquids at elevated pressures. AIChE J 19:409–411
60. Liquide L (1976) Gas encyclopaedia. Elsevier Scientific Publishing Co., Amsterdam, Netherlands
61. Livingston J, Morgan R, Owen FT (1911) The weight of a falling drop and the laws of tate. J Am Chem Soc 33:1713
62. Lydersen AL (1955) Estimation of critical properties of organic compounds. Eng. Exp. Stn. Rep. 3, University of Wisconsin College of Engineering, Madison.
63. Lyman TJ, Danner RP (1976) Correlation of liquid heat capacities with a four-parameter corresponding states method. AIChE J 22:759–765
64. Mamedov AM (1978) Thermal-conductivity of six aromatic hydrocarbons. Inzhenerno-Fizicheskii Zhurnal 34:465–470
65. Marsh K, Perkins R, Ramires MLV (2002) Measurement and correlation of the thermal conductivity of propane from 86 to 600 K at pressures to 70 MPa. J Chem Eng Data 47:932–940
66. McLinden MO, Klein SA, Perkins R (2000) An extended corresponding states model for the thermal conductivity of refrigerants and refrigerant mixtures. Int J Refrig 23:43–63
67. Miller JW, Jr., Gordon RS, Yaws CL (1976) Correlation constants for liquids – heat capacities. Chem Eng 83(25):129–131
68. Miller JW, Jr., McGinley JJ, Yaws CL (1976) Correlation constants for liquids – thermal conductivities. Chem Eng 83(25):133–135
69. Miller JW, Jr., Gordon RS, Yaws CL (1976) Correlation constants for chemical compounds – thermal conductivity of gas. Chem Eng 153–155
70. Miller JW, Jr., Gordon RS, Yaws CL (1976) Correlation constants for chemical compounds – gas viscosity. Chem Eng 86(24):155–157
71. Miller JW, Jr., Gordon RS, Yaws CL (1976) Correlation constants for chemical compounds – liquid viscosity. Chem Eng 86(24):157–159
72. Miller JW, Yaws CL, Shah PN, Schorr GR, Patel PM (1976) Chem Eng 83(25):153
73. Miller JW, Jr., Yaws CL (1976) Correlation constants for liquids – surface tension. Chem Eng 83(22):127–129
74. Misic D, Thodos G (1961) The thermal conductivity of hydrocarbon gases at normal pressure. AIChE J 7:264–267
75. Nabizadeh H, Mayinger F (1992) Viscosity of gaseous R123. High Temp. High Pres. 24:221–230
76. Needham DP, Ziebland H (1965) Ammonia and its anomalous behaviour in the vicinity of the critical point. Int J Heat Mass Transfer 8:1387–1411
77. Okada M, Higashi Y (1994) Surface tension correlation of HFC-134a and HCFC-123. Progress Report to IEA Annex 18, Boulder
78. Okada M, Higashi Y (1995) Experimental surface tensions for HFC-32, HCFC-124, HFC-125, HCFC-141b, HCFC-142b, and HFC-152a. Int J Thermophys 16:791–800
79. Okada M, Watanabe K (1988) Surface tension correlations for several fluorocarbon refrigerants. Heat Transf Jpn Res 17:35–52
80. Okubo T, Nagashima A (1992) Measurement of the viscosity of HCFC-123 in the temperature range 233–418 K and at pressures up to 20 MPa. Int J Thermophys 13:401–410
81. Overhoff U (2006) Development of a new equation of state for the fluid region of propene for temperatures from the melting line to 575 K with pressures to 1000 MPa as well as software for the computation of thermodynamic properties of fluids. Ph.D. Dissertation, Ruhr-University, Bochum, Germany
82. Pennington RE, Kobe KA (1957) The thermodynamic properties of acetone. J Am Chem Soc 79:300–305
83. Penoncello SG, Goodwin ARH, Jacobsen RT (1995) A thermodynamic property formulation for cyclohexane. Int J Thermophys 16:519–531
84. Perkins RA (2002) Measurement and correlation of the thermal conductivity of isobutane from 114 K to 600 K at pressures to 70 MPa. J Chem Eng Data 47:1272–1279
85. Perkins RA, Huber ML (2006) Measurement and correlation of the thermal conductivity of pentafluoroethane (R125) from 190 K to 512 K at pressures to 70 MPa. J Chem Eng Data 51:898–904
86. Perkins RA, Ramires MLV, Nieto de Castro CA, Cusco L (2002) Measurement and correlation of the thermal conductivity of butane from 135 K to 600 K at pressures to 70 MPa. J Chem Eng Data 47:1263–1271
87. Perry JH (1950) Chemical Engineer's Handbook, 3rd edn. McGraw-Hill, New York
88. Perry RH, Chilton CH (1973) Chemical Engineer's Handbook, 5th edn. McGraw-Hill, New York
89. Reid RC, Prausnitz JM, Sherwood TK (1977) The properties of gases and liquids, 3rd edn. McGraw-Hill, New York
90. De Reuck KM (1990) International thermodynamic tables of the fluid state-11 fluorine. International union of pure and applied chemistry, Pergamon Press, Oxford
91. De Reuck KM, Craven RJB (1993) International tables of the fluid state, vol. 12: Methanol. Hemisphere, London
92. Rihani DN, Doraiswamy LK (1965) Estimation of heat capacity of organic compounds from group contributions. Ind Eng Chem Fundam 4:17–21
93. Robbins LA, Kingrea CL (1962) Estimate thermal conductivity. Hyd Proc Pet Ref 41(5):133–136
94. Sakiadis BC, Coates J (1955) Studies in thermal conductivity of liquids. AIChE J 1:275–288
95. Sellschopp W (1935) Z Ver Dt Ing 75:69
96. Setzmann U, Wagner W (1991) A new equation of state and tables of thermodynamic properties for methane covering the range from the melting line to 625 K at pressures up to 1000 MPa. J Phys Chem Ref Data 20:1061–1155
97. Shah PN, Yaws CL (1976) Densities of liquids. Chem Eng 25:131–133
98. Smukala J, Span R, Wagner W (2000) A new equation of state for ethylene covering the fluid region for temperatures from the melting line to 450 K at pressures up to 300 MPa. J Phys Chem Ref Data 29:1053–1122

99. Soares VAM, Almeida BJVS, McLure IA, Higgins RA (1986) Surface tension of pure and mixed simple substances at low temperature. Fluid Phase Equilibria 32:9–16
100. Somayajulu GR (1988) A generalized equation for surface tension from the triple point to the critical point. Int J Thermophys 9:559–566
101. Somayajulu GR (1988) A new equation for enthalpy of vaporization from the triple point to the critical point. Int J Thermophys 9:567–574
102. Span R, Wagner W (2003) Equations of state for technical applications. II. Results for nonpolar fluids. Int J Thermophys 24:41–109
103. Stephan K, Hildwein H (1987) recommended data of selected compunds and binary mixtures. Chemistry data series, vol. 4: Part 1 + 0032, DECHEMA.
104. Stairs RA, Sienko MJ. (1956) Surface tension of ammonia and of solutions of alkali halides in ammonia. J Am Chem Soc 78:920–923
105. Stiel LI, Thodos G (1961) The viscosities of nonpolar gases at normal pressures. AIChE J 7:611–615
106. Stiel LI, Thodos G (1962) The viscosity of polar gases at normal pressures. AIChE J 8:229–232
107. Stiel LI, Thodos G (1964) The viscosity of polar substances in the dense gaseous and liquid regions. AIChE J 10:275–277
108. Stiel LI, Thodos G (1964) The thermal conductivities of nonpolar substances in the dense gaseous and liquid regions. AIChE J 10:26–29
109. Takahashi M, Yokoyama C, Takahshi S (1987) Viscosities of gaseous R13B1, R142b, and R152a. J Chem Eng Data 32:98–103
110. Technical Data Book-Petroleum Refining, American Petroleum Institute Division of Refining. Washington, DC, 1970
111. Tegeler Ch, Span R, Wagner W (1999) A new equation of state for argon covering the fluid region for temperatures from the melting line to 700 K at pressures up to 1000 MPa. J Phys Chem Ref Data 28:779–850
112. Tillner-Roth R, Harms-Watzenberg F, Baehr HD (1993) Eine neue Fundamentalgleichung für Ammoniak. DKV-Tagungsbericht 20:167–181
113. Tillner-Roth R (1995) A fundamental equation of state for 1,1-difluorethane (HFC-152a). Int J Thermophys 16:91–100
114. Tillner-Roth R, Baehr HD (1994) An international standard formulation for the thermodynamic properties of 1,1,1,2-tetrafluorethane (HFC-134a) for temperatures from 170 K to 455 K and pressures up to 70 MPa. J Phys Chem Ref Data 23:657–729
115. Thinh TP, Duran JL, Ramalho RS, Kaliaguine S (1971) Equations improve Cp° predictions. Hyd Proc 50:98–104
116. Timmermans J (1950) Physico- chemical constants of pure organic compounds. Elsevier Publishing Co., New York, pp 303–325
117. Touloukian YS, Makitu T (1970) Thermophysical properties of matter, vol. 6. IFI/Plenum, New York
118. Touloukian YS, Liley PE, Saxena SC (1970) Thermophysical properties of matter, vol. 3. IFI/Plenum, New York
119. Touloukian YS, Powell RW, Ho CY, Klemens PG (1970) Thermophysical properties of matter, vol. 1. IFI/Plenum, New York
120. Touloukian YS, Liley PE, Saxena SC (1970) Thermophysical properties of matter, vol. 6. IFI/Plenum, New York
121. Touloukian YS, Liley PE, Hestermans P (1975) Thermophysical properties of matter, vol. 11. IFI/Plenum New York
122. Touloukian YS, Saxena SC, Hestermans P (1975) Thermophysical properties of matter, vol. 11. IFI/Plenum, NewYork
123. Tsvetkov OB, Laptev YuA, Asambaev AG (1994) Thermal conductivity of refrigerants R123, R134a, and R125 at low temperatures. Int J Thermophys 15:203–214
124. Tufeu R, Clifford AA (1988) Thermal conductivity of gaseous and liquid ammonia. J Heat Transf 110:992–993
125. Vargaftik NB (1975) Tables on the thermophysical properties of liquids and gases, 2nd edn. Hemisphere Publishing Corp., Washington, DC
126. Van Velzen D, Cardozo RL, Langenkamp H (1972) A liquid viscosity temperature chemical constitution relation for organic compounds. Ind Eng Chem Fundam 11:20–25
127. Vines RG, Bennett LA (1954) The thermal conductivity of organic vapors. The relationship between thermal conductivity and viscosity, and the significance of the euken faktor. J Chem Phys 22:360–366
128. Vogel E, Kuechenmeister C, Bich E, Laesecke A (1998) Reference correlation of the viscosity of propane. J Phys Chem Ref Data 27:947–970
129. Vogel E, Kuechenmeister C, Bich E (1999) Viscosity for *n*-butane in the fluid region. High Temp High Press 31:173–186
130. Vogel E, Kuechenmeister C, Bich E (2000) Viscosity correlation for isobutane over wide ranges of the fluid region. Int J Thermophys 21:343–356
131. Wakeham WA, Fenghour A (1995) The viscosity of ammonia, persönliche Mitteilung. (Artikel im Druck bei J Phys Chem Ref Data)
132. Watson KM (1943) Thermodynamics of the liquid state. Ind Eng Chem 35:398–400
133. Yamamoto R, Matsuo S, Tanaka Y (1992) Thermal conductivity of halogenated ethanes HFC-134a, HFC-123 and HCFC-141b. Int J Thermophys 14:79–90
134. Yaws CL (1991) Calculate liquid heat capacity. Hyd Proc 73–77
135. Yoor P, Thodos G (1970) Viscosity of nonpolar gaseous mixtures at normal pressures. AIChE J 16:300–304
136. Younglove BA, McLinden MO (1994) An international standard equation of state for the thermodynamic properties of refrigerant 123. J Phys Chem Ref Data 23:731–779
137. Yuan TF, Stiel LI (1970) Heat capacity of saturated nonpolar and polar liquids. Ind Eng Chem Fundam 9:393–400

D4.1 Refrigerants: Regulations

Ewald Preisegger · Felix Flohr
Solvay Fluor GmbH, Hannover, Germany

1 Introduction

The refrigerants used in vapor compression refrigeration systems in the European Community (EC) today are

- Hydrochlorofluorocarbons (HCFCs), e.g., R22
- Hydrofluorocarbons (HFCs), e.g., R134a
- Ammonia (R717)
- Carbon dioxide (R744)
- Hydrocarbons (HCs), e.g., propane

The still mainly used halogenated refrigerants belonging to the group of HCFCs and HFCs are subject to comprehensive international legislation due to their ozone-depleting properties (in case of HCFCs), respectively, their potential effect on the climate (in case of HFCs) if released into the atmosphere.

The basic international instruments are

- The *Montreal Protocol* of 1987 regulating production and consumption of ozone-depleting substances (ODS) [1]
- The *Kyoto Protocol* of 1997 requiring measures to reduce greenhouse gas (GHG) emissions [2]

All subsequent regulations concerning production, placing on the market, and use of halogenated refrigerants are based on these international protocols with the aim to implement the requirements set in these protocols into national law of the signatory states.

1.1 Legislation for Ozone-Depleting Substances

1.1.1 Montreal Protocol

It regulates production and consumption of ODS, e.g., chlorofluorocarbons (CFCs) globally. Its basic requirements for industrialized and developing countries are described in brief in Table 1a.

EC Regulation 1005/2009 [3]

The EC implemented the Montreal Protocol with a detailed regulation going far beyond the requirements of the Montreal Protocol. The latest version is the recently published regulation EC 1005/2009 that replaced the previous regulation EC 2037/2000 by January 01, 2010. Since fully halogenated CFCs already had been phased out completely in the EC, special provisions have to be made in this new regulation on ODS only for HCFCs, as far as refrigeration and air conditioning (AC) applications are concerned.

This EC regulation is immediately applicable law in all Member States and does not require national implementations!

Some requirements are especially important for refrigeration systems still running with HCFC refrigerants:

Placing on the market and use

- The placing on the market and the use of controlled substances shall be prohibited (Art 5(1))
- Until December 31, 2014, only reclaimed and recycled HCFCs may be used for the maintenance or servicing of existing refrigeration, AC, and heat pump equipment with further restrictions according to Art 11(3 and 4)

Labeling and recording

- Cylinders containing reclaimed and recycled HCFCs as well as refrigeration, AC, and heat pump equipment have to be labeled according to Art 11(3 and 6)
- Operators of equipment have to keep records on HCFCs used for maintenance and servicing; service contractors are required to keep records on the sources of HCFCs used for servicing (Art 11(7))

Exports

- Exports of products and equipment containing HCFCs have to be authorized by the Commission on request of the competent authority of a Member State (Art 17(3))

Recovery of controlled substances

- Controlled substances contained in equipment shall be recovered for destruction, recycling, or reclamation (Art 22(1))

Leakage checks

- Companies shall take all precautionary measures practicable to prevent and minimize any leakages and emissions of controlled substances. Refrigeration, AC and heat pump

VDI-GVC (ed.), *VDI Heat Atlas*, DOI 10.1007/978-3-540-77877-6_13,

D4.1. Table 1a. *Montreal Protocol* (latest version 2008) regulates worldwide production and use ("consumption") of ODS

Basis	100% ODP-weighted HCFC consumption in 1989 + 2.8% ODP-weighted CFC consumption in 1989	
	Industrialized nations	Developing countries
CFCs	Phase-out 1996	Phase-out 2010
HCFCs	Freeze 2004	Freeze 2013 based on average 2009/2010 consumption
	2010: 75% reduction	2015: 10% reduction
	2015: 90% reduction	2020: 35% reduction
	2020: 99.5% reduction	2025: 67.5% reduction
	2030: phase out	2030: 97.5% reduction
		2040: phase out

D4.1. Table 1b. *Kyoto Protocol*

Basis	UN framework convention on climate change (UNFCCC)	
Target	Emission reduction of the GHGs	
	CO_2, CH_4, and N_2O (natural GHGs)	
	HFCs, PFCs, and SF_6 (industrial GHGs)	
Emission reduction targets	EC	−8%
	USA	−7%
	Japan	−6%
	Global average	−5.2%
Commitment period	2008–2012	
Baseline	For CO_2, CH_4, and N_2O: emissions in 1990	
	For HFCs, PFCs, and SF_6: emissions in 1995 (optional 1990)	
Entry into force: February 16, 2005		

equipment with a refrigerant charge of more than 3 kg has to be frequently checked for leakages with a checking frequency depending on the refrigerant charge. For each system records shall be maintained on the leakage checks as well as on the refrigerant charge and any quantities added or removed during maintenance or servicing (Art 23).

National Regulations

Some EC Member States may have implemented national regulations, e.g., for defining the minimum qualification requirements for the personnel carrying out, e.g., leak checking activities and refrigerant recovery, as it is the case, e.g., with the German "Chemikalien-Ozonschicht-Verordnung" [4].

European countries outside the EC, where the regulation 1005/2009 is not to be applied, need their own national legislation for ODS. As an example, the "Verordnung über umweltgefaehrdende Stoffe" [5] in Switzerland may be mentioned.

In both cases it therefore will be necessary to get acquainted with individual national regulations for each of these countries before starting activities at HCFC containing refrigeration, AC, and heat pump systems.

1.2 Legislation for Greenhouse Gases

1.2.1 Kyoto Protocol

It requires measures on a global basis to reduce emissions of the most important GHGs, carbon dioxide (CO_2), methane (CH_4), nitrogen oxide (N_2O) as well as emissions of the group of fluorinated gases. This group consists of HFCs, perfluorocarbons (PFCs), and sulfur hexafluoride (SF_6).

Its basic requirements for industrialized and developing countries are described in brief in Table 1b.

EC Regulation 842/2006 [6]

On July 4, 2006, the "Regulation EC 842/2006 of the European Parliament and of the Council on certain fluorinated greenhouse gases" [6] entered into force and therefore—as an immediately applicable law—has to be complied with by all 27 EC Member States. It represents the implementation of the Kyoto Protocol in the EC with regard to fluorinated gases.

Certain requirements of this regulation are concerning the persons and companies involved in operating and servicing of refrigeration, AC, and heat pump systems with HFC and PFC

refrigerants. In detail, the following legally binding measures have to be observed:

General requirements for emission reduction (Art 3(1))

Operators of refrigeration, AC, and heat pump systems containing HFC or PFC refrigerants generally have to take all measures which are technically and economically feasible

- To prevent leakage of these gases
- To repair any detected leakage as soon as possible

Requirements for leak testing (Art 3(2))

Art 3(2) lays down the following procedure for leak testing of refrigeration and AC systems:

- Systems with a HFC or PFC charge of 3 kg or more:
  - At least once every 12 months (does not apply to hermetically sealed systems labeled as such and containing less than 6 kg HFC or PFC)
- Systems with a HFC or PFC charge of 30 kg or more:
  - At least once every 6 months
- Systems with a HFC or PFC charge of 300 kg or more:
  - At least once every 3 months
  - For these applications leakage detection systems shall be installed and checked every 12 months to ensure their proper functioning.
  - *Basically valid*: Where a properly functioning leakage detection system is in place, the frequency of the leak checks shall be halved. After a leak has been repaired, the system shall be checked again within 1 month.

Logbook (Art 3(6))

This chapter imposes the operators of refrigeration and AC systems with more than 3 kg HFC or PFC refrigerant charge to keep records on the following data:

- Type and location of the system
- Type of HFC or PFC refrigerant used
- Refrigerant charge (nominal charge)
- Date and result of leak checks; name and employer of the testing person
- Date of servicing and maintenance; name and employer of the serviceman
- Quantity of HFC or PFC refrigerant added during servicing
- Quantity of HFC or PFC refrigerant recovered during servicing, maintenance, and final disposal of the system

Recovery (Art 4)

Operators of refrigeration and AC systems are responsible for the proper recovery of HFC and PFC refrigerants in order to ensure their recycling, reclamation, or destruction. Similarly this applies for the users of transport and storage containers for fluorinated GHGs like HFC refrigerants prior to scrapping.

Labeling (Art 7)

All refrigeration, AC, and heat pump systems with HFC or PFC refrigerants (as well as other products and equipment containing fluorinated gases covered by this regulation) only may be placed on the EC market if they carry a label with the chemical designation (accepted industry nomenclature, e.g., R134a), the nominal charge and a remark that it contains a fluorinated GHG covered by the Kyoto Protocol.

Training and certification (Art 5)

Activities mentioned in "Requirements for leak testing" and "Recovery" only shall be carried out by appropriately trained and certified personnel. The EC Commission has set minimum requirements [7] as the basis for corresponding measures that Member States had to implement until July 04, 2008. From July 04, 2009, only certified personnel involved in servicing of equipment or refrigerant recovery is allowed to take delivery of fluorinated GHGs!

Besides this, the Commission has published standard requirements regarding the methodology for leak testing as well as the labeling of products, equipment, and containers [8,9].

National Regulations

Some EC Member States may have implemented national regulations, e.g., for specifying in detail the criteria to be applied for leak checking activities or for setting necessary qualification standards for personnel involved in certain activities. An example is the German "Chemikalien-Klimaschutz-Verordnung" [10].

The EC Member States Austria and Denmark have additional national regulations on fluorinated GHGs in force which are partially stricter than the EC regulation 842/2006 [11–13].

European countries outside the EC, where the regulation 842/2006 is not applicable, have established own national legislation for fluorinated GHGs. As an example, the "Verordnung über umweltgefaehrdende Stoffe" [14] in Switzerland may be mentioned.

It will therefore be necessary to get acquainted with individual national regulations in each of these countries before starting activities at refrigeration, AC, and heat pump systems containing HFC or PFC refrigerants.

1.3 Legislation for Nonhalogenated Refrigerants

Since the refrigerants ammonia, carbon dioxide, and HCs are not ODS and their global warming potential is very low compared with HFCs and PFCs, no environment-related international or national regulations comparable with those in force for fluorinated gases are restricting their use. However, due to their safety-related properties regarding flammability and/or toxicity, comprehensive safety precautions have to be applied when using these gases as refrigerants.

The necessary requirements are laid down in the European Standard EN 378 (1-4) [15], which additionally contains provisions to protect the aquatic environment when handling ammonia.

Beyond this, the operation of refrigeration systems with ammonia and HCs is subject to various additional regionally differing requirements in the EC. The publication [16] provides an overview about the most important directives, regulations, and standards to be considered when planning and building an ammonia refrigeration plant in Germany (Tables 2a and 2b).

D4.1. Table 2a. Thermophysical properties of refrigerants

Refrigerant	Formula (ma.%)	Molar mass (kg/kmol)	Melting temperature or triple point temperature[a] (°C)	Normal boiling point (°C)	Temperature t_{crit} (°C)	Pressure p_{crit} (bar)	Boiling pressure		Pressure ratio	Specific volume of sat. vapor	Theoretical swept volume for 1 kWh (−15°C /30°C) (m^3/kWh)	Circulated refrigerant mass per kW (kg/min kW)	Circulated mass of sat. liquid per kW	Coefficient of performance[b]	Volumetric refrigeration capacity[b] (kJ/m^3)	Isentropic compressing end temperature[b]
							At −15°C (bar)	At +30°C (bar)	p_s (30°C)/p_s (−15°C) (–)	at −15°C (m^3/kg)			at 30°C (dm^3/min)	(−15°C/30°C) (–)		(−15°C/30°C) (°C)
R50 (methane)[c]	CH_4	16.04	−182.46	−161.48	−82.6	45.99	–/–	–/–	–/–	–/–	–/–	–/–	–/–	–/–	–/–	–/–
R14[c]	CF_4	88.01	−183.61	−128.05	−45.6	37.50	–/–	–/–	–/–	–/–	–/–	–/–	–/–	–/–	–/–	–/–
R1150 (ethylene)	CH_2=CH_2	28.05	−169.15	−103.77	9.3	50.40	28.89	–/–	–/–	–/–	–/–	–/–	–/–	–/–	–/–	–/–
Dinitrogen oxide	N_2O	44.01	−90.85	−88.45	36.5	71.60	22.96	64.10	2.79	0.0192	0.353	0.304	0.332	3.60	8378	64.1
R170 (ethane)	CH_3CH_3	30.07	−183.25	−88.65	32.3	48.80	16.31	47.07	2.89	0.0332	0.720	0.432	1.510	2.16	4834	50.2
R508A[c]	R23/R116 (39/61)	100.10	–/–	−87.63	10.2	36.51	18.60	–/–	–/–	–/–	–/–	–/–	–/–	–/–	–/–	–/–
R508B[c]	R23/R116 (46/54)	95.39	–/–	−87.60	11.2	37.72	18.76	–/–	–/–	–/–	–/–	–/–	–/–	–/–	–/–	–/–
R23[c]	CHF_3	70.01	−155.13	−82.02	26.1	48.32	16.27	–/–	–/–	–/–	–/–	–/–	–/–	–/–	–/–	–/–
R744 (carbon dioxide)[d]	CO_2	44.01	−56.56	−78.45[e]	31.1	72.95	22.89	71.92	3.14	0.0166	0.431	0.465	0.780	1.45	4320	71.0
R116[c]	CF_3CF_3	138.01	−100.05	−78.09	19.9	30.48	12.15	–/–	–/–	–/–	–/–	–/–	–/–	–/–	–/–	–/–
R32[c,d]	CH_2F_2	52.02	−136.81	−51.65	78.1	57.82	4.88	19.28	3.95	0.0747	1.049	0.234	0.249	4.52	3420	68.5
R410A[c,d]	R32/R125 (50/50)	72.59	–/–	−51.44	71.4	49.02	4.80	18.84	3.92	0.0540	1.160	0.358	0.346	4.39	3093	51.2
R428A[c]	R125/R143a/ R290/R600a (77.5/20/ 0.6/1.9)	107.53	–/–	−48.35	69.0	37.25	3.92	15.13	3.86	0.0450	1.662	0.615	0.580	4.03	2158	33.8
R125[c,d]	CHF_2CF_3	120.02	−100.63	−48.09	66.0	36.18	4.05	15.69	3.87	0.0391	1.641	0.700	0.604	4.00	2185	32.1
R1270 (propylene)[d]	CH_3CH=CH_2	42.08	−185.2	−47.62	91.1	45.55	3.63	13.05	3.60	0.1278	1.607	0.210	0.421	4.55	2233	42.1
R143a[c,d]	CH_3CF_3	84.04	−111.81	−47.24	72.7	37.61	3.77	14.34	3.80	0.0596	1.624	0.454	0.500	4.28	2209	37.6
R507A[c,d]	R125/R143a (50/50)	98.86	–/–	−46.74	70.6	37.05	3.77	14.59	3.87	0.0509	1.658	0.543	0.531	4.18	2163	35.3

R422A[c]	R125/R134a/R600a (85.1/11.5/3.4)	113.60	–/–	−46.50	71.7	37.46	3.49	14.05	4.02	0.0485	1.831	0.629	0.567	3.92	1959	33.8
R404A[c,d]	R125/R143a/R134a (44/52/4)	97.60	–/–	−46.22	72.0	37.29	3.61	14.14	3.92	0.0541	1.709	0.527	0.517	4.16	2099	36.0
R502	R22/R115 (48.8/51.2)	111.63	–/–	−45.34	81.5	40.17	3.44	13.05	3.80	0.0507	1.725	0.568	0.477	4.39	2079	37.1
R407C[c,d]	R32/R125/R134a (23/25/52)	86.20	–/–	−43.63	86.0	46.29	2.63	11.76	4.47	0.0870	1.989	0.381	0.342	3.91	1802	51.4
R422D[c]	R125/R134a/R600a (65.1/31.5/3.4)	109.94	–/–	−43.20	79.6	39.05	2.80	11.96	4.28	0.0637	2.123	0.555	0.496	3.88	1689	36.4
R427A[c]	R32/R125/R143a/R134a (15/25/10/50)	90.44	–/–	−42.96	85.3	43.92	2.57	11.42	4.44	0.0848	2.076	0.408	0.369	3.91	1727	47.7
R290 (propane)	$CH_3CH_2CH_3$	44.10	−187.62	−42.11	96.7	42.51	2.92	10.79	3.70	0.1533	1.978	0.215	0.444	4.55	1814	36.6
R22[c,d]	$CHClF_2$	86.47	−157.42	−40.81	96.1	49.90	2.96	11.92	4.02	0.0772	1.711	0.369	0.315	4.66	2096	52.9
R417A[c]	R125/R134a/R600a (46.6/50/3.4)	106.75	–/–	−39.07	87.1	40.36	2.33	10.32	4.44	0.0796	2.384	0.499	0.442	3.98	1504	37.5
R500	R12/R152a (73.8/26.2)	99.30	–/–	−33.60	102.1	41.68	2.15	8.78	4.08	0.0931	2.403	0.430	0.383	4.65	1493	40.7
R717 (ammonia)[d]	NH_3	17.03	−77.6	−33.33	132.3	113.33	2.36	11.67	4.94	0.5067	1.654	0.054	0.091	4.76	2167	99.1
R12[d]	CCl_2F_2	120.91	−157.05	−29.75	112.0	41.36	1.82	7.44	4.08	0.0915	2.817	0.513	0.397	4.70	1273	37.8
R134a[c,d]	CH_2FCF_3	102.03	−103.3	−26.07	101.1	40.59	1.64	7.70	4.70	0.1202	2.926	0.406	0.342	4.61	1226	36.6
RE170 (dimethyl ether)	$CH_3–O–CH_3$	46.07	−141.5	−24.81	127.2	53.41	1.52	6.80	4.46	0.2878	3.009	0.174	0.267	4.83	1191	45.1
R152a[c,d]	CH_3CHF_2	66.05	−118.59	−24.02	113.3	45.17	1.49	6.90	4.64	0.2056	3.037	0.246	0.278	4.78	1180	47.0
R227ea[c]	CF_3CHFCF_3	170.03	−126.8	−16.34	101.8	29.25	1.07	5.28	4.92	0.1111	[f]	[f]	[f]	[f]	[f]	[f]
R124[c]	$CHClFCF_3$	136.48	−199.15	−11.96	122.3	36.24	0.89	4.45	5.00	0.1689	[f]	[f]	[f]	[f]	[f]	[f]
R600a (isobutane)[c]	$CH(CH_3)_2–CH_3$	58.12	−159.42	−11.75	134.7	36.29	0.89	4.05	4.54	0.3975	5.441	0.228	0.419	4.36	659	30.0
R764 (sulfur dioxide)[c]	SO_2	64.06	−75.45	−10.02	157.5	78.84	0.81	4.62	5.73	0.4029	4.377	0.181	0.134	4.84	818	97.0
R142b[c]	CH_3CClF_2	100.50	−130.43	−9.12	137.1	40.55	0.79	3.93	4.95	0.2587	5.503	0.354	0.323	4.81	651	36.0

D4.1. Table 2a. (continued)

Refrigerant	Formula (ma.%)	Molar mass (kg/kmol)	Melting temperature or triple point temperature[a] (°C)	Normal boiling point (°C)	Temperature t_{crit} (°C)	Pressure p_{crit} (bar)	Boiling pressure		Pressure ratio	Specific volume of sat. vapor	Theoretical swept volume for 1 kWh (−15°C /30°C) (m^3/kWh)	Circulated refrigerant mass per kW (kg/min kW)	Circulated mass of sat. liquid per kW	Coefficient of performance[b]	Volumetric refrigeration capacity[b] (kJ/m^3)	Isentropic compressing end temperature[b]
							At −15°C (bar)	At +30°C (bar)	p_s (30°C)/p_s (−15°C) (–)	at −15°C (m^3/kg)			at 30°C (dm^3/min)	(−15°C/30°C) (–)		(−15°C/30°C) (°C)
R600 (butane)[c]	CH_3–CH_2–CH_2–CH_3	58.12	−138.26	−0.49	152.0	37.96	0.56	2.83	5.03	0.6350	[f]	[f]	[f]	[f]	[f]	[f]
R114[c]	$CClF_2CClF_2$	170.92	−92.52	3.59	145.7	32.57	n.d.f	n.d.f	n.d.f	n.d.f	n.d.f	n.d.f	n.d.f	n.d.f	n.d.f	n.d.f
R245fa[c]	$CHF_2CH_2CF_3$	134.05	−102.1	15.14	154.0	36.51	0.25	1.78	7.01	0.6154	[f]	[f]	[f]	[f]	[f]	[f]
R11	CCl_3F	137.37	−110.47	23.71	198.0	44.08	0.20	1.26	6.23	0.7602	17.555	0.385	0.263	5.03	204	42.8
R123[c,d]	$CHCl_2CF_3$	152.93	−107.15	27.82	183.7	36.62	0.16	1.10	6.99	0.8805	22.289	0.422	0.291	4.90	160	32.8
R601a (isopentane)[c,d]	$(CH_3)_2CH$–CH_2–CH_3	72.15	−160.5	27.83	187.2	33.78	0.17	1.09	6.32	1.6931	22.127	[f]	[f]	[f]	[f]	[f]
R141b[c]	CH_3CCl_2F	116.95	−103.47	32.04	204.4	42.12	0.14	0.94	6.97	1.3371	24.904	0.310	0.254	5.01	143	40.2
R601 (pentane)[c]	CH_3–CH_2–CH_2–CH_2–CH_3	72.15	−129.68	36.06	196.6	33.70	0.12	0.82	6.96	2.4892	[f]	[f]	[f]	[f]	[f]	[f]
R365mfc[c]	$CF_3CH_2CF_2CH_3$	148.07	−34.15	40.19	186.9	32.66	0.08	0.69	8.37	1.7305	[f]	[f]	[f]	[f]	[f]	[f]
R113	CCl_2FCClF_2	187.38	−36.22	47.58	214.1	33.92	0.07	0.54	7.87	1.6403	[f]	[f]	[f]	[f]	[f]	[f]
R718 (water)	H_2O	18.02	0	100.00	374.1	218.31	[f]	0.04	[f]	[f]	[f]	[f]	[f]	[f]	[f]	[f]

[a]Melting temperatures of blends are not listed, please check the melting temperatures of the single components
[b]For a single cycle with $p_o = -15°C$, $p_c = 30°C$, isentropic compression, $T_{superheat} = 0$ K, $T_{subcooled} = 0$ K
[c]Data acc. Refprop 8.0, 2007
[d]Compare ISO17584:2005
[e]Sublimation temperature
[f]Not available under conditions described under (b)
n.d.f. no data found

D4.1. Table 2b. Refrigerant properties of saturated liquid[a]

Refrigerant	Formula (% by weight)	Temperature (°C)	Pressure (bar)	Density (kg/m)	Specific heat capacity (kJ/kg K)	Thermal conductivity (W/m K)	Dynamic viscosity (mN s/m²)	Kinematic viscosity (μm²/s)	Temperature conductivity (10^{-8} m²/s)	Prandtl no.
R50 (Methane) Normal boiling point, °C −161.5	CH_4	−170	0.472	434.5	3.426	0.195	0.140	0.323	13.127	2.462
		−150	2.378	405.0	3.580	0.168	0.093	0.229	11.554	1.982
		−130	7.520	371.1	3.876	0.139	0.064	0.171	9.661	1.772
		−110	18.026	328.8	4.615	0.110	0.044	0.133	7.279	1.834
R14 Normal boiling point, °C −128.0	CF_4	−90	36.399	261.7	9.098	0.081	0.028	0.109	3.394	3.200
		−130	0.881	1613.7	0.899	0.097	0.242	0.150	6.700	2.240
		−110	3.088	1502.5	0.973	0.082	0.172	0.114	5.641	2.029
		−90	8.055	1375.2	1.078	0.068	0.127	0.092	4.586	2.014
		−70	17.348	1214.1	1.313	0.054	0.093	0.076	3.391	2.252
		−50	33.053	928.0	3.487	0.044	0.057	0.061	1.351	4.517
R1150 (ethylene) Normal boiling point, °C −103.8	CH_2=CH_2	−110	0.691	576.5	2.409	0.194	0.191	0.332	13.947	2.379
		−90	2.132	547.5	2.451	0.171	0.147	0.269	12.757	2.107
		−70	5.172	516.1	2.549	0.151	0.116	0.225	11.449	1.967
		−50	10.619	480.8	2.739	0.132	0.092	0.192	9.988	1.920
		−30	19.366	438.9	3.127	0.113	0.072	0.164	8.247	1.987
		−10	32.428	383.0	4.247	0.094	0.053	0.138	5.783	2.389
R170 (ethane) Normal boiling point, °C −88.6	CH_3CH_3	−100	0.523	557.9	2.397	0.178	0.193	0.345	13.308	2.593
		−70	2.499	519.8	2.530	0.150	0.133	0.256	11.381	2.253
		−40	7.774	476.4	2.767	0.123	0.095	0.199	9.351	2.130
		−10	18.588	422.6	3.275	0.099	0.067	0.158	7.134	2.210
		20	37.655	339.0	5.746	0.075	0.042	0.123	3.859	3.198
R508A Normal boiling point, °C −87.6	R23/R116 (39/61)	−100	0.468	1592.9	1.016	0.106	0.440	0.277	6.542	4.227
		−80	1.542	1506.5	1.060	0.093	0.305	0.202	5.846	3.457
		−60	3.954	1411.7	1.124	0.082	0.220	0.156	5.192	3.000
		−40	8.508	1302.6	1.224	0.072	0.160	0.123	4.518	2.727
		−20	16.160	1167.6	1.421	0.062	0.114	0.098	3.716	2.629
		0	28.123	964.9	2.232	0.050	0.072	0.075	2.339	3.189

D4.1. Table 2b. (continued)

Refrigerant	Formula (% by weight)	Temperature (°C)	Pressure (bar)	Density (kg/m)	Specific heat capacity (kJ/kg K)	Thermal conductivity (W/m K)	Dynamic viscosity (mN s/m²)	Kinematic viscosity (μm²/s)	Temperature conductivity (10^{-8} m²/s)	Prandtl no.
R508B Normal boiling point, °C −87.6	R23/R116 (46/54)	−100	0.467	1581.7	1.038	0.111	0.430	0.272	6.741	4.029
		−80	1.540	1496.5	1.081	0.097	0.298	0.199	6.026	3.307
		−60	3.952	1403.1	1.144	0.086	0.216	0.154	5.359	2.876
		−40	8.518	1296.1	1.244	0.075	0.159	0.122	4.675	2.620
		−20	16.214	1164.1	1.440	0.065	0.114	0.098	3.863	2.530
		0	28.275	969.5	2.190	0.053	0.073	0.075	2.503	3.016
R23 Normal boiling point, °C −82.0	CHF_3	−90	0.624	1475.7	1.225	0.142	0.349	0.237	7.877	3.002
		−65	2.474	1378.7	1.275	0.121	0.235	0.170	6.899	2.471
		−40	7.065	1269.7	1.371	0.104	0.166	0.131	5.994	2.182
		−15	16.265	1137.2	1.573	0.089	0.117	0.103	4.955	2.082
		10	32.438	946.7	2.300	0.071	0.076	0.081	3.248	2.480
		20	41.610	816.4	4.130	0.060	0.058	0.071	1.786	3.974
R744 (carbon dioxide) Triple point, °C −56.6 Values acc. ISO 17584:2005	CO_2	−50	6.823	1154.6	1.971	0.172	0.229	0.199	7.560	2.627
		−20	19.696	1031.7	2.165	0.135	0.139	0.135	6.027	2.241
		0	34.851	927.4	2.542	0.110	0.099	0.107	4.683	2.288
		20	57.291	773.4	4.264	0.086	0.066	0.086	2.598	3.292
		30	72.137	593.3	35.338	0.095	0.044	0.074	0.455	16.220
R116 Normal boiling point, °C −78.1	CF_3CF_3	−100	0.262	1697.9	0.893					
		−70	1.535	1568.5	0.963	0.073	0.360	0.229	4.800	4.775
		−40	5.403	1418.3	1.065	0.061	0.218	0.154	4.023	3.828
		−10	14.033	1222.3	1.276	0.049	0.129	0.105	3.118	3.383
		10	23.853	1015.6	1.910	0.040	0.079	0.078	2.046	3.803
R32 Normal boiling point, °C −51.7 Values acc. ISO 17584:2005	CH_2F_2	−60	0.650	1235.7	1.576	0.194	0.307	0.249	9.973	2.492
		−35	2.214	1165.7	1.619	0.174	0.225	0.193	9.204	2.094
		−10	5.826	1088.8	1.698	0.153	0.168	0.155	8.289	1.865
		15	12.808	1000.9	1.843	0.134	0.127	0.127	7.240	1.757
		40	24.783	893.0	2.163	0.115	0.095	0.106	5.932	1.793
		60	39.332	773.3	3.001	0.099	0.071	0.092	4.283	2.155

R410A Normal boiling point, °C −51.4 Values acc. ISO 17584:2005	R32/R125 (50/50)	−60	0.642	1376.3	1.359	0.140	0.353	0.257	7.460	3.441
		−40	1.755	1313.0	1.389	0.127	0.267	0.204	6.970	2.922
		−20	4.007	1245.1	1.439	0.115	0.207	0.166	6.414	2.589
		0	8.007	1170.0	1.519	0.103	0.161	0.138	5.799	2.380
		20	14.476	1083.1	1.658	0.092	0.126	0.116	5.111	2.274
		40	24.256	975.3	1.939	0.081	0.096	0.098	4.279	2.297
		60	38.418	815.5	3.153	0.071	0.067	0.082	2.753	2.986
R428A Normal boiling point, °C −48.3	R125/R143a/R290/R600a (77.5/20/0.6/1.9)	−60	0.558	1415.9	1.172	0.096	0.441	0.311	5.770	5.397
		−40	1.490	1350.9	1.211	0.087	0.323	0.239	5.306	4.505
		−20	3.344	1281.0	1.263	0.078	0.243	0.190	4.833	3.927
		0	6.589	1203.2	1.337	0.070	0.185	0.154	4.352	3.534
		20	11.774	1112.6	1.454	0.062	0.140	0.126	3.841	3.277
		40	19.537	997.7	1.698	0.054	0.102	0.103	3.217	3.190
		60	30.713	814.4	2.950	0.047	0.066	0.081	1.971	4.091
R125 Normal boiling point, °C −48.1 Values acc. ISO 17584:2005	CHF_2CF_3	−60	0.543	1555.7	1.091	0.097	0.499	0.321	5.705	5.626
		−30	2.281	1446.1	1.157	0.083	0.313	0.216	4.964	4.355
		0	6.705	1319.8	1.255	0.070	0.204	0.154	4.217	3.660
		30	15.685	1158.4	1.457	0.057	0.130	0.112	3.399	3.304
		60	31.703	872.1	3.139	0.046	0.067	0.077	1.675	4.589
R1270 (propylene) Normal boiling point, °C −47.6	$CH_3CH=CH_2$	−60	0.556	625.2	2.152	0.155	0.226	0.361	11.513	3.134
		−30	2.116	587.7	2.264	0.141	0.163	0.277	10.600	2.609
		0	5.841	546.1	2.436	0.126	0.121	0.222	9.478	2.344
		30	13.050	497.5	2.723	0.110	0.092	0.184	8.139	2.261
		60	25.281	433.7	3.397	0.093	0.067	0.154	6.345	2.433
		90	44.675	287.9	41.619	0.088	0.035	0.123	0.736	16.668
R143a Normal boiling point, °C −47.2 Values acc. ISO 17584:2005	CH_3CF_3 30	−60	0.531	1200.6	1.293	0.108	0.360	0.300	6.948	4.314
		−30	2.149	1117.9	1.375	0.094	0.234	0.210	6.086	3.444
		0	6.197	1024.3	1.495	0.081	0.160	0.156	5.265	2.965
		14.340	908.4	1.722	0.068	0.108	0.119	4.372	2.728	
		60	28.744	728.9	2.714	0.056	0.065	0.089	2.836	3.154

D4.1. Table 2b. (continued)

Refrigerant	Formula (% by weight)	Temperature (°C)	Pressure (bar)	Density (kg/m)	Specific heat capacity (kJ/kg K)	Thermal conductivity (W/m K)	Dynamic viscosity (mN s/m²)	Kinematic viscosity (μm²/s)	Temperature conductivity (10^{-8} m²/s)	Prandtl no.
R507A Normal boiling point, °C −46.7 Values acc. ISO 17584:2005	R125/R143a (50/50)	−60	0.511	1357.4	1.220	0.096	0.416	0.306	5.828	5.254
		−30	2.129	1263.2	1.279	0.084	0.266	0.210	5.173	4.066
		0	6.244	1156.3	1.381	0.072	0.178	0.154	4.491	3.428
		30	14.600	1022.6	1.589	0.060	0.118	0.115	3.723	3.100
		60	29.486	806.1	2.677	0.050	0.068	0.084	2.297	3.654
R422A Normal boiling point, °C −46.5	R125/R134a/ R600a (85.1/11.5/ 3.4)	−60	0.503	1468.4	1.144	0.100	0.492	0.335	5.965	5.614
		−30	2.109	1367.6	1.207	0.086	0.309	0.226	5.220	4.324
		0	6.205	1252.5	1.303	0.073	0.203	0.162	4.464	3.631
		30	14.521	1108.3	1.491	0.060	0.132	0.119	3.646	3.270
		60	29.263	875.5	2.464	0.048	0.074	0.085	2.232	3.792
R404A Normal boiling point, °C −46.2 Values acc. ISO 17584:2005	R125/R143a/ R134a (44/52/4)	−60	0.498	1348.0	1.229	0.098	0.418	0.310	5.925	5.232
		−30	2.078	1255.0	1.288	0.085	0.267	0.213	5.266	4.042
		0	6.102	1150.0	1.388	0.073	0.179	0.156	4.578	3.406
		30	14.283	1019.4	1.590	0.062	0.119	0.117	3.809	3.076
		60	28.849	813.0	2.543	0.051	0.070	0.086	2.447	3.507
R502 Normal boiling point, °C −45.3	R22/R115 (48.8/ 51.2)	−60	0.486	1525.6	0.964	0.098	0.445	0.292	6.682	4.369
		−30	1.964	1429.2	1.016	0.086	0.297	0.208	5.914	3.516
		0	5.658	1320.3	1.094	0.074	0.207	0.157	5.129	3.054
		30	13.047	1190.3	1.226	0.062	0.143	0.120	4.281	2.812
		60	25.942	1010.1	1.617	0.050	0.092	0.091	3.086	2.946
		80	38.964	737.6	9.630	0.049	0.051	0.069	0.685	10.144
R407C Normal boiling point, °C −43.6 Values acc. ISO 17584:2005	R32/R125/R134a (23/25/52)	−60	0.430	1430.0	1.292	0.128	0.486	0.340	6.926	4.904
		−30	1.871	1338.1	1.336	0.112	0.311	0.232	6.247	3.718
		0	5.679	1236.2	1.416	0.096	0.211	0.170	5.498	3.101
		30	13.591	1115.4	1.569	0.082	0.145	0.130	4.667	2.779
		60	27.692	951.1	2.001	0.068	0.094	0.099	3.555	2.788
		80	41.738	751.6	4.535	0.060	0.060	0.080	1.756	4.534
R422D Normal boiling point, °C −43.2	R125/R134a/ R600a (65.1/ 31.5/3.4)	−60	0.426	1454.6	1.180	0.105	0.526	0.361	6.111	5.914
		−30	1.818	1358.4	1.233	0.091	0.329	0.242	5.411	4.472
		0	5.431	1250.5	1.319	0.077	0.217	0.174	4.681	3.715
		30	12.860	1119.0	1.480	0.064	0.144	0.129	3.896	3.307
		60	26.090	926.1	2.033	0.052	0.087	0.094	2.761	3.407
		70	32.238	817.2	3.040	0.048	0.067	0.082	1.942	4.243

R427A Normal boiling point, °C −43.0	R32/R125/R143a/R134a (15/25/10/50)	−60	0.418	1420.2	1.275	0.121	0.492	0.346	6.698	5.173
		−30	1.808	1328.6	1.319	0.106	0.313	0.235	6.029	3.904
		0	5.464	1227.3	1.399	0.091	0.211	0.172	5.301	3.246
		30	13.046	1106.7	1.551	0.077	0.144	0.130	4.499	2.897
		60	26.555	941.8	1.982	0.064	0.093	0.099	3.418	2.895
		80	40.038	736.8	4.740	0.057	0.058	0.079	1.621	4.855
R290 (propane) Normal boiling point, °C −42.1	$CH_3CH_2CH_3$	−60	0.427	601.1	2.172	0.140	0.244	0.405	10.709	3.784
		−30	1.678	566.6	2.305	0.122	0.172	0.304	9.355	3.251
		0	4.745	528.6	2.493	0.106	0.126	0.238	8.041	2.955
		30	10.790	484.4	2.777	0.091	0.092	0.190	6.796	2.800
		60	21.168	428.0	3.337	0.078	0.066	0.153	5.489	2.795
		80	31.319	373.3	4.545	0.070	0.049	0.131	4.139	3.158
		90	37.641	328.8	7.623	0.067	0.039	0.118	2.678	4.408
R22 Normal boiling point, °C	$CHClF_2$	−50	0.645	1435.6	1.079	0.118	0.389	0.271	7.599	3.564
		−20	2.453	1346.5	1.123	0.104	0.270	0.200	6.865	2.917
		0	4.980	1281.5	1.169	0.095	0.216	0.169	6.323	2.665
Values acc. ISO 17584:2005	30	11.919	1170.7	1.281	0.081	0.155	0.133	5.416	2.452	
		60	24.275	1030.4	1.539	0.067	0.108	0.105	4.227	2.479
		90	44.423	780.1	3.981	0.052	0.061	0.078	1.675	4.642
R417A Normal boiling point, °C −39.1	R125/R134a/R600a (46.6/50/3.4)	−50	0.592	1414.2	1.224	0.106	0.466	0.330	6.098	5.409
		−20	2.279	1319.7	1.280	0.091	0.300	0.227	5.402	4.203
		0	4.658	1250.3	1.336	0.082	0.229	0.184	4.921	3.729
		30	11.246	1129.0	1.475	0.069	0.155	0.137	4.158	3.293
		60	23.117	962.2	1.856	0.056	0.098	0.102	3.162	3.221
		80	35.147	755.3	4.207	0.049	0.060	0.079	1.549	5.102
R115 Normal boiling point, °C −39.2	$CClF_2CF_3$	−50	0.609	1583.8	0.916	0.075	0.469	0.296	5.154	5.747
		−20	2.221	1477.2	0.972	0.065	0.307	0.208	4.511	4.604
		0	4.409	1398.7	1.022	0.059	0.236	0.169	4.099	4.122
		20	7.909	1310.3	1.089	0.053	0.182	0.139	3.687	3.764
		60	20.613	1067.6	1.455	0.041	0.097	0.091	2.655	3.439
		70	25.443	965.7	1.922	0.039	0.077	0.080	2.110	3.778
R500 Normal boiling point, °C −33.6	R12/R152a (73.8/26.2)	−50	0.462	1362.8	1.041	0.104	0.396	0.290	7.333	3.960
		−20	1.781	1281.6	1.093	0.091	0.269	0.210	6.521	3.218
		10	5.001	1191.4	1.166	0.080	0.190	0.160	5.732	2.788
		40	11.371	1085.7	1.283	0.068	0.136	0.125	4.913	2.545
		70	22.383	947.7	1.560	0.057	0.093	0.098	3.876	2.531
		100	40.107	657.9	8.924	0.052	0.047	0.071	0.883	8.074

D4.1. Table 2b. (continued)

Refrigerant	Formula (% by weight)	Temperature (°C)	Pressure (bar)	Density (kg/m)	Specific heat capacity (kJ/kg K)	Thermal conductivity (W/m K)	Dynamic viscosity (mN s/m²)	Kinematic viscosity (μm²/s)	Temperature conductivity (10^{-8} m²/s)	Prandtl no.
R717 (ammonia) Normal boiling point, °C −33.3 Values acc. ISO 17584:2005	NH_3	−40	0.717	690.2	4.414	0.688	0.281	0.408	22.590	1.804
		−10	2.907	652.1	4.564	0.590	0.190	0.292	19.832	1.471
		20	8.575	610.2	4.745	0.500	0.138	0.227	17.265	1.313
	50	20.340	562.9	5.064	0.416	0.104	0.184	14.607	1.262	
		100	62.553	456.6	6.991	0.285	0.063	0.138	8.920	1.552
		120	91.125	385.5	11.940	0.231	0.048	0.125	5.024	2.496
R12 Normal boiling point, °C −29.8 Values acc. ISO 17584:2005	CCl_2F_2	−40	0.641	1516.5	0.873	0.091	0.387	0.255	6.852	3.728
		−10	2.188	1427.6	0.917	0.079	0.273	0.191	6.070	3.152
		20	5.664	1328.9	0.976	0.069	0.199	0.149	5.307	2.817
		50	12.166	1213.0	1.072	0.059	0.144	0.119	4.504	2.637
		80	22.975	1061.4	1.302	0.048	0.099	0.093	3.481	2.685
		100	33.399	903.8	1.996	0.041	0.069	0.077	2.279	3.367
R134a Normal boiling point, °C −26.1 Values acc. ISO 17584:2005	CH_2FCF_3	−30	0.844	1388.4	1.273	0.106	0.401	0.289	5.985	4.825
		0	2.928	1294.8	1.341	0.092	0.267	0.206	5.299	3.884
		30	7.702	1187.5	1.446	0.079	0.183	0.154	4.599	3.353
		60	16.818	1052.9	1.660	0.066	0.124	0.117	3.781	3.105
		90	32.442	837.8	2.756	0.053	0.072	0.086	2.285	3.785
RE170 (dimethyl ether) Normal boiling point, °C −24.8	$CH_3–O–CH_3$	−30	0.804	742.3	2.217	0.179	0.209	0.282	10.881	2.590
		0	2.666	700.0	2.304	0.161	0.156	0.223	10.001	2.228
		30	6.795	653.3	2.442	0.143	0.122	0.187	8.971	2.081
		60	14.472	599.2	2.674	0.125	0.098	0.164	7.789	2.104
		90	27.219	530.2	3.196	0.106	0.079	0.149	6.284	2.379
		110	39.513	462.8	4.444	0.094	0.067	0.144	4.568	3.149
R152a Normal boiling point, °C −24.0 Values acc. ISO 17584:2005	CH_3CHF_2	−30	0.772	1023.5	1.610	0.123	0.322	0.315	7.474	4.211
		0	2.640	959.1	1.697	0.109	0.219	0.228	6.692	3.413
		30	6.898	886.6	1.826	0.096	0.154	0.174	5.921	2.931
		60	15.007	799.4	2.051	0.083	0.109	0.136	5.088	2.669
		90	28.780	678.5	2.703	0.071	0.073	0.107	3.870	2.765
		100	35.050	618.5	3.495	0.067	0.061	0.098	3.099	3.166

R227ea Normal boiling point, °C −16.3	CF_3CHFCF_3	−20	0.863	1556.9	1.072	0.073	0.446	0.286	4.353	6.581
		0	1.954	1486.0	1.114	0.067	0.337	0.227	4.067	5.581
		20	3.891	1408.4	1.166	0.062	0.256	0.182	3.766	4.833
		40	7.025	1320.9	1.236	0.056	0.194	0.147	3.451	4.256
		60	11.759	1216.5	1.346	0.051	0.144	0.118	3.110	3.804
		80	18.583	1078.2	1.596	0.046	0.101	0.093	2.664	3.508
R124 Normal boiling point, °C −12.0	$CHClFCF_3$	−20	0.715	1497.3	1.049	0.084	0.450	0.301	5.343	5.628
		10	2.341	1405.3	1.102	0.073	0.307	0.219	4.740	4.614
		40	5.935	1301.6	1.174	0.064	0.215	0.166	4.157	3.982
		70	12.620	1176.9	1.297	0.055	0.151	0.128	3.580	3.575
		100	23.787	1001.8	1.665	0.047	0.098	0.098	2.820	3.483
		110	28.831	912.1	2.135	0.045	0.081	0.088	2.318	3.818
R600a (isobutane) Normal boiling point, °C −11.7	$CH(CH_3)_2-CH_3$	−20	0.725	602.9	2.182	0.107	0.252	0.418	8.106	5.155
		10	2.206	568.9	2.338	0.095	0.178	0.312	7.125	4.380
		40	5.312	531.2	2.535	0.084	0.129	0.244	6.242	3.902
		70	10.875	487.0	2.812	0.075	0.095	0.196	5.450	3.588
		100	19.865	429.6	3.347	0.067	0.068	0.158	4.629	3.408
		120	28.366	372.0	4.585	0.062	0.050	0.134	3.648	3.666
R764 (sulfur dioxide) Normal boiling point, °C −10.0	SO_2	−10	1.014	1461.1	1.365					
		20	3.309	1381.6	1.389					
		50	8.418	1294.1	1.444					
		80	17.989	1193.9	1.552					
		110	33.944	1071.4	1.798					
		140	58.665	894.7	2.827					
R142b Normal boiling point, °C −9.1	CH_3CClF_2	−10	0.978	1194.6	1.231	0.094	0.342	0.286	6.416	4.461
		20	2.888	1123.7	1.300	0.083	0.243	0.216	5.688	3.802
		50	6.825	1044.2	1.393	0.073	0.176	0.169	4.990	3.386
		80	13.807	949.8	1.540	0.063	0.128	0.135	4.306	3.128
		100	20.743	871.5	1.727	0.057	0.101	0.116	3.792	3.056
		120	30.045	764.8	2.260	0.052	0.075	0.098	2.983	3.300
R600 (butane) Normal boiling point, °C −0.5	$CH_3–CH_2–CH_2–CH_3$	−10	0.696	611.4	2.267	0.120	0.225	0.367	8.641	4.252
		20	2.076	578.6	2.413	0.107	0.166	0.287	7.646	3.756
		50	4.958	542.3	2.598	0.095	0.125	0.231	6.736	3.432
		80	10.116	500.4	2.851	0.084	0.095	0.189	5.920	3.195
		110	18.456	447.9	3.285	0.075	0.069	0.155	5.119	3.024
		140	31.172	364.7	5.227	0.067	0.045	0.123	3.528	3.475

D4.1. Table 2b. (continued)

Refrigerant	Formula (% by weight)	Temperature (°C)	Pressure (bar)	Density (kg/m)	Specific heat capacity (kJ/kg K)	Thermal conductivity (W/m K)	Dynamic viscosity (mN s/m²)	Kinematic viscosity (μm²/s)	Temperature conductivity (10^{-8} m²/s)	Prandtl no.
R114 Normal boiling point, °C 3.6	$CClF_2CClF_2$	0	0.882	1528.4	0.958	0.066	0.367	0.240	4.536	5.297
		30	2.510	1439.1	1.000	0.060	0.259	0.180	4.169	4.312
		60	5.796	1338.7	1.058	0.054	0.187	0.139	3.793	3.675
		90	11.560	1218.2	1.153	0.048	0.133	0.109	3.383	3.236
		100	14.197	1170.3	1.205	0.045	0.118	0.101	3.220	3.132
		120	20.800	1051.9	1.408	0.041	0.089	0.085	2.778	3.045
R245fa Normal boiling point, °C 15.1	$CHF_2CH_2CF_3$	0	0.529	1404.0	1.274	0.096	0.573	0.408	5.362	7.615
		30	1.778	1324.9	1.333	0.087	0.382	0.289	4.899	5.890
		60	4.626	1236.8	1.413	0.077	0.266	0.215	4.403	4.890
		90	10.061	1133.3	1.532	0.067	0.186	0.164	3.880	4.237
		120	19.275	999.2	1.777	0.058	0.125	0.125	3.295	3.788
		150	33.946	744.6	4.720	0.054	0.064	0.086	1.541	5.587
R11 Normal boiling point, °C 23.7	CCl_3F	10	0.607	1511.3	0.867	0.091	0.467	0.309	6.955	4.443
		40	1.744	1440.0	0.896	0.083	0.343	0.238	6.397	3.726
		80	5.232	1334.7	0.951	0.072	0.237	0.178	5.641	3.153
		120	12.364	1210.1	1.041	0.061	0.165	0.136	4.830	2.824
		160	24.903	1044.6	1.266	0.050	0.108	0.104	3.759	2.760
		190	39.250	820.6	2.705	0.042	0.065	0.079	1.892	4.165
R123 Normal boiling point, °C 27.8 Values acc. ISO 17584:2005	$CHCl_2CF_3$	10	0.506	1501.6	1.002	0.081	0.499	0.332	5.365	6.191
		40	1.545	1424.8	1.038	0.072	0.352	0.247	4.891	5.057
		80	4.891	1311.2	1.100	0.063	0.231	0.176	4.343	4.048
		120	11.990	1174.4	1.207	0.054	0.153	0.131	3.801	3.436
		160	24.901	975.7	1.584	0.045	0.097	0.099	2.902	3.419
		180	34.506	765.9	4.549	0.040	0.064	0.084	1.140	7.363
R601a (isopentane) Normal boiling point, °C 27.8	$(CH_3)_2CH–CH_2–CH_3$	10	0.523	630.0	2.198	0.113	0.253	0.401	8.153	4.921
		40	1.515	599.4	2.355	0.102	0.187	0.312	7.230	4.319
		80	4.575	553.9	2.600	0.089	0.131	0.236	6.180	3.817
		120	10.864	498.6	2.933	0.077	0.091	0.182	5.292	3.447
		160	22.049	420.2	3.680	0.067	0.058	0.138	4.337	3.174
		180	30.233	349.8	6.221	0.064	0.040	0.113	2.919	3.887

R141b Normal boiling point, °C 32.0	CH_3CCl_2F	20	0.650	1243.4	1.147	0.092	0.432	0.348	6.451	5.392
		60	2.462	1163.2	1.209	0.081	0.281	0.241	5.769	4.182
		100	6.773	1072.5	1.298	0.071	0.190	0.177	5.122	3.455
		130	12.550	992.7	1.400	0.065	0.142	0.143	4.666	3.071
		160	21.320	893.9	1.591	0.059	0.104	0.116	4.171	2.793
		190	34.053	745.1	2.382	0.055	0.069	0.092	3.123	2.952
R601 (pentane) Normal boiling point, °C 36.1	$CH_3–CH_2–CH_2–CH_2–CH_3$	20	0.566	625.7	2.293	0.113	0.227	0.363	7.896	4.601
		60	2.145	584.6	2.493	0.099	0.164	0.280	6.781	4.135
		100	5.927	537.4	2.748	0.086	0.119	0.222	5.814	3.821
		130	11.035	494.8	3.014	0.077	0.092	0.187	5.167	3.614
		160	18.879	439.5	3.490	0.069	0.068	0.154	4.491	3.438
		190	30.476	342.1	6.849	0.063	0.041	0.120	2.676	4.469
R365mfc Normal boiling point, °C 40.2	$CF_3CH_2CF_2CH_3$	30	0.692	1246.3	1.387	0.086	0.463	0.372	4.967	7.485
		60	1.965	1178.6	1.453	0.073	0.324	0.275	4.281	6.416
		90	4.580	1103.2	1.535	0.063	0.233	0.211	3.728	5.663
		120	9.260	1014.4	1.653	0.055	0.167	0.165	3.278	5.037
		150	16.933	899.5	1.883	0.049	0.116	0.128	2.868	4.480
		180	29.006	699.2	3.559	0.047	0.066	0.094	1.885	4.987
R113 Normal boiling point, °C 47.6	CCl_2FCClF_2	30	0.544	1551.1	0.923	0.067	0.611	0.394	4.696	8.382
		60	1.502	1477.0	0.954	0.061	0.425	0.288	4.347	6.624
		90	3.428	1397.1	0.991	0.056	0.309	0.221	4.019	5.508
		120	6.807	1308.0	1.040	0.050	0.228	0.175	3.699	4.723
		150	12.201	1202.9	1.117	0.045	0.167	0.139	3.357	4.143
		180	20.267	1064.7	1.297	0.040	0.116	0.109	2.891	3.783
R718 (water) Normal boiling point, °C 100.0	H_2O	90	0.702	965.3	4.205	0.675	0.314	0.326	16.635	1.958
		140	3.615	926.1	4.283	0.683	0.197	0.212	17.228	1.232
		190	12.552	876.1	4.447	0.669	0.142	0.162	17.164	0.943
		240	33.469	813.4	4.772	0.632	0.111	0.136	16.279	0.837
		290	74.418	731.9	5.493	0.565	0.090	0.122	14.052	0.872
		340	146.007	610.7	8.208	0.469	0.070	0.115	9.347	1.234

[a]Data acc.Refprop 8.0, 2007

2 Bibliography

1. Montreal-protocol on substances that deplete the ozone layer, www.ozone.unep.org/Ratification_status/evolution_of_mp.shtml
2. Kyoto protocol to the United Nations framework convention on climate change, www.unfccc.int/essential_background/kyoto_protocol/items/1678.php
3. Regulation (EC) no 1005/2009 of the European Parliament and of the Council of 16 September 2009 on substances that deplete the ozone layer. Off J Eur Union, L 286/1, October 31, 2009
4. Verordnung über Stoffe, die die Ozonschicht schaedigen (Chemikalien-Ozonschichtverordnung – ChemOzonSchichtV) vom 13 November 2006. Bundesgesetzblatt Jahrgang 2006, Teil I Nr. 53, p 2638. Bonn. 22 November 2006
5. Schweiz (April 2003) Verordnung vom 9 Juni 1986 ueber umweltgefaehrdende Stoffe (Stoffverordnung, StoV). Systematische Sammlung des Bundesrechts SR 814.013. Aenderung vom 30, p 1345. Anhang 3.4, http://www.admin.ch/ch/d/as/2003/1345.pdf
6. Regulation (EC) No 842/2006 of the European Parliament and of the Council of 17 May 2006 on certain fluorinated greenhouse gases. Off J Eur Union, L 161/1, June 14, 2006
7. Commission Regulation (EC) No 303/2008 of 2 April 2008, establishing, pursuant to Regulation (EC) No 842/2006 of the European Parliament and of the Council, minimum requirements and the conditions for mutual recognition for the certification of companies and personnel as regards stationary refrigeration, air conditioning and heat pump equipment containing certain fluorinated greenhouse gases. Off J Eur Union, L 92/3. April 3, 2008
8. Commission Regulation (EC) No 1516/2007 of 19 December 2007, establishing pursuant to Regulation (EC) No 842/2006 of the European Parliament and of the Council, standard leakage checking requirements for stationary refrigeration, air conditioning and heat pump equipment containing certain fluorinated greenhouse gases. Off J Eur Union, L 335/10, December 20, 2007
9. Commission Regulation (EC) No 1494/2007 of 17 December 2007, establishing pursuant to Regulation (EC) No 842/2006 of the European Parliament and of the Council, the form of labels and additional labeling requirements as regards products and equipment containing certain fluorinated greenhouse gases. Off J Eur Union, L 332/25, December 18, 2007
10. Verordnung zum Schutz des Klimas vor Veraenderungen durch den Eintrag bestimmter fluorierter Treibhausgase (Chemikalien-Klimaschutzverordnung – ChemKlimaschutzV) vom 2. Juli 2008. Bundesgesetzblatt Jahrgang 2008, Teil I Nr. 27, p 1139, Bonn. 07 Juli 2008
11. 447. Verordnung des Bundesministers für Land- und Forstwirtschaft, Umwelt und Wasserwirtschaft ueber Verbote und Beschraenkungen teilfluorierter und vollfluorierter Kohlenwasserstoffe sowie von SF_6 (HFKW-FKW-SF_6-V). Bundesgesetzblatt fuer die Republik Oesterreich. Jahrgang 2002. Teil II. Dezember 2002
12. 139. Verordnung: Aenderung der Verordnung ueber Verbote und Beschraenkungen teilfluorierter und vollfluorierter Kohlenwasserstoffe sowie von SF_6 (HFKW-FKW-SF6-V). Bundesgesetzblatt fuer die Republik Oesterreich. Jahrgang 2007. Teil II. 21 Juni 2007
13. Statutory Order no. 552 of 2 July 2002, Regulating certain industrial greenhouse gases. Ministry of the Environment, Danish Environmental Protection Agency, Copenhagen
14. Schweiz (April 2003) Verordnung vom 9 Juni 1986 ueber umweltgefaehrdende Stoffe (Stoffverordnung, StoV). Systematische Sammlung des Bundesrechts SR 814.013. Aenderung vom 30, p 1345. Anhang 3.5, http://www.admin.ch/ch/d/as/2003/1345.pdf
15. EN 12693 (1996) Refrigerating systems and heat pumps – safety and environmental requirements. DIN EN 378-1-4. CEN European Committee for Standardization, Brussels
16. Schrempf B, Sontheim B (Stand Juni 2004) Planung und Betrieb von Ammoniak-Kaelteanlagen. TÜV Industrie Service GmbH, Muenchen. Axima Refrigeration GmbH, Lindau. Leitfaden auf Basis aktueller Regelwerke

D4.2 Cryostatic Bath Fluids, Aqueous Solutions, and Glycols

Gernot Krakat
FRAGOL Schmierstoffe GmbH & Co., Mülheim (Ruhr), Germany

Following synoptical tables (Table 1–6) will give an overview on current cryostatic bath fluids, aqueous heat transfer fluids, and glycols including their data. Most of the data are taken from manufacturer's product overviews and brochures based on recent informations.

They passed without obligation in comply with our best knowledge and experiences and the same to existing third person trade mark rights.

The trade names are mostly registered trade marks by the companies, so this explicit advice replace the identification of the circumstances.

D4.2. Table 1. Cryostatic bath fluids

Substance	Chemical formula	Melting point Boiling point (°C)	Range of application (°C)	Vapor pressure (bar)	Min/max		
					Density (kg/m³)	Specific heat capacity (kJ/kg K)	Kinematic viscosity (10^6 m²/s)
Methanol	CH_3OH	−97.65	−90	–	904	2.14	9.62
		64.65	60		755	2.69	0.46
Ethanol	C_2H_5OH	−114.05	−100	–	892	1.90	52.7
		78.35	78.3	1.01			
			100		716	3.45	0.46
Methylglycol	CH_3OCH_2–	−85	−80	–			120
	CH_2OH	122–127	−40		1,020		
			20			2.236	
			+50	0.06	935		17.0
Tetrachlormethane	CCl_4	−22.9	−20	–	1,672	0.834	1.20
		76.55	70	0.8	1,574	0.876	0.25
Trichlorethylene	C_2HCl_3	−86	−85	–	1,730	0.879	1.31
		87.25	80	99			
			100		1,340	1.005	0.26
Aliphatic hydrocarbons (e.g., B. Therminol D12)		–	−70		835	1.635	354.35
		192	260		550	3.100	0.25
Aliphatic hydrocarbons (e.g., therminol VLT)		−135	−100		849	1.352	36.1
		99.2	175		521	2.586	0.25
Benzine	C_6–C_8	Boiling range					
		25–80	−50		775	2.051	1.27
		135–220	100		650	2.386	0.30

D4.2. Table 1. (continued)

Substance	Chemical formula	Safety engineering data							Remark
		Flash point DIN ISO 2592 (°C)	Autoignition temperature DIN 51794 (°C)	Explosive limits vol. %		Temperature range ATEX 94/9/EG	Explosion group DIN EN 50 014	MAK-value (ppm)	
				Lower	Upper				
Methanol	CH_3OH	11	455	6	50	T1	II A	200	Toxic
Ethanol	C_2H_5OH	12	425	2.5	15	T2	II A	1.000	
Methylglycol	CH_3OCH_2–CH_2OH		290	2.5	20	T2	II A	16	
Tetrachlormethane	CCl_4							2.5	
Trichlorethylene	C_2HCl_3		410	8	52	T 2		50	
Aliphatic hydrocarbons		59	270	0.6	7	T 3	II A		Therminol D 12 (Solutia) [12]
Aliphatic hydrocarbons		−6.2				T 3	II A		Therminol VLT (Solutia) [12]
Benzine	C_6–C_8	<−20	∼280	1.2	7.5	T 3	II A		Petroleum ether
Benzine	C_6–C_8	>21/>55	∼240	0.6	6.5	T 3	II A		White spirit

D4.2. Table 2. Cryostatic bath fluids

Substance	Chemical formula	Temperature (°C)	Density (kg/m³)	Specific heat capacity (kJ/kg K)	Thermal conductivity (W/m K)	Dynamic viscosity (10^{-6} Ns/m²)	Kinematic viscosity (10^{-6} m²/s)	Thermal diffusivity (10^{-8} m²/s)	Prandtl number
Methanol [1]	CH_3OH	−100	905	2.135	0.244	16.00	17.70	12.6	140
		−75	900	2.193	0.235	4.86	5.42	11.9	45.5
		−50	858	2.240	0.227	2.27	2.65	11.8	22.5
		−25	833	2.294	0.217	1.28	1.54	11.4	13.5
		0	810	2.386	0.209	0.817	1.01	10.4	9.8
		20	792	2.495	0.202	0.584	0.74	10.3	7.2
		50	765	2.679	0.191	0.396	0.52	9.33	5.6
		100	714	3.014	0.172	0.245	0.345	9.80	4.3
Ethanol [1]	C_2H_5OH	−100	892	1.90	0.207	47.01	52.8	12.2	433
		−75	870	1.946	0.199	15.26	17.6	11.8	150
		−50	850	2.013	0.191	6.40	7.54	11.1	68
		−25	825	2.093	0.183	3.25	3.94	10.6	37
		0	806	2.231	0.174	1.78	2.22	9.72	22.9
		20	789	2.394	0.167	1.21	1.54	8.78	17.5
		50	763	2.800	0.159	0.701	0.92	7.44	12.4
		100	716	3.453	0.147	0.326	0.442	5.92	7.5
Tetrachlormethane [1]	CCl_4	−25	1,680	0.833	0.112	4.90	2.92	7.94	36.6
		0	1,633	0.841	0.109	1.33	0.81	7.94	10.2
		20	1,594	0.850	0.107	0.965	0.607	7.89	7.7
		50	1,534	0.862	0.106	0.651	0.425	8.00	5.3
		100	1,434	0.896	0.105	0.383	0.267	8.17	3.27

D4.2. Table 2. (continued)

Substance	Chemical formula	Temperature (°C)	Density (kg/m³)	Specific heat capacity (kJ/kg K)	Thermal conductivity (W/m K)	Dynamic viscosity (10^{-6} Ns/m²)	Kinematic viscosity (10^{-6} m²/s)	Thermal diffusivity (10^{-8} m²/s)	Prandtl number
Trichlorethylene [1]	C_2HCL_3	−85	1,730	0.879	0.138	2.26	1.310	9.11	14.4
		−75	1,710	0.887	0.137	2.01	1.180	9.06	13.1
		−50	1,660	0.900	0.135	1.40	0.845	9.03	9.4
		−25	1,610	0.921	0.133	0.981	0.610	8.92	6.9
		0	1,550	0.938	0.130	0.710	0.458	9.00	5.1
		20	1,507	0.950	0.128	0.576	0.391	9.17	4.27
		50	1,440	0.971	0.125	0.446	0.310	8.86	3.51
		100	1,340	1.005	0.120	0.343	0.256	8.89	2.88
Benzine [1]		−50	775	2.051	0.142	0.981	1.26	8.89	14.2
		−25	755	2.093	0.141	0.686	0.91	8.89	10.2
		0	735	2.135	0.140	0.510	0.695	8.89	7.8
		20	720	2.198	0.140	0.402	0.56	8.83	6.3
		50	690	2.260	0.143	0.294	0.425	9.17	4.65
		100	650	2.386	0.136	0.196	0.302	8.75	3.45
Therminol D 12 [12]		−85	835	1.635	0.124	295.88	354.35	9.08	3,901
		−50	811	1.805	0.119	12.07	14.889	8.13	183.2
		−20	790	1.941	0.116	3.23	4.094	7.56	54.12
		0	776	2.025	0.113	1.93	2.486	7.19	34.57
		20	762	2.108	0.110	1.29	1.697	6.85	24.78
		50	740	2.235	0.105	0.80	1.087	6.35	17.12
		100	702	2.445	0.096	0.45	0.642	5.59	11.48
		150	662	2.645	0.087	0.29	0.437	4.97	8.80
		200	615	2.857	0.076	0.20	0.327	4.33	7.56
		250	562	3.045	0.065	0.15	0.259	3.80	6.82
Therminol VLT [12]		−110	857	1.397	0.129	31.0	36.1	10.77	335.0
		−100	849	1.441	0.128	16.2	19.0	10.46	181.6
		−50	808	1.659	0.118	2.32	2.88	8.88	32.72
		−20	783	1.787	0.112	1.03	1.56	8.00	19.49
		0	766	1.871	0.108	0.876	1.14	7.53	15.13
		20	748	1.955	0.104	0.661	0.883	7.11	12.42
		50	722	2.080	0.097	0.460	0.460	6.46	9.86
		100	676	2.287	0.086	0.277	0.409	5.56	7.35
		150	626	2.497	0.073	0.177	0.283	4.67	6.06
		200	567	2.735	0.059	0.118	0.208	3.80	5.47

D4.2. Table 3a. Aqueous solution of anorganic substances (overview)

Substance	Chemical formula	Contents at minimal temperature (kg/kg)	Minimum temperature Ambient temperature (°C)	Density (kg/m³)	Specific heat capacity (kJ/kg K)	Kinematic viscosity (10^{-6} m²/s)	pH value	Physiological effect	Remarks
Sodium chloride	NaCl	−0.231	−21.2	1,192	3.300	60.4		nontoxic	[1]
			20	1,174	3.346	14.4			
Magnesium chloride	$MgCl_2$	0.206	−33.6	1,196	2.963	16.7		nontoxic	[1]
			20	1,183	3.083	2.4			

D4.2. Table 3a. (continued)

Substance	Chemical formula	Contents at minimal temperature (kg/kg)	Minimum temperature Ambient temperature (°C)	Density (kg/m³)	Specific heat capacity (kJ/kg K)	Kinematic viscosity (10^{-6} m²/s)	pH value	Physiological effect	Remarks
Calcium chloride	$CaCl_2$	0.299	−55	1,315	2.600	41.8		nontoxic	[1]; $CaCl_2$−special [6]
			20	1,277	2.783	2.75			
Magnesium chloride/ Calcium chloride	$MgCl_2$/ $CaCl_2$	0.225	−35	1,221	2.872	32.1	12.0	nontoxic	TK 8 grün [2] Reinhartin [6] Chlorisol [7]
			20	1,199	3.014	2.62			
Potassium carbonate	K_2CO_3	0.389	−35	1,434	2.587	41	12.2	nontoxic	Pa9 rot [2] Anticora [6] Karbosol [7]
			20	1,406	2.698	2.58			
	K_2CO_3 98–100% technical quality	0.40	−35	1,427	2.61	31.5		nontoxic	[3] 1,985 exact
			20	1,404	2.71	3.06			
Ammonia water	NH_4OH–H_2O	0.237	−50	939	4.37	27			
		0.763							

D4.2. Table 3b. Aqueous solution of anorganic substances (overview)

Substance	Chemical formula	Eutectic point					Remarks
		Proportional mass weight percentage (%)	Melting point/ freezing point (°C)	Density (g/m³)	Dynamic viscosity (10^{-3} Ns/m²)	Kinematic viscosity (10^{-6} m²/s)	
Sodium chloride	NaCl	23.4	−21.1	1,194	6.7	5.6	[4–6]
Magnesium chloride	$MgCl_2$	21.5	−33.6	1,205	25	20.7	[4–7]
Calcium chloride	$CaCl_2$	32	−49.7	1,342	80	59.6	[4–7]
Potassium carbonate	K_2CO_3	40	−37.5	1,435	55	38.3	[4–7]

D4.2. Table 4. Aqueous solution of anorganic substances

Solute substance and weight percentage (%)	Freezing point (°C)	Temperature (°C)	Density (kg/m³)	Specific heat capacity (kJ/kg K)	Thermal conductivity (W/m K)	Dynamic viscosity (10^{-6} Ns /m²)	Kinematic viscosity (10^{-6} m²/s)	Thermal diffusivity (10^{-8} m²/s)	Prandtl number
NaCl [1]									
7	−4.4	20	1,049	3.843	0.593	1.08	1.03	14.7	6.95
		10	1,052	3.835	0.576	1.41	1.345	14.3	9.4
		0	1,054	3.827	0.559	1.87	1.78	13.9	12.7
		−4	1,055	3.818	0.556	2.16	2.06	13.9	14.8
11	−7.5	20	1,079	3.697	0.593	1.15	1.06	14.8	7.18
		10	1,083	3.684	0.570	1.52	1.41	14.3	9.9
		0	1,084	3.676	0.556	2.02	1.87	14.0	13.4
		−5	1,085	3.672	0.549	2.44	2.26	13.8	16.4
		−7.5	1,086	3.672	0.545	2.65	2.45	13.8	17.8

D4.2. Table 4. (continued)

Solute substance and weight percentage (%)	Freezing point (°C)	Temperature (°C)	Density (kg/m³)	Specific heat capacity (kJ/kg K)	Thermal conductivity (W/m K)	Dynamic viscosity (10^{-6} Ns /m²)	Kinematic viscosity (10^{-6} m²/s)	Thermal diffusivity (10^{-8} m²/s)	Prandtl number
13.6	−9.8	20	1,098	3.609	0.593	1.23	1.115	15.0	7.45
		10	1,103	3.601	0.568	1.62	1.47	14.3	10.3
		0	1,106	3.588	0.554	2.15	1.95	14.1	13.9
		−5	1,108	3.584	0.547	2.61	2.37	13.9	17.1
		−9.8	1,110	3.580	0.540	3.43	3.13	13.7	22.9
16.2	−12.2	20	1,118	3.534	0.573	1.31	1.2	14.4	8.3
		10	1,122	3.525	0.569	1.73	1.57	14.4	10.9
		0	1,126	3.513	0.552	2.32	2.12	14.1	15.1
		−5	1,127	3.509	0.544	2.83	2.58	13.9	18.6
		−10	1,129	3.504	0.535	3.49	3.18	13.7	23.2
		−12.2	1,130	3.500	0.533	4.22	3.48	13.6	28.3
18.8	−15.2	20	1,138	3.462	0.581	1.43	1.26	14.8	8.5
		10	1,143	3.454	0.566	1.85	1.63	14.4	11.4
		0	1,147	3.442	0.550	2.56	2.25	14.0	16.1
		−5	1,149	3.433	0.542	3.12	2.74	13.9	19.8
		−10	1,151	3.429	0.533	3.87	3.4	13.7	24.8
		−15	1,152	3.425	0.525	4.78	4.19	13.5	31
21.2	−18.2	20	1,158	3.395	0.579	1.55	1.33	14.6	9.1
		10	1,163	3.383	0.563	2.01	1.73	14.4	12.1
		0	1,167	3.375	0.547	2.82	2.44	14.0	17.5
		−5	1,169	3.366	0.538	3.44	2.96	13.8	21.5
		−10	1,171	3.362	0.530	4.31	3.7	13.6	21.7
		−15	1,173	3.358	0.522	5.28	4.55	13.5	33.9
		−18	1,175	3.354	0.518	6.08	5.24	13.3	39.4
23.1	−21.2	20	1,174	3.345	0.565	1.67	1.42	14.7	9.6
		10	1,179	3.337	0.555	2.16	1.84	14.0	13.1
		0	1,183	3.324	0.544	3.04	2.59	13.9	18.6
		−5	1,185	3.320	0.536	3.75	3.2	13.7	23.3
		−10	1,187	3.312	0.528	4.71	4.02	13.6	29.5
		−15	1,189	3.308	0.520	5.75	4.9	13.4	36.5
		−21	1,191	3.303	0.514	7.75	6.6	13.2	50
$MgCl_2$ [1]									
7.2	−5	20	1,059	3.768	0.572	1.34	1.27	14.3	8.88
		10	1,062	3.756	0.558	1.73	1.63	14.0	11.6
		0	1,064	3.747	0.545	2.41	2.27	13.7	16.6
		−5	1,065	3.726	0.552	2.84	2.69	14.0	19.3
11.6	−10.3	20	1,099	3.509	0.566	1.65	1.5	14.6	10.3
		10	1,102	3.492	0.549	2.15	1.95	14.3	13.6
		0	1,104	3.475	0.535	3.10	2.8	14.1	20
		−5	1,106	3.462	0.528	3.73	3.39	13.9	24.4
		−10	1,107	3.450	0.521	4.56	4.16	13.7	30.4
13.8	−14.5	20	1,119	3.395	0.558	1.82	1.63	14.7	11.1
		10	1,121	3.375	0.544	2.47	2.2	14.4	15.2
		0	1,123	3.358	0.529	3.52	3.14	14.0	22.4
		−5	1,125	3.349	0.522	4.22	3.77	13.9	27.1
		−10	1,126	3.337	0.514	5.09	4.55	13.7	33.2
		−14	1,127	3.329	0.508	5.98	5.32	13.6	39.2

D4.2. Table 4. (continued)

Solute substance and weight percentage (%)	Freezing point (°C)	Temperature (°C)	Density (kg/m³)	Specific heat capacity (kJ/kg K)	Thermal conductivity (W/m K)	Dynamic viscosity (10^{-6} Ns /m²)	Kinematic viscosity (10^{-6} m²/s)	Thermal diffusivity (10^{-8} m²/s)	Prandtl number
17	−22.8	20	1,150	3.236	0.552	2.20	1.91	14.9	12.9
		10	1,152	3.215	0.537	3.05	2.65	14.5	18.3
		0	1,154	3.195	0.521	4.20	3.65	14.2	25.7
		−5	1,155	3.182	0.514	5.30	4.61	14.1	32.8
		−10	1,157	3.165	0.507	6.23	5.42	14.0	38.7
		−15	1,158	3.148	0.498	7.84	6.8	13.7	49.5
		−20	1,159	3.140	0.490	9.71	8.41	13.6	61.8
		−22	1,160	3.140	0.486	10.39	9.05	13.5	67
20.6	−33.6	20	1,183	3.081	0.545	2.85	2.41	15.0	16.1
		10	1,186	3.056	0.529	3.90	3.3	14.6	22.7
		0	1,188	3.035	0.513	5.49	4.64	14.3	32.5
		−5	1,189	3.014	0.505	6.77	5.71	14.1	40.5
		−10	1,190	3.006	0.497	8.37	7.07	14.0	50.7
		−15	1,192	2.998	0.487	10.36	8.72	13.7	63.8
		−20	1,193	2.981	0.479	12.93	10.9	13.6	80.5
		−25	1,194	2.973	0.470	16.27	13.7	13.3	103
		−30	1,195	2.964	0.461	19.91	16.8	13.1	128
		−33	1,196	2.956	0.454	22.55	19.05	13.0	147
$CaCl_2$ [1]									
14.7	−10.2	20	1,128	3.362	0.576	1.49	1.32	15.2	8.7
		10	1,131	3.349	0.563	1.86	1.64	14.9	11.05
		0	1,135	3.329	0.549	2.56	2.27	14.6	15.6
		−5	1,137	3.316	0.542	3.04	2.7	14.4	18.7
		−10	1,138	3.308	0.534	4.06	3.6	14.3	25.3
20.9	−19.2	20	1,188	3.077	0.569	2.00	1.68	15.5	10.9
		10	1,192	3.056	0.555	2.45	2.06	15.3	13.4
		0	1,196	3.044	0.542	3.28	2.76	14.9	18.5
		−5	1,198	3.014	0.535	3.82	3.22	14.9	21.5
		−10	1,199	3.014	0.527	5.07	4.25	14.7	28.9
		−15	1,202	3.014	0.521	6.59	5.53	14.7	38.2
25.7	−31.2	20	1,237	2.894	0.562	2.63	2.12	15.7	13.5
		10	1,242	2.883	0.548	3.22	2.51	15.3	16.5
		0	1,247	2.872	0.535	4.26	3.43	15.1	22.7
		−10	1,253	2.854	0.521	6.68	5.4	14.8	36.6
		−15	1,255	2.837	0.514	8.36	6.75	14.6	46.3
		−20	1,258	2.817	0.508	10.56	8.52	14.6	58.5
		−25	1,260	2.791	0.501	12.90	10.4	14.3	72
		−30	1,263	2.763	0.494	14.81	12.0	14.5	83
28.4	−43.6	20	1,272	2.805	0.557	3.14	2.47	15.6	15.8
		0	1,277	2.780	0.529	5.12	4.02	15.0	26.7
		−10	1,282	2.763	0.518	8.02	6.32	14.7	42.7
		−20	1,287	2.721	0.505	12.65	10.0	14.6	68.8
		−25	1,290	2.721	0.498	15.98	12.6	14.4	87.5
		−30	1,292	2.700	0.491	18.83	14.9	14.3	103.5
		−35	1,295	2.700	0.484	24.52	19.3	14.2	136.5
		−40	1,297	2.680	0.478	30.40	24	14.1	171

D4.2. Table 4. (continued)

Solute substance and weight percentage (%)	Freezing point (°C)	Temperature (°C)	Density (kg/m³)	Specific heat capacity (kJ/kg K)	Thermal conductivity (W/m K)	Dynamic viscosity (10^{-6} Ns /m²)	Kinematic viscosity (10^{-6} m²/s)	Thermal diffusivity (10^{-8} m²/s)	Prandtl number
29.9	−55	20	1,283	2.784	0.554	3.51	2.75	15.5	17.8
		0	1,293	2.738	0.528	5.69	4.43	15.0	29.5
		−10	1,298	2.700	0.515	9.04	7.04	14.8	47.5
		−20	1,304	2.680	0.502	14.42	11.23	14.6	77
		−30	1,309	2.659	0.488	22.55	17.6	14.3	123
		−35	1,311	2.638	0.483	28.44	22.1	14.2	156.5
		−40	1,313	2.638	0.476	35.30	27.5	14.1	196
		−45	1,315	2.617	0.470	43.15	33.5	13.9	240
		−50	1,318	2.617	0.463	50.99	39.7	13.8	290
		−55	1,321	2.596	0.456	64.72	50.2	13.6	368
$MgCl_2/CaCl_2$ (4:1) [2]									
10	−7.5	20	1,084	3.622	0.570	1.68	1.55	14.5	10.7
		15	1,086	3.613	0.562	1.87	1.73	14.3	12.1
		10	1,088	3.605	0.556	2.12	1.95	14.2	13.7
		5	1,090	3.596	0.549	2.42	2.22	14.0	15.9
		0	1,092	3.588	0.542	2.82	2.58	13.8	18.9
		−5	1,094	3.580	0.535	3.33	3.04	13.7	22.2
		−7.5	1,095	3.576	0.532	3.65	3.33	13.6	24.5
15	−15	20	1,130	3.425	0.558	2.01	1.77	14.4	12.3
		15	1,132	3.413	0.551	2.28	2.01	14.3	14.1
		10	1,134	3.402	0.544	2.63	2.32	14.1	16.5
		5	1,136	3.391	0.537	3.02	2.66	13.9	19.1
		0	1,138	3.379	0.530	3.51	3.08	13.8	22.3
		−5	1,140	3.367	0.523	4.16	3.65	13.6	26.8
		−10	1,142	3.356	0.516	4.97	4.35	13.5	32.2
		−15	1,144	3.345	0.509	6.08	5.31	13.3	39.9
17.3	−20	20	1,150	3.292	0.553	2.28	1.98	14.6	13.6
		10	1,154	3.265	0.542	2.98	2.58	14.4	17.9
		0	1,158	3.241	0.525	4.05	3.50	14.0	25
		−10	1,162	3.215	0.511	5.74	4.94	13.7	36.1
		−20	1,166	3.190	0.498	8.83	7.57	13.4	56.5
20	−26.7	20	1,174	3.136	0.546	2.75	2.34	14.8	15.8
		10	1,178	3.111	0.532	3.58	3.04	14.5	21.0
		0	1,182	3.085	0.518	4.58	4.10	14.2	28.9
		−10	1,186	3.061	0.505	6.89	5.81	13.9	41.8
		−20	1,190	3.034	0.493	10.6	8.91	13.7	65.0
		−25	1,192	3.021	0.484	13.5	11.3	13.4	84.3
22.5	−35.3	20	1,199	3.014	0.540	3.16	2.64	14.9	17.7
		10	1,203	2.989	0.526	4.22	3.51	14.6	24.0
		0	1,207	2.964	0.513	5.76	4.77	14.3	33.4
		−10	1,211	2.938	0.498	8.34	6.89	14.0	49.2
		−20	1,215	2.912	0.484	12.90	10.6	13.7	77.4
		−30	1,219	2.886	0.471	22.90	18.8	13.4	140
		−35.5	1,221	2.872	0.463	32.40	26.5	13.2	201

D4.2. Table 4. (continued)

Solute substance and weight percentage (%)	Freezing point (°C)	Temperature (°C)	Density (kg/m³)	Specific heat capacity (kJ/kg K)	Thermal conductivity (W/m K)	Dynamic viscosity (10^{-6} Ns /m²)	Kinematic viscosity (10^{-6} m²/s)	Thermal diffusivity (10^{-8} m²/s)	Prandtl number
K_2CO_3 [2]									
12.8	−5	20	1,140	3.542	0.586	1.26	1.11	14.5	7.66
		10	1,145	3.521	0.565	1.77	1.55	14.0	11.1
		0	1,150	3.500	0.544	2.51	2.18	13.5	16.1
		−5	1,154	3.492	0.534	2.99	2.59	13.2	19.6
21.2	−10	20	1,240	3.107	0.573	1.70	1.37	14.9	9.2
		10	1,245	3.084	0.554	2.42	1.94	14.4	13.5
		0	1,250	3.065	0.536	3.58	2.86	14.0	20.4
		−5	1,254	3.056	0.527	4.38	3.49	13.7	25.5
		−10	1,255	3.046	0.517	5.39	4.29	13.5	31.8
27	−15	20	1,290	2.964	0.561	2.11	1.64	14.7	11.2
		10	1,295	2.941	0.544	3.09	2.39	14.3	16.7
		0	1,300	2.920	0.528	4.66	3.58	13.9	25.8
		−5	1,302	2.908	0.520	5.76	4.45	13.7	32.5
		−10	1,305	2.897	0.511	7.26	5.56	13.5	41.2
		−15	1,307	2.889	0.503	9.07	6.94	13.3	52.2
31	−20	20	1,330	2.853	0.554	2.55	1.92	14.6	13.2
		10	1,335	2.830	0.538	3.73	2.79	14.2	19.6
		0	1,340	2.811	0.521	5.88	4.39	13.8	31.8
		−5	1,342	2.803	0.513	7.35	5.48	13.6	40.3
		−10	1,345	2.793	0.505	9.32	6.93	13.4	51.7
		−15	1,348	2.780	0.500	11.80	8.75	13.3	65.8
		−20	1,350	2.772	0.488	15.00	11.1	13.0	85.4
34	−25	20	1,360	2.782	0.547	2.94	2.16	14.5	14.9
		10	1,365	2.761	0.531	4.45	3.26	14.1	23.1
		0	1,370	2.738	0.515	6.91	5.04	13.7	36.8
		−10	1,375	2.721	0.499	11.08	8.06	13.3	60.6
		−15	1,377	2.713	0.491	14.22	10.3	13.1	78.6
		−20	1,380	2.705	0.484	18.34	13.3	13.0	102
		−25	1,382	2.692	0.476	24.00	17.4	12.8	136
36.6	−30	20	1,385	2.730	0.542	3.33	2.40	14.3	16.8
		10	1,390	2.709	0.526	5.15	3.70	14.0	26.4
		0	1,395	2.688	0.510	8.14	5.83	13.6	42.9
		−10	1,400	2.667	0.494	13.04	9.31	13.2	70.5
		−20	1,405	2.464	0.479	22.00	15.7	12.9	122
		−25	1,408	2.636	0.471	28.80	20.5	122.7	161
		−30	1,410	2.627	0.463	38.70	27.4	12.5	219
38.9	−35	20	1,406	2.696	0.537	3.68	2.62	14.2	18.5
		10	1,412	2.680	0.522	5.69	4.03	13.8	29.2
		0	1,417	2.656	0.506	9.02	6.37	13.4	47.5
		−10	1,422	2.638	0.490	14.70	10.3	13.1	78.6
		−20	1,427	2.615	0.474	24.70	17.3	12.7	136
		−30	1,432	2.596	0.459	43.60	30.4	12.3	247
		−35	1,434	2.583	0.451	60.00	41.8	12.2	343

D4.2. Table 4. (continued)

Solute substance and weight percentage (%)	Freezing point (°C)	Temperature (°C)	Density (kg/m³)	Specific heat capacity (kJ/kg K)	Thermal conductivity (W/m K)	Dynamic viscosity (10^{-6} Ns /m²)	Kinematic viscosity (10^{-6} m²/s)	Thermal diffusivity (10^{-8} m²/s)	Prandtl number
K_2CO_3 [3]									
10	−3.5	20	1,089	3.69	0.591	1.26	1.16	14.7	7.87
		10	1,091	3.67	0.574	1.60	1.47	14.3	10.2
		0	1,093	3.66	0.566	2.12	1.94	13.9	14.0
15	−5.8	20	1,135	3.50	0.586	1.45	1.28	14.8	8.66
		10	1,138	3.48	0.569	1.85	1.62	14.3	11.3
		0	1,141	3.47	0.552	2.40	2.10	13.9	15.1
		−5	1,142	3.46	0.544	2.85	2.50	13.7	18.2
20	−8.8	20	1,187	3.31	0.581	1.70	1.43	14.8	9.69
		10	1,190	3.29	0.564	2.15	1.81	14.4	12.6
		0	1,193	3.28	0.547	2.80	2.35	14.0	16.8
		−5	1,194	3.27	0.538	3.25	2.72	13.8	19.8
25	−12.8	20	1,238	3.12	0.576	2.05	1.66	14.9	11.1
		10	1,242	3.10	0.559	2.55	2.05	14.5	14.2
		0	1,245	3.09	0.542	3.35	2.59	14.1	19.1
		−5	1,247	3.08	0.534	3.90	3.13	13.9	22.5
		−10	1,249	3.07	0.526	4.60	3.68	13.7	26.8
30	−18	20	1,292	2.96	0.569	2.55	1.97	14.9	13.3
		10	1,295	2.94	0.553	3.25	2.51	14.5	17.3
		0	1,298	2.93	0.536	4.30	3.31	14.1	23.5
		−10	1,302	2.91	0.520	6.00	4.61	13.7	33.6
		−15	1,303	2.90	0.512	7.20	5.53	13.5	40.8
35	−26	20	1,350	2.82	0.563	3.25	2.41	14.8	16.3
		10	1,354	2.80	0.546	4.20	3.10	14.4	21.5
		0	1,358	2.79	0.530	5.65	4.16	14.0	29.7
		−10	1,361	2.77	0.514	8.05	5.91	13.6	43.4
		−20	1,362	2.75	0.498	12.10	8.87	13.3	66.8
		−25	1,366	2.74	0.490	15.50	11.35	13.1	86.7
40	−36	20	1,404	2.71	0.554	4.3	3.06	14.6	21.0
		10	1,408	2.69	0.538	5.65	4.01	14.2	28.3
		0	1,412	2.68	0.522	7.90	5.59	13.8	40.6
		−10	1,417	2.66	0.507	11.70	8.26	13.5	61.4
		−20	1,421	2.64	0.491	18.30	12.87	13.1	98.4
		−30	1,425	2.62	0.475	(32.00)	(22.5)	12.7	(177)
		−35	1,427	2.61	0.467	(45.00)	(31.5)	12.5	(252)

D4.2. Table 5a. Organic charge materials for aqueous solutions (overview)

Substance	Chemical formula	Contents at min. temperature (kg/kg^c)	Melting point ambient temperature (°C)	Density (kg/m^3)	Specific heat capacity (kJ/kg K)	Kinematic viscosity (10^{-6} m^2/s)	pH value
Methanol	CH_3OH	1	−97.65	904	2.14	9.62	
			20	792	2.495	0.737	
Ethanol	C_2H_5OH	1	−114.05	892	1.90	52.7	
			20	789	2.394	1.53	
Monoethylenglycol[a]	$C_2H_4(OH)_2$	0.65	−50				
			20	1,134	2.3	27	7.8–8.2
1.2 Propylenglycol[a]	$C_3H_6(OH)_2$	0.6	−40	1,100	2.3		
			20	1,050	2.5	71.4	7–9
Glycerin	$C_3H_6(OH)_3$	0.63	−40	1,190	2.53	840	
			20	1,162	3.00	11.2	
Potassium formiate-based (acc. safety data sheet Pekasol 2000) [7]	HCOOK	1	−56				
			−50	1,313	3.00	123	
			0	1,297	3.14	6.70	
			20	1,290	3.19	3.18	11.5–12

Substance	Chemical formula	Corrosiveness	Physiological number	Remarks
Methanol	CH_3OH	High corrosive	$LD_{50}{}^b$ = 0.34 g/kg MAK 200 ppm	
Ethanol	C_2H_5OH	High corrosive	MAK 1,000 ppm	
Monoethylenglycol[a]	$C_2H_4(OH)_2$	More corrosive as pure water; less corrosive when inhibited	$LD_{50}{}^b$ = 5.8 g/kg	For example, Antifrost B (AVIA) Antifrogen N (Clariant) Glythermin NF (BASF) Dowcal 10 (Dow) Tyfocor (Tyforop) Glykosol N (Prokühlsole) Fragoltherm W-EGA (Fragol) Fragoltherm W-EBS (Fragol)
Monoethylenglycol[a]	$C_2H_4(OH)_2$	Less corrosive when inhibited	Free of nitrite, amine, phosphate $LD_{50}{}^b > 2.0$ g/kg	For example, Zitrec M (Arteco)
1,2 Propylenglycol[a]	$C_3H_6(OH)_2$	Less corrosive when inhibited	$LD_{50}{}^b$ = 15 g/kg	For example, Antifrogen L (Clariant) Glythermin P 44 (BASF) Dowcal 20 (Dow) Dowcal N FDA-approved Tyfocor L (Tyforop) Pekasol L (Prokühlsole) Fragoltherm W-PGA (Fragol) Zitrec F (Arteco) NSF approved
1,2 Propylenglycol[a]	$C_3H_6(OH)_2$	Less corrosive when inhibited	Free of nitrite, amine, phosphate $LD_{50}{}^b$ = 15 g/kg	For example, Zitrec L (Arteco)
Potassium acetate	CH_3COOK	Low tested acc. ASTM D 1384; wastage rate <0.01 mm/year regarding the guidelines	$LD_{50}{}^b > 2.0$ g/kg MAK 200 ppm	based on potassium acetate which is approved as a food additive
Potassium acetate-potassium formiate-mix	CH_3COOK-HCOOK	Low tested acc. EMPA-SOP Nr. 1536: steel 0, carbon steel 0 g/m^2 weight loss; low, when inhibited	Free of nitrite, amine, phosphate $LD_{50}{}^b > 2.0$ g/kg MAK 200 ppm	[9] Institut Fresenius: contents components which are approved as food additives

D4.2. Table 5a. (continued)

Substance	Chemical formula	Corrosiveness	Physiological number	Remarks
potassium formiate-sodium propionate-mix	HCOOK- C_2H_5 COONa-mixture	Low, tested acc. ASTM D 1384; wastage rate <0.01 mm/year regarding the guidelines	Free of nitrite, amine, phosphate LD_{50}[b] > 2.0 g/kg	For example, Zitrec S (Arteco)
potassium formiate	HCOOK	Low, tested acc. ASTM D 1384; wastage rate <0.01 mm/year regarding the guidelines	Free of nitrite, amine, phosphate LD_{50}[b] > 2.0 g/kg MAK 200 ppm	Based on potassium acetate which is approved as a food additive

[a]Commercial coolants, anti corrosion inhibited
[b]LD_{50} (oral, rat)
[c]Contents kg substance/kg solution

D4.2. Table 5b. Organic charge materials for aqueous solutions (overview)

Substance	Chemical formula	Application concentration % (volume)	Application range (°C)	Density at 20°C (kg/m³)	Specific heat capacity at 20°C (kJ/kg K)
Methanol	CH_3OH	10–100	−90 to +20	792	2.945
Ethanol	C_2H_5OH	10–100	−100 to +20	798	2.394
Monoethylenglycol[a]	$C_2H_4(OH)_2$	5–90	−40 to +130	1,114	2.35
1,2 Propylenglycol[a]	$C_3H_6(OH)_2$	5–90	−30 to +130	1,036	2.50
Potassium acetate	CH_3COOK	60–90	−55 to +80[c]	1,100–1,240	3.55–2.95
Potassium acetate-potassium formiate-mixture	CH_3COOK–HCOOK	30–100	−60 to +60	1,289	2.668
Potassium formiate-sodium propionate-mixture	HCOOK–C_2H_5 COONa–Gemisch	Ready made	−55 to +80	1.089–1.312	3.63–2.5
Potassium formiate	HCOOK	Ready made	−60 to +80[c]	1,222–1,394	3.20–2.52

Substance	Chemical formula	Kinematic viscosity at 20°C (10^{-6} m²/s)	Corrosiveness (versus metals)	Physiological figures	Examples of commercial products with corrosion protection
Methanol	CH_3OH	0.737	In aqueous solutions High corrosive	LD_0 = 0.34 g/kg (oral, human) MAK: 200 ppm	
Ethanol	C_2H_5OH	1.53	In aqueous solutions High corrosive	LD_{50}[b] = 7.06 g/kg (oral, rat) MAK: 1,000 ppm	
Monoethylenglycol[a]	$C_2H_4(OH)_2$	19	Low, when anti-corrosive inhibited	LD_{50}[b] = 5.8 g/kg (oral, rat)	For example, Antifrost B (AVIA) Antifrogen N (Clariant) Glythermin NF (BASF) Tyfocor (Tyforop) Dowcal 10 (Dow) Glykosol N (Prokühlsole) Fragoltherm W-EGA (Fragol) Zitrec M (Arteco)

D4.2. Table 5b. (continued)

Substance	Chemical formula	Kinematic viscosity at 20°C (10^{-6} m²/s)	Corrosiveness (versus metals)	Physiological figures	Examples of commercial products with corrosion protection
1,2 Propyleneglycol[a]	$C_3H_6(OH)_2$	56	Low, when anti-corrosive inhibited	LD_{50}[b] = 15 g/kg (oral, rat)	For example, Antifrogen L (Clariant) Glythermin P 44 (BASF) Tyfocor L (Tyforop) Dowcal 20 (Dow) Dowcal N FDA approved Pekasol L (Prokühlsole) Fragoltherm W-PGA (Fragol) Zitrec L (Arteco) Zitrec F (Arteco)NSF approved
Potassium acetate	CH_3COOK	1.67 to −10	Low considering the guidelines	LD_{50}[b] > 2.0 g/kg MAK 200 ppm	Tyfoxit (Tyforop)
Potassium acetate-potassium formiate-mixture	CH_3COOK-HCOOK	1.29 to −9.8 2.95 to −60	Low considering the guidelines	Free of nitrite, amine, phosphate LD_{50}[b] > 2.0 g/kg MAK 200 ppm	Pekasol 2000 (Prokühlsole)
Potassium formiate-sodium propionate-mixture	HCOOK-C_2H_5 COONa		Low considering the guidelines	Free of nitrite, amine, phosphate	For example, Zitrec S (Arteco)
Potassium formiate	HCOOK	1.67 to −15 2.88 to −60	Low considering the guidelines	Free of nitrite, amine, phosphate	Tyfoxit F15–F60: ready made (Tyforop) Antifrogen KF (Clariant) Freezium (Kemira)

[a]Commercial coolants, anti-corrosion inhibited
[b]LD_{50} (oral, rat)
[c]Considering the guidelines

D4.2. Table 5c. Aqueous solution of organic substances

Solute substance and weight percentage (%)	Freezing point (°C)	Temperature (°C)	Density (kg/m³)	Specific heat capacity (kJ/kg K)	Thermal conductivity (W/m K)	Dynamic viscosity (10^{-6} Ns /m²)	Kinematic viscosity (10^{-6} m²/s)	Thermal diffusivity (10^{-8} m²/s)	Prandtl number
CH_3OH [1]									
10	−7.5	0	984	4.291	0.514	2.62	2.66	12.2	21.8
		−7.5	986	4.344	0.504	3.63	3.68	11.8	31.2
20	−16.5	0	972	4.072	0.469	3.53	3.63	11.8	30.8
		−10	976	4.072	0.458	5.39	5.52	11.5	48
		−16.5	978	4.072	0.452	6.91	7.07	11.3	62.6
30	−26	0	961	3.816	0.434	3.68	3.83	12.0	31.9
		−10	965	3.841	0.426	5.88	6.09	11.5	53
		−20	970	3.830	0.419	9.81	10.1	11.5	87.8
		−26	972	3.820	0.414	13.50	13.9	11.1	125
40	−39	0	946	3.653	0.400	3.73	3.94	11.6	34
		−10	951	3.632	0.397	5.59	5.88	11.5	51.1
		−20	956	3.611	0.394	8.92	9.33	11.4	81.8
		−30	962	3.588	0.391	15.40	16	11.3	142
		−39	966	3.567	0.388	27.50	28.5	11.3	252

D4.2. Table 5c. (continued)

Solute substance and weight percentage (%)	Freezing point (°C)	Temperature (°C)	Density (kg/m³)	Specific heat capacity (kJ/kg K)	Thermal conductivity (W/m K)	Dynamic viscosity (10^{-6} Ns /m²)	Kinematic viscosity (10^{-6} m²/s)	Thermal diffusivity (10^{-8} m²/s)	Prandtl number
50	−54.5	0	928.5	3.437	0.368	3.50	2.69	11.5	23.4
		−20	941.5	3.387	0.368	7.65	8.13	11.5	70.7
		−40	954.5	3.339	0.368	23.05	24.1	11.5	210
		−54.5	964	3.308	0.369	90.20	93.6	11.6	807
60	−74	0	908.5	3.224	0.335	2.94	3.24	11.4	28.4
		−20	923	3.174	0.339	6.08	6.59	11.6	56.8
		−40	937	3.128	0.343	9.41	10	11.7	85.5
		−60	951	3.077	0.347	56.90	59.8	11.9	503
		−74	961	3.046					
70	Below −80	0	887	3.025	0.305	2.43	2.74	11.4	24
		−20	902	2.978	0.313	4.50	4.99	11.7	42.6
		−40	917	2.931	0.321	9.40	10.3	11.9	86.6
		−60	932	2.878	0.330	27.50	29.5	12.3	240
		−75	943	2.843	0.337	99.00	105	12.6	833
		−80	948	2.831	0.339				
80	Below −80	0	863	2.826	0.277	1.83	2.12	11.4	18.6
		−20	878	2.774	0.288	3.10	3.53	11.8	29.9
		−40	894	2.727	0.298	5.88	6.58	12.2	53.9
		−60	910	2.680	0.309	14.00	15.4	12.7	121
		−75	926	2.642	0.317	36.30	39.2	13.0	302
		−80	927	2.627	0.320				
90	Below −80	0	810.5	2.604	0.251	1.37	1.69	11.9	14.2
		−20	828	2.559	0.263	2.12	2.56	12.4	20.6
		−40	845	2.512	0.276	3.56	4.21	13	32.4
		−60	863	2.460	0.289	7.20	8.34	13.6	61.3
		−75	876	2.424	0.298	15.00	17.1	14	122
		−80	880	2.418	0.302				
CH_3 OH [1]									
10	−6	0	985	4.375	0.535	3.24	3.29	12.4	26.5
		−6	988	4.396	0.529	3.92	3.79	12.2	31.1
20	−11.5	0	976	4.365	0.481	5.50	5.64	11.3	49.9
		−11.5	983	4.365	0.473	9.80	9.97	11.0	91
30	−17.5	0	966	4.291	0.430	7.16	7.41	10.4	71.2
		−10	972	4.176	0.425	12.75	13.1	10.5	125
		−17.5	977	4.134	0.422	20.60	21.1	10.4	203
40	−25.5	0	949	3.988	0.381	7.20	7.59	10.1	75.1
		−10	956	3.957	0.379	12.75	13.3	10.0	133
		−20	963	3.925	0.377	24.50	25.4	9.97	255
		−25.5	967	3.904	0.376	38.25	39.6	9.96	398
50	−33.5	0	930	3.695	0.341	6.47	6.96	9.92	70.2
		−10	937	3.663	0.340	11.00	11.7	9.91	118
		−20	944	3.642	0.338	20.00	21.2	9.83	216
		−30	952	3.590	0.337	40.70	42.8	9.86	434
		−33.5	955	3.571	0.337	56.00	58.6	9.88	593

D4.2. Table 5c. (continued)

Solute substance and weight percentage (%)	Freezing point (°C)	Temperature (°C)	Density (kg/m³)	Specific heat capacity (kJ/kg K)	Thermal conductivity (W/m K)	Dynamic viscosity (10^{-6} Ns /m²)	Kinematic viscosity (10^{-6} m²/s)	Thermal diffusivity (10^{-8} m²/s)	Prandtl number
60	−43	0	907	3.360	0.305	5.50	6.06	10.0	60.6
		−10	915	3.318	0.306	8.83	9.65	10.1	95.5
		−20	923	3.287	0.307	14.70	15.9	10.1	157
		−30	931	3.255	0.309	26.50	28.5	10.2	279
		−40	939	3.213	0.312	54.40	57.9	10.3	562
		−43	942	3.203	0.312	69.60	73.9	10.3	717
70	−55.5	0	884	3.060	0.277	4.56	5.16	10.2	50.6
		−10	893	3.025	0.279	5.03	5.63	10.3	54.7
		−20	901	2.985	0.283	7.16	7.95	10.5	75.7
		−30	909	2.952	0.286	11.20	12.3	10.7	115
		−40	917	2.914	0.290	17.35	18.9	10.9	173
		−50	926	2.878	0.293	53.30	57.6	11.0	524
		−55.5	930	2.860	0.294	86.30	92.8	11.1	836
80	−72	0	860	2.757	0.250	4.51	5.24	10.5	49.9
		−20	877	2.690	0.260	7.45	8.49	11.0	77.2
		−40	893	2.617	0.269	17.46	19.6	11.5	170
		−50	902	2.585	0.273	28.90	32.0	11.7	273
		−60	910	2.546	0.278	55.90	61.4	12.0	512
		−65	914	2.533	0.281	85.00	93.0	12.1	769
90	Below −80	0	834	2.481	0.2269	2.81	3.37	10.9	30.9
		−20	851	2.418	0.238	5.10	5.99	11.6	51.6
		−40	868	2.345	0.250	10.00	11.5	12.3	93.5
		−60	875	2.271	0.262	24.00	27.4	13.2	208
		−75	898	2.219	0.274	62.80	69.9	13.7	510

Solute substance and volume percentage (%)	Freezing point (°C)	Temperature (°C)	Density (kg/m³)	Specific heat capacity (kJ/kg K)	Thermal conductivity (W/m K)	Dynamic viscosity (10^{-6} Ns /m²)	Kinetic viscosity (10^{-6} m²/s)	Thermal diffusivity (10^{-8} m²/s)	Prandtl number	Vapor pressure (mbar)
Monoethylenglycol[a] [8, 10] $C_2H_4(OH)_2$										
20	−10	−10	1,038	3.85	0.498	5.19	5	12.5	40.1	
		0	1,036	3.87	0.502	3.11	3	12.5	23.98	
		20	1,030	3.90	0.512	1.65	1.6	12.7	12.6	
		40	1,022	3.93	0.521	1.02	1.0	13.0	7.69	
		60	1,014	3.96	0.531	0.71	0.7	13.2	5.29	180
		80	1,006	3.99	0.540	0.52	0.52	13.4	3.86	430
		100	997	4.02	0.550	0.41	0.41	13.7	2.99	850
34	−20	−20	1,069	3.51	0.462	11.76	11	12.3	89.3	
		0	1,063	3.56	0.466	4.89	4.6	12.3	37.4	
		20	1,055	3.62	0.470	2.32	2.2	12.3	17.9	
		40	1,044	3.68	0.473	1.57	1.5	12.3	12.2	
		60	1,033	3.73	0.475	1.01	0.98	12.3	7.93	150
		80	1,022	3.78	0.478	0.69	0.68	12.4	5.50	380
		100	1,010	3.84	0.480	0.51	0.51	12.4	4.12	800

D4.2. Table 5c. (continued)

Solute substance and volume percentage (%)	Freezing point (°C)	Temperature (°C)	Density (kg/m³)	Specific heat capacity (kJ/kg K)	Thermal conductivity (W/m K)	Dynamic viscosity (10^{-6} Ns /m²)	Kinetic viscosity (10^{-6} m²/s)	Thermal diffusivity (10^{-8} m²/s)	Prandtl number	Vapor pressure (mbar)
52	−40	−40	1,108	3.04	0.416	110.80	100	12.35	810	
		−20	1,100	3.11	0.409	27.50	25	12.0	290	
		0	1,092	3.19	0.405	10.37	9.5	11.6	81.7	
		20	1,082	3.26	0.402	4.87	4.5	11.4	39.5	
		40	1,069	3.34	0.398	2.57	2.4	11.1	21.6	
		60	1,057	3.41	0.394	1.59	1.5	10.9	13.8	130
		80	1,045	3.49	0.390	1.05	1.0	10.7	9.4	330
		100	1,032	3.56	0.385	0.72	0.7	10.5	6.68	660
1,2 Propylenglycol[a] [9, 10] $C_3H_6(OH)_2$										
25	−10	−10	1,032	3.93	0.466	10.22	9.9	11.5	86.2	
		0	1,030	3.95	0.470	6.18	6.0	11.55	51.9	
		20	1,024	3.98	0.478	2.86	2.8	11.7	23.8	
		40	1,016	4.00	0.491	1.42	1.4	12.1	11.6	72
		60	1,003	4.03	0.505	0.90	0.90	12.5	7.20	180
		80	986	4.05	0.519	0.67	0.68	13.0	5.24	420
		100	979	4.08	0.513	0.51	0.52	13.3	3.90	930
38	−20	−20	1,050	3.68	0.420	47.25	45	10.9	414	
		0	1,045	3.72	0.425	12.54	12	10.9	109.8	
		20	1,036	3.77	0.429	4.56	4.4	11.0	40.1	
		40	1,025	3.82	0.433	2.26	2.2	11.1	19.9	66
		60	1,012	3.88	0.437	1.32	1.3	11.1	11.7	170
		80	997	3.94	0.441	0.90	0.9	11.2	8.01	410
		100	982	4.0	0.445	0.69	0.7	11.3	6.18	910
47	−30	−30	1,066	3.45	0.397	160	150	10.8	1,390	
		−20	1,062	3.49	0.396	74.3	70	10.7	655	
		−10	1,058	3.52	0.395	31.7	30	10.6	283	
		0	1,054	3.56	0.395	19.0	18	10.5	171	
		20	1,044	3.62	0.394	6.26	6	10.4	57.6	
		40	1,030	3.69	0.393	2.99	2.9	10.3	28.0	53
		60	1,015	3.76	0.392	1.62	1.6	10.27	15.6	160
		80	999	3.82	0.391	1.10	1.1	10.25	10.7	370
		100	984	3.89	0.390	0.81	0.82	10.19	8.05	800

Solute substance and volume percentage (%)	Freezing point (°C)	Temperature (°C)	Density (kg/m³)	Specific heat capacity (kJ/kg K)	Thermal conductivity (W/m K)	Dynamic viscosity (10^{-6} Ns /m²)	Kinetic viscosity (10^{-6} m²/s)	Thermal diffusivity (10^{-8} m²/s)	Prandtl number
Glycerin [7]									
19.5	−5	40	1,038	3.880	0.548	1.07	1.03	13.61	7.6
		20	1,045	3.855	0.524	1.70	1.63	13.01	12.5
		10	1,048	3.840	0.511	2.35	2.24	12.70	17.7
		0	1,051	3.830	0.498	3.35	3.19	12.37	25.8
		−5	1,052	3.825	0.492	4.15	3.94	12.23	32.3
30.5	−10	40	1,066	3.690	0.504	1.55	1.45	12.81	11.3
		20	1,074	3.635	0.484	2.58	2.40	12.40	19.4
		10	1,078	3.610	0.473	3.50	3.25	12.15	26.7
		0	1,081	3.585	0.462	5.00	4.63	11.92	38.8
		−10	1,083	3.560	0.451	7.9	7.3	11.70	62.4
39.5	−15	40	1,088	3.560	0.470	2.02	1.86	12.13	15.3
		20	1,097	3.460	0.453	3.55	3.24	11.93	27.1
		10	1,102	3.415	0.444	5.03	4.56	11.80	38.7
		0	1,106	3.365	0.435	7.80	7.05	11.69	60.3
		−10	1,109	3.315	0.426	12.7	11.5	11.59	98.8
		−15	1,110	3.290	0.422	17	15	11.56	133

D4.2. Table 5c. (continued)

Solute substance and volume percentage (%)	Freezing point (°C)	Temperature (°C)	Density (kg/m³)	Specific heat capacity (kJ/kg K)	Thermal conductivity (W/m K)	Dynamic viscosity (10^{-6} Ns /m²)	Kinetic viscosity (10^{-6} m²/s)	Thermal diffusivity (10^{-8} m²/s)	Prandtl number
46.5	−20	40	1,107	3.440	0.444	2.65	2.39	11.66	20.5
		20	1,117	3.325	0.429	5.0	4.48	11.55	38.3
		10	1,121	3.265	0.421	7.2	6.42	11.50	55.8
		0	1,125	3.210	0.414	11.4	10.1	11.46	88.4
		−10	1,129	3.150	0.407	19	17	11.44	147
		−20	1,132	3.090	0.400	37	33	11.44	286
52	−25	40	1,122	3.340	0.426	3.45	3.07	11.37	27.0
		20	1,132	3.210	0.412	6.70	5.92	11.34	52.2
		10	1,137	3.145	0.405	9.90	8.71	11.33	76.9
		0	1,141	3.080	0.398	15.7	13.8	11.33	121
		−10	1,146	3.020	0.392	27.5	24.0	11.33	212
		−20	1,150	2.950	0.385	56	49	11.35	429
		−25	1,151	2.920	0.382	82	71	11.37	627
56	−30	40	1,132	3.270	0.411	4.30	3.80	11.10	34.2
		20	1,142	3.130	0.398	8.40	7.36	11.13	66.1
		10	1,147	3.060	0.392	12.8	11.2	11.17	99.9
		0	1,152	2.990	0.386	20.2	17.4	11.21	155
		−10	1,157	2.920	0.380	37	32	11.25	284
		−20	1,162	2.850	0.375	80	69	11.32	608
		−30	1,166	2.780	0.370	180	154	11.41	1,350
60	−35	40	1,143	3.200	0.397	5.40	4.72	10.85	43.5
		20	1,153	3.055	0.385	10.7	9.3	10.93	84.9
		10	1,159	3.980	0.380	16.0	13.8	11.00	125
		0	1,164	2.905	0.375	26	22	11.09	201
		−10	1,169	2.830	0.370	50	43	11.18	382
		−20	1,174	2.755	0.365	110	94	11.29	830
		−30	1,178	2.680	0.360	270	230	11.40	2,010
		−35	1,180	2.645	0.358	430	365	11.47	3,180
63	−40	40	1,151	3.150	0.388	6.40	5.56	10.70	52.0
		20	1,162	2.995	0.376	13.0	11.2	10.80	104
		10	1,168	2.920	0.371	20.0	17.1	10.88	157
		0	1,173	2.840	0.366	35	30	10.99	272
		−10	1,178	2.765	0.361	70	59	11.08	536
		−20	1,183	2.685	0.357	165	139	11.24	1,240
		−30	1,187	2.610	0.353	400	340	11.39	2,960
		−40	1,190	2.530	0.349	1,000	840	11.59	7,250

Solute substance and freezing point	Temperature (°C)	Density (kg/m³)	Specific heat capacity (kJ/kg)K	Thermal conductivity (W/m K)	Dynamic viscosity (10^{-6} Ns /m²)	Kinematic viscosity (10^{-6} m²/s)	Thermal diffusivity (10^{-8} m²/s)	Prandtl number
Freezium 15 [11]								
−15	−15	1,155	3.32	0.49	3.51	3.04	12.78	23.61
	−10	1,153	3.33	0.50	3.03	2.63	13.02	20.21
	0	1,149	3.34	0.51	2.20	1.92	13.29	14.32
	10	1,145	3.36	0.53	1.68	1.47	13.78	10.69
	20	1,141	3.37	0.54	1.33	1.17	14.04	8.30
	30	1,137	3.39	0.56	1.09	0.96	14.53	6.63
	40	1,133	3.40	0.57	0.89	0.79	14.80	5.37

D4.2. Table 5c. (continued)

Solute substance and freezing point	Temperature (°C)	Density (kg/m³)	Specific heat capacity (kJ/kg)K	Thermal conductivity (W/m K)	Dynamic viscosity (10^{-6} Ns /m²)	Kinematic viscosity (10^{-6} m²/s)	Thermal diffusivity (10^{-8} m²/s)	Prandtl number
Freezium 25								
−25	−25	1,229	3.00	0.47	6.49	5.28	12.75	41.56
	−20	1,227	3.01	0.47	5.45	4.44	12.73	34.63
	−10	1,223	3.03	0.49	3.71	3.03	13.22	23.11
	0	1,219	3.06	0.50	2.68	2.20	13.40	16.46
	10	1,215	3.08	0.51	2.05	1.69	13.63	12.34
	20	1,211	3.10	0.52	1.63	1.35	13.85	9.63
	30	1,207	3.12	0.54	1.33	1.10	14.34	7.73
	40	1,203	3.14	0.55	1.09	0.91	14.56	6.29
Freezium 30								
−30	−30	1,253	2.91	0.46	8.91	7.11	12.62	56.36
	−20	1,250	2.93	0.47	5.9	4.72	12.83	36.75
	−10	1,246	2.95	0.48	4.01	3.22	13.06	24.57
	0	1,242	2.97	0.49	2.92	2.35	13.28	17.52
	10	1,238	3.00	0.51	2.23	1.80	13.73	13.17
	20	1,234	3.02	0.52	1.76	1.43	13.95	10.29
	30	1,230	3.04	0.53	1.44	1.17	14.17	8.27
	40	1,226	3.07	0.54	1.19	0.97	14.35	6.74
Freezium 40								
−40	−40	1,304	2.71	0.44	18.49	14.18	12.45	113.47
	−30	1,301	2.74	0.45	11.33	8.71	12.62	68.55
	−20	1,297	2.76	0.46	7.15	5.51	12.85	42.60
	−10	1,293	2.79	0.47	4.86	3.76	13.03	28.58
	0	1,289	2.82	0.49	3.52	2.73	13.48	20.46
	10	1,285	2.85	0.50	2.68	2.09	13.65	15.42
	20	1,281	2.87	0.51	2.14	1.67	13.87	12.09
	30	1,277	2.90	0.52	1.75	1.37	14.04	9.75
	40	1,272	2.92	0.53	1.54	1.21	14.01	8.77
Freezium 60								
−60	−60	1,371	2.46	0.42	89.95	65.61	12.45	531.31
	−50	1,368	2.49	0.43	49.30	36.04	12.62	288.57
	−40	1,364	2.52	0.44	25.71	18.85	12.80	148.94
	−30	1,360	2.55	0.45	14.43	10.91	12.98	85.07
	−20	1,356	2.58	0.46	9.36	6.90	13.15	53.11
	−10	1,352	2.61	0.47	6.37	4.71	13.32	35.80
	0	1,348	2.65	0.48	4.62	3.43	13.44	25.73
	10	1,344	2.68	0.49	3.53	2.63	13.60	19.48
	20	1,340	2.71	0.50	2.80	2.09	13.77	15.34
	30	1,336	2.74	0.51	2.28	1.71	13.93	12.41
	40	1,332	2.77	0.52	1.89	1.42	14.09	10.19
Tyfoxit F15 [6]								
−15	−15	1,236	3.16	0.501	4.68	3.79	12.83	29.5
	−10	1,234	3.17	0.512	3.97	3.22	13.09	24.6
	0	1,230	3.18	0.523	3.01	2.45	13.37	18.3
	10	1,226	3.19	0.534	2.37	1.93	13.65	14.1
	20	1,222	3.20	0.546	2.04	1.67	13.96	12.0
	30	1,218	3.21	0.556	1.75	1.44	14.22	10.1
	40	1,214	3.22	0.567	1.53	1.26	14.50	8.69

D4.2. Table 5c. (continued)

Solute substance and freezing point	Temperature (°C)	Density (kg/m³)	Specific heat capacity (kJ/kg)K	Thermal conductivity (W/m K)	Dynamic viscosity (10^{-6} Ns /m²)	Kinematic viscosity (10^{-6} m²/s)	Thermal diffusivity (10^{-8} m²/s)	Prandtl number
Tyfoxit F20								
−20	−20	1,278	2.91	0.486	6.39	5.00	13.07	38.3
	−10	1,274	2.92	0.497	4.55	3.57	13.36	26.7
	0	1,270	2.93	0.508	3.28	2.58	13.65	18.9
	10	1,266	2.94	0.519	2.61	2.06	13.94	14.8
	20	1,262	2.95	0.531	2.18	1.73	14.26	12.1
	30	1,258	2.96	0.542	1.85	1.47	14.56	10.1
	40	1,254	2.97	0.553	1.62	1.29	14.85	8.69
Tyfoxit F30								
−30	−30	1,304	2.77	0.446	10.9	8.35	12.35	67.6
	−20	1,300	2.78	0.456	6.97	5.36	12.62	42.5
	−10	1,296	2.79	0.472	4.89	3.77	13.05	28.9
	0	1,292	2.80	0.485	3.54	2.74	13.41	20.4
	10	1,288	2.81	0.498	2.83	2.20	13.76	16.0
	20	1,284	2.82	0.511	2.30	1.79	14.11	12.7
	30	1,280	2.83	0.524	1.92	1.50	14.47	10.4
	40	1,276	2.84	0.537	1.70	1.33	14.82	8.97
Tyfoxit F40								
−40	−40	1,360	2.64	0.425	25.9	19.06	11.84	161
	−30	1,356	2.65	0.436	14.0	10.31	12.13	85.0
	−20	1,352	2.66	0.447	8.88	6.57	12.43	52.9
	−10	1,348	2.67	0.458	6.13	4.55	12.73	35.7
	0	1,344	2.68	0.469	4.37	3.25	13.02	25.0
	10	1,340	2.59	0.480	3.59	2.68	13.32	20.1
	20	1,336	2.70	0.491	2.74	2.05	13.61	15.1
	30	1,332	2.71	0.502	2.26	1.70	13.91	12.2
	40	1,328	2.72	0.513	1.98	1.49	14.20	10.5
Tyfoxit F50								
−50	−50	1,386	2.55	0.379	76.2	55.0	10.72	513
	−40	1,382	2.56	0.392	33.4	24.2	11.08	218
	−30	1,378	2.57	0.405	17.8	13.89	11.44	113
	−20	1,374	2.58	0.418	11.1	8.1	11.79	68.4
	−10	1,370	2.59	0.431	7.26	5.30	12.15	43.6
	0	1,366	2.60	0.443	5.29	3.87	12.47	31.0
	10	1,362	2.61	0.455	3.98	2.92	12.80	22.8
	20	1,358	2.62	0.468	3.20	2.36	13.15	17.9
	30	1,356	2.63	0.481	2.71	2.00	13.49	14.8
	40	1,360	2.64	0.493	2.35	1.73	13.73	12.6
Tyfoxit F60								
−60	−60	1,426	2.44	0.356	386	271	10.23	2,649
	−50	1,422	2.45	0.369	132	93.1	10.59	879
	−40	1,418	2.46	0.382	53.8	37.9	10.95	346
	−30	1,414	2.47	0.395	25.8	18.2	11.31	161
	−20	1,410	2.48	0.408	15.2	10.8	11.67	92.5
	−10	1,406	2.49	0.421	9.95	7.08	12.03	58.9
	0	1,402	2.50	0.434	6.80	4.85	12.38	39.2
	10	1,398	2.51	0.447	5.10	3.65	12.74	28.6
	20	1,394	2.52	0.460	4.01	2.88	13.09	22.0
	30	1,390	2.53	0.473	3.38	2.43	13.45	18.1
	40	1,386	2.54	0.486	2.84	2.05	13.81	14.8

D4.2. Table 5c. (continued)

Solute substance and freezing point	Temperature (°C)	Density (kg/m³)	Specific heat capacity (kJ/kg)K	Thermal conductivity (W/m K)	Dynamic viscosity (10^{-6} Ns /m²)	Kinematic viscosity (10^{-6} m²/s)	Thermal diffusivity (10^{-8} m²/s)	Prandtl number
Pekasol 2000 [7] 40 Vol%								
−14.1	−10	1,133	3.275	0.507	3.85	3.40	13.7	24.9
	0	1,131	3.301	0.517	2.74	2.42	13.8	17.5
	10	1,128	3.326	0.527	2.04	1.81	14.1	12.8
	20	1,124	3.349	0.538	1.58	1.41	14.2	9.9
	40	1,115	3.390	0.558	1.05	0.94	14.7	6.4
	60	1,105	3.418	0.579	0.75	0.68	15.5	4.4
Pekasol 2000 50 Vol.%								
−19	−10	1,164	3.124	0.492	4.4	3.8	13.53	28.1
	0	1,161	3.152	0.502	3.1	2.7	13.72	19.6
	20	1,154	3.202	0.521	1.8	1.6	14.10	11.1
	40	1,150	3.220	0.538	1.2	1.04	14.53	7.0
	60	1,139	3.250	0.556	0.84	0.74	15.02	4.9
Pekasol 2000 60 Vol.%								
−25	−20	1,198	2.960	0.468	7.8	6.5	13.20	49.4
	−10	1,195	2.993	0.477	5.2	4.3	13.34	32.4
	0	1,191	3.022	0.487	3.6	3.1	13.53	22.6
	20	1,183	3.073	0.506	2.1	1.8	13.92	12.7
	40	1,170	3.125	0.524	1.35	1.15	14.33	8.1
	60	1,160	3.151	0.540	1.05	0.91	14.77	6.1
Pekasol 2000 80 Vol.%								
−40	−40	1,263	2.655	0.425	36.3	28.7	12.67	226.4
	−30	1,260	2.701	0.434	19.5	15.5	12.75	121.5
	−20	1,256	2.741	0.443	11.5	9.2	12.87	71.3
	−10	1,252	2.775	0.451	7.4	5.9	12.98	45.3
	0	1,248	2.805	0.460	5.1	4.1	13.14	30.9
	20	1,238	2.853	0.477	2.8	2.3	13.50	16.9
	40	1,225	2.898	0.496	1.8	1.47	13.97	10.9
	60	1,214	2.930	0.512	1.3	1.07	14.39	7.0
Pekasol 2000 90 Vol.%								
−50	−50	1,295	2.515	0.407	104.6	80.8	12.50	647.1
	−40	1,292	2.567	0.415	48.3	37.4	12.51	299.0
	−30	1,288	2.612	0.423	25.0	19.4	12.57	154.1
	−20	1,283	2.650	0.431	14.3	11.1	12.68	87.7
	−10	1,279	2.683	0.440	8.9	7.0	12.82	54.5
	0	1,274	2.712	0.448	6.0	4.7	12.97	36.5
	20	1,264	2.757	0.464	3.3	2.6	13.31	19.5
	40	1,251	2.800	0.480	2.1	1.68	13.70	12.0
	60	1,240	2.830	0.497	1.45	1.17	14.16	8.1
Pekasol 2000 100 Vol.%								
−60	−60	1,327	2.397	0.389	404.5	304.8	12.23	2,492.4
	−50	1,323	2.449	0.399	152.4	115.2	12.31	940.4
	−40	1,319	2.495	0.405	66.1	50.1	12.31	407.3
	−30	1,314	2.535	0.413	32.5	24.7	12.40	199.4
	−20	1,310	2.570	0.420	17.9	13.6	12.47	109.1
	−10	1,305	2.600	0.428	10.8	8.3	12.61	65.8
	0	1,300	2.626	0.436	7.2	5.5	12.77	43.1
	20	1,289	2.668	0.452	3.8	3.0	13.14	22.5
	40	1,278	2.700	0.467	2.4	1.88	13.53	13.9
	60	1,265	2.732	0.483	1.65	1.30	13.98	9.0

D4.2. Table 5c. (continued)

Solute substance and freezing point	Temperature (°C)	Density (kg/m³)	Specific heat capacity (kJ/kg)K	Thermal conductivity (W/m K)	Dynamic viscosity (10^{-6} Ns /m²)	Kinematic viscosity (10^{-6} m²/s)	Thermal diffusivity (10^{-8} m²/s)	Prandtl number
Tyfoxit 1.10 [6]								
−10	−10	1,112	3.48	0.510	4.43	3.98	13.18	30.2
	0	1,108	3.50	0.517	3.09	2.79	13.33	20.9
	10	1,104	3.52	0.524	2.35	2.13	13.48	15.8
	20	1,100	3.55	0.531	1.84	1.67	13.60	12.3
	30	1,096	3.57	0.538	1.46	1.33	13.75	9.7
	40	1,092	3.59	0.546	1.29	1.18	13.93	8.5
Tyfoxit 1.15								
−20	−20	1,166	3.21	0.471	9.82	8.42	12.58	66.9
	−10	1,162	3.23	0.478	6.36	5.47	12.74	42.9
	0	1,158	3.25	0.485	4.22	3.64	12.89	28.2
	10	1,154	3.27	0.492	3.17	2.75	13.04	21.1
	20	1,150	3.30	0.499	2.42	2.10	13.15	16.1
	30	1,146	3.32	0.506	1.86	1.62	13.30	12.2
	40	1,142	3.34	0.513	1.60	1.40	13.45	10.4
Tyfoxit 1.20								
−40	−40	1,224	2.94	0.428	67.17	54.88	11.89	462
	−30	1,220	2.96	0.435	29.24	23.89	12.01	199
	−20	1,216	2.99	0.441	15.56	12.75	12.09	105
	−10	1,212	3.01	0.448	9.27	7.62	12.24	62.3
	0	1,208	3.03	0.455	6.28	5.18	12.39	41.8
	10	1,204	3.05	0.461	4.42	3.66	12.51	29.3
	20	1,200	3.08	0.468	3.40	2.82	12.62	22.3
	30	1,196	3.10	0.474	2.46	2.05	12.74	16.1
	40	1,192	3.12	0.481	2.06	1.72	12.89	13.3
Tyfoxit 1.24								
−55	−55	1,270	2.73	0.395	329	276	12.14	2,273
	−50	1,268	2.74	0.398	216	170	11.44	1,486
	−40	1,264	2.77	0.404	80.8	63.9	11.54	554
	−30	1,260	2.80	0.411	45.1	35.8	11.65	307
	−20	1,256	2.83	0.417	23.4	18.6	11.73	159
	−10	1,252	2.86	0.423	13.5	10.8	11.81	91.4
	0	1,248	2.90	0.429	9.05	7.25	11.85	61.2
	10	1,244	2.92	0.435	6.12	4.92	11.98	41.1
	20	1,240	2.95	0.442	4.53	3.65	12.08	30.2
	30	1,236	2.98	0.448	3.23	2.61	12.16	21.5
	40	1,232	3.00	0.455	2.61	2.12	12.31	17.2
Zitrec S-10 [11]	−10	1,102	3.59	0.5	4.67	4.24	12.64	33.86
	0	1,099	3.60	0.51	3.35	3.05	12.89	23.74
	10	1,094	3.62	0.52	2.42	2.21	13.13	16.78
	20	1,089	3.63	0.54	1.81	1.66	13.66	12.17
	30	1,085	3.65	0.55	1.40	1.29	13.89	9.31
	40	1,080	3.66	0.56	1.12	1.04	14.17	7.34
Zitrec S-25	−20	1,213	3.05	0.45	9.34	7.72	12.16	63.89
	−10	1,207	3.07	0.46	5.96	4.94	12.41	39.68
	0	1,202	3.08	0.47	4.07	3.39	12.70	26.62
	10	1,197	3.10	0.48	2.97	2.48	13.21	18.85
	20	1,191	3.11	0.50	2.26	0.50	13.50	14.11
	30	1,186	3.12	0.51	1.79	0.51	13.78	10.98
	40	1,181	3.14	0.52	1.46	0.52	14.02	8.80

D4.2. Table 5c. (continued)

Solute substance and freezing point	Temperature (°C)	Density (kg/m³)	Specific heat capacity (kJ/kg)K	Thermal conductivity (W/m K)	Dynamic viscosity (10^{-6} Ns /m²)	Kinematic viscosity (10^{-6} m²/s)	Thermal diffusivity (10^{-8} m²/s)	Prandtl number
Zitrec S-40	−40	1,293	2.68	0.41	34.79	26.91	11.83	227.48
	−30	1,288	2.70	0.42	20.22	15.70	12.08	130.06
	−20	1,282	2.71	0.43	11.67	9.10	12.38	73.49
	−10	1,277	2.73	0.44	7.37	5.77	12.62	45.32
	0	1,271	2.74	0.45	5.16	4.06	12.92	31.25
	10	1,265	2.76	0.47	3.83	3.03	13.46	22.71
	20	1,260	2.77	0.48	2.90	2.30	13.47	16.99
	30	1,254	2.79	0.49	2.21	1.76	13.72	12.72
	40	1,248	2.80	0.49	1.76	1.41	14.02	9.96
Zitrec S-55	−50	1,354	2.39	0.40	111.04	82.01	12.36	661.18
	−40	1,348	2.40	0.40	52.57	39.00	12.39	314.46
	−30	1,342	2.42	0.41	25.47	18.98	12.62	149.93
	−20	1,336	2.44	0.42	14.19	10.62	12.88	82.30
	−10	1,330	2.46	0.43	9.64	7.25	13.14	54.88
	0	1,324	2.47	0.44	6.34	4.79	13.45	35.47
	10	1,318	2.49	0.45	4.56	3.46	13.71	25.26
	20	1,312	2.50	0.46	3.40	2.59	13.72	18.84
	30	1,306	2.52	0.46	2.77	2.12	13.98	15.10
	40	1,300	2.53	0.47	2.30	1.77	14.29	12.33

[a]Commercial coolant, anti corrosion inhibited

D4.2. Table 6. Organic compounds water free (glycol, overview)

Substance or trade name	Chemical formula	Manufacturer	Melting or pour point /boiling point boiling range (°C)	Operative range (°C)	Vapor pressure (mbar)	Thermophysical properties of fluids at min. or max.		
						Density (kg/m³)	Specific heat capacity (kJ/kg)K	Kinematic viscosity (10^{-8} m²/s)
Triethylenglycol techn. rein	$C_6H_{14}O_4$	BASF	−8	0	-	1,138	2.00	130
		Clariant	280–350	180	30	1,088	2.93	1.2
Polyethylenglycol PEG-Typ 400 [8] 600 1000 1500 2000 3000 4000 6000	OH $(CH_2CH_2O)_n$ –H M_m = 380–400 570–630 950–1,050 1,400–1,600	BASF Dow Clariant Sasol Germany	 +4 to +8 17–22 35–40 44–48	40 200	<1	1,110 940		at 25°C in 50% aqueous solution 76–85 12–14 17–21 26–31
Polyglycol, comm.	s. PEG	Clariant	−50 to −35	20 250	<1	1,045 863	1.95 20°C	(3.3–70) * 10^3 15–2,700 at 160°C
	s. PEG	Clariant	−50	20 250	<1	10°C: 1,038 50°C 1,014	1.95	3,300 at −17.8°C 150 at 20°C 50 at 50°C 15 at 98.9°C
Polyalkylenglycol-heat transfer fluid Fragoltherm S 15 A		Fragol	−51	−35		1,059	1.55	600 at −20°C
			280–350	205	<100	866	2.51	1.5 at 200°C

D4.2. Table 6. (continued)

Substance or trade name	Chemical formula	Manufacturer	Melting or pour point /boiling point boiling range (°C)	Operative range (°C)	Vapor pressure (mbar)	Thermophysical properties of fluids at min. or max.		
						Density (kg/m^3)	Specific heat capacity (kJ/kg)K	Kinematic viscosity (10^{-8} m^2/s)
Polyalkylenglycol-heat transfer fluid Fragoltherm S 20 A		Fragol	−36	−25	<100	1,065	1.60	2,500 at −20°C
				240		858	2.56	2.5 at 200°C
Polyethylenglycol-heat transfer fluid Fragoltherm 250	s. PEG	Fragol	−5	20		1,125	2.10	100
				250	<100		2.80	1.2

Substance- or trade name	Flash point DIN 51376	Combustion point DIN 51758	Autoignition temperature DIN 51794	Temperature range ATEX 94/9/EG	pH value	Moisture content wt %	Physiological characteristics	Remarks
Triethylenglycol techn. pure	160–165	165–170	370	T 2	6.5–7.5	<0.5	LD_{50} = 17 g/kg	Can be stabilized by inhibitors
Polyethylenglycol PEG-type 400 600 1000 1500	240–245		340		10% aqueous solution 4–7	<0.5 water soluble	LD_{50} = 44 g/kg R - 42 g/kg R 51 g/kg R (R rat)	Max. 0.05 wt-% ash, is thermostable at average molecular weight 300–6,000 thermal properties can be stabilized by additives
Polyglycol, comm., e.g., 11/50	250		285–310	T 2		<0.5	LD_{50} = 2.5–>15 g/kg	by using adequate additives above 120–250°C
	250		310	T 2	10% aqueous solution 6–8	<0.5 water soluble	LD_{50} = 2.5 g/kg	Average molecular weight 1,200 max. 0.01 wt-% ash, lubricating properties under high pressure (3 kbar) as well
Heat transfer fluid based on polyalkylenglycol Fragoltherm S 15 A	>220		>300	T 2	7–9 2:1 water mix	<0.5 water soluble	LD_{50} > 10 g/kg	High-temperature stabilized polyalkylenglycol; material properties next chapter
Heat transfer fluid based on polyalkylenglycol Fragoltherm S 20 A	>260		>300	T 2	7–9 2:1 water mix	<0.5 water soluble	LD_{50} > 10 g/kg	High-temperature stabilized polyalkylenglycol; material properties next chapter
Heat transfer fluid based on polyethylenglycol Fragoltherm 250	>260	>270	>300	T 2	7–9 2:1 water mix	<0.5 water soluble	LD_{50} > 10 g/kg	High-temperature stabilized polyethylenglycol

1 Bibliography

1. Hofmann E (1959) Wärme- und Stoffübergang. In: Handbuch der Kältetechnik. Springer Verlag, Berlin, s. bes. S. 454 ff
2. Kühlsolen-Merkblätter 200, 400 u.a. Firmenschrift AKZO-Chemie. Düren 1979/1980
3. Melinder Å (1989) Köldbäre för värmepumptillämpningar (published by the Swedish State Council for Building Research) The Royal Institute of Technology, Stockholm; Document R 18; Melinder Å (1985) Applied thermodynamics and refrigeration. The Royal Institute of Technology, Stockholm; Document R 114: "Secondary refrigerants for heat pump applications" (published by the Swedish State Council for Building Research, Stockholm)
4. Melinder Å (1993) Thermodynamic properties of secondary refrigerants. Dept. of Energy Technology, The Royal Institute of Technology, Stockholm
5. Melinder Å, Granryd E Secondary Refrigerants for Heat pumps and low Temperature Refrigeration, Trita REFR Report No. 92/6
6. Product description of TYFOROP-Chemie GmbH, Hamburg, Germany
7. Product overview, Druckschrift der proKühlsole GmbH, Düren, Germany
8. Product description of Clariant GmbH, Division Surfactants, Werk Gendorf, Burgkirchen, Germany
9. Brochure Glythermin NF und P44 der BASF, ESB/AA-J550, Ludwigshafen, Germany
10. Product description of DOW Europe S.A., Horgen, Switzerland
11. Product overview of Arteco N.V., B-9052, Gent-Zwijnaarde, Belgium
12. Product description of Solutia S.A./N.V., B-1348 Louvain-la-Neuve, Belgium

D4.3 Oil-based and Synthetic Heat Transfer Media

Andreas Glück[1] · *Dietmar Hunold*[2]
[1]HTT Vertriebsbüro Süd GmbH, Ebersbach, Germany
[2]HTT Energy Systems GmbH, Herford, Germany

1 Introduction

The following synoptical tables with the most common heat transfer media currently available in the market including their properties shall offer the user a quick orientation. The predominant part of this compilation consists of producer information and procedure documentations. They correspond to the best knowledge and experiences and are passed in this sense – without being able to give the grade of exactness and without bindingness – also in regard to the existing proprietary rights of third parties. The trade names for the most part are registered as trademarks of companies. By this general remark, the designation of the fact is replaced.

Moreover, from basic considerations, heat transfer media known from the literature were included regardless the binding health and safety regulations in the meantime. Generally, it is to check for each heat transfer medium if the intended use is allowed according to the latest status.

To identify the optimum heat transfer medium for each application, indications of thermostability and the product life to be expected are to be inquired besides the price, which can vary strongly depending on delivery quantity and region. It is recommended to contact manufactorers of heat transfer plants with long-term experience besides the manufactorers of heat transfer fluids and its sales or distributing organisations. These companies can ensure a product-independent consultation and also specify various possibilities of a service life prolonging plant dimensioning and equipment.

At production and operation of plants with heat transfer media different acts, regulations, rules, standards, and directives depending on the location are to be observed. So for example, in Germany, there are to name among others the Immission Control Acts, Health and Safety Regulations, the Equipment Safety Statute or the Directive BGV D3 of the chemical industry (former VGB 64). As specific standard for heat transfer plants, the following have been established worldwide:

- DIN 4754: Heat transfer medium plants with other heat transfer media than water
- Directive VDI 3033: Heat transfer medium plants with other heat transfer media than water; design, operation, and maintenance
- Pressure Equipment Directive 97/23/EC
- AD-Merkblaetter of the workship "pressure vessels"
- Safety data sheet according to Directive 91/155/EEC for the heat transfer medium in use

Particularly, Anglo-Saxon influenced countries (British/Latin American) often use the following:

- American Society of Mechanical Engineers (ASME) Codes and Standards

The property collection corresponds in its coverage and content to one of the up-to-date German versions of the *VDI Wärmeatlas* (10. edition) and shall offer the reader a quick survey over the heat transfer media on mineral oil basis and/or synthetic heat transfer media basically suitable for his or her purpose.

At this point, it may be indicated explicitly that there are a number of additional heat transfer media with comparable properties available on the market. The VDI Heat Atlas, however, does not claim to offer a complete list of all products.

Due to the required space for it, the tables dispense with the indication of the usual Anglo-Saxon units. Instead, the essential conversion factors and formulas were prefixed in tabular form (Table 1).

The special field of the heat transfer technology was further ensured by the following standards:

DIN ISO 6743 Part 12 classification; family Q (heat transfer media)
DIN 51 522 Heat transfer media Q; specifications, checking
DIN 51 528 Determination of the thermostability of unused heat transfer media
DIN 51 529 Testing and assessment of used heat transfer media

Finally, it is pointed out to a *Wagner*-based property collection [1, 2], which also contains the appropriate safety data sheets.

Since the survey data named by the producers do not agree with extrapolations from the tabulated properties in all cases, the newest data should be obtained before making decisions.

2 Characteristics of Heat Transfer Media

To assess mineral-oil-based and synthetic heat transfer media the following characteristics are compared [1, 3]:

- *Aging.* All organic heat transfer substances are decomposed under the time influence of temperature, pressure, and

D4.3. Table 1. Conversion factors and formulas between metric and British/American units

Property	Brit./Am. unit	Metric unit	Metric unit	Brit./Am. unit
Temperature	x [°F]	5/9 · (x−32) [°C]	x [°C]	9/5 · (x + 18.5) [°F]
Pressure	1 psi	0.069 bar	1 bar	14.504 psi
Density	1 lb/ft^3	16.031 kg/m^3	1 kg/m^3	0.0624 lb/ft^3
Specific thermal capacity	1 Btu/(lb·°F)	4.179 kJ/(kg·K)	1 kJ/(kg·K)	0.239 Btu/(lb·°F)
Kinematic viscosity	1 lb/(ft·h)	0.403 mm^2/s	1 mm^2/s	2.482 lb/(ft·h)
Thermal conductivity	1 Btu/(ft·h·°F)	1.730 W/(m·K)	1 W/(m·K)	0.578 Btu/(ft·h·°F)
Enthalpy	1 Btu/lb	2.3235 kJ/kg	1 kJ/kg	0.4301 Btu/lb

oxygen; this decomposition rating can be reduced at best by targeted measures. Depending on the application, it is to distinguish between thermostability as the consistency of the molecules compared to the temperature free from oxygen and the oxidation stability as the consistency of the molecules compared to oxygen. The superordinated term of the disproportionation differs generally from the substance decomposition or substance conversion to products less suitable as heat transfer medium. Organic heat transfer media react with the oxygen of the ambient air at higher temperatures unless no inertization is planned. The oxidation products (e.g., organic acids or polymerization products) cause mostly an increase of viscosity as long as they remain in the solution. When the molar mass of these substances however exceeds a definite value, the oxidation products are deposited as mud. By the materials used at production of the heat transfer plant or by impurities in the plants, the oxidative aging can be advanced. When the specified temperature limits are observed as well as suitable materials and an inert gas superposition (e.g., N2) are used, an early oxidative damage to the substance can be avoided.

- "Aging is according to definition a production of substances that are not available in unused oil. The substances are created by the influence of atmospheric oxygen, heat, as well as excavation of metals and sealing materials" Zufall [4].
- At normal use of the heat transfer oils, the atmospheric oxygen supply in the plants according to DIN 4754 is either not possible due to inertization or planned only in the open but "cold" expansion vessel. The latter has no important influence on the aging.
- The already mentioned increase in viscosity mostly occurs at mineral oil fillings and only when inadmissible atmospheric air supply in larger quantities is possible. The main cause for this in most cases can be found in an expansion vessel, which is warmed up and open to the atmosphere. The inadmissible atmospheric air supply is mostly connected also with the formation of acid substances in such a large quantity that an appreciable neutralization value or similar can be measured.
- Cracking is the fission of the heat transfer medium molecules primarily in the boundary layer of the heating surface of the heater.
- This procedure can be minimized when the proceeding is according to DIN 4754 and the producer information to the admissible film temperature of the heat transfer medium at the design are observed.
- As an additional consequence of the thermal load, many heat transfer media form also small quantities of low boiling, benzine-like substances that have to be removed from the circuit by "boiling out" to avoid a critical lowering of the flash point and problems by cavitation.
- Polymerized substances (so-called heavy boiler) resulting from "cracking" are comparable in its effects on the plant to the above mentioned increase in viscosity and can lead to serious problems by deposits on the heating surfaces (fouling) or even choking. Therefore, special attention is to be paid to them when designing the plant and also at the annual checking of the heat transfer medium. Among others, the chronological course of the Conradson value is thereby of particular importance as a measure for the solid, not vaporable residues. At noticeable increase, it can signalize the beginning of formation of deposits. In each case, the careful and regular checking of the heat transfer medium is urgently recommended to the operator of a heat transfer plant. To avoid misinterpretation, a correct sampling is to be considered.
- *Thermostability and service life.* As an essential criteria for this feature, it is to state that the heat transfer medium flow temperature, which is to be expected under normal operating conditions, has a distance as large as possible to the maximum admissible flow temperature given by each producer. The following formulation may apply as rough guide value: A flow temperature reduced by 10 K leads to a doubling of the service life, particularly the usability of the heat transfer medium.
- *Corrosion.* Within the specified stated temperature limits, the ferrous materials are generally not affected.
- *Physiological properties.* In general, heat transfer media are not toxic. Arising decomposition products can, however, cause irritations to the respiratory tracts and mucous membranes; therefore, the regulations of the producer for handling are to be strictly observed. At toxicological effect, the maximum allowable concentration values will be determined by asking the producer in case of doubt. Maximum allowable concentration values are not included systematically.
- *Properties and methods of test.* Declaration of the properties listed in survey Tables 2a and 3a:

(Continued on page 500)

D4.3. Table 2a. Heat transfer media on mineral oil basis (survey, no. 1 to 13)

1	2	3	4	5	6	7	8	9	10	11	12	13	14	15	16
No.	Trade name	Composition key[a]	Producer	Pour point/ Boiling point (°C)	Application range (°C)	Vapor pressure (mbar)	Density (kg/m³)	Specific heat capacity (kJ/kgK)	Kinematic viscosity (mm²/s)	Thermal conductivity (W/m K)	Application limits		Flash point (°C)	Auto Ignition temperature (°C)	Former product/ explosive limit[b]
											Lower: filling and start-up (°C)	Upper: max. film temperature (°C)			
1	Farolin U	1	Aral	−12	−10	–	886	1.8	15.8	0.135	3	350	205	340	
				365	325	160	682	3.1	0.60	0.113	110				
2	Farolin S	2	Aral	−45	−25	–	931	1.66	1,396	0.129	3	320	180	335	
				340	305	120	710	2.93	0.52	0.113	87				
3	Farolin T	2	Aral	−42	−30	–	914	1.74	91.9	0.132	−15	300	145	340	
				315	300	150	695	2.84	0.56	0.111	70				
4	Thermofluid A	1,2,3	AVIA	<−60	−25	–	947	1.70	804	0.133	−25	280	140	330	AVILUB
				285	250	290	751	2.68	0.52	0.114	56				C-3826
5	Thermofluid B	1,2,3	AVIA	−2	0	–	878	1.81	300	0.136	−2	340	205	340	AVILUB
				310	310	230	688	2.94	0.59	0.113	96				B-3824
6	Transcal N	1	BP	−15	0	–	889	1.95	310	0.135	0	340	225	340	
				365	320	130	680	3.04	0.56	0.115	100				
7	Transcal LT	2	BP	−54	−20	–	900	1.80	300	0.136	−20	280	155	240	
				290	260	280	732	2.77	0.49	0.118	71				
8	Deacal A 12	1,2	Shell & DEA	<−36	0	–	882	1.75	82.6	0.135	−11	270	150		Texatherm A 12
				290	250		720	2.67	0.53	0.117	78				u. 0.6; o. 6.5
9	Deacal 32	1	Shell & DEA	<−24	0	–	887	1.78	310	0.135	1	290	200		Texatherm 32
				340	270	36	711	2.78	0.68	0.115	102				Regal Oil R032
															u. 0.6; o. 6.5
10	Deacal 46	1	Shell & DEA	<−24	0	–	885	1.80	604	0.133	0	300	200		u. 0.6; o. 6.9
				270	280	30	709	2.81	0.84	0.113	115				
11	Thermalöl S	2	Esso	−54	−10	–	893	1.80	47.3	0.134	−25	260	146	340	
				278	240	340	731	2.67	0.52	0.116	59				
12	Thermalöl T	1	Esso	−15	0	–	877	1.81	285	0.135	−2	340	210	315	
				355	320	180	670	3.01	0.60	0.112	102		PM[c]		
13	Finkotherm M 300	1	E. Finke Mineralölwerk	−12	0	–	880	1.89	300	0.135	0	340	215		u. 0.6; o. 6.5
				380	320	167	645	3.23	0.57	0.112	101				

D4.3. Table 2a. Heat transfer media on mineral oil basis (survey, no. 14 to 23)

1	2	3	4	5	6	7	8	9	10	11	12	13	14	15	16
No.	Trade name	Composition key[a]	Producer	Pour point/ Boiling point (°C)	Application range (°C)	Vapor pressure (mbar)	Density (kg/m³)	Specific heat capacity (kJ/kgK)	Kinematic viscosity (mm²/s)	Thermal conductivity (W/m K)	Application limits		Flash point (°C)	Auto Ignition temperature (°C)	Former product/ explosive limit[b]
											Lower: filling and start-up (°C)	Upper: max. film temperature (°C)			
14	Mobiltherm 594	2	Exxon	−69	−44	–	914	1.64	300	0.135	−44	280	122	300	
			Mobil	285	250	413	724	2.70	0.42	0.116	34				
15	Mobiltherm 603	1	Exxon	−19	−8	–	876	1.79	300	0.137	−8	300	188	340	
			Mobil	382	280	275	677	2.98	0.52	0.113	90				
16	Mobiltherm 605	1	Exxon	−12	−10	–	876	1.78	636	0.137	−1	345	204	n.b.	
			Mobil	n.b.	315	62	661	2.97	0.63	0.114	100				
17	HT 250	4	Fragol	−48	−40	–	869	1.86	816	0.135	−30	285	>150	239	
				305	270	150	656	2.97	0.53	0.096	55				
18	HT 300	1	Fragol	−12	0	–	890	1.90	300	0.134	0	340	>228	340	
				360	320	120	680	3.00	0.57	0.111	106				
19	ÖMV-Ö1 WT 15	2	ÖMV	−50	−9	–	892	1.79	143	0.133	−9	270	165	295	
				290	250	65	742	2.82	0.62	0.115	79				
20	ÖMV-Ö1 WT 32	1	ÖMV	−18	0	–	882	1.80	322	0.135	1	330	210	310	
				>360	310	160	694	3.09	0.58	0.112	103				
21	ÖMV-Ö1 WT 46	1	ÖMV	−15	0	–	889	1.79	570	0.133	8	340	225	320	
				>360	320	100	696	3.11	0.64	0.111	114				
22	Thermia Ö1 A	2	Shell & DEA	−60	−25	–	917	1.707	300	0.133	−25	280	140	330	Shell-Thermia-Ö1 11
				285	250	290	751	2.678	0.52	0.114	56				
23	Thermia Ö1 B	1	Shell & DEA	−15	−2	–	878	1.810	300	0.136	−2	340	205	340	Shell-Thermia-Ö1 27, C
				>360	310	130	688	2.934	0.59	0.113	96				

[a]1 paraffin-based; 2 naphthene-based; 3 aromatic hydrocarbons; 4 mineral selection raffinate
[b]u. = lower; o. = upper explosive limit
[c]Pensky-Martens

D4.3. Table 2b. Heat transfer media on mineral oil basis (no. 1 to 3)

No.	Substance (Trade name)	Temperature (°C)	Vapor pressure (mbar)	Density (kg/m³)	Specific heat capacity (kJ/kg K)	Thermal conductivity (W/mK)	Dynamic viscosity (10^{-3} Ns/m²)	Kinematic viscosity (10^{-6} m²/s)	Thermal diffusivity (10^{-8} m²/s)	Prandtl number
1	Farolin U	0		879	1.832	0.135	206.56	235	8.38	2,803
		15		870	1.881	0.134	87.00	100	8.19	1,221
		20		863	1.921	0.133	69.04	80.00	8.02	997
		40		852	1.996	0.132	25.56	30.00	7.76	386
		60		840	2.074	0.131	13.44	16.00	7.52	213
		80		826	2.151	0.129	7.85	9.50	7.26	131
		100		812	2.225	0.128	4.38	5.40	7.08	76.2
		150		781	2.436	0.124	2.03	2.60	6.52	39.9
		200		748	2.621	0.120	1.05	1.40	6.12	22.9
		250		714	2.827	0.117	0.68	0.96	5.80	16.6
		300		682	3.021	0.113	0.48	0.70	5.48	12.8
2	Farolin S	0		911	1.760	0.129	419	460	8.05	5,717
		15		905	1.821	0.128	103	114	7.77	1,467
		20		898	1.832	0.127	85.31	95.00	7.72	1,230
		40		884	1.910	0.126	25.64	29.00	7.46	389
		60		870	1.978	0.125	11.31	13.00	7.26	179
		80		857	2.064	0.124	5.91	6.90	7.01	98.4
		100		844	2.135	0.123	3.63	4.30	6.83	63.0
		150		810	2.320	0.119	1.46	1.80	6.33	28.4
		200		776	2.519	0.117	0.85	1.10	5.99	18.4
		250		710	2.712	0.113	0.50	0.70	5.87	11.9
3	Farolin T	0		896	1.781	0.132	71.68	80.00	8.27	967
		15		885	1.832	0.131	28.32	32.00	8.08	396
		20		882	1.861	0.130	22.05	25.00	7.92	316
		40		868	1.924	0.129	9.54	11.00	7.72	142
		60		854	1.982	0.128	5.12	6.00	7.56	79.3
		80		842	2.091	0.126	3.20	3.80	7.17	53.1
		100		828	2.176	0.125	2.15	2.60	6.94	37.5
		150		794	2.368	0.121	0.95	1.20	6.44	18.7
		200		762	2.568	0.118	0.53	0.70	6.03	11.6
		250		728	2.764	0.114	0.36	0.50	5.67	8.9
		300		695	2.961	0.111	0.33	0.48	5.39	8.9

D4.3. Table 2b. Heat transfer media on mineral oil basis (no. 4 to 6)

No.	Substance (Trade name)	Temperature (°C)	Vapor pressure (mbar)	Density (kg/m³)	Specific heat capacity (kJ/kg K)	Thermal conductivity (W/mK)	Dynamic viscosity (10^{-3} Ns/m²)	Kinematic viscosity (10^{-6} m²/s)	Thermal diffusivity (10^{-8} m²/s)	Prandtl number
4	Thermofluid A	−20		914	1.709	0.133	173	189	8.51	2,223
		0		902	1.785	0.131	41.5	46	8.14	565
		20		890	1.853	0.130	15.1	17	7.88	215
		50		872	1.960	0.128	5.49	6.3	7.49	84
		100	2	842	2.140	0.124	1.85	2.2	6.88	31.5
		150	15	811	2.319	0.121	0.89	1.1	6.43	17.1
		200	75	781	2.499	0.118	0.56	0.72	6.05	11.9
		250	290	751	2.678	0.114	0.39	0.52	5.67	9.2
		280	580	733	2.786	0.112	0.33	0.45	5.46	8.2
5	Thermofluid B	0		875	1.812	0.135	253	288.5	8.51	3,388
		20		863	1.882	0.134	65.7	75.9	8.25	921
		50		845	1.991	0.132	16.9	19.9	7.85	254
		100		815	2.173	0.128	4.09	5.01	7.23	69.3
		150		784	2.355	0.124	1.73	2.20	6.72	32.8
		200	5	754	2.538	0.121	0.98	1.30	6.32	20.6
		250	26	724	2.720	0.117	0.62	0.85	5.94	14.3
		300	100	694	2.902	0.114	0.43	0.62	5.66	11.0
		310	130	688	2.938	0.113	1.41	0.59	5.59	10.6
		340	260	669	3.048	0.111	0.35	0.52	5.54	9.6
6	Transcal N	0		884	1.92	0.134	284	321.3	7.89	4,069
		20		871	1.97	0.133	72.30	83.0	7.75	1,071
		40		858	2.05	0.131	26.60	31.0	7.44	416
		60		845	2.12	0.130	12.40	14.67	7.26	202
		80		833	2.19	0.129	6.91	8.30	7.07	117
		100	0.02	820	2.26	0.127	4.26	5.20	6.85	75.8
		150	0.29	788	2.43	0.124	1.78	2.26	6.48	34.9
		200	2.6	757	2.60	0.120	0.980	1.29	6.10	21.2
		250	16	725	2.77	0.116	0.623	0.86	5.78	14.9
		300	68	693	2.94	0.113	0.440	0.63	5.55	11.4
		320	120	680	3.00	0.111	0.387	0.57	5.44	10.5

D4.3. Table 2b. Heat transfer media on mineral oil basis (no. 7 to 9)

No.	Substance (Trade name)	Temperature (°C)	Vapor pressure (mbar)	Density (kg/m³)	Specific heat capacity (kJ/kg K)	Thermal conductivity (W/mK)	Dynamic viscosity (10^{-3} Ns/m²)	Kinematic viscosity (10^{-6} m²/s)	Thermal diffusivity (10^{-8} m²/s)	Prandtl number
7	Transcal LT	0		884	1.88	0.134	48	54.30	8.06	673
		20		871	1.95	0.133	17.30	19.96	7.83	254
		40		858	2.02	0.131	8.15	9.50	7.56	126
		60		845	2.08	0.130	4.56	5.40	7.40	73.0
		80		833	2.15	0.129	2.87	3.45	7.20	47.8
		100	1.0	820	2.22	0.127	1.97	2.40	6.98	34.4
		150	8.7	788	2.39	0.124	0.970	1.23	6.58	18.7
		200	50	757	2.56	0.120	0.582	0.77	6.19	12.7
		250	200	725	2.73	0.116	0.406	0.56	5.86	9.6
8	Deacal A 12	0		882	1.75	0.135	72.9	82.6	8.75	944.4
		20		869	1.83	0.134	23.6	27.2	8.43	322.8
		40		856	1.90	0.133	10.3	12.0	8.18	146.7
		60		843	1.97	0.131	5.40	6.40	7.89	81.1
		80		830	2.05	0.130	3.20	3.90	7.64	51.0
		100		817	2.12	0.128	2.30	2.80	7.39	37.9
		120		804	2.19	0.127	1.50	1.90	7.21	26.3
		140		791	2.27	0.125	1.10	1.40	6.96	20.1
		160		778	2.34	0.124	0.86	1.10	6.81	16.2
		180		765	2.41	0.122	0.69	0.90	6.62	13.6
		200		752	2.48	0.121	0.60	0.80	6.49	12.3
		220		739	2.56	0.120	0.48	0.65	6.34	10.3
		240		726	2.63	0.118	0.41	0.56	6.18	9.06
		250		720	2.67	0.117	0.38	0.53	6.13	8.64
9	Deacal 32	0	$2.81 \cdot 10^{-6}$	887	1.78	0.135	275	310	8.55	3,625
		20	$2.2 \cdot 10^{-5}$	874	1.86	0.133	73.4	84	8.18	1,028
		40	$1.37 \cdot 10^{-4}$	861	1.93	0.132	27.6	32	7.94	402.8
		60	$7.08 \cdot 10^{-4}$	848	2.00	0.131	12.7	15	7.72	194.2
		80	$3.12 \cdot 10^{-3}$	835	2.08	0.129	7.10	8.5	7.43	114.4
		100	$1.2 \cdot 10^{-2}$	822	2.15	0.128	4.60	5.6	7.24	77.3
		120	$4.11 \cdot 10^{-2}$	809	2.22	0.126	2.83	3.5	7.02	49.9
		140	0.127	796	2.30	0.125	1.99	2.5	6.83	36.6

D4.3. Table 2b. Heat transfer media on mineral oil basis (no. 9 to 11)

No.	Substance (Trade name)	Temperature (°C)	Vapor pressure (mbar)	Density (kg/m³)	Specific heat capacity (kJ/kg K)	Thermal conductivity (W/mK)	Dynamic viscosity (10^{-3} Ns/m²)	Kinematic viscosity (10^{-6} m²/s)	Thermal diffusivity (10^{-8} m²/s)	Prandtl number
9	Deacal 32 (continued)	160	0.366	783	2.37	0.123	1.49	1.9	6.63	28.7
		180	0.926	770	2.45	0.122	1.16	1.5	6.47	23.2
		200	2.24	757	2.52	0.120	0.91	1.2	6.29	19.1
		220		744	2.59	0.119	0.74	0.99	6.18	16.0
		240		731	2.67	0.117	0.61	0.84	5.99	14.0
		260		718	2.74	0.116	0.52	0.72	5.90	12.2
		270		711	2.78	0.115	0.48	0.68	5.81	11.6
10	Deacal 46	0	$1.85 \cdot 10^{-6}$	885	1.80	0.133	534.5	604	8.35	7,234
		20	$1.42 \cdot 10^{-5}$	872	1.87	0.132	116.9	134	8.09	1,655
		40	$8.69 \cdot 10^{-5}$	860	1.94	0.131	39.6	46	7.85	586
		60	$4.45 \cdot 10^{-4}$	847	2.01	0.129	17.8	21	7.58	277
		80	$1.95 \cdot 10^{-3}$	835	2.09	0.128	9.18	11	7.33	150
		100	$7.52 \cdot 10^{-3}$	822	2.16	0.126	5.59	6.8	7.10	95.8
		120	$2.58 \cdot 10^{-2}$	810	2.23	0.125	3.73	4.6	6.92	66.5
		140	$8.04 \cdot 10^{-2}$	797	2.30	0.123	2.63	3.3	6.71	49.2
		160	0.119	785	2.37	0.122	1.96	2.5	6.56	38.1
		180	0.603	772	2.45	0.121	1.47	1.9	6.40	29.7
		200	1.48	759	2.52	0.119	1.21	1.6	6.22	25.7
		220		747	2.59	0.118	0.971	1.3	6.10	21.3
		240		735	2.66	0.116	0.809	1.1	5.93	18.5
		260		722	2.74	0.115	0.693	0.96	5.81	16.5
		280		709	2.81	0.113	0.596	0.84	5.67	14.8
11	Esso Thermalöl S	0		886	1.80	0.134	42.00	47.40	8.40	564
		20		874	1.87	0.132	15.10	17.28	8.08	214
		40	0.02	861	1.94	0.131	7.20	8.36	7.84	107
		60		849	2.01	0.129	4.10	4.83	7.56	63.9
		80		836	2.09	0.128	2.60	3.11	7.33	42.5
		100	1.6	823	2.16	0.126	1.80	2.19	7.09	30.9
		150	250	790	2.34	0.123	0.90	1.14	6.65	17.1
		200	1,000	758	2.52	0.119	0.55	0.73	6.23	11.6
		250	5,000	725	2.70	0.116	0.38	0.52	5.93	8.8

D4.3. Table 2b. Heat transfer media on mineral oil basis (no. 12 to 14)

No.	Substance (Trade name)	Temperature (°C)	Vapor pressure (mbar)	Density (kg/m³)	Specific heat capacity (kJ/kg K)	Thermal conductivity (W/mK)	Dynamic viscosity (10^{-3} Ns/m²)	Kinematic viscosity (10^{-6} m²/s)	Thermal diffusivity (10^{-8} m²/s)	Prandtl number
12	Esso Thermalöl T	0		877	1.81	0.135	250.00	285.06	8.50	3,352
		20		865	1.88	0.134	66.00	76.30	8.24	926
		40		852	1.95	0.132	25.00	29.34	7.95	369
		60		840	2.03	0.131	12.10	14.40	7.68	187
		80		827	2.10	0.129	6.80	8.22	7.43	111
		100		814	2.17	0.128	4.20	5.16	7.25	71.2
		150	0.1	781	2.35	0.124	1.80	2.30	6.76	34.1
		200	1.0	749	2.53	0.121	1.00	1.34	6.39	20.9
		250	5.5	715	2.72	0.117	0.60	0.84	6.02	13.9
		300	25.0	682	2.90	0.113	0.40	0.59	5.71	10.3
		320	40.0	670	2.97	0.112	0.40	0.60	5.63	10.6
13	Finkotherm M 300	0		880	1.89	0.135	264.00	300	8.12	3,695
		20		867	1.97	0.133	68.50	79	7.79	1,014
		40		854	2.05	0.132	27.3	32	7.54	424
		60		841	2.14	0.131	12.10	14.39	7.28	198
		80		828	2.22	0.129	6.71	8.10	7.02	115
		100		815	2.30	0.128	4.16	5.10	6.83	74.7
		150	0.4	782	2.51	0.124	1.72	2.20	6.32	34.8
		200	2.6	745	2.72	0.121	0.89	1.19	5.97	20.0
		250	14	705	2.93	0.117	0.59	0.84	5.66	14.8
		300	69	660	3.14	0.113	0.42	0.63	5.45	11.7
		320	167	645	3.23	0.112	0.37	0.57	5.38	10.7
14	Mobiltherm 594	−10		892	1.76	0.135	22.7	25.4	8.60	296
		0		886	1.80	0.134	14.1	15.9	8.40	189
		20	0.01	847	1.901	0.137	7	8.63	8.5	102
		40	0.05	834	1.974	0.135	4	4.79	8.2	58
		60	0.19	820	2.048	0.134	2.5	3.03	8.0	38
		80	0.6	807	2.121	0.132	1.69	2.09	7.7	27
		100	1.7	794	2.195	0.131	1.22	1.54	7.5	21
		150	14	761	2.379	0.127	0.66	0.87	7.0	12
		200	72	728	2.563	0.123	0.428	0.59	6.6	9
		250	276	695	2.747	0.120	0.309	0.44	6.3	7

D4.3. Table 2b. Heat transfer media on mineral oil basis (no. 15 to 17)

No.	Substance (Trade name)	Temperature (°C)	Vapor pressure (mbar)	Density (kg/m³)	Specific heat capacity (kJ/kg K)	Thermal conductivity (W/mK)	Dynamic viscosity (10^{-3} Ns/m²)	Kinematic viscosity (10^{-6} m²/s)	Thermal diffusivity (10^{-8} m²/s)	Prandtl number
15	Mobiltherm 603	−10		877	1.78	0.137	319	364	8.79	4,142
		0		871	1.81	0.136	145.5	167	8.63	1,936
		20	0	859	1.887	0.135	42	49.1	8.3	590
		40	0	846	1.960	0.133	17	20.5	8.0	255
		60	0	833	2.033	0.132	8.8	10.6	7.8	135
		80	0	819	2.106	0.130	5.14	6.27	7.6	83
		100	0.09	806	2.179	0.129	3.32	4.12	7.3	56
		150	1.1	774	2.362	0.125	1.48	1.91	6.9	28
		200	8.5	741	2.545	0.122	0.839	1.13	6.5	18
		250	44	708	2.727	0.118	0.548	0.77	6.1	13
		300	171	675	2.910	0.114	0.392	0.58	5.8	10
16	Mobiltherm 605	−10	1.0	876	1.78	0.137	557	636	8.86	7,173
		0	8.1	867	1.82	0.137	241	278	8.69	3,197
		20	41	854	1.89	0.136	67	78	8.38	930
		40	71	841	1.97	0.134	25.9	30.8	8.1	380
		60		828	2.04	0.133	12.5	15.1	7.85	193
		80		814	2.12	0.131	7.0	8.6	7.61	113
		100		801	2.19	0.130	4.4	5.5	7.4	74
		150		768	2.37	0.126	1.8	2.4	6.91	35
		200		736	2.55	0.122	1.0	1.8	6.48	21
		250		704	2.73	0.118	0.65	0.92	6.13	15
		300		671	2.92	0.115	0.45	0.68	5.86	11
		320		657	2.99	0.114	0.40	0.61	5.79	10
17	HT 250	−40	3.0	869	1.86	0.135	709	816	8.34	9,786
		−20	20	855	1.94	0.133	101	118	8.04	1,471
		0	90	842	2.01	0.131	28	34	7.75	435
		20	190	829	2.08	0.129	11.6	14.0	7.47	187
		40		816	2.15	0.126	5.9	7.3	7.21	101
		60		803	2.22	0.124	3.5	4.4	6.96	63
		80		790	2.29	0.122	2.3	2.9	6.72	44
		100		777	2.36	0.119	1.7	2.1	6.49	32

D4.3. Table 2b. Heat transfer media on mineral oil basis (no. 17 to 20)

No.	Substance (Trade name)	Temperature (°C)	Vapor pressure (mbar)	Density (kg/m³)	Specific heat capacity (kJ/kg K)	Thermal conductivity (W/mK)	Dynamic viscosity (10^{-3} Ns/m²)	Kinematic viscosity (10^{-6} m²/s)	Thermal diffusivity (10^{-8} m²/s)	Prandtl number
17	HT 250 (continued)	150		743	2.54	0.113	0.87	1.2	5.97	20
		200		708	2.72	0.106	0.55	0.78	5.34	14
		250		671	2.90	0.100	0.39	0.58	5.11	11
		280		647	3.01	0.095	0.33	0.50	4.89	10
18	HT 300	0	20	890	1.9	0.134	267	300	7.92	3,784
		20	73	873	1.97	0.133	71	81	7.71	1,047
		40	120	858	2.05	0.132	27	31	7.50	413
		60		844	2.12	0.130	12.6	14.9	7.29	205
		80		831	2.19	0.129	7.0	8.4	7.09	119
		100		818	2.26	0.127	4.3	5.3	6.89	77
		150		788	2.43	0.124	1.78	2.3	6.45	36
		200		757	2.60	0.120	0.97	1.28	6.09	21
		250		725	2.77	0.116	0.61	0.85	5.80	15
		300		693	2.94	0.113	0.43	0.62	5.54	11
		320		680	3.01	0.111	0.38	0.56	5.44	10
19	ÖMV-Ö1 WT 15	0		892	1.79	0.133	127.9	143.4	8.33	1,721
		40		868	1.95	0.130	14.2	16.3	7.68	212.2
		80		844	2.12	0.127	4.1	4.87	7.10	69.0
		120	1	820	2.28	0.125	1.9	2.26	6.69	34.4
		160	4	796	2.45	0.122	1.03	1.32	6.26	20.8
		200	16	772	2.61	0.119	0.69	0.89	5.91	15.1
		240	58	748	2.78	0.116	0.49	0.66	5.58	11.8
		250	65	742	2.82	0.115	0.46	0.62	5.52	11.2
20	ÖMV-Ö1 WT 32	0		882	1.80	0.135	284	321.6	8.50	3,787
		40		858	1.97	0.132	27.0	31.45	7.81	403.4
		80		834	2.13	0.129	7.0	8.41	7.26	115.7
		120		810	2.30	0.126	2.9	3.64	6.76	53.2
		160	1	785	2.46	0.123	1.6	2.03	6.37	31.4
		200	3	761	2.63	0.120	0.99	1.31	6.00	21.7
		240	14	737	2.79	0.118	0.69	0.94	5.74	16.4
		280	55	713	2.96	0.115	0.51	0.72	5.45	13.2
		300	120	701	3.04	0.113	0.45	0.64	5.30	12.1
		310	160	694	3.09	0.112	0.42	0.58	5.25	11.6

D4.3. Table 2b. Heat transfer media on mineral oil basis (no. 21 to 23)

No.	Substance (Trade name)	Temperature (°C)	Vapor pressure (mbar)	Density (kg/m³)	Specific heat capacity (kJ/kg K)	Thermal conductivity (W/mK)	Dynamic viscosity (10^{-3} Ns/m²)	Kinematic viscosity (10^{-6} m²/s)	Thermal diffusivity (10^{-8} m²/s)	Prandtl number
21	2ÖMV-Ö1 WT 46	20	2	2,889	21.79	20.133	2,507	2,570	28.36	26,820
		40		865	1.96	0.131	39.8	45.7	7.73	595
		80		841	2.12	0.128	9.3	11.0	7.18	153
		120		817	2.28	0.125	3.7	4.48	6.68	67.4
		160	<1	792	2.45	0.122	1.9	2.40	6.29	38.2
		200	2	768	2.62	0.119	1.2	1.52	5.91	25.4
		240	9	744	2.78	0.117	0.82	1.07	5.66	19.5
		280	27	720	2.95	0.114	0.58	0.81	5.37	15.1
		320	100	696	3.11	0.111	0.45	0.64	5.13	12.5
22	Thermia Ö1 A	−20		914	1.709	0.133	173	189	8.51	2,223
		0		902	1.785	0.131	41.5	46	8.14	565
		20		890	1.853	0.130	15.1	17.0	7.88	215
		50		872	1.960	0.128	5.49	6.30	7.49	84.1
		100	2	842	2.140	0.124	1.85	2.20	6.88	31.9
		150	15	811	2.319	0.121	0.89	1.10	6.43	17.1
		200	75	781	2.499	0.118	0.56	0.72	6.05	11.9
		250	290	751	2.678	0.114	0.39	0.52	5.67	9.2
		280	580	733	2.786	0.112	0.33	0.45	5.46	8.2
23	Thermia Öl B	0		875	1.812	0.135	253	288.5	8.51	3,388
		20		863	1.882	0.134	65.7	75.9	8.25	921
		50		845	1.991	0.132	16.9	19.9	7.85	254
		100		815	2.173	0.128	4.09	5.01	7.23	69.3
		150		784	2.355	0.124	1.73	2.20	6.72	32.8
		200	5	754	2.538	0.121	0.98	1.30	6.32	20.6
		250	26	724	2.720	0.117	0.62	0.85	5.94	14.3
		300	100	694	2.902	0.114	0.43	0.62	5.66	11.0
		310	130	688	2.938	0.113	0.41	0.59	5.59	10.6
		340	260	669	3.048	0.111	0.35	0.52	5.44	9.6

D4.3. Table 3a. Synthetic heat transfer media (survey, no. 1 to 7)

1	2	3	4	5	6	7	8	9	10	11	12	13	14	15	19	20	21	22
No.	Trade name	Structure	Producer	Pour point/ boiling point (°C)	Appli-cation range min./ max. (°C)	Vapor pressure (mbar)	Density (kg/m³)	Specific thermal capacity (kJ/ kg K)	Kinematic viscosity (mm²/s)	Thermal conduc-tivity (W/mK)	Application limits		Flash point (°C)	Auto Ignition temper-ature (°C)	Explosive limit volume content (%)	Molar mass (kg/ kmol)	Possible appli-cation	Former product/ remark
											Lower: Filling and start-up (°C)	Upper: Max. film temperature (°C)						
1	Diphyl DT	Ditolylether, Synonyma: Dimethyldi-phenylether	Bayer/ Lanxess	−54	−20	–	1,067	1.45	61	0.138	<−25	340	135	545			B	
				284 bis 294	330	2,700	786	2.33	0.33	0.090	25							
2	Diphyl KT	Mixture of benzyl-toluol and di-benzyl-toluol	Bayer/ Lanxess	−60	−50	–	1,062	1.40	1,058	0.139	−43	370	144	490			B	
				285	350	3,200	745	2.58	0.34	0.089	37							
3	Diphyl THT	Partially hydrated terphenyl	Bayer/ Lanxess	−33	0		1,013	1.48	903	0.110	1	370	190	380			A	
				352	345	833	791	2.67	0.47	0.101	80							
4	Deacal HT 22	Mixture of linear alkali-benzols	Fuchs Europe	<−45	−20	–	938	.65	1,500	0.131	−5	320	>190	364			A	
				340	300	970	725	2.80	0.53	0.109	80							
5	Dowtherm G	Mixture of di- and tri-arylether	Dow	−25	−7	–	1,127	1.52	135	0.128	−15	385	137	432	u. 1.2	204.6 m	B	
				288	370	3,500	820	2.39	0.26	0.080	55				o. 3.3			
6	Dowtherm J	Mixture of isomers of alkylated aromatic compounds	Dow	−86	−80	–	930	1.57	10.65	0.150	<−84	340	58	420	u. 0.8	134 m	B	
				181	315	1,1940	570	3.01	0.28	0.065	−55				o. 9.0		C	
7	Dowtherm RP	Mixture of diaryl-alkyl components C_{14}–C_{30}	Dow	<0	0	–	1,043	1.56	41.3	0.134	<0	375	194	385	u. 0.33	236.4		
				353	350	960	785	2.60	0.2	0.089	72				o. 4.66			

D4.3. Table 3a. Synthetic heat transfer media (survey, no. 8 to 13)

1	2	3	4	5	6	7	8	9	10	11	12	13	14	15	19	20	21	22
No.	Trade name	Structure	Producer	Pour point/ boiling point (°C)	Application range min./ max. (°C)	Vapor pressure (mbar)	Density (kg/m³)	Specific thermal capacity (kJ/ kg K)	Kinematic viscosity (mm²/s)	Thermal conductivity (W/mK)	Application limits		Flash point (°C)	Auto Ignition temperature (°C)	Explosive limit volume content (%)	Molar mass (kg/ kmol)	Possible application	Former product/ remark
											Lower: Filling and start-up (°C)	Upper: Max. film temperature (°C)						
8	Dowtherm Q	Mixture of diphenyl thane and alkylated aromatic compounds	Dow	<−36	−35	–	1,010	1.48	49.7	0.126	<−40	355	120	411	u. 0.55	190 m	B	
				267	330	3,090	731	2.59	0.25	0.077					o. 5.5			
9	Finkotherm S 300	Alkali-benzol mixture (synth. Alkyl-substituted aromatic CH-compounds)	E. Finke	−50	−20	–	914	1.70	3,500	0.138	−4	330	200	360			A	
				360	300	800	693	3.46	0.60	0.111	88							
10	Ucotherm S 15 A	Polyalkylene glycol	Fragol	−51	−20	<100	1,047	1.84	600	0.160	−12	215	>260	>300			A	decom-position before boiling point
				s. Bem.	205		865	2.34	1.45	0.158	93							
11	Ucotherm S 20 A	Polyalkylene glycol	Fragol	−36	0		1,050	1.68	510	0.160	8	250	>170	>300			A	decom-position before boiling point
				s. Bem.	240		858	2.56	2.5	0.158	158							
12	Rhenotherm 350 S	Synthetic CH-compounds	Fuchs Europe	−30	−15		15 °C: 870				−2	370						
							674	3.12	0.36	0.08	87							
13	Marlotherm SH	Mixture of isomeric di-benzyl-toluol	SASOL Germany	−34	−5	–	1,061	1.46	380	0.134	−5	380	>200	450		272	A	previous product: Marlotherm S
				390	350	700	808	2.78	0.35	0.087	70							

D4.3. Table 3a. Synthetic heat transfer media (survey, no. 14 to 21)

1	2	3	4	5	6	7	8	9	10	11	12	13	14	15	19	20	21	22
No.	Trade name	Structure	Producer	Pour point/ boiling point (°C)	Appli-cation range min./ max. (°C)	Vapor pressure (mbar)	Density (kg/m³)	Specific thermal capacity (kJ/ kg K)	Kinematic viscosity (mm²/s)	Thermal conduc-tivity (W/mK)	Application limits		Flash point (°C)	Auto Ignition temper-ature (°C)	Explosive limit volume content (%)	Molar mass (kg/ kmol)	Possible appli-cation	Former product/ remark
											Lower: Filling and start-up (°C)	Upper: Max. film temperature (°C)						
14	Marlotherm N	Alkyl-substituted aromatic CH-compounds	SASOL Germany	−60[f]	−10	–	897	1.86	350	0.137	−10	330	ca. 180	ca. 33O		(320) m	A	Hüls
				340	300	716	668	2.99	0.38	0.112	70							
15	Marlotherm X	Mixture of isomers of alkyl-aromatic-compounds	SASOL Germany	<−70	−70	–	947	1.73	11.5	1.56	<−70	320	63[e]	410	u. 0.7	134	A	Hüls
				180[b]	300[c]	10,900	633	2.86	0.24	0.06	−54				o. 7.2		C	
					180[d]													
16	Cassida Fluid HT 32	Base oil, PAO-treated	Shell & DEA	−54	−30	–	795	1.96	365	0.151	−30	320	230	354				"USDA approval. group H[a]
				>360	320	25	669	3.04	0.85	0.136	185							
17	Therminol D12	Mixture of aliphatic CH-compounds	Solutia	<−85	−85	–	835	1.64	354	0.124	−80	275	59	277		180	B	Santotherm Gilotherm
				182	260	3,962	550	3.10	0.25	0.063	−22							
18	Therminol ADX-10	Alkyl-aryl CH-compounds	Solutia	−80	−45	–	901	1.66	493	0.132	−41	280	136	327		236	A	Santotherm Gilotherm
				293	250	370	686	2.72	0.39	0.090	33							
19	Therminol RD	Cross-linked alkyl benzol	Solutia	−55	−20	–	897	1.69	178	0.123	–	300	120	395		240	A	Santotherm Gilotherm
				283	270	728	697	2.93	0.49	0.094	48							
20	Therminol ALD	Alkyl-benzol mixture	Solutia	−30	7	–	879	1.90	323	0.114	7	340	168	390		320	A	Santotherm Gilotherm
				342	310	500	674	2.90	0.53	0.090	90							

D4.3. Table 3a. Synthetic heat transfer media (survey, no. 14 to 21)

1	2	3	4	5	6	7	8	9	10	11	12	13	14	15	19	20	21	22
No.	Trade name	Structure	Producer	Pour point/ boiling point (°C)	Appli-cation range min./ max. (°C)	Vapor pressure (mbar)	Density (kg/m³)	Specific thermal capacity (kJ/ kg K)	Kinematic viscosity (mm²/s)	Thermal conduc-tivity (W/mK)	Application limits		Flash point (°C)	Auto Ignition temper-ature (°C)	Explosive limit volume content (%)	Molar mass (kg/ kmol)	Possible appli-cation	Former product/ remark
											Lower: Filling and start-up (°C)	Upper: Max. film temperature (°C)						
21	Therminol SP/55	Alkyl-benzol mixture	Solutia	−40	−10	–	892	1.80	346	0.132	−10	335	177	366		320	A	Santotherm
				351	315	480	659	2.95	0.45	0.093	85							
22	Therminol 59	Alkyl-substituted aromatic CH-compounds	Solutia	−61	−39	–	1,016	1.49	440	0.125	−39	340	132	404		207	B	Santotherm 200 ppm max. humidity
				289	315	1,630	740	2.67	0.32	0.089	26							
23	Therminol 66	Hydrated terphenyl	Solutia	−32	0	–	1,021	1.50	1,297	0.118	10	375	170	399		252	A	Santotherm 100 ppm max. humidity
				359	345	780	787	2.74	0.42	0.088	88							
24	Therminol 68	Mixture of synthetic aromatic compounds	Solutia	−33	−10	–	1,048	1.53	307	0.126	−10	390	155	400		226	B	Santotherm 200 ppm max. humidity
				308	360	2,501	782	2.72	0.30	0.096	71							
25	Therminol 72	Mixture of synthetic Aromatic compounds	Solutia	−18	−10	–	1,106	1.47	346	0.144	−10	400	132	585		190	B	Santotherm
				271	380	5,736	753	2.53	0.19	0.096	45							MCS-2424 200 ppm max. humidity
26	Calflo AF	Semi-synthetic paraffinic components 2 HT (hydro treated)	(Petro Canada)	−18	−5	–	863	1.70	371	0.138	−3	315	204	343		365	A	Petro Canada
			Fragol	349	290	70	716	2.84	0.75	0.122	106							

D4.3. Table 3a. Synthetic heat transfer media (survey, no. 27 to 31)

1	2	3	4	5	6	7	8	9	10	11	12	13	14	15	19	20	21	22
No.	Trade name	Structure	Producer	Pour point/ boiling point (°C)	Appli-cation range min./ max. (°C)	Vapor pressure (mbar)	Density (kg/m³)	Specific thermal capacity (kJ/ kg K)	Kinematic viscosity (mm²/s)	Thermal conduc-tivity (W/mK)	Application limits		Flash point (°C)	Auto Ignition temper-ature (°C)	Explosive limit volume content (%)	Molar mass (kg/ kmol)	Possible appli-cation	Former product/ remark
											Lower: Filling and start-up (°C)	Upper: Max. film temperature (°C)						
27	Calflo FG	Base oil (hydro treated mineral oil)	(Petro Canada)	−18	−10	–	870	1.78	1,056	0.139	−4	343	209	350		380	A	HI-Zul. des USDA approval. group H1[a]
			Fragol	350	325	178	645	2.91	0.7	0.121	107							
28	Calflo HTF	Base oil (hydro treated mineral oil)	(Petro Canada)	−18	−18	–	877	1.78	8,086	0.141	−1	343	212	355		380	A	
			Fragol	380	325	140	703	2.91	0.65	0.122	112							
29	Ucotherm FG-8	Hydrated mineral oil	Fragol	−48	−45	–	872	1.85	1,573	0.136	−30	285	>150	239				
				305	270	150	656	2.97	0.53	0.096	50							
30	Ucotherm FG-33	Hydrated mineral oil	Fragol	−15	−10	–	855	2.07	702	0.156	0	345	>220	359				
				>390	325	200	640	3.16	0.7	0.129	110							
31	Therminol VLT	Methyl-cyclo-hexane + 2,2,4-tri-methyl-pentene	Solutia	<−135	−115	–	862	1.37	50	0.130	−115	210	−7	264				
				99	175	575	598	2.61	0.14	0.066	−70							

[a]FDA approved heat transfer medium for food processing
[b]Boiling point
[c]Fire point Cleveland Open Cup (COC)
[d]in liquid phase
[e]in vapor phase
[f]Setting point acc. DIN 51 583

D4.3. Table 3b. Synthetic heat transfer media (no. 1 to 2)

No.	Substance (Trade Name)	Temperature (°C)	Vapor Pressure (mbar)	Density (kg/m³)	Specific Heat Capacity (kJ/kg K)	Thermal Conductivity (W/mK)	Dynamic viscosity (10^{-3} Ns/m)²	Kinematic viscosity (10^{-6} m²/s)	Thermal Diffusivity (10^{-8} m²/s)	Prandtl Number
1	Diphyl DT	−20		1,067	1.450	0.138	66.35	61	8.92	682
		0		1,051	1.510	0.136	15.0	14.3	8.57	164
		20		1,053	1.580	0.133	6.65	6.32	8.13	77.1
		40		1,019	1.640	0.130	3.53	3.46	7.78	43.8
		60		1,002	1.700	0.127	2.35	2.35	7.46	30.7
		80		986	1.760	0.125	1.61	1.63	7.20	22.2
		100		970	1.820	0.123	1.22	1.26	6.97	17.4
		120		954	1.870	0.119	0.973	1.02	6.67	14.9
		140	14.8	938	1.930	0.116	0.784	0.836	6.41	12.8
		160	32.5	922	1.980	0.114	0.639	0.693	6.24	10.9
		180	64	906	2.030	0.111	0.536	0.592	6.04	9.6
		200	124	890	2.070	0.108	0.463	0.520	5.86	8.7
		220	224	874	2.120	0.106	0.401	0.458	5.72	7.9
		240	364	858	2.160	0.103	0.359	0.418	5.56	7.4
		260	609	842	2.200	0.100	0.326	0.387	5.40	7.1
		280	937	826	2.240	0.097	0.312	0.378	5.24	7.0
		300	1,480	810	2.280	0.094	0.289	0.357	5.09	6.9
		320	2,240	794	2.320	0.092	0.275	0.346	4.99	6.8
		330	2,680	786	2.335	0.091	0.269	0.342	4.93	6.8
		340	3,100	778	2.350	0.090	0.262	0.330	4.87	6.8
2	Diphyl KT	−50		1,062	1.40	0.139	1124.0	1058.4	9.35	11,320
		−40		1,054	1.43	0.137	278.0	236.76	9.09	2,902
		−20		1,039	1.49	0.135	45.00	43.31	8.72	497
		0		1,023	1.55	0.132	14.30	13.98	8.32	168
		20		1,007	1.61	0.130	6.55	6.50	8.02	81.0
		40	0.02	991	1.67	0.127	3.69	3.72	7.67	48.5
		60	0.1	975	1.73	0.125	2.38	2.44	7.41	32.9
		80	0.6	959	1.79	0.122	1.68	1.75	7.11	24.6
		100	1.9	943	1.84	0.120	1.26	1.34	6.92	19.4
		120	5.5	927	1.90	0.117	1.00	1.08	6.64	16.3
		140	14	911	1.96	0.115	0.81	0.89	6.44	13.8

D4.3. Table 3b. Synthetic heat transfer media (no. 2 to 3)

No.	Substance (Trade Name)	Temperature (°C)	Vapor Pressure (mbar)	Density (kg/m³)	Specific Heat Capacity (kJ/kg K)	Thermal Conductivity (W/mK)	Dynamic viscosity (10^{-3} Ns/m)²	Kinematic viscosity (10^{-6} m²/s)	Thermal Diffusivity (10^{-8} m²/s)	Prandtl Number
2	Diphyl KT (continued)	160	31	896	2.02	0.112	0.68	0.76	6.19	12.3
		180	62	880	2.08	0.110	0.59	0.67	6.01	11.1
		200	118	864	2.14	0.107	0.51	0.59	5.79	10.2
		220	208	848	2.20	0.105	0.45	0.53	5.63	9.41
		240	348	832	2.26	0.102	0.41	0.49	5.42	9.04
		260	554	816	2.31	0.100	0.37	0.45	5.31	8.47
		280	847	800	2.37	0.097	0.34	0.43	5.12	8.40
		300	1,248	784	2.43	0.095	0.31	0.40	4.99	8.02
		320	1,782	769	2.49	0.092	0.28	0.36	4.80	7.50
		340	2,474	753	2.55	0.090	0.26	0.35	4.69	7.46
		350	2,888	745	2.58	0.089	0.25	0.34	4.63	7.34
		360	3,350	737	2.61	0.087	0.25	0.34	4.52	7.52
		370	3,866	729	2.64	0.086	0.24	0.33	4.47	7.38
3	Diphyl THT	0		1,017	1.48	0.110	919	903	7.29	7,278
		20		1,004	1.54	0.109	101	101	7.06	1,077
		40		991	1.61	0.109	26.6	27	6.82	320
		60		978	1.68	0.108	10.8	11	6.60	143
		80		965	1.74	0.108	5.7	5.8	6.43	80.1
		100		952	1.81	0.107	3.5	3.6	6.24	52.6
		120		939	1.88	0.107	2.3	2.5	6.07	38.1
		140		926	1.95	0.106	1.7	1.8	5.91	29.6
		160	3	913	2.01	0.106	1.3	1.4	5.79	24.2
		180	7	900	2.08	0.105	1.1	1.2	5.65	20.6
		200	16	887	2.15	0.105	0.89	1.0	5.53	17.9
		220	32	874	2.22	0.104	0.75	0.86	5.41	16.0
		240	62	861	2.29	0.104	0.65	0.76	5.30	14.6
		260	111	848	2.36	0.103	0.57	0.68	5.20	13.5
		280	190	835	2.44	0.103	0.51	0.61	5.09	12.9
		300	312	822	2.51	0.102	0.46	0.56	5.01	12.1
		320	491	809	2.58	0.102	0.42	0.52	4.93	11.7
		340	746	796	2.65	0.101	0.38	0.48	4.86	11.0
		370	1,318	111	2.76	0.100	0.34	0.44	4.75	10.7

D4.3. Table 3b. Synthetic heat transfer media (no. 4 to 5)

No.	Substance (Trade Name)	Temperature (°C)	Vapor Pressure (mbar)	Density (kg/m^3)	Specific Heat Capacity (kJ/kg K)	Thermal Conductivity (W/mK)	Dynamic viscosity (10^{-3} Ns/m)^2	Kinematic viscosity (10^{-6} m^2/s)	Thermal Diffusivity (10^{-8} m^2/s)	Prandtl Number
4	Deacal HT 22	−20		938	1.65	0.131	1,407	1,500	8.46	17,722
		0	$9.01 \cdot 10^{-4}$	925	1.71	0.130	185	200	8.22	2,433
		20	$3.34 \cdot 10^{-3}$	912	1.79	0.129	44.7	49	7.90	620.1
		40	$1.05 \cdot 10^{-2}$	898	1.87	0.127	17.1	19	7.56	251.2
		60	$2.94 \cdot 10^{-2}$	885	1.94	0.126	7.96	9	7.34	122.6
		80	$7.48 \cdot 10^{-2}$	872	2.01	0.124	4.36	5	7.07	70.7
		100	0.178	859	2.10	0.123	2.92	3.4	6.82	49.9
		120	0.403	845	2.16	0.122	2.03	2.4	6.68	35.9
		140	0.887	832	2.23	0.120	1.50	1.8	6.47	27.8
		160	1.91	819	2.30	0.119	1.15	1.4	6.32	22.2
		180	4.03	805	2.38	0.117	0.966	1.2	6.11	19.7
		200	8.33	792	2.50	0.116	0.768	0.97	5.86	16.6
		220		779	2.52	0.115	0.654	0.84	5.86	14.3
		240		766	2.60	0.113	0.559	0.73	5.67	12.9
		260		752	2.67	0.112	0.489	0.65	5.58	11.7
		280		739	2.74	0.110	0.429	0.58	5.43	10.7
		300		725	2.80	0.109	0.384	0.53	5.37	9.87
		320		713	2.89	0.108	0.349	0.49	5.24	9.35
5	Dowtherm G	−5		1,125	1.51	0.128	121.95	108.40	7.46	1,452
		0		1,121	1.53	0.128	74.66	66.60	7.41	898
		20		1,105	1.58	0.126	18.92	17.12	7.20	238
		40		1,069	1.63	0.124	8.29	7.61	6.99	108.9
		60		1,072	1.67	0.122	4.76	4.44	6.80	65.3
		80	1	1,056	1.72	0.120	3.16	2.99	6.59	45.4
		100	3	1,040	1.77	0.118	2.27	2.18	6.40	34.1
		120	7	1,023	1.81	0.115	1.72	1.68	6.21	27.1
		140	16	1,007	1.86	0.113	1.35	1.34	6.03	22.2
		160	34	991	1.90	0.110	1.08	1.09	5.84	18.7
		180	68	975	1.95	0.108	0.88	0.90	5.66	16.0
		200	125	958	2.00	0.105	0.73	0.76	5.48	13.9

D4.3. Table 3b. Synthetic heat transfer media (no. 5 to 6)

No.	Substance (Trade Name)	Temperature (°C)	Vapor Pressure (mbar)	Density (kg/m^3)	Specific Heat Capacity (kJ/kg K)	Thermal Conductivity (W/mK)	Dynamic viscosity (10^{-3} Ns/m)^2	Kinematic viscosity (10^{-6} m^2/s)	Thermal Diffusivity (10^{-8} m^2/s)	Prandtl Number
5	Dowtherm G (continued)	220	217	942	2.04	0.102	0.61	0.65	5.31	12.2
		240	358	926	2.09	0.099	0.52	0.56	5.14	10.9
		260	566	909	2.13	0.096	0.44	0.48	4.97	9.7
		280	858	893	2.18	0.094	0.38	0.43	4.81	8.9
		300	1,261	877	2.23	0.091	0.33	0.38	4.64	8.1
		320	1,800	860	2.27	0.088	0.29	0.34	4.49	7.5
		340	2,498	844	2.32	0.085	0.26	0.31	4.33	7.1
		360	3,385	828	2.36	0.082	0.23	0.28	4.18	6.6
6	Dowtherm J	−80		935	1.570	0.150	9.96	10.65	10.22	104
		−60		921	1.616	0.146	5.12	5.56	9.81	56.7
		−40		907	1.664	0.142	2.88	3.18	9.41	33.7
		−20		893	1.716	0.138	1.80	2.02	9.01	22.4
		0		879	1.771	0.133	1.23	1.40	8.54	16.4
		20		864	1.830	0.129	0.91	1.05	8.16	12.9
		40		849	1.892	0.125	0.70	0.824	7.78	10.6
		60	10	833	1.956	0.120	0.56	0.672	7.36	9.1
		80	30	818	2.024	0.126	0.47	0.575	7.01	8.2
		100	80	801	2.093	0.112	0.40	0.499	6.68	7.5
		120	160	785	2.166	0.107	0.35	0.446	6.29	7.1
		140	320	767	2.240	0.103	0.31	0.404	6.00	6.7
		160	580	749	2.316	0.099	0.28	0.374	5.71	6.6
		180	980	731	2.394	0.094	0.25	0.342	5.37	6.4
		200	1,580	711	2.474	0.090	0.23	0.323	5.12	6.3
		220	2,430	691	2.560	0.085	0.22	0.318	4.81	6.6
		240	3,590	669	2.640	0.081	0.20	0.299	4.59	6.5
		260	5,130	646	2.721	0.077	0.19	0.294	4.38	6.7
		280	7,120	620	2.812	0.072	0.18	0.290	4.13	7.0
		300	9,640	592	2.918	0.068	0.17	0.287	3.94	7.3
		310	11,130	577	2.980	0.066	0.17	0.283	3.84	7.7
		315	11,940	569	3.014	0.065	0.16	0.281	3.79	7.4

D4.3. Table 3b. Synthetic heat transfer media (no. 7 to 8)

No.	Substance (Trade Name)	Temperature (°C)	Vapor Pressure (mbar)	Density (kg/m³)	Specific Heat Capacity (kJ/kg K)	Thermal Conductivity (W/mK)	Dynamic viscosity (10^{-3} Ns/m)²	Kinematic viscosity (10^{-6} m²/s)	Thermal Diffusivity (10^{-8} m²/s)	Prandtl Number
7	Dowtherm RP	0		1,043	1.56	0.134	221	212	8.24	2,573
		20		1,029	1.62	0.131	42.8	41.6	7.86	529
		40		1,015	1.68	0.129	14.9	14.7	7.57	194
		60		1,001	1.74	0.126	7.19	7.18	7.23	99.3
		80		987	1.80	0.124	4.20	4.26	6.98	61.0
		100		973	1.86	0.121	2.77	2.85	6.69	42.6
		120		959	1.92	0.118	1.98	2.06	6.41	32.1
		140		944	1.98	0.116	1.49	1.58	6.21	25.4
		160		930	2.04	0.113	1.18	1.27	5.96	21.3
		180	10	916	2.10	0.111	0.96	1.05	5.77	18.2
		200	20	901	2.16	0.108	0.80	1.89	5.55	16.0
		220	30	886	2.22	0.105	0.68	0.77	5.34	14.4
		240	60	871	2.27	0.103	0.58	0.67	5.21	12.9
		260	110	856	2.33	0.100	0.51	0.60	5.01	12.0
		280	200	841	2.39	0.0977	0.45	0.54	4.86	11.1
		300	330	825	2.45	0.0951	0.40	0.48	4.71	10.2
		320	520	809	2.51	0.0925	0.36	0.44	4.56	9.65
		340	790	793	2.57	0.0899	0.33	0.42	4.41	9.52
		350	960	785	2.60	0.0886	0.31	0.39	4.34	8.99
		360	1,160	777	2.63	0.0873	0.30	0.39	4.27	9.13
		370	1,400	768	2.66	0.0860	0.29	0.38	4.21	9.03
8	Dowtherm Q	−35		1,010	1.48	0.128	50.21	49.71	8.59	578.9
		−30		1,009	1.50	0.128	35.24	34.93	8.47	412.6
		−20		1,001	1.52	0.127	19.47	19.45	8.30	234.4
		−10		994	1.56	0.126	12.06	12.13	8.11	149.6
		0		986	1.59	0.124	8.09	8.20	7.93	103.5
		10		979	1.62	0.123	5.76	5.88	7.77	75.7
		20		971	1.65	0.122	4.30	4.43	7.60	58.3
		30		963	1.69	0.121	3.32	3.45	7.44	46.4
		40		956	1.72	0.120	2.64	2.76	7.28	37.9

D4.3. Table 3b. Synthetic heat transfer media (no. 8)

No.	Substance (Trade Name)	Temperature (°C)	Vapor Pressure (mbar)	Density (kg/m³)	Specific Heat Capacity (kJ/kg K)	Thermal Conductivity (W/mK)	Dynamic viscosity (10^{-3} Ns/m)²	Kinematic viscosity (10^{-6} m²/s)	Thermal Diffusivity (10^{-8} m²/s)	Prandtl Number
8	Dowtherm Q (continued)	50		948	1.75	0.118	2.15	2.27	7.13	31.8
		60		940	1.78	0.117	1.78	1.89	7.00	27.1
		70		933	1.81	0.116	1.50	1.61	6.83	25.5
		80		925	1.85	0.114	1.29	1.39	6.70	20.8
		90		917	1.88	0.113	1.11	1.21	6.56	18.4
		100		910	1.91	0.112	0.97	1.07	6.43	16.6
		110	10	902	1.94	0.110	0.86	0.95	6.30	15.1
		120		895	1.97	0.109	0.77	0.86	6.17	13.9
		130	20	887	2.00	0.107	0.69	0.78	6.05	12.9
		140		879	2.03	0.106	0.62	0.71	5.93	11.9
		150	30	872	2.06	0.104	0.56	0.64	5.81	11.1
		160	50	864	2.09	0.103	0.52	0.60	5.70	10.6
		170	70	856	2.12	0.101	0.47	0.55	5.58	9.8
		180	100	849	2.15	0.100	0.44	0.52	5.47	9.5
		190	130	841	2.18	0.098	0.40	0.48	5.35	8.9
		200	180	833	2.21	0.097	0.38	0.46	5.25	8.7
		210	240	826	2.24	0.095	0.35	0.42	5.15	8.2
		220	320	818	2.27	0.094	0.33	0.40	5.04	8.0
		230	420	811	2.30	0.092	0.31	0.38	4.94	7.7
		240	540	803	2.33	0.091	0.29	0.36	4.84	7.5
		250	680	795	2.36	0.089	0.27	0.34	4.74	7.2
		260	860	788	2.39	0.087	0.26	0.33	4.64	7.1
		270	1,060	780	2.42	0.086	0.25	0.32	4.55	7.0
		280	1,310	772	2.45	0.084	0.23	0.30	4.47	6.7
		290	1,610	765	2.47	0.083	0.22	0.29	4.37	6.6
		300	1,950	757	2.50	0.081	0.21	0.28	4.28	6.5
		310	2,350	749	2.53	0.080	0.20	0.27	4.20	6.4
		320	2,820	742	2.56	0.078	0.19	0.26	4.10	6.2
		330	3,350	734	2.59	0.077	0.18	0.25	4.03	6.1

D4.3. Table 3b. Synthetic heat transfer media (no. 9 to 11)

No.	Substance (Trade Name)	Temperature (°C)	Vapor Pressure (mbar)	Density (kg/m^3)	Specific Heat Capacity (kJ/kg K)	Thermal Conductivity (W/mK)	Dynamic viscosity (10^{-3} Ns/m)^2	Kinematic viscosity (10^{-6} m^2/s)	Thermal Diffusivity (10^{-8} m^2/s)	Prandtl Number
9	Finkotherm S 300	−20		914	1.70	0.138	3,199	3,500	8.88	39,410
		0		900	1.81	0.137	396	440	8.47	5,194
		20		886	1.93	0.135	78.40	88.49	7.89	1,121
		40		872	2.02	0.132	33.10	37.96	7.49	506
		60	0.1	858	2.14	0.131	15.40	17.95	7.13	252
		80	0.5	845	2.26	0.129	6.34	7.50	6.75	111
		100	1.6	832	2.37	0.127	4.16	5.00	6.44	77.6
		150	20	795	2.65	0.124	1.59	2.00	5.89	29.4
		200	95	762	2.92	0.119	0.991	1.30	5.35	24.3
		250	310	726	3.19	0.115	0.581	0.80	4.97	16.1
		300	800	693	3.46	0.111	0.416	0.60	4.63	13.0
		330	1,400	670	3.68	0.109	0.335	0.50	4.42	11.3
10	Ucotherm S 15 A	−20		1,047	1.63	0.160	628	600	9.38	6,400
		0		1,031	1.71	0.160	124	120	9.08	1,322
		20		1,015	1.80	0.160	41	40	8.76	457
		40		999	1.87	0.160	18	18	8.56	210
		60		983	1.95	0.159	9.8	10	8.29	121
		80		966	2.02	0.159	6.3	6.5	8.15	79.8
		100		950	2.10	0.159	4.4	4.6	7.97	57.7
		120		934	2.18	0.159	3.1	3.3	7.81	42.3
		140		918	2.26	0.159	2.4	2.6	7.66	33.9
		160		902	2.34	0.158	1.9	2.1	7.49	28.1
		180		885	2.42	0.158	1.6	1.8	7.38	24.4
		200		869	2.50	0.158	1.3	1.5	7.27	20.6
		220		853	2.57	0.158	1.1	1.3	7.21	18.0
11	Ucotherm S 20 A	0		1,050	1.88	0.160	536	510	8.11	6,292
		20		1,098	1.93	0.160	145	140	8.02	1,753
		40		1,020	1.97	0.160	57.1	56	7.98	703
		60		1,002	2.01	0.160	28.1	28	7.94	353
		80		987	2.05	0.160	15.8	16	7.92	202
		100		975	2.13	0.159	10.7	11	7.70	143
		120		955	2.17	0.159	7.64	8	7.69	104

D4.3. Table 3b. Synthetic heat transfer media (no. 11 to 13)

No.	Substance (Trade Name)	Temperature (°C)	Vapor Pressure (mbar)	Density (kg/m³)	Specific Heat Capacity (kJ/kg K)	Thermal Conductivity (W/mK)	Dynamic viscosity (10^{-3} Ns/m)²	Kinematic viscosity (10^{-6} m²/s)	Thermal Diffusivity (10^{-8} m²/s)	Prandtl Number
11	Ucotherm S 20 A (continued)	140		939	2.21	0.159	5.82	6.2	7.68	80.6
		160		929	2.25	0.159	4.27	4.6	7.67	60.8
		180		908	2.29	0.159	3.09	3.4	7.67	44.6
		200		890	2.33	0.159	2.67	3.0	7.68	39.6
		220		873	2.37	0.159	2.36	2.7	7.69	35.8
		240		858	2.42	0.158	2.15	2.5	7.63	33.7
12	Renotherm 350 S	20		890	1.86	0.1023	58.7	66	6.18	1,068
		100		802	2.39	0.0925	1.28	1.60	4.83	33.2
		150		835	2.20	0.0960	3.01	3.60	5.23	68.9
		250		735	2.76	0.0855	0.456	0.62	4.21	14.7
		300		701	2.95	0.0820	0.316	0.45	3.97	11.4
		350		674	3.12	0.0792	0.243	0.36	3.77	9.6
13	Marlotherm SH	0		1,058	1.48	0.133	340	321	8.49	3,779
		20		1,044	1.55	0.131	49	47	8.10	581
		40		1,030	1.62	0.128	17	16.5	7.67	338
		60		1,016	1.70	0.125	8.2	8.1	7.24	112
		80		1,001	1.77	0.123	4.7	4.7	6.94	67.6
		100		987	1.85	0.120	3.1	3.1	6.57	47.2
		120		973	1.92	0.117	2.2	2.3	6.26	36.1
		140	0.1	958	1.99	0.115	1.7	1.8	6.03	29.4
		160	0.5	944	2.07	0.112	1.3	1.4	5.73	24.0
		180	1.7	930	2.15	0.110	1.1	1.2	5.50	21.7
		200	5.0	915	2.22	0.107	0.84	0.92	5.27	17.4
		220	12.0	901	2.29	0.104	0.69	0.77	5.04	15.2
		240	27	887	2.37	0.102	0.58	0.65	4.85	13.5
		260	54	873	2.44	0.099	0.50	0.57	4.65	12.3
		280	98	858	2.52	0.096	0.43	0.50	4.44	11.3
		300	200	844	2.59	0.094	0.38	0.45	4.30	10.5
		320	315	830	2.67	0.091	0.33	0.40	4.11	9.7
		340	560	815	2.74	0.088	0.29	0.36	3.94	9.1
		360	860	801	2.82	0.086	0.26	0.32	3.81	8.5

D4.3. Table 3b. Synthetic heat transfer media (no. 14 to 15)

No.	Substance (Trade Name)	Temperature (°C)	Vapor Pressure (mbar)	Density (kg/m³)	Specific Heat Capacity (kJ/kg K)	Thermal Conductivity (W/mK)	Dynamic viscosity (10^{-3} Ns/m)²	Kinematic viscosity (10^{-6} m²/s)	Thermal Diffusivity (10^{-8} m²/s)	Prandtl Number
14	Marlotherm N	−20		904	1.82	0.137	720	796	8.33	9,556
		0		890	1.89	0.136	160	180	8.09	2,225
		20		877	1.97	0.135	45.6	52.0	7.81	666
		40		863	2.04	0.134	17.3	20.0	7.61	263
		60		850	2.11	0.132	7.99	9.40	7.36	128
		80		836	2.19	0.130	4.43	5.30	7.10	74.6
		100		823	2.26	0.129	2.80	3.40	6.94	49.0
		120		810	2.33	0.127	1.86	2.30	6.73	34.2
		140		796	2.41	0.125	1.43	1.80	6.52	27.6
		160	1	783	2.48	0.124	1.10	1.40	6.39	21.9
		180	4	769	2.55	0.122	0.85	1.10	6.22	17.7
		200	17	755	2.62	0.121	0.66	0.87	6.12	14.2
		220	48	743	2.74	0.119	0.56	0.73	5.93	12.3
		240	115	729	2.77	0.118	0.44	0.60	5.84	10.3
		260	235	716	2.84	0.116	0.36	0.50	5.70	8.77
		280	429	702	2.92	0.114	0.30	0.43	5.56	7.73
		300	716	688	2.99	0.112	0.26	0.38	5.44	6.99
15	Marlotherm X	−60		931	1.73	0.153	6.61	7.10	9.50	74.7
		−40		915	1.72	0.147	3.20	3.50	9.34	37.5
		−20		899	1.73	0.142	1.89	2.10	9.13	23.0
		0		885	1.74	0.137	1.24	1.40	8.90	15.7
		20	0.9	868	1.79	0.132	0.95	1.10	8.50	12.9
		40	3.6	851	1.80	0.126	0.72	0.85	8.23	10.3
		60	12	835	1.85	0.121	0.58	0.69	7.83	8.81
		80	32	819	1.92	0.116	0.46	0.56	7.38	7.59
		100	76	803	1.98	0.111	0.39	0.48	6.98	6.88
		120	161	787	2.06	0.106	0.33	0.42	6.54	6.42
		140	313	769	2.14	0.101	0.28	0.37	6.14	6.03
		160	564	752	2.23	0.095	0.25	0.33	5.67	5.82
		180	954	735	2.32	0.090	0.22	0.30	5.28	5.68
		200	1,600	718	2.41	0.085	0.21	0.29	4.91	5.91
		220	2,500	701	2.50	0.080	0.20	0.28	4.56	6.14

D4.3. Table 3b. Synthetic heat transfer media (no. 15 to 17)

No.	Substance (Trade Name)	Temperature (°C)	Vapor Pressure (mbar)	Density (kg/m^3)	Specific Heat Capacity (kJ/kg K)	Thermal Conductivity (W/mK)	Dynamic viscosity (10^{-3} Ns/m)^2	Kinematic viscosity (10^{-6} m^2/s)	Thermal Diffusivity (10^{-8} m^2/s)	Prandtl Number
15	Marlotherm X (continued)	240	3,800	684	2.59	0.075	0.18	0.27	4.23	6.38
		260	5,500	667	2.68	0.069	0.17	0.26	3.86	6.74
		280	7,900	650	2.77	0.064	0.16	0.25	3.55	7.04
		300	10,900	633	2.86	0.059	0.15	0.24	3.26	7.36
16	Cassida Fluid HT 32	0		835	2.07	0.150	182	218	8.68	2,512
		20		824	2.12	0.148	57.7	70.0	8.47	826
		60		799	2.29	0.146	12.0	15.0	7.98	188
		100		774	2.42	0.144	4.41	5.70	7.69	74.1
		150		742	2.55	0.141	1.99	2.68	7.45	36.0
		200		713	2.79	0.130	1.10	1.54	6.99	22.0
		250		683	2.92	0.137	0.70	1.03	6.87	15.0
		300		652	3.16	0.135	0.50	0.76	6.55	11.6
		340		628	3.28	0.134	0.39	0.62	6.51	9.58
17	Therminol D 12	−85		835	1.64	0.124	296	354	9.06	3,909
		−60		818	1.76	0.121	23.9	29.2	8.40	347
		−40		804	1.85	0.118	7.06	8.78	7.93	110.7
		−20		790	1.94	0.116	3.23	4.09	7.57	54.2
		0		776	2.03	0.113	1.93	2.49	7.17	34.9
		20	1	762	2.11	0.110	1.30	1.70	6.84	24.8
		40	3	748	2.20	0.107	0.93	1.24	6.50	18.5
		60	9	733	2.28	0.104	0.70	0.96	6.22	15.4
		80	23	717	2.36	0.100	0.56	0.78	5.91	13.2
		100	60	702	2.45	0.096	0.45	0.64	5.58	11.5
		120	124	687	2.53	0.093	0.38	0.55	5.35	10.3
		140	244	670	2.61	0.089	0.31	0.47	5.09	9.23
		160	443	653	2.69	0.085	0.27	0.41	4.84	8.47
		180	754	635	2.77	0.081	0.23	0.36	4.61	7.81
		200	1,223	615	2.86	0.076	0.20	0.33	4.32	7.64
		220	1,867	596	2.93	0.072	0.17	0.29	4.12	7.04
		240	2,768	574	3.01	0.067	0.15	0.27	3.88	6.96
		260	3,962	550	3.10	0.063	0.14	0.25	3.70	6.76

D4.3. Table 3b. Synthetic heat transfer media (no. 18 to 19)

No.	Substance (Trade Name)	Temperature (°C)	Vapor Pressure (mbar)	Density (kg/m³)	Specific Heat Capacity (kJ/kg K)	Thermal Conductivity (W/mK)	Dynamic viscosity (10^{-3} Ns/m)²	Kinematic viscosity (10^{-6} m²/s)	Thermal Diffusivity (10^{-8} m²/s)	Prandtl Number
18	Therminol ADX 10	−50		904	1.64	0.133	784	867	8.97	9,666
		−40		898	1.68	0.131	251	279	8.68	3,214
		−20		884	1.76	0.129	46	52.2	8.29	630
		0		871	1.84	0.126	14.4	16.5	7.86	210
		20		857	1.91	0.124	6.28	7.33	7.58	96.7
		40		843	1.99	0.121	3.40	4.03	7.21	55.9
		60		829	2.07	0.119	2.13	2.57	6.93	37.1
		80		815	2.14	0.116	1.47	1.80	6.65	27.1
		100		801	2.21	0.113	1.09	1.36	6.38	21.3
		150	20	765	2.39	0.106	0.62	0.80	5.80	13.8
		200	80	727	2.56	0.098	0.40	0.55	5.32	10.3
		220	160	711	2.62	0.095	0.34	0.48	5.10	9.41
		240	280	694	2.69	0.092	0.29	0.42	4.93	8.52
		260	470	677	2.75	0.088	0.26	0.38	4.78	7.95
		280	750	659	2.81	0.085	0.22	0.33	4.59	7.19
		290	940	650	2.85	0.083	0.21	0.32	4.48	7.14
19	Therminol RD	−30		905	1.61	0.124	561	619	8.51	2,092
		−20		897	1.65	0.123	160	178	8.31	2,142
		0		883	1.73	0.121	30.2	34.2	7.92	432
		20		869	1.81	0.119	10.5	12.1	7.57	160
		40		855	1.89	0.117	5.06	5.91	7.24	81.5
		60		841	1.97	0.115	2.95	3.51	6.91	50.7
		80		827	2.06	0.113	1.95	2.36	6.63	36.2
		100	1	813	2.14	0.111	1.40	1.72	6.38	26.6
		120	3	799	2.22	0.109	1.07	1.34	6.15	21.2
		140	9	785	2.30	0.107	0.85	1.09	5.93	18.4
		160	20	772	2.38	0.105	0.70	0.91	5.71	15.9
		180	44	758	2.46	0.103	0.60	0.79	5.52	14.3
		200	90	744	2.54	0.101	0.51	0.69	5.34	12.9
		220	174	731	2.62	0.099	0.45	0.62	5.15	12.0
		240	319	717	2.71	0.097	0.40	0.56	4.99	11.2
		260	559	704	2.79	0.095	0.36	0.51	4.84	10.5
		270	728	697	2.83	0.094	0.34	0.49	4.77	10.3

D4.3. Table 3b. Synthetic heat transfer media (no. 20 to 21)

No.	Substance (Trade Name)	Temperature (°C)	Vapor Pressure (mbar)	Density (kg/m^3)	Specific Heat Capacity (kJ/kg K)	Thermal Conductivity (W/mK)	Dynamic viscosity (10^{-3} Ns/m)^2	Kinematic viscosity (10^{-6} m^2/s)	Thermal Diffusivity (10^{-8} m^2/s)	Prandtl Number
20	Therminol ALD	−10		892	1.85	0.116	2,797	3,040	7.03	43,243
		0		884	1.88	0.115	631	714	6.92	10,318
		20		870	1.94	0.113	88.7	102	6.70	1,522
		40		856	2.01	0.112	25.2	29.4	6.51	452
		60		842	2.07	0.110	10.4	12.35	6.31	196
		80		828	2.13	0.109	5.41	6.53	6.18	106
		100		814	2.20	0.107	3.26	4.01	5.97	67.2
		150	3	779	2.36	0.103	1.36	1.74	5.60	31.1
		200	20	746	2.53	0.099	0.77	1.03	5.25	19.6
		250	90	713	2.69	0.095	0.51	0.72	4.95	14.5
		300	380	681	2.86	0.091	0.37	0.55	4.67	11.8
		310	490	674	2.90	0.090	0.36	0.53	4.60	11.5
21	Therminol SP/55	−20		916	1.75	0.141	2,600	2,840	8.80	32,287
		0		903	1.83	0.139	270	300	8.41	3,566
		20		890	1.90	0.137	67	75	8.10	926
		40	1	876	1.98	0.135	23	26	7.78	334
		60	2	863	2.05	0.133	11	13	7.52	173
		80	3	849	2.12	0.131	5.8	6.8	7.28	93.4
		100	5	836	2.20	0.129	3.7	4.4	7.01	62.7
		120	7	823	2.28	0.128	2.6	3.1	6.82	45.4
		140	12	809	2.35	0.126	1.9	2.3	6.63	34.7
		160	18	796	2.43	0.124	1.4	1.8	6.41	28.1
		180	29	782	2.50	0.122	1.2	1.5	6.24	24.0
		200	45	769	2.57	0.120	0.92	1.2	6.07	19.8
		220	73	756	2.65	0.118	0.77	1.02	5.89	17.3
		240	114	742	2.73	0.116	0.66	0.89	5.73	15.5
		260	180	729	2.81	0.114	0.57	0.78	5.57	14.0
		280	282	715	2.88	0.113	0.50	0.70	5.49	12.8
		300	450	702	2.96	0.111	0.46	0.65	5.34	12.2
		305	540	699	2.97	0.110	0.43	0.62	5.30	11.7

D4.3. Table 3b. Synthetic heat transfer media (no. 22 to 23)

No.	Substance (Trade Name)	Temperature (°C)	Vapor Pressure (mbar)	Density (kg/m³)	Specific Heat Capacity (kJ/kg K)	Thermal Conductivity (W/mK)	Dynamic viscosity (10^{-3} Ns/m)²	Kinematic viscosity (10^{-6} m²/s)	Thermal Diffusivity (10^{-8} m²/s)	Prandtl Number
22	Therminol 59	−50		1,025	1.46	0.126	2,504	2,443	8.42	29,014
		−40		1,017	1.49	0.125	454	446	8.25	5,407
		−20		1,003	1.55	0.125	53.3	53.1	8.04	660
		0		989	1.62	0.123	15.3	15.5	7.68	201.9
		20		974	1.68	0.121	6.86	7.04	7.39	95.2
		40		960	1.75	0.120	3.88	4.04	7.14	56.6
		60		945	1.81	0.118	2.50	2.65	6.90	38.4
		80		931	1.88	0.117	1.77	1.90	6.68	28.4
		100	3.9	916	1.94	0.115	1.32	1.44	6.47	22.3
		150	30	878	2.11	0.110	0.74	0.84	5.94	14.1
		200	130	840	2.27	0.104	0.48	0.57	5.45	10.4
		250	450	799	2.44	0.098	0.34	0.42	5.03	8.36
		300	1,240	755	2.62	0.091	0.25	0.33	4.60	7.17
		310	1,480	745	2.66	0.090	0.24	0.32	4.54	7.05
		320	1,760	736	2.69	0.088	0.23	0.31	4.44	6.97
23	Therminol 66	0		1,021	1.53	0.121	1,020	1,000	7.75	12,903
		20		1,008	1.60	0.120	100.6	100	7.44	1,344
		40		994	1.67	0.119	26.0	26.2	7.17	365.4
		60		980	1.74	0.118	11.3	11.5	6.92	166.2
		80		966	1.80	0.117	5.80	6.0	6.73	89.2
		100		953	1.88	0.115	3.52	3.7	6.42	57.6
		150	3	920	2.05	0.111	1.51	1.65	5.88	28.1
		200	25	885	2.22	0.107	0.87	0.99	5.45	18.2
		250	105	852	2.40	0.102	0.59	0.69	4.99	13.8
		300	340	818	2.58	0.096	0.43	0.53	4.55	11.65
		350	930	785	2.75	0.091	0.33	4.22	9.95	9.95
		370	1,360	768	2.83	0.087	0.31	0.40	4.00	9.99

D4.3. Table 3b. Synthetic heat transfer media (no. 24 to 25)

No.	Substance (Trade Name)	Temperature (°C)	Vapor Pressure (mbar)	Density (kg/m³)	Specific Heat Capacity (kJ/kg K)	Thermal Conductivity (W/mK)	Dynamic viscosity (10^{-3} Ns/m)²	Kinematic viscosity (10^{-6} m²/s)	Thermal Diffusivity (10^{-8} m²/s)	Prandtl Number
24	Therminol 68	−20		1,056	1.49	0.127	941	891	8.02	11,113
		0		1,042	1.56	0.125	134	129	7.69	1677.5
		20		1,027	1.62	0.123	65.2	34.7	7.39	469.4
		40	0.1	1,013	1.68	0.122	13.9	13.7	7.13	192.2
		60	0.3	998	1.75	0.120	6.94	6.95	6.87	100.4
		80	0.8	984	1.82	0.119	4.07	4.13	6.64	61.7
		100	2.2	970	1.88	0.117	2.66	2.74	6.42	42.1
		150	16.7	934	2.04	0.113	1.24	1.33	5.93	22.4
		200	82.4	898	2.20	0.109	0.73	0.81	5.52	14.7
		250	299.6	862	2.36	0.105	0.48	0.55	5.16	10.66
		300	869.4	826	2.53	0.101	0.34	0.41	4.83	8.49
		320	1,266	811	2.59	0.100	0.30	0.37	4.76	7.77
		340	1,799	797	2.65	0.098	0.26	0.33	4.62	7.14
		360	2,501	782	2.72	0.096	0.24	0.30	4.51	6.65
		370	2,925	775	2.75	0.096	0.23	0.29	4.50	6.44
25	Therminol 72	−20		1,115	1.46	0.144	208.6	187	8.84	2,116
		0		1,097	1.51	0.142	40.8	37.15	8.57	434
		20		1,079	1.56	0.139	13.6	12.6	8.26	153
		40		1,061	1.62	0.137	6.3	5.90	7.97	74.0
		60		1,043	1.67	0.134	3.5	3.36	7.69	44.2
		80		1,025	1.72	0.132	2.23	2.18	7.49	29.4
		100		1,007	1.78	0.130	1.56	1.55	7.25	22.1
		120		989	1.83	0.127	1.16	1.17	7.02	17.1
		140		970	1.88	0.125	0.89	0.92	6.85	13.4
		160		952	1.94	0.122	0.70	0.74	6.61	11.2
		180		934	1.99	0.120	0.57	0.61	6.46	9.44
		200	330	916	2.04	0.118	0.48	0.52	6.31	8.24
		220	450	898	2.10	0.115	0.40	0.44	6.10	7.21
		240	620	880	2.15	0.113	0.34	0.39	5.97	6.53

D4.3. Table 3b. Synthetic heat transfer media (no. 25 to 26)

No.	Substance (Trade Name)	Temperature (°C)	Vapor Pressure (mbar)	Density (kg/m^3)	Specific Heat Capacity (kJ/kg K)	Thermal Conductivity (W/mK)	Dynamic viscosity (10^{-3} Ns/m)^2	Kinematic viscosity (10^{-6} m^2/s)	Thermal Diffusivity (10^{-8} m^2/s)	Prandtl Number
25	Therminol 72 (continued)	260	860	862	2.20	0.110	0.29	0.34	5.80	5.86
		280	1,190	844	2.26	0.108	0.26	0.31	5.66	5.48
		300	1,640	825	2.31	0.106	0.23	0.28	5.56	5.04
		320	2,260	807	2.36	0.103	0.20	0.25	5.41	4.62
		340	3,120	789	2.42	0.101	0.18	0.23	5.29	4.35
		360	4,300	771	2.47	0.098	0.17	0.22	5.15	4.27
		380	5,930	753	2.52	0.096	0.15	0.20	5.06	3.96
26	Calflo AF	−10		866	1.68	0.139	628	726	9.56	7,592
		0		861	1.72	0.138	195	226	9.32	2,425
		20		851	1.79	0.137	55.3	65	8.99	723
		40		841	1.87	0.136	25.8	30.7	8.65	355
		60		831	1.95	0.137	12.0	14.4	8.33	173
		80		821	2.03	0.134	6.9	8.4	8.04	104
		100	0.1	811	2.10	0.133	4.5	5.5	7.81	70.4
		120	0.2	801	2.18	0.132	3.1	3.9	7.56	51.6
		140	0.5	791	2.26	0.130	2.3	2.9	7.27	39.9
		160	1.2	781	2.33	0.129	1.8	2.3	7.09	32.4
		180	2.6	771	2.41	0.128	1.4	1.8	6.89	26.1
		200	5.3	761	2.49	0.127	1.1	1.5	6.70	22.4
		220	10	751	2.57	0.126	0.98	1.3	6.53	19.9
		240	19	741	2.64	0.125	0.79	1.07	6.39	16.7
		260	33	731	2.72	0.124	0.68	0.93	6.24	14.9
		280	56	721	2.8	0.123	0.58	0.81	6.09	13.3
		300	91	711	2.88	0.122	0.50	0.71	5.96	11.9
		320	144	701	2.95	0.121	0.44	0.63	5.86	10.8
		340	220	691	3.03	0.120	0.39	0.56	5.73	9.77

D4.3. Table 3b. Synthetic heat transfer media (no. 27 to 28)

No.	Substance (Trade Name)	Temperature (°C)	Vapor Pressure (mbar)	Density (kg/m³)	Specific Heat Capacity (kJ/kg K)	Thermal Conductivity (W/mK)	Dynamic viscosity (10^{-3} Ns/m)²	Kinematic viscosity (10^{-6} m²/s)	Thermal Diffusivity (10^{-8} m²/s)	Prandtl Number
27	Ucotherm FG-8	−45	20	872	1.85	0.136	1,372	1,573	8.44	18,633
		−40	90	869	1.86	0.135	708.8	815.7	8.34	9,786
		−20	150	856	1.94	0.133	101.3	118.3	8.03	1,474
		0		843	2.00	0.131	28.42	33.72	7.75	435
		20		830	2.08	0.129	11.58	13.96	7.48	187
		40		816	2.15	0.126	5.93	7.27	7.18	101
		60		803	2.22	0.124	3.53	4.39	6.95	63
		80		790	2.29	0.122	2.33	2.95	6.74	44
		100		777	2.36	0.119	1.65	2.13	6.48	33
		150		743	2.54	0.113	0.87	1.17	5.98	20
		200		708	2.72	0.106	0.55	0.78	5.5	14
		250		672	2.90	0.099	0.39	0.58	5.09	11
		270		656	2.97	0.096	0.34	0.53	4.93	10
28	Ucotherm FG-33	−10	10	855	2.07	0.156	600.4	702.2	8.81	7,966
		0	60	849	2.11	0.154	254.2	299.5	8.60	3,483
		20	160	836	2.17	0.150	68.87	82.35	8.27	996
		40		824	2.23	0.146	26.71	32.42	7.95	408
		60		811	2.30	0.143	13.00	16.02	7.66	209
		80		799	2.36	0.139	7.37	9.23	7.37	125
		100		786	2.43	0.137	4.66	5.93	7.17	83
		150		755	2.59	0.131	2.00	2.66	6.70	40
		200		723	2.75	0.128	1.12	1.55	6.44	24
		250		690	2.91	0.127	0.73	1.05	6.32	17
		300		657	3.07	0.128	0.52	0.79	6.35	13
		320		644	3.14	0.129	0.46	0.72	6.38	11

D4.3. Table 3b. Synthetic heat transfer media (no. 29 to 30)

No.	Substance (Trade Name)	Temperature (°C)	Vapor Pressure (mbar)	Density (kg/m³)	Specific Heat Capacity (kJ/kg K)	Thermal Conductivity (W/mK)	Dynamic viscosity (10^{-3} Ns/m)²	Kinematic viscosity (10^{-6} m²/s)	Thermal Diffusivity (10^{-8} m²/s)	Prandtl Number
29	Thenninol VLT	−120	0.017	866	1.35	0.131	69.5	80.3	11.2	718
		−100	0.18	849	1.44	0.128	16.2	19.0	10.4	182
		−80	1.2	833	1.53	0.124	6.1	7.32	9.75	75
		−60	5.4	816	1.62	0.120	3.06	3.75	9.12	41
		−40	19	799	1.70	0.116	1.83	2.28	8.55	27
		−20	54.5	783	1.79	0.112	1.22	1.56	8.03	19
		0	134	766	1.87	0.108	0.88	1.14	7.55	15
		20	291	748	1.96	0.104	0.66	0.88	7.1	12
		40	572	731	2.04	0.099	0.52	0.71	6.68	11
		60	1,037	713	2.12	0.095	0.41	0.58	6.29	9
		80	3,492	695	2.20	0.090	0.34	0.48	5.91	8
		100	6,279	676	2.29	0.086	0.28	0.41	5.55	7
		150		626	2.50	0.073	0.18	0.28	4.69	6
		180		592	2.63	0.065	0.14	0.23	4.19	5
30	Calflo FG	−10		870	1.78	0.139	919	1,057	8.98	11,744
		0		863	1.82	0.138	357	414	8.79	4,714
		20		850	1.88	0.137	82.8	97.4	8.57	1,136
		40		836	1.95	0.136	28.6	34.2	8.34	410
		60		823	2.02	0.135	13.4	16.3	8.12	201
		80		809	2.08	0.134	7.43	9.18	7.96	115
		100		796	2.15	0.133	4.63	5.81	7.71	75.3
		120		782	2.22	0.132	3.13	4.00	7.55	53.1
		140		769	2.29	0.131	2.26	2.94	7.38	39.8
		160		756	2.35	0.130	1.71	2.27	7.26	31.2
		180		742	2.42	0.129	1.35	1.81	7.13	25.4
		200		729	2.49	0.128	1.09	1.50	7.00	21.4
		220		715	2.56	0.127	0.91	1.27	6.88	18.4

D4.3. Table 3b. Synthetic heat transfer media (no. 30 to 31)

No.	Substance (Trade Name)	Temperature (°C)	Vapor Pressure (mbar)	Density (kg/m³)	Specific Heat Capacity (kJ/kg K)	Thermal Conductivity (W/mK)	Dynamic viscosity (10^{-3} Ns/m)²	Kinematic viscosity (10^{-6} m²/s)	Thermal Diffusivity (10^{-8} m²/s)	Prandtl Number
30	Calflo FG (continued)	240	20	702	2.62	0.125	0.77	1.10	6.80	16.1
		260	30	688	2.69	0.124	0.66	0.96	6.70	14.4
		280	50	675	2.76	0.123	0.58	0.86	6.60	13.0
		300	90	662	2.82	0.122	0.52	0.78	6.54	11.9
		320	160	648	2.89	0.121	0.46	0.71	6.46	11.0
		340	260	635	2.96	0.120	0.42	0.66	6.38	10.3
31	Calflo HTF	−10		873	1.81	0.140	799	915	8.86	10,328
		0		868	1.84	0.139	239	275	8.70	3,160
		20		858	1.91	0.138	65.6	76.5	8.42	909
		40		848	1.97	0.137	30.0	35.4	8.20	432
		60		837	2.04	0.136	13.6	16.3	7.96	205
		80		827	2.11	0.135	7.8	9.4	7.74	121
		100		817	2.17	0.134	5.1	6.2	7.56	82.0
		120		807	2.24	0.133	3.6	4.4	7.36	59.8
		140	0.3	797	2.30	0.131	2.6	3.2	7.15	44.8
		160	0.8	787	2.37	0.130	2.0	2.5	6.97	35.9
		180	1.8	776	2.43	0.129	1.6	2.0	6.84	29.2
		200	3.9	766	2.50	0.128	1.2	1.6	6.68	23.9
		220	7.7	756	2.57	0.127	1.1	1.4	6.54	21.4
		240	15	746	2.63	0.126	0.90	1.2	6.42	18.7
		260	27	736	2.70	0.125	0.74	1.0	6.29	15.9
		280	46	726	2.76	0.124	0.63	0.87	6.19	14.1
		300	78	716	2.83	0.123	0.54	0.76	6.07	12.5
		320	126	705	2.89	0.122	0.47	0.67	5.99	11.2
		340	197	695	2.96	0.121	0.42	0.60	5.88	10.2

D4.3. Table 4a. Synthetic heat transfer media; mixtures (survey, no. 1 to 3)

1	2	3	4	5	6	7	8	9	10	11	12	13	14	15	19	20	21	22
No.	Trade name	Structure	Producer	Pour point/ Boiling point (°C)	Application range min./max. (°C)	Vapor pressure (mbar)	Density (kg/m³)	Specific heat capacity (kJ/kg K)	Kinematic viscosity (mm²/s)	Thermal conduc-tivity (W/m K)	Application limits		Flash Point	Auto Ignition temp. (°C)	Explosive limit volume content (°C)	Explosive limit volume content (%)	Possible applica-tion (kg/ kmol)	Former product/ remark
											Lower: Filling and start-up (°C)	Upper: Max. film temper-ature (°C)						
1	Diphyl	Eutectic mixture of 26.5% diphenyl and 73.5% diphenyloxide (mass content)	Bayer/ Lanxess	12.3[a]	20	–	1,062	1.549	4.12	0.138		410	115[b]	615[b]	108.5 ≙ 1.0	165.8	C	water content <200 mg/kg
				257	400	11,100	717	2.575	0.199	0.082	13				138.5 ≙ 3.5			
2	Dowtherm A	Eutectic mixture of 26.5% diphenyl and 73.5% diphenyloxide (mass content)	Dow	12.0[c]	15	–	1,066	1.55	4.05	0.140		430	113	615		166	C	
				257.1[d]	400	10,640	680	2.701	0.19	0.077	13							
3	Therminol VP 1	Eutectic mixture of 26.5% diphenyl and 73.5% diphenyloxide (mass content)	Solutia	12	12	–	1,071	1.52	5.12	0,137	13	430	124	621		166	c	Santotherm VP 1, Monsanto
				257	400	10,900	694	2.62	0.21	0.076								
4	Dowtherm J	Mixture of isomers of alkylated aromatic compounds	Dow	−80	−80	–	935	1.59	10.65	0.150	<−84	340	58	420	u. 0.8	134 m	C	properties see table 3b, No. 6″
				181	315	11,930	570	3.01	0.28	0.065	−55				o.9.0		B	

D4.3. Table 4a. Synthetic heat transfer media; mixtures (survey, no. 4 to 7)

1	2	3	4	5	6	7	8	9	10	11	12	13	14	15	19	20	21	22
No.	Trade name	Structure	Producer	Pour point/ Boiling point (°C)	Application range min./max. (°C)	Vapor pressure (mbar)	Density (kg/m³)	Specific heat capacity (kJ/kg K)	Kinematic viscosity (mm²/s)	Thermal conduc-tivity (W/m K)	Application limits		Flash Point	Auto Ignition temp. (°C)	Explosive limit volume content (°C)	Explosive limit volume content (%)	Possible applica-tion (kg/ kmol)	Former product/ remark
											Lower: Filling and start-up (°C)	Upper: Max. film temper-ature (°C)						
5	Marlotherm LH	Mixture of isomeric benzyl toluol	SASOL Germany	−30[e]	−30	–	1,034	1.45	40	0.137	−30	380	130[f]	450	123 ≙ 0.9	182	C	previous product: Marlotherm L
				280	360	4,800	703	2.75	0.26	0.092	10				178 ≙ 6.8			
6	Therminol LT	Alkyl substituted aromatic compounds	Solutia	−75	−73	–	938	1.45	10	0.142	−73	340	58	429		134	C	Santotherm MCS 2313. Monsanto
				185	315	15,000	561	2.98	0.19	0.064	−55							
7	Therminol VP-3	Cyclo-hexyl-benzol and bi-cyclo-hexyl	Solutia	2.4	2.4	–	942	1.52	5	0.120	–	357	104	351				
				243	330	6,930	641	3.00	0.25	0.076	2.4							

[a]Solidification point
[b]Without DIN indication
[c]Freeze point
[d]Boiling point
[e]Setting point acc. DIN 51 583
[f]Flash point DIN 51 758

D4.3. Table 4b. Synthetic heat transfer media; mixtures. Heat transfer in liquid and vapor phase (no. 1 to 2)

No.	Substance (Trade name)	Temperature (°C)	Vapor pressure (bar)	Density		Liquid					Vapor				
				Liquid (kg/m³)	Vapor (kg/m³)	Specific heat capacity (kJ/kg K)	Thermal conductivity (W/m K)	Dynamic viscosity (10^{-3} Ns/m²)	Kinematic viscosity (10^{-6} m²/s)	Thermal diffusivity (10^{-8}m²/s)	Prandtl number	Specific enthalpy		Enthalpy of vaporization (kJ/kg)	Dynamic viscosity (10^{-3} Ns/m²)
												kJ/kg	kJ/kg		
1	Diphyl	20	–	1,062	–	1.55	0.138	4.38	4.12	8.38	49.2	12.14	381.6	369.5	
		40	–	1,046	–	1.65	0.136	2.57	2.46	7.88	31.2	45.1	407.9	362.8	
		60	0.0004	1,029	0.0045	1.74	0.132	1.76	1.71	7.37	23.2	78.5	435.5	357.0	
		80	0.0016	1,013	0.0133	1.81	0.130	1.31	1.29	7.09	18.2	113.7	461.9	348.2	
		100	0.0049	996	0.0347	1.87	0.126	1.01	1.01	6.77	14.9	149.2	493.2	344.0	
		120	0.0134	979	0.0812	1.92	0.124	0.798	0.815	6.60	12.3	186.0	523.7	337.7	
		140	0.0310	962	0.1727	1.96	0.121	0.647	0.673	6.42	10.5	224.0	555.1	331.1	
		160	0.0666	945	0.3406	2.00	0.118	0.541	0.572	6.24	9.17	262.5	587.3	324.8	
		180	0.132	927	0.6301	2.03	0.115	0.461	0.497	6.11	8.13	302.6	620.3	317.7	
		200	0.242	909	1.0977	2.06	0.111	0.399	0.439	5.93	7.40	343.2	653.8	310.6	
		220	0.418	892	1.8157	2.10	0.109	0.347	0.389	5.82	6.68	385.0	688.0	303.0	
		240	0.686	873	2.8827	2.13	0.106	0.304	0.348	5.70	6.11	427.6	722.7	295.1	
		260	1.08	855	4.4000	2.17	0.103	0.270	0.316	5.55	5.69	471.1	757.8	286.7	
		280	1.62	836	6.5177	2.22	0.100	0.238	0.285	5.39	5.29	515.8	793.8	278.0	
		300	2.37	818	9.3397	2.26	0.097	0.210	0.257	5.25	4.90	561.4	829.8	268.4	
		320	3.35	798	13.16	2.31	0.094	0.189	0.237	5.10	4.65	608.2	866.2	258.0	
		340	4.63	779	17.98	2.37	0.092	0.172	0.221	4.98	4.44	655.4	902.0	246.6	
		360	6.24	759	24.23	2.43	0.088	0.159	0.209	4.77	4.38	704.3	938.0	233.7	
		380	8.25	738	32.19	2.50	0.086	0.151	0.205	4.66	4.40	753.6	973.1	219.5	
		400	10.7	717	42.35	2.57	0.082	0.143	0.199	4.45	4.47	804.2	1007.3	203.1	
2	Dowtherm A	20		1,060	0	1.57	0.140	4.29	4.05	8.40	48.2	12.6	1.573	402.9	–
		40		1,044	0	1.63	0.138	2.56	2.45	8.10	30.3	44.4	1.632	392.9	–
		60		1,028	3	1.69	0.135	1.72	1.67	7.77	21.5	77.8	1.690	383.3	–
		80		1,012	10	1.74	0.133	1.25	1.24	7.53	16.4	112.1	1.745	373.6	–
		100	0.01	995	27	1.80	0.131	0.97	0.97	7.32	13.3	147.3	1.799	364.8	–
		120	0.01	978	67	1.85	0.128	0.77	0.79	7.06	11.2	184.1	1.854	356.1	–

D4.3. Table 4b. Synthetic heat transfer media; mixtures. Heat transfer in liquid and vapor phase (no. 2 to 3)

No.	Substance (Trade name)	Temperature (°C)	Vapor pressure (bar)	Density		Liquid					Vapor				
				Liquid (kg/m³)	Vapor (kg/m³)	Specific heat capacity (kJ/kg K)	Thermal conductivity (W/m K)	Dynamic viscosity (10^{-3} Ns/m²)	Kinematic viscosity (10^{-6} m²/s)	Thermal diffusivity (10^{-8}m²/s)	Prandtl number	Specific enthalpy		Enthalpy of vaporization (kJ/kg)	Dynamic viscosity (10^{-3} Ns/m²)
												kJ/kg	kJ/kg		
2	Dowtherm A (continued)	140	0.03	961	151	1.91	0.126	0.64	0.67	6.87	9.7	221.8	1.908	347.3	–
		160	0.07	943	306	1.97	0.124	0.53	0.56	6.69	8.4	260.7	1.966	338.9	–
		180	0.13	925	579	2.02	0.121	0.46	0.50	6.47	7.7	300.4	2.021	330.1	–
		200	0.25	907	1,025	2.08	0.119	0.39	0.43	6.32	6.8	341.4	2.075	321.7	–
		220	0.43	888	1,717	2.13	0.117	0.34	0.38	6.17	6.2	383.3	2.134	313.4	–
		240	0.70	869	2,742	2.19	0.114	0.30	0.35	6.00	5.8	426.8	2.188	304.2	–
		260	1.10	849	4,194	2.25	0.112	0.27	0.32	5.86	5.4	471.1	2.251	295.0	–
		280	1.66	828	6,210	2.31	0.110	0.24	0.29	5.75	5.0	516.7	2.310	284.9	–
		300	2.43	807	8,911	2.37	0.107	0.21	0.26	5.59	4.7	563.6	2.372	274.1	–
		320	3.43	784	12,480	2.44	0.105	0.19	0.24	5.50	4.4	599.1	2.435	262.3	–
		340	4.72	761	17,120	2.49	0.102	0.17	0.22	5.39	4.1	660.7	2.485	250.2	–
		360	6.35	736	21,300	2.53	0.100	0.15	0.20	5.37	3.8	711.3	2.531	236.8	–
		380	8.37	709	30,870	2.58	0.098	0.14	0.20	5.35	3.7	762.7	2.582	222.6	–
		400	10.84	680	40,980	2.66	0.095	0.13	0.19	5.26	3.6	815.5	2.657	206.3	–
		420	13.81	648	54,510	2.77	0.093	0.11	0.17	5.17	3.3	870.3	2.774	187.4	–
3	Therminol VP 1	20	–	1,061	–	1.562	0.139	4.75	4.48	8.39	53.4	12.14	391.0	385.6	–
		40	–	1,046	–	1.612	0.137	2.95	2.82	8.12	34.7	43.12	422.9	377.2	–
		60	0.0005	1,030	–	1.666	0.134	1.90	1.84	7.81	25.6	77.87	448.8	370.9	–
		80	0.0016	1,016	–	1.721	0.131	1.40	1.38	7.49	18.4	110.1	476.9	364.7	–
		100	0.0069	998	–	1.775	0.128	0.99	0.99	7.23	13.7	146.5	505.3	358.0	–
		150	0.0441	957	–	1.913	0.121	0.56	0.59	6.61	8.93	242.0	579.9	340.8	–
		200	0.239	913	–	2.047	0.114	0.38	0.42	6.10	6.89	342.5	661.9	322.8	–
		250	0.865	866	–	2.186	0.107	0.272	0.31	5.65	5.49	446.3	749.4	302.7	–
		300	2.405	812	–	2.319	0.099	0.204	0.25	5.26	4.75	556.8	842.0	280.5	–
		350	5.476	755	–	2.453	0.092	0.163	0.22	4.97	4.43	681.6	932.8	253.3	–
		400	10.913	688	–	2.587	0.085	0.140	0.20	4.78	4.18	807.6	1,025	218.6	–

D4.3. Table 4b. Synthetic heat transfer media; mixtures. Heat transfer in liquid and vapor phase (no. 4 to 6)

No.	Substance (Trade name)	Temperature (°C)	Vapor pressure (bar)	Density		Liquid					Vapor				
				Liquid (kg/m³)	Vapor (kg/m³)	Specific heat capacity (kJ/kg K)	Thermal conductivity (W/m K)	Dynamic viscosity (10^{-3} Ns/m²)	Kinematic viscosity (10^{-6} m²/s)	Thermal diffusivity (10^{-8}m²/s)	Prandtl number	Specific enthalpy		Enthalpy of vaporization (kJ/kg)	Dynamic viscosity (10^{-3} Ns/m²)
												kJ/kg	kJ/kg		
4	Therminol VP-3	2,4	0.006	9.42	0.00004	1.52	0.120	5.00	5.31	8.33	64	−3.1	531.1	534.2	0.0067
		20	0.03	933	0.0002	1.60	0.117	2.94	3.15	7.86	40	24.4	550.7	526.3	0.0071
		40	0.15	923	0.0009	1.70	0.115	1.87	2.03	7.37	28	57.4	574.7	517.3	0.0076
		60	0.58	911	0.0034	1.79	0.112	1.33	1.46	6.94	21	92.3	600.3	508.0	0.0081
		80	1.94	899	0.0107	1.88	0.110	1.02	1.13	6.55	17	128.9	627.7	498.8	0.0087
		100	5.7	885	0.0296	1.96	0.107	0.82	0.92	6.2	15	167.3	656.7	489.4	0.0091
		150	52.7	847	0.242	2.16	0.101	0.54	0.64	5.46	12	270.2	736.2	466.0	0.0104
		200	300	803	1.24	2.34	0.094	0.38	0.48	4.88	10	382.6	825.2	442.6	0.0117
		250	1,220	750	4.6	2.52	0.087	0.28	0.37	4.45	8	503.9	922.4	418.5	0.0129
		300	3,820	687	13.7	2.75	0.080	0.20	0.29	4.13	7	634.9	1,026	391.1	0.0141
		330	6,930	641	24.5	3.00	0.076	0.16	0.25	4.03	6	720.7	1,090	369.3	0.0148
5	Dowtherm J	s. Tab. 8 b, Nr.8													
6	Marlotherm LH	−20	–	1,026	–	1.48	0.136	17	17	8.96	190	30.3	–	–	
		0	–	1,010	–	1.55	0.134	8.4	8.3	8.56	97	0	–	–	
		20	–	996	–	1.62	0.132	4.0	4.0	8.18	48.9	31.7	–	–	
		40	–	980	–	1.68	0.129	2.5	2.6	7.84	33.2	64.6	–	–	
		60	–	966	–	1.75	0.127	1.8	1.9	7.51	25.3	98.9	–	–	
		80	–	950	–	1.82	0.125	1.4	1.5	7.23	20.7	134.7	–	–	
		100	0.002	936	0.014	1.88	0.122	1.0	1.1	6.93	15.9	171.7	513	341	
		150	0.022	898	0.141	2.05	0.116	0.61	0.68	6.30	10.8	270.1	598	328	
		200	0.131	856	0.68	2.22	0.111	0.40	0.47	5.84	8.05	376.7	695	318	
		250	0.526	813	2.38	2.38	0.105	0.31	0.38	5.43	7.00	491.9	803	311	
		300	1.62	766	6.16	2.55	0.099	0.26	0.30	5.07	5.91	615.4	920	305	
		320	2.39	747	8.94	2.62	0.097	0.21	0.28	4.96	5.65	667.1	970	303	
		340	3.44	726	12.0	2.69	0.095	0.20	0.27	4.86	5.55	720.2	1,021	301	
		360	4.83	703	15.3	2.75	0.092	0.18	0.26	4.76	5.46	774.6	1,074	299	

D4.3. Table 4b. Synthetic heat transfer media; mixtures. Heat transfer in liquid and vapor phase (no. 7)

No.	Substance (Trade name)	Temperature (°C)	Vapor pressure (bar)	Density		Liquid					Vapor				
				Liquid (kg/m³)	Vapor (kg/m³)	Specific heat capacity (kJ/kg K)	Thermal conductivity (W/m K)	Dynamic viscosity (10^{-3} Ns/m²)	Kinematic viscosity (10^{-6} m²/s)	Thermal diffusivity (10^{-8}m²/s)	Prandtl number	Specific enthalpy		Enthalpy of vaporization (kJ/kg)	Dynamic viscosity (10^{-3} Ns/m²)
												kJ/kg	kJ/kg		
7	Therminol LT	−70	–	936	–	1.46	0.142	8.65	9.24	10.4	88.9	−113.1	368.4	481.5	
		−60	–	928	–	1.50	0.140	5.50	5.93	10.1	58.7	−98.3	374.8	473.1	
		−40	–	913	–	1.57	0.136	2.84	3.11	9.49	32.8	−67.2	393.3	460.5	
		−20	–	897	–	1.65	0.132	1.75	1.95	8.92	21.9	−34.4	413.6	448.0	
		0	–	882	–	1.73	0.129	1.21	1.37	8.45	16.2	0	435.4	435.4	
		20	–	866	–	1.80	0.125	0.89	1.03	8.02	12.8	35.9	458.8	422.9	
		40	–	850	0.0193	1.88	0.121	0.69	0.81	7.57	10.7	73.2	482.2	409.0	
		60	0.01	833	0.0546	1.95	0.117	0.55	0.67	7.20	9.31	111.9	508.8	396.9	
		80	0.03	817	0.1360	2.02	0.113	0.46	0.56	6.85	8.18	151.8	536.1	384.3	
		100	0.07	800	0.3050	2.09	0.109	0.38	0.48	6.52	7.36	192.9	564.7	371.8	
		150	0.42	755	1.62	2.27	0.099	0.26	0.35	5.78	6.06	301.2	642.4	341.2	
		200	1.67	706	5.95	2.45	0.089	0.19	0.27	5.15	5.24	417.3	726.7	309.4	
		250	5.06	651	17.50	2.63	0.078	0.15	0.22	4.56	4.82	543.4	817.2	273.8	
		300	12.5	583	45.60	2.88	0.068	0.11	0.20	4.05	4.94	680.9	909.1	228.2	
		310	14.7	567	55.30	2.95	0.066	0.11	0.19	3.95	4.81	710.5	927.0	216.5	
		315	15.9	558	60.90	3.00	0.065	0.11	0.19	3.88	4.90	725.2	935.4	210.2	

D4.3. Table 5a. Synthetic heat transfer media; silicone based media and perfluorinated organic carbon compounds (survey, no. 1 to 6)

1	2	3	4	5	6	7	8	9	10	11	12	13	14	15	16	17	18
No.	Trade name	Structure	Producer	Pour point/ Boiling point (°C)	Appli-cation range (°C)	Vapor pressure (mbar)	Vapor pressure ($kg/m^{3)}$	Specific heat capacity (kJ/kg K)	Kinematic viscosity (mm^2/s)	Thermal conductivity (W/m K)	Application limits		Flash point (°C)	Auto Ignition temp. (°C)	Molar mass (kg/ kmol)	Possible application	Remark/ former product
											Lower: Filling and start-up (°C)	Upper: Max. film temperature (°C)					
1	Sylthern XLT	Polydimethyl-siloxan (Silicon)		<−110	−100	–	950	1.34	36.8	0.113	<−100	288	47	350		B	USDA approval, group H1
					260	5,240	563	2.27	0.34	0.091	−37						
2	Sylthern 800	Polydimethyl-siloxan (Silicon)		<−55	−40	–	992	1.51	51.6	0.146	<−40	430	177	385	1,000	B	
					400		548	2.26	0.45	0.064	62						
3	Sylthern HF	Polydimethyl-siloxan (Silicon)	Dow	<−82	<−73		966	1.45	17	0.130	<−73		63[a]	355			[a]
					260	2,740	629	2.27	0.35	0.047	<−73		77[b]	Selfignition			[b]
4	Fluorinert FC-40	Perfluor-carbon	3M	−57	−40	–	1,989	0.96	170	0.068			–	–	650	C	inert liquid
				155													
5	Fluorinert FC-43	Perfluor-carbon	3M	−50	−40	–	2,000	0.96	450	0.068	−30		–	–	670	C	inert liquid
				174	300						10						
6	Fluorinert FC-70	Perfluor-carbon	3M	−25	−15	–	2,013	1.00		0.070	−15		–	–	820	C	water content 10 ppm
				215	300		1,403	1.47	0.22	0.067	61						

D4.3. Table 5a. Synthetic heat transfer media; silicone based media and perfluorinated organic carbon compounds (survey, no. 7 to 11)

1	2	3	4	5	6	7	8	9	10	11	12	13	14	15	16	17	18
No.	Trade name	Structure	Producer	Pour point/ Boiling point (°C)	Application range (°C)	Vapor pressure (mbar)	Vapor pressure (kg/m$^{3)}$	Specific heat capacity (kJ/kg K)	Kinematic viscosity (mm²/s)	Thermal conductivity (W/m K)	Application limits		Flash point (°C)	Auto Ignition temp. (°C)	Molar mass (kg/ kmol)	Possible application	Remark/ former product
											Lower: Filling and start-up (°C)	Upper: Max. film temperature (°C)					
7	Fluorinert FC-72	Perfluor-carbon	3M	−90	−40	12	1,844	0.96	1.25	0.064	<−40		–	–	338	C	water content 10 ppm
				56	300	$>10^5$					<−40						
8	Fluorinert FC-75	Perfluor-carbon	3M	−88	−60	<1	1,972	0.93	17	0.069	<−60		–	–	420	C	water content 10 ppm
				102	300	$8–10^4$					−40						
9	Fluorinert FC-77	Perfluor-carbon	3M	−110	−60	0.1	1,985	0.93	13	0.069	<−60		–	–	415	C	water content 10 ppm
				97	300	10^5					−42						
10	Fluorinert FC-84	Perfluor-carbon	3M	−95	−60	0.4	1,944	0.93	4.2	0.069	<−60		–	–	388	C	water content 11 ppm
				80	300	10^5					−70						
11	Fluorinert FC-87	Perfluor-carbon	3M	−101	−60	7	1,853	0.93	1.35	0.063	<−60		–	–	288	C	water content 11 ppm
				31	300						<−60						

[a]closed cup
[b]open cup

D4.3. Table 5b. Synthetic heat transfer media; silicone based media and perfluorinated organic carbon compounds (no. 1 to 2)

No.	Substance (Trade name)	Temperature (°C)	Vapor pressure (mbar)	Liquid						
				Density (kg/m³)	Specific heat capacity (kJ/ kg K)	Thermal conductivity (W/ m K)	Dynamic viscosity (10^{-3} Ns/m²)	Kinematic viscosity (10^{-6} m²/s)	Thermal diffusivity (10^{-8} m²/s)	Prandtl number
1	Syltherm XLT	−100		978	1.52	0.134	78.6	80.4	9.01	892
		−80		958	1.56	0.131	20.0	20.9	8.77	238
		−60		937	1.60	0.127	9.40	10.0	8.47	118
		−40		917	1.65	0.123	5.20	5.67	8.13	69.7
		−20		896	1.69	0.119	3.10	3.46	7.86	44.0
		0		876	1.73	0.115	2.00	2.00	7.59	26.4
		20	3	855	1.77	0.111	1.40	1.60	7.33	21.8
		40	6	835	1.81	0.109	1.00	1.20	7.21	16.6
		60	18	814	1.86	0.102	0.80	0.98	6.74	14.5
		80	47	794	1.90	0.0973	0.63	0.79	6.45	12.2
		100	106	773	1.94	0.0925	0.51	0.66	6.17	10.7
		120	215	753	1.98	0.0877	0.43	0.57	5.88	9.69
		140	401	732	2.02	0.0827	0.36	0.49	5.59	8.77
		160	695	711	2.07	0.0777	0.31	0.44	5.28	8.33
		180	1,135	691	2.11	0.0725	0.28	0.41	4.97	8.25
		200	1,762	670	2.15	0.0673	0.24	0.36	4.67	7.71
		220	2,619	650	2.19	0.0620	0.22	0.34	4.36	7.80
		240	3,751	629	2.23	0.0566	0.20	0.32	4.04	7.92
		260	5,203	609	2.28	0.0511	0.18	0.30	3.68	8.15
		280	7,018	588	2.32	0.0455	0.17	0.29	3.34	8.68
		290	8,074	578	2.34	0.0427	0.16	0.28	3.16	8.86
2	Syltherm HF	−73		966	1.45	0.130	16.5	17	9.28	183.19
		−70		963	1.46	0.129	14.9	15.5	9.18	169
		−60		953	1.48	0.127	10.8	11.3	9.00	126
		−40		932	1.53	0.122	6.20	6.65	8.56	77.7
		−20		912	1.58	0.117	3.88	4.25	8.12	52.3
		0		892	1.63	0.112	2.60	3.00	7.70	39.0
		20		872	1.68	0.107	1.84	2.10	7.30	28.8
		40		851	1.73	0.102	1.37	1.60	6.93	23.1

D4.3. Table 5b. Synthetic heat transfer media; silicone based media and perfluorinated organic carbon compounds (no. 2 to 3)

No.	Substance (Trade name)	Temperature (°C)	Vapor pressure (mbar)	Liquid						
				Density (kg/m³)	Specific heat capacity (kJ/ kg K)	Thermal conductivity (W/ m K)	Dynamic viscosity (10^{-3} Ns/m²)	Kinematic viscosity (10^{-6} m²/s)	Thermal diffusivity (10^{-8} m²/s)	Prandtl number
2	Syltherm HF (continued)	60	6	831	1.78	0.097	1.05	1.26	6.56	19.2
		80	14	811	1.83	0.092	0.83	1.02	6.20	16.5
		100	30	791	1.88	0.087	0.67	0.85	5.85	14.5
		120	80	771	1.93	0.082	0.56	0.73	5.51	13.2
		140	150	750	1.98	0.077	0.47	0.63	5.19	12.1
		160	280	730	2.03	0.072	0.40	0.55	4.86	11.3
		180	490	710	2.08	0.067	0.35	0.49	4.54	10.8
		200	800	690	2.12	0.062	0.31	0.45	4.24	10.6
		220	1,260	670	2.17	0.057	0.27	0.40	3.92	10.2
		240	1,890	649	2.22	0.052	0.24	0.37	3.61	10.2
		250	2,290	639	2.25	0.050	0.23	0.36	3.48	10.3
		260	2,740	629	2.27	0.047	0.22	0.35	3.29	10.6
3	Syltherm 800	−40		992	1.51	0.146	51.2	51.6	9.75	529
		−20		973	1.54	0.142	25.9	26.6	9.48	281
		0		954	1.58	0.139	15.4	16.1	9.22	175
		20		936	1.61	0.135	10.0	10.7	9.00	119
		40		918	1.64	0.131	7.0	7.6	8.70	87.3
		60		901	1.68	0.127	5.1	5.7	8.39	67.9
		80	14.6	883	1.71	0.124	3.9	4.4	8.21	53.6
		100	40.1	865	1.75	0.120	3.0	3.5	7.93	44.2
		120	93	847	1.78	0.116	2.4	2.8	7.69	36.4
		140	190	830	1.81	0.112	1.9	2.3	7.46	30.9
		160	350	811	1.85	0.109	1.5	1.9	7.26	26.2
		180	595	793	1.88	0.105	1.3	1.6	7.04	22.7
		200	946	774	1.92	0.101	1.1	1.4	6.80	20.6
		220	1,420	755	1.95	0.098	0.91	1.2	6.67	18.0
		240	2,050	735	1.99	0.094	0.74	1.0	6.43	15.7
		260	2,840	715	2.02	0.089	0.64	0.89	6.16	14.4
		280	3,800	694	2.05	0.086	0.54	0.78	6.04	12.9

D4.3. Table 5b. Synthetic heat transfer media; silicone based media and perfluorinated organic carbon compounds (no. 3 to 5)

No.	Substance (Trade name)	Temperature (°C)	Vapor pressure (mbar)	Liquid						
				Density (kg/m^3)	Specific heat capacity (kJ/ kg K)	Thermal conductivity (W/ m K)	Dynamic viscosity (10^{-3} Ns/m^2)	Kinematic viscosity (10^{-6} m^2/s)	Thermal diffusivity (10^{-8} m^2/s)	Prandtl number
3	Syltherm 800 (continued)	300	4,960	672	2.09	0.082	0.47	0.70	5.84	12.0
		320	6,310	649	2.12	0.079	0.41	0.63	5.74	11.0
		340	7,860	625	2.16	0.075	0.36	0.57	5.56	10.3
		360	9,620	601	2.19	0.071	0.31	0.52	5.39	9.65
		380	11,600	575	2.22	0.067	0.28	0.48	5.25	9.14
		400	13,700	548	2.26	0.064	0.25	0.45	5.17	8.70
4	Fluorinert FC-40	−60		2,032	0.93	0.068			3.60	
		−40		1,989	0.96	0.068	338	170	3.56	4,774
		−20		1,946	0.99	0.068	36	18.5	3.53	524
		0		1,903	1.02	0.067	10.7	5.6	3.45	162
		20		1,860	1.05	0.067	4.8	2.6	3.43	75.8
		40	10	1,817	1.08	0.067	2.8	1.56	3.41	45.7
		60	28	1,774	1.11	0.067	1.9	1.05	3.40	30.9
		80	69	1,731	1.14	0.067	1.25	0.72	3.40	21.2
		100	155	1,688	1.17	0.066	0.91	0.54	3.34	16.2
		120	321	1,645	1.20	0.066	0.69	0.42	3.34	12.6
		140	618	1,602	1.23	0.066	0.54	0.34	3.35	10.2
		160	1,120	1,559	1.26	0.066	0.45	0.29	3.36	8.63
		180	1,927	1,516	1.29	0.066	0.38	0.25	3.37	7.42
		200	3,166	1,473	1.32	0.065	0.34	0.23	3.34	6.89
		220	4,966	1,430	1.35	0.065	0.30	0.21	3.37	6.23
		240	7,608	1,387	1.38	0.065	0.26	0.19	3.40	5.59
		260	11,226	1,344	1.41	0.065	0.23	0.17	3.43	4.96
		280		1,301	1.44	0.065	0.21	0.16	3.47	4.61
5	Fluorinert FC-43	−60		2,044	0.93	0.068			3.58	
		−40		2,000	0.96	0.068	900	450	3.54	12,706
		−20		1,957	0.99	0.068	73.4	37.5	3.51	1,068
		0		1,913	1.02	0.067	16.3	8.5	3.43	248
		20	1.3	1,869	1.05	0.067	6.5	3.5	3.41	103
		40	4.4	1,826	1.08	0.067	3.5	1.9	3.40	55.9

D4.3. Table 5b. Synthetic heat transfer media; silicone based media and perfluorinated organic carbon compounds (no. 5 to 6)

No.	Substance (Trade name)	Temperature (°C)	Vapor pressure (mbar)	Liquid						
				Density (kg/m³)	Specific heat capacity (kJ/ kg K)	Thermal conductivity (W/ m K)	Dynamic viscosity (10^{-3} Ns/m²)	Kinematic viscosity (10^{-6} m²/s)	Thermal diffusivity (10^{-8} m²/s)	Prandtl number
5	Fluorinert FC-43 (continued)	60	13	1,782	1.11	0.067	2.1	1.2	3.39	35.4
		80	34	1,739	1.14	0.067	1.4	0.83	3.38	24.6
		100	81	1,695	1.17	0.066	1.03	0.61	3.33	18.3
		120	174	1,651	1.20	0.066	0.78	0.47	3.33	14.1
		140	350	1,608	1.23	0.066	0.59	0.37	3.34	11.1
		160	658	1,564	1.26	0.066	0.48	0.31	3.35	9.26
		180	1,171	1,521	1.29	0.066	0.41	0.27	3.36	8.04
		200	1,983	1,477	1.32	0.065	0.35	0.24	3.33	7.21
		220	3,219	1,433	1.35	0.065	0.30	0.21	3.36	6.25
		240	5,032	1,389	1.38	0.065	0.26	0.19	3.39	5.60
		260	7,606	1,345	1.41	0.065	0.24	0.18	3.43	5.25
		280	11,158	1,301	1.44	0.065	0.22	0.17	3.47	4.90
6	Fluorinert FC-70	−40		2,061	0.96	0.070			3.54	
		−20		2,023	0.99	0.070			3.50	
		0		1,984	1.02	0.070	357	180	3.46	5,202
		20		1,945	1.05	0.070	54.5	28	3.43	816
		40	0.4	1,907	1.08	0.070	16.2	8.5	3.40	250
		60	1.6	1,868	1.11	0.069	9.2	4.9	3.33	147
		80	5.1	1,830	1.14	0.069	4.0	2.2	3.31	66.5
		100	14	1,791	1.17	0.069	2.6	1.45	3.29	44.1
		120	36	1,752	1.20	0.069	1.75	1.00	3.28	30.5
		140	83	1,714	1.23	0.069	1.3	0.76	3.27	23.2
		160	176	1,675	1.26	0.068	0.97	0.58	3.22	18.0
		180	351	1,637	1.29	0.068	0.77	0.47	3.22	14.6
		200	661	1,598	1.32	0.068	0.62	0.39	3.22	12.1
		220	1,180	1,559	1.35	0.068	0.53	0.34	3.23	10.5
		240	2,016	1,520	1.38	0.068	0.46	0.30	3.24	9.26
		260	3,307	1,481	1.41	0.067	0.39	0.26	3.21	8.10
		280	5,234	1,442	1.44	0.067	0.35	0.24	3.23	7.43
		300	8,023	1,403	1.47	0.067	0.31	0.22	3.25	6.77

D4.3. Table 5b. Synthetic heat transfer media; silicone based media and perfluorinated organic carbon compounds (no. 7 to 8)

No.	Substance (Trade name)	Temperature (°C)	Vapor pressure (mbar)	Liquid						
				Density (kg/m^3)	Specific heat capacity (kJ/ kg K)	Thermal conductivity (W/ m K)	Dynamic viscosity (10^{-3} Ns/m^2)	Kinematic viscosity (10^{-6} m^2/s)	Thermal diffusivity (10^{-8} m^2/s)	Prandtl number
7	Fluorinert FC-72	−40	12.3	1,844	0.96	0.064	2.30	1.25	3.62	34.6
		−20	41.7	1,792	0.99	0.062	1.47	0.82	3.49	23.5
		0	118	1,740	1.02	0.060	1.01	0.58	3.38	17.2
		20	290	1,687	1.05	0.058	0.74	0.44	3.27	13.4
		40	636	1,636	1.08	0.056	0.57	0.35	3.17	11.0
		60	1,269	1,583	1.11	0.054	0.46	0.29	3.07	9.45
		80	2,340	1,531	1.14	0.051	0.38	0.25	2.92	8.56
		100	4,041	1,479	1.17	0.049	0.31	0.21	2.83	7.42
		120	6,600	1,427	1.20	0.047	0.27	0.19	2.74	6.93
		140	10,280	1,375	1.23	0.045	0.23	0.17	2.66	6.39
		160	15,375	1,322	1.26	0.043	0.20	0.15	2.58	5.81
		180	22,190	1,270	1.29	0.041	0.18	0.14	2.50	5.60
		200	31,040	1,218	1.32	0.038	0.16	0.13	2.36	5.51
		220	42,250	1,166	1.35	0.036	0.14	0.12	2.29	5.24
8	Fluorinert FC-75	−60		1,972	0.93	0.069	33.5	17	3.76	452
		−40		1,923	0.96	0.068	9.8	5.1	3.68	139
		−20	2.5	1,874	0.99	0.066	4.5	2.4	3.56	67.4
		0	10	1,825	1.02	0.065	2.6	1.4	3.49	40.1
		20	31	1,776	1.05	0.063	1.7	0.94	3.38	27.8
		40	85	1,727	1.08	0.062	1.2	0.68	3.32	20.5
		60	206	1,678	1.11	0.060	0.86	0.51	3.22	15.8
		80	455	1,629	1.14	0.059	0.65	0.40	3.18	12.6
		100	922	1,580	1.17	0.057	0.54	0.34	3.08	11.0
		120	1,738	1,531	1.20	0.056	0.44	0.29	3.05	9.51
		140	3,082	1,482	1.23	0.054	0.39	0.26	2.96	8.78
		160	5,180	1,433	1.26	0.053	0.33	0.23	2.94	7.82
		180	8,320	1,384	1.29	0.051	0.29	0.21	2.86	7.34
		200	12,840	1,335	1.32	0.050	0.25	0.19	2.82	6.74
		220	19,130	1,286	1.35	0.048	0.23	0.18	2.76	6.52

D4.3. Table 5b. Synthetic heat transfer media; silicone based media and perfluorinated organic carbon compounds (no. 9 to 10)

No.	Substance (Trade name)	Temperature (°C)	Vapor pressure (mbar)	Liquid						
				Density (kg/m³)	Specific heat capacity (kJ/ kg K)	Thermal conductivity (W/ m K)	Dynamic viscosity (10^{-3} Ns/m²)	Kinematic viscosity (10^{-6} m²/s)	Thermal diffusivity (10^{-8} m²/s)	Prandtl number
9	Fluorinert FC-77	−60	0.1	1,985	0.93	0.069	26	13	3.74	348
		−40	0.9	1,936	0.96	0.068	8.3	4.3	3.66	117
		−20	3.9	1,887	0.99	0.066	4.0	2.1	3.53	59.5
		0	14	1,838	1.02	0.065	2.3	1.25	3.47	36.0
		20	43	1,789	1.05	0.063	1.5	0.86	3.35	25.7
		40	114	1,740	1.08	0.062	1.08	0.62	3.30	18.8
		60	268	1,691	1.11	0.060	0.81	0.48	3.20	15.0
		80	568	1,642	1.14	0.059	0.62	0.38	3.15	12.1
		100	1,115	1,593	1.17	0.057	0.51	0.32	3.06	10.5
		120	2,044	1,544	1.20	0.056	0.43	0.28	3.02	9.27
		140	3,532	1,495	1.23	0.054	0.36	0.24	2.94	8.16
		160	5,803	1,446	1.26	0.053	0.32	0.22	2.91	7.56
		180	9,125	1,397	1.29	0.051	0.28	0.20	2.83	7.01
		200	13,810	1,348	1.32	0.050	0.24	0.18	2.81	6.41
		220	20,210	1,299	1.35	0.048	0.22	0.17	2.74	6.20
10	Fluorinert FC-84	−60	0.4	1,944	0.93	0.069	8.2	4.2	3.82	110
		−40	2.1	1,893	0.96	0.067	4.0	2.1	3.69	56.9
		−20	8.5	1,841	0.99	0.065	2.3	1.25	3.57	35.0
		0	29	1,790	1.02	0.063	1.5	0.85	3.45	24.6
		20	82	1,739	1.05	0.060	1.08	0.62	3.29	18.8
		40	206	1,687	1.08	0.058	0.81	0.48	3.18	15.1
		60	460	1,636	1.11	0.056	0.62	0.38	3.08	12.3
		80	940	1,584	1.14	0.054	0.51	0.32	2.99	10.7
		100	1,780	1,533	1.17	0.052	0.41	0.27	2.90	9.31
		120	3,160	1,482	1.20	0.049	0.36	0.24	2.76	8.70
		140	5,308	1,430	1.23	0.047	0.30	0.21	2.67	7.87
		160	8,490	1,379	1.26	0.045	0.26	0.19	2.59	7.34
		180	13,030	1,327	1.29	0.043	0.23	0.17	2.51	6.77
		200	19,280	1,276	1.32	0.041	0.20	0.16	2.43	6.58
		220	27,640	1,225	1.35	0.038	0.18	0.15	2.30	6.52

D4.3. Table 5b. Synthetic heat transfer media; silicone based media and perfluorinated organic carbon compounds (no. 11)

No.	Substance (Trade name)	Temperature (°C)	Vapor pressure (mbar)	Liquid						
				Density (kg/m^3)	Specific heat capacity (kJ/ kg K)	Thermal conductivity (W/ m K)	Dynamic viscosity (10^{-3} Ns/m^2)	Kinematic viscosity (10^{-6} m^2/s)	Thermal diffusivity (10^{-8} m^2/s)	Prandtl number
11	Fluorinert FC-87	–60		1,853	0.93	0.063	2.5	1.35	3.66	36.9
		–40		1,803	0.96	0.061	1.40	0.77	3.52	21.9
		–20		1,753	0.99	0.059	0.98	0.56	3.40	16.5
		0		1,703	1.02	0.057	0.75	0.44	3.28	13.4
		20		1,653	1.05	0.055	0.61	0.37	3.17	11.7
		40		1,603	1.08	0.053	0.51	0.32	3.06	10.5
		60		1,553	1.11	0.051	0.45	0.29	2.96	9.80
		80		1,503	1.14	0.048	0.41	0.27	2.80	9.64
		100		1,453	1.17	0.046	0.36	0.25	2.71	9.23
		120		1,403	1.20	0.044	0.32	0.23	2.61	8.81
		140		1,353	1.23	0.041	0.30	0.22	2.46	8.94
		160		1,303	1.26	0.039	0.27	0.21	2.38	8.82
		180		1,253	1.29	0.037	0.25	0.20	2.29	8.73
		200		1,203	1.32	0.035	0.24	0.20	2.20	9.09

D4.3. Table 6a. High temperature salts (HTS)

Substance (trade name):	Durferrit ASD heat transfer salt
Substance structure:	Eutectic melting, ternary mixture from alkali-nitrates and nitrites, in the literature designated as HTS-melting
Producer:	Houghton Durferrit GmbH; D-63408 Hanau
Melting range: max.	138°C up to 142°C
Application temperature:	620°C, reaction conversion too large, also corrosion-limited
Chemical main reaction:	In the salt melting reaction proceeds in the presence of air to the right only:
	$2NaNO_2 + O_2 \rightarrow NaNO_3$
	hermetically sealed:
	$5NaNo_2 \rightarrow NaNO_3 + Na_2O + N_2$
	In both cases decrease of nitrite volume, increase of the nitrate volume. N_2-superposition delayed, does however not avoid alteration
Temperature criteria:	$t \leq 450$°C, melting practical thermally stable
	$t < 450$°C, also for a short time, results in nitrite decomposition causing increase of the melting point; hardly any change of thermal transfer properties
	$t < 500$°C, HTS melting starts to convert with iron
	$t < 620$°C, conversion distinctive: $\vartheta_{max} = 620$°C
Chemical side reaction:	Absorption of carbon dioxide under formation of alkali carbonates, which fail when exceeding the solubility
Service life:	Producer informs on the basis of sent in HTS samples; from the operating data of the melting the decomposition rate can be predestinated
Regeneration salt:	Durferrit ASD regeneration salt; in most cases a reconstitution of the original salt properties is more advantageous than the exchange of the complete amount of salt
Materials:	Corrosion behavior of different materials at temperatures up to 600°C; (Fig. 1). Materials with less than 0.1 mm/a are considered to be constant. Up to 450°C unalloyed or alloy-treated steels will do if no local superheating occurs. Risk of intercrystalline corrosion. Copper, silver, cast iron, magnesium alloys as well as aluminium and its alloys may not be used. When using aluminium and magnesium explosive reactions can occur.
See the original brochure for further details, in particular precautions (toxicity, flammability, fire fighting, and information about melting down); make a request for safety data sheet.	

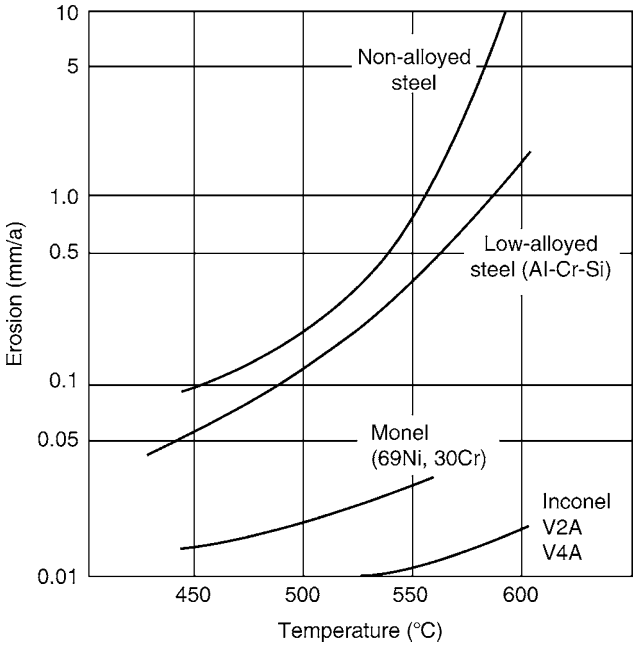

D4.3. Fig. 1. Material excavation in Durferrit ASD.

Column 5 top: Turbidity point, particularly yielding point according to DIN ISO 3016 (pour point) in °C.
Column 5 bottom: Boiling point to be established from the boiling progress, which is determined either according to DIN 51 751 at normal pressure (preferably at synthetic heat transfer media) or according to DIN 51 356 under reduced pressure and conversion to 1.013 bar (at mineral oils).

Boiling point is the first dropping off condensation drop in the test apparatus, which serves also to determine the boiling progress under normal pressure (DIN 51 751). According to the actual running progresses, this should be denominated rather as distillation point and distillation progress [4].
Column 6: Upper and lower category temperature for the application range; exclusively producer's indications.
Column 9: Indication of the true specific thermal capacity, demand of the middle specific thermal capacity [2, 3].
Column 12: Lower application temperatures according to *Wagner* [1]. It is about temperatures at which the kinematic viscosity has the following values:
Filling and start-up at maximum $300 \cdot 10^{-6}$ m^2/s,
Economical pump operation at maximum $5 \cdot 10^{-6}$ m^2/s.
Column 13: Maximum film temperature, admissible locally for a short time only in the boundary layer of the heating surface (remark else as column 6, upper category temperature), recalculation in heated tube according to DIN 4754, enclosure A1.
Column 14: Flash point: It is the lowest temperature based on 1.013 bar at which the vapors developed by the heat transfer medium flame up in presence of a pilot flame.
Methods of determination:

- Flash point according to DIN ISO 2592, determination in open cup according to Cleveland (COC);
- Flash point according to DIN 51 758, determination in closed cup according to *Pensky-Martens*. This method is used at heat transfer media since it is easier to prove low boilers in used oil.

According to DIN 51 522 "Heat transfer oils Q," the determination of the flash point according to DIN 51 758 is prescribed to check mineral oils and other combustible fluids. Provided that these values are available, they will be mentioned additionally in the tables. A decrease of the flash point is an indication of

D4.3. Table 6b. Physical properties

HTS melting	Temperature (°C)	Density (kg/m³)	Specific heat capacity (kJ/kg K)	Thermal conductivity (W/m K)	Dynamic viscosity (10^{-3} Ns/m²)	Kinematic viscosity (10^{-6} m²/s)	Thermal diffusivity (10^{-8} m²/s)	Prandtl number
Durferrit ASD	145	–	1.392	≈0.5	–	–	–	–
	150	1,972	1.395	≈0.5	18.68	9.47	18.2	52.1
	200	1,935	1.425	≈0.5	11.64	6.02	18.1	33.2
	300	1,860	1.486	≈0.5	5.98	3.21	18.1	17.8
	350	1,823	1.516	≈0.5	4.64	2.54	18.1	14.1
	400	1,786	1.547	≈0.5	(3.73)[a]	2.09	18.1	11.5
	450	1,748	1.577	≈0.5	(3.07)[a]	1.76	18.1	9.68
	500	1,711	1.607	≈0.5	(2.59)[a]	1.51	18.2	8.32

[a]Values in ( ) have been extrapolated

D4.3. Table 6c. Physical properties, supplementation. The properties depend on the aging grade, which varies from the property for new salt and for example, at a four-years period of use a melting aged to 20% $NaNO_2$

Density of layer:	1,150 to 1,200 kg/m³ according to DIN 53 912
Density of the HTS melting:	ρ = [1,972−0.745 (ϑ−150)/K] kg/m³, with ϑ as celsius temperature of the HTS melting
Melting temperature:	142°C of the pure ternary, eutectic melting salt mixture. With increasing water content k_{H2O} (in % of the mass) the melting point of the salt mixture drops along the liquid saturation temperature ϑ_{liq} (Fig. 2).
	ϑ_{liq} = 140.24 exp (−0.081 k_{H2O}), with ϑ in °C
Linear expansion coefficient:	$\beta = 4.95 \cdot 10^{-5}$ K^{-1} for the solid
Cubic expansion coefficient:	α = 0.745/[1972−0.745(ϑ−150)] K^{-1}, with ϑ as celsius temperature
Medium specific heat capacity:	c m [J/(kg K)] = 1303.9 + 0.60666 θ [°C]; 145°C < θ < 500°C
Melting heat:	approx. 84 kJ/kg
Thermal conductivity melting:	approx. 0.5 W/(mK)
Dynamic viscosity for new salt:	$\eta = 69.8958\ \vartheta^{-1.642}$
	η in Pa s, ϑ celsius temperature, measured in range 145°C < ϑ <350°C, (Fig. 3).
Specific electric resistance:	θ = 150°C: ρ = 19.0 x 10^8 Ω square mm/m

decomposition products and combustible gases that resulted from the cracking of the heat transfer medium.

Column 15: The autoignition temperature according to DIN 51 794 is the temperature at which the heat transfer medium autoignites without external ignition source at 1.013 bar.

"These temperature values are less interesting for the practical operation, they can partly be dangerous since they are much too high. More important is the remark that heat transfer oils on mineral oil basis can lead to autoignition at 100°C and higher when they have wetted insulating materials such as glass or mineral wool. In this case it is not important how strong the air flow is in this insulating materials" [4].

Table 3a and Table 4a still contain

Column 19: Explosive limit in % volume content l.: lower, u.: upper.

Indication of the system temperature t in °C, at which the limit concentration in the vapor phase just adjusts itself, for example, Table 4a, no. 6 Marlotherm L: 123 ≙ 0.9 means: at 123°C the lower explosive limit is attained in the vapor phase with 0.9% volume content.

Column 21: Application possibilities of the heat transfer medium:

Group A: The heat transfer medium decomposes (disproportionate) below or until the beginning of the boiling point at 1

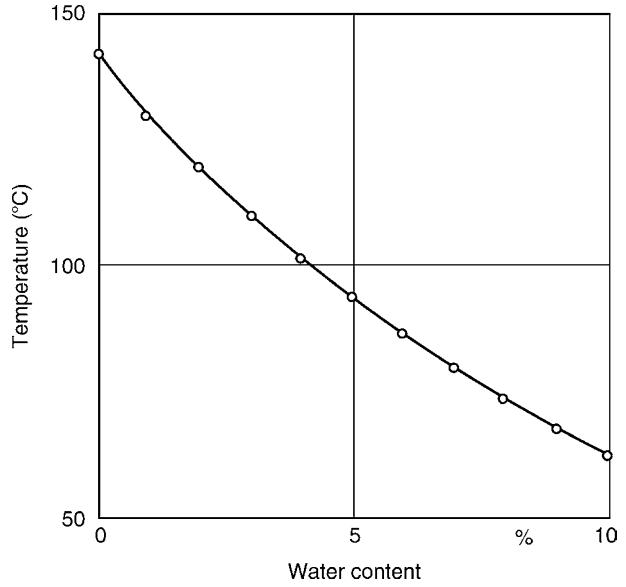

D4.3. Fig. 2. Liquid saturation temperature in dependence of water content.

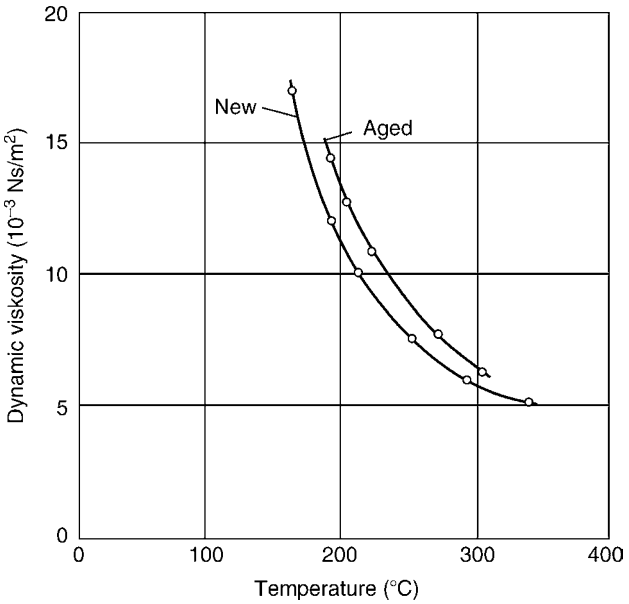

D4.3. Fig. 3. Temperature dependence of the dynamic viscosity of Durferrit ASD.

D4.3. Table 7. Aspects and criteria for selection of heat transfer media (summary)

1. Operational criteria for selection
– Toxicity and handling (maximum allowable concentration, etc.)
– Environmental compatibility: odor, biodegradable, costs for disposal of used product, taking back by the supplier, etc.
– Operation risks and operational safety
Hazard category
Combustibility and combustion behavior
Enthalpy of reaction (calorific value)
Auto Ignition behavior and self-ignition in air (of the vapors)
Reactions with existing operating fluids
Risk at leakages, leaking of product in the ambience or in counter circuits. When liquid enters, for example, in absorbing insulating materials, self-igniting explosive mixtures can be formed with air due to wicking action. For this reason not-absorbing insulation materials are to be used.
– Thermostability
– Security of supply regarding prices, quantities stored, and delivery periods
– Reference list about heat transfer plants in operation, collected operational experience, and recommendations of producers of the heat transfer plants.
2. Special criteria for selection
– Admissible temperature range, min./max. application temperatures, max. film temperature
– Low pour point
– High boiling temperature or late boiling point
– Small increase of vapor pressure with the temperature
– High specific thermal capacity
– Low viscosity at deep temperatures: criteria for start-up and filling as well as for economical pump operation according to *Wagner* [1]
– High thermal conductivity
– No unrequested formation of layer on the heat-exchanging surfaces that means no fouling factor that causes additional energy demand, flow reduction, and cleaning costs
– Aging and oxidation resistance; insensitive to catalytic acting foreign substances, for example, acids, salts, water, air humidity, metal shavings, rust or mounting fats (oils), in particular after the start-up
– Production of no corrosion signs
– Small volume dilatation when heating
– Requirement for regeneration for the heat transfer medium as low as possible

bar by separating mostly light parts. When exceeding ϑ_{max} the characteristics of the heat transfer medium changes constantly.

Group B: The use of the heat transfer medium at temperatures above the boiling point is possible when an inert-gas superposition is available to avoid evaporation. Arising vapors are not to be condensed to the actual substance anymore. The heat transfer medium changes constantly.

Group C: The heat transfer media do not change by evaporation and condensation; the original characteristics remain. The heat transfer media are therefore applicable for isothermal heating by condensing vapor.

In the following text, the most popular heat transfer oils are listed under the main criterion "applicable temperature range" (up to 300°C/larger 300°C) as well as the classic heat transfer media for heating–cooling–chilling processes without the claim to be complete.

3 Bibliography

1. Wagner W (2005) Wärmeträgertechnik mit organischen Fluiden. 7. Auflage. Vogel Industrie Medien GmbH&Co.KG, Würzburg
2 Wagner W (1993) WTS-Stoffdatenatlas. Eigenverl, St. Leon-Rot
3. Kilger H (1988) Zur Auswahl wirtschaftlicher Wärmeträger. Chem Ing Tech. 60(2):S94/102
4. Zufall S (1993) Persönliche Mitteilung vom 19.11.1993 an Prof. Dr. Ing. H. Kilger, Hamburg

D5.1 Calculation of Vapor–Liquid Equilibria

Andreas Pfennig
RWTH Aachen, Aachen, Germany

1 Introduction

For the design of processes, the knowledge of the vapor–liquid equilibrium (VLE) is essential in many cases, either to be able to detect the formation of a second phase or to quantitatively describe the properties of the coexisting phases in a two-phase process. The VLE of any given system depends strongly on composition as well as on temperature or pressure.

In this short chapter, only some basic fundamentals are presented. The principal thermodynamic relations forming the basis for VLE description are independent of the specifics of the substances dealt with. On the other hand, for models describing the substance-specific thermodynamic properties a variety of approaches are available and still under development. Here, only comparably simple systems can be dealt with, excluding e.g., polymers, electrolytes, surfactants, and biomolecules. The interested reader is referred to textbooks and specialized literature for further reading [1–6].

The model parameters are optimally based on experimental data for any system of interest. Extensive data sets can be found either in the original literature or in data collections [7–15], which are usually also available in digital form [16, 17]. Since experiments are often not available during the first steps of process and equipment design, today several prediction methods have been developed of which some are included in this chapter.

2 Phase Equilibria and Phase Diagrams

2.1 Composition in Multicomponent Systems

The composition of multicomponent systems can be described with different concentration measures. Typical measures are mass fraction, which is often used in technical applications, and molar concentrations, which are mostly used for chemical calculations and are also relevant for the description of mass transfer. In thermodynamic calculations, mol fractions are the measure of choice in most of the applications. Thermodynamics can in principle be built on any concentration measure. In most of the thermodynamic calculations the molar scale is relevant, taking the molecular picture into account which generally leads to a description that is physically more sound and thus, often more accurate. Mass fraction, often erroneously called weight fraction, is applied only for components that have no defined molar mass like polymers. Molar concentrations are used where the particles per volume are relevant for the microscopic description as e.g., in electrolyte solutions. The different concentration measures can be converted using density and/or molar mass. The details of the alternative descriptions can be found in the standard textbooks mentioned earlier. Here, only the most common description based on molar scale is presented.

The mol fraction x_i of component i is defined as

$$x_i = \frac{N_i}{N}, \tag{1}$$

where N_i is the amount of substance of component i, N the amount of substance in the system with

$$N = \sum_{i=1}^{K} N_i \tag{2}$$

and K the number of components. The convention is often followed that x_i denotes mol fraction of a liquid, y_i that of a vapor or gas, and z_i denotes an explicitly unknown state or the overall mol fraction in a multiphase system. From the definition of the x_i follows that

$$\sum_{i=1}^{K} x_i = 1 \tag{3}$$

i.e., in a mixture only $K - 1$ mol fractions can be chosen independently, the mol fraction of the Kth component results from Eq. (3).

VDI-GVC (ed.), *VDI Heat Atlas*, DOI 10.1007/978-3-540-77877-6_14,

2.2 Equilibrium Conditions and Phase Rule

If a system consists of π coexisting phases in equilibrium, the pressure p and temperature T in all phases have to be identical, constituting mechanical and thermal equilibrium. Additionally, for establishing material equilibrium, the chemical potentials μ_i of each component have to be identical in all phases, i.e.,

$$\mu_i^{\alpha} = \mu_i^{\beta} = \cdots = \mu_i^{\pi} \tag{4}$$

for all i. In deriving these conditions it is assumed that no external fields exist and the influence of interfaces can be neglected. Also, chemical reactions are not accounted for. It should be noted here that generally the indices are chosen to increase with decreasing volatility. Thus, usually component 1 is the one with the highest vapor pressure and component K, with the lowest.

If the independent variables describing the multiphase system in equilibrium, i.e., the compositions of all phases, pressure, and temperature are to be determined from these equilibrium conditions, it turns out that a certain number of conditions have to be specified in order to unequivocally determine the system state. This number of freedoms F is given by the Gibbs phase rule:

$$F = K - \pi + 2. \tag{5}$$

2.3 Useful Variables

For the description of VLE, some useful intermediate variables are often introduced. The partition coefficient or distribution ratio K_i describes the ratio of the mol fractions between the phases:

$$K_i = \frac{y_i}{x_i}. \tag{6}$$

The relative volatility $\alpha_{i,j}$ describes the ratio of the partition coefficients between the components regarded:

$$\alpha_{i,j} = \frac{K_i}{K_j}. \tag{7}$$

For a binary system, the relative volatility can be used to connect the vapor and the liquid equilibrium compositions:

$$y_1 = \frac{\alpha_{1,2} x_1}{\alpha_{1,2} x_1 + 1 - x_1}. \tag{8}$$

2.4 Ideal Systems

If the system regarded shows ideal behavior in the vapor as well as in the liquid phase, the chemical potentials of vapor (v) and liquid (l) are

$$\mu_i^{\mathrm{v}} - \mu_i^0 = \tilde{R} T \ln(y_i p) \tag{9}$$

and

$$\mu_i^{\mathrm{l}} - \mu_i^0 = \tilde{R} T \ln(x_i p_i^{\mathrm{s}}) \tag{10}$$

where the reference state is referred to by μ_i^0, which is chosen identical for both phases. Introducing these expressions for the chemical potentials into Eq. (4) results in Raoult's law:

$$y_i p^{\mathrm{s}} = x_i p_i^{\mathrm{s}}, \tag{11}$$

where superscript s indicates saturated conditions. p_i^{s} refers to the pure-component vapor pressure at the desired temperature T, and p^{s} to the vapor pressure of the mixed system at T, with the equilibrium compositions x_i in the liquid and y_i in the vapor. Since Eq. (3) applies for y_i as well:

$$p^{\mathrm{s}} = \sum_{i=1}^{K} x_i p_i^{\mathrm{s}}. \tag{12}$$

The principal behavior of an ideal binary system is depicted in Fig. 1, where the pressure is plotted against mol fraction. The individual contributions are shown, which are straight lines proportional to x_i running through p_i^{s} at the appropriate side of the diagram, according to the right-hand side of Eq. (11). The sum of both contributions obviously is a straight line connecting the pure-component vapor pressures. The y_i can then be obtained from Eq. (8), where for the ideal system follows

$$K_i = \frac{p_i^{\mathrm{s}}}{p^{\mathrm{s}}} \tag{13}$$

and

$$\alpha_{i,j} = \frac{p_i^{\mathrm{s}}}{p_j^{\mathrm{s}}}. \tag{14}$$

In Fig. 1 the dependence $p^{\mathrm{s}}(y_1)$ obtained with Eq. (8) also is shown. Figure 2 shows the corresponding $y_i = f(x_i)$ for different values of $\alpha_{1,2}$ as e.g., used for the construction of the McCabe–Thiele diagram in distillation.

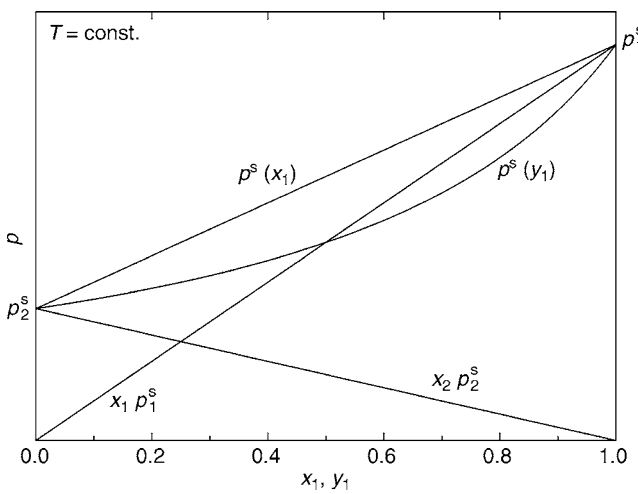

D5.1. Fig. 1. Pressure contributions and Raoult's law for an ideal system.

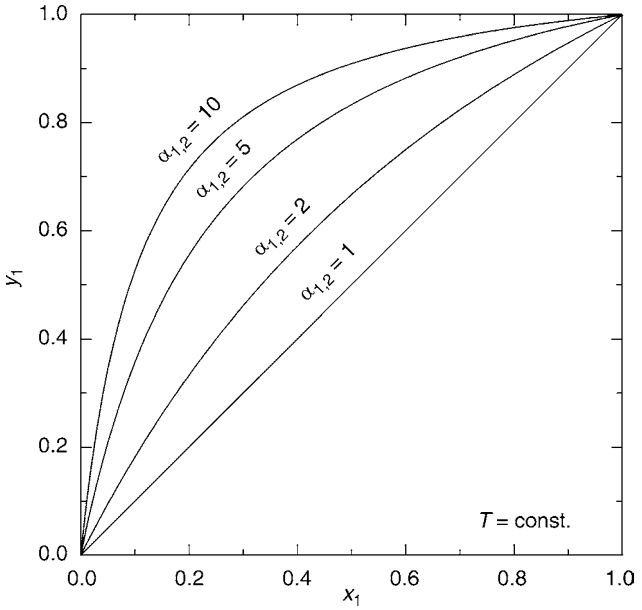

D5.1. Fig. 2. *yx*-diagram for varied relative volatility.

2.5 Graphical Representation of Nonideal Systems

VLE for a typical system with only little deviation from ideality is shown in Fig. 3 in three diagrams. The boiling-point and dew-point curves are specified as well as an example of tie lines connecting the representation of two phases in equilibrium which in this case are horizontal. Also it is shown how the *yx*-diagram can be constructed from the boiling-point and dew-point curves.

In Fig. 4, a binary azeotropic system is shown. At the azeotrope vapor and liquid compositions become identical,

$$x_{i,az} = y_{i,az} \tag{15}$$

and the slope of bubble-point and dew-point curves are horizontal, i.e., have an extreme point. Thus, both curves touch each other at their maximum or minimum. Maximum or minimum pressure or temperature azeotropes are possible, depending on the molecular interactions in the mixture as compared to the pure components. The isothermal and isobaric diagrams are linked such that a vapor–pressure maximum corresponds to a boiling-temperature minimum and vice versa. In the *yx*-diagram the equilibrium curve intersects the diagonal. The azeotrope depends on the conditions chosen, e.g., on the system pressure or temperature. Since distillation does not allow to overcome azeotropic compositions, extensive data collections exist for azeotropic data [10, 14, 15]. The azeotropic data for some selected systems are given in Table 1.

For systems displaying a miscibility gap a heteroazeotrope is frequently encountered. For systems of narrow or strongly asymmetric miscibility gap the azeotrope can be to the side of the miscibility gap. In the majority of cases, the azeotrope lies within the miscibility gap as shown in Fig. 5, which is called heteroazeotrope. If the miscibility gap is very wide, i.e., the components are only very slightly miscible as is the case in

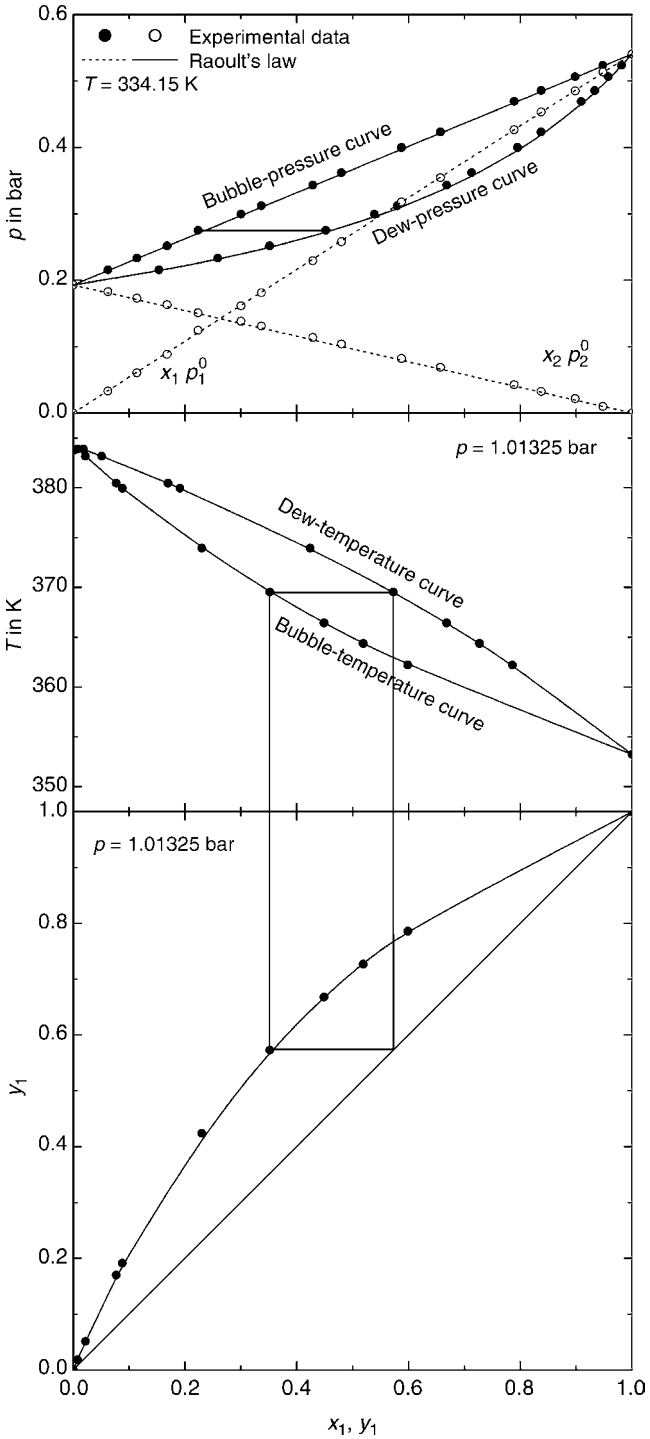

D5.1. Fig. 3. Isothermal and isobaric vapor–liquid equilibrium diagrams for the binary system benzene (1) and toluene (2). Comparison of experimental data with values determined with Raoult's law. Data are taken from [7].

many aqueous-organic systems, the vapor pressure of a binary heteroazeotrope can be approximated by

$$p_{az}^s = p_1^s + p_2^s \tag{16}$$

and the vapor composition of the heteroazeotrope by

$$y_{i,az} = \frac{p_i^s}{p_{az}^s}. \tag{17}$$

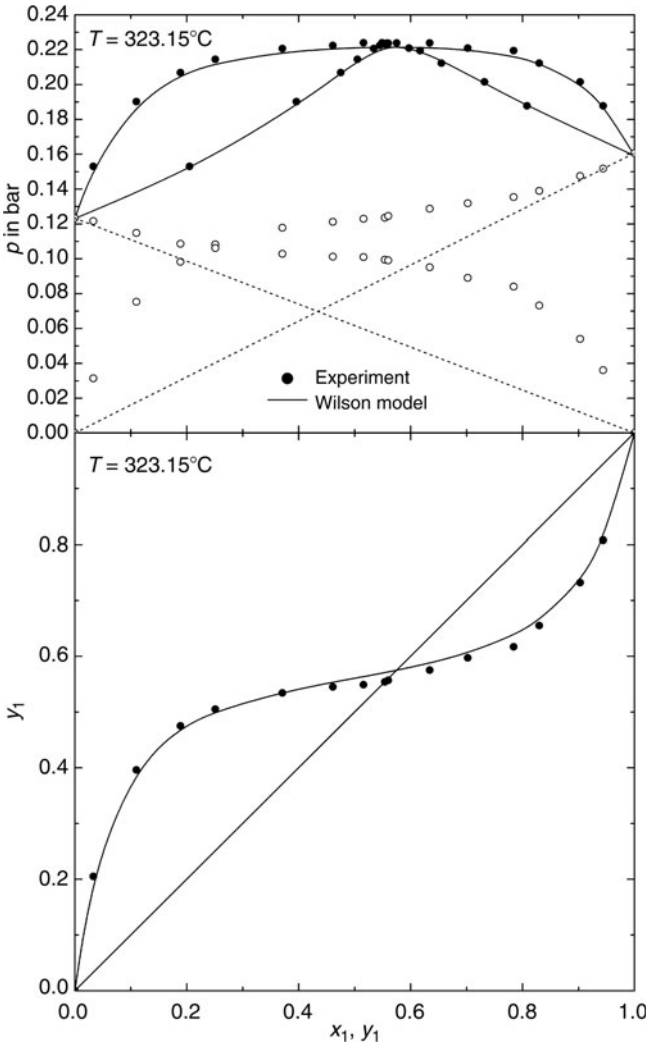

D5.1. Fig. 4. Isothermal vapor–liquid equilibrium data for the azeotropic binary system water (1) and 1,4-dioxane (2). Comparison of experimental values with results of the Wilson model. Data are taken from [7].

3 Modeling Vapor–Liquid Equilibria

To evaluate the equilibrium conditions for specific systems, two approaches are generally applied, one relying on equations of state (EOS), the other building on models for the excess Gibbs energy. Both approaches are briefly presented in the following.

3.1 Equations of State

EOS stem from the fundamental equation for the free (Helmholtz) energy of a system:

$$\tilde{a} = \tilde{a}(T, \tilde{v}, x_i), \tag{18}$$

where $\tilde{v}$ is the molar volume of the system. From this fundamental equation, the pressure and the chemical potential can be derived:

$$p(T, \tilde{v}, x_i) = -\left(\frac{\partial \tilde{a}(T, \tilde{v}, x_i)}{\partial v}\right)_{T, x_i} \tag{19}$$

and

$$\mu_i(T, \tilde{v}, x_k) = \left(\frac{\partial N\tilde{a}(T, \tilde{v}, x_k)}{\partial N_i}\right)_{T, N\tilde{v}, N_{j\neq i}}. \tag{20}$$

Other thermodynamic properties can be derived from the fundamental equation as well, as described in the standard text books. If the EOS is given as $p(T, \tilde{v}, x_i)$, Eq. (19) can be used to obtain $\tilde{a}(T, \tilde{v}, x_i)$ by integration. It should be noted that in practice not $\tilde{a}$ but rather the deviation from ideal-gas behavior is relevant for which the integration is generally possible even if it may be tedious.

When working with EOS, usually fugacities f_i of component i are introduced and defined by

$$\mu_i = \tilde{R}T \ln f_i. \tag{21}$$

Fugacity can be regarded as a partial pressure of component i in a mixture corrected for the deviation of the real component from the ideal-gas behavior. Fugacities thus have units of pressure. It is also customary to introduce fugacity coefficients φ_i with

$$f_i = \varphi_i x_i p, \tag{22}$$

which expresses this interpretation more explicitly. The fugacity coefficient can be derived directly from

$$\ln \varphi_i = \left(\frac{\partial N \frac{\tilde{a} - \tilde{a}^{ig}}{\tilde{R}T}}{\partial N_i}\right)_{T, N\tilde{v}, N_{j\neq i}} - \ln Z, \tag{23}$$

where the index ig refers to the ideal gas and Z is the compressibility factor

$$Z = \frac{p\tilde{v}}{\tilde{R}T}. \tag{24}$$

It is obvious that for an ideal gas with

$$Z = 1 \tag{25}$$

also

$$\varphi_i = 1 \tag{26}$$

and

$$f_i = y_i p = p_i, \tag{27}$$

where p_i is the partial pressure of component i. Since all components approach ideal-gas behavior at sufficiently low density, Eq. (25) has to be approached for any substance in this limit. This also has to hold for all EOS model equations properly describing the system behavior.

Substituting Eq. (21) into Eq. (4) it is easily realized that with fugacities VLE can be obtained from

$$f_i^{\mathrm{v}} = f_i^{\mathrm{l}} \tag{28}$$

which has to be satisfied for all components i simultaneously. With Eq. (22) follows

$$K_i = \frac{\varphi_i^{\mathrm{l}}}{\varphi_i^{\mathrm{v}}}. \tag{29}$$

D5.1. Table 1. Azeotropic data for some selected systems at 1.01325 bar [14, 15]. For extensive data sets, see [10, 14, 15]

Component 1	Component 2	Substance	Saturation temperature (°C)	Temperature of azeotrope (°C)	Azeotropic mol fraction
H_2O		Water	100		
	C_6H_6	Benzene	80.15	69.3	0.704
	C_7H_{16}	Heptane	98.45	79.2	0.548
	C_2H_6O	Ethanol	78.35	78.15	0.8943
	$C_4H_8O_2$	1,4-Dioxane	101.50	87.2	0.482
C_6H_{14}		Hexane	68.75		
	$CHCl_3$	Chloroform	61.15	59.95	0.650
	C_2H_6O	Ethanol	78.35	58.68	0.332
	C_3H_6O	Acetone	56.25	49.7	0.631
C_7H_8		Toluene	110.65		
	CH_4O	Methanol	64.65	63.6	0.880
	$C_2H_6O_2$	Ethylene glycol	197.25	110.3	0.090
	$C_2H_4O_2$	Acetic acid	118.00	100.6	0.632
$CHCl_3$		Chloroform	61.15		
	CH_2O_2	Formic acid	100.8	59.15	0.313
	C_3H_6O	Acetone	56.25	64.5	0.345

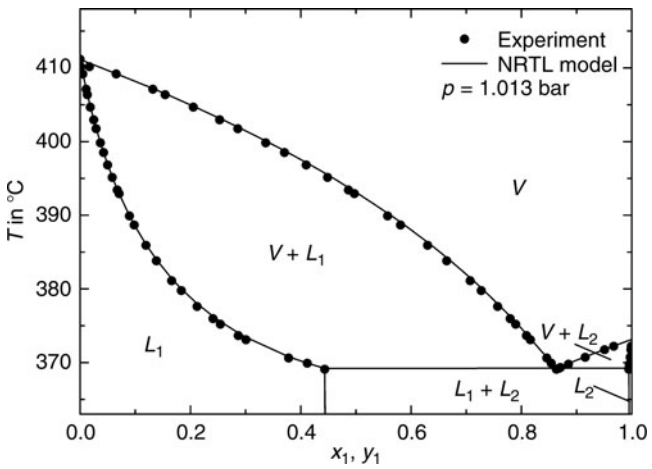

D5.1. Fig. 5. Isobaric vapor–liquid equilibrium data for the binary system water (1) and 1-pentanol (2) displaying a heteroazeotrope. Comparison of experimental values with the results of the NRTL model. Data are taken from [7].

These equilibrium conditions have to be evaluated numerically, where some algorithms can e.g., be found in [18, 19]. To give an example, a simple algorithm for bubble-pressure calculation is presented in Fig. 6.

In the following, some selected EOS are presented that allow for the calculation of the fugacities and fugacity coefficients. Since a variety of EOS are able to describe liquid as well as vapor phase, a single EOS can be used to calculate VLE consistently based on one single substance-specific mathematical equation. Another advantage is that most EOS allow for the description of the system behavior up to and also above the critical point. Thus, equilibria can be described in an extremely wide range of conditions including VL-critical behavior as well as supercritical phase equilibria between fluid phases.

A common disadvantage that will become obvious in the following lies in the simplicity of the correlations introducing the mixture effects for most EOS. This leads to significant problems if substances are to be modeled with EOS for which the molecular interactions differ significantly between pure components and in the mixture. Thus, EOS are generally applied for only moderately nonideal systems.

3.1.1 The Virial Equation

A very simple EOS is the virial equation which is a Taylor-series expansion in molar density ρ of the nonideal system behavior about the ideal-gas equation, which for technical application is generally truncated after the second term:

$$Z = 1 + \tilde{B}\tilde{\rho}, \tag{30}$$

where $\tilde{B}$ is the second virial coefficient, which depends only on temperature and composition, and

$$\tilde{\rho} = \tilde{v}^{-1}. \tag{31}$$

The virial equation can only describe the vapor or gas state. It is generally recommended that Eq. (30) should be used only up to roughly one third of the critical density, since above that the deviations may become unacceptably large. Special care should be taken for systems with carboxylic acids which can form dimers even in the vapor state, an effect that has to be accounted for explicitly. In a mixture $\tilde{B}$ is described by

$$\tilde{B} = \sum_{i=1}^{K}\sum_{j=1}^{K} y_i y_j \tilde{B}_{i,j}, \tag{32}$$

where the virial cross coefficient $\tilde{B}_{i,j} = \tilde{B}_{j,i}$ accounts for the interactions between components i and j. $\tilde{B}_{i,i}$ is the second virial coefficient of pure component i. With the virial equation the fugacity coefficient becomes

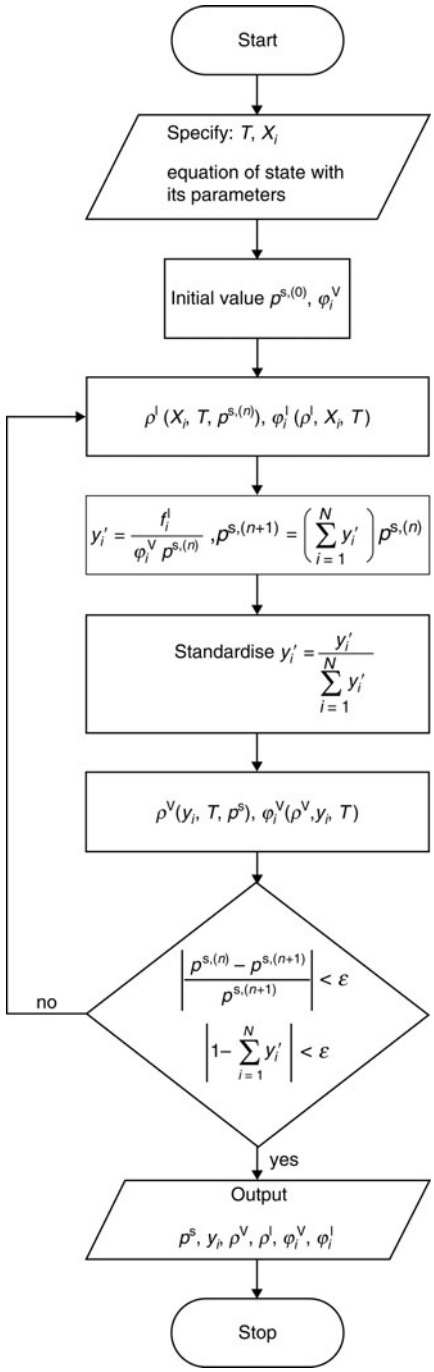

D5.1. Fig. 6. A simple algorithm for the calculation of bubble pressure with equations of state.

$$\ln \varphi_i = 2\rho \sum_{j=1}^{K} y_j \tilde{B}_{i,j} - \ln Z. \tag{33}$$

The second virial coefficients for many components are available in data banks and have been published, e.g., by Dymond and Smith [9]. If the second virial coefficients have to be estimated the method of Tsonopoulos [20–23] who derived a correlation based on the principle of corresponding states, is often applied for pure components, i.e., by taking reference to the critical point (c):

$$\frac{\tilde{B}_{ii} p_c}{\tilde{R} T_c} = f^{(0)} + \omega f^{(1)} + f^{(2)}, \tag{34}$$

where ω is the acentric or Pitzer factor

$$\omega = -\log \frac{p^s(T_r = 0.7)}{p_c} - 1 \tag{35}$$

with the reduced temperature

$$T_r = \frac{T}{T_c} \tag{36}$$

and the f-functions for nonpolar contributions given by

$$f^{(0)} = 0.1445 - \frac{0.330}{T_r} - \frac{0.1385}{T_r^2} - \frac{0.0121}{T_r^3} - \frac{0.000607}{T_r^8}, \tag{37}$$

$$f^{(1)} = 0.0637 + \frac{0.331}{T_r^2} - \frac{0.423}{T_r^3} - \frac{0.008}{T_r^8} \tag{38}$$

$f^{(2)}$ accounts for polar interactions. For components without hydrogen bonds

$$f^{(2)} = \frac{a}{T_r^s}. \tag{39}$$

For ketones, aldehydes, nitriles, and ethers a can be approximated with the reduced dipole moment μ_r

$$a = -2.14 \cdot 10^{-4} \mu_r - 4.308 \cdot 10^{-21} \mu_r^8 \tag{40}$$

with

$$\mu_r = \frac{\mu^2 p_c}{1.01325 \frac{\mathrm{Pa} D^2}{K^2} T_c^2}, \tag{41}$$

where μ is the dipole moment e.g., in Debye.

For polar components with hydrogen bonds

$$f^{(2)} = \frac{a}{T_r^6} - \frac{b}{T_r^8} \tag{42}$$

with $a = 0.0878$ for all alcohols and $a = 0.0279$ for water. For methanol $b = 0.0560$, for unbranched alcohols from C_2 to C_4 $b = 0.00908 + 0.0006957\mu_r$, and for water $b = 0.0229$.

If information is missing for the cross virial coefficients, their absolute value can be approximated by the Lorentz combining rule

$$|\tilde{B}_{i,j}| = \frac{1}{8}\left[\left(|\tilde{B}_{i,i}|\right)^{1/3} + \left(|\tilde{B}_{j,j}|\right)^{1/3}\right]^3. \tag{43}$$

This is a very rough approximation though, since $\tilde{B}_{i,j}$ can in principle lie outside the range between $\tilde{B}_{i,i}$ and $\tilde{B}_{j,j}$. If the signs of the pure-component virial coefficients are not identical, some arithmetic mean has to be chosen. For the correlation of Tsonopoulos, it is recommended to apply mixing rules for the critical properties and evaluate the correlations given earlier with those [24].

3.1.2 Cubic Equations of State

The so-called cubic EOS are capable of also describing the behavior of the liquid phase, thus allowing for the calculation of VLE

based on only one material equation. Two frequently used EOS are presented here, which are based on the EOS of van der Waals who was the first to suggest this principal model structure.

The Soave modification of the Redlich–Kwong EOS [25, 26], often abbreviated as SRK EOS or RKS EOS, is given by

$$p = \frac{\tilde{R}T}{\tilde{v} - b} - \frac{a(T)}{\tilde{v}(\tilde{v} + b)} \tag{44}$$

with the mixing rules for the parameters

$$a = \sum_{i=1}^{K} \sum_{j=1}^{K} z_i z_j a_{i,j}, \tag{45}$$

$$b = \sum_{i=1}^{K} z_i b_i. \tag{46}$$

The combining rule for $i \neq j$ is

$$a_{i,j} = (1 - k_{i,j}) \sqrt{a_{i,i} a_{j,j}}, \tag{47}$$

where $k_{i,j}$ is a binary parameter, usually close to zero, to be fitted to experimental data.

The pure-component parameters can be determined from the following correlation

$$a_{i,i}(T) = a_{c,i} \alpha_i(T), \tag{48}$$

$$\alpha_i(T) = \left[1 + m_i \left(1 - \sqrt{T_{r,i}}\right)\right]^2, \tag{49}$$

$$m_i = 0.480 + 1.574\omega_i - 0.176\omega_i^2. \tag{50}$$

From the conditions of the critical point, i.e., the critical isotherm having a saddle point, the following relations can be derived

$$a_{c,i} = \frac{1}{9(2^{1/3} - 1)} \frac{\tilde{R}^2 T_{c,i}^2}{p_{c,i}} \tag{51}$$

and

$$b_i = \frac{(2^{1/3} - 1)}{3} \frac{\tilde{R} T_{c,i}}{p_{c,i}}. \tag{52}$$

For the fugacity coefficient results

$$\ln \varphi_i = \frac{b_i}{b}(Z - 1) - \ln\left[Z\left(1 - \frac{b}{\tilde{v}}\right)\right] + \frac{1}{b\tilde{R}T}\left[\frac{ab_i}{b} - 2\sqrt{aa_i}\right] \ln\left(1 + \frac{b}{\tilde{v}}\right). \tag{53}$$

Equation (44) is called a cubic EOS because if T and p and the composition of the mixture are specified, a cubic equation results for the determination of the molar volume. In case this determining equation has three real roots larger than b, the lowest value corresponds to the liquid molar volume and the highest to the vapor molar volume. The intermediate value corresponds to an unstable state. Above the critical isotherm only one real root larger than b is found.

A second cubic EOS often applied is the Peng–Robinson EOS (PR EOS) [27], which is given by

$$p = \frac{\tilde{R}T}{\tilde{v} - b} - \frac{a(T)}{\tilde{v}^2 + 2b\tilde{v} - b^2} \tag{54}$$

with mixing and combining rules as well as the defining equations for $a_{i,i}(T)$ and $\alpha_i(T)$ being identical to that of the SRK EOS. m_i is given by

$$m_i = 0.37464 + 1.54226\omega - 0.26992\omega^2. \tag{55}$$

The pure-component parameters can be determined from the critical coordinates of a component by

$$a_{c,i} = 0.45724 \frac{\tilde{R}^2 T_{c,i}^2}{p_{c,i}} \tag{56}$$

and

$$b_i = 0.077796 \frac{\tilde{R} T_{c,i}}{p_{c,i}}. \tag{57}$$

For the fugacity coefficient results

$$\ln \varphi_i = \frac{b_i}{b}(Z - 1) - \ln\left[Z\left(1 - \frac{b}{\tilde{v}}\right)\right] + \frac{1}{b\tilde{R}T}\left[\frac{\sqrt{2}ab_i}{4b} - \sqrt{\frac{aa_i}{2}}\right] \ln\left(\frac{1 + \frac{b}{\tilde{v}}(1 + \sqrt{2})}{1 + \frac{b}{\tilde{v}}(1 - \sqrt{2})}\right). \tag{58}$$

In the 1970s and 1980s, many variations and generalizations of these equations have been proposed, most of which are hardly applied today.

For these cubic EOS, the binary parameters have been fitted and are published in the corresponding volumes of the DECHEMA Data Series [7].

3.1.3 Noncubic Equations of State

A variety of noncubic EOS are available in the literature. With noncubic EOS the densities for given $T, p,$ and z_i do not result from a cubic equation but rather have to be determined iteratively. A variety of algorithms have been proposed to quickly and safely find the roots of the EOS even in the very close vicinity of the critical point.

One class of noncubic EOS is the extended virial EOS. The Benedict–Webb–Rubin EOS (BWR EOS) [28, 29] or the Bender EOS [30] can e.g., be used to describe mixtures of components with very small molar mass like in natural gas. Other even generalized forms of this type of equation are available, e.g., by Lee and Kesler (LK EOS) [31].

In recent years, research aims at overcoming the deficiencies of the EOS presented here, which are mentioned earlier and are a result of the simple structure of the pure-component EOS as well as of the primitive mixing and combining rules. One very successful approach is the SAFT EOS, which has originally been proposed by Huang and Radosz [32, 33] directly in a formulation for the Helmholtz free energy. The SAFT EOS is currently investigated and extended by many authors e.g., to also include very strongly interacting components, polymers, and electrolytes.

3.2 $\tilde{g}^E$- or γ_i-Models

An alternative approach for calculating VLE is to describe the fugacities in the vapor with a possibly simple EOS and in the liquid based on a $\tilde{g}^E$- or γ_i-model:

$$f_i^l = \gamma_i x_i \varphi_i^{s,v} p_i^s \kappa_i, \tag{59}$$

where γ_i is the activity coefficient of component i in the liquid mixture, p_i^s is the pure-component vapor pressure at the specified temperature, $\varphi_i^{s,v}$ is the pure-component fugacity coefficient of the vapor at p_i^s, and κ_i is the so-called Poynting correction which accounts for the compression of the pure component between p_i^s and p^s of the mixture, where the latter is determined by the resulting VLE equilibrium condition which has to be fulfilled for each component:

$$\varphi_i y_i p^s = \gamma_i x_i \varphi_i^{s,v} p_i^s \kappa_i. \tag{60}$$

The Poynting correction can be approximated as

$$\kappa_i \approx \exp\left(\frac{\tilde{v}_i^l (p^s - p_i^s)}{\tilde{R}T}\right) \tag{61}$$

when the liquid is reasonably incompressible, which generally is the case, and where $\tilde{v}_i^l$ is the molar volume of the pure-component liquid at T and p_i^s.

The nonideality in the liquid is described by the activity coefficients which are strongly dependent on mixture composition and which can be determined from a $\tilde{g}^E$-model with

$$\mu_i^E(T,p,x_k) = \tilde{R}T \ln \gamma_i = \left(\frac{\partial N \tilde{g}^E(T,p,x_k)}{\partial N_i}\right) T, p, N_{j\neq i}, \tag{62}$$

where the superscript "E" refers to an excess property defined as the value of a mixture from which the value of an ideal mixture at the same T, p, and x_i has been subtracted. Since all relevant $\tilde{g}^E$-models assume incompressible liquids, the activity coefficients result to be pressure independent.

The fugacity coefficients of the vapor are generally described either with the virial equation or for intermediate and low pressures and temperatures above ambient, and it turns out that $\varphi_i^{s,v} \approx \varphi_i$ and their individual effect can be neglected. Under these conditions also the Poynting correction can usually be neglected ($\kappa_i = 1$), and the molar volume of the pure liquids would need to be known otherwise. With these simplifying assumptions the equilibrium condition simplifies to

$$y_i p^s = \gamma_i x_i p_i^s. \tag{63}$$

If the nonideality of the liquid mixture can also be neglected, which is only the case for components of similar molecular size and chemical structure such as isomers or close neighbors of a homologous series,

$$\gamma_i = 1, \tag{64}$$

which corresponds to Raoult's law, that has been discussed earlier.

For the pure-component vapor pressure any expression for the saturation-pressure curve can be used, often the Antoine equation is applied

$$\log \frac{p_s^s}{1\ \text{bar}} = A - \frac{B}{C+T} \tag{65}$$

for which the temperature coefficients for a variety of components can be found e.g., in Boublík et al. [7, 8, 24]. When the coefficients for the Antoine equation are adopted from the literature, care should be taken that the units of temperature and pressure as well as the base of the logarithm are identical to those for which the coefficients have been determined. If only the critical point and the acentric factor are known, generalized correlation functions can be used like that proposed by Lee and Kesler [31].

With the notation used here, which corresponds to the symmetrical normalization, the activity coefficients approach unity for any pure component. For a composition approaching infinite dilution, the activity coefficients generally deviate strongly from unity and are termed infinite-dilution activity coefficients γ_i^∞. The γ_i^∞ can thus be used to determine the adjustable model parameters of a $\tilde{g}^E$-model in the common case where there are only two adjustable parameters per binary mixture.

Some $\tilde{g}^E$-models are presented in the following. The model parameters of these models have to be fitted to experimental data, preferably VLE data. If the models have only two binary parameters, these can be backed out from both infinite-dilution activity coefficients for which many experimental data have been published [16, 17]. The parameters have been determined and are reported for a wide variety of systems in the DECHEMA Data Series [7]. A simple algorithm for calculating VLE with $\tilde{g}^E$-models is presented in Fig. 7.

3.2.1 Redlich–Kister Model

A simple approach taken by Redlich and Kister [34] is to expand $\tilde{g}^E$ in an appropriate series:

$$\tilde{g}^E = x_1 x_2 \left(\sum_{l=1}^{L} A_l (x_1 - x_2)^{l-1}\right), \tag{66}$$

where the A_i are substance-specific parameters to be fitted to experimental data. Without significant extension the Redlich–Kister model (RK) can only be applied to binary systems. It is mostly used in the cases where very accurate description of $\tilde{g}^E$ is required and a sufficient number of accurate experimental data are available. With Eq. (62) the following results for the activity coefficients are obtained:

$$\tilde{R}T \ln \gamma_1 = x_2^2 \sum_{i=1}^{L-1} (A_i + 2x_1 i A_{i+1})(x_1 - x_2)^{i-1} \tag{67}$$

and

$$\tilde{R}T \ln \gamma_2 = x_2^2 \sum_{i=1}^{L-1} (A_i - 2x_2 i A_{i+1})(x_1 - x_2)^{i-1}. \tag{68}$$

3.2.2 Wilson Model

The model proposed by Wilson [35] for the first time introduced the concept of local composition, i.e., the fact that the composition "seen" by one type of molecules in their close vicinity should generally not be identical to the overall composition due to energetic interactions, which leads to some neighborhoods being preferred over others. The Wilson model describes multicomponent mixtures:

$$\tilde{g}^E = -RT \sum_{i=1}^{K} x_i \ln\left(\sum_{j=1}^{K} x_i \Lambda_{i,j}\right), \tag{69}$$

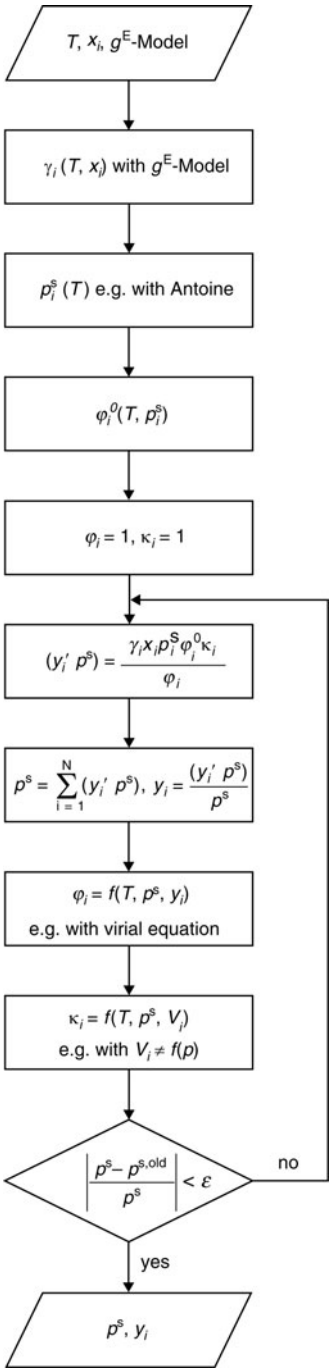

D5.1. Fig. 7. A simple algorithm for the calculation of bubble pressure with $\tilde{g}^E$-models.

where

$$\Lambda_{i,j} = \frac{\tilde{v}_j^L}{\tilde{v}_i^L} \exp\left(-\frac{\lambda_{i,j} - \lambda_{i,i}}{\tilde{R}T}\right) \tag{70}$$

and especially

$$\Lambda_{i,i} = 1. \tag{71}$$

The $\lambda_{i,j}$ are interaction energies between the molecules and $\tilde{v}_i^L$ is the pure-component liquid molar volume. In the beginning it had been discussed whether this molar volume should be treated as a variable, e.g., depending on T. Today, it is agreed that it can be used at any specified T; generally 293°C is used. With the Wilson model multicomponent mixtures can be described based only on the two binary parameters $(\lambda_{i,j} - \lambda_{i,i})$ for each binary subsystem. The feature that calculation of muticomponent mixtures can be described solely based on binary parameters holds for all models described in the following.

For the activity coefficient results

$$\ln \gamma_i = 1 - \ln\left(\sum_{j=1}^{K} x_j \Lambda_{i,j}\right) - \sum_{k=1}^{K} \frac{x_k \Lambda_{k,i}}{\sum_{j=1}^{K} x_j \Lambda_{k,j}}. \tag{72}$$

The Wilson model is able to describe strongly interacting components including polar and hydrogen-bonding substances. The Wilson model cannot describe liquid–liquid equilibria, due to its mathematical structure. This has to be taken into account and can sometimes even be an advantage, since it has to be kept in mind that all $\tilde{g}^E$-models only approximate system behavior. For systems that are strongly nonideal and close to demixing but do not show a miscibility gap, the Wilson model cannot erroneously predict liquid–liquid demixing, which may save computer time otherwise required for testing, if demixing is predicted for the conditions of interest.

3.2.3 NRTL Model

Also based on the local-composition concept, the NRTL model (nonrandom two liquids) has been derived by Renon and Prausnitz [36]:

$$\tilde{g}^E = \tilde{R}T \sum_{i=1}^{K} x_i \frac{\sum_{j=1}^{K} \tau_{j,i} G_{j,i} x_j}{\sum_{j=1}^{K} G_{j,i} x_j} \tag{73}$$

with

$$\tau_{j,i} = \frac{g_{j,i} - g_{j,i}}{\tilde{R}T} \tag{74}$$

and

$$G_{j,i} = \exp(-\alpha_{j,i} \tau_{j,i}). \tag{75}$$

Here, $g_{i,j}$ describes the interaction energy between molecules of type i and j which implies

$$g_{j,i} = g_{i,j} \tag{76}$$

$\alpha_{i,j}$ is the nonrandomness parameter which should lie between 0 and 1. Additionally, it is usually assumed that

$$\alpha_{j,i} = \alpha_{i,j} \tag{77}$$

resulting in

$$\tau_{i,i} = 0 \tag{78}$$

and

$$G_{i,i} = 1. \tag{79}$$

The activity coefficient is described by the following expression:

$$\ln \gamma_i = \frac{\sum_{j=1}^{K} \tau_{j,i} G_{j,i} x_j}{\sum_{j=1}^{K} G_{j,i} x_j} + \sum_{j=1}^{K} \frac{x_j G_{i,j}}{\sum_{k=1}^{K} G_{k,j} x_k} \left(\tau_{i,j} - \frac{\sum_{l=1}^{K} \tau_{l,j} G_{l,j} x_l}{\sum_{l=1}^{K} G_{l,j} x_l}\right). \tag{80}$$

For a binary system the parameters are two values of $(g_{j,i} - g_{i,i})$ as well as $\alpha_{i,j}$. Thus, the NRTL model has three binary parameters which allow relatively flexible fitting even for highly nonideal systems. For most systems though experimental information is not accurate enough to significantly determine the three independent parameters, thus often $\alpha_{i,j}$ is fixed to values of e.g., 0.2 or 0.3, which correspond to typical values of the nonrandomness parameter.

3.2.4 UNIQUAC Model

The UNIQUAC model was first derived by Abrams and Prausnitz [37] and later validated by Maurer and Prausnitz [38]. The expression for the molar Gibbs energy is divided into two expressions

$$\tilde{g}^{\mathrm{E}} = \tilde{g}^{\mathrm{E}}_{\mathrm{comb}} + \tilde{g}^{\mathrm{E}}_{\mathrm{res}}, \tag{81}$$

where the combinatorial part describes the effects of molecular size and shape and the residual part accounts for the effect of energetic interactions. For the combinatorial part, the Guggenheim–Staverman expression is used:

$$\tilde{g}^{\mathrm{E}}_{\mathrm{comb}} = \tilde{R}T \sum_{i=1}^{K} x_i \ln \frac{\varphi_i}{x_i} + \tilde{R}T \frac{z}{2} \sum_{i=1}^{K} q_i x_i \ln \frac{\psi_i}{\varphi_i}, \tag{82}$$

where z is the coordination number, $z = 10$ is assumed. φ_i is the volume fraction of component i in the system

$$\varphi_i = \frac{x_i r_i}{\sum_{j=1}^{K} x_j r_j} \tag{83}$$

and ψ_i its surface fraction:

$$\psi_i = \frac{x_i q_i}{\sum_{j=1}^{K} x_j q_j}, \tag{84}$$

with r_i the volume parameter and q_i the surface parameter determined from van der Waals volumes and surfaces obtained with the Bondi method [39], normalized with appropriate reference values given by Abrams and Prausnitz:

$$r_i = \frac{\tilde{v}_{\mathrm{vdW,Bondi},i}}{\tilde{v}_{\mathrm{ref}}} \quad \text{with } \tilde{v}_{\mathrm{ref}} = 15.17 \ \frac{\mathrm{cm}^2}{\mathrm{mol}}, \tag{85}$$

$$q_i = \frac{\tilde{a}_{\mathrm{vdW,Bondi},i}}{\tilde{a}_{\mathrm{ref}}} \quad \text{with } \tilde{a}_{\mathrm{ref}} = 2.5 \times 10^9 \ \frac{\mathrm{cm}^2}{\mathrm{mol}}. \tag{86}$$

The van der Waals volumes and surfaces can in principle be determined from the increment method given by Bondi [39], but the r_i and q_i can also be found directly in data collections such as [7].

The residual term of the UNIQUAC model accounts for interaction energies $u_{i,j}$:

$$\tilde{g}^{\mathrm{E}}_{\mathrm{res}} = -\tilde{R}T \sum_{i=1}^{K} x_i q_i \ln \sum_{j=1}^{K} \psi_j \tau_{j,i} \tag{87}$$

with

$$\tau_{j,i} = \frac{u_{j,i} - u_{i,i}}{\tilde{R}T}. \tag{88}$$

The expression for the activity coefficient is equally split into two contributions:

$$\ln \gamma_i = \ln \gamma_{i,\mathrm{comb}} + \ln \gamma_{i,\mathrm{res}} \tag{89}$$

with

$$\ln \gamma_{i,\mathrm{comb}} = 1 - \frac{\varphi_i}{x_i} + \ln \frac{\varphi_i}{x_i} - \frac{z}{2} q_i \left(1 - \frac{\varphi_i}{\psi_i} + \ln \frac{\varphi_i}{\psi_i}\right), \tag{90}$$

$$\ln \gamma_{i,\mathrm{res}} = q_i \left(1 - \ln \left[\sum_{j=1}^{K} \psi_j \tau_{j,i}\right] - \sum_{j=1}^{K} \frac{\psi_j \tau_{i,j}}{\sum_{k=1}^{K} \psi_k \tau_{k,j}}\right). \tag{91}$$

Also with the UNIQUAC model strongly nonideal and associating mixtures can be dealt with. Again, from the two parameters $(u_{j,i} - u_{i,i})$ for each binary subsystem the thermodynamic behavior of a multicomponent system can be described.

3.2.5 Group-Contribution Method UNIFAC

The model parameters of the $\tilde{g}^{\mathrm{E}}$-models presented so far have to be determined by fitting to experimental VLE information. It has been shown by Fredenslund et al. [40] that it is possible to consistently represent the thermodynamic behavior not by activity coefficients for the molecular species present in the system but rather for the chemical groups constituting them. This has the advantage that the resulting interaction-energy parameters, which correspondingly refer to the interactions between groups, can first be determined from data for characteristic substances, where the parameters are fitted simultaneously to data of many mixtures of components with the respective groups. The parameters can then be used for any system the components of which consist of these groups. This is obviously a tedious fitting task.

The UNIFAC model can be efficiently evaluated with the notation of Sørensen et al. [41]:

$$\ln(\gamma_i) = 1 - \bar{R}_i + \ln \bar{R}_i + q_i \left[1 - \ln \bar{Q}_i - \frac{z}{2}\left(1 - \frac{\bar{R}_i}{\bar{Q}_i} + \ln \frac{\bar{R}_i}{\bar{Q}_i}\right)\right] - \sum_{j=1}^{N} \left(\Theta_j \frac{S_{j,i}}{\eta_j} - G_{j,i} \ln \frac{S_{j,i}}{\eta_j}\right), \tag{92}$$

where j runs over all N structural groups. The individual variables in this equation follow from

$$r_i = \sum_{j=1}^{N} v_j^{(i)} R_j, \quad q_i = \sum_{j=1}^{N} v_j^{(i)} Q_j, \tag{93}$$

$$\bar{R}_i = \frac{r_i}{\sum_{k=1}^{K} x_k r_k}, \quad \bar{Q}_i = \frac{q_i}{\sum_{k=1}^{K} x_k q_k}, \tag{94}$$

$$G_{j,i} = Q_j v_j^{(i)}, \quad \Theta_j = \sum_{k=1}^{K} G_{j,k} x_k, \tag{95}$$

$$\tau_{m,j} = \exp\left(-\frac{a_{m,j}}{T}\right), \quad z = 10, \tag{96}$$

$$S_{j,i} = \sum_{m=1}^{N} G_{m,i} \tau_{m,j}, \quad \eta_j = \sum_{k=1}^{K} S_{j,k} x_k, \tag{97}$$

where index k counts the components, and indices j and m count the structural groups. $v_j^{(i)}$ is the number of groups of type j within molecule i. The meaning of the other variables closely corresponds to those of the UNIQUAC model. $a_{m,j}$ are the energy parameters corresponding to the interactions between the groups that have been fitted to an entire set of data for many systems of components with various structural groups. A small selection of the parameters is presented in Tables 2 and 3.

The original UNIFAC model has been modified by two groups leading to mod. UNIFAC (Lyngby) [42] and mod. UNIFAC (Dortmund) [43], where the latter appears to be relatively frequently applied. Both modifications take temperature-dependent parameters into account. The parameter base for mod. UNIFAC (Dortmund) is continually extended by Gmehling and coworkers funded by the so-called UNIFAC consortium. These parameters are regularly published with a certain time delay and are then available to the public (see [44] for the most recent set of parameters that can also be downloaded there. Published parameters can be found also in [45–47]).

3.2.6 Quantum-Chemical Predictions

In recent years, the COMSO-RS or COSMO-Therm method has been proposed and developed by Klamt [48, 49]. This model is based on quantum-chemical calculations for the charge distribution on the surface of the molecules. Then suitable thermodynamic expressions are applied to describe the molecules interacting via these surfaces. Thus, a method is available that allows purely predictive description of thermodynamic behavior of mixtures solely based on calculations without any experiments.

It is generally accepted that the COSMO approach gives reasonable values for many systems, where of course a lesser accuracy has to be expected as compared with the aforementioned methods, which are fitted to the experiment. Especially, when comparing different systems COSMO often gives the correct order for the thermodynamic behavior, making the method suitable for screening purposes. Currently, many investigations are under way to test the COSMO method for extreme systems such as e.g., ionic liquids.

Example 1

(a) Calculate the fugacity coefficient at the vapor pressure at $T = 232.15$ K for the pure components 1,4-dioxane (1) and water (2) according to the scheme of Tsonopoulos. The following properties are given:

$p_1^s = 0.159$ bar, $T_{c,1} = 588.15$ K, $p_{c,1} = 54.72$ bar, $\omega_1 = 0.288$, $\mu_1 = 0.45$ D and

$p_2^s = 0.123$ bar, $T_{c,2} = 647.3$ K, $p_{c,2} = 220.64$ bar, $\omega_2 = 0.344$.

(b) Calculate the fugacities in a corresponding gas mixture of dioxane and water at $y_1 = 0.4729$ and $p_1^s = 0.2079$ bar with the same assumptions using the Lorentz combining rule [Eq. (43)].

Solution

(a) With the correlation of Tsonopoulos, Eq. (34), the following values are obtained for the pure-component

D5.1. Table 2. Volume and surface parameters of UNIQUAC and UNIFAC for selected groups (A refers to aromatic, F to furan)

Main group	Subgroup	No.	R_j	Q_j	Examples for group assignment	
1 CH_2	CH_3	1	0.9011	0.848	Hexane	$2CH_3$, $4CH_2$
	CH_2	2	0.6744	0.540	2-methyl propane	$3CH_3$, 1CH
	CH	3	0.4469	0.228	2,2-dimethyl propane	$4CH_3$, 1C
	C	4	0.2195	0.000		
2 C=C	CH_2=CH	5	1.3454	1.176	1-hexene	$1CH_3$, $3CH_2$, $1CH_2$=CH
	CH=CH	6	1.1167	0.867	2-hexene	$2CH_3$, $2CH_2$, 1CH=CH
	CH_2=C	7	1.1173	0.988	2-methyl-1-butene	$2CH_3$, $1CH_2$, $1CH_2$=C
	CH=C	8	0.8886	0.676	2-methyl-2-butene	$3CH_3$, 1CH=C
	C=C	9	0.6605	0.485	2,3-dimethyl butene-2	$4CH_3$, 1C=C
3 ACH	ACH	10	0.5313	0.400	Benzene	6ACH
	AC	11	0.3652	0.120	Styrene	$1CH_2$=CH, 5ACH, 1AC
4 $ACCH_2$	$ACCH_3$	12	1.2663	0.968	Toluene	5ACH, $1ACCH_3$
	$ACCH_2$	13	1.0396	0.660	Ethyl benzene	$1CH_3$, 5ACH, $1ACCH_2$
	ACCH	14	0.8121	0.348	Cumene	$2CH_3$, 5ACH, 1ACCH
5 OH	OH	15	1.0000	1.200	2-propanol	$2CH_3$, 1CH, 1OH
6 CH_3OH	CH_3OH	16	1.4311	1.432	Methanol	$1CH_3OH$
7 H_2O	H_2O	17	0.9200	1.400	Water	$1H_2O$
8 ACOH	ACOH	18	0.8952	0.680	Phenol	5ACH, 1ACOH
13 CH_2O	CH_3O	25	1.1450	1.088	Dimethyl ether	$1CH_3$, $1CH_3O$
	CH_2O	26	0.9183	0.780	Diethyl ether	$2CH_3$, $1CH_2$, $1CH_2O$
	CH-O	27	0.6908	0.468	Diisopropyl ether	$4CH_3$, 1CH, 1CH-O
	FCH_2O	28	0.9183	1.100	Tetrahydrofuran	$3CH_2$, $1FCH_2O$

D5.1. Table 3. Group interaction parameters $a_{m,j}$ in K for describing vapor–liquid equilibrium. Note that $a_{m,j\neq a_{j,m}}$

$m\downarrow$ $j\rightarrow$	CH_2	C=C	ACH	$ACCH_2$	OH	CH_3OH	H_2O	ACOH	CH_2O
CH_2	0.00	86.02	61.13	76.50	986.50	697.20	1318.00	1333.00	251.50
C=C	−35.36	0.00	38.81	74.15	524.10	787.60	270.60	526.10	214.50
ACH	−11.12	3.45	0.00	167.00	636.10	637.35	903.80	1329.00	32.14
$ACCH_2$	−69.70	−113.60	−146.80	0.00	803.20	603.25	5695.00	884.90	213.10
OH	156.40	457.00	89.60	25.82	0.00	−137.10	353.50	−259.70	28.06
CH_3OH	16.51	−12.52	−50.00	−44.50	249.10	0.00	−181.00	−101.70	−128.60
H_2O	300.00	496.10	362.30	377.60	−229.10	289.60	0.00	324.50	540.50
ACOH	275.80	217.50	25.34	244.20	−451.60	−265.20	−601.80	0.00	−162.90
CH_2O	83.36	26.51	52.13	65.69	237.70	238.40	−314.70	−178.50	0.00

virial coefficients: $\tilde{B}_{1,1} = -1575\ \mathrm{cm^2/mol}$ and $\tilde{B}_{2,2} = -1674\ \mathrm{cm^2/mol}$. From this, the fugacities result as $\varphi_1 = 0.99067$ and $\varphi_2 = 0.99211$ with Eq. (33). Note that the equation of state has to be solved for molar volume or density at given temperature and pressure, leading to a quadratic equation resulting directly from Eq. (30).

(b) With the Lorentz combining rule $\tilde{B}_{1,2} = \tilde{B}_{2,1} = -1624\ \mathrm{cm^2/mol}$ is obtained, leading to $\tilde{B} = -1638\ \mathrm{cm^3/mol}$, $\varphi_1 = 0.98790$, and $\varphi_2 = 0.98714$.

Example 2

(a) Calculate the VLE for a mixture of 1,4-dioxane (1) and water (2), assuming ideal vapor phase and neglecting the Poynting correction. The nonideality of the liquid can be described with the UNIQUAC model. The following data are given, which can be obtained from the DECHEMA Data Series [7]:
$r_1 = 3.1854$, $q_1 = 2.64$, $r_2 = 0.92$, $q_2 = 1.4$, $z = 10$, $u_{2,1} - u_{1,1} = -1762.7\ \mathrm{J/mol}$, $u_{1,2} - u_{2,2} = 5516.2\ \mathrm{J/mol}$, $x_1 = 0.25$, and $T = 323.15\ \mathrm{K}$. The vapor pressures are specified in example 1.

It should be noted in passing that the DECHEMA values for the geometry parameters obviously do not take decrements for dioxane rings specified by Bondi [39] into account. Since the published parameters for the UNIQUAC model have been fitted assuming these geometry values, the slightly erroneous values have to be used consequently.

(b) Show that the vapor mixture of Example 1b corresponds to the saturated state in equilibrium with the liquid of (a) of this example, if the vapor nonidealities are accounted for with the virial equation and only the Poynting correction is neglected.

Solution

(a) From the UNIQUAC modelresults (Eqs. (89–91)) $\ln(\gamma_1) = 0.4135 + 0.4877$, $\ln(\gamma_2) = 0.1513 + 0.0152$, $\gamma_1 = 2.4626$, and $\gamma_2 = 1.1811$. From Eq. (63) results $p^s = x_1\gamma_1 p_1^s + x_2\gamma_2 p_2^s = 0.207\ \mathrm{bar}$ and $y_1 = 0.4733$.

(b) According to Eq. (60) it has to be shown that

$$x_i y_i p_i^s \varphi_i^{s,v} - y_i \varphi_i p^s \approx 0$$

for both components. With the values determined in Example 1 for the fugacity coefficients, it can be shown that this difference is close to 10^{-6} which can be regarded to be essentially zero compared to the individual terms.

Example 3

According to the DECHEMA Data Series [7], a typical set of VLE data is chosen for the system 1,4-dioxane (1) and water (2) at $T = 323.15\ \mathrm{K}$:

x_1	y_1	p^s
–	–	mbar
0.0000	0.0000	123.34
0.0330	0.2050	153.00
0.1100	0.3960	190.17
0.1890	0.4750	206.84
0.2510	0.5050	214.41
0.3710	0.5340	220.62
0.4610	0.5450	222.43
0.5160	0.5490	223.91
0.5540	0.5540	223.03
0.5600	0.5570	223.63
0.6340	0.5750	223.83
0.7020	0.5970	220.85
0.7840	0.6170	219.41
0.8300	0.6550	212.21
0.9030	0.7320	201.53
0.9440	0.8080	187.78
1.0000	1.0000	160.64

Assuming ideal vapor phase and neglecting Poynting correction, the parameters of the Wilson equation are to be determined from

(a) regression of all data points,
(b) only from the coordinates of the azeotrope, and
(c) from the activity coefficients at infinite dilution.

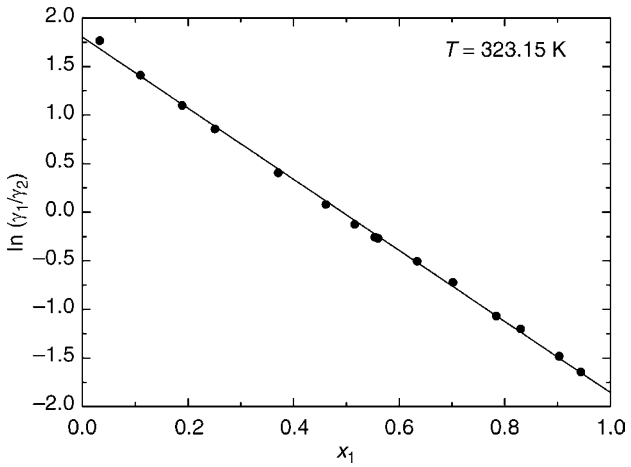

D5.1. Fig. 8. Graphical determination of infinite-dilution activity coefficients for the system 1,4-dioxane (1) and water (2).

Solution

The activity coefficients can be backed out with the assumptions from Eq. (63), where the pure-component vapor pressures are taken from Example 1.

The coordinates of the azeotrope are $x_{1,az} = y_{1,az} = 0.5540$ and $p^s_{az} = 223.03$ mbar. The activity coefficients at infinite dilution can be determined readily from a plot of $\ln(\gamma_1/\gamma_2)$ versus mol fraction in the liquid as shown in Fig. 8, where a linear dependence has been fitted. It has to be kept in mind that the activity coefficient of the component in excess tends toward unity in this limit. From the regression follows $\ln(\gamma_1^\infty) = 1.8023$ and $\ln(\gamma_2^\infty) = 1.8560$.

The resulting Wilson parameters are

Method of determination	$\Lambda_{1,2}$	$\Lambda_{2,1}$	γ_1^∞	γ_2^∞	Mean deviation Δp mbar	Mean deviation Δy_1 –
(a) All data	0.26048	0.29066	7.8035	7.2075	1.494	0.0082
(b) Azeotropic data	0.17655	0.35077	10.8415	6.4953	2.181	0.0089
(c) Values of γ_i^∞	0.33036	0.30532	6.0633	6.3983	7.429	0.0174

Besides the parameters the predicted infinite-dilution activity coefficients are shown [the exact values are those of solution (c)] as well as mean absolute deviations in the last two columns. It is obvious that quite accurate fitting is possible when all data are taken into account. The simplifying assumptions in (b) and (c) lead to reasonable results as well.

Example 4

Calculate the activity coefficients of the system 1,4-dioxane (1) and water (2) at $x_1 = 0.25$ and $T = 323.15$ K with the UNIFAC method. The following values for the intermediate variables are obtained.

Group j	R_j	Q_j	$v_j^{(1)}$	$v_j^{(2)}$
1 H_2O	0.9200	1.4000	0	1
2 CH_2	0.6744	0.5400	2	0
3 CH_2O	0.9183	0.7800	2	0

Group j	$G_{j,1}$	$G_{j,2}$	Θ_j
1 H_2O	0.0000	1.4000	1.0500
2 CH_2	1.0800	0.0000	0.2700
3 CH_2O	1.5600	0.0000	0.3900

Component i	r_i	q_i	$\bar{R}_i$	$\bar{Q}_i$
1	3.1854	2.6400	2.1431	1.5439
2	0.9200	1.4000	0.6190	0.8187

Group j	$a_{j,1}$(K)	$a_{j,2}$(K)	$a_{j,3}$(K)
1	0.0	300.0	540.5
2	1318.0	0.0	251.5
3	−314.7	83.4	0.0

Group j	$\tau_{j,1}$(K)	$\tau_{j,2}$(K)	$\frac{\tau_{j,3}}{K}$
1	1.0000	0.3952	0.1878
2	0.0169	1.0000	0.4592
3	2.6481	0.7726	1.0000

$S_{1,1}$	4.1494
$S_{2,1}$	2.2853
$S_{3,1}$	2.0559
$S_{1,2}$	1.4000
$S_{2,2}$	0.5533
$S_{3,2}$	0.2629

η_1	2.0873
η_2	0.9863
η_3	0.7111

It follows for $\gamma_1 = 1.8832$ and $\gamma_1 = 1.3145$. Comparing these values to Example 2, it is obvious that they capture the trend but for this strongly nonideal system certain deviations have to be expected.

4 Bibliography

1. Barthel JMG, Krienke H, Kunz W (1998) Physical chemistry of electrolyte solutions. Steinkopff, Darmstadt
2. Evans DF, Wennerström H (1994) The colloidal domain: Where physics, chemistry, biology, and technology meet. VCH Publishers, New York
3. Modell M, Reid RC (1983) Thermodynamics and its applications, 2nd edn. Prentice Hall, Englewood Cliffs
4. Pfennig A (2004) Thermodynamik der Gemische. Springer Verlag, Berlin
5. Sandler SI (1999) Chemical and engineering thermodynamics, 3rd edn. John Wiley & Sons, New York
6. Smith JM, Van Ness HC, Abbott M (2005) Introduction to chemical engineering thermodynamics, 7th edn. McGraw Hill, New York
7. DECHEMA Data Series with many volumes, starting with Gmehling J; Onken U (1977) Vapor–liquid equilibrium data collection. DECHEMA, Frankfurt

8. Boublík T, Fried V, Hála E (1973) The vapour pressures of pure substances. Elsevier, Amsterdam
9. Dymond JH, Smith EB (1980) The virial coefficients of pure gases and mixtures. Clarendon Press, Oxford
10. Gmehling J, Menke J, Krafczyk J, Fischer K (1994) Azeotropic data. VCH, Weinheim
11. Hirata M, Ohe S, Nagahama K (1975) Computer aided data book of vapor-liquid equilibria. Kodansha, Tokyo
12. Wichterle I, Linek J, Hála E (1973) Vapor-liquid equilibrium data bibliography. Elsevier, Amsterdam
13. Wohlfarth C (1994) Vapour-liquid equilibrium data of binary polymer solutions. Elsevier, Amsterdam
14. Landolt-Börnstein (1971/1977) Zahlenwerte und Funktionen. Vol. II, part 2a, Vol. IV, part 4, 6th ed., "new series", group IV, Vol. 3. Springer, Berlin
15. Horsley LH Azeotropic Data, Vol. 3; Advances in chemistry series 116. American Chemical Society, Washington, DC, 1952, 1962, 1973
16. DETHERM, DECHEMA, http://www.dechema.de (01.06.2009)
17. Dortmund Data Bank, DDBST, http://www.ddbst.de (01.06.2009)
18. Prausnitz JM, Chueh PL (1968) Computer calculations for high-pressure vapor-liquid equilibria. Prentice-Hall, Englewood Cliffs
19. Topliss RJ (1985) Techniques to facilitate the use of equations of state for complex fluid-phase equilibria. Ph.D. thesis, University of California, Berkeley
20. Tsonopoulos C (1974) An empirical correlation of second virial coefficients. AIChE J 20:263–272
21. Tsonopoulos C (1975) Second virial coefficients of polar haloalkanes. AIChE J 24:827–829
22. Tsonopoulos C (1978) Second virial coefficients of water pollutants. AIChE J 24:1112–1115
23. Tsonopoulos C (2003) Second virial coefficients of polar haloalkanes - 2002. Fluid Phase Equilib 211:35–49
24. Reid RC, Prausnitz JM, Poling BE (1987) The properties of gases ans liquids, 4th edn. McGraw-Hill, New York
25. Redlich O, Kwong JNS (1949) On the thermodynamics of solutions. V. An equation of state. Fugacities of gaseous solutions. Chem Rev 44:233–244
26. Soave G (1972) Equilibrium constants from a modified Redlich-Kwong equation of state. Chem Eng Sci 27:1197–1203
27. Peng D-Y, Robinson DB (1976) Two and three phase equilibrium calculations for systems containing water. Can J Chem Eng 54:595–599
28. Benedict M, Webb GB, Rubin LC (1940) An empirical equation for thermodynamic properties of light hydrocarbons and their mixtures. I. methane, ethane, propane and n-butane. J Chem Phys 8:334–345
29. Benedict M, Webb GB, Rubin LC (1942) An empirical equation for thermodynamic properties of light hydrocarbons and their mixtures. II. Mixtures of methane, ethane, propane and n-butane. J Chem Phys 10:747–758
30. Bender E (1973) The calculation of phase equilibria from a thermal equation of state applied to the pure fluids argon, nitrogen, oxygen and their mixtures. Verlag C.F. Müller, Karlsruhe
31. Lee BI, Kesler MG (1975) A generalized thermodynamic correlation based on three-parameter corresponding states. AIChE J 21:510–527
32. Huang SH, Radosz M (1990) Equation of state for small, large, polydisperse, and associating molecules. Ind Eng Chem Res 29:2284–2294
33. Huang SH, Radosz M (1991) Equation of state for small, large, polydisperse, and associating molecules: extension to fluid mixtures. Ind Eng Chem Res 30:1994–2005
34. Redlich O, Kister AT (1948) Algebraic representation of thermodynamic properties and the classification of solutions. Ind Eng Chem 40:345–348
35. Wilson GM (1964) Vapor–liquid equilibrium. XI. A new expression for the excess free energy of mixing. J Am Chem Soc 86:127–130
36. Renon H, Prausnitz JM (1968) Local compositions in thermodynamic excess functions for liquid mixtures. AIChE J 14:135–144
37. Abrams DS, Prausnitz JM (1975) Statistical thermodynamics of liquid mixtures: a new expression for the excess Gibbs energy of partly or completely miscible systems. AIChE J 21:116–128
38. Maurer G, Prausnitz JM (1978) On the derivation and extension of the UNIQUAC equation. Fluid Phase Equilib 2:91–99
39. Bondi A (1968) Physical properties of molecular crystals, liquids and glasses. John Wiley & Sons, New York
40. Fredenslund A, Jones RL, Prausnitz JM (1975) Group-contribution estimation of activity coefficients in nonideal liquid mixtures. AIChE J 21:1086–1099
41. Magnussen T, Sørensen JM, Rasmussen P, Fredenslund A (1980) Liquid-liquid equilibrium data: their retrieval, correlation and prediction Part III: prediction. Fluid Phase Equilib 4:151–163
42. Larsen BL, Rasmussen P, Fredenslund A (1987) A Modified UNIFAC group-contribution model for prediction of phase equilibria and heats of mixing. Ind Eng Chem Res 26:2274–2286
43. Weidlich U, Gmehling J (1987) A modified UNIFAC model. 1. Prediction of VLE, h^E and γ^∞.Ind Eng Chem Res 26:1372–1381
44. DDBST: http://unifac.ddbst.de/, 01.06.2009
45. Gmehling J, Li J, Schiller M (1993) A modified UNIFAC model. 2. Present parameter matrix and results for different thermodynamic properties. Ind Eng Chem Res 32:178–193
46. Gmehling J, Lohmann J, Jakob A, Li J, Joh R (1998) A modified UNIFAC (Dortmund) model. 3. Revision and extension. Ind Eng Chem Res 37:4876–4882
47. Gmehling J, Wittig R, Lohmann J, Joh R (2002) A modified UNIFAC (Dortmund) model. 4. Revision and extension. Ind Eng Chem Res 41:1678–1688
48. Klamt A, Schüürmann G (1993) COSMO: a new approach to dielectric screening in solvents with explicit expressions for the screening energy and its gradient. J Chem Soc Perkin Trans 2:799–805
49. Klamt A, Eckert F (2000) COSMO-RS: a novel and efficient method for the A priori prediction of thermophysical data of liquids. Fluid Phase Equilib 172:43–72

D5.2 Polymer Solutions: Vapor–Liquid Equilibrium and Diffusion Coefficients

Wilhelm Schabel
Karlsruher Institut für Technologie (KIT), Karlsruhe, Germany

1 Vapor–Liquid Equilibrium of Polymer Solutions

The phase equilibrium between a polymer solution and the solvent vapor is usually treated like a vapor–liquid equilibrium (VLE) even if the Many thermodynamic models for polymer solutions are available in the literature and in principle the models can be categorized in two groups: equations of state models for the description of both phases e.g., [1, 2] or lattice models for calculating the activity coefficients in the liquid phase. Activity coefficient models are usually easier to use for practical applications and calculations than equations of state. The well-known activity coefficients model for thermodynamics of polymers is the model of Flory [3] and Huggins of 1942 [4]. This (correlative) model is mathematically pretty simple to use and hence suited for practical calculations, but it generally requires tabulated fitting (correlative) parameters of interaction parameters to measured data. An overview of various methods of measuring the VLE of polymer solutions is given e.g., by Schabel et al [5].

On the other hand there are predictive group contribution methods which offer the advantage for the user that the activity coefficients can be calculated solely from known and tabulated group contributions of the molecular structure of the substances. The UNIFAC (Universal Functional Activity Coefficient), and UNIQUAC (Functional Group Activity Coefficients), (see Subchap. D5.1) represents a commonly used group contribution method that has proven its reliability for the determination of activity coefficients in liquid mixtures of low molecular weight. In mixtures of high molecular weight, e.g., polymer solutions, however, the predicted values for the activities are too low because of free-volume effects. Oishi and Prausnitz [6] therefore suggested extending the activity coefficients calculated with the UNIFAC method by an appropriate free-volume contribution named UNIFAC-free volume (UNIFAC-FV). In this chapter both methods (correlative and predictive) will be introduced and equations and examples are given to use them.

1.1 Flory–Huggins Model

The model of Flory [3] and Huggins [4] considers the polymer solution as a three-dimensional lattice of spheres. The solvent molecules are considered as single spheres, whereas the polymer is regarded as a chain of these.

Flory and Huggins calculated the combinatorial entropy of mixing based on statistical deliberations and they set the enthalpy of mixing to zero assuming an ideal athermal mixture.

For the activity a_i, i.e., the ratio of the partial pressure p_i of the solvent over the polymer solution and the saturation vapor pressure of the pure solvent p_{0i} (see also Subchap. D5.1 or, e.g., [7]), it can be written:

$$\ln a_i^{\text{entropy of mixing}} = \ln \frac{p_i}{p_{0i}} = \ln\ \phi_i + \left(1 - \frac{\tilde{\nu}_i}{\tilde{\nu}_\mathrm{P}}\right) \phi_\mathrm{P} \qquad (1)$$

ϕ is the volume fraction of the solvent (i) and the polymer (P), respectively, and $\tilde{\nu}\left(= \tilde{M}_i / \rho_i\right)$ is the molar volume of the component i (m^3/mol). The volume fraction for binary systems is calculated (neglecting excess volumes) from the mass fractions x_i and the densities of the pure substances ρ_i and ρ_P

$$1 - \phi_i = \phi_\mathrm{P} = \frac{x_\mathrm{P}}{x_i \rho_\mathrm{P} / \rho_i + x_\mathrm{P}} \qquad (2)$$

Usually volume fractions or mass fractions are used to determine the composition of polymer solutions. Molar fractions will yield values being close to 1, even at low solvent contents, due to the usually significantly different molar masses of the polymer and the solvent. Since attractive and repulsive forces are interacting between molecules, the exchange of one molecule in a mixture of component 1 against one molecule or parts of a chain of molecules of substance 2 requires work. This work is considered as enthalpy of mixing and contributes to the activity. According to Huggins [4] this contribution can be written as:

$$\ln a_i^{\text{enthalpy of mixing}} = \chi_{i\mathrm{P}}\, \phi_\mathrm{P}^2 \qquad (3)$$

with a Flory–Huggins interaction parameter χ_{iP}. This parameter was considered by this theory to be independent of the composition (entropic influence) but shows a dependence on temperature. Adding the two parts of the activity from Eqs. (1) and (3), the result is the well-known Flory–Huggins equation for the activity of the solvent (i) in a polymer (P).

$$\ln a_i = \ln \phi_i + (1 - \frac{\tilde{v}_i}{\tilde{v}_P}) \phi_P + \chi_{iP} \phi_P^2 \qquad (4)$$

For polymer solutions, the molar volume $\tilde{v}_i \left(= \tilde{M}_i/\rho_i\right)$ of the solvent and the polymer are significantly different $(\tilde{v}_i << \tilde{v}_P)$ and the form of the Flory–Huggins equation for polymer solutions that is usually found in literature is reduced to:

$$\begin{aligned} \ln a_i &= \ln \phi_i + \phi_P + \chi_{iP}\phi_P^2 \\ \text{or} \quad a_i &= \phi_i \exp\left(\phi_P + \chi_{iP}\phi_P^2\right) \end{aligned} \qquad (5)$$

According to Hildebrand and Scott [8], the Flory–Huggins interaction parameter χ_{iP} can be predicted for a polymer-solvent system (independently of the composition) using solubility parameters. Various experimental results of the past, however, show that the interaction parameter χ_{iP} is often dependent on the composition of the system [9–12] which has to be taken into account. This discrepancy can be explained by the assumption that the macromolecules are like a chain of spheres occupying certain lattice positions and, according to theory, the other lattice positions are readily accessible for the solvent molecules. But most polymer systems will create knots and entanglements making the free lattice positions on the inside inaccessible for the solvent molecules. Therefore an important assumption of the F–H Theory is not fulfilled and χ_{iP} has to include entropic influences that are dependent on the configuration and the composition within the lattice. Tapavicza and Prausnitz [13] and Flory [14] show that this entropic contribution has to be taken into account and can be significantly large. Therefore, it is usually not possible to predict the interaction parameters and they must be determined and fitted to measured data. Flory [14] proposes to fit the interaction parameter as a function of the volume fraction with the following empirical polynomial expression:

$$\chi_{iP}(\phi_P) = \chi_1 + \chi_2 \cdot \phi_P + \chi_3 \cdot \phi_P^2 \qquad (6)$$

In Table 1 the coefficients [The given parameters cannot be used for the calculation of the excess Gibbs energy (G^E).] for describing the concentration dependence of $\chi_{iP}(\phi_P)$ according to Eq. (6) are listed for some polymer-solvent systems. Further values and measured data can be found, e.g., in [9, 10, 15–17]. The temperature dependence of the interaction parameter can be described by the following equation according to Koningsveld and Kleintjens [18]:

$$\chi_{iP}(\phi_P, T) = \chi_{iP}(\phi_P) \cdot (1 + \beta/T + \gamma \cdot T + \delta \cdot \ln T) \qquad (7)$$

This equation can as well be used to describe phase separation of polymer solutions. Danner and High [10] has successfully described critical upper and lower separation temperatures (UCST and LCST) by fitting this equation to measured data. An extension of the Flory–Huggins equation for cross-linked polymers can be found, e.g., in [19]. The swelling of the polymer is accounted for by an additional summand in the exponent of Eq. (5). The values given here in this chapter and Table 1 are fitted to predict VLE and are not suited to predict phase separation by means of G^E models.

D5.2. Table 1. Coefficients[1] for describing the concentration dependence of the Flory–Huggins interaction parameter $\chi_{iP}(\phi_P)$ according to Eq. (6). For a few polymer–solvent systems the equilibrium data from [9, 11, 12], has been used to fit Eq. (6) for a defined temperature or a temperature interval

Polymer–solvent system (source)	T (°C)	χ_1	χ_2	χ_3
Benzene–PIB [9]	25	0.51	0.23	0.32
Cyclohexane–PIB [9]	25	0.44	−0.08	0.07
Cyclohexane–PS [9]	34	0.51	0.15	0.46
Toluene–PS [9]	25	0.43	−0.31	−0.04
Methylene chloride–CTA [9]	25	0.35	0.19	0.08
n-Octane–PDMS [9]	20	0.50	−0.04	0.04
Methanol–PVAc [11]	20–60	0.41	−0.25	1.21
Toluene–PVAc [11]	20–60	0.43	0.32	0.18
Benzene–PVAc [12]	20–50	0.42	–	–

CTA cellulose triacetate; *PDMS* polydimethylsiloxane; *PIB* polyisobutylene; *PS* polystyrene; *PVAc* polyvinyl acetate.

1.2 UNIFAC-FV Model

With the extension of the UNIFAC (Subchap. D5.1) method for polymers, UNIFAC-FV, vapor–liquid equilibrium of polymer-solvent systems can be predicted from group contributions of the molecules without having any experimental data. The model provides good results for organic solvents and (normal) polymers. It fails, however, for water as a solvent and for block copolymers and cross-linked polymers.

The UNIFAC model by Fredenslund and Gmehling is based on the assumption that the molecules of a mixture can be divided into functional groups. The interactions between the molecules are thought to be caused by the interactions of these groups. Some surface and volume interaction parameters are listed in Subchap. D5.1. In the UNIFAC-FV model the activity is the sum of a combinatorial, a residual and a free-volume contribution:

$$\ln a_i = \ln a_i^C + \ln a_i^R + \ln a_i^{FV} \qquad (8)$$

The third term $\left(\ln a_i^{FV}\right)$ takes the influence of the free-volume into account. This is the volume that is not occupied by molecules on a microscopic scale whereas it is part of the macroscopic volume of a substance. The free-volume is for instance also responsible for the thermal expansion behavior of liquids. The free-volume contribution can be neglected for the calculation of the activity of monomers and is therefore absent in the original UNIFAC model. However, it has to be considered when calculating an equilibrium involving a polymer component because polymer chains tend to form clusters making certain positions inaccessible for solvent molecules as it was explained above. Oishi and Prausnitz [6] used an equation of state

simplified by Flory to derive the contribution of the free-volume to the activity.

The combinatorial contribution (see Subchap. D5.1, vapor–liquid equilibium) can be written as follows:

$$\ln a_i^{\mathrm{C}} = \ln \varphi_i' + 1 - \frac{\varphi_i'}{\tilde{x}_i} + \frac{z}{2} \cdot \tilde{M}_i \cdot q_i \cdot \ln \frac{\theta_i}{\varphi_i'} - \frac{z}{2} \cdot \tilde{M}_i \cdot q_i \cdot \left(1 - \frac{\varphi_i'}{\theta_i}\right) \tag{9}$$

In a binary mixture of polymer and solvent it follows:

$$1 - \frac{\varphi_i'}{\tilde{x}_i} = \varphi_P' \left(1 - \frac{\tilde{v}_i}{\tilde{v}_P}\right) \approx \varphi_P' \tag{10}$$

With Eq. (10) the first two summands in Eq. (9) have the same form as the Flory–Huggins Eq. (4). The index ′, however, shows that the volume fractions are calculated differently. The reduced group volume r and the reduced group surface q are calculated as follows:

$$r_i = \frac{1}{\tilde{M}_i} \cdot \sum_k \nu_k^{(i)} R_k \tag{11}$$

$$q_i = \frac{1}{\tilde{M}_i} \cdot \sum_k \nu_k^{(i)} Q_k \tag{12}$$

with the number ν_k of functional groups of the type k in component i. Q and R are group parameters (See Subchap. D5.1). The volume fraction φ_i' and the surface fraction θ_i are defined by

$$\varphi_i' = \frac{x_i r_i}{\sum_j^n x_j r_j} \tag{13}$$

$$\theta_i = \frac{x_i q_i}{\sum_j^n x_j q_j} \tag{14}$$

with x_i being the mass fraction of component i in a mixture of n components. In Eq. (9), z is the coordination number. According to Oishi and Prausnitz [6] z can be set to 10.

The residual contribution of component i which is composed of groups with the index k is:

$$\ln a_i^{\mathrm{R}} = \sum \nu_k \left(\ln \Gamma_k - \ln \Gamma_k^{\text{pure } i}\right) \tag{15}$$

Here Γ_k is the residual group activity.

$$\ln \Gamma_k = Q_k \left(1 - \ln\left(\sum_m \Theta_m \Psi_{mk}\right) - \sum_m \frac{\Theta_m \Psi_{km}}{\sum_n \Theta_n \Psi_{nm}}\right) \tag{16}$$

with

$$\Theta_m = \frac{Q_m W_m / \tilde{M}_m}{\sum_n Q_n W_n / \tilde{M}_n} \tag{17}$$

and

$$W_m = x_i \frac{\nu_m^{(i)} \tilde{M}_m}{\tilde{M}_i} \tag{18}$$

$\tilde{M}_m$ is the molar mass of group m and W_m the mass fraction of this group. Ψ_{mn} is a group interaction parameter (see Subchap. D5.1) that is given by:

$$\Psi_{mn} = \exp\left(-\frac{a_{mn}}{T}\right) \tag{19}$$

a_{mn} is a group interaction parameter that can be found in Subchap. D5.1. It is not to be confused with the activity a.

The term $\Gamma_k^{\text{pure } i}$ in Eq. (15) is calculated using Eqs. (16) through (18) with a mass fraction x_i of 1. Its purpose is to ensure that the activity of the pure substance is 1.

The free-volume contribution to the activity can be calculated according to Oishi and Prausnitz [6] using the following formula:

$$\ln a_i^{\mathrm{FV}} = 3c_i \cdot \ln\left(\frac{\hat{v}_i^{1/3} - 1}{\hat{v}_{\mathrm{M}}^{1/3} - 1}\right) - c_i \cdot \frac{\hat{v}_i / \hat{v}_{\mathrm{M}} - 1}{1 - 1 \Big/ \hat{v}_i^{1/3}} \tag{20}$$

Here, $\hat{v}$ is the reduced volume of component i and the mixture M, respectively. It is a measure of the ratio of the free volume and the total volume. $\hat{v}_i$ can be calculated with the density and the molar group volume using the following empirical correlation [6]:

$$\hat{v}_i = \frac{1}{15.17 \cdot 1.28 \cdot r_i \cdot \rho_i / (\mathrm{g/cm^3})} \tag{21}$$

However, this correlation fails for aqueous solutions due to the anomalous expansion behavior of water.

The reduced volume of the mixture is given by [6]:

$$\hat{v}_{\mathrm{M}} = \frac{\sum_i x_i / \rho_i / (\mathrm{g/cm^3}) - 1}{15.17 \cdot 1.28 \cdot \sum_i r_i \cdot x_i} \tag{22}$$

c_i is a parameter derived from the perturbed hard-chain theory [1, 6] specifying the total number of external degrees of freedom. For solvents like methanol or ethanol c_i equals 1.1, for larger molecules a "somewhat larger value should be used" (quote [6]). For benzene $c_{\text{benzene}} = 1.54$ is found in [1], for toluene $c_{\text{toluene}} = 1.649$ in [20].

2 Diffusion Coefficients in Polymer Solutions

Values for diffusion coefficients in polymer-solvent systems can span several orders of magnitude. Depending on solvent concentration and temperature, they range from the values for diffusion in liquids ($\sim 10^{-9}$ m^2/s) to those for solids from (10^{-13} to $\sim 10^{-19}$ m^2/s) (see Fig. 3).

Common approaches for the calculation of diffusion coefficients in liquids such as those by Einstein [21], Wilke and Chang [22] and Reid et al [23] are therefore only applicable for very dilute polymer solutions. Their predictive power fails for high polymer concentrations because of the specific properties of the macromolecules.

Over the past decades the free-volume theory has established itself as an apt model for the description of the concentration and temperature dependence of diffusion coefficients in polymer solutions. This model has been based on the extension of the free-volume theory to liquids by Cohen and Turnbull [24]. They assumed that the volume of a liquid described by a

hard-sphere model can be divided into the volume that is occupied by molecules and a volume of vacancies which are distributed throughout the material (free volume). This free volume is continuously redistributed by thermal fluctuations. A diffusion step (jump) can occur if a sufficiently large free-volume element is adjacent to a molecule. These assumptions lead to the following expression for the self-diffusion coefficient in a pure liquid.

$$D_i = A \cdot \exp\left(-\gamma \frac{V^*}{V^f}\right) \tag{23}$$

Equation (23) resembles the Arrhenius equation and describes the probability that there is a free volume V^f next to a molecule which is larger than its size V^*. The volume of the liquid at 0 K is used for estimating the size of a molecule. The overlap factor γ is introduced because two molecules may share the same free volume. γ should lie between 0.5 and 1.

Fujita [25] has adapted the free-volume theory for the description of diffusion in polymer solutions. Vrentas and Duda [26] have refined and complemented this concept. They assume that not only an entire molecule can act as a jumping unit but also parts of a polymer chain. For the self-diffusion (Based on the original model for *pure* liquids [24], this expression is called self-diffusion coefficient even if used for solvents in polymers. Strictly speaking this nomenclature is only valid for diffusion processes of one component in itself and in absence of concentration gradients.) coefficient of solvents in polymers they present the following equation:

$$D_i = D_{0i} \cdot \exp\left(-\frac{x_i \hat{V}_i^* + \xi_{iP} \cdot x_P \hat{V}_P^*}{\hat{V}^{FH}/\gamma_{iP}}\right) \tag{24}$$

D_{0i} is a pre-exponential factor, $\hat{V}_i^*$ is the specific critical hole free volume of component i, ξ_{iP} is the ratio of the critical molar volume of solvent jumping units and the critical molar volume of polymer jumping units, and γ_{iP} is the overlap factor. $\hat{V}^{FH}$ is the specific average hole free volume of the polymer solution. It is additively composed of the hole free volume of the different components.

In polymers not the entire free volume is redistributed by thermal fluctuations. Therefore, Vrentas and Duda [26] classify the free volume in two parts: the interstitial free volume whose redistribution requires a large amount of energy and which is thus distributed evenly among the molecules of one species and the hole free volume which is continuously redistributed by thermal fluctuations and is therefore the critical variable in diffusion (see Fig. 1).

Below the glass transition temperature T_g a part of the hole free volume is "frozen" so that it is larger than the equilibrium value. Above the glass transition temperature of the polymer solution Vrentas and Duda [26] suggest the following equation for the specific average hole free volume $\hat{V}^{FH}$ in Eq. (24):

$$\begin{aligned}\hat{V}^{FH} &= x_i \hat{V}_{FH,i} + x_P \hat{V}_{FH,P} \\ &= x_i K_{I,i}\left(K_{II,i} - T_{gi} + T\right) + x_P K_{I,P}\left(K_{II,P} - T_{gP} + T\right)\end{aligned} \tag{25}$$

T_{gi} is the glass transition temperature of the component i, and T the temperature of the polymer solution in Kelvin. $K_{I,i}$ and $K_{II,i}$ are free volume parameters derived from other physical parameters describing the expansion behavior of component i.

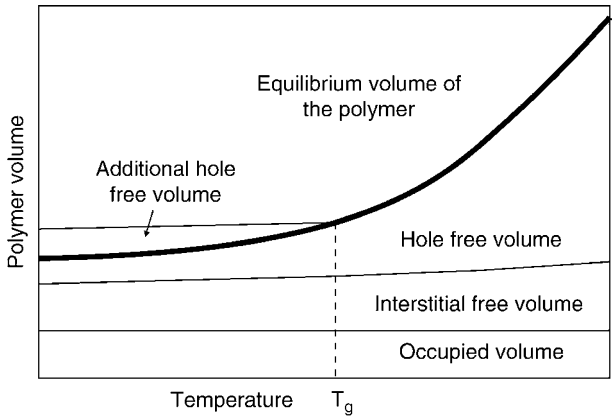

D5.2. Fig. 1. Schematic diagram of the free-volume as a function of temperature.

According to Zielinski and Duda [27] free-volume parameters can be predicted using data of pure substances and group contribution methods. For the pre-exponential factor D_{0i} and the ratio of the critical molar volumes of the jumping units ξ_{iP} varying values are found in the literature. As they have a significant influence on the precision of the diffusion coefficients, these two parameters are usually fitted to measured data [28].

In the literature often a thermodynamic factor θ is introduced into Eq. (23) leading to the following form:

$$D = D_i \cdot \theta = D_i \cdot (1-\varphi_i)^2 \cdot (1 - 2\chi_{iP}\varphi_i) \tag{26}$$

The factor θ is calculated with the Flory–Huggins interaction parameter χ_{iP}. This derivation, however, is only valid for a constant, concentration independent value for χ_{iP}. Table 1 shows that this is not the case for the majority of polymer-solvent systems. It must be noted that if using an average constant value for χ_{iP} the thermodynamic factor θ can also assume negative values. It is recommended to calculate diffusion coefficients exclusively using Eqs. (23) and (24). This has to be considered when fitting D_{0i} and ξ_{iP} in Eq. (23) to measured data. Free-volume parameters for some common solvents and polymers can be found in the literature [27, 29].

3 Examples

3.1 Example 1: Phase Equilibrium of Polymer Solutions

The activity of methanol in polyvinyl acetate (PVAc) is to be determined at 20°C and for a solvent ratio (kg solvent/kg polymer) of $X = 0.1$.

Calculation of the activity according to Flory–Huggins:

From Chap. D3: $\rho_1 = 0.792$ g/cm^3 and from [12] $\rho_P = 1.189$ g/cm^3. Equation (2) yields:

$$\phi_p = \frac{1}{0.1\left(1.186/0.792\text{g/cm}^3\right) + 1} = 0.869$$

The interaction parameters in Eq. (6) for the material system methanol–PVAc are taken from Table 1.

$$\chi_{lP} = 0.41 - 0.25\phi_P + 1.21\phi_P^2 = 1.106$$

The activity is calculated using Eq. (5):

$$a_1 = 0.131 \exp\left(0.869 + 1.106 \cdot 0.869^2\right) = 0.720$$

Calculation of the activity according to UNIFAC-FV:
Step 1: Breaking down the components into different functional groups and preparing the group parameters

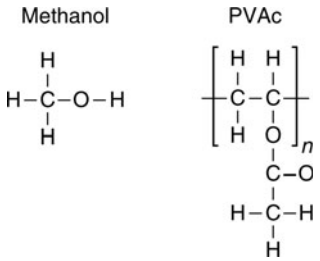

Component 1 is methanol:
$1 \times CH_3OH$ main group no. 6, sub-group no. 16 (not $1 \times CH_3$ and $1 \times$ OH!)
Component 2 is PVAc:
$1 \times CH_2$ – main group no. 1, sub-group no. 2
$1 \times CH$ – main group no. 1, sub-group no. 3
$1 \times COOCH_3$ – main group no. 11, sub-group no. 22
From Subchap. D5.1:

$R_2 = 0.6744 \quad Q_2 = 0.540 \quad \tilde{M}_2 = 14\,\text{g/mol}$
$R_3 = 0.4469 \quad Q_3 = 0.228 \quad \tilde{M}_3 = 13\,\text{g/mol}$
$R_{16} = 1.4311 \quad Q_{16} = 1.432 \quad \tilde{M}_{16} = 32\,\text{g/mol}$
$R_{22} = 1.9031 \quad Q_{22} = 1.728 \quad \tilde{M}_{22} = 59\,\text{g/mol}$
$a_{16} = 697.2\,\text{K} \quad a_{61} = 16.51\,\text{K}$
$a_{111} = 232.1\text{K} \quad a_{111} = 114.8\,\text{K}$
$a_{611} = -10.72\,\text{K} \quad a_{116} = 249.63\,\text{K}$

$(a_{1\,1} = a_{6\,6} = a_{11\,11} = 0)$
from [14]: $c_1 = 1.1$.

Step 2: Mass fractions

$$x_1 = \frac{0.1}{1+0.1} = 0.0909;\; x_2 = \frac{1}{1+0.1} = 0.9091$$

Step 3: Volume and surface fractions (p = degree of polymerization): Eqs. (11–14)

$$r_1 = \frac{1}{32} \cdot (1 \cdot 1.4311) = 0.04472$$

$$r_2 = \frac{1}{p \cdot 86} \cdot p \cdot (1 \cdot 0.6744 + 1 \cdot 0.4496 + 1 \cdot 1.9031) = 0.03517$$

$$q_1 = \frac{1}{32} \cdot (1 \cdot 1.432) = 0.04475$$

$$q_2 = \frac{1}{p \cdot 86} \cdot p \cdot (1 \cdot 0.540 + 1 \cdot 0.228 + 1 \cdot 1.1728) = 0.02902$$

$$\varphi_1' = \frac{0.0909 \cdot 0.04472}{0.0909 \cdot 0.04472 + 0.9091 \cdot 0.03517} = 0.1128$$

$$\varphi_2' = \frac{0.9091 \cdot 0.03517}{0.0909 \cdot 0.04472 + 0.9091 \cdot 0.03517} = 0.8872$$

$$\theta_1 = \frac{0.0909 \cdot 0.04475}{0.0909 \cdot 0.04475 + 0.9091 \cdot 0.02902} = 0.1336$$

Step 4: Combinatorial contribution to the activity Eq. (9):

$$\ln a_1^C = \ln 0.1128 + 0.8827 + \frac{10}{2} \cdot 32 \cdot 0.04475 \cdot \ln\frac{0.1336}{0.1128} - \frac{10}{2} \cdot 32 \cdot 0.04475 \cdot \left(1 - \frac{0.1128}{0.1336}\right) = -1.198$$

Step 5: Interaction parameters Eq. (19):

$$\Psi_{16} = \exp\left(-\frac{679.20\text{k}}{293.15\text{k}}\right) = 0.0927$$

$\Psi_{61} = 0.9452 \quad \Psi_{111} = 0.4531$
$\Psi_{111} = 0.6760 \quad \Psi_{611} = 1.0372$
$\Psi_{116} = 0.4268 \quad \Psi_{11} = \Psi_{66} = \Psi_{1111} = 1$

Step 6: Group mass fractions Eq. (18):

$$W_2 = 0.9091 \cdot \frac{p \cdot 14}{p \cdot 86} = 0.1480$$

$$W_3 = 0.9091 \cdot \frac{p \cdot 13}{p \cdot 86} = 0.1374$$

$$W_{16} = 0.0909 \cdot \frac{1 \cdot 32}{32} = 0.0909$$

$$W_{22} = 0.9091 \cdot \frac{p \cdot 59}{p \cdot 86} = 0.6237$$

Step 7: Group surface fractions Eq. (17):

$$\Theta_2 = \frac{0.540 \cdot (0.1480/14)}{0.540 \cdot (0.1480/14) + 0.228 \cdot (0.1374/13) + 1.432 \cdot (0.0909/32) + 1.728 \cdot (0.6237/59)} = 0.1875$$

$$\Theta_3 = \frac{0.228 \cdot (0.1374/13)}{0.540 \cdot (0.1480/14) + 0.228 \cdot (0.1374/13) + 1.432 \cdot (0.0909/32) + 1.728 \cdot (0.6237/59)} = 0.0791$$

$$\Theta_{16} = \frac{1.432 \cdot (0.0909/32)}{0.540 \cdot (0.1480/14) + 0.228 \cdot (0.1374/13) + 1.432 \cdot (0.0909/32) + 1.728 \cdot (0.6237/59)} = 0.1336$$

$$\Theta_{22} = \frac{1.728 \cdot (0.6237/59)}{0.540 \cdot (0.1480/14) + 0.228 \cdot (0.1374/13) + 1.432 \cdot (0.0909/32) + 1.728 \cdot (0.6237/59)} = 0.5998$$

Step 8: Residual group activity Eq. (16):

$$\ln \Gamma_{16} = 1.432 \cdot \left[1 - \ln(0.1875 \cdot 0.0927 + 0.0791 \cdot 0.0927 + 0.1336 \cdot 1 + 0.5998 \cdot 0.4268) - \frac{0.1875 \cdot 0.9452}{0.1875 \cdot 1 + 0.0791 \cdot 1 + 0.1336 \cdot 0.9452 + 0.5998 \cdot 0.6760} - \frac{0.0791 \cdot 0.9452}{0.1875 \cdot 1 + 0.0791 \cdot 1 + 0.1336 \cdot 0.9452 + 0.5998 \cdot 0.6760} - \frac{0.1336 \cdot 1}{0.1875 \cdot 0.0927 + 0.0791 \cdot 0.0927 + 0.1336 \cdot 1 + 0.5998 \cdot 0.4268} - \frac{0.5998 \cdot 1.0372}{0.1875 \cdot 0.4531 + 0.0791 \cdot 0.4531 + 0.1336 \cdot 1.0372 + 0.5998 \cdot 1}\right] = 0.7433$$

Pure comp. 1: $W_2 = W_3 = W_{22} = 0 \quad W_{16} = 1$;

$$\Theta_2 = \Theta_3 = \Theta_{22} = 0 \quad \Theta_{16} = 1.$$

$$\ln \Gamma_{16}^{\text{pure 1}} = 1.432 \cdot \left[1 - \ln(0 + 0 + 1 \cdot 1 + 0) - 0 - 0 - \frac{1 \cdot 1}{0 + 0 + 1 \cdot 1 + 0} - 0\right] = 0$$

Step 9: Residual contribution to the activity Eq. (15):

$$\ln a_1^R = 1 \cdot (0.7433 - 0) = 0.7433$$

Step 10: Reduced molar volumes Eqs. (21) and (22):

$$\hat{v}_1 = \frac{1}{15.17 \cdot 1.28 \cdot 0.04472 \cdot 0.792} = 1.4540$$

$$\hat{v}_M = \frac{(0.0909/0.792) + (0.9091/1.189)}{15.17 \cdot 1.28 \cdot (0.04472 \cdot 0.0909 + 0.03517 \cdot 0.9091)} = 1.2566$$

Step 11: Free volume contribution Eq. (20):

$$\ln a_1^{FV} = 3 \cdot 1.1 \cdot \ln\left(\frac{1.4540^{1/3} - 1}{1.2566^{1/3} - 1}\right) - 1.1 \cdot \frac{(1.4540/1.2566) - 1}{1 - (1/1.4540^{1/3})} = 0.2386$$

Step 12: Predicting the activity Eq. (8):

$$a_1 = \exp(-1.1980 + 0.7433 + 0.2386) = 0.806$$

(The result is approximately 10% higher than the measured values according to [11, 12]) (Fig. 2)

3.2 Example 2: Diffusion Coefficients in Polymer Solutions

The diffusion coefficient of methanol and toluene in PVAc at 40°C and at a solvent ratio of $X_i = 0.10$ are to be determined.

Calculating the diffusion coefficients with the free-volume theory [26]:

$$x_i = \frac{X_i}{(1 + X_i)} = \frac{0.1}{1 + 0.1} = 0.0909$$

The free-volume parameters of the systems methanol/toluene–PVAc from the literature are listed in Table 2.

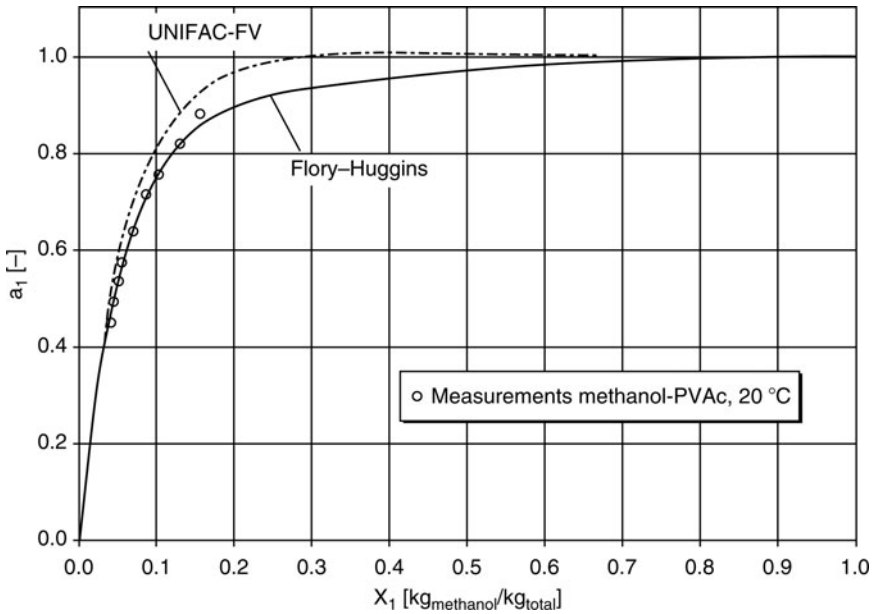

D5.2. Fig. 2. Activity a_1 of methanol in PVAc as a function of the mass fraction x_1. Measured values from [11] at 20°C are compared to the calculations with the Flory–Huggins and the Universal Functional Activity Coefficient (UNIFAC-FV) models of the example.

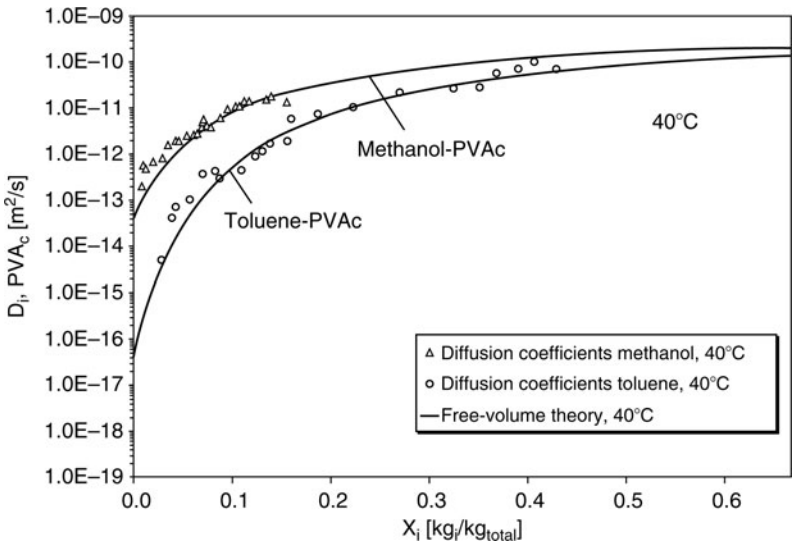

D5.2. Fig. 3. Diffusion coefficients of methanol and toluene in PVAc at 40°C as a function of the solvent ratio. The diagram shows measured values from [28] and the calculations using the free-volume theory of the example. The diffusion coefficient of the larger molecule toluene exhibits a stronger dependence on the composition than that of the smaller molecule methanol.

D5.2. Table 2. Free-volume parameters for methanol, toluene and polyvinyl acetate (PVAc) from [11, 27, 29]

FV-parameter(source)	PVAc	
	Methanol	Toluol
$\hat{V}_1^*$ (cm^3/g)	0.961 [29]	0.917 [27]
$\hat{V}_p^*$(cm^3/g)	0.728 [27]	
$K_{1,i}/\gamma_{iP}$ (cm^3/g K)	$1.17{\cdot}10^{-3}$ [29]	$1.45{\cdot}10^{-3}$ [29]
$K_{1,P}/\gamma_{iP}$ (cm^3/g K)	$0.433{\cdot}10^{-3}$ [27]	
$K_{II,i}$-T_{gi} (K)	−48.4 [29]	−86.32 [27]
$K_{II,P}$-T_{gP} (K)	−258.2 [27]	
D_{0i} (m^2/s)	$6.53{\cdot}10^{-9}$ [11]	$3.9{\cdot}10^{-9}$ [11]
ξ_{iP} (–)	0.39 [11]	0.60 [11]

With Eqs. (24) and (25) it can be calculated:
Methanol–PVAc:

$$\left(\frac{\hat{V}^{FH}}{\gamma_{iP}}\right) = 0.0909 \cdot 1.17 \cdot 10^{-3}(-48.4 + 313.15) + 0.9091 \cdot 0.433 \cdot 10^{-3}(-258.2 + 313.15)\,(cm^3/g) = 0.0498\ (cm^3/g)$$

$$D := 6.53 \cdot 10^{-9} \cdot \exp\left(-\frac{0.0909 \cdot 0.961 + 0.39 \cdot 0.9091 \cdot 0.728}{0.0498}\right)$$

$$(m^2/s) = 6.33 \cdot 10^{-12}\,(m^2/s)$$

Toluol–PVAc:

$$\left(\frac{\hat{V}^{FH}}{\gamma_{iP}}\right) = 0.0909 \cdot 1.45 \cdot 10^{-3}(-86.32 + 313.15) + 0.9091 \cdot 0.433 \cdot 10^{-3}(-258.2 + 313.15)(cm^3/g) = 0.0515\ (cm^3/g)$$

$$D = 3.9 \cdot 10^{-9} \exp\left(-\frac{0.0909 \cdot 0.917 + 0.6 \cdot 0.9091 \cdot 0.728}{0.0515}\right)$$

$$(m^2/s) = 3.48 \cdot 10^{-13}\,(m^2/s)$$

4 Bibliography

1. Beret S, Prausnitz JM (1975) Perturbed hard-chain theory: an equation of state for fluid containing small or large molecules. AIChE J 21:1123–1132
2. Gross J, Sadowski G (2001) Perturbed-chain saft: an equation of state based on a perturbation theory for chain molecules. Ind Eng Chem Res 40:1244–1260
3. Flory PJ (1942) Thermodynamics of high polymer solutions. J Chem Phy 10:51–61
4. Huggins ML (1942) Thermodynamic properties of solutions of long-chain compounds. Ann New York Acad Sci 43:1–32
5. Schabel W, Mamaliga I, Kind M (2003) Messungen von Sorptionsisothermen und Diffusionskoeffizienten in Polymerlösungen. Chemie Ingenieur Technik 75(1):36–41
6. Oishi T, Prausnitz JM (1978) Estimation of solvent activities in polymer solutions using a group contribution method. Ind Eng Chem Process Des Dev 17:333–339
7. Gmehling J et al (1977–2002) Vapor-liquid equilibrium data collection, 26 parts. DECHEMA Chemistry Data Series, Frankfurt
8. Hildebrand J, Scott R (1962) Regular solutions. Prentice-Hall, Englewood Cliffs, NJ
9. Brandrup J (1989) Polymer handbook, 3rd edn. Wiley, New York
10. Danner RP, High MS (1993) Handbook of polymer solution thermodynamics. AiChE, New York
11. Mamaliga I, Schabel W, Kind M (2004) Measurements of sorption isotherms and diffusion coefficients by means of a magnetic suspension balance. Chem Eng Process 43:753–763. doi:10.1016/S0255–2701(03)00077–1
12. Saure R, Schlünder EU (1995) Sorption isotherms for methanol, benzene and ethanol on poly(vinyl acetate) (PVAc). Chem Eng Process 34:305–316
13. Tapavicza S, Prausnitz JM (1975) Thermodynamik von Polymerlösungen: Eine Einführung. Chem Ing Techn 47:552–562
14. Flory PJ (1970) Thermodynamics of polymer solutions. Discuss Faraday Soc 49:7–29
15. Wohlfarth C (1994) Vapour-liquid equilibrium data of binary polymer solutions. In: Physical sciences data 44. Elsevier, Amsterdam
16. Young RJ, Lovell PA (1991). Introduction to polymers, 2nd edn. Chapmann & Hall, London
17. Wohlfarth C (2004) CRC handbook of thermodynamic data of aqueous polymer solutions. CRC Press
18. Koningsveld R, Kleintjens LA (1985) Liquid-liquid phase separation in multicomponent polymer systems. 22. Thermodynamics of statistical copolymers. Macromolecules 18:243–252
19. Gusler GM, Cohen Y (1994) Equilibrium swelling of highly cross-linked polymeric resins. Ind Eng Chem Res 33:2345–2357
20. Pretel EJ, Danner RP (1996) Vapor-liquid equilibrium properties for polymer-solvent mixtures using the perturbed soft chain theory. Fluid Phase Equil 115:1–23
21. Einstein A (1905) Annalen der Physik 17:549
22. Wilke CR, Chang PC (1955) AIChE J 1:264
23. Reid RC, Prausnitz JM, Sherwood TK (1977) The properties of gases and liquids, 3rd edn. McGraw-Hill, New York
24. Cohen MH, Turnbull D (1959) Molecular transport in liquids and glasses. J Chem Phys 31(5):1164–1169
25. Fujita H (1961) Fortschr Hochpolym Forsch 3:
26. Vrentas JS, Duda JL (1977) Diffusion in polymer-solvent systems I. J of Polym Sci Polym Phys Ed 15:403
27. Zielinski JM, Duda JL (1992) Predicting polymer/solvent diffusion coefficients using free-volume theory. AIChE J 38(3):405–415
28. Schabel W, Scharfer P, Müller M, et al (2003) Messung und Simulation von Konzentrationsprofilen bei der Trocknung binärer Polymerlösungen. Chemie Ingenieur Technik 75(9):1336–1344
29. Hong SU, Benesi AJ, Duda JL (1996) Use the solvent free-volume parameters from ^{13}c relaxations to study polymer/solvent diffusion behaviour. Polym Int 39(3):243–249

Further Reading

Goydan R, Reid RC, Tseng H-S (1989) Estimation of the solubilities of organic compounds in polymers by group-contribution methods. Ind Eng Chem Res 28:445–454

Kontogeorgis GM (1994) Equations of state and activity coefficient models for vapor-liquid equililibria calculations in polymer solutions. AIChE J 40:1711–1727

Hao W, Elbro HS, Alessi P (1992) Polymer solution data collection. Chemistry data series. Vol. 14, Pt. 2: Solvent activity coefficients at infinite dilution, Pt. 3: Liquid-liquid-equilibrium. DECHEMA, Frankfurt

D5.3 Vapor Pressures of Aqueous Salt Solutions

Hartwig Wolf
Alstom Switzerland Ltd., Baden, Switzerland

1 Introduction

Solving a nonvolatile salt (2) in water (1) results in a reduction of the vapor pressure p_1 of the solution compared to the saturation vapor pressure p_1^* of pure water. The lowering of the vapor pressure is considered as colligative property such as boiling point elevation, freezing point depression, and osmotic pressure, i.e., a property that depends only on the number of solved molecules. These phenomena are caused by the presence of the solved salt, which lowers the chemical potential of the solution compared to the solvent. If the interactions between the molecules of solute and solvent are the same as those between the molecules of each substance by itself, the solution is called an ideal solution and the lowering of the vapor pressure Δp_1 represents a pure entropy effect and is proportional to the mole fraction $\tilde{x}_2$ of the solute:

$$\Delta p_1 = \tilde{x}_2 p_1^*. \tag{1}$$

In case of salts, the calculation of $\tilde{x}_2$ has to take into account the amount of substance n_2 of the ions that are dissolved:

$$n_2 = n_{2,0}(1 + \alpha(i - 1)), \tag{2}$$

which is depended on the amount of substance of the salt $n_{2,0}$ in the solution, the degree of dissociation α, and the number of ions i of the salt molecule.

When interactions between like and unlike molecules are different, the solution shows a nonideal behavior. The lowering of the vapor pressure can be calculated using the extended Raoult's law:

$$\Delta p_1 = [1 - (1 - \tilde{x}_2)\gamma_1]p_1^*, \tag{3}$$

in which the activity coefficient γ_1 takes into account the deviation from ideal behavior. Both the degree of dissociation α and the activity coefficient γ_1 depend strongly on the mole fraction $\tilde{x}_2$ of the solute; thus, a prediction of the lowering of the vapor pressure relies strongly on experimental data.

2 Data and Approximations for Vapor Pressure Estimation

Boiling temperatures of different saturated salt solutions are shown in Tables 1a and 1b as a function of vapor pressure and salt precipitation. A further column lists the relative vapor pressure $\varphi = p_1/p_1^*\{T.\}$ above the salt solutions at a temperature of $T = 25°C$. In addition, parameters A and B for a basic approximation

$$p_1/[Pa] = \mathrm{A}\, 10^{10} \mathrm{e}^{-\frac{10^3\ \mathrm{B}}{273.15\ +\ T/[°\mathrm{C}]}}, \tag{4}$$

are given. The relative error of the approximation is less than 5% for all data used. The applicable temperature range for the exponential function is listed in the column aside.

Tables 2a–2d comprise the dependency of the temperatures of different unsaturated solutions on the vapor pressure and the salt concentration. Otherwise, the tables correspond to Tables 1a and 1b with respect to their structure.

The vapor pressures above different salt solutions at temperatures 25 and 100°C are indicated in Tables 3a–3c as a function of the salt concentration m. Likewise, the parameters of an elementary function, i.e., of a polynomial of third order, fit:

$$p_1 = p_1^* + A\, m + B\, m^2 + C\, m^3, \tag{5}$$

The underlying data are reflected with a relative error less than 5%, mostly less than 2%.

Finally, Table 4 covers values of vapor pressures for saturated salt solutions at high temperatures as a function of temperature. Table 5 contains data for temperatures of saturated solutions of salt mixtures under variation of the vapor pressure.

All the tables are based on the data from the literature listed in the chapter bibliography. The parameters of the approximations have been set using the least-squares method. Substances for which an insufficient number of data have been found and measured data, which have been recognized as not reliable were not considered within this article.

3 Enclosure A: Saturated Salt Solutions

D5.3. Table 1a. Vapor pressure above saturated salt solutions; given are the temperatures of the salt solution in °C as function of the vapor pressure p_1

Solute	Formula of precipitation	Vapor Pressure p1 (Pa)										ϕ (25°C)	$p_1/[Pa] = A\,10^{10} e^{-\frac{10^3 B}{273.15+T/[°C]}}$		Temperature range (°C)		
		100	200	500	1,000	2,000	5,000	10,000	20,000	50,000	100,000		A	B			
Silver nitrate	$AgNO_3$					20.1	37.9	52.9	69.4			0.82	1.8110	4.6979	10.0	..	72.0
Barium chloride	$BaCl_2 * 2H_2O$				8.0	19.0	35.1	48.4	63.0	84.3		0.90	8.9925	5.1488	5.0	..	90.0
Tartaric acid	$C_4H_6O_6$						37.1					0.87	1.2117	4.5607	22.7	..	46.3
Calcium bromide	$CaBr_2$	−6.1	5.5										0.1819	4.4646	−17.4	..	21.7
Calcium bromide	$CaCl_2 * 2H_2O$					49.4							2.0387	5.2056	45.0	..	55.0
Calcium bromide	$CaCl_2 * 4H_2O$				31.4								0.0298	3.8387	30.0	..	40.0
Calcium bromide	$CaCl_2 * 6H_2O$			11.3								0.30	0.0761	4.0491	5.0	..	25.0
Calcium hydrogen phosphate	$CaHPO_4 * 2H_2O$					18.1	33.8	46.9				0.95	11.8399	5.2128	10.0	..	50.0
Calcium nitrate	$Ca(NO_3)_2$				38.9	50.7							18.0344	5.9329	30.0	..	60.0
Calcium nitrate *)	$Ca(NO_3)_2 * 4H_2O$		−9.7	4.5	16.3	29.1						0.51	1.2639	4.7325	−17.6	..	31.1
Cadmium bromide	$CdBr_2 * 4H_2O$						35.8					0.89	3.8383	4.8979	24.0	..	41.5
Potassium acetate	CH_3COOK	−5.8	4.3	18.9	30.9							0.23	1.8710	5.0919	−17.6	..	31.1
Cobalt chloride	$CoCl_2 * 6H_2O$					24.2	44.9					0.66	0.2573	4.1825	18.0	..	52.3
Urea	$CO(NH_2)_2$					21.8	39.8					0.75	1.5441	4.6771	10.0	..	50.0
Chromium oxide	CrO_3				19.1	30.8	47.8	62.0				0.45	6.5546	5.2601	15.0	..	70.0
Cesium bromide	CsBr				8.9	20.1						0.84	7.2446	5.1044	5.0	..	25.0
Cesium fluoride	CsF	32.3	45.0	63.4	78.8								0.3776	5.3297	30.0	..	80.0
Cesium iodide	CsI				7.8	18.8						0.91	10.1786	5.1807	5.0	..	25.0
Copper chloride	$CuCl_2 * 2H_2O$		−9.7	2.8	13.0	24.1	40.1					0.67	12.4334	5.3336	−17.4	..	40.5
Copper sulfate	$CuSO_4 * 5H_2O$					18.8	33.5					0.94	41.8432	5.5932	9.8	..	38.7
Iron sulfate	$FeSO_4 * 7H_2O$					18.7						1.00	404.8582	6.2531	11.0	..	25.3
Oxalic acid	$H_2C_2O_4 * 2H_2O$		17.8	29.6	39.2	49.5						0.11	316.0015	6.8330	15.0	..	50.0
Potassium bromide	KBr				9.5	20.7	37.0	50.5	65.3			0.81	8.0135	5.1449	5.0	..	80.0
Potassium chloride *)	KCl				8.6	19.9	36.4	50.2	65.2	87.4		0.85	5.8807	5.0397	5.0	..	95.5
Potassium chlorate	$KClO_3$							46.5	61.2				7.3127	5.0524	40.0	..	80.0
Potassium thiocyanate	KCNS				17.2	31.6	53.1	71.5				0.46	0.2222	4.2428	15.0	..	72.0
Potassium carbonate	$K_2CO_3 * 2H_2O$			7.4	19.3	32.3	51.3	67.3				0.43	1.2235	4.7725	2.0	..	80.0
Potassium chromate	K_2CrO_4							49.3	64.1	86.0			6.9193	5.0784	40.0	..	90.0
Potassium dichromate	$K_2Cr_2O_7$						33.5	46.9	61.5			0.98	7.9803	5.0862	23.7	..	80.0
Potassium fluoride	KF						62.9	78.2					4.1613	5.3553	50.0	..	90.0
Potassium dihydrogen phosphate	KH_2PO_4					18.0	34.0	47.3				0.96	8.9189	5.1276	10.0	..	50.0
Potassium iodide	KI				11.7	23.5	40.7	55.1	70.9			0.69	3.5631	4.9524	5.0	..	90.0
Potassium nitrate	KNO_3				7.1	18.5	34.9	48.7				0.92	5.4804	4.9940	5.0	..	60.0

*The relative error between measured data and calculated data via indicated approximation exceeds partly values of 5%

D5.3. Table 1b. Vapor pressure above saturated salt solutions; given are the temperatures of the salt solution in °C as function of the vapor pressure p_1.

Solute	Formula of precipitation	Vapor pressure p1 (Pa)										ϕ (25°C)	$p_1/[Pa] = A\,10^{10} e^{\frac{10^3 B}{273.15+T/[°C]}}$		Temperature range (°C)		
		100	200	500	1,000	2,000	5,000	10,000	20,000	50,000	100,000		A	B			
Potassium hydroxide	KOH		17.4									0.08	6.431E-04	3.0157	10.0	..	40.0
Potassium sulfate	K_2SO_4				7.1	17.9	33.6	46.6				0.97	12.5927	5.2274	0.0	..	60.0
Lithium chloride	LiCl	1.9	13.3	29.8	43.7	58.9	81.5					0.12	0.3702	4.7926	−17.6	..	100.3
Lithium chloride	Li_2SO_4						35.6	49.0	63.6	85.1	103.3	0.87	8.5309	5.1410	24.7	..	110.0
Magnesium chloride	$MgCl_2 * 6H_2O$			12.8	24.5	37.1	55.5					0.33	2.5382	5.0742	0.0	..	62.3
Magnesium nitrate	$Mg(NO_3)_2 * 6H_2O$				15.7	28.4	47.1					0.53	1.3576	4.7442	5.0	..	50.0
Magnesium sulfate	$MgSO_4$						34.6	48.8	64.4	87.5		0.95	3.2891	4.8314	30.0	..	95.4
Manganese chloride	$MnCl_2 * 4H_2O$				14.4	25.0						0.63	30.8777	5.6218	10.6	..	25.4
Sodium bromide	$NaBr * 2H_2O$		−9.7	3.8	15.0	27.1	44.8	59.6	75.8			0.56	2.9383	4.9551	−17.6	..	80.0
Sodium chloride	NaCl			0.6	11.0	22.2	38.5	52.0	66.8	88.6		0.75	8.3028	5.1807	0.0	..	100.0
Sodium carbonate	$Na_2CO_3 * 10H_2O$					18.8						0.88	1.7753	4.6712	10.0	..	31.7
Sodium carbonate	$Na_2CO_3 * 7H_2O$											0.85	1.1443	4.5489	24.5	..	35.0
Sodium carbonate	$Na_2CO_3 * H_2O$						37.2	50.1	64.3	84.9			15.9355	5.3616	36.0	..	91.9
Sodium dichromate	$Na_2Cr_2O_7 * 2H_2O$			4.3	15.6	27.9	45.8					0.54	2.4046	4.9077	0.0	..	50.0
Sodium iodide	$NaI * 2H_2O$		−4.9	9.8	22.1	35.4						0.37	0.8933	4.7249	−12.1	..	45.0
Sodium nitrite	$NaNO_2$					24.7	41.9	56.3	72.1			0.64	3.8323	4.9946	20.0	..	80.0
Sodium nitrate	$NaNO_3$				10.4	22.2	39.5	54.0	69.8			0.74	3.2067	4.9003	5.0	..	72.5
Sodium hydroxide	NaOH		23.7	41.3								0.07	0.2408	4.8390	15.0	..	50.0
Sodium sulfite	Na_2SO_3						35.1	48.0	62.1	82.7	100.0	0.88	14.9876	5.3065	24.2	..	172.6
Sodium sulfite	$Na_2SO_3 * 7H_2O$						35.2	49.2	64.6	87.2	106.4	0.91	4.3182	4.9256	20.0	..	188.9
Sodium sulfate	Na_2SO_4						35.4	48.3				0.86	17.5087	5.3607	20.8	..	53.9
Sodium sulfate	$Na_2SO_4 * 10H_2O$				11.3	21.6						0.79	42.7477	5.6534	10.0	..	29.0
Ammonium chloride	NH_4Cl					21.4	38.1	52.1	67.4			0.78	4.9449	5.0138	10.0	..	70.0
Ammonium dihydrogen phosphate	$NH_4H_2PO_4$					18.4	34.5	48.0				0.93	7.8313	5.0976	10.0	..	50.0
Ammonium nitrate	NH_4NO_3				12.1	25.7	46.0					0.61	0.3791	4.3204	10.0	..	60.0
Ammonium sulfate	$(NH_4)_2SO_4$				9.9	20.9	37.0					0.80	10.0125	5.2139	0.0	..	50.0
Nickel chloride	$NiCl_2 * 4H_2O$						45.8						5.0234	5.1424	36.3	..	54.1
Nickel chloride	$NiCl_2 * 6H_2O$					28.2						0.53	1.0751	4.6708	19.8	..	45.2
Lead nitrate	$Pb(NO_3)_2$					17.9	34.3	47.9	62.8	84.9	103.5	0.95	5.9497	5.0083	10.0	..	130.0
Rubidium chloride	RbCl						39.7	54.4	70.7				2.4059	4.8133	30.0	..	90.0
Rubidium fluoride	RbF		32.6	50.0	64.4								0.5277	5.2252	30.0	..	80.0
Strontium chloride	$SrCl_2 * 6H_2O$		2.8	14.2	23.5	33.4						0.35	213.4587	6.3719	0.0	..	37.6
Strontium nitrate	$Sr(NO_3)_2$				8.3	19.7						0.86	5.4318	5.0130	5.0	..	25.0
Zinc sulfate	$ZnSO_4 * 7H_2O$					20.0						0.86	24.1680	5.4558	15.5	..	29.5

4 Enclosure B: Unsaturated Salt Solutions

D5.3. Table 2a. Vapor pressure above unsaturated salt solutions; given are the temperatures of the salt solution in °C as function of the vapor pressure p_1

Solute	Formula	Concentration $\left[\frac{\text{g anhydrous salt}}{100\ \text{g } H_2O}\right]$	Vapor pressure p1 (Pa)								$p_1/[Pa] = A\ 10^{10} e^{-\frac{10^3 B}{273.15+T/[°C]}}$		Temperature range (°C)		
			500	1,000	2,000	5,000	10,000	20,000	50,000	100,000	A	B			
Aluminum sulfate	$Al_2(SO_4)_3$	10.3					45.7	60.3	81.6	99.6	8.2376	5.078	40.0	..	100.0
		20.5					46.1	60.5	81.8		9.1307	5.1168	40.0	..	95.0
		39.4					47.4	61.9	83.2		9.2914	5.1434	40.0	..	95.0
Barium bromide	$BaBr_2$	29.7				33.6	46.9	61.3	82.6		9.2502	5.133	30.0	..	95.0
		50.6				34.7	48.0	62.5	83.9		9.0488	5.144	30.0	..	95.0
		74.3				36.1	49.5	64.2	85.7		8.6117	5.1525	30.0	..	95.0
Barium chloride	$BaCl_2$	10.5				33.4	46.4	60.6			12.0239	5.2102	30.0	..	70.0
		20.3				33.9	46.9	61.1			12.2011	5.2227	30.0	..	70.0
		28.9				34.4	47.5	61.6			13.1289	5.2548	30.0	..	70.0
Beryllium sulfate	$BeSO_4$	15.8				33.3	46.4	60.8	81.9		10.0911	5.1539	30.0	..	95.0
		31.5				34.5	47.6	62.0	83.0		10.8369	5.1963	30.0	..	95.0
		46.2						63.6	84.9		10.2427	5.2027	60.0	..	95.0
Calcium bromide	$CaBr_2$	20.1				33.7	47.0	61.5	82.9		8.7277	5.1169	30.0	..	100.0
		60.2				38.8	52.2	66.9	88.4		9.7696	5.2365	30.0	..	100.0
		91.9				44.9	58.5				10.7494	5.3697	30.0	..	70.0
Calcium chloride	$CaCl_2$	11.1				33.8	47.1	61.6	82.8		9.2929	5.1383	30.0	..	100.0
		45.4					54.9	70.0	92.3	111.3	6.5068	5.1457	49.6	..	125.4
		66.7	10.6	21.2	32.6	49.1	62.8	77.7	99.6	118.1	11.9292	5.4738	0.0	..	120.0
		87.5			38.4	54.9	68.7				15.0678	5.6499	30.0	..	70.0
		155.4						100.8	124.2		11.5306	5.8221	90.0	..	140.0

D5.3. Table 2a. (continued)

Solute	Formula	Concentration $\left[\frac{\text{g anhydrous salt}}{100\ \text{g } H_2O}\right]$	Vapor pressure p1 (Pa)								$p_1/[Pa] = A\,10^{10}e^{-\frac{10^3 B}{273.15+T/[°C]}}$		Temperature range (°C)		
			500	1,000	2,000	5,000	10,000	20,000	50,000	100,000	A	B			
Calcium iodide	CaI_2	33.4				34.1	47.2	61.4			12.0913	5.2241	30.0	..	70.0
		55.1				35.2	48.5	62.9			10.4897	5.1992	30.0	..	70.0
		85.7				37.8	51.2	65.8			9.7761	5.2202	30.0	..	70.0
Calcium nitrate	$Ca(NO_3)_2$	25.3				34.1	47.1				11.9573	5.2193	20.0	..	60.0
		98.8			24.6	40.7	54.1				11.805	5.3284	20.0	..	60.0
		200.0		24.9	36.5	53.3					10.5819	5.5063	20.0	..	60.0
		342.0	27.2	38.3	50.3						12.5465	5.808	20.0	..	60.0
Cobalt sulfate	$CoSO_4$	25.0				33.3	46.5	60.8	81.8	99.6	10.4655	5.1661	30.0	..	100.0
		45.0				34.1	47.4	61.9	83.1		9.3124	5.1437	30.0	..	100.0
Cesium bromide	CsBr	33.4				33.8	46.9	61.1			11.8257	5.2116	30.0	..	70.0
		74.2				34.8	48.0	62.5			9.9862	5.1764	30.0	..	70.0
		125.3				36.0	49.5	64.1			8.5351	5.1487	30.0	..	70.0
Cesium chloride	CsCl	30.0				34.1	47.3	61.7	82.9		10.1172	5.1692	30.0	..	100.0
		59.3				35.0	48.3	62.7			10.1866	5.1866	30.0	..	70.0
		92.5				36.2	49.6	64.3			8.2179	5.1392	30.0	..	70.0
		144.6				39.4	52.7	67.3			11.0385	5.2843	30.0	..	70.0
Cesium iodide	CsI	34.9				33.6	46.7	61.0			11.1334	5.1896	30.0	..	70.0
		67.4				34.3	47.5	61.9			10.1421	5.1726	30.0	..	70.0
Copper sulfate	$CuSO_4$	19.2						60.6	81.8		8.9318	5.1097	50.0	..	90.0
		30.3						61.1	82.3		9.3334	5.1321	50.0	..	90.0
Iron sulfate	$FeSO_4$	25.8						60.8	82.2		8.3763	5.0925	50.0	..	95.0
		45.6						61.7	83.0		8.7487	5.1198	50.0	..	100.0

D5.3. Table 2b. Vapor pressure above unsaturated salt solutions; given are the temperatures of the salt solution in °C as function of the vapor pressure p_1

Solute	Formula	Concentration $\left[\frac{\text{g anhydrous salt}}{100\ \text{g}\ H_2O}\right]$	Vapor Pressure p1 (Pa)								$p_1/[Pa] = A\,10^{10} e^{-\frac{10^3 B}{273.15 + T/[°C]}}$		Temperature range (°C)		
			500	1,000	2,000	5,000	10,000	20,000	50,000	100,000	A	B			
Potassium bromide	KBr	14.9				33.6	46.7	61.0			11.236	5.1933	30.0	..	70.0
		35.8				34.6	47.9	62.5	84.0		8.427	5.1201	30.0	..	100.0
		69.0							86.6		5.5272	5.0063	65.0	..	95.0
Potassium chloride	KCl	9.5				33.4	46.6	60.9			10.558	5.1703	30.0	..	70.0
		21.8				34.5	47.7	62.1			10.3175	5.1821	30.0	..	70.0
		32.0				35.5	48.8	63.3			9.6108	5.1762	30.0	..	70.0
Potassium chlorate	$KClO_3$	9.8							81.8		6.5014	4.9971	70.0	..	95.0
		14.7							81.9		6.1863	4.9809	70.0	..	95.0
Potassium thiocyanate	KCNS	19.4					46.9	61.5	83.0		7.9828	5.0863	40.0	..	90.0
		48.6					49.1	64.0	86.0		6.4585	5.0536	40.0	..	100.0
		77.8					51.3	66.5	89.0		5.1288	5.0129	40.0	..	100.0
Potassium carbonate	K_2CO_3	20.7				34.1	47.3	61.7	82.9		9.6007	5.1519	30.0	..	100.0
		110.6			30.6	47.1	60.9	75.9	97.9		10.1498	5.3889	30.0	..	100.0
Potassium chromate	K_2CrO_4	25.3						61.2	82.6		8.2834	5.0948	60.0	..	90.0
		69.9						64.0	85.6		7.8267	5.1175	60.0	..	90.0
Potassium fluoride	KF	11.6							83.1		6.8608	5.0342	70.0	..	100.0
		49.4				41.6	55.1	69.7			11.1269	5.3255	30.0	..	90.0
		69.7			31.2	47.5	61.0	75.7			13.8138	5.4936	30.0	..	90.0
Potassium iodide	KI	16.6				33.3	46.5	60.8	81.9		10.1415	5.156	23.0	..	90.0
		33.2				33.8	47.1	61.6	82.8		9.1772	5.134	23.0	..	90.0
		66.4				35.3	48.7	63.4	85.1		7.7964	5.1081	23.0	..	90.0
		93.8				36.7	50.3	65.1			7.3441	5.1133	30.0	..	70.0

D5.3. Table 2b. (continued)

Solute	Formula	Concentration $\left[\frac{\text{g anhydrous salt}}{100\ \text{g}\ H_2O}\right]$	Vapor Pressure p1 (Pa)								$p_1/[Pa] = A\,10^{10} e^{-\frac{10^3 B}{273.15+T/[°C]}}$		Temperature range (°C)		
			500	1,000	2,000	5,000	10,000	20,000	50,000	100,000	A	B			
Potassium nitrate	KNO_3	30.4				34.4	47.7	62.2	83.5		9.2216	5.1458	19.9	..	100.0
		101.1							86.7		4.8331	4.9594	70.0	..	100.0
		151.7							88.7		3.9841	4.9169	70.0	..	100.0
Potassium hydroxide	KOH	5.0		7.1	18.0	33.7	46.8	61.1	82.1	99.8	11.0377	5.1892	0.0	..	100.0
		40.0	3.4	14.0	25.4	41.9	55.6	70.6	92.6		7.9558	5.2235	0.0	..	100.0
		80.0	17.6	28.6	40.5	57.7	72.0	87.6			9.1612	5.5325	0.0	..	100.0
		120.0		46.4	58.5	76.1	90.6				16.8331	6.0526	40.0	..	100.0
Potassium phosphate	K_3PO_4	139.3					63.2	78.6			7.7913	5.3376	50.0	..	90.0
		605.7	51.8	62.3	73.6	89.6					195.0625	7.1764	50.0	..	90.0
		1864.6									1.7107E-05	2.385	50.0	..	90.0
Potassium sulfate	K_2SO_4	1.0		7.2	18.0	33.6	46.6	60.7	81.3	98.8	13.3937	5.2468	0.0	..	100.0
		5.0		7.4	18.2	33.8	46.7	60.9	81.6	99.0	13.2918	5.2471	0.0	..	100.0
		10.0				33.3	46.5	60.8	81.3	99.6	10.4017	5.1643	30.0	..	100.0
		15.0						60.8	82.3		7.5087	5.055	60.0	..	100.0
Lithium bromide	LiBr	5.0		6.9	17.8	33.5	46.6	60.8	81.7	99.4	11.3475	5.1939	0.0	..	100.0
		79.9	9.9	20.7	32.3	49.1	63.1	78.3			8.5071	5.3647	0.0	..	100.0
		200.0	43.3	55.8	69.2	88.9					4.4693	5.7944	40.0	..	100.0
Lithium chloride	LiCl	12.8				35.5	48.6	62.9			11.8318	5.2402	20.0	..	80.0
		21.2	0.9	11.1	22.2	38.2	51.5	66.0			11.0786	5.2659	0.0	..	80.0
		25.4			23.7	39.9	53.4	68.1	89.8		9.5555	5.2487	20.0	..	100.0

D5.3. Table 2c. Vapor pressure above unsaturated salt solutions; given are the temperatures of the salt solution in °C as function of the vapor pressure p_1

Solute	Formula	Concentration $\left[\frac{\text{g anhydrous salt}}{100\ \text{g } H_2O}\right]$	Vapor pressure p1 (Pa)								$p_1/[Pa] = A\,10^{10} e^{-\frac{10^3 B}{273.15+T/[°C]}}$		Temperature range (°C)		
			500	1,000	2,000	5,000	10,000	20,000	50,000	100,000	A	B			
Lithium chloride	LiCl	53.8			38.5	55.3	69.2				12.4376	5.5927	30.0	..	70.0
		78.2		38.7	50.5	67.6					17.8305	5.9247	30.0	..	70.0
Lithium iodide	LiI	10.7				33.3	46.4	60.8	81.9	99.7	10.0128	5.1514	30.0	..	100.0
		50.9				36.9	50.3	65.0	86.6		8.5469	5.163	30.0	..	95.0
		135.5			36.7	54.2	68.8				5.6155	5.3139	30.0	..	70.0
Lithium nitrate	$LiNO_3$	11.0				33.6	46.8	61.3	82.6		9.0641	5.1261	30.0	..	100.0
		38.2				37.6	51.2	65.9	87.7		8.0575	5.1572	30.0	..	100.0
		66.6				42.3	56.3	71.5	94.0		6.327	5.159	30.0	..	100.0
		121.4				52.8	67.2	82.9			6.8795	5.3582	40.0	..	100.0
Lithium sulfate	Li_2SO_4	5.5				33.4	46.5	60.8	81.7	99.4	11.1031	5.1859	20.0	..	100.0
		11.0				33.8	46.9	61.1	82.0	99.6	11.5948	5.2054	20.0	..	100.0
		15.4							82.8		8.5416	5.1077	65.0	..	90.0
Magnesium bromide	$MgBr_2$	18.4				34.0	47.2	61.6	82.8		9.8281	5.1576	30.0	..	100.0
		27.6				34.9	48.1	62.5			10.7446	5.2009	30.0	..	80.0
		55.2				39.2	52.7	67.3			9.8796	5.248	30.0	..	80.0
Magnesium chloride	$MgCl_2$	19.1				35.5	48.9	63.5	85.0		8.425	5.1355	30.0	..	100.0
		35.4				40.9	54.5	69.3	91.2		8.7407	5.2367	30.0	..	95.0
		45.7			30.1	46.5	60.1				11.2215	5.4105	30.0	..	70.0
Magnesium nitrate	$Mg(NO_3)_2$	12.9				33.9	46.8				14.6987	5.28	20.0	..	60.0
		49.0			22.9	38.9	52.2				12.1346	5.3061	20.0	..	60.0
		87.4					63.0				7.7284	5.3314	50.0	..	70.0
Magnesium sulfate	$MgSO_4$	12.0				33.4	46.5	60.8	81.8	99.5	10.7204	5.1747	20.0	..	100.0
		18.1				33.6	46.7	61.0	82.1	99.8	10.6617	5.1763	20.0	..	100.0
		24.1				33.9	47.0	61.3	82.3		10.8274	5.1858	20.0	..	100.0
Manganese sulfate	$MnSO_4$	30.2					46.4	60.9	82.2		8.8106	5.1099	40.0	..	100.0
		49.8					47.9	62.3	83.4		10.578	5.1927	40.0	..	95.0
Sodium bromide	NaBr	5.0		6.8	17.7	33.5	46.5	60.8	81.7	99.4	11.281	5.1913	0.0	..	110.0
		41.2				35.9	49.4	64.0	85.6		8.1994	5.1341	30.0	..	100.0
		90.0			25.0	41.8	55.8	71.2	93.8		5.7021	5.1175	20.0	..	110.0
Sodium chloride	NaCl	2.6		6.8	17.7	33.4	46.5	60.8	81.7	99.3	11.2163	5.1888	0.0	..	110.0
		16.0						62.4	84.0		7.2641	5.0678	50.0	..	100.0
		25.0		9.2	20.2	36.2	49.6	64.1	85.4	103.4	9.801	5.195	0.0	..	110.0
		36.0					51.9	66.8	88.6		7.9118	5.1637	50.0	..	100.0
Sodium chlorate	$NaClO_3$	5.0		6.8	17.7	33.4	46.5	60.7	81.6	99.3	11.3051	5.1911	0.0	..	100.0
		60.0		9.5	20.6	36.6	50.0	64.6	86.0		9.4261	5.1895	0.0	..	100.0
		100.0			22.2	38.6	52.3	67.2	89.2		7.3384	5.1443	20.0	..	100.0
Sodium carbonate	Na_2CO_3	5.3		6.9	17.8	33.5	46.6	60.9	81.8	99.5	11.1846	5.1898	0.0	..	100.0
		20.1				34.2	47.5	62.0	83.3		9.2428	5.1428	30.0	..	100.0
		29.7				35.1	48.4	62.8	84.1		9.8181	5.1762	30.0	..	95.0
		42.9					49.4	64.0	85.6		8.4146	5.1425	40.0	..	100.0

D5.3. Table 2d. Vapor pressure above unsaturated salt solutions; given are the temperatures of the salt solution in °C as function of the vapor pressure p_1

Solute	Formula	Concentration $\left[\frac{\text{g anhydrous salt}}{100\ \text{g } H_2O}\right]$	Vapor Pressure p1 (Pa)								$p_1/[Pa] = A\,10^{10} e^{-\frac{10^3 B}{273.15+T/[°C]}}$		Temperature range (°C)		
			500	1,000	2,000	5,000	10,000	20,000	50,000	100,000	A	B			
Sodium iodide[a]	NaI	10.0		6.9	17.8	33.7	46.9	61.3	82.5	100.3	9.8638	5.1545	0.0	..	141.0
		49.8		8.4	19.6	35.7	49.2	63.9	85.6	103.9	7.9494	5.122	0.0	..	141.0
		175.0			31.0	48.7	63.6	79.8	103.9	124.4	3.4021	5.0641	20.0	..	141.0
Sodium nitrate	$NaNO_3$	5.0		6.9	17.9	33.7	46.9	61.3	82.3	100.1	10.2202	5.1654	0.0	..	125.0
		90.0				38.2	52.1	67.3	89.8	108.8	5.4776	5.0469	25.0	..	125.0
Sodium hydroxide	NaOH	5.0		7.1	18.0	33.9	47.2	61.6	82.8	100.7	9.5727	5.1492	0.0	..	120.0
		40.0	7.6	18.1	29.3	45.6	59.1	73.8	95.4	113.6	12.4846	5.4289	0.0	..	120.0
		60.0	18.0	28.6	39.9	56.2	69.8	84.5	106.0		21.0347	5.7823	0.0	..	120.0
		100.0	40.4	51.2	62.8	79.5	93.3	108.2			51.1189	6.5039	20.0	..	120.0
Sodium sulfate	Na_2SO_4	5.3		6.9	17.7	33.4	46.5	60.7	81.6	99.2	11.6046	5.1998	0.0	..	100.0
		25.0		7.9	18.8	34.5	47.6	61.9	82.8		12.0139	5.2291	0.0	..	100.0
		42.8				35.1	48.4	62.9	84.2		9.4168	5.1627	20.0	..	100.0
		49.7					48.4	63.0	84.5		8.2775	5.1218	40.0	..	95.0
Ammonium bromide	NH_4Br	10.0		7.2	18.0	33.7	46.8	61.0	81.8	99.4	12.0698	5.2166	0.0	..	100.0
		60.0		9.8	20.9	37.0	50.4	65.0	86.4		9.3978	5.1948	0.0	..	100.0
		80.0		10.1	21.4	37.9	51.6	66.6	88.7		6.5456	5.0968	40.0	..	100.0
Ammonium chloride	NH_4Cl	10.0		7.6	18.5	34.4	47.5	61.8	82.8	100.6	10.9613	5.1977	0.0	..	110.0
		30.0		9.5	20.6	36.6	50.0	64.6	85.9	104.0	9.5436	5.1932	0.0	..	110.0
		50.0					52.0	67.2	89.6	108.5	5.6395	5.0545	50.0	..	110.0

Ammonium nitrate	NH_4NO_3	99.6						65.7	88.6		3.7708	4.8958	65.5	..	103.0
		152.1					52.7	67.3			9.7595	5.2435	40.0	..	80.0
		870.9							121.2		0.8823	4.7642	118.0	..	143.5
Ammonium sulfate[a]	$(NH_4)_2SO_4$	5.0		6.7	17.6	33.3	46.4	60.7	81.6	99.2	11.2021	5.1867	0.0	..	110.0
		70.0		9.6	20.7	36.8	50.1	64.7	86.1	104.2	9.4729	5.193	0.0	..	110.0
Nickel sulfate	$NiSO_4$	26.3				33.2	46.4	60.9	82.1		9.1272	5.1218	30.0	..	100.0
		44.9				34.1	47.4	61.8	83.0		9.6286	5.1536	30.0	..	95.0
Rubidium chloride	RbCl	18.1				33.7	46.8	61.1			10.9564	5.1863	30.0	..	70.0
		54.0				35.6	48.9	63.4			9.9384	5.1891	30.0	..	70.0
		84.0				38.0	51.3	65.9			10.4289	5.2432	30.0	..	70.0
Strontium bromide	$SrBr_2$	19.8				33.8	47.0	61.3	82.2		10.939	5.1881	30.0	..	90.0
		59.3				36.6	50.0	64.7	86.2		8.7181	5.1644	30.0	..	90.0
		82.6				39.6	53.1	67.9			9.1543	5.23	30.0	..	70.0
Strontium chloride	$SrCl_2$	10.5				33.4	46.5	60.8			10.8907	5.18	30.0	..	70.0
		28.5				35.2	48.4	62.8	84.0		10.1943	5.1888	30.0	..	90.0
		50.8				38.5	51.8	66.3			11.415	5.2812	30.0	..	70.0
Strontium iodide	SrI_2	33.1				34.0	47.1	61.4			11.2023	5.1987	30.0	..	70.0
		80.9				37.0	50.3	64.8			10.1994	5.2193	30.0	..	70.0
		141.9				43.3	57.0				8.9386	5.2847	30.0	..	70.0
Zinc sulfate	$ZnSO_4$	16.2		7.1	18.0	33.8	46.9	61.3	82.3		10.6976	5.1806	0.0	..	100.0
		30.7						61.0	82.3		9.3447	5.1323	50.0	..	95.0
		45.2						62.4	83.6		9.9253	5.1726	50.0	..	95.0

[a]The relative error between measured data and calculated data via indicated approximation exceeds partly values of 5%

D5.3. Table 3a. Vapor pressure above unsaturated salt solutions; given is the vapor pressure p_1 of the salt solution in 10^2 Pa as function of the salt concentration m at a temperature of 25°C

Solute	Formula	Concentration m (g anhydrous salt/kg H_2O)							$p1 = p_1^* + Am + Bm^2 + Cm^3$ $[p] = Pa$; $[m] = \frac{g\ anhydrous\ salt}{kg H_2O}$			Concentration range $\left[\frac{g\ anhydrous\ salt}{100\ g\ H_2O}\right]$		
		2	5	10	20	50	100	200	A	B	C			
Silver nitrate	$AgNO_3$					29.8	28.7	27.0	−4.49	1.88E-02	−3.80E-05	17.0	..	255.3
Barium chloride	$BaCl_2$	31.5	31.4	31.0	30.4				−6.46	4.70E-02	−2.17E-03	0.2	..	41.7
Calcium chloride	$CaCl_2$	31.5	31.1	30.2	27.8	17.8			−7.81	−6.53E-01	5.04E-03	1.1	..	79.7
Cadmium sulfate	$CdSO_4$		31.5	31.4	31.2	30.0			−2.30	−8.00E-04	−3.73E-04	2.1	..	75.1
Cesium bromide	CsBr		31.4	31.2	30.8	29.4	27.2		−4.54	3.00E-03	−2.30E-05	2.1	..	106.4
Cesium iodide	CsI		31.5	31.3	30.9	29.9			−3.86	8.20E-03	−4.00E-05	2.6	..	77.9
Cesium nitrate	$CsNO_3$	31.6	31.4	31.2	30.8				−5.28	6.80E-02	−7.00E-04	2.0	..	29.2
Copper sulfate	$CuSO_4$	31.6	31.5	31.3	31.0				−3.84	8.40E-02	−3.00E-03	1.6	..	22.3
Iron (II) chloride	$FeCl_2$				28.5	21.6			−9.52	−3.66E-01	3.10E-03	12.7	..	63.6
Potassium iodide	KI	31.6	31.4	31.1	30.5	28.7	25.3		−5.34	−1.54E-02	4.51E-05	1.7	..	141.1
Potassium nitrate	KNO_3				30.2				−9.17	8.62E-02	0	10.1	..	30.4
Lanthanum chloride	$LaCl_2$	31.6	31.4	31.2	30.5				−3.77	−1.04E-01	−5.38E-04	1.1	..	31.5
Lithium sulfate	Li_2SO_4			30.5	29.1				−11.33	−4.23E-02	−1.20E-03	5.5	..	33.1
Lithium hydroxide	LiOH		29.7	27.6					−40.20	1.12E-01	−1.39E-02	2.4	..	12.0
Magnesium chloride	$MgCl_2$		30.9	29.8	26.4	12.6			−9.66	−1.01E + 00	8.84E-03	4.8	..	52.4
Manganese sulfate	$MnSO_4$	31.6	31.5	31.3	30.9	28.5			−3.15	−1.18E-02	−9.70E-04	1.5	..	63.4
Sodium sulfate	Na_2SO_4			30.9	30.2				−8.67	9.85E-02	−1.71E-03	7.1	..	42.7
Sodium bromide	NaBr	31.5	31.2	30.7	29.6	25.3			−8.58	−9.64E-02	3.25E-04	1.0	..	92.6
Sodium chloride	NaCl				27.7				−16.63	−1.61E-01	4.90E-04	13.4	..	35.9
Sodium nitrate	$NaNO_3$		31.1	30.6	29.5	26.8			−11.35	3.57E-02	−9.70E-05	5.0	..	90.0
Sodium hydroxide	NaOH		30.5	28.9	25.0	11.2			−19.15	−9.01E-01	9.27E-03	4.0	..	72.2
Ammonium chloride	NH_4Cl	31.3	30.7	29.7	27.9				−19.68	4.16E-02	−3.78E-04	0.5	..	32.1
Nickel sulfate	$NiSO_4$	31.6	31.5	31.3	31.0				−3.76	5.89E-02	−2.39E-03	1.6	..	40.2
Rubidium bromide	RbBr	31.5	31.4	31.1	30.5	28.7			−6.05	4.53E-03	−4.17E-05	1.7	..	82.7
Rubidium chloride	RbCl	31.5	31.3	30.8	30.0	27.5			−8.24	3.40E-03	−1.01E-04	1.2	..	60.5
Rubidium iodide	RbI		31.4	31.2	30.7	29.3	27.0		−4.67	1.60E-03	−1.58E-05	2.1	..	106.2
Rubidium nitrate	$RbNO_3$	31.5	31.4	31.1	30.6	29.5			−6.59	6.50E-02	−3.58E-04	1.5	..	66.4
Trontium chloride	$SrCl_2$			30.7	29.5	23.9			−7.39	−1.91E-01	5.54E-04	6.3	..	55.8
Zinc sulfate	$ZnSO_4$	31.6	31.5	31.4	31.0	28.7			−3.05	3.83E-03	−1.24E-03	1.6	..	64.8

D5.3. Table 3b. Vapor pressure above unsaturated salt solutions; given is the vapor pressure p_1 of the salt solution in 10^5 Pa as function of the salt concentration m at a temperature of 100°C

Solute	Formula	Concentration m (g anhydrous salt/kg H_2O)							$p1 = p_1^* + Am + Bm^2 + Cm^3$ $[p] = Pa;\ [m] = \frac{\text{g anhydrous salt}}{\text{kg}H_2O}$			Concentration range $\left[\frac{\text{g anhydrous salt}}{100\ \text{g}\ H_2O}\right]$		
		2	5	20	50	100	200	A	B	C				
Aluminum sulfate	$Al_2(SO_4)_3$				0.993				−113.3	2.57	−9.91E-02	10.3	..	40.0
Barium bromide	$BaBr_2$				0.982	0.917	0.789		−125.5	−1.68	6.90E-03	11.9	..	130.8
Barium chloride	$BaCl_2$				0.968	0.886			−208.7	−0.91	2.00E-04	10.4	..	52.1
Barium chlorate	$Ba(ClO_3)_2$			1.000	0.986	0.937			−117.6	−1.04	6.90E-03	9.1	..	95.2
Calcium bromide	$CaBr_2$			0.991	0.960	0.820	0.525		−165.9	−5.58	2.36E-02	10.0	..	109.9
Calcium chloride	$CaCl_2$			0.956	0.891	0.665	0.309		−523.6	−5.13	3.32E-02	5.6	..	155.4
Calcium nitrate	$Ca(NO_3)_2$			0.985	0.954	0.854	0.677		−275.5	−1.13	5.20E-03	6.7	..	168.1
Cadmium chloride	$CdCl_2$			1.000	0.987	0.946	0.869		−136.0	0.18	−2.60E-03	9.6	..	102.7
Cadmium nitrate	$Cd(NO_3)_2$			0.994	0.974	0.908			−193.2	−0.09	−4.90E-03	7.1	..	94.6
Cadmium sulfate	$CdSO_4$				1.002				−53.4	−0.06	0	10.9	..	43.5
Cobalt chloride	$CoCl_2$			0.979	0.935	0.778			−282.3	−6.58	5.66E-02	6.5	..	58.4
Cobalt nitrate	$Co(NO_3)_2$			0.989	0.958	0.837	0.614		−207.5	−3.87	1.95E-02	9.5	..	128.1
Copper sulfate	$CuSO_4$				0.992	0.947			−98.6	−0.10	−1.16E-02	11.2	..	55.9
Iron (II) chloride	$FeCl_2$		0.997	0.977	0.930	0.758			−301.2	−6.59	4.82E-02	3.8	..	88.7
Iron sulfate	$FeSO_4$			1.005	0.994	0.951			−74.8	−1.08	2.00E-03	7.6	..	53.2
Potassium bromide	KBr				0.957	0.866	0.717		−263.6	−0.88	5.56E-03	11.9	..	107.1
Potassium chloride	KCl		0.993	0.972	0.928				−395.5	−1.97	2.34E-02	3.9	..	46.7
Potassium chlorate	$KClO_3$			0.990	0.967	0.906			−238.6	0.44	1.00E-03	6.1	..	57.6
Potassium thiocyanate	KCNS			0.976	0.940	0.837	0.688	0.478	−378.1	0.50	2.60E-04	7.8	..	262.4
Potassium oxalate	$K_2C_2O_4$			0.990	0.967	0.893			−235.6	0.51	−1.19E-02	8.3	..	74.8

D5.3. Table 3c. Vapor pressure above unsaturated salt solutions; given is the vapor pressure p_1 of the salt solution in 10^5 Pa as function of the salt concentration m at a temperature of 100°C

Solute	Formula	Concentration m (g anhydrous salt/kg H_2O)							$p1 = p_1^* + Am + Bm^2 + Cm^3$ $[p] = Pa$; $[m] = \frac{\text{g anhydrous salt}}{\text{kg}H_2O}$			Concentration range $\left[\frac{\text{g anhydrous salt}}{100\ \text{g}\ H_2O}\right]$		
		2	5	10	20	50	100	200	A	B	C			
Potassium carbonate	K_2CO_3			0.977	0.940	0.819	0.613		−348.7	−1.10	5.80E-03	7.2	..	146.5
Potassium chromate	K_2CrO_4				0.972	0.909			−233.3	2.14	−3.26E-02	10.1	..	54.4
Potassium fluoride	KF			0.956	0.892	0.684	0.361		−542.3	−3.57	2.47E-02	5.8	..	151.1
Potassium dihydrogen Phosphate	KH_2PO_4			0.995	0.978	0.939			−198.8	1.40	−7.70E-03	7.1	..	95.3
Potassium hydrogen sulfate	$KHSO_4$			0.992	0.971	0.909	0.808		−209.8	0.02	2.32E-04	7.1	..	122.6
Potassium iodide	KI			0.993	0.972	0.905	0.790		−200.0	−0.40	1.70E-03	8.7	..	199.2
Potassium nitrite	KNO_2		0.995	0.977	0.942	0.847	0.718	0.554	−374.6	0.87	−7.28E-04	4.4	..	229.8
Potassium nitrate	KNO_3			0.987	0.962	0.898	0.818	0.708	−272.3	0.94	−1.71E-03	5.1	..	242.7
Potassium hydroxide	KOH		0.977	0.938	0.851	0.561	0.236		−678.1	−8.07	7.08E-02	2.8	..	100.0
Potassium sulfate	K_2SO_4	1.009	1.002	0.992	0.973				−234.1	2.83	−6.28E-02	0.5	..	24.4
Potassium tungstate	K_2WO_4				0.989	0.943	0.848		−102.6	−0.87	2.40E-03	17.0	..	170.1
Lithium bromide[a]	LiBr		0.995	0.973	0.922	0.721	0.351		−332.7	−6.79	3.49E-02	4.3	..	140.0
Lithium chloride[a]	LiCl		0.966	0.913	0.795	0.414			−886.3	−12.98	1.35E-01	2.2	..	97.5
Lithium hydrogen sulfate	$LiHSO_4$			0.979	0.941	0.805			−316.5	−2.28	5.80E-03	5.4	..	57.2
Lithium nitrate[a]	$LiNO_3$		0.986	0.959	0.901	0.720	0.453		−523.7	−2.16	1.79E-02	3.5	..	127.6
Lithium hydroxide	LiOH	0.975	0.906						−1671.1	−154.64	1.19E + 01	1.2	..	6.7
Lithium sulfate	Li_2SO_4			0.980	0.946				−315.6	−1.35	1.03E-02	5.5	..	34.4
Magnesium bromide	$MgBr_2$			0.987	0.949	0.785			−205.9	−6.16	2.26E-02	7.4	..	92.1
Magnesium chloride	$MgCl_2$	1.006	0.992	0.960	0.869	0.483			−308.2	−24.51	1.90E-01	1.0	..	70.0
Magnesium dihydrogen sulfate	$MgH_2(SO_4)_2$			0.991	0.960				−179.9	−4.60	1.72E-02	6.6	..	48.1
Magnesium nitrate	$Mg(NO_3)_2$		0.998	0.979	0.934	0.748			−276.3	−6.44	2.74E-02	4.5	..	50.4
Magnesium sulfate	$MgSO_4$			1.000	0.987	0.907			−134.9	1.21	−5.56E-02	6.3	..	51.8
Manganese chloride	$MnCl_2$			0.979	0.938	0.796			−294.7	−4.99	4.38E-02	6.6	..	66.7
Manganese sulfate	$MnSO_4$		1.008	1.003	0.995				−125.3	2.90	−5.89E-02	4.5	..	40.8
Sodium bromide	NaBr		0.997	0.980	0.942	0.809	0.585		−307.0	−2.83	1.62E-02	5.0	..	123.5
Sodium bromate	$NaBrO_3$			0.991	0.968	0.896			−215.1	−0.63	4.80E-03	7.9	..	83.0

Sodium chloride	NaCl		0.990	0.962	0.893				−398.0	−13.33	1.64E-01	2.6	..	39.2
Sodium chlorate	$NaClO_3$		0.997	0.981	0.949	0.862	0.738	0.566	−331.6	0.59	−2.56E-04	5.0	..	202.2
Sodium carbonate	Na_2CO_3			0.979	0.946				−364.4	2.31	−4.16E-02	5.3	..	44.2
Sodium hydrogen phosphate	Na_2HPO_4			0.991	0.972	0.922			−236.5	1.78	−1.40E-02	7.1	..	88.9
Sodium dihydrogen phosphate	NaH_2PO_4			0.992	0.973	0.922	0.843		−218.9	0.93	−4.40E-03	6.3	..	132.0
Sodium hydrogen sulfate	$NaHSO_4$			0.987	0.960	0.879	0.752		−258.0	−0.41	3.80E-03	6.3	..	125.3
Sodium iodide	NaI			0.985	0.956	0.861	0.692	0.382	−272.6	−0.75	2.67E-03	7.8	..	303.4
Sodium nitrite	$NaNO_2$		0.989	0.966	0.919	0.788	0.619		−479.6	0.32	5.30E-03	3.6	..	110.4
Sodium nitrate	$NaNO_3$		0.995	0.977	0.941	0.845	0.710		−373.8	0.77	−6.00E-04	4.4	..	178.5
Sodium hydroxide[a]	NaOH	0.997	0.972	0.927	0.827	0.499	0.153		−783.8	−9.03	8.27E-02	2.0		100.0
Sodium sulfate	Na_2SO_4			0.990	0.968				−234.4	0.43	−6.50E-03	5.3	..	44.5
Sodium tungstate	Na_2WO_4			1.000	0.985	0.935	0.839		−124.6	−0.77	2.70E-03	8.8	..	122.6
Ammonium bromide	NH_4Br			0.979	0.946	0.851	0.706		−342.0	0.36	−9.00E-05	5.1	..	140.0
Ammonium chloride	NH_4Cl		0.983	0.954	0.897	0.743			−602.8	1.01	5.00E-03	2.8	..	70.0
Ammonium hydrogen sulfate	NH_4HSO_4			0.986	0.959	0.881	0.760		−274.2	0.15	6.00E-04	6.0	..	138.1
Ammonium iodide	NH_4I			0.989	0.965	0.895	0.784	0.595	−240.5	0.07	4.32E-04	7.6	..	210.2
Ammonium nitrate	NH_4NO_3		0.995	0.978	0.944	0.853	0.731	0.571	−362.0	0.89	−9.22E-04	4.2	..	400.0
Ammonium sulfate	$(NH_4)_2SO_4$		1.001	0.989	0.965	0.893	0.764		−247.3	0.28	−3.00E-03	5.0		100.0
Nickel chloride	$NiCl_2$			0.979	0.932	0.748			−274.6	−7.34	4.43E-02	6.5	..	64.8
Nickel nitrate	$Ni(NO_3)_2$			0.991	0.960	0.832			−181.3	−4.55	1.89E-02	9.1	..	82.2
Nickel sulfate	$NiSO_4$			1.004	0.997				−114.2	3.03	−7.41E-02	8.1	..	38.7
Rubidium chloride	RbCl				0.958	0.871	0.733		−265.7	−0.58	4.30E-03	18.1	..	120.9
Rubidium nitrate	$RbNO_3$				0.974	0.927			−219.7	1.24	−5.70E-03	10.3	..	85.5
Strontium bromide	$SrBr_2$			0.996	0.973	0.877	0.659		−148.9	−2.88	8.30E-03	9.9	..	113.8
Strontium chloride	$SrCl_2$			0.986	0.947	0.795			−213.7	−6.63	4.33E-02	7.9	..	85.6
Strontium nitrate	$Sr(NO_3)_2$			0.995	0.975	0.913			−179.4	−0.68	4.80E-03	6.4	..	88.3
Zinc chloride	$ZnCl_2$			0.996	0.974	0.887	0.673		−152.1	−2.15	2.70E-03	7.1	..	122.7
Zinc nitrate	$Zn(NO_3)_2$			0.989	0.959	0.838			−198.1	−4.22	2.33E-02	9.5	..	79.0
Zinc sulfate	$ZnSO_4$			1.006	0.997	0.959			−71.1	−0.34	−8.50E-03	8.4	..	77.5

[a]The relative error between measured data and calculated data via indicated approximation exceeds partly values of 5%

5 Enclosure C: High Temperature Data and Salt Mixtures

D5.3. Table 4. Vapor pressure above saturated salt solutions at higher temperatures; given is the vapor pressure p_1 of the salt solution in 10^5 Pa as function of the temperature

Solute	Formula of precipitation	Temperature (°C)						
		100	125	150	200	300	450	600
Silver nitrate	$AgNO_3$	0.51	0.89	1.24	0.62			
Potassium chloride	KCl				1.13	4.93	17.1	22.3
Potassium thiocyanate	KCNS	0.20	0.29	0.28				
Potassium fluoride	KF				4.22	24.6	102	179
Potassium carbonate	Na_2CO_3	0.83	1.90	5.28	15.2	88.8		
Sodium sulfite	Na_2SO_3	0.80	1.82	3.78	12.7			
Sodium sulfate	Na_2SO_4	0.88	2.15	4.38	14.4	83.7		
Sodium bromide	NaBr					39.8	127	158
Sodium chloride	NaCl	0.75	1.71	3.48	11.2	58.3	245	394
Sodium iodide	NaI				4.10	17.8	65.4	
Strontium chloride	$SrCl_2$					38.9	160	

D5.3. Table 5. Vapor pressure above saturated solutions of salt mixtures; given is the temperature of the salt solution in °C as function of the vapor pressure p_1

Solute	Initial weight[a] (mass% anhydrous salt)	Vapor pressure p1 (Pa)					
		1,000	2,000	5,000	10,000	20,000	50,000
Ammonium nitrate/lead-(IV)-nitrate	50/50	13.5	27.9	49.4	71.8		
Ammonium nitrate/sodium nitrate	78.2/21.8	15.7	30.5	52.5	81.6		
Ammonium nitrate/silver nitrate	30.7/69.3	12.2	25.4	47.2	73.3		
Lead-(IV)-nitrate/silver nitrate	20/80		21.1	39.1	54.3	71.5	101.9
Potassium bromide/potassium thiocyanate	27/73	18.5	32.6	54.0	73.9	101.8	
Potassium chloride/potassium thiocyanate	20/80	17.8	32.2	53.6	73.2	100.2	
Potassium chloride/sodium chloride	58.5/41.5			38.5	52.6	68.0	90.9
Potassium iodide/potassium thiocyanate	10.7/89.3	19.1	33.7	55.3	75.3	105.5	
Magnesium chloride/sodium chloride	98.85/1.15		36.9	56.4	72.9	91.1	
Ammonium nitrate/lead-(IV)-Nitrate/silver nitrate	29.8/7.5/62.7	16.3	30.8	58.6			
Potassium chloride/magnesium chloride/sodium chloride	16.3/77.9/5.8		36.3	53.2	68.2	84.5	
Potassium chloride/sodium chloride/sodium sulfate	58.3/36.3/5.4			37.8	52.1	67.8	91.1
Potassium chloride/magnesium chloride/magnesium sulfate/ sodium chloride[b]	20/57.1/14.3/8.6		30.0	44.3	58.3	74.1	96.8
Potassium chloride/magnesium chloride/magnesium sulfate/ sodium chloride[b]	38.1/26.2/11.9/23.8			40.2	54.1	70.0	93.0

[a]The composition of the salt solution or precipitation does not necessarily correspond to the composition of the initial weight due to the different solubility of the salt components

[b]Column 2 shows the mass fraction in percentage of the anhydrous salt in the solution

6 Bibliography

1. Acheson DT (1965) Vapor pressures of saturated aqueous salt solutions. Humidity Moisture 3:521–530
2. Adams RJ, Merz AR (1929) Hygroscopicity of fertilizer materials and mixtures. Ind Eng Chem 21(4):305–306
3. Apelblat A (1993) The vapour pressures of saturated aqueous lithium chloride, sodium bromide, sodium nitrate, ammonium nitrate, and ammonium chloride at temperatures from 283 K to 313 K. Chem Thermodyn 25:63–71
4. Apelblat A (1993) The vapour pressures of saturated aqueous solutions of potassium bromide, ammonium sulfate, copper(II) sulfate, iron(II) sulfate, and manganese(II) dichloride, at temperatures from 283 K to 308 K. Chem Thermodyn 25:1513–1520
5. Apelblat A (1992) The vapour pressures of water over saturated aqueous solutions of barium chloride, magnesium nitrate, calcium nitrate, potassium carbonate, and zinc sulfate, at temperatures from 283 K to 313 K. Chem Thermodyn 24:619–626
6. Applebey MP, Crawford FH, Gordon K (1934) Vapour pressures of saturated solutions. J Chem Soc 11:1665–1671

7. Badger WL, Baker EM (1920) Studies in evaporator design - IV. Chem Metall Eng 23(12):569–574
8. Barry JC, Richter J, Stich E (1988) Vapour pressures and ionic activity coefficients in the system KNO_3+H_2O from dilute solutions to fused salts at 425 K, 452 K, and 492 K. Ber Bunsen-Ges Phys Chem 92:1118–1122
9. Baxter GP, Lansing EL (1920) The aqueous pressure of some hydrated crystals. Oxalic acid, strontium chloride and sodium sulfate. J Am Chem Soc 42:419
10. Baxter GP, Cooper WC Jr. (1924) J Am Chem Soc 46:923
11. Bechtold MF, Newton RF (1940) J Am Chem Soc 62:1390
12. Bencowitz I, Hotchkiss HT Jr. (1926) Vapor pressure lowering as a function of the degree of saturation. II. J Phys Chem 30:643–657
13. Boryta DA, Maas AJ, Grant CB (1975) Vapor pressure-temperature-concentration relationship for system lithium bromide and water (40-70 % lithium bromide). J Chem Eng Data 20(3):316–319
14. Carr DS, Harris BL (1949) Solutions for maintaining constant relative humidity. Ind Eng Chem 41:2014
15. Chia-tsun Liu, Lindsay WT, Jr. (1972) Thermodynamics of sodium chloride solutions at high temperatures. J Solution Chem 1(1):45–69
16. Dean JA Lange's Handbook of Chemistry. 12. Auflage. New York: McGraw-Hill
17. Derby IH, Yngve V (1916) The dissociation tensions of certain hydrated chlorides and the vapor pressures of their saturated solutions. J Am Chem Soc 38(8):1439
18. Diesnis M (1937) Ann Chem 7:5
19. Dingemans P, Dijkgraaf LL (1946) The vapour pressure of solutions saturated with silver nitrate and with lead nitrate. Recl Trav Chim 65:477–484
20. Dingemans P, Dijkgraaf LL (1947) The system NH_4NO_3-$AgNO_3$-$Pb(NO_3)_2$-H_2O. Recl Trav Chim 66:239–246
21. Dingemans P, Dijkgraaf LL (1948) The vapour pressure of aqueous solutions, saturated with respect to ammonium nitrate and sodium nitrate. Recl Trav Chim 67:225–230
22. Dingemans P, Dijkgraaf LL (1948) The vapour pressure of saturated solutions of sodium nitrate in water. Recl Trav Chim 67:231–234
23. Dingemans P (1945) The vapour pressure of solutions saturated with lead nitrate and ammonium nitrate. Recl Trav Chim 64:199–204
24. Dingemans P (1943) Das System H_2O-NH_4NO_3-$AgNO_3$. Recl Trav Chim 62:88–95
25. Dingemans P, van den Berg K (1942) Die Dampfspannung gesättigter Silbernitratlösungen. Recl Trav Chim 61:605–615
26. Dingemans P (1941) Die Dampfspannung von gesättigten NH_4NO_3-Lösungen. Recl Trav Chim 60:319–328
27. Dingemans P (1939) Die Dampfspannung von Lösungen, gesättigt an Kaliumrhodanid und an Kaliumchlorid (bzw. -bromid und -jodid). Recl Trav Chim 58:574–581
28. Dingemans P (1945) The vapour pressure of saturated solutions of lead nitrate. Recl Trav Chim 64:194–198
29. Edgar G, Swan WO (1922) The factors determining the hygroscopic properties of soluble substances. I. The vapor pressures of saturated solutions. J Am Chem Soc 44:570
30. Ewing WW, Klinger E, Brandner JD (1934) Studies on the vapor pressure-temperature relations and on the heats of hydration, solution and dilution of the binary system magnesium nitrate-water. J Am Chem Soc 56:1053–1057
31. Gokcen NA (1951) Vapor pressures of water above saturated lithium chloride solution. J Am Chem Soc 73:3789
32. Goldberg RN, Nuttall RL (1978) Evaluated activity and osmotic coefficients for aqueous solutions: The alkaline earth metal halides. J Phys Chem Ref Data 7(1):263–310
33. Greenspan L (1977) Humidity fixed points of binary saturated aqueous solutions. J Res Nat Bur Stand Sect A 81A(1):89–96
34. Hartung EJ (1920) An accurate method for the determination of vapour pressure. Trans Farad Soc 15:150
35. Hayward AM, Perman EP (1931) Vapour pressure and heat of dilution. Part VII. Vapour pressures of aqueous solutions of sodium hydroxide and of alcoholic solutions of calcium chloride. Trans Farad Soc 27:59–69
36. Hedlin CP, Trofimenkoff FN (1965) Relative humidities over saturated solutions of nine salts in the temperature range from 0 to 90° F. Humidity Moisture 3:51–520
37. JRI Hepburn (1932) The vapour pressure of water over aqueous solutions of the chlorides of the alkaline-earth metals. Part IV. Evaluation of activity coefficients. J Chem Soc 1284–1292
38. Hüttig GF, Reuscher F (1924) Z Anorg Chem 137:155
39. Iyoki S, Iwasaki S, Uemura T (1990) Vapor pressures of the water-lithium bromide-lithium iodide system. J Chem Eng Data 35:429–433
40. Jänecke E, Rahlfs E (1930) Über das System NH_4NO_3-H_2O. Z. anorg. Z Anorg Chem 192:237–244
41. Jänecke E (1930) Über das System: NaOH-$NaNO_3$-H_2O. Z. anorg. Z Anorg Chem 188:72–89
42. Kangro W, Groeneveld A (1962) Konzentrierte wäßrige Lösungen, I. Z Phys Chem 32:110–126
43. Keevil MB (1942) High temperature vapor pressures of saturated salt solutions. J Am Chem Soc 64:841–850
44. Ketsko VA, Urusova MA, Valyashko VM (1984) Solubility and vapour pressure of solutions in the $CaCl_2$-H_2O system at 250-400 °C. Russ J Inorg Chem 29(9):1398–1399
45. Krumgal'z BS, Mashovets VP (1964) Vapor pressure of NaOH solutions (of over 45% concentration) at temperatures up to 400°. Zh Prikl Khim 37 (12):2712–2713
46. Landolt, Börnstein, Roth/Scheel: Physikalisch Chemische Tabellen. Dritter Ergänzungsband III. 5. Auflage 1936
47. Lax E D'Ans Lax, Taschenbuch für Chemiker und Physiker. Bd. 1: Makroskopische physikalisch- chemische Eigenschaften. 3. Auflage. Berlin: Springer
48. Leopold GH, Johnston J (1927) The vapor pressure of the saturated aqueous solutions of certain salts. J Am Chem Soc 49:1974–1988
49. Lide DR Handbook of chemistry and physics. 74. Auflage. London: CRC Press; 1993–1994
50. Lincoln AT, Klein D (1907) J Phys Chem 11:318
51. Lovelace BF, Frazer JCW, Sease VB (1921) Lowering of the vapor pressure of water, etc. J Am Chem Soc 43(I):102
52. Marcus Y, Soffer N (1988) Solubilities and vapour pressures in the quinquinary system NaCl-KCl-$MgCl_2$-$CaCl_2$-H_2O. J Chem Soc Farad Trans 1 84 (10):3575–3585
53. Matuzenko MYu, Zarembo VI, Puchkov LV (1982) Tensimetric study of the $MgSO_4$-H_2O and $CdSO_4$-H_2O systems at 383 to 443°K. Zh Prikl Khim 55:747–750
54. Mazghouni M, Kbir-Ariguib N (1981) Etude des equilibres solide-liquide-vapeur des systemes binaires K_3PO_4-H_2O et $Mg_3(PO_4)_2$-H_2O. Counioux: Thermochim Acta 47:125–139
55. Morey GW, Chen WT (1956) Pressure-temperature curves in some systems containing water and a salt. J Am Chem Soc 78:4249–4252
56. Newton RF, Tippetts EA (1936) J Am Chem Soc 58:280
57. Novikov BE, Korzhavina NA (1987) Thermodynamic study of water and vapor solutions of K_2CO_3 under conditions of phase equilibrium in a wide range of temperatures and concentrations. High Temp 25:350–354
58. O'Brien FEM (1948) The control of humidity by saturated salt solutions. J Sci Instrum 25:73–76
59. Ölander A, Liander H (1950) The phase diagram of sodium chloride and steam above the critical point. Acta Chem Scand 4:143–1445
60. Olynyk P, Gordon AR (1943) The vapor pressure of aqueous solutions of sodium chloride at 20, 25 and 30° for concentrations from 2 molal to saturation. J Am Chem Soc 65:224–226
61. Paranjpe B (1916) J. Indian Inst. Sci. 2
62. Patil KR, Chaudhari SK, Katti SS (1992) Thermodynamic properties of aqueous electrolyte solutions. 3. Vapor pressure of aqueous solutions of $LiNO_3$, LiCl + $LiNO_3$, and LiBr + $LiNO_3$. J Chem Eng Data 37:136–138
63. Patil KR, Tripathi AD, Pathak G, Katti SS (1990) Thermodynamic properties of aqueous electrolyte solutions. 1. Vapor pressure of aqueous solutions of LiCl, LiBr, and LiI. J Chem Eng Data 35:166–168
64. Patil KR, Tripathi AD, Pathak G, Katti SS (1991) Thermodynamic properties of aqueous electrolyte solutions. 2. Vapor pressure of aqueous solutions of NaBr, NaI, KCl, KBr, KI, RbCl, CsCl, CsBr, etc. J Chem Eng Data 36:225–230

65. Pearce JN, Pumplin GG (1937) The vapor pressures and activity coefficients of aqueous solutions of ammonium chloride at 25°. J Am Chem Soc 59:121–1220
66. Pearce JN, Taylor MD, Bartlett RM (1928) The vapor pressures of aqueous solutions of potassium iodide and sodium bromide at 25°. J Am Chem Soc 50:2951–2958
67. Petit MC (1965) J Chim Phys Phys-Chim Biol 62:1119
68. Ravich MI, Borovaya FE, Smirnova EG (1968) Solubility and vapour pressure in the potassium carbonate-water system at elevated temperatures. Russ J Inorg Chem 13(7):1000–1004
69. Ravich MI, Yastrebova (1963) Phase equilibria in the LiCl-H_2O system at high temperatures. Russ J Inorg Chem 8(1):102–105
70. Robinson RA, Bower VE (1965) An additivity rule for the vapor pressure lowering of aqueous solutions. J Res Nat Bur Stand Sect A 69A(4):365–367
71. Robinson RA, Jones RS (1936) The activity coefficients of some bivalent metal sulfates in aqueous solution from vapor pressure measurements. J Am Chem Soc 58:959–961
72. Robinson RA, Stokes RH (1940) Trans Farad Soc 36:733
73. Robinson RA (1937) The osmotic and activity coefficient data of some aqueous salt solutions from vapor pressure measurements. J Am Chem Soc 59:84–90
74. Saad D, Padova J, Marcus Y (1975) J Solut Chem 4:983
75. Sacchetto GA, Kodejs Z (1986) Solution properties of water in molten $AgNO_3$-$LiNO_3$ mixtures as derived from vapour-pressure measurements on $AgNO_3$-$LiNO_3$-H_2O melts. J Chem Soc Farad 82:1853–1864
76. Sakai W (1939) The study of urea, I. J Soc Chem Ind Jpn 43(4):104B–106B
77. Sako T, Hakuta T, Yoshitome H (1985) Vapor pressures of binary (H_2O-HCl, -$MgCl_2$, and -$CaCl_2$) and ternary (H_2O-$MgCl_2$-$CaCl_2$) aqueous solutions. J Chem Eng Data 30:224–228
78. Serowy F, Soika G, Wiss Z (1964) Tech Hochsch Chem Leuna-Merseburg 6:343
79. Simonson JM, Pitzer KS (1986) Thermodynamics of multicomponent, miscible, ionic systems: The system $LiNO_3$-KNO_3-H_2O. J Phys Chem 90:3009–3013
80. Sourirajan S, Kennedy GC (1962) The system H_2O-NaCl at elevated temperatures and pressures. Am J Sci 260:115–141
81. Speranski A (1910) Über den Dampfdruck der gesättigten Lösungen. Z Phys Chem 70:519
82. Speranski A (1912) Über den Dampfdruck und über die integrale Lösungswärme der gesättigten Lösungen. Z Phys Chem 78:86
83. Stokes RH, Robinson RA (1949) Standard solutions for humidity control at 25°C. Ind Eng Chem 41:2013
84. Stokes RH (1945) Trans Farad Soc 41:642
85. Thakker MT, Chi CW, Peck RE, Wasan DT (1968) J Chem Eng Data 13(4):553
86. Urusova MA, Ravich MI (1966) Phase equilibria in the potassium fluoride-water system at elevated temperatures. Russ J Inorg Chem 11(3):353–357
87. Urusova MA, Valyashko (1987) The vapour pressure and activity of water in concentrated aqueous solutions containing the chlorides of alkali metals (Li, K, Cs) and alkaline earth, etc. Russ J Inorg Chem 32(1):23–26
88. Urusova MA, Valyashko VM (1983) Solubility, vapour pressure, and thermodynamic properties of solutions in the $MgCl_2$-H_2O system at 300-350°C. Russ J Inorg Chem 28(7):1045–1048
89. Urusova MA, Valyashko VM (1984) Vapour pressure and thermodynamic properties of aqueous solutions of magnesium chloride at 250°C. Russ J Inorg Chem 29(9):1395–1396
90. Urusova MA (1974) Phase equilibria in the sodium hydroxide-water and sodium chloride-water systems at 350-550°C. Russ J Inorg Chem 19 (3):450–453
91. Urusova MA (1986) Vapour pressure in the $SrCl_2$-H_2O system at temperatures above 250°C. Russ J Inorg Chem 31(7):1104–1105
92. Valyashko VM, Urusova MA, Ketsko VA (1987) Phase equilibria and thermodynamic properties of solutions in the $MgCl_2$-H_2O, $CaCl_2$-H_2O, $SrCl_2$-H_2O, etc. Russ J Inorg Chem 32(11):1634–1639
93. Washburn EW (1926) International critical tables of numerical data, physics, chemistry and technology. Bd. I. New York: McGraw-Hill, pp 67–68
94. Washburn EW (1928) International critical tables of numerical data, physics, chemistry and technology. Bd. III. New York: McGraw-Hill, pp 292–300, u. 351–385
95. Wexler A, Hasegawa S (1954) Relative humidity-temperature relationships of some saturated salt solutions in the temperature range 0° to 50° C. J Res Nat Bur Stand 53(1)19–26

D6.1 Thermodynamic Properties of Pure Metals and Metal Alloys

Matthias Neubronner[1] · *Thomas Bodmer*[2]
[1]EON Energie, Munich, Germany
[2]Marl, Germany

Tables 1–7 indicate numeric values for various physical properties of materials often used in process equipment and plant engineering. The dependence on the temperature of these numeric values is indicated. Table 1 shows these properties for pure metals. Table 2 provides an overview of alloys, which can be categorized into different groups by their properties and their alloying constituents. Here, the group of steels is the most significant, which have, therefore, been subdivided according to their respective material properties. As well as two representative gray cast iron materials, some nonferrous materials have been listed. Out of these, the nickel alloys due to their acid resistance and the aluminum alloys are frequently employed in process equipment and plant engineering.

All materials are to be identified by their material numbers and – standard designations (DIN or EN) according to [1] for steels and according to [2] for nonferrous materials. Table 2 illustrates the chemical composition for all materials listed. Where no range is stated, the values shown are the respective maximum values of a constituent. The density at 20°C is also shown. The figures for steels have been taken from the sources [1, 3]. The chemical compositions of the nonferrous materials have been taken from the provided standards for each material, as stated in source [4]. The material numbers, designations, and chemical compositions for most of the materials shown here correspond to the standards as valid today. A small number of additional materials without currently valid standards have been listed, because they can still be found in plant operation. These materials have been labeled clearly in Table 2. The material properties shown in Tables 3–7 have, in some cases, been determined for older materials based on currently valid standards. The current materials listed in Table 2 generally only differ from their predecessors by terminology and a very minor variation in their chemical composition. Therefore, the thermodynamic properties in Tables 3–7 are also valid for these materials.

For these materials, Tables 3–7 contain the thermal conductivity, the specific heat capacity, the average thermal expansion coefficient between 20°C and the temperature, the dynamic modulus of elasticity and the Poisson's ratio for various temperatures.

The thermal conductivity significantly depends on the percentage by mass of the various alloying constituents. Furthermore, constituents, which only occur in trace quantities, can substantially influence the thermal conductivity. In general, the thermal conductivity is different for all materials. It has, therefore, been tabulated separately for each material.

The thermodynamic properties for heat capacity, thermal expansion, the modulus of elasticity, and the Poisson's ratio, show a lower dependence on the alloying constituents. In particular, for many steels for which the chemical composition does not differ greatly, these are very similar. Therefore, the figures for various steels have been combined in Tables 4–7. The dynamic Poisson's ratio, subject to temperature, can, by acceptable approximation, be described with the same numerical values for all steels. The indicated serial numbers in Tables 3–7 refer to Table 2.

The measuring errors for steels are ±7% for the thermal conductivity, ±3% for the specific heat and the Poisson's ratio, ±2% for the thermal expansion and approximately ±1% for the modulus of elasticity. Those thermodynamic properties put in brackets are uncertain values. They have either been extrapolated from measured values at other temperatures, or been determined for a similar material. The thermodynamic properties for steels have been taken from the literature [3–6]. The thermodynamic properties for the other materials can be found in [7–9]. Data for the dynamic Poisson's ratio are not available for all the materials listed here.

Further, thermodynamic properties can easily be estimated based on the values stated in the tables:

For any temperature in centigrade, the density can be determined by approximation from the density (20°C) according to Table 2 and the average thermal expansion coefficient between 20°C and, as in Table 5, according to the following correlation:

$$\rho(\vartheta) = \frac{\rho(20°\mathrm{C})}{[1+\tilde{\beta}(20°\mathrm{C},\vartheta)(\vartheta - 20°\mathrm{C})]^2}.$$

For the thermal diffusivity, the following correlation applies at any temperature:

$$a(\vartheta) = \frac{\lambda(\vartheta)}{\rho(\vartheta)c(\vartheta)}.$$

The density deviates only slightly from the density at 20°C. The thermal diffusivity can, therefore, be determined directly from the figures in the table by acceptable approximation:

$$a(\vartheta) \approx \frac{\lambda(\vartheta)}{\rho(20°\mathrm{C})c(\vartheta)}.$$

The heat penetration capacity has been defined as follows:

$$b(\vartheta) = \sqrt{\lambda(\vartheta)\rho(\vartheta)c(\vartheta)}.$$

Also, the heat penetration capacity can be approximated based on the density at 20°C.

VDI-GVC (ed.), *VDI Heat Atlas*, DOI 10.1007/978-3-540-77877-6_15,

D6.1. Table 1. Pure metals: The dependence on specific heat capacity c of the temperature in centigrade ϑ, also the heat of fusion ϑ, the density ρ, and the thermal conductivity λ at $\vartheta = 0°C$

Metal	ρ (0°C) kg/m³	ϑ_s °C	λ (0°C) W/(m K)	c J/(kg K)			
				0°C	200°C	400°C	600°C
Aluminum	2,700	600	236	837	984	1,080	1,210
Antimony	6,690	630.5	26	205	230	260	300
Beryllium	1,850	1,280	218	1,820	2,260	2,660	2,900
Lead	11,340	327	35.5	125	135	210fl	
Cadmium	8,650	321	104	230	250	258fl	
Chromium	6,930	1,845	95	435	509	535	570
Iron	7,870	1,537	84	435	519	603	754
Germanium	5,330	937	66	316	368	383	398
Gold	19,300	1,063	318	128	138	147	151
Indium	7,360	156.6	84	231	257fl	255fl	
Iridium	22,400	2,443	148	129	135	141	147
Potassium	860	63.6	104	742	838fl		
Copper	8,960	1,083	401	381	415	431	456
Lithium	534	180.5	79	3,485	4,370fl		
Magnesium	1,740	650	156	1,002	1,106	1,211	1,303
Molybdenum	10,220	2,610	139	250	262	275	289
Sodium	970	97.8	135	1,200	1,340fl	1,280fl	
Nickel	8,910	1,453	94	431	515	524	526
Niobium	8,550	2,415	53	269	276	284	292
Palladium	12,020	1,552	76	245	255	265	275
Platinum	21,450	1,769	7	131	138	143	148
Mercury	13,550	−38.9	8.2	140fl	136fl	136fl	
Ruthenium	12,300	2,250	117	231	244	258	271
Silver	10,500	961	428	236	242	251	263
Silicon	2,330	1,412	170	691	825	865	899
Tantalum	16,600	2,996	57	139	146	152	157
Titanium	4,510	1,680	22.5	513	576	607	630
Uranium	19,100	1,132	27	114	124	148	183
Vanadium	6,120	1,919	31.5	502	521	546	578
Tungsten	19,300	3,380	182	133	136	142	147
Zinc	7,130	419.5	121	385	418	456	519fl
Tin	7,280	213.9	68	226	244	238fl	

D6.1. Table 2. Designation of metallic materials, density ρ at 20°C and chemical composition

Ser. no.	Material number	Designation	Density at ρ at 20°C 10^3 kg/m^3	Chemical composition (ladle analysis) in % by mass																
				C	Si	Mn	P	S	Cr	Mo	Ni	Al	Fe	Cu	Mg	Zn	Ti	Pb	Sn	Other(s)
Temperature resistant steels, unalloyed																				
1	1.0305[a]	St 35.8	7.85	0.17	0.1–0.35	0.4–0.8	0.04	0.04					Rest							
2	1.0315[a]	St 37.8	7.85	0.17	0.1–0.35	0.4–0.8	0.04	0.04					Rest							
3	1.0405[a]	St 45.8	7.85	0.21	0.1–0.35	0.4–1.2	0.04	0.04					Rest							
4	1.0498[a]	St 42.8	7.85	0.21	0.1–0.35	0.4–1.2	0.04	0.04					Rest							
5	1.0345	P 235 GH	7.80	0.16	0.35	0.4–1.2	0.025–0.03	0.015–0.025	0.3	0.08	0.3	0.02	Rest	0.3				0.03–0.04		
6	1.0425	P 265 GH	7.80	0.2	0.40	0.5–1.4	0.025–0.03	0.075–0.025	0.3	0.08	0.3	0.02	Rest	0.3				0.03–0.04		
Temperature resistant steels, unalloyed																				
7	1.0481	P 295 GH	7.83	0.08–0.2	0.4	0.9–1.5	0.025–0.03	0.015–0.025	0.3	0.08	0.3		Rest	0.3				0.03		
8	1.0482[a]	19 Mn 5	7.83	0.17–0.22	0.3–0.6	1–1.3	0.04	0.04	0.3				Rest							
9	1.5415	15 Mo 3	7.85	0.12–0.2	0.35	0.4–0.9	0.025–0.03	0.035	0.0–0.3	0.25–0.35			Rest	0.3						
10	1.5423	16 Mo 5	7.85	0.12–0.2	0.15–0.5	0.5–0.8	0.04	0.04		0.45–0.65			Rest							
11	1.6210	15 MnNi 6 3	7.84	0.18	0.15–0.35	1.2–1.65	0.015	0.005	0.15	0.05	0.5–0.85	0.02–0.055	Rest	0.06				0.02		
12	1.6310	20 MnMoNi 5 5	7.85	0.17–0.23	0.15–0.3	1.2–1.5	0.012	0.008	<0.2	0.4–0.55	0.5–0.8	0.01–0.04	Rest	0.12						
13	1.6368	15 NiCuMoNb 5 (WB 36)	7.85	0.17	0.25–0.5	0.8–1.2	0.03	0.025	0.3	0.25–0.4	1–1.3		Rest	0.5–0.8						Nb 0.015–0.045
14	1.7335	13 CrMo 4 5	7.85	0.08–0.18	0.35	0.4–1.0	0.025–0.03	0.02	0.7–1.15	0.45–0.60			Rest	0.03–0.3						
15	1.7362	12 CrMo 19 5	7.77	0.15	0.3–0.6	0.3–	0.03	0.026	4–0.65	0.45–			Rest							
16	1.7380	10 CrMo9 10; GS-12 CrMo9 10	7.80	0.08–0.15	0.3–0.5	0.4–0.8	0.020–0.040	0.02	2–2.5	0.9–1.1			Rest	0.0–0.3						
17	1.7715	14 MoV 6 3	7.84	0.1–0.18	0.4	0.4–0.7	0.025	0.015	0.3–0.6	0.5–0.7		0.02	Rest							V 0.22–0.32

D6.1. Table 2. (continued)

Ser. no.	Material number	Designation	Density at ρ at 20°C 10^3 kg/m^3	Chemical composition (ladle analysis) in % by mass																
				C	Si	Mn	P	S	Cr	Mo	Ni	Al	Fe	Cu	Mg	Zn	Ti	Pb	Sn	Other(s)
Temperature resistant steels, highly alloyed																				
18	1.4903	X 10 CrMoVNb 9 1	7.77	0.08–0.12	0.5	0.3–0.74	0.025	0.015	8–9.5	0.85–1.05	0.4	0.04	Rest							Nb 0.06–0.1; V 0.18–0.25
19	1.4922	X 20 CrMoV 11-1	7.75	0.17–0.23	0.4	0.3–1	0.025	0.015	10–12.5	0.8–1.2	0.3–0.8		Rest							V 0.25–0.35
20	1.4981[a]	X 8 CrNiMoNb 16 16	8.01	0.04–0.1	0.3–0.6	1.5	0.035	0.015	15.5–17.5	1.6–2	15.5–17.5		Rest							Nb 0.4–1.2
21	1.7386	X 11 CrMo 9-1	7.77	0.08–0.15	0.25–1	0.3–0.6	0.025	0.02	8–10	0.9–1.1			Rest	<0.3						
High-temperature resistant steels																				
22	1.4910	X 3 CrNiMoBN 17-13-3	7.98	0.04	0.75	2	0.035	0.015	16–18	2–3	12–14		Rest							N 0.1–0.18; B 0.0015–0.005
23	1.4919	X 6 CrNiMoB 17-12-2	7.98	0.04–0.08	1	2	0.035	0.015	16.5–18.5	2–2.5	10–13		Rest							B 0.0015–0.005
24	1.4948	X 6 CrNi 18-10	7.90	0.04–0.08	1	2	0.035	0.015	17–19		8–11		Rest							
25	1.4949[a]	X 3 CrNiN 18-11	7.93	0.04	0.75	2	0.03	0.015	17–19	0.2–0.5	9.5–11.5		Rest							N 0.1–0.18
Heat-resisting steels																				
26	1.4713	X 10 CrAlSi 7	7.7	0.12	0.5–1	1	0.04	0.015	6–8			0.5–1	Rest							
27	1.4749	X 18 CrN 28	7.7	0.15–0.2	1	1	0.04	0.015	26–29				Rest							N 0.15–0.20
28	1.4828	X 15 CrNiSi 20-12	7.9	0.2	1.5–2.5	2	0.045	0.015	19–21		11–13		Rest							
29	1.4876	X 10 NiCrAlTi 32 21	8	0.12	1	2	0.03	0.015	19–23		30–34	0.15–0.6	Rest				0.15–0.6			
30	1.4877	X 5 NiCrCeNb 32 27	8	0.04–0.08	0.3	1	0.02	0.01	26–28		31–33	0.025	Rest							Ce 0.1; Nb 0.6–1.0
Stainless and acid-resistant steels																				
31	1.4016	X 6 Cr 17	7.7	0.08	1	1	0.04	0.015–0.03	6–8				Rest							
32	1.4057	X 17 CrNi 16-2	7.7	0.12–0.22	1	1.5	0.04	0.015–0.03	15.0–17.0		1.5–2.5		Rest							
33	1.4301	X 5 CrNi 18-10	7.9	0.07	1	2	0.045	0.015–0.030	17–19.5		8.5–10.5		Rest	0.0–1.0						
34	1.4510	X 3 CrTi 17	7.7	0.05	1	1	0.04	0.015–0.03	17–19				Rest				0.8			
35	1.4541	X 6 CrNiTi 18-10	7.9	0.08	1	2	0.045	0.015–0.03	17–19		9–12		Rest	0.0–1.0			<0.7			

36	1.4550	X 6 CrNiNb 18-10	7.9	0.08	1	2	0.045	0.015	17–19		9–12		Rest							Nb 0.8–1.0
37	1.4571	X 6 CrNiMoTi 17-12 2	7.98	0.08	1	2	0.045	0.015–0.03	16.5–18.5	2–2.5	10.5–13.5		Rest	0.0–1.0			0.7			
Case hardening and heat treatable steels																				
38	1.0402	C 22	7.85	0.17–0.24	0.4	0.4–0.7	0.045	0.045	0.40	0.10	0.40		Rest							Nb 0.05; V 0.05
39	1.1191	C 45 E	7.85	0.42–0.5	0.4	0.5–0.8	0.035	0.035	0.40	0.10	0.40		Rest							
Fine-grained structural and low-temperature steels																				
40	1.0461[a]	St E 255	7.85	0.18	0.4	0.5–1.3	0.035	0.03	0.03	0.8	0.3	0.02	Rest	0.2						Nb 0.05; V 0.05
41	1.8905	P 460 N	7.85	0.2	0.1–0.5	1.2–1.7	0.035	0.03	0.3		0.4–0.7		Rest							Nb 0.05; V 0.2
42	1.6217	13 MnNi 6 3	7.85	0.18	0.5	0.85–1.65	0.03	0.025			0.3–0.8	0.02 min	Rest							Nb 0.0.05; V 0.05
Aluminum alloys																				
43	EN AW-1200	EN AW–Al 99.0	2.71		(Si + Fe) < 1	0.05						Rest	(Si + Fe) < 1	0.05	0.05	0.1	0.05			
44	EN AW-3003	EN AW–AlMn 1 Cu	2.73		0.6	1–1.5						Rest	0.7	0.05–0.2		0.1				
45	EN AW-5052	EN AW–AlMg 2.5	2.68		0.25	0.1			0.15–0.35			Rest	0.4	0.1	2.2–2.8	0.1				
46	EN AW-5083	EN AW–AlMg 4.5 Mn 0.7	2.66		0.4	0.2–0.7			0.05–0.25			Rest	0.4	0.1	4.0–4.9	0.25	0.15			
47	EN AW-6061	EN AW–AlMg 1 SiCu	2.7		0.4–0.8	0.15			0.04–0.35			Rest	0.7	0.15–0.4	0.8–1.2	0.25	0.15			
48	EN AW-6060	EN AW–AlMg 1 Si	2.7		0.3–0.6	0.1			0.05			Rest	0.1–0.3	0.1	0.35–0.6	0.15	0.1			
Copper alloys																				
49	CW 352 H	CuNi 10 Fe 1 Mn	8.90	0.05		0.5–1	0.02	0.05			9–11		1–2	Rest		0.5		0.02	0.03	
50	CW 354 H	CuNi 30 Mn 1 Fe	8.90	0.05		0.5–1.5	0.02	0.05			30–32		0.4–1	Rest		0.5		0.02	0.05	
51	CW 614 H	CuZn 39 Pb 3 (Ms 58)	8.47								0.3	0.05	0.53	57–59		Rest		2.5–3.5	0.3	
52	CW 610 N	CuZn 39 Pb 0.5 (Ms 60 Pb)	8.40								0.3	0.05	0.2	59.0–60.5		Rest		0.2–0.8	0.2	
53	CW 706 R	CuZn 28 Sn 1 As (50 Ms 71)	8.56			0.1	0.01				0.1		0.07	70–72.5		Rest		0.05	0.9–1.3	As 0.02–0.06
54	CW 717 R	CuZn 38 Sn 1 (50 Ms 60)	8.35								0.2		0.1	59–62		Rest		0.2	0.5–1	
55	CW 702 R	CuZn 20 Al 2 As (50 Ms 76)	8.33			0.1	0.01				0.1	1.8–2.3	0.07	76–79		Rest		0.05		As 0.02–0.06

D6.1. Table 2. (continued)

Ser. no.	Material number	Designation	Density at ρ at 20°C 10^3 kg/m^3	Chemical composition (ladle analysis) in % by mass																
				C	Si	Mn	P	S	Cr	Mo	Ni	Al	Fe	Cu	Mg	Zn	Ti	Pb	Sn	Other(s)
56	CW 450 K	CuSn 4 (Phosphorus bronze)	8.90				0.01–0.4				0.2		0.1	Rest		0.2		0.02	3.5–4.5	
57	CW 303 G	CuAl 8 Fe 3 (Aluminum bronze)	7.70		0.2	1					1	6.5–8.5	1.5–3.5	Rest		0.5		0.05	0.1	
Nickel alloys																				
58	2.4066	Ni 99.2	8.90	0.1	0.25	0.35					>98.2		0.4	0.25	0.15		0.1			Co 1
59	2.4360	NiCu 30 Fe	8.80	0.15	0.5	2		0.02			>62.0	0.5	1–2.5	28–34			0.3			Co 1
60	2.4816	NiCr 15 Fe	8.43	0.025–0.1	0.5	1	0.02	0.015	14–17		>72.0	0.3	6–10	0.5			0.3			Co 1.5
61	2.4858	NiCr 21 Mo	8.10	0.025	0.5	1	0.02	0.015	19.5–23.5	2.5–3.5	38–46	0.2	Rest	1.5–3			0.6–1.2			Co 1
62	2.4856	NiCr 22 Mo 9 Nb	8.40	0.03–0.1	0.5	0.5	0.02	0.015	20–23	8–10	>58.0	0.4	5	0.5			0.4			Co 1; (Nb + Ta) 3.2–4.2
63	2.4819	NiMo 16 Cr 15 W	8.90	0.010	0.08	1	0.02	0.015	14.5–16.5	15–17	Rest		4–7	0.5						Co 2.5; V 0.35; W 3–4.5
64	2.4610	NiMo 16 Cr 16 Ti	8.60	0.015	0.08	1	0.025	0.015	14–18	14–17	Rest		3	0.5			0.7			Co 2
65	2.4617	NiMo 28	9.20	0.01	0.08	1	0.025	0.015	1	26–30	Rest		2	0.5						Co 1
Other materials																				
66	1.3912	Ni 36	8.20	0.1	0.5	0.5					35–37		Rest							
67	3.7165	TiAl 6 V 4	4.43	0.08								5.5–6.75	0.3				Rest			V 3.5–4.5
68	EN-JS 1030	EN-GJS-400-15	7.1	3.5–3.8	2.5–3.0	0.4	0.1	0.01					Rest		0.06–0.12					
69		GG (m. Lamellar graphite)	7.08	3.12	2.61	0.65	0.14	0.11	0.06		0.07		Rest	0.12						

[a]Material number invalid

D6.1. Table 3. Thermal conductivity dependent on temperature

Ser. no.	Material number	Temperature in °C													
		−200	−100	0	20	100	200	300	400	500	600	700	800	900	1000
1	1.0305				57	57	54	50	45	42	37				
2	1.0315				57	57	54	50	45	42	37				
3	1.0405				54	53	50	47	43	40	36				
4	1.0498				54	54	50	47	43	40	36				
5	1.0345				55	55	51	48	44	41					
6	1.0425				55	55	51	48	44	41					
7	1.0481				47	47	46	44	41	38	35				
8	1.0482				40	41	41	40	38	36	34				
9	1.5415				51	51	49	45	42	39	36				
10	1.5423				48	47	46	43	40	37	34				
11	1.6210				42	43	43	41	39	36					
12	1.6310				42	43	43	41	39	36					
13	1.6368				38	41	42	41	39	38	35				
14	1.7335				46	46	46	43	41	38	36				
15	1.7362				20	23	25	26	27	28	28				
16	1.7380				35	37	38	38	37	35	33				
17	1.7715				46	47	46	44	41	39	36				
18	1.4903				26	27	28	28	29	30	30				
19	1.4922				24	24	25	25	26	26	26				
20	1.4981				15	16	17	19	20	21	22	24	25		
21	1.7386				21	23	24	26	27	28	29				
22	1.4910				13	15	16	18	19	21	22	24	25		
23	1.4919				16	17	18	19	20	22	23	24			
24	1.4948				17	18	19	20	21	22	23	24			
25	1.4949				17	18	19	20	21	22	23	24			
26	1.4713				21	22	23	24	25	25	26	26			
27	1.4749				17										
28	1.4828				13	14	16	17	19	21	22	23	25	26	28
29	1.4876				12	13	15	16	18	20	21	23	24	26	27
30	1.4877				12					20					
31	1.4016				24	24	25	25	25	25	26	26	27	27	28
32	1.4057				25										
33	1.4301				15	16	18	19	21	22	24	25	26	28	29
34	1.4510				16	17	19	20	21	22	23	24	26	27	28
35	1.4541				15	16	18	20	21	22	24	25	27	28	29

D6.1. Table 3. (continued)

Ser. no.	Material number	Temperature in °C													
		−200	−100	0	20	100	200	300	400	500	600	700	800	900	1000
36	1.4550				15	16	18	19	20	22	23	24	26	27	28
37	1.4571				13	15	17	18	20	21	22	24	25		
38	1.0402				55–61						35–40				
39	1.1191				47–52						32–37				
40	1.0461				54	53	50	47	43	40					
41	1.8905				40	41	41	40	38	36					
42	1.6217				41										
43	EN AW-1200	327	242	235		240	237	232	226	219					
44	EN AW-3003			(202)		180	183	(177)	(171)						
45	EN AW-5052			(134)		146	155								
46	EN AW-5083			(113)		126	137								
47	EN AW-6061			(164)		172	176	(179)	(180)						
48	EN AW-6060			(209)		206	202	200	197						
49	CW 352 H				51.7	60.2	70	78.9	86.7	91.9	92	85.9	90	93.3	
50	CW 354 H				25.8	29.8	34.8	39.6	44.3	48.5	52.4	56.1	59.8	63.4	
51	CW 614 H				108	119	131	136	139	138					
52	CW 610 N			(68)		79	90	100	(111)						
53	CW 706 R		(99)	110		120	136	152							
54	CW 717 R	41	69	99		131	142	146	148	150	(151)				
55	CW 702 R		(87)	100		112	125	(138)							
56	CW 450 K		(65)	(77)		88.6	95.2	(112)							
57	CW 303 G		(61)	72		83	94	(105)							
58	2.4066		77.4	72.2		70	61.4	56.6	55.7	57.6	59.7	61.8	63.9	65.9	
59	2.4360	15.5	19.7	21.4		24.3	27.6	30.6	33.5	36.8	39.8	42.7	(45.6)	(49)	
60	2.4816		13.1	14.5		15.9	17.3	18.9	20.4	22.2	23.9	25.6	27.3	(29.1)	
61	2.4858		(9.7)	(11.4)		13.4	15.1	16.6	18.4	20	21.7	23.3	24.8	26.5	
62	2.4856		7.9	9.3		10.9	12.3	13.8	15.2	16.8	18.3	19.7	21.5	23.4	
63	2.4819		8.1	9.6		11.2	13	14.7	16.4	18.2	20	21.8	23.5	25.3	
64	2.4610		(7.6)	(9.6)		11.2	13.2	14.9	16.8	18.5	20.4	(22.7)	(24.7)	(26.8)	
65	2.4617		(10.1)	11.1		12.2	13.4	14.6	16	17.3	18.7	(19.9)	(21.2)	(22.5)	
66	1.3912				13	15	16	18	19						
67	3.7165				6.5	7.6	9.1	10.5	12	13.4	15				
68	EN-JS 1030				26.8	28.8	30.3	30.9	38.8	30.4					
69					42.5	41.8	40.8	39.6	38.2	36.7					

D6.1. Table 4. Specific heat capacity dependent on temperature

Ser. no.	Material number	Temperature in °C										
		20	100	200	300	400	500	600	700	800	900	1000
1–4; 7–14; 16–18; 21	1.0305; 1.0315; 1.0405; 1.0498; 1.0481; 1.0482; 1.5415; 1.5423; 1.6210; 1.6310; 1.6368; 1.7335; 1.7380; 1.7715; 1.4903; 1.7386	0.43	0.50	0.54	0.58	0.62	0.69	0.78				
5; 6	P 235 GH; P 265 GH	0.46	0.49	0.52	0.56	0.61	0.68					
15	1.7362	0.42	0.49	0.53	0.56	0.61	0.67	0.76				
19	1.4922	0.45	0.49	0.54	0.58	0.63	0.71	0.83				
20; 22–25	1.4981; 1.4910; 1.4919; 1.4948; 1.4949	0.45	0.50	0.53	0.54	0.55	0.58	0.61	0.61	0.61		
26	1.4713	0.43	0.49	0.53	0.56	0.61	0.67	0.77	0.92			
27	1.4749	0.50										
28; 29; 35–37	1.4828; 1.4876; 1.4541; 1.4550; 1.4571	0.47	0.50	0.53	0.53	0.56	0.58	0.60	0.61	0.61	0.62	0.64
30	1.4877	0.445										
31; 34	1.4016; 1.4510	0.45	0.50	0.54	0.58	0.64	0.74	0.88				
32	1.4057	0.46										
33	1.4301	0.47	0.50	0.53	0.53	0.56	0.58	0.60	0.61	0.61		
38; 39	1.0402; 1.1191	0.44	0.48	0.52	0.56	0.60	0.66	0.75				
40; 41	1.0461; 1.8905	0.43	0.50	0.54	0.58	0.62	0.69					
	See Below											
43	EN AW-1200											
47; 48	EN AW-6061; 6060	1.106										
49	CW 352 H	(0.362)	0.399	0.419	0.426	0.431	0.46	0.498	0.494	0.474	0.48	
50	CW 354 H	(0.354)	0.399	0.427	0.444	0.454	0.472	0.486	0.496	0.5	0.5	
51	CW 614 N	0.41										
52; 54	CW 610 N; CW 717 R											
55	CW 702 R	0.376										

D6.1. Table 4. (continued)

Ser. no.	Material number	Temperature in °C										
		20	100	200	300	400	500	600	700	800	900	1000
53	CW 706 R (mean value of cp between 0 °C u. ϑ)	0.376			0.399	0.405	0.413		0.442	0.453	0.46	
56	CW 450 K	0.368										
57	CW 303 G	0.435										
58	2.4066											
59	2.4360	0.428	0.441	0.459	0.478							
60; 61	2.4816; 2.4858; 2.4856											
62		(0.460)										
63; 64	2.4819; 2.4610; 2.4617											
65		(0.376)										
66	1.3912	0.477	0.52	0.566	0.524	0.508	0.506					
67	3.7165	(0.499)	0.565	0.592	0.606	0.619	0.657					
68	EN-JS 1030	0.461	0.527	0.569	0.593	0.606						
69	(GG)	0.468	0.519	0.569	0.616	0.662	0.713					
		Temperature in °C										
		−190	−150	−100	−50	−25	20					
42	1.6217	0.16	0.27	0.34	0.4	0.42	0.46					

D6.1. Table 5. Average linear thermal expansion coefficient β between 20°C and the temperature 10^{-6}/K

Ser. no.	Material number	Temperature in °C												
		−200	−100	0	100	200	300	400	500	600	700	800	900	1000
1–4; 7–10; 13; 14; 16; 17	1.0305; 1.0315; 1.0405; 1.0498; 1.0481; 1.0482; 1.5415; 1.5423; 1.6368; 1.7335; 1.7380; 1.7715													
					12.2	12.9	13.4	14	14.3	14.6				
5; 6	1.0345; 1.0445													
11; 12	1.6210; 1.6310				12.3	12.8	13.3	13.8	14.2					
15	1.7362				11.4	12	12.4	12.8	13.2	13.4				
18; 19	1.4903; 1.4922				10.9	11.3	11.7	12	12.3	12.6				
20; 22–25	1.4981; 1.4910; 1.4919; 1.4948; 1.4949				16.3	16.9	17.3	17.8	18.2	18.4	18.7	19		
21	1.7386				11.2	11.6	12	12.3	12.6	12.9				
26	1.4713				11.3	11.8	12.3	12.7	13	13.2				
27	1.4749							11				12.5		14
28; 35; 36	1.4828; 1.4541; 1.4550				16.7	17.2	17.7	18.1	18.4	18.8	19.1	19.4	19.7	20
29	1.4876				15.1	15.7	16.2	16.6	17	17.4	17.7	18	18.3	18.6
30	1.4877							16.2				17.7		18.4
31	1.4016				10	10	10.5	10.5	11					
32	1.4057				10	10.5	11	11	11					
33	1.4301				16.7	17.2	17.7	18.1	18.4	18.8	19.1	19.4		
34	1.4510				10.3	10.8	11.2	11.6	11.9	12.1	12.4	12.9		
37	1.4571				16.5	17.5	18.5	18.5	19					
38; 39	1.0402; 1.1191				12.5	13.2	13.7	14.2	14.6	14.9				
40; 41	1.0461; 1.8905				12	13	13	14	14					
	(No. 42 see below)													
43	EN AW-1200	20.5	21.5	22.5	23.5	24.5	25.4							
44	EN AW-3003		(21.2)	(22.2)	23.2	24.1	(25.1)							
45	EN AW-5052		(21.7)	(22.7)	23.8	24.8	(25.7)							
46	EN AW-5083		(22.1)	(23.0)	24.0	25.0	(25.9)							
47	EN AW-6061		(21.3)	(22.3)	23.3	24.3	(25.2)							
48	EN AW-6060		(21.4)	(22.4)	23.4	24.4	(25.4)							
49	CW 352 H				16.4	16.8	17.1	17.5	17.9	18.4	19	19.6	20.1	
50	CW 354 H				15.4	15.9	16.3	16.7	17.1	17.6	18.1	18.6	19.1	
51	CW 614 N			(19.3)	19.6	20.2	21.1							
52	CW 610 N			18.8	19.8	20.6	21.6	(22.4)						
53	CW 706 R		(19.4)	(19.6)	19.8	20	20.2	(20.3)						

D6.1. Table 5. (continued)

Ser. no.	Material number	Temperature in °C												
		−200	−100	0	100	200	300	400	500	600	700	800	900	1000
54	CW 717 R		18	18.9	19.8	20.7	21.6	22.5	23.4	24.3				
55	CW 702 R		(15.8)	(17.0)	18	19	20	(21)						
56	CW 450 K		(11.3)	(14.2)	16.2	17.1	18	(18.9)						
57	CW 303 G		(14.8)	(15.3)	15.8	16.4	16.9	(17.4)						
58	2.4066	9.3	10.9	12.2	13.3	13.8	14.3	14.8	15.2	15.5	15.8	16.1	(16.4)	
59	2.4360	10.9	12	13.1	14.1	15.5	15.8	15.9	16.2	16.6	16.9	17.4	(17.7)	
60	2.4816	(11.3)	11.9	12.5	13	13.6	14.1	14.5	14.9	15.3	15.7	16.1	(16.5)	
61	2.4858		(12.0)	(13.0)	14	14.8	15.1	15.5	15.7	16.3	16.8	17.3	17.7	
62	2.4856	9.5	11.3	12.2	12.8	13.1	13.3	13.6	14	14.5	15	15.5	16.1	
63	2.4819		(9.9)	(10.7)	11.3	12	12.7	13.1	13.3	13.8	14.4	15	15.7	
64	2.4610		(8.9)	(9.9)	10.8	11.8	12.5	13	13	13.4	13.5	14.5	15.1	
65	2.4617		(9.5)	9.9	10.4	10.8	11.2	11.4	11.7	(11.9)	(12.0)	(12.1)	(12.2)	
66	1.3912			(1.8)	2.2	3.3	6.2	8.7						
67	3.7165			(8.7)	9.2	9.5	9.7	9.9	10.3					
68	EN-JS 1030			(12.0)	12.4	12.8	13.2	13.5						
69	(GG)			(11.6)	12	12.4	12.7	13	13.3					
		Temperature in °C												
		−190	−150	−100	−50	−25								
42	1.6217	9	10	11	11	12								

D6.1. Table 6. Dynamic modulus of elasticity E in kN/mm^2

Ser. no.	Material number	Temperature in °C													
		−200	−100	0	20	100	200	300	400	500	600	700	800	900	1000
1–14; 38; 39	1.0305; 1.0315; 1.0405; 1.0498; 1.0345; 1.0425; 1.0481; 1.0482; 1.5414; 1.5423; 1.6210; 1.6310; 1.6368; 1.7335; 1.0402; 1.1191				211	207	200	192	184	175	165				
15	1.7362				217	212	205	198	189	180	168				
16; 17	1.7380; 1.7715				214	209	202	195	187	177	167				
18; 19; 21; 26; 34	1.4903; 1.4922; 1.7386; 1.4713; 1.4510				218	213	207	199	190	181	168				
20; 22–25	1.4981; 1.4910; 1.4919; 1.4948; 1.4949				199	194	185	176	166	158	150	142	133		
27	1.4749														
28	1.4828				196	190	182	174	166	158	150	142	134	127	120
29	1.4876				194	189	183	177	170	163	156	149	141	134	127
30	1.4877														
31	1.4016				220										
32	1.4057				216										
33; 35–37	1.4301; 1.4541; 1.4550; 1.4571				200	194	186	179	172	165					
40	1.0461				212	207	200	193	185	176					
41	1.8905				210	205	198	191	183	173					
	see below														
43	EN AW-1200	(77)	(73)	69.5		(66)	(58)	(47)							
44	EN AW-3003	76	72.7	69.5		65.5	(57.9)	(46.9)							
45	EN AW-5052	77	73.8	71		66.9	55.8	(42.7)							
46	EN AW-5083	78	74.8	71.4		68.6	60.7	(50.3)							
47	EN AW-6061	76	72.4	69.6		65.8	60.3	(52.4)							
48	EN AW-6060	(76)	(72.4)	69.6		65.8	57.9	(48.3)							
49	CW 352 H	134	129	124		118	112	106	100						
50	CW 354 H	159	156	153		(148)	(143)	(137)	(130)	(121)					
51	CW 614 N			111		108	104	99							
52	CW 610 N			(109)		96	83	(69)							
53	CW 706 R		112	110		107	94	79	59						
54	CW 717 R	103	101	97		94	90	85	79	(71)					
55	CW 702 R		(112)	110		(107)	(94)	(79)	(59)						
56	CW 450 K	115	114	109		103	94	83	67						
57	CW 303 G	112	112	109		(103)	(94)	(83)	(67)						

D6.1. Table 6. (continued)

Ser. no.	Material number	Temperature in °C													
		−200	−100	0	20	100	200	300	400	500	600	700	800	900	1000
58	2.4066		(217)	(214)		210	207	203	198	190	182	174	163	141	
59	2.4360		(179)	(179)		179	177	171	152	123	98	(81)			
60	2.4816		(228)	(220)		212	207	202	196	188	181	172	163	152	
61	2.4858		(203)	(197)		192	187	181	174	168	162	154	146	131	
62	2.4856		(210)	(207)		203	199	193	187	181	174	167	157	145	
63	2.4819		(212)	(207)		201	195	190	184	178	(172)	(167)	(161)	(155)	
64	2.4610		(219)	(214)		208	202	196	190	183	176	169	160	150	
65	2.4617		(222)	(217)		213	208	203	197	191	185	(179)	(172)	(165)	
66	1.3912			130		135	141	143	141	(136)					
67	3.7165			108		103	97	91	85	80	(75)				
68	EN-JS 1030			159		155.5	151	145.3	139.7	133.9					
69	(GG)			127.8		125.7	122.8	119.9	116.8	113.2					
		Temperature in °C													
		−190	−150	−100	−50	−25	20								
43	1.6217	221	219	217	215	214	212								

D6.1. Table 7. Poisson's ratio ν

Ser. no.	Material number	Temperature in °C						
		20	100	200	300	400	500	600
1–42		0.28	0.28	0.29	0.29	0.30	0.30	0.31
49	CW 352 H	0.35	0.36	0.36	0.36			
50	CW 354 H	0.33	0.33	0.33	0.33			
51	CW 614 N	0.41	0.41	0.41	0.38			
66	1.3912	0.28	0.29	0.27	0.28	0.27	0.28	
67	3.7165	0.26	0.26	0.26	0.26	0.26	0.26	
68	EN-JS 1030	0.27	0.27	0.28	0.28	0.28	0.29	
69	(GG)	0.26	0.26	0.26	0.26	0.27	0.27	

Bibliography

1. Stahlschlüssel (2004) Verlag Stahlschlüssel Wegst, 20. Auflage, Marbach
2. Deutsches Institut für Normung (1999) Werkstoff-Kurzzeichen und Werkstoffnummern für Nichteisenmetalle, DIN-Normen-heft 4, 3. Auflage, Beuth
3. Werkstoffblätter der Fa. Mannesmann Röhrenwerke AG, Düsseldorf
4. Richter F (1983) Physikalische Eigenschaften von Stählen und ihre Temperaturabhängigkeit. Stahleisen-Sonderberichte 10, Düsseldorf
5. Landolt-Börnstein (1991) Zahlenwerte und Funktionen aus Natur und Technik, Neue Serie, Band III/15, Teilband c. Springer-Verlag, Berlin
6. SEW 310 (1992) Physikalische Eigenschaften von Stählen, Stahl-Eisen-Werkstoffblätter des Vereins Deutscher Eisenhütten-leute, Verlag Stahleisen, Düsseldorf
7. Beaton CF (1985) Thermal and mechanical properties of heat exchanger construction material, Kap. 5.5.12 in Heat exchanger design handbook. Hemisphere Publ. Co., New York
8. Richter F (1991) Die physikalischen Eigenschaften von metallischen Werkstoffen. Metall Bd 45(6):S.582–S.589
9. Landolt-Börnstein (1967) Zahlenwerte und Funktionen aus Natur und Technik. Bände IV 4a, IV 2b, IV 2c. Springer-Verlag, Berlin
10. Touloukian YS (1970) Thermophysical properties of matter. vols 1,4. IFI/Plenum, New York

D6.2 Polymers

Christof Hübner · Paul Bernd Kempa
Fraunhofer-Institut für Chemische Technologie (ICT), Pfinztal, Germany

The tables in this section contain a selection of physical properties for different commonly used polymers and composites, some of them as a function of temperature.

Table 1 gives a survey over some polymers and their basic characteristics. The nomenclature follows DIN ISO 1629 [1] and DIN 7728 [2]. The polymers are divided into three groups: elastomers, thermoplastics, and thermosets depending on their chemical structure and mechanical properties (cf. DIN 7724 [3]).

Elastomers consist of slightly cross-linked macromolecules. They exhibit a rubber elastic behavior in their temperature range of use.

Thermoplastics and thermosets behave mainly elastic in the range of low deformations. Once thermoplastics, which consist of non-interlinked macromolecules, are heated above their application temperature, they exhibit viscoelastic flow behavior. At higher temperatures, they are decomposed. Cooling down again reverts this process and brings the thermoplastic material back into the state of elastic behavior.

Thermosets, which are heated over their temperature of application, show no flow behavior, because they consist of closely cross-linked macromolecules. At higher temperatures they are decomposed as well. Table 1 shows further characteristics such as morphology and the production process.

1 Properties

Table 2 shows the properties of the pure base polymers and of the reinforced polymers. In most applications, the base polymers are combined with fillers and reinforcements in order to tailor their mechanical, thermal, electrical, or magnetic properties. The fillers or further components can be softeners, talcum, soot, graphite or as reinforcements glass and carbon fibers or even natural fibers. The physical properties of the composites can be roughly estimated from the properties of their constituents and the percentage of the single constituents of the material with the help of mixing rules, which hold best in the range of small filler contents. For the exact determination of electrical, thermal, or mechanical properties, more detailed considerations of the structure of the fillers or reinforcements are necessary. In the case of reinforcing fibers their length and diameter as well as their spatial distribution (random distribution, fabrics, alignments...) must be considered. Especially for fiber reinforced materials, the processing plays an important role, because it strongly influences the orientation of the fibers in the matrix and therefore it normally produces highly anisotropic material properties.

In Table 1 some of the listed polymer types (e.g., polyamide, polyester, polycarbonate, polyurethane, epoxy resin) represent a complete group of polymers. For polyamides, the values are explicitly listed for PA6 and PA66 where data is available. The properties of the other polyamide types can be expected to be in a similar range. For polyesters, polycarbonates, polyurethanes, and epoxies, the grade is given as far as known from literature. In all the cases, the listed values are just recommended values, because the values within the groups can vary.

In Table 2 the maximum application temperatures for short-term use and for long-term use are listed [4, 13, 14]. Further, the density ρ, the modulus of elasticity E (Young's modulus) and Poisson's ratio ν, and the quotient of the lateral contraction and the elongation of a sample in a tensile test both expressed in terms of engineering strains, are given for a temperature of 20°C, where available. These values were taken from the literature [5–9].

Tables 3–5 show values for the thermal conductivity λ, the specific heat capacity c, and the linear differential coefficient of thermal expansion β for different temperatures θ. The values were taken from several works [6–8, 10–14]. For some polymers, no data for the differential coefficient of thermal expansion β is available, but only for the average linear coefficient of expansion $\overline{\beta}$ between the considered temperature and 20°C. Between these values the following relation holds

$$\overline{\beta}\,(\theta, 20^\circ\mathrm{C}) = \frac{1}{\theta - 20^\circ\mathrm{C}} \int_{20^\circ\mathrm{C}}^{\theta} \beta(\theta)\,\mathrm{d}\theta,$$

where $\beta(\theta) = \mathrm{d}L/L\,\mathrm{d}\theta$.

For many of the cited values in Tables 2–5, data sheets of different manufacturers and distributors of polymeric materials as well as different databases were used, which are not listed in the bibliography, because they were arbitrarily picked in order to achieve a representative survey but cannot be regarded as a complete research of all available sources. Many of the values from Tables 2–5 originate from the last volume 10 of the VDI Wärmeatlas [15]. They were verified and adopted where possible.

D6.2. Table 1. Survey of the basic characteristics of some polymers

Name of the polymer	DIN	Type	Structure	Synthesis
Polyethylene	LDPE	Thermoplastic	Semi-crystalline	Polymerization
Polyethylene	HDPE	Thermoplastic	Semi-crystalline	Polymerization
Polypropylene	PP	Thermoplastic	Semi-crystalline	Polymerization
Polymethylmethacetate	PMMA	Thermoplastic	Amorphous	Polymerization
Polystyrene	PS	Thermoplastic	Amorphous	Polymerization
Polyvinylchloride	PVC	Thermoplastic	Amorphous	Polymerization
Polytetrafluoroethylene	PTFE	Thermoplastic	Semi-crystalline	Polymerization
Polyoxymethylene	POM	Thermoplastic	Semi-crystalline	Polymerization
Polyamide	PA	Thermoplastic	Semi-crystalline	Polycondensation
Polyester	UP	Thermopl./Thermoset		Polycondensation
Polycarbonate	PC	Thermoplastic	Amorphous	Polycondensation
Polyurethane	PUR	Elastomer		Polyaddition
Epoxy resin	EP	Thermoset		Polyaddition
Hard natural rubber	NR (hard)	Elastomer		Vulcanization
Natural rubber	NR	Elastomer		Vulcanization

D6.2. Table 2. Maximum application temperature, density ρ, modulus of elasticity, and Poisson's ratio ν at 20°C

DIN	Maximum application temperature in °C		Density ρ at 20°C in 10^3 kg/m^3	Modulus of elasticity E at 20°C in kN/mm^2	Poisson's ratio ν at 20°C
	Short term	Long term			
LDPE	70–80	60–80	0.92	0.15–0.5	0.44
HDPE	90–120	60–80	0.95	0.6–1.4	0.44
PP	140	80–100	0.91	1.1–1.4	0.34
PP GF30	140	100	1.12	5.8–7	
PMMA	85–100	60–90	1.17–1.18	2.0–3.4	0.40
PS	60–80	50–70	1.04–1.09	3.3	0.38
PVC	80	70	1.30–1.40	2.0–3.0	0.36
PTFE	300	250	2.14–2.20	0.4–0.75	
POM	110–140	85–110	1.43–1.44	2.8–3.2	
POM GF30	140	100	1.6[a]	9.0	
PA	170	100	1.12–1.17	1.5–2.5	0.44
PA GF30	170–200	90–110	1.35	5.0–7.5	
UP	200	150	1.21	3.5	
PC	135	100–120	1.2	2.1–2.4	
PC GF30	145	110–135	1.42	7.5	
PUR	100–120	60–80	1.10–1.20	0.3–1.0	
EP	180	130	1.10–1.40	4.0	0.40
NR (hard)			1.13–1.18		
NR			0.91	0.0011	0.49

[a]For POM GF25.

D6.2. Table 3. Thermal conductivity λ in W/(m K) for different temperatures θ

DIN	Temperature θ (°C)								
	–150	–100	–50	0	20	50	100	150	200
LDPE	0.36	0.38	0.38	0.35		0.31	0.24	0.25	
HDPE	0.62	0.56	0.50	0.44		0.38	0.32	0.25	
PP	0.17	0.19	0.21	0.22		0.22	0.20		
PP GF30					0.22				
PMMA	0.16	0.18	0.19	0.19		0.19	0.20	0.19	0.18
PS	0.13	0.14	0.15	0.16		0.16	0.16	0.16	
PVC	0.13	0.15	0.15	0.16		0.17	0.17		
PTFE	0.23	0.24	0.25	0.25		0.26	0.26	0.26	
POM	0.47	0.45	0.43	0.42		0.41	0.38		
PA6	0.29	0.31	0.32	0.32		0.29	0.27	0.25	
PA6 GF30					0.28				
PA66	0.32	0.33	0.33	0.33		0.33	0.32		
PA66 GF30					0.27				
PA610	0.31	0.32	0.33	0.33		0.32	0.31		
UP					0.18				
PC	0.17	0.19	0.21	0.23		0.24	0.24	0.24	
PC GF30					0.26				
PUR	0.20	0.21	0.22	0.21		0.20	0.20		
EP				0.20	0.20	0.20	0.20		
NR (hard)	0.14	0.15	0.16	0.16		0.17	0.17		
NR	0.16	0.16	0.16	0.15		0.15	0.15		

D6.2. Table 4. Specific heat capacity c in J/(kg K) for different temperatures θ

DIN	Temperature θ (°C)									
	–200	–150	–100	–50	0	20	50	100	150	200
LDPE	550	840	1,100	1,430	1,990		2,730			
HDPE	550	840	1,100	1,340	1,640		2,050	2,860		
PP	460	770	1,030	1,280	1,570		1,920	2,350		
PP GF30										
PMMA	410	670	900	1,060	1,260		1,420	1,850		
PS	390	510	700	890	1,090		1,340	1,680	1,990	2,030
PVC	350	470	610	750	920		1,040	1,530	1,740	
PTFE	280	430	600	800	960		1,060	1,100	1,150	1,230
POM	470	650	820	1,080	1,270		1,460	1,850		
PA	470	730	930	1,150	1,360		1,680	2,150	2,600	
PA6 GF30						1,500				
PA66 GF30						1,500				
UP						1,200				
PC	360	500	700	900	1,100		1,300	1,500	1,900	2,000
PUR						1,800				
EP						1,000				
NR (hard)						1,380				
NR						1,880				

D6.2. Table 5. Linear differential coefficient of thermal expansion β in 10^{-6}/K for different temperatures θ

DIN	Temperature θ (°C)										
	–200	–150	–100	–50	0	20	50	100	150	200	250
LDPE											
HDPE	45	68	95	124		169	330	690			
PP		58	69	76	191	194	143	226	294		
PP GF30						35–80[a]					
PMMA		30	37	45	57	69	75	120	184		
PS	39	51	61	67		71	100	176	180	174	
PVC							75[b]				
PTFE	34	45	70	95	116	525	119	131	167	222	305
POM					90	95	100	165	410	230	
PA6			50	66	80	91	401	151	140	346	
PA6 GF30						20–30[c]					
PA66 GF30						20–30[c]					
UP	30	41	49	58	73	84	107	150			
PC						66					
PC GF30						30[c]					
PUR	99[b]	127[b]	160[b]	260[b]	200[b]						
EP	18	18	38	49	61	62	63	75	130		
NR (hard)						60	80[b]				
NR						220					

[a]Lower value for long-fiber reinforced material, higher value for short-fiber reinforced material.
[b]Average linear coefficient of thermal expansion $\overline{\beta}$ between 20°C and the temperatures θ in 10^{-6}/K.
[c]In the range of 23–55°C.

2 Bibliography

1. DIN ISO 1629: Kautschuke und Latices: Einteilung, Kurzzeichen. Deutsches Institut für Normung e.V. 2004-11
2. DIN EN ISO 1043-1: Kunststoffe - Kennbuchstaben und Kurzzeichen - Teil 1: Basis-Polymere und ihre besonderen Eigenschaften (ISO 1043-1:2001); Deutsche Fassung EN ISO 1043-1:2002. Deutsches Institut für Normung e.V. 2002–06
3. DIN 7724: Polymere Werkstoffe; Gruppierung polymerer Werkstoffe aufgrund ihres mechanischen Verhaltens. Deutsches Institut für Normung e.V. 1993–04
4. Carlowitz R (1995) Kunststofftabellen. 4. Auflage. Hanser Verlag, München
5. Van Krevelen DW (1990) Properties of polymers. Elsevier, Amsterdam
6. Blanke W (Hrsg.) (1989) Thermophysikalische Stoffgrößen. Springer-Verlag, Berlin
7. Kaye/Laby (1986) Tables of physical and chemical constants, vol. 15. Aufl. Longman, London
8. VDMA Fachgemeinschaft Gummi- und Kunststoffmaschinen (Hrsg.) (1979) Kenndaten für die Verarbeitung thermoplastischer Kunststoffe. Teil 1 Thermodynamik. Carl Hanser Verlag, München
9. Oberbach K (1980) Kunststoffkennwerte für Konstrukteure. 2. Auflage. Hanser Verlag, München
10. Landold-Börnstein (1967) Zahlenwerte und Funktionen aus der Natur und Technik, Band IV 4 b. Springer-Verlag, Berlin
11. Touloukian YS et al. (1970) Thermophysical properties of matter, vol. 1, 4. IFI/Plenum, New York
12. Brandrup J, Immergut EH (Hrsg.) (1989) Polymer handbook, vol. 3. Wiley, New York
13. Eyerer P, Elsner P, Hirth Th. (Hrsg.) (2005) Domininghaus - Die Kunststoffe und ihre Eigenschaften, vol. 6. Springer-Verlag, Berlin, Heidelberg
14. Oberbach K, Baur E, Brinkmann S, Schmachtenberg E, Saechtling H (2004) Saechtling-Kunststoff-Taschenbuch, vol. 29. Hanser Verlag, München
15. VDI Wärmeatlas (2006) 10. Auflage. Springer-Verlag, Berlin, Heidelberg

D6.3 Thermal Conductivity of Packed Beds

Evangelos Tsotsas
Otto-von-Guericke-Universität Magdeburg, Magdeburg, Germany

1 Introduction

The effective thermal conductivity of stagnant multiphase media depends on the thermal conductivities and volume fractions of the constituent phases. Consequently, the thermal conductivity of packed beds is a function of the thermal conductivity λ_p of the particles, the thermal conductivity λ_f of the fluid that fills the voids between particles, and the porosity ψ of the bed:

$$\lambda_{bed} = \lambda_{bed}(\lambda_p, \lambda_f, \psi) \tag{1a}$$

The quantities λ_p, λ_f, and ψ are called primary parameters. Apart from these, several secondary parameters may also have an influence, due to processes such as:

- Heat transfer by radiation: The intensity of heat transfer by radiation depends on temperature T, the optical properties of the fluid and the surface of particles, and the size of voids, which correlates with the particle diameter d.
- Pressure dependence: According to kinetic gas theory, the thermal conductivity of unconfined, dilute gas is independent of pressure. However, the thermal conductivity of gas surrounded by solid surfaces – as in a packed bed – decreases with decreasing pressure. The same happens with the thermal conductivity of the entire bed (Smoluchowski effect). Particle diameter d and the mean free path of the gas molecules – which depends on pressure, temperature, and thermodynamic properties – are important for the extent of this decrease.
- Heat transfer through flattened interparticle contacts: Particles can flatten around contact points due to external forces or due to their own weight of the packed bed. Deformation and heat transfer over the solid bridge depend, among others, on the mechanical properties of the solid and the morphology of particle surface.

Adding particle shape and particle size distribution to this list of secondary influence parameters, the functional dependence

$$\lambda_{bed} = \lambda_{bed}(\lambda_p, \lambda_f, \psi;\ p,\ T,\ d,\ \text{particle shape},\ \text{particle size distribution},\ \text{mechanical and optical properties of particles},\ \text{thermodynamic and optical properties of fluid},\ \text{and flattening of contacts}) \tag{1b}$$

is obtained.

2 Requirements to Models

It is the task of models to specify the functional relationships described in a general way by Eq. (1a) or (1b). A successful model should take all primary and as many secondary influence parameters as possible into account, possess some flexibility by appropriate fitting parameters, enable easy calculations, and reliably predict measured thermal conductivities. Furthermore, it should fulfill physically reasonable limiting cases. Such limiting cases can be expressed without the consideration of secondary influence parameters, that means on Eq. (1a), as follows:

$$\begin{aligned}
&1:\ \psi = 0 &&\curvearrowright\ \lambda_{bed} = \lambda_p,\\
&2:\ \psi = 1 &&\curvearrowright\ \lambda_{bed} = \lambda_f,\\
&3:\ \lambda_p = \lambda_f &&\curvearrowright\ \lambda_{bed} = \lambda_p = \lambda_f,\\
&4:\ \lambda_f \to \infty &&\curvearrowright\ \lambda_{bed} \to \infty,\\
&5:\ \lambda_p \to \infty &&\curvearrowright\ \lambda_{bed} \to \infty,\\
&6:\ \lambda_f \to 0 &&\curvearrowright\ \lambda_{bed} \to 0,\\
&7:\ \lambda_p \to 0 &&\curvearrowright\ \lambda_{bed}/\lambda_f = \delta_{bed}/\delta.
\end{aligned}$$

Most of these relationships are evident and do not require further explanation. The limiting case 5 presupposes point or area contacts between particles. Limiting case 6 is valid for particles that do not touch each other, or have point contacts. Finally, limiting case 7 means that the reduced thermal conductivity of a bed of nonconducting particles should be equal to the effective diffusion coefficient δ_{bed} of this bed divided by the molecular diffusivity δ. The ratio δ_{bed}/δ is relatively easy to measure, so that a basis for comparison and an assessment of model behavior are provided by the limiting case $\lambda_p \to 0$ (see Sect. 4.2).

3 Types of Models

Prediction of the thermal conductivity of packed beds is a topic of intensive research in physics and engineering since more than one century. The numerous models that have emerged can be classified into three categories according to a proposal by Tsotsas and Martin [1], as illustrated in Fig. 1.

Type I. In type I models, the Laplace equation for heat conduction is solved analytically or numerically to compute the temperature field in and around the particles. The oldest and simplest analytical solution of this kind has been provided by Maxwell in 1873. It can be expressed in the form

$$k_{bed} = (1 + 2\phi)/(1 - \phi), \tag{2a}$$

with

$$\phi = (1 - \psi)(k_p - 1)/(k_p + 2) \tag{2b}$$

and

$$k_{bed} = \lambda_{bed}/\lambda_f, k_p = \lambda_p/\lambda_f. \tag{3a, b}$$

Maxwell's solution is based on the assumption that individual particles do not exert any thermal influence on each other. Therefore, it is well suited for application to dilute suspensions und emulsions. In the case of packed beds, Eqs. (2a) and (2b) give reliable results only in the region of small values of the ratio λ_p/λ_f ($\lambda_p/\lambda_f < 20$).

Subsequent authors have tried to relax the assumption of infinite dilution. Analytical solutions can be derived only for regular packing structures and are mathematically demanding. Therefore, numerical computations have also been conducted as soon as digital computers became available. Wakao and Kato [2] calculated in a pioneering work the thermal conductivity of simple cubical and orthorhombic arrangements of spheres of equal size. Such regular packed beds have porosities of $\psi = 0.476$ and $\psi = 0.395$, respectively. Nowadays, fields of temperature can be calculated numerically even for relatively large, random assemblies of particles [3]. However, such calculations are not free of limitations (see Sect. 5) and hardly appropriate for everyday use.

Type II. Models of the second type (Ohmic analogs) introduce thermal resistances for conduction in the solid and the fluid phases; such resistances are combined in order to specify the functional relationship of Eq. (1a). The simplest possible combinations are the series arrangement of Fig. 2a with

$$k_I = \frac{\lambda_I}{\lambda_f} = \left(\psi + \frac{1 - \psi}{k_p}\right)^{-1} \tag{4a}$$

and the parallel arrangement of Fig. 2b with

$$k_{II} = \lambda_{II}/\lambda_f = \psi + (1 - \psi)k_p. \tag{4b}$$

For a given set of primary parameters λ_p, λ_f, and ψ the series combination has the lowest and the parallel combination has the highest possible conductivity (lower-bound and upper-bound solutions according to Wiener, 1904).

The usually broad region between upper bound and lower bound contains thermal conductivities of, among others, consolidated porous media and loose particle beds. To distinguish between them, at least one additional structural parameter is necessary. The relative proportion a of series arrangement plays this role in the Ohmic combination according to Fig. 2c, which has been proposed by Krischer [4]. The thermal conductivity of this combination is obtained to

$$k_{bed} = \left(\frac{a}{k_I} + \frac{1 - a}{k_{II}}\right)^{-1}. \tag{4c}$$

For packed beds, a value of $a = 0.20$ can be recommended [4]. The resistance scheme of Fig. 2c enables simple and quick estimations of packed-bed thermal conductivity. However, it is

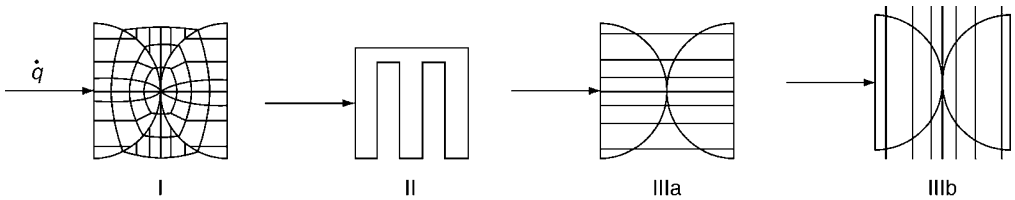

D6.3. Fig. 1. Types of models to predict the thermal conductivity of packed beds: Type I. Exact analytical or numerical computation of the temperature field. Type II. Combination of resistances. Type IIIa. Unit cell, parallel heat flux lines; Type IIIb. Unit cell, parallel isotherms.

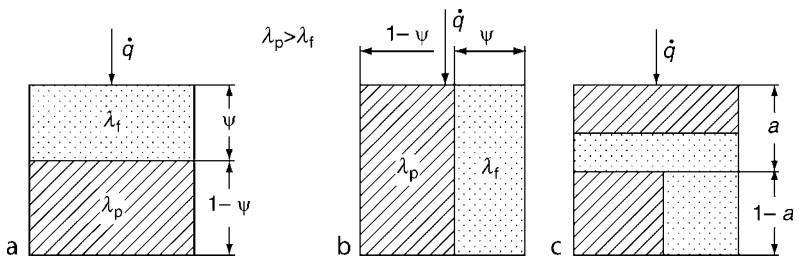

D6.3. Fig. 2. Plate model according to Krischer [4] for the thermal conductivity of dispersed fluid–solid systems: (**a**) Arrangement with maximal resistance (series combination); (**b**) Arrangement with minimal resistance (parallel combination); (**c**) Combination of (**a**) and (**b**).

not adequate for precise calculations, especially when secondary parameters have a relatively large influence. The same is true for most models of type II.

Type III. Models of this type calculate the thermal conductivity of a unit cell, which is then set equal to the thermal conductivity of the packed bed. For the sake of easy calculation, either parallel lines of heat flux (type IIIa) or parallel isotherms (type IIIb) are assumed (Fig. 1). Both assumptions are fulfilled exactly only at the trivial limit of $\lambda_p = \lambda_f$. Models of the third type are popular compromises between the realistic, but computationally expensive models of the first and the simple, but coarse models of the second type.

Tsotsas and Martin [1] evaluated many different models for the thermal conductivity of packed beds in terms of the requirements and criteria from Sect. 2, coming to the conclusion that type III models can be recommended for practical use. This is especially true for one model from this family that has been developed by Zehner, Bauer, and Schlünder. This model will be presented in some detail in Sect. 4.

4 The Model of Zehner/Bauer/Schlünder

4.1 General

The unit cell of the Zehner/Bauer/Schlünder model is depicted in Fig. 3. It consists of a cylindrical core, where two half particles are placed opposite to each other, and of an annular fluid-filled section around the core. The main idea of the model is to repair the incorrect assumption of parallel heat flux lines by using fictitious, nonspherical particles to simulate the thermal behavior of spherical ones. The contor of such "model particles" is defined by means of the deformation parameter B. In Sect. 4.2, a model version that considers only the primary parameters λ_p, λ_f, and ψ will be presented. This basis version will be extended in Sect. 4.3 in order to capture the influence of secondary parameters.

4.2 Influence of Primary Parameters

According to Fig. 3, the reduced thermal conductivity of the bed can be calculated to

$$k_{bed} = 1 - \sqrt{1-\psi} + \sqrt{1-\psi}\ \ k_c, \tag{5a}$$

with

$$k_c = \frac{2}{N}\left(\frac{B}{N^2}\frac{k_p - 1}{k_p}\ln\frac{k_p}{B} - \frac{B+1}{2} - \frac{B-1}{N}\right), \tag{5b}$$

and

$$N = 1 - \left(B/k_p\right), k_c = \lambda_c/\lambda_f. \tag{5c, d}$$

Here, λ_c is the thermal conductivity of the core of the unit cell [5]. The deformation parameter B is derived for spherical particles by putting the porosity of the unit cell equal to the porosity of the packed bed. This leads approximately to

$$B = 1.25\left(\frac{1-\psi}{\psi}\right)^{10/9}. \tag{5e}$$

Equations (5a)–(5e) fulfill the limiting cases 1–6 from Sect. 2. Due to the mentioned separation of the unit cell in a core and a margin zone (Fig. 3; Eq. (5a))

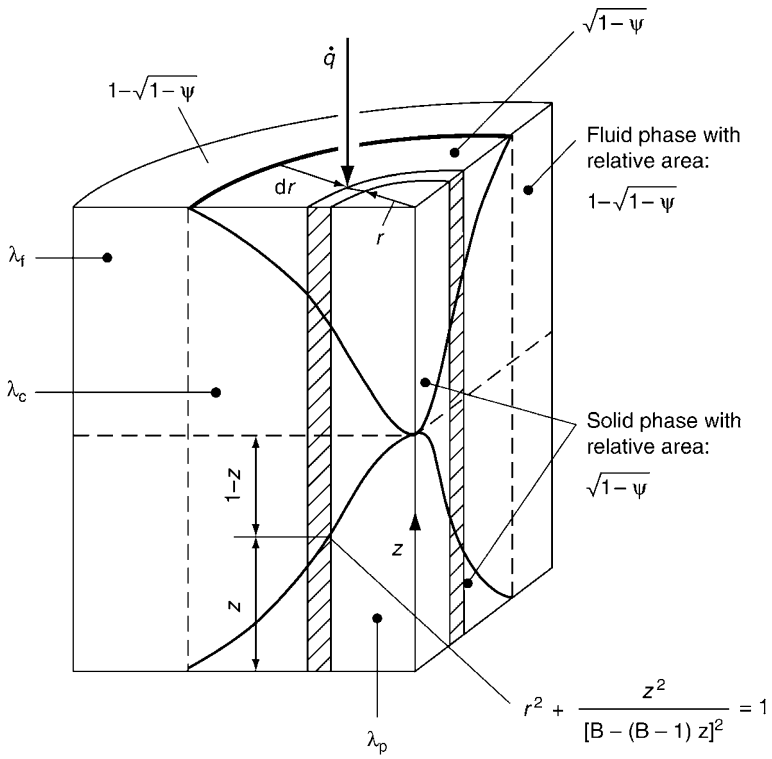

D6.3. Fig. 3. Unit cell of the model of Zehner/Bauer/Schlünder.

$$\lambda_p = 0, \text{ then } \lambda_{bed}/\lambda_f = \delta_{bed}/\delta = 1 - \sqrt{1-\psi} \qquad (6)$$

is obtained in limiting case 7.

Equation (6) can well describe diffusion coefficients measured by Currie [6], as in Fig. 4. To cover a broad range of porosities, Currie investigated not only monodispersed packed beds of spheres, but also polydispersed beds of spherical particles, beds of irregular particles, loose beds, and highly porous materials.

Taking into consideration only spheres of equal size reveals a slight underprediction of measured data by Eq. (6). This is illustrated in Fig. 5, which is based on a collection of effective diffusion coefficients for random, regular, and sintered beds from [1]. A still larger deviation between Eq. (6) and experimental results is observed for dilute solid–liquid suspensions and liquid–liquid emulsions. Respective data points are plotted in Fig. 6 [7, 8]. They stem from measurements of electrical conductivity, which does not make a difference, because diffusion and electrical conduction are described mathematically by the same equation. Excellent agreement is obtained with Maxwell in Fig. 6 (broken line according to Eq. (2) with $k_p = 0$).

The foregoing discussion shows that the ratio δ_{bed}/δ does not depend uniquely on porosity ψ (volume fraction of the continuous phase), but also on the structure of binary systems. The respective structural parameter, which has been denoted by a in the treatment of the model by Krischer, cannot, unfortunately, be predicted in an easy way. However, Eq. (6) does provide a good approximation for practical use if only packed beds or binary systems with a similar structure are considered.

The dependence of reduced packed bed thermal conductivity k_{bed} from the ratio $k_p = \lambda_p/\lambda_f$ at $\psi = 0.40$ is depicted in Fig. 7.

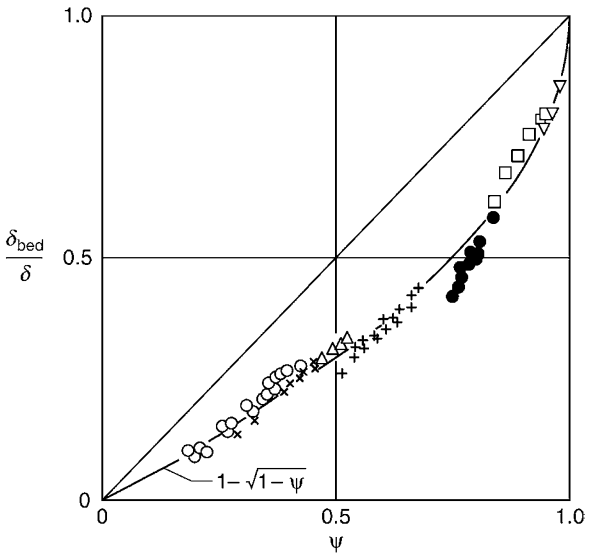

D6.3. Fig. 4. Reduced effective diffusion coefficients δ_{bed}/δ in dependence of porosity ψ according to measurements by Currie [6] for:
○ Glas spheres and sand (monodispersed beds and mixtures);
× Carborundum (monodispersed beds and mixtures);
Δ Salt (particles of irregular shape); + Soil crumbs; ● Kaolin; □ Celite;
▽ Steel wool. The solid curve corresponds to Eq. (6).

There is an excellent agreement between Eq. (5) and the previously mentioned numerical results for a regular, orthorhombic packing of spheres from Wakao and Kato [2]. On contrary, the models of Krischer and Maxwell agree with the numerical calculations only within certain ranges of k_p.

4.3 Influence of Secondary Parameters

Zehner/Schlünder [9] and Bauer/Schlünder [10] have extended the model by taking into consideration the secondary parameters listed in Sect. 1. The resulting equations are:

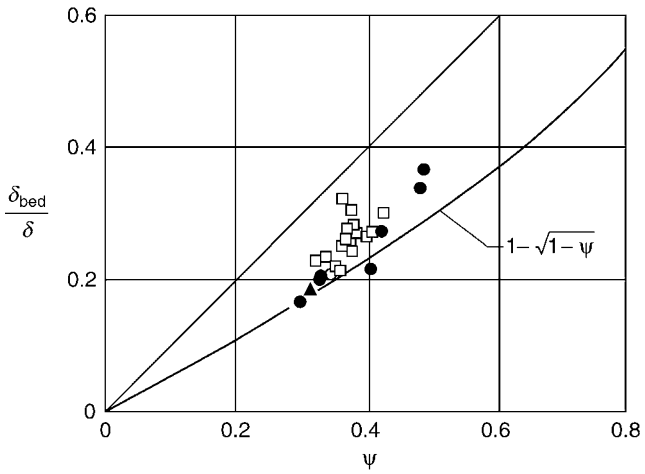

D6.3. Fig. 5. Reduced diffusion coefficients δ_{bed}/δ for assemblies of equally sized spheres against porosity ψ. Measured data of various authors [1] for: □ random beds; ● regular beds; ▲ sintered beds. The solid curve corresponds to Eq. (6).

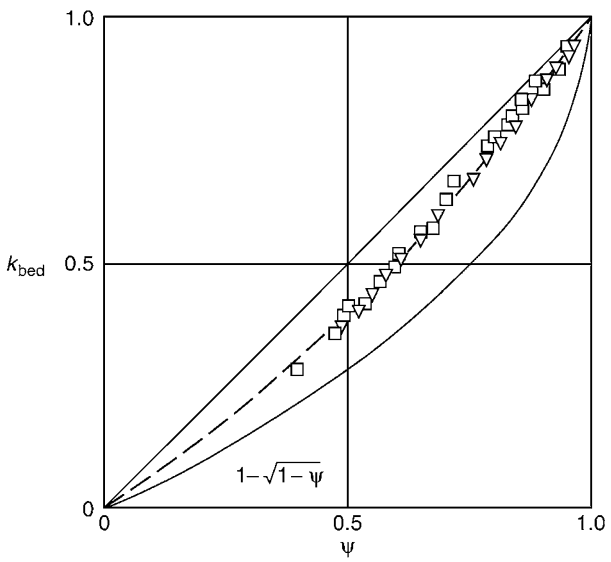

D6.3. Fig. 6. Reduced electrical conductivity k_{bed} of binary systems with nonconducting dispersed phase as a function of porosity ψ: □ solid–liquid suspensions (Turner [7]); ▽ liquid–liquid emulsions (Meredith and Tobias [8]). The solid curve corresponds to Eq. (6), the broken curve corresponds to the model of Maxwell (Eq. (2) with $k_p = 0$).

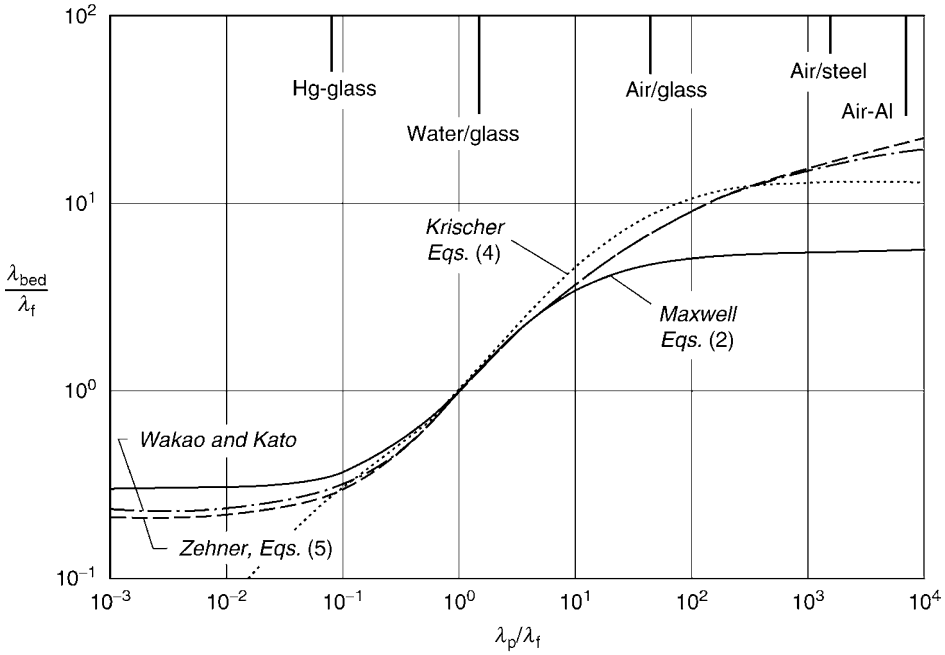

D6.3. Fig. 7. Influence of particle-to-fluid conductivity ratio $k_p = \lambda_p/\lambda_f$ on the reduced thermal conductivity of packed beds. Solid line: Maxwell, Eq. (2) with $\psi = 0.40$; Dashed line: Krischer, Eq. (4) with $a = 0.20$ and $\psi = 0.40$; Broken line: Zehner and Schlünder, Eq. (5) with $\psi = 0.40$; Broken-dashed line: numerical calculation by Wakao and Kato for orthorhombic packings of spheres ($\psi = 0.395$).

$$k_{bed} = \left(1 - \sqrt{1-\psi}\right)\psi\left[\left(\psi - 1 + k_G^{-1}\right)^{-1} + k_{rad}\right] + \sqrt{1-\psi}\left[\varphi k_p + (1-\varphi)k_c\right] \tag{7a}$$

with

$$k_c = \frac{2}{N}\left\{\frac{B(k_p + k_{rad} - 1)}{N^2 k_G k_p}\ln\frac{k_p + k_{rad}}{B\left[k_G + (1-k_G)(k_p + k_{rad})\right]} + \frac{B+1}{2B}\left[\frac{k_{rad}}{k_G} - B\left(1 + \frac{1-k_G}{k_G}k_{rad}\right)\right] - \frac{B-1}{Nk_G}\right\} \tag{7b}$$

$$N = \frac{1}{k_G}\left(1 + \frac{k_{rad} - Bk_G}{k_p}\right) - B\left(\frac{1}{k_G} - 1\right)\left(1 + \frac{k_{rad}}{k_p}\right) \tag{7c}$$

$$B = C_f[(1-\psi)/\psi]^{10/9} f(\zeta), \tag{7d}$$

$$k_{rad} = \frac{\lambda_{rad}}{\lambda_f} = \frac{4\sigma}{(2/\varepsilon) - 1}T^3\frac{d}{\lambda_f}, \tag{7e}$$

and

$$k_G = \lambda_G/\lambda_f = [1 + (l/d)]^{-1}. \tag{7f}$$

The influence of thermal radiation is taken into account by means of the quantity k_{rad}, Eq. (7e), where ε is the emissivity of particle surfaces, σ is the radiation coefficient of the black body ($\sigma = 5.67 \times 10^{-8}\,W/m^{-2}\,K^{-4}$), and T is the temperature in Kelvin. Pressure dependence (Smoluchowski effect) is expressed by the quotient k_G in Eq. (7f). The modified mean free path l of gas molecules can be calculated from Eq. (46) in ❯ Chap. M6. If the continuous phase is not a gas, one may set $k_G = 1$. Possible flattening around particle contacts is considered by the flattening coefficient φ in Eq. (7a). Although some proposals of modeling and computation exist in the literature (see Sect. 5), the coefficient φ in most cases will be determined empirically. Another model parameter that has to be gained by fitting to experimental data is C_f. The shape factor C_f describes in Eq. (7d) the influence of particle shape on packed-bed thermal conductivity. For random or regular orthorhombic beds made of equally large spheres the shape factor has a value of $C_f = 1.25$ (compare with Eq. (5e)). For the particle diameter d one should always use the diameter of a sphere of equal volume. Herein, intraparticle voids should be neglected.

Apart from the shape factor C_f, a distribution function $f(\zeta)$ is also foreseen in the calculation of the deformation parameter B by Eq. (7d). The idea of this function is to capture the influence of different particle sizes in the bed by correlating f with a parameter expressing the broadness of particle size distribution. The distribution parameter

$$\zeta = \left[\frac{\sum Q_i/d_i^2}{(\sum Q_i/d_i)^2} - 1\right]^{0.5} \tag{8}$$

can be used for this purpose. Here, Q_i is the volume fraction of particles with diameter d_i (sphere of equal volume) in the mixture. However, numerous experimental results with binary and polydispersed packed beds show [11–16] that thermal conductivities can be calculated quite accurately by setting the distribution function simply equal to unity:

$$f(\zeta) = 1. \tag{9}$$

In other words, polydispersed beds can be treated as monodispersed when calculating thermal conductivity – provided that the right value of bed porosity is used [11]. Bed porosity is

always smaller for a polydispersed bed than for a monodispersed one, and can be measured quite easily. Additionally, particle diameters calculated from

$$d = \left(\sum Q_i/d_i\right)^{-1} \tag{10}$$

should be used in the equations for k_{rad} and k_G when dealing with polydispersed packings.

Table 1 summarizes values for the shape factor C_f and the flattening coefficient φ according to Bauer [17].

Inserting into Eq. (7) $k_{rad} = 0$, $k_G = 1$, $\varphi = 0$, $C_f = 1.25$, and $f(\zeta) = 1$, again the simpler set of Eq. (5) is obtained, which does not account for the influence of secondary parameters on bed thermal conductivity.

The model is also applicable to particles covered with a thin solid layer. To this purpose, the ratio k_p should be replaced in model equations by

$$k_p^* = \frac{k_p}{1 + Bi} \tag{11a}$$

The *Biot* number is defined as

$$Bi = \frac{s}{\lambda_s}\frac{\lambda_p}{d} \tag{11b}$$

where s is the thickness and λ_s is the thermal conductivity of the coating. The coating may be applied on purpose, or it may be undesired. Thin oxide layers created spontaneously on metallic particles during contact with air are typical undesired coatings. In this case, Bauer [17] recommends the use of $s/\lambda_s = 0.15 \times 10^{-3}$ W^{-1} m^2 K in Eq. (11b).

Some examples for the influence of radiation and particle shape on the thermal conductivity of packed beds are given in Figs. 8–11. Experimental data have been taken from Yagi and Kunii [18] for spheres, cylinders, Raschig rings, and broken, irregular materials. The solid lines correspond to calculations with Eq. (7). As the figures show, thermal radiation is important for high temperatures and/or large particles (see Eq. (7e)). Pressure dependence is illustrated in Figs. 12 and 13 on the basis of data from [19]. Both the measured points and the solid curves from Eq. (7) have a characteristic sigmoid shape. Residual thermal conductivities at very low pressures are due to radiation and flattened particle contacts. Values of $k_{bed} = \lambda_{bed}/\lambda_f < 1$ can easily be reached in this region. This means that evacuated packed beds transport less heat than stagnant gas layers of the same thickness. Therefore, they can be used for the purpose of

D6.3. Table 1. Shape factors and flattening coefficients for Eq. (7); (d_i, d_o: inner and outer diameter, respectively).

Particle shape	C_f	φ	Material
Spherical	1.25	0.0013	Steel
		0.0077	Ceramic
		0.0253	Copper
Irregular (broken)	1.40	0.0010	Sand
Cylindrical	2.50	?	
Raschig rings	2.5 [1 + $(d_i/d_o)^2$]	?	

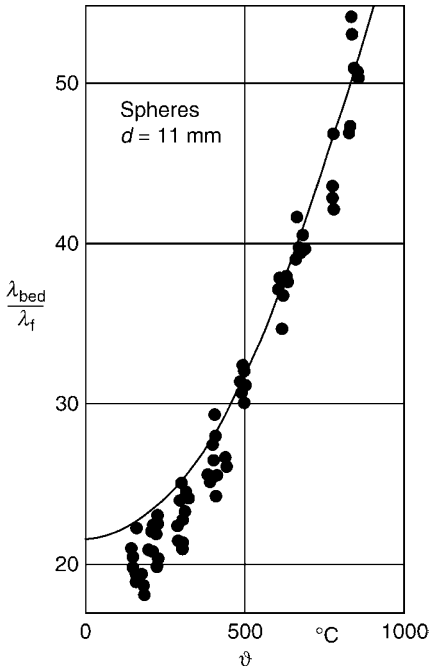

D6.3. Fig. 8. Temperature dependence of the reduced effective thermal conductivity $k_{bed} = \lambda_{bed}/\lambda_f$ for spherical steel particles (d = 11 mm, λ_p = 52 W m^{-1} K^{-1}, ε = 0.80, φ = 0.0013, ψ = 0.40) in air ($p = 10^5$ Pa). Experimental data: Yagi and Kunii [18]; calculation: Eq. (7).

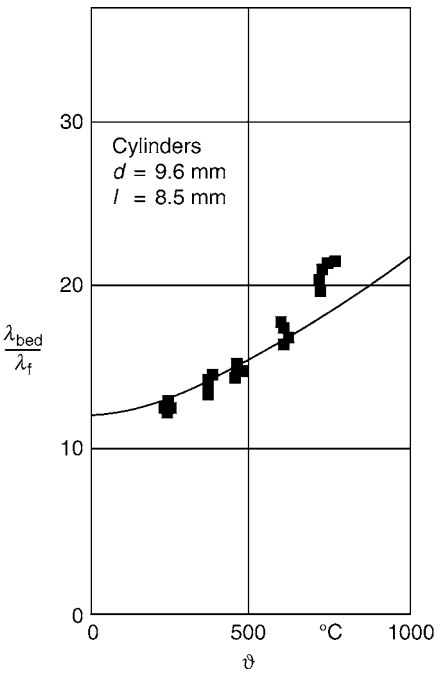

D6.3. Fig. 9. Temperature dependence of the reduced effective thermal conductivity $k_{bed} = \lambda_{bed}/\lambda_f$ for cylindrical ceramic particles (d = 9.6 mm, l = 8.5 mm, λ_p = 1.63 W m^{-1} K^{-1}, ε = 0.93, φ = 0.0077, ψ = 0.43) in air ($p = 10^5$ Pa). Experimental data: Yagi and Kunii [18]; calculation: Eq. (7).

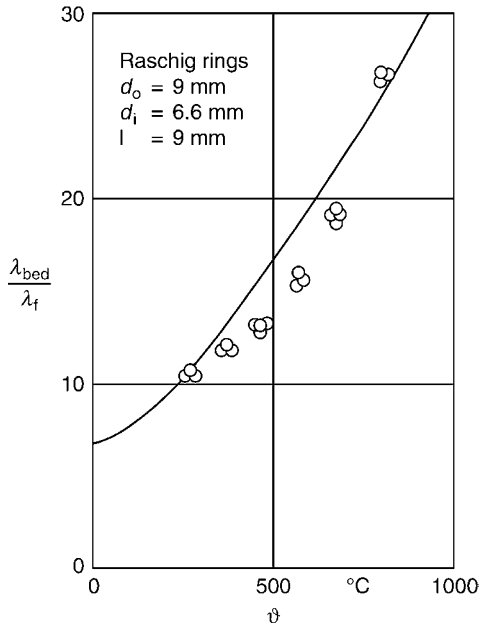

D6.3. Fig. 10. Temperature dependence of the reduced effective thermal conductivity $k_{bed} = \lambda_{bed}/\lambda_f$ for ceramic Raschig rings (d_o = 9 mm, d_i = 6.6 mm, l = 9 mm, λ_p = 1.63 W m^{-1} K^{-1}, ε = 0.93, φ = 0.0077, ψ = 0.72) in air ($p = 10^5$ Pa). Experimental data: Yagi and Kunii [18]; calculation: Eq. (7).

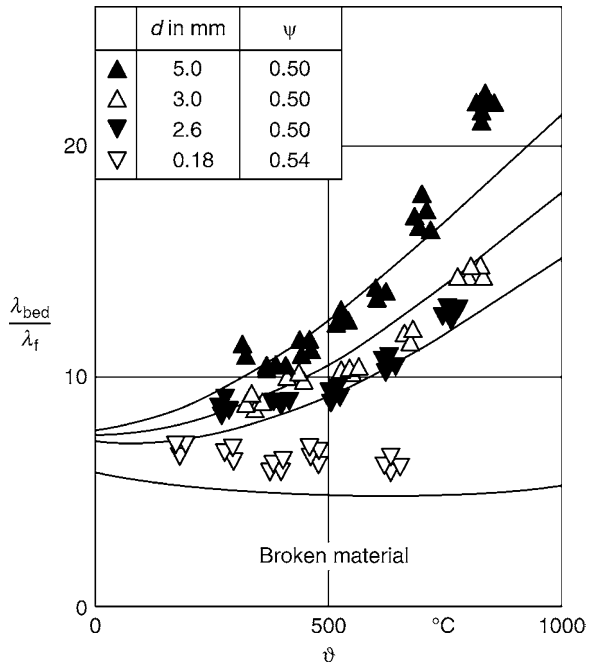

D6.3. Fig. 11. Temperature dependence of the reduced effective thermal conductivity $k_{bed} = \lambda_{bed}/\lambda_f$ for different size fractions of broken, irregularly shaped material (cement clinker, λ_p = 1.98 W m^{-1} K^{-1}, ε = 0.93, φ = 0.0077) in air ($p = 10^5$ Pa). Experimental data: Yagi and Kunii [18]; calculation: Eq. (7).

insulation (compare with Chap. K6). The high impact of flattened contacts on the residual thermal conductivity of packed beds is illustrated in Fig. 14 with calculated curves (φ = 0: point contacts, φ large: large flat areas). On the contrary, heat transfer over solid bridges is usually not very important at normal or elevated pressure.

4.4 Comparison with Experimental Data

The basis version of the model (Eq. (5)) has been compared to a large amount of experimental results measured by various authors by Zehner/Schlünder [5] and Tsotsas/Martin [1]. Tsotsas and Martin conducted their systematic comparison not only for packed beds, but also for emulsions (two liquid phases), suspensions (solid particles in a liquid), and dispersions (two solid phases). In almost all cases the model was found to predict the data with an accuracy of better than ±30%. A comprehensive control of the influence of secondary parameters (extended model version according to Eq. (7)) has been carried out by Bauer [17]. Again, good agreement was found between model predictions and the data.

5 Complementary Remarks

The entire previous discussion is based on the assumption that heat conduction in packed beds can be described with an effective thermal conductivity – similarly as in the case of a homogeneous body. This approach has been successful in practice. It is reasonable for all steady state and the majority of transient heat transfer problems. However, significant temperature differences may occur between the solid and the fluid phase in the course of very fast transient processes. If this happens, the packed bed cannot be considered any more as a continuum with the effective thermal conductivity λ_{bed}. Unfortunately, no general quantitative criteria are available for the validity of the continuum assumption. A specific situation, where the continuum approach fails, is the stepwise change of thermal boundary condition at the outer surface of a gas-filled packed bed. Defining the time of the change as $t = 0$ and considering the bed as a homogeneous body, leads to heat transfer coefficients between the boundary and the body that go to infinity as time goes to zero ($\alpha \to \infty$ for $t \to 0$, see Eq. (5) in Chap. M6). This is a wrong result. In reality, the heat transfer coefficient is limited to a certain maximal value by conduction through the gas gap between outer boundary of the bed and the adjoining, first particle layer. The respective thermal resistance is called a contact resistance and denoted by $1/\alpha_{ws}$. Its prediction and practical use are treated in Chap. M6. There, a criterion applicable to this specific case (a critical time) is also discussed.

Another assumption implicit to the previous discussion is that the effective thermal conductivity has the same value in every spatial direction. This is true for packed beds, but it is not true for anisotropic bodies with a preferential orientation of their structural elements. If the medium is periodic, a special

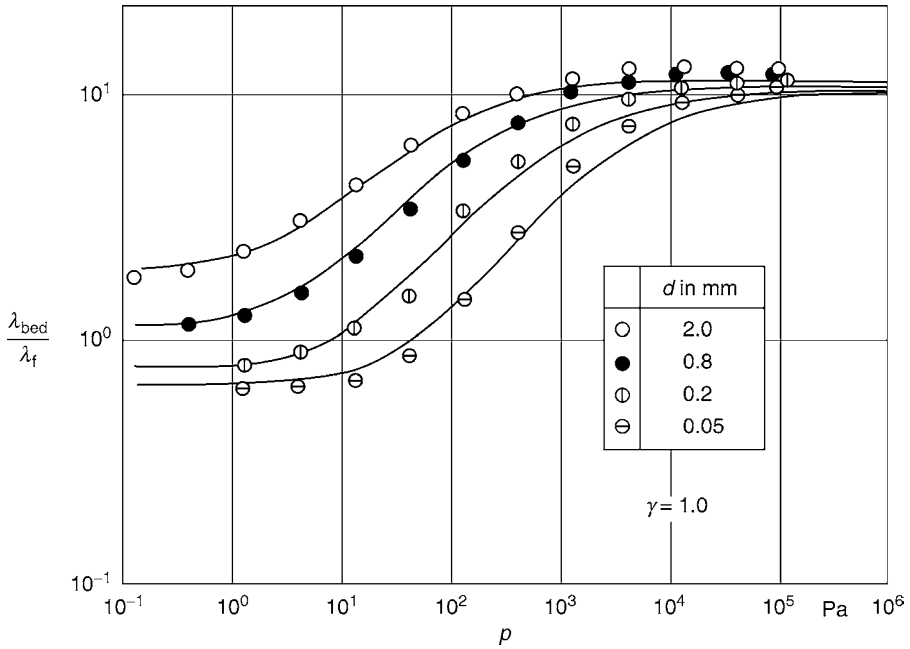

D6.3. Fig. 12. Pressure dependence of the reduced effective thermal conductivity $k_{bed} = \lambda_{bed}/\lambda_f$ of packed beds of spherical ceramic particles ($k_p = \lambda_p/\lambda_f = 104$, $\varepsilon = 0.90$, $\varphi = 0.0077$, $\psi = 0.39$) in Freon 12 (CF_2Cl, $\vartheta = 30°C$, $\gamma = 1.0$). Experimental data: Imura and Takegoshi [19]; calculation: Eq. (7).

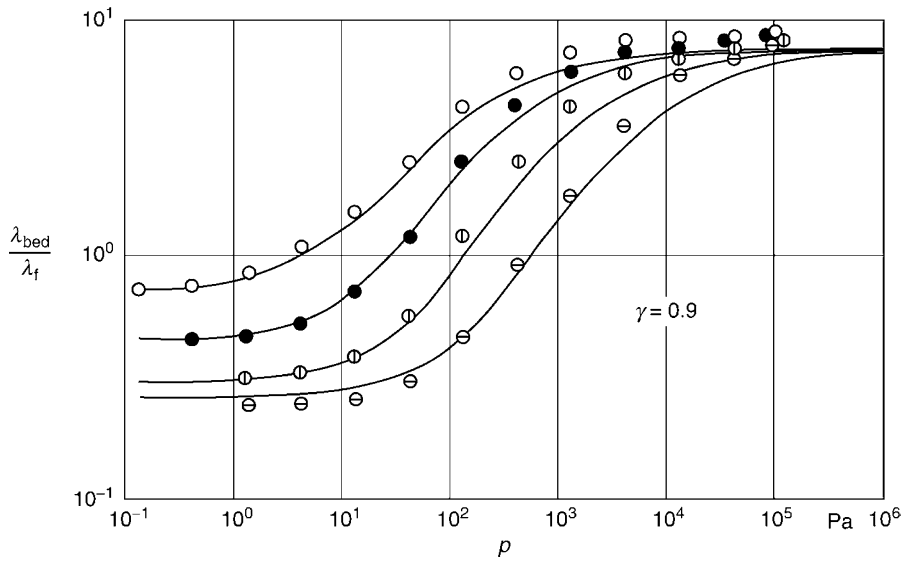

D6.3. Fig. 13. Continuation of Fig. 12 with nitrogen as the fluid ($k_p = \lambda_p/\lambda_f = 41$, $\gamma = 0.90$). All other conditions are the same.

mathematical technique called homogenization can be used to derive direction-dependent thermal conductivities [20]. The simplest possible example of anisotropy is that of the two parallel plates of Fig. 2. Applying homogenization to a respective unit cell leads to the upper-bound solution (Eq. (4b); Fig. 2b) in one direction and to the lower-bound solution (Eq. (4a); Fig. 2a) in the other.

As already discussed (Fig. 7), predictions of Eq. (5) are almost identical to the numerical results by Wakao and Kato [2] for the orthorhombic packing of spheres with $\psi = 0.395$. Such an excellent agreement is not obtained for the simple cubical packing ($\psi = 0.476$). Respective numerical calculations [2, 21] show a slight dependence of the factor in Eq. (5e) – that means of C_f – from the conductivity ratio k_p. This result is not really surprising, if it is remembered that the task of the deformation parameter B is to correct the inaccurate assumption about parallel lines of heat flux. Since the deviation of heat flux lines from linearity depends on $k_p = \lambda_p/\lambda_f$, it is reasonable to expect the same kind of dependence in B and, consequently, also in C_f. Numerical results for the simple cubical packing are predicted very well by replacing the factor $C_f = 1.25$ in Eq. (5e) with a value of $C_f \approx 1.8$ [21].

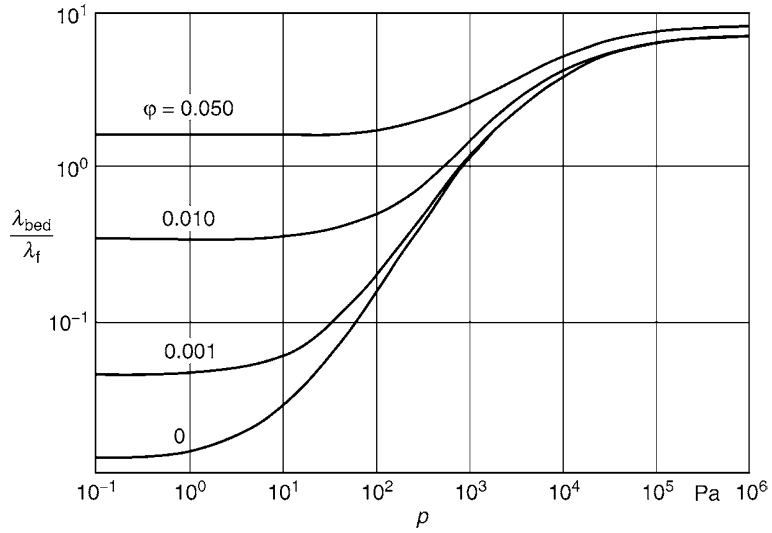

D6.3. Fig. 14. Influence of pressure on the reduced effective thermal conductivity $k_{bed} = \lambda_{bed}/\lambda_f$ at different flattening coefficients φ. Calculations after Eq. (7) for spherical particles in nitrogen with $d = 0.05$ mm, $k_p = \lambda_p/\lambda_f = 41$, $\varepsilon = 0.90$, $\psi = 0.39$, $\vartheta = 30°C$, $\gamma = 0.90$.

Field distortions due to different conductivities in the fluid and the particle phase depend on the arrangement of particles in space and are often called non-Maxwell or higher-order effects. The recommended model of Zehner, Bauer, and Schlünder accommodates such interactions by geometric distortion of the unit-cell particle. The same principle has been applied by other authors on the Maxwell formula [22] or on Ohmic cells [23]. Raghavan and Martin [23] show that Ohmic analogs can be equivalent to Maxwell's solution (Eq. (2)) under certain circumstances.

Concerning radiation, it should be noted that its remote influence has been neglected in Eq. (7). This is well justified for packed beds of opaque particles, but inaccurate in case of transparent particles or highly porous materials. Furthermore, heat transfer by radiation has been incorporated in Fourier's law, which is not exactly correct. A more fundamental treatment of such aspects can be found in publications that concentrate on thermal radiation in porous media [24–26].

The treatment of flattened contacts by the coefficient φ in the recommended model is also approximate. In case of dominance of this path of heat transfer, more detailed approaches that take particle roughness into account [27] may be used. Additionally, particle deformation may be considered as a function of local stress. This cannot be accomplished on a unit cell, but requires solution of the thermal and the coupled mechanical problem for the entire packed bed. Such solutions can be achieved by the thermal version of the discrete element method (thermal DEM) [28, 29]. Their benefit is that they make the influence of external loads and weight on thermal conductivity accessible – including inhomogeneous distributions of stress ("stress chains") that correlate with bed structure. The price to be paid is that conduction through flattened contacts is treated only approximately (by a deformation-dependent resistance or conductance), while other paths of heat transfer are neglected completely. A similar dilemma is connected with numerical computations of the temperature field in entire packed beds. Assessing the influence of an additional liquid phase (liquid bridges) is the benefit of such calculations in [3]. The price is a relatively low spatial resolution, which means less accuracy in the determination of non-Maxwell effects than in unit-cell computations.

Finally, it should be noticed that ψ can be replaced with $(1 - \psi)$, k_p with $1/k_p$, and k_{bed} with k_{bed}/k_p in either Eq. (2) or Eq. (5). This is called phase inversion, and gives estimates for the thermal conductivity of bodies that consist of a continuous solid and a dispersed fluid phase. A modification of the Zehner/Bauer/Schlünder model for such sponge-like materials or foams has been presented by Hsu et al. [30]. Carson et al. [31] discuss respective conductivity bounds. Models specific to ceramic or metallic foams can also be found in the literature (e.g., [32]).

6 Examples

Examples 1

Calculate the thermal conductivity of a monodispersed packed bed of ceramic spheres ($d = 2$ mm, $\lambda_p = 2$ W m^{-1} K^{-1}, $\varepsilon = 0.90$, $\psi = 0.40$) in air at a pressure of $p = 10^5$ Pa and a temperature of $\vartheta = 20°C$.

Subchap. D2.2 ↷ $\lambda_f = 25.69 \times 10^{-3}$ W m^{-1} K^{-1}, $c_{p,f} = 1{,}007$ J kg^{-1} K^{-1}, $\tilde{M} = 28.96$ kg kmol^{-1}

Chap. A1 ↷ $\tilde{R} = 8314.41$ J kmol^{-1} K^{-1}

Chap. M6, Eq. (47) ↷ $\gamma = 0.904$

Chap. M6, Eq. (46) ↷ $l = 2.62 \times 10^{-7}$ m

Eq. (7f) ↷ $k_G = 0.99987$, Eq. (7e) ↷ $k_{rad} = 0.364$

Furthermore, it is: $k_p = \lambda_p/\lambda_f = 77.85$.

Table 1 ↷ $C_f = 1.25$, $\varphi = 0.0077$.

Eq. (9), Eq. (7d) ↷ $B = 1.961$, Eq. (7c) ↷ $N = 0.9794$, Eq. (7b) ↷ $k_c = 10.76$, Eq. (7a) ↷ $k_{bed} = 8.99$, $\lambda_{bed} = 0.231$ W m^{-1} K^{-1}.

Neglecting the secondary influence parameters ($k_G = 1$, $k_{rad} = 0$, $\varphi = 0$) one can obtain

Eq. (5c) ↷ $N = 0.9748$, Eq. (5b) ↷ $k_c = 10.33$

Eq. (5a) ↷ $k_{bed} = 8.23$, $\lambda_{bed} = 0.211$ W m^{-1} K^{-1}

For comparison:
According to Maxwell:
Eq. (2) ↷ $\phi = 0.577$, $k_{bed} = 5.10$, $\lambda_{bed} = 0.131$ W m^{-1} K^{-1}
According to Krischer:
Eq. (4) ↷ $k_I = 2.45$, $k_{II} = 47.11$, $k_{bed} = 10.15$
$\lambda_{bed} = 0.261$ W m^{-1} K^{-1}

Example 2

Calculate the thermal conductivity of the same packed bed as in Example 1 at a pressure of $p = 10^2$ Pa and a temperature of $\vartheta = 700$°C. All other input data remain the same.
Subchap. D2.2 ↷ $\lambda_f = 66.46 \times 10^{-3}$ W m^{-1} K^{-1}
$c_{p,f} = 1137$ J kg^{-1} K^{-1}
Chap. M6, Eq. (47) ↷ $\gamma = 0.571$
Chap. M6, Eq. (46) ↷ $l = 2.22 \times 10^{-3}$ m
Eq. (7f) ↷ $k_G = 0.474$, Eq. (7e) ↷ $k_{rad} = 5.146$
Furthermore, it is: $k_p = \lambda_p/\lambda_f = 30.09$.
Eq. (7c) ↷ $N = -0.143$, Eq. (7b) ↷ $k_c = 7.18$
Eq. (7a) ↷ $k_{bed} = 6.22$, $\lambda_{bed} = 0.414$ W m^{-1} K^{-1}
Under consideration of just one secondary parameter at a time one would obtain
$k_G = 1$, $k_{rad} = 5.146$, $\varphi = 0.0077$ ↷ $k_{bed} = 10.33$
$k_G = 0.474$, $k_{rad} = 0$, $\varphi = 0.0077$ ↷ $k_{bed} = 0.812$
$k_G = 0.474$, $k_{rad} = 5.146$, $\varphi = 0$ ↷ $k_{bed} = 6.09$
Comparison with the right value of $k_{bed} = 6.22$ shows that thermal radiation and the Smoluchowski effect are now very important.

Example 3

Repeat the calculation of Example 2 for a binary mixture of irregular particles with $d_1 = 1$ mm, $d_2 = 5$ mm, $Q_1 = Q_2 = 0.50$, $\psi = 0.32$, and $\varphi = 0$. All other data remain the same.
Eq. (10) ↷ $d = 1.67$ mm
Eq. (7f) ↷ $k_G = 0.429$, Eq. (7e) ↷ $k_{rad} = 4.289$
Table 1 ↷ $C_f = 1.40$
With f(ζ) = 1 (Eq. (9)) it follows
$B = 3.235$, $N = -2.364$, $k_c = 5.42$, $k_{bed} = 4.75$ and
$\lambda_{bed} = 0.315$ W m^{-1} K^{-1}

7 Symbols

a	structural parameter (–)
B	deformation parameter (–)
c	specific heat capacity (J kg^{-1} K^{-1})
C_f	shape factor (–)
d	particle diameter (m)
$f(\zeta)$	distribution function (–)
k	reduced thermal conductivity ($k = \lambda/\lambda_f$) (–)
l	length of cylindrical particle (m)
l	modified mean free path of gas molecules (m)
$\widetilde{M}$	molar mass (kg kmol^{-1})
p	Pressure (Pa)
$\dot{q}$	heat flux (W m^{-2})
Q	volume fraction (–)
$\widetilde{R}$	universal gas constant (J kmol^{-1} K^{-1})
s	thickness of coating (m)
t	time (S)
T	thermodynamic temperature (K)
γ	accommodation coefficient (–)
δ	diffusion coefficient (m^2 s^{-1})
ε	emissivity (–)
ζ	distribution parameter (–)
ϑ	temperature (°C)
λ	thermal conductivity (W m^{-1} K^{-1})
σ	radiation coefficient of the black body (W m^{-2} K^{-4})
φ	flattening coefficient (–)
ϕ	Maxwell parameter (–)
ψ	porosity (–)

8 Indices

bed	packed bed
c	core of unit cell
f	fluid
G	considering pressure dependence
i	inner
i	single fraction in polydispersed bed
o	outer
p	particle
p	at constant pressure
rad	radiation
s	coating layer
I	series combination
II	parallel combination

9 Bibliography

1. Tsotsas E, Martin H (1987) Thermal conductivity of packed beds: A review. Chem Eng Process 22:19–37
2. Wakao N, Kato K (1969) Effective thermal conductivity of packed beds. J Chem Eng Jpn 2:24–33
3. Kohout M, Collier AP, Stepanek F (2004) Thermal conductivity of wet particle assemblies. Int J Heat Mass Transfer 47:5565–5574
4. Krischer O (1956) Die wissenschaftlichen Grundlagen der Trocknungstechnik, 1st edn. Springer: Berlin
5. Zehner P, Schlünder E-U (1970) Wärmeleitfähigkeit von Schüttungen bei mäßigen Temperaturen. Chem- Ing- Tech 42:933–941
6. Currie JA (1960) Gaseous diffusion in porous media. Br J Appl Phys 11:314–324
7. Turner JCR (1976) Two-phase conductivity: the electrical conductance of liquid-fluidized beds of spheres. Chem Eng Sci 31:487–492
8. Meredith RE, Tobias CW (1961) Conductivities of emulsions. J Electrochem Soc 108:286–290
9. Zehner P, Schlünder E-U (1972) Einfluß der Wärmestrahlung und des Druckes auf den Wärmetransport in nicht durchströmten Schüttungen. Chem- Ing- Tech 44:1303–1308
10. Bauer R, Schlünder E-U (1978) Effective radial thermal conductivity of packings in gas flow. Part II: Thermal conductivity of the packing fraction without gas flow. Int Chem Eng 18:189–204
11. Tsotsas E, Schlünder E-U (1991) The impact of particle size dispersity on the thermal conductivity of packed beds: Measurements, numerical simulations, prediction. Chem Eng Technol 14:421–427
12. Okazaki M, Yamasaki T, Gotoh S, Toei R (1981) Effective thermal conductivity of granular beds of various binary mixtures. J Chem Eng Jpn 14:183–189
13. Sordon G (1988) Über den Wärmetransport in Kugelschüttungen. Diss Univ Karlsruhe
14. Gurgel JM (1989) Contribution à l'étude expérimentale de la conductivité thermique de milieux granulaires (mono ou bidisperses avec ou sans adsorption). Thèse de Docteur, Univ. Pierre et Marie Curie Paris VI

15. Botterill JSM, Salway AG, Teoman Y (1989) The effective thermal conductivity of high temperature particulate beds. Part II: Model predictions and the implication of the experimental values. Int J Heat Mass Transfer 32:595–609
16. Gupta M, Yang J, Roy C (2003) Predicting the effective thermal conductivity of polydispersed beds of softwood bark and softwood char. Fuel 82:395–404
17. Bauer R (1976) Effektive radiale Wärmeleitfähigkeit gasdurchströmter Scüttungen mit Partikeln unterschiedlicher Form und Größenverteilung. Diss Univ Karlsruhe
18. Yagi S, Kunii D (1957) Studies of effective thermal conductivity in packed beds. AIChE J 3:373–381
19. Imura S, Takegoshi E (1974) Effect of gas pressure on effective thermal conductivity. Nippon Kikai Gakkai Rombunshu 40:489–497
20. Hornung U (1997) Homogenization and porous media. Springer: Berlin
21. Tsotsas E, Schlünder E-U (1990) Numerical calculation of the thermal conductivity of two regular bidispersed beds of spherical particles. Computers Chem Engng 14:1031–1038
22. Bauer TH (1993) A general analytical approach towards the thermal conductivity of porous media. Int J Heat Mass Transfer 17:4181–4191
23. Raghavan VR, Martin H (1995) Modelling of two-phase thermal conductivity. Chem Eng Process 34:439–446
24. Vortmeyer D (1980) Radiation in packed solids. Ger Chem Eng 3:124–138
25. Tien CL (1988) Thermal radiation in packed and fluidized beds. Trans ASME, J Heat Transfer 110:1230–1242
26. Gross U, Tran LTS (2004) Radiation effects on transient hot-wire measurements in absorbing and emitting porous media. Int J Heat Mass Transfer 47:3279–3290
27. Slavin AJ, Londry FA, Harrison J (2000) A new model for the effective thermal conductivity of packed beds of solid spheroids. Int J Heat Mass Transfer 43:2059–2073
28. Vargas WL, McCarthy JJ (2001) Heat conduction in granular materials. AIChE J 47:1052–1059
29. Siu WWM, Lee SH-K (2004) Transient temperature computation of spheres in three-dimensional random packings. Int J Heat Mass Transfer 47:887–898
30. Hsu CT, Cheng P, Wong KW (1994) Modified Zehner-Schluender models for stagnant thermal conductivity of porous media. Int J Heat Mass Transfer 37:2751–2759
31. Carson JK, Lovatt SJ, Tanner DJ, Cleland AC (2005) Thermal conductivity bounds for isotropic, porous materials. Int J Heat Mass Transfer 48:2150–2158
32. Bhattacharya A, Calmidi VV, Mahajan RL (2002) Thermophysical properties of high porosity metal foams. Int J Heat Mass Transfer 45:1017–1031

D6.4 Industrial Refractories

Axel Eschner
Osterode (Harz), Germany

1 Introduction

Refractories generally consist of crystalline phases, a glassy phase, and pores. Each of the phases and their chemical and mineralogical composition influence their thermal and physical properties. The chemical and mineralogical composition determines the specific heat and the thermal expansion. The quantity of crystalline phases and the quantity of the pores as well as their distribution within the material influence the thermal conductivity. The density (bulk density) of refractories is a result of their chemical–mineralogical composition and the porosity.

Refractory materials can be divided into two groups – shaped and burnt or thermally treated products (bricks), and unshaped products (castables, mortars, and mastics).

In the following typical values with rising temperature of the thermal conductivity, the specific heat capacity and the thermal linear expansion as well as the density are shown for diverse shaped products. Based on these values, the thermal diffusivity *a* for instationary calculations can be generated. The general references below the tables and figures should be taken into consideration.

2 Thermal Conductivity of Shaped Refractories

With rising temperature the thermal conductivity of crystalline dielectric material decreases ($\lambda \sim 1/T$), and in amorphous (glassy) material the thermal conductivity increases with temperature ($\lambda \sim T$). In the pores, thermal conductivity is determined by heat conduction (λg) and by a heat radiation ($a \sim T^3$). Depending on which component supersedes, thermal conductivity decreases with rising temperature, for example for products with a high content of crystalline phases such as magnesia, silicon carbide, corundum or zircon, or increases with rising temperature, for example for products with high X-ray amorphous phase – fireclay bricks or amorphous carbon containing bricks. Also the gas in the pores has an influence on the thermal conductivity. Normal air or combustion gases show a very low thermal conductivity, hydrogen increases thermal conductivity of refractory products especially with great open pores, as is the case of insulating bricks.

Because of the predominantly heterogeneous structure of refractories, thermal conductivity can be affected by the grain sizing, the contact conditions in the matrix, reformation or new formation during the burning process or in the application, and the conditions of the emission. There is a diversity of methods to investigate the thermal conductivity, which give results that partly differ from each other, depending on measuring of the thermal conductivity by the stationary method (panel steady-state method – according to American Society for Testing and Materials (ASTM) or method of plate comparison KLASSE) or by the instationary method (transient method – hot wire method). The lowest values for thermal conductivity are measured by the ASTM calorimeter method, the highest values by the hot wire method. The values for the KLASSE method are in between. In the following, properties are presented which have been investigated by the KLASSE method and the hot wire method. Because of the predominantly heterogeneous, coarse-grained structure of refractory materials, the Laser Flash method for determining the thermal diffusivity is only limited. The deviation between the results measured by each method can be up to 15%, especially for insulating refractory bricks.

In the following, the typical properties of the most eminent shaped and burnt, thermally treated refractory products are shown in the Figs. 1–8 and in Table 1. The properties correlate with the data given in the tables.

3 Thermal Conductivity of Unshaped Refractories (Monolithics)

Unshaped refractories (material for monolithic installations, castables, mortars, and mastics) have a thermal conductivity which is 20–50% lower than that of burnt or carbon-bond materials (see Table 1). The reduction of thermal conductivity varies according to the bond type, hydraulic, chemical, and pitch- or resin- bond. A hydraulic bond by alumina cement

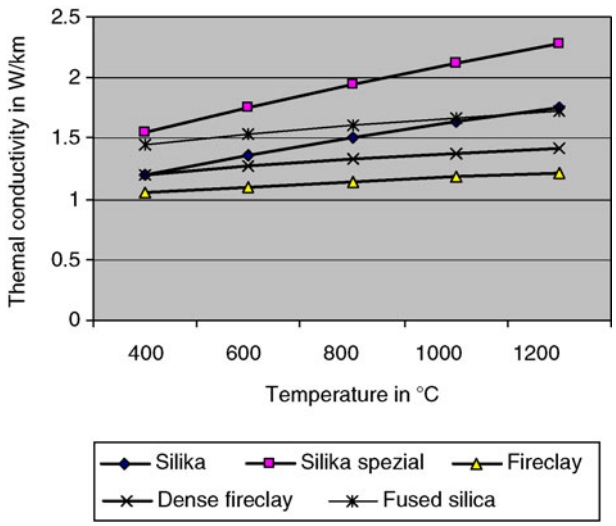

D6.4. Fig. 1. Typical values for thermal conductivity of silica bricks, fused silica bricks, and fireclay bricks. Silica bricks and fireclay bricks show an increase in thermal conductivity caused by elevated amount of X-ray amorphous phase.

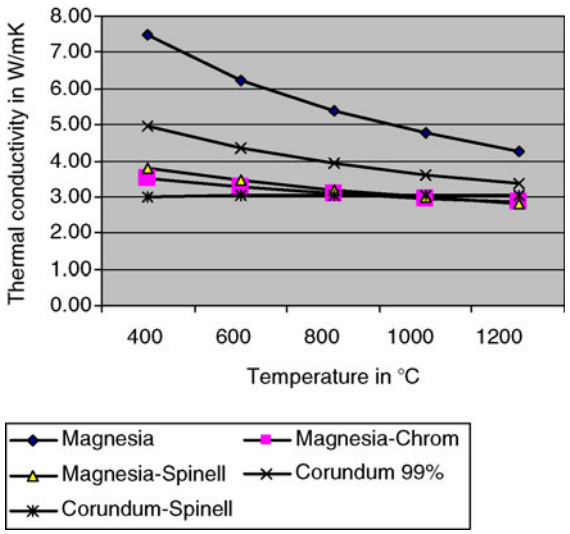

D6.4. Fig. 2. Typical values for thermal conductivity of magnesia bricks and corundum bricks. Pure magnesia and corundum bricks reveal a strong temperature dependence of thermal conductivity. With decreasing amount of the mineral phase Periklas (magnesia) and corundum in the products, the thermal conductivity and temperature dependence decrease.

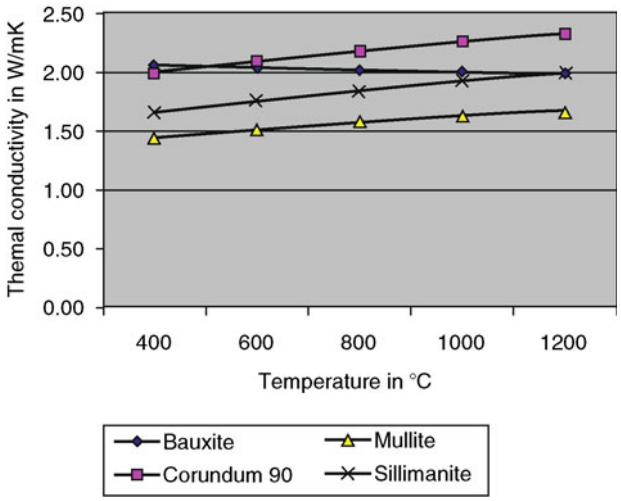

D6.4. Fig. 3. Typical values for thermal conductivity of sillimanite-, mullite-, bauxite- and corundum bricks. If the content of Al_2O_3 in bricks is lower than 90%, the thermal conductivity decreases and shows an increase or constant values at rising temperature compared to pure corundum bricks.

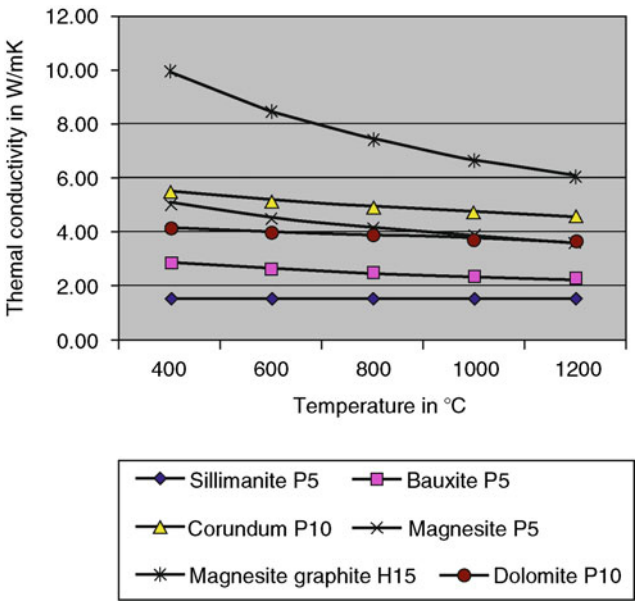

D6.4. Fig. 4. Typical values for thermal conductivity of bricks based on magnesia, dolomite, and alumina with carbon bond. P means pitch bond, H means resin bond; the following number indicates the contents of carbon after carbonization. If products on the basis of magnesia are bound with pitch or resin or impregnated later with tar and are finally coked, so that carbonization with carbon crystalline lattice emerges in the structure, thermal conductivity increases. If the product contains additional graphite, thermal conductivity significantly increases.

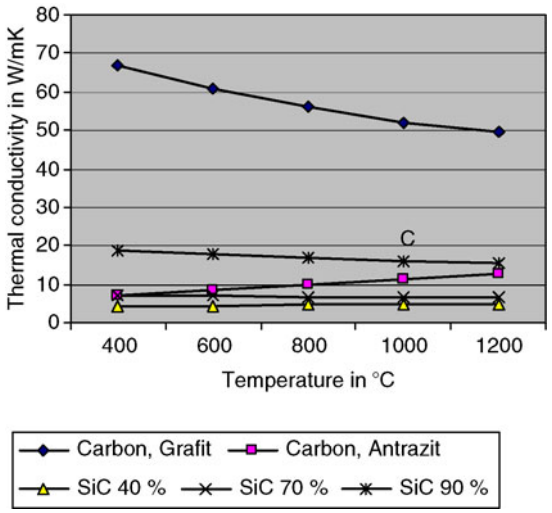

D6.4. Fig. 5. Typical values for thermal conductivity of carbon bricks and silicon carbide bricks. Products based on graphite and SiC have a high thermal conductivity. Graphite is characterized by anisotropy of thermal conductivity, which is dependent on the orientation of the graphite flakes to the direction of the heat flow. Parallel to the graphite flakes, thermal conductivity is extreme, and perpendicular to it, there are lower values. With regard to the example carbon/graphite, the thermal conductivity of a technical product with a predominant thermal alignment of the flakes is shown. The product based on anthracite has a sognificant content of amounts of amorphous carbon, which therefore shows an increase in thermal conductivity with temperature. Ceramic-bond silicon carbide shows an increase of thermal conductivity with rising SiC content. Also the correlation with temperature changes.

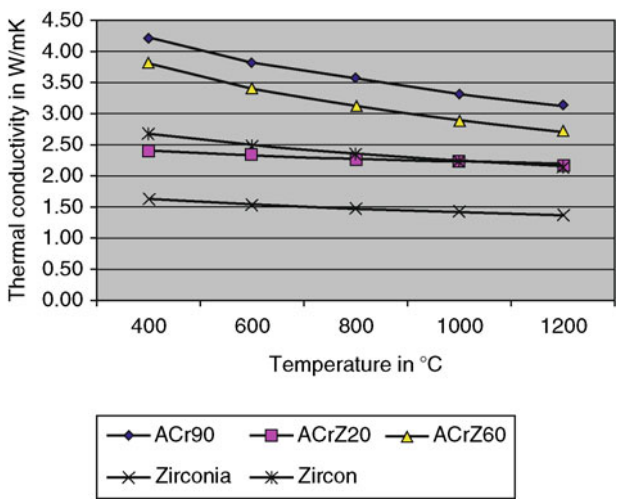

D6.4. Fig. 6. Typical values for thermal conductivity of alumina chrome bricks, alumina chrome zircon, zirconia, and zircon bricks. The number indicates the percentage of alumina. Materials based on alumina with chromium oxide or with chromium oxide and zirconia, zirconia, and zircon show the typical behaviour of refractory products with crystalline phases.

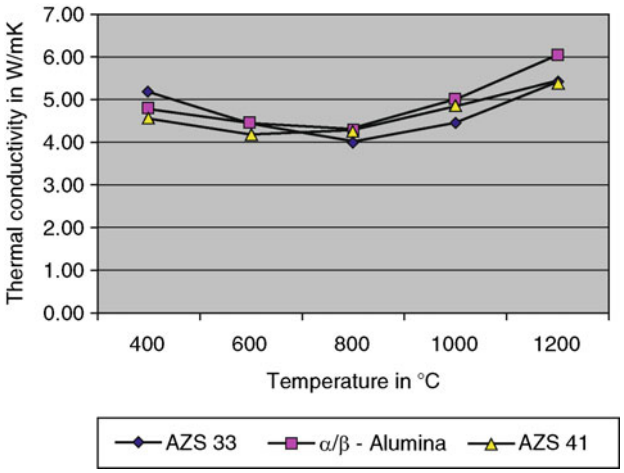

D6.4. Fig. 7. Typical values for thermal conductivity of fused bricks (A=Al_2O_3, S=SiO_2, and Z=ZrO_2). In fused products, there is a significant increase in the heat radiation starting from about 800°C, due to their high amount of glass phase and their lack of porosity.

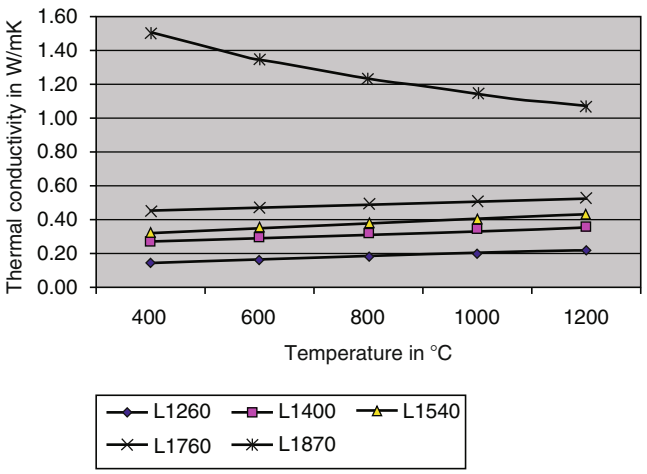

D6.4. Fig. 8. Typical values for thermal conductivity of lightweight fire bricks. The number indicates the classification temperature in °C. Due to the use of raw materials with higher alumina content, the classification temperature increases and the lightweight firebricks become more resistant to temperature. By this they become more dense with decreasing porosity. Consequently, thermal conductivity increases. The firelight brick L1870 consists of bubble alumina, thus showing the typical decrease of thermal conductivity of crystalline materials in relation to temperature. With rising classification temperature the porosity declines, which is the reason for an increase of thermal conductivity.

reduces thermal conductivity more significantly than a chemical bond (phosphate, water glass, etc.). As for the pitch- or resin-bond, the reduction of thermal conductivity is a minor one in comparison with burnt or soaked materials. The characteristics of thermal conductivity and its dependence on

D6.4. Table 1. Typical values of the thermal conductivity (W/mK) for different refractory product groups

Product group	Temperature (°C)				
	400	600	800	1000	1200
Silica	1.20	1.36	1.51	1.64	1.76
Silica special	1.55	1.76	1.95	2.12	2.28
Fused silica	1.44	1.53	1.61	1.67	1.73
Fireclay	1.05	1.10	1.15	1.18	1.22
High-duty fireclay	1.20	1.27	1.33	1.38	1.42
Sillimanite	1.66	1.76	1.84	1.92	1.98
Mullite	1.45	1.52	1.58	1.63	1.67
Corundum 90%	2.00	2.10	2.19	2.27	2.33
Bauxite	2.06	2.03	2.02	2.00	1.99
Corundum 99%	4.97	4.36	3.93	3.60	3.35
Corundum Spinel	3.01	3.02	3.03	3.04	3.05
ACr 90	4.20	3.81	3.52	3.30	3.12
ACrZ 20	2.40	2.33	2.27	2.22	2.18
ACrZ 60	3.80	3.40	3.11	2.89	2.71
Magnesite Chrome	3.50	3.27	3.10	2.96	2.85
Magnesia	7.50	6.23	5.37	4.75	4.28
Magnesite Spinel	3.80	3.44	3.18	2.98	2.82
Magnesite Graphite H15	9.96	8.46	7.44	6.68	6.10
Dolomite P10	4.17	3.99	3.92	3.75	3.66
Sillimanite P5	1.50	1.50	1.50	1.50	1.50
Bauxite P5	2.90	2.67	2.49	2.36	2.25
Corundum P10	5.49	5.19	4.96	4.78	4.62
Magnesite P5	5.05	4.53	4.15	3.86	3.63
Zirconia	1.63	1.54	1.48	1.43	1.38
Zircon	2.67	2.49	2.35	2.24	2.15
AZS 41	4.55	4.17	4.25	4.85	5.40
AZS 33	5.17	4.42	4.00	4.45	5.40
α/β-Alumina	4.78	4.45	4.30	5.00	6.05
SIC 40%	4.20	4.41	4.58	4.73	4.86
SIC 70%	7.00	6.81	6.67	6.55	6.45
SIC 90%	18.60	17.55	16.76	16.14	15.62
L1260	0.14	0.16	0.18	0.20	0.22
L1400	0.27	0.30	0.32	0.34	0.36
L1540	0.32	0.35	0.38	0.41	0.43
L1760	0.45	0.47	0.49	0.51	0.53
L1870	1.50	1.34	1.23	1.14	1.07
Carbon, anthracite	7.00	8.51	9.95	11.33	12.65
Carbon, graphite	67.00	60.67	56.06	52.01	49.46

temperature generally are the same within the material groups, whether they are bricks or monolithics. Due to the diversity of the binding possibilities in case of the unshaped refractory products, the presentation of typical properties of unshaped products is refrained.

Furthermore, it has to be considered that – in case of the design of a wall using unshaped products – a temperature gradient in the direction of the thermal flow performs that can lead to a distinctive sintered body, where the thermal conductivity on the side affected by temperature can be higher, due to sintering, than on the "cold" side.

4 Specific Heat Capacity

The mean specific heat capacity is indicated as a heat capacity in a temperature range, starting with 20°C. It can be calculated from the specific heat of the singular oxides. Tables 2 and 3 indicate the specific heat capacities of each of the oxides as well as of carbon.

D6.4. Table 2. Mean specific heat capacity of some refractory oxides (KJ/Kg K)

Oxide	SiO_2	Al_2O_3	Fe_2O_3	CaO
Temperature (°C)				
20–100	0.746	0.866	0.676	0.79
20–200	0.857	0.932	0.714	0.819
20–300	0.886	0.974	0.748	0.84
20–400	0.916	1.012	0.781	0.857
20–500	0.932	1.042	0.815	0.865
20–600	0.945	1.067	0.84	0.874
20–700	0.953	1.088	0.869	0.882
20–800	0.962	1.1	0.895	0.886
20–900	0.966	1.113	0.916	0.89
20–1000	0.97	1.126	0.932	0.865
20–1100	0.973	1.139	0.947	0.9
20–1200	0.98	1.152	0.96	0.904

D6.4. Table 3. Mean specific heat capacity of some refractory oxides and carbon (KJ/Kg K)

Oxide/element	MgO	Cr_2O_3	ZrO_2	C
Temperature (°C)				
20–100	0.983	0.722	0.501	0.875
20–200	1.012	0.739	0.542	0.96
20–300	1.033	0.748	0.571	1.038
20–400	1.054	0.756	0.601	1.116
20–500	1.075	0.76	0.623	1.186
20–600	1.096	0.764	0.645	1.256
20–700	1.113	0.769	0.66	1.383
20–800	1.134	0.773	0.675	1.383
20–900	1.151	0.777	0.685	1.442
20–1000	1.168	0.781	0.694	1.5
20–1100	1.184	0.785	0.703	1.557
20–1200	1.199	0.789	0.713	1.613

The mean heat capacity results from

$$c_{p_m} = \sum x_i * c_{p_i} \quad (1)$$

with

c_{p_m} = mean specific heat capacity in a temperature sector,
x_i = mass fraction of component i, and
c_{p_i} specific heat capacity of the component i

The specific heat capacity can be calculated regardless of the nature of the material type, it can be equally made for shaped and unshaped products.

Typical specific heat capacities for different product groups are shown in Fig. 9 and Table 4.

5 Density, Porosity, and Thermal Expansion

In Table 5, typical bulk densities of shaped refractory products as well as the thermal expansions for a defined temperature sector are assembled. Figure 10 shows the effects for silica bricks and unstabilized zirconia bricks.

The density comprises the porosities caused by their production process, which can vary from 0% for fused material and 80% for lightweight refractory bricks. Together with the thermal expansion, the densities of the products change. Thermal expansion is nearly independent from porosity.

The thermal conductivities shown in Table 1 refer to the porosities indicated in Table 4. If the porosity and consequently the density change, the alteration of the thermal conductivity for porosity deviations up to 5% can be approximately calculated by use of the following formula:

$$\lambda(\mathrm{P1}) = \lambda(\mathrm{P2})\frac{1-\mathrm{P1}[1+0.35(1-\mathrm{P1})]}{1-\mathrm{P2}[1+0.35(1-\mathrm{P2})]} \quad (2)$$

with λ(P1) the thermal conductivity concerning the new porosity P1

λ(P2) of the thermal conductivity concerning the well-known porosity P2

and

P1 and P2 are the porosities divided by 100.

Example: In case of porosity P2 = 12%, corundum (99%) has a thermal conductivity of 3.6 W/mK.

For a porosity of 15%, this will give accordingly Eq. (2):

$$\lambda(\mathrm{P1}) = 3.6\frac{1-0.15[1+0.35(1-0.15)]}{1-0.12[1+0.35(1-0.12)]} = 3.44\,\mathrm{W/mK}.$$

6 Thermal Diffusivity *a*

Typical values of the thermal diffusivity a are shown in Table 6

The thermal diffusivity a in m^2/h results from

$$a = \frac{\lambda}{p \times c_p} \quad (3)$$

with λ = thermal conductivity (W/mK)

p = density (Kg/m^3)

c_p = specific heat capacity (3.6 KJ/Kg K)

The rate of conversion 3.6 results from the conversion of the specific heat capacity of KJ/Kg K to Wh/Kg K.

The thermal diffusivity is needed for instationary temperature calculations and for the formation of the Fourier number Fo.

7 General Remarks Concerning the Application and Heat Engineering with Refractories

The properties indicated in the above chapters refer to the state of delivery of the refractories.

During use, especially in case of contact with liquid metals, slags, inorganic melts, or condensed vapours, the thermal properties may change. Infiltration of liquid metals may raise the thermal conductivity and the thermal diffusivity significantly. Slag has only a slight influence on the thermal properties; by diminishing the porosity, the thermal conductivity of the infiltrated zone increases by 10–20%. Gases, with the exception

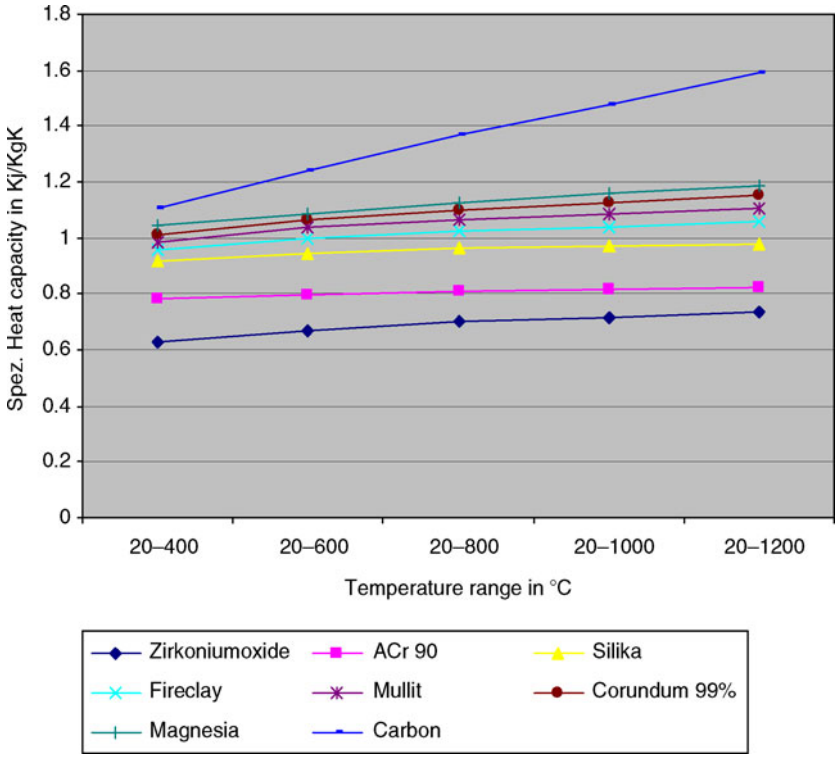

D6.4. Fig. 9. Typical values for specific heat capacity of some product groups.

of hydrogen, have only a slight changing effect on thermal conductivity.

In general, products according to ISO/R836 are "Refractories" if their melting or softening point is higher than 1500°C. But the refractories can also be affected and modified chemically and mineralogically far below their melting point. Normally, refractory lining is built up in several layers, for thermal and economic reasons. The inner layer, which borders the "reaction zone," must be resistible to the process reactions. The following layers in the wall serve to reduce the temperature and diminish thermal losses.

The diverse refractories used in wall designs have to be chosen with regard to their chemical and physical characteristics. Exemplary here is referred again to the example of the thermal expansion of the refractories. If the expansion of the refractories has not been considered in design e.g., by using expansion joints etc., the forces emerging may exceed the compressive strength of the refractories caused by preventing expansion in the heating process, which leads to self-destruction. Especially, refractories on the basis of silica and zirconia with irregular thermal expansion require specific heating programs.

8 Briefly Characterization of the Most Used Refractories

8.1 Silica Products

For silica products, their expansion anomaly caused by modifications and density alterations in connection with rising temperature has to be considered. Up to about 700°C, the products are highly sensitive to temperature cycling; they have to be heated up very slowly. Above 1000°C, they have a very good thermal shock resistance. Silica products have a high hot crushing strength up to 1700°C and have a good chemical consistency, except against alkali containing melts.

8.2 Fireclay- and Alumina-Rich Products

The properties of the products in the binary system SiO_2–Al_2O_3 are substantially characterized by the quantity of Al_2O_3. With increasing Al_2O_3 content, the density and thermal conductivity increase as well as their specific heat capacity.

The thermal shock resistance in this product group is good.

Fireclay products can be used up to 1500°C in accordance with their composition.

Products with a high amount of alumina, e.g., on the basis of bauxite, sintered mullite or fused mullite, and sintered or fused corundum show a high strength and good chemical resistance, except against basic reacting substances and slag or melts containing iron oxide FeO. Products with a high amount of alumina, too, are consequently manufactured by using graphite additives, pitch- or resin-bond, for the application in steel industry. Thermal conductivity and thermal diffusivities of products with a high amount of alumina, pitch- or resin-bond, are a little bit higher than for burnt products. They increase with the amount of graphite.

Alumina spinel products, with or without carbon (AMC products with pitch- or resin-bond) with supplements of magnesia, are used in metallurgy. The percentage of MgO can increase up to 30%. With increasing MgO content, the thermal conductivity rises.

D6.4. Table 4. Typical specific heat capacities (KJ/KgK) for different refractory product groups

Product group	Temperature sector from 20°C				
	400	600	800	1000	1200
Silica	0.915	0.944	0.961	0.969	0.979
Silica special	0.915	0.944	0.961	0.970	0.980
Fused silica	0.917	0.946	0.963	0.972	0.982
Fireclay	0.956	0.997	1.021	1.037	1.054
High-duty fireclay	0.958	0.999	1.024	1.040	1.058
Sillimanite	0.978	1.024	1.052	1.072	1.093
Mullite	0.987	1.035	1.065	1.087	1.109
Corundum 80%	0.993	1.043	1.072	1.095	1.118
Bauxite	0.994	1.045	1.077	1.100	1.124
Corundum 99%	1.011	1.066	1.099	1.124	1.150
Corundum spinel	1.013	1.067	1.100	1.126	1.152
ACr 90	0.782	0.794	0.806	0.816	0.825
ACrZ 20	0.772	0.789	0.804	0.814	0.825
ACrZ 60	0.905	0.945	0.970	0.990	1.010
Magnesia chrome	1.004	1.043	1.079	1.110	1.138
Magnesia	1.047	1.088	1.125	1.158	1.188
Magnesia spinel	1.050	1.093	1.131	1.164	1.194
Magnesia graphite H15	1.061	1.117	1.168	1.215	1.258
Dolomite P10	0.950	0.988	1.022	1.051	1.078
Sillimanite P5	0.986	1.037	1.070	1.095	1.120
Bauxite P5	1.000	1.056	1.092	1.121	1.149
Corundum P10	1.020	1.083	1.126	1.160	1.195
Magnesia P5	1.050	1.097	1.139	1.177	1.211
Zirconia	0.624	0.668	0.698	0.718	0.737
Zirconia	0.708	0.747	0.773	0.788	0.804
AZS 41	0.831	0.878	0.908	0.929	0.950
AZS 33	0.861	0.908	0.938	0.958	0.980
α/β-Alumina	0.989	1.044	1.080	1.107	1.133
SIC 40%	0.993	1.043	1.072	1.095	1.118
SIC 70%	0.998	1.049	1.079	1.103	1.126
SIC 90%	1.005	1.058	1.090	1.115	1.140
L1260	0.942	0.979	1.002	1.017	1.033
L1400	0.954	0.994	1.018	1.034	1.050
L1540	0.979	1.026	1.054	1.075	1.096
L1760	0.991	1.040	1.070	1.092	1.114
L1870	1.011	1.066	1.099	1.124	1.150
Carbon, anthracite	1.106	1.240	1.362	1.474	1.581
Carbon, graphite	1.108	1.244	1.366	1.479	1.588

Alumina products with quantities of chromium oxide and/or zirconia are used for specific requirements of thermal combustion of industrial waste and for special applications in the glass industry. Due to the additives, their densities increase whereas the thermal conductivities decrease by 10–30% compared to pure corundum bricks.

The resistance toward oxidation of the carbon products has to be taken in account.

8.3 Magnesia and Dolomite Products

Magnesia and dolomite products have a very high thermal expansion and are therefore extremely sensitive to thermal shock. Pure magnesia bricks show high thermal conductivity with a strong dependence upon rising temperature. According to their composition, they can be used up to 2000°C. They are resistible against basic slag and basic reacting products, for

D6.4. Table 5. Typical bulk density, porosity, and thermal expansions for different refractory product groups

Product group	Density (g/cm³)	Porosity (Volume-%)	Thermal expansion (%)	Thermal expansion Up to °C
Silica	1.82	21	1.3*	800
Silica special	1.91	16	1.3*	800
Fused silica	1.94	12	0.05*	1000
Fireclay	2.15	25	0.75	1400
High-duty fireclay	2.32	16.5	0.8	1400
Sillimanite	2.53	16.5	0.8	1400
Mullite	2.54	18	0.8	1400
Corundum 90%	2.83	18	0.8	1400
Bauxite	2.76	21	1	1400
Corundum 90%	2.83	12	1.2	1500
Corundum Spinel	3.10	20	0.8	1000
ACr 90	3.18	17	1.2	1500
ACrZ 20	3.78	17	1.1	1500
ACrZ 60	3.20	20	1.2	1500
Magnesia Chrome	3.06	16	1.8	1400
Magnesia	3	14	1.9	1400
Magnesia Spinel	2.85	18	1.7	1400
Magnesia Graphite H15	2.98	3	1.8	1400
Dolomite P10	2.97	5	1.7	1400
Sillimanite P5	2.74	4	0.7	1000
Bauxite P5	2.83	9	0.8	1000
Corundum P10	3.02	5	0.8	1000
Magnesia P5	2.92	6	1.9	1400
Zirconia	4.95	12.5	0.8*	1000
Zircon	3.94	20.5	0.65*	1500
AZS 41	4	0	0.65*	1000
AZS 33	3.72	0	0.8	1000
α/β-Alumina	3.2	0	0.8	1000
SIC 40%	2.4	22	0.8	1400
SIC 70%	2.6	15.5	0.7	1400
SIC 90%	2.68	13	0.7	1400
L1260	0.49	gr. 50	0.7	1100
L1400	0.79	gr. 50	0.7	1100
L1540	0.89	gr. 50	0.8	1100
L1760	1.27	gr. 50	0.9	1100
L1870	1.44	gr. 50	0.9	1100
Carbon, anthracite	1.54	13	0.38	1000
Carbon, graphite	1.55	26	0.27	1000

*Means that the development of the thermal expansion at rising temperature is not a steady one, but can prove significant deviations and steps, which is due to changes in modifications with temperature

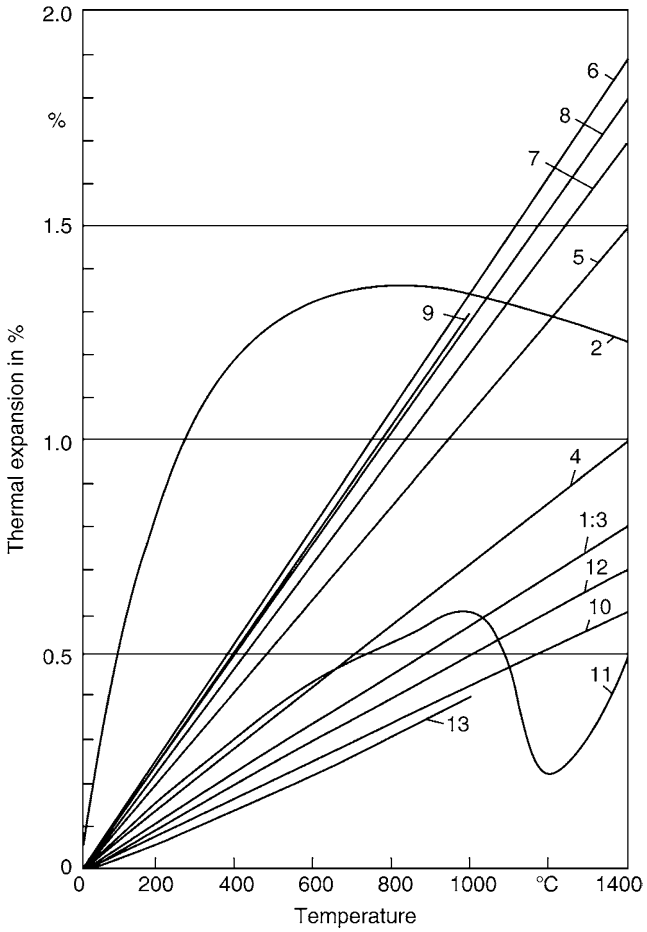

D6.4. Fig. 10. Thermal expansion in % of shaped refractory products: 1 high-duty firebrick, 2 silica brick, 3 sillimanite brick, 4 corundum brick, 5 forsterite brick, 6 magnesia brick, 7 magnesia spinel brick, 8 magnesia chrome brick, 9 doloma brick, 10 zircon brick, 11 zirconia brick (unstabilized), 12 silicon carbide brick, and 13 carbon brick.

instance in the production of cement and lime. They are irresistible against acid slags and acid reaction products. In order to improve their resistance against thermal shock and chemical attack, in magnesia products, chromium oxide, alumina (for the spinel formation), spinel, hercynite, gallaxit, or zirconia can be added. Burnt or carbon-bond products are in use. Quantities of carbon, especially graphite additives, increase the thermal conductivity; all the other additives reduce the thermal conductivity by 10–40%.

Dolomite products have a very poor hydration resistance and are normally impregnated by tar or pitch- or resin-bond. Like magnesia products, they have a high thermal conductivity. By the use of zirconia or carbon, their resistance against thermal shock can be improved.

Fortsterite products belong to basic products (Magnesia–Silicates). They have a high resistance against slag enriched by iron oxide. It is minor in use.

8.4 Carbon Products and Products with Higher Carbon Additives

Products based on carbon have a high thermal conductivity, especially products based on graphite, and low thermal expansion. Therefore, they provide an enormous thermal shock

D6.4. Table 6. Typical thermal diffusivity a (m^2/h) for different product groups. The values in the table have to be mulitpled by 10^{-3}

Product group	Thermal diffusivity a*1/1000 in m^2/h at				
	400°C	600°C	800°C	1000°C	1200°C
Silica	2.594	2.853	3.100	3.342	3.553
Silica special	3.191	3.513	3.819	4.119	4.381
Fused silica	2.916	3.001	3.092	3.190	3.266
Fireclay	1.838	1.851	1.879	1.909	1.931
High-duty fireclay	1.943	1.971	2.011	2.054	2.085
Sillimanite	2.416	2.446	2.489	2.548	2.578
Mullite	2.159	2.157	2.180	2.204	2.213
Corundum 90%	2.563	2.562	2.598	2.638	2.652
Corundum spinel	2.702	2.538	2.442	2.370	2.305
Corundum 99%	6.257	5.207	4.550	4.077	3.700
Corundum spinel	3.449	3.287	3.199	3.135	3.074
ACr 90	6.083	5.423	4.942	4.574	4.274
ACrZ 20	2.960	2.805	2.687	2.596	2.517
ACrZ 60	4.717	4.045	3.606	3.285	3.024
Magnesia chrome	4.103	3.688	3.380	3.137	2.946
Magnesia	7.793	6.358	5.377	4.664	4.322
Magnesia special	4.570	3.979	3.557	3.239	2.985
Magnesia graphite H15	8.982	10.032	10.917	11.680	12.364
Dolomite P10	5.323	4.893	4.651	4.325	4.116
Sillimanite P5	2.000	1.901	1.843	1.801	1.760
Bauxite P5	3.688	3.211	2.903	2.677	2.489
Corundum P10	6.419	5.710	5.252	4.906	4.613
Magnesia P%	5.923	5.087	4.493	4.048	3.697
Zirconia	1.897	1.680	1.539	1.445	1.364
Zirconia	3.448	3.043	2.779	2.599	2.447
AZS 41	4.925	4.278	4.213	4.701	5.118
AZS 33	5.808	4.707	4.128	4.493	5.335
α/β-Alumina	5.439	4.793	4.481	5.083	6.008
SIC 40%	6.346	6.345	6.406	6.481	6.523
SIC 70%	9.716	8.991	8.557	8.225	7.930
SIC 90%	24.854	22.273	20.537	19.443	18.406
L1260	1.092	1.217	1.338	1.453	1.555
L1400	1.290	1.360	1.432	1.501	1.558
L1540	1.322	1.392	1.466	1.535	1.592
L1760	1.287	1.292	1.311	1.329	1.342
L1870	3.709	3.144	2.788	2.528	2.319
Carbon, anthracite	14.795	16.045	17.083	17.969	18.708
Carbon, graphite	140.445	113.313	95.306	81.686	72.354

resistance. They will be only slightly or not infiltrated by slag. In oxidizing atmosphere they can be used up to 400°C because of their inconsistency against oxygen, steam, and carbon dioxide. In reducing atmosphere, the temperature limit of their appliance may rise up to 3000°C.

In the steel making processes, products on the basis of magnesia, alumina, and/or zirconia are used with a percentage of graphite and pitch- or resin-bond that amounts up to 30% carbon. Due to the amount of graphite, these products have a significantly improved structural flexibility and an excellent thermal shock resistance.

In extreme situations, they can be contacted cold with liquid steel.

8.5 Zirconia-Containing Products

During heating up, zirconia (Baddeleyite) performs three different modifications with different mole volumes that have a great influence on thermal expansion.

By adding certain metal oxides, normally magnesia oxide, calcium oxide, or yttrium oxide, the cubic high temperature modification remains nearly stable within the whole temperature range. The materials then show a nearly linear dependence of thermal expansion. A low thermal conductivity and a relatively high thermal expansion result in a low thermal shock resistance. Due to their high strength and resistance toward metal melts, zirconia products possess a high abrasion resistance when steel is cast or glass is melted.

Compared to zirconia products, zircon products have a lower thermal expansion and a higher thermal conductivity. That is why they have a slightly better thermal shock resistance. Zircon products are like zirconia products primarily used in steelmaking and in the glass industry because of their strong resistance to acid slag/melts.

8.6 Silicon Carbide Products

Silicon carbide products have a strong mechanical strength and hardness, a very high thermal conductivity and – due to their high thermal diffusivity – an enormous thermal shock resistance. They can be produced with ceramic bond (clay or alumina bonding) or nitrogen bond (silicon oxinitride, silicon nitride, or siliconaluminia-oxinitride). They have an excellent stability against fused lead, zinc, cadmium, and copper. Products containing silicon carbide are inconsistent against fused alkalies, basic slags, steam, hydrogen, carbon monoxide as well as chlorine gas. In an oxidizing atmosphere, silicon carbide disintegrates above 900°C and forms SiO_2 and CO or CO_2. Above 1250°C, a protective layer of SiO_2 is built up at the surface, which prevents further oxidation. Because of their high thermal conductivity, silicon carbide products are used in cooled furnace walls and as kiln furniture in the ceramic industry.

8.7 Fused Refractories

Fused refractories are fused in electric arc furnaces and then cast in shapes. They can be based on alumina, zirconia, alumina zirconia silica with or without chromium oxide, alumina chromium oxide, alumina magnesia chrome oxide, magnesia chromium oxide, alumina mullite, and alumina zirconia. Due to their dense structure, they have a low thermal shock resistance. The heating up process of fused castables has to proceed

slowly. Fused products are mainly used in glass melting furnaces. The corrosion resistance against glass melts is excellent.

Fused Silica is quite different from all the other fused refractories; it has an extremely low thermal expansion (nearly zero) and can be heated up extremely quickly without discomposure. But above 1250°C, it devitrifies and produces christobalite, developing the thermal properties of a silica product.

9 Bibliography

1. Eschner/Großkopf/Jeschke (1974) Erfahrungen mit dem Heißdrahtverfahren zur Bestimmung der Wärmeleitfähigkeit feuerfester Baustoffe. Tonidustrie-Zeitung 98, Nr. 9, S.212–S.219
2. Bisson, L (1986) Ein Verfahren zur Messung der Temperaturleitfähigkeit mittels Laserblitz. Ber DKG 63, Nr. 6 S.285–S.291
3. Routschka (2001) Taschenbuch Feuerfeste Werkstoffe. Vulkan Verlag, 3. Auflage
4. Didier-Werke AG (1997) Feuerfeste Werkstoffe und ihre Merkmale, 12. Auflage
5. Hagemann/Peters (1982) Thermal conductivity – comparison of methods: ASTM-method, hot wire-method and its variations. Interceram Nr. 2, S.131–S.135
6. Schulle (1990) Feuerfeste Werkstoffe. Deutscher verlag für Grundstoffindustrie
7. The technical association of refractories (1998) Refractories handbook. Japan
8. Eschner (1978) Die wämetechnischen Eigenschaften von Magnesiasteinen für Niedertarifheizungen und ihr Einfluss auf die Geometrie des Speichermaterials. Dissertation an der Technischen Universität Clausthal
9. Carnigia SC, Barna GL (1992) Handbook of industrial refractories technology. Principles, typesm properties and applications. Noyer Publications, Park Ridge, S.672
10. VDI-Richtlinie VDI 312B Blatt 4, Jan.1977. Induktive Erwärmung; Physikalische Stoffeigenschaften nichtmetallischer Werkstoffe (Ofenbaustoffe)
11. Traustel S, Panda J, Jacob P (1961) Ein Beitrag zur Erforschung des Wärmeleitvermögens von Mischkörpern aus Komponenten verschiedener Leitfähigkeit mit Hilfe der elektrischen Analogie. Tonindustrie-Zeitung 85: S.565–S.569
12. Krischer O, Kröll K (1963) Die wissenschaftlichen Grundlagen der Trocknungstechnik. Band 1, Springer-Verlag, Berlin

D6.5 Insulations Materials

Günther Kasparek
Munich, Germany

1 Introduction

The insulation performance of insulants is caused by the cell gas, usually air, which is enclosed in open or closed cells and by the reduction of thermal radiation by the solid material.

Heat transfer within the insulation material occurs not only over the solid particles and the gas enclosed in the cavities, but also through radiation between the surfaces of fibers or cell cavities.

The most important property of thermal insulation materials is their thermal conductivity. Due to the temperature dependent conductivity of air and thermal radiation, the thermal conductivity of insulants increases with increasing temperature. An exception are cellular plastics blown with blowing agents such as pentane or HCFCs. The characteristic saddle curves as seen in Fig. 1 result due to the condensation of these gases in the cells.

Because of their small dimensions local convection in the cells does not occur. However, global convection may occur in open cell (fibrous) insulants when great temperature differences exist.

Example, this is the case in the insulation of heat generators.

Reliable methods for precalculation of the thermal conductivity do not exist. Therefore, it must be determined by experiments, which are of international standards.

Moisture in the form of liquid water in the insulants has a significant influence on the conductivity. The conductivity already increases with low moisture contents.

In addition to the conductivity, other properties may be of interest. The most important are

- Apparent density which was named to distinguish from the density of the solid material.
- The service temperature range.
- Compressive strength or compressive stress.
- The dimensionless water vapor diffusion resistance factor to calculate water vapor diffusion processes.
- Fire behavior.
- Behavior with chemicals.
- Sound absorbing properties.

There is to be distinguished between open cell insulants e.g., mineral wool (MW) and closed cell materials e.g., extruded polystyrene or cellular glass (CG). Only open cell insulants have good sound attenuation properties. On the opposite, closed cell insulants have to be used for cold insulations.

Cellular plastics are usually driven with blowing agents whose conductivities are lower than that of air, e.g., pentane, CO_2, or HCFC. However, an exchange of gas due to diffusion takes place so that also in this case air is finally the cell gas. This "aging effect" must be accounted for in the conductivity declared by manufacturers.

For thermal insulation materials, applications for buildings and for industrial insulation have to be distinguished.

2 European Standardization

Insulants with application in the building sector or for industrial installations are subject to the European Construction Product Directive. For these products, there exist (the so-called harmonized) obligatory standards. For building application, these are the series EN 13162–EN 13171, and for industrial installations the drafts prEN 14303–prEN 14314 which have not been put into force yet. Furthermore, a series for in situ insulants which are made on site exists, which has not been put into force either. Conformity with these standards allows the products to obtain the CE mark, which is necessary for a free trade within Europe. To avoid fatal errors, it should be mentioned, that for all insulants which are delivered acc. to CEN or ISO standards the data for the product characteristics are written with decimal commas.

To designate the different insulation materials, a system of abbreviations has been installed as follows:

- MW mineral wool
- CG cellular glass
- FEF flexible elastomeric foam
- XPS extruded polystyrene foam
- EPS expanded polystyrene foam
- PUR polyurethane foam
- PIR polyisocyanurate foam
- CS calcium silicate
- PEF polyethylene foam
- PF phenolic foam
- EP expanded perlite
- EV vermiculite

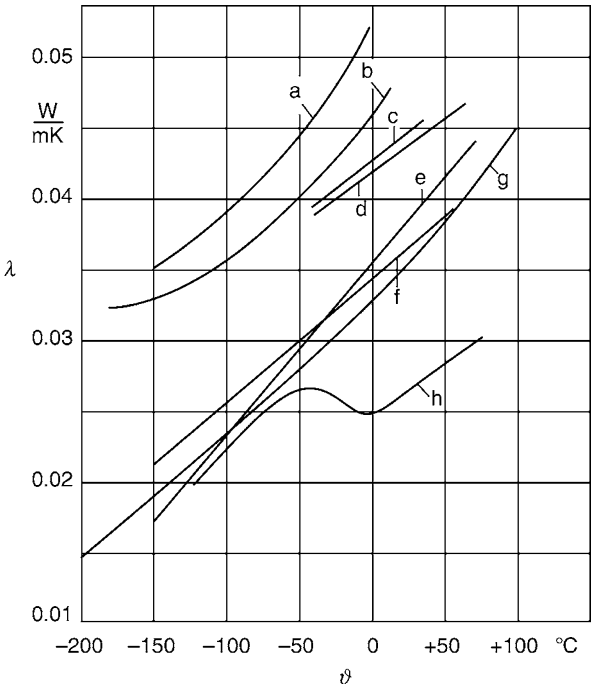

D6.5. Fig. 1. Thermal conductivity of cold insulants. Abscissae: temperature in °C, Ordinate: heat conductivity in W/(mK). a, cellular glass (CG) – sections; b, CG – boards; c, polyethylene; d, flexible elastomeric foam; e, polystyrene; f, cork – boards 100 kg/m^3; g, polyurethane (PUR) blown with CO_2; h, PUR blown with R142 b or pentane.

In contrast to the conventional norms as they had been installed in Germany for example, the European Norms do not standardize the insulants and their performances. They especially do not contain any requirements but only standardize how to describe the properties in the form of classes and levels and therefore, they are only a "frame of description," which has to be used by public bodies and comparable institutions when calling for tenders.

3 Building Application

The thermal conductivity of insulants for building application is declared for a reference mean temperature of 10°C. The "declared value" (Germ.: Nennwert) has to be given and guaranteed by the manufacturer. For design purposes, the declared value has to be transformed into a "design value" (Germ.: Bemessungswert). The rules to be applied are subject to national regulations. In Germany, DIN 4108–4 applies. DIN 4108–10 prescribes the minimum values of the properties depending on the field of application. In other countries, comparable prescriptions exist.

Table 1 shows reference values for some characteristics.

4 Industrial Installations

Since industrial application covers a wide temperature range, thermal conductivity is declared as a function of temperature.

D6.5. Table 1. Reference values of insulants for building application

	Declared thermal conductivity in W/(m*K) at 10 °C	Water vapor diffusion resistance factor μ	Apparent density in kg/m^3
Mineral wool	0.035–0.05	1	20–200
Expanded polystyrene	0.035–0.05	20–100	20–30
Extruded polystyrene	0.030–0.036	80–250	30–50
Rigid polyurethane	0.025–0.024	40–200	35–80
Cellular glass	0.045–0.055	Vapor tight	110–130
Flexible elastomeric foam	0.037–0.046	1,000–7,000	40–90
Phenolic foam	0.020–0.045	10–60	40–200
Wood wool products	0.060–0.065	2–5	60–200
Vermiculite	0.060–0.07		
Expanded perlite	0.045–0.07	3–5	65–80

While for flat products conductivity is given in dependence on the temperature, for cylindrical products conductivity is a function of the mean temperature of the hot and cold sides of the insulation. Attention must be paid to this fact when comparing data.

According to the AGI Working documents series Q [1], the manufacturer can give the thermal conductivity in the form of limitation curves.

The conversion of the declared value to the design value is described in VDI 2055 or the international standard EN ISO 23993. There the expression "design value" is replaced by "operational thermal conductivity" (Germ.: Betriebswärmeleitfähigkeit). Supplementary values for thermal bridges as joints, metallic substructure, or reinforcements on plane surfaces have to be taken into account.

4.1 Influences on the Thermal Conductivity

The most important characteristics which influence thermal conductivity are temperature and apparent density. As mentioned above, conductivity generally increases with increasing temperature due to the temperature dependence of gas conductivity and the contribution of thermal radiation.

The influence of the apparent density is different and is dependent upon the temperature. At low temperatures, the effect of the comparably high conductivity of the solid structure is predominant, so that with increasing apparent density the conductivity of the insulant increases as well.

By contrast, at high temperatures conductivity decreases with increasing apparent density. This is due to a higher amount of solid structure reducing thermal radiation.

Furthermore, moisture in the form of condensated water leads to high conductivities. This intensifies when ice formation occurs and may result in a total loss of the insulation property and destruction of the insulation system. The data in Figs. 1 and 2 are valid for dry insulants. For references about the influence of moisture, see [2–5 and Subchap. D6.6]

As mentioned before, it has been frequently discussed whether free convection in the insulants occurs. No convection takes place within the small cells or pores. However, with high temperature differences global convection movement occurs in air-permeable insulants such as MW and causes a significant additional heat loss. Effective countermeasures are the use of insulants with a longitudinal airflow resistance >50 kPa*s/m^2 and non–air-permeable foils at the faces of the insulant. Detailed investigations and calculation advice are given in [6].

4.2 Service Temperature Range

There is to be distinguished between the maximum service temperature and the service temperature, which is of practical interest. The former is determined according to standardized tests (EN 14706 and EN 14707) and given by the manufacturer on its product label, whereas the latter is a matter of experience.

For MW products, the service temperature is approximately 80–90% of the maximum service temperature.

Table 2 shows some relevant properties of insulants for industrial installations.

4.3 Insulation Materials for Cold Insulations

Cold insulations are defined as insulations where the medium temperature is below the ambient temperature. They have to reduce the heat ingress into the system to be insulated as well as to prevent dew formation on the surface of the insulation system and in the insulant itself.

Moisture in the insulation in the form of liquid water or ice increases the thermal conductivity and can damage the insulation.

For this purpose it is necessary that the two transport mechanisms – water vapor diffusion and air movement into the insulation – are prevented or reduced, respectively.

The water-vapor diffusion can be reduced by an insulant with a high water-vapor diffusion resistance factor, e.g., FEF, or by applying a vapor retarder onto the surface of the insulant. To prevent ingress of moisture by air movement into the insulation, a closed cell insulant has to be used.

Therefore, for cold insulations only closed cell materials have to be used. Exceptions exist for technical reasons e.g., insulation of air-treatment installations with MW or tanks for liquid natural gas insulated with perlite. In these cases, special means as double-skin coverings, which are soldered or welded air-tight, are necessary.

There is a contrast in the requirements for protection of sound. For this purpose, open cell insulation materials in combination with closed cell insulants are necessary.

The most important properties of cold insulants including their fire behavior are listed in Table 3.

The fire behavior refers to DIN 4102, which in future will be replaced by the European standard EN 13501.

Cold insulants can also be used as hot insulants in the service temperature range given in Table 3.

There does not exist any minimum service temperature caused by the properties of the insulants. The lower limit depends on the design of an insulation system.

Due to the German Rules and regulations of the accident prevention, the use of organic insulants is restricted to a temperature above −180°C because of explosion risk in the presence of liquid oxygen as far as the presence of air cannot be prevented definitely.

D6.5. Table 2. Properties of insulants for industrial installations

Insulant	Apparent density in kg/m^3	Service temperature in °C
Mineral wool		
Wired mats	70–90	520
	80–120	540
	100–160	580
Sections	50–160	450–680
Lamella mats, pressure resistant	40–60	500
Loose wool	60–170	550–750
Cellular glass	110–130	400
Calcium–magnesium–silicate fibers, mats	96–160	850
Calcium silicate	250–350	850
Microporous insulants	140–400	1,000
Expanded perlite	65–80	750

D6.5. Table 3. Insulants for cold insulations for industrial installations

Insulant	Apparent density in kg/m^3	Upper service temperature in °C	Fire behavior according to DIN 4102
Expanded polystyrene	20–30	80	B1, B2
Extruded polystyrene	30–50	80	B1, B2
Rigid polyurethane (PUR)	40–70	130	B1, B2
In situ PUR	40–60	100	B1, B2
Cellular glass	110–130	400	A1
Flexible elastomeric foam	40–90	105	B2, B1
Expanded cork (ICB)	80–120	100	B2, B1

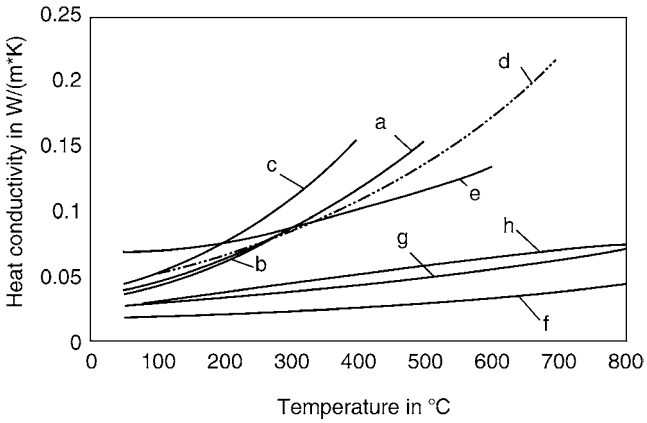

D6.5. Fig. 2. Thermal conductivity of hot insulants. Abscissae: temperature in °C, ordinate: heat conductivity in W/(m*K). a, mineral wool – mats; b, mineral wool – sections; c, cellular glass; d, calcium–magnesium–silicate fiber; e, calcium silicate; f, microporous insulant; g, microporous insulant (slatted panels); h, static air.

4.4 Insulation Materials for Hot Insulations

For hot insulations, all types of insulation materials can be used.

The apparent density and the service temperature are given in Table 2. Reference values for the thermal conductivity can be found in Fig. 2.

The actual service temperature depends on the operating conditions. The thermal conductivity as well as other properties can be influenced by the manufacturer through the production process. Therefore, values given by the manufacturer should be used.

By far the most common insulating material is MW. MW is the generic term for glass wool and stone wool. Slag wool is no longer used in Europe. Forms of delivery are wired mats, mats, sections, lamella mats, slabs/boards, felts, and loose wool.

CG is predominantly used when high compressive loads occur or a non–combustible insulant is required.

Calcium–magnesium–silicate (CMS) fibers are normally used in high temperature application as a preinsulation to reduce the temperature to values where MW can be installed.

D6.5. Table 4. Specific heat capacities of insulants

Insulant	kJ/(kg*K)
Mineral wool	0.84
Calcium silicate	1.1
Polyurethane	1.4
Polystyrene	1.2
Perlite	0.84
Cellular glass	0.84
Microporous insulants	1.05

CMS fibers replace the before used ceramic fibers which now are prohibited for heat insulation application due to the danger of cancer.

CS is a solid material which has a low thermal conductivity at high temperatures and high compressive strength.

A special case with thermal insulation materials are the microporous insulants, also called super isolation materials. In these materials, the distances between the particles respectively cell walls are smaller than the mean free path length of air. Due to the Smoluchowski effect, the conductivity of these materials is below that of static air.

Table 4 shows the specific heat capacity of insulants.

5 Bibliography

1. Working documents of Arbeitsgemeinschaft Industriebau (AGI), Series Q. Verlag Georg. D. Callwey GmbH. Lindau
2. Zehendner H (1979) Einfluss von Feuchtigkeit auf die Wärmeleitfähigkeit von Schaumkunststoffen im Bereich von -30 °C bis + 30°C, Kunststoff im Bau. 18–20
3. Achtziger J (1985) Einfluss des Wassergehalts und der Feuchtigkeitsverteilung auf die Wärmeleitfähigkeit der Dämmschicht. Bauphysik 7(2):121–124
4. Cammerer WF (1987) der Feuchtigkeitseinfluss auf die Wärmeleitfähigkeit von Bau- und Wärmedämmstoffen. Bauphysik 9(6):259–266
5. Technical Letter No. 11: Feuchte im Dämmsystem (Moisture in insulation systems), Hauptverband der Deutschen Bauindustrie, Berlin (2004)
6. Schreiner R, Zeitler M (1989) Einfluss der Konvektion auf die Wärmeübertragung in Dämmkonstruktionen. BWK 41(12):525–531

D6.6 Thermal Conductivity of Insulation Materials Depending on Moisture Content and Temperature

Fabian Ochs · Hans Müller-Steinhagen
Universität Stuttgart, Stuttgart, Germany

1 Introduction

In VDI Heat Atlas Subchap. D6.3 [1], most significant works related to the measurement and modelling of the thermal conductivity of porous media are listed, see also [2, 3]. In general, the availability of measured thermal conductivity data of (bulk) insulation at elevated moisture contents is very limited. Almost no measured data for the thermal conductivity of insulation materials can be found for temperatures above ambient.

2 Definitions

Bulk densities (ρ) of typical insulation materials range from 100 kg/m^3 to almost 400 kg/m^3, with reference thermal conductivities (λ_R) in the range from 0.05 to 0.12 W/(m K) according to DIN 4108 [4] or manufacturer information. The grain (particle) size (d) of the particular bulk insulation materials is 0–1, 2–4, 4–8 or 8–16 mm for expanded glass, expanded clay, and expanded perlite and 0/20, 0/60, 0/90 or 10/50 mm for foam glass gravel.

The fraction of open pores (accessible for water) and closed pores (non-accessible for water) are important parameters for the thermal conductivity. The total (or bulk) pore fraction (Ψ) can be determined using the total (bulk) density (ρ) and the density of the solid (ρ_s) according to the following equation.

$$\Psi = 1 - \frac{\rho}{\rho_s} \tag{1}$$

The macro-porosity, which corresponds to the fraction of the voids between the grains (Ψ_{macro}) and the fraction of closed pores (Ψ_{cl}) can be measured according to the method described in [5]:

$$\Psi_{op} = \Psi - \Psi_{cl} = \Psi_{macro} + \Psi_{micro} \tag{2}$$

The open porosity (Ψ_{op}) consists of the macro-porosity (Ψ_{macro}) and the micro-porosity (Ψ_{micro}). Micro-porosity is the fraction of open porosity and is, thus, used for water-accessible pores of the grain.

For a single grain, the porosity can be calculated using total porosity (Ψ) and macro-porosity (Ψ_{macro}).

$$\Psi_g = \frac{\Psi - \Psi_{macro}}{1 - \Psi_{macro}} \tag{3}$$

with

$$\Psi_{macro} = \frac{V_{macro}}{V} \tag{4}$$

The free saturation water content (u_{fs}) is determined as the drain weight according to DIN EN 13755 [6] see Table 1. It can be significantly lower than the maximum water content (u_{max}) which is obtained if 100% of the voids are filled with water:

$$u_{max} = \Psi_{op} \cdot \rho_w \tag{5}$$

3 Prediction of Thermal Conductivity

3.1 Thermal Conductivity of Moistened Porous Materials

The VDI Heat Atlas [1] distinguishes between three types of prediction models for the thermal conductivity of porous materials. Type I considers the temperature and heat flux profile of two particles which are in contact (unity cell). It is the most complex model in terms of calculation effort and has to be solved numerically. A simplification is presented by Type III.

D6.6. Table 1. Grain size (d), density (ρ), reference thermal conductivity (λ_R), density (ρ_s) and thermal conductivity (λ_s) of solid matrix, open (Ψ_{op}), and total (Ψ) void fraction and free saturation water content (u_{fs}) of bulk insulation material

Material	Grain size	Bulk density	Solid density	Reference thermal conductivity	Solid thermal conductivity	Total void fraction	Open void fraction	Free saturation
	d	ρ	ρ_s	λ_R	λ_s	Ψ	Ψ_{op}	u_{fs}
	(mm)	(kg/m³)		(W/(m K))		(–)		(kg/m³)
Expanded glass	4–8	185	2,480	0.08	1.16	0.93	0.61	500
Expanded clay	4–8	270	2,650	0.10	3.44	0.90	0.51	300

λ_R: reference thermal conductivity, dry at 10°C according to DIN 4108 [4] or manufacturer data; density (ρ): manufacturer information (ρ_s), and thermal conductivity (λ_s) of solid matrix from [4, 7], free saturation water content [8].

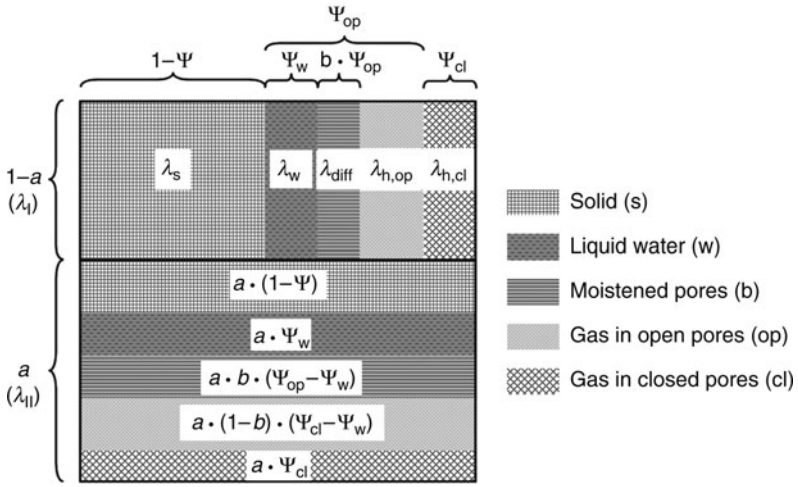

D6.6. Fig. 1. Extended layer model taking into account the fraction of closed and thus, by moisture unaffected pores.

Analog to Type I the unity cell is regarded, but instead of a grid of isotherms and heat flux lines either parallel isotherms or heat flux lines are considered. A frequently used representative is the model developed by Zehner, Bauer and Schlünder (see [2] for details). It describes thermal conductivity very well, if secondary parameters like the thermal contact resistance or flattening effects are considered.

According to a suggestion by Krischer [3], that is, prediction model type II, the thermal conductivity of (moistened) porous materials can be expressed in terms of an aggregation of serial and parallel layers consisting of solid (s), liquid water (w), humid air and dry air (a). Typical bulk insulation materials have a fraction of 23–44% of closed pores (see Sect. 2). It is advantageous to consider the closed pores as an additional layer as will be shown later. This leads to a five-layer model according to Fig. 1.

The summation of the serial layers yields the maximum thermal conductivity.

$$\lambda_I = (1-\Psi)\cdot\lambda_s + \Psi_w\cdot\lambda_w + b\cdot(\Psi_{op}-\Psi_w)\cdot(\lambda_p+\lambda_{diff}) + (1-b)\cdot(\Psi_{op}-\Psi_w)\cdot\lambda_p + \Psi_{cl}\cdot\lambda_{p,cl} \quad (6)$$

The minimum thermal conductivity is obtained by adding the parallel layers, which are weighted with the share of poor conductive layers (a). The maximum thermal conductivity in Eq. (7) is weighted accordingly with (1– a).

$$\lambda_{II} = \left(\frac{1-\Psi}{\lambda_s} + \frac{\Psi_w}{\lambda_w} + \frac{b\cdot(\Psi_{op}-\Psi_w)}{\lambda_p+\lambda_{diff}} + \frac{(1-b)\cdot(\Psi_{op}-\Psi_w)}{\lambda_p} + \frac{\Psi_{cl}}{\lambda_{p,cl}}\right)^{-1} \quad (7)$$

The addition of the weighted maximum (λ_I) and minimum (λ_{II}) thermal conductivity results in the effective thermal conductivity (λ_{eff}) of the porous medium.

$$\lambda_{eff} = \frac{1}{\frac{1-a}{\lambda_I} + \frac{a}{\lambda_{II}}} \quad (8)$$

For dry materials with air as pore gas, the number of layers in the model is reduced to two, that is, solid with the fraction ($1-\Psi$) and air with the fraction (Ψ).

$$\lambda_I = (1-\Psi)\cdot\lambda_s + \Psi\cdot\lambda_p \quad (9)$$

and correspondingly

$$\lambda_{II} = \frac{1}{\frac{1-\Psi}{\lambda_s} + \frac{\Psi}{\lambda_p}} \quad (10)$$

The thermal conductivity of the solid can be measured according to a method proposed in [7] if the literature data are not available. Here, data for glass, clay, perlite or sand/stone are given.

The effective thermal conductivity of the pore (p) consists of a contribution of molecular conduction of the pore gas (pg) and a contribution due to radiation (rad).

$$\lambda_p = \lambda_{pg} + \lambda_{rad} \tag{11}$$

In most cases, the pore gas is air. The thermal conductivity of air can be approximated using a second order polynomial [3].

$$\lambda_a = 0.0243 + 7.8421 \cdot 10^{-5}\vartheta - 2.0755 \cdot 10^{-8}\vartheta^2 \tag{12}$$

The effect of the radiation can be considered using Eq. (13).

$$\lambda_{rad} = \frac{4 \cdot \sigma_s \cdot d_m}{(2/\varepsilon) - 1} T^3 = c_{rad} \cdot T^3 \tag{13}$$

where σ_s is the blackbody radiation constant, ε the coefficient of emission of the particle surface, T the absolute temperature in K and d_m is the mean pore diameter. As the coefficient of emission is not available in most of the cases the parameters in Eq. (13) are lumped to the radiation constant (c_{rad}), which can be determined from experiments.

Using the Nelder-Mead method [9] the unknown parameters a and c_{rad} may be identified.

Convection can be neglected in the present application as, according to Zeitler [10], it only takes place when the Rayleigh number, defined in Eq. (14), exceeds the critical value $Ra_{crit} > 1708$:

$$Ra = Gr \cdot Pr = \frac{g \cdot \beta_{pg} \cdot \Delta T_p \cdot d_{p,m}^3}{\nu_{pg} \cdot a_{pg}} \tag{14}$$

Even for coarse-grained materials with mean grain diameters of 12 mm the Rayleigh number remains smaller than the critical value under the given boundary conditions.

3.2 Influence of Moisture as a Function of Temperature

In order to model the presence of moisture, the thermal conductivity of liquid water (λ_w) and of water saturated air ($\lambda_{a,sat}$) in Eqs. (6) and (7) have to be calculated. The thermal conductivity of water can be represented by a third order polynomial approach according to [3]. The thermal conductivity of water vapour (v) as a function of temperature is given by Quast [11]:

$$\lambda_v = \frac{1.713 \cdot 10^{-4} \cdot (1 + 0.0129 \cdot T) \cdot \sqrt{T}}{1 - 80.95/T} \tag{15}$$

Ackermann [12] provides an equation for the thermal conductivity of water saturated air with the saturation pressure p_{sat} according to Eq. (23) at an absolute pressure of $p_{amb} = 1$ bar.

$$\lambda_{a,sat} = 0.5 \cdot \left[p_{sat} \cdot \lambda_v + (1 - p_{sat}) \cdot \lambda_a + \left(\frac{p_{sat}}{\lambda_v} + \frac{1 - p_{sat}}{\lambda_a} \right)^{-1} \right] \tag{16}$$

The fraction of pores filled with liquid water can be estimated using the absolute moisture content (u).

$$\Psi_w = u/\rho_w \tag{17}$$

3.3 Thermal Conductivity Due to Pore Diffusion

For the moistened pores, the conductive terms of solid λ_s, of water λ_w and of dry air λ_a or saturated air $\lambda_{a,sat}$ are taken into account according to Eqs. (6) and (7). Additionally heat transfer due to evaporation at the warm side of a pore and condensation at the opposite cold side of the pore occurs (heat pipe effect). The effective thermal conductivity due to pore diffusion (λ_{diff}) is modelled introducing an additional term, which is added to the thermal conductivity of the pore λ_p.

$$\lambda_{p,op} = \lambda_p + \lambda_{diff} \tag{18}$$

The term (λ_{diff}) describing the heat transport due to pore diffusion is expressed in different ways in the literature. Krischer [3] who developed the original model proposed:

$$\lambda_{diff} = \frac{D_v}{R_v \cdot T} \cdot \frac{p_{amb}}{p_{amb} - p_{sat}} \cdot \frac{dp_{sat}}{d\vartheta} \Delta h_v \tag{19}$$

In the VDI Heat Atlas [13] a similar correlation can be found.

$$\lambda_{diff} = \frac{D_v}{R_v^2 T^2} \frac{p_{amb}}{p_{amb} - p_{sat}} \Delta h_v^2 \tag{20}$$

De Vries [14] suggests the following correlation for the thermal conductivity due to pore diffusion:

$$\lambda_{diff} = D_v \cdot \frac{dp_{sat}}{d\vartheta} \cdot \Delta h_v \tag{21}$$

Whereas the equations according to Krischer and VDI Heat Atlas provide similar results, the De Vries approach yields significant deviations above 70°C.

For the temperature-dependent parameters, the vapour diffusion coefficient (D_v) and the saturation vapour pressure (p_{sat}), different empirical correlations are suggested in the literature (Krischer [3], De Vries [14], Schirmer [15], Vos [16]): The following empirical function given in VDI Heat Atlas [13] is recommended:

$$D_v = \frac{2.252}{p_{amb}} \cdot \left(\frac{T}{273} \right)^{1.81} \tag{22}$$

Furthermore, different correlations for the vapour saturation pressure can be found in the literature (e.g., VDI Heat Atlas [13], Magnus [17] or the Antoine correlation [18]). The Antoine correlation was originally used by Krischer and is, thus, also used in this work

$$p_{sat} = 610.8 \cdot \exp\left(\frac{17.08085 \cdot \vartheta}{234.175 + \vartheta} \right) \tag{23}$$

It is valid in a temperature range from 0°C to 100°C. The derivation of the saturation pressure in Eq. (23) yields

$$\frac{dp_{sat}}{d\vartheta} = \frac{2.44314.10^6}{(234.175 + \vartheta)^2} \cdot \exp\left(\frac{17.08085 \cdot \vartheta}{234.175 + \vartheta} \right) \tag{24}$$

The gas constant of water vapour is R_v = 461.5 KJ/(kg K) and the specific heat of evaporation is Δh_v = 2260 kJ/kg.

3.4 Approximation of the Fraction of Moistened Pores

The moistened pores, that is, the pores in which diffusion takes place, can be determined by subtracting the share of water-filled pores from the share of open pores. Hence,

$$\Psi_{\mathrm{diff}} = b \cdot (\Psi_{\mathrm{op}} - \Psi_{\mathrm{w}}) \tag{25}$$

The fraction of the moistened pores (b) is, therefore, a function of the water content (u). Between water content zero (dry material) and the free saturation (u_{fs}), the parameter b can take values between 0 and 1. For free water saturation b becomes 1. If the free saturation water content (u_{fs}) is equal to the maximum water content, which applies in the case of open-porous materials such as mineral wool, no air remains in the pores of the material. Consequently, the fraction of moistened pores $\Psi_{\mathrm{op}} - \Psi_{\mathrm{w}}$ and thus Ψ_{diff} is zero: no pore diffusion takes place. The fraction b has to be determined by iterative curve-fitting using, for example, the Nelder-Mead algorithm [9]. For each data set of thermal conductivity as a function of temperature and moisture content (u) the corresponding b value has to be determined.

For the predictions of the fraction of moistened pores (b) as a function of water content (u), the following empirical correlation developed by Krischer [3] is suggested in the VDI Heat Atlas [13]:

$$b = 1 - \left(1 - \frac{u}{u_{\mathrm{fs}}}\right)^9 \tag{26}$$

However, the present measurements indicate that the fraction of pores (b) in which pore diffusion takes place does not depend on the free saturation water content only. Therefore, a more complex correlation may be required.

The correlation between (b) and the water content (u) is similar to the moisture storage function of porous materials (or water retention curve of soils) which describes the moisture content (u) as a function of the relative humidity (Φ). Thus, already known correlations may be applied. A one-parameter approach (model II) with the empirical factor (c) and the free saturation water content (u_{fs}) is given with Eq. (27) from [19]

$$b = \frac{u \cdot c}{u_{\mathrm{fs}} \cdot (1 - c) + u} \tag{27}$$

while better results can be achieved using an approach with two empirical parameters (m_1, m_2) according to Eq. (28) which is suggested in [20]

$$b = \exp\left(m_1 \cdot \left(\frac{u_{\mathrm{fs}}}{u} - 1\right)^{m_2}\right) \tag{28}$$

In Fig. 2, the comparison of the predictions of the three models and the experimental data (iteratively determined data $b(u)$ for expanded glass granules 4–8 mm and expanded clay 4–8 mm) is shown. The best agreement between model prediction and experimental data is obtained using model III, Eq. (28).

3.5 Temperature Dependence of the Closed Pore Fraction

By definition, closed pores are not accessible to water (see Sect. 2). Due to the decreasing dynamic viscosity (η) and surface tension (σ) of water with increasing temperature (ϑ), the fraction of non-accessible pores is assumed to decrease with increasing temperature according to the following equation:

$$\Psi_{\mathrm{cl}}(\vartheta) = \chi \cdot \Psi_{\mathrm{cl,ref}} \cdot \frac{\eta(\vartheta)}{\eta_{\mathrm{ref}}} \cdot \frac{\sigma(\vartheta)}{\sigma_{\mathrm{ref}}} \tag{29}$$

The dynamic viscosity and the surface tension can be approximated by polynomial functions according to [21]. Good agreement between calculated and experimental results can be achieved by setting the correction factor (χ) in Eq. (29) equal to 0.5.

4 Model Validation

The effective thermal conductivity of several different (bulk) insulation materials (expanded glass expanded clay, perlite, foam glass, mineral wool) was measured according to [22] in a temperature range from 20°C to 80°C for water contents between 0 and the free saturation water content (u_{fs}).

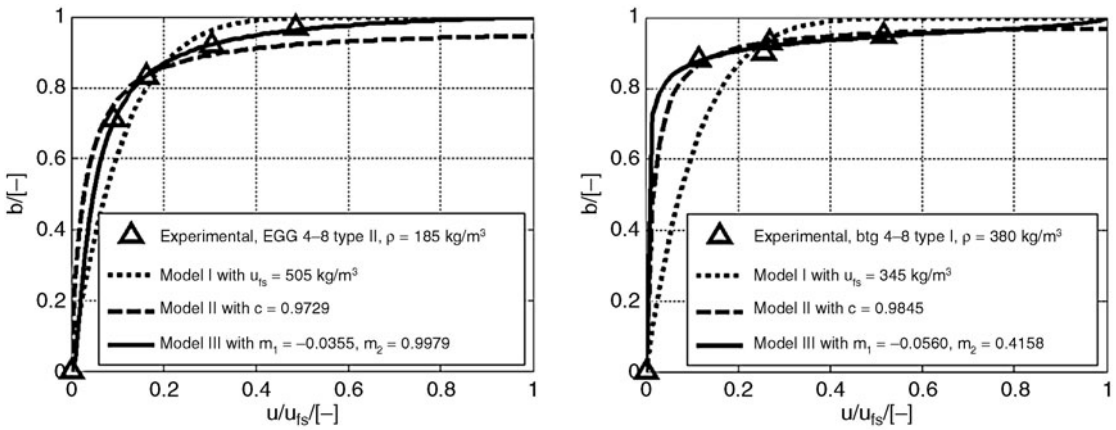

D6.6. Fig. 2. Comparison of model predictions and agreement with experimental results for the fraction of moistened pores (b); EGG: expanded glass granules 4–8 mm type II; btg: expanded clay 4–8 mm type I.

D6.6. Table 2. Fraction of serial and thus poor conductive layers (a) and corresponding values of the radiation constant (c_{rad}), determined using the Nelder-Mead iteration method

Material	Grain size d (mm)	Density ρ (kg/m^3)	Fraction of poor conductive layers a (–)	Radiation constant c_{rad} (W/(m K^4))	Parameter Eq. (28) m1 (–)	m2 (–)
Expanded glass	4–8	185	0.441	$3.9 \cdot 10^{-10}$	–0.0355	0.9979
Expanded clay	4–8	270	0.297	$1.0 \cdot 10^{-10}$	–0.0033	2.9097

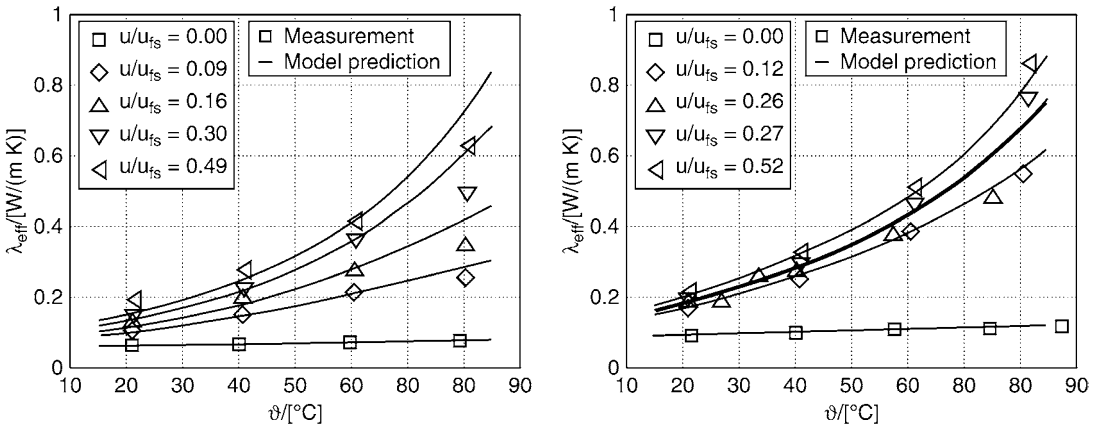

D6.6. Fig. 3. Model predictions and measured data for the thermal conductivity (λ_{eff}) of expanded glass granules 4–8 mm type II (EGG: *left*) and expanded clay 4–8 type I (EC: *right*) as a function of the temperature (ϑ) with normalised water content (u/u_{fs}) as parameter.

The lowest thermal conductivity was measured for expanded perlite with about 0.05 W/(m K) at 20°C. The highest value is 0.10 W/(m K) for expanded clay. All investigated porous bulk materials show a (nearly) linear increase of the effective thermal conductivity with temperature when dry, see [23] for details and further results.

The resulting fraction of serial layers (a) and the corresponding radiation constant (c_{rad}) of expanded glass granules and expanded clay are compared in Table 2.

In Fig. 3 model predictions are compared with measured results for expanded glass granules 4–8 mm type II and expanded clay 4–8 mm type I. Good agreement is obtained in the relevant temperature range. Nevertheless, there are deviations at 80°C. Measurement errors at higher temperatures, which are probably caused by heat losses from the guarded heating plate to the ambient, resulting in a measured value of the thermal conductivity that is too low.

5 Summary

An exponential increase of the thermal conductivity with increasing temperature can be recognised above moisture contents of about 50 kg/m^3 (corresponding to $u/u_{fs} \approx 0.1$). For expanded glass granules, the effective thermal conductivity (λ_{eff}) exceeds the reference value (dry, 10°C) of 0.08 W/(m K) by a factor of five at a temperature of 60°C and a moisture content of about 200 kg/m^3; at 80°C even by a factor of 10. A similar behavior can be recognised in the case of expanded clay.

The suggested model predicts the measured data and trends with good accuracy.

6 Symbols

Latin letters

a	fraction of poorly conductive layers (–)
a	thermal diffusivity (m $\cdot$ s^{-2})
b	fraction of moistened pores (–)
c	approximation factor for b(u), model II (–)
c_{rad}	radiation constant (W $\cdot$ m^{-1} $\cdot$ K^{-1})
d	diameter (m)
D	diffusion coefficient (m^2 $\cdot$ s^{-1})
g	acceleration due to gravity (m $\cdot$ s^{-2})
h_v	latent heat of evaporation (kJ $\cdot$ kg^{-1})
m_1, m_2	empirical parameter for b(u), model III (–)
p	pressure (Pa)
R	gas constant (J $\cdot$ (kg $\cdot$ K))$^{-1}$
T	absolute temperature (K)
u	(absolute) moisture content (kg $\cdot$ m^{-3})
V	volume (m^3)

Greek letters

β	coefficient of expansion (K^{-1})
Δ	difference (–)
ε	emissivity coefficient (–)
η	dynamic viscosity (kg $\cdot$ (m $\cdot$ s)$^{-1}$)
ϑ	Celsius temperature (°C)
λ	thermal conductivity (W $\cdot$ (m $\cdot$ K)$^{-1}$)

ν kinematic viscosity ($m \cdot s^{-1}$)
ρ (bulk) density ($kg \cdot m^{-3}$)
σ surface tension ($N \cdot m^{-1}$)
σ_s Boltzmann constant ($W \cdot m^{-2} \cdot K^{-4}$)
φ relative humidity (–)
χ empirical correction factor (–)
Ψ porosity (void fraction) (–)
Ψ_w volume related liquid water content (–)

Subscripts

I, II parallel, serial layer
a air
amb ambient
cl closed
diff diffusion
eff effective
fs free saturation
g grain (particle)
max maximum
m mean
op open
p pore
pg pore gas
s solid
sat saturation
v vapour
w water

7 Bibliography

1. VDI Heat Atlas (2009) D6.3, Thermal conductivity of packed beds (VDI-Wärmeatlas, Kapitel Dee, 10. Auflage), Springer Verlag, 2006
2. Schlünder E-U, Tsotsas E (1988) Wärmeübertragung in Festbetten, durchmischten Schüttgütern und Wirbelschichten, ISBN 3–13–713001–8. Georg Thieme Verlag, Stuttgart
3. Krischer O, Kast W (1992) Die wissenschaftlichen Grundlagen der Trocknungstechnik, 3. Auflage, Springer-Verlag/Heidelberg, ISBN: 3–540–08280–8
4. DIN 4108 Teil 4, Thermal insulation and energy economy in buildings - Part 4: Hygrothermal design values, Wärmeschutz und Energie-Einsparung in Gebäuden - Teil 4: Wärme- und feuchteschutztechnische Bemessungswerte, 2004
5. Walz K (ed) (1974) Merkblatt I für Leichtbeton und Stahlbeton mit geschlossenem Gefüge, Betonprüfung zur Überwachung der Leichtzuschlagherstellung, Betontechnische Berichte des Forschungsinstituts der Zementindustrie
6. DIN EN 13755 (2002) Determination of water absorption and saturation coefficient, Bestimmung der Wasseraufnahme unter atmosphärischem Druck
7. Bouguerra A, Laurent JP, Goual MS, Queneudec M (1997) The measurement of the thermal conductivity of solid aggregates using the transient plane source technique. J Phys D Appl Phys 30:2900–2904
8. DIN 52620 (1991) Determination of the reference moisture content of building materials, Bestimmung des Bezugsfeuchtegehalts von Baustoffen
9. Nelder JA, Mead R (1965) A simplex method for function minimization. Computer J 7:308–313
10. Zeitler MG (2000) Allgemeingültiges Modell zur Berechnung der Wärmeleitfähigkeit poröser Stoffe und Stoffschichten, Diss., Universität Essen, Essen
11. Quast U (1977) Wärme- und Stoffübertragung in Gegenstrom-Kühltürmen unter Berücksichtigung von Nebel- und Sprühtropfenbildung, TH Darmstadt, Diss., Darmstadt
12. Ackermann D (1972) Wärme- und Stoffübertragung bei der Kondensation eines turbulent strömenden Dampfes in Anwesenheit von Inertgas, Diss., Universität Stuttgart, Stuttgart
13. Tsotsas E (2009) VDI Heat Atlas, M6 Heat Transfer from tempered surfaces in fixed and partially fuidized beds (VDI-Wärmeatlas, Kapitel Mg 11, 10. Auflage), Springer Verlag, 2006
14. De Vries DA (1966) Heat transfer in soils. In: Van Wijk WR (ed). Physics of plant environment. North Holland, Amsterdam
15. Schirmer R (1938) Die Diffusionswiderstandszahl von Wasserdampf-Luftgemischen und die Verdampfungsgeschwindigkeit. VDI Beiheft Verfahrenstechnik 6:170
16. Andersson A-C (1985) Verification of calculation methods for moisture transport in porous building materials, Swedish Council for Building Research, D6:1985, Stockholm
17. Sonntag D, Heinze D (1982) Sättigungsdampfdruck- und Sättigungsdampfdichtetafeln für Wasser und Eis. (1. Aufl.), VEB Deutscher Verlag für Grundstoffindustrie
18. Reid RC, Prausnitz JM, Poling BE (1977) The properties of gases and liquids, 3rd edn. McGraw-Hill, New York
19. Künzel HM (1994) Verfahren zur ein- und zweidimensionalen Berechnung des gekoppelten Wärme- und Feuchtetransports in Bauteilen mit einfachen Kennwerten, Diss., Fraunhofer Institut für Bauphysik (IBP), Universität Stuttgart, Stuttgart
20. Holm A, Krus M, Künzel HM (2002) Approximation der Feuchtespeicherfunktion aus einfach bestimmbaren Kennwerten, IBP-Mitteilungen 406, 29. Fraunhofer Institut für Bauphysik (IBP), Stuttgart
21. Bednar T (2000) Beurteilung des feuchte- und wärmetechnischen Verhaltens von Bauteilen und Gebäuden, Weiterentwicklung der Meß- und Rechenverfahren, Diss., TU Wien, Wien
22 DIN 52 612 (1979), Determination of Thermal Conductivity by the Guarded Hot Plate Apparatus; Bestimmung der Wärmeleitfähigkeit mit dem Plattengerät, Testing of Thermal Insulating Materials
23. Ochs F, Heidemann W, Müller-Steinhagen H (2008) Effective thermal conductivity of moistened insulation materials as a function of temperature. Int J Heat Mass Transfer (online 2007) 51(3–4):539–552, Elsevier

D6.7 Thermal Conductivity of Building Materials

Hans Werner[1] · *Martin H. Spitzner*[2]
[1]Hochschule für Angewandte Wissenschaften (FH), München, Germany
[2]FIW München, Gräfelfing, Germany

1 Soil

In a totally dry condition, the porosity (ratio of pore volume to total volume) of a material is by far the most important influencing variable in view of the thermal conductivity. In general, soil is to be considered a granular material with a relatively high porosity. As the densities of the components do not vary within a broad range, the density of the dried soil is an appropriate quantity for evaluating the porosity. In practice, one has to expect water within the pores in most of the cases. Based on the test executed by Krischer [1], one can estimate the thermal conductivity of soil with different moisture contents according to Figs. 1 and 2. Concerning the natural moisture content of solid soil, the following empirical values apply:

Soil	Density kg/m3	Moisture content, in % by volume	
		Range of values observed	Usual condition
Argillaceous, clayey sandy	1,900–2,100	10–28	25
	1,600–1,800	4–14	10

The heat transport results from the thermal conduction in porous material. Here, the thermal conductivity λ is decisive. The dependence on temperatures is a result of the relatively weak and nearly linear part of the molecular thermal conductivity (cf. Fig. 3, characteristics of the thermal conductivity of dry material) and of the part of water vapor diffusion which, due to the virtually quadratic dependence on temperatures of the diffusion coefficient, determines the developing of the effective thermal conductivity in humid soils.

At a temperature of about 60°C the apparent thermal conductivity of the air in the humid material, independent of its water content, corresponds to the molecular thermal conductivity of water λ_w = 0.65 W/(m K) and thus, thermal conductivity of the humid material comes up to a value which corresponds to the total saturation of the pores. At still higher temperatures partially waterlogged material shows a higher thermal conductivity than in the case of the total pore saturation. In Fig. 3, the results of the measurements done on sand by Watzinger et al. [2] are shown. Provided the recorded curves are extrapolated beyond the measurement range up to a temperature of about 60°C, one can, based on what had been said earlier, assume that there is a common intersection point.

2 Wood and Derived Timber Products

If wood is in direct contact with air, the moisture content depends on the relative humidity of the air. The humidity of the wood reached after a certain time is referred to as equilibrium moisture content (The equilibrium moisture content is the average moisture content of a material to be expected during its application in practice. Scientifically, it is defined by the so-called sorption isotherm of 10°C for 80% relative humidity.) previously called practical moisture content (moisture content related to mass).

In general, one can assume that, in wood, there are the following relations between relative humidity of the air and equilibrium moisture content:

Relative humidity of air in %	20	40	60	80	100
Equilibrium moisture content at 20°C in % (related to mass)	4	7	11	17	33

According to DIN 1052-1 [3], the equilibrium moisture content depending on the use categories are as follows:

Use category	1	2	3
Equilibrium moisture content	5–15%[a]	10–20%[b]	12–24%

[a]In most of the coniferous woods, a mean equilibrium moisture content of 12% is not exceeded in use category 1.
[b]In use category 2, a mean equilibrium moisture content of 20% is not exceeded.

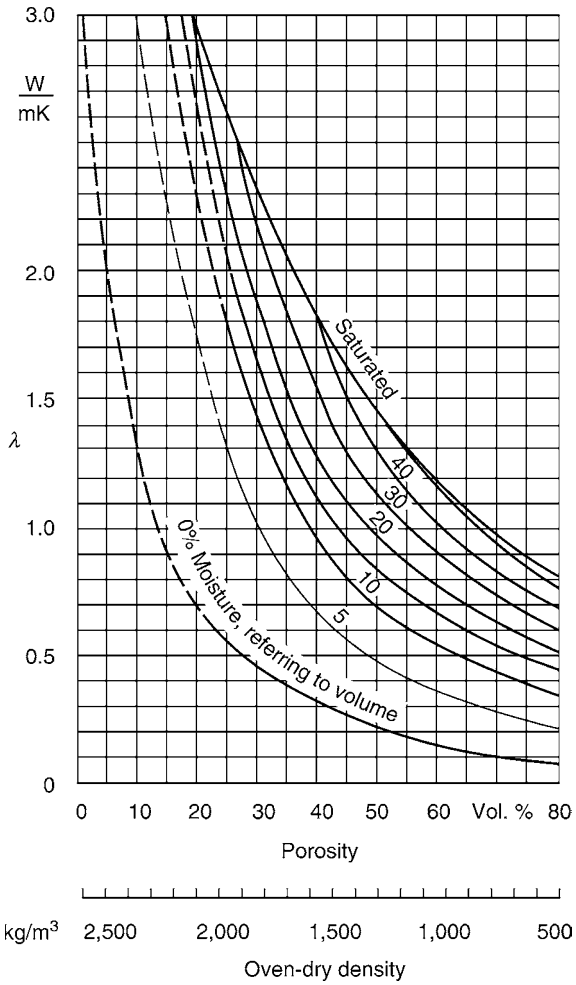

D6.7. Fig. 1. Thermal conductivity of soil at a temperature of 20°C.

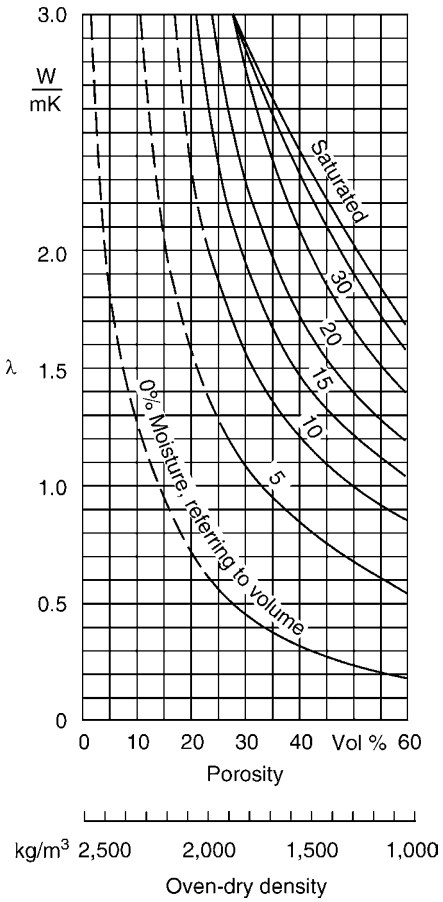

D6.7. Fig. 2. Thermal conductivity of siliceous sand at a temperature of 20°C.

Use categories are identified by equilibrium moisture contents in wood regarding certain application areas. A difference is made between:

Use category 1: Humidities in wood at an air temperature of 20°C and a relative humidity of the ambient air exceeding 65% only during a few weeks per year, e.g., inside all over closed and heated buildings.

Use category 2: Humidities in wood at an air temperature of 20°C and a relative humidity of the ambient air exceeding 85% only during a few weeks per year, e.g., in roofed open buildings.

Use category 3: Climate conditions leading to wood humidities in excess of those mentioned in utilization category 2, e.g., in constructions exposed to outside weather conditions.

Apart from the moisture content, the thermal conductivity of wood depends above all on the density. Figure 4 shows a diagram made by Koch [4], on which one can see the thermal conductivity perpendicular to the direction of the wood fibers in dependency of the moisture content and density. In the direction of the fibers, the values of the thermal conductivity are twice as high as the ones perpendicular to the direction of the fibers.

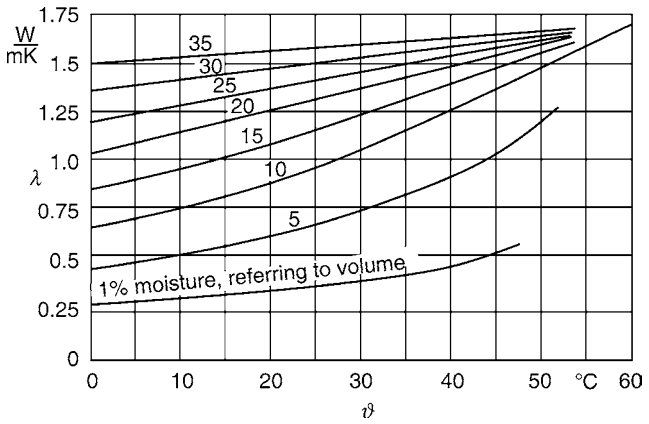

D6.7. Fig. 3. Thermal conductivity of humid sand depending on the temperature.

3 Common Building Materials

Thermal design values of construction material are to be found in DIN V 4108-4 (June 2007, [5]). The values indicated here are referred to as design values of thermal conductivity λ and take into consideration the influence of temperature, moisture

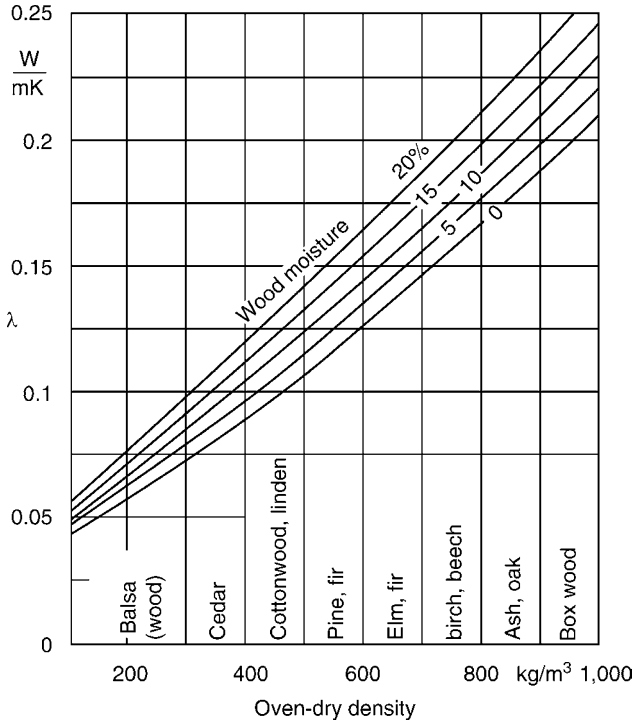

D6.7. Fig. 4. Thermal conductivity of wood perpendicular to the direction of the wood fibers in dependency of moisture content (%) and dry density (kg/m^3) according to [4].

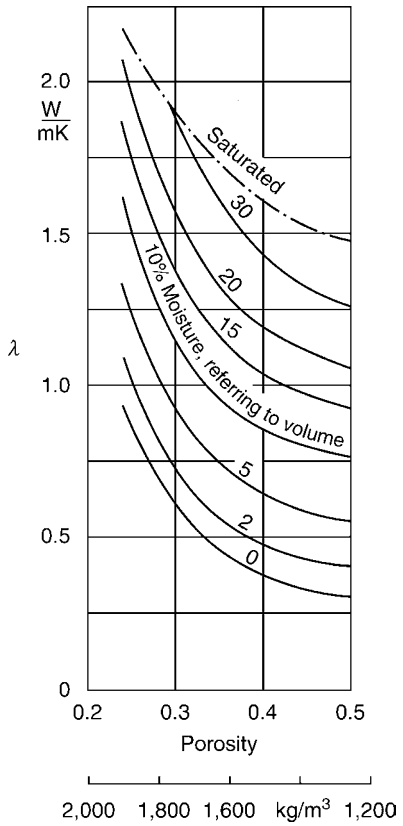

D6.7. Fig. 5. Thermal conductivity of humid bricks depending on the porosity at a temperature of about 20°C according to [8].

D6.7. Table 1. Equilibrium moisture content of building material according to DIN V 4108-4 [5]

Line		Construction material	Moisture content *u* kg/kg
1		Dense concrete with porous aggregate	0.13
2	2.1	Porous lightweight concrete with porous aggregate according to DIN 4226-1	0.03
	2.2	Porous lightweight concrete with porous aggregate according to DIN 4226-2	0.045
3		Gypsum and anhydrite	0.02
4		Melted asphalt and asphalt mastic	0
5		Wood, plywood, fiberboards, reed boards and mats, and organic fiber insulating material	0.15
6		Thermal insulation material out of plant fibers from sea weed, wood, turf, coco, and other fibers	0.15

Further equilibrium moisture contents are listed in Table 6 of DIN 12524:2000-07.

content, variations of the material characteristics, and ageing when applied in the conventional building constructions (cf. scope of DIN V 4108). The moisture content and the condition of application on which the design values are based are to be found in the standards referred to.

Table 1 reproduces the equilibrium moisture content of construction material according to DIN V 4108-4.

In the Tables 2–4, there is an abridged version of DIN V 4108-4 (2007-6) [5], cf. Tables 1 and 2 of this standard. The thermal conductivity of most of the building materials depends largely on their bulk density (mass in relation to the gross volume including all cavities). As most of the industrially fabricated building materials are produced in different apparent densities, thermal conductivity is given in DIN V 4108-4 for different density categories.

All values are only valid for application in conventional building constructions. In case of any other usage condition, there can be variations in view of the given design values.

An analysis of a multitude of research results concerning the influence of the moisture content onto the thermal conductivity of building and insulating materials is published in a paper by Achtziger and Cammerer [6].

The thermal conductivities of specific products (branded products manufactured by industry) can be found in Germany in the Bauregelliste (list of building rules) or in the Allgemeine bauaufsichtliche Zulassung (technical approval) of that product, both of which are published by the Deutsches Institut für Bautechnik (DIBt, German Institute for building technique).

Further tabulated design values are listed in DIN EN 12524 [3]. These values are used if there is no other data given in the national rules and regulations. There is an abridged version in Table 5.

D6.7. Table 2. Design values of thermal conductivity of building materials and masonry (abridged version of DIN V 4108-4 [5])

Line	Material	Density ρ kg/m³	Design thermal conductivity λ W/(m·K)
1	Rendering plasters, mortar, and floor pavement		
1.1	Rendering/plastering mortar		
1.1.1	Rendering/plastering mortar of lime, lime cement, and lean lime	1,800	1.0
1.1.2	Rendering/plastering mortar of lime-gypsum, gypsum, anhydrite, and lime-anhydrite		
1.1.3	Lightweight rendering/plastering mortar	<1,300	0.56
1.1.4	Lightweight rendering/plastering mortar	≤1,000	0.38
1.1.5	Lightweight rendering/plastering mortar	≤700	0.25
1.1.6	Gypsum rendering/plastering mortar without aggregate	1,200	0.51
1.1.7	Thermal insulating plaster according to DIN 18550-3		
	Thermal conductivity group		
	060	≥200	0.060
	070		0.070
	080		0.080
	090		0.090
	100		0.100
1.1.8	Resin plaster	1,100	0.70
1.2	Masonry mortar		
1.2.1	Cement mortar	2,000	1.6
1.2.2	General purpose masonry mortar	1,800	1.2
1.2.3	Thin layer masonry mortar	1,600	1.0
1.2.4	Lightweight masonry mortar according to DIN 1053-1	≤1,000	0.36
1.2.5	Lightweight masonry mortar according to DIN 1053-1	≤700	0.21
1.2.6	Lightweight masonry mortar	250	0.10
		400	0.14
		700	0.25
		1,000	0.38
		1,500	0.69
1.3	Floor pavement and screed		
1.3.1	Bitumen and asphalt	Cf. DIN EN 12524	
1.3.2	Cementitious screed	2,000	1.4
1.3.3	Anhydrite screed	2,100	1.2
1.3.4	Magnesite screed	1,400	0.47
		2,300	0.70
2	Concrete components		
2.1	Concrete according to DIN EN 206	Cf. DIN EN 12524	
2.2	Dense lightweight concrete and dense reinforced lightweight concrete according to DIN EN 206 and DIN 1045-2, produced using aggregates with porous structures according to DIN 4226-2, without additional siliceous sand	800	0.39
		900	0.44
		1,000	0.49
		1,100	0.55
		1,200	0.62
		1,300	0.70
		1,400	0.79
		1,500	0.89
		1,600	1.0
		1,800	1.3
		2,000	1.6

D6.7. Table 2. (continued)

Line	Material	Density ρ kg/m^3	Design thermal conductivity λ W/(m·K)
2.3	Autoclaved aerated concrete according to DIN 4223-1	400	0.13
		500	0.15
		550	0.18
		600	0.19
		700	0.22
		800	0.25
		1,000	0.31
2.4	Porous lightweight concrete		
2.4.1	With nonporous aggregates according to DIN 4226-1, e.g., gravel	1,600	0.81
		1,800	1.1
		2,000	1.4
2.4.2	With porous aggregates according to DIN 4226-2, without additional siliceous sand	600	0.22
		800	0.28
		1,000	0.36
		1,200	0.46
		1,400	0.57
		1,600	0.75
		2,000	1.2
2.4.2.1	Exclusive use of natural pumice	400	0.12
		500	0.15
		700	0.21
		800	0.24
		900	0.27
		1,000	0.32
		1,300	0.47
2.4.2.2	Exclusive use of expanded clay	400	0.13
		500	0.16
		600	0.19
		700	0.23
		800	0.26
		1,000	0.35
		1,200	0.44
		1,400	0.55
		1,600	0.68
		1,700	0.76
3	Building boards		
3.1	Autoclaved aerated concrete slabs and autoclaved aerated concrete panels unreinforced according to DIN 4166		
3.1.1	Autoclaved aerated concrete slabs with normal joint thickness and masonry mortar according to DIN 1053-1	400	0.20
		500	0.22
		600	0.24
		700	0.27
		800	0.29
3.1.2	Autoclaved aerated concrete panels laid with thin joints	400	0.13
		500	0.16
		600	0.19
		700	0.22
		800	0.25

D6.7. Table 2. (continued)

Line	Material	Density ρ kg/m^3	Design thermal conductivity λ W/(m·K)	
3.2	Lightweight concrete wallboards according to DIN 18162	800	0.29	
		900	0.32	
		1,000	0.37	
		1,200	0.47	
		1,400	0.58	
		600	0.29	
3.3	Gypsum blocks according to DIN 18163, also with pores, voids, or aggregates	750	0.35	
		900	0.41	
		1,000	0.47	
		1,200	0.58	
		900	0.25	
3.4	Gypsum plasterboards according to DIN 18180	900	0.25	
4	Masonry, including mortar joints			
4.1	Masonry made of clay masonry units according to DIN V 105-1 and DIN V 105-6 or clay masonry blocks according to DIN in connection with E DIN 20000-401 NM/DM			
4.1.1	Solid clinker, vitrified brick, vertically perforated clinker, and ceramic clinker	1,800	0.81	
		2,000	0.96	
		2,200	1.2	
		2,400	1.4	
4.1.2	Solid brick, vertically perforated or hollow clay masonry units, and filler brick	1,200	0.50	
		1,400	0.58	
		1,600	0.68	
		1,800	0.81	
		2,000	0.96	
		2,200	1.2	
		2,400	1.4	
			LM21/LM36	NM/DM
		600	0.28	0.33
		700	0.31	0.36
		800	0.34	0.39
4.1.3	Vertically perforated or hollow clay masonry unit with perforation A and B according to DIN 105-1 or thermal insulation bricks (LD) according to DIN EN 771-1 in connection with E DIN 20000-401	900	0.37	0.42
		950	0.38	0.44
		1,000	0.40	0.45
4.1.4	Vertically perforated or hollow clay masonry unit (HlzW) and thermal insulation brick (WDz) according to DIN 105-2, or thermal insulation brick (LD) according to DIN EN 771-1 in connection with E DIN 20000-401, nominal dimension h = 238 mm		LM21/LM36	NM
		600	0.20	0.23
		700	0.21	0.24
		800	0.23	0.26
		900	0.24	0.27
		1,000	0.26	0.29
4.1.5	Plane thermal insulation brick (PWDz) according to DIN 105-6, h = 248 mm	600	0.21	
		700	0.22	
		800	0.24	
		900	0.25	

D6.7. Table 2. (continued)

Line	Material		Density ρ kg/m^3	Design thermal conductivity λ W/(m·K)		
4.2	Masonry made of sand-lime blocks according to DIN V 106-1		1,000	0.50		
			1,200	0.56		
			1,400	0.70		
	Masonry made of sand-lime blocks according to DIN V 106-2		1,600	0.79		
			1,800	0.99		
	Masonry made of sand-lime blocks according to EN 771-2 in connection with E DIN 20000-402		2,000	1.1		
			2,200	1.3		
			2,000	0.47		
			2,200	0.52		
			2,400	0.58		
4.3	Masonry made of granulated slag blocks according to DIN 398		1,600	0.64		
			1,800	0.70		
			2,000	0.76		
4.4	Masonry made of plane autoclaved aerated concrete blocks (PP) according to DIN V 4165		350	0.11		
			400	0.13		
			450	0.15		
			500	0.16		
			550	0.18		
			600	0.19		
			650	0.21		
			700	0.22		
			750	0.24		
			800	0.25		
4.5	Masonry made of concrete masonry units					
4.5.1	Hollow blocks (Hbl) according to DIN V 18151, group 1		450	LM21[a] DM	LM36[a]	NM[a]
				0.20	0.21	0.24
			500	0.22	0.23	0.26
	width of stone, in cm number of compartments rows		550	0.23	0.24	0.27
			600	0.24	0.25	0.29
	17.5	≥ 2	650	0.26	0.27	0.30
	24	≥ 3	700	0.28	0.29	0.32
	30	≥ 4	800	0.31	0.32	0.35
	36.5	≥ 5	900	0.34	0.36	0.39
	49	≥ 6	1,000	–	–	0.45
4.5.2	Hbls according to DIN V 18151 and hollow boards according to DIN 18148, group 2 width of stone, in cm number of compartments rows		500	0.24	0.25	0.29
			600	0.27	0.28	0.32
			650	0.29	0.30	0.34
	11.5	1	700	0.30	0.32	0.36
	17.5	1	800	0.34	0.36	0.41
	24	2	900	0.37	0.40	0.46
4.5.2	Hbls according to DIN V 18151 and hollow boards according to DIN 18148, group 2		1,000	–	–	0.52
	Width of stone, in cm	Number of compartments rows				
	30	≤ 3	1,200	–	–	0.60
	36.5	≤ 4	1,400	–	–	0.72
	49	≤ 5	1,600	–	–	0.76

D6.7. Table 2. (continued)

Line	Material	Density ρ kg/m^3	Design thermal conductivity λ W/(m·K)		
4.5.3	Solid blocks (Vbl, S-W) according to DIN V 18152	450	0.14	0.16	0.18
		500	0.15	0.17	0.20
		550	0.16	0.18	0.21
		600	0.17	0.19	0.22
		650	0.18	0.20	0.23
		700	0.19	0.21	0.25
		800	0.21	0.23	0.27
		900	0.25	0.26	0.30
		1,000	0.28	0.29	0.32
4.5.4	Solid blocks (Vbl and Vbl-S) according to DIN V 18152, made of lightweight concrete with lightweight aggregates other than natural pumice or expanded clay	450	0.22	0.23	0.28
		500	0.23	0.24	0.29
		600	0.25	0.26	0.31
		700	0.27	0.28	0.33
		800	0.29	0.30	0.36
		900	0.32	0.32	0.39
		1,000	0.34	0.35	0.42
		500	0.22	0.23	0.32
		600	0.24	0.26	0.34
		650	0.25	0.27	0.35
4.5.5	Solid blocks (V) according to DIN V 18152	800	0.30	0.32	0.40
		1,000	0.36	0.38	0.46
		1,200	–	–	0.54
		1,600	–	–	0.74
		1,800	–	–	0.87
		2,000	–	–	0.99
4.5.6	Concrete masonry units according to DIN 18153	800	0.60		
		1,200	0.80		
		1,000	1.1		
		2,000	1.4		
		2,400	2.1		
5	Thermal insulation material — cf. Tables 2 and 6				
6	Timber and wood-based panels	cf. DIN EN 12524			
7	Coverings, sealant material, and sealant sheets				
7.1	Floor covering	cf. DIN EN 12524			
7.2	Sealant material	cf. DIN EN 12524			
7.3	Roof sheeting, roof sealant sheeting				
7.3.1	Bitumen roof sheeting according to DIN 52128	1,200	0.17		
7.3.2	Bare bitumen roof sheeting according to DIN 52129	1,200	0.17		
7.3.3	Bitumen roof sheeting with inlay of glass fiber fleece according to DIN 52143	–	0.17		
8	Other material in use				
8.1	Loose-fill, covered out of porous material:				

D6.7. Table 2. (continued)

Line	Material		Density ρ kg/m^3	Design thermal conductivity λ W/(m·K)
8.1.1	Expanded perlite	≤100	0.060	
	Mica mineral	≤100	0.070	
	Cork pellets, expanded	≤200	0.055	
	Pumice slag	≤600	0.13	
	Expanded clay, expanded shale	≤400	0.16	
	Pumice gravel	≤1,000	0.19	
	Lava foam	≤1,200	0.22	
		≤1,500	0.27	
8.1.2	Out of polystyrene cellular plastic particles	15	0.050	
8.1.3	Out of sand, gravel, split (dry)	1,800	0.70	
8.2	Tiles	cf. DIN EN 12524		
8.3	Glass			
8.4	Natural stones			
8.5	Clay building materials	600	0.17	
		800	0.25	
		1,000	0.35	
		1,200	0.47	
		1,400	0.59	
		1,800	0.91	
		2,000	1.1	

[a]NM General purpose mortar; Normal mortar.
LM21 Lightweight masonry mortar with λ&$$$; = 0.21 W/(m K).
LM36 Lightweight masonry mortar with λ&$$$; = 0.36 W/(m K).
DM Thin layer masonry mortar.

D6.7. Table 3. Thermal conductivity for thermal insulation materials according to harmonized European standards, according to Table 1, line 5 of DIN V 4108-4, or line 5 of the Table 2 above (abridged)

Line	Material	Category I		Category II	
		Nominal value λ_D	Design value λ_D	Limit value λ_{limit}	Design value λ_D
5.1	Mineral wool (MW) according to DIN EN 13162	0.03–0.035, . . . 0.05	0.036–0.042, . . . 0.06	0.029–0.0338, . . .0.048	0.03–0.035, . . . 0.05
5.2	Expanded polystyrene (EPS) according to DIN EN 13163	0.03–0.035, . . . 0.05	0.036–0.042, . . . 0.06	0.029–0.0338, . . . 0.048	0.03–0.035, . . . 0.05
5.3	Extruded polystyrene (XPS) according to DIN EN 13164	0.026–0.030, . . . 0.04	0.031–0.036, . . . 0.048	&$$$;,0.252–0.029, . . .&$$$; 0.0385	0.026–0.030, . . . 0.04
5.4	Polyurethane rigid foam according to DIN EN 13165e	0.020–0.025, . . .0.040	0.024–0.030, . . .0.048	0.0195–0.0242, . . . 0.0428	0.020–0.025, ... 0.045
5.5	Phenolic foam (PF) according to DIN EN 13166	0.020–0.025, . . . 0.045	0.024–0.03, . . . 0.054	0&$$$;,0.195–0.0242, . . .&$$$; 0.0428	0.020–0.025, . . . 0.045
5.6	Cellular glass (CG) according to DIN EN 13167	0.038–0.04, . . . 0.055	0.046–0.048, . . . 0.066	0.0366–0.0385, . . . 0.0529	0.038–0.04, . . . 0.055
5.7	Wood wool (WW) lightweight boards according to DIN EN 13168				
5.7.1	WW boards	0.060–0.065, . . . 0.10	0.072–0.078, . . . 0.12	0.0576–0.0623, . . . 0.0957	0.060–0.065, . . . 0.10
5.7.2	WW multilayer boards according to DIN EN 13168 (WW-C)				
	With EPS layer according to DIN EN 13163	0.030–0.035, . . . 0.050	0.036–0.042, . . . 0.060	0.0290–0.0338, . . . 0.0480	0.030–0.035, . . . 0.050

D6.7. Table 3. (continued)

Line	Material	Category I		Category II	
		Nominal value λ_D	Design value λ_D	Limit value λ_{limit}	Design value λ_D
	With MW core according to DIN EN 13162	0.030–0.035, . . . 0.05	0.036–0.042, . . . 0.06	0.0290–0.0338, . . . 0.048	0.030–0.035, . . . 0.05
	WW coating(s) according to DIN EN 13168	0.10–0.14	0.12–0.17	0.0957–0.1380	0.10–0.14
5.8	Expanded perlite boards according to DIN EN 13169	0.038–0.040, . . . 0.050	0.046–0.048, . . . 0.066	0.0366–0.0385, . . . 0.048	0.038–0.040, . . . 0.05
5.9	Expanded cork boards (ICB) according to DIN EN 13170	0.040–0.045, . . . 0.055	0.049–0.055, . . . 0.067	0.0385–0.0428, . . . 0.0529	0.040–0.045, . . . 0.055
5.10	Wood fiber insulation according to DIN EN 13171	0.032–0.040, . . . 0.060	0.043–0.053, . . . 0.072	0.0309–0.0385, . . . 0.0575	0.032–0.040, . . . 0.060

D6.7. Table 4. Thermal conductivity of thermal insulation material according to national standards (DIN V 4108-4, cf. Table 2)

Line	Material	Density ρ in kg/m³	Design thermal conductivity λ in W/(m · K)
1.	Cellular plastic, produced on-site		
1.1	In situ formed sprayed or dispensed rigid polyurethane foam according to DIN 18159-1 (blowing agent CO2)		
	Thermal conductivity group		
	035	(>45)	0.035
	040		0.040
1.2	In situ formed urea formaldehyde foam according to DIN 18159-2		
	Thermal conductivity group		
	035	(≥ 10)	0.035
	040		0.040
1.3	Wood fiber thermal insulation material according to DIN 68755		
	Thermal conductivity group	(110–450)	
	035		0.035
	040		0.040
	045		0.045
	050		0.050
	055		0.055
	060		0.060

3.1 Masonry

As a general rule, for masonry the design values according to DIN V 4108-4 [5] (having been determined according to DIN EN ISO 10456 [7]) or according to technical approvals (German Allgemeine bauaufsichtliche Zulassung) are applied. In this case, they are based on the moisture content at 23°C and 80% relative humidity. One has to focus on the fact that, with masonry, not only the thermal conductivity of the masonry blocks is taken into consideration in the design value but also that of the mortar and thus, of the resulting effect of thermal bridges.

Due to larger quantities of condensation water, an insufficient protection against driving rain, ground water, and such-like, the moisture content can be far higher than the equilibrium moisture content. This can lead to a negative effect on the thermal insulation of the masonry.

Figure 5 shows the evaluation of measurements on bricks having different densities at a temperature of about 20°C, according to Krischer and Rohnalter [8]. By means of Fig. 5, the influence of the moisture content onto the thermal conductivity of brick masonry can be estimated. Having evaluated the international literature, Cammerer [9] concludes a mean value determining the moisture influence on thermal conductivity of different construction materials for walls to be applied in practice (Table 6). A summing up of the influence of moisture onto the thermal conductivity of other building material as well is mentioned in Cammerer [10]. In practice, however, these fundamental dependencies are not that important as in DIN V 4108-4 [5] and the equilibrium moisture content has already

D6.7. Table 5. Design values for thermal conductivities and specific thermal capacities according to EN 12524-1 [3] for other materials

Material group or application	Density ρ kg/m³	Design thermal conductivity λ W/(mK)	Specific heat capacity c_P J/(kg K)
Asphalt and Bitumen	2,100	0.70	1,000
Pure	1,050	0.17	1,000
Felt/ sheet	1,100	0.23	1,000
Concrete			
Medium density	1,800	1.15	1,000
High density	2,400	2.00	1,000
Reinforced (with 2% of steel)	2,400	2.5	1,000
Floor coverings			
Rubber	1,200	0.17	1,400
Underlay, cellular rubber	270	0.10	1,400
Underlay, felt	120	0.05	1,300
Underlay, cork	<200	0.05	1,500
Carpet/textile flooring	200	0.06	1,300
Linoleum	1,200	0.17	1,400
Glass			
Soda lime glass (including float glass)	2,500	1.00	750
Quartz glass	2,200	1.40	750
Glass mosaic	2,000	1.20	750
Water			
Ice at −10°C	920	2.30	2,000
Ice at 0 °C	900	2.20	2,000
Snow, freshly fallen («30 mm)	100	0.05	2,000
Snow, soft (30–70 mm)	200	0.12	2,000
Snow, slightly compacted (70–100 mm)	300	0.23	2,000
Snow, compacted (<200 mm)	500	0.60	2,000
Metals			
Aluminum alloys	2,800	160	880
Bronze	8,700	65	380
Brass	8,400	120	380
Copper	8,900	380	380
Iron, cast	7,500	50	450
Lead	11,300	35	130
Steel	7,800	50	450
Stainless steel	7,900	17	460
Zinc	7,200	110	380
Plastics, solid			
Acrylic	1,050	0.20	1,500
Polycarbonates	1,200	0.20	1,200
Polytetrafluoroethylene	2,200	0.25	1,000
Polyvinylchloride (PVC)	1,390	0.17	900
Polymethylmethacrylate	1,180	0.18	1,500
Polyacetate	1,410	0.30	1,400
Polyamide (nylon)	1,150	0.25	1,600
Polyamide 6.6 with 25% glass fibers	1,450	0.30	1,600
Polyethylene/high density	980	0.50	1,800
Polyethylene/low density	920	0.33	2,200
Polystyrene	1,050	0.16	1,300
Polypropylene	910	0.22	1,800

D6.7. Table 5. (continued)

Material group or application	Density ρ kg/m^3	Design thermal conductivity λ W/(mK)	Specific heat capacity c_P J/(kg K)
Polypropylene with 25% glass fibers	1,200	0.25	1,800
Polyurethane	1,200	0.25	1,800
Epoxy resin	1,200	0.20	1,400
Phenolic resin	1,300	0.30	1,700
Polyester resin	1,400	0.19	1,200
Rubber			
Natural	910	0.13	1,100
Neoprene (Polychloroprene)	1,240	0.23	2,140
Butyl (isobutene),	1,200	0.24	1,400
Foam rubber	60–80	0.06	1,500
Hard rubber (Ebonite), solid	1,200	0.17	1,400
Ethylene propylene diene monomer	1,150	0.25	1,000
Sealant materials, weather stripping and thermal breaks			
Silica gel (desiccant)	720	0.13	1,000
Silicone, pure	1,200	0.35	1,000
Silicone, filled (as thermal break)	1,450	0.50	1,000
PVC with softener (PVC-P)	1,200	0.14	1,000
Gypsum			
Gypsum	600	0.18	1,000
Gypsum	900	0.30	1,000
Gypsum	1,200	0.43	1,000
Gypsum	1,500	0.56	1,000
Soils			
Clay or silt	1,200–1,800	1.5	1,670–2,500
Sand and gravel	1,700–2,200	2.0	910–1,180
Stones			
Natural, crystalline rock	2,800	3.5	1,000
Natural, sedimentary rock	2,600	2.3	1,000
Natural, sedimentary rock, light	1,500	0.85	1,000
Natural, porous e.g., lava	1,600	0.55	1,000
Basalt	2,700–3,000	3.5	1,000
Gneiss	2,400–2,700	3.5	1,000
Granite	2,500–2,700	2.8	1,000
Marble	2,800	3.5	1,000
Slate	2,000–2,800	2.2	1,000
Limestone, soft	1,800	1.1	1,000
Limestone, hard	2,200	1.7	1,000
Limestone, extra hard	2,600	2.3	1,000
Sandstone (silica)	2,600	2.3	1,000
Natural pumice	400	0.12	1,000
Artificial stone	1,750	1.3	1,000
Timber			
Spruce, pine	500	0.13	1,600
Hard wood	700	0.18	1,600
Wood-based panels			
Plywood	300	0.09	1,600
Plywood	500	0.13	1,600

D6.7. Table 5. (continued)

Material group or application	Density ρ kg/m³	Design thermal conductivity λ W/(mK)	Specific heat capacity c_P J/(kg K)
Plywood	700	0.17	1,600
Plywood	1,000	0.24	1,600
Cement-bonded particleboard	1,200	0.23	1,500
Particleboard	300	0.10	1,700
Particleboard	600	0.14	1,700
Particleboard	900	0.18	1,700
Oriented strand board	650	0.13	1,700

D6.7. Table 6. Mean values of the influence of moisture content onto their thermal conductivity according to W. F. Cammerer [10] for different types of masonry

Material	Density kg/m³	Increase of thermal conductivity in % per 1% of moisture content in volume in % of				
		1	3	5	10	20
Masonry in solid brick	1,200	21	19.5	19	17	14
	1,400	18	17.5	17	15	12.5
	1,600	16	15	14.5	13	11
	1,800	13	12.5	12	11	9
	2,000	10	9.5	9	8	6.5
Lime stone walls	1,700–1,850	—	17	12	9	—
Lightweight walls out of vertically perforated bricks	1,000–1,300	In average 15%			—	—
Horizontal coring clay brick	1,100	In average 10%			—	—
Lightweight building material such as aerated concrete and pumice construction material	500–800	—		12	10	8

been taken into consideration. Moisture contents, in practice which are higher than the equilibrium moisture content, need a testing by specialists. Recommendations concerning the then occurring thermal conductivity cannot be given offhand.

3.2 Specific Thermal Capacity

The specific thermal capacity of building materials is a relatively insignificant factor as it is only to be considered in conditions changing at short term (transient). In DIN V 4108-4 [5] these values are not indicated, as in practice only long-term mean values matter, for which near steady-state conditions apply. Only in DIN EN 12524 [3] specific thermal capacities are indicated. One recognizes that, for most of the building materials including industrially produced building materials out of clay, for mineral wool and air, the specific thermal conductivities are at about 1,000 J/(kg·K). Woods show about 1,600 J/(kg·K) and rigid foams about 1,450 J/(kg·K).

4 Bibliography

1. Krischer O (1934) Der Einfluss der Feuchtigkeit, Körnung und Temperatur auf die Wärmeleit-fähigkeit körniger Stoffe. (Die Leitfähigkeit des Erdbodens) München: Beihefte z. Ges. Ing. Reihe I, H. 33
2. Watzinger A, Kindem B, Michelsen B (1938) Untersökelser av Meddelser fra Veidirektoren Nr. 6
3. DIN EN 12524 (2000) Baustoffe und -produkte - Wärme- und feuchteschutztechnische Eigenschaften - Tabellierte Bemessungswerte, Beuth-Verlag
4. Koch, B (1950) Grundlagen des Wärmeaustausches (Stoffwerte). Dissen T. W.: Beucke
5. DIN V 4108-4 (2007) Wärmeschutz und Energieeinsparung von Gebäuden - Teil 4: Wärme- und feuchtigkeitstechnische Bemessungswerte, Beuth-Verlag
6. Achtziger J, Cammerer uJ (1984) Einfluss des Feuchtegehaltes auf die Wärmeleitfähigkeit von Bau- und Dämmstoffen. Forschungsvorhaben Nr. BIS-800183–4. Forschungsinstitut für Wärmeschutz e.V. München
7. DIN EN ISO 10456 (1999) Baustoffe und -produkte - Verfahren zur Bestimmung der wärme-schutztechnischen Nenn- und Bemessungswerte. Beuth-Verlag
8. Krischer O, Rohnalter uH (1940) Wärmeleitung und Dampfdiffusion in feuchten Gütern. VDI-Forschungsheft 402
9. Cammerer JS (1957) Der Einfluss der Feuchtigkeit auf die Wärmeleitzahl von Baustoffen nach dem derzeitigen internationalen Schrifttum. In: Cammerer JS, Schäcke uH. Feuchtigkeitsregelung, Durchfeuchtung und Wärmeleitfähigkeit bei Baustoffen und Bauteilen. Untersuchungen und Versuche im Auftrage des Bundesministers für Wohnungsbau. Wilhelm Ernst & Sohn, Berlin
10. Cammerer WF (1966) 10 Jahre Forschung im Wärmeschutz. Neue Erkenntnisse aus der Bauforschung. Erich Schmidt, Berlin, Bielefeld, München

Heat Conduction

E1 Steady-State Heat Conduction

Erich Hahne
Universität Stuttgart, Stuttgart, Germany

1 Introduction

Conduction heat transfer is the transfer of energy caused by interaction between adjacent molecules of a stagnant substance, gaseous, liquid, or solid, subject to a temperature difference between some solid boundaries, which means a difference of molecular kinetic energy. Unless they are confined to small spaces, gases and liquids tend to move when heated and transfer heat by the regime of "natural convection." Thus, heat conduction mostly occurs in solid bodies. The basic equation for the heat flow $\dot{Q}$ (rate of heat transferred) is the Fourier law of heat conduction equation (1):

$$\dot{Q} = -\lambda A \frac{\mathrm{d}T}{\mathrm{d}x}. \tag{1}$$

With λ being the thermal conductivity of the material, A the area of the body normal to the heat flow in the direction of x (one dimensional flow), and $\mathrm{d}T/\mathrm{d}x$ the temperature gradient. If there is no dependence on time, there is a steady flow i.e., steady conduction.

In the following, the temperature distribution as shown in Figs. 1 and 2 can be calculated by the given equations if the contacts between the layers are perfect i.e., there are no inhomogeneities (gaps due to roughness or enclosures) between them. These would cause a "contact resistance" with a temperature jump across the gap.

2 Temperature Distribution for Simple Geometries

Equation (1) can be applied to simple geometries such as plane walls, cylindrical, or spherical walls where the heat flow is one-dimensional. In all these cases, constant thermal conductivity is assumed.

2.1 Plane Walls

For plane and multilayered walls with surface A and n layers (Fig. 1), the Fourier equation is transformed into

$$\dot{Q} = \frac{A(T_1 - T_{n+1})}{\frac{s_1}{\lambda_1} + \frac{s_2}{\lambda_2} + \cdots + \frac{s_n}{\lambda_n}}. \tag{2}$$

The temperature distribution in any of the layers, e.g., the kth layer is

$$T = T_k - \frac{\dot{Q}}{A\,\lambda_k}(x - x_k). \tag{3}$$

(Note that $x > x_k$)

The temperature at the end of the kth layer is

$$T_{k+1} = T_k - \frac{\dot{Q}}{A\,\lambda_k} s_k, \tag{4}$$

with $x_{k+1} - x_k = s_k$.

2.2 Hollow Cylinders (Pipes)

In single- or multi-layered (e.g., insulated) pipes of length l, with n layers, (Fig. 2) the heat flow is

$$\dot{Q} = \frac{2\pi l(T_1 - T_{n+1})}{\frac{1}{\lambda_1}\ln\frac{r_2}{r_1} + \frac{1}{\lambda_2}\ln\frac{r_3}{r_2} + \cdots + \frac{1}{\lambda_n}\ln\frac{r_{n+1}}{r_n}}. \tag{5}$$

VDI-GVC (ed.), *VDI Heat Atlas*, DOI 10.1007/978-3-540-77877-6_16,

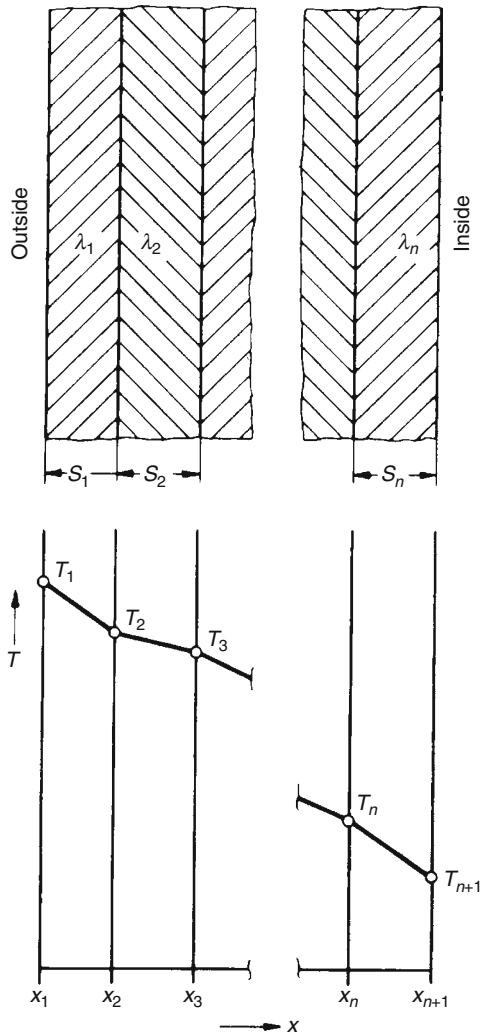

E1. Fig. 1. Temperature distribution in plane walls.

The temperature distribution in any of the layers, e.g., the kth layer is

$$T = T_k - \frac{\dot{Q}}{2\pi l \lambda_\kappa} \ln \frac{r}{r_k}. \tag{6}$$

The temperature at the end of the kth layer is

$$T_{k+1} = T_k - \frac{\dot{Q}}{2\pi l \lambda_\kappa} \ln \frac{r_{k+1}}{r_k}. \tag{7}$$

2.3 Hollow Spheres (Spherical Shells)

In single- or multi-layered (n layers) spherical shells (Fig. 2) the heat flow can be obtained from Eq. (8)

$$\dot{Q} = \frac{4\pi (T_1 - T_{n+1})}{\frac{1}{\lambda_1}\left(\frac{1}{r_1} - \frac{1}{r_2}\right) + \frac{1}{\lambda_2}\left(\frac{1}{r_2} - \frac{1}{r_3}\right) + \cdots + \frac{1}{\lambda_n}\left(\frac{1}{r_n} - \frac{1}{r_{n+1}}\right)}. \tag{8}$$

The temperature distribution in any of the layers e.g., the kth layer is

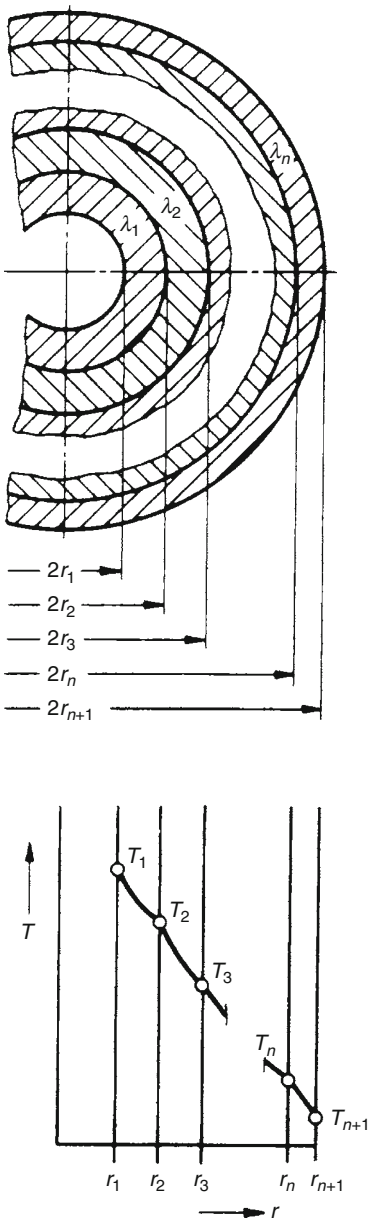

E1. Fig. 2. Temperature distribution in hollow cylinders and spheres.

$$T = T_k - \frac{\dot{Q}}{4\pi \lambda_\kappa}\left(\frac{1}{r_k} - \frac{1}{r}\right). \tag{9}$$

The temperature at the end of the kth layer is

$$T_{k+1} = T_k - \frac{\dot{Q}}{4\pi \lambda_\kappa}\left(\frac{1}{r_k} - \frac{1}{r_{k+1}}\right). \tag{10}$$

2.4 Examples

Example 1

A plane wall tempering furnace with an inside temperature of $T_1 = 1500°C$ is insulated with three layers: magnesite ($\lambda_1 = 2.9\,W/m\,K$), fireclay ($\lambda_2 = 0.8\,W/m\,K$), each 250 mm

thick, and diatomaceous earth ($\lambda_3 = 0.14\,\mathrm{W/m\,K}$) 150 mm thick (Fig. 3). The outside surface temperature was measured as $T_4 = 84°\mathrm{C}$.

What is the temperature distribution in the wall?

Since the temperature distribution is linear and perfect contact is assumed, it is enough to calculate the temperatures at the layer boundaries.

The transferred heat flux $\dot{Q}/A$ according to Eq. (2) is

$$\frac{\dot{Q}}{A} = \frac{1500 - 84}{\frac{0.25}{2.9} + \frac{0.25}{0.80} + \frac{0.15}{0.14}}\,\mathrm{W/m^2} = 963\,\mathrm{W/m^2}.$$

According to Eq. (4)

$$T_2 = \left(1500 - \frac{963}{2.9}0.25\right)°\mathrm{C} = 1417\,°\mathrm{C},$$

$$T_3 = \left(1417 - \frac{963}{0.80}0.25\right)°\mathrm{C} = 1116\,°\mathrm{C},$$

$$T_4 = \left(1116 - \frac{963}{0.14}0.15\right)°\mathrm{C} = 84\,°\mathrm{C}\text{ as given.}$$

Example 2

The outside temperature of an iron pipe with inside/outside diameter 37/40 mm is 600°C (Fig. 4). The pipe is insulated with two layers.

Layer 1: kieselguhr bricks 25 mm thick, $\lambda_1 = 0.14\,\mathrm{W/m\,K}$.

Layer 2: slag wool 45 mm thick, $\lambda_2 = 0.06\,\mathrm{W/m\,K}$

The outside surface temperature of the insulation is $T_3 = 35°\mathrm{C}$.

The temperature distribution should be calculated and drawn. According to Eq. (5) the heat flow per m length is

$$\frac{\dot{Q}}{l} = \frac{2\pi\,(600 - 35)}{\frac{1}{0.14}\ln\frac{0.09}{0.04} + \frac{1}{0.06}\ln\frac{0.18}{0.09}}\,\mathrm{W/m} = 205\,\mathrm{W/m}.$$

For the first layer, the temperature distribution is obtained according to Eq. (6)

$$T = 600°\mathrm{C} - \frac{205}{2\pi\,0.14}\ln\left(\frac{r}{0.02}\right)°\mathrm{C};\ \text{temperature distribution}$$

r in m	0.020	0.025	0.030	0.035	0.040	$0.045 = r_2$
T in °C	600	548	505	469	438	$411 = T_2$

For the second layer with $T_2 = 411°\mathrm{C}$ the temperature distribution is

$$T = 411°\mathrm{C} - \frac{205}{2\pi\,0.06}\ln\left(\frac{r}{0.045}\right)°\mathrm{C};\ \text{temperature distribution}$$

r in m	0.045	0.050	0.060	0.070	0.080	$0.090 = r_3$
T in °C	411	354	255	171	99	$35 = T_3$

3 Variable Thermal Conductivity

If the thermal conductivity depends on temperature, Eqs. (2), (5), and (8) can still be used, when the thermal conductivity between two temperatures T_k and T_{k+1} can be taken as a mean value according to Eq. (11)

$$\lambda_{k,k+1} = \frac{1}{T_k - T_{k+1}} \int_{T_{k+1}}^{T_k} \lambda\,(\Theta)\,\mathrm{d}\Theta. \qquad (11)$$

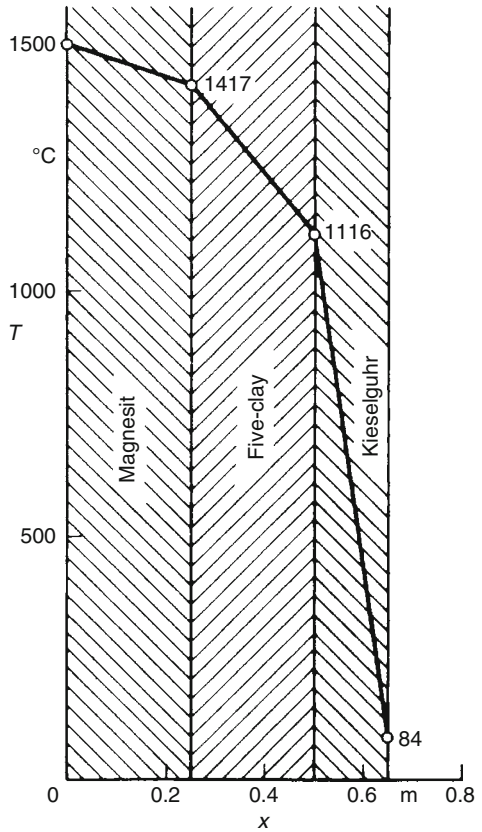

E1. Fig. 3. Temperature distribution in an insulated plane wall (example 1).

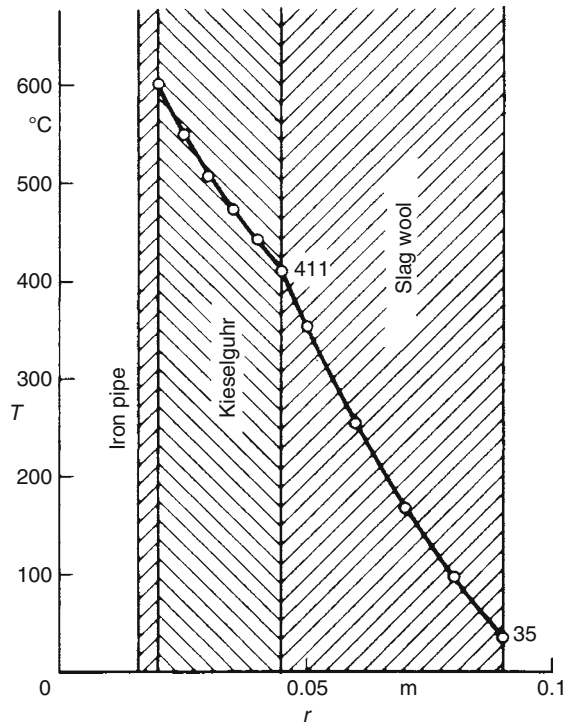

E1. Fig. 4. Temperature distribution within the insulation around an iron pipe (example 2).

In this case, the temperature distribution in a plane wall is no longer linear. If the temperature dependence of λ is linear

$$\lambda = \lambda_0 + aT. \tag{12}$$

Eq. (11) becomes

$$\lambda_{k,k+1} = \lambda_0 + a\frac{T_k + T_{k+1}}{2}. \tag{13}$$

This means in order to obtain the mean thermal conductivity of a layer, the arithmetic mean of the boundary temperatures has to be introduced.

The equation for the temperature distribution usually cannot be solved for T.

For an arbitrary temperature dependence of thermal conductivity one obtains for plane walls

$$x = x_k + \frac{A}{\dot{Q}}\int_{T}^{T_k} \lambda(\Theta)\,\mathrm{d}\Theta, \tag{14}$$

for hollow cylinders

$$\ln\frac{r}{r_k} = \frac{2\pi l}{\dot{Q}}\int_{T}^{T_k} \lambda(\Theta)\,\mathrm{d}\Theta, \tag{15}$$

for hollow spheres

$$\frac{1}{r} = \frac{1}{r_k} - \frac{4\pi}{\dot{Q}}\int_{T}^{T_k} \lambda(\Theta)\,\mathrm{d}\Theta. \tag{16}$$

The value Θ in these integrals is the temperature as integral variable.

Often (for metals) the temperature dependence of the thermal conductivity is linear (Eq. (13)); then the temperature distribution in a layer for any of the three aforementioned cases is

$$T = T_k - \frac{\lambda_\kappa}{a}\left(1 - \sqrt{1 - \frac{2a}{\lambda_\kappa^2}P}\right), \tag{17}$$

with λ_k being the thermal conductivity at T_k.

The heat flow per m length for the plane wall is

$$P = \frac{\dot{Q}}{A}(x - x_k), \tag{18}$$

for the hollow cylinder

$$P = \frac{\dot{Q}}{2\pi l}\ln\frac{r}{r_k}, \tag{19}$$

for the hollow sphere

$$P = \frac{\dot{Q}}{4\pi}\left(\frac{1}{r_k} - \frac{1}{r}\right). \tag{20}$$

In case that the thermal conductivity depends on location e.g., due to different moisture contents, it is often useful to integrate Eq. (1) numerically or divide the insulating layer into separate layers.

3.1 Example

Example 3

On the boundaries of a plane insulating layer, 250 mm thick, temperatures of $T_1 = 1000°C$ and $T_2 = 40°C$ were measured. The thermal conductivity of the material (kieselguhr) is $\lambda = (0.08 + 1.5 \cdot 10^{-4}/°C)$ W/m K (Fig. 5).

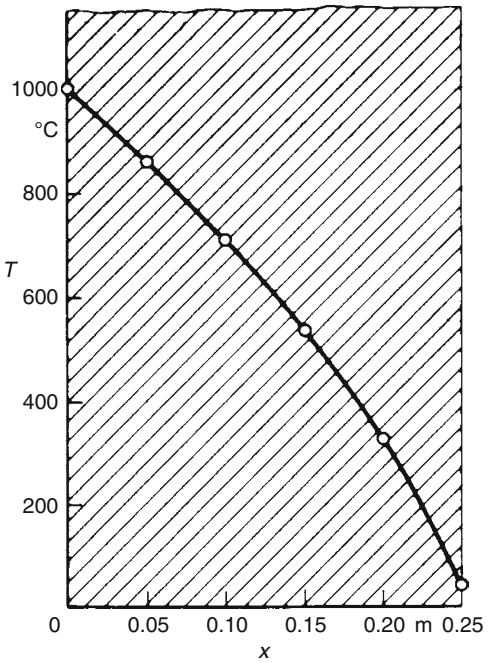

E1. Fig. 5. Temperature distribution in a plane insulating layer with variable thermal conductivity (example 3).

Calculate the heat flux (heat flow density) and the temperature distribution.

According to Eq. (13),

$$\lambda_{1000,40} = \left(0.08 + 1.5\frac{1000 + 40}{2}10^{-4}\right)\text{W/m K} = 0.158\,\text{W/m K}.$$

The heat flux according to Eq. (2) is

$$\frac{\dot{Q}}{A} = \frac{(1000 - 40)}{(0.25/0.158)}\,\text{W/m}^2 = 607\,\text{W/m}^2.$$

With Eq. (18) at $x_1 = 0$, we receive

$$P = 607 \times \text{W/m}^2$$

and with Eq. (17) and $\lambda_1 = (0.08 + 1.5 \cdot 10^{-4} \cdot 1000)$ W/m K $= 0.230$ W/m K

$$T = \left(1000 - \frac{0.230}{1.5 \cdot 10^{-4}}\left(1 - \sqrt{1 - \frac{2 \cdot 1.5 \cdot 10^{-4}}{0.230^2}607\,x}\right)\right)°\text{C},$$

$$T = \left(1000 - 1533\left(1 - \sqrt{1 - 3.44\,x}\right)\right)°\text{C}$$

x in m	0	0.05	0.10	0.15	0.20	0.25
T in °C	1000	862	709	535	324	40

This temperature distribution is shown in Fig. 5.

4 Two-Dimensional Heat Conduction [1, 2]

4.1 Introduction

The heat flow from an isothermal plane A_1 to another isothermal plane A_2 in arbitrary geometric configuration can be calculated from

$$\dot{Q} = -\lambda\int\int_{A_1}(\partial T/\partial n)_1\,\mathrm{d}A = \lambda\int\int_{A_2}(\partial T/\partial n)_2\,\mathrm{d}A_2. \tag{21}$$

Using the conduction *shape coefficient* S (given in a length m)

$$S = \frac{\iint\limits_{A_1} (\partial T/\partial n)_1 \, \mathrm{d}A_1}{T_2 - T_1} = \frac{\iint\limits_{A_2} (\partial T/\partial n)_2 \mathrm{d}A_2}{T_2 - T_1}, \qquad (22)$$

it follows

$$\dot{Q} = \lambda S(T_1 - T_2). \qquad (23)$$

If the shape coefficient is related to a characteristic length l or r, a *dimensionless shape factor* is obtained

$$S/l = S_l \text{ or } S/r = S_r.$$

And the heat flow per length is

$$\dot{Q}/l = \dot{Q}_l = \lambda S_l (T_1 - T_2). \qquad (24)$$

Shape factors for a variety of configurations are presented in Tables 1–4.

In all the figures, the heat is conducted from one isotherm to another through the hatched area only. Other boundaries are considered adiabatic. The two-dimensional configurations are assumed to be very long in depth (except the hollow spheres), so that three-dimensional end effects do not disturb.

4.2 Examples

Example 4

An airplane runway, $\delta = 20$ m wide, shall be heated to a constant temperature of $T_2 = 5°C$ when the surrounding ground surface is at $T_2 = 0°C$.

How big are conduction heat losses across the ground with $\lambda = 1$ W/m K, when on both sides along the runway the ground is covered by insulating material either (a) $b = 1$ m wide or (b) 5 m wide.

Assuming that heat losses through the insulating material and transient processes are negligible, an approximate calculation can be based on the configuration 4 in Table 1 and Fig. 6.

(a) For $b = 1$ m, we read from configuration 4 the value k and obtain for

$k^2 = [20/(2 + 20)]^2 = 0.83$ and from Fig. 6 $K'/K = 0.70$.

From configuration 4, Table 1 $S_l = 2/0.70 = 2.857$ and $\dot{Q}_l = 1 \cdot 2.857 \cdot 5$ W/m $= 14.29$ W/m.

(b) For $b = 5$ m, $k^2 = [20/(10 + 20)]^2 = 0.44$; $K/K' = 0.955$.

$S_l = 2 \cdot 0.955 = 1.910$; $\dot{Q}_l = 1 \cdot 1.910 \cdot 5 = 9.55$ W/m.

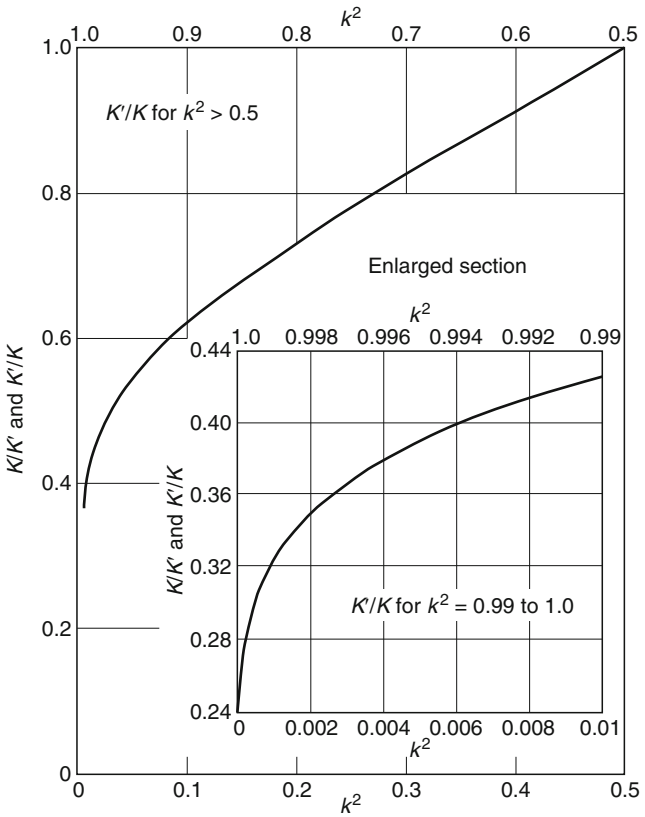

E1. Fig. 6. Relation K/K' or K'/K vs. k^2 for band-type configurations.

Example 5

A steam conduit ($r = 100$ mm) has 45 mm high fins on both sides in order to prevent the 150 mm thick insulation from sliding down. What is the shape factor of this configuration (Table 2, Nr. 7) compared to that without fins (Table 3, Nr. 1) or to the configuration Nr. 2, Table 3, when the insulating material has subsided by $e = 45$ mm? The insulation is shrouded by an isothermal metal sheet.

From Table 2, Nr. 7, we calculate $h/\delta = \frac{\ln 145/100}{\ln 250/100} = 0.45$; $2b/\delta = \frac{\pi}{\ln 50/100} = 3.429$.

From Fig. 7, we obtain $S_R = 0.1375$ (S_R is considered constant for $2b/\delta > 2.0$); for the configuration with fins we obtain $S_l = 2\,(3.429 + 0.2750) = 7.408$ (configuration 7); without fins $S_l = 2\pi/\ln(250/100) = 6.857$ (Table 3, Nr. 1); for eccentric pipes $S_l = 2\pi/\operatorname{arcosh} 1.4095 = 7.17$ (Table 3, Nr. 2).

5 Heat Losses from Walls and Pipes

5.1 Rough Estimate for Insulated Walls in Inside Rooms

An exact calculation of heat losses can be obtained from equations given in Chap. C2 together with equations for heat transfer coefficients from Part F. For the appropriate insulation thickness e.g., for containers or for an approximate determination of heat losses for hot room walls, an estimate can be obtained with Fig. 9. Here, it is assumed that the heat transfer in the container and the heat conduction through the container wall are high enough so that the respective temperature difference can be neglected. For the outside heat transfer coefficient, a mean value for natural convection (Eq. (25)) can be used:

$$\alpha_a = 1.6 \frac{\mathrm{W}}{\mathrm{m^2 K}} \sqrt[4]{\frac{T_w - T_u}{K}}, \qquad (25)$$

with T_w the outside wall temperature of the insulation, T_a the ambient temperature. The heat transfer by radiation is taken into account with the radiation number $C = 4.7$ W/(m^2 K^4), the ambient temperature with $T_a = 20°C$. Technical data of the thermal conductivity are given in Fig. 9 in parenthesis for the

E1. Table 1. Shape factors for plane walls and band-type configurations (length l; $S/l = S_l$; K/K' and K'/K according to Fig. 6)

Configuration (Nr)	Shape factor	Remarks
1 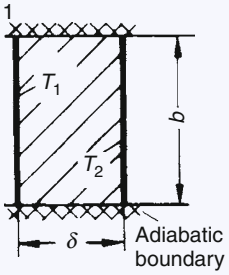	Plane wall: $S_l = b/\delta$	
2 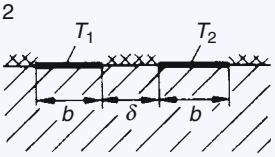	Aligned bands in a semi-infinite solid medium: $S_l = \frac{1}{2}K'/K$	$k = \delta/(2b + \delta)$
3 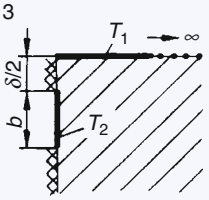	Band perpendicular to an isothermal boundary: $S_l = K'/K$	$k = \delta/(2b + \delta)$
4 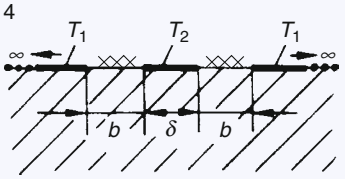	Band aligned between isothermal boundaries: $S_l = 2K/K'$	$k = \delta/(2b + \delta)$
5 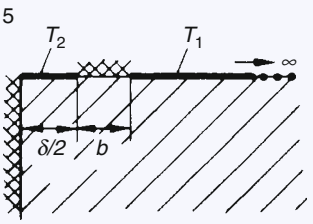	Band aligned to an isothermal boundary: $S_l = K/K'$	$k = \delta/(2b + \delta)$
6 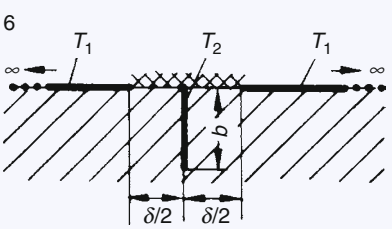	Band perpendicular between isothermal boundaries: $S_l = 2K/K'$	$k = \frac{1}{\sqrt{1 + (\delta/2b)^2}}$
7 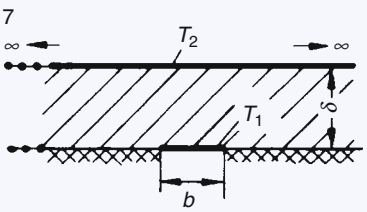	Band parallel to an isothermal boundary: $S_l = 2K'/K$	$k = \frac{1}{\cosh\left(\frac{\pi b}{4\delta}\right)}$

E1. Table 1. (continued)

Configuration (Nr)	Shape factor	Remarks
8 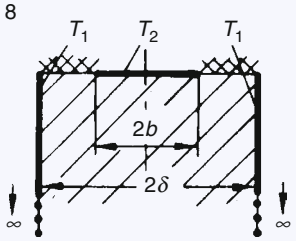	Band between perpendicular isothermal boundaries: $S_I = 2K'/K$	$k = \cos\left(\frac{\pi b}{2\delta}\right)$
9 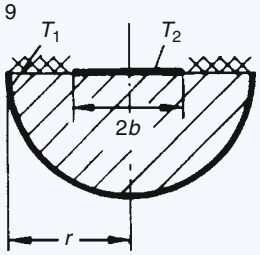	Band on a semicircular boundary: $S_I = 2K'/K$	$k = \frac{1-(b/r)^2}{1+(b/r)^2}$
10 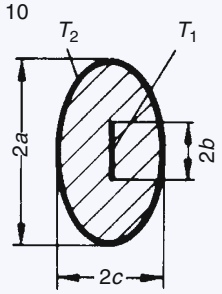	Band confocal in an elliptic tube: $S_I = \frac{2\pi}{\ln\frac{a+c}{b}}$	$b = \sqrt{a^2 - c^2}$

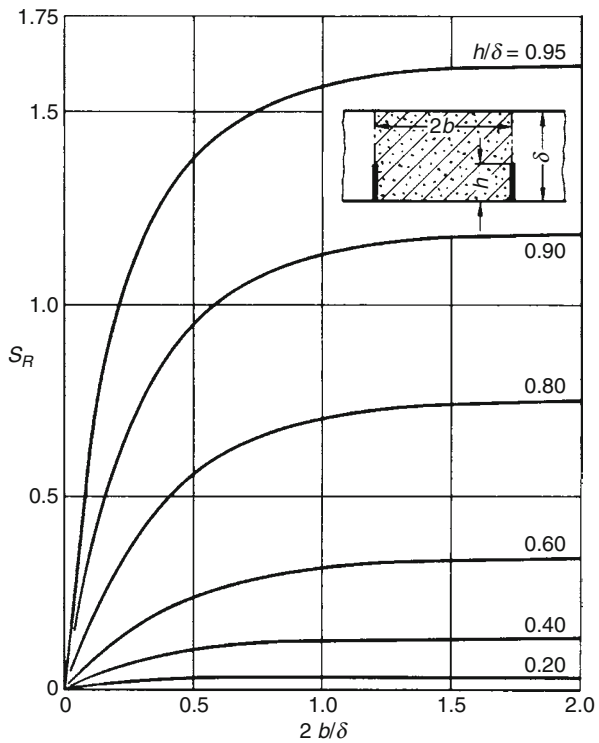

E1. Fig. 7. Fin factor S_R for a plane wall with inside fins on one side vs. the ratio $2b/\delta$ depending on h/δ.

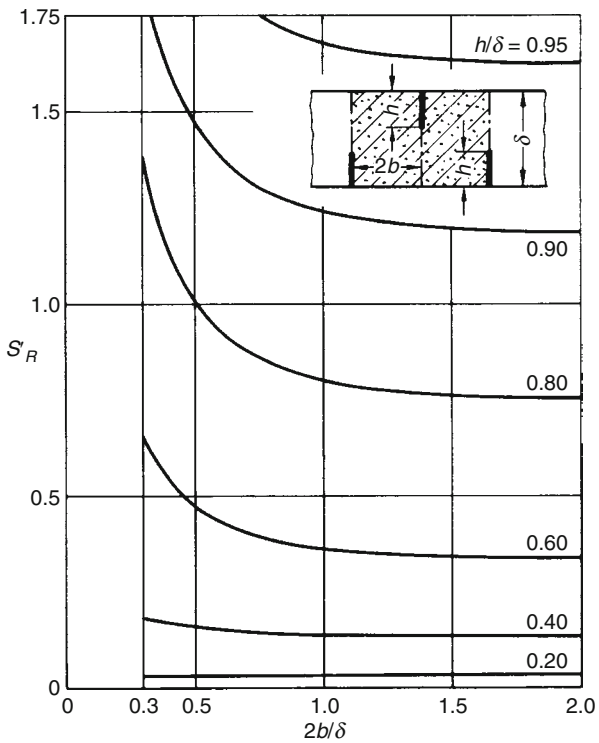

E1. Fig. 8. Fin factor S'_R for a plane wall with inside fins arranged alternately vs. the ratio $2b/\delta$ depending on h/δ.

E1. Table 2. Shape factors for straight isothermal fins (length l; $S/l = S_l$; S_R and S'_R according to Figs. 7 and 8) [2, 4]

Configuration (Nr)	Shape factor
1 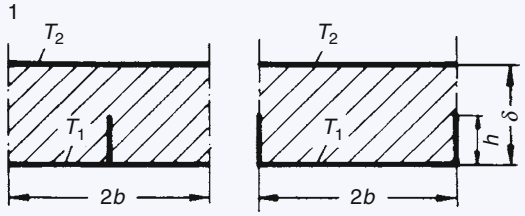	$S_l = \frac{2b}{\delta} + 2S_R$
2 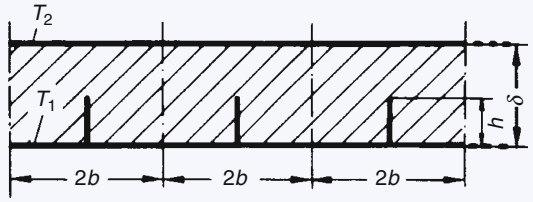	$S_{l,\text{ges}} = \Sigma S_l = n\left(\frac{2b}{\delta} + 2S_R\right)$ n number of fins
3 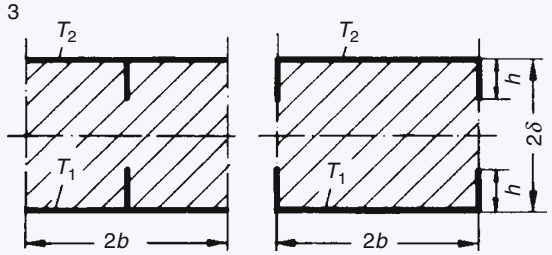	$S_l = \frac{b}{\delta} + S_R$
4 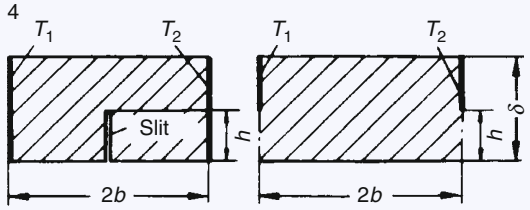	$S_l = \frac{1}{2b/\delta + 2S_R}$
5 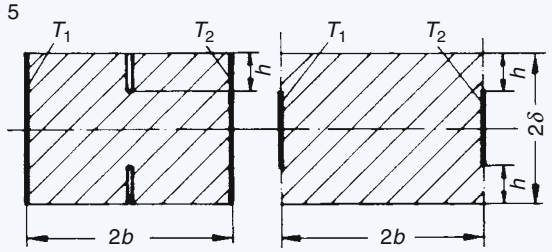	$S_l = \frac{1}{b/\delta + S_R}$
6 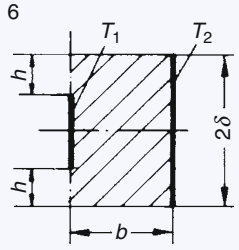	$S_l = \frac{2}{b/\delta + S_R}$

E1. Table 2. (continued)

Configuration (Nr)	Shape factor
7 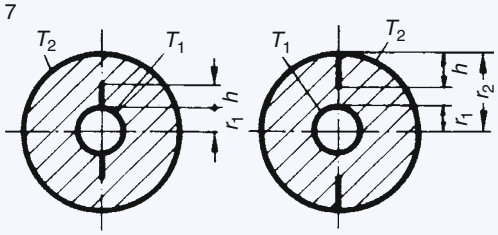	$S_l = n\left(\frac{2\pi/n}{\ln(r_2/r_1)} + 2S_R\right)$: $2b/\delta = \frac{2\pi/n}{\ln(r_2/r_1)}, h/\delta = \frac{\ln(r_1+h)/r_1}{\ln(r_2/r_1)}$ n number of fins
8 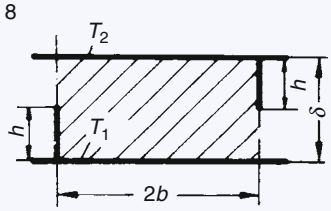	$S_l = \frac{2b}{\delta} + 2S'_R$
9 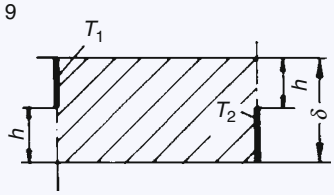	$S_l = \frac{1}{2b/\delta + 2S'_R}$
10 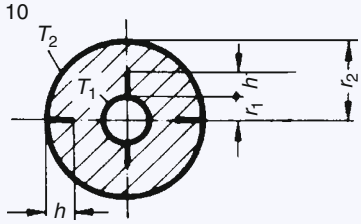	$S_l = \frac{2\pi}{\ln(r_2/r_1)} + 8S'_R$ $2b/\delta = \frac{\pi/2}{\ln(r_2/r_1)}, h/\delta = \frac{\ln(r_1+h)/r_1}{\ln(r_2/r_1)}$

E1. Table 3. Shape factors for pipes, pipe arrangements and wires (length l; $S/l = S_l$) [3, 4, 5]

Configuration (Nr)	Shape factor	Remarks
1 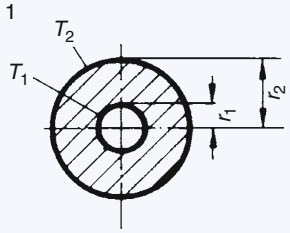	Concentric pipes: $S_l = 2\pi / \ln\frac{r_2}{r_1}$	
2 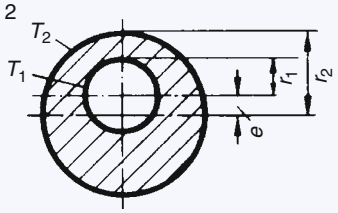	Excentric pipes: $S_l = \frac{2\pi}{\operatorname{arcosh}\frac{r_1^2 + r_2^2 - e^2}{2r_1 r_2}}$	$\operatorname{arcosh}\ u = \ln\left(u \pm \sqrt{u^2 - 1}\right)$

E1. Table 3. (continued)

Configuration (Nr)	Shape factor	Remarks
3 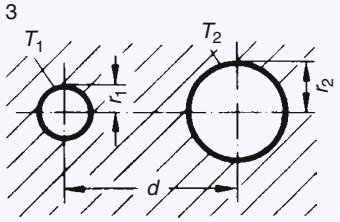	Pipes in extended medium: $S_l = \dfrac{2\pi}{\operatorname{arcosh}\dfrac{d^2 - r_1^2 - r_2^2}{2r_1 r_2}}$	
4 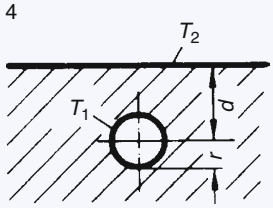	Pipe in the ground: $S_l = \dfrac{2\pi}{\operatorname{arcosh}(d/r)}$ $S_l = \dfrac{2\pi}{\ln(2d/r)}$	fur $d/r > 5$
5 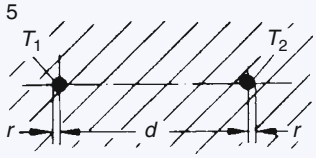	Wires in extended medium: $S_l = \dfrac{\pi}{\ln(d/r)}$	$d/r > 10$
6 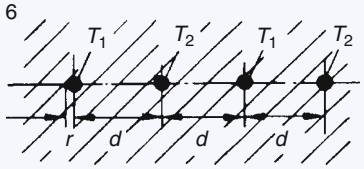	Wires of alternating different temperatures in extended medium: $S_l = \dfrac{2\pi}{\ln\dfrac{2d}{\pi r}}$	$r < d$
7 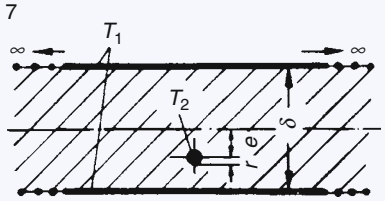	Wire excentric in a large plate: $S_l = \dfrac{2\pi}{\ln\cot\dfrac{\pi(e+\delta/2)}{2\delta} + \ln\dfrac{2\delta}{\pi r}}$	$r < \delta$
8 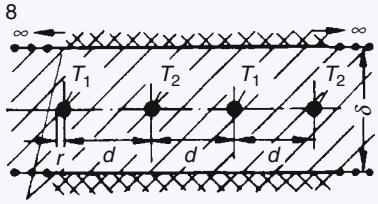 Adiabatic boundary	Wires of alternating different temperatures in a plate: $S_l = \dfrac{2\pi}{\dfrac{2\pi d}{\delta} + \ln\dfrac{\delta}{2\pi r}}$	$r < d, \delta$
9 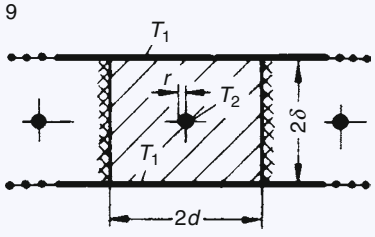	Wire in a piece of plane wall: $S_l = \dfrac{2\pi}{\dfrac{\pi\delta}{2d} + \ln\dfrac{d}{\pi r}}$	$r < d, \delta$

E1. Table 3. (continued)

Configuration (Nr)	Shape factor	Remarks
10 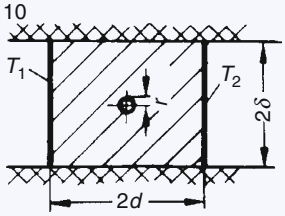 	Hole in a piece of a plane wall: $S_I = \frac{1}{2\pi}\left(\frac{\pi\delta}{2d} + \ln\frac{d}{\pi r}\right)$	$r < d, \delta$
11 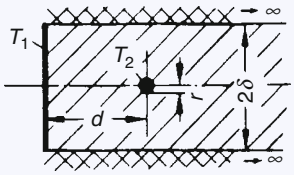 	Wire in a semi-infinite piece of a wall: $S_I = \frac{2\pi}{\frac{\pi d}{\delta} + \ln\frac{\delta}{\pi r}}$	$r < d, \delta$
12 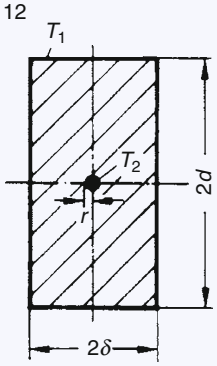 	Wire in the axis of a rectangular rod: $S_I = \frac{2\pi}{\ln\frac{4\delta}{\pi r} - C}$	$\delta/r \geq 10$ d/δ | C 1.00 | 0.1658 1.25 | 0.0793 1.50 | 0.0356 2.00 | 0.0075 2.50 | 0.0016 3.00 | 0.0003 ∞ | 0
13 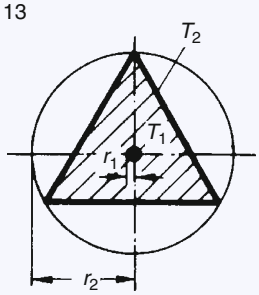 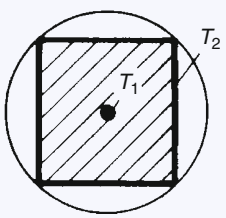 	Wire in the axis of an equilateral polygonal rod: $S_I = \frac{2\pi}{\ln r_2/r_1 - C}$	$r_2/r_1 > 10$ n number of corners n | C 3 | 0.5696 4 | 0.2708 5 | 0.1606 6 | 0.1067 8 | 0.0570 10 | 0.0354 ∞ | 0 for $n \rightarrow \infty$ see table 3, Nr.1
14 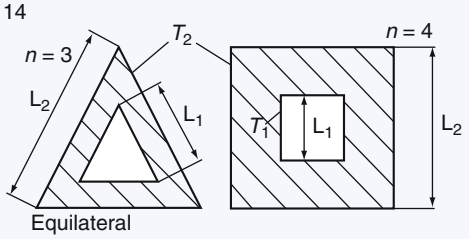 	Concentric polygonal pipes $S_I = n\left[\frac{2\cot(\pi\alpha)}{\ln(1/y)} \cdot \frac{1}{y + (1-y)/[\sin(\pi\alpha)]^q}\right]$ $\alpha = \frac{1}{2} - \frac{1}{n}$ *n number of polygon sides* $y = L_1/L_2$ $q = \frac{1}{1 - 0.75\ln(2\alpha)}$	$n = 3, 4, \ldots$ to ∞, (∞ see also table 3, fig 1) Lit [6]

E1. Table 3. (continued)

Configuration (Nr)	Shape factor	Remarks
15 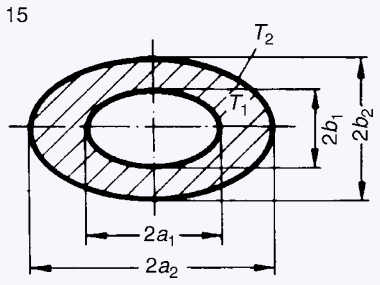	Confocal elliptic pipes $S_l = \dfrac{2\pi}{\ln \dfrac{a_2 + b_2}{a_1 + b_1}}$	$a_1^2 - b_1^2 = a_2^2 - b_2^2$

E1. Table 4. Shape factors for hollow spheres, sphere arrangements and disc-type configuration (radius r; S/r = S_r) [3]

Configuration (Nr)	Shape factor	Remarks
1 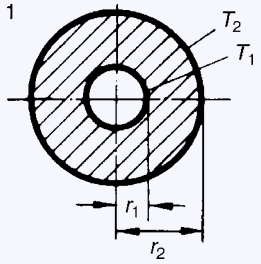	Hollow sphere $S_r = \dfrac{4\pi}{(r/r_1) - 1}$	$r_2 = r$
2 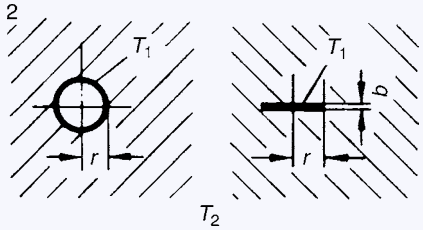	In extended medium: Single sphere $S_r = 4\pi$ Circular disc $S_r = 8$	T_2 very far away $b/r \approx 0$
3 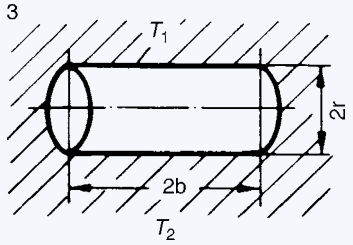	Cylindric stub: $S_r = S_r(b/r)$	b/r | S_r 0 | 8 0.25 | 10.42 0.5 | 12.11 1.0 | 14.97 2.0 | 19.97 4.0 | 27.84 T_2 far away
4 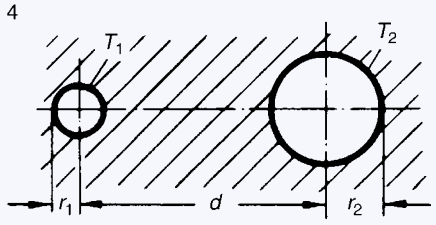	Spheres of different size: $S_r = \dfrac{4\pi}{\dfrac{r}{r_1} + \left[1 - \dfrac{(r/d)^4}{1 - (r/d)^2}\right] - \dfrac{2r}{d}}$	$r_2 = r$ $d/r \geq 5$

E1. Table 4. (continued)

Configuration (Nr)	Shape factor	Remarks
5 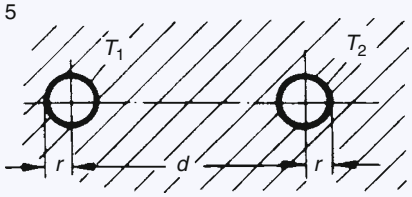	Spheres of equal size (large distance): $S_r = \frac{4\pi}{2(1 - r/d)}$	$d/r \geq 5$
6 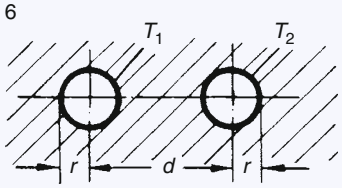	Spheres of equal size (small distance): $S_r = \frac{4\pi}{2}\left[1 + \frac{r}{d} + \left(\frac{r}{d}\right)^2 + \left(\frac{r}{d}\right)^3 + 2\left(\frac{r}{d}\right)^4 + 3\left(\frac{r}{d}\right)^5 + \ldots\right]$	$2 < \frac{d}{r} < 5$
7 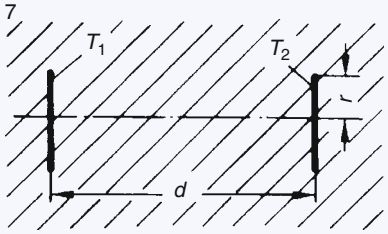	Parallel circular discs: $S_r = \frac{4\pi}{2\left[\frac{\pi}{2} - \arctan r/d\right]}$	$\frac{d}{r} \geq 5$
8 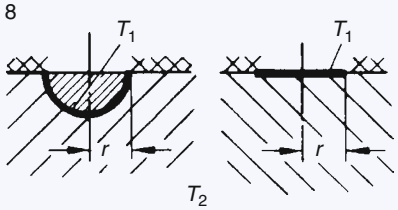	On top of a semi-infinite medium: Hemisphere $S_r = 2\pi$ Circular disc $S_r = 4$	T_2 very far away
9 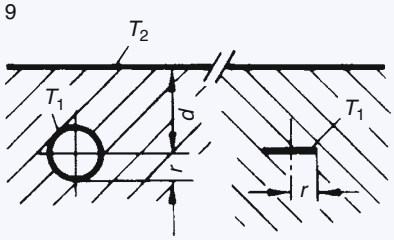	In semi-infinite medium: Sphere $S_r = \frac{4\pi}{1 - r/2d}$ Circular disc $S_r = \frac{4\pi}{\pi/2 - \arctan r/2d}$	$d/r > 2$
10 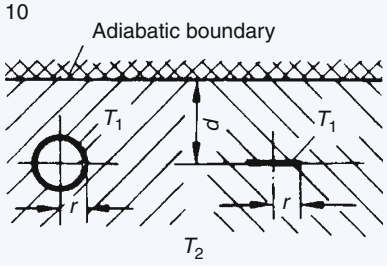	In semi-infinite medium with adiabatic top: Sphere $S_r = \frac{4\pi}{1 + r/2d}$ circular disc $S_r = \frac{4\pi}{\frac{\pi}{2} + \arctan\frac{r}{2d}}$	$d/r > 2$ T_2 very far away

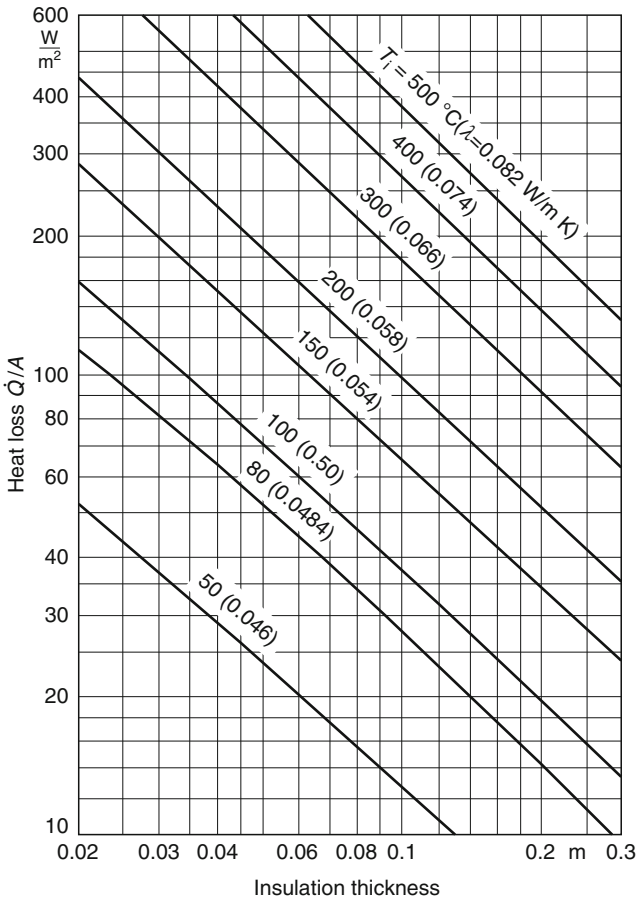

E1. Fig. 9. Heat loss of insulated outside walls vs. insulation thickness.

respective temperature region. The arithmetic mean of the surface temperatures is taken as reference temperature. Data of Fig. 9 are quite precise for thick insulations, for thin insulations larger deviations can occur due to inaccuracies of Eq. (25).

5.2 Heat Losses from Insulated Pipes

The exact calculation of such heat losses is performed with the equation for concentric multilayered pipes (Chaps. C2 and E1 in Sect. 2.2).

For a pipe 1 with two insulating layers, 2 and 3, as shown in Fig. 10, this equation is

$$\frac{\dot{Q}}{l} = \frac{\pi(T_\mathrm{i} - T_\mathrm{a})}{\frac{1}{\alpha_1 d_1} + \frac{1}{2\lambda_1}\ln\frac{d_2}{d_1} + \frac{1}{2\lambda_2}\ln\frac{d_3}{d_2} + \frac{1}{2\lambda_3}\ln\frac{d_4}{d_3} + \frac{1}{\alpha_3 d_4}}. \qquad (26)$$

The heat transfer coefficient α_i is calculated according to Chap. G1, the heat transfer coefficient α_a in stagnant air according to Part F and in moving air by Chap. G2. If relevant, radiation can be accounted for according to Chap. K1. Data for thermal conductivity are taken for a mean state of each insulating layer, e.g., the arithmetic mean of the bordering temperatures and the mean moisture content. For an anticipated strong temperature- or moisture drop/increase, it is recommended to subdivide the insulating layers and use graded thermal conductivities.

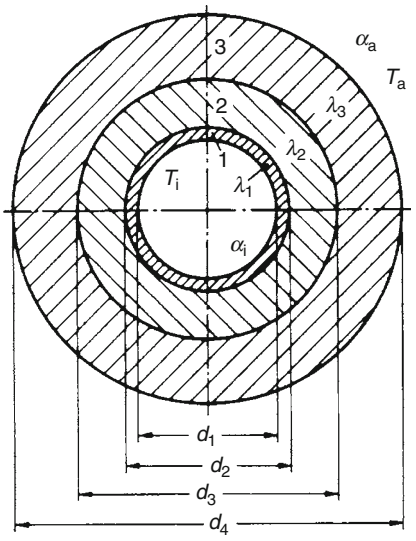

E1. Fig. 10. Cross section of a pipe (1) with two insulation layers (2,3) according to equ. (26).

5.3 Graphical Determination of Heat- and Cold-Losses in Stagnant Surrounding Air

The nomogram Fig. 11 can be used for a fast determination of such losses. The heat transfer coefficient on the outside layer can be obtained from the approximation

$$\alpha_\mathrm{a} = 8\frac{\mathrm{W}}{\mathrm{m^2K}} + 0.04\frac{\mathrm{W}}{\mathrm{m^2K^2}}\Delta T, \qquad (27)$$

with ΔT being the (positive) difference between wall and surrounding temperatures; Eq. (27) includes radiation and natural convection. It gives satisfactory results within $5\ \mathrm{K} \le \Delta T \le 100\ \mathrm{K}$ and $0.05\ \mathrm{m} \le d_{n+1} \le 1\ \mathrm{m}$ with d_{n+1} as outer diameter of the insulation. This equation provides a mean value of the theoretically calculated heat transfer coefficients for the given range [7]. An auxiliary value D is introduced in the nomogram that allows for all heat flow resistances except the outside heat transfer

$$D = d_{n+1}\left(\frac{1}{\alpha_1 d_1} + \frac{1}{2\lambda_2}\ln\frac{d_2}{d_1} + \frac{1}{2\lambda_2}\ln\frac{d_3}{d_2} + \cdots + \frac{1}{2\lambda_n}\ln\frac{d_{n+1}}{d_n}\right). \qquad (28)$$

As temperature difference, the positive difference between the inner temperature T_i and the ambient temperature T_a has to be taken.

5.3.1 Examples

Example 6

How big is the heat loss for a pipe 10 m long, inner/outer diameter 100/108 mm, insulation thickness 50 mm, with thermal conductivity 0.12 W/m K, ambient temperature 10°C; the pipe carries saturated steam of 120°C.

Neglecting the thermal resistance within the pipe and the wall, one obtains from Eq. (28)

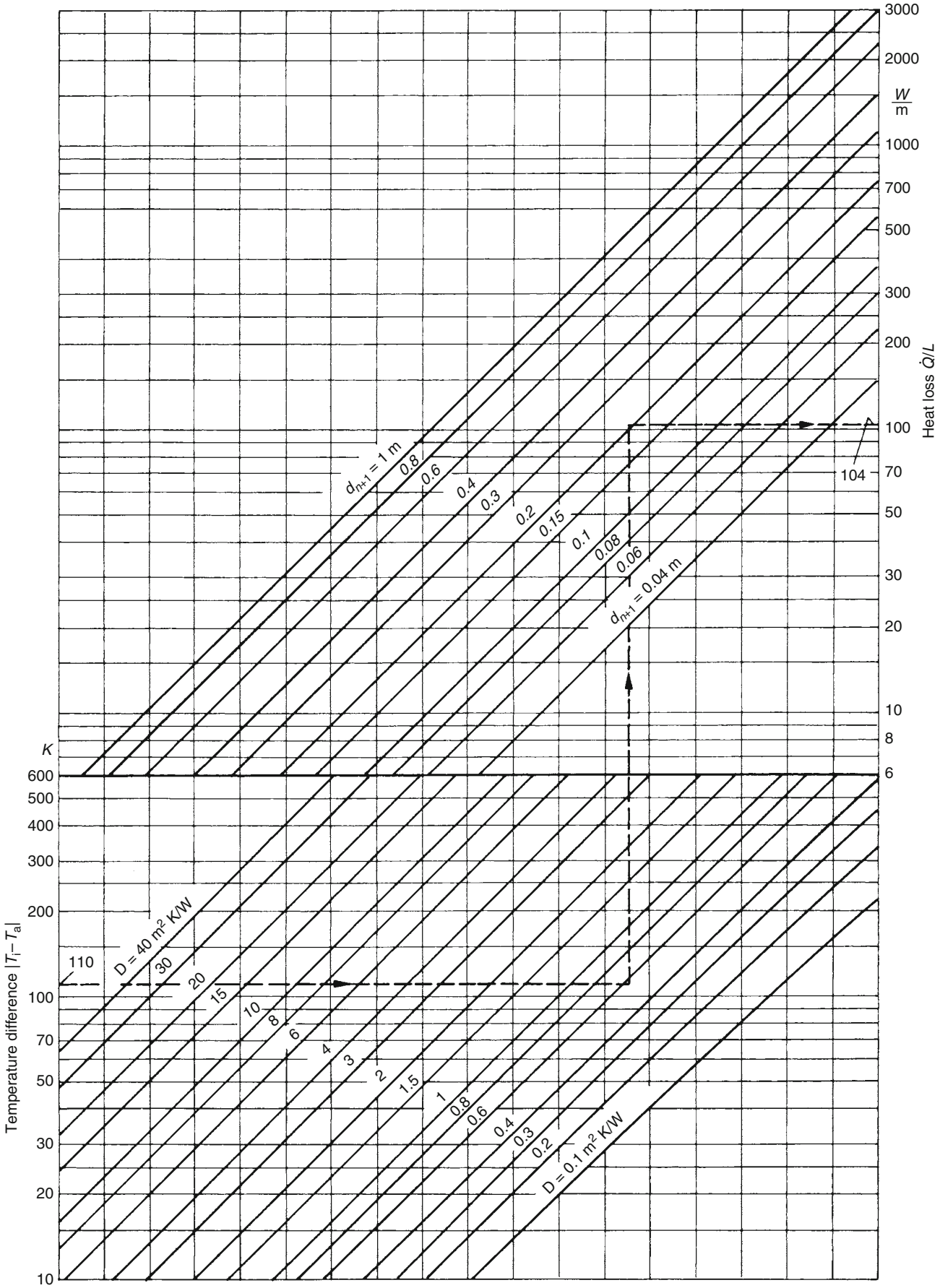

E1. Fig. 11. Nomogram for approximate determination of heat- and cold-losses of insulated pipes.

$$D = 0.208\left(\frac{1}{2 \cdot 0.12}\ln\frac{0.208}{0.108}\right)\frac{\mathrm{m^2K}}{\mathrm{W}} = 0.57\ \frac{\mathrm{m^2K}}{\mathrm{W}}.$$

As shown in the nomogram (Fig. 11, along the sketched line) starting at $T_i - T_a = 110$ K to $D = 0.57$ and $d_{n+1} = 0.208$ m gives $\dot{Q}/l = 104$ W/m heat loss per m and in total $\dot{Q} = 104$ W/m · 10 m = 1040 W.

Example 7

A pipe 200/216 mm inner/outer diameter is insulated with two layers, each 50 mm thick. The thermal conductivity of the inner layer is 0.14 W/m K, of the outer 0.07 W/m K. Gas of 500°C flows inside the pipe, the inside heat transfer coefficient is 60 W/m^2 K. The ambient air temperature is 20°C.

What is the heat loss per m length?

$$D = 0.416\left(\frac{1}{60 \cdot 0.216} + \frac{1}{2 \cdot 0.14}\ln\frac{0.316}{0.216} + \frac{1}{2 \cdot 0.07}\ln\frac{0.416}{0.316}\right)$$
$$= 1.41\ \frac{\mathrm{m^2K}}{\mathrm{W}}.$$

From the nomogram (Fig. 11), we obtain with $T_i - T_a = 480$ K and $d_{n+1} = 0.416$ the heat loss $Q/l = 405$ W/m.

5.4 Heat Losses with Wind

For moving air, the heat resistance on the outside is $1/\alpha_a$. This is given in Fig. 12 for various wind speeds and various outside diameters of the insulation, d_{n+1}. This figure also presents the wind forces according to the *Beaufort*-scale for the various ranges of wind speed. The heat transfer coefficient α_a can be calculated from relations for pipes in cross-flow [8], considering a mean heat transfer coefficient for radiation of 5 W/m^2 K.

The heat loss can be obtained from Eq. (26).

If the defined value D (Eq. (28)) is already known, it is easier to obtain the loss from

$$\frac{\dot{Q}}{l} = \frac{d_{n+1}\pi(T_i - T_a)}{D + 1/\alpha_a}. \tag{29}$$

5.4.1 Example

Example 8

The pipe of Example 6 is exposed to wind (w = 10 m/s). From Fig. 12, we obtain for w = 10 m/s and d_{n+1} = 0.208 m, $1/\alpha_a = 0.021$ m^{2}K/W and from Eq. (29)

$$\frac{\dot{Q}}{l} = \frac{0.208\pi 110}{0.57 + 0.021}\ \mathrm{W/m} = 122\ \mathrm{W/m},$$

$$\dot{Q} = 122\ \mathrm{W/m} \cdot 10\ \mathrm{m} = 1220\ \mathrm{W}.$$

5.5 Heat Losses of Pipes Inside Walls

A picture and symbols of such an arrangement are given in Fig. 13.With these data (according to [9]) Fig. 14 can be used to determine the losses (note that Fig. 13 assumes an isothermal wall, T_{a1}).The temperature difference ΔT accounts for possible different temperatures, T_{a1} and T_{a2} on either side of the wall:

$$\Delta T = T_i - T_{a1} + B(T_{a1} - T_{a2}). \tag{30}$$

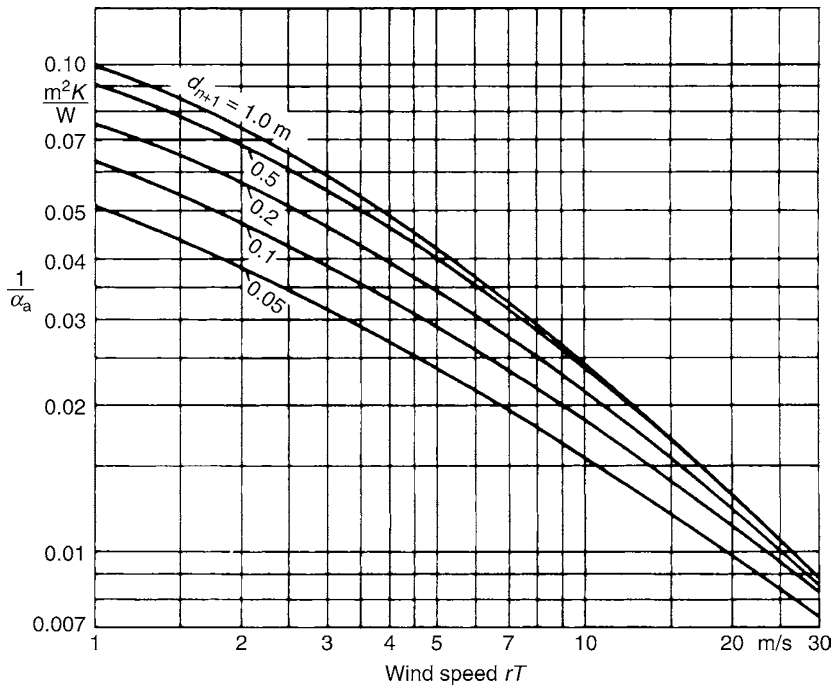

E1. Fig. 12. Determination of heat losses with wind: heat resistence vs. wind speed.

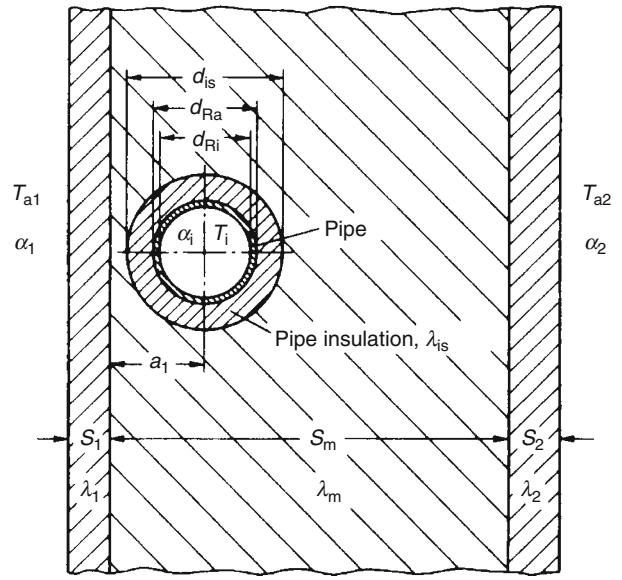

E1. Fig. 13. Pipe in a wall.

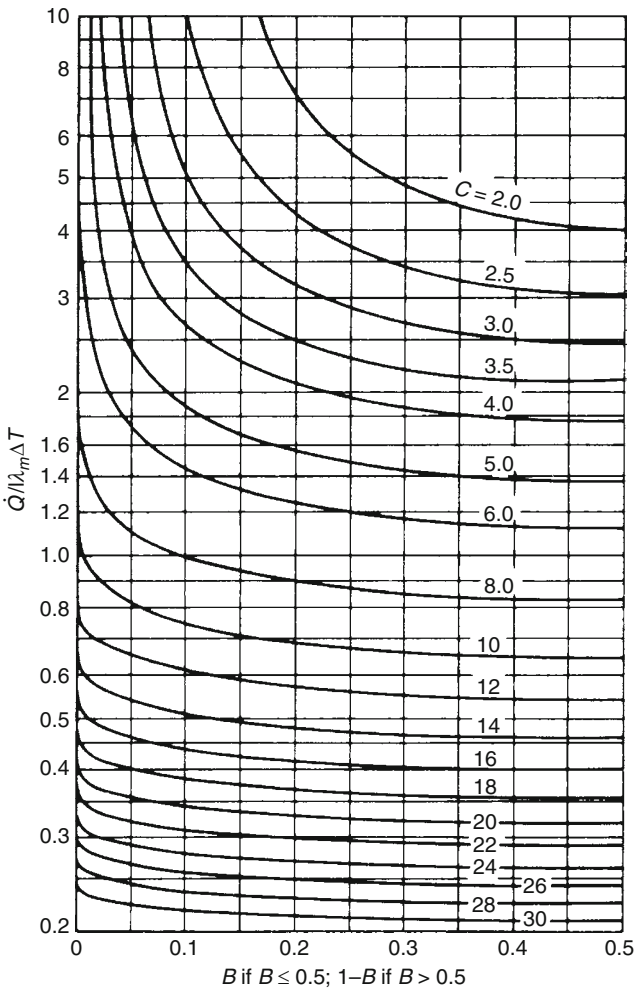

E1. Fig. 14. Determination of heat-and cold-losses for pipes in walls according to [9].

The auxiliary values B and C have to be calculated from

$$B = \frac{\frac{1}{\alpha_1} + \frac{s_1}{\lambda_1} + \frac{a_1}{\lambda_m}}{\frac{1}{\alpha_1} + \frac{s_1}{\lambda_1} + \frac{s_m}{\lambda_m} + \frac{s_2}{\lambda_2} + \frac{1}{\alpha_2}} \tag{31}$$

and

$$C = \frac{2\lambda_m}{\alpha_1 d_{Ri}} + \frac{\lambda_m}{\lambda_{ik}} \ln \frac{d_{is}}{d_{Ra}} + \ln\left[\frac{2\lambda_m}{d_{is}}\left(\frac{1}{\alpha_1} + \frac{s_1}{\lambda_1} + \frac{s_m}{\lambda_m} + \frac{s_2}{\lambda_2} + \frac{1}{\alpha_2}\right)\right]. \tag{32}$$

A temperature drop within the metallic pipe wall is neglected.

The data in Fig. 14 are based on the following equations [9]

$$\frac{\dot{Q}}{l\lambda_m \Delta T} = \frac{2\pi}{\ln(K + \sqrt{K^2 - 1})} \tag{33}$$

with

$$K = \frac{1}{\pi} e^C \left(1 + \frac{\pi^2}{4} e^{-2C}\right) \sin(\pi B). \tag{34}$$

For very thick walls or a pipe in the ground, the value B greatly reduces and the value C greatly increases. Then Eq. (34) becomes according to [10]

$$K = \frac{2\lambda_m}{d_{is}}\left(\frac{1}{\alpha_1} + \frac{s_1}{\lambda_1} + \frac{a_1}{\lambda_m}\right)\left(\frac{d_{is}}{d_{Ra}}\right)^{\lambda_m/\lambda_{is}} \exp\left(\frac{2\lambda_m}{\alpha_i d_{Ri}}\right). \tag{35}$$

5.5.1 Example

Example 9 (According to [11])
A heating pipe, outer diameter 21.3 mm, inside a ceiling, is surrounded by a 6 mm insulating layer. The ceiling is 160 mm thick, including a floor cover of 5 mm. The pipe axis is 35 mm distant from the lower side of the ceiling. Water of 80°C flows inside the pipe. The various conductivities are pipe insulation 0.04 W/m K, ceiling 2.0 W/m K, and floor cover 0.20 W/m K. The heat transfer coefficient from the ceiling top side is 12 W/m^{2}K, from the lower side 8 W/m^{2}K. The respective room temperatures are 18°C in the upper room and 22°C in the lower. How big is the heat loss per m pipe length?

According to Eq. (31)

$$B = \frac{\frac{1}{8} + 0 + \frac{0.035}{2.0}}{\frac{1}{8} + 0 + \frac{0.155}{2.0} + \frac{0.005}{0.20} + \frac{1}{12}} = 0.460$$

and Eq. (30)

$$\Delta T = 80\ \text{K} - 22\ \text{K} + 0.460(22 - 18)\ \text{K} = 59.8\ \text{K}.$$

According to Eq. (32) when the heat transfer resistances of the flowing water and the pipe wall are neglected,

$$C = 0 + \frac{2.0}{0.040} \ln \frac{33.3}{21.6} + \ln\left[\frac{2 \cdot 2.0}{0.0333}\left(\frac{1}{8} + 0 + \frac{0.155}{2.0} + \frac{0.005}{0.20} + \frac{1}{12}\right)\right] = 25.3.$$

E1. Table 5. Additions for valves and slide valves

kind of insulation		Inner diameter of pipe (mm)	Eqivalent length of the uninsulated pipe in m. at a pipe temperature of	
			100°C	400°C
inside rooms	stripped	100	6	16
		500	9	26
	1/4 stripped	100	2.5	5
	3/4 insulated	500	3	7.5
	1/3 stripped	100	3	6
	2/3 insulated	500	4	10
outside rooms	stripped	100	15	22
		500	19	32
	1/4 stripped	100	4.5	6
	3/4 insulated	500	6	8.5
	1/3 stripped	100	6	8
	2/3 insulated	500	7	11

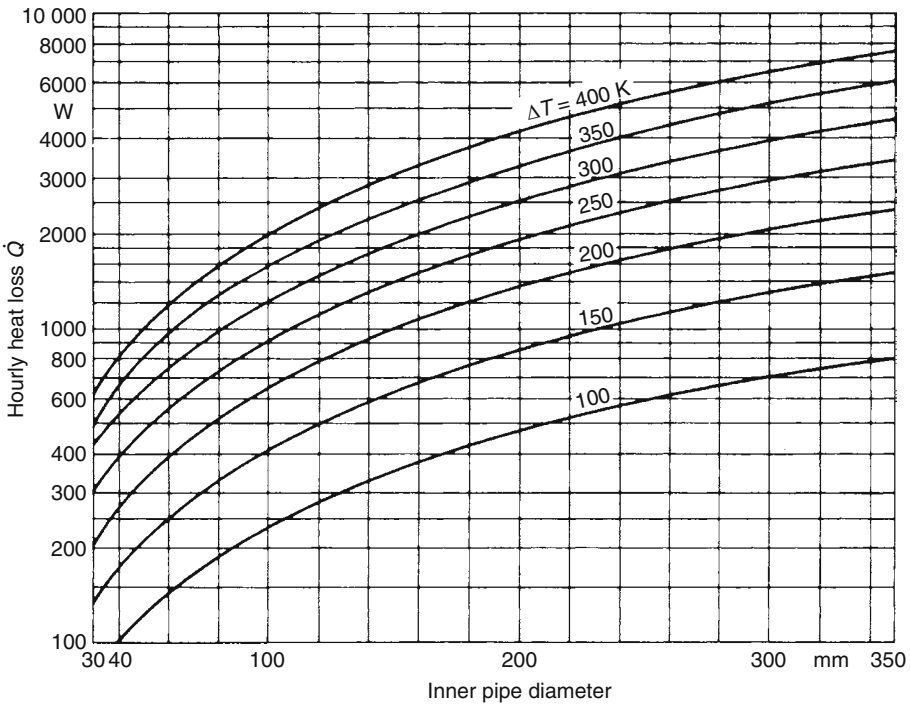

E1. Fig. 15. Determination of hourly heat losses of stripped flanges according to [12].

With B and C we obtain from Fig. 14 or from Eqs. (33) and (34)

$$\frac{\dot{Q}}{l\lambda_m \Delta T} = 0.25.$$

The heat loss per length is

$$\frac{\dot{Q}}{l} = 0.25 \cdot 2.0 \cdot 59.8 \text{ W/m} = 30 \text{ W/m}.$$

5.6 Additional Heat Losses of Insulated Pipes

Additional heat losses originate from flanges, valves, pipe suspensions, manifolds, and other auxiliary devices. A determination of such losses is inexact; the following data should only be considered estimates.

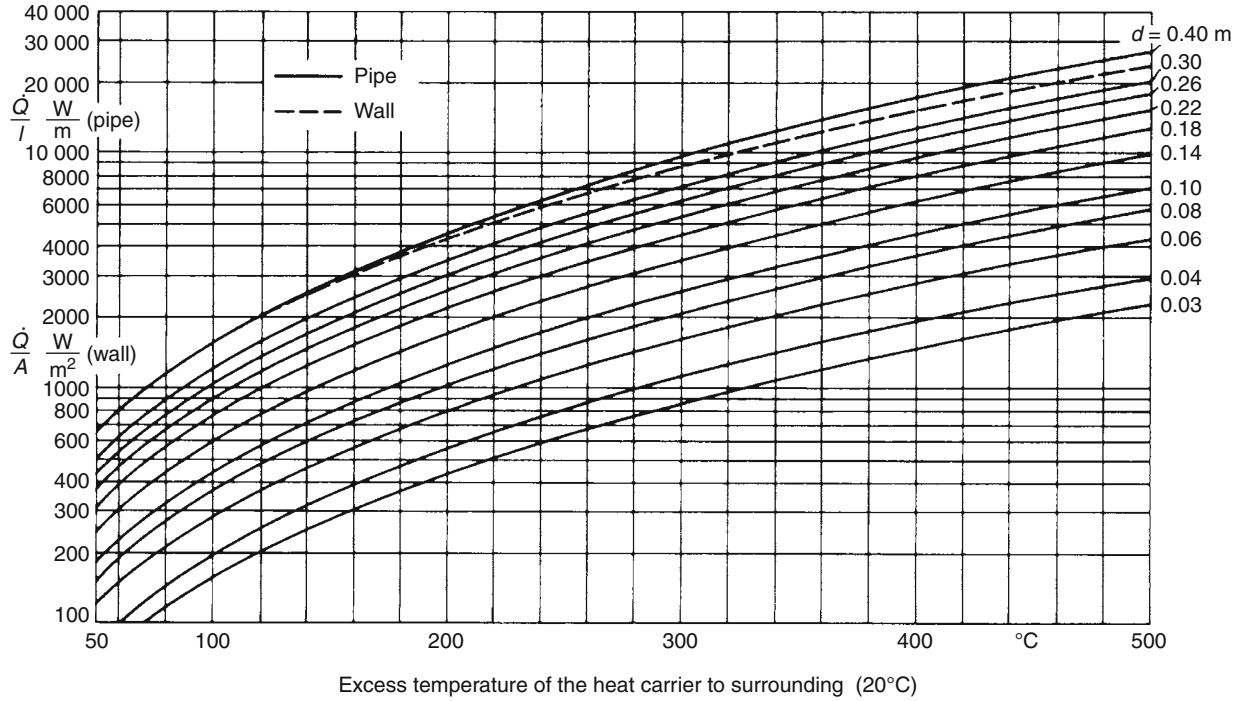

E1. Fig. 16. Determination of heat losses for uninsulated pipes and containers inside rooms.

Pipe suspensions: for chains and thin iron strips 10–15% should be added to the total pipe length; for heavy sleeve bearings, 20%.

Stripped flanges: data from Fig. 15 may be used for inside rooms [12] when fluids or saturated steam flows in the pipe with a high heat transfer coefficient. For gas flow with low heat transfer coefficients, the data from Fig. 15 should be reduced by 20%. For stripped flanges outside rooms, it is assumed that heat losses are equal to that of a stripped pipe of the same area.

Insulated flanges: for a continuous insulation with constant diameter, no additions are made. When flange caps are involved, 0.5–1 m insulated pipe length is added.

Valves and slide valves: additions according to Table 5 may be used.

5.7 Heat Losses of Noninsulated Pipes and Containers Inside Rooms

The exact calculation of heat losses for stripped surfaces in stagnant air can be obtained from Part F. The diagram Fig. 16 allows for a quick approximate determination of heat losses on stripped pipes. This is of interest when the economical advantage of an insulation is desired. This diagram is valid for inner rooms with 20°C air temperature and a radiation number of $C = 4.7\ \mathrm{W/m^2K^4}$ for the surface. The inner heat transfer is neglected as long as $\alpha_i \geq 1000\ \mathrm{W/m^2K}$. For other air temperatures, the following multiplication factor should be applied.

Air temperature in °C	−10	0	+10	+20	+30	+40
Factor *f*	0.88	0.91	0.96	1.00	1.05	1.10

6 Bibliography

1. Kutateladse SS (1963) Fundamentals of heat transfer. Edward Arnold, London
2. Hahne E, Schällig R (1972) Formfaktoren der Wärmeleitung für Anordnungen mit isothermen Rippen. Wärme-und Stoffübertragung 5:39–46
3. Hahne E, Grigull U (1974) A shape factor scheme for point source configurations. Int J Heat Mass Transf 17:267–273
4. Hahne E, Grigull U (1975) Formfaktor und Formwiderstand der stationären mehrdimensionalen Wärmeleitung. Int J Heat Mass Transf 18:751–767
5. Grigull U, Sandner H (1975) Wärmeleitung. Springer-Verlag, Berlin
6. Nickolay M, Cramer C, Martin H (2000) Analytical solution for the potential flow through the wall of n-sided hollow cylinders of regular polygonal cross section. Int J Heat Mass Transf 43:139–145
7. Cammerer JS (1962) Der Wärme-und Kälteschutz in der Industrie, 4. Auflage, Berlin
8. Hilpert R (1933) Wärmeabgabe von beheizten Drähten und Rohren im Luftstrom. Forschung Ing Wesen 4:215–224
9. Elgeti K (1971) Der Wärmeverlust eines in der Wand verlegten Rohres. HLH 22:109–113
10. Krischer O (1036) Das Temperaturfeld in der Umgebung von Rohrleitungen, die in der Erde verlegt sind. Gesundheitsingenieur 59:537–539
11. Maly F (1968) Die Wärmeabgabe von Heizungsrohren in Wohnungstrenndecken. Gesundheitsingenieur 89:203–208
12. Weyh W (1935) Wärmeersparnis durch Flanschisolierung. Arch Wärmewirt 16:151

E2 Transient Conduction in Stagnant Media

Holger Martin
Karlsruher Institut für Technologie (KIT), Karlsruhe, Germany

1 Basic Equations

Time-dependent temperature fields $T(r, t)$ play a crucial role in many technical applications. Their mathematical modeling enables us to predict the duration of a heating or cooling process, the heat taken up or released during the process, or the exact position inside a body where a maximum or a minimum temperature occurs at a certain time. The fundamentals needed for a calculation of such temperature fields are the first law of thermodynamics (applied as an energy balance of the system in question) and Fourier's law of heat conduction (as a rate equation, or an equation describing the "kinetics" of heat transfer). For the volume element of a stagnant incompressible medium, the (thermal) energy balance is

$$\rho c_p \frac{\partial T}{\partial t} = -\nabla \dot{q}. \tag{1}$$

Equation (1) states that the internal energy of the volume element is increased if the net heat flux out of the system is less than the heat flux entering the system. An additional increase of internal energy by adding power (work/time) (such as electric power) or an internal release of thermal energy from the dissipation of other energy forms has to be taken into account by an added term on the right-hand side of Eq. (1).

The kinetics of heat conduction (i.e., Fourier's law) relates the so far unknown heat flux to the gradient of the temperature field:

$$\dot{q} = -\lambda \nabla T. \tag{2}$$

Following Eq. (2), the direction of heat flux coincides with the direction of the negative temperature gradient. This is only true if the thermal conductivity λ does not depend on direction. Coupling the balance, Eq. (1), with the kinetics, Eq. (2), results in an equation to calculate the temperature field (Fourier's equation):

$$\rho c_p \frac{\partial T}{\partial t} = \nabla \lambda \nabla T. \tag{3}$$

For constant conductivity λ Eq. (3), with the thermal diffusivity $\kappa = \lambda/(\rho c_p)$, simplifies to

$$\frac{\partial T}{\partial t} = \kappa \nabla^2 T. \tag{3a}$$

Table 1 contains a comprehensive collection of the differential operations symbolized by the nabla operator, ∇, in Eqs. (1–3a) in the three main coordinate systems.

2 Initial and Boundary Conditions

Time-dependent temperature fields are caused by perturbations of a steady-state initial condition. Such a perturbation, in general, consists in a change of state of the surroundings at a moment $t = t_I$ [Conveniently, the time at the beginning of the heating or cooling process is set to $t_I = 0$, i.e., the time is counted at the moment, when the temperature of the surroundings is (suddenly) changed]. The temperatures $T(r, t)$ at any time later, $t > 0$, are then determined unambiguously, if the temperature field is known at $t = 0$

$$T(r, 0) = \varphi(r) \text{ initial condition} \tag{4}$$

and when the state of the surroundings is given for all times $t > 0$ (boundary conditions).

The boundary conditions in general form are

$$-\lambda \left(\frac{\partial T}{\partial n}\right)_0 = \dot{q}_0 \text{ boundary condition,} \tag{5}$$

where $\partial/\partial n$ means a differentiation in the direction outward, normal to the surface. Equation (5) relates the temperature gradient at the surface of the body to the heat flux through the surface, which in turn might be calculated via Eq. (2) from the temperature field of the surroundings. Strictly spoken, a coupled system of differential equations (3) for the temperature fields inside and outside the body in consideration had to be

VDI-GVC (ed.), *VDI Heat Atlas*, DOI 10.1007/978-3-540-77877-6_17,

solved. To avoid this difficulty, usually the heat flux at the surface $\dot{q}_0$ has to be specified somehow, for example, by Newton's "law of cooling"

$$\dot{q}_0 = \alpha_a (T_0 - T_\infty). \tag{6}$$

This form of the boundary condition with a constant outer heat transfer coefficient α_a and a given temperature of the surroundings $T_\infty = T_\infty (r_S, t)$ becomes very simple, if the outer heat transfer resistance $(1/\alpha_a)$ vanishes. In this case, as to be seen from Eq. (6), the surface temperature T_0 itself becomes a given quantity $(T_0 = T_\infty)$

$$T_0 = T_\infty (r, t). \tag{7}$$

Equation (7) is called a boundary condition "of the first kind." If the heat flux, however, is specified at the surface

$$-\lambda \left(\frac{\partial T}{\partial n} \right)_0 = \dot{q}_0 (r, t) \tag{8}$$

one speaks of a boundary condition of the second kind. The more general case, as given by Eqs. (5) and (6),

$$\left(\frac{\lambda}{\alpha_a} \frac{\partial T}{\partial n} + T \right)_0 = T_\infty (r, t) \tag{9}$$

is called a boundary condition of the third kind. From Eqs. (3–5) (in one of the forms corresponding to Eqs. (7–9) the time-dependent temperature field inside a stagnant incompressible medium (without internal energy dissipation) is determined unequivocally.

3 Analytical Solutions

For simply shaped bodies a great number of analytical solutions for transient temperature fields are known [1–4]. Some of the practically most important and simplest of these solutions are described in the following.

3.1 Step Change of State of the Surroundings

3.1.1 One-dimensional Heat Flux

The direction of the heat flux vector always coincides, in these cases, with a single direction of the coordinate system, as for example with the x-direction in a Cartesian system – the planes $x =$ const. are then isothermal faces, or with the r-direction in cylindrical or in spherical coordinates – in these cases the isothermal faces are cylindrical or spherical shells with $r =$ const. The temperature field equation (3a) simplifies accordingly (see also Table 1):

For the plane temperature field $T(x, t)$:

$$\frac{\partial T}{\partial t} = \kappa \frac{\partial^2 T}{\partial x^2} \tag{3b}$$

for the cylindrically symmetrical temperature field $T(r, t)$:

$$\frac{\partial T}{\partial t} = \frac{\kappa}{r} \frac{\partial}{\partial r} \left(r \frac{\partial T}{\partial r} \right) \tag{3c}$$

for the spherically symmetrical temperature field $T(r, t)$:

$$\frac{\partial T}{\partial t} = \frac{\kappa}{r^2} \frac{\partial}{\partial r} \left(r^2 \frac{\partial T}{\partial r} \right). \tag{3d}$$

The three equations (3b–d) can be written comprehensively in the form

$$\frac{\partial T}{\partial t} = \frac{\kappa}{r^n} \frac{\partial}{\partial r} \left(r^n \frac{\partial T}{\partial r} \right) \tag{3e}$$

with $n = 0$, 1, or 2 for plane, cylindrically or spherically symmetric temperature fields.

The simple shapes corresponding to the three aforementioned one-dimensional temperature fields are the following:

(a) $-X \le x \le X; -\infty < y, z < \infty;$

slab of thickness $2X$, infinitely extended in the y- and z-directions, in the following referred to as "the slab" for shortness:

(b) $0 \le r \le R; 0 \le \varphi \le 2\pi; -\infty < z < \infty;$

circular cylinder of diameter $2R$, infinitely extended in the z-direction, in the following referred to as "the cylinder" for shortness:

(c) $0 \le r \le R; 0 \le \varphi \le 2\pi; 0 \le \psi \le \pi;$

sphere of diameter $2R$.

As an initial condition, Eq. (4), the most simple case,

$$T(r, 0) = T_I = \text{const.} \tag{4a}$$

E2. Table 1. Vector operations in the three main coordinate systems

	Cartesian coordinates (x, y, z)	Cylinder coordinates (r, φ, z)	Spherical coordinates (r, φ, ψ)
Gradient ∇T	$e_x \frac{\partial T}{\partial x} + e_y \frac{\partial T}{\partial y} + e_z \frac{\partial T}{\partial z}$	$e_r \frac{\partial T}{\partial r} + e_\varphi \frac{1}{r} \frac{\partial T}{\partial \varphi} + e_z \frac{\partial T}{\partial z}$	$e_r \frac{\partial T}{\partial r} + e_\varphi \frac{1}{r \sin\psi} \frac{\partial T}{\partial \varphi} + e_\psi \frac{1}{r} \frac{\partial T}{\partial \psi}$
Divergence $\nabla \dot{q}$	$\frac{\partial \dot{q}_x}{\partial x} + \frac{\partial \dot{q}_y}{\partial y} + \frac{\partial \dot{q}_z}{\partial z}$	$\frac{1}{r^2} \frac{\partial}{\partial r} (r \dot{q}_r) + \frac{1}{r} \frac{\partial \dot{q}_\varphi}{\partial \varphi} + \frac{\partial \dot{q}_z}{\partial z}$	$\frac{1}{r^2} \frac{\partial}{\partial r} (r \dot{q}_r) + \frac{1}{r \sin\psi} \frac{\partial \dot{q}_\varphi}{\partial \varphi} + \frac{1}{r \sin\psi} \frac{\partial}{\partial \psi} (\dot{q}_\psi \sin\psi)$
Laplacian $\nabla^2 T$	$\frac{\partial^2 T}{\partial x^2} + \frac{\partial^2 T}{\partial y^2} + \frac{\partial^2 T}{\partial z^2}$	$\frac{1}{r^2} \frac{\partial}{\partial r} \left(r \frac{\partial T}{\partial r} \right) + \frac{1}{r^2} \frac{\partial^2 T}{\partial \varphi^2} + \frac{\partial^2 T}{\partial z^2}$	$\frac{1}{r^2} \frac{\partial}{\partial r} \left(r^2 \frac{\partial T}{\partial r} \right) + \frac{1}{r^2 \sin^2\psi} \frac{\partial^2 T}{\partial \varphi^2} + \frac{1}{r^2 \sin\psi} \frac{\partial}{\partial \psi} \left(\sin\psi \frac{\partial T}{\partial \psi} \right)$
	Relations to the Cartesian coordinates	$x = r \cos\varphi$	$x = r \cos\varphi \sin\psi$ **e** unit vector
		$y = r \sin\varphi$	$y = r \sin\varphi \sin\psi$
		$z = z$	$z = r \cos\psi$

is chosen here, and as a boundary condition, following Eq. (9):

$$\left(\frac{\lambda}{\alpha_a}\frac{\partial T}{\partial r}+T\right)_{r=R}=\begin{cases}T_I & \text{for } t\le 0\\ T_\infty & \text{for } t>0\end{cases} \tag{9a}$$

that is, a single step change of the temperature of the surroundings from T_I to T_∞ at $t = 0$.

The field equation (3e) together with the initial and boundary condition equations (4a) and (9a) can be written in dimensionless form using the following definitions.

The normalized temperature:

$$\Theta\equiv\frac{T-T_\infty}{T_I-T_\infty}; \tag{10}$$

the normalized distance from the center of symmetry:

$$\xi\equiv\frac{r}{R}\ \text{or}\ \frac{x}{X}; \tag{11}$$

the dimensionless time (or Fourier number):

$$\tau\equiv\frac{\kappa t}{R^2}\quad\text{or}\quad\frac{\kappa t}{X^2}; \tag{12}$$

and the ratio of the internal conductive resistance (R/λ) to the outer heat transfer resistance $(1/\alpha_a)$, or the Biot number:

$$\mathrm{Bi}=\frac{\alpha_a R}{\lambda}\quad\text{or}\quad\frac{\alpha_a X}{\lambda}. \tag{13}$$

With Eqs. (10–13) one obtains

$$\frac{\partial\Theta}{\partial\tau}=\frac{\kappa}{\xi^n}\frac{\partial}{\partial\xi}\left(\xi^n\frac{\partial\Theta}{\partial\xi}\right) \tag{14}$$

with $n = 0$ for the slab, $n = 1$ for the cylinder, and $n = 2$ for the sphere.

Initial condition:

$$\Theta(\xi,0)=1; \tag{15}$$

boundary condition:

$$\left(\frac{1}{\mathrm{Bi}}\frac{\partial\Theta}{\partial\xi}+\Theta\right)_{|\xi|=1}=\begin{cases}1 \text{ for } \tau\le 0,\\ 0 \text{ for } \tau>0.\end{cases} \tag{16}$$

In this normalized form, it makes no difference whether a heating or a cooling problem is treated. The normalized temperature given in Eq. (10) decreases from 1 at the beginning $(\tau = 0)$ to 0 for sufficiently high values of time $(\tau\to\infty)$.

Figure 1 shows an example for such a transient temperature field. The fact that all the tangents at the instantaneous temperature curves at the surface $(\xi = 1)$ have a common intersection at a point outside the body is remarkable and very helpful for plotting these curves. It follows immediately from the boundary condition equation (16). The coordinates of this point of intersection ("pole") are $(\Theta = 0,\ \xi = 1 + 1/\mathrm{Bi})$.

If the outer heat transfer resistance tends toward zero (that means $1/\mathrm{Bi}\to 0$), the pole comes immediately to the surface and the boundary condition of the first kind is reached, that is $\Theta\ (\xi = 1;\ \tau > 0) = 0$. In this case, the temperature differences inside the body are the greatest possible. This is asymptotically reached in heating or cooling of big bodies made of poorly conducting material (stone, sand, plastics, or the like) with a high outside heat transfer coefficient (well-mixed water, evaporation, or condensation).

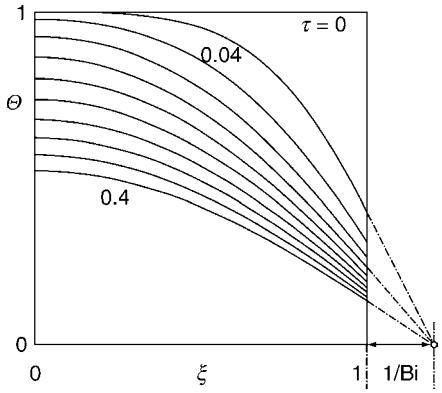

E2. Fig. 1. Temperature field $\Theta(\xi, \tau, \mathrm{Bi})$ for a slab with a boundary condition of the third kind.

If the outer resistance, however, compared to the inner conductive resistance, becomes more important, the pole moves outward from the surface. The wall tangents and therefore the whole temperature curves become increasingly flatter. From a simple geometric consideration the maximum inside temperature difference max $\Theta\ (\xi = 0) - \Theta(\xi = 1) \equiv \Delta\Theta_{\max}$ can be estimated. One finds

$$\Delta\Theta_{\max}<\frac{\mathrm{Bi}}{1+\mathrm{Bi}}. \tag{17}$$

For Biot numbers $\mathrm{Bi} < 0.1$, the central and surface temperatures differ by <9% of the initial difference $(\Theta_I - \Theta_\infty)$ to the surroundings. An example for such a case is the cooling or heating of small well-conducting bodies (metals) in stagnant gas (small outer heat transfer coefficient).

Further from Fig. 1 it can be seen that the temperature field for short times τ shows significant changes only in a narrow zone under the surface of the body. It has a typical boundary layer behavior. The thickness ($2X$ or $2R$) has no influence on the field; the body may be regarded as half-infinitely extended in this time-range. It is more convenient then to have the origin of the length coordinate at the surface. The new coordinate becomes $y = X - x$, or $R - r$. The dimensionless numbers, τ, and Bi, no longer contain X, or R, since these dimensions have no influence on the temperatures. A more reasonable length-scale in the short-time range is the term $\sqrt{\kappa t}$, which enters the dimensionless numbers:

$$\eta\equiv\frac{y}{2\sqrt{\kappa t}}\quad\left(=\frac{1-\xi}{2\sqrt{\tau}}\right), \tag{18}$$

$$\mathrm{Bi}^*\equiv\frac{\alpha_a\sqrt{\kappa t}}{\lambda}\quad\left(=\mathrm{Bi}\sqrt{\tau}\right). \tag{19}$$

The solution for the temperature field $\Theta\ (\eta, \mathrm{Bi}^*)$ in this case is found to be [1]

$$\Theta=\mathrm{erf}\ \eta+\mathrm{e}^{-\eta^2}\mathrm{e}^{(\eta+\mathrm{Bi}^*)^2}\{1-\mathrm{erf}\,(\eta+\mathrm{Bi}^*)\}. \tag{20}$$

The error function erf (z) is defined as

$$\mathrm{erf}\,(z)=\frac{2}{\sqrt{\pi}}\int_0^z\mathrm{e}^{-\zeta^2}\mathrm{d}\zeta. \tag{21}$$

The graph of this function is shown in Fig. 2. For bodies of finite thickness, Eq. (20) is to be seen as an asymptotic solution for short times τ.

The surface temperature $\Theta_0 = \Theta(\eta = 0)$ follows from Eq. (20) as

$$\Theta_0 = e^{Bi^{*2}}\{1 - \text{erf}\,(Bi^*)\}. \tag{22}$$

For large values of Bi^*, Eq. (22) can be written as

$$\Theta_0 = \frac{1}{\sqrt{\pi}\,Bi^*}\,(\text{error} < 1\%\ \text{for}\ Bi^* > 3). \tag{23}$$

For $Bi^* \to \infty$, $\Theta_0 = 0$, that is, to a boundary condition of the first kind, and Eq. (20) reduces to the first term:

$$\Theta = \text{erf}\ \eta\ (Bi^* \to \infty). \tag{24}$$

From Eq. (24), one can calculate the instantaneous heat flux through the surface with Eq. (2):

$$\dot{q}_{0,t} = \frac{\sqrt{\lambda\rho c_p}}{\sqrt{\pi\, t}}\,(T_I - T_0). \tag{25}$$

The heat flux is therefore inversely proportional to the square root of time, t. It is proportional to the square root of the product $\lambda\rho c$.

The mean integral value of the heat flux from $t = 0$ to t, $\dot{q}_0 = (1/t)\int_0^t \dot{q}_{0,t}\,dt$, turns out to be just twice the instantaneous flux at t:

$$\dot{q}_0 = 2\frac{\sqrt{\lambda\rho c_p}}{\sqrt{\pi\, t}}\,(T_I - T_0). \tag{25a}$$

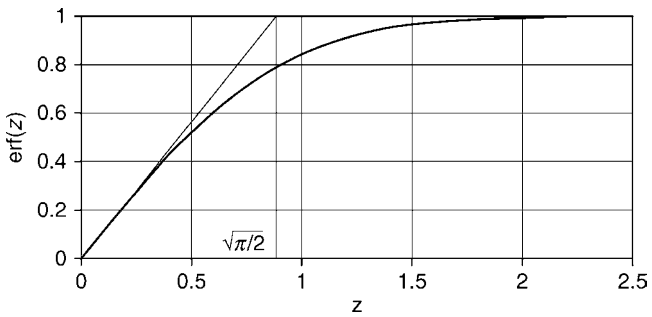

E2. Fig. 2. Graph of the error function.

For sufficiently longer times τ, the temperature profiles inside the body of finite thickness tend to become similar to each other (see Fig. 1). They now can all be described by a single function of position $f(\xi)$ that is scaled down with increasing time:

$$\Theta = g(\tau)\, f(\xi). \tag{26}$$

Introducing this multiplicative ansatz into the differential equation (14) yields the same time-function, $g(\tau)$, irrespective of the shape of the body (or the value of n):

$$g(\tau) = \exp(-m^2\tau). \tag{27}$$

Here, m is a constant that is to be determined from the boundary conditions. The function of position, $f(\xi)$, however, depends on the shape, or the value of n (see Table 2, last column). These functions alone are not sufficient to describe the temperature field for short times, especially not the initial temperature distribution. This requires the use of an infinite series of these functions:

$$\sum_{i=1}^{I} C_i(m_i)\, f(m_i\xi).$$

The coefficients C_i of this series are calculated in order to make each finite series fit the initial temperature distribution, $\Theta(\xi, 0) = 1$, with a minimum of the sum of the squares of errors, and to converge, with increasing number, I, of the summands, against the initial temperature distribution.

The eigenvalues m_i are the roots of the transcendental equations given in the second column of Table 2. These equations can easily be solved graphically or with a numerical solver. In Table 3 the first four eigenvalues m_1–m_4, for a slab, a cylinder, and a sphere are given as functions of the Biot number. For the given problem, all these roots m_i are equal or greater than zero and tend to $\pi + m_{i-1}$ for large numbers i. The fourth eigenvalue is therefore always greater than or equal to 3π, the fourth term of the series equation (28) contains a time-scale factor $\exp(-m_4^2\tau)$, which, even for relatively short times τ, becomes very small. For example, it is <0.00014 for $\tau = 0.1$. For $\tau > 0.1$, a calculation of the first three terms of the series equation (28) will suffice. For $\tau > 0.5$, the first term alone is often exact enough.

E2. Table 2. Temperature field for one-dimensional transient heat flow in a slab, a cylinder, and a sphere after a step change of the temperature of the surroundings from the constant initial temperature of the body, T_I, to a fixed value, T_∞, at a prescribed constant value of the outer heat transfer coefficient, α_a (boundary condition of the third kind)

	m_i to be determined from	$C_i\,(m_i)$	$D_i\,(m_i)$	$f(m_i\,\xi)$
Slab	$m_i = \frac{\alpha_a X}{\lambda}\frac{\cos(m_i)}{\sin(m_i)}$	$2\frac{\sin(m_i)}{m_i + \sin(m_i)\cos(m_i)}$	$1\frac{\sin(m_i)}{m_i}$	$\cos\left(m_i\frac{x}{X}\right)$
Cylinder	$m_i = \frac{\alpha_a R}{\lambda}\frac{J_0(m_i)}{J_1(m_i)}$	$2\frac{J_1(m_i)}{m_i(J_0^2(m_i) + J_1^2(m_i))}$	$2\frac{J_1(m_i)}{m_i}$	$J_0\left(m_i\frac{r}{R}\right)$
Sphere	$m_i = \left(1 - \frac{\alpha_a R}{\lambda}\right)\frac{\sin(m_i)}{\cos(m_i)}$	$2\frac{\sin(m_i) - m_i\,cos(m_i)}{m_i - \sin(m_i)\cos(m_i)}$	$3\frac{\sin(m_i) - m_i\cos(m_i)}{m_i^3}$	$\frac{\sin\left(m_i\frac{r}{R}\right)}{m_i\frac{r}{R}}$

E2. Table 3. The first four roots m_i of the transcendental equations in Table 2

Bi	Slab				Cylinder				Sphere			
	m_1	m_2	m_3	m_4	m_1	m_2	m_3	m_4	m_1	m_2	m_3	m_4
0	0.000	π	2π	3π	0.000	3.832	7.016	10.174	0.000	4.493	7.725	10.904
0.001	0.032	3.142	6.283	9.425	0.045	3.832	7.016	10.174	0.055	4.494	7.725	10.904
0.002	0.044	3.12	6.284	9.425	0.063	3.832	7.016	10.174	0.077	4.494	7.725	10.904
0.005	0.071	3.143	6.284	9.425	0.100	3.833	7.016	10.174	0.122	4.495	7.726	10.905
0.01	0.100	3.145	6.285	9.426	0.141	3.834	7.017	10.175	0.173	4.496	7.727	10.905
0.02	0.141	3.148	6.286	9.427	0.200	2.837	7.019	10.176	0.242	4.498	7.78	10.906
0.05	0.222	3.157	6.291	9.430	0.314	3.845	7.023	10.178	0.385	4.504	7.732	10.908
0.1	0.311	3.173	6.299	9.435	0.442	3.858	7.030	10.183	0.542	4.516	7.739	10.913
0.2	0.433	3.204	6.315	9.446	0.617	3.884	7.044	10.193	0.759	4.538	7.761	10.923
0.5	0.653	3.292	6.362	9.477	0.941	3.959	7.086	10.222	1.166	4.604	7.790	10.950
1.0	0.861	3.426	6.437	9.529	1.256	4.079	7.156	10.271	$\pi/2$	$3\pi/2$	$5\pi/2$	$7\pi/2$
2.0	1.079	3.644	6.578	9.630	1.599	4.292	7.288	10.366	2.030	4.913	7.979	11.085
5.0	1.314	4.034	6.910	9.893	1.990	4.713	7.617	10.622	2.569	5.354	8.303	11.335
10	1.428	4.305	7.229	10.200	2.180	5.034	7.957	10.936	2.836	5.717	8.659	11.658
20	1.498	4.491	7.495	10.513	2.288	5.257	8.253	11.268	2.986	5.978	8.983	12.003
50	1.536	4.619	7.703	10.783	2.357	5.411	8.484	11.562	3.079	6.158	9.239	12.320
∞	$\pi/2$	$3\pi/2$	$5\pi/2$	$7\pi/2$	2.405	5.520	8.653	11.792	π	2π	3π	4π

The Fourier series are

$$\Theta = \sum_{i=1}^{\infty} C_i(m_i)\, f(m_i\xi)\, \exp(-m_i^2\tau), \tag{28}$$

$$\overline{\Theta} = \sum_{i=1}^{\infty} C_i(m_i)\, D_i(m_i)\, \exp(-m_i^2\tau). \tag{29}$$

Figures 3–11 show the normalized center- and surface temperatures Θ_m and Θ_0 according to Eq. (28) with $\xi = 0$ and $\xi = 1$, respectively, and the normalized caloric mean temperature $\overline{\Theta}$ according to Eq. (29). These diagrams have been calculated by Soininen and Heikkilä [5] using the first 20 eigenvalues of the series solutions. The term $(1 - \overline{\Theta})$ corresponds to the heat released or taken up in relation to the initial enthalpy difference $\rho c_p\, V(T_I - T_\infty)$:

$$Q(t) = \rho c_p V(T_I - T_\infty) \cdot (1 - \overline{\Theta}). \tag{30}$$

The average temperature $\overline{T}$ is defined as an integral caloric mean value:

$$\overline{T} \equiv \int_V (\rho c_p T) dV \Big/ \int_V (\rho c_p) dV. \tag{31}$$

For constant properties ρc for a slab, a cylinder, and a sphere ($n = 0, 1, 2$) one obtains

$$\overline{\Theta} = (n+1) \int_0^1 \Theta(\xi)\xi^n d\xi. \tag{32}$$

The values $D_i(m_i)$ in Table 2 are calculated from Eq. (32). For sufficiently large values of time τ, the first of these values tends to

$$D_1(m_1) = \overline{\Theta}/\Theta_c. \tag{33}$$

In the limiting case $1/\mathrm{Bi} \to 0$ (the boundary condition of the first kind) the eigenvalues m_i can be found directly, and the first terms of the series in Eqs. (28) and (29) as a long-time asymptotic solution (practically for $\tau > 0.5$) reads

Slab:

$$\Theta(x,t) = \frac{4}{\pi}\cos\left(\frac{\pi}{2}\frac{x}{X}\right)\exp\left(-\left(\frac{\pi}{2}\right)^2\frac{\kappa t}{X^2}\right), \tag{34}$$

$$\overline{\Theta}(t) = \frac{2}{(\pi/2)^2}\exp\left(-\left(\frac{\pi}{2}\right)^2\frac{\kappa t}{X^2}\right). \tag{35}$$

Cylinder:

$$\Theta = 1.613 J_0\left(2.405\frac{r}{R}\right)\exp\left(-(2.405)^2\frac{\kappa t}{R^2}\right), \tag{36}$$

$$\overline{\Theta} = \frac{4}{(2.405)^2}\exp\left(-(2.405)^2\frac{\kappa t}{R^2}\right). \tag{37}$$

Sphere:

$$\Theta = 2\frac{\sin(\pi r/R)}{(\pi r/R)}\exp\left(-(\pi)^2\frac{\kappa t}{R^2}\right), \tag{38}$$

$$\overline{\Theta} = \frac{6}{(\pi)^2}\exp\left(-(\pi)^2\frac{\kappa t}{R^2}\right). \tag{39}$$

In these cases, the heat flux at the surface can also be calculated directly as in Eq. (25a):

$$\dot{q}_0 = \frac{\lambda}{X/2}\exp(-(\pi/2)^2\tau)\cdot(T_I - T_\infty), \tag{40}$$

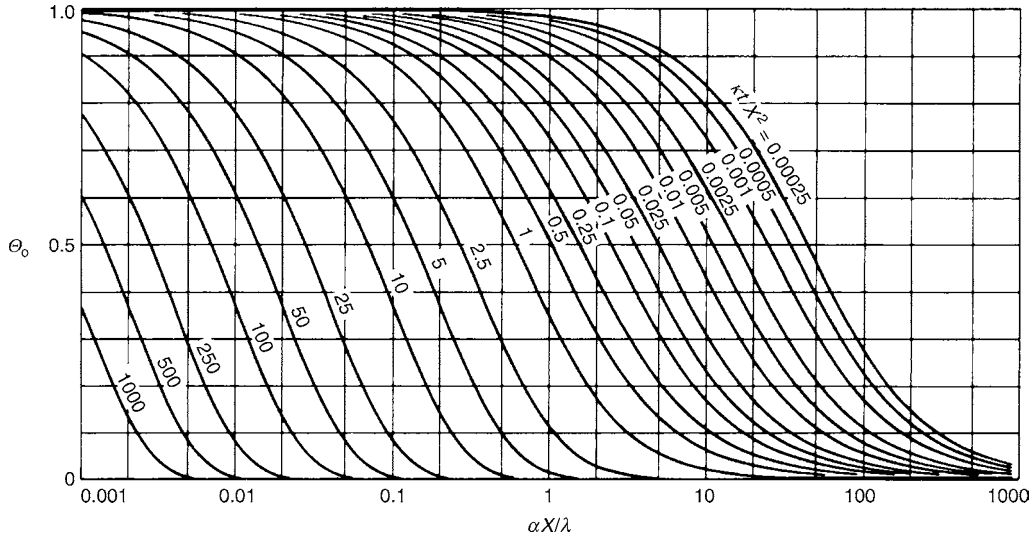

E2. Fig. 3. Normalized temperature Θ_0 at the surface of a slab.

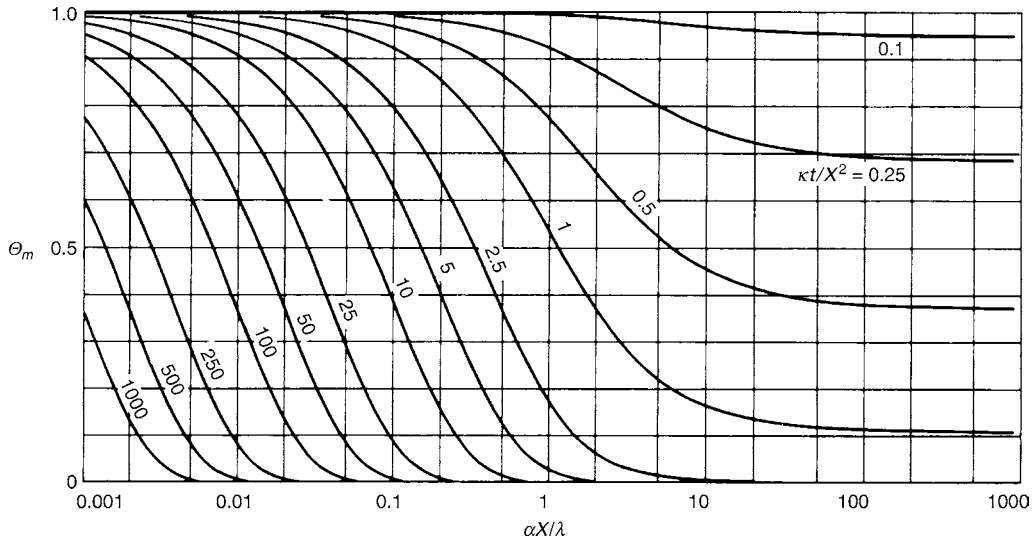

E2. Fig. 4. Normalized temperature Θ_m at the center of a slab.

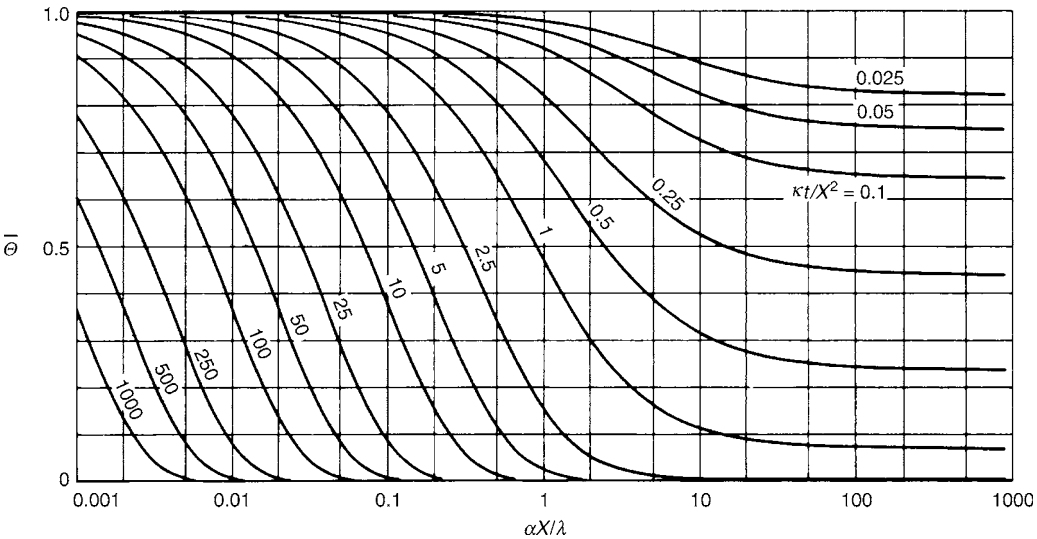

E2. Fig. 5. Normalized caloric average temperature $\overline{\Theta}$ of a slab.

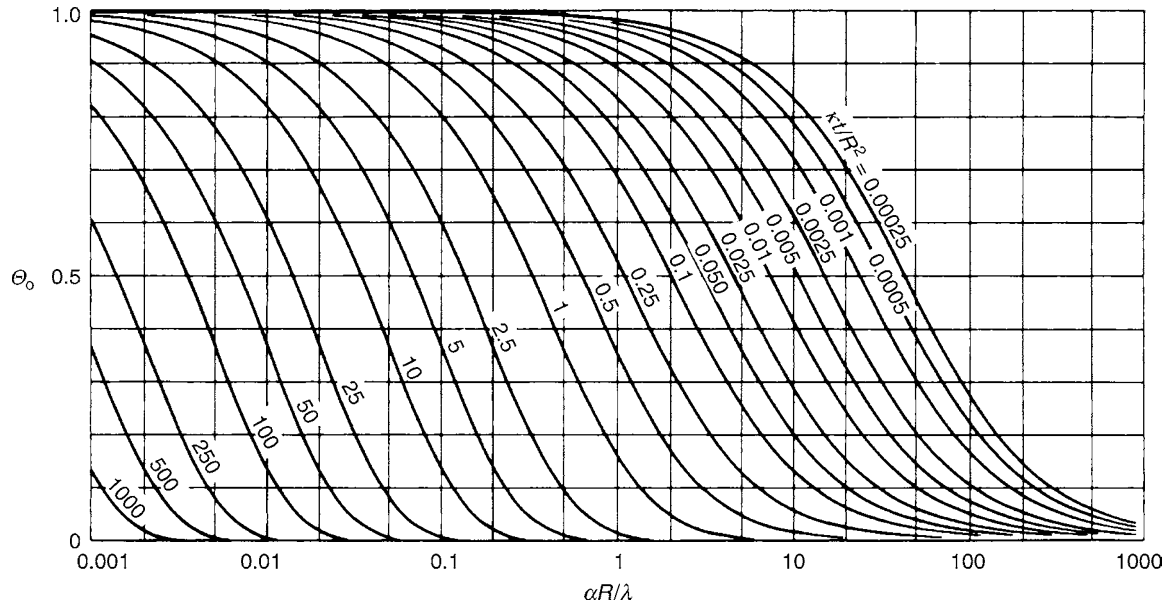

E2. Fig. 6. Normalized temperature Θ_0 at the surface of a cylinder.

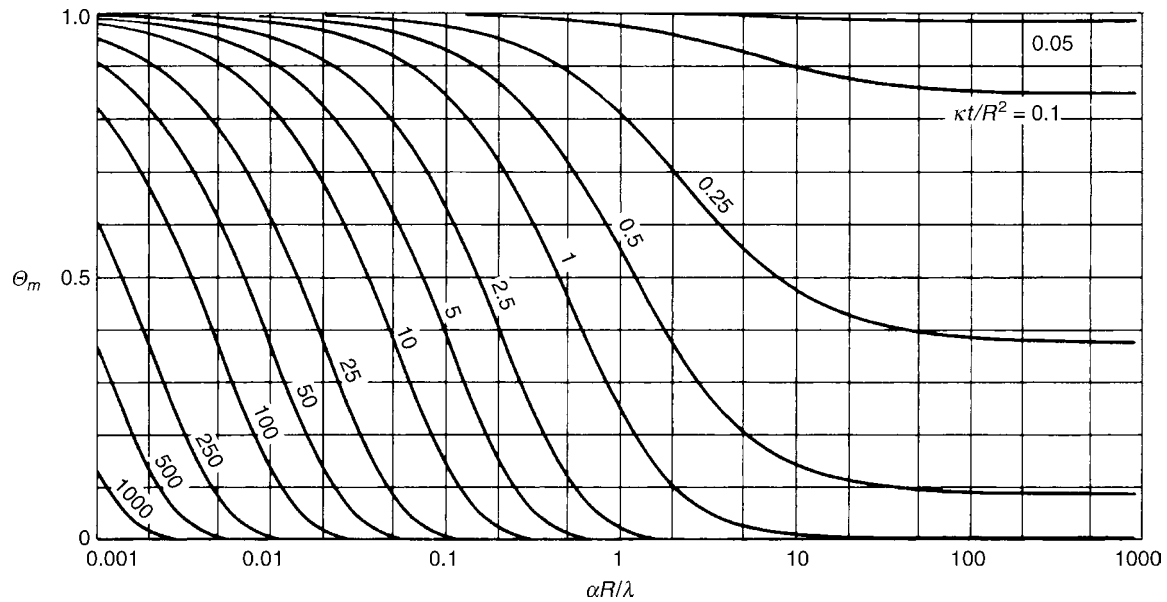

E2. Fig. 7. Normalized temperature Θ_m at the center of a cylinder.

$$\dot{q}_0 = \frac{\lambda}{R/2}\ \exp(-(2.405)^2\tau)\cdot(T_I - T_\infty), \tag{41}$$

$$\dot{q}_0 = \frac{\lambda}{R/2}\ \exp(-(\pi)^2\tau)\cdot(T_I - T_\infty). \tag{42}$$

For a slab (40), a cylinder (41), and a sphere (42), $(1/\mathrm{Bi}) = 0$ and $\tau > 0.5$.

Asymptotic approximations for practical calculations of transient conduction problems – *The use of internal (time-dependent) heat transfer coefficients* – [6]:

The temperature field $\Theta = \Theta(\tau, \xi, \mathrm{Bi}, a_V^*)$ can be found from the analytical solution, Eq. (28), as a functions of time, position, the outer heat transfer coefficient (in Bi), and the shape of the body. The latter enters the equation via the number $n = 0, 1, 2$, or the number $a_V^* = AR/V$ (or AX/V) that is the product of surface area and radius (or half-thickness) divided by the volume of the body, which has the values $(n+1)$, that is $a_V^* = 1, 2, 3$ for a slab, a cylinder, and a sphere, respectively.

Defining an internal heat transfer coefficient α_i for transient conduction in a stagnant body as

$$\alpha_i = \frac{\dot{Q}}{A(\overline{T} - T_0)}, \tag{43}$$

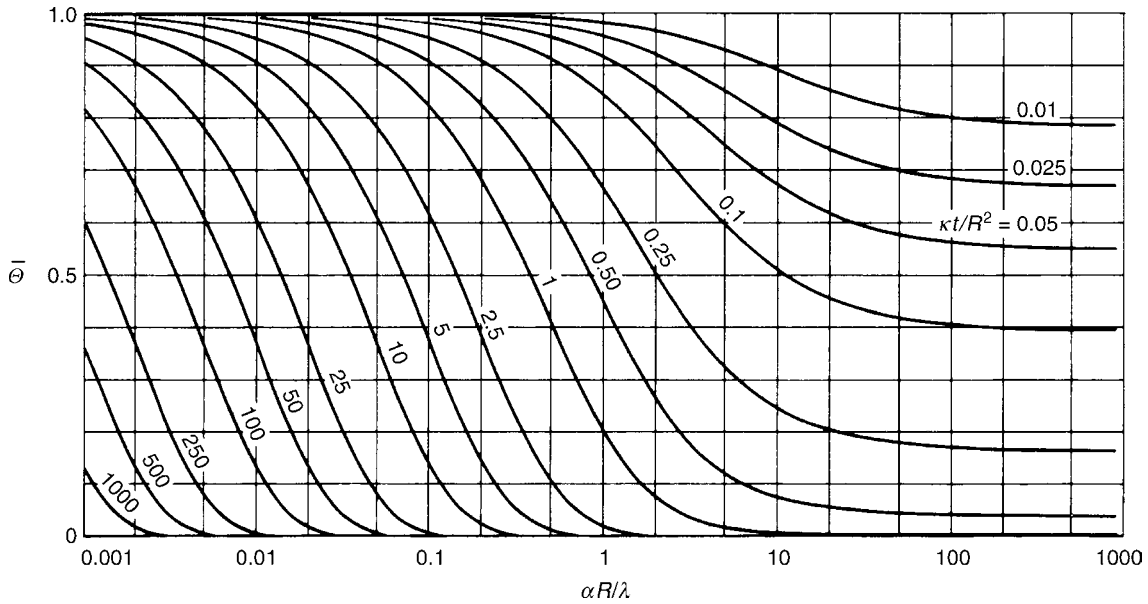

E2. Fig. 8. Normalized caloric average temperature $\overline{\Theta}$ of a cylinder.

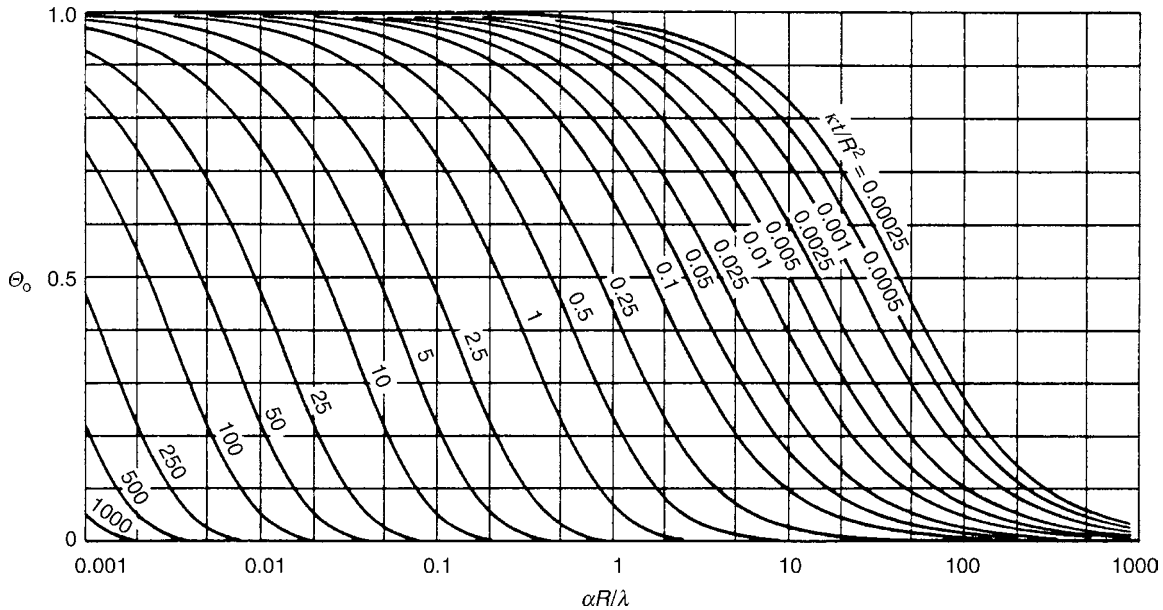

E2. Fig. 9. Normalized temperature Θ_0 at the surface of a sphere.

which can be expressed in dimensionless form as a Nusselt number $\mathrm{Nu} = \alpha_i R/\lambda$ (or $\alpha_i X/\lambda$) by relatively simple asymptotic equations for long and for short times.

Asymptotic Nusselt numbers for long times:

$$\mathrm{Nu}_\infty = \frac{a_V^* + 2 + \mathrm{Bi}}{1 + a_V^* \mathrm{Bi}/m_1^2} \qquad \begin{array}{c|ccc} & \text{slab} & \text{cylinder} & \text{sphere} \\ a_V^* & 1 & 2 & 3 \\ m_1 & \pi/2 & 2.4048 & \pi \end{array} \quad . \tag{44}$$

Asymptotic mean Nusselt numbers for short times:

$$\mathrm{Nu}_0\sqrt{\tau} = \frac{\sqrt{\pi} + 10\mathrm{Bi}\sqrt{\tau}}{1 + 5\mathrm{Bi}\sqrt{\pi\tau}}. \tag{45}$$

Smooth interpolation between the asymptotes (*approximately valid for all times*):

$$\mathrm{Nu} = \sqrt{\mathrm{Nu}_\infty^2 - b^2 + (\mathrm{Nu}_0 + b)^2} \qquad b = 0.2 \tag{46}$$

From these formulae one can now approximately calculate the average temperature $\overline{\Theta}$:

$$\overline{\Theta}(\tau) = \exp\left\{\frac{a_V^* \tau}{1/\mathrm{Bi} + 1/\mathrm{Nu}(\tau, \mathrm{Bi})}\right\} \tag{47}$$

In order to calculate also the surface temperature – from the ratio of resistances k/α_a, with $1/k = 1/\alpha_a + 1/\alpha_{it}$ – instantaneous heat transfer coefficients are needed here, no time-averaged ones as given by Eq. (45).

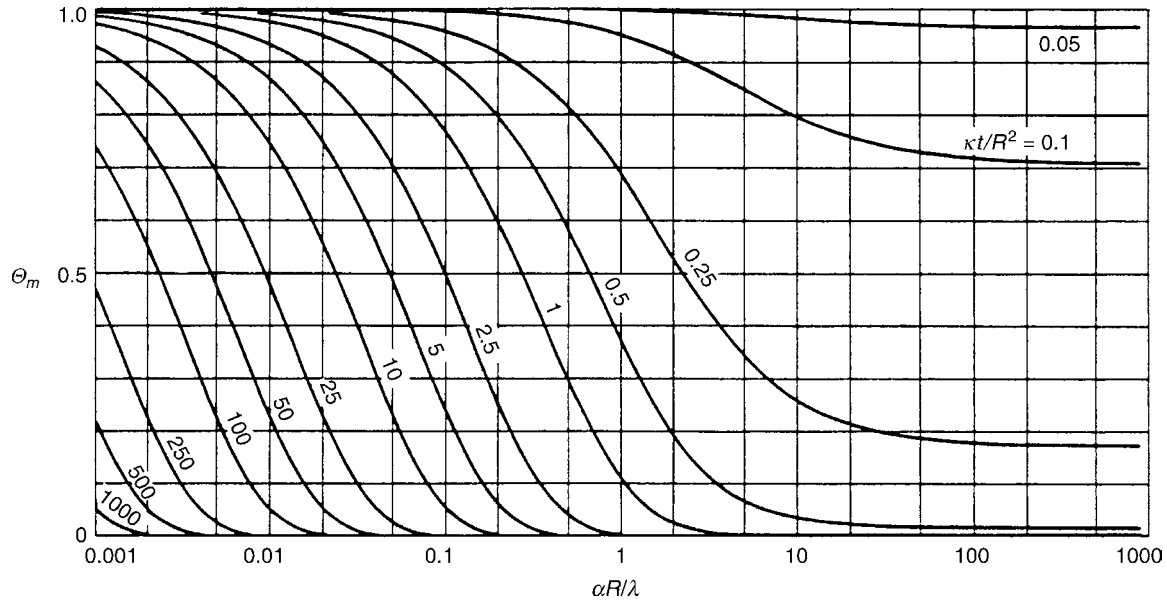

E2. Fig. 10. Normalized temperature Θ_m at the center of a sphere.

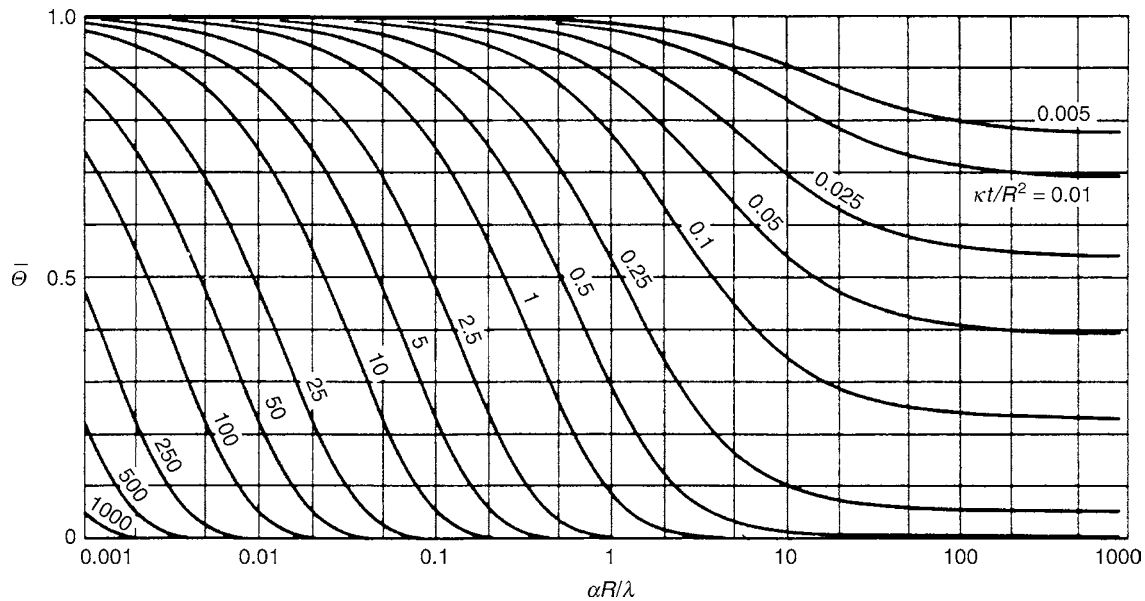

E2. Fig. 11. Normalized caloric average temperature $\overline{\Theta}$ of a sphere.

Instantaneous asymptotic Nusselt numbers for short times:

$$\mathrm{Nu}_{0t}\sqrt{\tau} = \frac{2.3\sqrt{\pi} + 2\mathrm{Bi}\sqrt{\tau}}{2\,(2.3 + \mathrm{Bi}\sqrt{\pi\tau})}. \tag{48}$$

Smooth interpolation between the asymptotes:

$$\mathrm{Nu}_t = \sqrt{\mathrm{Nu}_\infty^2 - b_t^2 + (\mathrm{Nu}_{0t} + b_t)^2} \qquad b_t = -0.2. \tag{49}$$

The surface temperature follows from this as

$$\Theta_0(\tau) = \Theta(\tau, \xi = 1) = \frac{\overline{\Theta}}{1 + \mathrm{Bi}/\mathrm{Nu}_t(\tau)}. \tag{50}$$

The temperature $\Theta_c = \Theta(\xi = 0)$ in the center shows a lag in its variation with time, which can be taken into account by a new time-scale $\tau_c = (\tau - \Delta\tau)$ with the variable time lag $\Delta\tau$.

$$\begin{aligned} &(0 < \Delta\tau < \Delta\tau_\infty \text{ for } 0 < \tau < \infty): \\ &\Delta\tau = \left\{1/\Delta\tau_\infty^m + 1/\tau^m\right\}^{-1/m} \end{aligned} \tag{51}$$

with

$$m = \frac{30 + \mathrm{Bi}}{10.8 + \mathrm{Bi}/4} + \frac{0.16}{\sqrt{\tau}}, \tag{52a}$$

$$\frac{1}{\Delta\tau_\infty} = 4 + \frac{6 + a_V^* + 2\mathrm{Bi}}{6 + a_V^* + (2.71 + 0.03a_V^*)\mathrm{Bi}}\,2a_V^*. \tag{52b}$$

From this, the center temperature is found with $\tau_c = (\tau - \Delta\tau)$:

$$\Theta_c(\tau) = \Theta(\tau, \xi = 0) = \exp\left\{-\frac{a_V^*\tau_c}{1/\mathrm{Bi} + 1/\mathrm{Nu}(\tau_c)}\right\}. \tag{53}$$

The argument of the exponential function in Eq. (47) is $kAt/(\rho cV)$, that is, a dimensionless time, which is called NTU (number of transfer units) in other contexts.

The deviations of the temperatures calculated from the approximate equations (44–53) compared to the exact solution in form of the Fourier's series, Eq. (28) are between +2.6% and −1% of the initial temperature difference in the most unfavorable case (for the center temperature of a sphere at large Biot numbers). The corresponding errors for the average temperature or for the surface temperature are always $< \pm 2\%$.

Example 1

An internal wall in an industrial oven consists of brickwork, 120 mm thick, with the physical properties $\lambda = 1.2$ W/mK, $c = 840$ J/kg K, and $\rho = 1600$ kg/m^3. It has a uniform initial temperature of $T_I = 370°C$. To cool it down, air of 20°C is blown into the oven. The heat transfer coefficient from the wall to the air is $\alpha_a = 10$ W/m^2 K. What are the surface, average, and center temperatures of the wall, after 2.8 h of cooling?

First, the dimensionless time τ (or the Fourier number) is calculated:

$$\tau \equiv \frac{\kappa t}{X^2} = \frac{\lambda t}{\rho c X^2} = \frac{1.2 \cdot 2.8 \cdot 3600}{1600 \cdot 840 \cdot 60^2 \cdot 10^{-6}} = 2.50.$$

The Biot number is

$$\mathrm{Bi} \equiv \frac{\alpha_a X}{\lambda} = \frac{10 \cdot 60 \cdot 10^{-3}}{1.2} = 0.50.$$

From the approximate equations (44–53) one calculates for a slab with $a_V^* = 1$, $m_1 = \pi/2$, and for $\mathrm{Bi} = \alpha_a X/\lambda = 0.5$ and $\tau = \kappa t/X^2 = 2.50$:

$\mathrm{Nu}_\infty = 2.91$, $1/\Delta\tau_\infty = 5.912$, $m = 2.893$, $\tau_c = 2.331$.

$\mathrm{Nu}_t = 2.939$, $\Theta_0 = 0.292$, $T_0 = (20 + 350{\cdot}0.292)°C = 122°C$.

$\mathrm{Nu}(\tau) = 3.059$, $\overline{\Theta} = 0.341$, $\overline{T} = (20 + 350{\cdot}0.341)°C = 139°C$.

$\mathrm{Nu}(\tau_m) = 3.069$, $\Theta_m = 0.367$, $T_c = (20 + 350{\cdot}0.367)°C = 148°C$.

From the diagrams, Figs. 3–5, the normalized average, surface, and center temperatures can be read for Bi = 0.5, and Fo = 2.5 as well. The results are practically the same.

3.1.2 Multi-dimensional Heat Flux

Solutions for some simple multi-dimensional temperature fields can be obtained by multiplication of the appropriate one-dimensional solutions.

In Cartesian coordinates, the temperature field $\Theta(x, y, z, t)$ with the initial condition

$$\Theta(x, y, z, 0) = 1 \tag{54}$$

and the boundary conditions

$$\left.\begin{aligned} \left(\frac{\lambda}{\alpha_1}\frac{\partial\Theta}{\partial x} + \Theta\right)_{|x|=X} &= 0 \\ \left(\frac{\lambda}{\alpha_2}\frac{\partial\Theta}{\partial y} + \Theta\right)_{|y|=Y} &= 0 \\ \left(\frac{\lambda}{\alpha_3}\frac{\partial\Theta}{\partial z} + \Theta\right)_{|z|=Z} &= 0 \end{aligned}\right\} \; t > 0 \tag{55}$$

is given by

$$\Theta(x, y, z, t) = \Theta_1(x, t) \cdot \Theta_2(y, t) \cdot \Theta_3(z, t), \tag{56}$$

where Θ_1, Θ_2, and Θ_3 are solutions of the corresponding one-dimensional problems with the initial and boundary conditions as given earlier.

Examples

For the quarterspace ($x > 0$, $y > 0$, $-\infty < z < \infty$), that is, a two-dimensional rectangular corner, with a boundary condition of the first kind, one obtains

$$\Theta(x, y, t) = \mathrm{erf}\,\frac{x}{\sqrt{\kappa t}}\,\mathrm{erf}\,\frac{y}{\sqrt{\kappa t}} \tag{57}$$

(see Eq. (24) for the one-dimensional solution).

For the octant ($x > 0$, $y > 0$, $z > 0$), that is, a three-dimensional rectangular corner with a boundary condition of the first kind, the field is

$$\Theta(x, y, z, t) = \mathrm{erf}\,\frac{x}{\sqrt{\kappa t}}\,\mathrm{erf}\,\frac{y}{\sqrt{\kappa t}}\,\mathrm{erf}\,\frac{z}{\sqrt{\kappa t}}. \tag{58}$$

For the (infinitely) long bar of rectangular cross section ($-X < x < X$, $-Y < y < Y$, $-\infty < z < \infty$), with a boundary condition of the third kind, one finds

$$\Theta(x, y, t) = \Theta_1(x, t) \cdot \Theta_2(y, t) \tag{59}$$

$\Theta_1(x, t)$ from Eq. (28) (slab), $\Theta_2(y, t)$ from Eq. (28) with $x \to y$, $X \to Y$.

And for the rectangular parallelepiped ($-X < x < X$, $-Y < y < Y$, $-Z < z < Z$):

$$\Theta(x, y, z, t) = \Theta_1(x, t) \cdot \Theta_2(y, t) \cdot \Theta_3(z, t) \tag{60}$$

$\Theta_{1,2,3}$ from Eq. (28) (slab).

In cylinder coordinates, the field $\Theta(r, z, t)$, with the initial condition

$$\Theta(r, z, 0) = 1 \tag{61}$$

and the boundary conditions

$$\left.\begin{aligned} \left(\frac{\lambda}{\alpha_1}\frac{\partial\Theta}{\partial r} + \Theta\right)_{|r|=R} &= 0 \\ \left(\frac{\lambda}{\alpha_3}\frac{\partial\Theta}{\partial z} + \Theta\right)_{|z|=Z} &= 0 \end{aligned}\right\} \; t > 0 \tag{62}$$

the temperature field within a finite cylinder ($0 \le r < R$, $-Z < z < Z$) is

$$\Theta(r, z, t) = \Theta_1(r, t) \cdot \Theta_2(z, t) \tag{63}$$

with

$\Theta_1(r, t)$ from Eq. (28) (cylinder)

$\Theta_2(z, t)$ from Eq. (28) (slab with $x \to z$, $X \to Z$).

Especially the last two cases, the parallelepiped, with the special case $X = Y = Z$ (cube), and the finite cylinder are of practical importance. A mathematical proof that the aforementioned multiplicative expressions are in fact solutions of the differential equation (3a) and the given boundary conditions may be found in the textbooks [1, 4]. The simple multiplication of one-dimensional solutions to get the multi-dimensional

solution is also valid for the average temperature $\overline{\Theta}$, that is, one can also apply the approximate solution from Eq. (47) correspondingly.

Example 2

An aqueous solid foodstuff ($\kappa = 0.16{\cdot}10^{-6}$ m^2/s; $\lambda = 0.6$ W/mK) in thin-walled cylindrical cans of height H ($=2X$) = 50 mm and diameter D ($=2R$) = 100 mm is to be sterilized in hot water of $T_\infty = 150$°C (under pressure). The heat transfer coefficient from the water to the cans is estimated to be $\alpha_a = 600$ W/m^2 K. How long must the cans be kept in the hot water, if they enter the bath at $T_I = 20$°C and shell reach an average temperature of 100°C?

For the finite cylinder from Eq. (63) one gets with

$\overline{\Theta}_1(t) = \overline{\Theta}\left(\frac{\kappa t}{R^2}, \frac{\alpha_a R}{\lambda}\right)$, infinite cylinder of diameter $2R$,

$\overline{\Theta}_2(t) = \overline{\Theta}\left(\frac{\kappa t}{X^2}, \frac{\alpha_a X}{\lambda}\right)$, slab of thickness $2X$.

As the time is the unknown here, the solution could be found only by iteration from the diagrams (Figs. 5 and 8) or from Eq. (29).

Even the approximate solution equation (47) cannot be solved explicitly for the time. Its iterative solution, however, is rather simple and converges quite rapidly. With the time $\tau = \tau_2 = \kappa\, t/X^2$ (with the half-thickness of the slab) as a variable, and $\tau_1 = \kappa\, t/R^2 = (H/D)^2\, \tau$ (cylinder) for $H/D = 0.5$, one finds, with $\mathrm{Bi}_2 = \alpha_a X/\lambda = 600{\cdot}0.025/0.6 = 25$, $\mathrm{Bi}_1 = \alpha_a\, R/\lambda = 50$, and $\tau_1 = 0.25\tau$, the values $\bar{\Theta}_2(\tau, \mathrm{Bi}_2)$ and $\bar{\Theta}_1(\tau_1, \mathrm{Bi}_1)$ from Eq. (47) and the product $\bar{\Theta}(\tau) = \bar{\Theta}_2\ (\tau, \mathrm{Bi}_2)\ \bar{\Theta}_1(\tau_1, \mathrm{Bi}_1)$ until the required normalized average temperature of $\bar{\Theta}(\tau) = (100 - 150)/(20 - 150) = 50/130 = 0.3846$ is reached. The final values are shown below:

	a_V^*	Bi	τ	Θ_c center	$\overline{\Theta}$ average	Θ_0 surface
$\Theta_{slab} = \Theta_2$	1	25	**0.1481**	0.8988	0.5983	0.0613
$\Theta_{cyl} = \Theta_1$	2	50	0.0370	0.9978	0.6428	0.0493
$\Theta_1 \cdot \Theta_2$				0.8968	**0.3846**	0.0030

From this the time required is found as $t = \tau X^2/\kappa = 0.1418{\cdot}25^2/0.16$ s = 578 s. So a can ought to be kept for about 10 min in the hot water, to heat its content to the required average temperature of 100°C. In the center, however, the foodstuff is only heated to $(150 - 130 \cdot 0.8968)$°C = 33.4°C, while it had already reached 149°C at the outer wall.

3.1.3 Coupled Systems

It is often found that boundary conditions cannot easily specified immediately at the surface of a single body: the volume under consideration, for which the boundary conditions can be given, may contain several bodies with different physical properties (namely λ, ρ, c_p). Again assuming that these properties are constant within each of these several bodies, the Eq. (3a) has to be applied to each of these separately. At the interfaces between these bodies the fields are coupled by the interfacial condition equations (64) and (65).

$$T_i = T_{i+1} \text{ (at the interface of body } i \text{ and } i+1). \tag{64}$$

For real interfaces of solid bodies this condition need not be strictly satisfied. Due to the incompleteness of contact, roughness, and oxide and sorptive layers, additional contact resistances might require appropriate modifications of Eq. (64)

$$\lambda_i \left(\frac{\partial T}{\partial n}\right)_i = \lambda_{i+1} \left(\frac{\partial T}{\partial n}\right)_{i+1} \text{ (at the interface of body } i \text{ and } i+1). \tag{65}$$

The unsteady change of the conductivity, λ, at the interface results in corresponding unsteady changes in the temperature gradients. The heat fluxes entering and leaving the interface have to be the same (see Eq. (65)), because the interface has no mass and therefore, no heat capacity.

A prototype example of this kind is the contact of two semi-infinite bodies of different initial temperatures T_1 and T_2 with the plane $x = 0$ as their common interface (The same is valid for the short-time contact of two bodies of finite thickness) (Fig. 12).

Instantaneously (at least within the frame of Fourier's theory) the temperature at the interface changes to the common contact temperature T_0. Thus, for each of the two temperature fields, a boundary condition of the first kind applies. The solutions from Eq. (24) are

$$\frac{T - T_0}{T_1 - T_0} = -\mathrm{erf}\,\frac{x}{\sqrt{\kappa_1 t}} \quad (x < 0), \tag{66}$$

$$\frac{T - T_0}{T_2 - T_0} = \mathrm{erf}\,\frac{x}{\sqrt{\kappa_2 t}} \quad (x > 0). \tag{67}$$

The so far unknown contact temperature T_0 follows from these solutions with Eq. (65)

$$T_0 = \frac{T_1 + \vartheta_{21} \cdot T_2}{1 + \vartheta_{21}}, \quad \vartheta_{21} = \frac{\sqrt{\lambda \rho c}_2}{\sqrt{\lambda \rho c}_1}. \tag{68}$$

The contact temperature (for given initial temperatures) depends on the ratio ϑ_{21} of the two coefficients $\sqrt{\lambda \rho c}_{1,2}$ only.

T_0 is always closer to the initial temperature of the body with the higher of these coefficients.

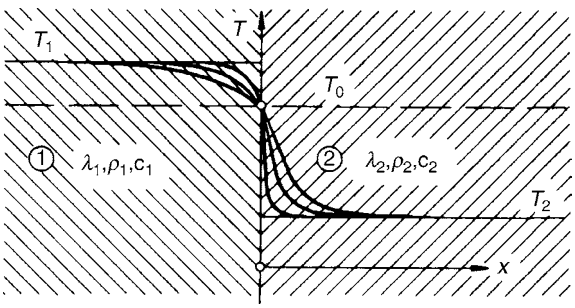

E2. Fig. 12. Temperature field during contact of two semi-infinite solids.

The temperature differences $(T_1 - T_0)$ and $(T_0 - T_2)$ are inversely related to the corresponding coefficients:

$$\frac{T_1 - T_0}{T_0 - T_2} = \vartheta_{21}. \tag{68a}$$

This is the reason that wood feels cooler (warmer) than metals if both materials have the same temperature above (below) the hand temperature.

Solutions for other coupled temperature fields, as occurring in multilayered bodies, or in solids in contact with a well-stirred fluid of limited heat capacity, can be found in [1, 2]. Analytical solutions for such cases can often be obtained via the method of Laplace transforms.

3.1.4 Phase Change – Melting and Solidification of Geometrically Simple Bodies

If inside a body a phase-change point, T_P, is crossed, the isothermal surface, $T = T_P$, subdivides the body into two regions of different states (or two phases). In this case, there are also coupled systems, as in the previous Sect. 3.1.3. As an additional complication, however, the position of the interface changes with time, and at this interphase there is an enthalpy change at a constant temperature (for pure components). Exact analytical solutions for this kind of problem are known only for a limited number of special cases [1, 3, 4]. The details of the coupled temperature fields are not usually practically important in these cases, but the times for complete or partial solidification (or melting) of a body. Solidification times can be approximately calculated in a relatively simple and straightforward way if the enthalpy of the solidified shell can be neglected against the phase change enthalpy. In the following only the solidification is treated, the results may, however, be applied to melting problems as well.

Figure 13 shows the problem. It is assumed that the liquid (subscript "1") is already at the phase change temperature T_P at the beginning. The energy balance for the liquid under these conditions is

$$-\dot{Q} \approx \rho_1 \Delta h_{12} \frac{\mathrm{d}V_1}{\mathrm{d}x}\frac{\mathrm{d}x}{\mathrm{d}t}, \tag{69}$$

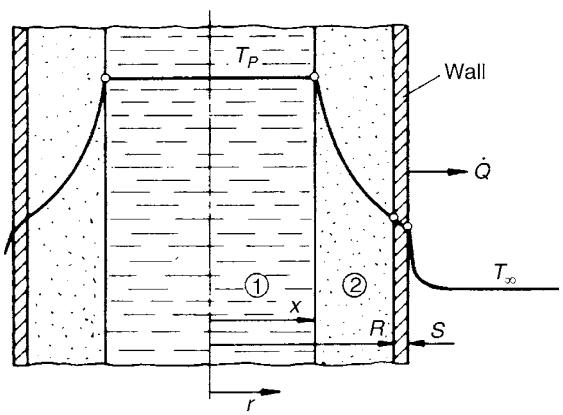

E2. Fig. 13. Phase change: solidification or melting of a simply shaped body.

where x denotes the position, and $\mathrm{d}x/\mathrm{d}t$ the velocity of the moving phase boundary. The change of enthalpy of the solid shell (subscript "2") is neglected during the solidification process ($c_{p2}\,(T_P - T_\infty) << \Delta h_{12}$). In this case it may be assumed that a (quasi-) steady-state temperature profile exists in the solid shell at each instant. The heat flow $\dot{Q}$ is to be expressed as

$$\dot{Q} = kA \cdot (T_P - T_\infty) \tag{70}$$

with

$$\frac{1}{k} = \frac{1}{\alpha_i(x)} + \underbrace{\left(\frac{s}{\lambda}\right)_{\text{wall}} + \frac{1}{\alpha_a}}$$

or

$$\frac{1}{k} = \frac{1}{\alpha_i(x)} + \frac{1}{k_a} \tag{71}$$

The inner conductive resistance $1/\alpha_i$ for the quasi-steady-state temperature profiles is

$$\frac{1}{\alpha_i(x)} = \frac{R}{\lambda_2}\left(1 - \frac{x}{R}\right) \text{ for a slab,} \tag{72}$$

$$\frac{1}{\alpha_i(x)} = \frac{R}{\lambda_2}\ln\left(\frac{R}{x}\right) \text{ for a cylindrical shell,} \tag{73}$$

$$\frac{1}{\alpha_i(x)} = \frac{R}{\lambda_2}\left(\frac{R}{x} - 1\right) \text{ for a spherical shell.} \tag{74}$$

From Eqs. (69–74) an ordinary differential equation for the velocity of the interface, $\mathrm{d}x/\mathrm{d}t$, is obtained. In dimensionless form, it reads

$$1 + \mathrm{Ph}\left\{\frac{1}{\mathrm{Bi}} + \frac{1}{\mathrm{Nu}(\xi)}\right\}\xi^n \frac{\mathrm{d}\xi}{\mathrm{d}\tau} = 0, \tag{75}$$

where Ph is a phase change number

$$\mathrm{Ph} \equiv \frac{\rho_1 \Delta h_{12}}{\rho_2 c_{p2}(T_P - T_\infty)}, \tag{76}$$

Bi is the Biot number

$$\mathrm{Bi} \equiv \frac{k_a R}{\lambda_2}, \tag{77}$$

ξ is the normalized coordinate of the position of the interface

$$\xi \equiv \frac{x}{R}, \tag{78}$$

τ is the dimensionless time (Fourier number)

$$\tau \equiv \frac{\lambda_2 t}{\rho_2 c_{p2} R^2} \tag{79}$$

and the dimensionless internal resistance $1/\mathrm{Nu}(\xi)$ follows from Eqs. (72–74):

$$\frac{1}{\mathrm{Nu}(x)} = \begin{cases} 1 - \xi & \text{slab} & n = 0, \\ -\ln \xi & \text{cylinder} & n = 1, \\ 1/\xi - 1 & \text{sphere} & n = 2. \end{cases} \tag{80}$$

The integration of Eq. (75) with Eq. (80) in the limits $\xi = 1$ to $\xi = 0$ gives the time of solidification τ_s. Due to the neglected change of enthalpy of the solid shell, this calculation gives a minimum time of solidification $\tau_{s,min}$:

$$\tau_{s,min} = \frac{Ph}{n+1}\left\{\frac{1}{2}+\frac{1}{Bi}\right\}. \tag{81}$$

Real times of solidification (or melting) are as much higher than the minimum calculated from Eq. (81), the smaller the phase change number Ph and the bigger the Biot number Bi is. The ratio $\tau_s/\tau_{s,min}$, that is, the factor by which the minimum time is to be multiplied to get the real solidification time is shown in Fig. 14 for slab ($n = 0$), cylinder ($n = 1$), and sphere ($n = 2$) versus $(n + 1)$/Ph, with Bi as a parameter.

There is an exact analytical solution for the slab (Neumann's solution [1]):

$$\tau_{s,plate}(Bi \to \infty) = \frac{1}{4\nu^2}, \tag{82}$$

where the parameter ν is to be calculated implicitly from

$$Ph\sqrt{\pi}\cdot \nu e^{\nu^2}\operatorname{erf}\nu = 1. \tag{83}$$

Values calculated from Eqs. (82) and (83) are shown in Fig. 14 as the open circles. The curves in this figure were calculated from an analytical approximation as shown in the figure. For the cylinder and the sphere the broken lines in Fig. 14 are based on values numerically calculated by Tao [8].

Example 3

For freezing of water (or substances containing high amounts of water, such as many foodstuffs) at a temperature of the refrigerant of $T_\infty = -18°C$, the phase change number, with the physical properties:

$\rho_1 = 1000$ kg/m^3, $\rho_2 = 917$ kg/m^3, $\Delta h_{12} = 333$ kJ/kg, $c_{p2} = 2.05$ kJ/kg K, and $T_p = 0°C$, becomes

$$Ph = \frac{1000\cdot 333}{917\cdot 2.05\cdot(0-(-18))} = 9.84.$$

And the reciprocal is 1/Ph = 0.102. The freezing time can therefore be well calculated from the simple equation (81). The correction required, even in the worst case (sphere, Bi = ∞), remains below 15% (see Fig. 16). The freezing time of a plane shell of thickness X (with the heat removal over one side and a high overall heat transfer coefficient k_a) is

$$t_{s,min}(Bi = \infty) = \frac{\rho_2 c_{p2}}{\lambda_2}\frac{1}{2}X^2\frac{\rho_1\Delta h_{12}}{\rho_2 c_{p2}(T_P - T_\infty)}.$$

With the data given earlier, and with $\lambda_2 = 2.2$ W/(K m) this results in

$$t_{s,min} = 4.2\cdot\left(\frac{X}{mm}\right)^2 s \quad (T_\infty = -18°C,\ k_a >> \lambda_2/X).$$

A layer of water of 10 mm thickness takes at least 420 s, or 7 min, to freeze under the given conditions. To reach a frozen layer of 100 mm the time needed is 4.2 10^4 s = 11 h 40 min.

Much lower values of the phase change number, Ph, than those for water are found for metals and for organic materials. From [7] one finds for example, at $T_\infty = 20°C$

	Tin	Aluminum	Copper	Steel
Ph ≈	1.1	0.54	0.40	0.27

The required corrections of the minimum solidification time become considerably greater in these cases. Because of the high conductivity of the metals, the Biot number is usually small, however, so that the corrections again tend to be not greater than 1.

3.2 Periodic Change of Temperature of the Surroundings

Another boundary condition playing an important role in some applications is the periodic change of the temperature of the surroundings. Examples are the daily and annual changes of solar irradiation on soil and buildings, the periodic thermal load of cylinder walls of combustion engines, the temperature

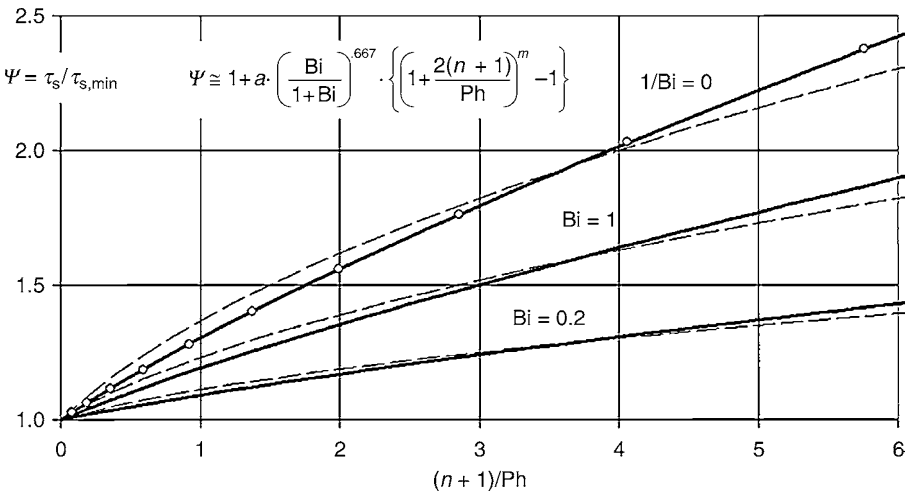

E2. Fig. 14. Ratio of the time of solidification to the minimum time of solidification. Circles: Neumann's solution. Full lines: $a = 0.224$, $m = 0.778$ (slab), broken lines: $a = 0.5$, $m = 0.5$ (cylinder and sphere).

control (on–off control) by thermostats, and the periodic heat transfer in regenerators.

A simple form to specify boundary conditions of this kind is to prescribe the temperature of the surroundings (boundary condition of the third kind) as a harmonic oscillation around a constant average T_{av}, with a constant amplitude ($T_{\infty,\,max} - T_{av}$):

$$T_\infty(t) = T_{av} + (T_{\infty,max} - T_{av})\sin(\omega t). \tag{84}$$

Assuming that this boundary condition has already been maintained long enough so that the disturbances from an initial condition vanish ($t >> t_P$, with $t_P = 2\pi/\omega$), the temperature distribution inside the body becomes

$$T(x,t) = T_{av} + (T_{\infty,max} - T_{av})\hat{A}\sin(\omega t + \varphi). \tag{85}$$

Amplitude $\hat{A}$ and phase φ of this temperature wave are functions of the normalized distance from the center ξ (see Eq. (11)), the Biot number Bi (Eq. (13)), and a number M defined as

$$M \equiv \sqrt{\frac{\pi R^2}{\kappa\, t_P}} \quad \text{or} \quad M \equiv \sqrt{\frac{\pi X^2}{\kappa\, t_P}} \tag{86}$$

which might be seen as (the square root of) a reciprocal Fourier number with the time of a period $t_P = 2\pi/\omega$. For small values of M, that is, for slow changes of the temperature of the surroundings (with a great time period $t_P >> \pi R^2/\kappa$), the amplitude $\hat{A}$ is close to 1 and the phase φ is close to 0. The temperatures inside the body practically completely follow the oscillations of the surroundings. For large values of M, that is, for fast changes of the surrounding temperatures the amplitude $\hat{A}$ greatly decreases from the surface ($\xi = 1$) to the center ($\xi = 0$) of the body, accompanied by a similarly increasing negative phase lag in this direction. For sufficiently large values of M only a small zone under the surface of the body can follow the outer temperature oscillations.

The analytical expressions for the amplitude and the phase can be written for a slab, a cylinder, and a sphere in the general form

$$\hat{A}(\xi, M, \mathrm{Bi}) = \sqrt{\frac{F_R^2(M\xi) + F_I^2(M\xi)}{G_R^2(M,\mathrm{Bi}) + G_I^2(M,\mathrm{Bi})}}, \tag{87}$$

$$\varphi(\xi, M, \mathrm{Bi}) = \arctan\left(\frac{F_I G_R - F_R G_I}{F_R G_R + F_I G_I}\right). \tag{88}$$

The meaning of the functions F_R, F_I, G_R, and G_I is given in Table 4. Figures 15–20 show the amplitudes and phases at the surface of the body ($\xi = 1$) as a function of M with $\mathrm{Bi}_M \equiv (\alpha_a/\lambda)\sqrt{\kappa\, t_P/\pi}$ as a parameter for slab (15, 16), cylinder (17, 18), and sphere (19, 20).

Due to the outer heat transfer resistance, $1/\alpha_a$, the harmonic oscillation of the temperature of the surroundings (according to Eq. (84)) is transferred to the surface with a reduced amplitude and a negative phase lag as shown in Fig. 21:

$$T_0(x,t) = T_{av} + (T_{\infty,max} - T_{av})\hat{A}_0\sin(\omega t + \varphi_0). \tag{89}$$

The time lag of the surface temperature against the temperature of the surroundings can be as large as one quarter of one time period in the extreme case of very thin bodies ($M \to 0$) and poor outer heat transfer ($\mathrm{Bi}/M \to 0$) ($\varphi_0 = -\pi/2$). In that case, the amplitude of the surface temperature oscillation, however, tends to zero.

The amplitudes and phases in the center of a body can be read from Figs. 22 and 23. So the most important quantities of the temperature field are determined.

For large values of $M\xi$ (a semi-infinite body) Eqs. (87) and (88) can be simplified with

$$\eta \equiv M(1-\xi) = \sqrt{\frac{\pi}{\kappa\, t_P}}\, y \tag{90}$$

with the coordinate y inwardly directed, with the origin at the surface, and

$$\mathrm{Bi}_M \equiv \frac{\alpha_a}{\lambda}\sqrt{\frac{\kappa\, t_P}{\pi}} \tag{91}$$

to

$$\hat{A}(\eta, \mathrm{Bi}_M) = \frac{\mathrm{e}^{-\eta}}{\sqrt{1 + 2/\mathrm{Bi}_M + 2/\mathrm{Bi}_M^2}}, \tag{92}$$

$$\phi(\eta, \mathrm{Bi}_M) = -\left(\eta + \arctan\frac{1}{1 + \mathrm{Bi}_M}\right). \tag{93}$$

E2. Table 4. Functions to calculate the amplitude and the phase from Eqs. (87) and (88) at a periodic change of the temperature of the surroundings

	Slab	Cylinder[a]	Sphere
$F_R\,(M\,\xi)$	$\cosh\,(M\,\xi)\cos\,(M\,\xi)$	$\mathrm{ber}\left(\sqrt{2}M\xi\right)$	$\dfrac{\sinh(M\xi)}{\xi}\cos(M\xi)$
$F_I(M\,\xi)$	$\sinh\,(M\,\xi)\sin\,(M\,\xi)$	$\mathrm{bei}\left(\sqrt{2}M\xi\right)$	$\cos(M\xi)\dfrac{\sinh(M\xi)}{\xi}$
$\left.\dfrac{\mathrm{d}F_R}{\mathrm{d}(M\xi)}\right\|_{\xi=1}$	$\sin\,M\cos\,M$ $-\cosh\,M\sin\,M$	$\mathrm{ber}_1\left(\sqrt{2}M\right) + \mathrm{bei}_1\left(\sqrt{2}M\right)$ $\left[= \sqrt{2}\,\mathrm{ber}'\left(\sqrt{2}M\right)\right]$	$\left(\cosh M - \dfrac{\sinh M}{M}\right)\cos M - \sinh M\sin M$
$\left.\dfrac{\mathrm{d}F_I}{\mathrm{d}(M\xi)}\right\|_{\xi=1}$	$\cosh\,M\sin\,M$ $+\sinh\,M\cos\,M$	$\mathrm{bei}_1\left(\sqrt{2}M\right) + \mathrm{ber}_1\left(\sqrt{2}M\right)$ $\left[= \sqrt{2}\,\mathrm{bei}'\left(\sqrt{2}M\right)\right]$	$\sinh M\sin M + \left(\cos M - \dfrac{\sinh M}{M}\right)\cos M$

$G_R(M,\,\mathrm{Bi}) \equiv \left\{F_R(M\xi) + \dfrac{M}{\mathrm{Bi}}\dfrac{\mathrm{d}F_R}{\mathrm{d}(M\xi)}\right\}_{\xi=1}$ $\quad G_I(M,\,\mathrm{Bi}) \equiv \left\{F_I(M\xi) + \dfrac{M}{\mathrm{Bi}}\dfrac{\mathrm{d}F_I}{\mathrm{d}(M\xi)}\right\}_{\xi\approx 1}$

[a]Tables and graphs of the functions ber, bei, ber_1, bei_1 (Kelvin's functions) can be found in [14] and [15]

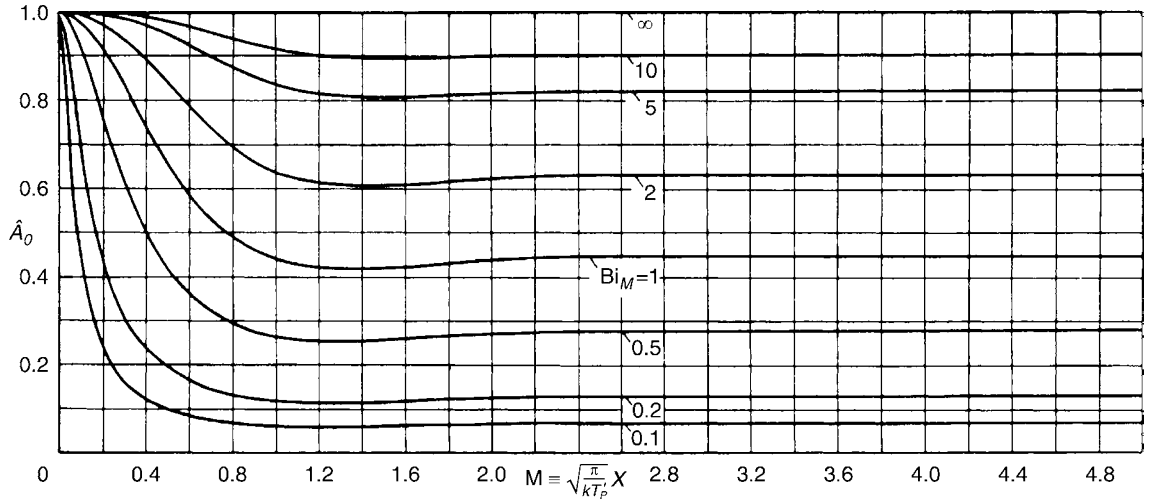

E2. Fig. 15. Amplitudes $\hat{A}_0$ of the temperature wave at the surface of a slab as functions of M, with the parameter $\mathrm{Bi}_M \equiv (\alpha_a/\lambda)\sqrt{\kappa t_P/\pi}$.

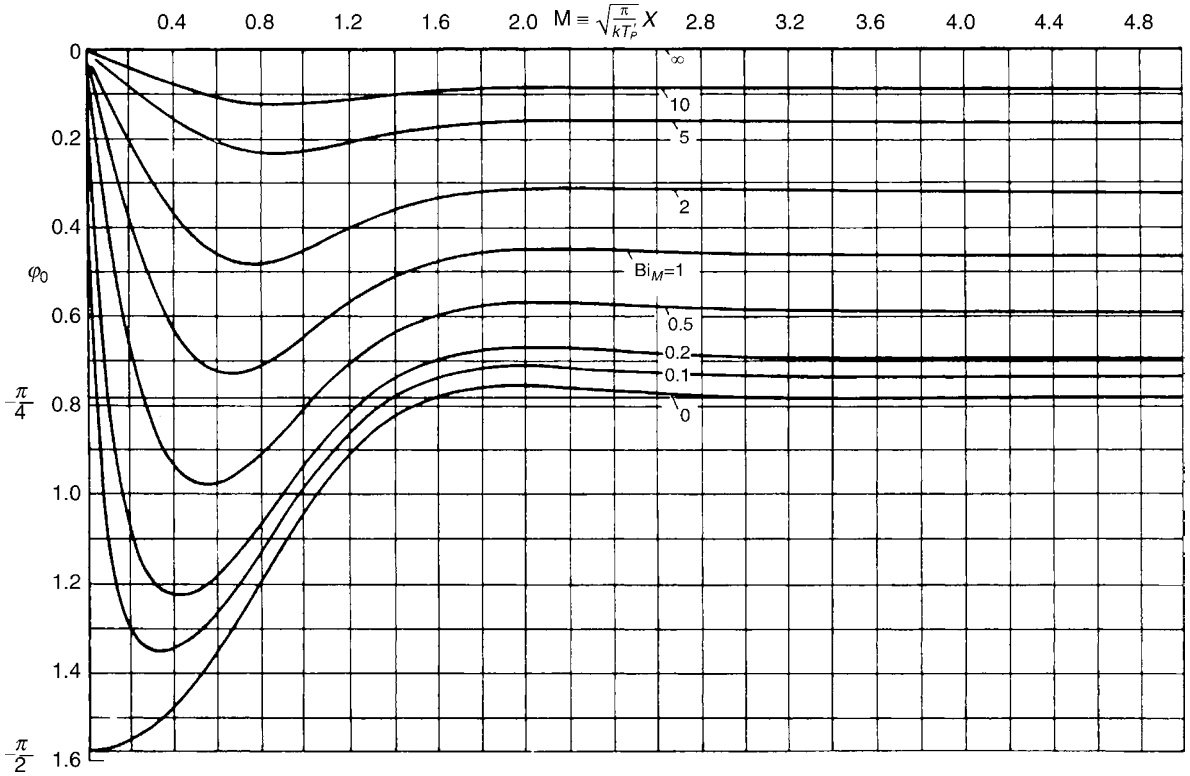

E2. Fig. 16. Phase shift φ_0 of the temperature wave at the surface of a slab as functions of M, with the parameter $\mathrm{Bi}_M \equiv (\alpha_a/\lambda)\sqrt{\kappa t_P/\pi}$.

With the periodic boundary condition, Eq. (84), the direction of heat flux is changed after each half-period. The instantaneous heat flux changes, as the temperature, in a harmonic oscillation. Integrating over a half-period gives the amount of heat stored during this time span as internal energy, and which is given back to the surroundings within the next half-period. Using the abbreviations,

$$F'_R \equiv \left.\frac{\mathrm{d}F_R(M\xi)}{\mathrm{d}(M\xi)}\right|_{\xi=1}, \tag{94}$$

$$F'_I \equiv \left.\frac{\mathrm{d}F_I(M\xi)}{\mathrm{d}(M\xi)}\right|_{\xi=1} \tag{95}$$

(see Table 4) after some rearrangement, one obtains

$$Q_{t_p/2} = A\frac{\lambda}{\sqrt{\kappa t_P/\pi}}\sqrt{\frac{F'^2_R + F'^2_I}{G'^2_R + G'^2_I}}\frac{2}{\pi}(T_{\infty,\max} - T_{\mathrm{av}})\frac{t_P}{2}. \tag{96}$$

Defining an overall heat transfer coefficient k by

$$Q_{t_p/2} = kA\,\Delta T_{\mathrm{av}}\frac{t_P}{2}, \tag{97}$$

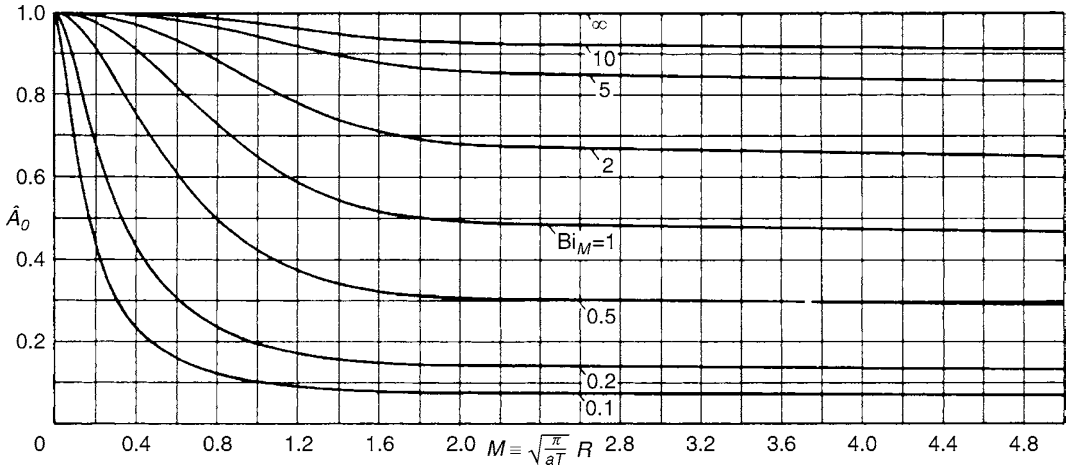

E2. Fig. 17. Amplitudes $\hat{A}_0$ of the temperature wave at the surface of cylinder as functions of M, with the parameter $\mathrm{Bi}_M \equiv (\alpha_a/\lambda)\sqrt{\kappa t_P/\pi}$.

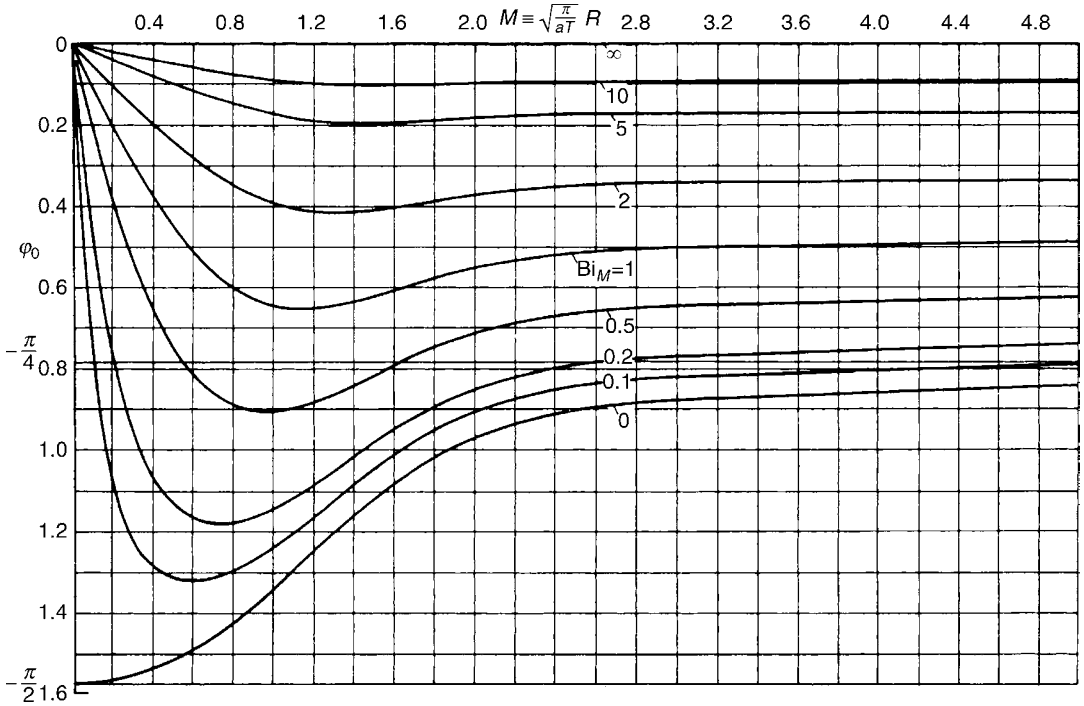

E2. Fig. 18. Phase shift φ_0 of the temperature wave at the surface of cylinder as functions of M, with the parameter $\mathrm{Bi}_M \equiv (\alpha_a/\lambda)\sqrt{\kappa t_P/\pi}$.

where the time-averaged temperature difference, ΔT_{av}, can be found from Eq. (84)

$$\Delta T_{\mathrm{av}} \equiv \frac{1}{t_P/2}\int_0^{t_P/2}(T_\infty - T_{\mathrm{av}})\,\mathrm{d}t = \frac{2}{\pi}(T_{\infty,\max} - T_{\mathrm{av}}) \qquad (98)$$

a comparison of Eqs. (96) and (97) gives

$$\frac{k\sqrt{\kappa t_P/\pi}}{\lambda} = \sqrt{\frac{F_R'^2 + F_I'^2}{G_R'^2 + G_I'^2}}. \qquad (99)$$

The right-hand side of Eq. (99) is a function of M and Bi_M. For $\mathrm{Bi}_M \to 0$ (i.e., the inner heat transfer resistance is negligible against the outer one), from Eqs. (94) and (95) and Table 4 one finds

$$\lim_{\mathrm{Bi}_M \to 0} \frac{k\sqrt{\kappa t_P/\pi}}{\lambda} = \mathrm{Bi}_M \qquad (100)$$

or with Eq. (91)

$$\lim_{\mathrm{Bi}_M \to 0} k = \alpha_a. \qquad (101)$$

In the other limit, $\mathrm{Bi}_M \to \infty$, k tends to the inner heat transfer coefficient α_i:

$$\frac{\alpha_i\sqrt{\kappa t_P/\pi}}{\lambda} = \sqrt{\frac{F_R'^2 + F_I'^2}{G_R'^2 + G_I'^2}}. \qquad (102)$$

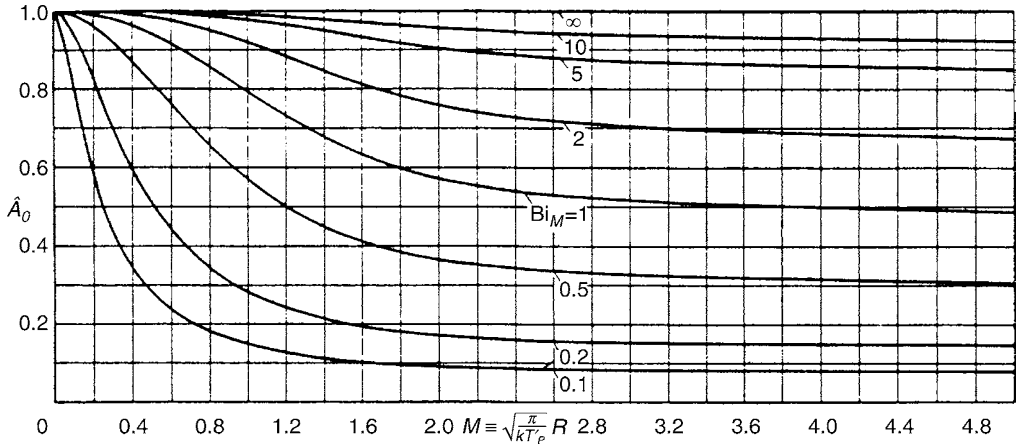

E2. Fig. 19. Amplitudes $\hat{A}_0$ of the temperature wave at the surface of a sphere as functions of M, with the parameter $\mathrm{Bi}_M \equiv (\alpha_a/\lambda)\sqrt{\kappa t_P/\pi}$.

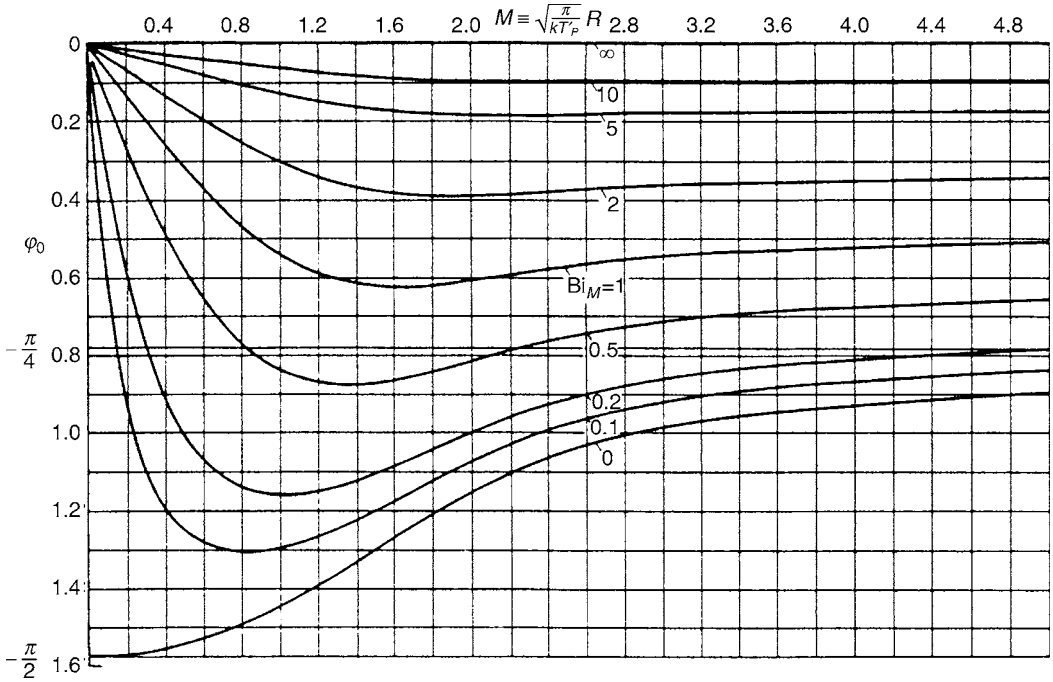

E2. Fig. 20. Phase shift of the temperature wave at the surface of a sphere as function of M, with the parameter $\mathrm{Bi}_M \equiv (\alpha_a/\lambda)\sqrt{\kappa t_P/\pi}$.

This inner heat transfer coefficient α_i or rather the corresponding Nusselt number

$$\mathrm{Nu}_{i,M} \equiv \frac{\alpha_i\sqrt{\kappa\, t_P/\pi}}{\lambda} \tag{103}$$

is shown in Fig. 24 for a slab, a cylinder, and a sphere versus M. For great values of M, $\mathrm{Nu}_{i,M}$ tends toward the constant value:

$$\lim_{M\to\infty} \mathrm{Nu}_{i,M} = \sqrt{2} \quad \text{or} \quad \lim_{M\to\infty} \alpha_i = \sqrt{\frac{2\pi}{t_P}}\sqrt{\lambda\rho\, c}. \tag{104}$$

For small values of M, the limiting values for a slab, a cylinder, and a sphere are (see Table 4)

$$\lim_{M\to 0} \mathrm{Nu}_{i,M} = \begin{cases} 2M & \text{slab,} \\ M & \text{cylinder,} \\ (2/3)M & \text{sphere,} \end{cases} \tag{105}$$

or

$$\lim_{M\to 0} \alpha_i = \begin{cases} 2\pi\dfrac{\lambda}{\kappa\, t_P}X & \text{slab,} \\ \pi\dfrac{\lambda}{\kappa\, t_P}R & \text{cylinder,} \\ \frac{2}{3}\pi\dfrac{\lambda}{\kappa\, t_P}R & \text{sphere.} \end{cases} \tag{105a}$$

For a slab the inner heat transfer coefficient α_i for a fixed period t_P goes through a maximum with increasing thickness of the slab (at $M = 1.2$ in Fig. 24). This wall thickness $2X_{M=1.2}$, with the greatest storage capacity, for a period of $t_P = 2\mathrm{h}$, for example, and fire-clay ($\kappa = 16 \cdot 10^{-4}\ \mathrm{m^2/h}$; [3, p. 96]) turns out to be

$$2X_{M=1.2} = 2 \cdot 1.2\sqrt{\kappa\, t_P/\pi} = 76\ \mathrm{mm}.$$

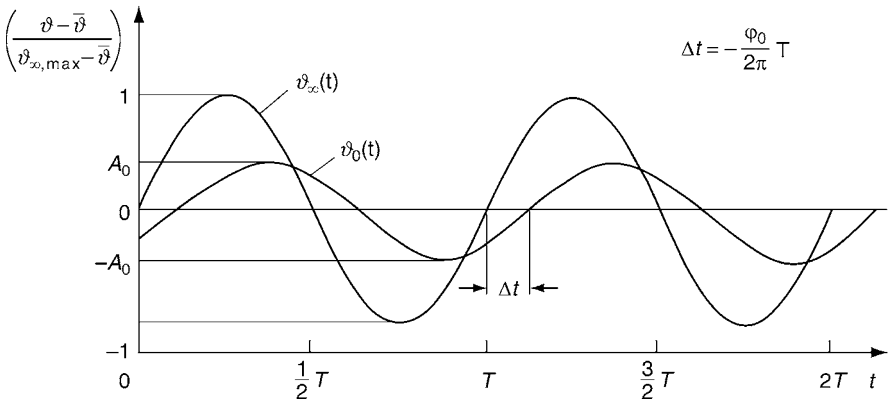

E2. Fig. 21. Time lag Δt of the surface temperature T_0 of a slab for a harmonic oscillation of the ambient temperature T_∞, at $M = 1$, and Bi = 1.

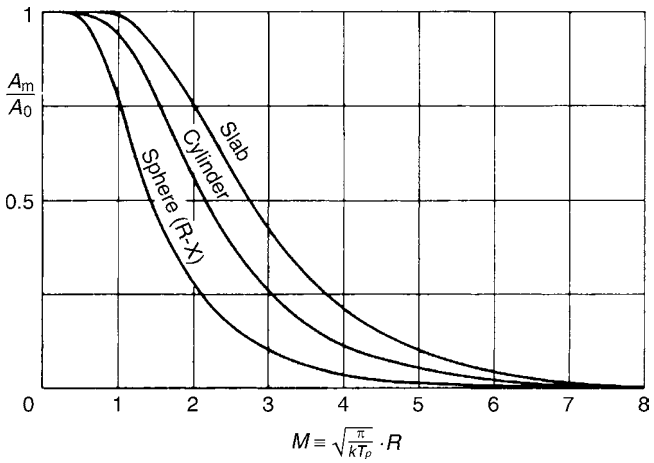

E2. Fig. 22. Amplitudes in the center of the body as functions of M.

In practice, the boundary conditions are more or less different from the simple harmonic oscillation as given in Eq. (84). By a Fourier analysis, however, they can be expressed as sums of harmonic oscillations. Equation (85) together with Eqs. (87) and (88) and Table 4 are then to be applied to each single oscillation of the Fourier analysis, and the resulting temperature variation is found from a summation of such particular solutions.

4 Finite Difference Methods (FD)

For more complex geometries and boundary conditions it might be rather difficult, if not impossible to apply analytical. In these cases numerical calculations offer an alternative, though often more tedious, way of prediction. In this chapter, only a few relatively simple numerical methods are treated. They give the reader a possibility to carry out their own numerical calculations by spreadsheet programs, for example, or may give the users of commercial software some basic information about the principles. The numerical methods used in commercial software are, partly, based on the same principles, but other numerical techniques also used in commercial software, as finite element, or finite volume methods are not treated here. These latter methods are usually less easily applied without professional help of experts.

4.1 The Explicit FD Equation

The most simple and straightforward example of the numerical methods is an explicit FD scheme for one-dimensional heat conduction, based on a difference approximation of a differential equation, as derived from Eq. (3e):

$$\frac{1}{\kappa}\frac{\partial T}{\partial t} = \frac{\partial^2 T}{\partial x^2} + \frac{n}{x}\frac{\partial T}{\partial x}, \tag{106}$$

where x stands for the direction of the heat flux in the Cartesian ($n = 0$), in cylindrical ($n = 1$, $x = r$) or in spherical coordinates ($n = 1$, $x = r$). The continuous time and space coordinates (t, x) are therefore replaced by discrete points in time, $t_{I+1} = t_I + \Delta t$ and space $x_{K+1} = x_K + \Delta x$, and the space derivatives in Eq. (106) are replaced by central differences, while the time derivative is replaced by a forward difference: $(T_{I+1} - T_I)/\Delta t$:

$$T_{I+1,K} \cong m\left(1 - \frac{n\Delta x}{2r_K}\right)T_{I,K-1} + (1-2m)T_{I,K} + m\left(1 + \frac{n\Delta x}{2r_K}\right)T_{I,K+1}, \tag{107}$$

where

$$m = \frac{\kappa\,\Delta t}{(\Delta x)^2} \tag{108}$$

is a kind of Fourier number relating the time step Δt to the square of the chosen spatial step divided by the thermal diffusivity $(\Delta x)^2/\kappa$. This dimensionless time step, or "grid Fourier number," is often called the *module* of the difference scheme.

From the special choice of approximating the time derivative (on the left-hand side of Eq. (106) by a forward difference, the temperature T_{I+1}, at the new time level enters the difference equation just once, so that it can be explicitly solved for this "new" temperature in terms of three "old" temperatures at the positions $K-1$, K, and $K+1$. From the middle term on the right-hand side of Eq. (107) it can easily be found that the method

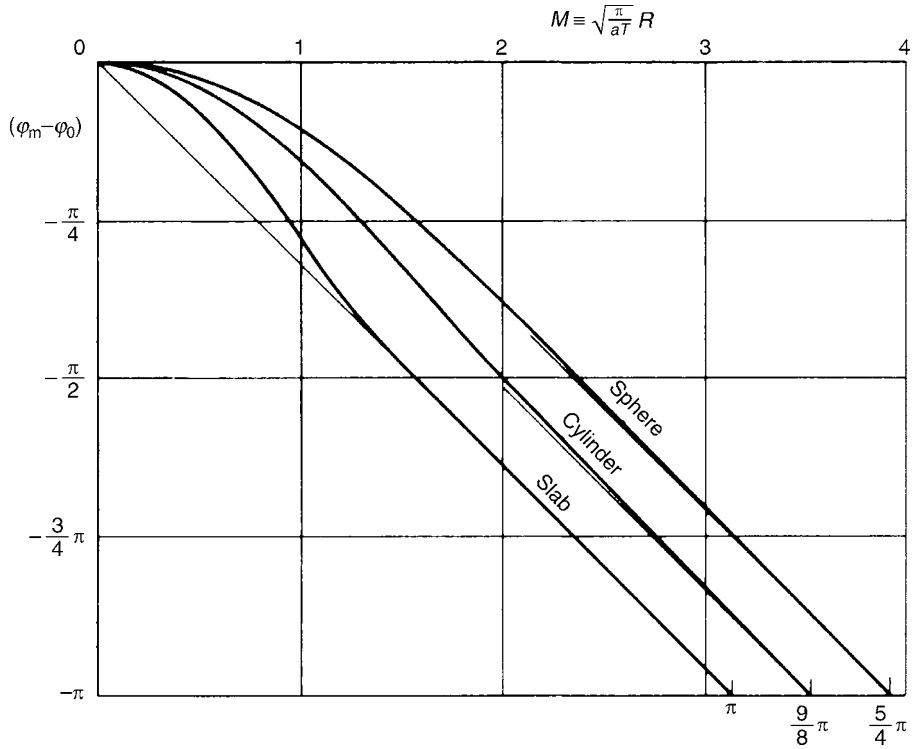

E2. Fig. 23. Phase shift in the center of the body as functions of *M*.

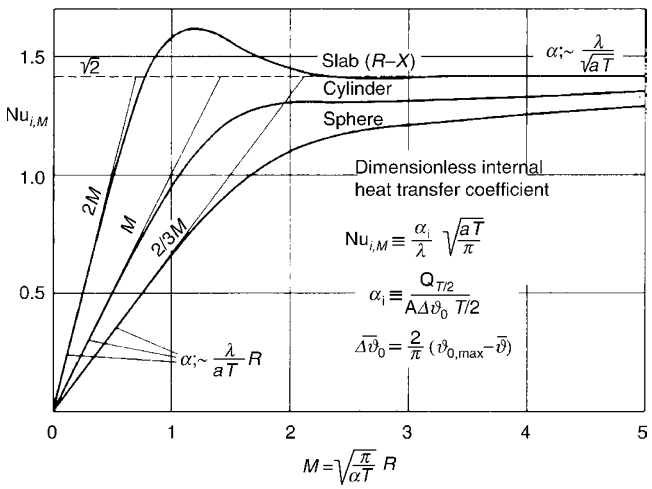

E2. Fig. 24. Dimensionless internal heat transfer coefficient $Nu_{i,M}$ as a function of *M*.

becomes unstable if the module, *m*, exceeds a value of 1/2. If time steps greater than $\Delta t_{max} = (1/2)\ (\Delta x)^2/\kappa$ are chosen, the calculation diverges leading to artificial temperature oscillations. For Cartesian coordinates ($n = 0$), the difference scheme becomes extremely simple:

$$T_{I+1,K} \cong m\,T_{I,K-1} + (1 - 2m)T_{I,K} + m\,T_{I,K+1}. \qquad (107a)$$

Using the maximum possible time step, so that $m = 1/2$ results in finding the new temperature $T_{I+1,K}$ from the arithmetic mean of the temperatures at x_{K-1} and x_{K+1} at the time t_I.

$$T_{I+1,K} = (T_{I,K-1} + T_{I,K+1})/2 (n = 0, m = 1/2). \qquad (107b)$$

This scheme has earlier been used in a graphic method [9] to construct transient temperature fields by ruler and pencil. Though $m = 1/2$ is stable in principle for one-dimensional heat flow, better results are obtained for smaller values of *m*. Especially, the choice of $m = 1/3$ makes the calculation nearly as easy, and the new temperature is found as the arithmetic mean of the three old temperatures:

$$T_{I+1,K} = (T_{I,K-1} + T_{I,K} + T_{I,K+1})/3 (n = 0, m = 1/3). \qquad (107c)$$

When using Eq. (107) for the one-dimensional problems with $n = 0, 1, 2$, the spatial coordinate should be chosen as shown in Fig. 25.

$$r_K = \Delta x(K - 1/2) \qquad (109)$$

the body of thickness *2X*, with symmetrical boundary conditions, is thus subdivided into K^* shells of thickness Δx, and

$$\Delta x/X = \Delta\xi = 1/K^*. \qquad (110)$$

To apply the boundary conditions, the positions $K = 0$ ($\Delta x/2$ left of the center) and $K = K^* + 1$ ($\Delta x/2$ right of the surface) are needed (Fig. 25). For the temperatures at these positions one finds

$$T_{I,0} = T_{I,1}\ (\text{symmetry}), \qquad (111)$$

$$T_{I,K^*+1} = T_{I,K^*}\frac{1 - b_x/2}{1 + b_x/2} + T_\infty \frac{b_x}{1 + b_x/2}, \qquad (112)$$

with $b_x = \mathrm{Bi}\Delta x$, $\mathrm{Bi} = \alpha_a X/\lambda$; $\Delta\xi = \Delta x/X$ (boundary condition of the third kind).

If there is no central symmetry, and the Cartesian coordinates are applied, it might be easier to use a half-shell (of thickness $\Delta x/2$) at the outermost part of the body, so that the surface temperature itself occurs in the difference scheme. A boundary condition of the third kind can then be expressed in the FD scheme as

$$T_{I,K^*+1} = b_x T_{I,K^*} + (1 - b_x) T_\infty \quad (b_x = \mathrm{Bi}\Delta\xi = \alpha_a \Delta x/\lambda). \tag{112a}$$

The module m in the term $m\,(T_{K-1} + T_{K+1})$ of an FD scheme, however, has to be doubled for $K = K^*$ to $2m$, because the volume of the outermost shell is only one half of that of an inner shell.

For a constant temperature of the surroundings, the temperatures can be normalized to make $\Theta_\infty = 0$, so that the second terms on the right-hand side of Eqs. (112) and (112a) vanish.

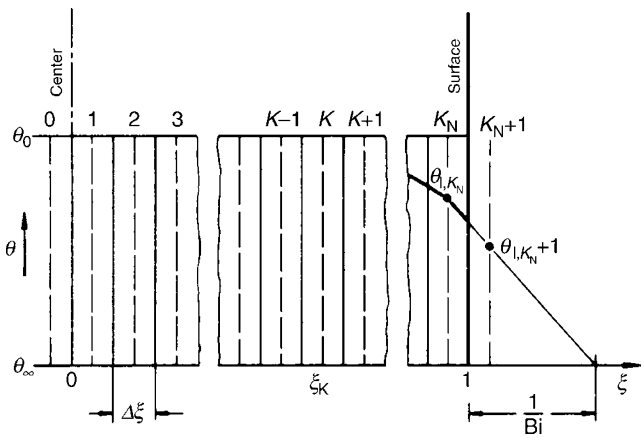

E2. Fig. 25. Subdivision of a body in K^* shells of thickness $\Delta\xi$ for a finite difference calculation.

For the intermediate temperatures, from $K = 1$ to K^* (or $K^* - 1$, if the surface temperature itself occurs in the scheme), Eq. (107) with Eq. (109) can be used

$$T_{I+1,K} \cong m\left(1 - \frac{n}{2K-1}\right) T_{I,K-1} + (1 - 2m) T_{I,K} + m\left(1 + \frac{n}{2K-1}\right) T_{I,K+1}. \tag{113}$$

Using Eqs. (111–113), all the problems treated analytically in Sect. 3.1.1 for a slab, a cylinder, and a sphere can also be solved numerically. Moreover, these equations can be used to calculate one-dimensional temperature fields in spherical shells, in cylindrical walls, or in slabs with unsymmetric boundary conditions (such as different temperatures and different heat transfer coefficients) and even melting or solidification problems [8].

The application of the one-dimensional form of the explicit FD equations is demonstrated in Example 4.

Example 4

The cooling (or heating) of a solid sphere with a constant initial temperature ($\Theta_{0,K} = 1$), in an environment of constant temperature ($\Theta_{I,\infty} = 0$) and a constant ambient heat transfer coefficient $\alpha_a = \lambda_i/R$ ($\mathrm{Bi} = 1$). The temperature distribution at (the dimensionless) time $\tau = 0.25$ is to be calculated.

A rather coarse subdivision of the sphere into four shells ($K^* = 4$) is chosen. Thus, the relative shell thickness becomes $\Delta\xi = 1/4$, and the time step has to be less than or equal to $\Delta\tau_{\max} = 1/2(\Delta\xi)^2$; or $\Delta\tau_{\max} = 1/32$. To get the temperature distribution at $\tau = 0.25$, one has to calculate at least 8 time steps ($8\Delta\tau = 8/32 = 0.25$). The calculation is done with the limiting time step to show that the method works even at this limiting value of the module $m = 1/2$. How to carry out the calculations is shown in Table 5. In the first row, the terms for $\Theta_{I,K}$ or $\Theta_{I+1,K}$ resulting from Eqs. (111) to (113) are given. In the last column additionally the temperature at the surface, $\Theta_{I,s}$, is shown, which does not directly appear in the difference scheme (It is calculated as the arithmetic mean of Θ_{I,K^*} and Θ_{I,K^*+1}. In the last row, the analytically calculated temperatures – as obtained from Eq. (28) – are given for comparison.

E2. Table 5. Numerical calculation of the cooling of a sphere by the explicit finite difference scheme

I + 1 I	$\Theta_1 = \frac{-\Theta_1+3\Theta_2}{2}$	$\Theta_2 = \frac{\Theta_1+5\Theta_3}{6}$	$\Theta_3 = \frac{3\Theta_2+7\Theta_4}{10}$	$\Theta_4 = \frac{5\Theta_3+7\Theta_4}{14}$	$\Theta_s = \frac{8\Theta_4}{9}$
0	1	1	1	1	
1	1	1	1	0.857	0.762
2	1	1	0.900	0.786	0.689
3	1	0.917	0.850	0.714	0.635
4	0.875	0.875	0.775	0.661	0.587
5	0.875	0.792	0.725	0.607	0.540
6	0.750	0.750	0.663	0.563	0.500
7	0.750	0.677	0.619	0.513	0.460
8	0.641	0.641	0.566	0.480	0.427
8 (analytical)	0.681	0.647	0.582	0.491	0.436

The Cartesian explicit FD scheme, Eq. (107a), can easily be generalized for 2D and 3D temperature fields. In place of indicating time and position by subscripts *I*, *K*, *L*, and *M*, in three-dimensional problems, it might be more appropriate to use relative space indications (related to the actual position, the temperature without a space index), such as *W*–*E*, *S*–*N*, and *D*–*U* (for west–east, south–north, down–up). The space steps are chosen equally in all directions ($\Delta x = \Delta y = \Delta z$):

$$T_{\text{new}} \cong [m\,(T_W + T_E) + (1 - 2m)T]_{\text{old}} \quad (1D,\, m \le 1/2), \tag{107d}$$

$$T_{\text{new}} \cong [m\,(T_W + T_E + T_S + T_N) + (1 - 4m)T]_{\text{old}} \quad (2D,\, m \le 1/4), \tag{114}$$

$$T_{\text{new}} \cong [m\,(T_W + T_E + T_S + T_N + T_D + T_U) + (1 - 6m)T]_{\text{old}} \quad (3D,\, m \le 1/6). \tag{115}$$

From these schemes one can see that the limiting module, $m_{\max}$, for stable calculation becomes 1/4 for 2D, and 1/6 for 3D problems. Again it might be safer to use values of 1/5 for 2D and 1/7 for 3D problems, also resulting in simple arithmetic means of the 4 + 1, or the 6 + 1 temperatures at adjacent positions, including the central position.

4.2 Implicit FD Schemes

4.2.1 The Basic Implicit FD Scheme

The explicit FD scheme, as treated in Sect. 4.1, has the advantage of being practically applied quite easily (for example, in a spreadsheet program, or a program in a higher programming language that can be written without deeper knowledge of mathematics).

A severe disadvantage, however, is caused by the stability condition (see Eqs. (107d), (114) and (115)). The time step, Δt, must always be chosen less than or equal to (1/2) $(\Delta x)^2/\kappa$ (for two or three space coordinates even with the factor 1/4 or 1/6, respectively, in place of 1/2). With a thermal diffusivity typically being in the order of magnitude of $\kappa = 10^{-6}$ m^2/s, and a subdivision of a slab of $X = 1$ cm into only 10 parallel elements, that is, $\Delta x = 10^{-3}$ m, the maximum time step for a stable calculation is half a second. Increasing the number of spatial elements by a factor 10 (for higher accuracy) reduces this maximum time step by a factor of 1/100 to 5 ms. Thus, very large numbers of time steps have to be calculated to reach a reasonable finite heating or cooling time.

This disadvantage can be avoided: Replacing the spatial derivatives on the right-hand side of Eq. (106) by corresponding FD terms not at the *I*th, but at the $I + 1$th time step (that means an approximation of the time derivative by a backward time difference). In place of Eq. (113) one gets

$$\begin{aligned} &-\left(1 - \frac{n}{2K-1}\right) m \cdot T_{K-1} + (1 + 2m) \\ &T_K - \left(1 + \frac{n}{2K-1}\right) m \quad \cdot T_{K+1}\Big|_{I+1} = T_{K,I} \end{aligned} \tag{116}$$

or shorter:

$$[a_K\ T_{K-1} + b_K\ T_K + c_K\ T_{K+1}]_{I+1} = d_K. \tag{117}$$

Equation (117), written for each grid-point, $K = 1$ to K^*, results in a system of linear equations for the K^* unknown temperatures $T_{K,I+1}$:

$$\begin{bmatrix} b_1 & c_1 & & & & & \\ a_2 & b_2 & c_2 & & & & \\ & a_3 & b_3 & c_3 & & & \\ & & & \cdot & & & \\ & & & & \cdot & & \\ & & & & & \cdot & \\ & & & & & a_{K^*} & b_{K^*} \end{bmatrix}_I \times \begin{bmatrix} T_1 \\ T_2 \\ T_3 \\ \cdot \\ \cdot \\ \cdot \\ T_{K^*} \end{bmatrix}_{I+1} = \begin{bmatrix} d_1 \\ d_2 \\ d_3 \\ \cdot \\ \cdot \\ \cdot \\ d_{K^*} \end{bmatrix}_I . \tag{118}$$

The coefficient matrix **A**, multiplied by the column vector of the unknown temperatures, is equal to the column vector of the right sides, d_K, of the linear equations:

$$\mathbf{A}_I \times \vec{T}_{K,I+1} = \vec{d}_{K,I}. \tag{118a}$$

The solution can be easily found by matrix multiplication of the inverted matrix and the vector on the right-hand side:

$$\vec{T}_{K,I+1} = \mathbf{A}_I^{-1} \times \vec{d}_{K,I}. \tag{119}$$

Matrix inversion and matrix multiplication can be done by using appropriate tools, now widely available, even in common spreadsheet programs, for example, the functions MINV (matrix) and MMULT(matrixA; matrixB) in Excel can be used to invert the Matrix **A**, and to carry out the multiplication in Eq. (119).

The coefficients of the matrix are constant for a given time step, or module, *m*. The module, however, can be changed without stability problems. Much fewer time steps are needed for equal or better accuracy, compared with the explicit scheme.

On the right-hand side, d_K, because of $d_K = T_{K,I}$, has to be newly calculated for each time step.

How to do the calculations is shown again for a sphere, $n = 2$, with only $K^* = 4$ shells, and a Biot number of Bi = 1, as in Example 4 (Sect. 4.1).

With Eqs. (110) and (111) (symmetry, $T_0 = T_1$), (112) (the boundary condition), and (116) (the implicit difference scheme), one finds the coefficients of the matrix:

$$\begin{aligned} &K = 1,\, T_{K-1} = T_K, \\ &b_1 = 1 + (1 + n)m;\, c_1 = -(1 + n)m, \end{aligned} \tag{120}$$

$$\begin{aligned} &K = 2, \text{to } K^* - 1, \\ &a_K = -[1 - n/(2K - 1)]m;\, b_K = 1 + 2m; \\ &\quad c_K = -[1 + n/(2K - 1)]m \end{aligned} \tag{121}$$

$$\begin{aligned} &K = K^*, \\ &a_{K^*} = -[1 - n/(2K^* - 1)]m; \\ &\quad b_{K^*} = 1 + 2m - [1 + n/(2K^* - 1)]m(T_{K^*+1}/T_{K^*}). \end{aligned} \tag{122}$$

With $n = 2$, and Bi = 1, Eq. (112) gives $T_{K^*+1}/T_{K^*} = (2K^* - 1)/(2K^* + 1)$, and $b_{K^*} = 1 + m$; so the coefficient matrix in this example becomes

$$A = \begin{bmatrix} 1 + 3m & -3m & & \\ -m/3 & 1 + 2m & -5m/3 & \\ & -3m/5 & 1 + 2m & -7m/5 \\ & & -5m/7 & 1 + m \end{bmatrix}. \tag{123}$$

Choosing the same time step as in the explicit scheme, $m = 1/2$, for the first four steps, the temperatures at $\tau = 0.125$ (=4/32, or $I = 4$ in Table 5) are found to be

$$\Theta_1 = 0.887, \Theta_2 = 0.858, \Theta_3 = 0.794, \Theta_4 = 0.685;$$

they differ by less than 4% from the corresponding values found with the explicit scheme. Now, it is possible to continue the calculation with two larger time steps of $m = 1$ (without changing the spatial steps) to reach the same final time of $\tau = 0.25$ (=8/32, $I = 8$ in Table 5), to get:

$$\Theta_1 = 0.695, \Theta_2 = 0.664, \Theta_3 = 0.601, \Theta_4 = 0.509.$$

Still these values are relatively close to the analytical results. The greater time step, however, does not lead to divergent numerical results. Even a single time step ($m = 4$), eightfold the maximum possible of the explicit scheme, can be safely used to get a less accurate but still an approximate solution.

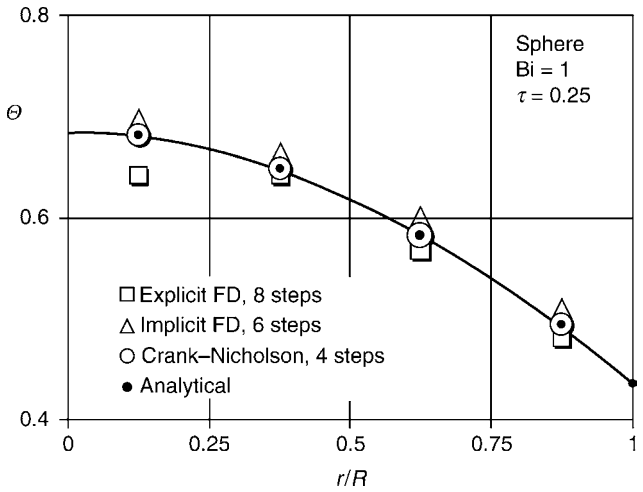

E2. Fig. 26. Comparison of FD calculations with the analytical solution.

4.2.2 The Crank–Nicholson Implicit FD Scheme

A higher accuracy can be obtained with the implicit FD scheme first given by Crank and Nicholson [10]. In this scheme, the right-hand side of Eq. (106) is replaced by the arithmetic mean of the corresponding difference terms at times I and $I+1$ so that the time derivative is a central difference as well (not a forward or a backward difference, as in the two preceding treated schemes). Again, a system of linear equations in the form of Eq. (117) has to be solved, but with coefficients and right sides:

$$a_K = -[1 - n/(2\ K - 1)]\ K = 2, 3, \ldots K^*,$$

$b_1 = 1 + n + 2/m\ K = 1$ (symmetry),
$b_K = 2\ (1 + 1/m)\ K = 2, 3, \ldots, K^* - 1$,
$b_{K^*} = 2(1 + 1/m) - [1 + n/(2\ K^* - 1)]\ (\Theta_{K^*+1}/\Theta_{K^*})$ (boundary condition),
$c_K = -\ [1 + n/(2\ K - 1)], K = 1, 2, \ldots, K^* - 1$,
$d_1 = [(2/m) - 1 - n)\ \Theta_1 + (1 + n)\ \Theta_2]\ K = 1$ (symmetry),
$d_K = [-\ a_K\ \Theta_{K-1} + (b_K - 4)\ \Theta_K - c_K\ \Theta_{K+1}]$
$K = 2, 3, \ldots, K^*$.

The calculation with the Crank–Nicholson scheme, using only four time steps, with $m = 1$ (i.e., twice the stable limit of the explicit scheme) gives the temperatures

$$\Theta_1 = 0.681, \Theta_2 = 0.648, \Theta_3 = 0.582, \Theta_4 = 0.491,$$

which almost perfectly agree with the analytic results (the relative deviations are less than + 0.09%, and −0.07%). Again, the scheme is stable for arbitrary values of m. Even with a single time step ($m = 4$), the relative errors are in the order of + 10%, and −11%.

The results for temperatures in the sphere obtained with the three FD schemes are shown in a plot of temperature versus radial position in Fig. 26.

4.2.3 The Alternating Directions Implicit (ADIP) Scheme for Two-Dimensional Temperature Fields

Two- or three-dimensional transient temperature fields can be solved by the explicit scheme (given in Sect. 4.1). The stability limit of the time step, however, might be a reason to look for alternatives without such time step limitations.

To apply an implicit FD scheme to two- (or even three-) dimensional problems, the method of alternate directions [11, 12], applied in two consecutive time steps, I+1, and I+2, reduces the problem to one dimension at each single step. Starting from a two-dimensional differential equation in Cartesian coordinates:

$$\frac{1}{\kappa}\frac{\partial T}{\partial t} = \frac{\partial^2 T}{\partial x^2} + \frac{\partial^2 T}{\partial y^2}. \tag{124}$$

Its FD approximation is chosen as

$$\begin{aligned} \frac{T_{I+1} - T_I}{\kappa \Delta t} &= \left.\frac{(T_E - T) - (T - T_W)}{(\Delta x)^2}\right|_{I+1} \\ &\quad + \left.\frac{(T_N - T) - (T - T_S)}{(\Delta y)^2}\right|_{I}, \\ \frac{T_{I+2} - T_{I+1}}{\kappa \Delta t} &= + \left.\frac{(T_N - T) - (T - T_S)}{(\Delta y)^2}\right|_{I+2} \\ &\quad + \left.\frac{(T_E - T) - (T - T_W)}{(\Delta x)^2}\right|_{I+1}. \end{aligned} \tag{125}$$

With equal spatial steps, $\Delta x_{(W-E)} = \Delta y_{(N-S)}$, and the module $m = \kappa \Delta t/(\Delta x)^2$, this can be rearranged to give

$$\begin{aligned} -T_W + (2 + 1/m)T - T_E|_{I+1} &= T_S - (2 - 1/m)T + T_N|_I \\ -T_S + (2 + 1/m)T - T_N|_{I+2} &= T_W - (2 - 1/m)T + T_E|_{I+1} \end{aligned}. \tag{126}$$

Example 5 shows a relatively simple application of this 2D FD scheme.

Example 5

The transient temperatures in the wall of a tube of square cross section, as shown in Fig. 27, are to be calculated for the case that the inner wall is suddenly brought to a temperature of $T_i = 1$, while the outer wall is kept at the constant initial temperature $T_o = 0$. The ratio of outer to inner side lengths is $2a/2b = 2$. Due to the symmetry of the geometry and the boundary

conditions, only 1/8 of the cross section suffices for a calculation. The subdivision of the wall thickness $s = a - b$ is chosen to be $\Delta x = \Delta y = s/3$. It is reasonable to use $m = 1/2$, that is, twice the stability limit of the explicit scheme for a two-dimensional problem, see Eq. (114). This makes the coefficients in the linear equation (126) equal to (−1, 4, −1), while the right-hand side reduces to the sums of the two neighboring temperatures $(2 - 1/m) = 0$. The constant temperatures (1 at the inner, and 0 at the outer sides of the wall appear in the last column vector, not in the matrix, so only the fifth line in the matrix contains three nonzero coefficients (see Fig. 25).

$$\begin{bmatrix} 4 & & & & -1 & & & & & & \\ & 4 & & & & -1 & & & & & \\ & & 4 & & & & -1 & & & & \\ & & & 4 & & & & -1 & & & \\ & & & -1 & 4 & & & & -1 & & \\ -1 & & & & & 4 & & & & & \\ & -1 & & & & & 4 & & & & \\ & & -1 & & & & & 4 & & & \\ & & & -1 & & & & & 4 & & \\ & & & & -1 & & & & & 4 & -1 \\ & & & & & & & & & -1 & 4 \end{bmatrix}_1 \times \begin{bmatrix} T_1 \\ T_2 \\ T_3 \\ T_4 \\ T_5 \\ T_6 \\ T_7 \\ T_8 \\ T_9 \\ T_{10} \\ T_{11} \end{bmatrix}_{I+1} = \begin{bmatrix} 1+2T_2 \\ 1+T_1+T_3 \\ 1+T_2+T_4 \\ 1+T_3+T_5 \\ T_4+T_{10} \\ 2T_7 \\ T_6+T_8 \\ T_7+T_9 \\ T_8+T_{10} \\ T_9+T_{11} \\ T_{10} \end{bmatrix}_I, \tag{127}$$

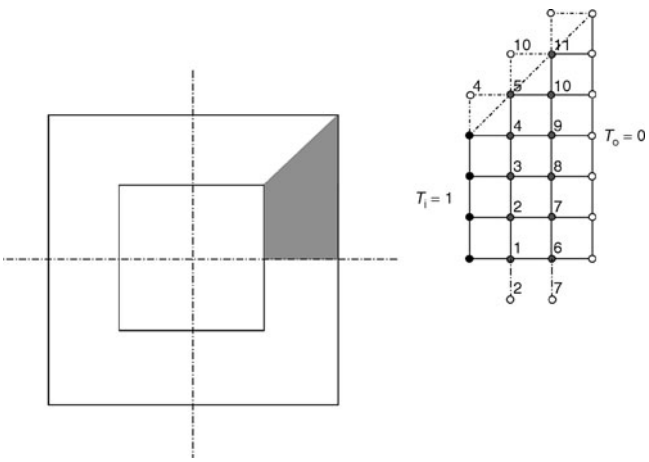

E2. Fig. 27. Geometry and spatial discretization for Example 5.

$$\begin{bmatrix} 4 & -2 & & & & & & & & & \\ -1 & 4 & -1 & & & & & & & & \\ & -1 & 4 & -1 & & & & & & & \\ & & -1 & 4 & -1 & & & & & & \\ & & & -1 & 4 & & & & & -1 & \\ & & & & & 4 & -2 & & & & \\ & & & & & -1 & 4 & -1 & & & \\ & & & & & & -1 & 4 & -1 & & \\ & & & & & & & -1 & 4 & -1 & \\ & & & & & & & & -1 & 4 & -1 \\ & & & & & & & & & -1 & 4 \end{bmatrix}_2 \times \begin{bmatrix} T_1 \\ T_2 \\ T_3 \\ T_4 \\ T_5 \\ T_6 \\ T_7 \\ T_8 \\ T_9 \\ T_{10} \\ T_{11} \end{bmatrix}_{I+2} = \begin{bmatrix} 1+T_6 \\ 1+T_7 \\ 1+T_8 \\ 1+T_9 \\ T_4+T_{10} \\ T_1 \\ T_2 \\ T_3 \\ T_4 \\ T_5 \\ T_{10} \end{bmatrix}_{I+1}. \tag{128}$$

The solution of these systems of linear equations (127) and (128) has to be found alternately from matrix inversion and multiplication:

$$\vec{T}_{K,I+1} = \mathbf{A}_1^{-1} \times \vec{d}_{K,I} \text{ (for each odd number } I = 1, 3, 5, \ldots), \tag{129}$$

$$\vec{T}_{K,I+2} = \mathbf{A}_2^{-1} \times \vec{d}_{K,I+1} \text{ (for each even number } I = 2, 4, 6, \ldots). \tag{130}$$

These can again be done by hand calculation, using easily available mathematical tools, such as the MINV(matrix) and MMULT (matrixA;matrixB) functions in Excel (as mentioned earlier). The results of such a calculation are shown in Table 6.

The time steps, because of $\Delta\xi = 1/3$ and $m = 1/2$, are $\Delta\tau = 1/18$, so the dimensionless time is obtained directly from the number I, divided by 18. The characteristic length is the wall thickness. Table 6 gives the 11 temperatures for the time steps, I, specified in the first line.

The last two lines give the dimensionless heat flows into the wall and out of the wall:

$$Q_i^* = 8 \cdot [(1 - \Theta_1)/2 + (1 - \Theta_2) + (1 - \Theta_3) + (1 - \Theta_4)], \tag{131}$$

$$Q_o^* = 8 \cdot [\Theta_6/2 + \Theta_7 + \Theta_8 + \Theta_9 + \Theta_{10} + \Theta_{11}]. \tag{132}$$

Initially, the flow out of the wall is zero. With increasing time the two flows become equal to each other. A final steady state is reached asymptotically. For this final steady state, the

E2. Table 6. Results of the 2D calculation by the implicit alternating directions implicit scheme (Example 5)

I	0	1	2	3	4	5	6	7	8	9	10	13	18
Θ_1	0	0.267	0.530	0.565	0.599	0.620	0.641	0.646	0.651	0.653	0.655	0.656	0.657
Θ_2	0	0.267	0.526	0.561	0.595	0.616	0.636	0.640	0.646	0.648	0.650	0.651	0.652
Θ_3	0	0.267	0.509	0.541	0.575	0.594	0.613	0.618	0.624	0.626	0.628	0.630	0.631
Θ_4	0	0.267	0.442	0.466	0.509	0.527	0.547	0.553	0.560	0.562	0.564	0.566	0.567
Θ_5	0	0.071	0.194	0.264	0.302	0.330	0.347	0.358	0.364	0.369	0.371	0.374	0.375
Θ_6	0	0.067	0.132	0.207	0.278	0.292	0.306	0.312	0.318	0.320	0.322	0.324	0.324
Θ_7	0	0.067	0.132	0.205	0.274	0.288	0.302	0.308	0.314	0.316	0.318	0.319	0.320
Θ_8	0	0.067	0.127	0.196	0.257	0.271	0.285	0.291	0.297	0.299	0.301	0.303	0.303
Θ_9	0	0.067	0.111	0.161	0.214	0.230	0.244	0.250	0.256	0.259	0.261	0.263	0.263
Θ_{10}	0	0.018	0.050	0.098	0.134	0.151	0.163	0.170	0.175	0.178	0.180	0.182	0.182
Θ_{11}	0	0.004	0.017	0.037	0.058	0.071	0.078	0.083	0.086	0.088	0.089	0.091	0.091
Q_i^*	28	20.5	14.1	13.2	12.2	11.6	11.1	10.9	10.8	10.7	10.6	10.6	10.58
Q_0^*	0	2.0	4.0	6.4	8.6	9.2	9.8	10.1	10.3	10.4	10.5	10.6	10.57

temperatures can be obtained more easily from the explicit scheme, see Eq. (114), with $T_{new} = T_{old}$, or $T = (T_E + T_N + T_W + T_S)/4$. This FD equivalent of Laplace equation can be carried out in a spreadsheet by a simple iteration process. The steady-state values of the dimensionless heat flows are the same as the so-called shape factors (see Chap. E1).

An exact analytical solution for the shape factors of n-sided hollow cylinders of regular polygonal cross section can be found in [13]. With $n = 4$, and $y = b/a = 0.5$, the shape factor from this analytical solution is $S = 10.23$. The FD result with the relatively coarse grid, $\Delta\xi = 1/3$, gives a slightly higher dimensionless flux of $S = Q^* = 10.58$ (+3.4%).

5 How to Account for Temperature-Dependent Physical Properties

In case that the temperature dependency of the physical properties, λ, and ρc_p cannot be neglected, Eq. (3) can also be brought into the form of Eq. (3a) (for constant properties) when introducing a new temperature scale by

$$\vartheta = \int_{T_0}^{T} \{\lambda/\lambda(T_0)\}\mathrm{d}T, \tag{133}$$

$$\frac{\partial\vartheta}{\partial t} = \kappa(\vartheta)\,\nabla^2\vartheta. \tag{134}$$

If the temperature dependency of λ, for example, can be given in a power law form:

$$\lambda = \lambda_0 \cdot (T/T_0)^n \tag{135}$$

one finds (for $n \neq -1$)

$$\vartheta = \frac{T_0}{n+1} \cdot \left[\left(\frac{T}{T_0}\right)^{n+1} - 1\right] \tag{136}$$

and

$$\lambda(\vartheta) = \lambda_0 \cdot \left[1 + (n+1)\frac{\vartheta}{T_0}\right]^{n/n+1}. \tag{137}$$

In a numerical calculation using FD schemes the thermal diffusivity, $\kappa = \lambda/(\rho c_p)$, $\kappa(\vartheta)$ must be kept constant for a time step, or, when using ADIP, correspondingly for two time steps with the alternating directions. Because of the narrow stability limits of the explicit scheme, the implicit methods in these cases are preferred.

6 Bibliography

1. Carslaw HS, Jaeger JC (1946) Conduction of heat in solids, 1st edn. Clarendon Press, Oxford; 2nd edition 1959, reprinted 1960, 1962, 1965, 1967
2. Tautz H (1971) Wärmeleitung und Temperaturausgleich. Verl. Chemie, Weinheim
3. Gröber EG (1961) Die Grundgesetze der Wärmeübertragung, 3rd edn. Springer, Berlin
4. Grigull U, Sandner H (1982) Heat conduction. Springer, Berlin
5. Soininen M, Heikkilä P (1981) Transient heat transfer in an infinite plate, in an infinite cylinder and in a sphere. Åbo Akademi, Inst. f. anl. tekn. Mittl. Nr. 48, Turku
6. Martin H, Saberian M (1994) Improved asymptotic approximations for transient conduction and diffusion processes. Chem Eng Process 33: 205–210
7. Megerlin F (1967) Die analytische Behandlung von Gefriervorgängen. Kältetechn Klimatisierung 19(12):386–391
8. Tao LC (1967) Generalized numerical solutions of freezing a saturated liquid in cylinders and spheres. AIChE J 13(1):165–169
9. Schmidt E (1924) Über die Anwendung der Differenzenrechnung auf technische Anheiz- und Abkühlungsprobleme. Beiträge zur technischen Mechanik und technischen Physik (August Föppl-Festschrift). Springer, Berlin, pp 179–189
10. Crank J, Nicholson P (1947) A practical method for numerical evaluation of solutions of partial differential equations of the heat-conduction type. Proc Camb Phil Soc 43
11. Peaceman PW, Rachford HH Jr (1955) The numerical solution of parabolic and elliptic differential equations. J Soc Ind Appl Math 3:28–44
12. Douglas J Jr, Rachford HH Jr (1956) On the numerical solution of heat conduction problems in two and three space variables. Trans Am Math Soc 82:421–439
13. Nickolay M, Cramer C, Martin H (2000) Analytical solution for the potential flow through the wall of n-sided hollow cylinders of regular polygonal cross-section. Int J Heat Mass Trans 43:139–145
14. Jahnke/Emde/Lösch (1966) Tables of higher functions, 7th edn. Teubner, Stuttgart
15. Abramowitz M, Stegun Irene A (eds) (1965) Handbook of mathematical functions. Dover Publications, New York

Free Convection

F1 Heat Transfer by Free Convection: Fundamentals

André Thess
Technische Universität Ilmenau, Ilmenau, Germany

1 Formulation of the Problem

Free convection refers to the fluid flow which is driven by a spatially nonuniform distribution of density [1]. The nonuniformity of density can be either a result of inhomogeneous temperature distribution or nonuniform concentration of an admixture such as salt concentration in seawater. The present overview is exclusively devoted to free convection due to temperature differences.

The general formulation of heat transfer problems as relevant to practical applications is shown in Fig. 1, where Fig. 1a is for *external flows* and Fig. 1b is for *internal flows*. For external flows the heat transfer problem consists in computing the total heat flow $\dot{Q}$ from a hot body to the surrounding fluid for given values of the uniform surface temperature T_S of the hot body and of the temperature of the fluid T_∞ far away from the body. For internal flows the heat transfer problem consists in computing the total heat flow $\dot{Q}$ for given values of the uniform temperature T_1 on one part of the boundary of the fluid and of the uniform temperature T_2 on another part. Defining $\Delta T = T_S - T_\infty$ for external and $\Delta T = T_1 - T_2$ for internal flow, the heat transfer problem for free convection is equivalent to computing the dependence $\dot{Q}(\Delta T)$. This is referred to as the *constant temperature case*. A related but different problem is the *constant heat flux case* which consists in assuming a constant heat flux density at the surface of a body and computing the maximum of the (non-uniform) surface temperature. The present overview is restricted to the constant temperature case.

By virtue of the linearity of the heat transport equation the desired relation can be written in the form

$$\dot{Q} = \alpha A \Delta T \tag{1}$$

where α is the heat transfer coefficient [1] and A is the surface area of the heated body (for external flow) or the area of the heated part of the boundary (for internal flow). The present heat transfer problem is then equivalent to the computation of the heat transfer coefficient. In contrast to forced convection, where the flow field is known, the flow field in free convection is set up by ΔT, hence the heat transfer coefficient is a function of the applied temperature difference. The ultimate goal of free-convection heat transfer calculation is therefore to determine $\alpha(\Delta T)$.

The heat transfer problem under consideration can either be solved by a full numerical simulation using computational fluid dynamics (CFD) software or by using empirical correlations based on experiments and numerical simulations. The present overview is exclusively concerned with the second method which provides an approximate solution to the heat transfer problem.

2 Physical Parameters

The best documented case is that of small temperature differences, described by the condition $\Delta T \ll T_*$ where T_* is any of the quantities T_S, T_∞, T_1, and T_2 defined in Fig. 1 or the reference temperature defined by Eqs. (3) or (4) below. This case can be treated within the framework of the Boussinesq approximation where all thermophysical properties of the fluid are considered as temperature-independent except for the density in the buoyancy term of the Navier–Stokes equation. In the framework of the Boussinesq approximation the solution of the heat transfer problem requires the following quantities to be given:

ρ - density
ν - kinematic viscosity
κ - thermal diffusivity
β - isobaric volume expansion coefficient
λ - thermal conductivity
L - characteristic length
ΔT - temperature difference
g - acceleration of gravity.

The quantities have to be given at a reference temperature T_*. The isobaric volume expansion coefficient is defined as

$$\beta = \frac{1}{\rho}\left(\frac{\partial \rho}{\partial T}\right)_p . \tag{2}$$

If the fluid under consideration is an ideal gas, its isobaric expansion coefficient can be approximated by the formula $\beta = 1/T_*$ [4].

If the condition $\Delta T \ll T_*$ is not satisfied, the full temperature dependence of the thermophysical data, i.e. $\rho(T)$, $\nu(T)$, $\kappa(T)$,

VDI-GVC (ed.), *VDI Heat Atlas*, DOI 10.1007/978-3-540-77877-6_18,

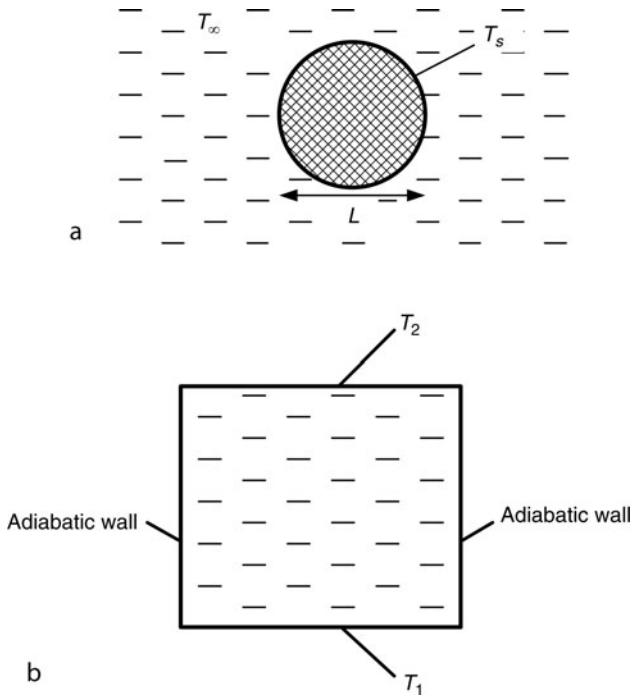

F1. Fig. 1. Schematic of two canonical problems in free convection, (**a**) external flow around a heated sphere ($T_s > T_\infty$), (**b**) internal flow in a horizontal fluid large heated from below ($T_1 > T_2$). Gravity acts downward in both figures.

and $\lambda(T)$ has to be taken into account. For a general treatment of the problem with fully temperature-dependent material properties see [2, 3]. If such an approach is too expensive computationally or if high accuracy is not necessary, the problem with temperature-dependent thermophysical data can be approximated by a problem with temperature-independent material properties evaluated at the reference temperatures

$$T_* = \frac{1}{2}(T_S + T_\infty) \tag{3}$$

for external flow and

$$T_* = \frac{1}{2}(T_1 + T_2) \tag{4}$$

for internal flow. Assuming steady-state conditions, the goal of heat transfer calculation in the framework of the Boussinesq approximation is to determine the function

$$\alpha(\rho, \nu, \kappa, \beta, \lambda, L, \Delta T, g). \tag{5}$$

3 Nondimensional Groups

The problem of the computation of the heat transfer coefficient α is equivalent to determining the functional relationship

$$\mathrm{Nu}(\mathrm{Ra}, \mathrm{Pr}) \tag{6}$$

between the nondimensional groups Ra, Pr, and Nu, called Rayleigh-, Prandtl-, and Nusselt number, respectively. They are given as

$$\mathrm{Ra} = \frac{\beta g \Delta T L^3}{\nu\kappa}, \tag{7}$$

$$\mathrm{Pr} = \frac{\nu}{\kappa}, \tag{8}$$

$$\mathrm{Nu} = \frac{\alpha L}{\lambda}. \tag{9}$$

In literature, the Nusselt number is often expressed in the form

$$\mathrm{Nu}(\mathrm{Gr}, \mathrm{Pr}) \tag{10}$$

instead of Eq. (6), where Gr = Ra/Pr is the Grashof number. Equations (6) and (10) contain the same information and can be converted into eachother by either substituting Ra = GrPr in Eq. (6) or Gr = Ra/Pr in Eq. (10).

4 Methodology

The methodology for solving heat transfer problems with free convection involves the following steps.

1. Compile the input parameters ρ, ν, κ, β, λ, and ΔT, g
2. Compute the nondimensional groups Ra and Pr,
3. Compute Nu(Ra, Pr) using the formulas given in the VDI Heat Atlas,
4. Compute α from Nu using Eq. (9),
5. Compute $\dot{Q}$ from α using Eq. (1).

This methodology is illustrated using the following two examples.

Example 1 (External flow)

A spherical body with a diameter of $D = 5\,\mathrm{cm}$ and a surface temperature of $T_S = 100\,^\circ\mathrm{C}$ is placed in a large vessel containing water with a temperature $T_\infty = 20\,^\circ\mathrm{C}$. What is the total heat flow $\dot{Q}$ from the body to the water?

Step 1 - compilation of input parameters: With $\Delta T = 80\,\mathrm{K}$ and $T_* = 333\,\mathrm{K}$, the condition $\Delta T \ll T_*$ for neglecting the temperature depends of the material properties is not satisfied. Nevertheless, it is appropriate to start the analysis using this simplified approach and setting $T_* = (T_S + T_\infty)/2 = 60\,^\circ\mathrm{C}$. For this temperature Chap. D2 provides the values $\rho = 983.2\,\mathrm{kg/m^3}$, $\nu = 4.750 \times 10^{-7}\,\mathrm{m^2/s}$, $\kappa = 1.591 \times 10^{-7}\,\mathrm{m^2/s}$, $\beta = 5.232 \times 10^{-4}\,K^{-1}$, and $\lambda = 0.6544\,\mathrm{W/(mK)}$. Moreover, $L = 5 \times 10^{-2}\,\mathrm{m}$, $\Delta T = 80\,\mathrm{K}$, $g = 9.81\,\mathrm{m/s^2}$.

Step 2 - computation of Ra *and* Pr: With the foregoing input parameters the nondimensional groups are readily calculated as $\mathrm{Ra} = 6.792 \times 10^8$ and $\mathrm{Pr} = 2.98$.

Step 3 - computation of the Nusselt number: Using the empirical correlation $\mathrm{Nu} = 2 + 0.589\mathrm{Ra}^{1/4}/[1 + (0.469/\mathrm{Pr})^{9/16}]^{4/9}$ given in Chap. F2 the Nusselt number is obtained as Nu = 84.98.

Step 4 - computation of the heat transfer coefficient: Inserting the Nusselt number and the material properties into Eq. (9) one obtains $\alpha = 1112\,\mathrm{W/(m^2K)}$.

Step 5 - computation of the heat flux: The total heat flux is obtained by applying Eq. (1) with the surface area $A = \pi L^2$ and the computed heat transfer coefficient. The result is $\dot{Q} = 698.7\,\mathrm{W}$.

Comment: Given the approximate nature of the empirical correlation used in step 3, the results of steps 3, 4, and 5 should be considered as accurate to at most two decimal places. This provides the final result Nu $\approx$ 85, $\alpha \approx 1.1\,\mathrm{kW/(m^2K)}$, and $\dot{Q} \approx 700\,\mathrm{W}$.

Example 2 (Internal flow)
Air in a cylindrical vessel with height $L = 3.70\,\mathrm{m}$ and diameter $D = 3.70\,\mathrm{m}$ is heated from below by an isothermal bottom plate with temperature $T_1 = 30\,^\circ\mathrm{C}$ and cooled from above by an isothermal plate with $T_2 = 10\,^\circ\mathrm{C}$. There is no heat loss through the sidewall. What is the total heat flow $\dot{Q}$ from the heating to the cooling plate?

Step 1 - compliation of input parameters: With $\Delta T = 20\,\mathrm{K}$ and $T_* = 293\,\mathrm{K}$ the condition $\Delta T \ll T_*$ for neglecting the temperature dependence of the material properties is satisfied. The material properties are therefore evaluated at $T_* = (T_1 + T_2)/2 = 20\,^\circ\mathrm{C}$. For this temperature Chap. D2 provides the values $\rho = 1.188\,\mathrm{kg/m^3}$, $\nu = 1.535 \times 10^{-5}\,\mathrm{m^2/s}$, $\kappa = 2.147 \times 10^{-5}\,\mathrm{m^2/s}$, $\beta = 3.421 \times 10^{-3}\,K^{-1}$, and $\lambda = 2.569 \times 10^{-2}\,\mathrm{W/(mK)}$. Moreover, $L = 3.70\,\mathrm{m}$, $\Delta T = 20\,\mathrm{K}$, and $g = 9.81\,\mathrm{m/s^2}$.

Step 2 - computation of Ra *and* Pr: With the foregoing input parameters the nondimensional groups are readily calculated as $\mathrm{Ra} = 1.032 \times 10^{11}$ and $\mathrm{Pr} = 0.715$. The aspect ratio, to be defined in Chap. F3, is an additional parameter of the problem. Its value is $\Gamma = 1$.

Step 3 - computation of the Nusselt number: The Prandtl number of air is similar to that of helium. Therefore, the data from Chap. F3 (Sect. 2.1) can be used. Using Table 2 for $\mathrm{Ra} = 1.04 \times 10^{11}$ and $\mathrm{Pr} = 0.74$ the Nusselt number is obtained as $\mathrm{Nu} = 270$.

Step 4 - computation of the heat transfer coefficient: Inserting the Nusselt number and the material properties into Eq. (9) one obtains $\alpha = 1.875\,\mathrm{W/(m^2K)}$.

Step 5 - computation of the heat flux: The total heat flux is obtained by applying Eq. (1) with the surface area $A = \pi D^2/4$ and the computed heat transfer coefficient. The result is $\dot{Q} = 403\,\mathrm{W}$.

Comment: Given the fact that the data from Table 2 used in step 3 are not exactly for the Rayleigh and Prandtl numbers at hand, the result should be considered as accurate to at most two decimal places. This provides the final result $\dot{Q} \approx 400\,\mathrm{W}$.

5 Bibliography

1. Incropera FP, De Witt DP (1996) Fundamentals of heat and mass transfer. Wiley, New York
2. Herwig H (1986) Approximate method of treating the effect of variable properties in the calculation of plane laminar boundary layer flows past cylindrical bodies. Int Chem Eng AIChE J 27:25–33
3. Herwig H, Schäfer P (1996) A combined perturbation/finite-difference procedure applied to temperature effects and stability in a laminar boundary layer. Arch Appl Mech 66:264–272
4. Moran MJ, Shapiro HN (1995) Fundamentals of engineering thermodynamics. Wiley, New York

F2 Heat Transfer by Free Convection: External Flows

Werner Kast[2] · *Herbert Klan*[2] (*Revised by André Thess*[1])
[1]Technische Universität Ilmenau, Ilmenau, Germany
[2]Technische Universität Darmstadt, Darmstadt, Germany

1 Vertical Surfaces

The average dimensionless heat transfer coefficient [1, 2] for laminar and turbulent flows near a vertical surface in the range from $\mathrm{Ra} = 10^{-1}$ to $\mathrm{Ra} = 10^{12}$ is defined by [3]

$$\mathrm{Nu} = \left\{0.825 + 0.387[\mathrm{Ra} f_1(\mathrm{Pr})]^{1/6}\right\}^2 \tag{1}$$

The function $f_1(\mathrm{Pr})$ allows for the effect of the Prandtl number in the range $0.001 < \mathrm{Pr} < \infty$ [4]:

$$f_1(\mathrm{Pr}) = \left[1 + \left(\frac{0.492}{\mathrm{Pr}}\right)^{9/16}\right]^{-16/9} \tag{2}$$

Its numerical values for some Prandtl numbers are presented in Table 1.

The value to be inserted for the characteristic length L in Eqs. (7) and (9) of Chap. F1 for Ra and Nu is that of the height of the surface.

Equation (1) does not exactly represent the behavior in the zone of transition between laminar and turbulent flows ($10^8 \le \mathrm{Ra} \le 10^9$). However, its accuracy is adequate for engineering applications in the entire range of Rayleigh numbers.

If an error of up to 4% is permissible, Eq. (1) can also be applied for constant rates of heat flux through the surface and for the associated temperature distribution. The temperature at the center of the surface should be inserted for T_s if the heat flow rate is constant.

The following equation has been developed for heat transfer from a vertical cylinder [5]. It allows the Nusselt number for the cylinder to be determined from its height-to-diameter ratio h/D and the Nusselt number for a vertical plate of the same height, i.e.,

$$\mathrm{Nu} = \mathrm{Nu}_{\mathrm{plate}} + 0.97\frac{h}{D} \tag{3}$$

Example 1

A uniform temperature of $T_s = 40°\mathrm{C}$ is maintained over the entire surface of a vertical wall of height $h = 0.8$ m and width $b = 0.5$ m. At what rate is the heat transferred from this wall to the surrounding air ($T_\infty = 20°\mathrm{C}$)?

The properties of air at $T_* = 30°\mathrm{C}$ can be obtained from Subchap. D2.2, i.e.,

$$\lambda = 0.0268\ \mathrm{W/mK}; \quad \nu = 16.1 \times 10^{-6}\ \mathrm{m^2/s}; \quad \text{and } \mathrm{Pr} = 0.70.$$

Since $T_\infty = 273$ K, we have $\beta = 1/T_\infty = 1/293\ \mathrm{K^{-1}}$.

The characteristic length is $L = h$. Thus, the Rayleigh number is

$$\mathrm{Ra} = \frac{gl^3\beta(T_s - T_\infty)}{\nu \times \kappa} = 9.26 \times 10^8.$$

The effect of the Prandtl number is obtained from Eq. (2). Thus, $f_1(\mathrm{Pr}) = 0.345$.

Inserting the above obtained values in Eq. (1) gives

$$\mathrm{Nu} = 120,$$
$$\alpha = \frac{\mathrm{Nu}\lambda}{L} = 4.01\frac{\mathrm{W}}{\mathrm{m^2\ K}}.$$

Hence, the rate of convective heat flow is

$$\dot{Q} = A\alpha(T_s - T_\infty) = 0.8 \times 0.5 \times 4.01(40 - 20)\ \mathrm{W} = 32.1\ \mathrm{W}.$$

2 Inclined Plane Surfaces

The transfer of heat from inclined plane surfaces depends on whether the heat loss is upward or downward. If it is downward, the boundary layer hugs the plane of the surface; and if heat is transferred upward, the boundary layer separation occurs downstream after an entrance length. The following applies for heated and cooled plane surfaces.

1. No separation occurs if a heated surface transmits heat downward or if a cooled surface absorbs heat from above.
2. Separation may occur if a heated surface transmits heat upward or if a cooled surface absorbs heat from below.

VDI-GVC (ed.), *VDI Heat Atlas*, DOI 10.1007/978-3-540-77877-6_19,

F2. Table 1. Numerical values for the function f_1 (Pr)

Pr	0.01	0.70	7	100	∞
f_1(Pr)	0.0168	0.345	0.698	0.916	1

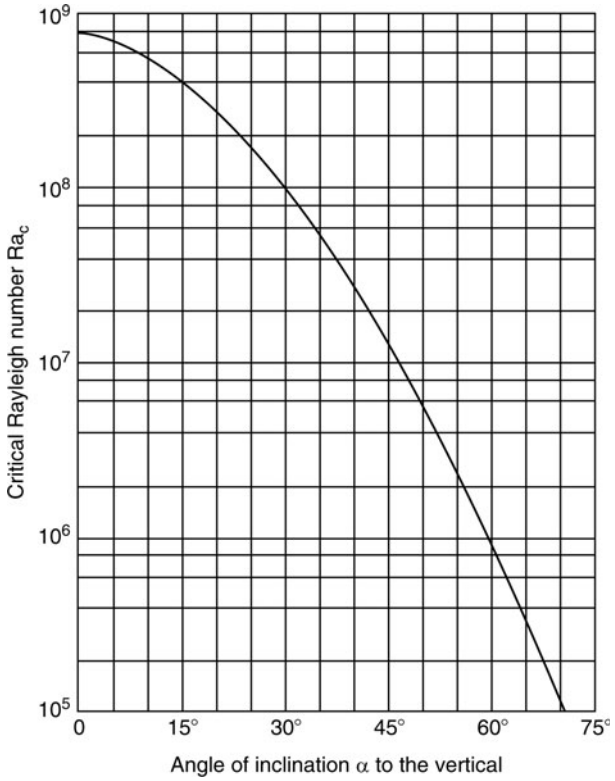

F2. Fig. 1. Upper limit Ra_c for the laminar range as a function of the angle of inclination α in free convection at heated upper surfaces or at cooled lower surfaces [a suitable approximation is given by $Ra_c = 10^{(8.9 - 0.00178\ a\ 1.82)}$].

In Case 1, an approximate figure for the dimensionless heat transfer coefficient can be obtained from the equations for vertical surfaces by introducing the term $g \cos \alpha$, the component of gravity parallel to the vertical surface, instead of g, the acceleration due to gravity [6, 7]. Thus, the term Ra_α is substituted for Ra in Eq. (1), where

$$Ra_\alpha = Ra \cos \alpha \tag{4}$$

The only cases in which the simple generalization expressed by Eq. (1) is not valid for turbulent flow arise if heat transfer occurs at heated upper surfaces or cooled lower surfaces, i.e., for Case 2. Owing to the separation of the boundary layer, the transition into turbulent flow in these cases takes place at critical Rayleigh numbers Ra_c that are lower than their counterparts on vertical surfaces (cf. Fig. 1). The following relationship, which has been derived from the measurements in water (Pr = 7), has been proposed for the turbulent range [7]:

$$Nu = 0.56(Ra_c \cos \alpha)^{1/4} + 0.13(Ra^{1/3} - Ra_c^{1/3}) \tag{5}$$

The value of Ra_c to be inserted in this equation for a given angle of inclination α can be obtained from Fig. 1.

Example 2

A pane of glass in a solar collector is inclined at an angle of 50° to the vertical. The temperature at its surface is $T_s = 30°C$, and that of the stationary surrounding air is $T_\infty = 10°C$. The length of the pane is $h = 2$ m; and the width, $b = 1$ m. What are the heat losses by convection at the upper side of the glass pane in the collector?

The properties of air at $T_\infty = 20°C$ (Subchap. D2.2) are

$$\lambda = 0.0260 \text{ W/mK}, \quad \nu = 15.1 \times 10^{-6} \text{ m}^2/s,$$
$$\text{Pr} = 0.70, \qquad \beta = \frac{1}{T_\infty} = \frac{1}{283} \text{K}^{-1}$$

The characteristic length is $L = h = 2$ m. Hence,

$$\text{Ra} = \frac{gl^3\beta(\vartheta_s - \vartheta_\infty)}{\nu^x} = 1.703 \times 10^{10}$$

According to Fig. 1, the upper limit for the zone of laminar flow at an angle of inclination of 50° is $Ra_c = 5.5 \times 10^6$. Hence, according to Eq. (5),

$$\text{Nu} = 0.56(5.5 \times 10^6 \cos 50°)^{1/4} + 0.13[(1.703 \times 10^{10})^{1/3} - (5.5 \times 10^6)^{1/3}] = 338.$$

It follows from Eq. (9) in Chap. F1 that

$$\alpha = \frac{\text{Nu}\lambda}{l} = 4.37 \text{ W/m}^2 \text{ K}.$$

The heat losses by free convection above the pane of glass in the collector are

$$\dot{Q} = A\alpha(T_s - T_\infty) = 175 \text{ W}.$$

3 Horizontal Plane Surfaces

There are two cases of heat transfer at horizontal plane surfaces: First, upward transport of heat from a heated surface and downward transport of heat from a cooled surface of semi-infinite extent; Second, downward heat transfer from a heated surface and upward heat transfer from a cold surface. The form of the relationship for the dimensionless heat transfer coefficient is

$$\text{Nu} = f(\text{Pr},\ \text{Geometry})\text{Ra}^{1/5} \tag{6}$$

The term "Geometry" in this case refers to the shape of the plane surface. The index 1/5 has been derived from solutions of boundary layer equations for horizontal surfaces of semi-infinite extent and a stable (laminar) boundary layer. If the temperature difference is not too great, flow becomes stable in the boundary layers of plane surfaces of finite length and must be symmetrical at the centre of the surface. The characteristic length L is

$$L = \frac{ab}{2(a+b)}, \text{ for rectangular surfaces}$$

and $L = d/4$, for circular discs.

3.1 Heat Emission at Upper Surface (Lower Surface Cooled)

The equation for laminar flow [8], i.e., $\mathrm{Ra} f_2(\mathrm{Pr}) \lesssim 7 \times 10^4$, is

$$\mathrm{Nu} = 0.766[\mathrm{Ra} f_2(\mathrm{Pr})]^{1/5} \tag{7}$$

and that for turbulent flow, i.e., $\mathrm{Ra} f_2(\mathrm{Pr}) \gtrsim 7 \times 10^4$, is

$$\mathrm{Nu} = 0.15[\mathrm{Ra} f_2(\mathrm{Pr})]^{1/3} \tag{8}$$

The surface at which heat transfer takes place is considered to be part of a plane of infinite extent, in both cases.

The function f_2 (Pr) describes the effect of the Prandtl number over the entire range $0 < \mathrm{Pr} < \infty$ and is given by

$$f_2(\mathrm{Pr}) = \left[1 + \left(\frac{0.322}{\mathrm{Pr}}\right)^{11/20}\right]^{-20/11} \tag{9}$$

Its numerical values for a few Prandtl numbers are presented in Table 2.

Equations (7) and (8) are unsuitable if the conditions of the surrounding inflow depart considerably from the boundary conditions. An example of where this arises is a room with floor heating, in which case the flow of air within the room is also governed to a great extent by the transport of heat and momentum to the surroundings.

Example 3

The surface of the water in a rectangular swimming pool of $C = 10$ m length and $B = 6$ m width is covered by a floating plastic film. The temperature of the film is $T_s = 20°\mathrm{C}$, and that of the ambient air is $T_\infty = 10°\mathrm{C}$. How much heat does the film release by convection to the air?

The properties listed in Subchap. D2.2 for air at $\vartheta_m = 15°\mathrm{C}$ are

$$\lambda = 0.0257\ \mathrm{W/mK}, \quad \nu = 14.7 \cdot 10^{-6}\ \mathrm{m^2/s},$$
$$\mathrm{Pr} = 0.70; \qquad \beta = \frac{1}{T_\infty} = \frac{1}{283}\mathrm{K}^{-1}.$$

The characteristic length is

$$L = \frac{CB}{2(C+B)} = 1.875\mathrm{m}.$$

The dimensionless numbers are

$$\mathrm{Ra} = 7.402 \times 10^9$$
$$f_2(\mathrm{Pr}) = 0.401.$$

Convection is turbulent, because $\mathrm{Ra}\, f_2\,(\mathrm{Pr}) > 7 \times 10^4$. Applying Eqs. (8) and (9) thus gives

$$\mathrm{Nu} = 215.4,$$
and
$$\alpha = 2.95\ \mathrm{W/m^2K}$$

The film transfers heat by convection to the surrounding air at a rate of

$$\dot{Q} = A\alpha(T_s - T_\infty) = 1770\ \mathrm{W}.$$

3.2 Heat Emission at Lower Surface (Upper Surface Cooled)

In this case, the only known relationship [9] for the range of laminar flow, i.e., $10^3 < \mathrm{Ra}\, f_1\,(\mathrm{Pr}) < 10^{10}$, is

$$\mathrm{Nu} = 0.6[\mathrm{Ra} f_1(\mathrm{Pr})]^{1/5} \tag{10}$$

The term f_1 (Pr) in this equation is defined by Eq. (2).

The surface at which heat transfer takes place is considered to be a plane of infinite extent.

4 Horizontal Curved Surfaces

4.1 Cylinders

In analogy to Eq. (1), the relationship that applies to the average dimensionless heat transfer coefficient for free convection around a horizontal cylinder [10] is

$$\mathrm{Nu} = \{0.60 + 0.387[\mathrm{Ra} f_3(\mathrm{Pr})]^{1/6}\}^2 \tag{11}$$

The characteristic length L from which the Nusselt and Rayleigh numbers are calculated is

$$L = D \tag{12}$$

The function f_3 (Pr) describes the effect of the Prandtl number over the entire range $0 < \mathrm{Pr} < \infty$ and is given by

$$f_3(\mathrm{Pr}) = \left[1 + \left(\frac{0.559}{\mathrm{Pr}}\right)^{9/16}\right]^{-16/9} \tag{13}$$

Its numerical values for some Prandtl numbers are presented in Table 3.

4.2 Spheres

If the diameter D is taken as the characteristic length L, free convection around spheres can be described by the equations that apply to vertical planes [11]. If the temperature difference or the sphere diameter is small, the average dimensionless heat transfer coefficient tends asymptotically toward a limit, i.e.,

$$\mathrm{Nu} \to 2 \quad \text{if } \mathrm{Ra} \to 0.$$

F2. Table 2. Numerical values for the function f_2(Pr)

Pr	0.01	0.70	7	100	∞
f_2(Pr)	0.0242	0.401	0.736	0.927	1

F2. Table 3. Numerical values for the function f_3(Pr)

Pr	0.01	0.70	7	100	∞
f_3(Pr)	0.015	0.325	0.681	0.911	1

In other words, Eq. (1) is no longer valid for spheres if $\mathrm{Ra} < 10^3$. A better approximation is as follows [12]:

$$\mathrm{Nu} = 0.56\left[\left(\frac{\mathrm{Pr}}{0.846+\mathrm{Pr}}\right)\mathrm{Ra}\right]^{1/4} + 2 \tag{14}$$

4.3 Cubes

The dimensionless heat transfer coefficient for a cube is given by [13]

$$\mathrm{Nu} = 5.748 + 0.752\left(\frac{\mathrm{Ra}}{f_4(\mathrm{Pr})}\right)^{0.252} \tag{15}$$

The characteristic length in this case is $L = A/D$ and $D = 4\ V/A$, where A is the total area and V is the volume of the cube. The function $f_4(\mathrm{Pr})$ is given by

$$f_4(\mathrm{Pr}) = \left(1 - \left(\frac{0.492}{\mathrm{Pr}}\right)^{9/16}\right)^{16/9} \tag{16}$$

Example 4

The temperature at the surface of an uninsulated horizontal pipe of outer diameter $D = 0.108$ m is $T_s = 180°\mathrm{C}$. At what rate per unit length of pipe is the heat transferred by convection to a stationary atmosphere at $T_\infty = 20°\mathrm{C}$?

The properties of air at $T_* = 100°\mathrm{C}$ (cf. Subchap. D2.2) are

$$\lambda = 0.0318\ \mathrm{W/mK}; \quad \nu = 23.15 \times 10^{-6}\ \mathrm{m^2/s}$$
$$\mathrm{Pr} = 0.69, \quad \beta = \frac{1}{T_\infty} = \frac{1}{293}\mathrm{K^{-1}}.$$

The characteristic length is $L = D = 0.108$ m.

$$\mathrm{Ra} = 8.7 \times 10^6$$
$$f_3(\mathrm{Pr}) = 0.323.$$

Inserting the above obtained values in Eq. (11):

$$\mathrm{Nu} = 27.0$$
$$\alpha = 7.95\ \mathrm{W/m^2K}.$$

Thus, the heat losses per pipe length L are

$$\dot{Q}/L = \pi D\alpha(T_s - T_\infty) = 432\ \mathrm{W/m}.$$

4.4 Finned Tubes

Numerous types of finned tubes are encountered in practice. Smooth tubes with circular fins of constant thickness have been taken as an example in this case. Few results of measurements on free convection around horizontal finned tubes have been published [14–17]. An analysis of these reveals that the values for all the tubes with circular fins that were investigated do not depart by more than ±25% from the figures obtained by the following equation:

$$\mathrm{Nu} = 0.24\left(\mathrm{Ra}\frac{b}{d}\right)^{1/3} \tag{17}$$

where b is the fin spacing and d is the diameter of the tube.

In this case, an effective diameter $d_e = d + h$, where h is the height of the fins, is inserted for the characteristic length L in Eqs. (7) and (9) of Chap. F1 for the determination of the Rayleigh and Nusselt numbers. The value inserted for the temperature difference is T_s, the average temperature at the surface of the core tube. The measured values from which Eq. (17) was derived cover the $10^3 < \mathrm{Ra} < 10^7$ range. All the experiments were carried out in air (Pr = 0.70).

The only cases in which Eq. (17) should be applied are those in which the material of construction for both the tube and fins has a thermal conductivity equal to or greater than that of steel. Moreover, there should be no gaps between the tube and the fins. The values for the heat transfer external area, i.e., α determined from Eq. (17), must be expressed in terms of the total external area, i.e.,

$$\alpha = \frac{\dot{Q}}{A_{\mathrm{tot}}(T_s - T_\infty)} \tag{18}$$

Example 5

The dimensions of a horizontal steel finned tube are as follows:

Diameter of tube	$d = 0.050$ m
Height of fins	$h = 0.030$ m
Thickness of fins	$s = 0.002$ m
Fin spacing	$b = 0.020$ m.

The temperature of the tube is $T_s = 80°\mathrm{C}$, and that of the surrounding air, $T_\infty = 20°\mathrm{C}$. How much more convective heat is given off per unit time and unit length from this tube than from a smooth tube with an effective diameter $d_e' = 0.080$ m?

Properties of air at $T_* = 50°\mathrm{C}$ (cf. Subchap. D2.2):

$$\lambda = 0.0282\ \mathrm{W/mK}; \quad \nu = 19.3 \cdot 10^{-6}\mathrm{m^2/s};$$
$$\mathrm{Pr} = 0.69 \quad \beta = 1/T_\infty = 1/293\ \mathrm{K^{-1}}.$$

The effective diameter is $d_e = d + h = 0.080$ m.

$$\mathrm{Ra}_{d_e} = \frac{g d_e^3 \beta(T_0 - T_\infty)}{\nu^x} = 1.905 \times 10^6$$
$$\frac{b}{d} = \frac{0.02\ \mathrm{m}}{0.05\ \mathrm{m}} = 0.4.$$

The number of fins per unit length is

$$n = \frac{1}{b+s} = \frac{1}{(0.02+0.002)\mathrm{m}} = 45.5/\mathrm{m}.$$

The total area of heat-emitting surface per unit length L_0 of the finned tube is

$$\frac{A_{\mathrm{tot}}}{L_0} = \pi d(1 - sn) + n\frac{\pi}{2}[(d+2h)^2 - d^2] + n\pi s(d+2h),$$
$$\frac{A_{\mathrm{tot}}}{L_0} = 0.860\frac{\mathrm{m^2}}{\mathrm{m}}.$$

Inserting in Eq. (30):

$$\mathrm{Nu} = 0.24\left(\mathrm{Ra}_{d_e}\frac{b}{d}\right)^{1/3} = 21.9,$$
$$\alpha = \frac{\mathrm{Nu}\lambda}{d_e} = 7.73\frac{\mathrm{W}}{\mathrm{m^2K}}.$$

The convective heat flow rate per unit length L_0 of the finned tube is

$$\frac{\dot{Q}}{L_0} = \frac{A_{tot}}{L_0}\alpha(T_s - T_\infty) = 399\frac{W}{m}.$$

The figure is to be compared to that for convective heat transfer around a smooth tube of $d = d_e = 0.08$ m and a characteristic length of $L = d = 0.08$ m. The latter can be obtained from Eqs. (3), (24), and (26). Thus,

$$Nu = 17.33 \text{ and } \quad \alpha = 6.11\ W/m^2K.$$

The convective heat flow rate per unit length of finned tube is

$$\frac{\dot{Q}}{L_0} = \frac{A}{L_0}\alpha(T_s - T_\infty) = 92.1\frac{W}{m}.$$

Thus, the rate of convective heat loss from the finned tube is more than four times as much as that from a smooth tube with the same effective diameter.

5 Superimposed Free and Forced Convection

If buoyancy forces act in the same direction as a forced convection, the velocities and their gradients in the boundary layers increase. As a consequence, the heat transfer is generally increased. On the other hand, it was observed [18] that superimposing forced convection on predominantly free convection initially retarded the transition to turbulence because the boundary layer separation was thus restricted. The additive effect of superimposing did not become evident until higher Rayleigh numbers were attained. Since this complex behavior was not investigated in sufficient depth, the following method must be regarded merely as a rough approximation.

The following equation applies for the case in which the free convection is in the same direction as a forced vertical convection current and is derived from experimental results [19]:

$$Nu^3 = Nu_{forced}^3 + Nu_{free}^3 \qquad (19)$$

In analogy, the following applies for the case in which the free convection is in the direction opposite to the vertical current:

$$Nu^3 = \left|Nu_{forced}^3 - Nu_{free}^3\right| \qquad (20)$$

If the forced convection current is vertical, this method may be adopted for the vertical plate, the horizontal cylinder, and the sphere. The Nusselt numbers applicable to the term that allows for the forced convection can be obtained from Chaps. G1 (plate), G5 (cylinder), and G8 (individual sphere).

Superimposing free convection on *non* vertical forced convection has been the subject of such little study that it still cannot be verified whether the above method could also be adopted in this case.

Example 6

Wind flows upward over the longitudinal plane of the pane of glass in the solar collector described in Example 2. The velocity parallel to the plane and beyond the boundary layer is $u_\infty = 1$ m/s. What heat losses now result from convection on the upper side of the collector?

Let the effect of free convection be described by the Nusselt number determined in Example 2, i.e., $Nu_{free} = 338$.

The Reynolds number that applies for the effect of forced convection is

$$Re = \frac{u_\infty l}{\nu} = 1.32 \cdot 10^5.$$

This figure lies in the transition between turbulent and laminar flows. The Nusselt number that can be read off against it in the diagrams in Chap. C1 is $Nu_{forced} = 440$.

Equation (19) thus becomes

$$Nu^3 = (440^3 + 338^3)^{1/3} = 498.$$

It is thus evident that the wind, which was assumed to flow at a low velocity, increases the convective heat losses by almost 50%.

Example 7

A heat transfer unit in the form of a plate (height $h = 0.5$ m; breadth $b = 0.3$ m) is suspended vertically in a tunnel through which air flows upward at an average velocity of $u_\infty = 1$ m/s and a temperature of $T_\infty = 20°C$. The temperature on both sides of the plate is $T_s = 60°C$. Owing to baffles, flow in the channel is turbulent. At what rate does the unit emit heat by convection?

The properties of air at $T_m = 40°C$ (cf. Subchap. D2.2) are

$$\lambda = 0.0275\ W/mK, \quad \nu = 18.81 \cdot 10^{-6}\ m^2/s,$$
$$Pr = 0.69, \quad \beta = \frac{1}{T_\infty} = \frac{1}{293}\ K^{-1},$$
$$f_1(Pr) = 0.343.$$

The characteristic length is $L = h = 0.5$ m, and thus,

$$Ra = 3.26 \times 10^8$$
$$Re = \frac{u_\infty l}{\nu} = \frac{1 \cdot 0.5}{18.81 \cdot 10^{-6}} = 2.66 \cdot 10^4.$$

Equation (20) gives

$$Nu_{forced} = 144; \quad Nu_{free} = 100,$$
$$Nu = \{\left|Nu_{forced}^3 - Nu_{free}^3\right|\}^{1/3} = 126.$$

Thus,

$$\alpha = \frac{Nu\lambda}{l} = 6.9\ W/m^2K.$$

Consequently, the surfaces on both sides of the plate transfer heat by convection at the following rate to the air flowing in the channel:

$$\dot{Q} = A\alpha(T_s - T_\infty) = 82.8\ W.$$

6 Bibliography

1. Incropera FP, DeWitt DP (1996) Fundamentals of heat and mass transfer. Wiley & Sons, New York
2. Incropera FP, DeWitt DP (1996) Fundamentals of heat and mass transfer. Wiley & Sons, New York
3. Churchill W, Chu HHS (1975) Correlating equations for laminar and turbulent free convection from a vertical plate. Int J Heat Mass Tran 18:1323–1329
4. Churchill W, Usagi R (1972) A general expression for the correlation of rates of transfer and other phenomena. AIChE J 18:1121–1128

5. Fujii T, Uehara H (1970) Laminar natural-convective heat transfer from the outer surface of a vertical cylinder. Int J Heat Mass Tran 13:607–615
6. Vliet GC (1969) Natural convection local heat transfer on constant-heat-flux inclined surfaces. J Heat Tran 91C:511–516
7. Fujii T, Imura H (1972) Natural-convection heat transfer from a plate with arbitrary inclination. Int J Heat Mass Trans 15:755–767
8. Stewartson K (1958) On the free convection from a horizontal plate. Z Angew Math Phys 9:276–281
9. Churchill W (1983) Free convection around immersed bodies. Chapter 2.5.7 in heat exchanger design handbook. VDI-Verl, Düsseldorf
10. Churchill W, Chu HHS (1975) Correlating equations for laminar and turbulent free convection from a horizontal cylinder. Int J Heat Mass Trans 18:1049–1053
11. Kast W, Krischer O, Reinicke H, Wintermantel K (1974) Konvektive Wärme- und Stoffübertragung. Springer-Verl, Berlin
12. Raithby GD, Hollands KGT (1975) A general method of obtaining approximate solutions to laminar and turbulent free convection problems. Adv Heat Trans 11:265–315
13. Sparrow EM, Stretton AJ (1985) Natural convection from variously oriented cubes and from other bodies of unity aspect ratio. Int J Heat Mass Trans 28:741–752
14. Bradike F (1950) Die Wärmeabgabe von Rippenrohren bei freier Konvektion. Heizung-Lüftung-Haustechnik 1(3):51–58
15. Kast W, Krischer O (1959) VDI-Forschung, vol. 474.
16. Knudsen JG, Pan RB (1963) Natural convection heat transfer from transverse finned tubes. Chem Eng Progr 59(7):45–50
17. Tsubouchi T, Masuda H Natural convection heat transfer from horizontal finned circular cylinder. Rep. Inst. of High Speed Mechanics, Tohoku University, Sendai, Japan. 20 (1968/69), 57–82; 23 (1971), 21–25; 25 (1972), 143–173
18. Hall WB, Price PH (1970) Mixed forced and free convection from a vertical heated plate to air. In: Proceedings of 4th International Heat Transfer Conference, vol 4. Paris, Versailles, paper NC 3.3
19. Churchill W (1977) A comprehensive correlating equation for laminar, assisting, forced and free convection. AIChE J 10:10–16

F3 Heat Transfer by Free Convection: Internal Flows

André Thess
Technische Universität Ilmenau, Ilmenau, Germany

1 General Relationships

The general formulation of the heat transfer problem for internal flow has been described in Chap. F1 (see in particular Fig. 1b). For a comprehensive explanation of the governing equations, similarity parameters, and empirical correlations the reader is referred to [1]. The present equations are for heat transfer in the absence of radiation.

If the temperatures of the surfaces involved are fixed, the rates at which heat is transferred by convection, conduction, and radiation can be determined separately and independently. Thus, the total heat flow rate $\dot{Q}$ is given by

$$\dot{Q} = A\lambda_{\mathrm{CCR}}/L(T_1 - T_2),$$

where $\lambda_{\mathrm{CCR}} = \lambda_{\mathrm{R}} + \lambda_{\mathrm{CC}}$ is the total thermal conductivity equivalent, $\lambda_{\mathrm{R}} = 4\, s\, C_{12} T_{\mathrm{m}}^3$ is the thermal conductivity equivalent for radiation (C_{12} is the radiation transfer factor defined in Chap. K1), and $\lambda_{\mathrm{CC}} = \mathrm{Nu}_s\lambda$ is the thermal conductivity equivalent for convection and conduction.

Under different boundary conditions, the heat transfer mechanisms interact. As a rule, the integrodifferential equations that describe the problem are difficult to solve (cf. *Thermal radiation*).

2 Plane Horizontal Layers

The most extensively documented case of free convection in internal flows is that of the Rayleigh–Bénard convection. The term Rayleigh–Bénard convection refers to the buoyancy driven flow of a fluid enclosed between two horizontal plates, where the lower plate is heated and the upper plate is cooled, i.e. $T_1 > T_2$. Rayleigh–Bénard convection in cylindrical containers with height L and diameter D and adiabatic sidewalls is characterized by the Rayleigh number Ra, Prandtl number Pr (both being defined in Chap. F1) as well as by the aspect ratio $\Gamma = D/L$. The known properties of the Nusselt number Nu(Ra, Pr, Γ) are summarized next. Detailed information about the turbulent regime $\mathrm{Ra} > 10^5$ is provided in the review articles [2, 3].

If $\mathrm{Ra} < 0$, which corresponds to heating from above, the fluid is stably stratified. In this case, there is no flow and Nu = 1. If the fluid is heated from below and

$$0 \le \mathrm{Ra} < \mathrm{Ra}_c(\Gamma) \qquad (1)$$

the fluid is unstably stratified but hydrodynamically stable. The velocity is zero and Nu = 1. The critical Rayleigh number Ra_c (which is independent of Pr but which depends on Γ) can be computed using hydrodynamic stability theory [4, 5]. For isothermal solid upper and lower walls and adiabatic sidewalls, $\mathrm{Ra}_c(\Gamma) \approx 1{,}707$ if $\Gamma \gg 1$.

For $\mathrm{Ra} > \mathrm{Ra}_c$, there is convection inside the layer and hence, $\mathrm{Nu} > 1$. The spatial and temporal structure of the flows varies widely, involving weakly nonlinear (steady, oscillatory, and chaotic) regimes [6, 7] and strongly nonlinear (turbulent) regimes [2, 3]. At present there exists no formula for Nu(Ra, Pr, Γ) which is simple, accurate, and covers the whole parameter space $\mathrm{Ra}_c < \mathrm{Ra} < \infty$, $0.005 \le \mathrm{Pr} < \infty$, and $0 < \Gamma < \infty$. (The lower bound for the Prandtl number is that for sodium.) The following subsections provide three types of data. Sect. 2.1

VDI-GVC (ed.), *VDI Heat Atlas*, DOI 10.1007/978-3-540-77877-6_20,

contains selected experimental data for water, helium, and mercury which are highly accurate but cover only a restricted range of the parameter space. These data are given explicitly for water and helium and as a power law for mercury. Sect. 2.2 provides references to empirical correlations covering a large range of parameters but involving complex mathematical expressions. The expressions are not given explicitly. Sect. 2.3 contains empirical correlations which are simple and cover a large portion of the parameter space but whose accuracy is limited.

2.1 Accurate Experimental Reference Data

Table 1 contains selected results of accurate experiments on Rayleigh–Bénard convection in water carried out in cylindrical cells with nearly adiabatic sidewalls [8, 9]. For more data including a wide range of Γ, see [8–10].

Table 2 lists selected results of accurate experiments on Rayleigh–Bénard convection in helium carried out in cylindrical cells with aspect ratios $\Gamma = 1$ and $\Gamma = 0.5$ [11, 12]. Since helium has similar Prandtl number as air, these data can be used as reference data for air as well.

For mercury Pr = 0.025 and $\Gamma = 1$ ref. [13], gives the following data:

$$\mathrm{Nu} = (0.140 \pm 0.005)\mathrm{Ra}^{(0.26 \pm 0.02)} \quad \text{for } 7.0 \times 10^6 \le \mathrm{Ra} \le 4.5 \times 10^8, \tag{2}$$

$$\mathrm{Nu} = (0.044 \pm 0.015)\mathrm{Ra}^{(0.20 \pm 0.02)} \quad \text{for } 4.5 \times 10^8 \le \mathrm{Ra} \le 2.1 \times 10^9. \tag{3}$$

For experimental data with mercury in cells with other aspect ratios see [14].

The data listed in this Section of Part F represent the most accurate experiments available today (2009). They should, therefore, be considered reference data. For older experimental data as well as data for other than cylindrical geometries, see the review articles [2, 3].

2.2 Accurate Empirical Correlations

For Rayleigh–Bénard convection with aspect ratio $\Gamma \approx 1$, empirical correlations for Nu(Pr, Ra) have been developed in [15, 16] (see also [3]). These correlations are valid for the turbulent flow regime ($\mathrm{Ra} > 10^5$) and cover all technically relevant Prandtl numbers [15] (or at least $\mathrm{Pr} > 0.6$ [16]). The correlations are given in implicit form, i.e., as $f(\mathrm{Pr}, \mathrm{Ra}, \mathrm{Nu}) = 0$. Here, they are not listed explicitly. Their numerical evaluation requires a root-finding algorithm and the computation of elementary functions.

F3. Table 1. Selected results of accurate measurements of the Nusselt number in Rayleigh–Bénard convection in water in cylindrical cells with $\Gamma \approx 1$ (extrapolated to the case of heating and cooling plates with infinite heat conductivity)

Γ	Pr	Ra	Nu	Source
0.967	4.38	1.846×10^7	20.33	[8]
0.967	4.38	1.2444×10^8	35.50	[8]
1.003	4.38	1.13×10^9	66.6	[8]
1.003	4.38	1.113×10^{10}	134.5	[8]
0.982	4.38	1.040×10^{11}	283.3	[8]
1	4.29	4.900×10^{11}	446.82	[9]
1	4.29	1.065×10^{12}	568.06	[9]

2.3 Rough Empirical Correlations

The relationship $\mathrm{Nu} = f(\mathrm{Ra})$ for the average dimensionless heat transfer coefficient is presented graphically in Fig. 1.

For $\mathrm{Ra} > \mathrm{Ra}_c$

the following equations apply [17]: for laminar boundary layers,

$$1{,}708 < \mathrm{Ra} < 2.2 \times 10^4 : \ \mathrm{Nu} = 0.208(\mathrm{Ra})^{0.25} \tag{4}$$

and for turbulent boundary layers,

$$\mathrm{Ra} < 2.2 \times 10^4 : \ \mathrm{Nu} = 0.092(\mathrm{Ra})^{0.33}. \tag{5}$$

More involved relationships exist for air and water [18]. The values lie within the range of scattering in Fig. 1. Ra_{cr} depends on the geometry of the layer and the thermal boundary conditions. The effect of sidewalls increases the critical Rayleigh number [19, 20]. If the flow of heat is downward, Nu = 1 provided that boundary effects do not preponderate.

F3. Table 2. Selected results of accurate measurements of the Nusselt number in the Rayleigh–Bénard convection in helium in cylindrical cells

Γ	Pr	Ra	Nu	Source
1	0.68	5.97×10^6	16.2	[11]
1	0.68	1.88×10^7	22.9	[11]
1	0.68	1.56×10^8	41.7	[11]
1	0.69	1.48×10^9	78.5	[11]
1	0.69	1.02×10^{10}	133	[11]
1	0.74	1.04×10^{11}	270	[11]
1	0.92	1.48×10^{12}	681	[11]
1	1.30	1.39×10^{13}	1,510	[11]
1	3.81	2.10×10^{14}	3,843	[11]
1	9.33	1.08×10^{15}	7,446	[11]
0.5	0.66	1.23×10^5	3.05	[12]
0.5	0.66	1.33×10^6	11.7	[12]
0.5	0.67	1.19×10^7	20.0	[12]
0.5	0.69	1.47×10^8	38.5	[12]
0.5	0.72	1.83×10^9	82.5	[12]
0.5	1.1	1.35×10^{10}	151	[12]
0.5	1.1	1.09×10^{11}	292	[12]
0.5	3.4	1.69×10^{12}	897	[12]
0.5	4.0	1.10×10^{13}	1,660	[12]
0.5	15	1.25×10^{14}	3,890	[12]

3 Inclined Plane Layers [21–25]

The relationship $\mathrm{Nu} = f(\mathrm{Ra})$ for the average dimensionless heat transfer coefficient is represented in Fig. 2. The following expression has been quoted for upward flow of heat [21]:

$$\mathrm{Nu} = C(\mathrm{Ra})^{0.33}\,\mathrm{Pr}^{0.074} \tag{6}$$

C depends on the angle α formed to the vertical, i.e.,

α	0°	30°	45°	60°	90°
C	4.9×10^{-2}	5.7×10^{-2}	5.9×10^{-2}	6.5×10^{-2}	6.9×10^{-2}

The following applies for the $5 \times 10^3 > \mathrm{Ra} < 10^8$ range and for downward flow of heat at an angle $\alpha = 45°$ [21]:

$$\mathrm{Nu} = 1 + \frac{0.025(\mathrm{Ra})^{1.36}}{\mathrm{Ra} + 1.3 \times 10^4}. \tag{7}$$

Other relationships that cover the range of scattering have been given for layers of air [22, 23]. The values quoted for $\alpha = 0°$ and $\alpha = 90°$ do not agree with those for the vertical and horizontal layers, respectively. This indicates the uncertainty of the relationships.

Critical Rayleigh numbers at which the onset of heat transfer by free convection can first be anticipated and other relationships to the angle of inclination are given in the literature [24, 25].

4 Vertical Layers [26–29]

In this case, Fig. 3 represents the relationship for the average dimensionless heat transfer coefficient $\mathrm{Nu} = f(\mathrm{Gr}, \mathrm{Pr}, h/L)$, in which h is the height of the vertical layer. The following equations for gases and liquids [26] can be considered most reliable in the $h/L < 80$ range:

$$\mathrm{Nu} = 0.42\mathrm{Pr}^{0.012}(\mathrm{Ra})^{0.25}\left(\frac{h}{L}\right)^{-0.25} \quad (10^4 < \mathrm{Ra} < 10^7),$$
$$\mathrm{Nu} = 0.049(\mathrm{Ra})^{0.33} \quad (10^7 < \mathrm{Ra} < 10^9). \tag{8}$$

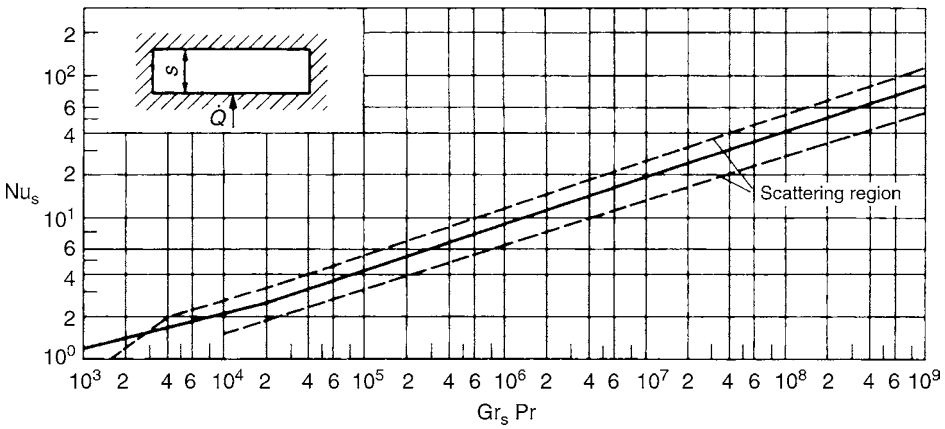

F3. Fig. 1. Average dimensionless heat transfer coefficient Nu as a function of GrPr for heat transfer in horizontal rectilinear enclosures.

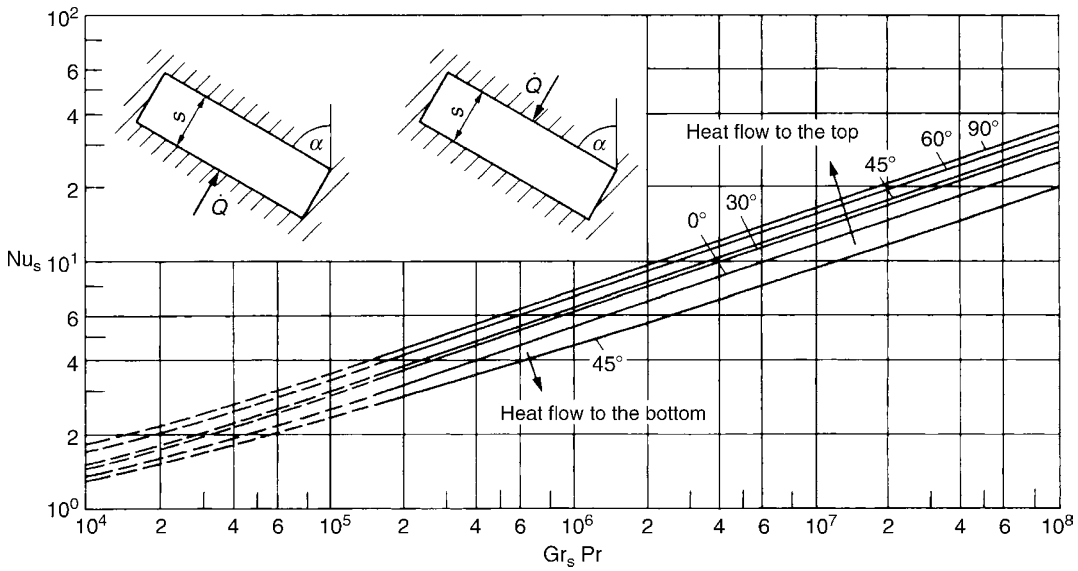

F3. Fig. 2. Average dimensionless heat transfer coefficient Nu as a function of Ra for heat transfer in inclined rectilinear enclosures.

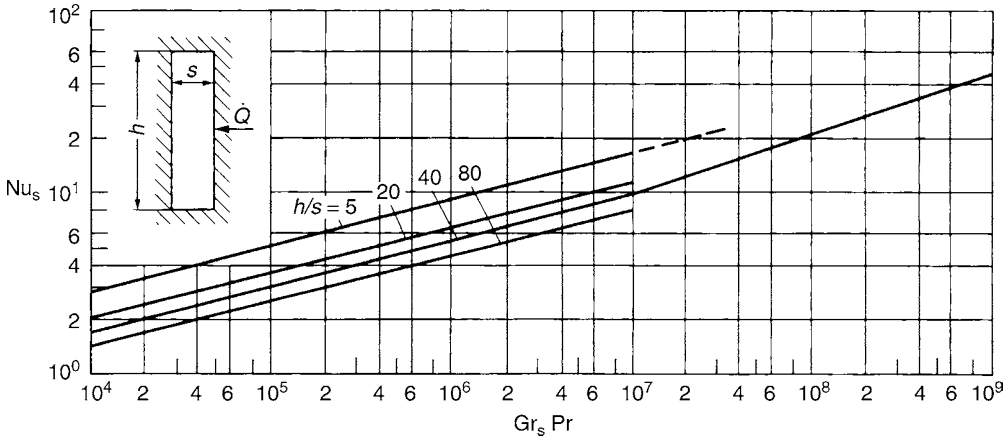

F3. Fig. 3. Average dimensionless heat transfer coefficient Nu as a function of Ra for heat transfer in vertical rectilinear enclosures.

The results obtained for $h/L = 1$, $h/L < 1$, and wider ranges of parameters have been compiled and compared [29]. No verified results are available for the range $h/s > 80$.

5 Special Cases of Plane Layers

Partitions: The following equation shows [30] the relationship between the dimensionless heat transfer coefficient Nu, the number of partitions N, the total height h, and the layer thickness L in vertical plane layers that have been divided into several partitions:

$$\mathrm{Nu}_s = 0.297\mathrm{Ra}^{1/4}(h/L)^{-1/4}(N+1)^{-1}. \qquad (9)$$

If there are 2–5 layers, the amount of heat transferred by convection can be reduced by 70–90%. Equations have been drawn up for the case in which the divisions do not extend all the way upward [31, 32].

Inclined parallelograms: Relationships have been established between heat transfer, the Rayleigh number relating to depth s of the layer, and the angle of inclination to the horizontal [33].

Honeycombs: Figures have been published for the average dimensionless heat transfer coefficient in cases when partitions of thermal insulating material in the form of cells are inclined at various angles to the horizontal [34].

5.1 Horizontal Annuli [35–38]

The dimensionless average heat transfer coefficient in this case is given by

$$\mathrm{Nu}_s = f\left(\mathrm{Ra}, \frac{r_0}{r_i}\right).$$

The relationship is presented graphically in Fig. 4. Equation (10) applies for the $\mathrm{Ra} > 7.1 \times 10^3$ range, heat flow from the inside to the outside, and $r_0/r_i \leq 8$:

$$\mathrm{Nu}_s = 0.20(\mathrm{Ra})^{0.25}\left(\frac{r_0}{r_i}\right)^{0.5}. \qquad (10)$$

In the range from $r_0/r_i = 6$ to $r_0/r_i = 8$, the relationship tends toward that for a horizontal tube.

Heat transfer coefficients are altered by vertical eccentricities e, i.e., the spacing between the axis of the cylinder that has been trued horizontally and the axis of the inner cylinder that has been displaced vertically upward or downward. If the inner cylinder has been displaced vertically upward in a ratio of $e(r_0 - r_i) = 2/3$, the heat transfer coefficient is reduced by 5%, expressed in terms of the value for a horizontally trued inner cylinder; and, if the displacement has been vertically downward in a ratio of $e/(r_0 - r_i)$, the heat transfer coefficient is increased by 10% [36].

The value for Nu in internally heated annuli inclined at an angle of 45° to the horizontal can also be obtained from Eq. (10).

5.2 Vertical Annuli [39–41]

The average dimensionless heat transfer coefficient in this case is given by

$$\mathrm{Nu}_s = f\left(\mathrm{Ra}, \frac{h}{L}, \frac{h}{r_i}, \frac{h}{r_a}\right),$$

where h is the height of the vertical annular gap. The relationship is represented graphically in Fig. 5. If the flow of heat is from the inside to the outside, the following applies:

$$\mathrm{Nu}_s = \frac{C_1 \mathrm{Gr}_s\ \mathrm{Pr}(h/L)^2}{C_2(h/r_0)^4(r_i/h) + \left[\mathrm{Gr}_s\ \mathrm{Pr}(h/L)^3\right]^{n_1}(r_i/h)^{n_2}} \qquad (11)$$

The factors C_1 and C_2 and the exponents n_1 and n_2 depend, as shown in the table below, on the magnitude N, which is given by

$$N = \left[\mathrm{Gr}_s\ \mathrm{Pr}\left(\frac{h}{L}\right)^3\right]^{-0.25}\left(\frac{h}{r_i}\right) \qquad (12)$$

	C_1	C_2	n_1	n_2
$N < 0.2$	0.48	854	0.75	0
$0.2 < N < 1.48$	0.93	1646	0.84	0.36
$1.48 < N$	0.49	862	0.95	0.80

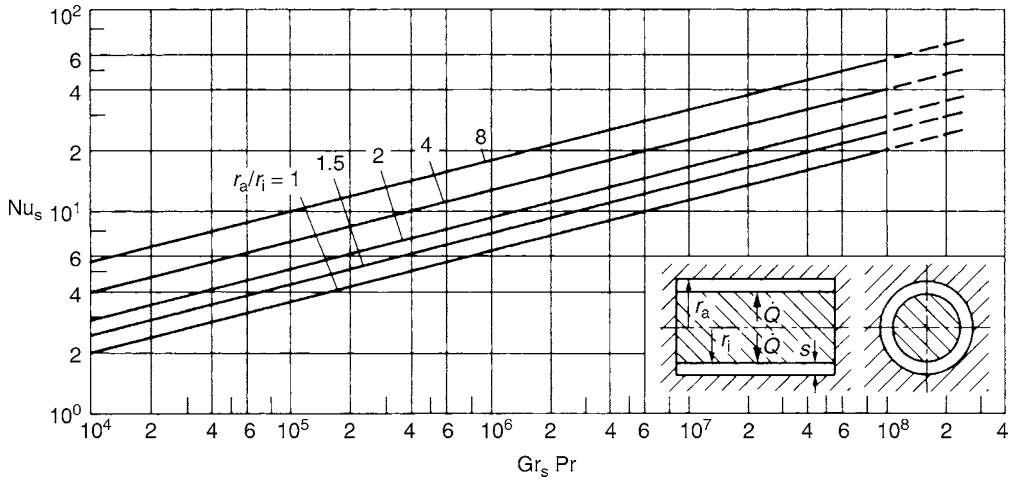

F3. Fig. 4. Average dimensionless heat transfer coefficient Nu as a function of Ra for heat transfer in horizontal concentric annuli.

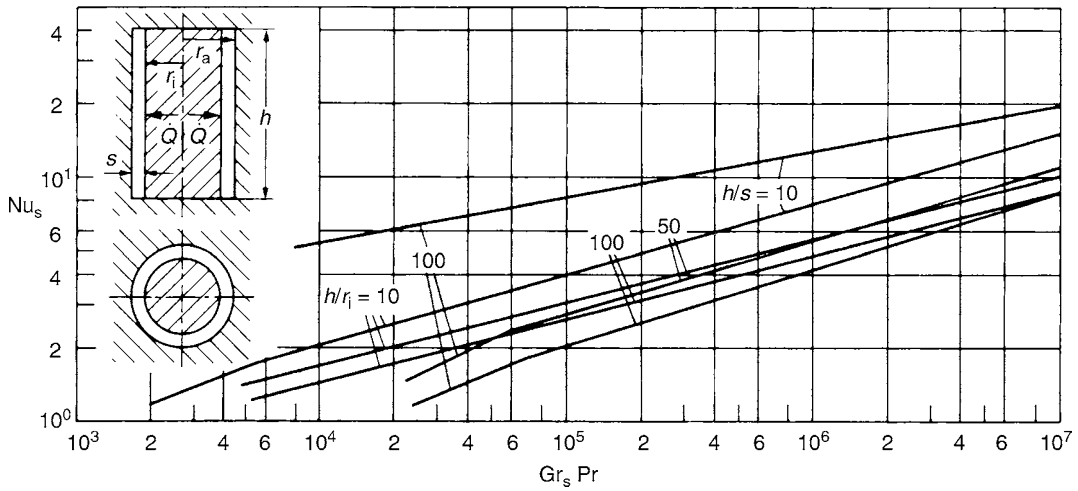

F3. Fig. 5. Average dimensionless heat transfer coefficient Nu as a function of Ra for heat transfer in vertical concentric annuli.

5.3 Spherical Gaps [42]

Equations have been devised for the determination of the average dimensionless heat transfer coefficient

$$\mathrm{Nu} = f(\mathrm{Ra}_{r_0}, \mathrm{Pr}, L/r_0)$$

applicable to externally heated spherical gaps in the range between conduction and heat transfer by free convection [42].

5.4 Porous Layers [43–50]

Other parameters must be introduced in order to describe free convection in porous layers saturated with fluid. A characteristic that can be adopted is the porosity, as defined by

$$\psi = V_{\text{interstices}}/V_{\text{total}}. \tag{13}$$

The permeability can be described by the porosity thus defined and by the diameter d of the particles in the bed, i.e.,

$$K = (d^2/150)[\psi^3/(1-\psi)^2]. \tag{14}$$

In some studies, about 180 figures have been cited instead of 150 for the first divisor. Allowance for the effect of the porous medium can be made by introducing the Darcy number $\mathrm{Da} = K/L^2$, in which L is the thickness of the layer, as a modified Rayleigh number, i.e.,

$$\mathrm{Ra}^* = \mathrm{RaDa}. \tag{15}$$

The corresponding values must be inserted for the properties of the medium. The dimensionless coefficients can then be defined as follows:

$$\mathrm{Nu}_s = \alpha s/\lambda_{\text{sat}},$$
$$\mathrm{Pr}^* = \nu_{\mathrm{F}}/a_{\text{sat}},$$
$$\mathrm{Ra}^* = g\beta_{\mathrm{F}}\Delta\vartheta LK/\nu_{\mathrm{b}}a_{\mathrm{b}},$$

where $a_{\mathrm{b}} = \lambda_{\mathrm{b}}/(\rho c_{\mathrm{p}})_{\mathrm{F}}$.

The subscript b refers to the entire porous bed saturated with the fluid, and the subscript F refers to the fluid fraction.

The thermal conductivity of the porous layer saturated with fluid λ_{sat} must be determined separately. The quotient of λ_{sat} and the known value for λ_{F} can be obtained as described in

Chap. D6. Other methods described elsewhere [50] may be adopted for simpler cases, such as those that are adequate for free convection. As a result of the difference in heat transport, the dimensionless heat transfer coefficient in porous layers is generally less than that in homogeneous layers subject to the same thermal and geometric boundary conditions. This effect reduces as the Rayleigh number increases.

5.5 Inclined Porous Rectangular Layers

The following equations have been cited in the literature [46] for the dimensionless heat transfer coefficient in porous layers inclined at angles of $\alpha' = 0$–$180°$ to the horizontal (Fig. 6). They are valid for dimensionless ratios of $h/L = 5$–32.7 and for particles of various diameters d in the bed.

$$0° < \alpha' < 15°, \leftarrow 60 < \mathrm{Ra}^* \cos(\alpha' - 60) < 4.5 \times 10^2 :$$
$$\mathrm{Nu}_s = 0.053 \mathrm{Pr}^{*0.13} (d/L)^{-0.020} [\mathrm{Ra}^* \cos(\alpha' - 60°)]^{0.72}; \tag{16a}$$

$$15° < \alpha' < 120°, \leftarrow 60 < \mathrm{Ra}^* \cos(\alpha' - 60) < 4.5 \times 10^2 :$$
$$\mathrm{Nu} = 0.024 \mathrm{Pr}^{*0.13} (h/L)^{-0.34} [\mathrm{Ra}^* \cos(\alpha' - 60°)]^{0.52}; \tag{16b}$$

$$0° < \alpha' < 60°, \leftarrow 4.5 \cdot 10^2 < \mathrm{Ra}^* \cos\alpha' < 3 \times 10^4 :$$
$$\mathrm{Nu} = 0.067 \mathrm{Pr}^{*0.13} (d/L)^{-0.65} (\mathrm{Ra}^* \cos\alpha')^{0.52}; \tag{16c}$$

$$60° < \alpha' < 120°, \leftarrow 4.5 \cdot 10^2 < \mathrm{Ra}^* \sin\alpha' < 3 \times 10^4 :$$
$$\mathrm{Nu} = 0.062 \mathrm{Pr}^{*0.13} (h/L)^{-0.52} (\mathrm{Ra}^* \sin\alpha')^{0.64}. \tag{16d}$$

Equations are not given for larger angles of inclination, because they entail that, if the heated side faces downward, there would be no convection and only pure conduction would prevail.

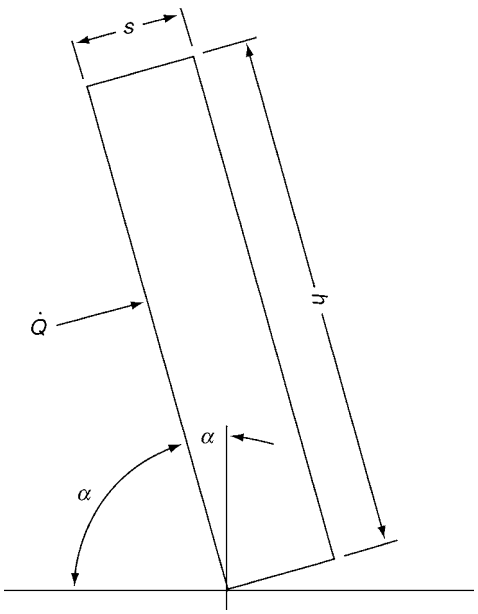

F3. Fig. 6. Inclined porous enclosure.

5.6 Horizontal Porous Annuli

The following equation has been submitted for the determination of the average dimensionless heat transfer coefficient Nu in this case [48]:

$$\mathrm{Nu} = 0.255 \mathrm{Ra}^{*0.45}. \tag{17}$$

It is valid for the $10 < \mathrm{Ra}^* < 10^3$ range.

5.7 Vertical Porous Annuli

The case of a vertical annulus that is filled with a porous medium saturated with a fluid under the same geometrical boundary conditions as those illustrated in Fig. 5 has been described [34]. If the heat flux remains constant, the equation for the average dimensionless heat transfer coefficient is

$$\mathrm{Nu} = C \, \mathrm{Ra}^{nm} (h/L)^{-n}. \tag{18}$$

Numerical values for the indices and the constants in this equation are listed in Table 3.

If the direction of the constant heat flux $\dot{q}$ is from the inside to the outside, the correspondingly modified Rayleigh number Ra is given by

$$\mathrm{Ra}'' = g\beta_\mathrm{F} K L^2 \dot{q} / (\nu_\mathrm{F} a_\mathrm{b} \lambda_\mathrm{b}). \tag{19}$$

The increase in heat transfer depends greatly on the h/L ratio, particularly if the Rayleigh number is low. If the inner wall of the cylinder is isothermal, heat transfer is slightly impaired. Various other cases with peculiar geometric boundary conditions have been mentioned in the literature.

F3. Table 3. Exponents and constants for the determination of the dimensionless heat transfer coefficient by Eq. (18)

r_0/r_i	h/L	C	m	n	$\mathrm{Ra}_s'' \geq$
	1	0.312	0.413	0	100
1	2	0.411	0.368	0	100
	$5 < h/L < 50$	0.662	0.345	0.328	500
	1	0.430	0.393	0	100
2	2	0.520	0.395	0	100
	$5 < h/L < 20$	0.812	0.339	0.319	500
	1	0.512	0.382	0	100
3	2	0.589	0.354	0	200
	$5 < h/L < 20$	0.917	0.333	0.311	500
	1	0.617	0.371	0	200
5	2	0.719	0.340	0	200
	$5 < h/L < 20$	1.096	0.320	0.301	500
	1	0.873	0.344	0	200
10	2	0.989	0.326	0	500
	$5 < h/L < 20$	1.512	0.293	0.279	1,000
20	$5 < h/L < 10$	2.052	0.269	0.244	1,000

5.8 Other Thermal and Geometric Boundary Conditions

5.8.1 Internal Heat Sources [51–56]

Internal heat sources within an enclosed fluid initiate currents in the form of convection cells. Heat is removed through the surfaces of the cooled walls in accordance with the temperature difference.

5.8.2 Thermal Radiation [51–56]

Consider the case of heat transfer in enclosures by simultaneous free convection and radiation with boundary conditions of the second or third kind. As a result of the superimposed heat radiation, the differences in temperature between the surfaces at which heat is exchanged are reduced. The consequence of this is that the coefficients of convective heat transfer decrease as the fraction of heat transported by radiation increases. The total heat flux thus rises.

The effect of radiation increases with the wall temperatures and the wall temperature differences. If radiation from the walls is augmented by gas radiation in molecular gases and vapors, the heat transfer as a whole somewhat decreases.

5.8.3 Mass Transfer [57–62]

No relationships of general validity can be offered for combined heat and mass transfer brought about by the differences in concentration and free convection. A few cases relating to vertical plane layers have been described in the literature.

Heat is not transferred solely by conduction during melting. Convection also sets in within the melt during the phase transition. Time-dependent dimensionless heat transfer equations are given in the literature for special boundary conditions.

5.8.4 Unsteady Free Convection [63]

Special cases have appeared in the literature to describe the complex relationships that exist in heat transfer by unsteady free convection in enclosures. They do not allow presentation in a generalized form.

6 Bibliography

1. Incropera FP, DeWitt DP (1996) Fundamentals of heat and mass transfer. Wiley & Sons, New York
2. Siggia E (1994) High Rayleigh number convection. Annu Rev Fluid Mech 26:137–168
3. Ahlers G, Grossmann S, Lohse D (2009) Heat transfer and large scale dynamics in turbulent Rayleigh-Benard convection. Rev Mod Phys 81:503–537
4. Chandrasekhar S (1981) Hydrodynamic and hydromagnetic stability. Dover, New York
5. Busse F (1985) Hydrodynamic instabilities and the transition to turbulence. In: Swinney HL, Gollub JP (eds) Topics in applied physics, vol. 45. Springer-Verlag, Berlin, pp 97–133
6. Cross MC, Hohenberg PC (1993) Pattern formation outside of equilibrium. Rev Mod Phys 65:851–1112
7. Bodenschatz E, Pesch W, Ahlers G (2000) Recent developments in Rayleigh–Bénard convection. Annu Rev Fluid Mech 32:709–778
8. Funfschilling D, Brown E, Nikolaenko A, Ahlers G (2005) Heat transport by turbulent Rayleigh–Bénard convection in cylindrical samples with aspect ratio one and larger. J Fluid Mech 536:145–154
9. Sun C, Ren LY, Song H, Xia K-Q (2005) Heat transport by turbulent Rayleigh–Bénard convection in 1m diameter cylindrical cells of widely varying aspect ratio. J Fluid Mech 542:165–174
10. Nikolaenko A, Brown E, Funfschilling D, Ahlers G (2005) Heat transport by turbulent Rayleigh–Bénard convection in cylindrical cells with aspect ratio one and less. J Fluid Mech 523:251–260
11. Niemela JJ, Sreenivasan KR (2003) Confined turbulent convection. J Fluid Mech 481:355–384
12. Chavanne X, Chilla F, Chabaud B, Castaing B, Hebral B (2001) Turbulent Rayleigh–Bénard convection in gaseous and liquid helium. Phys Fluids 13:1300–1320
13. Cioni S, Ciliberto S, Sommeria J (1997) Strongly turbulent Rayleigh–Bénard convection in mercury: comparison with results at moderate Prandtl number. J Fluid Mech 335:111–140
14. Glazier JA, Segawa T, Naert A, Sano M (1999) Evidence against 'ultrahard' thermal turbulence at very high Rayleigh numbers. Nature 398:307–310
15. Grossmann S, Lohse D (2000) Turbulent thermal convection: a unifying view. J Fluid Mech 407:27–56
16. Hölling M, Herwig H (2006) Asymptotic analysis of heat transfer in turbulent Rayleigh–Bénard convection. Int J Heat Mass Trans 49:1129–1136
17. Probert D, Brooks RG, Dixon M (1970) Chem Process Eng Heat Trans Survey 35–42
18. Hollands KGT, Raithby GD, Konicek L (1975) Int J Heat Mass Trans 19:879–884
19. Catton I, Edwards DK (1967) J Heat Trans 89:295–299
20. Churchill W (1983) Heat exchanger design handbook, Hemisphere, Washington, DC, Chapter 2.5.8
21. Dropkin D, Somerscales E (1965) Trans ASME 87:77
22. Hollands KGT, Unny TE, Raithby GD, Konicek L (1976) Trans ASME J Heat Trans 98:189–193
23. Randall KR, Mitchell JW, El-Wakil MM (1979) Trans ASME J Heat Trans 101:120–125
24. Hollands KGT, Konicek L (1973) Int J Heat Mass Trans 16:1467–1476
25. Inaba H (1984) Int J Heat Mass Trans 27:1127–1139
26. MacGregor RK, Emery AF (1969) Trans ASME, J Heat Trans Ser C 91:391–403
27. Yin H, Wung TY, Chen K (1978) Int J Heat Mass Trans 21:307–315
28. Markatos NC, Pericleous KA (1984) Int J Heat Mass Trans 27:755–772
29. Merker GP, Mey S (1988) Wärme- & Stoffübertragung 22:291–301
30. Nishimura T, Shiraishi M, Nagasawa F, Kawamura Y (1988) Int J Heat Mass Trans 31:1679–1686
31. Bajorek M, Lloyd JR (1982) J Heat Trans 104:527–532
32. Nansteel MW, Greif R (1981) J Heat Trans 103:623–629
33. Seki N, Fukusako S, Yamaguchi A (1983) J Heat Trans 105:433–439
34. Smart DR, Hollands KGT, Raithby GD (1980) J Heat Trans 102:75–80
35. Itoh M, Fujuta T, Nishiwaki N, Firata M (1970) Int J Heat Mass Trans 13:1364S–1368S
36. Kühn TH, Goldstein RJ (1976) Int J Heat Mass Trans 19:1126–1134
37. Hessami MA, Polland A, Rowe RD, Ruth DW (1985) J Heat Trans 107:603–610
38. Projahn U, Beer H (1985) Wärme- & Stoffübertragung 19:248–254
39. Nagendra HR, Tirunarayanan MA, Ranachandran A (1970) Chem Eng Sci 25:605–610
40 Keyhani M, Kulacki FA, Christensen RN (1983) J Heat Trans 105:454–459
41. Prasad V, Kulacki FA (1985) J Heat Trans 107:596–602
42. Wright JL, Douglas RW (1986) Int J Heat Mass Trans 29:725–739
43. Himasekhar K, Bau HH (1986) Int. J. Heat Mass Trans 20:702–712
44. Prasad A, Kulacki FA (1985) J Heat Trans 107:147–154
45. Beckermann C, Ramadhyami S, Viskanta R J. Heat Trans109:363–370
46. Inaba H, Sugawara M, Blumenberg J (1988) Int J Heat Mass Trans 31:1365–1374
47. Jonsson T, Catton I (1987) J Heat Trans 109:371–377

48. Rao YF, Fukuda K, Hasegawa S (1987) J Heat Trans 109:919–927
49. Prasad V (1986) Numer Heat Trans 29: 841–853
50. Krischer O, Kast W (1978) Trocknungstechnik, vol. 1. Berlin: Springer-Verlag
51. Acharya S, Goldstein RJ (1985) J Heat Trans 107:855–866
52. Cheung FB (1977) Int J Heat Mass Trans 20:499–506
53. Kikuchi Y, Kawasaki T, Shioyama T (1982) Int J Heat Mass Trans 25:363–370
54. Kulacki FA, Goldstein RJ (1972) J Fluid Mech 55:271–287
55. Lee J-H, Goldstein RJ (1988) J Heat Trans 110:345–349
56. Yücel A, Acharya S, Williams ML (1989) Numer Heat Trans 15:261–278
57. Ranganathan P, Viskanta R (1988) Numer Heat Trans 14:35–59
58. Trevisan OV, Bejan A (1987) Heat Trans 109:104–112
59. Jany P, Bejan A (1988) Int J Heat Mass Trans 31:1221S–1235S
60. Lacroix M (1989) Numer Heat Trans 15B:191–210
61. Betzel T, Beer H (1988) Wärme & Stoffübertragung 22:335–344
62. Riviere PH, Beer H (1987) Int Comm Heat Mass Trans 14:155–165
63. Patterson J, Imberger J (1980) J Fluid Mech 100:65–85

F4 Heat Transfer by Free Convection: Special Cases

Werner Kast[2] · *Herbert Klan*[2] (*Revised by André Thess*[1])
[1]Technische Universität Ilmenau, Ilmenau, Germany
[2]Technische Universität Darmstadt, Darmstadt, Germany

1 Vertical Systems [1, 2]

Heated vertical channels act as chimneys, i.e., buoyancy forces cause the surrounding fluid to flow toward the inlet and through the channel itself. Assume a channel with a constant wall temperature T_w, a heated section of height h, and a longitudinal cross section of area f extending from the inlet to the outlet; and let fluid flow through the channel with a velocity distribution u. Then the heat transferred from the channel walls to the fluid is given by

$$\dot{Q} = \rho c_p \left[\int_0^f u(T - T_E)\, \mathrm{d}f \right]_h = A\alpha(T_w - T_E), \qquad (1)$$

where A is the area of the heated surface, T_E is the temperature of the fluid entering the channel, and ϑ is the outlet temperature distribution. The average heat transfer coefficient for the entire channel is

$$\alpha = \frac{\dot{Q}}{A(T_w - T_E)}. \qquad (2)$$

It is described by the following relationship for vertical channels:

$$\mathrm{Nu_S} = \mathrm{Nu_S}(\mathrm{Gr_S^*Pr}), \qquad (3)$$

where

$$\mathrm{Nu_S} = \frac{\alpha s}{\lambda}, \qquad (4)$$

$$\mathrm{Gr_S^*} = \frac{g\beta(T_w - T_E)s^3}{\nu^2}\frac{s}{h}, \qquad (5)$$

$$Pr = \frac{\nu}{a}. \qquad (6)$$

The coefficient of volume expansion β is determined as described in ◉ Chap. F1. The reference temperature for the properties is $\frac{1}{2}(T_w + T_E)$. If the channel is planar and heated on one side, as illustrated in Fig. 1a, the characteristic length s from which Nu and Gr are calculated is the width of the channel, i.e., $s = d$. In plane channels heated on two sides, as illustrated in Fig. 1b, the characteristic length is half the channel width, i.e., $s = d/2$; and in heated tubes, as illustrated in Fig 1c, it is the channel radius $s = r = d/2$. The heat transfer area A and the channel cross section f can then be obtained from the channel length b. The following thus apply:

Fig. 1a $A = bh$
Fig. 1b $A = 2bh$
Fig 1c $A = \pi dh$; $f = \pi d^2/4$.

The relationship $\mathrm{Nu_S} = \mathrm{Nu_S}(\mathrm{Gr_S^*Pr})$ is represented graphically for vertical tubes and plane channels in Fig. 2. In the range of low $\mathrm{Gr_S^*}$ numbers ($\mathrm{Gr_S^*} < 1$), the function $\mathrm{Nu_S}(\mathrm{Gr_S^*Pr})$ in Eq. (3) is given by

$$\mathrm{Nu_S} = C_1(\mathrm{Gr_S^*Pr}) \qquad (7)$$

where

$C_1 = 1/12 = 0.0833$ in the case shown in Fig. 1a
$C_1 = 1/3 = 0.3333$ in the case shown in Fig. 1b
$C_1 = 1/6 = 0.0625$ in the case shown in Fig 1c.

In the range of high $\mathrm{Gr^*_S}$, the function $\mathrm{Nu_S}(\mathrm{Gr_S^*Pr})$ in Eq. (3) is given by

$$\mathrm{Nu_S} = C_2(\mathrm{Gr_S^*Pr})^{1/4} \qquad (8)$$

where

$C_2 = 0.61$ in the case shown in Fig. 1a
$C_2 = 0.69$ in the case shown in Fig. 1b
$C_2 = 0.52$ in the case shown in Fig 1c.

Within this range the heat transfer coefficient α is independent of the channel width s. Owing to the change in the direction of flow at the inlet, however, the asymptotes do not agree

VDI-GVC (ed.), *VDI Heat Atlas*, DOI 10.1007/978-3-540-77877-6_21,

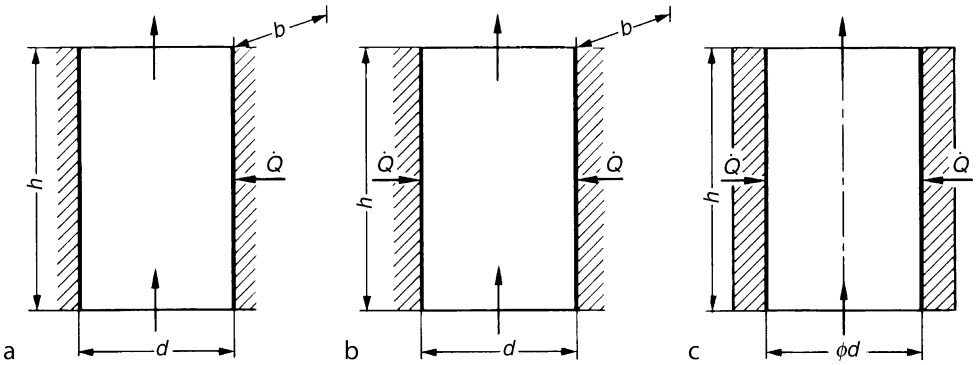

F4. Fig. 1. (**a**) Vertical rectilinear channel heated on one side; characteristic dimension $s = d$. (**b**) Rectilinear channel heated on two sides; characteristic dimension $s = d/2$. (**c**) Heated tube; characteristic length $s = r = d/2$.

with the equations in Chap. F2. As a consequence, a finite vertical velocity remains at the leading edge, even if the channel walls are widely spaced.

Heat transfer in the entire Gr_S^*Pr range can be approximately represented by the following equation (Fig. 3):

$$Nu_S = \left[\frac{1}{(C_1 Gr_S^* Pr)^{3/2}} + \frac{1}{[C_2 (Gr_S^* Pr)^{1/4}]^{3/2}}\right]^{-2/3} \quad (9)$$

2 Inclined Systems [2]

The following relationship applies for channels that are inclined at an angle of $\alpha = 45°$ or less to the vertical and are heated from above, from below, or from both above and below

$$Nu_S = C_2 (Gr_S^* Pr \cos\alpha)^{1/4} \quad (10)$$

where

$C_2 = 0.673$

$2 \times 10^2 < Gr_S^* Pr < 2 \times 10^5$

$0.0437 < s/h < 0.109$.

3 Open Vertical Annulus

The characteristic dimension for a vertical annulus (Quoss. H.: Study No. 45, Technical University of Darmstadt, 1977) of height h is (Fig. 4)

$$s = \sqrt{r_0 r_i}\ln(r_0/r_i) \quad (11)$$

Various cases of heating exist. Heat transfer also depends on the ratio of the radii, and the only studies that have been made on the subject have been in the following range:

$$1 < r_0/r_i < 10 \quad (12)$$

If $Gr_S^* < 10^2$, the dimensionless heat transfer coefficient that applies for isothermal heating of both walls at a temperature T_w is

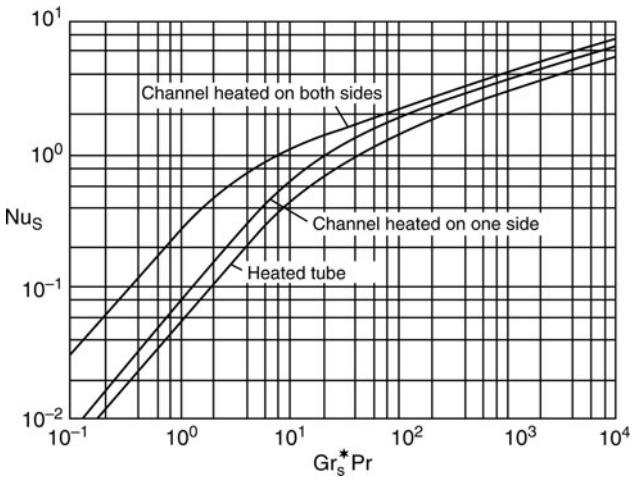

F4. Fig. 2. Nu_S as a function of Gr_S^*Pr for rectilinear vertical channels and vertical tubes.

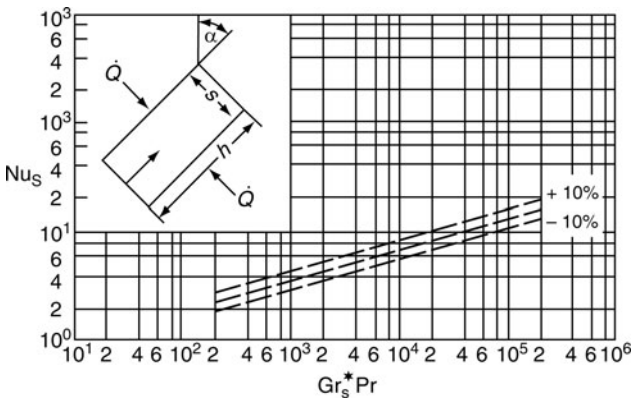

F4. Fig. 3. Average dimensionless heat transfer coefficient in inclined rectangular channels heated from below, from above, and from both above and below.

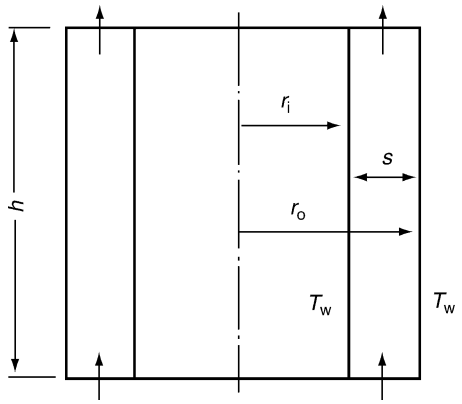

F4. Fig. 4. Open vertical annulus.

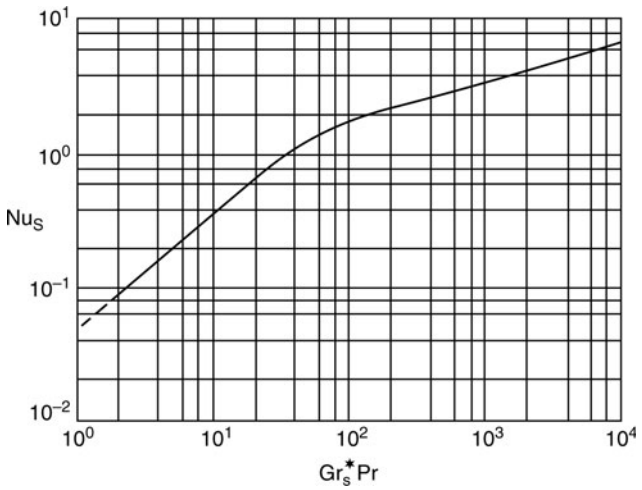

F4. Fig. 5. Average dimensionless heat transfer coefficient for heating both the tubes forming an annulus.

$$Nu_S = C_1(Gr_S^* Pr) \tag{13}$$

where $C_1 = 0.0463$.

The relationship that applies if $Gr_S{}^* Pr > 10^2$ is

$$Nu_S = C_2(Gr_S^* Pr)^{0.25} \tag{14}$$

where $C_2 = 0.631$ (Fig. 5).

The dimensionless heat transfer coefficient for the case of isothermal heating of the outer tube and an adiabatic inner tube and for $Gr_S{}^* < 10$ is

$$Nu_S = C_1(Gr_S^* Pr) \tag{15}$$

where $C_1 = 0.0824$ for $r_0/r_i \to 1$ and $C_1 = 0.0463$ for $r_0/r_i \to 10$.

The relationship that applies if $Gr_S{}^* Pr > 10^2$ is

$$Nu_S = C_2(Gr_S^* Pr)^{0.25} \tag{16}$$

where $C_2 = 0.631$ (Fig. 6).

If the inner tube is isothermally heated at a temperature T_w and the outer tube is adiabatic, the dimensionless heat transfer coefficient for $Gr^*{}_S Pr < 10$ is given by

$$Nu_S = C_1(Gr_S^* Pr) \tag{17}$$

where $C_1 = 0.0858$ for $r_0/r_i \to 1$ and $C_1 = 0.5020$ for $r_0/r_i \to 10$.

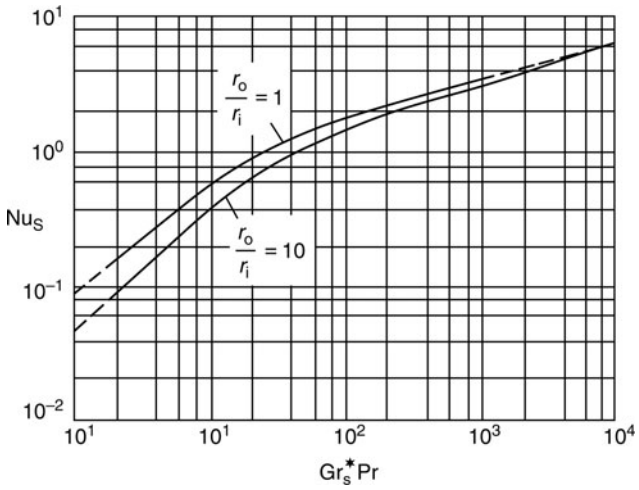

F4. Fig. 6. Average dimensionless heat transfer coefficient for heated outer tube and adiabatic inner tube.

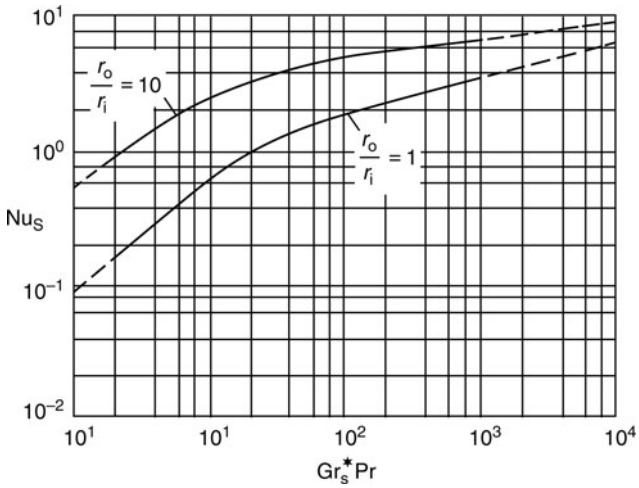

F4. Fig. 7. Average dimensionless heat transfer coefficient for heated inner tube and adiabatic outer tube.

If $Gr_S{}^* Pr > 10^2$,

$$Nu_S = C_2(Gr_S^* Pr)^{0.25} \tag{18}$$

where $C_2 = 0.631$ for $r_0/r_i \to 1$ and $C_2 = 0.8$ for $r_0/r_i \to 10$ (Fig. 7).

The following dimensionless relationship may be adopted for the entire range:

$$Nu_S = \left[\frac{1}{(C_1 Gr_S^* Pr)^{3/2}} + \frac{1}{[C_2(Gr_S^* Pr)^{0.25}]^{3/2}}\right]^{-2/3} \tag{19}$$

4 Other Geometric and Thermal Boundary Conditions

4.1 Superimposed Forced Convection [3]

Suppose that buoyancy forces drive a free convection current upward against a downward forced turbulent current in a vertical channel with a hydraulic diameter D_h. The relationship of

the dimensionless heat transfer coefficient to the Reynolds and Grashof numbers in this case is as follows:

$$\mathrm{Nu_{Dh}} = 0.0115\mathrm{Re_{Dh}^{0.8}Pr^{0.5}} \cdot \left\{1 + \left[1 - \frac{696}{\mathrm{Re_{Dh}^{0.6}}} + \frac{8300\ \mathrm{Gr_{Dh}}}{\mathrm{Re_{Dh}^{2.6}(Pr^{0.5}+1)}}\right]^{0.39}\right\} \quad (20)$$

It is valid for $0.7 < \mathrm{Pr} < 7$; for $10^4 < \mathrm{Re_{Dh}} < 2 \times 10^4$; and for $10^6 < \mathrm{Gr_{Dh}} < 2 \times 10^9$.

Heat transfer is improved by the superimposed free convection.

5 Convergent Channels [4]

Imagine that heat transfer takes place in a convergent vertical channel that is heated on both sides. The angle at which the converging walls are inclined toward the vertical lies in the $\alpha = 0°–15°$ range. In this case, the difference between the average dimensionless heat transfer coefficient and the values calculated from Eqs. (7) and (8) is negligible if the characteristic channel width is taken to be one half of the gap width at the lower end of the channel.

6 Partially Heated Channels [5]

If $\mathrm{Gr_S^*} > 100$, heat transfer in vertical channels that are heated on the one side can be improved by alternating, i.e., by applying the heat to the one side at the lower end of the channel, and to the other side at the upper end.

7 Half-open Layers

This case concerns various layouts of the heated surfaces with apertures of a thermosiphon that is exposed on the one side to the surroundings. The relationship that is given in the literature for the average dimensionless heat transfer coefficient in this case is

$$\mathrm{Nu_S} = f(\mathrm{Gr_S}, \mathrm{Pr}, h/s) \quad (21)$$

where h is the height of the heated surface and s is the depth of the layer. If the walls are inclined, the angle of inclination must again be taken into account.

8 Bibliography

1. Klan H (1976) Über den Wärmeübergang bei freier Konvektion von Luft in beheizten senkrechten Kanälen. Dissertation, Tech. University of Darmstadt
2. Azevedo LFA, Sparrow EM (1985) J Heat Transf 107:893–901
3. Swanson LW, Catton I (1987) J Heat Transf 109:943–946
4. Sparrow EM, Ruiz R, Azevedo LFA (1988) Int J Heat Mass Transf 31:907–915
5. Tanda G (1988) Wärme- u. Stoffübertragung 23:307–312

F5 Thermal Output of Heating Appliances Operating with Hot Water

Werner Kast[2] · *Herbert Klan*[2] (*Revised by André Thess*[1])
[1]Technische Universität Ilmenau, Ilmenau, Germany
[2]Technische Universität Darmstadt, Darmstadt, Germany

1 Thermal Output of Space Heating Appliances (Radiators)

Radiators are intended to provide heating in buildings, which can be determined as laid down in German standard DIN 4701. This document is available in English. The appliances transmit heat by radiation and/or convection.

1.1 Types of Space Heating Appliances

Space heating systems and appliances are classified as follows without regard to their shape and material of construction:

(a) Sectional radiators
(b) Panel radiators
(c) Column radiators
(d) Special heating systems
(e) Panel heating

1.2 Thermal Output

The thermal output of a space heater $\dot{Q}$ is proportional to the average excess temperature of the heated surface ΔT^n. The numerical value of the exponent n is generally from $n = 1.25$ to $n = 1.4$; for panel heating it is from $n = 1.0$ to $n = 1.1$. The excess temperature is determined from the inlet and outlet water temperatures T_i and T_o, respectively, and the air temperature T_a, i.e.,

$$\Delta T = \frac{T_i - T_o}{\ln[(T_i - T_a)/(T_o - T_a)]}.$$

An arithmetic mean excess temperature T_m can be adopted if the temperature difference $T_i - T_o$ is small, i.e., as long as

$$\frac{T_o - T_a}{T_i - T_a} > 0.7.$$

Thus,

$$\Delta T = T_m - T_n \quad \text{where } T_m = \frac{T_i + T_0}{2}.$$

A standard rating for the thermal output $\dot{q}_n$ is adopted in German standards. It is based on the thermal output at an excess temperature of $\Delta T_n = 60$ K, i.e., at $T_1 = 90°C$, $T_r = 70°C$, and $T_a = 20°C$, and can be converted into a rating at other temperatures by the relationship

$$\frac{\dot{q}}{\dot{q}_n} = \left(\frac{\Delta T}{\Delta T_n}\right)^n.$$

The thermal output of floor heating panels is restricted by a physiologically tolerable temperature at the surface of $T_{F,\,max} = 29°C$ in living rooms, $T_{F,\,max} = 35°C$ in edge zones, and $T_{F,\,max} = 33°C$ in bathrooms. The rating for the thermal output in this case is quoted for $T_{F,\,max} = 29°C$ and a room temperature of 20°C.

Slight differences, which depend on the nature of the heating system, occur between the comfort value of the room temperature and that of the air temperature. Other factors are the layout of the rooms, differential gaps in the controllers, and heat losses. In view of all these, the areas of the heaters are made 15% greater than the design values.

Values for the thermal output of conventional heating appliances are listed in the following tables. They are expressed in terms of the length of the radiator, the number of sections in the radiator, or the area of the floor heating panels. Rough figures that can be adopted for calculation are $n = 1.3$ for radiators and $n = 1.0$ for floor heating.

The figures quoted for the output ratings are valid for radiators in which the hot water inlet is connected at the top; and the outlet (whether on the same or the opposite side), at the bottom. A considerable reduction in the thermal output can be expected if the connections are otherwise.

Paints pigmented with metal powders may considerably impair the thermal efficiency. Thus, they give rise to a decrease in thermal output of at least 4%, if the radiators are installed in niches; of at least 4%, if there is a sill above the radiator; and of at least 10%, if the radiator is covered at the front.

2 Thermal Output of Sectional Radiators

See Tables 1–5.

VDI-GVC (ed.), *VDI Heat Atlas*, DOI 10.1007/978-3-540-77877-6_22,

F5. Table 1. Cast iron radiators; T_m = 80°C and T_a = 20°C, *H* height; *D* depth; *L* length

Dimensions of radiator	H	280	430	430	430	430	580	580	580	580	680	980	980	980
	D	250	70	110	160	220	70	110	160	220	160	70	160	220
Standard thermal output per gill in W		92	55	70	93	122	68	92	126	162	147	111	204	260

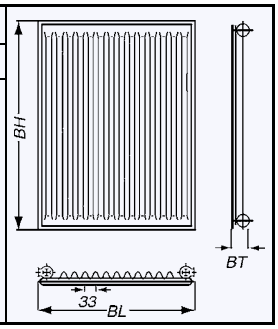

F5. Table 2. Steel radiators; T_m = 80°C and T_a = 20°C

Dimensions of radiator	H	300	300	400	400	400	600	600	600	1000	1000	1000
	D	160	250	110	160	220	110	160	220	110	160	220
Standard thermal output per section in W		50	77	55	74	99	73	99	128	122	157	204

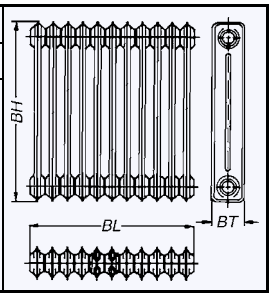

F5. Table 3. Tubular steel radiators; T_m = 80°C and T_a = 20°C. Diameter of tubes 25 mm. Length of section 46 mm

	Standard thermal output per Section in W				
	2-Row	3-Row	4-Row	5-Row	6-Row
D	64	101	139	177	215
H					
190	19	27	35	41	47
300	29	41	53	64	76
350	34	48	63	74	88
400	38	55	70	85	100
450	44	62	78	97	113
500	49	69	87	107	126
550	55	74	95	117	138
600	59	81	104	127	151
750	74	101	128	157	184
900	90	119	150	185	219
1,000	98	131	166	204	241
1,100	107	143	181	221	263
1,200	116	156	197	240	280
1,500	142	192	242	288	335
1,800	167	228	287	343	399
2,000	188	254	319	378	442
2,500	233	316	395	465	541
2,800	261	352	440	516	602

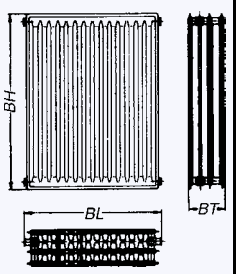

F5. Table 4. Column radiators with $\Delta T = 60$ K

Dimensions of radiator	H	472	572	672	972	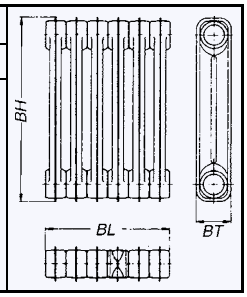
	D	72	72	72	72	
Rated thermal output per gill in W		45	54	63	92	

F5. Table 5. Fold radiators with $\Delta T = 60$ K. Length of section 30 mm

Dimensions of radiator	H	450			600			1000			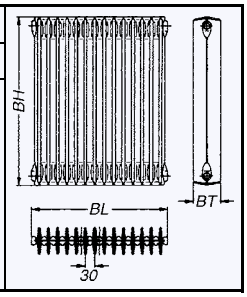
	D	40	80	100	40	80	100	40	80	100	
Standard thermal output per section in W		904	1,352	1,525	1,149	1,704	1,951	1,809	2,689	3,077	

F5. Table 6. Panel radiators with $\Delta T = 60$ K. Smooth walls, panels of 25 ± 3 mm thickness, and ≥ 35 mm(internal) width (without cover grill)

Height in mm		200	300	400	500	600	700	800	900
Standard thermal output in W/m	Single-plate	267	400	525	650	773	893	1,010	1,125
	Double-plate	454	673	881	1,078	1,263	1,436	1,599	1,750
	Triple-plate	641	946	1,237	1,506	1,753	1,979	2,188	2,357

3 Thermal Output of Panel Radiators

See Tables 6–13.

4 Thermal Output of Floor Heating

The heat flux $\dot{q}$ emitted by the floor heating panels installed by conventional dry and wet construction techniques can be determined as a function of the excess temperature ΔT of the hot water. It lies between $\dot{q} = 50\ \mathrm{W/m^2}$ and $\dot{q} = 90\ \mathrm{W/m^2}$ for living rooms at $T = 20°\mathrm{C}$. The actual value depends on the pipe spacing, the thickness of the concrete slab, the tube diameter, the method adopted for laying the floor, the floor covering, etc.

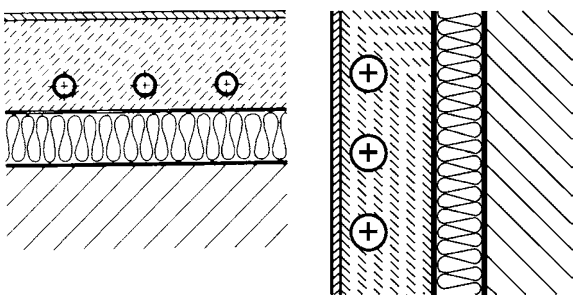

F5. Table 7. Panel radiators with $\Delta T = 60$ K. Vertically profiled; panels of 18 $\pm$ 3 mm thickness. Developed length of profiles at least 10% longer than the length of the panels; height of profiles $\geq$ total height $-$ 100 mm (without cover grill); (internal width) $\geq$ 35 mm

Height in mm		200	300	400	500	600	700	800	900	1,000
Standard thermal output in W/m	Single-plate	294	425	556	684	810	935	1,058	1,180	1,300
	Double-plate	500	727	945	1,157	1,360	1,556	1,744	1,924	2,093
	Triple-plate	706	1,029	1,334	1,630	1,910	2,177	2,430	2,668	2,886

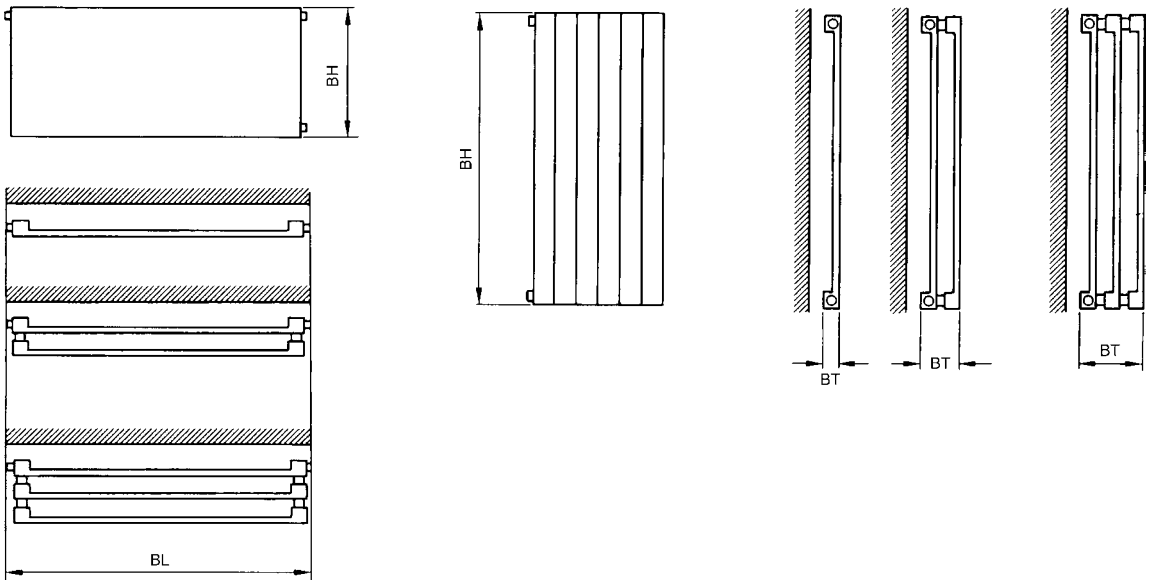

F5. Table 8. Panel radiators; vertically profiled; sheet-metal convector (SMC) welded onto corrugations; panels of 18 mm thickness (without cover grill); $\Delta T = 60$ K

	Standard thermal output in W/m				
H	350	500	600	900	
Single-plate with 1 SMC, B 43 mm	670	925	1,087	1,549	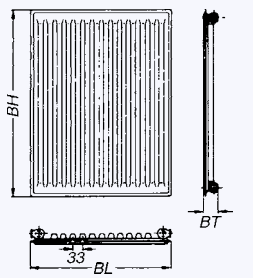
Double-plate with 2 SMCs, D 80 mm	1,211	1,586	1,870	2,850	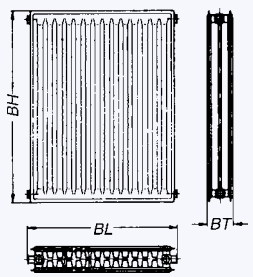
Triple-plate with 3 SMCs, D 142 mm	1,773	2,460	2,882	3,956	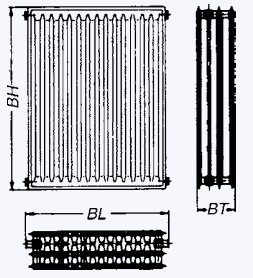

F5. Table 9. Panel radiators; vertically profiled; sheet-metal convector (SMC) welded onto water channels; panels of 15 mm thickness (without cover grill); $\Delta T = 60$ K

	Standard thermal output in W/m					
H	260	390	520	650	900	
Single-plate with 2 SMCs, D 60 mm	787	1,125	1,433	1,705	2,129	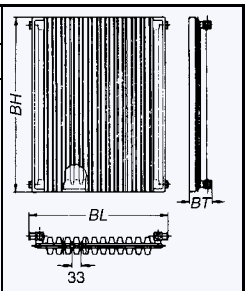
Double-plate with 4 SMCs, D 130 mm	1,456	2,018	2,540	2,999	3,732	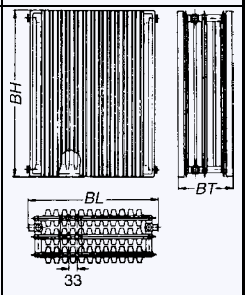
Triple-plate with 6 SMCs, D 190 mm	2,129	2,848	3,575	–	–	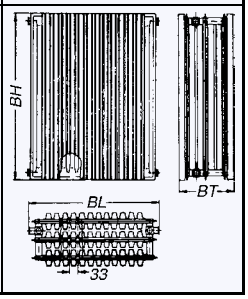

F5. Table 10. Horizontal tubular steel radiators with smooth walls; $\Delta T = 60$ K

Pipe diameter		Standard thermal output in W per tube and unit length (m)		
Inch	mm	Single tube	Tiers of tubes	
1	25	87	77	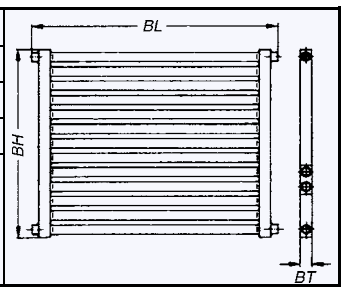
1.5	40	120	100	
2	50	144	116	

F5. Table 11. Finned-tube convectors of 70 mm height. Single bank with shaft of *SH* mm height. $\Delta T = 60$ K

	Standard thermal output in W/m (total length)						
SH	D	50	100	150	200	250	300
300		311	641	927	1,166	1,355	1,499
600		521	1,080	1,553	1,967	2,358	2,745
1200		657	1,343	1,971	2,583	3,186	3,769

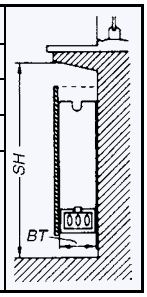

F5. Table 12. Finned-tube convectors of 160 mm height. Two banks with shaft of *SH* mm height. $\Delta T = 60$ K

	Standard thermal output in W/m (total length)					
SH	D	100	150	200	250	300
300		884	1,152	1,384	1,589	1,767
600		1,422	1,962	2,475	2,925	3,294
1,200		1,895	2,678	3,432	4,167	4,890

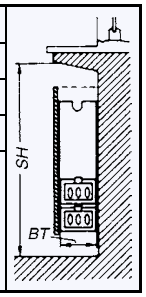

F5. Table 13. Radiant ceiling heating panel installed at a height of 6 m. Heat emission only downward. Spacing between tubes *Sp*; breadth of panels *B*. $\Delta T = 60$ K

	Standard thermal output in W/m						
Sp	150				250		
B	450	600	750	900	485	720	955
Standard thermal output in W/m	287	358	445	527	219	320	420

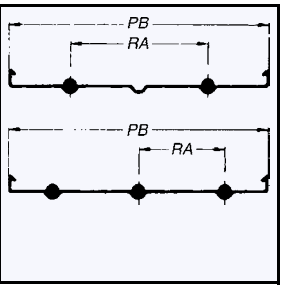

Forced Convection

G1 Heat Transfer in Pipe Flow

Volker Gnielinski
Karlsruher Institut für Technologie (KIT), Karlsruhe, Germany

1 Flow Through Pipes, Critical Reynolds Number

Pipe flow is always laminar if the Reynolds number is less than Re = 2300, and is said to be turbulent at higher values. There is no doubt that turbulent flow sets in at $\mathrm{Re} > 10^4$. In the transition region of $2300 < \mathrm{Re} < 10^4$, the type of flow is influenced by the nature of the inlet stream and the form of the pipe inlet.

2 Definition of Heat Transfer Coefficient

The average heat transfer coefficient α over a length l of a pipe is defined by

$$\dot{q} = \alpha \, \Delta T_{\mathrm{LM}}$$

The variable ΔT_{LM} is the logarithmic mean temperature difference and is given by

$$\Delta T_{\mathrm{LM}} = \frac{(T_{\mathrm{w}} - T_{\mathrm{i}}) - (T_{\mathrm{w}} - T_{\mathrm{o}})}{\ln \dfrac{T_{\mathrm{w}} - T_{\mathrm{i}}}{T_{\mathrm{w}} - T_{\mathrm{o}}}}$$

where T_{i} and T_{o} are the inlet and outlet temperatures of the flowing medium and T_{w} is the constant pipe wall temperature. The average heat transfer coefficient α is obtained by integration of the local coefficient, that is,

$$\alpha = \frac{1}{l} \int_0^l \alpha_x \mathrm{d}x.$$

3 Heat Transfer in Laminar Flow

3.1 Constant Wall Temperature

3.1.1 Hydrodynamically Developed Laminar Flow

Many authors have proposed numerical methods for determining heat transfer in thermally and hydrodynamically developed laminar flow (in long pipes) and in thermally developing and hydrodynamically developed laminar flow (the Nusselt-Graetz problem).

The asymptotes for the *local Nusselt number* at a point x, as measured from the point at which heating or cooling commences, are given by

$$\mathrm{Nu}_{x,T,1} = 3.66 \tag{1}$$

for small values of $\mathrm{Re}\,\mathrm{Pr}\,(d_{\mathrm{i}}/x)$ and

$$\mathrm{Nu}_{x,T,2} = 1.077 \sqrt[3]{\mathrm{Re}\,\mathrm{Pr}\,(d_{\mathrm{i}}/x)} \tag{2}$$

for high values of $\mathrm{Re}\,\mathrm{Pr}\,(d_{\mathrm{i}}/x)$.

Local Nusselt numbers for the range between the two asymptotes have been determined numerically and tabulated by Shah and London [1].

Local Nusselt numbers in the entire $0 < \mathrm{Re}\,\mathrm{Pr}(d_{\mathrm{i}}/x) < \infty$ range, with a deviation that attains a maximum at 6% at $10 < \mathrm{Re}\,\mathrm{Pr}\,d_{\mathrm{i}}/x < 100$ and is otherwise much smaller, can be obtained from

VDI-GVC (ed.), *VDI Heat Atlas*, DOI 10.1007/978-3-540-77877-6_23,

$$\mathrm{Nu}_{x,T} = \left\{ \mathrm{Nu}_{x,T,1}^3 + 0.7^3 + [\mathrm{Nu}_{x,T,2} - 0.7]^3 \right\}^{1/3} \quad (3)$$

The asymptotes for the *mean Nusselt number* in a tube of the length l as measured from the point, at which heating or cooling commences, are

$$\mathrm{Nu}_{\mathrm{m},T,1} = 3.66 \quad (4)$$

for low values of $\mathrm{Re}\,\mathrm{Pr}\,d_\mathrm{i}/l$ and

$$\mathrm{Nu}_{\mathrm{m},T,2} = 1.615\ \sqrt[3]{\mathrm{Re}\,\mathrm{Pr}\,\mathrm{d_i}/\mathrm{l}} \quad (5)$$

for high values of $\mathrm{Re}\,\mathrm{Pr}\,d_\mathrm{i}/l$.

As has been demonstrated in the literature [2], the numerically determined and tabulated mean Nusselt numbers [1] in the entire $0 < \mathrm{Re}\,\mathrm{Pr}\,d_\mathrm{i}/l < \infty$ range can be represented, with deviations of less than 1%, by the following equation:

$$\mathrm{Nu}_{\mathrm{m},T} = \left\{ \mathrm{Nu}_{\mathrm{m},T,1}^3 + 0.7^3 + [\mathrm{Nu}_{\mathrm{m},T,2} - 0.7]^3 \right\}^{1/3} \quad (6)$$

3.1.2 Hydrodynamic and Thermal Development of Flow

As a result of friction between the fluid and the pipe wall, a velocity profile commences to build up at the pipe inlet. If, at the same time, heat is transferred, a temperature profile also sets in. Boundary layers are thus formed, and heat transfer in this zone is calculated in the light of the boundary layer theory.

The *local Nusselt number* can be determined from Eq. (7), which was proposed by Pohlhausen [3] for parallel flow over a flat plate and has been transformed here to apply for pipe flow.

$$\mathrm{Nu}_{x,T} = 0.332\ \sqrt[3]{\mathrm{Pr}}\sqrt{\mathrm{Re}d_\mathrm{i}/x} \quad (7)$$

The factor 0.332 in Eq. (7) is a good approximation for $\mathrm{Pr} > 0.1$. The relationship between the Prandtl number, even if it assumes small or large values, and the heat transfer coefficient is better defined by a rough equation put forward by Martin [4], that is,

$$\mathrm{Nu}_{x,T,3} = \frac{1}{2}\left(\frac{2}{1+22\,\mathrm{Pr}}\right)^{1/6} (\mathrm{Re}\,\mathrm{Pr}\,d_\mathrm{i}/x)^{1/2} \quad (8)$$

Equations (7) and (8) are valid for high values of d_i/x. As the length of the flow path x becomes greater, d_i/x becomes progressively less, and higher values for the Nusselt number are obtained from Eq. (3) than from Eqs. (7) and (8). In this case, the values that are valid are those calculated from Eq. (3).

Equation (9), which was suggested by Martin [4], yields the local values of the Nusselt number at any point x in a pipe in which laminar flow is developing thermally and hydrodynamically.

$$\mathrm{Nu}_{x,T} = \left\{ \mathrm{Nu}_{x,T,1}^3 + 0.7^3 + [\mathrm{Nu}_{x,T,2} - 0.7]^3 + \mathrm{Nu}_{x,T,3}^3 \right\}^{1/3} \quad (9)$$

where $\mathrm{Nu}_{x,T,1}$ is obtained from Eq. (1), $\mathrm{Nu}_{x,T,2}$ from Eq. (2), and $\mathrm{Nu}_{x,T,3}$ from Eq. (8).

Simultaneous thermal and hydrodynamic development of laminar flow is so rapid that the mean Nusselt number over the length l departs from the figure determined by Eq. (6) only for short pipes ($d_\mathrm{i}/l > 0.1$).

The asymptotes for the *mean Nusselt numbers* for large values of d_i/l, that is, for short pipes, are obtained by integrating Eq. (7) or Eq. (8) over the length l to give

$$\mathrm{Nu}_{\mathrm{m},T} = 0.664\ \sqrt[3]{\mathrm{Pr}}\sqrt{\mathrm{Re}\ d_\mathrm{i}/l} \quad (10)$$

and

$$\mathrm{Nu}_{\mathrm{m},T,3} = \left(\frac{2}{1+22\,\mathrm{Pr}}\right)^{1/6} (\mathrm{Re}\,\mathrm{Pr}\,d_\mathrm{i}/l)^{1/2} \quad (11)$$

Equation (11) is a good approximation for the relationship between the Nusselt and the Prandtl numbers, even if $\mathrm{Pr} < 1$. The equation proposed by Stephan [5] for the average Nusselt number in hydrodynamic and thermal development of laminar flow transforms into Eqs. (10) and (11) if the flow path is short.

As has been demonstrated [2], an equation that is valid for all lengths of pipes can be derived for the mean Nusselt number during thermal and hydrodynamic development of flow. One that has been suggested by Martin [4] is as follows:

$$\mathrm{Nu}_{\mathrm{m},T} = \left\{ \mathrm{Nu}_{\mathrm{m},T,1}^3 + 0.7^3 + [\mathrm{Nu}_{\mathrm{m},T,2} - 0.7]^3 + \mathrm{Nu}_{\mathrm{m},T,3}^3 \right\}^{1/3} \quad (12)$$

where $\mathrm{Nu}_{\mathrm{m},T,1}$ is obtained from Eq. (4), $\mathrm{Nu}_{\mathrm{m},T,2}$ from Eq. (5), and $\mathrm{Nu}_{\mathrm{m},T,3}$ from Eq. (11).

3.1.3 Definitions, the Effect of Temperature-Dependent Property Variations

The dimensionless groups are defined as follows:

$$\mathrm{Nu} = \frac{\alpha\, d_\mathrm{i}}{\lambda}; \qquad \mathrm{Re} = \frac{w\, d_\mathrm{i}}{\nu}.$$

In the theoretical derivation of the equations presented in Sects. 3.1.1 and 3.1.2, it was assumed that the properties of the medium remain constant. The equations can be adopted in practice if the properties are referred to the mean temperature of the medium $T_\mathrm{m} = (T_\mathrm{i} + T_\mathrm{o})/2$.

If the properties depend on temperature, the direction of the heat flux (heating or cooling) affects heat transfer. Experiments on laminar gas flow of air, nitrogen, and helium [6–8] in the $0.5 < T/T_\mathrm{w} < 20$ range – where T is the mean gas temperature and T_w is the wall temperature, both in Kelvin – have revealed that the heat transfer coefficient differs by less than 10%.

Sieder and Tate [9] allowed for this effect in liquids by introducing the factor $(\eta/\eta_\mathrm{w})^{0.14}$, in which η is the dynamic viscosity of the liquid at T_m and η_w is that at the wall temperature. Recent practice favors the adoption of the Prandtl number ratio instead of the viscosity ratio for the liquid at corresponding temperatures. Hufschmidt and Burck [10] found a factor of $(\mathrm{Pr}/\mathrm{Pr_w})^{0.11}$ for turbulent flow. Since the values measured by Sieder and Tate are scattered quite considerably and it is worthwhile to bring the correction factor into line with that for turbulent flow, a factor of $(\mathrm{Pr}/\mathrm{Pr_w})^{0.11}$ should also be taken for laminar flow. (Pr is the Prandtl number at T_m; and $\mathrm{Pr_w}$, that at the wall temperature.)

In Eqs. (6) and (12) $(\mathrm{Pr}/\mathrm{Pr_w})$ is equated to unity. Hence,

$$\mathrm{Nu} = \mathrm{Nu}_{\mathrm{m},T}\left(\frac{\mathrm{Pr}}{\mathrm{Pr_w}}\right)^{0.11} \tag{13}$$

3.2 Constant Heat Flux

3.2.1 Hydrodynamically Developed Laminar Flow

Theoretical relationships for the heat transfer coefficient also exist for the boundary condition of constant heat flux, i.e., $\dot{q}$ = const., along the length of the plate. An example where this occurs is the electric heating of tubes.

In thermally and hydrodynamically developed laminar flow (low values of $\mathrm{Re\,Pr}\, d_\mathrm{i}/x$, i.e., long pipes), the asymptote for the *local Nusselt number* at a point located at a distance x from the pipe inlet is given by

$$\mathrm{Nu}_{x,q,1} = 4.354 \tag{14}$$

If the flow is still developing thermally and has been developed hydrodynamically, the asymptote is given by Eq. (15). The conditions in this case are that the value of $\mathrm{Re\,Pr}\, d_\mathrm{i}/x$ is high, heating does not commence until the end is reached of the section in which hydrodynamic development takes place, and x is measured from the point at which heating commences.

$$\mathrm{Nu}_{x,q,2} = 1.302\ \sqrt[3]{\mathrm{Re\,Pr}\, d_\mathrm{i}/x} \tag{15}$$

Local Nusselt numbers in the range between the two asymptotes have been determined numerically and tabulated by Sha and London [1].

The local Nusselt numbers in the entire $0 < \mathrm{Re\,Pr}\, d_\mathrm{i}/x < \infty$ range can be obtained from Eq. (16). The maximum deviation in this case is –4% in the $100 < \mathrm{Re\,Pr}\, d_\mathrm{i}/x < 1000$ range; otherwise it is less or even positive.

$$\mathrm{Nu}_{x,q} = \left\{\mathrm{Nu}_{x,q,1}^3 + 1 + [\mathrm{Nu}_{x,q,2} - 1]^3\right\}^{1/3} \tag{16}$$

The asymptotes for the *mean Nusselt number* in a pipe of length l are

$$\mathrm{Nu}_{\mathrm{m},q,1} = 4.364 \tag{17}$$

for low values of $\mathrm{Re\,Pr}\, d_\mathrm{i}/l$ and

$$\mathrm{Nu}_{\mathrm{m},q,2} = 1.953\ \sqrt[3]{\mathrm{Re\,Pr}\, d_\mathrm{i}/l} \tag{18}$$

for high values of $\mathrm{Re\,Pr}\, d_\mathrm{i}/l$.

Equation (19) allows the same mean Nusselt numbers as those determined numerically [1] to be obtained over the entire $0 < \mathrm{Re\,Pr}\, d_\mathrm{i}/l$ range. The deviation is less than 1%.

$$\mathrm{Nu}_{\mathrm{m},q} = \left\{\mathrm{Nu}_{\mathrm{m},q,1}^3 + 0.6^3 + [\mathrm{Nu}_{\mathrm{m},q,2} - 0.6]^3\right\}^{1/3} \tag{19}$$

3.2.2 Hydrodynamic and Thermal Development of Flow

Gauler [11] has calculated the *local Nusselt number* for the thermal and hydrodynamic development of flow, which is explained in the first paragraph of Sect. 3.1.2, for the case of parallel flow over a flat plate. Rearrangement of his equation to apply for flow through a pipe gives

$$\mathrm{Nu}_{x,q} = 0.459\ \sqrt[3]{\mathrm{Pr}}\sqrt{\mathrm{Re}\ d_\mathrm{i}/x}\quad \text{for}\quad \mathrm{Pr} \approx 1 \tag{20}$$

and

$$\mathrm{Nu}_{x,q} = 0.464\ \sqrt[3]{\mathrm{Pr}}\ \sqrt{\mathrm{Re}\ d_\mathrm{i}/x}\quad \text{for}\quad \mathrm{Pr} \to \infty \tag{21}$$

For practical purposes, the equation applicable to $\mathrm{Pr} > 0.7$ can be obtained with sufficient accuracy by taking the average of the two factors in Eqs. (20) and (21), i.e.,

$$\mathrm{Nu}_{x,q,3} = 0.462\ \sqrt[3]{\mathrm{Pr}}\ \sqrt{\mathrm{Re}\ (d_\mathrm{i}/x)}\ \text{for}\ \mathrm{Pr} > 0.7 \tag{22}$$

Equation (22) is applicable for large values of (d_i/x). Increasing flow length results in small values of (d_i/x), and one obtains from Eq. (22) smaller values of the local Nusselt number than from Eq. (16).

Spang [12] numerically calculated local Nusselt numbers for thermally and hydrodynamically developing laminar flow with $\dot{q}$ = const. The values for $0.7 < \mathrm{Pr} < 1{,}000$ are very well represented by

$$\mathrm{Nu}_{x,q} = \left\{\mathrm{Nu}_{x,q,1}^3 + (\mathrm{Nu}_{x,q,2} - 1)^3 + \mathrm{Nu}_{x,q,3}^3\right\}^{1/3} \tag{23}$$

with $\mathrm{Nu}_{x,q,1}$ from Eq. (14), $\mathrm{Nu}_{x,q,2}$ from Eq. (15), and $\mathrm{Nu}_{x,q,3}$ from Eq. (22).

Laminar flow develops very quickly. Therefore, for $(d_\mathrm{i}/l) > 0.1$, *mean Nusselt numbers* in flows with simultaneous thermal and hydrodynamic development differ only slightly from the values calculated from Eq. (19), which was for the case where fully developed flow was established before heating started. The asymptote for the mean Nusselt number for simultaneous development at large values of (d_i/l) (i.e., for short tubes) results from an integration of Eq. (22) over the length of the tube, giving the following equation:

$$\mathrm{Nu}_{\mathrm{m},q,3} = 0.924\ \sqrt[3]{\mathrm{Pr}}\ \sqrt{\mathrm{Re}\,(d_\mathrm{i}/l)} \tag{24}$$

A comparison with the calculated values of Spang [12] shows that an equation for the thermally and hydrodynamically developing flow for all tube lengths can be obtained from

$$\mathrm{Nu}_{\mathrm{m},q} = \left\{\mathrm{Nu}_{\mathrm{m},q,1}^3 + 0.6^3 + (\mathrm{Nu}_{\mathrm{m},q,2} - 0.6)^3 + \mathrm{Nu}_{\mathrm{m},q,3}^3\right\}^{1/3} \tag{25}$$

with $\mathrm{Nu}_{\mathrm{m},q,1}$ from Eq. (17), $\mathrm{Nu}_{\mathrm{m},q,2}$ from Eq. (18), and $\mathrm{Nu}_{\mathrm{m},q,3}$ from Eq. (24).

3.2.3 Explanations, Effect of Temperature-Dependent Property Variations

The explanations given in Sect. 3.1.3 also apply in this case. Herwig [13] published a theoretical study on the effect exerted on heat transfer by temperature-dependent property variations for the case of completely developed pipe flow at $\dot{q}$ = const. The results practically correspond to those obtained from Eq. (13). Since no experimental data can be found in the literature that would allow the effect of variations in properties to be

determined, the procedure recommended is precisely that described in Sect. 3.1.3.

4 Heat Transfer in Turbulent Flow Through Pipes

4.1 Nusselt Number for Fully Developed Turbulent Flow

Transition from laminar to turbulent flow starts at Re = 2100 to Re = 2300. The flow is fully turbulent at Re $\geq 10^4$. If the flow is turbulent, almost the same Nusselt number applies for the two boundary conditions: "constant wall temperature" and "constant heat flux."

An equation put forward by Gnielinski [14] for heat transfer during turbulent flow of gases and liquids through pipes is

$$\mathrm{Nu_m} = \frac{(\xi/8)\,\mathrm{Re\,Pr}}{1 + 12.7\sqrt{\xi/8}\left(\mathrm{Pr}^{2/3} - 1\right)}\left[1 + \left(d_\mathrm{i}/l\right)^{2/3}\right] \qquad (26)$$

where

$$\xi = \left(1.8\log_{10}\mathrm{Re} - 1.5\right)^{-2} \qquad (27)$$

Equation (26) was obtained by modifying an equation that was derived from the theory of momentum transport by Petukhov and Kirillov [15] and is valid for completely developed pipe flow. It was enlarged by a factor proposed by Hausen [16] to take into account the dependence of the heat transfer coefficient from the length of the pipe. According to Konakov [17], the friction factor for turbulent flow in smooth pipes may be calculated from Eq. (27).

Explanations and ranges of validity are as follows:

$$\mathrm{Nu_m} = \frac{\alpha\, d_\mathrm{i}}{\lambda};\ \mathrm{Re} = \frac{w d_\mathrm{i}}{\nu};\ 10^4 \leq \mathrm{Re} \leq 10^6;$$
$$0.1 \leq \mathrm{Pr} \leq 1000;\ d_\mathrm{i}/l \leq 1.$$

The physical properties of the fluids are referred to the mean temperature $T_\mathrm{m} = (T_\mathrm{i} + T_\mathrm{o})/2$.

Section 4.4 deals with the effect of the temperature dependence of the physical properties on the heat transfer coefficient.

On a large number of experimental data, Gnielinski [14] has tested the validity of Eq. (26). The Prandtl numbers of the data were between 0.6 and 1,000. Martin [18] compared the Nusselt numbers resulting from Eq. (26) with those from a new calculation procedure for the heat transfer with turbulent flow in tubes from Churchill and Zajic [19]. He found that the results of this calculation procedure agree very well with those from Eq. (26) up to a Prandtl number of Pr = 0.1. The range of validity of Eq. (26) may therefore be widened up to Pr = 0.1.

From Eq. (26), it may be inferred that the Nusselt number for fully developed turbulent flow depends markedly from the length of the tube only at the entrance. The *local Nusselt number* results from a differentiation of Eq. (26), giving

$$\mathrm{Nu_x} = \frac{(\xi/8)\ \mathrm{Re\,Pr}}{1 + 12.7\sqrt{\xi/8}\ \left(\mathrm{Pr}^{2/3} - 1\right)}\left[1 + \frac{1}{3}\left(d_\mathrm{i}/x\right)^{2/3}\right] \qquad (28)$$

with ξ from Eq. (27).

4.2 Nusselt Number in the Transition Region Between Laminar and Fully Developed Turbulent Flow

After the critical Reynolds number (approximately 2300) is exceeded, the development of turbulence depends on many influencing factors, for example, the shape of the entrance of the tube, the manner in which the fluid flows towards the tube entrance and the disturbances in the velocity of the flow.

Rotta [20] observed that water entering a tube from a container was changing at short intervals between laminar and turbulent flow. To describe the temporal sequences, he introduced an "intermittency factor" γ, where $\gamma = 1$ if the flow is turbulent permanently, and $\gamma = 0$ if the flow is permanently laminar.

According to these observations, Gnielinski [21] proposed an equation to describe by interpolation the regime between permanent laminar and turbulent flow. This equation represents very well the experimental data of numerous authors. The equation is as follows:

$$\mathrm{Nu} = (1-\gamma)\,\mathrm{Nu}_{\mathrm{lam},2300} + \gamma\,\mathrm{Nu}_{\mathrm{turb},10^4} \qquad (29)$$

where γ is given by

$$\gamma = \frac{\mathrm{Re} - 2300}{10^4 - 2300}, \quad \text{and} \quad 0 \leq \gamma \leq 1 \qquad (30)$$

$\mathrm{Nu_{lam,2300}}$ is the Nusselt number at Re = 2300 calculated from Eq. (12) or Eq. (25) according to the boundary condition. $\mathrm{Nu_{turb,10^4}}$ is the Nusselt number from Eq. (26) at $\mathrm{Re} = 10^4$.

Therefore, one gets:

For *constant wall temperature* laminar flow, from Eq. (12)

$$\mathrm{Nu}_{\mathrm{m},T,2300} = \left\{49.371 + \left(\mathrm{Nu}_{\mathrm{m},T,2,2300} - 0.7\right)^3 + \mathrm{Nu}^3_{\mathrm{m},T,3,2300}\right\}^{1/3} \qquad (31)$$

with

$$\mathrm{Nu}_{\mathrm{m},T,2,2300} = 1.615\ (2300\,\mathrm{Pr}\,d_\mathrm{i}/l)^{1/3} \qquad (32)$$

and

$$\mathrm{Nu}_{\mathrm{m},T,3,2300} = \left(\frac{2}{1 + 22\,\mathrm{Pr}}\right)^{1/6}(2300\,\mathrm{Pr}\,d_\mathrm{i}/l)^{1/2} \qquad (33)$$

For *constant heat flux*, laminar flow, from Eq. (25)

$$\mathrm{Nu}_{\mathrm{m},q,2300} = \left\{83.326 + \left(\mathrm{Nu}_{\mathrm{m},q,2,2300} - 0.6\right)^3 + \mathrm{Nu}^3_{\mathrm{m},q,3,2300}\right\}^{1/3} \qquad (34)$$

with

$$\mathrm{Nu}_{\mathrm{m},q,2,2300} = 1.953\ (2300\,\mathrm{Pr}\,d_\mathrm{i}/l)^{1/3} \qquad (35)$$

and

$$\mathrm{Nu}_{\mathrm{m},q,3,2300} = 0.924\ (\mathrm{Pr})^{1/3}(2300\ d_\mathrm{i}/l)^{1/2} \qquad (36)$$

For *constant wall temperature or constant heat flux* and turbulent flow from Eq. (26)

$$\mathrm{Nu}_{\mathrm{m},10^4} = \frac{(0.0308/8)10^4\,\mathrm{Pr}}{1 + 12.7\sqrt{0.0308/8}\left(\mathrm{Pr}^{2/3} - 1\right)}\left[1 + \left(d_\mathrm{i}/l\right)^{2/3}\right] \qquad (37)$$

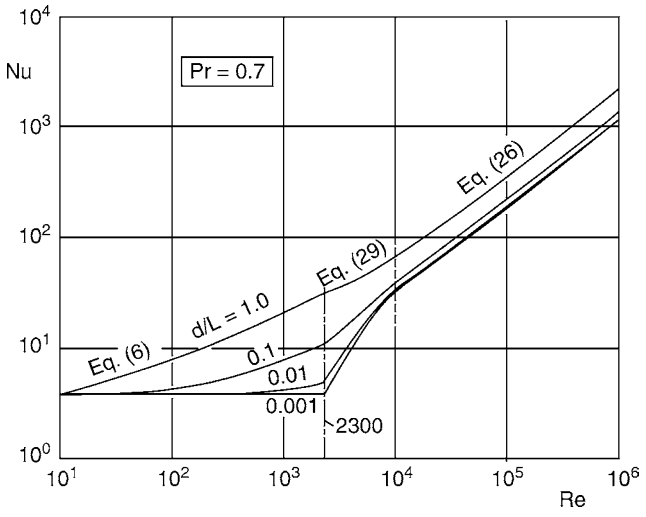

G1. Fig. 1. Nu_m in dependence of Re according to the Eqs. (6), (26), and (29) for heat transfer in circular pipes at Pr = 0.7.

Range of validity:

$$2300 \leq Re \leq 10^4; \quad 0.6 \leq Pr \leq 1000; \quad d_i/l \leq 1.$$

This equation of interpolation avoids the "jump" at Re = 2300 in the Nusselt number resulting from the equation included in the former edition of this handbook. A continuous calculation of the Nusselt number is achieved by using Eq. (29) combined with the other equations. This is demonstrated in Fig. 1 for the boundary condition "constant wall temperature" and Pr = 0.7.

The physical properties of the fluids are referred to the mean temperature $T_m = (T_i + T_o)/2$.

4.3 Nusselt Number for Approximate Calculations

For estimate purposes, less complicated equations are often sufficient. As it is shown in [14], the following equations also represent a large number of experimental data in the transition region. The equations are as follows:

For $0.5 \leq Pr \leq 1.5$

$$Nu_m = 0.0214\left(Re^{0.8} - 100\right)Pr^{0.4}\left[1 + \left(d_i/l\right)^{2/3}\right] \qquad (38)$$

and for $1.5 < Pr < 500$

$$Nu_m = 0.012\left(Re^{0.87} - 280\right)Pr^{0.4}\left[1 + \left(d_i/l\right)^{2/3}\right] \qquad (39)$$

Note that these approximate equations give considerably higher values of the Nusselt number than does Eq. (29) for small values of (d_i/l). They should not be used in this region.

4.4 Effect of Temperature Dependent Property Variations

If the properties of the medium are affected by temperature, the direction of the heat flux (heating or cooling) influences heat transfer. Allowance for this effect in *liquids* can be made – as it is in laminar flow – by the factor $(Pr/Pr_w)^{0.11}$, where Pr is the Prandtl number at T_m and Pr_w is that at the wall temperature T_w. In Eqs. (26), (38), and (39), Pr/Pr_w has been equated to unity.

Hence the following applies for liquids:

$$Nu = Nu_m\left(\frac{Pr}{Pr_w}\right)^{0.11} \qquad (40)$$

Equation (40) is valid for $0.1 < Pr/Pr_w < 10$.

Hackl and Gröll [22] measured the heat transferred from hot oils to a cooled pipe wall in order to determine the effect of temperature-dependent property variations up to $Pr/Pr_w = 10^{-4}$. They suggested two empirical equations to represent the results of their experiments.

These results have also been the subject of comments by Hausen [23], and were developed by Gregorig [24] into a correction function, which he recommended for the case of cooling liquids with high Prandtl numbers, e.g., viscous oils.

The Prandtl number of *gases* depends very little on temperature. Consequently, a factor $(T/T_w)^n$ is adopted to allow for the effect on heat transfer exerted by the variations in properties. In this case,

$$Nu = Nu_m(T/T_w)^n \qquad (41)$$

where T is the average gas temperature and T_w is the wall temperature of the pipe, both in Kelvin.

If the gas is cooled, i.e., $T/T_w > 1$, the exponent n becomes $n = 0$. If it is heated, i.e., $T/T_w < 1$, the exponent depends on the nature of the gas. Gnielinski [14] correlated values measured in the $1 > T/T_w > 0.5$ range with $n = 0.45$. A value quoted in the literature for carbon dioxide in the same T/T_w range is $n = 0.12$. Heinmann [25] quotes a value of $n = -0.18$ for superheated steam at $1 > T/T_w > 0.67$ and at pressures between 21 bar and 100 bar. Gregorig [26] drew up a nomogram that allows for the variations in properties over a wide range of temperatures.

5 Example of a Calculation

Water of a temperature at the inlet of $T_i = 10°C$ is flowing in a tube with an inner diameter of $d_i = 10$ mm and a length of 1,000 mm with a velocity of $w = 0.5$ m/s. The tube is heated from the outside by condensing steam of water in a way that the temperature at the inner wall has a constant temperature of $T_w = 100°C$. How large is the temperature of the water at the outlet of the tube?

Solution

To calculate the dimensionless numbers in the equations, the physical properties of the water are needed. Because of the temperature dependence of these properties, the problem can be solved only by iteration.

1. Approximate calculation of the Reynolds number to see whether the flow is laminar or turbulent or the Reynolds number is within the transition region $2300 \leq Re \leq 10^4$: $Re = wd_i/\nu$; at 20°C is $\nu = 1.004 \times 10^{-6} m^2/s$, therefore $Re = 0.5 \times 0.01/1.004 \times 10^{-6} = 4980$. The Reynolds

number is within the transition region. The heat transfer coefficient α has to be calculated from the Sects. 4.2 and 4.4.
2. The physical properties of the water have to be taken from Subchap. D2.1.
3. The Prandtl number at the wall temperature $\vartheta_i = 100°C$ remains at $Pr_w = 1.757$. The heat transfer area of the tube is $A = \pi\, d_i\, l = \pi \times 0.01 \times 1.0 = 0.0314\ m^2$.
4. For the further steps of calculation, see Table 1.

Because the physical properties at the reference temperature $T_m = 31.1°C$ differ only marginally from that at 31.0°C, a further step of iteration is not necessary. The temperature of the water at the end of the tube is therefore $T_o = 52.2^0C$.

6 Effect of the Shape of the Tubes Inlet

Equations (12), (26), and (29) yield mean Nusselt numbers for tubes fitted without fillets in a tube support plate, as is illustrated in Fig. 2. The effect of the shape of the tube inlet on the local Nusselt number was investigated by Grass [27] and by Boelter et al. [28].

7 Noncircular Pipes

There are no standard equations for *laminar* flow in pipes of noncircular cross section. Information on the heat transfer coefficient in these cases can be obtained from the literature [1].

According to statements from the literature, the Nusselt numbers for heat transfer in *turbulent* flow in smooth straight ducts of noncircular cross section can also be calculated from Eq. (26) by using the hydraulic diameter of the duct in evaluating Nu, Re, and d_i/l. The hydraulic diameter is defined as

$$d_h = \frac{4S}{P} \tag{42}$$

where S is the flow cross-sectional area and P is the wetted perimeter of the duct.

G1. Table 1. Steps of iteration for the example of a calculation

Step of iteration	1. Step	2. Step
T_o (approximately)	50	52
T_i	10	10
$T_m = \frac{T_i + T_o}{2}$	30	31
$\nu\,(T_m)\,/10^{-6}m^2/s$	0.801	0.786
$\lambda\,(T_m)\,/W/(m\ K)$	0.6155	0.6171
$\rho\,(T_m)/kg/m^3$	995.65	995.33
$c_p\,(T_m)/J/(kg\ K)$	4,177	4,177
$Pr\,(T_m)$	5.414	5.296
Laminar portion		
Equation (32) $Nu_{m,T,2,2300} = 1.615\,(2300\,Pr\,d_i/l)^{1/3}$	8.065	8.006
Equation (33) $Nu_{m,T,3,2300} = \left(\frac{2}{1+22\,Pr}\right)^{1/6} (2300\,Pr\,d_i/l)^{1/2}$	5.639	5.598
Equation (31) $Nu_{m,T,2300}$	8.564	8.503
Turbulent portion		
Equation (37) $Nu_{m,10^4} = \frac{(0.0308/8)\ 10^4\,Pr}{1+12.7\sqrt{0.0308/8}\,\left(Pr^{2/3}-1\right)}\left[1+(d_i/l)^{2/3}\right]$	82.57	81.86
$Re = w \cdot d_i/\nu\ (T_m)$	6242.2	6,361
Equation (30) $\gamma = \frac{Re - 2300}{10^4 - 2300}$	0.512	0.527
Equation (29) $Nu = (1-\gamma)\,Nu_{lam,2300} + \gamma\,Nu_{turb,10^4}$	46.46	47.16
Equation (40) $Nu = Nu_m \cdot \left(\frac{Pr(T_m)}{Pr_w}\right)^{0.11}$	52.58	53.25
$\alpha = \frac{Nu \cdot \lambda\,(T_m)}{d_i}$	3,236 W/(m² K)	3,286 W/(m² K)
$\Delta T_m = \frac{(T_w - T_i) - (T_w - T_o)}{\ln \frac{(T_w - T_i)}{(T_w - T_o)}}$	68.06	66.8
$\dot{Q} = \alpha \cdot A \cdot \Delta\, T_m$	6914.6	6892.5
$T_o = \frac{\dot{Q}}{w \cdot \pi \cdot \frac{d_i^2}{4} \cdot \rho(T_m) \cdot c_p(T_m)} + T_i$	52.3	52.2

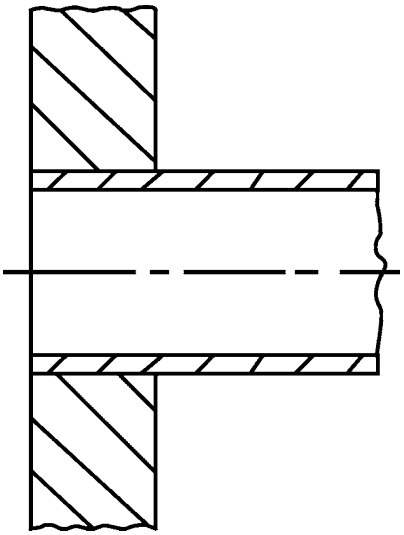

G1. Fig. 2. Tube inlet in a support plate.

8 Bibliography

1. Sha RK, London AL (1978) Laminar flow forced convection in ducts. Academic Press, New York/San Francisco, CA/London
2. Gnielinski V (1989) Zur Wärmeübertragung bei laminarer Rohrströmung und konstanter Wandtemperatur. Chem-Ing-Techn 61:160–161
3. Pohlhausen E (1921) Der Wärmeaustausch zwischen festen Körpern und Flüssigkeiten mit kleiner Reibung und kleiner Wärmeleitung. Z angew Math Mech 1:115–121
4. Martin H (1990) Lecture on heat transfer II. Universitaet Karlsruhe (TH), Karlsruhe, Germany
5. Stephan K (1959) Wärmeübergang bei turbulenter und bei laminarer Strömung in Rohren und ebenen Spalten. Chem-Ing-Techn 31:773–778
6. Kays WM, Nicoll WB (1963) Laminar flow heat transfer to a gas with large temperature differences. J Heat Transfer 85:329/338
7. Davenport ME, Leppert G (1965) The effect of transverse temperature gradients on the heat transfer and friction for laminar flow of gases. J Heat Transfer 87:1919–1996
8. Bankstone CA, Sibbit WL, Skoglund VJ (1966) Stability of gas flow distribution among parallel heated channels, 2nd Propulsion Joint Specialist Conf., Colorado Springs, AIAA Paper No. 66–589
9. Sieder EN, Tate GE (1936) Heat transfer and pressure drop of liquids in tubes. Ind Eng Chem 8:1429–1435
10. Hufschmidt W, Burck E (1968) Einfluss temperaturabhängiger Stoffwerte auf den Wärmeübergang bei turbulenter Strömung von Flüssigkeiten in Rohren bei hohen Wärmestromdichten und Prandtlzahlen. Int J Heat Mass Transfer 11:1041–1048
11. Gauler K (1972) Wärme- und Stoffübertragung an eine mitbewegte Grenzfläche bei Grenzschichtströmung. Universitaet Karlsruhe (TH), Karlsruhe, Germany
12. Spang B (1996) Einfluss der thermischen Randbedingungen auf den laminaren Wärmeübergang im Kreisrohr bei hydrodynamischer Einlaufströmung. Heat Mass Transfer 31:199–204
13. Herwig H (1985) The effect of variable properties on momentum and heat transfer in a tube with constant heat flux across the wall. Int J Heat Mass Tranf 28:423–431
14. Gnielinski V (1976) New equations for heat and mass transfer in turbulent pipe and channel flow. Int Chem Eng 16:359–368
15. Petukhov BS, Kirillov VV (1958) On heat exchange at turbulent flow of liquids in pipes (in Russian). Teploenergetika 4:63–68
16. Hausen H (1943) Darstellung des Wärmeüberganges in Rohren durch verallgemeinerte Potenzbeziehungen. Verfahrenstechn, Z VDI-Beiheft 8 (4):91–98
17. Konakov PK (1946) A new correlation fort he friction coefficient in smooth tubes. Berichte der Akademie der Wissenschaften der UdSSR. Band LI 51:503–506
18. Martin H (2003) Lecture on heat transfer I. Universitaet Karlsruhe (TH), Karlsruhe, Germany
19. Churchill SW, Zajic S (2002) Prediction of fully developed turbulent convection with minimal explicit empiricism. AIChE-J 48:927–940
20. Rotta JC (1972) Turbulente Strömungen. Verlag Teubner, Stuttgart, Germany
21. Gnielinski V (1995) Ein neues Berechnungsverfahren für die Wärmeübertragung im Übergangsbereich zwischen laminarer und turbulenter Rohrströmung. Forsch im Ing-Wes 61:240–248
22. Hackl A, Gröll W (1969) Zum Wärmeübergangsverhalten zähflüssiger Öle. Verfahrenstechn 3:141–145
23. Hausen H (1969) Comments to [22]. Verfahrenstechn 3:355/480
24. Gregorig R (1976) The effect of nonlinear temperature dependent Prandtl number on heat transfer of fully developed flow of liquids in a straight tube. Wärme- und Stoffübertragung 9:61–72
25. Heinemann JB. Argonne National Laboratory, ANL–213, 196.
26. Gregorig R (1973) Wärmeaustausch und Wärmeaustauscher. Verlag Sauerländer, Aarau u. Frankfurt/M, Germany, p 171
27. Grass G (1956) Wärmeübergang an turbulent strömende Gase im Rohreinlauf. Allg Wärmetechn 7:58–64
28. Boelter LMK, Young G, Iversen HW (1948) An investigation of aircraft heaters, XXVII-distribution of heat transfer rate in the entrance section of a circular tube. Nat Adv Comm Aeron NACA TN 1451, Washington

G10 Impinging Jet Flow Heat Transfer

Wilhelm Schabel · Holger Martin
Karlsruher Institut für Technologie (KIT), Karlsruhe, Germany

1 Introduction: Impinging Jets from Round and Slot Nozzles

Heating, cooling of products, and drying of coatings with large surface area is often carried out in devices consisting of arrays of round or slot nozzles through which liquid or gas jets (most frequently air) impinge vertically upon the product surface.

Figure 1 shows the different cases of impinging flow that are subsequently discussed. It is assumed that the jets consist of the same fluid as the surrounding fluid. The flow pattern of impinging jets can be subdivided into three characteristic regions (Fig. 2).

At the exit of the nozzle, a *free jet* is formed which is widened and decelerated due to mixing with the surrounding fluid. At a certain distance over the surface, the free jet is transformed into a *stagnation flow* where the vertical component of the velocity is reduced to zero, whereas the horizontal component increases from zero to a maximum value at a certain distance from the stagnation point. The stagnation flow is transformed into a *wall jet* which, like the free jet, is characterized by widening and deceleration [1].

For most technically relevant applications, the flow will be turbulent. Exact information regarding the limits of laminar impinging flow cannot be found in the literature. The Reynolds number is written with the average velocity at the exit of the nozzle w and hydraulic diameter of the nozzle D:

$$\mathrm{Re} = \frac{wD}{\nu} \tag{1}$$

Even for small values of $\mathrm{Re} \geq 100$, the jet flow will be turbulent. For round nozzles, the hydraulic diameter is equal to the (inner) diameter of the nozzle opening. For slot nozzles with the slot width B and the slot length $L_s >> B$, the hydraulic diameter is defined as

$$D = 2B \tag{2}$$

2 Definitions in Heat and Mass Transfer

Average heat transfer coefficients at a surface impinged upon by jets are defined as the heat flux divided by the difference of the fluid temperatures at the exit of the nozzle (N) and the surface (S) of the material which is below the nozzle at a distance H:

$$\alpha = \frac{\dot{Q}}{A(T_\mathrm{N} - T_\mathrm{S})} \tag{3}$$

Local heat transfer coefficients $\alpha(x)$ or $\alpha(r)$ at a substrate surface are technically relevant if the material underneath the nozzle array does not move. Detailed information and recent experimental results regarding this topic can be found in Hofmann et al. [2]. Diagrams with measured local heat and mass transfer coefficients and further details can be found in a review on this subject published in 1977 [1].

The dimensionless numbers used in this chapter are

$$\mathrm{Nu} = \frac{\alpha D}{\lambda} \quad \text{or} \quad \mathrm{Sh} = \frac{\beta D}{\delta} \tag{4}$$

$$\mathrm{Re} = \frac{wD}{\nu},$$

see Eq. (1)

$$\mathrm{Pr} = \frac{\nu}{a} \quad \text{or} \quad \mathrm{Sc} = \frac{\nu}{\delta} \tag{5}$$

VDI-GVC (ed.), *VDI Heat Atlas*, DOI 10.1007/978-3-540-77877-6_32,

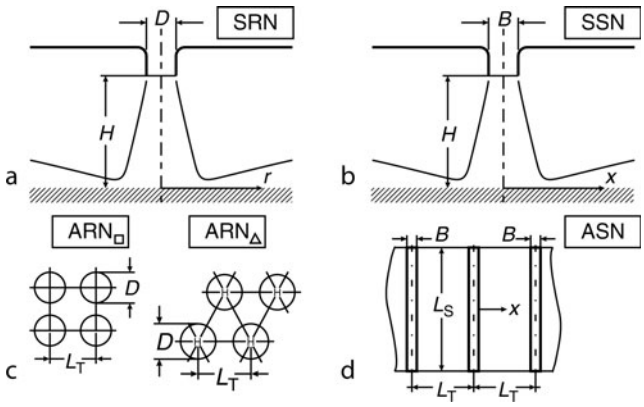

G10. Fig. 1. Arrays of nozzles. (**a**) The single round nozzle (SRN), (**b**) the single slot nozzle (SSN), (**c**) the array of round nozzles (ARNs), and (**d**) the array of slot nozzles (ASNs).

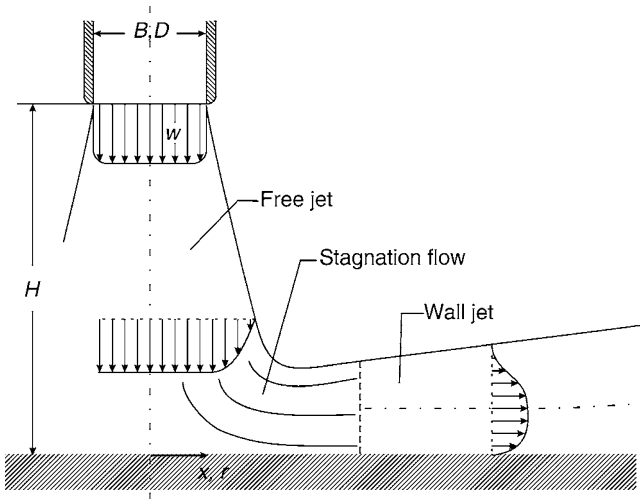

G10. Fig. 2. Impinging flow from round and slot nozzles.

For the calculation of these numbers, the temperature dependent properties should be used at the arithmetic mean temperature of the fluid between the nozzle exit (N) and the surface (S) $T_m = (T_N + T_S)/2$. The average mass transfer coefficient can be calculated analogously from the equations for the average heat transfer coefficient if Nu is replaced by Sh, and Pr by Sc (Part A).

3 Single Round Nozzle (SRN) and Single Slot Nozzle (SSN)

For a SRN, the integral heat and mass transfer coefficients, i.e. the mean value over a circle of the radius r around the stagnation point, can be expressed as follows:

$$\mathrm{Nu_{SRN}} = \frac{1 - 1.1/r^*}{r^* + 0.1(h^* - 6)} \cdot F(\mathrm{Re}) \cdot \mathrm{Pr}^{0.42} \qquad (6)$$

$$F(\mathrm{Re}) = 2[\mathrm{Re}(1 + 0.005 \cdot \mathrm{Re}^{0.55})]^{0.5}$$

Range of validity:

$$2.5 \le (r^* = r/D) \le 7.5,$$
$$2.0 \le (h^* = H/D) \le 12,$$
$$2\,,\,000 \le \mathrm{Re} \le 400,\,000.$$

Equation (6) from Schlünder and Gnielinski [3] is based on their own experimental results and on the evaluation of data from other sources. The function $F = F(Re)$ was originally graphically correlated, then described by power-law correlations in three different ranges of the Reynolds number $F = a\mathrm{Re}^m$ [4, 5]. According to Martin [1] it can be described by the aforementioned equation over the complete range of Reynolds numbers investigated.

For the SSN with $D = 2B$, the empirical equation for integral heat and mass transfer coefficients over the area of a rectangle $2x \cdot L_s$ (around the stagnation line at $x = 0$) is given according to Schlünder et al. [4] by:

$$\mathrm{Nu_{SSN}} = \frac{1.53 \cdot \mathrm{Re}^m}{x^* + h^* + 1.39} \cdot \mathrm{Pr}^{0.42} \qquad (7)$$

$$m = 0.695 - \frac{1}{x^* + h^{*1.33} + 3.06}$$

Here the exponent m of the Reynolds number depends on the geometric ratios and varies from 0.56 to 0.68 within the range of validity given next.

Range of validity:

$$2 \le (x^* = x/D) \le 25,$$
$$2 \le (h^* = H/D) \le 10,$$
$$3,\,000 \le \mathrm{Re} \le 90,\,000.$$

4 Arrays of Round Nozzles

For ARNs (see Fig. 1c) an empirical equation for integral average heat and mass transfer coefficients at the surface is given by Krötzsch [5] and in a modified form by Martin [1] as

$$\mathrm{Nu_{ARN}} = G \cdot \mathrm{Re}^{\frac{2}{3}} \cdot \mathrm{Pr}^{0.42}$$

$$G = \frac{d^* \cdot (1 - 2.2d^*)}{1 + 0.2 \cdot (h^* - 6) \cdot d^*} \cdot \left[1 + \left(\frac{10 \cdot h^* \cdot d^*}{6}\right)^6\right]^{-0.05} \qquad (8)$$

Range of validity:

$$0.004 \le (d^{*2} = f) \le 0.04,$$
$$2 \le (h^* = H/D) \le 12,$$
$$2,000 \le \mathrm{Re} \le 100,000.$$

Equation (8) is also recommended by Polat [6]. In Eq. (8) $d^* = \sqrt{f}$, where f is the relative nozzle area, i.e. the ratio of nozzle exit cross-sectional area to surface area of the product. For a square-shaped arrangement ($\mathrm{ARN}_\square$, from Fig. 1) it can be found that

$$f = \frac{\pi}{4}\frac{D^2}{L_T^2} \qquad (9)$$

$$d^* = \sqrt{f} = 0.8862 \frac{D}{L_T} \tag{10}$$

and for the triangle arrangement (ARN_Δ, Fig. 1),

$$f = \frac{\pi}{2\sqrt{3}} \frac{D^2}{L_T^2} \tag{11}$$

$$d^* = \sqrt{f} = 0.9523 \frac{D}{L_T} \tag{12}$$

5 Arrays of Slot Nozzles (ASN)

For arrays of slot nozzles (ASN see Fig. 1d, $D = 2B$), the relative nozzle area is simply:

$$f = \frac{B}{L_T} \tag{13}$$

$$d^* = f = 0.5 \frac{D}{L_T} \tag{14}$$

The integral average heat and mass transfer coefficients at the product surface are empirically expressed by Martin [1] based on his own experimental results [7] and evaluation of data from other sources.

$$\mathrm{Nu_{ASN}} = \frac{2}{3} f_o^{3/4} \left(\frac{2\mathrm{Re}}{f/f_o + f_o/f} \right)^{2/3} \mathrm{Pr}^{0.42} \tag{15}$$

$$f_o = \left[60 + 4 \cdot (h^* - 2)^2 \right]^{-1/2}$$

Range of validity:

$$0.008 \le (f = B/L_T) \le 2.5 \cdot f_o,$$
$$1 \le (h^* = H/D) \le 40 \quad \text{with } D = 2B,$$
$$1,500 \le \mathrm{Re} \le 40,000.$$

Equation (15) and the other equations given in this chapter are recommended by Polat [6] for practical applications as well.

6 Optimization of the Nozzles Spacing and Geometry

The problem of optimizing the nozzle arrangement with regard to the expense in fan power per product area means to identify the array that yields the highest average heat and mass transfer coefficient at the product surface at a given fan power per unit area. It was addressed by Krötzsch [8] for ARNs and by Martin [7] and Martin and Schlünder [9] for ASNs. A detailed summary of these calculations of optimization can be found in Martin's work [1]. The results of this optimization are also recommended by Polat [6] as a starting point for design. An absolute optimum for this problem cannot be found. The three main geometric nozzle parameters are

1. the hydraulic diameter of the nozzles D,
2. the nozzle-to-plate distance H and
3. the nozzle-to-nozzle spacing L_T,

which characterize a periodic array of round or slot nozzles. All three dimensions should be chosen in proper relation to each other. Variation of D with fixed values for the ratios H/D, L_T/D, however, cannot lead to an optimal value for the nozzle diameter. It can be easily seen that minimization of all three lengths leads to a monotonic increase of the heat and mass transfer coefficients especially due to reducing the flow distance to the product surface ($L_T/2$). In order to obtain a meaningful optimum, i.e., a maximum mean heat or mass transfer coefficient for a given fan power per unit surface area, it is necessary that one of the lengths has to fixed and is given as a secondary condition. The optimal ratios of the other two lengths and the one given as a secondary condition can then be determined unambiguously so that the best heat and mass transfer possible under the chosen conditions can be achieved. For safety reasons, most often the nozzle-to-plate distance H is the length limiting the optimization problem. In technical applications, less than a few centimeters of distance between a fast moving, maybe sagging or even flagging, product sheet and the nozzles can probably not be achieved. Particularly for coated products in the first drying regime the viscosity of the liquid film is too low and surface defects occur due to the impact of the impinging flow. A proper distance, H, has to be determined e.g. experimentally. From my experience in coating industry, a range of distances between 1 cm to 10 cm can be obtained and found in practical applications.

With the secondary condition H = constant the approximate optimum values for the nozzle geometry for arrays of round and slot nozzles are given [1] as

$$D_{opt} \approx \frac{1}{5} H \tag{16}$$

$$L_{Topt} \approx \frac{7}{5} H \tag{17}$$

The optimum values for the relative nozzle areas that can be derived analytically from the given equations are

$$f_{opt\ ARN} = 1.52\% \tag{18}$$

$$f_{opt\ ASN} = 7.18\% \tag{19}$$

(The approximate Eqs. (16) and (17) result with Eqs. (9–12) in slightly differing values of $f_{opt} \approx 1.6\%$ for the squared arrangement of an $ARN_\square$ (1.85% for ARN_Δ) and for the triangle arrangement $f_{opt} \approx 7.14\%$ for ASN.) From the result of this optimization, it can be deducted that for achieving the same heat and mass transfer coefficients with the same fan power, an optimal ARN requires a smaller volume flow and a higher velocity at the nozzle exit, whereas an optimal ASN requires a higher volume flow but a lower velocity at the nozzle exit as following:

$$w_{ARN} = 1.68 \cdot w_{ASN} \tag{20}$$

$$\dot{V}_{ASN} = 2.82 \cdot \dot{V}_{ARN} \tag{21}$$

Therefore, ASNs should be preferably used for products that might be damaged by too high flow velocities, such as polymeric thin film coatings at the early stage of drying (constant rate period), where the viscosity is low.

The factors 1.68 and 2.28 in Eqs. (20) and (21) are derived from $\left(f_{opt\ ASN}/f_{opt\ ARN}\right)^{1/3} = 1.68$ and the square of this value [1].

If it is taken into account that a part of the total pressure drop is needed for overcoming the flow resistances within the

air supply system and is therefore not available at the nozzles, the optimum relative nozzle areas f_{opt} become smaller than the values obtained from Eqs. (18) and (19), as Steinberg [10] has shown.

The ratio of the pressure drop available at the nozzles and the total pressure drop can be written as

$$\frac{\Delta p_{nozzle}}{\Delta p_{total}} = \frac{1}{1 + K \cdot f^2} \tag{22}$$

Here the resistance constant K is the ratio of the pressure drop $\Delta p_s = \Delta p_{total} - \Delta p_{nozzle}$ of the air supply system and the dynamic pressure of the incident flow towards the nozzle $(\rho/2)(w * f)^2$ with

$$K = \frac{\Delta p_s}{(\rho/2)(w * f)^2}.$$

The constant K in its denominator contains the square of the very small incident flow velocity $w * f$ in the plenum chamber above the nozzles. Depending on the design of the air supply system with filters, perforated plates, baffles, etc., K may well reach values in the order of 1,000–10,000. To find the optimal ratios of the geometric parameters, taking a constant resistance number; K, of the air supply system into account, the maximum of the function $G_H(f, h^*)$ has to be determined with K as a parameter. This function can be derived by applying the optimization conditions: constant fan power per unit area of transfer surface

$$P = \Delta p \frac{wfA}{A} = \text{const.}$$

and constant nozzle-to-plate distance H

$$H = \text{const.}$$

to Eqs. (8) and (15) for the heat transfer for impinging flow from arrays of round and slot nozzles [1, 10].

$$\frac{\alpha H}{\lambda}\left(\frac{\rho \xi_{nozzle}}{2P}\right)^{2/9}\left(\frac{\nu}{H}\right)^{2/3}\mathrm{Pr}^{-0.42} = G_H(f, h^*) \tag{23}$$

For ARNs, i.e., $f = d^{*2}$, $h^* = H/D$, it follows from Eq. (8)

$$\begin{aligned} G_{H,\,ARN} &= G_1 G_2 G_3 \\ G_1 &= h^{*1/3}\frac{d^*(1 - 2.2 \cdot d)}{1 + 0.2 \cdot (h^* - 6) \cdot d^*} \\ G_2 &= \left[1 + \left(10\frac{h^* \cdot d^*}{6}\right)^6\right]^{-0.05} \\ G_3 &= \left[f\left(1 + Kf^2\right)\right]^{-2/9} \end{aligned} \tag{24}$$

For ASNs, i.e., $f = B/L_T$, $h^* = H/(2B)$ and $f_o = \left[60 + 4 \cdot (h^* - 2)^2\right]^{-1/2}$ Eq. (15) yields

$$\begin{aligned} G_{H,\,ASN} &= G_1 G_2 G_3 \\ G_1 &= \frac{2}{3} h^{*1/3} f_o^{3/4} \\ G_2 &= \left(\frac{2}{f/f_o + f_o/f}\right)^{2/3} \\ G_3 &= \left[f\left(1 + Kf^2\right)\right]^{-2/9} \end{aligned} \tag{25}$$

The maximum of G_H can be found numerically or analytically from Eq. (24) or (25) for given values of the air supply system flow resistance number K. For $K = 0$ the solution results in the same ratios of geometric parameters as given earlier in Eqs. (16) and (17).

Tables 1 and 2 show values that were obtained by evaluating Eqs. (24) and (25). They can be used to find an optimal spatial arrangement of the nozzles. It can be seen in Table 1 that the ratio $(L_T/H)_{opt}$ is nearly constant for ARN:

$(L_T/H)_{opt} \approx 1.3$ for square spacing and

G10. Table 1. Optimal spatial arrangement for arrays of round nozzles with a constant fan power per unit area of transfer surface P, constant nozzle-to-plate distance H, and a constant flow resistance number K of the air supply system $\left(1/h^* = D/H,\ d^* = \sqrt{f}\right)$

K	f(%)	d^*(%)	D/H	$(L_T/H)_\varepsilon$	$(L_T/H)_\Delta$	α/α_{max}
0	1.521	12.33	0.1842	1.324	1.423	1.000
10	1.503	12.26	0.1831	1.324	1.422	0.999
20	1.486	12.19	0.1820	1.323	1.422	0.999
50	1.439	12.00	0.1970	1.323	1.421	0.998
100	1.373	11.72	0.1747	1.321	1.420	0.995
200	1.271	11.27	0.1679	1.320	1.418	0.992
500	1.082	10.40	0.1544	1.316	1.414	0.983
1,000	0.913	9.56	0.1415	1.313	1.410	0.973
2,000	0.743	8.62	0.1273	1.309	1.407	0.960
5,000	0.541	7.35	0.1082	1.304	1.401	0.938
10,000	0.414	6.44	0.0945	1.301	1.398	0.918
20,000	0.312	5.59	0.0818	1.297	1.394	0.897
50,000	0.210	4.59	0.0669	1.294	1.390	0.866
100,000	0.154	3.93	0.0572	1.291	1.388	0.841
200,000	0.112	3.35	0.0488	1.289	1.385	0.816

G10. Table 2. Optimal spatial arrangement for arrays of slot nozzles with a constant fan power per unit area of transfer surface P, constant nozzle-to-plate distance H, and a constant flow resistance number K of the air supply system $(1/h^* = 2B/H,\ f = B\,L_T)$

K	f(%)	(B/H)(%)	L_T/H	α/α_{max}	kf^2
0	7.183	9.926	1.382	1.000	0.000
20	6.537	9.424	1.442	0.980	0.085
50	5.937	8.909	1.501	0.958	1.176
100	5.315	8.320	1.565	0.931	0.282
200	4.590	7.551	1.645	0.895	0.421
500	3.564	6.289	1.765	0.835	0.635
1,000	2.803	5.198	1.855	0.783	0.786
2,000	2.108	4.073	1.932	0.730	0.889
5,000	1.364	2.732	2.003	0.662	0.930
10,000	0.956	1.944	2.034	0.615	0.913
20,000	0.665	1.366	2.053	0.571	0.885

$(L_T/H)_{opt} \approx 1.4$ for triangular spacing

For ASNs $(L_T/H)_{opt}$ ranges from 1.4 for $K = 0$ to nearly 2 for large values of K (Table 2). The ratio of the pressure drop of the air supply system and the actual pressure drop in the nozzles $(\Delta p_s/\Delta p_{nozzle} = kf^2$ according to Eq. (22)) under these optimal conditions is lower than 1.

7 Influence of Downstream Flow Conditions

Optimal arrays of nozzles have a relatively small nozzle spacing $(L_{T\,opt} \approx 1.4H)$. Therefore, it can be difficult to provide sufficiently large cross-sectional areas for the downstream flow [9]. The problems linked to a lateral downstream flow leading to increasing and inhomogeneous heat transfer coefficients in cross web direction and in directions to the edges, are addressed in detail by Martin [1].

An upward downstream flow between the nozzles is in any case more favorable for the heat and mass transfer but cannot always be implemented easily.

8 Influence of the Nozzle Shape

It is known that the design of the nozzles influences the relation between the impressed pressure drop Δp and the velocity of the fluid w at the exit of the nozzle.

$$\Delta p = \frac{\xi \rho w^2}{2} \tag{26}$$

For a well-designed nozzle, the coefficient ξ has the value $\xi_{nozzle} \approx 1.0$. For sharp-edged orifices (holes in a perforated plate) it can reach values of up to

$$\xi_{orifice} \approx 2.69 \tag{27}$$

(In [1] instead of ξ the term $(1 + \zeta_D)$,with $0 \le \zeta_D \le 1.69$, was used). The expression

$$\mu = \frac{1}{\sqrt{\xi}} \tag{28}$$

is also called *discharge coefficient* C_D in the review by Polat [6]. For sharp-edged round and slot orifices, the jet is constricted and the cross-sectional area reduces by the factor ε (see Fig. 3). For the diameter of a round jet from an orifice it can, therefore, be written as

$$D' = \sqrt{\varepsilon} \cdot D \tag{29}$$

The width of a planar jet from a slot orifice is analogously

$$B' = \varepsilon \cdot B \tag{30}$$

Therefore, the speed of the contracted jet is increased to

$$w' = \frac{w}{\varepsilon}. \tag{31}$$

For sharp-edged orifices the contraction coefficient has the value

$$\varepsilon_{orifice} = 0.61 \tag{32}$$

For this limiting case, the value of ε is the same as the value of the discharge coefficient μ [11]. If for the calculations concerning orifice plates, the increased velocity at the smallest cross-section w' is taken instead of the exit velocity w, it follows from Eqs. (26), (27), (31), and (32) that:

$$\xi'_{orifice} \approx 2.69 \cdot (0.61)^2 = 1.00 \tag{33}$$

The significantly larger coefficient for orifices $\xi_{orifice} \approx 2.69$ (when referring to w and the cross section at the nozzle exit) therefore, only results from the contraction of the jet and not from frictional losses. Friction only plays a role for nozzles (without flow separation) with increasing length of the nozzle (ξ_{nozzle} will be slightly larger than 1, e.g. 1.05 for short and 1.15 for long nozzles), whereas for orifice plates the flow is virtually inviscid. For more detailed calculations of the fluid dynamics, experimental values for the coefficient ξ should be used if possible.

If in the equations for Nu (or Sh) the diameter D, the slot width B, and the exit velocity w are replaced by the corresponding variables for the smallest cross-sectional area D', B', w' they can also be applied for calculation of the round and slot orifice plates which are much easier to manufacture [1, 6].

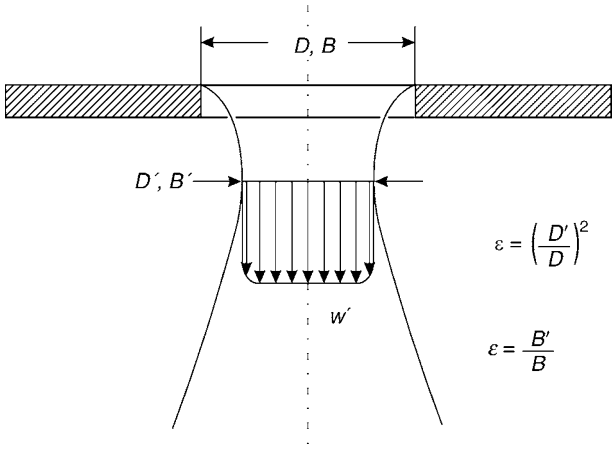

G10. Fig. 3. Jet contraction at hole and slot aperture plates.

9 Examples

9.1 Example 1

An ARN is to be designed with a given nozzle-to-plate distance H = 40 mm. The resistance of the air supply system can be neglected ($kf^2 << 1$).

According to Eq. (16), the optimal diameter of the nozzle is $D_{opt} = (1/5) \cdot 40\ \text{mm} = 8\text{mm}$.

The optimal relative nozzle area is, according to Eq. (18), $f = 0.0152$.

With $H/D = h^* = 5$, $f^{1\backslash 2} = d^* = (0.0152)^{1/2} = 0.1233$

the value of the geometry function from Eq. (8) can be calculated as

$$G = 0.09212 \cdot 0.9619 = 0.08861$$

If the nozzle exit velocity of the air is w = 48 m/s and the air from the nozzles has a temperature of 120°C, whereas the product surface has a temperature of 40°C, the material properties of air are to be calculated at an average temperature $T_m = (120 + 40)/2°\text{C} = 80°\text{C}$. According to Chap. D2,

$$\lambda = 0.0300\ \text{W/mK},\ \nu = 21.4 \cdot 10^{-6}\,\frac{\text{m}^2}{\text{s}},\ \text{Pr} = 0.708$$

thus

$$\text{Re} = 48 \cdot 8\,000/21.4 = 17\,944$$

and

$$\text{Nu}_{\text{ARN}} = \text{G} \cdot \text{Re}^{2/3} \cdot \text{Pr}^{0.42} = 52.53.$$

Finally, the heat transfer coefficient is found to be $\alpha_{\text{ARN}}(48\ \text{m/s}) = 197\,\text{W}/(\text{m}^2\,\text{K})$.

9.2 Example 2

For an optimal ASNs with the reduced exit velocity according to Eq. (20) $w = 48/1.68\,\text{m/s} \approx 29\,\text{m/s}$, H = 40 mm and $D(= 2B)$ = 8 mm (that is B = 4 mm), thus

$$H/D = h^* = 5$$

and according to Eq. (19) $f = 0.0718$

with Eq. (15) $f_0 = [60 + 4 \cdot (h^* - 2)]^{-1/2} = 0.1021$

$$\text{Nu}_{\text{ASN}} = 0.1000 \cdot \text{Re}^{2/3}$$

$$\text{Re} = 29 \cdot 8\,000/21.4 = 10\,841\,, \quad \text{Nu}_{\text{ASN}} = 48.99.$$

The resulting heat transfer coefficient is only 6.5% lower than that for the ARN

$$\alpha_{\text{ASN}}(29\ \text{m/s}) = 184\,\text{W}/(\text{m}^2\,\text{k}).$$

As α is proportional to $w^{2/3}$ for arrays of round and slot nozzles, the velocity

$$w = (197/184)^{3/2} \cdot 29\,\text{m/s} \approx 32\,\text{m/s}$$

results in the same values for α for both kinds of arrays:

$$\alpha_{\text{ASN}}(32\ \text{m/s}) = \alpha_{\text{ARN}}(49\ \text{m/s}) = 197\,\text{W}/(\text{m}^2\text{K})$$

9.3 Example 3

If the array from example 1 were made from perforated plates instead of an ARN, the contraction coefficient of the orifices would be $\varepsilon = 0.610$ according to Eq. (32). In order to obtain the same heat transfer coefficient (as in example 1 with the round nozzles), D and w in Eq. (8) have to be replaced by $D' = 8$ mm and $w' = 48$ m/s, respectively. The orifices would have to have a diameter of

$$D = \frac{D'}{\sqrt{\varepsilon}} = \frac{8\ \text{mm}}{\sqrt{0.61}} = 10.25\ \text{mm}$$

leading to a higher relative nozzle area of $f = \frac{f'}{\varepsilon} = \frac{0.0152}{0.61} = 0.0249$, and a correspondingly lower (nominal) outlet velocity of $w = \varepsilon w' = 29.3$ m/s, so that the velocity, $w' = 48$ m/s, in the narrowest cross section of the jet has the same value as at the outlet of the nozzles (with $\varepsilon_{\text{nozzle}} = 1$) from example 1.

The spacing L_T according to Eq. (10) or (11) would stay the same, e.g. for ARN_Δ:

$$L_T = D' \cdot \frac{0.9523}{\sqrt{f'}} = D \cdot \frac{0.9523}{\sqrt{f}} = 61.79\ \text{mm}.$$

9.4 Example 4

The corresponding array of slot orifices (as in example 2 with slot nozzles) has the slot width $B = B'/\varepsilon = 4\ \text{mm}/0.61 = 6.56\,\text{mm}$ (for the same value for ε) and a relative nozzle area of

$$f = \frac{f'}{\varepsilon} = \frac{0.0718}{0.61} = 0.118.$$

The spacing L_T also stays unchanged:

$$L_T = \frac{B}{f} = \frac{B'}{f'} = \frac{4\ \text{mm}}{0.0718} = 55.7\ \text{mm}.$$

9.5 Example 5

The design of the air supply system (see Chaps. L1–L3 and handbooks on fluid dynamics) for the array of slot orifices in example 4 is such that the resistance number K for the whole system, except for the nozzles, is $k \approx 500$. If the spatial arrangement and the geometry of the nozzles are left unchanged, i.e. $H = 40$ mm, $B = 40$ mm, and $L_T = 55.7$ mm, at a constant fan power per unit area of product surface it can be found from Eqs. (23) and (25):

$$\frac{\alpha}{\alpha_{max}} = \frac{G_H}{G_{Hmax}} = \frac{(1 + Kf'^2)^{-2/9}}{1} = \frac{1}{(1 + 500 \cdot 0.0718^2)^{2/9}}$$

$$= \frac{1}{3.578^{2/9}} = 0.753$$

$$\alpha = 0.753 \cdot 184 \frac{W}{m^2 K} = 139 \frac{W}{m^2 K}$$

The result is a heat transfer coefficient which is approximately 25% lower. In order to obtain the same heat transfer as in examples 4 and 2, the fan power would have to be increased by the factor $1/(0.753)^{9/2} = 3.58$ according to Eq. (23).

If instead the optimal spatial arrangement for $K = 500$ from Table 2 is taken $f' = 3.564\%$, $B' = 0.06289 \cdot H$ and $B = B'/\varepsilon = B'/0.61$ and $L_T = 1.765 \cdot H$ with $H = 40$ mm

$$B = 4.12 \text{ mm and } L_T = 70.6 \text{ mm}$$

The result is a more favorable ratio of $\alpha/\alpha_{max} = 0.835$ and therefore,

$$\alpha = 0.835 \cdot 184 \ W/m^2 K = 154 \ W/m^2 K.$$

This means that the heat transfer is only reduced by 16% compared to the ideal case ($K = 0$). Accordingly, the fan power would have to be increased by the factor $1/(0.835)^{9/2} = 2.25$ in order to achieve the same heat transfer coefficient of 184 W/(m² K) as in example 2 for K = 500 instead of factor 3.58 for the unchanged spatial arrangement.

10 Further Information

Heat transfer in impinging flow can also apply to jets of liquid or multiphase (spray) jets. In combustion technology, impinging jet flames are used. *The equations given in this chapter are mostly based on experimental investigations on air jets.* In principle, they are also applicable to liquid jets in a liquid environment. For liquid jets in a gaseous environment, for spray jets, and for impinging jet flames, other works from literature should be consulted. An overview of the literature can be found in some works [1, 6] as well as in a more recent article by Viskanta [12] with 103 references before 1992.

11 Bibliography

1. Martin H (1977) Heat and mass transfer between impinging gas jets and solid surfaces. In: Hartnett JP, Irvine TF (eds) Advances in heat transfer, vol 13. Academic Press, New York, pp 1–60
2. Hofmann HM, Kind M, Martin H (2007) Measurements on steady state heat transfer and flow structure and new correlations for heat and mass transfer in submerged impinging jets. Int J Heat Mass Tran 50:3957–3965
3. Schlünder EU, Gnielinski V (1967) Wärme- und Stoffübertragung zwischen Gut und aufprallendem Düsenstrahl. Chem Ing Tech 39:578–584
4. Schlünder EU, Krötzsch P, Hennecke FW (1970) Gesetzmässigkeiten der Wärme- und Stoffübertragung bei der Prallströmung aus Rund- und Schlitzdüsen. Chem Ing Tech 42:333–338
5. Krötzsch P (1968) Wärme- und Stoffübergang bei Prallströmung aus Düsen- und Blendenfeldern. Chem Ing Tech 40:339–344
6. Polat S (1993) Heat and mass transfer in impingement drying. Dry Technol 11:1147–1176
7. Martin H (1973) Stoffübergangsversuche und strömungstechnische Berechnungen zur Ermittlung einer optimalen Schlitzdüsenanordnung für Prallstrahltrockner. Ph. D. thesis. Univ. Karlsruhe
8. Krötzsch P (1970) Über die Optimierung von Runddüsentrocknern. Verfahrenstechnik 3:291–294
9. Martin H, Schlünder EU (1973) Optimierung von Schlitzdüsentrocknern auf Grund neuer Versuchsergebnisse über den Wärme- und Stoffübergang in solchen Apparaten. Chem Ing Tech 45:290–294
10. Steinberg NI (1995) Design of an efficient air impingement nozzle array. Chem Eng Progress 91: 52–55
11. Huesmann K (1966) Druckverlust- und Durchflußkoeffizienten von senkrecht angeströmten perforierten Platten. Chem Ing Tech 38:877–879
12. Viskanta R (1993) Heat transfer to impinging isothermal gas and flame jets. Exp Therm Fluid Sci 6:113–134

G2 Heat Transfer in Concentric Annular and Parallel Plate Ducts

Volker Gnielinski
Karlsruher Institut für Technologie (KIT), Karlsruhe, Germany

1 Introduction

The simplest form of a two-fluid heat exchanger is a double pipe made up of two concentric circular tubes. One fluid flows through the inside tube and the other in co-current- or countercurrent flow through the annular passage. Heat exchangers of this type are common practice if liquids at high and very high pressures have to be either heated or cooled.

Beside separate double-pipe heat exchangers, heating or cooling jackets for tubes are of this type. But annular passages may also occur as heat exchangers in other types, for example, to heat a fluid by electricity, either a heating-rod is put into the middle of a circular tube, or the fluid in the annulus is heated or cooled from the outer tube, and an inert rod is placed in the middle of the tube to increase the velocity of the fluid in the gap. Finally, the fluid flowing in the annulus is either heated or cooled from both sides, from the inner tube and from the outside of the outer tube.

2 Flow in the Annulus; Hydraulic Diameter

When a fluid is flowing in the annulus between two concentric tubes, the characteristic dimension to be taken for the determination of the amount of heat transferred between it and the walls of the tubes is the hydraulic diameter, which is given by

$$d_h = d_o - d_i \tag{1}$$

where d_o is the inner diameter of the outer tube and d_i is the outer diameter of the inner tube. Annular flow is laminar at Reynolds numbers less than Re = 2,300, and is considered to be turbulent at higher values. The annular flow is most certainly turbulent at Re $>10^4$. In the transition zone $2{,}300 < \mathrm{Re} < 10^4$, the inlet conditions decide the type of the flow.

Annuli are geometrically similar only if they have the same diameter ratio

$$a = (d_i / d_o) \tag{2}$$

Heat transfer coefficients are dependent on this ratio because of the shape of the velocity profile. With annular flow, the maximum velocity is shifted to the inner wall of the duct as $a = (d_i/d_o)$ decreases. According to the theory, the lesser the radius of the curvature of a surface, the thinner the boundary layer under otherwise identical conditions. Hence, the smaller the diameter ratio, the greater the heat transfer coefficient on the inner side of the annulus. If d_i becomes infinitely small – $a = (d_i/d_o) \rightarrow 0$ – (an infinitesimal thickness wire at the center) the heat transfer coefficient α on the inner side becomes

VDI-GVC (ed.), *VDI Heat Atlas*, DOI 10.1007/978-3-540-77877-6_24,

infinitely large. Nevertheless, heat transport at the inner side would become negligibly small, because the area of the inner tube thus tends to be zero.

The coefficient on the outer side, on the other hand, decreases with the diameter ratio. The limiting case $a = 1$ is the parallel-plate geometry.

3 Definition of Heat Transfer Coefficient and the Dimensionless Numbers

The definition of the average heat transfer coefficient α over a length l is the same as in pipe flow (cf. Chap. G1). The dimensionless numbers are defined as follows:

$$\mathrm{Nu} = \frac{\alpha\, d_\mathrm{h}}{\lambda};\ \mathrm{Re} = \frac{w\, d_\mathrm{h}}{\nu}.$$

The physical properties are referred to the mean fluid temperature $T_\mathrm{m} = (T_\mathrm{in} + T_\mathrm{out})/2$.

4 Boundary condition

Heat can be transferred to the fluid flowing in the annulus:

- From the inner tube, in which case the outer tube is insulated
- From the outer tube, in which case the inner tube is insulated
- From both the inner and the outer tubes, in which case it is assumed that the temperatures on the two walls are equal, that is, $T_\mathrm{wi} = T_\mathrm{wo}$.

These boundary conditions are reviewed in Fig. 1. Others are dealt with in the literature together with any effects that may be exerted by any eccentricity of the tubes on heat transfer in laminar flow [1, 2].

5 Heat Transfer in Laminar Flow, Constant Wall Temperature

5.1 Hydrodynamically Developed Laminar Flow

For the thermal boundary condition of constant wall temperature, Stephan [3] has calculated asymptotic values of the Nusselt number for the thermally and hydrodynamically developed laminar flow. In Fig. 2, Stephan's solutions are presented graphically as a function of $a = (d_\mathrm{i}/d_\mathrm{o})$ for the three boundary conditions.

Martin [4] has developed approximate expressions for the three curves on Fig. 2 which are:

Boundary condition 1 (inner surface heated):

$$\mathrm{Nu}_{1,\mathrm{i}} = 3.66 + 1.2\, a^{-0.8} \tag{3}$$

Boundary condition 2 (outer surface heated):

$$\mathrm{Nu}_{1,\mathrm{o}} = 3.66 + 1.2\, a^{0.5} \tag{4}$$

Boundary condition 3 (both surfaces heated at equal wall temperatures):

$$\mathrm{Nu}_{1,\mathrm{b}} = 3.66 + \left[4 - \frac{0.102}{a + 0.02}\right] a^{0.04} \tag{5}$$

In the same paper Stephan [3] also calculated the mean fluid temperatures and Nusselt numbers for thermally developing and hydrodynamically developed laminar flow in annuli and drew up equations for their approximate determination.

The asymptotes to the calculated data for large values of $\mathrm{Re\ Pr\ d_h}/l$ for the different boundary conditions are obtained from the equation

$$\mathrm{Nu}_2 = f_g \sqrt[3]{\mathrm{Re\ Pr}\ d_\mathrm{h}/l} \tag{6}$$

where f_g is given by [3]

Boundary condition 1:

$$f_{g\,\mathrm{i}} = 1.615\, \left[1 + 0.14\, a^{-1/2}\right] \tag{7}$$

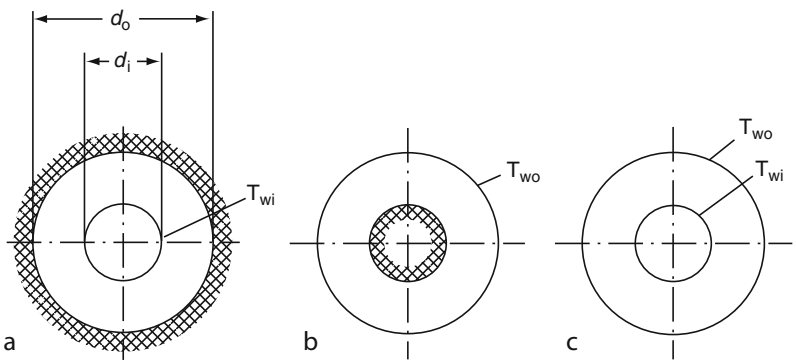

G2. Fig. 1. Boundary conditions for heat transfer in an annular gap 1. Heat transferred at the inner tube (subscript i); the outer tube insulated 2. Heat transferred at the outer tube (subscript o); the inner tube insulated 3. Heat transferred at both tubes (subscript b); the walls of each are at the same temperature $T_\mathrm{wi} = T_\mathrm{wo}$.

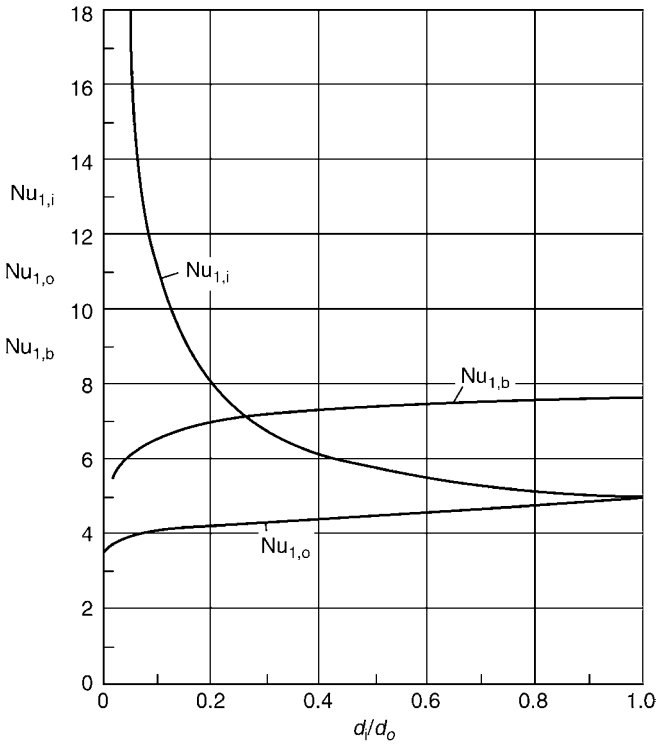

G2. Fig. 2. Graphical representation of Eqs. (3), (4), and (5) for the determination of Nu_1 as a function of(d_i/d_o) ratio for the three boundary conditions.

Boundary condition 2:

$$f_{g\,o} = 1.615\left[1 + 0.14a^{1/3}\right] \tag{8}$$

Boundary condition 3:

$$f_{g\,b} = 1.615\left[1 + 0.14\,a^{0.1}\right] \tag{9}$$

From the following Eq. (10), mean Nusselt numbers can be calculated for hydrodynamically developed and for both thermally developing and thermally developed flow. The length l in this case is measured from the point at which heating or cooling commences.

$$\mathrm{Nu_m} = \left(\mathrm{Nu_1^3} + \mathrm{Nu_2^3}\right)^{1/3} \tag{10}$$

Nu_1 and Nu_2 are to be calculated from the Eqs. (3–9) according to the boundary conditions.

The effect of temperature dependent variations in physical properties is as described in Chap. G1. Hence

$$\mathrm{Nu} = \mathrm{Nu_m}\left(\frac{\mathrm{Pr}}{\mathrm{Pr_w}}\right)^{0.11} \tag{11}$$

Pr is the Prandtl number at T_m; and Pr_w, that at the wall temperature.

5.2 Thermally and Hydrodynamically Developing Flow

At the annulus inlet, a velocity profile begins to build up as a result of friction between the fluid and the walls. If, at the same time, heat is transferred, a temperature profile also begins to form. Hydrodynamic and thermal boundary layers develop simultaneously. In this region heat transfer can be determined from the boundary layer theory.

The asymptote for large values of $\mathrm{RePr}(d_h/l)$ is

$$\mathrm{Nu_3} = \left\{\frac{2}{1 + 22\mathrm{Pr}}\right\}^{1/6}(\mathrm{RePr}d_h/l)^{1/2} \tag{12}$$

The following equation, in analogy to those for pipe flow, was proposed by Martin [4] for the mean Nusselt number for thermally and hydrodynamically developing flow:

$$\mathrm{Nu_m} = \left(\mathrm{Nu_1^3} + \mathrm{Nu_2^3} + \mathrm{Nu_3^3}\right)^{1/3} \tag{13}$$

Nu_1, Nu_2 and Nu_3 are to be calculated from the Eqs. (3–9) and (12) for the boundary conditions concerned.

Allowance for the variation in physical properties with temperature is made by Eq. (11).

6 Heat Transfer for Turbulent Flow

6.1 Fully Developed Turbulent Flow

Transition to turbulent flow in annular ducts starts at Re = 2, 300. The flow is fully turbulent at $\mathrm{Re} \geq 10^4$ Heat transfer coefficients for turbulent flow in concentric annular ducts are dependent on the ratio $a = (d_i/d_o)$ in addition to Re, Pr, and (d_h/l), since annuli are not geometrically similar unless the diameter ratio a is identical. Furthermore, they are dependent on the boundary conditions mentioned at the beginning of this Chapter and shown in Fig. 1.

According to Gnielinski [5], a great number of data on heat transfer for fully developed turbulent flow can be correlated by a modified equation of Petukhov and Kirillov [6]. The modified equation reads

$$\mathrm{Nu_m} = \frac{(\xi_{\mathrm{ann}}/8)\mathrm{Re\ Pr}}{k_1 + 12.7\sqrt{\xi_{\mathrm{ann}}/8}\,(\mathrm{Pr}^{2/3} - 1)}\left[1 + \left(\frac{d_h}{l}\right)^{2/3}\right]F_{\mathrm{ann}} \tag{14}$$

with

$$k_1 = 1.07 + \frac{900}{\mathrm{Re}} - \frac{0.63}{(1 + 10\mathrm{Pr})} \tag{15}$$

The friction factor ξ_{ann} of an annular duct differs from the friction factor of a circular tube (cf. Eq. (27) of Chap. G1). Because of the different velocity profile in annular flow ξ_{ann} itself depends on the ratio $a = (d_i/d_o)$.

Comparing a large number of experimental data on the friction factor of annular duct flows, Gnielinski [7] found

$$\xi_{\mathrm{ann}} = \left(1.8\log_{10}(\mathrm{Re}^*) - 1.5\right)^{-2} \tag{16}$$

with

$$\mathrm{Re}^* = \mathrm{Re}\frac{[1 + a^2]\ln a + [1 - a^2]}{[1 - a]^2 \ln a} \tag{17}$$

For the boundary condition "heat transfer at the inner wall, outer wall insulated" (Fig. 1a), the best correlation of the experimental data was to be achieved with

$$F_{\mathrm{ann,i}} = 0.75\,a^{-0.17} \tag{18}$$

and for the boundary condition "heat transfer at the outer wall, inner wall insulated" (Fig. 1b)

$$F_{\mathrm{ann,o}} = (0.9 - 0.15\, a^{0.6}) \tag{19}$$

No experimental data could be found for heat transfer from both walls to the annular flow (Fig. 1c). Following the proposal of Stephan [3] one gets for this boundary condition

$$F_{\mathrm{ann,b}} = \frac{0.75\, a^{-0.17} + (0.9 - 0.15\, a^{0.6})}{1 + a} \tag{20}$$

In the above equations, the ranges of validity are $10^4 \le \mathrm{Re} \le 10^6$, $0.6 \le \mathrm{Pr} \le 1000$, $0 \le (d_\mathrm{h}/l) \le 1$. The physical properties used in the equations have to be calculated at the mean bulk temperature of the fluid $T_\mathrm{m} = (T_\mathrm{in} + T_\mathrm{out})/2$.

6.2 Effect of Temperature Dependent Property Variations

The direction of heat flux (heating or cooling the fluid) influences the heat transfer when the physical properties are temperature-dependent. No special investigations for annular ducts about this influence are known. Therefore, the correction factors for the circular tubes (Chap. G1, Sect. 4.4) are adopted. According to this the factor K is introduced. For liquids

$$K = \left(\frac{\mathrm{Pr}}{\mathrm{Pr_w}}\right)^{0.11} \tag{21}$$

Pr is the Prandtl number at T_m; and $\mathrm{Pr_w}$, that at the wall temperature.

For gases the variation of fluid properties with temperature can be taken into account by simple power laws. The correction factor K as multiplier to Eq. (14) can be written in the principal form

$$K = \left(\frac{T_\mathrm{m}}{T_\mathrm{w}}\right)^{n} \tag{22}$$

Where T_m is the absolute bulk temperature of the gas ($T_\mathrm{m} = (T_\mathrm{m} + 273.1)/K$) and T_w is the absolute wall temperature.

The exponent n is n = 0 in the case of cooling the gas [$(T_\mathrm{m}/T_\mathrm{w}) > 1$]. Heating the gas [$(T_\mathrm{m}/T_\mathrm{w}) < 1$] leads to different values for each gas. Gnielinski [8] correlated the data he collected for gases by taking $n = 0.45$ in the range $0.5 < (T_\mathrm{m}/T_\mathrm{w}) < 1.0$. According to the literature n should be approximately 0.12 for carbon dioxide and –0.18 for overheated steam in the same temperature ratio.

The effect of variable physical properties is therefore taken into account with

$$\mathrm{Nu} = \mathrm{Nu_m} K \tag{23}$$

6.3 Transition Region Between Laminar and Fully Developed Turbulent Flow, $2{,}300 \le \mathrm{Re} \le 10^4$

Chap. G1, Sect. 4.2 reports on the development of turbulence in tubes. The same relationships may be assumed for concentric annular ducts. Nusselt numbers experimentally determined in the transition region can be represented by the same equation suggested for the tube case:

$$\mathrm{Nu_m} = (1 - \gamma)\, \mathrm{Nu_{lam,2300}} + \gamma\, \mathrm{Nu_{turb,10^4}} \tag{24}$$

with

$$\gamma = \frac{\mathrm{Re} - 2{,}300}{10^4 - 2{,}300} \quad \text{and} \quad 0 \le \gamma \le 1 \tag{25}$$

$\mathrm{Nu_{lam,2300}}$ is the Nusselt number for the appropriate boundary conditions for laminar flow at Re = 2,300 (see Eq. (13)) and $\mathrm{Nu_{turb,10^4}}$ is the Nusselt number for turbulent flow and the same boundary conditions at fully developed turbulent flow at $\mathrm{Re} = 10^4$.

6.3.1 Heat Transfer from the Inner Tube with Outer Tube Insulated

For the boundary condition in Fig. 1a, where heat transfer is at the inner tube wall with outer tube insulated, the Nusselt number is calculated from Eq. (24) with the laminar term is estimated as follows:

$$\mathrm{Nu_{lam,2300,i}} = \left(\mathrm{Nu_{1,i}^3} + \mathrm{Nu_{2,2300,i}^3} + \mathrm{Nu_{3,2300}^3}\right)^{1/3} \tag{26}$$

where $\mathrm{Nu_{1,i}}$ is calculated from Eq. (3)

$$\mathrm{Nu_{1,i}} = 3.66 + 1.2\, a^{-0.8} \tag{27}$$

and where $\mathrm{Nu_{2,2300,i}}$ is calculated from Eq. (6)

$$\mathrm{Nu_{2,233,i}} = f_{g,\mathrm{i}}(2300\mathrm{Pr}\ d_\mathrm{h}/l)^{1/3} \tag{28}$$

with $f_{g,\mathrm{i}}$ from Eq. (7), $\mathrm{Nu_{3,2300,i}}$ is given by Eq. (12)

$$\mathrm{Nu_{3,2300}} = \left\{\frac{2}{1 + 22\mathrm{Pr}}\right\}^{1/6} (2{,}300\mathrm{Pr}d_\mathrm{h}/l)^{1/2} \tag{29}$$

The turbulent term in Eq. (24) is estimated from the expressions

$$\mathrm{Nu_{turb,10^4,i}} = \frac{(\xi_\mathrm{ann}/8)\, 10^4\mathrm{Pr}}{k_1 + 12.7\sqrt{\xi_\mathrm{ann}/8}\,(\mathrm{Pr}^{2/3} - 1)} \left[1 + \left(\frac{d_\mathrm{h}}{l}\right)^{2/3}\right] \left(0.75\, a^{-0.17}\right) \tag{30}$$

with ξ_ann from Eq. (16) at

$$\mathrm{Re}^* = 2{,}300\, \frac{[1 + \mathrm{a}^2]\ln \mathrm{a} + [1 - \mathrm{a}^2]}{[1 - \mathrm{a}]^2 \ln \mathrm{a}} \tag{31}$$

and k_1 from Eq. (15) at

$$k_1 = 1.07 + \frac{900}{2{,}300} - \frac{0.63}{(1 + 10\mathrm{Pr})} \tag{32}$$

6.3.2 Heat Transfer from the Outer Tube with Inner Tube Insulated

For the boundary condition in Fig. 1b, where heat transfer is from the outer tube with inner tube insulated, Eq. (24) may be used again with the laminar expression:

$$\mathrm{Nu_{lam,2300,o}} = \left(\mathrm{Nu_{1,o}^3} + \mathrm{Nu_{2,2300,o}^3} + \mathrm{Nu_{3,2300}^3}\right)^{1/3} \tag{33}$$

where $Nu_{1,o}$ is calculated from Eq. (4)

$$Nu_{1,o} = 3.66 + 1.2\, a^{0.5} \tag{34}$$

and where $Nu_{2,2300,o}$ is calculated from Eq. (6)

$$Nu_{2,o} = f_{g,o}\sqrt[3]{Re\ Pr}\ d_h/l \tag{35}$$

with $f_{g,o}$ from Eq. (8). $Nu_{3,2300}$ is given by Eq. (29).

The turbulent term in Eq. (24) is calculated from the expression

$$Nu_{turb,10^4,o} = \frac{(\xi_{ann}/8)\,10^4 Pr}{k_1 + 12.7\sqrt{\xi_{ann}/8}\,(Pr^{2/3}-1)}\left[1+\left(\frac{d_h}{l}\right)^{2/3}\right](0.9 - 0.15\, a^{0.6}) \tag{36}$$

with ξ_{ann} from Eqs. (16) and (31) and k_1 from Eq. (32).

6.3.3 Heat Transfer from Both Surfaces (Equal and Constant Wall Temperature)

For the boundary condition in Fig. 1c, where heat transfer is from the inner and the outer tube, with equal and constant wall temperatures, one may again use Eq. (24) with the laminar term being calculated from:

$$Nu_{lam,2300,b} = \left(Nu_{1,b}^3 + Nu_{2,2300,b}^3 + Nu_{3,2300}^3\right)^{1/3} \tag{37}$$

where $Nu_{1,b}$ is calculated from Eq. (5)

$$Nu_{1,b} = 3.66 + \left[4 - \frac{0.102}{a + 0.2}\right] a^{0.04} \tag{38}$$

and where $Nu_{2,2300,b}$ is calculated from Eq. (6)

$$Nu_{2,b} = f_{g,b}\sqrt[3]{Re\ Pr\ d_h/l} \tag{39}$$

with $f_{g,b}$ from Eq. (9). $Nu_{3,2300}$ is given by Eq. (29).

The turbulent term in Eq. (24) is calculated from the expression

$$Nu_{turb,10^4,b} = \frac{(\xi_{ann}/8)\,10^4 Pr}{k_1 + 12.7\sqrt{\xi_{ann}/8}\,(Pr^{2/3}-1)}\left[1+\left(\frac{d_h}{l}\right)^{2/3}\right]\left\{\frac{0.75\, a^{-0.17} + (0.9 - 0.15\, a^{0.6})}{1 + a}\right\} \tag{40}$$

with ξ_{ann} from Eqs. (16) and (31) and k_1 from Eq. (32).

7 Example of Calculation

Within a double pipe, the heat exchanger decane shall be heated from 0°C to 40°C. The mass flow rate of the decane is (a) 0.05 kg/s, (b) 1 kg/s, (c) 0.2 kg/s. The inner diameter of the outer tube is d_o = 40 mm and the outer diameter of the inner tube is d_i = 20 mm. Hot water runs through the inner tube so that the mean wall temperature of the tube is adjusted to 100°C. The outer tube is insulated. How long must the double pipe be?

Solution: The problem concerns a heat transfer in an annular duct, the boundary condition is 1.

List of the given data:

$$T_{in} = 0°C;\ d_i = 0.02m \quad (a)\ \dot{M} = 0.05kg/s$$

$$T_{out} = 40°C;\ d_o = 0.04\,m \quad (b)\ \dot{M} = 1kg/s$$

$$T_w = 100°C;\ d_h = 0.02\,m \quad (c)\ \dot{M} = 0.2kg/s$$

$$a = d_i/d_o = 0.5$$

The physical properties of decane at $T_m = (T_{in} + T_{out})/2 = 20°C$ and $T_w = 100°C$ are taken from Part D. They are given in Table 1.

The heat transfer coefficients to be calculated are dependent on the length of the double pipe. Therefore, the calculation must be done iteratively.

Because the temperatures at the entrance and the exit together with the wall temperature are given, the logarithmic mean temperature difference ΔT_{LM} remains a constant during the iteration and can be calculated in advance:

$$\Delta T_{LM} = \frac{(T_w - T_{in}) - (T_w - T_{out})}{\ln\dfrac{T_w - T_{in}}{T_w - T_{out}}}$$

$$\Delta T_{LM} = \frac{(100-0) - (100-40)}{\ln\dfrac{100-0}{100-40}} = 78.3\,K.$$

To find out which equations have to be used to calculate the heat transfer coefficients for problems (a), (b), and (c), the Reynolds numbers must be known:

$$Re = \frac{w \cdot d_h}{\nu} = \frac{\dot{M}(d_o - d_i)\cdot 4}{\pi(d_o^2 - d_i^2)\cdot\eta} = \frac{\dot{M}\cdot 4}{\pi(d_o + d_i)\eta};$$

(a) $Re = \dfrac{0.05 \cdot 4 \cdot 10^5}{\pi \cdot 0.06 \cdot 92.1} = 1,152$ laminar,

(b) $Re = \dfrac{1 \cdot 4 \cdot 10^5}{\pi \cdot 0.06 \cdot 92.1} = 23,041$ fully turbulent,

(c) $Re = \dfrac{0.2 \cdot 4 \cdot 10^5}{\pi \cdot 0.06 \cdot 92.1} = 4,608$ transition region $2{,}300 < Re < 10^4$

Calculations to (a)

The steps of iteration are included in Table 2.

Comment: Only the indicated decimal numbers were used.

Calculations to (b)

Not from the length of the tube-dependent values:

Equation (15)

$$k_1 = 1.07 + \frac{900}{Re} - \frac{0.63}{(1 + 10Pr)} = 1.07 + \frac{900}{23,041} - \frac{0.63}{1 + 10 \cdot 15.88}$$

$$= 1.1051$$

G2. Table 1. Phsysical properties of Decane

T	T_m = 20°C	T_w = 100°C
λ/W/m K	0.126	0.104
$\eta 10^5$/N s/m^2	92.1	36.4
c_p/J/kg K	2173	2474
ρ/kg/m^3	730	667
$Pr = \eta \cdot c_p/\lambda$	15.88	8.66

Equation (17)

$$\mathrm{Re}^* = \mathrm{Re}\frac{[1+\mathrm{a}^2]\ln \mathrm{a} + [1-\mathrm{a}^2]}{[1-\mathrm{a}]^2 \ln \mathrm{a}} = 23,041\frac{[1+0.5^2]\ln 0.5 + [1-0.5^2]}{[1-0.5]^2 \ln 0.5} = 23,041 \cdot 0.672 = 15,481.59$$

Equation (16)

$$\xi_{\mathrm{ann}} = (1.8\log_{10}(\mathrm{Re}^*) - 1.5)^{-2} = (1.8\log_{10}(\mathrm{Re}^*) - 1.5)^{-2} = 0.02740$$

Equation (18)

$$F_{\mathrm{ann,i}} = 0.75\ a^{-0.17} = 0.75 \cdot 0.5^{-0.17} = 0.8438$$

Equation (21)

$$K = [\mathrm{Pr}(T_\mathrm{m})/\mathrm{Pr}(T_\mathrm{w})]^{0.11} = 1.069$$

Steps of iteration to (b)

The steps of iteration are included in Table 3

Calculations to (c)

Not from the length of the tube-dependent values:

Equation (3)

$$\mathrm{Nu}_{1,\mathrm{i}} = 3.66 + 1.2\ a^{-0.8} = 3.66 + 1.2 \cdot 0.5^{-0.8} = 5.75$$

Equation (7)

$$f_{g\,\mathrm{i}} = 1.615\ \left[1 + 0.14\ a^{-1/2}\right] = 1.615\left(1 + 014 \cdot 0.5^{-1/2}\right) = 1.935$$

Equation (15)

$$k_1 = 1.07 + \frac{900}{\mathrm{Re}} - \frac{0.63}{(1+10\mathrm{Pr})} = 1.07 + \frac{900}{10^4} - \frac{0.63}{1+10 \cdot 15.88} = 1.156$$

Equation (17)

$$\mathrm{Re}^* = \mathrm{Re}\frac{[1+\mathrm{a}^2]\ln \mathrm{a} + [1-\mathrm{a}^2]}{[1-\mathrm{a}]^2 \ln \mathrm{a}} = 10^4\frac{[1+0.5^2]\ln 0.5 + [1-0.5^2]}{[1-0.5]^2 \ln 0.5} = 10^4 \cdot 0.671915 = 6719.15$$

Equation (16)

$$\xi_{\mathrm{ann}} = (1.8\log_{10}(\mathrm{Re}^*) - 1.5)^{-2} = (1.8\log_{10}(\mathrm{Re}^*) - 1.5)^{-2} = 0.03443$$

Equation (18)

$$F_{\mathrm{ann,i}} = 0.75\ a^{-0.17} = 0.75 \cdot 0.5^{-0.17} = 0.8438$$

Equation (21)

$$K = [\mathrm{Pr}(T_\mathrm{m})/\mathrm{Pr}(T_\mathrm{w})]^{0.11} = 1.069$$

G2. Table 2. Steps of iteration to (a)

Step of iteration	1	2	3
Length of the annular tube	20 m	19 m	18.8 m
Eq. (3): $\mathrm{Nu}_{1,\mathrm{i}} = 3.66 + 1.2\,a^{-0.8}$	5.75	5.75	5.75
Eq. (7): $f_{g\,\mathrm{i}} = 1.615\ \{1 + 0.14\,a^{-1/2}\}$	1.935	1.935	1.935
Eq. (6): $\mathrm{Nu}_{2,\mathrm{i}} = f_{g,\mathrm{i}}\sqrt[3]{\mathrm{Re\ Pr\ d_h/l}}$	5.10	5.19	5.20
Eq. (12): $\mathrm{Nu}_3 = \left\{\frac{2}{1+22\mathrm{Pr}}\right\}^{1/6}(\mathrm{Re\ Pr\ d_h/l})^{1/2}$	1.81	1.86	1.86
Eq. (13): $\mathrm{Nu_{m,i}} = (\mathrm{Nu}_{1,\mathrm{i}}^3 + \mathrm{Nu}_{2,\mathrm{i}}^3 + \mathrm{Nu}_{3,\mathrm{i}}^3)^{1/3}$	6.9	6.95	6.96
Eq. (11): $\mathrm{Nu_i} = \mathrm{Nu_{m,i}}(\mathrm{Pr/Pr_w})^{0.11}$	7.38	7.43	7.44
$\alpha = \mathrm{Nu_i} \cdot \lambda(T_{\mathrm{m})/\mathrm{d}}\mathrm{h}$	46.5 W/m^{2}K	46.8 W/m^{2}K	46.9 W/m^{2}K
$\dot{Q} = \alpha \cdot \pi \cdot d_\mathrm{i} \cdot l \cdot \Delta T_{\mathrm{LM}}$	4575.4 W	4374.6 W	4337.8 W
$T_{\mathrm{out}} = T_{\mathrm{in}} + \dot{Q}/(\dot{M} \cdot c_\mathrm{p}(T_\mathrm{m})$	42.1°C	40.3°C	39.9°C

Result: To heat 0.05 kg/s decane from 0°C to 40°C in the described double-pipe heat exchanger, a length of 19 m is needed.

G2. Table 3. Steps of iteration to (b)

Steps of iteration	1	2	3
Length of the annular tube	10	11.5	11.8
Eq. (14) $\mathrm{Nu_i} = \frac{(\xi_{\mathrm{ann}}/8)\mathrm{Re\ Pr}}{k_1 + 12.7\sqrt{\xi_{\mathrm{ann}}/8}\,(\mathrm{Pr}^{2/3} - 1)}\left[1 + \left(\frac{d_h}{l}\right)^{2/3}\right]F_{\mathrm{ann}}K$	239.20	238.86	238.81
$\alpha = \mathrm{Nu_i} \cdot \lambda(T_\mathrm{m})/d_\mathrm{h}$	1,506.94	1,504.84	1,504.48
$\dot{Q} = \alpha \cdot \pi \cdot d_\mathrm{i} \cdot l \cdot \Delta T_{\mathrm{LM}}$	74,137.34	85,139.42	87,339.25
$T_{\mathrm{out}} = T_{\mathrm{in}} + \dot{Q}/(\dot{M} \cdot c_\mathrm{p}(T_\mathrm{m})$	34.12	39.18	40.19

Result: To heat 1.0 kg/s decane from 0°C to 40°C in the described double pipe heat exchanger, a length of 11.8 m is needed.

Equation (25)

$$\gamma = \frac{\mathrm{Re} - 2,300}{10^4 - 2,300} = \frac{4,608 - 2,300}{10^4 - 2,300} = 0.3$$

Steps of iteration to (c)

The steps of iteration are included in Table 4

8 Parallel Plate Duct

8.1 Hydraulic Diameter; Boundary Conditions

A parallel plate duct (rectilinear gap) is formed between two plates with a constant spacing s between them. The characteristic dimension for flow through the gap, corresponding to the hydraulic diameter, is twice the gap width, that is,

$$d_\mathrm{h} = 2\,\mathrm{s} \tag{41}$$

The critical Reynolds number up to which the flow in the gap is laminar lies between 2,200 and 3,600. It depends greatly on the inlet conditions, for example, sharp or rounded edges.

There are a number of boundary conditions that apply for heat transport from the gap walls to the flowing medium, and they have been dealt with in detail in the literature for the case of laminar flow [1, 2]. Those that are considered here relate to the case of $d_\mathrm{i}/d_\mathrm{o} = 1$ in Sects. 1–7.

In the boundary condition represented by Fig. 3a, one side of the gap is maintained at a constant temperature T_{w1}, and the other side is insulated. In that represented in Fig. 3b, both walls of the gap are heated to the same temperature $T_{\mathrm{w1}} = T_{\mathrm{w2}}$. This corresponds to the boundary condition 3 illustrated in Fig. 1 for a concentric annulus.

8.2 Definition of Heat Transfer Coefficient and the Dimensionless Numbers

The definition of the average heat transfer coefficient α over a length l is the same as in pipe flow (cf. Chap. G1). The dimensionless numbers are defined by

$$\mathrm{Nu} = \frac{\alpha\, d_\mathrm{h}}{\lambda};\ \mathrm{Re} = \frac{w\, d_\mathrm{h}}{\upsilon};$$

The values for the physical properties must be referred to the main liquid temperature $T_\mathrm{m} = (T_\mathrm{in} + T_\mathrm{out})/2$.

8.3 Heat Transfer in Laminar Flow

8.3.1 Hydrodynamically Developed Laminar Flow

Many authors have determined the Nusselt number for laminar flow that has been fully developed thermally and hydrodynamically.

G2. Table 4. Steps of iteration to (c)

Step of iteration	1	2	3
Length of the annular tube	14 m	13 m	13.6 m
Eq. (28) $\mathrm{Nu}_{2,2300,i} = f_{\mathrm{g,i}}(2300\ \mathrm{Pr}\ d_\mathrm{h}/l)^{1/3}$	7.23	7.41	7.30
Eq. (29) $\mathrm{Nu}_{3,2300} = \left\{\frac{2}{1+22\mathrm{Pr}}\right\}^{1/6}(2300\ \mathrm{Pr}\ d_\mathrm{h}/l)^{1/2}$	3.05	3.17	3.10
Eq. (26) $\mathrm{Nu}_{\mathrm{lam},2300,\mathrm{i}} = \left(\mathrm{Nu}_{1,\mathrm{i}}^3 + \mathrm{Nu}_{2,2300,\mathrm{i}}^3 + \mathrm{Nu}_{3,2300}^3\right)^{1/3}$	8.42	8.57	8.48
Eq. (30) $\mathrm{Nu}_{\mathrm{turb},10^4,\mathrm{i}} = \frac{(\xi_\mathrm{ann}/8)\,10^4\mathrm{Pr}}{k_1 + 12.7\sqrt{\xi_\mathrm{ann}/8}\,(\mathrm{Pr}^{2/3}-1)}\left[1+\left(\frac{d_\mathrm{h}}{l}\right)^{2/3}\right]F_{\mathrm{ann,i}}$	108.78	108.85	108.80
Eq. (24) $\mathrm{Nu}_\mathrm{m} = (1-\gamma)\,\mathrm{Nu}_{\mathrm{lam},2300} + \gamma\,\mathrm{Nu}_{\mathrm{turb},10^4}$	38.53	38.65	38.57
$\mathrm{Nu} = ((1-\gamma)\,\mathrm{Nu}_{\mathrm{lam},2300} + \gamma\,\mathrm{Nu}_{\mathrm{turb},10^4})\,K$	41.18	41.32	41.23
$\alpha = \mathrm{Nu}_\mathrm{i}\cdot\lambda(T_\mathrm{m})/d_\mathrm{h}$	259.46	260.31	259.79
$\dot{Q} = \alpha\cdot\pi\cdot d_\mathrm{i}\cdot l\cdot\Delta T_{\mathrm{LM}}$	17,870.8	16,648.4	17,382.1
$T_\mathrm{out} = T_\mathrm{in} + \dot{Q}/(\dot{M}\cdot c_\mathrm{p}(T_\mathrm{m}))$	41.1	38.3	40.0

Result: To heat 0.2 kg/s decane from 0°C to 40°C in the described double pipe heat exchanger, a length of 13.6 m is needed.

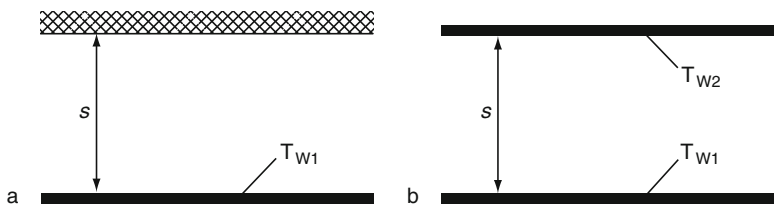

G2. Fig. 3. Boundary conditions for heat transfer in a parallel plate duct (in an annular gap for the case of $(d_\mathrm{i}/d_\mathrm{o}) = 1$). Boundary condition (a): Heat transferred from one side of the duct. Boundary condition (b): Heat transferred at both sides of the duct, each at the same wall temperature $T_{\mathrm{w1}} = T_{\mathrm{w2}}$.

The equation that applies for the boundary condition shown in Fig. 3a is

$$\mathrm{Nu}_{1,\mathrm{I}} = 4.861 \tag{42}$$

and that for the boundary condition shown in Fig. 3b is

$$\mathrm{Nu}_{1,\mathrm{II}} = 7.541 \tag{43}$$

These equations are practically the same as Eqs. (3), (4), and (5) for the case $d_\mathrm{i}/d_\mathrm{o} = 1$.

Under the boundary conditions illustrated in Fig. 3a and b, the asymptote for high values of $\mathrm{RePrd_h}/l$ in thermally developing and hydrodynamically developed flow is

$$\mathrm{Nu}_2 = 1.841\sqrt[3]{\mathrm{RePrd_h}/l}. \tag{44}$$

If laminar flow is hydrodynamically developed and thermally developing or developed, the mean Nusselt number in parallel plate ducts is given by the following equation, in which the length l is measured from the point at which heat transfer commences:

$$\mathrm{Nu_m} = (\mathrm{Nu}_1^3 + \mathrm{Nu}_2^3)^{1/3} \tag{45}$$

Nu_1 and Nu_2 for the applicable boundary conditions can be determined by solving Eqs. (42)–(44). Equation (45) which has been derived from Eq. (10) and the boundary conditions corresponding to Eqs. (3–9) when $d_\mathrm{i}/d_\mathrm{o} = 1$, yields values of $\mathrm{Nu_m}$ that agree very well with the tabulated figures [1] applicable to the same boundary conditions. The greatest difference is about 4%, and occurs for $20 < \mathrm{Re\ Pr}\ d_\mathrm{h}/l < 200$.

8.3.2 Hydrodynamic and Thermal Development of Flow

If heating commences at the inlet to the parallel plate duct, a temperature as well as a velocity profile is formed. The mean liquid temperatures and Nusselt numbers for the boundary conditions shown in Fig. 3a) have been calculated by Stephan [9]. An equation suggested by Mercer et al. [10] yields values that agree with these figures to within 7% in the $0.1 < \mathrm{Pr} < 10$ range:

$$\mathrm{Nu_{mI}} = 4.86 + \frac{0.061\{\mathrm{Re\ Pr}\ d_\mathrm{h}/l\}^{1.2}}{1 + 0.091\{\mathrm{Re\ Pr}\ d_\mathrm{h}/l\}^{0.17}} \tag{46}$$

Stephan [11] also determined mean liquid temperatures and Nusselt numbers for the boundary conditions shown in Fig. 3b) and submitted the following equation for the Nusselt numbers:

$$\mathrm{Nu_{m,II}} = 7.55 + \frac{0.024\{\mathrm{RePr}d_\mathrm{h}/l\}^{1.14}}{1 + 0.0358\{\mathrm{RePr}d_\mathrm{h}/l\}^{0.64}Pr^{0.17}} \tag{47}$$

The range quoted for the validity is $0.1 < \mathrm{Pr} < 1{,}000$.

The asymptote to the Nusselt numbers calculated for high values of $\mathrm{Re\ Pr}\ d_\mathrm{h}/l$ from the boundary theory for thermal and hydrodynamic development is the same as that applicable to concentric annuli (cf. Eq. (12)), that is,

$$\mathrm{Nu}_3 = \left\{\frac{2}{1 + 22\mathrm{Pr}}\right\}^{1/6}(\mathrm{Re\ Pr}\ d_\mathrm{h}/l)^{1/2} \tag{48}$$

The Nusselt numbers obtained from Eq. (49) represent, with only slight deviations the boundary conditions given by the Eqs. (46) and (47) and tabulated figures [1].

$$\mathrm{Nu_m} = (\mathrm{Nu}_1^3 + \mathrm{Nu}_2^3 + \mathrm{Nu}_3^3)^{1/3} \tag{49}$$

Nu_1 is obtained from Eq. (42) or (43); Nu_2, from Eq. (44); and Nu_3, from Eq. (48).

8.4 Heat Transfer in Turbulent Flow

It has been shown [2] that the equation presented for turbulent pipe flow in Chap. G2 can also be applied for the determination of Nusselt numbers in parallel plate ducts. In this case it is valid in the $0.5 < \mathrm{Pr} < 100$ range for the boundary condition illustrated in Fig. 3b and for $3 \cdot 10^4 \leq \mathrm{Re} < 10^6$; the friction factor is the same as for circular tubes, and the hydraulic diameter of the parallel plate duct should be inserted for the diameter of the tube.

9 Bibliography

1. Sha RK, London AL (1978) Laminar flow forced convection in ducts. Academic Press, New York/San Francisco/London
2. Kakac S, Sha RK, Aung W (eds) (1987) Handbook of single phase convective heat transfer. Wiley, New York
3. Stephan K (1962) Wärmeübergang bei turbulenter und laminarer Strömung in Ringspalten. Chem -Ing -Techn 34:207–212
4. Martin H (1990) Lecture on Heat transfer II, GermanyUniversitaet Karlsruhe (TH),
5. Gnielinski V (2009) Heat transfer coefficients for turbulent flow in concentric annular ducts. Heat Transfer Engng 30(6):431–436
6. Petukhov BS, Kirillov VV (1958) On heat exchange at turbulent flow of liquids in pipes (in Russian). Teploenergetika 4:63–68
7. Gnielinski V (2007) Berechnung des Druckverlustes in glatten konzentrischen Ringspalten bei ausgebildeter laminarer und turbulenter Strömung. Chemie -Ing Techn 79:91–95
8. Gnielinski V (1976) New equations for heat and mass transfer in turbulent pipe and channel flow. Int Chem Eng 16:359–368
9. Stephan K (1960) Wärmeübertragung laminar strömender Stoffe in einseitig beheizten oder gekühlten Kanälen. Chem Ing Techn 32:401–404
10. Mercer WE, Pearce WM, Hitchcock JE (1967) Laminar forced convection in the entrance region between parallel flat plates. J Heat Transfer 89:251–267
11. Stephan K (1959) Wärmeübergang und Druckabfall bei nicht ausgebildeter Laminarströmung in Rohren und in ebenen Spalten. Chem Ing Techn 31:773–778

G3 Heat Transfer in Helically Coiled Tubes

Volker Gnielinski
Karlsruher Institut für Technologie (KIT), Karlsruhe, Germany

1 Introduction

Centrifugal forces in a fluid flowing through a curved pipe cause secondary flows circulating outward into the core region of the pipe to form a pair of symmetric vortices. The combination of both the main and the secondary flows creates a flow pattern in which the maximum velocity is shifted outward from the center of the tube. The secondary flow produces a transverse transport of the fluid over the cross section of the pipe. This additional convective transport improves heat transfer between the fluid and the wall of the pipe but increases the pressure drop when compared to that in a straight tube. The differences are particularly apparent in laminar flows.

2 Determination of the Average Diameter of Curvature

The intensity of the secondary flow depends on the relative curvature (d/D) of the coil, where d is the inner diameter of the tube and D the diameter of the curvature. The average diameter of a spiral with n turns and a pitch h formed from a tube of the length l is

$$D_S = \frac{l}{n\,\pi} \tag{1}$$

The projected diameter of a winding D_c in the coil illustrated in Fig. 1 results from the relations of a right-angled triangle (Pythagorus).

$$D_C = \sqrt{D_S^2 - \left(\frac{h}{\pi}\right)^2} \tag{2}$$

The average diameter of the curvature D of the coil, that is, the value to be inserted in the ratio (d/D), is

$$D = D_C\left[1 + \left(\frac{h}{\pi D_C}\right)^2\right] \tag{3}$$

Appreciable differences between D and D_c result only for strongly curved tubes and large pitches. For most practical cases, the difference is negligible as h is small compared to D_c.

3 Critical Reynolds Number

The secondary flow has a stabilizing effect on the laminar flow. Any disturbances are apparently damped by the secondary flow. Therefore, the transition from laminar to turbulent flow is shifted to higher Reynolds numbers with increasing relative curvature (d/D).

The critical Reynolds number according to Schmidt [1] is

$$\mathrm{Re}_{crit} = 2300\left[1 + 8.6\left(\frac{d}{D}\right)^{0.45}\right] \tag{4}$$

This equation is based on a value for the critical Reynolds number of $\mathrm{Re}_{crit} = 2300$ for the straight tube.

4 Definition of the Heat Transfer Coefficient

The average heat transfer coefficient α is defined in terms of the heat flux $\dot{q}$ and the logarithmic mean of the temperature difference

$$\alpha = \dot{q}/\Delta T_{LM} \tag{5}$$

The logarithmic mean temperature difference $\Delta\, T_{LM}$ is given by

$$\Delta T_{LM} = \frac{(T_{w,in} - T_{in}) - (T_{w,out_w} - T_{out})}{\ln\dfrac{T_{w,in} - T_{in_i}}{T_{w,out} - T_{out}}} \tag{6}$$

where T_{in} and T_{out} are the inlet and outlet bulk fluid temperatures and $T_{w,in}$ and $T_{w,out}$ are the tube wall temperatures at the inlet and at the outlet of the coil, respectively.

The temperature T_{out} may be calculated from

$$T_{out} = T_{in} + \frac{\dot{Q}}{\dot{M}\,c_p} \tag{7}$$

Where $\dot{Q}$ is the total rate of heat transfer to the fluid as it passes through the coil and $\dot{M}$ is the mass flow rate of the fluid. If $\dot{Q}$ is not known, the equation can be rewritten as

$$T_{out} = T_{in} + \frac{\alpha\, A\, \Delta T_{LM}}{\dot{M}\,c_p} \tag{8}$$

VDI-GVC (ed.), *VDI Heat Atlas*, DOI 10.1007/978-3-540-77877-6_25,

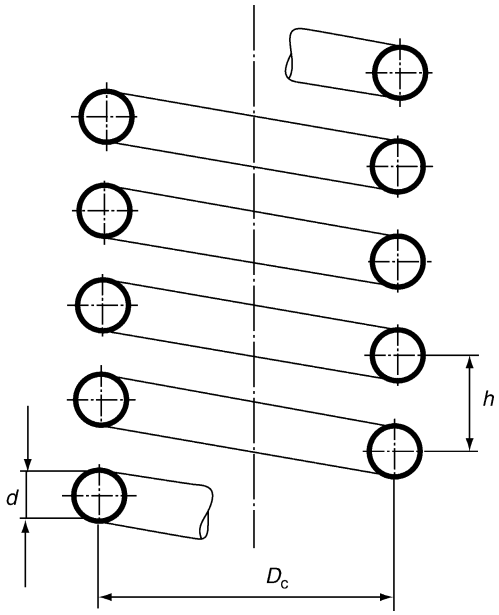

G3. Fig. 1. Geometry of a coil.

where A is the total heat transfer area. Since T_{out} appears in ΔT_{LM}, a trial and error solution is required to obtain T_{out}.

The Nusselt number is calculated from

$$\mathrm{Nu} = \frac{\alpha d}{\lambda} \tag{9}$$

with λ the thermal conductivity of the fluid. The Reynolds number is calculated from

$$\mathrm{Re} = \frac{\dot{m} d}{\eta} \tag{10}$$

where $\dot{m}$ is the mass flow per unit area and η the dynamic viscosity of the fluid. The physical properties are evaluated at the mean temperature of the fluid:

$$T_m = (T_{in} + T_{out})/2. \tag{11}$$

5 Heat Transfer in Laminar Flow

Heat transfer coefficients in the region of thermally and/or hydrodynamically developing flow depend on the tube length l. The effect of the thermal and fluid dynamic inlet conditions on the heat transfer coefficient in laminar flow has been the subject of numerical analysis, for example, by Bauermeister and Brauer [2] and Janssen and Hoogendorn [3]. They included the factor (l/d). The figures thus calculated for the heat transfer coefficient are considerably less than those determined by experiment.

Experiments have failed to reveal any effect exerted by the relative length of flow path concerned (l/d) on the coefficient. In fact, many research workers maintain that, as a result of the secondary current in the spiral, the temperature and velocity profiles are already formed after a very short relative length (l/d).

In any case, not very many measurements have been made of the heat transfer coefficient in coils, and none is known in which the number of turns and the length of flow path have been systematically varied. Consequently, it is more reliable to adopt the Bauermeister and Brauer equations [2] to analyze the zone for which no experimental verifications exist, for example, for coils with numerous turns and long flow paths (l/d). The equations themselves are too complex to be dealt with here.

Values are quoted in the literature for measurements performed on water ($2 < \mathrm{Pr} < 5$) and oil ($100 < \mathrm{Pr} < 200$) in coils heated by condensing steam.

The geometry of the coils was as follows:

d/D	0.2	0.14	0.098	0.069	0.049	0.024	0.012
l/d	231	165	365	205	477	579	636
n	15.5	8.9	11.5	5	7.5	4.5	2.5

It has been shown [4] that, if the Schmidt equation [1] is applied, these measured values conform with a deviation of ± 15% to the following equation:

$$\mathrm{Nu} = 3.66 + 0.08\left[1 + 0.8\left(\frac{d}{D}\right)^{0.9}\right]\mathrm{Re}^{m}\mathrm{Pr}^{1/3}\left(\frac{\mathrm{Pr}}{\mathrm{Pr}_w}\right)^{0.14} \tag{12}$$

with $m = 0.5 + 0.2903\,(d/D)^{0.194}$.

The Prandtl number Pr is evaluated at the mean fluid temperature T_m and Pr_w at the wall temperature. The factor $(\mathrm{Pr}/\mathrm{Pr}_w)^{0.14}$ was introduced into the original equation by Schmidt to take into account the temperature dependence of the physical properties. Equation (12) applies for $\mathrm{Re} \le \mathrm{Re}_{crit}$, as defined by Eq. (4).

6 Heat Transfer in Turbulent Flow for $\mathrm{Re} > 2.2 \times 10^4$

Schmidt [1] found a transition region for heat transfer between the critical Reynolds number, Re_{crit}, and fully developed flow at $\mathrm{Re} > 2.2 \times 10^4$. It is described in the following paragraph. The measured values were determined on air (Pr = 0.7) and water ($2 < \mathrm{Pr} < 5$). According to Gnielinski [4] they conform to a deviation of ± 15% to the following equation if $\mathrm{Re} > 2.2 \times 10^4$:

$$\mathrm{Nu} = \frac{(\xi/8)\mathrm{RePr}}{1 + 12.7\sqrt{\xi/8}\left(\mathrm{Pr}^{2/3} - 1\right)}\left(\frac{\mathrm{Pr}}{\mathrm{Pr}_w}\right)^{0.14}. \tag{13}$$

The friction factor for turbulent flow in helically coiled tubes is given by Mishra and Gupta [5] as

$$\xi = \left[\frac{0.3164}{\mathrm{Re}^{0.25}} + 0.03\left(\frac{d}{D}\right)^{0.5}\right]\left(\frac{\eta_w}{\eta}\right)^{0.27} \tag{14}$$

The correction factor $(\eta_w/\eta)^{0.27}$ in Eq. (14), where η_w is the dynamic viscosity of the fluid at wall temperature and η that at T_m, was added by Gnielinski [6] to the original equation given by Mishra and Gupta [5] to take into account the temperature dependence of the dynamic viscosity and is based entirely on the experimental results for heating.

7 Heat Transfer in the Transition Region

Gnielinski [4] has shown that a linear interpolation of the Nusselt numbers between Re_{crit} and $Re = 2.2 \times 10^4$ suffices for the determination of the Nusselt numbers in the transition zone $Re_{crit} < Re < 2.2 \times 10^4$. The corresponding equations are

$$Nu = \gamma\, Nu_l(Re_{crit}) + (1 - \gamma)\, Nu_t(Re = 2.2 \times 10^4) \qquad (15)$$

where $Nu_1(Re_{crit})$ = Nu as in Eq. (12) if $Re = Re_{crit}$ and Nu_t ($Re = 2.2. \times 10^4$) = Nu as in Eq. (13) if $Re = 2.2 \times 10^4$ and

$$\gamma = \frac{2.2 \cdot 10^4 - Re}{2.2 \cdot 10^4 - Re_{crit}} \qquad (16)$$

8 Bibliography

1. Schmidt EF (1967) Wärmeübergang und Druckverlust in Rohrschlangen. Chem -Ing -Techn 39:781–789
2. Bauermeister K, Brauer H (1979) Laminare Strömung und Wärmeübergang in Rohrwendeln und Rohrspiralen. VDI Forschungsh., no. 593, 49 pp., VDI-Verlag Düsseldorf
3. Janssen LAM, Hoogendorn CJ (1978) Laminar convective heat transfer in helically coiled tubes. Int J Heat Mass Transfer 21:1197–1206
4. Gnielinski V (1986) Heat transfer and pressure drop in helically coiled tubes. Proc 8th Int Heat Transfer Conf, San Francisco, Hemisphere, Washington DC, vol. 6, pp. 2847–2854
5. Mishra P, Gupta SN (1979) Momentum transfer in curved pipes. I. Newtonian fluids. Ind Eng Chem Process Des Dev 18:130–137
6. Gnielinski V (1986) Correlations for pressure drop in helically coiled tubes. Int Chem Eng 26:36–44

G4 Heat Transfer in Flow Past a Plane Wall

Volker Gnielinski
Karlsruher Institut für Technologie (KIT), Karlsruhe, Germany

1 Introduction

Brauer and Sucker [1] dealt with the mass transfer in parallel laminar flow along a flat plate. From the numerical solutions to the complete set of differential equations for the concentration field, smoothed curves for average Sherwood numbers were derived. In view of the analogy between heat and mass transfer, these curves can also be applied to heat transfer. For Reynolds numbers Re $<$ 100, they yield higher values of the Nusselt number than those calculated by Pohlhausen [2] and Kroujiline [3] from the boundary layer theory (cf. Eq. (2)). If Re $>$ 100, the results obtained by both methods practically agree.

2 Parallel Flow Along a Flat Plate with Laminar Boundary Layer

The stream adjacent to the plate is retarded when a fluid of uniform velocity is flowing over a plate. If the leading edge of this plate is streamlined, a laminar boundary layer is formed outward from it. The thickness of the laminar boundary layer increases with increasing distance x from the leading edge. At a length x_{crit}, the forces between the streaming particles are not sufficient enough to keep them inline, and a transition to a turbulent boundary layer starts. The critical length x_{crit} is determined by the critical Reynolds number.

$Re_{x,crit} = w\, x_{crit}/\nu$, which depends on, among other factors, the degree of turbulence in the inflowing stream and the roughness of the plates surface. A figure of $Re_{x,crit} = 5 * 10^5$ is assumed. It may be higher if there is little turbulence at the inlet, or much lower if there is much turbulence.

2.1 Entire Surface at Uniform Temperature

Equations for the local and the average value of the Nusselt number were derived by Pohlhausen [2] and Kroujiline [3]. The *local value* of the Nusselt number $Nu_{x,lam}$ at a position x from the leading edge of the plate can be calculated from

$$Nu_{x,lam} = 0.332 \sqrt{Re_x}\ \sqrt[3]{Pr} \tag{1}$$

Where $Nu_{x,lam} = \frac{\alpha x}{\lambda}$ and $Re_x = \frac{wx}{\nu}$

The *average Nusselt* number $Nu_{l,lam}$ for a flat plate of the length l results from integrating Eq. (1)

$$Nu_{l,lam} = 0.664 \sqrt{Re_l}\ \sqrt[3]{Pr} \tag{2}$$

with $Nu_{l,lam} = \frac{\alpha l}{\lambda}$ and $Re_l = \frac{wl}{\nu}$.

A weak dependence of the factors 0.332 in Eq. (1) and 0.664 in Eq. (2) on Pr is ignored. According to Presser [4], the factor 0.664 increases to 0.703 for Pr = 1,000.

2.2 Uniform Heat Flux on the Surface of the Plate

According to Gauler [4], the local value of the Nusselt number at a position x from the leading edge is calculated from

$$Nu_{x,lam} = 0.460 \sqrt{Re_x}\ \sqrt[3]{Pr} \tag{3}$$

The range of validity of Eqs. (1–3) is $Re_x < 10^5$.

$Re_l < 10^5$ with the above-mentioned dependencies. Pr = 0.6 – 2000.

Physical properties are evaluated at the mean temperature $T_m = (T_{in} + T_{out})/2$ of the fluid.

3 Parallel Flow Along a Flat Plate with Turbulent Boundary Layer

If the plate has a blunt or obtuse-angled leading edge, a turbulent boundary layer will spread out from it. Presser [5] has investigated the effect exerted by the shape of the leading edge. According to Petukhov and Popov [6], the value of the Nusselt number for a flat plate at a constant wall temperature with

VDI-GVC (ed.), *VDI Heat Atlas*, DOI 10.1007/978-3-540-77877-6_26,

physical properties evaluated at the bulk temperature T_m of the fluid can be calculated from

$$\mathrm{Nu_{turb}} = \frac{(\zeta/8)\mathrm{RePr}}{1 + 12.7\sqrt{(\zeta/8)}(\mathrm{Pr}^{2/3} - 1)} \tag{4}$$

For the *local Nusselt number*, $\mathrm{Nu}_{x,\mathrm{turb}}$, the drag coefficient ζ presented by Schlichting [7] for a plate with turbulent boundary layer, to be used in Eq. (4) is

$$(\zeta/8) = 0.296\,\mathrm{Re}_x^{-0.2} \tag{5}$$

thus resulting in

$$\mathrm{Nu}_{x,\mathrm{turb}} = \frac{0.0296\mathrm{Re}_x^{0.8}\mathrm{Pr}}{1 + 2.185\mathrm{Re}_x^{-0.1}(\mathrm{Pr} - 1)} \tag{6}$$

For the *average Nusselt number* the average friction factor given by Schlichting [7] for a plate with turbulent boundary layer to be used in Eq. (4) is

$$(\zeta/8) = 0.037\,\mathrm{Re}_l^{-0.2} \tag{7}$$

yielding

$$\mathrm{Nu}_{l,\mathrm{turb}} = \frac{0.037\mathrm{Re}_l^{0.8}\mathrm{Pr}}{1 + 2.443\mathrm{Re}_l^{-0.1}(\mathrm{Pr}^{2/3} - 1)} \tag{8}$$

The range of validity of Eqs. (6) and (8) is $5{*}10^5 < \mathrm{Re} < 10^7$ and $0.5 < \mathrm{Pr} < 2000$. The physical properties are evaluated at the mean temperature $T_m = (T_{in} + T_{out})/2$ of the fluid.

4 Combined Correlation for Average Coefficients For Both Turbulent and Laminar Flow Over a Plate

In practical applications, a blunt leading edge and higher degrees of turbulence prevent the formation of a laminar boundary layer over the entire length of the plate, even if the Reynolds number lies within the range of medium values. No sudden change of the Nusselt number given by Eq. (2) to those resulting from Eq. (8) is observed. Krischer and Kast [8] have presented a graph correlating collected data of heat transfer for air at a flat plate from $10^1 < \mathrm{Re_l} < 10^6$. As shown by Gnielinski [9], the following equation represents not only the graph of Krischer and Kast [8], but also measures the heat transfer coefficients in a wide range of Prandtl numbers.

$$\mathrm{Nu_{l,0}} = \sqrt{\mathrm{Nu_{l,lam}^2} + \mathrm{Nu_{l,turb}^2}} \tag{9}$$

where $\mathrm{Nu_{l,0}} = \alpha\, l/\lambda$ and $\mathrm{Nu_{l,lam}}$ from Eq. (2) and $\mathrm{Nu_{l,turb}}$ from Eq. (8).

Equation (9) holds for average Nusselt numbers from $10^1 < \mathrm{Re} < 10^7$ and $0.5 < \mathrm{Pr} < 2000$. Physical properties are evaluated at the mean temperature $T_m = (T_{in} + T_{out})/2$ of the fluid.

Figure 1 demonstrates the course of Eq. (9) for Pr = 0.7.

To test a computer program for Eq. (9) the result for Re = 5000 and Pr = 0.7 is $\mathrm{Nu_{l,0}} = 51.51$.

5 Dependence of the Heat Transfer on the Length of an Unheated Initial Portion of the Plate

The heat transfer from a plate will be influenced by the presence of an unheated section preceding the heated section.

After Brauer [10], the effect of an unheated initial section of the plate in case of a laminar boundary layer can be taken into account by extending Eq. (2) to

$$\mathrm{Nu_{l,lam}} = 0.664\sqrt{\mathrm{Re_l}}\,\sqrt[3]{\mathrm{Pr}}\,\frac{\left[1 - (1 - l_0/l)^{3/4}\right]^{2/3}}{l_0/l} \tag{10}$$

and computing $\mathrm{Nu_{l,lam}}$ and $\mathrm{Re_l}$ with the total length l of the plate, where l_0 denotes the heated length of the plate.

According to Zukauskas and Ambrazyavichyus [11], however, this effect may be neglected in the case of a turbulent boundary layer if $\mathrm{Nu_{l,turb}}$ and $\mathrm{Re_l}$ in Eq. (8) are calculated with the length l_0 of the heated portion and if the ratio l_0/l is between 1 and 0.1.

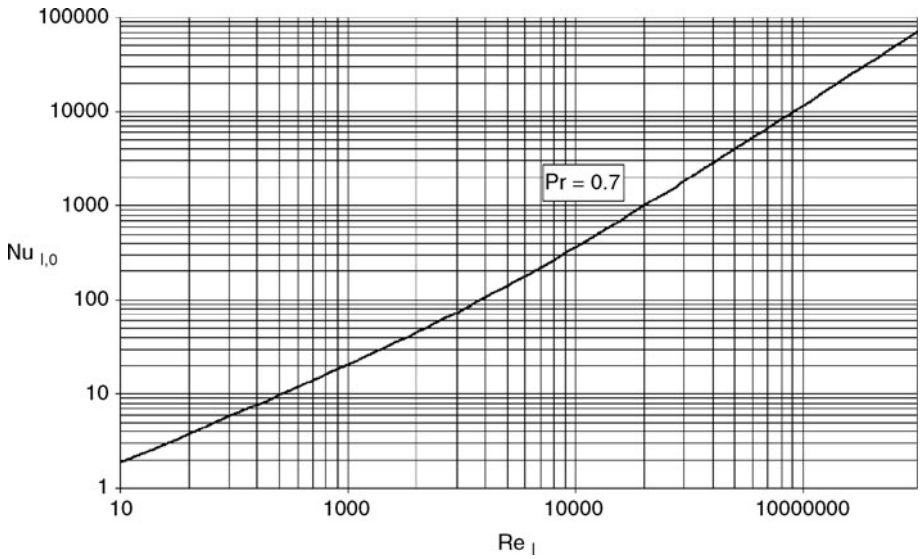

G4. Fig. 1. Course of Eq. (9) for Pr = 0.7.

6 Effect of the Direction of Heat Flux

The direction of heat flux – that is, heating or cooling the plate – affects the heat transfer in case of temperature-dependent fluid properties. For liquids this effect can be taken into account, according to Zukauskas and Ambrazyavichyus [11], by introducing a factor

$$K = K_l = \left(\frac{\mathrm{Pr}}{\mathrm{Pr_w}}\right)^{0.25} \tag{11}$$

Pr and $\mathrm{Pr_w}$ are the Prandtl numbers of the liquid at the mean fluid temperature T_m and at the wall temperature, respectively.

For gases this effect may be allowed for, according to Churchill and Brier [12], by using the factor

$$K = K_g = \left(\frac{T_m}{T_w}\right)^{0.12} \tag{12}$$

T_m and T_w are the absolute temperatures of the gas at mean gas temperature and of the wall temperature, respectively.

As K is introduced in Eq. (9), the consideration of heat flux gives

$$\mathrm{Nu_l} = K\mathrm{Nu_{l,0}} \tag{13}$$

7 Bibliography

1. Brauer HD, Sucker D (1976) Stoff- und Wärmeübergang an umströmten Platten, Zylindern und Kugeln. Chem Ing Techn. 48(9):737–741
2. Pohlhausen E (1921) Wärmeaustausch zwischen festen Körpern und Flüssigkeiten mit kleiner Reibung und kleiner Wärmeleitung. Z Angew Math Mech 1(2):115–121
3. Kroujiline G (1936) Investigation de la Couche –limite Thermique. Techn Phys USSR 3 183:311
4. Gauler K (1972) Wärme- und Stoffübertragung an eine mitbewegte Grenzfläche bei Grenzschichtströmung. Dr.-Ing. Diss, Universitaet Karlsruhe (TH), Germany
5. Presser KH (1968) Experimentelle Prüfung der Analogie zwischen konvektiver Wärme- und Stoffübertragung bei nichtabgelöster Strömung. Wärme- & Stoffübertragung. 1(4):225–236
6. Petukhov BS, Popov VN (1963) Theoretical calculation of heat exchange and frictional resistance in turbulent flow in tubes of incompressible fluid with variable physical properties. High Temperature 1(1):69–83
7. Schlichting, H. (1958) Grenzschicht-Theorie, 3rd edn. Verl.G. Braun, Karlsruhe
8. Krischer O, Kast W (1978) Die wissenschaftlichen Grundlagen der Trocknungstechnik, 3rd ed. Springer, Berlin
9. Gnielinski V (1975) Berechnung mittlerer Wärme- und Stoffübergangskoeffizienten an laminar und turbulent überströmten Einzelkörpern mit Hilfe einer einheitlichen Gleichung. Forsch Ing Wes 41:145–150
10. Brauer H (1971) Stoffaustausch einschl. Chem Reaktion, Aarau, Frankfurt/M, Verl. Sauerländer.
11. Zukauskas AA, Ambrazyavichyus AB (1961) Heat transfer of a plate in a liquid flow. Int J Heat Mass Transf 3: 305–309
12. Churchill SW, Brier JC (1955) Convective heat transfer from a gas stream at high temperature to a circular cylinder normal to the flow. Chem Engng Progr Symp Ser 51(17):57–65

G5 Heat Transfer to Single Cylinders, Wires, and Fibers in Longitudinal Flow

Holger Martin[1] · *Bernhard Gampert*[2]
[1]Karlsruher Institut für Technologie (KIT), Karlsruhe, Germany
[2]Universität Duisburg-Essen, Essen, Germany

1 Circular Cylinders in Longitudinal Flow

Heat transfer between a circular cylinder and a fluid flowing parallel to its axis is determined by the thermal and the hydrodynamic boundary layer. The following problems refer to the laminar boundary layers and single circular cylinders, that means, the flow is assumed to be not influenced by the walls or by other cylinders. Natural convection is not considered.

In principle the following cases are possible:

1.1 Longitudinal Flow over a Circular Cylinder at Rest

In order to calculate the heat transfer rates, the steady-state boundary layer equations have to be solved for the velocity and the temperature fields. For longitudinal flow over a circular cylinder at rest, the boundary conditions for the fluid dynamic layer are (see Fig. 1)

$$r = r_w = d/2\; x_A \le x \le x_E:\; u = u_w = 0,$$
$$r \to \infty\; u = u_\delta \neq 0$$
$$x_A = 0,\; x_E = L;\; x_A,\; x_E = \text{const.}$$

1.2 The Finite Circular Cylinder Axially Moving Through a Fluid at Rest

Longitudinal flow in this case is due to the motion of the cylinder. The boundary conditions for the calculation of the velocity field are (see Fig. 2)

$$r = r_w = d/2\; x_A(t) \le x \le x_E(t):\; u = u_w \neq 0,$$
$$r \to \infty\; u = u_\delta = 0$$
$$x_A(t) = u_w t,\; x_E(t) = L + u_w t$$

This case can be reduced to the previous one (Sect. 1.1) by using a coordinate system moving with the cylinder. So the heat transfer results for the cylinder at rest as given in Sect. 3 may be used as well for this case.

1.3 The Infinite Circular Cylinder Axially Moving in a Fluid at Rest

A case that is different from those in Sects. 1.1 and 1.2 is an infinitely long cylinder moving axially through a stagnant fluid. Problems of this kind arise for fibers coming from a nozzle and going out of the cooling process after a certain residence time (see Fig. 3) [1–3]. The boundary conditions for this problem are

$$r = r_w = d/2\; x_A \le x \le x_E:\; u = u_w \neq 0,$$
$$r \to \infty\; u = u_\delta = 0$$
$$x_A = 0,\; x_E = L$$

1.4 The Infinite Circular Cylinder Axially Moving in a Longitudinal Flow

A combination of cases 1.1 and 1.3 will be found if the infinite cylinder axially moves in a longitudinal fluid flow. The boundary conditions in this case are

$$r = r_w = d/2\; x_A \le x \le x_E:\; u = u_w \neq 0,$$
$$r \to \infty\; u = u_\delta \neq 0$$
$$x_A = 0,\; x_E = L$$

Heat transfer (and flow resistance) at the cylinder surface, in this case, do not only depend upon the relative velocity as used by Gampert [2, 3] $u_r = |u_\delta - u_w|$; but also upon the ratio of these two velocities, u_w/u_δ. In place of this ratio, u_w/u_δ, a parameter

VDI-GVC (ed.), *VDI Heat Atlas*, DOI 10.1007/978-3-540-77877-6_27,

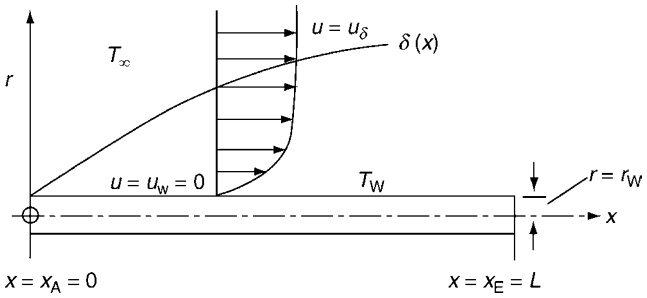

G5. Fig. 1. Longitudinal flow over a circular cylinder at rest.

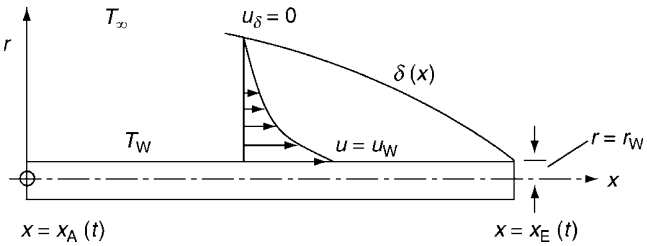

G5. Fig. 2. A finite circular cylinder axially moving through a fluid at rest.

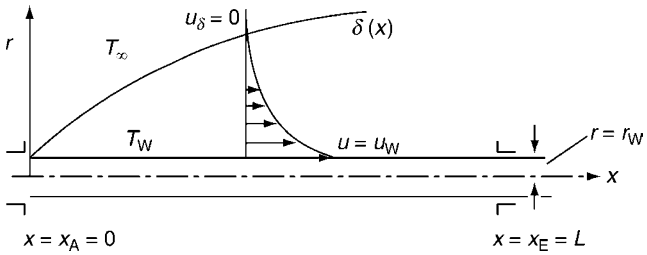

G5. Fig. 3. The infinite circular cylinder axially moving in a fluid at rest.

$$w = \frac{u_w/u_\delta}{1 + u_w/u_\delta} \tag{1}$$

can be used which varies from 0 to 1 and clearly distinguishes between the three cases:

Case 1.1 (=1.2): $w = 0$, case 1.3: $w = 1$, and case 1.4: $0 < w < 1$. In place of the relative velocity u_r, the sum of the two velocities, $(u_\delta + u_w)$, seems to be a more reasonable variable to describe the dependency of heat transfer on fluid flow in this case.

$$u_{sum} = u_\delta + u_w \tag{2}$$

The reason for this choice can be easily explained by the fact that the case of vanishing relative velocity $u_r = 0$, that is, $u_\delta = u_w$ does not mean that heat transfer tends to zero. Actually, this case of vanishing relative velocity corresponds to a "frictionless" (plug flow) case of transient conduction (in a coordinate system moving with the velocity $u_\delta = u_w$) where the heat transfer coefficient α is inversely proportional to the residence time to the power of $-1/2$:

$$Nu = \frac{1}{\sqrt{\pi Fo}} \qquad Fo = \kappa t / r_w^2 \quad t = x/u \tag{3}$$

G5. Table 1. Heat transfer at the circular cylinder axially moving in a longitudinally flowing fluid [$w = 0$, $w = 0.5/1.5$, $w = 0.9/1.9$, and $w = 1/2$ (approximation of the analytical solution from Carslaw & Jaeger [4, §13.5, Eqs. (8–10)]), $w = 1$, and Pr = 0.7]

$w = u_w/(u_\delta + u_w)$	A	B	C	u_w/u_δ
0	0.547	0.951	0	0
0.3333	0.590	0.901	0	0.5
0.4737	0.620	0.863	0	0.9
0.5000	0.622	0.855	0	1
1	0.674	0.690	0.035	∞

in case of negligible curvature. The corresponding case for the infinite region bounded internally by the circular cylinder is treated in the work by Carslaw and Jaeger [4], paragraph 13.5, and it is used in an approximate form in Table 1 ($w = 0.5$, $u_w/u_\delta = 1$).

2 Definitions

Heat transfer at the cylinder in longitudinal flow is treated in the following for constant wall temperature, T_w, and constant temperature of the surroundings, T_∞.

The local heat transfer coefficient is defined as

$$\alpha_x = \frac{\dot{q}_x}{T_w - T_\infty} \tag{4}$$

The local Nusselt number is defined with the fluid conductivity, λ, measured at the wall temperature, $\lambda\,(T_w)$.

$$Nu = \frac{\alpha_x d}{\lambda} \tag{5}$$

The viscosity in the Reynolds number, $Re_d = u_r\, d/\nu$, is measured at the ambient temperature, T_∞.

3 Heat Transfer to a Circular Cylinder in Longitudinal Flow

The difference between a cylinder in longitudinal flow and a flat plate is due to the curvature of the cylinder wall. This influence depends upon the ratio of boundary layer thickness and radius of the cylinder. It can be taken into account via the length (or residence time, or curvature) parameter, X.

$$X = \frac{\nu x}{(d/2)^2\, u_{sum}} \qquad \left(= 4\frac{x/d}{Re_{sum}}\right) \tag{6}$$

In the formulae for mean Nusselt numbers, $x = L$ is to be used in X.

3.1 Heat Transfer to a Circular Cylinder for Low Values of the Curvature Parameter

If X is small enough the influence of curvature may be neglected, and the heat transfer coefficients can be calculated for a flat plate.

For the cylinder at rest ($w = 0$) in longitudinal flow (cases 1.1 and 1.2) in this limit (see also Chap. G4, and Gauler [5]) the solution is found to be

$$\mathrm{Nu} = 0.332 \frac{\mathrm{Pr}^{1/3}}{\sqrt{X/4}} (w = 0)(0.5 < \mathrm{Pr} < 500) \qquad (7)$$

for the local values (at a position x), and twice this value (0.664 in place of 0.332 in Eq. (2)) for the integral mean value, $\mathrm{Nu_m}$ (from $x = 0$ to L).

The errors to be expected (compared to the solution accounting for the curvature, as given in the Sect. 4) are about

$$2\% \text{ for } X = 0.001,$$
$$15\% \text{ for } X = 0.01,$$
$$35\% \text{ for } X = 0.1$$

The infinite circular cylinder axially moving in a fluid at rest (case 1.3, $w = 1$) in this limit (negligible curvature, flat plate) leads to [5]

$$\mathrm{Nu} = 0.4437 \frac{\mathrm{Pr}^{2/3}}{\sqrt{X/4}} (w = 1)(0.5 < \mathrm{Pr} < 5) \qquad (8)$$

The special situation $w = 1/2$ of case 1.4 ($0 < w < 1$), that is, $u_r = |u_\delta - u_w| = 0$ corresponds to plug flow (frictionless flow). In this case the local Nusselt number for negligible curvature is found from [5] as

$$\mathrm{Nu} = \frac{1}{\sqrt{\pi}} \sqrt{\frac{u_w d^2}{\kappa x}} \; (w = 1/2)(0 < \mathrm{Pr} < \infty) \qquad (9)$$

for all Prandtl numbers $\mathrm{Pr} = \nu/\kappa$.

3.2 Heat Transfer to a Circular Cylinder for Larger Values of the Curvature Parameter (Lean Cylinder, Fiber)

Gampert [2] has numerically calculated the Nusselt numbers for the cases 1.1, (=1.2), 1.3, and 1.4, using a highly accurate finite difference method. For small and large values of the curvature parameter the numerical result could be compared with analytical solutions.

The results are shown graphically in Fig. 4 for a Prandtl number of Pr = 0.7 (air). For case 1.3 ($w = 1$), Fig. 5 also shows the corresponding curves for other Prandtl numbers Pr = 0.1, 0.7, 1.0, and 10.

The local and integral mean Nusselt numbers can be correlated by the general formulae

$$\mathrm{Nu} = \frac{A}{\sqrt{X}} + \frac{B}{X^{0.1}} + C \qquad (10)$$

$$\mathrm{Nu_m} = 2\frac{A}{\sqrt{X}} + \frac{10}{9}\frac{B}{X^{0.1}} + C \qquad (11)$$

where the "constants" A, B, and C depend upon the case (i.e., on the parameter w) and the Prandtl number, Pr.

The Tables 1 and 2 give the numerical values of A, B, and C to be used in Eqs. (10) and (11).

4 Example

A thin cylindrical wire of the radius $r_w = 10^{-4}$ m moves continuously with a velocity u_w through air flowing in the same direction with a velocity u_δ. This corresponds to case 1.4, and the parameters A, B, and C for the local Nusselt number [Eq. (10)] can be found in Table 1.

Two cases shall be investigated (which have the same relative velocity $u_r = |u_\delta - u_w| = 10$ m/s).

Case 1: Air velocity $u_\delta = 100$ m/s and wire velocity $u_w = 90$ m/s.

The sum of the velocities $u_s = u_\delta + u_w = 190$ m/s and the ratio $u_w/u_\delta = 0.9$.

Case 2; Air velocity $u_\delta = 20$ m/s and wire velocity $u_w = 10$ m/s.

The sum of the velocities $u_s = u_\delta + u_w = 30$ m/s and the ratio $u_w/u_\delta = 0.5$.

The local Nusselt number at position $x = 0.55$ m is to be calculated.

Assuming an air temperature of $T_\infty = 50°\mathrm{C}$, the kinematic viscosity, ν is found from Part D, to be $\nu = 18.2 \cdot 10^{-6} \mathrm{m^2/s}$.

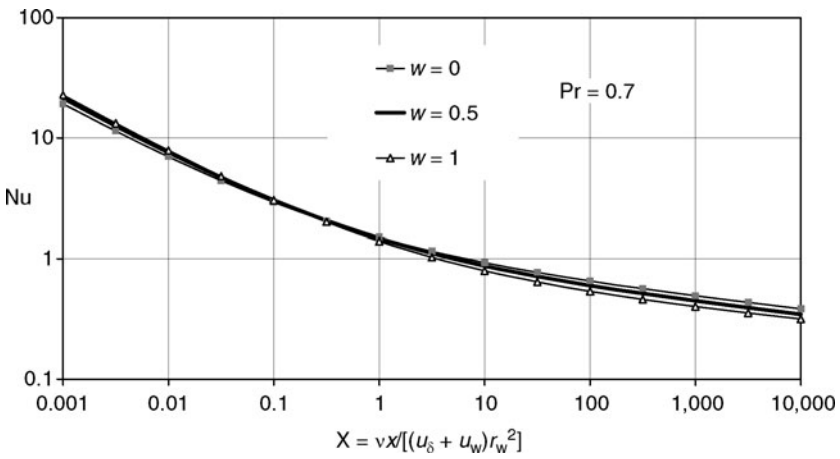

G5. Fig. 4. Heat transfer at the circular cylinder in longitudinal flow. Local Nusselt number, Nu, versus the curvature parameter, X [Eq. (5)] for Pr = 0.7, parameter $w = u_w/(u_w + u_\delta)$, where u_w is the velocity of the moving cylinder and u_δ is the air velocity parallel to the axis of the cylinder.

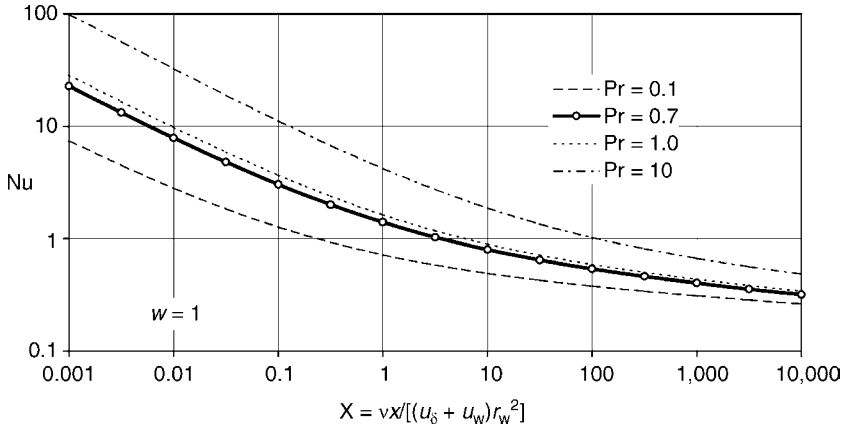

G5. Fig. 5. Heat transfer at the continuously moving circular cylinder without forced air flow (case 1.3: $u_\delta = 0$, $w = 1$). Local Nusselt numbers, Nu, versus the curvature parameter, X [Eq. (6)] for different Prandtl numbers.

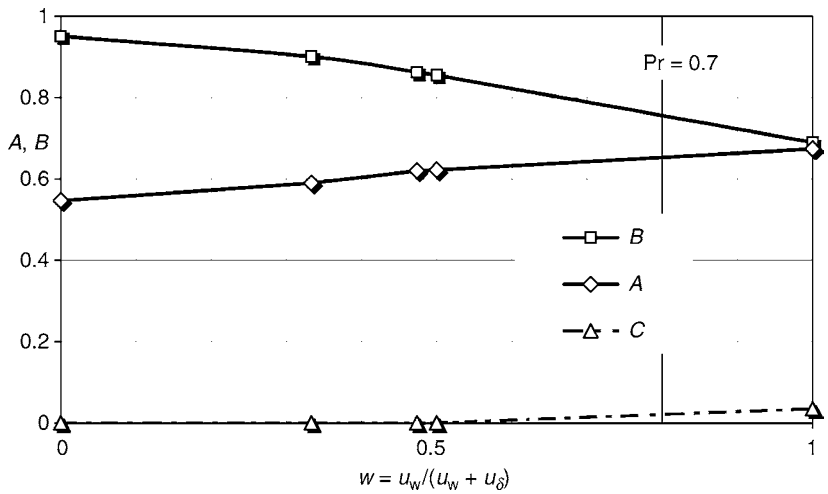

G5. Fig. 6. Heat transfer at the continuously moving circular cylinder in longitudinal air flow (Pr = 0.7). Values of the parameters A, B, and C to be used in Eqs. (10) and (11). The constants were recalculated from Gampert [3].

G5. Table 2. Heat transfer at infinite circular cylinder axially moving in a fluid at rest (case 1.3: w =1, Pr = 0.1, 0.7, 1.0, and 10)

Pr	A		B		C		Range
0.1	0.206	0.211*	0.415	0.395*	0.086	0.095*	$10^{-3} \le X \le 10^4$
0.7	0.674		0.690		0.035		$10^{-3} \le X \le 10^4$
1.0	0.857		0.732		0.040		$10^{-3} \le X \le 10^4$
10	3.075		1.135		0		$10^{-2} \le X \le 10^3$
$w = 1$	Local	Mean*	Local	Mean*	Local	Mean*	

*values of A, B, C to be used in Eq. (11)

From Eq. (6), the value of the curvature parameter, X, becomes

$$X = (18.2\,10^{-6}\,\mathrm{m^2/s} \cdot 0.55\,\mathrm{m})/(10^{-8}\,\mathrm{m^2} \cdot 190\,\mathrm{m/s}) = 5.268\ (\mathrm{Case\ 1})$$

$$X = (18.2\,10^{-6}\,\mathrm{m^2/s} \cdot 0.55\,\mathrm{m})/(10^{-8}\,\mathrm{m^2} \cdot 30\,\mathrm{m/s}) = 33.367\ (\mathrm{Case\ 2})$$

From Eq. (9) and Table 1 (for air: Pr = 0.7), one finds

$$\mathrm{Nu_d}\,(5.268,\ 0.9) = 1.00 \text{ for } (\mathrm{w} = 9/19)\ u_\mathrm{w}/u_\delta = 0.9, \text{ and}$$
$$\mathrm{Nu_d}\,(33.367,\ 0.5) = 0.74 \text{ for } (\mathrm{w} = 1/3)\ u_\mathrm{w}/u_\delta = 0.5.$$

In spite of the same relative velocity in both cases, the higher sum velocity and the higher ratio lead to a higher heat transfer coefficient. At a relative velocity of $u_\mathrm{r} = |u_\delta - u_\mathrm{w}| = 0\,\mathrm{m/s}$, and

the sum $u_s = u_\delta + u_w = 190\,\mathrm{m/s}$, the Nusselt number is very nearly the same as for Case 1 Nu (5.268, 1) = 0.995 for ($w = 1/2$) $u_w/u_\delta = 1$.

5 Bibliography

1. Sakiadis BC (1961) Boundary-layer behavior on continuous solid surfaces: III the boundary layer on a continuous cylindrical surface. AIChE J 7:467–472
2. Gampert B (1973) Grenzschichttheoretische Probleme des aerodynamischen Schmelzspinnprozesses, Dissertation TU Berlin
3. Gampert B (2006) Abschnitt Ge, Wärmeübertragung an einzelnen längsüberströmten Zylindern, Drähten und Fäden, in: VDI-Wärmeatlas, 10. Aufl, Springer-Verlag, Berlin
4. Carslaw HS, Jaeger JC (1967) Conduction of heat in solids. Clarendon Press, Oxford, 2nd edn. 1959, reprinted
5. Gauler K (1972) Wärme- und Stoffübertragung an eine mitbewegte ebene Grenzfläche bei Grenzschichtströmung, Dissertation Universität Karlsruhe

G6 Heat Transfer in Cross-flow Around Single Tubes, Wires, and Profiled Cylinders

Volker Gnielinski
Karlsruher Institut für Technologie (KIT), Karlsruhe, Germany

1 Average Nusselt Number

According to Krischer and Kast [1] the equations for determining the average Nusselt number in cross-flow over tubes, wires, and profiled cylinders are the same as those over a flat plate (Chap. G4) if the characteristic length used in the calculation of the Reynolds and Nusselt numbers is the "streamed length." This streamed length is the length of the entire path traversed by a particle in flowing over the surface presented to it by the body concerned. It is defined by Pasternak and Gauvin [2] as the total surface area A of the body divided by the maximum perimeter l_c perpendicular to the flow:

$$l = \frac{A}{l_c} \tag{1}$$

The streamed length is shown in Fig. 1. For a long tube of the diameter d and the length L according to Eq. (1), we get

$$l = \frac{\pi\, dL}{2L} = \frac{\pi}{2} d \tag{2}$$

The equation suggested by Gnielinski [3] for the average Nusselt number in cross-flow over tubes, wires, and profiled cylinders arranged as in standard engineering practice is

$$\mathrm{Nu}_{l,0} = 0.3 + \sqrt{\mathrm{Nu}_{l,\mathrm{lam}}^2 + \mathrm{Nu}_{l,\mathrm{turb}}^2} \tag{3}$$

where

$$\mathrm{Nu}_{l,\mathrm{lam}} = 0.664\sqrt{\mathrm{Re}_l}\,\sqrt[3]{\mathrm{Pr}} \tag{4}$$

and

$$\mathrm{Nu}_{l,\mathrm{turb}} = \frac{0.037\,\mathrm{Re}^{0.8}\,\mathrm{Pr}}{1 + 2.443\mathrm{Re}_l^{-0.1}\left(\mathrm{Pr}^{2/3} - 1\right)} \tag{5}$$

The minimum value of $\mathrm{Nu}_{l,0}$ in Eq. (3) results from the fact that, in practice, the length of a cylinder in cross-flow is always finite. Consequently, if the surrounding is at rest, the heat flux attains a minimum. The average Nusselt number for a cylinder thus asymptotically approaches a minimum, which is assumed to be $\mathrm{Nu}_{\min} \approx 0.3$ [3].

The relevant definitions are

$$\mathrm{Nu}_l = \alpha\, l/\lambda,$$

$$\mathrm{Re}_l = wl/\nu;\ 10 < \mathrm{Re}_l < 10^7$$

$$\mathrm{Pr} = 0.6 - 1000$$

$T_m = (T_{in} + T_{out})/2$ is the mean fluid temperature to which the properties are referred.

Equation (3) is presented graphically for air (Pr = 0.7) and water at 20°C (Pr = 7) Fig. 2.

If the Reynolds number is low, for example, in cross-flow over thin wires, the relationship $\mathrm{Nu}_{\min} = 0.3$ cannot be used since the thickness of the boundary layer is not small when compared with the dimension of the object. However, the Nusselt number in this range can be determined from the Sucker and Brauer equation [4].

2 Cylinder in a Restricted Channel

It has been proved [3] that the Nusselt number for a cylinder in a narrow channel can also be determined from Eq. (3) if the velocity taken to calculate the Reynolds number is the integral mean value w along the surface of the cylinder. It is determined from the fluid velocity w_0 in the cross section of the empty channel, as is illustrated in Fig. 3, and the void fraction of the

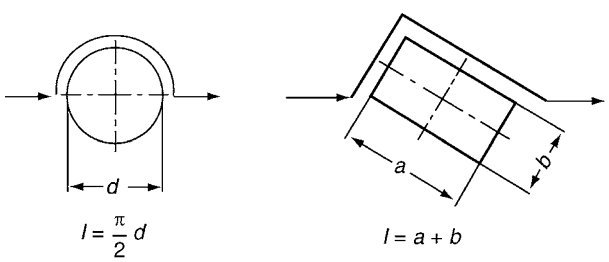

G6. Fig. 1. Definition of the streamed length.

VDI-GVC (ed.), *VDI Heat Atlas*, DOI 10.1007/978-3-540-77877-6_28,

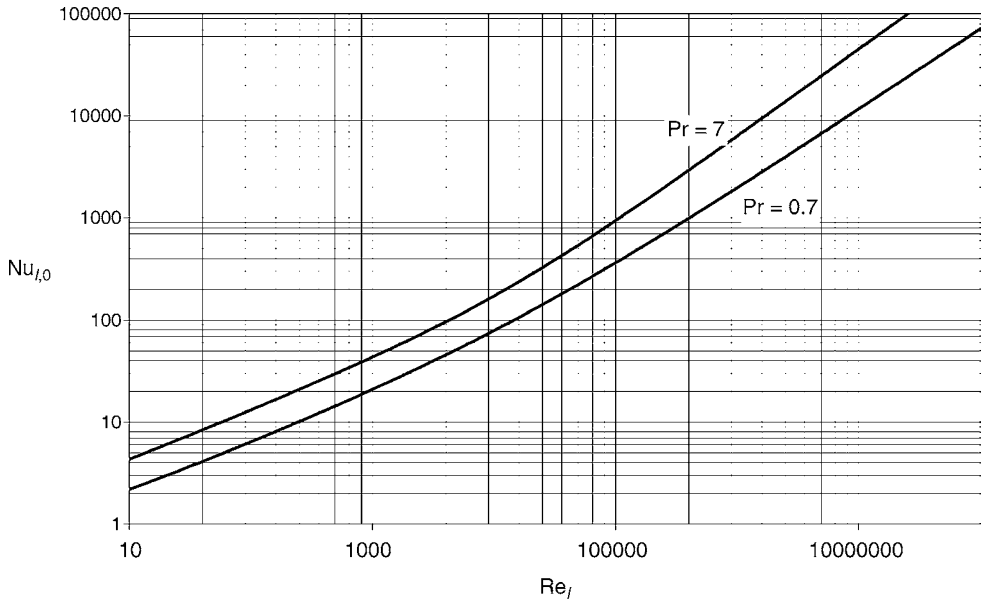

G6. Fig. 2. Course of Eq. (3) for air (Pr=0.7) and water at 20 °C (Pr=7).

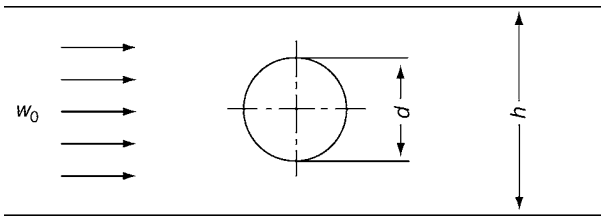

G6. Fig. 3. Cylinder in a restricted channel.

flow channel over the length of the cylinder. Thus

$$w = w_0/\psi \tag{6}$$

if the height of the channel is h,

$$\psi = 1 - \frac{\pi d}{4h} \tag{7}$$

3 The Effect of Temperature-dependent Variations in Properties

The direction of heat flux (heating or cooling) affects heat transfer if the properties depend on temperature. A factor K is taken to allow for this [3], that is,

$$\mathrm{Nu}_l = \mathrm{Nu}_{l,0}\, K \tag{8}$$

For liquids, K is given by

$$K = K_\mathrm{F} = (\mathrm{Pr}/\mathrm{Pr}_\mathrm{w})^{0.25} \tag{9}$$

where Pr is the Prandtl number at T_m; and Pr_w, is that at the wall temperature at T_w.

For gases, K is given by

$$K = K_\mathrm{G} = (T_\mathrm{m}/T_\mathrm{w})^{0.12} \tag{10}$$

where T_m is the temperature of the gas, and T_w is the temperature of the wall, both in Kelvin.

4 Effect of an Inclined Flow to the Cylinder

Experiments by Vornehm [5] have shown that Nu_l decreases with the vertical angle between the direction of flow and the axis of the cylinder. The relationship is as follows:

ϕ	90°	80°	70°	60°	50°	40°	30°	20°
$\mathrm{Nu}_{l,\phi}/\mathrm{Nu}_l$	1.0	1.0	0.99	0.95	0.86	0.75	0.63	0.5

5 Bibliography

1. Krischer O, Kast W (1978) Die wissenschaftlichen Grundlagen der Trocknungstechnik, 3rd edn. Springer, Berlin
2. Pasternak IS, Gauvin WH (1960) Turbulent heat and mass transfer from stationary particles. Can J Chem Eng 38:35–42
3. Gnielinski V (1975) Berechnung mittlerer Wärme- und Stoffübergangskoeffizienten an laminar und turbulent überströmten Einzelkörpern mit Hilfe einer einheitlichen Gleichung. Forsch -Ing Wes 41(5):145–153
4. Sucker D, Brauer H (1976) Wärme- und Stoffübertr.: Stationärer Stoff- und Wärmeübergang an Stationär quer angeströmten. Zylindern 9(1):1–12
5. Vornehm L (1936) Einfluss der Anströmrichtung auf den Wärmeübergang. Z VDI 80(22):702–703

G7 Heat Transfer in Cross-flow Around Single Rows of Tubes and Through Tube Bundles

Volker Gnielinski
Karlsruher Institut für Technologie (KIT), Karlsruhe, Germany

1 Definition of the Heat Transfer Coefficient

The average coefficient of heat transfer α at the surface of a row of tubes and in a tube bundle is defined by

$$\dot{q} = \alpha \, \Delta T_{\mathrm{LM}}$$

The variable ΔT_{LM} is the logarithmic mean temperature difference and is given for a constant wall temperature boundary condition by

$$\Delta T_{\mathrm{LM}} = \frac{(T_{\mathrm{w}} - T_{\mathrm{in}}) - (T_{\mathrm{w}} - T_{\mathrm{out}})}{\ln (T_{\mathrm{w}} - T_{\mathrm{in}_{\mathrm{i}}})/(T_{\mathrm{w}} - T_{\mathrm{out}})},$$

where T_{in} and T_{out} are the inlet and outlet temperatures, respectively, of the flowing medium, and T_{w} is the wall temperature.

2 Determination of the Heat Transfer Coefficient for a Single Row of Tubes

The average Nusselt number for cross-flow over a single row of tubes can be calculated from Eq. (3) in Chap. G6 for the single tube, if the characteristic velocity in the Reynolds number in Eq. (3) is replaced by the average velocity in the void between the tubes in the row. The void fraction, which depends on the transverse pitch ratio $a = s_1/d_{\mathrm{o}}$ in the row, as is illustrated in Fig. 1, is given by

$$\psi = 1 - \frac{\pi}{4a} \tag{1}$$

Thus, the following applies for $\mathrm{Nu}_{\mathrm{O,row}}$ according to Chap. G6:

$$\mathrm{Nu}_{O,\mathrm{row}} = 0.3 + \sqrt{\mathrm{Nu}^2_{l,\mathrm{lam}} + \mathrm{Nu}^2_{l,\mathrm{turb}}} \tag{2}$$

where

$$\mathrm{Nu}_{l,\mathrm{lam}} = 0.664 \sqrt{\mathrm{Re}_{\psi,l}} \sqrt[3]{\mathrm{Pr}} \tag{3}$$

$$\mathrm{Nu}_{l,\mathrm{turb}} = \frac{0.037 \, \mathrm{Re}^{0.8}_{\psi,l} \, \mathrm{Pr}}{1 + 2.443 \mathrm{Re}^{-0.1}_{\psi,l} \, (\mathrm{Pr}^{2/3} - 1)} \tag{4}$$

$$\mathrm{Nu}_{0,\mathrm{row}} = \frac{\alpha \, l}{\lambda} \tag{5}$$

$$\mathrm{Re}_{\psi,l} = \frac{w \, l}{\psi \, \nu} \qquad 10 < \mathrm{Re}_{\psi,l} < 10^6 \tag{6}$$

$$\mathrm{Pr} = \frac{\nu}{a} \qquad 0.6 < \mathrm{Pr} < 10^3 \tag{7}$$

$l = (\pi/2) d_0$ is the streamed length, i.e., the length of the flow path traversed over a single tube (see Fig. 1 of Chap. G6), and w is the velocity of the flowing medium in the free cross section of the row. $T_{\mathrm{m}} = (T_{\mathrm{in}} + T_{\mathrm{out}})/2$ is the mean temperature at which the physical properties of the flowing medium are evaluated.

If the turbulence in the inflowing medium is low, e.g., if there is pronounced acceleration in the channel inlet or if diffusers have been installed to ensure steady flow, deviations in the Nusselt number of up to 40% may occur in the $10^4 < \mathrm{Re}_{\psi,l} < 10^6$ range, as has also been observed in a cross-flow over a single tube [1].

3 Determination of the Heat Transfer Coefficient in a Tube Bundle

The average Nusselt number in a cross-flow over a bundle of smooth tubes can be calculated from that in a cross-flow over a single tube [2]. However, if the flow velocity is the same in both cases, the Nusselt number for a tube in a bundle is higher than that for a single tube exposed to this velocity in free flow. The enhancement depends on the longitudinal pitch and the

VDI-GVC (ed.), *VDI Heat Atlas*, DOI 10.1007/978-3-540-77877-6_29,

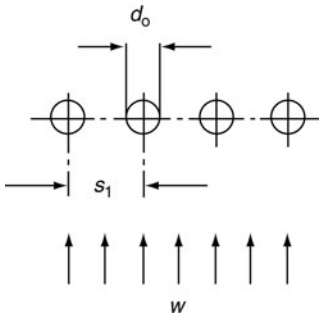

G7. Fig. 1. Lateral spacing in a row of tubes.

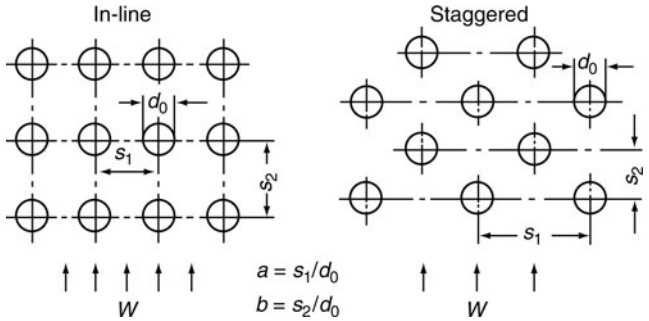

G7. Fig. 2. Lateral and longitudinal spacing in tube bundles.

transverse pitch of the bundle. The Nusselt number of the single tube in cross-flow can be determined from Eq. (3) in Chap. G6 if the Reynolds number is selected in the same way as that for an individual row of tubes, i.e., if the characteristic velocity for the flowing medium is the average in the void fraction of a row over a length corresponding to the tube diameter. The following applies in this case [2]:

$$\mathrm{Nu}_{0,\mathrm{bundle}} = f_\mathrm{A}\mathrm{Nu}_{l,0} \tag{8}$$

The void fraction and the arrangement factor f_A depend on the transverse pitch ratio $a = s_1/d_o$ and the longitudinal pitch ratio $b = s_2/d_o$ in the tube bundle.

The determination of a and b for various arrangements of the tube bundle is illustrated in Fig. 2. The void fraction is given by

$$\psi = 1 - \frac{\pi}{4\,a} \qquad \text{for } b \geq 1 \tag{9}$$

$$\psi = 1 - \frac{\pi}{4\,a\,b} \qquad \text{for } b < 1 \tag{10}$$

According to Eq. (3) in Chap. G6, $\mathrm{Nu}_{l,0}$ is given by

$$\mathrm{Nu}_{l,0} = 0.3 + \sqrt{\mathrm{Nu}^2_{l,\mathrm{lam}} + \mathrm{Nu}^2_{l,\mathrm{turb}}} \tag{11}$$

where

$$\mathrm{Nu}_{l,\mathrm{lam}} = 0.664\,\sqrt{\mathrm{Re}_{\psi,l}}\,\sqrt[3]{\mathrm{Pr}} \tag{12}$$

$$\mathrm{Nu}_{l,\mathrm{turb}} = \frac{0.037\;\mathrm{Re}^{0.8}_{\psi,l}\;\mathrm{Pr}}{1 + 2.443\;\mathrm{Re}^{-0.1}_{\psi,l}\;(\mathrm{Pr}^{2/3} - 1)} \tag{13}$$

$$\mathrm{Nu}_{0,\mathrm{bundle}} = \frac{\alpha\;l}{\lambda} \tag{14}$$

$$\mathrm{Re}_{\psi,l} = \frac{w\;l}{\psi\;\nu} \qquad 10 < \mathrm{Re}_{\psi,l} < 10^6 \tag{15}$$

$$\mathrm{Pr} = \frac{\nu}{a} \qquad 0.6 < \mathrm{Pr} < 10^3 \tag{16}$$

$l = (\pi/2)d_0$ is the streamed length of a single tube, w is the velocity of the flowing medium in the free cross section outside the bundle, and $T_\mathrm{m} = (T_\mathrm{i} + T_\mathrm{o})/2$ is the mean temperature of the flowing medium at which the physical properties are evaluated.

The factor f_A for in-line tube arrangement is given by

$$f_{\mathrm{A,in\text{-}line}} = 1 + \frac{0.7\;(b/a - 0.3)}{\psi^{1.5}(b/a + 0.7)^2}, \tag{17}$$

where ψ is given by Eq. (9).

Equation (17) was derived from experimental measurements with $b \geq 1.2$; the available measurements with $b < 1.2$ have a ratio $(b/a) \geq 1$.

Tube bundles with an in-line tube arrangement and a longitudinal pitch ratio $b < 1.2$ behave – according to the available data [1] for $\mathrm{Re}_{\psi,l} < 10^4$ – more like parallel channels, which are formed by the tube rows, with the tubes lying narrowly behind one another. An expected increase in the heat transfer coefficient due to the turbulence enhancement caused by the tube rows, which is expressed by Eq. (17), does not occur or is insignificant. Due to the lack of experimental data, no better information can be given.

The factor for the staggered tube arrangement is

$$f_{\mathrm{A,stag}} = 1 + \frac{2}{3\,b}. \tag{18}$$

$f_{\mathrm{A,in\text{-}line}}$ is shown as a function of the transverse pitch ratio a and the longitudinal pitch ratio b in Fig. 3; and $f_{\mathrm{A,stag}}$ is shown as a function of the longitudinal pitch ratio b in Fig. 4.

An alternative calculation method, which does not need the empirical factors $f_{\mathrm{A,in\text{-}line}}$ and $f_{\mathrm{A,stag}}$ from Eqs. (17) and (18), respectively, for the enhancement of the heat transfer in a bundle, as compared to a single tube, was suggested, in 2000, by Martin and Gnielinski [3], and, in a slightly improved version, in 2002, by Martin [4]. This newer method, based on the so-called Lévêque analogy (see Martin [5]), allows to calculate heat (or mass) transfer coefficients from the frictional pressure drop. Shah and Sekulic [6] recommend this newer method [4] in their Fundamentals of Heat Exchanger Design of 2003.

Here in Part G, the earlier empirical method is still presented in order to be consistent within all the Chaps. G6, G7, G8, and G9, which depend upon each other. The new method [4] may well be used for tube bundles in a pure cross-flow, but the application in the more complex configurations on the shell side of baffled shell-and-tube heat exchangers (Chap. G8) cannot be recommended at the present state of knowledge. A lot of additional testing and comparison will be needed before the newer method is used in the whole Part G.

4 Partly Staggered Tube Bundles

The pitch ratios a, b, and c in a partly staggered tube bundle are illustrated in Fig. 5. The average Nusselt number for these

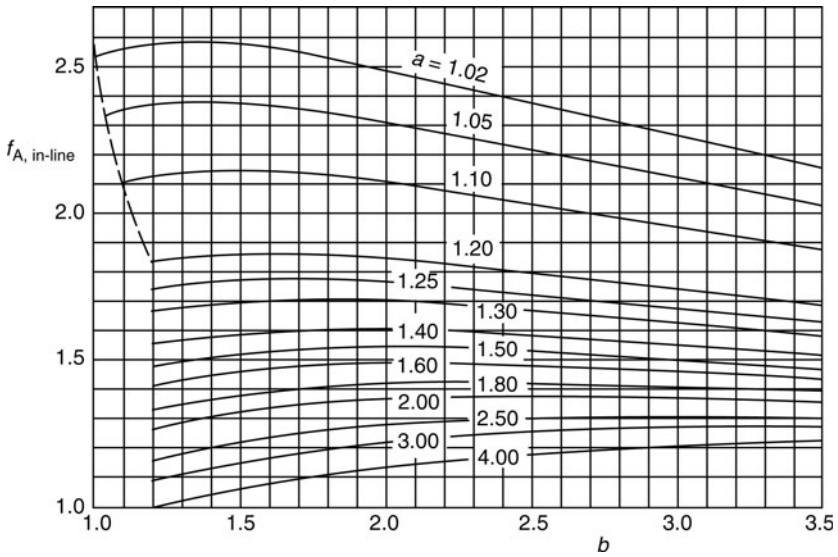

G7. Fig. 3. Factor $f_{A,\text{in-line}}$ for tubes arranged in-line as a function of the lateral and longitudinal spacing ratios.

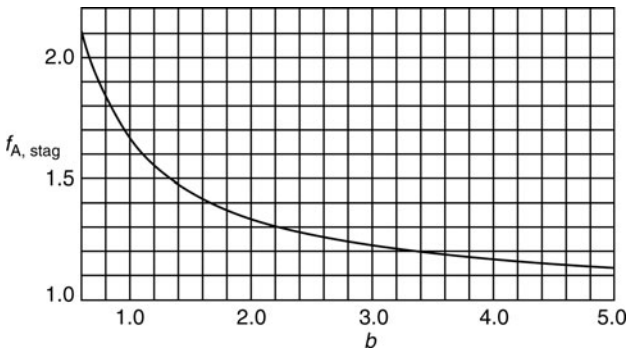

G7. Fig. 4. Factor $f_{A,\text{stag}}$ for staggered arrangements of tubes as a function of longitudinal spacing ratio.

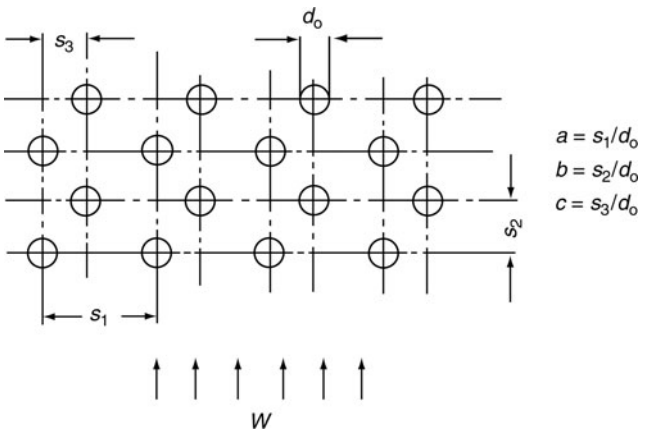

G7. Fig. 5. Spacing ratios for partly staggered tube bundles.

arrangements can also be determined from Eq. (8) if those with pitch ratios $c < a/4$ are regarded as in-line; and those with $c \geq a/4$ as completely staggered. Thus,

$$f_{A,\text{part.stag}} = f_{A,\text{in-line}} \quad \text{for } c < a/4 \tag{19}$$

$$f_{A,\text{part.stag}} = f_{A,\text{stag}} \quad \text{for } c \geq a/4 \tag{20}$$

5 Effect of the Number of Rows

The value of the heat transfer coefficient measured for a tube row in a bundle depends on the number of preceding rows. It increases from the first row to about the fifth row and then remains constant. If the average Nusselt number has to be determined for bundles with ten or more rows, the effect of the first few rows needs no longer to be taken into consideration. In other words, Eq. (8) is valid for the Nusselt number in any row of a bundle with a large number of rows after the inlet effects have diminished and also for the average Nusselt number in a bundle of ten or more rows. If the number of rows is less then ten, the average Nusselt number can be approximately determined from

$$\text{Nu}_{0,\text{bundle}} = \frac{1 + (n-1)f_A}{n} \text{Nu}_{l,0} \tag{21}$$

where n is the number of rows.

6 Effect of Temperature-Dependent Variations in Properties

The direction of heat flux (heating or cooling) affects heat transfer. This can be taken into consideration by introducing a correction factor K as follows [2]:

$$\text{Nu}_{\text{row}} = \text{Nu}_{0,\text{row}}\, K \tag{22}$$

$$\text{Nu}_{\text{bundle}} = \text{Nu}_{0,\text{bundle}}\, K \tag{23}$$

The factor K for liquids with $\text{Pr}/\text{Pr}_W > 1$, i.e., liquid heating, is given by

$$K = K_L = (\text{Pr}/\text{Pr}_W)^{0.25} \tag{24}$$

where Pr is the Prandtl number for the liquid at T_m, and Pr_W is the Prandtl number at the wall temperature T_W.

If $\text{Pr}/\text{Pr}_W < 1$, i.e., liquid cooling, then

$$K = K_L = (\text{Pr}/\text{Pr}_W)^{0.11} \tag{25}$$

The effect of temperature-dependent property variations on heat transfer in gases can be described within certain limits by

$$K = K_G = (T_m/T_W)^n \tag{26}$$

where T_m is the mean gas temperature in Kelvin ($T_m = (T_m/^\circ C + 273.1\ K)$ and T_W the Kelvin temperature of the tube wall.) The index n in Eq. (26) depends on the gas.

There have been very few studies in which the T_m/T_W ratio has been systematically varied. A value of $n = 0$ has been reported for cooling of air in a cross-flow over a tube bundle [7]; and a value of $n = 0.12$ for the cooling of nitrogen in a cross-flow over a single cylinder [8].

7 Effect of Turbulence

The degree of turbulence affects the heat transfer coefficient in the first few rows of a tube bundle. It was found experimentally that the heat transfer coefficient in the first row increased by about 42% when the degree of turbulence in the air flowing through the tube bundle was increased (by installing coarse screens at inlet) from 0.008 (very smooth flow) to 0.25 [9].

The enhancement in the heat transfer coefficient decreased from one row to the other and became negligible after the fifth row. Significant improvements in heat transfer can thus be achieved by increasing artificially the degree of turbulence in front of the tube bundle; this leads, however, to an increase in the pressure drop. Therefore, it is applied only in bundles with a few number of rows.

8 Oblique Flow Over Tube Bundles

Several studies [10–12] have revealed that the coefficient of heat transfer in oblique flow over tube bundles can be determined if the effective velocity of the flowing medium is taken to be the component perpendicular to the axes of the tubes. In this case, Eq. (15) becomes $Re_{\psi,l} = (w \sin\theta)\, l/(\psi\, \nu)$, where θ is the angle between the direction of flow and the axes of the tubes. In transverse flow, $\theta = 90^\circ$ and $\sin\theta = 1$.

9 Example of a Calculation

Water flows through a tube bundle placed in a rectangular channel at a mass flow rate of $\dot{M} = 100$ kg/s and an inlet temperature of 20°C. The tube bundle has an in-line tube arrangement with a transverse pitch of 30 mm and a longitudinal pitch of 26 mm. The tube bundle has six rows; each row has ten tubes with an outside diameter of 20 mm and a tube length of 2 m. The distance between the axis of the outermost tubes of the bundle and the adjacent channel sides amounts to 15 mm. The channel cross section is thus 0.3 m wide and 2 m long. The tubes of the bundle are heated from inside; they have a wall temperature of 100°C.

It is required to calculate the water temperature at the outlet of the channel.

Because of the temperature dependence of the properties of the water, the problem can be solved only iteratively.

List of the given data:

$\dot{M} = 100$ kg/s	$n = 6$ rows of tubes
$T_{in} = 20^\circ C$	$d_O = 0.02$ m
$T_w = 100^\circ C$	$l = (\pi/2)0.02$ m
$L = 2$ m	$s_1 = 0.03$ m
$z = 10$ tubes/row	$s_2 = 0.026$ m

Calculation of the geometrical data:

$$a = s_1/d_o = 30/20 = 1.5;\ b = s_2/d_o = 26/20 = 1.3$$

Exchange area $A = \pi\, d_o\, z\, n\, L = 7.54\ m^2$;

Free cross section in front of the bundle: $S = z\, s_1\, L = 10 \cdot 0.03 \cdot 2 = 0.6\ m^2$,

$$\psi = 1 - \frac{\pi}{4 \cdot 1.5} = 0.4764 \text{ (Eq. (9))}$$

Factor for the arrangement of the tubes: in-line tubes

$$f_{A,\text{in-line}} = 1 + \frac{0.7\ (1.3/1.5 - 0.3)}{0.4764^{1.5}(1.3/1.5 + 0.7)^2} = 1.491$$

The physical properties are taken from Subchap. D2.1.

Steps of interation for the example are given in Table 1.

G7. Table 1. Steps of iteration for the example of a calculation

Step of iteration	1. Step	2. Step	3. Step
$T_{in}/^\circ C$	20	20	20
$T_{out}/^\circ C$	90	30	29.6
$T_m = (T_{in} + T_{out})/2$	55	25	24.8
$\nu(T_m)/10^{-6}\, m^2/s$	0.512	0.893	0.897
$\lambda(T_m)/W/(mK)$	0.6492	0.6072	0.6068
$\rho(T_m)/kg/m^3$	985.69	997.05	997.09
$c_p(T_m)/J/(kg\,K)$	4,182	4,179	4,179
$Pr(T_m)$	3.248	6.128	6.163
Pr_w	1.757	1.757	1.757
$w = \dot{M}/(\rho(T_m) \cdot S/m/s)$	0.169	0.167	0.167
Eq. (15): $Re_{\psi,l} = w\, l/(\psi\, \nu(T_m))$	21,767	12,332	12,277
Eq. (12): $Nu_{l,lam} = 0.664(Re_{\psi,l})^{1/2}\, Pr\,(T_m)^{1/3}$	145.1	134.9	134.9

G7. Table 1. (continued)

Step of iteration	1. Step	2. Step	3. Step
Equation (13): $Nu_{l,turb} = \frac{0.037 Re_{\psi,l}^{0.8} Pr(T_m)}{1+2.443 Re_{\psi,l}^{-0.1} (Pr(T_m)^{2/3}-1)}$	171.1	131.3	131.0
Equation (11): $Nu_{l,0} = 0.3 + (Nu_{l,lam}^2 + Nu_{L,turb}^2)^{1/2}$	224.6	188.5	188.3
Equation (21): $Nu_{0,bundle} = \frac{1+(n-1)f_{A,in-line}}{n} Nu_{l,o}$	316.5	265.6	265.3
Equation (23): $Nu_{bundle} = Nu_{0,bundle}(Pr(T_m)/Pr_w)^{0.25}$	369.1	363.0	363.1
$\alpha = Nu_{bundle}\, \lambda(T_m)/l/W/(m^2K)$	6015.4	7016.0	7013.3
$\Delta T_{LM} = \frac{(T_w-T_{in})-(T_w-T_{out})}{\ln T_w-T_{in_i}/T_w-T_{out}}$	33.66 K	74.89 K	75.10 K
$\dot{Q} = \alpha\, A\, \Delta T_{LM}/W$	1,526,686.9	3,961,728.9	3,971,309.2
$T_{out} = \frac{\dot{Q}}{\dot{M} c_p(T_m)} + T_{in}$	23.7°C	29.5°C	29.5°C

The physical properties of the water do not change at a mean temperature of $T_m = (20 + 29.5)/2 = 24.75°C$ compared with 24.8°C. Therefore, no additional step of iteration is necessary. The temperature of the water at the exit is 29.5°C.

10 Bibliography

1. Gnielinski V (1975) Berechnung mittlerer Wärme- und Stoffübergangskoeffizienten an laminar und turbulent überströmten Einzelkörpern mit Hilfe einer einheitlichen Gleichung. Forsch Ing-Wesen 41(5):145–153
2. Gnielinski V (1979) Equations for calculating heat transfer in single tube rows and banks of tubes in transverse flow. Int Chem Eng 19(3):380–390
3. Martin H, Gnielinski V (2000) Calculation of heat transfer from pressure drop in tube bundles. Proceedings of 3rd European thermal sciences conference, Heidelberg, pp 1155–1160
4. Martin H (2002) The generalized Lévêque equation and its practical use for the prediction of heat and mass transfer rates from pressure drop. Chem Eng Sci 57:3217–3223
5. Martin H (1996) A theoretical approach to predict the performance of chevron-type plate heat exchangers. Chem Eng Process 35:301–310
6. Shah RK, Sekulic DP (2003) Fundamentals of heat exchanger design. John Wiley & Sons, New York
7. Preece RJ, Lis J, Brier JC (1975) Effect of gas-side physical property variations on the heat transfer to a bank of tubes in cross-flow. Proc Inst Mech Eng 189:69–75
8. Churchill SW, Brier JC (1955) Convective heat transfer from a gas stream at high temperature to a circular cylinder normal to the flow. Chem Eng Prog Symp Ser 51:57–65
9. Traub D (1986) Dr.-Ing. Diss. Universität Stuttgart
10. Groehn HG (1980) Thermal and hydraulic investigation of yawed tube bundle heat exchangers. Advanced Study Institute on Heat Exchangers ASI Proceedings, Istanbul
11. Groehn HG (1982) Influence of the yaw angle on heat transfer and pressure drop of tube bundle heat exchangers. Proceedings of the 7th international heat transfer conference, München, Paper HX 8
12. Yanez Moreno AA, Sparrow EM (1987) Heat transfer, pressure drop, and fluid flow patterns in yawed tube banks. Int J Heat Mass Transf 30:1979–1995

G8 Shell-Side Heat Transfer in Baffled Shell-and-Tube Heat Exchangers

Edward S. Gaddis[1] · *Volker Gnielinski*[2]
[1]Technische Universität Clausthal, Clausthal-Zellerfeld, Germany
[2]Karlsruher Institut für Technologie (KIT), Karlsruhe, Germany

1 Introduction

The method described in this chapter for calculating the mean heat transfer coefficient on the shell-side of a baffled shell-and-tube heat exchanger is based on the corresponding method for calculating the mean heat transfer coefficient in a tube bundle with a cross flow. However, the flow configuration on the shell-side of a baffled shell-and-tube heat exchanger leads to a number of deviations from the case of a flow across a tube bundle. The geometry of the baffles in the heat exchanger shell – as shown in Fig. 1 – generates a main stream through the heat exchanger tube bundle, which is partly across and partly parallel to the tubes. Unavoidable clearances between the outer surface of the tubes and the holes in the heat exchanger baffles, as well as between the baffles and the inside shell surface lead to leakage streams, which participate in heat transfer, but not to the same extent as the main stream. Since the tubes in the tube bundle cannot be brought uniformly and very close to the shell, bypass streams occur in the gaps between the outer tubes of the bundle and the inside surface of the heat exchanger shell; such bypass streams do not participate effectively in heat transfer. These geometrical factors dictated by the design of a shell-and-tube heat exchanger lead to deviations between the heat transfer in a tube bundle and that on the shell-side of a baffled heat exchanger; they can be taken into account by means of correction factors. The correction factors described hereafter are based on data given by Bell [1]. The presented method of calculation was checked by Gnielinski and Gaddis [2] through a large number of experimental measurements available in the open literature.

2 Required Geometrical Data

The following geometrical parameters are required for the calculation of the mean shell-side heat transfer coefficient:

D_i	Shell inside diameter
D_1	Baffle diameter
D_B	Tube bundle diameter
d_o	Outer diameter of tubes
d_B	Diameter of holes in baffles
H	Height of baffle cut
L_E	Sum of the shortest connections e and e_1 (see Fig. 3, $L_E = 2e_1 + \Sigma e$)
n_T	Total number of tubes in heat exchanger including blind and support tubes
n_W	Number of tubes in both upper and lower windows (baffle cuts)
n_S	Number of pairs of sealing strips
n_{MR}	Number of main resistances in cross flow between adjacent baffles (needed only if $n_S \neq 0$, see Fig. 6 for the determination of n_{MR})
S	Baffle spacing (assumed constant, otherwise see Sect. 4.4)
s_1	Transverse pitch
s_2	Longitudinal pitch

Tube arrangement: in-line or staggered.

VDI-GVC (ed.), *VDI Heat Atlas*, DOI 10.1007/978-3-540-77877-6_30,

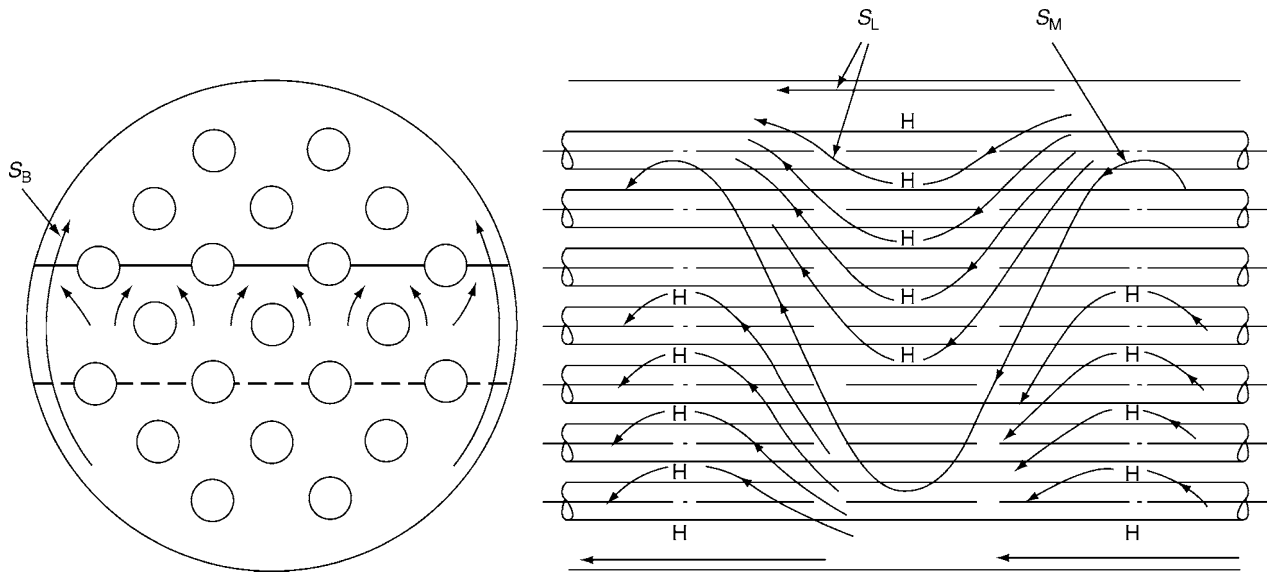

G8. Fig. 1. Fluid flow on the shell-side of a baffled shell-and-tube heat exchanger. S_M Main stream (partly across and partly parallel to the tubes). S_L Leakage stream. S_B Bypass stream.

3 Mean Shell-Side Heat Transfer Coefficient

3.1 Definition of Mean Shell-Side Heat Transfer Coefficient

Heat transfer between the shell-side flow and the outer surface of the tubes of a tube bundle in a baffled shell-and-tube heat exchanger is given by

$$\dot{Q} = \alpha A \Delta T_{LM}. \tag{1}$$

ΔT_{LM} in Eq. (1) is the logarithmic mean temperature difference. For a constant wall temperature boundary condition, the logarithmic mean temperature difference is calculated from the fluid inlet temperature T_{in}, the fluid outlet temperature T_{out}, and the wall temperature T_w by

$$\Delta T_{LM} = \frac{(T_{in} - T_w) - (T_{out} - T_w)}{\ln\left(\frac{T_{in} - T_w}{T_{out} - T_w}\right)} = \frac{T_{in} - T_{out}}{\ln\left(\frac{T_{in} - T_w}{T_{out} - T_w}\right)}. \tag{2}$$

Equations (1) and (2) define the mean shell-side heat transfer coefficient α.

3.2 Determination of Mean Shell-Side Heat Transfer Coefficient

The mean shell-side heat transfer coefficient α is calculated from dimensionless correlations determined experimentally. The dimensionless number that comprises the mean shell-side heat transfer coefficient is the mean shell-side Nusselt number defined by

$$Nu_{shell} = \frac{\alpha l}{\lambda}. \tag{3}$$

The characteristic length l in the mean shell-side Nusselt number in Eq. (3) is the length of a stream line over the tube surface (half tube circumference) and is given by

$$l = \frac{\pi}{2} d_o. \tag{4}$$

Equations for calculating the mean shell-side Nusselt number are presented hereafter. The mean shell-side heat transfer coefficient is thus calculated from

$$\alpha = \frac{Nu_{shell} \lambda}{l}. \tag{5}$$

4 Mean Shell-Side Nusselt Number

The mean shell-side Nusselt number Nu_{shell} of a baffled shell-and-tube heat exchanger can be calculated from the mean Nusselt number Nu_{bundle} of a tube bundle with a cross flow; its numerical value differs from that of the tube bundle because of the flow configuration on the shell-side. To allow for the deviations caused by this flow configuration, a correction factor f_W is introduced as follows:

$$Nu_{shell} = f_W Nu_{bundle}. \tag{6}$$

A procedure for calculating Nu_{bundle} is given hereafter (see also Chap. G7). Equations for calculating the correction factor f_W are presented in Sect. 4.3.3.

4.1 Mean Nusselt Number of a Tube Bundle

The mean Nusselt number Nu_{bundle} of a tube bundle under real operating conditions can be calculated from the mean Nusselt

number $Nu_{0,bundle}$ of an ideal tube bundle by introducing correction factors as follows:

$$Nu_{bundle} = f_N f_P Nu_{0,bundle}. \quad (7)$$

The correction factor f_N takes into consideration the influence of the number of tube rows in the tube bundle and the correction factor f_P the influence of the change in the physical properties of the fluid in the thermal boundary layer near the tube surface due to temperature changes during heating or cooling. A procedure for calculating $Nu_{0,bundle}$ is given hereafter. Equations for calculating f_N and f_P are given in Sects. 4.3.1 and 4.3.2 respectively.

4.2 Mean Nusselt Number of an Ideal Tube Bundle

An ideal tube bundle is defined arbitrarily as follows: Number of tube rows is $n_R \geq 10$, number of tubes per row is ≥ 10, ratio of tube length to tube diameter is ≥ 10, physical properties of fluid is independent of temperature, fluid velocity in the free cross section at the inlet of the tube bundle is uniform and perpendicular to the free cross section and smooth tube surface. Large deviations from the idealized situation can be accounted for by introducing correction factors. The Nusselt number $Nu_{0,bundle}$ of an ideal tube bundle is based on the procedure given in Chap. G7 and is calculated from

$$Nu_{0,bundle} = f_A Nu_{l,0} \quad (8)$$

with

$$Nu_{l,0} = 0.3 + \sqrt{Nu_{l,lam}^2 + Nu_{l,turb}^2}, \quad (9)$$

where

$$Nu_{l,lam} = 0.664 \sqrt{Re_{\psi,l}} \sqrt[3]{Pr} \quad (10)$$

and

$$Nu_{l,turb} = \frac{0.037 Re_{\psi,l}^{0.8} Pr}{1 + 2.443 Re_{\psi,l}^{-0.1} \left(Pr^{2/3} - 1\right)} \quad (11)$$

with

$$Re_{\psi,l} = \frac{wl}{\psi \nu} \quad \text{(Reynolds number)} \quad (12)$$

and

$$Pr = \frac{\nu}{a} \quad \text{(Prandtl number)}. \quad (13)$$

The characteristic length l in the Reynolds number in Eq. (12) is defined by Eq. (4) and the characteristic velocity w is given by

$$w = \frac{\dot{V}}{A_f}. \quad (14)$$

The cross sectional area A_f required to calculate the characteristic velocity w from the fluid flow rate $\dot{V}$ is calculated from

$$A_f = D_i S. \quad (15)$$

S is the baffle spacing assumed constant in all heat exchanger channels; if the baffle spacing of the end channels differs from that of the central channels see Sect. 4.4. According to Chap. G7, the void fraction ψ in Eq. (12) is a function of the transverse pitch ratio $a = s_1/d_o$ and the longitudinal pitch ratio $b = s_2/d_o$ and is given by

$$\psi = 1 - \frac{\pi}{4a} \quad \text{for } b \geq 1 \quad (16)$$

and

$$\psi = 1 - \frac{\pi}{4ab} \quad \text{for } b < 1 \quad (17)$$

The tube arrangement factor f_A in Eq. (8) is calculated from the following equations:
For in-line tube arrangement:

$$f_A = 1 + \frac{0.7((b/a) - 0.3)}{\psi^{1.5}((b/a) + 0.7)^2}. \quad (18)$$

For staggered tube arrangement:

$$f_A = 1 + \frac{2}{3b}. \quad (19)$$

The factor f_A for in-line and for staggered tube arrangements in dependence on a and b or on b respectively can also be evaluated from diagrams presented in Chap. G7. The ranges of the pitch ratios, which were examined for developing the above equations, are given in Chap. G7.

4.3 Correction Factors

Equations for evaluating the correction factors f_N, f_P, and f_W are given hereafter.

4.3.1 Correction Factor for Number of Tube Rows

A tube bundle in a cross flow with a number of tube rows n_R<10 has a mean Nusselt number, which differs from that for a tube bundle with $n_R \geq 10$. This is due to the fact that the fluid flow and the level of turbulence are not yet fully developed in the first few rows of the tube bundle. Equations for calculating the correction factor f_N in dependence on the number of tube rows are given in Chap. G7. However, the flow structure in the first few rows in a tube bundle between adjacent segmental baffles in a shell-and-tube heat exchanger with a large number of segmental baffles – because of the frequent change in the flow direction – differs from that in a tube bundle with a cross flow. For that reason, the correction factor f_N is ignored. Thus, in Eq. (7)

$$f_N = 1 \quad (20)$$

is substituted irrespective of the number of tube rows in the tube bundle.

4.3.2 Correction Factor for Temperature Dependence of Physical Properties

Heating or cooling the fluid through the tube bundle influences the fluid temperature in the thermal boundary layer near the

surface of the tubes. To account for the change in the physical properties of the fluid in that layer due to change of temperature a correction factor f_P is introduced as follows:
For heating of liquids $[(\mathrm{Pr}/\mathrm{Pr}_w) > 1]$:

$$f_P = \left(\frac{\mathrm{Pr}}{\mathrm{Pr}_w}\right)^{0.25}. \tag{21}$$

For cooling of liquids $[(\mathrm{Pr}/\mathrm{Pr}_w) < 1]$:

$$f_P = \left(\frac{\mathrm{Pr}}{\mathrm{Pr}_w}\right)^{0.11}. \tag{22}$$

For gases approximately:

$$f_P = \left(\frac{T_m}{T_w}\right)^{n_P}. \tag{23}$$

The exponent n_P in Eq. (23) depends on the type of gas used; very limited data about n_P are available in the literature ($n_P \approx 0$ for cooling of air and ≈ 0.12 for cooling of nitrogen; see Chap. G7).

To account for the change of the fluid temperature in the flow direction, the physical properties in the presented equations are to be evaluated at the mean fluid temperature T_m given by

$$T_m = \frac{T_{in} + T_{out}}{2}. \tag{24}$$

4.3.3 Correction Factor for Shell-Side Flow Configuration

The correction factor f_W for the shell-side flow configuration is formed as a multiplication of the geometry correction factor f_G, the leakage correction factor f_L, and the bypass correction factor f_B, or

$$f_W = f_G f_L f_B. \tag{25}$$

Equations for evaluating the correction factors f_G, f_L, and f_B are given hereafter.

Geometry Correction Factor

The geometry correction factor f_G takes in consideration the deviation of the mean Nusselt number for a baffled shell-and-tube heat exchanger from that of a real tube bundle described in Sect. 4.1. This deviation is due to the specific shell-side flow, which is partly across the tube bundle in the space between adjacent baffles and partly parallel to the tubes in the upper and lower windows (baffle cuts) of the heat exchanger. According to K. J. Bell, V. Gnielinski and E. S. Gaddis [1, 2], f_G can be calculated from

$$f_G = 1 - R_G + 0.524 R_G^{0.32}, \tag{26}$$

where

$$R_G = \frac{n_W}{n_T}. \tag{27}$$

In Eq. (27), n_W is the number of tubes in both upper and lower windows; tubes that lie on the edges of the baffles and are thus partly in the cross flow between the baffles and partly in the parallel flow in the windows count as half tubes. n_T is the total number of tubes in the heat exchanger. Figure 2 may be used to calculate the geometry correction factor f_G.

Leakage Correction Factor

The leakage correction factor f_L is calculated from

$$f_L = 0.4\frac{A_{GTB}}{A_{SG}} + \left(1 - 0.4\frac{A_{GTB}}{A_{SG}}\right)\exp(-1.5R_L), \tag{28}$$

where A_{SG} is the sum of the areas of all gaps between the tubes and the holes in a baffle and between the shell and a baffle, or

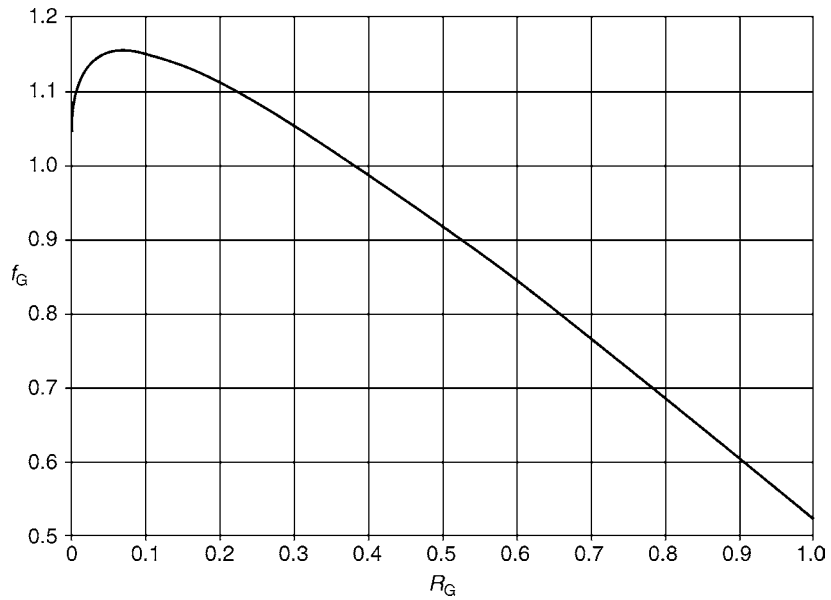

G8. Fig. 2. Geometry correction factor f_G as a function of the parameter R_G.

$$A_{SG} = A_{GTB} + A_{GSB}. \tag{29}$$

The area A_{GTB} of all gaps between the tubes and the holes in a baffle is given by

$$A_{GTB} = \left(n_T - \frac{n_W}{2}\right)\frac{\pi\left(d_B^2 - d_o^2\right)}{4} \tag{30}$$

and the area A_{GSB} of the gap between the shell and a baffle is given by

$$A_{GSB} = \frac{\pi}{4}\left(D_i^2 - D_1^2\right)\frac{360 - \gamma}{360}, \tag{31}$$

where γ is the central angle of a baffle cut (see Fig. 9) measured in degrees and is given by

$$\gamma = 2\cos^{-1}\left(1 - \frac{2H}{D_1}\right). \tag{32}$$

The ratio R_L is calculated from

$$R_L = \frac{A_{SG}}{A_E}, \tag{33}$$

where A_E is the area for the cross flow between two baffles measured in the row of tubes on or near the diameter of the shell that is parallel to the edge of the windows, or

$$A_E = SL_E. \tag{34}$$

L_E is the sum of the shortest connections e between adjacent tubes and e_1 between the outermost tubes in the bundle and the shell, measured in the row of tubes on or near the diameter of the shell that is parallel to the edge of the windows ($L_E = 2e_1 + \Sigma e$). Figure 3 illustrates the meaning of L_E, e and e_1; equations for the calculation of e for different tube bundle geometries are also given in the figure. The baffle spacing S is assumed constant, otherwise see Sect. 4.4. While the leakage streams that flow through the gaps between the tubes and the holes in the baffles contribute to heat transfer, the leakage streams that flow through the gaps between the shell and the baffles do not participate in heat transfer; therefore the gap area A_{GSB} should be kept as small as possible. Figure 4 may be used to calculate the leakage correction factor f_L.

Bypass Correction Factor

Bypass streams between the inner surface of the shell and the outermost tubes of the tube bundle do not participate effectively to heat transfer. Sealing strips – as shown in Fig. 5 – can be fixed in the tube bundle to reduce the level of bypass streams. This is particularly important in shell-and-tube heat exchangers with floating-heads, where the gaps responsible for the bypass streams are relatively large. The bypass correction factor f_B is given by

$$f_B = \exp\left[-\beta R_B\left(1 - \sqrt[3]{\frac{2n_S}{n_{MR}}}\right)\right] \quad \text{for } n_S \le \frac{n_{MR}}{2} \tag{35}$$

and

$$f_B = 1 \quad \text{for } n_S > \frac{n_{MR}}{2}, \tag{36}$$

where

$$\beta = 1.5 \text{ for laminar flow } (\mathrm{Re}_{\psi,1} < 100)$$

and

$$\beta = 1.35 \text{ for transition region and turbulent flow } (\mathrm{Re}_{\psi,1} \ge 100)$$

The ratio R_B is given by

$$R_B = \frac{A_B}{A_E}. \tag{37}$$

In Eq. (35), n_S is the number of pairs of sealing strips (in Fig. 5, $n_S = 2$) and n_{MR} is the number of main resistances in cross flow and thus the number of the shortest connections, which the flow

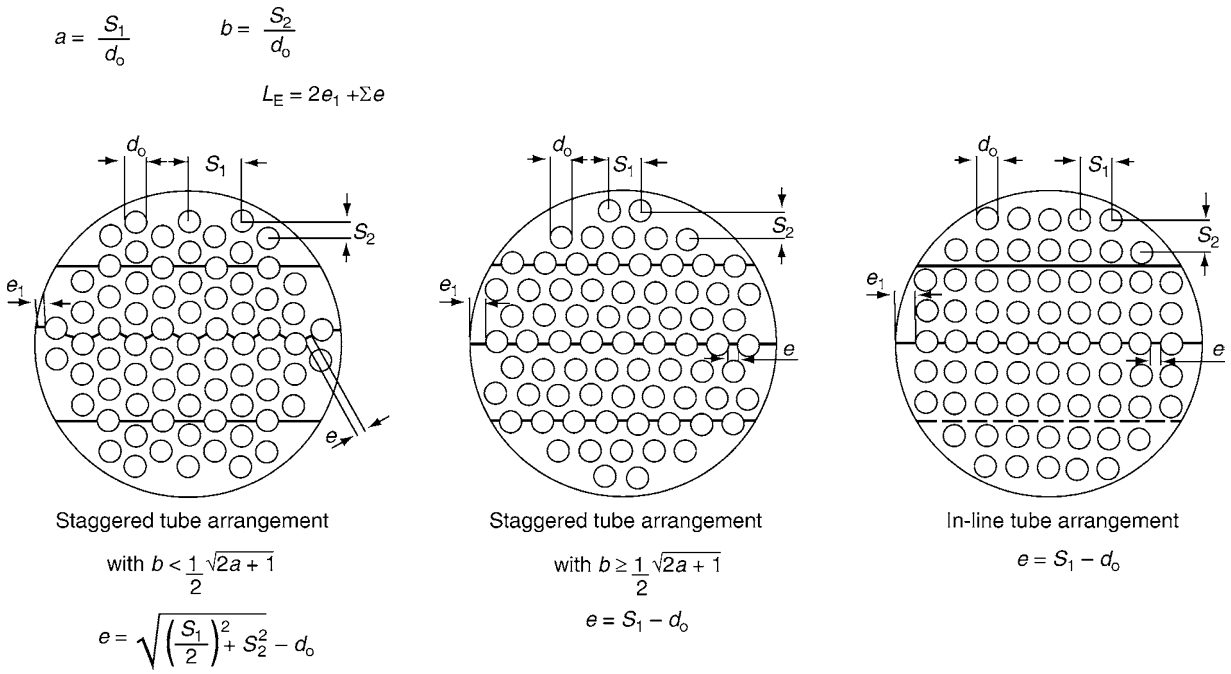

G8. Fig. 3. Illustration of the shortest connection L_E.

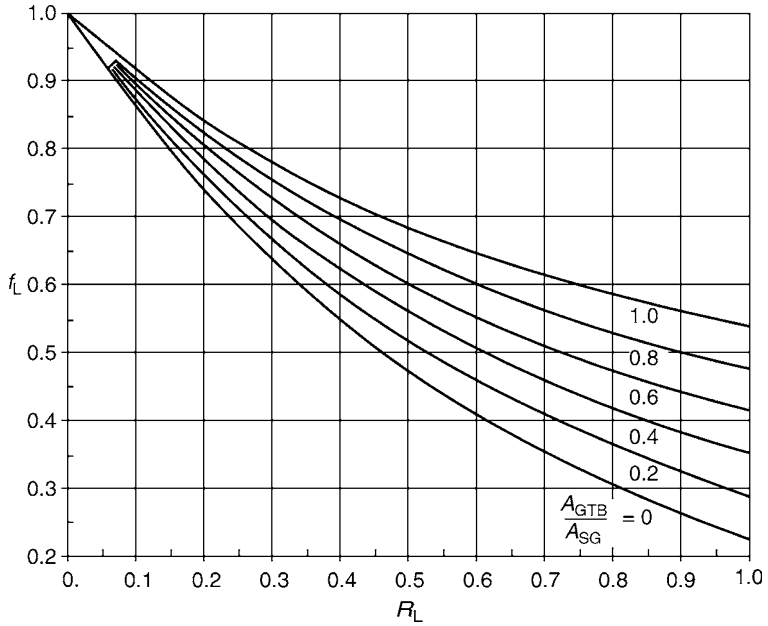

G8. Fig. 4. Leakage correction factor f_L as a function of R_L with the ratio A_{GTB}/A_{SG} as a parameter.

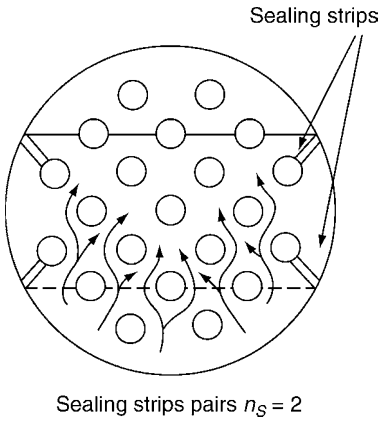

G8. Fig. 5. Reduction of bypass streams by means of sealing strips.

crosses on its way between the upper and the lower edges of adjacent baffles. Figure 6 illustrates the determination of n_{MR}. The area A_E in Eq. (37) is calculated from Eq. (34) and the area A_B is the cross sectional area that is responsible for the bypass streams and is given by

$$A_B = S(D_i - D_B - e) \text{ for } e < (D_i - D_B) \tag{38}$$

and

$$A_B = 0 \text{ for } e \geq (D_i - D_B). \tag{39}$$

The tube bundle diameter D_B is the diameter of a circle, which touches the outermost tubes in the space between the upper and lower edges of adjacent baffles (see Fig. 9). Figure 7 may be used to calculate the bypass correction factor f_B.

4.4 End Effects in Baffled Shell-and-Tube Heat Exchangers

In many cases, the dimensions of the heat exchanger nozzles necessitate larger inlet and outlet baffle spacing (spacing between heat exchanger sheets and first or last baffle) compared with the central baffle spacing. This leads to a different mean heat transfer coefficient in the end channels (inlet and outlet channels) compared with the central channels. The mean heat transfer coefficient α_E in the end channels and the mean heat transfer coefficient α_C in the central channels can be calculated separately from the previous equations using the baffle spacing S_E for the end channels and the baffle spacing S_C for the central channels. The mean heat transfer coefficient α for the whole heat exchanger can be calculated from

$$\alpha = \frac{2S_E\alpha_E + (L - 2S_E)\alpha_C}{L}, \tag{40}$$

where L is the total tube length. Other factors that influence the mean heat transfer coefficient in end channels are

- Velocity distribution at inlet of inlet channel and outlet of outlet channel dictated by the construction of the nozzles particularly the inlet nozzle
- Absence of parallel flow at inlet of inlet channel and at outlet of outlet channel
- Absence of leakage streams through the heat exchanger sheets

However, these deviations are relatively small in a baffled shell-and-tube heat exchanger with a large number of baffles ($L \gg 2S_E$).

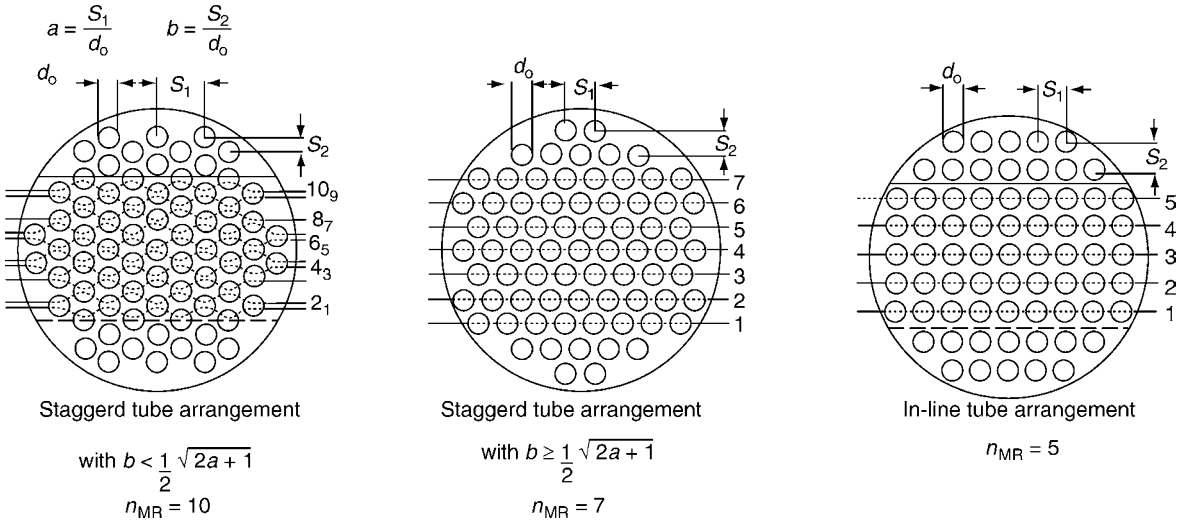

G8. Fig. 6. Determination of the number on main resistances n_{MR} in cross flow.

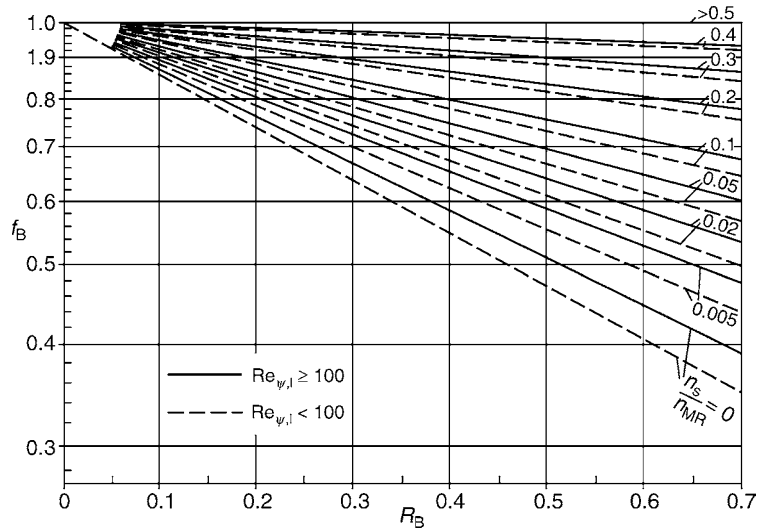

G8. Fig. 7. Bypass correction factor f_B in dependence on R_B and the ratio n_S/n_{MR}.

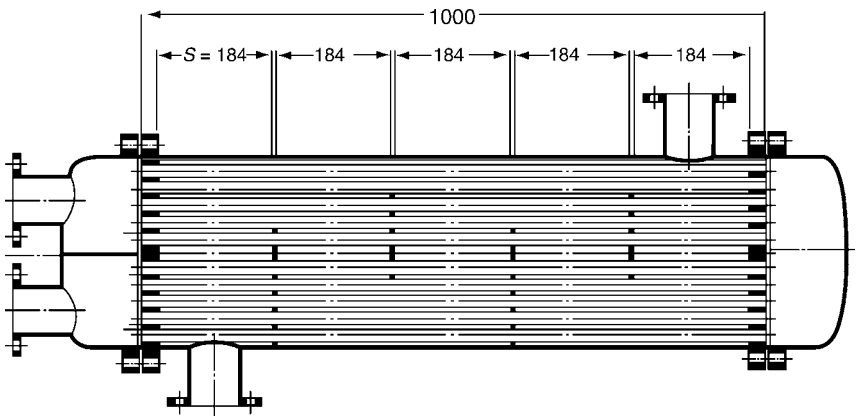

G8. Fig. 8. Longitudinal section of the heat exchanger in the example (dimensions in mm).

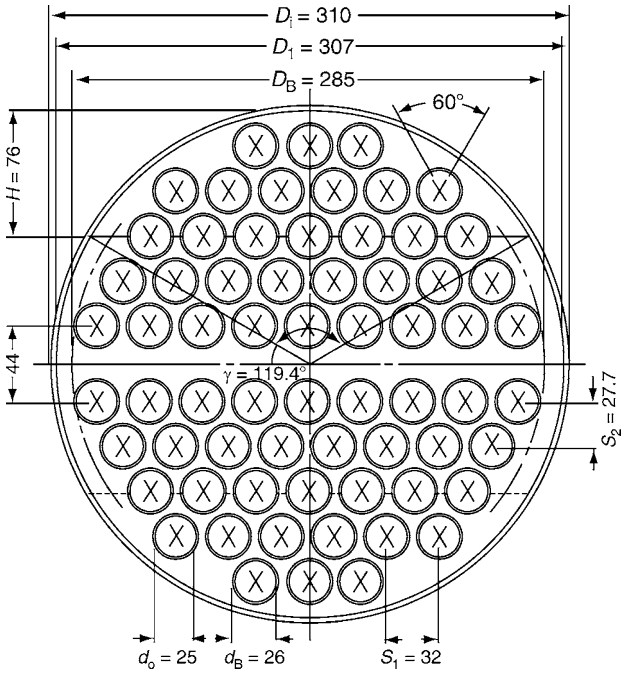

G8. Fig. 9. Cross-section of the heat exchanger in the example (dimensions in mm).

4.5 Limitations of the Proposed Calculation Procedure

A large number of experimental measurements obtained from shell-and-tube heat exchangers with segmental baffles and different geometries are available in the literature and were considered to check the calculation procedure presented in this chapter. The tested heat exchangers had staggered tube arrangement with different transverse and longitudinal pitch ratios as follows:

- Staggered square: with a pitch ratio $t/d_o = 1.2$, corresponding to a transverse pitch ratio $a = 1.697$ and a longitudinal pitch ratio $b = 0.849$
- Equilateral triangle: with pitch ratios in the range $1.2 \leq (t/d_o) \leq 2.2$ corresponding to transverse pitch ratios in the range $1.2 \leq a \leq 2.2$ and longitudinal pitch ratios in the range $1.039 \leq b \leq 1.905$, the ratio(b/a) is constant and is equal to 0.866

Measurements with in-line tube arrangement were not available.

The experimental measurements were made with different flow rates, different physical properties and during heating or cooling the shell-side fluid; the fluids used were water and oil with different viscosities. Measurements with gases were not available. The operating conditions during the experiments covered the following ranges:

- Reynolds number: $10 < \mathrm{Re}_{\psi,1} < 10^5$
- Prandtl number: $3 < \mathrm{Pr} < 10^3$

Measurements obtained at low Reynolds numbers ($\mathrm{Re}_{\psi,1} < 10^2$) with a high Prandtl number ($\mathrm{Pr} \approx 10^3$) showed high deviations between experimental measurements and theoretical predictions. In this range of operation, as well as with gases, care must be taken (i.e., higher factors of safety).

The above procedure of calculation is valid for heat exchangers with geometrical parameters that lie within the following ranges:

$$R_G \leq 0.8$$
$$R_L \leq 0.8$$
$$R_B \leq 0.5$$
$$0.2 \leq S/D_i \leq 1$$

Heat exchangers with geometrical ratios outside the above ranges, led to high deviations between experimental measurements and theoretical predictions. Also, heat exchanger geometries leading simultaneously to small numerical values of the correction factors f_G, f_L and f_B (i.e., a very small numerical value for f_W from Eq. (25)) showed high deviations. Thus, in addition to the above limitations, the calculation procedure should be used only for heat exchangers that have a correction factor for the shell-side flow configuration f_W, which lies within the following range:

$$f_W \geq 0.3.$$

5 Example

The shell-and-tube heat exchanger shown in Figs. 8 and 9 has two tube passes and four baffles with equal baffle spacing. Water with a volumetric flow rate of $\dot{V} = 20\ \mathrm{m^3\ h^{-1}}$ is cooled in the shell-side from an inlet temperature $T_{in} = 63.3\ ^\circ\mathrm{C}$ to an outlet temperature $T_{out} = 56.7\ ^\circ\mathrm{C}$. The wall temperature of the tubes is constant at $T_w = 50\ ^\circ\mathrm{C}$. The heat exchanger has the following geometrical data:

Shell inside diameter	$D_i = 310$ mm
Baffle diameter	$D_1 = 307$ mm
Tube bundle diameter	$D_B = 285$ mm
Outer diameter of tubes	$d_o = 25$ mm
Hole diameter in baffles to accommodate the tubes	$d_B = 26$ mm
Baffle cut	$H = 76$ mm
Total number of tubes	$n_T = 66$
Number of tubes in upper and lower windows	$n_W = 25$
(Tubes that lie on the edges of the baffles count as half tubes)	
Number of pairs of sealing strips	$n_S = 0$
Baffle spacing	$S = 184$ mm
Transverse pitch	$s_1 = 32$ mm
Longitudinal pitch	$s_2 = 27.7$ mm

Tube arrangement: staggered

Other dimensions are given in Figs. 8 and 9. It is required to calculate the mean shell-side heat transfer coefficient.

Solution:

Mean water temperature:

Equation (24): $T_m = \frac{T_{in}+T_{out}}{2} = \frac{63.3+56.7}{2} = 60\ ^\circ\mathrm{C}$

Physical properties of water:

At mean temperature $T_m = 60\ ^\circ\mathrm{C}$:

Kinematic viscosity $\nu = 0.471 \times 10^{-6}\ \mathrm{m^2\ s^{-1}}$

Thermal conductivity $\lambda = 654 \times 10^{-3}\ \mathrm{W\ m^{-1}\ K^{-1}}$

Prandtl number $\mathrm{Pr} = 2.96$

At wall temperature $T_w = 50\ ^\circ C$:

Prandtl number $Pr_w = 3.54$

Calculation of the mean Nusselt number $Nu_{0,bundle}$ for an ideal tube bundle:

$$a = \frac{s_1}{d_o} = \frac{32}{25} = 1.28$$

$$b = \frac{s_2}{d_o} = \frac{27.7}{25} = 1.11$$

Equation (16): $\psi = 1 - \frac{\pi}{4a} = 1 - \frac{\pi}{4\times 1.28} = 0.386$ (since $b > 1$)

Equation (4): $l = \frac{\pi}{2} d_o = \frac{\pi}{2} \times (25 \times 10^{-3}) = 0.03927$ m

Equation (15): $A_f = D_i S = (310 \times 10^{-3}) \times (184 \times 10^{-3}) = 0.05704\ m^2$

Equation (14): $w = \frac{\dot{V}}{A_f} = \frac{(20/3600)}{0.05704} = 0.0974\ m\ s^{-1}$

Equation (12): $Re_{\psi,l} = \frac{wl}{\psi\nu} = \frac{0.0974 \times 0.03927}{0.386 \times (0.471 \times 10^{-6})} = 21038$

Equation (10): $Nu_{l,lam} = 0.664\sqrt{Re_{\psi,l}}\sqrt[3]{Pr} = 0.664\sqrt{21038}\sqrt[3]{2.96} = 138.3$

Equation (11): $Nu_{l,turb} = \frac{0.037 Re_{\psi,l}^{0.8} Pr}{1 + 2.443 Re_{\psi,l}^{-0.1}(Pr^{2/3} - 1)} = \frac{0.037 \times 21038^{0.8} \times 2.96}{1 + 2.443 \times 21038^{-0.1}(2.96^{2/3} - 1)} = 160.7$

Equation (9): $Nu_{l,0} = 0.3 + \sqrt{Nu_{l,lam}^2 + Nu_{l,turb}^2} = 0.3 + \sqrt{138.3^2 + 160.7^2} = 212.3$

Calculation of the tube arrangement factor f_A:

Equation (19): $f_A = 1 + \frac{2}{3b} = 1 + \frac{2}{3\times 1.11} = 1.6$ (staggered tube arrangement)

Equation (8): $Nu_{0,bundle} = f_A Nu_{l,0} = 1.6 \times 212.3 = 339.7$

Calculation of the mean Nusselt number Nu_{bundle} (real tube bundle):

Calculation of the correction factor f_N for the number of tube rows:

The correction factor f_N is ignored (see Sect. 4.3.1), and therefore

Equation (20): $f_N = 1$ is used.

Calculation of the correction factor f_P for temperature dependence of physical properties:

Equation (22): $f_P = \left(\frac{Pr}{Pr_w}\right)^{0.11} = \left(\frac{2.96}{3.54}\right)^{0.11} = 0.981$ (cooling of liquid)

Equation (7): $Nu_{bundle} = f_N f_P Nu_{0,bundle} = 1.0 \times 0.981 \times 339.7 = 333.2$

Calculation of the mean shell-side Nusselt number Nu_{shell}:

Calculation of the geometry correction factor f_G:

Equation (27): $R_G = \frac{n_W}{n_T} = \frac{25}{66} = 0.379$

Equation (26): $f_G = 1 - R_G + 0.524 R_G^{0.32} = 1 - 0.379 + 0.524 \times 0.379^{0.32} = 1.005$

Calculation of the leakage correction factor f_L:

Equation (30): $A_{GTB} = \left(n_T - \frac{n_W}{2}\right)\frac{\pi\left(d_B^2 - d_o^2\right)}{4} = \left(66 - \frac{25}{2}\right)\frac{\pi(26^2 - 25^2)}{4} = 2143\ mm^2$

Equation (32): $\gamma = 2\cos^{-1}\left(1 - \frac{2H}{D_i}\right) = 2\cos^{-1}\left(1 - \frac{2\times 76}{307}\right) = 119.4^\circ$

Equation (31): $A_{GSB} = \frac{\pi}{4}\left(D_i^2 - D_l^2\right)\frac{360-\gamma}{360} = \frac{\pi}{4}(310^2 - 307^2)\frac{360-119.4}{360} = 972\ mm^2$

Equation (29): $A_{SG} = A_{GTB} + A_{GSB} = 2143 + 972 = 3115\ mm^2$

Calculation of the sum of the shortest connections L_E after Fig. 3:

Check: $b \geq \frac{1}{2}\sqrt{2a+1}$? $\rightarrow$ $1.11\text{mm} \geq \frac{1}{2}\sqrt{2\times 1.28 + 1} = 0.943\text{mm} \rightarrow$ yes

According to Fig. 3: $e = s_1 - d_o = 32 - 25 = 7$ mm

e_1 can be determined from the drawings; in this example e_1 can be calculated from the following equation:

$$e_1 = \frac{D_i - D_B}{2} = \frac{310 - 285}{2} = 12.5\ \text{mm}$$

According to Fig. 9: number of shortest connections e between the tubes in tube bundle = 8

$$L_E = 2e_1 + \Sigma e = 2 \times 12.5 + 8 \times 7 = 81\ \text{mm}$$

Equation (34): $A_E = SL_E = 184 \times 81 = 14904\ mm^2$

Equation (33): $R_L = \frac{A_{SG}}{A_E} = \frac{3115}{14904} = 0.209$

Equation (28): $f_L = 0.4\frac{A_{GTB}}{A_{SG}} + \left(1 - 0.4\frac{A_{GTB}}{A_{SG}}\right)\exp(-1.5R_L)$

$$= 0.4\frac{2143}{3115} + \left(1 - 0.4\frac{2143}{3115}\right)\exp(-1.5 \times 0.209)$$

$$= 0.805$$

Calculation of the bypass correction factor f_B:

$\frac{n_S}{n_{MR}} = 0$ (no sealing strips)

Check: $e(D_i - D_B)$? $\rightarrow$ [$e = 7$ mm, $(D_i - D_B) = (310 - 285) = 25$ mm] $\rightarrow$ yes

Equation (38): $A_B = S(D_i - D_B - e) = 184(310 - 285 - 7) = 3312\ mm^2$

Equation (37): $R_B = \frac{A_B}{A_E} = \frac{3312}{14904} = 0.222$

Check: $(Re_{\psi,1} \geq 100)$? $\rightarrow$ yes $\rightarrow \beta = 1.35$

Equation (35): $f_B = \exp\left[-\beta R_B\left(1 - \sqrt[3]{\frac{2n_S}{n_{MR}}}\right)\right] = \exp[-1.35 \times 0.222(1 - \sqrt[3]{2\times 0})] = 0.741$ (since $n_S < \frac{n_{MR}}{2}$)

Calculation of the factor f_W for shell-side flow configuration:

Equation (25): $f_W = f_G f_L f_B = 1.005 \times 0.805 \times 0.741 = 0.599$

The mean shell-side Nusselt number Nu_{shell} can be calculated from

Equation (6): $Nu_{shell} = f_W Nu_{bundle} = 0.599 \times 333.2 = 199.6$

Calculation of the mean shell-side heat transfer coefficient α:

Equation (5): $\alpha = \frac{Nu_{shell}\lambda}{l} = \frac{199.6\times 654\times 10^{-3}}{0.03927} = 3324\ W\ m^{-2}\ K^{-1}$

The procedure of evaluating the thermal performance on the shell-side of an existing shell-and-tube heat exchanger is based usually on the knowledge of the volumetric flow rate $\dot{V}$ of the shell-side fluid (or the mass flow rate), the fluid inlet temperature T_{in}, the wall temperature T_w and the total heat transfer area A as well as the other dimensions of the heat exchanger. The heat transfer calculations yield in this case the fluid outlet temperature T_{out}. On the other hand, dimensioning a new heat exchanger to fulfill the requirements of a particular process is based usually on the knowledge of $\dot{V}$, T_{in}, T_{out}, and T_w. The heat transfer calculations yield in this case the total heat transfer area A required to fulfill the process requirements on the shell-side. Moreover, in each case the wall temperature T_w can be determined only in conjunction with the thermal and fluid dynamic conditions of the fluid inside the heat exchanger tubes. In both cases (performance evaluation of an existing heat exchanger or dimensioning of a new heat exchanger for a particular job), one of the parameters used in the example (T_{out} or A) is not known a priori; it has to be assumed, checked,

and corrected if necessary. Thus, the calculations are based most probably on iteration. The given example represents only a single step in the iteration procedure.

6 Symbols

Latin Letters

A	Total surface ara of all tubes in a shell-and-tube head exchanger ($m^2(mm^2)$).
A_B	Area responsible for bypass streams (m^2 (mm^2))
A_E	Smallest area for cross flow between two baffles measured in the row of tubes on or near the diameter of the shell that is parallel to the edge of the baffles (m^2 (mm^2))
A_f	Cross sectional area defined by Eq. (15) (m^2 (mm^2))
A_{GSB}	Area of gap between the shell and a baffle (m^2 (mm^2))
A_{GTB}	Area of all gaps between the tubes and the holes in a baffle (m^2 (mm^2))
A_{SG}	sum of the areas of all gaps between the tubes and the holes in a baffle and between the shell and a baffle (m^2 (mm^2))
a	Thermal diffusivity (in the definition of Prandtl number, Eq. (13)) ($m^2\ s^{-1}$)
a	Transverse pitch ratio ($= s_1/d_o$) (l)
b	Longitudinal pitch ratio ($= s_2/d_o$) (l)
D_l	Baffle diameter (m (mm))
D_B	Tube bundle diameter (m (mm))
D_i	Shell inside diameter (m (mm))
d_B	Diameter of holes in baffles to accommodate the tubes (m (mm))
d_o	Outer diameter of tubes (m (mm))
e	Shortest connection between adjacent tubes in the same tube row or in adjacent tube rows (see Fig. 3) (m (mm))
e_1	Shortest connection between the outermost tube in the bundle and the shell measured in the tube row on or near the diameter of the shell that is parallel to the edge of the baffles (see Fig. 3) (m (mm))
f_A	Tube arrangement factor (l)
f_B	Bypass correction factor (l)
f_G	Geometry correction factor (l)
f_L	Leakage correction factor (l)
f_N	Correction factor for number of tube rows (l)
f_P	Correction factor for change in physical properties in the thermal boundary layer near the surface of the tubes (l)
f_W	Correction factor for shell-side flow configuration (l)
H	Height of baffle cut (m (mm))
L	Total length of heat exchanger tubes (m (mm))
L_E	Sum of the shortest connections e and e_1 measured in the row of tubes on or near the diameter of the shell that is parallel to the edge of the baffles (see Fig. 3) (m (mm))
l	Half circumference of tube (m (mm))
$Nu_{0,bundle}$	Mean Nusselt number of an ideal tube bundle (see Eq. (8)) (l)
Nu_{bundle}	Mean Nusselt number of a tube bundle under real operating conditions (see Eq. (7)) (l)
$Nu_{l,0}$	Mean Nusselt number for a single tube (l)
$Nu_{l,lam}$	Mean Nusselt number for a single tube with laminar flow (l)
$Nu_{l,turb}$	Mean Nusselt number for a single tube with turbulent flow (l)
Nu_{shell}	Mean shell-side Nusselt number ($= \alpha l/\lambda$) (l)
n_{MR}	Number of main resistances in cross flow between adjacent baffles (see Fig. 6) (l)
n_P	Exponent of temperature ratio in Eq. (23) (l)
n_R	Number of tube rows in cross flow in a tube bundle between adjacent baffles (l)
n_S	Number of pairs of sealing strips (l)
n_T	Total number of tubes in heat exchanger including blind and support tubes (l)
n_W	Number of tubes in both upper and lower windows (baffle cuts) (l)
Pr	Prandtl number ($= \nu/a$) (l)
Pr_w	Prandtl number at wall temperature T_w (l)
$\dot{Q}$	Heat flow rate between the shell-side fluid and the outer surface of the tubes (W)
R_B	Ratio A_B/A_E (see Eq. (37)) (l)
R_G	Ratio n_W/n_T (see Eq. (27)) (l)
R_L	Ratio A_{SG}/A_E (see Eq. (33)) (l)
$Re_{\psi,l}$	Reynolds number for a tube bundle ($= wl/\psi\nu$) (l)
S	Baffle spacing (in the case of same baffle spacing in all channels) (m (mm))
S_B	Bypass stream (see Fig. 1)
S_C	Baffle spacing in central channels (m (mm))
S_E	Baffle spacing in end channels (inlet and outlet channels) (m (mm))
S_L	Leakage stream (see Fig. 1)
S_M	Main stream (see Fig. 1)
s_1	Transverse pitch (m (mm))
s_2	Longitudinal pitch (m (mm))
T	Absolute temperature ($T = T + 273.1$) (K)
T_w	Absolute wall temperature ($T_w = T_w + 273.1$) (K)
t	Pitch for an equilateral triangle or a staggered square tube arrangement (m (mm))
w	Characteristic velocity in the definition of the Reynolds number ($m\ s^{-1}$)
$\dot{V}$	Fluid flow rate ($m^3\ s^{-1}$ ($m^3\ h^{-1}$))

Greek Letters

α	Mean shell-side heat transfer coefficient in heat exchanger ($W\ m^{-2}\ K^{-1}$)
α_C	Mean shell-side heat transfer coefficient in central channels ($W\ m^{-2}\ K^{-1}$)
α_E	Mean shell-side heat transfer coefficient in end channels (inlet and outlet channels) ($W\ m^{-2}\ K^{-1}$)
β	Constant in Eq. (35) (l)
γ	Central angle of a baffle cut (◦)
T	Fluid temperature (°C)

T_w	Wall temperature of tubes (°C)
ΔT_{LM}	Logarithmic mean temperature difference (°C)
λ	Thermal conductivity ($W\,m^{-1}\,K^{-1}$)
v	Kinematic viscosity ($m^2 s^{-1}$)
ψ	Void fraction (see Eqs.(16) and (17))(1)

Subscripts

in	At inlet
m	Mean value
out	At outlet

Notice: The units between brackets (mm, mm^2, and $m^3\,h^{-1}$) are not consistent with the M.K.S. units system; they are used in the example for convenience.

7 Bibliography

1. Bell KJ (1963) Final report of the cooperative research program on shell and tube heat exchangers. University of Delaware, Engineering Experimental Station, Bulletin No. 5, Newark, Delaware
2. Gnielinski V, Gaddis ES (1978) Berechnung des mittleren Wärmeübergangskoeffizienten im Außenraum von Rohrbündelwärmeaustauschern mit Segment-Umlenkblechen. vt verfahrenstechnik 12(4):211–217

G9 Fluid-Particle Heat Transfer in Flow Through Packed Beds of Solids

Volker Gnielinski
Karlsruher Institut für Technologie (KIT), Karlsruhe, Germany

1 Introduction

Heat transfer coefficients between particles and fluid in packed beds are one of the basic pieces of information needed for unit operations and chemical reactor design. Heat transfer is of interest, for example, in chemical reactors with fixed beds of catalysts in which large amounts of heat are absorbed or released, or in fixed beds used as regenerative heat exchangers. Particles of very different shapes, such as spheres, cylinders, Raschig rings or Berl saddles are used as packing material. Chap. G9 deals with the calculation of heat transfer coefficients between a fluid flowing through a packed bed and the particles of the packed bed.

2 Definition of the Heat Transfer Coefficient

The average coefficient of heat transfer between the solid particles in a bed and a fluid flowing through the bed is defined by

$$\dot{q} = \alpha \, \Delta T_{\mathrm{LM}}$$

The logarithmic mean temperature difference is given by

$$\Delta T_{\mathrm{LM}} = \frac{(T_{\mathrm{w}} - T_{\mathrm{in}}) - (T_{\mathrm{w}} - T_{\mathrm{out}})}{\ln \dfrac{T_{\mathrm{w}} - T_{\mathrm{in_i}}}{T_{\mathrm{w}} - T_{\mathrm{out}}}}$$

where T_{in} and T_{out} are respectively, the inlet and the outlet temperatures of the fluid and T_{w} is the wall temperature.

3 Determination of the Heat Transfer Coefficient

The coefficient of heat transfer between a fluid and the particles in a bed of solids through which it flows is greater than that for flow over individual particles of the same shape.

According to Gnielinski [1, 2], it can be predicted by means of a form factor f_{a} and a Nusselt number equation that applies for flow over a single sphere. Thus,

$$\mathrm{Nu} = f_{\mathrm{a}} \, \mathrm{Nu}_{\mathrm{sphere}} \tag{1}$$

where

$$\mathrm{Nu}_{\mathrm{sphere}} = 2 + \sqrt{\mathrm{Nu}_{\mathrm{lam}}^2 + \mathrm{Nu}_{\mathrm{turb}}^2} \tag{2}$$

$$\mathrm{Nu}_{\mathrm{lam}} = 0.664 \sqrt{\mathrm{Re}_\psi} \sqrt[3]{\mathrm{Pr}} \tag{3}$$

$$\mathrm{Nu}_{\mathrm{turb}} = \frac{0.037 \, \mathrm{Re}_\psi^{0.8} \, \mathrm{Pr}}{1 \times 2.443 \mathrm{Re}_\psi^{-0.1} (\mathrm{Pr}^{2/3} - 1)} \tag{4}$$

$$\mathrm{Nu} = \frac{\alpha \, d_{\mathrm{S}}}{\lambda} \tag{5}$$

$$\mathrm{Re}_\psi = \frac{w_{\mathrm{free}} \, d_{\mathrm{S}}}{\nu \, \psi} \tag{6}$$

$$\mathrm{Pr} = \frac{\nu}{a} \tag{7}$$

and

$$d_{\mathrm{S}} = \sqrt{\frac{A_{\mathrm{P}}}{\pi}} \tag{8}$$

The diameter of a sphere of the same area as that of a particle in the bed is determined from the geometrical area A_{P} of an individual particle with the aid of Eq. (8). The area A_{P} is calculated from the area per unit volume of the bed and the number of particles per unit volume. If the bed consists of spheres of the same diameter d, then $d_{\mathrm{S}} = d$.

w_{free} is the superficial velocity above the bed. The void fraction ψ is obtained from the volume V of the vessel containing the bed and the volume V_{F} of all particles in the bed, i.e.,

$$\psi = \frac{V - V_{\mathrm{F}}}{V} \tag{9}$$

The following numerical values can be inserted for the form factor f_{a}:

For a bed consisting of spheres of the same size,

$$f_{\mathrm{a}} = 1 + 1.5(1 - \psi) \tag{10}$$

VDI-GVC (ed.), *VDI Heat Atlas*, DOI 10.1007/978-3-540-77877-6_31,

for cylindrical particles with a length l to diameter d ratio of $0.24 < l/d < 1.2$,

$$f_a = 1.6 \tag{11}$$

for cubes,

$$f_a = 1.6 \tag{12}$$

for Raschig rings,

$$f_a = 2.1 \tag{13}$$

and for Berl saddles,

$$f_a = 2.3 \tag{14}$$

The values to be inserted for the physical properties of the fluid in Eqs. (5–7) must be referred to the mean temperature of the fluid, i.e., $T_m = (T_{in} + T_{out})/2$.

4 Validity and Other Methods for Calculation

The validity of Eq. (1) has been checked by heat and mass transfer measurements in the following ranges:

For beds of spherical particles,
$10^{-1} < \mathrm{Re}_\psi < 10^4$, and Pr or $Sc = 0.6 - 1000$;
for cylinders,
$10^2 < \mathrm{Re}_\psi < 10^4$, and Pr or $Sc = 0.6 - 1300$;
for cubes,
$10^2 < \mathrm{Re}_\psi < 10^4$, and $\mathrm{Pr} = 0.7$; and
for Berl saddles and Raschig rings,
$10^2 < \mathrm{Re}_\psi < 10^4$, and $Sc = 0.6$ and $Sc = 2.5$.

In the literature, the Nusselt numbers cited for packed beds and for Peclet numbers in the $\mathrm{Pe} = \mathrm{Re}_\psi \mathrm{Pr}$ range below 500–1000 are much less than the corresponding values obtained from Eq. (1): Many of these values have been collated by Kunii and Suzuki [3]. A mathematical model that has been suggested by Schlünder [4] was taken as a basis by Martin [5] to explain the difference between the experimental and calculated values in the light of flow irregularities that result from different void fractions in the packed bed.

The model is based on a packed bed that consists of particles of equal size and has an average void fraction of ψ. A larger void fraction is assumed for part of the cross section. Since both parts give rise to the same pressure drop, the fluid velocity is greater in the part of the bed with the larger void fraction. Hence the two parts of the bed have different NTUs. These differences are particularly pronounced if the Péclet numbers are small.

Equation (1) is valid for the coefficients of heat transfer between the particles and the fluid in both parts of the bed. However, the values that it yields are much higher than those obtained by combining the various values of NTU for the two components of the flow. The apparent Nusselt numbers thus determined are related in the same way as the measured values given in the list [3] to the Péclet number and the ratio of the particle diameter to the height of the bed.

5 Bibliography

1. Gnielinski V (1981) Equations for the calculation of heat and mass transfer during flow through stationary spherical packings at moderate and high Peclet numbers. Int Chem Eng 21(3):378–383
2. Gnielinski V (1982) Berechnung des Wärme- und Stoffaustauschs in durchstömten ruhenden Schüttungen. Verfahrenstechnik 16(1):36–39
3. Kunii D, Suzuki M (1967) Particle –to-fluid heat and mass transfer in packed beds of fine particles. Int J Heat Mass Transfer 10:840–852
4. Schlünder EU (1976) Über den Mechanismus der Stoffübertragung in Kontaktapparaten. Verfahrenstechnik 10(10):645–650
5. Martin H (1978) Low Peclet number particle-to fluid heat and mass transfer in packed beds. Chem Engn Sci 33:913–919

Boiling

Despite the large number of studies on boiling heat transfer, the prediction of heat transfer coefficients is still based on empirical or semiempirical methods. The reason is the lack of a coherent theory of the complex interactions of the various heat and mass transport processes on the various characteristic length scales involved in boiling heat transfer. The aim of Part H "Boiling" is to present and explain the state of the art of the empirical or semiempirical methods for pool boiling and flow boiling situation in Chaps. H2 and H3, respectively. The specific theoretical background which helps understanding and applying the methods is included in these sections, too. Any boiling process, pool or flow boiling, starts with the formation of individual bubbles. Important empirical parameters, e.g., active nucleation site density, are controlled by this basic process. Therefore, an introductory Chap. H1 on fundamentals of bubble formation is put infront.

Peter Stephan

H1 Fundamentals of Bubble Formation

Karl Stephan
Universität Stuttgart, Stuttgart, Germany

Heat transfer in boiling is more easily understood when we know how the vapor bubbles form on the hot surface.

The following considerations hold for the equilibrium of a vapor bubble, assumed to be spherical, Fig. 1, with the liquid surrounding it. Between the gaseous bubble (gas = index G) and the surrounding liquid (liquid = index L), *thermal equilibrium* exists

$$\vartheta_G = \vartheta_L = \vartheta\,. \tag{1}$$

If a surface element of the spherical shell is cut out of the vapor bubble, as depicted in the right side of Fig. 1, with side lengths $r\,\mathrm{d}\varphi$, the forces $\sigma r\,\mathrm{d}\varphi$ exerted by the surface tension σ (σ is force per unit length) act upon the edges. The resultant F_R of these forces is given by

$$\mathrm{d}^2F_R = 2\sigma r\,\mathrm{d}\varphi^2\,.$$

The forces resulting from the gas and liquid pressure are also of influence

$$p_L(r\,\mathrm{d}\varphi)^2 + \mathrm{d}^2F_R = p_G(r\,\mathrm{d}\varphi)^2\,.$$

From this, the condition of *mechanical equilibrium* follows

$$p_G = p_L + 2\sigma/r\,. \tag{2}$$

Finally, the condition for *equilibrium with respect to mass exchange* between the gaseous and liquid phase also holds. This leads, as illustrated, for instance, in [1], to

$$p_L = p_0 - \frac{\varrho'}{\varrho' - \varrho''}\,\frac{2\sigma}{r} \tag{3}$$

or with to

$$p_G = p_0 - \frac{\varrho'}{\varrho' - \varrho''}\,\frac{2\sigma}{r}\,. \tag{4}$$

Equation (3) or (4) is known as *Thomson's equation*. It produces a relationship between the vapor pressure $p_0(\vartheta)$ at a flat phase interface, the liquid pressure $p_L(\vartheta, r)$ and the vapor pressure $p_G(\vartheta, r)$ at the surface of a vapor bubble of radius r. These relationships are illustrated in Fig. 2. At a given temperature ϑ, the vapor pressure p_G, corresponding to (Subchap. H1.4), is smaller by

$$p_0 - p_G = \Delta p_G = \frac{\varrho''}{\Delta\varrho}\,\frac{2\sigma}{r} = \frac{\varrho''}{\varrho' - \varrho''}\,\frac{2\sigma}{r}\,,$$

than the vapor pressure p_0 at the flat phase boundary. As the surface tension σ is temperature dependent, the curves for the vapor pressure p_G and the liquid pressure p_L do not run exactly but only approximately parallel to the vapor pressure curve p_0 at the phase interface.

If, instead of stipulating the boiling temperature ϑ, the pressure p_0 of a liquid–vapor bubble system is given, then the liquid has to be superheated by $\Delta\vartheta = \vartheta - \vartheta_S$ in comparison to the system with a flat phase boundary, so that a vapor bubble of radius r is in equilibrium with the liquid, as shown in Fig. 2. In addition, it is clear that the required degree of superheating $\Delta\vartheta = \vartheta - \vartheta_S$ is larger, if the radius r of the vapor bubble is the smaller, therefore, for small radii $r^* < r$ the curves for the vapor pressure $p_G(\vartheta, r^*)$ and the liquid pressure $p_L(\vartheta, r^*)$ in Fig. 2 are shifted further to the right. Conversely, for a given degree of superheating $\Delta\vartheta$, a vapor bubble of definite radius r is in equilibrium with the superheated liquid. For the approximate calculation of the required superheating, we assume that the curves $p_0(\vartheta)$ and $p_L(\vartheta, r)$ in Fig. 2 run parallel. This gives

$$\frac{\mathrm{d}p_L}{\mathrm{d}\vartheta} = \frac{\mathrm{d}p_0}{\mathrm{d}\vartheta}\,. \tag{5}$$

The differential $dp_0/d\vartheta$ is the slope of the vapor pressure curve $p_0(\vartheta)$. It can be calculated from the Clausius-Clapeyron equation

$$\frac{\mathrm{d}p_0}{\mathrm{d}\vartheta} = \frac{\Delta h_v \varrho'' \varrho'}{T_s\,(\varrho' - \varrho'')}\,. \tag{6}$$

On the other hand, with (3)

$$\frac{\mathrm{d}p_L}{\mathrm{d}\vartheta} \cong \frac{p_0 - p_L}{\Delta\vartheta} \cong \frac{1}{\Delta\vartheta}\,\frac{\varrho'}{\varrho' - \varrho''}\,\frac{2\sigma}{r}\,. \tag{7}$$

From these equations, the bubble radius r is calculated as a function of the superheating $\Delta\vartheta = \vartheta - \vartheta_S$, to be approximately

$$r \cong \frac{2\sigma T_S}{\varrho'' \Delta h_v \Delta\vartheta}\,. \tag{8}$$

According to this, for a particular degree of liquid superheating $\Delta\vartheta$ a definite bubble radius exists, at which the bubble is in equilibrium with the liquid. Bubbles whose radii are $r^* < r$ are in equilibrium with the liquid only if the superheating is $\Delta\vartheta^* > \Delta\vartheta$, as shown in Fig. 2. A liquid superheated by $\Delta\vartheta$ is too cold. Therefore, bubbles that are too small will condense again. Bubbles of radius $r^* > r$ are in liquid that is superheated, and they can continue to grow. However, in reality the residence time of bubbles, in particular those close to the wall, is so small that equilibrium is never reached and the actual superheating of the fluid is many times greater than $\Delta\vartheta$. A particular critical bubble radius also belongs to this actual superheating. In boiling water at 1 bar, according to Eq. (8), the bubble diameter is $2r \cong 0.155$ mm, based on superheating in the core of the liquid by 0.4 K. A bubble of this size is then able to form and can grow. A bubble of this type contains around $3{\cdot}10^{20}$ water molecules. However, it is difficult for so many molecules with the high energy of vapor molecules to collect coincidentally at a certain position inside the liquid, form a bubble and then grow. This raises the question of how vapor bubbles are actually formed.

Observations have taught us that no bubbles form in a completely pure, carefully degassed liquid, unless the liquid is

VDI-GVC (ed.), *VDI Heat Atlas*, DOI 10.1007/978-3-540-77877-6_33,

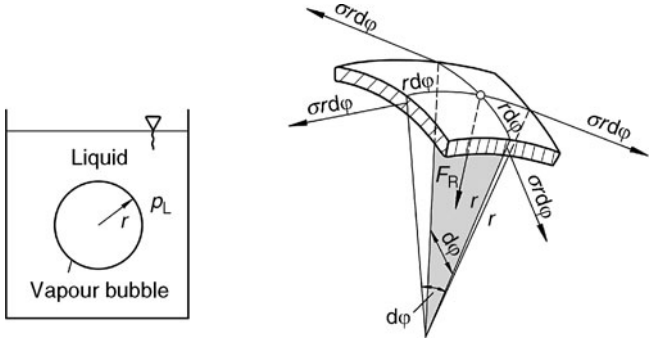

H1. Fig. 1. Mechanical Equilibrium between a spherical vapor bubble and the liquid surrounding it.

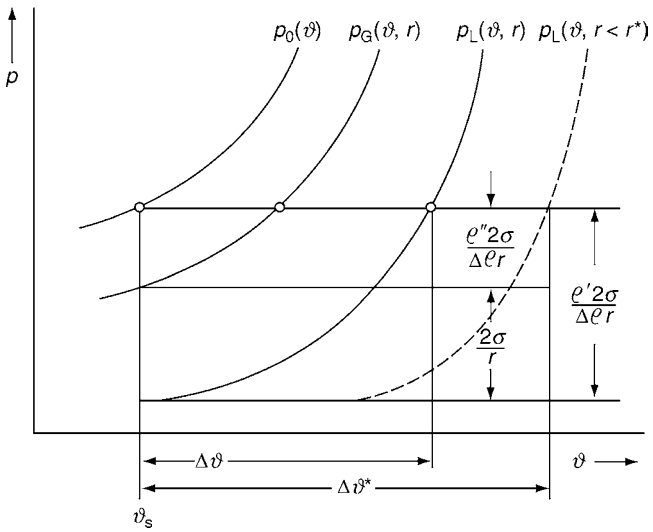

H1. Fig. 2. Vapor and liquid pressure between a liquid and a spherical vapor bubble.

extremely superheated or, for example, ionising beams are sent through it. Furthermore, over a long time, the bubbles reappear at the same place on the heated surface, with a varying frequency that can be approximated to an error function. Obviously, this has something to do with highly active centers that catalyze the transformation from unstable superheated liquid to stable vapor. These centres are the remains of gas or vapor in depressions in the surface that have not been driven out by the liquid, because even with good wetting ability it cannot completely fill the fine depressions on the surface. When heated, the gas or vapor remnants expand until a critical size is reached that corresponds to the size of a viable bubble. Then a vapor bubble can grow further as a result of the superheating of the fluid, until finally the adhesion force becomes smaller than the buoyancy and dynamic forces and the bubble detaches itself from the heated surface. After the bubble breaks off, further gas or vapor remains enclosed in the depression. This will be cooled by cold liquid flowing from the centre of the fluid to the wall, and then subsequently, by additionally heating from the wall. A new nucleus for the growth of a vapor bubble forms. These considerations explain why the surface structure is an influential quantity for heat transfer.

Vapor bubbles almost always develop at favourable positions on solid surfaces or on suspended particles. Therefore, it is generally *heterogeneous nuclei formation* that prevails. The *homogeneous nuclei formation*, with bubbles formed by "themselves" as a result of the natural fluctuations of the molecules, plays a very minor role.

Bibliography

1. Stephan, K. (1992) Heat transfer in condensation and boiling. Berlin: Springer, 127–128.

H2 Pool Boiling

Dieter Gorenflo[1] · *David Kenning*[2]
[1]Universität Paderborn, Paderborn, Germany
[2]Brunel and Oxford Universities, UK

1 Pool Boiling Regimes

In industrial applications, heat is transferred to a boiling liquid from heated walls or tube bundles in a boiler, as shown schematically in Fig. 1. The heat source may be a fluid, chemical, electric, or nuclear energy. The geometry of the heating elements varies widely. Much of the former data and all of the new material for the update of this chapter were derived from experiments with single, horizontal, copper cylinders with embedded electrical heating elements and thermocouples, immersed in a large pool of saturated liquid.

If the temperature T_w of such an element is raised to a value above the saturation temperature T_{sat} corresponding to the system pressure p, the relationship between the heat flux $q = Q/A$ and the temperature difference $\Delta T = T_w - T_{sat}$ will be similar to that shown in Fig. 2 [1–3].

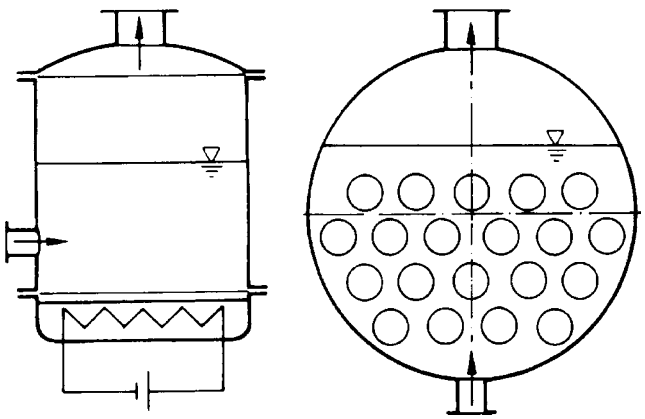

H2. Fig. 1. Evaporator in which the heated surfaces are flat walls, tube bundles, or assemblies of metal rods.

The diagram (Fig. 2a) on the left applies to an intermediate reduced pressure $p^* = p/p_c$ and (Fig. 2b) on the right to a reduced pressure close to the critical point. Both logarithmic diagrams include grids of straight lines corresponding to constant values of the surface coefficient of heat transfer α, which is defined by

$$q = \alpha \Delta T \tag{1}$$

It can be seen in Fig. 2a that for small increases in the temperature difference in free convection without bubble formation (line A–B), the increase in heat flux q is somewhat more than directly proportional to ΔT, that is, α increases with ΔT. At a certain temperature difference (point C), which depends on the pressure and the characteristics of the heating surface, vapor bubbles start to form at the heated surface, causing q to increase with increasing ΔT much more rapidly than in free convection, shown by the interpolation lines drawn between the data points indicated by solid dots in Fig. 2a and b. These lines are nearly straight in many cases, indicating a power-law relationship between q and ΔT (and α).

The pronounced nonlinear increase in q with ΔT is characteristic of heat transfer during nucleate boiling. Vapor bubbles are formed at gas or vapor filled cavities on technically rough heating surfaces, with radii r of a few microns, similar to the sizes of the cavities. Because of surface tension σ, the pressure inside a vapor nucleus of radius r must be higher than the pressure in the adjacent liquid by an amount given approximately by

$$\Delta p \sim 2\sigma / r. \tag{2}$$

This requires the liquid to be superheated by an amount that can be estimated from the slope of the equilibrium vapor pressure curve $(dp/dT)_{sat}$. When this superheat is exceeded, the vapor nucleus becomes unstable and grows by evaporation, with heat supplied from the superheated liquid and wall by several mechanisms that are discussed in [4] and in Chap. H1.

VDI-GVC (ed.), *VDI Heat Atlas*, DOI 10.1007/978-3-540-77877-6_34,

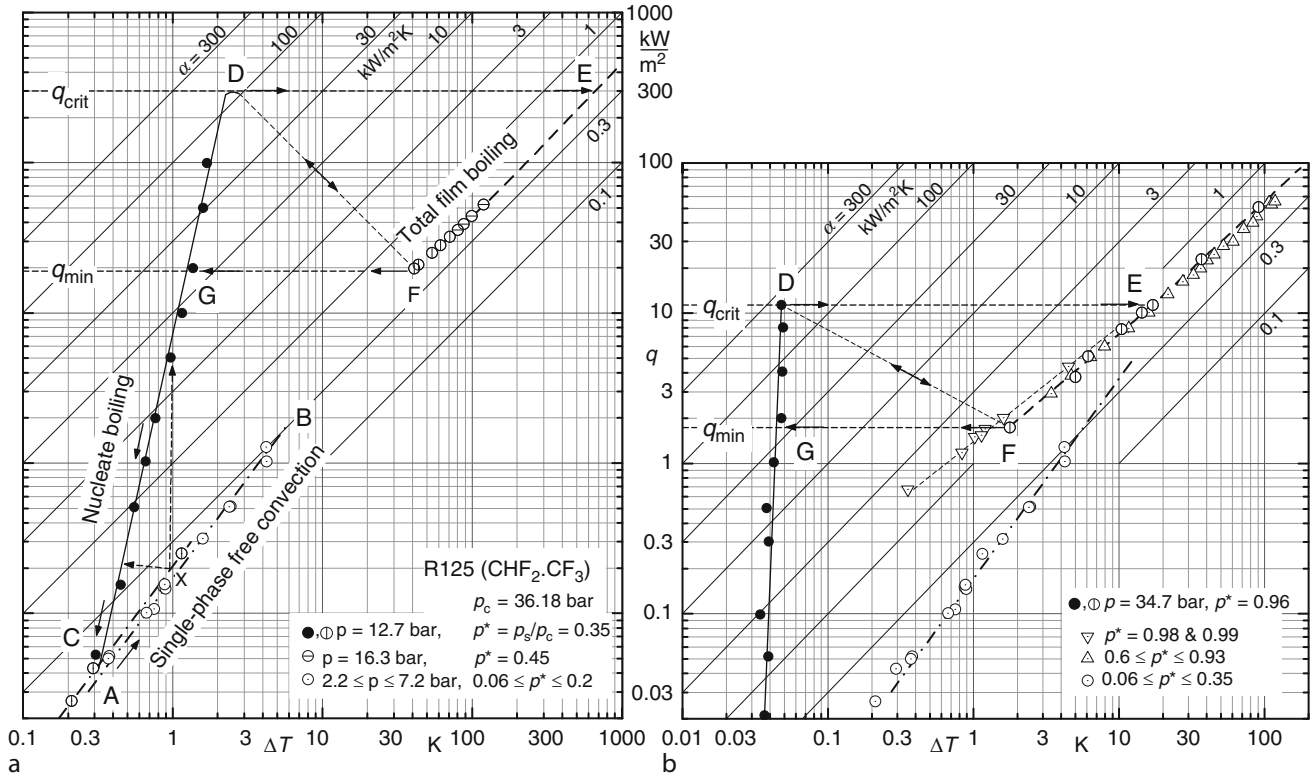

H2. Fig. 2. Heat flux q as a function of the temperature difference ΔT in nucleate and film boiling and in single-phase free convection. Fluid: Refrigerant R125 (CHF_2CF_3); heated surface: horizontal copper tube with 25 mm OD and sandblasted surface (according to [3], extended).

An increase in wall superheat activates an increasing number of smaller nucleation sites, leading to the nonlinear increase in q.

The number of active nucleation sites at a given ΔT also increases with a rise in the saturation pressure, because the surface tension σ decreases and the slope $(dp/dT)_{sat}$ increases. An example is given by comparing the continuous lines with solid dots in Fig. 2a and b, which present numerical values that are typical for many organic liquids. It can thus be seen that if the pressure is raised from 35% to 96% of the critical value, the temperature difference required to effect a given heat flux is reduced by an order of magnitude.

The activation of increasing numbers of nucleation sites by increases in wall superheat and/or system pressure can only occur if appropriate sizes of cavities are present on the heating surface. This depends on its microgeometry (roughness) and cleanliness. The examples in Fig. 2 are for a clean refrigerant boiling on a clean copper surface that had been sandblasted with fine corundum powder. The very steep increase of q with ΔT at near-critical pressure is caused by the activation of many tiny cavities of similar size and shape that release extremely small bubbles, as seen in the photographs in [3].

Nucleate boiling allows heat to be transferred at comparatively high rates by applying small temperature differences. However, there is a limit to the extent that the heat flux can thus be increased. The temperature difference ΔT at which this maximum (or critical) heat flux q_{crit} (point D in Fig. 2) occurs depends on the saturation pressure. In this regime of very intense nucleate boiling, a coherent film of vapor starts to form on parts of the heated surface, leading to a new regime of total film boiling when the surface is completely covered. There, the heat flux increases again with ΔT, at first with slightly decreasing heat transfer coefficient and then at a rate corresponding to a gradual increase in α, as in Fig. 2a at very high superheats, mainly as a result of growing turbulence in the film of vapor and the gradual increase in heat transfer by radiation. The absence of contact between the liquid and the heating surface reduces the influence of the surface properties, compared to nucleate boiling.

It is worth noting that the heat transfer coefficient and the maximum heat flux in nucleate boiling and the minimum heat flux in film boiling depend considerably on pressure, whereas heat transfer in total film boiling and in single-phase free convection is only slightly influenced by the pressure (and thus the temperature) in the saturated state. The only exception arises in the vicinity of the critical point, owing to the large changes in some properties with very small changes in temperature and pressure, illustrated by the fine dashed line for $p^* = 0.98$ and 0.99 in Fig. 2b with higher heat transfer coefficients than the bold dashed line for $p^* = 0.96$ and lower pressures.

The above is a somewhat simplified description of pool boiling that sets out some of the problems that have to be addressed in providing information for industrial design: nonlinearity between heat flux and temperature difference, dependence on fluid properties and pressure, dependence on surface properties that are difficult to define, and transitions between regimes with entirely different heat transfer characteristics.

These transitions are of potential importance in industrial applications because “hysteresis” occurs, dependent on whether the heat flux is increasing or decreasing and on the nature of the

heat source. Heating by the rapid flow of a fluid at a controlled inlet temperature approximates to controlling the temperature of the heating surface; heating by electrical or nuclear energy approximates to controlling the heat flux.

At first, the onset of nucleate boiling from single-phase free convection at a certain superheat is discussed that depends on the size of nucleation cavities available on the surface. With fluid heating, an attempt to increase the wall temperature activates more of the available sites, leading to an increase in the heat flux following the nearly vertical dashed line from point X in Fig. 2a. With electrical or nuclear heating, an attempt to increase the heat flux requires the activation of more sites, and this may result in a reduction in the wall temperature that in the limit follows the nearly horizontal dashed line starting from the same point X.

The particular path in both cases depends on hysteresis operating at the level of individual cavities, some of which may depend on "seeding" by vapor from bubbles formed at adjacent cavities, or may remain active at lower superheats than are required initially. Once the heat flux has been increased to a high value ("fully developed nucleate boiling"), all the available nucleation sites have been activated, and subsequent changes in q move up and down the line A–D in a repeatable manner. For this reason, data in the nucleate boiling region are conventionally reported for experimental conditions in which the heat flux is gradually reduced from a high value.

A different sort of hysteresis occurs in the transition between nucleate and film boiling. For fluid heating with a progressive change in wall temperature, there is a broad transition region D–F with patches of nucleate and film boiling on the heated surface. The point F of minimum heat flux and minimum wall temperature in total film boiling is called the Leidenfrost point. This transition is important during the cooldown of cryogenic systems, and during the metallurgical quenching of components with a large thermal capacity. For electrical or nuclear heating of systems with a low thermal capacity, the transition from nucleate boiling (point D) to film boiling (point E) following a small increase in heat flux (above q_{crit}) occurs rapidly, with the next stable equilibrium between heating element and boiling liquid occurring at very high superheat ("burnout"), if reduced pressures are not too high (Fig. 2a).

Transition back from film boiling to nucleate boiling with decreasing heat flux, however, occurs at a much lower minimum heat flux starting from the Leidenfrost point F and ending at G. Industrial systems employing electrical or nuclear heating are designed to avoid the hysteresis loop D–E–F–G. (More details on interactions between the characteristics of the heating element and the boiling liquid are given in fundamental studies by Stephan [5, 6] and in more recent publications [7, 8].)

So far, it has been assumed that the liquid pool is at the saturation temperature corresponding to the system pressure. This is a necessary condition at the free surface of the pool. The increased hydrostatic pressure below the free surface leads to slight subcooling ($T < T_{sat}$) of the liquid near the heater, which may have significant effects at pressures close to p_c. Substantial subcooling occurs at the start of heating a cold pool (without a free surface, or in contact with a gas) but is difficult to maintain unless there is a continuous supply of cold liquid to the vessel. For this reason, the effects of subcooling are discussed in Chap. H3 on "Flow Boiling."

2 Single-Phase Free Convection

Single-phase free convection without bubble formation may occur in regions of evaporators where the heating surface operates at small wall superheats or low heat fluxes below the onset of nucleate boiling, for example, in refrigeration, line A–B in Fig. 2a. The predictive equations are then those that are used generally for free convection (Fig. 3), with the heat transfer

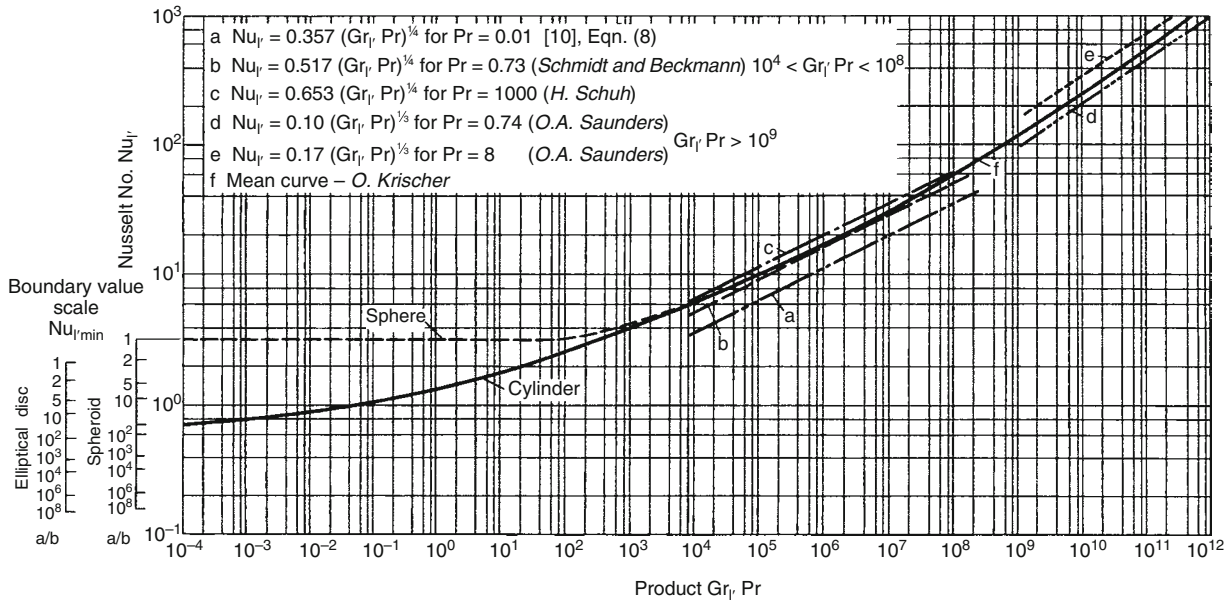

H2. Fig. 3. Experimental and theoretical results in free convection heat transfer around bodies of various geometries and Prandtl numbers [10]. (Taken from 3rd German ed. of VDI-Heat Atlas, 1977.)

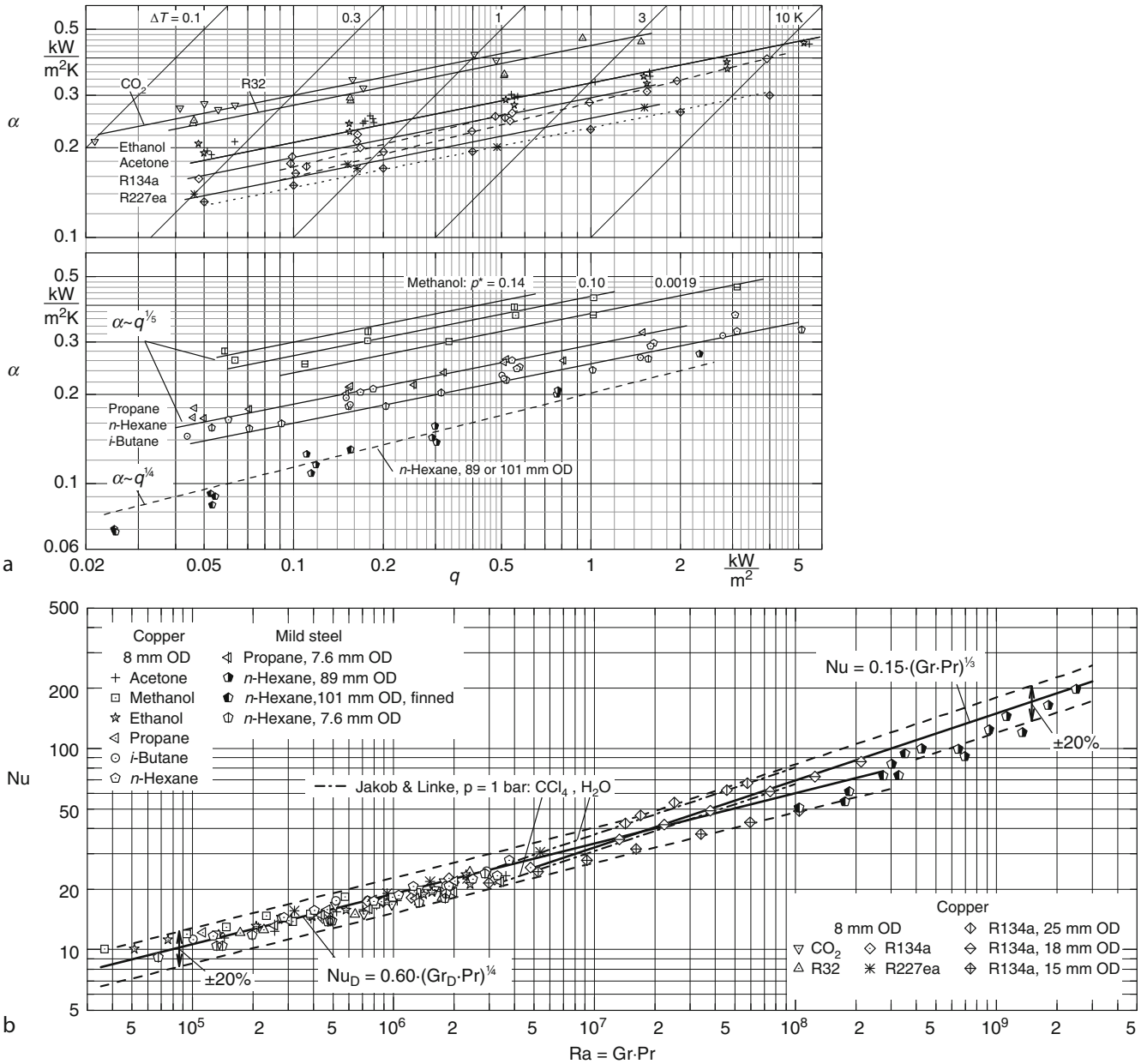

H2. Fig. 4. Single-phase free convective heat transfer without bubble formation from horizontal tubes with different diameters to various fluids (from [11–13, 15–20]). (**a**) Heat transfer coefficient as a function of the heat flux with the superheat ΔT as parameter; (**b**) Nusselt number as a function of the Rayleigh number. Dashed lines: error limits. Dot-dashed lines for water and tetrachloromethane according to Jakob and Linke [13].

coefficient α averaged over the surface, and the fluid properties evaluated for the saturated liquid state. These are for laminar or turbulent flow in the boundary

$$\mathrm{Nu_D} = 0.60(\mathrm{Gr_D\,Pr})^{1/4} \quad \text{(laminar)} \tag{3}$$

$$\mathrm{Nu} = 0.15(\mathrm{Gr\,Pr})^{1/3} \quad \text{(turbulent)}, \tag{4}$$

valid in both cases for Prandtl numbers lying in the range 2–100. The two equations predict the same Nusselt number Nu when the Rayleigh number Ra = product of Grashof number Gr and Prandtl number Pr is slightly less than 2×10^7, so the transition from turbulent to laminar flow probably occurs in the range $10^7 < \mathrm{GrPr} < 10^8$. The transition from laminar to turbulent flow may be shifted toward much higher values of GrPr in special cases in which laminar flow is favored by the geometry and finish of the heating surface.

In turbulent flow, the heat transfer coefficient is unaffected by the characteristic length scale, which has a weak effect in laminar flow. For horizontal cylinders, the diameter D is used for this length. It may also be the *Krischer* length of flow path [9] for other simple geometries, Fig. 3, which also shows the limiting values of Nu for small values of $\mathrm{GrPr} < 10^4$. The variation of ±20% between data is typical of the combined effect of experimental scatter and of accuracy to be expected from simple correlations for free convection. The relations between heat transfer coefficient α, heat flux q, and length scale D

corresponding to Eqs.(3) and (4) are laminar $\alpha \sim (q/D)^{1/5}$ (3a), turbulent $\alpha \sim q^{1/4}$ (4a).

The relationships are illustrated in Fig. 4a for ten saturated liquids at pressures ranging from less than 0.2% to more than 30% of the critical pressure, obtained during studies of pool boiling on horizontal cylinders with different diameters and of different materials since 1993 [11, 12, 15–20]. Lines of constant temperature difference ΔT have been plotted in Fig. 4a to indicate its magnitude in relation to q. The nondimensional plot of Nu vs. Ra = (GrPr) in Fig. 4b with D as characteristic length confirms that the data agree with Fig. 3 and Eqs.(3) and (4) to ±20%, ranging from laminar flow to above the laminar-turbulent transition.

In the laminar flow regime, it can be seen from the solid lines in Fig. 4a and b that the values of α for all the liquids vary only by a factor of 2 at a given q and $D = 8$ mm. For a particular fluid, for example, methanol (with by far the biggest variation in pressure), α decreases by only 20% as the pressure is reduced by a factor of 70.

The influence of diameter is illustrated in Fig. 4a for R134a, see key in Fig. 4b, on copper cylinders of diameter 8 mm (solid line), 15 mm with gold-plated surface [11] (dotted line), 18 and 25 mm (dashed lines). The 8 and 15 mm data follow the smaller slope characteristic of laminar flow, although the 15 mm data lie in the transition region. The values differ by a ratio slightly greater than predicted by Eq. (3), and the 15 mm data lie on the lower limit of the laminar correlation in Fig. 4b. The data for 18 and 25 mm follow the larger slope characteristic of turbulent flow, although they too lie in the broad transition region. The values of α are similar to those for the 8 mm cylinder in laminar flow.

The effect of much larger changes in D is illustrated in Fig. 4a by data for *n*-hexane on cylinders of diameter 7.6 mm (solid line, laminar flow) and 89 mm (dashed line, turbulent flow), showing that it is possible for α to be lower in turbulent flow on a large cylinder than in laminar flow on a small cylinder at the same heat flux. This example also includes data for a *finned* tube of external diameter 101 mm (root diameter 89 mm; fin spacing 5 mm), using the wetted area of the fins to calculate q. The data for the smooth and finned cylinders are then the same within experimental uncertainty. This confirms earlier findings for low-fin copper tubes of various geometries with fin heights of 1.5–3.5 mm, spacing 1.3–3.8 mm [2, 14], but may not hold for fin spacing below 1 mm.

From the above evidence, Eqs.3 and 4 may be used to predict to ±20% the heat transfer coefficients in single-phase free convection on horizontal cylinders with smooth and low-fin surfaces (including operation in the transition zone between laminar and turbulent flow), which frequently precedes (or follows) pool boiling. They may also be used to estimate heat transfer coefficients for other simple geometries.

3 Nucleate Boiling of Pure Substances

3.1 Summary of Calculation Method for α

Despite the large number of treatises that have appeared on the subject in the literature (see, e.g., recent review articles [4, 21–23]) no coherent theory yet exists that would allow heat transfer coefficients during nucleate boiling to be predicted from first principles to the accuracy required in engineering.

Thus, in the light of the current state of the art, only empirical or semiempirical correlations can be applied in practice. Their development has proved that it is expedient to treat separately the influence on α of the main groups of variables, that is, the properties of the liquids, the nature of the heated surfaces, and the operating parameters (namely, the heat flux q and pressure p). This concept has been applied to establish a reduced heat transfer coefficient α/α_0 of the form

$$\alpha/\alpha_0 = F_q F_{p^*} F_w \tag{5}$$

where α_0 is the heat transfer coefficient for a *specific* fluid at a reference state that is the same for *all* fluids, and the functins F are independent nondimensional functions applicable to *all* fluids (with a very small number of exceptions), representing the *relative* influences on α of the heat flux q, the reduced pressure p^* (caused by the change in fluid properties with p^*, see [17, 24, 25]), and wall properties. In previous editions of the *Heat Atlas*, it has been shown that experimental data for a large number of fluids are correlated successfully by this concept. The reference conditions are chosen to be typical mid-range values for fully developed nucleate boiling in industrial applications: $q_0 = 20$ kW/m^2 and $p_0^* = 0.1$. The reference state for the heater is defined as a copper cylinder with an intermediate value $R_{a0} = 0.4$ µm of the arithmetic mean roughness height of the surface (as defined in ISO 4287/1:1984), which lies within the range common for heater surfaces manufactured in practice.

The concept with respect to the variation of heat flux and pressure (in terms of reduced pressure) from the reference state is illustrated in Fig. 5 for *i*-butane boiling on a copper tube. The influences of the four independent parameters in Eq. (5) will be discussed in detail in Sects. 3.2, 3.3, and 3.4.

In this edition of the *Heat Atlas*, the functions F_q and F_{p*} have been updated using new experimental data. A new simple method for determining α_0 is presented and a more rational form of Eq. (5) is proposed, using the new concept of a reference fluid.

3.2 Effect of Heat Flux and Pressure

In Eq. (5), the terms

$$F(q) = (q/q_0)^n \tag{6}$$

and

$$F(p) = F(p^*) \tag{7}$$

express the relationships between the heat transfer coefficient α and the heat flux q at constant reduced pressure (see, e.g., α_1, α_2 or α_3, α_4 in Fig. 5) and between α and reduced pressure p^* at constant q (see, e.g., α_1 and α_4 in Fig. 5). The relations $\alpha(q)$ and $\alpha(p^*)$ in the fourth German edition of the *VDI-Heat Atlas* (1984) were adopted for the first English edition (1993), and had been established empirically from experiments for many fluids. The updated forms of the two relations have been developed using also the new experimental results of the past 20 years.

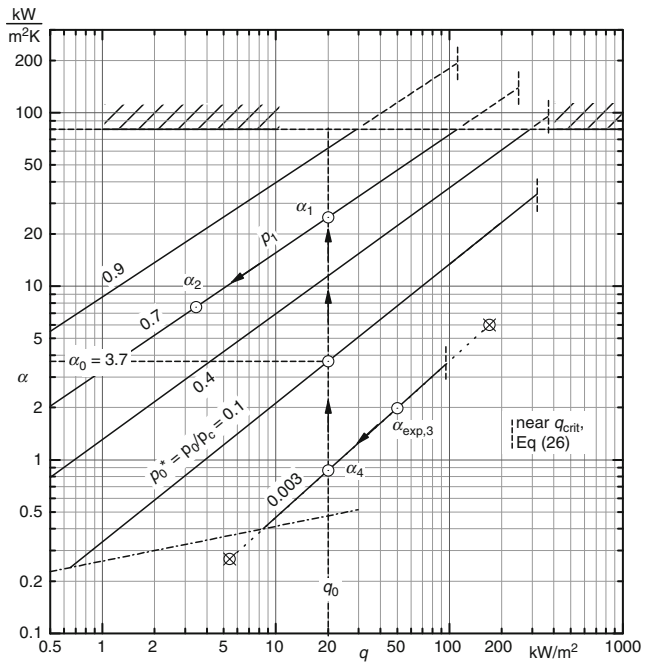

H2. Fig. 5. Conversion of measured or calculated heat transfer coefficients into the corresponding values at other pressures and heat fluxes taking *i*-butane boiling on a copper tube as an example. Dot-dashed line: single-phase free convection; vertical dashed lines: maximum heat flux q_{crit} in nucleate boiling; arrows indicating how α_2 can be calculated from α_0 or from $\alpha_{exp,3}$.

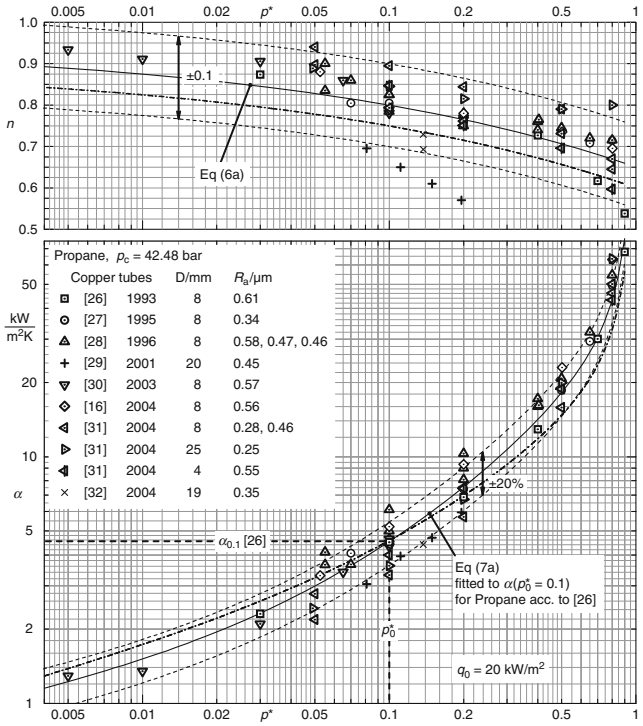

H2. Fig. 6. Heat transfer coefficient α and exponent n as functions of the reduced pressure p^* for propane. Example for the determination of the reference value, $\alpha_{0.1}$ for each individual source in Fig. 7, from measured values.

In Fig. 6, the update procedure is demonstrated for measurements of propane boiling on horizontal copper tubes with different diameters D and mean roughness heights R_a. Corresponding new data for other organic fluids are shown in Fig. 7 where the values $\alpha_{0.1}$ at $p_0^* = 0.1$, q_0, but $R_a = R_{a,exp}$ (to treat the sources as authentically as possible) had been interpolated for each fluid and roughness of the heated wall (e.g., $\alpha_{0.1}$ for [26] in Fig. 6) and were used to determine the *relative* pressure dependence of α in the lower diagrams, and the exponent n in the upper represents the slopes of the straight lines in loglog-plots of α over q as in Fig. 5.

The update results in somewhat steeper increases of α with q or p^*, respectively, as follows from comparing the dot-dashed lines for the former with the full lines for the new relations according to

$$n(p^*) = 0.95 - 0.3p^{*0.3} \tag{6a}$$

and

$$F(p^*) = 0.7p^{*0.2} + 4p^* + (1.4p^*)/(1 - p^*). \tag{7a}$$

As can be seen from Fig. 7, the dot-dashed lines from the former versions of Eqs. (6a) and (7a) remain within the experimental scatter of the new data and approach the upper border of the scatter for very small reduced pressures in the lower diagrams, while passing slightly beyond the lower border at very high reduced pressures.

No reliable new measurements have been found in the literature for cryogenic fluids so the former experimental results are shown in Figs. 8 and 9. The experimental scatter for these fluids is very high, as can be seen particularly from the big differences in α for nitrogen and helium at atmospheric pressure (N_2: circles at $p^* = 0.03$ in Fig. 8; He: all symbols at $p^* = 0.44$ in Fig. 9). On the one hand, this will be caused by the much greater difficulties for measurements at very low saturation temperatures; on the other, it is caused by using different heating elements (tubes, plates, wires) and wall materials (the question on whether it is permissible to apply results of measurements on thin wires is dealt with in the discussion of Fig. 12 in Sect. 3.5).

For these fluids, no update of the calculation method (Eqs. (6) and (7)) is given and the former equations shown in the diagrams should be applied. In the case of helium, the reference heat flux is $q_0 = 1$ kW/m^2 (lower diagram of Fig. 9) because nucleate boiling no longer exists at $q = 20$ kW/m^2 for this fluid, and furthermore, it cannot be decided if Eq. (6a) may be used, due to the very high experimental scatter in the upper diagram of Fig. 9.

For water, relationships $n(p^*)$ and $F(p^*)$ according to

$$n(p^*) = 0.9 - 0.3p^{*0.15} \tag{6b}$$

and

$$F(p^*) = 1.73p^{*0.27} + 6.1p^{*2} + \left(0.68p^{*2}\right)/\left(1 - p^{*2}\right) \tag{7b}$$

had been established from the former measurements (Fig. 10) that differed somewhat from those for the other fluids. As no new experimental results have been found to support an update for water, Eqs. (6b) and (7b) should continue to be applied. Suggestions of *Fritz* in the *VDI-Heat Atlas* of 1963 (dot-dashed lines in the upper and lower parts of Fig. 10) for both

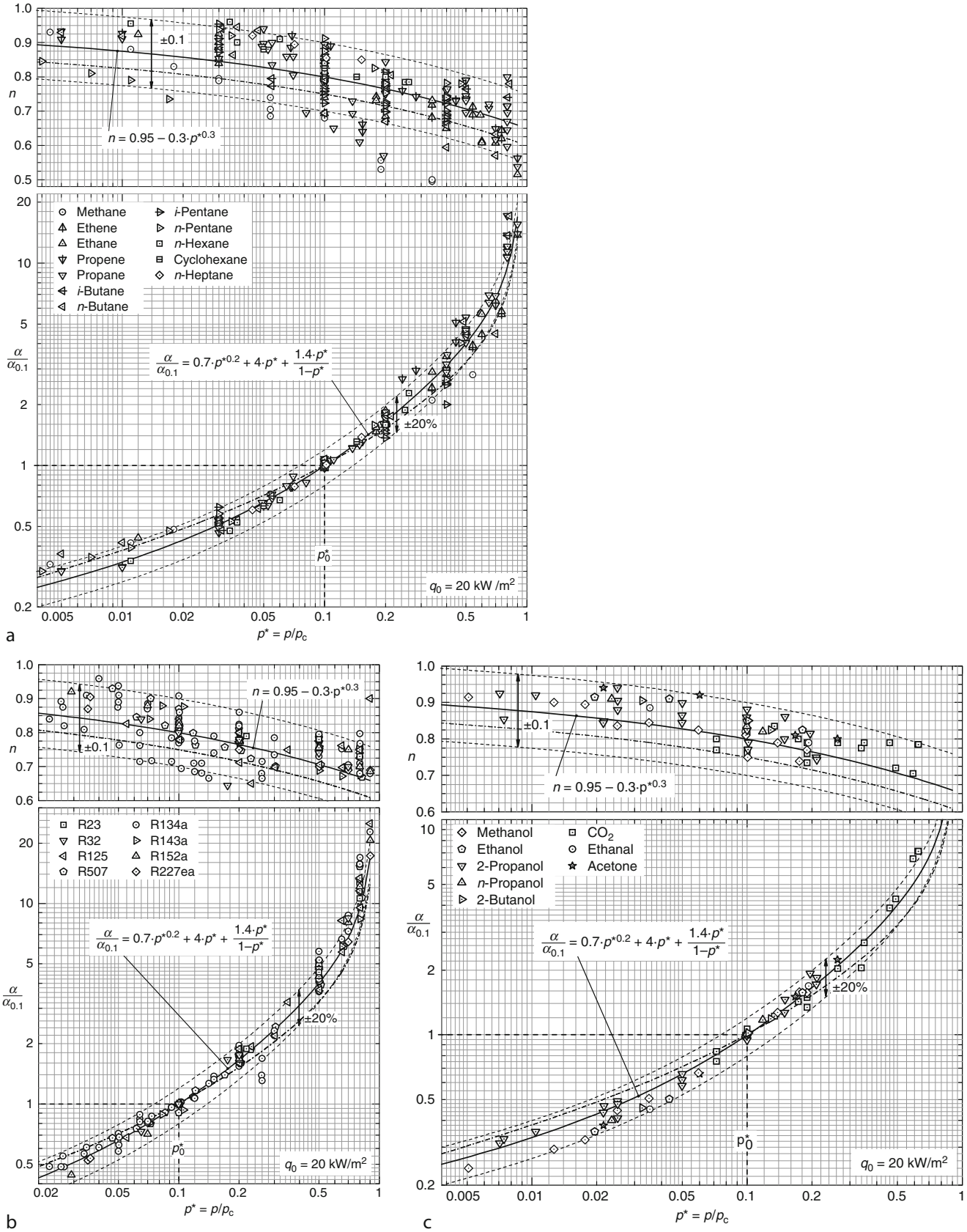

H2. Fig. 7. Pressure dependence of the exponent n and of α for nucleate boiling of three groups of fluids on single horizontal copper cylinders. Full curves according to Eqs. (6a) and (7a), dot-dashed curves from calculation method before the update. (**a**) (top, left): Hydrocarbons (from [17, 18, 26–39]). (**b**) (bottom, left): Partly fluorinated hydrocarbons = HFC-refrigerants (from [11, 15–18, 20, 31, 40–45]). (**c**) (bottom, right): Alcohols and other organic fluids (from [17–20, 31, 33, 46–49]).

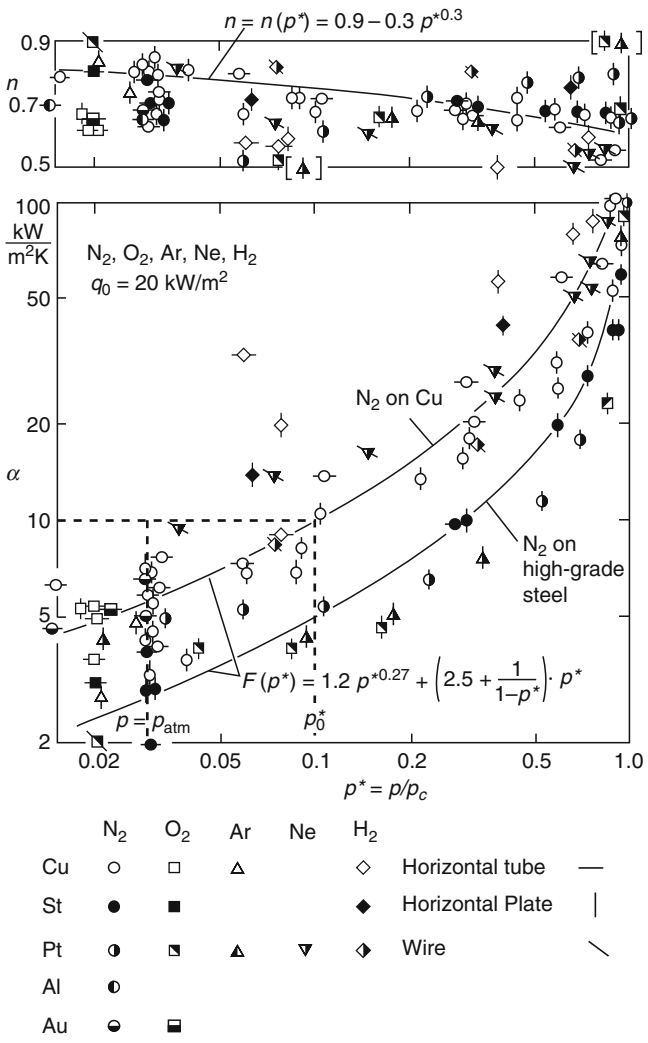

H2. Fig. 8. Heat transfer coefficient α and exponent *n* as functions of the reduced pressure *p** for cryogenic fluids taken from the former edition of the *Heat Atlas* (from [50–72]). The curves in both diagrams represent the former calculation method.

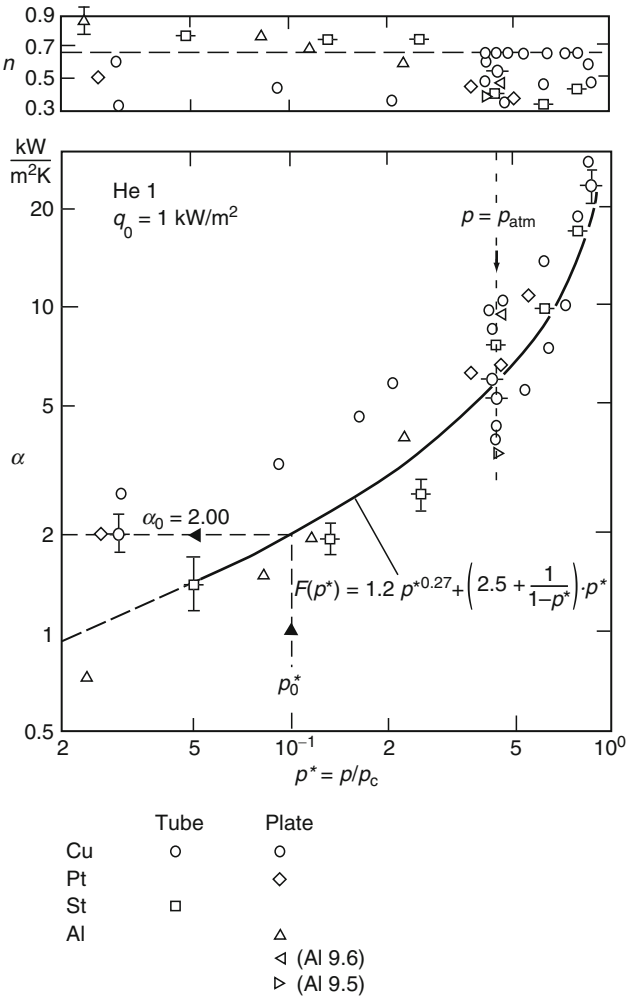

H2. Fig. 9. Heat transfer coefficient α and exponent *n* as functions of the reduced pressure *p** for helium taken from the former edition of the *Heat Atlas* (from [60, 63, 73–82]). The curve in the lower diagram represents the former calculation method.

relationships practically agree with Eqs. (6b) and (7b) within the limited pressure range previously investigated ($0.001 < p^* < 0.1$ or $0.22 < p < 22$ bar, respectively).

Comments on Eqs. (6) and (7):

A. The *upper limit* for the validity of Eqs. (6) and (7) is given by $p^* = 0.9$, because measured values for $p^* > 0.9$ are scanty and are also unreliable owing to the very small superheat of the wall surfaces at these pressures (cf. Fig. 2b). Another reason is that pressures of $p^* > 0.9$ are of little interest in practice at present. The *lower limit* recommended is an absolute pressure of $p = 0.1$ bar (the lowest line in Fig. 5 almost corresponds to this pressure), because nucleation at even lower pressures differs drastically from that at higher pressures; for instance, bubbles with diameters larger than 10 mm at the instant of detachment are often formed. An alternative update of Eq. (6) was proposed by Ribatski and Saiz Jabardo in 2003 [96] (see also [45]), based on their own measurements, by modifying the exponent of p^* from 0.3 to 0.2, instead of modifying the first term from 0.9 to 0.95 as

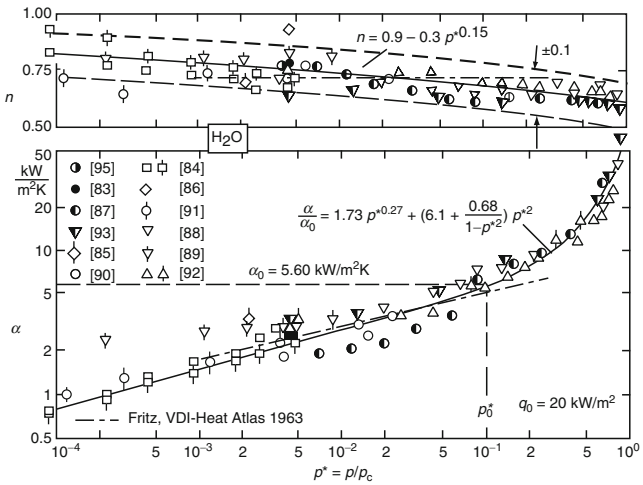

H2. Fig. 10. Heat transfer coefficient α and exponent *n* as functions of the reduced pressure *p** for water taken from the former edition of the *Heat Atlas* (from [83–95]). The curves in both diagrams represent the former (and new) calculation method for water according to Eqs. (6b) and (7b).

done in Eq. (6a). This results in almost the same n-values as in the former Eq. (6a) at the upper limit of $p^* = 0.9$ (with $n = 0.606$ updated from 0.609) and a somewhat larger change at the lower limit of approximately $p^* = 0.003$ ($n = 0.806$ updated from 0.847).

B. Straight lines for α at $p^* = \text{const.}$ as in Fig. 5 end in free convection without bubble formation (dot-dashed line) or at the maximum heat flux q_{crit} of nucleate boiling (dashed vertical lines in Fig. 5). Unlike the straight extrapolations to q_{crit} in Fig. 5, the slope n may decrease during the approach to q_{crit}. Evaporators are usually designed to operate at a heat flux well below q_{crit}. For operating conditions close to this limit, it would be advisable to verify the calculations by experiment.

C. The steep increase of α with p^* according to Eq. (7) also follows from Eq. (2) and the pressure dependencies of surface tension and slope of the vapor pressure cuve in a calculation model given in [17, 24, 25], which also implies that the exponent n is incorporated in F_p of Eq. (5), if this function is determined using properties of the fluid instead of the empirical function $F(p^*)$ given in Eq. (7). Furthermore, the $\alpha(q)$-increase according to Eq. (6) also depends on the distributions in size and spatial arrangement of the active nucleation sites, that is, on the roughness pattern of the heated surfaces [20, 45, 96, 97]. These interrelations between the $\alpha(q)$, $\alpha(p)$, and $\alpha(R_a)$ dependencies show that the assumption of *separate* influences of the various groups of parameters on α in Eq. (5) is only a first order approach.

3.3 Effect of the Properties of the Fluid

In the concept Eq. (5) is based upon, the influence of the properties of the fluid are (arbitrarily) separated in two parts, the one related to the variation of pressure is represented within F_{p*} or Eq. (7), respectively, and the other at the constant reduced reference pressure p_0^* is expressed by α_0 (Fig. 11). This latter part is presented in Table 1 in the form of the column for the updated experimental values $\alpha_{0,exp}$ from Figs. 6 and 7 (and pertaining references). When the experimental surface roughness $R_{a,exp}$ differed from the reference roughness R_{a0}, $\alpha_{0,1}$ of the figures was adjusted by means of Eq. (9), as discussed in Sect. 3.4. Superscript *d* denotes fluids for which experimental data are sparse; *f* denotes fluids without update. The experimental values from the *Heat Atlas* 1991/1993 are also tabulated, to show the effect of the update. While all new data are for copper tubes as heating elements, the data preceding the update were predominantly for tubes (and for copper as wall material) and a few other geometries (and materials).

In the two upper diagrams of Fig. 11, the updated and former values of $\alpha_{0,exp}$ are shown by large shaded and open circles respectively and the experimental results from the various new sources are shown by small open circles, plotted in logarithmic scales against the property ratio P_f. As can be seen, the data are correlated well by the power law

$$\alpha_{0,calc} = 3.58 P_f^{0.6}, \text{ with } P_f = (dp/dT)_{sat}/\sigma \qquad (8)$$

where $(dp/dT)_{sat}$ is the slope of the vapor pressure curve and σ is the surface tension, both at the reference pressure $p_0^* = 0.1$.

This representation, used first in [18], results from considerations in [24] (also discussed in [2, 17, 25]) and from former plots employing P_f in its reciprocal form [33, 97]). As can be seen from comparing the new averaged experimental heat transfer coefficients $\alpha_{0,exp}$ for each of the 28 updated fluids in the upper two diagrams of Fig. 11 and the pertaining values in Table 1 with $\alpha_{0,calc}$ determined from Eq. (8), the maximum deviation of the calculated, from any of the experimental values, is less than $\pm 9\%$ (except for ethene), with a mean deviation below $\pm 4\%$.

In Fig. 11 (third from the top), Eq. (8) is compared with the updated values for the 28 fluids above (closed symbols) and 26 not yet updated fluids of Table 1, together with water and ammonia, but without helium (open symbols). It follows that the mean deviation for all the fluids of Table 1, again excluding helium, rises to slightly below $\pm 10\%$, because the mean deviation of the 26 not updated fluids (excluding helium) is significantly higher, (below $\pm 15\%$, open circles).

As before the update, it is recommended that $\alpha_{0,exp}$ be used instead of $\alpha_{0,calc}$ for all fluids with reliable experimental values in Table 1 (without superscript *d* or *f*), particularly in those cases where the values calculated with Eq. (8) are higher than the experimental ones.

Because of the extended principle of corresponding states, the success of this correlation with a dimensional constant does not imply that $(dp/dT)_{sat}$ and σ are the only properties that would appear in a mechanistic model for α_0.

A further development of the correlation is to employ a reference fluid, together with the reference wall material, so that Eq. (8) may be written in the dimensionless form (see the diagram at the bottom of Fig. 11)

$$\alpha_0/\alpha_{0,ref} = \left(P_f/P_{f,ref}\right)^{0.6} \qquad (8a)$$

A suitable reference is a fictitious fluid with the intermediate experimental $\alpha_0(P_f)$-relation of Eq. (8) and the fluid parameter $P_f = 1\ (\mu m\ K)^{-1}$, which lies in the middle of the P_f-variation for the fluids important in practice ($0.5 < P_f < 2$) except for the cryogenics and liquid metals. Thus for this fluid boiling on a copper surface with the reference roughness, the fluid reference values are $\alpha_{0,ref}$ ($= \alpha_{0,exp}$) $= 3.58$ kW/m^{2}K, $P_{f,ref} = 1.000\ (\mu m\ K)^{-1}$. As can be seen from Table 1, also the three fluids *i*-butane, *n*-pentane, and R12 could be used as reference fluids because the calculated and experimental α_0-values for each of them are the same (and their P_f being in the intermediate range).

In a separate column of Table 1, values of $\alpha_{0,calc}$ have been determined using the former calculation method in which the Stephan/Preusser correlation [83] at $p^* = 0.03$ (near p_{atm}) and Eq. (7) are applied (using the new form of Eq. (7) and recent sources for the many properties of the fluids incorporated in the correlation). Also for this calculation method, the mean deviation from the experimental data is only slightly higher, but the new method in Eqs. (8) and (8a) has the advantage that it contains only two thermophysical properties of the fluids. It is up to the user to determine which of the two Eqs. (8) or (8a) to apply because the calculations result in the same values. Equation (8a) allows now to rewrite Eq. (5) in a more consistent way

$$\alpha/\alpha_{0,ref} = F_q F_{p*} F_f F_w \qquad (5a)$$

with $\alpha_{0,ref}$ being the fixed value given above (and included in Eq. (8)), and the influence of the fluid properties at p_0^*

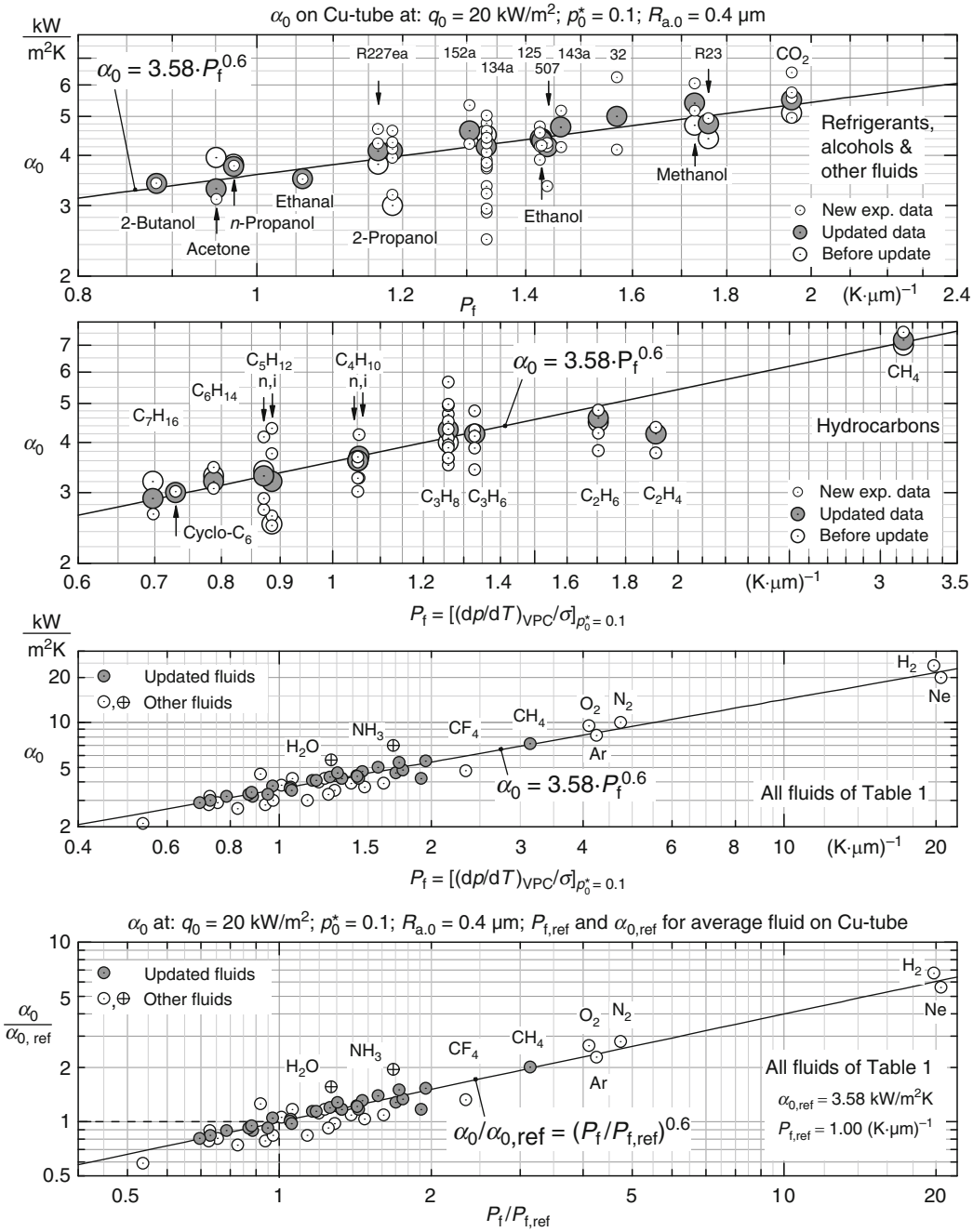

H2. Fig. 11. Heat transfer coefficient α_0 at the reference conditions as function of the property ratio P_f. Upper two diagrams: Comparison of Eq. (8) with the data for 28 fluids before and after the update (open or shaded big circles), together with the experimental data from the various new sources (small open circles). Lower two diagrams: Comparison of Eqs. (8) and (8a) with the updated values for the 28 fluids above (shaded circles) and the 28 other fluids of Table 1 (open circles), excluding helium.

being represented by F_f (or the right-hand side of Eq. (8a), respectively), in *relative* form as for the other three groups of parameters.

3.4 Effect of the Properties of the Heater

The quantitative effect exerted by the material of the heated wall and the texture of its surface on the heat transfer coefficient over a wide range of pressures in nucleate boiling is far less well understood than the three groups of effects discussed in Sects. 3.2 and 3.3 above (see, e.g.,[19, 20, 28, 45, 49, 98]. Consequently a method of general validity for the determination of the function F_W in Eq. (5) cannot be submitted.

In the following, the limited experimental evidence available at present is used to develop a preliminary method of representing separately the influences of the material of the heated wall and the roughness texture of its surface, thus

$$F_W = F_{WR} \cdot F_{WM}. \quad (9)$$

For this separation, it is essential to have an appropriate quantitative specification of the surface texture. It cannot be

H2. Table 1. Properties used in Eq. (8) and heat transfer coefficients α_0 for various fluids boiling on single horizontal copper tubes at $p_0^* = 0.1$, $q_0 = 20$ kW/m^2, $R_{a,0} = 0.4$ µm

Fluid	Formula	ASRHAE	Critical pressure	Data at $p_s = 0.1\ p_c$ [a]				α_0 in kW/(m^{2}K)			
								Heat Atlas 1991/1993		*Heat Atlas* update 2009	
			p_c [a] bar	T_s °C	σ mN/m	$\frac{dp}{dT}$ [b] kPa/K	$P_f = \frac{dp/dT}{\sigma}$ [c] [µm·K]$^{-1}$	$\alpha_{0,\,calc}$	$\alpha_{0,\,exp}$	$\alpha_{0,\,exp}$	$\alpha_{0,\,calc}$
Methane	CH_4		45.99	−139.3	8.286	26.039	3.142	8.95	7.00	7.20	7.13
Ethene	C_2H_4		50.42	−70.6	10.540	20.167	1.913	6.75	—	4.20	5.29
Ethane	C_2H_6		48.72	−53.4	10.600	18.064	1.704	5.78	4.50	4.60	4.94
Propene	C_3H_6		45.55	−8.1	10.905	14.504	1.330	4.90	—	4.20	4.25
Propane	C_3H_8		42.51	−3.5	10.595	13.361	1.261	4.44	4.00	4.30	4.12
n-Butane	C_4H_{10}		37.96	40.1	10.076	10.599	1.052	3.66	3.60	3.60	3.70
i-Butane	C_4H_{10}		36.29	26.2	8.972	9.459	1.054	3.57	—	3.70	3.70
n-Pentane	C_5H_{12}		33.70	76.6	10.003	8.713	0.871	3.30	3.40	3.30	3.30
i-Pentane	C_5H_{12}		33.78	67.9	9.962	8.822	0.886	3.26	2.50	3.20	3.33
n-Hexane	C_6H_{14}		30.34	108.3	9.419	7.416	0.787	3.13	3.30	3.20	3.11
Cyclohexane	C_6H_{12}		40.75	135.4	12.082	8.815	0.730	2.69	—	3.00	2.97
n-Heptane	C_7H_{16}		27.36	136.2	9.207	6.422	0.697	2.69	3.20[d]	2.90	2.89
Benzene	C_6H_6		48.94	141.6	13.790	10.430	0.756	3.03	—[e]	2.90[e,f]	3.03
Toluene	C_7H_8		41.26	168.7	11.718	8.499	0.725	3.21	—[e]	2.80[e,f]	2.96
Diphenyl	$C_{12}H_{10}$		38.47	327.0	11.475	6.159	0.537	2.25	2.10[d]	2.10[d,f]	2.47
Methanol	CH_3OH		82.16	129.1	12.680	21.923	1.729	5.14	—[e]	5.40	4.98
Ethanol	CH_3CH_2OH		61.31	132.4	11.940	17.048	1.428	4.28	4.40	4.35	4.44
n-Propanol	$CH_3CH_2CH_2OH$		50.50	148.5	13.824	13.435	0.972	3.44	3.80	3.75	3.52
i-Propanol	$CH_3CHOHCH_3$		47.60	128.0	12.584	14.912	1.185	3.24	3.00	4.10	3.97
n-Butanol	$CH_3CH_2CH_2CH_2OH$		44.10	170.0	12.492	11.185	0.895	2.86	2.60[d]	2.60[d,f]	3.35
i-Butanol	$CH_3CH_3CHCH_2OH$		42.95	154.4	12.291	11.286	0.918	3.26	4.50[d]	4.50[d,f]	3.41
2-Butanol	$CH_3CHOHCH_2CH_3$		41.94	143.5	13.055	11.519	0.882	2.96	—	3.40	3.33
Ethanal	CH_3CHO		55.50	78.2	13.013	13.780	1.059	—	—	3.50	3.71
Acetone	CH_3COCH_3		47.0	109.3	12.036	11.443	0.951	3.63	—[e]	3.30	3.48
Carbon dioxide	CO_2		73.77	−48.1	15.058	29.390	1.952	4.33[g]	5.10[d]	5.50	5.35
Trifluoromethane	CHF_3	R23	48.32	−49.8	11.183	19.673	1.759	5.41	4.40[d]	4.80	5.03
Difluoromethane	CH_2F_2	R32	57.82	−10.2	12.814	20.104	1.569	5.86	—	5.00	4.70
Pentafluoroethane	CHF_2CF_3	R125	36.18	−18.1	9.338	13.308	1.425	3.88	—	4.40	4.43
1,1,2-Tetrafluoroethane	CH_2FCF_3	R134a	40.59	9.4	10.226	13.630	1.333	3.92	4.50	4.20	4.26
1,1,1-Trifluoroethane	CH_3CF_3	R143a	37.61	−15.1	9.048	13.232	1.462	4.44	—	4.70	4.50
1,1-Difluoroethane	CH_3CHF_2	R152a	45.17	15.9	10.970	14.315	1.305	4.25	—	4.60	4.21
2,3,3,3-Tetrafluoroprop-1-ene	$H_2C{=}CFCF_3$	R1234yf	32.18	0.9	9.589	10.902	1.137	—	—	3.00[d,f]	3.87

H2. Table 1. (continued)

Fluid	Formula	ASRHAE	Critical pressure	Data at $p_s = 0.1\ p_c$[a]				α_0 in kW/(m²K)			
								Heat Atlas 1991/1993		*Heat Atlas* update 2009	
			p_c[a] bar	T_s °C	σ mN/m	$\frac{dp}{dT}$[b] kPa/K	$P_f = \frac{dp/dT}{\sigma}$[c] [µm·K]$^{-1}$	$\alpha_{0,\ calc}$	$\alpha_{0,\ exp}$	$\alpha_{0,\ exp}$	$\alpha_{0,\ calc}$
Heptafluoropropane	$CHF_2CF_2CF_3$	R227ea	29.25	11.3	8.555	9.956	1.164	3.10	3.80[d]	4.10	3.93
R125/R143a, azeotrope	R125/R143a	R507	37.05	−15.5	9.241	13.285	1.438	4.04	—	4.20	4.46
Cyclooctafluorobutane	C_4F_8	RC318	27.78	21.4	8.596	9.137	1.063	2.82	4.20	4.20[f]	3.72
Tetrafluoromethane	CF_4	R14	37.50	−106.3	8.272	19.391	2.344	5.00	4.75[d]	4.75[d,f]	5.98
1,1-Dichloro-2,2,2-trifluoroethane	$CHCl_2CF_3$	R123	36.62	68.9	10.174	9.895	0.973	2.89	—	3.00[d,f]	3.53
Fluorotrichloromethane	$CFCl_3$	R11	44.08	73.0	11.799	11.082	0.939	2.99	2.80	2.80[f]	3.45
Difluorodichloromethane	CF_2Cl_2	R12	41.36	9.3	10.546	12.644	1.199	3.64	4.00	4.00[f]	4.00
Trifluorochloromethane	CF_3Cl	R13	38.79	−52.0	9.373	15.099	1.611	4.34	3.90	3.90[f]	4.77
Trifluorobromomethane	CF_3Br	R13B1	39.70	−24.2	10.679	13.764	1.289	3.75	3.50	3.50[f]	4.17
Difluorochloromethane	CHF_2Cl	R22	49.90	0.1	11.688	16.237	1.389	4.34	3.90	3.90[f]	4.37
Trifluorotrichloroethane	$CF_2ClCFCl_2$	R113	33.92	89.6	10.249	8.489	0.828	2.42	2.65	2.65[f]	3.20
Tetrafluorodichloroethane	CF_2ClCF_2Cl	R114	32.57	38.7	9.361	9.472	1.012	2.89	3.80	3.80[f]	3.61
Pentafluorochloroethane	CF_2ClCF_3	R115	31.29	−10.4	8.722	10.747	1.232	3.32	4.20	4.20[f]	4.06
R22/R115, azeotrope	R22/R115	R502	40.17	−10.5	10.223	12.799	1.252	3.22	3.30	3.30[f]	4.10
Chloromethane	CH_3Cl		66.79	30.4	14.371	18.597	1.294	5.32	4.40	4.40[f]	4.18
Tetrachloromethane	CCl_4		45.60	137.0	13.179	9.615	0.730	2.58	—[e]	3.20[e,f]	2.97
Sulfur hexafluoride	SF_6		37.55	−37.5	9.547	14.104	1.477	2.65[g]	3.70	3.70[f]	4.53
Water	H_2O		220.64	217.4	33.670	42.694	1.268	5.99	5.60	5.60	4.13
Ammonia	NH_3		113.33	29.0	20.180	33.948	1.682	8.73	7.00	7.00	4.90
Oxygen	O_2		50.43	−164.2	8.635	35.492	4.110	8.82	9.50[d]	9.50[d,f]	8.37
Nitrogen	N_2		33.96	−183.8	6.233	29.559	4.743	9.64	10.0	10.0[f]	9.12
Argon	Ar		48.63	−167.7	8.152	34.663	4.252	8.33	8.20[d]	8.20[d,f]	8.54
Neon	Ne		26.79	−242.4	3.075	62.890	20.452	22.92	20.0[d]	20.0[d,f]	21.9
Hydrogen	H_2		12.96	−251.9	1.805	35.725	19.789	24.27	24.0[d]	24.0[d,f]	21.5
Helium	He		2.27	−270.2	0.217	34.978	161.537	2.01[h,i]	2.00[i]	2.00[i,f]	75.8[i]

While all new data are for copper tubes, data preceding the update had predominantly been for copper tubes.

[a]Sources used in this table: Refprop 8.0; VDI Heat Atlas; DIPPR database.

[b]For vapour pressure curve.

[c]Ratio of properties for calculating new α_0-values.

[d]Very few experimental data available.

[e]Very high scatter of experimental data.

[f]No update.

[g]Stephan/Preusser equation solved for pressure at Triple Point.

[h]Stephan/Preusser equation solved for pressure at $p^* = 0.3$ ($p = 0.68$ bar).

[i]Figures valid for $q = 1$ kW/m², as no pool boiling at 20 kW/m².

assumed that the same texture will be represented by the same value of a single roughness parameter, or that a particular surface treatment will result in the same texture for different wall materials. The influence of unknown differences in the roughness may be interpreted erroneously as part of the influence of the material.

Stephan [95] in 1963 found that $\alpha \propto R_a^{2/15}$, expressed here in terms of the reference roughness R_{a0}:

$$F_{WR} = (R_a/R_{a0})^{2/15}. \quad (9a)$$

Originally, a different parameter in the former German standard DIN 4762/1:1960 was chosen by Stephan because it could be related to the volume of vapor trapped in the roughness cavities of the heating surface. This relationship is not implied, however, in any of the parameters defined in the new standard ISO 4287/1:1984.

From comparative measurements on metal surfaces that had been finished in a variety of ways (drawn, turned, milled, emeried, and sandblasted), see [99] and former editions of the *VDI-Heat Atlas*, it was shown that a power law relationship exists between the former parameter and R_a that is valid over a large range of R_a-values $0.1 < R_a < 10$ µm, and that $R_{a,0} = 0.4$ µm is a representative value for metal surfaces, for which R_a generally lies in the range $0.2 < R_{a,m} < 0.6$ µm. Therefore, Eq. (9a) can be written in terms of R_a as has been done here, and the reference value chosen is $R_{a,0} = 0.4$ µm.

Subsequently, other correlations have been developed for $\alpha(R_a)$, either with a slight influence of the reduced pressure [100,101] but about the same *average* $\alpha(R_a)$-dependency as in Eq. (9a), or without the influence of p^* [45] but with a somewhat more pronounced increase of α with R_a. For the sake of simplicity and a "conservative" approach (because roughness will mostly be higher in industrial applications than for laboratory specimens), Eq. (9a) is recommended for use until the influences of surface texture are better understood.

Among the properties of the *wall material*, the effusivity $b = (\lambda\rho c)^{0.5}$, the square root of the product of thermal conductivity λ, density ρ, and specific heat capacity c is particularly important for the transient conduction of heat in the wall to the active nucleation sites on its surface. In Table 2, heat transfer coefficients are compared for five heaters with defined surface roughness and made of four different materials. From the data it can be concluded that the influence of the wall material may be represented very approximately by

$$\alpha \propto (\lambda\rho c)^{0.25} = b^{0.5} \text{ or } F_{WM} = (b/b_{Cu})^{0.5}, \quad (9b)$$

if the influence of the surface roughness has been eliminated by Eq. (9a) (in a similar approximation). The heaters are four tubes with different diameters and a thin wire, the wall materials are copper, mild steel St35.8, high-grade steel, and platinum. The fluids are propane and the refrigerant R134a boiling at $p_0{}^* = 0.1$, and the results for three heat fluxes are given (50, 20, and 5 kW/m^2).

All the experimental values in Table 2 were first converted to the same arithmetic mean roughness height $R_{a,0} = 0.4$ µm by

H2. Table 2. Approximate representation of the influence of the wall material (and surface roughness) on the heat transfer coefficient in Eq. (9) shown for experiments with horizontal heaters of different diameters and wall material as examples. Boiling liquids: Propane and R134a at $p^*_0 = 0.1$

Heater [Heating element]		Copper tube		Mild steel tube (St 35.8)		Stainless steel tube	Platinum wire		
Diameter D in mm		8.0		7.6	88.4	2.0	0.1		
Effusivity b in kWs$^{0.5}$/m^{2}K		35.35		13.4		7.73	15.9		
Arithmetic mean roughness height R_a in µm		0.47	0.59	0.20	0.18	0.78	0.06		
Fluid		Propane	R 134a	Propane		R 134a	Propane	R 134a	
Reference(s)		[97]	[102]	[103]		[104]	[105]	[104]	[106]
Heat transfer coefficient		kW/m^{2}K		kW/m^{2}K		kW/m^{2}K	kW/m^{2}K		
α_{exp} at $p^*_0 = 0.1$ and at three heat fluxes q = 50, 20, 5 kW/m^2:	50[a]	10.70	10.80	6.50	6.70	6.99	5.20	5.31	5.33
	20[a]	5.00	5.30	3.05	3.27	3.28	2.63	2.77	2.63
	5[a]	1.57	1.80	0.96	1.09	1.05	0.95	1.04	0.90
$\alpha_{0,4} = \alpha_{(R_{a0}=0.4)} = \alpha_{exp}\left(\frac{R_{a0}}{R_{a,exp}}\right)^{0.133}$	50	10.47	10.26	7.13	7.45	6.39	6.70	6.84	6.86
	20	4.89	5.03	3.35	3.64	3.00	3.39	3.57	3.39
	5	1.54	1.71	1.05	1.22	0.96	1.22	1.33	1.16
$(\alpha_{0.4})_j = (\alpha_{0.4})_{Cu}\left(\frac{b_j}{b_{Cu}}\right)^{0.5}$	50	$\alpha_{0,4}$	$\alpha_{0,4}$	6.46		4.80	7.03	6.88	
	20	$\alpha_{0,4}$	$\alpha_{0,4}$	3.02		2.35	3.29	3.28	
	5	$\alpha_{0,4}$	$\alpha_{0,4}$	0.95		0.80	1.03	1.15	
$\frac{\alpha_{0.4\,exp} - \alpha_{0.4\,calc}}{\alpha_{0.4\,exp}}$		%	%	%	%	%	%	%	
	50	0	0	9.4	13.4	25.0	−5.0	−0.6	−0.3
	20	0	0	9.8	17.0	21.6	3.0	5.3	0.3
	5	0	0	10.0	22.2	16.4	16.6	13.8	1.4

[a]Some of the values interpolated from experimental data for other heat fluxes, but uncertainty for this within experimental limits of error.

means of Eq. (9a) and then the α-values for the different metals were calculated using Eq. (9b) and the $\alpha_{0.4}$-data of the copper tube. As can be seen, the α-values calculated at the reference heat flux $q_0 = 20$ kW/m^2 are conservatively lower than the measured values by 0–20% and the same holds approximately for the two other heat fluxes – but only for *conversion* in the above direction, that is, *starting from copper*. Equation (9b) has been included in the German editions of the *Heat Atlas* since 1994.

In preceding editions of the *Heat Atlas*, average experimental α_0-values for stainless steel and platinum besides those for copper were also listed in Table 1 for the three cryogenic fluids oxygen, nitrogen, and argon boiling at $p_0^* = 0.1$ and $q_0 = 20$ kW/m^2. As no information about surface roughness was found at that time, the data were assigned to $R_{a,0} = 0.4$ µm. Also for these fluids, Eq. (9b) was used to convert the data for copper to the other metals, and the deviations remained within the limits given above, despite the additional uncertainty about the roughness (Table 3).

From the above, the function F_W in Eqs. (5) and (10) can be written as

$$F_W = (R_a/R_{a0})^{2/15}\left[(\lambda\rho c)/(\lambda\rho c)_{Cu}\right]^{0.25}. \qquad (9c)$$

The reference conditions are $R_{a,ref} = R_{a,0} = 0.4$ µm and $(\lambda\rho c)_{ref} = (\lambda\rho c)_{Cu}$. It is convenient to use copper as reference wall material because most of the data in the literature were measured with copper heaters. The geometrical characteristics of the wall, such as the diameter of horizontal tubes, do not appear in F_W. The data of Table 2, corrected for the influences of roughness and wall material by Eq. (9), verify the outcome of other recent investigations [20, 103, 107] that the diameter of the tubes, within a wide range of variation, has little influence on α at intermediate heat fluxes, if the average superheat of the circumference is used in the definition of α (Eq. (1)). This may also be seen already from the experimental values for the two tubes with $D = 7.6$ or 88.4 mm, with the same wall material and almost the same surface roughness (Table 2).

As follows from detailed examinations in [20], the effect of different heater diameters on nucleate boiling heat transfer mainly consists of convective influences of the bubbles, which slide along the heated surface and improve heat transfer with increasing heater diameter, particularly at small to intermediate heat fluxes and not too elevated reduced pressures, by providing additional vapor–liquid interface for evaporation near the heated surface. This may be incorporated in Eq. (6) in the future as more systematic evidence becomes available.

Comments (A, B) on Eq. (9a) and (C, D) on Eq. (9b):

A. There is experimental evidence that the single *mean* roughness parameter used in Eq. (9a) is not sufficient to determine the influence of surface roughness on the heat transfer coefficient in nucleate boiling. For instance, a few cavities with reentrant internal shapes that are particularly suited for trapping small amounts of vapor during bubble detachment will increase heat transfer at small heat fluxes (and not too elevated reduced pressures) without affecting the R_a-value of an otherwise very smooth surface. On the other hand, the great number of tiny cavities produced by sandblasting with fine grain will improve heat transfer at high heat fluxes and reduced pressures in comparison with a smooth emery-ground surface with the same small R_a-value.

B. For very rough surfaces (e.g., $R_a > 3$ to 5 µm), the increase of α with R_a according to Eq. (9a) may be found up to very high R_a-values of about 10 µm at high heat fluxes and is even more pronounced at lower fluxes [28] on surfaces that have been sandblasted with coarse steel particles of irregular shape, because tiny cavities are produced along with the large cavities that dominate R_a. By contrast, blasting with coarse glass beds, as in [45], will also result in large cavities and high R_a-values, but only a few small cavities with reentrant characteristics will be formed. Thus, the increase according to Eq. (9a) will exist only at the lowest q-values but vanish or change in the opposite direction at high heat fluxes [45].

It follows from (A) and (B) that more roughness parameters should enter Eq. (9a) to characterize the shape and size distribution of the cavities within the roughness texture, as Stephan has pointed out already in his pioneering work of 1963. Applying R_a with more fitting parameters (e.g., as in [28]) will not predict the behavior of surfaces differing from those fitted.

C. Equation (9b) should only be applied to convert heat transfer coefficients from copper to metals with lower effusivity

H2. Table 3. Equation (9b) applied to experimental data in former editions of the Heat Atlas for cryogenic liquids boiling on heaters made of different metals at $p^*_0 = 0.1$, $q_0 = 20$ kW/m^2

Material of heater		Copper			Platinum			Stainless steel
Effusivity b in kWs^{0,5}/m^2 K			35.35[a]			15.9		7.73[c]
Arithmetic mean roughness height R_a in µm			0.4[b]			0.4[b]		0.4[b]
Fluid		O_2	N_2	Ar	O_2	N_2	Ar	N_2
$\alpha_{0,4\ exp}$	in kW/m^{2}K	9.50	10.00	8.20	7.20	7.00	6.70	5.00
$\alpha_{0,4\ calc}$	in kW/m^{2}K	$= \alpha_{0,4\ exp}$	$= \alpha_{0,4\ exp}$	$= \alpha_{0,4\ exp}$	6.38	6.71	5.50	4.68
$\frac{\alpha_{exp} - \alpha_{calc}}{\alpha_{exp}}$	in %	0	0	0	11.3	4.1	17.8	6.5

[a] Material properties of copper assumed as included in Table 2.
[b] $R_a = R_{a,0} = 0.4$ µm assumed as no data on roughness available.
[c] Properties of high-grade steel as in Table 2 applied. Using properties of two common qualities of high-grade steel, as given in Part D of the *Heat Atlas*, would reduce deviation from 6.5 to 4.2% or −1.5%.

because the positive deviations in Tables 2 and 3 indicate that its influence may be overestimated somewhat. Its use for conversion in the opposite direction would result in nonconservative overprediction of the heat transfer coefficient on a copper surface.

D. Special care has to be taken when using Eq. (9b) for metal alloys. The examples in Tables 2 and 3 indicate that the prediction is no worse than for pure metals. However, it should not be used without experimental verification for alloys that contain components with highly different thermal conductivity (or effusivity), as is the case for CuNi10 or different grades of brass (Cu with 20–40% Zn). For all these copper alloys, heat transfer coefficients no smaller than for copper have been found in some reliable measurements [31, 35, 37, 45]. Variations in properties on a crystalline microscale may influence transient conduction processes between closely spaced nucleation sites. Another weakness of Eq. (9b) is that at present it does not consider the wetting properties of the system metal – fluid at the fluid-solid boundary.

3.5 Effect of Industrial Scale Evaporators

Including the effects discussed above, Eq. (5) can be rearranged to give

$$\alpha/\alpha_{0,\mathrm{ref}} = (q/q_0)^{n(p^*)} F(p^*) \left(P_f/P_{f,\mathrm{ref}}\right)^{0.6} (R_a/R_{a0})^{2/15} \left[(\lambda\rho c)/(\lambda\rho c)_{\mathrm{Cu}}\right]^{1/4}. \quad (10)$$

Examples of parameters, other than those embraced by Eq. (10), that may affect the performance of industrial-scale free-convection evaporators are

- The geometry of the individual heating elements (e.g., finned tubes and tubes with surfaces to augment boiling) and the entire layout of the evaporator (tube bundles; horizontal and inclined flat walls; etc.);
- Additives and adulterants in the boiling liquid (e.g., wetting agents, oils, or dissolved substances that are deposited on the heated surfaces);
- The operation of the plant (e.g., the admission of subcooled liquid and intermittent operation with on–off control.

Calculating the heat transfer coefficient α_{10} from Eq. (10) for fully developed nucleate boiling *on a single horizontal copper tube*, allowance for these effects can be made by introducing an average heat transfer coefficient $\bar{\alpha}$ and appending appropriate corrections, that is,

$$\bar{\alpha}/\alpha_{10} = C_{\mathrm{G}} C_{\mathrm{Ad}} C_{\mathrm{Op}} \quad (11)$$

where C_{G} is the correction for the geometry; C_{Ad}, for the adulterants in the boiling liquid; and C_{Op}, for the particular mode of operation.

The design of large shell-and-tube evaporators is hampered by the lack of reliable information in the literature. One reason for the scantiness of reliable data is the factor of uncertainty involved in scaling up the results obtained in research setups. Another reason is that the three parameters for which corrections are allowed usually occur simultaneously in large pilot plants and cannot be separated. Hence, the results obtained on individual items or equipment or their assemblies cannot be presented, even to a limited extent, in a generalized form.

Thus very approximate correlations will be proposed in the sections that follow only for the first factor in Eq. (11), while the others will be discussed in the form of hints for making rough estimates. (Priority in the near future must be devoted to the improvement of Eq. (9c), while the factors in Eq. (11) should be verified by experiment in each case for the individual items of equipment or assemblies.)

3.5.1 Geometry

With respect to their geometry, there are no significant differences *in the relative increases* of the heat transfer coefficient α with the heat flux q or reduced pressure p^* between horizontal tubes and horizontal flat plates or wires. For plates, this has been shown in former editions of the *Heat Atlas* (and is evident also from Fig. 14); for thin tubes (D = 2 mm) and wires, it is demonstrated in Fig. 12 by comparing new experimental results with Eq. (6a) or (7a), respectively.

On the other hand, differences may occur *in the absolute values of* α for horizontal tubes and those for flat plates or thin wires. In the case of flat plates, flow development and edge effects exert influences that are absent for horizontal tubes. In the case of thin horizontal wires, the differences may be caused by the entirely different ratio between the diameters of the heating element and the detaching bubbles, in comparison with tubes. This ratio becomes similar to the normal conditions

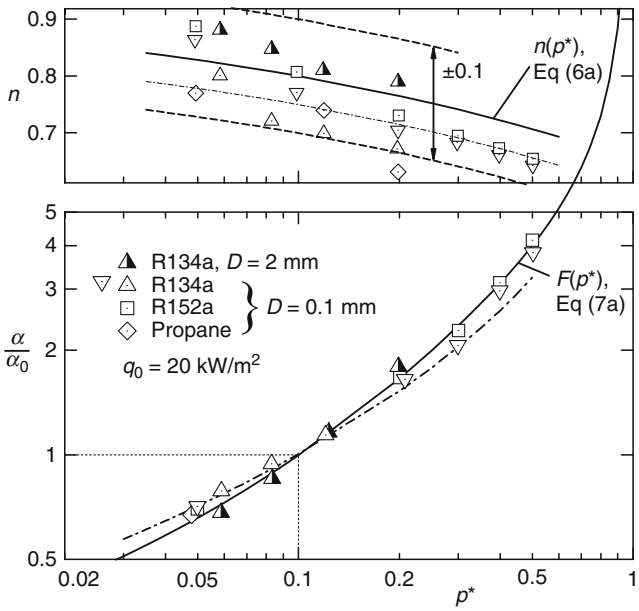

H2. Fig. 12. Relative pressure dependence of α and the exponent n for various fluids boiling on a thin tube and wires ([104–106]) in comparison to Eqs. (6a) and (7a), shown as solid lines, or the calculation method in previous editions of the *Heat Atlas* (dot-dashed lines).

for tubes at lower reduced pressures only at very high reduced pressures $p^* > 0.9$ with bubble radii < 50 µm [3].

Roughly, the same applies to vertical heated surfaces, because an improvement in heat transfer brought about by additional convection at the lower end is accompanied by an impairment at the upper end due to the restriction imposed by the rising cloud of bubbles on the liquid inflow. In some cases, the flow velocity at the lower end of vertical heated surfaces or through horizontal tube bundles may greatly exceed the upward velocity of the free-flowing bubbles. Under these circumstances, heat transfer must be determined by the methods described in Chap. H3 (Flow Boiling) for forced-circulation evaporators.

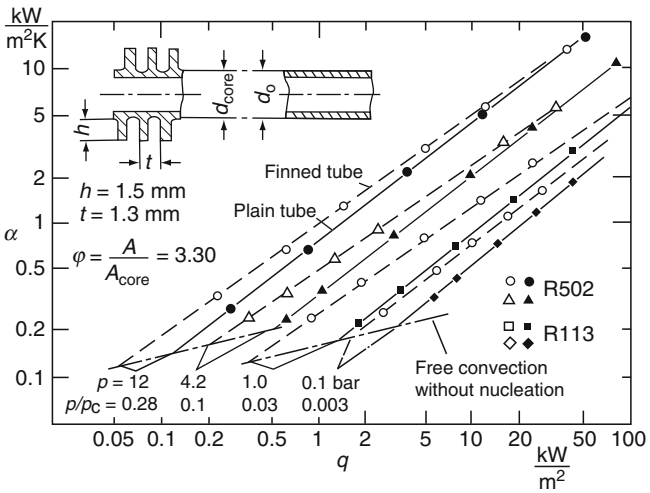

H2. Fig. 13. α as a function of q for a finned and a plain tube of the same core diameter. Parameter: Pressure p or reduced pressure p^*. Both α and q expressed in terms of the total outer area of the respective tube.

3.5.2 Finned Tubes and Tubes with Artificial Cavities

Within the range of initial nucleate boiling where the heat flux is low, horizontal evaporator tubes with external fins (as sketched in Fig. 13) transfer heat more efficiently than plain tubes. This is illustrated in Fig. 13 for the range of pressures extending from 0.3 to 30% of the value at the critical point and in Fig. 14 for a flat plate with similar fins at p^* near 0.1.

Throughout almost the entire range of heat flux concerned, the finned tube has a higher heat transfer coefficient, expressed in terms of the external area, than the plain tube. (In Fig. 13 and in all further general considerations on finned tubes, the heat transfer coefficient defined by Eq. (1) was not derived from the temperature at the actual surface but from that at the base of the fins. It is thus referred to as the "apparent heat transfer coefficient.")

The increase in α can be ascribed to the great roughness at the crests of the fins and the additional convection caused by the bubbles that rise along the flanks of the fins. Both kinds of influences increase heat transfer at low heat fluxes more than at higher, so the effect of the heat flux on α is weaker for finned tubes than for plain. And the same holds for the (relative) effect of pressure because the augmentation of α by convection is (almost) independent of pressure.

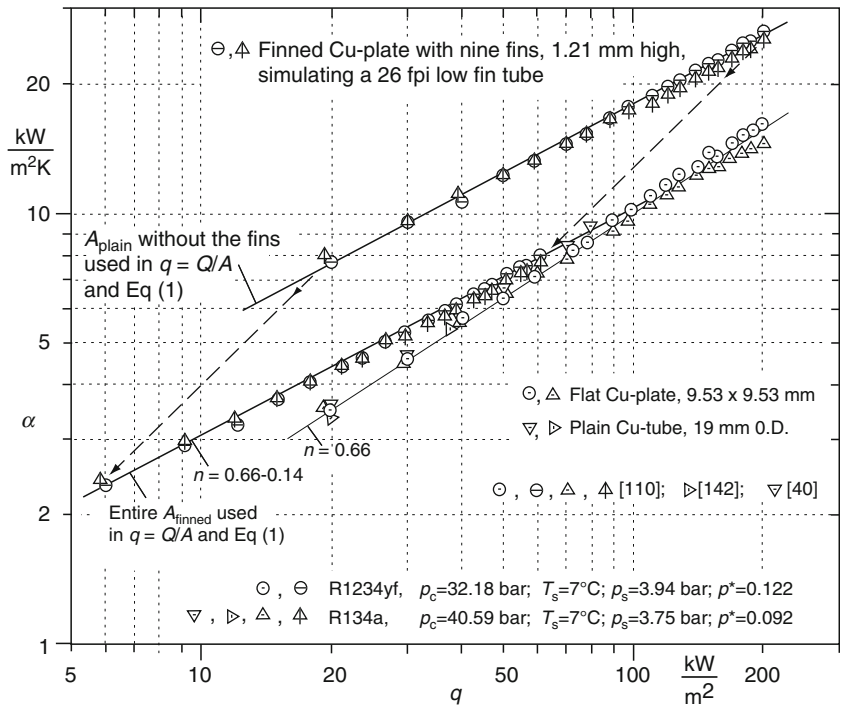

H2. Fig. 14. $\alpha(q)$-dependency for R134a and the new refrigerant R1234yf boiling on flat plain or finned copper plates ([110], extended).

As a consequence, the exponent n will be less than that for a plain tube, and the pressure dependence of $F(p^*)$ will be weaker. A rough estimate for the *effect of the heat flux on finned tubes* can be obtained from

$$n_f(p^*) = n(p^*) - 0.1\, h/t_l \tag{6c}$$

where n_f and n are the indices in the terms for the heat flux ratio – in Eq. (5) or (10) – for the finned and plain tubes respectively and $n(p^*)$ can be obtained from Eqs. (6a) and (6b); h is the height of the fins; and t_l is the free spacing between fins. Approximate allowance can be made for the *effect of the reduced pressure* by substituting the term $(p^*/\sqrt{\varphi})$ for (p^*) in $F(p^*/\sqrt{\varphi})$ or $F(p^*)$ of Eqs. (7a) and (7b), that is,

$$F_{f,p^*} = F(p^*/\sqrt{\varphi}) \tag{7c}$$

where φ is the ratio of the surface area of the finned tube to that of a plain tube of the same core diameter.

If no experimental data are available for verification, Eqs. (6c) and (7c) should not be used except for copper tubes of conventional dimensions (trapezoid-shaped – also called K-shaped – fins as sketched in Fig. 13 and t_l not much smaller than 1 mm), and unless the pressure is within the range $0.02 > p^* < 0.3$ (or from somewhat below 1 bar to not much above 10 bar).

Allowance for the roughness of finned tubes should not be in the form of Eq. (9), because the great dissimilarities in the surface structure of the fin crests and the other parts of the tubes produce conditions completely different to those encountered for plain tubes. However, a great allowance has already been introduced by the modifications made in the relationship between the heat transfer coefficient, the heat flux, and the pressure.

A fact that can be exploited in estimating the *reference value* $\alpha_{0,f}$ *for finned tubes* is that the heat transfer coefficients for both finned and plain copper tubes, are approximately the same at a heat flux of about 100 kW/m^2 and reduced pressures near $p^* = 0.1$:

$$\alpha_{100,\text{finned}} = \alpha_{100,\text{plain}} \text{ at } q = 100 \text{ kW/m}^2 \text{ and } p_0^* = 0.1. \tag{8c}$$

This is evident from Figs. 13 and 14. Thus, the first step will be to calculate the heat transfer coefficient $\alpha_{100,\text{plain}}$ that applies for both tubes from α_0 using Eq. (8) or Table 1 and from $n(p^*)$ applying Eq. (6). $\alpha_{0,f}$ can then be derived from $\alpha_{100,\text{finned}}$ using Eq. (6c), see Example 2 and Fig. 20.

The method suggested here yields results that agree well with measured values (cf. Figs. 17b, c and 20). Equally good agreement is achieved by a calculation method devised by Slipcevic [108] (also discussed in [109]).

The differences in n and α that exist between plain and integral-fin (K-shaped) tubes and are used in the method discussed above have also been verified in very recent experiments [110] with R134a and the new refrigerant R1234yf (see Table 1) boiling on small flat plain or finned copper plates that can be applied in the cooling of electronic chips (Fig. 14). As in the method, the (somewhat extrapolated) line for the finned plate and the interpolation line for the plain intersect near 100 kW/m^2 and the difference of 0.14 in n corresponds to 0.1 h/t_l in good approximation. The absolute values of α measured in [110] lie at the lower limit of the experimental scatter, as shown in [39] also for other fluids investigated by this group.

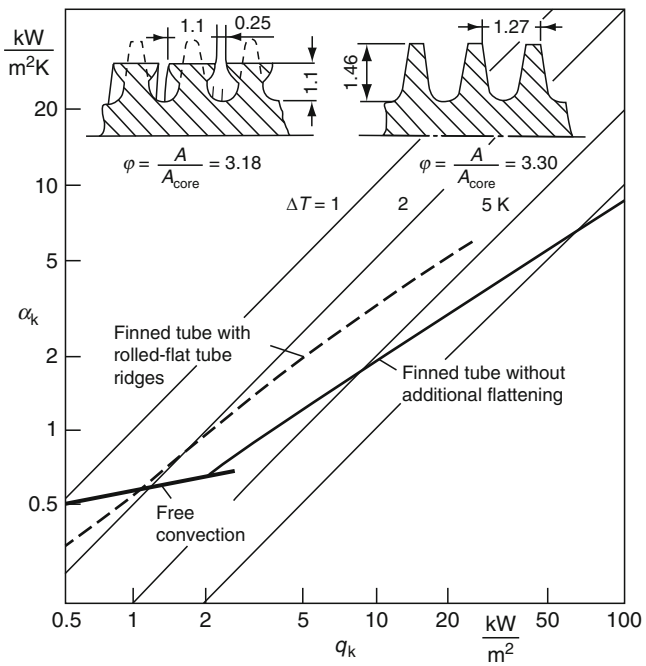

H2. Fig. 15. Heat transfer coefficient as a function of the heat flux in nucleate boiling of Refrigerant R11 at a pressure of 1.3 bar for two tubes with fins of the same basic structure, but one with the ridges of the fins flattened by rolling (α_k and q_k expressed in terms of the area A_{core}).

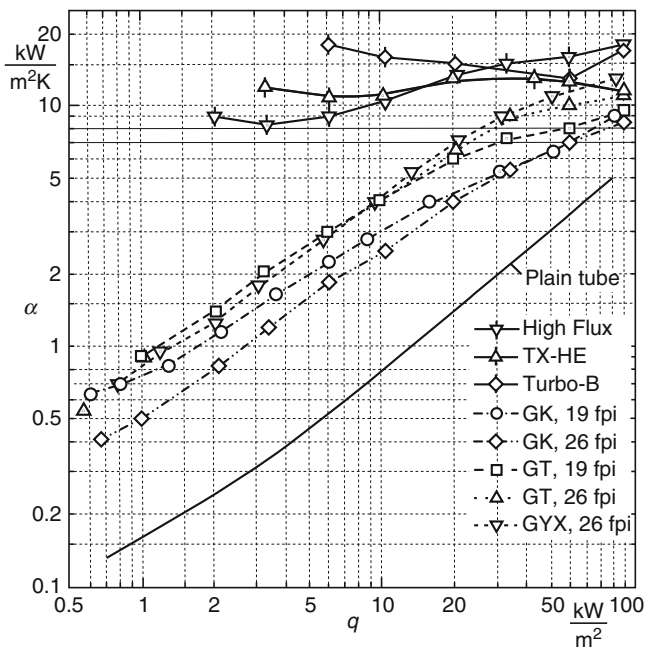

H2. Fig. 16. Heat transfer coefficient as a function of the heat flux for Refrigerant R114 boiling at 1 bar on different structured and porous surfaces (from [115], modified in [111]).

In the past decades, a great variety of evaporator tubes with enhanced surfaces containing artificial nucleation sites have been developed (see, e.g., the reviews in [111–114] and Figs. 15 and 16), that can be divided into two main groups, one based on integral-fin tubes with modified fins to form reentrant grooves or tunnels ("structured surfaces," e.g., the T-type in Fig. 15 or the four types with broken interpolation lines in Fig. 16), and another based on plain tubes with sintered porous metallic matrix bonded to the tube surface ("porous surfaces," e.g., the three types with solid interpolation lines in Fig. 16).

The examples in Figs. 15 and 16 demonstrate the typical improvement of heat transfer from *structured* surfaces over plain tubes for pressures near atmospheric. The improvement by the porous surfaces is much better, but their α, q-behavior is entirely different (also for higher pressures [116]), thus ending up with basically the same heat transfer coefficients for all kinds of surfaces at high heat fluxes near 100 kW/m^2.

The few examples of nucleate boiling heat transfer from tubes with artificial reentrant cavities shown in Figs. 15 and 16 give an impression of the difficulties in the development of calculation methods for enhanced boiling heat transfer from the many complex commercially used surface configurations. In the reviews cited above, a great number of correlations are discussed, but their application without experimental verification is not yet safe, if extrapolation to configurations other than the particular one used in the development of the method is required.

3.5.3 Horizontal Tube Bundles

If the heat flux is low or moderate, the average heat transfer coefficient in nucleate boiling on the outer surfaces of horizontal tubes in a bundle is higher than that for a single tube. One reason for this is that the liquid inlet is designed to cope with the requirements for the entire bundle, with the result that the flow rate over the lowermost bank of tubes is higher than that over a single tube. Another reason is the rising cloud of bubbles within the bundle.

A significant number of proposals have appeared in the literature for the calculation of the contributions thus made toward heat transfer [117–125]. In the discussion on Eq. (11), attention was drawn to the problems involved in the interpretation of experimental results and to their application in the design of tube-bundle evaporators. In view of these remarks, there would be no justification for a complicated mathematical outlay; for this reason, the following simple method, analogous to those described elsewhere [117, 118], is recommended for horizontal tube bundles operating under the restricted condition that the flow velocity of the cloud of bubbles within the bundle is similar to that for the swarm of bubbles leaving a single horizontal tube. If it is much higher, the calculation methods of two-phase flow should be employed [126–130] (see also the remarks at the end of Sect. 4 on the effect of bubbles coming from lower tube banks).

First, the average heat transfer coefficient $\bar{\alpha}$ for the tube bundle is separated in a purely formal manner into the

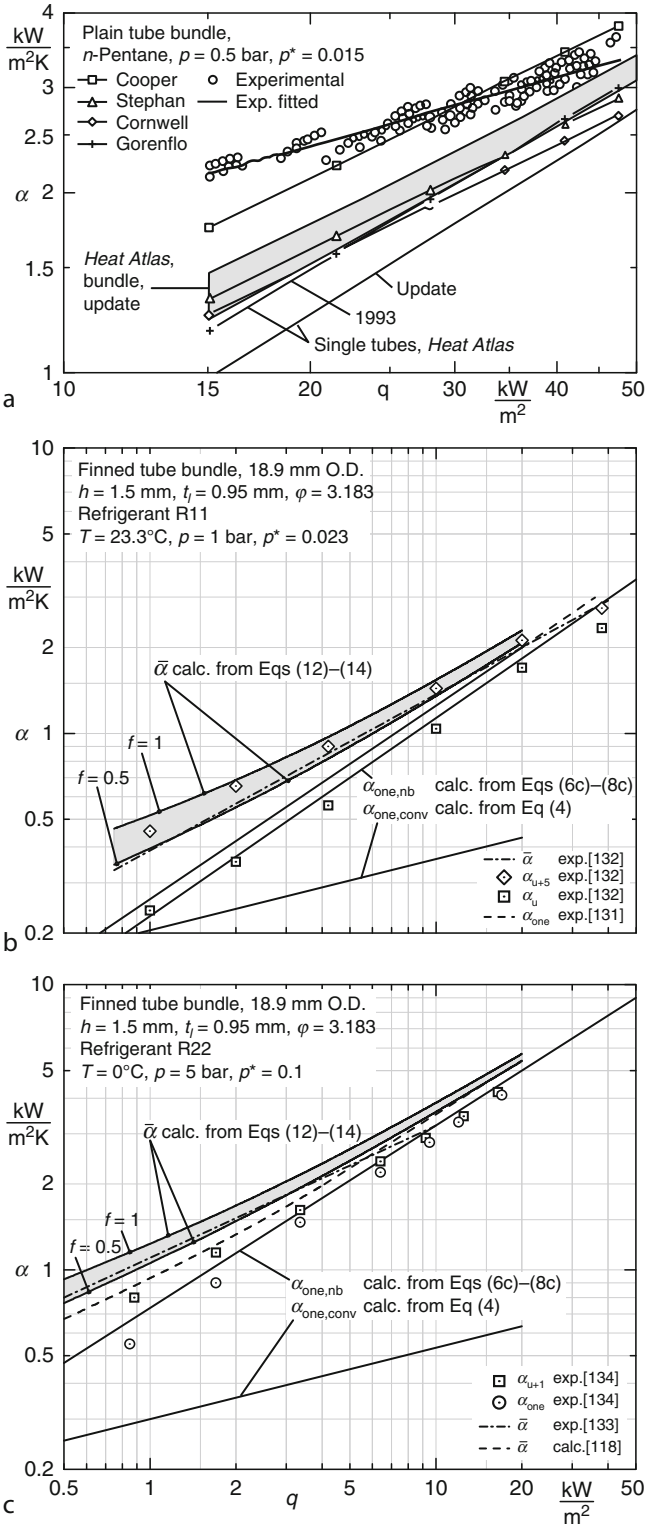

H2. Fig. 17. Calculated and measured values of the heat transfer coefficient as functions of the heat flux for tube bundles. (**a**) *n*-Pentane boiling on a plain tube bundle at $p = 0.5$ bar (according to [120], extended). (**b**), (**c**) Refrigerants R11 or R22 boiling on finned tube bundles. The indices $u + 1$ and $u + 5$ denote the bank of tubes as counted from the undermost (see specimen calculation in Example 2 and Fig. 20).

coefficient α_u for the undermost row and the relative improvement $(\bar{\alpha}/\alpha_u)$ within the bundle. Thus,

$$\bar{\alpha} = \alpha_u(\bar{\alpha}/\alpha_u). \tag{12}$$

α_u is calculated by additive superposition of the heat transfer coefficient $\alpha_{one,nb}$ and the convective contribution $\alpha_{one,conv}$, both for a single tube, that is,

$$\alpha_u = \alpha_{one,nb} + f\alpha_{one,conv} \tag{13}$$

where the factor f depends on the size of the tube bundle and the anticipated inlet flow velocity, where $0.5 \leq f \leq 1$.

The evaluation of data extracted from the literature gives the following approximate *dimensional* expression for $(\bar{\alpha}/\alpha_u)$:

$$(\bar{\alpha}/\alpha_u) = 1 + (2 + q\varphi)^{-1} \tag{14}$$

where q is the heat flux in kW/m^2 on the *total outer surface area* of the tubes, and φ is the area ratio (φ = 1 for plain tubes). Equation (14) applies for $(q\varphi)$ between ca. 1 and 20 kW/m^2 and for near-atmospheric pressure, that is, about 0.5–10 bar. The evaluation of Eqs. (12)–(14) for bundles of plain and finned tubes is illustrated in Fig. 17 and, in connection with Example 2, in Fig. 20. For the sake of simplicity and in the light of the restriction mentioned above, $\alpha_{one,conv}$ is calculated there for natural convection from Eqs. (3) and (4). A better approximation would be to estimate the rising velocity of the cloud of bubbles within the bundle from the vapor volume varying with heat flux and pressure.

A condition that has been assumed in the derivation of these equations is that q = constant for the entire tube bundle. This is certainly not satisfied if the bundles are heated by a liquid. In this case, the heat flux for the individual segments or rows in the bundle must be estimated from the difference between the temperature of the heating medium and that of the boiling liquid at the inlet to each segment of the bundle [132, 135].

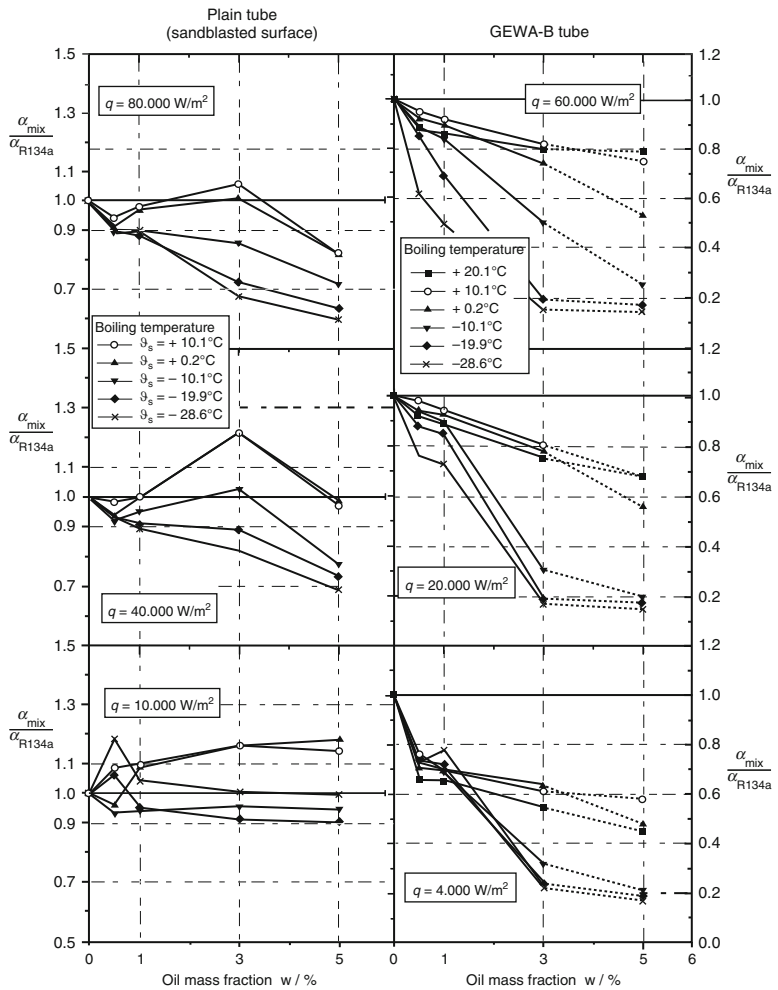

H2. Fig. 18. Relative variation of the heat transfer coefficient for R134a/SE55 oil mixtures boiling on a plain tube with fine sandblasted surface (*left*) or an enhanced (GEWA-B) tube (*right*) versus oil mass fraction at different pressures and heat fluxes (according to [140], modified).

3.5.4 Impurities

As a rule, adulteration of the boiling liquid by another impairs heat transfer (cf. Sect. 4). The only impurities that can increase the transfer of heat above that of the pure liquid are surface active agents, if they are added in low concentrations, but the improvement is usually slight [134, 136–139]. The increase can be ascribed to the decrease in surface tension and the associated reduction in the energy required to produce viable bubbles. Typical new results obtained by Spindler and Hahne [140] on adding oil to refrigerants boiling on plain or enhanced tubes are shown in Fig. 18. It is evident that the oil may augment (by surface active ingredients) or reduce heat transfer in the case of the plain tube as has been found for many refrigerants mixed with different lubricating oils in the literature (various new sources are given in [140]); on the other hand, only degradation of heat transfer occurs in Fig. 18 for the enhanced tube.

Impurities in the form of dissolved or suspended additives that are deposited on the heated surface usually give rise to heat transfer coefficients that are lower than those for nucleate boiling of the pure liquid.

Apart from the presentation of results of individual measurements, no method yet exists for estimating the effect of impurities on the heat transfer coefficient in nucleate boiling.

3.5.5 Evaporator Operation

All the experimental results that have been described up to now in Sect. 3 and the calculation methods developed from them apply to the case in which the potential nucleation sites are fully activated at the wall superheat and the liquid is in the saturated state associated with the reigning pressure at some distance from the heated surface. If the operation of the evaporator does not allow these conditions to be adhered to, the heat transfer coefficients in the range of initial nucleate boiling are lower than those that would be expected from Eqs. (5) to (10).

On–off controllers or gradual increments in heat flux increase the likelihood that nucleation is not completely activated. As a consequence, an operating point is reached between fully activated nucleation and free convection without bubble formation, as is illustrated by the hatched zone in Fig. 19.

A corresponding effect is brought about by the entry of subcooled liquid. In this case, therefore, Eq. (3) or (4) should be used instead of Eq. (5) in order to allow a safeguard, even if the heat flux or superheat is somewhat higher than that corresponding to the commencement of nucleate boiling.

3.5.6 Examples

Example 1

Calculate the length of a single cylindrical rod of 10 mm outer diameter required to transfer 1 kW for the evaporation of water at $p = 100$ bar. The superheat is $\Delta T = 3$ K.

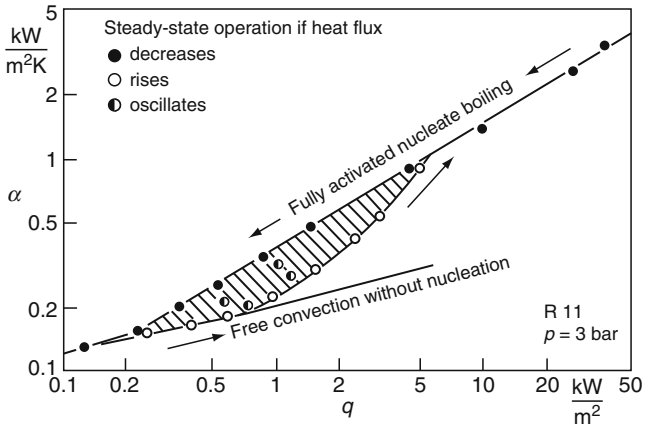

H2. Fig. 19. Effect of the mode of operation on the heat transfer coefficient at initial nucleate boiling of Refrigerant R11 on a finned tube at $p = 3$ bar [141] (similar results in [135, 136]).

$Q = 1$ kW $= \pi\ D\ L\ \alpha\ \Delta T$. The desired length is $L = Q/\pi\ D\ \alpha\ \Delta T$.

The heat transfer coefficient is calculated in the following steps:

a. According to Table 1, the reference value is $\alpha_{0,\mathrm{exp}} = 5.60$ kW/m^{2}K at $q_0 = 20$ kW/m^2 and $p_0^* = 0.1$. A value of 4.13 kW/m^{2}K, that is, ca. 26% lower, is obtained from Eq. (8). For the highly associating fluid water, the experimental value is preferred to the principle of corresponding states.
b. Conversion into the value at $p_1 = 100$ bar: Since $p_c = 220.64$ bar (Table 1), $p_1^* = 0.453$. Equation (7b) then gives $\alpha_1/\alpha_0 = F(p_1^*) = 2.186$ or $\alpha_1 = 2.186\alpha_0 = 15.77$ kW/m^{2}K (at $p_1 = 100$ bar and $q_1 = 20$ kW/m^2).
c. $\alpha(q)$ at p_1: Equation (6b) gives $n(p_1^*) = 0.634$; thus, $\alpha \sim q^{0.634}$ at p_1.
d. $\alpha(\Delta T)$ at p_1: $\alpha \sim q^{0.634} = (\alpha\Delta T)^{0.634}$ according to Eq. (1); therefore, $\alpha \sim \Delta T^{1.73}$.
e. α_2 at $\Delta T_2 = 3$ K and $p_2 = p_1$: $\alpha_2/\alpha_1 = (\Delta T_2/\Delta T_1)^{1.73} = 4.442$, as $\Delta T_1 = q_1/\alpha_1 = 1.267$ K. Thus $\alpha_2 = 4.442\ \alpha_1 = 70.0$ kW/m^{2}K and $q_2 = 210$ kW/m^2.

Since α_2 is near 100 kW/m^{2}K, it should be checked how close the heat flux q_2 is to the maximum in nucleate boiling (Fig. 5). It follows from Sect. 5 that $q_{\mathrm{crit}} > 1000$ kW/m^2 $>> q_2$. (The values of the maximum heat flux that can be obtained for water are much higher than those for most organic liquids.)

The length of rod required is thus $L = (1/0.01 \times 70 \times 3 \times \pi)$ m $= 15.1$ cm.

Example 2

An evaporator has to be designed in which Refrigerant R22 boils at −30°C (Fig. 20). The tubes have fins of $h = 1.5$ mm height spaced at $t_l = t - b = 0.95$ mm. The area ratio is $\varphi = 3.18$. Determine $\alpha(q)$ for the tube bundle; that is, $\alpha_f(q)$ has to be developed for the saturation pressure of R22 at −30°C,

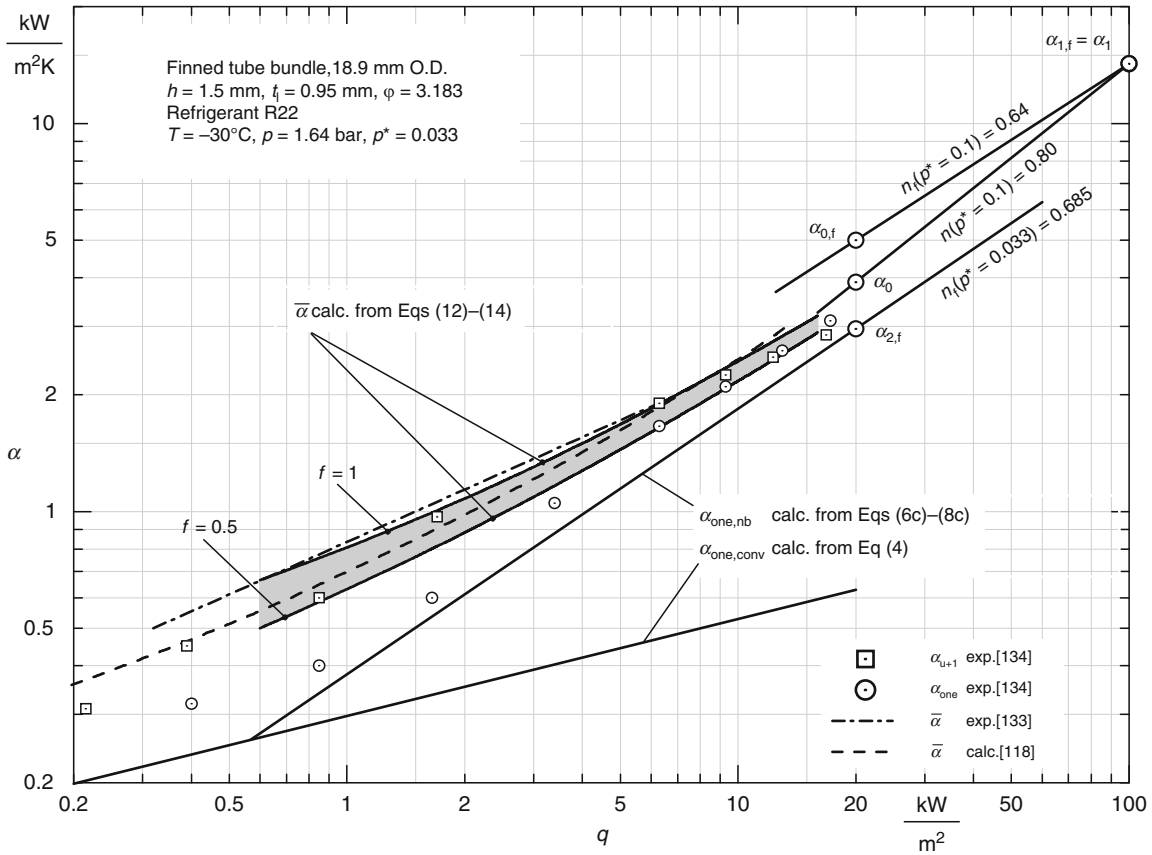

H2. Fig. 20. α as a function of q, as calculated from Eqs. (4) to (14) (see Example 2). Comparison with experimental data [133, 134] and with a calculation method [118]. $u + 1$ denotes the bank of tubes immediately above the undermost.

p = 1.64 bar or $p/p_c = p^* = 0.0329$ (with p_c = 49.9 bar from Table 1).

The calculation proceeds in the following steps:

a. α_0 for a single plain tube:
According to Table 1, the reference value is $\alpha_{0,\text{exp}} = 3.90$ kW/m^{2}K at $q_0 = 20$ kW/m^2 and $p_0^* = 0.1$. A value of 4.37 kW/m^{2}K, that is, 12% higher, is obtained from Eq. (8). For a safe design, $\alpha_{0,\text{exp}}$ is preferred.

b. $\alpha_{0,f}$ for a single finned tube:
According to Eq. (8c), $\alpha_{1,\text{finned}} = \alpha_{1,\text{plain}}$ at $q_1 = 100$ kW/m^2 and $p_0^* = 0.1$.
$\alpha_{1,\text{plain}}$ follows from Eq. (10) and $\alpha_{0,\text{exp}}$ at $p_0^* = 0.1$:
$\alpha_1/\alpha_0 = (q_1/q_0)^n = (100/20)^n = 3.624$, with $n(p^* = 0.1) = 0.800$ from Eq. (6a).
So $\alpha_1 = 3.624\ \alpha_0 = 14.13$ kW/m^{2}K $= \alpha_{1,f}$. $\alpha_{0,f}$ for the finned tube is obtained in the same way backward:
$\alpha_{0,f}/\alpha_{1,f} = (20/100)^{n_f} = 0.3558$, with n_f $(p^* = 0.1) = 0.642$ from Eq. (6c), and $\alpha_{0,f} = 0.3558\ \alpha_{1,f} = 5.03$ kW/m^{2}K.

c. $\alpha_{2,f}$ at $p_2 = 1.64$ bar or $p_2^* = 0.0329$:
According to Eq. (7c), $\alpha_{2,f}/\alpha_{0,f} = F_{2,f,p^*}(p*/\sqrt{\varphi})/F_{0,f,p^*}(p*/\sqrt{\varphi}) = 0.5922$.
Hence $\alpha_{2,f} = 0.5922\ \alpha_{0,f} = 2.98$ kW/m^{2}K, with $n_{2,f} = 0.684$ from Eq. (6c).

Thus, the following applies for a single tube at $p_2^* = 0.0329$:
$\alpha_{\text{one,nb}} = C_{\text{nb}}\, q^{0.684}$, where $C_{\text{nb}} = \alpha_{2,f}/q^{n_{2,f}} = 0.384$ and $\alpha_{\text{one,conv}} = C_{\text{conv}}\, q^{0.25}$ with $C_{\text{conv}} = 0.30$ from Eq. (4) and the properties listed for R22 in Part D.

d. Determination of $\alpha(q)$ for the tube bundle from Eqs. (12) to (14):

$$\bar{\alpha} = \alpha_u(\bar{\alpha}/\alpha_u) = \left(\alpha_{\text{one,nb}} + f\alpha_{\text{one,conv}}\right)\left[1 + (2 + q\varphi)^{-1}\right],$$
$$\bar{\alpha} = \left(0.384\, q^{0.684} + 0.30 f q^{0.25}\right)\left[1 + (2 + q\varphi)^{-1}\right].$$

If the upper and lower limits for the estimate are taken to be $f = 1$ and $f = 0.5$ respectively, the hatched zone in Fig. 20 will be obtained. The unit to which the numerical values for α pertain throughout the entire calculation is kW/m^{2}K; and for q, kW/m^2.

4 Nucleate Boiling of Mixtures

4.1 Experimental Evidence

It is found experimentally that the heat transfer coefficient α_{mix} in nucleate boiling of zeotropic binary mixtures is less than an

"ideal" heat transfer coefficient $\alpha_{id,m}$, defined by the molar average of the heat transfer coefficients α_1 and α_2 for the pure components, Eq. (15):

$$\alpha_{id,m} = x_1\alpha_1 + x_2\alpha_2 = x_1\alpha_1 + (1 - x_1)\alpha_2 \qquad (15)$$

where x_1 and x_2 are the molar fractions of components 1 and 2. This was established by Bonilla and Perry for a great number of zeotropic mixtures [143] and has since been confirmed in many other studies that have been reviewed (cf., e.g., [41, 144]. It is also demonstrated by the lowest diagrams of Figs. 21–24 (α_{id} may be defined for constant saturation pressure (Fig. 21d) or constant *reduced* pressure (Figs. 23–25); the latter will be used in Sect. 4 because it is more appropriate for a unified discussion of the results (see also [41, 147]).

Alternatively, the "ideal" heat transfer coefficient α_{id} for mixtures can be defined by using the molar average ΔT_{id} in Eq. (1):

$$\Delta T_{id} = q/\alpha_{id,T} = x_1\Delta T_1 + x_2\Delta T_2 \qquad (15a)$$

where ΔT_1 and ΔT_2 are the temperature differences required to transfer q to the pure components 1 and 2 respectively. Thus,

$$q/\alpha_{id,T} = x_1(q/\alpha_1) + x_2(q/\alpha_2) \text{ or } 1/\alpha_{id,T} = (x_1 + \alpha_1) + (x_2/\alpha_2). \qquad (15b)$$

As can easily be verified, $\alpha_{id,T} = \alpha_{id,m}$, if $\alpha_1 = \alpha_2$, and the maximum difference between the ideal coefficients is only about ±5% if α_1 and α_2 vary by about a factor of two, as for the updated list of substances other than cryogens for Eq. (8), in the range $0.7 < P_f < 2$, or $2.89 < \alpha < 5.43$ kW/m^{2}K (Table 1).

By analogy with pure fluids, the actual heat transfer coefficient α_{mix} defined by Eq. (1a) is

$$\alpha_{mix} = q/\Delta T = q/[T_W - T_{sat}(p, x_1)] \qquad (1a)$$

where $T_{sat}(p, x_1)$ is the bubble temperature corresponding to the bulk liquid composition and the system pressure p. In a zeotropic mixture, the equilibrium composition of the vapor differs from that of the liquid, $y_1 \neq x_1$, which is illustrated in Figs. 21–24. Consequently, during evaporation at a finite rate, the *lower* boiling component evaporates preferentially to provide

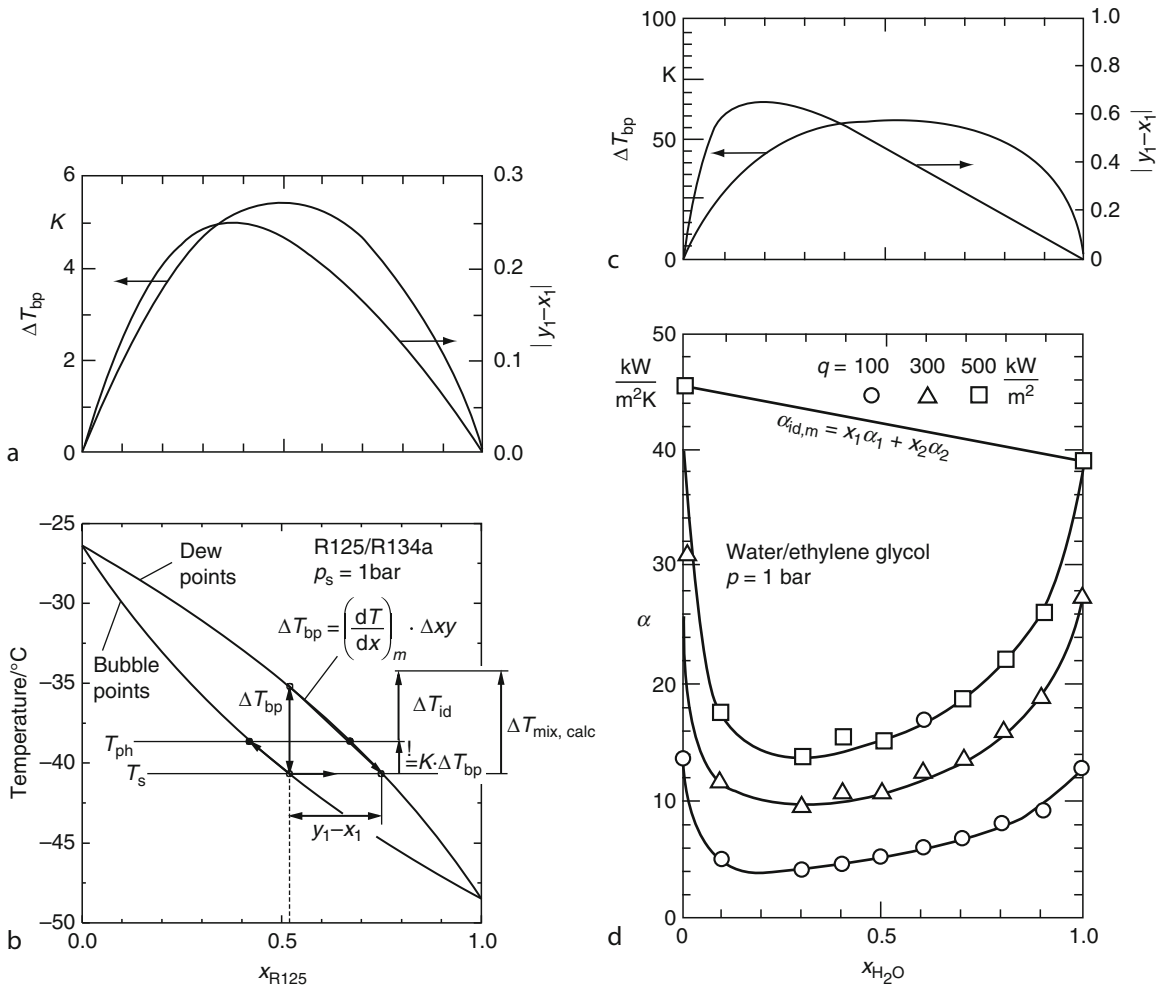

H2. Fig. 21. Diagrams on the left: (**a**) Nearly symmetrical dependence of the two characteristic features of the vapor/liquid equilibrium, Δxy and ΔT_{bp}, on the composition x of the liquid and (**b**) relationship of these features to the superheat ΔT of the heated wall for the binary refrigerant system R125/R134a (modified from [41]). Diagrams on the right: (**c**) Markedly asymmetrical x-dependence of Δxy and ΔT_{bp} compared with (**d**) the asymmetrical x-dependence of α_{mix} for the binary system water/ethylene glycol (from [145], according to [41]).

the enrichment of this component in the bubbles growing on the heated wall, with an accompanying enrichment of the *higher* boiling component in the liquid within the boundary layer near the wall.

Thus, the temperature T_{ph} of the liquid–vapor interface is elevated over the saturation temperature $T_{sat}(p, x_l)$ (Fig. 21b), and the effective temperature difference ΔT for heat transfer from the surface of the wall through the adjacent liquid to the bubbles is diminished. This causes the reduction in α_{mix} below $\alpha_{id,m}$. The value of T_{ph} depends on processes of mass transfer in the liquid boundary layer, which oppose the local enrichment of the higher boiling component. Simple estimates for T_{ph} form the basis of the calculation methods for the heat transfer coefficients of boiling mixtures discussed in Sect. 4.2.

It follows that the heat transfer coefficient α_{mix} should not fall below the molar average α_{id} if the composition of the vapor (y) in the growing vapor bubbles is the same as that of the undisturbed liquid (x), as in *azeotropic* mixtures. This premise has been confirmed to a good approximation by measurements on such systems. This can also be seen in Fig. 24 for the mixtures of R22/R115 along the azeotropic line [148, 149] and in Fig. 22c, where the α-values for the azeotropic refrigerant R507 are the same as for its components R125 and R143a within the whole pressure range investigated [41, 144].

In the case of binary systems that form an azeotrope, the azeotropic mixture can be regarded as a new pure component, and the system can be divided into two separate binary subsystems. For ternary or multicomponent systems, the definitions of ΔT_{id}, $\alpha_{id,m}$, and $\alpha_{id,T}$ have to be extended to

$$\Delta T_{id} = \sum_i x_i \Delta T_i, \qquad \alpha_{id,m} = \sum_i x_i \alpha_i$$
$$\text{and} \quad 1/\alpha_{id,T} = \sum_i x_i/\alpha_i. \tag{15c}$$

The two binary systems in Figs. 23 and 24 have been taken as examples to illustrate the dependencies of the heat transfer coefficient α on the heat flux q (through the exponent n), reduced pressure p^* (obtained from the experimental value

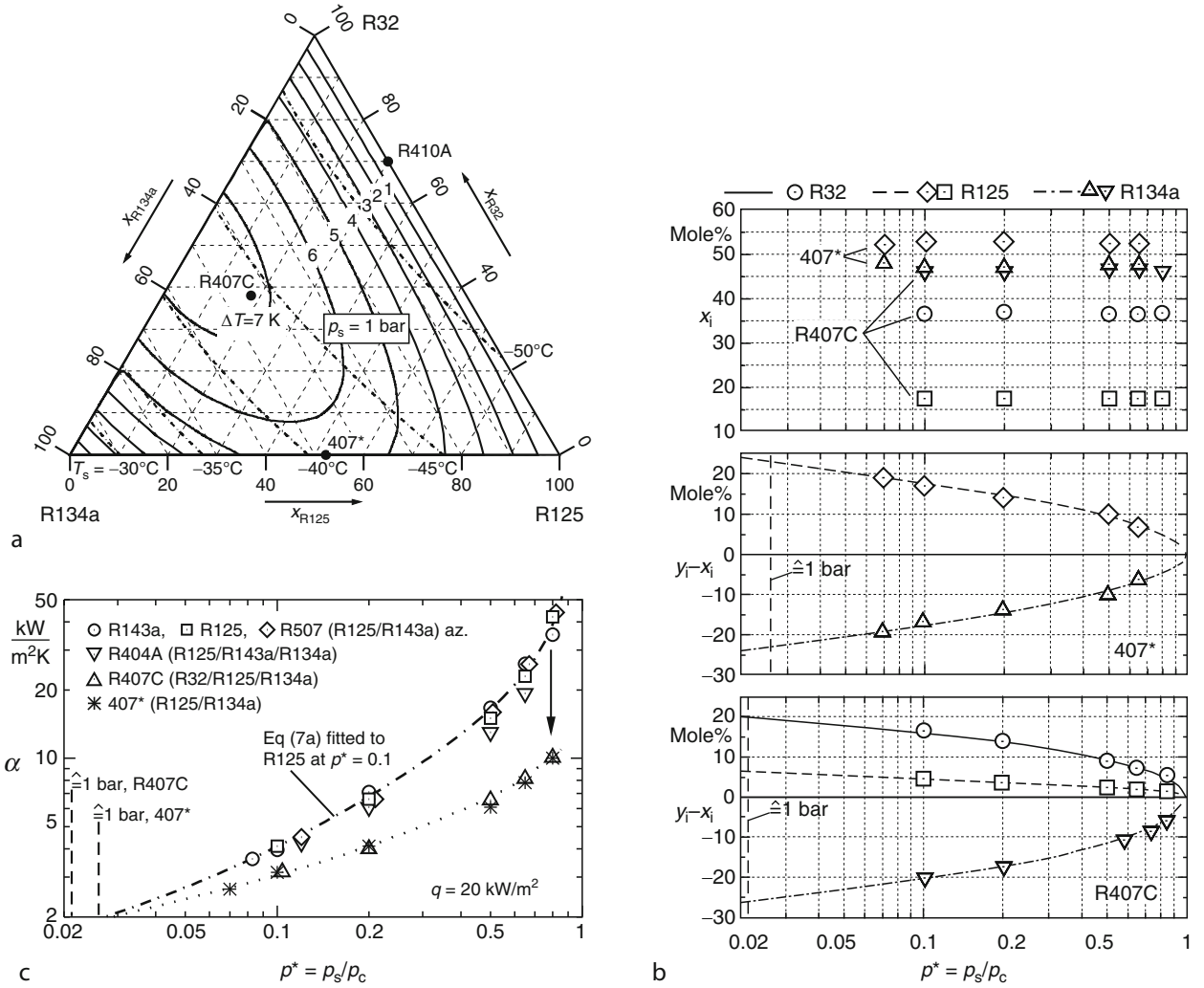

H2. Fig. 22. (**a**) Composition of the liquid and ΔT_{bp} for the ternary mixture R407C and the binary 407* with (almost) the same molar fraction of the higher boiling component R134a. (**b**) Pressure dependence of composition x and shift Δxy for the two mixtures. (**c**) Pressure dependence of α for the two mixtures, for two of the components, for the azeotropic mixture R507, and the ternary R404A (containing only a small fraction of the highest boiling R134a). (Modified from [41], see also [144]).

for the critical pressure p_c for each of the mixtures), and composition x of the liquid.

From the diagrams for n, it can be seen that the increase of α with q for zeotropic mixtures is always less than for the pure components; the effect is highest at intermediate compositions and increases with reduced pressure. For the mixtures with compositions along the azeotropic line in Fig. 24, however, n is the same as for the pure components (within experimental error, as also holds for the absolute values of α, diagram below), demonstrating that nucleate boiling heat transfer for azeotropes does not differ from that of the pure components. On the other hand, it also shows that a mixture with fixed composition behaves like an azeotrope only at a certain pressure, while there is zeotropic behavior with at least some difference in the compositions of the vapor and liquid phases at all other pressures.

The diagrams in Figs. 21c, d; 23d, e and 24 b–d show that the enrichment $(y_1 - x_1) = (\Delta xy)_1$ of the lower boiling component in the vapor phase and the deterioration of heat transfer in mixture boiling, $\alpha_{id} - \alpha_{mix}$, are greatest for intermediate compositions of the mixtures. A more thorough examination reveals, however, that narrow limits exist for the analogy between the x-dependency of the ratio α_{mix}/α_{id} and those of the difference Δxy and of the "temperature glide" ΔT_{bp} between the dew point and bubble point temperatures at constant x. The two

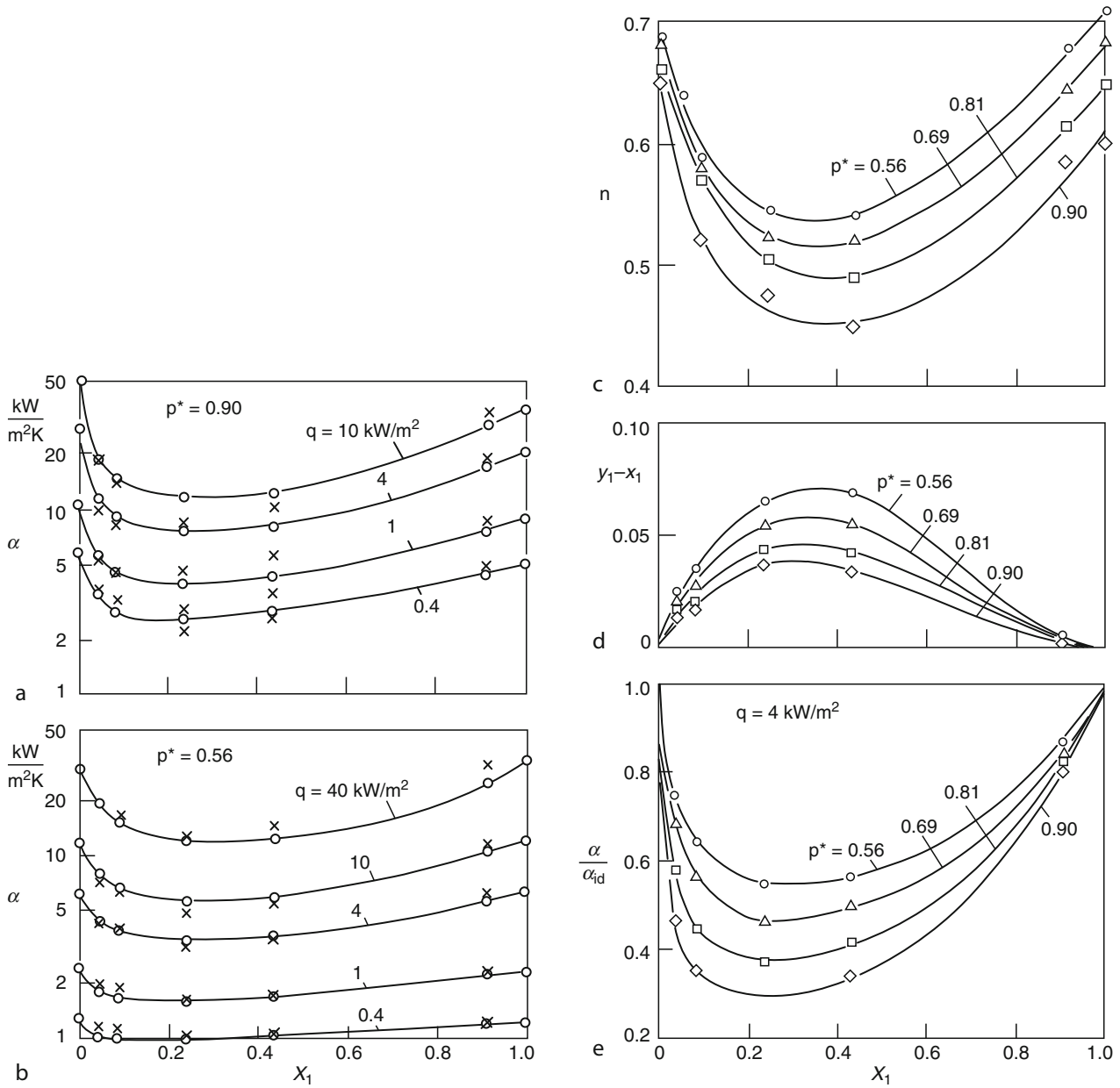

H2. Fig. 23. Boiling of the binary system sulfur hexafluoride/R13B1 at elevated reduced pressures. Diagrams on the left (**a**), (**b**): $\alpha(x)$-dependence for two reduced pressures with heat flux q as parameter. Diagrams on the right: (**c**) Exponent n of the $\alpha(q)$-relationship, (**d**) shift Δxy of vapor/liquid compositions, and (**e**) ratio α_{mix}/α_{id} as functions of the molar fraction x_1 of the more volatile component SF_6 (parameter: p^*). According to [146, 147], but with slightly modified values of $n(p^*)$. Crosses (x) in the upper two diagrams: α_{calc} from Eq. (21a) with $B_0/\beta_l = 10^4$ s/m ($B_0 = 2$) for $p^* = \text{const}$.

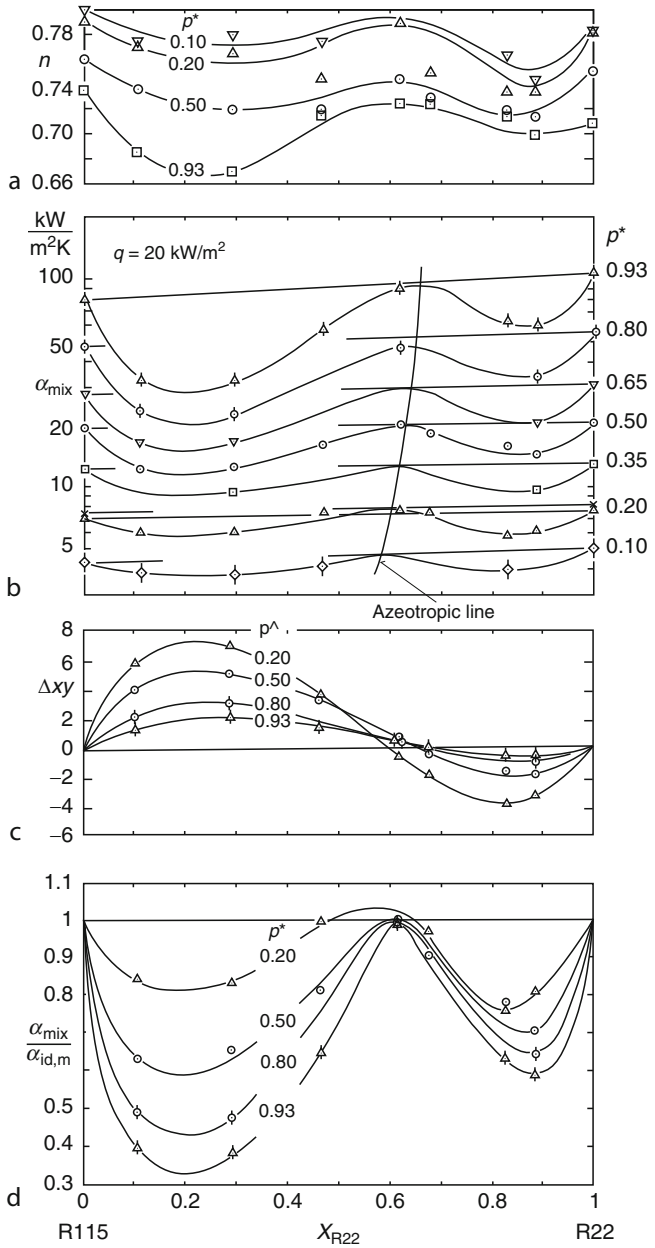

H2. Fig. 24. *x*-dependence of α for the refrigerant system R22/R115 at seven reduced pressures (together with the *x*, *p**-dependence of the azeotropic compositions = "azeotropic line") and of the exponent *n*, shift Δ*xy*, and ratio α_{mix}/α_{id} at four selected *p**-values. From [148] (see also [149]).

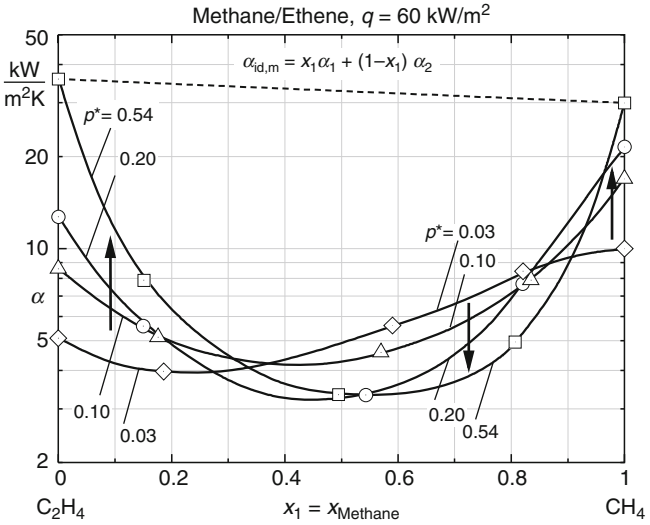

H2. Fig. 25. Variation of α with composition x_1 and reduced pressure *p** for the system methane/ethene at constant, high heat flux (according to [30]).

characteristic phase equilibrium properties can be connected to a good approximation (Fig. 21b) by

$$\Delta T_{bp} = (dT/dx)_m \Delta xy \qquad (16)$$

The main differences in the *x*-dependencies of Δ*xy* and α_{mix}/α_{id} are

a. The minima of α_{mix}/α_{id} occur at significantly lower fractions x_1 than the maxima of Δ*xy* and
b. The impairment of heat transfer in mixture boiling becomes continuously more pronounced as the critical point is approached, whereas the difference in the molar fractions of vapor and liquid decreases (Figs. 22b, c; 23d, e and 24c, d).

The fact that deterioration of heat transfer tends to vanish despite the increasing difference in the molar fractions toward very low reduced pressures, which is particularly obvious from Fig. 22b and c, is due to a vigorous remixing effect of the liquid in the superheated boundary layer near the heated wall, because (1) big, fast growing bubbles are formed and (2) the density difference between vapor and liquid is large. Both effects result in high acceleration of the vapor *and the liquid* in the immediate vicinity of the heated wall at the detachment of the bubbles and afterward, when they are sliding upward along the tube surface.

With increasing reduced pressure, however, bubble size and the vapor–liquid density difference diminish continuously. Therefore, the turbulent motion of the liquid near the heated wall steadily decreases and the enrichment of the higher boiling component in the liquid within the boundary layer cannot be compensated any longer, even though the difference Δxy decreases continuously, too.

For very wide boiling binaries, deterioration of heat transfer increases drastically with rising reduced pressure, thus compensating or even overcoming the strong increase of α with p^* according to Eq. (7) for the pure components. The latter can be seen in the example of Fig. 25 at intermediate to high fractions of the lower boiling component. This "negative" pressure dependence of α existing here – and for other wide boiling binaries reviewed in [30] – is not a peculiarity, but a continuous trend that may occur for this kind of binary and depends on heat flux and pressure.

4.2 Calculation Methods

Most of the correlations for nucleate boiling heat transfer to mixtures proposed in the past and collected in [41, 144] attempt

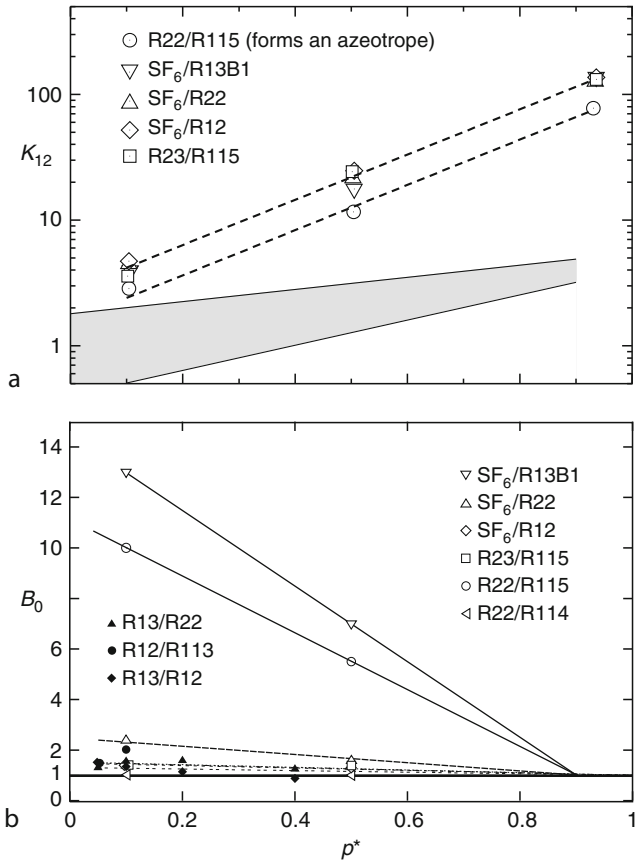

H2. Fig. 26. (**a**) Pressure dependence of the parameter K_{12} in Eqs. (18) and (19) as fitted in [151] (symbols) and as given originally (shaded area). (**b**) Pressure dependence of the parameter B_0 in Eqs. (21a) and (23) for various binary refrigerant systems according to [30].

to model the deterioration of heat transfer in terms of the ratio α_{mix}/α_{id} and relate it to the vapor/liquid phase equilibrium by one of its characteristic features Δxy or ΔT_{bp}, respectively.

In an early approach given by Stephan and Körner [150], the superheat ΔT_{mix} in Eq. (1a) is broken down into the ideal component ΔT_{id} and an excess component ΔT^E by analogy to the modeling of the "real" thermophysical properties of fluids, that is,

$$\Delta T_{mix} = \Delta T_{id} + \Delta T^E \text{ or } \Delta T_{mix}/\Delta T_{id} = 1 + \Delta T^E/\Delta T_{id} \quad (17)$$

and $\Delta T^E/\Delta T_{id}$ is linked to Δxy by

$$\Delta T^E/\Delta T_{id} = K_{12}\Delta xy. \quad (18)$$

Combining Eqs. (17) and (18) with (15a) and (15b) yields

$$\alpha_{id,T}/\alpha_{mix} = 1 + K_{12}\Delta xy. \quad (19)$$

(The reciprocal relationship of the ratio α_{mix}/α_{id} mentioned above and shown in Figs. 23 and 24 is used in the following to simplify the form of the equations.)

The parameter K_{12} has been fitted at constant heat flux (q = 20 kW/m^2) to various binary systems of refrigerants in [151] – also comprising the two of Figs. 23 and 24 – resulting in a strong increase of K_{12} with reduced pressure (Fig. 26a), which is similar for the five binary systems investigated and reveals a trend of K_{12} increasing with the distance ΔT_{sN} of the normal boiling points of the components (cf. Fig. 27) that can be seen well at the intermediate value of p^* = 0.5 in Fig. 26a.

Using the modified K_{12}-values of Fig. 26a, the representation of experimental data is nearly as good as for recent more sophisticated approaches, particularly at high heat fluxes, as has been shown in [151]. (Originally, values for K_{12} at atmospheric pressure were given in [150, 152–154] together with a much weaker

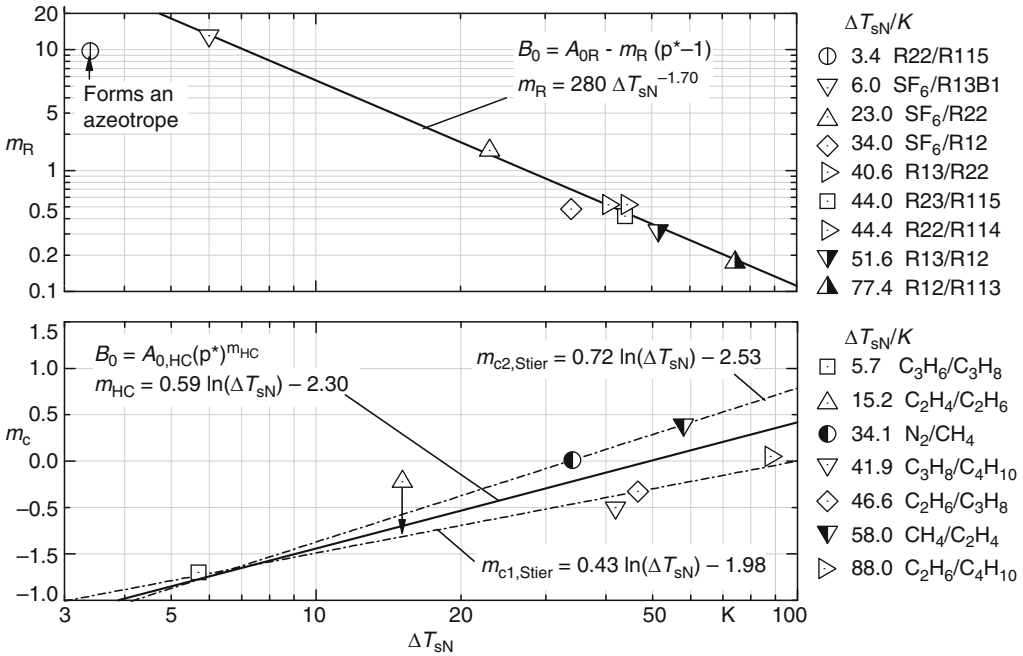

H2. Fig. 27. Connection of the parameter B_0 with the distance ΔT_{sN} of the normal boiling points of the pure components for mixtures of halocarbon refrigerants (*top*) and hydrocarbons (*bottom*) according to [30].

pressure dependence, the shaded area in Fig. 26a, which restricted the method to near-atmospheric pressures, $p^* < 0.05$).

Employing the measurements on SF_6/R13B1 shown in Fig. 23 and on various other binary systems up to high reduced pressures [147], Schlünder developed a promising calculation method based on the mass transfer by diffusion that takes place in the liquid layer near the heated wall [155] (cf. [156, 157]). Introducing some simplifications that start with the assumption (Fig. 21b)

$$T_w - T_{ph} = \Delta T_{id}, \tag{20}$$

so that the effective temperature difference for heat transfer in the mixture is the same as in the pure components and there are no differences in the mechanisms for bubble formation and release between pure substances and mixtures, then

$$\Delta T_{mix}/\Delta T_{id} = \alpha_{id,T}/\alpha_{mix} = \left[\Delta T_{id} + \left(T_{ph} - T_s\right)\right]/\Delta T_{id} = 1 + \left(T_{ph} - T_s\right)/\Delta T_{id}. \tag{21}$$

Next, modeling $(T_{ph} - T_s)$ by diffusion leads to

$$\left(T_{ph} - T_s\right)] \approx (dT_{sat}/dx_1)(\Delta xy)_1[1 - \exp(-\Phi)] \tag{22}$$

so that Eq. (21) finally becomes

$$\alpha_{id,T}/\alpha_{mix} = 1 + [1 - \exp(-\Phi)](dT_{sat}/dx_1)(\Delta xy)_1/\Delta T_{id} \tag{21a}$$

where

$$\Phi = B_0 q/\beta_l \rho_l \Delta h_v \tag{23}$$

β_l and ρ_l are the mass transfer coefficient and density in the liquid, Δh_v is the enthalpy of vaporization, and B_0 is a parameter that Schlünder approximated to unity but which can be used for fitting experimental results. When doing so at a constant intermediate heat flux (mostly $q = 20$ kW/m^2), B_0 is found to be a function of the reduced pressure p^*, particularly for narrow boiling binary systems ($\Delta T_{sN} < 10$ K) as can be seen for various binary refrigerant systems in Fig. 26b.

The result generally obtained at the highest pressure, that is, $B_0 = 1$, obviously confirms close to the critical point the assumption of diffusion controlled heat transfer that was made in deriving the model for Eqs. (21) and (21a) and also the numerical value that was inserted in Eq. (23): $\beta_l = 2 \cdot 10^{-4}$ m/s = 0.2 mm/s. Only the order of magnitude for β_l is known, viz. 0.1–0.5 mm/s, deduced from absorption measurements [156]. Hence, the quotient B_0/β_l can also be regarded as a fitting parameter, as had been done in the preceding editions of the *Heat Atlas*.

For wide boiling systems, that is, those for which the normal boiling points of the components are widely spaced ($\Delta T_{sN} >$ 30 K), the value of B_0/β_l remains approximately the same if fitted to moderate or high heat fluxes, even at low pressures (Fig. 26b). However, it increases if ΔT_{sN} is small as mentioned above, or if the heat flux is small [151, 158, 159]. In the latter case, a calculation method that was developed for pure substances [160–162] and applied to binary mixtures by Bier and Bayer [151] should be more appropriate because heat transfer by natural convection is included for those parts of the heated surface where no bubbles are produced [159].

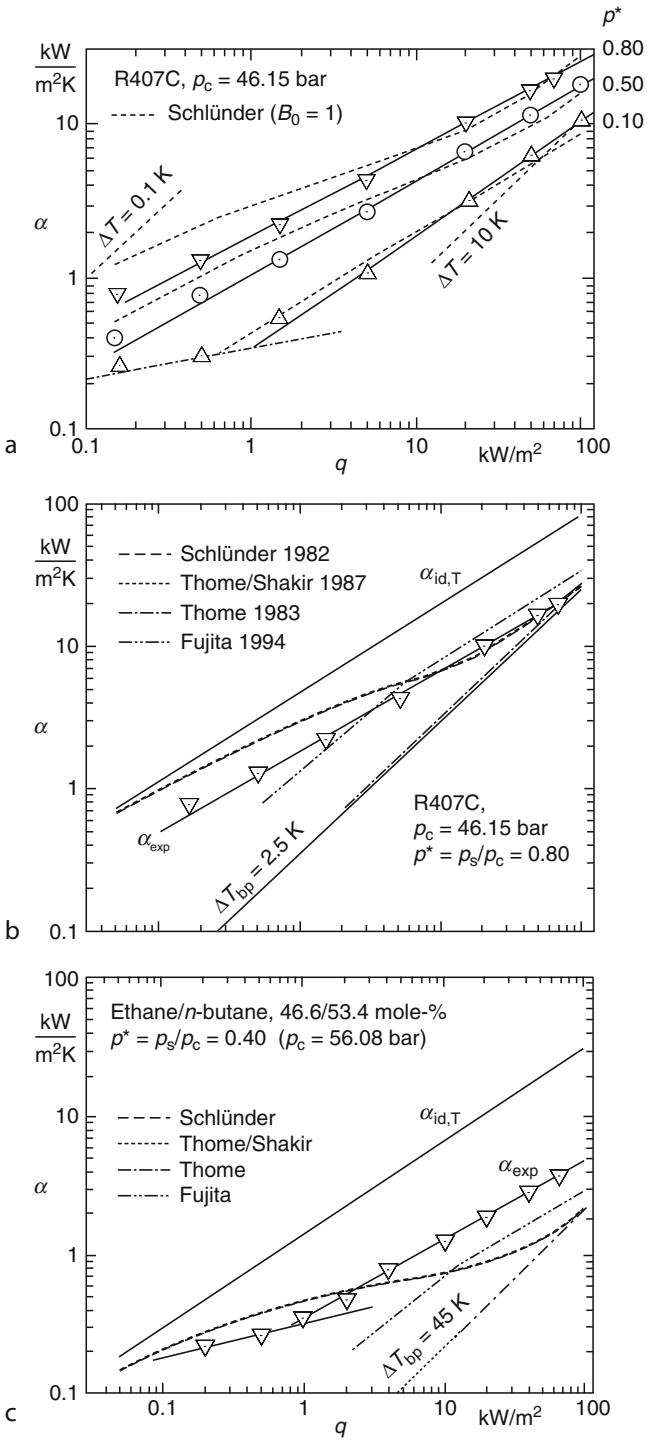

H2. Fig. 28. α-values calculated with Eqs. (21a) and (24) and two more correlations [165, 166] in comparison with experimental data for the narrow boiling ternary R407C [41, 144] (*upper two diagrams*) and the very wide boiling C_2H_6/C_4H_{10} [26, 144] (*lowest diagram*).

Values calculated from Eq. (21a) have been plotted in the diagrams on the left of Fig. 23 (crosses). They reproduce fairly well the deterioration that was determined experimentally, despite the fact that only one numerical value of $B_0/\beta_l = 10^4$ s/m ($B_0 = 2$) was taken for all the heat fluxes and both pressures (corresponding approximately, however, to the average value

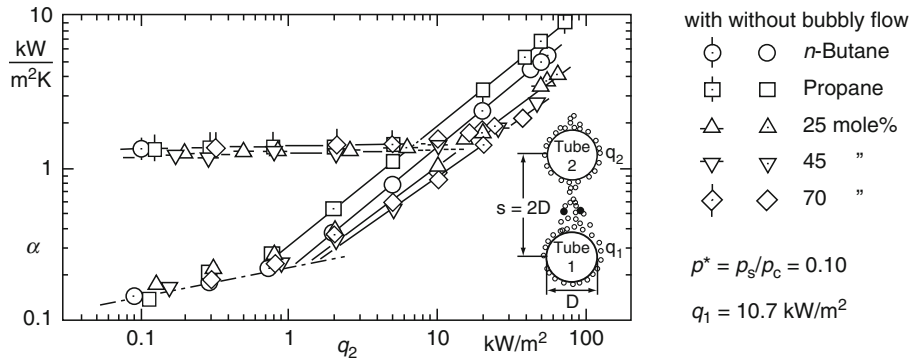

H2. Fig. 29. Simulation of convective improvement of α by bubbles streaming upward from lower tube banks in a bundle for propane/*n*-butane mixtures (from [168]).

following from Fig. 26b for this system and the comparatively high reduced pressures). If a function of q and p^* were to be substituted for B_0/β_l, the measured values would be better reproduced (see [146] for other systems), but the predictive capability would be lost.

Following earlier attempts [151, 159, 163], B_0 was modeled in [30] as a function of ΔT_{sN} (Fig. 27) for refrigerants and hydrocarbons in order to improve the predictive quality. It turns out that reproduction of experimental data is similar to using the interpolation lines in Fig. 26b [30]. In the case of the refrigerants, also the two systems with "negative" pressure dependence (half-closed symbols) are interpolated by the common line, while a different correlation was fitted in [30] to the two hydrocarbons with this behavior. It can be concluded, however, from the good representation of the experiments for C_2H_4/C_2H_6 by the lowest line instead of the triangle on its base in Fig. 27, that using the common full line for all the hydrocarbon systems shown will not increase the deviations of calculated and measured values significantly.

Introducing the temperature glide ΔT_{bp} at total vaporization into Eq. (22) by applying the approximate Eq. (16) results in

$$\left(T_{ph} - T_{sat}\right) = \Delta T_{bp}[1 - \exp(-\Phi)] \tag{22a}$$

and Eq. (21a) in the correlation of Thome and Shakir proposed some years later [164]

$$\alpha_{id,T}/\alpha_{mix} = 1 + [1 - \exp(-\Phi)]\Delta T_{bp}/\Delta T_{id}. \tag{24}$$

If the "mixture factor" K that has been defined (see Fig. 21b) by

$$\Delta T_{mix} = \Delta T_{id} + K\Delta T_{bp} \tag{25}$$

is used for expressing many of the correlations for mixture boiling in a uniform way [41, 144], Eq. (24) can be written as

$$\Delta T_{mix}/\Delta T_{id} = \alpha_{id,T}/\alpha_{mix} = 1 + K\Delta T_{bp}/\Delta T_{id} \text{ with}$$
$$K_{Thome/Shankir} = 1 - \exp(-\Phi). \tag{24a}$$

In Fig. 28, α-values calculated with Eqs. (21a) and (24) or (24a) and two more correlations [165, 166] are compared with experimental data for the narrow boiling ternary R407C [41, 144] and the very wide boiling C_2H_6/C_4H_{10} [26, 144]. As can be seen from Fig. 28a, deviations between the measurements and the values calculated by Eq. (21a) are small for the lowest pressure and all heat fluxes. This is mainly due to the fact that the "mixture effect" is small for this narrow boiling system at low reduced pressures, see Fig. 22c. The same will hold for all of the mixed refrigerants actually used in practice because they are similarly narrow boiling.

Representation of the experimental data is also very good for the two higher pressures at high heat fluxes, but the experiments are significantly overpredicted at the highest pressure and small heat fluxes. (In the calculation for the ternary system, Eq. (21a) has been used in the form extended to multicomponent mixtures as explained in [157], and the same procedure has been applied for the other correlations.)

Results would be the same for Eq. (24), as can be concluded from Fig. 28b. For the very wide boiling binary in Fig. 28c, however, the prediction of neither correlation is satisfactory. The best results are obtained by the correlation of Fujita and Tsutsui [166] for both systems at the intermediate to high reduced pressures shown. Recently, it has been recommended that Eqs. (21a) and (24) be combined to improve prediction for wide boiling binary systems with markedly asymmetric vapor/liquid equilibrium, for example, NH_3/H_2O [167].

Comments on calculation methods for mixture boiling:

a. On the whole, calculation methods for mixture boiling heat transfer are less satisfactory than those discussed in Sect. 3 for pure substances, except for narrow boiling systems at low reduced pressures when Δxy is small and the remixing effect of the bubbles within the boundary layer near the heated wall is high. In a tube bundle, the same effect will be produced by the bubbles rising from the lower banks of tubes, at least at low to intermediate heat fluxes, see Fig. 29 [168]. From the comparison with the pure components it is obvious that the reduction of heat transfer for the mixtures is entirely compensated within the domain where heat transfer is convection controlled, and it may even be improved both for mixtures and their components. The same holds for additional flow of liquid [169]. At higher fluxes, however, the additional convection has no visible influence.
b. The p, T, x phase diagram for systems with closely spaced normal boiling points ($\Delta T_{sN} < 10$ K), and particularly for those with azeotropes, is an important prerequisite for the calculation methods discussed above and must therefore be accurately known.

5 Critical Heat Flux and Film Boiling

5.1 Critical Heat Flux in Nucleate Boiling

According to Kutateladze [170] and Zuber et al. [171–173], the maximum heat flux q_{crit} in saturated pool nucleate boiling (point D in Fig. 2) on horizontal flat plates or plain tubes can be calculated from

$$q_{crit} = K_1 \Delta h_v \rho_v^{0.5} [\sigma(\rho_l - \rho_v)g]^{0.25} \quad (26)$$

where Δh_v is the enthalpy of vaporization, σ is the surface tension, and ρ_v and ρ_l are the densities of the vapor and the liquid respectively.

Zuber derived a numerical value of 0.13 for the factor K_1 from a simplified model for the development of instability in the counterflow of liquid and vapor normal to a horizontal plate. Kutateladze obtained $K_1 = 0.13$ to 0.16 by fitting to measured values.

The pressure dependence of q_{crit} for water according to Eq. (26) has been plotted in Fig. 30. It is similar for all fluids, with a maximum near $p^* = 0.3$. The absolute values, however, are lower by a factor of approximately 10 for organic liquids (as e.g., in Figs. 5 and 32).

As $\sigma \sim (\rho_l - \rho_v)^4$ to a good approximation, the liquid–vapor density difference is represented in Eq. (26) to the power of 1.25. The only other properties in the equation are the enthalpy of vaporization and the vapor density. Many other correlations exist in the literature for the calculation of q_{crit}; most of them contain the terms $\Delta h_v \rho_v^{0.5}$ and $(\rho_l - \rho_v)^m$ in which the exponent m is given by $1.25 < m < 1.5$ [170–177].

Of all the parameters important for q_{crit}, the effect of the pressure has been investigated most. From studies by Borishanskij [178] and Mostinskij [179] and the existing experimental data on q_{crit}, the following function can be interpolated for the relative pressure dependence of q_{crit}, which is analogous to Eq. (7) for the $\alpha(p^*)$-relationship

$$q_{crit}/q_{crit,0} = 2.8\, p^{*0.4}(1 - p^*) \quad (27)$$

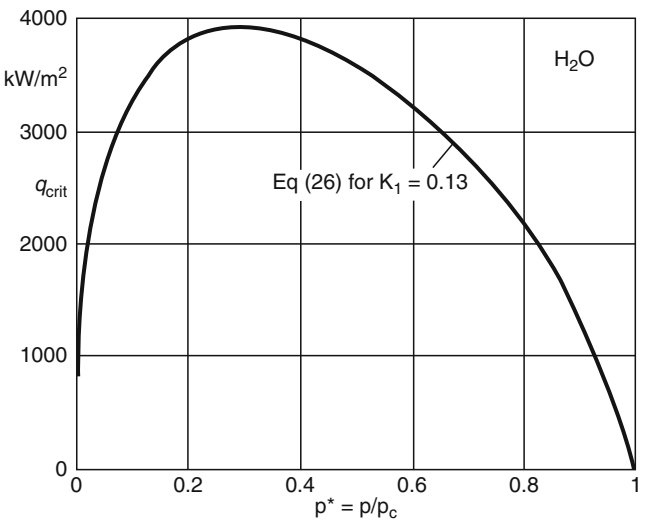

H2. Fig. 30. Maximum heat flux q_{crit} in the nucleate boiling of water as determined from Eq. (26).

where $q_{crit,0}$ is the value for the maximum heat flux at the reference pressure $p_0^* = 0.1$.

In Fig. 31, the relative pressure dependence of q_{crit} according to Eq. (27) is compared with experimental data. It can be seen that the solid line for Eq. (27) lies between the center and the lower limit of the range of experimental scattering. The curve of q_{crit} for water, as determined from Eq. (26), has been included in the diagram in the form of a dashed line. For $0.001 < p^* < 0.6$, it deviates by less than 5% from the values determined from Eq. (27), but at higher p^*, q_{crit} determined from Eq. (26) is considerably higher than many of the experimental data at these pressures, particularly in the case of organic fluids [182, 183, 185–187] (and in [142], also for p^* near 0.1).

Therefore, it is it is recommended that q_{crit} be calculated from Eq. (27) and the reference value $q_{crit,0}$ be determined from experimental data for a particular system fluid – wall at any (reduced) pressure available and to fit the parameter A in

$$q_{crit}/q_{crit,0} = A\, p^{*0.4}(1 - p^*) \quad (27a)$$

to the measured value. If measurements do not exist, then $q_{crit,0}$ should be calculated from Eq. (26) for p_0^*.

Labuntsov [188] demonstrated that, at *very low* reduced pressures, the relative pressure dependence is noticeably less pronounced than following from Eqs. (26) and (27). According to the results of his measurements on water and ethanol at heated walls of various geometries and properties, the relationship is similar to that for liquid metals, which can be described by $q_{crit} \sim p^{*m}$ where $0.15 < m < 0.20$. Consequently, the exponent 0.4 in Eq. (27) is somewhat too high for very low reduced pressures as can also be concluded from the left edge of Fig. 31. (For this reason, it is recommended to divide the pressure range into two [189], e.g., $(q_{crit}/q_{crit,1}) = A_1\, p^{*0.4}(1 - p^*)$ for $p^* \geq 0.1$, and $(q_{crit}/q_{crit,2}) = A_2(p^{*0.2} + p^{*0.5})$ for $p^* \leq 0.1$.)

Equation (26) does not depend on the characteristic dimension L of the heated wall. If $L' = L/[\sigma/(\rho_l - \rho_v)g]^{0.5} < 2$, Lienhard and Dhir [177] proposed a correction

$$q_{crit,L} = K_2 q_{crit,26} \quad (28)$$

where

$$K_2 = 1.19(L')^{-0.25} \quad (29)$$

and $q_{crit,26}$ is the maximum heat flux as determined from Eq. (26). Equation (28) is valid for $0.1 \leq L' \leq 2$. Examples of the upper limits for the correction of Eq. (26) by Eqs. (28) and (29) are $L_{max} = 5$ mm for water at $p = 1$ bar ($p^* = 0.0045$) and $L_{max} = 1$ mm for R125 at $p = 19$ bar ($p^* = 0.53$).

For spheres and horizontal cylinders, the radius, and for fins, the height should be used as characteristic dimensions. The effect of the correction factor K_2 is indicated in Fig. 31 by the shift in the results of measurements on thin wires [185] at $p^* = \text{const.}$ (points marked by a cross are shifted to points marked by a plus sign). It can be seen that the correction reduces the systematic deviations in the results for thin wires.

Many other factors that affect the maximum heat flux in nucleate boiling are not embraced by Eqs. (26)–(29). Subcooling of the bulk liquid may produce a large increase in the

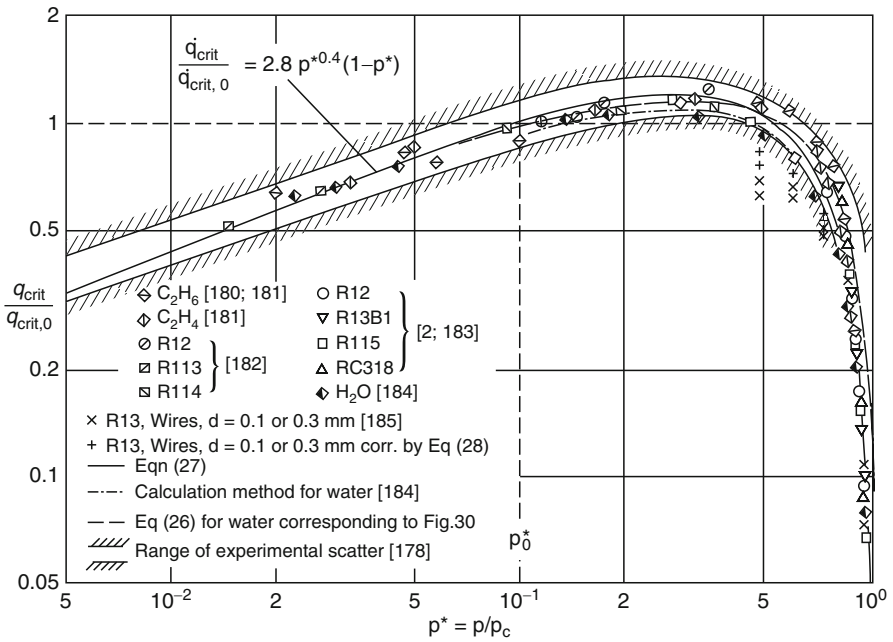

H2. Fig. 31. Relative pressure dependence of q_{crit} from Eqs. (26) and (27) compared with experimental data fitted to the values at $p^*_0 = 0.1$. If this pressure is not included in the range of measurements, the values have been fitted to the lowest experimental pressure [182] or to $p^* = 0.9$ [2, 185].

maximum heat flux, initially increasing linearly with subcooling, then approaching an asymptote. However, as noted in Sect. 1, subcooled conditions are difficult to sustain in pool boiling, unless there is a continuous flow of cold liquid into the vessel. Motion or agitation of the bubbly mixture that directs liquid toward the heated wall may also increase the maximum heat flux. Factors that modify the maximum heat flux in saturated pool boiling include the roughness of the heated surface [190], the type of heating [182], and impurities and the wetting of the heated surface [187]. The results of studies on these effects are inconsistent, so they cannot yet be included in correlations. Therefore, all that can be derived from Eqs. (26)–(29) is an approximate estimate for the maximum heat flux in saturated pool nucleate boiling.

Typical values measured for q_{crit} in nucleate boiling of *binary mixtures* have been plotted in Fig. 32. They lie between or above the corresponding values for the pure components to an extent that depends on the properties of the mixture and the pressure [181]. In analogy to the deterioration in heat transfer, the highest values of q_{crit} frequently occur at intermediate compositions, as can be seen from the curve for 49 mass% C_2H_4 in Fig. 32. The trend that the *relative* difference becomes particularly large at $p^* > 0.9$ (lowest closed rhomb in Fig. 32) is also found in experiments at even higher p^* with SF_6/R13B1 [191].

The same phenomena that are responsible for the impairment in heat transfer (i.e., the additional resistance to heat transport caused by diffusion and the lower numbers of bubbles) retard the coalescence of bubbles to form a film and thus provide a qualitative explanation. Bubble coalescence is further influenced by Marangoni flows driven by local variations in surface tension. Coalescence is opposed or promoted,

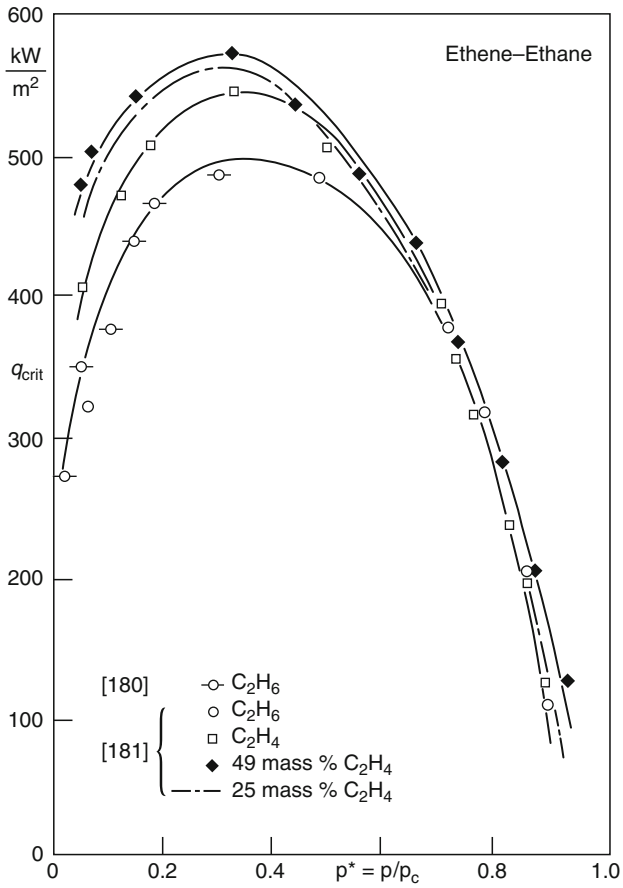

H2. Fig. 32. Maximum heat flux q_{crit} as a function of the reduced pressure for ethane, ethene, and two of their mixtures [181].

depending on whether surface tension increases (positive mixture) or decreases (negative mixture) with increasing fraction of the less volatile fluid [192].

Equation (26) can also be used to calculate q_{crit} for binary mixtures. The reservations are the same as those for the individual components, and the values to be inserted for the properties are those of the mixture. The same recommendation has been submitted by Stephan and Preusser [83], whose measured values for q_{crit} at near-atmospheric pressure always lie between those for the pure components. If the values for the mixture are higher, Eq. (26) yields a conservative estimate.

5.2 Film Boiling

In total film boiling there is no direct contact between the liquid phase and the heated surface so the surface and bulk properties of the heated wall are unimportant. On surfaces with a sloping component (inclined plates, cylinders, and spheres), the vapor in the film flows upward due to gravity and is eventually discharged to the pool. Heat transfer across the vapor film is influenced by the hydrodynamic conditions at the liquid–vapor boundary, including wave formation by Rayleigh–Taylor or Kelvin–Helmholtz instabilities. There is a weak dependence on the characteristic length of the system L. In large systems, the vapor flow may become turbulent. On horizontal surfaces with L larger than the wavelength for Rayleigh–Taylor instability, the vapor is discharged as large periodic bubbles at the wave nodes. (This is consistent with the condition $L/[\sigma/(\rho_l - \rho_v)\, g]^{0.5} > 2$ for the maximum heat flux in nucleate boiling q_{crit} given by Eq. (26) to be independent of L). Subcooling of the bulk liquid increases the heat transfer coefficient in film boiling and influences its stability.

Theoretical and experimental studies of film boiling for a wide range of conditions were reviewed in [197]. In applications aimed at achieving high heat transfer coefficients in boiling on tubes, designers try to avoid film boiling and the relatively simple methods described below may be used to estimate the low heat transfer coefficients for film boiling in saturated pool boiling.

Total film boiling including the effects of radiation was investigated by Bromley in theoretical studies backed up by experiments with carbon tubes (D = 5 to 12 mm) [193, 194] starting at comparatively large wall superheats. The result of his studies in pool boiling [193] is the following implicit relationship between the heat transfer coefficient α in film boiling, the coefficient α_{cond} for heat transport purely by conduction across a laminar film of vapor and the coefficient α_{rad} purely for radiation through the film of vapor:

$$\alpha = \alpha_{cond}(\alpha_{cond}/\alpha)^{1/3} + \alpha_{rad}. \tag{30}$$

His approximate explicit equation for the range which is of interest in engineering, $0 < \alpha_{rad} < 10\ \alpha_{cond}$, is

$$\alpha = \alpha_{cond} + \alpha_{rad}[(3/4) + (1/4)/(1 + 2.62\,\alpha_{cond}/\alpha_{rad})]. \tag{30a}$$

A more exact calculation by Roetzel [195] led to an equation that yields values for α a few percent higher than those obtained from Eq.(30a).

The heat transfer coefficient α_{rad} for the radiation component is obtained from Eq.(1) by substituting q_{rad} for q, where $q_{rad} = C_{12}\,(T_w^{\,4} - T_l^4)$, given in Chap. K1. The transport of heat by conduction through the laminar vapor film is given by

$$\alpha_{cond} = K_f (L\Delta T)^{-1/4} \left(\lambda_v^3 \rho_v\, \Delta h\, \Delta\rho\, g/\eta_v\right)^{1/4} \tag{31}$$

where λ_v, ρ_v, η_v are the thermal conductivity, density, and dynamic viscosity of the vapor, evaluated at $T_m = 0.5\,(T_w + T_l)$, and $\Delta\rho = \rho_l\,(T_{sat}) - \rho_v\,(T_m)$, $\Delta h = h_l\,(T_{sat}) - h_v(T_m)$ are the differences in density and specific enthalpy between the vapor and the liquid. $\Delta T = T_w - T_l$ (with $T_l = T_{sat}$) is the superheat of the wall, L is the characteristic dimension of the heater ($L = D$

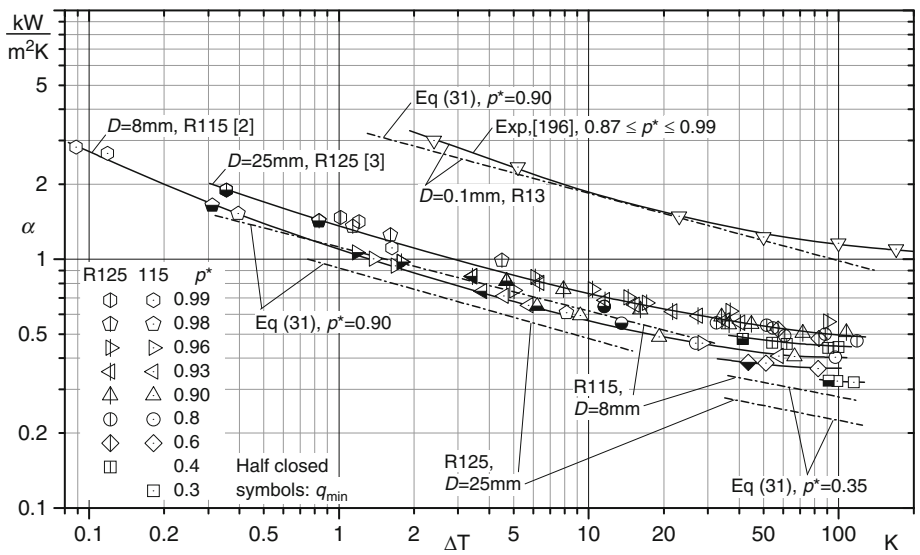

H2. Fig. 33. Comparison of heat transfer coefficients calculated from Eq.(31) with experimental data for film boiling of refrigerants on a thin Pt-wire or copper tubes with different diameters at small superheats ΔT.

for horizontal tubes; $L = H$ for vertical walls). The empirical parameter for horizontal heaters is $K_f = 0.62 \pm 0.04$ [193]; and for vertical walls, 0.8 [195].

Most of the experimental data on which these equations are based have been obtained in experiments at low reduced pressures. Examples of measurements for p^* up to 0.99 are shown in Fig. 33 for refrigerants R115 and R125 on 8 and 25 mm diameter horizontal tubes and R13 on a 0.1 mm wire. Unfilled symbols correspond to total film boiling; half-filled symbols indicate the lower limit q_{min}. For these conditions, the superheats ΔT and the absolute temperatures of the interfaces for film boiling are comparatively small, so α_{rad} is only a few % of α_{cond}.

In this logarithmic plot of α vs. ΔT, the heat transfer coefficients calculated from Eq.(31), approximately straight dot-dashed lines, are compared with the experimental data (slightly curved solid interpolation lines) in the range $0.3 < p^* < 0.99$. For the 0.1 mm wire and the 8 mm tube at intermediate values of ΔT, Eq.(31) is in close agreement with the experimental data, indicating that it continues to represent well the influences of ΔT, D, and fluid properties at large values of p^*. For a given fluid, the change in the combination of properties in Eq.(31) with pressure is small and the experimental data for R115 and R125 in the range $0.8 < p^* < 0.99$ lie on the same line within experimental uncertainty, with only a comparatively small decrease at $p^* < 0.6$.

At small and large values of ΔT, the experimental values of α become larger than the predictions of Eq.(31). For the 25 mm tube, the predictions are exceeded by approximately 50%, even at intermediate superheats.

Photographs and high-speed videos of the large tube reveal waves on the liquid – vapor interface. Waves are also visible for smaller tubes and ΔT's at very high p^*. Enhancement of the conduction assumed in Eq.(31) by convection and/or turbulence is then to be expected, as reviewed in [197].

A somewhat more pronounced influence of pressure than that predicted by Eq.(31) has been found in [198] for the entire range of existence of the liquid phase between triple point and critical point for CO_2 boiling on thin wires of $D = 0.05$, 0.1, and 0.4 mm diameter. Pitschmann and Grigull [199] extended Bromley's theory particularly to thin wires and developed a correlation that has been well confirmed by experiment [185, 187, 198].

A calculation method that has been proposed for film boiling of *binary mixtures* on vertical heater surfaces [200] includes the effect of diffusion on the temperature at the surface of the film and on the heat transfer coefficient (see also [201]).

The surface condition and bulk properties of the wall conditions have a strong effect on the reversion of film boiling to transition boiling and then nucleate boiling at a minimum heat flux q_{min} during transient cooling and this leads to variations between the results of different studies that are important in processes that involve quenching, such as heat treatment, cooldown of cryogenic systems, and firefighting. When the superheated surface is liquid and the evaporating liquid is subcooled, hydrodynamic instabilities of both interfaces at q_{min} may lead to an explosive increase in the generation of vapor, with potentially disastrous consequences in severe nuclear accidents, continuous casting, and spills of cryogenic fluids on water.

Theoretical predictions of this lower limit (point F in Fig. 2 and half-closed symbols in Fig. 33), reviewed in [185, 187], differ widely from one another and from measured values [183, 187]. It can be shown from measurements at reduced pressures $p^* \geq 0.6$ that the ratio of the maximum heat flux q_{crit} in nucleate boiling and the minimum heat flux q_{min} in film boiling is roughly independent of pressure and the properties of the fluid [2, 3, 182, 183, 202]. Thus

$$q_{crit}/q_{min} = 8 \pm 2. \tag{32}$$

Together with Eqs. (26) and (27), this relationship provides a first approximation for q_{min} at $p^* > 0.6$ in saturated pool boiling.

6 Bibliography

1. Nukijama S (1934) Maximum and minimum values of heat transmitted from metal to boiling water under atmospheric pressure. J Soc Mech Eng 37:53–54, 367–374
2. Gorenflo D (1977) Wärmeübergang bei Blasensieden, Filmsieden und einphasiger freier Konvektion in einem großen Druckbereich. Abh. deutsch. Kälte- und Klimatechn. Ver. Nr. 22. Verl. C. F. Müller, Karlsruhe
3. Gorenflo D, Baumhögger E, Herres G (2010) Natural convective heat transfer near the critical state. In: Proceedings of 3rd IIR Conference on thermophysical properties and transfer processes of refrigerants, Boulder, CO, 2009, paper # 193; cf. also: Nucleate boiling, film boiling and single-phase free convection at pressures up to the critical state. Part I: Integral heat transfer for horizontal copper cylinders. Part II: Circumferential variation of the wall superheat for a horizontal 25 mm copper cylinder. Int J Refrig 33(7)
4. Kenning DBR (1999) What do we really know about nucleate boiling? In: IMechE conference transactions, 6th UK National heat transfer conference, Edinburgh, pp 143–167
5. Stephan K (1965) Stabilität beim Sieden. BWK 17:571–578
6. Stephan K (1966) Übertragung hoher Wärmestromdichten an siedende Flüssigkeiten. Chem Ing Techn 38:112–117
7. Auracher H (1990) Transition boiling. Proceedings of the 9th international heat transfer conference, Jerusalem, vol 1, pp 69–90
8. Dhir VK (1990) Nucleate and transition boiling heat transfer under pool and external flow conditions. Proceedings of the 9th international heat transfer conference, Jerusalem, vol 1, pp 129–156
9. Krischer O (1963) Die wissenschaftlichen Grundlagen der Trocknungstechnik, 2 Aufl. Springer-Verlag, Berlin
10. Börner H (1977) Über den Wärme- und Stoffübergang an umspülten Einzelkörpern bei Überlagerung von freier und erzwungener Strömung. VDI-Forsch.-Heft 513. Düsseldorf: VDI-Verl. 1965 and: VDI-Wärmeatlas, Abschn. Fa. 3. Auflage. VDI-Verl, Düsseldorf
11. Barthau G, Hahne E (2001) Nucleate pool boiling of R134a on a gold-plated copper test tube. In: Proceedings of the 1st IIR Conference on thermophysical properties and transfer processes of refrigerants, Paderborn, pp 372–379
12. Sokol P, Schömann H, Rott W, Caplanis S, Gorenflo D (1990) Wärmeübergang beim Blasensieden neuer Kältemittel. DKV-Tagungsbericht, pp 323–340
13. Jakob M, Linke W (1935) Der Wärmeübergang beim Verdampfen von Flüssigkeiten an senkrechten und waagerechten Flächen. Phys Zeitschr 36:267–280
14. Gorenflo D (1967) Influence of pressure on heat transfer from horizontal tubes to boiling refrigerants. Proceedings of the 12th international congress of refrigeration, Madrid, vol 2, pp 587–598
15. Mohrlok K (2005) Wärmeübergang beim Behältersieden von Kältemittel/Öl-Gemischen an einem Glattrohr und einem Hochleistungsrohr. DKV-Forschungsbericht Nr.71, Ph.D. thesis, University of Stuttgart
16. Caplanis S (1997) Wärmeübertragung und Blasenbildung an Hochleistungs-Verdampferrohren. University (GH) of Paderborn
17. Gorenflo D, Chandra U, Kotthoff S, Luke A (2004) Influence of thermophysical properties on pool boiling heat transfer of refrigerants. Int J Refrig

27:492–502. (extended version of a presentation at 8th UK national heat transfer conference, Oxford, 2003)
18. Kotthoff S, Gorenflo D (2005) Influence of the fluid on pool boiling heat transfer of refrigerants and other organic substances. In: Proceedings of the 2nd IIR conference on thermophysical properties and transfer processes of refrigerants, Vicenza, paper #TP47
19. Gorenflo D, Kotthoff S (2005) Review on pool boiling heat transfer of carbon dioxide. Int J Refrig 28:1169–1185
20. Kotthoff S, Gorenflo D (2009) Heat transfer and bubble formation on horizontal copper tubes with different diameters and roughness structures. Heat Mass Transf 45:893–908
21. Gorenflo D, Luke A, Danger E (1998) Interactions between heat transfer and bubble formation in nucleate boiling. Proceedings of the 11th int. heat transfer conf., Kyongju, vol 1, pp 149–174
22. Dhir VK (2006) Mechanistic prediction of nucleate boiling heat transfer – achievable or a hopeless task? J Heat Transfer 128:1–12
23. Stephan P, Fuchs T (2009) Local heat flow and temperature fluctuations in wall and fluid in nucleate boiling systems. Heat Mass Transfer 45:919–928
24. Bier K, Gorenflo D, Wickenhäuser G (1973) Zum Wärmeübergang beim Blasensieden in einem weiten Druckbereich. Chem Ing Techn 45:935–942
25. Bier K, Gorenflo D, and Wickenhäuser G (1977) Pool boiling heat transfer at saturation pressures up to critical. In: Heat transfer in boiling. Hemisphere Publishing Corporation, Washington, London, pp 137–158
26. Bednar WH (1993) Wärmeübergang beim Blasensieden von binären Kohlenwasserstoffgemischen. PhD thesis, University (TH) of Karlsruhe, see also: Bednar W, Bier K (1993) Wärmeübergang beim Behältersieden von Propan/n-Butan-Gemischen. DKV-Tagungsbericht 20, Bd. II. 1, pp 323–340
27. Pinto A (1995) Wärmeübergang und Blasenbildung beim Sieden von Propan an einem geschmirgelten Kupferrohr in einem großen Druckbereich. PhD thesis, University of Paderborn
28. Luke A (1996) Beitrag zum Einfluss der Mikrostruktur von Heizflächen auf den Wärmeübergang beim Blasensieden. PhD thesis, University of Paderborn; cf. also: Luke A (1997) Pool boiling heat transfer from horizontal tubes with different surface roughness. Int J Refrig 20:561–574
29. Mertz R (2001) Beitrag zum Behältersieden von Kohlenwasserstoffen an Rohren mit hinterschnittenen Oberflächen. PhD thesis, University of Stuttgart
30. Stier K-H (2003) Beitrag zur Druckabhängigkeit des Wärmeübergangs beim Blasensieden von binären Gemischen. DKV-Forschungsbericht Nr. 69, PhD thesis, University (TH) of Karlsruhe; cf. also: Span R, Buljina I, Gorenflo D (2005) Review on pool boiling heat transfer of wide boiling binary refrigerant mixtures. In: Proceedings of the 2nd IIR conference on thermophysical properties and transfer processes of refrigerants, Vicenza, paper #TP48
31. Danger E (2004) Wärmeübergang und Blasenbildung beim Sieden. DKV-Forschungsbericht Nr. 70, PhD thesis, University of Paderborn
32. Jung D, Lee H, Bae D, Oho S (2004) Nucleate boiling heat transfer coefficients of flammable refrigerants. Int J Refrig 27:409–414
33. Bier K, Lambert M (1990) Heat transfer in nucleate boiling of different low boiling substances. Int J Refrig 13:293–300
34. Gorenflo D, Sokol P, Caplanis S (1990) Pool boiling heat transfer from single plain tubes to various hydrocarbons. Int J Refrig 13:286–292
35. Siebert M (1987) Untersuchung zum Einfluß des Wandmaterials und des Rohrdurchmessers auf den Wärmeübergang von horizontalen Rohren an siedende Flüssigkeiten, PhD thesis, University (TH) of Karlsruhe
36. Gorenflo D, Kotthoff S, Chandra U (2004) New measurements of pool boiling heat transfer with hydrocarbons and other organics for update of VDI-Heat Atlas calculation method. In: Proceedings of the 6th IIR-Gustav Lorentzen conference, Glasgow, paper 1/C/1.00
37. Braun R (1992) Wärmeübergang beim Blasensieden an der Außenseite von geschmirgelten und sandgestrahlten Rohren aus Kupfer, Messing und Edelstahl, PhD thesis, University (TH) of Karlsruhe
38. Hübner P (2000) Zum Wärmeübergang beim Blasensieden an Rippenrohren. PhD thesis, University (GH) of Paderborn
39. Kotthoff S, Gorenflo D (2008) Pool boiling heat transfer to hydrocarbons and ammonia: A state-of-the-art review. Int J Refrig 31:573–602
40. Jung D, Kim Y, Ko Y, Song K (2003) Nucleate boiling heat transfer coefficients of pure halogenated refrigerants. Int J Refrig 26:240–248
41. Köster R (2001) Phasengleichgewicht und Wärmeübergang beim Sieden von Gemischkältemitteln. DKV-Forschungsbericht Nr. 64, PhD thesis, University of Paderborn; cf. also: Köster R, Kotthoff S, Gorenflo D (2001) Pool boiling heat transfer and phase equilibrium: equimolar binary R125/134a compared with ternary R407C. In: Proceedings of the 1st IIR conference on thermophysical properties and transfer processes of refrigerants, Paderborn, pp 344–353
42. Baumhögger E, Buljina I, Gorenflo D (2008) Wärmeübergang beim Sieden von R125 ($CHF_2.CF_3$) in freier Konvektion bis in den kritischen Zustandsbereich. DKV-Tagungsbericht, Bd.II.1, pp 127–153
43. Barthau G, Hahne E (2000) Nucleation site density and heat transfer in nucleate pool boiling of refrigerant R134a in a wide pressure range. In: Proceedings of the 3rd European thermal sciences conference, Heidelberg, vol 2, pp 731–736
44. Park K-J, Jung D (2007) Boiling heat transfer enhancement with carbon nanotubes for refrigerants used in building air conditioning. Energy Build 39:1061–1064
45. Saiz Jabardo JM, Ribatski G, Stelute E (2009) Roughness and surface material effects on nucleate boiling heat transfer from cylindrical surfaces to refrigerants R134a and R123. Exp Therm Fluid Sci 33:579–590
46. Kotthoff S (2005) Unpublished experimental results, ThEt, University of Paderborn
47. Maxwell H (2005) Einfluss der Stoffeigenschaften auf den Wärmeübergang beim Blasensieden. Diplomarbeit, ThEt, University of Paderborn
48. Kotthoff S, Chandra U, Gorenflo D, Luke A (2004) New measurements of pool boiling heat transfer for carbon dioxide in a wide temperature range. In: Proceedings of the 6th IIR-Gustav Lorentzen conference, Glasgow, paper 2/A/3.30
49. Loebl S, Kraus WE (2004) Pool boiling heat transfer of carbon dioxide on a horizontal tube. In: Proceedings of the 6th IIR-Gustav Lorentzen conference, Glasgow, paper 1/A/1.20; cf. also: (2004) Zum Wärmeübergang bei der Verdampfung von Kohlendioxid am horizontalen Rohr. DKV-Tagungsbericht, Bd.II.1, 219–232
50. Bier K, Rüthlein H (1988) Apparatus for precise measurements of pool boiling heat transfer in the temperature range of liquid nitrogen. Int J Refrig 11:321–328
51. Belyakov VP, Orlov VK (1987) Heat transfer at boiling of nitrogen under subatmospheric pressure and its intensification. In: Bougard J, Afgan N (eds) Heat and mass transfer in refrigeration and cryogenics. Washington, Hemisphere Publishing, pp 547–552
52. Levterov AI, Semena M, Zaripov VK, Gershuni AN (1983) Boiling of nitrogen on a porous surface. Therm Eng 30(3):174–177
53. Kravchenko VA, Ostrovskij YN (1979) Effect of surface roughness on boiling heat transfer to light hydrocarbons and nitrogen. Heat Transfer Sov Res 11:133–137
54. von Hofmann TME (1977) Wärmeübergang beim Blasensieden verflüssigter Gase und ihrer binären Gemische. PhD thesis, ETH Zürich; cf. also: Wärme- und Stoffübertragung 11:189–193
55. Thome LR, Bald WB (1978) Nucleate pool boiling in cryogenic binary mixtures. In: Proceedings of the 7th international cryogenic engineering conference, London, pp 523–530
56. Akhmedov FD, Grigorev VA, Dudkevich AS (1974) The boiling of nitrogen at pressures from atmospheric to critical. Teploenergetika 21 (1):84–85
57. Grigorev VA, Pavlov YM, Ametistov EV (1973) Correlating experimental data on heat transfer with pool boiling of several cryogenic liquids. Teploenergetika 20(9):57–63
58. Ackermann H, Bewilogua L, Vinzelberg H (1975) Bubble boiling from heated surfaces of different material in liquid nitrogen. Cryogenics 15:677–678
59. Ackermann H, Bewilogua L, Jahn A, Knöner R, Vinzelberg H (1976) Heat transfer in nitrogen-methane mixtures under pressure with film boiling. Cryogenics 16:497–499
60. Bewilogua L, Knöner R, Vinzelberg H (1975) Heat transfer in cryogenic liquids under pressure. Cryogenics 15:121–125
61. Verkin BI, Kirichenko YA, Charkin AI (1976) Cryogenic liquid boiling in inhomogeneous magnetic field. In: Proceedings of the 6th international cryogenic engineering conference, Grenoble, pp 292–294
62. Bland ME, Bailey CA, Davey G (1973) Boiling from metal surfaces immersed in liquid nitrogen and liquid hydrogen. Cryogenics 13:651–657

63. Lyon DN (1968) Pool boiling of cryogenic liquids. Chem Eng Progr Symp Ser 64(87):82–92
64. Kosky PG, Lyon DN (1968) Pool boiling heat transfer to cryogenic liquids. AIChE J 14:372–387
65. Astruc JM, Perroud P, Lacaze A, Weil L (1967) Pool boiling heat transfer in liquid neon. In: Advances in cryogenic engineering, vol 12. New York, Plenum Press, pp 387–394
66. Lyon DN (1964) Peak nucleate boiling heat fluxes and nucleate boiling heat transfer coefficients for liquid N_2, liquid O_2 and their mixtures in pool boiling at atmospheric pressure. Heat Mass Transfer 7:1097–1116
67. Mulford RN, Nigon JP, Dash JG, Keller WE (1963) Heat exchange between a copper surface and liquid hydrogen and nitrogen. Ext. from secret Doc. LAMS-1443. Aus: Vance RW (1963) Cryogenic technology. Wiley, New York/London
68. Hodge, Brickwede from Richards RJ, Steward WG, Jacobs RB (1961) A survey of the literature on heat transfer from solid surfaces to cryogenic fluids. NBS TN 122, Boulder Laboratories, October 1961. From: Vance RW (1963) Cryogenic technology. Wiley, New York/London
69. Claas CR, DeHaan JR, Piccone M, Cost RB (1960) Boiling heat transfer to liquid hydrogen from flat surfaces. Adv Cryog Eng 5:254–261
70. Weil L, Lacaze A (1955) Heat exchanges in liquid hydrogen boiling under pressure. In: Proceedings of the 9th international congress of refrigeration, Paris, vol I, Paper 1.13, pp 1024–1027
71. Blanchero JT, Barker GE, Boll RH (1951) Heat transfer characteristics of boiling oxygen, fluorine and hydrazine. Engineering research institute, University of Michigan. From: Vance RW (1963) Cryogenic technology. Wiley, New York/London
72. Haselden GG, Peters JI (1949) Heat transfer to boiling liquid oxygen and liquid nitrogen. Trans Inst Chem Eng (Lond) 27:201–208
73. Shugaev VA, Pavlov YM, Potekhin SA (1983) Certain principles of heat transfer with nucleate boiling of helium. Therm Eng 30(8):487–490
74. Grigorev VA, Klimenko VV, Pavlov YM, Ametistov YV, Klimenko AV (1977) Characteristic curve of helium pool boiling. Cryogenics 17:155–156
75. Deev VI, Keilin E, Kovalev IA, Kondratenko AK, Petrovichev VI (1977) Nucleate and film pool boiling heat transfer to saturated liquid helium. Cryogenics 17:557–562
76. Verkin BI, Kirichenko YA, Kozlov SM, Levchenko NM (1976) Heat transfer in helium I. In: Proceedings of the 6th international cryogenic engineering conference, Grenoble, pp 289–291
77. Jergel M, Stevenson R (1974) Contribution to the static heat transfer to boiling liquid helium. Cryogenics 14:431–433
78. Jergel M, Stevenson E (1971) Static heat transfer to liquid helium in open pools and narrow channels. Int J Heat Mass Transfer 14:2099–2107
79. Holdredge RM, McFadden PW (1970) Heat transfer from horizontal cylinders to a saturated helium I bath. In: Proceedings of the 16th cryogenic engineering conference, Kitakyushu, pp 352–358
80. Smith RV (1969) Review of heat transfer to helium. I. Cryogenics 9:11–19
81. Lyon DN (1965) Boiling heat transfer and peak nucleate boiling fluxes in saturated liquid helium between the lambda and critical temperatures. Adv Cryog Eng 10b:371–379
82. Karagounis A (1956) Heat transfer coefficient for liquid helium. Bull Inst Intern Froid, Annexe 2:195–199
83. Stephan K, Preußer P (1979) Wärmeübergang und maximale Wärmestromdichte beim Behältersieden binärer und ternärer Flüssigkeitsgemische. Chem Ing Techn MS 649–679, Synopse Chem Ing Techn 51:37
84. Gorodov AK, Kabankov ON, Martinov YK, Yagov VV (1979) Effect of the material and of the thickness of the heating surface on the heat transfer rate in boiling of water and ethanol at subatmospheric pressures. Heat Transfer Sov Res 11(3):44–52
85. Happel O (1975) Wärmeübergang bei der Verdampfung binärer Gemische im Gebiet des Blasen- und Übergangssiedens. PhD thesis, Ruhr-Universität Bochum
86. Lorenz JJ, Mikic BB, Rohsenow WM (1974) The effect of surface conditions on boiling characteristics. Proceedings of the 5th int. heat transfer conf., Tokyo, vol 4, pp 35–39
87. Fedders H (1971) Messung des Wärmeübergangs beim Blasensieden von Wasser an metallischen Rohren. Kernforschungsanlage Jülich, Jül-740 RB
88. Borishanskij VM, Bobrovich GI, Minchenko FP (1969) Heat transfer from a tube to water and to ethanol in nucleate pool boiling. In: Kutateladze SS (ed) Problems of heat transfer and hydraulics of two-phase media. Pergamon Press, Oxford, pp 85–106
89. Minchenko FP, Firsova EV (1969) Heat transfer to water and water-lithium salt solutions in nucleate pool boiling. In: Kutateladze SS (ed) Problems of heat transfer and hydraulics of two-phase media. Pergamon Press, Oxford, pp 137–151
90. Körner M (1967) Beitrag zum Wärmeübergang bei der Blasenverdampfung binärer Gemische. PhD thesis, TH Aachen
91. Raben IA, Beaubœuf RT, Commerford GE (1965) A study of heat transfer in nucleate pool boiling of water at low pressure. Chem Eng Progr Symp Ser 61(57):249–257
92. Borishanskij VM, Kozyrev AP, Svetlova LS (1964) Heat transfer in the boiling of water in a wide range of saturation pressure. Teplofiz Vysok Temp 2(1):119–121
93. Golowin VS, Koltschugin BA, Labunzow DA (1963) Experimentelle Untersuchungen des Wärmeübergangs und der kritischen Wärmestromdichte beim Sieden von Wasser bei freier Konvektion (russ.). Ing Fiz Journ 6(2):3–7
94. Fritz W, Wanninger W (1963) Blasenverdampfung im Sättigungszustand der Flüssigkeit an einfachen Heizflächen. VDI-Wärmeatlas, Abschn. Hb, 1. Aufl
95. Stephan K (1963) Beitrag zur Thermodynamik des Wärmeübergangs beim Sieden. Abh. deutsch. Kältetech. Ver. Nr. 18. Karlsruhe: Verlag C. F. Müller; cf. also: Chem Ing Techn 35:775–784
96. Ribatski G, Saiz Jabardo JM (2003) Experimental study of nucleate boiling of halocarbon refrigerants on cylindrical surfaces. Int J Heat Mass Transfer 46:4439–4451
97. Gorenflo D, Sokol P, Caplanis S (1991) Zum Wärmeübergang beim Blasensieden von Kohlenwasserstoffen und Halogen-Kältemitteln an einem Glattrohr und einem Hochleistungs-Rippenrohr. Wärme- und Stoffübertragung 26:273–281
98. Gorenflo D, Schömann H, Sokol P, Caplanis S (1990) Zum Einfluß der Oberflächenrauhigkeit und des Rohrdurchmessers beim Blasensieden an einzelnen Glatt- und Rippenrohren. Wärme- u. Stoffübertr 25:265–272
99. Schömann H (1994) Beitrag zum Einfluß der Heizflächenrauhigkeit auf den Wärmeübergang beim Blasensieden. PhD thesis, University (GH) of Paderborn
100. Nishikawa K, Fujita Y, Ohta H, Hidaka S (1982) Effect of the surface roughness on the nucleate boiling heat transfer over the wide range of pressure. In: Proceedings of the 7th international heat transfer conference, München, vol 4, pp 61–66
101. Cooper MG (1984) Heat flow rates in saturated nucleate boiling – a wide ranging examination using reduced properties. Adv Heat Transfer 16:157–239
102. Gorenflo D, Sokol P, Caplanis S (1991) Pool boiling heat transfer to new refrigerants. In: Proceedings of the 18th international congress of refrigeration, Montreal, vol II, pp 423–428
103. Sokol P (1994) Untersuchungen zum Wärmeübergang beim Blasensieden an Glatt- und Rippenrohren mit großem Außendurchmesser. PhD thesis, University (GH) of Paderborn
104. Möller C, Groß U, Hahne E (1992) Einfluß von Öl auf den Wärmeübergang beim Sieden neuer Kältemittel. DKV-Statusbericht 12:81–87
105. Hahne E, Shen J, Spindler K (November 1993) Blasensieden von Propan am Draht. Unveröffentlichte Messungen am Institut f. Thermodynamik und Wärmetechnik, Universität Stuttgart
106. Shi K (1989) Wärmeübergang beim Sieden am waagerechten Draht. PhD thesis University of Stuttgart; cf. also: Shi K, Hahne E, Möller C, U. Groß U (1990) Untersuchungen des Wärmeüberganges beim Sieden der Ersatzkältemittel R134a und R152a. DKV-Tagungsbericht 17, pp 313–321 and Shi K, Hahne E, Groß U (1991) Pool boiling heat transfer in HFC-134a, HFC-152a and their mixtures. In: Proceedings of the 18th international congress of refrigeration, Montreal, vol II, pp 459–463
107. Kaupmann P (1999) Durchmessereinfluß und örtlicher Wärmeübergang beim Blasensieden an horizontalen Stahlrohren. PhD thesis, University (GH) of Paderborn; cf. also: Kaupmann P, Gorenflo P, Luke A (2001) Pool boiling heat transfer on horizontal steel tubes with different diameters. Multiphase Sci Technol 12:14–26
108. Slipcevic B (1983) Sieden von Halogen-Kältemitteln an einzelnen Rippenrohren. Maschinenmarkt 89:2090–2093

109. Fath W, Gorenflo D (1986) Zum Einsatz von Rippenrohren in überfluteten Verdampfern bei hohen Siedедrücken. DKV-Tagungsbericht 13, pp 315–332
110. Park K-J, Jung D (2010) Nucleate boiling heat transfer coefficients of R1234yf on plain and low fin surfaces. Int J Refrig 33:553–557
111. Kotthoff S, Gorenflo D, Danger E, Luke A (2006) Heat transfer and bubble formation in pool boiling: Effect of basic surface modifications for heat transfer enhancement. Int J Therm Sci 45:217–236
112. Manglik RM, Bergles AE (2004) Enhanced heat and mass transfer in the new millenium: A review of the 2001 literature. J Enhanced Heat Transfer 11:87–118
113. Webb RL, Kim NH (2005) Pool boiling. In: Principles of enhanced heat transfer, 2nd edn. Taylor & Francis
114. Thome JR (1990) Enhanced boiling heat transfer. Hemisphere, Washington, DC
115. Memory SB, Sugiyama DC, Marto PJ (1995) Nucleate pool boiling of R114 and R114-oil mixtures from smooth and enhanced surfaces – I. Single tubes. Int J Heat Mass Transfer 38:1347–1361
116. Ribatski G, Thome JR (2006) Nucleate boiling heat transfer of R134a on enhanced tubes. Appl Therm Eng 26:1018–1031
117. Bier K, Engelhorn HR, Gorenflo D (1976) Wärmeübergang an tiefsiedende Halogenkältemittel. Ki, Klima + Kälte-Ing 4, pp 399–406
118. Slipcevic B (1975) Wärmeübergang bei der Blasenverdampfung von Kältemitteln an glatten und berippten Rohrbündeln. Ki, Klima- u. Kälteingenieur 3, pp 279–86
119. Palen JW, Taborek J, Yilmaz S (1981) Comments to the application of enhanced boiling surfaces in tube bundles. In: International sem advancements in heat exchangers, September 1981, ICHMT Dubrovnik
120. Roser R, Thonon B, Mercier P (1999) Experimental investigations on boiling of n-pentane across a horizontal tube bundle: two-phase flow and heat transfer characteristics. Int J Refrig 22(7):536–547
121. Kramer W (2000) Cross flow and pool boiling of Ethanol-Water mixtures on the outside of horizontal smooth and enhanced tubes. Fortschr.-Ber. VDI Reihe 3 Nr. 640. VDI-Verlag, Düsseldorf
122. Aprin L, Mercier P, Tadrist L (2002) Analysis of experimental results of n-pentane and propane boiling across a horizontal tube bundle. In: Proceedings of the 12th international heat transfer conference, Grenoble
123. Aprin L, Mercier P, Tadrist L (2007) Experimental analysis of local void fraction measurements for boiling hydrocarbons in complex geometry. Int J Multiphase Flow 33:371–393
124. Thonon B (2008) A review of hydrocarbon two-phase heat transfer in compact heat exchangers and enhanced geometries. Int J Refrig 31:633–642
125. Ribatski G, Saiz Jabardo JM, Fockink da Silva E (2008) Modeling and experimental study of nucleate boiling on a vertical array of horizontal plain tubes. Exp Therm Fluid Sci 32:1530–1537
126. Bell KJ (1981) Heat exchangers with phase change. In: Proceedings of the international seminar on advancements in heat exchangers, September 1981, ICHMT, Dubrovnik
127. Palen JW, Jarden A, Taborek J (1972) Characteristics of boiling outside largescale horizontal multitube bundles. AIChE Symp 68:50–61
128. Grant IDR, Chisholm D (1979) Horizontal two-phase flow across tube banks baffled shell-and-tube heat exchanger. J Heat Transfer 101:38–42
129. Grant IDR, Chisholm D (1980) Horizontal two-phase flow across tube banks. Int J Heat Fluid Flow 2:97–100
130. Grant IDR, Colchin CD, Chisholm D (1981) Tube submergence and entrainment on the shell-side of heat exchangers. In: Proceedings of the international seminar on advancements in heat exchangers, September 1981, ICHMT, Dubrovnik
131. Gorenflo D (1966) Zum Wärmeübergang bei der Blasenverdampfung an Rippenrohren. PhD thesis, TH Karlsruhe
132. Müller J, Hahne E (1980) Boiling heat transfer in finned tube bundles. In: Proceedings all union heat transfer conference, Minsk
133. Danilowa GN, Djundin VA (1971) Wärmeübergang bei der Verdampfung von R 12 und R 22 an Rippenrohrbündeln (russ.). Cholod Techn 48:40–46
134. Zimmermann F (1982) Messung der Wärmeübergangskoeffizienten von verdampfenden Kältemitteln bei überfluteter Verdampfung. Ki, Klima-Kälte-Heizung 10:11–17
135. Güttinger M (1970) Die Verbesserung des Wärmeübergangs bei der Verdampfung. In: Proceedings of the 4th int. heat transfer conference, Paris-Versailles, vol 1, Paper HE 2.4.
136. Stephan K, Mitrović J (1981) Heat transfer in natural convective boiling of refrigerant-oil-mixtures in bundles of T-shaped finned tubes. In: 20th national heat transfer conference. Milwaukee
137. Burkhardt J, Hahne E (1979) Influence of oil on the nucleate boiling of refrigerant 11. In: XVth international congress of refrigeration, Venezia, vol 2, pp 537–544
138. Sauer HJ, Gibson K, Chongrungreong S (1978) Influence of oil on the nucleate boiling of refrigerants. In: Proceedings of the 6th int. heat transfer conference, Toronto, vol 1, pp 181–186
139. Stephan K (1964) Einfluß des Öls auf den Wärmeübergang von siedendem Frigen 12 und Frigen 22. Kältetechnik 16:152–166
140. Spindler K, Hahne E (2009) The influence of oil on nucleate boiling heat transfer. Heat Mass Transfer 45:979–990
141. Gorenflo D (1968) Zur Druckabhängigkeit des Wärmeübergangs an siedende Kältemittel bei freier Konvektion. Chem Ing Techn 40:757–762
142. Kang DG, Park KJ, Jung D (2009) Nucleate boiling heat transfer coefficients of halogenated refrigerants up to critical heat fluxes. In: Proceedings of the 3rd IIR conference on thermophysical properties and transfer processes of refrigerants, Boulder, CO, paper # 195
143. Bonilla CF, Perry CW (1941) Heat transmission to boiling binary liquid mixtures. Trans AIChE 37:685–705
144. Gorenflo D, Köster R (1999) Pool boiling heat transfer from horizontal tubes to mixtures. In: Mayinger F, Lehner M (eds) Convective flow and pool boiling. Taylor & Francis, Philadelphia, pp 3–22. (Presented at 3rd international conference on boiling heat transfer, Irsee, 1997)
145. Fujita Y, Bai Q, Tsutsui M (1996) Heat transfer of binary mixtures in nucleate pool boiling. In: Proceedings of 2nd European thermal sciences conference, Roma, vol 2, pp 1639–1646
146. Bier K, Schmadl J, Gorenflo D (1982) Pool boiling heat transfer to mixtures of SF_6 and R13B1 at elevated saturation pressures. In: Proceedings of the 7th int. heat transfer conf., München, vol. 4, pp 35–40; cf. also: vt 16 S. 708–10 and Chem Eng Fund 1:79–102
147. Schmadl J (1982) Zum Wärmeübergang bei der Blasenverdampfung binärer Stoffgemische unter hohem Druck. PhD thesis, Universität Karlsruhe (TH)
148. Bieling V (1987) Zum Wärmeübergang beim Blasensieden des Kältemittelstoffsystems R22/R115 in einem großen Druckbereich. PhD thesis, University (GH) of Paderborn
149. Gorenflo D, Bieling V (1987) Heat transfer at pool boiling of mixtures. In: Heat and mass transfer in refrigeration and cryogenics. Hemisphere Publishing, New York, pp 243–257
150. Stephan K, Körner M (1969) Berechnung des Wärmeübergangs verdampfender binärer Flüssigkeitsgemische. Chem Ing Techn 41:409–416
151. Bayer A (1988) Untersuchungen zum Blasensieden von binären Stoffgemischen in einem großen Druckbereich. PhD thesis, University (TH) of Karlsruhe; cf. also: Bier K, Bayer A (1989) Pool boiling heat transfer to binary mixtures in a wide range of saturation pressures. Eurotherm seminar no. 8, Paderborn, pp 150–162
152. Stephan K (1980) Wärmeübertragung beim Verdampfen von Gemischen in natürlicher Strömung. Verfahrenstechnik 14:470–474
153. Preußer P (1978) Wärmeübergang beim Verdampfen binärer und ternärer Flüssigkeitsgemische. PhD thesis, Ruhr-Universität Bochum
154. Stephan K, Preußer P (1978) Heat transfer in natural convection boiling of polynary mixtures. In: Proceedings of the 6th int. heat transfer conf., Toronto, vol 1, pp 187–192
155. Schlünder EU (1982) Über den Wärmeübergang bei der Blasenverdampfung von Gemischen. vt verfahrenstechnik 16:692–698
156. Gropp U, Schlünder EU (1986) The influence of liquid side mass transfer and selectivity during surface and nucleate boiling of liquid mixtures in a falling film. Chem Eng Process 20:103–114
157. Schlünder EU (1986) Heat transfer in nucleate boiling of mixtures. In: Proceedings of the 8th international heat transfer conference, San Francisco. vol 4, pp 2073–2079
158. Gorenflo D, Blein P, Herres G, Rott W, Schömann H, Sokol P (1988) Heat transfer at pool boiling of mixtures with R 22 and R 114. Int J Refrig 11:257–263

159. Rott W (1990) Zum Wärmeübergang und Phasengleichgewicht siedender R22/R114 Kältemittel-Gemische in einem großen Druckbereich. PhD thesis, University (GH) of Paderborn
160. Bier K, Gorenflo D, Salem MI, Tanes YM (1978) Pool boiling heat transfer and size of active nucleation centers for horizontal plates with different surface roughness. In: Proceedings of the 6th int. heat transfer conf., Toronto, vol 1, pp 151–156
161. Gorenflo D, Knabe V, Bieling V (1986) Bubble density on surfaces with nucleate boiling – its influence on heat transfer and burnout heat flux at elevated saturation pressures. In: Proceedings of the 8th international heat transfer conference, San Francisco, vol 4, pp 1995–2000
162. Blöchl R (1986) Zum Einfluß der Oberflächenstruktur unterschiedlich bearbeiteter Heizflächen auf die Wärmeübertragung beim Blasensieden. PhD thesis, University (TH) of Karlsruhe
163. Jungnickel H, Wassilew P, Kraus WE (1980) Investigations of the heat transfer of boiling binary refrigerant mixtures. Int J Refrig 3:129–133
164. Thome JR, Shakir S (1987) A new correlation of nucleate pool boiling of aqueous mixture. AIChE Symp Series 83:46–51
165. Thome JR (1983) Prediction of binary mixture boiling heat transfer coefficients using only phase equilibrium data. Int J Heat Mass Transfer 26:965–974
166. Fujita Y, Tsutsui M (1994) Nucleate pool boiling of binary mixtures. Inst Chem Eng Symp Series 135:129–134
167. Táboas F, Vallès M, Bourouis M, Coronas A (2007) Pool boiling of ammonia/water and its pure components: comparison of experimental data in the literature with the predictions of standard correlations. Int J Refrig 30:778–788
168. Gorenflo D, Kaupmann P, Köster R, Buschmeier M (1995) Pool boiling heat transfer of propane/i-butane/n-butane mixtures: example for other ternary mixtures as new refrigerants. In: Proceedings of the 19th international congress of refrigeration, Den Haag, vol IVa, pp 238–245
169. Buschmeier M, Sokol P, Pinto AD, Gorenflo D (1994) Pool boiling heat transfer of propane/n-butane mixtures at a single tube with superimposed convective flow of bubbles or liquid. In: Proceedings of the 10th international heat transfer conference, Brighton, vol V, pp 69–74, see also: Buschmeier M, Luke A, Sokol P, Gorenflo D (1993) Wärmeübergang beim Blasensieden von Propan/n-Butan-Gemischen mit Queranströmung, DKV-Tagungsbericht 20, Bd. II.1, S. 341–354
170. Kulaleladze SS (1959) Kritische Wärmestromdichte bei einer unterkühlten Flüssigkeitsströmung. Energetika 7:229–239; cf. also: Kulaleladze SS (1951) Izvestia Akademia Nauk Otdelinie Tekhnicheski Nauk 4:529
171. Zuber N (1958) On the stability of boiling heat transfer. J Heat Transfer 80:711
172. Zuber N, Tribus M (1958) Further Remarks on the stability of boiling heat transfer. UCLA Report 58–5, University of California, Los Angeles
173. Zuber N, Tribus M, Westwater JW (1961) Hydrodynamic crisis in pool boiling of saturated and subcooled liquids. In: Proc. of the int. heat transfer conference. Boulder, CO, paper no. 27, pp 230–236
174. Borishanskij VM (1956) An equation generalizing experimental data on the cessation of bubble boiling in a large volume of liquid. J Tekh Fiz 26:452–456
175. Noyes RC (1963) An experimental study of sodium pool boiling heat transfer. J Heat Transfer 85:125–131
176. Moissis R, Berenson PJ (1963) On the hydrodynamic transition in nucleate boiling. J Heat Transfer 85:221–229
177. Lienhard JH, Dhir VK (1973) Hydrodynamic prediction of peak pool-boiling heat fluxes from finite bodies. J Heat Transfer 95:152–158
178. Borishanskij VM (1969) Correlation of the effect of pressure on the critical heat flux and heat transfer rates using the theory of thermodynamic similarity. In: Kutateladze SS (ed) Problems of heat transfer and hydraulics of two-phase media. Pergamon Press, Oxford, pp 16–37
179. Mostinskij IL (1963) Anwendung des Korrespondenzprinzips zur Berechnung der Wärmeübertragung und der kritischen Wärmestromdichte für siedende Flüssigkeiten. Teploenergetika 10(4):66–71
180. Sciance CT, Colver CP, Sliepcevich CM (1967) Nucleate pool boiling and burnout of liquefied hydrocarbon gases. Chem Eng Progr Symp Ser 63(77):109–114
181. Wright RD, Colver CD (1969) Saturated pool boiling burnout of ethane-ethylene-mixtures. Chem Eng Prog Symp Ser 65:204–210
182. Hesse G (1972) Wärmeübergang bei Blasenverdampfung, bei maximaler Wärmestromdichte und im Übergangsbereich zur Filmverdampfung. PhD thesis, Techn. Universität Berlin
183. Bier K, Engelhorn HR, Gorenflo D (1977) Heat transfer at burnout and Leidenfrost points for pressures up to critical. In: Hahne E, Grigull U (eds) Heat transfer in boiling. Hemisphere Publishing, Washington, DC, pp 85–98
184. Tolubinskij VI, Kichigin AM, Povsten SG (1979) The critical heat flux density in free-convection boiling of water. Heat Transfer Sov Res 11:6–11
185. Feurstein G (1974) Der Einfluß des Druckes und der Geometrie auf den Wärmeübergang beim Behältersieden nahe dem kritischen Punkt. PhD thesis, Techn. Universität München
186. Hesse G (1973) Heat transfer in nucleate boiling, maximum heat flux and transition boiling. Int J Heat Mass Transfer 16:1611–1627
187. Hahne E, Feurstein G (1977) Heat transfer in pool boiling in the thermodynamic critical region: effect of pressure and geometry. In: Hahne E, Grigull U (eds) Heat transfer in boiling. Hemisphere Publishing, Washington, DC, pp 159–206
188. Labuntsov DA, Jagov VV, Gorodov AK (1978) Critical heat fluxes in boiling at low pressure region. In: Proceedings of the 6th int. heat transfer conf., Toronto, vol 1, pp 221–225
189. Gorenflo D (1982) Stand der Berechnungsmethoden zum Wärmeübergang bei der Verdampfung von Kältemitteln in freier Konvektion. DKV-Tagungsbericht 9 Essen, pp 213–240
190. Diesselhorst T, Grigull U, Hahne E (1977) Hydrodynamic and surface effects of the peak heat flux in pool boiling. In: Hahne E, Grigull U (eds) Heat transfer in boiling. Hemisphere Publishing, Washington, DC, pp 99–136
191. Alpay HE, Gorenflo D (1983) Burnout heat transfer to SF_6/R13B1-mixtures at near-critical saturation pressures. In: Proceedings of the 16th international congress of refrigeration, Paris, vol 2, pp 155–162
192. Fujita Y, Bai Q (1997) Critical heat flux of binary mixtures in pool boiling and its correlation in terms of Marangoni number. Int J Refrig 20:616–622
193. Bromley LA (1950) Heat transfer in stable film boiling. Chem Eng Progr 46:221–227
194. Bromley LA, Norman RL, Robbers JA (1953) Heat transfer in forced convection film boiling. Ind Eng Chem 45:2639–2646
195. Roetzel W (1979) Berechnung der Leitung und Strahlung bei der Filmverdampfung an der ebenen Platte. Wärme- u. Stoffübertragung 12:1–4
196. Grigull U, Abadzic E (1968) Heat transfer from a wire in the critical region. Proc Inst Mech Engrs 182(Pt 31):52–57
197. Nishio S, Auracher H (1999) Film and transition boiling. In: Kandlikar SG, Shoji M, Dhir VK (eds) Handbook of phase change; boiling and condensation, Chap 7. Taylor & Francis, Philadelphia, PA
198. Hesse G, Sparrow EM, Goldstein RJ (1976) Influence of pressure on film boiling heat transfer. J Heat Transfer 98:166–172
199. Pitschmann P, Grigull U (1970) Filmverdampfung an waagerechten Zylindern. Wärme- u. Stoffübertragung 3:75–84
200. Marschall E (1976) Filmsieden eines Zweistoffgemischs. Wärme- u. Stoffübertragung 9:167–172
201. Happel O, Stephan K (1974) Heat transfer from nucleate to the beginning of film boiling in binary mixtures. In: Proceedings of the 5th int. heat transfer conf., Tokyo, vol 4, pp 340–344
202. Sciance CT, Colver CP, Sliepcevich CM (1967) Pool boiling of methane between atmospheric pressure and the critical pressure. Adv Cryog Eng 12:395–408

H3 Flow Boiling – An Introduction

Matthias Kind
Karlsruher Institut für Technologie (KIT), Karlsruhe, Germany

This and the following subchapters are about heat transfer from a wall of an evaporator to a flowing and boiling subcooled, saturated or superheated liquid–vapor system. Flow boiling is an effective means to achieve high heat transfer rates at moderate temperature differences and is used in a multitude of technical applications like power plants, refrigerators, chemical and nuclear reactors, and evaporators in process industry.

A liquid (pure substance or mixture) is subcooled at point z in the direction of flow, if its average temperature is below the equilibrium temperature T_{sat} corresponding to the local pressure p. Saturation of a two-phase flow is reached when its average temperature is equal to the equilibrium temperature T_{sat}. The mixture may be superheated in the case that droplets evaporate into superheated steam as is the case at the end of an evaporation process.

The quality of two-phase flow at point z in the direction of flow is described by the local value of the vapor mass fraction $\dot{x}$, which is defined as the ratio of the local area specific mass flow rate of vapor $\dot{m}_V$ to the total area specific mass flow rate $\dot{m}$. (For special symbols used in flow boiling, see Subchap. H3.8.)

$$\dot{x} \equiv \frac{\dot{m}_V}{\dot{m}}. \tag{1}$$

At thermodynamic equilibrium the vapor mass fraction $\dot{x}$ at point z in the direction of flow can be obtained from the local specific enthalpies of the saturated liquid h' and of the two-phase fluid h using the enthalpy of evaporation Δh_{LV},

$$\dot{x} = \dot{x}_{eq} \equiv \frac{h - h'(p)}{\Delta h_{LV}(p.)} \tag{2}$$

$\dot{x}_{eq}$ is the only value that can be predicted by an energy balance and thus can be used for evaporator design. A schematic comparison between this value and the actual vapor mass fraction $\dot{x}$ is shown in Fig. 1. The greatest differences between these values occur at low and high values of $\dot{x}$ depending on various parameters. Generally, in the medium range of $\dot{x}_{eq}$, the difference is negligible, and is thus been completely ignored in the following sections, i.e., no distinction is made between $\dot{x}$ and $\dot{x}_{eq}$.

Below the critical heat flux, the following two boiling mechanisms can be observed: the so-called convective flow boiling mechanism and the nucleate flow boiling mechanism. The mechanism of convective flow boiling is characterized by the phenomenon that no vapor bubbles emerge at the wall. Rather, the vapor is generated close to or at the existing liquid–vapor interface. The mechanism of nucleate flow boiling is characterized by the phenomenon that steadily new vapor bubbles are nucleated at the wall due to sufficiently high superheating at the wall.

The parameters that decide which of the two mechanisms will predominate are the heat flux $\dot{q}$, the pressure p, the mass velocity $\dot{m}$, the vapor mass fraction $\dot{x}$, and the inner diameter d and the angle of inclination of the tube. A clear distinction between the two regimes can be drawn from Fig. 2. Thus in convective flow boiling, the heat transfer coefficient α does not depend on the heat flux $\dot{q}$ or the temperature difference $\Delta T = T_w - T_{eq}$ between the wall and the thermodynamically equilibrated two-phase fluid. If, however, α depends significantly on the heat flux, the nucleate boiling mechanism predominates.

A schematic diagram of the phenomena that occur within a horizontal evaporator tube at a moderate mass velocity is presented in Fig. 3. The flow patterns are sketched for low heat flux between $\dot{x}_{eq} = 0$ and $\dot{x}_{eq} = 1$. Under these circumstances the flow patterns are practically identical to those in an unheated tube.

For subcooled liquids up to $\dot{x}_{eq} = 0$ and at low heat fluxes (no nucleate boiling), heat transfer is convective and the value of the heat transfer coefficient is $\alpha(z)_{conv} = \alpha_{L0}$. Beyond $\dot{x}_{eq} = 0$ the heat transfer coefficient $\alpha(z)_{conv}$ commences to increases rapidly, because the convective flow boiling mechanism becomes active. However, a considerable impairment of $\alpha(z)_{conv}$ takes place in the stratified-wavy flow regime owing to incomplete wetting. In the flow regimes of slug and annular flow, wetting is so effective that the heat transfer coefficient $\alpha(z)_{conv}$ again increases with $\dot{x}$ until the onset of partial dry out, after which $\alpha(z)_{conv}$ drops rapidly to the value α_{G0} for pure vapor flow.

Figure 3 also includes a curve for the heat transfer coefficient in nucleate boiling $\alpha(z)_{nb}$, which occurs if the heat flux is correspondingly high. This curve also embraces the subcooled boiling regime, i.e., vapor generation before the point $\dot{x}_{eq} = 0$ is attained. Before the end of the tube is reached, the vapor mass fraction becomes so large that the critical boiling regime (point A) is attained.

Also in Fig. 3 the temperature profile versus the length of the tube $T(z)$ is shown. Below $\dot{x}_{eq} = 0$ the temperature rises until $T_{eq}\ (p)$ is reached at $\dot{x}_{eq} = 0$. If due allowance is made for the pressure drop, $T_{eq}(p)$ can be obtained for $\dot{x}_{eq} > 0$ with the aid of the vapor pressure curve. For $\dot{x}_{eq} > 1$ no more liquid is present and the temperature of the fluid (pure vapor) rises steadily. In the case of exceeding the critical boiling point (point A), the temperature deviates from $T_{eq}\ (p)$ as is shown by the dashed line. Owing to entrained liquid droplets, in this case the actual vapor mass fraction $\dot{x}$ deviates from the theoretical value $\dot{x}_{eq}$.

Since in the nucleate boiling regime $\alpha(z)_B = f(\dot{q})$, and since $\alpha(z)_{conv}$, $\alpha(z)_B$, and T_{eq} are functions of the tube length z, it is justified to restrict the prediction of the corresponding heat transfer coefficients to local values in the direction of flow z. By definition, $\alpha(z)$ is given by

VDI-GVC (ed.), *VDI Heat Atlas*, DOI 10.1007/978-3-540-77877-6_35,

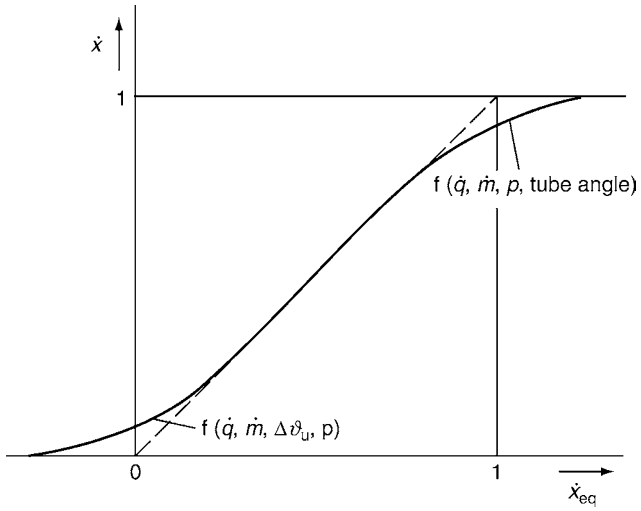

H3. Fig. 1. Relationship between actual and thermodynamic vapor fraction.

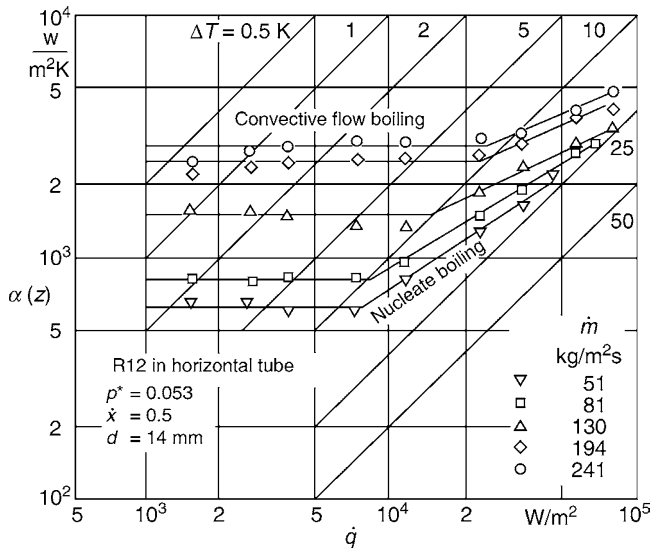

H3. Fig. 2. Parameter-averaged heat transfer coefficient as a function of heat flux (measurements on R 12 in horizontal tubes [R18]).

$$\alpha(z) = \frac{\dot{q}(z)}{T_w(z) - T_{sat}(p(z.))} \qquad (3)$$

The temperature of the inner wall and the heat flux are averaged over the circumference of the tube. In other words, the heat transfer coefficient $\alpha(z)$ is a perimeter-averaged value. This fact must be particularly borne in mind in predictions for nonvertical tubes, the circumferences of which are generally incompletely wetted. If the tubes are vertical, $\alpha(z)$ is uniform over the entire circumference.

The numerical value for the perimeter-averaged heat transfer coefficient depends on the extent to which the tube is wetted. Hence, the flow pattern, i.e., the description of the phase distribution, must also be taken into account in the determination of heat transfer. In Subchap. H3.1, a method to predict the flow patterns in an evaporator tube is given.

Another prerequisite is the knowledge about the local pressure p in the evaporator tube which can be evaluated from the pressure drop in the evaporator tube (Subchap. H3.2).

Subcooled nucleate flow boiling (Subchap. H3.3) occurs, if a liquid, which in average is subcooled, flows in an evaporator tube under high heat flow conditions and vapor bubbles occur at the wall.

Saturated nucleate flow boiling (Subchap. H3.4) takes place, if a saturated liquid–vapor mixture flows in an evaporator tube at moderate heat fluxes below the critical heat flux, and either convective or nucleate boiling occur.

Above the critical heat flux critical boiling states occur (Subchap. H3.5). Here either a vapor film interrupts the direct

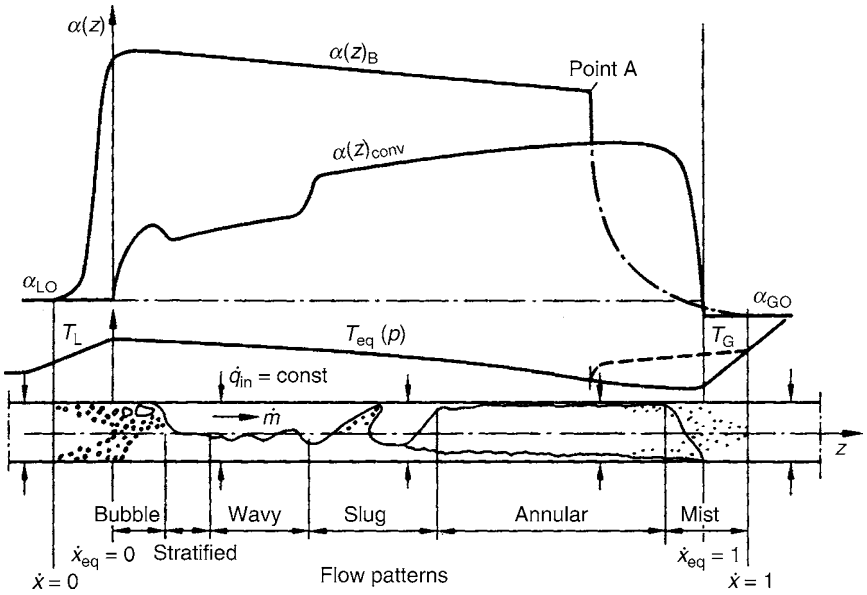

H3. Fig. 3. Schematic diagram illustrating flow patterns and the profiles for the fluid temperature and the perimeter-averaged heat transfer coefficient in a horizontal tube.

thermal contact of the liquid with the wall (film boiling, departure from nucleate boiling), or film dryout takes place.

Heat transfer beyond the critical heat flux (Subchap. H3.6) depends on the occurrence of either of these two phenomena.

In Subchap. H3.7, the treatment of heat transfer during flow boiling is extended to multicomponent systems.

H3.1 Flow Patterns in Evaporator Tubes

Dieter Steiner† · *Matthias Kind*
Karlsruhe, Germany

Phase distribution can be described by the observation of flow patterns in unheated sight glasses, and the patterns can be predicted by flow regime maps. The regimes formed by the dividing lines in the maps represent idealized states because, in reality, continuous transitions occur between the individual flow patterns.

1 Flow Patterns in Vertical Tubes

Upward flow patterns that have been observed are sketched in Fig. 1. Up to now, measurements of upward and downward flows in vertical tubes have failed to reveal any effect of the flow patterns on heat transfer. Since the heated wall is always, except in mist flow, completely wetted, there is no point in reproducing flow pattern maps here. Maps for upward and downward flows can be found in the literature [1–4]. (For literature and special symbols, see Subchap. H3.8.)

2 Flow Patterns in Horizontal and Slightly Inclined Tubes

In horizontal and slightly inclined tubes and under certain flow conditions, stratification of two phases occurs due to gravity.

Flow patterns for horizontal and slightly inclined tubes (angle of inclination to the horizontal $\Theta = \pm 10°$ at the most) are sketched in Fig. 2. For hydraulic reasons, only part of the heated wall is wetted in stratified, wavy, and slug flows. Since incomplete wetting exerts an effect on the heat transfer coefficient, a knowledge of the flow pattern is essential. Steiner [5] adapted a publication by Taitel and Dukler [6] as a basis for revising the regime transitions for wavy flow into slug, plug, and annular flow regimes and in checking them against measured data. Accordingly, the flow pattern map reproduced in Fig. 3 applies for liquids with low and medium boiling points.

2.1 Application of the Flow Pattern Map

The following scheme is advised for application of the map.

(a) Determination of the *Martinelli* parameter X

$$X = \frac{\left|(\mathrm{d}p/\mathrm{d}z)_\mathrm{L}\right|}{\left|(\mathrm{d}p/\mathrm{d}z)_\mathrm{G}\right|} = \left(\frac{1-\dot{x}}{\dot{x}}\right)^{0.875}\left(\frac{\rho_\mathrm{G}}{\rho_\mathrm{L}}\right)^{0.5}\left(\frac{\eta_\mathrm{L}}{\eta_\mathrm{G}}\right)^{0.125} \quad (1)$$

with index "G" for vapor and "L" for liquid.

(b) If Θ is the angle of inclination to the horizontal, the four dimensionless numbers are given by

$$\left(\mathrm{Re_L Fr'_G}\right)^{0.5} = \left(\frac{\dot{m}^3\dot{x}^2(1-\dot{x})}{\rho_\mathrm{G}(\rho_\mathrm{L}-\rho_\mathrm{G})\eta_\mathrm{L} g\cos\Theta}\right)^{0.5}, \quad (2)$$

$$\mathrm{Fr}^{0.5}_{\mathrm{G}m} = \left(\frac{\dot{m}^2\dot{x}^2}{gd\rho_\mathrm{L}\rho_\mathrm{G}}\right)^{0.5}, \quad (3)$$

$$\left(\mathrm{Fr\,Eu}\right)^{0.5}_\mathrm{L} = \left(\frac{\xi_\mathrm{L}\dot{m}^2(1-\dot{x})^2}{2d\rho_\mathrm{L}(\rho_\mathrm{L}-\rho_\mathrm{G})g\cos\Theta}\right)^{0.5}, \quad (4)$$

$$\left(\frac{\mathrm{We}}{\mathrm{Fr}}\right)_L = \frac{gd^2\rho_\mathrm{L}}{\sigma}. \quad (5)$$

The *Reynolds* number and the friction factor are obtained from the following equations:

$$\mathrm{Re_L} = \frac{\dot{m}(1-\dot{x})d}{\eta_\mathrm{L}}, \quad (6)$$

$$\xi_\mathrm{L} = \frac{0.3164}{\mathrm{Re}^{0.25}_\mathrm{L}}. \quad (7)$$

(c) The next step is to sound out the limiting conditions in the light of the actual value of the *Martinelli* parameter X. The following magnitudes with the subscript "lim" correspond to the limiting curves in Fig. 3. In order to obtain a definite result it is essential that the limiting conditions are sounded out in the following sequence.

†Deceased

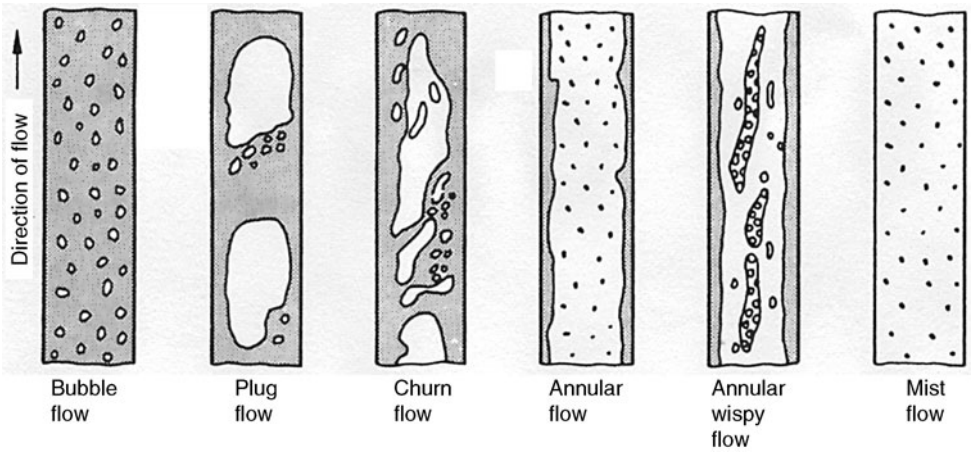

H3.1. Fig. 1. Flow patterns for upward flow in vertical tubes.

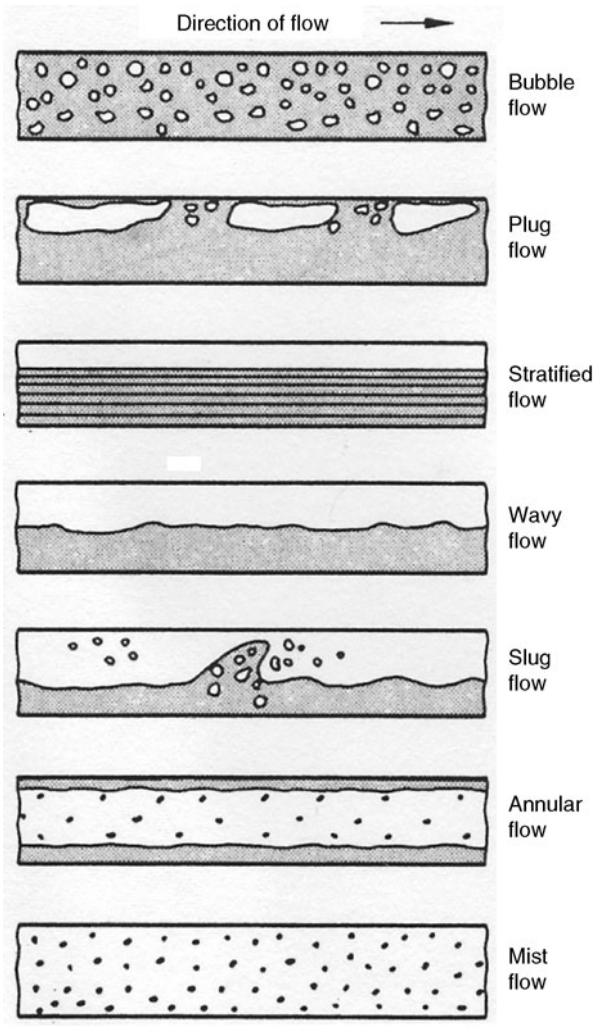

H3.1. Fig. 2. Flow patterns in horizontal tubes.

Flow is stratified if

$$\left(\mathrm{Re_L Fr'_G}\right)^{0.5} \leq \left(\mathrm{Re_L Fr'_G}\right)^{0.5}_{\mathrm{tt,lim}}.$$

If $(\mathrm{We/Fr})_\mathrm{L}$ is taken into consideration, the condition for wavy flow is

$$\mathrm{Fr}_\mathrm{G}^{0.5} \leq (\mathrm{Fr}_{\mathrm{G}m})^{0.5}_{\mathrm{tt,\,lim\ 1}}.$$

Bubble flow exists if

$$(\mathrm{Fr\,Eu})_\mathrm{L}^{0.5} \geq (\mathrm{Fr\,Eu})^{0.5}_{\mathrm{L,lim}}.$$

Under the following conditions, plug or slug flow exists:

$$X \geq 0.34 \quad \text{and} \quad \mathrm{Fr}_{\mathrm{G}m}^{0.5} > (\mathrm{Fr}_{\mathrm{G}m})^{0.5}_{\mathrm{tt,\,lim\ 1}}.$$

Dependent on $(\mathrm{We/Fr})_\mathrm{L}$, the condition for mist flow is

$$X < 0.51 \quad \text{and} \quad \mathrm{Fr}_{\mathrm{G}m}^{0.5} \geq (\mathrm{Fr}_{\mathrm{G}m})^{0.5}_{\mathrm{lim\ 2}}.$$

The final alternative is annular flow, and it is defined by more than one boundary curves.

The limits for turbulent flow of both the gas and the liquid (subscript "t,t") and also for laminar liquid and turbulent gas flow (subscript "l,t") are indicated in Fig. 3. Since the differences are of no significance in practice, the only equations that have been given are those that apply to the turbulent case. Exemptions are cited in the literature [5].

Example 1

Refrigerant R 12 flows in a horizontal evaporator tube of $d = 14$ mm at a pressure of $p = 1.51$ bar at its boiling point ($T_\mathrm{eq} = -20°\mathrm{C}$). The area-specific mass flow rate is $\dot{m} = 80\ \mathrm{kg/(m^2\ s)}$. Determine the flow patterns that are formed at the following values of $\dot{x}$: 0.01; 0.02; 0.1; 0.2; 0.3; 0.5; 0.7; 0.8; and 0.9.

It is assumed that the heat flux is moderate, i.e., $\dot{q} \leq 5\ \mathrm{kW/m^2}$, so that the flow patterns formed can be roughly determined from Fig. 3 for unheated tubes. The required properties of R12 are

$$\rho_\mathrm{L} = 1459.9\,\mathrm{kg/m^3}, \quad \eta_\mathrm{L} = 3.25 \cdot 10^{-4}\,\mathrm{kg/(m\,s)},$$
$$\rho_\mathrm{G} = 9.15\,\mathrm{kg/m^3}, \quad \eta_\mathrm{G} = 1.08 \cdot 10^{-5}\,\mathrm{kg/(m\,s)},$$
$$\sigma = 1.43 \cdot 10^{-2}\,\mathrm{kg/s^2}, \quad \Theta = 0°.$$

The solution is obtained from Eqs. (1–7) and the flow pattern map (Fig. 3). The sequence stipulated above must be adhered to in sounding out the likely flow patterns. The results are listed in Table 1.

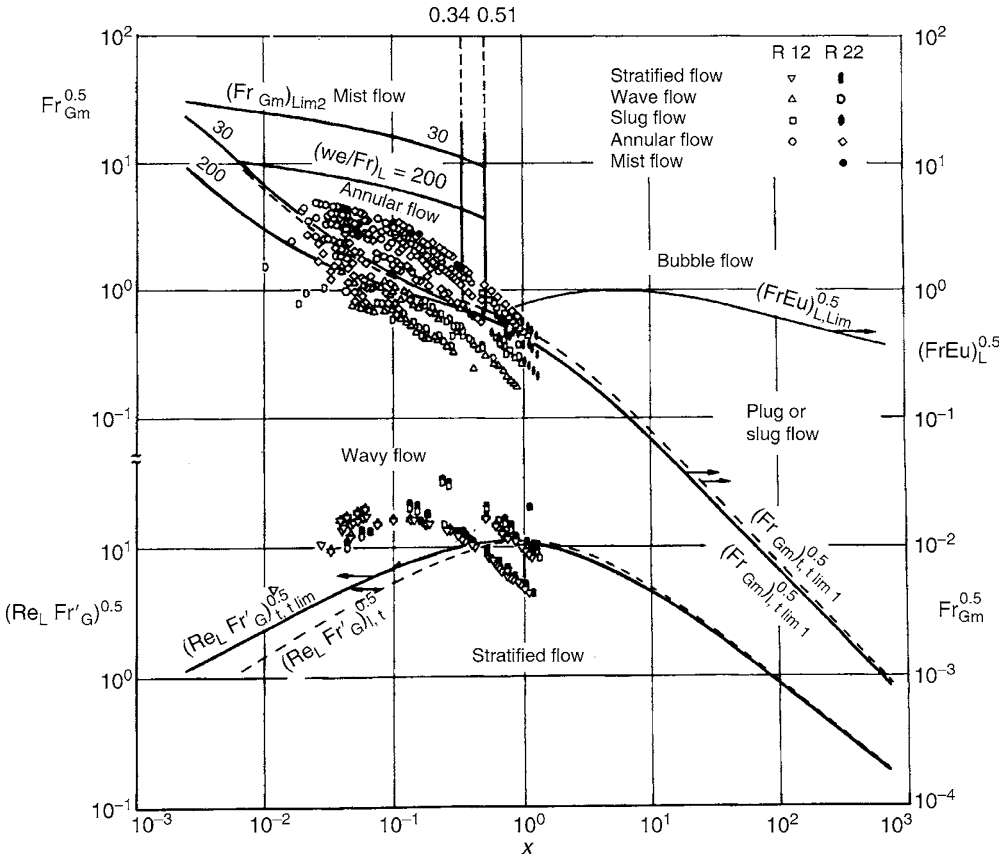

H3.1. Fig. 3. Flow pattern map for horizontal pipe flow ($\Theta = 0°$).

H3.1. Table 1. Results obtained in specimen calculation (Example 1)

$\dot{x}$	0.01	0.02	0.1	0.2	0.3	0.5	0.7	0.8	0.9
X	6.75	3.65	0.83	0.41	0.25	0.12	0.058	0.036	0.018
$(\mathrm{Re_L Fr'_G})^{0.5}$	1.09	2.18	10.44	19.69	27.62	–	–	–	–
$\mathrm{Fr}^{0.5}_{Gm}$	0.019	0.037	0.187	0.374	0.561	0.934	1.31	1.5	1.68
$(\mathrm{FrEu_L})^{0.5}$	0.021	0.021	0.019	–	–	–	–	–	–
$(\mathrm{We/Fr})_L$	–	–	–	–	–	–	196	196	196
$\mathrm{Re_L}$	3412.7	3378.3	3102.5	–	–	–	–	–	–
ξ_L	0.0414	0.0415	0.0424	–	–	–	–	–	–
Result (cf. Fig. 3)	Stratified flow	Stratified flow	Stratified flow	Wavy flow[a]	Wavy flow	Wavy flow	Annular flow	Wavy flow	Wavy flow

[a]According to Subchap. H3.4 the stratified–wavy flow range occurs at $\dot{x} = 0.2$, because $(\mathrm{Re_L Fr'_G})^{0.5} \leq 2(\mathrm{Re_L Fr'_G})^{0.5}_{\mathrm{lt,lim}}$. If, in accordance with the criteria for sounding out the boundaries, the other dimensionless numbers are not required, the numerical values are not listed in the table.

2.2 Determination of the Boundary Curves in the Flow Pattern Map

The requisite correlations with X must be known for the computer plotting of the boundary curves and for sounding out the anticipated flow pattern. The relationships between the given parameters and the equations for the dimensionless numbers have already been formulated [Eq. (1) and Eqs. (2–7), respectively]. Another relationship that applies is

$$X^2 = \left[\left(\frac{\tilde{U}_G + \tilde{U}_i}{\pi}\right)^{0.25}\left(\frac{\pi^2}{64\,\tilde{A}_G^2}\right)\left(\frac{\tilde{U}_G + \tilde{U}_i}{\tilde{A}_G} + \frac{\tilde{U}_i}{\tilde{A}_L}\right) - \frac{1}{(\mathrm{Fr\,Eu})_G}\right] \cdot \left(\frac{\pi}{\tilde{U}_L}\right)^{0.25}\left(\frac{64\,\tilde{A}_L^3}{\pi^2\,\tilde{U}_L}\right), \quad (8)$$

where

$$(\mathrm{Fr\,Eu})_G = \frac{\xi_G(\dot{m}\dot{x})^2}{2dg\rho_G(\rho_L - \rho_G)\sin\Theta}, \quad (9)$$

$$\xi_G = \frac{0.3164}{Re_G^{0.25}}, \tag{10}$$

$$Re_G = \frac{\dot{m}\dot{x}\, d}{\eta_G}. \tag{11}$$

The other dimensionless variables that are required for an analysis can be derived from the geometry (see Fig. 4) for a given height h of liquid or for a given relative liquid level $\tilde{h}_L$, which is given by

$$\tilde{h}_L = \frac{h}{d}. \tag{12}$$

The subscripts "L," "G," and "i" in the following equations indicate the liquid and gas (vapor) phases and the phase interface. The one that is appropriate for the case in question should be inserted in the equation concerned.

$$\tilde{U}_{L,G,i} = \frac{U_{L,G,i}}{d}, \tag{13}$$

$$\tilde{A}_{L,G} = \frac{A_{L,G}}{d^2}. \tag{14}$$

For $0 \le \tilde{h}_L \le 1$ is

$$\tilde{U}_i = 2\sqrt{\tilde{h}_L\left(1 - \tilde{h}_L\right)}. \tag{15}$$

Case $\tilde{h}_L \le 0.5$, with $\psi = 360° - \varphi$ (φ see Fig. 4):

$$\psi = 2\,\mathrm{Arcsin}\,\tilde{U}_i, \tag{16}$$

$$\tilde{U}_L = \frac{\psi}{2}, \tag{17}$$

$$\tilde{U}_G = \pi - \tilde{U}_L, \tag{18}$$

$$\tilde{A}_L = \frac{\psi - \sin(\psi 180/\pi)}{8}, \tag{19}$$

$$\tilde{A}_G = \frac{\pi}{4} - \tilde{A}_L. \tag{20}$$

Case $\tilde{h}_L > 0.5$:

$$\varphi = 2\,\mathrm{Arcsin}\,\tilde{U}_i, \tag{21}$$

$$\tilde{U}_G = \frac{\varphi}{2}, \tag{22}$$

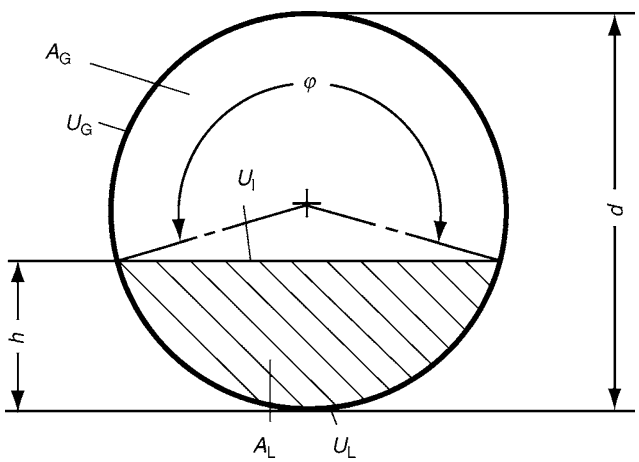

H3.1. Fig. 4. Cross-sectional and peripheral fractions in a circular tube.

$$\tilde{U}_L = \pi - \tilde{U}_G, \tag{23}$$

$$\tilde{A}_L = \frac{\varphi - \sin(\varphi 180/\pi)}{8}, \tag{24}$$

$$\tilde{A}_L = \frac{\pi}{4} - \tilde{A}_G. \tag{25}$$

Since $\tilde{U}_{L,G,i} = f(\tilde{h}_L)$ and $\tilde{A}_{L,G} = f(\tilde{h}_L)$, the average reference liquid height $\tilde{h}_L(X)$ can be obtained from Eq. (8) by iteration. For this purpose, a suitable approximate solution should generally be known. Apart from the case of $\tilde{h}_L \approx 0.5$, a reliable approximate value also permits a decision to be taken on whether $\tilde{h}_L \le 0.5$ or $\tilde{h}_L \ge 0.5$ and thus on which equations are valid.

The mean liquid height in stratified flow patterns can be obtained from the void fraction ε as defined in Chap. H3. The following correlation proposed by Rouhani [7] agrees well with the measured values [8]:

$$\varepsilon = \frac{\dot{x}}{\rho_G}\left[(1 + 0.12(1-\dot{x}))\left(\frac{\dot{x}}{\rho_G} + \frac{1-\dot{x}}{\rho_L}\right) + \frac{1.18(1-\dot{x})(g\sigma(\rho_L - \rho_G))^{0.25}}{\dot{m}\rho_L^{0.25}}\right]^{-1}. \tag{26}$$

The angle φ in radians subtended by the unwetted surface is obtained by iteration from ε, i.e.,

$$\varphi = 2\pi\varepsilon + \sin\left(\varphi\frac{180}{\pi}\right). \tag{27}$$

Then with this value of ε, the appropriate value for $\tilde{h}_{L,o}$ can be determined

$$\tilde{h}_{L,o} = \frac{15\,\pi\,(1-\varepsilon)}{8(3\ \sin\ \varphi/2\ +\ 4\ \sin\ \varphi/4)} \tag{28}$$

The limiting curves can now be delineated by inserting the known values for the relative liquid height $\tilde{h}_L(X)$ in the required functions $\tilde{A}_L$, $\tilde{A}_G$, and $\tilde{U}_i$. In doing so, it is essential to adhere to the following sequence in sounding out the boundary conditions in order to obtain a unique result.

Stratified flow:

$$Re_L Fr'_G \le \left(Re_L Fr'_G\right)_{tt,lim} = \frac{(226.3)^2}{\pi^3}\tilde{A}_L\tilde{A}_G^2. \tag{29}$$

Wavy flow:

$$Fr_{Gm} \le (Fr_{Gm})_{tt,lim\ 1} = \frac{16\tilde{A}_G^3}{\pi^2\sqrt{1 - \left(2\tilde{h}_L - 1\right)^2}}\left[\frac{\pi^2}{25\tilde{h}_L^2}\left(\frac{Fr}{We}\right)_L + \frac{1}{\cos\Theta}\right]. \tag{30}$$

Bubble flow:

$$(Fr\,Eu)_L \ge \left[(Fr\,Eu)_L\right]_{lim} = \frac{128\tilde{A}_G\tilde{A}_L^2}{\pi^2\tilde{U}_i}. \tag{31}$$

Plug or slug flow:

If $X \ge 0.34$, $Re_L \ge 1{,}187$, and $Re_G \ge 1{,}187$, the following must apply:

$$Fr_{Gm} > (Fr_{Gm})_{tt,lim\ 1}. \tag{32}$$

The following conditions must be satisfied for turbulent gas and laminar liquid flow, i.e., $Re_G \geq 1{,}187$ and $Re_L < 1{,}187$:

$$X \geq 0.51 \quad \text{and} \quad Fr_{Gm} \geq (Fr_{Gm})_{tt,lim\ 1}. \tag{33}$$

Mist flow:

$$X < 0.51$$

and

$$Fr_{Gm} \geq (Fr_{Gm})_{lim\ 2} = \frac{7680\,\tilde{A}_G^2}{\pi^2 \xi_{Ph}} \left(\frac{Fr}{We}\right)_L, \tag{34}$$

where

$$\xi_{Ph} = \left[1.138 + 2\,\log\left(\frac{\pi}{1.5\,\tilde{A}_L}\right)\right]^{-2}. \tag{35}$$

Annular flow:

The conditions that must be satisfied in this case are

$$X < 0.51$$

and

$$(Fr_{Gm})_{tt,lim\ 1} < Fr_{Gm} < (Fr_{Gm})_{lim\ 2}. \tag{36}$$

All the properties denoted by the subscript "L" for boiling liquid/vapor mixtures without inert components are identical to the corresponding properties of the saturated liquid. All values denoted by the subscript "G" apply to the saturated vapor.

Slight angles of inclination, i.e., $\Theta \geq 0.5°$, suffice for a significant shift in the limits. This applies to the boundary between stratified and wavy flow and from wavy to plug or slug and annular flow. The mathematically predicted transitions agree quite well with the observations by Bornea et al. [9].

If the tubes are not circular, acceptable approximations for determining the flow pattern can be obtained by substituting the hydraulic diameter d_h for the diameter d in all the above dimensionless numbers. Thus,

$$d_h = \frac{4\,A}{U}, \tag{37}$$

where U is the wettable periphery in the assumed case that the entire cross-sectional area A is filled by the liquid.

Recently, Katan et al. [10] and Thome and El Hajal [11] have reconsidered the above procedure and transformed the above dimensionless representation of the limiting curves into non-dimensionless representations of mass flow density $\dot{m}$ versus quality $\dot{x}$. Charts produced in this manner are more easy to read than Fig. 3, nevertheless, they are only valid for a single system at a given pressure.

H3.2 Pressure Drop in Evaporator Tubes

Jogindar Mohan Chawla[1,†] · *Matthias Kind*[2]
[1]Ettlingen, Germany
[2]Karlsruhe, Germany

The pressure drop of flows through evaporator tubes is composed of three components: the frictional and the static pressure drops, and the pressure drop due to acceleration.

$$\Delta p = (\Delta p)_{\text{friction}} + (\Delta p)_{\text{static}} + (\Delta p)_{\text{acceleration}} \tag{1}$$

1 Frictional Pressure Drop

The total pressure drop due to friction can be found by integrating over the whole pipe length $l = l_2 - l_1$:

$$(\Delta p)_{\text{friction}} = \int_{l_1}^{l_2} \left(\frac{\mathrm{d}p}{\mathrm{d}l}\right)_{\text{friction}} \mathrm{d}l, \tag{2}$$

where $(\mathrm{d}p/\mathrm{d}l)_{\text{friction}}$ is the local gradient of the pressure drop due to friction.

This results from the momentum transfer among the liquid and vapor phases themselves and between them and the pipe wall. The equations for the determination of the local frictional pressure drop gradients are given in Table 1. It must be distinguished between the cases where the vapor phase is continuous or dispersed [1]. (For literature and special symbols, see Subchap. H3.8.)

2 Static Pressure Drop

The total static pressure drop can be calculated similar to the frictional pressure drop by integration of the local pressure drop gradient over the whole pipe length l:

$$\left(\frac{\mathrm{d}p}{\mathrm{d}l}\right)_{\text{static}} = \left[\rho_{\text{l}}(1-\varepsilon) + \rho_{\text{g}}\varepsilon\right] g \sin\theta, \tag{3}$$

where θ denotes the angle of inclination of the tube. The local gradient of the static pressure drop is calculated by superposition of the contribution of the liquid and vapor phases. The equations for the determination of the vapor volume fraction ε in the above equation are given in Table 2. Like in the previous case of local frictional pressure drop gradient it must be distinguished whether the vapor phase is dispersed or not [1].

3 Pressure Drop due to Acceleration

The component of the pressure drop which is due to acceleration arises from momentum change of both of the flowing phases after heat supply. With the knowledge of the mean flow velocities of both phases this can be calculated rather accurately. The local pressure drop due to acceleration is given by the following equation that takes the change $\mathrm{d}\dot{x}$ of vapor content with the change of momentum flow $\mathrm{d}(I)/\mathrm{d}(t)$ into consideration:

$$(\mathrm{d}p)_{\text{acceleration}} = \frac{\mathrm{d}(I)/\mathrm{d}(t)}{\pi d^2/4} = \frac{\mathrm{d}(\dot{I})}{\pi d^2/4}. \tag{4}$$

The flow of momentum is

$$\dot{I} = \frac{\pi d^2}{4}\dot{m}^2\left[\frac{\dot{x}^2}{\varepsilon\rho_{\text{g}}} + \frac{(1-\dot{x})^2}{(1-\alpha)\varepsilon\rho_{\text{l}}}\right]. \tag{5}$$

Then, the total pressure drop caused by acceleration becomes

$$(\Delta p)_{\text{acceleration}} = \dot{m}^2 \int_{\dot{I}_1}^{\dot{I}_2} d\left[\frac{\dot{x}^2}{\varepsilon\rho_{\text{g}}} + \frac{(1-\dot{x})^2}{(1-\varepsilon)\rho_{\text{l}}}\right] \tag{6}$$

$$(\Delta p)_{\text{acceleration}} = \dot{m}^2 \left|\frac{\dot{x}^2}{\varepsilon\rho_{\text{g}}} + \frac{(1-\dot{x})^2}{(1-\varepsilon)\rho_{\text{l}}}\right|_{x_1}^{x_2}. \tag{7}$$

For a complete evaporation, the vapor content changes from 0 to 1 and the pressure drop is

$$(\Delta p)_{\text{acceleration}} = \dot{m}^2\left(\frac{1}{\rho_{\text{g}}} - \frac{1}{\rho_{\text{l}}}\right). \tag{8}$$

[†]Deceased

H3.2. Table 1. Calculation procedure for the local pressure drop gradient due to friction

Dispersed vapor phase, see [1, 2]

$$\frac{1}{\beta}=\frac{\dot V_g}{\dot V_l}=\frac{\dot x\,\rho_l}{(1-\dot x)\,\rho_g}\le\frac{12\sqrt{Fr}}{1+\sqrt{Fr}/7} \tag{T1.1}$$

$$\left(\frac{dp}{dl}\right)_{friction}=\xi\frac{\dot m^2}{2\,\rho_g\,d}\left[1+\dot x\left(\frac{\rho_l}{\rho_g}-1\right)\right]\cdot\left[1-\dot x\left(\frac{\rho_l}{\rho_g}-1\right)(K_2-1)\right] \tag{T1.2}$$

with the friction coefficient [3] to be determined by iteration from

$$\frac{1}{\sqrt{\xi}}=-2\,\log\left(\frac{k/d}{3.7}+\frac{2.51}{Re_{ZP}\sqrt{\xi}}\right), \tag{T1.3}$$

and

$$Re_{ZP}=\frac{\dot m\,d}{\eta_l\left[1-\dot x\left(1-\frac{\eta_g}{\eta_l}\right)\right]}, \tag{T1.4}$$

if $Re_{ZP}>2300$. And

$$K_2=1+0.09\beta \text{ for } \beta\le 0.4, \tag{T1.5a}$$

or

$$\frac{1}{K_2}=1-\frac{2.97/\beta^{2/3}+1}{6\left(1.83/\beta^{2/3}+1\right)\left(3.43/\beta^{2/3}+1\right)} \text{ for } \beta>0.4. \tag{T1.5b}$$

Continuous vapor phase, see [4–6]

$$\frac{1}{\beta}=\frac{\dot V_g}{\dot V_l}=\frac{\dot x\,\rho_l}{(1-\dot x)\,\rho_g}>\frac{12\sqrt{Fr}}{1+\sqrt{Fr}/7} \tag{T1.6}$$

$$\left(\frac{dp}{dl}\right)_{friction}=\xi_g\frac{\dot m^2\dot x^2}{2\,\rho_g\,d}\,\Phi \tag{T1.7}$$

with friction coefficient for smooth pipes with $Re_g>2300$ [7]

$$\frac{1}{\sqrt{\xi_g}}=2\,\log\left(Re_g\sqrt{\xi_g}\right)-0.8, \tag{T1.8}$$

and

$$\Phi=\left(\frac{1}{1-(1-E)\gamma_F-E\gamma_E}\right)^2, \tag{T1.9}$$

and

$$E=1.857+0.815\,\log\left[\left(\frac{\dot m\,\dot x}{\rho_g\,a_g}\right)^2\left(1+\frac{4575\,\rho_g^2}{\rho_l^2}\right)\right] \tag{T1.10}$$

and with,

$$\gamma_F=1-\left(1+\frac{(1-\dot x)\,\rho_g}{\dot x\,\varepsilon\,\rho_l}\right)^{-1.19} \tag{T1.11a}$$

$$\gamma_E=\left(1+\frac{6.67}{\left(\frac{1-\dot x}{\dot x}\right)^{0.45}(1+3\,\dot x^4)\left(\frac{\eta_l}{\eta_g}-1\right)^{0.25}}\right)^{-1}, \tag{T1.11b}$$

and

$$\varepsilon^{-3}=\varepsilon_1^{-3}+\varepsilon_2^{-3}, \tag{T1.12}$$

whereas for smooth pipes with $k/d<5\cdot10^{-4}$

$$\varepsilon_1=1.71\,\psi^{0.2}\left(\frac{1-\dot x}{\dot x}\right)^{0.15}\left(\frac{\rho_g}{\rho_l}\right)^{0.5}\left(\frac{\eta_g}{\eta_l}\right)^{0.1} \tag{T1.13a}$$

and for rough pipes with $k/d\ge5\cdot10^{-4}$

$$\varepsilon_1=1.71\,\psi^{0.2}\left(\frac{1-\dot x}{\dot x}\right)^{0.15}\left(\frac{\rho_g}{\rho_l}\right)^{0.5}\left(\frac{\eta_g}{\eta_l}\right)^{0.1}\left(\frac{5\cdot10^4}{k/d}\right)^{0.13} \tag{T1.13b}$$

and

$$\varepsilon_2=9.1\,\psi \tag{T1.14}$$

with

$$\psi=\frac{1-\dot x}{\dot x}(Re_l\,Fr_l)^{-1/6}\left(\frac{\rho_l}{\rho_g}\right)^{-0.9}\left(\frac{\eta_l}{\eta_g}\right)^{-0.5}. \tag{T1.15}$$

H3.2. Table 2. Calculation procedure for the static pressure drop gradient

Dispersed vapor phase, i.e.,	Continuous vapor phase, i.e.,
$\frac{1}{\beta}=\frac{\dot{V}_g}{\dot{V}_l}=\frac{\dot{x}\,\rho_l}{(1-\dot{x})\,\rho_g}\le\frac{12\sqrt{Fr}}{1+\sqrt{Fr}/7}$ (T2.1)	$\frac{1}{\beta}=\frac{\dot{V}_g}{\dot{V}_l}=\frac{\dot{x}\,\rho_l}{(1-\dot{x})\,\rho_g}>\frac{12\sqrt{Fr}}{1+\sqrt{Fr}/7}$ (T2.4)
$\varepsilon=\frac{K}{1+\beta}$ (T2.2)	$\varepsilon=1-H$ (T2.5)
with $K=1-\frac{30.4/\beta^{2.3}+11}{60\left(1.6/\beta^{2.3}+1\right)\left(3.2/\beta^{2.3}+1\right)}$ (T2.3)	If $500>\frac{1}{\beta}>\frac{12\sqrt{Fr}}{1+\sqrt{Fr}/7}$, then
	$H^{-3}=H_1^{-3}+H_2^{-3}$ (T2.6)
	with
	$H_1=\exp\left[2-0.1335\,\ln\frac{\eta_l}{\eta_g}+\left(1.1-0.08534\,\ln\frac{\eta_l}{\eta_g}\right)\ln\varepsilon\right]$ (T2.7a)
	and
	$H_2=\frac{\chi_{tt}}{1+\chi_{tt}}$ (T2.7b)
	and with $\chi_{tt}=\left(\frac{1-\dot{x}}{\dot{x}}\right)^{7/8}\left(\frac{\eta_l}{\eta_g}\right)^{1/8}\left(\frac{\rho_g}{\rho_l}\right)^{1/2}$. (T2.7c)
	If $10^4>\frac{1}{\beta}>500$, then [8]
	$H=464\,\beta^{5/3}$. (T2.8)
	If $\frac{1}{\beta}>10^4$, then
	$H=\frac{\beta}{1+\beta}$. (T2.9)

H3.3 Subcooled Boiling

Matthias Kind[1] · *Jens-Jürgen Schröder*[2,†]
[1]Karlsruher Institut für Technologie (KIT), Karlsruhe, Germany
[2]Hannover, Germany

This chapter considers boiling during the transfer of high heat fluxes to a subcooled flowing liquid. It demonstrates how the associated changes in wall temperature, density, and pressure can be quantitatively predicted. An important application is in reactor technology, when information has to be acquired on the average vapor flow rate per unit of cross-sectional area that can be obtained from a given heat flux.

As a general rule, subcooled boiling frequently gives rise to two-phase instability and fluctuations in mass flow rate in process circuits.

1 Description of the Phenomena

When a liquid, which is undercooled with respect to its boiling point, flows through a heated channel, as illustrated in Fig. 1, subcooled boiling commences at the point where the first bubbles are formed on the wall. This point is referred to as the initial point (subscript *i*). In most of the cases that have been investigated up to now, the initial point is not followed immediately by a significant increase in the vapor volumetric fraction per unit area of cross-section, referred to as the void fraction ε (Fig. 1, Part C), where (for literature and special symbols, see Subchap. H3.8)

$$\varepsilon = A_G/A. \tag{1}$$

The reason for this is that the bubbles collapse either at the wall itself or in its near vicinity immediately after they have been formed. Thus, heat transfer is improved. The rise in wall temperature, thus, decreases and may even become negative (Fig. 1, Parts A and B). (The purpose of presenting two separate dimensionless temperature profiles – the one for purely laminar flow (Part A) and the other for completely developed turbulent flow (Part B) – will be evident in many of the passages that follow.) The decrease is caused by simultaneous evaporation and condensation: the bubbles act as a heat pipe in the boundary layer. Another reason is the increased turbulence in the layer of liquid close to the wall and downstream from the initial point. The superheating of the wall prior to the initial point may be an undesirable phenomenon, for instance, during evaporative cooling of electronic parts by wetting liquids [1–4].

Afterwards, the bubbles slide along the wall [5] and do not enter the bulk of the liquid until a point further downstream is reached at which the temperature of the bulk has also risen to the vicinity of the boiling point. Penetration of the bubbles into the bulk is accompanied simultaneously by a decided increase in the void fraction and the commencement of net vapor generation (subscript *n*). At this point, the vapor mass fraction $\dot{x}$ commences to rise (Fig. 1, Part D), where

$$\dot{x} = \dot{m}_G/\dot{m}. \tag{2}$$

†Deceased

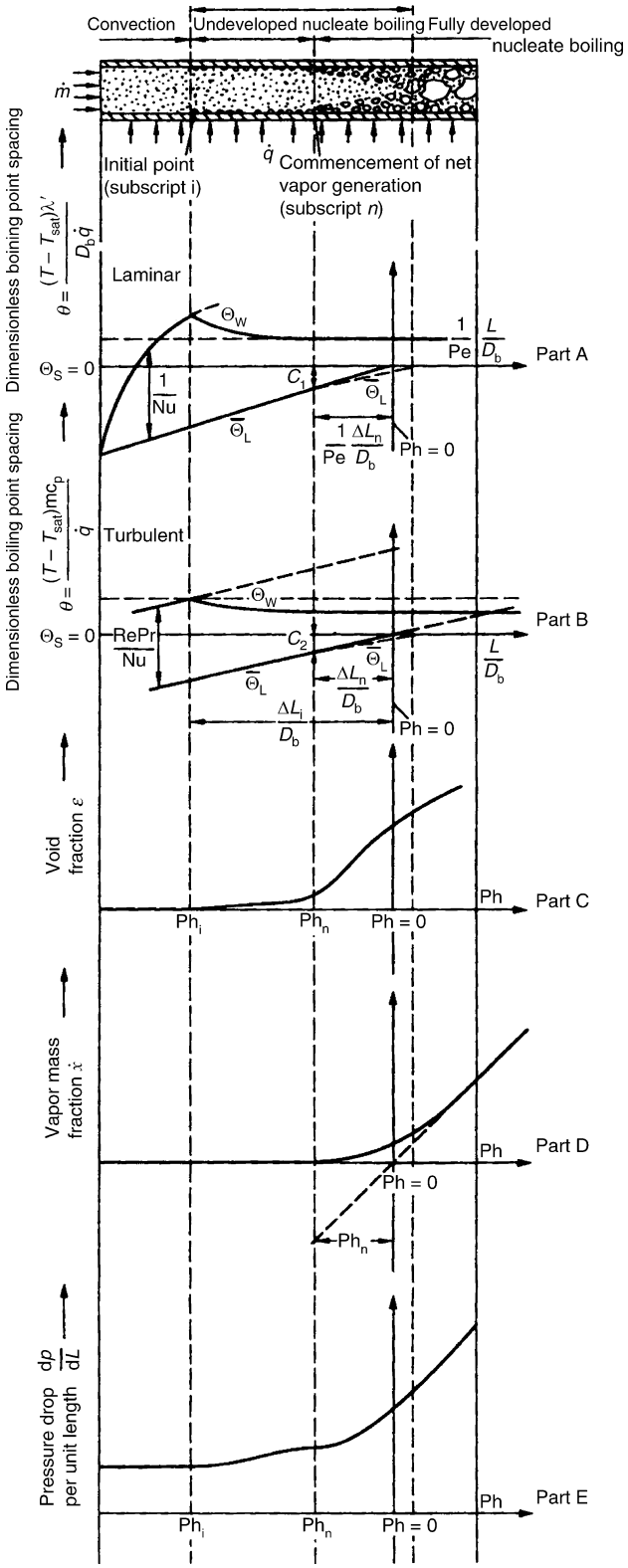

H3.3. Fig. 1. Phenomena occurring during heat transfer in a heated channel.

Still further downstream, recondensation is no longer a significant factor, and the heat transfer mechanism commences to develop in the same way as forced-convection saturation boiling (see Subchap. H3.4).

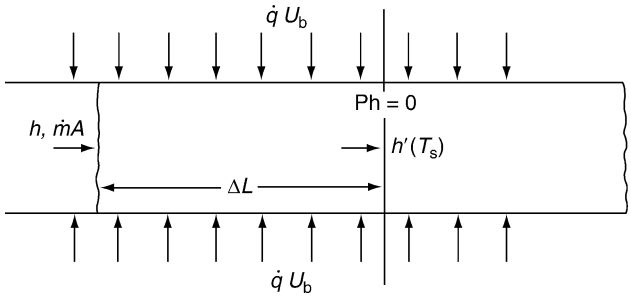

H3.3. Fig. 2. Energy balance for subcooled flow through a channel.

1.1 Location of Points in the Heated Channel

If the mean heat flux in the direction of flow is $\dot{q}_m$ and the mass velocity in the cross-sectional area A is $\dot{m}$, the following relationship can be obtained from an energy balance between any one point in the channel through which the subcooled liquid flows (Fig. 2) and the point at which the saturation enthalpy h' is attained:

$$\frac{\dot{m}(h' - h)}{4\dot{q}_m} = \frac{\Delta L}{D_b}, \tag{3}$$

where D_b is a characteristic length derived from the cross-sectional area A and the heated periphery U_b, that is,

$$D_b = \frac{4A}{U_b}. \tag{4}$$

If the channel is a tube that is heated uniformly over its entire circumference, D_b is its diameter.

Hence, $\Delta L/D_b$ is the dimensionless distance between the cross-section at any given point and the cross-section with the caloric mean saturation temperature. The enthalpy h is also taken to be the caloric mean value at the cross-section in question.

In the following analysis, the point at which the enthalpy h is attained, is identified by the phase number Ph, which is a dimensionless boiling point spacing, that is,

$$\mathrm{Ph} \equiv \frac{h - h'}{\Delta h_v}. \tag{5}$$

If $h' \le h \le h''$, which is a case that is not considered here, Ph is identical to the vapor mass fraction at thermodynamic equilibrium, that is, the vapor quality. It is a caloric dimension that is not necessarily proportional to $\Delta L/D_b$. This can be demonstrated by substituting $\mathrm{Ph}\Delta h_v$ for $(h - h')$ on the left of Eq. (3) and multiplying by the term N_{bm} which is given by

$$N_{bm} \equiv \frac{\dot{q}_m}{\dot{m}\,\Delta h_v}. \tag{6}$$

The relationship, thus, obtained is

$$-\frac{\mathrm{Ph}}{4\,\Delta h_v} = \frac{\Delta L}{D_b}. \tag{7}$$

N_{bm} is the boiling number, that is, a dimensionless expression for the mean heat load in a given stretch of boiling liquid. As a rule, it is not a constant.

Equation (7) can be applied to the balance between any two points in the channel, in which it becomes

$$-\frac{(\mathrm{Ph}_1 - \mathrm{Ph}_2)}{4\,N_{bm\,1,2}} = \frac{\Delta L_{1,2}}{D_b}. \tag{7a}$$

If the two points are the channel inlet and $\mathrm{Ph} = 0$, Eq. (7) becomes

$$-\frac{\mathrm{Ph}_0}{4\,N_{bm\,0}} = \frac{\Delta L_0}{D_b}. \tag{7b}$$

1.2 Initial Conditions

The generation of vapor bubbles in subcooled liquids on a heated wall is closely connected to the temperature profile. Thus, if single-phase heat transfer is assumed, the first step in a calculation is to determine the temperature profile in the wall T_W (if it is not already given) and that in the inflowing liquid.

In practice, the conditions will lie between two limiting cases: purely laminar flow of the heated liquid ($\mathrm{Re} < 2 \times 10^3$) and completely turbulent flow ($\mathrm{Re} > 10^5$). If the hydrodynamic profile is fully developed, both cases are quite easy to calculate. Parts A and B in Fig. 1 illustrate qualitatively the characteristic wall temperature and the mean liquid temperature profiles in a generalized dimensionless form for a constant heat flux $\dot{q}$. They extend to the initial point i, which can be determined as described in Chap. G1.

A distinction has been drawn between the definition for the dimensionless boiling point spacing in purely laminar flow (Part A) and that in fully turbulent flow (Part B). It allows for the fact that, in the first case, it is the molecular term λ' that is responsible for heat transport that is not brought about by vapor bubbles; and, in the second case, it is the turbulent term $\lambda' \mathrm{Pe}$.
Clausse and Lahey [6] have demonstrated that the occurrence of subcooled boiling also depends on whether the thermal conditions allow hydrodynamic flow to develop at as early a stage as possible.

1.3 Laminar Flow ($\mathrm{Re} < 2 \times 10^3$)

(Fully developed hydrodynamic profile; the section for thermal development is generally very long.)

The following applies for tubular cross-sections in which $d = D_b = D_h$ (hydraulic diameter);
For $\dot{q}$ = constant,

$$\mathrm{Nu}(l) = \frac{\alpha(l)\,d}{\lambda} = 4.36\left[1 + \left(0.0292\mathrm{Pe}\,\frac{d}{l}\right)^2\right]^{0.15}\left(\frac{\mathrm{Pr}}{\mathrm{Pr}_w}\right)^{0.14}. \tag{8a}$$

For T_W = constant, the local coefficient $\alpha(l)$ is

$$\mathrm{Nu}(l) = \frac{\alpha(l)\,d}{\lambda} = \frac{3.66^3 + 2/3(1.61^3\mathrm{Pe}\cdot d/l)}{(3.66^3 + 1.61^3\mathrm{Pe}\cdot d/l)^{2/3}}\left(\frac{\mathrm{Pr}}{\mathrm{Pr}_w}\right)^{0.14} \tag{8b}$$

and the average coefficient is

$$\mathrm{Nu}(l) = \frac{\alpha(l)\,d}{\lambda} = \left(3.66^3 + 1.61^3\mathrm{Pe}\cdot d/l\right)^{1/3}\left(\frac{\mathrm{Pr}}{\mathrm{Pr}_w}\right)^{0.14}. \tag{8c}$$

Mathematical methods for other cross-sections have been proposed by Kay [7].

1.4 Turbulent flow ($\mathrm{Re} < 10^5$)

For $\dot{q}$ = constant,

$$\frac{\mathrm{Nu}(l)}{\mathrm{Pe}} = \frac{\alpha(l)}{\dot{m}\cdot c_p} = \frac{\xi/8}{1 + 12.7\sqrt{\xi/8}\,(\mathrm{Pr}^{2/3} - 1)}\left[1 + \left(\frac{d}{l}\right)^{2/3}\right]\left(\frac{\mathrm{Pr}}{\mathrm{Pr}_w}\right)^{0.14}. \tag{9a}$$

For T_W = constant, the local coefficient $\alpha(l)$ is

$$\frac{\mathrm{Nu}(l)}{\mathrm{Pe}} = \frac{\alpha(l)}{\dot{m}\cdot c_p} = \frac{\xi/8}{1 + 12.7\sqrt{\xi/8}\,(\mathrm{Pr}^{2/3} - 1)}\left[1 + \frac{1}{3}\left(\frac{d}{l}\right)^{2/3}\right]\left(\frac{\mathrm{Pr}}{\mathrm{Pr}_w}\right)^{0.14}. \tag{9b}$$

For the average coefficient $\alpha(l)$, see Eq. (9a) where

$$\xi = (0.790\ln\mathrm{Re} - 1.64)^{-2}. \tag{10}$$

The length of the section l is measured from the point at which heating commences. All the properties must be referred to the average liquid temperature, which is obtained from the wall temperature, for which an estimate must be made first. However, Pr_w must be referred to the wall temperature. The full Gnielinski [8] equation (Eq. (24) in Chap. G1) must be resorted to for the transition between purely laminar and fully developed turbulent flow. Thus,

$$T_W - T_L = \frac{\dot{q}}{\alpha}. \tag{11}$$

2 Nucleate Boiling Incipience

The length l_i that is traversed by the liquid before nucleate boiling commences, is obtained from

$$\frac{l_i}{D_b} = \frac{\Delta L_0}{D_b} - \frac{\Delta L_i}{D_b},$$

where ΔL_0 is the length of the channel between the inlet and the point at which saturation enthalpy is attained, $\Delta L_0/D_b$ is obtained from Eq. (3) by substituting the enthalpy at the inlet cross-section for h, and $\Delta L_i/D_b$ follows from Eq. (7) if $\mathrm{Ph}_i = (h_i - h)/\Delta h_v$ is known.

There are special cases in which Ph_i can be determined directly from empirical equations [9]. The following procedure must be adopted in other cases.

If $T_L(l_i)$ is the average temperature of the liquid at the initial point, the corresponding enthalpy h_i is obtained from

$$h' - h_i = c_p[T_{sat} - T_L(l_i)]. \tag{12}$$

Since $\dot{q} = \alpha(l_i)\,[T_W - T_L\,(l_i)]$, Eq. (12) can be transformed into

$$\begin{aligned} h' - h_i &= c_p\,[(T_W - T_L(l_i)) - (T_W - T_{sat})_i], \\ h' - h_i &= c_p\left[\frac{\dot{q}}{\alpha(l_i)} - (T_W - T_{sat})_i\right]. \end{aligned} \tag{12a}$$

Inserting Ph_i from Eq. (5) gives

$$\mathrm{Ph}_i = \frac{h_i - h'}{\Delta h_v} = -\frac{c_p}{\Delta h_v}\left[\frac{\dot{q}}{\alpha(l_i)} - (T_W - T_{sat})_i\right]. \tag{12b}$$

The terms $\alpha(l_i)$ and $(T_W - T_{sat})_i$ must be known in order to determine the length l_i up to the initial point. $\alpha(l_i)$ is derived from Eqs. (8a), (8b), (9a), or (9b); the choice depends on how the heat is transferred. The wall superheat $(T_W - T_{sat})_i$ can then be calculated either from empirical equations [10] or from theoretical models [11].

2.1 Determination of the Initial Point from Residual Subcooling of Water in Turbulent Flow and Elevated Pressures in Vertical Tubes

The term $\overline{T}_L$ in the expression $(T_L - T_{sat})_i$ for residual subcooling is the caloric mean liquid temperature corresponding to h. Even if the wall temperature profile is unknown, the initial point for a given heat flux can be determined from a relationship suggested by Hodgson [9] for $(7 \le p \le 138$ bar), that is,

$$141\left(N_{b,i}\right)^{0.7} = (-\mathrm{Ph}_i)^{0.55} H_b^{0.08}. \tag{13}$$

The term H_b allows for the effect of pressure:

$$H_b = -\frac{\Delta h_v}{c'_p} \frac{d\left(\frac{\rho'}{\rho''}\right)\Big/ \mathrm{d}p}{\mathrm{d}T_b/\mathrm{d}p} \approx \frac{\Delta h_v^2}{c'_p T\, v'\, p}. \tag{14}$$

The following relationship applies for water:

$$H_b^{0.08} \approx 1.25\left(\frac{p}{p_c}\right)^{-0.1}, \tag{14a}$$

where p_c is the critical pressure.

The location of the point associated with Ph_i is determined from Eq. (7) or (7a). Equation (13) was derived by extrapolating the ratio of heat transfer coefficients α/α_1 obtained from measurements toward a limit of unity, that is, $\alpha/\alpha_1 \to 1$. It has been checked by Guglielmini et al. [12] in the light of measurements, inc1uding those by other authors, and has also been confirmed by data extracted from more recent literature (cf. Fig. 3).

Almost the same exponential relationship, namely, $N_{bi} \sim \mathrm{Ph}_i^{0.773}$, as opposed to $N_{bi} \sim \mathrm{Ph}_i^{0.786}$, was determined by Bräuer and Mayinger [14] in their experiments on R 12 in an annulus. The results also revealed that the constant of proportionality depends slightly on the Reynolds number.

Bucher [15], Müller-Steinhagen et al. [16], You et al. [4], and other authors studied the effect of dissolved inert gases on the initial point.

2.2 Determination of the Initial Point from the Wall Superheat in Boiling Water at Elevated Pressures in Vertical Tubes

As long as free convection can be neglected, an effect of vertical flow cannot be determined [17, 18].

Good results for water have been obtained with an empirical equation developed by Bergles and Rosenow [10]. At pressures

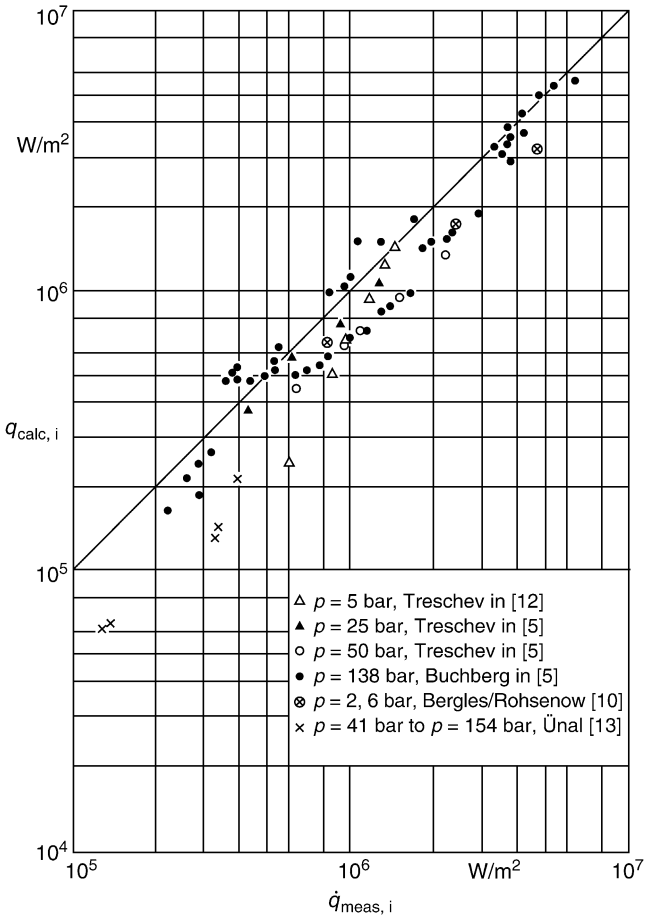

H3.3. Fig. 3. Comparison of values of heat flux calculated from Eq. (13) with measured values.

of 1–140 bar, the wall superheat for $\dot{q}$ = constant at the initial point is given by

$$(T_W - T_{sat})_i = \frac{5}{9}\left[\left(\frac{\dot{q}}{1120}\right)^{0.463} p^{-0.535}\right]^{p^{0.0234}}, \tag{15}$$

where $(T_W - T_{sat})_i$ is in K, $\dot{q}$ in W/m^2, and p in bar. This relationship for water has proved to be independent of the properties of the heated surface.

2.3 Initial Point in Boiling Water at Elevated Pressures in Horizontal and Inclined Tubes

In these cases, boiling may commence earlier if free convection within the liquid is a significant factor. The subject has been dealt with by Hein et al. [19].

2.4 Wall Superheat in Boiling Water ($p \sim 1$ bar), Organic Liquids, Refrigerants, and Liquefied Gas

Refer to Subchap. H2.2 "Physical conditions for the initiation of the bubble formation" and the respective equation, given there.

Example 1

Determine $(T_W - T_{sat})_i$ for water under the following conditions: $T_{sat} = (273 + 200)\ K = 473\ K$; $p = 15.55$ bar; $\dot{q} = 2\ MW/m^2$.

Inserting the corresponding values for the properties, which can be obtained in Subchap. H2.2, Eq. (17) gives $(T_W - T_{sat})_i \approx 5.3$ K. This agrees well with the figure obtained from Eq. (15), namely, $(T_W - T_{sat})_i \approx 4.8$ K. Inserting the values for the properties in Eq. (16) gives $r_{crit,i} = 1\ \mu m$. Since water is generally a very poor wetting agent, there is no doubt that a nucleation site of this order will be present on a technically rough heated surface. Hence, the first bubbles are very likely to appear at a wall superheat of approximately 5 K.

3 Onset of Net Vapor Generation

A quantitative description can be obtained with the aid of a simple model developed by Saha and Zuber [20]. According to this, net vapor generation commences when, owing to slight subcooling $(T - T_{sat})$, recondensation of the vapor bubbles close to the wall no longer suffices to remove the applied heat. Since the latent heat of condensation is removed by conductivity in purely laminar flow, the following equation holds:

$$\frac{1}{C_1}\left(T_{sat} - \overline{T}_L\right)_n \frac{\lambda'}{D_b} = \dot{q}. \tag{16}$$

Alternatively, if $\dot{q}$ = constant, Eq. (7) can be applied to give

$$\frac{\left(T_{sat} - \overline{T}_L\right)_n \lambda'}{\dot{q} D_b} = -\frac{1}{Pe}\frac{Ph_0}{N_b} = 4\frac{N_{bm}}{N_b}\frac{1}{Pe}\frac{\Delta L_n}{D_b} = C_1.$$

Heat transfer is much more intensive in completely developed turbulent flow. As a first approximation, the ratio of the turbulent to the molecular component is proportional to the Péclet number, that is,

$$\frac{1}{C_2}\left(T_{sat} - \overline{T}_L\right)_n \frac{\lambda'}{D_b} Pe = \dot{q}. \tag{17}$$

Alternatively, if $\dot{q}$ = constant, Eq. (7) can be applied to give

$$\frac{\left(T_{sat} - \overline{T}_L\right)_n \dot{m} c_p}{\dot{q}} = -\frac{Ph_n}{N_b} = 4\frac{N_{bm}}{N_b}\frac{\Delta L_n}{D_b} = C_2.$$

Since the nucleation sites have already been completely activated, it can be expected that the proportionality constants C_1 and C_2 hardly depend any longer on the specific properties of the heated surfaces and thus, remain the same in all cases that are otherwise physically similar.

Hence C_1 and C_2 characterize specifically similar caloric states and can be uniquely described only if Ph_n and the type of flow (laminar or turbulent) are given. There is no similarity to the $\Delta L_n/D_b$ model unless $\dot{q}$ = constant or $N_{bm} = N_b$.

In the light of the experimental results at their disposal, Saha and Zuber [20] arrived at the following figures:

$1/C_1 = 455$ for $Pe \le 70,000$ and $1/C_2 = 0.0065$ for $Pe \ge 70,000$.

The evaluation of other experimental data indicates the following relationship for the transition zone between purely laminar and completely developed turbulent flow:

$$\frac{1}{C_2} = \left[\left(\frac{455}{Pe}\right)^2 + 0.0065^2\right]^{1/2}. \tag{18}$$

In Fig. 4, values calculated from this equation are compared with experimental results.

In the turbulent region ($Pe > 70,000$), experimental data for refrigerant R 113 lie below the constant $C_2 = 1/0.0065$ given by Saha and Zuber [20]. In this case, they are approximated better by $C_2 = 1/0.0033$.

Bartolomei et al. [34] derived a purely empirical equation for the phase number Ph_n. It permits the conclusion that C_2 possibly still depends on pressure and, to a slight extent, on the heat and mass fluxes.

In the experiments on annular channels in the *Slowpoke* project, Rogers et al. [32] discovered that subcooling at the point n increased with the velocity, although the Péclet number was $Pe < 70,000$. As can be seen from Fig. 5, this does not affect the Saha and Zuber relationship in the first instance.

4 Improvement in Heat Transfer and the Wall Temperature Profile

4.1 Constant Heat Flux

A measure for any improvement is the following ratio:

$$\frac{T_W - \overline{T}_L}{\left(T_W - \overline{T}_L\right)_i} = \frac{\alpha_i}{\alpha}.$$

4.1.1 Determination on the Basis of Experimental Data: Water at Elevated Pressure ($7 \le p \le 138$ bar)

The Hodgson [9] empirical equation is valid in this range, that is,

$$\frac{\alpha_i}{\alpha} = 0.0152\left(\frac{\Delta L}{D_b}\right)^{0.55} N_b^{-0.15} H_b^{0.03}, \tag{19}$$

where α_i is as determined from Eq. (9) and

$$\frac{\Delta L_n}{D_b} < \frac{\Delta L}{D_b} \le \frac{\Delta L_i}{D_b}.$$

Since Eq. (19), which is analogous to Eq. (13), was derived from measurements on very short tubes, α_i/α can be regarded as a local ratio. Figures calculated from the equation correspond to within ±20% to values measured by Hodgson [9] and other authors. It does not allow for the hysteresis that is observed between rising and falling values of heat flux.

In this range of pressures, $H_b^{0.08}$ is given by

$$H_b^{0.08} \approx 1.25\left(\frac{p}{p_c}\right)^{-0.10}. \tag{20}$$

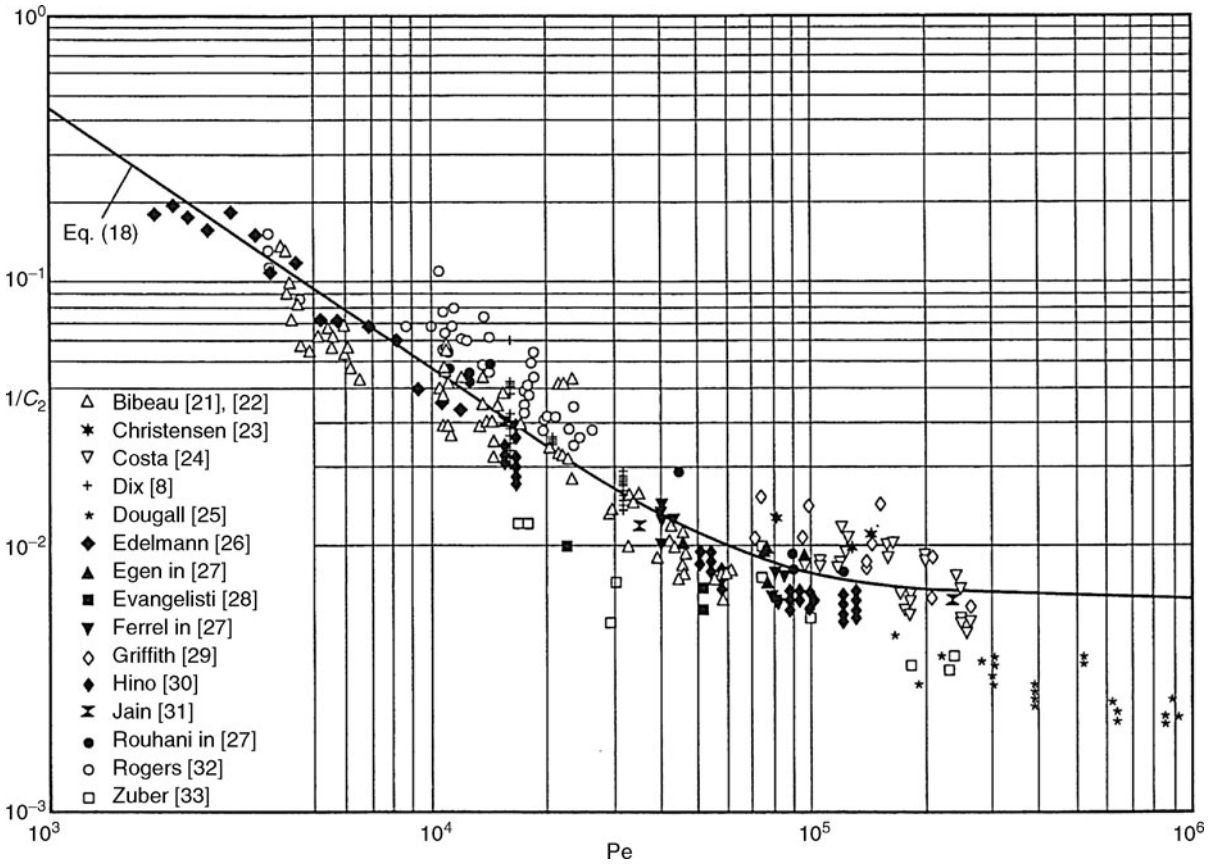

H3.3. Fig. 4. Comparison of measured values with figures calculated from Eq. (21). (Many of the data plotted in this diagram are dealt with in greater detail by Saha and Zuber [20].)

4.1.2 Determination on the Basis of Experimental Data: Other Liquids and Water at $p \cong 1$ bar

Equation (21) has been suggested by Moles and Shaw [35] for water and other liquids. It was derived from numerous measurements on short tubes:

$$\frac{\alpha_i}{\alpha} = 0.0254 \left(\frac{\Delta L}{D_b}\right)^{0.50} N_b^{-0.17} \mathrm{Pr}^{0.46} \left(\frac{\rho'}{\rho''}\right)^{0.03}, \qquad (21)$$

where

$$\frac{\Delta L_n}{D_b} < \frac{\Delta L}{D_b} \leq \frac{\Delta L_i}{D_b}.$$

This equation yields figures that conform to within ± 40% with 90% of all values measured on water, ethanol [36], 1-butanol [19], ammonia [19], and hydrazine [37]. It also gives good results for R 12 [36].

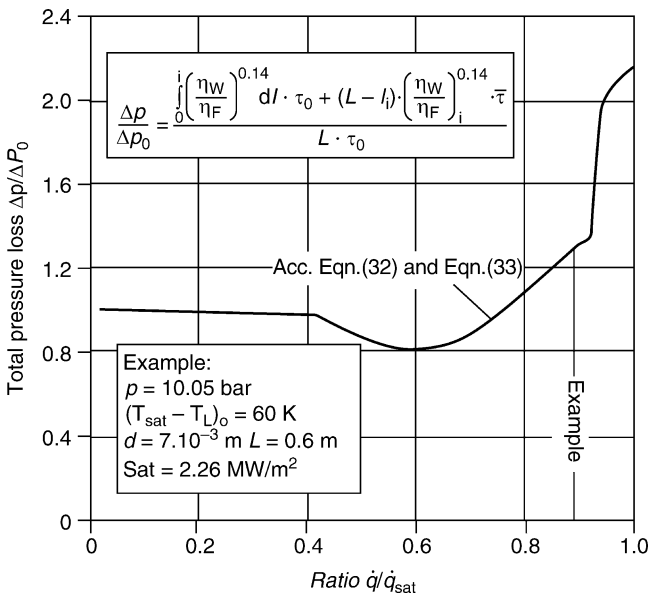

H3.3. Fig. 5. Example 2f: total pressure loss.

4.1.3 Determination on the Basis of Experimental Saturation Boiling Data: All Substances

Justification of the mathematical method presented here exists in the fact that its results agree well with those obtained for water from Eq. (19). In fact, in a check against values determined for R 12 [38], it proved to be superior to other mathematical methods given in the literature. In any case, it continuously phases into the method described in Subchap. H3.4 for the determination of heat transfer during the boiling of saturated liquids.

The entire heat flux is split up into a hydrodynamic component and a component that is described by a boiling point curve that is independent of the mass flux and its vapor fraction. The local heat flux is given by

$$\dot{q}(l) = \dot{q}_{\mathrm{conv}}(l) + \dot{q}_B(l), \tag{22}$$

where $\dot{q}_{\mathrm{conv}} = \alpha_i(l)(T_W - T_L)$, $\dot{q}_B = \alpha_B(l)\,(T_W - T_{sat})$, and $\alpha_B(l)$ is given in Subchap. H3.4.

Remarks

The method suggested by Chen [39] and adopted by Bergles et al. [40] for convective saturation boiling generally cannot be recommended for subcooled boiling, despite the explicitly worded findings of Gungor and Winterton [41, 42] about its suitability. The method based on an equation derived by Forster and Zuber [43] for saturated pool boiling makes use of a bubble suppression factor S that depends on Reynolds number. The aim of this factor is to allow for the fact that the thermal boundary layer becomes progressively thinner as the Reynolds number increases, with the result that bubble formation is impeded. If the method is applied to the results of experiments performed at high heat fluxes, it can be seen that S must be substantially greater than unity ($S >> 1$, cf. [38]). In addition, heat transfer must be largely independent of Reynolds number. This has been demonstrated by Del Valle and Kenning [44] in more recent measurements on subcooled water at high heat fluxes and at ambient pressure.

Furthermore, in the case of very high supercooling measurements [44] show an explicit improvement of the heat transfer rate. This can only be explained by a further boiling mechanism, which is described in Subchap. H2.2, Eq. (28). This mechanism is active at Ja-numbers >100. It cannot be described with Eq. (60) in Subchap. H3.4. Bergles and Rohsenow [10] found massive hydrodynamic instabilities for slowly flowing water at 2.6 bar and subcoolings $60\ \mathrm{K} < (T - T_{sat}) < 90\ \mathrm{K}$. These instabilities must be attributed to the above-mentioned further boiling mechanism.

4.1.4 Determination of Wall Temperature Profile

The wall temperature has to be determined by iteration. The first step is to determine the wall superheat on the assumption that the entire heat flux $\dot{q}$ is still transferred barely by convection, that is,

$$\left(T_W - \overline{T}_L\right)_i = \frac{\dot{q}}{\alpha_i}. \tag{23}$$

(The subscript i has been inserted because the equation corresponds to the conditions at the initial point.)

Afterward, the wall superheat is calculated on the assumption that the entire heat flux is transferred by saturation boiling, that is,

$$\left(T_W - \overline{T}_L\right)_i = \frac{\dot{q}}{\alpha_B(\dot{q})}. \tag{24}$$

Thus, the wall temperature corresponding to T_L, is

$$1 - \left[\frac{T_W - T_{sat}}{(T_W - T_{sat})_B}\right]^{1/(1-n)} = \frac{T_W - \overline{T}_L}{\left(T_W - \overline{T}_L\right)_i}. \tag{25}$$

The value to be chosen for the term n in the exponent is the same which describes the relationship between the heat transfer coefficient and the heat flux as given in Subchap. H3.4.

4.2 Constant Wall Temperature

It can be assumed as a first approximation that the heat is linearly related to the residual subcooling between the initial point Ph_i and the point at which the saturation enthalpy is reached. In this case, the length of the heated section required to transfer heat from Ph_i to $\mathrm{Ph} = 0$ can be calculated from Eq. (7).

The average heat flux is taken for the determination of the boiling number N_{bm} and is given by

$$\dot{q}_m = \frac{\dot{q}_{\max} - \dot{q}_{\min}}{\ln(\dot{q}_{\max}/\dot{q}_{\min})}, \tag{26}$$

where $\dot{q}_{\max} = (\alpha_i + \alpha_B)\,(T_W - T_{sat})$, $\dot{q}_{\min} = \alpha\left(T_W - \overline{T}_{L,it}\right)$, and α_B is a function of $(T_W - T_{sat})$ as described in Sect. 4.1.2.

5 Void Fraction

Rouhani [45] has proved by experiment that the void fraction ε increases only slightly after the initial point (cf. Part C in Fig. 1). It does not commence to increase rapidly until bubbles are generated in large numbers within the bulk of the flow at a point that is characteristic for the onset of net vapor generation. The development of the void fraction has been described in the form of semiempirical equations by Rouhani [46] for water at elevated pressure.

5.1 Approximation for $\varepsilon < \varepsilon_n$

An equation for interpolation in this range has been derived by Jain et al. [31] from their measurements on R 113, that is,

$$\varepsilon = \varepsilon_n \left(\frac{\mathrm{Ph} - \mathrm{Ph}_i}{\mathrm{Ph}_n - \mathrm{Ph}_i}\right)^{0.6} \left[1 - \exp\left(\frac{1}{4}\left(\frac{\Delta L_n}{D_b} - \frac{\Delta L_i}{D_b}\right)\right)\right], \tag{27}$$

$$\mathrm{Ph}_i < \mathrm{Ph} < \mathrm{Ph}_n.$$

The following applies for water [46]

$$\varepsilon_n = 9.74 \frac{10^{-3}}{D_b}\, p^{-0.237}, \tag{28}$$

where D_b is in meters and p is in $\mathrm{N/m^2}$.

The following figures apply for refrigerants: $\varepsilon_n = 0.005 - 0.01$ [31].

5.2 Approximation for $\varepsilon > \varepsilon_n$

The further development of the void fraction, with an allowance for buoyancy in vertical tubes, can be estimated from an equation derived by Zuber and Findlay [33], that is,

$$\varepsilon - \varepsilon_n = \frac{\dot{x}}{\rho''}\left\{C\left(\frac{\dot{x}}{\rho''} + \frac{1-\dot{x}}{\rho'}\right) + \frac{1.18}{\dot{m}}\left[\frac{\sigma g(\rho' - \rho'')}{\rho'^2}\right]^{1/4}\right\}^{-1}. \tag{29}$$

Rouhani [46] determined the following numerical values for C by comparing the figures calculated from the above equation with the results of his measurements: $C = 1.54$ for almost laminar flow and $C = 1.12$ for turbulent flow.

6 Vapor Mass Fraction

In the light of experimental data, Levy [27] demonstrated that the vapor mass fraction $\dot{x}$ (Part D in Fig. 1) can be adequately represented in almost all cases by a simplified model, that is,

$$\dot{x} = \mathrm{Ph} - \mathrm{Ph}_n \exp\left(\frac{\mathrm{Ph}}{\mathrm{Ph}_n} - 1\right). \tag{30}$$

The case of $\mathrm{Ph} > \mathrm{Ph}_n$ (negative) corresponds to Eq. (5). Firstly, $\dot{x}$ is calculated from Eq. (30); and, secondly, $\varepsilon - \varepsilon_n$ from Eq. (29).

7 Pressure Drop

An improvement of heat transfer in subcooled boiling along a given heated surface is accompanied by an increase in the total pressure drop (Part E in Fig. 1). As is shown in Subchap. H3.2, a momentum balance in the form of a separated flow model for an element $\mathrm{d}L$ of the flow path is given by

$$-\frac{\mathrm{d}p}{\mathrm{d}L} = \frac{\tau_W U}{f} + \dot{m}^2 \frac{\mathrm{d}}{\mathrm{d}L}\left[\frac{\dot{x}^2}{\varepsilon\rho''} + \frac{(1-\dot{x})^2}{1-\varepsilon}\frac{1}{\rho'}\right] + g(\varepsilon\rho'' + (1-\varepsilon)\rho')\sin\gamma. \tag{31}$$

If the flow channel is horizontal, $\gamma = 0°$. Provided that heat transfer is single phase, τ_W can be determined as described in Subchap. H3.2 if due allowance is made for the changes in properties that are caused by heating. Thus,

$$\tau_W = \tau_0\left(\frac{\eta_W}{\eta_F}\right)^m. \tag{32}$$

If the tube and annulus are heated internally, the value for the index $m = 0.14$; and if the annulus is heated externally and internally, $m = 0.25$.

τ_W increases when the first coherent bubbles appear, as denoted by the subscript i. In this case, the second term in Eq. (31) remains comparatively insignificant. When the first bubbles are detached and emerge from the boundary layer (subscript n), τ_W decreases again as the wall becomes more densely covered by bubbles, whereas the second term commences to rise rapidly. In this range, instability and fluctuations in flow may arise.

Very few investigations have been made on pressure drop in subcooled boiling, and they have mainly been restricted to water [24, 44, and 47]. For the development of a computer code, Hoffmann and Wong [48] subdivide the heated pipe into sections according to their respective boiling phenomena. Bartolomei and Kovrizhnykh [49] give an overall equation which takes into account data by Tarasova et al. [50]:

$$\frac{\bar{\tau}}{\tau_{Wi}} = 1 + 170 N_b^{0.7}\left(\frac{\rho'}{\rho''}\right)^{0.3}\left(\frac{w^2}{g\cdot l_0}\right)^{-0.15}\left(1 - \frac{\mathrm{Ph}(L)}{\mathrm{Ph}_i}\right)^{1.5}, \tag{33}$$

with $\mathrm{Ph}_i < \mathrm{Ph}(L)$, where $\mathrm{Ph}(L)$ can be positive as well as negative. The characteristic length

$$l_0 = \sqrt{\frac{\sigma}{g(\rho' - \rho'')}}$$

is proportional to the size of bubble detachment. Thus, it can be seen that, since $\tau_{Wi} < \tau_0$, the total pressure drop may, in practice, be less than the pressure drop that would occur if the liquid were to continue to flow adiabatically under the conditions at the evaporator tube inlet (inlet condition τ_0). This would be the case if the liquid were still strongly undercooled at the outlet, although subcooled boiling had already taken place [51] and Fig. 5.

At high system pressures, the relationship between the pressure drop, the mass flow rate, and the boiling number N_b is not so pronounced as it is at ambient pressure. This is because the difference in density between steam and water, and the resultant forces of acceleration are less. The factor $(\rho'/\rho'')^{0.3} N_b^{0.7}$ makes due allowance for the great significance that is attached at low total pressures to the amount of heat transferred to the stream of subcooled liquid and the ratio of the liquid to the vapor density.

On the basis of experimental data for various refrigerants and for water, Hahne et al. [52] give a correlation for the pressure loss as a function of boiling number and subcooling.

Example 2

Water flows at a rate of $\dot{m} = 3 \times 10^3$ kg/(m^{2}s) and an average pressure of $p = 10.05$ bar($T_{sat} = 180°$C) through a vertical, electrically heated tube ($\dot{q} = 2 \times 10^6$ W/m^2; D = D_b = 7 × 10^{-3} m; L = 0.6 m). The subcooling at the inlet is $(\overline{T}_L - T_{sat})_0 = -60$ K. (The inlet is indicated by the subscript 0.)

(a) Where is the initial point located?
(b) At which point does the onset of net steam generation occur?
(c) What is the magnitude of $\dot{x}(L)$?
(d) What is the magnitude of $\varepsilon(L)$?
(e) What is the wall temperature profile or how great is $\alpha(l)$?
(f) How much is the pressure drop $\Delta p/\Delta p_0$ greater than if the tube were unheated?

Properties at $T = 120°$C:

$$\eta = 0.232 \times 10^{-3}\,\mathrm{kg/ms};\ c_p = 4245\ \mathrm{J/kg\,K};$$
$$\lambda = 0.683\,\mathrm{W/m\,K};\ \rho = 943\,\mathrm{kg/m^3}.$$

Properties at $T = 180°C$:

$$\Delta h_v = 2014\ \text{kJ/kg};\ \rho' = 887\ \text{kg/m}^3;\ \rho'' = 5.16\ \text{kg/m}^3;$$
$$Pr' = 0.976.$$

(a) Location of the initial point:

$$\text{Re} = \dot{m}D_b/\eta = 91{,}300\ \text{(turbulent flow)};\ \text{Pr} = \eta c_p/\lambda = 1.44;$$
$$\text{Pe} = \text{Re Pr} = 1.31 \times 10^5;$$

$$N_b = \dot{q}/\dot{m}\Delta h_v = 0.331 \times 10^{-3};$$
$$\text{Ph}_0 = c_{pi}/\Delta h_v \cdot (T_\text{L} - T_\text{sat})_0 = -0.126;$$

$$\frac{\Delta L_0}{D_b} = -\frac{\text{Ph}_0}{4 \cdot N_b} = 95 \rightarrow \Delta L_0 = 0.665\ \text{m};\ \text{Ph}_i = -0.114;$$
$$\frac{\Delta L_i}{D_b} = -\frac{\text{Ph}_i}{4 \cdot N_b} = 86 \rightarrow \Delta L_i = 0.60\ \text{m};$$
$$l_i = \Delta L_0 - \Delta L_i = 0.065\ \text{m}.$$

(b) Location of onset of net steam generation:

$$\frac{1}{C_2} = 0.0074;\ Ph_n = -0.045;\ \frac{\Delta L_n}{D_b} = 34 \rightarrow \Delta L_n = 0.24\ \text{m};$$
$$l_n = \Delta L_0 - \Delta L_n = 0.425\text{m}.$$

(c) Vapor mass fraction $\dot{x}$ at pipe length L:

$$\text{Ph}(L) = -0.0123 \rightarrow \dot{x}(L) = 0.0094.$$

(d) Vapor void fraction at pipe length L

$$\varepsilon_n = 0.053;\ \varepsilon(L) - \varepsilon_n = 0.544 \rightarrow \varepsilon(L) \approx 0.6.$$

(e) Heat transfer at initial point:

$$\text{Re}_{120} = 91{,}300;\ \text{Pr}_{120} = 1.44;\ \text{Pr}_{180} = 0.976;\ l_i/D = 9.3;$$
$$\xi = 0.0183;$$

$$\text{Nu}(l_i) = \alpha_i D/\lambda = 327 \rightarrow \alpha_i = 32.1\ \text{kW/m}^2\,\text{K};$$
$$\Delta T_i = 62.3\ \text{K}.$$

Indirectly follows:

$$(T_\text{W} - T_\text{S})_i = (T_\text{W} - T_\text{L})_i - (T_\text{L} - T_\text{S})_i$$
$$= \Delta T_i + \text{Ph}_i \Delta h_v/c_p$$
$$= 62.3\ \text{K} - 54.4\ \text{K} = 7.8\ \text{K}.$$

Directly with Eq. (15), it follows:

$$(T_\text{W} - T_\text{S})_i = 5.9\ \text{K}.$$

Using Eq. (XX) in Chap. H2, it follows:

$$(T_\text{W} - T_\text{S})_i = 6.8\ \text{K}$$

between initial point i and point n of net vapor generation

$$\frac{\alpha_i}{\alpha} = \frac{T_\text{W} - \overline{T}_\text{L}}{(T_\text{W} - T_\text{L})_i} = \left(\frac{\Delta L/D_b}{\Delta L_i/D_b}\right)^{0.55}$$

in particular can be estimated

$$\left(T_\text{W} - \overline{T}_\text{L}\right)_n = 0.6\left(T_\text{W} - \overline{T}_\text{L}\right)_i = 37.4\ \text{K}$$

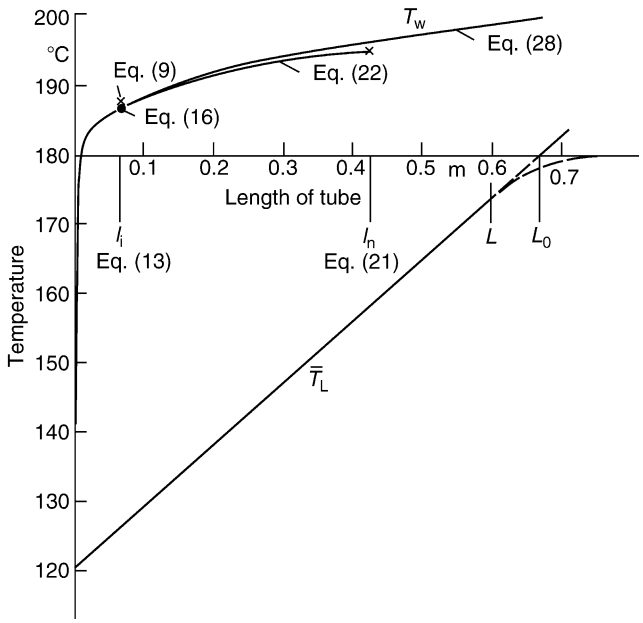

H3.3. Fig. 6. Wall pressure determined in Example 2f.

From there, it follows directly, that

$$(T_\text{W} - T_\text{S})_n = (T_\text{W} - T_\text{L})_i + \text{Ph}_n \Delta h_v/c_p = 15.4\ \text{K}$$

between point n of net vapor generation and Ph = 0.

Using Subchap. H3.4, the following can be estimated

$$\dot{q} = 2 \times 10^6\ \text{W/m}^2;\ \alpha(L)_B = 88{,}090\ \text{W/m}^2\,\text{K} \text{ and } n = 0.69,$$
$$\text{and } \left(T_\text{W} - \overline{T}_\text{L}\right)_i = 62.3\ \text{K},\ \text{and } (T_\text{W} - T_\text{S})_0 = 22.7\ \text{K}.$$

With this, it follows:

$$1 - ((\vartheta_\text{W} - 180)/22.7)^{3.25} = \left(\vartheta_\text{W} - \bar{\vartheta}_\text{L}\right)/62.3.$$

For given $\bar{\vartheta}_\text{F} = 180°C$ or Ph = 0, it can be found by iteration, that

$$\vartheta_\text{W} = 200°C.$$

With this information, the wall temperature profile between i and Ph = 0 can be sketched, as is shown in Fig. 6 as expected, water shows on technical surfaces no particular superheating to commence boiling (as is shown in the general sketch, Fig. 1). Vapor mass fraction $\dot{x}$ has no influence.

(f) Pressure drop in comparison to the unheated pipe:

Up to the initial point, the shear stress at the wall can be estimated using the wall temperature profile, estimated above.

Furthermore, is $\bar{\tau}/\tau_{\text{W}i} = 1.98$, and

$$\frac{\Delta p}{\Delta p_0} = \frac{(\Delta L_0 - \Delta L_i)\bar{\tau}_{1\text{ph}} + (L - (\Delta L_0 - \Delta L_i))\bar{\tau}}{L\tau_0} \approx 1.27.$$

H3.4 Saturated Flow Boiling

Matthias Kind[1] · *Yasushi Saito*[2]
[1]Karlsruher Institut für Technologie (KIT), Karlsruhe, Germany
[2]Kyoto University, Osaka, Japan

1 Convective Flow Boiling of Pure Liquids

Two-phase forced convective boiling, which has also been referred to as convective flow boiling [G1] (for literature and special symbols, see Subchap. H3.8), occurs if the thermal resistance of the boundary layer is less than that in nucleate boiling. In this case, superheat in the liquid on the wall no longer suffices to meet the conditions for the activation of nucleation sites and for bubble formation. Evaporation, thus, results at the liquid–vapor phase boundary.

If the tube walls are wetted, the thermal resistance in the boundary layer is governed by the mechanisms that take place in the liquid phase (cf. *Dukler* [G2], *Hewitt* [G3], and *Steiner* [G4]). Owing to the extent to which the cross-section is occupied and the drag effect exerted by the vapor, the average liquid velocity w' in the two-phase flow is generally higher than that in the single-phase flow at the same mass velocity of the liquid itself. Likewise, the hydraulic diameter d_h is less than the tube inner diameter.

1.1 Convective Flow Boiling in Vertical Tubes

In all flow patterns below the critical boiling state (cf. Subchap. H3.5) in vertical tubes (Fig. 1 in Subchap. H3.1), the heated wall is completely wetted. The following (The term $(1-\dot{x})^{0.01}$ and $\dot{x}^{0.01}$ have been introduced in order to obtain a value of unity for $\dot{x}=0$ and a value of α_{GO}/α_{LO} for $\dot{x}=1$ in Eq. (1).) applies for the vapor mass fraction over the entire range from $\dot{x}=0$ to $\dot{x}=1$:

$$\frac{\alpha(z)_{conv}}{\alpha_{LO}} = \left\{(1-\dot{x})^{0.01}\left[(1-\dot{x})^{1.5}+1.9\dot{x}^{0.6}\left(\frac{\rho'}{\rho''}\right)^{0.35}\right]^{-2.2} + \dot{x}^{0.01}\left[\frac{\alpha_{GO}}{\alpha_{LO}}\left(1+8(1-\dot{x})^{0.7}\left(\frac{\rho'}{\rho''}\right)^{0.67}\right)\right]^{-2}\right\}^{-0.5}. \quad (1)$$

In Eq. (1), α_{LO} and α_{GO} are the local single-phase heat transfer coefficients to be determined at a point z. They are based on a mass velocity $\dot{m}$ that represents the total flow for the liquid (L) or the vapor (G), respectively. They can be determined from the equations given in Sect. 4 (Appendix) or in Chap. G1, for the corresponding hydrodynamic conditions (flow at the inlet or fully developed flow), the thermal boundary conditions ($\dot{q}$ = constant; T_w = constant), and the following values for the Reynolds number:

$$Re_{LO} = \frac{\dot{m}d_h}{\eta_L} \text{ and } Re_{GO} = \frac{\dot{m}d_h}{\eta_G}. \quad (2)$$

The equations to be selected depend on the shape of the cross-section. Thus, the results of measurements on rectangular tubes [W6] and concentric annuli [W7, W8] indicate that the value to be inserted for the hydraulic diameter d_h is that determined by Eq. (37) in Subchap. H3.1.

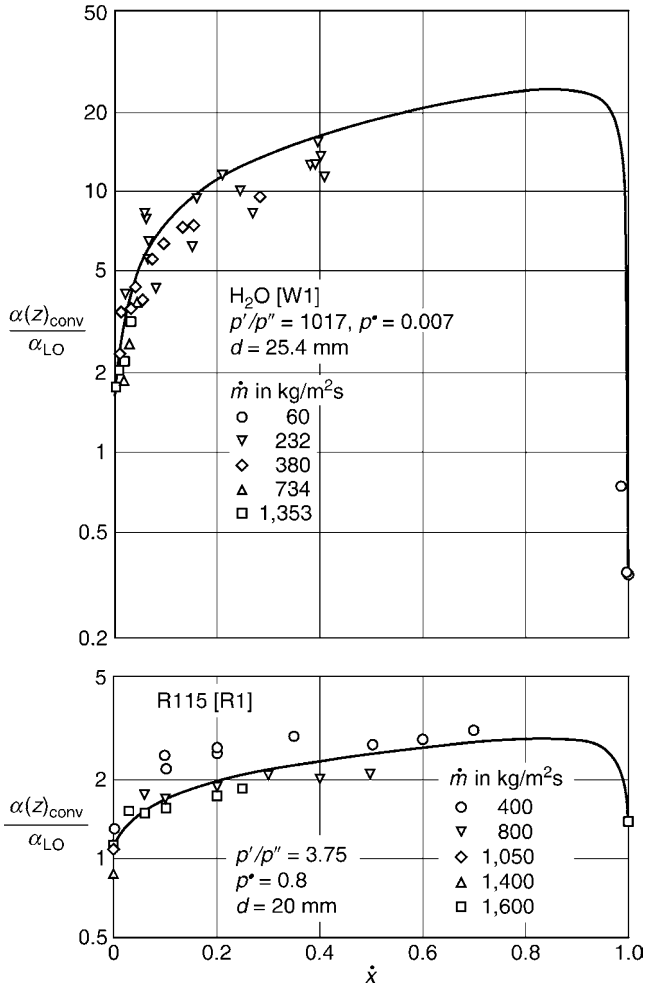

H3.4. Fig. 1. Relative heat transfer coefficient as a function of the vapor mass fraction in a vertical tube.

1.1.1 Values for the Properties

All the values required for calculation are those for the properties at saturation, for example, $\eta_L = \eta'$ and $\eta_G = \eta''$.

The range of validity is $3.5 \leq \rho'/\rho'' \leq 5000$.
The range of reduced pressures ($p^* = p/p_c$) for the liquids investigated is $10^{-3} \leq p^* \leq 0.8$.

The studies were performed on tubes and annuli of $3 \leq d_h/mm \leq 25.4$. The results of the measurements at low and high values of reduced pressure are shown in Fig. 1. No systematic relationship could be determined between the $\alpha(z)_{conv}/\alpha_{LO}$ ratio and the mass velocity [W1–W6, R1–R4, H2].

1.1.2 Effect of Bends and Elbows

The equations submitted in Sect. 1.1 of this chapter apply solely to straight tubes. They do not embrace disturbances in the two-phase flow, such as secondary currents brought about by gravity and centrifugal forces in bends and elbows. The magnitude of the centrifugal forces depends on the radius of curvature and the velocities of the two phases in the main direction of flow. Together with the force of gravity, they are responsible for some degree of stratification in the liquid phase, with the consequence that partial dryout may occur downstream in vertical tubes of l/d = 5–10 relative length. In other words, the heat transfer coefficient may be reduced in this region.

Measurements were performed by *Pujol* [R3] on R 113 in hairpin rows of vertical tubes at mass velocities of $\dot{m} = 200$–1800 kg/m²s, vapor mass fraction of $\dot{x} = 0$–1, and reduced pressures of $p^* = 0.03$–0.13. They revealed that heat transfer is no longer disturbed if the relative length exceeds l/d = 20. The figures for the heat transfer coefficient on the outer surfaces of the heated bends ($R/d \approx 4.1$) were always higher than those on the inside. Nevertheless, the inner surfaces did not dryout, even at the bend outlets, that is, no significant decrease in the local heat transfer coefficients was observed.

1.2 Convective Flow Boiling in Horizontal Tubes

The liquid phase may be stratified by gravity (cf. Subchap. H3.1) with the result that the heated wall is not completely wetted and that heat transfer to the vapor phase is generally poor. Hence, if the heat flux applied at the circumference $\dot{q}$ is kept constant, the temperatures at the upper surfaces of the tube are considerably higher than those at the lower surfaces. The effects of stratification on the wall temperature distribution over the circumference of tubes has been demonstrated in studies by *Styrikovich* et al. [W11, W12] on water and in measurements by *Chaddock* and *Noerager* [R10] on R 12.

Accordingly, the average heat transfer coefficient around the circumference depends on the degree of wetting and heat conduction $\lambda_w s$ of the tube wall, and attention to these relationships has been drawn by various authors [G5, G6, W15, W17, R14].

Another aspect has been brought up in heat transfer measurements performed by *Chawla* [R11], *Bandel* [R6], *Naganagoudar* and *Steiner* [R23], *Iwicki* and *Steiner* [R18], *Müller-Steinhagen* [C13], and *Schmidt* [R26]. They demonstrated that the only case of convective boiling in which incomplete wetting has a significant effect on the perimeter-averaged heat transfer coefficient is that in which according to Fig. 3 in Subchap. H3.1, there is a stratified or a stratified-wavy flow pattern (Stratified-wavy flow is the name given to the range of wavy flow in which $\left(\mathrm{Re}_L \mathrm{Fr}'_G\right)^{0.5} \leq 2\left(\mathrm{Re}_L \mathrm{Fr}'_G\right)^{0.5}_{\mathrm{tt,lim}}$ is approximately valid.). In all the other flow patterns, the mass velocity does not have a systematic effect on the $\alpha(z)_{conv}/\alpha_{LO}$ ratio. The following applies over the entire range of vapor mass fractions (The term $(1-\dot{x})^{0.01}$ and $\dot{x}^{0.01}$ have been introduced in order to obtain a value of unity for $\dot{x}$ = 0 and a value of α_{GO}/α_{LO} for $\dot{x}$ = 1 in Eq. (1)):

$$\frac{\alpha(z)_{conv}}{\alpha_{LO}} = \left\{ (1-\dot{x})^{0.01} \left[(1-\dot{x}) + 1.2\dot{x}^{0.4} \left(\frac{\rho'}{\rho''} \right)^{0.37} \right]^{-2.2} + \dot{x}^{0.01} \left[\frac{\alpha_{GO}}{\alpha_{LO}} \left(1 + 8(1-\dot{x})^{0.7} \left(\frac{\rho'}{\rho''} \right)^{0.67} \right) \right]^{-2} \right\}^{-0.5} . \quad (3)$$

In Eq. (3), α_{LO} and α_{GO} are the local single-phase heat transfer coefficients to be determined at a point z. They are based on a mass velocity $\dot{m}$ that represents the total flow for either the liquid (L) or the vapor (G), respectively. The pertinent Reynolds numbers for the liquid and the vapor are given by

$$\mathrm{Re}_{LO,GO} = \frac{\dot{m} d_h}{\eta_{L,G}}.$$

According to measurements by *Davis* and *David* [W13], the value to be inserted for d_h is that determined from Eq. (37) in Subchap. H3.1. Equations for the determination of α_{LO} and α_{GO} under given hydrodynamic and boundary conditions are presented in Sect. 4 (Appendix), and in Chap. G2. They depend on the shape of the cross-section. The values to be taken for the properties of the pure substances are those for the liquid and the vapor at saturation.

The range of validity is $3.5 \leq \rho'/\rho'' \leq 1500$.
These density ratios correspond to reduced pressures of $5{\cdot}10^{-5} \leq p^* \leq 0.8$.

Up to $p^* = 0.8$, the values determined by this method agree well with those obtained by the measurements of *Niederkrüger* [G7].

The measurements [W9, W10, R2, R4, R6, R8, R11, R18, R23, C13] adopted to fit the parameters in Eq. (3) were performed in tubes of $6 \leq d_h/\mathrm{mm} \leq 25$ diameter. The results obtained at a low and a moderate reduced pressure are shown in Fig. 2. A striking feature is that the slope of the curve for $\alpha(z)_{conv}/\alpha_{LO}$ in the 0–0.2 range of values for the vapor mass fraction is much steeper than that for vertical tubes (cf. Fig. 1). It is in this range that the difference between flow patterns in vertical tubes and those in horizontal tubes is most pronounced. At even higher vapor mass fractions, annular and transition flow patterns also occur in horizontal tubes. However, the thickness of the layer at the crest differs from that at the base of the tube.

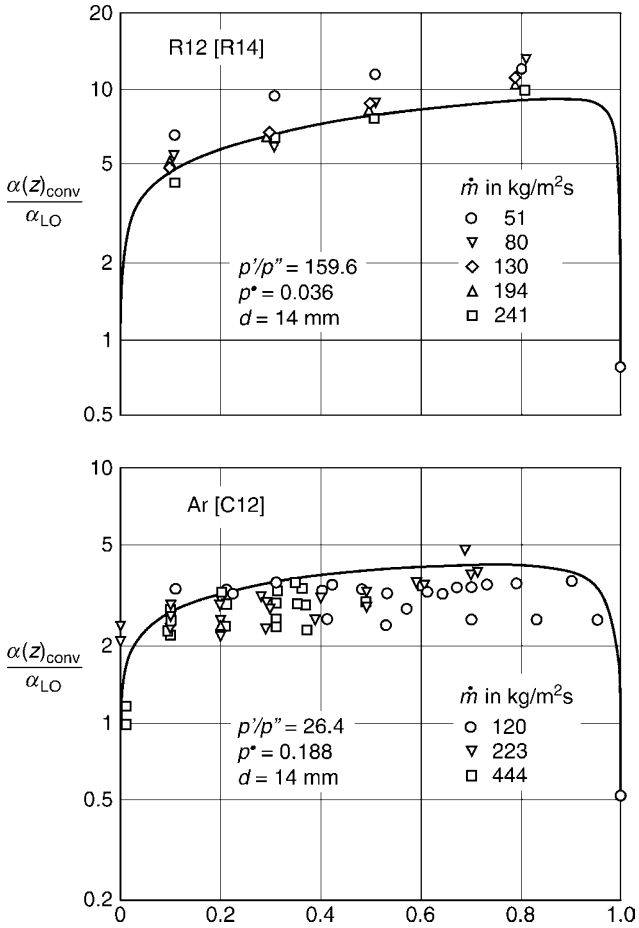

H3.4. Fig. 2. Relative heat transfer coefficient as a function of the vapor mass fraction in a horizontal tube.

1.2.1 Effects of Incomplete Wetting

The perimeter-averaged heat transfer coefficient in *stratified* and *stratified-wavy flow* is reduced by incomplete wetting. As is shown in Fig. 4 in Subchap. H3.1, φ is the angle subtended at the center by the unwetted arc. The coefficient α_G for the heat transferred from this arc to the vapor is usually lower than the coefficient α_{Lb} for the wetted arc, which is equal to the value for $\alpha(z)_{conv}$ determined from Eq. (3), that is, $\alpha_{Lb} = \alpha(z)_{conv}$.

The reference length of the unwetted arc is given by

$$\Phi = \varphi/2\pi. \tag{4}$$

The ratio a of the local heat transfer coefficient in the unwetted to that in the wetted section at the point z is given by

$$a = \alpha_G/\alpha_{Lb}. \tag{5}$$

M is a characteristic that defines the fins and is given by

$$M = \frac{\alpha_{Lb} d}{\lambda_w} \cdot \frac{\pi^2 d_m}{4s}, \tag{6}$$

where $d_m = d + s$, s is the wall thickness, and λ_w is the thermal conductivity of the tube.

According to *Martin* [G8], the perimeter-averaged heat transfer coefficient for the *boundary condition of* $\dot{q}$*= constant* is given by

$$\frac{\alpha(z)_{conv}}{\alpha_{Lb}} = \frac{1-(1-a)\Phi}{\psi}, \tag{7}$$

where

$$\psi = 1 + \Phi(1-\Phi)\frac{(1-a)^2}{a}\left[1 - \frac{1-(1-a)\Phi}{f_1+f_2}\right], \tag{8}$$

where

$$f_1 = a\sqrt{M}\Phi(1-\Phi)\coth\left(\sqrt{M}(1-\Phi)\right),$$
$$f_2 = a\sqrt{M}\Phi(1-\Phi)\coth\left(\sqrt{aM}\Phi\right).$$

The factor ψ is shown as a function of M for $\Phi = 0.5$, that is, for a half-wetted tube, in Fig. 3. A point to note is that M is large, particularly if the tubes have poor thermal conductivity and thin walls, with the consequence that the decrease in the perimeter-averaged heat transfer coefficient may not be neglected.

If the *boundary condition* is T_w = *constant* or $\dot{q}$ = *constant* and the tubes have good thermal conductivity ($\lambda_w s \geq 1$W/K; or, to be more precise, $M \leq 1$) and if $\psi = 1$, Eq. (7) becomes

$$\alpha(z)_{conv} = \alpha_{Lb}(1-\Phi) + \alpha_G\Phi. \tag{9}$$

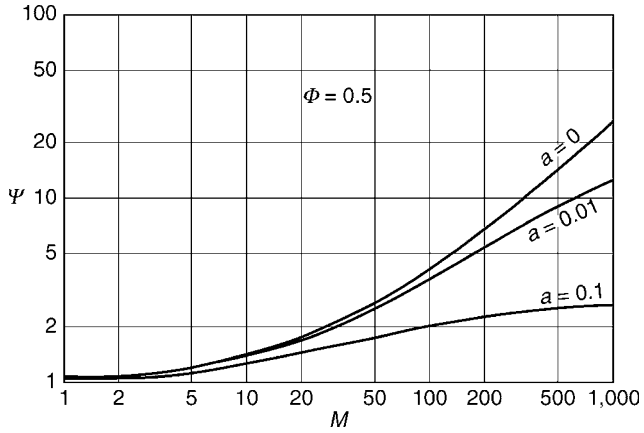

H3.4. Fig. 3. Relationship between ψ and the fin characteristic M.

The heat transfer coefficient α_G is obtained from the equations given in Sect. 4 (Appendix), in which case the value for the hydraulic diameter d_{hG} of the gas phase to be inserted in the expression for the Nusselt and Reynolds numbers is

$$d_{hG} = d\left(\frac{\varphi - \sin\left(\frac{180}{\pi}\varphi\right)}{\varphi + 2\sin\left(\frac{90}{\pi}\varphi\right)}\right). \tag{10}$$

The Reynolds number at the point z is given by

$$\mathrm{Re}_G = \frac{\dot{m}\,\dot{x}\,d_{hG}}{\eta''\,\varepsilon}, \tag{11}$$

where ε is the void fraction as determined from Eq. (26) in Subchap. H3.1.

1.2.2 Determination of the Length of the Unwetted Arc φ

The relationship of the flow parameters to the length of the unwetted arc in stratified flow is unknown. The longest unwetted arc is obtained by assuming a flat phase boundary layer, that is, by neglecting the contact angle and the interfacial tension. It can be determined by iteration from Eq. (26) in Subchap. H3.1, and the relationship between ε and φ given by Eq. (27) in Subchap. H3.1, that is,

$$\varphi_g = 2\pi\varepsilon + \sin\left(\varphi_g 180/\pi\right). \tag{12}$$

The heat transfer coefficient corresponding to the boundary condition of $\dot{q} = constant$ or $T_w = constant$ can then be obtained from Eq. (7) or (9). It is the smallest value possible, because interfacial tension and the effect of the contact angle in the two-phase flow cause the tube to be wetted much more effectively, as has been verified by observations [R18, R26, R29].

With organic and inorganic fluids and with mixtures *Niederkrüger* et al. [G7, G9] proved acceptable agreement between experiment and calculation, if the unwetted arc is approximated by

$$\varphi = 0.5\varphi_g. \tag{13}$$

In addition, it was shown that the flow patterns and wetting limits in heated tubes may differ from those in unheated tubes. Studies by *Zahn* [R29] on R22 in heated glass tubes (T_w approximately constant) and by *Schmidt* [R26] on R12 in copper and nickel tubes have revealed by using γ-ray densitometry that some of the flow patterns observed no longer agree with the values predicted for adiabatic vapor–liquid flow from the flow pattern maps.

Consequently, the conclusion may not be drawn that the flow patterns obtained from maps for unheated tubes (Fig. 3 in Subchap. H3.1) remain unchanged when the tube is heated. The additional patterns indicated by the foregoing equations serve as criteria on how $\alpha(z)_{conv}$ should be calculated. The figures, thus, determined agree to within about ±30% with the results of the experiments that have been mentioned [W9, W10, R2, R4, R6, R8, R11, R18, R23, R26, C13, G7, G9].

1.2.3 Improvement in Wetting

Certain measures exist for counteracting, either entirely or partially, the substantial reduction in the perimeter-averaged heat transfer coefficient that is brought about by incomplete wetting. They include tubes with internal fins, for example, integral internal fins or twisted-tape inserts [R17, R25]. Smooth tube walls can be completely wetted by inducing helical flow, for example, by fitting internal coiled strips or machining helical grooves in the inner surface. This has been demonstrated by *Brendeng* [R7], who fitted a coiled strip into a tube through which R12 flowed with a mass velocity of $\dot{m}$ = 86 kg/m^{2}s (The ratio of the coil pitch to the tube inner diameter was 6.3.). The heat transfer coefficient was, thus, increased, under otherwise identical conditions, by a factor of 2.2. The disadvantage of improving heat transfer by these methods is that they involve a higher pressure drop.

Another possibility to improve wetttablity of the inner tube wall is the installation of a displacement tube, to produce a ring gap flow. In studies of *Geskes* [W35] with water, air, and water vapor, it has been found that by the eccentric arrangement of a displacement tube, the wettability effect can be optimized. At the same time, the pressure drop was not so greatly increased.

1.2.4 Effect of Bends and Elbows

The equations submitted in Sect. 1.2 for the determination of the heat transfer coefficient do not embrace the effects of disturbances in two-phase flow brought about by bends, elbows, branches, etc. An example of these effects arose in studies by *Lis* and *Strickland* [W15] on the flow of water in annular flow pattern through a horizontal tube. It was observed that the crest of the tube became dry when a *vertical* assembled bend of R/d = 3 was installed upstream. The relative horizontal length within which dryout occurred depended on the applied heat flux $\dot{q}$, which gave rise to convective boiling, and lay between l/d = 15 and l/d = 65. The relative length of this zone of disturbance l/d was greatly decreased when the bend radius was reduced to R/d = 1.4. When the obstruction was replaced

by a *horizontal* assembled bend of $R/d = 3$ in an otherwise identical experimental layout, hardly any dryout could be observed. The values of reduced pressure under which the experiments were performed, lay between $p^* = 0.068$ and $p^* = 0.3$.

Zahn [R29] studied flow through hairpin rows of horizontal tubes connected by bends of $R/d = 2.35$. The medium was R22, the mass velocity was $\dot{m} = 96$–256 kg/m^{2}s, and the vapor mass fraction was $\dot{x} = 0.2$–0.99 at $p^* = 0.13$. The disturbance in the two-phase flow observed at the tube inlets downstream from the bends extended over a relative length of between $l/d = 10$ and $l/d = 20$. This length was roughly the same in both upward and downward flow through the vertical assembled hairpin rows.

1.3 Convective Flow Boiling in Inclined Tubes and Helical Coils

1.3.1 Inclined Tubes

Stratification of the liquid in tubes inclined at an angle Θ to the horizontal is caused by the gravity component $g \cos \Theta$. Studies by *Cumo* et al. [W30] on R12 at $p^* = 0.77$ and by *Kefer* [W34] on water revealed that the critical boiling regime at the crest of the tube continuously depends on the angle of inclination and passed through a minimum at $\Theta = 0$. *Styrikovich* et al. [W12] investigated the effect of the angle of inclination on the boiling of water at reduced pressures of $p^* = 0.15$–0.4 and noted that the crest of the tube was no longer overheated if $\Theta \geq 10°$. In view of the scanty information on the subject, the only suggestions that can be made for the determination of the perimeter-averaged heat transfer coefficient in inclined tubes are as follows:

If the angle of inclination is $\Theta = 0°$–$30°$, the equations to apply are those for horizontal tubes (Sect. 1.2); and if $\Theta > 30°$, the equations for vertical tubes (Sect. 1.1).

1.3.2 Helical Coils

The centrifugal forces that occur in flow through bends give rise to secondary currents in the form of double vortices. In the three-dimensional bends of helical coils, the direction of flow changes continuously, and a twist flow is superimposed on the double vortices. The vapor velocity that results from the high density ratio ρ'/ρ'' at moderate reduced pressures ensures that the double vortex and the twist flow suffice to wet the tube wall entirely in most of the applications that occur in engineering practice.

This has been confirmed in studies by *Bell* and *Owhadi* [W16, W17] on water at $p^* \approx 0.006$, $\dot{m} = 70$–310kg/m^{2}s, and $\dot{x} = 0.13$–0.96 at the outlet in coils described by $d/D_w = 0.024$ and $d/D_w = 0.05$ (cf. Chap. G3). The points at which the greatest threat of burnout arose at applied heat fluxes of up to $\dot{q} = 250{,}000$ W/m^2 were the crests and the bases of the tubes. They were both dry at vapor mass fractions of 0.8–0.95, whereas the inside and the outside of the coil frequently remained wetted at values of up to $\dot{x} = 0.99$.

In the light of these results, it is suggested that perimeter-averaged heat transfer coefficients at $p^* \leq 0.3$ be calculated by Eq. (1). If $p^* > 0.3$, Eq. (1) should not be applied unless the mass velocity is $\dot{m} \geq 500$ kg/m^{2}s, because there is risk of incomplete wetting at lower values of $\dot{m}$. If incomplete wetting is likely, the equations to apply are those for a horizontal tube (Sect. 1.2; Incomplete wetting).

The relationships given for helical coils in Chap. G3, should be inserted in all equations for the single-phase heat transfer coefficients α_{LO} and α_{GO}. The values to be inserted for the properties are those for the saturated state of the liquid and the vapor.

1.3.3 Effect of Impurities (Applicable to Sects. 1.1–1.3)

Impurities in the liquid phase are solutions of oils, wetting agents, or other liquids in low concentrations. It must be ensured that the correct values for the properties of the mixture are inserted in the equations for convective flow boiling. If the composition of the liquid is known, the properties of the mixture can be calculated as indicated in Chap. D1. The behavior of the mixtures is dealt with in Subchap. H3.7.

2 Nucleate Flow Boiling of Pure Liquids

Heat transfer during evaporation in the nucleate boiling regime is governed by the activation of nucleation sites, bubble growth, and bubble departure. As has been demonstrated by *Koumoutsos* et al. [G10], superimposed forced convection exerts a direct effect on bubble departure. Allowance must also be made for the change in the temperature profile from that in the nucleate boiling of flowing liquid–vapor mixtures to that in free convection.

By introducing the S-factor, *Chen* [G11] explained this change of the temperature profile in the boundary layer, which affects the bubble growth and the number of the nucleation site.

No theory has yet been formulated that allows the heat transfer coefficient in nucleate boiling of flowing liquid–vapor mixtures to be calculated. For this reason, one will refer here to extensions of the equations that *Borishanskii* et al. [G12] derived by applying thermodynamic similarity in the determination of heat transfer in pool boiling.

2.1 Nucleate Flow Boiling in Vertical Tubes

2.1.1 Upward Flow in a Vertical Tube

As long as the critical boiling regime (cf. Subchap. H3.5) is not transgressed, the heated wall of vertical tubes is completely wetted by the liquid in all flow patterns. The heat transfer coefficient can be obtained from the following equation:

$$\frac{\alpha(z)_B}{\alpha_0} = C_F \left(\frac{\dot{q}}{\dot{q}_0}\right)^n F(p^*) F(d) F(W) F(\dot{m}, \dot{x}), \qquad (14)$$

in which the properties of the liquid are embraced by the factor C_F; the properties of the heated wall, by $F(W)$; the dimensions of the tube, by $F(d)$; the flow parameters, by $F(\dot{m},\dot{x})$; and the effect of pressure, by $F(p^*)$. The relationship to heat flux is defined by the term $\dot{q}^n$. The reference value α_o is the same as in Chap. H2, Eq. (5). For selected systems reference values α_o are given in Table 2.

2.1.2 The Effect of Heat Flux and Pressure in Nucleate Boiling

The characteristic $\alpha - \dot{q}$ curves shown in Fig. 4 can be obtained by plotting measurements on all substances in the nucleate boiling regime. It can be clearly seen that the slope of the curve becomes less as the reduced pressure p^* increases. In other words, the exponent n in Eq. (14) depends on pressure.

Practical considerations in the nucleate boiling of flowing liquid–vapor mixtures necessitate the division of media into four groups: (1) Inorganic substances, (2) Hydrocarbons and halocarbons, (3) Cryogenic substances with boiling point $\leq$180K with the exception of ethane and methane, and (4) Helium as the sole representative of its group (cf. Table 2).

It has also been demonstrated by experiment that the exponent n in Eq. (14) becomes less as the critical heat flux (cf. Subchap. H3.5) is approached. No equation has yet been derived to allow for this effect.

For *inorganic fluids*, for example, water and ammonia; and for *hydrocarbons*, for example, *n*-butanol and *halocarbons*, for example, R22, R134a, and R227 n can be estimated by

$$n = 0.8 - 0.1 \cdot 10^{(0.76\,p^*)}. \qquad (15)$$

With the exception of methane and ethane, *cryogenic fluids* (with boiling points $\leq$ 180 K), for example, nitrogen, hydrogen, and helium, display a less pronounced relationship to pressure. At reduced pressures of $p^* < 0.6$, the values of n are also less than those for the inorganic substances mentioned above. The following correlation is suggested for cryogenic fluids:

$$n = 0.7 - 0.13 \cdot 10^{(0.48p^*)}. \qquad (16)$$

The pressure exerts a significant effect on heat transfer, particularly at the lower and higher values of p^*, and its relationships must be known for the determination of $\alpha(z)_B$. These relationships can be defined by the function $F(p^*)$, which takes into account the allocation into the four groups and the *reference heat flux* $\dot{q}_o$ for the *specific substances* (cf. Table 2). $F(p^*)$ is given by

$$F(p^*) = 2.816p^{*0.45} + \left(3.4 + \frac{1.7}{1 - p^{*7}}\right)p^{*3.7}. \qquad (17)$$

The results of measurements [W4, W23, W26, W27, A1, R4, R30, R31, R33, R34, C1, C2, C5] were taken to determine the pressure function. They are compared in Fig. 5, where it can be seen that the deviation of any one substance, for example, water, from the mean curve, does not differ from that of the other substances. In other words, the deviations are not restricted to specific substances.

2.1.3 Effect of Mass Velocity, the Vapor Mass Fraction, and the Tube Diameter

In the literature on flow nucleate boiling in vertical tubes [G1, G11, G13–G17, G25], differences exist in the equations relating

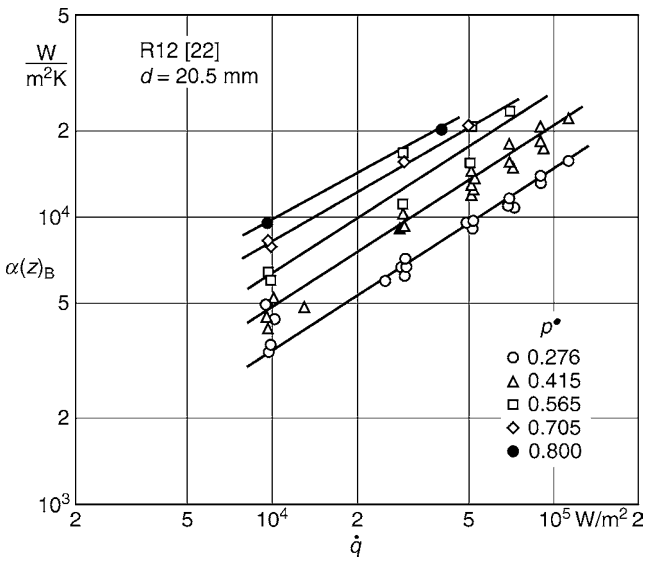

H3.4. Fig. 4. Heat transfer coefficient $\alpha(z)_B$ as a function of the heat flux in a vertical tube.

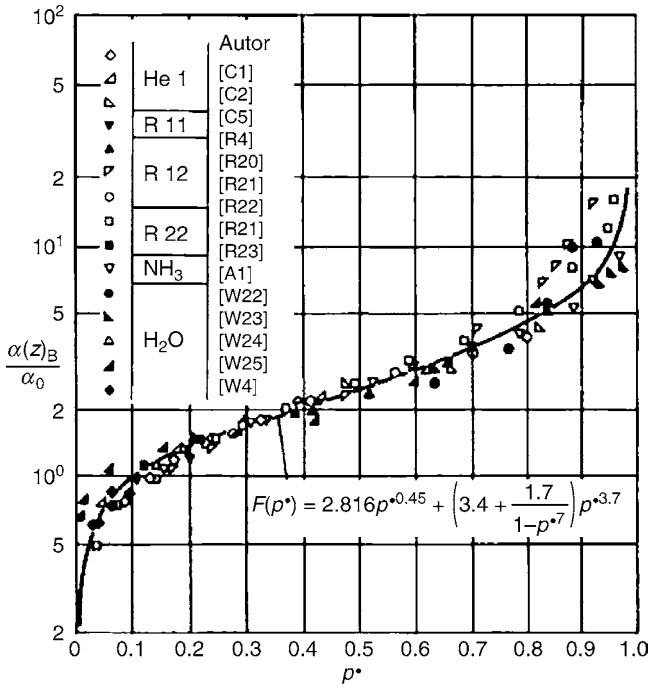

H3.4. Fig. 5. Relative heat transfer coefficient as a function of the reduced pressure for nucleate boiling in a vertical tube and $\dot{q}_0$ for values of relating to the substances concerned.

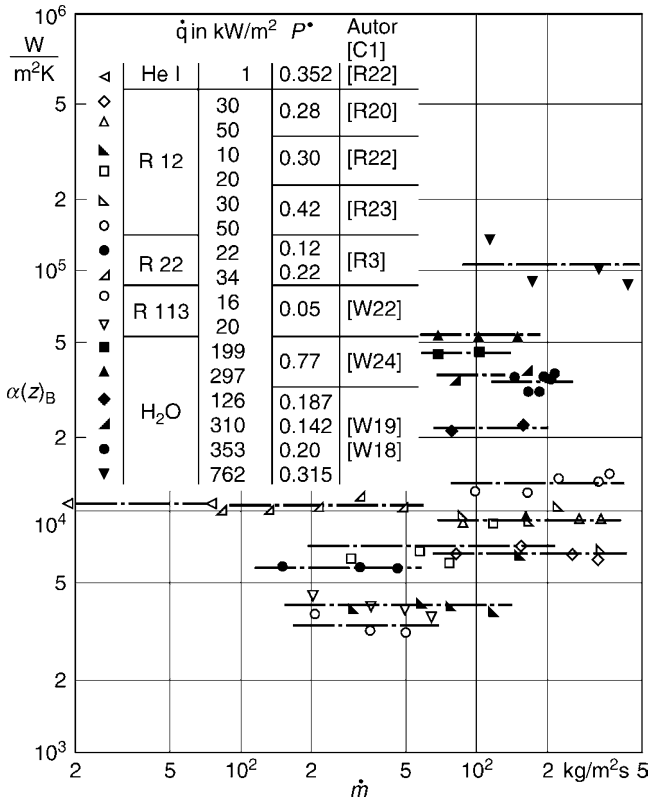

H3.4. Fig. 6. Heat transfer coefficient as a function of mass velocity for nucleate boiling in vertical tubes.

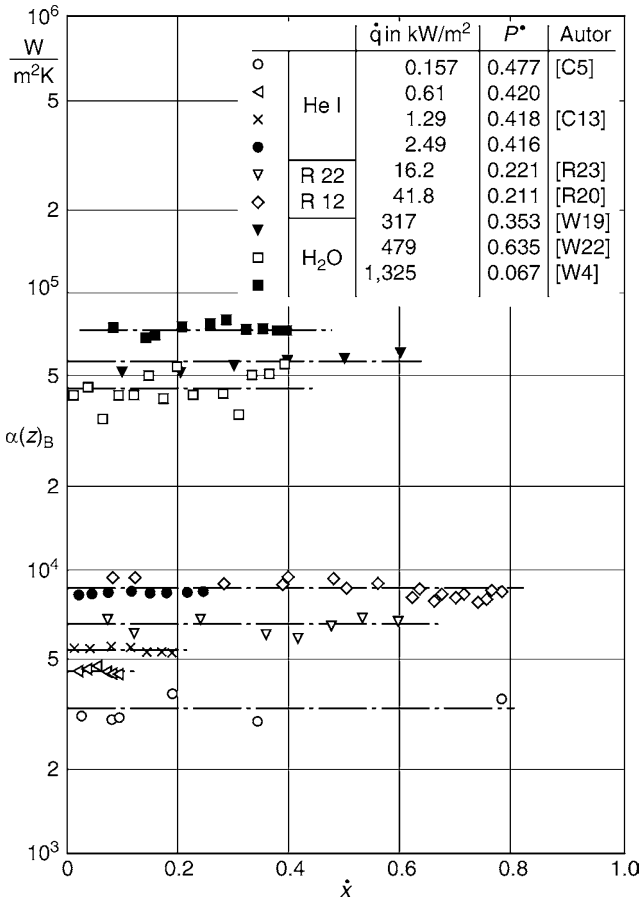

H3.4. Fig. 7. Heat transfer coefficient as function of the vapor mass fraction for nucleate boiling in vertical tubes.

the heat transfer coefficient to the flow parameters $\dot{m}$ and $\dot{x}$. In order to find an explanation for these contradictions, the measurements concerned [W18, W20, W23, W24, W26, R3, R30, R33, R34, C1] were evaluated. All the other parameters were the same in each case. The graph thus obtained is reproduced in Fig. 6. According to this, heat transfer during nucleate boiling in vertical tubes is not affected by the mass velocity, even at values as high as 4,500 kg/m^{2}s.

The velocity profile for the liquid is substantially altered by an increase in the vapor mass fraction and drag by the vapor. Figure 7 shows that the vapor mass fraction does not have any effect on the heat transfer coefficient within the range in which it was measured, that is, $\dot{x}$ = 0–0.8.

Hence, the heat transfer coefficient in nucleate flow boiling cannot depend on the flow parameters $\dot{m}$ and $\dot{x}$ or on characteristics that contain them, that is,

$$F(\dot{m}, \dot{x}) = 1. \tag{18}$$

Various authors [W3, W23, W24, R4] have performed experiments on evaporator test units of different internal diameters in the same test loop in order to determine the effect of d on the heat transfer coefficient. Some authors [C1–C5] measured heat transfer coefficients of helium I in tubes with different diameters, while the other parameters were the same. All the results are reproduced in Fig. 8. It can be seen that, if the other parameters are kept constant, the heat transfer coefficient in nucleate boiling decreases with an increase in the tube diameter. The average relationship in the range of validity is

$$F(d) = (d_o/d)^{0.4}, \tag{19}$$

where $d_o = 10^{-2}$ m.

2.1.4 Effect of the Properties of the Heated Wall

Details are not yet known as to which properties of a heated wall govern the heat transfer coefficient. *Stephan* [G18] submitted the following relationship that applies in pool boiling for surfaces finished by turning or drawing:

$$\alpha_{PB} \sim R_p^{0.133},$$

where R_p is the smooth depth as defined in DIN 4762, Part 1/08.60 (cf. Subchap. H2.3).

Systematic measurements were made by *Takagi* [W14] and *Müller* [W27] to determine the effect of roughness on heat transfer in nucleate boiling of flowing liquid–vapor mixtures. *Takagi* used a rectangular horizontal channel in which the lower wall was heated and which was always completely wetted, whereas *Müller* performed his experiments in vertical tubes. The results which are presented in Fig. 9 confirm – on an average – the relationship submitted by *Stephan*.

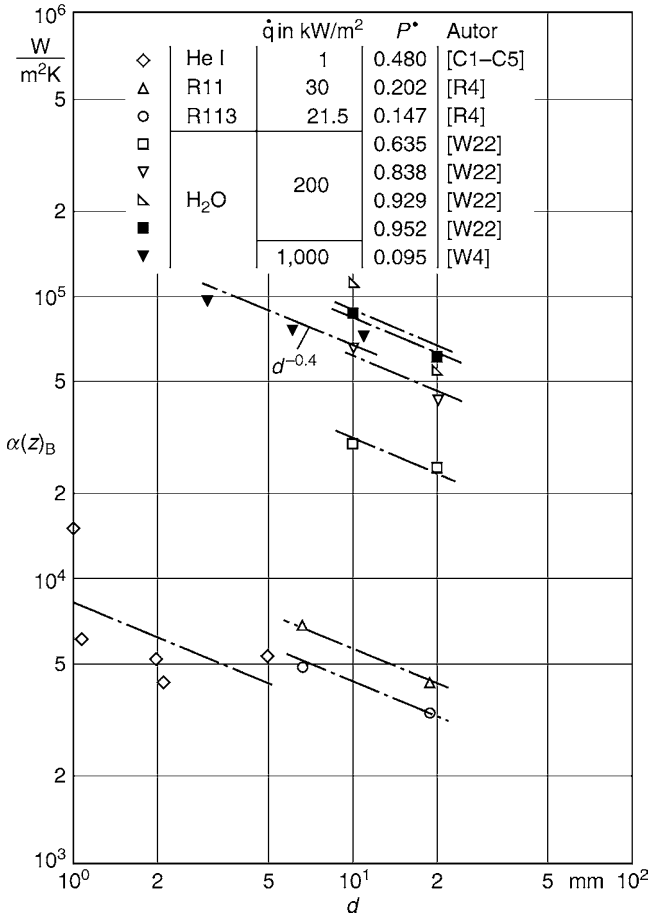

H3.4. Fig. 8. Heat transfer coefficient as a function of tube diameter for nucleate boiling in vertical tubes.

In Subchap. H2.3, the *arithmetic mean roughness height* R_a was proposed as the reference magnitude in nucleate and flow boiling. Its relationship to the smooth depth R_p for machined and emery-polished surfaces was determined as $R_a = 0.4R_p$ by *Gorenflo* et al. (cf. Subchap. H2.3). A somewhat different correlation, that is, $R_a = 0.6R_p$, was derived from measurements on drawn copper and nickel tubes in the $0.06 \leq R_a \leq 0.7$ range of roughness heights. Consequently, the following equation will be adopted until further results are available:

$$F(W) = (R_a/R_{ao})^{0.133}. \tag{20}$$

If $R_{ao} = 1$ µm is taken as the reference value, the choice of R_a in preference to R_p in Eq. (21) entails that the heat transfer coefficient is, purely theoretically, 7% (if $R_a = 0.6\ R_p$) or 13% (if $R_a = 0.4R_p$) higher. This increase was not taken into consideration and, therefore, leads to a conservative design of heat transfer equipment. According to DIN 4766 Part 2/03.81, a value of R_{ao} can be achieved by most finishing techniques.

If the effects discussed are taken into account, the heat transfer coefficient in upward flow through vertical tubes in the subatmospheric to elevated pressure range can be obtained from

$$\frac{\alpha(z)_B}{\alpha_0} = C_F \left(\frac{\dot{q}}{\dot{q}_0}\right)^{n(p^*)} \cdot \left[2.816p^{*0.45} + \left(3.4 + \frac{1.7}{1-p^{*7}}\right)p^{*3.7}\right] \cdot \left(\frac{d_o}{d}\right)^{0.4} \left(\frac{R_a}{R_{ao}}\right)^{0.133}. \tag{21}$$

The exponent $n(p^*)$ is determined from Eq. (15) or (16) according to the nature of the fluid. If the design value is close to that for $\dot{q}_{cr}$ (cf. Subchap. H3.5), account must be taken of the fact that the exponent $n(p^*)$ is smaller than the figure calculated

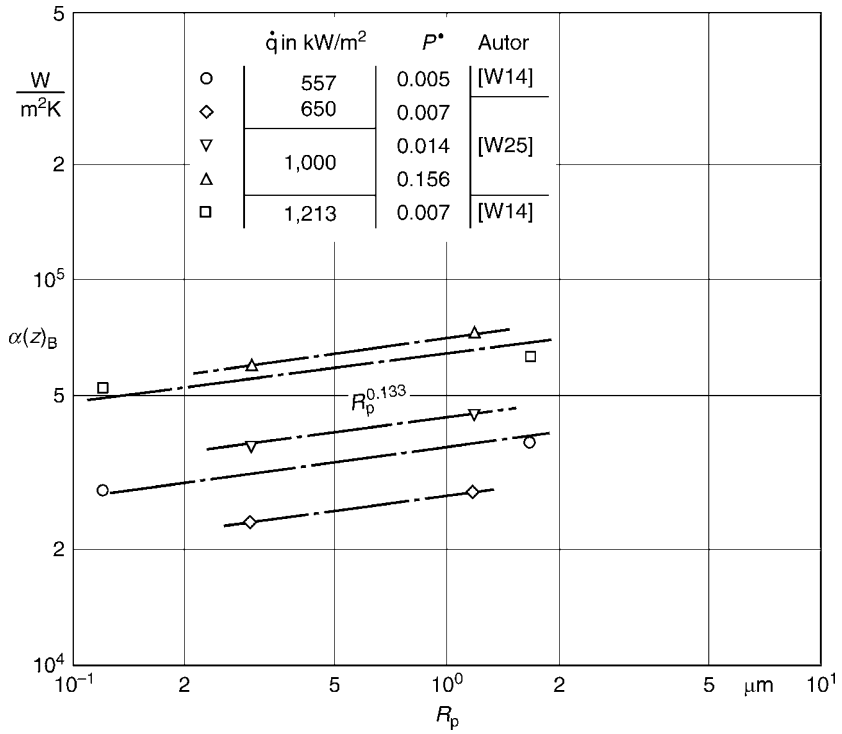

H3.4. Fig. 9. Effect of the roughness of tube surfaces on the heat transfer coefficient in nucleate boiling.

from Eq. (15) or (16). Thus, the degree of uncertainty in the calculation will become greater.

Symbols with the subscript *o* denote reference values:

$d_o = 1 \cdot 10^{-2}$ m and $R_{ao} = 1 \cdot 10^{-6}$ m; α_o is the reference value at $p_o^* = p/p_c = 0.1$ and $R_{ao} = 1 \cdot 10^{-6}$ m. α_o is listed in Table 2 against the values of $\dot{q}_o$ for *specific substances*.

The factor C_F for various substances has been derived from measurements [W4, W18, W20, W21, W23, W26, A1, R3, R4, R30, R33, R34, C1–C7, G7, G19], and some of the results are listed in Table 1 under the headings "H_2 (Para)" to "R113".

Range of validity of Eq. (21) is:
$0.01 \leq p^* \leq 0.985$; $1 \leq d/\text{mm} \leq 32$; $0.05 \leq R_a/\mu\text{m} \leq 5$.

The roughness values were obtained in measurements on drawn and welded normal and high-precision tubes, including types that were cold-drawn or cold-rolled after welding.

The relationship that can be established between the values of C_F listed in Table 1 and the molar mass $\tilde{M}$ allows the C_F values for other substances to be determined, that is,

$$C_F = 0.435\left(\tilde{M}/\tilde{M}_{H2}\right)^{0.27}. \quad (22)$$

where $\tilde{M}_{H2} = 2.016$g/mol is the molar mass of H_2.

Results that have been obtained up to now indicate that an upper limit of $C_F \leq 2.5$ should be observed.

Equation (22) has been applied to various hydrocarbons [R4, H2, H3, H5, H6], and some of the results obtained are listed in Table 1 in the subcolumns headed "Methanol" to "R11". They are compared with the standard deviation determined for the corresponding measured values. The agreement is good.

Heat transfer data obtained in nucleate boiling experiments in *annular channels* [W7, W8, W18, W22] agreed adequately with calculated values in which d_h, as defined by Eq. (37) in Subchap. H3.1, was substituted for d in Eq. (21).

Heat transfer coefficients for substances not listed in Table 2 can be obtained by determining the reference value α_o ($p_o^* = 0.1$) for $R_a = 1 \cdot 10^{-6}$ m in the following steps, cf. Chap. H2.

(a) Determination of $\alpha_{0.03}$ at the saturation pressure $p^* = 0.03$ with the physical properties at saturation and for a heat flux of $\dot{q} = 20\,000$ W/m^2

(b) Conversion of the value for $\alpha_{0.03}$ ($p^* = 0.03$) to the value $\alpha_{0.03}$ at $p_o^* = 0.1$ by inserting the value of $F(p^*)$ (cf. Example 2, Sect. 4 of this Chapter).

(c) If α_o, corresponding to the specified group of substances in Table 2, has to be determined from a value of $\dot{q}$ that differs from 20,000 W/m^2, the exponent n must be calculated.

2.1.5 Downward Flow in Vertical Tubes

Pujol [R3] studied the effect exerted by the direction of flow on heat transfer to R113 during nucleate boiling in vertical tubes. The bank of tubes in the experiments was designed so that all the measured values for the parameters could be evaluated equally well at an adequate distance from the tube bends. The results are presented in Fig. 10. They reveal that the heat transfer coefficient in downward flow is less than that in upward flow in accordance with the relationship

$$\alpha(z)_{B,\text{down}} = 0.75\alpha(z)_B, \quad (23)$$

where $\alpha(z)_B$ is the value for upward flow as given by Eq. (21).

Kattan et al. [R35] studied flow boiling of R134a in downward and upward flow by using an experimental loop with rotatable test tube. Measurements were performed at mass velocities of $\dot{m}$= 310–1540 kg/m^{2}s and at a reduced pressure of p^* =0.1. Their measurement results showed a significant decrease in the heat transfer coefficients in downward flow at a vapor mass fraction of $\dot{x}$ = 0.07–0.5, which can be fairly calculated by Eq. (23). The effect of upflow and downflow on nucleate boiling of R12 was also investigated by *Hahne* et al. [R36]. The relative lengths of the tubes upstream from the section in which the measurements were made, were $l/d \geq 100$. A significant effect of the flow direction on heat transfer was not observed at $\dot{m}$= 310–1540 kg/m^{2}s, and at $\dot{x}$ = 0–0.17. The results that have been obtained up to now do not permit a definite conclusion to be drawn. For this reason, it is recommended for safety's sake that Eq. (23) also be applied to other substances and other parameters in downward flow.

2.2 Nucleate Flow Boiling in Horizontal Tubes

If the heated wall in horizontal tubes is constantly and completely wetted, the heat transfer coefficient is approximately the same as that in a vertical tube [G20]. This flow pattern

H3.4. Table 1. C_F factor and standard deviation σ[a] for the substance investigated

Substance	H_2 (Para)	He	NH_3	H_2O	N_2	R 22	R 12	R 113
C_F	0.35	0.86	1.24	0.72	0.8	1.2	1.21	2.2
Σ	0.11	0.31	0.23	0.26	0.77	0.36	0.14	0.8
No. of measurements	41	97	128	10,262	82	256	524	302
Substance	Methanol	Ethanol	*n*-Butanol	Benzene	Cyclohexane	*n*-Pentane	*n*-Heptane	R 11
C_F[b]	0.918	1.013	1.151	1.168	1.191	1.143	1.249	1.36
σ	0.15	0.1	0.39	0.18	0.22	0.2	0.22	0.58
No. of measurements	123	99	154	111	115	113	126	92

[a] σ is a measure for the scatter of experimental values around the mean. If normal distribution is assumed, 68% of the experiments lie within the $C_F \pm \sigma$ interval
[b] Calculated from Eq. (22)

H3.4. Table 2. Heat transfer coefficients α_0 at $p_o^* = 0.1$, $R_{ao} = 1 \cdot 10^{-6}$ m and the normalized values of heat flux $\dot{q}_o$ for various fluids. Further data can be found in Chap. H2, Table 1

Substance	Formula		p_c bar	$\tilde{M}$ kg/kmol	$\dot{q}_o$ W/m²	α_o W/m²K
Methane	CH_4		46.0	16.04	20,000	8,060
Ethane	C_2H_6		48.8	30.07	20,000	5,210
Propane	C_3H_8		42.4	44.10	20,000	4,000
n-Butane	C_4H_{10}		38.0	58.12	20,000	3,300
n-Pentane	C_5H_{12}		33.7	72.15	20,000	3,070
Isopentane	C_5H_{12}		33.3	72.15	20,000	2,940
n-Hexane	C_6H_{14}		29.7	86.18	20,000	2,840
n-Heptane	C_7H_{16}		27.3	100.20	20,000	2,420
Cyclohexane	C_6H_{12}		40.8	84.16	20,000	2,420
Benzene	C_6H_6		48.9	78.11	20,000	2,730
Toluene	C_7H_8		41.1	92.14	20,000	2,910
Diphenyl	$C_{12}H_{10}$		38.5	154.21	20,000	2,030
Methanol	CH_4O		81.0	32.04	20,000	2,770
Ethanol	C_2H_6O		63.8	46.07	20,000	3,690
n-Propanol	C_3H_8O		51.7	60.10	20,000	3,170
Isopropanol	C_3H_8O		47.6	60.10	20,000	2,920
n-Butanol	$C_4H_{10}O$		49.6	74.12	20,000	2,750
Isobutanol	$C_4H_{10}O$		43.0	74.12	20,000	2,940
Acetone	C_3H_6O		47.0	58.08	20,000	3,270
Trichlorofluoromethane	$CFCl_3$	(R11)	44.0	137.37	20,000	2,690
Dichlorodifluoromethane	CF_2Cl_2	(R12)	41.6	120.91	20,000	3,290
Chlorotrifluoromethane	CF_3Cl	(R13)	38.6	104.47	20,000	3,910
Bromotrifluoromethane	CF_3Br	(R13 B 1)	39.8	148.93	20,000	3,380
Chlorodifluoromethane	CHF_2Cl	(R22)	49.9	86.47	20,000	3,930
Trifluoromethane	CHF_3	(R23)	48.7	70.02	20,000	4,870
Trichlorotrifluoroethane	$C_2F_3Cl_3$	(R113)	34.1	187.38	20,000	2,180
Dichlorotetrafluoroethane	$C_2F_4Cl_2$	(R114)	32.6	170.92	20 000	2,460
Chloropentafluoroethane	C_2F_5Cl	(R115)	31.3	154.47	20,000	2,890
1.1- Dichloro-2.2.2-trifluoroethane	$C_2HCl_2F_3$	(R123)	36.7	152.93	20,000	2,600[a]
1.1.1.2- Tetrafluoroethane	$C_2H_2F_4$	(R134 a)	40.6	102.03	20,000	3,500[a]
l.1-Difluoroethane	$C_2H_4F_2$	(R152 a)	45.2	66.05	20,000	4,000[a]
Hexafluorochloropropane	C_3HF_6Cl	(R226)	30.6	186.48	20,000	3,700
Heptafluoropropane	C_3HF_7	(R227)	29.3	170.03	20,000	3,800[a]
Cyclooctafluorobutane	C_4F_8	(RC318)	28.0	200.03	20,000	2,710
Chlorodifluoromethane/ Chloropentafluoroethane	CHF_2Cl/C_2F_5Cl	(R502)	40.8	111.6	20,000	2,900
Chloromethane	CH_3Cl		66.8	50.49	20,000	4,790
Tetrachloromethane	CCl_4		45.6	153.82	20,000	2,320
Tetrafluoromethane	CF_4		37.4	88.0	20,000	4,500
Helium I	He		2.275	4.0	1,000	1,990
Hydrogen (Para)	H_2		12.97	2.02	10,000	12,220[a]
Neon	Ne		26.5	20.18	10,000	8,920
Nitrogen	N_2		34.0	28.02	10,000	4,380
Argon	Ar		49.0	39.95	10,000	3,870
Oxygen	O_2		50.8	32.0	10,000	4,120

H3.4. Table 2. (continued)

Substance	Formula		p_c bar	$\tilde{M}$ kg/kmol	$\dot{q}_o$ W/m²	α_o W/m²K
Water	H_2O		220.64	18.02	150,000	25,580
Ammonia	NH_3		113.0	17.03	150,000	36,640
Carbon dioxide	CO_2		73.8	44.01	150,000	18,890
Sulfur hexafluoride	SF_6		37.6	146.05	150,000	12,230

[a]Properties not exactly known in all cases

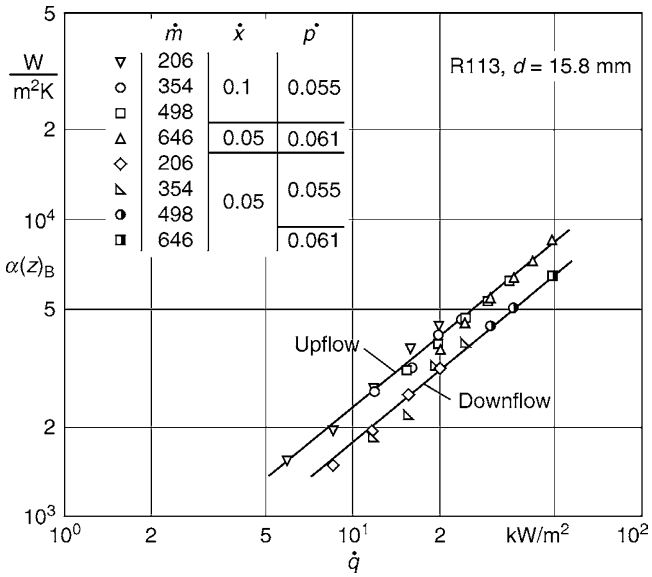

H3.4. Fig. 10. Heat transfer coefficient during upward and downward flow in a vertical tube (measurements on R 113 [R3]).

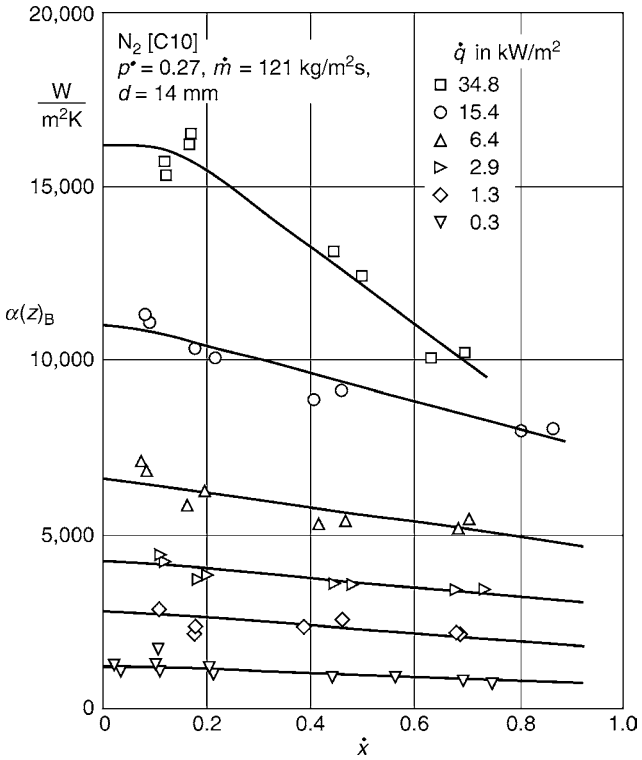

H3.4. Fig. 11. Heat transfer coefficient as a function of the vapor mass fraction for nucleate boiling in a horizontal tube.

cannot be achieved frequently, because the thickness of the film is more or less asymmetrical even in annular flow [G26]. One of the consequences is that critical boiling (Subchap. H3.5) sets in at the crest of horizontal tubes at a much earlier stage than it does in vertical tubes under otherwise comparable conditions [W34]. Therefore, this boundary must be taken into account in evaporators with high power density.

Incomplete wetting or the thermally effective wetting limit (Sect. 1.2) is also very pronounced during heat transfer in the nucleate boiling regime. An example is given in Fig. 11, in which the effect of incomplete wetting in a copper tube of $\lambda_w s = 0.95$ W/K is illustrated. It can be seen that the extent to which the perimeter-averaged heat transfer coefficient decreases with the vapor mass fraction becomes greater as the heat flux increases.

Another point in which nucleate boiling in horizontal tubes differs from that in vertical tubes is that measurements have revealed a relationship between the perimeter-averaged heat transfer coefficient and the flow parameters $\dot{m}$ and $\dot{x}$. The perimeter-averaged heat transfer coefficient in nucleate boiling is an approximation. A physically justified prediction ought to be based on local heat transfer coefficients (determined point-by-point) and relative wetting functions similar. These values are not yet available.

This relationship can be ascribed to partial drying. The following function was determined from measurements [R11, R18, R23, C11–C13] in copper tubes with $\lambda_w s \geq 0.7$ W/K:

$$F(\dot{m}, \dot{x}) = \left(\frac{\dot{m}}{\dot{m}_0}\right)^{0.25} \left[1 - p^{*0.1}\left(\frac{\dot{q}}{\dot{q}_{cr,PB}}\right)^{0.3} \dot{x}\right], \qquad (24)$$

where

$$\dot{q}_{cr,PB} = 2.79\dot{q}_{cr;0.1}p^{*0.4}(1 - p^*) \qquad (25)$$

and

$$\dot{q}_{cr;0.1} = 0.13\Delta h_{v0}\left(\rho_0''\right)^{0.5}\left(\sigma_0 g\left(\rho_0' - \rho_0''\right)\right)^{0.25}. \qquad (26)$$

$\dot{m}_o$ is a reference value; in this case, $\dot{m}_o = 100$ kg/m²s. All properties in Eq. (26) must be determined at a reference pressure of $p_o^* = 0.1$.

Equations (25) and (26) are used to determine the maximum heat flux in pool boiling in Chap. H2. The term $\dot{q}_{cr,PB}$ in

Eq. (24) is merely a reference value, and its application does not permit the conclusion that the critical boiling regime in horizontal tubes can be determined from Eqs. (25) and (26).

It has been demonstrated by measurements [W10, R11, R18, R23, R26, C11–C13] that the relationship of $\alpha(z)_B$ to pressure can no longer be described by the equation for vertical tubes, that is, Eq. (17) in Sect. 2.1. The results of the measurements have been plotted in Fig. 12, which also shows the curve for the following function:

$$F(p^*) = 2.692p^{*0.43} + \frac{1.6p^{*6.5}}{1 - p^{*4.4}}. \tag{27}$$

The experiments also reveal an effect of dryout on the relationship between the heat transfer coefficient and the mass velocity. Thus, the exponent n is less than that in vertical tubes, even if the horizontal tubes are thick and have good thermal conductivity ($\lambda_w s > 0.7$ W/K). A point that strikes attention is that, at $p^* \geq 0.1$, the experiments performed by *Riedle* et al. [R4] in stainless steel tubes of ($\lambda_w s < 0.1$ W/K gave rise in several cases to much lower values of n than those obtained in copper tubes. In the experiments on cryogenic fluids, all the sections in which the measurements were performed, consisted of copper with a wall heat conduction of $\lambda_w s > 0.7$ W/K.

If $\lambda_w s \geq 0.7$ W/K, the relationship for *inorganic substances*, *hydrocarbons*, and *halocarbons* is

$$n = 0.9 - 0.36 \cdot p^{*0.13}; \tag{28}$$

and that for *cryogenic fluids*,

$$n = 0.9 - 0.44 \cdot p^{*0.085}. \tag{29}$$

Müller-Steinhagen and *Schlünder* [G21] solved the thermal conductivity equation numerically for given wetting limits and for the heat transfer coefficient at given points. It was, thus, demonstrated that the perimeter-averaged heat transfer coefficient, expressed as a function of the wall heat conduction $\lambda_w s$, decreases with an increase in the diameter of horizontal tubes. In view of the fact that $\alpha(z)_B \sim d^{-0.4}$ in a vertical tube, a closer relationship to the diameter can be expected for a horizontal tube. The following equation has been derived from the experiments concerned [R4, R11], which yielded the results plotted in Fig. 13:

$$F(d) = (d_o/d)^{0.5}, \tag{30}$$

where $d_o = 10^{-2}$ m.

Heat transfer in tubes with a high wall heat conduction ($\lambda_w s \geq 0.7$ W/K)

Boundary condition $\dot{q}_o$*= constant.* A review of all the relationships discussed gives rise to the following equation for nucleate boiling in horizontal tubes for $\lambda_w s \geq 0.7$ W/K

$$\frac{\alpha(z)_B}{\alpha_0} = C_F \left(\frac{\dot{q}}{\dot{q}_0}\right)^{n(p^*)} \left[2.692p^{*0.43} + \frac{1.6p^{*6.5}}{1 - p^{*4.4}}\right] \cdot \left(\frac{d_0}{d}\right)^{0.5} \left(\frac{R_a}{R_{a0}}\right)^{0.133} \left(\frac{\dot{m}}{\dot{m}_0}\right)^{0.25} \cdot \left[1 - p^{*0.1}\left(\frac{\dot{q}}{\dot{q}_{cr,PB}}\right)^{0.3} \dot{x}\right]. \tag{31}$$

Whether $n(p^*)$ is determined from Eq. (28) or (29) depends on the fluid. Equation (25) is taken to calculate $\dot{q}_{cr,PB}$; and $\dot{q}_{cr,01}$ is obtained from Table 3 or Eq. (26). The reference values normally indicated by the subscript o are $d_o = 1 \cdot 10^{-2}$ m, $\dot{m}_o = 100$ kg/m^{2}s, and $R_{ao} = 1 \cdot 10^{-6}$ m. The reference values $\dot{q}_o$ and α_o (at $p_o^* = p/p_c = 0.1$) and $R_{ao} = 1 \cdot 10^{-6}$ m are taken from Table 2. The factor C_F was determined from measurements [W10, W14, R2, R4, R6, R8–R11, R18, R23, R26, C9–C13, G7, G9], and the C_F-value for $\lambda_w s \geq 0.7$ W/K is given in Table 3.

Boundary condition T_w *= constant.* The correction ψ for stratified and wavy flow can be obtained from Fig. 14 up to the limit $\lambda_w s \to \infty$ ($\psi = 0.86$). This value has to be inserted in Eqs. (31) and (35). All the other equations remain unchanged, and no correction is required for other flow patterns.

Range of validity for Eq. (31):

$0.03 \leq p^* \leq 0.93$ (cryogenic fluids)

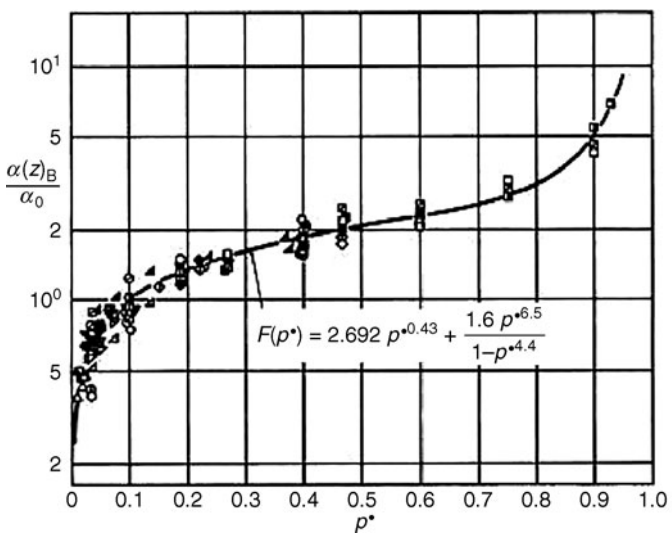

		$\dot{m}$ in kg/m^{2}s	Autor
○	Ar	125	[C12]
◔		220	
◑		450	
◕		797	
●		998	
◎		122	[C11]
●		460	
□	N_2	45	[C11]
⊟		72	
⊡		127	
▣		232	
■		473	
◇		119	[C10]
◈		222	
◆		453	
○		122	[C12]

		$\dot{m}$ in kg/m^{2}s	Autor
◣	R11	26.7	[R10]
◺		36.5	
◭		37.6	
▲		82.5	
▽	R12	51	[R14]
▾		81	
◤		241	
◿		130	[R18]
◢		567	
▽	R22	83	[R16]
▿		133	
▼		276	
◪	H_2O	587	[W10]
◥		1,038	

H3.4. Fig. 12. Relative heat transfer coefficient as a function of the reduced pressure p^* for nucleate boiling in horizontal tubes and for values of $\dot{q}_0$ relating to the substances concerned.

$0.005 \leq p^* \leq 0.85$ (all other liquids)
$4 \leq d/\text{mm} \leq 25$
$0.05 \leq R_a/\mu\text{m} \leq 5$.

The range of roughness values is valid for drawn tubes and precision tubes, welded tubes, and welded precision tubes that have been cold-drawn or cold-rolled after welding.

A relationship exists between the molar mass $\widetilde{M}$ and C_F within the range of scattering. Thus, C_F for substances that are not listed in Table 3, can be obtained approximately from the following correlation:

$$C_F = 0.789\left(\widetilde{M}/\widetilde{M}_{H2}\right)^{0.11}, \tag{32}$$

where $\widetilde{M}_{H2} = 2.016$ g/mol is the molar mass of H_2.

Results that have been obtained up to now indicate that an upper limit of $C_F \leq 2.5$ should be observed.

Heat transfer in tubes with low wall heat conduction ($\lambda_w s < 0.7$ W/K).

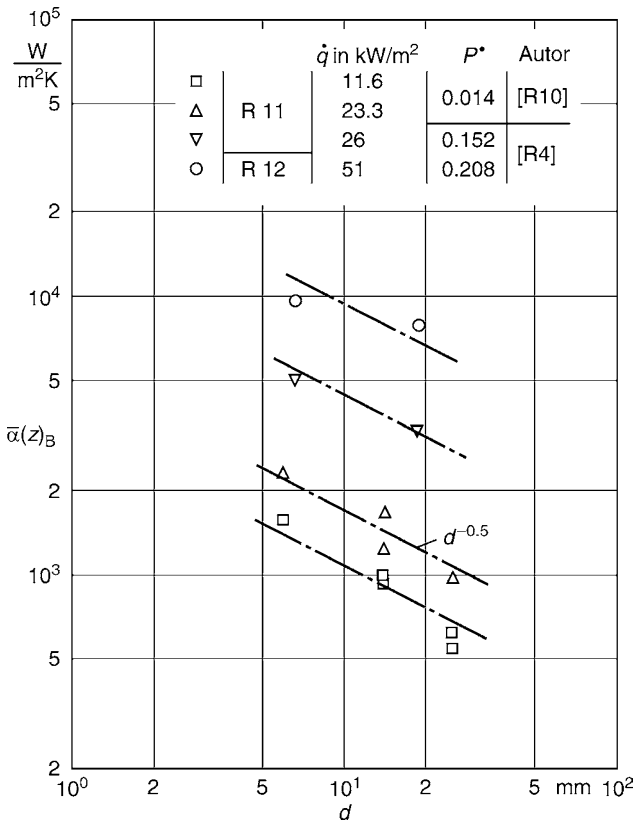

H3.4. Fig. 13. Heat transfer coefficient as a function of tube diameter for nucleate boiling in horizontal tubes.

Boundary condition $\dot{q}$ = *constant.* Incomplete wetting has an even greater effect in tubes with thin walls and poor wall heat conduction $\lambda_w s$. The following amendments in the correlations have been derived from the few measurements that are available [R4, R6, R18, R26] for evaluation.

(a) The exponent n in the term for the heat flux decreases almost independently of the flow pattern. Allowance for this change is made by the factor κ, a plot of which is shown in Fig. 14.
(b) The heat transfer coefficient is less than that relating to $\lambda_w s \geq 0.7$ W/K under otherwise identical conditions. The extent of the decrease depends on the flow pattern observed in the unheated sight glass. The requisite correction is made by the factor ψ, which is shown as a function of $\lambda_w s$ in Fig. 14.

The dependency shown in Fig. 14 can be formulated as follows:
For all flow patterns, the factor κ can be written by

$$\kappa = 0.675 + 0.325\tanh\left(3.711\left(\lambda_w s - 3.24\cdot 10^{-2}\right)\right). \tag{33a}$$

The value of ψ to be taken as an approximation depends on the flow pattern.

Stratified and wavy flow

$$\psi = 0.46 + 0.4\tanh\left(3.387\left(\lambda_w s - 8.62\cdot 10^{-3}\right)\right) \tag{33b}$$

Slug flow

$$\psi = 0.671 + 0.329\tanh\left(3.691\left(\lambda_w s - 8.42\cdot 10^{-3}\right)\right) \tag{33c}$$

Annular flow

$$\psi = 0.755 + 0.245\tanh\left(3.702\left(\lambda_w s - 1.25\cdot 10^{-2}\right)\right) \tag{33d}$$

Thus, if $\lambda_w s < 0.7$ W/K, the value of n to be taken as an approximation instead of Eq. (28),

$$n = \kappa\left(0.9 - 0.36\cdot p^{*0.13}\right); \tag{34a}$$

and instead of Eq. (29),

$$n = \kappa\left(0.9 - 0.44\cdot p^{*0.085}\right). \tag{34b}$$

C_F in this case, is given by

$$C_F = \psi C_F(\lambda_w s \geq 0.7 W/K). \tag{35}$$

C_F ($\lambda_w s \geq 0.7$ W/K) can be obtained from Table 3 or Eq. (32).

Boundary condition T_w = *constant.* The correction ψ for stratified and wavy flow can be obtained from Fig. 14 up to the limit $\lambda_w s \to \infty$ ($\psi = 0.86$). This value has to be inserted in Eq. (35). All the other equations remain unchanged, and no correction is required for other flow patterns.

H3.4. Table 3. Factor C_F, standard deviation α, and reference value $\dot{q}_{cr,0.1}$

Substance	H_2 (Para)	H_2O[a]	Ne	N_2	Ar	R 22	R 12	R 11
C_F	0.79	0.72	0.95	1.67	0.93	1.23	1.06	1.87
α	0.17	0.29	0.09	0.30	0.34	0.18	0.30	0.32
$\frac{\dot{q}_{cr,0.1}}{W/m^2}$	79,410	3,293,350	126,870	230,000	295,220	429,580	324,150	363,400
No. of measurements	12	1,008	89	1,310	965	819	1182	1,207

[a]Some of the values measured for water have been taken from Mumm [W10], in which $\lambda_w s = 0.01$ W/K. The corrections are $\kappa = 1$ and $\psi = 1$ [Eqs. (33) and (34)]

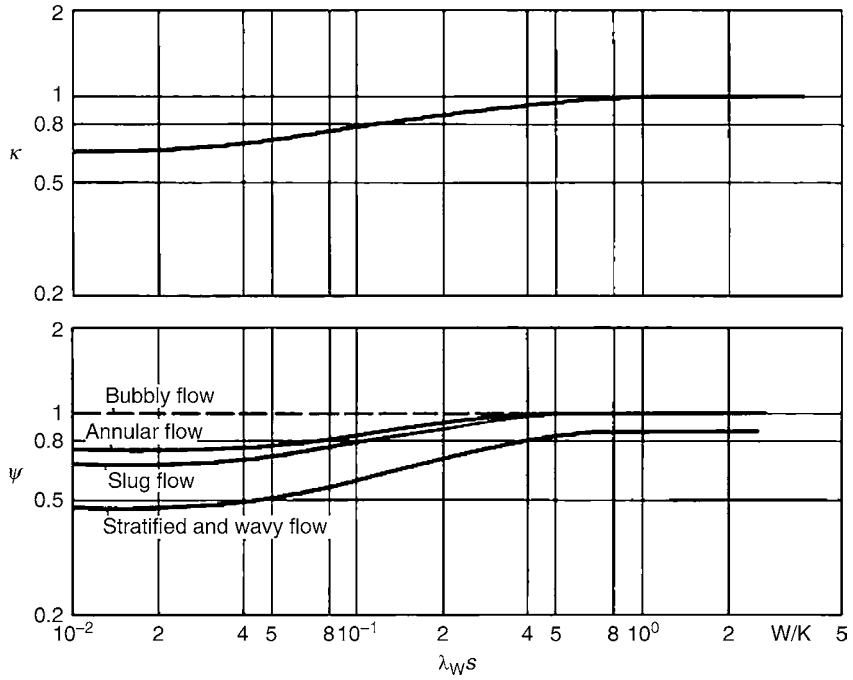

H3.4. Fig. 14. Correlation factors κ and ψ as functions of the heat conduction $\lambda_W s$ of the tube wall.

2.2.1 Limit for the Effect of Mass Velocity

From a given mass velocity upward, the value for $\alpha(z)_B$ determined from Eq. (31) no longer depends on the term $(\dot{m}/\dot{m}_0)$. This case arises if the value for $\alpha(z)_B$ determined from Eq. (31) is higher than that calculated from Eq. (21). If the limiting value of $(\dot{m}/\dot{m}_0)^{0.25}$ is expressed as $Y = (\dot{m}/\dot{m}_0)^{0.25}_{lim}$ and calculated on condition that Eq. (31) is equal to that determined from Eq. (21), the following equations are obtained:

$$Y = \frac{\left[\alpha(z)_B\right]_{Eq.(21)}}{\left[\alpha(z)_B \text{ at } (\dot{m}/\dot{m}_0) = 1\right]_{Eq.(31)}}. \quad (36)$$

and if $\left(\alpha(z)_B\right)_{Eq.(31)} > \left(\alpha(z)_B\right)_{Eq.(21)}$,,

$$\alpha(z)_B = \left(\alpha(z)_B\right)_{Eq.(21)}. \quad (37)$$

$n(p^*)$ is determined for the fluid concerned, and $\dot{q}_{cr,PB}$ is calculated as before.

2.2.2 Effects of Bends and Elbows (Sects. 2.1 and 2.2)

The equations given for the determination of $\alpha(z)_B$ in vertical and horizontal tubes do not allow for the disturbances in two-phase flow that are caused by bends, elbows, etc. *Pujol's* measurements [R3] on R 113 in hairpin rows of vertical tubes also embraced nucleate boiling. No disturbances were detected after a relative length $l/d = 20$ had been traversed downstream from a bend with a curvature of $R/d \approx 4.1$ (Sect. 1.1). It can generally be expected that asymmetric film thickness at high heat fluxes causes a partial dryout, that is, a reduction in the heat transfer coefficient over a relative length of $l/d = 5$ to $l/d = 10$, behind conventional bends.

No investigations have been made on the effect of bends, elbows, etc. in horizontal tubes on the heat transfer coefficient in the nucleate boiling regime. It can be concluded from the results discussed in Sect. 1.2, that the phase distribution changes over a relative length of $l/d = 5$–10 behind conventional bends with a curvature of $R/d = 2$–10. Since it is not yet known whether this type of disturbance intensifies the effect of already existent dryout, further reductions in the heat transfer coefficient should not be taken into account.

2.2.3 Effect of Surface Treatment (Sects. 2.1 and 2.2)

Additional roughness caused by sintered coatings or sandblasting cannot be embraced by the function $F(W)$ defined by Eq. (20). The inner surface of the tube used by *Haffner* [R31] in studies on nucleate boiling was sandblasted with aluminaoxide and had an average roughness height of $R_a = 0.33$ µm. The heat transfer coefficients determined for R12 and R22 in this tube were, on an average, higher by a factor of 1.7 than those calculated from Eq. (21) for $R_a = 0.33$. However, the relationships to $\dot{q}$ and p^* agreed satisfactorily with those given by Eq. (21).

2.2.4 Effect of Impurities (Sects. 2.1 and 2.2)

Impurities are solutions of wetting agents, oils, or other liquids that are present in low concentrations in the liquid phase. In nucleate boiling, they exert a considerable effect on heat

transfer. Thus, the presence of oils in refrigerants either increases or decreases the heat transfer coefficient to an extent that depends on the concentration [R22]. The fouling caused by the deposition of the dissolved substances onto the heated surfaces may give rise to great difficulties (cf. Chap. C4). In an example that occurred, the heat transfer coefficient in a horizontal tube during nucleate boiling of argon containing 40 ppm of residual components of air, was reduced in the course of time to one-third of its original value [C13].

2.2.5 Determination of C_F from Measurements

Values of C_F more accurate than those read off from Tables 1 and 3 or calculated from Eqs. (22) and (32) can be derived by inserting values measured on the given liquid/tube wall system in Eqs. (21), (31), or (37) and solving for C_F. Equations (22) and (32) may then be resorted to for extrapolating to other conditions, because the relationships to $\dot{q}$, p, d, $\dot{m}$, and $\dot{x}$ can be regarded as verified by measurements [G7, G9].

2.3 Nucleate Flow Boiling in Inclined Tubes and Helical Coils

2.3.1 Inclined Tubes

Only a few measurements on water are available for the analysis of nucleate boiling in inclined tubes. The parameters in *Bogdanov's* study [W28] on a tube inclined at an angle of 45° were d = 20 mm, $\dot{m}$= 200–3000 kg/m^{2}s, and p^* = 0.045–0.55. *Gilli*'s measurements [W29] in tubes inclined at an angle of 15° to the horizontal were performed at mass velocities of $\dot{m}$ = 200–860 kg/m^{2}s and reduced pressures of p^* = 0.07 and p^* = 0.13. The data, thus, obtained were too scanty to permit any correlations to be established for inclined tubes. Therefore, until further measurements become available, it is suggested that the perimeter-averaged heat transfer coefficient for tubes inclined at an angle of Θ = 0–30° to the horizontal be calculated from the equations for horizontal tubes (Sect. 2.2); and that for tubes inclined at an angle of $\Theta > 30°$, from the equations for vertical tubes (Sect. 2.1).

2.3.2 Helical Coils

Studies on nucleate boiling in helical tubes have been reported in the literature [W16, W17, W31–W33]. *Carver* et al. [W31] performed most of their measurements under conditions of critical boiling. *Gilli* et al. [W32] suggested that the perimeter-averaged heat transfer coefficient for water at $\dot{m}$ = 300–3300 kg/m^{2}s and for reduced pressures of p^* = 0.3–0.86 be calculated from the following equation:

$$\alpha(z)_B = 26 \cdot 10^3 \left(\frac{h_{cr}}{h_{cr} + \Delta h_v}\right)^5 \cdot \left(0.86 \cdot 10^{-3}\dot{q}\right)^{0.57(\Delta h_v/h_{cr})^{0.16}} \left(1 - \frac{d}{D_w}\right)^{-2.4}, \quad (38)$$

where D_w is the average coil diameter, Δh_v is the specific enthalpy of vaporization corresponding to the boiling pressure p, and for water h_{cr} = 2107. 4 kJ/kg.

Very few or no experiments at all have been carried out on water under conditions other than those outlined above or on other liquids. According to *Steiner* [G4], the equation for nucleate boiling in vertical tubes can also be applied to helical coils. It can be deduced from Sect. 1.3 that this approximation is valid only as long as the tube wall is completely wetted. If observation of the phase distribution reveals that flow is already stratified in unheated coils, the equations for horizontal tubes (Sect. 2.2) should be resorted to for the determination of $\alpha(z)_B$.

3 Summary of Heat Transfer in Flow Boiling of Pure Substances

The methods for determining the perimeter-averaged heat transfer coefficient in convective and nucleate boiling during the flow of liquid/vapor mixtures through tubes have been described in Sects. 1 and 2. They were based on measurements on various pure substances under various conditions, and different correlations are required to describe the heat transfer coefficient in each of the two boiling regimes [G22]. Inclusion of the transition boiling regime was avoided, as far as possible, in evaluating the experimental results. Observations by *Gouse* and *Coumou* [R15] and *Gouse* and *Dickson* [R16] on heated glass tubes demonstrated that both convective and nucleate boiling, that is, a definite number of activated nucleation sites, occurred in the transition regime. Results of measurements in transition boiling have been published by many authors [W4, R6, R11, R18, R23, R26].

If the criteria for the onset of nucleate or convective boiling are left out of consideration and if transition boiling is taken into account, the perimeter-averaged heat transfer coefficient, which depends on the inclination of the tubes, is given by

$$\alpha(z) = \sqrt[3]{\alpha(z)_{conv}^3 + \alpha(z)_B^3}, \quad (39)$$

where $\alpha(z)_{conv}$ is defined in Sects. 1.1–1.3, and $\alpha(z)_B$ is defined in Sects. 2.1–2.3. If the heat flux is very small, $\alpha(z)_B$ cannot be determined by the method described in Sect. 2 and inserted into Eq. (39). A certain superheat, that is, heat flux $\dot{q}_{onb}$ is required for the onset of boiling in the liquid near the wall. If it is not attained, only convective boiling should be taken into account in Eq. (39). Particular attention must be devoted to this point in the $\dot{x}$ = 0–0.3 range of vapor mass fractions.

The heat flux at the onset of nucleate boiling can be estimated from

$$\dot{q}_{onb} = \frac{2\sigma T_{sat}\alpha_{LO}}{r_{cr}\rho'' \Delta h_v}, \quad (40)$$

where $r_{cr} = 0.3 \cdot 10^{-6}$ m for all heated surfaces with a permissible roughness as defined in Sect. 2; α_{LO} is the local single-phase heat transfer coefficient at the point z = 0 and for a liquid mass velocity of $\dot{m}$. If the Reynolds number, the hydrodynamic conditions, and the thermal boundary conditions

($\dot{q}$ = constant; T_w = constant) are known, α_{LO} for a given tube cross-section can be calculated from the equations presented in Sect. 4 (Appendix) or in Chap. G4. The value to insert for the Reynolds number in this case is

$$\mathrm{Re}_{LO} = \frac{\dot{m} d_h}{\eta_L}. \tag{41}$$

The value for α_{LO} for helical coils can be determined by the method described in Chap. G3.

The values to be taken for the properties are those corresponding to saturation at the pressure p.

4 Appendix – Local Heat Transfer Coefficient in Forced Single-Phase Flow

The local heat transfer coefficient at the point z in the direction of flow is defined by

$$\alpha(z) = \frac{\dot{q}(z)}{(T_W - T_{sat}(p))_z}. \tag{A1}$$

Flow in the tube is always laminar below the critical Reynolds number of Re = 2300, and becomes turbulent above this value. In the $2300 \le \mathrm{Re} \le 5{\cdot}10^4$ transition range, the equations for laminar heat transfer in a short length of tube, that is, $d/z > 0.01$, may yield higher values of the Nusselt number Nu_z than those obtained from turbulent flow equations. This depends on the Prandtl number. In such cases, it must always be ensured that the highest value obtained for Nu_z is taken.

According to *Gnielinski* [G23], the following equations apply.

Laminar flow:
Boundary condition T_w=constant
Hydrodynamic inflow:

$$\mathrm{Nu}_z = 0.332 \sqrt[3]{\mathrm{Pr}} \sqrt{\mathrm{Re} \cdot d/z} \tag{A2}$$

Hydrodynamically developed flow:

$$\mathrm{Nu}_z = \sqrt[3]{3.66^3 + 1.077^3 \mathrm{Re}\,\mathrm{Pr} \cdot d/z} \tag{A3}$$

If $d/z \ge 1$, the numerical value to insert in Eqs. (A2) and (A3) is $d/z = 1$.

Boundary condition $\dot{q}$ = constant

According to *Shah* and *London* [G24], the following approximations apply.
Hydrodynamic inflow:

$$\mathrm{Nu}_z = 0.455 \sqrt[3]{\mathrm{Pr}} \sqrt{\mathrm{Re} \cdot d/z} \tag{A4}$$

Hydrodynamically developed flow:

$$\mathrm{Nu}_z = \sqrt[3]{4.36^3 + 1.302^3 \mathrm{Re}\,\mathrm{Pr} \cdot d/z} \tag{A5}$$

If $d/z \ge 1$, the numerical value to insert in Eqs. (A4) and (A5) is $d/z = 1$.

Turbulent flow:

According to *Gnielinski* [G23], the equations for turbulent flow under the boundary condition T_w = constant or $\dot{q}$ = constant do not differ significantly from each other.
Hydrodynamic inflow (sharp edges)

If $d/z \ge 1$, Nu_z can be obtained approximately from the following equation:

$$\mathrm{Nu}_z = \frac{4}{3} \mathrm{Nu}_\infty. \tag{A6}$$

If $d/z < 1$,

$$\mathrm{Nu}_z = \mathrm{Nu}_\infty \left[1 + \frac{1}{3} (d/z)^{2/3} \right], \tag{A7}$$

where

$$\mathrm{Nu}_\infty = \frac{(\xi/8)(\mathrm{Re} - 1000)\,\mathrm{Pr}}{1 + 12.7\sqrt{(\xi/8)}\left(\mathrm{Pr}^{2/3} - 1\right)} \tag{A8}$$

Hydrodynamically developed flow

$$\mathrm{Nu}_z = \mathrm{Nu}_\infty \tag{A9}$$

Explanations

$$\mathrm{Nu}_z = \frac{\alpha(z) d}{\lambda} \tag{A10}$$

$$\mathrm{Pr} = \frac{\eta c_p}{\lambda} \tag{A11}$$

$$\xi = \left(1.82 \log_{10} \mathrm{Re} - 1.64\right)^{-2}. \tag{A12}$$

The Reynolds numbers are obtained from Eq. (39) in Sect. 1.1 or from Sect. 1.2. If the tube cross-section is not circular, the hydraulic diameter d_h must be substituted for the diameter d in the equations for the Nusselt and Reynolds numbers.

The values to be inserted for the properties have to be determined in accordance with the instructions given in Sects. 1.1 and 1.2. The same applies to the determination of the local heat transfer coefficient for a liquid, in which case the properties of the liquid concerned must be inserted in Eqs. (A10) and (A11). The corresponding procedure is adopted in calculating $\alpha(z)$ for a vapor.

Example 1

n-Butanol is to be evaporated at an average pressure of $p = 4.82$ bar in a natural-circulation evaporator with vertical copper tubes (d_o = 30 mm, s = 1.5 mm, R_a = 2 µm). The average heat flux is $\dot{q}$= 60 kW/m^2, and the mass velocity in the tubes is $\dot{m}$= 250 kg/m^2 s. The *n*-butanol enters the tubes at saturation, and the vapor mass fraction at the outlet is $\dot{x}_{out}$= 0.3. The heat transfer coefficient has to be determined step by step, and $\Delta\dot{x}$= 0.05 is given.

Properties at $p = 4.82$ bar $T_w = 446.5$ K

$\rho' = 640$ kg/m^3; $\eta' = 2.308 \cdot 10^{-4}$ kg/m s;
$\lambda' = 1.126 \cdot 10^{-1}$ W/m K; $\rho'' = 12.5$ kg/m^3;
$\eta = 1.14 \cdot 10^{-5}$ kg/m s; $\lambda' = 2.82 \cdot 10^{-2}$ W/m K;
$c'_p = 4420$ J/kg K; $\Delta h_v = 509\,700$ J/kg;
$c''_p = 2140$ J/kg K; $\sigma = 1.23 \cdot 10^{-2}$ kg/s^2.

The inlet to the tube bundle has sharp edges. The heat transfer coefficients in single-phase flow are to be determined for the case of hydrodynamic inflow under the boundary condition $\dot{q}$ = constant. The equations concerned are given by Eqs. (A4), (A6–A8), and (A10–A 12).

At $z = 0$, $\alpha_{LO} = 1271$ W/m^2 K.

The heat flux at the onset of nucleate boiling [Eq. (40)] is

$$\dot{q}_{onb} = \frac{2\sigma T_{sat}\alpha_{LO}}{r_{cr}\rho''\Delta h_v}$$
$$= \frac{2 \cdot 1.23 \cdot 10^{-2}\text{kg/s}^2 \cdot 446.5\text{K} \cdot 1271\text{W/m}^2\text{K}}{0.3 \cdot 10^{-6}\text{m} \cdot 12.5\text{kg/m}^3 \cdot 509700\text{Ws/kg}} = 7304\text{W/m}^2.$$

In accordance with the remarks in Sect. 3, both convective and nucleate boiling occur because $\dot{q} > \dot{q}_{onb}$.

α_0 for *n*-butanol in nucleate boiling is taken from Table 2.

The heat transfer coefficient in nucleate boiling $\alpha(z)_B$ is determined by the method described in Sect. 2; and the coefficient in convective flow boiling is determined by the method described in Sect. 1. The figures thus obtained are listed in Table 4.

Determination of the length of tube required to evaporate *n*-butanol from $\dot{x}_{in} = 0$ to $\dot{x}_{out} = 0.3$:

The energy balance yields

$$\dot{m}f\,\Delta\dot{x}\,\Delta h_v = \dot{q}\,\pi\,d\,l, l = \frac{\dot{m}f\Delta\dot{x}\Delta h_v}{\dot{q}\pi d}$$
$$= \frac{250\text{kg/m}^2\text{s} \cdot 5.73 \cdot 10^{-4}\text{m}^2 \cdot 0.3 \cdot 509,700\text{Ws/kg}}{60,000\text{W/m}^2 \cdot \pi \cdot 2.7 \cdot 10^{-2}\text{m}} = 4.3\text{m}.$$

Thus, a section of length $\Delta l = 0.717$ m is required for each change in the vapor fraction by an amount $\Delta\dot{x} = 0.05$.

Example 2

Refrigerant R12 is to be completely evaporated at $\theta_{sat} = -20°C$ in a single-pass injection evaporator designed for cooling brine.

The mass velocity in each tube is 80 kg/m^2 s, and the inlet vapor mass fraction behind the expansion valve is $\dot{x}_{in} = 0.1$. The dimensions of the horizontal tube are $d_o = 18$ mm and $s = 2$ mm, and the roughness is $R_a = 1.5$ µm. The average heat flux to be transferred is $\dot{q} = 9$ kW/m^2. The heat transfer coefficient has to be determined step by step, and $\Delta\dot{x} = 0.1$ is given.

Properties at $p = 1.51$ bar and $\theta_{sat} = -20°C$

$\rho' = 1459.9$ kg/m^3; $\eta' = 3.249 \cdot 10^{-4}$ kg/m s;
$\lambda' = 8.562 \cdot 10^{-2}$ W/m K; $\rho'' = 9.15$ kg/m^3;
$\eta'' = 1.08 \cdot 10^{-5}$ kg/m s; $\lambda'' = 7.34 \cdot 10^{-3}$ W/m K;
$c'_p = 904.9$ J/kg K; $\Delta h_v = 161\,780$ J/kg;
$c''_p = 600.1$ J/kg K; $\sigma = 1.43 \cdot 10^{-2}$ kg/s^2.

Flow is hydrodynamically undeveloped at the inlet to the evaporator tube, that is, downstream from the expansion valve and the refrigerant distributor. The values for α_{LO}, α_{GO}, and α_G have to be determined for hydrodynamic inflow at $\dot{q}$ = constant from Eqs. (A4), (A6–A8), and (Al0–A12).

At $z = 0$, $\alpha_{LO} = 246.5$ W/m^2 K. Hence, the heat flux at the onset of nucleate boiling [Eq. (40)] is $\dot{q}_{onb} = 4019$ W/m^2. Since $\dot{q} = 9000$ W/m^2 $> \dot{q}_{onb}$, both convective and nucleate boiling occur.

Convective Flow Boiling

According to the criterion given in Sect. 1 and to the flow pattern map, stratified or stratified-wavy flow exists at $\dot{x} = 0.1$ and $\dot{x} = 0.2$ (Table 5). The angle subtended at the center by the unwetted surface φ is obtained from H3.1, Eqs. (26) and (27) in Subchap. H3.1; and the hydraulic diameter for the vapor phase d_{hG}, from Eq. (10). The value to be inserted for the thermally effective unwetted arc in the determination of $\alpha(z)_{conv}$ need only be half as much as the figure determined from Eq. (13).

The values for $\alpha(z)_{conv}$ and the fin characteristic M are as follows:

$\dot{x}$	M	$\alpha(z)_{conv}$ W/m^2 K
0.1	0.98	779
0.2	0.65	503

Since $M < 1$, the above figures for $\alpha(z)_{conv}$ are approximations, as determined from Eq. (9). The values obtained from Eq. (8) are listed in Table 5. A comparison reveals that the values

H3.4. Table 4. Calculation results for the natural-convective evaporator (Example 1)

$\dot{x}$	z m	α_{LO} W/m^2 K	α_{GO} W/m^2 K	$\frac{\alpha(z)_{conv}}{\alpha_{LO}}$	$\alpha(z)_{conv}$ W/m^2 K	$\alpha(z)_B$ W/m^2 K	$\alpha(z)$ W/m^2 K
0	0[a]	1274	1188	1	1274	4570	4603
0.05	0.717	992	924	2.350	2330	4570	4764
0.1	1.434	978	912	3.038	2972	4570	4956
0.15	2.15	973	907	3.592	3495	4570	5169
0.2	2.867	970	904	4.072	3950	4570	5396
0.25	3.584	968	902	4.505	4361	4570	5629
0.3	4.3	967	901	4.904	4740	4570	5867

[a]At $z = 0$ m the value $z = 10^{-5}$ m is assumed

H3.4. Table 5. Calculation results for the single-pass injection evaporator (Example 2)

$\dot{x}$	z m	Flow pattern	α_{LO} W/m² K	α_{GO} W/m² K	α_G W/m² K	d_{hG} m	$\frac{\alpha(z)_{conv}}{\alpha_{LO}}$	α_{Lb} W/m² K	ε	φ^0	Φ	Ψ	$\alpha(z)_{conv}$ W/m² K	ψ	$\alpha(z)_B$ W/m² K	$\alpha(z)$ W/m² K
0.1	0[a]	Stratified flow	247	148	30.5	$1.16\cdot10^{-2}$	4.621	1137	0.775	233.2	0.324	1.021	764	0.849	927	1075
0.2	0.503	Wavy flow[b]	131	115	37.6	$1.24\cdot10^{-2}$	5.771	754	0.85	251.6	0.35	1.015	498	0.849	901	949
0.3	1.007	Wavy flow	130	113			6.585						853	0.849	875	1089
0.4	1.51	Wavy flow	129	113			7.231						933	0.849	850	1125
0.5	2.013	Wavy flow	129	113			7.773						1000	0.849	824	1160
0.6	2.517	Annular flow	129	112			8.239						1059	0.995	935	1261
0.7	3.02	Annular flow	128	112			8.646						1110	0.995	905	1283
0.8	3.523	Wavy flow	128	112			8.994						1153	0.849	746	1249
0.9	4.027	Wavy flow	128	112			9.215						1181	0.849	720	1264
1	4.53		128	112			0.875						112		–	112

[a] At $z = 0$ m the value $z = 10^{-5}$ m is assumed
[b] At $\dot{x} = 0.2$ the condition $Re_L Fr'_G \leq 4\left(Re_L Fr'_G\right)_{lim}$ is fulfilled. Therefore, the convective heat transfer coefficient is to be calculated as if it were stratified flow with partial wetting

obtained from Eq. (9) are sufficiently accurate for the boundary condition $\dot{q}$=constant and for $M \leq 1$.

Nucleate Boiling in the Horizontal Tube

At $\theta_{sat} = -20°C$, $\lambda_w = 320$ W/m K. The correction factors for the change in n and C_F for stratified and wavy flow can be read off from Fig. 14: thus, $\kappa = 0.993$ and $\psi = 0.849$.

The heat transfer coefficient for vertical tubes [Eq. (21)] is $\alpha(z)_B = 1337$ W/m² K. It is higher than the corresponding value calculated for horizontal tubes at all values of $\dot{x}$. Consequently, the limit defined by Eq. (36) is not reached at which heat transfer no longer depends on the mass velocity.

The energy balance yields $\dot{m} f \, \Delta\dot{x} \, \Delta h_v = \pi \, d \, l \, \dot{q}$. Hence, the length of the tube is

$$l = \frac{80\text{kg/m}^2\text{s} \cdot 1.54 \cdot 10^{-4}\text{m}^2 \cdot 0.9 \cdot 161780\text{J/kg}}{9000\text{W/m}^2 \cdot \pi \cdot 1.4 \cdot 10^{-2}\text{m}} = 4.53\text{m}.$$

In other words, the one pass suffices. The length of the section of tube required to effect a change of $\Delta\dot{x}$= 0.1 in the vapor mass fraction is $\Delta l = 0.503$.

The values obtained are listed in Table 5.

Example 3

Determine the rate of heat transfer into the water in the evaporation tubes of a forced-circulation boiler. The evaporation section consists of seamless steel (13 CrMo 44) tubes of $d_o = 31.8$ mm and $s = 4.5$ mm. The length of a straight section in the string of tubes is 3.5 m, and the spacing is 64 mm. The tubes are horizontal and are welded to the wall formed by the fins.

In view of the layer of magnetite formed during operation, the average roughness height that can be anticipated is $R_a = 5$ µm. The boiler is operated at a pressure of $p = 160$ bar and a mass velocity of $\dot{m}$= 800 kg/m² s. The furnace is designed to allow a heat flux of $\dot{q}$= 200 kW/m² to be applied uniformly over the circumference of the tubes. The water is heated to saturation in the economizer, that is,it enters the evaporator tubes at $\dot{x}_{in} = 0$.

H3.4. Table 6. Flow pattern in horizontal evaporator tubes acc. to Subchap. H3.1 (Example 3)

$\dot{x}$	z m	Flow pattern
0.01	0	Plug flow
0.1	2.12	Slug flow
0.2	4.23	Slug flow
0.3	6.35	Slug flow
0.4	8.47	Slug flow
0.5	10.59	Slug flow
0.6	12.7	Annular mist flow
0.7	14.82	Mist flow
0.8	16.94	Mist flow
0.9	19.06	Mist flow

The heat transfer coefficients and the wall superheat are to be determined in steps of $\Delta\dot{x} = 1$. The steps are continued up to the state of critical boiling if it has not already been reached, or to complete evaporation.

Properties at $p = 160$ bar and $\theta_{sat} = 347.34°C$:

$\rho' = 584$ kg/m³; $\eta' = 6.69 \cdot 10^{-5}$ kg/m s;
$\lambda' = 4.427 \cdot 10^{-1}$ W/m K; $\rho'' = 107.87$ kg/m³;
$\eta'' = 2.34 \cdot 10^{-5}$ kg/m s; $\lambda'' = 1.282 \cdot 10^{-1}$ W/m K;
$c'_p = 9597.1$ J/kg K; $\Delta h_v = 928\,644$ J/kg;
$c''_p = 14\,878.8$ J/kg K; $\sigma = 4.2 \cdot 10^{-3}$ kg/s².

The length of the tubes derived from the energy balance $\dot{m} f \, \Delta\dot{x} \, \Delta h_v = \dot{q} \, \pi \, d \, l$ is

$$l = \frac{800\text{kg/m}^2\text{s} \cdot 4.083 \cdot 10^{-4}\text{m}^2 \cdot 928,664\text{J/kg}}{200,000\text{W/m}^2 \cdot \pi \cdot 2.28 \cdot 10^{-2}\text{m}} = 21.17\text{m}.$$

A section of length Δl= 2.12 m is required to cause a change of $\Delta\dot{x}$= 0.1 in the vapor mass fraction. The number of the tube rows is n = 21.17 m/3.5 m ≈ 6.

H3.4. Table 7. Calculation results for the evaporator tube (Example 3)

$\dot{x}$	z m	α_{LO} W/m² K	α_{GO} W/m² K	$\frac{\alpha(z)_{conv}}{\alpha_{LO}}$	$\alpha(z)_{conv}$ W/m² K	ψ	$\alpha(z)_B$ W/m² K	$\alpha(z)$ W/m² K	ΔT K
0	0	12,176	12,270	1	12,176	1	75,163	75,270	2.66
0.1	2.12	12,176	12,270	1.896	23,079	0.825	58,335	59,515	3.36
0.2	4.23	12,176	12,270	2.110	25,694	0.825	55,456	57,237	3.49
0.3	6.35	12,176	12,270	2.235	27,209	0.825	52,577	54,902	3.64
0.4	8.47	12,176	12,270	2.313	28,168	0.825	49,698	52,548	3.81
0.5	10.59	12,176	12,270	2.363	28,768	0.825	49,385	52,446	3.81
1	21.17	12,176	12,270	1.008	12,270	–	–	12,270	16.3

No allowance is made for evaporation in the bends, which have a curvature of $R/d = 1.4$ and an average length of about 0.1 m. Since the relative length of the economizer tubes is $l/d \geq 20$, flow is hydrodynamically developed. The equations for the determination of the heat transfer coefficient in single-phase flow are Eqs. (A8) and (A9– A12).

At $\alpha_{LO} = 12\,176$ W/m² K, the minimum heat flux required for the onset of nucleate boiling is $\dot{q}_{onb} = 2112$ W/m². Since a value of $\dot{q} = 200$ kW/m² is given, both convective and nucleate boiling must be taken into account.

Convective Boiling

The flow patterns determined by the method described in Subchap. H3.1 are entered in Table 6. The likelihood of a reduction in $\alpha(z)_{conv}$ in the convective boiling regime can be ignored, because stratified or stratified-wavy flow does not occur throughout the entire $\dot{x}$ range. The disturbance in the two-phase flow that is caused by the bends with a curvature of $R/d = 1.4$ within a length of $l/d \approx 25$, can be ignored in the case of slug and mist flow.

Nucleate Boiling in Horizontal Tubes

$\lambda_w = 30$ W/m K and $\lambda_w s = 0.135$ W/K apply if $\theta = 350°$C. The correction factor obtained from Eq. (33a) is $\kappa = 0.792$, and the values for ψ have been entered in Table 7.

If the tubes are horizontal, no allowance need be made for the effect of bends in further reducing the heat transfer coefficient in nucleate boiling.

The heat transfer coefficient in nucleate boiling is $\alpha(z)_B = 75{,}523$ W/m² K, as determined by Eq. (60) for vertical tubes. The figure or $\alpha(z)_B$ determined by Eq. (31) for the horizontal tube is less than 75,523 W/m² K at all vapor mass fractions $\dot{x}$. Consequently, the limit at which $\alpha(z)_B$ no longer depends on the mass velocity, is not reached.

Critical Boiling State

According to the method described in Subchap. H3.5, the critical heat flux should first be determined for upward flow in a vertical tube. A figure of $\dot{x}_{cr} = 0.405$ at dryout is obtained from H3.5, Eq. (3).

The values at which the critical state occurs in a horizontal tube ($\cos\varphi = 1$) can then be determined from H3.5, Eqs. (5–7). Thus,

$$\mathrm{Fr} = \frac{\frac{\dot{x}_{cr}\dot{m}}{\rho''}}{\sqrt{\frac{gd\cos\varphi(\rho'-\rho'')}{\rho''}}} = \frac{\frac{0.405 \cdot 800\,\mathrm{kg/m^2 s}}{107.87\,\mathrm{kg/m^3}}}{\sqrt{\frac{9.81\,\mathrm{m/s^2} \cdot 2.28 \cdot 10^{-2}\,\mathrm{m}(584-107.87)}{107.87}}} = 3.02.$$

In other words, a critical state will arise. The crisis in boiling at the upper ($\dot{x}_{cr,up}$) or lower ($\dot{x}_{cr,low}$) side of the tube can be expected to occur at the following vapor mass fractions:

$$\dot{x}_{cr,up} = \dot{x}_{cr} - \Delta\dot{x}_{cr}/2 = 0.405 - 0.63/2 = 0.09,$$
$$\dot{x}_{cr,low} = \dot{x}_{cr} + \Delta\dot{x}_{cr}/2 = 0.405 + 0.63/2 = 0.72,$$

$\Delta\dot{x}_{cr}$ is obtained from H3.5, Eq. (6), that is,

$$\Delta\dot{x}_{cr} = 16/(2 + \mathrm{Fr})^2 = 0.63.$$

The flow patterns in the unheated tubes can be determined as described in Subchap. H3.1. It can be seen from Table 6 that slug flow occurs at $\dot{x} = 0.1$–0.5, that is, the two-phase flow is stratified. As a result of the heat applied, slug flow is thermally suppressed, and the stratification effect is intensified [R26]. For the purpose of the calculation, it is, therefore, assumed that the critical state is reached from $\dot{x}_{cr,low} = \dot{x} = 0.5$ onward. Values for $\dot{x} = 0$ to $\dot{x} = 0.5$ are listed in Table 7.

H3.5 Critical Boiling States in Flowing Liquids

Hein Auracher[1] · *Oliver Herbst*[2]
[1]Stuttgart, Germany
[2]AREVA NP GmbH, Erlangen, Germany

1 Introduction

Boiling allows large heat fluxes to be transferred at small temperature differences from a wetted wall to a liquid, but an upper limit is imposed on the flow rate of the heat thus transferred. If certain boundary conditions are transgressed, the heat transfer mechanism undergoes a change, referred to as the boiling crisis. This critical state in boiling can be recognized by one of the following characteristics:

- If the heat flux is applied to the system by electric heaters, radiators, nuclear energy, or other independent sources, a critical value $\dot{q}_{cr}$ exists at which a slight increase in $\dot{q}$ gives rise to a sudden leap in the wall temperature.
- A slight increase in the set temperature of a wall heated by an exchanger, condenser, or similar system causes a pronounced decrease in the heat flux.

The reason for the deterioration in heat transport in these cases is that the liquid loses direct contact with the wall. As a consequence, heat is transferred to the vapor and no longer to the liquid phase.

The boiling curve for a heated surface/liquid system is shown in Fig. 1. Its shape and thus the value for the critical heat flux depend on

- The nature of the liquid.
- The flow pattern (liquid pool or flowing liquid).
- The thermodynamic state of the liquid, for example, subcooling and the void fraction.
- The geometry of the heated surface.
- The material from which the heated wall has been constructed.
- The finish on the heated surface.

Two different physical mechanisms lead to the boiling crisis. They are described below.

- Film boiling

  If the void fraction in the stream is low, that is, if the liquid is the continuous phase, a vapor film is formed at the point where the boiling crisis occurs, and it separates the liquid from the heated surface. Owing to the poor thermal conductivity of the vapor, heat transfer is greatly impaired, and heat is imparted to the liquid by film boiling. The mechanism, which is illustrated in Fig. 2a, is referred to as departure from nucleate boiling (DNB). An increase in heat flux in this case shifts the initiation of the boiling crisis in the direction of lower vapor mass fractions.

- Dryout of the heated surfaces

  If the void fraction is high enough to cause annular flow, the liquid film is torn off or dries out at the point where the boiling crisis occurs. This case is illustrated in Fig. 2b. Under these circumstances, the deterioration in heat transfer is less than that in film boiling, because the high vapor mass fraction is responsible for convective cooling of the heated surface. The critical mass fraction of vapor is almost independent of the heat flux. In the range of low heat fluxes, however, the number of entrained liquid droplets that are redeposited on the heated surface may increase. In this case, the boiling crisis is referred to as deposition-controlled burnout.

The attention that must be paid to the following factors in the boiling crisis depends on the application:

- The (critical) vapor mass fraction.
- The (critical) heat flux.

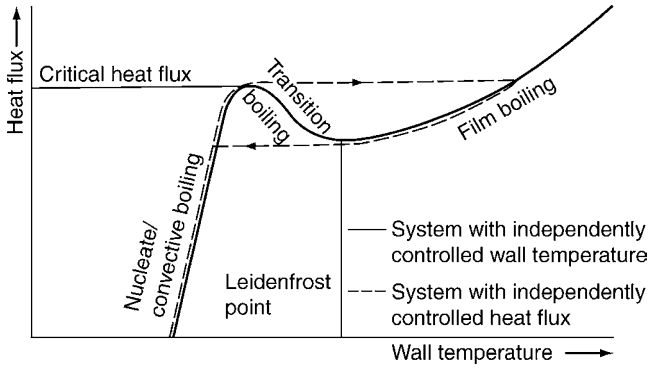

H3.5. Fig. 1. Heat transfer mechanisms in two-phase flow.

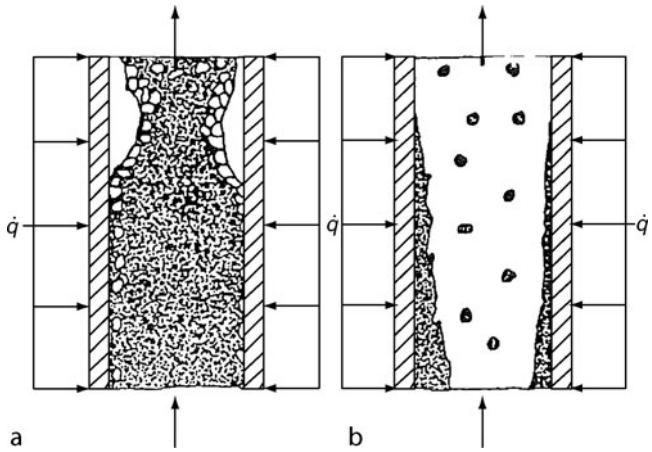

H3.5. Fig. 2. Boiling crisis mechanisms. (**a**) Film boiling (DNB). (**b**) Dryout.

The curve obtained by plotting the critical heat flux against the vapor mass fraction can be divided into three characteristic sections [1], as is shown in Fig. 3.

The effect of the boiling crisis depends on the interplay between the liquid and the heated surface as well as on the thermodynamic parameters. It is represented schematically in Fig. 4 for a water–steel system. Burnout or physical damage of the heated surface can be anticipated if the heat flux lies within the hatched section above the full-line curve in the diagram. It is also evident that a boiling crisis need not necessarily lead to damage if the vapor mass fraction is high, particularly if the medium is a refrigerant.

2 Flow of Water

2.1 Flow through Tubes

2.1.1 Upward Flow through Vertical Tubes

Two fundamental difficulties are encountered in determining the critical heat flux:

- In deciding the form of boiling crisis that can be anticipated, that is, film boiling or dryout.

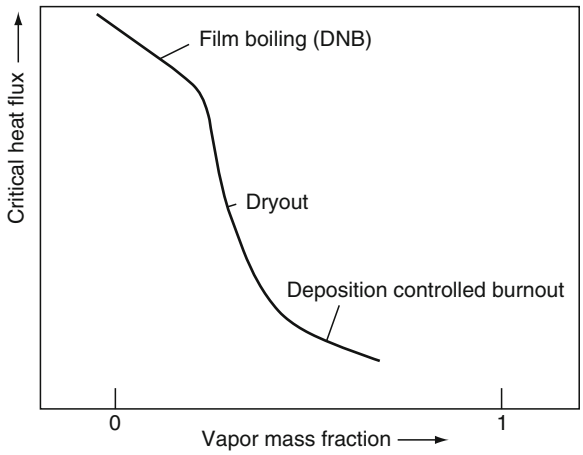

H3.5. Fig. 3. Typical relationship between the critical heat flux and the vapor mass fraction or "quality" [1].

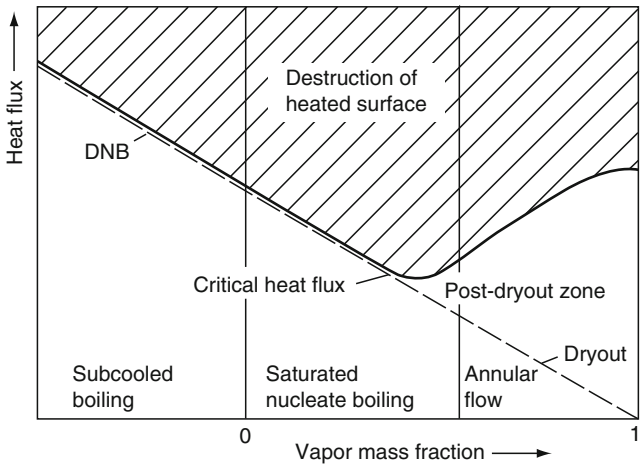

H3.5. Fig. 4. Effect of the boiling crisis on the heated surface for a water–steel system.

- In selecting the equation applicable to a particular case from the numerous empirical correlations, most of which are valid only within narrow ranges of the parameters concerned.

Figure 5 may serve as a guide for the recommended calculation procedure within the respective limits of validity, collectively covering a very large range of parameters.

The case for which high pressure parameters are coupled with large mass fluxes (Zone 3 in Fig. 5) is accounted for in the following method. It largely disregards the physical mechanisms involved, instead utilizing equations that are valid over a wide range of parameters for film boiling and dryout.

In the light of a comparison of about 3,000 measured values, Drescher and Köhler [2] demonstrated that the tables compiled by Doroshchuk et al. [3,4] are superior to the correlations extant. In practice, however, it is simpler to use the empirical equation for water that *Doroshchuk* derived *for film boiling* from the tables. The loss in accuracy that it entails can be reasonably accepted. The equation is

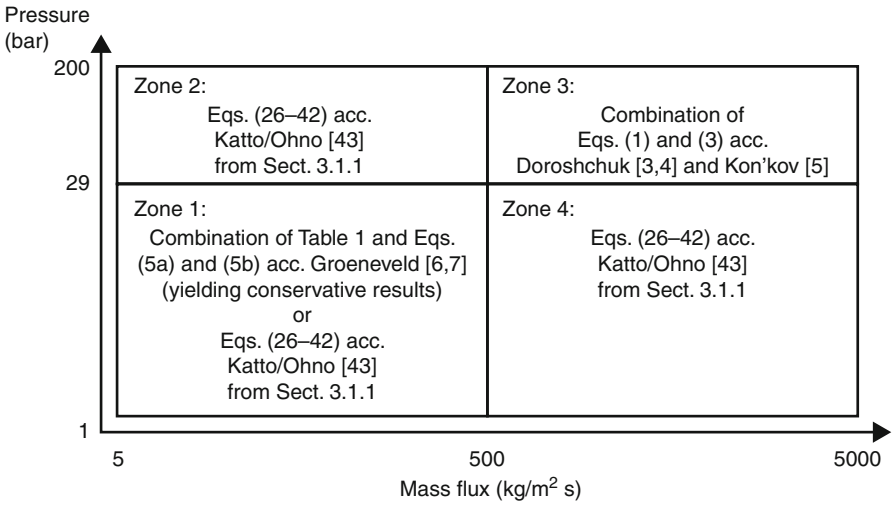

H3.5. Fig. 5. Parameter domains and their respective calculation procedures.

$$\dot{q}_{cr} = 10^3 \left[10.3 - 17.5\left(\frac{p}{p_c}\right) + 8\left(\frac{p}{p_c}\right)^2\right]\left(\frac{8\cdot 10^{-3}}{d}\right)^{0.5} \cdot \left(\frac{\dot{m}}{1000}\right)^{0.68\left(\frac{p}{p_c}\right)-1.2\dot{x}-0.3} \cdot e^{-1.5\dot{x}}. \quad (1)$$

The ranges within which the equation is valid are

$$29 \text{ bar} \le p \le 200 \text{ bar},$$
$$500 \text{ kg/m}^2\text{s} \le \dot{m} \le 5000 \text{ kg/m}^2\text{s},$$
$$0 \text{ K} \le \Delta\vartheta_{sub} \le 75 \text{ K},$$
$$4\cdot 10^{-3} \text{ m} \le d \le 25\cdot 10^{-3} \text{ m}.$$

The critical vapor mass fraction is given by

$$\dot{x}_{cr} = \frac{\ln\left(\frac{\dot{m}}{1000}\right)\left(0.68\frac{p}{p_c} - 0.3\right) - \ln(\dot{q}_{cr}) + \ln(C)}{1.2\ln\left(\frac{\dot{m}}{1000}\right) + 1.5} \quad (2a)$$

where

$$C = 10^3\left[10.3 - 17.5\left(\frac{p}{p_c}\right) + 8\left(\frac{p}{p_c}\right)^2\right]\left(\frac{8\cdot 10^{-3}}{d}\right)^{0.5}. \quad (2b)$$

Equation (1) was checked by taking the quotient of the calculated and measured values of the critical heat flux. The mean was found to be 0.99 with a standard deviation of 16% [2].

The *Kon'kov* equation for water [5] has been recommended for the range in which the heated surface *dries out* [2, *loc. cit.*]. Thus,

$$\begin{aligned} \dot{q}_{cr} &= 1.8447\cdot 10^8 \dot{x}^{-8}\dot{m}^{-2.664} \cdot (d\cdot 1{,}000)^{-0.56} e^{0.1372p} && \text{Range of pressures } p \\ &&& 4.9-29.4 \text{ bar} \\ \dot{q}_{cr} &= 2.0048\cdot 10^{10} \dot{x}^{-8}\dot{m}^{-2.664} \cdot (d\cdot 1{,}000)^{-0.56} e^{-0.0204p} && \\ &&& 29.4-98 \text{ bar} \\ \dot{q}_{cr} &= 1.1853\cdot 10^{12} \dot{x}^{-8}\dot{m}^{-2.664} \cdot (d\cdot 1{,}000)^{-0.56} e^{-0.0636p} && \\ &&& 98-196 \text{ bar}. \end{aligned} \quad (3)$$

Range of parameters covered by the equation

$$200 \text{ kg/m}^2\text{s} \le \dot{m} \le 5{,}000 \text{ kg/m}^2\text{s},$$
$$4\cdot 10^{-3} \text{ m} \le d \le 32\cdot 10^{-3} \text{ m}.$$

The critical vapor mass fraction of water is given by

$$\begin{aligned} \dot{x}_{cr} &= 10.795\, \dot{q}^{-0.125}\dot{m}^{-0.333} \cdot (d\cdot 1{,}000)^{-0.07} e^{0.01715p} && \text{Range of pressures } p \\ &&& 4.9-29.4 \text{ bar} \\ \dot{x}_{cr} &= 19.398\, \dot{q}^{-0.125}\dot{m}^{-0.333} \cdot (d\cdot 1{,}000)^{-0.07} e^{-0.00255p} && \\ &&& 29.4-98 \text{ bar} \\ \dot{x}_{cr} &= 32.302\, \dot{q}^{-0.125}\dot{m}^{-0.333} \cdot (d\cdot 1{,}000)^{-0.07} e^{-0.00795p} && \\ &&& 98-196 \text{ bar}. \end{aligned} \quad (4)$$

Equation (3) was checked by taking the difference between the calculated and the measured values of the critical vapor mass fraction [2]. The mean deviation was found to be −0.04; and the standard deviation, 0.10.

The application of the above equations presumes stable flow. If fluctuations occur in the mass flow rate, the boiling crisis may be triggered off at a much earlier stage.

It can be seen in Fig. 3 that the curve obtained by plotting the critical heat flux against the vapor mass fraction has a much greater downward slope in the dryout range than in the range of film boiling. Hence the boundary between the two critical boiling mechanisms is the intersect of Eqs. (1) and (3). This implies that the critical heat flux must be calculated from both equations and that the lower value thus obtained should be taken.

Consequently, the decision can be made which form of boiling crisis – film boiling or dryout – is to be anticipated:

The value to be taken for $\dot{q}_{cr}$ is the lower of that obtained from Eq. (1) and that from Eq. (3).

Likewise, the value to be taken for $\dot{x}_{cr}$ is the lower of that obtained from Eq. (2) and that from Eq. (4).

Diagrams are presented in Figs. 6–11 for the determination of the heat flux during the upward flow of water in vertical tubes of 10 and 20 mm diameter. The corresponding values for tubes

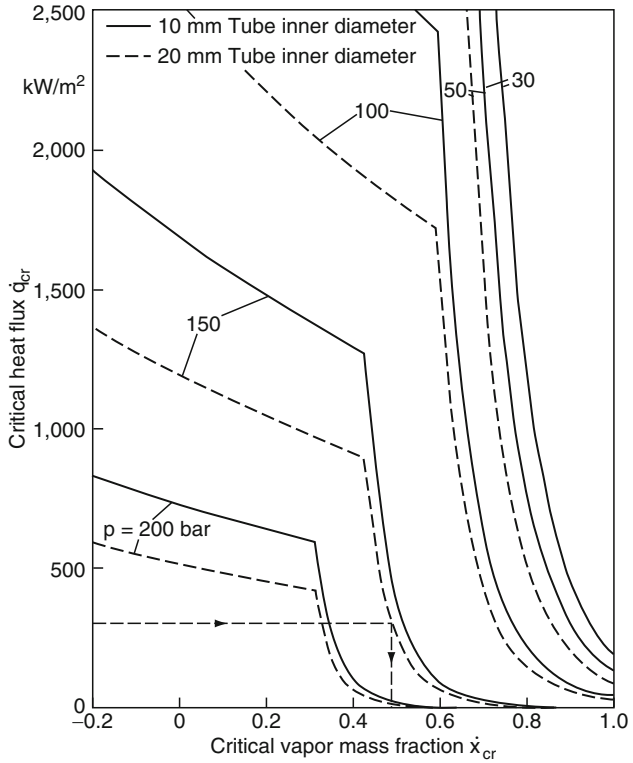

H3.5. Fig. 6. Critical heat flux as a function of the critical vapor mass fraction (mass velocity 500 kg/m^2 s).

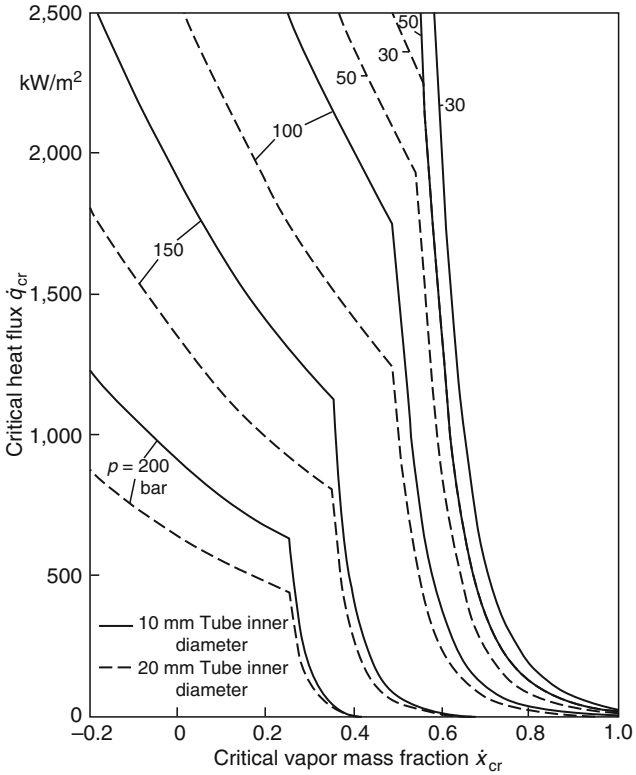

H3.5. Fig. 8. Critical heat flux as a function of the critical vapor mass fraction (mass velocity 1000 kg/m^2 s).

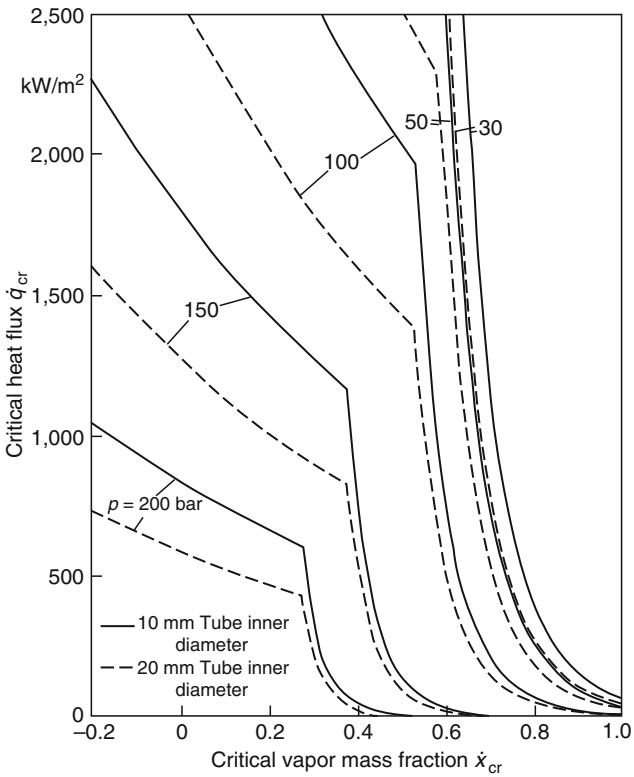

H3.5. Fig. 7. Critical heat flux as a function of the critical vapor mass fraction (mass velocity 750 kg/m^2 s).

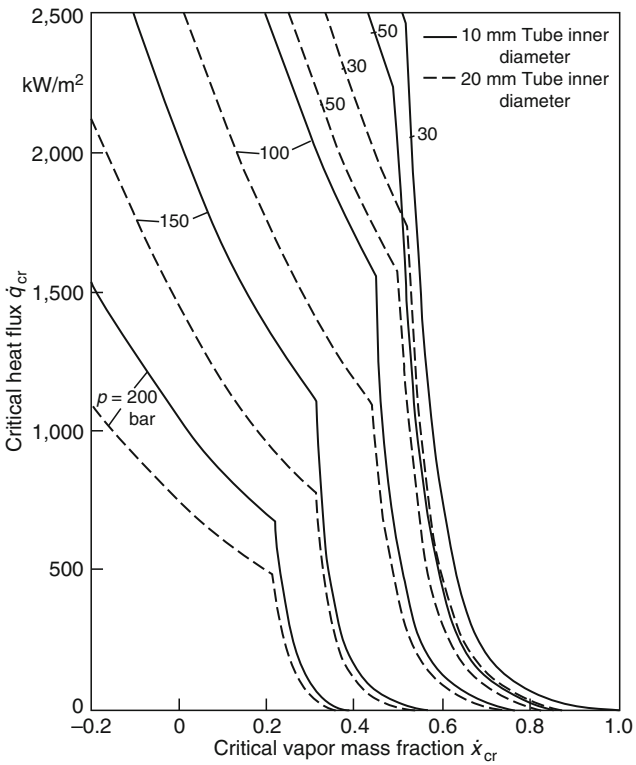

H3.5. Fig. 9. Critical heat flux as a function of the critical vapor mass fraction (mass velocity 1,500 kg/m^2 s).

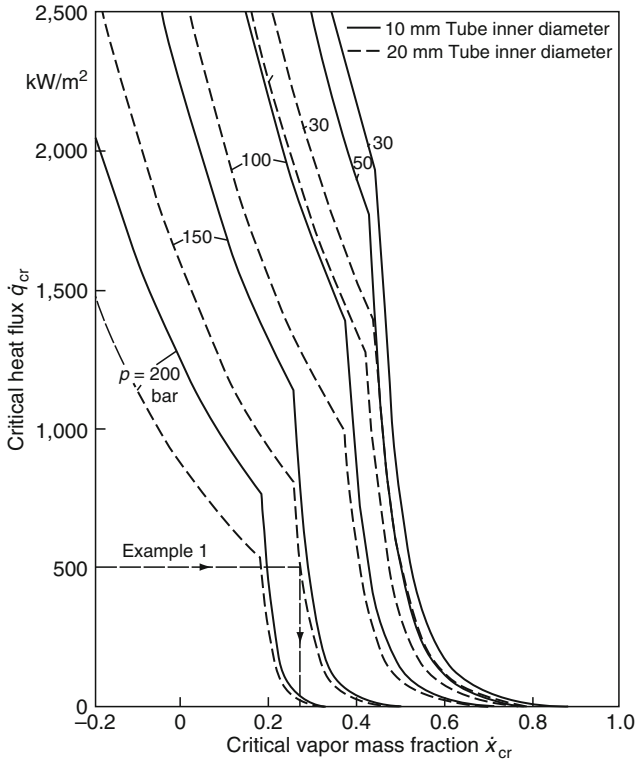

H3.5. Fig. 10. Critical heat flux as a function of the critical vapor mass fraction (mass velocity 2,500 kg/m^2 s).

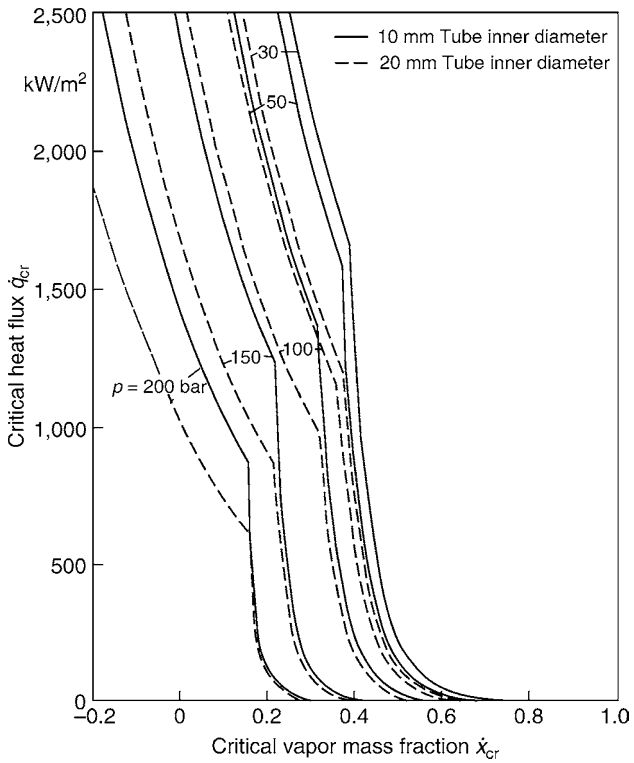

H3.5. Fig. 11. Critical heat flux as a function of the critical vapor mass fraction (mass velocity 4,000 kg/m^2 s).

in the 4–25 mm diameter range can be obtained by interpolation or extrapolation.

For parameters within the domain

$$p < 29 \text{ bar},$$
$$\dot{m} < 500 \text{ kg/m}^2\text{s},$$

the combination of Eqs. (1) and (3) is not valid (Zone 1 in Fig. 5). In this case, the critical heat flux for $l/d > 80$ and $-0.5 < \dot{x}_{inl} < 0$ can be extracted from Table 1. Table 1 is an excerpt from "1995 Tables of Critical Heat Fluxes" developed by Groeneveld et al. [6]. Table 1 displays the critical heat flux in discrete steps of pressure, mass flux and critical vapor mass fraction for the parameter ranges considered here.

The table developed by Groeneveld et al. [6] is based upon approximately 23,000 values for upwards flow in vertical tubes covering the range of $1 \le p \le 200$ bar, $6 \le \dot{m} \le 8{,}000$ kg/m^{2}s, $-0.5 \le \dot{x}_{cr} \le 1.0$, $3 \cdot 10^{-3} \le d \le 40 \cdot 10^{-3}$ m and $80 \le l/d \le 2{,}485$. The accuracy of the table totaled to a RMS error of 7.8% and an average relative error of 0.69%. Only data incorporating a heated length to diameter ratio of greater than 80 was used to ensure that the underlying "local conditions hypothesis" is valid. This hypotheses assumes that the local values of the proper system parameters (p, $\dot{m}$, $\dot{x}_{cr}$, and d) explicitly determine the critical heat flux.

All of the values in Table 1 are valid for tubes with an inner diameter of 8 mm and can be adjusted to suit alternate diameters by applying Eq. (5a):

$$\frac{\dot{q}_{cr,d}}{\dot{q}_{cr,d=8\text{ mm}}} = \left(\frac{d}{8 \cdot 10^{-3}}\right)^{-0.5} \quad \text{for} \quad 3 \cdot 10^{-3}\text{ m} \le d \le 25 \cdot 10^{-3}\text{ m}$$
$$\frac{\dot{q}_{cr,d}}{\dot{q}_{cr,d=8\text{ mm}}} = 0.6 \quad \text{for} \quad 25 \cdot 10^{-3}\text{ m} < d \le 40 \cdot 10^{-3}\text{ m}. \tag{5a}$$

Parameters which are not explicitly tabulated in Table 1 may be linearly interpolated between the displayed values. Here it must be noted that the empty cells in Table 1 correspond to such highly subcooled fluid enthalpies that their respective values are smaller than at the point of freezing.

For smaller heated tube lengths that are in the range of $5 \le l/d < 80$, the heated length influences the critical heat flux, necessitating the correction of the values in Table 1 using the following method [7]:

$$\frac{\dot{q}_{cr,\,l/d<80}}{\dot{q}_{cr,\,l/d\ge 80}} = K_l \tag{5b}$$

with

$$K_l = \exp\left(\frac{d}{l} \cdot e^{2\cdot\varepsilon_{hom}}\right)$$

and the volumetric vapor fraction according to the homogenous model:

$$\varepsilon_{hom} = \frac{\rho_l \cdot \dot{x}}{\rho_l \cdot \dot{x} + \rho_g \cdot (1 - \dot{x})}. \tag{5c}$$

For very small mass fluxes ($\dot{m} \le 100$ kg/m^{2}s), the critical heat fluxes specified by *Groeneveld* are afflicted with certain uncertainties. This is because they are based upon comparatively smaller numbers of measured data [6]. For this reason, measurements by Köhler et al. [8] on an electrically heated tube at

H3.5. Table 1. Critical heat fluxes $\dot{q}_{kr}$ in (kW/m^2) for smaller pressures and mass fluxes acc. Groeneveld [6] for tubes with an inner diameter of 8 mm, $l/d \geq 80$

Pressure (bar)	Mass flux (kg/m^2 s)	Vapor mass fraction																						
		−0.5	−0.4	−0.3	−0.2	−0.15	−0.1	−0.05	0	0.05	0.1	0.15	0.2	0.25	0.3	0.35	0.4	0.45	0.5	0.6	0.7	0.8	0.9	1
1	0[a]					4,593	3,419	2,247	1,066	421	298	207	158	142	130	120	111	103	99	84	74	68	67	0
1	50					4,940	3,881	2,618	1,526	787	754	683	635	620	609	600	591	582	570	513	401	288	253	0
1	100					5,206	4,124	2,942	1,947	1,159	1,137	1,123	1,107	1,093	1,084	1,078	1,070	1,060	1,037	961	747	550	416	0
1	300					5,232	4,206	3,475	2,792	1,693	1,665	1,651	1,598	1,536	1,502	1,475	1,378	1,243	1,151	979	751	626	550	0
1	500					5,261	4,305	3,768	3,204	2,040	1,887	1,883	1,875	1,798	1,725	1,714	1,615	1,486	1,463	1,188	752	558	415	0
3	0[a]				5,024	4,349	3,432	2,433	1,596	1,575	1,029	665	467	317	234	194	178	171	170	149	143	143	90	0
3	50				5,644	4,951	3,882	2,842	2,003	1,987	1,443	1,123	938	813	745	708	686	660	642	601	472	391	300	0
3	100				6,174	5,211	4,235	3,225	2,431	2,076	1,574	1,291	1,258	1,230	1,211	1,190	1,168	1,118	1,081	1,026	857	669	473	0
3	300				6,403	5,447	4,544	3,889	3,371	2,433	2,095	2,071	1,995	1,895	1,828	1,771	1,636	1,494	1,418	1,203	866	695	564	0
3	500				6,414	5,498	4,667	4,234	3,832	2,863	2,479	2,435	2,333	2,185	2,072	1,869	1,700	1,539	1,447	1,155	764	574	521	0
5	0[a]				4,879	4,200	3,469	2,595	1,783	1,697	1,174	786	535	374	278	226	207	191	183	151	150	149	140	0
5	50				5,568	4,962	3,983	3,168	2,424	2,249	1,728	1,380	1,145	1,005	921	865	826	793	754	611	493	476	359	0
5	100				6,195	5,267	4,489	3,688	2,975	2,478	1,780	1,683	1,623	1,566	1,525	1,492	1,440	1,391	1,292	1,158	1,045	875	539	0
5	300				6,589	5,783	5,098	4,547	4,089	3,396	2,921	2,801	2,679	2,527	2,409	2,050	1,799	1,552	1,489	1,188	1,049	919	607	0
5	500				6,629	5,876	5,250	4,853	4,452	3,784	3,247	3,074	2,888	2,695	2,498	2,187	1,887	1,593	1,414	959	774	622	554	0
10	0[a]			5,619	4,685	4,058	3,564	2,859	2,175	1,910	1,438	1,030	717	519	389	312	286	270	556	198	188	181	175	0
10	50			6,371	5,523	4,991	4,436	3,928	3,323	2,944	2,469	2,071	1,752	1,559	1,414	1,307	1,230	1,157	1,076	876	806	804	700	0
10	100			6,981	6,252	5,685	5,281	4,851	4,268	3386	2,799	2,651	2,531	2,415	2,292	2,184	2,041	1,891	1,703	1,312	1,291	1,250	732	0
10	300			7,492	7,295	7,089	6,901	6,766	6,620	6,215	5,289	4,760	4,456	4,120	3,432	2,600	2,151	1,924	1,708	1,343	1,289	1,215	660	0
10	500			7,577	7,464	7,327	7,177	7,110	7,048	6,818	5,771	5,094	4,660	4,233	3,856	2,754	2,284	1,979	1,659	1,035	825	767	589	0
30	0[a]	6,583	5,927	5,252	4,544	4,205	3,891	3,536	3,022	2,429	2,009	1,564	1,145	892	699	568	502	452	413	321	275	266	256	0
30	50	7,307	6,575	5,972	5,386	5,107	4,857	4,570	4,135	3,478	3,061	2,653	2,266	2,041	1,865	1,722	1,614	1,521	1,418	1,409	1,400	1,392	1,000	0
30	100	7,888	7,106	6,580	6,114	5,897	5,708	5,479	5,057	4,121	3,502	3,326	3,186	3,051	2,926	2,796	2,625	2,467	2,367	2,191	1,936	1,587	1,015	0
30	300	8,463	7,476	7,307	7,303	7,302	7,300	7,298	7,255	6,954	5,922	5,380	5,211	4,936	4,635	3,997	3,322	3,177	3,173	2,865	2,078	1,536	953	0
30	500	8,655	7,674	7,578	7,560	7,554	7,641	7,627	7,621	7,496	7,000	6,400	5,660	5,269	4,807	4,297	3,392	3,376	3,324	2,745	1,841	1,320	835	0

[a]Values required for interpolations within the range $0\,\mathrm{kg/m^2\,s} < \dot{m} \leq 50\,\mathrm{kg/m^2\,s}$ made available by [6,7]

pressures of 1 and 1.35 bar, mass fluxes from 5 to 40 kg/m^{2}s and heated length-to-diameter ratios of less than 80 are shown in Fig. 12. They are compared with values extracted from Table 1 and adjusted using Eqs. (5a) and (5b). Virtually all values lie within a tolerance of ±20%, which qualify as excellent on the grounds that the mass fluxes under investigation were extremely small. Hence, the values in Table 1 are verified for $\dot{m} \leq$ 100 kg/m^{2}s.

For practical purposes, it is easier on one hand to work with equations than with Table 1, which in most cases necessitates additional interpolation calculations. On the other hand, no approximation equations were put forward by *Groeneveld*. Therefore, extensive parameter variations for comparison of his tabulations [6] and the method acc. to Katto and Ohno [43] were undertaken. This method is introduced in Sect. 3.1.1. When applying Eqs. (26–42), it is necessary to use the physical properties for water and steam.

In the calculation of the critical heat flux for water, Fig. 13 compares the results of *Katto/Ohno* with those of Table 1 and Eq. (5b). The results are compared over a domain of $1 \leq p \leq 30$ bar, $5 \leq \dot{m} \leq 500$ kg/m^2 s and $38 \leq l/d \leq 700$ for an evaporator tube of $d = 8 \cdot 10^{-3}$ m. Over a wide range of parameters, excellent agreement is observed within a tolerance of −10% to +30%. Therefore, the method acc. to *Katto* and *Ohno* (Eqs. 26–42) can be applied for the approximation of the critical heat fluxes given in Table 1. However, it emerges from Fig. 13 that the values calculated by *Katto/Ohno* for pressures of 1–5 bar are on average higher than those in Table 1. Therefore, for security relevant considerations in the range of smaller pressures and mass fluxes, it is prudent to use the values in Table 1 and adjust the results using Eqs. (5a) and (5b) as necessary.
For parameters within the range

$$29 \leq p \leq 200\,\text{bar},$$
$$\dot{m} < 500\ \text{kg/m}^2\text{s},$$

i.e., for higher pressures coupled with smaller mass fluxes (Zone 2 in Fig. 5) the combination of Eqs. (1) and (3) is not valid. In this case, the procedure developed by *Katto/Ohno* [43] (Eqs. 26–42) can be applied for $l/d > 5$ and $-0.5 < \dot{x}_{\text{inl}} < 0$ to approximate the critical heat fluxes given in the tables developed by Groeneveld [6]. For evaporator tubes with $d = 8 \cdot 10^{-3}$ m, the critical heat fluxes calculated by *Katto/Ohno* and the values given in the *Groeneveld* tables are in very good agreement. Results lie within a tolerance of ±30% over the domain $50 \leq p \leq 200$ bar, $20 \leq \dot{m} \leq 500$ kg/m^2 s and $12 \leq l/d \leq 700$.
For parameters within the range

$$p < 29\ \text{bar},$$
$$\dot{m} \geq 500\ \text{kg/m}^2\text{s},$$

i.e., for smaller pressures coupled with higher mass fluxes (Zone 4 in Fig. 5) the combination of Eqs. (1) and (3) is likewise invalid. For $l/d > 100$ und $-0.5 < \dot{x}_{\text{inl}} < 0$, the procedure developed by Katto and Ohno [43] (Eqs. 26–42) can also be applied to approximate the critical heat fluxes given in the tables developed by Groeneveld [6]. For evaporator tubes of $d = 8 \cdot 10^{-3}$ m, the equations developed by *Katto/Ohno* for the critical heat flux and the values in the *Groeneveld* tables are in good agreement. Results lie within a tolerance of ±30% for the parameter range $1 \leq p \leq 30$ bar, $500 \leq \dot{m} \leq 4{,}000$ kg/m^{2}s and $100 \leq l/d \leq 700$. Stronger scattering may develop when water-steam flow of smaller pressures take on higher mass fluxes approaching the speed of sound (at the corresponding critical vapor mass fraction). This makes both the occurrence and therefore the forecasting of a critical heat flux impossible.

Consequently, there exists a complete calculation method for the determination of the critical heat flux for upwards flows through vertical tubes. This is applicable over a wide range of parameters, i.e. pressures from 1 to 200 bar and mass fluxes from 5 to 5,000 kg/m^2 s (refer to Fig. 5).

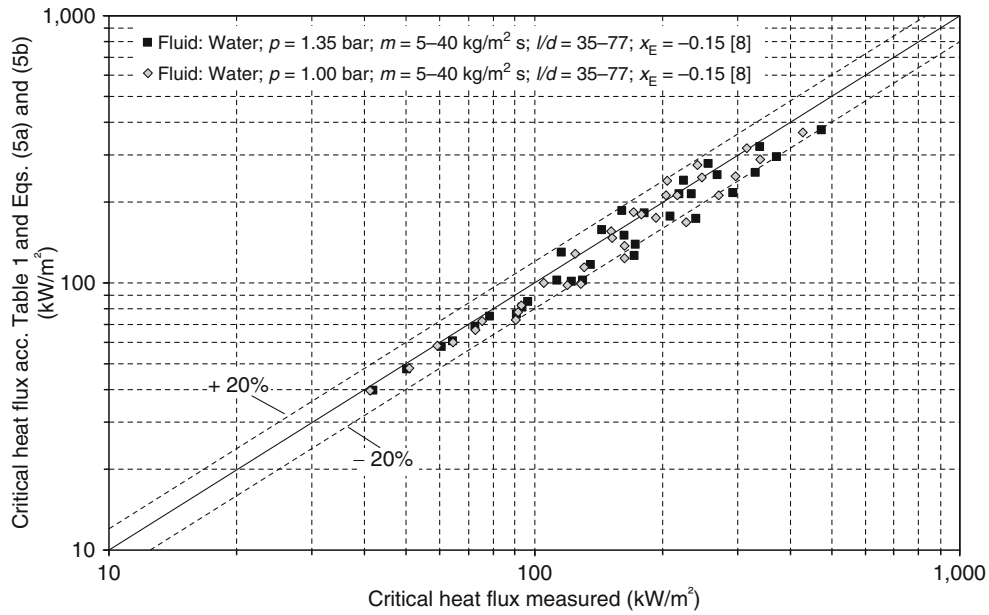

H3.5. Fig. 12. Comparison of measured critical heat fluxes and the values of Table 1 (acc. *Groeneveld* [6]) for water.

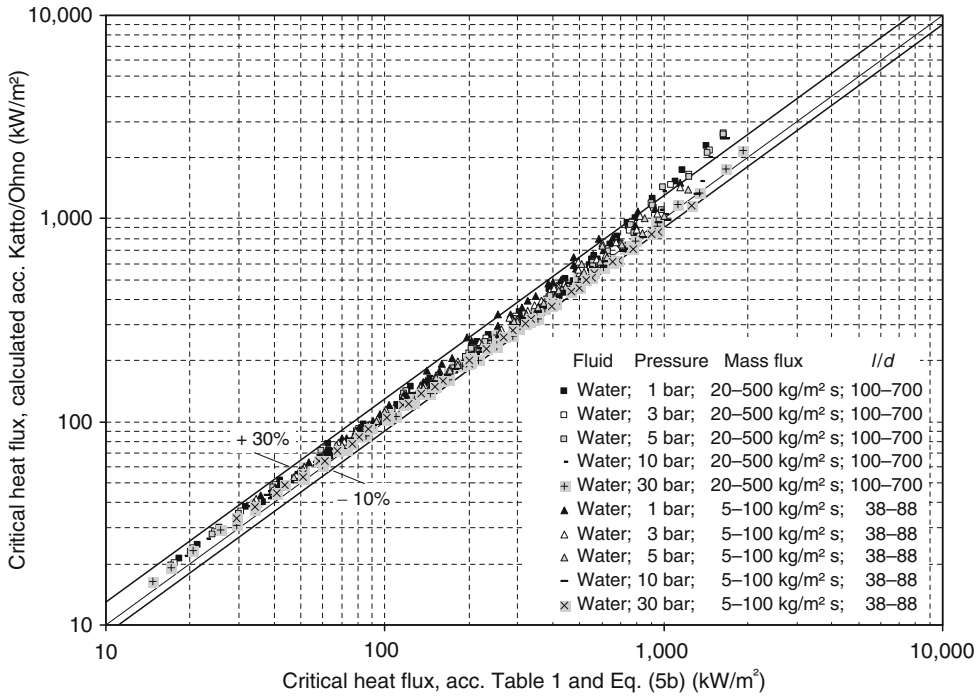

H3.5. Fig. 13. Comparison of critical heat fluxes acc. *Katto/Ohno* [43] and the values of Table 1 (acc. *Groeneveld* [6]) for water.

Figure 14 shows the critical heat fluxes determined from the *Groeneveld* tables [6] and Eqs. (1) and (3) at the transition from Zone 2 to 3 and from 3 to 4. As an example, subcooled-water with an equilibrium vapor mass fraction of −0.20 flows into a 20 mm inner diameter evaporator tube. It is heated over the length of 6 and 10 m (top and bottom diagrams respectively in Fig. 14).

Concerning the transition from Zone 2 to 3 (left diagrams), the heat flux is plotted for pressures of 30, 100, 150, and 200 bar, respectively, at the limiting mass flux of 500 kg/m^2 s. The point of intersection with each straight heat balance line gives the heat flux for which the boiling crisis is initiated exactly at the tube exit. The heat balance lines describe the linear relationship between the heat flux and the vapor mass fraction at the exit of a uniformly heated tube. There are small relative deviations from +1.3% to +16.7%, a larger relative deviation of +27.6% becoming evident only at 200 bar and l/d = 500 where the critical heat fluxes are small. The relative deviations are defined to be between the respective heat fluxes at the points of their intersection with the heat balance lines. Only the values which lie along these lines explicitly correspond to the system defined by the parameters (l, d, $\dot{x}_{\mathrm{inl}}$, p, $\dot{m}$) and the condition (*boiling crisis directly at the tube exit*).

Regarding the transition from Zone 3 to 4 (right diagrams), the heat flux is plotted for 500, 1,500, and 4,000 kg/m^2 s, respectively, at a pressure of 30 bar, together with the heat balance lines. Here also, there are small relative deviations from −10.8% to +10.6%. Additionally, the parameter combination of 200 bar and 4,000 kg/m^2 s is illustrated in these diagrams (bold text in legend; lines with triangle symbols). Large relative deviations of +36.7% and +61.9% becoming evident at the heated length of 6 and 10 m, respectively. This fact shows that when higher pressures are coupled with higher mass fluxes (Zone 3 in Fig. 5) the calculation by *Doroshchuk* and *Kon'kov* produces considerably conservative values and should therefore be retained – especially for security relevant considerations.

Example 1

Water at saturation enters an evaporator tube that is uniformly heated in the axial direction. At what point in the tube does the boiling crisis occur?

Tube inner diameter $d = 20 \cdot 10^{-3}$ m
Length of tube $l = 8$ m
Pressure $p = 150$ bar
Mass flow rate $\dot{M} = 0.8$ kg/s
Heat flow rate $\dot{Q} = 250$ kW

Determination of heat flux

$$\dot{q} = \frac{\dot{Q}}{d\pi l} = \frac{250\ \mathrm{kW}}{\pi \cdot 0.02\ \mathrm{m} \cdot 8\ \mathrm{m}} = 497.4\ \mathrm{kW/m^2}.$$

Determination of mass velocity

$$\dot{m} = \frac{4\dot{M}}{\pi d^2} = \frac{4 \cdot 0.8\ \mathrm{kg/s}}{4 \cdot 10^{-4}\pi\ \mathrm{m^2}} = 2546.5\ \mathrm{kg/m^2\,s}.$$

A comparison of Fig. 10 with Fig. 3 reveals that the boiling crisis for these parameters is attained by dryout of the heated surface. Hence, the critical vapor mass fraction should be determined from Eq. (4). The figure thus obtained is $\dot{x}_{\mathrm{cr}} = 0.269$. It must now be checked whether the boiling crisis is actually attained by dryout. Thus, substituting $\dot{x}_{\mathrm{cr}} = 0.269$ for $\dot{x}$ in Eq. (1) gives

$$\dot{q}_{\mathrm{cr}} = 767\ \mathrm{kW/m^2} > 497.4\ \mathrm{kW/m^2}.$$

that is, the assumption is confirmed.

The critical vapor mass fraction is attained at the point z. Since $\pi dzq = M(\dot{x}_{\mathrm{cr}} - \dot{x}_{\mathrm{inl}})$ and $\dot{x}_{\mathrm{inl}} = 0$,

$$z = \frac{\dot{M}\dot{x}_{\mathrm{cr}}\Delta h_{\mathrm{v}}}{d\pi\dot{q}} = \frac{0.8\ \mathrm{kg/s} \cdot 0.269 \cdot 1{,}004\ \mathrm{kJ/kg}}{0.02\pi\ \mathrm{m} \cdot 497.4\ \mathrm{kW/m^2}} = 6.91\ \mathrm{m}.$$

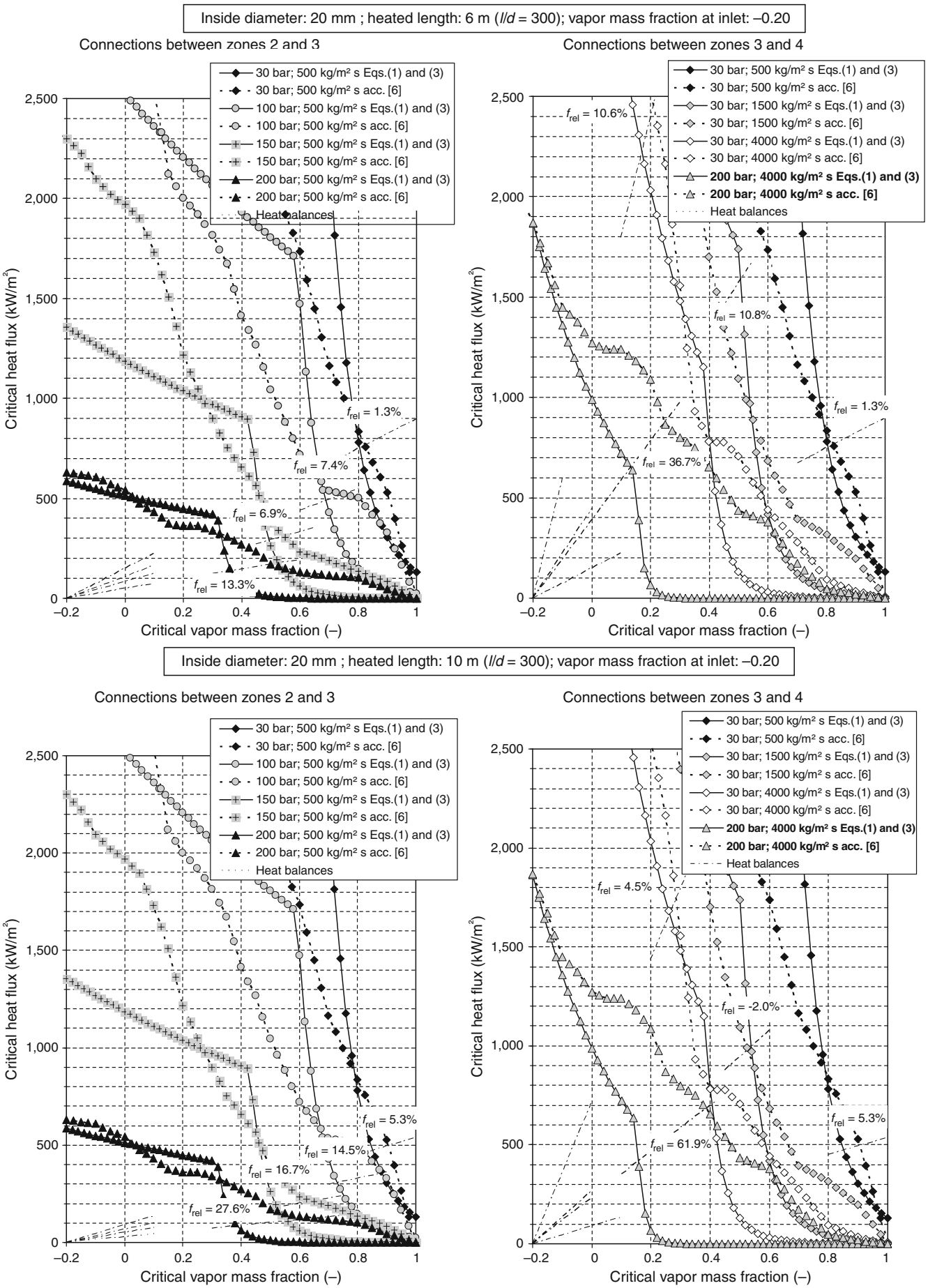

H3.5. Fig. 14. Transition between the individual zones.

Example 2

A straight vertical tube with an inner diameter of 12 mm and a length of 1.0 m is uniformly, electrically heated. Water flows through the tube at 300 kg/m^2 s, 0.3 MPa (3 bar) and $\vartheta_{inl} = 100°C$. At what heat flux does the boiling crisis occur?

The vapor mass fraction at the inlet $\dot{x}_{inl}$ is given by:

$$\dot{x}_{inl} = \frac{h_{inl} - h'}{\Delta h_v} = \frac{419.0 - 561.2}{2161.9} = -0.066.$$

In other words, the water is subcooled when it enters the tube. The critical heat flux at the upper end of the tube is determined below.

The relevant parameters are located in Zone 1 of Fig. 5. Hence, the critical heat flux can be extracted from Table 1 and converted for the actual diameter using Eq. (5a). The heated length to inner diameter ratio is given by:

$$\frac{l}{d} = \frac{1.0}{12 \cdot 10^{-3}} = 83.3 > 80$$

Equation (5b) must not be applied in this case because the ratio is greater than 80.

The critical heat flux is dependant upon the vapor mass fraction, which at the upper end of the tube is in turn dependant on the adjusted heat flux. Therefore, the solution can only be found using iteration. This is completed with the use of an energy balance:

$$\dot{q} \cdot \pi \cdot d \cdot l = \dot{m} \cdot \frac{\pi}{4} \cdot d^2 \cdot (\dot{x}_{out} - \dot{x}_{inl}) \cdot \Delta h_v,$$

solving for $\dot{x}_{out}$:

$$\dot{x}_{out} = \frac{\dot{q} \cdot 4 \cdot l}{\dot{m} \cdot d \cdot \Delta h_v} + \dot{x}_{inl}.$$

The vapor mass fraction at the tube outlet is determined for a range of heat fluxes. Values of the critical heat flux corresponding to these vapor mass fractions are then extracted from Table 1. For 3 bar, 300 kg/m^2 s and a vapor mass fraction of, for example, 0.4, a value of 1,636 kW/m^2 can be read from Table 1. Since $d < 25$ mm, this value is then converted to suit the actual diameter using Eq. (5a):

$$\dot{q}_{cr,d=12\text{ mm}} = \dot{q}_{cr,d=8\text{ mm}} \cdot \left(\frac{12}{8}\right)^{-0.5}$$
$$= 1636 \cdot 1.5^{-0.5}\ \text{kW/m}^2 = 1335.8\ \text{kW/m}^2$$

The following table of values is obtained by varying the value of the heat flux:

$\dot{q}$ (kW/m^2)	$\dot{x}_{out}$ (–)	$\dot{q}_{cr,d=8\text{ mm}}$ from Table 1 (kW/m^2)	$\dot{q}_{cr,d=12\text{ mm}}$ using Eq. (5a) (kW/m^2)
525	0.20	1,995	1628.9
625	0.26	1,895	1547.3
700	0.30	1,828	1492.6
800	0.35	1,771	1446.0
925	0.41	1,636	1335.8
1,000	0.45	1,494	1219.8
1,100	0.50	1,418	1157.8
1,131	0.52		1130.6[a]
1,300	0.60	1,203	982.2

[a]Interpolated

Plotted versus $\dot{x}_{out}$, the solution is located at the intersection of the energy balance line with $\dot{q}_{cr,d=12\text{ mm}}$:

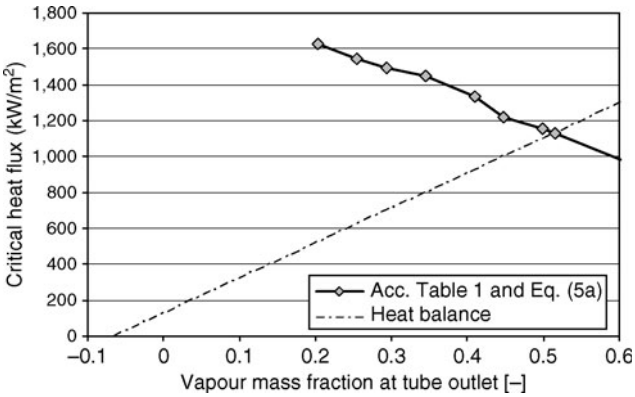

The critical heat flux is 1,131 kW/m^2.

2.1.2 Horizontal and Inclined Tubes

Owing to the phase separation caused by gravity, the vapor mass fractions at which the boiling crisis occurs are lower in horizontal and inclined tubes than they are in vertical tubes. In most cases, the crisis sets in at the crest of the tube while the lower wall remains wetted. An example of a temperature profile in a horizontal, uniformly heated evaporator tube is presented in Fig. 15. It differs from that in a vertical tube uniformly heated in the axial direction. In the vertical tube, the boiling crisis usually commences at the tube outlet and migrates upstream when more heat is applied. In the example shown in Fig. 15 for a horizontal tube, the boiling crisis already occurs at low vapor mass fractions and disappears again downstream. The incipient boiling crisis in this example can be explained by the transition from nucleate to stratified flow, in which case the crest of the tube may dry out.

As the vapor mass fraction and thus the rate of mixing increase, the crest of the tube is rewetted. This can be ascribed to a change from stratified to slug or annular flow. In the latter case, the film on the crest of the tube is thinner than that on the underside. Consequently, the dryout that results when the water film evaporates commences at the crest of the tube. As can be seen in Fig. 15, very large differences may exist between the vapor mass fractions at the first and last occurrences of the boiling crisis. The higher the ratio of the force of gravity to the forces applied during turbulent mixing, the greater the difference between flow in horizontal tubes to that in vertical tubes. The ratio increases if the specific mass flow rate is reduced or the tube diameter is increased. If the mass velocity is higher than 4,000–6,000 kg/m^2 s, the inclination of the tube no longer has any effect on the point at which the boiling crisis occurs.

Published comparisons between vertical and inclined tubes [9–12] are mostly based on measurements performed within a narrow range of parameters. Extensive measurements on evaporator tubes were made by Kefer [13]. The effect of the inclination of the tubes is described qualitatively in Fig. 16.

The following procedure is recommended for estimating the effect of inclination on the occurrence of the boiling crisis.

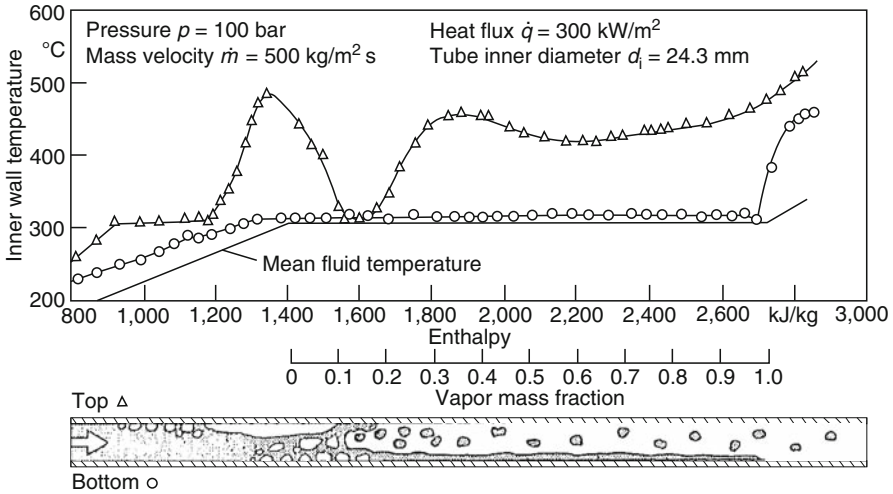

H3.5. Fig. 15. Effect of gravity on heat transfer in horizontal tubes.

It was derived from a suggestion by Wallis [87] to the effect that stratification during two-phase flow in a horizontal tube could be represented by a dimensionless group, in which the inertia force is the numerator and the buoyancy of the vapor is the denominator. Together with the vapor mass fraction $\dot{x}_{cr}$ at which the boiling crisis would occur in vertical tubes (cf. Sect. 2.1.1), this characteristic forms the following modified Froude number:

$$Fr = \frac{\dot{x}_{cr}\dot{m}}{\sqrt{gd(\varrho' - \varrho'')\cos\varphi}} \qquad (6)$$

where φ is the angle of inclination of the tube to the horizontal.

If the numerical value of Fr obtained from this equation is higher than $Fr = 10$, the angle of inclination of the tube has practically no effect on the boiling occurrence. Very pronounced stratification effects can be anticipated if $Fr < 3$. The boiling crisis occurs on the crest of horizontal tubes at very low vapor mass fractions, whereas the underside remains wetted until the liquid has almost completely evaporated.

According to Kefer [13], the difference between the critical vapor mass fraction at the crest and that at the underside of horizontal tubes can be determined with the aid of the modified Froude number defined by Eq. (6). The equation that he suggested is

$$\Delta\dot{x}_{cr} = \dot{x}_{cr,low} - \dot{x}_{cr,up} = \frac{16}{(2 + Fr)^2}. \qquad (7)$$

It has been checked that Eq. (7) covers the following ranges of parameters:

$$25 \le p \le 200 \text{ bar}$$
$$500 \le \dot{m} \le 2{,}500 \text{ kg/m}^2\text{s}$$
$$200 \le \dot{q} \le 600 \text{ kW/m}^2.$$

It can be seen from Fig. 17 that the figures calculated from Eq. (7) for various angles of inclination agree well with measured values. The diagram also shows that stratification effects become much more pronounced and that the measured values are more scattered if the value of Fr is reduced to below 4–5. For this reason, it is recommended that Froude numbers higher than $Fr = 10$ should be selected in order to avoid stratification.

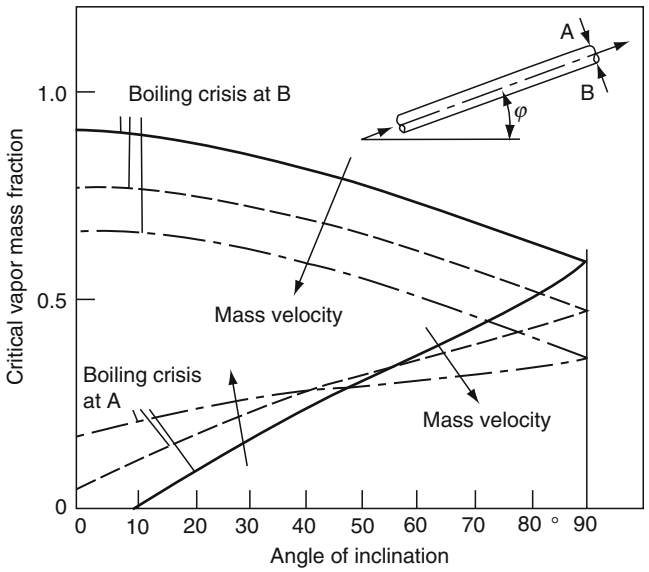

H3.5. Fig. 16. Effect of the angle of inclination on the critical vapor mass fraction.

Figure 18 shows that even better agreement can be obtained between the figures calculated from Eq. (7) and measured values. The improvement is achieved by inserting an average value for $\dot{x}_{cr}$ in Eq. (6) for the determination of the modified Froude number. The average in this case is that derived from the measured values for the critical vapor mass fractions responsible for dryout at the crest and underside respectively of the tube. In other words, the value inserted for $\dot{x}_{cr}$ in Eq. (6) can be regarded as the mean vapor mass fraction at which the crest and underside of the tube dry out. Thus, the critical vapor mass fractions in horizontal and inclined tubes are given by

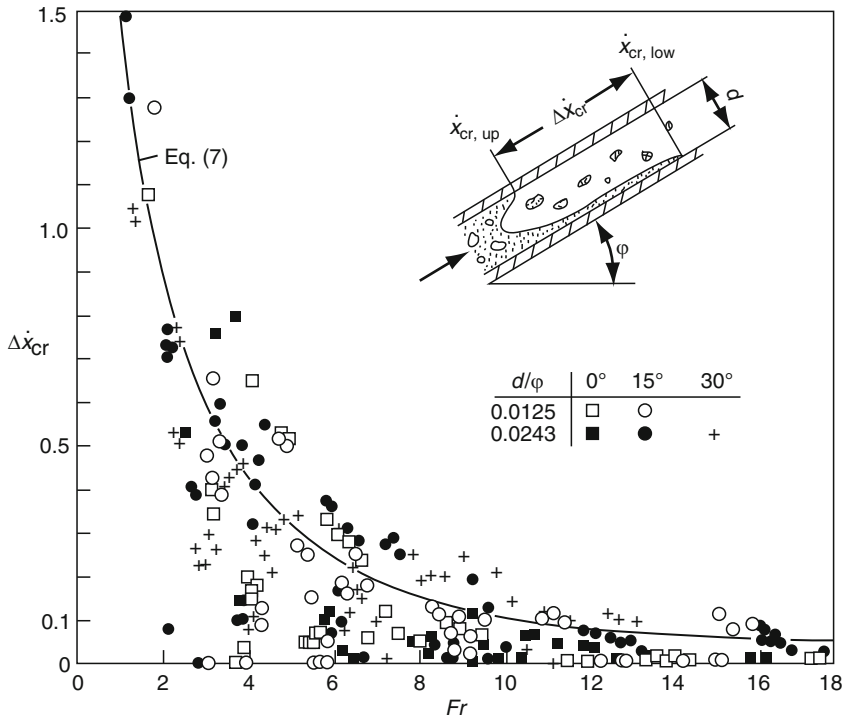

H3.5. Fig. 17. Difference between the critical vapor mass fraction during dryout on the crest and that during dryout on the underside of a horizontal or inclined tube {*Fr* calculated from Eq. (6) with values of $\dot{x}_{cr}$ obtained as described in Sect. 2.1.1}.

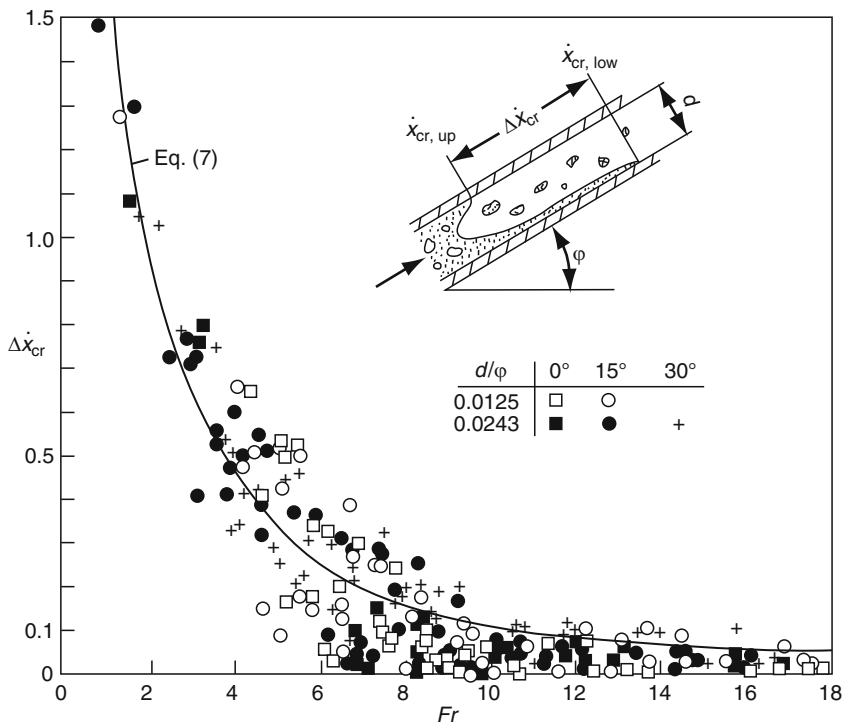

H3.5. Fig. 18. Difference between the critical vapor mass fraction during dryout on the crest and that during dryout on the underside of a horizontal or inclined tube {*Fr* calculated from Eq. (6) with values of $\dot{x}_{cr}$ obtained from measurements}.

$$\dot{x}_{cr,up} = \dot{x}_{cr} - \frac{\Delta\dot{x}_{cr}}{2},$$
$$\dot{x}_{cr,low} = \dot{x}_{cr} + \frac{\Delta\dot{x}_{cr}}{2}. \quad (8)$$

If the value calculated for $\dot{x}_{cr,low}$ is higher than unity, the figure to be taken is $\dot{x}_{cr,low} = 1$.

Initiation of the boiling crisis in horizontal tubes is associated with a slight rise in temperature, which is not the case

during flow through vertical tubes. One of the reasons for this lower increase is the flow of heat in the tube wall from the unwetted crest to the wetted underside.

Example 3

Determine the critical vapor mass fraction at the crest and underside of a horizontal evaporator tube through which water flows.

Parameters

Inner diameter of tube $d = 20 \cdot 10^{-3}$

Pressure $p = 150$ bar

Mass velocity $\dot{m} = 500$ kg/m^2 s

Heat flux $\dot{q} = 300$ kW/m^2

According to Fig. 6, the critical vapor mass fraction for upward flow through a vertical tube is $\dot{x}_{cr} = 0.49$. The densities for the vapor and the water at 150 bar are $\varrho'' = 96.71$ kg/m^3 and $\varrho' = 603.17$ kg/m^3 respectively.

The Froude number determined from Eq. (6) is

$$Fr = \frac{\dot{x}_{cr}\dot{m}/\sqrt{\varrho''}}{\sqrt{gd(\varrho' - \varrho'')\cos\varphi}} = \frac{0.49 \cdot 500/\sqrt{96.71}}{\sqrt{9.81 \cdot 20 \cdot 10^{-3}(603.17 - 96.71)1}} = 2.50.$$

The difference between the critical vapor mass fraction during dryout at the crest and that at the underside is obtained as follows from Eq. (7):

$$\Delta\dot{x}_{cr} = \frac{16}{(2 + Fr)^2} = \frac{16}{(2 + 2.50)^3} = 0.79.$$

Thus the critical vapor mass fractions during dryout at the crest and the underside respectively of the evaporator tube are obtained as follows from Eq. (8):

$$\dot{x}_{cr,up} = \dot{x}_{cr} - \frac{\Delta\dot{x}_{cr}}{2} = 0.49 - \frac{0.79}{2} = 0.095,$$

$$\dot{x}_{cr,low} = \dot{x}_{cr} + \frac{\Delta\dot{x}_{cr}}{2} = 0.49 + \frac{0.79}{2} = 0.885.$$

In this case, the boiling crisis at the crest occurs at very low vapor mass fractions, whereas the underside remains wetted until the liquid has almost completely evaporated.

2.1.3 Helical Coils

Flow patterns in coiled or bent tubes are formed by buoyancy, centrifugal forces, and secondary cross-flows caused by pressure gradients perpendicular to the main direction of flow. The boiling crisis is affected by separation effects that depend on the geometry of the helical coil. In analogy to the case in horizontal tubes (cf. Sect. 2.1.2), initial and final boiling crises, that is, first and last occurrences, can be observed.

It is demonstrated schematically in Fig. 19 that, at elevated operating pressures ($p > 100$ bar), the boiling crisis in a helical coil with a vertical axis is mainly influenced by the mass velocity. The centrifugal forces that arise at $\dot{m} > 850$ kg/m^3 s crowd the liquid toward the outside of the coil, and the boiling crisis occurs on the inside [14,60]. At low mass fluxes, the force of

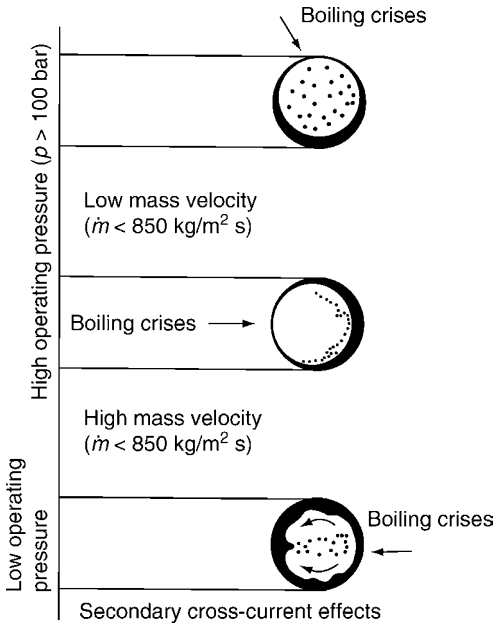

H3.5. Fig. 19. Location of the flow boiling crisis in coiled tubes [60].

gravity predominates, and the boiling crisis thus occurs initially at the upper end of the coil. At low operating pressures and high mass velocity, secondary cross-flows transport the liquid phase from the outside to the inside of the coil; in this case, the initial boiling crisis is mainly observed on the outside of the coil.

The boiling crisis in coiled tubes has not been the subject of many experimental and theoretical studies, and the data that can be found on the subject in the literature are scanty [14–23]. Ünal [14,20] performed experiments with the following operating parameters:

$$0.44 < p/p_c = p_r < 0.92,$$

$$100 \text{ kg/m}^2\text{s} < \dot{m} < 3{,}500 \text{ kg/m}^2\text{s},$$

$$0.08 < \dot{x}_{cr} < 1.0 \text{ and}$$

$$38 < D_w/d < 90.$$

He thus derived the following empirical correlation for the critical vapor mass fraction and the points in the coil at which it occurred:

$$\dot{x}_{cr} = 3.88 K_h K_p K_D K_\delta K_m + \dot{x}_{inl} \quad (9)$$

where

$$K_h = 1 + 3.8(1 - h_{inl}/h')$$

$$K_p = 0.114 - 0.041 \ln(1 - p_r)$$

$$K_D = 1 + 0.44 \exp(-0.056\, D_w/d)$$

(for the first boiling crisis)

$$K_D = 1 + 0.56 \exp(-0.011\, D_w/d)$$

(for the last boiling crisis)

$$K_\delta = \left(\frac{2\delta}{d}\right)^{0.32},$$

$$K_m = \frac{\left(\frac{l_{cr}}{d}\right) + 4.59\left(\frac{l_{cr}}{d}\right)^{-0.2}}{\left(\frac{l_{cr}}{d}\right) + 28 Fr^{0.44}}.$$

The location of the boiling crisis within the coil can be calculated from the heat balance, that is,

$$\frac{l_{cr}}{d} = \frac{\dot{m}\Delta h_v}{4\dot{q}}(\dot{x}_{cr} - \dot{x}_{inl}). \quad (10)$$

By definition, the Froude number is given by $Fr = \dot{m}/(\varrho'\sqrt{gd})$.

The critical vapor mass fraction $\dot{x}_{cr}$ at the point l_{cr} where the boiling crisis occurs is determined by iteration. The first approximations for $\dot{x}_{cr}$ and l_{cr} in the iteration can be obtained from Eqs. (9) and (10). It is evident from Eq. (9) that the effect of the factor D_w/d on $\dot{x}_{cr}$ can be neglected if $D_w/d > 40$.

Equation (9) is not valid for operating parameters in the following ranges:

$$p < 5 \text{ bar}$$
$$\dot{m} < 500 \text{ kg/m}^2\text{s}$$
$$80 < l/d < 250$$
$$10 < D_w/d < 20$$
$$-0.25 < \dot{x}_{inl} < 0,$$

An empirical equation that can be resorted to for calculating the final boiling crisis when these parameters apply is that derived by Babarin [22] and Alad'yev [23], that is,

$$\dot{q}_{cr} = k\left(\frac{\dot{m}}{l/d}\right)^{0.9}[1 + C_w(0.75 + \dot{x}_{inl})] \quad (11)$$

The numerical value of the factor k in this equation is 585 for water. The relationship between the factor C_w and the mass velocity $\dot{m}$ is shown in Fig. 20, which was plotted from the following points:

$\dot{m}$ (kg/m^2 s)	50–200	300	400	500
C_w	−0.660	0.395	0.925	1.270

Example 4

Water flows at a rate of 250 kg/m^2 s, a pressure of 0.3 MPa (3 bar), and a temperature of ϑ_{int} = 100°C through an electrically heated, coiled tube of 12 mm inner diameter and 1.0 m length. Determine the heat flux at which the boiling crisis occurs in the tube.

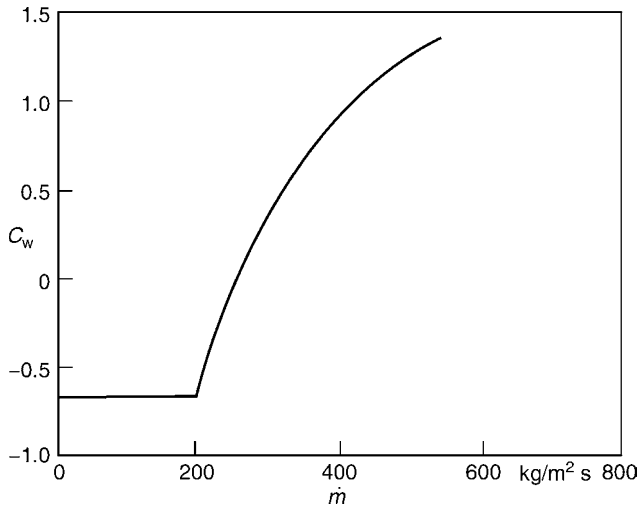

H3.5. Fig. 20. C_w factor in Eq. (11) as a function of the mass velocity $\dot{m}$.

The inlet vapor mass fraction is

$$\dot{x}_{inl} = \frac{h_{inl} - h'}{\Delta h_v} = \frac{419.0 - 561.2}{2161.9} = -0.066.$$

The critical heat flux, as determined from Eq. (11), is

$$\dot{q}_{cr} = 585\left(\frac{250}{83.3}\right)^{0.9}[1 - 0.06(0.75 - 0.066)] \text{ kW/m}^2$$
$$= 1{,}510 \text{ kW/m}^2.$$

Example 5

An evaporator heated by a helical coil is operated at a system pressure of 16.0 MPa (160 bar). The outer diameter of the coil is D_{wo} = 1.8 m; and the inner diameter, D_{wi} = 0.63 m. The outer diameter of the coiled tube is d_o = 0.022 m; and the inner diameter, d = 0.016 m. The water enters at a temperature of ϑ_{in} = 300°C and a mass velocity of $\dot{m}$ = 1,500 kg/m^2 s. It is assumed that the heat flux remains constant at $\dot{q}$ = 600 kW/m^2 over the entire length of the coil. Determine the location of the points at which the first and the last boiling crises occur within the inner and outer coils.

Applying Eq. (9) gives

$$K_h = 1 + 3.8\left(1 - \frac{1336.7}{1648.5}\right) = 1.719;$$

$$K_p = 0.114 - 0.041 \ln\left(1 - \frac{160}{221.3}\right) = 0.166;$$

$$K_\delta = \left(\frac{2 \cdot 0.003}{0.016}\right)^{0.32} = 0.731;$$

$$\dot{x}_{inl} = \frac{1336.7 - 1648.5}{929.9} = -0.335$$

$$Fr = \frac{1500}{583.8\sqrt{9.8065 \cdot 0.016}} = 6.486.$$

(a) Outer coil (D_{wo} = 1.8 m)

The following applies for the first boiling crisis:

$$K_D = 1 + 0.44 \exp\left(-0.056\frac{1.8}{0.016}\right) = 1.0008 \approx 1.0;$$

and the following applies for the last boiling crisis:

$$K_D = 1 + 0.56 \exp\left(-0.011\frac{1.8}{0.016}\right) = 1.162.$$

As a first approximation, $\dot{x}_{cr}$ = 0.4. Applying Eq. (10) gives

$$l_{cr} = \frac{1500 \cdot 929.9}{4 \cdot 600}(0.4 + 0.335) = 427.2.$$

The next step is to determine K_m. Thus

$$K_m = \frac{427.2 + 4.59(427.2)^{-0.2}}{427.2 + 28 \cdot 6.486^{0.44}} = 0.873.$$

It then follows from Eq. (9) that

$$x_{cr} = 3.88 \cdot 1.719 \cdot 0.166 \cdot 1 \cdot 0.731 \cdot 0.873 - 0.335 = 0.372.$$

Repeating the calculation with $\dot{x}_{cr} = 0.37$ gives

$$\dot{x}_{cr} = 0.367; \quad l_{cr} = 6.53 \text{ m}.$$

Determination of the final boiling crisis

A value of $\dot{x}_{cr} = 0.367 \cdot 1.162/1.0 \approx 0.43$ is taken as a first approximation for the iteration, and the calculation then proceeds in the same way as that for the first boiling crisis. Thus

$$\frac{l_{cr}}{d} = \frac{1500 \cdot 929.9}{4 \cdot 600}(0.43 + 0.335) = 444.6;$$

$$K_m = \frac{444.6 + 4.59(444.6)^{-0.2}}{444.6 + 28 \cdot 6.486^{0.44}} = 0.877;$$

$\dot{x}_{cr} = 3.88 \cdot 1.719 \cdot 0.166 \cdot 1.162 \cdot 0.731 \cdot 0.877 - 0.335 = 0.49$. The calculation is repeated with the new value for the critical vapor mass fraction, and the following is obtained after two iteration stages:

$$\dot{x}_{cr} = 0.478; \quad l_{cr} = 7.75 \text{ m}.$$

(b) Inner coil ($D_w = 0.63$ m)

The procedure for determining the first boiling crisis is similar to that adopted under heading (a) for the outer coil. Thus

$$K_D = 1 + 0.44 \exp\left(-0.056 \cdot \frac{0.63}{0.016}\right) = 1.048.$$

Likewise, for the final boiling crisis,

$$K_D = 1 + 0.56 \exp\left(-0.011 \cdot \frac{0.63}{0.016}\right) = 1.363.$$

Determination of the first boiling crisis

In view of the results obtained for the outer coil, the first approximation to be taken for the iteration is $\dot{x}_{cr} = 0.367 \cdot 1.048 = 0.38$, and the desired root is again obtained in two stages, that is,

$$\dot{x}_{cr} = 0.385; \quad l_{cr} = 6.88 \text{ m}.$$

Determination of the final boiling crisis

The first approximation made in this case is

$$\dot{x}_{cr} = 0.478 \cdot \frac{1.363}{1.162} \approx 0.56.$$

The following figures are obtained after three stages in the iteration:

$$\dot{x}_{cr} = 0.640; \quad l_{cr} = 9.25 \text{ m}.$$

For the purpose of the calculation, the pressure drop in the coil is neglected. The values for the properties of the fluid can be referred to the system pressure of 16.0 MPa.

2.1.4 Effect of Nonuniform Heating

Nonuniform Heating in the Circumferential Direction

If evaporator tubes are heated by radiation on the one side, a roughly cosinusoidal profile can be assumed for the heat flux on the inside of the tube, as is shown in Fig. 21. The maximum heat flux at the commencement of the boiling crisis is greater than that for the case of uniform heating, but the average value, that is, the transmittable heat flux, is less. A model that was devised by Butterworth [24] and is illustrated in Fig. 22 allows the effect of nonuniform heating on the critical heat flux to be determined.

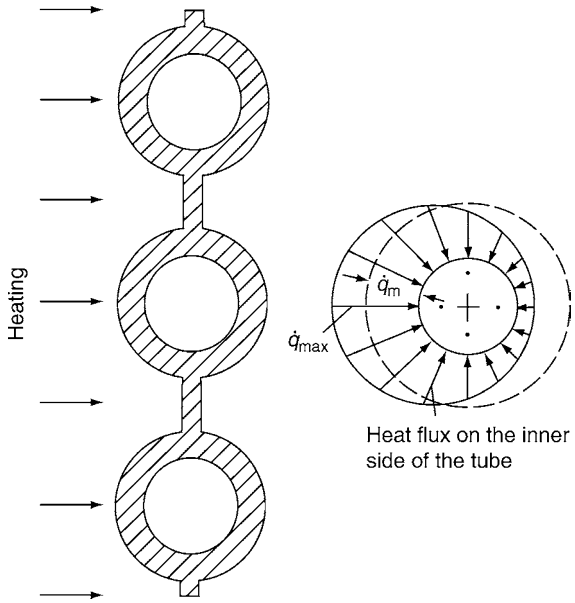

H3.5. Fig. 21. Distribution of heat flux inside a tube heated on the one side.

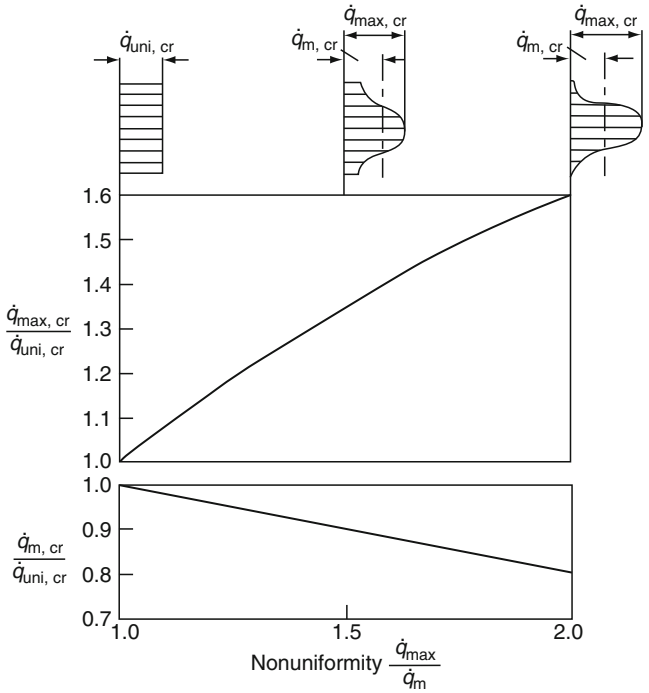

H3.5. Fig. 22. Effect of nonuniformity on the average and maximum critical heat fluxes expressed as a function of the critical heat flux under conditions of uniform heating.

Nonuniform Axial Heating

The axial heat applied to a cooling medium is often nonuniform. In this case, the occurrence of the boiling crisis may be governed solely by the local parameters (a case referred to as the local conditions hypothesis). An additional factor that is inherent in the heating system is its memory effect, which depends on the nature of the heat applied and on the pressure, the mass flux, and the vapor mass flux fraction.

As a general rule, local parameters suffice for determining the boiling crisis in the subcooled regime, for example, under the conditions in pressurized water reactors, and the memory effect in the heating system is a significant factor in regimes with high vapor mass fractions, for example, steam generators. Nonuniform axial heating causes water droplets to be detached from the film on the wall under conditions that differ from those encountered in uniform heating. As a consequence, dryout of the liquid film on the wall may, in turn, be influenced [25–29].

(a) Local conditions hypothesis

The assumption made in the local conditions hypothesis is that the boiling crisis in tubes with nonuniform axial heating occurs at the same combination of local heat flux and local vapor mass fraction as it does in tubes with uniform axial heating.

A heat flux profile that can be assessed by the local conditions hypothesis is shown in Fig. 23. Here, the critical heat flux at a given point B would be exceeded if the combination of the local heat flux $\dot{q}_B$ and the local vapor mass fraction $\dot{x}_B$ were to give rise to a boiling crisis in a uniformly heated tube, that is, if $\dot{q}_B > \dot{q}_{cr,B}$.

This is not the case in the example shown. Even if the point B were to be placed in other positions, the local heat flux would be less than the value calculated by the method described in Sect. 2.1.1. It is evident from Fig. 23 that the margin of safety against critical boiling depends greatly on the axial position in the flow channel.

(b) Integral power hypothesis

In the integral power hypothesis, it is assumed that the power that must be applied in a tube with nonuniform axial heating before the boiling crisis is reached is the same as that applied in a uniformly heated tube.

Figure 24 shows a heat flux profile that can be assessed by the integral power hypothesis. If the combination of the mean heat flux $\dot{q}_{m,\,AB}$ and the local vapor mass fraction $\dot{x}_B$ were to cause a boiling crisis in a uniformly heated tube, that is, if $\dot{q}_{m,\,AB} > \dot{q}_{cr,\,B}$, the boiling crisis in the nonuniformly heated tube would occur between the points A and B. This is not the case in the example shown. However, the margin of safety against critical boiling is less than that determined by the local conditions hypothesis.

The point of reference A that is frequently selected for the commencement of the regime investigated is that at which the liquid reaches saturation. In this case, the section AB is referred to as the "boiling length."

When the critical heat flux is calculated by both methods, the smaller of the two values obtained should be taken. If the maximum power lies within the zone at the commencement of the heated section, the integral power hypothesis should be applied; and if it lies at the end of the heated section, the local conditions hypothesis should be applied.

2.2 Complex Geometries

2.2.1 Annular Channels

A cross section through an annular channel is shown in Fig. 25. Heat may be applied in three different ways, that is,

- Through the wall of the outer tube (inner diameter d_o).
- Through the wall of the inner tube (inner diameter d).
- Through the walls of both tubes.

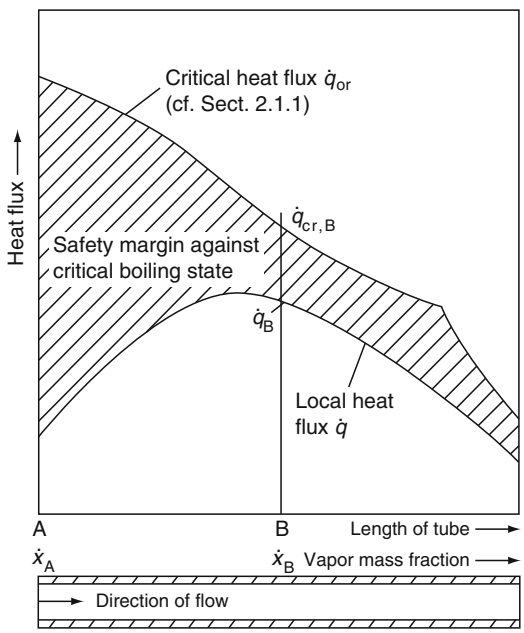

H3.5. Fig. 23. Determination of the boiling crisis by the local conditions hypothesis.

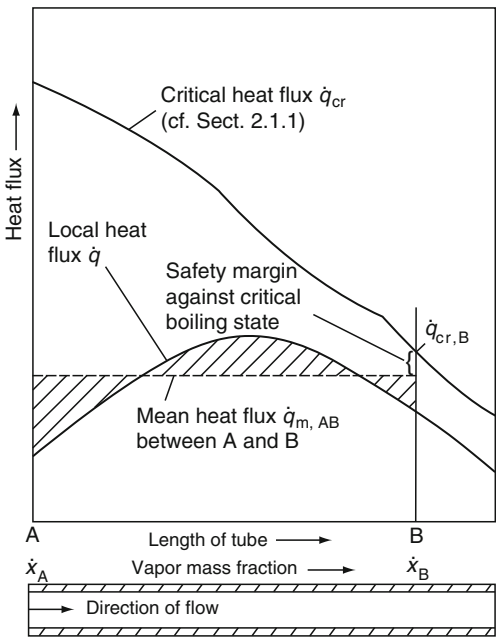

H3.5. Fig. 24. Determination of the boiling crisis by the integral power hypothesis.

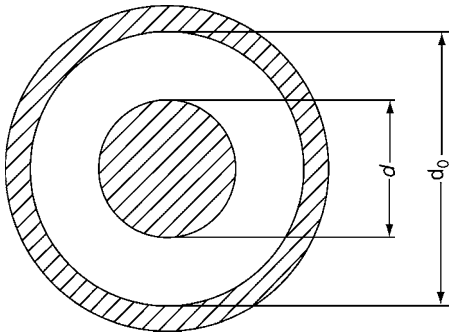

H3.5. Fig. 25. Cross section through annular channel.

Heat Applied through the Wall of the Outer Tube

In this case, the critical heat flux $\dot{q}_{cr}$ or the critical vapor mass fraction $\dot{x}_{cr,o}$ can be determined as a first approximation by inserting the diameter of the outer tube in the equations given in Sect. 2.1.1.

Example 6

Water flows at a pressure of 70 bar and a mass velocity $\dot{m}$ = 1,000 kg/m^2 s through an annular gap ($d_o = 21.3 \cdot 10^{-3}$ m, $d = 12 \cdot 10^{-3}$ m and a heated length of 3 m). If the inlet temperature ϑ_{inl} = 275.8°C and the outer tube is uniformly heated axially, what is the maximum rate at which heat can be fed $\dot{Q}_{act}$ without the occurrence of critical boiling? What would happen if the mass velocity were to be increased to $\dot{m}$ = 4,000 kg/m^2 s?

The following figures can be read off against 70 bar in steam tables:

$$h' = 1267.4 \text{ kJ/kg}$$
$$\Delta h_v = 1506.0 \text{ kJ/kg}$$
$$h_{inl} = 1217.4 \text{ kJ/kg}.$$

The heat flux is obtained from the energy balance, that is,

$$\dot{q} = \frac{(d_o^2 - d^2)\dot{m}\Delta h_v}{4 d_o l}\left(\dot{x}_{cr,o} - \dot{x}_{inl}\right),$$
$$\dot{x}_{inl} = (h_{inl} - h')/\Delta h_v = -0.035.$$

If d_o is substituted for d in Eq. (4) and if $\dot{x}_{cr,o}$ = 0.5 (from Fig. 8) is taken as the first approximation in the iteration, the following will be obtained in a few stages:

$$\dot{q}_{cr} = 1{,}066 \text{ kW/m}^2 \quad \text{and} \quad \dot{x}_{cr,o} = 0.549.$$

It can be seen from Fig. 8 that the value to be determined from Eq. (1) is $\dot{q}_{cr} > 1{,}066$ kW/m^2 and thus that the conditions for critical boiling are not reached.

If a standard deviation of $\Delta x = 0.1$ for the measured values is laid down as a safety measure [2], the figures finally obtained are

$$\dot{x}_{max} = 0.549 - 0.1 = 0.449 \quad \text{and} \quad \dot{q}_{max} = 883.1 \text{ kW/m}^2.$$

The maximum rate of heat flow through the annulus is

$$\dot{Q}_{act} = 883.1 \cdot 21.3 \cdot 10^{-3}\pi \cdot 3 \text{ kW} = 177.3 \text{ kW}.$$

Inserting $\dot{m}$ = 4,000 kg/m^{2}s for the mass velocity in Eq. (4) gives

$$\dot{q}_{cr} = 2{,}524 \text{ kW/m}^2 \quad \text{and} \quad \dot{x}_{cr,o} = 0.311.$$

As can be seen from Fig. 11, $\dot{q}_{cr} < 2{,}500$ kW/m^2 if $\dot{x}_{cr,o}$ = 0.311. Therefore, the critical data must be determined from Eq. (1). Since the energy balance and Eq. (1) conform for $\dot{q}_{cr}$ = 1,653 kW/m^2 and $\dot{x}_{cr,o}$ = 0.191, these values represent the conditions for the occurrence of critical boiling.

If a standard deviation of 16% for the measured values is laid down as a safety measure [2], the following figures are obtained:

$$\dot{q}_{max} = 1{,}653(1 - 0.16) = 1{,}388 \text{ kW/m}^2$$
$$\dot{x}_{max} = 0.155.$$

Hence the peak value of the power that can be transmitted through the annular gap is

$$\dot{Q}_{act} = 1{,}388 \cdot 21.3 \cdot 10^{-3}\pi \cdot 3 \text{ kW} = 278.6 \text{ kW}.$$

Heat Applied through the Wall of the Inner Tube

The critical heat fluxes $\dot{q}_{cr}$ that apply if heat is transmitted only through the inner wall of the annulus do not differ from those that occur if the outer wall is heated. Therefore, in the cases in which Eq. (1) or Eq. (2) is valid, the characteristic diameter for the determination of $\dot{q}_{cr}$ is $d = d_o$.

If Eq. (3) or Eq. (4) is adopted, $\dot{x}_{cr,o}$ must also be determined for $d = d_o$ first of all. The critical vapor mass fraction $\dot{x}_{cr,i}$ that applies for the case in which the inner tube of the annulus is heated is then obtained by multiplying $\dot{x}_{cr,o}$ by the diameter ratio d/d_o, that is,

$$\dot{x}_{cr,i} = \dot{x}_{cr,o}\frac{d}{d_o}. \tag{12}$$

In each case, the "poorer" of the results obtained by the two methods is taken.

Example 7

Under the conditions quoted in Example 6, what is the rate of heat flow $\dot{Q}_{act}$ if the inner and not the outer tube is heated?

The energy balance for the heat flux yields

$$\dot{q} = \frac{(d_o^2 - d^2)\dot{m}\Delta h_v}{4dl}\left(\dot{x}_{cr,i} - \dot{x}_{inl}\right),$$
$$\dot{x}_{inl} = \frac{(h_{inl} - h')}{\Delta h_v},$$
$$\dot{x}_{cr,i} = \frac{d}{d_a}\dot{x}_{cr,o},$$

If d_o is substituted for d in Eq. (4) and if $\dot{x}_{cr,o}$ = 0.5 is taken as the first approximation in the iteration (as in Example 6), the following will be obtained in a few stages:

$$\dot{q}_{cr} = 1{,}111 \text{ kW/m}^2, \ \dot{x}_{cr,o} = 0.546, \text{ and } \dot{x}_{cr,i} = 0.308.$$

It is immediately evident from Fig. 8 that critical boiling, as defined by Eq. (1), does not occur under these conditions. If a standard deviation of Δx = 0.1 for the measured values is laid down as a safety measure [2], the following values are obtained:

$$\dot{x}_{max,o} = 0.546 - 0.1 = 0.446$$
$$\dot{x}_{max,i} = 12/21.3 \cdot 0.046 = 0.251$$
$$\dot{q}_{max} = 927.2 \text{ kW/m}^2.$$

The peak value of the power that can be transmitted through the annular gap is

$$\dot{Q}_{act} = 927.2 \cdot 12 \cdot 10^{-3}\pi \cdot 3 \text{ kW} = 104.9 \text{ kW}.$$

The method indicated by Eqs. (4) and (12) initially yields the following results for a mass velocity of $\dot{m} = 4{,}000$ kg/m^2 s:

$$\dot{q}_{cr} = 2{,}703 \text{ kW/m}^2,\ \dot{x}_{cr,o} = 0.308, \text{ and } \dot{x}_{cr,i} = 0.174.$$

These figures are higher than those calculated from Eq. (1), namely,

$$\dot{q}_{cr} = 2{,}502 \text{ kW/m}^2 \text{ and } \dot{x}_{cr,i} = 0.123.$$

If a standard deviation of 16% is laid down for the measured values as a safeguard [2], the following values are obtained:

$$\dot{q}_{max} = 2{,}052(1 - 0.16) \text{ kW/m}^2 = 1{,}724 \text{ kW/m}^2$$
$$\dot{x}_{max,i} = 0.098.$$

Thus the maximum rate at which heat can be transmitted through the annular gap is

$$\dot{Q}_{act} = 1724 \cdot 12 \cdot 10^{-3}\pi \cdot 3 \text{ kW} = 195 \text{ kW}.$$

Heat Applied through Both Walls

In Fig. 26, the critical vapor mass fraction $\dot{x}_{cr}$, as determined from measurements by Becker and Letzter [30], has been plotted against the ratio y of the power fed through the wall of the outer tube to the total power fed, that is, $y = \dot{Q}_o/(\dot{Q}_o + \dot{Q}_i)$. Values for $\dot{x}_{cr}$ determined in the previous sections have been included in the diagram, namely, those for heat fed solely through the wall of the outer tube ($y = 1$; symbol ▲) and those for heat fed solely through the wall of the inner tube ($y = 0$; symbol •). The agreement with the measured values for the boundary case is good.

If heat is applied through the walls of both the inner and outer tubes, the experimental results (Fig. 26) can be closely approximated by considering the critical vapor mass fraction to be constant in the $0.8 < y \leq 1.0$ range and by equating $\dot{x}_{cr} = \dot{x}_{cr,o}$. In the $0 < y \leq 0.8$ range, $\dot{x}_{cr}$ can be obtained by linear interpolation from $\dot{x}_{cr,i}$ and $\dot{x}_{cr,o}$.

The power peak that can be fed to the annular channel is given by

$$\dot{Q}_{act} = (\dot{x}_{cr} - \dot{x}_{inl})\Delta h_v \dot{m} f. \tag{13}$$

The heat flux transferred from the outer tube is

$$\dot{q}_o = \frac{y\dot{Q}_{act}}{\pi d_o l}; \tag{14}$$

and that transferred from the inner tube is

$$\dot{q}_i = \frac{(1.0 - y)\dot{Q}_{act}}{\pi d l}. \tag{15}$$

Example 8

Under the conditions quoted in Example 6, what is the maximum power $\dot{Q}_{act}$ that can be fed to the annulus if both tube walls are heated? The outer tube supplies 60% of the power.

If the selected safeguards are taken into consideration, the critical vapor mass fractions corresponding to $\dot{m} = 1{,}000$ kg/m^{2}s are

in Example 6, $\dot{x}_{cr,o} = 0.449$

in Example 7, $\dot{x}_{cr,i} = 0.251$.

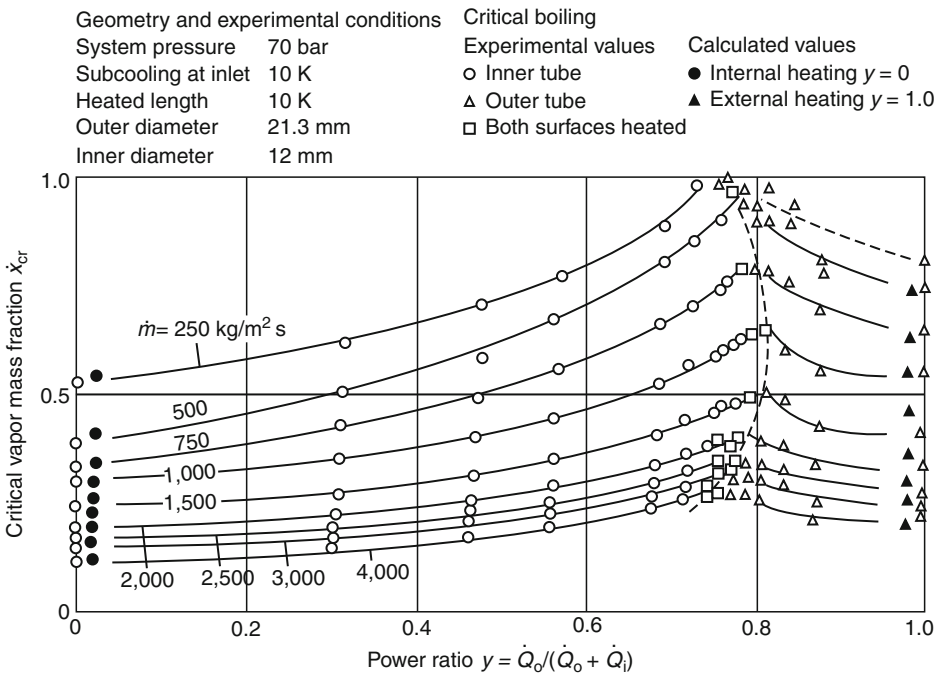

H3.5. Fig. 26. Critical vapor mass fraction in an annular channel as a function of the ratio of the power applied to the outer tube to the total power [30].

The cross sectional area of the annulus is

$$A = \pi/4(d_o^2 - d^2) = \pi(21.3^2 - 12^2)10^{-6}\ \mathrm{m}^2 = 2.43 \cdot 10^{-4}\ \mathrm{m}^2.$$

Since $y < 0.8$, $\dot{x}_{cr}$ is obtained by interpolation, that is,

$$\dot{x}_{cr} = \left(\frac{\dot{x}_{cr,o} - \dot{x}_{cr.i}}{0.8}\right)0.6 + \dot{x}_{cr,i} = 0.400$$

The power peak that can be transmitted is given by Eq. (13), that is,

$$\dot{Q}_{act} = (0.400 + 0.035)1506 \cdot 1{,}000 \cdot 2.43 \cdot 10^{-4}\ \mathrm{kW} = 159.3\ \mathrm{kW}.$$

The heat flux from the outer tube is given by Eq. (14), that is,

$$\dot{q}_o = \frac{0.6 \cdot 159.3}{\pi \cdot 21.3 \cdot 10^{-3} \cdot 3}\ \mathrm{kW/m^2} = 476\ \mathrm{kW/m^2}.$$

The heat flux from the inner tube is given by Eq. (15), that is,

$$\dot{q}_i = \frac{0.4 \cdot 159.3}{\pi \cdot 12 \cdot 10^{-3} \cdot 3}\ \mathrm{kW/m^2} = 563\ \mathrm{kW/m^2}.$$

If the selected safeguards are taken into consideration, the critical vapor mass fractions corresponding to $\dot{m} = 4{,}000\ \mathrm{kg/m^2 s}$ are

in Example 6, $\dot{x}_{cr,o} = 0.155$

in Example 7, $\dot{x}_{cr,i} = 0.098$.

$$\dot{x}_{cr} = \left(\frac{\dot{x}_{cr,o} - \dot{x}_{cr,i}}{0.8}\right)0.6 + \dot{x}_{cr.i} = 0.141.$$

The power peak that can be transmitted is given by Eq. (13), that is,

$$\dot{Q}_{act} = (0.141 + 0.035) \cdot 1506 \cdot 4{,}000 \cdot 2.43 \cdot 10^{-4}\ \mathrm{kW} = 257.6\ \mathrm{kW}.$$

The heat flux from the outer tube is given by Eq. (14), that is,

$$\dot{q}_o = \frac{0.6 \cdot 257.6}{\pi \cdot 21.3 \cdot 10^{-3} \cdot 3}\ \mathrm{kW/m^2} = 770\ \mathrm{kW/m^2}.$$

The heat flux from the inner tube is given by Eq. (15), that is,

$$\dot{q}_1 = \frac{0.4 \cdot 257.6}{\pi \cdot 12 \cdot 10^{-3} \cdot 3}\ \mathrm{kW/m^2} = 911\ \mathrm{kW/m^2}.$$

2.2.2 Axial Rod Bundles

General

The thermohydraulic conditions that relate to axial flow within multirod clusters permit a greater degree of freedom in the geometry and the heating system than the conditions that apply to flow through tubes. Cheng and Müller have conducted a review of the relevant effects [31]. In the first place, the cross-sectional area available for flow between the heated rods may vary; and, in the second place, the heat flux may differ from the one rod to another. As a result, there will always be a zone within rod clusters that is particularly threatened by the occurrence of critical boiling.

These threatened zones can generally occur at high heat and low mass fluxes. The conditions in the cooling medium are often determined by subchannel analysis with the aid of a computer program [32–40]. These methods, in common with those adopted for flow through tubes, are mostly based on the local conditions hypothesis, but resort is occasionally taken to the integral power hypothesis (cf. Sect. 2.1.4).

The procedure described below permits safety margins for boiling crises to be approximately determined without a computer [41].

The first point to note is that the occurrence of the critical boiling state depends on local conditions in the cooling medium, for example, the local vapor mass fraction $\dot{x}$ or degree of subcooling, the local mass velocity $\dot{m}$, and the pressure p. It does not depend on the system variables, for example, the temperature at the inlet to the rod cluster or the length l of the cluster. If the ratio of the distance between spacers t and the wetted hydraulic diameter d_h is sufficiently large, that is, $t/d_h > 20$, the experimental determination can be regarded as reliable, or at least for the film-boiling regime. Controversy still exists on the application of this method to the dryout of heater surfaces.

Another requirement is to express axial flow through the bundle in terms of flow through an equivalent tube. For this purpose, it is assumed that the rods are arranged in groups of four so that the lines drawn through their centers form a rectangular grid. The flow channels can then be regarded as the circles inscribed within the individual squares of the grid, as is illustrated in Fig. 27; and the equivalent tube consists of the four rod quadrants that form the corners of each square and are pieced together as is shown in the diagram.

The critical heat flux can also be influenced by the spacers within the rod bundle. The pressure drop caused by the spacers must be as small as possible, and the following requirements are imposed on the rectangular grid formed by the rods in order to obviate critical boiling.

- The ratio of the flow cross section to the area of the surface of the heated tube must remain constant.
- The rods must be uniformly arranged, and protuberant fittings such as spring attachments must be as small as possible.
- Springs and protuberances should preferably be located in the narrow gap between the heated tubes.

Uniform design of the rod bundle cross section and spacers is of great importance in avoiding boiling crises, because weak points will adversely affect the performance of the entire assembly.

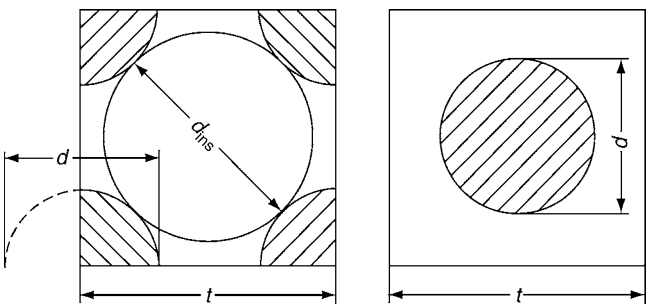

H3.5. Fig. 27. Basic element in flow around the outside of a multirod cluster. t, spacing in square grid; d, outer diameter of the equivalent tube; d_{ins}, diameter of the inscribed circle.

If spacers are sufficiently well designed to have no influence on the occurrence of the critical boiling state, the equations and diagrams presented in Sect. 2.1.1 for upward flow through vertical tubes can also be applied to flow along the vertical axis of a multirod cluster assembly. For this purpose, the inlet parameters must be modified as described below.

Inlet Parameters

Mass velocity $\dot{m}_j$

(a) Equation (16) applies if all the subchannels (subscript j) consist of identical elements and conform to Fig. 27:

$$\dot{m}_j = \dot{m}_m = \frac{\dot{M}}{A} \tag{16}$$

where

$\dot{M}$ is the total mass flow rate through the tube bundle

A is the total cross sectional area through which the medium flows

(b) If the bundle is nonuniformly heated in the radial direction, for example, if the heater rating for each tube differs or if the cooling channels have different hydraulic diameters, the assumption of equal pressure drops in parallel channels gives rise to the following equation:

$$\dot{m}_j = \dot{m}_m \frac{\sqrt{\frac{d_{h,j}}{\Phi_j^2}}}{\sum_{j=1}^{n} \sqrt{\frac{d_{h,j}}{\Phi_j^2}} \frac{A_j}{A}} \tag{17}$$

where

A_j is the cross sectional area of the subchannel

$U_{wet,\,j}$ is the wetted periphery of the subchannel

$d_{h,\,j}$ is the wetted hydraulic diameter $= 4A_j/U_{wet,\,j}$

Φ_j^2 is the two-phase multiplier expressed as the average over the heated length of tube (cf. Subchap. H3.2)

n is the number of parallel channels

The vapor mass fraction $\dot{x}$ is given by

$$\dot{x}_j = \frac{h_{inl} - h' + \Delta h_j}{\Delta h_v}. \tag{18}$$

(a) If the heating is the same in all the tubes and the hydraulic diameters are the same in all the subchannels j, the enthalpy difference is given by

$$\Delta h_j = \Delta h_m = \frac{\dot{q}_m U_{htd} l}{\dot{m}_m f}. \tag{19}$$

(b) Equation (20) applies for tube bundles that are nonuniformly heated in the radial direction and/or have different hydraulic diameters:

$$\Delta h_j = \Delta h_m \left[\left(\frac{\dot{q}_j}{\dot{q}_m} \frac{(U_{htd}/f)_j}{(U_{htd}/f)_m} \frac{\dot{m}_m}{\dot{m}_j} - 1 \right) \psi + 1 \right]. \tag{20}$$

The term $\dot{m}_m/\dot{m}_j$ is calculated from Eq. (17).

The geometry of the system ($U_{htd}/A; \dot{m}_m/\dot{m}_j$) and the heating parameters ($\dot{q}_j/\dot{q}_m; \dot{m}_m/\dot{m}_j$) give rise to differences in the rate at which the medium is heated up. The extent to which these differences are phased out by admixture with the coolant is expressed by the factor ψ, which depends on the design of the spacers. Under normal conditions, values in the $0.65 < \psi < 0.75$ range can be taken for spacers in tube bundles with a ratio $t/d \approx 1.3$ (where t is the bar spacing as illustrated in Fig. 27). Values of down to $\psi = 0.35$ at $t/d \approx 1.3$ can also be reached in unsaturated bulk flow ($\dot{x}_j < 0$) by fitting the spacers with devices that promote turbulence. If the vapor mass fraction is positive, that is, $\dot{x}_j > 0$, these devices must be designed so that they do not interfere with the film of water on the heated surfaces and thus give rise to a premature boiling crisis. Otherwise, the gain that could be anticipated from better mixing ($\dot{x}_j < 0$) would be annulled by the increased accumulation of liquid droplets ($\dot{x}_j > 0$).

Tube Diameter *d*

The characteristic length that is mostly suggested in the literature is similar to that adopted in the determination of pressure drop, that is, the wetted hydraulic diameter d_h. In some instances, the only means of calculating the recommended hydraulic diameter is based on the heated peripheries, but this assumption could lead to errors, as in the case of annular gaps. If the rods are arranged to form a regular square grid, much better results are obtained by selecting the diameter of the largest inscribed circle d_{ins} (cf. Fig. 27) as the reference magnitude in the $8 \cdot 10^{-3} \le d_{ins} \le 30 \cdot 10^{-3}$ range. The diameter d_{ins} of the circle inscribed in a square grid is obtained from the rod spacing t and the rod diameter d, that is,

$$d_{ins} = t\sqrt{2} - d. \tag{21}$$

If the rods are very closely spaced or arranged to form a hexagonal grid or if the pressure is less than 100 bar, Eq. (21) should be treated with reserve.

Uniform Axial Heating

Avoidance of film boiling

The method for determining the critical heat flux $\dot{q}_{cr,j}$ for each subchannel j in a cluster with uniform axial heating is that described in Sect. 2.1.1:

$$\dot{q}_{cr,j} = \dot{q}_{cr}(p, \dot{m}_j, d_j, \dot{x}_j). \tag{22}$$

The factor that decides whether or not film boiling will occur is the minimum ratio of the critical heat flux $q_{cr,j}$ to the maximum heat flux $\dot{q}_j$ on the heated surface of channel K, that is,

$$\left(\frac{\dot{q}_{cr}}{\dot{q}}\right)_K = \min\left(\frac{\dot{q}_{cr,j}}{\dot{q}_j}\right). \tag{23}$$

The term $(\dot{q}_{cr}/\dot{q})_K$ must be substantially higher than 1.0 if film boiling is to be avoided.

According to Drescher and Köhler [2], the standard deviation of figures determined by Eq. (1) from the values measured in flow through tubes is 16%.

Avoidance of dryout

The critical vapor mass fraction $\dot{x}_{cr,j}$ in each subchannel j is determined by the method described in Sect. 2.1.1:

$$\dot{x}_{\mathrm{cr,j}} = \dot{x}_{\mathrm{cr}}(p, \dot{m}_{\mathrm{j}}, \dot{q}_{\mathrm{j}}). \tag{24}$$

The limiting value that decides whether or not the heated surfaces will dry out is the minimum difference between the critical vapor mass fraction and the actual vapor mass fraction in the channel K, that is,

$$\Delta\dot{x}_{\mathrm{K}} = \min(\dot{x}_{\mathrm{cr,j}} - \dot{x}_{\mathrm{j}}). \tag{25}$$

If dryout is to be prevented, the term $\Delta\dot{x}_{\mathrm{K}}$ must be significantly greater than zero. Drescher and Köhler [2] submitted a figure of 0.10 for the standard deviation from the difference between calculated and measured values of the vapor mass fraction in flow through tubes. For this reason, $\Delta\dot{x}_{\mathrm{K}} > 0.10$ is recommended.

Nonuniform Axial Heating

The method that has been described for nonuniform axial heating is to divide the tube bundle up into sections, in each of which the heating is constant. The minima defined by Eqs. (23) and (25) indicate the margins that separate the conditions from those in critical boiling.

Special Cases

If no measurements are available for the grid selected, care must be exercised in evaluating the results obtained by the above methods. This applies particularly if

- Great differences exist in the spacing within the bundle.
- The nonuniformity of the axial power distribution is very pronounced.
- The surfaces in the subchannel illustrated in Fig. 27 are unheated or are heated to very different extents (cf. Sect. 2.2.1).
- The system pressure is low, that is, $p < 50$ bar, and the vapor mass fraction is positive. In this case, the likelihood of unstable flow within the bundle cannot always be excluded, even if acceptable results are obtained from Eqs. (23) and (25). As a consequence of the instability, the boiling crisis may occur [42].
- If the design of the spacers leaves room for doubt (cf. Sect. 2.2.1).

Example 9

The 5 × 5 rod cluster illustrated in Fig. 28 is subjected to uniform axial heating. The diameter of the rods is $10.8 \cdot 10^{-3}$, the spacing is $14.3 \cdot 10^{-3}$, and the heated length is 2.985 m; the rods are accommodated in a square housing of $77 \cdot 10^{-3}$ m side. Water flows through the assembly at a pressure of 160 bar, an inlet temperature of 296.0°C, and an average mass flux of 3,660 kg/m^2 s. The power ratios $\dot{q}_{\mathrm{j}}/\dot{q}_{\mathrm{m}}$ for the rods are

6 rods – mean value · 1.1800
19 rods – mean value · 0.9432.

If the power rating for the cluster is $\dot{Q}_{\mathrm{act}} = 3{,}750$, can the likelihood of a boiling crisis be excluded?

The types of channel and the geometries are listed in Table 2.

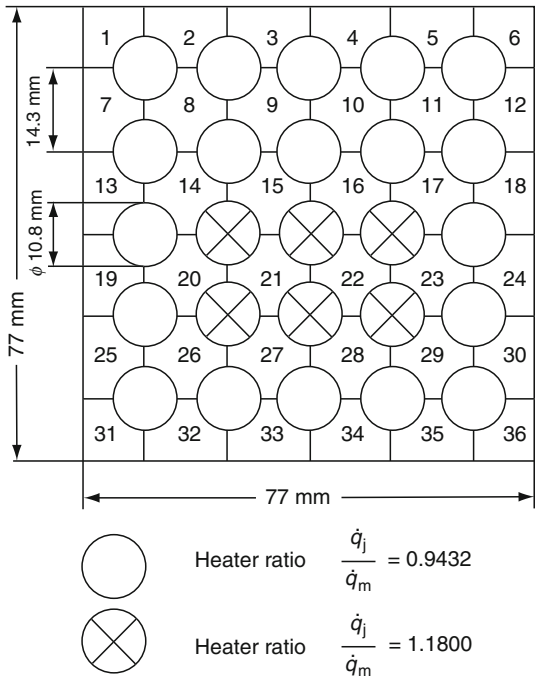

H3.5. Fig. 28. Cross section through a 5 × 5 rod bundle.

H3.5. Table 2. Types of channel and their geometry

Channel number in Fig. 28		No.	Wetted hydraulic diameter (10^{-3} m)	Heated periphery (10^{-3} m)	Area (10^{-6}) m²
I	1, 6, 31, 36	4	10.62	8.48	75.11
II	2, 3, 4, 5, 7, 12, 13, 18, 19, 24, 25, 30, 32, 33, 34, 35	16	12.25	16.96	95.77
III	8, 9, 10, 11	4	13.3	33.93	112.88
IV	14, 17, 26, 29	4	13.3	33.93	112.88
V	15, 16, 20, 23, 27, 28	6	13.3	33.93	112.88
VI	21, 22	2	13.3	33.93	112.88
		36		848.16	3638.84

The diameter d_{ins} of the inscribed circle depicted in Fig. 27 is

$$d_{\mathrm{ins}} = \left(\sqrt{2} \cdot 14.3 \cdot 10^{-3} - 10.8 \cdot 10^{-3}\right) \mathrm{m} = 9.42 \cdot 10^{-3} \mathrm{m}.$$

The mean heat flux is

$$\dot{q}_{\mathrm{m}} = \frac{3{,}750}{25 \cdot \pi \cdot 10.8 \cdot 10^{-3} \cdot 2.985} \mathrm{kW/m^2} = 1{,}481 \mathrm{kW/m^2}.$$

The mean enthalpy difference, as determined from Eq. (19), is

$$\Delta h_{\mathrm{m}} = \frac{3{,}750}{3{,}660 \cdot 3638.84 \cdot 10^{-6}} \mathrm{kJ/kg} = 281.6 \mathrm{kJ/kg}.$$

If $\Phi_j^2 = 1$ in Eq. (17),

$$\sum_{j=1}^{n} \frac{f_j}{f} \sqrt{d_{h,j}} = 0.112(\mathrm{m})^{1/2}.$$

The results of the following steps in the calculation are entered in Table 3.

The following figures can be read off against 160 bar in steam tables:

$$h' = 1650.5 \text{ kJ/kg}$$
$$\Delta h_v = 934.3 \text{ kJ/kg}$$
$$h_{inl} = 1316.0 \text{ kJ/kg}.$$

Table 4 lists the parameters that have been calculated from these variables and inserted in Eq. (18) and that are required for the determination of critical boiling by means of Eqs. (1) and (4).

The correlation for $\dot{x}_j$ is

$$\dot{x}_j = \frac{\Delta h_m}{\Delta h_v} \left(\frac{\Delta h_j}{\Delta h_m} \right) + \dot{x}_{inl}.$$

Since the vapor fractions $\dot{x}_j$ are small, there is no need to correct the two-phase multiplier Φ^2, which was initially assumed to be $\Phi^2 = 1$. If higher values of $\dot{x}_j$ occur, the ratio $\dot{m}_j/\dot{m}_m$ must be corrected by iteration.

Values obtained from Eqs. (22) and (24) are listed in Table 5. The figures listed in the $\dot{q}_{max,j}$ column represent the maximum heat flux in each type of channel. The minimum value is obtained from Eq. (23). Thus

$$\left(\frac{\dot{q}_{cr}}{\dot{q}} \right)_{v1} = \frac{1{,}883}{1{,}748} = 1.077.$$

The lowest value $\dot{q}_{cr}/\dot{q} = 1.077$ in the cluster lies within the standard deviation of 16% for measurements performed on tubes [2]. Hence the possibility of film boiling cannot be entirely excluded. Although the critical heat flux of 1,883 kW/m^2 is higher than the heat flux actually applied, that is, 1,748 kW/m^2, the safety margin of 135 kW/m^2 does not suffice to cover the range of scatter of the measurements [2]. In this case, the remedy would be to reduce the heat input or the inlet temperature or to increase the mass flux.

The minimum value determined from Eq. (25) is

$$\Delta \dot{x}_{v1} = 0.196 - 0.0453 = 0.151.$$

In this case, therefore, the likelihood of dryout can be excluded.

H3.5. Table 3. Values for $\psi = 0.7$, $\Phi = 1.0$, and the geometric parameters in Eqs. (17) and (20)

Type of channel	No.	$\dot{q}_j/\dot{q}_m$	$\frac{(U_{htd}/f)_j}{(U_{htd}/f)_m}$	$\dot{m}_j/\dot{m}_m$	$\Delta h_j/\Delta h_m$
I	4	0.9432	0.484	0.917	0.648
II	16	0.9432	0.760	0.985	0.809
III	4	0.9432	1.289	1.026	1.129
IV	4	1.0024	1.289	1.026	1.182
V	6	1.0616	1.289	1.026	1.234
VI	2	1.18	1.289	1.026	1.338

H3.5. Table 4. Parameters for the determination of critical boiling state

Type of channel	$\dot{x}_j$	$\dot{m}_j$(kg/m^2 s)	$d_{ins,j}$ (10^{-3} m)
I	−0.162	3356	9.42
II	−0.114	3,606	9.42
III	−0.0177	3,755	9.42
IV	−0.0017	3,755	9.42
V	0.0139	3,755	9.42
VI	0.0453	3,755	9.42

3 Flow of Other Liquids

3.1 Pure Liquids

3.1.1 Upward or Downward Flow in Vertical Tubes

Subcooled or Saturated Liquids at the Tube Inlet

According to Katto and Ohno [43], the critical heat flux during upward flow in uniformly heated, vertical tubes can be determined from the following equation:

$$\dot{q}_{cr} = \dot{q}_{cr,n}(1 - K\dot{x}_{inl}) \quad (26)$$

where $\dot{q}_{cr,o}$ is the critical heat flux for liquid that is saturated when it enters the flow channel; $\dot{x}_{inl} = (h_{inl} - h_s)/\Delta h_v$ is the vapor mass fraction at the inlet cross section of the tube; in this case, h_s is the saturation enthalpy corresponding to the pressure at the tube inlet, h_{inl} is the enthalpy of the liquid, and Δh_v is the enthalpy of vaporization; K is the subcooling parameter.

Equation (26) is not valid unless the liquid in the tube inlet is subcooled ($\dot{x}_{inl} < 0$) or – in the limiting case – barely saturated. A different mathematical approach is required if the liquid does contain vapor when it enters the tube, but this will be dealt with at a later stage.

Data obtained in measurements on R 12 [43] are presented graphically in Fig. 29 as an example. They verify the linear relationship expressed by Eq. (26) between $\dot{q}_{cr}$ and the extent of subcooling for a constant mass velocity $\dot{m}$ and a given pressure p. The only cases in which pronounced departures from the linear relationship normally occur [44] arise if the liquid velocity is low ($u_1 < 0.2$–0.3 m/s) at the inlet to short tubes or if the vapor mass fraction at the tube outlet does not differ significantly from zero, that is, $\dot{x}_{cr} \approx 0$. Other cases of departure from a

H3.5. Table 5. Values obtained from Eqs. (22) and (24)

Type of channel	$\dot{q}_{cr,j}$ (kW/m^2)	$\dot{q}_{max,j}$(kW/m^2)	$\dot{x}_{cr,j}$
I	3,428	1,397	0.210
II	3,046	1,397	0.205
III	2,293	1,397	0.202
IV	2,182	1,748	0.196
V	2,080	1,748	0.196
VI	1,883	1,748	0.196

linear relationship were observed in experiments that were performed at high pressures and very high mass velocities, for example, $\dot{m} > 3{,}800$ kg/m^2 s, on R 12 in tubes of 1,000 mm length, and 3 and 5 mm diameter [45].

Equations (27–41) allow $\dot{q}_{cr,o}$ and K to be determined. The ranges of parameters within which they are valid are discussed in the following section.

$$q_1^* = C(\sigma^*)^{0.043}\frac{1}{\ell^*} \tag{27}$$

$$q_2^* = 0.1(0^*)^{0.133}(\sigma^*)^{1/3}\frac{1}{1+0.0031\ell^*} \tag{28}$$

$$q_3^* = 0,098(\varrho^*)^{0.133}(\sigma^*)^{0.433}\frac{(\ell^*)^{0.27}}{1+0.0031\ell^*} \tag{29}$$

$$q_4^* = 0.234(\varrho^*)^{0.513}(\sigma^*)^{0.433}\frac{(\ell^*)^{0.27}}{1+0.0031\ell^*} \tag{30}$$

$$q_5^* = 0.0384(\varrho^*)^{0.6}(\sigma^*)^{0.173}\frac{1}{1+0.28(\sigma^*)^{0.233}\ell^*} \tag{31}$$

The dimensionless quantities in Eqs. (27–31) are defined as follows:

$$q_1^* = \frac{\dot{q}_{cr,o}}{\dot{m}\Delta h_v} \tag{32}$$

$$\sigma^* = \frac{\sigma\varrho_\ell}{\dot{m}^2\ell} \tag{33}$$

$$\ell^* = \frac{\ell}{d} \tag{34}$$

$$\varrho^* - \frac{\varrho_z}{\varrho_\ell}. \tag{35}$$

The subscript i in Eq. (32) represents the subscripts 1–5 in Eqs. (27–31). The significance of the symbols in Eqs. (27–35) is as follows: $\dot{m}$ mass velocity; σ surface tension; ϱ_g and ϱ_l density of the gas/vapor and the liquid; l heated length of tube; and d inner diameter of tube.

All the values for the properties of the fluid must be referred to the saturation temperature corresponding to the inlet pressure.

The following applies for the dimensionless parameter C in Eq. (27):

$$C = 0.25 \text{ for } \ell^* < 50; \tag{36}$$

$$C = 0.25 + 9\cdot 10^{-4}(\ell^* - 50) \text{ for } \ell^* \text{ for } \ell^* = 50{-}150; \tag{37}$$

$$C = 0.34 \text{ for } \ell^* > 150. \tag{38}$$

Measured values of $\dot{q}_{cr,o}$ for Refrigerant R 12 [43] are compared in dimensionless form with figures calculated from Eqs. (27–38) in Fig. 30. A corresponding diagram in which values measured at a lower pressure by Groeneveld [46] are compared with the calculations is presented in Fig. 31.

Equations (39–41) allow the subcooling parameter K to be expressed in terms of the quantities defined by Eqs. (33–35) and in terms of the parameter C {Eqs. (36–38)}. The choice of equation depends on the range of parameters involved.

$$K_1 = \frac{1.043}{4C(c^*)^{0.043}} \tag{39}$$

$$K_2 = \frac{5}{6}\cdot\frac{0.0124 + 1/\ell^*}{(\varrho^*)^{0.130}(\sigma^*)^{1/3}} \tag{40}$$

$$K_3 = 1.12\cdot\frac{1.52(\sigma^*)^{0.223} + 1/\ell^*}{(\varrho^*)^{0.6}(\sigma^*)^{0.173}} \tag{41}$$

A comparison of figures calculated from Eqs. (39–41) with values obtained by measurement on R 12 [43] is presented in Fig. 32. The measured values plotted were determined from the slopes of the curves that are reproduced in Fig. 29 and that fit Eq. (26).

An idea of the accuracy of Eqs. (39–41) can be obtained from Figs. 33 and 34, in which the calculated values are compared with measurements performed by various authors on some refrigerants.

Ranges of Validity for the Equations

The ranges of the parameters within which Eqs. (27–41) are valid are reviewed in Figs. 30–33, and rules for their delimitation are

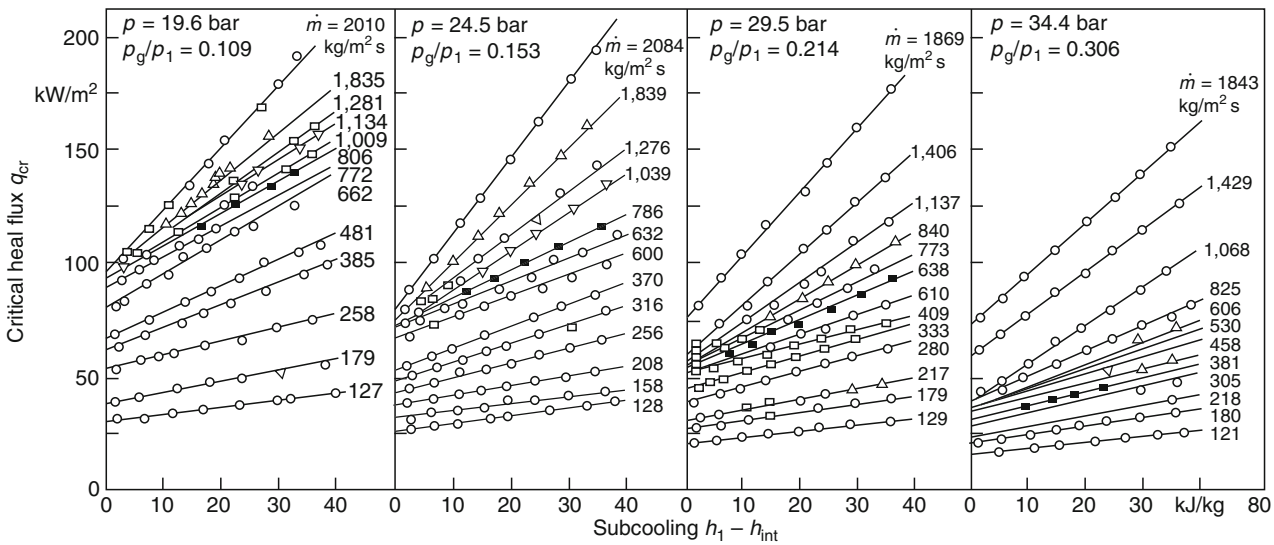

H3.5. Fig. 29. Measured values of the critical heat flux $\dot{q}_{cr}$ for R 12 (d = 0.01 m; ℓ/d = 100) [43].

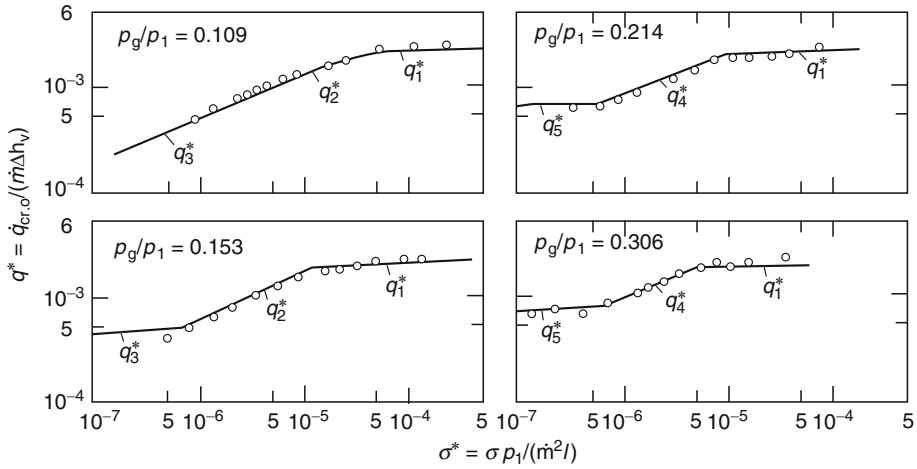

H3.5. Fig. 30. Comparison between values measured on R 12 and figures calculated from Eqs. (27) and (35) for q_i^* (i = 1–5; d = 0.01 m; ℓ/d = 100) [43].

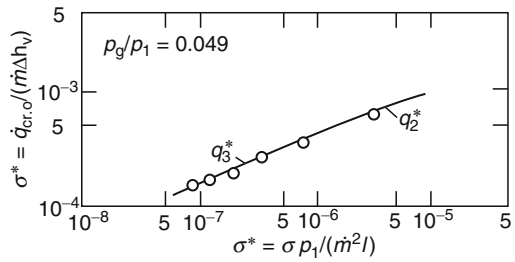

H3.5. Fig. 31. Comparison between values measured on R 12 and figures calculated from Eqs. (28), (29), and (32–35) for q_2^* and q_3^* (d = 7.8 mm; ℓ/d = 176.9) [46].

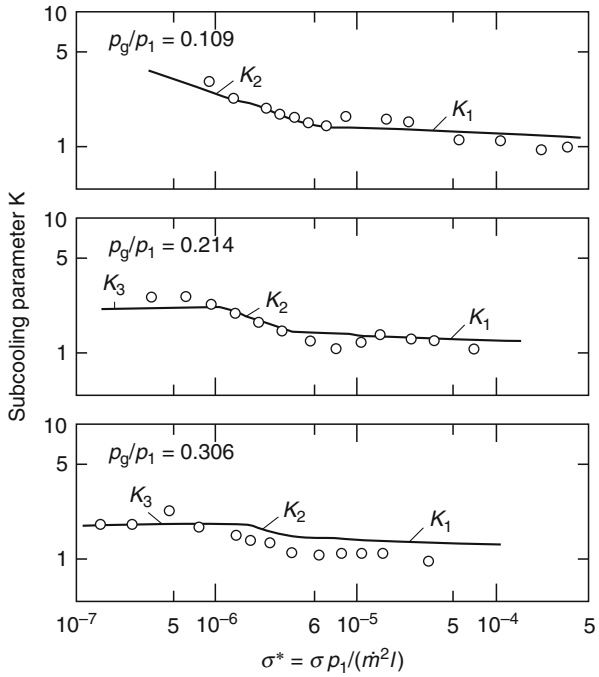

H3.5. Fig. 32. Comparison between values measured on R 12 and figures calculated from Eqs. (39) and (41) for the subcooling parameter K_i (i = 1–3; d = 0.01 m; ℓ/d = 100) [43].

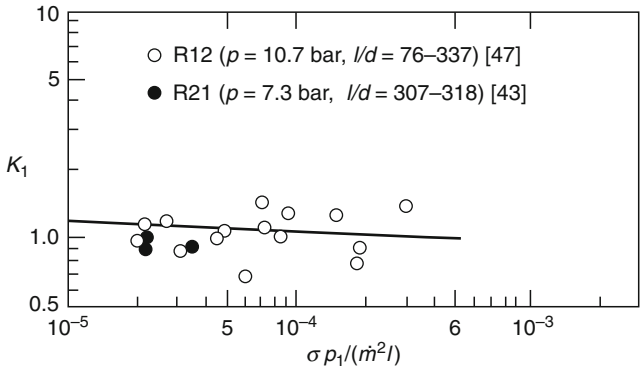

H3.5. Fig. 33. Comparison between measured values and figures calculated from Eq. (39) for the subcooling parameter K_1.

submitted below. A distinction is drawn between two pressure ranges, each represented by a pressure ratio.

(a) Determination of the critical heat flux for

$$\varrho^* = \left(\frac{\varrho_\ell}{\varrho_\ell}\right) \leq 0.15$$

In this range, the following rule applies to the calculation of $\dot{q}_{cr}$ by means of Eqs. (27–29):

$$\begin{aligned} q_1^* \leq q_2^* : &\quad q^* = q_1^* \\ q_1^* > q_2^* : &\quad q_2^* \leq q_3^* \rightarrow q^* = q_1^*, \\ &\quad q_2^* > q_3^* \rightarrow q* = q_3^*. \end{aligned}$$

The associated values for the subcooling parameter K are determined as follows from Eqs. (39) and (40):

$$\begin{aligned} K_1 \geq K_2 : &\quad K = K_1, \\ K_1 < K_2 : &\quad K = K_2. \end{aligned}$$

(b) Determination of the critical heat flux for

$$\varrho^* = (\varrho_\ell/\varrho_\ell) > 0.15.$$

For this range, Eqs. (27), (30), and (31) are applied as follows:

$$\begin{aligned} q_1^* \le q_4^* : &\quad q^* = q_1^*, \\ q_4^* > q_4^* : &\quad q_4^* \ge q_5^* \rightarrow q^* = q_4^*, \\ &\quad q_4^* < q_5^* \rightarrow q^* = q_5^*. \end{aligned}$$

The following rule applies to the determination of the subcooling parameter K from Eqs. (39–41):

$$\begin{aligned} K_1 \ge K_2 : &\quad K = K_1, \\ K_1 < K_2 : &\quad K_2 \le K_3 \rightarrow K = K_2, \\ &\quad K_2 > K_3 \rightarrow K = K_3. \end{aligned}$$

Critical Vapor Mass Fraction

The critical vapor mass fraction is derived from an energy balance. Thus

$$\dot{x}_{cr} = \frac{4\dot{q}_{cr}}{\dot{m}\Delta h_V}\frac{\ell}{d} + \dot{x}_{inl}. \qquad (42)$$

If critical boiling occurs at the end of the heated section, the value to be inserted for ℓ in Eq. (42) is the total length. Otherwise, it is the length of the section up to the occurrence of the boiling crisis.

Comparison with Measured Data

Equations (26–41) were developed from a dimensional analysis [47] and were reconciled with numerous values obtained from measurements by various authors [43–55]. The substances on which the measurements were performed were R 12, R 21, R 22, R 113, R 114, hydrogen, nitrogen, and helium (I). As a rule, only the measured values for the critical heat flux $\dot{q}_{cr,\,o}$ referred to $\dot{x}_{inl}$ were adopted for reconciliation and comparison. In most cases, the agreement between the measured values and the values of q^* calculated from Eqs. (27–31) was satisfactory.

Calculated and measured values of $\dot{q}_{cr}$ for various fluids are compared in Figs. 35 and 36, in order to impart an idea on the reliability of Eq. (27), which is more generally valid and in which an allowance has been made for any subcooling that might occur in the inlet cross section.

Figure 35 presents the values measured on halocarbon refrigerants. A total of 2,046 measurements was taken from six different data banks to check the *Katto* and *Ohno* correlation. It must be noted that the data were not selected from the standpoint of their reliability. Space considerations precluded the inclusion of some of the measured values with a tolerance of ±20% in this diagram. In view of the wide range of parameters embraced by the data investigated, the agreement between the measurements and the calculations must be regarded as very good.

The corresponding comparison for helium (I), hydrogen, nitrogen, potassium, and ammonia is presented in Fig. 36. Five data banks with a total of 438 measured values were available. The data were not selected any further. The overwhelming majority of the measured values lay within a tolerance of ±30%. In this case, too, not enough space was available to allow all of the data to be entered in the diagram. The values of $\dot{q}_{cr}$ represented range from about 10^{-1}–10^4 kW/m^2, and the main system parameters in some cases were varied within wide limits.

The refrigerants (CFCs, HCFCs) used in Fig. 35 to test the reliability of Katto/Ohno's method are now (CFCs) or soon (HCFCs) only allowed for research purposes. They are forbidden for practical application because of their ozone depletion potential. Test with refrigerants allowed for practical application (HFCs) show a similar reliability as those used in Fig. 35. This holds also for nonfluorocarbon refrigerants which are not used for the reliability test in Fig. 36 namely, e.g., propane, butane, and CO_2. The conclusion that can thus be drawn is that the Katto/Ohno method is very reliable for nonaqueous fluids.

Restrictions on the Validity

Under the following conditions, the mathematical method described in Sect. 3.1.1 does not yield reliable values; or, at least, it is not adequately supported by data derived from measurements.

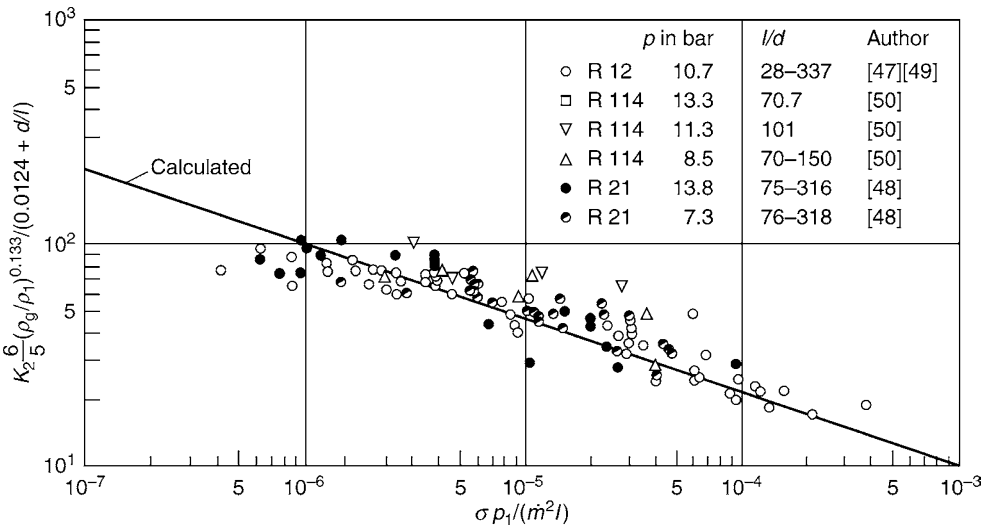

H3.5. Fig. 34. Comparison between measured values and figures calculated from Eq. (40) for the subcooling parameter K_2.

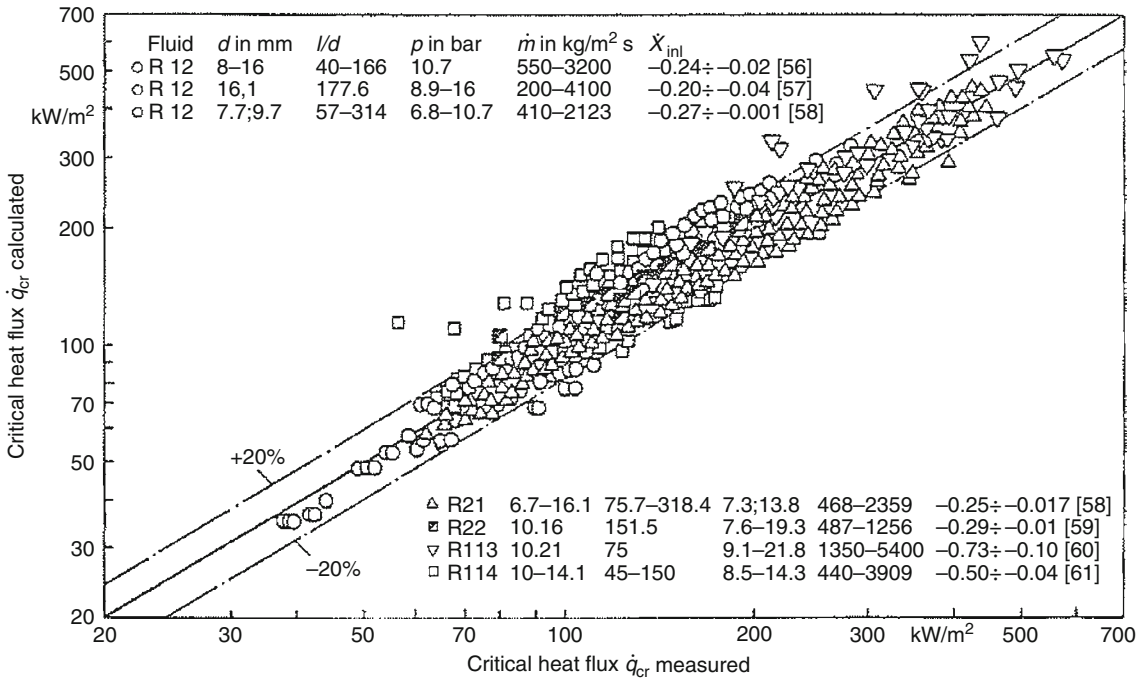

H3.5. Fig. 35. Comparison between measured values and figures calculated by the *Katto/Ohno* method for the critical heat flux of fluorocarbon refrigerants.

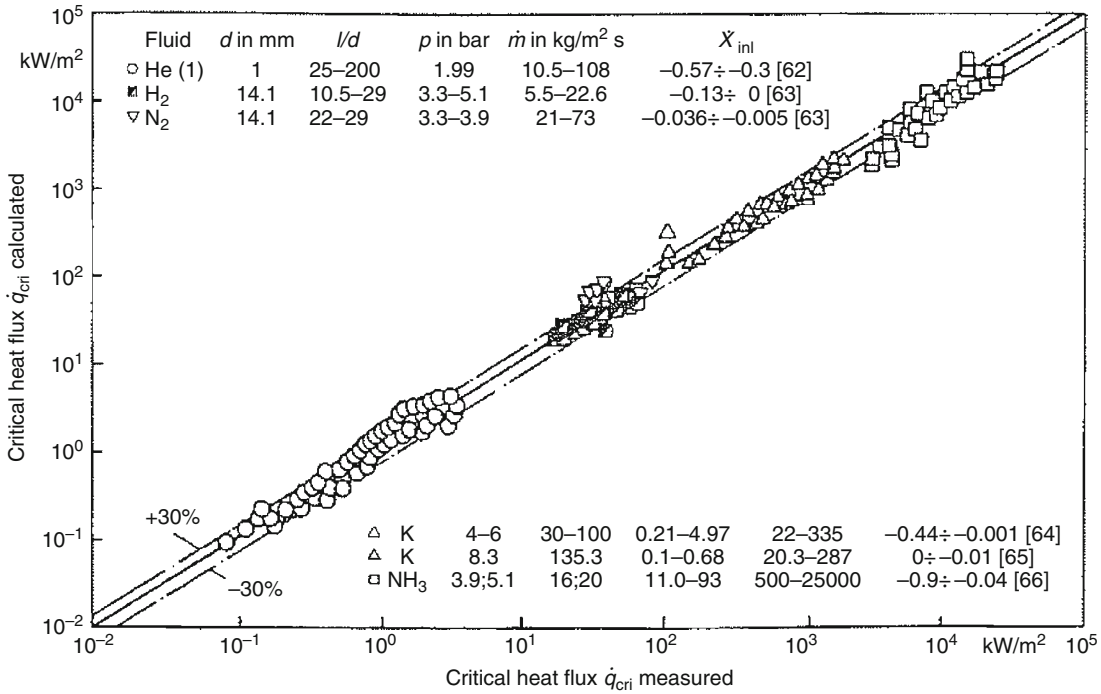

H3.5. Fig. 36. Comparison between measured values and figures calculated by the *Katto/Ohno* method for the critical heat flux for helium (I), hydrogen, nitrogen, potassium, and ammonia.

- The system is instable. If there are fluctuations in the pressure or the mass flux, the boiling crisis may occur at considerably smaller heat fluxes.
- The vapor mass fraction at the tube inlet is greater than zero ($\dot{x}_{inl} > 0$). In this case, the method presented in Sect. 2.1.1 should be chosen; it can be applied to other fluids by the *Ahmad* procedure, which is described in the last part of Sect. 3.1. Although some of the data plotted in Fig. 36 apply to $\dot{x}_{inl} > 0$, they fit the correlation just as accurately as the other measured values. Further measurements are required to determine whether this finding applies in general.

- The vapor mass fraction at the end of the heated section is less than zero ($\dot{x}_{cr} < 0$). This situation may arise in short lengths of tube if the mass flux is high and subcooling occurs. In this case, too, the method described in Sect. 2.1.1 should be adopted and modified by the *Ahmad* procedure when appropriate. Attention is drawn to the fact that the values plotted for R 113 in Fig. 35 and those plotted for ammonia in Fig. 36 mostly correspond to a negative $\dot{x}_{cr}$. Here, too, it would appear that the *Katto/Ohno* yields reliable results. However, the general validity of this statement must continue to be questioned until more measured values become available for comparison.
- If the length-to-diameter ratio of the tube is very large ($\ell/d > 600$), Eqs. (28) and (29) no longer yield reliable results. Again, preference should be given to the method given in Sect. 2.1.1 and by *Ahmad*.

Downward Flow through Tubes

The effect exerted by the direction of flow on the critical heat flux has been studied by Cumo et al. [67], and the results that they obtained on Refrigerant R 12 are presented in Fig. 37. On an average, the values determined for upward flow are 11% higher than those for downward flow. Equation (27) yields results that correspond comparatively accurately with the measured values in the $\dot{m}$ = 120–325 kg/m^2 s range; and the values of $\dot{q}_{cr,o}$ calculated from Eq. (28) are somewhat too high in the $\dot{m}$ = 503–1,043 kg/m^2 s range. An explanation for this phenomenon has been offered by Katto [44]. On the whole, the results obtained by Eqs. (26–41) correspond well to all the measured values (Figs. 35 and 36). Consequently, there is no point in modifying Eq. (28) to accommodate the data presented in Fig. 37.

In the light of the accuracy with which the correlations given can conform to the measured values, the studies by *Cumo* et al. demonstrate that the critical heat flux is not significantly altered by the direction of flow. For practical purposes, it is recommended that the values for the critical heat flux determined by Eqs. (26–41) be reduced by 10% if flow is downward.

Example 10

Nitrogen at a pressure of 5 bar flows with a mass velocity of 30 kg/m^2 s through a vertical evaporator tube of 1.0 m length and 12 mm inner diameter. The inlet temperature is 85 K, and the tube is heated axially at a rate of 40 kW/m^2. Determine the location of the boiling crisis and the associated vapor mass fraction.

The following applies for nitrogen: $h_{inl} = -105.5$ kJ/kg, h' (5 bar) = −87.3 kJ/kg, and Δh_v (5 bar) = 173.8 kJ/kg. Hence,

$$\dot{x}_{inl} = \frac{-105.5 - (-87.3)}{173.8} = -0.1$$

Other properties of nitrogen at 5 bar are $\varrho_\ell = 724.4$ kg/m^3, $\varrho_g = 20.23$ kg/m^3 and $\sigma = 5.3 \cdot 10^{-3}$ N/m.

The location of the boiling crisis is determined by iteration commencing with, say, $\ell = 0.5$, which results in $\dot{q}_{cr} < 40$ kW/m^2. ℓ is then reduced stepwise until the set value $\dot{q}_{cr} = 40$ kW/m^2 is attained. The value obtained after a few stages in the iteration is $\ell = 0.364$ m. The calculation proceeds as follows.

$$\text{Eq. (33)}: \sigma^* = \frac{5.3 \cdot 10^{-3}\ \text{N/m} \cdot 724.4\ \text{kg/m}^3}{30^2\ \text{kg}^2/\text{m}^4\ \text{s}^2 \cdot 0.364\ \text{m}} = 0.0117;$$

$$\text{Eq. (34)}: \ell^* = \frac{0.364}{0.012} = 30.3; \quad \text{Eq. (35)}: \varrho^* = \frac{20.23}{724.4} = 0.0279;$$

$$\text{Eq. (36)}: C = 0.25, \ \text{da}\ \ell^* < 50.$$

Since $\varrho^* < 0.15$, the range of validity given under the heading (a) applies. Thus

$$\text{Eq. (27)}: \quad q_1^* = 6.81 \cdot 10^{-3}; \ \text{Eq. (28)}: \ q_2^* = 12.87 \cdot 10^{-3}.$$

$$q_1^* < q_2^* \rightarrow q^* = q_1^*.$$

$$\text{Eq. (39)}: K_1 = 1.26; \ \text{Eq. (40)}: K_2 = 0.269. \ K_1 > K_2 \rightarrow K = K_1.$$

$$\text{Eq. (32)}: \dot{q}_{cr,o} = q_1^* \dot{m} \Delta h_v = 6.81 \cdot 10^{-3} \cdot 30\ \text{kg/m}^2\ \text{s}$$

$$173.8\ \text{kJ/kg} = 35.5\ \text{kW/m}^2.$$

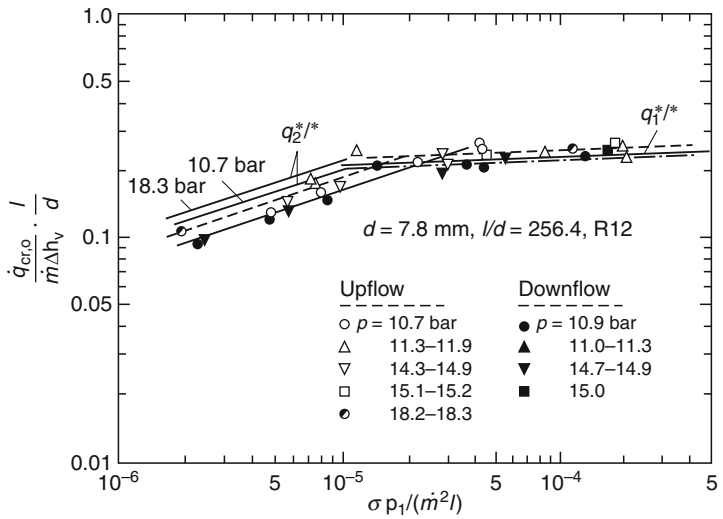

H3.5. Fig. 37. Comparison between upward and downward flow in vertical tubes [67].

Eq. (26) : $\dot{q}_{cr} = 35.5\ \mathrm{kW/m^2} \cdot [1 - 1.26(-0.1)] = 40\ \mathrm{kW/m^2}$.

The critical vapor mass fraction can then be obtained from Eq. (42), that is,

$$\dot{x}_{cr} = \left(\frac{4 \cdot 40\ \mathrm{kW/m^2}}{30\ \mathrm{kg/m^2\ s} \cdot 173.8\ \mathrm{kJ/kg}} \right) \cdot 30.3 - 0.1 = 0.83.$$

Example 11

Refrigerant R 12 flows upward in a vertical evaporator tube subjected to uniform axial heating. Determine the critical heat flux and the critical vapor mass fraction.

Inner diameter of tube	$d = 14 \cdot 10^{-3}$ m	
Length of tube	$\ell = 2$ m	
Pressure	$p = 10$ bar	
Mass flow rate	$\dot{M} = 0.17$ kg/s	
Inlet temperature	$\vartheta_{inl} = 28.94°C$	
Properties of R 12	$\vartheta_s = 41.5°C$;	$\varrho_\ell = 1245.6$ kg/m^3;
(at 10 bar)	$\varrho_g = 56.90$ kg/m^3;	$h' = 240.2$ kJ/kg;
	$\Delta h_v = 128.3$ kJ/kg.	

Specific heat capacity of the liquid between ϑ_{inl} and ϑ_s:

$$c = 1.02\ \mathrm{kJ/kg\ K}; \quad \sigma = 6.5 \cdot 10^{-3}\ \mathrm{N/m}.$$

Vapor mass fraction at the inlet cross section:

$$h_{inl} = h' - c(\vartheta_s - \vartheta_{inl}).$$

$$\begin{aligned} \text{Hence } \dot{x}_{inl} &= -c(\vartheta_s - \vartheta_{inl})/\Delta h_v \\ &= [1.02\ \mathrm{kJ/kg\ K}\ (41.5 - 28.94)\ \mathrm{K}]/128.3\ \mathrm{kJ/kg} \\ &= -0.1. \end{aligned}$$

$$\text{Mass velocity } \dot{m} = \frac{4\dot{M}}{\pi d^2} = \frac{4 \cdot 0.17\ \mathrm{kg/s}}{\pi\, 0.014^2\ \mathrm{m^2}} = 1{,}104\ \mathrm{kg/m^2\ s}.$$

The calculation proceeds as follows (cf. Example 10).

$$\sigma^* = 3.33 \cdot 10^{-6}; \ell = 142.9; \varrho^* = 0.0457.$$

Since ℓ^* lies between 50 and 150, Eq. (37) yields $C = 0.33$.

Since $\varrho^* < 0.15$, the range of validity given under the heading (a) applies.

$$q_1^* = 1.36 \cdot 10^{-3};\ q_2^* = 0.686 \cdot 10^{-3};\ q_1^* > q_1^*;$$
$$q_3^* = 0.731 \cdot 10^{-3};\ q_2^* < q_3^* \rightarrow q^* = q_2^*.$$
$$K_1 = 1.34;\ K_2 = 1.63;\ K_1 < K_2 \rightarrow K = K_2.$$

$$\dot{q}_{cr,\ell} = 0.686 \cdot 10^{-3} \cdot 1104\ \mathrm{kg/m^2\ s} \cdot 128.3\ \mathrm{kJ/kg} = 97.2\ \mathrm{kW/m^2}.$$

$$\dot{q}_\ell = 97.2\ \mathrm{kW/m^2}\ [1 - 1.63(-0.1)] = 113\ \mathrm{kW/m^2}.$$

$$\dot{x}_{cr} = \left(\frac{4 \cdot 113\ \mathrm{kW/m^2}}{1{,}104\ \mathrm{kg/m^2\ s} \cdot 128.3\ \mathrm{kJ/kg}} \right) \cdot 142.9 - 0.1 = 0.36.$$

3.1.2 Horizontal and Inclined Tubes

The peculiarities of the boiling crisis in nonvertical tubes have already been dealt with in Sect. 2.1.2. There is no qualitative difference between the behavior of water and that of other fluids. For this reason and also because systematic studies have, as yet, been confined to water, the mathematical method described in Sect. 2.1.2 should also be adopted for other fluids. The figures thus obtained apply to water and can be converted into the corresponding figures for the fluid by the method proposed by *Ahmad* (Sect. 3.1.7). The procedure is as follows:

- Conversion of the properties of the fluid into the corresponding figures for water as laid down in Sect. 3.1.7.
- Determination of the Froude number from Eq. (6) with the figures thus obtained for water. The critical vapor mass fraction $\dot{x}_{cr}$ is calculated as described in Sect. 2.1.1.
- If $Fr > 10$, the angle of inclination of the tube does not have any effect on the boiling crisis. As a first approximation, this will also apply to the fluid concerned. Consequently, the boiling crisis should be determined by the method given in Sect. 3.1.1.
- If $Fr < 10$, the angle of inclination of the tube is likely to exert an effect. In this case, the values for water obtained as described above should be taken for the determination of the boiling crisis.

Details of this procedure are given in Example 14.

Note. In a study on the critical heat flux of water and Refrigerant R 12 in horizontal and vertical tubes, Merilo [10] observed that very good results were obtained by adopting the Ahmad method for converting the conditions for critical boiling in vertical tubes. In horizontal tubes, however, the equivalent critical heat flux for R 12, that is, the value of $\dot{q}_{cr}$ obtained by converting the conditions for water, was always less than that for water. At the most, the figures differed by a factor of 1.7. It cannot be said at present whether this finding is of general validity, and further studies on the subject would be required to clarify the matter. For this reason, a corresponding safety factor should be included in the values of the critical heat flux calculated for other fluids if $Fr < 10$.

3.1.3 Microchannels

Flow boiling in microchannels are often used as a cooling method for high heat flux systems such as electronic chips or laser diodes. Studies with microchannel tubes [68] and rectangular microchannels [69] revealed strong dependence of the critical heat flux on mass velocity, heated length and equivalent microchannel diameter but – in contrast to macrochannels – no significant influence of liquid subcooling.

Wojtan et al. [68] carried out experiments with refrigerants R 134a and R 245fa flowing in tubes of 0.5 and 0.8 mm internal diameter. Other experimental system conditions were : heated length 1 : 20–70 mm, mass velocity $\dot{m}$: 400–1,600 kg/m^2 s, heat flux $\dot{q}$: 3.2–600 kW/m^2, saturation temperature : 30°C, 35°C, inlet subcooling : 2–15 K, *We*-number: 293–21,044, ϱ_g/ϱ_ℓ: 0.009–0.041, l/d : 25-141. The authors proposed the following modified Katto/Ohno correlation

$$\dot{q}_{cr} = 0.437\ \dot{m}\ \Delta h_v\, We^{-0.24} \left(\frac{\varrho_g}{\varrho_\ell} \right)^{0.073} \left(\frac{l}{d} \right)^{-0.72} \qquad (43)$$

with the liquid Weber number

$$We = \frac{\dot{m}^2 l}{\varrho_\ell \sigma} \tag{44}$$

Wojtan et al.'s experimental data are predicted with the mean absolute error of 7.6 % with 82.4 % of data falling within a ±15 % error band.

Park and Thome [69] carried out experiments with refrigerants R 134a, R 236fa, and R 245fa flowing in arrays of vertically arranged rectangular micro channels. One test section had 20 parallel rectangular channels, 467 µm wide and 4,052 µm deep, a second one had 29 channels, 199 µm wide 756 µm deep. They found that using the heated equivalent diameter $d_{eq} = d$ defined as : (4x flow area)/heated perimeter and the actual mass velocity $\dot{m} = \dot{M}/(\text{width} \times \text{depth})$ their data matched well with the correlation of Wojtan et al., Eqs. (43) and (44).

3.1.4 Helical Coils

No qualitative difference exists between the effect of water and that of other fluids on the boiling crisis in helical coils (cf. Sect. 2.1.3). Since design data derived from systematic studies on other fluids are not yet available, the method of calculation recommended is that devised by Jensen and Bergles [70]. This method has been based on measurements with Refrigerant R 113. It differs from, say, the *Katto/Ohno* method (Sect. 3.1.1) in that the authors assume the validity of the local conditions hypothesis, which states that the critical heat flux is uniquely defined by the local values of the main system parameters.

The critical heat flux in subcooled boiling ($\dot{x}_{cr} \leq -0.1$) can be determined from the following equation:

$$\dot{q}_{cr} = KG\dot{m}\Delta h_v Re^{-0.6}[1.234 - 3.873 \cdot 10^{-6} Re_\ell + (-1.367 - 3.15 \cdot 10^{-6} Re_\ell)\dot{x}]. \tag{45}$$

The dimensionless K in Eq. (45) allows for the effect of the centrifugal forces in the coil and is given by

$$K = 0.769\left(\frac{\dot{m}^2}{\varrho_\ell^2 g D_W}\right)^{-0.26} \quad \text{for} \quad \frac{\dot{m}^2}{\varrho_\ell^2 g d} > 10 \tag{46}$$

and

$$K = 1 \quad \text{for} \quad \frac{\dot{m}^2}{\varrho_\ell^2 g d}. \tag{47}$$

At low fluid velocities, allowance must be made for the effect of the buoyancy of the vapor in the two-phase mixture. Thus, Eq. (45) contains a factor C that is a function of the Reynolds and Grashof numbers and is defined by

$$C = 0.4(Gr/Re_\ell^2)^{-0.21} \quad \text{for } Gr/Re_\ell^2 \geq 0.0127 \tag{48}$$

and

$$C = 1 \quad \text{for } Gr/Re_\ell^2 < 0.0127 \tag{49}$$

The Reynolds and Grashof numbers in Eqs. (45), (48), and (49) are given by

$$Re_\ell = \frac{\dot{m} d}{\eta_\ell} \tag{50}$$

and

$$Gr = \frac{g d^3 (\varrho_\ell - \varrho_g)\varrho_\ell}{\eta_\ell^2}. \tag{51}$$

On an average, figures calculated from Eq. (45) deviated by 7.4% from values obtained in measurements. The maximum deviation was 45.3%.

The equation that applies for the boiling crisis in saturated boiling ($\dot{x}_{cr} \geq 0.1$) for $\dot{m} > 950$ kg/m^2 s is

$$\dot{q}_{cr} = 1.713 \cdot 10^4 Re_g^{-1.143} \dot{x}^{-0.436} \cdot (d/D_W)^{0.31} \dot{m}\Delta h_v \tag{52}$$

The corresponding equation for $\dot{m} \leq 950$ kg/m^2 s is

$$\dot{q}_{cr} = 4.09 \cdot 10^{-6} Re_g^{0.5} \dot{x}^{-0.460} (d/D_W)^{0.17} \dot{m}\Delta h_v \tag{53}$$

In this case, too, the Reynolds number is defined by Eq. (50) except that the dynamic viscosity of the vapor η_g is substituted for that of the liquid.

On an average, figures calculated from Eqs. (52) and (53) deviated by 3% from measured values. The maximum deviation was 14.1%. All the values for the fluid properties expressed in Eqs. (45–53) apply to the conditions at saturation.

No data could be obtained by measurement in the $-0.1 < \dot{x}_{cr} < 0.1$ range, in which the transition from bubble to annular flow occurs. In this case, the boiling crisis cannot be uniquely located, because it may occur several times along the path formed by the coil [70]. Jensen and Bergles [70] demonstrated that the only means of avoiding operating conditions of this nature in evaporator coils is to take resort to one of the following alternatives:

- Ensuring that the critical vapor mass fraction at the end of the helical tube is less than −0.1 ($\dot{x}_{cr} < -0.1$).

  or

- Ensuring that the critical heat flux in saturated boiling {Eqs. (52) and (53)} is lower than that in subcooled boiling {Eqs. (45–51)} when $\dot{x} = -0.1$.

The *Jensen* and *Bergles* method has been derived solely from measurements on the one fluid (R 113), at the one pressure (9.4 bar), and in tubes of the same diameter (d = 7.62 mm). The other system parameters were varied as follows: $\dot{m}$ = 570–5,470 kg/m^{2}s; $\dot{q}_{cr}$ = 54–800 kW/m^2; $\dot{x}_{cr}$ = −0.55–0.94; D_w = 117.5–409.6 mm; ℓ = 635–1,295 m; $\Delta T = T_s - T_{inl}$ = 0–110 K. (ΔT is the subcooling at the inlet.)

The term $\dot{q}_{cr}/\dot{m}\Delta h_v$, which was also introduced by *Katto* and *Ohno*, allows Eqs. (45), (52), and (53) to be expressed in a dimensionless form. Nevertheless, the restricted range of parameters within which the measurements were performed detracts from the concept of general validity for this method of calculation. The reliability must still be verified by future measurements. Therefore, larger factors of safety must be allowed in the design of evaporator coils that have to cope with parameters that differ significantly from those in the experiments mentioned above [70].

Example 12

R 12 is to be evaporated at a system pressure of $p = 1$ bar in a helical-tube evaporator. The mass velocity is 2,000 kg/m^{2}s, and the refrigerant is subcooled when it enters the evaporator ($\dot{x}_{\text{inl}} = -0.15$). The diameter of the windings in the helical coil is $D_w = 0.5$ m, the length of the tube is $\ell = 6$ m, and the tube inner diameter is $d = 10 \cdot 10^{-3}$. The heat flux remains constant over the length of the coil. What would its value be if the boiling crisis were to occur just at the end of the coil?

Properties of R 12 at 1 bar

$$\vartheta_\ell = -30^\circ\text{C}; \varrho_\ell = 1489.3 \text{ kg/m}^3; \varrho_g = 6.22 \text{ kg/m}^3;$$
$$\Delta h_v = 166.1 \text{ kJ/kg}; \quad \eta_\ell = 370.5 \cdot 10^{-6} \text{ Pa s};$$
$$\eta_g = 10.14 \cdot 10^{-6} \text{ Pa s}.$$

The Reynolds number is determined from Eq. (50), but the value to be inserted for the dynamic viscosity is that of the vapor because saturated boiling occurs ($\dot{x}_{\text{cr}} > 0.1$). Thus

$$Re_g = \frac{2{,}000 \text{ kg/m}^2 \text{ s} \cdot 10 \cdot 10^{-3} \text{ m}}{10.14 \cdot 10^6 \text{ Pa s}} = 1.97 \cdot 10^6.$$

Since the boiling crisis in this case occurs during saturated boiling, Eq. (52) applies. The critical value must be taken for the vapor mass fraction, and it is related to $\dot{q}_{\text{cr}}$ through the energy balance. Inserting Eq. (42) in Eq. (52) gives rise to an implicit equation for $\dot{x}_{\text{cr}}$, which can be solved by iteration. The following figures are obtained after a few stages: $\dot{x}_{\text{cr}} = 0.76$ and $\dot{q}_{\text{cr}} = 126.4$ kW/m^2.

Check for instability:

The critical heat flux $\dot{q}_{\text{cr}}$ in saturated boiling must be less than that in subcooled boiling (indicated below by the symbol $\dot{q}_{\text{cr,sub}}$) if $\dot{x} = -0.1$ is inserted in Eq. (45).

Determination of the dimensionless numbers in Eq. (45) Eqs. (46) and (47):

$$\frac{\dot{m}^2}{\varrho_\ell^2 g d} = 18.38 > 10 \rightarrow$$

$$K = 0.769 \left(\frac{2{,}000^2 \text{ kg}^2/\text{m}^4 \text{ s}^2}{1489.3^2 \text{ kg}^2/\text{m}^6 \cdot 9.81 \text{ m/s}^2 \cdot 0.5 \text{ m}} \right)^{-0.26} = 0.997;$$

Eqn (51):

$$Gr = \frac{9.81 \text{ m/s}^2 \cdot 10^{-6} \text{ m}^3 (1489.3 - 6.22) \cdot 1489.3 \text{ kg}^2/\text{m}^6}{370.5^2 \cdot 10^{-12} \text{ Pa}^2 \text{ s}^2}$$
$$= 1.58 \cdot 10^8;$$

$$\text{Eq. (50)}: \quad Re_\ell = \frac{2{,}000 \text{ kg/m}^2 \text{ s} \cdot 10 \cdot 10^{-3} \text{ m}}{370.5 \cdot 10^{-6} \text{ Pa s}} = 5.4 \cdot 10^4;$$

Eqn (48) and (49):

$$Gr/Re_\ell^2 \simeq 0.054 > 0.0127 \rightarrow C = 0.4 \cdot 0.054^{-0.21} = 0.74.$$

Eq. (45):

$$\dot{q}_{\text{cr,sub}} = 0.997 \cdot 0.74 \cdot 2{,}000 \text{ kg/m}^2 \text{ s} \cdot 166.1 \text{ kJ/kg}$$
$$\cdot (5.4 \cdot 10^4)^{-0.6} [1.234 - 3.873 \cdot 10^{-6} \cdot 5.4 \cdot 10^4$$
$$+ (-1.367 - 3.15 \cdot 10^{-6} \cdot 5.4 \cdot 10^4)(-0.1)]$$
$$= 417 \text{ kW/m}^2.$$

Since $\dot{q}_{\text{cr}} < \dot{q}_{\text{cr,sub}}$, instability does not occur.

3.1.5 Effect of Nonuniform Heating

Nonuniform Peripheral Heating

The method presented in Sect. 2.1.4 for the determination of the critical heat flux in nonuniformly heated tubes can also be applied to liquids other than water.

Nonuniform Axial Heating

The procedure to adopt in this case is the same as that described in Sect. 2.1.4. Both the "local conditions" and the "integral power" hypotheses can be adopted, and the smaller of the two values thus obtained should be taken as the critical heat flux. The ranges of parameters within which the equations are valid are given in Sect. 3. Thus, the first step is to vary the value of ℓ for a uniformly heated tube in order to determine the critical heat flux as a function of the length. The next step is to apply the two hypotheses (Figs. 23 and 24) to check the margin of safety between the figures calculated and the conditions for critical boiling. In this case it is advisable to locate the reference point A at the commencement of the heated length.

3.1.6 Flow through Vertical Annuli

The procedure to adopt in this case is that given in Sect. 2.2.1.

Heat Applied through the Wall of the Outer Tube

The critical heat flux is determined from Eqs. (26–41). The value to insert for the tube diameter is that of the outer tube (d_o in Fig. 25). The critical vapor mass fraction at the end of the heated section is obtained from the energy balance, that is,

$$\dot{x}_{\text{cr,o}} = \frac{4\dot{q}_{\text{cr}}}{\dot{m}\Delta h_v} \frac{\ell}{d_o} \frac{1}{1 - \left(\frac{d}{d_o}\right)^2} + \dot{x}_{\text{inl}}. \tag{54}$$

Heat Applied through the Wall of the Inner Tube

As a first approximation, the critical heat flux in the inner tube is identical to that in the wall of the outer tube. Hence Eqs. (26–41) are again adopted for the determination of $\dot{q}_{\text{cr}}$, and the value to be inserted for the diameter is again $d = d_o$. The critical vapor mass fraction at the end of the heated section is then given by

$$\dot{x}_{\text{cr,i}} = \frac{4\dot{q}_{\text{cr}}}{\dot{m}\Delta h_v} \frac{\ell}{d} \frac{1}{1 - \left(\frac{d_o}{d}\right)^2 - 1} + \dot{x}_{\text{inl}}. \tag{55}$$

Heat Applied through Both Tube Walls

Here, too, the method to be adopted is that given in Sect. 2.2.1. The procedure is as follows:

- The critical heat flux is determined from Eqs. (26–41) on the assumption that $d = d_o$.
- The critical vapor mass fractions $\dot{x}_{\text{cr,o}}$ and $\dot{x}_{\text{cr,i}}$ are calculated from Eqs. (54) and (55).
- The true critical vapor mass fraction $\dot{x}_{\text{cr}}$ is determined by interpolation as recommended in Sect. 2.2.1.
- The maximum heat flow rate that can be transferred $\dot{Q}_{\text{act}}$ and the heat fluxes $\dot{q}_o$ and $\dot{q}_i$ in the inner and outer tube walls are calculated from Eqs. (13–15).

Example 13

Refrigerant R 114 flows upward in a vertical annulus of $d_o = 25 \cdot 10^{-3}$ m, $d = 15 \cdot 10^{-3}$ m, and a heated length of 4 m. The pressure is $p = 5$ bar; and the mass velocity $\dot{m} = 2{,}500$ kg/m^2 s. The fluid at the inlet cross section is subcooled, that is, $\dot{x}_{inl} = -0.05$, and the annulus is heated through both tube walls {power ratio $y = \dot{Q}_o/(\dot{Q}_o + \dot{Q}_i) = 0.5$}. The total heat applied must be 80% of the maximum feasible. What are the values for the heat flux in the outer and inner tubes?

Properties of R 114 at 5 bar

$$\vartheta_s = 54^\circ C; \varrho_\ell = 1361.4\,\text{kg/m}^3; \varrho_g = 36.07\,\text{kg/m}^3$$

$$\Delta h_v = 115.49\,\text{kJ/kg}; \sigma = 9.2 \cdot 10^{-3}\,\text{N/cm}.$$

Procedure (cf. Example 10)

$$\sigma^* = 5.0 \cdot 10^{-7}; \ell^* = \ell/d_0 = 160; \varrho^* = 0.0265.$$

Since $\ell^* > 150$, Eq. (38) applies and yields $C = 0.34$.

Since $\varrho^* > 0.15$, the range of validity given under the heading (a) applies

$$q_1^* = 1.14 \cdot 10^{-3}; q_2^* = 0.327 \cdot 10^{-3}; q_3^* = 0.297 \cdot 10^{-3}.$$

Therefore, $q_1{}^* > q_2{}^*$ and $q_2{}^* > q_3{}^* \rightarrow q^* = q_3{}^*$.

$$K_1 = 1.43 \text{ and } K_2 = 3.17; K_1 < K_2 \longrightarrow K = K_2.$$

$\dot{q}_{cr,o} = 0.297 \cdot 10^{-3} \cdot 2{,}500\,\text{kg/m}^2\text{s} \cdot 115.49\,\text{kJ/kg} = 85.9\,\text{kW/m}^2$;
$\dot{q}_{cr} = 85.9\,\text{kW/m}^2[1 - 3.17(-0.05)] = 99.5\,\text{kW/m}^2$.

Applying Eq. (54) for the critical vapor mass fraction $\dot{x}_{cr,o}$:

$$\dot{x}_{cr,o} = \frac{4 \cdot 99.5\,\text{kW/m}^2 \cdot 4\,\text{m}}{2{,}500\,\text{kg/m}^2\,\text{s} \cdot 115.49\,\text{kJ/kg} \cdot 25 \cdot 10^{-3}\,\text{m}\,[(15/25)^2]} - 0.05 = 0.295.$$

Applying Eq. (55) for $\dot{x}_{cr,i}$:

$$\dot{x}_{cr,i} = \frac{4 \cdot 99.5\,\text{kW/m}^2 \cdot 4\,\text{m}}{2{,}500\,\text{kg/m}^2\,\text{s} \cdot 115.49\,\text{kJ/kg} \cdot 15 \cdot 10^{-3}\,\text{m}\,[(15/25)^2 - 1]} - 0.05 = 0.157.$$

Since $0 < y < 0.8$, the following linear interpolation yields $\dot{x}_{cr}$:

$$\dot{x}_{cr} = \left(\frac{\dot{x}_{cr.o} - \dot{x}_{cr.i}}{0.8}\right) \cdot 0.5 + \dot{x}_{cr.i} = 0.243.$$

Maximum rate at which heat can be transferred {Eq. (13)}:

$$\dot{Q}_{act,max} = (\dot{x}_{cr} - \dot{x}_{in1})\Delta h_v \dot{m} f = (0.243 + 0.05) \cdot 115.49\,\text{kJ/kg} \cdot 2{,}500\,\text{kg/m}^2\,\text{s}\,(\pi/4) \cdot (25^2 - 15^2) \cdot 10^{-6}\,\text{m}^2 = 26.58\,\text{kW}.$$

Heater setting: $\dot{Q}_{act} = 0.8 \cdot \dot{Q}_{actmax} = 21.26$ kW.

Heat fluxes in the outer and inner tube walls:

$$\text{Eq. (14)}: \quad \dot{q}_o = \frac{y\dot{Q}_{act}}{\pi d_o \ell} = 33.84\,\text{kW/m}^2;$$

$$\text{Eq. (15)}: \quad \dot{q}_i = \frac{(1-y)\dot{Q}_{act}}{\pi d \ell} = 56.39\,\text{kW/m}^2.$$

3.1.7 Application to Other Liquids by Converting the Results Obtained on Water (Ahmad Method)

The theory of mathematical similarity has been applied for converting the parameters that describe the boiling crisis in water, which is by far the liquid that has been most frequently investigated, into the corresponding parameters for other fluids. The *Ahmad* method [71] is currently the best of these, and it was specially developed for the conversion of the critical boiling parameters involved in upward flow through vertical channels [72–74]. The requirements that must be met to establish similarity in this method are listed in Table 6. The stipulation is that the system parameters for the fluids concerned must be selected so that the dimensionless numbers required for the calculation agree. The dimensionless number for converting the mass velocity is ψ, which is defined by

$$\psi = \frac{\dot{m} d_h}{\eta'} \left(\sqrt{\frac{\gamma}{\varrho'}} \frac{\eta'}{d_h}\right)^{2/3} (\eta'/\eta'')^{1/8} \tag{56}$$

where

$$\gamma = \left|\frac{d(\varrho'/\varrho'')}{dp}\right|. \tag{57}$$

The critical heat flux $\dot{q}_{cr}$ and vapor mass fraction $\dot{x}_{cr}$ at the point where the boiling crisis is located are related as follows through the energy balance for the channel:

H3.5. Table 6. Conditions for similarity in the *Ahmad* method for upward flow in vertical tubes

Parameter	Dimensionless number	Range of validity [72–74]	
		Tube and annulus[a]	Rod bundle 4, 9, 19, 25 rods
System pressure	ϱ_ℓ/ϱ_g	7 to 980	3 to 20
Mass velocity	ψ {Eq. (56)}	5 to 100	5 to 40
Vapor mass fraction at boiling crisis	$\dot{x}_{cr}$	−0.4 to 0.9	−0.35 to 0.9
Critical heat flux	$\dot{q}_{cr}/(\dot{m}\Delta h_v)$	No limit	No limit
Geometry (remains unchanged)			
Vapor mass fraction at channel inlet	$\dot{x}_{inl}$	−0.02 to 0.8	−0.04 to −0.8
Ratio of heated length to hydraulic diameter	ℓ/d_h	60 to 310	60 to 250
Fluids (used for the test; the validity for other fluids is not excluded)		Water, Refrigerant R 12, R 21, R 22, R 113, R 114, CO_2	Water, Refrigerant R 12

[a]The only liquids for which the annular channel was checked were water and R 12

$$\dot{x}_{cr} - \dot{x}_{inl} = \frac{A_{hld}}{A} \frac{\dot{q}_{cr}}{\dot{m} \Delta h_v}. \quad (58)$$

where A_{htd} is the area of the heated surface and A is the cross-sectional area of the flow channel.

An example for the conversion of the critical boiling parameters in a 5 × 5 rod bundle (cf. Sect. 2.2.2) is illustrated in Fig. 38. The curves shown have been drawn through points that represent the critical vapor mass fraction for water corresponding to three inlet conditions $\dot{x}_{inl}$ for the liquid at a constant density ratio. The diagram allows the critical vapor mass fractions for the fluid concerned, for example, R 12, to be read off against the value of ψ calculated from Eq. (56). The critical heat flux for a geometrically similar channel, e.g. one through which R 12 flows, can then be determined from Eq. (58).

If the necessary experimental values for water are not available, the system parameters for the fluid concerned must first of all be converted into the equivalent values for water under similar conditions, as listed in Table 6. These values allow the critical boiling parameters $(\dot{q}_{cr}; \dot{x}_{cr})$ for water to be determined as described in Sect. 2. The conversion of these parameters, in turn, into the corresponding values for the fluid concerned proceeds in accordance with the instructions implied in Table 6.

The *Ahmad* method can be successfully applied if the correlations for heat transfer in single-phase flow of water are also the same as those for the fluid concerned. If this is not the case, for example, for molten metals, the method involves greater errors.

Example 14

R 12 flows under the following conditions in a horizontal, uniformly heated tube:

Tube inner diameter $d = 20 \cdot 10^{-3}$m	
Pressure	p = 25 bar
Mass velocity	$\dot{m} = 500\,kg/m^2s$
Heat flux	$\dot{q} = 34\,kW/m^2$

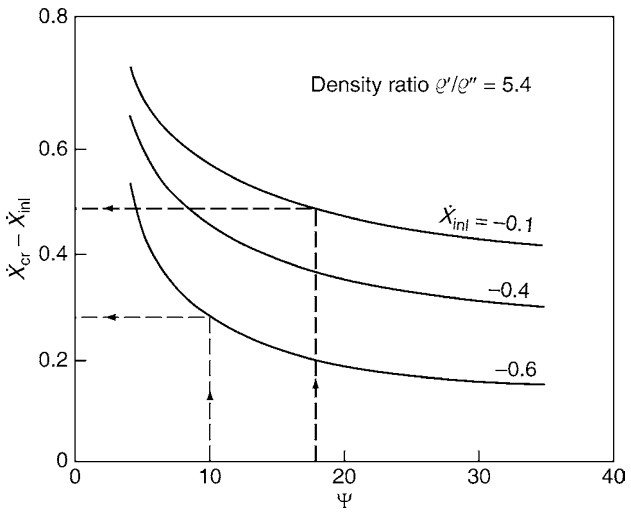

H3.5. Fig. 38. Determination of the conditions for critical boiling by the *Ahmad* method.

What is the length of the path through which the fluid must flow before the boiling crisis occurs on the crest and underside of the tube?

The first step is to convert the system parameters for the flow of R 12 into the corresponding values for water by means of Table 6.

Inner diameter of tube

Since the geometry remains the same, $d = d_h = 20 \cdot 10^{-3}$m.

Properties of R 12 at 25 bar

$$\vartheta_\ell = 83.4°C; \varrho_\ell = \varrho' = 1032.9\,kg/m^3; \Delta h_v = 90.52\,kJ/kg;$$
$$\eta_\ell = \eta' = 157.9 \cdot 10^{-6}\,Pa\,s; \eta_g = \eta'' = 17.42 \cdot 10^{-6}\,Pa\,s.$$

Pressure. The density ratio ϱ_ℓ/ϱ_g for R 12 at 25 bar is the same as that for water at 147.5 bar.

Properties of water at 147.5 bar; $\vartheta_s = 340.8°C; \varrho_\ell = \varrho' = 607.66\,kg/m^3; \varrho_g = \varrho'' = 94.24\,kg/m^3; \Delta h_v = 1{,}016\,kJ/kg;$ $\eta_\ell = \eta' = 75.22 \cdot 10^{-6}$ Pa s; $\eta_g = \eta'' = 25.31 \cdot 10^{-6}$ Pa s.

Mass velocity. The dimensionless number ψ {Eq. (56)} must be the same for both fluids. Inserting values taken from steam tables in Eq. (57) gives

$$|\gamma|_{R12} = 0.424\,l/bar; \quad |\gamma|_{H_2O} = 0.0869\,l/bar.$$

Therefore,

$$\psi_{R12} = \left(\frac{500\,kg/m^2\,s \cdot 0.02\,m}{157.9 \cdot 10^{-6}\,Pa\,s}\right)\left[\sqrt{\frac{0.424\,l/bar}{1032.9\,kg/m^3}} \cdot \left(\frac{157.9 \cdot 10^{-6}\,Pa\,s}{0.02\,m}\right)\right]^{2/3} \cdot \left(\frac{157.9}{17.42}\right)^{1/8} = 5.3.$$

Inserting $\psi = \psi_{R\ 12}$ and the appropriate values for water in Eq. (56) and solving for $\dot{m}$ gives $\dot{m}_{H2O} = 638\,kg/m^2\,s$.

Critical heat flux. The *Ahmad* method requires that the dimensionless number $\dot{q}_{cr}/\dot{m}\ \Delta h_v$ must be the same for both fluids. It therefore follows that

$$\dot{q}_{cr.H_2O} = \frac{34\,kW/m^2 \cdot 638\,kg/m^2\,s \cdot 1016.1\,kJ/kg}{500\,kg/m^2\,s \cdot 90.52\,kJ/kg} = 487.1\,kW/m^2.$$

The critical vapor mass fraction is calculated from Eq. (1) or Eq. (4). In this case, it is Eq. (4) that applies. Thus

$$\dot{x}_{cr} = 32.302 \cdot 487.1^{-0.125} \cdot 638^{-0.333} \cdot 20^{-0.07} \cdot e^{-0.00795 \cdot 147.5} = 0.44.$$

Equation (6) yields

$$Fr = \frac{0.44 \cdot 638\,kg/m^2\,s}{\sqrt{94.24\,kg/m^3 \cdot 9.81\,m/s^2 \cdot 0.02\,m\,(607.66 - 94.24)\,kg/m^3}} = 2.85.$$

Since $Fr < 10$, it can be expected that the inclination of the tube exerts an effect. Thus inserting the numerical value for Fr in Eq. (7) gives $\Delta\dot{x}_{cr} = 16/(2 + 2.85)^2 = 0.68$.

Equation (8) yields

$$\dot{x}_{cr,up} = 0.44 - \frac{0.68}{2} = 0.095 \quad \text{and} \quad \dot{x}_{cr,low} = 0.44 + \frac{0.68}{2} = 0.78.$$

It follows from the energy balance {Eq. (42)} that

$$\ell = \frac{\dot{m}\Delta h_v}{\dot{q}_{cr}} \frac{d}{4}(\dot{x}_{cr} - \dot{x}_{inl}).$$

According to definition, the numerical values for the terms in the equation for ℓ are the same in both cases. Hence, the following applies for the flow of R 12 and water:

$$\ell_{cr,up} = \left(\frac{500\,\text{kg/m}^2\,\text{s} \cdot 90.52\,\text{kJ/kg}}{34\,\text{kW/m}^2}\right)\left(\frac{0.02\,\text{m}}{4}\right)(0.095 + 0.1)$$
$$= 1.3\,\text{m};$$
$$\ell_{cr,low} = 5.8\,\text{m}.$$

3.2 Binary Mixtures

The critical heat flux in a binary mixture can be determined by the critical heat fluxes of the individual components – calculated for the same pressure p, mass flux $\dot{m}$ and quality $\dot{x}$ – and by the molar fraction of the more volatile component within the liquid phase (cf. the Stephan–Körner equation for the determination of heat transfer during boiling of binary mixtures [75]):

$$\dot{q}_{cr}^{Mix} = \dot{q}_{cr,\,id}^{Mix}(1 + X) \tag{59}$$

with

$$\dot{q}_{cr,\,id}^{Mix} = [\dot{q}_{cr}^{MV}\tilde{x} + \dot{q}_{cr}^{LV}(1 - \tilde{x})]. \tag{60}$$

$\dot{q}_{cr}^{MV}$ and $\dot{q}_{cr}^{LV}$ are the critical heat fluxes of the pure more volatile and less volatile components with the lower and higher boiling point, respectively (Fig. 39), determined by the method described in Sect. 2 or Sect. 3.1. X is a factor for which the following is true: $X \geqq 0$.

3.2.1 Refrigerant Mixtures

Based on measurements of *Marroquin Nisch* with mixtures of the refrigerants R 114/R 13B1 and R 142b/R 22 [76] the following relationship has been derived for X in Eq. (59):

$$X = \left\{3.2 \cdot 10^5 \frac{(|\tilde{y} - \tilde{x}|)^{2.7}}{Re_l^{LV}} + 9.6 \frac{(|\tilde{y} - \tilde{x})^{1.9}}{(Re_l^{LV})^{0.1}} \cdot \left[\frac{T_s^{MV}}{T_s^{Mix} - T_s^{MV}}\right] P*^{2.2}\right\} \cdot e^{-3(0.2+\dot{x}_A)} \tag{61}$$

with

$$Re_l^{LV} = \frac{\dot{m}\,d_h}{\eta_l^{LV}} \tag{62}$$

and

$$P^* = \frac{1}{2}\left(\frac{P}{P_c^{LV}} + \frac{P}{P_c^{MV}}\right) \tag{63}$$

$\tilde{y}$ and $\tilde{x}$ are the molare fractions of the liquid and vapor phase, respectively, in the more volatile component, T_s^{Mix} is the temperature of the mixture on the boiling point curve calculated by the method given in Subchap. D5.1 "Calculation of Vapour liquid equilibria" and T_s^{MV} is the boiling point of the more volatile component, calculated by the method given in Subchap. D5.1 "Calculation of Vapour liquid equilibria", both temperatures in K (Fig. 39, $\vartheta_s = T_S - 273.15$ K). $\dot{x}_A$ is the quality at the outlet of the evaporator section. d_h in eqn. (62) is the hydraulic diameter of the flow channel and η_l^{LV} the dynamic viscosity of the liquid phase of the less volatile component at T_s^{Mix}. P_c^{LV} and P_c^{MV} in Eq. (63) are the critical pressures of the individual components.

Equation (61) is based on measurements with mixtures of the refrigerants R 114/R 13B1 and R 142b/R 22 [75] in the parameter ranges $0.26 \leq p/p_c \leq 0.61$; $-0.2 \leq \dot{x}_A \leq +0.2$; $1{,}000 \leq \dot{m} \leq 2{,}000$ kg/m^2 s; $3.4 \leq l/d \leq 38.8$, with l as the heated channel length and d as the tube diameter.

The outlet quality $\dot{x}_A$ can be determined in accordance with Eq. (1), Subchap. H3.4, under the assumption of

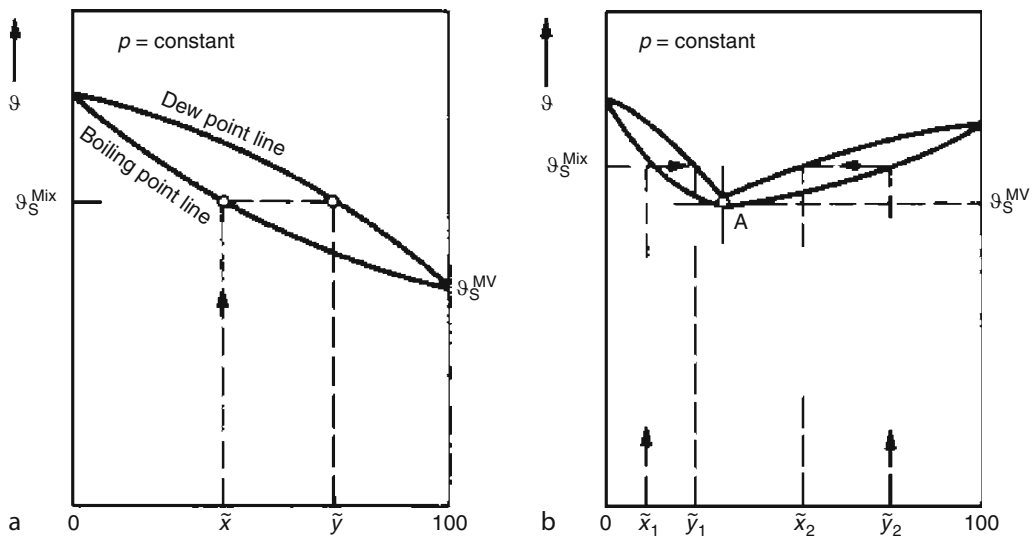

H3.5. Fig. 39. Equilibrium curves for binary mixtures: (**a**) without and (**b**) with an azeotropic point A and a boiling point minimum.

thermodynamic equilibrium. Equations (61–63) represent an extension of a method proposed by Sterman et al. [77], which has been developed solely based on measurements with a subcooled mixture (Mono isopropyl diphenyl-benzene-mixture; vertical annular channel: length 110 mm, outer/inner diameter 16 mm/10 mm; p = 0.2 MPa; $25 \leq \Delta\vartheta_u \leq 70$ K; $4 \leq u_E \leq 12$ m/s).

Figure 40 shows a typical measurement result for $\dot{x}_A = -0.2$ in comparison with calculated values according to Eqs. (59–63). The relative increase of the critical heat flux compared to the linearly interpolated value (Eq. 60) in accordance with $(\dot{q}_{cr}^{Mix} - \dot{q}_{cr,id}^{Mix})/\dot{q}_{cr}^{Mix} = X/(1+X)$ is plotted in the lower part of the ordinate. The upper part shows the trend of $(\tilde{y} - \tilde{x})$ of both mixtures. The higher $(\tilde{y} - \tilde{x})$, the higher is the relative increase of the critical heat flux. This is also true for increasing subcooling at the outlet. By contrast, Fig. 41 shows that a relative increase is no longer detectable at $\dot{x}_A = 0.1$, that is $X \approx 0$.

3.2.2 Accuracy and Scope of Eqs. (59–63)

A comparison of calculated values with all data measured by *Marroquin Nisch* is shown in Fig. 42. The majority of data lies within a tolerance range of ±25%. Measurements of Celata et al. [79] for a mixture of the refrigerants R 114/ R12 are included in the same range. These data have been investigated in the following parameter ranges: $0.24 \leq p/p_c \leq 0.86$; $0 \leq \dot{x}_A \leq 1$; $400 \leq \dot{m} \leq 1{,}600$ kg/m^2 s; l/d = 277.4. Hence, Eqn. (59–63) have been verified by measurements with three different mixtures of refrigerants for a wide parameter range. These equations enable the calculation of critical heat fluxes within a tolerance range of ±25%. This is true for outlet qualities between $-0.2 \leq \dot{x}_A \leq 1$. For higher subcooling at the outlet, Eq. (64) has to be used instead of Eqs. (61–63).

3.2.3 Other Mixtures

For mixtures of nonrefrigerants, measurements of Marroquin Nisch [76] and Tolubinskiy and Matorin [78] are available. In [76], the data of a *n*-propanol–acetone mixture are presented for the parameter ranges p = 0.11 MPa; $\dot{x}_A = 0$ and 0.1; $\dot{m} = 100$ and 500 kg/m^2 s and $3.4 \leq l/d \leq 38.8$. *Tolubinskiy and Matorin* have performed measurements with water–ethyl alcohol, water–acetone, water–ethylene glycol and benzene–ethyl alcohol in short vertical tubes ($l/d \approx 15$) for the parameter ranges $0.3 \leq p \leq 1.3$ MPa; inlet velocity $2.5 \leq u_E \leq 10$ m/s; inlet subcooling 10 K $\leq \Delta\vartheta_U \leq$ 110 K. Figure 43 shows typical results of their

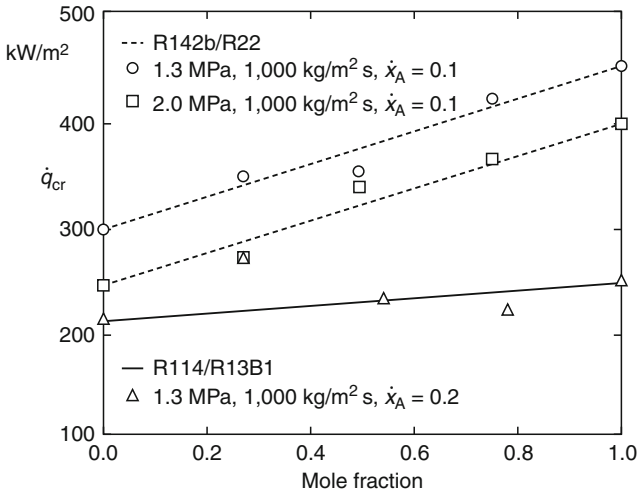

H3.5. Fig. 41. Measured values of *Marroquin Nisch* [76] for the critical heat fluxes of saturated binary mixtures of refrigerants.

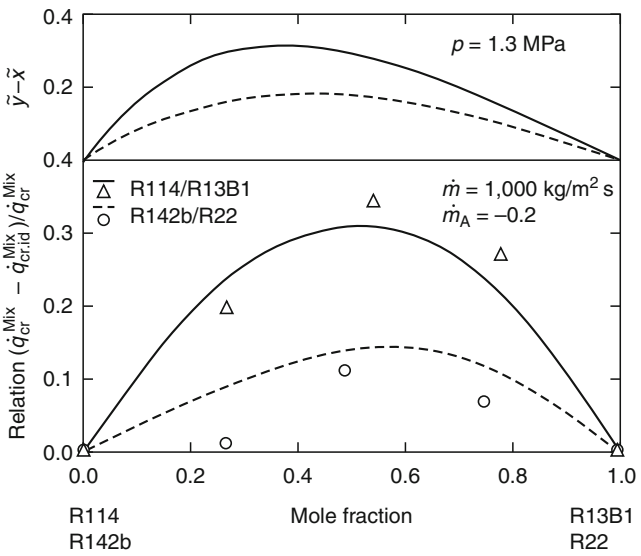

H3.5. Fig. 40. Critical heat flux of subcooled binary mixtures of refrigerants. △ and ○: Measured values of *Marroquin Nisch* [76]. - - - - and –: calculated values in accordance with Eqs. (59–63).

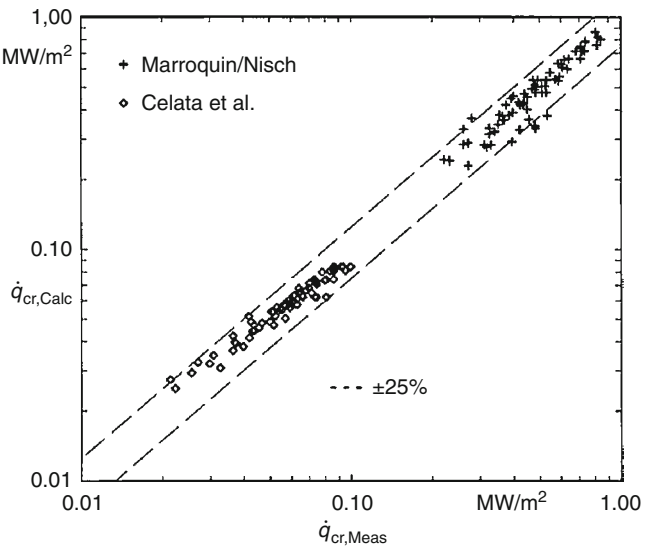

H3.5. Fig. 42. Comparison of measured and calculated values in accordance with Eqs. (59–63). Mixtures of refrigerants: Marroquin Nisch [76] and Celata et al. [79].

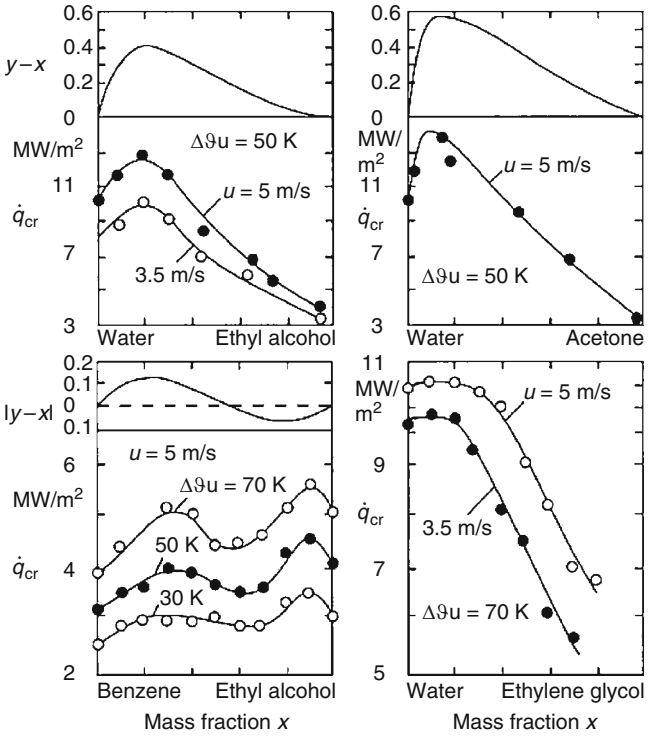

H3.5. Fig. 43. Critical heat flux of subcooled binary mixtures at 0.66 MPa acc. to Tolubinskiy and Matorin [78].

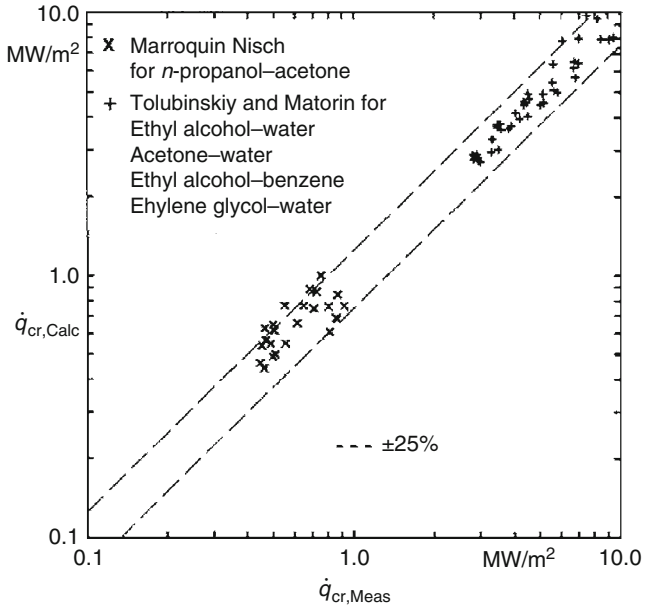

H3.5. Fig. 44. Comparison of measured and calculated values in accordance with Eqs. (59), (60), and (64).

investigations, which prove the fact, that an increase of the critical heat flux compared to the linearly interpolated value ($X > 0$ in Eq. (59)) emerges – especially at high inlet subcooling in the short tubes. However, *Marroquin Nisch* found also values $X > 0$ in comparatively long tubes and at saturation condition of the mixture which he has investigated.

An equation of type (59) and (60) is proposed in [78]:

$$X = 1.5\,(|\tilde{y} - \tilde{x}|)^{1.8} + 6.8(|\tilde{y} - \tilde{x}|)\left[\frac{T_S^{Mix} - T_S^{MV}}{T_S^{MV}}\right] \qquad (64)$$

The symbols used correspond to those of Eq. (61). If the binary mixture forms an azeotrope at a minimum boiling point A, as shown in Fig. 39, the temperature at this point is taken to be T_S^{MV} ($\vartheta_S = T_S - 273.15$ K). Figure 44 demonstrates, that both the data of *Tolubinskiy and Matorin* and the data of *Marroquin Nisch* can be reproduced by this method within a tolerance range of approx. ±25%. Hence, Eqs. (59), (60), and (64) can be recommended for the determination of the critical heat fluxes of mixtures of nonrefrigerants.

It has to be pointed out, that Eqs. (59–64) have been developed empirically due to a comparatively low number of measured data. However, all measurements, available up to now, have shown that the critical heat flux of a binary mixture is not less than the value resulting from the linear interpolation performed in Eq. (60). Hence, the critical heat flux estimated by this method is, at least, not too low.

Equations (59), (60), and (64) have to be used, if $\dot{x}_A < -0.2$ is valid for the subcooling of the mixture at the outlet of the evaporator channel.

Example 15

An acetone/1-propanol – mixture with the molar fraction of $\tilde{x} = 0.5$ is flowing through an evaporator channel with $d = 20 \cdot 10^{-3}$ m vertically upward. The pressure is $p = 0.15$ MPa, the mass flux $\dot{m} = 1{,}000$ kg/m² s. One has to calculate the relative increase of the critical heat flux $(\dot{q}_{cr}^{Mix} - \dot{q}_{cr,id}^{Mix})/\dot{q}_{cr}^{Mix} = X/(1+X)$ compared to the linearly interpolated value in accordance with Eq. (60) for the following conditions:

a. Subcooling of the mixture at tube outlet: $\Delta\vartheta = 34.9$ K. Therefore $\dot{x}_A$ at the tube outlet has to be determined additionally.
b. Quality at tube outlet: $\dot{x}_A = +0.22$.

Fluid properties at $p = 0.15$ MPa for the more volatile component (acetone): $T_S^{MV} = 342.1$ K. At $\tilde{x} = 0.5$: $T_S^{Mix} = 353.15$ K.

a. In accordance with Subchap. H3.4, Eqn. (1), $\dot{x}_A = (h(z) - h'(p))/\Delta h_v(p)$; data of the mixture acc. to Lee, Kesler, and Plöcker (LKP), D5.1 and Dfa 4 [86]. $h(z) = 180.85$ kJ/kg, $h'(p) = 275.3$ kJ/kg, $\Delta h_v(p) = 590.3$ kJ/kg.

One gets $\dot{x}_A = -0.16$. For $p = 0.15$ MPa and $\tilde{x} = 0.5$, LKP leads to $\tilde{y} - \tilde{x} = 0.28$.

Equation (64) is valid: $X = 0.21$. Relative increase: $X/(1+X) = 0.17$.

b. No change, since $\dot{x}_A$ is not affecting Eq. (64).

4 Symbols

A	cross sectional area (m²)
A_{htd}	area of heated surface (m²)
C	dimensionless parameter (–)
d	inner diameter of tube; rod diameter (m)

d_h	hydraulic diameter (m)
d_{ins}	diameter of inscribed circle (cf. Fig. 27) (m)
D_w	diameter of winding in a coil; spacing of tube centers (m)
f_{rel}	relative error (–)
Fr	Froude number (–)
g	acceleration due to gravity (m/s^2)
Gr	Grashof number (–)
h	enthalpy (kJ/kg)
Δh	enthalpy difference (kJ/kg)
Δh_v	specific enthalpy of vaporization (kJ/kg)
K	subcooling parameter (–)
K_l	correction factor for heated length (–)
ℓ	length (m)
$\dot{m}$	mass velocity (kg/m^2 s)
$\dot{M}$	mass flow rate (kg/s)
p	pressure (bar)
p_c	critical pressure (bar)
p_r	reduced (reference) pressure ($p_\tau = p/p_c$)(–)
$\dot{q}$	heat flux (kW/m^2)
$\dot{q}_{cr}$	critical heat flux (kW/m^2)
$\dot{q}_{cr,o}$	critical heat flux if saturated fluid enters the channel (kW/m^2)
$\dot{q}_{uni}$	heat flux if heating is uniform (kW/m^2)
$\dot{Q}$	heat flow rate (kW)
Re	Reynolds number (–)
t	rod spacing (m)
u	velocity (m/s)
U_{htd}	heated periphery (m)
U_{wel}	wetted periphery (m)
x	mass fraction (–)
$\dot{x}$	vapor mass fraction (or "quality") on the assumption of thermodynamic equilibrium (–)
$\dot{x}_{cr}$	critical vapor mass fraction on the assumption of thermodynamic equilibrium (–)
$\dot{x}_{cr,o}$	critical vapor mass fraction on the assumption of thermodynamic equilibrium, when heat is applied through the outer tube of an annulus (–)
$\dot{x}_{cr,i}$	critical vapor mass fraction on the assumption of thermodynamic equilibrium, when heat is applied through the inner tube of an annulus (–)
$\dot{x}_{cr,up}$	vapor mass fraction when the boiling crisis occurs on the upper surface of a horizontal or inclined tube (–)
$\dot{x}_{cr,low}$	vapor mass fraction when the boiling crisis occurs on the lower surface of a vertical or inclined tube (–)
$\Delta\dot{x}_{cr}$	difference between the critical vapor mass fraction on the lower surface of a horizontal or inclined tube and that on the upper surface (–)
$\Delta\dot{x}$	margin of safety against boiling crisis (–)
$\tilde{x}$	molar fraction of the liquid phase (–)
$\tilde{y}$	molar fraction of the vapor phase (–)
y	power ratio $\{y = Q_o/Q_o + Q_i)\}$ (–)
z	coordinate (m)
γ	Barnett number (1/bar)
δ	thickness of tube wall (m)
η	dynamic viscosity (kg/ms)
ϑ	Celsius temperature (°C)
$\Delta\vartheta_u$	subcooling at inlet (K)
ϱ	density (kg/m^3)
σ	surface tension (N/m)
φ	angle of inclination to horizontal (°)
Φ^2	two-phase multiplier (–)
ψ	dimensionless mass flux; reduction factor (–)
Subscripts	
act	Actual condition
cr	condition for critical boiling state
d	related to actual diameter
g	gas or vapor phase
hom	acc. homogeneous model
i	internal heating
inl	condition at channel inlet
j	with reference to a subchannel
K	with reference to the entire channel
ℓ	liquid phase
m	expressed in terms of the mean value
max	maximum value
o	outer heating
sat	saturation
sub	relating to subcooling
Superscripts	
HB	high-boiling
LB	low-boiling
mixt	mixture
$'$	saturated state of the liquid
$''$	saturated state of the vapor

5 Bibliography

(a) Literature on specialized subjects

1. Cumo M, Palazzi G, Urbani GC (1979) On the limiting critical quality and the "deposition controlled" burnout. CNEN-RT/ING (79):4
2. Drescher G, Köhler W (1981) Die Ermittlung kritischer Siedezustände im gesamten Dampfgehaltsbereich für innen-durchströmte Rohre. BWK 33 (10):416–422
3. Doroshchuk VE, Levitan LL, Lantsmann FP (1975) Recommendations for calculating burnout in a round tube with uniform heat release. Teploenergetika 22(12):66–70
4. Academy of Sciences, USSR (1977) Tabular data for calculating burnout when boiling water in uniformly heated round tubes. Thermal Eng 23 (9):77–79
5. Kon'kov AS (1965) Experimental study of the conditions under which heat exchange deteriorates when a steam–water mixture flows in heated tubes. Teploenergetika 13(12):77
6. Groeneveld DC, Leung LKH, Kirillov PL, Bobkov VP, Smogalev IP, Vinogradov VN, Huang XC, Royer E (1996) The 1995 look-up table for critical heat flux in tubes. Nucl Eng Des 163:1–23
7. Groeneveld DC, Cheng SC, Doan T (1986) 1986 AECL-UO critical heat flux lookup table. Heat Transfer Eng 7(1–2):46–62
8. Köhler W, Herbst O, Kastner W (1994) Thermal-hydraulic behavior of a safety condenser. In: Proceedings of the international conference on new trends in nuclear system thermo-hydraulics, vol I, Pisa, Italy, May 30–June 2, 1994
9. Cumo M, Fabrizi F, Palazzi G (1978) The influence of inclination on CHF in steam generators channels. CNEN-RT/ING (78):11
10. Merilo M (1977) Critical heat flux experiments in a vertical and horizontal tube with both Freon 12 and water as coolant. Nucl Eng Des 44:1–16

11. Chojnowski B, Wilson PW, Whitcutt RDB (1974) Critical heat flux for inclined steam generating tubes. In: Symposium on multiphase flow systems, Univ. Strathelyde Paper E 3, Published in I. Chem. E. Symp. Series No. 38
12. Watson GB, Lee RA, Wiener M (1974) Critical heat flux in inclined and vertical smooth and ribbed tubes. In: 5th International heat transfer conference, Tokyo, 1974, Paper B6.8
13. Kefer V (1989) Strömungsformen and Wärmeübergang in Verdampferrohren unterschiedlicher Neigung. Dissertation Tech. Univ. Munich
14. Ünal HC (1981) Some aspects of two-phase flow heat transfer and dynamic instabilities in medium and high pressure steam generators. Dissertation Tech. Univ. Delft
15. Roumy R (1971) Dryout in helically coiled tubes with boiling Freon 12. In: European two-phase flow group meeting, Copenhagen, 1971
16. Campolunghi F, Cumo M, Ferrari G, Palazzi G (1975) Full scale tests and thermal design correlations for coiled once-through steam generators. CNEN-RT/ING (75):11
17. Cumo M, Farello GE, Ferrari G (1972) The influence of curvature in post dryout heat transfer. Int J Heat Mass Transfer 15:2045–2062
18. Naitoh M, Nakamura A, Ogasawara H (1974) Dryout in helically coiled tube of sodium heated steam generator. ASME 74-WA/HT-48
19. Duchatelle L, De Nucheze L, Robin MG (1973) Departure from nucleate boiling in helical tubes of liquid metal heated steam generators. ASME 73-HT-57
20. Ünal HC, van Gasselt MLG, van T'Verlaat PM (1981) Dryout and two-phase flow pressure drop in sodium heated helically coiled steam generators tubes at elevated pressures. Int J Heat Mass Transfer 24:285–298
21. Miropol'skiy ZL, Pikus VY (1969) Critical boiling heat fluxes in curved channels. Heat Transfer Sov Res 1(1):74–79
22. Babarin VP, Sevat'yanov RI, Alad'yev IT, Khudyakow VF, Tzachev VA (1971) Critical heat flux in tubular coils. Heat Transfer Sov Res 3(4):85–90
23. Alad'yev IT, Petrov VI, Rzayev AI, Khudyakov VF (1976) Heat transfer in a sodium-potassium heat exchanger (potassium boiler) made of helically coiled tubes. Heat Transfer Sov Res 8(3):1–16
24. Butterworth D (1971) A model for predicting dryout in a tube with a circumferential variation in heat flux. AERE-M 2436, Harwell
25. Cumo M, Palazzi G, Urbani G, Frazolli FV (1980) Full scale tests on axial profile heat flux. Influence on the critical quality in PWR steam generators. CNEN-RT/ING (80):5
26. Cocilovo M, Cumo M, Palazzi G (1979) On DNB location with axially disuniform heat flux. CNEN-RT/ING (79):21
27. Doroshchuk VE, Levitan LL et al (1978) Investigations into burnout mechanism in steam-generating tubes. In: 6th International heat transfer conference, Toronto, August 7–11, 1978, Paper FB-21
28. Peskov OL, Remizoo OV, Sudnitsyn OA (1978) Some features of heat transfer burnout in tubes with non-uniform axial heat flux distribution. In: 6th International heat transfere conference, Toronto, August 7–11, 1978, Paper NR-10
29. Keeys RKF, Ralph IC, Roberts DN (1972) Post-burnout heat transfer in high pressure steam–water mixtures in a tube with cosine heat flux distribution. Progr Heat Mass Transfer 6:99–118
30. Becker KM, Letzter A (1975) Burnout measurements for flow of water in an annulus with two-sided heating. In: European two-phase flow group meeting, Haifa, 1975. KTH-NEL-23
31. Cheng X, Müller U (2003) Review on critical heat flux in water cooled reactors, Institut für Kern- und Energietechnik, Forschungszentrum Karlsruhe GmbH, Karlsruhe, FZKA 6825
32. Zernick W, Currin HB, Elyash E, Previti G (1962) THINC, A thermal hydrodynamic interaction code for a semi-open or closed channel core. WCAP-3704
33. Chelemer H, Weismann J, Tong LS (1967) Subchannel thermal analysis of rod bundle core. WCAP-7014
34. Bowring RW (1967) HAMBO – a computer program for the subchannel analysis of the hydraulic and burnout characteristics of rod clusters. AEEW R 524
35. Rowe DS (1967) Crossflow mixing between parallel flow channels during boiling. Part 1: COBRA – computer program for coolant boiling. BNWL-371, Part 1
36. Rowe DS (1973) COBRA IIIC: a digital computer program for steady state and transient thermal-hydraulic analysis of rod bundle nuclear fuel elements. BNWL-1965
37. Hochreiter LE, Chelemer H (1973) Application of the THINC-IV program to PWR design. WCAP-8195
38. Ulrych G (1976) Strömungsvorgänge mit unterkühltem Sieden in Brennstabbündeln wassergekühlter Kernreaktoren. Dissertation, Tech. Univ. of Brunswick
39. Burtak F, Heinecke J, Glück M, Kronenberg J, Kollmann T (2006) Advanced thermal hydraulic core and fuel assembly design with state-of-the-art subchannel codes. In: TOPFUEL, Salamanca, Spain, October 22–26, 2006
40. Glück M (2007) Sub-channel analysis with F-COBRA-TF – code validation and approaches to CHF prediction. Nucl Eng Des 237:655–667
41. Suchy P, Ulrych G, Kemner H, Kurz E (1979) Application of tables of critical heat fluxes to rod bundles. CONF-790519
42. Lahey RT, Drew DA (1980) An assessment of the literature related to LWR instability modes. NUREG/CR-1414
43. Katto Y, Ohno H (1984) An improved version of the generalized correlation of critical heat flux for the forced convective boiling in uniformly heated vertical tubes. Int J Heat Mass Transfer 27(9):1641–1648
44. Katto Y (1979) A generalized correlation of critical heat flux for the forced convection boiling in vertical uniformly heated round tubes – a supplementary report. Int J Heat Mass Transfer 22:783–794
45. Katto Y, Yokoya S (1982) CHF of forced convection boiling in uniformly heated vertical tubes: experimental study of hp-regime by the use of refrigerant 12. Int J Multiphase Flow 8:165–181
46. Groeneveld DC (1974) The occurrence of upstream dryout in uniformly heated channels. In: Proceedings of the 5th international heat transfer conference, Tokyo, Japan, vol 4, pp 265–269
47. Katto Y (1978) A generalized correlation of critical heat flux for the forced convection boiling in vertical uniformly heated round tubes. Int J Heat Mass Transfer 21:1527–1542
48. Katto Y (1979) An analysis of the effect of inlet subcooling on critical heat flux of forced convection boiling in vertical uniformly heated tubes. Int J Heat Mass Transfer 22:1567–1575
49. Katto Y (1980) General features of CHF of forced convection boiling in uniformly heated vertical tubes with zero inlet subcooling. Int J Heat Mass Transfer 23:493–504
50. Katto Y (1980) Critical heat flux of forced convection boiling in uniformly heated vertical tubes (correlation of CHF in HP-regime and determination of CHF-regime map). Int J Heat Mass Transfer 23:1573–1580
51. Katto Y (1982) A study on limiting exit quality of CHF of forced convection boiling in uniformly heated vertical channels. Trans Am Soc Mech Engrs Ser C J Heat Transfer 104:40–47
52. Katto Y (1981) On the heat-flux/exit-quality type correlation of CHF of forced convection boiling in uniformly heated vertical tubes. Int J Heat Mass Transfer 24:533–539
53. Katto Y, Ashida S (1982) CHF in high-pressure regime for forced convection boiling in uniformly heated vertical tube of low length-to-diameter ratio. In: Proceedings of the 7th international heat transfer conference, vol 4, pp 291–296
54. Nishikawa K, Yoshida S, Yamada A, Ohno M (1982) Experimental investigation of critical heat flux in forced convection boiling of Freon in a tube at high subcritical pressure. In: Proceedings of the 7th international heat transfer conference, vol 4, pp 321–326
55. Katto Y (1982) An analytical investigation on CHF of flow boiling in uniformly heated vertical tubes with special reference to governing dimensionless groups. Int J Heat Mass Transfer 25:1353–1361
56. Groeneveld DC (1969): Freon dryout correlations and their applicability to water. AECL 3418
57. Ilic V (1974) The effect of pressure on burnout in a round tube cooled by Freon 12. AAEC/E325
58. Barnett P G, Wood RW (1965) An experimental investigation to determine the scaling laws of forced convection boiling heat transfer. Part 2: an examination of burnout data for water, Freon 12 and Freon 21 in uniformly heated round tubes. AEEW-R443
59. Staub FW (1969) Two phase fluid modelling – the critical heat flux. Nucl Sci Eng 35: 190–199
60. Purcupile JC, Gouse W (1972): Reynolds flux model of critical heat flux in subcooled forced convection boiling. ASME-72-HT-4
61. Dix GE (1970): Freon-water modelling of the CHF in round tubes. ASME 70-HT-26

62. Katto Y, Yokoya S (1984) Critical heat flux of liquid helium (I) in forced convective boiling. Int J Multiphase Flow 10(4):401–413
63. Lewis JP, Goddykoontz JH, Kline JF (1962): Boiling heat transfer to liquid hydrogen and nitrogen in forced flow. NASA, Techn. Note D-1314
64. Alad'yev T, Gorlov IG, Dodonov LD, Fedynskiy O (1969) Heat transfer to boiling potassium in uniformly heated tubes. Heat Transfer Sov Res 1 (4):14–26
65. Hoffman HW, Krakoviak AI (1964) Convective Boiling with Liquid Potassium. In: Proceedings of the 1964 Heat Transfer and Fluid Mechanics Institute, Oak Ridge National Laboratory, Oak Ridge, pp 19–37
66. Noel MB (1966) Experimental investigation of the forced-convection and nucleate-boiling heat-transfer characteristics of liquid ammonia. JPL-Tech. Notes Report No. 32–125
67. Cumo M, Bertoni R, Cipriani R, Palazzi G (1977) Up-flow and down-flow burnout. In: Institution of mechanical engineers conference publication 1977–1978, pp 183–192
68. Wojtan L, Revellin R, Thome JR (2006) Investigation of saturated critical heat flux in a single, uniformly heated microchannel. Exp Thermal Fluid Sci 30:765–774
69. Park JE, Thome JR (2010) Critical heat flux in multi-microchannel copper elements with low pressure refrigerants. Int J Heat Mass Transfer 53:110–122
70. Jensen MK, Bergles A (1981) Critical heat flux in helically coiled tubes. J Heat Transfer 103:660–666
71. Ahmad Y (1973) Fluid-to-fluid modelling of CHF: a compensated distortion model. Int J Heat Mass Transfer 16:641–662
72. Katsaounis A (1981) Literaturbewertung zur Fluidähnlichkeit für die kritische Heizflächenbelastung. GKSS 81/E/10
73. Katsaounis A (1980) Verification of Ahmad's fluid-to-fluid scaling law by bundle experiments. In: Winter annual meeting of ASME, Chicago, HDT-vol 14
74. Katsaounis A (1981) Comparison of various CHF-data performed in different fluids and test sections with various CHF-correlations. In European two-phase flow group meeting, Eindhoven, 1981 and GKSS 81/E/35
75. Stephan K, Körner M (1969) Berechnung des Wärmeübergangs verdampfender binärer Flüssigkeitsgemische. Chem Ing Techn. 41:409–434
76. Marroquin Nisch A (1998) Kritische Wärmestromdichte und minimale Wärmestromdichte des Filmsiedens binärer Gemische im zwangsdurchströmten senkrechten Rohr. Fortschr.-Ber. VDI, Reihe 3, Nr. 541. Düsseldorf: VDI-Verl. 1998
77. Sternman L, Abramov A, Checheta G (1968) Investigation of Boiling Crisis at Forced Motion of High Temperature Organic Heat Carriers and Mixtures. Int. Symposium on Research into Co-current Gas-Liquid Flow. Univ. of Waterloo, Canada, paper E2
78. Tolubinskiy VI, Matorin A (1973) Forced convection boiling heat transfer crisis with binary mixture. Heat Transfer Sov Res 5(2):98–101
79. Celata GP, Cumo M, Setaro T (1994) Critical Heat Flux in Upflow-Convective Boiling of Refrigerant Binary Mixtures. Int J Heat Mass Transfer 37:1143–1153

(b) General literature

80. Tong LS (1972) Boiling crisis and critical heat flux. AEC Critical Review Series. TID-25 887, 1972
81. Bergles AE (1975) Burnout in boiling heat transfer. Part I: pool-boiling System. Nucl Safety 16(1):29–42
82. Bergles AE (1977) Burnout in boiling heat transfer. Part II: subcooled and low-quality forced-convection systems. Nucl Safety 18(2):154–167
83. Bergles AE (1979) Burnout in boiling heat transfer. Part III: high-quality forced-convection systems. Nucl Safety 20(6):671–689
84. Hewitt GF (1978) Critical heat flux in flow boiling. In: International heat transfer conference, Toronto, Aug. 1978, vol 6, Paper KS-13
85. Collier JG (1972) Convective boiling and condensation. McGraw-Hill, London
86. Hewitt GF, Hall Taylor N (1970) Annular two-phase flow. Pergamon Press, Oxford
87. Wallis GB (1969) One-dimensional two-phase flow. McGraw-Hill, New York
88. Bergles AE et al (1981) Two-phase flow and heat transfer in the power and process industries. Hemisphere Publishing Corporation, Washington
89. Butterworth D, Hewitt GF (1977) Two-phase flow and heat transfer. Oxford University Press, Oxford

H3.6 Postdryout Heat Transfer in Flow Boiling

Anastassios Katsaounis[1] · *Matthias Kind*[2]
[1]Beuth Hochschule für Technik Berlin, Berlin, Germany
[2]Karlsruher Institut für Technologie (KIT), Karlsruhe, Germany

1 Introduction

The equations submitted in this subchapter are valid if the boiling crisis or critical heat flux, as defined in Subchap. H3.5, has been exceeded. (For literature and special symbols, see Subchap. H3.8.) They are also checked here for their validity under the given boundary conditions, e.g., independently controlled wall temperature or heat flux.

1. Transition boiling

Transition boiling occurs if the wall temperature is lower than the maximum or the Leidenfrost-temperature (cf. Sect. 4). It is characterized by periodic wetting of the heated wall, i.e., the wall is contacted alternately by the boiling liquid and the vapor. If the heated wall is not wetted, a distinction is made between the two regimes "film boiling" and "postdryout heat transfer."

2. Film boiling

If the bulk of the liquid phase is subcooled, i.e., if the thermodynamic vapor mass fraction is negative, or if the vapor mass fraction is small (bubble flow), a film of vapor is formed at the wall while the bulk liquid continues to flow. This condition can be regarded as the inverse annular flow. If the heat flux is independently controlled, the poor heat transfer within the film of vapor, which has a lower thermal conductivity than that of the liquid, gives rise to a high wall temperature; or, if the wall temperature is given, a low heat flux is transferred. This condition is referred to as "film boiling."

3. Postdryout heat transfer

Postdryout heat transfer, also known as the dispersed-droplet regime, occurs if an excessively high wall temperature causes large quantities of vapor to be formed and thus forces the liquid film away from the surface. It also arises as a sequel to film boiling if an increase in the evaporation rate causes the flow pattern to change into one in which liquid droplets are dispersed in a fast-flowing vapor core. Owing to the presence of the liquid droplets, heat transfer in this case is generally better than that in film boiling.

There are many evaporation processes in which heat is transferred after the critical boiling state has been transgressed. Examples can be found in conventional and nuclear evaporators, cooling systems for liquid-propelled rockets, metalworking techniques, and refrigeration equipment. Others arise in the chemical industry, in which case the wall temperature is often independently controlled and it must always be checked whether or not the maximum or the Leidenfrost temperature is exceeded.

Postdryout heat transfer occurs most frequently in evaporation processes and has been the subject of numerous studies [1–6].

For steam–water flow inside vertical tubes, a temperature-based look-up table for heat-transfer coefficients has been compiled by Groeneveld et al. [7], providing an alternative to the calculation procedures outlined in parts 2 and 3. This look-up table is based on more than 20.000 fully developed film-boiling data points selected from a databank on film boiling at the University of Ottawa. It covers the following range of parameters:

$$\begin{aligned} 0.1 \le p &\le 200\ \text{MPa}, \\ 0 \le \dot{m} &\le 7,000\ \text{kg/m}^2\text{s}, \\ -0.2 \le \dot{x}_{\text{eq}} &\le 2, \\ 50 \le (T_{\text{w}} - T_{\text{sat}}) &\le 1,200\ \text{K}. \end{aligned}$$

2 Determination of Postdryout Heat Transfer During Droplet Flow

In Fig. 1, the wall and vapor temperature profiles are schematically shown for the case of constant heat flux at postdryout conditions. Furthermore, the vapor mass fractions at equilibrium

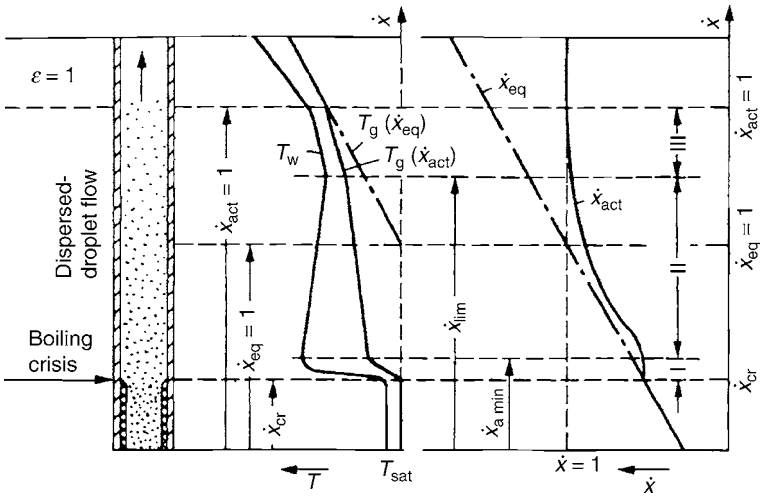

H3.6. Fig. 1. Schematic diagram showing the postdryout wall and vapor temperature profiles and vapor mass fractions under actual condition and at equilibrium.

and at actual boiling conditions are given. It is assumed that in Stage I ($\dot{x}_{cr} < \dot{x} \leq \dot{x}_{\alpha\,min}$), directly after the occurrence of the boiling crisis, the active vapor mass fraction $\dot{x}_{act}$ does not increase significantly, because here heat is transferred from the wall to the vapor phase. But, further downstream, the wall temperature increases rapidly because of the poor heat transfer between the wall and the vapor. Thereafter, the adjacent vapor is superheated, with the result that the droplets evaporate and the vapor mass fraction, the vapor velocity, and the heat transfer coefficient between the wall and the vapor increase (Stage II, $\dot{x}_{\alpha\,min} < \dot{x} < \dot{x}_{lim}$). In this stage, the wall temperature rises more slowly or, under certain conditions (in a vertical tube), even reduces. By experiments it has been demonstrated [8] that this regime of reduced increase of wall temperature rise comes to an end once a certain equilibrium vapor mass fraction $\dot{x}_{lim}$ is reached. Thereafter, the third stage (Stage III) follows, in which the surface area of the droplets decreases with an attendant reduction in the rate of evaporation.

For the calculation of rates of heat transfer, two limiting cases are assumed: thermodynamic equilibrium and thermodynamic nonequilibrium.

Thermodynamic equilibrium

In this case, both the vapor and the liquid droplets are at the saturation temperature, i.e., $T_g = T_d = T_{sat}$. The heat applied is completely consumed in evaporating the liquid droplets, and the vapor mass fraction steadily increases. The resultant increase in the vapor velocity and the improvement in heat transfer give rise to a reduction of the wall temperature, as can be seen in Fig. 2. This limiting condition can be expected at high mass velocities if the operating pressure is high, i.e., in the vicinity of the critical pressure [3–6].

Thermodynamic nonequilibrium

In thermodynamic nonequilibrium, only part of the heat is consumed in evaporating the liquid droplets at the saturation temperature $T_d = T_{sat}$. The remainder serves to superheat the vapor, the temperature of which thus steadily rises ($T_g > T_{sat}$). If it is assumed that all the heat applied is consumed solely in

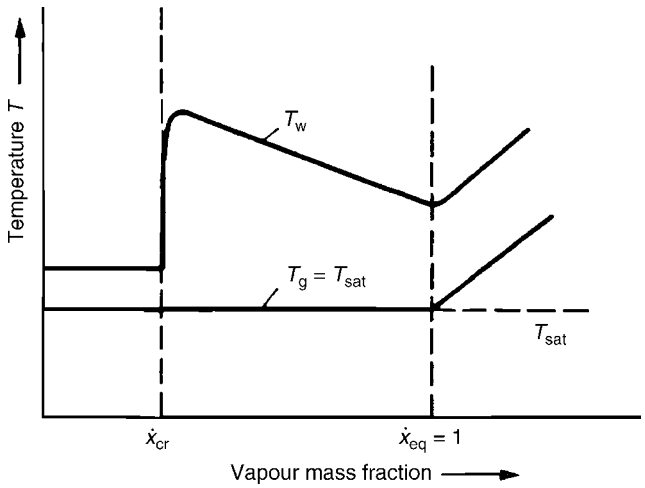

H3.6. Fig. 2. Temperature profile for evaporation in tubes at thermodynamic equilibrium.

superheating the vapor, the wall and the vapor temperature profiles will be as shown in Fig. 3. This condition arises in Stage I, $\dot{x}_{cr} < \dot{x} \leq \dot{x}_{\alpha\,min}$, illustrated in Fig. 1. In most cases, the values determined for the heat transfer coefficient under the assumption of thermodynamic nonequilibrium agree with measured values better and over a wider range of parameters than the corresponding figures calculated under the assumption of thermodynamic equilibrium.

2.1 Upward Flow Through Straight Vertical Tubes Under Thermodynamic Nonequilibrium

As a consequence of thermodynamic nonequilibrium, the enthalpy of the vapor is higher than the value at saturation, i.e., $h_g > h''(p)$. Thus, the active vapor mass fraction $\dot{x}_{act}$ is

$$\dot{x}_{act} = \frac{h - h'(p)}{h_g - h'(p)} = \frac{h - h'(p)}{\Delta h_v(p) + h_g - h''(p)}, \qquad (1)$$

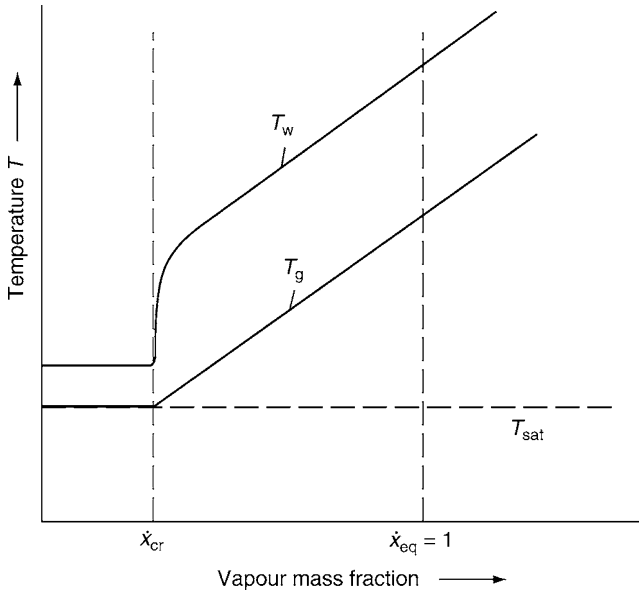

H3.6. Fig. 3. Temperature profile for evaporation in tubes at thermodynamic nonequilibrium.

whereas, using

$$h = \frac{\dot{q} A_{htd}}{\dot{m} A} + h_{inl} \tag{2}$$

for the enthalpy, the vapor mass fraction at equilibrium is obtained from

$$\dot{x}_{eq} = \frac{h - h'(p)}{\Delta h_v(p)}. \tag{3}$$

The active vapor mass fraction $\dot{x}_{act}$ is less than the value at equilibrium $\dot{x}_{eq}$, and the ratio $\dot{x}_{act}/\dot{x}_{eq}$ is referred to as the nonequilibrium factor $\dot{\omega}$, i.e.,

$$\dot{\omega} = \frac{\dot{x}_{act}}{\dot{x}_{eq}} \quad (0 \le \dot{\omega} \le 1) \tag{4}$$

Hein and Köhler [8–10] proposed the following equation for the determination of $\dot{\omega}$:

$$\dot{\omega} = \frac{2}{1 + \sqrt{1 + 4 \dfrac{c_{pg}}{\Delta h_v} \dfrac{\dot{q}}{(\alpha_{gd} A_d / A_{htd})}}}. \tag{5}$$

The term "$\alpha_{gd} A_d$" in Eq. (5), i.e., the product of the coefficient of heat transfer α_{gd} between the vapor and the liquid droplets and the area A_d of the evaporating droplets, is unknown.

The following relationships were derived by Hein and Köhler from the experimental values:

(a) For $\dot{m}/b < 1,767 \cdot 10^3$:

$$\alpha_{gd} \frac{A_d}{A_{htd}} = 1.473 \cdot 10^{-7} (\dot{m}/b)^{1.33}. \tag{6}$$

(b) For $\dot{m}/b \ge 1,767 \cdot 10^3$:

$$\alpha_{gd} \frac{A_d}{A_{htd}} = 3.078 \cdot 10^{-24} (\dot{m}/b)^4, \tag{7}$$

where b is the Laplace coefficient, as defined by

$$b = \left(\frac{\sigma}{g(\rho' - \rho'')} \right)^{0.5}. \tag{8}$$

The units for $\dot{m}$ and α_{gd} in Eqs. (6) and (7) are kg/m^2 s and kW/m^2 K, respectively.

The active vapor mass fraction $\dot{x}_{act}$ is calculated from Eq. (4); and the enthalpy of the superheated vapor h_d from Eq. (1). The temperature of the vapor in dispersed-droplet flow can then be obtained from Eq. (9):

$$T_g = T_{sat} + \frac{\Delta h_v}{c_{pg}} \left(\frac{1}{\dot{\omega}} - 1 \right). \tag{9}$$

Here, the specific heat capacity is defined by Eq. (10) and has to be calculated by an iteration procedure:

$$c_{pg} = \frac{h_g - h''}{T_g - T_{sat}}. \tag{10}$$

The wall temperature is given by

$$T_w = T_g + \frac{\dot{q}}{\alpha_{wg}}, \tag{11}$$

where α_{wg} is the heat transfer coefficient between the tube wall and the stream of vapor (gas). The method recommended by Hein and Köhler for the determination of α_{wg} is described in Chap. G2 [11]. The Reynolds number that pertains to this method is for two-phase flow, i.e.,

$$\mathrm{Re} = \mathrm{Re}_g \left\{ \dot{x}_{act} + (1 - \dot{x}_{act}) \frac{\rho_g}{\rho_l} \right\}, \tag{12}$$

where $\mathrm{Re} = \dot{m} d_h / \eta_g$ is the Reynolds number for the vapor stream.

The temperature to which the properties of the fluid are referred, for the determination of the heat transfer coefficient α_{wg}, is the average in the boundary layer, which corresponds to the arithmetic mean of the vapor and the wall temperatures. However, the density ρ_g in Eq. (12) must be referred to the vapor temperature T_g.

The vapor mass fraction $\dot{x}_{\alpha\,min}$ at the point where the heat transfer coefficient is a minimum (see Fig. 1) is given by

$$\dot{x}_{\alpha\,min} = \frac{\dot{x}_{cr}}{\dot{\omega}}. \tag{13}$$

$\dot{x}_{cr}$ in Eq. (13), e.g., for water, is obtained from Eq. (3) in Subchap. H3.5; and $\dot{\omega}$, from Eq. (5).

The point at which Stage III in Fig. 1 commences is fixed by the following correlation:

$$\begin{aligned} \dot{x}_{lim} &= 1.16 - 0.125 \log_{10}(\rho'/\rho'') \quad \text{for } \rho'/\rho'' \le 3, \\ \dot{x}_{lim} &= 1.25 - 0.320 \log_{10}(\rho'/\rho'') \quad \text{for } 3 < \rho'/\rho'' \le 26, \\ \dot{x}_{lim} &= 0.97 - 0.120 \log_{10}(\rho'/\rho'') \quad \text{for } 26 < \rho'/\rho''. \end{aligned} \tag{14}$$

Using this information about $\dot{x}_{lim}$ the range of validity for Stage II, $\dot{x}_{\alpha\,min} < \dot{x}_{eq} \le \dot{x}_{lim}$, is known.

The model recommended above was verified [3] together with four others taken from the literature [12–15] by comparing the calculated results with the measured values for water [9,16,17], refrigerant R12 [18], and hydrogen [19].The range of parameters within which the experiments were performed is listed in Table 1. It was thus demonstrated [3] that the best agreement with the experimental values over the entire range of verification was achieved by the *Hein and Köhler* method.

H3.6. Table 1. Experiments to verify the model calculations

Fluid	Pressure (bar)	ρ'/ρ'' (–)	$\dot{m}$ (kg/m²s)	$\dot{q}$ (kW/m²)	d (mm)	l (m)	Data points (–)
Hydrogen [19]	1.7–3.6	32–15	620–1,650	629–1,650	7.9	0.305	141
R12 [18]	9.3–27.9	24–5.3	326–1,280	10–63	12.5; 24.3	6.07	244
Water [17]	30–200	54–2.8	500–3,000	90–1,250	10.0–24.7	7.0	10,600
Water [16]	140–210	7.1–2.2	700–2,000	100–2,000	10.0; 20.0	3.0–8.5	2,080
Water [8]	50–200	30–2.8	300–2,500	150–600	12.5–24.3	6.1	3,500

Figures 4a, b and 5 are intended to facilitate calculations in the case of water (see Example 1).

Example 1

Water enters a vertical evaporator tube of 12 mm inner diameter at a pressure of 15 MPa (150 bar), at a heat flux of $\dot{q} = 1,000\ \mathrm{kW/m^2}$, and at an inlet velocity of $u = 3$ m/s. Determine the postdryout heat transfer coefficient α_{conv} and tube inner wall temperature T_w for $\dot{x}_{eq} = 0.8$ under the assumption of thermodynamic nonequilibrium.

According to Subchap. H3.5, $\dot{q} > \dot{q}_{cr}$. A value of $\dot{\omega} = 0.82$ can be read off against $\dot{m} = 603.1\ \mathrm{kg/m^3} \cdot 3\ \mathrm{m/s} = 1,810\ \mathrm{kg/m^2 s}$ in Fig. 4b. The value of the steam superheat that can be read off at $\dot{\omega} = 0.82$ in Fig. 5 is 28°C. Hence, $T_g = (342.1 + 28)^\circ\mathrm{C} \approx 370^\circ\mathrm{C}$. The same results can be obtained by applying Eqs. (4), (5), and (9), in which case the specific heat capacity c_{pg} must be determined by iteration. Inserting the values for η_g and for $\dot{x}_{act} = \dot{\omega} \cdot \dot{x}_{eq} = 0.82 \cdot 0.8 = 0.66$ in Eq. (12) then yields the Reynolds number for the two-phase mixture:

$$\mathrm{Re} = \frac{603.1 \cdot 3 \cdot 0.012}{2.36 \cdot 10^{-5}} \left[0.66 + (1 - 0.66)\frac{74.2}{603.1}\right] = 6.46 \cdot 10^5.$$

Iteration is commenced at $T_m = T_g$, and a value of Nu_g is read at $d/l \approx 0$ from the diagram in Chap. G2. From this, it follows that $\alpha_{wg} = 10.0\ \mathrm{kW/m^2\,K}$ and $T_w = T_g + \dot{q}/\alpha_{wg} = (370 + 100)^\circ\mathrm{C} = 470^\circ\mathrm{C}$. If the temperature-dependent properties, i.e., Pr and λ, are taken into account, then a wall temperature of 506°C is obtained after three steps in the iteration.

In this example, the values for the properties of water were taken from the literature [20].

2.2 Upward Flow Through Straight Vertical Tubes and Annular Gaps Under Thermodynamic Equilibrium

The empirical correlation proposed by Groeneveld [21] applies for high system pressures ($\rho'/\rho'' \leq 6$) and high mass flow rates ($\dot{m} > 2{,}000\ \mathrm{kg/m^2\,s}$) and assumes thermodynamic equilibrium. It has been demonstrated [3,22] that this correlation yields values for the postdryout heat transfer coefficient that still agrees with the measured values listed in Table 1. Hence, by virtue of its simplicity, it can be adapted for a rough determination of heat transfer coefficients within the given range of parameters. Note that it does not encompass the $\dot{x}_{cr} < \dot{x} \leq \dot{x}_{\alpha\,min}$ range, i.e., Zone I in Fig. 1.

Groeneveld [21] expanded the empirical relationship proposed by Miropol'skiy [23]:

$$\mathrm{Nu}'' = A\left(\mathrm{Re}''\frac{\dot{x}_{eq}}{\varepsilon_{hom}}\right)^B \mathrm{Pr}_w^C\, Y^D, \tag{15}$$

where $A = 0.00327$, $B = 0.9$, $C = 1.32$, and $D = -1.5$ for tubes and annular channels.

The Nusselt number is defined by

$$\mathrm{Nu}'' = \frac{\alpha_{conv} d_h}{\lambda''}. \tag{16}$$

The hydraulic diameter d_h is given by

$$d_h = \frac{4A}{U}. \tag{17}$$

The Reynolds number for the saturated vapor is calculated from the total mass velocity, i.e.,

$$\mathrm{Re}'' = \frac{\dot{m} d_h}{\eta''}. \tag{18}$$

Pr_w is the Prandtl number for the vapor at the wall temperature.

The heat flux is given by

$$\dot{q} = \alpha_{conv}(T_w - T_{sat}). \tag{19}$$

The term

$$\varepsilon_{hom} = \frac{\dot{x}_{eq}}{\dot{x}_{eq} + (\rho''/\rho')(1 - \dot{x}_{eq})} \tag{20}$$

is the void fraction in the homogeneous flow, i.e., the vapor velocity corresponds to that of the dispersed phase.

If thermodynamic equilibrium is assumed, the vapor mass fraction $\dot{x}_{eq}$ is obtained from the enthalpy balance expressed by Eq. (3).

The term "Y" is given by

$$Y = 1 - 0.1\left[\left(\frac{\rho'}{\rho''} - 1\right)(1 - \dot{x}_{eq})\right]^{0.4}. \tag{21}$$

Values of the Nusselt number Nu'' measured on vertical rod bundles (3 and 19 heated rods) were found to be much higher in some cases than the corresponding values calculated from Eq. (15) [21]. Another comparison between the figures calculated from Eq. (15) and measurements on horizontal and vertical three-rod assemblies immersed in refrigerant R 12 confirmed that the equation could be applied for vertical sections, if $\dot{x}_{eq} > 0.15$. The values for the Nusselt number Nu'' obtained in measurements over a horizontal section were, without exception, higher than the figures calculated from Eq. (15) [24].

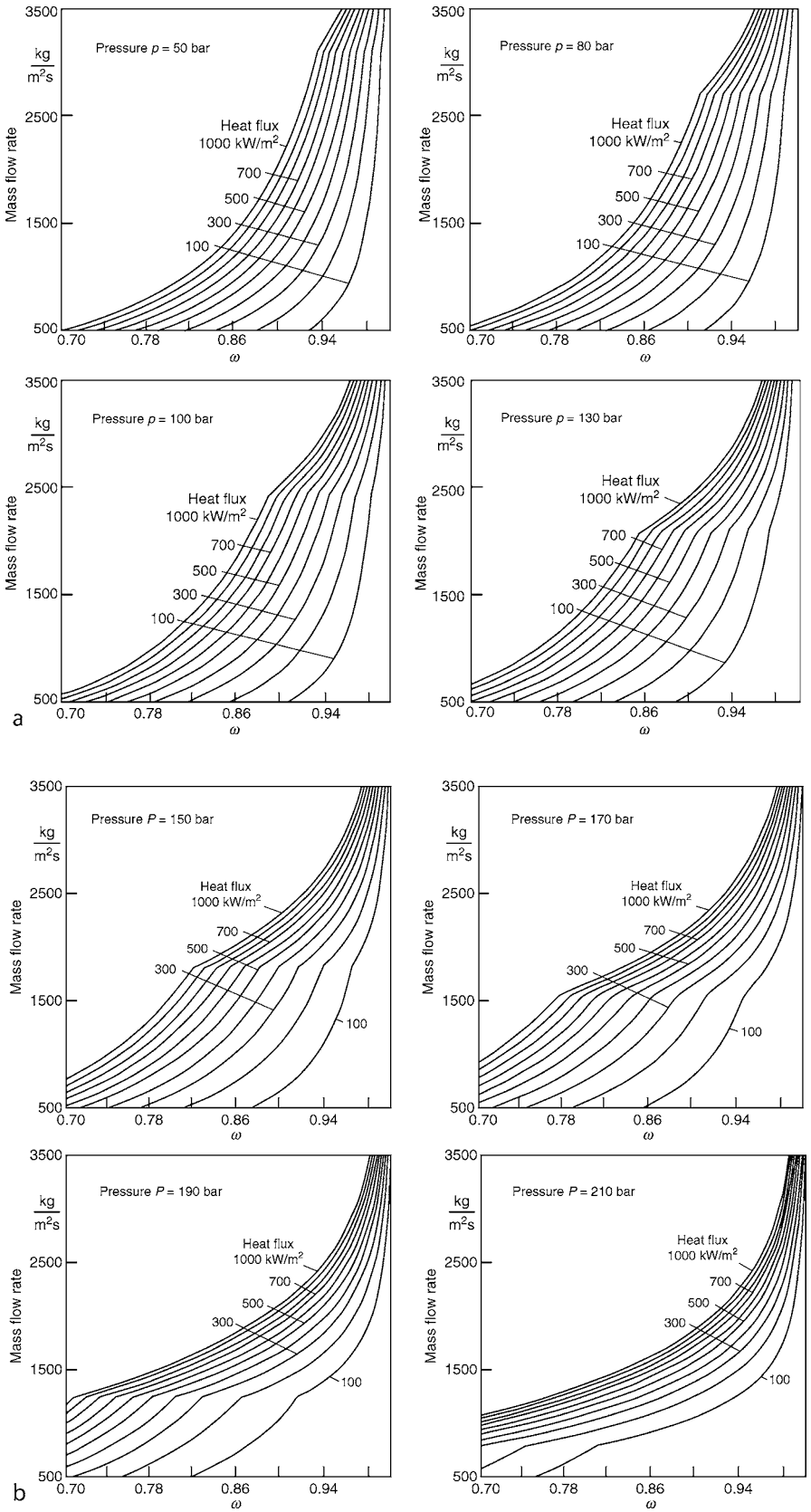

H3.6. Fig. 4. Thermal nonequilibrium factor $\dot{\omega}$ at various pressures, calculated for water [9], as a function of heat flux and mass velocity.

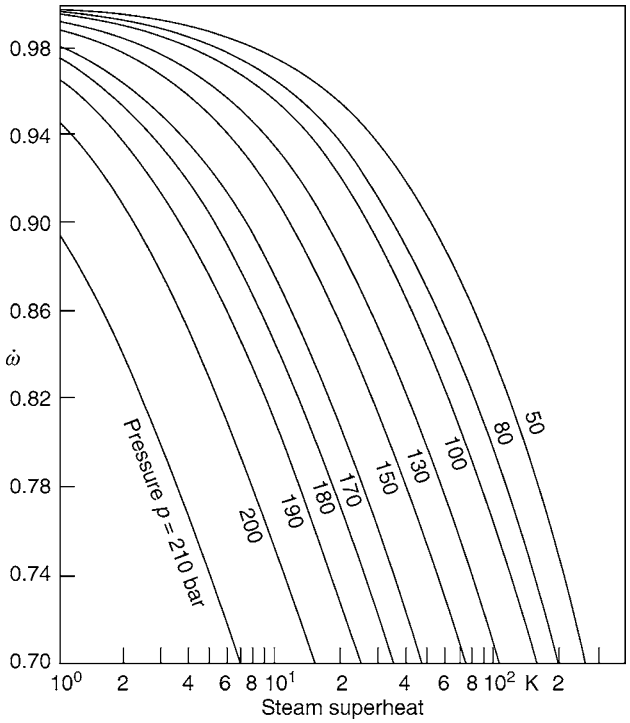

H3.6. Fig. 5. Steam superheat as a function of the thermal nonequilibrium factor $\dot{\omega}$ and the operating pressure.

Correlations derived for the determination of postdryout heat transfer coefficients and based on values obtained in measurements on methane, propane, and R 12 are cited in the literature [25,26]. They have also been checked by the author for their applicability to water and nitrogen within a restricted range of parameters. The results of other studies on heat transfer in the liquid-deficient regime on water and R 12 in horizontal tubes have been published [18,22,27].

The example presented in Fig. 6 illustrates how the Nusselt number Nu″ can be determined by graphical iteration.

Example 2

If the data are the same as those given in Example 1 but if thermodynamic equilibrium is assumed, determine the heat transfer coefficient and wall temperature for (a) $\dot{x}_{eq} = 0.4$ and (b) $\dot{x}_{eq} = 0.8$. The required properties of water can be obtained from the literature [20].

(a) Equation (21) gives

$$Y = 1 - 0.1\left[\left(\frac{603.1}{96.7} - 1\right)(1 - 0.4)\right]^{0.4} = 0.842.$$

It follows from Eq. (20) that

$$\varepsilon_{hom} = \frac{0.4}{0.4 + \frac{96.7}{603.1}(1 - 0.4)} = 0.806.$$

The Prandtl number at the saturation temperature, i.e., Pr″, is taken as a first approximation for Pr_w in solving Eq. (15) by iteration. Equation (15) thus becomes

$$Nu'' = 0.00327\left(\frac{603.1 \cdot 3 \cdot 0.012 \cdot 0.4}{2.28 \cdot 10^{-5} \cdot 0.806}\right)^{0.9} 2.48^{1.32} \cdot 0.842^{-1.5} = 1,796.$$

The heat transfer coefficient is then obtained from

$$\alpha_{conv} = \frac{Nu''\lambda''}{d_h} = \frac{1,796 \cdot 0.1164}{0.012} = 17.4 \cdot 10^3 \ W/m^2\,K.$$

Hence, the wall temperature is

$$T_w = T_{sat} + \frac{\dot{q}}{\alpha_{conv}} = 342.1 + \frac{1,000}{17.4} = 399.6°C.$$

A wall temperature of $T_w = 399.6°C$ corresponds to $Pr_w = 1.30$, and the calculation is repeated with this value. After four steps in the iteration, each of which is performed solely to determine the Prandtl number Pr_w, values of $\alpha_{conv} = 3.78$ kW/m² K and $T_w = 607°C$ are obtained.

(b) The same procedure as in (a) is adapted. In this case, a heat transfer coefficient of $\alpha_{conv} = 5.4$ kW/m²K and a wall temperature of $T_w = 527.3°C$ are obtained after three steps in the iteration.

2.3 Flow Through Straight Horizontal and Upward Inclined Tubes

Gravity and inertia forces cause the flow patterns in two-phase flow through horizontal tubes to differ from those formed in upward flow through vertical tubes (cf. Subchaps. H3.4 and H3.5). The flow patterns in horizontal tubes depend on whether the gravity or inertia predominates and on the vapor mass fraction in the stream. Thus various forms may be assumed, e.g., bubble, stratified, plug, slug, or annular flow. It can be derived from the literature [28,29] that the transition from stratified and wavy to annular flow is characterized by a modified Froude number, i.e., the ratio of the inertia forces to gravity.

Hein et al. [27,30], Köhler [8], and Kefer et al. [31] performed extensive measurements relating to the boiling crisis and to heat transfer in vertical, horizontal, and inclined evaporator tubes—predominantly in the annular and dispersed-droplet flow regimes. If the Froude number calculated from the measured values by the method described in Subchap. H3.5, Sect. 2.1.2, is higher than 10, the angle of inclination of the tube does not exert a significant effect on the location of the critical boiling state.

If flow is stratified or if the liquid film formed on the crest of a horizontal tube during annular flow is very thin, the boiling crisis first occurs at the upper surface of the tube, where the vapor mass fraction $\dot{x}_{cr,up}$ is lowest [27,30]. It has also been determined by measurements [8,30] that the maximum temperature on the inner wall at the crest of a horizontal tube is less than that in a vertical tube under otherwise identical conditions. This can be ascribed to the fact that the temperature at the unwetted upper surface, which is cooled by suspended droplets, is higher than that at the wetted lower surface, which is cooled

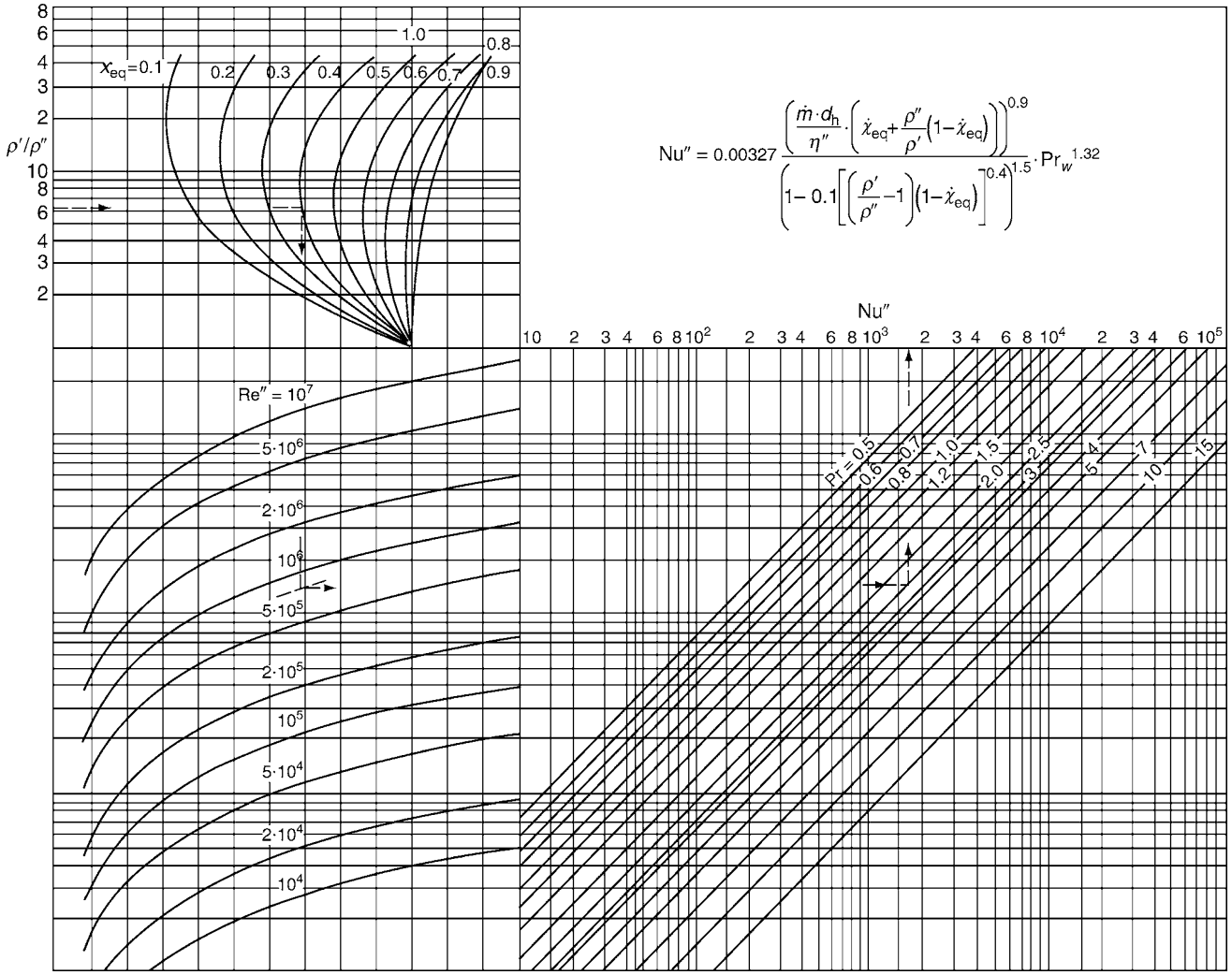

H3.6. Fig. 6. Groeneveld [21] diagram for the postdryout heat transfer at thermodynamic equilibrium in vertical cylindrical tubes and annular gaps. The Nusselt number Nu″ was determined from Eq. (15).

more efficiently by nucleate boiling. Thus, heat is conducted over the circumference from the crest to the lower side of the tube. The boiling crisis occurs sooner at the crest of a horizontal tube, i.e., at a lower vapor mass fraction, than it does under otherwise identical conditions in upward flow through a vertical tube. The effect is more pronounced in measurements of the critical boiling state and on heat transfer in horizontal tubes that are heated only on the upper side [32].

Another fact that can be derived from the literature [9] is that, if the conditions are the same, heat transfer in a horizontal tube is equal to that in a vertical tube whenever the boiling crisis occurs at the same position on the upper ($\dot{x}_{cr,up}$) and lower ($\dot{x}_{cr,low}$) horizontal surfaces, i.e., if $\dot{x}_{cr,up} \approx \dot{x}_{cr,low} \approx \dot{x}_{cr}$ and if $\dot{x}_{cr}$ is the critical vapor mass fraction under the same conditions in a vertical tube.

In the dispersed-droplet flow regime ($\dot{x} > \dot{x}_{cr,low}$), the vapor forms a continuous phase and water droplets accumulate in the lower section of the horizontal tube. It can therefore be assumed that the thermal disequilibrium is less in the lower section of the tube than in the upper [18]. Dispersed-droplet flow differs from the flow of liquids in that the natural convection has practically no effect on the temperature distribution in the wall of the tube [8].

The first step in analyzing heat transfer during flow through straight, horizontal, or inclined tubes is to determine the Froude number Fr by the method described in Subchap. H3.5, Sect. 2.1.2, and the dryout point on the upper ($\dot{x}_{cr,up}$) and lower ($\dot{x}_{cr,low}$) surfaces of the tube. The following three cases must then be taken into consideration.

1. If Fr $\geq$ 10 or if $\dot{x}_{cr,low} - \dot{x}_{cr,up} \leq 0.1$, heat transfer can be determined as described in Sect. 2.1 [22].
2. If the vapor mass fraction $\dot{x}$ in the stream lies within the $\dot{x}_{cr,up} \leq \dot{x} \leq \dot{x}_{cr,low}$ range and if Fr < 10, heat transfer cannot be easily determined. The material and wall thickness of the tube and the ratio of the wetted to the unwetted area of the inner walls exert a significant effect on heat transport [8,30]. Comprehensive calculations that involve the

two-dimensional Fourier differential equation for thermal conductivity and its solution (cf. Chap. E2) are required for this range of parameters [31].

3. Heat transfer in the $\dot{x} > \dot{x}_{cr,low}$ range of pure dispersed-droplet flow can be determined by the method given in Sect. 2.1.

3 Determination of Heat Transfer During Transition and Film Boiling

At negative or very low vapor fractions of the flow ($\dot{x} \leq 0.2$ [33] respectively $\varepsilon \leq 0.3$ [1]) and after the boiling crisis happened, transition or film boiling appears. Also, film boiling is observed before rewetting of superheated surfaces by flooding. Partial film boiling, named transition boiling, can be observed in the region between boiling crisis and minimal heat flux if the wall temperature is imposed. In this case, the minimal heat flux $\dot{q}_{min}$ corresponds to the maximum temperature T_{max} of the heated surface. The maximum temperature at flow boiling corresponds to the lowest temperature, which allows stable film boiling. A slight reduction of this maximum wall temperature leads to transition boiling or partial film boiling.

3.1 Transition Boiling

Transition boiling is observed at low or negative vapor mass fractions and is characterized by random alternating contact with the heating surface by the vapor and then the liquid.

In the near-transition boiling range, the boiling curve (heat flux versus temperature difference) plotted on a log-log scale is approximately linear. Consequently, a rough prediction of the behavior in transition boiling can be achieved by interpolation if the conditions at the critical boiling state ($\dot{q}_{cr}$; ΔT_{cr}) and the minimum heat flux ($\dot{q}_{min}$; ΔT_{max}) are known. The following equation is adapted in this case [1,31]:

$$\ln\left(\frac{\dot{q}_{TB}}{\dot{q}_{min}}\right) = \ln\left(\frac{\dot{q}_{cr}}{\dot{q}_{min}}\right) \cdot \frac{\ln(\Delta T_{max}/\Delta T_{TB})}{\ln(\Delta T_{max}/\Delta T_{cr})}. \qquad (22)$$

No information is given in the literature on how the temperature difference $\Delta T_{cr} = T_{cr} - T_{sat}$ and the heat transfer coefficient α_{cr} can be calculated. If neither of these values is available from measurements, ΔT_{cr} can be obtained as a first approximation from

$$\Delta T_{cr} = f_{corr} \frac{\dot{q}_{cr}}{\alpha_B}, \qquad (23)$$

where f_{corr} is a correction factor.

However, the condition $\Delta T_{cr} < \Delta T_{max}$ must apply, in which case $\alpha_{cr} = \alpha_B / f_{corr}$.

The method of determination for the critical heat flux $\dot{q}_{cr}$ is given in Subchap. H3.5; and for the heat transfer coefficient in developed nucleate boiling α_B, in Subchap. H3.4.

Nucleate boiling correlations do not allow for the decrease in the slope of the boiling curve before the critical boiling state is reached (cf. Fig. 1 in Subchap. H3.5). The temperature difference on the occurrence of the critical boiling state is actually greater, and allowance is made for this fact by the correction factor f_{corr} ($f_{corr} > 1$).

Auracher [33] performed measurements in the $0 \leq \dot{x} \leq 0.2$ range of vapor mass fractions on R 114 (dichlorotetrafluoroethane [$C_2F_4Cl_2$]) in vertical tubes. The results were reevaluated in order to determine the heat transfer coefficient in developed nucleate boiling α_B in Subchap. H3.2, and the correction factor $f_{corr} = \alpha_B/\alpha_{cr}$ was thus obtained. It can be seen from Fig. 7 that f_{corr} is independent of pressure within the observed range. The value shown for the correction factor in the diagram still has to be verified by measurements on other fluids. Nevertheless, it is recommended that a figure of $f_{corr} \approx 1.2$ be used in calculations until reliable results obtained on several fluids become available.

From atmospheric pool boiling experiments with water in a vertical plate [34], it is known that the properties of the surface of the plate (roughness, stain, oxidation) influence ΔT_{cr} considerably. Furthermore, it is known from steady-state [35] and transient [36] water measurements in a short vertical pipe at low pressure and low mass flow rates, that ΔT_{cr} is a function of pressure, mass flow rate, and subcooling of the fluid (see procedures to estimate $\dot{q}_{cr}$ and α_{cr} given in Subchaps. H3.4 and H3.5). Katsaounis [37] evaluated flow boiling measurements of Auracher [33] (R 114 in vertical pipes) and Weber [35,38] (water in short vertical pipes) according to the relations given by France et al. [39] for the heat flux

$$\frac{\dot{q}_{TB}}{\dot{q}_{cr}} = \exp[-K \cdot (\Delta T_{TB} - \Delta T_{cr})], \qquad (24)$$

and the heat transfer coefficient

$$\frac{\alpha_{TB}}{\alpha_{cr}} = \frac{\Delta T_{cr}}{\Delta T_{TB}} \cdot \exp[-K \cdot (\Delta T_{TB} - \Delta T_{cr})] \qquad (25)$$

(see Table 2). For these calculations ΔT_{cr} was evaluated by Eq. (23), and due to the specifics of these two measurements, Katsaounis [37] took the critical heatflux used for estimating ΔT_{cr} either from Auracher's measured data or from an empirical relation based on Weber's data. For estimating the respective maximum temperatures at transitional boiling (Leidenfrost-temperatures), Eq. (43) from Schroeder-Richter [40] was used.

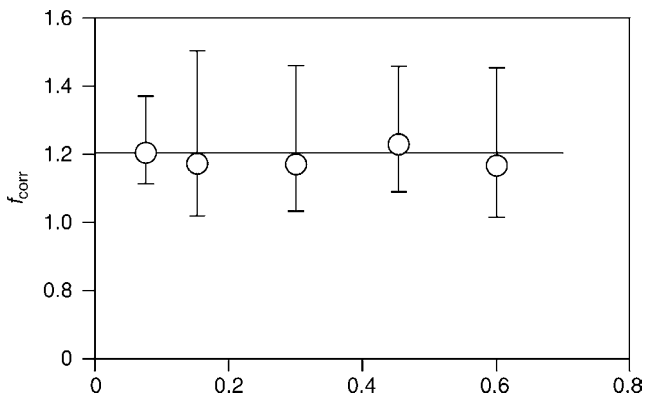

H3.6. Fig. 7. f_{corr} for R 114 as a function of the reduced pressure.

H3.6. Table 2. Experimental data versus calculation procedure of Katsaounis [37]

Fluid	Pressure (bar)	$\dot{m}$ (kg/m²s)	ψ	ΔT_{sub}, $\dot{x}$ (K, –)	d (mm)	l (m)	Data points (Eq. (26))
Water [38]	2.5–12	10–500	0.38–19.2	$5 \leq \Delta T \leq 50$	9.7	50.0	750
R 114 [33]	2.5–20	500–3,000	5.1–103.0	$0 \leq \dot{x} \leq 0.2$	14.0	87.0	970

Factor K in Eqs. (24) and (25) is obtained as a function of the dimensionless flow rate ψ

$$K = 0.033 + 8.4 \cdot 10^{-4} \cdot \psi - 9.1 \cdot 10^{-6} \cdot \psi^2 \qquad (26)$$

with ψ to be calculated from Eq. (54) in Subchap. H3.5 as follows:

$$\psi = \dot{m} \cdot \frac{d}{\eta'} \cdot \left(\sqrt{\frac{\gamma}{\rho'}} \cdot \frac{\eta'}{d} \right)^{2/3} \cdot \left(\frac{\eta'}{\eta''} \right)^{1/8} \qquad (27)$$

with

$$\gamma = \left| \frac{\mathrm{d}(\rho'/\rho'')}{\mathrm{d}p} \right| \qquad (28)$$

given as Eq. (55) in the same subchapter.

As was shown by Katsaounis [37], neither there is (for R 144) a significant dependence of Eq. (26) on vapor mass fraction $\dot{x}$ at the locus of measurement, nor there is (for water) a dependence on the subcooling of the fluid ΔT_{sub} at the entrance of measurement section.

Equations (24–28) show acceptable agreement with the correlations of France et al. [39] for $\dot{q}_{TB}$. Furthermore, measured data of Ragheb et al. [41] and Cheng et al. [42] can be reproduced well by the above equations if $\dot{q}_{cr}$ and ΔT_{cr} are given.

In the case of the transient measurements of Huang [36] in the regime of transitional boiling, Katsaounis [37] shows that the K-factor is lower than predicted by Eq. (26) for steady-state experiments. Thus, heat transfer coefficients from transient measurements of transitional film boiling (quenching experiments) are higher than the ones taken from steady-state experiments. This result is in accordance with the differences of critical heat fluxes from steady-state and from transient experiments [43]. The transient experiments of Huang [36] were carried out in the same measurement device and under the same variation of the experimental parameters as the experiments carried out by Weber [35].

Advice for the use of the equations

The following advices are given as how to apply Eqs. (22) and (24) respectively Eq. (25) for the estimation of the heat flux and the heat transfer coefficient in the transitional boiling regime. An approximation of the heat flux in the transitional boiling regime can be obtained from Eq. (22), if $\dot{q}_{cr}$ - and ΔT_{cr} -data (boiling crisis) and $\dot{q}_{min}$ - and ΔT_{max} -data at the state of minimal heat flux are known.

A more precise estimation of the heat flux is obtained from Eqs. (24–28) within the parameter range of Table 2. To do so, $\dot{q}_{cr}$ must be calculated by the procedures given in Subchap. H3.5, and ΔT_{cr} must be calculated from Eq. (23). For water, the maximum temperature for transition boiling is to be calculated from Eq. (44) respecting the range of validity of this equation.

In case, the maximum temperature is not known from measurements, the Leidenfrost-temperature must be estimated using Eq. (43). The influences of the different parameters on the Leidenfrost-temperature (see Sect. 4.2) bring about, that the maximum temperature is higher than the Leidenfrost-temperature according to Eq. (43) (see Example 3).

3.2 Film Boiling During Flow Through Vertical Cylindrical Tubes

Results of heat transfer measurements on film boiling are fewer and less accurate than those published on dispersed-droplet flow (cf. Sect. 2). For instance, correlations quoted in the literature are of restricted validity [1,2,44–49]. A recommendation often encountered in the literature is that the heat transfer coefficient in developed convective film boiling can be calculated from the same equations as those for pool boiling. This can be accepted provided that laminar flow can be assumed in the vapor film and if the mass flow rate is low ($\dot{m} < 500\,\mathrm{kg/m^2s}$). The overall heat transfer coefficient α_0 for saturated boiling can thus be obtained from the equations given in Sect. 5 of Subchap. H2.2. Alternatively, Eqs. (33–37) in this subchapter can be applied, in which case a factor of 0.8 must be substituted for the factor 0.62 that precedes the square bracket on the right-hand side of Eq. (34) in order to allow for the vertical position of the tube.

The characteristic length to insert in the expression for the Nusselt number is

$$d \equiv L = 2\pi \left[\frac{\sigma}{g(\rho' - \rho'')} \right]^{0.5}. \qquad (29)$$

It can be derived from the literature [1,2,34,42,47–54] that film boiling incurs much higher heat fluxes in subcooled (α_{sub}) than in saturated (α_0) liquids under otherwise identical conditions. In common with other authors [55,56], Groeneveld [45] recommended the following equation for determining the effect of liquid subcooling on the heat transfer coefficient:

$$\alpha_{sub} = \alpha_0 (1 + 0.025 \Delta T_{sub}). \qquad (30)$$

Although this empirical equation was derived from measurements on water, it can be adapted as a first approximation for other fluids if the flow velocity is less than 1 m/s [22,52,57].

As the liquid phase progressively evaporates downstream in the cylindrical tube, the liquid bulk in inverse annular flow disintegrates into droplets, with the result that dispersed-droplet flow gradually sets in and the heat transfer mechanism alters accordingly. The heat transfer coefficient and the wall temperature in dispersed-droplet flow are calculated as described in Sect. 2.

The boundary between the two heat transfer mechanisms, fully developed film flow and dispersed-droplet flow, is thus the intersect of the values for the heat fluxes determined by the two methods. This implies that the heat flux should be calculated by both methods and that the highest value should be taken [45], i.e.,

$$\dot{q} = \max\left[\alpha(T_w - T_{sat}); \alpha_{wg}(T_w - T_g)\right] \tag{31}$$

where α is the heat transfer coefficient in film boiling and α_{wg} is the heat transfer coefficient in dispersed droplet flow as in Sect. 2.1.

Example 3

Water flows through a boiler tube of 12 mm inner diameter with a mass flow rate of 500 kg/m^2 s, a pressure of 15 MPa (= 150 bar), and a saturation temperature of $T_{sat} = 342.1°C$. It is assumed that the critical boiling state occurs at $\dot{x}_{eq} = 0.01$ and that the inner wall temperature rises from the value at the boiling crisis T_{cr} to $T_w = 540°C$. Determine the heat transfer coefficients and the corresponding heat fluxes in the entire temperature range (T_{cr} to 540°C).

The first step is to determine the critical heat flux at $p_r = 150/221.1 = 0.678$ and $\dot{x} = 0.01$ by the method described in Subchap. H3.5. Thus,

$$\dot{q}_{cr} = 10^3\left[10.3 - 17.5 \cdot 0.678 + 8(0.678)^2\right] \cdot \left(\frac{0.008}{0.012}\right)^{0.5} \cdot \left(\frac{500}{1,000}\right)^{0.68p_r - 1.2 \cdot 0.01 - 0.3} \cdot e^{-1.5 \cdot 0.01} = 1,532\,\text{kW/m}^2.$$

The heat transfer coefficient in nucleate boiling in tubes with a slightly oxidized surface and a roughness height of $R_a = 0.8$ µm is determined by the method given in Subchap. H3.4. Thus,

$$\alpha_B = 0.72 \cdot 25.58\left(\frac{1,532}{150}\right)^{(0.8 - 0.1 \cdot 10^{0.76p_r})} \cdot \left[2.816 \cdot 0.678^{0.45} + \left(3.4 + \frac{1.7}{1 - 0.678^7}\right)0.678^{3.7}\right] \cdot \left(\frac{10}{12}\right)^{0.4}\left(\frac{0.8}{1}\right)^{0.133} = 179.5\,\text{kW/m}^2\,\text{K}.$$

The temperature difference at the dryout point can now be determined from Eq. (23), i.e.,

$$\Delta T_{cr} = 1.2 \cdot \frac{1,532}{179.5} = 10.2\ \text{K}.$$

It follows that $T_{cr} = 342.1 + 10.2 = 352.3°C$ (Point 1 in Fig. 8).

From Fig. 9, it can be seen that in this example the maximum temperature T_{max} at transitional boiling attains a value between the Leidenfrost-temperature $T_L = 374.15°C$ (Eq. (43)) and the regression line through the measured data ($T^*_{max} = 440°C$).

Thus, in the temperature range between $T_{cr} = 352.3°C$ and T_{max} heat transfer occurs in the partial film boiling regime. In order to calculate heat fluxes by Eqs. (24–28), system properties have to be taken from Chap. D2 for $p = 150$ bar and $T_s = 342.1°C$: $\eta' = 69.49 \cdot 10^{-6}$ kg/(m s), $\eta'' = 23.03 \cdot 10^{-6}$ kg/(m s), $\rho'(150\,\text{bar}) = 603.17$ kg/m^3, $\rho''(150\,\text{bar}) = 97.07$ kg/m^3, and $\rho'(151\,\text{bar}) = 601.3$ kg/m^3, $\rho''(151\,\text{bar}) = 98.15$ kg/m^3.

The calculation is as follows:

$$\gamma \approx \frac{\Delta(\rho'/\rho'')}{\Delta p} = \frac{603.17/97.07 - 601.3/98.15}{(151 - 150)\text{bar}} = 0.0874\ \text{bar}^{-1} = 0.0874 \cdot 10^{-5}\left(\text{m s}^2/\text{kg}\right),$$

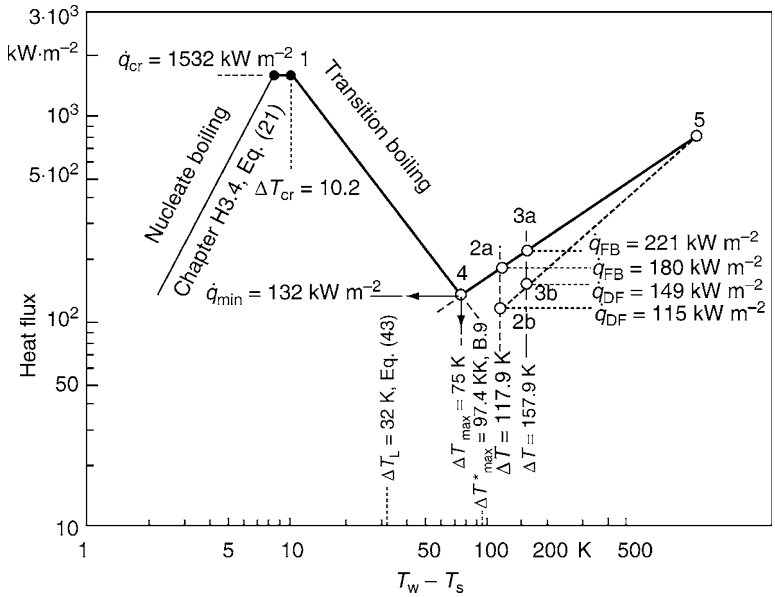

H3.6. Fig. 8. Boiling curve plotted from calculated values. Heat flux as a function of $T_w - T_{sat}$.

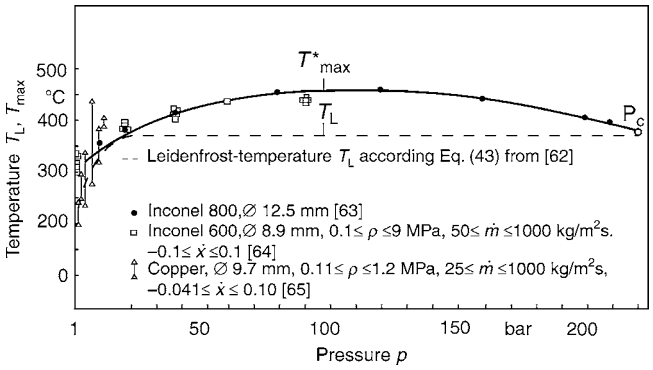

H3.6. Fig. 9. Maximum temperature for water as a function of pressure. Curve plotted from measured values [73–75].

$$\psi = \frac{500 \cdot 0.012}{69.49 \cdot 10^{-6}} \cdot \left[\sqrt{\frac{0.0874 \cdot 10^{-5}}{603.17}} \cdot \left(\frac{69.49 \cdot 10^{-6}}{0.012} \right) \right]^{2/3} \cdot \left(\frac{69.49 \cdot 10^{-6}}{23.03 \cdot 10^{-6}} \right)^{1/8} = 3.617,$$

$$K = 0.033 + 8.4 \cdot 10^{-4} \cdot 3.617 - 9.1 \cdot 10^{-6} \cdot 3.617^2 = 0.03592.$$

The following table is computed using

$$\frac{\dot{q}_{TB}}{\dot{q}_{cr}} = \exp[-0.03592 \cdot (\Delta T_{TB} - \Delta T_{cr})].$$

ΔT_{TB} (K)	$\dot{q}_{TB}/\dot{q}_{cr}$ (–)	$\dot{q}_{TB}$ (kW/m²)
20	0.7033	1,077.4
40	0.3429	525.3
60	0.1672	256.1
80	0.0815	124.8

These data are plotted in Fig. 8.

If the wall temperature exceeds T_{max}, the wall can no longer be wetted. Then, the heat transfer solely occurs by film boiling or droplet flow. The following calculations have to be carried out for determining the intersection No. 4 (ΔT_{max}; $\dot{q}_{min}$) between the calculated line for transition film boiling and that of fully developed film boiling rep. droplet flow (Fig. 8).

(a) Determination of the heat transfer coefficient on the assumption of fully developed film boiling

The reference length for the heat transfer coefficient is obtained from Eq. (29). Thus,

$$L = 2\pi \left[\frac{5.23 \cdot 10^{-3}}{9.81(603.1 - 96.7)} \right]^{0.5} = 6.45 \cdot 10^{-3} \text{m}.$$

The heat transfer coefficient α_{conv} corresponding to a wall temperature of $T_w = 460°C$, which lies between the Leidenfrost-point and the given temperature of 540°C, is determined from Eq. (34) in Sect. 3.3. But the average temperature of the vapor film, to which the properties of the stream are referred [20], must first be calculated, i.e., $T_m = 0.5(342.1 + 460) \approx 401°C$. Hence,

$$\rho_g = 63.6 \text{ kg/m}^3, \quad \eta_g = 25.0 \cdot 10^{-6} \text{ Pa s},$$
$$c_{pg} = 4.14 \text{ kJ/kg K}, \quad \lambda_g = 79.8 \cdot 10^{-3} \text{ W/mK},$$
$$\text{Pr}_g = 1.296, \quad \text{Pr}_w = 1.118.$$

The difference between the temperature of the wall and that of the liquid is $\Delta T_{wl} = 460 - 342.1 = 117.9$ K. Inserting in Eq. (37) gives

$$\Delta h_v^* = 1,004 \left[1 + \frac{0.4 \cdot 4.14 \cdot 117.9}{1,004} \right] = 1,432.4 \text{ kJ/kg}$$

The convective heat transfer coefficient for laminar flow in the vapor film is calculated from Eq. (34), i.e.,

$$\alpha_{conv} = 0.8 \left[\frac{79.8^3 \cdot 10^{-9} \cdot 9.81 \cdot 63.6 \cdot (603.1 - 63.6) \cdot 1,432.4 \cdot 10^3}{25.0 \cdot 10^{-6} \cdot 4.45 \cdot 10^{-3} \cdot 117.9} \right]^{0.25} = 1,515.8 \text{ W/m}^2\text{K}.$$

The radiation component of the heat transfer coefficient is obtained from Eq. (35), i.e.,

$$\alpha_{rad} = 0.79 \cdot 5.67 \cdot 10^{-8} \frac{460^4 - 342.1^4}{117.9} = 11.8 \text{ W/m}^2\text{K}.$$

The coefficient of total heat transfer in film boiling is then obtained from Eq. (33). Thus,

$$\alpha = 1,515.8 + \frac{3}{4} \cdot 11.8 \approx 1,524.7 \text{ W/m}^2\text{K}.$$

The corresponding heat flux is $\dot{q}_{FB} = \alpha \Delta T_{wl} = 1.525 \cdot 117.9 \approx 180$ kW/m² (Point 2a in Fig. 8).

(b) Determination of the heat transfer coefficient on the assumption of dispersed-droplet flow

From an energy balance and with an assumed mean heat flux of $\dot{q} = 856$ kW/m² the vapor mass fraction is estimated at a distance of 200 mm after the locus of critical heat flux in the evaporator pipe to be

$$\dot{x}_{eq} = \dot{x}_{inl} + 4 \cdot \frac{\dot{q}}{\dot{m} \cdot \Delta h_v} \frac{l}{d} = 0.123.$$

The heat transfer coefficient at droplet flow is determined following Sect. 2.1 with $T_w - T_{eq} = 117.9$ K and $\dot{q} = 180$ kW/m²:

With

$$b = \sqrt{\frac{5.224 \cdot 10^{-3} \text{ N/m}}{9.81 \text{ m/s}^2 \cdot (603.1 - 97.07) \text{ kg/m}^3}} = 1.0257 \cdot 10^{-3} \text{m}$$

and

$$\frac{\dot{m}}{b} = \frac{500}{1.0257 \cdot 10^{-3}} = 487.4 \cdot 10^3 \text{ kg/(m}^3\text{ s)} < 1,767 \cdot 10^3 \text{ kg/(m}^3\text{ s)}$$

is

$$\alpha_{gd} \frac{A_d}{A} = \left(1.473 \cdot 10^{-7} \left(\text{kW m}^{1.33} \text{ s}^{1.33}\right)/\left(\text{kg}^{1.33} \text{ K}\right)\right) \cdot \left(487.4 \cdot 10^3 \text{ kg/(m}^3\text{ s)}\right)^{1.33} = 5.41 \text{ kW/m}^2\text{K}.$$

Inserting $\dot{\omega} = 0.6$ and $c_{pg} = 4.13$ kJ/(kg K) the gas temperature is determined to be

$$T_g = 342.1 + \frac{1,004}{4.14}\left(\frac{1}{0.6} - 1\right) = 503.8°C.$$

From that follows $h_g(150\ \text{bar},\ 503.8°C) = 3,312\ \text{kJ/kg}$ and $h''(150\ \text{bar}) = 2,615\ \text{kJ/kg}$,

$$c_{pg} = \frac{(3,312 - 2,615)\text{kJ/kg}}{(503.8 - 342.1)\text{K}} = 4.31\ \text{kJ/(kg K)}.$$

Further, the following data are to be determined:

$$\dot{\omega} = \frac{2}{\left[1 + \sqrt{1 + \left(\frac{4{\cdot}4.31\ \text{kJ/kg K}}{1,004\ \text{kJ/kg}}\right) \cdot \frac{180\ \text{kW/m}^2}{(5.41\ \text{kW/m}^2\,\text{K})}}\right]} = 0.887,$$

$$\dot{x}_{act} = \dot{\omega}\dot{x}_{eq} = 0.887 \cdot 0.123 = 0.109,$$

and

$$\text{Re}_g = \frac{500 \cdot 0.012}{25.0 \cdot 10^{-6}}\left[0.109 + (1 - 0.109)\frac{63.6}{603.17}\right] = 4.87 \cdot 10^4.$$

With $\xi = \left[1.82 \cdot \log_{10}(4.87 \cdot 10^4) - 1.64\right]^{-2} = 0.021$, $\left(\text{Pr}_g/\text{Pr}_w\right)^{0.11} = 1.0164$, and $d/l \approx 1$, the value for Nu_g is either determined from the nomogram given in Chap. G1, or it is calculated from

$$\text{Nu}_g = \frac{(0.021/8) \cdot (4.87 \cdot 10^4 - 10^3) \cdot 1.296}{\left[1 + 12.7 \cdot \sqrt{0.021/8} \cdot (1.296^{2/3} - 1)\right]} \cdot 1.0164 = 147.$$

The heat transfer coefficient at fully developed droplet flow is

$$\alpha_{wg} = 147 \cdot \frac{79.8 \cdot 10^{-3}\ \text{W/(m K)}}{0.012\ \text{m}} = 977.5\ \text{W/(m}^2\,\text{K)}.$$

Hence, the heat flux is $\dot{q}_{FB} = 977.5\ \text{W/m}^2\text{K} \cdot 117.9\ \text{K} = 115.2\ \text{kW/m}^2$.

After a second iteration using the new $\dot{q}_{FB}$-value, one obtains $T_g = 371.7°C$, $\dot{\omega} = 0.907$, $\dot{q}_{act} = 0.112$, $\text{Re}_g = 49,300$, $\text{Nu}_g = 147.8$, and thus $\alpha_{wg} = 982.4\ \text{W/m}^2\,\text{K}$ and $\dot{q}_{FB} = 115.8\ \text{kW/m}^2$ (see point 2b in Fig. 8). Thereafter, the calculations from procedure shown in (a) and (b) has to be repeated for some other wall temperature, e.g., $T_w = 500°C$, which ought to be in between T_{max} and $T_w = 540°C$.

(a) The heat transfer coefficient at film boiling is now $\alpha = 1,400\ \text{W/m}^2\,\text{K}$ and the heat flux is $\dot{q}_{FB} = 1.4 \cdot 157.9 = 221.0\ \text{kW/m}^2$ (see point 3a in Fig. 8)

(b) After three iterations the heat transfer coefficient for droplet flow is calculated to be $\alpha_{wg} = 943.6\ \text{W/m}^2\,\text{K}$ which leads to a heat flux of $\dot{q}_{DF} = 0.9436 \cdot 157.9 = 149.0\ \text{kW/m}^2$ (see point 3b in Fig. 8).

The intersection between the line $\overline{2a\ 3a}$ and the heat flux at partial film boiling gives the maximum temperature $T_{max} = T_{sat} + \Delta T_{max} = 342.1 + 75 = 417.1°C$ and the corresponding heat flux $\dot{q}_{min} = 132.0\ \text{kW/m}^2$. This maximum temperature lies between the Leidenfrost-temperature according to Eq. (43), $T_L = 374.15°C$ ($\Delta T_L = T_w - T_{sat} = 32.0\ \text{K}$), see Fig. 8.

Furthermore, from Fig. 8 it can be read that the two straight lines $\overline{2b\ 3b}$ and $\overline{2a\ 3a}$ intersect in point 5. To the right of this point heat transfer occurs in the droplet flow regime, and to the left it occurs in the film boiling regime.

3.3 Film Boiling During Flow over Horizontal Cylinders

The heat transfer coefficient α_{conv} for forced convection in a direction perpendicular to the axis of a cylinder depends on the Froude number [57], which is defined by

$$\text{Fr} = \frac{u_l}{\sqrt{gd}}. \tag{32}$$

If $\text{Fr} \leq 1$, the total heat transfer coefficient is given by

$$\alpha = \alpha_{conv} + \frac{3}{4}\alpha_{rad}. \tag{33}$$

The term "α_{conv}" is the convection component and is given by

$$\alpha_{conv} = 0.62\left[\frac{\lambda_g^3 g \rho_g \left(\rho' - \rho_g\right)\Delta h_v^*}{\eta_g d \Delta T_{wl}}\right]^{1/4}. \tag{34}$$

The term "α_{rad}" is the radiation component and is defined by

$$\alpha_{rad} = C_{wl}\left(T_w^4 - T_l^4\right)/\Delta T_{wl}. \tag{35}$$

C_{wl} and h_v^* are defined by Eqs. (36) and (37):

$$C_{wl} = \frac{\sigma}{1/\varepsilon_w + 1/\varepsilon_l - 1}, \tag{36}$$

$$\Delta h_v^* = \Delta h_v\left(1 + \frac{0.4 c_{pg}\Delta T_{wl}}{\Delta h_v}\right). \tag{37}$$

σ is Stefan's constant for black body radiation, and ε_w and ε_l are the emissivities of the heated surface and the liquid. If ε_l cannot be obtained from tables [58], a value of $\varepsilon \approx 1$ is taken. Δh_v is the enthalpy of vaporization, and the mean temperature of the vapor film is $T_g = 0.5(T_w + T_l)$.

If $\text{Fr} \geq 2.0$, the Nusselt number is calculated from the following relationship:

$$\overline{\text{Nu}} = 2.7\left(\text{RePr}^* \frac{\nu_l}{\nu_g}\right)^{0.5}. \tag{38}$$

Nu and Pr^* are defined by Eqs. (39) and (40)

$$\overline{\text{Nu}} = \frac{\alpha_{conv} d}{\lambda_g}, \tag{39}$$

$$\text{Pr}^* = \frac{\eta_g \Delta h_v^*}{\lambda_g \Delta T_{wl}}. \tag{40}$$

The Reynolds number is given by

$$\text{Re} = \frac{u_l \rho_l d}{\eta_l}. \tag{41}$$

The numerical values to be inserted for the properties in Eq. (41) are those relating to the temperature of the liquid.

The correlation for the total heat transfer coefficient for the case of $\text{Fr} \geq 2$ allows for the radiation component, i.e.,

$$\alpha = \alpha_{conv} + \frac{7}{8}\alpha_{rad}. \tag{42}$$

Equation (38) has been checked in the $2 \leq \text{Fr} \leq 15$ range with various liquids, viz. benzene, carbon tetrachloride, ethanol, and *n*-hexane [57]. The diameter of the heaters in the experiments ranged between 9.8 and 16.2 mm.

All the properties of the vapor film (subscript "g") must be referred to the mean film temperature $T_g = 0.5(T_w + T_l)$.

The heat transfer coefficient in the $1 < Fr < 2$ range is obtained by linear interpolation of the boundary values for Fr = 1 and Fr = 2.

Studies by Motte and Bromley [59] on ethanol, benzene, *n*-hexane, and carbon tetrachloride demonstrated that heat transfer can be significantly improved through subcooling and the flow velocity. The effect of flow velocities of up to 4 m/s in these liquids has been presented in diagrams [22,59], and the effect of subcooling at low velocities ($u_l \leq 1$ m/s) can be derived from Eq. (30).

Example 4

What is the heat transfer coefficient between a slightly oxidized, horizontal heated rod of 12 mm diameter and liquid nitrogen flowing at a velocity of 3 m/s? The wall temperature is 900 K; the liquid is saturated, and the pressure in the system is 1 MPa (= 10 bar).

The properties of nitrogen can be obtained from the literature [60]. At $p = 10$ bar, $T_{sat} = T_l = 103.7$ K. Hence the difference in temperature between the wall and the liquid is $\Delta T = 796.3$ K and is thus greater than the temperature difference at the Leidenfrost-point (Sect. 4). Consequently, the film boiling occurs and the Froude number is

$$Fr = \frac{3}{\sqrt{9.81 \cdot 0.012}} = 8.7.$$

The equation to apply is therefore Eq. (38).

The properties of nitrogen at $T_l = 103.7$ K are

$$\rho_l = 668.9 \text{ kg/m}^3, \quad \eta_l = 6.57 \cdot 10^{-5} \text{ Pa s},$$
$$\Delta h_v = 153.9 \text{ kJ/kg}, \quad \nu_l = 0.98 \cdot 10^{-7} \text{ m}^2/\text{s},$$
$$Re = \frac{3 \cdot 668.9 \cdot 0.012}{6.57 \cdot 10^{-5}} = 3.67 \cdot 10^5.$$

The average temperature is

$$T_g = 0.5(900 + 103.7) \text{ K} = 501.9 \text{ K} \approx 502 \text{ K}.$$

Properties at T_g and $p = 10$ bar

$$\rho_g = 6.68 \text{ kg/m}^3, \quad \eta_g = 2.59 \cdot 10^{-5} \text{ Pa s},$$
$$\lambda_g = 0.039 \text{ W/mK}, \quad \nu_g = 3.88 \cdot 10^{-6} \text{ m}^2/\text{s},$$
$$c_{pg} = 1.06 \text{ kJ/kg K}, \quad \Delta h_v^* = 153.9(1 + 0.4 \cdot 1.06 \cdot 796.3/153.9)^2 = 1,569.9 \text{ kJ/kg},$$
$$Pr^* = \frac{2.59 \cdot 10^{-5} \cdot 1,569.9 \cdot 10^3}{0.039 \cdot 796.3} = 1.31,$$
$$\overline{Nu} = 2.7\left(3.67 \cdot 10^5 \cdot 1.31 \frac{0.98 \cdot 10^{-7}}{3.88 \cdot 10^{-6}}\right)^{0.5} = 297.0,$$
$$\alpha_{conv} = \frac{297.0 \cdot 0.039}{0.012} = 965.4 \text{ W/m}^2 \text{ K}.$$

The radiation component is obtained by inserting $\varepsilon_l \approx 1$ and $\varepsilon_w = 0.79$ in Eqs. (35) and (36). Thus,

$$\alpha_{rad} = 0.79 \cdot 5.67 \cdot 10^{-8} \frac{900^4 - 103.1^4}{796.3} = 36.8 \text{ W/m}^2 \text{ K}.$$

Inserting in Eq. (42) gives

$$\alpha = \left(965.4 + \frac{7}{8} \cdot 36.8\right) \text{ W/m}^2 \text{ K} = 997.7 \text{ W/m}^2 \text{ K}.$$

4 Determination of the Maximum Temperature at Which a Surface Is Wetted (Leidenfrost-Point)

Leidenfrost [61] was the first to observe the wetting of a surface heated to a temperature substantially higher than the saturation temperature of the wetting liquid. In describing the evaporation of water droplets on a red-hot metallic body, he noted that the droplets did not wet the surface of the metal until the temperature fell below a certain point, which is known as the Leidenfrost-temperature and is denoted by T_L. This point marks the boundary between transition and fully developed film boiling and is thus referred to as the "departure from film boiling (DFB)." The associated heat flux is known as the "minimum film boiling heat flux ($\dot{q}_{min}$)"; and the associated Leidenfrost-temperature as the "maximum film boiling temperature (T_{max})."

Wetting occurs frequently in engineering practice, e.g., in metallurgical processes, in hardening steel during quenching, in cryogenic engineering during filling, and in the operation of conventional and nuclear steam generators or heat exchangers.

4.1 Calculation of the Leidenfrost-Temperature of a Heated Surface

Schroeder-Richter and Bartsch [40,62] propose a thermomechanical model for the calculation of the Leidenfrost-temperature, assuming stable transition boiling in a situation of forced upward flow and using nonequilibrium thermodynamic principles. The fundamental assumption of this model is that the liquid surrounding the vapor film and the vapor at the heated wall are at equilibrium at their respective pressures. This presumes a situation of mechanical nonequilibrium and thus a relevant overpressure at the heated wall. Considering the conservation laws for mass, momentum and energy at the phase boundary between vapor and liquid at the locus of the Leidenfrost-phenomenon, they derive

$$h''(T_{sat}) - h'(T_L) = 0.5 \cdot [\nu''(T_{sat}) - \nu''(T_L)] \cdot [p(T_L) - p(T_{sat})], \quad (43)$$

which can be interpreted as a new way of defining the Leidenfrost-temperature.

Assuming stagnant vapor at the heated surface, this temperature replaces the temperature derived from the spinodal (see Subchap. H3.5, Fig. 1). The Leidenfrost-temperature T_L can be determined by iteration, using T_{sat} (p) as the equilibrium temperature of the fluid at pressure p in the body of the flow. For example, such an iterative calculation gives for water at $p = 1$ a Leidenfrost-temperature of $T_L = T_{sat} + 150$ K. The advantage of this equation is that it is valid for any fluid [40].

4.2 Calculation of the Maximum Temperature for Wetting of Isothermal Heated Surfaces

Figure 9 shows the Leidenfrost-temperature for water after Schroeder-Richter in comparison to measured data of Hein et al. [63], Groeneveld and Stewart [64], and Feng [65]. It can be seen, that the measured maximum temperature at transitional boiling is higher than the one defined by Eq. (43). This deviation can be justified by influences of the properties of the heating surface, and by differences in the thermodynamic properties of the flowing fluid at the core temperature and the stagnant fluid at the wall which is at maximum temperature.

The influence of the wall material on the wall temperature at wetting may only then be neglected, if isothermal or quasi-isothermal conditions exist at the wall, i.e., $(\lambda\rho c_p)_w \gg (\lambda\rho c_p)_l$. If this is not the case and the thermophysical properties of the liquid are comparable to those of the wall material, i.e., if $(\lambda\rho c_p)_w \approx (\lambda\rho c_p)_l$, then transient wetting phenomena exert larger local fluctuations of the wall temperature. In this case, thermophysical properties of the wall have to be considered for the calculation of the wall temperature.

Hitherto existing investigations about the maximum temperature have shown the influence of the following experimental parameters on the wetting temperature:

- Surface properties, i.e., roughness, stain, and oxidation [66–69].
- System pressure. Figure 9 shows the measured data of the maximum temperature. They are in good agreement with the data published elsewhere by Emmerson and Snoek [70]. Up to the critical pressure, these data show the maximum temperature of brass surfaces during partial wetting by droplets of R 12, R 113, chloroform, and carbon tetrachloride.
- Mass flow rate. Auracher [33] with R 114 and Feng and Johannsen [65,71] with water investigated the influence of the mass flow rate on the maximum temperature during transition flow boiling in tubes. Measurements by Feng [65] show that in the pressure range between 0.1 to 1.2 MPa the maximum temperature increases with increasing mass flow rate, see Fig. 10 [37].

The empirical equation proposed by Groeneveld [1,22,64] has been transformed into a dimensionless form and validated with measured data given by Feng [65] in short vertical tubes with water in the parameter range of $0.11 \le p \le 1.2$ MPa, $-0.041 \le \dot{x} \le 0.10$, and $25 \le \dot{m} \le 1,000$ kg/m^2 s. From this, the relationship

$$\frac{T_{max}(\text{in °C})}{T_{crit}(\text{in °C})} = \left[0.760 + 2.607 \cdot p_r - 4.865 \cdot p_r^2 - \frac{26.727 \cdot \dot{x}}{2.82 + 26.986 \cdot p_r}\right] \cdot f(\dot{m}) \quad (44)$$

was developed. It is the equation given by Groeneveld and Stewart [64] and expanded in [37] by the term

$$f(\dot{m}) = 0.943 + 5.87 \cdot 10^{-4} \cdot \dot{m} \quad (45)$$

is developed for the given parameter range, see Fig. 11. In this equation $\dot{x} = (h - h'(p))/\Delta h_v$ is to be set, with h being the specific enthalpy of the liquid in the bulk of the flow. Considering the range of its validity, Eq. (44) of Groeneveld and Stewart can be used to calculate the maximum temperature during flow boiling of water in tubes within the parameter range of $0.1 \le p \le 6.0$ MPa, $25 \le \dot{m} \le 1{,}000$ kg/m^2 s, and $-0.1 \le \dot{x} \le 0.1$, see Fig. 9 [37].

Subcooling the liquid ($T_l < T_{sat}$) has a significant effect on the Leidenfrost-point. This is evident from Eq. (43) and from the results plotted in Fig. 12 of measurements on various materials in water at low pressures ($p \le 0.5$ MPa). The following empirical equation, derived from the results of measurements in water [53,66,72], can be recommended for use in industry:

$$T_{max} - T_{sat} = 200\text{K} + 6.15(T_{sat} - T_l). \quad (46)$$

It is valid for surfaces in the range of $5 \cdot 10^3 \le (\lambda\rho c)_w^{1/2} \le 10^4$ W s$^{1/2}$/m^2 K, e.g., stainless steel and Zircaloy.

The best straight line drawn through points representing measurements on silver surfaces wetted with water has also been included in Fig. 12.

4.3 Calculation of the Maximum Temperature for Wetting of Nonisothermal Heated Surfaces

Henry [73] recommended the following equation for the determination of the maximum temperature for the case of clean

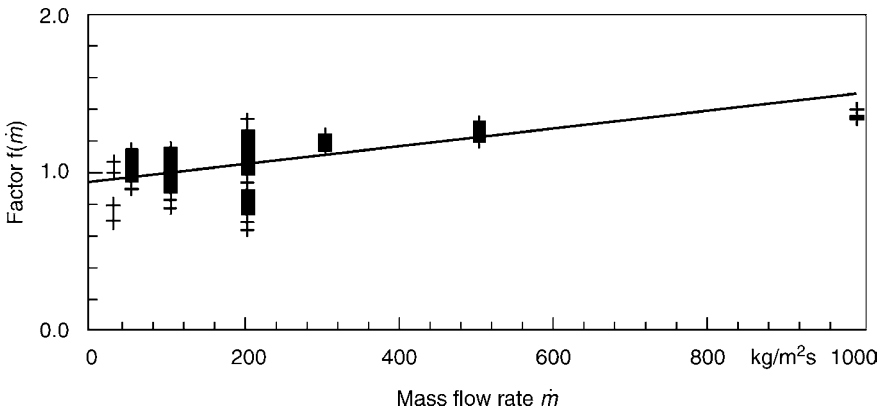

H3.6. Fig. 10. Dependence of the factor $f(\dot{m})$, Eq. (44) on the mass flow rate. Measured data from Feng [65].

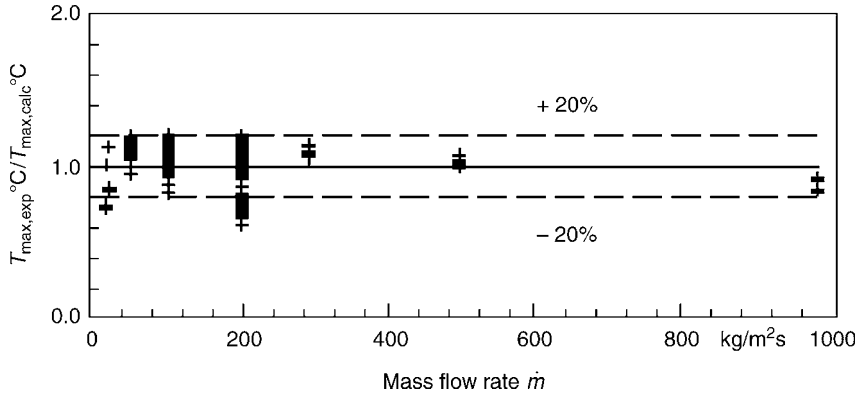

H3.6. Fig. 11. Measured data from Feng [65] compared to Eq. (44), in °C.

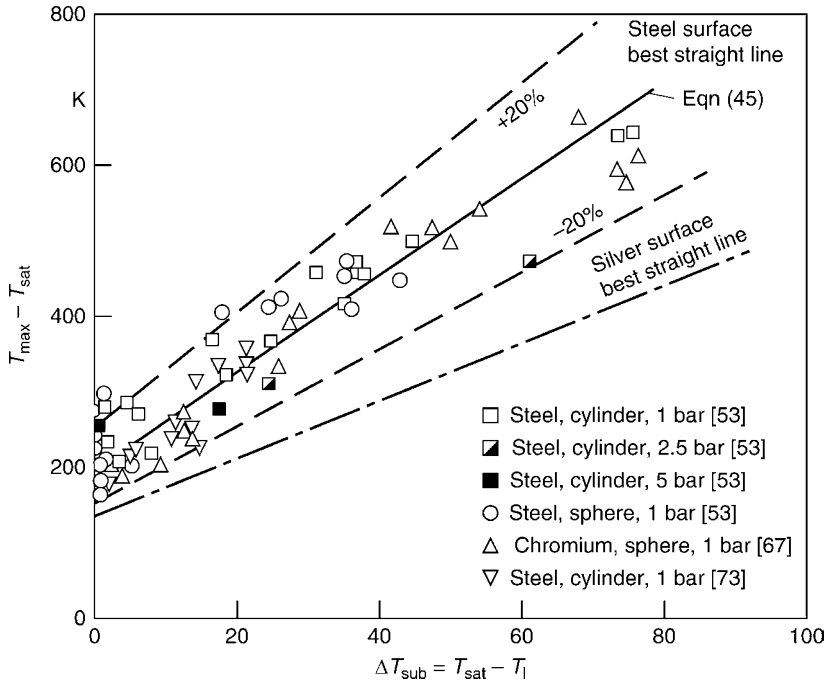

H3.6. Fig. 12. Leidenfrost-point as a function of liquid subcooling with the material or construction as parameter [47,48,55,72].

surfaces and liquids with a high surface tension, e.g., molten metals and water at near-atmospheric pressure:

$$\frac{T_{max} - T_{max-iso}}{T_{max-iso} - T_l} = 0.42 \left[\sqrt{\frac{(\lambda\rho c_p)_l}{(\lambda\rho c)_w}} \frac{\Delta h_v}{c_w \Delta T_{L-iso}} \right]^{0.6}, \qquad (47)$$

where $T_{max-iso}$ is the maximum temperature for an isothermal surface and is given by the Berenson equation [74], i.e.,

$$\Delta T_{max-iso} = T_{max-iso} - T_{sat} = 0.127 \frac{\rho_g \Delta h_v}{\lambda_g} \cdot \left[\frac{g(\rho_l - \rho_g)}{\rho_l + \rho_g} \right]^{2/3} \cdot \left[\frac{\sigma}{g(\rho_l - \rho_g)} \right]^{1/2} \left[\frac{\eta_g}{g(\rho_l - \rho_g)} \right]^{1/3}. \qquad (48)$$

The properties of the vapor must be referred to the average temperature of the vapor film $T_g = 0.5(T_w + T_l)$.

Kalinin et al [75] studied the effect of liquids with good wetting properties (contact angle $\beta_0 \approx 0$) within the following range of parameters:

$$0.02 \le p_r \le 0.60, \quad \frac{T_{sat} - T_l}{T_{crit} - T_{sat}} \le 1.5, \quad 10^{-3} \le \sqrt{\frac{(\lambda\rho c_p)_l}{(\lambda\rho c)_w}} \le 1.0 \qquad (49a)$$

$$d_h \sqrt{\frac{g(\rho_l - \rho_g)}{\sigma}} \ge 10.0, \quad u_l \left[\frac{\rho_l - \rho_g}{g\sigma} \right]^{1/4} \le 160, \quad \frac{\rho_l u_l d_h}{\eta_l} \le 1.4 \cdot 10^6 \qquad (49b)$$

The correlation that he recommended is

$$\frac{T_{max} - T_{sat}}{T_{crit} - T_l} = 1.65\left\{0.1 + 1.5\left[\frac{(\lambda\rho c_p)_l}{(\lambda\rho c)_w}\right]^{0.25} + 0.6\frac{(\lambda\rho c_p)_l}{(\lambda\rho c)_w}\right\} \quad (50)$$

It has been checked against measurements [75] in vertical tubes and annular gaps constructed from various materials (copper, Duralumin, stainless steel, magnesium alloys, titanium alloys, steel, and fluorocarbon polymers). The geometric configuration (tubes and rod bundles of various diameters) and the roughness were varied. The fluids were nitrogen, R 12, R 13, R 22, and water in free and forced convection. The scatter between the measured values and the figures calculated from Eq. (50) was ±30%. According to the publication [75], Eq. (50) is also valid for rod bundles.

Figure 13 presents a comparison between the values calculated from Eq. (50) and measurements performed by Hein [66] in R 12. The measured values are greatly scattered, particularly in the lower range of pressures. Scattering of the measurements of the Leidenfrost-temperature has been observed in all the experiments known (see Fig. 12) and can by no means be ascribed to experimental error. In view of this fact, Komnos [76] suggested that the stability of the vapor film formed before wetting occurs is of crucial importance in deciding the wetting temperature. He thus developed a mathematical model based on the mass and energy balances at the liquid/vapor film boundary. The intersect of the curves for these balances is regarded as a theoretical Leidenfrost-temperature. The scatter of the measured values is thus explained as random hydrodynamic instabilities at the liquid/vapor film phase boundary. These instabilities may cause the wall to be prematurely wetted if turbulence in the vapor film is increased. Alternatively, they may be suppressed by the surface tension in the liquid phase or by an increase in the rate of evaporation, which would bring the phase boundary closer toward the heated wall. In view of the attendant increase in density and decrease in buoyancy, it may be assumed that the film becomes more stable at elevated pressures [77].

Example 5

A high-temperature steel tube of 25 mm diameter in a steam generator is heated to $T_w = 500°C = 773.1$ K by interrupting the flow of cooling water. It is then flooded by readmitting the cooling water at a mass flow rate of $\dot{m} = 500$ kg/m^2 s, a temperature of $T_l = 160°C = 433.15$ K, and a pressure of 1 MPa. At what temperature is the wall of the tube wetted by the water?

The values for the properties of the water at T_1 are [20] $h = 675.7$ kJ/kg, $c_p = 4.337$ kJ/kgK, $\lambda_l = 0.689$ W/mK, $\rho_l = 907.5$ kg/m^3, $\eta_l = 1.72.10^{-4}$ kg/ms, and $\sigma = 0.04658$ N/m. The boiling point of water at 1 MPa is $T_{sat} = 179.9°C = 453.0$ K, and the corresponding enthalpy and latent heat of vaporization are $h' = 762.6$ kJ/kg and $\Delta h_v = 2{,}013.6$ kJ/kg. The density of the steam film at T_g is $\rho_g = 3.6$ kg/m^3.

The values for the properties of the steel tube at $T_w = 500°C$ are [58] $c_w = 0.595$ kJ/kg K; $\rho_w = 7{,}800$ kg/m^3; and $\lambda_w = 37.0$ W/m K.

For water: $(\lambda\rho c_p)_l = 0.689 \cdot 907.5 \cdot 4{,}337 = 2.71 \cdot 10^6$ W^{2}s/m^4 K^2.
For steel tube: $(\lambda\rho c)_w = 37.0 \cdot 7{,}800 \cdot 595 = 1.72 \cdot 10^8$ W^{2}s/m^4 K^2.

Although $(\lambda\rho c)_w > (\lambda\rho c_p)_l$, the maximum temperature should still be determined by Eq. (50). First of all, Eqs. (49a) and (49b) must be applied to verify whether Eq. (50) is valid within the given range of parameters. Thus,

$$p_r = \frac{1}{22.12} = 0.045, \quad \text{i.e., } p_r > 0.02,$$

$$\frac{T_{sat} - T_l}{T_{crit} - T_{sat}} = \frac{453.0 - 433.1}{647.3 - 453.0} = 0.102 < 1.5,$$

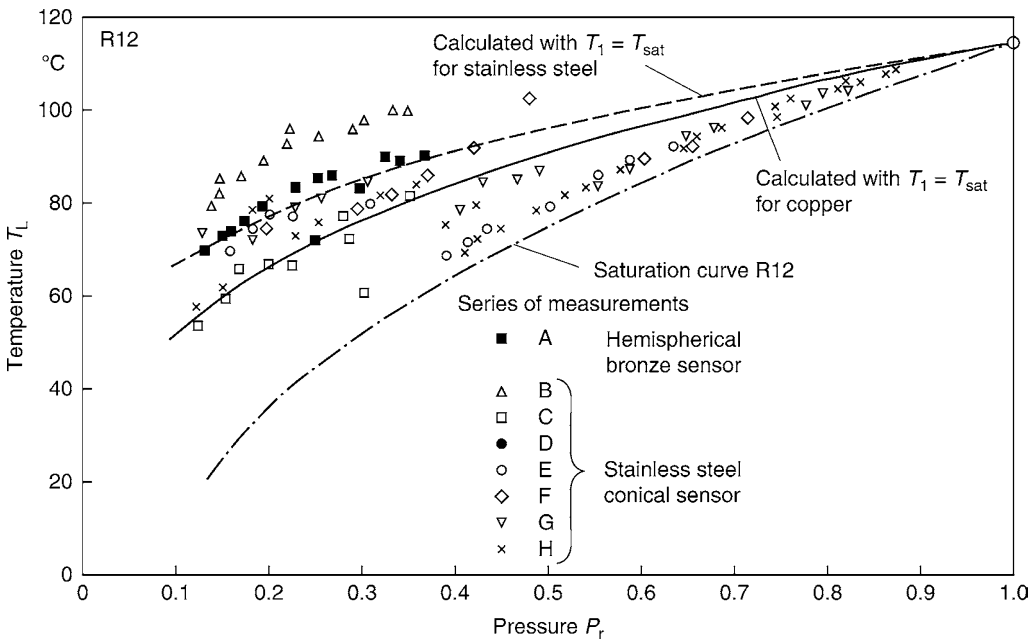

H3.6. Fig. 13. Equation (50) in comparison to data measured by Hein [66].

$$10^{-3} \le \sqrt{\frac{2.71 \cdot 10^6}{1.72 \cdot 10^8}} \le 1,$$

$$0.025\sqrt{\frac{9.81(907.5-3.6)}{46.58 \cdot 10^{-3}}} = 10.9 > 10,$$

$$u_l = \frac{500}{907.5} = 0.55 \text{ m/s},$$

$$0.55\left[\frac{907.5-3.6}{9.81 \cdot 0.04658}\right]^{1/4} = 3.6 < 160,$$

$$\frac{907.5 \cdot 0.55 \cdot 0.025}{1.72 \cdot 10^{-4}} = 7.25 \cdot 10^4 < 1.4 \cdot 10^6.$$

Hence, all the conditions stipulated in Eq. (49) are satisfied, and Eq. (50) may be applied for the determination of the maximum temperature. Thus,

$$\frac{T_{max}-T_{sat}}{T_{crit}-T_l} = 1.65\left[0.1 + 1.5\left(\frac{2.71 \cdot 10^6}{1.72 \cdot 10^8}\right)^{1/4} + 0.6 \cdot \left(\frac{2.71 \cdot 10^6}{1.72 \cdot 10^8}\right)\right] = 1.65 \cdot 0.641 = 1.057.$$

The maximum temperature is, therefore,

$$T_{max} = 453.0 + 1.057(647.3 - 433.1) = 679.4 \text{ K}.$$

The maximum temperature can also be determined from Eq. (44) to allow a comparison. The check for validity yields

$$\frac{h - h'(p)}{\Delta h_v} = \frac{675.7 - 762.6}{2,013.6} = -0.043.$$

This value lies within the verified range. Thus,

$$T_{max} = 557.6 + 44.1 \cdot 1 - 3.72 \cdot 1^2 - \frac{10^4}{2.82 + 1.22 \cdot 1}\left[\frac{675.7 - 762.6}{2,013.6}\right] = 704.4 \text{ K}.$$

Therefore, the maximum temperature determined by the two methods differ by 25 K, i.e., by only about 3.5%, and the tube is rewetted at about 700 K or 427°C.

The calculation of the maximum temperature is done with and without taking into account the influence of the mass flow according to Eq. (44) with $f(\dot{m}) = 0.943 + 5.87 \cdot 10^{-4}$ m² s/kg· 500 kg/m² s = 1.236. With $p_r = 1.0/22.12 = 0.04521$ follows

$$\frac{T_{max}(\text{in°C})}{T_{crit}(\text{in°C})} \cdot \frac{1}{f(\dot{m})} = \left[0.760 - 2.607 \cdot 0.04521 - 4.865 \cdot 0.04521^2 - \frac{26.727 \cdot (-0.043)}{2.82 + 26.986 \cdot 0.04521}\right] = 1.153.$$

When neglecting the influence of the mass flow rate according to Eq. (50), the maximum temperature is calculated to T_{max} = 0.917·374.15 = 343.1°C (= 616.1 K). This value differs by 63 K to the value according to Eq. (50), which means that in this case the difference is rather big. But, accounting for the influence of the mass flow rate according to Eq. (44), then T_{max}/T_{crit} = 0.917·1.236 = 1.133, or T_{max} = 1.133·374.15 = 423°C (= 697 K). Now, the difference between both calculations is only 18 K.

Example 6

A tantalum sphere heated to 1,700 K comes into contact with liquid sodium at 1,150 K and 0.1 MPa. At what temperature is the sphere wetted by the sodium?

The values for the properties of sodium at T_l = 1,150 K and p = 0.1 MPa are [53] $\lambda_l = 49.9$ W/m K, $\rho_l = 743.0$ kg/m³, $c_p = 1.28$ kJ/kg K, and $\sigma = 0.092$ N/m. The values relating to $T_g = 0.5(1,700 + 1,150) = 1,425$ K are $\rho_g = 0.199$ kg/m³, $\eta_g = 3.03 \cdot 10^{-5}$ kg/m s, $\lambda_g = 0.0456$ W/m K, and $\Delta h_v = 3,896.6$ kJ/kg. The critical pressure and the corresponding temperature of the sodium are p_{crit} = 37 MPa and T_{crit} = 2,500 K. The saturation temperature of sodium at 0.1 MPa is T_{sat} = 1,153 K.

The values for the properties of tantalum at the temperature at the surface of the sphere are $\lambda_w = 72.2$ W/m K, $\rho_w = 16,650$ kg/m³, and $c_w = 0.15$ kJ/kg K [52].

For sodium: $(\lambda\rho c_p)_l = 49.9 \cdot 743.0 \cdot 1,280 = 4.74 \cdot 10^7$ W² s/m⁴ K².
For tantalum: $(\lambda\rho c)_w = 72.2 \cdot 16,650 \cdot 150 = 1.8 \cdot 10^8$ W² s/m⁴ K².

Thus, $(\lambda\rho c_p)_l$ and $(\lambda\rho c)_w$ are of the same order, i.e., $(\lambda\rho c_p)_l \approx (\lambda\rho c)_w$. Since, in addition, $p_r = 0.1/37 < 0.02$, i.e., <0.02, and the liquid has a high surface tension; Eqs. (47) and (48) should be taken to calculate the maximum temperature. Equation (48) becomes

$$T_{max-iso} = T_{sat} + 0.127\frac{0.199 \cdot 3,896.6 \cdot 10^3}{0.04556} \cdot \left[\frac{9.81 \cdot (743.0 - 0.199)}{743.0 + 0.199}\right]^{2/3} \cdot \left[\frac{0.092}{9.81 \cdot (743.0 - 0.199)}\right]^{1/2} \cdot \left[\frac{3.03 \cdot 10^{-5}}{9.81 \cdot (743.0 - 0.199)}\right]^{1/3},$$

$$T_{max-iso} = 1153 + 56.5 = 1,209.5 \text{ K}.$$

The maximum temperature then follows from Eq. (47), i.e.,

$$\frac{T_{max} - T_{max-iso}}{T_{max-iso} - T_l} = 0.42\left[\sqrt{\frac{4.74 \cdot 10^7}{1.8 \cdot 10^8}} \cdot \frac{3,896.6}{0.15 \cdot 56.5}\right]^{0.6} = 11.14,$$

or

$$T_{max} = 1,209.5 + 11.14(1,209.5 - 1,150) = 1,872.3 \text{ K} = 1,599°\text{C}.$$

It can be derived from tables compiled by various authors [22] that the value of T_{max} thus calculated differs by no more than ±15% from the measured values. Accordingly, the tantalum sphere will be wetted immediately on its immersion in the sodium.

H3.7 Flow Boiling of Mixtures

Dieter Steiner[1,†] · *Matthias Kind*[1] · *Yasushi Saito*[2]
[1]Karlsruher Institut für Technologie (KIT), Karlsruhe, Germany
[2]Kyoto University, Osaka, Japan

The heat transfer coefficient for mixtures *without miscibility gap* is defined by

$$\alpha(z) = \frac{\dot{q}(z)}{\overline{T}_w(z) - T_{sat}(p(z))} \qquad (1)$$

(identical to Eq. (3) in Chap. H3), in which the boiling point T_{sat} is the equilibrium temperature at pressure p of the system when the molar composition of the liquid phase is $\underline{\tilde{x}}$ at a point z in an evaporator tube.

If due consideration is given to the real behavior of the components j in the mixed phase, the term $T_{sat}(z) = T_{sat}(p, \underline{\tilde{x}})$ can be obtained by iteration as described in Subchap. D5.1 (see also Example 2). The boiling temperature of pure substances steadily decreases as a result of the pressure drop; however, $T_{sat}(z)$ for mixtures may even increase, because the less volatile components become more concentrated along the length of the flow path z.

1 Convective Flow Boiling of Mixtures

It has been established by various studies [1–26] (see Subchap. H3.8) that convective and nucleate boiling occur together in mixtures. Niederkrüger [23] and Wettermann [24] demonstrated this most clearly by local measurements. The results obtained by Wettermann on a binary mixture for mass velocities between 80 and 400 kg/m^2 s are presented in Fig. 1.

In the light of these results, both the heat transfer coefficient in the convective boiling regime $\alpha(z)_{conv}$ and the local single-phase heat transfer coefficients $\alpha(z)_{L0}$ and $\alpha(z)_{G0}$ can be determined from the equations given in Subchap. H3.4. The appropriate properties for the mixture to be inserted in the equations can be obtained from Chap. D1. The composition of the mixture is calculated as described in Sect. 4. Methods for determining the values for the properties of refrigerant–oil mixtures without miscibility gaps [27–31] are presented in Chap. D1. In this case, the values to insert for the refrigerant are those corresponding to saturation at the system pressure; and the values for the oil are those at the boiling point $T_{sat}(p)$ of the refrigerant.

1.1 Vertical Tubes

All points on the inner wall of the tube are wetted, and $\alpha(z)_{conv}$ can be calculated from Subchap. H3.4, Eq. (1).

1.2 Horizontal Tubes

Subchap. H3.4, Eq. (3) is used to determine $\alpha(z)_{conv}$ for all flow patterns with the exception of stratified and stratified-wavy flows. In the latter two cases, incomplete wetting must be taken into consideration and therefore, Subchap. H3.4, Eqs. (3–11) for the boundary conditions $\dot{q}$ = constant and T_w = constant are used. The *flow pattern* is determined from the flow pattern map (see Subchap. H3.1) and the boundary conditions that define them. The values to be inserted for the properties in all the dimensionless numbers and equations are those for the mixture.

It was demonstrated by Gropp [20] that the resistance to mass transfer on the liquid side has comparatively little effect in convective boiling of mixtures with normal viscosity. If the mixture has a high viscosity, the resistance to mass transfer on the liquid side exerts a significant effect, even in convective boiling, as has been demonstrated by Palen [21] with mixtures of ethylene glycol/water and propylene glycol/water. In this case the measured heat transfer coefficients are considerably lower than the coefficients estimated by linear averaging the coefficients calculated for the pure substances according to Eq. (2), see below. Nevertheless, Numrich [25] shows that a good agreement between experiment and calculation can be obtained, if $\alpha(z)_{conv}$ is estimated by Subchap. H3.4, Eqs. (1–8), and if properties of the mixture are used in these equations.

2 Nucleate Boiling of Mixtures in Pipe Flow

The upper limit in nucleate boiling of mixtures is the critical boiling state (cf. Subchap. H3.5). Vertical tubes in evaporators are always completely wetted up to this point, whereas

[†]Deceased

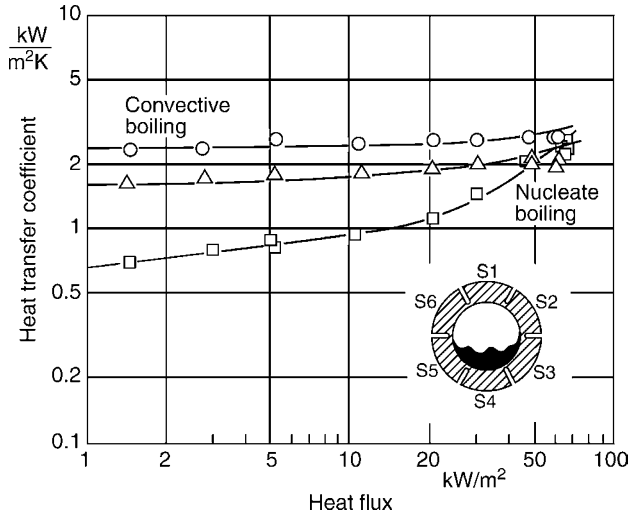

H3.7. Fig. 1. Local heat transfer coefficient in segment S4 as a function of the heat flux. System $C_2F_6/C_2H_2F_4$, $p = 11$ bar, vapor mass fraction 0.65, composition 23 mol% C_2F_6.

horizontal tubes may already be incompletely wetted before the critical boiling state is reached. Consequently, the heat transfer equations for vertical tubes differ from those for horizontal. In both cases, it is essential to arrange the components of the mixture in the sequence of their boiling points, i.e., the subscript $j = 1$ is allotted to the component with the lowest boiling point, and the subscript $j = K$, to the component with the highest boiling point.

2.1 Nucleate Boiling in Vertical Tubes

According to the literature [3–21] and according to own results of extensive systematic measurements [22–24], the best agreement between mathematical models given by [2,26] and experimental data is obtained with the help of the following equations:

$$\frac{1}{\alpha(z)_{\mathrm{id,B}}} = \sum_{j=1}^{K} \frac{\tilde{x}_j}{\alpha_{\mathrm{B},j}}. \tag{2}$$

The heat transfer $\alpha_{\mathrm{B},j}$ for the pure substances j at the point z are obtained by inserting the local parameters in Eq. (21), Subchap. H3.4.

Mixtures at their azeotropic composition boil like pure substances. Therefore, $\alpha_{\mathrm{id,B}}$ -values of azeotrope forming mixtures, which are not at their azeotropic composition, have to be estimated from Eq. (1) using $\alpha_{\mathrm{B},j}$ -values for the azeotrope and for the pure substance.

Using Eq. (2) the heat transfer coefficient of a mixture at nucleate boiling is estimated from

$$\frac{\alpha(z)_{\mathrm{B}}}{\alpha_{\mathrm{id,B}}} = \frac{1}{1 + \frac{\alpha_{\mathrm{id,B}}}{\dot{q}} \left[\sum_{j=1}^{K-1} \left(T_{\mathrm{sat},K} - T_{\mathrm{sat},j}\right)\left(\tilde{y}_j - \tilde{x}_j\right)\left(1 - \exp\frac{-B_0 \dot{q}}{\beta_{\mathrm{L}} \tilde{\rho}_{\mathrm{L}} \Delta\tilde{h}_{\mathrm{v}}}\right) \right]}. \tag{3}$$

In this model, which was proposed by Schlünder [2], B_0 is a parameter, which considers the fraction of heating power, required for nucleate boiling, with respect to the total heating power. β_{L} is the mass transfer coefficient on the liquid side of the phase boundary.

The terms in Eq. (3) are defined by the following equations:

$$\tilde{\rho}_{\mathrm{L}} = \left(\sum_{j=1}^{K} \tilde{x}_j \tilde{v}_j \right)^{-1}. \tag{4}$$

The molar volumes for the pure substances $\tilde{v}_j$ are determined at $T_{\mathrm{sat}}(z)$ and p. If the molar densities of the pure substances at $T_{\mathrm{sat}}(z)$ and p are known, which is often the case, the following applies:

$$\tilde{v}_j = \left(\tilde{\rho}_j\right)^{-1}. \tag{5}$$

The molar enthalpies for the liquid $\tilde{h}'_j$ and the vapor $\tilde{h}''_j$ must also be determined for the pure substances in the saturated state at $T_{\mathrm{sat}}(z)$ and p. Thus, the molar enthalpy of vaporization is given by

$$\Delta\tilde{h}_{\mathrm{v}} = \sum_{j=1}^{K} \tilde{y}_j \tilde{h}''_j - \sum_{j=1}^{K} \tilde{x}_j \tilde{h}'_j \tag{6}$$

with $\tilde{y}_j$ the mole fraction corresponding to $\tilde{x}_j$ at equilibrium.

If the saturation enthalpies $\tilde{h}'$ and $\tilde{h}''$ are unknown, the following approximation can be used:

$$\Delta\tilde{h}_{\mathrm{v}} = \sum_{j=1}^{K} \Delta\tilde{h}_{\mathrm{v}j}\left(T_{\mathrm{sat},j}(p)\right)\tilde{x}_j. \tag{7}$$

For mixtures of halogenated hydrocarbons and for mixtures of a halogenated hydrocarbon with an organic substance, the following relation is confirmed for a wide parameter range [22–24]:

$$\frac{B_0}{\beta_{\mathrm{L}}} \cdot \frac{\alpha_{\mathrm{id,B}}}{c_{\mathrm{pL}}\rho_{\mathrm{L}}} = 40.6 \left(\frac{\dot{q}}{\dot{q}_0}\right)^{1.19} \left(\frac{\dot{m}}{\dot{m}_0}\right)^{-0.77} \dot{x}^{-0.15} \tag{8}$$

with $\dot{q}_0 = 20,000\ \mathrm{W/m^2}$ and $\dot{m}_0 = 100\ \mathrm{kg/m^2\,s}$. Good agreement is shown with literature data [11,17,18]. For rough estimations, the value $B_0/\beta_{\mathrm{L}} = 5 \cdot 10^3\ \mathrm{s/m}$ may be assumed.

Because the above equations are derived in general terms, it is reasonable to assume that they can also be applied to ternary and multicomponent mixtures.

2.2 Nucleate Boiling in Horizontal Tubes

According to the current knowledge on the subject, incomplete wetting is to be treated with the help of perimeter-averaged heat transfer coefficient $\alpha_{\mathrm{B},j}$ of the pure substances. A more physical prediction of heat transfer coefficients would have to consider local conditions at the incompletely wetted surfaces. This method has been elaborated for a limited number of mixtures by Wettermann [24]. The following applies for a horizontal tube:

$$\frac{1}{\alpha_{\mathrm{id,B}}} = \sum_{j=1}^{K} \frac{\tilde{x}_j}{\alpha_{\mathrm{B},j}}. \tag{9}$$

The heat transfer coefficients $\alpha_{\mathrm{B},j}$ for the pure substances j are obtained from the local parameters at the point z, as defined by

Subchap. H3.4, Eqs. (30), (31), and (33–37), with due allowance for the flow pattern and boundary conditions ($\dot{q}$ = constant; T_w = constant).

Studies by Niederkrüger [23] and Wettermann [24] on binary mixtures in various states demonstrated that the flow pattern map, see Subchap. H3.1, and the boundary conditions that define them also permit useful predictions for mixtures, provided that the values inserted for the properties in all the dimensional numbers and equations are those for the mixture (cf. Chap. D1). Thus, the flow pattern determined for the mixture at the point z must be used to calculate the value of $\alpha_{B,j}$ for the pure substances j.

The *heat transfer coefficient for the mixture* $\alpha(z)_B$ can then be obtained from Eq. (3). The value of $\alpha_{id,B}$ that is used on both sides of Eq. (3) is determined from Eq. (9).

Experimental studies have allowed the above equations to be checked only for binary and ternary mixtures. It can be assumed from the results obtained by Zizyukin and Aèrov [6] on ternary mixtures that the equations can also be applied to multicomponent mixtures.

3 Total Heat Transfer Coefficient in Flow Boiling of Mixtures

As was previously stated, a given wall superheat or a given heat flux $\dot{q}_{onb}$ is required for onset of nucleate boiling. This also pertains to mixtures, and the following equation approximately applies for T_{sat} at $z = 0$:

$$\dot{q}_{onb} = \frac{2\,\sigma\,T_{sat}\,\alpha_{L0}}{r_{cr}\,\tilde{\rho}''\,\Delta\tilde{h}_v}. \tag{10}$$

All the values to be inserted for the properties are those for the mixture, and Eq. (3) applies for the molar density of the mixed vapor $\tilde{\rho}''$. The molar enthalpy of vaporization for the mixture is calculated from Eq. (4), and the surface tension, by the method given in Chap. D1. The numerical value $r_{cr} = 0.3 \cdot 10^{-6}$ m also applies for mixtures. The term α_{L0} is the local single-phase heat transfer coefficient at the point $z = 0$ (cf. Sect. 4 of Subchap. H3.4) for the liquid mass velocity $\dot{m}$. The properties used for the determination of α_{L0} are those for the liquid mixture.

If the heat flux to be transferred at the point z is $\dot{q}(z) \geq \dot{q}_{onb}$, the total perimeter-averaged heat transfer coefficient can be calculated from

$$\alpha(z) = \sqrt[3]{\alpha(z)_{conv}^3 + \alpha(z)_B^3} \tag{11}$$

and

$$\alpha(z) = \frac{\dot{q}(z)}{T_w(z) - T_{sat}(z)}. \tag{12}$$

If $\dot{q}(z) \leq \dot{q}_{onb}$, only the convective component needs to be taken into consideration, i.e., $\alpha(z) = \alpha(z)_{conv}$.

4 Changes in the State of Mixtures

The relationship between the instantaneous composition of the liquid $\underline{\tilde{x}}$ and the mass flow rate of the remaining liquid $\dot{M}_L$ at the point z can be determined if the heat transferred per element of length Δz of evaporator tube is known. The following definitions apply.

The molar flow rates of liquid and vapor are determined from the mass flow rates $\dot{M}_L$ and $\dot{M}_G$ and the molar masses $\widetilde{M}_L$ and $\widetilde{M}_G$, i.e.,

$$\dot{N}_L = \frac{\dot{M}_L}{\widetilde{M}_L(\underline{\tilde{x}})}, \tag{13}$$

$$\dot{N}_G = \frac{\dot{M}_G}{\widetilde{M}_G(\underline{\tilde{y}})}. \tag{14}$$

If the remaining liquid at any point z in the direction of flow is assumed to be in equilibrium with the vapor at that point, the following applies

$$K_j(T_{sat}(z), \underline{\tilde{x}}) \equiv \frac{\tilde{y}_j}{\tilde{x}_j}. \tag{15}$$

The phase equilibrium constant K_j is determined by the methods described in Chap. D5. If component j is the volatile component, then $K_j > 1$; otherwise $K_j < 1$. For azeotropic mixtures $K_j = 1$.

In the case of saturated liquid entering the tube, balancing of component j is done by

$$\dot{N}_{L,in}\tilde{x}_{j,in} = \dot{N}_{L,out}\tilde{x}_{j,out} + \dot{N}_{G,out}\tilde{y}_{j,out}. \tag{16}$$

Insertion of Eqs. (13) and (14) leads to

$$\frac{\dot{M}_{L,out}}{\widetilde{M}_{L,out}}\tilde{x}_{j,out} + \frac{\dot{M}_{G,out}}{\widetilde{M}_{G,out}}\tilde{y}_{j,out} - \frac{\dot{M}_{L,in}}{\widetilde{M}_{L,in}}\tilde{x}_{j,in} = 0. \tag{17}$$

Taking into consideration, that

$$\dot{M}_{L,in} = \dot{m}A, \tag{18}$$

$$\dot{M}_{L,out} = \dot{m}A(1 - \dot{x}_{out}), \tag{19}$$

$$\dot{M}_{G,out} = \dot{m}A\dot{x}_{out}, \tag{20}$$

the following objective function OF is obtained:

$$OF = \frac{(1 - \dot{x}_{out})}{\widetilde{M}_{L,out}}\tilde{x}_{j,out} + \frac{\dot{x}_{out}}{\widetilde{M}_{G,out}}\tilde{y}_{j,out} - \frac{1}{\widetilde{M}_{L,in}}\tilde{x}_{j,in} = 0. \tag{21}$$

Using Eq. (15), this equation can be solved by iteration for a given pressure. By this at any locus z the values for $\tilde{x}_{j,out}$ and $\tilde{y}_{j,out}$ are found.

Measurements by Wettermann [24] validate the above procedure for a wide parameter range, see Fig. 2.

Example 1. Local Heat Transfer Coefficients at Forced Convection Boiling of a Binary Mixture

Consider a mixture of ethanol (1)/*n*-butanol (2) (no azeotrope) with feed composition $x_1 = 0.065$, which is partially evaporated in a 4 m long vertical tube of a forced convection evaporator. The saturated mixture enters the copper tube ($d_{out} \times s = 38$ mm $\times$ 1.5 mm) at 1.5 bar and at a mass flow rate of $\dot{m} = 560\ \mathrm{kg/(m^2\ s)}$.

The thermal conductivity of copper is 300 W/(K m). The inner wall temperature of the tube is kept constant by condensing steam which is kept 30°C above the boiling temperature of the feed mixture.

Upon neglecting pressure changes in the tube, calculate the following values in steps of 5 m tube length: local heat transfer coefficient, transferred heating power, composition, and vapor mass fraction. Furthermore, calculate the mean heat transfer coefficient $\alpha_m = \Sigma\Delta Q/(\pi d_{out} l(T_{steam} - T_{out}(p_{out}))$ averaged over the entire tube length (T_{steam} temperature of the steam at the outside of the tube, T_{out} temperature of the mixture at the outlet of the tube at p_{out}.).

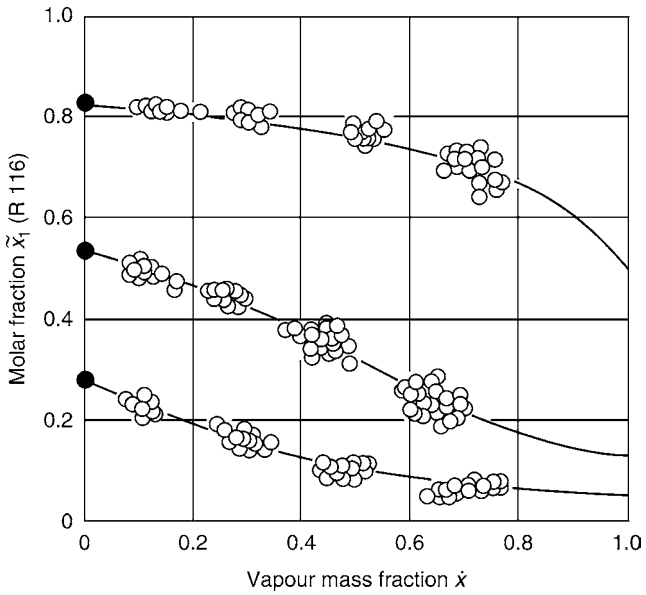

H3.7. Fig. 2. Molar fraction $\tilde{x}_1$ of the low boiling component "1" as a function of vapor mass fraction $\dot{x}$ for three initial compositions (·).System $C_2F_6/C_2H_2F_4$, closed batch evaporation, p = 11 bar, $\dot{m}$ = 74 − 426 kg/m^2 s.

Results:

See Tables 1 and 2, and

$$\alpha_m = \frac{\sum \Delta\dot{Q}}{\pi \cdot d_{out} \cdot l \cdot (T_{steam} - T_{out}(p_{out}))} = \frac{126.2\ \text{kW}}{\pi \cdot 0.038\ \text{m} \cdot 4\ \text{m} \cdot (425.25\ \text{K} - 398.72\ \text{K})} = 10.0\ \text{kW}/(\text{m}^2\ \text{K}).$$

Example 2. Required Length of Evaporator Tubes for Total Evaporation at Forced Convection Boiling of a Ternary Mixture

Consider an evaporator with an horizontal heater in which a ternary mixture (no azeotrope) is to be totally evaporated, i.e., vapor mass fraction $\dot{x}_{out} = 1$.

The feed consists of C_2F_6 ($\tilde{x}_1 = 0.35$), SF_6 ($\tilde{x}_2 = 0.25$), and $C_2H_2F_6$ ($\tilde{x}_3 = 0.4$). Its mass flow density is $\dot{m} = 300$ kg/(m^2 s). It is saturated ($\dot{x}_{in} = 0$) at $p = 10$ bar. The tubes with the dimensions of $d_{out} \times s = 16$ mm × 1 mm are made of electrolyte copper with thermal conductivity of $\lambda = 394$ W/(Km).

The required length of the horizontal tubes is to be computed stepwise by applying a heat transfer coefficient which is averaged with respect to the circumference of the tubes. A constant specific heat flow rate of 30 kW/m^2 is assumed. The step width with respect to vapor mass fraction ought to be 0.1. The composition of the "last droplet" at the exit of the tubes is to be calculated.

Remarks: The effect of partial wetting at slug flow is to be taken into consideration by $\psi = 1$. Ring-slug-flow shall be treated as ring-flow.

Results:

See Tables 3 and 4, and $\tilde{x}_{1,out} = 0.097$, $\tilde{x}_{2,out} = 0.075$, $\tilde{x}_{3,out} = 0.828$.

H3.7. Table 1. Example 1 – properties of ethanol and *n*-butanol

l (m)	ρ' (kg/m^3)	$\tilde{\rho}'$ (mol/m^3)	ρ'' (kg/m^3)	$\tilde{\rho}''$ (mol/m^3)	λ' (W/m K)	λ'' (W/m K)	η' (kg/m s)	η'' (kg/m s)	h' (J/kg)	h'' (J/kg)	Δh_v (J/kg)	$\Delta\tilde{h}_v$ (J/mol)	c'_p (J/kgK)	c''_p (J/kgK)	σ (N/m)
0.0	711	9,973	3.20	48.46	0.1247	0.0227	3.75 E−04	9.32 E−06	129,680	726,574	596,893	42,610	3,292	1,920	1.51 E−2
0.5	711	9,973	3.20	48.46	0.1247	0.0227	3.75 E−04	9.32 E−06	131,083	726,574	595,490	42,610	3,292	1,920	1.51 E−2
1.0	708	9,875	3.24	48.24	0.1244	0.0227	3.72 E−04	9.28 E−06	115,878	709,148	593,270	42,554	3,305	1,920	1.50 E−2
1.5	707	9,827	3.26	48.13	0.1242	0.0227	3.71 E−04	9.26 E−06	109,962	701,139	591,176	42,528	3,312	1,921	1.49 E−2
2.0	705	9,783	3.28	48.05	0.1240	0.0227	3.69 E−04	9.24 E−06	104,449	693,717	589,267	42,503	3,318	1,921	1.49 E−2
2.5	704	9,743	3.29	47.90	0.1239	0.0228	3.68 E−04	9.22 E−06	99,454	687,010	587,556	42,482	3,324	1,921	1.48 E−2
3.0	703	9,707	3.30	47.80	0.1238	0.0228	3.67 E−04	9.21 E−06	94,903	680,937	586,033	42,462	3,329	1,921	1.48 E−2
3.5	702	9,674	3.31	47.73	0.1237	0.0228	3.66 E−04	9.19 E−06	90,793	675,479	584,685	42,445	3,333	1,921	1.48 E−2
4.0	701	9,645	3.33	47.68	0.1236	0.0228	3.65 E−04	9.18 E−06	87,137	670,625	583,487	42,430	3,337	1,922	1.47 E−2

H3.7. Table 2. Example 1 – results

l (m)	$\Delta\dot{Q}$(W)	$\sum\Delta\dot{Q}$(W)	$\dot{q}(W/m^2)$	$\dot{x}$	$\tilde{x}_1$	x_1	T_s (K)	ΔT_{bp} (K)	α_{L0} (W/(m^2 K))	α_{G0} (W/(m^2 K))	$\alpha(z)_{conv}$ (W/(m^2 K))	$\alpha(z)_{conv}/\alpha_{L0}$	$\alpha_{id,B}$ (W/(m^2 K))	B_0/β_L (s/m)	$\alpha(z)_B$ (W/(m^2 K))	$\alpha(z)$ (W/(m^2 K))	ΔT (K)
0		0		0	0.101	0.065	395.25	4.826	1,221	1,551	1,221	1	6,977	402,790[a]	5,898	5,915	31.11
0.5	10,116	10,116	183,999	0.042	0.093	0.060	395.76	4.501	1,222	1,553	3,794	3.105	6,975	81,751	5,958	6,432	28.61
1	12,133	22,249	220,691	0.090	0.085	0.055	396.29	4.166	1,224	1,555	5,349	4.370	8,053	78,290	6,990	7,909	27.91
1.5	13,856	36,105	252,034	0.144	0.078	0.050	396.79	3.840	1,226	1,557	6,720	5.481	8,944	76,956	7,872	9,249	27.25
2	15,384	51,489	279,815	0.202	0.071	0.045	397.26	3.534	1,227	1,559	7,989	6.511	9,714	76,253	8,652	10,500	26.65
2.5	16,783	68,272	305,269	0.264	0.065	0.041	397.68	3.257	1,229	1,560	9,197	7.483	10,405	75,845	9,365	11,695	26.10
3	18,085	86,357	328,942	0.330	0.059	0.038	398.07	3.001	1,230	1,562	10,361	8.424	11,036	75,584	10,027	12,847	25.61
3.5	19,314	105,670	351,298	0.399	0.055	0.035	398.41	2.770	1,232	1,563	11,492	9.328	11,624	75,415	10,648	13,967	25.15
4	20,491	126,161	372,715	0.471	0.050	0.032	398.72	2.565	1,233	1,564	12,599	10.218	12,180	75,314	11,238	15,065	24.74

[a]For the evaluation of B_0/β_L, the vapor fraction is taken to be $\dot{x} = 1 \cdot 10^{-6}$.

H3.7. Table 3. Example 2 – properties of R116 (C_2F_6), R846 (SF_6), and R134a ($C_2H_2F_6$) at 10 bar

$\dot{x}$	ρ' (kg/m^3)	$\tilde{\rho}'$(mol/m^3)	ρ'' (kg/m^3)	$\tilde{\rho}''$ (mol/m^3)	λ' (W/(m K))	λ'' (W/(m K))	η' (kg/(m s))	η'' (kg/(m s))	h' (kJ/kg)	h'' (kJ/kg)	Δh_v (kJ/kg)	$\Delta\tilde{h}_v$ (J/mol)	c'_p (J/(kg K))	c''_p (J/(kg K))	σ (N/m)
0	1,402	11,164	77.553	577	0.0701	0.0122	$2.25{\cdot}10^{-4}$	$1.34{\cdot}10^{-5}$	197	285	88.726	13,650	1,261	865	$7.12{\cdot}10^{-3}$
0.1	1,400	11,220	77.307	576	0.0709	0.0122	$2.27{\cdot}10^{-4}$	$1.34{\cdot}10^{-5}$	197	286	88.799	13,795	1,262	865	$7.31{\cdot}10^{-3}$
0.2	1,396	11,287	77.003	574	0.0720	0.0122	$2.29{\cdot}10^{-4}$	$1.34{\cdot}10^{-5}$	198	287	88.929	13,971	1,263	865	$7.53{\cdot}10^{-3}$
0.3	1,391	11,364	76.602	573	0.0732	0.0123	$2.31{\cdot}10^{-4}$	$1.34{\cdot}10^{-5}$	199	288	89.158	1,418	1,264	865	$7.78{\cdot}10^{-3}$
0.4	1,385	11,453	76.042	570	0.0747	0.0123	$2.32{\cdot}10^{-4}$	$1.34{\cdot}10^{-5}$	200	289	89.565	14,460	1,266	865	$8.07{\cdot}10^{-3}$
0.5	1,376	11,553	75.247	566	0.0763	0.0124	$2.35{\cdot}10^{-4}$	$1.35{\cdot}10^{-5}$	201	291	90.273	14,800	1,270	865	$8.38{\cdot}10^{-3}$
0.6	1,363	11,659	74.060	560	0.0781	0.0125	$2.36{\cdot}10^{-4}$	$1.36{\cdot}10^{-5}$	203	295	91.494	15,213	1,275	866	$8.70{\cdot}10^{-3}$
0.7	1,346	11,754	72.371	552	0.0800	0.0126	$2.35{\cdot}10^{-4}$	$1.37{\cdot}10^{-5}$	206	299	93.474	15,677	1,283	868	$8.95{\cdot}10^{-3}$
0.8	1,325	11,817	70.198	542	0.0813	0.0128	$2.31{\cdot}10^{-4}$	$1.38{\cdot}10^{-5}$	209	306	96.342	16,115	1,294	873	$9.07{\cdot}10^{-3}$
0.9	1,305	11,838	67.846	532	0.0820	0.0131	$2.25{\cdot}10^{-4}$	$1.39{\cdot}10^{-5}$	213	313	99.865	16,450	1,307	881	$9.02{\cdot}10^{-3}$
1	1,287	11,828	65.679	523	0.0823	0.0133	$2.18{\cdot}10^{-4}$	$1.40{\cdot}10^{-5}$	217	321	103.599	16,670	1,320	891	$8.88{\cdot}10^{-3}$

H3.7. Table 4. Example 2 – results

$\dot{x}$	z (m)	Flow regime	$\tilde{x}_1$	$\tilde{x}_2$	T_s (K)	α_{L0} (W/(m^2 K))	α_{G0} (W/(m^2 K))	$\alpha(z)_{conv}$ (W/(m^2 K))	$\alpha(z)_k/\alpha_{L0}$	$\alpha_{id,B}$ (W/(m^2 K))	ΔT_{bp} (K)	B_0/β_L (s/m)	$\alpha(z)_B$ (W/(m^2 K))	$\alpha(z)$ (W/(m^2 K))	ΔT (K)
0	0	Plug[a]	0.35	0.25	264.5	526	491	526	1	11,502	18.0	34,482	1,455	1,479	20.3
0.1	0.33	Slug	0.333	0.244	264.8	528	491	1,315	2.56	10,538	19.3	6,682	1,782	1,994	15.0
0.2	0.67	Slug	0.313	0.236	265.2	531	491	1,541	2.90	9,987	20.6	6,343	1,718	2,059	14.6
0.3	1.01	Slug	0.291	0.226	265.8	535	491	1,694	3.17	9,433	22.1	6,304	1,626	2,093	14.3
0.4	1.36	Ring-slug	0.265	0.212	266.6	540	492	1,814	3.36	8,956	23.7	6,340	1,537	2,125	14.1
0.5	1.74	Ring	0.235	0.195	267.7	546	493	1,914	3.51	8,393	25.2	6,517	1,446	2,157	13.9
0.6	2.15	Ring	0.203	0.172	269.4	554	494	2,005	3.62	7,833	26.5	6,760	1,373	2,200	13.6
0.7	2.61	Ring	0.170	0.144	271.9	564	497	2,088	3.70	7,289	27.0	7,054	1,329	2,254	13.3
0.8	3.14	Ring	0.140	0.116	275.2	575	501	2,157	3.75	6,774	26.5	7,390	1,325	2,312	13.0
0.9	3.73	Ring	0.115	0.092	279.0	586	507	2,159	3.68	6,300	25.0	7,763	1,353	2,323	12.9
1	4.35		0.097	0.075	282.5	597	513	513	0.86	6,300	23.0	7,763	0	513	58.5

[a]For the evaluation of B_0/β_L, the vapor fraction is taken to be $\dot{x} = 1{\cdot}10^{-6}$.

H3.8 Special Symbols and References Used and Cited in Subchaps. H3.1–H3.7

Matthias Kind
Karlsruher Institut für Technologie (KIT), Karlsruhe, Germany

Note: Most of the symbols used in Subchaps. H3.1–H3.7 are listed in Chap. A1 "Symbols and Units". Here only special symbols are listed.

Symbols

A	m^2	area, cross-sectional area
a	–	ratio of values for α
b	m	Laplace coefficient
B_0	–	nucleate boiling parameter
C	–	dimensionless parameter
C_F	–	factor
C_{wl}	$W/m^2\,K$	radiation coefficient
d	m	tube inner diameter
d_e	m	diameter of the inscribed circle (cf. Subchap. H3.5, Fig. 27)
d_h	m	hydraulic diameter
D_W	m	average diameter of winding in helical coil
f	m^2	cross-sectional area
f_{rel}	–	relative error
F	–	function
Δh	kJ/kg	enthalpy difference
Δh_v	kJ/kg	specific enthalpy of vaporization
K	–	equilibrium constant
K	–	subcooling parameter
K_l	–	correction factor for heated length
$\dot{m}$	$kg/(m^2\,s)$	mass flow rate
M	–	fin characteristic
n	–	exponent in term for heat flux
r_{crit}	m	parameter for heated surface
R	m	mean radius
R_a	m	arithmetic mean roughness height (ISO 4287)
s	m	wall thickness
t	m	rod spacing
U	m	periphery, or total periphery occupied by the fluid
$\dot{x}$	–	vapor mass fraction
$\dot{x}_{cr,i}$	–	critical vapor mass fraction on the assumption of thermodynamic equilibrium, when heat is applied to the inner tube of an annulus
$\dot{x}_{cr,o}$	–	critical vapor mass fraction on the assumption of thermodynamic equilibrium, when heat is applied to the outer tube of an annulus
$\dot{x}_{cr,lo}$	–	vapor mass fraction when the boiling crisis occurs on the lower surface of a horizontal or inclined tube
$\dot{x}_{cr,up}$	–	vapor mass fraction when the boiling crisis occurs on the upper surface of a horizontal or inclined tube
$\Delta\dot{x}_{cr}$	–	difference between the critical vapor mass fraction on the lower surface of a horizontal or inclined tube and that on the upper surface
$\Delta\dot{x}$	–	margin of safety against boiling crisis
$\underline{\tilde{x}}$	–	mole fraction vector $(\tilde{x}_1, \ldots, \tilde{x}_k)$ (liquid)
X	–	Martinelli parameter
$\underline{\tilde{y}}$	–	mole fraction vector $(\tilde{y}_1, \ldots, \tilde{y}_k)$ (vapor)
Y	–	mass flux ratio
z	m	coordinate in direction of flow
$\dot{q}_{uni}$	kW/m^2	heat flux if heating is uniform
Z	–	atomic number
σ	$W/m^2\,K^4$	Stephan's constant
$\dot{\omega}$	–	nonequilibrium factor $\dot{x}_{act}/\dot{x}_{eq}$
γ	l/bar	Barnett number
δ	m	thickness of tube wall
$\Delta\vartheta_u$	°C, K	subcooling at inlet
φ	°	angle of inclination to horizontal
Φ^2	–	two-phase multiplier
ψ	–	dimensionless mass flux, reduction factor
ε	–	void fraction

Θ	°	angle of inclination
κ	–	factor
ξ	–	pressure drop coefficient
$\tilde{\rho}$	kmol/m^3	molar density
σ	–	standard deviation
φ	–	unwetted arc or angle subtended by it at the centre of the tube cross-section
Φ	–	normalized unwetted arc
ψ, Ψ	–	factor
$\mathrm{Re_l} = \dfrac{\dot{m}(1-\dot{x})}{\eta_\mathrm{l}}$	–	Reynolds number for liquid phase
$\mathrm{Re_g} = \dfrac{\dot{m}\,\dot{x}\,d}{\eta_\mathrm{g}}$	–	Reynolds number for vapor phase
$\mathrm{Fr} = \left(\dfrac{\dot{m}\,\dot{x}}{\rho_\mathrm{l}}\right)^2 \dfrac{\rho_\mathrm{l}}{\rho_\mathrm{g}\,g\,d}$	–	Froude number
$\mathrm{Fr_g} = \dfrac{\dot{m}^2\,\dot{x}^2}{\rho_\mathrm{g}^2\,g\,d}$	–	Froude number for vapor phase
$\mathrm{Eu} = \dfrac{\Delta p}{\rho w^2}$	–	Euler number

Subscripts

act	actual condition
α min	location of minimum heat transfer coefficient
B	nucleate boiling
conv	convective
cr	critical boiling state
crit	critical
d	related to actual diameter
d	droplet
eq	equilibrium
G, g	vapor
h, htd	heated
hom	homogeneous model
i	interface
i	initial point of bubble formation
i	internal heating
inl	inlet conditions
iso	isothermal
j	with reference to a subchannel
K	heaviest component
K	with reference to the entire channel
lt	laminar-turbulent
L, l	liquid
L	Leidenfrost point
m	mean
max	maximum value
n	beginning of netto vapor production
o	outer heating
onb	onset of nucleate boiling
rad	radiation
sat	saturated
sub	subcooled condition
tt	turbulent-turbulent
TB	transition boiling
u	subcooled
W, w	at the wall
wet	wetted
0	normal, reference
0	at the beginning of the heated section
1, 2	any two points on the heated section
1 ph	single phase

Superscripts

HB	high-boiling
LB	low-boiling
FB	film boiling
DF	droplet flow
$'$	liquid in boiling state
$''$	vapor in condensing state
–	mean, averaged

Bibliography

References cited in Subchap. H3.1

1. Butterworth D, Hewitt GF (1978) Two-phase flow and heat transfer. Oxford University, Oxford
2. Collier JG, Thome JR (2001) Convective boiling and condensation, 3rd edn. (in paperback, repr.). Clarendon, Oxford
3. Mayinger F (1982) Strömungen und Wärmeübergang in GasFlüssigkeits-Gemischen. Springer, Vienna/New York
4. Taitel Y, Bornea D, Dukler AE (1980) Modelling flow pattern transitions for steady upward gas-liquid flow in vertical tubes. AIChE J 26 (3):345–354
5. Steiner D (1996) Wärmeübergang beim Strömungsverdampfen von Reinstoffen und von Mischungen. Habilitation, University of Karlsruhe
6. Taitel Y, Dukler AE (1976) A model for predicting flow regime transitions in horizontal and near horizontal gas-liquid flow. AIChE J 22(1):47–55
7. Rouhani Z (1969) Modified correlations for void fraction and two-phase pressure drop. AB Atomenergi Sweden, AE-RTV-841, pp 1–10
8. Bonn W (1980) Wärmeübergang und Druckverlust bei der Verdampfung von Stickstoff und Argon im durchströmten horizontalen Rohr sowie Betrachtungen über die tangentiale Wärmeleitung and die maximal mögliche Flüssigkeitsüberhitzung. Dissertation, Techncal University Karlsruhe
9. Bornea D, Shohan O, Taitel Y et al (1980) Flow pattern transition for horizontal and inclined pipes; experimental and comparison with theory. Int J Multiphase Flow 6:217–225
10. Kattan N, Thome JR, Farvat D (1995) Boiling of R134a and R123 in a microfin tube. In: Proceedings of the 19th international congress on refrigeration, Den Haag, the Netherlands, 20–25 August 1995, vol IVa, pp 337–344
11. Thome JR, El Hajal J (2004) Two phase flow pattern map for evaporation in horizontal tubes: latest version. Heat Transfer Eng 24(6):3–10

References cited in Subchap. H3.2

1. Moussalli G, Chawla JM (1976) Dampfvolumenanteil und Druckabfall in der Blasenströmung. Forsch Ing Wes 42:149–153
2. Moussalli G (1975) Dampfvolumenanteil und Druckabfall in der Blasenströmung. Dissertation,University of Karlsruhe
3. Moody LF, Princeton NJ (1944) Friction factors for pipe flow. J Heat Transfer, Trans ASME Ser C 66(11):671–684
4. Chawla JM (1967) Wärmeübergang und Druckabfall in waagerechten Rohren bei der Strömung von verdampfenden Kältemitteln. VDI-Forsch-Heft, 523
5. Kesper B (1974) Wandschubspannung und konvektiver Wärmeübergang bei Zweiphasen-Flüssigkeits-Dampfströmung hoher Geschwindigkeit. Dissertation, University of Karlsruhe
6. Kesper B, Chawla JM (1976) Reibungsdruckabfall bei adiabater Zweiphasen-Flüssigkeits-Dampfströmung hoher Geschwindigkeit. Forsch Ing-Wes 42:177–183
7. Schlichting H (1958) Grenzschichttheorie. Braun, Karlsruhe
8. Böckh VP (1975) Ausbreitungsgeschwindigkeit einer Druckstörung und kritischer Durchfluß in Flüssigkeits/Gas-Gemischen. Dissertation, University of Karlsruhe

References cited in Subchap. H3.3

1. Bar-Cohen A, Simon TW (1988) Wall superheat excursions in the boiling incipience of dielectric fluids. Heat Transfer Eng 9:19–31
2. You SM, Simon TW, Bar-Cohen A, Tong W (1990) Experimental investigation of nucleate boiling incipience with a highly-wetting dielectric fluid (R-113). Int J Heat Mass Transfer 33(1):105–117
3. Tong W, Bar-Cohen A, Simon TW, You SM (1990) Contact angle effects on boiling incipience of highly-wetting liquids. Int J Heat Mass Transfer 33 (1):91–103
4. You SM, Simon TW, Bar-Cohen A (1990) Experiments on boiling incipience with highly-wetting dielectric fluid; effects of pressure, subcooling and dissolved gas content. In: Proceedings of the 9th international heat transfer conference, Jerusalem, August 1990, vol 2, pp 337–342
5. Dix GE (1971) Vapor void fraction for forced convection with subcooled boiling at low flow rates. PhD thesis, University of California, Berkeley
6. Clausse A, Lahey RT Jr (1990) The influence of flow development on subcooled boiling. Int Commun Heat Mass Transfer 17:545–554
7. Kays WM (1966) Convective heat and mass transfer. McGraw-Hill, New York
8. Gnielinski V Heat transfer in pipe flow
9. Hodgson AS (1968) Forced convection subcooled boiling heat transfer with water in an electrically heated tube at 100 to 550 lb/in. Trans Inst Chem Eng 46:25–31
10. Bergles AE (1964) The determination of forced-convection surface boiling heat transfer. J Heat Transfer 86:365–372
11. Hahne E, Spindler K, Shen N (1990) Incipience of flow boiling in subcooled well wetting fluids. In: Proceedings of the 9th international heat transfer conference, Jerusalem, August 1990, vol 2, pp 69–74
12. Guglielmini G, Nannei E, Pisoni C (1980) Survey of heat transfer correlations in forced convection boiling. Wärme-und Stoffübertragung 13:177–185
13. Ünal HC (1977) Void fraction and incipient point of boiling during the subcooled nucleate flow boiling of water. Int J Heat Mass Transfer 20:409–419
14. Bräuer H, Mayinger F (1988) Subcooled boiling heat transfer to R12 in an annular vertical channel. Chem Eng Technol 11:320–327
15. Bucher B (1979) Beitrag zum Siedebeginn beim unterkühlten Sieden mit Zwangskonvektion. Dissertation, University of Hanover
16. Müller-Steinhagen H, Epstein N, Watkinson AP (1988) Effect of dissolved gases on subcooled flow boiling heat transfer. Chem Eng Process 23:115–124
17. Bartolini R, Guglielmini G, Nannei E (1983) Experimental study on nucleate boiling of water in vertical upflow and downflow. Int J Multiphase Flow 9 (2):161–165
18. Sudo Y et al (1986) Experimental study of incipient nucleate boiling in narrow vertical rectangular channel simulating subchannel of upgraded JRR-3. J Nucl Sci Technol 23(1):73–82
19. Kreith F, Summerfield M (1950) Pressure drop and convective heat transfer with surface coiling at high heat flux; data for aniline and n-butyl alcohol. J Heat Transfer 72:869–879
20. Saha A, Zuber N (1974) Point of net vapor generation and vapor void fraction in subcooled boiling. In: Proceedings of the fifth international heat transfer conference, Tokyo, vol IV, pp 175–179
21. Bibeau EL, Salcudean M (1990) The effect of flow direction on void growth at low velocities and low pressures. Int Commun Heat Mass Transfer 17:19–25
22. Bibeau EL, Salcudean M (1993) Subcooled void growth for finned and circular annular geometries at low pressures and low velocities. Exp Heat Transfer 3:1183–1190
23. Staub FW (1968) The void fraction in subcooled boiling – prediction of the initial point of net vapor generation. J Heat Transfer 90:151–156
24. Costa J (1967) Mesure de la perle de pression par acceleration et étude de l'apparition du taux de vide en ébullition locale à basse pression. Note TT No. 244, Ceng, Grenoble, France
25. Dougall RS, Lippert TE (1971) Net vapour generation point in boiling flow of trichlorotrifluoroethane at high pressures. NASA Contractor Report No. 2241
26. Edelmann Z, Elias E (1981) Void fraction distribution in low flow rate subcooled boiling. Nucl Eng Des 66:375–382
27. Levy S (1967) Forced convection subcooled boiling – prediction of vapor volumetric fraction. Int J Heat Mass Transfer 10:951–965
28. Evangelisti R, Lupoli P (1969) The void fraction in an annular channel at atmospheric pressure. Int J Heat Mass Transfer 12:699–711
29. Griffith P, Clark JA, Rohsenow WM (1958) Void volumes in subcooled boiling systems. ASME Paper, No. 58-HT-19
30. Hino R, Ueda T (1985) Studies on heat transfer and flow characteristics in subcooled flow boiling, Part 1: Boiling characteristics. Int J Multiphase Flow 11(3):269–281
31. Jain PK, Nourmohammadi K, Roy RP (1980) A study of forced convective subcooled boiling in heated annular channels. Nucl Eng Des 60:401–411
32. Rogers JT, Salcudean M, Abdullah Z, McLeod D, Poirier D (1987) The onset of significant void in up-flow of water at low pressure and velocities. Int J Heat Mass Transfer 30(11):2247–2260
33. Zuber N, Findlay JA (1965) Average volumetric concentration in two-phase flow systems. J Heat Transfer 87:453–468
34. Bartolomei CG, Chun LT, Huo NC (1985) Heat Transfer Sov Res16(4): 60–63
35. Moles FD, Shaw JFC (1972) Boiling heat transfer to subcooled liquids under conditions of forced convection. Trans Inst Chem Eng 50:76–84
36. Badiuzzaman M (1967) The Pakistan Engineer 7:759
37. Noel MB (1961) Experimental investigation of the forced-convection and nucleate boiling heat transfer characteristics of liquid ammonia. Technical Report 32/125, California Institute of Technology, Pasadena
38. Spindler K, Shen N, Hahne E (1990) Vergleich von Korrelationen zum Wärmeübergang beim unterkühlten Sieden. Wärme-und Stoffübertragung 25(2):101–109
39. Chen JC (1996) Correlation for boiling heat transfer to saturated fluids in convective flow. I EC Process Des Dev 5(3):322–329
40. Bergles AE, Collier JG et al (1981) Two-phase flow and heat transfer in the power and process industries. Hemisphere, Washington/New York/ London
41. Gungor KE, Winterton RHS (1986) A general correlation for flow boiling in tubes and annuli. Int J Heat Mass Transfer 29:351–358
42. Gungor KE, Winterton RHS (1987) Simplified general correlation for saturated flow boiling and comparisons of correlations with data. Chem Eng Res Des 65:148–179
43. Forster HK, Zuber H (1955) Dynamics of vapour bubbles and boiling heat transfer. AIChE J 9(4):531
44. Del Valle VH, Kenning DBR (1985) Subcooled flow boiling at high heat flux. Int J Heat Mass Transfer 28:1907–1920
45. Rouhani SZ (1966) Void measurements in the region of subcooled low quality boiling. Part II, AE-RTL-849
46. Rouhani SZ (1979) Experimental and theoretical studies of vapour volume fraction in two-phase flow. Dissertation, Norwegen
47. Mayinger F, Bärmann D, Hein D (1968) Hydrodynamische Vorgänge und Stabilität der Strömung bei unterkühltem Sieden. Chem Ing Tech 40 (11):515 ff
48. Hoffman MA, Wong CF (1992) Prediction of pressure drops in forced convection subcooled boiling water flows. Int J Heat Mass Transfer 35:3291–3299
49. Bartolomei GG, Kovrizhnykh VP (1991) Correlation of experimental data on hydraulic resistance with subcooled boiling. Therm Eng 38(12): 669–672
50. Tarasova NV, Orlov VM (1962) Teploenergetika 6:48–52
51. Dormer J, Bergles AE (1964) Pressure drop with surface boiling in small-diameter tubes. Rep. No. 8767-31, Massachusetts Institute of Technology
52. Hahne E, Spindler K, Skok H (1993) A new pressure drop correlation for subcooled flow boiling of refrigerants. Int J Heat Mass Transfer 36 (17):4267–4274

References cited in Subchap. H3.4

General literature

G1. Mayinger F (1982) Strömungen und Wärmeübergang in GasFlüssigkeits-Gemischen. Springer, Vienna/New York

G2. Dukler AE (1960) Fluid mechanics and heat transfer in falling film systems. Chem Eng Prog Symp Ser 56(30):1

G3. Hewitt GF (1961) Analysis of annular two-phase flow; application of the Dukler analysis to vertical upward flow in a tube. Atomic Energy Research Establishment, Report AERE-R 3680

G4. Steiner D (1996) Wärmeübergang beim Strömungsverdampfen von Reinstoffen und von Mischungen. Habilitation, Universität Karlsruhe
G5. Bonn W (1980) Wärmeübergang und Druckverlust bei der Verdampfung von Stickstoff und Argon im durchströmten horizontalen Rohr sowie Betrachtungen über die tangentiale Wärmeleitung and die maximal mögliche Flüssigkeitsüberhitzung. Dissertation, Technical University Karlsruhe
G6. Bonn W, Iwicki J, Steiner D et al (1980) Über die Auswirkungen der Ungleichverteilung des Wärmeübergangs am Rohrumfang bei der Verdampfung im waagerecht durchströmten Rohr. Wärme-und Stoff übertragung 13:265–274
G7. Niederkrüger M (1991) Strömungssieden von reinen Stoffen und binären zeotropen Gemischen im waagerechten Rohr bei mittleren und hohen Drücken. Fortschr-Ber VDI-Z. Reihe 3:245
G8. Martin H (1980) Published by Bonn, W. Dissertation, Universität Karlsruhe (cf. [G9])
G9. Niederkrüger M, Steiner D Schlünder E-U (1992) Horizontal flow boiling experiments of saturated pure components and mixtures of R846/R12 at high pressures. Int J Refrig 15(1):48–58
G10. Koumoutsos N, Moissis R Spyridonos A (1968) A study of bubble departure in forced-convection boiling. J Heat Transfer 5:223–230
G11. Chen JC (1966) Correlation for boiling heat transfer to saturated fluids in convective flow. Ind Eng Chem Process Des Dev 5(3):322–329
G12. Borishanskii VM, Novikov II, Kutateladze SS (1961) Use of thermodynamic similarity in generalizing experimental data of heat transfer. In: Proceedings of the 1961–1962 heat transfer conference, Boulder, 28 August–1 September 1961, ASME, pp 475–482
G13. Tong LS (1967) Boiling heat transfer and two-phase flow. Wiley, New York
G14. Butterworth D, Hewitt GF (1978) Two-phase flow and heat transfer. Oxford University, Oxford
G15. Isbin HS, Kvamme A, Yamazaki Y et al (1961) Heat transfer to steam-water flows. In: Proceedings of the 1961 Heat Transfer and Fluid Mechanics Institute, Stanford University, Stanford, CA, pp 70–78
G16. Collier JG, Thome JR (2001) Convective boiling and condensation, 3rd edn. (in paperback, repr.). Clarendon, Oxford
G17. Shah MM (1976) A new correlation for heat transfer during boiling flow through pipes. ASHRAE Trans 82(2):66–86
G18. Stephan K (1964) Beitrag zur Thermodynamik des Wärmeübergangs beim Sieden. Abh. des Deutschen Kältetechnischen Vereins No. 18, Verl. C. F. Müller, Karlsruhe
G19. Wettermann M (1999) Würmeübergang beim Sieden von Gemischen bei Zwangskonvektion im horizontalen Verdampferrohr. Fortschr-Ber VDI, Reihe 3:625
G20. Collier JG (1983) Convective boiling inside horizontal tubes. In: EU, Schlünder KJ Bell et al (eds) HEDH – heat exchanger design handbook. Hemisphere & VDI, Washington
G21. Müller-Steinhagen HM, Schlünder EU (1984) Über den Einfluß des Wärmeleitvermögens der Rohrwand auf den urnfangsgemittelten Wärmeübergangskoeffizienten beim Sieden im horizontalen Verdampferrohr. Chem Eng Process 18:303–316
G22. Steiner D, Taborek J (1992) Flow boiling heat transfer in vertical tubes correlated by an asymptotic model, Heat Trans Eng 13(2):43–69
G23. Gnielinski V (1983) Forced convection in ducts. In: Schlünder EU, Bell KJ et al (eds) HEDH – heat exchanger design handbook. Hemisphere & VDI, Washington
G24. Shah RK, London AL (1978) Laminar flow forced convection in ducts. Academic, New York
G25. Ginoux JJ (1978) Two-phase flows and heat transfer with application to nuclear reactor design problems. Hemisphere, Washington
G26. Butterworth D (1972) Air-water annular flow in a horizontal tube. Prog Heat Mass Transfer 6:235–251

Studies on water

W1. Dengler CE (1952) Heat transfer and pressure drop for evaporation of water in a vertical tube. Sc D thesis in Chem Eng, Massachusetts Institute of Technology
W2. Katsuki N, Sekoguchi K et al (March 1979) Momentum and heat transfer in flow-boiling (orig. Japanese). Master thesis, Kyushu University
W3. Sani RL (1960) Downflow boiling and nonboiling heat transfer in a uniformly heated tube. Master thesis, University of California, Lawrence Radiation Lab. Report UCRL-9023
W4. Schrock VE, Grossman LM (1959) Forced convection boiling studies – forced convection vaporization project – final report. Institute of Engineering Research, University of California. Series No. 73308-UCX 2182, TID-14 632
W5. Wright RM (1961) Downflow forced convection boiling of water in uniformly heated tubes. PhD thesis, University of California, Lawrence Radiation Lab. Report UCRL-9744
W6. Yanai M (1971) Flow boiling heat transfer in a vertical channel (orig. Japanese). Dr thesis, Kyoto University
W7. Bennett JAR, Collier JG, Pratt HRC et al (1961) Heat transfer to two-phase gas-liquid systems. Part I. Steam-water mixtures in the liquid-dispersed region in an annulus. Report AERE-R 3159 (1959) and Trans Inst Chem Eng 39:113–126
W8. Collier JG, Lacey PMC Pulling DJ (1964) Heat transfer to two-phase gas-liquid systems. Part II. Further data on steam/water mixtures in the liquid dispersed region in an annulus. Report AERE-R 3809 (1962) and Trans Inst Chem Eng 42:T 127–T 139
W9. Isbin HS, Kvamme A, Yamazaki Y et al (1961) Heat transfer to steam-water flows. In: Proceedings of the 1961 Heat Transfer and Fluid Mechanics Institute. Stanford University Press, Stanford, CA, pp 70–78
W10. Mumm JF (1954) Heat transfer to boiling water forced through a uniformly heated tube. Argonne National Laboratory, Report, ANL-5276
W11. Styrikovich MA, Miropolskii ZL (1950) Phase separation in high-pressure water-steam streams in heated horizontal tubes. DokI Akad Nauk SSSR 71 (2):279–282
W12. Styrikovich MA, Miropolskii ZL (1955) The temperature regime for operational horizontal and inclined steam-generating tubes at high pressures. In: Styrikovich MA (ed) Hydrodynamics and heat transfer during boiling in high pressure boilers. Moskau, pp 244–272
W13. Davis EI, David MM (1961) Heat transfer to high-quality steam-water mixtures flowing in a horizontal rectangular duct. Can J Chem Eng 39 (3):99–105
W14. Takagi T (1967) Critical heat flux in horizontal boiling channel (orig. Japanese). Dr thesis, Osaka University
W15. Lis J, Strickland JA (1970) Local variations of heat transfer in a horizontal steam evaporation tube. Heat Transfer Paris Versailles 4(6):1–12
W16. Owhadi A, Bell KI, Crain B (1968) Forced convection boiling inside helically-coiled tubes. Int J Heat Mass Transfer 11:1179–1193
W17. Bell KJ, Owhadi A (1969–1970) Local heat-transfer measurements during forced-convection boiling in a helically coiled tube. Proc Inst Mech Eng 184:52–58
W18. Bertoletti S, Lesarge J, Lombardi C et al (1961) A research program in two-phase flow. Part II. Work on the heat transfer loop. CISE-Report R-36, pp 1–221
W19. Cicchitti A, Lombardi C, Silvestri M et al (1960) Two-Phase cooling experiments: Pressure drop, heat transfer and burnout measurements. Energia Nucleare 7(6):407–425
W20. Campolunghi FM, Cumo G, Ferrari et al (1974) Boiling heat transfer in L.M.F.B.R. steam generators. Comitato Nazionale Energia Nucleare, CNEN-Report, RT/ING (74)17
W21. Campolunghi F, Cumo M, Palazzi G et al (1977) Subcooled and bulk boiling correlations for thermal design of steam generators. Comitato Nazionale Energia Nucleare, CNEN-Report, RT/ING (77)10
W22. Era A, Gaspari GP, Hassid A et al (1966) Heat transfer data in the liquid-deficient region for steam water mixtures at 70 kg/cm^2 flowing in tubular and annular conduits. CISE-Report R-184
W23. Herkenrath H, Mörk-Mörkenstein P, Jung U et al (1967) Wärmeübergang an Wasser bei erzwungener Strömung im Druckbereich von 140 bis 250 bar. Euratom, Report EUR 3658 d
W24. Herkenrath H, Mörk-Mörkenstein P (1969) Die Wärmeübergangskrise von Wasser bei erzwungener Strömung unter hohen Drücken. Part 1: Darstellung und Vorausbestimmung der kritischen Wärmestromdichte für Drücke von 170 bis 215 bar. Atomkernenergie 14 (1969) No. 3, 163/70. Part 2: Der Wärmeübergang im Bereich der Krise. Atomkernenergie 14:403–407

W25. Hein D, Köhler W, Krätzer W (1979) Experimentelle und analytische Untersuchungen zum Wärmeübergang in Dampferzeugerrohren. Kraftwerk Union AG, Bericht KWU-R513 für Benson-Lizenznehmer. Released for publication by KWU
W26. Morozov VG (1969) Heat transfer during the boiling of water in tubes. In: Borishansky VM, Paleev II (eds) Convective heat transfer in two-phase and one-phase flows. Israel Program for Scientific Translations, Jerusalem
W27. Müller F (1967) Wärmeübergang bei der Verdampfung unter hohen Drücken. VDI-Forsch.-H. 522. VDI, Düsseldorf
W28. Bogdanov VV (1955) Investigation of the effect of the rate of motion of the water current on the heat exchange coefficient on boiling in an inclined tube (orig. Russian). Izvestiya Akademii Nauk, Otdelenie Tekhnicheskikh Nauk (4):136–140 and AERE Lib/Trans 596
W29. Gilli PR (1963) Forschungen auf dem Gebiet der Filmverdampfung. Mitteilungen der VGB, H. 86:288–300
W30. Cumo M, Fabrizi F, Palazzi G (1978) The influence of inclination on CHF in steam generators channels. Comitato Nazionale Energia Nucleare, CNEN-Report RT/ING (78)11
W31. Carver JR, Kakerale CR, Slotnik J (1964) Heat transfer in coiled tubes with two-phase flow. USAEC-Report TID20983
W32. Gilli PV, Edler A, Halozan H et al (1975) Probleme des Wärrneüberganges, Druckverlustes und der Strömungsstabilität in thermisch hochbeanspruchten Dampferzeugerrohren. VGB Kraftwerkstechnik 55H. (9):589–600
W33. Schaup P (1973) Wärmeübergang und Wärmeübergangskrise der Zweiphasenströmung in Schraubenrohren. Dissertation, Technical University Graz
W34. Kefer V (1989) Strömungsformen and Wärmeübergang in Verdampferrohren unterschiedlicher Neigung. Dissertation, Technical University of Munich
W35. Geskes P (1998) Zweiphasenströmung in Ringkanälen solarer Dampferzeugerrohre. Fortschr. Ber. VDI, Reihe 7(347):1–118

Studies on ammonia

A1. Barthau G Experimental investigation of ammonia flow boiling at high pressures (orig. Russian). Fifth All-Union Heat and Mass Transfer Conference, Minsk 1976, vol III-1, pp 220–225; Unpublished measurements at the Thermodynamics and Heat Technics Institute of Stuttgart University
A2. Gronnerud R (1974) Two-phase heat resistance in boiling refrigerants – Calculations and influence on evaporator design. Institutt for Kjøleteknikk, Norges Tekniske Høgskole, Trondheim, pp 1–28

Studies on refrigerants (halocarbons)

R1. Haβdenteufel W (1983) Wärmeübergang und Druckverlust bei Zweiphasenströmung. Dissertation, University of Stuttgart
R2. Lavin JG (1963) Heat Transfer to refrigerants boiling inside plain tubes and tubes with internal turbulators. D thesis, University of Michigan
R3. Pujol L (1968) Boiling heat transfer in vertical upflow and downflow tubes. PhD thesis, Lehigh University
R4. Riedle K, Purcupile JC et al (1973) Experimental and analytical investigation – boiling heat transfer in evaporator tubes horizontal flow. Carnegie-Mellon University, NSF-Grant 257, CMU, No. 1–55 307 (1971); Experimental investigation boiling heat transfer in evaporator tubes-vertical flow. In: AIChE Preprint 18, 14th national heat transfer conference, Atlanta
R5. Altman M, Norris RH, Staub FW (1960) Local and average heat transfer and pressure drop for refrigerants evaporating in horizontal tubes. J Heat Transfer Trans ASME 82(3):189–198
R6. Bandel J (1973) Druckverlust und Wärmeübergang bei der Verdampfung siedender Kältemittel im durchströmten waagerechten Rohr. Dissertation, Universität Karlsruhe
R7. Brendeng E (1983) Influence of internal turbulators on heat transfer in evaporator tubes. In: 16th international congress of refrigeration, I.I.R. Paris, 1–459, pp 686–690
R8. Bryan WL, Seigel LG (1955) Heat transfer coefficients in horizontal tube evaporators. Refrig Eng 63:36–45
R9. Johnston RC, Chaddock JB (1964) Heat transfer and pressure drop of refrigerants evaporating in horizontal tubes. ASHRAE Trans 70: 163–71
R10. Chaddock JB, Noerager JA (1966) Evaporation of refrigerant 12 in a horizontal tube with constant wall heat flux. ASHRAE Trans 72:90–103
R11. Chawla JM, (1967) Wärmeübergang und Druckabfall in waagerechten Rohren bei der Strömung von verdampfenden Kältemitteln. VDI-Forsch.-H. 523. VDI, Düsseldorf
R12. Djatchkow FN (1977) Heat transfer and pressure drop studies in the evaporation of R 22 in inside-finned tubes (orig. Russian). Cholodilnaja Technika 7:22–28
R13. Djatchkow FN, Kalnin IM, Krotkow WN (1977) Generalization of experimental values on heat transfer and hydrodynamics during flow of Freon 22 in inside-finned tubes (orig. Russian). Cholodilnaja Technika 7:22–28
R14. Fuchs PH (1975) Influence of tube material and external heat load on heat transfer coefficients with separated flow in evaporators. In: XV international congress of refrigeration, Venice, 1979, 1–43, pp 1–4; Pressure drop and heat transfer during flow of evaporating liquid in horizontal tubes and in return bends (orig. Norwegian). D thesis, Institutt for Kjøleteknikk, Norges Tekniske Høgskole, Trondheim
R15. Gouse W, Coumou KG (1965) Heat transfer and fluid flow inside a horizontal tube evaporator: Phase I. ASHRAE Trans 71:152–160
R16. Gouse W, Dickson AJ (1966) Heat transfer and fluid flow inside a horizontal tube evaporator: Phase H. ASHRAE Trans 72:104–114
R17. Hofmann E (1972) Efficiency of dry expansion evaporators with bare and inside-finned tubes. Bulletin de l'Institute International du Froid, Freudenstadt, Annexe 1972–1, pp 305–318
R18. Iwicki J, Steiner D (1979) Einfluß des Massenstroms und des Rohrdurchmessers auf den Druckverlust und Wärmeübergang verdampfender Kältermittel im durchströmten Rohr-Aufklärung von Widersprüchen zwischen bekannten Berechnungsmethoden und neuen experimentellen Ergebnissen. Arbeitsgemeinschaft Industrieller Forschungsvereinigungen. AIF-Report No. 20:3531/3, Cologne
R19. Kesper B (1974) Wandschubspannung und konvektiver Wärmeübergang bei Zweiphasen-Flüssigkeits-Dampfströmung hoher Geschwindigkeit. Dissertation, Universität Karlsruhe
R20. Lorentzen G, Gronnerud R (1970) Investigation of liquid holdup, flow resistance and heat transfer in an R 12-evaporator coil with recirculation. In: Proceedings of the XIIIth international congress of refrigeration, Washington, I.I.F. Annexe 1970-1, pp 193–203
R21. Malischev AA, Danilowa GN, Azarskow WM et al (1982) Effect of flow pattern on heat transfer during boiling in horizontal tubes (orig. Russian). Cholodilnaja Technika 8:30–34
R22. Malek A (1983) Influence de la presence d'huile dans le fluide frigorigene sur le transfer de chaleur ä l'evaporation dans un tube horizontal (orig. French). In: 16th International congress of refrigeration. I.I.R. Paris, 1–489, pp 585–588
R23. Naganagoudar CD, Steiner D (1977) Einfluß des Massenstroms und des Rohrdurchmessers auf den Druckverlust und Wärmeübergang verdampfender Kältemittel im durchströmten Rohr. Arbeitsgemeinschaft Industrieller Forschungsvereinigungen, AIF-Report No. 20, pp 3531–3532
R24. Pierre B (1955) Wärmeübergangszahl bei verdampfendem F 12 in horizontalen Rohren. Kältetechnik 7(6):163–166; Pierre B (1953) Heat transfer to boiling F 12 in horizontal tubes (orig. Swedish). Kylteknisk Tidskrift 6:76–81
R25. Schlünder EU, Chawla JM (1969) Örtlicher Wärmeübergang und Druckabfall bei der Strömung verdampfender Kältemittel in innenberippten, waagerechten Rohren. Kältetechnik 21(5):136–139
R26. Schmidt H (1986) Beitrag zum Verständnis des Wärmeübergangs im horizontalen Verdampferrohr. Fortschr.-Ber. VDI-Z. Reihe 19(6):1–161
R27. Uchida H, Yamaguchi (1966) Heat transfer in two-phase flow of refrigerant 12 through horizontal tube. In: Proceedings of the third international heat transfer conference, Chicago, vol 5, pp 69–79
R28. Worsøe-Schmidt P (1959) Some characteristics of flow pattern and heat transfer of Freon 12 evaporating in horizontal tubes. Ingeniøren Int Ed 3(3):98–104
R29. Zahn WR (1961) A visual study of two-phase flow while evaporating in horizontal tubes. J Heat Transfer 417–429
R30. Ahrens KH, Mayinger F (1978) Boiling heat transfer in the transition region from bubble flow to annular flow. In: Proceedings in two-phase

energy and chemical systems, International Centre for Heat and Mass Transfer, Dubrovnik
R31. Haffner H (1970) Wärmeübergang an Kältemittel bei Blasenverdampfung, Filmverdampfung und überkritischem Zustand des Fluids. Bundesministerium für Bildung und Wissenschaft, Forschungsber. K 70–24
R32. Jallouk PA (1974) Two-phase flow pressure drop and heat transfer characteristics of refrigerants in vertical tubes. PhD thesis, University of Tennessee
R33. Kaufmann WD (1974) Untersuchung des Wärmeübergangs und des Druckverlustes bei der Zweiphasenströmung von R 12 im senkrechten Rohr. Dissertation, Dissertation No. 5196, Tech Univ of Zürich
R34. Zuber N, Staub FW, Bijwaard G et al (1967) Steady state and transient void fraction in two-phase flow systems. In: Final report for the programme of two-phase flow investigation, GEAP-5417, EURAEC-1949 1 and 2
R35. Kattan N, Thome JR, Favrat D (1995) Flow boiling in horizontal and vertical tubes: The effect of tube orientation on heat transfer. In: Eng found conf, convective flow boiling, Banff, Canada, pp 1–6
R36. Hahne E, Shen N Spindler K (1989) Fully developed nucleate boiling in upflow and downflow. Int J Heat Mass Transfer 32:1799–1808

Studies on hydrocarbons

H1. Bennett DL (1976) A study of internal forced convective boiling heat transfer for binary mixture. PhD thesis, Lehigh University
H2. Talty RD (1953) A study of heat transfer to organic liquids in natural circulation vertical-tube boilers. PhD thesis, University of Delaware
H3. Somerville GF (1962) Downflow boiling of n-butanol in a uniformly heated tube. M thesis, University of California, Lawrence Radiation Lab., Report UCRL-10 527
H4. Shock RAW, Wadekar VV, Kenning DBR (1984) Flow boiling of ethanol and cyclohexane in a vertical tube. In: Proceedings UK-national heat transfer conference, Leeds
H5. Calus WF, Denning RK, di Montegnacco A Gadsdon J (1973) Heat transfer in a natural circulation single tube reboiler. Part I: Single component. Chem Eng 6:233–250
H6. Robertson JM, Wadekar VV (1988) Vertical upflow boiling of ethanol in a 10 mm diameter tube. In: 2nd UK national heat transfer conference, vol I, C 198/88, pp 67–77

Studies on cryogenic fluids

C1. Hildebrandt G (1971) Der Wärmeübergang an siedendes Helium I bei erzwungener Strömung im senkrechten Rohr. Dissertation, Technical University of Berlin
C2. Hildebrandt U (1971) Experimentelle Untersuchung des Wärmeübergangs an Helium I bei Blasenverdampfung in einem senkrechten Rohr. Wärme- and Stoffübertragung 4(3):142–151
C3. Johannes C (1972) Studies of forced convection heat transfer to helium I. Adv Cryogen Eng 17:352–360
C4. Keilin VE, Kovalev IA, Likov VV et al (1975) Forced convection heat transfer to liquid helium I in the nucleate boiling region. Cryogenics 15 (3):141–145
C5. Ogata H, Sato (1974) Forced convection heat transfer to boiling helium in a tube. Cryogenics 14:375–180
C6. Lewis JP, Goodykoontz PH, Kline JF (1962) Boiling heat transfer to liquid hydrogen and nitrogen in forced flow. National Aeronautics and Space Administration. Technical Note D-1314, pp NASA1–56
C7. Deew WU, Archipow WW, Nowikow WN (1984) Heat transfer during forced convection boiling of nitrogen (orig. Russian). Teploenergetika (3):26–29
C8. Shorin N, Sukhov VI, Shevyakova A et al (1973) Experimental determination of heat boiling of oxygen in vertical tubes and channels (Orig. Russian). Inzh-fizich zh 25(5):773–79
C9. Wright CC, Walters HH (1959) Single tube heat transfer tests gaseous and liquid hydrogen. Wright Air Development Center, WADC Technical Report 59-423, pp 1–46
C10. Mohr V (1975) Verdampfung von Neon in horizontalen Rohren. Dissertation, Universität Stuttgart
C11. Steiner D (1975) Wärmeübergang und Druckverlust von siedendem Stickstoff bei verschiedenen Drücken im waagerecht durchströmten Rohr. Dissertation, Universität Karlsruhe
C12. Bonn W (1980) Wärmeübergang und Druckverlust bei der Verdampfung von Stickstoff und Argon im durchströmten horizontalen Rohr sowie Betrachtungen über die tangentiale Wärmeleitung und die maximal mögliche Flüssigkeitsüberhitzung. Dissertation, Universität Karlsruhe
C13. Müller-Steinhagen H (1984) Wärmeübergang und Fouling beim Strömungssieden von Argon und Stickstoff im horizontalen Rohr. Fortschr-Ber VDI-Z Reihe 6(143):1–252
C14. Klein G (1975) Wärmeübertragung und Druckverlust bei der Strömung von verdampfendem Stickstoff im waagerechten Rohr. Dissertation, Technical University of Aachen
C15. Petukhov BS, Zhukov VM, Shieldcret VM (1983) Investigation of heat transfer and hydrodynamics in the helium two-phase flow in a vertical channel. In: Heat exchangers – theory and practice. Hemisphere, Washington, pp 251–262

References cited in Subchap. H3.5

Literature on specialized subjects

1. Cumo M, Palazzi G, Urbani GC (1979) On the limiting critical quality and the "deposition controlled" burnout. CNEN-RT/ING (79)4
2. Drescher G, Köhler W (1981) Die Ermittlung kritischer Siedezustände im gesamten Dampfgehaltsbereich für innendurchströmte Rohre, BWK 33, 10
3. Doroshchuk VE, Levitan LL, Lantsmann FP (1975) Recommendations for calculating burnout in a round tube with uniform heat release. Teploenergetika 22(12):66–70
4. Academy of Sciences, USSR (1977) Tabular data for calculating burnout when boiling water in uniformly heated round tubes. Therm Eng 23(9):77–79
5. Kon'kov AS (1965) Experimental study of the conditions under which heat exchange deteriorates when a steam-water mixture flows in heated tubes. Teploenergetika 13(12):77
6. Groeneveld DC, Leung LKH, Kirillov PL, Bobkov VP, Smogalev IP, Vinogradov VN, Huang XC, Royer E (1996) The 1995 look-up table for critical heat flux in tubes. Nucl Eng Des 163:1–23
7. Groeneveld DC, Cheng SC, Doan T (1986) AECL-UO critical heat flux lookup table. Heat Transfer Eng 7(1–2)
8. Köhler W, Herbst O, Kastner W (1994) Thermal-hydraulic behavior of a safety condenser. In: Proceedings international conference on new trends in nuclear system thermo-hydraulics, Pisa, Italy, vol I, 30 May–2 June 1994
9. Cumo M, Fabrizi, FG Palazzi (1978) The influence of inclination on CHF in steam generators channels. CNEN-RT/ING (78)11
10. Merilo M (1977) Critical heat flux experiments in a vertical and horizontal tube with both Freon-12 and water as coolant. Nucl Eng Des 44:1–16
11. Chojnowski B, Wilson PW, Whitcutt RDB (1974) Critical heat flux in inclined steam generating tubes. In: Symp multiphase flow systems, Univ Strathelyde Paper E 3. Published in I Chem E Symp Series No. 38
12. Watson G, Lee RA, Wiener M (1974) Critical heat flux in inclined and vertical smooth and ribbed tubes. In: 5th international heat transfer conference, Tokyo, Paper B 6.8
13. Kefer V (1989) Strömungsformen und Wärmeübergang in Verdampferrohren unterschiedlicher Neigung. Dissertation, Technical University München
14. Ünal HC (1981) Some aspects of two-phase flow heat transfer and dynamic instabilities in medium and high pressure steam generators. Dissertation, Technische Hochschule Delft
15. Roumy R (1971) Dryout in helically coiled tubes with boiling Freon 12. In: European two-phase flow group meeting, Copenhagen
16. Campolunghi F, Cumo M, Ferrari G, Palezzi G (1977) Full scale tests and thermal design correlations for coiled once-through steam generators. CNEN-RT/ING (75):11
17. Cumo M, Farello GE, Ferrari G (1972) The influence of curvature in post dryout heat transfer. Int J Heat Mass Transfer 15:2045–2062
18. Naitoh M, Nakamura A, Ogasawara H (1974) Dryout in helically coiled tube of sodium heated steam generator. ASME 74-WA/HT-48
19. Duchatelle L, De Nucheze L, Robin MG (1973) Departure from nucleate boiling in helical tubes of liquid metal heated steam generators. ASME 73-HT-57
20. Ünal HC, van Gasselt MLG, van T'Verlaat PM (1981) Dyrout and two-phase flow pressure drop in sodium heated helically coiled steam generators tubes at elevated pressures. Int J Heat Mass Transfer 24:285–298

21. Miropol'skiy ZL, Yu Pikus V (1969) Critical boiling heat fluxes in curved channels. Heat Transfer Sov Res 1(1)
22. Babarin VP, Sevat'yanov RI, Alad'yev IT, Khudyakow VF, Tzachev VA (1971) Critical heat flux in tubular coils. Heat Transfer Sov Res 3(4)
23. Alad'yev IT, Petrov CI, Rzayev AI, Khudyakov VF (1976) Heat transfer in a sodium-potassium heat exchanger (potassium boiler) made of helically-coiled tubes. Heat Transfer Sov Res 8(3)
24. Butterworth D (1971) A model for predicting dryout in a tube with a circumferential variation in heat flux. AERE-M 2436, Harwell
25. Cumo M, Palazzi G, Urbani G, Frazolli FV (1980) Full scale tests on axial profile heat flux. Influence on the critical quality in PWR steam generators. CNEN-RT/ING (80)5
26. Cocilovo M, Cumo, M, Palazzi G (1979) On DNB location with axially disuniform heat flux. CNEN-RT/ING (79)21
27. Doroshchuk CE, Levitan LL et al (1978) Investigations into burnout mechanism in steam-generating tubes. In: 6th international heat transfer conference, Toronto, 7–11 August 1978, Paper FB-21
28. Peskov OL, Remizoo OV, Sudnitsyn OA (1978) Some features of heat transfer burnout in tubes with non-uniform axial heat flux distribution. In: 6th international heat transfer conference, Toronto, 7–11 August 1978, Paper NR-10
29. Keeys RKF, Ralph IC, Roberts DN (1972) Post-burnout heat transfer in high pressure steam-water mixtures in an tube with cosine heat flux distribution. Prog Heat Mass Transfer 6:99–118
30. Becker KM, Letzter A (1975) Burnout measurements for flow of water in an annulus with two-sided heating. In: European two-phase flow group meeting, Haifa, KTH-NEL-23
31. Cheng X, Müller U (2003) Review on critical heat flux in water cooled reactors. Institut für Kern-und Energietechnik, Forschungszentrum Karlsruhe GmbH, Karlsruhe, FZKA 6825
32. Zernick W, Currin HB, Elyath E, Previti G (1962) THINC: a thermal hydrodynamic interaction code for a semi-open or closed channel core. WCAP-3704, Febr
33. Chelemer H, Weisman J, Tong LS (1967) Subchannel thermal analysis of rod bundle core. WCAP 7014, June 1967
34. Bowring RW (1967) HAMBO – a computer program for the subchannel analysis of the hydraulic and burnout characteristics of rod clusters. AEEW R 524
35. Rowe DS (March 1967) Crossflow mixing between parallel flow channels during boiling. Part 1: COBRA – computer program for coolant boiling. BNWL-371, Pt. 1
36. Rowe DS (March 1973) COBRA IIIC: a digital computer program for steady state and transient thermal-hydraulic analysis of rod bundle nuclear fuel elements. BNWL 1965
37. Hochreiter T, Chelemer Y (September 1973) Application of the THINC-IV program to PWR design. WCAP 8195
38. Ulrych (1976) Strömungsvorgänge mit unterkühltem Sieden in Brennstabbündeln wassergekühlter Kernreaktoren. Dissertation, TU Braunschweig
39. Burtak F, Heinecke J, Glück M, Kronenberg J, Kollmann T (2006) Advanced thermal hydraulic core and fuel assembly design with state-of-the-art subchannel codes. In: TOPFUEL, Salamanca, Spain, 22–26 October 2006
40. Glück M (2007) Sub-channel analysis with F-COBRA-TF – code validation and approaches to CHF prediction. Nucl Eng Des. 237:655–667
41. Suchy P, Ulrych G, Kemner H, Kurz E Application of tables of critical heat fluxes to rod bundles. In: Transactions of the ENC '79 conference of the European Nuclear Society
42. Lahey RT, Drew DA (1980) An assessment of the literature related to LWR instability modes. NUREG/CR-1414, April 1980
43. Katto Y, Ohno H (1984) An improved version of the generalized correlation of critical heat flux for the forced convective boiling in uniformly heated vertical tubes. Int J Heat Mass Transfer 27(9):1641–1648
44. Katto Y (1979) A generalized correlation of critical heat flux for the forced convection boiling in vertical uniformly heated round tubes – a supplementary report. Int J Heat Mass Transfer 22:783–794
45. Katto Y, Yokoya S (1982) CHF of forced convection boiling in uniformly heated vertical tubes: experimental study of HP-Regime by the use of refrigerant 12. Int J Multiphase Flow 8:165–1681
46. Groeneveld DC (1976) The occurrence of upstream dryout in uniformly heated channels. In: Proceedings of the 5th international heat transfer conference, vol 4, pp 265–269
47. Katto Y (1978) A generalized correlation of critical heat flux for the forced convection boiling in vertical uniformly heated round tubes. Int J Heat Mass Transfer 21:1527–1542
48. Katto Y (1979) An analysis of the effect of inlet subcooling on critical heat flux of forced convection boiling in vertical uniformly heated tubes. Int J Heat Mass Transfer 22:1567–1575
49. Katto Y (1980) General features of CHF of forced convection boiling in uniformly heated vertical tubes with zero inlet subcooling. Int J Heat Mass Transfer 23:493–504
50. Katto Y (1980) Critical heat flux of forced convection boiling in uniformly heated vertical tubes (correlation of CHF in HP-Regime and determination of CHF-Regime map). Int J Heat Mass Transfer 23:1573–1580
51. Katto Y (1982) A study of limiting exit quality of CHF of forced convection boiling in uniformly heated vertical channels. Trans Am Soc Mech Eng Ser C J Heat Transfer 40–47
52. Katto Y (1981) On the heat-flux/exit-quality type correlation of CHF of forced convection boiling in uniformly heated vertical tubes. Int J Heat Mass Transfer 24:533–539
53. Katto Y, Ashida S (1982) CHF in high-pressure regime for forced convection boiling in uniformly heated vertical tube of low length-to-diameter ratio. In: Proceedings 7th international heat transfer conference, vol 4, pp 291–296
54. Nishikawa K, Yoshida S, Yamada A, Ohno M (1982) Experimental investigation of critical heat flux in forced convection boiling of Freon in a tube at high subcritical pressure. In: Proceedings 7th international heat transfer conference, vol 4, pp 321–326
55. Katto Y (1982) An analytical investigation on CHF of flow boiling in uniformly heated vertical tubes with special reference to governing dimensionsless groups. Int J Heat Mass Transfer 25:1353–1361
56. Groeneveld DC (xxx) Freon dryout correlations and their applicability to water. Atomic Energy of Canada Limited AECL Report No. 3418
57. Ilic V (xxx) The effect of pressure on burnout in a round tube cooled by Freon 12. AAEC/E 325
58. Barnett PG, Wood RW (1965) An experimental investigation to determine the scaling laws of forced convection boiling heat transfer, Part 2: An examination of burnout data for water, Freon 12 and Freon 21 in uniformly heated round tubes. AEEW-R443
59. Staub FW (1969) Two phase fluid modelling – the critical heat flux. Nucl Sci Eng 35:190–199
60. Purcupile JC, Gouse SW Reynolds flux model of critical heat flux in subcooled forced convection boiling. ASME-72-HT-4
61. Dix GE Freon-water modelling of the CHF in round tubes. ASME 70-HT-26
62. Katto Y, Yokoya S (1984) Critical heat flux of liquid helium (I) in forced convective boiling. Int J Multiphase Flow 10(4):401–413
63. Lewis JP, Goodykoontz JH, Kline JF (xxx) Boiling heat transfer to liquid hydrogen and nitrogen in forced flow. NASA, Techn Note D-1314
64. Alad'yev T, Gorlov IG, Dodonov LD, Fedynskiy OS (1969) Heat transfer to boiling potassium in uniformly heated tubes. Heat Transfer Sov Res 1(4)
65. Hoffman HW, Krakoviak AI (1964) Convective boiling with liquid potassium. Oak Ridge National Laboratory, Oak Ridge
66. Noel MB Experimental investigation of the forced-convection and nucleate-boiling heat-transfer characteristics of liquid ammonia. JPL-Tech. Notes Report No. 32-125
67. Cumo M, Bertoni R, Cipriani R, Palazzi G (1977) Up-flow and down-flow burnout. Inst Mech Eng Conf, Publ 1977-8, pp 183–192
68. Jensen MK, Bergles A (1981) Critical heat flux in helically coiled tubes. J Heat Transfer 103:660–666
69. Ahmad SY (1973) Fluid-to-fluid modelling of CHF: a compensated distortion model. Int J Heat Mass Transfer 16:641–662
70. Katsaounis A Literaturbewertung zur Fluidähnlichkeit für die kritische Heizflächenbelastung. GKSS 81/E/10
71. Katsaounis A (1980) Verification of Ahmad's fluid-to-fluid scaling law by bundle experiments. In: Winter annual meeting of ASME, Chicago, HDT, vol 14
72. Katsaounis A (1981) Comparison of various CHF-data performed in different fluids and test sections with various CHF-correlations. In: European two-phase flow group meeting, Eindhoven, 1981 und GKSS 81/E/35
73. Marroquin Nisch A (1998) Kritische Wärmestromdichte und minimale Wärmestromdichte des Filmsiedens binärer Gemische im zwangsdurchströmten senkrechten Rohr. Fortschr.-Ber. VDI, Reihe 3, Nr. 541.VDI, Düsseldorf

74. Stephan K, Körner M (1969) Berechnung des Wärmeübergangs verdampfender binärer Flüssigkeitsgemische. Chem-Ing Techn 409–434
75. Sterman L, Abramov A, Checheta G (1968) Investigation of boiling crisis at forced motion of high temperature organic heat carriers and mixtures. In: International symposium on research into co-current gas-liquid flow. University of Waterloo, Canada, Paper E2
76. Celata GP, Cumo M, Setaro T (1994) Critical heat flux in upflow-convective boiling of refrigerant binary mixtures. Int J Heat Mass Transfer 37:1143–1153
77. Tolubinskiy VI, Matorin AS (1973) Forced convection boiling. Heat Transfer Sov Res 5(2)

(b) General literature

78. Tong LS (1972) Boiling crisis and critical heat flux. AEC Crit Rev Ser, TID-25 887
79. Bergles AE (1975) Burnout in boiling heat transfer. Part I: Pool-boiling system. Nucl Safety 16(1)
80. Bergles AE (1977) Burnout in boiling heat transfer. Part II: Subcooled and low-quality forced-convection systems. Nucl Safety 18(2)
81. Bergles AE (1979) Burnout in boiling heat transfer. Part III: High-quality forced-convection systems. Nucl Safety 20(6)
82. Hewitt GF Critical heat flux in flow boiling. In: International heat transfer conference, Toronto, August 1978, vol 6, Paper KS-13
83. Collier JG (1972) Convective boiling and condensation. McGraw-Hill, London
84. Hewitt GF, Hall-Taylor NS (1970) Annular two-phase flow. Pergamon, Oxford
85. Wallis GB (1969) One-dimensional two-phase-flow. McGraw-Hill, New York
86. Bergles AE et al (1981) Two-phase flow and heat transfer in the power and process industries. Hemisphere, Washington
87. Butterworth D, Hewitt GF (1977) Two-phase flow and heat transfer. Oxford University, Oxford

References cited in Subchap. H3.6

1. Groeneveld DC, Snoek CW (1986) Comprehensive examination of heat transfer correlations suitable for reactor safety analysis. In: Hewitt GF, Delhaye JM, Zuber N (ed) Multiphase science and technology, Chap 3, vol 2. Hemisphere, Washington
2. Mayinger F (1984) Strömung und Wärmeübertragung in GasFlüssigkeitsgemischen. Springer, Wien
3. Katsaounis A (1987) Post-dryout correlations and models compared to experimental data from different fluids. In: Proceedings of the XVIII international symposium on heat and mass transfer in cryoengineering and refrigeration, Hemisphere, Washington, ICHMT-Symposium, September 1986, Dubrovnik, Yugoslavia. Preprint GKSS 86/E/41
4. Bergles AE, Collier IG, Delhaye IM, Hewill GF, Mayinger F (1981) Two-phase flow and heat transfer in the power and process industries. Hemisphere, Washington
5. Collier JG (1976) Post-dryout heat transfer -a review of the current position. Advanced Study Institute on Two-Phase Flows and Heat Transfer, Istanbul
6. Hetsroni G (1982) Handbook of multiphase systems. Hemisphere, Washington
7. Groeneveld DC, Leung LKH, Vasic AZ, Guo YJ, Cheng SC (2003) A look-up table for fully developed film-boiling heat transfer. Nucl Eng Des 225:83–97
8. Köhler W (1984) Einfluß des Benetzungszustandes der Heizflache auf Wärmeübergang und Druckverlust in einem Verdampferrohr. Diss Chair A of Thermodynamics, Technical University of Munich
9. Hein D, Köhler W (1977) The role of thermal non-equilibrium in post-dryout heat transfer. In: European two-phase flow group meeting, Grenoble
10. Hein D, Köhler W (1986) A simple-to-use post-dryout heat transfer model accounting for thermal non-equilibrium. In: Proceedings of the 1st international workshop on fundamental aspects of post dryout heat transfer, Salt Lake City
11. Gnielinski V (1975) Neue Gleichungen für den Wärme-und den Stoffübergang in turbulent durchströmten Rohren and Kanälen. Forsch-Ing Wes 41 (1):8–16
12. Groeneveld DC, Delorme GGJ (1976) Prediction of thermal non-equilibrium in the post-dryout regime. Nucl Eng Des 36:17–26
13. Saha P (1980) A non-equilibrium heat transfer model for dispersed droplet post-dryout regime. Int J Heat Mass Transfer 23:483–492
14. Chen JC, Ozkaynak FT, Sundaram RK (1979) Vapor heat transfer in post-CHF region including the effect of thermodynamic non-equilibrium. Nucl Eng Des 51:143–155; A phenomenological correlation for post-CHF heat transfer. Nuclear Regulatory Commission of USA, NUREG-0237 (1977)
15. Webb W, Chen JC, Sundaram RK (1982) Vapor generation rate in non-equilibrium convective film boiling. In: International heat transfer conference, Munich, vol 4, p 45
16. Herkenrath H, Mörk-Mörkenstein P, Jung K, Weckermann FI (1967) Wärmeübergang am Wasser bei erzwungener Strömung im Bereich von 140 bis 250 bar. EUR 3658d
17. Becker KM, Hedberg CHL, Strand G (1983) An experimental investigation of the post dryout heat transfer. Royal Institute of Technology, Stockholm, KTH-NEL 33
18. Schnittger RB (1982) Untersuchungen zum Wärmeübergang bei vertikalen und horizontalen Rohrströmungen im Post-dryoutBereich. Dissertation, Technical University of Hannover 1982, cf. Chem-Ing Techn 54(10)
19. Hendricks RC, Graham RW, Hsu YY, Medeiros AA (1962) Correlation of hydrogen heat transfer in boiling and supercritical pressure states. ARS J 244–252 and NASA Technical Notes D-765, May 1961
20. Grigull K (1982) Zustandsgrößen von Wasser und Wasserdampf in SI-Einheiten. Springer, Berlin
21. Groeneveld DC (1969) An investigation of heat transfer in the liquid-deficient regime. Atomic Energy of Canada Limited AECL-3281
22. Katsaounis A Zur Berechnung der Wärmeübertragung nach der Siedekrise. GKSS Research Center Report GKSS 88/E/46
23. Miropol'skiy ZL (1963) Heat transfer in film boiling of a steamwater mixture in steam generating tubes. Teploenergetika 10(5):49–53
24. Dimmick GR (1979) Measurements of drypatch spreading and post-dryout temperatures in a 3-rod bundle cooled by Freon 12 in vertical and horizontal orientation. Atomic Energy of Canada Limited AECL-6683
25. Hynek L, Rohsenow WM, Bergles AB (1969) Forced convection dispersed flow film boiling. Massachusetts Institute of Technology -Heat Transfer Lab. Report No. DSR-70586, 63
26. Plummer DN, Iloeje OC, Rohsenow WM, Griffith P, Ganic E (1974) Post-critical heat transfer to flowing liquid in a vertical tube. Department of Mechanical Engineering, Massachusetts Institute of Technology, Report No. 72718-91
27. Hein D, Kastner W, Köhler W (1982) Influence of the orientation of a flow channel on the heat transfer in a boiler tube. In: European two-phase flow group meeting, Paris
28. Taitel Y, Dukler AE (1976) A model for predicting flow transition in horizontal and near horizontal gas-liquid flow. AIChE J 22(1):47–95 and 900
29. Wallis GB (1969) One-dimensional two-phase flow. McGraw-Hill, New York
30. Hein D, Kastner W, Köhler W (1982) Einfluß der Rohrlänge auf den Wärmeübergang in einem Verdampferrohr. Brennst Wärme-Kraft 34:489–493
31. Kefer V, Köhler W, Kastner W (1989) Critical heat flux (CHF) and post-CHF heat transfer in horizontal and inclined evaporator tubes. Int J Multiphase Flow 15(3):386–392
32. Kanzaka M, Iwabuchi M, Matsuo T, Haneda H, Yamamoto (1986) Heat transfer characteristics of horizontal smooth tube in high pressure region. In: International heat transfer conference, San Francisco, vol 5, pp 2173–2178
33. Auracher H (1987) Partielles Filmsieden in Zweiphasenströmungen. Fortschr-Ber VDI, Reihe 3, Nr. 142, VDI, Düsseldorf
34. Bui TD, Dhir VK (1985) Transition boiling heat transfer on a vertical surface. Trans ASME J Heat Transfer 107:756–763
35. Weber P (1990) Experimentelle Untersuchungen zur Siedekrise und zum Übergangssieden von strömendem Wasser unter erhöhtem Druck. Dissertation, TU-Berlin. Fortschr-Ber VDI, Reihe 3, Nr. 226, VDI, Düsseldorf
36. Huang X (1993) Vergleichende Untersuchung von Siedevorgängen aus temperaturgeregelten Messungen und Quenchingversuchen bei erzwungener Strömung von Wasser. Dissertation, TZ-Berlin. Fortschr-Ber VDI, Reihe 19, Nr. 65, VDI, Düsseldorf
37. Katsaounis A (1996) A prediction method of the transition boiling heat transfer in vertical tubes during forced convection in comparison to experimental data. In: Proceedings of the 2nd European thermal-science conference, Rome, vol 1, pp 425–432, 29–31 May 1996

38. Weber P, Johannsen K (1990) Convective transition boiling of water at medium pressure. In: Proceedings of the ninth international heat transfer conference, Jerusalem, Israel, vol 6, pp 35–40
39. France DM, Chan IS, Shin SK (1987) High-pressure transition boiling in internal flows. J Heat Transfer Trans ASME 109:498–502
40. Schroeder-Richter D (1991) Ein analytischer Beitrag zur Anwendung der Thermodynamik irreversible Prozesse auf Siedephänomene. Dissertation, TU-Berlin. Fortschr-Ber VDI, Reihe 3, Nr. 251, VDI, Düsseldorf
41. Ragheb HS, Cheng SC, Groeneveld DC (1981) Observations in transition boiling of subcooled water under forced convective conditions. Int J Heat Mass Transfer 24:1127–1137
42. Cheng SC, Ng WWL, Heng KT (1987) Measurement of boiling curves of subcooled water under convective conditions. Int J Heat Mass Transfer 21:1387–1392
43. Katsaounis A, Fulfs H, Kreubig M (1982) Experimental results of critical heat flux measurements in 25-rod bundles with different types of grid spacers. In: Bankoff SG, Afgan NH (eds) Proceedings of heat transfer in nuclear reactor safety. International Centre for Heat and Mass Transfer. Hemisphere, Washington
44. Breem BP, Westwater IW (1962) Effect of diameter of horizontal tubes on film boiling heat transfer. Chem Eng Prog 58:67–72
45. Groeneveld DC (1984) Inverted annular and low quality film boiling. A state-of-the-art report. In: Proceedings of the 1st International workshop on fundamental aspects of post-dryout heat transfer, Salt Lake City
46. Leonard JE, Sun KH, Dix GE Low flow film boiling heat transfer on vertical surfaces. Solar Nucl Heat Transfer AIChE Symp Ser No. 164 73
47. Denham MK (1950) Inverted annular film boiling and the Bromley model. United Kingdom Atomic Energy Authority, AEEW-R, 1983
48. Bressler RG (1972) A review of physical models and heat transfer correlations for free-convection film boiling. Adv Cryogen Eng 17(K-2): 382–406
49. Hsu YY (1972) A review of film boiling at cryogenic temperatures. Adv Cryogen Eng 17:361–381
50. Sparrow EM, Cess RD (1962) The effect of subcooled boiling on laminar film boiling. Trans ASME J H Transfer 84:149–156
51. Nishikawa KT, Ito T (1966) Two-phase boundary layer treatment of free convective-film boiling. Int J Heat Mass Transfer 9:103–115
52. Greitzer EM, Abernathy FH (1972) Film boiling on vertical surfaces. Int J Heat Mass Transfer 15:475–491
53. Lauer H (1976) Untersuchung des Wärmeübergangs und der Wiederbenetzung beim Abkühlen heißer Metallkörper. EUR. 5702d
54. Lauer H, Hufschmidt W (1976) Heat transfer and surface rewet during quenching. In: Advanced Study Institute on two-phase flow and heat transfer, Istanbul
55. Sudo Y (1980) Film boiling heat transfer during reflood phase in postulated PWR-LOCA. J Nucl Sci Technol 7:516–530
56. Stewart JIC, Groeneveld DC (1981) Low quality and subcooled film boiling of water at elevated pressures. Nucl Eng Des 67:259–272
57. Bromley LA, Leroy NR, Robbers JA (1953) Heat transfer in forced convection film boiling. Ind Eng Chem 45(I):2639–2646
58. Raznjevic K (1977) Thermodynamische Tabellen. VDI, Düsseldorf
59. Motte EI, Bromley LA (1957) Film boiling of flowing subcooled liquids. Ind Eng Chem 49(II):1921–1928
60. Vargaftik NB (1975) Tables on the thermo physical properties of liquids and gases. Hemisphere, Washington
61. Leidenfrost JG (1966) On the fixation of water in diverse fire. Int J Heat Mass Transfer 9:1153–1166
62. Schroeder-Richter DG (1990) Bartsch: the Leidenfrost phenomenon caused by a thermodynamical effect of transition boiling: a revised problem of non-equilibrium thermodynamics. In: Witte LC, Avedisian CT (eds) Proc. fund. of phase change, boiling and condensation, New York, ASME-HTD, vol 136, pp 13–20
63. Hein D, Kefer V, Liebert H (1984) Maximum wetting temperatures up to critical pressure. In: Proceedings of the 1st international workshop of fundamental aspects of post-dryout heat transfer, Salt Lake City
64. Groeneveld DC, Stewart JC (1982) The minimum film boiling temperature for water during film boiling collapse. In: International heat transfer conference, Munich, Paper FB 37, vol 4, pp 393–398
65. Feng Q (1991) Experimentelle Untersuchungen zur maximalen Temperatur des Übergangssiedens bei erzwungener Wasserströmung bis 1,2 MPa. Dissertation, TU-Berlin. Fortschr-Ber VDI, Reihe 3, Nr. 265, VDI, Düsseldorf
66. Hein D (1981) Modellvorstellungen zum Wiederbenetzen durch Fluten. Dissertation, Technical University of Hanover
67. Yao S, Henry RE (1978) An investigation of the minimum film boiling temperature on horizontal surfaces. Trans ASME J Heat Transfer 100:260–267
68. Michiyoshi I, Makino K (1978) Heat transfer characteristics of evaporation of a liquid droplet on heated surfaces. Int J Heat Mass Transfer 21:605–613
69. Chowdhury K, Winterton RH (1984) Transition boiling on surfaces of different surface energy. In: Proceedings of the 1st international workshop on fundamental aspects of post-dryout heat transfer, Salt Lake City
70. Emmerson GS, Snoek CW (1978) The effect of pressure on the Leidenfrost point of discrete drops of water and Freon on a brass surface. Int J Heat Mass Transfer 21:1081–1086
71. Feng Q, Johannsen K (1990) The high-temperature limit of the transition boiling regime for water in vertical upflow at medium pressure. In: Proceedings of the ninth international heat transfer conference, Jerusalem, Israel, vol 6, pp 29–34
72. Bradfield WS (1967) On the effect of subcooling on wall superheat in pool boiling. J Heat Transfer ASME 89:269–270
73. Henry RE A correlation of the minimum film boiling temperature. Heat Transfer Res Des AIChE Symp Ser No. 138 70
74. Berenson PJ (1961) Film-boiling heat transfer from a horizontal surface. Trans ASME J Heat Transfer 83:351–358
75. Kalinin EK, Yarkho A, Berlin II, Kochelaev Yu, Kostyuk VV (1969) Investigations of the crisis of film boiling channels. In: Proceedings of the two-phase flow and heat transfer in rod bundles. ASME-winter annual meeting, Los Angeles
76. Komnos A (1981) Ein thermohydrodynamisches Modell zur Wiederbenetzung. Dissertation, A. Institute of Thermodynamics, Technical University of Munich
77. Kefer V (1982) Der Einfluß des Druckes auf das Benetzungsverhalten. Diploma thesis A. Institute of Thermodynamics, Technical University of Munich

References cited in Subchap. H3.7

1. Bennett DL, Chen JC (1980) Forced convective boiling in vertical tubes for saturated pure components and binary mixtures. AIChE J 26 (3): 454–461
2. Schlünder EU (1982) Über den Wärmeübergang bei der Blasenverdampfung von Gemischen. Verfahrenstechnik (vt) 16(9):692–698
3. Arora CP (1967) Boiling heat transfer data for pure and mixed refrigerants. Proceedings of the XII international congress of refrigeration, Madrid, vol 11, pp 411–417
4. Shock RAW (1973) The evaporation of binary mixtures in forced convection. PhD thesis, University of Oxford
5. Calus WF, di Montegnacco A, Dennig RK (1973) Heat transfer in a natural circulation single tube reboiler. Part II: Binary liquid mixtures. Chem Eng J 6:251–264
6. Zizyukin VK, Aérov MÉ (1975) Heat transfer to certain boiling hydrocarbons during their forced motion in a horizontal tube. Translated from Teoreticheskie Osnovy Khimicheskoi Technologii 9(1):54–59
7. Mishra MP, Varma HK, Sharma CP (1981) Heat transfer coefficients in forced convection evaporation of refrigerant mixtures. Lett Heat Mass Transfer 8:127–136
8. Varma HK, Sharma CP, Mishra MP (1979) Heat transfer coefficients during forced convection evaporation of R 12 and R 22 mixtures in annular flow regime. In: Proceedings of the XV international congress of refrigeration, Venice, vol II, pp 479–484
9. Singal LC, Sharma CP, Varma HK (1983) Experimental heat transfer coefficient for binary refrigerant mixtures of R 13 and R 12. ASHRAE Trans 1A:175–188
10. Singal LC, Sharma CP, Varma HK (1983) Correlations for averaged heat transfer coefficients in flow boiling of refrigerant 12 and 13 mixtures. In: Proceedings of the XVI international congress of refrigeration, Paris, vol B.1, pp 159–164

11. Toral H (1979). Flow boiling heat transfer in mixtures. PhD thesis, University of Oxford
12. Toral H, Kenning DBR, Shock RAW (1982) Flow boiling of ethanol/cyclohexane mixtures. In: 7th international heat transfer conference, Munich, vol 4, pp 255–260
13. Jain VK, Dhar DL (1983) Studies on flow boiling of mixtures of refrigerants R 12 and R 13 inside a horizontal tube. In: Proceedings of the XVI international congress of refrigeration, Paris, vol 1, pp 287–293
14. Ross H (1985) An investigation of horizontal flow boiling of pure and mixed refrigerants. PhD thesis, University of Maryland, College Park
15. Radermacher R, Ross H, Didion D Experimental determination of forced convection evaporative heat transfer coefficients for non-azeotropic refrigerant mixtures. In: ASME national heat transfer conference, Report ASME 83-WA/HT54, pp 1–7
16. Ross H, Radermacher R (1987) Suppression of nucleate boiling of pure and mixed refrigerants in turbulent annular flow. Int J Multiphase Flow 13 (6):759–772
17. Ross H, Radermacher R, DiMarzo M, Didion D (1987) Horizontal flow boiling of pure and mixed refrigerants. Int J Heat Mass Transfer 30 (5):979–992
18. Jung DS, McLinden M, Radermacher R, Didion D (1989) Horizontal flow boiling heat transfer experiments with a mixture of R 22/R 114. Int J Heat Mass Transfer 32(1):131–145
19. Kaiser EP (1988) Wärmeübertragung beim Sieden von binären Gemischen im Naturumlaufverdampfer. Dissertation, Dissertation No. 8504, Technical University of Zürich
20. Gropp U (1985) Wärme-und Stoffübergang bei der Oberflächenverdampfung und beim Blasensieden eines binären Kältemittelgemisches am Rieselfilm. Dissertation, Universität Karlsruhe
21. Palen JW (1988) Falling film evaporation of wide-boiling-range mixtures inside a vertical tube. PhD dissertation, Lehigh University
22. Niederkrüger M, Steiner D, Schlünder EU (1992) Horizontal flow boiling experiments of saturated pure components and mixtures of R 846/R 12 at high pressures. Int J Refrig 15(1):48–58
23. Niederkrüger M (1991) Strömungssieden von reinen Stoffen und binären zeotropen Gemischen im waagerechten Rohr bei mittleren und hohen Drücken. Fortschr-Ber VDI-Z Reihe 3(245)
24. Wettermann M (1999) Wärmeübergang beim Sieden von Gemischen bei Zwangskonvektion im horizontalen Verdampferrohr. Fortschr-Ber VDI-Z Reihe 3(625)
25. Numrich R (1996) Falling film evaporation of soluble mixtures. In: Convective flow boiling. Taylor & Francis, Washington, pp 335–338
26. Thome JR (1989) Prediction of the mixture effect on boiling in vertical thermosyphon reboilers. Heat Transfer Eng 10(2):29–38
27. Gronnerud R (1974) Two-phase heat resistance in boiling refrigerants – Calculations and influence on evaporator design. Institutt for Kjøleteknikk, Norges Tekniske Høgskole, Trondheim, pp 1–28
28. Lorentzen G, Gronnerud R Investigation of liquid holdup, flow resistance and heat transfer in an R 12-evaporator coil with recirculation. In: Proceedings of the XIIIth international congress of refrigeration, Washington, I.I.F. Annexe 19701, pp 193–203
29. Malek A (1983) Influence de la presence d'huile dans le fluide frigorigene sur le transfer de chaleur ä l'evaporation dans un tube horizontal (orig. French). In: 16th international congress of refrigeration, I.I.R. Paris, vol B1-489, 585–588
30. Pierre B (1953) Wärmeübergangszahl bei verdampfendem F 12 in horizontalen Rohren. Kältetechnik 7 (1955) No. 6, 163–166; Heat transfer to boiling F 12 in horizontal tubes (orig. Swedish). Kylteknisk Tidskrift 6:76–81
31. Worsøe-Schmidt P (1959) Some characteristics of flow pattern and heat transfer of Freon 12 evaporating in horizontal tubes. Ingeniøren Int Ed 3(3):98–104

Condensation

J1 Filmwise Condensation of Pure Vapors

Reiner Numrich[1] · *Jürgen Müller*[2]
[1]Paderborn, Germany
[2]BASF AG Ludwigshafen, Germany

1 Introduction

When a vapor comes into contact with a surface, the temperature of which is below the temperature of thermodynamic equilibrium, the vapor at this surface turns from the gaseous state to the liquid state. This process is known as condensation. Associated with the change of aggregate status is a significant production of heat.

If the condensation is caused by direct contact with the liquid phase, it is referred to as mixed or injection condensation. In the case of sufficient supercooling of the vapor and/or in the presence of condensation nuclei (e.g., tiny dust particles, small droplets), a mist can already be formed in the gas phase through spontaneous condensation.

Technically relevant in most applications is indirect condensation on cooled solid surfaces. Here, drops of liquid first start to form around individual condensation nuclei, becoming larger as the condensation process proceeds. This is known as drop condensation. If boundary layer conditions exist, which permit complete wetting of the wall, the vapor no longer condenses on the solid wall but on the surface of a liquid film. This type of condensation is known as film condensation.

The most common type under technical conditions is film condensation. This condensation type is taken as the basis for the description and calculation of condensation processes in the following. An essential feature is that the heat of condensation released at the condensation film surface must be transported to the cooled wall by the condensate film.

In the following, the general procedure for the design of condensers is described and information is provided on the use of material values, averaged or local reference values, and coefficient equations. According to condenser geometries used in practice, calculation methods are first described for the condensate film running down the vertical pipe due to gravitation. If necessary, the influence of the vapor flow on the heat transfer in the condensate film must be taken into account. The second classic setup is the horizontal or slightly inclined pipe where the condensation takes place on the outside of the pipe, usually in the mantle space of a horizontal tube nest apparatus, or inside the externally cooled pipe. In conclusion, special questions regarding the film condensation of metal vapors and superheated vapors are dealt with.

2 Calculation Methods

2.1 Definition of Heat Transfer Coefficients

The local temperature profile in a condensate film is shown in Fig. 1.

VDI-GVC (ed.), *VDI Heat Atlas*, DOI 10.1007/978-3-540-77877-6_36,

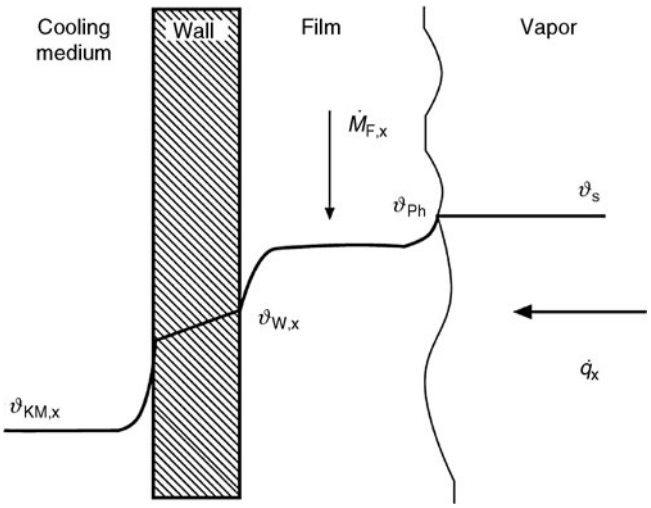

J1. Fig. 1. Schematic temperature profile for condensation of pure vapors.

The local heat transfer coefficient of the condensate film $\alpha_{F,x}$ is defined as

$$\alpha_{F,x} = \frac{\dot{q}_x}{\vartheta_{Ph} - \vartheta_{W,x}} \tag{1}$$

with the local heat flux density $\dot{q}_x$ transferred vertical to the wall, and the temperatures at the film surface ϑ_{Ph}, corresponding to the case of the condensation of pure vapors with the boiling temperature ϑ_S at the relevant system pressure, and at the wall $\vartheta_{W,x}$.

The local heat transfer coefficient is presented nondimensionally as a Nusselt number

$$\mathrm{Nu}_{F,x} = \frac{\alpha_{F,x}\mathcal{L}}{\lambda_F} \tag{2}$$

formed with the characteristic length of the film flow

$$\mathcal{L} = \sqrt{\frac{\nu_F^2}{g}}. \tag{3}$$

2.2 Calculation Using Local Data

The differential energy balance for a volume element of the condenser is

$$k_x(\vartheta_S - \vartheta_{KM,x})\mathrm{d}A = \Delta h_v \mathrm{d}\dot{M}_F. \tag{4}$$

The heat condensation of released at the phase boundary must be conducted to the cooling medium KM. The condensation area required A follows from the integration of Eq. (4) to

$$A = \int_0^{\dot{M}_{F,L}} \frac{\Delta h_V \mathrm{d}\dot{M}_F}{k_x(\vartheta_S - \vartheta_{KM,x})} \tag{5}$$

with the heat transfer coefficient k_x according to Chap. C2.

For a surface without curves, this is

$$\frac{1}{k_x} = \frac{1}{\alpha_{F,x}} + \frac{s}{\lambda_W} + \frac{1}{\alpha_{KM,x}} + R_f. \tag{6}$$

Here, s/λ_w is the heat transfer resistance of the wall, $\alpha_{KM,x}$ is the heat transfer coefficient on the coolant side, and R_f is the fouling resistance. All values must be assigned in relation to the axial coordinate x.

During condensation, the fouling resistance can have a significant influence on the heat transfer area required. Calculation in advance is currently not possible. Empirical values are known from the literature. Indicative values are shown in Chap. O1.

2.3 Calculation Using Average Data

If the heat transfer coefficient is only weakly dependent on the axial coordinate, Eq. (5) can be directly integrated at constant boiling temperature ϑ_S and, for area A of the condenser

$$A = \frac{\Delta h_v \dot{M}_F \langle x = L \rangle}{k(\vartheta_S - \vartheta_{KM})_{log}} \tag{7}$$

with the overall heat transfer coefficient k we obtain

$$\frac{1}{k} = \frac{1}{\alpha_F} + \frac{s}{\lambda_W} + \frac{1}{\alpha_{KM}} + R_f \tag{8}$$

and the mean temperature difference

$$(\vartheta_S - \vartheta_{KM})_{log} = \frac{(\vartheta_S - \vartheta_{KM,ein}) - (\vartheta_S - \vartheta_{KM,aus})}{\ln \dfrac{\vartheta_S - \vartheta_{KM,ein}}{\vartheta_S - \vartheta_{KM,aus}}}. \tag{9}$$

The condensate mass flow $\dot{M}_F$ must be assigned at the point $x = L$, i.e., at the outlet of the condenser. This procedure is suitable for a preliminary rough estimate of the transfer area of a condenser. For precise design, a calculation on the basis of local values is usually necessary.

3 Condensation in Vertical Tubes

3.1 Local Heat Transfer Coefficients Without Vapor Flow

In the *laminar flow area*, the local Nusselt number for the smooth film is calculated ignoring the vapor shear stress according to Nusselt [1]

$$\mathrm{Nu}_{F,x,1} = \frac{a_{F,x,1}\mathcal{L}}{\lambda_F} = 0.693 \left(\frac{1 - \rho_D/\rho_F}{\mathrm{Re}_{F,x}}\right)^{1/3}. \tag{10}$$

Here, the Reynolds number is obtained:

$$\mathrm{Re}_{F,x} = \frac{\dot{\Gamma}_X}{\eta_F} = \frac{\dot{M}_{F,x}}{\pi\, d\, \eta_F} = \frac{\dot{M}_{F,x}}{b\, \eta_F} \tag{11}$$

with the local trickle density Γ_x, i.e., the mass flow of film liquid in relation to the pipe circumference πd or to the width of the

cooling area b. The material properties must be assigned for the temperature of the phase boundary (boiling temperature) of the condensate film.

The *waviness of the film flow* at the surface improves the heat transfer. This effect is taken into account by a waviness correction f_{well}. Various approaches exist from different authors, which do not differ greatly. At this point, the approach of Kutateladze and Gogonin [2] is recommended:

$$f_{well} = \frac{Nu_{F,x,l,well}}{Nu_{F,x,l}} = \begin{cases} 1 & \text{for } Re_{F,x} < 1, \\ Re_{F,x}^{0.04} & \text{for } Re_{F,x} \geq 1. \end{cases} \quad (12)$$

In the case of *turbulent flow*, the Nusselt number of the condensate film is obtained from the arrangement in series of a heat transfer resistance near the wall and phase boundary [3, 4]. Experimental data for this have been measured by Yüksel [5] and Müller [3] in a Prandtl number range from 3 to 52 and, with the help of analogy observations applied to the basic processes of film evaporation and absorption. The local Nusselt number for the turbulent condensate film, according to Müller [3], is

$$Nu_{F,x,t} = \frac{\alpha_{F,x,t}\mathcal{L}}{\lambda_F} = \frac{0.0283 Re_{F,x}^{7/24} Pr_F^{1/3}}{1 + 9.66 Re_{F,x}^{-3/8} Pr_F^{-1/6}}. \quad (13)$$

3.1.1 Influence of Temperature-Dependent Properties

The influence of temperature-dependent material properties can be taken into account, according to Müller [3], by a correction factor f_η:

$$f_\eta = \left(\frac{\eta_{F,S}}{\eta_{F,W}}\right)^{1/4}. \quad (14)$$

It is valid for the laminar and the turbulent flow region and has a pronounced effect when the temperature difference in the film is large, e.g., in the case of intensive condensation processes of substances with high Prandtl numbers.

3.1.2 Combined Presentation

The equations shown above can be superimposed as follows:

$$Nu_{F,x} = \sqrt[2]{(f_{well} Nu_{F,x,l})^2 + Nu_{F,x,t}^2} \cdot f_\eta \quad (15)$$

This quadratic superimposition describes the equations of Müller [3] very well.

Figure 2 shows the local Nusselt number for the condensate film in relationship to the Reynolds number. The Prandtl number is shown as a parameter. The calculations were carried out according to Eq. (15) with $f_\eta = 1$.

Range of validity:

$Nu_{F,x}$ acc. to Eq. (15), $Re_{F,x} < 10{,}000, 0.5 < Pr_F < 500, 0.2 < \eta_{F,S}/\eta_{F,W} < 5$.

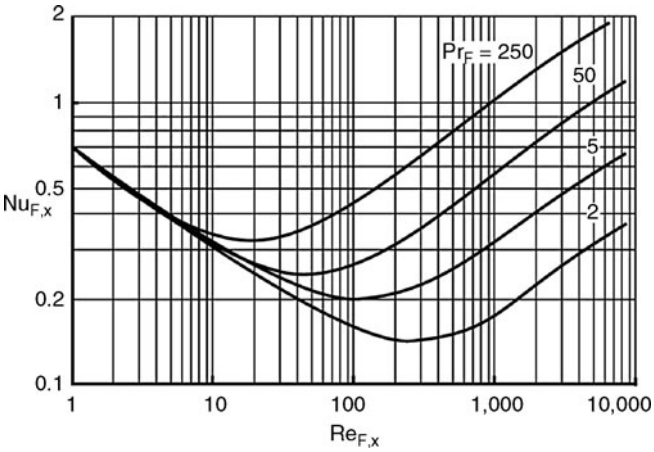

J1. Fig. 2. Local Nusselt number for filmwise condensation in a vertical tube as a function of Reynolds number and Prandtl number.

3.2 Mean Heat Transfer Coefficients Without Vapor Flow

Nusselt numbers averaged over the cooling area length are obtained by integration of the local values from the previous section. The following equations result for the average Nusselt numbers.

Laminar range:

$$Nu_{F,l} = \frac{\alpha_{F,l}\mathcal{L}}{\lambda_F} = \frac{4}{3} Nu_{F,x=L,l} = 0.925 \left(\frac{1 - \rho_D/\rho_F}{Re_{F,L}}\right)^{1/3}. \quad (16)$$

Turbulent range:

$$Nu_{F,t} = \frac{\alpha_{F,t}\mathcal{L}}{\lambda_F} = \frac{0.020 Re_{F,L}^{7/24} Pr_F^{1/3}}{1 + 20.52 Re_{F,L}^{-3/8} Pr_F^{-1/6}}. \quad (17)$$

Here, the Reynolds number is obtained with the trickle density Γ_L or the condensate mass flow $\dot{M}_{F,L}$ at the outlet of the condenser:

$$Re_{F,L} = \frac{\dot{\Gamma}_L}{\eta_F} = \frac{\dot{M}_{F,L}}{\pi d \eta_F} = \frac{\dot{M}_{F,L}}{b \eta_F}. \quad (18)$$

3.2.1 Combined Presentation

Laminar and turbulent regions can be superimposed as follows:

$$Nu_F = \sqrt[1,2]{(f_{well} Nu_{F,l})^{1,2} + (Nu_{F,t})^{1,2}} \cdot f_\eta \quad (19)$$

In the calculation of the average heat transfer coefficients, Eq. (12) can also be used as *waviness correction* f_{well}. The deviation can be ignored.

In order to take account of the *influence of temperature-dependent material properties*, Eq. (14) is also recommended in the case of average heat transfer coefficients.

The validity range of the equations for the local heat transfer applies here as well.

3.3 Heat Transfer with Significant Vapor Flow

In the case of high vapor velocities, there is a significant interaction between the gas and the fluid phases, expressed by the shear stress τ_D acting on the condensate film surface, which can have a considerable influence on the heat transport in the condensate film. For design in such cases, a general distinction must be made between flow with the current and counterflow.

3.3.1 Cocurrent Flow of Gaseous and Liquid Phases

Heat Transfer

If the gas and the fluid phases are both flowing in the same direction, the transport resistance is reduced in principle as a result of two different physical processes: first, through modification of the laminar sublayer near the wall and, second, through the excitation of turbulences in the boundary layer near the surface.

First, the effect of the shear stress at the phase boundary area on the heat transfer in the layer near the wall is considered (shown by the exponent +). The shear stress increases the mean velocity $\bar{u}_F$ in the liquid phase. As a result, the condensate film becomes thinner, as the Reynolds number Re_F remains constant locally, i.e., $\bar{u}_F \cdot \delta_F = \text{const}$. (Fig. 3).

The relationship of the Nusselt numbers with (exponent +) and without consideration of the shear stress can be represented by

$$\frac{Nu^+_{F,x,l}}{Nu_{F,x,l}} = K_W = \left(1 + 1.5\tau^*_D\right)^{1/3}. \tag{20}$$

Here, τ^*_D is a nondimensional shear stress in the form

$$\tau^*_D = \frac{\tau_D}{\rho_F g \delta^+_F} \text{ with } \tau_D = \frac{\xi_r}{8}\rho_D \bar{u}^2_D. \tag{21}$$

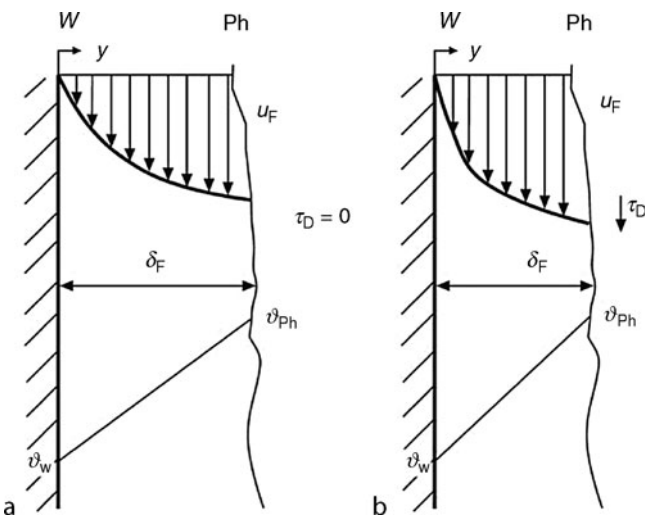

J1. Fig. 3. Velocity and temperature profiles with and without superimposed vapor flow at laminar film flow.

The calculation of the shear stress τ_D at the condensate film surface and the film thickness δ^+_F is explained under *pressure loss and shear stress*. In the turbulent flow region, the existing laminar sublayer is similarly influenced by the higher average condensate film velocity. From Numrich [8], we obtain the relationship (22)

$$\frac{Nu^+_{F,x,t}}{Nu_{F,x,t}} = K_{W,t} = \left(1 + \tau^*_D\right)^{1/3}. \tag{22}$$

Equation (22) has been confirmed by Müller [3] in a later work.

The description of the shear stress influence in Eq. (22) is sufficiently accurate for the whole flow region, using the superimposition function of Eq. (15). It is recommended to calculate uniformly in the whole flow region with

$$K_{W,l} = K_{W,l} = K_W = \left(1 + \tau^*_D\right)^{1/3} \tag{23}$$

so that, generally,

$$Nu^+_{F,x} = Nu_{F,x}\left(1 + \tau^*_D\right)^{1/3}. \tag{24}$$

Figure 4 shows a comparison of Nusselt numbers measured and calculated according to Eq. (24).

In systems with material properties other than water or water vapor, e.g., hydrocarbons with higher Prandtl numbers, the equations shown are inadequate for showing the influence of the shear stress. A comparison with experiments by different authors [9–11] shows that, as the Prandtl number rises, i.e., as the thermal conductivity of the fluid used falls, the heat transfer is up to 100% greater than that obtained with Eq. (24).

Figure 5 shows the relationship of measured Nusselt numbers to values calculated according to Eq. (24) as a function of the nondimensional shear stress.

The additional increase in the heat transfer with rising shear stress can be explained by a modification of the quasi-laminar layer at the phase boundary. The shear stress intensifies the exchange of impulses at the phase boundary which leads to the amplification of turbulent fluctuations in the condensate film. In the laminar flow region, the exchange of impulses increases the surface roughness of the condensate films, i.e., additional

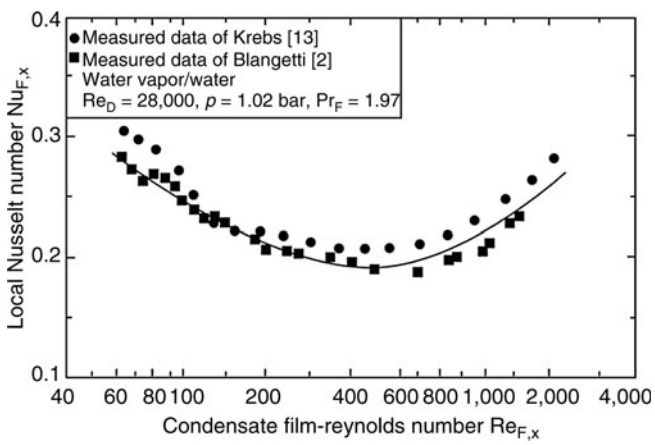

J1. Fig. 4. Comparison of measured data from Blangetti and Krebs with data according to Eq. (24) calculated Nusselt numbers.

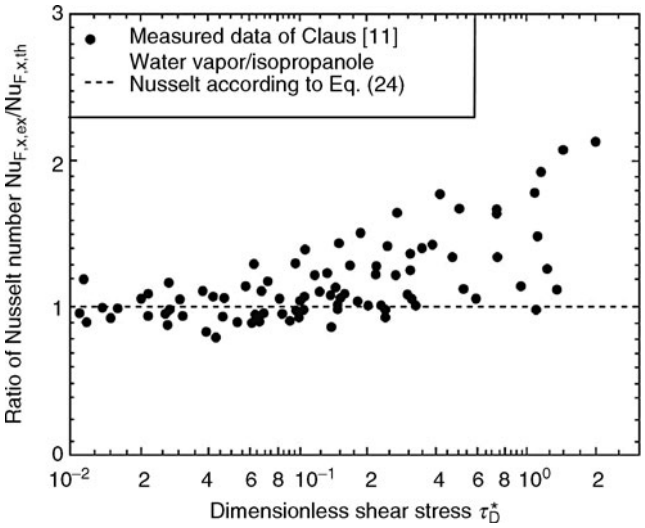

J1. Fig. 5. Comparison of measured Nusselt numbers with Eq. (24).

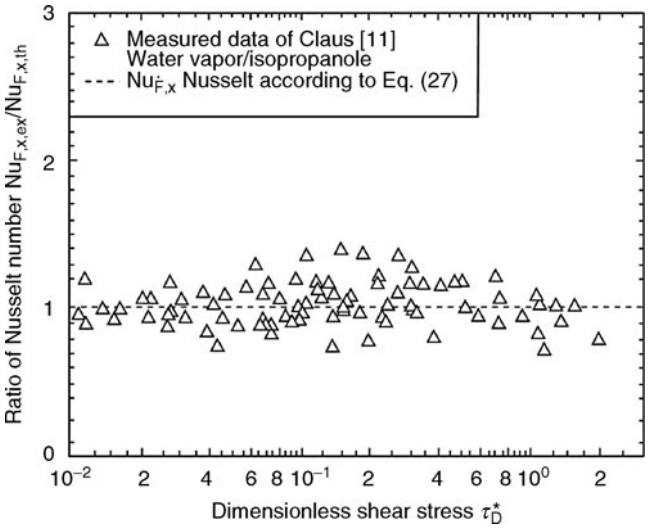

J1. Fig. 7. Comparison of measured Nusselt numbers with Eq. (27).

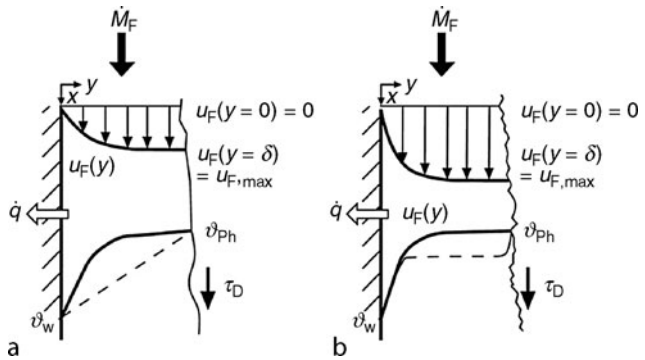

J1. Fig. 6. Velocity and temperature profiles in the presence of significant vapor flow.

turbulent fluctuations are excited on the surface (Fig. 6a). In the turbulent flow region, the laminar boundary layer near the surface is so influenced that the thickness of this layer is reduced in dependence on the shear stress and the heat transfer is also improved in this way (Fig. 6b).

As the influence of the shear stress between laminar and turbulent flow conditions in the condensate film differs significantly, two correction factors K_{Ph} must be introduced [12]:

- laminar flow regime:

$$K_{Ph,l} = 1 + \left(Pr_F^{0.56} - 1\right) \tanh \tau_D^*, \tag{25}$$

- turbulent flow regime:

$$K_{Ph,t} = 1 + \left(Pr_F^{0.08} - 1\right) \tanh \tau_D^*. \tag{26}$$

The following method is recommended:

$$Nu_{F,x}^{\bullet} = \sqrt{\left[\left(K_{Ph,l} Nu_{F,x,l}^{+}\right)^2 + \left(K_{Ph,t} Nu_{F,x,t}^{+}\right)^2\right]}. \tag{27}$$

Figure 7 shows the comparison from Fig. 5 with Eq. (27).

Pressure Loss and Shear Stress

As a rule, a downward directed two-phase ring flow exists in practice, in which the gas and liquid phases are separated. In the vertical pipe, assuming an adiabatic ring flow (represented by the exponent °), the relationship between friction pressure drop per length $(dp/dx)^\circ$ and the shear stress τ_D° at the condensate film surface ($\delta_F^+ \ll d$):

$$\left(\frac{dp}{dx}\right)^\circ = -\tau_D^\circ \frac{4}{d}. \tag{28}$$

The shear stress is defined by

$$\tau_D^\circ = \frac{\xi_r^\circ}{8} \rho_D \bar{u}_{D-F}^2. \tag{29}$$

Here, ξ_r° is the resistance coefficient of the condensate film surface and $\bar{u}_{D-F}$ is the average velocity of the gas phase in relation to the liquid phase. While, in the case of low pressures and the associated low condensation rates, it is often possible to calculate with the average gas velocity $\bar{u}_D = \bar{u}_{D-F}$, this results in very considerable deviations at higher pressures and high condensation rates, so that an estimate of the speeds is always necessary.

For calculation of the resistance coefficient ξ_r°, which governs the shear stress and the pressure loss, numerous approaches exist, some of which differ greatly under certain process conditions. A comparison with extensive experimental data shows that a modified approach in accordance with Andreussi [13] gives the best agreement [14]:

$$\xi_r^\circ = \xi_g^\circ \left(1 + 550F \cdot \tau_D^{*a}\right). \tag{30}$$

Herein are

$$\xi_g^\circ = 0.184 Re_{D-F}^{-0.2} \text{ with } Re_{D-F} = \frac{\bar{u}_{D-F} \cdot d_h}{\nu_D}. \tag{31}$$

The friction factor of a smooth tube,

$$F = \frac{\max\left\{\left(2Re_{F,x}\right)^{0.5}; 0.132 Re_{F,x}^{0.9}\right\}}{Re_{D-F}^{0.9}} \frac{\eta_L}{\eta_D} \sqrt{\frac{\rho_D}{\rho_L}} \tag{32}$$

a flow parameter

$$a = 0.85 \text{ for } \tau_D^* \le 1,$$
$$a = 0.3 \text{ for } \tau_D^* > 1 \tag{33}$$

an exponent for the description of the relationship between shear stress and gravity of the film. The required film thickness is also determined with the flow parameter F as

$$\frac{\delta_F^+}{d} = \frac{6.59F}{\sqrt{1 + 1,400F}}. \tag{34}$$

This is a calculated value which is only valid in combination with Eqs. (30–33) [15]. Strictly speaking, this should be δ_F^+, but in practice, $d_h \approx d$ is sufficiently accurate. Figure 8 shows qualitatively the relationships between ξ_r^o and the Reynolds numbers of the gas and liquid phases, taking as an example the system isopropanol–carbon dioxide.

The wall normal mass transport $\dot{m}_n$ toward the condensate film surface leads to an additional increase in the exchange of impulses. This is taken into account by the factor C_τ:

$$\xi_r = C_\tau \xi_r^o. \tag{35}$$

According to the ideas of film theory, this factor results in

$$C_\tau = \frac{a_\tau}{1 - e^{-a_\tau}} \text{ with } a_\tau = \frac{\dot{m}_n \cdot \bar{u}_{D-F}}{\tau_D^o}. \tag{36}$$

As the incorporation of this factor means a great deal of calculation work and the value of C_τ only plays a role with regard to pressure loss at high condensation rates, a prior estimate is recommended. In most cases, $C_\tau = 1$ can be set, so that $\xi_r = \xi_r^o$ or $\tau_D = \tau_D^o$. This simplification results in larger dimensioning than necessary.

Incidentally, when determining the whole pressure gradient, it is important that, in addition to friction pressure loss and gravity, the impulse gain due to the deceleration of the vapor flow is taken into account. While the gravity portion may be significant at very high gas densities, the deceleration portion of the total pressure drop

$$\left(\frac{dp}{dx}\right)_v \approx \frac{d(\rho_D \bar{u}_D)^2}{dx} \tag{37}$$

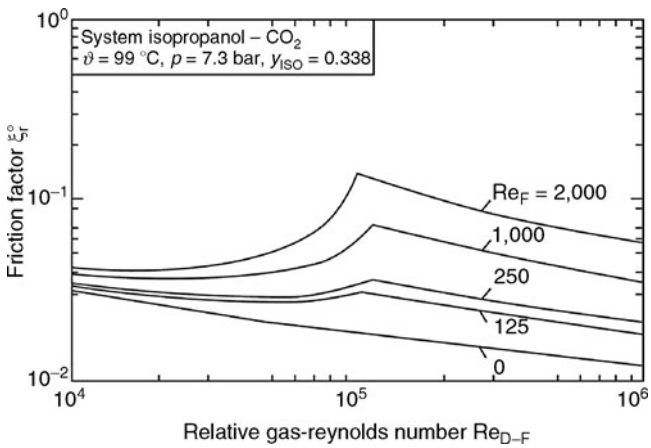

J1. Fig. 8. Friction factor ξ_r^o of gas flow at different Reynolds numbers of liquid phase for isopropanol und carbon dioxide.

may be of the same magnitude as the friction pressure loss, particularly in the case of almost complete condensation.

Limits, Entrainment

In the literature, e.g., [13], it is often pointed out that, when a limit value is exceeded for high vapor and liquid loading, droplet entrainment may occur. In the case of film condensation of pure vapors flowing in the same direction, this is of minor importance. The reason is that although, on entry into the condenser, the vapor velocity is at its highest, the condensate film has not yet formed or is very thin. Only from a specific Reynolds number of the liquid phase entrainment does occur, even at the highest vapor velocities [16]. While, as the condensation progresses, the quantity of condensate increases, the quantity of vapor and thus the square of the shear stress decrease. The rapid reduction of the flow velocity causes quick accumulation of the dispersed droplets. So this effect can usually be ignored, as its influence on heat transfer is negligible.

3.3.2 Countercurrent Flow of Gaseous and Liquid Phases

Heat Transfer

In the case of counterflow, the influence on the near-wall laminar sublayer and the intensification of the heat transfer in the near-surface layer act in exactly the opposite direction. In the case of counterflow, the gas phase causes the liquid film to slow down, thus increasing the thickness of the condensate film. We thus obtain the relationship according to Eq. (24) for $\tau_D^* < 2/3$:

$$Nu_{F,x}^+ = K_W \cdot Nu_{F,x} = Nu_{F,x}\left(1 - \tau_D^*\right)^{1/3}. \tag{38}$$

For $\tau_D^* > 2/3$, the unidirectional upward flow case exists. The influence on the layer near the surface can be shown in an analogue manner as in Eqs. (25) and (26). Equation (27) is correspondingly applicable. Altogether, the influence of the gas flow is first smaller in the case of counterflow. It must be remembered, however, that the interaction, i.e., the shear stress, is already many times greater at low vapor flow velocities than it is in the case of unidirectional flow.

Pressure Loss and Shear Stress

In analogy to Sect. 3.3.1, the pressure loss (Eq. (28)) and the shear stress (Eq. (29)) can be determined, remembering that, in addition to the changed coordinate direction, $\bar{u}_{D-F}$ no longer represents the difference between gas and liquid phases, but the sum

$$\bar{u}_{D-F} = \bar{u}_D + \bar{u}_F.$$

Even at low vapor velocities, the shear stress can be very high. This is due to the resistance coefficient ξ_r^o which, according to Henstock and Hanratty [15], is determined as

$$\xi_r^o = \xi_g^o(1 + 1,400F). \tag{39}$$

Limits, Entrainment, Backups

The maximum condensation performance that can be achieved does not depend on the heat transfer, but is limited by the hydrodynamics. In the case of counterflow, in contrast to

unidirectional flow, the greatest condensate mass flow and the greatest vapor mass flow occur at the same time at the lower inlet of the pipe. At this point, the influence on the condensate films of the flowing vapor phase is correspondingly at its greatest. As a backup or discharge of liquid must be avoided, the backup point must not be exceeded at this point. Before this point is reached, however, entrainment starts, the occurrence of which can be estimated with the modified Weber number

$$\mathrm{We}^* = \frac{\tau_D^o \cdot \delta_F^+}{\sigma_F}$$

τ_D^o can be obtained in accordance with Eq. (29). For δ_F^+, as an approximation, equations for the freely running trickle film can be used. As a critical limit value, which should not be exceeded in the design, the value $\mathrm{We}_C^* = 0.017$ is recommended, below which entrainment is not to be expected [13].

4 Condensation at Horizontal Tubes

4.1 Single Tube

For the condensation on horizontal pipes, Nusselt [1] has given circumferentially averaged heat transfer coefficients for the laminar region. At constant temperature of the outer wall of the condenser pipe and negligible vapor flow

$$\mathrm{Nu}_{F,1} = \frac{\alpha_{F,1}\mathcal{L}}{\lambda_F} = 0.959\left(\frac{1-\rho_D/\rho_F}{\mathrm{Re}_F}\right)^{1/3}. \quad (40)$$

The Reynolds number is also obtained here with the trickle density Γ:

$$\mathrm{Re}_F = \frac{\dot{\Gamma}}{\eta_F} = \frac{\dot{M}_F}{L\eta_F}, \quad (41)$$

in which the condensate mass flow $\dot{M}_F$ is related to the pipe length L. The material data should be inserted here at the average film temperature $(\vartheta_S + \vartheta_W)/2$.

4.2 Tube Bundle

According to Nusselt [1], for a vertically aligned row of pipes in which the condensate from the upper pipe drops on the next pipe below, there exists the following relationship of the average Nusselt number of row $\mathrm{Nu}_{F,1,RR}$ with η_R pipes with the circumferentially averaged Nusselt number of a single pipe $\mathrm{Nu}_{F,1}$:

$$\frac{\mathrm{Nu}_{F,1,RR}}{\mathrm{Nu}_{F,1}} = n_R^i \quad (42)$$

with $i = -1/4$. The heat transfer thus becomes worse as the number of pipes rises, since the liquid film becomes thicker below and the heat transfer resistance also becomes greater.

On the other hand, experimental data show a weaker relationship with the number of pipes in a row. The reasons for this are, for example:

- effects of the vapor shear stress on the heat transfer and
- splashing of the condensate from the pipes.

The experimentally determined exponents for Eq. (42) range from $i = -1/6$ to 0. For the practical calculation of heat transfer coefficients, the value $i = -1/6$ is recommended.

4.3 Tube Bundle, Influence of Gas Flow

In the case of tube bundles, the influence of the vapor shear stress on the heat transfer in the horizontal pipe must normally also be taken into account. Methods from various authors exist in the literature for taking account of the vapor flow.

For a single horizontal pipe with vapor flow from top to bottom, Fujii et al. [17] have published the equation

$$\mathrm{Nu}_{F,1} = \frac{\alpha_{F,1}\mathcal{L}}{\lambda_F} = C\chi\left(1 + \frac{0.276\ \mathrm{Pr}_F}{\chi^4 \mathrm{Fr}\,\mathrm{Ph}}\right)^{1/4}\sqrt{\mathrm{Re}_{GS}}\cdot\frac{\mathcal{L}}{d}. \quad (43)$$

Here $\chi = 0.9(1+G^{-1})^{1/3}$,

$$G = \frac{\mathrm{Ph}}{\mathrm{Pr}_F}\left(\frac{\rho_F\eta_F}{\rho_D\eta_D}\right)^{0,5}, \qquad \mathrm{Ph} = \frac{C_{\rho F}(\vartheta_S - \vartheta_W)}{\Delta h_v},$$

$$\mathrm{Re}_{GS} = \frac{\bar{u}_D d}{\nu_F}, \qquad \mathrm{Fr} = \frac{\bar{u}_D^2}{gd}, \quad C = 1.$$

In Fig. 9 the expression $\mathrm{Nu}_{F,1}/\sqrt{\mathrm{Re}_{GS}}$ is represented as a function of the parameter G. In the case of high values for $\mathrm{Pr}_F/\mathrm{Fr}\,\mathrm{Ph}$, i.e., at low gas flow velocities, the relationship according to Nusselt [1] (Eq. (40)) is reached.

The influence of the angle of incidence of the vapor flow on to the condenser pipe is variously discussed in the literature. Fujii [18] finds almost no influence on the heat transfer in a horizontal pipe. The equations given are also suitable for the calculation of pipe nests. In the case of Fujii et al. [19], calculation according to Eq. (43) is recommended for an offset array of pipes, and a reduction by 20% of the values calculated according to Eq. (43) is recommended for an aligned array:

$$C = \begin{cases} 0.8 & \text{in row,} \\ 1 & \text{displaced.} \end{cases}$$

For more precise calculations, multidimensional treatments must be drawn upon. As a result of condensation, the vapor

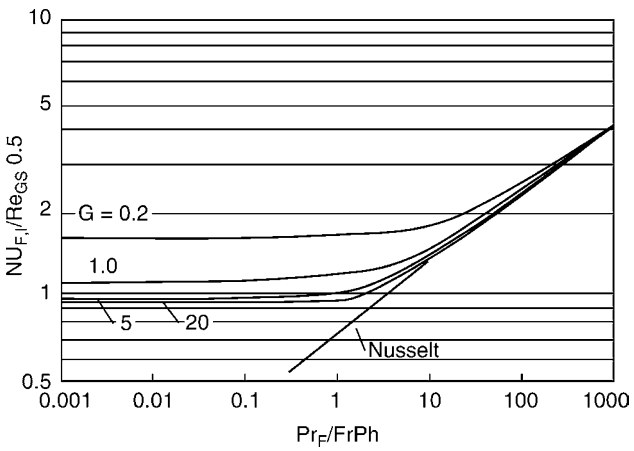

J1. Fig. 9. Influence of vapor flow on the heat transfer at horizontal tubes.

velocity and the system pressure are subject to strong variations which can be studied by splitting the condenser, according to incident flow, into individual lines or rings with constant flow conditions and monitoring these using balance sheets. In any case, however, it must be ascertained whether the work involved in more extensive calculations is justified, particularly with regard to uncertainties in the determination of the fouling resistance.

5 Condensation in Horizontal Tubes

The condensation process and, thus, the calculation of the heat transfer in the horizontal or slightly inclined pipe are essentially determined by the constant change in the flow distribution of the vapor and the liquid phase along the condensation section. Assuming pure vapor on entry at a relatively high velocity, an almost uniformly thin condensate film will form around the circumference. This liquid film becomes continuously thicker as the condensation progresses and, because of gravity, becomes more unevenly distributed. At the same time, the vapor velocity and, thus, the interaction between the vapor and the liquid phase are reduced. A mixture of annular and stratified flow forms which, according to condensation conditions, develops into a surge flow, a slug flow, or even a single phase (liquid) flow.

In order to assess the flow distribution, flow maps are employed, which are presented in many different ways. Figure 10 shows a simplified flow map according to Breber et al. [20], in which a modified Froude number (44)

$$\mathrm{Fr}_{\mathrm{G}}^{*} = \sqrt{\frac{\rho_{\mathrm{D}}}{\rho_{\mathrm{F}} - \rho_{\mathrm{D}}}} \frac{\bar{u}_{\mathrm{D},0}}{\sqrt{d \cdot g}}. \tag{44}$$

is shown in relation to the flow parameter F according to Eq. (32).

It is essential for the practical calculation that, on the basis of this map, a distinction is made between separated flows (annular, stratified, or wavy stratified flow) and purely discontinuous flow forms (bubble, surge, and slug flows). For assessment, the distribution of the gas and liquid phases in the pipe is still important, as described by the volumetric vapor content $\varepsilon = V_{\mathrm{D}}/(V_{\mathrm{D}} + V_{\mathrm{F}})$. The value of ε is given, according to Owen and Lee [21], as a function of the flow parameter F

$$\varepsilon = 1 - \frac{1}{1 + \dfrac{1}{8.48\,F}}. \tag{45}$$

As F is, in fact, a function of the flow vapor content $\dot{x} = \dot{M}_{\mathrm{D}}/(\dot{M}_{\mathrm{D}} + \dot{M}_{\mathrm{F}})$, the result is the relationship between ε and x in Fig. 11 for different density conditions $\rho_{\mathrm{D}}/\rho_{\mathrm{F}}$. Equation (45) has been verified for a large number of substance pairs [21].

5.1 Heat Transfer

On the basis of previous statements on the vertical pipe, the transfer resistance also exists only in the condensed phase, so that, in principle, the equations in Sect. 3 can be used for the laminar and turbulent Nusselt number according to Eqs. (10) and (13) together with the corresponding coefficients.

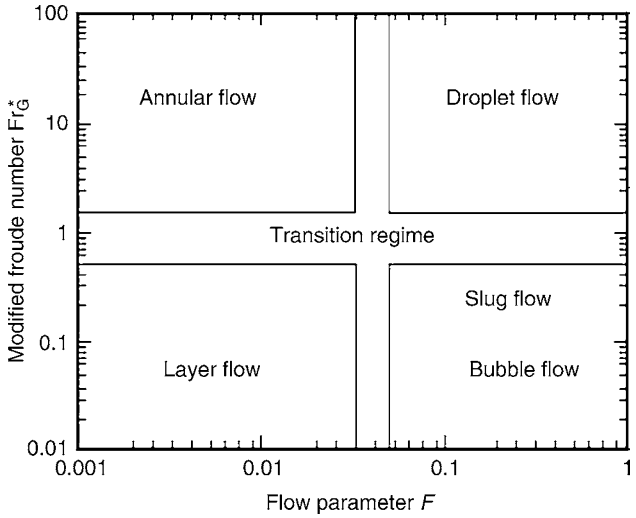

J1. Fig. 10. Flow map according to Breber et al. [20].

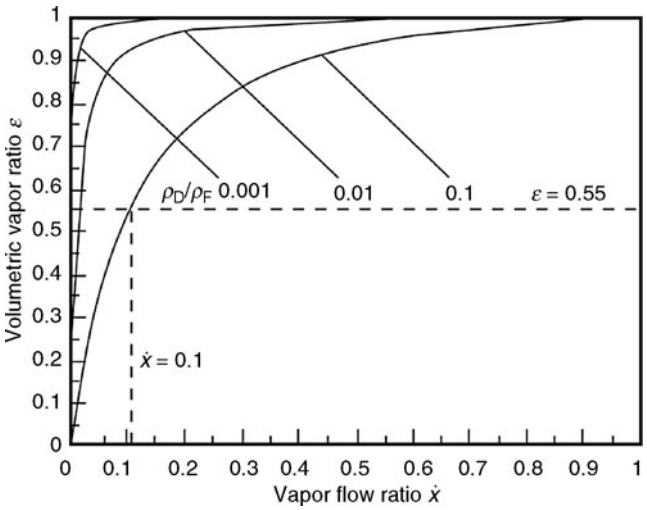

J1. Fig. 11. Volumetric vapor content ε as a function of vapor flow x with various density ratios $\rho_{\mathrm{D}}/\rho_{\mathrm{F}}$.

It should be noted here that the shear stress in the condensate film is eliminated by the gravitational force. The Nusselt numbers and the heat transfer coefficients of the vertical condensate film must be correspondingly modified. This is carried out by a shear stress correction K_{W}, which, for the horizontal pipe, derived from a simple balance of forces, gives

$$K_{\mathrm{W}} = \tau_{\mathrm{D}}^{*1/3}. \tag{46}$$

This approach takes into account the improvement in heat transfers at high shear stresses and the deterioration of the heat transfers for the case where the shear stress τ_{D} acting on the condensate film is smaller than the comparable gravitational stress in the vertical case.

It should also be noted that, for the relative shear stress τ_D^*, the film thickness δ_F^+ must be substituted by the circumferentially averaged thickness of the liquid cross section δ_A^+, which, with a good approximation for $\varepsilon \geq 0.67$, gives

$$\delta_A^+ = \frac{1-\varepsilon}{4} d \tag{47}$$

especially as the shear stress is only significant in the case of very high volumetric vapor contents. The relative shear stress is therefore

$$\tau_D^* = \frac{\tau_D}{\rho_F g \delta_A^+}. \tag{48}$$

The improvement in the heat transfer due to the increase in turbulence in the liquid phase resulting from the vapor shear stress τ_D can be described in analogy to Eqs. (25) and (26). For die, Nusselt number in the laminar flow region:

$$\mathrm{Nu}_{F,x,l}^{\bullet} = K_{Ph,l} \cdot \mathrm{Nu}_{F,x,l}^{+} \tag{49}$$

or in the turbulent region

$$\mathrm{Nu}_{F,x,t}^{\bullet} = K_{Ph,t} \cdot \mathrm{Nu}_{F,x,t}^{+}. \tag{50}$$

$\mathrm{Nu}_{F,x}^{+}$ is obtained in both equations with the correction factor according to Eq. (46).

Here, the superimposition according to Eq. (27) also applies.

5.2 Pressure Loss and Shear Stress

Under the assumption of separated flow, the aforementioned statements on shear stress and pressure loss are valid. The resistance coefficient required is calculated according to Henstock and Hanratty [15] as

$$\xi_r^{\circ} = \xi_g^{\circ}(1 + 850\, F), \tag{51}$$

where ξ_g° and F are obtained according to Eqs. (31) and (32) The shear stress τ_D° is obtained in analogy to Eq. (29) (also see the calculation examples). As far as entrainment is concerned, the same statements apply in principle as for unidirectional flow, with the possibility of occurrence already shown in the flow maps.

6 Special Points

6.1 Additional Resistance at Phase Layer Between Vapor and Liquid Phases

In the case of metal vapor, highly superheated vapor, or nonvolatile substances, an additional molecular heat transfer resistance may occur at the liquid–vapor phase boundary. The mass flow density at the phase boundary, according to Rohsenow et al. [22], is

$$\dot{m} = \frac{\sigma_{Akk}}{1 - 0.5\sigma_{Akk}} \sqrt{\frac{\widetilde{M}}{2\pi\tilde{R}}} \left(\frac{p_D}{T_D^{1/2}} - \frac{p_{Ph}}{T_{Ph}^{1/2}} \right). \tag{52}$$

For the accommodation coefficient, $\sigma_{Acc} = 1$ can be used.

By taking a balance at the phase boundary, the unknown temperature T_{Ph} can be determined iteratively:

$$\alpha_F(\vartheta_{Ph} - \vartheta_W) = \frac{\sigma_{Akk}}{1 - 0.5\,\sigma_{Akk}} \sqrt{\frac{\widetilde{M}}{2\pi\tilde{R}}} \left(\frac{p_\infty}{T_\infty^{1/2}} - \frac{p_{Ph}}{T_{Ph}^{1/2}} \right) \Delta h_v. \tag{53}$$

The deterioration in the condensation performance on the occurrence of a significant phase boundary resistance (PBR) is then given by

$$\frac{\dot{q}_{PGW}}{\dot{q}s} = \frac{\vartheta_{Ph} - \vartheta_W}{\vartheta_\infty - \vartheta_W}. \tag{54}$$

6.2 Condensation of Metal Vapors

In the case of the condensation of metal vapors, with their high thermal conductivity in the liquid ($\mathrm{Pr}_F < 0.1$), the acceleration elements in the balance equations of the laminar film condensation can no longer be ignored. A correction of the heat transfer coefficient obtained according to *Nusselt* is therefore necessary. According to Chen [23], this correction φ is dependent on the phase transition number $\mathrm{Ph} = c_{p,F}(\vartheta_D - \vartheta_W)/\Delta h_v$ and the Prandtl number $\mathrm{Pr}_F = \eta_F c_{p,F}/\lambda_F$

$$\varphi = \frac{\mathrm{Nu}_{F,x,l,\,Pr\to 0}}{\mathrm{Nu}_{F,x,l}} = \left(\frac{1 + 0.68\,\mathrm{Ph} + 0.02\,\mathrm{Ph}^2/\mathrm{Pr}_F}{1 + 0.85\,\mathrm{Ph}/\mathrm{Pr}_F - 0.15\,\mathrm{Ph}^2/\mathrm{Pr}_F} \right). \tag{55}$$

Figure 12 shows the correction term φ in relation to the Prandtl and the phase transition numbers. In some cases, an additional resistance at the liquid–vapor phase boundary has to be taken into account (Sect. 6.1).

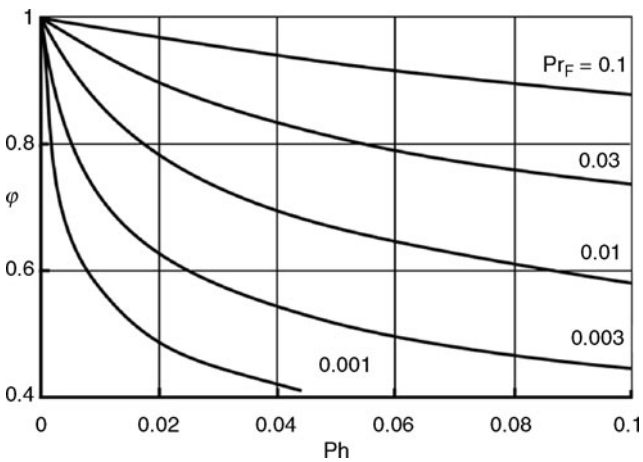

J1. Fig. 12. Influence of small Prandtl numbers ($\mathrm{Pr}_F < 0.1$) on heat transfer during filmwise condensation.

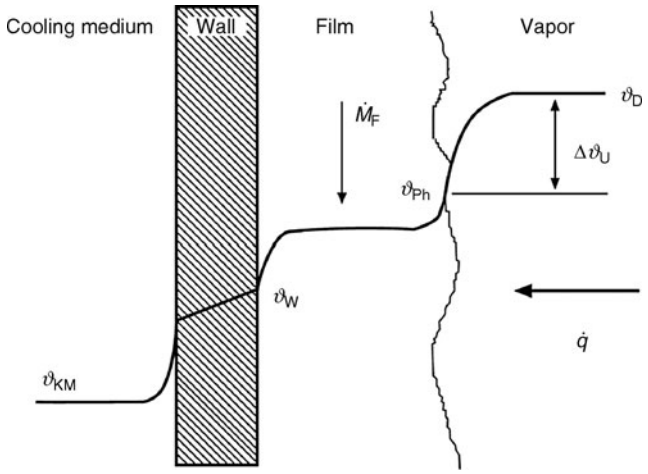

J1. Fig. 13. Schematic temperature profile during condensation of superheated vapor.

6.3 Condensation of Superheated Vapor

When superheated vapor comes into contact with a cold surface, condensation occurs if the temperature of the surface is below the saturation value at the corresponding system pressure. Figure 13 shows a qualitative temperature profile.

In addition to the latent heat, sensible heat is also transferred. For calculation of the heat transfer, instead of the evaporation enthalpy, the total difference of the specific enthalpies of vapor and liquid must be used:

$$\Delta h = \Delta h_v + C_{pD}(\vartheta_D - \vartheta_S) = \Delta h_v + c_{pD}\Delta\vartheta_{\ddot{U}}. \qquad (56)$$

Thus, the condensation area required according to Eq. (5)

$$\frac{A_{\ddot{U}}}{A} = \left(1 + \frac{c_{pD}\Delta\vartheta_{\ddot{U}}}{\Delta h_v}\right) \qquad (57)$$

generally increases only slightly in comparison with the condensation of dry saturated vapors, so this may normally be ignored.

In the case of strong superheating, the heat and material transfer processes in the gas–vapor phase must be taken into account. Here, the reader is referred to Subchap. J2.1 (particularly Sect. 3.4.4), which also applies correspondingly for the condensation of pure vapors.

7 Calculation Examples

Example 1

Condensation of isopropanol vapor in a vertical tube

Inlet conditions (saturation state)

Vapor flow	$\dot{M}_{D,E} = 0.04$ (kg/s) $\hat{=}$ 144 (kg/h)
Pressure	$p = 2.0$ bar = const
Temperature	$\vartheta = 100°C$ = const

Cooling conditions

Heat transfer coefficient	$a_{KM} = 6{,}500$ W/m^{2}K
Heat transfer wall	$\left(\frac{\lambda}{s}\right)_W = 10{,}000$ W/m^{2}K
Temperature of cooling fluid	$\vartheta_{KM} = 50°C \approx$ const

Properties at saturation state

Liquid	Density	$\rho_F = 712.7$ (kg/m^3)
	Dynamic viscosity	$\eta_F = 0.376{\cdot}10^{-3}$ Pa s
	Specific heat capacity	$c_{p,F} = 3{,}550$ J/(kg K)
Vapor	Density	$\rho_D = 4.15$ kg/m^3
	Dynamic viscosity	$\eta_D = 9.8{\cdot}10^{-6}$ Pa s
Condensation enthalpy		$\Delta h_v(\vartheta = 100\,°C) = 627.9$ kJ/kg

Solution

The calculation of the heat exchange area A and the tube length L is done by using local data according to Sect. 3 with following consumptions:

$$1 - \frac{\rho_D}{\rho_F} \approx 1; \quad f_\eta \approx 1; \quad \delta_F^+ \ll d.$$

The relative velocity between vapor and condensate is approximately the absolute velocity of the vapor, and the shear stress of vapor is neglected.

Mass flux normal to the wall is neglected.

Local condensate flow rates $\dot{M}_{F,x}$

$$\dot{M}_{F,1} = 1 \text{ kg/h}; \quad \dot{M}_{F,2} = 25 \text{ kg/h};$$
$$\dot{M}_{F,3} = 75 \text{ kg/h}; \quad \dot{M}_{F,4} = 144 \text{ kg/h}.$$

The way of calculation is shown at the local value $\dot{M}_{F,2}$. The results are presented in Table 1. The calculation neglects the influence of vapor flow to liquid phase

- Local condensate Reynolds numbers $Re_{F,x}$

$$Re_{F,x} = \frac{\dot{M}_F}{\pi d \eta_F} = \frac{25}{3{,}600 \cdot \pi \cdot 0.03 \cdot 3.76 \cdot 10^{-4}} = 196, \quad \text{Eq. (11)}$$

- Local Nusselt numbers $Nu_{F,x}$

$$\text{laminar: } Nu_{F,x,l} = 0.7 Re_{F,x}^{-0.29} = 0.7 \cdot 196^{-0.29} = 0.151, \quad \text{Eqs. (10, 12)}$$

$$\text{turbulent: } Nu_{F,x,t} = \frac{0.0283 Re_{F,x}^{-0.292} Pr_F^{0.333}}{1 + 9.66 Re_{F,x}^{-0.375} Pr_F^{-0.167}}, \quad \text{Eq. (13)}$$

- Prandtl number

$$Pr_F = \frac{\eta_F c_{p,F}}{\lambda_F} = \frac{3.76 \cdot 10^{-4} \cdot 3{,}550}{0.124} = 10.76,$$

$$Nu_{F,x,t} = \frac{0.0283 \cdot 196^{0.292} \cdot 10.76^{0.333}}{1 + 9.66 \cdot 196^{-0.375} \cdot 10.76^{-0.167}} = 0.152,$$

$$Nu_{F,x} = \sqrt{Nu_{F,x,t}^2 + Nu_{F,x,t}^2} = \sqrt{0.151^2 + 0.152^2} = 0.214, \quad \text{Eq. (15)}$$

J1. Table 1. Example: vertical tube

Condensate flow rate	Condensate film Reynolds number	Nusselt numbers			Heat transfer coefficient	Overall heat transfer coefficients		Tube length
						Local	Between 2 coordinates	
$\dot{M}_{F,x}$ in $\frac{kg}{h}$	$Re_{F,x}$	$Nu_{F,x,l}$	$Nu_{F,x,t}$	$Nu_{F,x,t}$	$\alpha_{F,x}$ in $\frac{W}{m^2K}$	k_x in $\frac{W}{m^2K}$	k_x in $\frac{W}{m^2K}$	ΔL in m
1	8	0.383	0.029	0.384	1561	1118	916	0.97
15	196	0.151	0.152	0.214	870	713	790	2.34
75	588	0.110	0.250	0.273	1110	866	949	2.69
144	1129	0.091	0.332	0.344	1398	1032	$L = \Sigma\Delta L = 6.0$ m	

- Local heat transfer coefficient $\alpha_{F,x}$

$$Nu_{F,x,t} = \frac{a_{F,x} \cdot \mathcal{L}}{\lambda_F}.$$

- Characteristic length

$$\mathcal{L} = \left(\frac{\eta_F^2}{\rho_F^2 g}\right)^{1/3},$$

$$\mathcal{L} = \left(\frac{(3.76 \cdot 10^{-4})^2}{712.7^2 \cdot 9.81}\right)^{1/3} \text{m} = 3.05 \cdot 10^{-5} \text{ m}$$

$$a_{F,x} = \frac{Nu_{F,x} \cdot \lambda_F}{\mathcal{L}} = \frac{0.214 \cdot 0.124}{3.05 \cdot 10^{-5}} \text{ W/m}^2\text{K} = 870 \text{ W/m}^2\text{K}.$$

- Local overall heat transfer coefficient k_x:

$$\frac{1}{k_x} = \frac{1}{\alpha_{F,x}} + \left(\frac{s}{\lambda}\right)_W + \frac{1}{\alpha_{KM}},$$

$$\frac{1}{k_x} = \left(\frac{1}{870} + \frac{1}{10{,}000} + \frac{1}{6{,}500}\right) \text{m}^2\text{K/W} = 1.4 \cdot 10^{-3} \text{ m}^2\text{K/W}$$

$$\Rightarrow k_x = 713 \text{ W/m}^2\text{K}.$$

- Heat transfer coefficient between 1 and 2:

$$\bar{k}_{1,2} = \frac{1}{2}(k_1 + k_2) = \frac{1}{2}(1{,}118 + 713) \text{ (W/m}^2\text{ K)}$$
$$= 916 \text{ (W/m}^2\text{ K)}.$$

- Necessary length $\Delta L_{1,2}$ between 1 and 2 according to Eq. (7):

$$\Delta L_{1,2} = \frac{1}{\pi d} \cdot \frac{(\dot{M}_{F,2} - \dot{M}_{F,1}) \cdot \Delta h_v}{\bar{k}_{1,2} \cdot \Delta\vartheta}.$$

Due to the assumption of $\Delta\vartheta = 50$ K = constant it is valid

$$\Delta L_{1,2} = \frac{1}{\pi \cdot 0.03} \cdot \frac{(25 - 1) \cdot 627.9 \cdot 10^3}{3{,}600 \cdot 916 \cdot 50} \text{m} = 0.97 \text{ m}$$

- The total length is given by summation of the different elements to $L = 6.00$ m. The length from 0 to 1 is neglected.

Example 2

Condensation of water vapor at horizontal tubes.

Saturated water vapor with $\vartheta_D = 100°C$ flows outside over a cooled horizontal single tube.

- Influence of gas velocity is negligible.
- Geometry: $d_a = 25$ mm, $s = 1$ mm, $\lambda_R = 21$ W/(mK), $L = 1$ m.
- Cooling water: $\bar{u}_{KW} = 2$ m/s, $\vartheta_{KW,ein} = 20°C$,
  properties: $\rho_{KW} = 998$ kg/m^3, $c_{p,KW} = 4{,}180$ J/(kg K),
  $\nu_{KW} = 0.9 \cdot 10^{-6}$ m^2/s, $\lambda_{KW} = 0.60$ W/(mK),
  fouling factor $R_{f,KW} = 0.09$ K m^2/kW acc. to Chap. O1
- Condensate:
  Properties: $\rho_F = 965$ kg/m^3,
  $c_{p,F} = 4{,}205$ J/(kg K), $\nu_F = 0.29 \cdot 10^{-6}$ m^2/s,
  $\lambda_F = 0.68$ W/(mK), $\Delta h_v = 2{,}250$ kJ/kg.

Solution

- Geometry: $A_a = \pi d_a L = 0.079$ m^2, $A_i = \pi(d_a - 2s)$ $L = 0.072$ m^2.
- Calculation of cooling fluid acc. to Part G:

$$\dot{M}_{KW} = \rho_{KW} \frac{\pi}{4} d_i^2 \bar{u}_{KW} = 0.829 \text{ kg/s};$$

$$\text{with Re} = \frac{\bar{u}_{KW} d_i}{\nu_{KW}} = 51{,}111 \quad \text{and} \quad \text{Pr} = \frac{\rho_{KW} \nu_{KW} c_{p,KW}}{\lambda_{KW}} = 6.26;$$

it follows that

$$\text{Nu} = \frac{\alpha_{KW} d_i}{\lambda_{KW}} = 346 \text{ resp. } \alpha_{KW} = \frac{\text{Nu}\lambda_{KW}}{d_i} = 9{,}018 \text{ W/(m}^2\text{K)}.$$

- Calculation of condensate fluid:

Because the heat transfer coefficient for condensate α_F and also the outlet temperature of the cooling water $\vartheta_{KW,aus}$ is unknown, an iterative method becomes necessary.

Starting value: $\alpha_F = 10{,}000$ W/(m^2 K).

With balance and transfer equation we can obtain:

$$M_{KW} c_{p,KW} (\vartheta_{KW,aus} - \vartheta_{KW,ein}) = k A_a \Delta\vartheta_{log}$$

With

$$\frac{1}{kA_a} = \left(\frac{1}{\alpha_{KW}} + R_{f,KW}\right) \frac{1}{A_i} + \frac{s \ln (A_a/A_i)}{\lambda_R (A_a - A_i)} + \frac{1}{\alpha_F A_a}.$$

Now we can calculate the outlet temperature:

$\vartheta_{KW} = 24.78°C$.

Calculation of α_F:

$$\dot{Q}_F = \dot{Q}_{KW} = \dot{M}_{KW} c_{p,KW} (\vartheta_{KW,aus} - \vartheta_{KW,ein})$$
$$= 0.829 \text{ kg/s} \cdot 4{,}180 \text{ J/(kg K)} \cdot (24.78 - 20.00) \text{ K};$$
$$\dot{Q}_F = 16{,}551 \text{W};$$
$$\dot{M}_F = \dot{Q}_{KW}/\Delta h_v = 16{,}551 \text{ W}/2{,}250 \text{ kJ/kg} = 7.4 \text{ g/s};$$
$$\text{Re}_F = \dot{M}_F / L \rho_F \nu_F = 25.9;$$
$$\text{Nu}_F = 0.954 \text{Re}_F^{-1/3} \text{ according to Eq. (40)}.$$

As a first estimation, we get

$$\alpha_F = \mathrm{Nu}_F \lambda_F / \left(\nu_F^2/g\right)^{1/3} = 10{,}565\ \mathrm{W/(m^2\,K)}.$$

This value is used for the calculation of the cooling water outlet temperature.

After further iterative steps, the final result is
$\alpha_F = 10{,}519\ \mathrm{W/(m^2\,K)}$;
cooling temperature $\vartheta_{KW,aus} = 24.83°\mathrm{C}$;
condensate flow rate $\dot{M}_{KW} = 26.8\ \mathrm{kg/h}$.

Example 3

Condensation of R22 vapor in a horizontal tube.

Inlet conditions (saturation state)

Vapor flow	$\dot{M}_{D,E} = 0.1\ \mathrm{kg/s} \triangleq 360\ \mathrm{kg/h}$
Pressure	$p = 9.58\ \mathrm{bar}$
Temperature	$\vartheta = 22°\mathrm{C}$

Conditions for cooling water

Heat transfer coefficient		$\alpha_{KM} = 5{,}000\ \mathrm{W/m^2K}$
Heat transfer wall		$\left(\frac{\lambda}{s}\right)_W = 7{,}500\ \mathrm{W/m^2\,K}$
Temperature		$\vartheta_{KM} = 0°\mathrm{C}$
Properties at saturation state		
Liquid	Density	$\rho_F = 1{,}206\ \mathrm{kg/m^3}$
	Dynamic viscosity	$\eta_F = 2.04 \cdot 10^{-4}\ \mathrm{Pa\,s}$
	Thermal conductivity	$\lambda_F = 0.0866\ \mathrm{W/m\,K}$
	Heat capacity	$c_{p,F} = 1.24\ \mathrm{kJ/kg\,K}$
Vapor	Density	$\rho_D = 40.6\ \mathrm{kg/m^3}$
	Dynamic viscosity	$\eta_D = 1.32 \cdot 10^{-5}\ \mathrm{Pa\,s}$

Solution

The calculation of the heat exchange area A and the tube length L is done by using local data according to Sect. 3 with the following consumptions:

- $1 - \frac{\rho_D}{\rho_F} \approx 1; \quad f_n \approx 1; \quad \delta_F^+ \ll d.$
- The relative velocity between vapor and condensate is approximately the absolute velocity of the vapor, and the shear stress of vapor is neglected.
- Mass flux normal to the wall is neglected.

Definition of local points:
Local vapor contents $\dot{x}_1 = 0.99$; $\dot{x}_2 = 0.9$; $\dot{x}_3 = 0.5$; $\dot{x}_4 = 0.1$; $\dot{x}_5 = 0.01$.

The way of calculation is shown at the local value $\dot{x}_2$. The results are presented in Tables 2 and 3. The calculation neglects the influence of vapor flow to liquid phase according to Sect. 3.1.

The flow rates for liquid phase $\dot{M}_{F,x}$and vapor phase $\dot{M}_{D,x}$ are defined:

$$\dot{x}_2 = \frac{\dot{M}_{D,2}}{\left(\dot{M}_{F,x} + \dot{M}_{D,x}\right)} \Rightarrow \dot{M}_{D,2} = \dot{x}_2 \cdot \left(\dot{M}_{F,x} + \dot{M}_{D,x}\right)$$
$$= 0.9 \cdot 360\ \mathrm{kg/h} = 324\ \mathrm{kg/h}$$
$$\Rightarrow \dot{M}_{F,2} = 36\ \mathrm{kg/h}.$$

- Calculation of Reynolds numbers

$$\mathrm{Re}_{F,x} = \frac{\dot{M}_{F,x}}{\pi d \eta_F} = \frac{36}{3{,}600\pi \cdot 0.025 \cdot 2.04 \cdot 10^{-4}} = 624$$

$$\mathrm{Re}_{D,x} = \frac{4\dot{M}_{D,x}}{\pi d \eta_D} = \frac{4 \cdot 324}{3{,}600\pi \cdot 0.025 \cdot 1.32 \cdot 10^{-5}} = 347{,}247.$$

Simplification: $d_h = \varepsilon d \approx d$.

- Flow parameter F (Eq. (32))

$$F = \frac{\max\left(\left(2\mathrm{Re}_{F,x}\right)^{0.5}; 0.132\mathrm{Re}_{F,x}^{0.9}\right)}{\mathrm{Re}_{D,x}\,0.9}, \frac{\eta_F}{\eta_D}\sqrt{\frac{\rho_D}{\rho_F}},$$

$$F = \frac{0.132.624^{0.9}}{347{,}247^{0.9}} \cdot \frac{2.04 \cdot 10^{-4}}{1.32 \cdot 10^{-5}} \sqrt{\frac{40.6}{1{,}206}} = 1.27 \cdot 10^{-3},$$

- calculation of volumetric vapor content ε

$$\varepsilon = 1 - \frac{1}{1 + \frac{1}{8.48F}} = 1 - \frac{1}{1 + \frac{1}{8.48 \cdot 1.27 \cdot 10^{-3}}} = 0.9893,$$

Eq. (45)

- calculation of film thickness δ_F

$$\delta_F^+ = \frac{1}{4}(1-\varepsilon)d = \frac{1 - 0.9907}{4} \cdot 0.025\ \mathrm{m} = 0.067 \cdot 10^{-3}\ \mathrm{m}.$$

- Nusselt number of condensate film:
  Characteristic length

$$\mathcal{L} = \left(\frac{\eta_F^2}{\rho_F^2 g}\right)^{1/3} = \left(\frac{2.04^2 \cdot 10^{-8}}{1{,}206^2 \cdot 9.81}\right)^{1/3}\ \mathrm{m} = 1.43 \cdot 10^{-5}\ \mathrm{m},$$

- laminar Nusselt number $\mathrm{Nu}_{F,x,l}$

$$\mathrm{Nu}_{F,x,l} = 0.7 \cdot \mathrm{Re}_{F,x}^{-0.29} = 0.7 \cdot 624^{-0.29} = 0.108,$$

- turbulent Nusselt number $\mathrm{Nu}_{F,x,t}$

$$\mathrm{Nu}_{F,x,t} = \frac{0.0283 \cdot \mathrm{Re}_{F,x}^{+0.292}\,\mathrm{Pr}_F^{0.333}}{1 + 9.66 \cdot \mathrm{Re}_{F,x}^{-0.375}\,\mathrm{Pr}_F^{-0.167}}$$
$$= \frac{0.283 \cdot 624^{+0.292} \cdot 2.92^{0.333}}{1 + 9.66 \cdot 624^{-0.375} \cdot 2.92^{-0.167}} = 0.154,$$

Eq. (13)

$$\mathrm{Nu}_{F,x} = \sqrt{\mathrm{Nu}_{F,x,l}^2 + \mathrm{Nu}_{F,x,l}^2} = \sqrt{0.108^2 + 0.154^2} = 0.188,$$

Eq. (15)

- Calculation shear stress

$$\tau_D = \frac{\xi_r}{8}\rho_D u_D^2$$

  - friction factor (rough) $\xi_r = \xi_g\,(1 + 850F)$, Eq. (51)
  - friction factor (smooth)

$$\xi_g = 0.184\ \mathrm{Re}_{D,x}^{-0.2} = 0.184 \cdot 347{,}247^{-2} = 0.0143,$$

  - velocity u_D ($\delta_F < d$)

J1. Table 2. Example 3: values at different points

Coordinate	Mass flow rates		Reynolds numbers		Flow parameter	Volumetric vapor ratio	Film thickness
$\dot{x}$	$\dot{M}_{F,x}$ in $\frac{kg}{h}$	$\dot{M}_{D,x}$ in $\frac{kg}{h}$	$Re_{F,x}$	$Re_{D,x}$	F	ε	δ_F^4 in 10^{-3}m
0.99	3.6	356.4	62.4	381,972	$0.30 \cdot 10^{-3}$	0.9945	0.034
0.9	36	324	624	347,247	$1.27 \cdot 10^{-3}$	0.9893	0.067
0.5	180	180	3120	192,915	$9.14 \cdot 10^{-3}$	0.9281	0.449
0.1	324	36	5616	38,583	$66.10 \cdot 10^{-3}$	0.6408	2.245
0.01	356.4	3.6	6178	3,858	$571.8 \cdot 10^{-3}$	0.1709	5.182

J1. Table 3. Example 3: continuing Table 3

Coordinate	Nusselt numbers			Shear stress	Correction	Heat transfer coefficient	Overall heat transfer coefficient		Tube lengths
$\dot{x}$	$Nu_{F,x,l}$	$Nu_{F,x,t}$	$Nu_{F,x}$	τ_D in $\frac{N}{m^2}$	K_w	$\alpha^{\bullet}_{F,x}$ in $\frac{W}{m^2K}$	k_x in $\frac{W}{m^2K}$	k_x in $\frac{W}{m^2K}$	ΔL in m
0.99	0.209	0.050	0.215	2.24	1.77	2,304	1,303	1,214	0.79
0.9	0.108	0.154	0.188	3.13	1.58	1,799	1,125	1,138	3.76
0.5	0.068	0.304	0.311	5.23	0.99	1,864	1,150	1,001	4.27
0.1	0.057	0.381	0.385	3.60	0.51	1,189	852	727	1.32
0.01	0.056	0.396	0.400	1.87	0.31	751	601	Total tube length: 10.14 m	

$$u_D = \frac{4\dot{M}_{D,x}}{\rho_D \cdot \pi(d - 2\delta_F^+)^2},$$

$$u_D = \frac{4 \cdot 324}{3{,}600 \cdot 40.6\pi(0.025 - 2 \cdot 0.067 \cdot 10^{-3})^2}\ \text{m/s} = 4.56\ \text{m/s}.$$

- Correction for shear stress

$$K_W = \left(\frac{\tau_D}{\rho_F g \delta_F^+}\right)^{1/3} = \left(\frac{313}{1{,}206 \cdot 9.81 \cdot 0.067 \cdot 10^{-3}}\right)^{1/3} = 1.58.$$

- Heat transfer coefficient $\alpha^{\bullet}_{F,x}$

$$\alpha^{\bullet}_{F,x} = \frac{K_W \cdot Nu_{F,x} \cdot \lambda_F}{\mathcal{L}} = \frac{1.58 \cdot 0.188 \cdot 0.0866}{1.43 \cdot 10^{-5}}\ \text{W/m}^2\text{K}$$
$$= 1{,}799\ \text{W/m}^2\text{K}.$$

- Overall heat transfer coefficient k

$$\frac{1}{k_x} = \frac{1}{\alpha^{\bullet}_{F,x}} + \left(\frac{s}{\lambda}\right)_W + \frac{1}{\alpha_{KM}}$$
$$= \left(\frac{1}{1{,}799} + \frac{1}{7{,}500} + \frac{1}{5{,}000}\right)\ \text{m}^2\text{K/W} \Rightarrow k_x = 1{,}125\ \text{W/m}^2\text{K}.$$

- Overall heat transfer coefficient between two points

$$\bar{k}_x = \frac{k_{x,1} + k_{x,2}}{2} = \frac{1{,}303 + 1{,}125}{2}\ \text{W/m}^2\text{K} = 1{,}214\ \text{W/m}^2\text{K}.$$

- Necessary tube length

$$\Delta L = \frac{\Delta M_{F,x} \cdot \Delta h_v}{\pi d \cdot \bar{k}_x \Delta\vartheta},$$

with $\Delta\vartheta = 22\ \text{K} = \text{const}$.

$$\Delta L = \frac{(36 - 3.6) \cdot 185200}{3{,}600\pi \cdot 0.025 \cdot 1{,}214 \cdot 22}\ \text{m} = 0.68\ \text{m}.$$

- Pressure loss (Step 1→2)

$$\Delta p = \frac{\tau_{D1} + \tau_{D2}}{2} \cdot \frac{4\Delta L}{d - (\delta_{F_1}^+ + \delta_{F_2}^+)}$$
$$= \frac{2.24 + 3.13}{2} \cdot \frac{4 \cdot 0{,}68}{0.025 - (0.034 + 0.067) \cdot 10^{-3}}\ \text{Pa}.$$
$$= 340\ \text{Pa}$$

Step 2 → 3: $\Delta p = 2{,}568$ Pa.
Step 3 → 4: $\Delta p = 3{,}380$ Pa.
Step 4 → 5: $\Delta p = 822$ Pa.
Total pressure loss $\Delta p = 7{,}710$ Pa $\triangleq$ 71.1 mbar.

8 Symbols

A	exchange area (m^2)
b	length of condensation area (m)
C	constant, correction factor (–)
c_p	specific heat capacity (J/kg/K)
d	tube diameter (m)
e	factor (–)
f	correction factor (–)
F	flow parameter acc. to Eq. (32) (–)
g	gravitational acceleration (m/s^2)
G	factor acc. to Eq. (43) (–)
h	specific enthalpy (J/kg)
Δh_v	evaporation/condensation enthalpy (J/kg)
i	factor (–)

k overall heat transfer coefficient (W/(m^2 K))
K correction factor (–)
L length (m)
$\mathcal{L}$ characteristic length $\left(\mathcal{L} = \sqrt[3]{\nu_F^2/g}\right)$ (m)
$\dot{m}$ mass flux (kg/(m^2 s))
$\dot{M}$ mass flow (kg/s)
$\tilde{M}$ molar mass (kg/mol)
n number (–)
p pressure (bar)
$\dot{q}$ heat flux (W/m^2)
$\tilde{R}$ general gas constant (J/(mol K))
R_f fouling factor (m^2 K/W)
s wall thickness (m)
T temperature (K)
u_D vapor velocity (m/s)
x coordinate in main velocity direction (m)
α heat transfer coefficient (W/(m^2 K))
Γ trickle density (kg/(ms))
δ film thickness (m)
ε Volumetric vapor content (–)
η dynamic viscosity (kg/(ms))
ϑ temperature (°C)
λ thermal conductivity (W/(m K))
ν kinematic viscosity (m^2/s)
ξ friction factor (–)
ρ density (kg/m^3)
σ surface tension (N/m)
σ_{Akk} accumulation coefficient (–)
τ hear stress (N/m^2)
φ correction factor acc. to Eq. (55) (–)
χ factor acc. to Eq. (43) (–)

Dimensionless numbers

Fr, Fr* Froude number, modified Froude number acc. to Eq. (44)
Nu Nusselt number
Ph change of phase number
Pr Prandtl number
Re Reynolds number
We* modified Weber number

Indices

aus outlet
D vapor
ein inlet
F film
GS flowing gas phase
KM cooling substance
L tube length at $x = L$
l laminar
log logarithmic
o without mass flow
PGW phase layer resistance
Ph phase layer
r rough surface
RR tube bundle
S evaporation state
t turbulent
Ü superheated
W wall
well laminar wavy film
x local value
τ related to shear stress
* dimensionless value
– average value
• with influence to phase layer

9 Bibliography

1. Nusselt W (1916) Die Oberflächenkondensation des Wasserdampfes. Z VDI 60:541–546, 569–575
2. Kutateladze SS, Gogonin II (1979) Heat transfer in film condensation of slowly moving vapor. Int J Heat Mass Transfer 22:1593–1599
3. Müller J (1992) Wärmeübergang bei der Filmkondensation und seine Einordnung in Wärme- und Stoffübertragungsvorgänge bei Filmströmungen. Fortsch Ber VDI, Reihe 3(270)
4. Numrich R (1994) Stoff-, Wärme- und Impulsaustausch bei der Kondensation von Ein- und Mehrkomponentensystemen. Verlag Shaker, Aachen
5. Yüksel L (1987) Wärme- und Stoffübergang bei der nichtisothermen Absorption am Rieselfilm. Fortschr Ber VDI, Reihe 3(133)
6. Blangetti F (1979) Lokaler Wärmeübergang bei der Kondensation mit überlagerter Konvektion im vertikalen Rohr. Dissertation, Universität Karlsruhe (TH)
7. Krebs R (1984) Kondensation von Dampf in Anwesenheit nichtkondensierbarer Gase in turbulent durchströmten senkrechten Kondensatorrohren. Fortschr Ber VDI, Reihe 6(153)
8. Numrich R (1990) Influence of gas flow on heat transfer in film condensation. Chem Eng Technol 13:136–143
9. Kellenbenz J (1994) Wärmeübergang bei der Kondensation von strömenden Dämpfen reiner Stoffe und binärer Gemische. Fortsch Ber VDI, Reihe 3(365)
10. Lange J (1994) Die partielle Kondensation zweier im flüssigen Zustand löslicher Komponenten aus einem Gas/Dampf- Gemisch im senkrechten Rohr bei erhöhtem Druck. Dissertation, Universität GH Paderborn
11. Claus N (1996) Kondensation strömender reiner Dämpfe im senkrechten Rohr bei Drücken bis 15 bar. Dissertation, Universität GH Paderborn
12. Numrich R, Claus N, Hadley M (1995) Influence of gas flow on condensation process. Eurotherm Seminar, Paris
13. Andreussi P (1980) The onset of droplet entrainment in annular downward flows. Can J Chem Eng 58(4):267–270
14. Hadley M (1996) Kondensation binärer Dampfgemische unter dem Einfluß der turbulenten Gasströmung bei Drücken bis 15 bar. Dissertation, Universität GH Paderborn
15. Henstock W, Hanratty T (1975) The interfacial drag and the height of the wall layer in annular flows. AIChE J 21:990–1000
16. Ishii M, Grolmes MA (1975) Inception criteria for droplet entrainment in two- phase cocurrent film flow. AIChE J 21(2):308–318
17. Fujii T, Uehara H, Kurata C (1972, I) Laminar filmwise condensation of flowing vapour on a horizontal cylinder. Int J Heat Mass Transfer 15: 235–246
18. Fujii T (1982) Condensation of steam and refrigerant vapors. 7th International Heat transfer conference, München
19. Fujii T, Uehara H, Hirata K, Oda K (1972, II) Heat transfer and flow resistance in condensation of low pressure steam flowing through tube banks. Int J Heat Mass Transfer 15:246–260
20. Breber G, Palen JW, Taborek J (1980) Prediction of horizontal tubeside condensation of pure components using flow regime criteria. J Heat Transfer 102:471–476
21. Owen RG, Lee WC (1983) Some recent developments in condensation theory. Chem Eng Res Des 61(11), 335–361
22. Rohsenow WM, Hartnett JP, Ganic EN (1985) Handbook of heat transfer fundamentals, 2nd edn. McGraw Hill, New York
23. Chen MM (1961) An analytical study of laminar film condensation. Part 1: flat plate; Part 2: single and multiple tubes. J Heat Transfer C 38:48–60

J2 Film Condensation of Binary Mixtures with and without Inert Gas

Ernst-Ulrich Schlünder
Universität Karlsruhe (TH), Institut für Thermische Verfahrenstechnik, Karlsruhe, Germany

1 Introduction

Gaseous substances in a specified thermodynamic state can be subdivided into vapors and inert gases. Vapors are condensable at the respective specified coolant temperatures, but inert gases are not. In the condensation of binary mixtures, both components may be vapors or one component may be an inert gas. In both cases, in addition to the heat transfer resistance in the condensate film, heat transfer and mass transfer resistances also occur in the gas phase, leading to a reduction of condensation.

In the following, the basic equations for calculation of the condensation curve and a general calculation method for the design of a condenser are explained.

In many cases, an estimate of the distribution of the resistances to the gas phase, to the condensate film, and to the coolant, by ignoring one or the other, permits an appreciable simplification of the calculation. The approximate design of a condenser (Sects. 3.4 and 4.3) is primarily justified if important parameters like the gas volume flow, its temperature and composition, and the material values in the condensate film and in the gas phase are also known only approximately.

2 General Principles

The equations describing the condensation process follow from the mass, component, and energy balance equations for the gas and liquid phases in combination with the kinetic theorems for heat and mass transfer [1].

2.1 Integral Mass and Energy Balances

According to Fig. 1, the mass balance for the overall segment shown reads

$$\dot{N}_{GE} - \dot{N}_{GA} = \dot{N}_{FA} \qquad (1)$$

VDI-GVC (ed.), *VDI Heat Atlas*, DOI 10.1007/978-3-540-77877-6_37,

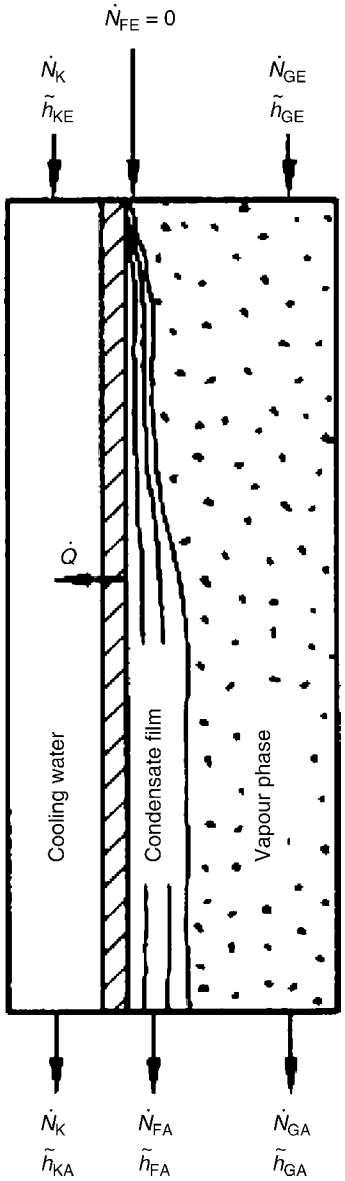

J2. Fig. 1. Condenser segment with cocurrent (parallel) coolant flow.

and the energy balance for the condensing phase and for the coolant (index K) reads

$$\dot{N}_{GE}\tilde{h}_{GE} - \dot{N}_{GA}\tilde{h}_{GA} = \dot{N}_{FA}\tilde{h}_{FA} + \dot{Q}, \tag{2}$$

$$\dot{Q} = \dot{N}_K(\tilde{h}_{KA} - \tilde{h}_{KE}). \tag{3}$$

If the mixture components behave ideally, the enthalpy of mixing vanishes and the enthalpy value for each substance can be normalized to be 0 at 0°C (liquid state):

$$\tilde{h}_F = \tilde{c}_{pF} T_F, \tag{4}$$

$$\tilde{h}_G = \Delta h_v\{0°C\} + \tilde{c}_{pG} T_G, \tag{5}$$

$$\Delta\tilde{h}_v\{T\} = \Delta\tilde{h}_v\{0°C\} + (\tilde{c}_{pG} - \tilde{c}_{pF})T, \tag{6}$$

with the enthalpy of evaporation

$$\Delta\tilde{h}_v\{T\} = \tilde{h}_G\{T\} - \tilde{h}_F\{T\}. \tag{7}$$

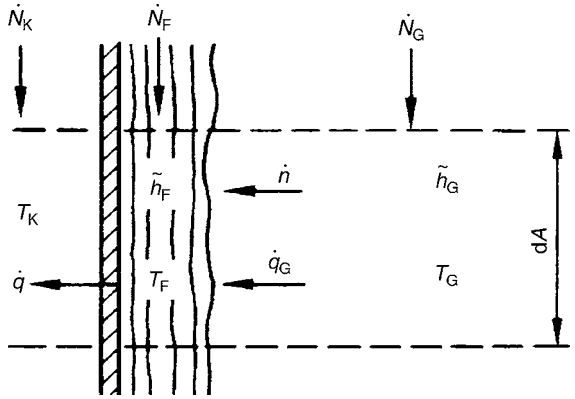

J2. Fig. 2. Local (differential) mass, component, and energy flows.

Here the temperatures T, T_G, and T_F must be inserted in °C. From Eq. (2), it follows that

$$\dot{Q} = \dot{N}_{GE}\tilde{c}_{pG}(T_{GE} - T_{GA}) + (\dot{N}_{GE} - \dot{N}_{GA})\Delta h_v\{T_{GA}\} + \dot{N}_{FA}\tilde{c}_{pF}(T_{GA} - T_{FA}). \tag{8}$$

The total heat flow $\dot{Q}$ to be transferred to the coolant is composed of the cooling of the gas flow from T_{GE} to T_{GA}, the condensation of the vapor at T_{GA}, and the supercooling of the condensate film to T_{FA}. The energy gain of the coolant is given by Eq. (3):

$$\dot{Q} = \dot{N}_K\tilde{c}_{pK}(T_{KA} - T_{KE}). \tag{9}$$

2.2 Differential Mass and Energy Balances

The mass, the component, and energy balances according to Fig. 2 are based on a so-called single-component boundary layer of constant thickness (film model).

Mass balances

$$\dot{N}_G = \dot{N}_{G1} + \dot{N}_{G2}, \tag{10}$$

$$\dot{N}_F = \dot{N}_{F1} + \dot{N}_{F2}, \tag{11}$$

$$\dot{n} = \dot{n}_1 + \dot{n}_2, \tag{12}$$

$$d\dot{N}_G - \dot{n}\,dA = 0, \tag{13}$$

$$d\dot{N}_{G1} - \dot{n}_1\,dA = 0, \tag{14}$$

$$d\dot{N}_F - \dot{n}\,dA = 0, \tag{15}$$

$$d\dot{N}_{F1} - \dot{n}_1\,dA = 0. \tag{16}$$

Energy balances

$$d(\dot{N}_G\tilde{h}_G) + \dot{q}_G\,dA + \dot{n}\tilde{h}_G\,dA = 0, \tag{17}$$

$$d(\dot{N}_F\tilde{h}_F) + \dot{q}\,dA - \dot{q}_G\,dA - \dot{n}\tilde{h}_G\,dA = 0. \tag{18}$$

Linkage of mass and energy balances

$$\dot{N}_G\tilde{c}_{pG}\frac{dT_G}{dA} + \dot{q}_G - \dot{n}\tilde{c}_{pG}(T_G - T_F) = 0, \tag{19}$$

$$\dot{N}_F\tilde{c}_{pF}\frac{dT_F}{dA} + \dot{q} - \dot{q}_G - \dot{n}\Delta\tilde{h}_v\{T_F\} = 0. \tag{20}$$

2.3 Theorems for Heat and Mass Transfer

Figure 3 shows the driving temperature and concentration gradients for the heat and mass transfer.

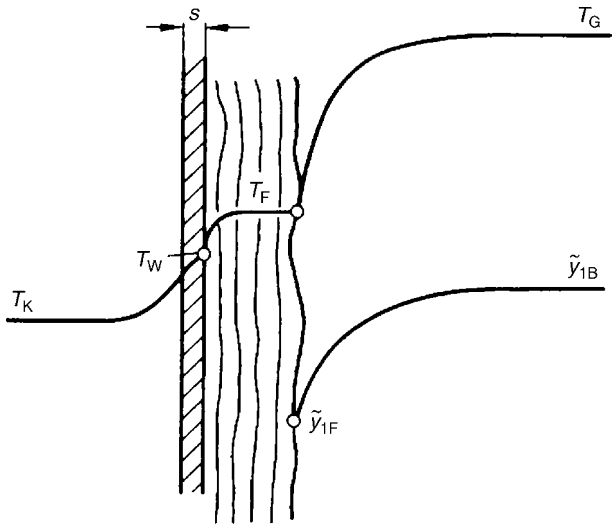

J2. Fig. 3. Temperature and concentration profiles in and close to the condensate film.

2.3.1 Heat Transfer

The heat flow to be removed locally to the coolant is

$$\dot{q} = k'(T_F - T_K); \tag{21}$$

here, the heat transfer coefficient k' is composed of the heat transfer coefficients of the condensate film, the conduction resistance of the pipe wall, and the heat transfer coefficient on the coolant side:

$$\frac{1}{k'} = \frac{1}{\alpha_F} + \frac{s}{\lambda_R} + \frac{1}{\alpha_K}. \tag{21a}$$

The heat flow $\dot{q}_G$ transferred from the gas is, according to the kinetic theorem of coupled heat and mass transfer:

$$\dot{q}_G = \alpha_G E_T (T_G - T_F), \tag{22}$$

with the Ackermann correction factor [2]

$$E_T = \frac{\phi_T}{1 - \exp(-\phi_T)}, \tag{22a}$$

$$\phi_T = \frac{\dot{n}\tilde{c}_{pG}}{\alpha_G}. \tag{22b}$$

The Ackermann correction is to account for the mass transfer occurring parallel to the heat transfer. The local heat transfer coefficient α_F in the condensate film is calculated as described in Chap. J1, the heat transfer coefficients α_G and α_K in the gas or in the coolant according to the design of the condenser – e.g., in the case of a flow through pipes, as described in Chap. G1 and in the case of cross flow around pipe bundles, as described in Chap. G6.

2.3.2 Mass Transfer

In the case of condensation of a pure vapor in the presence of an inert gas, a mass transfer resistance only occurs in the gas phase, as the condensate film only consists of one component. The mass transfer resistance in the condensate film in the case of condensation of a binary vapor mixture is explained in Sect. 4.

The locally condensing mass flow is determined by the concentration gradient between the core (bulk) of the flow and the condensate film surface (Fig. 3):

$$\dot{n} = n_G \beta_G \ln\left(\frac{\dot{r}_1 - \tilde{y}_{1F}}{\dot{r}_1 - \tilde{y}_{1B}}\right), \tag{23}$$

with

$$\dot{r}_1 = \frac{\dot{n}_1}{\dot{n}} \tag{23a}$$

and

$$\tilde{y}_{1B} = \frac{\dot{N}_{G1}}{\dot{N}_G}. \tag{23b}$$

The mass transfer coefficient β_G follows from the same formal relationships with which the heat transfer coefficient α_G is calculated, if the Nusselt and Prandtl numbers are replaced by the Sh and Sc numbers. This is because of the analogy of convective heat and mass transfer, as the basic transport mechanisms are similar and the resulting differential equations have the same form.

This is also the basis for the Lewis relationship, an approximation which links the heat and mass transfer coefficients in the gas phase:

$$\alpha_G = n_G \beta_G \tilde{c}_{pG} \mathrm{Le}^{0.6}, \tag{24}$$

with the Lewis number

$$\mathrm{Le} = \frac{\kappa_G}{\delta_G} = \frac{\lambda_G}{n_G \tilde{c}_{pG} \delta_G}. \tag{25}$$

3 Condensation of a Pure Vapor in the Presence of an Inert Gas

During the condensation of pure vapor from a gas–vapor flow, the vapor fraction and the temperature of the gas–vapor flow decrease along the condensation line. This reduces the driving concentration and temperature gradients. For determination of the local mass flow $\dot{n}$ and the local heat flow $\dot{q}$, knowledge of the local condensate film temperature T_F is necessary. The determination of the transfer area of the condenser must therefore take place by a step-by-step calculation method. An estimate of the heat and mass transfer resistances in the coolant, in the condensate film, and in the gas phase shows that closed derivable, limiting cases can often be drawn for the calculation of the transfer area. This can give an appreciable reduction of the calculation work in individual cases.

3.1 Determination of the Condensate Film Temperature

During the condensation of pure saturated vapors, the whole heat transfer resistance is in the condensate film and in the coolant. If there is also an inert gas (e.g., air) in the vapor, this accumulates at the condensation boundary, entrained by the vapor flow. As a result, the partial vapor pressure p_1 or the vapor mole fraction $\tilde{y}_{1F}$ at the condensate surface is reduced. This reduces the temperature gradient $T_F - T_K$ between condensate

film and coolant and thus also the condenser's performance. The temperature of the condensate film T_F can be determined with the coupled balance equation (20):

$$\dot{N}_F \tilde{c}_{pF} \frac{dT_F}{dA} + k'(T_F - T_K) = \dot{n} \Delta \tilde{h}_{v1}(T_F) + \alpha_G E_T (T_G - T_F). \quad (26)$$

If the vapor is assigned the index 1 and the inert gas the index 2, it follows, with

$$\dot{n}_2 = 0 \quad (27)$$

the relationships $\dot{n}_1 = \dot{n}$ and $\dot{r}_1 = 1$, that

$$\dot{n}_1 = n_G \beta_G \ln\left(\frac{1 - \tilde{y}_{1F}(T_F)}{1 - \tilde{y}_{1B}}\right) \quad (28)$$

or, because $\tilde{y}_1 + \tilde{y}_2 = 1$,

$$\dot{n}_1 = n_G \beta_G \ln\left(\frac{\tilde{y}_{2F}(T_F)}{\tilde{y}_{2B}}\right). \quad (28a)$$

If there is equilibrium at the condensate film surface and the air is saturated,

$$\tilde{y}_{1F} = \frac{p_1^*(T_F)}{p}. \quad (28b)$$

The saturated vapor pressure $p_1^*(T_F)$ associated with the condensate film temperature can be calculated, for example, with the simple Antoine vapor pressure equation

$$\ln p_1^* = A - \frac{B}{C + T/°C}. \quad (29)$$

The values for A, B, and C for almost all technically important substances can be found in the literature [3, 4].

In most cases, it is permissible, in the determination of the condensate film temperature, to ignore the change in the molar enthalpy of the condensate film. So, from Eq. (26), the iterative resolution for the condensate film temperature T_F is

$$k'(T_F - T_K) = n_G \beta_G \Delta \tilde{h}_{v1} \ln\left(\frac{\tilde{y}_{2F}(T_F)}{\tilde{y}_{2B}}\right) + \alpha_G E_T (T_G - T_F) \quad (30)$$

or

$$k'(T_F - T_K) = \alpha_G \phi_T \left(\frac{\Delta \tilde{h}_{v1}}{\tilde{c}_{pG1}} + \frac{T_G - T_F}{1 - \exp(-\phi_T)}\right), \quad (31)$$

with

$$\phi_T = \frac{n_1 \tilde{c}_{pG1}}{\alpha_G} = \frac{n_G \beta_G \tilde{c}_{pG1}}{\alpha_G} \ln \frac{\tilde{y}_{2F}(T_F)}{\tilde{y}_{2B}}. \quad (31a)$$

Using the Lewis relationship (Eq. (24)), it follows that

$$\phi_T = \frac{\tilde{c}_{pG1}}{\tilde{c}_{pG} Le^{0.6}} \ln\left(\frac{\tilde{y}_{2F}}{\tilde{y}_{2B}}\right). \quad (31b)$$

If the condensate film temperature T_F is known, the locally condensing component flux $\dot{n}_1$ (Eq. (28)) and the removed heat flux $\dot{q}$ (Eq. (21)) can be calculated (Example 1).

Example 1

Part A

The condensate film temperature T_F of a water vapor/air mixture with a mole fraction of water vapor at the inlet $\tilde{y}_{1B} = 0.5$ and temperature $T_G = 100°C$ at pressure $p = 1$ bar is to be calculated. The coolant water temperature is $T_K = 20°C$.

Convective heat transfer coefficient: $\alpha_G = 20$ W/m^2 K.
Overall heat transfer coefficient: $k' = 1{,}000$ W/m^2 K.
Properties are to be inserted at a temperature of 50°C.

The temperature dependence of the material values may be ignored for the iterative determination of the condensate film temperature T_F. The values for this case are

$$\Delta \tilde{h}_{v1} = 42{,}800 \text{ J/mol}, \quad \tilde{c}_{pG1} = 34.2 \text{ J/mol K},$$
$$\tilde{c}_{pG1}/(\tilde{c}_{pG} Le^{0.6}) = 1.3.$$

The vapor pressure dependence in the case of water is described by the Antoine equation

$$\ln \frac{p_1^*}{\text{bar}} = 11.9648 - 3984.923/(233.426 + T/°C),$$

while the dewpoint temperature $T_T(\tilde{y}_{1B})$ is 81.4°C.

Iteration

Following Eq. (31), the iteratively resolved equation for T_F is

$$T_F = T_K + 25K \cdot \phi_T + 0.02\,\phi_T \cdot (T_F - T_F)/(1 - \exp(-\phi_T)),$$

with

$$\phi_T = 1.3 \ln\left[2\left(1 - \frac{p_1^*}{p}\right)\right]$$

according to Eq. (31b). In place of the mole flow $\dot{n}_1$, the mass flow $\dot{m}_1$ can also be determined from the nondimensional mass flow ϕ_T according to Eq. (31a):

$$\dot{m}_1 = \alpha_G \phi_T / c_{pG1}$$

	T_F (°C)	p_1^* (bar)	φ_T (–)	T_F' (°C)	$\dot{m}_1$ (10^{-3} (kg/m^2 s))
1. Estimate	50	0.1231	0.730	39.6	7.68
2. Estimate	40	0.0736	0.802	41.8	8.44
Result	41.5	0.0797	0.793	41.5	8.35

Part B

Influence of gas and coolant temperature: In the case of strong superheating of the gas at the inlet, while the condensate film temperature T_F rises appreciably, the locally condensing mass flow $\dot{m}_1$ nevertheless decreases only slightly in this case, as can be seen in the following table (lines 1–3).

Line	T_G (°C)	T_K (°C)	T_F (°C)	φ_T (–)	$\dot{m}_1$ (10^{-3} (kg/m^2 s))	k'/α_{GD} (Eq. (38))
1	100	20	41.5	0.793	8.35	1.86
2	200	20	44	0.777	8.18	1.56
3	500	20	51	0.721	7.59	0.98
4	$T_G = T_F$	60	70	0.417	4.39	1.14
5	$T_G = T_F$	40	56.5	0.661	6.96	1.51
6	$T_G = T_F$	20	40	0.802	8.44	2.07
7	$T_G = T_F$	0	22	0.880	9.26	2.70

In the absence of heat flow $\dot{q}_G$, i.e., at $T_G = T_B$, Eq. (31) can be simplified to Eq. (39):

$$T_F = T_K + 32.5\,\mathrm{K} \cdot \ln\left(\frac{\tilde{y}_{2F} - (T_F)}{\tilde{y}_{2B}}\right).$$

The condensing mass flow only increases by 1% (lines 6 and 1).

A reduction of the coolant temperature T_K and thus the condensate film temperature T_F causes a reduction of the vapor pressure p_1^* and thus an increase in the driving concentration gradients and the locally condensing mass flow $\dot{m}_1$. As the vapor pressure p_1^* is exponentially dependent on the condensate film temperature T_F (Eq. (29)), its influence on the condensate mass flow $\dot{m}_1$ decreases, the lower the temperature T_F is, as shown in the table.

For the vapor pressure $p_1^* = 0$, the driving concentration gradient and the locally condensing mass flow are at a maximum. This is determined by the vapor or inert gas content in the core $\tilde{y}_{1B}$:

$$\phi_{T\,max} = \frac{\tilde{c}_{pG1}}{\tilde{c}_{pG}\mathrm{Le}^{0.6}} \ln\left(\frac{1}{1-\tilde{y}_{1B}}\right) = 1.3 \cdot \ln 2 = 0.901,$$

$$\dot{m}_{1\,max} = 9.48 \cdot 10^{-3}\,(\mathrm{kg/m^2\,s}).$$

3.2 General Method for Determination of the Transfer Area

The condenser performance or the transfer area can generally only be calculated step-by-step according to the program flowchart in Fig. 4. For this purpose, the total area A of the condenser is divided into a number of small area elements ΔA. The magnitude of ΔA can be estimated, for example, with the minimum required transfer area (Eq. (44)) and the number of sampling points. On the basis of the given entry conditions, the change in the gas and condensate mass flow can then be calculated. The step-by-step procedure is stopped when the specified total area or the required residual vapor fraction is reached. Corresponding methods are described in [5, 6].

3.2.1 Determination of Local Mass Flows

The change in the gas and condensate mass flow between two consecutive sampling points i and $i + 1$ is described by the differential balance equations (Eqs. (10–20)) in the form of differential equations:

$$\dot{N}_{G,i+1} = \dot{N}_{G,i} - \dot{n}_i \Delta A, \tag{32}$$

$$\dot{N}_{F,i+1} = \dot{N}_{F,i} + \dot{n}_i \Delta A. \tag{33}$$

As the inert gas flow $\dot{N}_{G2}$ is constant in the course of the condensation, the local inert gas content is given by

$$\tilde{y}_{2B,i} = \frac{\dot{N}_{G2}}{\dot{N}_{G,i}} = \frac{\dot{N}_{G2}}{\dot{N}_{G,1,i} + \dot{N}_{G2}}. \tag{34}$$

The respective, locally condensing mass flow $\dot{n}_i$ and the heat flow to be removed $\dot{q}_i$ are calculated with the help of the iteratively determined condensate film temperature $T_{F,i}$. For this purpose, the local temperatures of the gas–vapor mixture $T_{G,i}$, the coolant $T_{K,i}$, and the local material values and transport coefficients are needed.

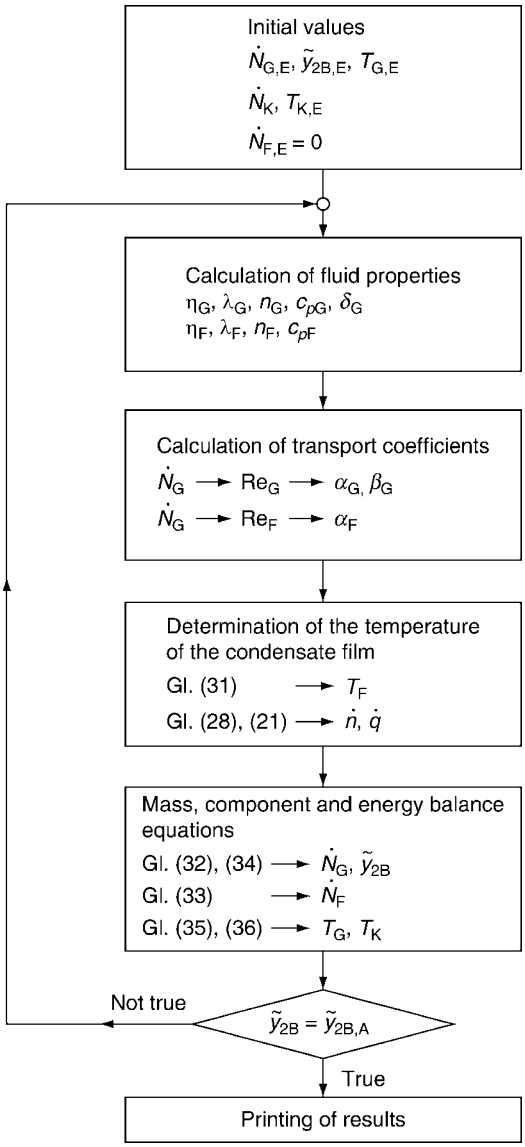

J2. Fig. 4. Program flowchart for the stepwise determination of the transfer area of a condenser for a pure condensate from a mixture of vapor and inert gas.

3.2.2 Determination of the Local Temperature of the Gas–Vapor Mixture T_G

If the gas–vapor mixture is saturated, the local mixture temperature $T_{G,i}$ in the bulk of the flow is equal to the dewpoint temperature $T_T(\tilde{y}_{1B,i})$ at each point corresponding with the local vapor fraction, which can be determined with the help of Eq. (29). If the mixture is superheated, the drop in the gas temperature T_G can be determined with the help of Eq. (19):

$$T_{G,i+1} = T_{G,i} - \frac{\dot{n}_i/\dot{N}_{G,i}}{\exp\,\phi_T - 1}(T_{G,i} - T_{F,i})\Delta A. \tag{35}$$

If the temperature at any point is below the dewpoint temperature T_T, small droplets may show up to form mist or fog. It is therefore recommended, when the dewpoint temperature is reached, to regard the gas–vapor mixture in the further course of the condensation as saturated and to calculate T_G according to Eq. (29).

3.2.3 Determination of the Local Coolant Temperature $T_{K,i}$

If the cooling takes place through a pure evaporating medium, the coolant temperature T_K remains constant along the condensation line. If the temperature rise is ignored in the case of cooling water, for a parallel flow between gas and coolant

$$T_{K,i+1} = T_{K,i} + \frac{\dot{q}_i}{\dot{N}_K c_{pK}} \Delta A. \tag{36}$$

If the coolant water flows in the opposite direction, i.e., countercurrent flow, the coolant water exit temperature must be calculated with the help of the total balance (Eqs. (8) and (9)), ignoring or estimating the cooling of the gas–vapor flow and the condensate film. In the case of cross-current flow, as in a pipe bundle system, for example, segment-wise constant coolant temperature may be assumed.

3.2.4 Properties

As the mixture cools down, passes through the condensation line, and the inert gas is enriched, the temperature and concentration dependence of the fluid property values must be taken into account if necessary. The material values of liquids, gases, and vapors are contained in Chap. D3 and their temperature dependence is described in Chap. D1. The material values of the mixture can be obtained from the material values of the vapor and of the inert gas. The thermal capacity may be simply calculated additively according to mole or mass fractions:

$$\tilde{c}_{pG} = \tilde{y}_1 \tilde{c}_{pG1} + \tilde{y}_2 \tilde{c}_{pG2} \tag{37a}$$

or

$$c_{pG} = y_1 c_{pG1} + y_2 c_{pG2}. \tag{37b}$$

For the calculation of the thermal conductivity λ_G and the viscosity η_G of the mixture, a simple addition of the values of the pure substances can lead to major errors. Special theorems are therefore necessary in these cases (Chap. D1). For the calculation of the mass transfer coefficient β_G or the Le number, the diffusion coefficient δ_G can be determined as described in Sect. 10.1 from Chap. D1.

3.2.5 Heat and Mass Transfer Coefficients

Reference is made to the equations for calculation of the transport coefficients α_K, α_F, α_G, and β_G in Sect. 2.3.

In many cases, as the controlling resistances are generally in the gas phase or in the coolant, a heat transfer coefficient of the condensate film α_F averaged over the condensation line and a constant heat transfer coefficient k' between condensate film and coolant may be assumed. For an estimate of α_F, in order to simplify the calculation, the influence of the vapor shear stress ($\tau^*_{DK} = 0$ in Chap. J1) can often be ignored.

Because of the decrease in the temperature and in the mass flow of the gas–vapor mixture along the condensation line, the heat and the mass transfer coefficient in the gas phase α_G and β_G must be calculated with the local fluid property values and the local Re numbers. It should be noted that a change in the cross-sectional area (e.g., as a result of pipe division in a pipe bundle system) also influences the gas velocity and thus the heat and mass transfer coefficients.

3.3 Distribution of Resistances Among the Gas Phase, the Condensate Film, and the Coolant

The individual resistances which are controlling the condensation are shown in Fig. 5. The heat transport here is from the inside (vapor space) outwards, i.e., from right to left (Fig. 1). The parallel heat and mass transfer resistances $1/\alpha_G$ and $1/\beta_G$ in the gas phase and the heat transfer resistances in the film $1/\alpha_F$, in the pipe wall s/λ_R and in the coolant $1/\alpha_K$ are arranged in series.

A simplified circuit diagram is obtained by introducing the heat transfer coefficients k and k' and the hypothetical heat transfer coefficients for the gas–vapor mixture α_{GD} (see Fig. 5). After calculation of the condensate film temperature T_F (Eq. (31)), using

$$\dot{q} = k(T_T - T_K) = k'(T_F - T_K) = \alpha_{GD}(T_T - \tilde{y}_{1B} - T_F) \tag{38}$$

the ratios of the resistances can be determined. The condensate film temperature must be above the coolant and below the dewpoint temperature ($T_K < T_F < T_T$). The resistance in the gas phase is controlling, if the relationship

$$\frac{k'}{\alpha_{GD}} = \frac{T_T - \tilde{y}_{1B} - T_F}{T_F - T_K} \tag{38a}$$

is large ($k' >> \alpha_{GD}$, $k \approx \alpha_{GD}$, $T_F \approx T_K$).

Correspondingly, the total resistance $1/k$ is on the coolant-side ($k \approx k'$), if the relationship k'/α_{GD} is small ($k' << \alpha_{GD}$, $T_F \approx T_T$).

3.3.1 Estimation of the Individual Resistances

If there is no excessive superheating of the gas–vapor mixture, the heat flow $\dot{q}_G$ can generally be ignored in the comparison with

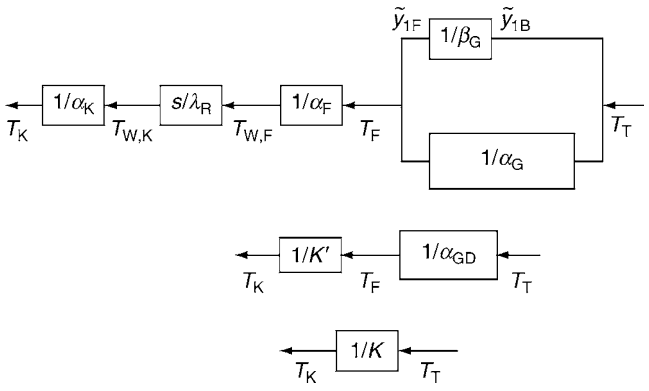

J2. Fig. 5. Heat and mass transfer resistances in the gas phase, in the condensate film and in the coolant. The second line summarizes the first line; the third row summarizes the second.

the enthalpy flow $\dot{n}_1 \Delta\tilde{h}_{v1}$ (Example 1, Part B). The calculation of the condensate film temperature can then be simplified to

$$T_F - T_K = C_T \ln\left(\frac{\tilde{y}_{2F}(T_F)}{\tilde{y}_{2B}}\right), \tag{39}$$

with

$$C_T = \frac{n_G \beta_G \Delta\tilde{h}_{v1}}{k'} \cong \frac{\alpha_G \Delta\tilde{h}_{v1}}{k' \tilde{c}_{pG} Le^{0.6}}. \tag{39a}$$

At high values of C_T and low inert gas contents $\tilde{y}_{2B}$, the condensation is heat transfer controlled.

At low values of C_T and high inert gas content, the resistance on the gas side is controlling; the condensation is mass transfer controlled. As the temperature difference $T_T - T_K$ increases, the resistance on the gas side increases in comparison with the resistance on the coolant side (Example 1, Part B).

The influence of the coolant temperature T_K and thus the condensate film temperature T_F on the locally condensing mass flow $\dot{n}_1$ is small in this case, as the driving concentration gradient is hardly changed. For the vapor pressure $p_1^* = 0$, the driving concentration gradient and the locally condensing mass flow is at its maximum (Example 1, Part B). The condenser performance is therefore primarily determined by the inert gas content. So, a marked increase in the condenser performance with high inert gas content cannot be achieved by a decrease in the coolant temperature T_K, but only by an improvement of mass transfer, i.e., in general, by an increase in the flow velocity of the gas–vapor mixture.

3.4 Simplified Methods for Determination of the Transfer Area

The level of the condensate film temperature T_F between the gas temperature T_G and the coolant temperature T_K depends on the distribution of the heat and mass transfer resistances among the gas phase, the condensate film, and the coolant. The distribution of these resistances changes in the course of the condensation, as the inert gas in the gas–vapor mixture is enriched. In many cases, by calculation of the condensate film temperature at the inlet T_{FE} and at the outlet T_{FA} of the condenser, it is possible to state whether the whole condensation process is controlled by heat or mass transfer. In these cases, simplified methods can be derived for determination of the transfer area [6].

3.4.1 Heat Transfer Controlled Condensation

As the smallest fraction of residual vapor, or the largest fraction of inert gas, is present at the gas outlet of the condenser, it must be determined whether the heat transfer resistance at the outlet is dominant. As a rule of thumb, it can be said that the whole condensation process is heat transfer controlled if the relationship

$$\left(\frac{k'}{\alpha_{GD}}\right)_A < 0.5$$

is true at the outlet. This condition is fulfilled in the case of low inert gas contents and high C_T values, i.e., at high α_G and β_G values or high gas velocities. The transfer area A of the condenser can then be determined according to the equation

$$A = \frac{\dot{Q}}{k' \Delta T_m}. \tag{40}$$

The mean driving temperature difference ΔT_m is calculated, according to the flow arrangement (Chap. C1), from the inlet and outlet temperatures of the condensate film T_{FE} or T_{FA} and the coolant T_{KE} or T_{KA}.

The total heat flow to be removed $\dot{Q}$ is calculated from the integral energy balance according to Eq. (8). If the gas outlet temperature is not known, it may be assumed as a first approximation that it is equal to the dewpoint temperature at the outlet:

$$T_{GA} = T_{TA}(\tilde{y}_{1B,A}).$$

It then follows from Eq. (8)

$$\begin{aligned}\dot{Q} &= \dot{N}_{FA}(\Delta\tilde{h}_{v1}(T_{TA}) + \tilde{c}_{pF}(T_{TA} - T_{FA})) \\ &\quad + \dot{N}_{GE}\tilde{c}_{pG}(T_{GE} - T_{TA}),\end{aligned} \tag{41}$$

with the condensate volume flow

$$\dot{N}_{FA} = \dot{N}_{GE} - \dot{N}_{GA} = \dot{N}_{GE}\left(1 - \frac{\tilde{y}_{2B,E}}{\tilde{y}_{2B,A}}\right). \tag{41a}$$

3.4.2 Mass Transfer Controlled Condensation

As the inert gas is enriched in the course of the condensation, the mass transfer resistance increases. Therefore, it must first be determined whether the mass transfer resistance is already dominant at the inlet of the condenser. With the condensate film temperature T_{FE} at the inlet, the ratio of the resistances $(k'/\alpha_{GD})_E$ can be calculated according to Eq. (38a). For the case

$$\left(\frac{k'}{\alpha_{GD}}\right)_E > 2,$$

the calculation procedure described below can be used. This condition is generally fulfilled at high inert gas contents or low C_T values (Eq. (39a)).

3.4.3 Condensation at Constant Condensate Film Temperature

With a knowledge of the condensate film temperature T_F, the locally condensing mole flux $\dot{n}_1$ and the resulting decrease in the gas volume flow $\dot{N}_G$ can be calculated. It is seen that, with the assumption of constant condensate film temperature T_F and thus constant inert gas content at the film surface $\tilde{y}_{2F}$, the differential mass balance can be obtained by integration. From the differential component balance equations

$$d\dot{N}_G = -\dot{n}_1 \, dA, \tag{13}$$

$$\dot{N}_{G2} = N_G \tilde{y}_{2B} \tag{34}$$

and the theorem for the mass transfer

$$\dot{n}_1 = n_G \beta_G \ln\frac{\tilde{y}_{2F}}{\tilde{y}_{2B}}, \tag{28}$$

it follows for the nondimensional transfer area, assuming constant gas density and constant mass transfer coefficient for simplification, that

$$\frac{n_G \beta_G A}{\dot{N}_{G2}} = -\frac{1}{\tilde{y}_{2F}} \int_{x_E}^{x_A} \frac{dx}{\ln x}, \tag{42}$$

with

$$x = \frac{\tilde{y}_{2F}}{\tilde{y}_{2B}}. \tag{42a}$$

With the parameter giving the number of transfer units

$$NTU_{G2} \equiv \frac{n_G \beta_G A}{\dot{N}_{G2}} \tag{42b}$$

and the integral logarithm

$$Li(x) = \int \frac{dx}{\ln x} = \ln(\ln x) + \ln x + \frac{(\ln x)^2}{2 \cdot 2!} + \frac{(\ln x)^3}{3 \cdot 3!} + \cdots \tag{42c}$$

this then gives

$$NTU_{G2} = \frac{1}{\tilde{y}_{2F}} [Li(x_E) - Li(x_A)]. \tag{43}$$

The series already converges, in the region of interest here ($x < 5$), after four or five series elements.

3.4.4 The Minimum Required Transfer Area

From Eq. (43), with the given gas contents at inlet and outlet, the minimum required transfer area can be calculated. As the temperature of the coolant medium falls, the vapor pressure $p_1^*(T_F)$ and thus the vapor content $\tilde{y}_{1F}$ at the condensate surface also falls. In the limit case, we have $\tilde{y}_{1F} = 0$ or $\tilde{y}_{2F} = 1$. The driving concentration gradient and thus the condensing mass flow is then at a maximum. The minimum required transfer area is then given by

$$A_{min} = \frac{\dot{N}_{G2}}{n_G \beta_G} \left[Li\left(\frac{1}{\tilde{y}_{2B,E}}\right) - Li\left(\frac{1}{\tilde{y}_{2B,A}}\right) \right], \tag{44}$$

with $\tilde{y}_{2B,E}$ and $\tilde{y}_{2B,A}$ as the inert gas contents of the gas–vapor mixture at the inlet and the outlet of the condenser.

3.4.5 Determination of the Transfer Area When the Film Temperature is not Constant

A more accurate value for the transfer area is obtained with the expedient selection of a suitable mean value for the inert gas content at the condensate surface $\bar{\tilde{y}}_{2F}$. An average value $\bar{\tilde{y}}_{2F}$ obtained from the inlet and outlet concentrations can lead to negative concentration gradients $\bar{\tilde{y}} - \bar{\tilde{y}}_{2B,A}$. It is therefore recommended to calculate an integral logarithm, to apply the inert gas content $\tilde{y}_{2F,A}$ at the outlet and the arithmetical mean of inlet and outlet concentrations in the prefactor. The transfer area is then given by

$$A = \frac{\dot{N}_{G2}}{n_G \beta_G} \frac{1}{\bar{\tilde{y}}_{2F}} \left[Li\left(\frac{\tilde{y}_{2F,A}}{\tilde{y}_{2B,E}}\right) - Li\left(\frac{\tilde{y}_{2F,A}}{\tilde{y}_{2B,A}}\right) \right], \tag{45}$$

with

$$\bar{\tilde{y}}_{2F} = \frac{1}{2}(\tilde{y}_{2F,E} + \tilde{y}_{2F,A}). \tag{45a}$$

By the use of $\tilde{y}_{2F,A}$, a locally greater driving gradient than that actually present is assumed and, therefore, the transfer area calculated is too small.

In the case of mass transfer controlled condensation, however, the influence on the condensing mass flow and the transfer area is small (Example 1, Part B).

If low residual vapor fractions $\tilde{y}_{1B,A}$ are required, the driving concentration gradient at the outlet becomes very small, so the transfer area becomes very large. In this case, it makes little difference whether the condensation at the inlet is already mass transfer controlled or even heat transfer controlled, as the transfer area is then determined by the low mass flows at low concentration gradients (Li (1,1) = −2.25; Li (1.01) = −4.60).

By linearization of the theorem for the mass transfer

$$\dot{n} = n_G \beta_G \frac{\tilde{y}_{1B} - \tilde{y}_{1F}}{1 - \tilde{y}_{1F}} \tag{46}$$

we obtain a simpler equation for calculation of the transfer area:

$$A = \frac{\dot{N}_{G2}}{n_G \beta_G \bar{\tilde{y}}_{2F}} \left[\frac{\tilde{y}_{2F,A}}{\tilde{y}_{2B,E}} - \frac{\tilde{y}_{2F,A}}{\tilde{y}_{2B,A}} + \ln \frac{\frac{\tilde{y}_{2F,A}}{\tilde{y}_{2B,E}} - 1}{\frac{\tilde{y}_{2F,A}}{\tilde{y}_{2B,A}} - 1} \right]. \tag{47}$$

As the linearized theorem gives lower mass flows, Eq. (47) results in larger transfer areas than Eq. (45). In many cases, this even cancels out the approximation error of Eq. (45) and leads to better results.

For determination of the transfer area, the mass transfer coefficient β_G can be expressed with the help of the Lewis relationship (Eq. (24)) by the heat transfer coefficient α_G:

$$A = \frac{\dot{N}_{GE} \tilde{c}_{pG} Le^{0.6}}{\alpha_G} \tilde{y}_{2B,E} NTU_{G2}. \tag{48}$$

For the transport coefficients α_G, β_G and the mass values, values averaged over the transfer area should be used.

3.4.6 Determination of the Transfer Area

In the first step, an assessment is made of whether the whole condensation process is heat or mass transfer controlled, by calculation of the condensate film temperatures at the inlet T_{FE} and at the outlet T_{FA} of the condenser according to Eq. (31). For this purpose, knowledge of the coolant and gas temperatures at the inlet and the outlet is required. The gas outlet temperature can in most cases be set equal to the dew-point temperature: $T_{GA} = T_{TA}(\tilde{y}_{1B,A})$. When coolant water is used, its heating-up is determined with the help of the integral energy balance (Eqs. (9) and (41)). Then, using Eq. (38), the ratio of the resistances at the inlet $(k'/\alpha_{GD})_E$ and at the outlet $(k'/\alpha_{GD})_A$ is determined. As the inert gas is enriched in the course of the condensation, the mass transfer resistance increases: $(k'/\alpha_{GD})_E < (k'/\alpha_{GD})_A$. Therefore, the condensation process for $(k'/\alpha_{GD})_A < 0.5$ may be regarded as heat transfer controlled and the transfer area calculated according to Eq. (40).

For $(k'/\alpha_{GD})_E > 2$, the whole process is mass transfer controlled, and the transfer area is given by Eq. (45) or (47).

Example 2 illustrates the procedure for the calculation of the transfer area in the case of heat transfer controlled (Part A) and mass transfer controlled condensation (Part B).

In some cases, the condensation at the inlet of the condenser is heat transfer controlled and, at the outlet, mass transfer controlled. As the calculation according to Eq. (40) generally leads to too high values and the calculation according to Eq. (45) (or Eq. (47)) to too low values for the transfer area, the transfer area can often be determined very satisfactorily by the application of both methods and averaging the results. The step-by-step calculation method naturally gives more reliable values, but it is also considerably more complicated.

3.4.7 Superheating of the Gas–Vapor Mixture

In a comparison of the condensation of a saturated gas–vapor mixture, more heat has to be removed in the case of superheating of the mixture. The condensate film temperature T_F is higher and the condensing mass flow is smaller (Example 1, Part B). Therefore, a larger transfer area is required.

It is frequently suggested that the transfer area is to be calculated in two steps in the case of condensation of a superheated mixture: In the first step, a fraction of the area is determined for cooling down to the dewpoint temperature and, in the second step, a further fraction of the area for the condensation of the saturated mixture. One part of the condenser is thus regarded as a simple gas cooler and designed accordingly. As the heat transfer coefficient α_G of a gas flow is generally very small, the area calculated for gas cooling may greatly exceed that required for condensation.

It is therefore advisable to check whether the condenser is actually working as a gas cooler or whether condensation is already taking place at the entry of the gas–vapor mixture. The condition for this is that the temperature of the cooling area (e.g., of the pipe wall) at the inlet of the condenser is below the dewpoint temperature:

$$T_{WE} < T_{TE}(y_{1B,A}). \tag{49}$$

The temperature is calculated from the energy balance equation

$$k''(T_{WE} - T_{KE}) = \alpha_G(T_{GE} - T_{WE}), \tag{50}$$

with

$$\frac{1}{k''} = \frac{s}{\lambda_R} + \frac{1}{\alpha_K} \tag{50a}$$

for flat walls or thin-walled pipes.

This results in the condition

$$\frac{T_{KE} + \frac{\alpha_G}{k''} T_{GE}}{1 + \frac{\alpha_G}{k''}} < T_{TE}(y_{1B,E}). \tag{51}$$

In practice, as the heat transfer in the gas is significantly poorer than the heat transfer to the coolant ($\alpha_G \ll k''$), condensation already occurs at the inlet. If not, the coolant temperature T_K and/or the heat transfer coefficient k'' should be adjusted accordingly.

As the heat to be dissipated from the superheating is generally much smaller than the condensation heat, superheating of the gas has little effect on condenser performance. The influence of the superheating of the gas is taken into account in the calculation of the condensate film temperature T_F and the total heat flow to be dissipated $\dot{Q}$. The simplified method for the determination of the transfer area according to Eq. (40) or (45) can therefore also be used for superheated gas–vapor mixtures. It is therefore clearly inadvisable to design a part of the condenser as a gas cooler. This can lead, in many cases, to the calculation of much too large transfer areas.

Example 2

The transfer area for the condensation of water vapor from a water vapor–air mixture in a condenser tube ($d = 0.03$ m) is to be determined. The coolant temperature is constant at $T_K = 20°C$; the overall heat transfer coefficient of coolant and pipe wall is $k'' = 1{,}000$ W/m^2 K.

Part A

From a gas–vapor flow of $M_{GE} = 10^{-2}$ kg/s with an entry temperature of $T_{GE} = 100°C$, an inert gas content on entry $y_{2B,E} = 0.152$ and at pressure $p = 1$ bar, 75% of the water vapor is to be condensed.

The conversion to molar values gives $\dot{N}_{GE} = 0.524$ mol/s, $\tilde{y}_{2B,E} = 0.10$, and $\dot{N}_{G2} = 0.0524$ mol/s; in addition, $T_{TE} = 96.7°C$.

The mass flow at the outlet is calculated from

$$\tilde{y}_{2B,A} = \frac{\dot{N}_{G2}}{\dot{N}_{G2} + 0.25\dot{N}_{G1,E}} = 0.308,$$

$\dot{N}_{GA} = 0.170$ mol/s.

Temperature T_{TA} is 90°C.

Calculation of the heat transfer coefficient gives

$$\mathrm{Re}_G = \frac{4\dot{M}_G}{\pi d\,\eta_G}, \quad \mathrm{Re}_{GE} = 3.2 \cdot 10^4, \quad \mathrm{Re}_{GA} = 1.0 \cdot 10^4.$$

Sect. 4 from Chap. G1 gives the pressure loss coefficient ξ, with Pr = 1, the Nu number and the heat transfer coefficient α_G:

$$\xi_E = 0.0232, \quad \mathrm{Nu}_E = 90, \quad \alpha_{GE} = 78.5\,\mathrm{W/m^2K};$$
$$\xi_A = 0.0315, \quad \mathrm{Nu}_A = 35, \quad \alpha_{GA} = 32.5\,\mathrm{W/m^2K};$$

$k'_E = k'' = 1{,}000$ W/m^2 K. It follows from Chap. J1, ignoring the vapor shear stress, $\alpha_{FA} = 4{,}000$ W/m^2 K and thus $k'_A = 800$ W/m^2 K.

Determination of the resistance distribution at inlet and outlet: With the help of Eq. (31), the values for the condensate film temperature can be calculated iteratively: $T_{FE} = 94.2°C$, $T_{FA} = 72.0°C$.

It follows from Eq. (38) that $(k'/\alpha_{GD})_E = 0.03$ and $(k'/\alpha_{GD})_A = 0.34$. The condensation process is thus heat transfer controlled.

Determination of the transfer area: Eq. (8) and/or Eq. (14) gives the total heat flow to be removed $\dot{Q} = 15.8$ kW.

The mean driving temperature difference in the case of parallel flow is

$$\Delta T_m = \frac{T_{FE} - T_{FA}}{\ln\left(\frac{T_{FE} - T_K}{T_{FA} - T_K}\right)} = 62.44\,\mathrm{K}.$$

With $\bar{k}' = 900\ \mathrm{W/m^2\,K}$, it follows from Eq. (40) that

$$L = \frac{Q}{\bar{k}'\Delta T_m \pi d} = 3.0\ \mathrm{m}.$$

The calculation of the tube length required according to Eq. (45) (mass transfer controlled) gives $L = 2.2$ m and, by the step-by-step calculation method, $L = 2.8$ m.

Part B

From a gas–vapor flow of $\dot{M}_{GE} = 2 \cdot 10^{-3}$ kg/s at an inlet temperature of $T_{GE} = 100°C$ and an inert gas content at the inlet of $y_{2B,E} = 0.617$, at pressure $p = 1$ bar, 75% of the water vapor is to be condensed.

Calculations corresponding to Part A

$$\dot{N}_{GE} = 0.085\ \mathrm{mol/s}, \quad \tilde{y}_{2B,E} = 0.5, \quad \dot{N}_{G2} = 0.0425\ \mathrm{mol/s},$$
$$T_{TE} = 81.4°C,$$
$$\dot{N}_{GA} = 0.053\ \mathrm{mol/s}, \quad \tilde{y}_{2B,A} = 0.8, \quad T_{TA} = 60.1°C,$$
$$\alpha_{GE} = 17\ \mathrm{W/m^2\,K}, \quad \alpha_{GA} = 10.5\ \mathrm{W/m^2\,K},$$
$$k'_E = 1,000\ \mathrm{W/m^2K}, \quad k'_A = 800\ \mathrm{W/m^2\,K},$$
$$T_{FE} = 38.6°C, \quad (k'/\alpha_{GD})_E = 2.3,$$
$$T_{FE} = 25.4°C, \quad (k'/\alpha_{GD})_A = 6.4.$$

The condensation process is thus mass transfer controlled.

Determination of the transfer area: With $\tilde{y}_{2F,A} = 0.968$ and $\bar{\tilde{y}}_{2F} = 0.95$, it follows according to Eq. (45) that

$$\mathrm{Li}(\tilde{y}_{2F,A}/\tilde{y}_{2B,E}) = 0.37,$$
$$\mathrm{Li}(\tilde{y}_{2F,A}/\tilde{y}_{2B,E}) = -1.46, \quad \mathrm{NTU}_{G2} = 1.93.$$

with $\bar{\alpha}_G = 14\ \mathrm{W/m^2K}$, $\bar{\tilde{c}}_{pG} = 32\ \mathrm{J/mol\,K}$ and $\mathrm{Le}^{0.6} = 0.84$

which gives the required tube length as

$$L = \frac{\dot{N}_{G2}\bar{\tilde{c}}_{pG}\mathrm{Le}^{0.6}}{\bar{\alpha}_G \pi d}\mathrm{NTU}_{G2} = 1.67\ \mathrm{m}.$$

According to Eq. (47), $\mathrm{NTU}_{G2} = 2.22$ or $L = 2.03$ m. A calculation of the tube length required with a step-by-step method gives the value $L = 1.85$ m.

4 Condensation of a Binary Vapor Mixture

In the condensation of a binary vapor mixture, the less volatile and therefore preferentially condensing component in the vapor phase is reduced, while the more volatile is enriched. As a result of mass and heat transfer resistances in the vapor phase, the composition of the vapor and the vapor temperature in the core (bulk) of the vapor flow and at the condensate film surface are not equal, as seen in Fig. 6. The mass and heat transfer resistances in the vapor phase, together with the heat transfer resistances in the condensate film and in the coolant, determine the performance of the condenser.

The general procedure for the determination of the transfer area of the condenser is the same as that for the condensation of a pure vapor in the presence of an inert gas. The local condensate film temperature T_F must also be determined iteratively in order to find the local mass flow $\dot{n}$ and the local heat flow $\dot{q}$.

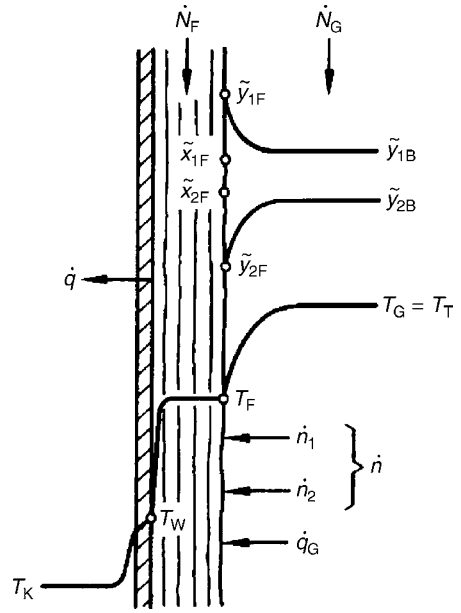

J2. Fig. 6. Concentration and temperature profiles in the condensation film of a binary vapor mixture. 1 – more readily boiling component. 2 – less readily boiling component.

The change in the vapor mass flow $\dot{N}_G$ and the vapor composition $\tilde{y}_{jB}$ and the vapor temperature T_G in the course of the condensation are then calculated by a step-by-step method. A description of the general procedure can therefore be restricted to the differences which occur in the condensation of a binary vapor mixture as opposed to the condensation of pure vapor in the presence of an inert gas.

An examination of the distribution of the resistances in the coolant, in the condensate film, and in the gas phase shows that, at high temperature differences, the condensation is heat transfer controlled. The vapor mixture then condenses almost like pure vapor. In this case, the required transfer area is easy to determine.

If selective condensation, i.e., a separation of the vapor mixture, is desired, small temperature differences and, thus, large transfer areas are necessary. In this case, the calculation of such an area (e.g., that of a dephlegmator) can be carried out by a step-by-step calculation method.

4.1 General Method for Determination of the Transfer Area

If, also in this case, the cooling of the condensate film is at first ignored, it follows according to Eq. (30) that

$$\dot{q} = k'(T_F - T_K) = \dot{n}\Delta\tilde{h}_v(T_F) + \alpha_G E_T(T_G - T_F). \qquad (52)$$

The kinetic theorem for the mass transfer in the gas phase is

$$\dot{n} = \dot{n}_1 + \dot{n}_2 = n_G\beta_G \ln\left(\frac{\dot{r}_1 - \tilde{y}_{1F}}{\dot{r}_1 - \tilde{y}_{1B}}\right). \qquad (23)$$

The mass transfer in the liquid phase can be described as in the gas phase. In general, however, it is assumed for simplicity that

the local composition of the liquid at the condensate surface is determined by the local mass flux [8]:

$$\tilde{x}_{1F} = \dot{r}_1. \tag{53}$$

This hypothesis presupposes a stratified, unmixed condensate film. In the opposite case, i.e., a completely mixed condensate film, the condensate film concentration can be determined from the condensate mass flux:

$$\tilde{x}_{1F} = \frac{\dot{N}_{F1}}{\dot{N}_F}. \tag{54}$$

This limiting case, however, is not usually taken as a basis, as condensate films mostly have a laminar flow and diffusion in the liquid alone does not generally lead to significant mixing.

It is also assumed that the liquid and vapor mixture at the condensate film surface is in thermodynamic equilibrium. Then (Sect. 2.3 from ◉ Subchap. D5.1)

$$\tilde{y}_{1F} = \gamma_1 (\tilde{x}_{1F}) \tilde{x}_{1F} \frac{p_1^*(T_F)}{p} \text{ is true.} \tag{55}$$

The parameters for the calculation of the vapor pressure curves $p_1^*(T_F)$ (Eq. (29)) and the activity coefficients $\gamma_1(\tilde{x}_{1F})$ (◉ Subchap. D5.1) can be found in the literature [3, 4].

4.1.1 Iterative Determination of the Condensate Film Temperature

Equations (23), (52), and (53) are combined to give the equation for the determination of the condensate film temperature T_F:

$$k'(T_F - T_K) = \alpha_G \phi_T \left(\frac{\Delta \tilde{h}_v}{c_{pG}} + \frac{T_G - T_F}{1 - \exp(-\phi_T)} \right), \tag{56}$$

with

$$\phi_T = \frac{\dot{n} \tilde{c}_{pG}}{\alpha_G} = \frac{n_G \beta_G \tilde{c}_{pG}}{\alpha_G} \ln \left(\frac{\tilde{x}_{1F} - \tilde{y}_{1F}}{\tilde{x}_{1F} - \tilde{y}_{1B}} \right). \tag{56a}$$

Using the Lewis relationship (Eq. (24)), it follows that

$$\phi_T = \mathrm{Le}^{-0.6} \ln \left(\frac{\tilde{x}_{1F} - \tilde{y}_{1F}}{\tilde{x}_{1F} - \tilde{y}_{1B}} \right). \tag{56b}$$

The iteration in to Eq. (56) is more complicated than that in to Eq. (31), as in this case, a value triplet must be determined for $\tilde{x}_{1F}, \tilde{y}_{1F}$, and T_F, fulfilled by Eq. (56). It is convenient to set the liquid composition $\tilde{x}_{1F}$ and to calculate the associated boiling temperature and vapor composition according to Example 6, ◉ Subchap. D5.1. The equilibrium diagram in Fig. 7 shows such a value triplet.

4.1.2 Determination of the Transfer Area

The determination of the transfer area is carried out according to the calculation scheme (Fig. 4) described in Sect. 3.2. With the help of the condensate film temperature T_F calculated according to Eq. (56), the local mass flow $\dot{n}$ and the local heat flow $\dot{q}$ and thus the decrease in the vapor volume flow (Eq. (32)) and the

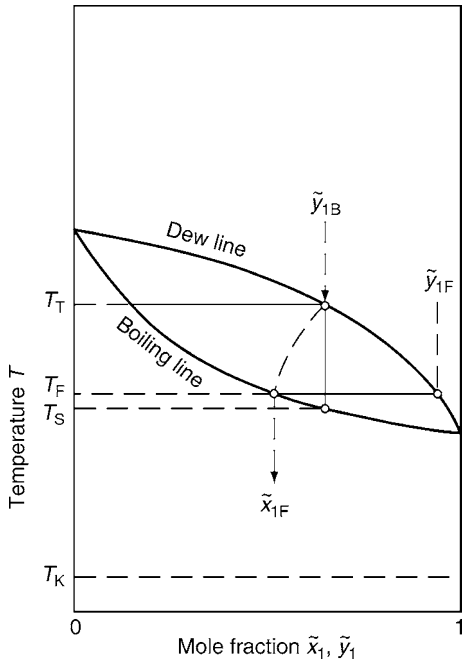

J2. Fig. 7. Boiling equilibrium of a binary mixture.

vapor temperature (Eq. (35)) along the condensation line can be calculated. The change in vapor composition between two consecutive sampling points i and $i+1$ follows from the component balance equation for component 1 (Eqs. (13) and (14)):

$$\tilde{y}_{1B,i+1} = \tilde{y}_{1B,i} + (\tilde{y}_{1B,i} - \tilde{x}_{1F,i}) \frac{\dot{n}_i}{\dot{N}_{Gi}} \Delta A. \tag{57}$$

4.2 Limiting Cases in the Condensation of Binary Vapor Mixtures

The level of the condensate film temperature T_F determines the distribution of resistances between the condensate film and the gas phase:

$$\dot{q} = k(T_T - T_K) = k'(T_F - T_K) = \alpha_{GD}(T_T - T_F). \tag{38}$$

It can be seen from the level of the boiling and dew lines in Fig. 7 that the condensate film temperature T_F must be between the dewpoint and boiling point of the mixture at vapor concentration $\tilde{y}_{1B}$:

$$T_S < T_F < T_T.$$

From this fact, two limiting cases for the condensation of binary vapor mixtures can be derived [9].

- Condensation in equilibrium ($T_F = T_T$)
  In the case of vanishingly small mass flows ($\dot{n} \to 0$) and temperature differences ($T_T - T_K \to 0$), the temperature and concentration profile in the gas phase is compensated. Only in this limiting case is it true that the liquid and the vapor compositions in the core are in equilibrium with each other as in Fig. 8. The difference between the liquid and the vapor composition – the selectivity – is then at a maximum.
- Local total condensation ($T_F = T_S$).

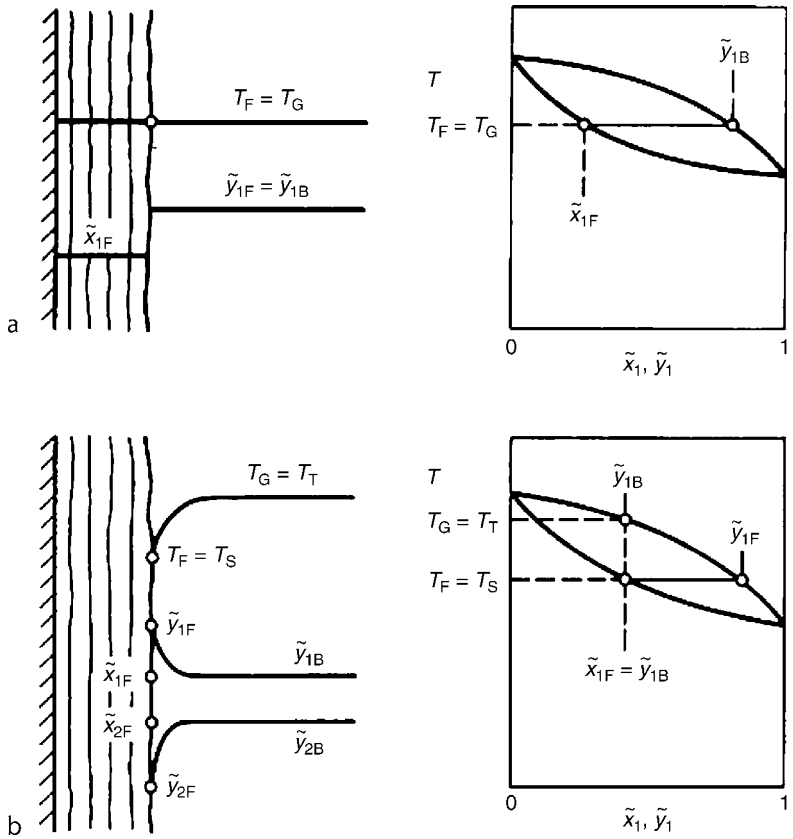

J2. Fig. 8. Limiting cases in the condensation of binary vapor mixtures: (a) condensation in equilibrium and (b) total condensation.

For very large mass flows ($\dot{m} \to \infty$) and temperature differences ($T_F - T_K \to \infty$), the vapor composition in the bulk is the same as the liquid composition, as shown in Fig. 8b, i.e.,

$$\tilde{x}_{1F} = \tilde{y}_{1B}, \tag{58}$$

and the condensate film temperature is the same as the associated boiling temperature:

$$T_F = T_S(\tilde{x}_{1F} = \tilde{y}_{1B}). \tag{59}$$

The vapor mixture condenses without a change in composition; a local total condensation takes place. From

$$\frac{k}{k'} = 1 - \frac{T_T - T_S}{T_T - T_K} \tag{60}$$

it follows that, in the limiting case $(T_T - T_K) \to \infty$, the total resistance of the condensation equals the sum of the heat transfer resistances in the condensate film and in the coolant: $k = k'$. The vapor mixture then condenses like pure vapor.

4.3 Simplified Methods for Determination of the Transfer Area

If – for example, in a dephlegmator – selective condensation, i.e., a separation of the vapor mixture, is desired, small temperature differences and thus large transfer areas are required. The limiting case of condensation in equilibrium can then be almost fulfilled. In this case, use of the step-by-step calculation method described in Sects. 3.1 and 4.1 is recommended.

If condensation without separation is required, high temperature differences $T_T - T_K$ are permissible. As the condensate film temperature must be above the boiling temperature of the vapor mixture ($T_F > T_S$), the influence of the mass transfer resistance in the gas phase is limited. If the temperature difference $T_T - T_K$ is significantly greater than the difference between dewpoint and boiling point ($T_T - T_S$), as in Fig. 6, the limiting case of local total condensation exists in practice. The condensation process is then heat transfer controlled ($k' << \alpha_{GD}$), the vapor mixture condenses almost like pure vapor, but not at the dewpoint temperature $T_T(\tilde{y}_{1B})$, but at boiling point $T_S(\tilde{y}_{1F} = \tilde{y}_{1B})$.

As a rough rule of thumb, it can be said that the condensation is heat transfer controlled, if

$$(T_T - T_K) > (T_T - T_S). \tag{61}$$

The transfer area is determined in this case as described in Chap. J1.

Presupposing an almost constant or averaged heat transfer coefficient k', the transfer area is given by

$$A = \frac{\dot{Q}}{k' \Delta T_m}. \tag{40}$$

The mean driving temperature difference ΔT_m is calculated according to flow routing (Chap. C1) from the inlet and outlet temperatures of the coolant medium T_{KE} or T_{KA} and the constant boiling temperature of the vapor mixture $T_S(\tilde{x}_{1F} = \tilde{y}_{1B})$. If the temperature of the coolant is constant or its heating is negligible,

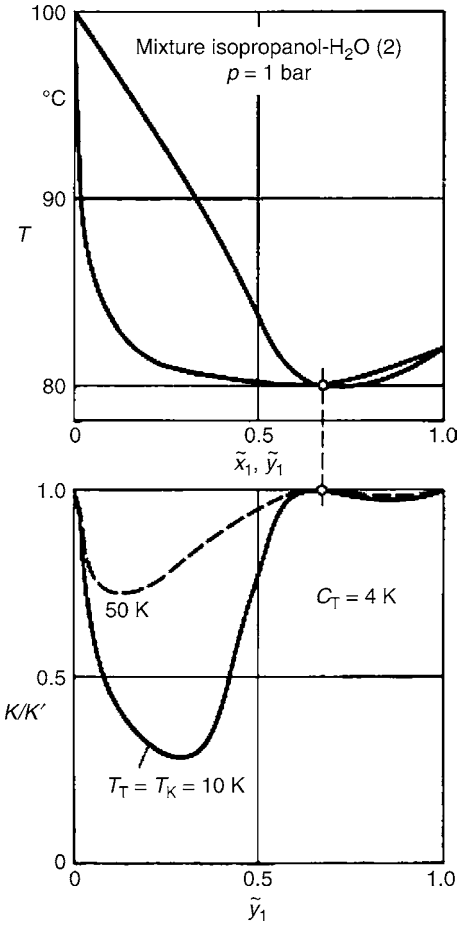

J2. Fig. 9. Boiling equilibrium and resistance distribution in the condensation of isopropanol–water vapor mixtures.

$$\Delta T_m = T_S - T_K. \tag{62}$$

The heat flow $\dot{Q}$ is given by the integral energy balance (Eq. (8)).

Taking as an example the condensation of an isopropanol (1)–water vapor(2) mixture, the influences of the phase equilibrium, the mass transfer, and the applied temperature difference $T_T - T_K$ can be illustrated [9]. Figure 9 shows the phase equilibrium of the mixture with the azeotropic point at $\tilde{x}_1 = \tilde{y}_1 = 0.68$ and the ratio of the total resistance to the heat transfer resistance on the coolant side k/k'. For this purpose, the condensate film temperature is calculated according to Eq. (56) and the resistance distribution according to Eq. (38). The parameter C_T (Eq. (39a)) has been set as

$$C_T = \frac{n_G \beta_G \Delta \tilde{h}_v}{k'} = 4 \text{ K}.$$

It can be seen that it is not the absolute temperature difference $T_T - T_K$, but the ratio to the difference between dewpoint and boiling point $T_T - T_S$ (Eq. (60)) which determines the distribution of the resistances.

An azeotropic vapor mixture always condenses like pure vapor ($k = k'$). But close-boiling mixtures, for example, those in the range $0.6 < \tilde{y}_1 < 1$, condense, practically regardless of the applied temperature difference $T_T - T_K$, almost like pure vapor. In the range $\tilde{y}_1 < 0.5$, the influence of the temperature difference on the distribution of resistances is clear. Thus, for example, for $\tilde{y}_1 = 0.2$, the values $k/k' = 0.33$ at $T_T - T_K = 10$ K and $k/k' = 0.75$ at $T_T - T_K = 50$ K; the difference between dewpoint and boiling point temperature at this point is $T_T - T_S = 12.4$ K. The determination of the transfer area according to Eq. (40) thus leads to good results in the case of a small temperature difference of $T_T - T_K = 10$ K in the range $\tilde{y}_1 > 0.5$, but can naturally not be applied, for example, for $\tilde{y} = 0.2 (T_K > T_S)$. Assuming a normal coolant water temperature of approx. 20°C, the applied temperature difference $T_T - T_K$ is greater than 50 K. For the temperature difference $T_T - T_K = 50$ K, Eq. (40) already supplies exact values for the required transfer area, as the ratio of the temperature differences in the whole concentration range

$$\frac{T_S - T_K}{T_F - T_K} > 0.99.$$

The condensate film temperature T_F is thus practically equal to the boiling point T_S ($\tilde{y}_{1F} = \tilde{y}_{1B}$). The limiting case of local total condensation on which Eq. (40) is based is nearly fulfilled.

5 Symbols

A	transfer area (m^2)
A, B, C	constants of the Antoine equation (Eq. (29)) (−)
C_T	constant (Eq. (39a)) (−)
$\tilde{c}_p$	molar heat capacity (J/mol K)
E_T	Ackermann correction (Eq. (22a)) (−)
$\tilde{h}$	molar enthalpy (J/mol)
$\Delta \tilde{h}_v$	molar evaporation enthalpy (J/mol)
k, k', k''	heat transfer coefficients (W/m^2 K)
Le	Lewis number (Eq. (25)) (−)
$\dot{M}$	mass flow (kg/s)
$\dot{m}$	locally condensing mass flow (kg/m^2 s)
$\dot{N}$	molar flow (mol/s)
$\dot{n}$	locally condensing molar flow (mol/m^2 s)
n	molar density (mol/m^3)
NTU	nondimensional transfer area (Eq. (42b)) (−)
p	pressure (Pa, bar)
p^*	saturated vapor pressure (Pa, bar)
$\dot{Q}$	heat flow (W)
$\dot{q}$	local heat flow (W/m^2)
$\dot{r}_1$	relative mass flow (Eq. (23a)) (−)
s	pipe wall thickness (M)
T	temperature (°C)
$\tilde{x}$	mole fraction in the condensate (−)
$\tilde{y}$	mole fraction in the gas phase (−)
y	mass fraction in the gas phase (−)
α	heat transfer coefficient (W/m^2 K)
β	mass transfer coefficient (m/s)
Γ	activity coefficient (−)
δ	binary diffusion coefficient (m^2/s)
κ	temperature conductivity (m^2/s)
λ	thermal conductivity (W/m K)
ξ	pressure loss coefficient (Example 2) (−)
φ_T	nondimensional mass flow (Eq. (22b)) (−)

Indices

1, 2, j	component
i	sampling point (Sect. 3.2)

A	outlet
B	core of flow (bulk)
E	inlet
F	condensate film
G	gas
K	coolant
S	boiling point
T	dewpoint
W	wall

6 Bibliography

1. Carey V (2008) Liquid–vapor phase change phenomena, 2nd edn. Taylor & Francis, New York
2. Ackermann G (1937) Wärmeübergang und molekulare Stoffübertragung im gleichen Feld bei großen Temperatur- und Partialdruckdifferenzen. VDI-Forsch.-Heft Nr. 382. VDI-Verl., Düsseldorf
3. Gmehling J, Onken U, Arlt W (1977) Dechema chemistry data series, Frankfurt
4. Wichterle I (1973) Antoine vapor pressure constants of pure compounds. Prag, Academia
5. Marschall E (1967) Wärmeübergang bei der Kondensation von Dämpfen aus Gemischen mit Gasen. Abhandlung Deutscher Kältetechnischer Verein, Nr. 19, C. F. Müller-Verl., Karlsruhe
6. Dallmeyer H, Gerhart K (1970) Stoff- und Wärmeübergang bei Kondensation aus Gas-Dampfgemischen. VDI-Forsch.-Heft Nr. 539. VDI-Verl, Düsseldorf
7. Fullarton D, Schlünder EU (1984) Näherungsweise Bestimmung der Austauschfläche bei der Kondensation von Gas-Dampfgemischen. Chem Eng Process 18
8. Colburn AP, Drew TB (1937) The condensation of mixed vapors. Trans Am Inst Chem Eng. Bd. 13:S. 197–S. 215
9. Fullarton D, Schlünder EU, Yüksel L (1984) Kondensation eines Isopropanol-Wasserdampf-Gemisches. Chem Eng Process 18

J3 Dropwise Condensation

Alfred Leipertz
Friedrich-Alexander-Universität Erlangen-Nürnberg, Erlangen, Germany

1 Introduction

Pure vapor condenses when it contacts a solid surface whose temperature is below the saturation temperature of the vapor T_s. Dropwise, filmwise and mixed forms of condensation with distinctly differing heat transfer performances can be observed, for example, the heat transfer coefficients for ideal dropwise condensation can be up to one order of magnitude that is larger than those for the filmwise mode. In this contribution, dropwise condensation is analyzed from a phenomenological point of view, and concerns heat transfer characteristics important for apparatus design.

2 Prerequisites and Appearance

The condensation form that appears mainly depends on the wettability of the surface which results from the free surface energy of the wall material and the surface tension of the condensing fluid. The wettability can be expressed in terms of the equilibrium contact angle γ_{eq} which is formed between a surface and a droplet lying on it. For ideal surfaces, a balance of the interfacial tensions σ between solid (S), liquid (L), and vapor (V) at the three phase contact line yields Young's Law [1]

$$\cos\gamma_{eq} = \frac{\sigma_{SV} - \sigma_{SL}}{\sigma_{LV}}. \quad (1)$$

Incomplete wettability, which mostly results in dropwise condensation, is given for contact angles of more than 90° [2]. However, contact angles of 60° and larger can also lead to dropwise condensation phenomena, which tend to pass into mixed condensation forms with increasing surface subcooling [3].

With decreasing surface tension σ_{LV} of the condensing fluid, the contact angles also become smaller. In comparison with other fluids of technical interest like organics (<50 mN·m^{-1}) or refrigerants (<10 mN·m^{-1}), water has a large surface tension of about 60 mN·m^{-1} at 100°C. Thus, the largest contact angles and the strongest tendency to dropwise condensation can be expected in steam systems.

On wall materials with good wettability, e.g., pure metallic surfaces with σ_{SG} values of 0.5 up to 5 N·m^{-1}, dropwise condensation can still be achieved by

(a) Adding to the vapor a non-wetting substance which is adsorbed on the condenser surface
(b) Applying hydrophobic materials like fatty acids or waxes to the surface
(c) Coating the surface with materials possessing low free surface energy, e.g., polymers or amorphous layers of hydrogenated carbon
(d) Direct modification of the metal surface in order to reduce its surface energy, e.g., by ion irradiation

The methods (a) and (b) can only be used for short-term applications. Both of the other methods have the potential for realization in industrial scales in case the coating according to method (c) satisfies a broad requirement profile [3] and the ion irradiation process mentioned in method (d) is adequately applied. Intensive research concerning heat transfer characteristics and long-term stability of these types of surface modification is done at present. Since the year 1989, a power plant condenser consisting of ion irradiated brass tubes is applied in China, achieving mean heat transfer coefficients of more than 6,000 W·m^{-2}·K^{-1} [4].

Figure 1 exemplarily shows a partially coated copper disk, on which dropwise condensation is induced by a promoter with a contact angle of 90° and pure filmwise condensation takes place on the untreated metal surface [5].

Mixed condensation can be observed when the wettability is not sufficiently reduced by the promoter, see, e.g., Fig. 2, with a contact angle of 74° and a surface subcooling of about 15 K [3]. When coatings are used to promote dropwise condensation, their additional heat transfer resistance has to be taken into account. For the hard coating used on the sample shown in Fig. 1, a thermal conductivity of 0.2 W·m^{-1}·K^{-1} was measured [5].

Although gold and silver with large free surface energies inhering good wettability are expected to show filmwise condensation, Westwater and coworkers [6, 7] observed dropwise condensation on these noble metals. This phenomenon was explained by the adsorption of organic substances with

VDI-GVC (ed.), *VDI Heat Atlas*, DOI 10.1007/978-3-540-77877-6_38,

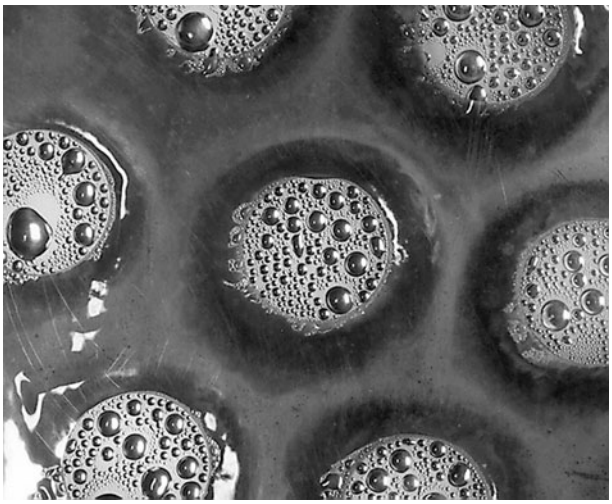

J3. Fig. 1. Dropwise and filmwise condensation on a partially coated copper disk; dropwise condensation only on the hard coated surface, filmwise condensation on the uncoated parts (diameter of the coated areas: 10 mm, layer thickness: 1.1 μm).

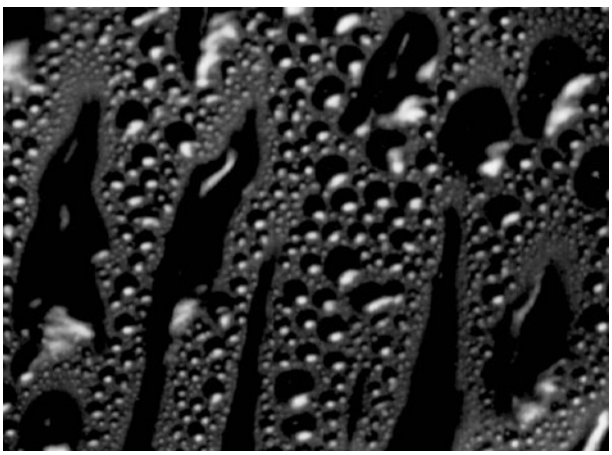

J3. Fig. 2. Mixed condensation for a contact angle of 74° [3] (original photograph: 40 × 54 mm).

hydrophobic characteristics on the surface, promoting dropwise condensation. In experiments under high cleanliness conditions, the expected good wettability and filmwise condensation were verified [8].

3 Dropwise Condensation Process and Models

In spite of the large number of studies on dropwise condensation carried out in the past decades, differing models are still discussed, partially associated with different dependencies in experimentally and theoretically acquired results, e.g., for the dependency of the heat transfer coefficient from the wall subcooling. During the last years, several review articles concerning dropwise condensation have been published [4, 9–11].

The transient process of droplet formation, growth, and drainage on the whole surface is a characteristic of the

J3. Fig. 3. Transient process of dropwise condensation on a hard coated copper disk showing a contact angle of 90° [3].

appearance of dropwise condensation, see Fig. 3. At first, small droplets are formed on locations with local minima of free surface energy. Due to condensation, these droplets grow and coalesce with neighboring droplets. When a certain size is reached, the gravitational force of the droplet and/or shear forces exerted by the vapor flow exceed the adhesive force between the droplet and the condensation surface. Thus, the droplet begins to roll along the surface and wipes other droplets off, which results in new "clean" surface areas, where smaller droplets can be formed again. This process of wiping and formation of new small droplets exhibiting low heat transfer resistance is considered to be the reason for the large heat transfer coefficients observed for dropwise condensation.

Concerning the mechanism of dropwise condensation, three different models are discussed:

(a) The vapor condenses between the droplets in almost droplet-free areas. The condensate is transported to the droplets by surface diffusion within an adsorbed film. Here, the boundary layer's thickness associated with heat conduction resistances can be neglected, which is the reason for the very large heat transfer coefficients [12]. According to this model, heat transfer takes place both at an extremely thin liquid film and at the droplets. Optical dynamic measurements of the film thickness [13] confirm this model with respect to the existence of a thin film between the droplets, but also model (b) is corroborated.

(b) According to this model, the vapor condenses as a thin film between the droplets as well, which can be regarded as filmwise condensation at first. When the film reaches a critical thickness, it breaks up and small droplets are formed. The major part of the heat transfer takes place at the very thin condensate film, while the droplets mainly act as liquid collectors [14, 15]. The models (a) and (b) are often combined to one model due to their strong similarities.

(c) The droplets are formed at individual nucleation sites, while the area between the droplets is regarded to be inactive with respect to condensation. The heat transfer occurs only through the droplets and is limited by their heat conduction resistance [16, 17]. In contrast to the works of Song et al. [13], optical investigations by Umur and Griffith [18] as well as studies on magnesium surfaces by Liu et al. [19] show that the area between the droplets is dry.

4 Heat Transfer Measurement and Calculation

The heat transfer measurement as a function of the wall subcooling $T_s - T_w$ is difficult due to temporally and locally fluctuating surface temperature of the condenser wall. In practice, only a mean surface temperature can be gained by extrapolation of the temperature profile inside the wall as far as one-dimensional thermal conduction can be proved by conformance of several heat balances [12, 20]. When additional promoter layers are present on the condenser surface, this procedure becomes more complex.

In addition, the influence of inert gases in the vapor is distinctly stronger for dropwise than for filmwise condensation. Beside problems with the stability of applied promoters, this phenomenon may be one of the main reasons for the wide variety of research results published. Especially concerning the dependence of the heat transfer coefficient on the wall subcooling, the diversity of statements is astonishing. Tanner et al. [21] and Rose and coworkers [20, 22, 23] found an increase in the heat transfer coefficient with increasing subcooling, and confirmed their theoretical predictions [4, 24]. In contrast, Shea and Krase [25], Welch and Westwater [15], Takeyama and Shimizu [26] as well as Koch et al. [3] and Rausch et al. [27] in later works showed a decreasing course similar to filmwise condensation. These results correspond to a Nu-correlation for a defined condensation system set up by Peterson and Westwater [28].

The diagram in Fig. 4 exemplarily compares heat transfer coefficients for filmwise condensation with measurement data acquired during dropwise condensation of steam at atmospheric pressure on vertically oriented condenser walls. The applied copper samples were coated with diverse hard coatings showing different contact angles [3, 12]. For small subcoolings, the measured heat flux values for dropwise condensation are up to 14 times larger than those for filmwise condensation.

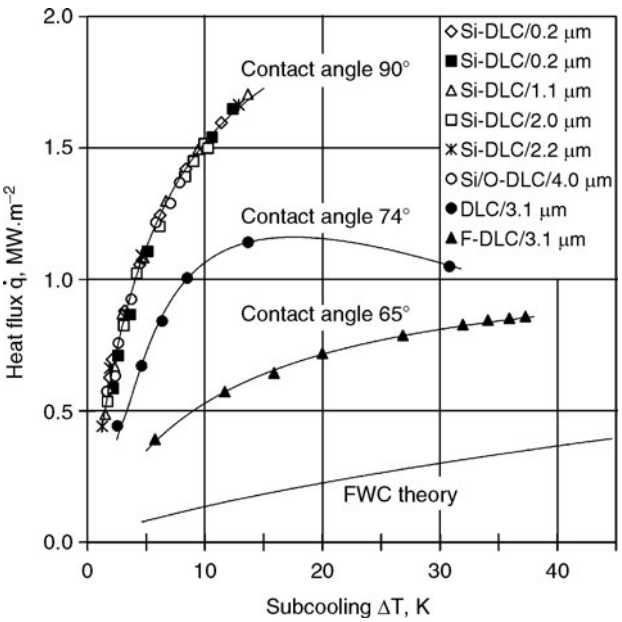

J3. Fig. 4. Measured heat flux as a function of the wall subcooling $\Delta T = T_s - T_w$ for various hard coatings on copper disks showing different contact angles (T_s = 373 K) [3, 12]. Choosing an appropriate coating (Si-DLC, 90°), the additional heat transfer resistance caused by the layer obviously has negligible effects on the achievable heat flux.

The heat transfer calculation depends on the applied model and is governed by the existing heat transfer resistances caused in the single steps of the heat transfer [9], namely phase transition and thermal conduction through the droplet or a film between the droplets. A constriction resistance originating from the heat flow around the thermally inactive surface underneath the big droplets has also to be taken into account. Furthermore, the additional thermal conduction resistance of the promoter layer and the thermal conductivity of the wall material need consideration. In case of a vapor consisting of different components, another resistance associated with the mass transport of the condensing component to the surface occurs. In this contribution, apart from some special remarks, only pure vapor is considered.

Detailed modeling based on droplet formation due to a heterogeneous nucleation process corresponding to model (c) or in a modified form in model (a) to obtain heat transfer equations was done by various research groups. For this, the droplet size distribution must be known, which is not easily available for most of the interesting systems. For pure steam with an empirically acquired droplet size distribution, Rose [4, 29] obtained results for the heat flux and the heat transfer coefficient using quite complicated calculation methods. One example is shown in Fig. 5, where the heat flux is given in dependence on the subcooling for several saturation temperatures on a vertical copper wall. Compared with the experimentally obtained values for fully developed dropwise condensation at a contact angle of 90° given in Fig. 4, it can be seen that the calculated values correspond very well in spite of the mentioned measuring problems and the assumptions made for the calculations.

In contrast, the values for the heat transfer coefficient do not correspond. While for the measurements [3, 12] in Fig. 4 for fully developed dropwise condensation (90°)

$$\alpha = \frac{\dot{q}}{T_s - T_w} \tag{2}$$

yields a decreasing heat transfer coefficient with increasing subcooling corresponding to

$$\alpha = -98.7 \ln(T_s - T_w) + 381 \text{ in } \mathrm{kW \cdot m^{-2} \cdot K^{-1}}, \tag{3}$$

the results in Fig. 5 show an inverse tendency represented by

$$\alpha = \vartheta^{0,8}[5 + 0.5(T_s - T_w)] \text{ in } \mathrm{kW \cdot m^{-2} \cdot K^{-1}}, \tag{4}$$

in a form which is dimensionless for the temperatures given by Rose [10]. For steam in the range of ϑ = 40...100°C for the actual fluid core temperature and for $\Delta T = T_s - T_w$ up to 8 K, a modified form with the factor 0.3 (instead of 0.5) in the brackets was introduced [4].

Several correlations for the heat transfer coefficient were suggested [14, 28], e.g., for steam and ethylene glycol on a hydrophobic coating in the form [28]

$$\mathrm{Nu} = 1.46 \cdot 10^{-6} \mathrm{Re}^{*-1.63} \pi_k^{1.16} \mathrm{Pr}_L^{0.5} \tag{5}$$

with

$$\mathrm{Nu} = \frac{2\alpha\sigma_{LV}\, T_s}{\rho_L \Delta h_v \lambda_L (T_s - T_w)}, \tag{6}$$

$$\mathrm{Re}^* = \frac{\lambda_L (T_s - T_w)}{\eta_L \Delta h_v}, \tag{7}$$

$$\pi_k = \frac{2\sigma_{LV}\, T_s}{\eta_L^2 \Delta h_v} \left(\frac{d\sigma_{LV}}{dT} \right), \tag{8}$$

and the Prandtl number of the liquid phase (Δh_v is the heat of vaporization in J·kg^{-1}). This correlation is recommended for $1.75 \leq \mathrm{Pr}_L \leq 23.6$; $7.8 \cdot 10^{-4} \leq \pi_k \leq 2.65 \cdot 10^{-2}$, and $2 \cdot 10^{-4} \leq \mathrm{Re}^* \leq 3 \cdot 10^{-2}$ [9] and is approximately valid outside these intervals as well. It must be kept in mind that such correlations were set up for defined condensation systems and their transferability to other systems is doubtable [9]. A discussion of heat transfer correlations for condensation can be found in a review article by Merte [30].

For the dependence of heat transfer coefficients on the subcooling, $\alpha \sim (T_s - T_w)^{-0.63}$ follows from Eq. (5). Corresponding to Eq. (3) and the measurement results in Fig. 4 and in contrast to Eq. (4), it gives a decreasing coefficient with increasing subcooling. As dropwise condensation is still in a testing phase, it is too early to decide which tendency is correct. However, it is recommended to apply Eq. (3), especially for subcoolings larger than 3 K, as Eq. (4) delivers too large and Eq. (5) yields distinctly too small heat transfer coefficients. In a calculation example given in Sect. 6, this is demonstrated in form of the obtained results.

For a technical application and its demands concerning long-term stability, the attainable heat transfer performance after a possible damage of the non-wetted coating is very important. Investigations with partially coated surfaces as given in Fig. 1 showed that for base materials with a large thermal conductivity only 20% of the surface have to be modified in order to obtain integral heat flows which make up about 80% of those for completely coated surfaces [5, 12]. Due to the high heat transfer performance on areas with fully developed dropwise condensation, the inactive part of the surface does not play an important role, even when it makes up more than half of the complete surface area. So damage to the promoter layer obviously has no decisive effect on the attainable heat transfer performance.

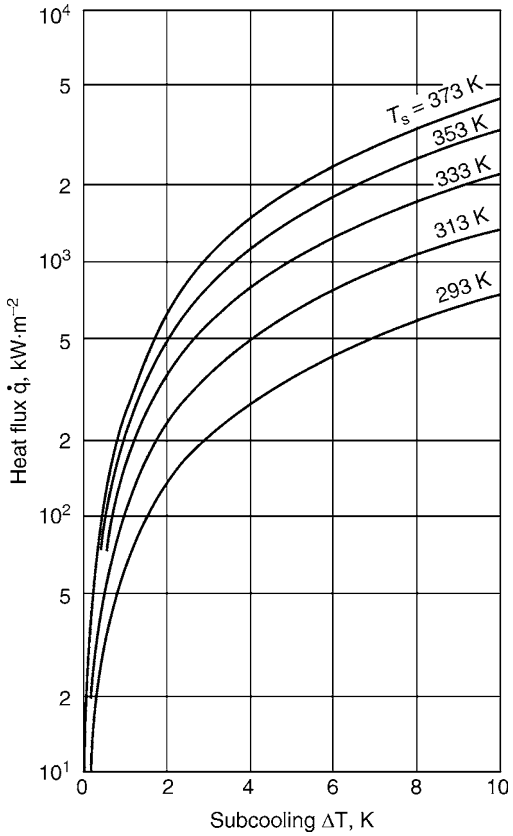

J3. Fig. 5. Calculated heat flux in dependence on the subcooling for various vapor saturation temperatures corresponding to [29].

5 Influence of Base Material, Inert Gas Concentration, and Wall Inclination

When instead of copper a different base material with a smaller thermal conductivity λ_w is used as condensation wall, the achievable heat transfer coefficients decrease. In Fig. 6, this dependency on the thermal conductivity of the base material is shown for aluminum, brass, and steel by mean values taken from several published results [31–33]. These mean values can be represented by the empirical equation

$$\alpha(\lambda_w) = f(\lambda_w) \cdot \alpha_{copper}. \tag{9}$$

In the range of 24 W·m^{-1}·K^{-1} $\leq \lambda_w \leq$ 400 W·m^{-1}·K^{-1}, $f(\lambda_w)$ can be described with

$$f(\lambda_w) = 3.75 \cdot 10^{-9} \lambda_w^3 - 8.11 \cdot 10^{-6} \lambda_w^2 + 4.61 \cdot 10^{-3} \lambda_w + 0.212 \tag{10}$$

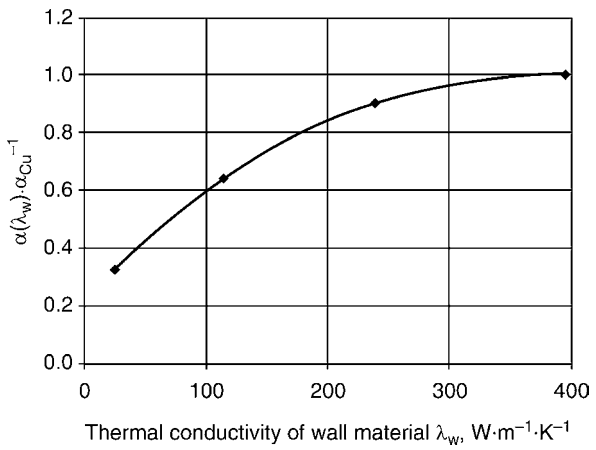

J3. Fig. 6. Empirical function of the dependence of the heat transfer coefficient $\alpha(\lambda_w)$ on the thermal conductivity of the condenser wall material λ_w in comparison with the heat transfer coefficient with copper α_{copper}.

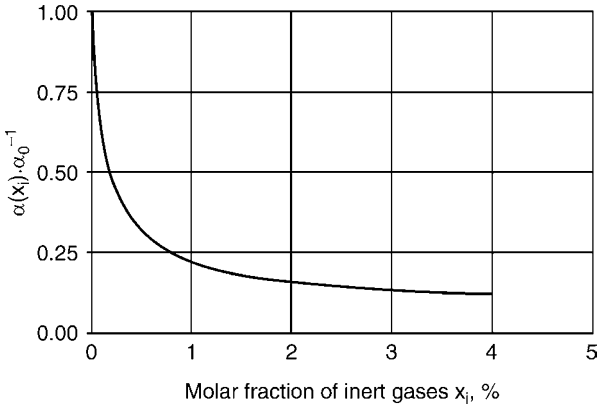

J3. Fig. 7. Reduction of the heat transfer coefficient in dependence on the molar fraction of inert gases x_i in % corresponding to [35].

in a good approximation. In a simpler form compared to other published results, this dependence can be expressed by

$$\frac{\alpha(\lambda_w)}{\alpha_{copper}} = \left(\frac{\lambda_w}{\lambda_{copper}}\right)^{0.42} \quad (11)$$

The exponent 0.42 is between previously published values of 0.5 [32, 34] and 0.33 [10].

In the presence of non-condensing gas components, the heat transfer coefficient decreases in dependence on the molar inert gas fraction x_i as shown by the measurements of Abdul-Hadi [35] in Fig. 7.

Maximum heat transfer coefficients are obtained for vertically oriented condenser wall surfaces. When the wall is inclined, the coefficient changes differently for forward (hanging droplets) and backward (lying droplets) inclinations. With the inclination angle β (horizontal surface: 0° for condensation on top and 180° for condensation on the undersurface), an empirical function in the form [5]

$$\frac{\alpha(\beta)}{\alpha(90°)} = (\sin\beta)^n. \quad (12)$$

with n = 0.270 for $0° \le \beta \le 90°$ and n = 0.176 for $90° \le \beta \le 180°$ was found.

The transferability of measured heat transfer coefficients in the case of dropwise condensation outside the horizontal tubes is of great interest for technical applications, e.g., tube bundle heat exchangers. Integration of the measurement results for the wall inclination range from 0° to 90° gives heat transfer coefficients on the horizontal tube of 87.6% compared with the values obtained on vertical walls for equal heat flux densities. For laminar filmwise condensation, the corresponding value is 86.4% [36].

6 Calculation Example

Steam condenses at a pressure of $p = 1.01325$ bar on the outside of a horizontal brass tube with hydrophobic coating. The outside wall temperature is 92°C. At a molar inert gas fraction of 1%, the heat transfer coefficient α is to be determined using the equation by Koch et al. [3].

From Eq. (3) by Koch with the subcooling $\Delta T = 8$ K follows

$$\alpha_{copper} = 175.8\,kW \cdot m^{-2} \cdot K^{-1}.$$

Consideration of the wall material brass with $\lambda_{brass} = 113$ $W \cdot m^{-1} \cdot K^{-1}$ using Eqs. (9) and (10) gives

$$\alpha_{brass} = 111.1\,kW \cdot m^{-2} \cdot K^{-1}.$$

For the influence of the molar inert gas fraction of 1%, Fig. 7 delivers $\alpha_i \cdot \alpha_0^{-1} = 0.225$ and thus

$$\alpha = 24.7\,kW \cdot m^{-2} \cdot K^{-1}.$$

The geometrical conversion from a vertical plain wall to a horizontal tube is taken into account by the factor 0.876 and gives the demanded value

$$\alpha_{tube} = 21.655\,kW \cdot m^{-2} \cdot K^{-1}.$$

Using the calculation equation by Rose, Eq. (4), instead of the equation by Koch,

$$\alpha_{tube} = 44.147\,kW \cdot m^{-2} \cdot K^{-1}.$$

would have been the result. Application of the correlation equation by Peterson and Westwater, Eq. (5), would have delivered a distinctly smaller value of

$$\alpha_{tube} = 2.071\,kW \cdot m^{-2} \cdot K^{-1}.$$

7 Bibliography

1. Young T (1805) An essay on the cohesion of fluids. Philos Trans R Soc London 95:65–87
2. Kast W (1965) Theoretische und experimentelle Untersuchung der Wärmeübertragung bei Tropfenkondensation. Fortschritt-Berichte VDI, Reihe 3: Verfahrenstechnik, Nr. 6, Düsseldorf, Aachen, Germany
3. Koch G, Zhang D, Leipertz A (1998) Study on plasma enhanced CVD coated material to promote dropwise condensation. Int J Heat Mass Transfer 41:1899–1906
4. Rose JW (1998) Interphase matter transfer, the condensation coefficient and dropwise condensation. In Proceedings of 11th International Heat Transfer Conference, Kyongju, Korea, 1998, vol 1, pp 89–104
5. Koch G, Zhang D, Leipertz A (1997) Condensation of steam on the surface of hard coated copper discs. Heat and Mass Transfer 32:149–156
6. Neill GA, Westwater JW (1984) Dropwise condensation of steam on electroplated silver surfaces. Int J Heat Mass Transfer 27:1539–1549
7. Woodruff DW, Westwater JW (1981) Steam condensation on various gold surfaces. J Heat Transfer 103:685–692
8. Wilkins DG, Bromley LA, Read SM (1973) Dropwise and filmwise condensation of water vapor on gold. AIChEJ 19:119–123
9. Carey VP (1992) Liquid vapor phase change phenomena. Taylor & Francis, Bristol
10. Rose JW (1998) Dropwise condensation. In: GF (ed) Hewitt Heat exchanger design handbook. Begell House, New York, Sect. 2.6.5, pp 1–11
11. Sadhal SS, Ayyaswamy PM, Chung JN (1997) Transport phenomena with drops and bubbles. Springer, New York
12. Koch G (1996) Untersuchungen zur Tropfenkondensation auf metallischen, hartstoffbeschichteten Oberflächen. Berichte zur Energie- und Verfahrenstechnik (BEV), Heft 96.4. ESYTEC, Erlangen, Germany
13. Song Y, Xu D, Lin J (1991) A study on the mechanism of dropwise condensation. Int J Heat Mass Transfer 34:2827–2831
14. Sugawara S, Katsuta K (1966) Fundamental study of dropwise condensation. In Proceedings of 3rd International Heat Transfer Conference, Chicago (USA), 1966, vol 2, pp 354–361

15. Welch JF, Westwater JW (1961) Microscopic study of dropwise condensation. In Proceedings of 2nd International Heat Transfer Conference, Boulder (USA), 1961, vol 2, pp 302–309
16. Gose EE, Mucciardi AN, Baer E (1967) Model for dropwise condensation on randomly distributed sites. Int J Heat Mass Transfer 10:15–21
17. Reisbig RL, Lay JE (1970) A nucleation theory and experimental study of dropwise condensation. In Proceedings of 4th International Heat Transfer Conference, Paris-Versailles (France), 1970, vol 6, Sect. Cs 1.2, pp 1–11
18. Umur A, Griffith P (1965) Mechanism of dropwise condensation. J Heat Transfer 87:275–282
19. Liu T, Mu C, Sun X, Xia S (2007) Mechanism study on formation of initial condensate droplets. AIChEJ 53:1050–1055
20. LeFevre EJ, Rose JW (1965) An experimental study of heat transfer by dropwise condensation. Int J Heat Mass Transfer 8:1117–1133
21. Tanner DW, Potter CJ, Pope D, West D (1965) Heat transfer in dropwise condensation. Int J Heat Mass Transfer 8:413–418
22. Citakoglu E, Rose JW (1968) Dropwise condensation - some factors influencing the validity of heat-transfer measurements. Int J Heat Mass Transfer 11:523–537
23. Stylianou SA, Rose JW (1980) Dropwise condensation on surfaces having different thermal conductivities. J Heat Transfer 102:477–482
24. LeFevre EJ, Rose JW A (1966) Theory of heat transfer by dropwise condensation. In Proceedings of 3rd International Heat Transfer Conference, Chicago (USA), 1966, vol 2, pp 362–372
25. Shea FL, Krase NW (1940) Dropwise and filmwise condensation of steam. Trans Am Inst Chem Eng 35:463–490
26. Takeyama T, Shimizu S (1974) On the transition of dropwise-film condensation. In Proceedings of 5th International Heat Transfer Conference, Tokyo (Japan), 1974, vol 3, Sect. Cs 2.5, pp 274–278
27. Rausch MH, Fröba AP, Leipertz A (2008) Dropwise condensation heat transfer on ion implanted aluminum surfaces. Int J Heat Mass Transfer 51:1061–1070
28. Peterson AC, Westwater JW (1966) Dropwise condensation of ethylene glycol. Chem Eng Prog Symp Ser 62:135–142
29. Rose JW (1976) Further aspects of dropwise condensation theory. Int J Heat Mass Transfer 19:1363–1369
30. Merte H (1973) Condensation heat transfer. Adv Heat Transfer 9:181–272
31. Koch G, Leipertz A (1997) Einsatz PTFE-ähnlicher Hartstoffschichten bei der Tropfenkondensation von Wasserdampf. Chem Ing Tech 69:122–125
32. Sadhal SS, Plesset MS (1979) Effect of solid properties and contact angle in dropwise condensation and evaporation. J Heat Transfer 101:48–54
33. Waas P (1981) Wärmeübergang bei Tropfenkondensation. PhD Thesis. München, Germany, Technische Universität,
34. Griffith P (1985) Dropwise condensation. In: Rohsenow WM, Hartnett JP, Ganic EN (eds) Handbook of heat transfer fundamentals, 2nd edn. McGraw-Hill, New York, pp 37–49
35. Abdul-Hadi MI (1979) Dropwise condensation of different steam-air mixtures on various substrate materials. Can J Chem Eng 57:451–458
36. Stephan K (1988) Wärmeübergang beim Kondensieren und beim Sieden. Springer, Berlin

J4 Mixing and Spray Condensation

Ulrich Hochberg
Hochschule Offenburg, University of Applied Sciences, Offenburg, Germany

1 Introduction

Spray condensers are condensers in which the steam to be condensed is immediately brought into contact with the cooling medium [1].

Compared to surface condensers, mixing condensers offer a number of advantages:

- low investment costs,
- large specific heat transfer surface,
- low fouling,
- easy maintenance,
- high operational reliability,
- low cooling water requirement,
- can be designed in materials that are not suitable for surface condensers.

The most important disadvantage of a spray condenser is the fact that the applications are limited because in many cases the contact of the condensate with the cooling medium is not allowed.

Mixing condensers are primarily used [2–9]:

- in connection with steam jet vacuum pumps,
- in demineralization systems,
- in connection with evaporation plants, in particular in the sugar and potash industry,
- in steam jet cooling systems,
- as water heaters,
- to condense the turbine steam in power stations, in connection with dry cooling towers.

When using alternative energy sources (geothermal, ocean thermal energy conversion) the use of mixing condensers is favorable [10, 11], since here only small temperature differences are obtained.

In special cases, it is reasonable to cool the heated mixture of cooling medium and condensate that is discharged from the mixing condenser in a liquid–liquid heat exchanger and to reuse it as cooling medium [12].

In mixing condensers operated in industrial, large-scale applications, the heat transfer resistance in the gaseous phase can normally be neglected when compared to the heat transfer resistance in the liquid phase. To dimension the mixing condensers, it can be restricted to the consideration of the heat transfer in the liquid. The temperature on the phase boundary can be calculated as saturation temperature corresponding to the partial pressure of the condensing liquid.

Gas coolers (quenches) as frequently used in technical applications are not discussed in this chapter. In these gas coolers, mostly a part of the cooling liquid evaporates, and here, the heat transfer resistance in the gaseous phase must not be neglected. The possible simplifications for the calculation of these units essentially differ from possible simplifications for the calculation of mixing condensers [13].

Different mixing condenser designs are described in [14].

For the preliminary calculation of mixing condensers a certain experience is required because there are many influences and condenser constructions; only if there are sufficient measured values for special condenser types, a reliable design will be possible. Therefore, the following equations can only be used for a first assessment.

The energy balance of a mixing condenser will be as follows, if the heat transfer to the environment is neglected:

$$\frac{\mathrm{d}U}{\mathrm{d}t} = (\dot{H}_{\mathrm{l,In}} + \dot{H}_{\mathrm{g,In}}) - (\dot{H}_{\mathrm{l,Out}} + \dot{H}_{\mathrm{g,Out}}). \qquad (1)$$

The following shall apply: $\dot{H}_{\mathrm{l,In}}$ and $\dot{H}_{\mathrm{l,Out}}$ are the enthalpy flows of feed and discharge of cooling medium and $\dot{H}_{\mathrm{g,In}}$ and $\dot{H}_{\mathrm{g,Out}}$ are the enthalpy flow of the feed and discharge of steam and inert gases, respectively.

The enthalpy flow of the discharged steam and gases $\dot{H}_{\mathrm{g,Out}}$ must not be neglected for many mixing condensers, because it is essential to discharge steam and gases from the condenser ("ventilation steam") in order to avoid excessive inert gas concentrations. The mass flow of the gas to be discharged strongly depends on the type of mixing condenser; it can be assessed, for example, according to [2].

The timely change of the internal energy $\mathrm{d}U/\mathrm{d}t$ of the mixing condenser and its contents only has to be taken into consideration for the simulation of transient conditions.

In the stationary case, the following shall apply, neglecting steam superheating and condensate subcooling, and for constant properties of the cooling medium

$$\dot{Q} = \dot{m}_{\mathrm{l}} c_{\mathrm{pl}} (T_{\mathrm{Out}} - T_{\mathrm{In}}) \qquad (2)$$

VDI-GVC (ed.), *VDI Heat Atlas*, DOI 10.1007/978-3-540-77877-6_39,

and for a given condenser pressure for the max. transferable heat flow

$$\dot{Q}_m = \dot{m}_l c_{pl}(T_S - T_{In}). \quad (3)$$

In order to simplify the calculation, the dimensionless discharge temperature of the condensate-cooling medium mixture is introduced as quotient of these temperatures:

$$\bar{\theta} = \frac{T_{Out} - T_{In}}{T_S - T_{In}}. \quad (4)$$

2 Condensation on Freely Falling Plane or Round Liquid Jets

If there is no inert gas, the heat transfer coefficient between steam and liquid is very high; therefore, the condensation of freely falling liquid jets is determined by the heat transfer in the liquid. The characteristic key figure to calculate the heat transfer is the Stanton figure:

$$St = \frac{\alpha}{\rho c_{pl} w}. \quad (5)$$

α is a fictional heat transfer coefficient to the liquid, related to the fictional surface F that is formed by the wetted circumference of the liquid discharge and the jet length L, ρ is the density and c_{pl} is the specific heat capacity of the liquid, and w is the speed in the discharge cross section A.

The dimensionless discharge temperature θ can be calculated according to the following formula if the Stanton figure is known:

$$\bar{\theta} = 1 - \exp\left(-\frac{F}{A}St\right). \quad (6)$$

The following shall apply to the round liquid jet:

$$\frac{F}{A} = 4\frac{L}{d}. \quad (7)$$

The following shall apply to the plain liquid jet with very large gaps:

$$\frac{F}{A} = 2\frac{L}{d}, \quad (8)$$

if d is the discharge diameter or the width of the discharge gap.

After a certain decomposition length, the liquid jet is dissolved into individual droplets [15–18]; this process has to be taken into consideration for the calculation of the Stanton figure.

The following shall apply to the Stanton number in general:

St = f (Ph, Pr, We, Fr, Re, geometry, flow arrangement).

The dimensionless parameters are explained in Chap. A2.

Numerous equations were published [10, 18–25] regarding the mathematical formulation of the dependence of the Stanton figure on its influencing variables.

Sometimes, these equations reflect the influence of the parameters on the Stanton figure in a qualitatively different way. As long as the number of measured values is not sufficient to be able to determine the influence of the parameters by means of equations, measured values of the design of mixing condensers shall be directly taken as a basis.

A first assessment of the Stanton figure is possible with the equation by Theofanous [10]:

$$St = 0.02\left(\frac{L}{d}\right)^{-0.5}. \quad (9)$$

The heat transfer on the liquid jet can be considerably increased by means of periodic transient liquid feed [26].

3 Heat Transfer on the Individual Drop

The highest volume-related heat flow densities can be achieved if the condensation takes place on individual drops as in this case the surface of the cooling medium is very large. The most important application is the condensation of water steam on liquid water. The growth of the drops due to condensation can be neglected in this case if the difference between cooling water inlet temperature and saturation temperature of the steam is smaller than 100 K. The most popular theories assume that the radius of the drops is constant and that the heat transfer resistance in the resulting condensate layer can be neglected [27–29].

If the cooling medium is a fluid, which has a miscibility gap with the cooling medium, the thermal conduction of the resulting condensate layer has to be taken into consideration as well [29]. The preliminary calculation of such condensers, however, is very inaccurate; there are studies showing that the accommodation coefficient is then unequal to 1 [30] (and the assumption of a thermodynamic equilibrium at the phase boundary is not justified).

In the following, it is assumed that the cooling medium is the same substance as the condensing vapor, the drop growth can be neglected, and there will be a thermodynamic equilibrium ($T_{ph} = T_s(p)$) on the phase boundary, i.e., the heat transfer coefficient of the steam is very high.

The introduction of the dimensionless temperature

$$\bar{\theta} = \frac{T - T_{In}}{T_S - T_{In}} \quad (10)$$

facilitates the calculation of the heat transfer.

When determining the heat transfer on the basis of the sprayed drops, it is assumed that the drops do not influence each other [27, 28, 31]. The heat transfer in drops is calculated in the same way as the thermal conduction in a rigid ball. The temperature of the ball is constant for time $t < 0$, and the surface temperature of the ball equals T_S for $t > 0$.

In case of a high relative speed between drop and steam, the measured heat transfer is higher than the heat transfer calculated for a rigid ball from mere thermal conduction. The increased heat transfer can be explained by the flow inside the drop [32–34] and by the oscillation of the drop [35].

If the thermal conductance in the individual drop is calculated in the same way as the thermal conductance in a rigid ball, and assuming a thermodynamic equilibrium on the ball surface,

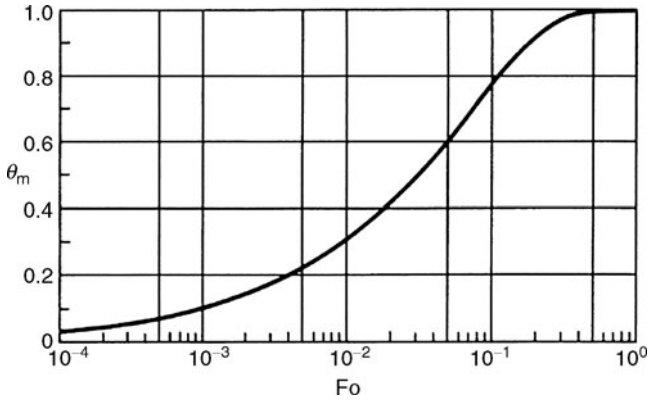

J4. Fig. 1. Standardized average temperature of a drop depending on the Fourier number.

the dimensionless mean temperature θ_m of the drop will result [36] as

$$\theta_m = 1 - \frac{6}{\pi^2}\sum_{n=1}^{\infty}\frac{1}{n^2}e^{-n^2\pi^2 Fo}, \tag{11}$$

with the Fourier number

$$Fo = \frac{\lambda t}{\rho c_{pl} r^2}. \tag{12}$$

The solution of Eq. (11) is shown in Fig. 1.

Although the sum in Eq. (11) converges rapidly, it is easier for practical application to determine the average temperatures via the proximity equation [37]

$$\theta_m = \sqrt{1 - e^{-\pi^2 Fo}}. \tag{13}$$

The proximity equation deviates from the exact solution according to Eq. (11) by less than 0.02.

Celata and others performed measurements of individual drops in technically interesting ranges from $r = 0.16$ mm to $r = 1.4$ mm [38]. It turned out that faults due to neglect of flow inside the drop and due to the oscillation of the drop are much more important than that assumed up to now. The measurements are limited to drop path lengths of less than 0.1 m. Velata and others propose to use the empiric correlation

$$Fo \cdot 0.21 \cdot \left(r \cdot \left|\vec{v}_g - \vec{v}_e\right| \cdot \frac{\rho c_{pl}}{\lambda} \cdot \frac{\eta_g}{\eta_e + \eta_g} \right)^{0.454} \tag{14}$$

in Eqs. (11–13) instead of the Fourier figure. For large mixing condensers, however, Eqs. (11–13) result in excessive values for the average temperature.

The Fourier number ("dimensionless residence time") (Eq. (12)) depends not only on the drop radius r, but also on the residence time t of a drop in the mixing condenser. In order to calculate the residence time, the equation of motion of the drop has to be solved.

On the assumption that the condensation does not essentially influence the trajectory of the drop and neglecting the buoyant force, Ref. [39] shall apply

$$\frac{d\vec{v}_l}{dt} = \frac{9}{2}\frac{\eta}{\rho_l r^2}\frac{c_d Re}{24}(\vec{v}_g - \vec{v}_l) + \vec{g}, \tag{15}$$

with

$$\frac{c_d\ Re}{24} = 1 + 0.197\ Re^{0.63} + 2.6 \cdot 10^{-4}\ Re^{1.38} \tag{16}$$

and

$$Re = \frac{2\left|\vec{v}_g - \vec{v}_l\right| r \rho_g}{\eta_g}. \tag{17}$$

Because of

$$\frac{d\vec{x}}{dt} = \vec{v}_l \tag{18}$$

this is a system of ordinary, nonlinear differential equations that can be solved with differential solvers, which are available in most of the standard program libraries. With the initial and boundary conditions given by the units (condenser geometry, initial drop speed according to the speed of the liquid in the tightest cross section), the result is the residence time of the drops in the mixing condenser.

The temperature of the liquid in the condenser discharge is the average temperature of all drops. Knowing the density of the volume distribution of the drops dv/dt, the temperature $\bar{\theta}$ can be calculated according to

$$\bar{\theta} = \sum_0^{\infty}\frac{dv}{dr}\theta_m(Fo)dr. \tag{19}$$

Manufacturers of spray nozzles frequently indicate the density of the drop size distribution $dN(r)/dr$. If atomization is done by means of hollow cone nozzles, the drop size distribution can be estimated according to [40]. These values can be taken as rough estimates, however, in case of high condensation rates, the jet geometry will change considerably, and this might result in the reduction of the heat transfer [41]. On the basis of the density of the drop size distribution, it is possible to calculate the volume distribution according to

$$\frac{dv}{dr} = \frac{r^3 dN(r)}{d} \Big/ M_3 \tag{20}$$

with the third moment of distribution [42]

$$M_3 = \int_0^{\infty} r^3 \frac{dN(r)}{dr} dr. \tag{21}$$

The equation by Mugele and Evans [43] proved itself [29, 31, 44] for the description of measured values of drops. It well represents the measured average diameter. The required constants are easy to adjust. Mugele and Evans assume that with a given flow field there is a maximum, stable drop radius r_m. With this maximum drop radius r_m and the adjustable parameter a the dimensionless function y of drop size r is formed:

$$y = \ln\frac{ar}{r_m - r}. \tag{22}$$

According to Mugele and Evans, y shall be distributed in a normal manner:

$$\frac{dv}{dy} = \frac{\delta}{\sqrt{\pi}}e^{-\delta^2 y^2}, \tag{23}$$

$$\frac{dv}{dr} = \frac{r_m}{(r_m - r)r} \cdot \frac{\delta}{\sqrt{\pi}}e^{\delta^2 y^2}, \tag{24}$$

with δ as distribution parameter.

If the density of the volume distribution dv/dr is known, the dimensionless discharge temperature can be calculated by means of a numerical or graphical evaluation of Eq. (19).

Example

Given: We assume that there is a mixing condenser with a width of 3 m for water steam with a saturation temperature $T_S = 40°C$. The steam speed, vertically from the bottom to the top, amounts to 2 m/s. Drops from a flat jet nozzle flow horizontally into the steam chamber, with an initial speed of 6 m/s. The inert gas rate can be neglected. We assume that the distribution according to Mugele and Evans the drops are distributed with $r_m = 0.8$ mm, $a = 0.4$, and $\delta = 0.5$. What is the average standardized discharge temperature of the cooling water?

On solving Eq. (15), we get the flight path of the drops. Figure 2 shows the graphical representation of the flight paths of some drops with different radii. For the numerical evaluation, the substance data of water at 40°C were used. The residence time of the drops and the volume distribution density are shown above the radius in Fig. 3. The graphical or numerical evaluation of Eq. (19) results in $\bar{\theta} = 0.94$.

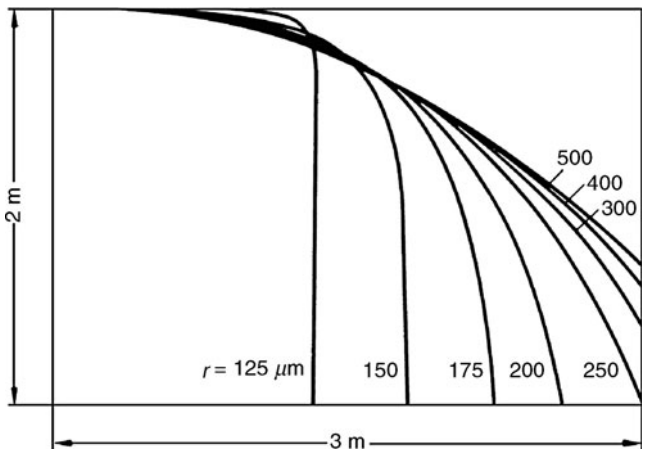

J4. Fig. 2. Example of the flight paths of drops of different radii.

4 Inert Gas Influence

The presence of inert gas reduces the capacity of the mixing condenser. In the literature, e.g., [45–50], this phenomenon is exclusively ascribed to the fact that the inert gas enriches on the phase boundary surface. Therefore, the partial pressure of the steam reduces on the phase boundary surface, and as a result, the condensation temperature that corresponds to the saturation temperature for this partial pressure decreases as well.

The decreasing capacity of a mixing condenser can be described in a first approximation by the fact that the reduction of the partial pressure on the phase boundary surface and thus, the reduction of the condensation temperature T_{Ph} are taken into consideration. (As already mentioned, other physical phenomena have to be taken into consideration in case of gas cooling by means of liquid injection.)

Taking into consideration the Clausius–Clapeyron equation, according to Schlünder [48] the saturation temperature T_{Ph} on the phase boundary surface under steady-state conditions can be calculated according to

$$0 = T_{In} - T_{Ph} + \Phi \frac{\Delta h_v}{c_{pg}} \cdot \ln \frac{\tilde{y}_I + \frac{\Delta h_v}{RT_{sv}^2}(T_{sv} - T_{Ph})}{\tilde{y}_I}, \qquad (25)$$

if the specific volume of the liquid and the real gas behavior of the steam are neglected. $T_{In} - T_{ph}$ is the driving temperature difference for the heat transfer through the condensate, Δh_v is the evaporation enthalpy, and c_{pg} is the specific heat of the steam. T_{sv} is the saturation temperature of the steam in the core flow, and R is the gas constant. It has to be observed that the temperatures in Eq. (25) have to be in kelvin. The mole fraction $\tilde{y}_I$ can be calculated on the basis of the weight fraction of the inert gas y_I according to

$$\tilde{y}_I = \frac{y_I}{y_I + (1 - y_I)M_I/M_g}, \qquad (26)$$

with molecule masses M_I and M_g of the inert gas and of the steam, respectively.

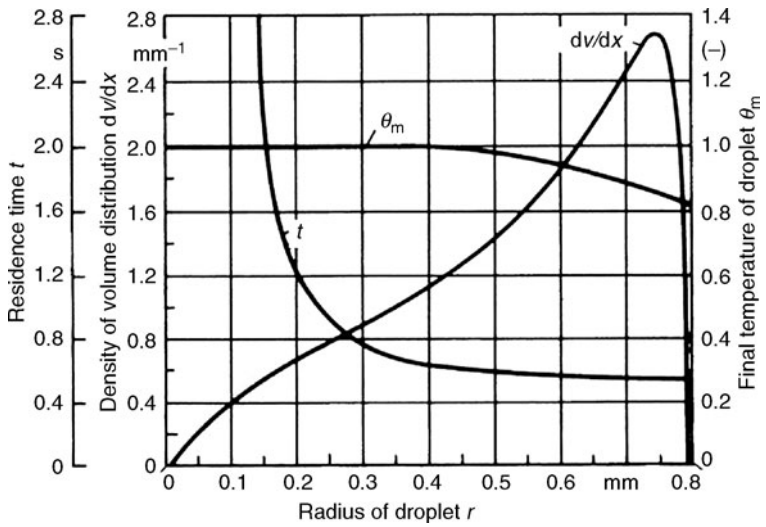

J4. Fig. 3. Final temperature, residence time, and volume distribution of the drops.

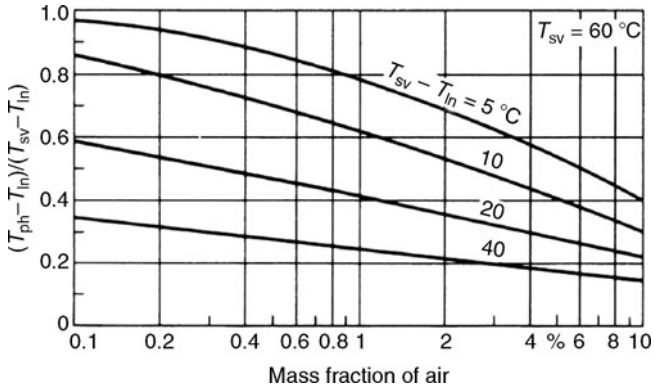

J4. Fig. 4. Influence of the air as inert gas to the condensation of water steam at $\Phi = 1.5 \cdot 10^{-3}$.

Φ is approximately the ratio of the heat transfer coefficient of the gas to that of the liquid.

Although the thermal conduction in the condensate is transient, Eq. (25) can even be applied if Φ is considered an adjustable constant. For many condensers and operating conditions, Φ ranges between 1 and $2 \cdot 10^{-3}$.

In the calculation of T_{Ph} according to Eq. (25) convergence problems might occur due to the stiffness of the problem with algorithms which converge with higher order. Simpler solvers avoid such problems.

Condensers for steam–inert gas mixtures can then be designed as condensers for pure steam, if T_S is the temperature on the phase boundary surface T_{Ph}. For a first assessment of the inert gas influence, Fig. 4 shows the relation of $(T_{Ph} - T_{In})/(T_{sv} - T_{In})$ over the inert gas concentration. The figure applies to water with $T_{sv} = 60°C$ and air as inert gas.

The important influence of the temperature difference $T_{sv} - T_{In}$ and thus, the heat flow density can be recognized. The higher the steam flow to the phase boundary surface, the higher the inert gas concentration on the phase boundary surface and thus, the reduction of the condensation temperature T_{Ph} on the phase boundary surface.

Equation (25) does not consider the compression of inert gas in the condenser and the heating of the cooling medium. In case of strong compression of the inert gas and (or) strong heating of the cooling medium, the condenser has to be calculated in steps [44].

5 Symbols

A	discharge surface of a liquid jet (m^2)
a	distribution parameter (–)
c_d	resistance coefficient (Eq. (14)) (–)
c_{pl}, c_{pg}	specific efficient heat capacity of the liquid or of the steam (J/kg K)
d	diameter or gap width (m)
F	fictional surface (see text) (m^2)
Fo	Fourier figure (Eq. (12)) (–)
$\vec{g}$	acceleration of gravity 9.81 m/s^2 (m/s^2)
Δh_v	evaporation enthalpy (J/kg)
$\dot{H}$	enthalpy flow (J/s)
L	jet length (m)
$\dot{m}_l$, $\dot{m}_g$	mass flow of the cooling medium or of the steam (kg/s)
M_I, M_g	molecular weight of the inert gas or of the steam (g/mol)
M_3	third moment of distribution of number (Eq. (21)) (–)
$N(r)$	distribution of total number (–)
$\dot{Q}$	heat flow (J/s)
$\dot{Q}_m$	max. transferable heat flow (J/s)
R	gas constant (J/kg K)
Re	Reynolds figure (Eq. (17)) (–)
r	drop radius (m)
r_m	max. drop radius (m)
St	Stanton value (Eq. (5)) (–)
T_{Out}	discharge temperature of the cooling medium (K)
T_{In}	inlet temperature of the cooling medium (K)
T_{sv}	saturation temperature of the steam in the core flow (K)
T_{Ph}	saturation temperature of the steam on the phase boundary (K)
T_S	saturation temperature of the steam for the condenserpressure (K)
t	time (s)
$\vec{v}\,(r)$	distribution of the volume total (–)
$\vec{v}$, $\vec{v}_g$	vector of the drop or gas speed (m/s)
w	speed of the cooling water (m/s)
$\vec{x}$	coordinate of a liquid drop (m/s)
y	dimensionless function of the drop size (–)
$\tilde{y}_I$, y_I	molecular or mass portion of the inert gas (–)
α	liquid-side heat transfer coefficient (W/m^2 K)
δ	distribution parameter (–)
η_g	gas viscosity (kg/m s)
θ	standardized temperature (Eq. (10)) (–)
$\bar{\theta}$	standardized caloric average temperature of the cooling medium (–)
θ_m	standardized caloric average temperature of a drop (–)
Φ	constant for the calculation of the inert gas influence (–)
ρ_g, ρ_l	density of gas or liquid (kg/m^3)

6 Bibliography

1. Holland-Merten EL (1953) Handbuch der Vakuumtechnik. VEB Wilhelm Kapp Verlag, Halle (Saale)
2. GEA Wiegand GmbH (1985) Strahlpumpen und Strahlwäscher, Arbeitsblätter. GEA Wiegand GmbH, Einsteinstraße 9–15, D-76275 Ettlingen
3. Bow WJ Direct contact steam condenser. US-Schutzrecht 3 814 398
4. Liebisch H (1968) Bedeutung und Entwicklungsstand der Mischkondensation von Dämpfen. Energietechnik 18(2):S. 67–S. 71
5. Heller L (1950) Condensation by means of air for steam turbines equipped with injection condensers. 4th world power conference, vol 3, Section E3, Paper 7
6. Bakay A, Jaszay T (1978) High performance jet condensers for steam turbines. Paper EC10, Sixth international heat transfer conference, Toronto, pp S. 61–S. 65
7. Heeren H, Holly L (1971) Trockenkühler entlasten Gewässer. Energie 23(10):S. 298–S. 304
8. Othmer DP, Benenati RP, Goulandris GG (1962) Vapor reheat, sea water desalination without metallic heat surfaces. Dechema-Monographien Nr. 47, S. 73–S. 98, Weinheim/Bergstraße

9. Kopp JH (1965) Über den Wärme- und Stoffaustausch bei Mischkondensation. Promotionsarb. ETH Zürich, Julius-Verlag, Zürich
10. Sam RG, Patel BR (1984) An experimental investigation of OC-OTEC direct-contact condensation and evaporation processes. J Solar Energy Eng 106:S. 120–S. 127
11. Minart P Condenseur à mélange, notament pour l'exploitation de l'énerga thermique des mers. EP-Schutzrecht 0 189 029-AI
12. Billet R (1973) Zum Wärme- und Stoffaustausch bei der partiellen Gegenstrom-Direktkondensation. Chem Ing Techn 45(13):S. 887–S. 891
13. Fair JR (1971) Process heat transfer by direct fluid-phase contact. IChE Symp. Series, vol 118(68), pp S. 1–S. 11
14. GEA Wiegand GmbH. Vakuum durch Kondensation. TKI 7, GEA Wiegand GmbH, Einsteinstra ße 9–15, D-76275 Ettlingen, Germany
15. Lee SY, Tankin RS (1984) Study of liquid spray (water) in a condensable environment (steam). Int J Heat Transfer 27(3):S. 363–S. 374
16. Iciek I (1982) The hydrodynamics of a free liquid jet and their influence on direct contact heat transfer. Part I. Int J Multiphase Flow 8(3):S. 239–S. 249
17. Iciek I (1982) The hydrodynamics of a free liquid jet and their influence on direct contact heat transfer. Part 2. Int J Multiphase Flow 8(3):S. 251–S. 260
18. Iciek I (1983) The hydrodynamics of a free liquid jet and their influence on direct contact heat transfer. Part 3. Int J Multiphase Flow 9(2):S. 167–S. 179
19. De Salve M, Panella B, Scorta G (1986) Heat and mass transfer of steam on a subcooled turbulent water jet. Proceeding of the 8th international Heat Transfer, San Francisco, pp S. 1653–S. 1658
20. Benedek S (1976) Heat transfer at the condensation of steam on a turbulent water jet. Int J Heat Mass Transfer 19:S. 448–S. 450
21. Mills AF, Kim S, Leininger T, Ofer S, Pesaran A (1982) Heat and mass transfer in turbulent liquid jets. Int J Heat Mass Transfer 25:S. 889–S. 897
22. Barathan D, Olson DA, Green HJ, Johnson DH (1982) Measured performance of direct contact jet condensers. Solar Energy Research Inst. Golden, Co. (USA), SERI/TP, pp 252–1437
23. Sklover GG, Rodivilin MD (1976) Condensation on water jets with a cross flow of steam. Teploenergetika 23:S. 48–S. 51
24. Isachenko VP, Solodov AP, Samoilovich YuZ, Kushnyrev VI, Sotskov SA (1971) Investigation of heat transfer with steam condensation on turbulent liquid jets. Teploenergetika 18(2):S. 7–S. 10
25. Isachenko VP, Solodov AP (1972) Heat transfer with steam condensation on continuous and on dispersed jets of liquid. Teploenergetika 19(9):S. 24–S. 27
26. Karapansios TD, Karabelas AJ (1995) Direct-contact condensation in the presence of noncondensables over free-falling films with intermittent liquid feed. Int J Heat Mass Transfer 38(5):S. 795–S. 805
27. Isachenko VP, Kushnyrev VI (1974) Condensation heat transfer in dispersed liquid spray. 5. International heat transfer conference, vol 3, Tokio, pp S. 217–S. 225
28. Ford JD, Lekic A (1973) Rate of growth of drops during condensation. Int J Heat Mass Transfer 16:S. 61–S. 64
29. Lekic A, Bajramovic R, Ford JD (1976) Droplet size distribution: an improved method for fitting experimental data. Can J Chem Eng 54(10): S. 399–S. 402
30. Maa JR, Hickman K (1972) Direct condensation of steam on a modified oil coolant. Desalination 10:S. 95–S. 111
31. Lekic A, Ford JD (1980) Direct contact condensation of vapor on a spray of subcooled liquid droplets. Int J Mass Transfer 23:S. 1531–S. 1537
32. Chung JN, Ayyaswamy PS, Sadhal SS (1984) Laminar condensation on a moving drop. Part 1. J Fluid Mech 139:S. 105–S. 131
33. Chung JN, Ayyaswamy PS, Sadhal SS (1984) Laminar condensation on a moving drop. Part 2. J Fluid Mech 139:S. 131–S. 144
34. Ohba K, Nishiguchi A, Kitada H (1982) Direct contact condensation of steam on a high speed spray jet of subcooled water. Technol Rep Kansai Univ 23(3):S. 13–S. 30
35. Hijikata K, Mori Y, Kawaguchi S (1984) Direct contact of vapor to falling cooled droplets. Int J Heat Mass Transfer 27(9):S. 1631–S. 1640
36. Carslaw HS, Jaeger JC (1959) Conduction of heat in solids, 2. Auflage. Clarendon Press, Oxford
37. Schlünder EU (1981) Einführung in die Wärmeübertragung. Skriptum. Braunschweig, Vieweg-Verl
38. Celata GP, Cumo M, D'Annibale F, Farello GE (1991) Direct contact condensation of steam on droplets. Int J Multiphase Flow 17(2): S. 191–S. 211
39. Mason BJ (1957) The physics of clouds. Oxford University Press, Oxford
40. Dahl HD, Muschelknautz E (1994) Zerstäubung mit Hohlkegeldüsen. VDI-Wärmeatlas, Abschnitt Jda, 7. Auflage. VDI-Verl
41. Mayinger F, Chávez A (1992) Measurement of direct-contact condensation of pure saturated vapour on an injection spray by applying pulsed laser holography. Int J Heat Mass Transfer 35(3):S. 691–S. 702
42. Kreyszig E (1968) Statistische Methoden und ihre Anwendungen, 3. Auflage. Vandenhoeck & Ruprecht, Göttingen
43. Mugele RA, Evans HD (1951) Droplet size distribution in sprays. Ind Eng Chem 43(6):S. 1317–S. 1324
44. Dombiowski N, Wolfsolnn DL (1972) The atomization of water by swirl spray pressure nozzles. Trans Inst Chem Eng 50:S. 259–S. 269
45. Taitel Y, Tamir A (1969) Condensation in the presence of a noncondensable gas in direct contact. Int J Heat Mass Transfer 12:S. 1157–S. 1169
46. Hassoa D, Luss D, Peck R (1964) Theoretical analyses of vapor condensation on laminar liquid jets. Int J Heat Transfer 7:S. 969–S. 981
47. Hassoa D, Luss D, Navoa U (1964) An experimental study of steam condensation on a laminar water sheet. Int J Heat Mass Transfer 7: S. 983–S. 1001
48. Schlünder EU (1984) Einführung in die Stoffübertragung. G. Thieme-Verl, Stuttgart, New York
49. Maa JR, Chuang HK (1978) On the design of cooler condenser for mixed vapor contuning uncondensable gas. Lett Heat Mass Transfer 5:S. 379–S. 389
50. Kashiwagi T, Oketani K (1980) Direct contact condensation on cooled fluid jets. Basic Mech. in two-phase flow and heat transfer. Presented at the winter annual meet of ASME, Chicago, vol III, Nov. 16–21, 1980. Publ. by ASME, New York, pp S. 87–S. 94

Radiation

K1 Radiation of Surfaces

Stephan Kabelac[1] · *Dieter Vortmeyer*[2]
[1]Helmut-Schmidt-Universität, Universität der Bundeswehr Hamburg, Hamburg, Germany
[2]Munich, Germany

1 Introduction

All substances, regardless of shape and consistency, emit and absorb radiation energy when their temperature is above absolute zero ($T > 0$ K). For nontransparent opaque bodies, the absorption and emission processes are confined to their surfaces. Thermal radiation energy can be regarded as electromagnetic waves carrying energy and entropy in the wavelength range between 0.1 µm and about 1000 µm (0.1 µm $< \lambda <$ 1000 µm). Because of these emission and absorption processes in all substances (solids, liquids, and gases) around there will be a net transfer of energy between those bodies which face each other and whose surfaces have different temperatures. This net thermal radiation energy is, from a thermodynamic view, a heat flux, as its only driving force is a temperature difference and as it carries entropy. In thermal equilibrium situations, the emission and absorption processes still exist, but the net radiation energy will be zero. The calculation of thermal radiation energy fluxes is derived in this chapter. These radiation fluxes typically appear in addition to convective heat fluxes and thus have to be worked out separately and added to give the overall heat flux. For more introductory literature, see [1–5].

1.1 The Black Body

The black body serves as a baseline for all calculations concerning thermal radiation, because only for this specific body an exact and simple physical description is known. A black body is a hypothetical radiating body, the surface of which absorbs *all* incoming radiation. No reflection or transmission occurs. Because of this the black body of a given temperature T will emit a maximum amount of radiation energy, no other body with the same temperature will emit more radiation in any wavelength interval. This black body radiation shows a characteristic spectral distribution which can be derived from quantum physics [2].

The spectral intensity M_λ^b, i.e., the radiation energy flux within an infinitely small wavelength interval dλ at a wavelength λ emitted from a small surface segment dA of a black body into the surrounding hemisphere is calculated by the formula first derived by Max Planck [6]:

$$M_\lambda^b(\lambda, T) = \frac{c_1}{\lambda^5[\exp(c_2/\lambda \cdot T) - 1]} \tag{1}$$

The constants c_1 and c_2 are not empirical numbers but products of basic nature constants. They result as

$$c_1 = 2\pi h c_0^2 = 3.74177107 \cdot 10^{-16}\,\mathrm{W\,m^2} \text{ and}$$
$$c_2 = h c_0 / k = 14387.75\,\mu\mathrm{m\,K}.$$

If the wavelength λ is introduced in µm, the second version of c_1 must be used and $M_\lambda{}^b$ results in $\mathrm{W{\cdot}m^{-2}{\cdot}\mu m^{-1}}$.

In Fig. 1, the spectral intensity $M_\lambda{}^b$ of a black body is shown as a function of wavelength λ for four different temperatures. The spectral intensity emitted by the surface of any real body having the same temperature T will be lower than the curves shown in Fig. 1.

Integration of Eq. (1) over all wavelengths gives the intensity of the black body

$$M^b = \int_0^\infty M_\lambda^b(\lambda, T)\mathrm{d}\lambda = \sigma \cdot T^4 \tag{2}$$

This equation is called the Stefan–Boltzmann equation, and σ is the Stefan–Boltzmann constant:

$$\sigma = \frac{2\pi^5 k^4}{15\, c_0\, h^3} = 5.67040 \times 10^{-8}(\mathrm{W/m^2\,K^4}).$$

The temperature T in Eqs. (1) and (2) is the thermodynamic temperature of the black body in the vicinity of the emitting body surface, given in Kelvin K with $T\,(\mathrm{K}) = T\,(^\circ\mathrm{C}) + 273.15$ K. For a quick lookup, Table 1 gives values of the intensity of black body radiation as a function of temperature as calculated by Eq. (2).

VDI-GVC (ed.), *VDI Heat Atlas*, DOI 10.1007/978-3-540-77877-6_40,

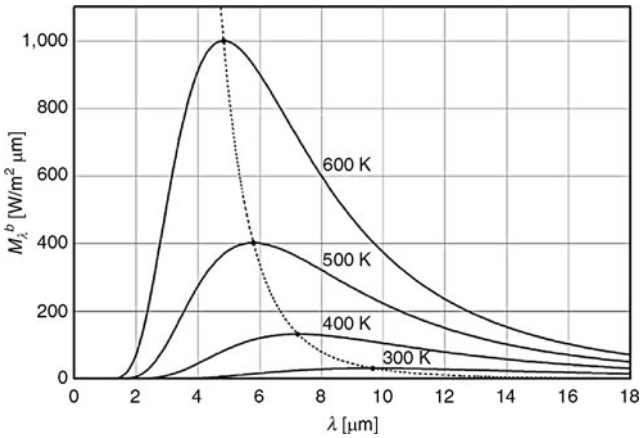

K1. Fig. 1. Spectral intensity M_λ^b of a black body for four different temperatures. The dotted line gives the position of the maximum intensity as calculated by Wien's law.

K1. Table 1. Intensity of black body radiation as a function of temperature and M^b

Temperature T		M^b W/m²
°C	K	
−100	173	50
−50	223	140
0	273	314
50	323	617
100	373	1,097
150	423	1,815
200	473	2,838
250	523	4,242
300	573	6,112
350	623	8,541
400	673	11,631
450	723	15,493
500	773	20,244
550	823	26,012
600	873	32,933
650	923	41,151
700	973	50,819
750	1,023	62,099
800	1,073	75,159
850	1,123	90,178
900	1,173	107,343
950	1,223	126,849
1,000	1,273	148,900
1,050	1,323	173,709
1,100	1,373	201,495
1,150	1,423	232,489
1,200	1,473	266,927
1,250	1,523	305,058
1,300	1,573	347,134

K1. Table 1. (continued)

Temperature T		M^b W/m²
°C	K	
1,350	1,623	393,420
1,400	1,673	444,188
1,450	1,723	499,717
1,500	1,773	560,296
1,550	1,823	626,224
1,600	1,873	697,805
1,650	1,923	775,354
1,700	1,973	859,194
1,750	2,023	949,656
1,800	2,073	1,047,080
1,850	2,123	1,151,815
1,900	2,173	1,264,217
1,950	2,223	1,384,652
2,000	2,273	1,513,494

1.2 Radiation Intensity of Real Bodies

ΔE is the radiation energy flux within the wavelength gap λ and $\lambda + \Delta\lambda$ emitted into the solid angle element $\Delta\Omega$ of an arbitrary body at temperature T as shown in Fig. 2. This radiation flux is composed of radiation of all wavelengths heading in all directions into the hemisphere above the emitting piece of area ΔA. The direction of a ray is represented by an element of solid angle $\Delta\Omega$ given in steradiant (sr), which is calculated from the polar angle β and the azimuth angle φ as $\Delta\Omega = \sin\beta{\cdot}\Delta\beta{\cdot}\Delta\varphi$, see Fig. 2. Thus, for an exact calculation of the radiation flux emitted by the surface area element ΔA of a real body all rays have to be integrated over all wavelengths and solid angles. The energy of one single basic ray is given as a spectral directional intensity L_λ

$$L_\lambda = \frac{\Delta^3 E}{\cos\beta\Delta A\Delta\Omega\Delta\lambda} \tag{3}$$

ΔE is the radiation energy flux within the wavelength gap λ and $\lambda + \Delta\lambda$ emitted into the solid angle element $\Delta\Omega$ per projected area element $\cos\beta{\cdot}\Delta A$. L_λ is typically given in W m^{-2} µm^{-1} sr^{-1}.

Integration of the spectral directional intensity L_λ over all directions of the hemisphere ($0 \le \beta \le 90°$; $0 \le \varphi \le 360°$) as described by the solid angle $\Omega = 2\pi$ results in the spectral intensity $M_\lambda(\lambda, T)$

$$M_\lambda(\lambda, T) = \int_{\Omega} L_\lambda(\lambda, T, \beta, \varphi)\cos\beta \mathrm{d}\Omega \tag{4}$$

One more integration summing up all possible wavelengths ($0 \le \lambda \le \infty$) gives the intensity M

$$M(T) = \int_0^\infty M_\lambda(\lambda, T)\mathrm{d}\lambda \tag{5}$$

If the temperature Tor radiation properties (optical properties) vary along the surface of a real body, each surface element ΔA has to be treated separately, and all surface elements have to be integrated to give the overall radiation emitted by the body under consideration.

When the spectral directional intensity L_λ is first integrated over all wavelengths ($0 \leq \lambda \leq \infty$) the directional intensity L independent of wavelength results

$$L(\beta, \varphi, T) = \int_0^\infty L_\lambda(\lambda, \beta, \varphi, T)\mathrm{d}\lambda \qquad (6)$$

which in turn will give the intensity $M\,(T)$ when integrated over the solid angle $\Omega\ (\beta, \varphi)$. $M\,(T)$ is the integral value giving the overall radiation energy flux emitted by a surface element of a real body in W/m^2. The spectral directional intensity L_λ will be conserved along its line of traveling as long as no scattering or absorption of molecules or particles takes place. Thus, an energy balance equation for radiation, the radiative transport Eq. (7), uses the spectral directional intensity L_λ as the base value. In technical radiative heat transfer calculations usually only spectral intensities M_λ or overall intensities M are considered, very few calculations take into account a directional dependence of radiation fluxes. This is allowed as most real bodies do not show a strong dependency of emitted radiation on the solid angle. Figure 3 gives the directional dependence of emissivity of some nonconducting materials as a function of the polar angle β. The emissivity ε is explained in Eq. (7). Electric conductors such as metals show a different behavior on behalf of solid angles as demonstrated in Fig. 4. They typically have a low emissivity for all polar angles except low polar angles close to the normal direction.

Surfaces which show no or negligible dependence of radiation intensities in a direction are called diffusive radiators or diffusive surfaces. For a diffusive surface, integration over the solid angle according to Eq. (4) gives

$$M_\lambda(\lambda, T) = \pi \cdot L_\lambda(\lambda, T)$$

for the spectral intensity, or

$$M(T) = \pi \cdot L(T)$$

for the overall intensity. The radiation energy flux emitted from a diffuse surface element $\Delta\Omega$ seen in a polar angle β reads

$$\Delta^2 E = L(T) \cdot \cos\beta \Delta A \Delta\Omega.$$

This relation is called the Lambert's cosine law, and it is used for the definition of a diffuse surface. The black body is a diffuse radiator.

The spectral distribution of radiation emitted by real bodies is complicated and cannot be cast into simple mathematical formulas. This spectral distribution depends on the atomic structure of the surface region of the body, it is something like a fingerprint of each individual substance, it can be calculated in principle on the basis of electromagnetic theory if the complex refractive index of the substance forming the uppermost molecular layer of the radiating body under consideration is known and if the exact topology of the surface is known [7, 8]. So the radiative emission of real bodies is tied to the emission of the black body by empirical correlations. The directional spectral degree of emission

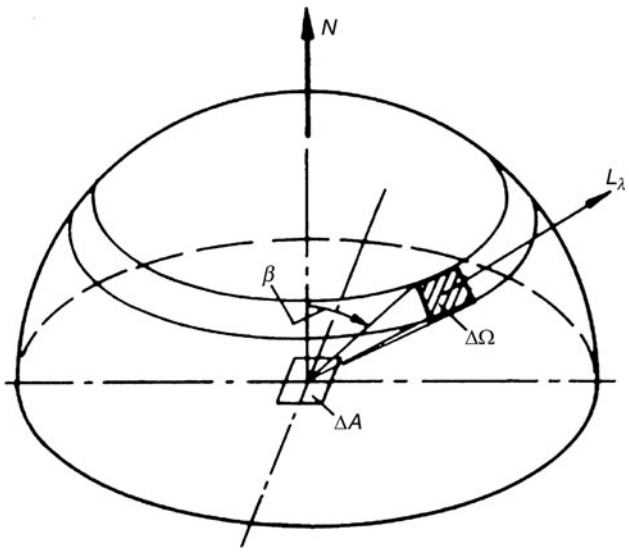

K1. Fig. 2. Radiation of a surface element ΔA.

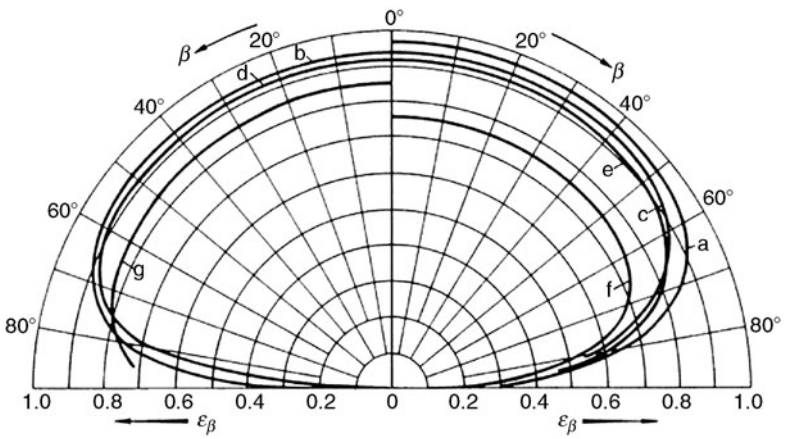

K1. Fig. 3. Directional emissivity of some nonconducting materials [3]: (*a*) ice, (*b*) wood, (*c*) glass, (d) paper, (e) clay, (f) copper oxide, (g) rough corundum.

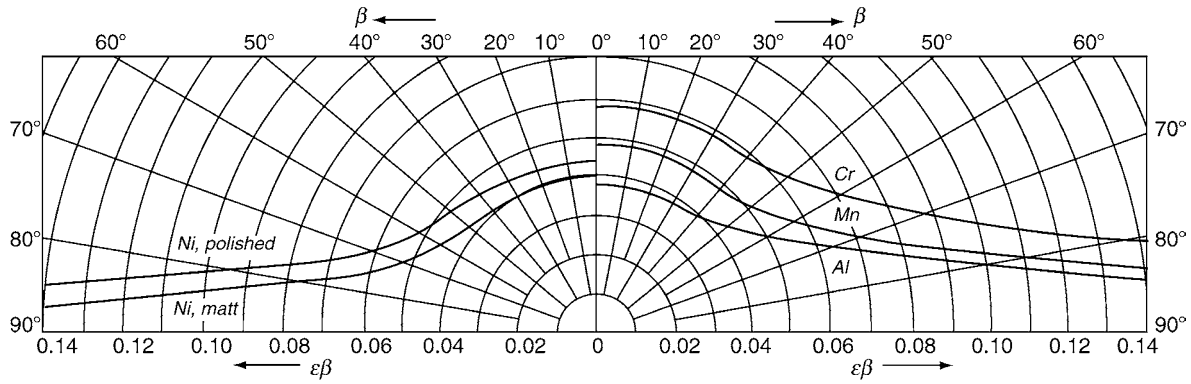

K1. Fig. 4. Directional emissivity of some metals with polished surfaces [3].

$$\varepsilon'_\lambda(\lambda, T, \beta, \varphi) := \frac{L_\lambda(\lambda, T, \beta, \varphi)}{L^b_\lambda(\lambda, T)} \tag{7}$$

gives the directional and spectral distribution of the radiation emitted by a real body as compared to the spectral intensity $L^b_\lambda = M^b_\lambda/\pi$ of a black body having exactly the same temperature as the real body. In the same manner

a hemispherical spectral degree of emission

$$\varepsilon_\lambda(\lambda, T) := \frac{M_\lambda(\lambda, T)}{M^b_\lambda(\lambda, T)} = \frac{1}{\pi}\int \varepsilon'_\lambda(\lambda, T, \beta, \varphi)\cos\beta \mathrm{d}\Omega$$

and a directional spectral degree of emission

$$\varepsilon'_\lambda(T, \beta, \varphi) := \frac{L(T, \beta, \varphi)}{L^b(T)} = \frac{\pi}{\sigma T^4}\cdot L(T, \beta, \varphi)$$

can be defined. All these degrees of emissivity have values between zero and one, $0 < \varepsilon_\lambda \leq 1$. As wavelength- and/or direction-dependent calculations are still too involved for most heat transfer calculations, the overall hemispherical degree of emission is defined as

$$\varepsilon(T) := \frac{M(\lambda, T)}{M^b(\lambda, T)} = \frac{M(\lambda, T)}{\sigma \cdot T^4}, \tag{8}$$

which is the ratio of the intensity emitted by the real body at a temperature T and the intensity of the black body at the same temperature T. If the degree of emission ε for a real body at temperature T is known, the intensity of the radiation of this body is calculated by

$$M(T) = \varepsilon(T)\cdot M^b(T) = \varepsilon(T)\cdot\sigma\cdot T^4 = \int_0^\infty \varepsilon_\lambda(\lambda, T) M^b_\lambda(\lambda, T)\mathrm{d}\lambda. \tag{9}$$

Table 1 can be used here to find values for the black body intensity $M^b(T)$. A body which is not black but which has a constant spectral degree of emission $\varepsilon_\lambda = \text{const.} = \varepsilon \leq 1$ is called a gray body. Typically, the Lambert's cosine law is additionally assumed to be valid for gray bodies. Figure 5 shows the spectral intensity M_λ ($T = 473$ K) for a black, a gray, and a real body.

Table 2 gives the hemispherical degree of emission $\varepsilon(T)$ for different materials. In some cases, the directional degree of

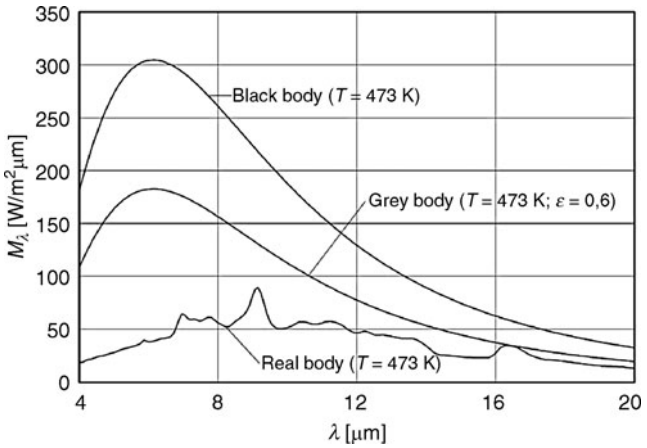

K1. Fig. 5. The spectral intensity M_λ for a black body, a gray body $\varepsilon = 0.6$, and some arbitrary body, each at $T = 473$ K.

emission $\varepsilon_n = \varepsilon'$ ($\beta = 0°$) for a direction normal to the surface is given. The approximate conversion of ε_n into ε is shown in Fig. 6, which depicts the ratio of these two values for metals (curve b) and nonconducting materials (curve a). Note that emissivities are very sensitive to different surface finishings, so you may find for some materials values for ε which deviate from the values given in Table 2. More degrees of emissivity can be found in the literature [9–13].

Other parameters which characterize the optical properties of a material are the degree of absorption a, the degree of reflection r, and the degree of transmission τ. These parameters are *not* connected to the black body characteristics but are ratios based on the overall incoming radiation energy flux E. The overall incoming radiation flux E is the area-specific radiation impinging on a surface, integrated over all directions (i.e., the hemisphere) and all wavelengths. According to the hemispherical spectral intensity M_λ, we can introduce a spectral incoming radiation flux, also called radiosity, E_λ, so that

$$E = \int_0^\infty E_\lambda(\lambda)\mathrm{d}\lambda.$$

Contrary to black bodies, real bodies will not absorb all incoming radiation. Some radiation will be reflected, some may go

K1. Table 2. Degrees of emissions ε or directional degrees of emission ε_n ($\beta = 0°$) for some materials as a function of temperature T

Material	T (K)	ε_n	ε
Metals			
Aluminum, rolled	443	0.039	0.049
	773	0.05	
Highly polished	500	0.039	
	850	0.057	
Polished	373	0.095	
Roughly polished	373	0.18	
Oxidized at T = 872 K	472	0.11	
	872	0.19	
Strongly oxidized	366	0.2	
	777	0.31	
Lead, gray oxidized	297	0.28	
Not oxidized	400	0.057	
	500	0.075	
Oxidized at T = 422 K	472	0.63	
Bronze, 4–7% Al			
Polished	422	0.03	
	1,089	0.052	
Oxidized	422	0.08	
	1,089	0.144	
Chrome, polished	423	0.058	0.071
	1,089	0.36	
Cobalt, polished	422	0.1	
	1,089	0.225	
Oxidized	589	0.15	
	1,089	0.3	
Gold, highly polished	500	0.018	
	900	0.035	
Copper, polished	293	0.03	
Slightly turned	293	0.037	
Strongly black oxidized	293	0.78	
Oxidized	403	0.76	
Rubbed to a fine degree	293	0.07	
Inconel, rolled	1,089		0.69
Sand blasted	1,089		0.79
Iron and steel			
Highly polished	450		0.052
	500		0.064
Polished	700		0.144
	1,300		0.377
Rubbed with sandpaper	293		0.242
Cast-iron, polished	473		0.21
Caste steel, polished	1,044		0.52
	1,311		0.56
Iron, roughly polished	373		0.17
Oxidized surfaces:			
Iron sheet metal, rusty	293		0.612
Strong rusty	292		0.685
From rolling	294		0.657
Cast iron, oxidized at 866 K	472		0.64
	872		0.78
Steel, oxidized at T = 866 K	472		0.79
	872		0.79
Steel sheet with a strong			
Layer of oxide	297		0.8
Cast iron with a rough surface			
Strongly oxidized	311–512		0.95
Geschmolzene Oberflächen:			
Cast iron, molten	1,572	0.29	
Pure iron, molten	1,789	0.42	
	2,044	0.45	
Steel, 0.25–1.2% C			
Lightly oxidized	1,833	0.27	
Molten	1,983	0.39	
Magnesium, polished	311	0.07	
	811	0.18	
Brass, not oxidized	298	0.035	
	373	0.035	
Oxidized	473	0.61	
	873	0.59	
Molybdenum	1,000	0.096	
	2,866	0.292	
	373		0.071
	1,673		0.17
Nickel, not oxidized	298		0.045
	373		0.06
Oxidized	473		0.37
	873		0.478
Niob, not oxidized	1,089		0.19
	1,366		0.24
Palladium	422	0.026	
	1,089	0.094	
Platinum	422	0.022	
	1,089	0.123	
Mercury, not oxidized	298	0.1	
	373	0.12	
Rhodium, polished	422	0.012	
	1,089	0.068	
Silver, polished	311	0.022	
	644	0.031	
Tantalum, polished	422	0.03	
	1,089	0.07	
Oxidized	422	0.42	
	1,089	0.42	
Titanium, oxidized	644		0.54

K1. Table 2. (continued)

Material	T (K)	ε_n	ε
	1,089		0.59
Bismuth, shiny	353	0.34	0.366
Tungsten	298		0.024
	773		0.071
	1,273		0.15
	1,773		0.23
Zinc, pure, polished	500	0.045	
	600	0.055	
Iron sheet with zinc surface			
Shiny	301	0.228	
Gray oxidized	297	0.276	
Tin, not oxidized	298		0.043
	373		0.05
Iron, tin covered, shiny	297		0.06
Non Metals			
Aluminum oxide	366		0.9
	673		0.76
	1,073		0.623
	1,600		0.4
Asbestos, cartonnage	296	0.96	
Paper	311	0.93	
	644	0.94	
Asphalt	300		0.93
Concrete, rough	273–366		0.94
Roofing felt	294	0.91	
Plaster (gypsum)	293	0.8–0.9	
Glass	293	0.94	
Quartz glass (7 mm thickness)	555	0.93	
	1,111	0.47	
Rubber	293	0.92	
Wood, oak plane ironed	273–366		0.9
Beech	343		0.91
Carbon black, non oxidized	298		0.81
	773		0.79
Carbon fibers	533		0.95
Graphite fibers	373		0.76
	773		0.71
Corundum, rough sand	353	0.85	0.84
Lacquers, paints			
Oil-based paint, black	366		0.92
Green	366		0.95
Red	366		0.97
White	366		0.94
Lacquer, white	373	0.925	
Matte black	353	0.97	
Bakelite lacquer	353	0.935	
Mennig paint	373	0.93	
Radiator surface paint	373	0.925	
Enamel, white or iron	292	0.897	
Magnesium oxide	550	0.55	
	1,100	0.2	
Marble, gray, polished	273–366		0.9
Paper	273		0.92
	366		0.94
Porcelain (china clay), white	295		0.924
Fire brick (quartz)	473		0.84
	1,073		0.56
	1,673		0.47
Silicon oxide	473		0.82
	1,073		0.52
	1,473		0.39
Thorium oxide	716	0.58	
	1,100	0.21	
Clay, glazed	298		0.9
Matte	298		0.93
Uranium oxide	1,300		0.79
	1,600		0.78
Water	273	0.95	
	373	0.96	
Ice, smooth with water	273	0.966	0.92
Rough, frosted	273	0.985	
Snow	273		0.8
Clay brick, red	273–366		0.93

This table shows measured values. Most values have been measured in normal direction to the surface, so ε_n is given. This value can be converted to a hemispherical value ε by using Fig. 6. More values are given in [9–13]

through the body (transmission), and only the rest will be absorbed and converted into internal energy of the body.

The overall hemispherical degree of absorption

$$a(T) = \frac{1}{E}\int_0^\infty a_\lambda(\lambda, T)E_\lambda(\lambda)\mathrm{d}\lambda$$

gives the part of the incoming radiation which is absorbed by the body when $a_\lambda(T, \lambda)$ is the spectral degree of absorption and $a(T)$ is the overall degree of absorption. The spectral as well as the overall degrees of absorption attain a value of one for the black body, for real bodies they are between zero and one. A directional spectral degree of absorption $a'_\lambda(\lambda, T, \beta, \varphi)$ could also be introduced. According to the first and second laws of thermodynamics, the directional spectral degree of absorption has to be equal to the directional spectral degree of emission [14]

$$a'_\lambda(\lambda, T, \beta, \varphi) = \varepsilon'_\lambda(\lambda, T, \beta, \varphi) \qquad (10)$$

for any body of temperature T. Equation (10) is known as the law of Kirchhoff, and it gives a powerful tool to calculate the degrees of absorption from the measured degrees of emission.

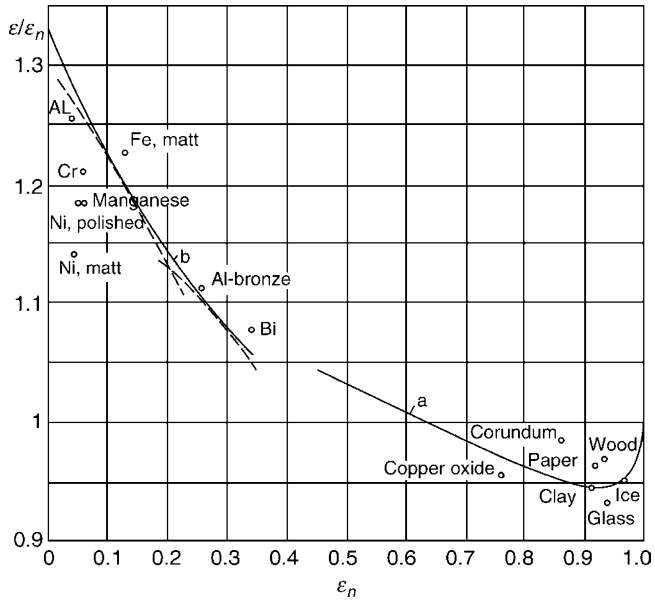

K1. Fig. 6. The overall degree of emission ε shown as a function of ε_n for the same material. Curve (a) is for nonconducting materials and curve (b) for metals.

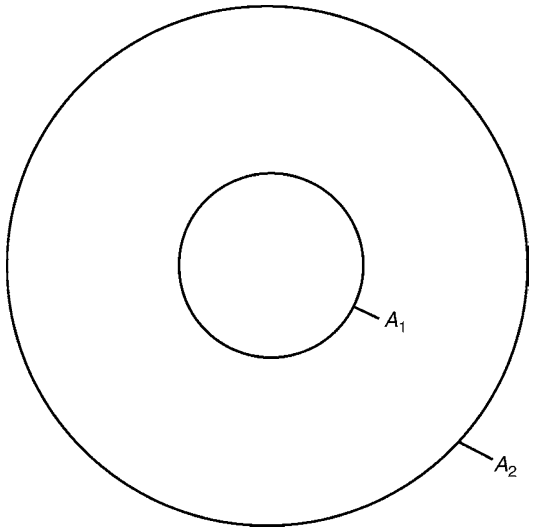

K1. Fig. 7. Two concentric pipes 1 and 2.

If the real body behaves like a diffuse radiator according to Lambert's law, Eq. (10) can be extended to spectral hemispherical quantities $a_\lambda = \varepsilon_\lambda$. If the body is a gray body, Eq. (10) finally gives $a(T) = \varepsilon(T)$.

Another optical property is the degree of reflection r. The hemispherical degree of reflection is defined as

$$r(T) = \frac{1}{E}\int_0^\infty r_\lambda(\lambda, T)E_\lambda(\lambda)\mathrm{d}\lambda r_\lambda$$

as the reflected part of the incoming radiation energy flux E impinging onto a surface. $r_\lambda(T, \lambda)$ is the spectral degree of reflection. The directional spectral degree of reflection r_λ' $(T, \lambda, \beta, \varphi)$ can be measured using an ellipsometer [3].

Finally, the spectral degree of transmission τ_λ is introduced which gives the fraction of the incoming specific spectral radiation energy E_λ which passes through a body. An energy balance equation for an irradiated body gives the important relation

$$a_\lambda(\lambda, T) + r_\lambda(\lambda, T) + \tau_\lambda(\lambda, T) = 1.$$

Extensive tables that include these optical properties for many different material are, for e.g., shown in [9].

2 Radiation Heat Transfer Between Surfaces

2.1 Simple Cases

If two parallel surfaces 1 and 2 of equal size, each having black body characteristics (thus they are called black surfaces) but different temperatures, face each other, the net thermal energy transferred from the hotter surface to the colder surface is

$$\dot{Q}_{12} = \sigma A\left(T_1^4 - T_2^4\right). \tag{11}$$

For Eq. (11) to be valid the linear extension of the surfaces has to be much larger than the distance between them, also the space between the plates must be free of any participating media. If these surfaces are gray surfaces having emissivities ε_1 and ε_2, the radiation transfer between the plates becomes more complicated. This is because of the reflection which comes into play and which has to be considered by ray tracing. The equation for the net heat transfer between the gray plates now becomes

$$\dot{Q}_{12} = C_{12}A\left(T_1^4 - T_2^4\right). \tag{12}$$

in W, where the radiation exchange factor [5]

$$C_{12} = \frac{\sigma}{\frac{1}{\varepsilon_1} + \frac{1}{\varepsilon_2} - 1} \tag{13}$$

shows the influence of geometry and emissivities. Equation (13) is valid for parallel plates only. The temperatures in Eqs. (11) and (12) are absolute temperatures in Kelvin, as in all equations regarding radiation energy transfer.

Another special geometric case is the concentric pipe situation shown in Fig. 7. The cylinders are supposed to be gray bodies again, now the radiation exchange factor is

$$C_{12} = \frac{\sigma}{\frac{1}{\varepsilon_1} + \frac{A_1}{A_2}\left(\frac{1}{\varepsilon_2} - 1\right)}. \tag{14}$$

For the calculation of the net heat flux $\dot{Q}_{12}$ from body 1 to body 2, the surface area A has to be used in Eq. (12).

Two special cases can be derived from Eq. (14). If $A_1 << A_2$, as in the case of a pipe within a big room (which does not have to be cylindrical any more), the radiation exchange factor reduces to $C_{12} = \varepsilon_1\sigma$. If on the other side, $A_1 \approx A_2$, i.e., the pipe surfaces are close to each other, the radiation exchange factor turns into the parallel plate case, Eq. (13):

$$C_{12} = \frac{\sigma}{\frac{1}{\varepsilon_1} + \frac{1}{\varepsilon_2} - 1}$$

2.2 View Factors

The two radiation heat transfer cases treated in the foregoing section were special cases in which all radiation emitted from object 1 reached object 2. In a standard thermal radiation situation with arbitrary sized and oriented surfaces A_1 and A_2, only a fraction of the radiation emitted by A_1 actually hits A_2, and vice versa only a different fraction of all radiation emitted by A_2 reaches A_1. This fraction of radiation departing from a body i of area A_i reaching the surface of another body k with the surface area A_k, divided by all the radiation emitted by surface i, is called view factor φ_{ik}

$$\varphi_{ik} = \frac{\text{radiation energy from surface } i \text{ reaching surface } k}{\text{all radiation emitted by surface } i}.$$

The view factor φ_{ik} is a purely geometrical value, and it is defined as

$$\varphi_{21} = \frac{1}{\pi A_1} \int_{A_1} \int_{A_2} \frac{\cos\beta_1 \cos\beta_2}{s^2} \mathrm{d}A_1 \, \mathrm{d}A_2.$$

This equation is further explained in Chap. K2, which is dedicated to view factors of many different geometrical situations. The net radiation energy exchanged between two black surfaces A_1 and A_2, which is equal to the net heat flux, is calculated as the difference of the absolute radiation energies to and from these surfaces

$$\dot{Q}_{12} = \varphi_{12} \, A_1 \sigma T_1^4 - \varphi_{21} \, A_2 \sigma T_2^4. \tag{15}$$

In case of thermal equilibrium $T_1 = T_2$, the resulting net energy exchange must be zero. Thus, we have

$$\varphi_{21} = \frac{A_1}{A_2} \varphi_{12}. \tag{16}$$

Using this relation, Eq. (15) can be written as

$$\dot{Q}_{12} = \varphi_{12} \, A_1 \sigma \left(T_1^4 - T_2^4\right). \tag{17a}$$

For gray surfaces part of the radiation reaching A_2 will be reflected back to A_1. For this situation ray tracing methods have to be applied. Only for gray surfaces having degrees of emissivity ε_1 and ε_2 a simple solution can be gained by infinite series methods which reads

$$\dot{Q}_{12} = \frac{\sigma \varepsilon_1 \varepsilon_2 A_1 \varphi_{12}}{1 - (1 - \varepsilon_1)(1 - \varepsilon_2)\varphi_{12}\varphi_{21}} \left(T_1^4 - T_2^4\right). \tag{17b}$$

One of the main problems in radiation heat transfer calculation is getting the appropriate view factors. As these are of purely geometrical nature, these view factors are tabulated for many technical situations. Some of these are given in Chap. K2. Before these are introduced some important rules for handling the view factors are given.

(a) *Reciprocal relation*: As shown earlier, we have

$$A_i \varphi_{ik} = A_k \varphi_{ki} \tag{18}$$

for all situations, this is known as the reciprocal relation.

(b) *Extended reciprocal relation*: This extension of Eq. (18) refers to Fig. 8, and it is valid for surfaces which are parallel to each other or which have a common border line

$$A_1 \varphi_{14} = A_2 \varphi_{23} = A_3 \varphi_{32} = A_4 \varphi_{41}. \tag{19}$$

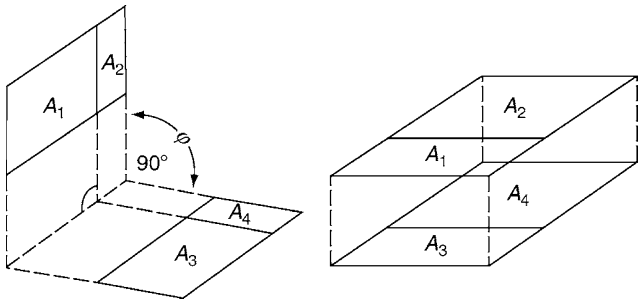

K1. Fig. 8 Extended reciprocal relation.

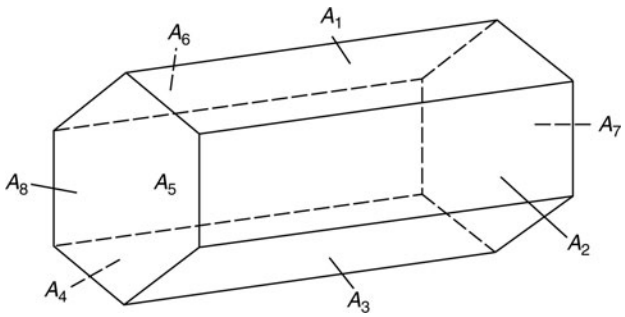

K1. Fig. 9. Summarizing relation.

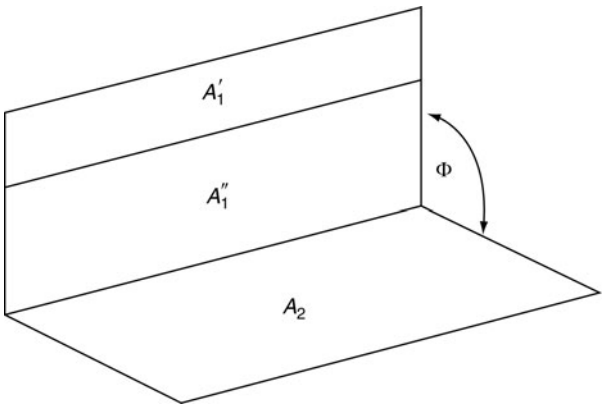

K1. Fig. 10. Splitting relation.

(c) Summarizing relation: If the hemisphere which is seen by surface i is completely surrounded by other surfaces k, all the radiation leaving surface i hit one of these other surrounding surfaces. The energy conservation equation then gives the summarizing relation

$$\sum_{k=1}^{n} \varphi_{ik} = 1. \tag{20}$$

which is shown in Fig. 9. Considering, for example, surface $i = 1$, the summarizing relation reads

$$\varphi_{12} + \varphi_{13} + \varphi_{14} + \varphi_{15} + \varphi_{16} + \varphi_{17} + \varphi_{18} = 1.$$

If a surface has a curvature it may happen that part of this surface can see itself. This would be true for a convex-shaped surface like the inner side of a bowl. In this situation,

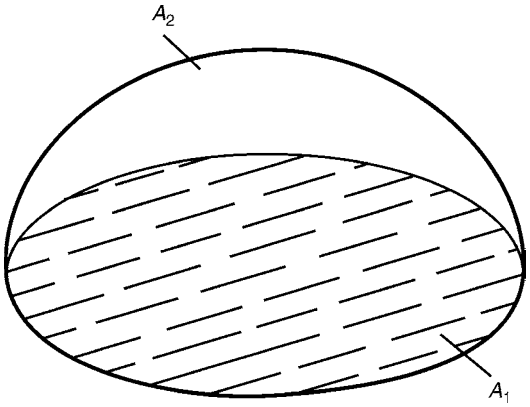

K1. Fig. 11. Surfaces considered in example 1.

it has its own view factor $\varphi_{ii} > 0$. A plane surface or a concave surface always has a view factor $\varphi_{ii} = 0$.

(d) *Splitting relation*: For a situation shown in Fig. 10, we have

$$A_1 = A_1' + A_1''.$$

Then the reciprocal relation, Eq. (18), gives

$$A_1\varphi_{12} = A_1'\varphi_{12}' + A_1''\varphi_{12}'' \tag{21}$$

for all angles Φ

Example 1

A volume is surrounded by a hemisphere and a circular plane as shown in Fig. 11. The view factors for these two surfaces are calculated as

$$\varphi_{11} = 0; \qquad \varphi_{12} = 1$$

$$\varphi_{21} = \frac{A_1}{A_2}\,(\text{reciprocal relation})$$

and

$$\varphi_{22} = 1 - \frac{A_1}{A_2}\,(\text{summarizing relation})$$

3 Radiation Heat Transfer Between Two or More Surfaces

3.1 Enclosure Method

In general, calculation of radiative heat transfer is extremely involved as for one surface the net radiation energy from *all* the surrounding environment in the view of this surface has to be considered a function of wavelength and solid angle. One big step to simplify such calculations is adopting the merits of a gray surface for all surfaces under consideration, so Lambert's cosine law accounts for the directional dependence and the black body spectrum, downscaled by the constant degree of emission ε, accounts for the simplified spectral behavior of each surface. The other problem, the interaction of a surface under consideration with all the surrounding surfaces in visual contact with this specific surface, can only be simplified if two surfaces have temperatures higher than the temperature of the other surfaces. Only then the Eqs. (17b) or (14) of the foregoing Sect. 2 can be applied to calculate the net radiative heat flux of a surface. If other surfaces have also to be considered, the enclosure method is recommended [3, 5].

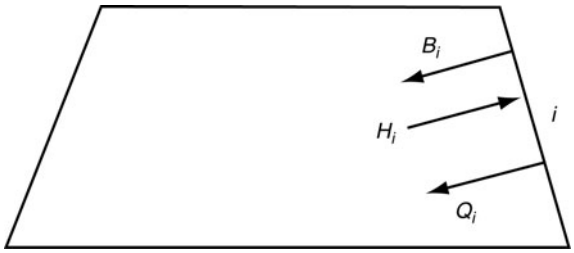

K1. Fig. 12. The definition of some new variables needed for the enclosure method.

According to Fig. 12, some definitions have to be introduced here beforehand:

H_i sum of all radiation fluxes approaching a surface i (incoming radiation, brightness) in W/m^2

B_i sum of all radiation fluxes leaving a surface i (outgoing radiation) in W/m^2, which is the reflected part $(1 - a_i) \cdot H_i$ plus the own emission E_i. Transmission is not considered.

$\dot{Q}_i^c$ conductive or convective thermal heat flux to or from surface i in W.

With these definitions and an equation for energy conservation of surface I we get a set of n algebraic equations to solve the radiative exchange between these n surfaces forming the enclosure:

$$H_i = \sum_{k=1}^{n} B_k\varphi_{ki} \tag{22}$$

$$B_i = E_i + (1 - \varepsilon_i)\sum_{k=1}^{n} B_k\varphi_{ki} \tag{23}$$

$$Q_i^c = (B_i - H_i) \cdot A_i \text{ for } \varepsilon_i \leq 1 \tag{24}$$

$$Q_i^c = \frac{A_i}{1 - \varepsilon_i}(E_i - \varepsilon_i B_i) \text{ for } \varepsilon_i < 1. \tag{25}$$

These equations hold true for the stationary case when all surfaces of the enclosure are assumed to be gray surfaces and no volumetric gas radiation is considered within the enclosure. For adiabatic surfaces within the enclosure we have

$$\dot{Q}_i = O \text{ and } H_i = B_i. \tag{26}$$

Example 2

In this example the radiative net energy flux between the two parallel planes A_1 and A_2 (see Fig. 13) is to be calculated using the enclosure method. The influence of the side surfaces A_3 and A_4 is to be neglected. The area $A_1 = A_2 = A$, the emissivities ε_1 and ε_2 as well as the temperatures T_1 and T_2 are given. Thus, we have for the view factors

$$\varphi_{11} = \varphi_{22} = 0 \text{ and } \varphi_{12} = \varphi_{21} \simeq 1 \text{ and}$$
$$\varphi_{13} = \varphi_{23} = \varphi_{14} = \varphi_{24} \simeq 0$$

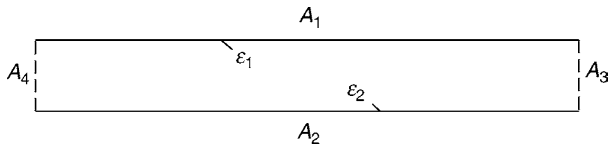

K1. Fig. 13. Radiative heat exchange between two parallel plates addressed in example 2.

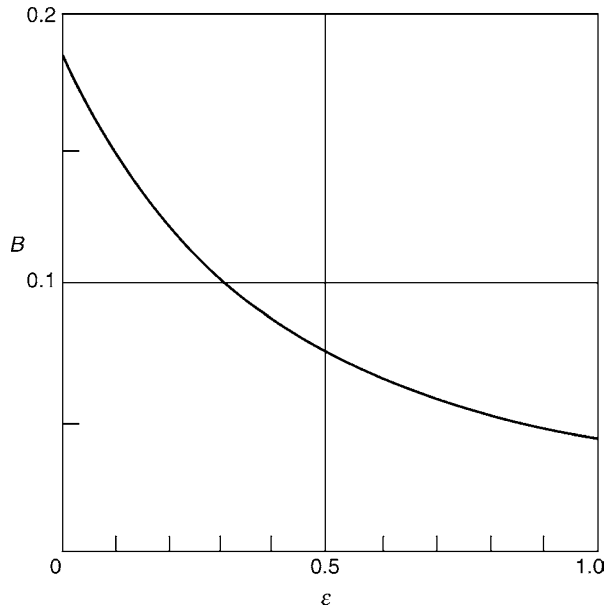

K1. Fig. 14. The radiation transmission factor in Eq. (28) as a function of particle emissivity ε [18].

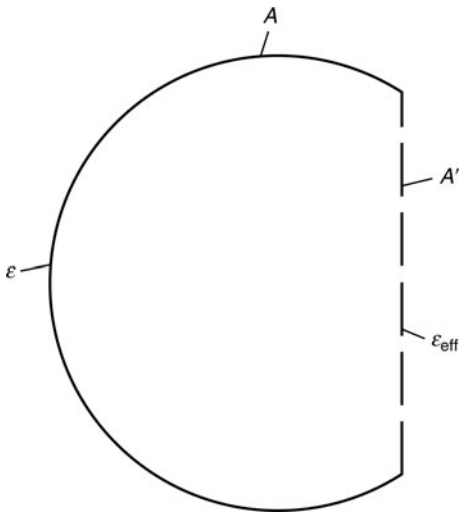

K1. Fig. 15. Effective emissivity of a hollow sphere.

Equation (23) gives

$$B_1 = E_1 + (1-\varepsilon_1)\cdot B_2 \cdot \varphi_{21} \text{ and } B_2 = E_2 + (1-\varepsilon_2)\cdot B_1 \cdot \varphi_{12}.$$

This gives the overall outgoing emission B_1 and B_2 of each surface:

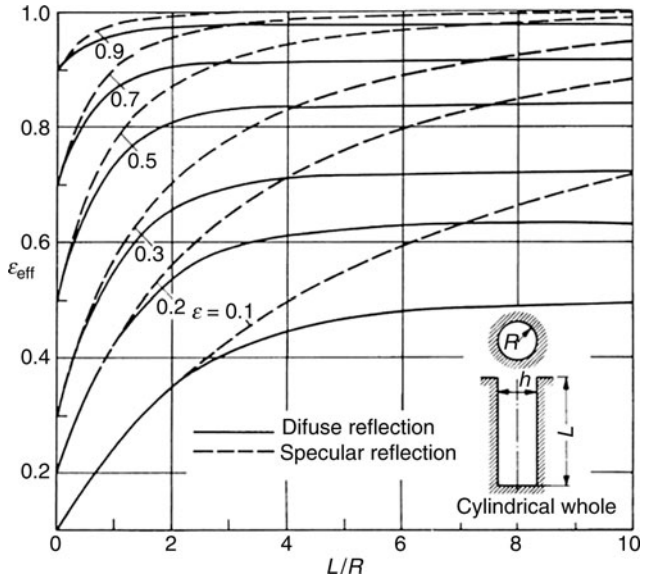

K1. Fig. 16. Effective degree of emission for cylindrical holes as a function of the aspect ratio L/R and the degree of emission of the wall [17].

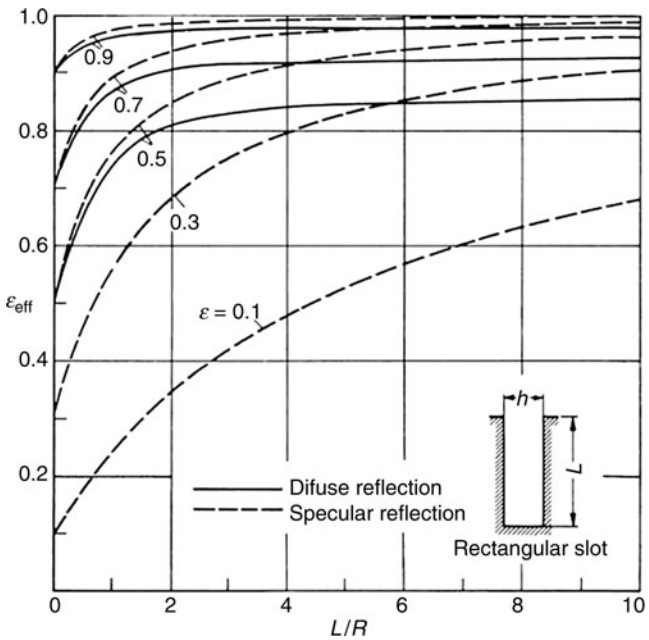

K1. Fig. 17. Effective degree of emission for rectangular cavities as a function of the aspect ratio L/h and the degree of emission of the wall [17].

$$B_1 = \frac{E_1 + (1-\varepsilon_1)\cdot E_2}{\varepsilon_1 + \varepsilon_2 - \varepsilon_1\varepsilon_2} \quad \text{and} \quad B_2 = \frac{E_2 + (1-\varepsilon_2)\cdot E_1}{\varepsilon_1 + \varepsilon_2 - \varepsilon_1\varepsilon_2}$$

The net heat flux Q_i^c for surface 1 for example results from Eqs. (24) and (22)

$$\dot{Q}_1 = (B_1 - H_1)A_1 = (B_1 - B_2)A_1 = \frac{\varepsilon_2 E_1 - \varepsilon_1 E_2}{\varepsilon_1 + \varepsilon_2 - \varepsilon_1\varepsilon_2} A_1 \text{ or}$$

$$\dot{Q}_1 = \frac{\sigma A_1}{\frac{1}{\varepsilon_1} + \frac{1}{\varepsilon_2} - 1}\left(T_1^4 - T_2^4\right)$$

In this special case having parallel plates the result is the same as given by Eq. (12), even though Q_i^c and Q_{12} have different definitions.

3.2 Radiation Heat Transfer in Packed Beds

At elevated temperatures radiation heat transfer between the particles of a packed bed becomes important, especially if other heat transfer modes such as conduction and convection are low. Typically, if the particle diameter d is much larger than wavelength λ, $d >> \lambda$, a packed bed behaves like an optical dense material where the mean free length of a photon is in the order of a particle diameter. As Vortmeyer [15] has shown the radiative heat transfer may then be calculated by Fourier's law of heat conduction, using an effective radiation conductivity λ_s:

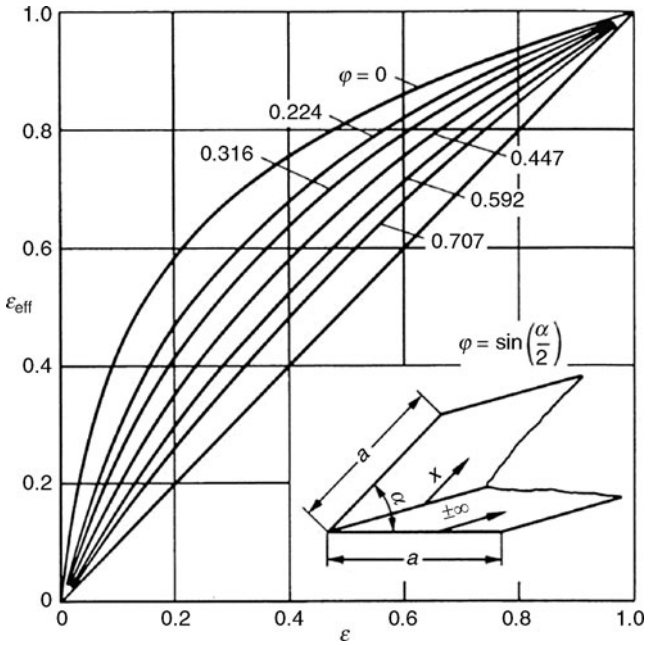

K1. Fig. 18. Effective emissivity for a wedge-type cavity of infinite length as a function of wall emissivity [19].

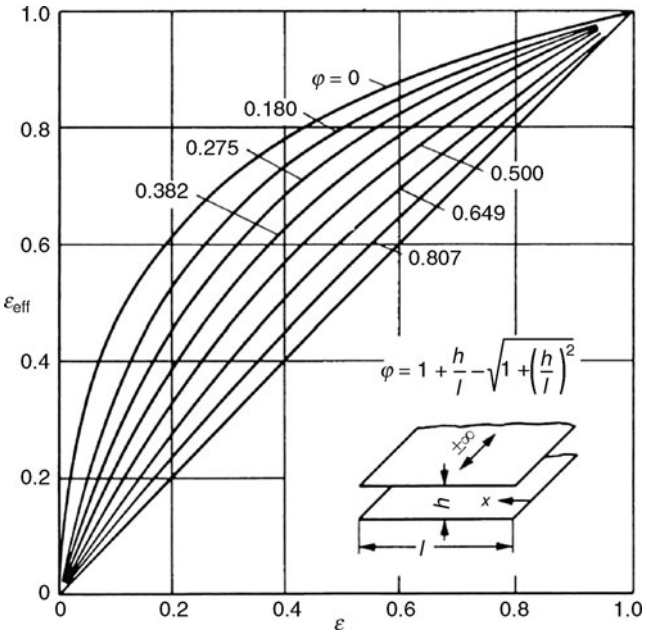

K1. Fig. 20. Effective degree of emission for a parallel wall cavity of infinite length [19].

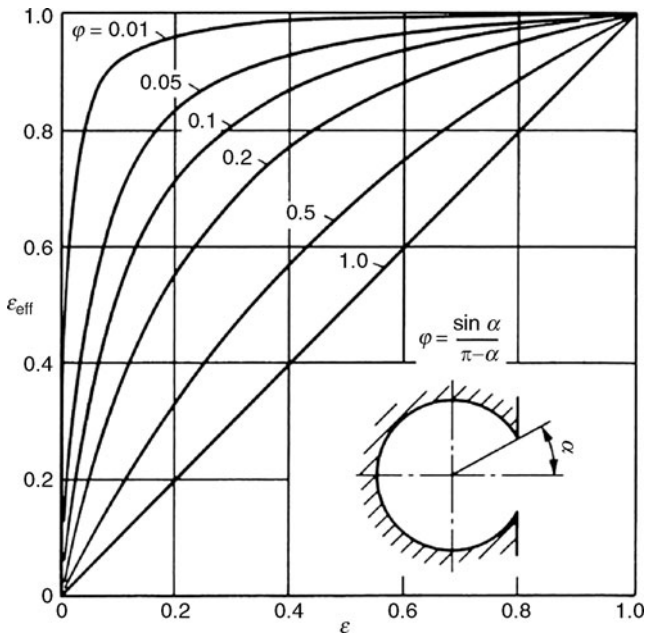

K1. Fig. 19. Effective degree of emission for a cylindrical shaped cavity of infinite length [19].

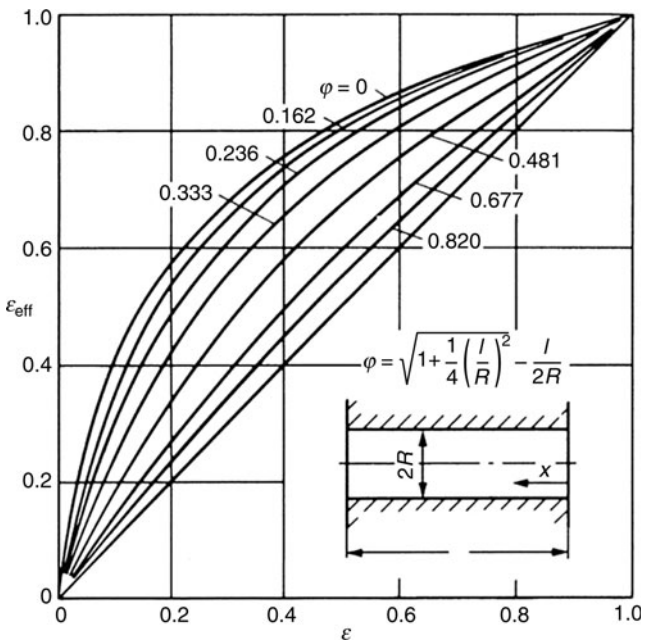

K1. Fig. 21. Effective degree of emission for a cylindrical hole with two open ends [19].

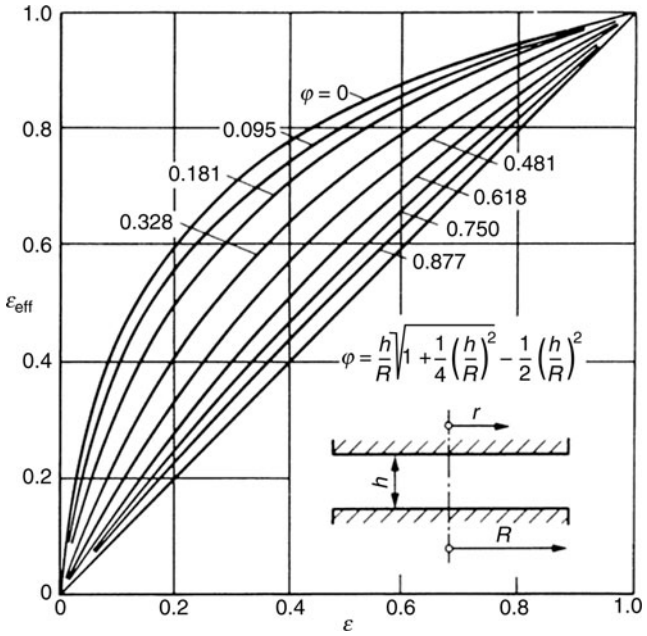

K1. Fig. 22. Effective degree of emission for parallel circle-shaped planes [19].

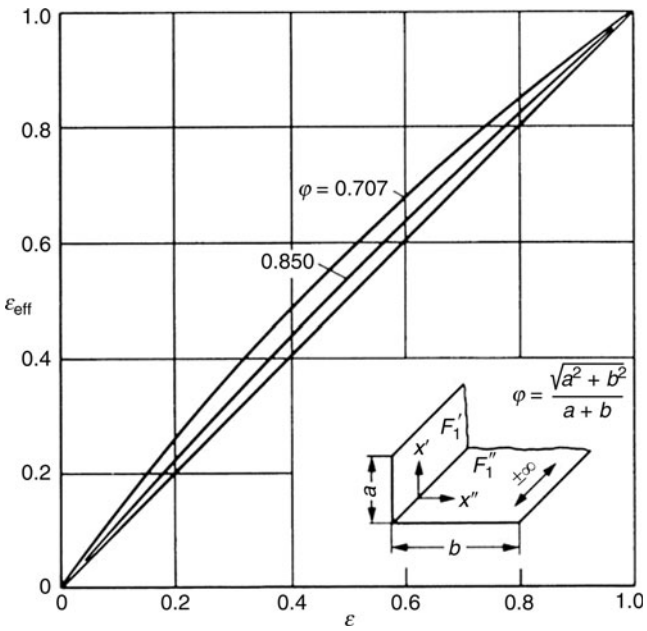

K1. Fig. 23. Effective degree of emission for an edge with perpendicular walls and infinite length [19].

The area specific heat flux $\dot{q}$ in W/m^2 reads

$$\dot{q} = -\lambda_s \cdot \frac{\mathrm{d}T}{\mathrm{d}x}, \tag{27}$$

were x is the coordinate along the main axis of the packed bed. The radiation conductivity λ_s is calculated by

$$\lambda_s = \frac{2B + \varepsilon(1 - B)}{2(1 - B) - \varepsilon(1 - B)} \sigma 4T^3 d, \text{ in W/(m K)}. \tag{28}$$

In Eq. (28) we have

ε emissivity of a particle within the packed bed
B radiation transmission factor (see Fig. 14)
d mean particle diameter
σ Stefan–Boltzmann constant, see Eq. (2).

The radiation transmission factor B actually also depends on the porosity of the packed bed. For the dependency on the particle degree of emission ε shown in Fig. 14 a mean porosity of 40% was assumed.

The derivation of Eq. (28) is based on the assumption that the particles of the packed bed have a high thermal conductivity λ. So this equation deviates from that of packed beds having solid particles with low thermal conductivity. More details as well as other theories on effective heat transfer within packed beds may be found in Chap. K4 and in [16].

3.3 Radiation from Cavities

Radiation escaping from an isothermal enclosure having only a small opening gives black body radiation in good approximation ($\varepsilon_{eff} \simeq 1$), independently of the degree of emissivity of the cavity surrounding material. This is because the black body radiation is physically related to "Hohlraum" radiation, i.e., radiation within any isothermal cavity. If a surface has cavities with large openings, such as a mounting table with drilling holes or slots, the degree of emissivity of this surface will be smaller than a black body surface but larger than the emissivity of the plane wall material ε. The effective degree of emissivity of a spherical cavity shown in Fig. 15, for example, is given by Eckert [17] to be

$$\varepsilon_{eff} = \frac{\varepsilon}{\varepsilon + \frac{A'}{A}(1 - \varepsilon)}.$$

Figures 16 through 23 give the effective degree of emission for cavities with different geometrical shapes, as cylindrical holes or triangular gaps. The radiation escaping from these cavities is typically *not* diffusive radiation, so Lambert's cosine law will not be truly valid even though the wall material itself may be a gray body.

4 Symbols

a degree of absorbance
A area, in m^2
B_i sum of all radiation fluxes leaving surface I in the enclosure approach, in W/m^2
c_0 speed of light in vacuum, $c_0 = 299\,792\,458$ m/s
C_{ik} radiation exchange factor
E radiation energy flux impinging onto a surface, in W/m^2
ΔE radiation energy flux, in W
h Planck constant, $h = 6.626\,068\,76 \times 10^{-34}$ J s
H_i sum of all radiation fluxes approaching surface i in the enclosure approach, in W/m^2
k Boltzmann constant, $k = 1.380\,650\,3 \times 10^{-23}$ J/K
L directional intensity
M radiation energy flux emitted by a surface, in W/m^2
Q_{ik} net radiative heat flux between surfaces i and k, in W

r degree of reflection
T thermodynamic temperature, in K
β polar angle between the normal of a surface and the radiation ray under consideration, in rad
ε degree of emission
φ azimuth angle
φ_{ik} view factor between surface i and k
λ wavelength, in µm
Ω solid angle, in sr
σ Stefan–Boltzmann constant, $\sigma = 5.67040 \times 10^{-8}\ \mathrm{W/m^2K^4}$
τ degree of transmission

Indices

b black body
λ spectral quantity, directional quantity

5 Bibliography

1. Modest M (2003) Radiative heat transfer, 2nd edn. Academic Press, Amsterdam
2. Mahan J (2002) Radiation heat transfer: a statistical approach. Wiley, New York
3. Siegel R, Howell JR (2002) Thermal radiation heat transfer, 4th edn. Taylor & Francis, New York
4. Brewster MQ (1992) Thermal radiative transfer and properties. John Wiley & Sons, New York
5. Baehr H-D, Stephan K (2006) Heat and mass transfer, 2nd rev. edn., chapt. 5. Springer, Berlin
6. Planck M (1901) Ueber das Gesetz der Energieverteilung im Normalspectrum. Annalen der Physik 4:553–563
7. Jordan EC (1968) Electromagnetic waves and radiating systems, 2nd edn. Prentice- Hall, London
8. Dimmena RA, Buckius RO (1994) Electromagnetic theory predictions of the directional scattering from triangular surfaces. J Heat Trans 116:S.639–S.645
9. Touloukian YS (1962) Thermophysical properties of matter. Vols. 7–9. IFI Plenum, New York. Tables of emissivity of surfaces. Int J Heat Mass Trans 5:67–76
10. Gubareff, J, Torborg (1960) Thermal radiation properties. Honeywell Research Center, Minneapolis, MN
11. Sala A (1986) Radiant properties of materials. Elsevier Science Publishers, Amsterdam
12. Kirchhoff R (1999) Bestimmung der spektralen Emissionsgrade feuerfester Baustoffe und keramischer Spezialerzeugnisse. Cuvillier Verlag, Goettingen
13. Landolt- B (1985) Zahlenwerte und Funktionen aus Naturwissenschaften und Technik, Vol. 15, Springer, Berlin
14. Kabelac S (1994) Thermodynamik der Strahlung. F. Vieweg & Sohn, Braunschweig
15. Vortmeyer D (1966) Fortschr.- Ber. VDI, Reihe 3, Nr. 9; Habilitation Thesis from July 28th, 1965. Düsseldorf: VDI- Verlag, 1966. See also: Vortmeyer, D.: Chem Ing Techn 38:404
16. Vortmeyer D (1980) Radiation in packed solids. Germ Chem Eng 3:124–138
17. Sparrow EM, Cess RD (1970) Radiation heat transfer. Brooks/Cole Publishing Co, Belmont/Calif
18. Vortmeyer D, Börner B (1966) Emissionsgrade aufgrund von Hohlräumen. Chem Ing Tech 38:1077–1079
19. Kast W (1965) Fortschr.- Ber. VDI, Reihe 6, Nr. 5. VDI- Verlag, Düsseldorf

K2 View Factors

Dieter Vortmeyer[1] · *Stephan Kabelac*[2]
[1]Munich, Germany
[2]Helmut-Schmidt-Universität, Universität der Bundeswehr Hamburg, Hamburg, Germany

1 Determination of View Factors

The view factor φ_{12} is a purely geometrical value which describes the fraction of the total radiation from a surface 1 that hits another surface 2; see Sect. 2.2 in Chap. K1. So in almost all cases of thermal radiation heat transfer, the first step in the calculation procedure is to determine the view factor which is valid for the two surfaces under consideration. The general formula for the view factor is

$$\varphi_{12} = \frac{1}{\pi A_1} \int_{A_1} \int_{A_2} \frac{\cos\beta_1 \cos\beta_2}{s^2} \, \mathrm{d}A_1 \, \mathrm{d}A_2, \tag{1}$$

where s is the length of the straight line which connects two differential area elements, one on each surface (Fig. 1). β_1 and β_2 are the polar angles between the normal line of these differential elements and the connecting line. Equation (1) holds true for two arbitrary surfaces obeying Lamberts cosine law, i.e., ideal diffuse radiating surfaces. As the evaluation of Eq. (1) is elaborate and as only geometrical parameters are involved, a number of solutions of Eq. (1) exist for different groupings of surfaces. These solutions are ready for application; they are explained in the following.

If one of the surfaces under consideration is small when compared to the second surface, this surface may be taken to be area element ΔA_1, so one integration is omitted and Eq. (1) simplifies to

$$\varphi_{12} = \frac{1}{\pi} \int_{A_2} \frac{\cos\beta_1 \cos\beta_2}{s^2} \, \mathrm{d}A_2. \tag{2}$$

Also for Eq. (2), special solutions exist which are introduced in the following section. The solutions given here are valid for simple geometrical settings and common technical situations. In some more complicated situations, the surfaces under consideration can be subdivided to find solutions given in this chapter. This also holds true for situations for large surfaces of nonuniform temperatures. More view factors and other methods of solution of Eq. (1), as for example the Monte–Carlo method, are described in [1–4].

The reciprocal relation [see Eq. (18) in Chap. K1]

$$A_i \varphi_{ik} = A_k \varphi_{ki} \tag{3}$$

should be kept in mind, as well as the summarizing relation

$$\sum_{k=1}^{n} \varphi_{ik} = 1 \tag{4}$$

[see Eq. (20) in Chap. K1].

2 Determination of the View Factor for Radiative Transfer from a Finite Surface to a Small Area Element

As long as the Lambert cosine law applies (see Sect. 1.2 in Chap. K1), view factors for small diffuse area elements can be determined by the graphical and analytical methods as described in this section.

2.1 Graphical Method [5]

The graphical procedure is illustrated in Fig. 2. Thus draw a plane (x, y-plane) through the element of area ΔA_1, and describe a hemisphere around the center O. O is the center point of area element ΔA. Connect O to points on the circumference of the surface A_2 at which the radiation is intercepted, e.g., to the points a_2, b_2, c_2, and d_2 on the rectangle shown in Fig. 1, so that the straight lines Oa_2, Ob_2, Oc_2, and Od_2 intersect the hemisphere surface at the points a_0, b_0, c_0, and d_0. Then project the surface formed by these points vertically onto the x, y plane to obtain the hatched area a_1, b_1, c_1, and d_1. The ratio of this area to the area of the circle formed by the intersection of the hemisphere with the x, y plane is the view factor φ_{12} to be determined.

2.2 Analytical Method

In some comparatively simple cases, the view factor φ_{12} of the area element ΔA_1 from which radiation is emitted to the surface

VDI-GVC (ed.), *VDI Heat Atlas*, DOI 10.1007/978-3-540-77877-6_41,

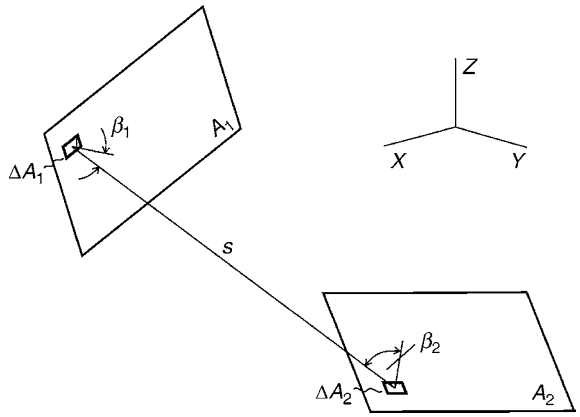

K2. Fig. 1. Two arbitrary surfaces A_1 and A_2 in space.

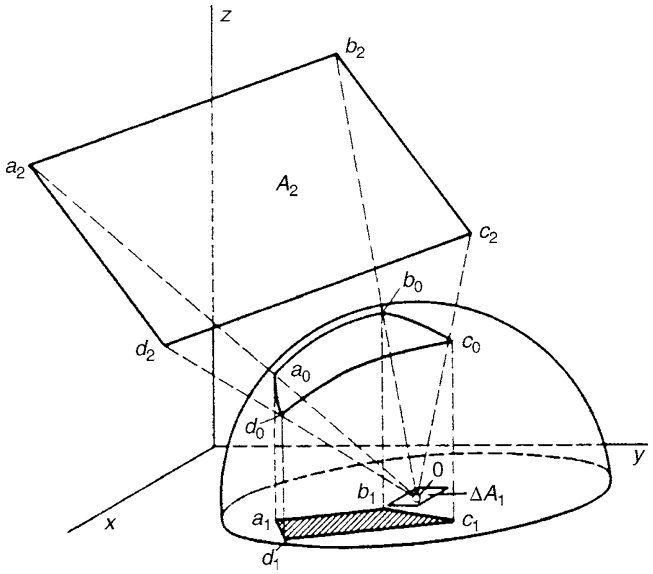

K2. Fig. 2. Graphical determination of the view factor φ_{12}.

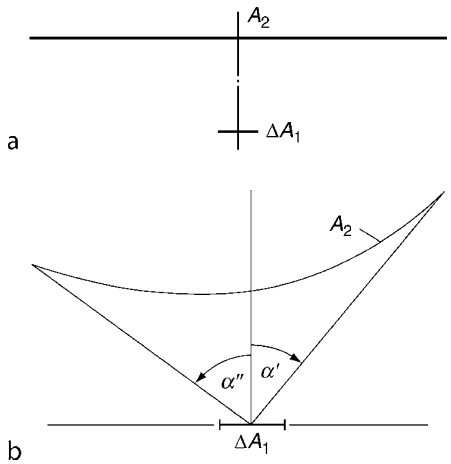

K2. Fig. 3. (**a**) Plane parallel to ΔA_1 and of large extent as compared to the distance between ΔA_1 and A_2. In this case we have (**b**) infinitely long surface of any given profile within the space limited by the tangents drawn from the element for area ΔA_1.

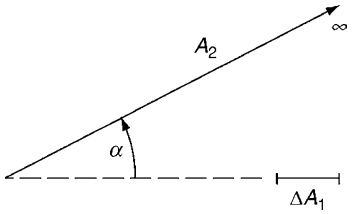

K2. Fig. 4. Surface of infinite extent that intersects the plane of the element of area ΔA at an angle α.

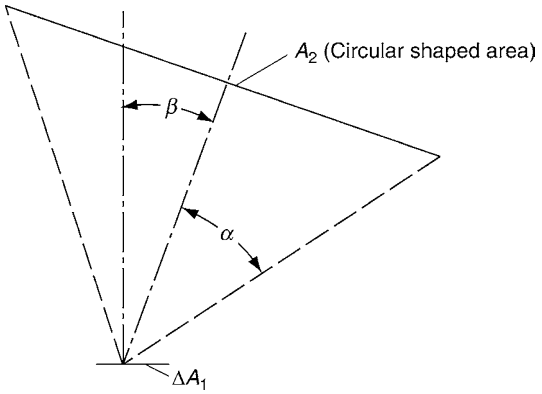

K2. Fig. 5. Surface A_2 of circular shape arranged so that the line normal to its center passes through the element of area ΔA_1.

A_2 can be determined from the following equations or diagrams. The shape of the area A_2 and its position relative to ΔA_1 are shown in the diagrams given in each case, and the symbols used should be clear as given within Figs. 3–11:

$$\varphi_{12} = 1. \tag{5}$$

From Fig. 3b,

$$\varphi_{12} = \frac{\sin\alpha' + \sin\alpha''}{2}. \tag{6}$$

From Fig. 4, we have

$$\varphi_{12} = \frac{1}{2}(1 + \cos\alpha). \tag{7}$$

From Fig. 5,

$$\varphi_{12} = \sin^2\alpha \cdot \cos\alpha, \quad \text{if } (\alpha + \beta) \leq 90°,$$

or

$$\varphi_{12} = \frac{\alpha - \sin\alpha \cdot \cos\alpha}{\pi}, \quad \text{for } \beta = 90°. \tag{8}$$

In other words, the circle A_2 is perpendicular to ΔA_1 in the second case. In this case, only the upper semicircle A_2 above the horizon of ΔA_1 is exposed to the radiation.

From Fig. 6,

$$B = \frac{b}{a}, \quad R = \frac{r}{a},$$

$$\varphi_{12} = \frac{1}{2} - \frac{1 + B^2 - R^2}{2\sqrt{B^4 + 2B^2(1 - R^2) + (1 + R^2)^2}}. \tag{9}$$

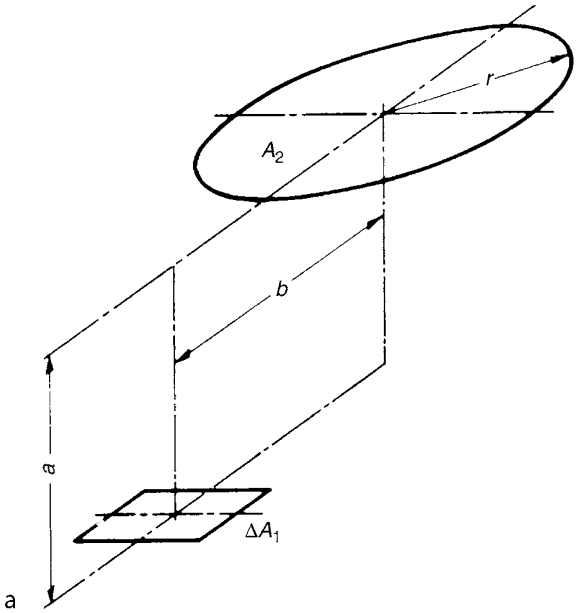

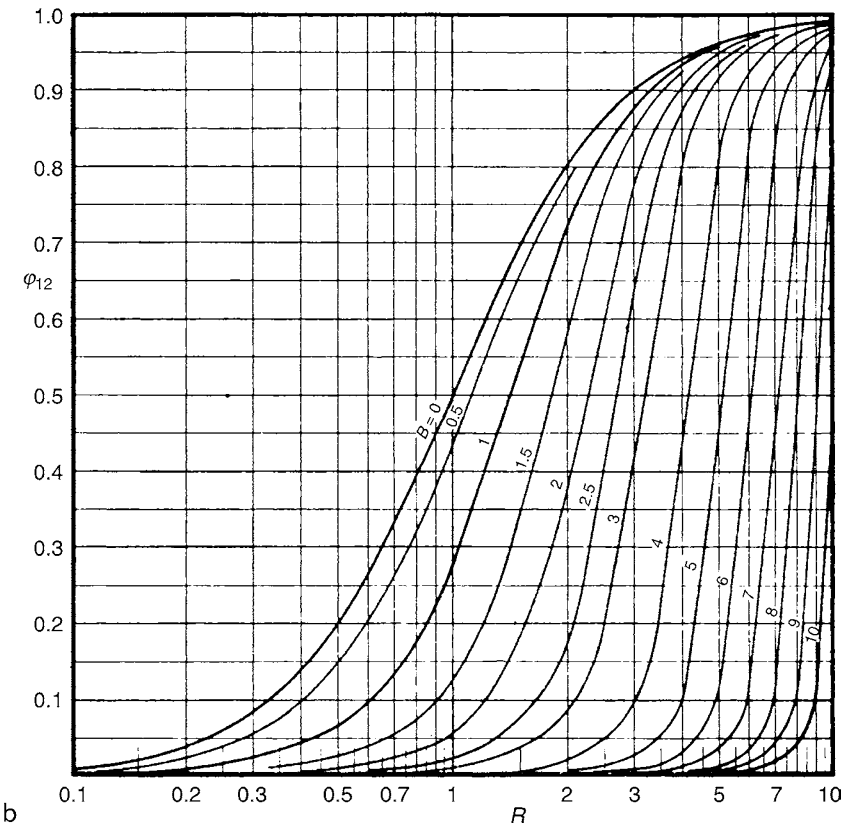

K2. Fig. 6. (**a**) Circular surface parallel to the element of area ΔA_1; (**b**) view factor φ_{12} as a function of R and B for the radiation emanating from an element of area onto a circular surface parallel to that element.

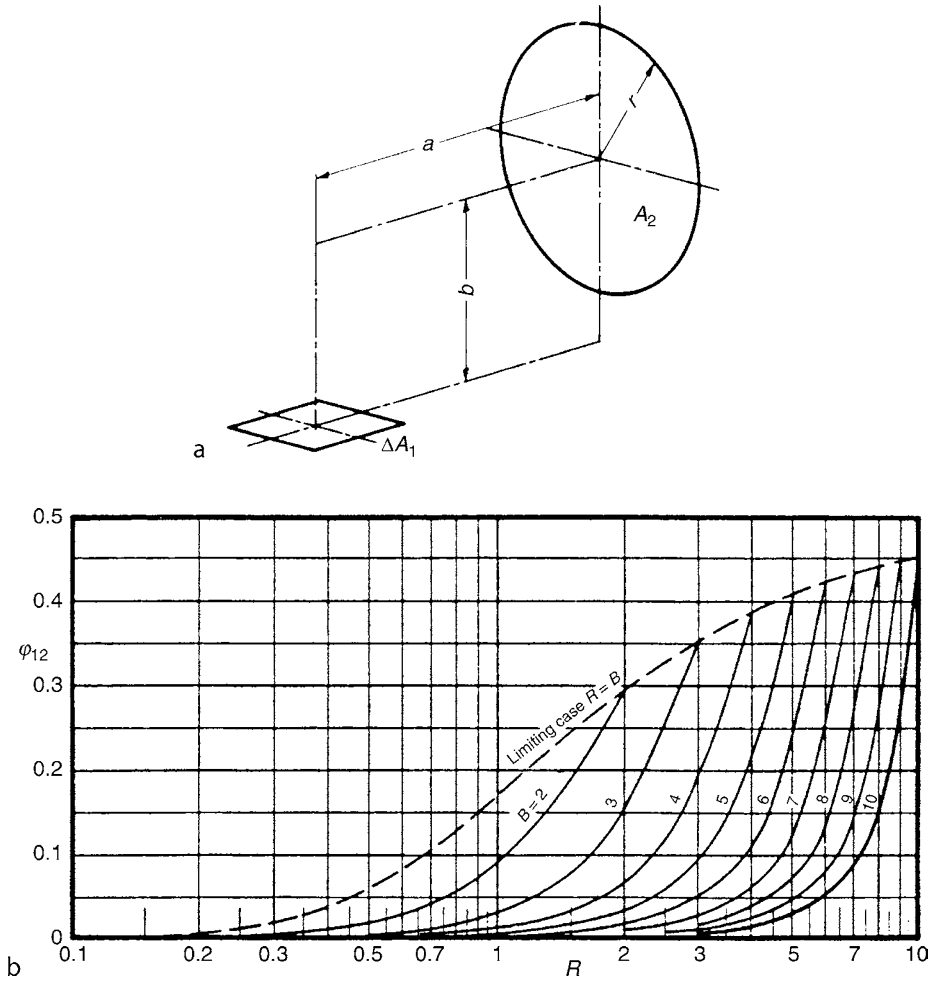

K2. Fig. 7. (**a**) Circular surface perpendicular to the element of area; (**b**) view factor φ_{12} as a function of R and B for the radiation emanating from an element of area onto a circular surface perpendicular to that element (see Fig. 7a).

From Fig. 7,

$$B = \frac{b}{a}, \quad R = \frac{r}{a},$$

$$\varphi_{12} = \frac{1}{2B}\left[\frac{1 + B^2 + R^2}{\sqrt{B^4 + 2B^2(1 - R^2) + (1 + R^2)^2}} - 1\right]. \qquad (10)$$

Equation (7) and Fig. 7b are not valid unless $b \geq r$ which means unless the circle lies above the horizon of ΔA_1.

From Fig. 8,

$$B = \frac{b}{a}, \quad C = \frac{c}{a},$$

$$\varphi_{12} = \frac{1}{2\pi}\left(\frac{B}{\sqrt{1+B^2}}\arctan\frac{C}{\sqrt{1+B^2}} + \frac{C}{\sqrt{1+C^2}}\arctan\frac{B}{\sqrt{1+C^2}}\right). \qquad (11)$$

If the rectangle A_2 does not have any of its corners exactly on the normal line to the element of area ΔA_1, it can be subdivided into a number of smaller rectangles with a common corner that lies on the normal. Alternatively, it can be represented as the sum and difference of rectangles with a common corner of this nature. In this case, the view factors for each part of the rectangle can be determined by repeated application of Eq. (11) or Fig. 8b, and the desired value for φ of the area A_2 can be obtained by appropriate addition or subtraction.

The procedure for rectangles in a general position perpendicular to the element of area ΔA_1 as shown in Fig. 9a is similar to that stated for parallel rectangles.

From Fig. 9,

$$B = \frac{b}{a}, \quad C = \frac{c}{a},$$

$$\varphi_{12} = \frac{1}{2\pi}\left(\arctan B - \frac{1}{\sqrt{1+C^2}}\arctan\frac{B}{\sqrt{1+C^2}}\right). \qquad (12)$$

From Fig. 10,

$$A = \frac{a}{r}, \quad B = \frac{b}{r},$$
$$X = (1 + B)^2 + A^2,$$

and

$$Y = (1 - B)^2 + A^2,$$

$$\varphi_{12} = \frac{1}{\pi B}\arctan\frac{A}{\sqrt{B^2 - 1}} + \frac{A}{\pi}\left[\frac{X - 2B}{B\sqrt{XY}}\arctan\sqrt{\frac{X(B-1)}{Y(B+1)}} - \frac{1}{B}\arctan\sqrt{\frac{B-1}{B+1}}\right]. \qquad (13)$$

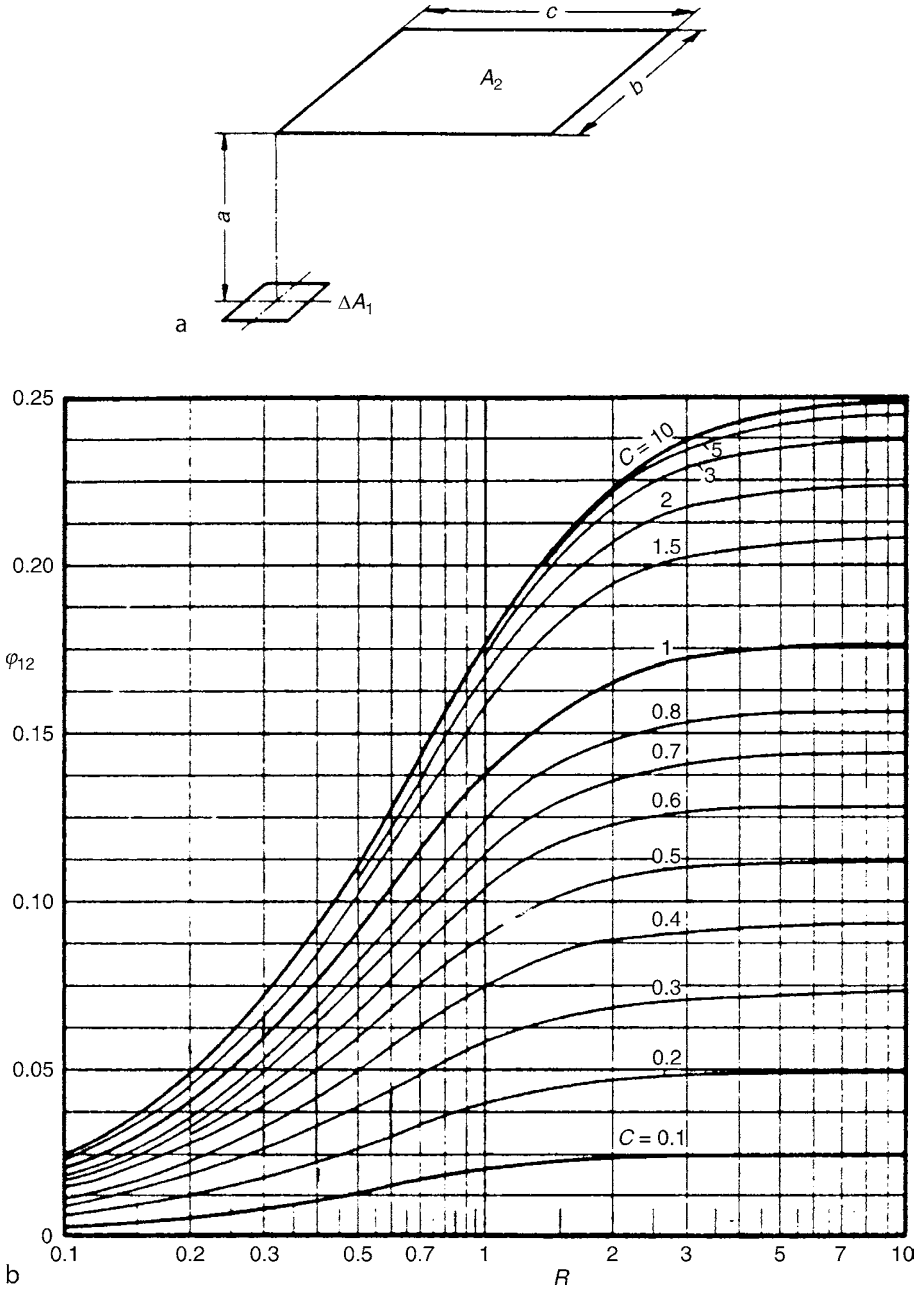

K2. Fig. 8. (**a**) Parallel rectangular surface A_2 with a corner that lies on the vertical to the center of the element of area ΔA_1; (**b**) view factor φ_{12} as a function of B and C for the radiation emanating from an element of area ΔA_1 onto a rectangular surface A_2 parallel to that element.

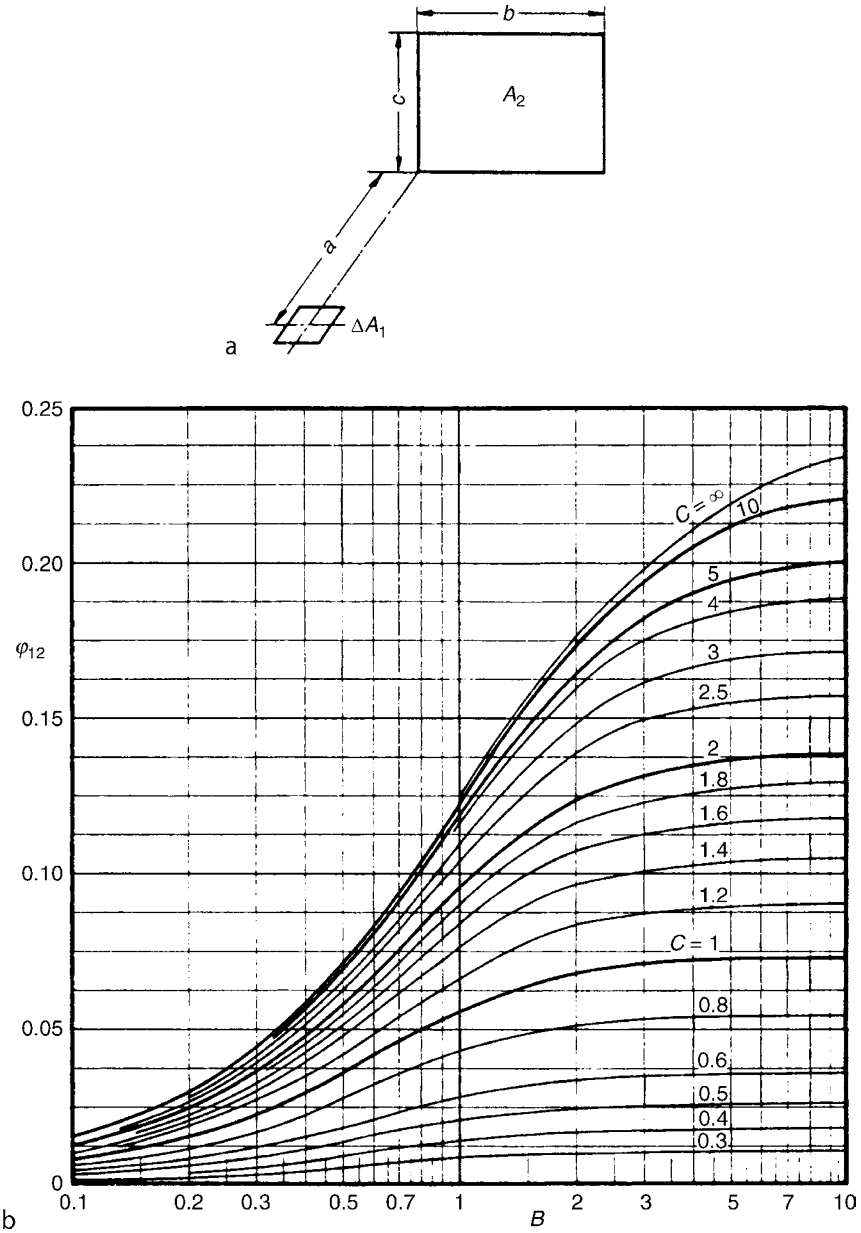

K2. Fig. 9. (**a**) Rectangular surface A_2 perpendicular to the element of area ΔA with the one side in the plane of the element and with one corner which is the normal to the line that passes through ΔA_1; (**b**) view factor φ_{12} as a function of B and C for the radiation emanating from an element of area onto a rectangular surface perpendicular to that element (see Fig. 9a).

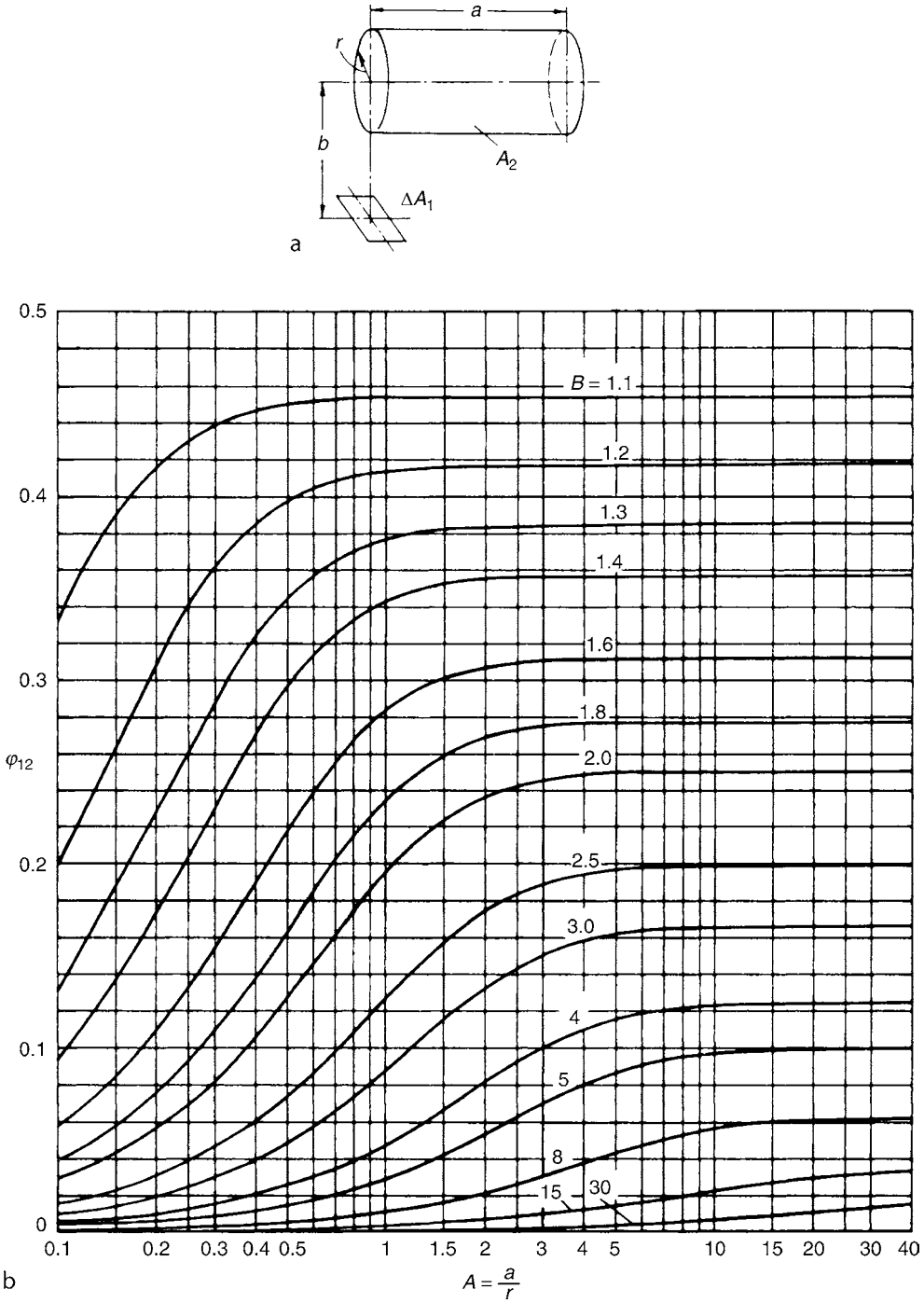

K2. Fig. 10. (**a**) Cylinder with the circumferential surface A_2 and the axis parallel to the element of area ΔA_1. The vertical line through the center of the element ΔA_1 intersects the axis at one front face of the cylinder; (**b**) view factor φ_{12} as a function of A and B for radiation between an element of area ΔA_1 and a cylinder (see Fig. 10a).

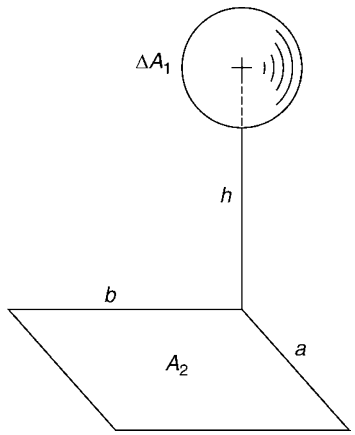

K2. Fig. 11. Radiation between a plane surface A_2 and a small differential spherical surface ΔA_1 [8].

From Fig. 11,

$$A = \frac{a}{h}, \quad B = \frac{b}{h},$$
$$\varphi_{12} = \frac{1}{8} - \frac{1}{4\pi} \arctan \sqrt{\frac{1 + A^2 + B^2}{A^2 B^2}}. \tag{14}$$

More solutions for the view factor of different geometrical situations can be found in literature [1–4].

3 Determination of the View Factor φ_{12} for Radiative Transfer Between Finite Surfaces

In Sect. 2, the view factor φ_{12} was given for cases where one of the two surfaces exchanging radiation was small as compared to the other surface. In this situation, which is favorable in cases where one surface has to be subdivided into small surface elements, Eq. (2) has to be solved. Now cases are described in this section below, where both areas A_1 and A_2 are of finite size. In these cases, Eq. (1) could be solved and complete solutions for the entire surfaces are available. The heat flux transferred by radiation is then calculated by means of Eqs. (17a) or (17b) in Chap. K1.

From Fig. 12,

$$R_1 = \frac{r_1}{a}, \quad R_2 = \frac{r_2}{a},$$
$$\varphi_{12} = \frac{1}{2R_1^2}\left(1 + R_1^2 + R_2^2 - \sqrt{(1 + R_1^2 + R_2^2)^2 - 4R_1^2 R_2^2}\right). \tag{15}$$

Circles of the same radius are regarded as a special case, i.e., $r_1 = r_2 = r$; $R = r/a$

$$\varphi_{12} = \frac{1}{2R^2}\left(1 + 2R^2 - \sqrt{1 + R^2}\right). \tag{16}$$

From Fig. 13,

$$B = \frac{b}{a}, \quad C = \frac{c}{a},$$
$$\varphi_{12} = \frac{1}{\pi}\left[\frac{1}{BC}\ln\frac{(1+B^2)(1+C^2)}{1+B^2+C^2} - \frac{2}{B}\arctan C - \frac{2}{C}\arctan B + \frac{2}{C}\sqrt{1+C^2}\arctan\frac{B}{\sqrt{1+C^2}} + \frac{2}{B}\sqrt{1+B^2}\arctan\frac{C}{\sqrt{1+B^2}}\right]. \tag{17}$$

A special case of parallel rectangles of the same size is shown in Fig. 13c:

$$B = \frac{b}{a}, \quad C = \frac{c}{a} = \infty,$$
$$\varphi_{12} = \sqrt{\frac{1 + B^2 - 1}{B}}. \tag{18}$$

Note that the length c is infinite.

From Fig. 14,

$$B = \frac{b}{a}, \quad C = \frac{c}{a},$$
$$\varphi_{12} = \frac{1}{\pi}\left(\frac{C}{\sqrt{1+C^2}}\arctan\frac{B}{\sqrt{1+C^2}} + \frac{\sqrt{1+B^2}}{B}\arctan\frac{C}{\sqrt{1+B^2}} - \frac{1}{B}\arctan C\right). \tag{19}$$

If the two sides of each surface A_1 and A_2 do not lie one above the other, the aim of the calculation can be achieved by applying the last equation or diagram twice. Whether the two values of φ_{12} thus obtained have to be added or subtracted depends on the position of A_1.

From Fig. 15,

$$B = \frac{b}{a}, \quad C = \frac{c}{a},$$
$$\varphi_{12} = \frac{1}{\pi}\left[\arctan\frac{1}{B} - \frac{B}{\sqrt{B^2+C^2}}\arctan\frac{1}{\sqrt{B^2+C^2}} - \frac{B}{2}\ln\frac{(B^2+C^2)(1+B^2)}{(1+B^2+C^2)B^2}\right]. \tag{20}$$

From Fig. 16,

$$B = \frac{b}{a}, \quad C = \frac{c}{a},$$
$$\varphi_{12} = \frac{1}{\pi B}\left\{B\cdot\arctan\frac{1}{B} + C\cdot\arctan\frac{1}{C} - \sqrt{B^2+C^2}\arctan\frac{1}{\sqrt{B^2+C^2}} + \frac{1}{4}\left[B^2\ln\frac{(1+B^2+C^2)B^2}{(B^2+C^2)(1+B^2)} + C^2\ln\frac{(1+B^2+C^2)C^2}{(B^2+C^2)(1+C^2)} - \ln\frac{1+B^2+C^2}{(1+B^2)(1+C^2)}\right]\right\}. \tag{21}$$

Figure 16c is an example for the general case of two vertical rectangular surfaces at a right angle to one another.

The above equation must be applied several times in this case in order to obtain the desired result:

$$\varphi_{12} = \varphi_{A_1A_2} = \frac{B''(\varphi_{B''C''} - \varphi_{B''C'}) - B'(\varphi_{B'C''} - \varphi_{B'C'})}{B'' - B'}. \tag{22}$$

The individual view factors involved in this equation become clear by the subscripts and by referring to Fig. 16c.

From Fig. 17,

$$\varphi_{12} = \frac{\cos\beta_1 \cos\beta_2}{\pi s^2} A_2 = \frac{n_1 n_2}{\pi s^4} A_2, \tag{23}$$

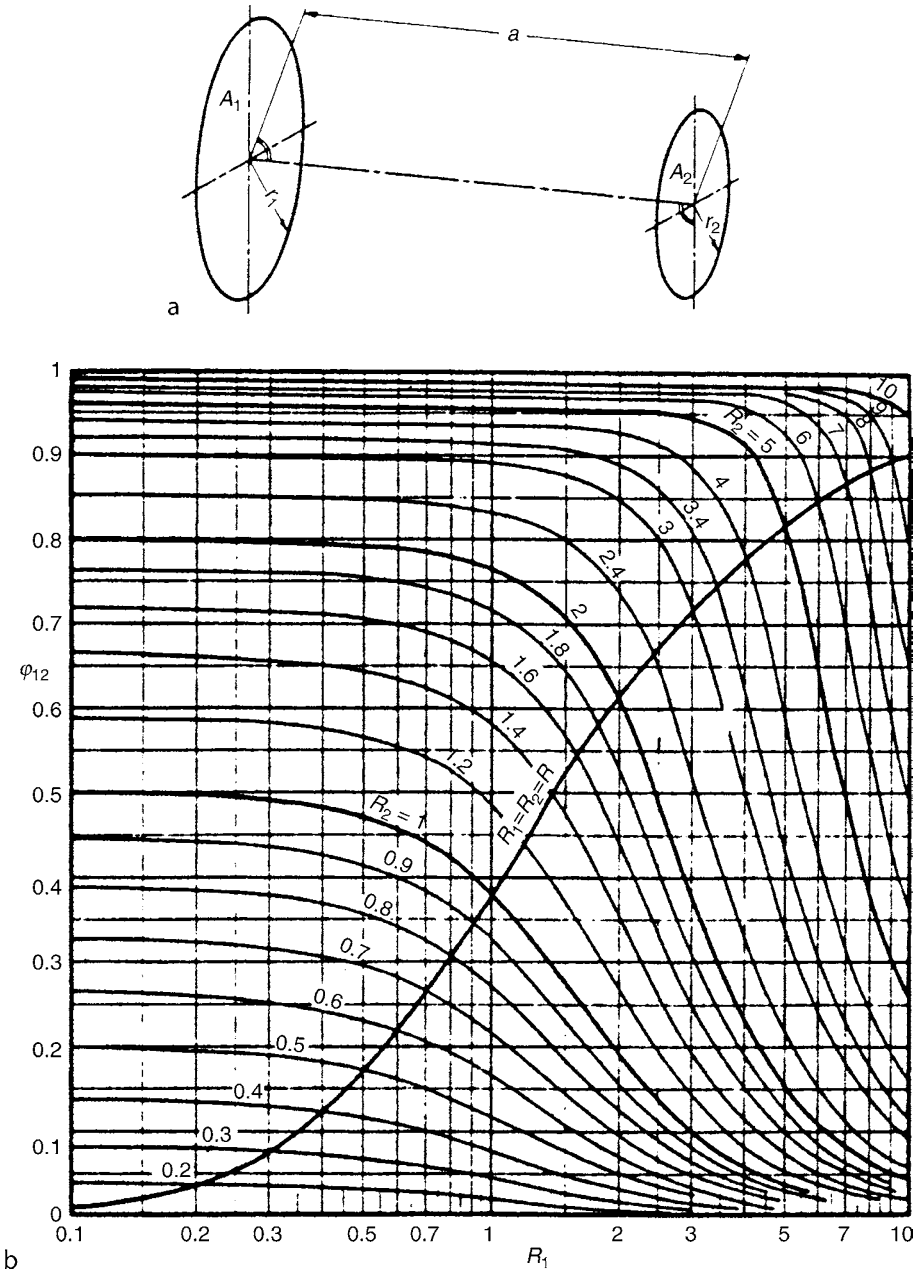

K2. Fig. 12. (**a**) Radiation between two parallel circular surfaces with a common vertical line through their centers; (**b**) view factor φ_{12} as a function of R_1 and R_2 for radiation between parallel circular surfaces with a common vertical line through their centers (see Fig. 12a).

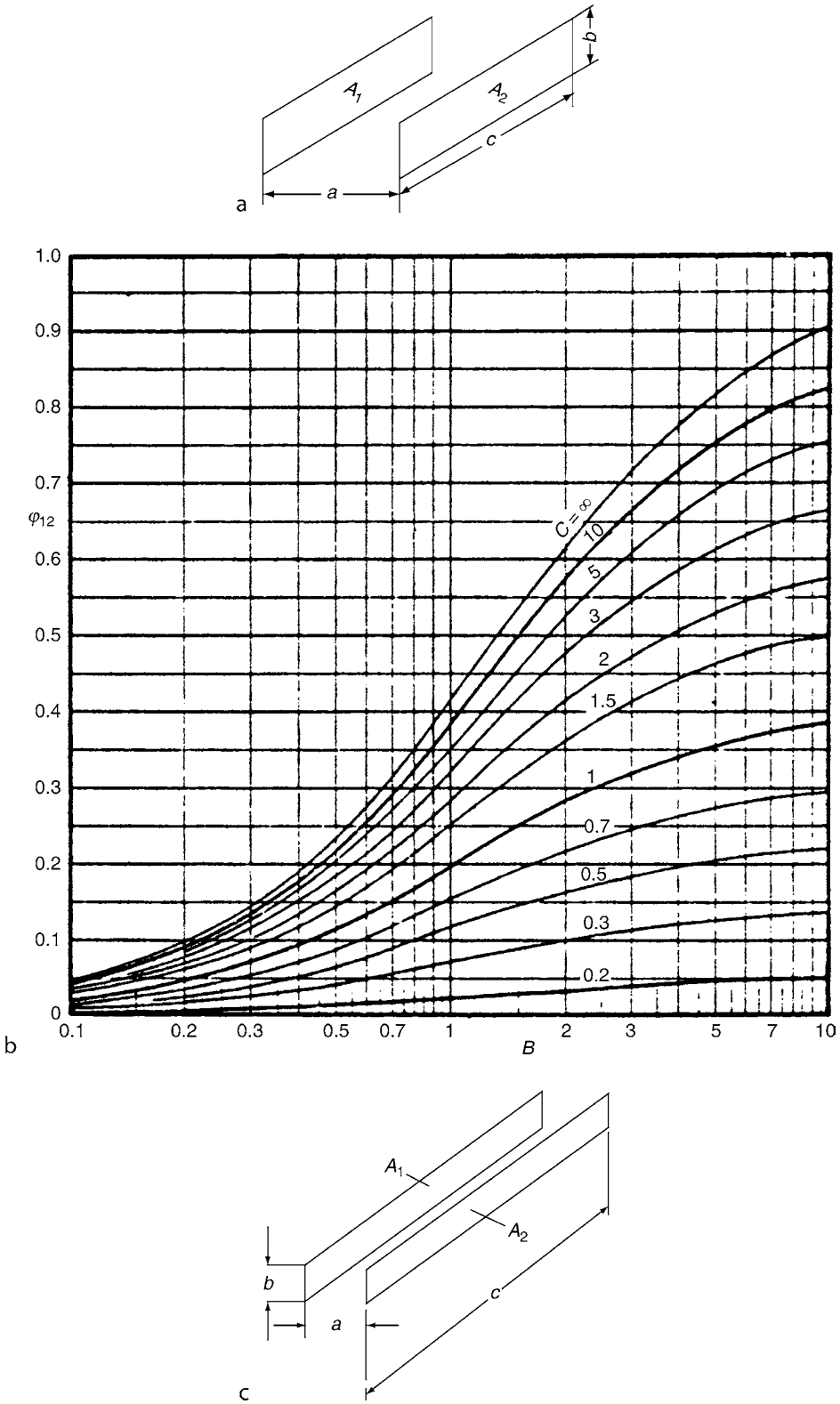

K2. Fig. 13. (**a**) Radiation between two parallel and opposite rectangular surfaces of the same size; (**b**) view factors φ_{12} as a function of B and C for radiation between two parallel and opposite rectangular surfaces of the same size; (**c**) special case of pairs of strips, where the length c of both stripes is infinite.

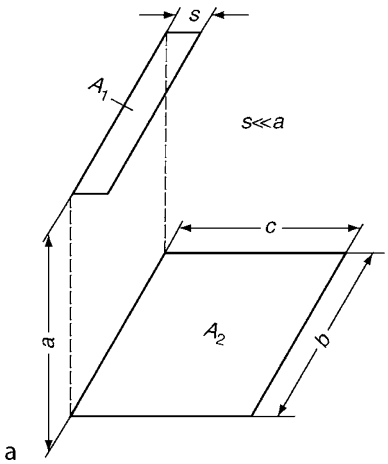

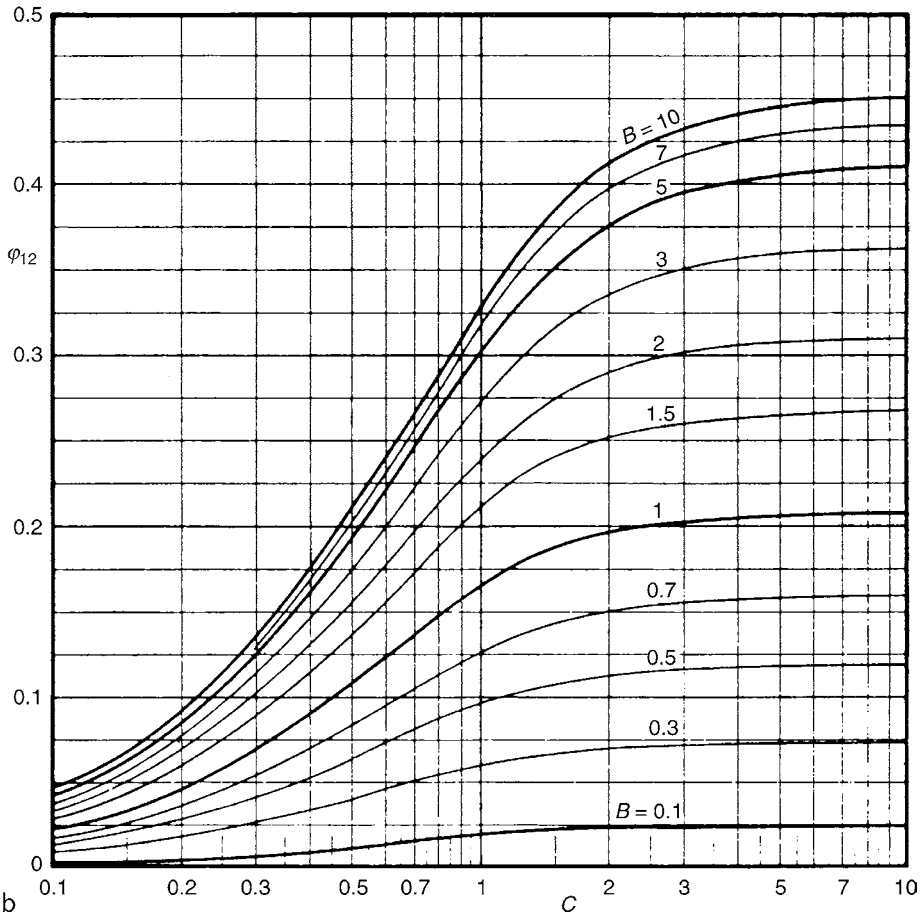

K2. Fig. 14. (**a**) Radiation from a stripe A_1 onto a parallel rectangular surface A_2 with the same length of side; (**b**) view factor φ_{12} as a function of B and C for radiation from a stripe onto a parallel rectangular surface with the same length of side (see Fig. 14a).

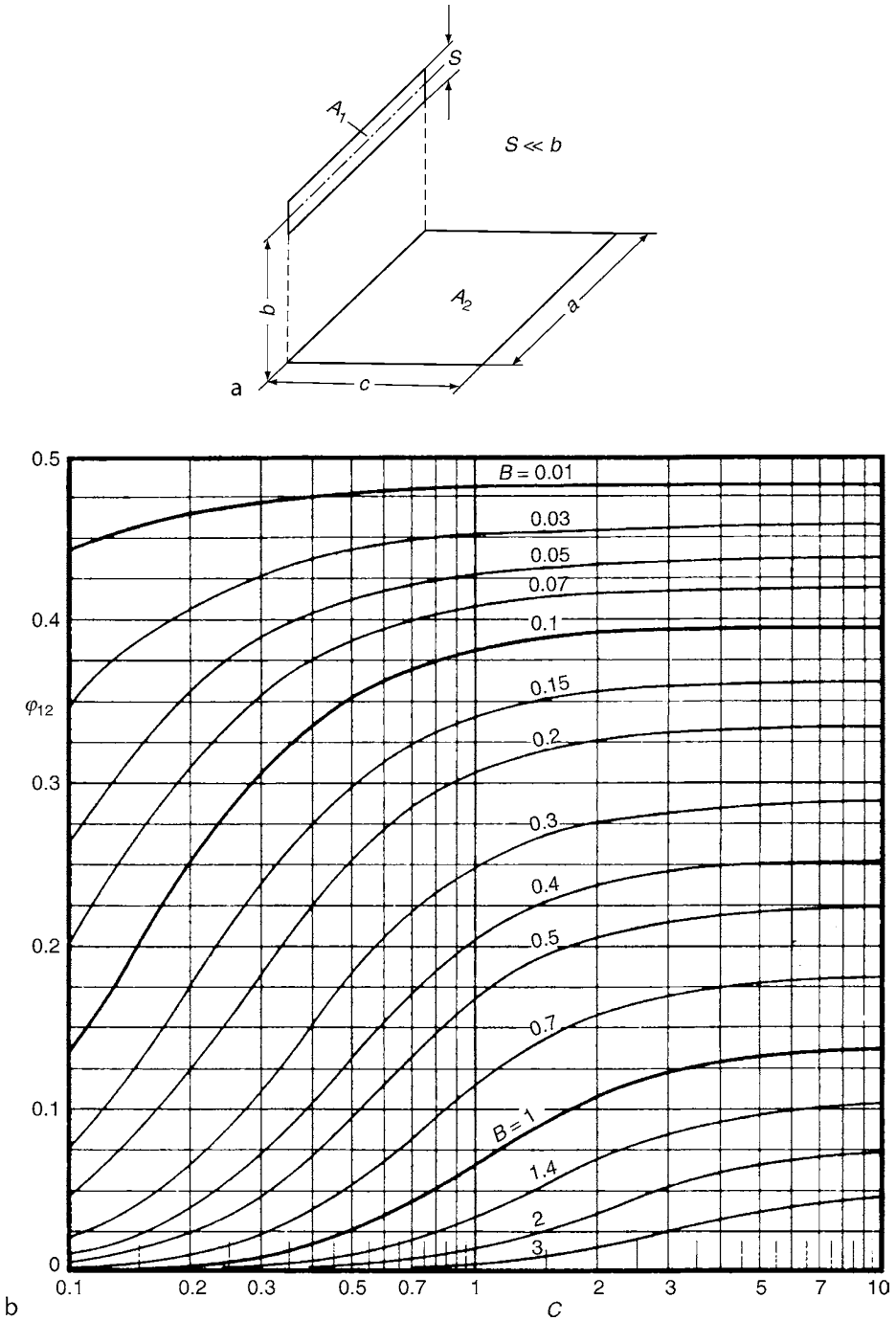

K2. Fig. 15. (**a**) Radiation between a plane stripe A_1 and a vertical rectangular surface A_2 with the same length of side and in a perpendicular position; (**b**) view factor φ_{12} as a function of B and C for radiation between a plane stripe and a rectangular surface at a right angle to it (see Fig. 15a).

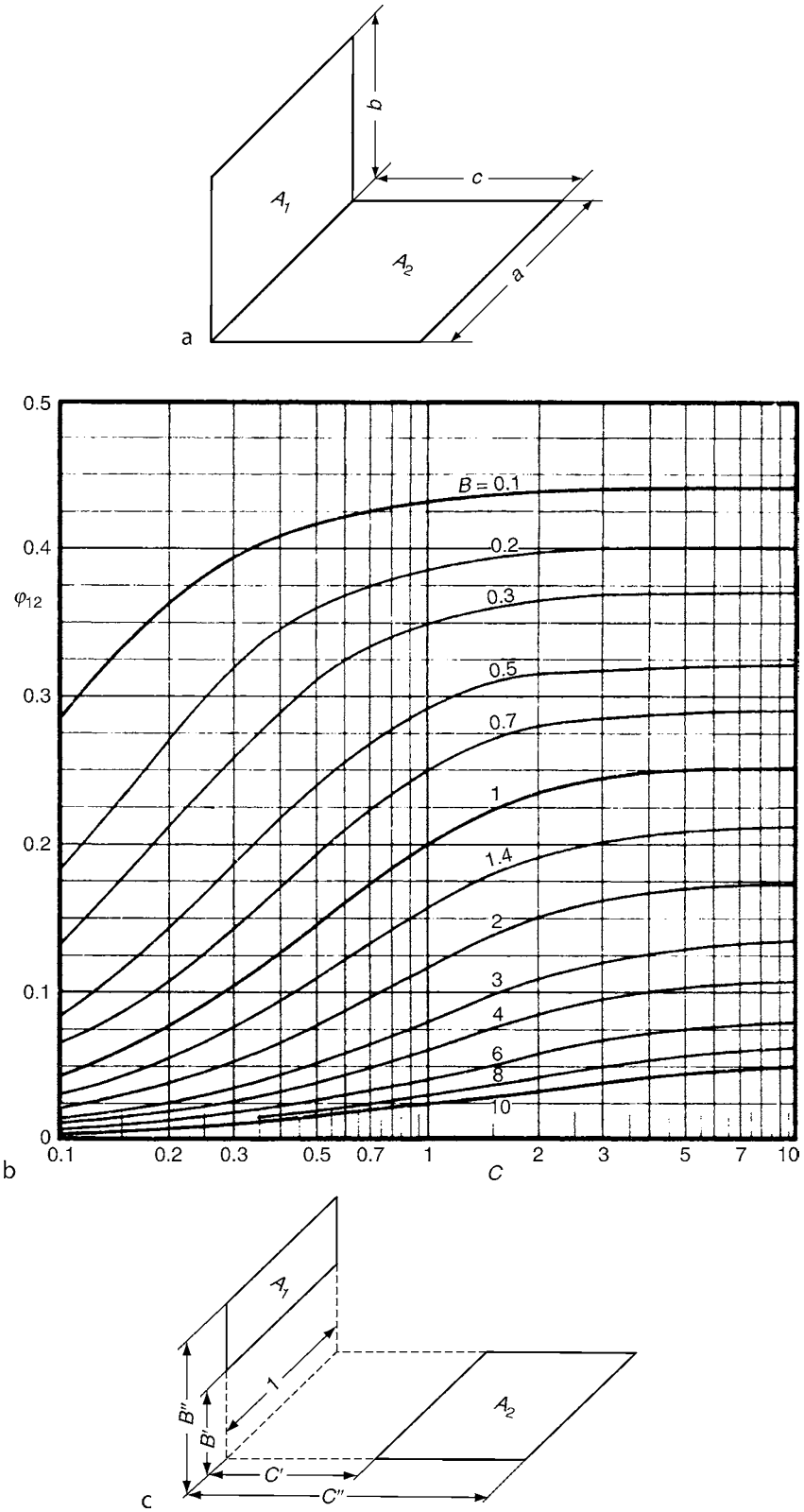

K2. Fig. 16. (**a**) Radiation between two surfaces A_1 and A_2 joined at a right angle to one another having one common side; (**b**) view factor φ_{12} as a function of B and C for radiation between two rectangular surfaces with a common side meeting at a right angle (see Fig. 16a); (**c**) general case for two rectangular surfaces A_1 and A_2 at a right angles to one another.

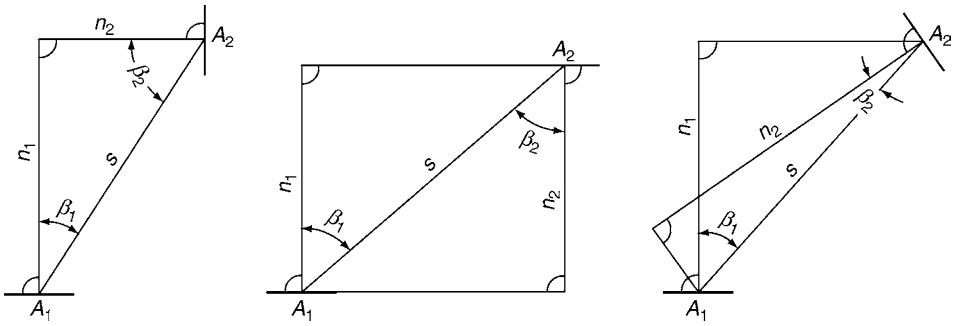

K2. Fig. 17. Radiation between surfaces that are small compared to the spacing between them.

where β_1 (or β_2) is the angle between the normal to the surface of A_1 (or A_2) and the straight line s joining the centers of the two surfaces. n_1 (or n_2) is the vertical distance between the plane at the surface of A_1 (or A_2) and the center of A_2 (or A_1).

These conditions are sketched in Fig. 17 for the special case in which the verticals to the center points of both surfaces lie within one plane.

From Fig. 18,

$$X = \frac{b}{a}, \quad Y = \frac{c}{a},$$

$$A = Y^2 + X^2 - 1, \quad B = Y^2 - X^2 + 1,$$

$$\varphi_{11} = 1 - \frac{1}{X} + \frac{2}{\pi X}\arctan\frac{2\sqrt{X^2-1}}{Y} - \frac{Y}{2\pi X}\left\{\frac{\sqrt{4X^2+Y^2}}{Y}\arcsin\left[\frac{4(X^2-1)+\frac{Y^2}{X^2}(X^2-2)}{Y^2+4(X^2-1)}\right] - \arcsin\frac{X^2-2}{X^2} + \frac{\pi}{2}\left(\frac{\sqrt{4X^2+Y^2}}{Y} - 1\right)\right\}, \tag{24}$$

$$\varphi_{12} = \frac{1}{X} - \frac{1}{\pi X}\left\{\arccos\frac{B}{A} - \frac{1}{2Y}\left[\sqrt{(A+2)^2-4X^2}\cdot\arccos\frac{B}{XA} + B\cdot\arcsin\frac{1}{X} - \frac{\pi A}{2}\right]\right\}, \tag{25}$$

$$\varphi_{13} = \frac{1}{2}(1 - \varphi_{12} - \varphi_{11}). \tag{26}$$

Note that in this case radiation from surface A_1, i.e., the inner surface of the outer cylinder, sees itself, so part of this radiation from A_1 will hit other parts of A_1 and thus φ_{11} is not zero.

From Fig. 19,

$$\varphi_{12} = \frac{(\overline{AA'D} + \overline{BC'C}) - (\overline{AC} + \overline{BD})}{2AB}. \tag{27}$$

From Fig. 20,

$$A = \frac{r_2}{r_1}, \quad B = \frac{s}{r_1}, \quad C = 1 + A + B,$$

$$\varphi_{12} = \frac{1}{2\pi}\left[\pi + \sqrt{C^2-(A+1)^2} - \sqrt{C^2-(A-1)^2} + (A-1)\arccos\left(\frac{A}{C} - \frac{1}{C}\right) - (A+1)\arccos\left(\frac{A}{C} + \frac{1}{C}\right)\right]. \tag{28a}$$

For the special case of $r_2 = r_1$, the view factor φ_{12} is simplified to give

$$\varphi_{12} = \frac{1}{2\pi}\left[\pi + \sqrt{C^2-4} - C - 2\arccos\left(\frac{2}{C}\right)\right]. \tag{28b}$$

From Fig. 21,

$$A = \frac{a}{r}, \quad B = \frac{b}{r}, \quad C = \frac{c}{r},$$

$$\varphi_{12} = \frac{1}{B-A}\left(\arctan\frac{B}{C} - \arctan\frac{A}{C}\right). \tag{29}$$

From Fig. 22,

$$A = \frac{a}{r}, \quad B = \frac{b}{r}, \quad C = \frac{c}{r},$$

$$X = A^2 + C^2 + g^2 - 1,$$

$$Y = C^2 - A^2 - g^2 + 1,$$

$$\varphi_{12} = \frac{2}{B}\int_0^{B/2} f(g)\,\mathrm{d}g, \tag{30a}$$

$$f(g) = \frac{A}{A^2+g^2} - \frac{A}{\pi(A^2+g^2)}\cdot\left\{\arccos\frac{Y}{X} - \frac{1}{2C}\left[\sqrt{X^2+4C^2}\arccos\frac{Y}{X\sqrt{A^2+g^2}} + Y\arcsin\frac{1}{\sqrt{A^2+g^2}} - \frac{\pi X}{2}\right]\right\}. \tag{30b}$$

After inserting the dimensionless numbers A, B, C and the dependent variables X and Y into Eq. (30b), the view factor φ in Eq. (30a) can be determined by a simple numerical integration along the variable g.

4 Radiation from Tube Banks

An important factor in the design of boilers and furnaces is the heat transferred by radiation onto the banks of tubes that line the walls or that are integrated into them. The method of

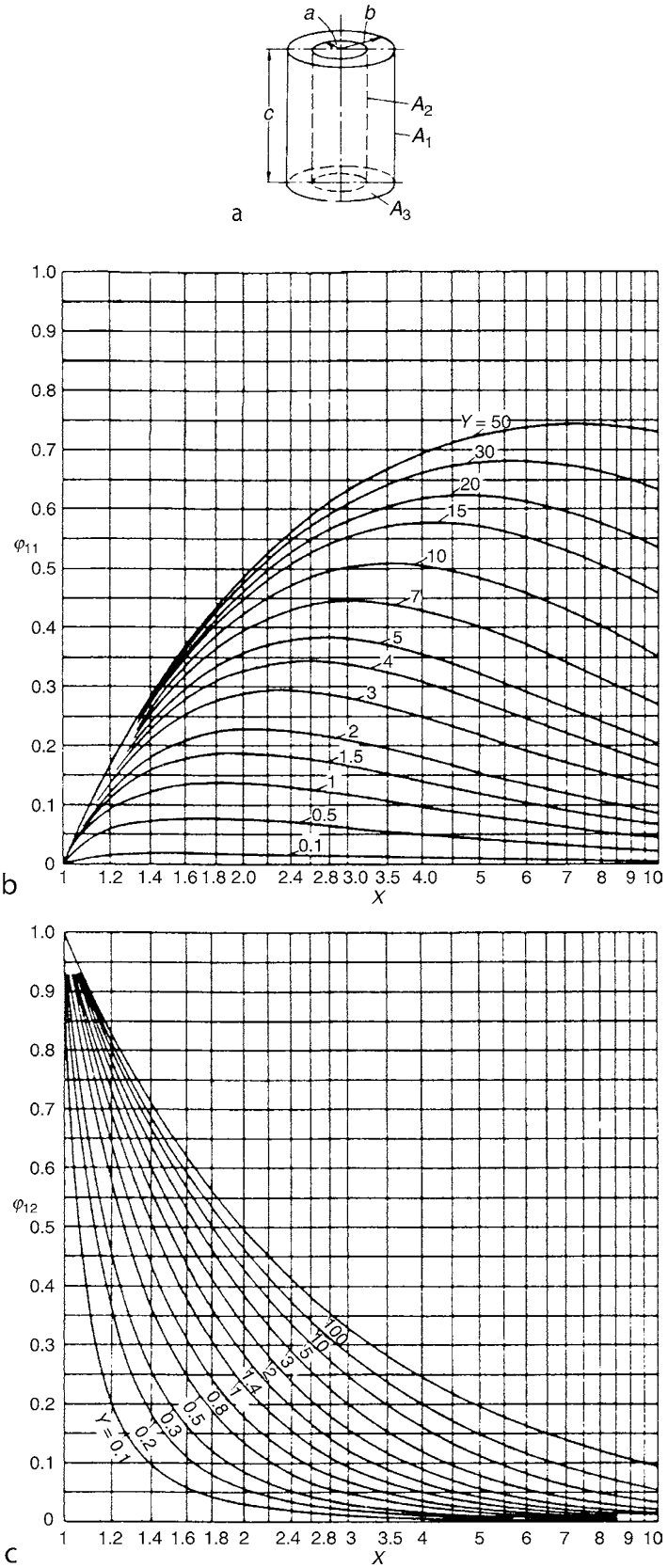

K2. Fig. 18. (**a**) Radiation between the surfaces of two concentric cylinders A_1 and A_2 of finite length c; (**b**) view factor φ_{11} as a function of X and Y for radiation from the outer cylinder onto itself; (**c**) view factor φ_{12} as a function of X and Y for radiation from the outer cylinder onto the inner cylinder A_2 (see Fig. 18a).

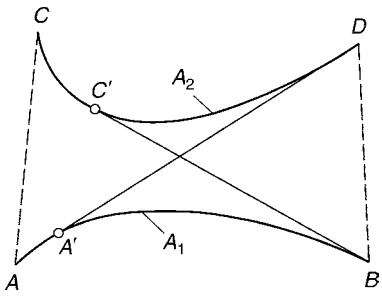

K2. Fig. 19. Radiation between curved surfaces A_1 and A_2 with parallel surface generating lines $\overline{AC}$ and $\overline{BD}$ and of infinite longitudinal extent.

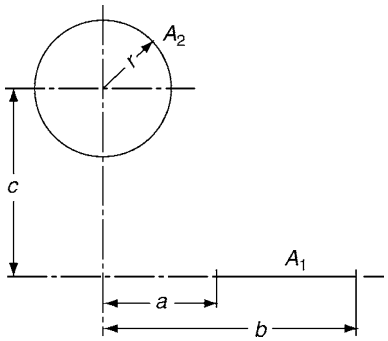

K2. Fig. 21. Radiation between a cylinder A_2 and a surface stripe A_1 that is parallel to the cylinder and of infinite extent.

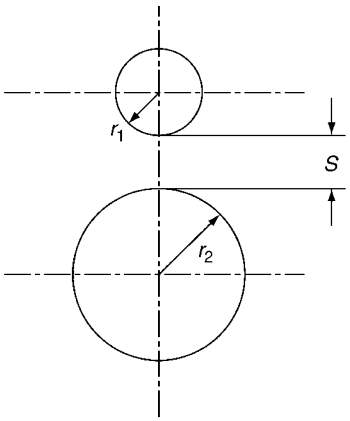

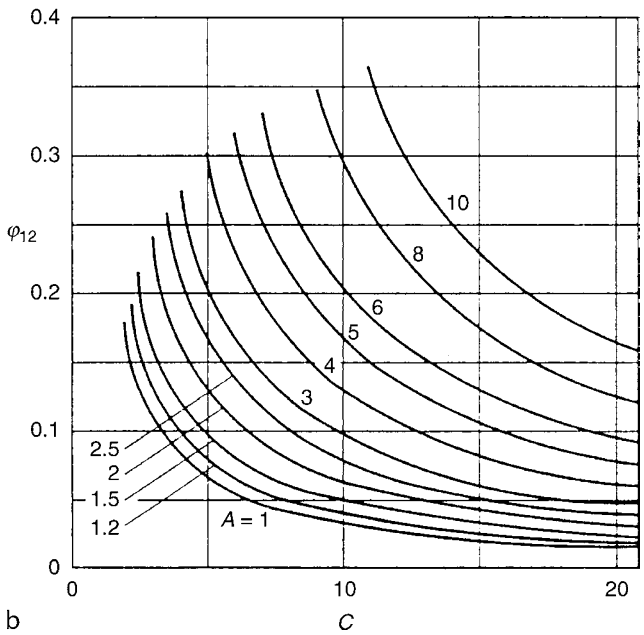

K2. Fig. 20. (**a**) Radiation between two parallel tubes of infinite length; (**b**) view factor φ_{12} as a function of C and A for two parallel tubes (see Fig. 20a).

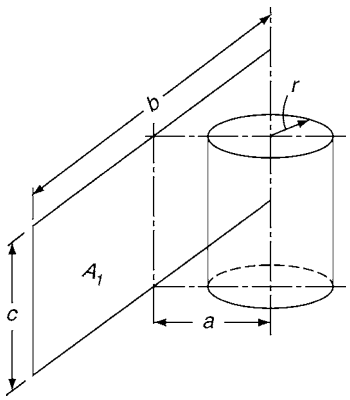

K2. Fig. 22. Radiation between a cylinder and a finite rectangular surface A_1 that is parallel to it.

calculation is analogous to that adopted for the radiation from electric rod resistance heaters in electric ovens. View factors calculated by Eckert [6] and Hottel [7] are presented in Figs. 23–25 for the determination of the radiant flux emanating from a radiating surface and intercepted by banks of tubes. In this particular case, the view factor φ_{12} is also referred to as the area ratio $\bar{\Psi}$.

In using these diagrams, a distinction must be made between the view factors that apply to the direct exchange between the wall and the tubes and those that refer to the *overall* total energy exchange. The derivation of the latter has been based on the assumption that the refractory wall behind the tube banks is adiabatic, i.e., it throws back all incident radiation, and that the tubes and the emitting surface are black body radiators.

Experience has shown that the emissivity of the tubes ε_R and that of the radiating wall ε_w are close to unity, i.e., black bodies. Consequently, if the reflected fractions are ignored, the heat flux brought about by radiation can be written as

$$\dot{q}_W = \varepsilon_W \varepsilon_R \sigma \bar{\Psi} \, (T_W^4 - T_R^4), \qquad (31)$$

where $\dot{q}_W$ is the heat flux per unit area of the radiating wall.

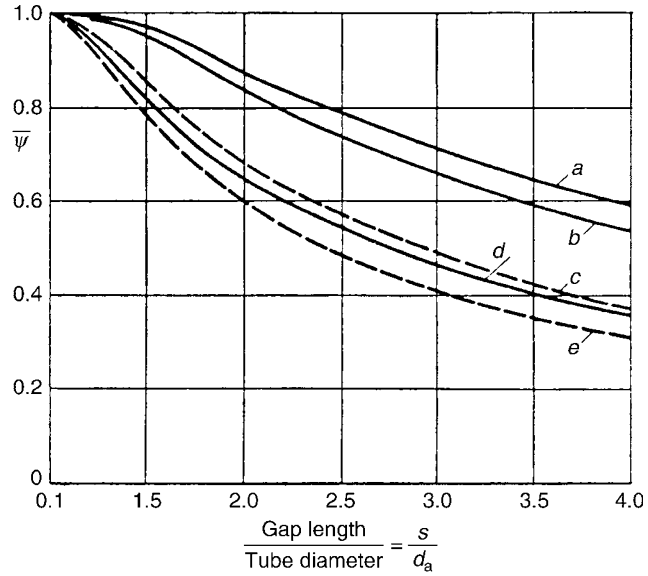

Case 1: $e > s$ 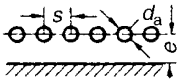 Curve *a*, *d*

Case 2: $e < s$ 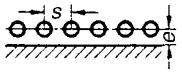 Curve *b*, *d*

Case 3: $e = 0$ 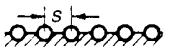 Curve *c*, *e*

K2. Fig. 23. Area ratio $\bar{\Psi}$ for a surface *A* covered by a bank of tubes [2]

Curve *a*	Total overall radiation incident on bank as in case 1 with $e > s$
Curve *b*	As in Case 2
Curve *c*	As in Case 3
Curve *d* or *e*	Direct radiation onto the wall surface as in Cases 1 and 2 or Case 3 for curve *e*.

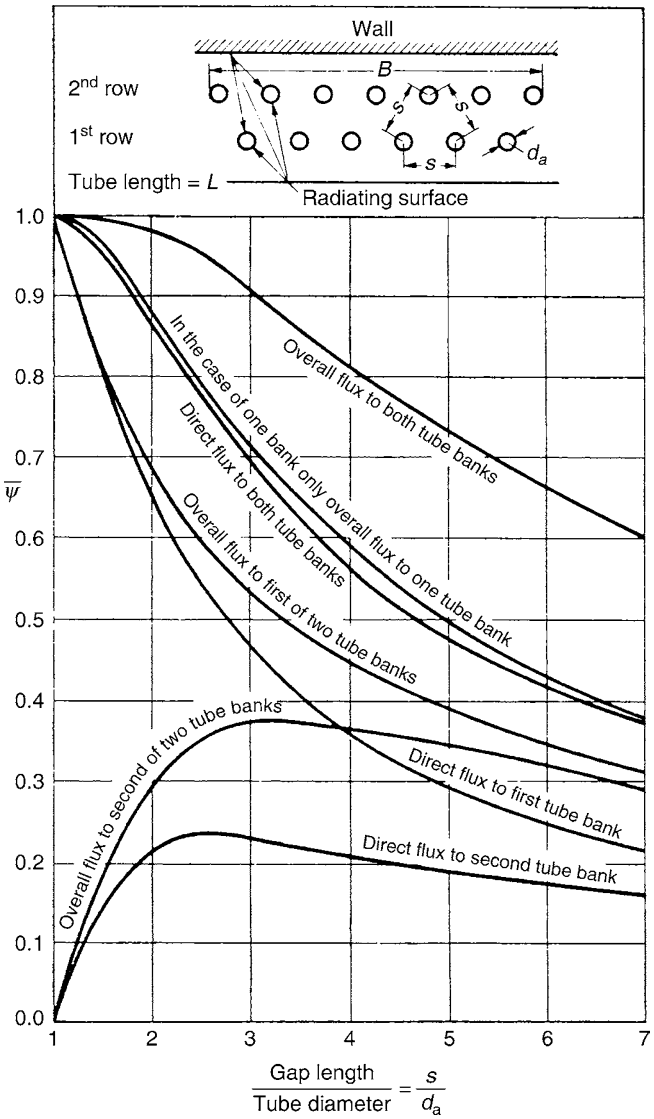

K2. Fig. 24. Area ratio $\bar{\Psi}$ for surface $A = B \times L$ lined by a tube bank consisting of two staggered rows [6, 7]. The width of the surface is *B*, the length is *L*.

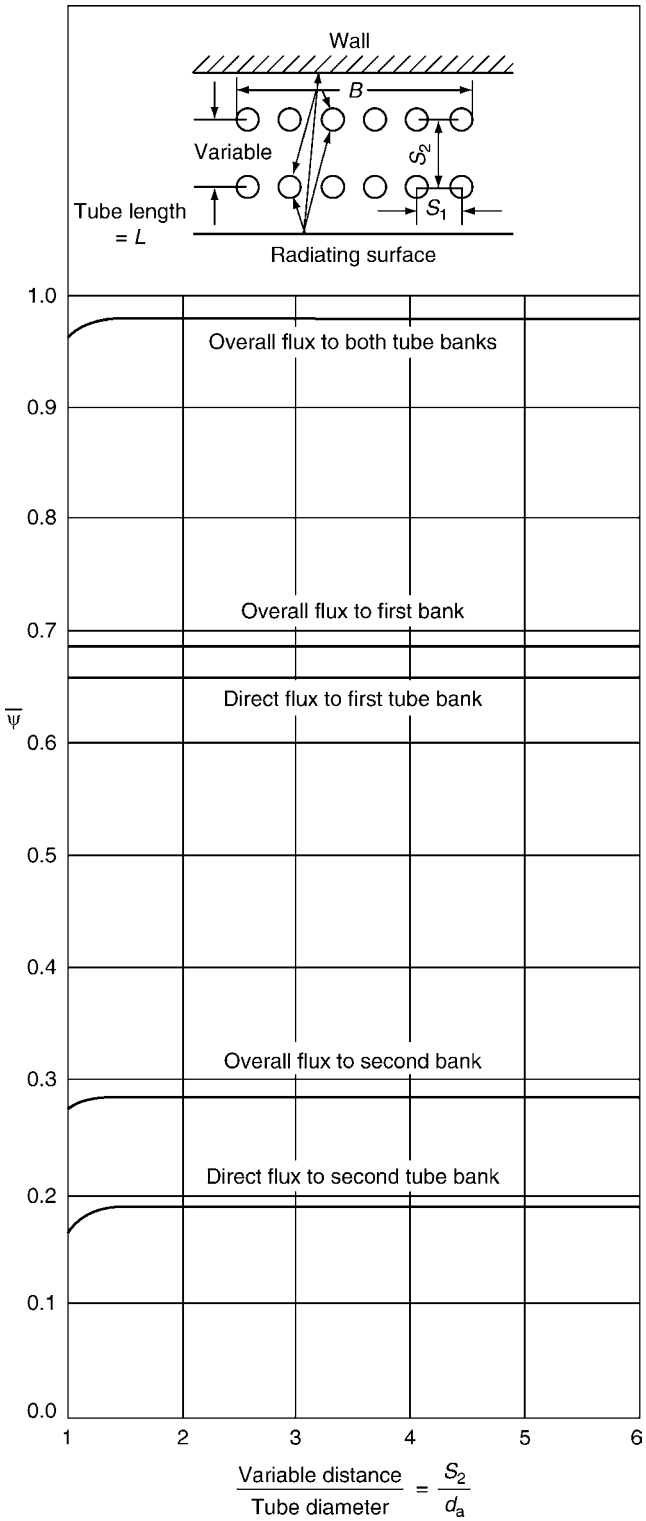

K2. Fig. 25. Area ratio $\bar{\Psi}$ for surface $A = B \times L$ lined by a row of tubes or by two rows arranged in line (spacing $s_1 = 2d_a$) [7].

If s is the center-to-center distance between the tube axes, as shown in Fig. 23, the radiant energy transferred per unit area of tube surface by the one bank of tubes is

$$\dot{q}_R = \frac{\dot{q}_W s}{d_a \pi}, \tag{32a}$$

and by two banks of tubes,

$$\dot{q}_R = \frac{\dot{q}_W s}{2 d_a \pi}. \tag{32b}$$

The values of $\bar{\Psi}$ for each of the two rows in a double bank of tubes can be obtained from Figs. 24 and 25. The heat applied to each row can be then determined from these figures.

5 Bibliography

1. Howell JR (1982) Radiation configuration factors. McGraw Hill, New York
2. Siegel R, Howell JR (1991) Thermal radiation heat transfer, 4th edn. Taylor Francis, New York, 2002; Teil 2, Springer-Verlag
3. Rao V, Sastri VM (1996) Efficient evaluation of diffuse view factors for radiation. Int J Heat Mass Transf 329(6):1281–1286
4. Clarksean R, Solbrig G (1994) Minimization of the effect of errors in approximate radiation view factors. Nucl Eng Des 149(1–3):431–440
5. Nußelt W (1928) Zeitschrift VDI 72 S. 673
6. Eckert E (1932) Archiv für Wärmewirtsch Bd. 13 S. 241
7. Hottel HC (1931) Trans Amer Mech Eng Bd. 53 S. 241
8. Eckert E (1937) Technische Strahlungsaustauschrechnungen und ihre Anwendung in der Beleuchtungstechnik und beim Wärmeaustausch. VDI-Verlag, Berlin

K3 Gas Radiation: Radiation from Gas Mixtures

Dieter Vortmeyer[1] · *Stephan Kabelac*[2]
[1]Munich, Germany
[2]Helmut-Schmidt-Universität, Universität der Bundeswehr Hamburg, Hamburg, Germany

Gases emit thermal radiation, just as liquids and solids do, when they are at a temperature $T > 0$ K. Radiation from gases is typically much less intense, as the volumetric density of the source of radiation, the molecules, is low. According to Kirchhoff's law, see ❯ Chap. K1, gases that emit radiation also absorb radiation. Unfortunately, the intensity and wavelength of emittance and absorbance are dependent on the structure of the gas molecules and are quite complicated. Dry air, elementary gases – e.g., O_2, N_2, H_2, – and the noble gases are practically diathermanous, i.e., transparent to thermal radiation. Other gases and vapors – e.g., H_2O, CO_2, CO, O_3, SO_2, HCl, NH_3, and CH_4 are selective radiators, i.e., they emit and absorb within narrow wavelength bands. Hydrocarbons also display characteristic emissivity and absorption to an extent that increases with the number of atoms in their molecules. In general, the spectral absorption and emission is a fingerprint of molecular structures which is used extensively for chemical spectroscopic analysis.

1 Radiant Intensity

Intensity is an important expression in formulating the laws of absorption and emission. If $\Delta\dot{E}$ is the radiant energy emitted from the small area ΔA within the beam formed by the solid angle $\Delta\Omega$ as is shown in Fig. 1, the intensity is defined by

$$I = \frac{\Delta\dot{E}}{(\Delta A \cos\beta\Delta\Omega)_{\Delta A,\Delta\Omega\to 0}} . \tag{1}$$

If the emission is within a vacuum, the intensity remains constant regardless of the distance from the radiating surface. It is for this reason that the laws of absorption are always formulated in terms of the intensity.

2 Absorption and Radiation in Gases at Constant Temperature

The decrease in intensity dI along a path ds is given by *Bouguer's law*, i.e.,

$$\mathrm{d}I = -aI\ \mathrm{d}s. \tag{2}$$

Equation (2) can be written in a spectral way as follows to show the dependence on wavelength λ:

$$\mathrm{d}I_\lambda = -a_\lambda I_\lambda \mathrm{d}s.$$

Thus, the decrease in intensity is proportional to the incident intensity multiplied by the element of length ds of the path traversed through the absorbing medium. The constant of proportionality a is known as the linear absorption coefficient. It contains the spectral absorptance a_λ and is dependent on temperature and pressure. With the assumption that a is proportional to the number of absorbing molecules in a given volume and that this number, in accordance with the ideal gas law, is related to the pressure, *Beer* converted the constant a into a product kp to obtain the law named after him, i.e.,

$$\mathrm{d}I = -kpI\mathrm{d}s. \tag{3}$$

If absorption takes place in gases at a constant temperature, the integration of Eqs. (2) and (3) gives

$$I = I_0 \mathrm{e}^{-as} \tag{4}$$

VDI-GVC (ed.), *VDI Heat Atlas*, DOI 10.1007/978-3-540-77877-6_42,

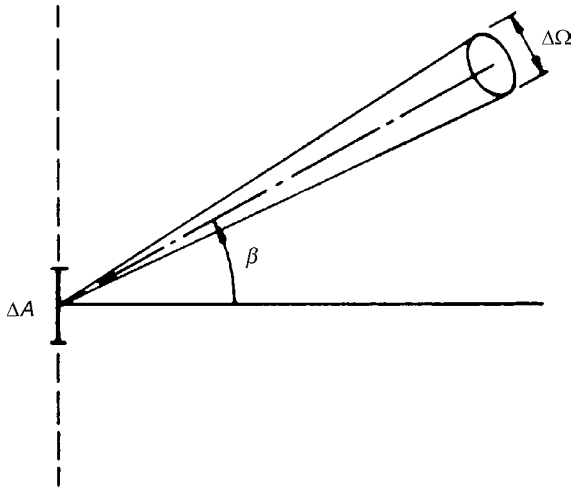

K3. Fig. 1. Definition of radiant intensity (see Eq. (1)).

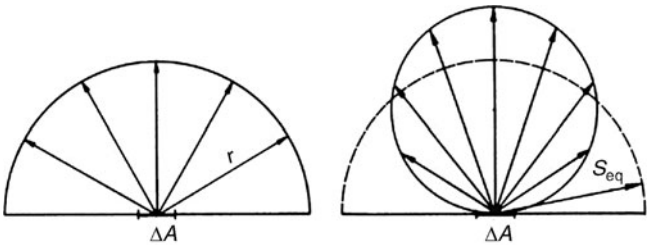

K3. Fig. 2. Effect of gas space geometry on the radiative exchange between the (a) wall element dA and (b) gas.

or

$$I = I_0 e^{-kps}. \tag{5}$$

The total intensity absorbed along the path s is

$$I_0 - I = I_0(1 - e^{-kps}). \tag{6}$$

Equation (6) describes the absorption of thermal radiation energy along a given "beam of intensity." However, the exchange of diffuse radiation between a diffuse radiating wall and the gas involves the additional problem of the geometry of the gas volume. To get the radiation energy flux exchange between an element dA of the wall and the gas, it has to be integrated along all the gas volume which is seen by the wall element. A hemisphere and a sphere have been taken as examples to illustrate the effect of the geometry.

In the hemisphere case (Fig. 2a), all the "beams of intensity" emitted by the element of area ΔA traverse paths of the same length r, but in the spherical space (Fig. 2b), the paths are each of different length. On its passage through the hemispherical gas volume, the energy emitted by ΔA is reduced by the amount absorbed, i.e.,

$$(1 - e^{-ar}). \tag{7}$$

It would be useful if the aforementioned notation for the absorptances, which are exactly valid only for the hemisphere case (Fig. 2a), could be applied to other geometries. This can be achieved by introducing an equivalent radius or the equivalent layer thickness s_{eq} (Fig. 2b) for r in Eq. (7).

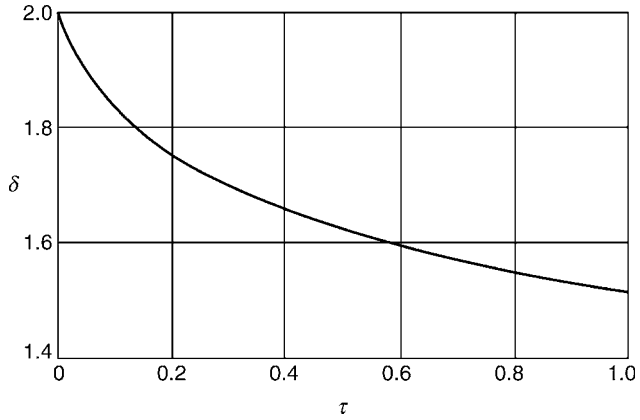

K3. Fig. 3. Layer of infinite extent between two parallel walls with distance D as an example to illustrate the relationship between the equivalence factor δ and the optical density τ, i.e., $\delta = s_{eq}/D$.

Thus

$$A_v = 1 - e^{-as_{eq}}, \tag{8}$$

where A_v is the geometry-dependent absorptance.

The equivalent layer thickness for the sphere shown in Fig. 2b, which may be regarded as representative for various other geometries, is the radius of the hemisphere that absorbs exactly the same amount of radiation as a hemisphere with radius $s_{eq.}$ A major disadvantage of this method is that s_{eq} for a given geometry still depends on the optical density of the absorbing gas medium. This is demonstrated by Fig. 3, in which exact values for $s_{eq}/D = \delta$ have been plotted against the optical density τ for a plane gas volume between two parallel walls with D being the distance between the walls, i.e., the beam length in this case.

Typical values derived from calculations of this nature are listed in Table 1, which are valid for optical densities of the order of about $\tau = 0.2$.

An approximate value for the equivalent radius s_{eq} for geometries not included in the table can be obtained from the equation

$$s_{eq} = 0.9\frac{4V}{A}, \tag{9}$$

where V is the gas volume under consideration and A is the wall area around the gas body.

The aforementioned remarks on absorption apply equally well to the emission of radiation from gas volumes at constant temperature.

The optical density is the product of a beam length s and the absorptance a and is designated by $\tau =$ s.a.

2.1 Emissivity of Carbon Dioxide and Water Vapor at a Total Pressure of $p = 1$ bar

Radiation by carbon dioxide and water vapor is an extremely important factor in thermal engineering design. Basically, the total radiant energy emitted by a gas of a given volume can be calculated if the spectral emissivity ε_λ is known, which has to be

K3. Table 1. Equivalent layer thickness $s_{eq} = \delta D$ for various gas bodies and for $\tau \approx 0.2$ (valid only for surfaces that emit diffuse radiation).

Gas body and nature of incident radiation	Characteristic dimension	Equivalence factor δ
Sphere	Diameter	0.63
Cylinder of infinite length		
Radiation onto circumference	Diameter	0.94
Radiation onto center of base		0.9
Radiation onto entire base		0.65
Cylinder $h = D$		
Radiation onto center of base	Diameter	0.71
Radiation onto entire surface		0.6
Cylinder $h = 0.5D$		
Radiation onto a base	Diameter	0.43
Radiation onto circumference		0.46
Radiation onto entire surface		0.45
Cylinder $h = 2D$		
Radiation onto both faces	Diameter	0.6
Radiation onto circumference		0.76
Radiation onto entire surface		0.73
Cylinder of infinite length with semicircular cross section		
Radiation onto center line of flat side	Radius	1.26
Cube	Length of side	0.6
Rectangle with sides of 1×4 length	Shortest side	
Radiation on 1×4 surface		0.82
Radiation on 1×1 surface		0.71
Radiation on entire surface		0.81
Rectangle with sides of $1 \times 2 \times 6$ length	Shortest side	
Radiation on 2×6 surface		
Radiation on 1×6 surface		1.06
Radiation on 1×2 surface		
Radiation on entire surface		
Plane layer of infinite extent between parallel walls	Wall spacing	1.76
Infinite space around tube bundles		
Center point of tubes on equilateral triangles	Inner spacing	2.8
Outer tube diameter = inner spacing		2.8
Outer tube diameter = half inner spacing		3.8
Center point of tubes on squares	Inner spacing	3.5
Outer tube diameter = inner spacing		

integrated over wavelength λ. The corresponding methods were developed by Nusselt [1], Schack [2], Hottel [3], Hertel [4], Goody [5], and Plass [6]. A summary of these methods is given in [7]. The need for these emissivities gave rise to extensive measurements at the temperatures, pressures, and layer thicknesses encountered in engineering practice. Thus, measurements performed by Schmidt, Eckert, Hottel, Mangelsdorf, Egbert [8–11], and others are still of fundamental significance.

The total emissivity ε_g was determined by experiment for various gases. It depends on the temperature, the thickness of the layer, the partial pressure p_g of the radiant gas, and – to a varying extent – on the total pressure p of the gas mixture.

According to Beer's law, see Eq. (3), the emission should depend solely on the product of the partial pressure and the thickness of the layer ($p_g s_{eq}$), but this could not be confirmed in all cases. Consequently, Hottel and Egbert compiled diagrams that retained the product $p_g s_{eq}$ as an important parameter but applied corrections for water vapor and carbon dioxide. Thus, Fig. 4 contains emissivities for carbon dioxide at a total pressure of $p = 1$ bar and for all partial pressures ($p_{CO_2} < 1$bar). Fig. 5b applies to water vapor with corrections given as a correction parameter f in accordance with Fig. 5a.

Figures 6–8 give the overall emissivity for the gases ammonia NH_3, sulfur dioxide SO_2, and methane CH_4, respectively, at a pressure of $p = 1$ bar.

2.2 Emissivity of Carbon Dioxide and Water Vapor at Elevated Total Pressures

Cheng and Nguyen [15] recommend a method that was developed by Leckner [16] for the determination of emissivity at elevated pressures. It consists of applying a correction factor for elevated pressures to the figures for the emissivity at $p = 1$ bar.

The following procedure applies for the emissivity of water vapor at elevated pressure $p > 1$ bar:

$$\varepsilon_{H_2O}(p) = f_{p,H_2O} \cdot \varepsilon_{H_2O}(p_{H_2O} s_{eq}, \text{Fig. 4}). \tag{10}$$

The correction parameter f_{p,H_2O} is given by

$$f_{p,H_2O} = 1 + (A-1)\exp\left[-0.5\left(\log\frac{0.132(T_g/1{,}000)^2}{p_{H_2O} s_{eq}}\right)^2\right], \tag{11}$$

$$A = \frac{(1{,}888 - 2{,}053\log\tau)p\left(1 + 4.9\frac{p_{H_2O}}{p}\sqrt{\frac{273}{T_g}}\right) + 1.10\left(\frac{T_g}{1{,}000}\right)^{-1.4}}{0.888 - 2{,}053\log\tau + p\left(1 + 4.9\frac{p_{H_2O}}{p}\sqrt{\frac{273}{T_g}}\right) + 1.10\left(\frac{T_g}{1{,}000}\right)^{-1.4}}, \tag{12}$$

where

$$\begin{aligned} &\tau = 0.75 \text{ for } T_g \le 750 \text{ K and} \\ &\tau = T_g/1{,}000 \text{ for } T_g > 750 \text{ K}. \end{aligned} \tag{13}$$

If the number for f_{p,H_2O} determined from Eq. (11) is higher than that for A determined from Eq. (12), the value to be taken is $f_{p,H_2O} = A$.

The method is recommended for the $1 \le p \le 100$ bar pressure range and for temperatures $T_g \ge 700$ K. There is no need to apply a correction for the partial pressure that relates to a total pressure of $p = 1$ bar, as indicated in Fig. 5a, because allowance

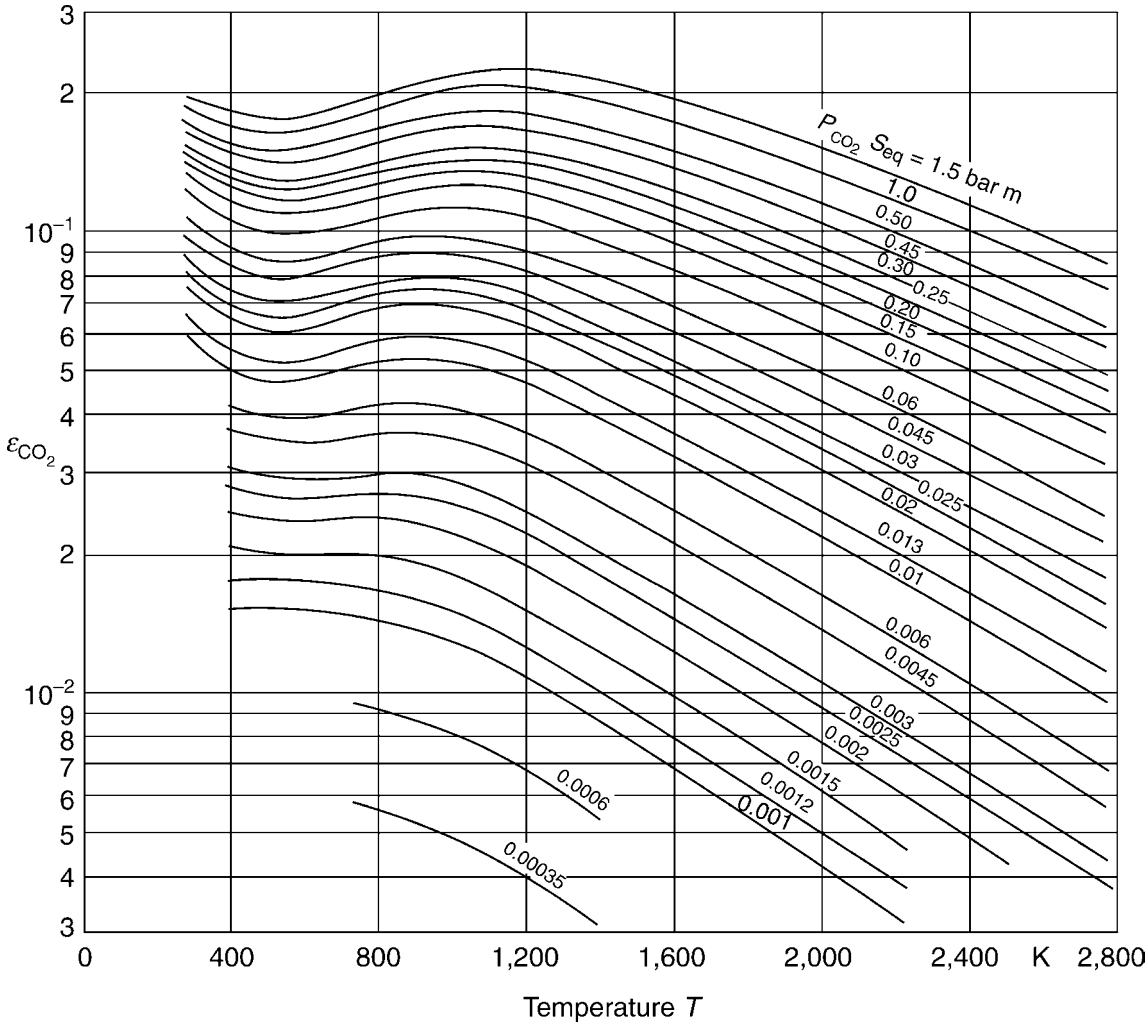

K3. Fig. 4. Emissivity ε_{CO_2} of carbon dioxide at a total pressure of 1 bar as a function of temperature and the product of $p_{H_2O}s_{eq}$ [12].

for the relationship between the correction factor and the partial pressure has been already been made in Eqs. (11) and (12).

2.2.1 Carbon dioxide

The emissivity of carbon dioxide at elevated pressures is given by

$$\varepsilon_{CO_2}(p) = f_{p,CO_2} \cdot \varepsilon_{CO_2}(p_{CO_2} s_{eq}, \text{Fig. 5}). \tag{14}$$

The pressure correction factor f_{p,CO_2} is given by

$$f_{p,CO_2} = 1 + (A-1)\exp\left[-0.5\left(\log\frac{B}{100 p_{CO_2} s_{eq}}\right)^2\right], \tag{15}$$

$$A = \frac{\left[0.1\left(\frac{T_g}{1{,}000\text{K}}\right)^{-1.45}+1\right]p\left(1+0.28\frac{p_{CO_2}}{p}\right)+0.23}{0.1\left(\frac{T_g}{1{,}000\text{K}}\right)^{-1.45}+p\left(1+0.28\frac{p_{CO_2}}{p}\right)+0.23}, \tag{16}$$

$$B = 0.225\left(\frac{T_g}{1{,}000\text{K}}\right)^2 \text{ for } T_g \geq 700 \text{ K},$$

$$B = 0.054\left(\frac{T_g}{1{,}000\text{ K}}\right)^2 \text{ for } T_g \leq 700 \text{ K}. \tag{17}$$

If the figure for f_{p,CO_2} determined by Eq. (15) is greater than that for A determined by Eq. (16), the value to be taken is $f_{p,CO_2} = A$. The method can be applied in the $0 \leq p \leq 100$ bar pressure range and for temperatures $T_g \geq 600$ K.

3 Radiative Exchange Between Gas and Wall

The following equation applies for the net flow rate of thermal radiation energy between a volume of gas and the wall that encloses the gas space:

$$\dot{Q}_{gw} = A\sigma\frac{\varepsilon_w}{1-(1-\varepsilon_w)(1-A_v)}(\varepsilon_g T_g^4 - A_v T_w^4). \tag{18}$$

It is valid only if the temperature, density, and concentration of the gas are constant in space, and its application requires a knowledge of the gas emissivity and absorptance. The emissivity depends solely on the equivalent layer thickness s_{eq} and the state of the gas (T_g, total pressure p, and partial pressure p_g of the gas

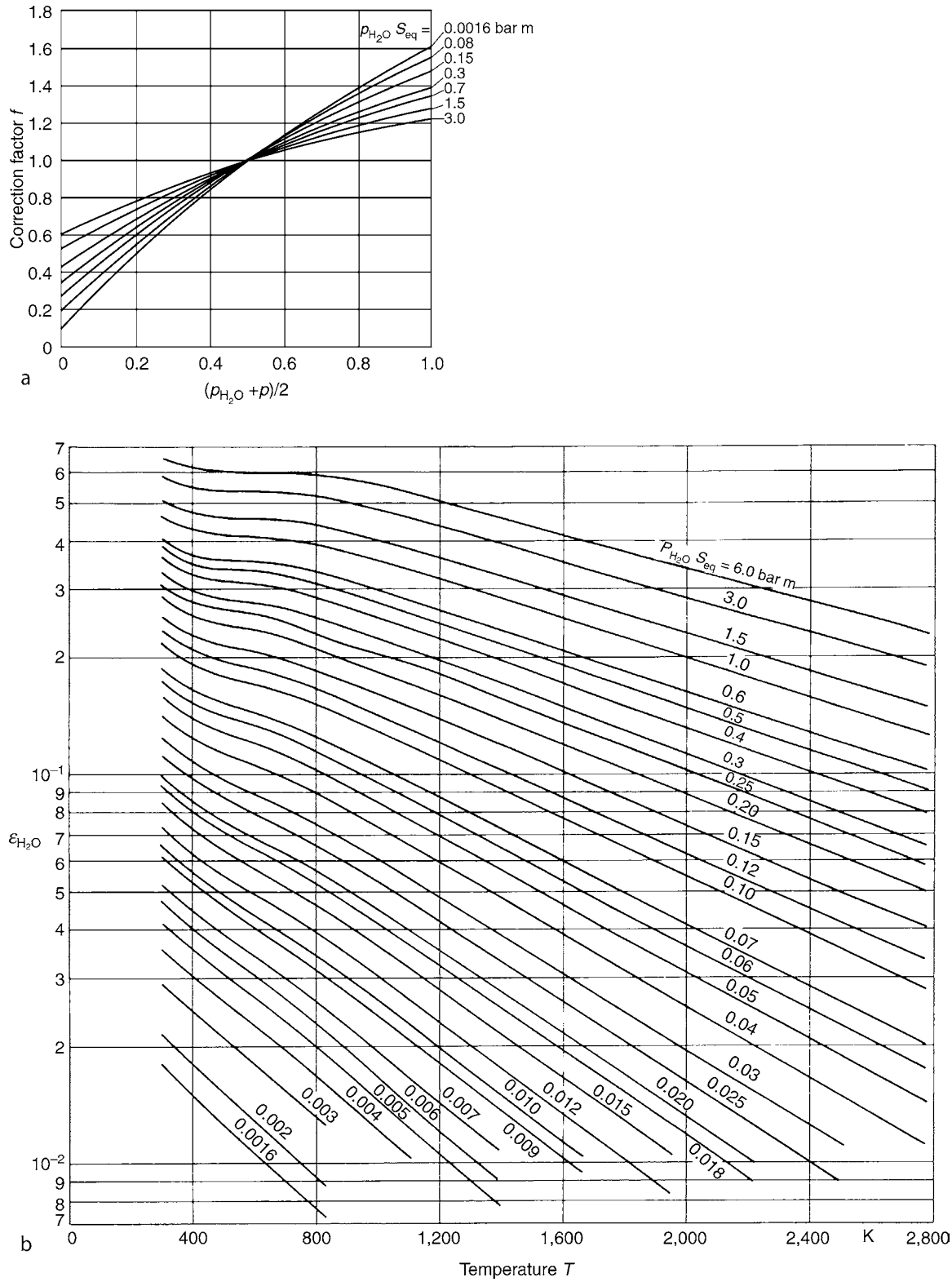

K3. Fig. 5. (**a**) Correction factor f for water vapor (total pressure $p \leq 1$ bar) [12]; (**b**) emissivity ε_{H_2O} of water vapor at a total pressure of 1 bar as a function of temperature and the product $p_{H_2O}s_{eq}$.

components). The absorptance however, also depends on the wall temperature T_w. Thus,

$$\varepsilon_g = \varepsilon_g(p, T_g, s_{eq}p_g),$$

$$A_v = A_v(p, T_g, T_w, s_{eq}p_g).$$

In all other cases reference is made to the corrections proposed by Hottel and Sarofim [17].

3.1 Water Vapor

$$A_v = \varepsilon_{gw}\left(\frac{T_g}{T_w}\right)^{0.45} \text{ for } p = 1 \text{ bar}.$$

The emissivity ε_{gw} can be read from Fig. 5b by taking into account the wall temperature T_w and the water vapor partial pressure $p_{H_2O}(T_w/T_g)$ which is converted to the value at the wall temperature

$$A_v = \left(\frac{T_g}{T_w}\right)^{0.45} \cdot \varepsilon_g\left(T_w; s_{eq} \cdot p_{H_2O} \cdot \frac{T_w}{T_g}\right) \text{ for } p = 1 \text{ bar}. \quad (19)$$

A correction factor f must be introduced to allow for the effect of the total pressure and the water vapor partial pressure on the wavelength ranges of spectral emission. This correction factor is shown in Fig. 5a for a pressure of up to 1 bar, and can be calculated from Eq. (11) for a pressure of $p > 1$ bar:

$$A_v = f\left(\frac{T_g}{T_w}\right)^{0.45} \cdot \varepsilon_g\left(T_w; s_{eq} \cdot p_{H_2O} \cdot \frac{T_w}{T_g}\right). \quad (20)$$

3.2 Carbon dioxide

$$A_v = f_{p,CO_2}\left(\frac{T_g}{T_w}\right)^{0.65} \cdot \varepsilon_g\left(T_w; s_{eq} \cdot p_{CO_2} \cdot \frac{T_w}{T_g}\right), \quad (21)$$

in which f_{p,CO_2} is given by Eq. (15) or $f_{p,CO_2} = 1$ for $p = 1$ bar.

3.3 Sulfur dioxide

$$A_v = \left(\frac{T_g}{T_w}\right)^{0.5} \cdot \varepsilon_g\left(T_w; s_{eq} \cdot p_{SO_2} \cdot \left(\frac{T_w}{T_g}\right)^{1.5}\right) \quad (22)$$

for $p = 1$ bar.

No corrections are known for other total pressures.

3.4 Ammonia and Methane

Emissivities for ammonia and methane can be obtained from Figs. 6 and 8. No formulae yet exist for converting A_v for these

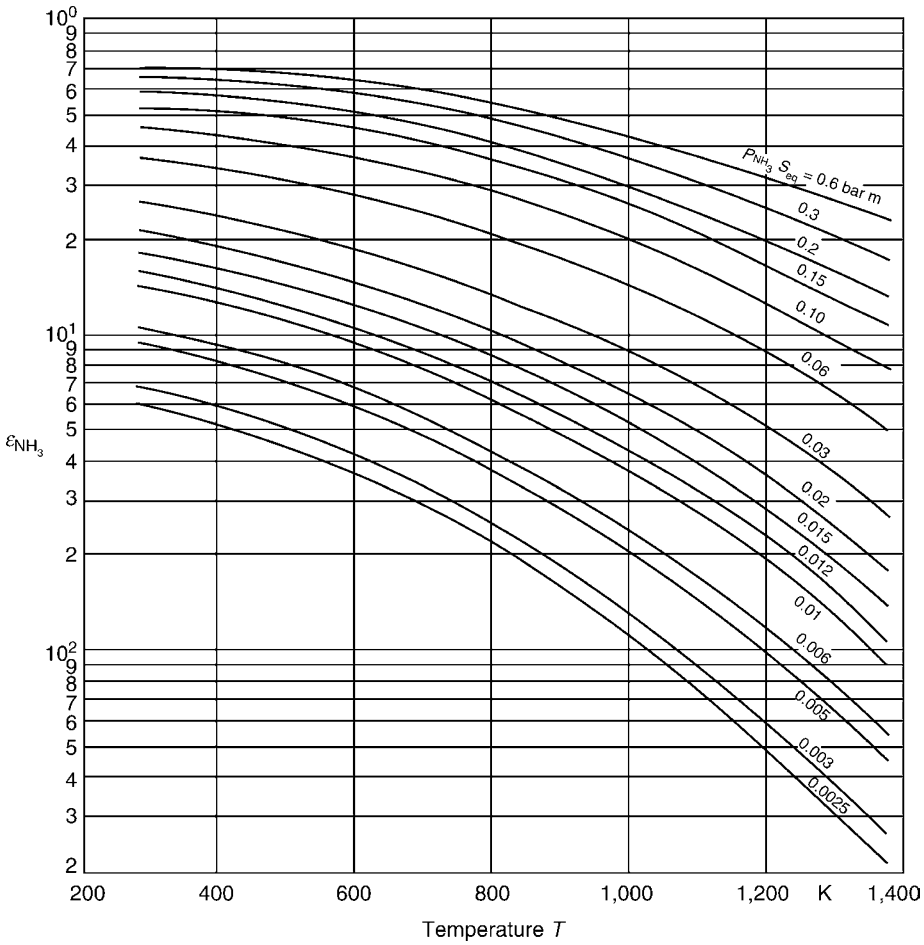

K3. Fig. 6. Emissivity of ammonia at a total pressure of 1 bar as a function of temperature and $p_{NH_3}s_{eq}$ [12].

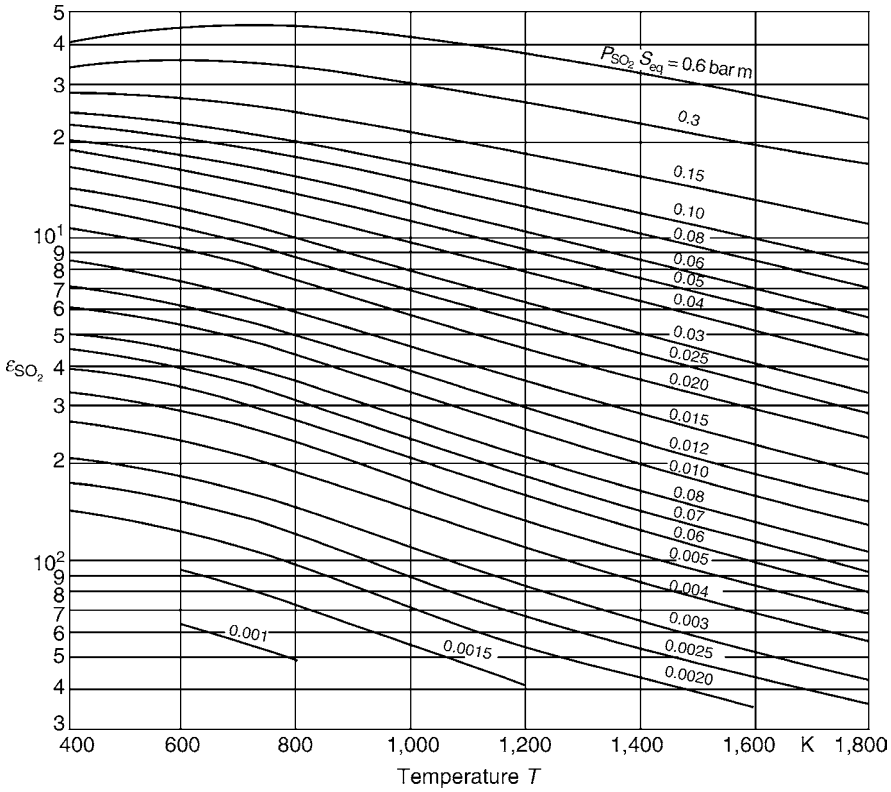

K3. Fig. 7. Emissivity of sulfur dioxide at a total pressure of 1 bar as a function of temperature and $p_{SO_2} s_{eq}$ [13].

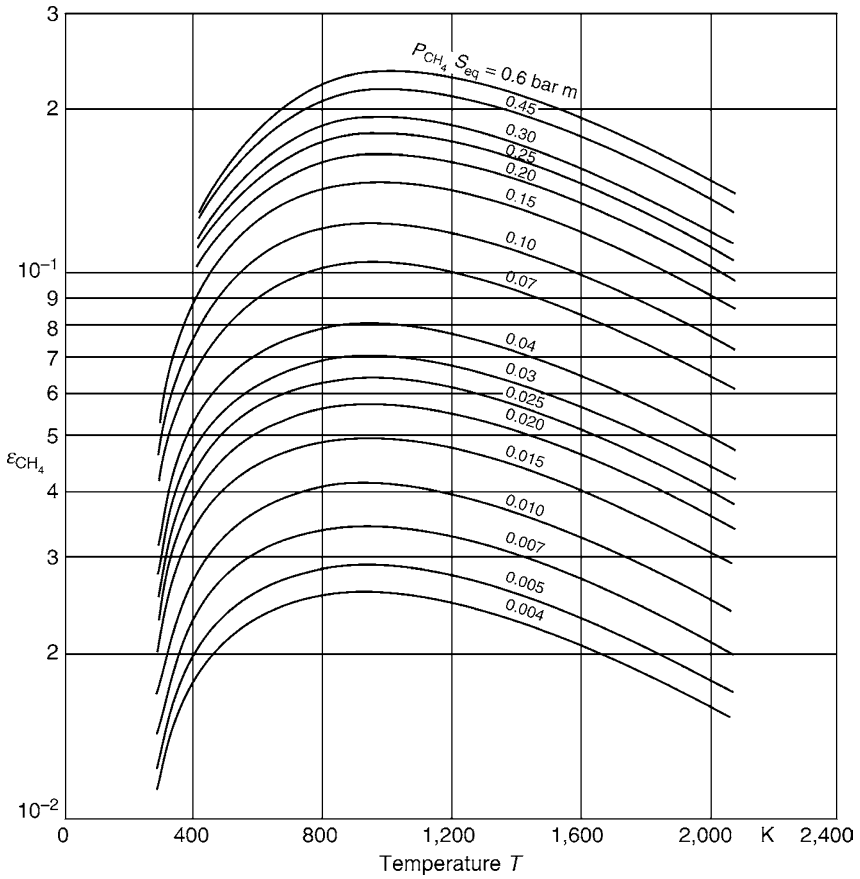

K3. Fig. 8. Emissivity of methane at a total pressure of 1 bar as a function of temperature and $p_{CH_4} s_{eq}$ [14].

gases, nor are there any correction factors for pressures other than 1 bar. For this reason, the relationship $\varepsilon_g = A_v$ should be adopted in radiative exchange calculations for these gases.

Other methods for the calculation of the radiant heat flux $\dot{Q}_{gw}$ have been suggested by Eckert [9] and – in an improved form – by Elgeti [18]. The results thus obtained for carbon dioxide and water vapor agree satisfactorily with those determined by Eq. (18).

4 Gas Mixtures

Hottel and Egbert [11] have suggested the following equations for the determination of the emissivity and absorptance of mixtures consisting of carbon dioxide, water vapor, and nonradiant components:

$$\varepsilon_g = \varepsilon_{H_2O} + \varepsilon_{CO_2} - (\Delta\varepsilon)_g, \tag{23a}$$

$$A_v = A_{vH_2O} + A_{vCO_2} - (\Delta\varepsilon)_w. \tag{23b}$$

The values of $(\Delta\varepsilon)_g$ and $(\Delta\varepsilon)_w$ at the corresponding gas and wall temperatures are obtained from Fig. 9a–c. This correction is necessary because of the overlap of the individual emission bands of the gases involved. The emissivities and absorptances for each of the components are read from the diagrams given earlier for the partial pressures at hand.

Example 1

Determine the net flow rate of radiant energy in a cube filled with gas under the following conditions:

Length of side of cube	$D = 1$ m
Wall temperature	$T_w = 600°C$
Gas temperature	$T_g = 1{,}400°C$
Wall emissivity	$\varepsilon_w = 0.9$

The gas contains 11% of water vapor and 10% of carbon dioxide (by volume). The rest is a nonradiant component. The total pressure is 1 bar.

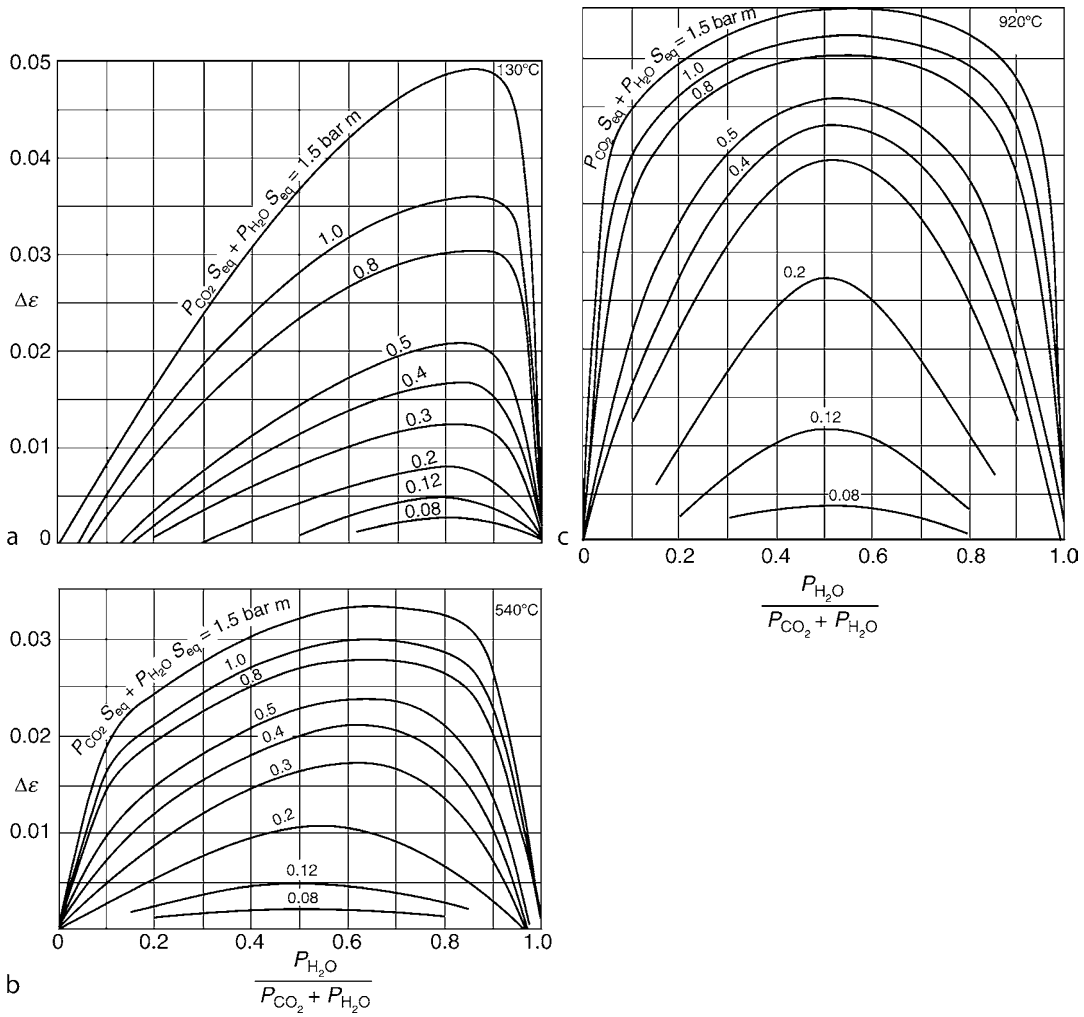

K3. Fig. 9. Correction $\Delta\varepsilon$ for mixtures of carbon dioxide and water vapor at (**a**) 130°C, (**b**) 540°C, and (**c**) 920°C and above [14].

From Table 1 the equivalent length for a cube is $s_{eq} = 0.6D$.

$$p_{CO_2} s_{eq} = 0.06 \text{ bar} \cdot \text{m} \text{ and } p_{H_2O} s_{eq} = 0.066 \text{ bar m}.$$

The following values for ε_{CO_2} and ε'_{H_2O} can be read from the diagrams in Figs. 4 and 5:

$$\varepsilon'_{H_2O} = 0.052 \text{ (uncorrected) and } \varepsilon_{CO_2} = 0.063.$$

Applying the correction factor f_{H_2O} obtained from Fig. 5a gives

$$\varepsilon_{H_2O} = 0.052 \cdot 1.08 = 0.0562.$$

The total emissivity of the gas, as obtained from Fig. 9c and Eq. (25), is $\varepsilon_g = 0.108$.

The absorptance of the individual gases is determined from Eqs. (19) and (21). First of all, the emissivities $(\varepsilon_{H_2O})_w$ and $(\varepsilon_{CO_2})_w$ are read off from Figs. 4, 5, and 5a, but in this case against the wall temperature and the corrected product of the partial pressure and the equivalent thickness of the layer. Thus,

$$(\varepsilon_{CO_2})_w = 0.078; \quad (\varepsilon_{H_2O})_w = 0.079.$$

It follows that $A_{vCO_2} = 0.119$ and $A_{vH_2O} = 0.106$.

The term for correcting the total absorptance of the mixture is read off against the wall temperature T_w in Fig. 9b. Thus, $(\Delta\varepsilon)_w = 0.005$.

Therefore, the total absorptance is $A_{vtot} = 0.22$.

Inserting this value in Eq. (18) gives a net radiant energy flow rate of $\dot{Q}_w = 238$ kW.

Example 2

A gas at a temperature $T = 1{,}600$ K and a pressure $p = 10$ bar contains 20% of water vapor. Determine the emissivity for an equivalent layer thickness $s_{eq} = 0.1$ m.

An emissivity of $\varepsilon_{H_2O}(p = 1 \text{ bar}) = 0.122$ can be read for a temperature $T = 1{,}600$ K and $p_{H_2O} \cdot s_{eq} = 0.2$ bar m.

From Eq. (13) $\tau = 1.6$; and from Eq. (12), $A = 1.4095$. Inserting this value for A in Eq. (11) $f_{p,H_2O} = 1{,}399$ for the pressure correction factor. Hence, the emissivity is $\varepsilon_{H_2O}(p = 10 \text{ bar}) = 1{,}399 \cdot 0.122 = 0.171$.

5 Analytical Calculation of the Emissivities of H_2O, CO_2 and their Mixtures

For computer-based calculations the total emissivities and absorptivities of real gases can be determined using the "gray-and-clear gas approximation" [17] (also called "weighted sum of gray gases model"). For carbon dioxide CO_2 at a total gas pressure of $p = 1$ bar and a partial pressure of 0.01 mbar $< p_{CO_2} s_{eq} <$ 10 mbar and at temperatures between 300 K $< T_g <$ 1,800 K [19], we have

$$\varepsilon_{CO_2} = Z - \sum_{i=1}^{6} a_i \exp(-k_i p_{CO_2} s_{eq}),$$

$$Z = c_1 + c_2 \frac{T_g}{1{,}000 \text{ K}} + c_3 \left(\frac{T_g}{1{,}000 \text{ K}}\right)^2,$$

$$a_i = b_{1i} + b_{2i} \frac{T_g}{1{,}000 \text{ K}} + b_{3i} \left(\frac{T_g}{1{,}000 \text{ K}}\right)^2. \quad (24)$$

The values of the coefficients in Eq. (24) are summarized below.

i	b_{1i}	b_{2i}	b_{3i}	k_i (1/mbar)
1	0.1074	−0.10705	0.072727	0.036
2	0.027237	0.10127	−0.043773	0.3586
3	0.058438	−0.001208	0.0006558	3.06
4	0.019078	0.037609	−0.015424	14.76
5	0.056993	−0.025412	0.0026167	102.28
6	0.0028014	0.038826	−0.020198	770.6

$c_1 = 0.27769$, $c_2 = 0.03869$ and $c_3 = 1.4249 \cdot 10^{-5}$.

For water vapor H_2O at a total gas pressure of $p = 1$ bar, temperatures between 700 K $< T_g <$ 1,500 K, and partial pressures between 0.05 mbar $< p_{H_2O} s_{eq} <$ 0.5 mbar or 0.5 mbar $< p_{H_2O} s_{eq} <$ 2 mbar [19] we have

$$\varepsilon_{H_2O} = Z - a \exp(-k p_{H_2O} s_{eq}),$$

$$Z = b_1 + b_2 \frac{T_g}{1{,}000 \text{ K}},$$

$$a = b_3 + b_4 \frac{T_g}{1{,}000 \text{ K}}. \quad (25)$$

The coefficients in Eq. (25) are as follows:

$p_{H_2O} s_{eq}$	0.05 . . . 0.5	0.5 . . . 2
b_1	0.43265	0.66439
b_2	−0.1089	−0.17389
b_3	0.3273	0.4572
b_4	−0.043821	−0.1317
k (1/mbar)	3.5829	0.84652

For a mixture of H_2O and CO_2 at a total pressure of $p = 1$ bar for $p_{H_2O}/p_{CO_2} = 1$, temperatures between 1,100 K $< T_g <$ 1,800 K, and equivilant layer thickness between 0.2 m $< s_{eq} <$ 6 m [20] we have

$$\varepsilon_{H_2O+CO_2} = \sum_{i=1}^{3} a_i \left[1 - \exp\left(-k_i (p_{H_2O} + p_{CO_2}) s_{eq}\right)\right],$$

$$a_i = b_{1i} + b_{2i} \frac{T_g}{1{,}000 \text{ K}}. \quad (26)$$

The coefficients for Eq. (26) are as follows:

i	b_{1i}	b_{2i}	k_i (1/mbar)
1	0.130	0.265	0
2	0.595	−0.15	0.824
3	0.275	−0.115	25.91

The corresponding degrees of absorption are readily calculated by using the same Eqs. (24–26) when the temperature of the emitting wall T_w is used instead of the temperature of the gas T_g.

6 Radiation from Gas Volumes at Nonuniform Temperatures

No simple solutions can be offered for this very difficult mathematical task, and reference must be taken to the literature [17, 21, 22]. However, the publications available are concerned more with the solutions of one-dimensional than of three-dimensional problems. An interesting contribution in this connection was made by Pandaya [23], who observed that the radiation in a space through which gas flowed and in which the temperature profile was curved (i.e., the temperature at the center was higher than that at this sides) could be adequately described by the arithmetic mean temperature.

Another subject that attracts great attention is radiation from luminous flames, in which case the emission from the carbon dioxide and water vapor is considerably augmented by that from small particles of incandescent soot. The formation of carbon particles depends on the entire conditions and still defies mathematical analysis. Another difficulty is the determination of the exact temperature of particles that can still enter into chemical reactions. In view of the importance attached to the problem, numerous studies have been performed on flames, with the consequence that at least some information is available on the estimation of radiation effects for certain types of flame. Details are given in publication by Hottel [17] and Schack [2, 24].

7 Combined Heat Transport by Conduction and Radiation in Gases, Liquids, and Molten Glass

A mathematical description of this subject entails integral–differential equations. Simplifications can be made if the radiant medium is optically dense, and transport by radiation can therefore be determined by a Fourier-type equation for thermal radiation (diffusion approximation). The first fundamental studies in this sector were performed on molten glass by Czerny and Genzel [25, 26] and Walther et al. [27].

More information on combined heat transport calculations is given by Sparrow and Cess [21].

It is not surprising that the proportion of radiation in the total heat flux becomes greater at high temperatures. However, Poltz [28] and Schödel and Grigull [29] have demonstrated that substantial proportions of radiation are present in the heat flux from liquids at temperatures of the order of 298 K. These proportions depend on the radiation characteristics of the liquid and geometric factors. The authors last cited made use of interferometry in order to present the hook-shaped temperature profile determined mathematically by Walther et al. [27] in a visible form.

8 Symbols

T_g	gas temperature (K)
T_w	wall temperature (K)
ε_g	emissivity of the gas (–)
ε_w	emissivity of the wall which surrounds the gas (–)
ε'_g	emissivity of the gas without pressure correction (–)
ε_{gw}	emissivity of the gas, based on wall temperature (–)
$\Delta\varepsilon$	correction parameter for calculating gas mixtures (–)
A_v	absorptance of the gas, being a function of geometry (–)
T	optical density (–)
R	radius (m)
s_{eq}	equivalent layer thickness (m)
p_g	partial pressure of a gas component (bar)
I	intensity (W m^{-2} sr^{-1})
$\dot{Q}_{gw}$	radiation heat flux between gas body and wall (W)
Δ	equivalence ratio (–)
D	characteristic length (m)
A	degree of absorption (–)

9 Bibliography

1. Nußelt W (1923) Der Wärmeübergang in der Verbrennungskraftmaschine. VDI-Forsch.-Heft Nr. 264. VDI-Ver, Düsseldorfl
2. Schack A (1924) Z Techn Phys 15:267
3. Hottel HC (1927) Trans Am Inst Chem Eng 19:173
4. Hertel T (1992) Ein Modell für die Berechnung der Gasstrahlung. (A model for calculation of gas radiation). Diss., TH Darmstadt
5. Goody RM (1952) Quart J R Meteorol Soc 78:165
6. Plass GN (1958) J Opt Soc Am 48:690–703
7. Siegel R, Howell JR (2002) Thermal radiation heat transfer, 4th edn. Taylor & Francis, New York
8. Schmidt E, Eckert E (1937) Forsch Ing Wes 8:87
9. Eckert E (1937) Messung der Gesamtstrahlung von Wasserdampf and Kohlensäure mit nichtstrahlenden Gasen bei Temperaturen bis zu 1 300 K. VDI-Forsch.-Heft 387
10. Hottel HC, Mangelsdorf HG (1935) Trans Am Inst Chem Eng 31:517
11. Hottel HC, Egbert RB (1942) Trans Am Inst Chem Eng 38:581
12. Port FJ (1940) Sc. D. Thesis in Chemical Engineering. MIT Cambridge, MA
13. Guerrieri SA (1932) S. M. Thesis in Chemical Engineering. MIT Cambridge, MA
14. Lee RHC, Happel J (1967) Ind Eng Chem Fundam 3:167
15. Cheng SCh, Nguyen C (1989) Emissivity of water vapour at elevated pressures. Int Commun Heat Mass Transfer 16:723–729
16. Leckner B (1972) Spectral and total emissivity of water vapor and carbon dioxide. Comb Flame 19:33–48
17. Hottel HC, Sarofim AF (1967) Radiative transfer. McGraw-Hill, New York
18. Elgeti K (1962) BWK 14:1–6
19. Farag IH (1982) Non luminous gas radiation: approximate emissivity models. Proceedings of the 7th international heat transfer conference, Munich, Germany, vol R6, pp 481–492
20. Johnson TF, Beér JM (1973) The zone method analysis of radiant heat transfer: A model for luminous radiation. J Inst Fuel 46:301–309
21. Sparrow EM, Cess RD (1978) Radiation heat transfer, Augm. Ed. Hemisphere Publ., Washington
22. Siegel R, Howell JR (2002) Thermal radiation heat transfer, 4th edn. Taylor & Francis, New York
23. Pandaya SB (1961) Untersuchung über die Strahlung von Gaskörpern ungleicher Temperatur (Study on the radiation of gas volumes with nonuniform temperature). Diss., RWTH Aachen
24. Schack A (1962) Der Industrielle Wärmeübergang. Stahleisen Publications, Düsseldorf
25. Czerny M, Genzel L (1952) Glastechn Ber 25:387–392
26. Genzel L (1953) Glastechn Ber 26:69–71
27. Walther A, Dörr J, Eller E (1953) Glastechnische Ber 26:133–140
28. Poltz H (1965) Int J Heat Mass Transfer 8:609–620; 515–527
29. Schödel G, Grigull U (1970) Proceedings of the 4th international heat transfer conference, vol 111. Paper R. 2.2

K4 Thermal Radiation of Gas–Solids–Dispersions

Hans-Gerd Brummel
Siemens Power Generation, Berlin, Germany

1 Introduction

Particles, e.g., fly ash entrained in the combustion gas flow of a steam generator, can considerably increase the radiant energy emitted by those hot gases. Depending on the wavelength as well as on the spectral optical properties (i.e., the complex refractive index) and size distribution of the particles, thermal radiation is being emitted, absorbed and scattered by the dispersed solids. For the emissivity of the dispersed particles their concentration in the gas (in the following referred to as "load") is the most governing parameter.

Two mathematical models, designed for different applications and boundary conditions, are presented in this section for the determination of the emissivity of a particle cloud.

The particle load represents the parameter, which has the highest impact on the emissivity of the dispersed solids. In cases, where the load of particles is low, as found in combustion chambers of oil and pulverized coal fired steam generators, a simple model can be applied with good accuracy, which is only taking into account the absorption/emission of the particles, neglecting any sort of radiation scattering by those solids.

This simple radiation model shall be presented here at first (see Sect. 2 of this chapter). It is comparable with the particle radiation approach of Chap. K5 ("Thermal Radiation in Combustion Environments"), which combines the heat transfer phenomena resulting from gas, soot, fly ash, and coal/coke radiation.

For technical processes which are characterized by small particle sizes combined with higher particle loads, a more complex radiation model will be presented in Sect. 3 of this Chapter, which also takes into account scattering effects, caused by those particles. This model fully includes the above-mentioned simple model as a special case, it is generally applicable, but is characterized by a slightly higher calculation effort.

After dealing with the particle radiation in greater detail (see in particular various calculation examples in Sect. 4 of this Chapter), the combination of particle and carrier gas radiation (topic of Chap. K3) will be covered subsequently in Sects. 5 and 6 of this Chapter.

2 Particle Radiation: Simplified Thermal Radiation Model for Low Particle Loads

For applications with operating conditions, where the exponent in Eqs. (1) or (2) does not exceed a limiting absolute value of 0.5, which is usually the case in conventional pulverized coal-fired boilers with combustion chambers of small to medium size, the emissivity of the particle cloud can be determined by a simple absorption model [1], neglecting any scattering of radiation by the particles (see Sect. 7 of this Chapter for symbol definitions).

$$\varepsilon_\mathrm{p} = 1 - \exp(-\bar{Q}_\mathrm{abs} A L_\mathrm{p} l_\mathrm{mb}) \tag{1}$$

or

$$\varepsilon_\mathrm{p} = 1 - \exp\left(-k \frac{3}{2\rho_\mathrm{p}} d_\mathrm{p}^{-2/3} L_\mathrm{p} l_\mathrm{mb}\right), \tag{2}$$

with

$$d_\mathrm{p} = \frac{3}{2\rho_\mathrm{p} A} \tag{3}$$

and

$$k = \bar{Q}_\mathrm{abs} d_\mathrm{p}^{-1/3}. \tag{4}$$

VDI-GVC (ed.), *VDI Heat Atlas*, DOI 10.1007/978-3-540-77877-6_43,

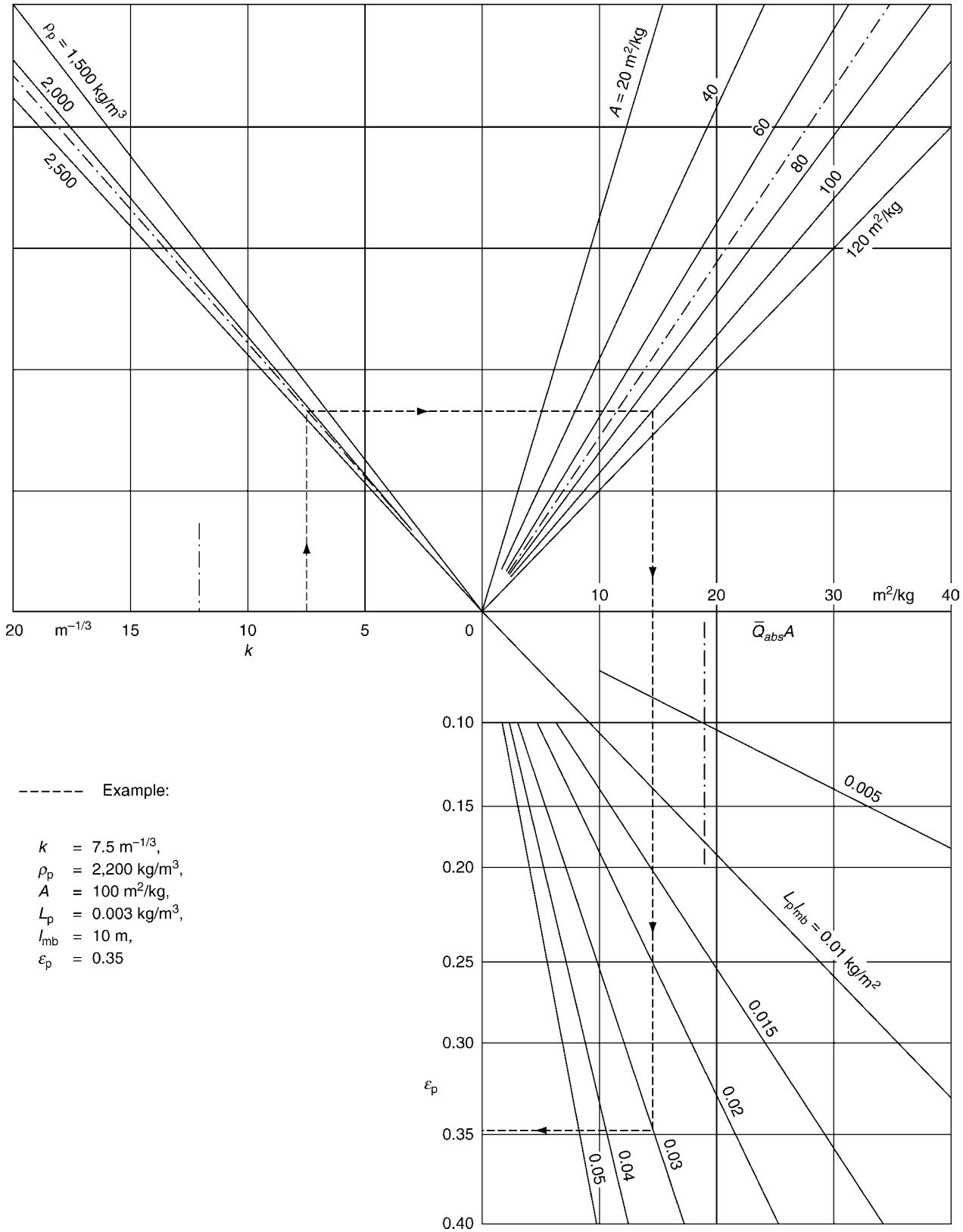

K4. Fig. 1. Nomogram for the determination of the dispersed particles emissivity ε_p as a function of the particle substance constant k (in $m^{-1/3}$) or the effective absorption projection area $\bar{Q}_{abs}A$ (in m^2/kg), respectively, the material density ρ_p, the particle load L_p (in kg/m^3), and the mean beam length l_{mb} (in m).

The nomogram shown in Fig. 1 can be applied alternatively to Eqs. (1) or (2).

The data required for the application of this calculation model or the nomogram were determined by Biermann and Vortmeyer [1] in studies on fly ash, compiled in Table 1. Data for particle load L_p and density of the fly ash material ρ_p were the easiest to obtain. The fly ash density was measured by means of a pycnometer (see VDI 2031). The surface measurements for the determination of the specific projection area of the particles A and the mean particle diameter d_p were performed with the Blaine permeabilimeter (by VDI 2031 method, other methods may result in different figures). The only way of determining the parameters $\bar{Q}_{abs}$ or k, respectively, characterizing the absorption of the particles, was by means of emission measurements. A wide range of data for $\bar{Q}_{abs}$, which actually were found independent of temperature (investigated range 723–1,323 K), are listed in Table 1. It has to be noted that these data are only valid for the related mean particle diameter d_p, also listed in the table.

Remarks

These data for the mean relative absorption efficiency $\bar{Q}_{abs}$ (or the substance constant k, respectively), which are compiled in Table 1 for 20 fly ashes cannot be used directly any longer, because most of the coal mines do not exist anymore and blending of imported coal nowadays is a common practice.

Nevertheless, the figures are still valid to provide an orientation concerning the range of the mean relative absorption efficiencies for coal ashes in general.

These data were also used as basis to derive representative optical properties for fly ashes in conjunction with the more complex radiation model presented in the following section.

3 Particle Radiation Model for Higher Particle Loads

Experiences have shown [1, 9] that the equations presented above in Sect. 2 of this Chapter show a tendency to overestimate the heat transfer from clouds of small ash particles to heating surfaces for processes with higher loads than found in conventional atmospheric pulverized coal fired boilers, such as fluidized bed combustion, entrained pressurized coal gasification, and pressurized pulverized coal combustion.

The root cause for this overestimation is the scattering of the radiation by the particles. The backwards scattered fraction attenuates the radiation heat transfer to the enclosure walls.

Figure 2 shows schematically the angular intensity distribution of the radiation, scattered by a spherical particle in dependency of the particle size parameter p, which is defined as a function of the diameter of the sphere d_{sph} and the wavelength λ of the incident radiation.

In the context of his experimental studies (see Sect. 2 of this Chapter above), Biermann together with Vortmeyer developed also a two-flux model [1] for the determination of the particle

K4. Table 1. Data on various types of fly ashes and limestone particles (Biermann and Vortmeyer [1])

Serial no.	Origin of fly ash		ρ_p, kg/m³	A, m²/kg	d_p, 10^{-6} m	$\bar{Q}_{abs}A$, m²/kg	$\bar{Q}_{abs}$	k, $m^{-1/3}$
	Coal	Firing						
1	Ruhr-Westerholt	Slag-tap	2,110	113.0	6.3	40.6	0.360	19.5
2	Ruhr + US	Slag-tap	2,220	74.8	9.0	30.5	0.408	19.6
3	Lower Rhine/Lohberg	Slag-tap	2,130	79.0	8.9	17.5	0.221	10.7
4	Lower Rhine/Lohberg	Slag-tap	2,290	87.0	7.5	17.6	0.202	10.3
5	Ruhr blend	Grate	2,200	56.0	12.2	14.4	0.257	11.2
6	Saar	Dry bottom	2,230	111.7	6.0	15.8	0.142	7.8
7	Ruhr-Gneisenau	Dry bottom	2,270	42.8	15.4	13.3	0.310	12.5
8	Upper Palatinate Lignite	Dry bottom	2,360	99.5	6.7	24.5	0.246	13.1
9	Saar	Cyclone	2,050	47.0	15.6	14.3	0.305	12.2
10	Ruhr-Marl	Cyclone	2,330	70.0	9.2	16.0	0.229	10.9
11	Saar	Dry bottom	2,370	55.2	11.5	17.4	0.315	14.0
12	Ruhr blend	Cyclone	2,550	73.1	8.1	18.0	0.246	12.3
13	Ruhr-Gneisenau	Cyclone	2,250	120.0	5.6	22.9	0.191	10.8
14	Ruhr blend	Dry bottom	1,930	82.0	9.5	21.3	0.260	12.3
15	Lignite Helmstedt	Dry bottom	2,580	33.6	17.3	9.94	0.295	11.4
16	West Virginia	Dry bottom	1,980	59.3	12.8	23.5	0.396	16.9
17	Ruhr-Prosper + Brassert	Cyclone	2,360	69.0	9.2	8.9	0.128	6.15
18	Ruhr-Marl	Cyclone	2,100	67.3	10.6	21.4	0.318	14.5
19	Hungarian Lignite I	Dry bottom	1,640	42.3	21.6	16.6	0.392	14.1
20	Hungarian Lignite II	Dry bottom	1,660	30.5	29.6	9.3	0.305	9.86
21	Limestone		2,700	38.7	14.4	5.84	0.150	6.17

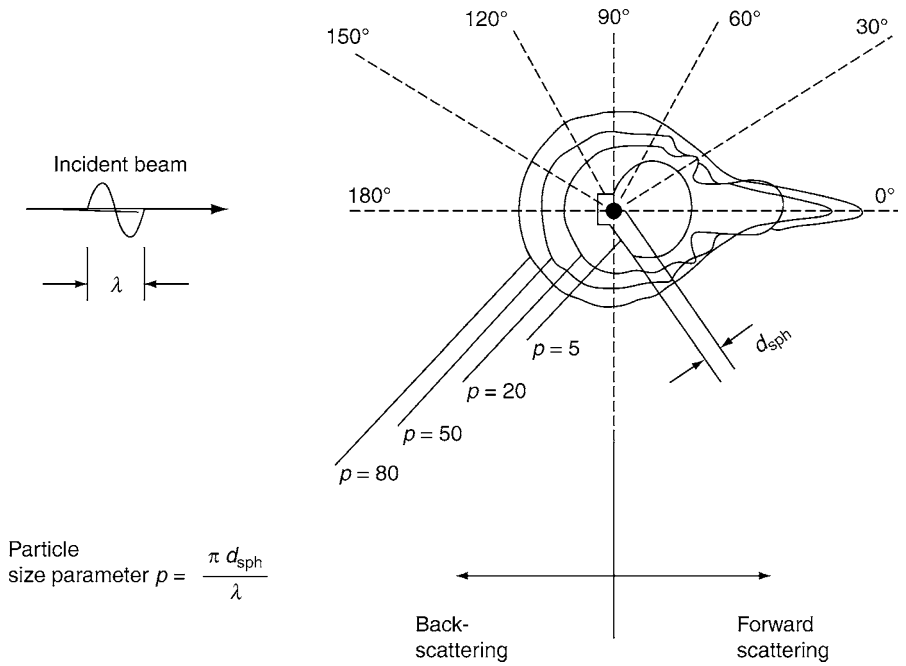

K4. Fig. 2. Angular distribution of the scattered intensity of incident radiation of wavelength λ hitting a spherical particle, in dependency of the particle size parameter p. Principal diagram of intensity distribution, taken from [10].

emissivity, taking scattering into account. Here the total scattered radiation is split into a forward and a backward fraction (backscattering). Forward scattering is treated in the model as having no impact on the radiation (in a two-flux model incident radiation and scattered radiation have the same direction), but backward scattering attenuates the emissivity, redirecting part of the radiation in the opposite direction.

In principle, the angular scattering distribution and also the radiation absorption of a particle can be calculated by means of the generally applicable electromagnetic theory published by Mie [2] in 1908 for scattering and absorption of radiation, caused by homogeneous spheres of arbitrary size. Scattering in the backward direction becomes significant when the wavelength of the radiation and the size of the sphere are of the same magnitude. For larger spheres forward scattering is dominant.

The backscattering fraction for the two-flux model can be obtained by integration of the angular scattered intensities over the backward-oriented hemisphere. At the time of the formulation of the two-flux model, it could hardly be used in practice, as complex Mie-calculations were very time consuming for the computers of the late 1960s. Even more important, there were no properties available at that time to describe the scattering characteristics of fly ashes.

In the second half of the 1980s, Brummel and Kakaras developed a thermal radiation model for gas–solid-dispersions, which incorporated the full Mie-algorithms [3], but still there were only very rare data available for the complex refractive indices of fly ashes, the most important input parameter needed for the Mie-calculations.

Therefore, Brummel reversed the calculation procedure (see [5, 13] for details). He determined mean complex indices of refraction iteratively in a comprehensive calculation procedure including the Mie-theory, using those singular data points for the mean relative efficiency absorption $\bar{Q}_{abs}$ as basis, which have been determined experimentally earlier by Biermann and Vortmeyer [1] and which are compiled in Table 1.

It was found that nearly half of the fly ashes listed there had very similar optical properties. Therefore, it was possible to work out representative curves for fly ash for the mean relative efficiencies for absorption $\bar{Q}_{abs}$ and even more important also for backscattering $\bar{Q}_{bsc}$, which are needed as input parameters in the above-mentioned two-flux model of Biermann and Vortmeyer [1]. By application of the full Mie-theory, these figures could not only be determined for the concrete mean particle diameters of the Biermann investigations (there is only one mean diameter listed per fly ash species – compare Table 1) but also for all other particle sizes with the same relative size distribution (see Figs. 3 and 4).

For estimates of the radiation by dispersed particles, i.e., without knowing the actual values for the mean relative efficiencies $\bar{Q}_{abs}$ and $\bar{Q}_{bsc}$ for the fly ash of interest, these curves can be taken as representative for coal ashes in general, as those efficiencies are located almost in the center of the bandwidth for all ashes of the experimental investigations carried out by Biermann.

For limestone, which is an additive in fluidized bed combustion, the figures differ from those of the representative fly ashes and therefore have been plotted separately in Figs. 3 and 4.

The displayed range for the mean particle diameter d_p from 0 to $100 \cdot 10^{-6}$ m in Figs. 3 and 4 covers the fly ash sizes found in the technical applications “pulverized coal combustion” and

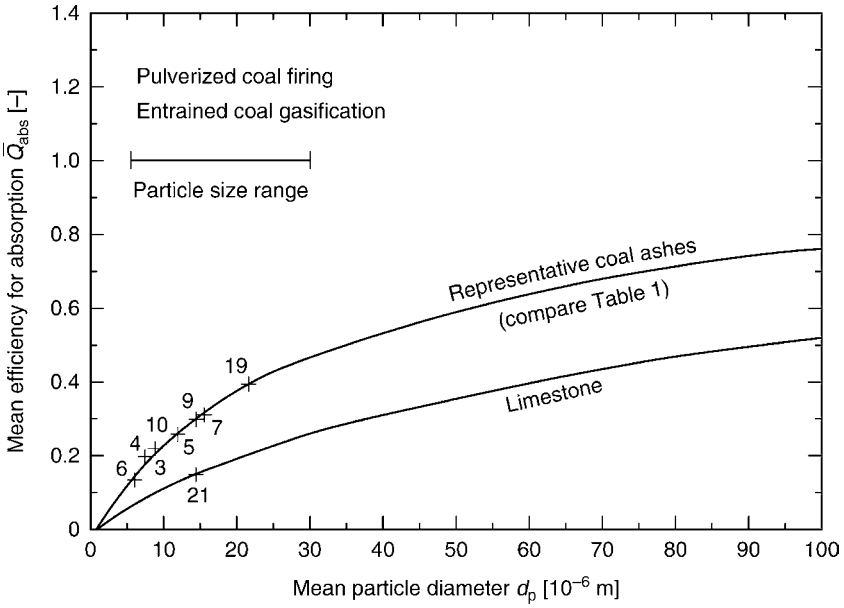

K4. Fig. 3. Calculated mean relative absorption efficiency $\bar{Q}_{abs}$ for representative fly ashes and limestone as a function of the mean particle diameter d_p according to [4, 5, 13] (compare Table 1, curves match well with the measured data points "+" for fly ash nos. 3, 4, 5, 6, 7, 9, 10, and 19 of the Biermann investigations [1]).

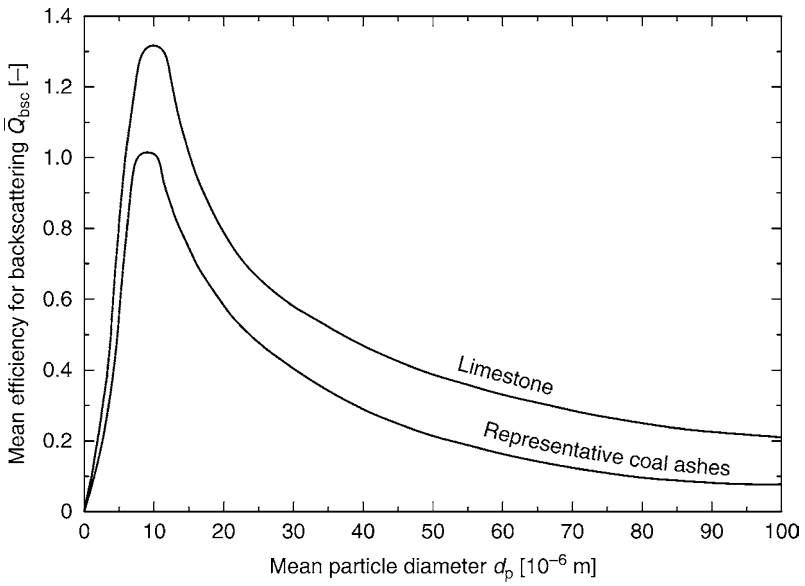

K4. Fig. 4. Calculated mean relative backscattering efficiency $\bar{Q}_{bsc}$ for representative fly ashes and limestone as a function of the mean particle diameter d_p (acc. to [4, 5, 13]).

"entrained coal gasification" to the full extend. For fluidized beds with much larger mean particle diameters, Table 2 has to be applied.

With the $\bar{Q}_{abs}$ and $\bar{Q}_{bsc}$ data for limestone from Figs. 3 and 4 and Table 2, the dispersed particles emissivities for ashes from circulating fluidized beds, which were determined experimentally by Stapper [6], could be reproduced with good accuracy (see [5] for more details).

Investigations by Neubronner and Vortmeyer [7, 11], dealing in particular with analyses of the chemical compositions and size distributions for ashes from numerous pulverized coal fired power plants, combined with Mie-calculations based on spectral optical properties for fly ash components measured by Goodwin and Mitchner [8, 12], show under certain conditions a strong impact of the actual size distribution of the fly ash on the mean relative backscattering efficiency.

K4. Table 2. Calculated mean relative efficiencies for absorption $\bar{Q}_{abs}$ and backscattering $\bar{Q}_{bsc}$ for representative fly ashes and limestone listed for a range of larger mean particle diameters d_p (acc. to [4, 5]). Applicable for fluidized bed combustion. To obtain data for mean particle sizes not directly listed, linear interpolation can be applied

Mean particle diameter d_p (10^{-6} m)	Representative coal ashes		Limestone	
	$\bar{Q}_{abs}$ (–)	$\bar{Q}_{bsc}$ (–)	$\bar{Q}_{abs}$ (–)	$\bar{Q}_{bsc}$ (–)
100	0.768	0.086	0.530	0.226
200	0.872	0.034	0.713	0.094
350	0.904	0.022	0.822	0.045
500	0.905	0.020	0.864	0.028
>1,000	0.906	0.020	0.897	0.021

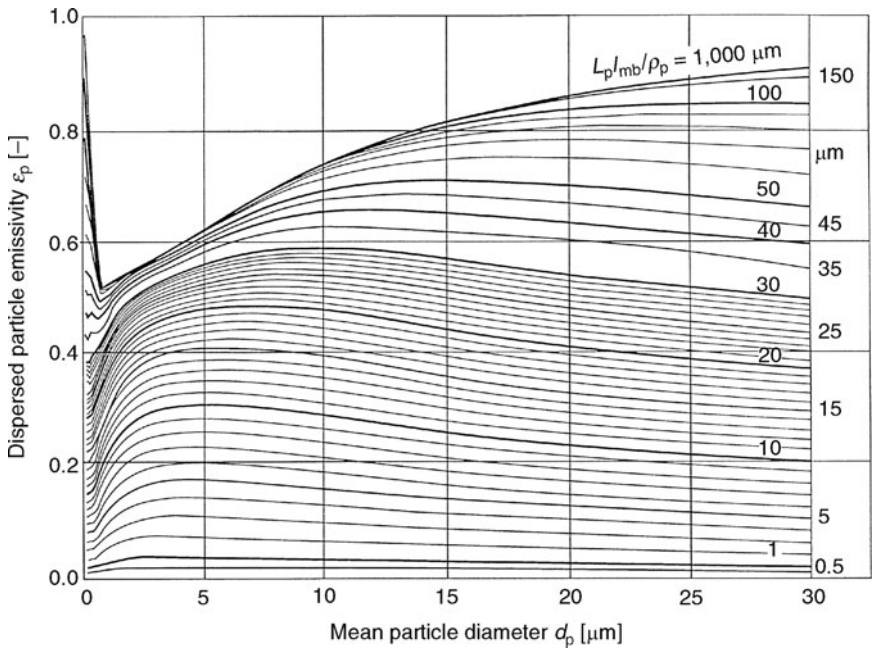

K4. Fig. 5. Diagram for the determination of the dispersed particles emissivity based on the radiation properties of representative fly ashes (acc. to [5, 13], application range 0 µm $\leq L_p l_{mb} \rho_p^{-1} \leq$ 1,000 µm).

3.1 Model Equations

According to the two-flux-model by Biermann and Vortmeyer [1] the dispersed particles emissivity under consideration of backward scattering can be expressed as

$$\varepsilon_p = (1-\beta)\left(\frac{1-\exp(-\Phi_p)}{1+\beta\exp(-\Phi_p)}\right), \tag{5}$$

with

$$\gamma = \left(1+\frac{2\bar{Q}_{bsc}}{\bar{Q}_{abs}}\right)^{1/2}, \tag{6}$$

$$\beta = \frac{\gamma-1}{\gamma+1}, \tag{7}$$

$A = \dfrac{3}{2\rho_p d_p}$ derived from Eq. (3), see Sect. 2 of this Chapter

$$\Phi_p = \bar{Q}_{abs} A L_p l_{mb} \gamma. \tag{8}$$

Data for $\bar{Q}_{abs}$ can be taken from Fig. 3 and data for $\bar{Q}_{bsc}$ can be taken from Fig. 4, as a function of the mean particle diameter. For larger mean particle diameters, $d_p > 100 \cdot 10^{-6}$ m data for $\bar{Q}_{abs}$ and $\bar{Q}_{bsc}$ are listed in Table 2.

Under negligence of backscattering, which is viable for values of the product $\Phi_p = \bar{Q}_{abs} A L_p l_{mb} < 0.5$, Eqs. (1) or (2) for the simplified model, described in Sect. 2 of this Chapter, can be derived as a special case from the set of Eqs. (5–8).

For mean particle diameters $d_p \leq 30$ µm, i.e., in particular for the technical applications pulverized coal combustion and entrained coal gasification, Figs. 3 and 4 as well as Eqs. (5–8) have been combined to a diagram (Fig. 5) for practical use. With known data for the fly ash density, particle load, and mean

beam length, which are generally easy to obtain, the dispersed particles emissivity can directly be read from the diagram in dependency from the mean "Sauter" particle diameter (derived from Eq. (3)).

Calculation example: d_p = 15 µm; ρ_p = 2,400 kg/m^3, L_p = 0.02 kg/m^3, and l_{mb} = 2.6 m. The mathematical term $L_p l_{mb} \rho_p^{-1}$ results in 21.67 µm and a dispersed particles emissivity ε_p of 0.48 can be read from the diagram (Fig. 5).

4 Particle Radiation: Calculation Examples

4.1 Simplified Dispersed Particles Radiation Model (See Sect. 2 of this Chapter)

Example 1: Low particle load
Application of simple model [Eqs. (2) and (3) or nomogram (Fig. 1)]

k = 9.5 m$^{-1/3}$,
ρ_p = 2,200 kg/m^3,
A = 100 m^2/kg,
L_p = 0.001 kg/m^3,
l_{mb} = 10 m.

Results

$d_p = 6.8 \cdot 10^{-6}$ m	acc. to Eq. (3)
ε_p = 0.165	acc. to Eq. (2)
ε_p = 0.17	acc. to nomogram Fig. 1 alternatively

Example 2: Increased particle load
Application of simple model [Eqs. (2) and (3) or nomogram (Fig. 1)]

k = 9.5 m$^{-1/3}$,
ρ_p = 2,200 kg/m^3,
A = 100 m^2/kg,
L_p = 0.02 kg/m^3,
l_{mb} = 10 m.

Results

$d_p = 6.8 \cdot 10^{-6}$ m	acc. to Eq. (3)
ε_p = 0.973	acc. to Eq. (2)

The simplified model, Eqs. (1) or (2) or nomogram (Fig. 1) cannot be applied anymore, due to the model-based overestimation of the emissivity (criterion: Absolute value of exponent in Eq. (2) > 0.5, see Sect. 2 of this chapter).

4.2 Dispersed Particle Radiation Model with Integration of the Mie-Theory (See Sect. 3.1 of this Chapter)

Application of the more sophisticated calculation model taking backward scattering into account.

Dispersed particles emissivity ε_p determination acc. to Eqs. (5–8) and Figs. 3 and 4.

Example 3: Low particle load, same input data as for Example 1
ρ_p = 2,200 kg/m^3,
A = 100 m^2/kg,
L_p = 0.001 kg/m^3,
l_{mb} = 10 m.

Particle substance: Fly ash

Results

$d_p = 6.8 \cdot 10^{-6}$ m	acc. to Eq. (3)
$\bar{Q}_{abs}$ = 0.18	read from Fig. 3
$\bar{Q}_{bsc}$ = 0.245	read from Fig. 4
ε_p = 0.164	acc. to Eqs. (5)–(8)

At low particle loads there is hardly any difference between the results obtained by the simple model (compare Example 1) and by the more complex model, which takes backward scattering into account.

Example 4: Increased particle load, same input data as for Example 2
ρ_p = 2,200 kg/m^3,
A = 100 m^2/kg,
L_p = 0.02 kg/m^3,
l_{mb} = 10 m.

Particle substance: Fly ash

Results

$d_p = 6.8 \cdot 10^{-6}$ m	acc. to Eq. (3)
$\bar{Q}_{abs}$ = 0.18	read from Fig. 3
$\bar{Q}_{bsc}$ = 0.245	read from Fig. 4
ε_p = 0.682	acc. to Eqs. (5–8)

The dispersed particles emissivity calculated by means of the complex Mie particle radiation model yields a result, which is only approximately 2/3 of the figure obtained by the simple model (compare Example 2), as the Mie-model takes into account the attenuation of the radiation caused by backscattering.

Example 5: Even more increased particle load
ρ_p = 2,200 kg/m^3,
A = 100 m^2/kg,
L_p = 0.2 kg/m^3,
l_{mb} = 10 m.

Particle substance: Fly ash

Results

$d_p = 6.8 \cdot 10^{-6}$ m	acc. to Eq. (3)
$\bar{Q}_{abs}$ = 0.18	read from Fig. 3
$\bar{Q}_{bsc}$ = 0.245	read from Fig. 4
ε_p = 0.683	acc. to Eqs. (5–8)

If backward scattering is taken into account, the dispersed particles emissivity asymptotically approaches a limiting figure <1 (compare Examples 3, 4, and 5; see [3, 5] for details).

By application of the simplified model the dispersed particles emissivity asymptotically approaches a figure of 1, which is the emissivity of a black body, which may lead to a significant overestimation of the radiative heat transfer.

The calculation examples 1–5 show that in particular for small mean particle diameters in the range of $10 \cdot 10^{-6}$ m and higher particle loads the more sophisticated model has to be applied, as in those cases, backscattering has a strong impact on the thermal radiation by the particles. For larger mean particle diameters ($d_p > 100 \cdot 10^{-6}$ m), backward scattering does not play a significant role. Here the results of the simplified model and the more sophisticated calculation procedure again match closer.

This fits well to the general scattering theory formulated by Mie. Highest scattering occurs, when particle size and wavelength are of the same magnitude. For larger particles scattering occurs mainly in the forward directions.

4.3 Thermal Radiation of Mixtures of Dispersed Particles

Example 6

The dispersed particles emissivity of a mixture of 20 wt% limestone with a mean particle diameter of $200 \cdot 10^{-6}$ m and 80 wt% fly ash (fly ash no. 7 from Table 1) with a mean particle diameter of $30 \cdot 10^{-6}$ m has to be determined. The overall particle load should equal 0.1 kg/m^3 and the mean beam length is assumed as 3.0 m.

(*Remark*: The input data of this example are fictitious with the goal to primarily describe the calculation procedure, the data do not refer to any real technical application.)

Due to the magnitude of the particle load the use of the sophisticated dispersed particles radiation model is necessary.

Particle substance 1: Fly ash (Index "1")

$\rho_{p\ 1}$ = 2,270 kg/m^3	taken from Table 1 "fly ash no. 7"
A_1 = 22.03 m^2/kg	acc. to Eq. (3)
$\bar{Q}_{abs\ 1}$ = 0.47	read from Fig. 3
$\bar{Q}_{bsc\ 1}$ = 0.087	read from Fig. 4

Particle substance 2: Limestone (Index "2")

$\rho_{p\ 2}$ = 2,700 kg/m^3	taken from Table 1 "limestone"
A_2 = 2.78 m^2/kg	acc. to Eq. (3)
$\bar{Q}_{abs\ 2}$ = 0.715	read from Table 2
$\bar{Q}_{bsc\ 2}$ = 0.030	read from Table 2

Averaging of the specific projection area and the mean relative efficiencies by weight is recommended for practical applications (index: "tot" for total):

A_{tot} = (80 wt% · 22.03 m^2/kg + 20 wt% · 2.78 m^2/kg)/100 wt%
= 18.18 m^2/kg,
$\bar{Q}_{abs\ tot}$ = 0.519,
$\bar{Q}_{bsc\ tot}$ = 0.076,

leads to the following result:

$\varepsilon_{p\ tot}$ = 0.896 acc. to Eqs. (5–8).

5 Combined Gas and Dispersed Particle Radiation

Also for the coupling of gas and particle phase radiation it makes sense to differentiate between low and higher particle loads.

5.1 Low Particle Load

If the thermal radiation of the gas body (see Chap. K3) is not scattered significantly by the dispersed particles, which is only the case for rather small particle loads ($L_p \leq 0.005$ kg/m^3), the total emissivity of the gas–solids–mixture can be described by the following equation, where the dispersed particles as well as the gas are assumed as gray bodies

$$\varepsilon_{g+p} = \varepsilon_g + \varepsilon_p - \varepsilon_g \varepsilon_p. \tag{9}$$

For absorption calculations the total absorptance is

$$\alpha_{g+p} = A_v + \varepsilon_p - A_v \varepsilon_p. \tag{10}$$

The radiative heat transfer between the gas–solid mixture and a wall can be described by the following correlation analogue Eq. (18) in Chap. K3

$$\dot{q}_{g+p,w} = \frac{\varepsilon_w}{\alpha_{g+p} + \varepsilon_w - \alpha_{g+p}\varepsilon_w} \sigma [\varepsilon_{g+p} T_g^4 - \alpha_{g+p} T_w^4]. \tag{11}$$

5.2 Increased Particle Load

At higher particle loads again the situation gets more complex. Regarding exclusively the radiation of the dispersed particles (solid phase) according to Eqs. (5–8), with increasing load or optical thickness, respectively, the dispersed particles emissivity will asymptotically approach a limiting value <1.

So due to backward scattering the thermal radiation of the particle phase cannot be raised by a further increase of the particle load.

For a mixture of gas phase and solid phase, this limiting dispersed particles emissivity (asymptote) is also the limiting value for the total emissivity of the gas–solid mixture. If more particles cannot increase the emissivity, the additional gas present also cannot raise it.

Nevertheless, applying the radiation coupling correlations for the gas and particle phases Eqs. (9) and (10), this will result in contrast to the statements above to increased figures for emissivity and absorptance even in that asymptotic range. This is shown in Fig. 6, where conditions of a medium particle load are displayed exemplarily.

To simulate the phenomena more realistically according to the laws of physics, a modified calculation procedure has to be applied, which will be described in the following.

By means of Eqs. (14) and (15), the absorption coefficients of the gas body $K_{emi,\ g}$ and $K_{abs,\ g}$ can be calculated, if the mean beam length l_{mb}, the emissivity ε_g, and the absorptance A_v of the gas body are known.

The parameters ε_g and A_v can be determined, as described in detail in Chap. K3, via the diagrams by Hottel et al. as a

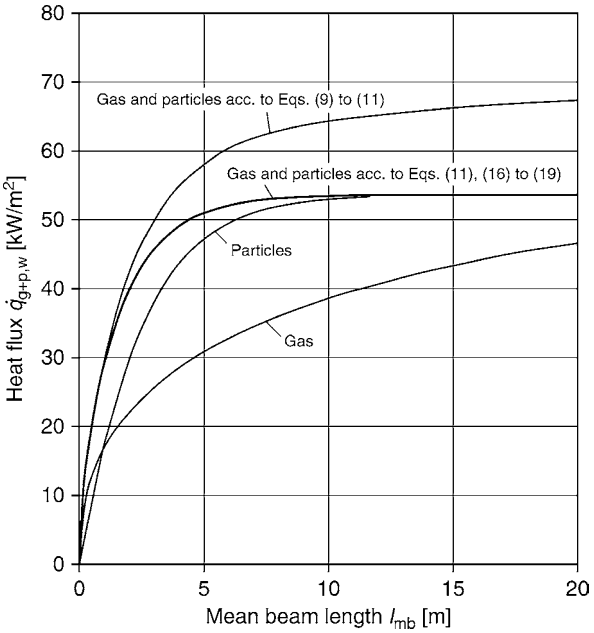

K4. Fig. 6. Superimposition of the thermal radiation of the gas and the dispersed particle phase for a medium particle load as a function of the mean beam length. Comparison of the coupling correlations for low particle loads (Eqs. (9–11)) with a more realistic coupling method, which also takes into account the scattering of gas radiation at the particles (Eqs. (11) and (16–19)).

function of temperature, the partial pressures of the gas components, and the mean beam length.

Finally, the mean beam length l_{mb} can be calculated using the geometry data of the enclosure for the gas–solid mixture (see Chap. K3, Eq. (9)).

Based on the definition equations for the emissivity of a gas body ε_g

$$\varepsilon_g = 1 - \exp(-K_{emi,g} l_{mb}) \tag{12}$$

and for the absorptance A_ν (compare Chap. K3, Eq. (8))

$$A_\nu = 1 - \exp(-K_{abs,g} l_{mb}), \tag{13}$$

the emission and absorption coefficients for the gas phase can be determined as

$$K_{emi,g} = -\ln(1 - \varepsilon_g)/l_{mb}), \tag{14}$$

$$K_{abs,g} = -\ln(1 - A_\nu)/l_{mb}). \tag{15}$$

As the absorption and emission coefficients of the gas and the solid phases can be coupled in an additive manner (under the assumption of an identical mean beam length l_{mb} for both phases), Eqs. (5–8), which were originally derived for a cloud of dispersed particles exclusively, can now be transferred into the following terms.

The total emissivity of the gas–solid mixture can be described similar to Eq. (5) in Sect. 3.1 of this Chapter

$$\varepsilon_{g+p} = (1 - \beta)\left(\frac{1 - \exp(-\Phi_{emi,g+p})}{1 + \beta \exp(-\Phi_{emi,g+p})}\right), \tag{16}$$

with the auxiliary terms

$$\gamma = \left(1 + \frac{2\bar{Q}_{bsc}}{\bar{Q}_{abs}}\right)^{1/2} \quad \text{see Sect. 3.1} \qquad \text{Eq. (6)}$$

and

$$\beta = \frac{\gamma - 1}{\gamma + 1} \quad \text{see Sect. 3.1,} \qquad \text{Eq. (7)}$$

and the optical thickness for the gas–solid mixture (compare Eq. (8) for the particle phase)

$$\Phi_{emi,g+p} = (\bar{Q}_{abs} A L_p + K_{emi,g}) l_{mb} \gamma. \tag{17}$$

The total absorptance of the gas–solid mixture can be described analogously by the following correlation

$$\alpha_{g+p} = (1 - \beta)\left(\frac{1 - \exp(-\Phi_{abs,g+p})}{1 + \beta \exp(-\Phi_{abs,g+p})}\right) \tag{18}$$

again with the auxiliary terms

$$\gamma = \left(1 + \frac{2\bar{Q}_{bsc}}{\bar{Q}_{abs}}\right)^{1/2} \quad \text{and} \quad \beta = \frac{\gamma - 1}{\gamma + 1}$$

and the optical thickness for absorption

$$\Phi_{abs,g+p} = (\bar{Q}_{abs} A L_p + K_{abs,g}) l_{mb} \gamma. \tag{19}$$

For the resulting heat flux $\dot{q}_{g+p,w}$ between a hot gas–solid mixture and a cooled wall.

Eq. (11) is valid, which shall be repeated here for reasons of clarity

$$\dot{q}_{g+p,w} = \frac{\varepsilon_w}{\alpha_{g+p} + \varepsilon_w - \alpha_{g+p}\varepsilon_w} \sigma[\varepsilon_{g+p} T_g^4 - \alpha_{g+p} T_w^4].$$

Remark

It is generally recommended to apply the more sophisticated coupling calculation model even for operating conditions with low particle loads, as in the age of powerful personal computers the additional calculation effort is not an issue anymore, as it was some decades ago.

5.3 Calculation Examples

The total heat flux density resulting from the thermal radiation exchange between a hot, particle laden flue gas of homogeneous temperature and cooled enclosure walls, will be determined, whereas again two cases with different particle loads shall be analyzed.

Case 1 (low particle load)

Input data

ε_g = 0.43	acc. to Chap. K3
A_ν = 0.58	acc. to Chap. K3
l_{mb} = 7.5 m	
A = 68.5 m²/kg	
L_p = 0.001 kg/m³	reference volume in operational state (at actual temperature and pressure)
d_p = 10 · 10⁻⁶ m	
ε_w = 0.7	
T_{g+p} = 1,073 K	
T_w = 673 K	

The mean efficiencies for the dispersed fly ash particles can be taken from Figs. 3 and 4 (Sect. 3 of this Chapter)

$\bar{Q}_{abs} = 0.22$,
$\bar{Q}_{bsc} = 0.21$.

Results

$\varepsilon_p = 0.1062$	acc. to Eqs. (5–) to (8) with Figs. (3) and (4) or acc. to Fig. 5 alternatively
$K_{emi,g} = 0.0749\ m^{-1}$	acc. to Eq. (14)
$K_{abs,g} = 0.1157\ m^{-1}$	acc. to Eq. (15)
$\varepsilon_{g+p} = 0.4668$	acc. to Eqs. (16) and (17)
$\alpha_{g+p} = 0.5722$	acc. to Eqs. (18) and (19)
$\dot{q}_{g+p,w} = 22828.3\ W\ m^{-2}$	acc. to Eq. (11)

The application of Eqs. (9–11), which are valid only for low particle loads, would result in a heat flux of 23351.9 W m^{-2}, an overestimation of just 2.3%.

Case 2 (high particle load)
Input data

$\varepsilon_g = 0.43$	acc. to Chap. K3
$A_v = 0.58$	acc. to Chap. K3
$l_{mb} = 7.5$ m	
A = 68.5 m^2/kg	
$L_p = 0.2$ kg/m^3	reference volume in operational state (at actual temperature and pressure)
$d_p = 10 \cdot 10^{-6}$m	
$\varepsilon_w = 0.7$	
$T_{g+p} = 1073$ K	
$T_w = 673$ K	

The mean efficiencies for the dispersed fly ash particles can be taken from Figs. 3 and 4 (Sect. 3 of this Chapter)

$\bar{Q}_{abs} = 0.22$,
$\bar{Q}_{bsc} = 0.21$.

Results

$\varepsilon_p = 0.7392$	acc. to Eqs. (5–8) with Figs. (3) and (4) or acc. to Fig. 5 alternatively
$K_{emi,g} = 0.0749\ m^{-1}$	acc. to Eq. (14)
$K_{abs,g} = 0.1157\ m^{-1}$	acc. to Eq. (15)
$\varepsilon_{g+p} = 0.7392$	acc. to Eqs. (16) and (17)
$\alpha_{g+p} = 0.7392$	acc. to Eqs. (18) and (19)
$\dot{q}_{g+p,w} = 35662.1\ W\ m^{-2}$	acc. to Eq. (11)

The formal application of Eqs. (9–11), which are valid only for low particle loads, would result in this case in a heat flux of 38815.7 W m^{-2}, an overestimation of 8.8%.

6 Closing Remarks

At higher figures for the (geometrically determined) mean beam length and very high particle loads, a thermal insulation of the hot core zone of a gas–solid mixture can occur. The radiation of the core zone cannot reach the enclosure walls anymore, as the layer of the gas solids mixture close to the walls turns out to be opaque, insulating as well gas as particle radiation from the core zone. This insulation effect is even higher, when relatively cold particles trickle downwards in that region next to the enclosure walls. These phenomena are covered in greater detail in [5].

7 Symbols

ε_p	dispersed particles emissivity (–)
$\bar{Q}_{abs}$	mean relative absorption efficiency of a particle (integrated over the wavelength spectrum) (–)
L_p	particle load at operation conditions (i.e., at given temperature and pressure) (kg/m^3)
A	specific projection area of the dispersed particles (m^2/kg)
l_{mb}	mean beam length (m)
d_p	mean particle diameter (definition acc. to Eq. (3)) (m)
k	substance constant linked with $\bar{Q}_{abs}$ (definition acc. to Eq. (4)) ($m^{-1/3}$)
ρ_p	density of the substance of the particles (material density) (kg/m^3)
β, γ	calculation parameters acc. to Eqs. (6) and (7) (–)
Φ_p	optical thickness of particle cloud (–)
$\bar{Q}_{bsc}$	mean relative backscattering efficiency of a particle (integrated over the wavelength spectrum) (–)
ε_{g+p}	total emissivity of a particle laden gas (–)
ε_g	emissivity of the gas body (–)
ε_p	emissivity of the dispersed particles (–)
α_{g+p}	total absorptance of a particle laden gas (–)
A_v	geometry-dependent absorptance of the gas body (–)
$\dot{q}_{g+p,w}$	radiative heat flux between particle laden gas and enclosure wall (W m^{-2})
ε_w	wall emissivity (–)
σ	Stefan–Boltzmann constant $5.67 \cdot 10^{-8}$ W m^{-2} K^{-4} (W m^{-2} K^{-4})
T_g	homogeneous gas (and particle) temperature (K)
T_w	wall temperature (K)
$K_{emi,g}$	emission coefficient of the gas phase (m^{-1})
$K_{abs,g}$	absorption coefficient of the gas phase (m^{-1})
$\Phi_{emi,g+p}$	optical thickness of the gas solid dispersion for emission (–)
$\Phi_{abs,g+p}$	optical thickness of the gas solid dispersion for absorption (–)

8 Bibliography

1. Biermann P, Vortmeyer D (1969) Wärmestrahlung staubhaltiger Gase. Wärme- und Stoffübertr 2:S193–S202
2. Mie G (1908) Beiträge zur Optik trüber Medien, speziell kolloider Metallösungen. Ann Phys 25:S377–S445
3. Brummel H-G, Kakaras E (1990) Wärmestrahlungsverhalten von Gas-Feststoff-Gemischen bei niedrigen, mittleren und hohen Staubbeladungen. Wärme- und Stoffübertr 25:S129–S140
4. Brummel H-G, Vortmeyer D (1994) Die Berechnung der Wärmestrahlung aus Gaskörpern mit Feststoffbeladungen. Chem Ing Techn 66 (3):S377–S380

5. Brummel H-G (1995) Berechnung der Temperaturstrahlung von Gas-Feststoff-Gemischen bei höheren Partikelbeladungen. Diss., TU München
6. Stapper B (1993) Zum Strahlungswärmeübergang in feststoffbeladenen Systemen. Diss., Univ. Dortmund. Fortschr.-Ber. VDI, R. 6, Nr. 288
7. Neubronner M, Vortmeyer D (1994) Thermal radiation of fly ashes – dependence on size distribution and chemical composition. In: Hewitt GF (ed) Heat transfer, Proceedings of 10th international heat transfer conference, Brighton, vol 2, pp 117–122
8. Goodwin DG, Mitchner M (1989) Flyash radiative properties and effects on radiative heat transfer in coal-fired systems. Int J Heat Mass Transfer 32(4): pp 627–638
9. Köneke D (1983) Kühlung und Erhitzung von Gas-Feststoff-Strömen in Wärmetauschern bei höheren Temperaturen. Diss., Univ. Dortmund
10. Smoot LD, Pratt DT (eds) (1979) Pulverized-coal combustion and gasification. Plenum Press, New York
11. Neubronner M (1995) Strahlungswärmeübertragung von Aschepartikeln aus Kohlefeuerungen. Diss., TU München. Fortschr.-Ber. VDI, R. 6, Nr. 331
12. Goodwin DG (1986) Infrared optical constants of coal slags. Ph.D. thesis, Stanford University, HTGL-Report T-255
13. Brummel H-G, Vortmeyer D (1998) Thermal radiation of gas–solid-dispersions at higher particle loadings. In: Proceedings of the 2nd International. Symposium. on radiation transfer. Begell House, Inc., New York, pp 511–527

K5 Heat Radiation in Furnaces

Wolfgang Richter[1,†] · *Klaus Görner*[2]
[1]Essen, Germany
[2]Universität Duisburg-Essen, Essen, Germany

1 Introduction

The exchange of energy by radiation in a flame or a furnace is the result of a complex radiation interaction in the furnace or combustion chamber including emission, absorption, reflection, and scattering within the suspension (flue gas) and between this and the walls of the combustion chamber. For simplifying nomenclature, subsequently the expressions "flue gas suspension" and "furnace" are used.

A calculation of this radiation energy transport presumes knowledge of the optical properties of the flue gas suspension and of the walls, as well as of the local temperature distribution in the calculation space and at the embracing walls. The optical properties depend on the composition of the flue gas suspension taking into account both gaseous and particulate species.

The temperature distribution depends on the interaction of flow, reaction, and burn-out processes. These variables are described by the flow (velocity) field and the concentration fields of the single species, resulting in an interaction as pointed out schematically in Fig. 1 [1].

Referring to the temperature distribution, it has to be taken into account additionally that gas and the particles could show differences in temperatures and in concentration distributions too, caused by locally high rates of heat release.

From the mathematical point of view, this is a system with distributed parameters which, due to the above-described dependencies, shows a strong coupling within and between the subsystems.

The spatial distribution of radiation heat fluxes inside the furnace and the net heat flow to the walls of the furnace are obtained from (radiation) energy balance equations for finite volume and surface regions of the furnace.

Often, it is not possible to predict the temperature distribution within the flue gas suspension or at the walls of the furnace. It is rather for the determination of these temperature distributions that the calculation of heat transfer is carried out. In this case, it is necessary to specify at first the flow field of flow and the location of energy release in the furnace as well as the convective heat exchange coefficients, then one has to compute the balance equations for radiation energies and also the total energy balance for finite volume and surface regions. A combined solution of total and radiation energy balance equations then leads to the wanted temperature field and simultaneously to total and radiation heat profiles corresponding to this temperature distribution.

On one hand, the knowledge of the local properties of the components contributing to the radiation in the furnace is usually incomplete. On the other hand, the calculation of the radiation energy exchange for furnaces with a geometry even close to reality is already insolvable in a straight forward mathematical way even for a homogeneous distribution of radiating components. Therefore, procedures for the computation of heat transfer in furnaces are mainly based on simplifications. These procedures are so-called mathematical furnace models.

Radiation models are mainly divided into flux and zone models (Fig. 2). Zone models include the so-called Monte Carlo models by which the radiation energy emitted per zone is divided into discrete single beams and the direction of which is determined by random numbers [2].

2 Radiation Properties of the Flue Gas Suspension and their Simplified Mathematical Modelling

The main thermal radiation emitting and absorbing components within a flame or a furnace fuelled by fossil fuels are the

[†]Deceased

VDI-GVC (ed.), *VDI Heat Atlas*, DOI 10.1007/978-3-540-77877-6_44,

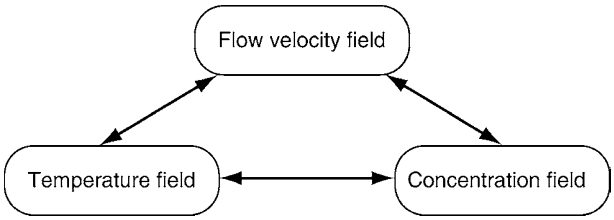

K5. Fig. 1. Interactions in the furnace.

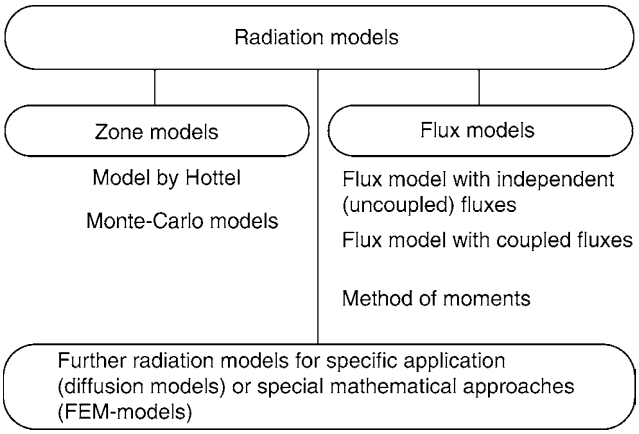

K5. Fig. 2. Classification of radiation models.

gaseous components steam (H_2O) and carbon dioxide (CO_2) – to a smaller extent also methane (CH_4) and carbon monoxide (CO) – and suspended particulate matter, e.g., soot, char (carbon), and ash particles. Triatomic gas phase species, like CO_2 and H_2O, show in single spectral areas large absorption coefficients. At other frequencies, no absorption/emission interaction with thermal radiation is observed, they are spectral diatherm (or diabate) in these areas. With respect to this overall behavior, this type of thermal radiator is called a narrow band radiator. Otherwise, the spectral degree of absorption of particulate flue gas components and of the embracing walls shows small or no frequency dependence, they are the so-called gray radiators. Both types of radiators contribute in the flue gas suspension to the total radiation.

With the exception of soot particles, particulate matter causes a not negligible scattering of the radiation. Their selective radiation of the gas components and the continuous radiation of the particulate matter in the furnace is superimposed by the gray radiation of hot areas of the walls of the furnace. Subsequently, based on and supplementary to Chaps. K3 and K4 treating physical principles of radiation of gases and dust particles, basic mathematical approaches are presented describing the properties and the interaction of the above-mentioned radiation sources in furnaces. Thereby, it is favorable to formulate the radiation properties of the suspension additively from those of the pure gas and the particulate phase.

2.1 Radiation Properties of Gaseous Combustion Room Components

For simplified calculations of radiation energy exchanges in a furnace including gas radiation, it is usually sufficient assuming contributions to thermal radiation only by H_2O and CO_2, and that each of these components shows uniform partial pressures within the whole combustion space. The partial pressures p_{H_2O} and p_{CO_2} are determined by stoichiometric calculation based on the fuel composition and on the air fuel ratio λ for fixed values of burn-out (common assumption: complete burn-out).

In Table 1, columns 10 and 11, CO_2 and H_2O partial pressures of the combustion gases of some solid fuels types are given for a total pressure of 1 bar in the furnace. The stoichiometric calculation is presented for complete burn-out and 30% air surplus. The small SO_2 partial pressures of the combustion gases of the solid fuels are covered by the CO_2 partial pressures.

Columns 12 and 14 in Table 1 show the degree of emission ε_G, for the combustion gases of each fuel, as determined from data and diagrams of Chap. K3 exemplarily for a uniform furnace temperature of 1,600 K and for two different equivalent layer thicknesses of s_{eq} = 0.6 m and 3.86 m. According to the approximate equation (9) given in Chap. K3, s_{eq} = 0.6 m is the equivalent layer thickness of a cubic gas volume with an edge length of 1 m; s_{eq} = 3.86 m is the equivalent layer thickness of a parallelepiped with the dimensions of 5 m × 5 m × 15 m. Calculating the exchange of radiation within a furnace for which gas radiation plays a role equivalent to that of the radiation of suspended particles or of wall radiation, it has been proved to be advantageous to approach the degree of emission of a radiating gas component depending on p_G s_{eq} by the following sum formula [4]:

$$\begin{aligned}\varepsilon_G &= \sum_{i=1}^{3} a_j\left(1 - e^{-k_{Gi} p_G s_{eq}}\right)\\ &= \sum_{i=1}^{3} a_j \varepsilon_{Gi}.\end{aligned} \tag{1}$$

With

$$\varepsilon_{Gi} = \left(1 - e^{-k_{Gi} p_G s_{eq}}\right).$$

ε_{Gi} has to be considered a fictitious variable. The coefficients a_i and k_{Gi} of Eq. (1) have to be adapted so that ε_G values calculated by Eq. (1) are in best agreement with the measured results presented in Chap. K3. It emerges that each of the three weighting factors a_i may be described by

$$a_i = b_{0i} + b_{1i} T_G \tag{2}$$

with the auxiliary condition

$$\sum_{1}^{3} a_i = 1. \tag{3}$$

The volumetric absorption coefficients k_{Gi} are not considered to be temperature dependent.

Eq. (1) is also applicable to gas radiation emitted from gas mixtures. Coefficients b_{0i}, b_{1i}, and k_{Gi} calculated by Johnson and Beér [3] for overlapping CO_2- and H_2O radiation and their validity limits are presented in Table 2. The conditions are in fair agreement with those of real furnaces. Eq. (1) has to be modified to

$$p_g = p_{H_2O} + p_{CO_2}.$$

K5. Table 1. Properties of coals: Composition of coals, concentration of the radiating gas phase species CO_2 and H_2O and degrees of emission for $s_{eq} = 0.6$ m and $s_{eq} = 3.86$ m at $T_G = 1{,}600$ K and 1 bar total pressure (30% air surplus; air half-saturated with water vapor at 289 K; SO_2 concentration taken into account by surplus CO_2; according to Sarofim and Hottel [3])

1	2	3	4	5	6	7	8	9	10	11	12	13	14	15
		C	H	O	S	N	Ash	Humidity			ε_G $S_{eq} = 0,6\ m$		$S_{eq} = 3,86\ m$	
No.	Coal type	Mass fraction (dry coal)						% Mass fraction	P_{CO_2} bar	P_{H_2O} bar	According to K3	According to Eq. (1)	According to K3	According to Eq. (1)
1	Lignite coal, Rheinland, Germany	49.6	3.6	18.7	0.4	0.4	27.3	56.0	0.114	0.251	0.166	0.149	0.355	0.335
2	Gassing coal (long-flame coal), Ruhr, Germany	79.2	5.1	5.7	0.7	1.5	7.8	10.0	0.132	0.071	0.108	0.121	0.248	0.260
3	Gassing coal (long-flame coal) Pennsylv., USA	79.5	5.2	6.1	1.3	1.4	6.5	1.4	0.133	0.062	0.105	0.120	0.238	0.257
4	Bituminous coal (gas coal) Saar, Germany	75.7	4.8	8.6	1.4	1.1	8.4	5.0	0.135	0.065	0.107	0.120	0.241	0.258
5	Fat (rich) coal, Ruhr, Germany	80.7	4.6	3.7	0.6	1.5	8.9	10.0	0.134	0.066	0.106	0.120	0.242	0.258
6	Anthracite (hard) coal	85.9	3.4	2.4	0.7	1.3	6.3	4.0	0.141	0.047	0.102	0.118	0.222	0.251

K5. Table 2. Constants for the degree of emission of the pure gas phase for Eq. (1), according to Johnson and Beér [5] with the validity limits $p_{Ges} = 1$ bar and $0.5 < p_{H_2O}/p_{CO_2} < 2$

i	b_{oi} (–)	b_{1i} (1/K)	k_{Gi} (1/(m bar))
1	0.130	+0.000265	0.0
2	0.595	–0.000150	0.824
3	0.275	–0.000115	25.907

A comparison with the data of columns 12 and 13 in Table 1 demonstrates that degrees of emission calculated by the methods given by Chap. K3 are in good agreement with that determined by Eq. (1).

As described for the degree of emission, the degree of absorption may be approximated in a similar way by a sum of exponential functions using absorption diagrams (Fig. 3):

$$A_v = \sum_{i=1}^{3} a_{Wi}\,(1 - e^{-k_{Gi} p_G s_{eq}}). \tag{4}$$

In this case, the weighting factors a_{Wi} are functions of the temperature T_W of the radiation source and to a smaller extent of the gas temperature T_G. For further simplification of calculations of the radiation exchange, it is recommended to determine A_v from Eq. (1) instead of Eq. (4). Then the degree of absorption A_v of the gas layer is equal to the layer's degree of emission ε_G at the radiation source's temperature T_W, i.e.,

$$a_{Wi}\,(T_W) \approx a_i\,(T_W) \tag{5a}$$

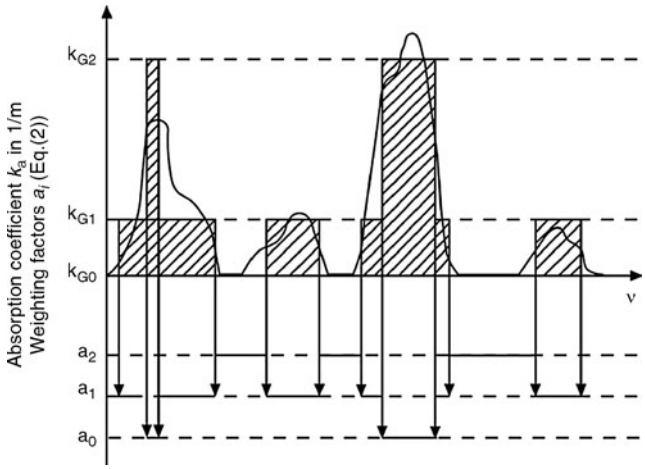

K5. Fig. 3. Basic spectral emissivity curve of a band radiator and its approximation by Eq. (1).

with

$$a_i\,(T_W) = b_{0i} + b_{1i} T_W \tag{5b}$$

and b_{0i} and b_{1i} are according to Table 2.

The given approximations for ε_G and A_v are in no way thought to substitute the exact emission diagrams or their interpolation formulas (Chap. K3, Eqs. (23)–(26b)). However, Eqs. (1) and (4) exhibit the advantage of using temperature-independent absorption coefficients $k_{Gi}\,p_G$, which correspond to gray radiation. This allows the application of precalculated irradiation numbers for the calculation of radiation exchange between the absorbing volume of the furnace and the furnace

walls. These irradiation numbers are given, for instance in [4] for various values of absorption coefficients and different geometric shapes and arrays of surface and volume radiators in diagrams and tables. Hence, during computation or progress of iterations, the matrix of irradiation numbers remains constant and needs not to be recalculated for each step.

Equations (1) and (4) are especially adapted to (cf. Fig. 2) zone procedures by which the radiation exchange in furnaces with inhomogeneous temperature distributions can be calculated. Further on, by means of the sum approaches it is easier to approximate the superposition of selective (discrete) gas radiation and continuous radiation of solids. Finally, the volumetric absorption of reflected radiation can better be taken into account. This could be of importance for the accuracy of radiation exchange calculations for stronger reflecting furnace walls. The degrees of emission and absorption calculated by Eqs. (1), (4), and (5) may be directly inserted into Eq. (18), Chap. K3, to calculate the radiation exchange between an isothermal furnace volume and the surrounding walls. A more realistic approach, however, is achieved, especially for stronger reflecting walls, if Eq. (18) of Chap. K3 is modified accordingly to

$$\dot{Q}_{GW} = A\sigma \sum_{i=1}^{3} \frac{\varepsilon_W \varepsilon_{Gi}}{1 - (1 - \varepsilon_W)(1 - \varepsilon_{Gi})} \cdot [a_i (T_G) T_G^4 - a_i (T_W) T_W^4] \tag{6a}$$

with

$$\varepsilon_{Gi} = (1 - e^{-k_{Gi} p_G s_{eq}}) \tag{6b}$$

in agreement with Eq. (1). For the special case of only one gray gas with $a_i = 1$, and $\varepsilon_G = A_v$, Eq. (6) turns into Eq. (18), Chap. K3.

2.2 Radiation Properties of Suspended Particulate Matter

Disregarding previous loads with particulate matter of the incoming fuel and the combustion air during the combustion of gaseous fuels, usually no particulate matter has to be taken into account. Soot formation can then be neglected for normal operating conditions.

The fuel from oil combustion is already charged with unburnable matter (ash). Because of the usually low absolute concentrations (below 20 mg/m^3 at standard temperature and pressure (STP) conditions), its contribution can be neglected. For insufficient spray atomization, for quenching processes, or for low-NO_x-operation with strongly understoichiometric conditions in sub-areas of the flame or the furnace, reasonable concentrations of soot or char may occur. This problem may also arise with light gas oil fuel (gas oil type L) and may become more severe with heavy gas oil fuel H or oils of even poorer quality (e.g., vacuum residual fuel oils) with high concentrations of asphaltenes. With respect to coal combustion, besides crude coal, coke or coal residues and ash have to be taken into account as optical relevant constituents. Always, if several gray-body-radiators have to be considered, it is necessary to aim at an approximation also for the particulate matter phase for the radiation properties to be as simple as possible by summation of the degrees of emission without considering possible overlapping effects.

This leads to the simplest possible approximation for the absorption coefficients $k_{a,S}$ of the flue gas suspension [1]:

$$k_{a,S} = k_{a,G} + k_{a,P}, \tag{7}$$

where $k_{a,G}$ describes the approximated absorption coefficient of the gas phase, while $k_{a,P}$ represents the summary influence of the particulate matter, such as soot, char, coal, or coke particles resulting in the simplified expression:

$$k_{a,P} = k_{a,R} + k_{a,C} + k_{a,A}, \tag{8}$$

where the indices S, R, C, and A represent suspension, soot, coal/char, and ash.

2.2.1 Radiation by Soot Particles

Soot particles are understood as particulate matter consisting mainly of carbon particles originated from the gas phase combustion of hydrocarbons. The mean diameter of the spherical nonagglomerated soot particles is between $30 \cdot 10^{-9}$ and $65 \cdot 10^{-9}$ m [3]. The soot particles cause the yellow shining of flames; they contribute especially to the energy exchange by radiation in the infrared spectrum. A determination of the spectral and total degree of emission of homogeneous layers of suspended soot particles is possible by means of theoretical approaches if the mass loading B_R of the layers (e.g., in kg/m^3), the density ρ_R, and the optical constants of the soot particulate matter are known [3, 5–7].

An approximate solution of the theoretical approaches for the wavelength-dependent soot radiation leads to the frequently used relation

$$\varepsilon_R = 1 - e^{-k_{a,R} \cdot B_R \cdot s_{eq}}, \tag{9a}$$

with

$$k_{a,R} = a_R \cdot T_R \text{ in m}^2/\text{kg}. \tag{9b}$$

ε_R is independent of the soot particles' diameter. Data in literature for the factor a_R (in m^2/kg K) for gas oil fuel L vary between 0.47 and 2.09 [8]. This fluctuation range is partially explained by the fact that a_R includes both ρ_R and other optical constants. These factors depend as well on the type of fuel as on the conditions at which the particles are formed (combustion regime). Based on work by Johnson and Beér [5] and by Tietze [8], a_R = 1.49 m^2/kg K appears to be a suitable value for oil flames. Figure 4 shows the emission diagram $\varepsilon_R = f(B_R\, s_{eq})$ with the temperature T_R of the radiating soot particles as a parameter calculated by means of this factor together with Eq. (9).

A possible relationship of $\varepsilon_R = f(B_R\, s_{eq})$ to Eq. (1) has been given by Johnson and Beér [5] in the form of the weighted sum of exponential functions:

$$\varepsilon_R = \sum_{i=1}^{3} a_i (1 - e^{k_{R,i} \cdot B_R \cdot s_{eq}}). \tag{10}$$

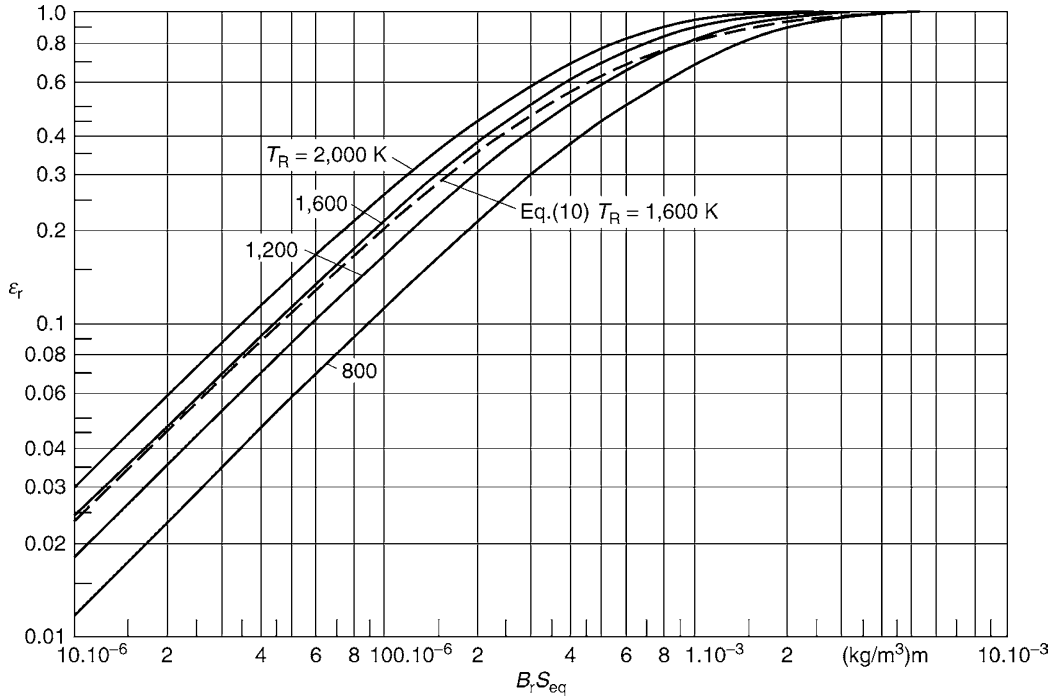

K5. Fig. 4. Degree of emission ε_R for suspensions of soot particles, according to Eq. (9) with a_R = 1.49 m^2/(kg K) as a function of B_R s_{eq} and in comparison with the approach following Eq. (10).

K5. Table 3. Constants for the degree of emission by soot, according to Eq. (10) [5]

i	b_{oi} (–)	b_{li} (1/K)	k_{Ri} (m^2/kg)
1	0.130	+0.000265	3,460
2	0.595	–0.000150	960
3	0.275	–0.000115	960

The specific absorption coefficients, which were temperature independent in opposition to Eq. (9a), have been determined by the authors in such a manner, that it was possible to use for the weighting factors $a_i = f(T_R)$ the same coefficients as computed in Table 2 for a H_2O/CO_2 mixture. The constants for the soot radiation result from Table 3.

If ε_R is approximated by Eq. (10), the radiation exchange between an isothermal, soot radiation emitting volume and the surrounding walls may best be formulated by Eq. (6). When calculating the net heat transfer due to soot emission, by far the greatest uncertainty is because of the unknown soot concentration in the furnace volume. A quantitative theory that would allow for the prediction of the formation of soot depending on the kind of fuel, temperature and pressure, air/fuel ratio, and mixing behavior [3] is not known. The problem is still increased by the effect that usually soot loading within a furnace is extremely inhomogeneous. Maxima of soot loading are to be found in flames themselves, and usually in the flame core at areas near to the burner.

In areas of the furnace with oxygen surplus, soot can burn off again at sufficiently high temperatures and adequate residence times. For low-NO_x operation mode, usually one of these conditions is not fulfilled.

Table 4 compiles some experimental results of soot concentrations averaged over flame cross sections. Related mean flame temperatures T_F and diameters D_F have been used to determine by Eq. (9) the degree of emission ε_R of the soot layers (without gas radiation). For these calculations, s_{eq} has been equated to the mean flame diameter. Because of the many influencing factors and the special flame conditions, which have not been taken into account, an uncritical transfer of the results from Table 4 may lead to considerable errors.

The small soot concentrations in natural gas flames are of no importance for the calculation of radiation exchange in small furnaces, although they may cause noticeable shining.

Approximate values for mean soot concentrations in heavy gas oil flames may be (with some caution) 500–1,000 mg/m^3 (at STP conditions), according to 100–200 mg/m^3 at 1,400 K. Local concentration maxima are at 7,000 mg/m^3 (at STP), according to about 1,350 mg/m^3 at 1,400 K.

Frequently, the CO concentration is used as an indicator and as an indirect measured quantity, instead of the soot concentration, because CO is also applied as a characteristic measure for incomplete burn-out (e.g., hydrocarbons). For a first coarse orientation, Tietze [8] presents a relation between local CO concentration and soot loading developed by him accordingly to Fig. 5 for a place downstream from the place of highest radiation density for heavy oil flames with air atomiser at STP. Also, the data given by Fig. 5 are only correct for the specific case. Generalizations may lead to major errors.

The volume of gas oil flames, i.e., the area in which shining soot radiation is emitted, can be calculated approximately by

K5. Table 4. Characteristic properties of technical flames of different thermal power (mean flame temperatures, mean soot concentrations, and soot emission degrees ε_R, according to Eq. (9) for different flame cross sections)

Flame type	Thermal power (MW)	Distance between burner (m)	Flame diameter D_F in m	Average flame temperature T_F (K)	Average soot loading B_R (kg/m^3)	$\varepsilon_R = f(B_R, D_R)$. Eq. (7) with a_R = 1.49 m^2/(kg K)	Origin of data
Natural gas, no. swirling	2.565	2.65	0.64	1273	$2.6 \cdot 10^{-6}$	0.0032	[8]
		4.65	1.02	1298	$2.5 \cdot 10^{-6}$	0.0049	
Gas oil fuel, type H no swirling air atomization	3.19	2.65	0.64	1483	$552 \cdot 10^{-6}$	0.5416	[8]
		4.65	1.28	1378	$99 \cdot 10^{-6}$	0.2295	
	0.638	1.70	0.65	1282	$394 \cdot 10^{-6}$	0.3417	[8]
		3.84	≈ 1.00	1046	$74 \cdot 10^{-6}$	0.1089	
		0.5	0.52	1345	$600 \cdot 10^{-6}$	0.4649	
	0.727	1.0	0.49	1400	$160 \cdot 10^{-6}$	0.1502	[14]
		2.0	1.00	1280	$65 \cdot 10^{-6}$	0.1166	
		2.75	0.50	1583	$860 \cdot 10^{-6}$	0.6373	
	1.5	3.50	0.62	1549	$394 \cdot 10^{-6}$	0.5963	[6]
		5.00	0.85	1498	$73 \cdot 10^{-6}$	0.1504	
Gas oil fuel, type H no swirling pressurized atomization	1.5	2.75	1.22	1465	$67 \cdot 10^{-6}$	0.1639	[6]
Gas oil fuel, type H swirling pressurized atomization	3.0	1.00	≈ 1.00	1508	$217 \cdot 10^{-6}$	0.3859	[11]

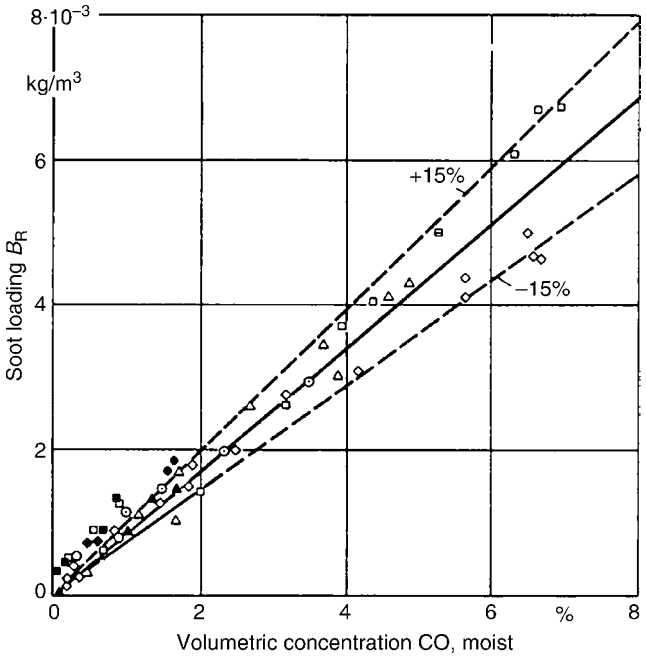

K5. Fig. 5. Basic relation between soot loading B_R and CO concentration in heavy oil flames (jet burner [8]).

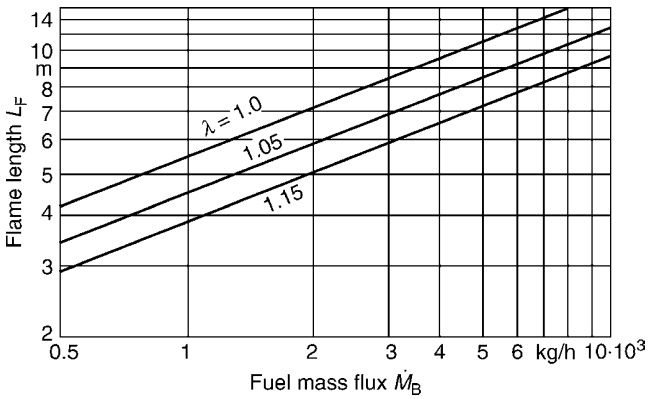

K5. Fig. 6. Flame length L_F as a function of fuel throughput $\dot{M}_B$ for each burner (gas oil fuel L) and of the air-ratio number λ (empirical approach [9]).

means of the empirical relations (11) and (12) or with the related diagrams in Figs. 6 and 7 [9]:

$$L_F = 1.5\dot{M}_B^{0.379}\left[0.36 + 0.128\ (e^{-16(\lambda-1)} - 1)\right]\ (\text{m}), \qquad (11)$$

$$D_F = \dot{M}_B^{0.387}\left[0.147 + 0.025\ (e^{-22(\lambda-1)} - 1)\right]\ (\text{m}). \qquad (12)$$

These are solely equations for numerical values in which the fuel throughput $\dot{M}_B$ has to be inserted in units of kg/h. In these equations and diagrams, the flame length L_F and the flame diameter D_F are empirically correlated with fuel throughput $\dot{M}_B$ for each burner with the air ratio number λ as a parameter. The approaches have been generated from data by various burner manufacturers [9]. The data refer to flames of swirl burners in which gas oil is usually atomized by atomizer steam or pressurized air.

Depending on degree of swirling and atomizer construction, deviations ±30% are to be expected. Eqs. (11) and (12) are not applicable to flames with smaller fuel throughput. Flames without swirling are by a factor of 2–3 longer than swirling flames

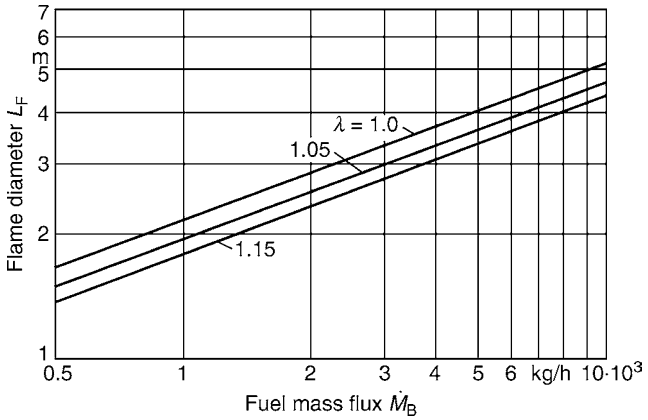

K5. Fig. 7. Flame diameter D_F as a function of fuel throughput $\dot{M}_B$ for each burner (gas oil fuel L) and of the air-ratio number λ (empirical approach [9]).

and accordingly slimmer. Also, low-NO_x flames (gas and oil) are about 20% longer, due to the softer combustion aimed at.

2.2.2 Radiation of Coal and Char Particles

In contrast to the emission of a layer of a soot particle suspension, the emission of clouds of coal and char particles, like that of clouds of ash, which is discussed subsequently, depends on the diameter of the single particles. While larger particles (>20 µm) may be treated at least approximately by the fundamentals of geometric optics, this is no longer the case for smaller particles. As is the case for soot, not-gray radiation behavior is dominant here.

For a common grinding of hard coal dust with a mean weight diameter of about 50 µm or an R 0.09 of 10% (i.e., the residue on the 90 µm sieve is 10 or 90% of the particles show diameters below 90 µm), the assumption of gray radiation for coal and char particles can be accepted as sufficiently exact.

For the degree of emission is also influenced by the particle size distribution [3], which is usually not known, and which is shifted to smaller diameters during the combustion process, in this section the degree of emission ε_K is given for constant particle diameters only

$$\varepsilon_K = 1 - \exp\left(-\bar{Q}_{abs,K} \cdot \frac{3}{2\rho_K \bar{x}_K} \cdot B_K \cdot s_{eq}\right) \qquad (13)$$

and ε_K for the Rosin–Rammler distribution

$$\varepsilon_K = 1 - \exp\left(-\bar{Q}_{abs,K} \cdot \frac{3}{2\rho_K \bar{x}_K} \cdot \frac{\pi}{n \sin(\pi/n)} \cdot B_K \cdot s_{eq}\right) \qquad (14)$$

with

$\bar{x}_K$	mean weighted diameter of the Rosin–Rammler distribution [3]
$\bar{Q}_{abs,K}$	mean relative effective cross section for the absorption of coal/char particles (constant, due to the assumption of a gray radiator)
	$0.8 \leq \bar{Q}_{abs,K} \leq 1.0$ for larger coal/char particles [3, 6, 8]
ρ_K	apparent density of coal/char particles 1,200 to 1,400 kg/m³ for coal
	600 to 1,000 kg/m³ for char
B_K	particle loading
s_{eq}	equivalent layer thickness
n	scattering parameter of Rosin–Rammler distribution

It may be noticed that Eq. (13) is identical with Eq. (1) of Chap. K4. The dependency of the degree of emission ε_K of the product of particle loading and layer thickness, according to Eq. (14) is given for various values of the parameter n from Fig. 8. The correlations have been determined based on $\bar{Q}_{abs,K} = 0.85$, $\rho_K = 1{,}000$ kg/m³, and $\bar{x}_K = 50 \cdot 10^{-6}$ m. In practical applications, Fig. 8 can be used only for estimations because the calculation is based on a pure Rosin–Rammler distribution between $x_K = 0$ and ∞. With such a distribution, for $n \to 1$ the influence of the smallest particle fractions for which Eq. (14) is not valid, will be overestimated.

It is not possible to present absolute values for the loading of furnaces with coal and char particles because these data depend much on the kind of coal and combustion and also on the combustion processing. A basic, very rough estimation can be made if a homogeneous mass distribution over the combustion room and flame zones is assumed, accordingly to the added mass flows, and if a certain burnout is anticipated. It has to be taken into consideration that the density ρ_K and usually also the particle size distribution may change depending on degassing and on burnout of the particles' cloud [6, 10].

Burnout calculations for coal and char particle clouds with a finer zone division can be found in the works of Field et al. [7]. From calculations of this type, which, however, would exceed the scope of the presented section, it is possible to derive local distributions of absorption coefficients in particle clouds with an accuracy sufficiently for radiation exchange calculations [11].

2.2.3 Radiation of Ash Particles

The relations in Eqs. (13) and (14) are similarly valid for the rough calculation of the degree of emission ε_A for ash particles. Problems with the description of radiation from ash particles are especially connected with the determination of the representative mean relative efficiency cross sections $\bar{Q}_{abs,A}$ for the absorption and in the estimation of the particle size distribution (see also Chap. K4, Table 1). Absorption indices of particulate matter of ash may be depending on the kind of combustion eventually strongly influenced by wavelengths [3, 12]. Further on, a considerable amount of ash particles is very small (<10 µm), so that the parameter $\bar{Q}_{abs,A}$ depends on particle diameters. For these reasons, the assumption of gray radiation of the ash particle cloud is only roughly justified. A systematic calculation of $\bar{Q}_{abs,A}$ depending on the kind of coal and combustion processing is not possible until now, it is suggested to consider the radiation of ash particles also as gray and to calculate with either one of the two relations in Eqs. (13) and (14). In agreement with the work of Sarofim and Hottel [3] and Table 1 of Chap. K4 values of $\bar{Q}_{abs,A} = 0.2$ and $\rho_A = 2{,}200$ kg/m³ may be used as representative. For more, differentiated calculations may be referred to Fig. 3 of Chap. K4.

For a Rosin–Rammler distribution with $n = 1{,}5$, ε_A values have been calculated for three different mean diameters of ash

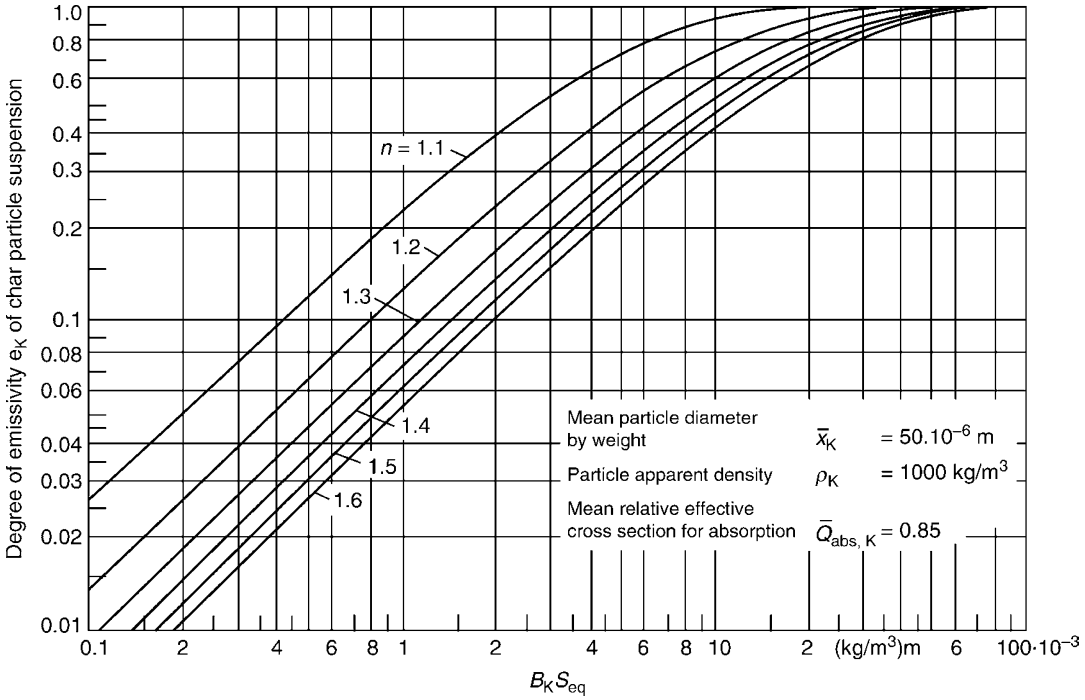

K5. Fig. 8. Degree of emission ε_K of char particle suspensions, according to Eq. (14) as a function of $B_K\, s_{eq}$ and the scattering parameter n of Rosin–Rammler distribution of the char particle size.

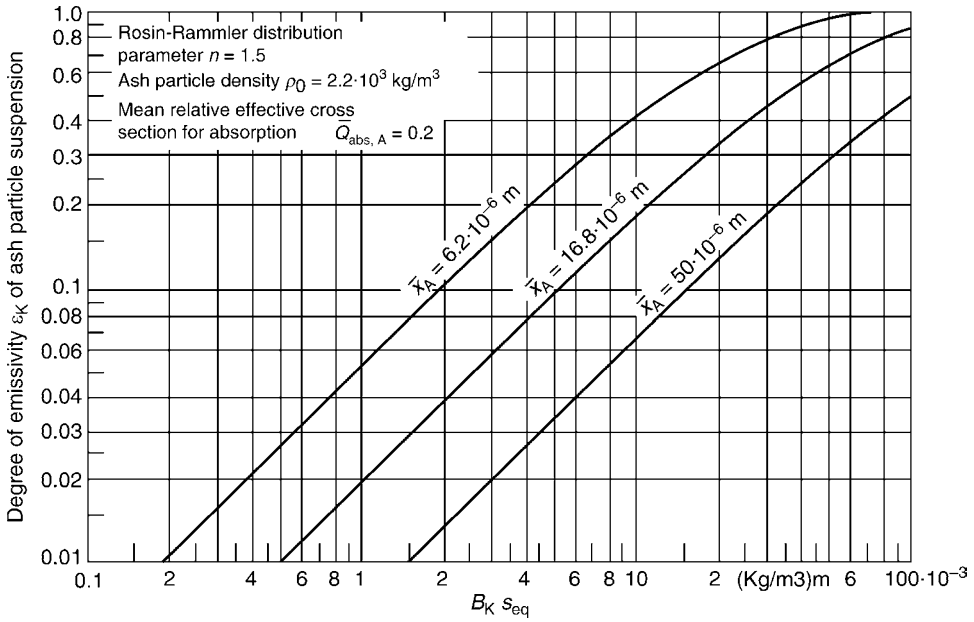

K5. Fig. 9. Emission degree ε_A of suspensions of ash particles as a function of $B_A\, s_{eq}$ for three mean ash particle diameters $\bar{x}_A$.

particles according to Eq. (14). Figure 9 shows the dependency of these values of $B_A\, s_{eq}$.

In Fig. 9, the distributions of the weighted diameters of ash particles for the upper and the lower curve may be regarded as limiting cases. Therefore, it is recommended to choose the curve $\varepsilon_A = f(B_A\, s_{eq})$ calculated with $\bar{x}_A = 16.8 \cdot 10^{-6}$ m for fly-ashes with an unknown particle size distribution.

As already mentioned in connection with coal and char particles, the influence of extremely small particles on ε_A is overestimated using the ideal Rosin–Rammler distribution for $n \to 1$.

As a first approximation for calculating the ash loading B_A, it can be assumed that the mass distribution of ash in the combustion room is constant neglecting agglomeration, segregation, and inhomogeneities in the flame zones.

It may be noticed that ash particles (to a minor part also coal and char particles) could influence the radiation exchange by scattering [13, 14]. This scattering of radiation causes minor furnace radiation and hence counteracts the influence of higher absorption coefficients in hot particle loaded layers. The effect of scattering increases with ash loading, with the size of the equivalent layer thickness, with the part of ash particles with diameters between 1 and 15 µm, and with decreasing absorption indices of the ash material. Taking into account these scattering effects, degrees of emission for ash particles can be approximated by Eqs. (5)–(8) in Chap. K4.

However, the simplest approximation is the assumption of a constant absorption coefficient neglecting the spectral dependency completely with

$$k_{a,A} = K_{a,A} \cdot B_A, \tag{15}$$

where the factor $K_{a,A}$ (m^2/kg) takes values between 10 and 50 for hard coal ashes and von 9–25 for lignite ashes [1]. B_A is the loading of the flue gas suspension with ash (continuum density, [kg/m^3]).

2.3 Radiation Properties of the Flue Gas Suspension

If the radiation of all particles is considered as gray, the degree of emission ε_S of the suspension can be expressed similarly to Eq. (9), Chap. K4, by

$$\varepsilon_S = 1 - (1 - \varepsilon_G)(1 - \varepsilon_R)(1 - \varepsilon_K)(1 - \varepsilon_A). \tag{16}$$

ε_R can be calculated accordingly to Eq. (9), ε_K and ε_A accordingly to Eqs. (13) or (14). The absorption ratio for the superimposed real gas and as gray assumed particle radiation can be approximated accordingly to Eq. (10) in Chap. K4, due to the relation

$$\alpha_S = 1 - (1 - A_v)(1 - \varepsilon_R)(1 - \varepsilon_R)(1 - \varepsilon_K)(1 - \varepsilon_A). \tag{17}$$

The advantage of formulating the degree of emission of a flue gas suspension, in which the single components show different radiation characteristics, by a weighted sum of exponential functions similar to Eqs. (1) and (10) has already been pointed out. ε_S is described in this case, e.g., by

$$\varepsilon_S = \sum_{i=1}^{3} a_i \left(1 - \exp\{-[K_{Gi}(p_{H_2O} + p_{co_2}) + k_{Ri} B_R + k_K B_K + k_K B_A] S_{eq}\}\right). \tag{18}$$

The coefficients for the calculation of a_i as well as k_{Gi} and k_{Ri} are given by Tables 2 and 3. Because coal or char and ash particles are considered as gray, their specific absorption coefficients k_K or k_A show the same values for each of the three additive terms of the right-hand side of Eq. (18).

These can be determined for constant particle diameters analogous to Eq. (13) by means of the relation

$$k_K = \bar{Q}_{abs,K} \frac{3}{2\rho_K x_K} \tag{19}$$

or

$$k_A = \bar{Q}_{abs,A} \frac{3}{2\rho_K x_K}. \tag{20}$$

With a known Rosin–Rammler distribution, the relations for k_K and k_A according to Eq. (14) are given by

$$k_K = \bar{Q}_{abs,K} \frac{3}{2\rho_K \bar{x}_K} \frac{\pi}{n \sin(\pi/n)} \tag{21}$$

and

$$k_A = \bar{Q}_{abs,A} \frac{3}{2\rho_A \bar{x}_A} \frac{\pi}{n \sin(\pi/n)}. \tag{22}$$

Similar to the soot radiation, the above-mentioned approach has possibly to be extended for the not gray character of the ash radiation.

Using the sum approach in Eq. (18), the radiation exchange between an isothermal furnace volume and the surrounding walls has to be calculated according to Eq. (6).

3 Calculation Examples

3.1 Basic Procedure

The use of the data presented in the two previous sections will be explained by two examples for typical calculations. For reasons of simplicity and clarity, these are based on the model of the stationary ideally stirred reactor. This model, that can by no ways substitute the more accurate multidimensional models, allows only a rough calculation of the total heat output $\dot{Q}_{GW}$ of a firing system, the efficiency η_F of the furnace, and the calculation of the furnace exit temperature T_G, which depends on these aforementioned values.

It is assumed that the combustion gases are mixed and that partial pressures, mass concentrations, and temperatures are distributed homogeneously all over the furnace and each is characterized by the corresponding values of p_j or m_j and T_G (system with concentrated parameters). The outlet values of the combustion room are identical with these mean values:

$$p_{j,ex} = p_j, \tag{23a}$$

$$m_{j,ex} = m_j, \tag{23b}$$

$$T_{ex} = T_G. \tag{23c}$$

For the easiest case, it is assumed further on that the furnace walls with the surface area A have a given constant surface temperature T_W on the furnace side and a known homogeneous degree of emission ε_W.

The partial pressures p_j or concentrations m_j of the combustion gases in the furnace are determined by means of the supplied mass streams and by the properties of fuel and air by a combustion calculation (not further explained here, see for e.g. [14]). It is convenient to assume complete burnout. The assumption of ideal mixing does implicitly mean that the fuel's chemically bound energy $\dot{Q}_c$ is homogeneously released in the flame or the furnace.

To determine T_G (=T_{ex}), a total energy balance for the combustion volume is necessary.

For stationary conditions, the balance equation reads:

$$f(T_G) = \dot{Q}_F + \dot{Q}_{K,GW} + \dot{Q}_{S,GW} - \dot{Q}_c = 0. \tag{24}$$

$\dot{Q}_F$ is the difference between added and removed convective enthalpy stream, $\dot{Q}_{K,GW}$ and $\dot{Q}_{S,GW}$ are the heat fluxes transferred to the walls by convection and radiation.

The terms in Eq. (24) can be calculated as follows:

$$\dot{Q}_F = \dot{M}_{VG}\left[\bar{c}_P\Big|_{T_U}^{T_G}(T_G - T_U) - \bar{c}_P\Big|_{T_U}^{T_0}(T_0 - T_U)\right], \quad (25)$$

$$\dot{Q}_{K,GW} = A\alpha(T_G - T_W). \quad (26)$$

$\dot{Q}_{S,GW}$ has to be determined accordingly to Eq. (18) of Chap. K3 or Eq. (11), Chap. K4 or accordingly to Eq. (6), Chap. K5. Further on, the chemical energy released by the fuel is

$$\dot{Q}_c = \dot{M}_B H_u. \quad (27)$$

The variables used are:

$\dot{M}_{VG}$	mass flow of the combustion gases in kg/s,
$\dot{M}_B$	mass flow of the fuel in kg/s,
$\bar{c}_P$	mean specific heat capacity of the combustion gas mixture at constant pressure in kJ/(kg K),
T_0	temperature of the incoming mass flows in K,
T_U	surrounding temperature in K,
T_G	temperature of the combustion room in K.

3.1.1 Solution of the Total Energy Balance for T_G

In Eq. (24), the absolute temperature T_G appears linear and also to the fourth order. Hence, the following iteration procedure is suggested to solve for T_G:

$$T_{G,n} = T_{G,n-1} - \frac{f(T_{G,n-1})}{f'(T_{G,n-1})} \quad (28a)$$

with

$$\dot{Q}_F + \dot{Q}_{K,GW} + \dot{Q}_{S,GW} - \dot{Q}_c = f(T_G). \quad (28b)$$

Here the index n refers to the nth iteration step. For incomplete convergence: $f(T_{G,n-1}) \neq 0$ and $T_{G,n} \neq T_{G,n-1}$. When the term for the radiation exchange in Eq. (21) has been determined accordingly to Eq. (18) in Chap. K3, the derivative of the energy in Eq. (24) with respect to T_G becomes approximately

$$f'(T_G) = \frac{df}{dT_G} \approx \dot{M}_{VG}\bar{c}_P\Big|_{T_U}^{T_G} + A\alpha + 4Ac_1\varepsilon_G\sigma T_G^3, \quad (29a)$$

with

$$c_1 = \frac{\varepsilon_W}{1-(1-\varepsilon_W)(1-A_v)}. \quad (29b)$$

If the dependencies $\bar{c}_P(T_G)$, $\varepsilon_G(T_G)$, or $A_v(T_G)$ are taken into account and if analytical descriptions are used therefore, the corresponding derivatives in Eq. (29a) may be used additionally to accelerate convergence.

3.1.2 Combustion or Firing Efficiency

The combustion or firing efficiency η_F is understood as the ratio of the sum of the heat flows delivered to the heat sinks related to the sum of incoming fuel energy and sensible heat energy:

$$\eta_F = \frac{\Sigma\dot{Q}_W}{\dot{Q}_c + \dot{Q}_{Fo}} = 1 - \frac{\dot{M}_{VG}\bar{c}_P\Big|_{T_U}^{T_G}(T_G - T_U)}{\dot{Q}_c + \dot{Q}_{Fo}}, \quad (30a)$$

with

$$\dot{Q}_{Fo} = \dot{M}_{VG}\bar{c}_P\Big|_{T_U}^{T_0}(T_0 - T_U). \quad (30b)$$

The heat totally transferred to the walls $\Sigma\dot{Q}_W$ may be divided into useful heat $\dot{Q}_n$ and heat losses dissipated outside $\dot{Q}_v$. The furnace efficiency, according to Günther [15] then results in

$$\eta_{Often} = \frac{\dot{Q}_n}{\dot{Q}_n + \dot{Q}_v} = \frac{\dot{Q}_n}{\Sigma\dot{Q}_W} \quad (31)$$

and the total efficiency (gross) η_{ges} is

$$\eta_{ges} = \frac{\dot{Q}_n}{\dot{Q}_c + \dot{Q}_{Fo}} = \eta_F\eta_{Often}. \quad (32)$$

3.2 Calculation Example 1: Gas Combustion

The example deals with a gas-fuelled steam generator combustion system, for which the furnace is approximated by an ideally stirred reactor (system with concentrated parameters). The following data are assumed as boundary conditions:

Furnace geometry	5 m × 5 m × 15 m,
Fuel	methane,
Lower heating value	H_u = 50,409 kJ/kg,
Heat introduced by the fuel	$\dot{Q}_c$ = 117,000 kW,
Combustion conditions	30% air surplus, no soot formation,[1])
Temperatures of the incoming mass flows	T_0 = 298.15 K,
Surrounding ambient temperature	T_U = 298.15 K,
Wall temperature	T_W = 700.00 K,
Degree of emission of the walls	ε_W = 0.8,
Convective heat transfer coefficient	$\alpha = 5.8 \cdot 10^{-3}$ kW/(m^2 K),
Stefan–Boltzmann constant	$\sigma = 5.67 \cdot 10^{-11}$ kW/(m^2 K^4).

3.2.1 Looking for the Furnace Exit Temperature T_G and Combustion Efficiency η_F

The calculation of radiation exchange is to be carried out according to the instructions of Chap. K3; ε_G and A_v are

then to be determined at T_G = 1,600 K. Further on, the specific heat capacity c_p of the combustion products is needed. This may be calculated by using temperature dependent values for the mixture, if available, or by the approximation given below:

$$\bar{c}_P \Big|_{T_U}^{T_G} = 1.2603\,\text{kJ/(kg K)} \text{ (at } 1,600 \text{ K)}$$

A combustion calculation, not further described here, gives the following partial pressures for the mentioned combustion conditions:

$$p_{CO_2} = 0.074\,\text{bar}, \quad p_{N_2} = 0.724\,\text{bar},$$
$$p_{H_2O} = 0.158\,\text{bar}, \quad p_{O_2} = 0.044\,\text{bar}$$

and the mass flow of the combustion gases $\dot{M}_{VG}$ = 54,319 kg/s. The mean thickness of the layer of the combustion volume is according to Eq. (9), Chap. K3

$$s_{eq} = 0.9\frac{4V}{A} = 0.9 \cdot \frac{4 \cdot 375}{350}\ \text{m} = 3.86\ \text{m}.$$

With T_G = 1,600 K and the data given for p_{CO_2}, p_{H_2O}, and s_{eq} for the degree of emission or absorption values of ε_G = 0.291 and A_v = 0.543 are obtained accordingly to the explanations in Chap. K3.

The energy balance equation (24) for T_G is solved by iteration by means of Eq. (28).

In the case of convergence, the calculation shows the following results:

$$\dot{Q}_F = 86,862\ \text{kW}; \quad \dot{Q}_{K,GW} = 1,760\ \text{kW};$$
$$\dot{Q}_{S,GW} = 28,378\ \text{kW}; \quad T_G = 1,567\ \text{K}.$$

For the combustion efficiency η_F, the result is, according to Eq. (30),

$$\eta_F = \frac{1,760 + 28,378}{117,000} = 0.2576.$$

3.3 Calculation Example 2: Coal Dust Firing

The example deals with a coal dust fuelled steam generator combustion, for which the furnace is approximated by an ideally stirred reactor (system with concentrated parameters). The boundary conditions are assumed to be the same as for Example 1, with the following exceptions:

Fuel	highly volatile hard coal dust,
Composition of fuel	according to Table 1, No. 3,
Lower heating value	H_u = 31,506 kJ/kg$_{wf}$,
Combustion conditions	according to Table 1, No. 3.

Looking for the furnace exit temperature T_G and for combustion efficiency η_F for the case

(a) that only gaseous combustion products of the coal dust are radiating, and for the case
(b) that this radiation is superimposed by the radiation of ash, coal, and soot particles.

The calculation of radiation exchange is to be carried out in both cases by means of the approach of the weighted three gray gases, according to Eqs. (6) and (6a) or Eq. (18). The specific heat capacity of the mixture of the combustion products should have in both cases a constant value of [1]).

$$\bar{c}_P \Big|_{T_U}^{T_G} = 1.18\,\text{kJ/(kg K)} \text{ (at } 1,500\,\text{K)}$$

For (b) the following, additional assumptions are made:

density of the mixture of the combustion products[2])	ρ_{VG} = 0.241 kg/m^3(at 1,500 K)
density of the ash particulate matter	ρ_A = 2,200 kg/m^3
mean weighted diameter of the ash particles	$\bar{x}_A = 16.8 \cdot 10^{-6}$ m
scattering parameter of the Rosin–Rammler distribution of the ash particles	n = 1.5
mean relative effective cross section for absorption of ash particle radiation	$\bar{Q}_{abs,A}$ = 0.2
effective mass concentration of char particles	one tenth of the mixed, but not reacted coal particles
density of char particulate matter	ρ_K = 850 kg/m^3
mean weighted diameter of the char particles	$\bar{x}_K = 65 \cdot 10^{-6}$ m
scattering parameter of the distribution of the char particles	n = 1.5
mean relative effective cross section for absorption of char particle radiation	$\bar{Q}_{abs,K}$ = 0.85
effective soot loading (at STP conditions)	B_R = 163.5 10^{-6} kg/m^3

A combustion calculation, not further described here, gives the following partial pressures for the mentioned combustion conditions:

$$p_{CO_2} = 0.133\,\text{bar}^3, \quad p_{O_2} = 0.046\,\text{bar},$$
$$p_{H_2O} = 0,062\,\text{bar}, \quad p_{N_2} = 0.759\,\text{bar}.$$

The mass flow of the combustion products results from this combustion calculation as $\dot{M}_{VG}$ = 55.50 kg/s.

To (a): *Pure gas radiation:* Based on the determined partial pressures, on the equivalent layer thickness of the combustion suspension s_{eq} = 3.86 m, and on the coefficients given in Table 2, the following expressions can be summarized for the calculation of the gas–wall radiation exchange according to Eqs. (6) and (6a):

$$\sum_{i=1}^{3} \frac{a_i(T_G)\varepsilon_W\varepsilon_{Gi}}{1-(1-\varepsilon_W)(1-\varepsilon_{Gi})} = 0.4664 - 0.000154\,T_G/\text{K}$$
$$\sum_{i=1}^{3} \frac{a_i(T_W)\varepsilon_W\varepsilon_{Gi}}{1-(1-\varepsilon_W)(1-\varepsilon_{Gi})} = 0.4664 - 0.000154\,T_W/\text{K}$$
$$= 0.3586.$$

The iterative computation of the total energy balance in Eq. (24)

of the combustion room carried out according to Example 1, however, by including the above-given temperature dependencies leads to the following convergent solution:

$$T_G = 1{,}625\ \text{K}; \qquad \dot{Q}_F = 86{,}909\ \text{kW};$$
$$\dot{Q}_{K,GW} = 1{,}878\ \text{kW}; \qquad \dot{Q}_{S,GW} = 28{,}213\ \text{kW}.$$

From this, the combustion efficiency can be determined to be

$$\eta_F = \frac{1,878 + 28,213}{117,000} = 0.2572.$$

To (b): Inclusion of radiation by ash, char, and soot particles: At first, for ideal mixing and for the other already mentioned assumptions, mass concentrations m_j of the particles in the combustion room are calculated.

Ash particles: The fuel stream is given by $\dot{M}_B = \dot{Q}_c/H_u = 3{,}714\ \text{kg}_{wf}/\text{s}$. With the portion of ash from Table 1 and the total mass flow $\dot{M}_{VG}$, it is obtained

$$m_A = 0.065\,\dot{M}_B/\dot{M}_{VG} = 0.00435\ \text{kg/kg}.$$

Char particles:

$$m_K = 0.1\frac{1}{1-0.014}\dot{M}_B/\dot{M}_{VG} = 0.00679\,\text{kg/kg}.$$

The loading with particles is calculated from the given density ρ_{VG}[4]) of the combustion products:

$$B_A = m_A\rho_{VG} = 0.00435 \cdot 0.241\text{kg/m}^3 = 1{,}048 \cdot 10^{-3}\text{kg/m}^3,$$
$$B_K = m_K\rho_{VG} = 0.00679 \cdot 0.241\ \text{kg/m}^3 = 1{,}636 \cdot 10^{-3}\ \text{kg/m}^3.$$

The soot loading at 1,500 K is

$$B_R = 163.5 \cdot 10^{-6} \cdot (273/1{,}500)\ \text{kg/m}^3 = 29.76 \cdot 10^{-6}\ \text{kg/m}^3.$$

The radiation exchange between furnace volume and wall is calculated accordingly to Eq. (6); the degrees of emission ε_{Si} for the three gray parts of the proposed sum approach for the radiation of the suspension are calculated by Eq. (18).

With the exception of k_K and k_A, the coefficients can be taken from Tables 2 and 3. The values of k_K and k_A are determined by means of Eqs. (21) and (22):

$$k_K = 0.85 \cdot \frac{3}{2} \cdot \frac{2.42}{850 \cdot 65 \cdot 10^{-6}}/(\text{kg/m}^3) = 55{,}846/(\text{kg/m}^3)\ \text{m},$$
$$k_A = 0.2 \cdot \frac{3}{2} \cdot \frac{2.42}{2{,}200 \cdot 16.8 \cdot 10^{-6}}/(\text{kg/m}^3)\,\text{m} = 19{,}643/(\text{kg/m}^3)\,\text{m}.$$

The temperature dependence of the radiation exchange coefficients can be summarized accordingly to the pure gas radiation (case (a)) and Eq. (6), as follows:

$$\sum_{i=1}^{3}\frac{a_i(T_G)\varepsilon_W\varepsilon_{Gi}}{1-(1-\varepsilon_W)(1-\varepsilon_{Si})} = 0.6331 - 0.00004905\,T_G/\text{K},$$
$$\sum_{i=1}^{3}\frac{a_i(T_W)\varepsilon_W\varepsilon_{Gi}}{1-(1-\varepsilon_W)(1-\varepsilon_{Si})} = 0.6331 - 0.00004905\,T_W/\text{K} = 0.5988.$$

The solution of the total energy balance in Eq. (24) for the flue gas suspension corresponds – accordingly to the assumptions of the task – with the following temperatures and heat flows:

$$T_G = 1{,}417\ \text{K}; \qquad \dot{Q}_F = 73{,}284\ \text{kW};$$
$$\dot{Q}_{K,GW} = 1{,}456\ \text{kW}; \qquad \dot{Q}_{S,GW} = 42{,}260\ \text{kW}.$$

The combustion efficiency is

$$\eta_F = \frac{1,456 + 42,260}{117,000} = 0.3736.$$

For the case of coal dust combustion, the presence of particles leads to a 45% increase of heat release in comparison to case (a), which neglects particle radiation. Evidently, this value depends on the assumptions about concentrations and sizes of particles. However, it has to be noticed that relevant differences for the heat release by flames with and without solid particles occur only in boiler (steam generator) firings, as these are the only ones, which are surrounded by relatively cold surfaces.

4 Bibliography

1. Görner K (1991) Technische Verbrennungssysteme. Springer, Berlin
2. Görner K, Dietz U (1990) Strahlungsaustauschrechnung mit der Monte-Carlo-Methode. Chem. Ing. Techn. 62(1):23–33
3. Sarofim AF, Hottel HC (1978) Proceedings of 6th International Heat Transfer Conference vol 6, pp 199–217
4. Hottel HC, Sarofim AF (1967) Radiative transfer. Mc Graw-Hill, New York
5. Johnson TR, Beér JM (1973) J. Inst. Fuel. 46:388
6. Hemsath KH (1969) Zur Berechnung der Flammenstrahlung. PhD thesis, Stuttgart
7. Field MA, Gill DW, Morgan BB, Hawksley PWG (1967) Combustion of pulverised coal, BCURA, Leatherhead
8. Tietze H (1978) Strahlungsverhalten von Gas- and Ölflammen. PhD thesis, Karlsruhe
9. Schumacher A, Waldmann H (1972) Wärme- und Strömungstechnik im Dampferzeugerbau. Vulkan, Essen
10. Hein K (1972) Beitrag zum Wärmeübergang in feststoffbeladenen Gasströmen technischer Staubfeuerungen. PhD thesis, Stuttgart
11. Michelfelder S, Lowes TM (1974) International Flame Research Foundation (IFRF), Doc. nr. F 36/a/4
12. Lowe A, Stewart I McC, Wall TF (1979) Proceedings of the 17th Symposium (Int.) on Combustion, pp. 105–114
13. Wall TF, Lowe A, Wibberley LJ, Stewart I McC (1979) Prog. Energy Combust. Sci. 5:1–29
14. Brummel HG (1995) Berechnung der Temperaturstrahlung von Gas-Feststoff- Gemischen bei höheren Partikelbeladungen. PhD thesis, TU, München
15. Günther R (1984) Verbrennung und Feuerungen. Springer, Berlin

K6 Superinsulations

Harald Reiss
Julius-Maximilians-Universität Würzburg, Würzburg, Germany

1 Introduction

This chapter describes theoretical and experimental methods for determining heat transport through superinsulations, that is, thermal insulations with a permeability to heat significantly less than that of motionless air. One means of satisfying this condition is to evacuate beds of finely divided solids. Considerably less heat flows through evacuated, highly specular metal foils that are available either as rolls or blankets. This type also referenced as "multilayer superinsulations" with a discontinuous structure, includes Dewar (thermos) flasks and locally supported insulations. Thermal transport through multilayer insulations will be described in the first part of this chapter. The second part concerns superinsulations with a continuous structure, for example, evacuated powders and fibers, like in panel superinsulations.

Figure 1 compares the thermal "pseudo"-conductivity of different types on superinsulations, with approximately same thickness. "Pseudo" thermal conductivity, λ', is provisionally used in Fig. 1 to compare continuous with discontinuous, or non-transparent with transparent types of superinsulations, respectively. For the latter, total heat flow, $\dot{Q}_{Total}$, includes radiative contributions that cannot be described by the conduction law, $\dot{Q} = \lambda\ A\ \Delta T/D$. Thickness, D, of the insulations by which λ' was derived from $\dot{Q}$ must be specified in these cases, or comparison made for samples of the same thickness (cf. Appendix A1). Classification is made with respect to discontinuous and continuous superinsulations.

This chapter is focussed on *nontransparent*, industrial-scale (i.e., not miniature) superinsulations used in energy technology, cryostats, superconducting magnets, or transformers. This also includes evacuated panels. Heat transfer in transparent insulations will be considered at the end of this chapter.

Reviews on the thermal properties and the flow of heat through superinsulations that exceed the scope of this chapter have been published by Kaganer [1], with a very large variety of experimental data and analysis, and Tien [2], both for cryogenic temperature, and by Glaser [3] for both low and high temperatures. These traditional (not necessarily old-fashioned) references may be consulted in case the reader is not familiar with superinsulations. A large variety of publications that shows measured total heat flow or total thermal conductivity of insulations is available, but only a minority of them report separation of heat flow and conductivity into gaseous, solid–solid contact and radiation components.

VDI-GVC (ed.), *VDI Heat Atlas*, DOI 10.1007/978-3-540-77877-6_45,

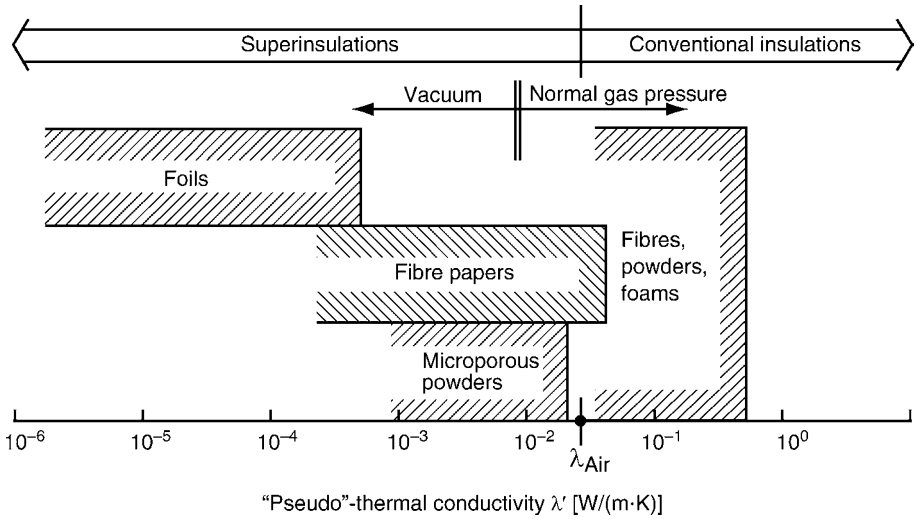

K6. Fig. 1. Thermal conductivity attainable by superinsulations at low temperatures; for explanation of the "Pseudo"-conductivity, λ′, compare footnote 1 and Appendix A1.

2 Superinsulations of Discontinuous Structures (Multilayers)

The purpose of this type of insulation is to minimize total heat flow losses $\dot{Q}_{Total}$ by reducing its components $\dot{Q}_{Gas}$, $\dot{Q}_{sc}$, and $\dot{Q}_{Rad}$, i.e.,

- To prevent heat flow, $\dot{Q}_{Gas}$, that otherwise would occur as a result of gases or ambient air by evacuating the insulated space to a residual gas pressure of less than 1 Pa.
- To avoid solid heat bridges as much as possible (solid–solid contacts between neighbouring metal foils or spacer materials, or through supports) and therefore heat flow losses, $\dot{Q}_{sc}$.
- To counteract radiation losses, $\dot{Q}_{Rad}$, by mirror coating the walls of a container (Dewar flasks) or by installing highly reflective metal foils (multilayer insulations).

If all these measures are adopted together and eventually additional actions taken such as reduction of the temperature of the warm wall by enclosing a vessel containing LH_2 or LH_e with a sheath cooled by LN_2, or by installation of intermediate vapour cooled, radiation shields, the total heat flow losses at all temperatures can be reduced to the minimum feasible in the light of the current state of the art. To increase the standby period of containers or pipings operating at low or medium temperature, application of phase change materials (latent heat storage) can be another option.

Methods for the separate determination, or at least estimates, of the heat loss currents $\dot{Q}_{Gas}$. $\dot{Q}_{sc}$, and $\dot{Q}_{Rad}$ are presented in the following section. Under *optimum* operating conditions in evacuated multilayer insulations the $\dot{Q}_{Gas}$ and $\dot{Q}_{sc}$-components are negligibly small as compared to $\dot{Q}_{Rad}$. However, heat leakages in multilayers by solid–solid contacts, the influence of disturbances such as gaps, or uncontrolled wrapping of the foils, play an important role on their thermal performance.

K6. Table 1. Constants C_1 and C_2 (data are from [5]) for calculation of mean free path, l_{Gas}, between two molecule/molecule collisions, by Eq. (1)

Gas	C_1 (p_0) [μm]	C_2 [K]
H_2	105.6	76
N_2	61	112
O_2	68.7	132
He	160	79
Ne	111.9	56
Ar	70.3	169
Kr	59.6	143
Xe	48.7	252
H_2O	95	600
CO	60.2	100
CO_2	57	273

C_1 applies for a gas pressure p_0 = 133 Pa. For a given value, $p_{Gas} \neq p_0$, the relationship that applies is $C_1(p_{Gas}) = (p_0/p_{Gas})\ C_1(p_0)$

2.1 Determination of $\dot{Q}_{Gas}$

The first step is to determine the mean free path, l_{Gas}, of the gas molecules between collisions, at a given residual gas pressure p_{Gas}, in the insulations. According to Sutherland [4], l_{Gas} is given by

$$l_{Gas} = \frac{C_1(p_{Gas})}{1 + C_2/T}\,[\mathrm{m}] \qquad (1)$$

where T is the absolute temperature in Kelvin, and C_1 and C_2 are constants for specific gases, some values for which are presented in Table 1. Example 1 for the determination of l_{Gas}. is given in Sect. 3.1. For air at atmospheric pressure and room temperature, $l_{Gas} \approx 0.06$ μm.

The next step is to estimate the average foil spacing δ. As a rule, $l_{Gas} >> \delta$, for this type of insulations. In other words, the

mean free path l_{Gas} is restricted not so much by intermolecular collisions as by the average foil spacing δ, i.e., by interactions with the solid components of the insulations.

The thermal conductivity of the residual gas λ_{Gas} is given by Kaganer [1], p. 6:

$$\lambda_{Gas}(p_{Gas}) = \frac{\lambda_0}{1 + 2 \times \beta \times Kn} [W/(m \cdot K)] \quad (2a)$$

where λ_0 is the thermal conductivity of the gas at atmospheric pressure (see Tables in Chap. D1, Subchap. D3.1), and Kn is the Knudsen number. The term β is a weighting factor that contains a correction, k, for the specific heat of the gas (figures are listed in Table 2), the well-known specific heat ratio $\kappa = c_p/c_v$ at constant pressure and volume, and the accommodation coefficient α, that is,

$$\beta = \frac{2 \times k}{\kappa + 1} \times \frac{2 - \alpha}{\alpha} \quad (3)$$

The figure for air is $\beta \approx 1.63$.

Accurate figures for the accommodation coefficient are not always available: $\alpha \approx 0.3$ for light gases (hydrogen and helium), and α is very close to unity for heavy gases, e.g., nitrogen (cf. [6]).

The Knudsen number in Eq. (2a) is given by

$$Kn = \frac{l_{Gas}}{\delta} \quad (4)$$

It is evident from Eq. (2a) that λ_{Gas} is small if

- λ_0 is as small as possible (in some special technical applications, inert gases would be suitable candidates for filling the space between the foils, after previous evacuation)
- The Knudsen number, Kn, is as large as possible, by reducing the foil clearance, δ, and by evacuation. However, a too high density of foils and/or spacers, per unit length, could lead to undesirable solid–solid contact conduction, and extend evacuation periods.

The lower the pressure, the greater the Knudsen number, Kn, or the less the value for λ_{Gas} simply because evacuation increases l_{Gas}. It follows from Eq. (4) that high Knudsen numbers can also be achieved in beds of very finely divided solids and very fine pore diameters, δ. The thermal conductivity component λ_{Gas} can then be completely eliminated, on an industrial scale, by evacuation and selection of small values for δ. A specimen calculation for λ_{Gas} is presented in Sect. 3.1.

The heat flow losses $\dot{Q}_{Gas}$ are obtained from the usual rule for heat conduction, i.e., $\dot{Q} = \lambda\ A\ \Delta T/D$ (Fourier's empirical law). Combining with Eq. (2a) gives

$$\dot{Q}_{Gas}(p_{Gas}) = \lambda_{Gas}(p_{Gas}) A \Delta T / D \quad (5)$$

where A is the area of the insulations, ΔT is the difference between the temperature of the heated wall and that of the cold wall, and D is the wall spacing. Note that Eq. (5) does not take into account coupling between the different heat transfer modes. Accordingly, Eq. (5) is an approximation that is the better fulfilled the lower the gas pressure.

If the residual gas pressure p_{Gas} is very low, λ_{Gas} as given in Eq. (2a) is converted into an expression for the free molecular thermal conductivity, that is, without intermolecular collisions, which is directly proportional to p_{Gas}.

2.2 Estimation of $\dot{Q}_{sc}$

There is no mathematical expression of general validity that allows heat transfer by solid–solid contacts, $\dot{Q}_{SC}$, in foil insulations to be estimated. Benefit of finite differences or finite element numerical methods in this case is comparatively small. The absolute number, or the density, of punctiform, or of line-wise or area-like solid–solid contacts between neighboring foils or spacers, is largely subject to the wrapping procedure and depends on the compressive load or, in case of cylindrical geometry, on the wrapping force (and the own weight of the foils plus spacers) under which the multilayer structure (foils plus spacers) is prepared. While in some cases an *overall* compressive load on the multifoil structure can be estimated, it is hardly possible to specify *local* compressive load distribution, which would be needed to estimate contact radii under local elastic or inelastic deformation of foils and spacers.

K6. Table 2. Correction factors, k, (applied to specific heat, c_v) for calculation of β, in dependence of temperature (Data are from [7])

Gas	T [K]						
	90.6	194.8	273.2	373.2	473.2	573.2	673.2
H_2	2.35		2.03		2.12		2.19
N_2			1.95				
O_2			1.915				
Air		1.94	1.95	1.945	1.943		
CO			1.865				
CO_2		1.805	1.67	1.6	1.56	1.55	
H_2O				1.41	1.395	1.41	1.425
He			2.43				
Ne			2.5				
Ar			2.49				
Kr			2.49				
Xe			2.54				

Metallic contacts between radiation foils are frequently obviated by layers of woven glass fabrics, nettings of polyester materials, thin fiber-glass paper spacers, or even punctiform ceramic coatings on metal foils, the latter for high temperature applications (Fig. 2). Modern spacers are produced in net form (tulle), with high porosity and with filament diameter in the order of 50 μm. Another means is to apply dimpled or crinkled metallic foils (Fig. 3b, c) that make spacers superfluous and avoid or reduce area-like solid–solid metallic contacts.

The same purpose is served by vacuum-metallized plastic films, e.g., Terepthalate (Mylar), with a thickness of polymer film and metallization of 6 μm and at least 40 nm, respectively. Compared to massive Al-foils, with thickness in the order of 10 μm, this not only reduces compressive loads, under their own weight, but also reduces conductive or radiative heat flow parallel to the foil surface; this aspect is important, for example, concerning the insulations of the neck or other feed-throughs of a cryostat.

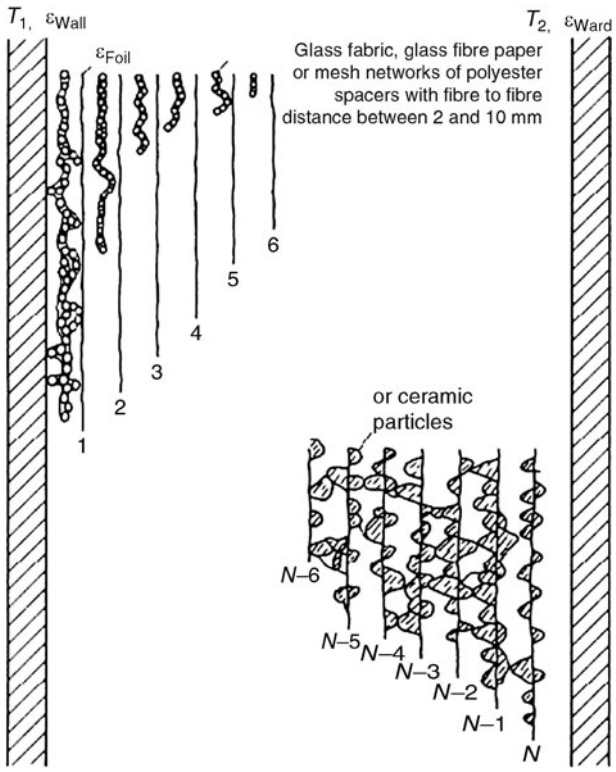

K6. Fig. 2. Structure (not to scale) of a multilayer superinsulation. Depending on the specific application (temperature), foil materials, for use at cryogenic to high temperatures, comprise either thin (in the order of 10 μm thickness), massive, flat (with appropriate spacers), crinkled or dimpled (to avoid area-like solid–solid contacts between neighboring foils, then without spacers) or perforated (to speed up evacuation) Al-foils, or, preferentially (because of low specific weight), very thin, smooth (to optical surface quality) polymer (Mylar, Kapton, PTFE) foils (6–12 μm thickness, for cryogenic applications) that are aluminized on one or on both sides, with Al-coating thickness per foil between 25 and 80 nm (one side coatings should have thickness of at least 40 nm), with spacers (mostly nettings, but sometimes also using very thin glass fiber paper). Both kind of foils (massive Al, aluminized polymer foils) are available from rolls or, concerning aluminized polymer foils, in form of mats (blankets) of 10–40 single polymer layers. Mechanical stabilization of foils and spacers is made by punctiform thermo-fixation and/or adhesive strips again composed of aluminized polyester foils with adhesives suitable for use at cryogenic temperatures.

If the number of foils increases, the radiation transmittance of the superinsulations decreases, but there would be more solid–solid contacts and greater heat flow losses Q_{SC}. Consequently, there is an optimum figure for the number per unit length of foils (Fig. 4).

Heat losses through multilayer insulations may increase significantly if the foils are subjected to compressive loads (Fig. 5, see also [8], a comprehensive study of the influence of all sorts of degradations onto the thermal performance of multilayer superinsulations), which could result from their own weight or from the winding procedure. An effective method to avoid compression of multifoils on cylindrical surfaces is spiral winding of foils and spacers, simultaneously from two rolls. More recommendations for the winding of multifoils can be found in Kaganer [1], pp. 121–123.

If atmospheric pressure were to act on flat outer side walls of an evacuated insulation space, locally supported foil insulations has been suggested for avoiding deformation of the walls. Thus the strain may be taken up by thin ceramic pegs, microporous powder insulation supports, or fiberglass paper spacers.

The strength of the usual construction materials for the walls (stainless steel, in many applications) entails that the spacing between supports must be less than 10 cm. Hence many additional thermal bridges, which detract from the insulation efficiency, are formed per unit of area. Foil insulations supported by ceramic pegs could be taken as an example to demonstrate this: Consider a high temperature multifoil superinsulation. If there are 50 highly reflective radiation foils in a completely evacuated space, and the wall temperatures are T_1 = 600 K and T_2 = 300 K, the heat flux will be $\dot{q}_{Total} = \dot{Q}_{Total}/A \approx$ 7–10 W/m^2. Let the diameter of a ceramic support be 3 mm. Then, if the wall spacing is 20 mm and the thermal conductivity of the ceramic is λ_S = 1 [W/(m · K)], the heat losses over this single support will be

$$\dot{Q}_{SC} = \frac{1 \cdot (0.0015^2 \cdot \pi) \cdot 300}{0.020} \left[\frac{\mathrm{W \cdot m^2 K}}{\mathrm{m \cdot K \cdot m}}\right] = 0.1\,\mathrm{W}.$$

Thus 100 ceramic supports per square meter cause the total heat losses through the peg-supported, high temperature foil insulations to be twice as much of the undisturbed case (in reality, even more supports would have to be installed).

Also, an increase in the thickness of the outer walls would entail considerable increase in mass. Accordingly, application of ceramic pegs, except for special cases, does not seem to be a favorable solution.

Instead, compressive loads on radiation foils can be avoided by fitting them in recesses in microporous insulation panels, as is illustrated in Fig. 6a. However, owing to the comparatively high thermal conductivity of the solid contacts in the microporous supporting material, viz. ca 5 [mW/(m · K)] in vacuum and at low or cryogenic temperatures, the attendant total heat

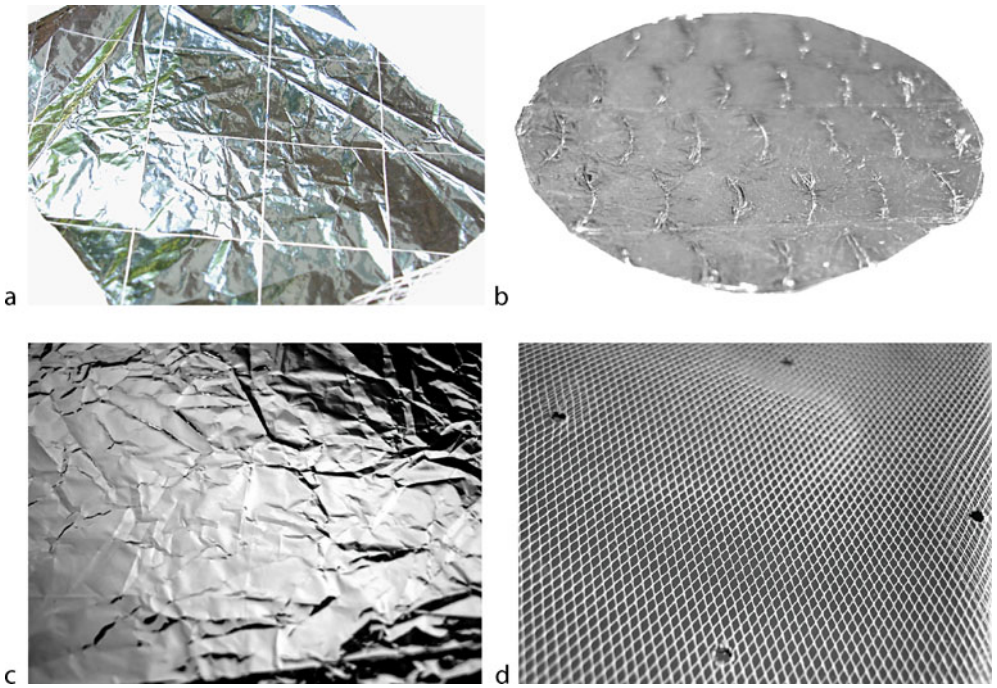

K6. Fig. 3. (**a**–**d**) Multifoil insulation materials; (**a**) One-sided aluminized (40 nm) polyethylene therephthalate film (Mylar) of 3.5 μm thickness, with broken-up metallization into 10 mm squares obtained by electromachining with narrow (0.2 mm) grooves, to interrupt induction loops; Patent EN 8114868 – 10/07/81, courtesy Cryomat S. A. R. L., Mormant, France; (**b**) dimpled Al-foil, courtesy Linde AG, Höllriegelskreuth, Germany (sample diameter about 40 mm); (**c**) crinkled metallized Mylar foil (sample size about 40 × 60 mm^2, and (**d**) spacer netting (tulle) using monofilament polyester filaments, surface density about 5–7 g/m^2, mesh size about 2 mm; (**c**) and (**d**) courtesy Jehier S. A., Chemille, France; (**d**) also shows perforation holes of about 2 mm diameter, in-line distance between holes 50 mm, to speed-up evacuation.

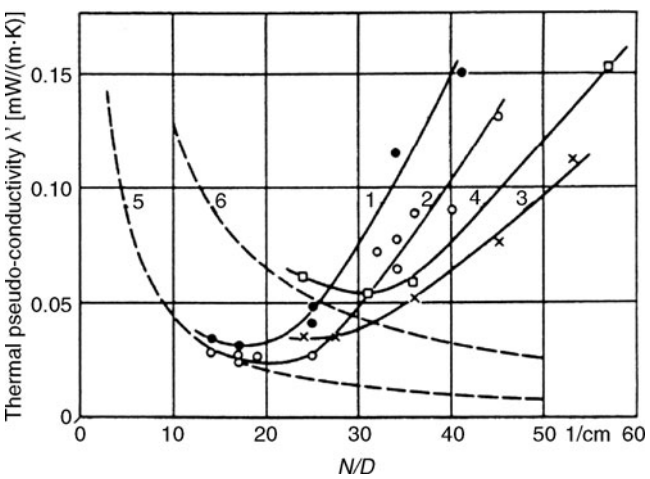

K6. Fig. 4. "Pseudo"- thermal conductivity, λ', of multifoil superinsulations, as a function of the number of foils, N, per unit thickness of insulation, D. The figure is from [1]. Curves 1- 3: aluminum foil with fiberglass paper of various thicknesses; Curve 4: vacuum-aluminized Dracon film with woven glass fabric, Curves 5 and 6: theoretical values (with no allowance for solid-contact conduction) calculated from ε_{Foil} = 0.04 and 0.12. Wall temperatures T_1 = 293 K and T_2 = 90 K.

losses still are at least twice as high as those for purely metallic foil on which there is no compressive load.

A more favorable solution (Figs. 6b and 7a, b) is offered by supports produced from fiberglass paper (conditioned, if necessary, by a thermo-fixation process, under mechanical pressure; this process has successfully been applied also to glass wool or, at high temperatures, to silica fibers). The very low total conductivity of the conditioned fiberglass material (fiberglass boards) hardly increases even under compression of up to 5 bar and especially at high temperatures ([9]). A ratio of 1:5 to 1:10 of the supported area to the total area appears to be realistic. A ratio of 1:10 would restrict the total heat flux losses to 10^{-12} W/m^2 at ΔT = 300 K and D = 20 mm ([10]); in other words, the unsupported, high temperature foil's resistance to heat would hardly be impaired.

As an example, Fig. 7a, b ([11]) shows the "k-value" associated with the total heat losses, i.e., $k = \dot{Q}_{Total}/(A\ \Delta T)$ in [W/(m^2 · K)], for a locally supported superinsulation (Curve 1) that consists of square supports (35 × 35 mm^2, with an average spacing of 70 mm) and ten continuous aluminium foils with intervening fiberglass layers. Curve 2 is obtained if the aluminium foils are left out. The measured values have been plotted against the mean radiation temperature, T^{*3} or T_{Rad}, as defined by Eq. (21) in Sect. 3.3.1. The corresponding k-values for unsegmented

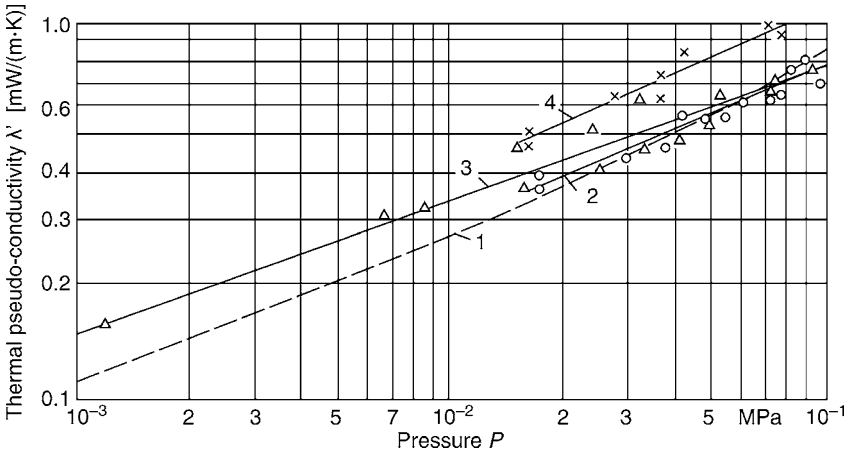

K6. Fig. 5. "Pseudo"- thermal conductivity, λ', of aluminium multifoil superinsulations, as a function of the compressive load, *p*. The figure is from [1]. Spacer materials for Curves 1 and 2: fiberglass paper of various thicknesses; for Curve 3: woven glass fabric, for Curve 4: perforated fiber-glass paper. Wall temperatures as in Fig. 4.

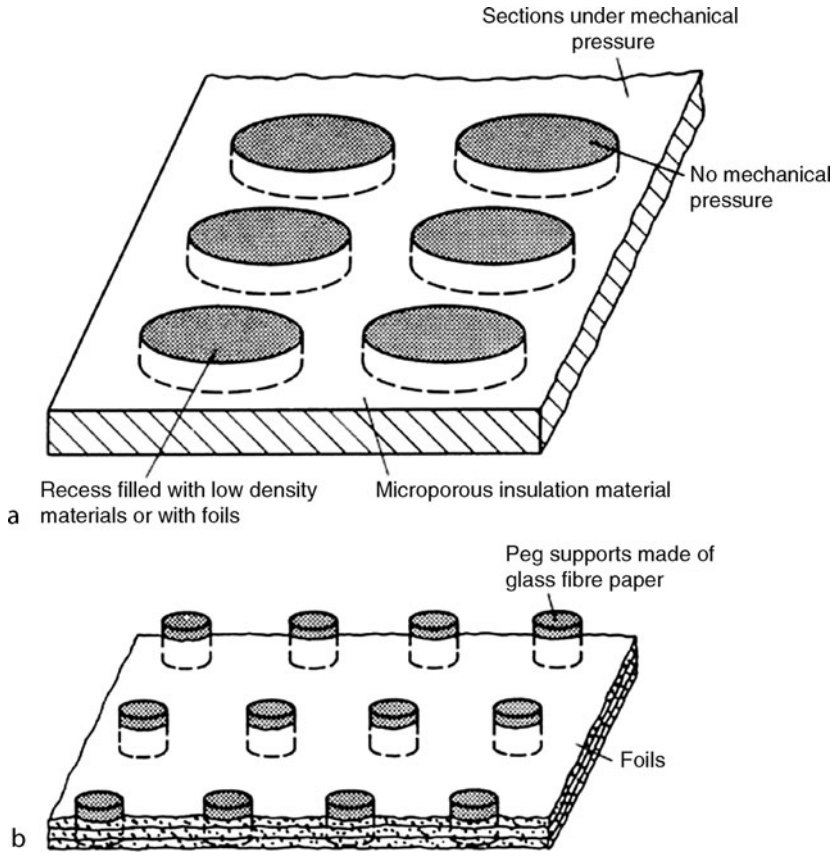

K6. Fig. 6. (**a**, **b**) Locally supported insulations (not to scale); (**a**) Microporous insulations with non-loadbearing circular recesses to accommodate the foils (or dispersed insulating material of very low density); (**b**) Supports, e.g., fiberglass material.

insulations consisting solely of fiberglass (Curve 3) have been included as a comparison. The thermal superiority of the segmented superinsulations can be clearly recognized. All the measured values plotted in this diagram were recorded under a pressure of 1.16 bar.

Heat losses can be considerably increased by direct contact between the warm and the cold sides of the foil assembly (Fig. 8a) by lateral conduction and radiation tunnelling caused by "cold ends" of the film when forming edge jointing. These heat losses can be avoided by staggering the layers of foil (Fig. 8b–d) or by shingled multilayer insulations. In shingled multilayers, one end of each shingle is attached to the inner tank wall and overlaps with a neighboring shingle; this also speeds up evacuation.

A very effective support structure that does not rely on supports (crinkling, nettings, papers) *between* neighboring foils

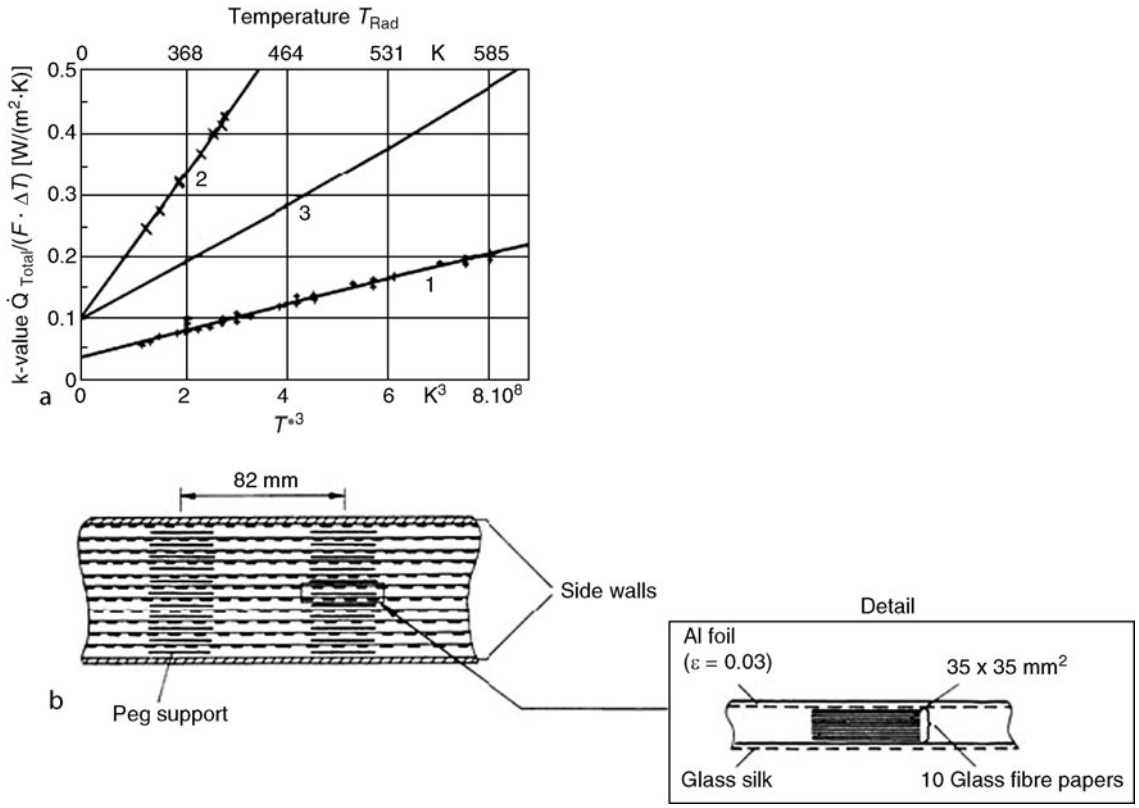

K6. Fig. 7. (**a**) k-Values associated with total heat losses for locally supported and unsegmented, load-bearing superinsulations subjected to compressive load as a function of the average temperature of radiation, T^{*3} {as defined by Eq. (21)}, or of $T_{Rad}{}^3$; the figure is from [11]. Curve 1: superinsulation with local fiberglass paper supports and 10 continuous strips of aluminum foil with intervening layers of woven glass fabric (Fig. 7b); area occupied by the supports as a percentage (18%) of the total area of insulation, average spacing between supports 70 mm; thickness of insulation D = 15.9 mm. Curve 2: same supports but without Al foil; D = 15.2 mm. Curve 3: unsegmented purely fiberglass insulations (fit with measured values, [9]); D = 15 mm. All measured values are determined at a pressure of 1.16 bar exerted by a compressive load. (**b**) Schematic diagram of locally supported superinsulations (Curve 1 in Fig. 7a) with fiberglass paper supports and continuous strips of aluminum foil (10 μm thickness; hemispherical emissivity $\varepsilon \approx 0.03$). Average density of insulations $\rho \approx 90$ kg/m^3 (The figure is from [11]).

but applies inner and outer corrugated tubes, rings, and thin rods (fiber-reinforced material) to support a *stack* of foils, or a blanket, of a multilayer insulation has been reported by Neumann [12], compare Fig. 9. In this concept, radiative exchange between neighboring stacks or blankets will not be increased by the supports, because the radiation exchanging surface of the rods and rings is small (a small percentage of the foil surfaces, contrary to e.g., fiber glass papers), while the non-radiative (solid conduction) paths become rather long due to large distances between neighboring support to blanket contacts. Further, the contacts, either punctiform or as lines, on the upper half-circle are subject to only the small weight of the blankets and on both half-circles only to some tension remaining from winding.

But heat losses over thermal bridges, between inner and outer tank of a container for cryogenic liquids, mostly at the front surfaces, may greatly exceed loss through the foils. This aspect is important also for long, vacuum-insulated tubes for the transport of cryogenic liquids, for superconducting power cables or, as occasionally considered, for medium temperature applications like large diameter pipings in district heating. Long hold times of a LHe cryostat are obtained using vapor-cooled shields for the inner liquid helium tank and a multifoil superinsulation for the outer liquid nitrogen tank. The inner tank can be supported using Kevlar cords, compare, e.g., [13]. Cords, straps, or struts are used in commercially available cryogenic containers. Thermal conductivity, tensile or compressive properties of these materials are critical.

Vapor cooling is applied not only to shields but also to current supply (feed-throughs) into containers housing superconducting magnets [15] or even for bushings in superconducting transformers. An example for calculation of the efficiency of vapor-cooled radiation shields from heat balance conditions is reported in Kaganer ([1], pp. 102–103).

As a completely different concept to support the inner against the outer tank of a container for LH_2, Walter [14] suggests to apply levitation forces between superconductors (melt-textured YBCO or melt-cast BSCCO 2212) and permanent magnets. While in the warm state of the tank, memory-metal actuators serve as supports between both tanks, this concept avoids any solid–solid contacts between both tanks in the cold phase; what remains is the interconnection between inner and outer tank at the neck of a storage unit. When the container is filled, the superconductor is field-cooled which

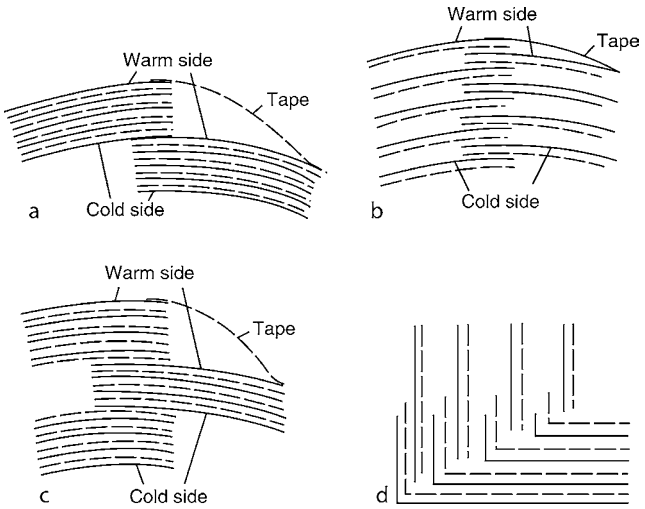

K6. Fig. 8. Overlap in multifoil superinsulations (schematic, following Langer [17]; (**a**) Simple overlap (greatest heat losses); (**b**) Layer-for-layer overlap; (**c**) Multiple-layer (blanket) overlap; (**d**) Edge joints (indentations). The total losses in a cylindrical tank with layer-for-layer and multiple-layer overlaps are 7% and 2%, respectively, less than those in tanks with simple overlaps [17]. However, these improvements depend on the configuration.

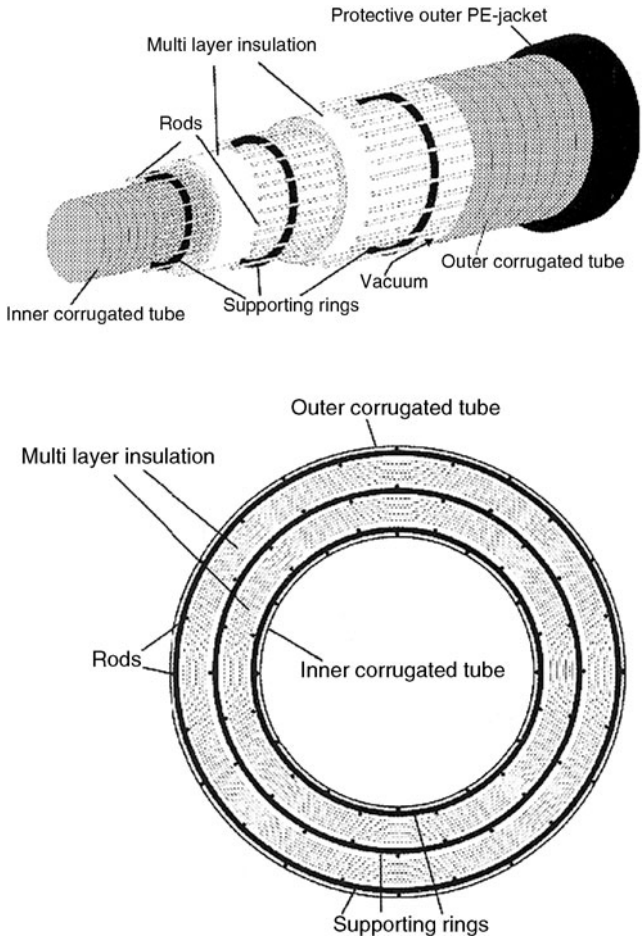

K6. Fig. 9. Mechanical support applied to shields in a multilayer insulation to prevent solid–solid contacts between neighboring shields (The figure is from [12]).

means its position is stabilized ("frozen") against displacements, by means of Lorentz forces between the magnetic field and shielding supercurrents, like in levitation experiments. As reported in [14], the heat loss component, $\dot{Q}_{SC}$, of the LH_2-container was reduced to 0.35 W by this concept, in comparison to the $\dot{Q}_{SC}$ of 2.1 W of a conventional storage unit (total heat losses were reduced from 4.5 to about 2.6 W; certainly, there is potential for further reduction).

2.3 Determination of $\dot{Q}_{Rad}$

Without using multifoils as radiation shields, suppression of radiative heat leakage in Dewar flasks is obtained solely by the extremely small thermal emissivity of mirror-finished glass or metallic walls. Radiative heat leakage in Dewar flasks can be estimated using the relations for multilayers given in the following by simply assuming the number N of foils to $N = 0$.

A standard choice for storage cryostats, cryostats for space missions, or stratospheric balloon experiments is to surround the inner liquid helium tank by an outer liquid nitrogen tank, with an intermediate temperature shield in-between. The shield is convectively cooled by evaporated helium. The radiative load on the liquid nitrogen tank is reduced by means of a multilayer insulation. Metallic walls of the inner tank, shield and outer tank that face each other can be designed simply as a Dewar flask provided they can be given a very small emissivity.

Consider the case of N highly specular foils, e.g., aluminum, nickel, or other metals of very low emissivity, between infinitely extended, *plane* parallel walls of temperatures T_1 and T_2 at right angles to the temperature gradient in an evacuated insulated space. Assume that ε_W is the hemispherical thermal emissivity of the two walls of area A and that it is independent of temperature and wavelength. It is also assumed that ε_{Foil} is the corresponding emissivity of the foils. Also let $\eta_W = \varepsilon_W/(2 - \varepsilon_W)$ and $\eta_{Foil} = \varepsilon_{Foil}/(2 - \varepsilon_{Foil})$ be the corresponding reduced emissivities. The radiant flux $\dot{q}_{Rad} = \dot{Q}_{Rad}/A$ (cf. [1], pp. 33–35) will then be given by

$$\dot{q}_{Rad} = \frac{\dot{q}_{Rad,0}}{1 + N \times \frac{\eta_W}{\eta_{Foil}}} \left[W/m^2\right]. \tag{6}$$

It is assumed that ε is the same for all the foils. The term $\dot{q}_{Rad,0}$ in Eq. (6) is the radiant flux without the foils and is defined by

$$\dot{q}_{Rad,0} = \varepsilon_{eff} \times \sigma \times (T_1^4 - T_2^4)\,[W/m^2] \tag{7a}$$

where T_1 and T_2 are absolute temperatures in Kelvin and

$$\varepsilon_{eff} = \frac{1}{2/\varepsilon_W - 1} = \eta_W \tag{8}$$

The term σ is the Stefan-Boltzmann constant, σ = 5.67040 10^{-8} [W /(m^2 K^4)]. Numerical values for the thermal emissivity, ε, can be found on pages from Chap. K1 or in the traditional literature and in some examples reported in Appendix A2 of this chapter.

It should be noted that the expression for $\dot{q}_{Rad,0}$ in Eq. (7a), and thus that for $\dot{q}_{Rad}$ in Eq. (6), are not in accordance with the structure of the normal thermal conductivity relationship $\dot{Q} = \lambda\ A\ \Delta T/D$, in which the thermal conductivity applies exclusively to specific substances. Thus it is not always possible to report a "radiation conductivity" λ_{Rad} (cf. Sect. 3.3 and Appendix A1).

If the inner surfaces of the walls are mirror-finished, e.g., by electro-polishing, $\varepsilon_W \approx \varepsilon_F$. In this case, the relationship for infinitely extended, *plane* parallel walls is

$$\dot{q}_{Rad} = \frac{\dot{q}_{Rad,0}}{1+N} = \frac{1}{1+N} \times \frac{\sigma \times (T_1^4 - T_2^4)}{2/\varepsilon - 1}\ [W/m^2]. \quad (9)$$

If there are no foils, i.e., if $N = 0$, Eq. (9) becomes

$$\dot{q}_{Rad} = \frac{\sigma \times (T_1^4 - T_2^4)}{2/\varepsilon - 1}\ [W/m^2] \quad (7b)$$

This expression is also valid (approximately, because it was assumed the walls are infinitely extended in length) for the side walls of cylindrical Dewar flasks if the two inner surfaces are mirror-finished to the same extent. However, if the reflection from the second wall is diffuse, regardless of that of the first wall, Eq. (7b) is transformed into Eqs. (12–14) of Chap. K1, Sect. 2.1.

The case of infinitely extended, concentric *cylindrical* walls is considered in Appendix A1 of this chapter, Eqs. (A1) and (A4).

2.4 Total Heat Losses in Evacuated Foil Insulations

A good, though not rigorous expression for the total heat losses is given by

$$\dot{Q}_{Total} = \dot{Q}_{Gas} + \dot{Q}_{SC} + \dot{Q}_{Rad} \quad (10)$$

if $\dot{Q}_{Gas}$ is obtained from Eqs. (2a) and (5); and $\dot{Q}_{Rad}$ from Eqs. (6–9). $\dot{Q}_{SC}$ is estimated as described in Sect. 3. The likelihood of free convection losses can be excluded if the foil insulation is evacuated (and if the foil spacing is not too large). In cases of doubt, the Rayleigh number must be estimated as described in Part. F.

The approximation to $\dot{Q}_{Total}$ given in Eq. (10) is based on the assumption that the individual components of heat flow $\dot{Q}_{Gas}$, $\dot{Q}_{SC}$, and $\dot{Q}_{Rad}$ can be determined separately from one another, as has been described here, and then simply be added. If the residual gas pressures are very low and the number of foils is large (conditions that are usually realized in foil insulations), the approximation is justified. However, the following reservations must be observed:

(a) If the residual gas pressures are significant, the heat currents caused by solid contacts may be greater than estimated, as has been observed by Fricke [16]. This can be interpreted as an apparent enlargement of the contact surfaces.

(b) Rigorously, the law of conservation of energy couples all the components of heat flow by means of the temperature profile in the superinsulations, in accordance with their respective relationships to temperature. Consequently, coupling between the different, temperature-dependent heat transport mechanisms must be observed in very accurate analyses. Nevertheless, the approximation obtained by Eq. (10) suffices for the description of regular superinsulations in the majority of applications.

In Sect. 3, a method for experimental separation of heat flow components, $\dot{Q}_{SC}$ and $\dot{Q}_{Rad}$, in *continuous* insulations will be outlined. The question is whether this is also possible in multilayers.

First, a plot of $\dot{Q}_{Total}$ against the residual gas pressure, p_{Gas} (Fig. 10, from [17]), yields the S-curves observed in multifoil insulations; curves of this type are typical also of dispersed insulations (or of any dispersed medium exposed to heat flow, if $\dot{Q}_{Total}$ is measured as a function of residual gas pressure). This can be explained by the fact that $\dot{Q}_{Gas}$ is the dominant component at high gas pressures, in which range λ_{Gas} is constant, i.e., independent of p_{Gas} (if there is no convection that would transfer λ_{Gas} into increased, "effective" values). Hence $\dot{Q}_{Gas}$ and thus $\dot{Q}_{Total}$ are also independent of p_{gas} at high gas pressures. At very low gas pressures, on the other hand, $\dot{Q}_{Gas}$ is negligibly small, and all that remains to be measured is the sum of $\dot{Q}_{SC}$ and $\dot{Q}_{Rad}$ which then does not depend on the residual gas pressure. As can be seen from Fig. 10, $\dot{q}_{Total}$ is reduced to values below 10 W/m^2 in this region. Between these two ranges of pressure, the $\dot{Q}_{Gas}$ component decreases with p_{Gas}, as is described in Sect. 2.1. A separation of $\dot{Q}_{Gas}$ from $\dot{Q}_{SC} + \dot{Q}_{Rad}$ in this intermediate range of p_{Gas}, and of $\dot{Q}_{SC}$ from $\dot{Q}_{Rad}$ in the whole range of pressure, is not possible from the diagram $\dot{Q}_{Total}$ versus residual gas pressure.

An experimental method to separate $\dot{Q}_{SC}$ (thermal bridges between foils and by other solid–solid contacts) from $\dot{Q}_{Rad}$ (solely radiation heat flow through the foils) in multilayer superinsulations has been suggested by Kaganer [1] (pp.164–167). It is based on transient measurements of heat losses, $\dot{Q}_{Total}$,

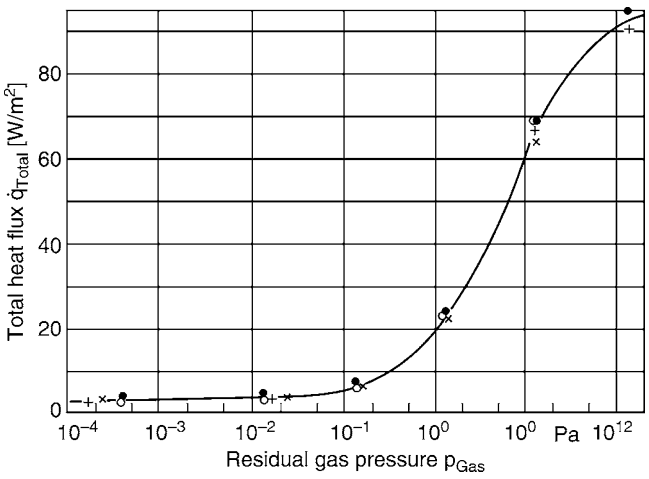

K6. Fig. 10. Total heat losses $\dot{q}_{Total} = \dot{Q}_{Total}/A$ in foil insulations as a function of the residual gas pressure p_{Gas} (data are from [17]); solid circles: 9 μm aluminium foil and glass tissue, crosses x: 0.25 μm aluminum on both sides of 12 μm polyester film and glass tissue, crosses + : 0.25 μm aluminum on both sides of 6 μm polyester film and polyester nonwoven, open circles: 0.25 μm aluminum on both sides of 12.5 μm polyimide film and polyester nonwoven.

during cool-down of a cryostat. Since this requires measurement of evaporation rates of a completely filled cryostat, there are hardly experimental values available other than those reported by Kaganer. Instead, the author has performed a numerical experiment (see Appendix A3) to check the suggested method.

Note that the components of $\dot{Q}_{\text{Total}}$ in Eq. (10) are calculated with given temperatures of warm and cold walls, at coordinates $x = \text{D}$ and $x = 0$, respectively. Conversely, if heat flux, $\dot{q}$, is given as boundary condition, i.e., not $T(\text{D})$ and $T(0)$, but $\lambda\, \text{d}T/\text{d}x$, on either wall plus the temperature of one wall, either $T(\text{D})$ or $T(0)$, the other temperature, $T(0)$ or $T(\text{D})$, respectively, can be calculated, from conservation of energy (see below). This means that temperature profiles can be calculated, which subsequently allows calculation also of the heat flux components.

Application of the second boundary conditions option (heat flux, plus one wall temperature) allows to account for coupling between radiation and conduction heat transfer (for an application of the following, see, e.g., [18]). Assume N concentric radiation shields of wrapped around an inner container of infinite length. Heat flow parallel to the cylindrical surfaces is neglected. This assumption can be justified if clearance between the shields and cross section of each shield is very small. Heat exchange between neighboring shields is by radiation and, because of some mechanical contacts, by conduction. Under stationary conditions, the energy balance for each of the $1 \le \text{j} \le \text{N}$ shields, with respect to its neighbours, $1 \le k \le N$, $j \ne k$, reads

$$\dot{Q}_{\text{j,k}} = (T_{\text{j}} - T_{\text{k}})/R_{\text{Cond (j,k)}} + (T_{\text{j}}^4 - T_{\text{k}}^4)/R_{\text{Rad(j,k)}} \qquad (11)$$

In Eq. (11), the first and second terms describe conduction and radiation contributions, respectively. The $R_{\text{Cond(j,k)}}$ and $R_{\text{Rad(j,k)}}$ are the corresponding thermal resistances to conduction and radiation between shields j and k. Assume that the shields $j = 1$ and $j = \text{N}$ are surrounded by outer and inner concentric walls, $j = 0$ and $j = \text{N} + 1$ (index a), respectively. The temperature of the outer wall, T_{a}, roughly equals ambient temperature $T_{\text{a}} > T_{\text{j=1}}$, while the temperature of the inner wall, T_0, equals temperature of a stored cryogenic liquid, T_2. Thus two additional equations like Eq. (11) take into account boundary conditions, either

$$\dot{Q}_{\text{1,a}} = (T_{\text{a}}^4 - T_1^4)/R_{\text{Rad(1,a)}} \qquad (12a)$$

or

$$\dot{Q}_{\text{N,0}} = (T_{\text{N}}^4 - T_0^4)/R_{\text{Rad(N,0)}} \qquad (12b)$$

For definition of the conductive and radiative resistances in Eqs. (11), (12a), and (12b), see Sect. 2.5 dealing with resistance networks. If using for radiative resistances between neighboring foils the relation $R_{\text{Rad}} = \Delta T/\dot{Q}_{\text{Rad}}$ with $\dot{Q}_{\text{Rad}}$ from Eq. (7b), that describes concentric cylinders of *infinite* length, a correction with respect to finite length of the container has to be introduced. If all materials parameters (conductivities and emissivities of shields and walls) are considered as independent of temperature, and the emissivities of all (mirror-finished) shields and walls identical, the resistances incorporate only geometry (size of the N + 1 surfaces).

Since all $\dot{Q}$ in Eqs. (11), (12a), and (12b) are equal, by conservation of energy we have a system of N + 1 interdependent, algebraic equations that can easily be solved. A check of this method can be made using thermal resistance networks (see Sect. 2.5). It is also possible to consider temperature-dependent conductivities and emissivities, but then solutions of the system of equations have to be found in iterations.

Values determined by experiment for the total heat losses $\dot{q}_{\text{Total}} = \dot{Q}_{\text{Total}}/A$ in foil insulations are listed in Tables 3 and 4. They are valid for various materials for foils and spacers in cryogenic and high-temperature insulations, various grades of perforations of the foils (to reduce the time required for gas removal), and winding forces. The tables have been extracted from Langer's comprehensive documentation [17], again a traditional source of data.

The recently published, detailed compilation ([8], Sects. 3–5) investigates experimentally the influence of the whole catalogue of degradations on thermal performance of multifoil superinsulations. The study includes interruptions like flanges, turns, gaps, fissures and edge jointing, the increase of heat transmission by mechanical pressure on multilayers, and longitudinal (parallel to foils) thermal conduction, all for a variety of materials and in the cryogenic range of temperatures including LHe. Advantages of winding versus mat technology is discussed also, and best results obtained so far for $\dot{Q}_{\text{Total}}$ of large cryogenic installations are reported in Sect. 6 of this reference.

2.5 Thermal Network Calculations Applied to Multilayer Superinsulations

Estimation of $\dot{Q}_{\text{SC}}$ in Sect. 2.2 and of $\dot{Q}_{\text{Rad}}$ using Eq. (6) and determination of $\dot{Q}_{\text{Total}}$ using Eq. (10) or Eqs. (11) and (12a, b), are restricted to heat flow components *perpendicular* to surfaces of foils and spacers. Lateral heat flow is not taken into account by these methods. However, lateral heat flow can be important at cryogenic and high-temperature multilayer insulations with respect to heat leakage through the neck of cryostats, through mechanical supports, or other penetrations (insulated evacuation channels or current feed-through). Further, the methods presented in the previous sections, except for Eqs. (11) and (12a, b), do not consider coupling between the different heat transfer mechanisms (gaseous or solid–solid contact conduction, radiation); this is because they do not take into account the temperature profiles, and accordingly, the temperature dependence of the conductivities or corresponding thermal resistances.

A practical method that allows to take into account not only heat flow of any origin and in *any* direction and coupling between conduction and radiation, by temperature-dependent material's properties like thermal conductivity (at least in intervals), is available from thermal network calculations.

Thermal networks are a generalization of electrical networks. The method is similar to Finite Element calculations using 1D-elements (differences occur in the applied solution schemes of the corresponding conduction and load matrices). Thermal networks have been applied successfully to power electronics, pipings for transport of hot fluids, motors and generators, power electronics, and superconducting transformers.

K6. Table 3. Total heat losses, $\dot{q}_{Total}$, through multilayer superinsulations; residual gas pressure $\leq 10^{-3}$ Pa, at cryogenic temperatures (Data are from [17]). The figures for the winding forces apply to foil of 70 cm width

Foil material	Spacer material	Thickness of insulations [mm]	ΔT [K]	$\dot{q}_{Total}$ [W/m^2]
(A) 0.25-μm aluminium one-sided on 6-μm polyester, $N = 5$, perforation 0.5%, 0.4 N winding force	Fibrex H 3204[a]	1.4	212	4.1
	Fibrex H 3002[a]	1.5	213	4.1
	Gevetex 2[b]	3.6	211	3.6
	Glass tissue[c]	1.9	211	3.5
	Interglass fabric[d]	2.1	210	4.3
	Perlon fabrics[e]	2.9	212	4.8
	Polyester Nonwoven 1751[f]	2.2	211	3.6
(B) as for (A) but with crimpled foil	Nil	4.9	210	4.4
	Nil	5.8	208	3.7
(C) as for (A) but different grades of perforation	Polyester Nonwoven 1751[f]			
0.1%		2.4	211	3.4
2.5%		2.5	212	4.2
(D) as for (A) but different winding forces	Polyester Nonwoven 1751[f]			
2 N		1.8	211	4.2
9.8 N		0.7	210	5.5
19.6 N		0.6	209	6.6
34.3 N		0.5	210	6.9
44.1 N			208	9.1
54.0 N			207	9.7
(E) 0.25 μm aluminium two-sided on 6 μm polyester. Otherwise as for (A).	Polyester Nonwoven 1751[f]	2.7	210	2.7
0.25 μm aluminium two-sided on 12.5 μm Kapton (polyamide), perforation 0.1%. Otherwise as for (A).	Polyester Nonwoven 1751[f]	2.5	212	3.0

[a]Heat-bonded polyester fibers (average thickness 30–50 μm; weight per unit area 20 g/m^2)
[b]Alkali-free glass silk (40 μm; 27 g/m^2); Dexol
[c]Boron silicate fiberglass paper (23 μm; 4 g/m^2)
[d]Alkali-free glass silk (40 μm; 27 g/m^2)
[e]Perlon fibers (100 μm; 17 g/m^2)
[f]Polyester fibers with binder (89 μm; 20 g/m^2)

To outline the principle, consider a cylindrical storage unit as indicated schematically in Fig. 11. It consists of a super-insulated inner tank and an outer container (shield to ambient) and a super-insulated neck. A thin-walled bellow is used as the inner tube of the neck, to reduce axial conductive heat losses to the surroundings. Assume N radiation shields are wrapped around the inner container, over its entire length and on its upper and lower front sides, with spacer materials in-between.

The method applies a suitable division of the solid components of the cryostat into length or volume sections, and the center of each section is denoted by a "node." In Fig. 11, in total M = 46 nodes have been defined. Finer divisions of the wall or shields volumes would significantly increase the number of nodes and thus calculation efforts, without substantially improving the accuracy needed for an overall analysis of the thermal performance of the cryostat. The thermal network could perhaps be a first step taken before detailed finite differences or finite element calculations are performed; actually, they could be made superfluous by results from a suitably designed thermal network.

2.5.1 Stationary Conditions

Consider in Fig. 11 a particular node, j. Thermal resistances, R_{jk}, are located between this and each of its neighboring nodes, k. Heat flow between each node (conduction, radiation, and even convection between solid components and stored liquid) follows the law $\dot{Q}_{jk} = \Delta T_{jk}/R_{jk}$ with ΔT_{jk} denoting the temperature difference between nodes j and k; the thermal resistances, R_{jk}, are explained below. Under stationary conditions, summation over all incoming and outgoing heat flow components at any of the nodes, j, equals zero, for stationary conditions (compare Kirchhoff's law in electrical circuits). A corresponding algebraic equation thus can be written for each node.

Consider as an example the node $j = 3$ located on the wall of the inner tank. Temperature at node 3 is T_3, and T_{Fluid} denotes

K6. Table 4. Total heat losses, $\dot{q}_{Total}$, through multilayer superinsulations at medium and high temperatures. The figures for the winding forces apply to foil of 70 cm width. Measured values A + to C from [17]

Foil material	Spacer material	Insulation thickness [mm]	T_1 [°C]	ΔT [K]	$\dot{q}_{Total}$ [W/m^2]
(A) 0.25 µm aluminum one-sided on 6 µm polyester, $N = 5$, perforation 0.1%, winding force 0.4 N	Polyester Nonwoven 1751[a]	1.8	50	34.2	2.1
		1.8	100	72.8	6.8
(B) 9 µm aluminum foil, $N = 5$, perforation 0.1%, winding force 13 N	Dexiglass paper[b]	1.5	50	31.8	1.9
		1.5	100	68.6	4.9
		1.5	150	102	9.0
		1.5	200	131.9	15.2
		1.5	250	158.4	24.7
(C) 9 µm Aluminum foil, $N = 5$, no perforations, plane layers, $p_{Gas} \leq 1.6 \times 10^3$ Pa	Quartz tissue[c]	0.8	197.5	162.5	42.7*
12.7 µm Nickel foil, $N = 5$, cold-rolled, no perforations, plane layers, $p_{Gas} \leq 1.4 \times 10^{-3}$ Pa	Quartz tissue[c]	1.2	349.3	300	99.3*
		1.2	501.1	417.4	227*
		1.2	647.5	515	416*
		1.2	790.0	595.3	688*
(D) Embossed aluminum foil, $N = 42$ (Linde cryoinsulation) $p_{Gas} \leq 2 \times 10^{-4}$ Pa	Woven glass fabric	20	307	270	12

[a]Polyester fibers with binder (average thickness 89 µm; weight per unit area 20 g/m^2)
[b]Boron silicate fiberglass paper (76 µm; 16 g/m^2)
[c]Quartz fibers (100 µm; 20 g/m^2)
The measured values marked by an asterisk can serve solely as a guide for estimating $\dot{q}_{Total}$

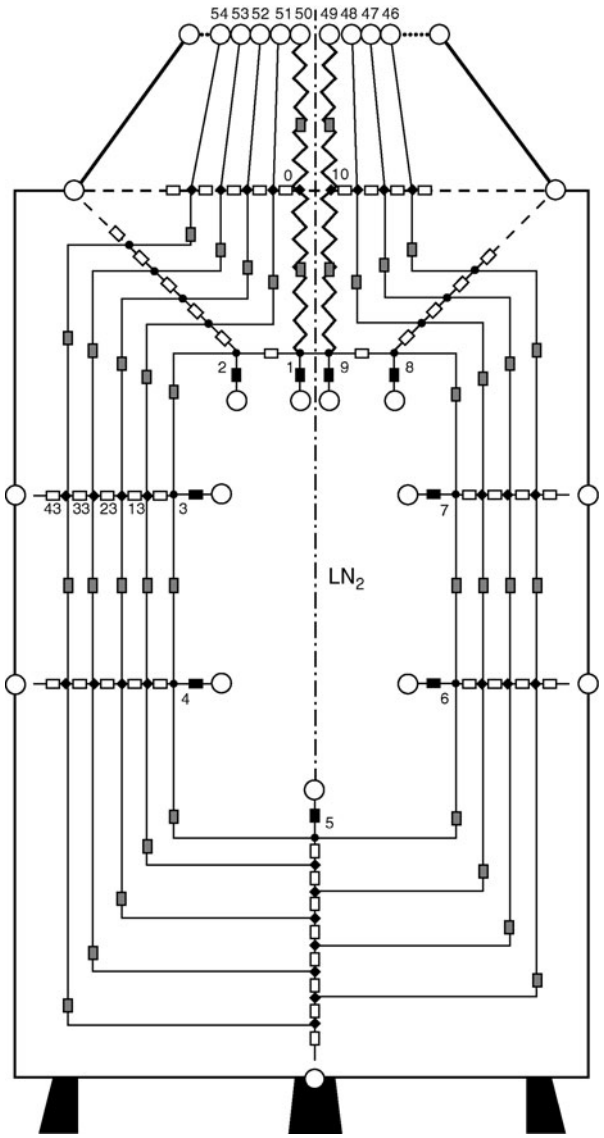

K6. Fig. 11. Thermal network of a cryogenic storage tank (the figure is from [19]; schematic, strongly simplified tank geometry, Klöpper design at top and bottom of inner and outer containers and filling pipe not indicated, dimensions at the neck enlarged). Dashed-dotted line: symmetry axis, thick solid lines: walls of containers and neck, thin solid lines: radiation shields and spacers (the solid lines thus also represent heat flow paths between nodes). Small solid circles: positions where temperatures are calculated in the network, large open circles: positions where boundary conditions are given; open, dotted, or full rectangles: thermal resistances concerning radiation, conduction and boiling, or convection, respectively.

the temperature of the stored liquid. With respect to the immediate neighbors of node 3, we have the equation

$$(T_2 - T_3)/R_{2,3} + (T_{13} - T_3)/R_{13,3} = (T_3 - T_4)/R_{3,4} + (T_3 - T_{Fluid})/R_{3,Fluid} \quad (13a)$$

Resistances $R_{2,3}$ and $R_{3,4}$ describe solid thermal conduction while $R_{13,3}$ is the radiative resistance between the innermost foil and the wall of the inner tank; $R_{3,Fluid}$ denotes heat transfer, by free convection or boiling, from the wall to the liquid.

Accordingly, $R_{2,3}$ takes the form

$$R_{2,3} = D_{2,3}/(\lambda_S A_{2,3})\ [\mathrm{K/W}] \quad (14a)$$

with $D_{2,3}$ the distance between nodes 2 and 3, λ_S the thermal conductivity of the stainless steel wall of the inner tank, and $A_{2,3}$ the cross section of the heat flow path between both nodes.

The radiative resistance, $R_{13,3}$ is given by

$$R_{13,3} = (T_{13} - T_3)/\dot{Q}_{Rad(13,3)}\ [\mathrm{K/W}] \quad (14b)$$

using Eq. (6) for determination of the radiative heat flow $\dot{Q}_{Rad(13,3)}$. For simplicity, Eq. (6) that describes radiative

exchange between parallel walls and shields has been taken for $\dot{Q}_{\mathrm{Rad}(13,3)}$; for the cylindrical case see [1], pp. 33–35. Because of the strong dependence on temperature of $\dot{Q}_{\mathrm{Rad}(13,3)}$, the temperatures T_{13} and T_3 have to be iteratively determined from solutions of the algebraic system of equations, see below.

The radiative resistance $R_{13,3}$ can be re-formulated to also integrate resistances parallel to radiation, that is, a resistance to solid–solid contact heat flow or to thermal conduction by the residual gas between foils and spacers.

For the convective thermal resistance, $R_{3,\mathrm{Fluid}}$, we have

$$R_{3,\mathrm{Fluid}} = 1/(\alpha F)[K/W] \tag{14c}$$

using α for the heat transfer coefficient and F the wetted surface of the inner container.

Assuming M nodes means we have a set of M interdependent, algebraic equations of the type Eq. (13a), for determination of the temperatures T_j $(1 \le j \le M)$. Thermal conductances, that is, the inverse of thermal resistances, constitute the coefficients in the conduction matrix. The calculated T_j have to be interpreted as mean values averaged over corresponding volumes (the above-mentioned sections) of the walls of inner container, of the bellow, and of the shields. Temperatures of the outer container and of the outer wall of the neck are given as boundary conditions (or if convection on the outer surface shall be modeled, ambient temperature and a corresponding heat transfer coefficient must be taken into account).

Solutions are easily found using standard methods to solve systems of algebraic equations (Kramer's scheme, or matrix methods). For more details of the network, of the resistances and the solution, see [19].

With the obtained temperature distribution T_j $(1 \le j \le M)$, the heat flow, $\dot{Q}_{jk}$, between any two nodes j and k, and the total heat loss, $\dot{Q}_{\mathrm{Total}}$, of the container accordingly is calculated using

$$\dot{Q}_{jk} = (T_j - T_k)/R_{jk} \tag{15a}$$

$$\dot{Q}_{\mathrm{Total}} = \sum \dot{Q}_{jk} \tag{15b}$$

The summation taken between the nodes of the inner wall $(1 \le j \le 9$ in Fig. 11) and the fixed node, k, indicated by an open circle, the fluid.

Total heat losses, $\dot{Q}_{\mathrm{Total}}$, and total conductive losses, $\dot{Q}_{\mathrm{Cond}}$ can be determined only at appropriate boundaries of the network. In Fig. 11, we have two boundaries: the first with the nodes $1 \le j \le 9$ separates the inner container from the stored liquid, and the second is identified between nodes $46 \le j \le 54$ located near the upper end of the bellow, and ambient. $\dot{Q}_{\mathrm{Cond}}$ is the heat that is delivered only by conduction from the ambient to the insulations material, to walls of the storage unit, and to the bellow before it is distributed in the insulations by radiation and solid–solid contact conductivity. Accordingly, separation of radiative and conductive losses is possible from network calculations.

2.5.2 Unsteady-State Conditions

Extension of the thermal resistance method to transient problems can be useful to analyze cool-down of a superinsulated container. For this purpose, terms $C_j\ \mathrm{d}T_j/\mathrm{d}t$, again for each node, j, have to be introduced into Eq. (13a); C_j denotes the heat capacity of the corresponding section of walls or foils. For node $j = 3$ (Fig. 11), we have

$$(T_2 - T_3)/R_{2,3} + (T_{13} - T_3)/R_{13,3} + (T_4 - T_3)/R_{4,3} + (T_{\mathrm{liq}} - T_3)/R_{\mathrm{Liq},3} = C_3 \mathrm{d}T_3/\mathrm{d}t \tag{13b}$$

This changes the calculation scheme from a system of interdependent, algebraic to a corresponding system of interdependent differential equations. If we take also into account temperature-dependent material properties, after elementary transformations, Eq. (13b) and the corresponding other $M - 1$ heat balances together yield the set

$$T_j(t) \times \sum k_{jk}(T) + \sum k_{jk}(T) \times T_k(t) - \dot{Q}_j(t) = C_j \times \mathrm{d}T_j(t)/\mathrm{d}t \qquad 0 \le j, k \le M, \text{ with } j \ne k. \tag{13c}$$

In Eq. (13c), the symbols $\sum k_{jk}(T)$ denote summations over temperature-dependent coefficients, the inverse of the corresponding thermal resistances, $R_{jk}(T)$, and $C_j(T) = \rho_j \times c_{p,j}(T) \times V_j$ the heat capacities, with density, specific heat, and volume, ρ_j, $c_{p,j}(T)$, and V_j, respectively, at the nodes, j; we further have source terms, $\dot{Q}_j(t)$, that in this simulation contain summations over constant temperatures (the boundary conditions) and inverse of heat resistances.

In the closed form, analytical integration would be possible with constant k_{jk}, C_j, and $\dot{Q}_j$, the solution scheme to Eq. (13c) has to apply numerical integration. The procedure is similar to solution steps in finite element problems.

The set Eq. (13c) can be rewritten in matrix form as $[\mathrm{k}] \times \{\mathrm{T}\} - \{\dot{\mathrm{Q}}\} = [\mathrm{C}] \times \{\mathrm{d}T/\mathrm{d}t\}$, with the conduction (or "stiffness") matrix, [k], the temperature column vector, {T}, the source column vector, $\{\dot{\mathrm{Q}}\}$, the heat capacity matrix, [C], and the temperature derivatives column vector, $\{\mathrm{d}T/\mathrm{d}t\}$. The elements of all these matrices and column vectors are functions of time, t. [k] and [C] are $M \times M$ matrices, and the column vectors have M rows. For each t, the matrix [k] equals its transposed matrix. The matrix [C] has only diagonal elements. Calculation of the inverse, $[\mathrm{C}^{-1}]$ of [C], and multiplication of the left side of Eq. (13c) by $[\mathrm{C}^{-1}]$ and by finite time steps, Δt, yields the column vector $\{\Delta T\}$ that has to be added to $\{T\}$ to yield the node temperatures, $\{T_k(t + \Delta t)\}$, obtained after one time step. The new T_k then are applied to recalculate the elements of the matrices [k], $[\dot{\mathrm{Q}}]$, and [C], to continue with the stepwise procedure. For an example, compare [20].

The method can be generalized to fluid networks, for calculation of stationary or transient distributions of residual gas pressures between foils and spacers, e.g., for modeling evacuation periods. Nodes have to be positioned in evacuation channels established by the open spaces between foils, spacers, and walls. In the system of algebraic or differential equations, respectively, temperatures, T_j, at the nodes, j, accordingly have to be replaced by residual gas pressures, p_j, likewise, thermal resistances, R_{jk}, by resistances to fluid flow, Z_{jk}, under *molecular* gas flow. While restriction to molecular gas flow conditions seems to be a drawback of the method, this flow condition is reached very quickly, usually after a few seconds during evacuation of multifoil superinsulations. Evacuation to final residual gas pressure, in the order

of 10^{-6} mbar, on the other hand, usually takes hours so that the missing initial degassing period does not play a big role.

For estimation of the fluid flow resistances, Z_{jk}, consult standard literature of vacuum technology, like [21] or [22], or the examples in [19] and [23].

Residual gas pressures in evacuated insulations are frequently measured at singular points only, mostly with closed valves. After individual waiting periods, it is assumed that the detected residual gas pressure is the same for all sections of the insulations. However, this is not fulfilled if sources like desorption of gas molecules from wall, foil or spacer surfaces, or permeation of gas molecules from ambient or from stored liquids, in particular hydrogen, through the outer or inner walls of the container, and/or sinks like getters in the evacuated space contribute to local variations of the residual gas pressure; this is the case in particular if the width of the evacuation channels (described by corresponding hydraulic diameters) is small. Such local variations can be modeled with the fluid networks like in [23].

3 Superinsulations of Continuous Structure (Powders, Fibers, Panels)

Heat transport through beds of dispersed solids in which the particle diameter is decidedly greater than the wavelength of thermal radiation has been described in Subchap. D6.3. The following concerns heat transport through media of considerably smaller particle size, e.g., evacuated powder and fiber insulations. Foamed material falls outside the scope of this study.

If the diameter of the particles or their interstices is, at the most, equal to the wavelength of radiant heat that is emitted by the source to be insulated, i.e., 1–500 µm, the insulating substance can be regarded as a continuum with respect to the propagation of radiation (cf. Sect. 3.3). As was the case in Sect. 1, the total heat losses are determined as the sum of individually estimated components, again in an approximation the validity of which has to be checked carefully.

3.1 Determination of $\dot{Q}_{Gas}$

$\dot{Q}_{Gas}$ is calculated by the same methods as those described in Sect. 2.1. After the mean free path l_{Gas} has been obtained from Eq. (1), the average pore diameter δ, that is, the mean diameter of the interstices between particles, is determined. Values of δ should be taken that have been verified by experiment, e.g., from measurements of capillary depression with a non-wetting liquid, BET adsorption isotherms, capillary condensation, or by light scattering experiments. If these are not available, a very rough estimate of δ can be made, for spherical particles or for fibers, using the following (traditional) equation ([24]) or Kaganer [1], p. 75,

$$\delta = C_3\, d/(1-\Pi)[\mathrm{m}] \qquad (16a)$$

where C_3 is a constant ($C_3 = 2/3$ for spherical particles and $C_3 = \pi/4$ for fibers), d is the particle diameter [m] and Π is the porosity of the insulations. But for spherical particles, Kaganer [1], p. 14, also reports

$$\delta = (2/3)\, d\,\Pi/(1-\Pi)\ [\mathrm{m}] \qquad (16b)$$

Equation (16a) applies only in an intermediate range of porosities, Π, while Eq. (16b) at least reproduces the case $\Pi = 0$ but also fails for $\Pi \to 1$. Neither formula is very convincing, so that experimental values of δ should be preferred; in case these are given as a function of the Knudsen number, it should be checked how the pore diameter was determined.

Example 1

Determine λ_{Gas} for nitrogen at 1/100th atmospheric pressure and $T = 300$ K in a bed of spherical particles (particle diameter 1 µm; powder density $\rho_P = 300$ kg/m^3; density of solid material $\rho_S = 5000$ kg/m^3).

Solution

Since $p_{Gas} = 10^3$ Pa, it follows from Table 1 that

$$\begin{aligned} C_1(p_{Gas}) &= (133\times 10^{-3})61\ \mu\mathrm{m} \\ &= 8.1\ \mu\mathrm{m}. \\ \text{Also } C_2 &= 112\ \mathrm{K}. \\ \text{Hence } l_{Gas} &= 8.1/(1+112/300)\ \mu\mathrm{m} \\ &= 5.9\ \mu\mathrm{m}. \end{aligned}$$

The porosity is $\Pi = 1 - \rho_P/\rho_S = 1 - 300/5000 = 0.94$. Inserting $C_3 = 0.667$, $d = 10^{-6}$, and $\Pi = 0.94$ in Eq. (16a) gives $\delta = 0.667 \times 10^{-6}/(1-0.94) = 1.11 \times 10^{-5} = 11.1$ µm. The Knudsen number is therefore Kn = 5.9/11.1 = 0.53.

The correction obtained from Table 2 for nitrogen at 300 K is $k = 1.95$. The ratio $\kappa = c_p/c_v$ for the bi-atomic gas molecule N_2 with $f = 5$ degrees of freedom is $(f+2)/f = 1.4$.

Therefore, if $\alpha = 1$, $\beta = (2 \times 1.95/(1.4+1) = 1.63$.

From the tables (e.g., in Subchap. D2.3), λ_0 for nitrogen at $T = 300$ K is $\lambda_0 = 0.026$ [W/(m · K)]. Equation (2a) then gives

$$\begin{aligned} \lambda_{Gas} &= \lambda_0/(1+2\times 1.63\times 0.53) \\ &= 0.026/2.73 \\ &= 0.0095\ [\mathrm{W/(m\cdot K)}]. \end{aligned}$$

The term Π in Eq. (16a, b), the porosity, is due to the interstices between particles. This is the only form of porosity that exists in beds of mono-dispersed particles and in fiber insulations (the intergrain porosity). However, if the particles themselves are micro-porous, for example, silica aerogel, corresponding allowance must be made by introducing a second porosity term Π' in Eq. (2a) (cf. [1], pp. 67, 68 and 71–75, Eq. (125)). In this case, Eq. (2a) transforms into

$$\lambda_{Gas} = C_{IGP}/(1+2\beta\,\mathrm{Kn}_{IGP}) + C_{MPP}/(1+2\,\beta\,\mathrm{Kn}_{MPP}) \qquad (2b)$$

with constants C_{IGP} and C_{MPP} and Kn_{IGP} and Kn_{MPP} the Knudsen numbers for the intergranular (index IGP) and microporous porosities (MPP), respectively. Addition of the gaseous conductivity components in Eq. (2b) indicates that the corresponding thermal conduction resistances are parallel.

As was the case in Sect. 2.1, $\dot{Q}_{Gas} = \lambda_{Gas}\, A\, \Delta T/D$ Eq. (5).

3.2 Determination of $\dot{Q}_{SC}$

Since the particles applied in thermal superinsulations are of much smaller diameter than those considered in Subchap. D6.3, the resistance to contact heat flow is an important factor in heat transfer. The following expressions for thermal conductivity by contact, λ_{SC}, have been derived by relating the conductivity of the solid material, λ_S, to the contact radii calculated from elasticity theory. The equation for λ_{SC} also includes the number of contacts between the particles in the bed of insulating material.

Let λ_S [W/(m · K)] be the thermal conductivity of the solid material from which the particles of insulations have been produced, and let p (Pa = N/m^2) be the mechanical pressure that acts on the insulations. Then, if the surfaces of the particles undergo elastic deformation in the zones of contact, the thermal conductivity by solid contact, λ_{SC}, for a bed of spherical particles (index "Spheres") will be given by Eq. (17) ([1], pp. 18–21), and for a regular network of fibers (index "Fibers"), compare Fig. 12a (another idealization), by Eq. (18) ([1], pp. 22–25):

$$\lambda_{SC,Spheres} = 3.44\,(1-\Pi)^{4/3}[(1-\gamma^2)/Y]^{1/3}\,\lambda_S\,p^{1/3}[W/(m\cdot K)] \tag{17}$$

$$\lambda_{SC,Fibers} = [16(1-\Pi)^2/\pi^2]\,\lambda_S\{[1/(1.86\,a\,p^{1/3})] + 1/[4(1-\Pi)]\}^{-1}[W/(m\cdot K)] \tag{18}$$

where γ is Poisson's ratio (about 0.22 for ceramic particles or glass fibers), Y is Young's modulus of elasticity for the solid material, and $a = \{(1-\gamma^2)/Y(1-\Pi)^2\}^{1/3}$.

Fiberglass paper (Fig. 12b) has a somewhat similar structure to that of the ideal network (Fig. 12a).

Values of λ_{SC} determined by Eqs. (17) and (18) for spherical particles and glass fibers have been plotted against temperature in Fig. 13. It is evident from these equations that λ_{SC} is independent of the particle diameter. See also [1], pp. 15–18 for more (traditional) expressions to estimate simultaneous gaseous and solid–solid contact heat flow through beds.

Example 2

Determine λ_{SC} for the bed of spherical particles described in Example 1 in Sect. 3.1 under the assumption that $\gamma = 0.22$, $Y = 6.7\times 10^{10}$ Pa (the value for boron silicate glass at $T = 300$ K), $\lambda_S = 1$ [W/(m · K)] and $p = 10^5$ Pa.

Solution

Inserting the above values in Eq. (17) yields

$$\lambda_{SC} = 3.44(1-0.94)^{4/3}\{[(1-0.22^2)/6.7\times 10^{10}]\,10^5\}^{1/3} = 9.1\times 10^{-4}[W/(m\cdot K)].$$

It is evident from Eqs. (17) and (18) that λ_{SC} for spherical and fibrous particles subjected to elastic deformation is related to the cube root of the applied pressure, p [Pa]. The relationship has been confirmed by experiments performed on insulations that was produced from evacuated fiberglass paper and subjected to low compressive loads (Fig. 14, from [9]). If the deformation is inelastic, λ_{SC} is more likely to be related to the square root of the applied pressure, *p*.

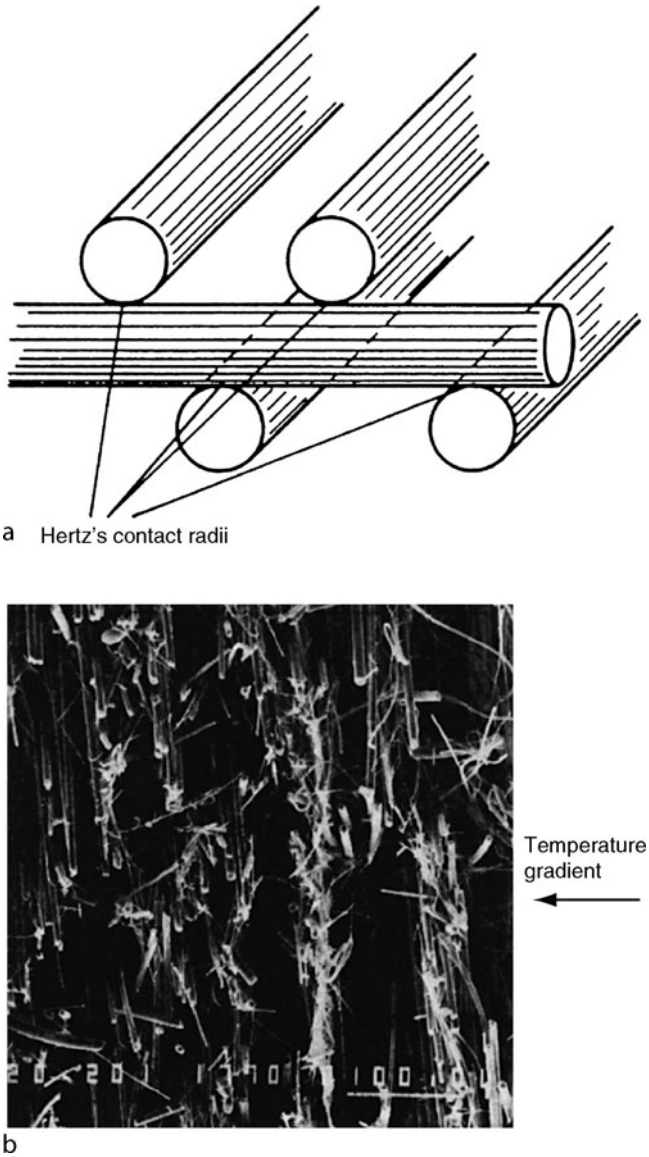

K6. Fig. 12. (**a**) Regular fiber network (schematic), for calculation of solid conduction conductivity assuming ideal orientation of fibers in a fiberglass insulations, (**b**) Scanning electron micrograph of a fiberglass paper (side view). The horizontal bar in the right corner below represents a length of 100 μm.

Calculation of λ_{SC} for expanded materials (foams) lies outside the scope of this chapter.

$\dot{Q}_{SC}$ is obtained from λ_{SC} by applying the normal rule for heat conduction, like in Eq. (5).

3.3 Determination of $\dot{Q}_{Rad}$

The method presented here differs significantly from that given for dispersed beds (cf. Part D). In the latter, radiation was expressed in terms of properties at the *surface*, i.e., the emissivity ε and the effective radiation path X_R, and was described as energy *exchange*. Here, instead, the small grain size entails that the penetration of radiation *into* the particles must also be taken into consideration, i.e., radiation energy *transport* is involved.

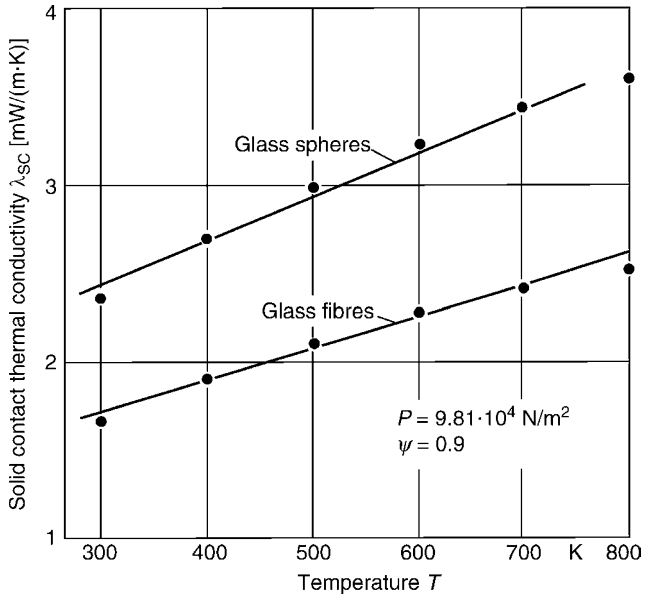

K6. Fig. 13. Thermal conductivity by solid contact, λ_{SC} (calculated values), as a function of temperature T, in a bed of spherical particles and in a regular network of fibers. Determined from Eqs. (17) and (18) for $\Pi = 0.9$, $\gamma = 0.22$, $p = 9.81 \times 10^4$ Pa, and temperature-dependent values of Y and λ_S.

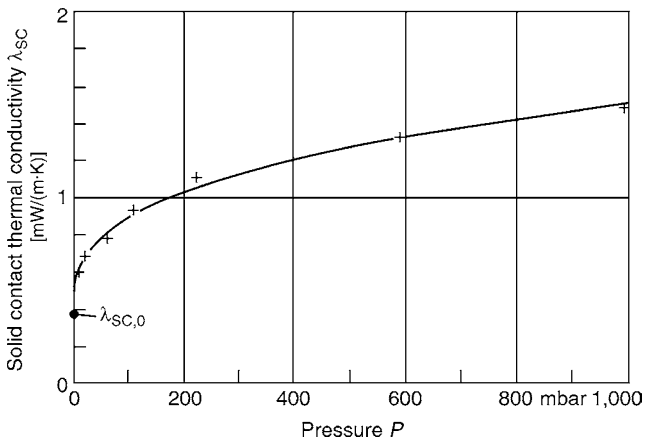

K6. Fig. 14. Thermal conductivity by solid contact, λ_{SC} (measured values), as a function of low values of the pressure p applied by a compressive load. Plotted from values determined by experiment (the figure is from [9]). The curve fits the relationship $\lambda_{SC} = \lambda_{SC,0} + a\, p^{1/3}$ by the method of least squares; $\lambda_{SC,0} = 0.37$ [mW/(m · K)] and $a = 0.11$ [mW/(m · K mbar$^{1/3}$)].

In the perfectly nontransparent case, the transport mechanism may even be regarded as diffusion. Therefore, the main parameters for the determination of heat flux by radiation are not restricted to the exchange of energy between surfaces but must also embrace the entire effect exerted by the particles on the extinction of radiation along a mean free path, l_{Rad}.

Radiative flow, $\dot{Q}_{Rad}$, as a transport process, is considerably more difficult to determine than the other components. Thus, it must first of all be determined whether or not the fine-grained insulating material is transparent or nontransparent in the range of wavelengths that is important for a heat balance within the thermal spectrum. If it is nontransparent, the heat losses can be expressed as a thermal conductivity in the form of λ_{Rad}, from a diffusion model (cf. Sect. 3.3.1 and Appendix A1). If the material is transparent (cf. Sect. 3.3.2), using an expression of this nature would involve a considerable error.

A substance of continuous structure is *nontransparent* if its optical thickness τ_0 is much larger than unity, i.e., $\tau_0 \geq 15$ (an explanation for this limit is given in Appendix A1). The optical thickness, $\tau_0(\Lambda\}$ at a given wave length, Λ, is defined by

$$\tau_0(\Lambda) = \int_0^D E(\Lambda) \times \mathrm{d}s \qquad (19)$$

where D [m] is the thickness of the insulations, which is to be considered constant in this case, and $E(\Lambda)$ [1/m] is the spectral linear extinction coefficient.

As a first approximation, it may be assumed that the dispersed insulating material scatters radiation isotropically, i.e., equally in all directions. This is usually assumed for the linear extinction coefficient, E, in the Lambert-Beer law. *Anisotropic* scattering, however, which is displayed by many real insulating materials, can be allowed for by converting E into an effective coefficient E^* (cf. Example 5).

In homogeneous media, the linear extinction coefficient is independent of position, i.e., $\tau_0(\Lambda\} = E(\Lambda)\, D$. If it is also independent of wavelength, i.e., in "gray" bodies, the optical thickness can simply be given by $\tau_0 = E\, D$, for all wavelengths. However, media of this nature represent, at the most, exceptions to the spectral behavior of the overwhelming majority of real substances.

Experience has shown that the mathematical method outlined in Sect. 3.3.1 yields values that agree weIl with those obtained in experiments, provided that $\tau_0(\Lambda\}$ is at least about 15 for *all* wavelengths, Λ.

Example 3

The extinction spectrum $E(\Lambda\}$ for glass fiber insulations with a continuous homogeneous structure is presented, in a very rough approximation in the form of a bar diagram in Fig. 15 (specialists are kindly asked to tolerate this for the moment). Calculate how thick the insulations must be if $\tau_0(\Lambda)$ is to be at least 100 at all wavelengths within the $1 \leq \Lambda \leq 20$ µm range.

Solution

The lowest values, $E(\Lambda) = 10^3$ m^{-1}, occur in the $6 \leq \Lambda \leq 8$ µm and $15 \leq \Lambda \leq 19$ µm ranges. Since $\tau_0(\Lambda) = E(\Lambda)\, D$, the minimum required thickness of the insulations is $D = \tau_0(\Lambda)/E(\Lambda) = 10^1/10^3$ m^{-1} = 0.1 m. This value obviously is too large for many practical applications. Accordingly, "opacifiers" have to be used to close the radiative "windows" of this material, see below.

In many cases, there will be no empirically determined extinction spectra available on which decisions of this nature can be based. It may be possible to find out whether at least a transmission spectrum for the substance concerned exists in the literature, compare e.g., in Nyquist [25]. Ranges of wavelengths in which the linear extinction coefficient is small or the

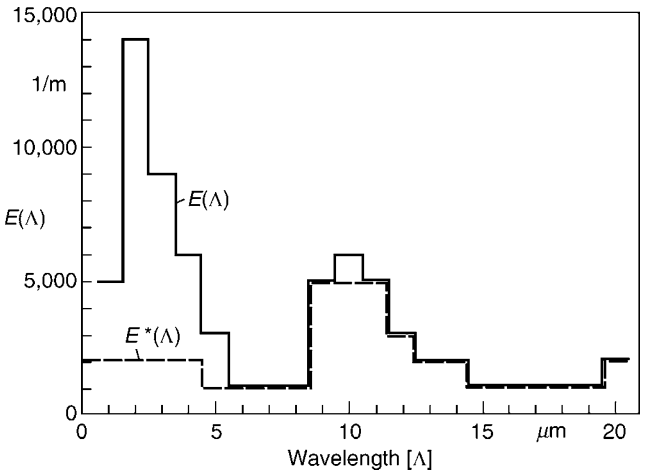

K6. Fig. 15. Extinction spectra (roughly corresponding to spectra of glass fibers) $E(\Lambda)$ and $E^*(\Lambda)$, as functions of wavelength, Λ. Presented in the form of a bar diagram to simplify calculation of minimum required optical thickness in the Examples 3, 5, and 6.

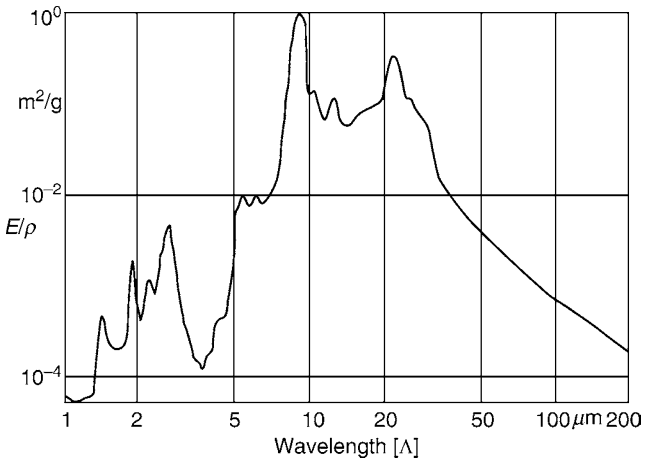

K6. Fig. 16. Linear extinction coefficient per unit density E/ρ, for silica aerogel as a function of wavelength, Λ (the figure is from [26]). ρ denotes density of the insulations.

transmission coefficient is correspondingly large, can be immediately recognized as transmission "windows" in the spectra. Examples are the $6 \leq \Lambda \leq 8$ μm range in the extinction spectrum in Fig. 15 and the $1 \leq \Lambda \leq 5$ and $\Lambda \geq 30$ μm ranges in the extinction spectrum for silica aerogel in Fig. 16 (from [26]; note the logarithmic scales). These windows account for particularly great radiant heat losses, and it must be determined whether components of black body radiation fall within them.

For this purpose, the spectral position, Λ_{max}, at a given temperature, at which the Planck radiation curve culminates, is determined from Fig. 17. If Λ_{max} lies within a window that cannot be closed by an opacifier (cf. Sect. 4, for selection of opacifiers), or by increasing the thickness of the insulations

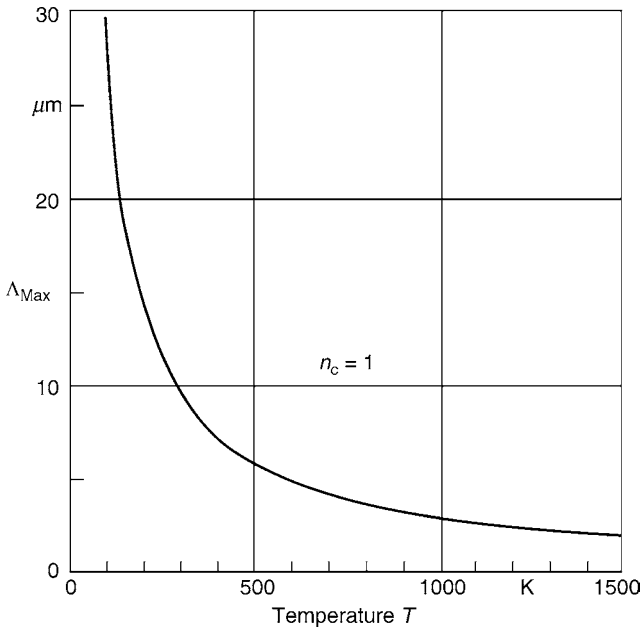

K6. Fig. 17. Wavelength Λ_{max} corresponding to the maximum on the Planck radiation curve at the given temperature T (Wien's displacement law). Determined for emission in vacuo (refractive index in a vacuum $n_c = 1$).

(see above example), great reserve must be shown in applying the expressions for λ_{Rad} given in Sect. 3.3.1. Conversely, values of λ_{Rad} calculated for nontransparent insulations always agree well with those obtained by measurement.

3.3.1 $\dot{Q}_{Rad}$ for Nontransparent Insulations

The solution of the classical Rosseland radiation diffusion model [28] can be adopted to calculate λ_{Rad} if the optical thickness $\tau_0(\Lambda) \geq 15$ for all the wavelengths that are of importance, i.e.,

$$\lambda_{Rad} = \frac{16 \times \sigma \times n^2}{3 \times E} \times T_{Rad}^3 [\mathrm{W/(m \cdot K)}] \qquad (20)$$

where σ the Stefan-Boltzmann constant, $\sigma = 5.67040 \times 10^{-8}$ $[\mathrm{W/(m^2 \cdot K)}]$, n the real part of the complex (effective) refractive index for the dispersed insulating structure, which is always close to unity if the porosity is high, and T_{Rad} is an (average) radiation temperature that is given by

$$\begin{aligned} T_{Rad}^3 &= \frac{T_1^4 - T_2^4}{4 \times (T_1 - T_2)} \\ &= \left(T_1^2 + T_2^2\right) \times (T_1 + T_2)/4 \\ &= \frac{T^{*3}}{4} \left[\mathrm{K^3}\right]. \end{aligned} \qquad (21)$$

where T_1 and T_2 are again the wall temperatures. Corresponding terms for the average radiation temperature found in the literature are T_{Rad}^3 or T^{*3}.

If the linear extinction coefficient, E, is known to be within sufficient accuracy, Eq. (20) together with Eq. (21) yields reliable results in the $120 \leq T_1 \leq 700$ K and $1 \leq T_2 \leq 300$ K ranges.

In a gray body, E is simply a constant that is independent of radiation temperature (but there may be materials properties of the corresponding material other than extinction coefficient of radiation that depend on temperature). If the medium is not a gray body radiator, the requisite value of $E(\Lambda)$ is $E_R(T)$, which is the average over the range of wavelengths concerned and is thus dependent on radiation temperature. Values calculated for this average, referred to as the Rosseland average, per unit density ρ, for some insulating materials have been plotted against the particle diameter d and the radiation temperature T in Fig. 18a–d.

In Fig. 18a–d, the asterisk in the Rosseland mean per unit density, E_R^*/ρ, indicates that allowance has been made for anisotropic scattering (cf. Example 5). The values plotted for E_R^*/ρ remain valid without major corrections (up to a maximum of 20%) within the $\Pi \geq 0.8$ porosity range ([26]). However, as compaction increases, "dependent scattering" and thus a reduction in E_R^*/ρ become evident.

The values for $E_R^*(T)$ are read off from these diagrams against $T = T_{Rad}$.

Example 4

A thermal insulations of continuous structure consists of glass fibers of $d = 4$ µm diameter, and the density is $\rho = 200$ kg/m^3. The temperatures at the walls are $T_1 = 485.6$ K and $T_2 = 300$ K. Determine T_{Rad}, and thus $E_R^*(T_{Rad})$ from Fig. 18a, and consequently calculate $\lambda_{Rad}\,(T_{Rad})$.

Solution

The first step is to determine T_{Rad} from Eq. (21). Thus T_{Rad}, $= [(485.6^2 + 300^2)\,(485.6 + 300)/4]^{1/3} = 400.0$ K.

$E_R^*(T_{Rad}) \approx 1.6 \times 10^4$ m^{-1} can then be read off against $d = 4$µm and $\rho = 200$ kg/m^3 in Fig. 18a.

If the extinction spectrum is fairly smooth, the Rosseland average does not depend very much on radiation temperature.

When the desired average linear extinction coefficient cannot be found from Fig. 18a–d, it may be obtained as follows from any spectral values of $E^*(\Lambda)$ that might be available ([34], p. 474):

$$\frac{1}{E_R^*(T)} = \frac{\sum_{\Delta\Lambda} \frac{1}{E^*(\Lambda)} \times f_\Lambda(T) \times \Delta\Lambda}{\sum_{\Delta\Lambda} f_\Lambda(T) \times \Delta\Lambda}\,[\mathrm{m}] \qquad (22)$$

This entails adding all the values in the wavelength intervals $\Delta\Lambda$ in which known figures for the spectral linear extinction coefficients are available, e.g., from spectroscopic measurements. The weighting functions, $f_\Lambda(T)$, are given by the same reference as

$$f_\Lambda(T) = \frac{\pi \times C_4 \times C_5}{2 \times \Lambda^6} \times \frac{1}{\sigma \times T^5} \times \frac{\exp\left(\frac{C_5}{\Lambda \times T}\right)}{\left[\exp\left(\frac{C_5}{\Lambda \times T}\right) - 1\right]^2}\,[1/\mathrm{m}] \quad (23)$$

where $C_4 = 5.9544 \times 10^{-17}$ W m^2 and $C_5 = 1.4388 \times 10^{-2}$ m K.

The relationship between the weighting factor $f_\Lambda(T)$ and the wavelength, Λ, at various temperatures is shown in Fig. 19.

Example 5

By means of Eqs. (22) and (23) or Fig. 19, determine $E_R(T_{Rad})$ and $\lambda_{Rad}(T_{Rad})$, one after the other, in the $1 \leq \Lambda \leq 20$ µm range of wavelengths. The wall temperatures are the same as in Example 4, and the extinction spectrum is that denoted by $E(\Lambda)$ in Fig. 15. Note: $E(\Lambda)$ {*without* asterisk} in this example implies the *erroneous* assumption of isotropic scattering by glass fibers.

Solution

$T_{Rad} = 400.0$ K and Eq. (22) give

$$\frac{1}{E_R(T_{Rad})}$$

$$= \frac{\frac{1}{5\cdot10^3} \cdot 5.54 \cdot 10^{-4} + \frac{1}{1.4\cdot10^4} \cdot 5.6 \cdot 10^2 + \cdots \frac{1}{2\cdot10^3} 8.611 \cdot 10^3}{5.54 \cdot 10^{-4} + 5.6 \cdot 10^2 + \cdots + 8.611 \cdot 10^3},$$

from which $E_R(T_{Rad}) = 1.679\ 10^3$ [1/m]

Using this value, and with $n^2 = 1$ (usually fulfilled in dispersed media) we have

$$\lambda_{Rad} = \frac{16 \cdot 5.669 \cdot 10^{-8}}{3 \cdot 1.679 \cdot 10^3} \cdot 400^3 \left[\frac{\mathrm{W} \cdot \mathrm{K}^3}{\mathrm{m}^2 \cdot \mathrm{K}^4 \cdot 1/\mathrm{m}} = [\mathrm{W/(m \cdot K)}]\right]$$
$$= 0.0115\,[\mathrm{W/(m \cdot K)}].$$

If neither calculated values of $E_R{}^*(T)$ nor $E(\Lambda)$ or $E^*(\Lambda)$ spectra are available, the relevant linear extinction coefficients E^*/ρ listed in Table 6 can be taken as approximations to calculate E in Eq. (20). The coefficients in Table 6 have been compiled from calorimetric or spectroscopic measurements or have been calculated from the Mie theory, which means they can be obtained from three different, independent methods.

Although isotropic scattering has been preferentially treated in older literature, it is the exception rather than the rule and applies only approximately in special cases, e.g., very small dielectric particles. A general rule is that anisotropic forward scattering increases with the particle size and leads to the reduction of $E(\Lambda)$ and thus E_R to effective values $E^*(\Lambda)$ and $E_R{}^*(T)$ respectively (as related to *single* scattering, this is *not* identical with dependent scattering, a phenomenon that goes back to the presence of closely located, neighboring particles). Likewise, backward scattering causes an increase in $E(\Lambda)$ and E_R. Forward scattering is particularly pronounced for glass fibers in the $1 \leq \Lambda \leq 6$ µm range of wavelengths {cf. $E(\Lambda)$ and $E^*(\Lambda)$ in Fig. 15). The effect of scattering on the linear extinction coefficient depends on the orientation of the fibers relative to the direction of the temperature gradient within the insulations (cf. caption to Fig. 18a–d). As opposed to this, scattering by very finely divided primary silica particles is more likely to be isotropic. In this case, therefore, $E^*(\Lambda)$ is equal to the $E(\Lambda)$ in Beer's law, and the same applies to the Rosseland average.

The potential effect of anisotropic scattering on the calculated value for λ_{Rad} is evident from the following example.

Example 6

In analogy to Example 5, calculate $E_{Rad}^*(T_{Rad})$ from the $E^*(A)$ values (with asterisk) in Fig. 15 and thus determine the correct value for $\lambda_{Rad}(T_{Rad})$.

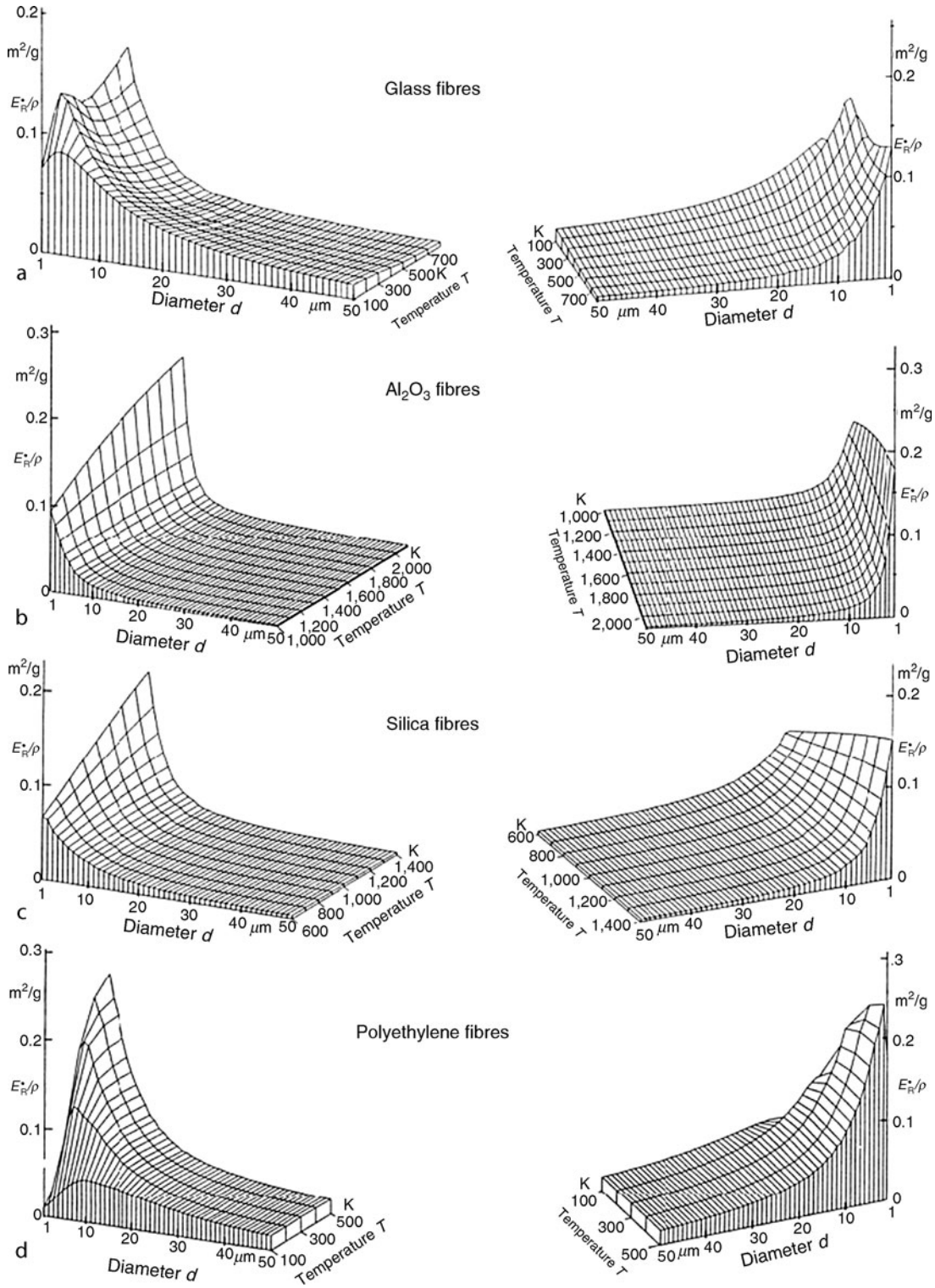

K6. Fig. 18. (**a**–**d**) Wavelength-averaged, effective linear extinction coefficient per unit density, E_R^*/ρ, for fibrous insulations as a function of the particle diameter, d, and the radiation temperature, T_{Rad}; E_R^*/ρ is calculated by the Mie theory using complex refractive indices. Diagrams (**a**) Glass fibers, (**b**) Ceramic fibers, (**c**) Silica fiber, (**d**) Polyethylene fibers. The calculations apply to vertical (non-polarized) radiation incidence, i.e., the axis of the fibers is at right angles to the direction of incident radiation. This condition can be roughly met for fiber papers (cf. Fig. 12b). If instead the insulations consists of glass or rock wool with the fiber axes in a random arrangement, the figures obtained for E_R^*/ρ must be corrected by multiplying with a factor ϕ, which has a numerical value of $\phi = 2/3$ for pure scattering. If the fibers were strongly absorbent, the numerical value would be about $\phi = 4/5$ ([26]) (ϕ also depends on fiber diameter and temperature [27]. The experimental values for the refractive indices originate from the literature: (**a**) [29], (**b**) [30] and [31], (**c**) [32], and (**d**) [33].

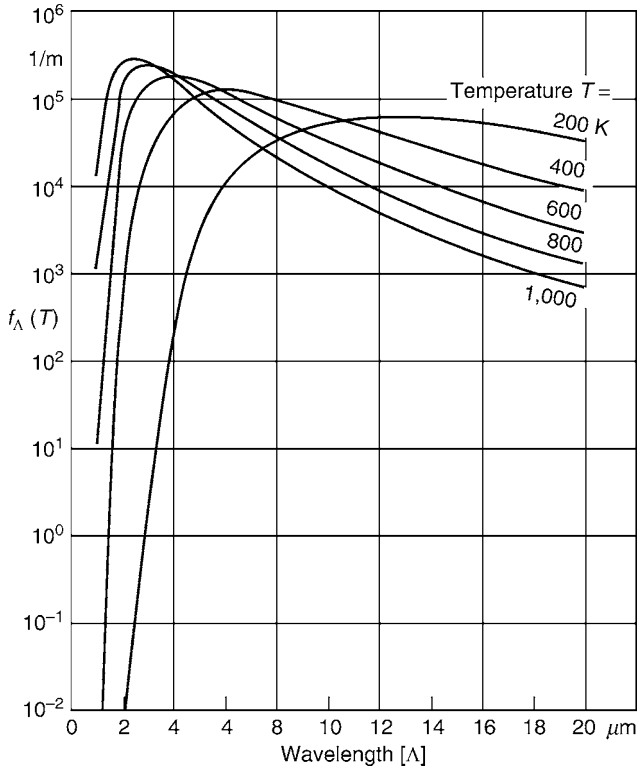

K6. Fig. 19. Weighting function $f_\Lambda(T)$ defined by Eq. (23) as a function of wavelength, Λ, with temperature T as parameter.

Solution

$$\frac{1}{E_R^*(T_{Rad})} = \frac{\frac{1}{2\cdot10^3}\cdot 5.54\cdot10^{-4} + \frac{1}{2\cdot10^3}\cdot 5.6\cdot10^{2} + \cdots \frac{1}{2\cdot10^3}\,8.611\cdot10^{3}}{5.54\cdot10^{-4} + 5.6\cdot10^{2} + \cdots + 8.611\cdot10^{3}}$$

Inserting this value in Eq. (20) with $n^2 = 1$ gives

$$\lambda_{Rad} = \frac{16\cdot5.669\cdot10^{-8}}{3\cdot1.413\cdot10^{3}}\cdot 400^3\left[\frac{W\cdot K^3}{m^2\cdot K^4\cdot 1/m} = [W/(m\cdot K)]\right]$$
$$= 0.0137\,[W/(m\cdot K)].$$

Thus the allowance for the importance of forward scattering caused by glass fibers has increased the radiation conductivity, λ_{Rad}, to a value about 20% higher than that obtained in Example 5.

Many of the linear extinction coefficients cited in the literature have been derived on the assumption of isotropic scattering. Hence, in order to avoid serious errors, they must be converted into the corresponding effective values before they are inserted in Eq. (20). Details of this conversion is the subject of specialized publications (e.g., [26]) and would be impossible without a knowledge of the complex refractive indices. The corrections necessary for the individual wavelengths may be as much as 90% of $E(\Lambda)$. However, since an average is taken in the Rosseland mean over a range of wavelengths, the corresponding error in E_R is reduced, and the deviation from E_R^* is thus usually 10–20%.

$\dot{Q}_{Rad}$ using the Rosseland diffusion mean is calculated using the value of λ_{Rad} in the usual rule for heat conduction, compare Eq. (5) (provided it is a nontransparent insulation).

3.3.2 $\dot{Q}_{Rad}$ for Insulations with IR-Transparent Zones

Insulation that is transparent in the visible and, partly, in the infrared spectrum, includes silica aerogels and highly dispersed Silicas. Aerogels are eminently suitable for solar energy systems ([35]) but are responsible for heat losses owing to their IR-transparency. Transparent insulations are also becoming integrated parts of façades of buildings, with the intention to contribute to development of "zero energy houses."

If no extinction spectra $E^*(\Lambda)$ but only average values of E^*/ρ (cf. Table 6) are available, the radiation losses, $\dot{Q}_{Rad}$, can be approximately determined in the same way as that for a homogeneous bed of transparent gray body radiators with small optical thicknesses, $\tau_0^* = E^* D$, between infinitely extended, plane parallel walls ([34], p. 480), i.e.,

$$\dot{q}_{Rad} = \frac{\dot{Q}_{Rad}}{F} = \frac{\sigma\times\left(T_1^4 - T_2^4\right)}{\frac{2}{\varepsilon_W} - 1 + \frac{3}{4}\times\tau_0^*}\,[W/m^2] \qquad (24)$$

where T_1 and T_2 are absolute temperatures in Kelvin. Methods that involve a more accurate description of radiation propagation in aerogels have been suggested by Caps [26].

If IR-transparency is pronounced, i.e., if $\tau_0(\Lambda) \ll 1$, heat transport by radiation cannot be described in terms of thermal conduction. In this case, figures for the total thermal conductivity, sometimes calculated from numerical results for the total heat flux or from its measurement, are not authentic, because they are not constants for the material concerned but depend on the thickness, D, of the layer and/or on the emissivity ε of the wall (compare Appendix A1), i.e., on the measuring instruments. A conductivity determined from Eq. (24) accordingly is a "pseudo"-radiative conductivity, λ'_{Rad}, and if it is summed up with other conductivity components to a total thermal conductivity, e.g., $\lambda_{Total} = \lambda_{Gas} + \lambda_{SC} + \lambda_{Rad}$, the total thermal conductivity, λ_{Total}, is a pseudo-conductivity, λ'_{Total}, too.

3.4 Total Heat Losses in Nontransparent Continuous Superinsulations

The total thermal conductivity, λ_{Total}, in nontransparent insulations is given by

$$\lambda_{Total} = \lambda_{Gas} + \lambda_{SC} + \lambda_{Rad} \qquad (25)$$

The loss components are obtained as follows: Eq. (2a) or (2b) using Eqs. (1) and (16a) or (16b) to determine Kn; Eq. (17) or (18) for λ_{SC}; and Eq. (20) for λ_{Rad}. As was stated in the remarks on Eq. (10), the likelihood of free convection losses can be excluded. Likewise, the restrictions on "additive approximation" appended to these remarks must be correspondingly applied to the thermal conductivity components. In this case, the lower the residual gas pressure and the greater the linear extinction coefficient, the better the approximation. If very accurate analyses are required, the principle of the conservation of energy (divergence of $\dot{q}_{Total} = 0$) must be applied to determine the temperature profile and the temperature-dependent thermal conductivity components.

If the components λ_{Gas} and λ_{SC} are combined to form a constant, a, that is roughly independent of temperature, Eq. (20) is extended to

$$\lambda_{Total} = a + \frac{16 \times \sigma \times n^2}{3 \times E^*} \times T_{Rad}^3 = a + b \times T_{Rad}^3 \qquad (26)$$

in which also b is a constant, and T_{Rad}^3 is given by Eq. (21). The plots of the measured values of λ_{Total} against T_{Rad}^3 are close approximations to straight lines (Fig. 20a–d). The sum of λ_{Gas} and λ_{SC} can be read off against the intersect at $T_{Rad}^3 = 0$, and the linear extinction coefficient for an average temperature and thickness can be obtained from the slope. Calorimetric values λ_{SC} and E^*/ρ listed in Tables 5 and 6, respectively, were determined in this way.

The remarkable agreement between measured λ_{Total} and the linear equation $\lambda_{Total} = a + b\ T_{Rad}^3$, Eq. (26), or using T^{*3} instead of using T_{Rad}^3, Eq. (21), is found not only with evacuated superinsulations (Fig. 20a–d) but also with non-evacuated, microporous powder insulations as demonstrated in Fig. 21. Like the insulations of Fig. 20c and d the non-evacuated insulations in Fig. 21 are also load-bearing ("load-bearing" means the compression of these insulations, under a mechanical pressure of 1 bar, i.e., during evacuation, could be kept below 10% of the original thickness). These insulations provide a thermal conductivity below that of motionless air, even at elevated temperatures. Following the classification made in Fig. 1, these insulations, too, can be considered "superinsulations."

The same applies to organic monolithic aerogels, or to aerogels doped with opacifiers that render these materials non-transparent. They exhibit very small thermal conductivity also under ambient pressure ([38]), with values even below the data reported in Fig. 21 (the samples of Fig. 21 were pressed to load-bearing boards, under high pressures, however).

3.5 Superinsulated Panels

A superinsulated panel consists of a pressure-resistant core (a board) that is prepared from microporous materials (powders, fibers), and vacuum-tight envelopes that encapsulate the core to safely protect its vacuum. The envelopes apply thin polymer foils, for medium to low temperature insulations, or stainless steel foils at elevated temperatures. Superinsulating properties of the panels rely on very small thermal conductivity of the evacuated core material. Heat leakage through the core material can be estimated following the relations given in the foregoing sections.

Thickness of the microporous core and of polymer foils is in the order of 10 mm or 100 µm, respectively. Accordingly, superinsulated panels are composed of materials not only of strongly differing thermal transport and mechanical properties but also of very strongly differing dimensions of its components. As a consequence, prediction of heat flow through, and temperature profiles in the panel and on its surfaces, is difficult. This applies in particular to analysis made by numerical methods (standard finite element codes do not like these conditions), and also to analysis of the mechanical behavior of the thin foils when they are exposed to mechanical load, as is the case during evacuation, or if they are wound around tubes, or under large temperature gradients.

Flat panel geometry presently dominates, but panels may be applied also for superinsulations of pipings and cylindrical vessels.

Thermal leakage through joints between neighboring panels may seriously degrade the thermal resistance of panel insulations, in particular if the foils are metallic or are metallized to provide improved, vacuum-tight barriers. Further, local temperature variations in the envelope materials can be responsible for mechanical load from differential thermo-contraction or expansion.

3.5.1 Flat Panel Geometry

Temperature of the envelopes is critical with regard to materials properties (vacuum thightness) under thermal load and lifetime of the insulations. Temperature distributions in envelope materials in indented panels can approximately be determined as suggested by Caps [48]): Assume a flat plate panel insulation, with two neighboring one-layer panels of thickness, D, that overlap over a distance (indentation length), L_i, (compare Fig. 22a; the case "blunt joins" is approximated by $L_i \to 0$).

To obtain the temperature profile of the foils in the horizontal section, path s_2, of the indentation, $-L_i/2 \le x \le L_i/2$, combine the two parallel foils into one. Heat flux components, $\dot{q}_1(x)$ and $\dot{q}_2(x)$, perpendicular through the surfaces of panels 1 and 2, serve as source and sink terms, respectively, for the divergence of the horizontal, local heat flux, $\dot{q}_{2Foils}(x)$, in the two foils. With constant (temperature-independent and homogeneous) thermal resistances, $R_{1,2}$ [K m^2/W], to the components $\dot{q}_1(x)$ and $\dot{q}_2(x)$ through the core material, we have

$$\dot{q}_1(x) = (1/R_1)[T_1 - T(x)]\left[\mathrm{W/m^2}\right] \qquad (27a)$$

$$\dot{q}_2(x) = (1/R_2)[T(x) - T_2]\left[\mathrm{W/m^2}\right] \qquad (27b)$$

Assuming the panels have a unit length, $L_z = 1$ m, in z-direction, a cross section of the foils of $A = d_{2Foil}\ x\ L_z$, the heat flux, $\dot{q}_{2Foils}(x)$, in the overlap region reads

$$\dot{q}_{2Foils}(x) = -\lambda_{Foil}\, d_{2Foils}\, \mathrm{d}T(x)/\mathrm{d}x\left[\mathrm{W/m^3}\right] \qquad (28)$$

using the solid thermal conductivity, λ_{Foil}, of the foils. Conservation of energy requires

$$[\dot{q}_2(x) - \dot{q}_1(x)]/d_{2Foils} = \mathrm{d}/\mathrm{d}x[\dot{q}_{2Foils}(x)]\left[\mathrm{W/m^3}\right] \qquad (29)$$

This yields a second order, inhomogeneous differential equation defining the temperature profile, T(x), in the foils by

$$\mathrm{d}^2/\mathrm{d}x^2[T(x)] - K_1 T(x) + K_2 = 0 \qquad (30)$$

using the constants $K_1 = \lambda_{Foil}\, d_{2Foils}\, R_m$ and $K_2 = K_1\ T_m$, with $R_m = R_1R_2/(R_1 + R_2)$ and $T_m = (T_1R_2 + T_2R_1)/(R_1 + R_2)$. Boundary conditions are

$$T(x = +L_i/2) = T_1 \qquad (31a)$$

$$T(x = -L_i/2) = T_2 \qquad (31b)$$

Two limiting cases, $\lambda_{Foil} \to \infty$ and $\lambda_{Foil} \to 0$, respectively, can be considered: In the first case, Eq. (30) reduces to

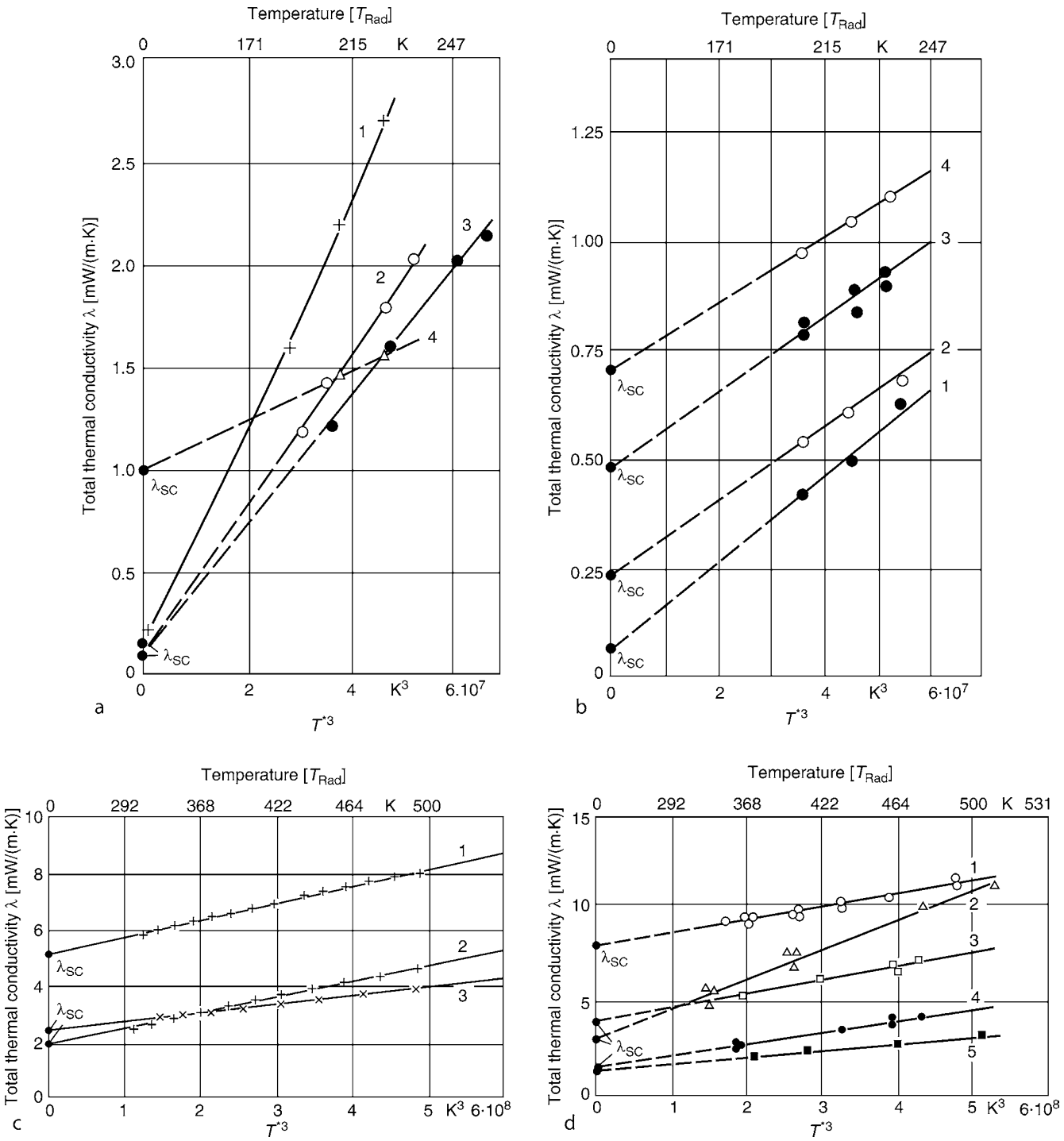

K6. Fig. 20. (**a**) Total thermal conductivity, λ_{Total}, of pure silica aerogel in a vacuum at cryogenic temperatures and various densities, ρ; the figure is from [1]. Curves 1–4: ρ = 70, 105, 125, and 457 kg/m^3. (**b**) Total thermal conductivity, λ_{Total}, in a vacuum of silica aerogel doped with an opacifier (45 wt% of bronze powder) at cryogenic temperatures and various densities, ρ; the figure is from [1]. Curves 1–4: ρ = 66, 87, 105, and 112 kg/m^3. (**c**) Total thermal conductivity, λ_{Total}, of powder and fiber insulations in a vacuum, at moderate and high temperature, prepared under mechanical pressure of about 1 bar; the figure is from [9]. Curve 1: Powder insulations: fumed silica + 16 wt% of Fe_3O_4 (density ρ = 270 kg/m^3, Π = 0.9), curve 2: pure boron silicate fiberglass paper (ρ = 300 kg/m^3, Π = 0.885), curve 3: boron silicate fiberglass paper doped with 30 wt% Fe_3O_4 powder (ρ = 330 kg/m^3). The diameter of the fibers in each case is 3–5 μm. (**d**) Total thermal conductivity, λ_{Total}, of powder and fiber insulations in a vacuum ($p_{Gas} \leq 1$ Pa), at moderate and high temperatures, and under approximately atmospheric pressure; measurements are from [36]. Curve 1: Minileit powder insulations (fumed silica + $FeTiO_3$, Grünzweig + Hartmann AG. Ludwigshafen, Germany), Curve 2: Pyrostop fiber insulations (40% alumina, 51% silica, fiber paper, fiber diameter 3–4 μm, Didierwerke AG, Wiesbaden, Gemany), Curve 3: ceramic fibers (99% alumina, nonwoven mats, fiber diameter 5 μm, Didierwerke AG, Wiesbaden, Germany), Curve 4: boron silicate fiberglass paper (fiber diameter 0.6 μm, Lydall Inc.), Curve 5: as for Curve 4, but with 33 wt% Fe_3O_4 powder as opacifier.

K6. Table 5. Solid/solid contact component, λ_{SC}, of thermal conductivity for various types of continuous superinsulations

Material	Density [kg/m^3]	λ_{sc} [mW/(m · K)]	Reference
Silica aerogel	70	0.14	Kaganer [1], p. 77
Silica aerogel (Santocel A)		0.06	Cockett [40]
Silica aerogel	457	1.0	Kaganer [1], p. 77
Silica aerogel + 45 wt% bronze powder	87	0.23	Kaganer [1], p. 97
Silica aerogel + 45 wt% bronze powder	105	0.48	Kaganer [1], p. 97
Silica aerogel + 45 wt% bronze powder	112	0.70	Kaganer [1], p. 97
Silica aerogel + 29 wt% Al powder		0.14	Kaganer [1], p. 92
Silica aerogel + 40 wt% Al powder		0.18	Kaganer [1], p. 92
Silica aerogel + 50 wt% Al powder		0.18	Kaganer [1], p. 92
Silica aerogel (Santocel A) + 40 wt% Al powder		0.13	Cockett [40]
Calcium silicate (Microcel E)		0.35	Cockett [40]
Carbon black, d = 0.1 μm	250	4.0	Serebryanyi [41]
Cement, d = 5 μm	1500	4.0	Serebryanyi [41]
Perlite	100	0.1	Kaganer [1], p. 78
Perlite	150	0.16	Kaganer [1], p. 78
Perlite	360	0.8	Kaganer [1], p. 78
Fumed Silica + 16 wt% Fe_3O_4	270	5.1*	Büttner [42]
Fumed Silica + 8 wt% TiO_2 + 8 wt % Fe_3O_4	270	5.9*	Büttner [42]
Minileit (Fumed Silica + $FeTiO_3$), Grünzweig + Hartmann AG, Ludwigshafen, Germany	260	7.8*	Ziegenbein [36]
Pure boron silicate glass fibers	300	1.9*	Büttner [9]
Ceramic fibers (99% Al_2O_3), Didier AG Wiesbaden, Germany	330	4.0*	Ziegenbein [36]
Boron silicate glass fibers + 30 wt% Fe_3O_4	330	2.4*	Büttner [9]

The measured values marked by an asterisk were obtained under mechanical (atmospherical) pressure load and under vacuum

K6. Table 6. Effective linear extinction coefficients, E^*/ρ (per unit density and averaged over a range of wavelengths) for various types of superinsulations. They were derived from calorimetric and spectroscopic measurements or calculated from the Mie theory

Material	Calorimetric E^*/ρ [m^2/g]	Spectroscopic E_R^*/ρ [m^2/g]	Theory E_R^*/ρ [m^2/g]
(a) Nontransparent insulations			
Fumed Silica + 16% Fe_3O_4	0.046[a]	0.042[b]	
Pure boron silicate glass fibers, d = 3–5 μm	0.058[a]	0.06[c]	0.06[c]
Fiberglass-bonded mats, d = 14 μm	0.011[d]	0.0087[d]	
Fibral (Al_2O_3 fibers), d = 5 to 10 μm	0.019[e]	0.014 [e]	
Boron silicate glass fibers + 30 wt % Fe_3O_4	0.077[a]		
Boron silicate glass fibers + 33 wt % Fe_3O_4	0.067[f] *(E /ρ)*	0.058[f]	
Polyester fibers			
d = 40 μm	0.0135[g]	0.0138[g]	
d = 26 μm	0.0229[g]	0.0253[g]	0.0247[g]
d = 16 μm	0.0407[g]	0.0422[g]	0.0401[g]
Polypropylene fibers			
d = 20 μm, pure		0.0328[g]	
Vacuum metallized on one side with			
0.05 μm Al		0.106[g]	
0.10 μm Al		0.112[g]	
(b) Insulation with transparent zones			
Silica aerogel, $\rho \leq 125$ kg/m^3, $T_1 \leq 300$ K	0.0199[h]		

[a] [42]
[b] [43]
[c] [44]
[d] [45]
[e] [46]
[f] [36]. The E/ρ values cited lie close to the E^*/ρ values, because absorption preponderates in glass fibers doped with Fe_3O_4
[g] [47]
[h] [1], p. 77; these E^*/ρ values are valid only for low densities and cryogenic temperatures
The authors assumed isotropic scattering in Cases [d] to [f]. In addition, the calorimetric measurements in Cases [d] and [e] were not performed in a vacuum Consequently, these E^*/ρ can serve solely as estimates
All opacifier addition rates are expressed as percentages in terms of the mass fraction

$$d^2/dx^2[T(x)] = 0 \tag{32a}$$

which indicates a linear temperature profile in the foils, $T(x) = K_3\, x + K_4$, with constants K_3 and K_4.

In the second case, the variation $d^2/dx^2\ [T(x)]$ can be neglected in the interval $-L_i/2 < x < L_i/2$, at positions, x, sufficiently distant from the boundaries. This yields

$$K_1[-T(x) + T_m] = 0 \tag{32b}$$

with the solution $T(x) = T_m$, the constant mean foil temperature at these positions.

In-between the two limiting cases, $T(x)$ may be curved, in dependence of conductivity, λ_{Foil}, and thickness, d, of the foils. While integration of Eq. (30) is straightforward, determination

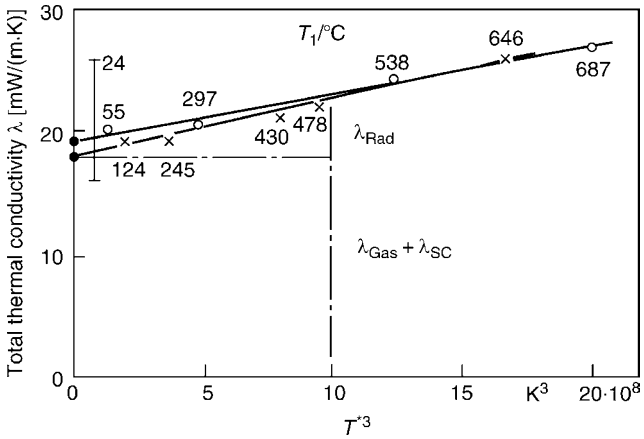

K6. Fig. 21. Total thermal conductivity, λ_{Total}, of two nonevacuated, microporous powder insulations (symbols and linear approximations) and, for comparison, of a sample of polyurethane foam expanded with fluoro-tri-chloro-rmethane (vertical bar), plotted vs. $T^{*3} = 4T_{Rad}{}^3$ [37]. Data for the powders (crosses and open circles) are from Micropore Europe N. V., Stint Niklaas, Belgium, for a density of 254 kg/m^3, and from Wacker Chemie GmbH, Kempten, Germany, for a density of 344 kg/m^3, respectively. Data were reported by Forschungsinstitut für Wärmeschutz e. V., München, Germany. Numbers attached to the data points and to the bar indicate temperature T_1 (in deg C) of the hot wall of the measuring installation. Full circles at $T^{*3} = 0$ indicate $\lambda_{Total} = \lambda_{Gas} + \lambda_{SC}$ obtained from a least squares fit to the data. The length of the vertical bar indicates ageing of the foam material over a 5 year-period [38].

of the integration constants from the boundary conditions is laborious; preference should be given to numerical solutions that also would allow temperature-dependent material properties, or applications of solvers like *Mathematica*.

The approach made in Eq. (30) has some drawbacks:

(a) Thermal conductivity of all solid components of the panels (foils and core material) is assumed constant (independent of temperature) and homogeneous
(b) Boundary conditions Eq. (31a, b) introduce a thermal short-circuit which leads to an overestimate of $\dot{Q}_{Total}$ (in reality, thin polymer foils constitute thermal resistance against heat flow parallel to their surface)
(c) The influence of surface temperature that in turn depends on convection or radiation on the upper and/or lower panel surfaces cannot be taken into account in his scheme because surface temperatures are given as a boundary conditions; contrary to this, thermal resistance networks, or finite element simulations (below) yield also surface temperatures (Fig. 23b and Figs. 26b–31b), because convection is modelled and heat flow, instead of temperature, is given as boundary condition
(d) Joints and gaps (and their filling, to suppress convection) between neighboring panels are neglected; taking joints or gaps into account, or extending the method to more than a single layer panel insulation, would enormously complicate the solution.

More suitable methods comprise thermal resistance networks (compare Sect. 2.5) and finite element calculations, see below. With reasonable fine divisions of the solid components of panels and joints, thermal resistance networks can take into account temperature dependency of conductivity or inhomogeneous materials properties. The situation for the one-layer panel insulation is comparatively simple, but this method becomes laborious with two or three layers, in particular, if the scheme would also be extended to 3D. In this case, at the latest, the advantage of finite element programs, in comparison to both Eq. (30) and resistance networks, with "top to bottom"-modeling tools and solution strategies becomes obvious.

However, the prediction for the temperature profile on the foils for the first limiting case, $\lambda_{Foil} \to \infty$, of Eq. (30) is nicely confirmed by 2D finite element calculations (Fig. 22b) using Al-foils of 50 µm thickness. On the other hand, the curves in Fig. 22c, d only gradually approach the second limiting case, $\lambda_{Foil} \to 0$, using PE-foils (c) or assuming, as a hypothetical case (d), a foil material with a conductivity identical to the conductivity of the core material (in Fig. 22b–d, identical foil thickness of 50 µm has been assumed to facilitate comparison of the results). Note (1): the case (d), "no foils," is not identical to the case "no joints," see, below, because microporous filling of the gap and of the two joints still remains, (2): the *s-coordinates* (the total path length, abscissa in Fig. 22b–d) of the upper foil (belonging to the left panel) are not identical to the s-coordinates of the lower foil (the right panel), compare Fig. 22a; at the same *x-coordinates*, foil temperature of the upper foil (open symbols in Fig. 22b–d), is always larger than foil temperature of the lower foil, of course. Boundary temperatures are 293.2 and 253.3 K, with convective boundary conditions on the upper surface and with a global temperature gradient of about 40 K over 15 mm panel thickness.

In summary, calculation of temperature profiles in indented panel insulations may be based on Eq. (30) if the conductivity of the foils is large, while for low conductivity envelope materials, it should be based on finite difference or finite element calculations. Once the temperature profiles are determined, they can be used for calculations of thermal contraction or expansion to yield stress in the foils (v. Mises average stress, to be compared with experimental values of maximum allowable stress at the corresponding temperatures). With regard to thermally induced stress, note from Fig. 22b–d that the temperature gradients in path sections s_1 and s_3 increase if the conductivity of the foils decreases.

Total heat loss, $\dot{Q}_{Total,}$ from 2D finite element calculation for indented, flat plate, one layer panel insulation, in dependence of indentation length, L_i, is shown in Fig. 23a using standard polymer foils with total thickness in the order of 100 µm. Such foils comprise one to three aluminized polymer foils as thin barriers against penetration of N_2, O_2, Ne, and H_2O-vapor, adhesive layers and a 50 µm polymer sealing layer that serves for welding the envelope at the joints to a vacuum-tight compound.

Figure 23a shows that $\dot{Q}_{Total}$ depends only weakly on indentation length. From the same analysis, in dependence of joint width, B, of the indented joints, Fig. 23b shows minimum temperature on the upper surface under convection if $T_1 = T_{ambient}$ and T_2 are 293 and 253 K, respectively (as before, the global temperature gradient is 40 K over a thickness of 15 mm. The insulations should be thick enough to avoid surface temperatures below dew point.

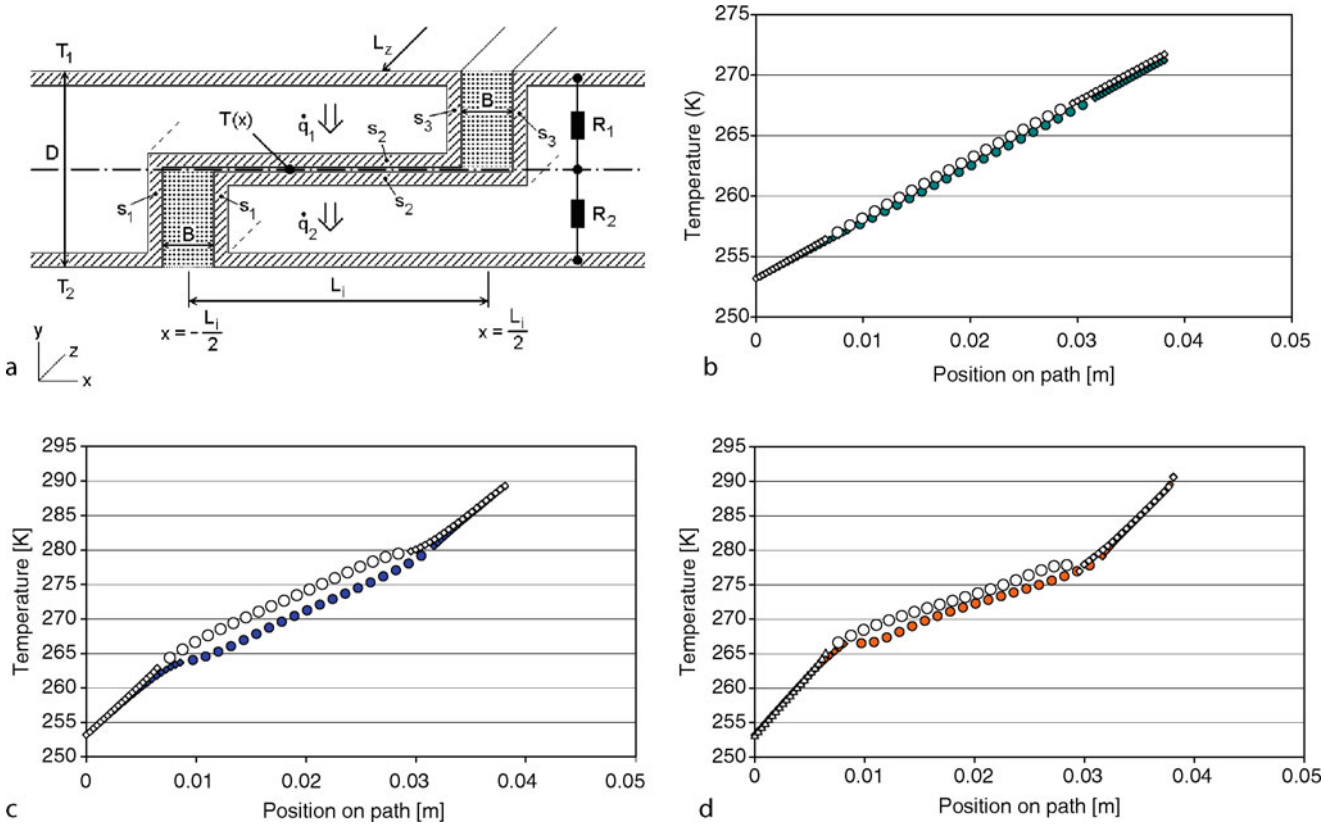

K6. Fig. 22. (**a**–**d**) Heat transfer in a flat plate, single layer panel insulation with indented joints; (**a**) Heat flow paths (schematic, rounded panel edges neglected in the diagram) in the overlap region, with shaded and dotted areas denoting envelope or filling material, respectively; the diagram (**a**) serves for finite element analysis in (**b**), (**c**), and (**d**), in Figs. 23a, b and 24a–c) and for application of Eqs. (27a, b–32a, b). Total path length, *s*, used for presentation of the finite element calculation results, runs from the lower vertical (s_1) over the horizontal (s_2) to the upper vertical sections (s_3) of the foils; in-between is a gap filled with a microporous filling, like in the joint sections; (**b**) and (**c**): Temperature of Al- or polyethylene foils, respectively; (**d**): Temperature if hypothetically assuming thermal conductivity of the foil would be identical to conductivity of the core material (evacuated fiberglass board); foil thickness in (**b**), (**c**), and (**d**) is identical 50 μm, to facilitate comparison with respect to the strongly different thermal transport properties of these materials. Foil temperature is plotted versus total path length, *s*, with solid symbols for the foils of the left, open symbols for the foils of the right panel; compare (**a**) for definition of s: diamonds denote sections s_1 and s_3, circles denote section s_2 of the total *s*. Note that the *total path length, s* (the abscissa in Fig. 22b–d), is not identical for the upper (left panel) and the lower foils (right panel), compare (**a**). For *identical x-coordinates*, foil temperature of the upper foil is always larger than temperature of the lower foil.

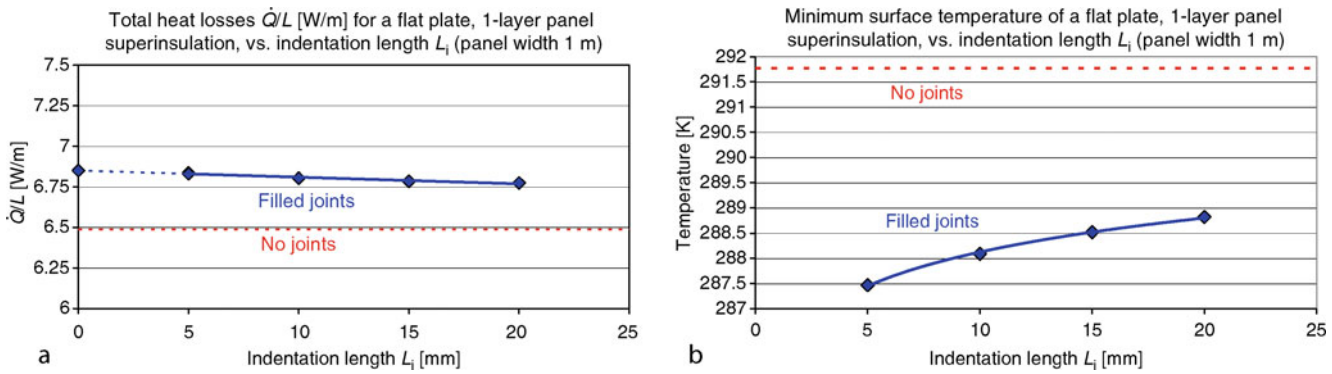

K6. Fig. 23. (**a**, **b**) Total heat losses, $\dot{Q}_{Total}$, and minimum surface temperatures, using standard polymer foils (in the order of 100 μm total thickness); (**a**) and (**b**) are plotted versus indentation length, L_i. Panel thickness is 15 mm, temperatures T_1 (293.2 K, of ambient air, for convection boundary condition on the upper insulation surface) and T_2 (253.2 K of bottom, temperature boundary condition), respectively.

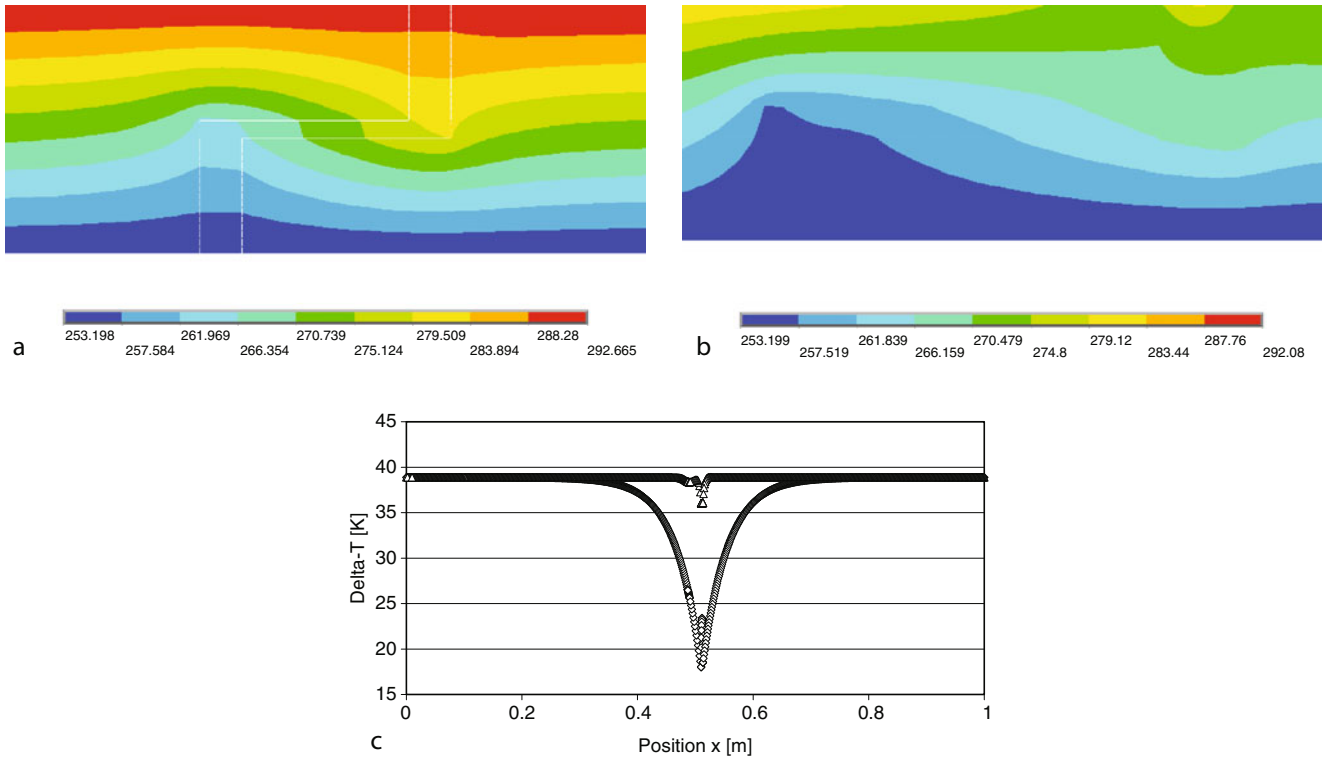

K6. Fig. 24. (**a**–**c**) Temperatures profiles, from 2D finite element calculations in the overlap region of an indented, single layer panel insulation; (**a**) and (**b**): Overall temperature profiles in the cross section of both panels using polyethylene (**a**) or Al-foils **(b)**, with identical foil thickness of 50 μm (again to facilitate comparison of the results); the dashed lines in (**a**) schematically identify positions of the overlap region; (**c**) temperature difference, ΔT, between upper and lower panel surfaces, versus x-coordinate of the insulation, when using polyethylene or Al-foils, respectively.

In all finite element calculations of this Subchapter, a thermal conductivity, λ, of the core material of 2.0, 2.25, 2.75, and 3.5 [mW/(m · K)], at temperatures 73, 173, 273, and 373 [K], respectively, has been applied. This conductivity may be considered representative for evacuated, load-bearing glassfiber boards. Results for the contributions to total heat flow by the *joints*, see below, does not depend much on the particular choice for the *core* materials conductivity.

Figure 24a, b show temperature profiles in the cross section of the indented panel insulations of Fig. 22a–c. Without a joint, the temperature profiles would be stratified homogenously over the total width of the panel. But the joint strongly disturbes stratified temperature distribution. This is also seen from Fig. 24c that reports temperature difference, ΔT, between the upper and lower surface. Note the strong variation of ΔT in the overlap region. For this reason, assumption of a homogeneous temperature difference over the total panel surfaces is approximately fulfilled only if the envelope material is of low thermal conductivity.

Using in the following standard polymer foils (thickness in the order of 100 μm), under variation of the width, **B,** of joints filled with a microporous material, and of the indentation length, $\mathbf{L_i}$ heat losses of panel insulations of the indented (and, later, blunt) joints have been condensed into algebraic relationships, see below. Figure 25a schematically describes heat flow paths in a blunt joint, and Fig. 25b illustrates positions of a minimum number of blunt joints in one-, two and three layer panel insulations (the latter diagram serves for identification of the following 2D finite element calculations for flat panel insulations).

For the dependence of $\dot{Q}_{\mathrm{Total}}/L_z$ on joint width, B, we have

$$\begin{aligned}\dot{Q}_{\mathrm{Total}}/L_z(\mathbf{B})\,[\mathrm{W/m}] &= C_{\mathrm{B1}}\{\Delta T[\mathrm{K}]\times L[\mathrm{m}]\times\lambda[\mathrm{W/(m\cdot K)}]/D[\mathrm{m}]\}\times \\ &\quad \mathbf{B}[mm]+C_{\mathrm{B2}}\{\Delta T[\mathrm{K}]\times L[\mathrm{m}]/D[\mathrm{m}]\}+C_{\mathrm{B3}}\end{aligned} \tag{33a}$$

and for the dependence of $\dot{Q}_{\mathrm{Total}}/L_z$ on indentation length, L_i

$$\begin{aligned}\dot{Q}_{\mathrm{Total}}/L_z(\mathbf{L_i})[\mathrm{W/m}] &= C_{\mathrm{Li1}}\{\Delta T[\mathrm{K}]\times L[\mathrm{m}]\times\lambda[\mathrm{W/(m\cdot K)}]/D[\mathrm{m}]\} \\ &\quad \times L_i[\mathrm{mm}]+C_{\mathrm{Li2}}\{\Delta T[\mathrm{K}]\times L[\mathrm{m}]/D[\mathrm{m}]\}+C_{\mathrm{Li3}}\end{aligned} \tag{33b}$$

The three terms in Eq. (33a, b) are explained as follows: The *first* term

$$C_{\mathrm{Bl}}\{\Delta T[K]\times L[\mathrm{m}]\times\lambda[\mathrm{W/(m\cdot K)}]/D[\mathrm{m}]\}\times\mathbf{B}[\mathrm{mm}],\text{or}$$
$$C_{\mathrm{Lil}}\{\Delta T[K]\times L[\mathrm{m}]\times\lambda[\mathrm{W/(m\cdot K)}]/D[\mathrm{m}]\}\times\mathbf{L_i}[\mathrm{mm}],$$

respectively, describes the contribution $\dot{Q}_{\mathrm{Joint}}/L_z$ by *indented* joints (envelopes plus filling material) that depends on joint width, **B** (at constant L_i) or on indentation length, $\mathbf{L_i}$ (at constant B), respectively, to total heat loss. The symbols C_{B1} and C_{Li1} indicate constants preceding the parameters ΔT, L, λ, and D^{-1} and the variables B or L_i, respectively, in Eq. (33a, b).

In the first term, ΔT [K] denotes temperature difference between warm and cold sides, taken over the *total* thickness of the insulations (note that convective boundary conditions on

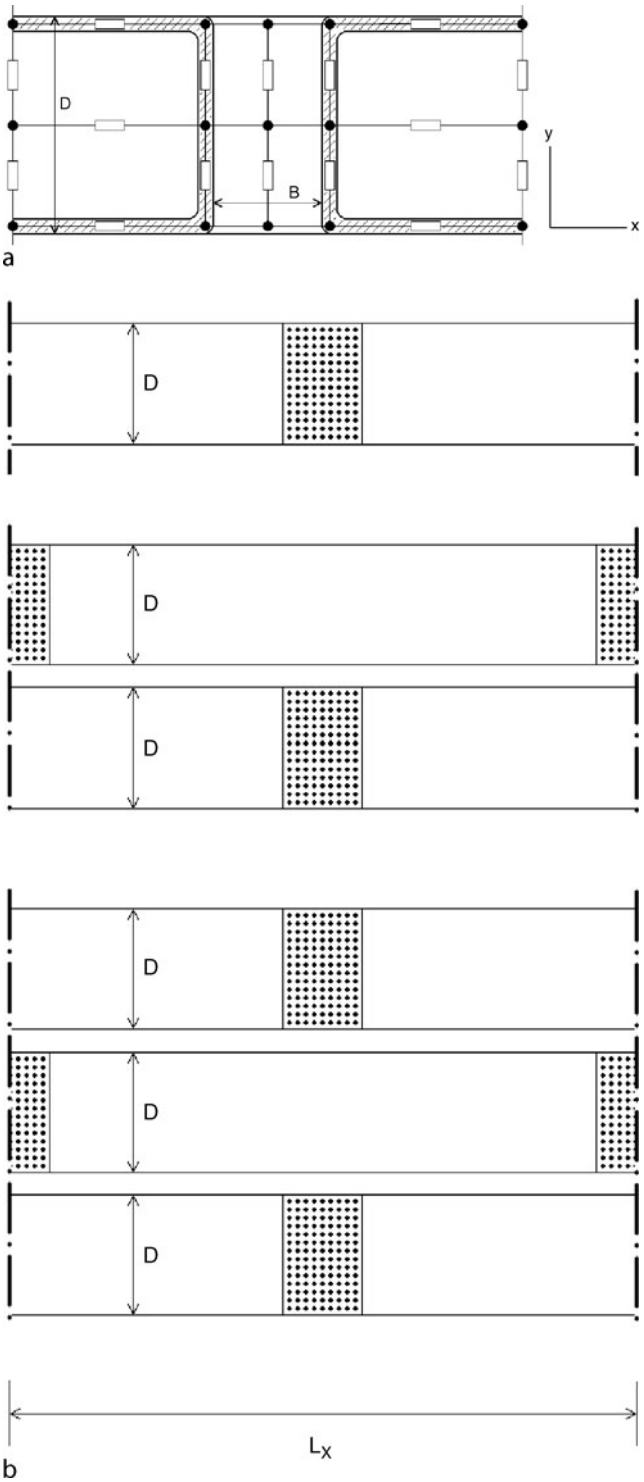

K6. Fig. 25. (**a**, **b**) 2D-thermal network (schematic) for calculation of heat flow through blunt joints in flat plate, one- or multiple layer panel insulations; (**a**) one-layer panel insulation with thermal resistances parallel and normal to global temperature gradient (*y*-direction), (**b**) positions of a minimum number of joints in one-, two-or three-layer panel insulations (dotted areas indicate the filling of the joints; analogous filling of the horizontal gap between upper and lower neighbouring panels could be preferable but is not indicated in the diagram); the figure serves also to identify the 2D finite element calculations in Figs. 26a, b–28a, b.

the warm side have been assumed in the finite element calculations, which means temperature of the warm side is air temperature). The symbol L [m] in the first term denotes *total* length of the joints, i.e., if there are two joints in z-direction, we have L = 2 m in the one-layer insulation. The thermal conductivity of the material filling the joints is indicated by λ [W/(m · K)]. The symbol D [m] indicates the thickness of *one* panel, also in case the insulation is two- or three-layer panel insulation (sample positions of a minimum number of indented or blunt joints in one-, two or three-layer panel insulations are schematically shown in Fig. 25b). Finally, B [mm] is the width of the joints filled with a microporous material, and L_i [mm] the indentation length.

If the width, B, of the joints is zero; this is not identical to the case "no joints". If $B = 0$, we still have some heat flow through foil sections oriented in vertical directions, at the corresponding edges (end positions) of the panels (compare the paths s_1 and s_3 in Fig. 22a), i.e., parallel to global temperature gradient, though there are no longer a contributions from *filling* of the joints.

The *second* term in Eq. (33a, b)

$$C_{B2} \times \{\Delta T[\mathrm{K}] \times L[\mathrm{m}]/D[\mathrm{m}]\} \text{ or}$$
$$C_{Li2} \times \{\Delta T[\mathrm{K}] \times L[\mathrm{m}]/D[\mathrm{m}]\}$$

with constants C_{B2} and C_{Li2} preceding the parameters, ΔT, L and D^{-1}, describes the contribution $\dot{Q}_{Joint}/L_z$ ($B = 0$) to total heat loss by the *indented* joints (only envelope material) that does *not* depend on joint width, B, or on indentation length, L_i, respectively.

The *third* term in Eq. (33a, b), constants C_{B3} and C_{Li3}, respectively, indicates the heat losses with no joints at all (no foil sections on panel edges, no filling materials).

Alternatively to the finite element result, the third term in Eq. (33a, b) can be estimated using the thermal resistances of each layer in the well-known analytical expression

$$\dot{Q}_0 = \Delta T/\left(\Sigma[D_i/(\lambda_i^* A)] + [1/(\alpha^* A)]\right) \qquad (34a)$$

with the summation index, i, running over all thermal conduction resistances of the multilayer structure, and α the heat transfer coefficient describing convection plus radiation on the outer surface. Instead of the thermal conductivity, λ, of evacuated, load-bearing glass fiber boards (see above), the conductivity of other core materials can be taken for calculation of $\dot{Q}_0$ without seriously affecting the results for the heat flow contribution by the joints obtained with the first and second terms in Eq. (33a, b).

The constants C_{Bk} and C_{Lik} ($1 \le k \le 3$; k denotes term number) for i*ndented* joints in Eq. (33a, b) are given in Table 7. For $\dot{Q}_{Total}/L_z$ (B), they apply to constant L_i = 5 mm, while for $\dot{Q}_{Total}/L_z$ (L_i), they apply to constant B = 3 mm. With these constants, applicability of Eq. (33a, b) is within $35 \le \Delta T \le 45$ [K], with the temperature of the warm side at 293 K, $0.015 \le \lambda \le 0.025$ [W/(m · K)], $0.01 \le D \le 0.02$ [m], $0.5 \le B \le 12$ [mm] and $1 \le L_i \le 20$ [mm]. Total heat losses, $\dot{Q}_{Total}/L_z$, in Eq. (33a, b) are given for a unit length of 1 m in z-direction of the insulations (compare Fig. 22a for the co-ordinate system). Note that B and L_i are to be introduced in Eq. (33a, b) in millimetres.

K6. Table 7. Constants C_{Bk} and C_{Lik} ($1 \leq k \leq 3$; k indicates term number in Eq. (33a, b)) for calculation of heat losses, $\dot{Q}_{Total}/L_z$, of superinsulated, *flat plate* panels with indented joints (joint positions according to Fig. 22); constants are given for a one-layer panel insulation

Constants	Dimensions	Values
C_{B1}	1/m	8.837E-04
C_{B2}	[W/(m · K)]	5.405E-05
C_{B3}	W/m	6.488
C_{Li1}	1/m	−1.287E-05
C_{Li2}	[W/(m · K)]	6.804E-05
C_{Li3}	W/m	6.488

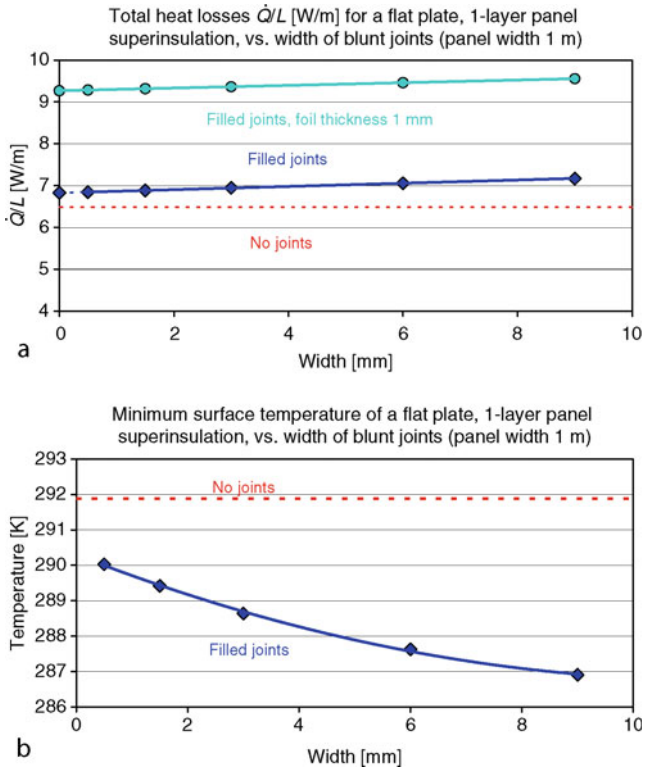

K6. Fig. 26. (**a**, **b**) Heat losses, $\dot{Q}_{Total}$, and minimum temperatures for a flat plate, one-layer panel superinsulation with blunt joints; results are obtained from 2D-finite element simulation. Open circles in Fig. 26a refer to a polymer foil thickness of 1 mm. Panel thickness is 15 mm.

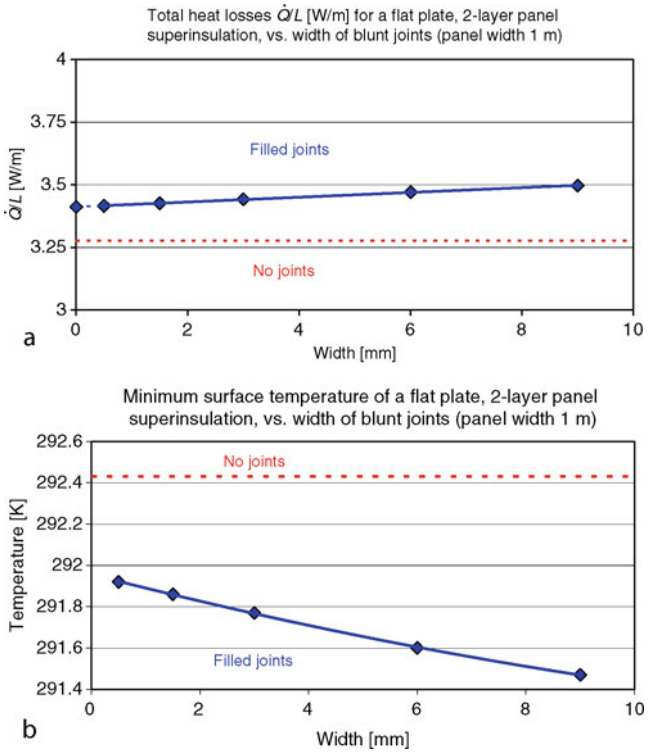

K6. Fig. 27. (**a**, **b**) Heat losses, $\dot{Q}_{Total}$, and minimum temperatures for a flat plate, two-layer panel superinsulation with blunt joints; results are obtained from 2D-finite element simulation. Thickness of each panel is 15 mm.

The results of 2D finite element-calculations for total heat losses, $\dot{Q}_{Total}/L_z$, of *blunt* joins, again using standard polymer foils (thickness in the order of 100 µm) under variation of the width, B, are shown in Figs. 26a, 27a and 28 a. Again, a temperature gradient of 40 K over the corresponding total thicknesses (15, 30, and 45 mm, respectively) of the insulations has been assumed in the calculations. The results have been condensed into the algebraic relationship indicated in Eq. (33a).

The constants C_{Bk} ($1 \leq k \leq 3$; k denotes term number) for *blunt* joints in Eq. (33a) are given in Table 8. With these constants, applicability of Eq. (33a) is within $35 \leq \Delta T \leq 45$ [K], with the temperature of the warm side at 293 K, $0.015 \leq \lambda \leq 0.025$ [W/(m · K)], $0.01 \leq D \leq 0.02$ [m], $0.5 \leq B \leq 12$ [mm] and $1 \leq L_i \leq 20$ [mm]. Total heat losses, $\dot{Q}_{Total}/L_z$, in Eq. (33a, b) are given for a unit length of 1 m in z-direction of the insulations (compare Fig. 22a for the co-ordinate system). Note again that B and L_i must be introduced in millimetres.

It is again assumed that the joints are filled with a microporous material to avoid solid–solid contacts between neighbouring panels, and convection (the whole structure could be open to air flow). Note that the heat losses increase very strongly if a polymer foil thickness of 1 mm would be used (Fig. 26a). Again, if the width, B, of the joints is zero; this is not identical to the case "no joints".

From the same finite element analysis, Figs. 26b, 27b, and 28b show minimum temperature on the upper surface under convection if $T_1 = T_{ambient}$ and T_2 are 293 and 253 K, respectively. Results are given for one, two and three layer, flat panel insulations with blunt joints. The insulations should be thick enough to avoid surface temperatures below dew point.

Total heat losses, $\dot{Q}_{Total}/L_z$, can be converted into "U-values" describing heat transmission by

$$U = (\dot{Q}_{Total}/L_z)/L_x [W/(m^2 \cdot K)] \qquad (35a)$$

Contrary to *k*-values (compare e.g., Fig. 7a, b), *U*-values not only include the thermal resistance of the insulations but also resistances due to convection with the environment or to a storage volume. Of particular interest are ΔU-values for heat

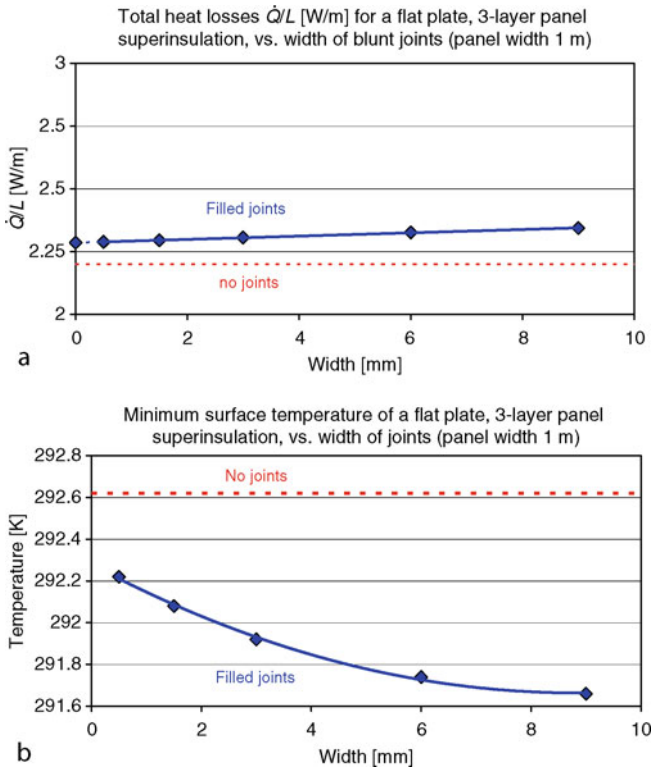

K6. Fig. 28. (**a**, **b**) Heat losses, $\dot{Q}_{Total}$, and minimum temperatures for a flat plate, three-layer panel superinsulation with blunt joints; results are obtained from 2D-finite element simulation. Thickness of each panel is 15 mm.

K6. Table 8. Constants C_{Bk} ($1 \le k \le 3$; k indicates term number in Eq. (33a, b)) for calculation of heat losses, $\dot{Q}_{Total}/L_z$, of superinsulated, *flat plate* panels with blunt joints (joint positions according to Fig. 24b); the constants are given for one-, two- and three-layer panel insulation

Number of layers	Constants	Dimensions	Values
1	C_{B1}	1/m	7.171E-04
	C_{B2}	[W/(m · K)]	1.277E-04
	C_{B3}	W/m	6.486
2	C_{B1}	1/m	8.961E-05
	C_{B2}	[W/(m · K)]	2.524E-05
	C_{B3}	W/m	3.277
3	C_{B1}	1/m	4.0928E-05
	C_{B2}	[W/(m · K)]	1.0679E-05
	C_{B3}	W/m	2.200

losses arising from contributions by the joints, which can be calculated from the first and second terms in Eq. (33a, b). Concerning the dependence on joint thickness, B, we formally have

$$\Delta U = [(C_{B1} \times \{\Delta T[\mathrm{K}] \times L[\mathrm{m}] \times \lambda[\mathrm{W/(m \cdot K)}]/D[\mathrm{m}]\} \times B[\mathrm{mm}] + C_{B2} \times \{\Delta T[\mathrm{K}] \times L[\mathrm{m}]/D[\mathrm{m}]\})L_x]/(A\Delta T) \quad (35b)$$

As given by Eq. (35b), ΔU is an overall correction averaged over the whole panel surface, A, and assuming for ΔT a uniform temperature difference taken over undisturbed and disturbed surface sections. It is clear that this can only yield an approximation to the real case because the surface temperature is lower at the positions of the joints compared to the undisturbed area (compare Fig. 24c). Nevertheless, this approach is frequently used, compare, e.g., Fricke [49], pp. 65–67, and literature cited therein, and can be justified if, as Fig. 24c confirms, the conductivity of the enevelope materials is small.

Example 7

Calculate total heat loss, $\dot{Q}_{Total}$, the corresponding U-value and the contribution ΔU by joints through a square, flat plate, one-layer panel superinsulation with blunt joints running around the panel. The panel has a thickness $D = 15$ mm, and the joints a width $B = 6$ mm. The thermal conductivity, λ, of the material filling the joints is 0.02 [W/(m · K)]. Standard polymer foils with thickness in the order of 100 µm are taken as envelope housing the core made of an evacuated, load-bearing fiberglass board.

Solution

With the materials specifications, we can take the results of the 2D-finite element simulations reported in Eq. (33a) for $\dot{Q}_{Total}$ and the constants from Table 7. For the one-layer panel insulation with $L_z = 1$ m, $\Delta T = 40$ K, $\lambda = 0.02$ [W/(m · K)], $D = 0.015$ m, $B = 6$ mm and $L_x = 1$ m, we have a total length of the joints of $L = 2$ m around the panel, a total panel surface $A = L_z \times L_x = 1$ m^2 including undisturbed and disturbed regions. Total heat loss, $\dot{Q}_{Total}$, from Eq. (33a) then amounts to

$$\dot{Q}_{Total} = (7.171\mathrm{E}-04 \times 2 \times 0.2/0.015) \times 6 + 1.227\mathrm{E}-04 \times 40 \times 2/0.015 + 6.486\,[\mathrm{W/(m^2 \cdot K)}] = 7.627\,\mathrm{W}$$

According to Eq. (35a), this yields an averaged total U-value,

$$U_{Total} = 7.627/(A\Delta T) = 7.627/(1 \times 40)\,[\mathrm{W/(m^2 \cdot K)}] = 0.191\,[\mathrm{W/(m^2 \cdot K)}]$$

which is rather small due to the very small thermal conductivity of the core material.

The contribution $\Delta\dot{Q}_{Joints}$ from the joints is given by terms 1 and 2 of Eq. (33a), or simply as

$$\Delta\dot{Q}_{Joints} = (7.627 - 6.486)\,\mathrm{W} = 1.140\,\mathrm{W}$$

Averaged over the total panel surface, A, and assuming uniform temperature difference, ΔT, also over the joints, the ΔU-value is

$$\Delta U = \Delta\dot{Q}_{Joints}/(A\Delta T) = 1.140/(1 \times 40)\,[\mathrm{W/(m^2 \cdot K)}] = 0.0285\,[\mathrm{W/(m^2 \cdot K)}]$$

A correction that in percentage of the losses of the undisturbed region amounts to

$$\Delta U\,[\%] = [0.0285/(0.191 - 0.0285) \times 100] = 17.6\%$$

The rather large percentage is due to the very low heat losses of the undisturbed region, in relation to the losses of the joints.

U-values for flat panels, and corrections ΔU for contributions by the joints, for different foil materials, panel thicknesses and widths of joints, all for applications near room temperature, are reported in Fricke [49], pp. 65–71. This reference also describes additional measures to reduce losses by thermal bridges like the joints in panel insulations. The same reference, p. 104, contains a comprehensive list of presently available, industrially produced panel insulations.

3.5.2 Cylindrical Geometry

As before, results will be calculated over a unit length, $L_z = 1$ m. A large part of presently produced panels extends to smaller length, which means not only axial but also circumferential joints have to be been taken into account, over the distance L_z. Fig. 29 schematically shows the geometry of axial and radial joints in a cylindrical, three-layer panel insulation. The circumferential positions of the axial joints have been chosen to obtain minimum heat leakage. It is again assumed that the joints are filled with a microporous material.

Figures 30a und 31a show total heat loss through two and three layer panel insulations positioned around a piping of 200 mm inner diameter; the data are obtained in detailed 3D finite element calculations. In these examples, $T_1 = T_{ambient}$ and $T_2 = 77$ K. At cryogenic temperatures, polymer foils used as envelopes could be subject to severe thermo-mechanical materials problems, however (embrittlement, strongly differing thermal expansion coefficients of polymers and core materials) which means leakage by pinholes, pores or cracks and, in the long run, increase of residual gas pressure in the core if not additional measures (integrating several aluminized polymer layers into the compound, compare, e.g., Fricke [49], or new materials) are taken to guarantee long-term vacuum-tightness of the envelope materials also under these temperature boundary conditions.

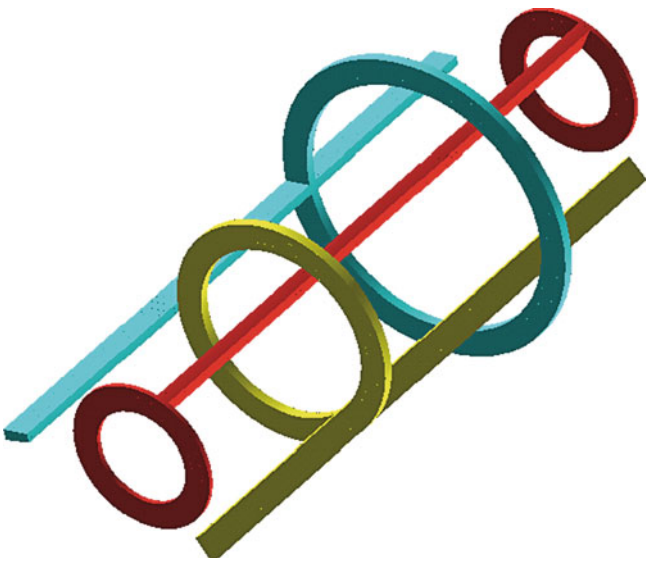

K6. Fig. 29. Position of circumferential and axial joints in a three-layer panel insulation (schematic).

The results again are condensed into the algebraic expressions given in Eq. (33a). If the width, B, of the joints is zero; this is not identical to the case "no joints".

The constants $C_{B,k}$ ($1 \le k \le 3$; k again denotes term number) to apply for *blunt* joints in Eq. (33a) are given in Table 9. With these constants, applicability of Eq. (33a) to the cylindrical geometry is within $200 \le \Delta T \le 180$ [K], with the temperature of the warm side at 293 K (note the convective boundary condition), $0.015 \le \lambda \le 0.025$ [W/(m · K)], $0.01 \le D \le 0.02$ [m] and $0.5 \le B \le 12$ [mm].

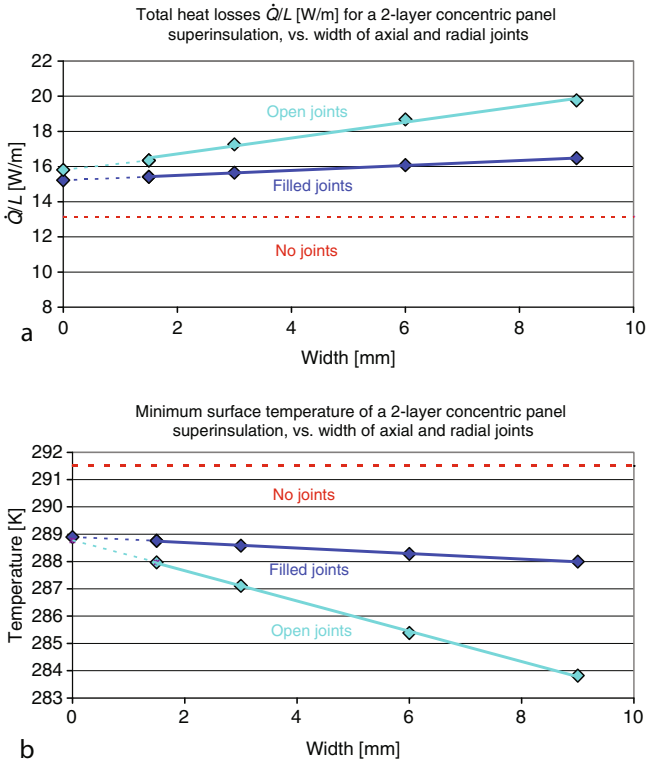

K6. Fig. 30. (**a**, **b**) Heat losses, $\dot{Q}_{Total}$, and minimum temperatures for a cylindrical, two-layer panel superinsulation with blunt joints; results are obtained from 3D-finite element simulation. Thickness of each panel is 15 mm.

K6. Table 9. Constants C_{Bk} ($1 \le k \le 3$; k indicates term number in Eq. (33a, b)) for calculation of heat losses, $\dot{Q}_{Total}/L_z$, of superinsulated, *concentric* panels for tube insulations with circumferential and axial blunt joints (joint positions according to Fig. 29); the constants are given for two- and three-layer panel insulations

Number of layers	Constants	Dimensions	Values
2	C_{B1}	1/m	1.364E-04
	C_{B2}	[W/(m · K)]	4.003E-05
	C_{B3}	W/m	13.150
3	C_{B1}	1/m	5.517E-05
	C_{B2}	[W/(m · K)]	1.727E-05
	C_{B3}	W/m	9.381

The total length, L, of the joints has to be taken over circumferential plus axial joints, again for the whole insulation. As before, D the thickness of *each* panel, and B the width of the joints (it is assumed the width is identical for all radial and axial joints).

Like for the flat geometry, the first term in Eq. (33a) describes the contribution $\dot{Q}_{\text{Joint}}/L$ by the joints to total heat loss. The second term, $\dot{Q}_0/L$, indicates that part of the losses that does not depend on joint width, B. The heat leakage for the case "no foils" can be estimated from the corresponding analytical expression, now for cylindrical geometry,

$$\dot{Q}_{\text{Cyl}} = 2\pi^* \Delta T/(\Sigma(1/\lambda_i)^* \ln(r_{i+1}/r_i) + (1/(\alpha^* A))) \qquad (34b)$$

with the summation index, i, running over all thermal conduction resistances of the multilayer structure, and α the heat transfer coefficient describing convection plus radiation on the outer surface.

Instead of the thermal conductivity, λ, of evacuated, load-bearing glass fiber boards (see above), the conductivity of other core materials can be taken for calculation of $\dot{Q}_0$ without affecting the results obtained with the first and second terms in Eq. (33a).

For two- and three-layer cylindrical panel insulations, Figs. 30b and 31b indicate the corresponding minimum surface temperatures. They are calculated assuming a temperature gradient of 216 K over the corresponding thicknesses (30 and 45 mm, respectively) of the two- or three-layer panel insulation of the tube. It is not possible to indicate simple closed form expressions for this purpose. Minimum values will always be found near the radial joints of the outer panel.

The dashed curves in Figs. 30a, b and 31a, b indicate heat losses and surface temperatures if the joints were to be left open (not be filled with a microporous material; the results indicate a worst case scenario). In view of the strongly increased heat losses and reduced surface temperatures, open joints should be avoided.

Figure 32 (materials from [50]) and Fig. 33 (data from [52]) show experimental values as examples for heat losses of panel superinsulations.

The lower data points in Fig. 32 have been obtained with silica aerogels doped with opacifiers (MnO_2, Fe_2O_3, or Fe_3O_4, TiO_2) and accordingly follow a linear relationship, compare Eq. (26). Instead, the upper data points refer to a panel that has been prepared without opacifier. Due to the smaller extinction coefficient, and because of the infrared "windows" of silica aerogel (Fig. 16), the approximation is no longer linear but by its curvature indicates transparency of the panel to thermal radiation. As a consequence, E_R^*/ρ is no longer a constant, for given temperature and particle diameter, but becomes dependent on radiation temperature. Reference to Eqs. (26) and (21) shows that in this case not a linear but a curved profile will result in the λ_{Total} versus T_{Rad}^3 diagram.

Experimental data by Caps [52] demonstrate small thermal conductivity, λ_{Total}, of an evacuated panel using pyrogenic silica as core material, in dependence of residual gas pressure. If the gas pressure increases to atmospheric pressure, the total thermal conductivity of the panel is still below the conductivity of motionless air. The increase of the thermal conductivity of this panel series can be described by $\lambda_{\text{Total}} = \lambda_{\text{sc}} + \lambda_{\text{Rad}} + 26/(1 + p_{1/2}/p_{\text{Gas}})$ with $p_{1/2} = 675$ mbar. Based on extremely

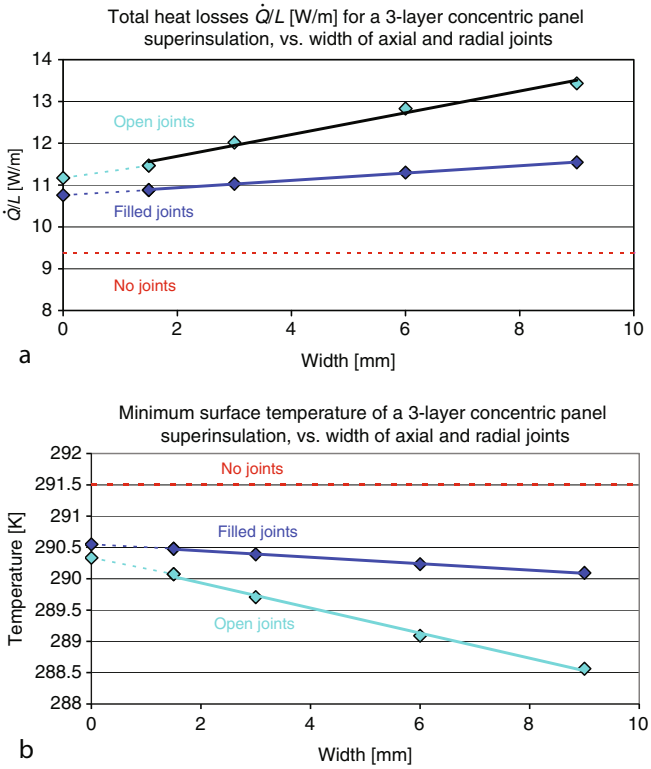

K6. Fig. 31. (**a**, **b**) Heat losses, $\dot{Q}_{\text{Total}}$, and minimum temperatures for a cylindrical three-layer panel insulation with blunt joints; results are obtained from 3D-finite element simulation. Thickness of each panel is 15 mm.

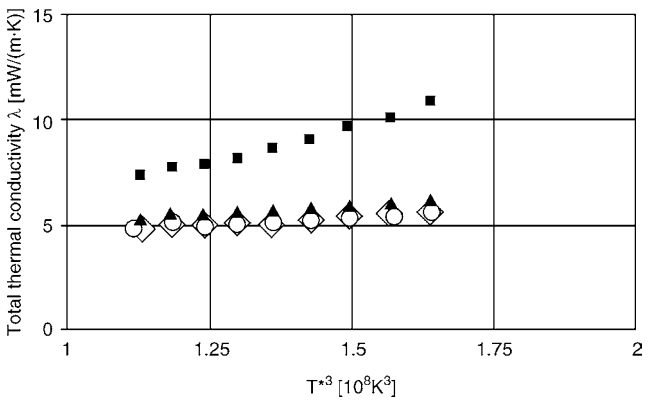

K6. Fig. 32. Experimental values for total thermal conductiviy, λ_{Total}, of four evacuated panels, versus $T^{*3} = 4T_{\text{Rad}}^3$; samples are from Degussa AG, Hanau, Germany [50]. The SiO_2 aerogel was compacted to a density of about 200 kg/m^3. Residual gas pressure of the fresh panel was below 1 mbar, residual humidity below 1%, one side of the samples was coated with Al. Data are measured by Fraunhofer Institut für Solare Energiesysteme, Freiburg, Germany [51] using $39.5 \leq T_1 \leq 118$°C $20.8 \leq T_2 \leq 22$°C. Open diamonds, open circles and solid triangles: opacified with MnO_2, Fe_3O_4 and TiO_2, respectively (concentrations not reported); full squares: without opacifier. The samples were delivered to the author by 1992 and have mainted vacuum since then.

small gas permeability of foils and joints reported in the same reference, the supplier expects a lifetime of such a panel safely above 30 years.

4 Improvement of Thermal Insulations

4.1 Optimum Choice of Materials Properties

It can be derived directly from Eqs. (2a, b), (17), or (18) and (6) or (20) how thermal insulations, of discontinuous or continuous types, can be improved. Minimum values for $\dot{Q}_{Total}$ or λ_{Total} are obtained as follows:

- For multilayer insulations, by selecting a large number of foils N with low emissivities ε_{Wall} and ε_{Foil}, in accordance with Eq. (6)
- For microporous insulations, by using particulate solid materials with low solid state thermal conductivities, λ_S, and high Young's moduli, Y, of elasticity and by avoiding compressive loads, p /(cf. Eqs. (17) or (18)), and
- By ensuring high linear extinction coefficients, E, in accordance with Eq. (20).
- In both types of insulations, by making sure that high Knudsen numbers, Kn, are obtained; this is realized by evacuating and reducing clearance between foils and spacers, or the pore diameter, δ, respectively, as indicated by Eq. (2a, b); if for continuous insulations experimental values are available for δ, these should be preferred over estimates using Eq. (16a, b)
- For evacuated panels, by using envelope material of as low as possible thermal conductivity, as far as available, to reduce heat losses at the joints. Note, however, increasing temperature gradients in the path sections s_1 and s_3 (Fig. 22b–d) if conductivity of the foils decreases, which can lead to substantial thermal contraction or expansion in this material. For the same reason, sharp edges of the panels should be avoided.

High linear extinction coefficients can be achieved by increasing the density, ρ, of the insulations (Fig. 18a–d) and by means of infrared opacifiers, if available with optimum particle diameters (see below, Fig. 36a–c). In almost all cases, an optimum density (Fig. 34, [1]) or an optimum opacifier concentration can be found (Fig. 35, [38]). If the density or concentration is too low, radiation is still is transmitted through the substance, with the result that λ'_{Rad} assumes high values. Conversely, if the density or

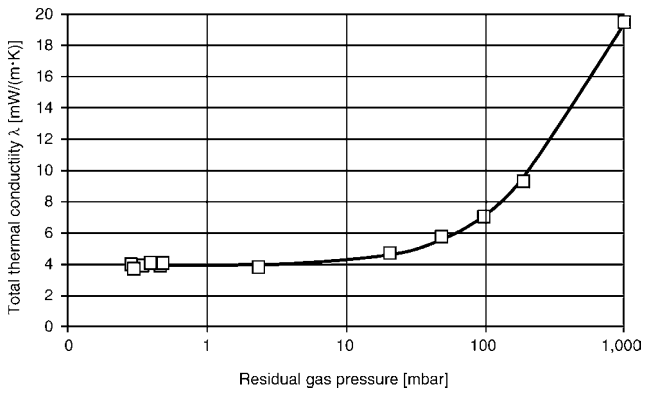

K6. Fig. 33. Experimental values for total thermal conductivity, λ_{Total}, of evacuated panels in dependence of residual gas pressure (The figure is from [52]).

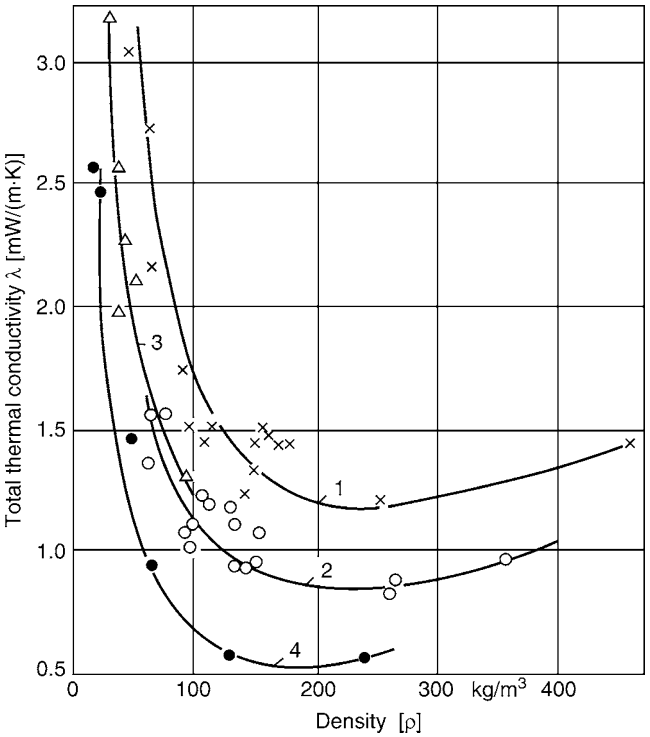

K6. Fig. 34. Total thermal conductivity, λ_{Total}, of evacuated powder and fiber insulations as a function of density ρ; the figure is from [1]. Curves 1: Silica aerogel, 2: Perlite, 3: Foamed material, 4: Glass wool (fiber diameter 1.2 μm); wall temperatures T_1 = 293 K and T_2 = 90 K; curve 1 for the pure Silica aerogel possibly indicates a pseudo-conductivity.

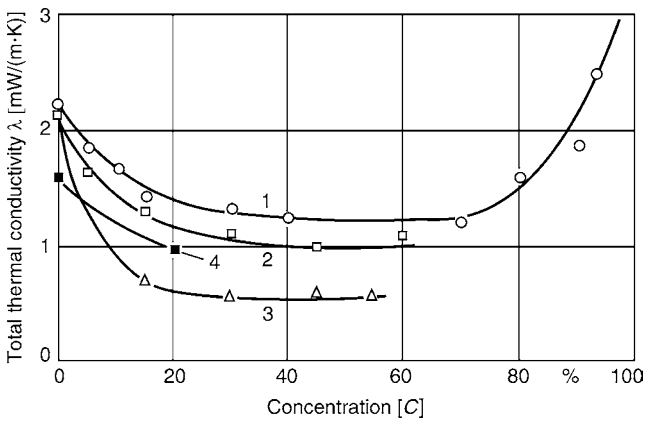

K6. Fig. 35. Total thermal conductivity, λ_{Total}, of evacuated powders ($p_{Gas} \leq 0.1$ Pa) at cryogenic temperatures as a function of concentration C (mass fraction) of opacifier (aluminium particles); data are from [38]; curves 1: Silica aerogel with aluminium flakes, 2: Perlite with aluminium powder, 3: Silica aerogel with aluminum powder, 4: Perlite with aluminium powder.

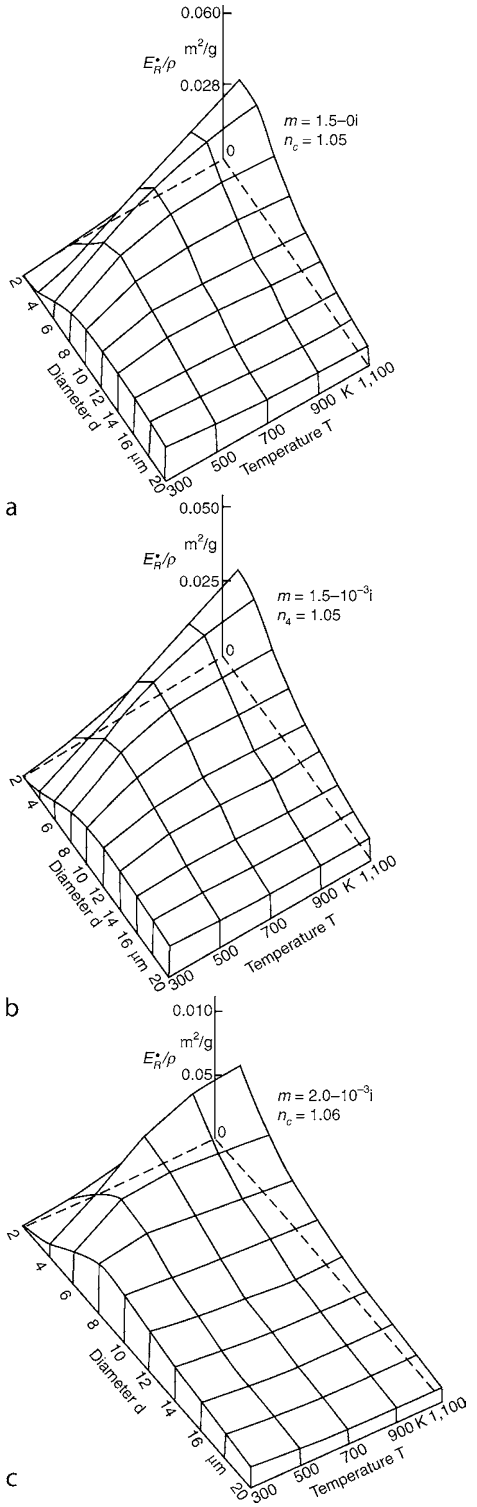

K6. Fig. 36. (**a**–**c**) Wavelength-averaged, effective linear extinction coefficients, E_R^*/ρ, per unit density, $\rho = \rho_{Particles}$, of spherical particles, as a function of particle diameter, *d*, and radiation temperature, T_{Rad}, for the estimation of the optimum diameter of opacifiers. The diagrams are calculated by the Mie theory using complex, *wavelength-independent* refractive indices, $m = n - ik$, and a density, ρ_S, of the basic solid material the particles are made from, of 5000 kg/m^3. The index $m = 1.5–10^{-3}$ i corresponds roughly to silica; and $m = 2–10^{-3}i$ to titanium dioxide. The relationships for $m = 1.5–0$i (the effect of the absorption coefficient *k*) have been included as a comparison. To approximately determine from these diagrams the extinction coefficient, *E*, for real opacifiers, the indices, *m*, applied in the calculations, should approximate the m of the real materials, in relevant wavelength intervals, $\Delta\Lambda$. If so, *E* can then be obtained using the given E_R^*/ρ by multiplication with the factor ($\rho_{Particles}$ 5000/ρ_S). n_c is the refractive index of the continuum surrounding the particles.

concentration is too high, the greater number of solid contacts affects an increase in λ_{SC}.

The criterion to be adopted in selecting an opacifier, e.g., aluminum powder, metal oxides, or carbon black, is its extinction spectrum as determined by experiment or by application of the Mie theory. In the latter case ([26]), the spectral complex refractive indices must be known, and reliable information on the particle diameter is required.

Optimum particle diameters, which can be read off from Fig. 36a–c, exist for dielectric spherical particles that are not strongly absorbent. The Rosseland averages, $E_R^*(T)/\rho$, entered in these diagrams were determined from the Mie theory by allowing for anisotropic scattering (ρ is the density of the powder). Strictly speaking, the applied complex indices of refraction are *sample* ones, but they approach the infrared optical properties of real materials, at least in certain wavelength intervals. Also, the diagrams have been calculated assuming a density, $\rho_S = 5000$ kg/m^3, identical for the three substances, of the basic solid materials from which the hypothetic opacifying powders were prepared. The calculations, accordingly, demonstrate existence of optimum particle diameters of opacifying materials for a certain range of indices of refraction. Analogous diagrams showing the existence of optimum particle diameters in a *real* substance (Fe_3O_4) have been published by Bauer [53].

4.2 Improvements by Latent Heat Storage

Extended standby periods of superinsulated devices can be achieved not only from improvement of the proper superinsulations (mostly by variations of its materials composition) but also from a combination with latent heat storage. Cool-down time of low, medium, or high temperature storage units, or of pipings in case of a production breakdown, can considerably be extended by this means. The method is not restricted to superinsulations.

Layers of latent heat storage material are integrated between the inner tube and thermal insulations, as shown e.g., in Fig. 37, which is a cross section (schematic) of a superinsulated pipe furnished with latent heat storage material. The latent heat storage material is located between the inner steel tube (2) and a separator (4) that in case of a superinsulation must be vacuum-tight. It is assumed that the fluid temperature, T_F, exceeds melting temperature, T_m, of the phase change material and ambient temperature, T_a; accordingly, it is assumed that the phase change material during normal operation of the pipe is in liquid state. Phase change of the storage material, between liquid and solid states, during cool-down of the fluid occurs at

the position $r_{int}(t)$ of the cross section, i.e., at a definite radius, under ideal conditions. Since the temperature profile across the pipe changes with time, t, the position of the liquid–solid interface (dashed curve in Fig. 37) changes accordingly, from the outer surface of the inner tube to the inner surface of the separator. These positions denote fully charged or fully discharged states of the storage material, respectively.

In case of a "normal" (non-evacuated) insulation, the position of the phase change material in the cross section of the pipe, with respect to position of the thermal insulations depends on the specific problem (quality of the insulations, temperatures): instead of being surrounded by the thermal insulations, the phase change material could surround the insulations in this case. Which of the two options shall or can be realized has to be concluded from thorough thermal analysis, for example, based on thermal network calculations of heat losses and temperature excursions (clearly, if superinsulation is used, the phase change material will be surrounded by the insulations). Note that heat transfer in phase change materials may be complicated by inhomogenous solidification and hysteresis after numerous cycles.

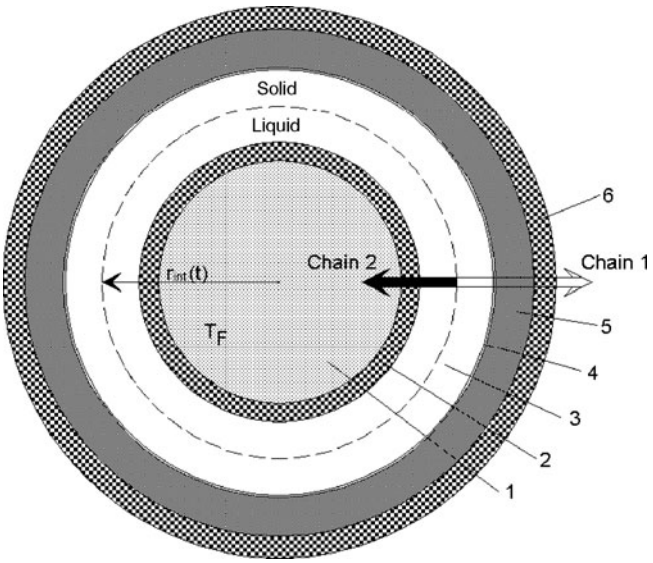

K6. Fig. 37. Cross section (schematic) of a pipe with superinsulations and incorporated latent heat storage material; components are indicated as follows: (1) fluid, (2) inner tube, (3) latent heat storage material, (4) vacuum tight separator, (5) thermal insulations, (6) outer tube. The thin dashed line indicates an (ideal) interface between solid and liquid phases of the storage material. The large arrows indicate directions (chains) of heat flow from the latent heat storage material [from the interface at which phase change occurs, with the radius $r_{int}(t)$] to ambient (Chain 1) or to fluid (Chain 2).

Figure 38 schematically shows a thermal resistance network (compare Sect. 2.5) that is designed according to Fig. 37. Heat transfer occurs through two chains. The origin of both chains is the interface between solid and liquid phase of the storage material.

Chain 1 directed outwards is located between phase change interface and ambient, via separator and thermal superinsulations. In this chain, we have thermal conduction and radiation resistances (storage material that is already solidified, separator, insulations, outer tube) and a convective resistance between outer surface of the outer tube and ambient. Chain 2 directed inwards is located between interface and fluid, with conductive resistances given by the storage material still being in liquid state and the inner tube, and with a convective resistance between inner surface of the inner tube that is wetted by the fluid.

Heat flow $\dot{Q}_S$(W) from the storage material along both chains is described by the first of the following two equations (the indices "PCM" and "F" denote phase change material, and fluid, respectively):

$$\rho^*_{PCM} c^*_{PCM} \mathrm{d}T_{PCM}/dt = \dot{Q}_{Chain\,1} + \dot{Q}_{Chain\,2} \qquad (36a)$$

$$\rho^*_{F} c^*_{F} \mathrm{d}T_{F}/dt = \dot{Q}_{chain\,2} \qquad (36b)$$

with opposite orientation of $\dot{Q}_{Chain\,1}$ and $\dot{Q}_{Chain\,2}$. In Eq. (36a, b), the symbols ρ and c denote density and specific heat of storage material and fluid, respectively. During phase change, the temperature of the storage material is constant, and the term $\rho_{PCM}{}^* c_{PCM}{}^* \mathrm{d}T_{PCM}/\mathrm{d}t$ in Eq. (36a) then has to be replaced by the change with time of the latent heat content of the storage unit as long as this content is above zero (during discharge; or below its maximum value during charging).

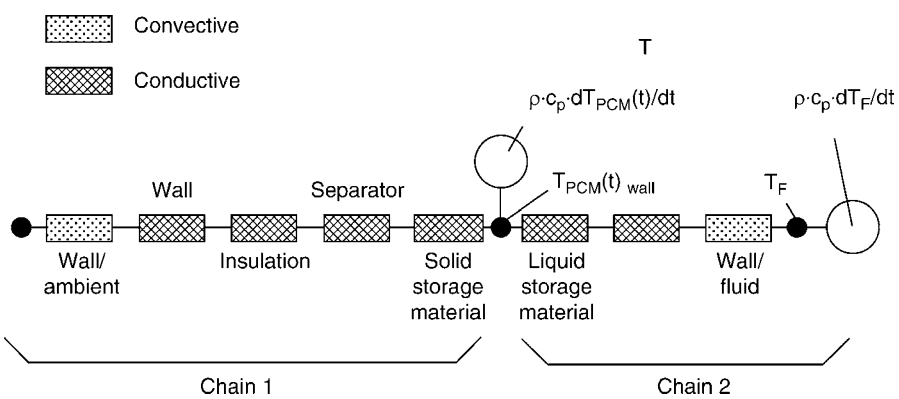

K6. Fig. 38. Thermal resistance network (1D chains) for calculation of temperature excursions of fluid (index F) and storage (index PCM) unit, with the definitions of the thermal resistances of Chains 1 and 2.

Using only these two equations is an approximation to the real case: also the other N-2 components of the pipe (tube materials, insulations, etc.) have heat capacities (and, accordingly, stored thermal energy) so that a number of in total N equations, like Eq. (36a, b), would be necessary to completely describe the energy household of the pipe. In most cases, the contribution of the heat capacities of the other N-2 components is small and in a good approximation can be neglected in Eq. (36a, b). Problems could come up only in exceptional (and unrealistic) cases when the thickness of the storage material would be extremely small in comparison to the thickness of the insulations. This means solution of both equations yield values of temperature excursions averaged over the volumes of fluid and storage material and neighboring tube or insulation components.

Both chains are composed of terms like $\Delta T_{i,j}(t)/R_{i,j}$, where $\Delta T_{i,j}(t)$ and $R_{i,j}$ denote temperature difference and thermal conductive resistances, between two neighboring surfaces i and j, or a convective resistance between surfaces and ambient or fluid, respectively. While most of the $R_{i,j}$ may be considered as constant (independent of temperature and time), this is not valid for the resistance between the phase change interface and the neighboring surface of separator (Chain 1) and between the interface and the outer surface of the inner tube (Chain 2), because the thickness of solid and liquid partial volumes of the storage material changes with time. Accordingly, $\dot{Q}_{\text{Chain1}}$ and $\dot{Q}_{\text{Chain2}}$ are not constant but functions of time, i.e., $\dot{Q}_k = \dot{Q}_k[T(t),t]$, with k = Chain 1 or Chain 2, which means it is not possible to separate both variables in Eq. (36a, b). Instead, a stepwise (numerical) integration of the two equations is necessary.

In a rough approximation, all materials data may be considered as constant (independent of temperature).

Figure 39 shows temperature excursions obtained from thermal network calculations assuming a hot liquid originally at 60°C is cooled down in an insulated pipe that is located in a cold environment (4°C). The figure demonstrates that standby periods can extended considerably.

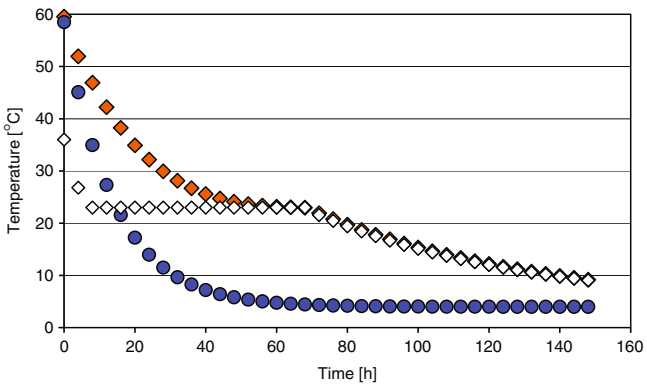

K6. Fig. 39. Temperature excursion of latent heat storage material (open diamonds) and of the fluid with (red diamonds) and without (blue circles) integration of a phase change material into the cross section of a pipe. Results are from thermal network calculation (compare Fig. 38), using temperatures of fluid, T_F, and ambient temperature, T_a, of 60°C and 4°C, respectively. Heat of solidification of the phase change material is 1.3 x 10^5 Ws/(kg), thickness about 75 mm, in a tube of about 250 mm inner diameter, with a conventional thermal insulation of 40 mm thickness and 0.2 W/(m · K) thermal conductivity (Courtesy ABB Corporate Research, Ladenburg, Germany (2008)).

Instead of assuming a sharp interface between solid and liquid phases, stratification and convection in the liquid storage material and in the fluid, and enthalpy diagrams taking account also hysteresis of the storage materials must also be considered for a rigorous analysis.

5 Symbols

Alpha-numeric symbols

a, b	Constants in Eq. (26)
A	Area (cross section in equations for calculation of heat flow) (m^2)
B	Width of joints (mm)
C	Specific heat (W s K^{-1} kg^{-1})
C	Constants in Eqs. (1) and (33a, b)
D	Panel thickness or thickness of insulations (compare text) (m)
d	Particle diameter (m)
E	Linear extinction coefficient (including scattering) in the Lambert-Beer law (m^{-1})
E^*	Effective value of E corrected for anisotropic scattering (m^{-1})
E_R^*	Rosseland average taken over spectral E^* values (m^{-1})
f	Degree of freedom, to calculate specific heat
k	k-Value; $k = \dot{Q}_{\text{Total}}/(A\,\Delta T)$, or correction factor in Table 2 (W $m^{-2}K^{-1}$)
k	Imaginary part of complex index m of refraction
K	Constants in Eq. (30)
Kn	Knudsen number defined by Eq. (4)
Li	Length of indentations of joints (m)
rn	Complex refractive index of a dispersed material or of opacifiers
M	Number of algrebraic equations in thermal network
n	Effective value of the real part of the complex refractive index, m
N	Number of foils or number of algebraic equations
p	Pressure exerted by compressive load or gas pressure (Pa)
$\dot{q}$	Heat flux (W m^{-2})
R	Thermal resistance (conduction, radiation, convection) (K/W)
s	path sections in Fig. 22a–d
$\dot{Q}$	Heat flow (W)
T	Absolute temperature (K)
T_1, T_2	Wall temperatures, $T_1 > T_2$ (K)
T_{Rad}	Mean temperature of radiation Eq. (21) (K)
U	U-value (heat transmission) defined in Eq. (35a) [W/(m^2 · K)]
ΔU	Correction to undisturbed U-value by contributions from joints to heat losses [W/(m^2 · K)]
Y	Young's modulus of elasticity (Pa)

Greek symbols

α	Accommodation coefficient for a gas at a wall, or heat transfer coefficient

β	Weight applied to Knudsen number, Kn, cf. Eq. (3)
γ	Poisson's ratio
δ	Foil spacing, or pore diameter in dispersed media (μm)
ε	Wavelength-averaged, hemispherical thermal emissivity
φ	Correction factor concerning angle of incidence of radiation on fiber axis
Λ	Wavelength (μm)
Λ_{max}	Wavelength at which black body radiant intensity is a maximum (μm)
λ	Thermal conductivity [W m^{-1} K^{-1}]
λ_0	Thermal conductivity of a gas at standard pressure [W m^{-1} K^{-1}]
λ'	Thermal pseudo-conductivity (compare footnote 1 and Appendix A1 [W m^{-1} K^{-1}]
Π	Porosity; $\Pi = 1 - (\rho/\rho_S)$
ρ	Density of dispersed media like powders or fibers (kg m^{-3})
σ	Stefan-Boltzmann constant, $\sigma = 5.67040 \times 10^{-8}$ [W/(m^{2}K^4)] [W m^{-2} K^{-4}]
τ_0	Optical thickness, cf. Eq. (19)

Subscripts

a or ambient	Ambient condition, e.g., room temperature
B_k	Subscript to constant C in Eq. (33a) that refers to width, B, of joints; k is an index running over the terms in this equation
c	continuum
Chain 1,2	Heat flow directions in Figs. 37 and 38
e	Electron
E	Electromagnetic
F	Fluid
Foil	Index to thermal conductivity or emissivity, λ
Gas	Residual gas
i	Index running over thermal resistances switched in series in Eq. (34a, b)
IGP	Intergranular porosity
Lik	Subscript to constant C in Eq. (33b) that refers to length, L_i, of an indentation; k is an index running over terms in this equation
MPP	Micropore porosity
p	(constant) pressure
P	Powder
PCM	Phase change (latent heat storage) material
Rad	Radiation
S	Solid
SC	Solid–solid contact conduction
V	Volume
W	Wall
0	Conductivity at normal (ambient pressure) or zero conditions (zero foils)

Superscripts

$*$	The asterix applied to extinction coefficients indicates that the quantity specified in this way is corrected for anisotropic scattering. If applied to temperature, the asterix indicates a radiative (mean) temperature, cf. Eq. (21).

6 Appendices

6.1 Appendix A1: Pseudo-conductivity, Minimum Optical Thickness for Non-transparency

6.1.1 Pseudo-conductivity

If a completely transparent medium (optical thickness $\tau_0 \to 0$) is placed between infinitely extended, planar parallel walls 1 and 2 of same thermal emissivity, $\varepsilon_1 = \varepsilon_2 = \varepsilon$, radiative flux, $\dot{q}_{Rad}$, is given by Eq. (7b),

$$\dot{q}_{Rad} = \frac{\sigma \cdot \left(T_1^4 - T_2^4\right)}{2/\varepsilon - 1} \left[\mathrm{W/m^2}\right]$$

Note that $\dot{q}_{Rad}$ does not depend on the wall separation, D. The definition of thermal conductivity, as a materials *constant* (or, better, as a physical quantity) in Fourier's empirical conduction law,

$$\dot{Q} = \lambda A \Delta T / D$$

cannot be applied for calculation of a radiative conductivity, λ_{Rad}, i.e.,

$$\lambda_{Rad} = \dot{q}_{Rad}\, D/\Delta T$$

because *this* quantity would not be constant but depend on wall separation, D, and on emissivity, ε.

The same applies if the optical thickness of a dispersed medium is small, Eq. (24),

$$\dot{q}_{Rad} = \frac{\dot{Q}_{Rad}}{F} = \frac{\sigma \times \left(T_1^4 - T_2^4\right)}{\frac{2}{\varepsilon_w} - 1 + \frac{3}{4} \times \tau_0^*} \left[\mathrm{W/m^2}\right]$$

In this case, the dependence of λ_{Rad} on D and would be smaller than in the case considered before, but still be detectable. This means that a quantity λ_{Rad} in a dispersed medium of small optical thickness, if conductivity is understood in the original sense of Fourier's conduction law, does not exist. If yet λ_{Rad} is calculated from either equations for $\tau_0 \to 0$ or for very small, but non-vanishing τ_0, it is a "pseudo"-radiative conductivity, λ'_{Rad}, that would be meaningless for a user if wall separation, D, and emissivity, ε, are not specified. A radiative conductivity exists only if optical thickness is so large that radiation at any position, x, within the medium has its origin at *this* position. Radiation emitted from walls surrounding the medium cannot be seen within the medium.

The same applies to *cylindrical* geometry. Assume two infinitely extended, concentric walls of which No. 1 is the inner, wall 2 the outer wall, again of the same thermal emissivity, $\varepsilon_1 = \varepsilon_2 = \varepsilon$, without foils in-between, $N = 0$. Radiative flow, $\dot{q}_{Rad}$, is given by

$$\dot{Q}_{Rad,0} = \sigma A_1 \left(T_1^4 - T_2^4\right) / [1/\varepsilon + (A_1/A_2)(1/\varepsilon - 1)] \quad \text{(A1)}$$

Compare this with the usual conduction law, now in cylindrical geometry,

$$\dot{Q} = \pi L (T_1 - T_2)/[(1/2\lambda)\ln(r_2/r_1)] \quad \text{(A2)}$$

(compare Chap. E1), with L the length of the cylinders and r_1, r_2 the corresponding radii. Solving for a λ yields

$$\lambda'_{\text{Rad},0} = \sigma r_1 \{\ln(r_2/r_1)/[1/\varepsilon + (r_1/r_2)(1/\varepsilon - 1)]\} 4T^3_{\text{Rad}} \quad \text{(A3)}$$

using $A_{1,2} = 2\pi r_{1,2} L$, and $4T^3_{\text{Rad}} = (T_1^4 - T_2^4)/(T_1 - T_2)$, from Eq. (21).

Also in this geometry, λ'_{Rad}, the radiative conductivity, depends on geometry by the factor $r_1 \ln(r_2/r_1)$ and on emissivity and thus is a pseudo-conductivity. If we keep r_1 constant, we have a dependence of λ'_{Rad} on $\ln(r_2)$, which is weaker, but detectable, than in the planar geometry.

If there are N foils between walls 1 and 2, the radiative flow reads

$$\dot{Q}_{\text{Rad,N}} = \dot{Q}_{\text{Rad},0} \Big/ \left\{1 + (\eta_W/\eta_{\text{Foil}}) r_1 \sum 1/[r_1 + (n/(N+1))(r_2 - r_1)]\right\} \quad \text{(A4)}$$

using the reduced emissivities, $\eta_i = \varepsilon_i/(2 - \varepsilon_i)$ like in Sect. 2.3 (i = W or Foil) and the summation taken over $1 \le n \le N$; compare Kaganer [1], pp. 33–34, for the denominator $1 + (\eta_W/\eta_{\text{Foil}}) r_1 \sum 1/[r_1 + (n/(N+1))(r_2 - r_1)]$. If this is set equal to the heat flow, $\dot{Q}$, in Eq. (A2), we have

$$\lambda'_{\text{Rad}} = \lambda'_{\text{Rad},0} \Big/ \left\{1 + (\eta_W/\eta_{\text{Foil}}) r_1 \sum 1/[r_1 + (n/(N+1))(r_2 - r_1)]\right\} \quad \text{(A5)}$$

of which the dependency on geometry is more complicated but again weaker compared to the previous cases. This is confirmed by Kaganer [1], p. 106, Table 19: Experimental values of the pseudo-conductivity of multilayer insulations, at residual gas pressure below 0.01 Pa, depend only weakly on thickness.

If instead of infinitely extended planar or cylindrical walls the case of walls of *finite* lengths is considered, the situation is quite analogous, with the same principal conclusions on λ'_{Rad} as before, but radiative exchange factors between the planar or cylindrical surfaces and end-faces have to be considered in the derivation of $\dot{Q}_{\text{Rad}}$; this is beyond the scope of this Appendix.

Assume now, in planar or cylindrical geometry, that the nonradiative components in the total thermal conductivity, λ_{Total}, as given in Eq. (25), are independent of wall separation, D (even this condition is not fulfilled if likewise the residual gas pressure would be very small). Now if λ'_{Rad} is a pseudo-conductivity, which means the radiative component is substantial, the same applies to λ_{Total} if λ'_{Rad} is introduced into Eq. (25). Like for λ_{Rad}, values given for λ_{Total} are meaningless for a user unless D and ε are specified.

Accordingly, total thermal conductivity, λ_{Total}, exists only if *all* its components exist, in the meaning of Fourier's conduction law. It is not possible to define a total thermal conductivity for a container that is filled with a transparent gas. Rather, a gaseous conductivity, independent of wall separation, may exist if the pressure is high enough that the mean collision distance between gas molecules is small compared with the wall distance. Therefore, "thermal conductivity" of transparent gases is at the most a partial conductivity, and values of λ_{Gas} given in the literature must have been cleaned from nonlocal, i.e., radiative, contributions (compare Tsederberg [54], p. 88, on the work of Wilner and Borelius). As a consequence, a large optical thickness at all wavelengths is imperative for the existence of total thermal conductivity.

Another conductivity that is mentioned frequently in the literature is "apparent conductivity." This expression is used if a strong curvature of $T(x)$ or if large temperature gradients $dT(x)/dx$ are expected in a planar medium near its boundaries. Calculating conductivity as usual from measured total $\dot{Q}$ gives only approximate values since local values of $dT(x)/dx$ can differ strongly from $-\Delta T/D = -(T_1 - T_2)/D$. The existence of large temperature gradients near the boundaries is due to weak thermal coupling of the medium to its surroundings, for example, to the walls (in the very special case of a nonconducting medium, even a temperature jump can be observed; see [55] and literature cited therein.

Weak thermal coupling to the wall occurs if the optical thickness of the medium is small. Therefore the real background for "pseudo-conductivity" and "apparent conductivity" seems to be the same. However, if one speaks of apparent conductivity, it is implicitly assumed that $dT(x)/dx$, though strongly varying, exists everywhere in the medium. In a medium for which a pseudo-conductivity has been calculated, $dT(x)/dx$ might not exist at all, e.g., in a Dewar vessel. On the other hand, "true" conductivity is associated with $dT(x)/dx$ that exists everywhere in the medium and is identical, or is at least very close, to $-(T_1 - T_2)/D$.

The literature is full of confusion about conductivity, pseudo-conductivity and apparent conductivity, up to present; it is not astonishing that a "thickness problem" was broadly discussed in 1980s in publications dealing with microporous insulations. Pseudo- and apparent conductivity neither are synonyms nor are they identical with "true" conductivity that does not depend on specific properties of the device (surface, thickness, emissivity of the walls) by which it was measured. A pseudo-conductivity may be defined for a Dewar vessel (as an extreme case) or for evacuated multifoil insulations but there is no continuous or differentiable temperature field at all. Even if gas pressure is high, radiative contributions can be substantial.

6.1.2 Minimum Optical Thickness

Minimum optical thickness, $\tau_0 \ge 15$, required in Sect. 3.3 for definition of a nontransparent medium results from a Monte Carlo simulation (compare Caps [26] or standard literature on radiative transfer), in dependence of optical thickness, of radiation transmitted by scattering through a homogeneous

medium. A strongly *anisotropic* radiation source (like laser radiation) has been assumed in this simulation. *Isotropic* distribution of the residual radiation was obtained if $\tau_0 \geq 15$. Isotropic distribution of radiation means that the radiation source, at these positions, τ_0, no longer can be identified. If this is fulfilled also at all wavelengths, the medium is nontransparent.

6.2 Appendix A2: Experimental Values of the Thermal Emissivity, ε, of Solids and Thin Foils

Touloukian [56] is one of the traditional data sources that in addition to Chap. K1 can be consulted for experimental values of the integrated, hemispherical emissivity, ε, of solids. For Al-surfaces,

7) "Alcoa No. 2 reflector plate measured in vacuum": ε. = 0.026 at 76 K

8) "Alcoa No. 2 reflector plate sanded with fine emery": ε. = 0.032 at 76 K

9) "Alcoa No. 2 reflector plate cleaned with alkali" ε. = 0.035 at 76 K

12) "sheet, liquid honed" ε. = 0.14 at 76 K

31) "plate hand-polished" ε. = 0.06 at 227

While these data demonstrate the dependence of the emissivity of the solid Al on its surface quality (morphology), these data, and the emissivities given in Chap. K1, *cannot* provide automatically the emission properties also of thin Al films, in particular of aluminized thin polymer foils. In general, thermal transport properties of thin films are not the same as of bulk material. This concerns thermal conductivity as well as emissivity of the films.

With respect to conductivity, thin films do not grow under thermodynamic equilibrium conditions, which means the concentration of defects can be very large. Further, at cryogenic temperatures, the mean free path, l_e, of electrons may be much larger than the thickness, d, of Al-coatings on Mylar foils, and the thermal conductivity may be strongly reduced by scattering at interfaces, imperfections, textures and grain boundaries. At room temperature, l_e in very pure Al amounts to about 0.04 μm, just the usual thickness of a one-side Al-film on Mylar foil.

Second, if l_e is large in comparison to the penetration depth, l_E, of the electromagnetic field, the electrons are subject to variations of field strength in the film (anomalous skin-effect). This results in an increase of the thermal emissivity of the Al-film, if the thickness is very small.

Radiative properties of thin films can be found in the elder literature, e.g., Turner [57], and, specialized on Al-coated polymer foils, in recent publications, e.g., [58] or [59]. Musilova specifies very small emissivity values for Al-coated polyester foils, between $0.012 \leq \varepsilon \leq$ and 0.018, at temperatures between 30 and 140 K.

Concerning single- or double sided metallizations on polymer foils, emittance of an uncoated side is higher than that of a coated side. Al-coatings with thickness less than 40 nm are partly transparent to infrared radiation. This means an infrared "observer" sees the emissive properties of the underlying polymer film. Kutzner [18], p. 400, Table 1, correlates coating thickness of vapor-deposited Al films with electrical surface resistance.

The presence of spacers requires a correction of the emissivity of the foils to "effective values" if their surface density is substantial. Tien [60] reports thermal emissivity of *continuous* Mylar foil of about $\varepsilon = 0.4$. The surface density of modern spacer materials amounts to only about 5 g/m^2 polyester, i.e., Mylar tulles, with 50 μm filaments and mesh size of about 2 mm. The contribution to the effective emissivity of a multilayer insulations by this material accordingly will be very small. This may be quite different if fiberglass papers or other spacer materials with higher surface densities are applied.

6.3 Appendix A3: Transient Experimental Method to Separate $\dot{Q}_{sc}$ from $\dot{Q}_{Rad}$ in Multilayer Superinsulations

To describe the method, let $\dot{Q}_{Total,st}$ and $\dot{Q}_{Shields,st}$ denote total *stationary* heat losses of a storage tank and *stationary* heat losses through its multi-foil insulations, respectively. Thermal bridges, $\dot{Q}_{Bridge,st}$, also stationary, comprise thermal contacts of the shields to the ambient and the bellow of the cryostat (compare Fig. 11) but without supports of the inner tank. We have

$$\dot{Q}_{Total,st} = \dot{Q}_{Shields,st} + \dot{Q}_{Bridge,st} \tag{A6}$$

Kaganer [1] pp. 164–167, derives Eq. (A6) for *transient* evaporation rates, $\dot{Q}_{Total}(t)$,

$$\begin{aligned} &\mathrm{In}\left[\left(\dot{Q}_{Total}(t) - \dot{Q}_{Total,st}\right)/\dot{Q}_{Total,st}\right] \\ &\quad = \mathrm{In}\left(2\dot{Q}_{Shields,st}/\dot{Q}_{Total,st}\right) - \pi^2\, a\, t/D^2 \end{aligned} \tag{A7}$$

In Eq. (A7), the symbol a denotes thermal diffusivity of the insulations, and D its thickness. By plotting the experimental $\dot{Q}_{Total}(t)$ in the co-ordinates

$$\dot{Q}(t) = \mathrm{In}\left[\left(\dot{Q}_{Total}(t) - \dot{Q}_{Total,st}\right)/\dot{Q}_{Total,st}\right] \tag{A8}$$

versus time, t, the curve, $\dot{Q}(t)$, shows a straight part at large times so that the diffusivity, a, of the insulations and the heat losses $\dot{Q}_{Shields}$ can be determined from slope and intercept with the ordinate at $t = 0$, respectively. If density and heat capacity of the foils are known, a radiative "pseudo"-conductivity can be calculated from the corresponding "pseudo-diffusivity."

Rough, order of magnitude agreement is found for the diffusivity, with values typical for multilayer superinsulations, and for $\dot{Q}_{Shields,st}$ [20]. Successful application of Kaganer's method significantly depends on existence of a wide linear portion of the curve $\dot{Q}(t)$, and, consequently, on the quality of linear fits to the data.

Laboratory experiments should be performed for further check of the method.

7 Bibliography

1. Kaganer MG (1966) Thermal insulation in cryogenic engineering. Engl. translation by A. Moscona, Israel Progr. Sci. Transl. Jerusalem (1969) from Teplovaya Izolyatsiya v Tekhnike Nizkikh Temperatur, Izdatel'stvo "Mashinostroenie", Moscow
2. Tien CL, Cunnington GR (1973) Cryogenic insulation heat transfer. In: Irvine TF Jr., Hartnett JP (eds) Ad Heat Transfer 9:349–417

3. Glaser PE, Black IA, Lindstrom RS, Ruccia FE (1967) Thermal Insulation Sytems - A Survey. NASA SP–5027
4. Sutherland W (1893) The viscosity of gases and molecular force. Phil Mag 36:507–531
5. v. Ardenne M (1973) Tabellen zur Angewandten Physik, Vol III. VEB Deutscher Verlag der Wissenschaften, Berlin
6. Wakao N, Vortmeyer D (1971) Pressure dependency of effective thermal conductivity of packed beds. Chem Eng Sci 26:1753–1765
7. Eucken A (1949) Allgemeine Gesetzmäßigkeiten über das Wärmeleitvermögen verschiedener Stoffarten und Aggregatzustände. Forschg Geb Ing Wes 11:6–20
8. Lehmann W (2000) Superisolation (SI) – Deren Qualität und Degradierung bei Anwendungen in der Kryotechnik, Deutscher Kälte- und Klimatechnischer Verein e. V. (DKV), DKV-Tagungsbericht Bremen, 27. Jahrg., Band I
9. Büttner D, Fricke J, Reiss H (1985) Thermal conductivity of evacuated load-bearing powder and fiber insulations - Measurements with the improved 700 x 700 mrn^2 variable load guarded hot plate device. Proceedings 9th Europ Conf Thermophys Prop, Manchester (1984), High Temperatures - High Pressures 17:333–341
10. Schäfer L (1986) Untersuchungen zur Wärmeleitfähigkeit von bereichsweise gestützten Folienisolationen anhand eines dynamischen Meßverfahrens. Diploma thesis, Phys Institute, Univ, Würzburg
11. Büttner D, Kreh A, Fricke J, Reiss H (1989) Recent advances in thermal superinsulations. Proceedings 11 th Europ Conf Thermophys Prop, Umea (1988), High Temperatures - High Pressures 21:39–50
12. Neumann H (2004) Concept for thermal insulation arrangement within a flexible cryostat for HTS power cables. Cryogenics 44:93–99
13. Masi S, Cardoni P, de Bernardis P, Piacentini F, Raccanelli A, Scaramuzzi F (1999) A long duration cryostat suitable for balloon borne photometry. Cryogenics 39:217–224
14. Walter H, Bock J, Siems SO, Canders WR, Freyhardt HC, Kesten M, Fieseler H (2003) Kryobehälter mit HTS-Lagerung, Tagungsband 8. Statusseminar Supraleitung und Tieftemperaturtechnik, Garmisch-Partenkirchen, Germany, Verein Deutscher Ingenieure, VDI Technologiezentrum, Düsseldorf, Germany
15. Wilson MN (1986) Superconducting magnets. Oxford Science Publications, Oxford University Press, reprinted in paperback
16. Fricke J, Caps R, Hümmer E, Döll, G, Arduini MC, De Ponte F (Dec. 1987) Optically thin fibrous insulations. ASTM C 16 Meeting, Bal Harbour, Florida
17. Langer H, Rust W (Dec. 1975) Wärmeisolierung durch Superisolation. Forschungsbericht T 75–42, BMFT
18. Kutzner K, Schmidt F, Wietzke I (July 1973) Radiative and conductive heat transmission through superinsulations – experimental results for aluminium coated plastic foils. Cryogenics 396–404
19. Reiss H (2004) A coupled numerical analysis of shield temperatures, heat losses and residual gas pressures in an evacuated super-insulation using thermal and fluid networks, Part I: Stationary conditions. Cryogenics 44:259–271
20. Reiss H (2006) A coupled numerical analysis of shield temperatures, heat losses and residual gas pressures in an evacuated super-insulation using thermal and fluid networks, Part II: Unsteady-state conditions (cool-down period). Cryogenics 46:864–872
21. Roth A (1990) Vacuum technology, 3rd edn. North Holland, Elsevier Science B. V., Amsterdam, NL
22. Wutz M (2000) Handbuch Vakuumtechnik. Theorie und Praxis. Vieweg, Wiesbaden, Gebundene Ausgaben
23. Reiss H (2006) A coupled numerical analysis of shield temperatures, heat losses and residual gas pressures in an evacuated super-insulation using thermal and fluid networks, Part III: Unsteady-state conditions (evacuation period). Cryogenics 46:873–880
24. Verschoor JD, Greebler P (Aug. 1952) Heat transfer by gas conduction and radiation in fibrous insulations. J Heat Transfer 74:961–968
25. Nyquist RA, Kagel RO (1971) Infrared spectra of inorganic compounds (3800–45 cm^{-1}). Academic Press, New York/London
26. Caps R (1985) Strahlungswärmeströme in evakuierten thermischen Superisolationen. Ph.D. thesis, Phys Institute, Univ., Würzburg
27. Mathes R, Blumenberg J, Keller K (1990) Radiative heat transfer in insulations with random fibre orientation. Int J Heat Mass Transfer 33:767–770
28. Rosseland S (1931) Astrophysik auf atomtheoretischer Grundlage. In: Born M, Franck J, (ed) Struktur der Materie in Einzeldarstellungen. Verlag von Julius Springer, Berlin
29. Hsieh CK, Su KC (1979) Thermal radiative properties of glass from 0.32 to 206 µm. Solar Energy 22:3–43
30. Harris L (1955) Preparation and infrared properties of aluminum oxide films. J Optical Soc Am 45:27–29
31. Harris L, Piper J (1962) Transmittance and ref1ectance of aluminum oxide films in the far infrared. J Optical Soc Am 52:223–224
32. Gaskell PH, Johnson DW (1976) The optical constants of quartz, vitreous silica and neutron-irradiated vitreous silica (1). J Non-Cryst Solids 20:153–169
33. McKay NL, Timusk T, Farnworth B (1984) Determination of optical properties of fibrous thermal insulation. J Appl Phys 55:4064–4071
34. Siegel R, Howell JR (1972) Thermal radiation heat transfer. McGraw Hill Kogakusha Ltd., Tokyo
35. Fricke J (ed) (1986) Aerogels. Springer Proc. in Phys. 6:Springer- Verlag, Berlin/Heidelberg
36. Ziegenbein B (1983) Evacuated high-temperature insulations for electrochemical batteries. Proceedings 8th Europ Conf Thermophys Prop, Baden-Baden (1982). High Temperatures - High Pressures 15:329–334
37. Reiss H (1992) Wärmeströme in thermischen Isolierungen. Phys Bl 48:617–22
38. Landolt-Börnstein (1972) Zahlenwerte und Funktionen, 6th edn, vol. IV. Eigenschaften der Materie in ihren Aggregatzuständen, 4. Teil, Wärmetechnik. Springer-Verlag, Berlin
39. Lu X, Wang P, Arduini-Schuster MC, Kuhn J, Büttner D, Nilsson O, Heinemann U, Fricke J (1992) Thermal transport in organic and opacified silica monolithic aerogels. J Non-Cryst Solids 145:207–210
40. Cockett AH, Molnar W (September 1960) Recent improvements in insulants. Cryogenics:21–26
41. Serebryanyi GL, Zarudnyi LB, Shorin SN (1968) Measurement of the heat conductivity coefficient of vacuum-powder insulation at high temperatures. Engl translation from Teplofizika Vysokikh Temperatur 6 (1968), 547–548 Plenum Publ Corp, New York
42. Büttner D, Fricke J, Krapf R, Reiss H (1983) Measurement of the thermal conductivity of evacuated load-bearing, high- temperature powder and glass board insulations with a 700 × 700 mm^2 guarded hot plate device. Proceedings 8th Europ Conf Thermophys Prop, Baden-Baden (1982). High Temperatures -High Pressures 15:233–240
43. Caps R, Büttner D, Fricke J, Reiss H (1983) Improving the ex- tinction properties of an evacuated high temperature powder insulation. Proceedings 8th Europ Conf Thermophys Prop, Baden Baden (1982). High Temperatures - High Pressures 15:225–232
44. Caps R, Trunzer A, Büttner D, Fricke J, Reiss H (1984) Spectral transmission and reflection properties of high temperature insulation materials. Int J Heat Mass Transfer 27:1865–1872
45. Cabannes F, Maurau J-C, Hyrien H, Klarsfeld SM (1979) Radiative heat transfer in fibreglass insulating materials as related to their optical properties. High Temperatures - High Pressures 11:429–434
46. Cabannes F (1980) Propriétés infrarouges et conductivite thermique par rayonnement des isolants thermiques a fibres refractaires. Rev Int hautes Temper Refract, Fr 17:120–133
47. Mayer G (1989) IR-optische Untersuchungen an Faserdämmstoffen. Diploma thesis, Phys. Institute, Univ., Würzburg, Report E 21–0589–3
48. Caps R (2004) private communication
49. Fricke J, Beck A, Binder M (2007) Vakuum-Isolations-Paneele für Gebäude – ein Lehrbuch. ZAE Bayern, Würzburg, Germany ISBN 978–3–00–022618–2
50. Degussa AG Zweigniederlassung Wolfgang, Hanau, Germany, VIP VR 224/255
51. Dengler J, Helde A, Wirth H (1995) Wärmeleitfähigkeitsmessungen an Vakuumisolationsplatten Ber. TOS 3- 9512- JJD- E07. Fraunhofer- Institut für Solare Energiesysteme, Freiburg, Germany
52. Caps R (2006) Vacuum insulation panels for buildings and technical applications, EPIC Conference, Lyon, France
53. Bauer A (1990) Analytische Modellierung des Strahlungswärmestromes in Superisolationen. Diplomarbeit, Lehrstuhl C für Thermodynamik der TU München, Germany
54. Tsederberg NV (1965) Thermal conductivity of gases and liquids, transl. by Scripta Technica, Cess R D (ed) MIT Press, Cambridge, MA

55. Reiss H (1988) Radiative transfer in nontransparent, dispersed media. Springer Tracts in Modern Physics 113
56. Touloukian YS, DeWitt DP (1970) Thermophysical properties of matter, Thermal radiative properties, Metallic elements and alloys. IFI/Plenum, New York/Washington
57. Turner AF (1962) Reflectance properties fo thin films and multilayers. In: Blau H, Fischer H (eds) Radiative transfer from solid materials. Macmillan, New York, pp 24–60
58. Musilova V, Hanzelka P, Kralik T, Srnka A (2005) Low temperature radiative properties of materials used in cryogenics. Cryogenics 45:529–536
59. Heaney JB (July 1998) Efficiency of aluminized mylar insulation at cryogenic temperatures. SPIE 3435:150–157
60. Tien CL, Cunnington GR (1972) Cryogenic insulation heat transfer, ibid; the authors refer to the original work of Tien CL, Chan CK, Cunnington GR. J Heat Transfer 94C:41

Fluid Dynamics and Pressure Drop

L1.1 Pressure Drop in Single Phase Flow in Pipes

Werner Kast[2] (*Revised by Hermann Nirschl*[1])
[1]Karlsruher Institut für Technologie (KIT), Karlsruhe, Germany
[2]Technische Universität Darmstadt, Darmstadt, Germany

1 General Pressure Drop Equation

Energy requirements for flow through a heat exchanger are related to the heat transfer coefficient α. If adequate pressure is available, high values of α, and thus small transfer areas, can be achieved. In equipment design, the capital and running costs must be weighed up against one another to determine the most economic system.

As a rule, determination of performance cannot be restricted to the calculation of pressure drop within the tubes or in the space surrounding the tube bundle, because it represents only a fraction of the flow losses in equipment. The calculation must include connections, extensions, and restrictions to flow, valves, bends, elbows, and baffles outside the tube bundle. Data for this purpose are presented in the following pages.

In the chapters that follow, the general term "fluid" embraces compressible gases with pronounced fluctuations in density and liquids that undergo only slight changes in density and have little compressibility. Application of similarity rules is valid only for substances that obey Newton's law, that is, whose viscosity is independent of shear. The many fluids that do not conform to this requirement, that is, non-Newtonian liquids, constitute a separate branch of study [1]. Strongly diluted gases also do not exhibit Newtonian flow. In this case, the mean free path of the molecules can be likened to the dimensions of a tube, and the friction is largely governed by the frequency of collisions between the particles and the fixed walls. Hence, special treatment is required for flow studies in a high vacuum [1, 2].

The following equation for the determination of pressure drop applies to all kinds of flow patterns, for example, laminar or turbulent:

$$\Delta p = \zeta a \frac{\rho w^2}{2} \qquad (1)$$

with ζ as the drag coefficient and a as a factor that depends on the nature of the flow problem.

Thus, for flow through pipes and ducts,

$$a = f(l/d_i)\ (\mathrm{l} = \text{length of pipe});$$

for flow through valves and pipeline fittings,

$a = 1$;

for crossflow over tube bundles,

$$a = f(n, l/d_i) \quad (n = \text{number of tubes}).$$

The average values for the density ρ and the velocity w in the direction of flow should be inserted in Eq. (1). If the change in density caused by the pressure drop is significant, the calculation should be performed in a number of steps. The same procedure is usually adopted in practice for non-isothermal flow. More accurate equations that allow for the expansion of gases and vapors and for heat losses during flow can be found in the literature [3, 4].

The principles of fluid dynamics lie outside the scope of Part L, although a close relationship exists between them and the determination of pressure drop. Attention is thus drawn to the works of reference on this subject [5–7].

2 Bibliography (Subchaps. L1.1, L1.2, L1.3)

1. Schiller L, Hahnemann HW, Linke W (1955) Strömung durch Rohre. In: Schmidt E (ed) Landolt-Börnstein, 6th edn, vol. 4, Springer, Berlin
2. Dushman S (1949) Scientific Foundation of vacuum technique. Wiley, New York
3. Richter H (1971) Rohrhydraulik, 5th edn. Springer, Berlin
4. Herning F (1966) Stoffströme in Rohrleitungen, 4th edn. VDI-Verl, Düsseldorf
5. White FM (1991) Viscous fluid flow, 2nd edn. McGraw Hill, Singapore
6. Perry RH (1997) Chemical engineers handbook, 7th edn, Sect. 5, Fluid and particle dynamics. McGraw Hill, New York
7. Baehr HD, Kabelac S (2009) Thermodynamik, 14th edn. Springer, Berlin
8. Roetzel W (1973) Calculation of single phase pressure drop in heat exchangers considering the change of fluid properties along the flow path. Wärme- und Stoffübertragung 6:3–13
9. Hausen H (1976) Wärmeübertragung im Gegenstrom, Gleichstrom und Kreuzstrom, 2nd edn. Springer-Verlag, Berlin
10. Gnielinski V (1986) Correlations for the pressure drop in helically coiled tubes. International Chemical Engineering 26:36–44
11. Mishra P, Gupta SN (1979) Momentum transfer in curved pipes. 1. Newtonian Fluids. Ind Eng Chem Process Des Dev 18:130–137
12. Schmidt EF (1967) Wärmeübergang und Druckverlust in Rohrschlangen. Chemie-Ing.-Techn. 39:781–789
13. Schiller L (1923) Über den Strömungswiderstand von Rohren verschiedenen Querschnitts and Rauhigkeitsgrades. Z Angew Math Mech 3, 2–13/ & VDI-Z 67, 623
14. Fromm K (1923) Resistance to flow in rough pipes. Z Angew Math Mech 3:329
15. Tiedt W (1966) Tech. Report No. 4 issued by the Institute for Hydraulics and Hydrology in Tech. Univ. of Darmstadt, March
16. Gnielinski V (2007) Berechnung des Druckverlustes in glatten konzentrischen Ringspalten bei ausgebildeter laminarer und turbulenter isothermer Strömung. Chemie-Ing. Techn. 79:91–95

VDI-GVC (ed.), *VDI Heat Atlas*, DOI 10.1007/978-3-540-77877-6_46,

17. Stephan K (1959) Wärmeübergang und Druckabfall laminarer Strömungen im Einlauf von Rohren und ebenen Spalten. Diss. Tech. Univ. of Karlsruhe
18. Kays WM (1950) Loss coefficients for abrupt changes in flow cross section with low Reynolds number flow in single and multiple tube systems.Trans. ASME 72:1067–1074
19. Linke W (1955) Untersuchungen über Rohrbündel-Wärmeübertrager. Chemie Ing. Techn. 27(3):142–148
20. Gnielinski V (2006) Widerstandsbeiwerte der mantelseitigen Ein- und Austrittsstutzen von Rohrbündelapparaten bei turbulenter Durchströmung. Chemie-Ing.-Techn. 78:90–93
21. Zimmermann E (1938) Der Druckabfall in geraden Stahlrohrleitungen. Arch Wärmewirtschaft 19(10):243–247

L1.2 Pressure Drop in Flow Through Pipes

Werner Kast[2] (*Revised by Hermann Nirschl*[1])
[1]Karlsruher Institut für Technologie (KIT), Karlsruhe, Germany
[2]Technische Universität Darmstadt, Darmstadt, Germany

1 Pressure Drop in Flow Through Pipes of Circular Cross-section

The pressure drop in pipe flow is given by

$$\Delta p = \zeta \frac{l}{d_i} \frac{\rho w_i^2}{2} \tag{1}$$

The drag coefficient ζ depends on the Reynolds number for flow within the tube, that is,

$$\mathrm{Re_i} = \frac{w_i \rho d_i}{\eta} \tag{2}$$

The properties η and ρ of the fluid and the velocity w_i refer to the average pressure $(p' + p'')/2$ and the average temperature $(\vartheta' + \vartheta'')/2$ in the tube. They may change considerably in the direction of flow; in this case, it is advisable to calculate the pressure drop in the individual sections.How heat transfer can be determined if allowance is made for the relationship of the physical properties to temperature was demonstrated in Chap. C2. Likewise, the pressure drop can be reliably calculated in streams with large fluctuations in temperature if it is determined together with the heat transfer coefficient at two points at the least [8].

Below the critical Reynolds number $\mathrm{Re_i} \approx 2320$, flow is laminar; above it, turbulent flow is likely. In the transition range of $\mathrm{Re_i} \approx 2320$ to $\mathrm{Re_i} \approx 8000$, flow may still be laminar in tubes with smooth inner surfaces if the inflow is quite calm and the tube inlet is well finished. As the pipe surfaces become rougher, the transition from laminar to turbulent flow is shifted in the direction of lower Reynolds numbers, but it never falls below a value of 2,320.

1.1 Laminar Flow

The Hagen-Poiseuille law, which is described by (Eq. 3), applies very accurately to smooth (glass, brass, or copper) tubes; it is also valid for rough tubes of up to $k = 0.07$, that is, slightly rusted steel or cast iron tubes:

$$\Delta p = \frac{32 \eta w_i l}{d_i^2} \tag{3}$$

The law can also be expressed in terms of the drag coefficient by combining (Eqs. 1–3), that is,

$$\zeta = \frac{64}{\mathrm{Re_i}} \tag{4}$$

1.2 Turbulent Flow

The roughness of the tube wall is an important factor. The only surfaces for which an accurate rule can be quoted for the resistance are those that are technically smooth (glass, drawn brass, copper tubes. etc.).

According to Blasius, the following simple formula applies in the $\mathrm{Re_i} \approx 3{,}000$ to $\mathrm{Re_i} \approx 100{,}000$ range:

$$\zeta = \frac{0.3164}{\sqrt[4]{\mathrm{Re_i}}} \tag{5}$$

The Hermann equation is convenient for the higher range from $\mathrm{Re_i} \approx 2 \cdot 10^4$ to $\mathrm{Re_i} \approx 2 \cdot 10^6$:

$$\zeta = 0.00540 + \frac{0.3964}{\mathrm{Re_i}^{0.3}} \tag{6}$$

For even higher Reynolds numbers ($\mathrm{Re} > 10^6$), ζ can be obtained from the Prandtl and von Kármán equation, that is,

$$\frac{1}{\sqrt{\zeta}} = -0.8 + 2 \log\left(\mathrm{Re_i} \sqrt{\zeta}\right) \tag{7}$$

1.3 Effect of Roughness

Much greater resistance to flow is encountered if the surfaces are rough. It depends solely on the roughness in turbulent flow; but, in the transition zone, it also depends on the Reynolds number $\mathrm{Re_i}$. The numerous observations that have been made have failed to establish a general relationship between pressure drop and roughness that would embrace the multiplicity of cases that are likely to occur in practice. In other words, a factor of uncertainty is attached to the determination of pressure drop in rough pipes. The following instructions may lead to greater accuracy, and are preceded by some brief explanations to ensure that they are correctly applied.

There are essentially two forms of roughness:

- Extended undulations and
- Slight protuberances

The latter may be rounded off and uniformly distributed, or they may be sharp and angular and distributed at random. At low Reynolds numbers, the boundary layer of the fluid is often thick enough to cover all projections. Although the pressure drop in this case is somewhat higher than that in a smooth tube, the relationship to Re_i is subject to much the same laws. As the Reynolds number increases, the boundary layer becomes thinner, so that the protuberances are exposed in the sequence of their sizes, and the turbulence is progressively increased until the relationship is quadratic. Hence the shape of the resistance curves derived from measurements gives an idea of the roughness. Likewise, changes in the shape over long running periods can indicate the thickness and nature of any deposits. The roughness depends on the material from which the inner surfaces of the tube have been formed and progresses from undulatory to protuberant in roughly the following sequence: vitreous, bituminized, drawn, sandblasted, galvanized, briefly stored, rusted, fouled after long periods of operation, and covered by scale.

Regardless of the numerous forms that roughness can assume and how it is distributed, it can be defined in general terms by a "relative roughness," which is given by

$$\varepsilon = \frac{K}{d_i} \tag{8}$$

where K is the average height of all the projections. Values that can be adopted as a guide for pipes are listed in Table 1. If flow is completely governed by roughness, the quadratic relationship for the resistance applies, and ζ is independent of Re_i. The Prandtl/Kármán equation for this case is

$$\frac{1}{\sqrt{\zeta}} = 2\log\left(\frac{d_i}{K}\right) + 1.14 \tag{9}$$

The relationship to both Re_i and K/d_i is allowed for in the Colebrook and White equation for the transition between flow over smooth and flow over rough surfaces, that is,

$$\frac{1}{\sqrt{\zeta}} = -2\log\left[\frac{2.51}{Re_i\sqrt{\zeta}} + \frac{K/d_i}{3.71}\right] \tag{10}$$

For practical convenience, (Eqs. 9) and (10) are presented graphically in Fig. 1.

The roughness in drawn steel tubes is predominantly undulatory, but the extent appears to differ with the diameter. The drag coefficient for this common type of tube can be obtained from the Hausen diagram, which is reproduced in Fig. 2.

The pressure drop Δp can be determined by inserting in (Eq. 1) the drag coefficient obtained from Figs. 1 or 2.

A rough estimate of the pressure drop in coolers can be derived from Figs. 3 and 4. Figure 3 applies for smooth tubes, for example, brass, copper, and glass; Fig. 4, for drawn steel tubes; and values of ζ are obtained from Fig. 2 (steel tubes) and Eqs. (5–7) (brass tubes). The water temperature in all cases is 25°C, and no allowance has been made for inlet and outlet losses.

L1.2. Table 1. Absolute roughness in millimeters for various materials

Drawn glass, lead, copper and brass tubes		0–0.0015
Drawn steel tubes	New	0.04 (0.02–0.1)
	Cleaned after long service	0.15–0.20
	Moderately rusted or slightly fouled	$\leq$ 0.40
	Heavily fouled	$\leq$ 3.0
Galvanized sheet steel	Smooth (air ducts)	0.07
Galvanized steel tubes	Normally galvanized	0.15
Welded steel pipes	New	0.05 (up to 0.1)
	New, bituminized	0.05
	Used, cleaned	0.15–0.20
	Uniformly rusted	$\leq$ 0.40
	Slightly fouled	1–1.5
	Heavily fouled	2–4
Riveted steel pipe		0.9 (0.5–10)
Cast iron pipes	New	0.26 (up to 1)
	New, bituminized	0.10–0.15
	Slightly rusted	1.0–1.5
	Fouled	1.5–4.0
Concrete conduits	Smooth finish	0.3 (up to 0.8)
	Rough	1.2 (up to 3)
Fibrous concrete pipes	(Eternit; Toschi)	0.05–0.1
Wooden boards	Unplaned	0.7
	Planed	0.2
Brickwork	Normal bonds	1.3
Plastic tubes		$\leq$ 0.0015

Figures 5–13 are valid for air at 50°C in steel pipes of standard diameters. The relevant drag coefficients are obtained from Fig. 2. These diagrams can also be applied to obtain approximations for any other gas, provided that any changes in the Reynolds number have only a slight effect on ζ. No allowance has been made for inlet and outlet losses. The approximate transition from laminar to turbulent flow, as determined from (Eq. 10), is indicated in the diagrams.

Values submitted as a guide in estimating the velocity w of various media in tubes are listed in Table 2.

However, the optimum velocity in any particular case must be determined by a profitability study, in which the peculiarities of the entire process may frequently prove to be the deciding factor.

1.4 Coils

As is evident from Fig. 14, the geometry of a coil can be described by the inner diameter d_i of the tube that has been wound into the form of a coil, the average diameter D_w of the winding, and the pitch h.

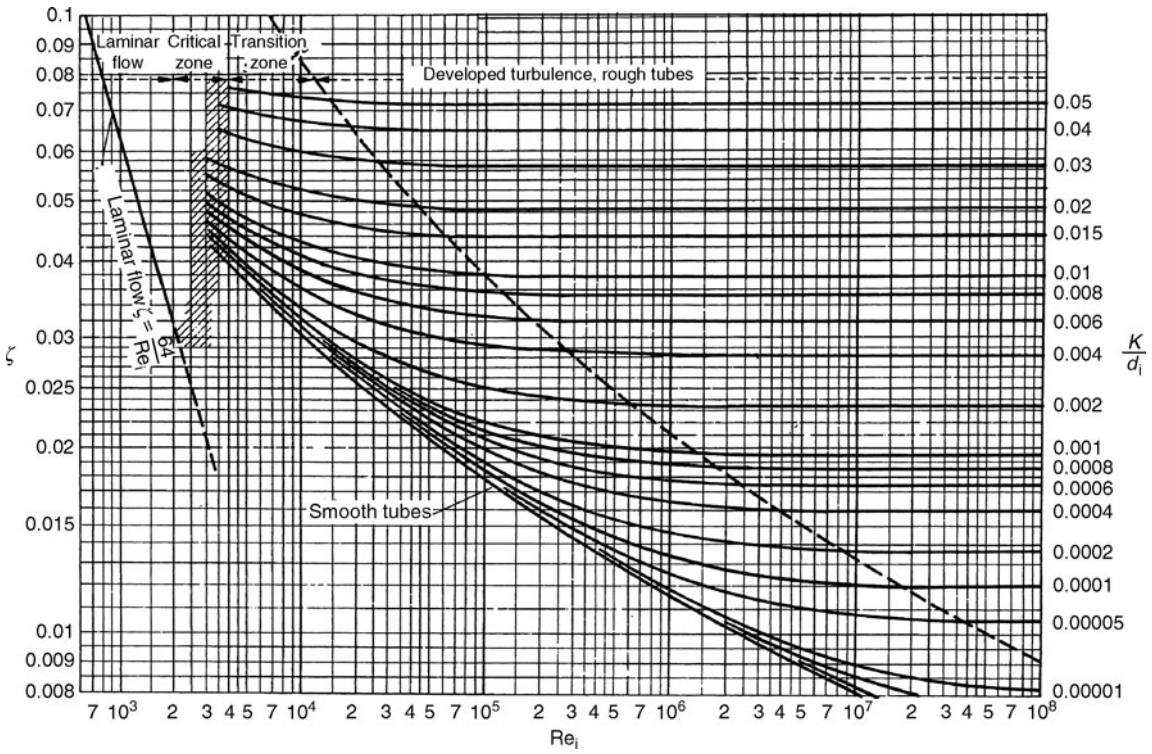

L1.2. Fig. 1. Drag coefficient ζ for rough tubes as a function of the roughness K/d_1 and the Reynolds number Re_i.

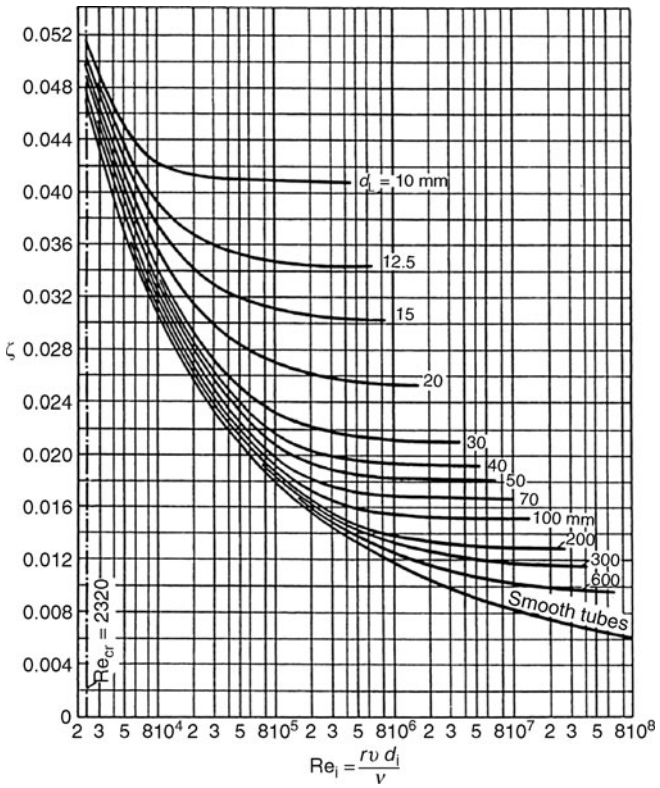

L1.2. Fig. 2. Drag coefficient ζ for freshly drawn steel tubes. Compiled by Hausen [9] from experimental values submitted by various research workers.

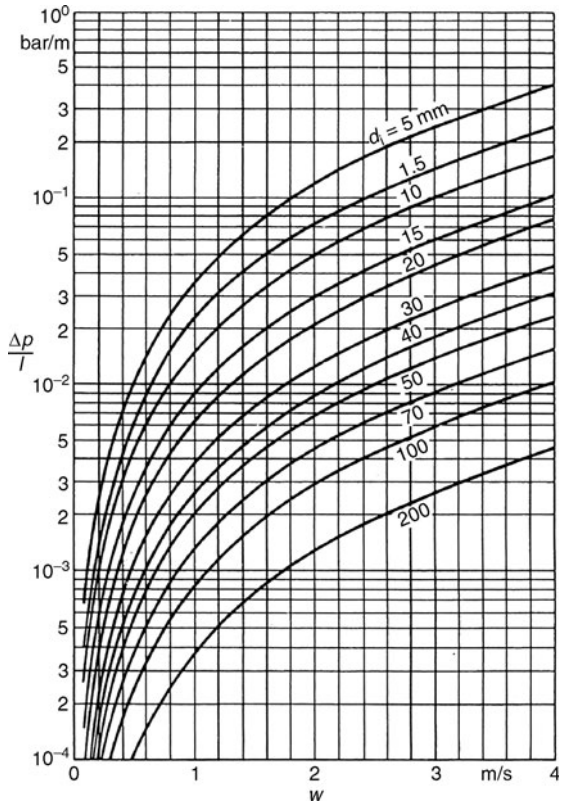

L1.2. Fig. 3. Pressure drop for water at 25°C in smooth tubes, e.g., brass, copper, or glass.

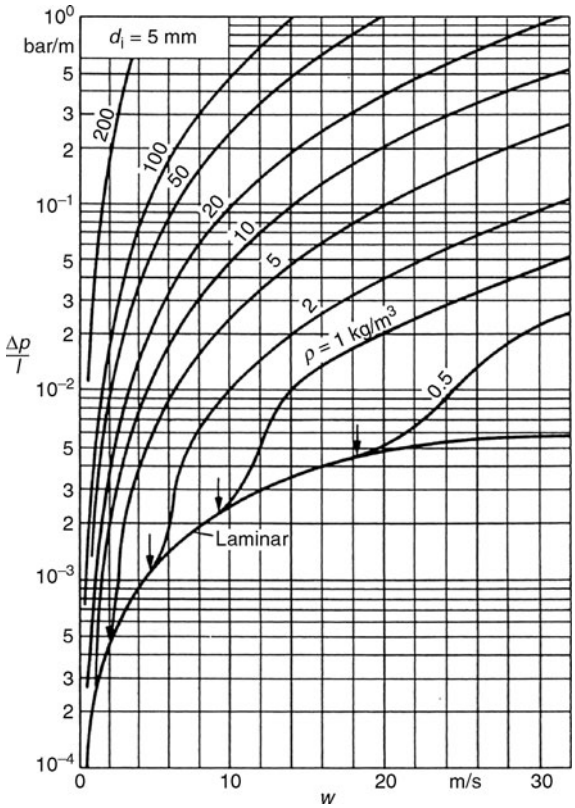

L1.2. Fig. 5. Pressure drop for air flow at 50°C in drawn steel tubes (d_i = 5 mm).

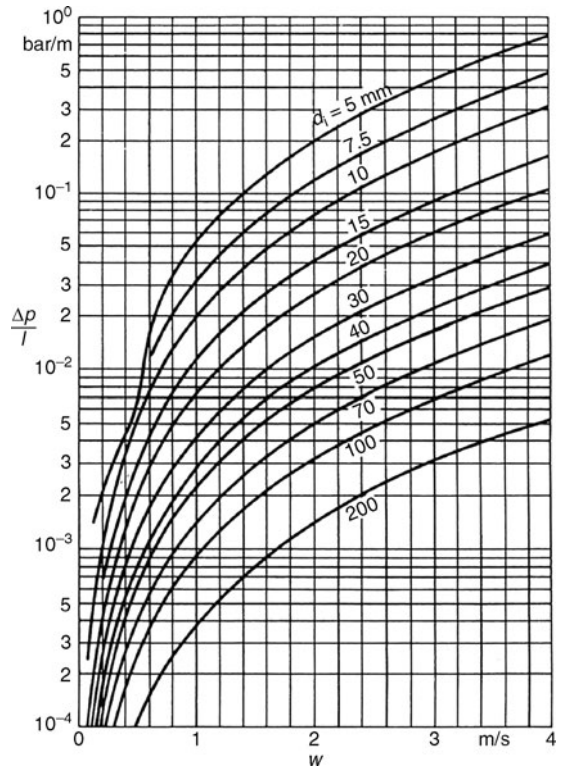

L1.2. Fig. 4. Pressure drop for water at 25°C in drawn steel tube.

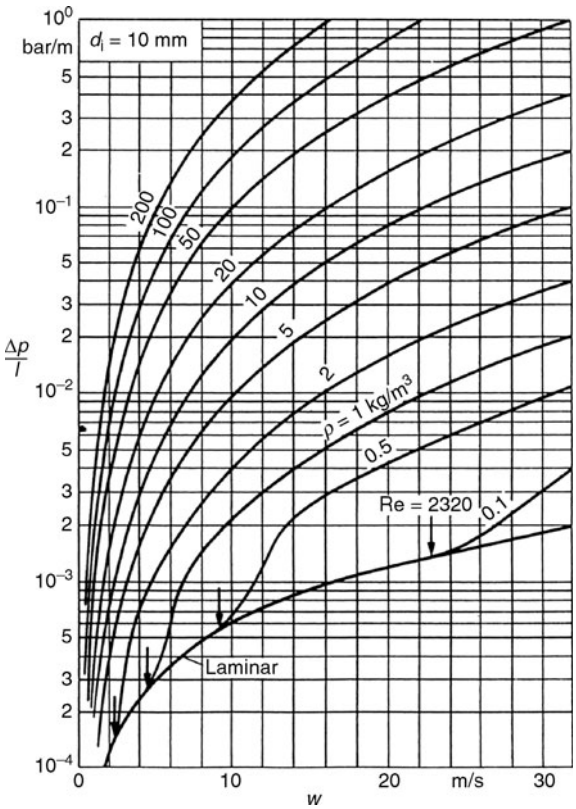

L1.2. Fig. 6. Pressure drop for air flow at 50°C in drawn steel tubes (d_i = 10 mm).

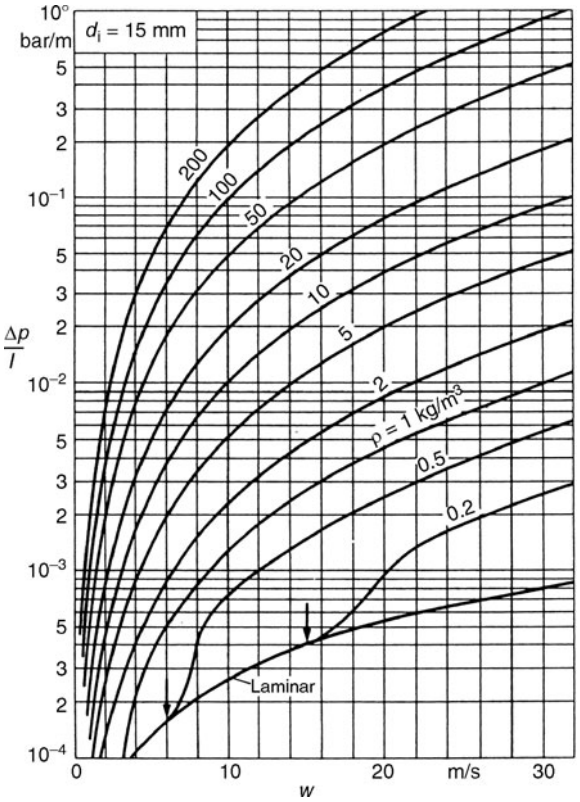

L1.2. Fig. 7. Pressure drop for air flow at 50 °C in drawn steel tubes (d_i = 15 mm).

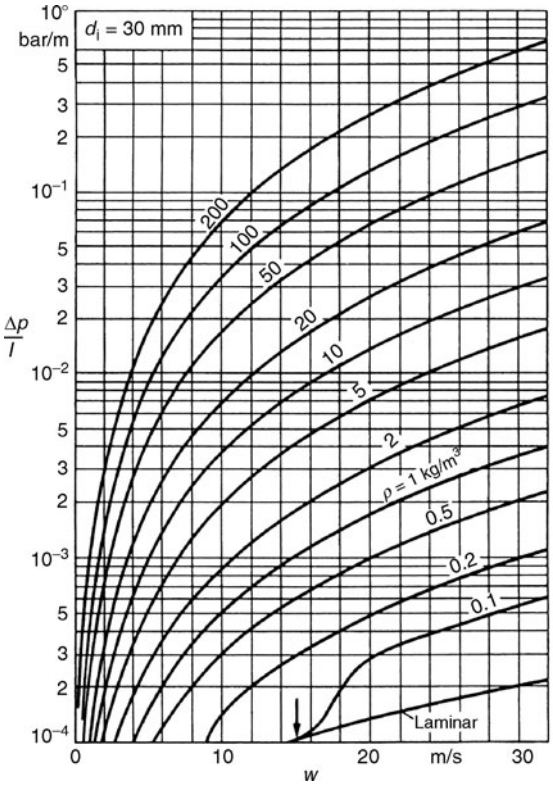

L1.2. Fig. 9. Pressure drop for air flow at 50°C in drawn steel tubes (d_i = 30 mm).

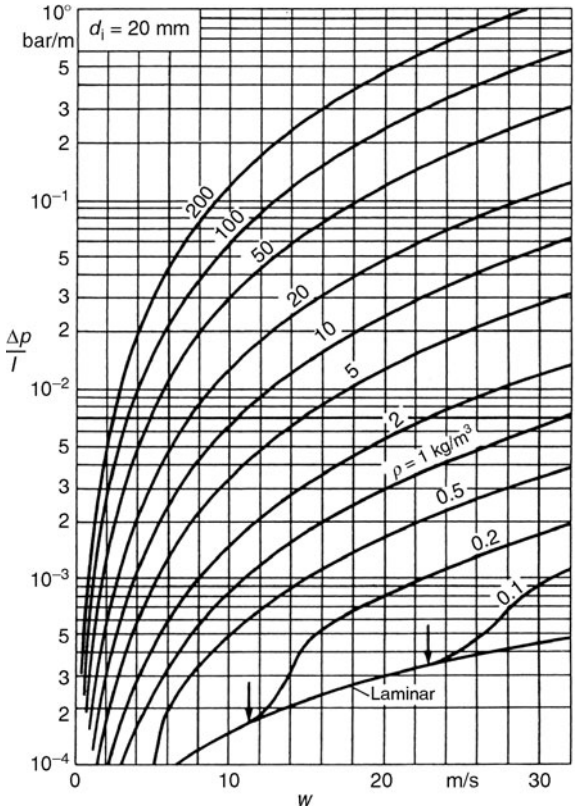

L1.2. Fig. 8. Pressure drop for air flow at 50 °C in drawn steel tubes (d_i = 20 mm).

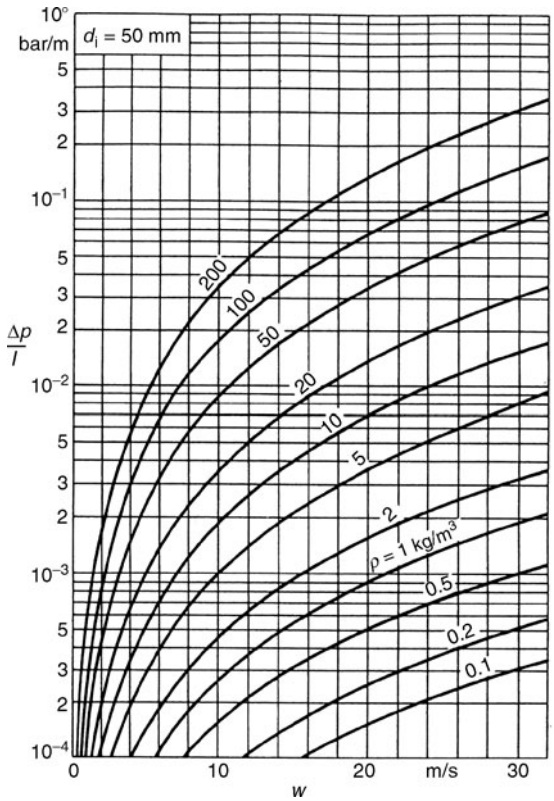

L1.2. Fig. 10. Pressure drop for air flow at 50°C in drawn steel tubes (d_i = 50 mm).

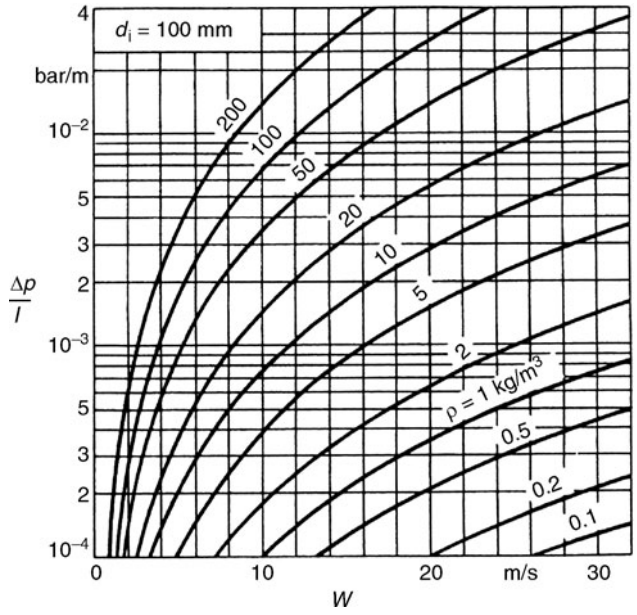

L1.2. Fig. 11. Pressure drop for air flow at 50°C in drawn steel tubes (d_i = 100 mm).

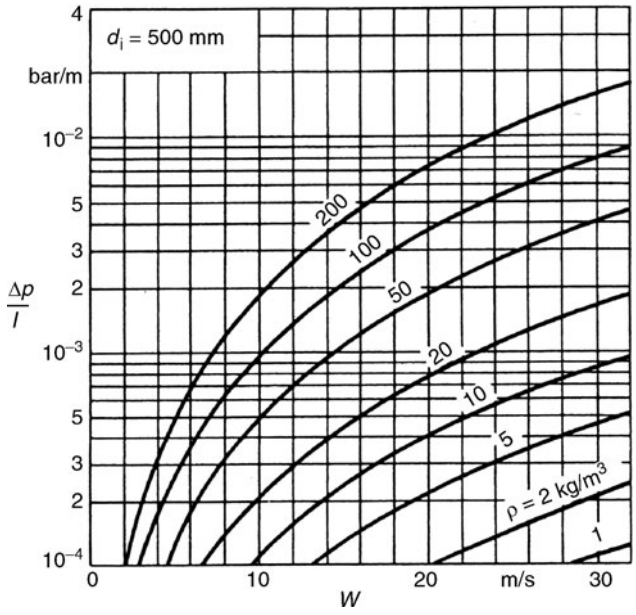

L1.2. Fig. 13. Pressure drop for air flow at 50°C in drawn steel tubes (d_i = 500 mm).

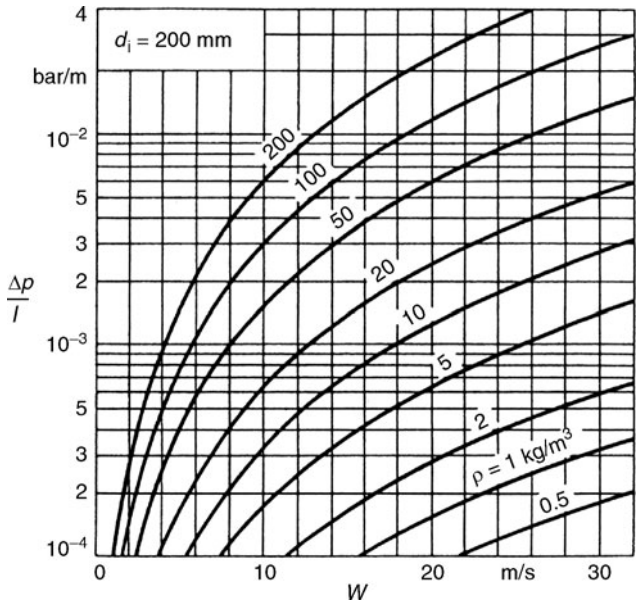

L1.2. Fig. 12. Pressure drop for air flow at 50°C in drawn steel tubes (d_i = 200 mm).

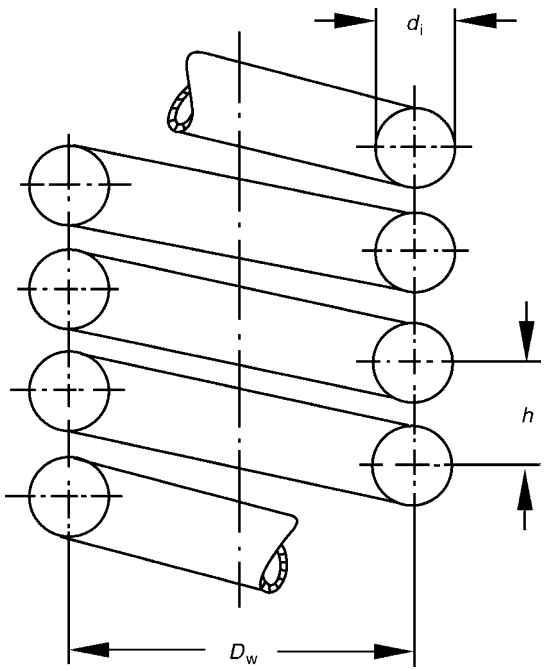

L1.2. Fig. 14. Geometry of a coil.

Owing to the tube's curvature, centrifugal forces are initiated during flow and give rise to a secondary current in the form of a double vortex. The pressure drop is thus greater than that in a straight tube and, in analogy to (Eq. 1), is given by

$$\Delta p = \zeta_w \frac{l}{d_i} \frac{\rho w_i^2}{2} \qquad (1a)$$

where l is the length of the coiled tube.

The drag coefficient ζ_w defined by this equation depends on the Reynolds number Re_i, as given by (Eq. 2), and on the d_i/D ratio, where D is the average diameter of curvature of the coil and is obtained from

$$D = D_w \left[1 + \left(\frac{h}{\pi D_w}\right)^2\right].$$

Significant differences between D and D_w exist only if the tubes are strongly bent and the pitch h of the coils is large. If $h < D_w$, it can be safely assumed that $D = D_w$ in the determination of pressure drop.

Gnielinski [10] compared the measured values determined by many research workers and came to the conclusion that the drag coefficients in isothermal laminar and isothermal

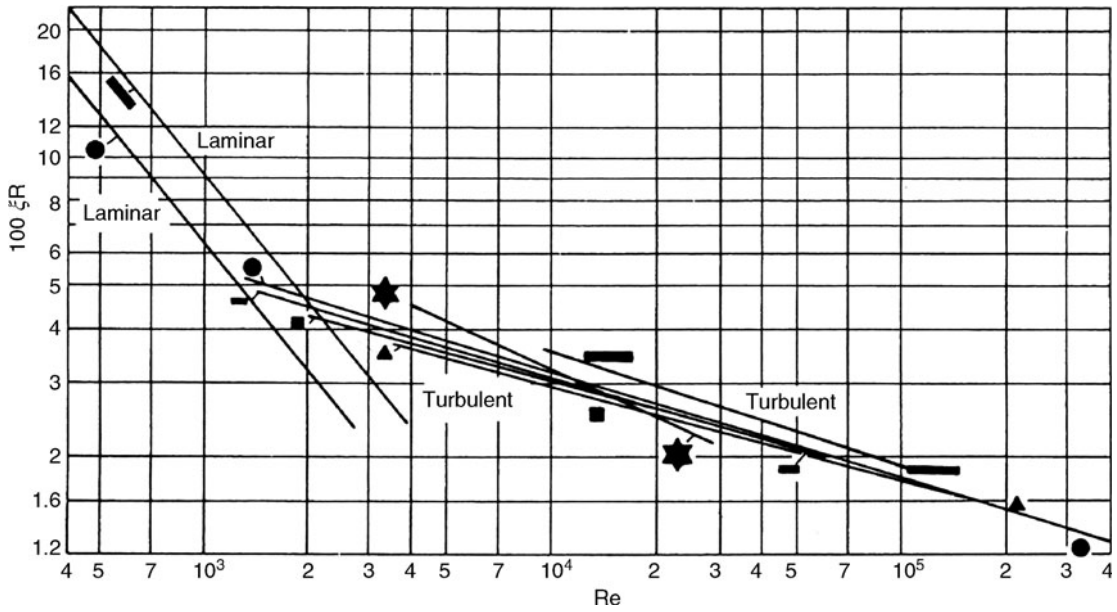

L1.2. Fig. 15. Drag coefficient for flow in smooth straight tubes of various cross-sections (Schiller [13]).

L1.2. Table 2. Velocities of various media in tubes

Oil	In oil lines	*w* in m/s
		1–2
Water	In lines of some length	0.5–1
	In heat exchanger tubes	1–3
	Downstream from reciprocating pumps	1–2
	Downstream from centrifugal pumps	1.5–3
	Upstream from turbines	2–7
Gases	At low pressures	5–30
	At moderate pressures	5–20
	At high pressures	3–6
Compressed air	In ducts	2–4
Steam	1–10 bar	15–20
	10–40 bar	20–40
	40–125 bar	30–60

turbulent flow could be calculated from the Mishra and Gupta [11] equations. That for laminar flow in the $1 < \{\mathrm{Re_i}\sqrt{d_i/D}\} < \{\mathrm{Re_{i,crit}}\sqrt{d_i/D}\}$ range is

$$\zeta_w = \frac{64}{\mathrm{Re_i}}\left[1 + 0.033\left(\log_{10}\left\{\mathrm{Re_i}\sqrt{\frac{d_i}{D}}\right\}\right)^{4.0}\right] \qquad (11)$$

The corresponding equation for turbulent flow in the $\mathrm{Re_{i,crit}} < \mathrm{Re_i} < 10^5$ range is

$$\zeta_w = \frac{0.3164}{\mathrm{Re_i^{0.25}}}\left[1 + 0.095\left(\frac{d_i}{D}\right)^{1/2}\mathrm{Re_i^{1/4}}\right] \qquad (12)$$

As the curvature ratio d_i/D increases, the transition from laminar to turbulent flow is shifted in the direction of higher Reynolds numbers. It would appear that flow disturbances are initially attenuated by the secondary stream and do not effect a transition to turbulence until the flow velocity reaches a certain high value that depends on the curvature.

An equation suggested by Schmidt [12] is valid for the critical Reynolds number:

$$\mathrm{Re_{i,crit}} = 2300\left[1 + 8.6\left(\frac{d_i}{D}\right)^{0.45}\right].$$

Equations (11) and (12) may not be applied to short bends because the energy consumption is increased at the start of the bend as a result of the cross-currents formed and the attendant complete rearrangement of the velocity profile. Consequently, the drag coefficient for a 90° bend is much higher than the figure calculated from these equations.

2 Pressure Drop in Flow Through Pipes of Noncircular Cross-section

2.1 Turbulent Flow

According to Schiller [13] and Fromm [14], the hydraulic diameter d_h allows (Eq. 5) to be applied for any given cross-section. It is given by

$$d_h = 4A/U \qquad (13)$$

where A is the cross-sectional area and U is the length of the participating periphery.

A plot of the drag coefficient ζ against Reynolds number Re for pipes of various cross-sections is reproduced in Fig. 15, and the relationship for flow through an annulus is shown in Fig. 16. Gnielinski [16] gives an equation for the drag

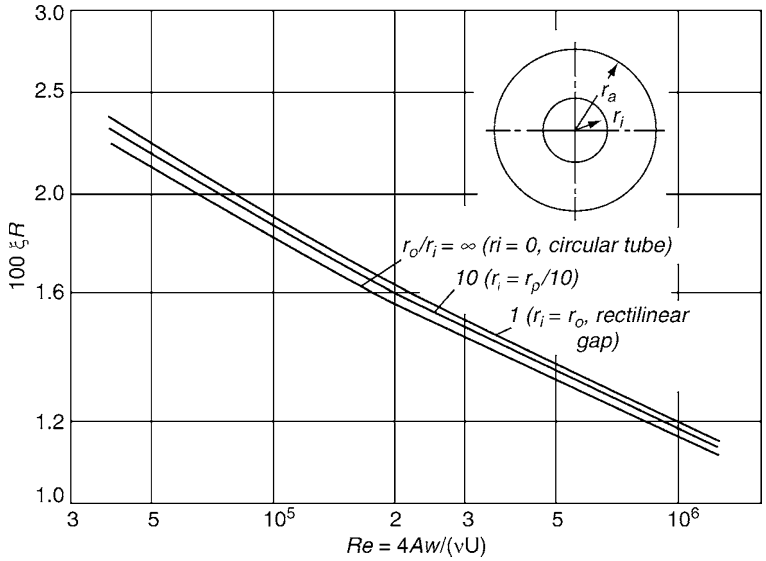

L1.2. Fig. 16. Drag coefficient for flow in the annulus of smooth concentric tubes of various diameters (Tiedt [15]).

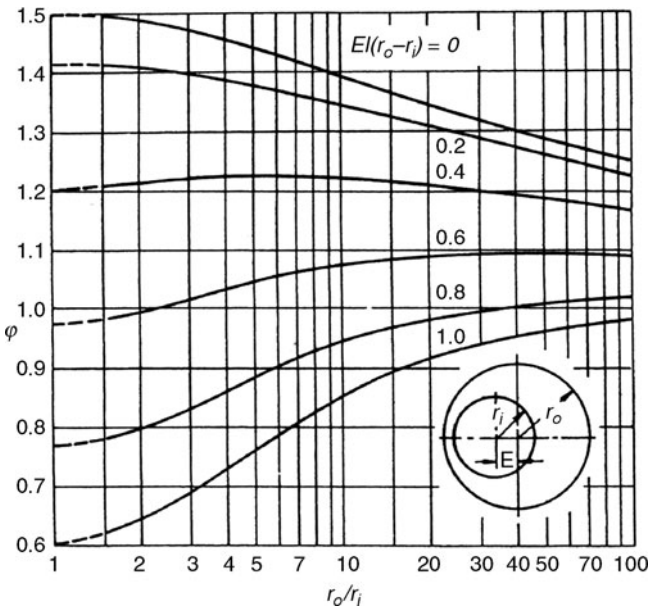

L1.2. Fig. 17. Relationship between φ and r_o/r_i for laminar flow in the annulus of concentric $\{E/(r_o - r_i) = 0\}$ and excentric $\{E/(r_o - r_i) > 0\}$ tubes. $\varphi = 1.0$ for $r_o/r_i = \infty$.

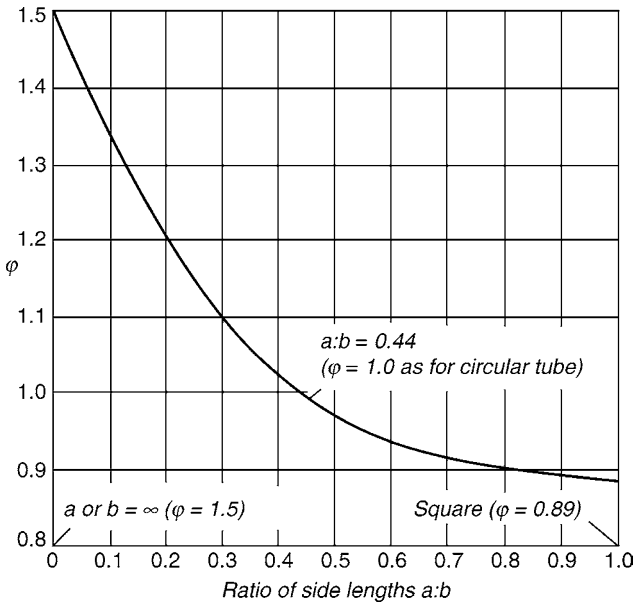

L1.2. Fig. 18. Factor φ for laminar flow in tubes of rectangular cross-section.

coefficient depending on Reynolds number for an annulus $\zeta = (1,8 \log \mathrm{Re}^* - 1,5)^{-2}$ with the Reynolds number Re^* modified with the diameter ratio which is arbitrary. For details see [16].

2.2 Laminar Flow

For the determination of the drag coefficient in laminar flow, a factor φ, which depends on the geometry of the cross-section, is introduced into (Eq. 4), that is,

$$\zeta = \varphi \frac{64}{\mathrm{Re}} = \varphi \frac{16\nu U}{wA} \tag{14}$$

It can be obtained from Figs. 17 and 18. For an annulus $\zeta = \frac{64}{\mathrm{Re}^*}$. For details see again [16].

For references, see Subchap. L1.1.

L1.3 Pressure Drop in Flow Through Pipes of Changing Cross-section

Werner Kast[2] (*Revised by Hermann Nirschl*[1])
[1]Karlsruher Institut für Technologie (KIT), Karlsruhe, Germany
[2]Technische Universität Darmstadt, Darmstadt, Germany

1 Abrupt Restrictions in Cross-section

Flow into a sudden restriction or from the head of a heat exchanger into tube bundle entails the following pressure drop in addition to the Bernoulli equation:

$$\Delta p = \zeta_{in} \frac{\rho w_i^2}{2}. \quad (1)$$

The additional pressure drop is caused by the vena contracta at the inlet and by the vortices that attenuate after a length of about 8 d_i to 10 d_i has been traversed in the tube. According to Stephan [17], a much longer attenuation path l_A has to be traversed before the final smooth flow profile is attained. Thus, if flow is laminar,

$$l_A \approx 0.13 \mathrm{Re}_i d_i. \quad (2)$$

If flow is turbulent,

$$l_A \approx 0.0575 \mathrm{Re}_i d_i. \quad (3)$$

Initially, the flow velocity is the same over the entire cross-section. Within the length l_A, it is decreased at the tube walls owing to the deceleration caused by increased friction and the kinetic (shear) energy required to establish the flow profile. Thus, the pressure drop is greater than the linear values obtained from Eqs. (1) and (3) on Subchap. L1.2.

All these effects are embraced by the term ζ_{in}.

If the fluid mass at the tube inlet is stationary or flows at a very low velocity, energy must be applied to accelerate it to the average velocity w_i, and the entire pressure drop is

$$\Delta p = (\zeta_{in} + 1) \frac{\rho w_i^2}{2}. \quad (4)$$

1.1 Narrowed Tubes

According to Kays [18], if the reduction in the diameter of the tube is abrupt as is shown in Fig. 1, ζ_{in} can be obtained from Fig. 2, in which it is shown as a function of the area ratio A_2/A_1 of the two cross-sections with the Reynolds number Re_i as parameter.

1.2 Inflow in Tube Bundles

Studies by Linke [19] have revealed that ζ_{in} depends on the spacing ratio s/d_i in the tube bundle (cf. Fig. 3) if flow is turbulent and Re > 20,000. If flow is laminar, ζ_{in} can be estimated by analogy from Fig. 2. Gnielinski [20] also gives values for ζ on the jacket side of the inlet and outlet ports of a double pipe heat exchanger.

1.3 Outflow from Vessels

It can be seen from Fig. 4, which was drawn up from data compiled by Weisbach, that the drag coefficient ζ_{in} greatly depends on the conditions at the tube inlet.

The values given can be transferred into Fig. 2 by entering them on the $A_2/A_1 = 0$ ordinate and connecting them to the zero ordinate at $A_2/A_1 = 1.0$ by the closest approximation to a straight line.

2 Continuous Reduction in Cross-sectional Area

If the cross-section is continuously reduced as is illustrated in Fig. 5, the stream of liquid in the jet is not separated provided that $\alpha < 40°$. The pressure drop is very low and of the order of

$$\Delta p = 0.04 \frac{\rho w_2^2}{2}. \tag{5}$$

Hence, almost the entire pressure is converted into kinetic energy in convergent tubes.

As the angle α increases, the case approaches that of an abrupt transition, in which the pressure drop is substantially greater. Long conical nipples are supplied for small angles α. In this case, the additional length must be calculated, for example, to obtain the average values for A and w.

If the inner surfaces of the tube are smooth and the Reynolds numbers are high, a factor of even less than 0.04 may be inserted in (Eq. 5).

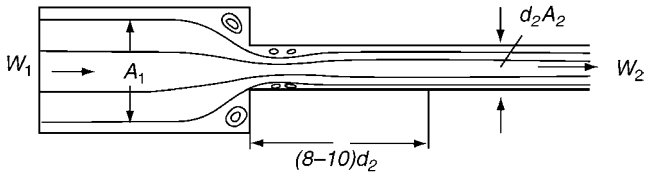

L1.3. Fig. 1. Abrupt reduction in tube diameter.

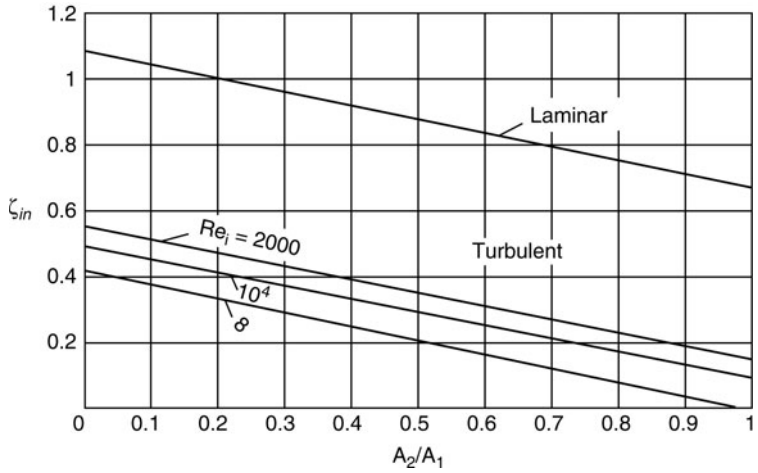

L1.3. Fig. 2. Drag coefficient ζ_{in} for the inlet pressure drop at an abrupt reduction in tube diameter.

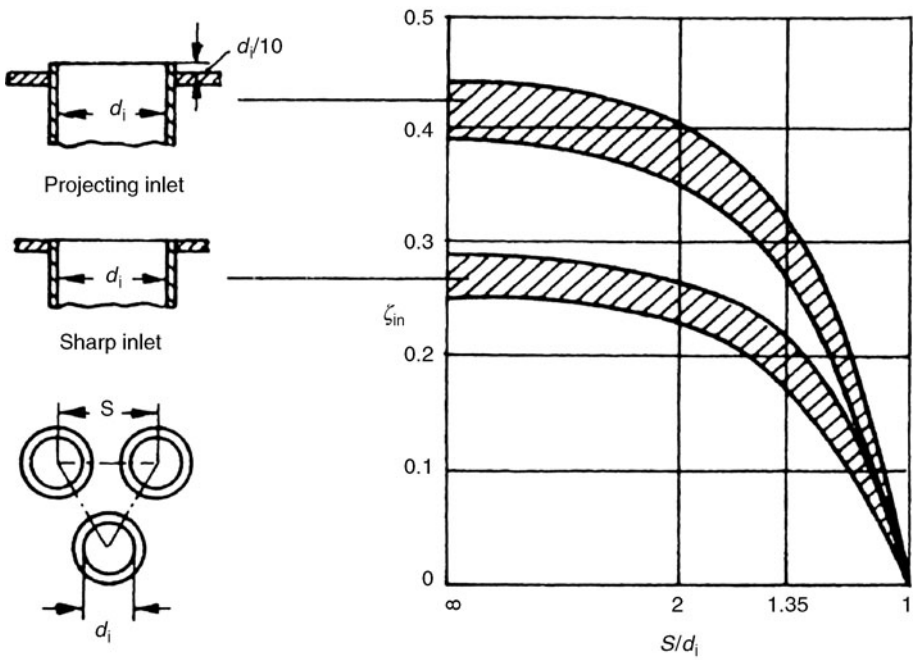

L1.3. Fig. 3. Drag coefficient ζ_{in} for tube bundle inlets when the tubes have sharp edges.

Angular inlet	Very sharp Normal chamfer	$\zeta_{in} = 0.5$ $\zeta_{in} = 0.25$	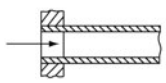
Widely projecting angular inlet	Very sharp Normal chamfer	$\zeta_{in} = 3$ $\zeta_{in} = 0.56$	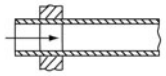
Rounded inlet	Depending on Smoothness Normal	$\zeta_{in} = 0.005$ ζ_{in} up to 0.06 $\zeta_{in} = 0.05$	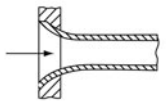
Angular inlet inclined at angle δ	$\zeta_{in} = 0.5 + 0.3 \cos \delta + 0.2 \cos^2 \delta$		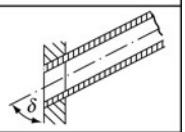

L1.3. Fig. 4. Drag coefficient ζ_{in} for outflow from vessels containing a stationary liquid.

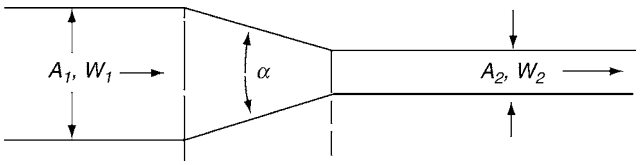

L1.3. Fig. 5. Continuous reduction in cross-sectional area.

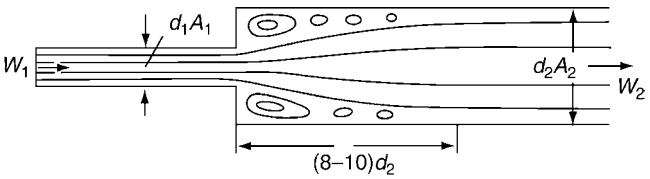

L1.3. Fig. 6. Sudden widening of cross-section.

3 Abrupt Widening of Cross-section

Figure 6 illustrates the flow of a liquid from a tube into a wide space, for example, the head of a heat exchanger or into a broader tube. An expanding jet with pronounced turbulence is thus formed. After it has traversed a length of 8 d_2 to 10 d_2, it is again accommodated against the walls of the tube. This outlet pressure drop is given by

$$\Delta p = (1 - A_1/A_2)^2 \cdot \frac{\rho w_i^2}{2}. \qquad (6)$$

where w_i is the velocity and ρ the density of the liquid in the tube. (Equation 6) is valid for turbulent flow. A correlation for the corresponding pressure drop in laminar flow has been established by Kays [18].

4 Continuous Widening of Cross-section

In continuously expanded tubes, as illustrated in Fig. 7, wall friction and turbulence do not permit ideal conversion of kinetic into pressure energy in accordance with the Bernoulli equation. The pressure drops in this case are given by

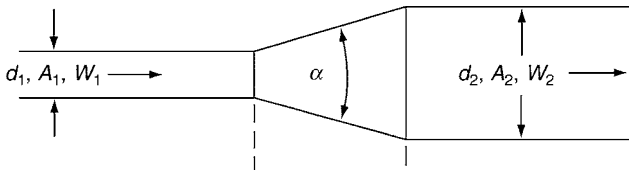

L1.3. Fig. 7. Continuous widening of cross-section.

$$\Delta p = \zeta' \left(1 - \frac{A_1}{A_2}\right)^2 \frac{\rho w_i^2}{2}. \qquad (7)$$

$$\Delta p = \zeta' \left(\frac{A_2}{A_1} - 1\right)^2 \frac{\rho w_i^2}{2}. \qquad (8)$$

where ζ' is a drag coefficient that is related to the angle of divergence as is indicated in Fig. 8.

The minimum pressure drop occurs at low angles, which depend as follows on the degree of turbulence:

Re	0.5	1.0	1.5	2.0	10^5
α	10	8.4	7.6	7.1	°

At even higher Reynolds numbers, the angle must be reduced to 5–6°. Another factor to observe is the roughness of the walls. For instance, the preferred angle for smooth walls ($K = 0.02$) is 7°; and for rough surfaces ($K = 0.04$), 9°.

5 Orifice, Nozzle, and Venturi meters

A schematic diagram illustrating flow through an orifice meter is presented in Fig. 9. The pressure drop is less than the differential pressure that can be read off on the gauge, because a large proportion of the kinetic energy is reconverted into pressure energy. The remaining pressure drop is given by

$$\Delta p = b(p_i' - p_2'),$$

where $p'_1 - p'_2$ in N/mm^2 is the differential pressure recorded on the instrument; b is a correction factor for orifice, nozzle, and

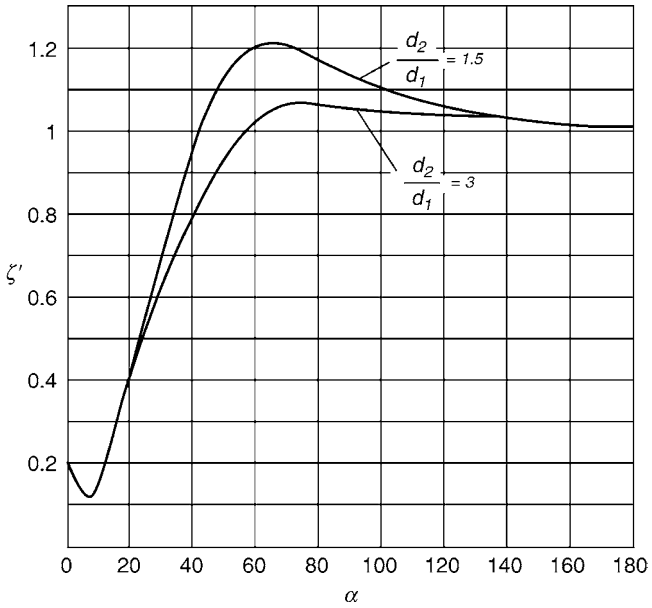

L1.3. Fig. 8. Drag coefficient ζ for expanded sections of tubes as a function of the angle of divergence and the tube diameter ratio d_2/d_1.

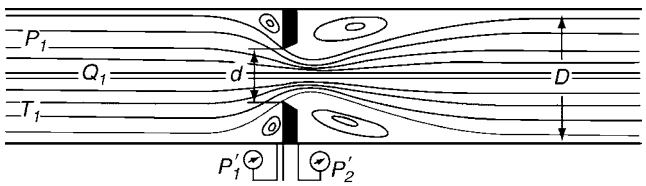

L1.3. Fig. 9. Flow through an orifice meter.

venturi meters and can be obtained from Fig. 10, in which it is shown as a function of the diameter ratio $m = (d/D)^2$.

6 Tees and Oblique Junctions

The drag coefficients that occur in the following are valid for turbulent flow and can be regarded as being independent of Re_i. Laminar flow is rarely encountered in practice, and does not set in until $Re_i < 1{,}000$. The values for ζ increase considerably with a decrease in Re_i. (Equations 1–3) apply to the additional pressure drop caused by impact and vortices during demixing and mixing. Consequently, the frictional resistance in the tubes must be calculated up to the intersect of the tee-axes. If w_z is the velocity of the entire stream G_z, the pressure drop in the branch G_a will be given by (Eq. 9), and in the branch G_d, by (Eq. 10):

$$\Delta p_a = \zeta_a \frac{\rho w_z^2}{2}. \tag{9}$$

$$\Delta p_d = \zeta_d \frac{\rho w_z^2}{2}. \tag{10}$$

The drag coefficients ζ_a and ζ_d are presented in Figs. 11 and 12. They are valid for tubes of circular cross-section, branches of the same diameter as that of the header, and junctions with sharp edges. If the edges are rounded off, the coefficients become

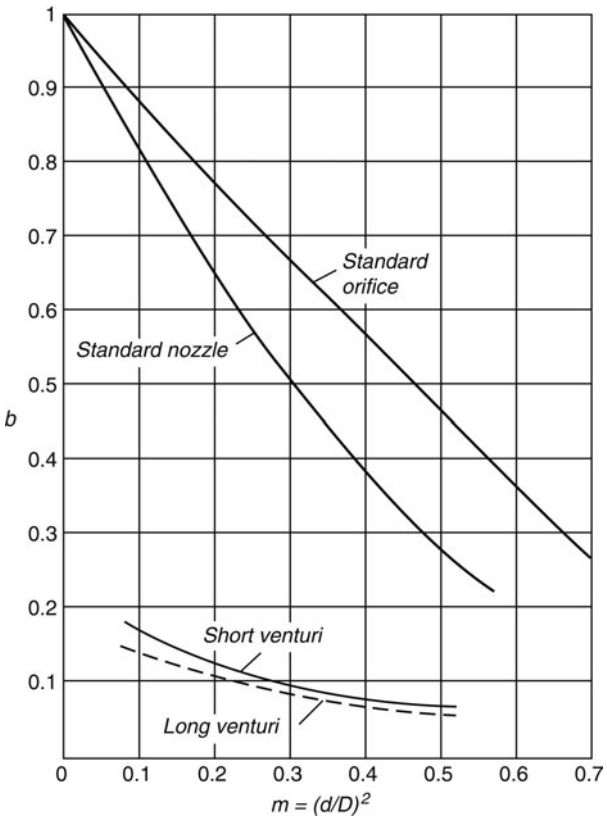

L1.3. Fig. 10. Correction factor b for the determination of the remaining pressure drop at orifice, nozzles, and venturis.

somewhat smaller. The reduction may be about 10–30% if the radius of curvature is large, that is, $r = 0.1\ d_a$. Values for junctions at different angles can be obtained by interpolation.

For a flow into a junction in which the one branch has been blanked off, the effect of the angle between the branch and the header and the diameter ratio $m = (d_1/d_2)^2$ is shown in Fig. 13.

Values for the pressure drop on Y-junctions and tees of the types illustrated in Figs. 11, 12, and 14 can be represented by

$$\Delta p = \zeta_v \frac{\rho w_v^2}{2}. \tag{11}$$

where w_v is the velocity in the limbs.

The sum of the cross-sectional areas of the two limbs in the relevant experiments was 1.1 times the cross-sectional area of the header, and the edges were slightly rounded. In the one case, each of the convergent or divergent streams accounted for one half of the flow rate. In the other case, one limb was blanked off, and the entire stream flowed into or out of the other.

Drag coefficients for tees and Y-junctions are listed in Table 1.

7 Changes in the Direction of Flow

Pressure drops additional to those caused by wall friction occur as a result of flow separation and cross-currents when flow is diverted through bends. They are given by

$$\Delta p = \zeta_b \frac{\rho w^2}{2}.$$

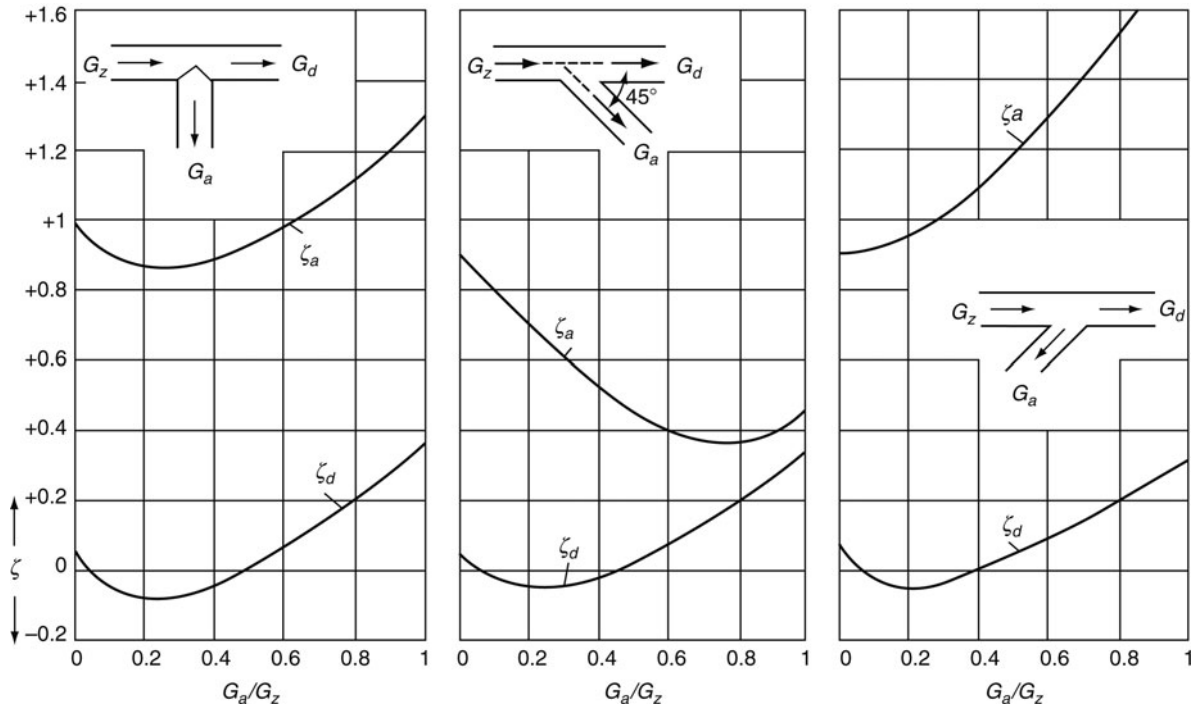

L1.3. Fig. 11. Flow divergence – drag coefficients ζ_a and ζ_d as functions of the flow rate ratio G_a/G_z.

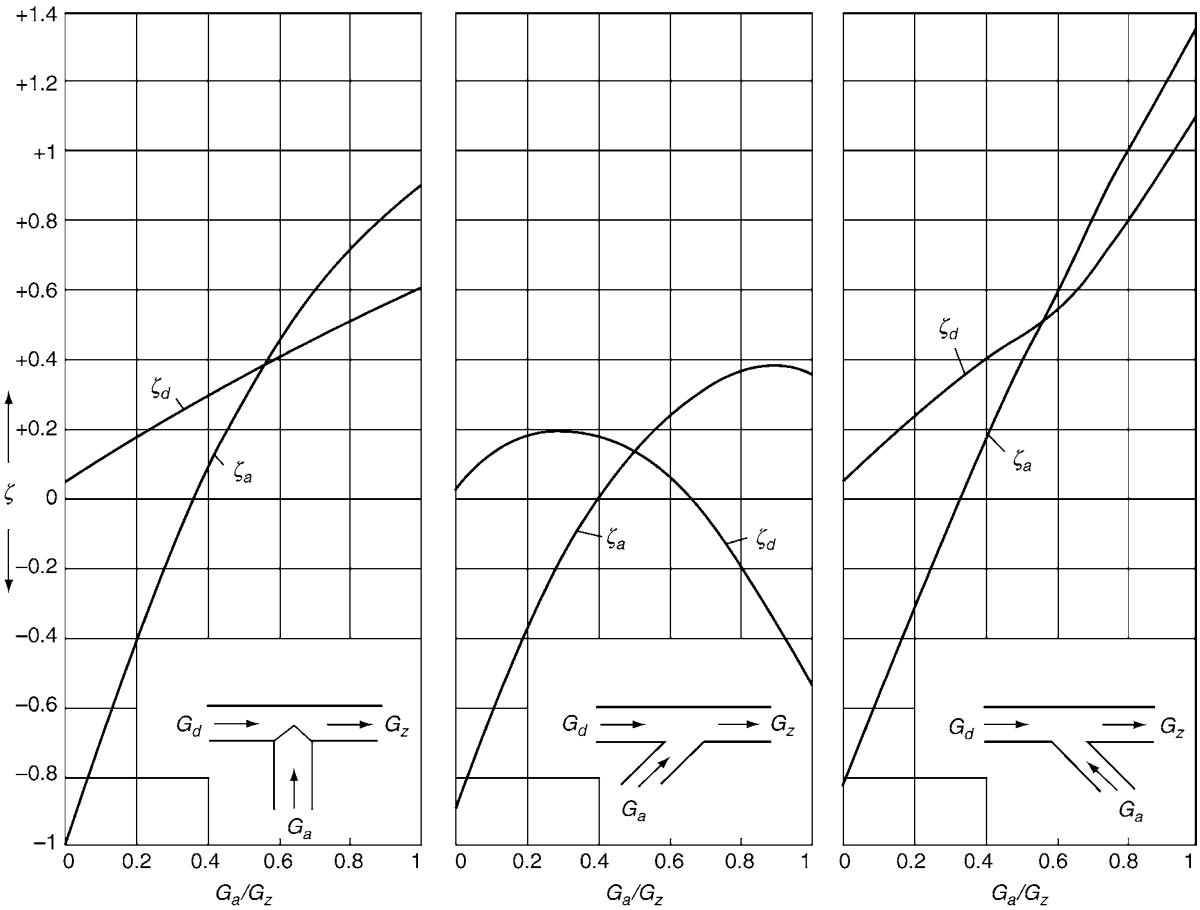

L1.3. Fig. 12. Flow convergence – drag coefficients ζ_a and ζ_d as functions of the flow rate ratio G_a/G_z.

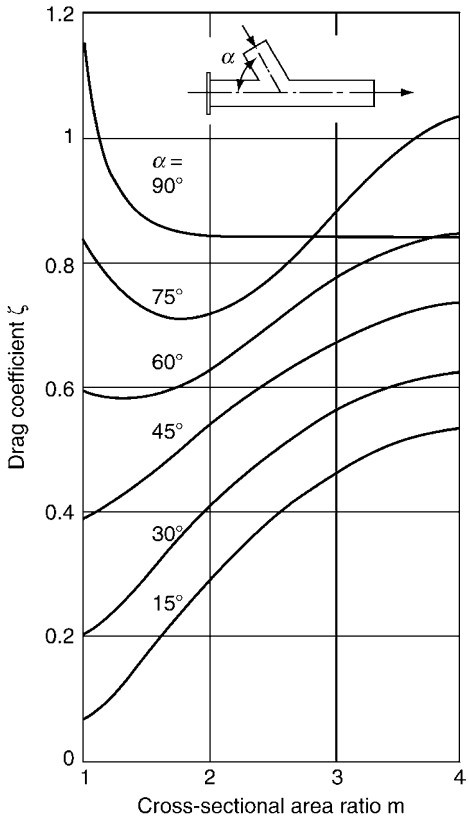

L1.3. Fig. 13. Drag coefficient ζ_a for flow into a tee with a blind flange on the one branch.

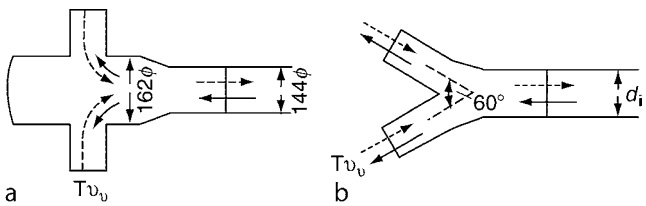

L1.3. Fig. 14. Tee (**a**) and Y-piece (**b**) for divergent and convergent flow. — divergent flow; ––– convergent flow.

L1.3. Table 1. Drag coefficients for tees and Y-junctions

		Values of ζ_v for symmetrical	
		Divergence	Convergence
Y-junction	d_i = 350 mm	0.067	0.17
	d_i = 140 mm	0.035	0.08
Tee	d_i = 144/162 mm	2.87	1.56
		Values of ζ_v for lateral	
		Outflow	Inflow
Y-junction	d_i = 350 mm	0.19	0.24
	d_i = 140 mm	0.25	0.24
Tee	d_i = 144/162 mm	0.72	0.99

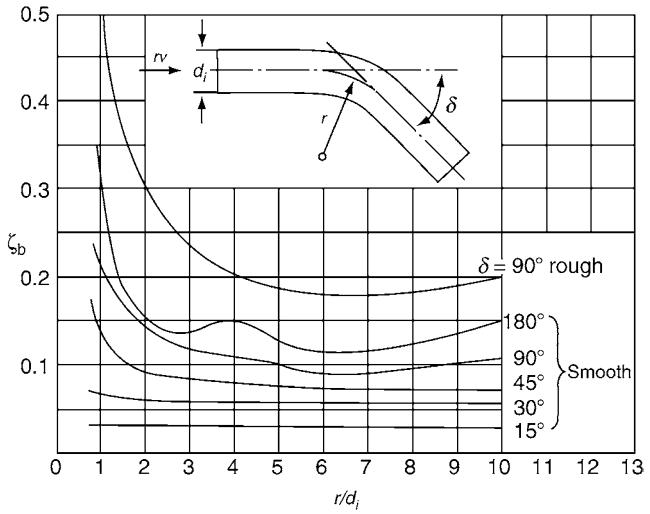

L1.3. Fig. 15. Drag coefficient ζ_b for high Reynolds numbers in bends (Re $> 10^5$).

7.1 Bends

The drag coefficient ζ_b increases with the angle δ through which the stream is diverted. Another major factor is the ratio of the bend radius r to the tube inner diameter d_i. The results obtained for Re $> 10^5$ are shown in Fig. 15.

It is evident form Fig. 16 that the drag coefficient for 90°-bends increases significantly with a decrease in Reynolds number.

The drag coefficient for three-dimensional curvature can be obtained by adding the values of ζ_b for the individual sections of curved pipe, but this applies only if each is separated from the other by a straight tube of more than 10 d_i length. The closer they are spaced, the more confused the flow pattern. However, the total pressure drop is less than that of the sum for the individual curves, as can be seen by comparing the coefficients for 90° and 180° bends in Fig. 17. According to Zimmermann [21], the procedure to adopt for 90° bends connected in series is that illustrated in Fig. 17.

7.2 Bends with Sharp Edges

As a result of the sharp diversion of flow in bends, pronounced turbulence occurs and gives rise to high values for ζ_b.

For water pipes with bolted connections at both ends the following figures for 90° bends are available.

d_i	14	20	25	34	39	49	mm
ζ_b	1.7	1.7	1.3	1.1	1.0	0.83	
	Fillet with sharp edges on the inside; bends rounded on the outside						
ζ_b	1.2	1.1	0.86	0.53	0.42	0.51	
	Bends						

Herning [6] submitted the following for 90° cast iron bends:

d_i	50	100	300	200	400	500	mm
ζ_b	1.3	1.5	1.8	2.1	2.2	2.2	

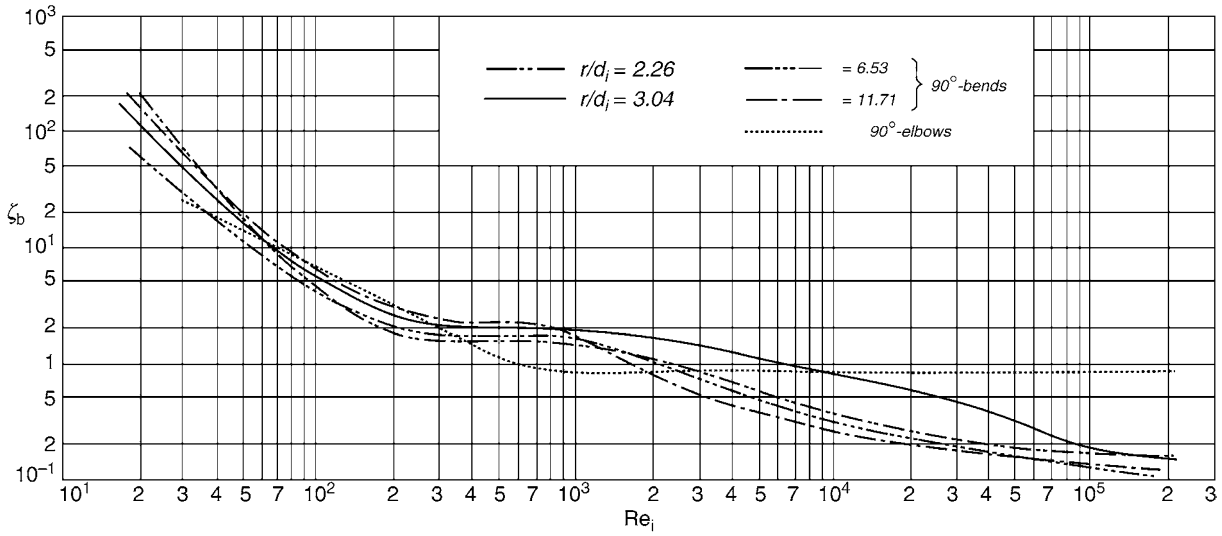

L1.3. Fig. 16. Drag coefficient ζ_b for smooth-walled 90°-bends as a function of Reynolds number Re_i.

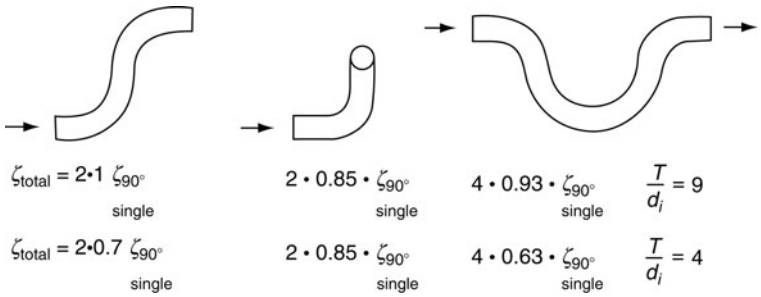

L1.3. Fig. 17. Drag coefficient ζ_b for three-dimensional bends.

7.3 Elbows

Turbulence in elbows is even greater than that in sharp bends, and results in very high values of ζ_b. As can be seen from Fig. 16, these values remain constant over a wide Re_i range ($Re_i > 500$). The effect of the angle δ can be seen in Fig. 18. Drag coefficients ζ_b for segmented bends are smaller than the sum of the values for the individual segments. Relevant figures are presented in Fig. 19, which is reproduced from Richter's [5] compilations of values obtained by Schubart and Kirchbach. A pronounced minimum pressure drop is evident at certain relative elbow spacings a/d.

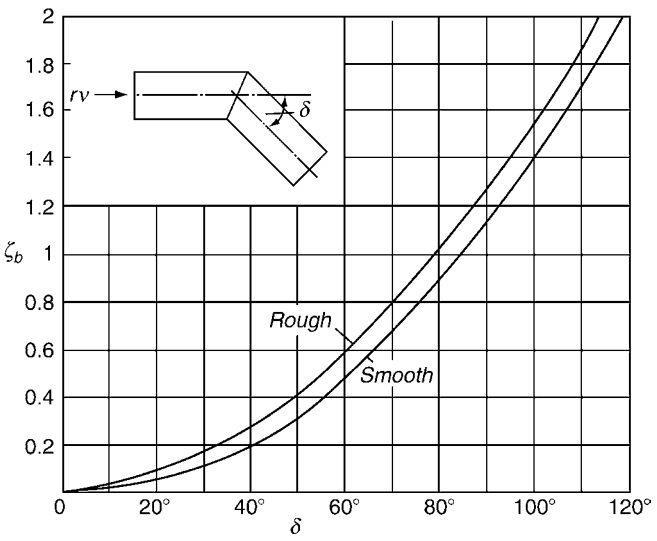

L1.3. Fig. 18. Drag coefficients ζ_b for single elbows as a function of the angle δ.

8 Valves

The pressure drop of valves is given by

$$\Delta p = \zeta_v \frac{\rho w^2}{2}$$

where w is the velocity in the cross-section taken through the rated pipe diameter.

The drag coefficients ζ_v are constant over a wide range of Reynolds numbers, because flow is almost completely turbulent. Laminar flow does not set in until the Reynolds number is less than Re = 100 to Re = 500. The drag coefficients ζ_v increase rapidly with a decrease in Reynolds number. The data that follow can serve merely as a guide because of the great

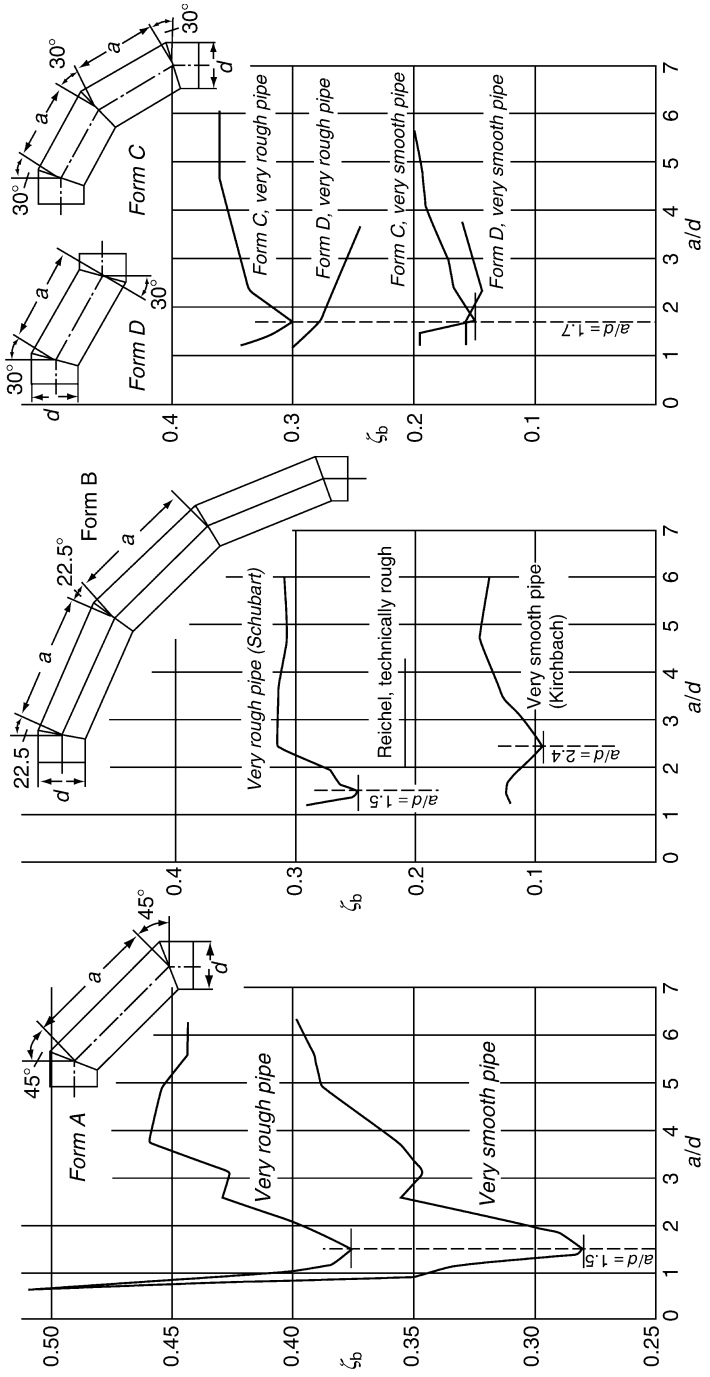

L1.3. Fig. 19. Drag coefficients ζ_b for segmented bends as a function of the a/d ratio.

differences in machining and design that exist between the various types of valves on the market.

8.1 Regulating Valves

The more the changes in the direction of the flow and in the cross-section and the more the projecting edges that give rise to turbulence and eddy currents, the higher the resistance to flow offered by a valve. This is evident from the sketches of well-known types of valves that are reproduced in Fig. 20.

The effect of the diameter differs. The drag coefficient ζ_v for Koswa and full-bore valves decreases as the rated diameter increases; and that for the German Standard DIN valve, which has an unfavorable hydraulic characteristic, becomes somewhat higher. The relationship which was plotted from measurements

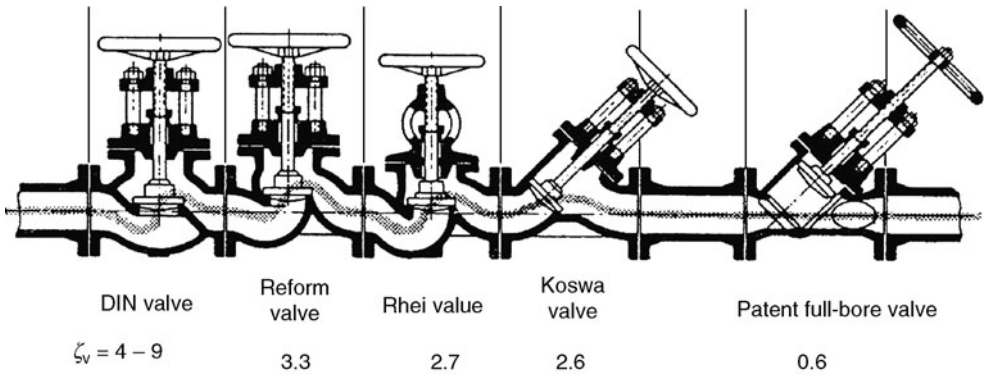

L1.3. Fig. 20. Drag coefficients ζ_v for some types of valves with rated diameters of 100 mm.

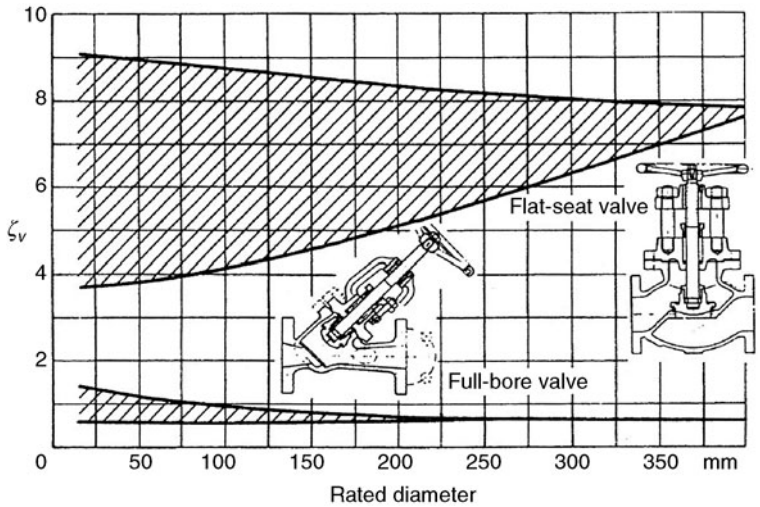

L1.3. Fig. 21. Drag coefficients ζ_v for completely opened regulating valves of various rated diameters.

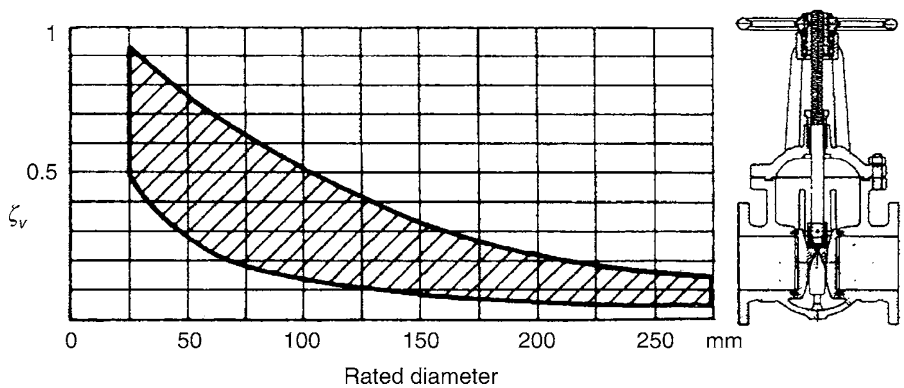

L1.3. Fig. 22. Drag coefficients ζ_v for completely opened double-disc parallel-gate valves with straight passages.

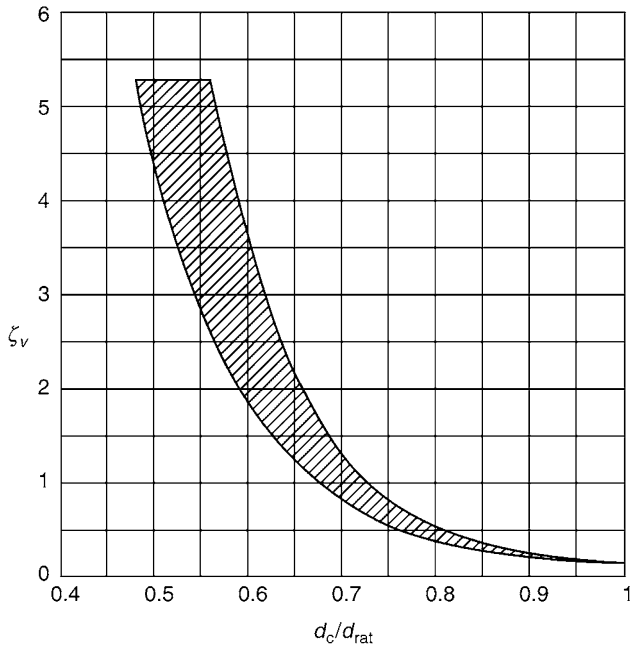

L1.3. Fig. 23. Drag coefficients ζ_v for completely opened gate valves with restriction to flow.

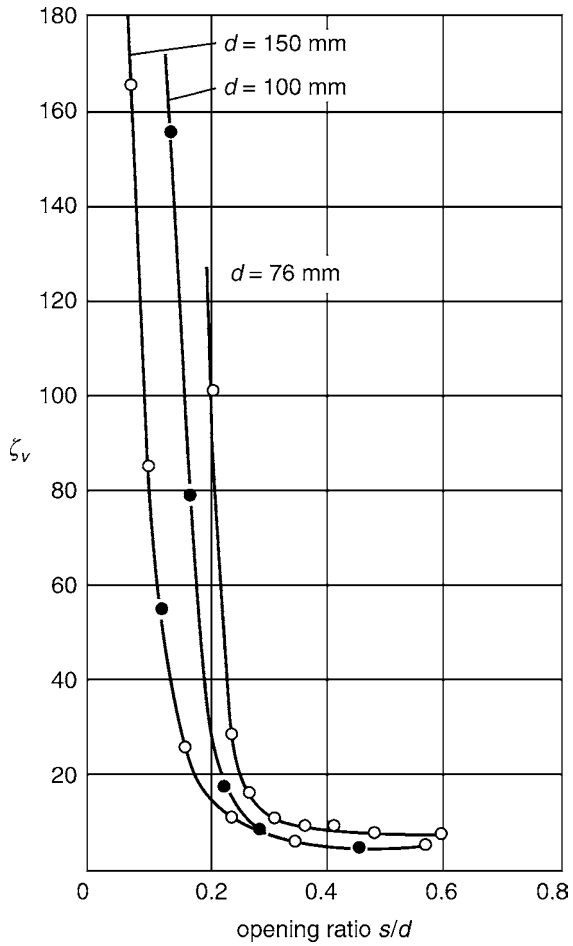

L1.3. Fig. 24. Throttling characteristic for a flat-seat valve of the design illustrated in Fig. 21.

performed by various research workers is shown in Fig. 21. Herning [6] submitted the following values of ζ_v for angle valves:

Rated diameter	50	100	200	300	400	mm
ζ_v	3.3	4.1	5.3	6.2	6.6	

The values for ζ_v published by Richter [3] are somewhat lower, i.e., $2 > \zeta_v > 3$.

8.2 Gate Valves

Double-disc parallel-gate valves are shutoff devices that offer the least resistance to flow. Relevant values of ζ_v, compiled

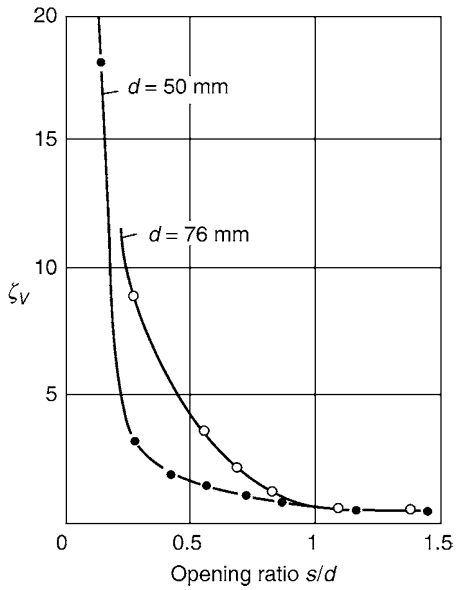

L1.3. Fig. 25. Throttling characteristic for a full-bore valve of the design illustrated in Fig. 21.

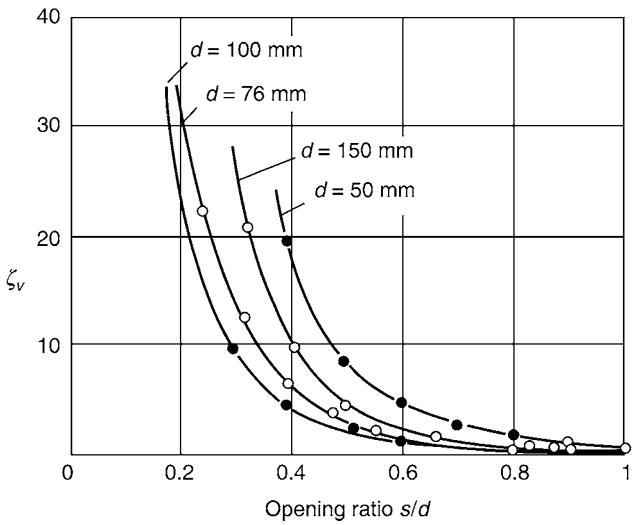

L1.3. Fig. 26. Throttling characteristic for a gate valve of the design illustrated in Fig. 22.

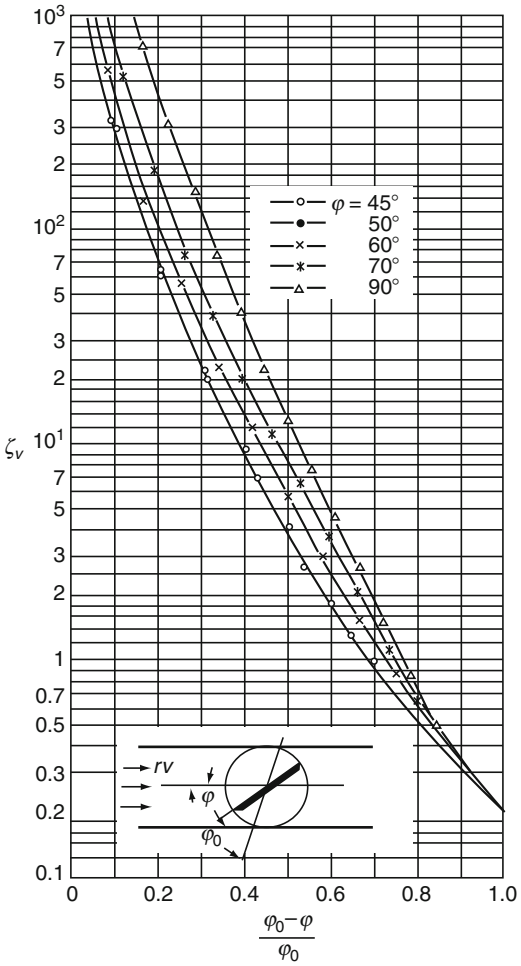

L1.3. Fig. 27. Characteristic for a butterfly valve.

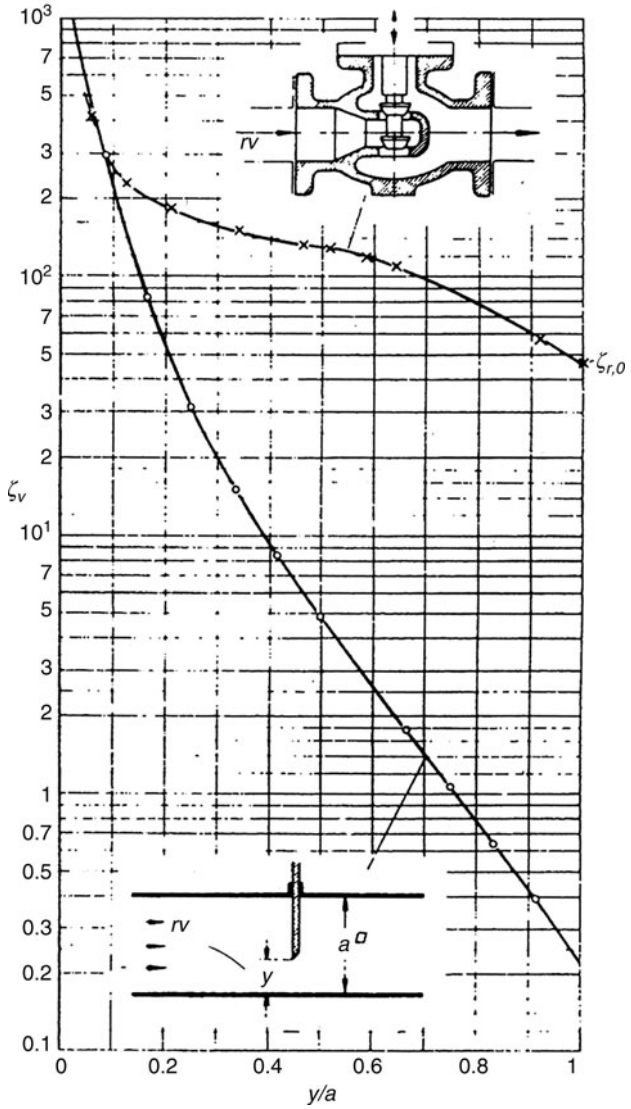

L1.3. Fig. 28. Characteristics for a gate and a control valve.

from measured values, have been plotted in Fig. 22. Those for gate valves with constrictions, for example, pressure-valves, increase rapidly with the constriction ratio d_c/d_{rat}, where d_c is the diameter of the constriction and d_{rat} is the rated diameter. This is demonstrated in Fig. 23, in which the hatched area represents data obtained from the literature and manufacturers' leaflets.

8.3 Throttle Valves and Gates

As a rule, the drag coefficient ζ_v does not increase noticeably until the opening lift s is less than one half. Appropriate curves are reproduced in Figs. 24–26.

8.4 Cocks

ζ_v for cocks with straight or widened passages is $\zeta_v = 0.6$–1.0. Considerably higher coefficients, for example, up to $\zeta_v = 4$, may result from constrictions or intersections.

8.5 Butterfly Valves and Gates

The relationship between ζ_v and the position of the flap can be seen from Figs. 27–28 for square channels. It would appear permissible to apply these values to pipes. Drag coefficients for a control valve have been included in Fig. 28.

ζ_v for other pipe fittings

Nonreturn valves	6
Water separator with baffle	7
Water separator without baffle	4
Nutating-disk water meters	8
Oscillating-piston water meters	12
Turbine water meters	6

For references, see Subchap. L1.1.

L1.4 Pressure Drop of Tube Bundles in Cross Flow

Edward S. Gaddis
Technische Universität Clausthal, Clausthal-Zellerfeld, Germany

1 Tube Bundles with Circular Tubes

1.1 Parallel Arrangement of Tube Rows

1.1.1 Introduction

Figure 1 shows the dependence of the drag coefficient ξ on the Reynolds number Re for a flow across a tube bundle with parallel arrangement of tube rows; the tube bundle has circular tubes with in-line or staggered tube arrangement. Five different regions are clear in Fig. 1. At low Reynolds number ($Re < 100$), the flow is laminar and the drag coefficient can be represented by the relation $\xi \propto Re^{-1}$. In the turbulent range, between $Re \approx 10^4$ and a critical Reynolds number $Re_{crit.}$, the drag coefficient – according to measurements made by different authors – may be represented with a good accuracy by the relation $\xi \propto Re^{-m}$ ($m << 1$). In the transition region between laminar and turbulent flow, the drag coefficient has a minimum for in-line tube arrangement [1]; such a minimum was not noticed with staggered tube arrangement. In the critical region between $2 \times 10^5 < Re_{crit.} < 6 \times 10^5$, there is a minimum for staggered tube arrangement and a second minimum for in-line tube arrangement [2, 3]. The flow at Reynolds numbers higher than the critical Reynolds number is usually denoted as trans-critical flow.

The equations presented hereafter for the prediction of the pressure drop for a flow across a tube bundle with in-line or with staggered tube arrangement are valid for a wide range of Reynolds numbers, covering the laminar, the transition, and the turbulent range nearly up to the critical Reynolds number. The equations are based on superposition of the equations of Bergelin et al. for laminar flow in a modified form [4, 5] and the equations of Gaddis and Gnielinski [5] for turbulent flow.

1.1.2 Determination of Pressure Drop

The pressure drop Δp across the tube bundle due to friction and flow separation in the wake region behind the individual tubes may be calculated from

$$\Delta p = \xi n_{MR} \frac{\rho w_e^2}{2}. \quad (1)$$

In Eq. (1), ξ is the drag coefficient, n_{MR} the number of main resistances in the flow direction, ρ the density and w_e the mean flow velocity in the narrowest cross section. For in-line tube arrangement and for staggered tube arrangement with the narrowest cross section between adjacent tubes in the same row (i.e., $b \geq 0.5\sqrt{2a+1}$), the number of the main resistances in the flow direction n_{MR} is identical with the number of the tube rows n_R. For staggered tube arrangement with the narrowest cross section in the diagonal between tubes in adjacent tube rows (i.e., $b < 0.5\sqrt{2a+1}$), the number of the main resistances in the flow direction may be calculated from the equation $n_{MR} = n_R - 1$. Figure 2 shows the position of the narrowest cross section in the different tube bundles and its relation to a and b.

The drag coefficient ξ is a function of the Reynolds number Re, the transverse pitch ratio a and the longitudinal pitch ratio b, where

$$Re = \frac{w_e d_o \rho}{\eta},$$
$$a = \frac{s_1}{d_o},$$
$$b = \frac{s_2}{d_o}.$$

1.1.3 Determination of Drag Coefficient

Definition of an Ideal Tube Bundle

An ideal tube bundle is defined arbitrarily as follows: Physical properties of fluid independent of temperature, number of tube rows $n_R \geq 10$, number of tubes per row ≥ 10, ratio of tube length to tube diameter ≥ 10, fluid velocity in the free cross section at inlet of tube bundle is uniform and perpendicular to the free cross section and smooth tube surface. Deviations from the ideal situation can be taken into account by means of correction factors.

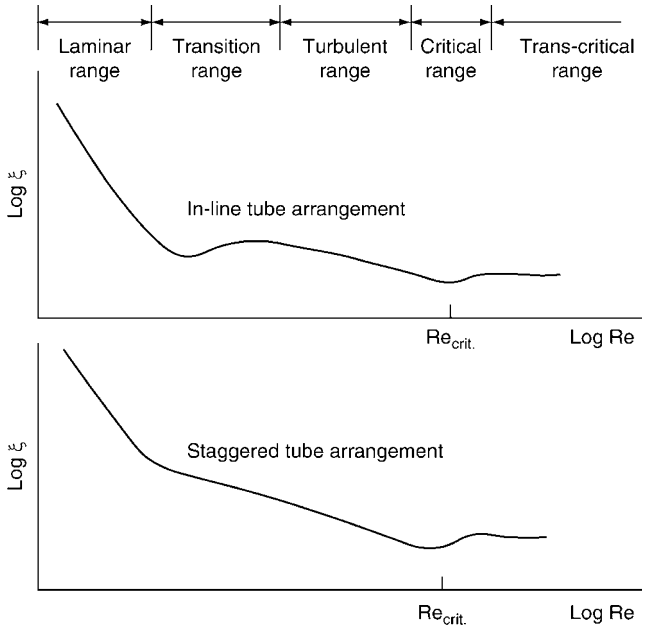

L1.4. Fig. 1. Schematic presentation of the dependence of the drag coefficient ξ on the Reynolds number Re.

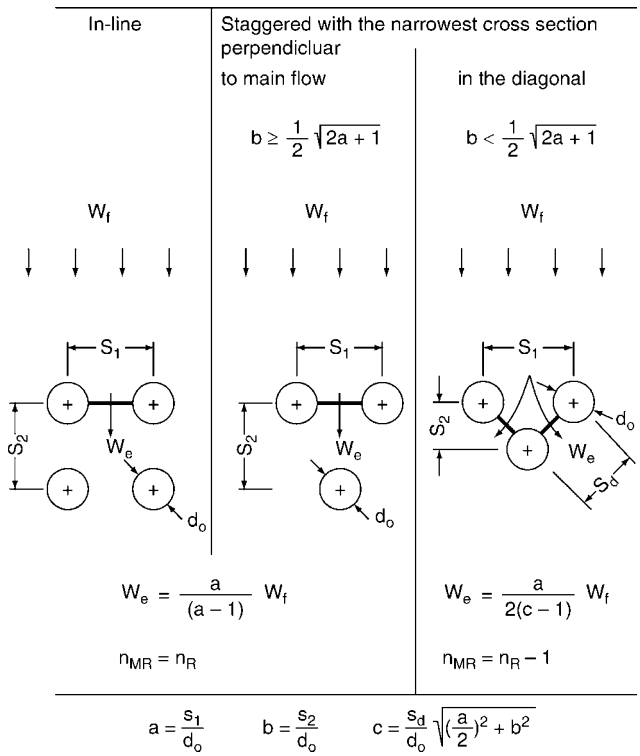

L1.4. Fig. 2. Illustration of the concept 'narrowest cross section,' which is presented with a thick line.

Drag Coefficient for an Ideal Tube Bundle

In-line tube arrangement The drag coefficient for an ideal tube bundle with in-line tube arrangement may be calculated from the following equations [5]:

$$\xi = \xi_{\text{lam}} + \xi_{\text{turb}} F_f \tag{2a}$$

with

$$F_f = 1 - \exp\left(-\frac{\text{Re} + 1000}{2000}\right). \tag{2b}$$

The drag coefficient ξ_{lam} for laminar flow is given by

$$\xi_{\text{lam}} = \frac{f_{\text{a,l,f}}}{\text{Re}} \tag{3}$$

with

$$f_{a,l,f} = \frac{280\pi\left[(b^{0.5} - 0.6)^2 + 0.75\right]}{(4ab - \pi)a^{1.6}}. \tag{4}$$

The drag coefficient ξ_{turb} for turbulent flow is given by

$$\xi_{\text{turb}} = \frac{f_{\text{a,t,f}}}{\text{Re}^{0.1(b/a)}} \tag{5}$$

with

$$f_{\text{a,t,f}} = \left[0.22 + 1.2\frac{\left(1 - \frac{0.94}{b}\right)^{0.6}}{(a - 0.85)^{1.3}}\right] \times 10^{0.47((b/a)-1.5)} + [0.03(a-1)(b-1)]. \tag{6}$$

Staggered tube arrangement The drag coefficient for an ideal tube bundle with staggered tube arrangement may be calculated from the following equations [5]:

$$\xi = \xi_{\text{lam}} + \xi_{\text{turb}} F_v \tag{7a}$$

with

$$F_{\text{v}} = 1 - \exp\left(-\frac{\text{Re} + 200}{1000}\right). \tag{7b}$$

The drag coefficient ξ_{lam} for laminar flow is given by

$$\frac{\xi_{\text{lam}} = f_{\text{a,l,v}}}{\text{Re}} \tag{8}$$

with

$$f_{\text{a,l,v}} = \frac{280\pi\left[(b^{0.5} - 0.6)^2 + 0.75\right]}{(4ab - \pi)a^{1.6}} \quad \text{for } b \geq 0.5\sqrt{2a+1} \tag{9}$$

and

$$f_{\text{a,l,v}} = \frac{280\pi\left[(b^{0.5} - 0.6)^2 + 0.75\right]}{(4ab - \pi)c^{1.6}} \quad \text{for } b < 0.5\sqrt{2a+1}. \tag{10}$$

The drag coefficient ξ_{turb} for turbulent flow is given by

$$\xi_{\text{turb}} = \frac{f_{\text{a,t,v}}}{\text{Re}^{0.25}} \tag{11}$$

with

$$f_{\text{a,t,v}} = 2.5 + \left(\frac{1.2}{(a - 0.85)^{1.08}}\right) + 0.4\left(\frac{b}{a} - 1\right)^3 - 0.01\left(\frac{a}{b} - 1\right)^3. \tag{12}$$

The diagonal pitch ratio c in Eq. (10) may be calculated from

$$c = \left((a/2)^2 + b^2\right)^{0.5}.$$

Physical Properties of Fluid The physical properties in the above equations are based on the fluid temperature ϑ and the fluid pressure p. In a tube bundle with a gaseous medium and a very large number of tube rows, the pressure may differ considerably between the inlet and outlet of the tube bundle; in such cases the physical properties are evaluated at the mean gas pressure $p_m = (p_{in} + p_{out})/2$. A change in the gas density ρ in the main flow direction from the gas density at inlet of the tube bundle – due to a change in the gas pressure – leads to a change in the gas velocity in the narrowest cross section w_e. The quantities ρ and w_e are related to one another through the continuity equation by the relation ρw_e = constant (the narrowest cross section does not change in the tube bundle). Thus, in conjunction with the mean gas density ρ_m corresponding to the mean gas pressure p_m, the mean velocity in the narrowest cross section $w_{e,m}$ should be used. Since the gas pressure at outlet of the tube bundle is not known *a priori*, an iteration procedure is required. An alternative for calculating the pressure drop in tube bundles with a very large number of tube rows ($n_R >> 10$) and changing medium density in the flow direction is to calculate the pressure drop row by row using Eq. (1) with $n_{MR} = 1$ and modified physical properties and gas velocity w_e at each row. The pressure drop across the tube bundle is then a summation of the calculated values. The computations according to this last procedure reduce calculation errors but are lengthier.

Graphical Presentation of the Equations

Figures 3, 4, 7, and 9 enable a quick evaluation of the factors $f_{a,l,f}$, $f_{a,t,f}$, $f_{a,l,v}$, and $f_{a,t,v}$, Fig. 5 enables the evaluation of the factors F_f and F_v and Fig. 8 shows the position of the narrowest cross section for staggered tube arrangement. Figures 6 and 10 give the drag coefficient ξ as a function of the Reynolds number Re for six commonly used ideal tube bundles; Fig. 6 is for three in-line and Fig. 10 for three staggered tube arrangements.

Correction Factor for Temperature Dependence of Physical Properties

Heating or cooling of the tube bundle leads to a change in the physical properties in the thermal layer near the tube surface; it can be allowed for by multiplying the drag coefficient ξ_{lam} for laminar flow by a correction factor $f_{z,l}$ and the drag coefficient ξ_{turb} for turbulent flow by a correction factor $f_{z,t}$.

In the laminar flow range, the correction factor $f_{z,l}$ may be calculated from [4]

$$f_{z,l} = \left(\frac{\eta_w}{\eta}\right)^{\overline{\left[\left(\frac{4ab}{\pi} - 1\right)\mathrm{Re}\right]^{0.25}}} \qquad (13)$$

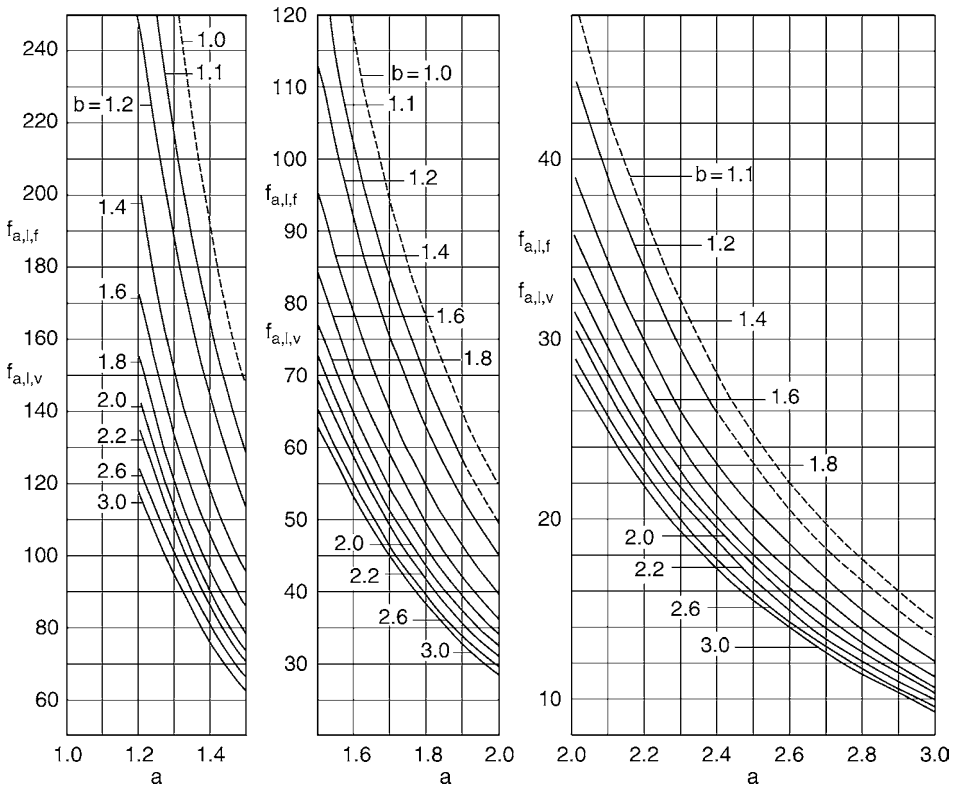

L1.4. Fig. 3. Dependence of $f_{a,l,f}$ and $f_{a,l,v}$ on a and b for in-line tube arrangement and for staggered tube arrangement with $b \geq 0.5\sqrt{2a+1}$ according to Eqs. (4) and (9) respectively.

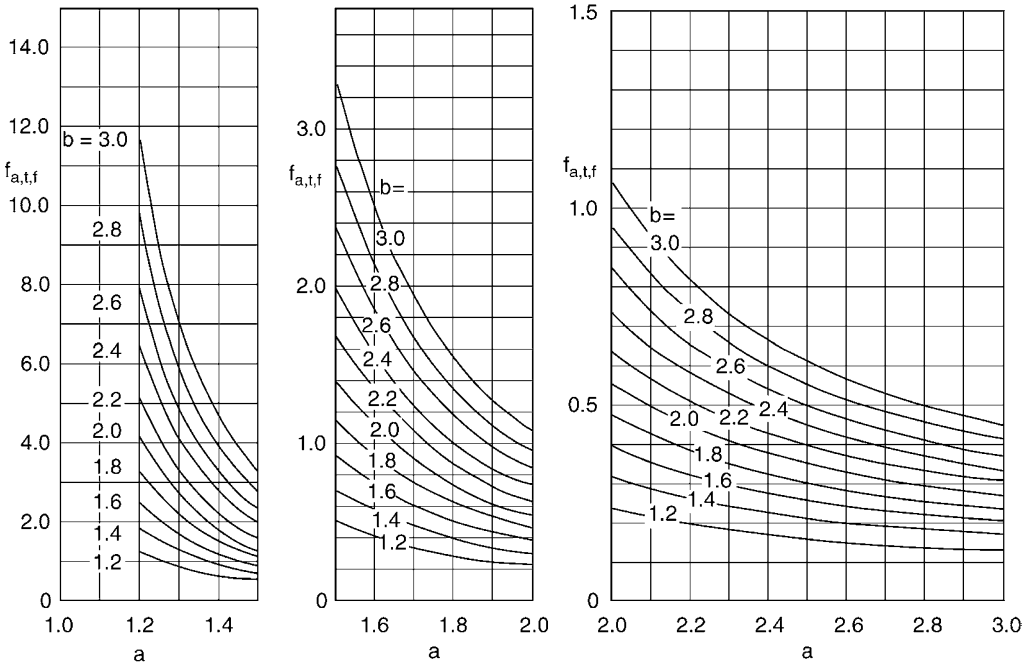

L1.4. Fig. 4. Dependence of $f_{a,t,f}$ on a and b for in-line tube arrangement according to Eq. (6).

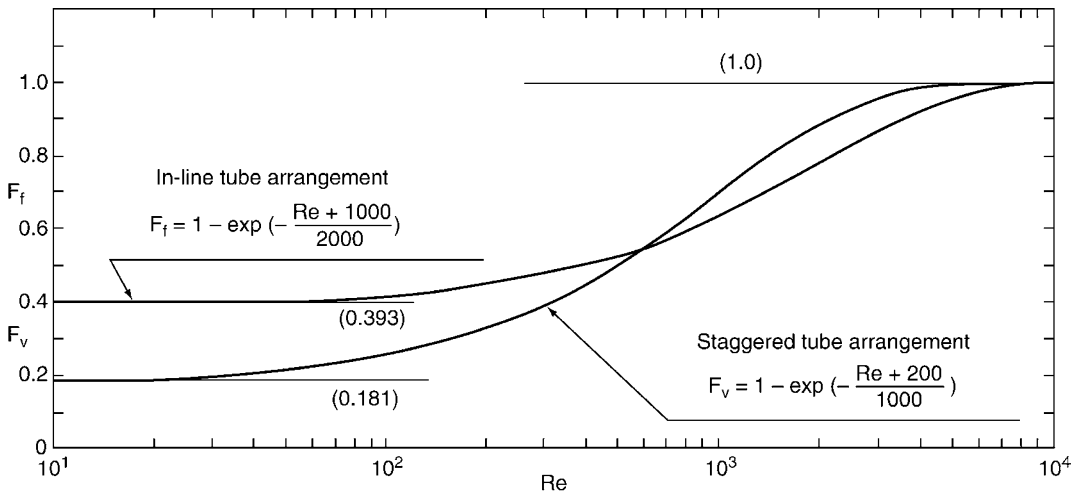

L1.4. Fig. 5. Dependence of the factors F_f and F_v appearing in Eqs. (2a), (2b), (7a) and (7b) on Re.

and in the turbulent flow range, the correction factor $f_{z,t}$ introduced by Sieder and Tate [6] for flow through circular tubes may be used, or

$$f_{z,t} = \left(\frac{\eta_w}{\eta}\right)^{0.14}. \tag{14}$$

In the above equations, the dynamic viscosity η and the density ρ under non-isothermal flow conditions are evaluated at the mean fluid temperature $\vartheta_m = (\vartheta_{in} + \vartheta_{out})/2$ and the dynamic viscosity η_w at the mean wall temperature ϑ_w.

Correction Factor for Small Number of Tube Rows

According to Bergelin et al. [4], the number of tube rows has an effect on the drag coefficient for the tube bundle in the laminar flow range only if the flow is non-isothermal and the number of tube rows n_R is less than 10. This effect can be allowed for by multiplying the drag coefficient ξ_{lam} in Eqs. (2a) and (7a) by the correction factor $f_{zn,l}$ [4], where

$$f_{zn,l} = \left(\frac{\eta_w}{\eta}\right)^{\frac{0.57\left(\frac{\eta_R}{10}\right)^{0.25}}{\left[\left(\frac{4ab}{\pi} - 1\right)Re\right]^{0.25}}} \quad \text{for } n_R < 10 \tag{15}$$

and

$$f_{zn,l} = f_{z,l} \text{ for } n_R \geq 10 \quad (\text{see, Eq.}(13) \text{ for } f_{z,l}). \tag{16}$$

The correction factor $f_{zn,l}$ given by Eq. (15) takes into consideration at the same time the influence of temperature change under non-isothermal conditions. Thus, in the case of a non-isothermal flow and $n_R < 10$ Eq. (13) becomes redundant.

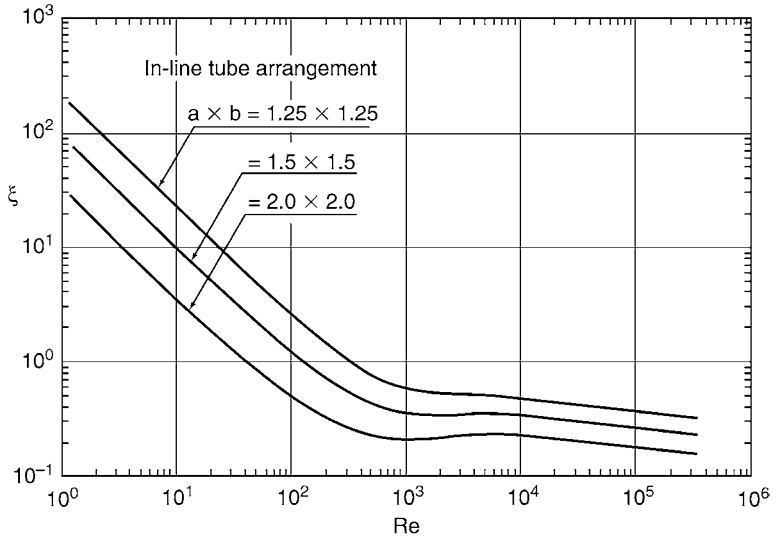

L1.4. Fig. 6. Dependence of the drag coefficient ξ on the Reynolds number Re for three commonly used ideal tube bundles with in-line tube arrangement.

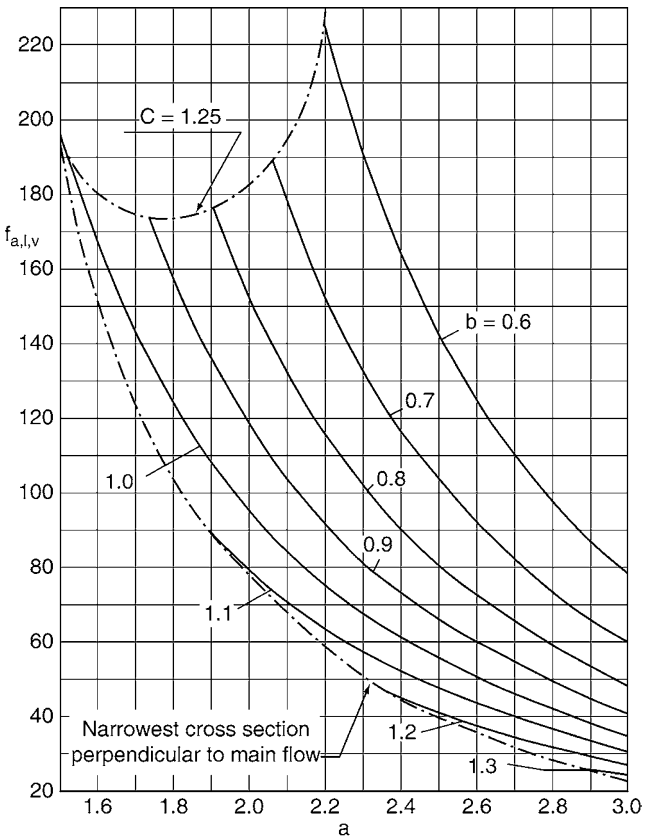

L1.4. Fig. 7. Dependence of $f_{a,l,v}$ on a and b for staggered tube arrangement with $b < 0.5\sqrt{2a+1}$ according to Eq. (10).

In the turbulent flow range, the change in the drag coefficient ξ_{turb} for a tube bundle with change in the number of tube rows between 5 and 10 is small [7] and may be ignored. However, sudden expansion of the flow area from that of the last tube row to the total available free area in the tube bundle leads to an additional pressure drop, which is negligible for a tube bundle with a large number of tube rows but may be remarkable in a tube bundle with a small number of tube rows. This may be compensated for by adding a correction factor $f_{n,t}$ to the drag coefficient ξ_{turb} in case of an isothermal flow or to the corrected drag coefficient $\xi_{turb} f_{z,t}$ in case of a non-isothermal flow [5], where

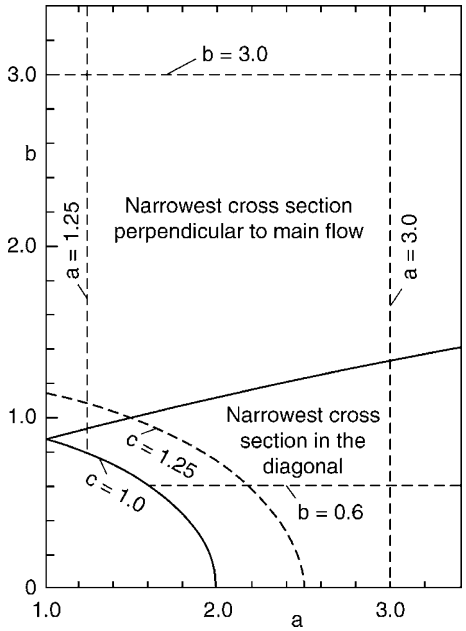

L1.4. Fig. 8. Position of the narrowest cross section for staggered tube arrangement in dependence on *a* and *b*.

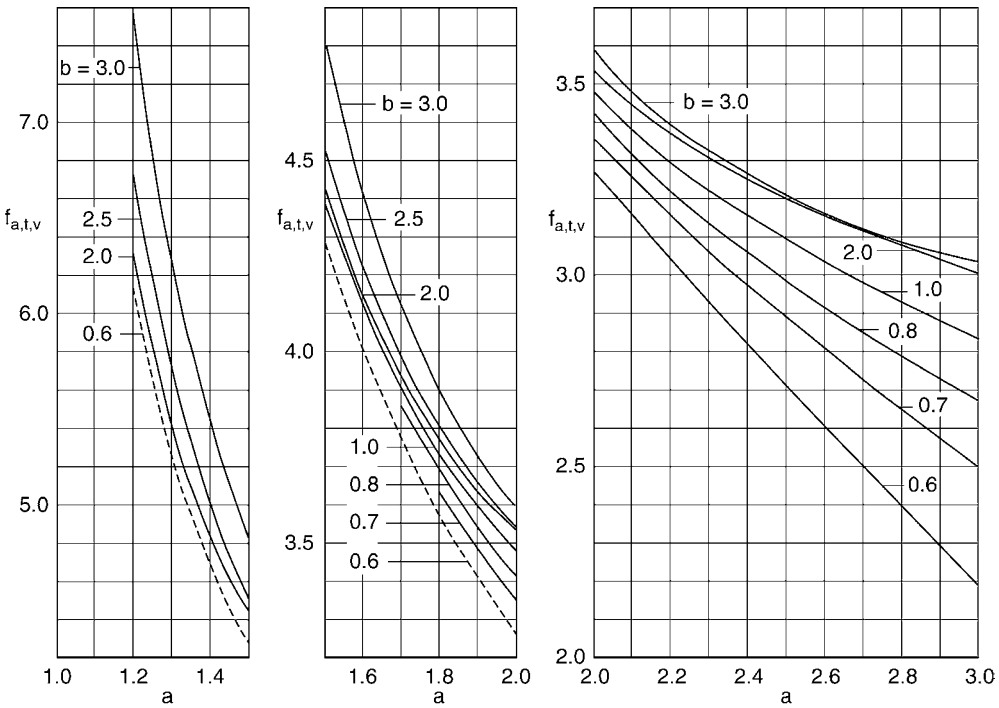

L1.4. Fig. 9. Dependence of $f_{a,t,v}$ on *a* and *b* for staggered tube arrangement according to Eq. (12).

$$f_{n,t} = \xi_0 \left(\frac{1}{n_R} - \frac{1}{10} \right) \text{ for } 5 \leq n_R < 10 \tag{17}$$

and

$$f_{n,t} = 0 \text{ for } n_R \geq 10. \tag{18}$$

For a tube bundle with in-line tube arrangement or with staggered tube arrangement and the narrowest cross section perpendicular to the main flow, the coefficient ξ_o due to sudden expansion of the flow area may be calculated from

$$\xi_o = \frac{1}{a^2} \tag{19}$$

and for a tube bundle with staggered tube arrangement and the narrowest cross section in the diagonal, ξ_o may be calculated from

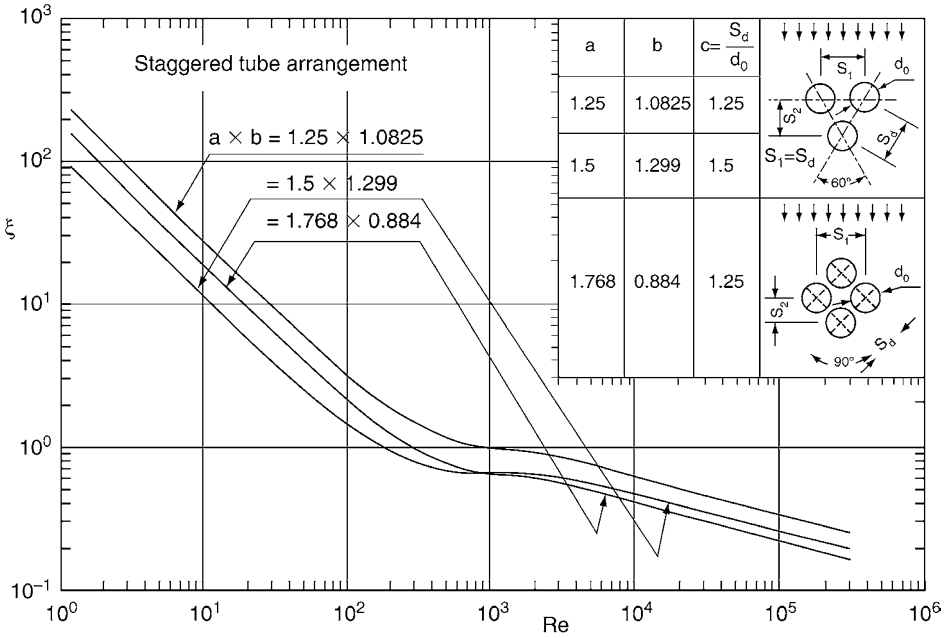

L1.4. Fig. 10. Dependence of the drag coefficient ξ on the Reynolds number Re for three commonly used ideal tube bundles with staggered tube arrangement.

$$\xi_o = \left[\frac{2(c-1)}{a(a-1)}\right]^2. \tag{20}$$

General Equations for Drag Coefficient

The general equations for calculating the drag coefficient for the non-isothermal case considering at the same time tube bundles with a smaller number of tube rows than that given in the definition of an ideal tube bundle are as follows:

For in-line tube arrangement:

$$\xi = \xi_{lam} f_{zn,l} + \left(\xi_{turb} f_{z,t} + f_{n,t}\right) F_f. \tag{21}$$

For staggered tube arrangement:

$$\xi = \xi_{lam} f_{zn,l} + \left(\xi_{turb} f_{z,t} + f_{n,t}\right) F_v. \tag{22}$$

To reduce computational effort (e.g., when using a hand calculator) the drag coefficient for small Reynolds numbers ($Re \leq 10$), may be calculated only from the laminar term ($\xi_{lam} f_{zn,l}$) and for high Reynolds numbers ($10^4 \leq Re \leq 3 \times 10^5$) only from the turbulent term ($\xi_{turb} f_{z,t} + f_{n,t}$) of the equations; in that last case, the factors F_f and F_v are effectively equal to unity.

Validity Range of Equations

The available experimental measurements used to develop the above equations covered the following ranges:

Reynolds number: $1 \leq Re \leq 3 \times 10^5$
and number of tube rows: $n_R \geq 5$.

The tube bundles used in the experimental investigations had transverse and longitudinal pitch ratios as follows:

In the range $Re < 10^3$:

For in-line tube arrangement: $a \times b = 1.25 \times 1.25, 1.5 \times 1.5, 2.0 \times 2.0$.

For staggered tube arrangement: $a \times b = 1.25 \times 1.0825, 1.5 \times 1.299, 1.768 \times 0.884$.

In the range $Re \geq 10^3$:

For in-line tube arrangement: $1.25 \leq a \leq 3.0, 1.2 \leq b \leq 3.0$.

For staggered tube arrangement: $1.25 \leq a \leq 3.0, 0.6 \leq b \leq 3.0$, $c \geq 1.25$.

Experimental measurements made at high Reynolds numbers and with gas as flow medium had always a flow velocity in the narrowest cross section of the tube bundle, which was much less than the sound velocity. Thus, density changes within the narrowest cross section can be ignored. The above ranges give the range of validity of the equations.

Example 1

A heat exchanger with a rectangular cross section has a tube bundle with 11 tube rows and in-line tube arrangement. Each tube row has ten circular tubes with an external diameter of 19.05 mm and a tube length of 0.4 m. Other dimensions of the heat exchanger are given in Fig. 11. The heat exchanger is used to cool oil of a volumetric flow rate $\dot{V}$ of 62 $m^3\ h^{-1}$ from the inlet temperature $\vartheta_{in} = 80.4\ °C$ to the outlet temperature $\vartheta_{out} = 78.8°C$. The mean wall temperature ϑ_w of the tubes amounts to 40.9°C. It is required to calculate the pressure drop Δp due to friction and flow separation. The following data for the physical properties of oil are given:

At a mean oil temperature $\vartheta_m = (80.4 + 78.8)/2 = 79.6°C$,
oil density $\rho = 837\ kg\ m^{-3}$ and
oil dynamic viscosity $\eta = 1.72 \times 10^{-2}$ Pas
and at the mean wall temperature $\vartheta_w = 40.9°C$,
oil dynamic viscosity $\eta_w = 8.55 \times 10^{-2}$ Pas.

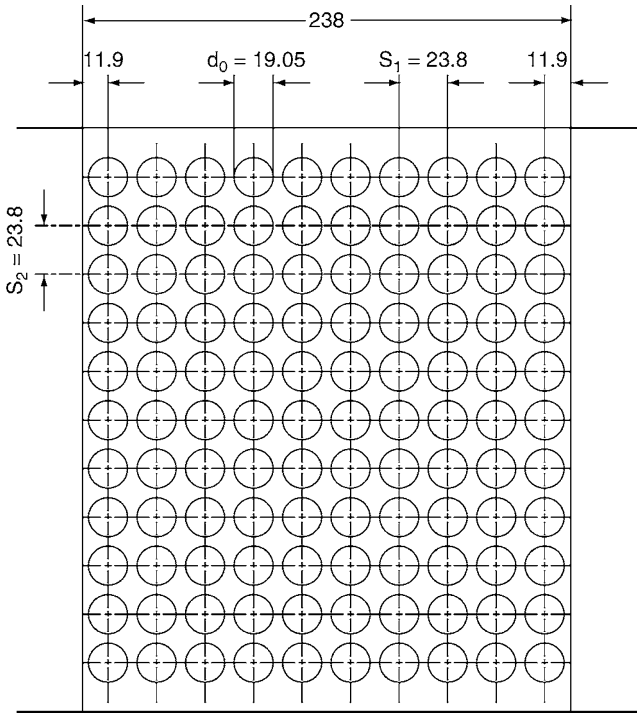

L1.4. Fig. 11. Dimensions of the heat exchanger in the example (dimensions in mm).

Solution:

The following quantities are calculated:

$$w_f = \frac{\dot{V}}{F} = \frac{62/3600}{0.238 \times 0.4} = 0.181\,\mathrm{m\,s^{-1}}$$

$$a = \frac{s_1}{d_o} = \frac{23.8}{19.05} = 1.25$$

$$b = \frac{s_2}{d_o} = \frac{23.8}{19.05} = 1.25$$

$$w_e = \frac{a}{a-1} w_f = \frac{1.25}{1.25-1} \times 0.181 = 0.905\,\mathrm{m\,s^{-1}} \text{ (see Fig. 2)}$$

$$\mathrm{Re} = \frac{w_e d_o \rho}{\eta} = \frac{0.905 \times (19.05 \times 10^{-3}) \times 837}{1.72 \times 10^{-2}} = 839$$

Equation (4):

$$f_{a,l,f} = \frac{280\pi\left[(b^{0.5} - 0.6)^2 + 0.75\right]}{(4ab - \pi)a^{1.6}}$$

$$= \frac{280 \times \pi \times \left[(1.25^{0.5} - 0.6)^2 + 0.75\right]}{(4 \times 1.25 \times 1.25 - \pi) \times 1.25^{1.6}} = 201.7$$

Equation (3):

$$\xi_{lam} = \frac{f_{a,l,f}}{\mathrm{Re}} = \frac{201.7}{839} = 0.24$$

Equation (13):

$$f_{z,l} = \left(\frac{\eta_w}{\eta}\right)^{\frac{0.57}{\left[\left(\frac{4ab}{\pi}-1\right)\mathrm{Re}\right]^{0.25}}} = \left(\frac{8.55 \times 10^{-2}}{1.72 \times 10^{-2}}\right)^{\frac{0.57}{\left[\left(\frac{4\times1.25\times1.25}{\pi}-1\right)\times839\right]^{0.25}}} = 1.19$$

Equation (6):

$$f_{a,t,f} = \left[0.22 + 1.2\frac{\left(1 - \frac{0.94}{b}\right)^{0.6}}{(a-0.85)^{1.3}}\right] \times 10^{0.47((b/a)-1.5)} + [0.03(a-1)(b-1)]$$

$$= \left[0.22 + 1.2 \times \frac{\left(1 - \frac{0.94}{1.25}\right)^{0.6}}{(1.25-0.85)^{1.3}}\right] \times \left[10^{0.47\left(\frac{1.25}{1.25}-1.5\right)}\right] + [0.03 \times (1.25-1) \times (1.25-1)] = 1.13$$

Equation (5):

$$\xi_{turb} = \frac{f_{a,t,f}}{Re^{0.1(b/a)}} = \frac{1.13}{(839)^{0.1\times(1.25/1.25)}} = 0.576$$

Equation (14):

$$f_{z,t} = \left(\frac{\eta_w}{\eta}\right)^{0.14} = \left(\frac{8.55 \times 10^{-2}}{1.72 \times 10^{-2}}\right)^{0.14} = 1.25$$

Equation (18):

$$f_{n,t} = 0 \text{ (since } n_R > 10)$$

Equation (2b):

$$F_f = 1 - \exp\left(-\frac{\mathrm{Re} + 1000}{2000}\right) = 1 - \exp\left(-\frac{839 + 1000}{2000}\right) = 0.601$$

Equation (16):

$$f_{zn,l} = f_{z,l} = 1.19 \text{ (since } n_R > 10)$$

Equation (21):

$$\xi = \xi_{lam} f_{zn,l} + \left(\xi_{turb} f_{z,t} + f_{n,t}\right) F_f = 0.24 \times 1.19 + (0.576 \times 1.25 + 0) \times 0.601 = 0.718$$

$$n_{MR} = n_R = 11 \quad \text{(in-line tube arrangement)}$$

The pressure drop Δp due to friction and flow separation is calculated from Eq. (1), or

$$\Delta p = \xi n_{MR} \frac{\rho w_e^2}{2} = 0.718 \times 11 \times \frac{837 \times 0.905^2}{2} = 2.71 \times 10^3 \text{ Pa} = 2.71 \times 10^3 \times 10^{-5} = 2.71 \times 10^{-2} \text{ bar}.$$

1.1.4 Other Components of Pressure Change

In case of a gaseous medium, the flow velocity may change considerably between the inlet and outlet of the tube bundle due to change in gas density. A change in gas density can be due to heating or cooling and/or due to pressure drop across the tube bundle. The change in velocity between inlet and outlet of the tube bundle causes an additional pressure change Δp_{mom} due to change in momentum flow rate, which may be calculated from $\Delta p_{mom} = (\rho w_f^2)_{out} - (\rho w_f^2)_{in}$. At the same time, the hydrostatic pressure difference $\Delta p_s = \rho h_s g$ between inlet and outlet of the tube bundle – in case of a high density medium (liquid) and a large tube bundle inclined to the horizontal – should also be considered. These two factors contribute to the pressure at the outlet of the tube bundle, which can be calculated from $p_{out} = p_{in} - \Delta p \pm \Delta p_{mom} \pm \Delta p_s$. While the term Δp always represents a pressure drop in the flow direction, both terms Δp_{mom} and Δp_s can be positive, negative or have a zero value.

Example 2

The heat exchanger used in Example 1 has a height $h_s = 0.3$ m and the direction of the flow is vertical downwards; the oil pressure at the inlet is 1.5 bar. It is required to calculate the oil pressure at the heat exchanger outlet.

Solution:

The change in the oil velocity in the free cross section between the inlet and outlet of the heat exchanger – due to change in density – is negligible. Thus, the change in oil pressure Δp_{mom} due to change in momentum flow rate is given by

$$\Delta p_{mom} = \left(\rho w_f^2\right)_{out} - \left(\rho w_f^2\right)_{in} = 0 \text{ bar}.$$

The hydrostatic head of the oil h_s is 0.3 m and the oil density ρ at mean liquid temperature ϑ_m is 837 kg m^{-3} (see Example 1). Thus, the change in oil pressure Δp_s due to the hydrostatic head of oil is given by

$$\Delta p_s = \rho h_s g = 837 \times 0.3 \times 9.81 = 2.46 \times 10^3 \text{ Pa} = 2.46 \times 10^3 \times 10^{-5} = 2.46 \times 10^{-2} \text{ bar}$$

and is positive in flow direction.

The pressure drop Δp due to friction and flow separation is calculated in Example 1 as

$$\Delta p = 2.71 \times 10^{-2} \text{ bar}$$

and is negative in flow direction.

Thus, the oil pressure p_{out} at the heat exchanger outlet is given by

$$p_{out} = p_{in} - \Delta p + \Delta p_{mom} + \Delta p_s = 1.5 - 2.71 \times 10^{-2} + 0 + 2.46 \times 10^{-2} = 1.5 \text{ bar}.$$

In the example, the irreversible pressure drop due to friction and flow separation is fully equalized through the pressure gain due to the available hydrostatic head of liquid; the oil pressure at the outlet is equal to that at the inlet.

1.1.5 Reference to Special Cases

Extreme Large Reynolds Numbers

Measurements of the drag coefficient in tube bundles for Reynolds numbers in critical and trans-critical ranges are reported from Hammeke et al. [8], Achenbach [2, 9, 10], and Poshkas et al. [11]. The experimental measurements are presented in tabular or graphical forms.

Rough Tubes

The tube roughness has an effect on the critical Reynolds number and on the drag coefficient in the critical and trans-critical ranges [9, 10]. Experimental measurements in a tube bundle with a staggered tube arrangement ($a = 2.0$, $b = 1.4$) show that an increase in the relative roughness of the tube surface leads to a decrease in the critical Reynolds number and to an increase in the drag coefficient in the trans-critical range [9]. A tube bundle with in-line tube arrangement and the same pitch ratios a and b shows a different performance; at high Reynolds numbers ($Re > 2 \times 10^6$), the drag coefficient decreases with increasing surface roughness [10]. At Reynolds numbers $Re < Re_{crit}$, the roughness of the tube surface in the examined ranges has practically no influence on the drag coefficient [9, 10].

Extreme Small Pitch Ratios

A number of tube bundles with very small transverse and longitudinal pitch ratios (for in-line tube arrangement: $1.01 \le a \le 1.06$, $b = a$, and for staggered tube arrangement: $a \times b = 1.03 \times 0.89$) were examined by Samoshka et al. [12] in the range $Re > 10^4$. The tube bundle with staggered tube arrangement has a higher drag coefficient than that with in-line tube arrangement and the same transverse pitch ratio. All examined tube bundles have in the range $10^4 < Re < 10^5$ for the dependence of ξ on Re in double logarithmic presentation a higher inclination than that for commonly used pitch ratios (larger exponent m for $\xi \propto Re^{-m}$).

Oblique Flow Over Tube Bundles

Under otherwise similar conditions, the following relation holds [13, 14]:

$$f_s = \frac{(\Delta p)_{\varphi < 90^o}}{(\Delta p)_{\varphi = 90^o}} < 1.0,$$

where φ is the angle between the flow direction and the tube axis. A comparison between own experimental measurements and theoretical predictions for f_s is given by Groehn [15].

Part Staggered Tube Arrangement

Bressler [16] and Niggeschmidt [3] examined tube bundles with part staggered tube arrangement under turbulent flow conditions. The dependence of the drag coefficient on the degree of deviation from the normal staggered case was reported.

1.2 Cross Arrangement of Tube Rows

Tube bundles with cross arrangement of tube rows and in-line or staggered tube arrangement according to Fig. 12 were examined by London et al. [17], Brauer [18], Klier [19], and Hammeke et al. [8]. While London et al. and Brauer examined tube bundles with the least possible longitudinal pitch ratio $b = s_2/d_o = 1$, Klier and Hammeke et al. examined tube bundles with a longitudinal pitch ratio $b > 1$. In addition, Brauer examined the influence of the cross angle β between tubes in adjacent rows on the pressure drop; the experimental measurements show that the pressure drop is maximum, when the cross angle $\beta = 60°$.

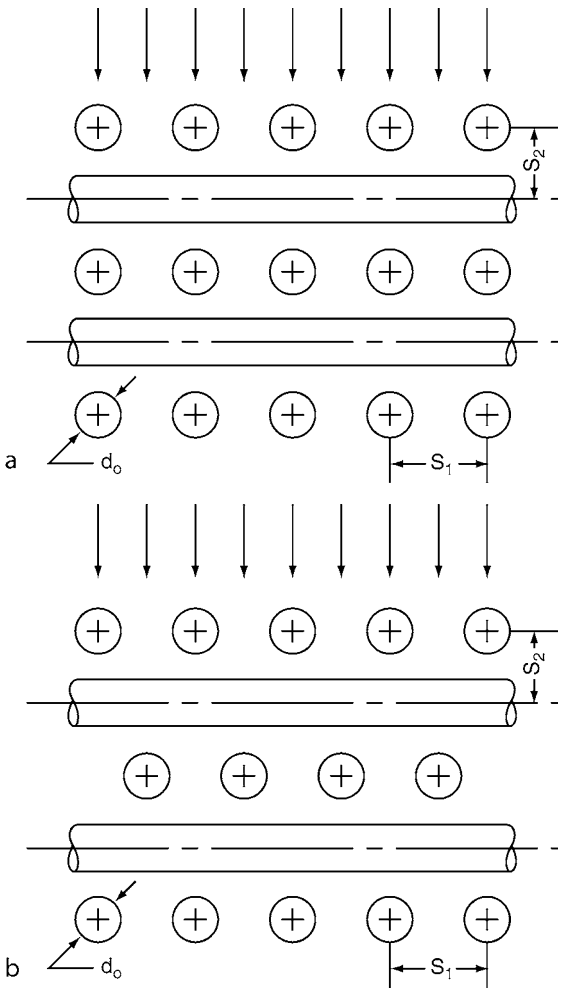

L1.4. Fig. 12. Tube bundles with cross arrangement of tube rows (cross angle $\beta = 90°$): (**a**) In-line cross arrangement; (**b**) Staggered cross arrangement.

According to Brauer [18], the pressure drop for an in-line tube arrangement or for a staggered tube arrangement with a longitudinal pitch ratio $b = s_2/d_o = 1$ may be calculated from

$$\Delta p = \xi_h \frac{4L}{d_h} \frac{\rho w_h^2}{2}. \tag{23}$$

The mean flow velocity w_h in the tube bundle is given by

$$w_h = \frac{\dot{V}}{F_h}. \tag{24}$$

The hydraulic cross section F_h and the length of the tube bundle L are calculated from

$$F_h = F\frac{V_f}{V} = n_a n_b s_1^2 \left(1 - \frac{\pi d_o}{4 s_1}\right) \tag{25}$$

and

$$L = n_R d_o. \tag{26}$$

The drag coefficient ξ_h in Eq. (23) for tube bundles with a cross angle $\beta = 90°$ is calculated from the following equations:
For in-line tube arrangement:

$$\xi_h = \frac{C_f}{Re_h^{0.09}} \text{ for } 5 \times 10^3 \le Re_h \le 10^5 \tag{27}$$

and for staggered tube arrangement (with $b = 1$):

$$\xi_h = \frac{C_v}{Re_h^{0.15}} \text{ for } 4 \times 10^3 \le Re_h \le 10^5. \tag{28}$$

The Reynolds number in Eqs. (27) and (28) is defined by

$$Re_h = \frac{w_h d_h \rho}{\eta} \tag{29}$$

and the hydraulic diameter d_h is calculated from

$$d_h = \left(\frac{4 s_1}{\pi d_0} - 1\right) d_o. \tag{30}$$

The factors C_f and C_v in Eqs. (27) and (28), which are presented in graphical form [18], depend on the transverse pitch ratio $a = s_1/d_o$ and are given in Table 1 approximately for discrete values of a in the range $1.25 \le a \le 5.0$. For intermediate values of a, the constants C_f and C_v can be calculated by interpolation. Table 1 shows that C_f and C_v have a minimum at about $a \approx 1.5$.

Brauer used his own experimental measurements as well as those of London et al. for developing the above equations. The tube bundles used in the experimental investigations had a total number of tube rows $n_R \ge 10$.

According to Hammeke et al., the pressure drop for an in-line tube arrangement with a transverse pitch ratio $a = 2.06$, a longitudinal pitch ratio $b = 1.37$, and constant medium density is given by

$$\Delta p = \xi n_R \frac{\rho w_e^2}{2}, \tag{31}$$

where

$$\xi = \frac{2.64}{Re^{0.21}} \text{ for } 5 \times 10^3 \le Re \le 5 \times 10^4 \tag{32}$$

and

L1.4. Table 1. Dependence of the constants C_f and C_v in Eqs. (27) and (28) on a

a	C_f	C_v
1.25	0.50	0.80
1.50	0.38	0.62
2.00	0.55	0.75
3.00	0.62	1.28
4.00	0.61	1.74
5.00	0.60	2.17

$$\xi = \frac{0.892}{\mathrm{Re}^{0.11}} \text{ for } 5 \times 10^4 \leq \mathrm{Re} \leq 2 \times 10^5. \quad (33)$$

The Reynolds number Re in Eqs. (32) and (33) is formed – as in Sect. 1.1.2 – with the tube diameter d_o and the flow velocity in narrowest cross section w_e. The examined tube bundle had a tube diameter $d_o = 51$ mm and a total number of tube rows $n_R = 10$. The working medium was gas at different pressures.

At Reynolds numbers in the range $2 \times 10^5 \leq \mathrm{Re} \leq 10^6$, Hammeke et al. presented the dependence of ξ on Re in a graphical form; the experimental measurements show that at $\mathrm{Re} > 10^6$ the drag coefficient ξ is nearly constant ($\xi \approx 0.325$). Further experimental measurements indicate that, the roughness of the tube surface at $\mathrm{Re} > 2 \times 10^5$ has a considerable effect on the pressure drop performance of the tube bundle.

Klier examined tube bundles with different geometries than those used by Brauer and Hammeke et al. and recommends in conjunction with Eq. (31) the following equations for predicting the drag coefficient ξ:

For in-line tube arrangement:

$$\xi = \frac{0.879}{\mathrm{Re}^{0.12}} \text{ for } a = 2.0 \quad (34)$$

and

$$\xi = \frac{1.482}{\mathrm{Re}^{0.147}} \text{ for } a = 1.5. \quad (35)$$

According to Klier, the pressure drop for in-line tube arrangement in the examined range of the longitudinal pitch ratio ($1.5 \leq b \leq 4.5$) does not depend on b.

For staggered tube arrangement:

$$\xi = \frac{1.048}{\mathrm{Re}^{0.131}} \text{ for } a = b = 2.0 \quad (36)$$

and

$$\xi = \frac{1.522}{\mathrm{Re}^{0.146}} \text{ for } a = b = 1.5. \quad (37)$$

Klier used tube bundles with $n_R = 10$ and varied the Reynolds number in the range $2.0 \times 10^3 \leq \mathrm{Re} \leq 1.5 \times 10^4$ to develop Eqs. (34–37). The Reynolds number in the previous equations is formed – as in Sect. 1.1.2 – with the tube diameter d_o and the flow velocity in the narrowest cross section w_e.

2 Tube Bundles with Oval Tubes

Oval tubes with the major diameter parallel to the flow direction have a favorable fluid dynamic performance compared with circular tubes. As seen in Fig. 13, the point of separation of the boundary layer around an oval tube – under otherwise similar flow conditions – moves downwards in the flow direction; this leads to a smaller turbulent wake behind the oval tube and hence to a smaller loss of energy in comparison with that for the circular tube. The associated form pressure drop is thus smaller. However, the difference in pressure drop between a tube bundle with oval tubes and that with circular tubes is not as large as that for single tubes. Oval tubes are also more expensive in the production and their fixation in the tube sheets of a heat exchanger is difficult and more costly.

The number of parameters, that are required for geometrical similarity of bundles with oval tubes, is higher than that required for bundles with circular tubes. While three parameters (transverse pitch ratio, longitudinal pitch ratio, and tube arrangement, i.e., in-line or staggered) are sufficient for geometrical similarity of commonly used circular tube bundles, additional parameters as the ratio of major diameter to minor diameter, the form of the tube cross section, and the position of the major and minor diameters relative to the flow are required for geometrical similarity of oval tube bundles. General equations similar to those presented in Sect. 1.1.3 for circular tube bundles are not available for oval tube bundles. Nevertheless, many authors carried out experimental measurements and presented empirical correlations for predicting the pressure drop in oval tube bundles; it must however be emphasized that these correlations are only valid for the specific geometrical parameters and the operating conditions examined by the authors.

Brauer [20] uses the following equation to calculate the pressure drop Δp in a tube bundle with oval tubes:

$$\Delta p = \xi_B n_R \frac{\rho w_e^2}{2} \quad (38)$$

with w_e the fluid velocity in the narrowest cross section. Figures 14 and 15 show the position of the narrowest cross section in the tube bundle.

For the drag coefficient ξ_B, Brauer gives different equations for tube bundles with different geometrical ratios as follows:

For the tube bundles No. 1, 2 in Table 2 (tube bundles with different dimensions but nearly geometrically similar)

$$\xi_B = \frac{12.4}{\mathrm{Re}_B^{0.24}} \text{ for } 5 \times 10^3 \leq \mathrm{Re}_B \leq 10^5 \quad (39)$$

and for the tube bundle No. 3 in Table 2

$$\xi_B = \frac{36.8}{\mathrm{Re}_B^{0.27}} \text{ for } 5 \times 10^3 \leq \mathrm{Re}_B \leq 10^5. \quad (40)$$

The tube bundle No. 4 in Table 2 has oval tubes with a higher ratio of the major diameter to the minor diameter ($d_{k,1}/d_{k,2} = 2.57$) compared to that for the tube bundles No. 1 and No. 2 ($d_{k,1}/d_{k,2}$=1.84, 2.00 respectively); the transverse pitch ratio ($s_1/d_{k,2}$) and the longitudinal pitch ratio ($s_2/d_{k,1}$) are nearly the same for the three tube bundles. This tube bundle shows a higher drag coefficient in the range $6 \times 10^4 \leq \mathrm{Re}_B \leq 10^5$ and

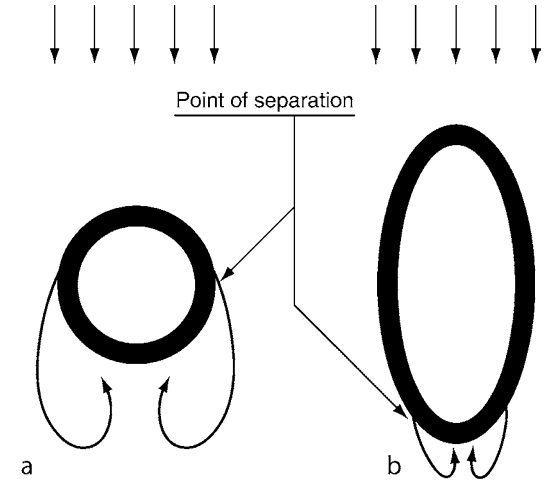

L1.4. Fig. 13. Turbulent wake behind a tube: (**a**) a circular tube; (**b**) an oval tube with the major diameter parallel to the flow direction.

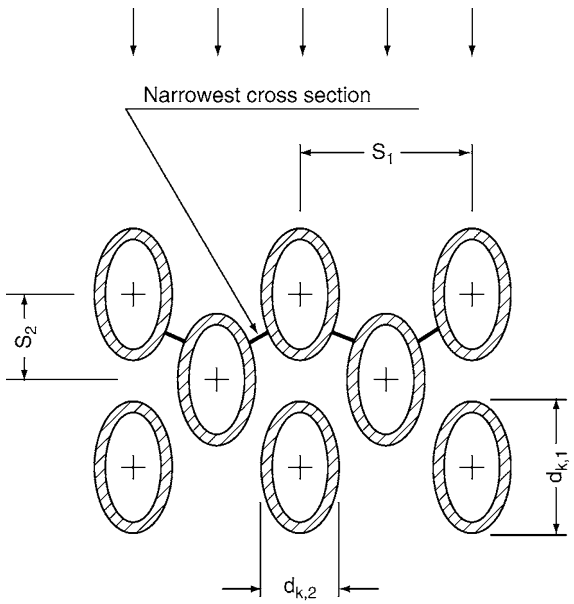

L1.4. Fig. 14. Arrangement of the tube bundles No.1, 2 and 4 in Table 2.

the inclination of the function $\xi_b = f(\mathrm{Re}_b)$ in a double logarithmic presentation is steeper. At a Reynolds number of about $\mathrm{Re} \approx 10^5$, the three tube bundles have almost the same drag coefficient.

The tube bundles No. 4 and 5 have the same dimensions of the tubes. However, the tubes have been arranged in tube bundle No. 5 – different to the commonly used arrangement – such that the main flow is parallel to the minor diameter. The pressure drop for tube bundle No. 5 is basically form pressure drop; experimental measurements yield for that bundle

$$\xi_{\mathbf{B}} = 0.53 \text{ for } 8 \times 10^3 \leq \mathrm{Re}_B \leq 5 \times 10^4. \tag{41}$$

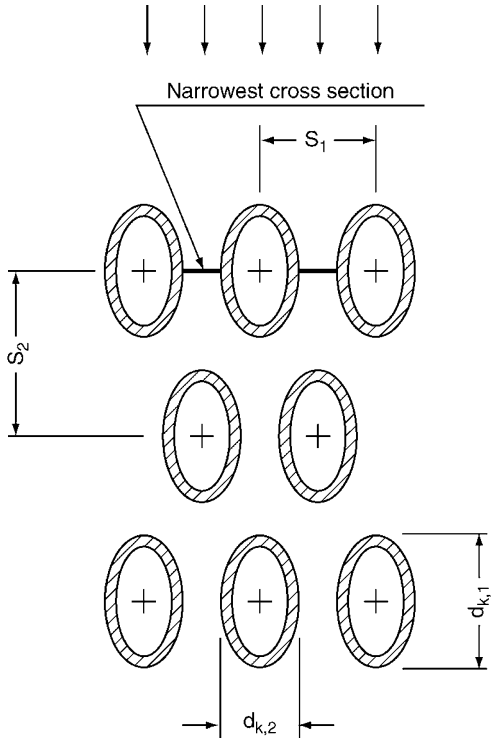

L1.4. Fig. 15. Arrangement of the tube bundle No. 3 in Table 2.

The Reynolds number in Eqs. (39) and (40) is formed by

$$\mathrm{Re}_B = \frac{w_e d_{h,o} \rho}{\eta} \tag{42}$$

and the hydraulic diameter $d_{h,o}$ is given by

$$d_{h,o} = \frac{4F_R}{U} = \frac{4V_f}{A_{tot}}. \tag{43}$$

Figures 14 and 16 show schematically the arrangement of the tube bundles used in this investigation.

Merker and Hanke [21] give for an oval tube bundle the following equation (Fig. 17):

$$\Delta p = \xi_{M,H} n_R \frac{s_1^2 U}{s_e^3} \frac{\rho w_f^2}{2} = \xi_{\mathbf{M,H}} n_R \frac{U}{s_e} \frac{\rho w_e^2}{2} \tag{44}$$

with

$$s_e = 2s_{10} \text{ for } \frac{s_2}{d_{k,1}} = 1 \tag{45}$$

and

$$s_e = 2s_{20} \text{ for } \frac{s_2}{d_{k,1}} = 0.67. \tag{46}$$

According to Merker and Hanke, the drag coefficient $\xi_{\mathbf{M,H}}$ is independent of the transverse pitch ratio $s_1/d_{k,2}$ in the examined ranges; The following equation is recommended to calculate $\xi_{\mathbf{M,H}}$:

$$\xi_{\mathbf{M,H}} = \frac{K}{\mathrm{Re}_{\mathbf{M,H}}^m} \tag{47}$$

L1.4. Table 2. Dimensions and details of the oval tube bundles examined by Brauer

No.	$d_{k,1}$ mm	$d_{k,2}$ mm	$\frac{d_{k,1}}{d_{k,2}}$	n_R	s_1 mm	s_2 mm	$\frac{s_1}{d_{k,2}}$	$\frac{s_2}{d_{k,1}}$
1	46	25	1.84	10	78	28	3.12	0.61
2	38	19	2.00	10	60	23	3.16	0.61
3	46	25	1.84	10	39	56	1.56	1.22
4	36	14	2.57	14	44	22	3.14	0.61
5	36	14	2.57	14	52	22	–	–

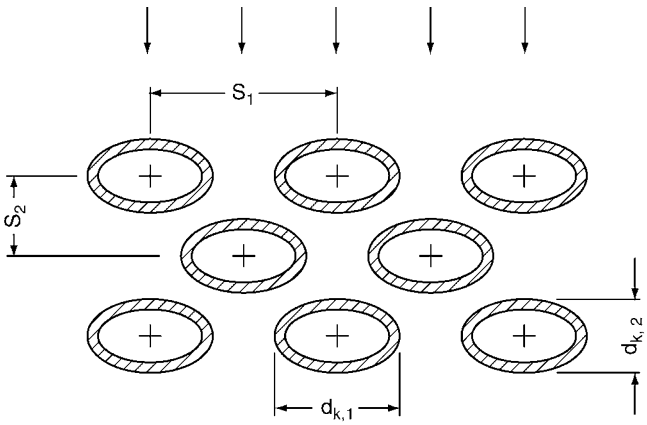

L1.4. Fig. 16. Arrangement of the tube bundle No. 5 in Table 2 (flow direction parallel to minor axis).

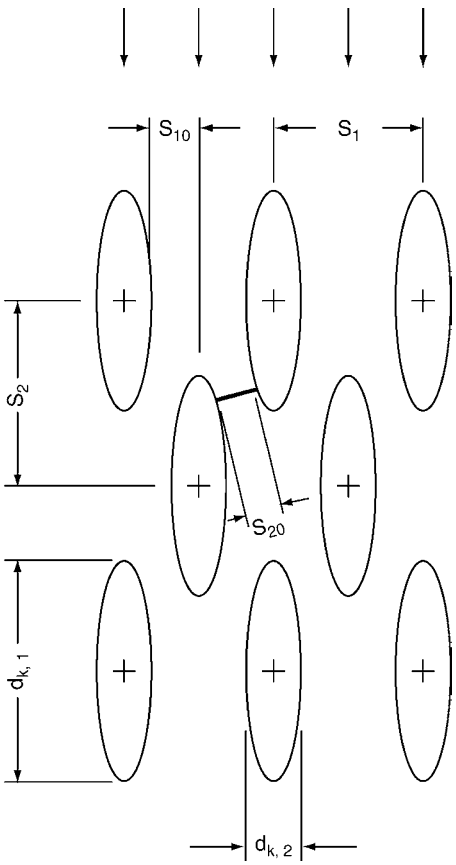

L1.4. Fig. 17. Arrangement of the tube bundle after Merker and Hanke showing the detailed dimensions of the tube bundle.

with

$$\mathrm{Re}_{\mathrm{M,H}} = \frac{w_e l \rho}{\eta} \tag{48}$$

and

$$l = \frac{U}{2}. \tag{49}$$

The constant K and the exponent m in Eq. (47) depend on the longitudinal pitch ratio $s_2/d_{k,1}$; their numerical values at different ranges of the Reynolds number $Re_{\mathrm{M,H}}$ are given in Table 3.

The measurements were made mostly with tube bundles with $n_R = 8$. Some measurements were made with a smaller number of tubes. The experimental results show that the flow after a few tube rows (between five and seven) is fully developed. The number of tube rows to achieve a fully developed flow depends on the longitudinal pitch ratio $s_2/d_{k,1}$. Tube bundles with a higher number of tube rows have a mean pressure drop per tube row, which practically does not depend on the number of the tube rows. The examined tube bundles had a major diameter $d_{k,1} = 30.2$ mm and a minor diameter $d_{k,2} = 7.6$ mm.

Ruth [22] examined three different tube bundles with tubes having an unconventional lenticular shape. The cross section of the tubes was formed from two circular arcs joined together as shown in Fig. 18. The following equation is given for calculating the pressure drop across the tube bundle:

$$\Delta p = \xi_{\mathrm{R}} \frac{S}{F} \frac{\rho w_e^2}{2} = \xi_{\mathrm{R}} n_{\mathrm{R}} \frac{U}{s_1} \frac{\rho w_e^2}{2}. \tag{50}$$

The examined lenticular tubes were made from segments of circular tubes with a chord $C = 51$ mm and a height $h = 6.4$ mm (h = half thickness of a lenticular tube); the tube bundles had in all cases distances $s_{10} = s_{20}$ and different ratios $s_{10}/h = s_{20}/h =$ 1.0, 1.91, and 3.5 (see, Fig. 18).

For the tube bundle with $s_{10}/h = s_{20}/h = 1.91$ and $n_{\mathrm{R}} = 5$, Ruth recommends for calculating the drag coefficient the following equation:

$$\xi_{\mathrm{R}} = \frac{0.56}{\mathrm{Re}_{\mathrm{R}}^{0.27}} \tag{51}$$

with the Reynolds number

$$\mathrm{Re}_{\mathrm{R}} = \frac{w_e (2 s_{10}) \rho}{\eta}. \tag{52}$$

The Reynolds number was varied in the range $2 \times 10^3 \leq \mathrm{Re}_{\mathrm{R}} \leq 5 \times 10^4$.

L1.4. Table 3. Values of K and m in Eq. (47)

$\frac{s_2}{d_{k,1}}$	K	m	Range of $Re_{M,H}$	Examined ratios $\frac{s_1}{d_{k,2}}$
1.00	1.668	0.479	$3.0 \times 10^3 \rightarrow 7.5 \times 10^3$	1.97, 2.26, 2.63, 3.16
	0.216	0.250	$7.5 \times 10^3 \rightarrow 3.0 \times 10^4$	
0.67	0.691	0.359	$4.0 \times 10^3 \rightarrow 1.0 \times 10^4$	2.63, 3.16
	0.251	0.250	$1.0 \times 10^4 \rightarrow 4.0 \times 10^4$	

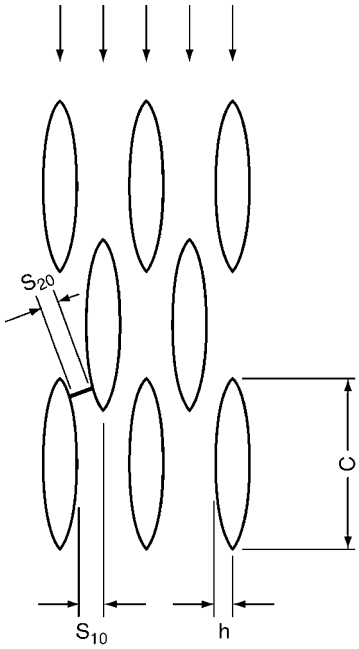

L1.4. Fig. 18. Tube bundle with lenticular tubes examined by Ruth.

The Reynolds number of the other tube bundles was varied only in a narrow range; the drag coefficient was given in a tabular form [22]. For a tube bundle with five tube rows, the following equations are valid approximately:
For $s_{10}/h = s_{20}/h = 1.0$

$$\xi_R = 0.033(2.3 \times 10^4 \leq Re_R \leq 3.2 \times 10^4) \quad (53)$$

and for $s_{10}/h = s_{20}/h = 3.5$

$$\xi_R = 0.051(2.5 \times 10^4 \leq Re_R \leq 2.6 \times 10^4). \quad (54)$$

The deviations between the given mean values and the experimental measurements lie within ± 5 %. Drag coefficients for tube bundles with a number of tube rows less than five are also presented by Ruth [22].

3 Symbols

Latin letters

A_{tot} outer surface of all tubes in bundle (m^2)
a transverse pitch ratio for a tube bundle with circular tubes (1)
b longitudinal pitch ratio for a tube bundle with circular tubes (l)
C chord of a lenticular tube (see Fig. 18) (m (mm))
C_f factor in Eq. (27) (l)
C_v factor in Eq. (28) (l)
c diagonal pitch ratio in a tube bundle with circular tubes (l)
d_o outside tube diameter (m (mm))
d_h hydraulic diameter for a tube bundle with cross arrangement of tube rows (see Eq. 30) (m (mm))
$d_{h,o}$ hydraulic diameter of an oval tube bundle (see Eq. 43) (m (mm))
$d_{k,1}$ major outside diameter of an oval tube (see Figs. 14–17) (m (mm))
$d_{k,2}$ minor outside diameter of an oval tube (see Figs. 14–17) (m (mm))
F frontal area of a tube bundle (m^2)
F_h hydraulic cross section of a tube bundle (see Eq. (25)) (m^2)
F_f factor (see Eq. (2b)) (l)
F_R free area per tube in the cross section of a tube bundle perpendicular to the tube axis (see Eq. (43)) (m^2)
F_v factor (see Eq. (7b)) (l)
$f_{a,l,f}$ factor (see Eq. (4)) (l)
$f_{a,l,v}$ factor (see Eqs. (9) and (10)) (l)
$f_{a,t,f}$ factor (see Eq. (6)) (l)
$f_{a,t,v}$ factor (see Eq. (12)) (l)
f_s factor for pressure drop reduction in case of oblique flow over tube bundles (l)
$f_{n,t}$ correction factor for sudden expansion of flow at outlet of tube bundle (see Eqs. (17) and (18)) (l)
$f_{z,l}$ temperature correction factor for laminar flow (see Eq. (13)) (l)
$f_{zn,l}$ correction factor for number of tube rows in a bundle with laminar flow (see Eqs. (15) and (16)) (l)
$f_{z,t}$ temperature correction factor for turbulent flow (see Eq. (14)) (l)
g acceleration due to gravity ($m\ s^{-2}$)
h half thickness of lenticular tube (see Fig. 18) (m (mm))
h_s hydrostatic head of liquid in a tube bundle (m (mm))
K constant in Eq. (47) (see Table 3) (l)
l half circumference length of an oval tube (see Eq. (49)) (m (mm))
L length of tube bundle in flow direction (m (mm))
m exponent of Reynolds number in $\xi \propto Re^{-m}$ (l)
n_a number of tubes in a row for a tube bundle with cross tube arrangement (l)
n_b number of tubes in the next row for a tube bundle with cross tube arrangement (see n_a) (l)
n_{MR} number of main resistances in flow direction (l)
n_R number of tube rows in a tube bundle; in case of a tube bundle with cross arrangement of tube rows n_R is the total number of tube rows in both directions (l)
p fluid pressure (Pa (bar))
Δp pressure drop across a tube bundle due to friction and flow separation (Pa (bar))
Δp_{mom} pressure change across a tube bundle due to change in flow momentum (Pa (bar))

Δp_s pressure change across a tube bundle due hydrostatic liquid head (Pa (bar))
Re Reynolds number for a tube bundle with circular tubes and parallel or cross arrangement of tube rows ($\mathrm{Re} = w_e d_o \rho/\eta$) (l)
$\mathrm{Re_B}$ Reynolds number for a tube bundle with oval tubes after Brauer (see Eq. (42)) (l)
$\mathrm{Re_{crit.}}$ critical Reynolds number Re(1)
$\mathrm{Re_h}$ Reynolds number for a tube bundle with circular tubes and cross arrangement of tube rows after Brauer (see Eq. (29)) (l)
$\mathrm{Re_{M,H}}$ Reynolds number for a tube bundle with oval tubes after Merker and Hanke (see Eq. (48)) (l)
$\mathrm{Re_R}$ Reynolds number for a tube bundle with lenticular tubes after Ruth (see Eq. (52)) (l)
S wetted area of all tubes in bundle ($\mathrm{m^2}$)
s_1 transverse pitch for a tube bundle with circular or oval tubes and parallel or cross arrangement of tube rows (see Figs. 2, 12, and 14–18) (m (mm))
s_2 longitudinal pitch for a tube bundle with circular or oval tubes and parallel or cross arrangement of tube rows (see Figs. 2, 12, and 14–18) (m (mm))
s_{10} dimension in oval or lenticular tube bundles (see Figs. 17 and 18) (m (mm))
s_{20} dimension in oval or lenticular tube bundles (see Figs. 17 and 18) (m (mm))
s_d diagonal pitch in a tube bundle with circular tubes (see Fig. 2) (m (mm))
s_e dimension in oval tube bundles (see Eqs. (45) and (46)) (m (mm))
U outside circumference of an oval tube (m (mm))
V volume of a tube bundle ($\mathrm{m^3}$)
V_f free volume in a tube bundle ($\mathrm{m^3}$)
$\dot{V}$ volumetric flow rate of fluid through tube bundle ($\mathrm{m^3\ s^{-1}}$ ($\mathrm{m^3\ h^{-1}}$))
w_e mean flow velocity in the narrowest cross section in a tube bundle with circular or oval tubes (see Fig. 2) ($\mathrm{m\ s^{-1}}$)
w_f flow velocity in the free cross section of a tube bundle (see Fig. 2) ($\mathrm{m\ s^{-1}}$)
w_h mean flow velocity in a tube bundle with cross arrangement of tube rows (see Eq. (24)) ($\mathrm{m\ s^{-1}}$)

Greek letters

β cross angle between tubes in adjacent rows in cross arrangement of tube rows (°)
φ angle between flow direction and tube axis (°)
η dynamic viscosity at mean fluid temperature (Pa s)
η_w dynamic viscosity at mean wall temperature (Pa s)
ϑ fluid temperature (°C)
ϑ_w mean wall temperature (°C)
ξ drag coefficient for a tube bundle with circular tubes and parallel or cross arrangement of tube rows (see Eqs. (1), and (31)) (l)
ξ_B drag coefficient for a tube bundle with oval tubes after *Brauer* (see Eq. (38)) (l)
ξ_h drag coefficient for a tube bundle with circular tubes and cross arrangement of tube rows after Brauer (see Eq. (23)) (l)
$\xi_{M,H}$ drag coefficient for a tube bundle with oval tubes after Merker and Hanke (see Eq. (44)) (l)
ξ_R drag coefficient for a tube bundle with lenticular tubes after Ruth (see. Eq. (50)) (l)
ξ_o coefficient to take in consideration the sudden expansion of flow area at exit of tube bundle (see Eqs. (19) and (20)) (l)
ρ density at mean fluid temperature ($\mathrm{kg\ m^{-3}}$)

Subscripts

in at inlet of tube bundle
lam for laminar flow
m mean value
out at outlet of tube bundle
turb for turbulent flow

The units between brackets (mm, bar, and $m^3\ h^{-1}$) are not consistent with the M.K.S. units system; they are used in some places in the text and in the examples for convenience

4 Bibliography

1. Bell KJ (1963) Final Report of the Cooperative Research Program on Shell and Tube Heat Exchangers. University of Delaware – Engineering Experimental Station, Bulletin No. 5, Newark, Delaware
2. Achenbach E (1969) Investigations on the flow through a staggered tube Bundle at Reynolds numbers up to Re=10^7. Wärme- und Stoffübertragung 2(1):47–52
3 Niggeschmidt W (1975) Druckverlust und Wärmeübergang bei fluchtenden, versetzten und teilversetzten querangeströmten Rohrbündeln, Dissertation, TH Darmstadt.
4. Bergelin OP, Colburn AP, Hull HL (1950) Heat transfer and pressure drop during viscous flow across unbaffled tube banks. University of Delaware, Engineering Experimental Station, Bulletin No. 2, Newark, Delaware
5. Gaddis ES, Gnielinski V (1983) Druckverlust in querdurchströmten Rohrbündeln. vt "verfahrenstechnik" 17(7):410–418
6. Sieder EN, Tate GE (1936) Heat transfer and pressure drop of liquids in tubes. Indl Engg Chem 28(12):1429–1435
7. Scholz F (1968) Einfluss der Rohrreihenzahl auf den Druckverlust und Wärmeübergang von Rohrbündeln bei hohen Reynoldszahlen. Chemie-Ing.-Tech. 40(20):988–995
8. Hammeke K, Heinecke E, Scholz F (1967) Wärmeübergangs- und Druckverlustmessungen an querangeströmten Glattrohrbündeln, insbesondere bei hohen Reynoldszahlen. Int J Heat Mass Transfer 10:427–446
9. Achenbach E (1971) Influence of surface roughness on the flow through a staggered tube bank. Wärme- und Stoffübertragung 4:120–126
10. Achenbach E (1971) On the cross flow through in-line tube banks with regard to the effect of surface roughness. Wärme- und Stoffübertragung 4:152–155
11. Poshkas PS, Yu Survila V, Zukauskas AA (1980) Drag and flow patterns for a tube in various rows of bundles with lateral cross flow of air at high Reynolds numbers. Intl Chem Engg 20(3):503–512
12. Samoshka PS, Makaryavichyus VI, Shlanchyauskas AA, Zhyugzhda II, Zukauskas AA (1968) Heat transfer and pressure drop for closely spaced tube banks in water flows. Intl Chem Engg 8(3):388–392
13. Michejew MA (1961) Grundlagen der Wärmeübertragung. VEB Verlag Technik, Berlin, p. 232

14 Idel´chik IE (1966) Handbook of hydraulic resistance, AEC-TR 6630, pp. 332–334
15 Groehn HG (1980) Thermal hydraulic investigation of yawed tube bundle heat exchangers. Proceedings: Advanced Study Institute on "Heat Exchangers, Thermal-Hydraulic Fundamentals and Design" Istanbul/Turkey 4–15
16. Bressler R (1958) Die Wärmeübertragung einzelner Rohrreihen in querangeströmten Rohrbündeln mit kleinen Versetzungsverhältnissen. Forsch.-Ing.-Wes. 24(3):90–103
17. London AL, Mitchell JW, Sutherland WA (1960) Heat-transfer and flow-friction characteristics of crossed-rod matrices, Transactions of the ASME. J Heat Transfer 82:199–213
18. Brauer H (1964) Strömungswiderstand und Wärmeübergang bei quer angeströmten Wärmeaustauschern mit kreuzgitterförmig angeordneten glatten und berippten Rohren. Chemie-Ing.-Techn. 36(3):247–260
19. Klier R (1964) Wärmeübergang und Druckverlust bei quer angeströmten, gekreuzten Rohrgittern. Int J Heat Mass Transfer 7:783–799
20 Brauer H (1961) Untersuchungen an Querstrom-Wärmeaustauschern mit verschiedenen Rohrformen, Sonderdruck aus Mitteilungen der Vereinigung der Grosskesselbesitzer, H. 73, August
21. Merker GP, Hanke H (1986) Heat transfer and pressure drop on the shell-side of tube-banks having oval-shaped tubes. Int J Heat Mass Transfer 29 (12):1903–1909
22. Ruth EK (1983) Experiments on a crossflow heat exchanger with tubes of lenticular shape, Transactions of the ASME. J Heat Transfer 105:571–575

L1.5 Pressure Drop in the Outer Shell of Heat Exchangers

Edward S. Gaddis
Technische Universität Clausthal, Clausthal-Zellerfeld, Germany

1 Shell-and-Tube Heat Exchangers with Segmental Baffles

1.1 Introduction

The flow in the shell-side of a shell-and-tube heat exchanger with segmental baffles is very complex. The segmental baffles lead to a main stream S_M inside the shell, as shown in Fig. 1, which is partly across and partly parallel to the tubes. Unavoidable gaps between the tubes and the holes in the baffles, and between the baffles and the heat exchanger shell cause leakage streams S_L, which may modify the main stream significantly. Since the tubes of the heat exchanger cannot be brought very close to the shell, bypass streams S_B may exist, which also influence the main stream. The flow direction of the main stream relative to the tubes is different in the window sections created by the baffle cuts from that in the cross flow sections existing between the segmental baffles. To calculate the pressure drop in the window sections different equations are needed than those used in the cross flow sections. The spacing between the heat exchanger sheets and the first and the last baffles, which is mostly dictated by the diameter of the inlet and outlet nozzles, differs in many cases from the spacing between two adjacent baffles and some of the aforementioned streams are not present in the first and the last heat exchanger sections. This adds to the complexity of the problem.

The procedure described in this chapter for calculating the shell-side pressure drop in shell-and-tube heat exchangers with segmental baffles is based principally on the Delaware method [1], in which the shell-side is divided into a number of sections. The pressure drop in the different sections is calculated separately and the total pressure drop in the heat exchanger is obtained as a summation of the individual pressure drops. The influence of leakage streams and bypass streams on the pressure drop is taken into consideration by means of correction factors. Unlike the Delaware method the pressure drop across the tube bundle is not obtained from diagrams, but from the equations presented in Subchap. L1.4. The modified calculation procedure is examined through a large number of experimental measurements available in the open literature [2].

1.2 Required Geometrical Data

The following geometrical parameters are required for the calculation of the total pressure drop in a shell-and-tube heat exchanger with segmental baffles:

D_B,D_{BE}	Tube bundle diameters (in most cases $D_{BE} \approx D_B$)
D_i	Inside shell diameter
D_1	Baffle diameter
d_o	Outer diameter of tubes
d_B	Diameter of holes in baffles
d_N	Nozzle diameter
H	Height of baffle cut
L_E	Sum of the shortest connections e and e_1 (see Fig. 4,$L_E = 2e_1 + \Sigma e$)
n_T	Total number of tubes in heat exchanger including blind and support tubes
n_W	Number of tubes in both upper and lower windows (baffle cuts)
n_{RW}	Number of tube rows in a window section
n_S	Number of pairs of sealing strips
n_B	Number of baffles
n_{MR}	Number of main resistances in a central cross flow section
n_{MRE}	Number of main resistances in an end cross flow section
S	Baffle spacing between adjacent baffles
S_E	Baffle spacing between heat exchanger sheets and adjacent baffles (in many cases $S_E = S$)
s_1	Transverse pitch
s_2	Longitudinal pitch

Tube arrangement: in-line or staggered.

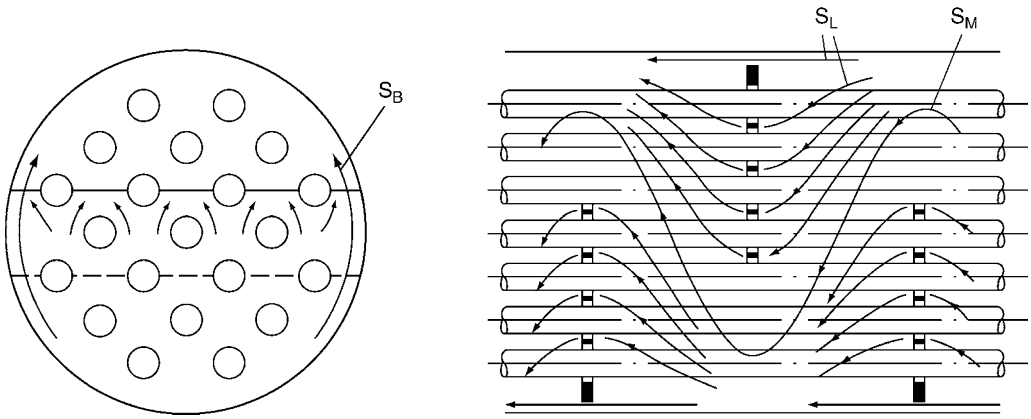

L1.5. Fig. 1. Fluid flow in the shell-side of a shell-and-tube heat exchanger with segmental baffles, S_M Main stream (partly across and partly parallel to the tubes), S_L Leakage stream, S_B Bypass stream.

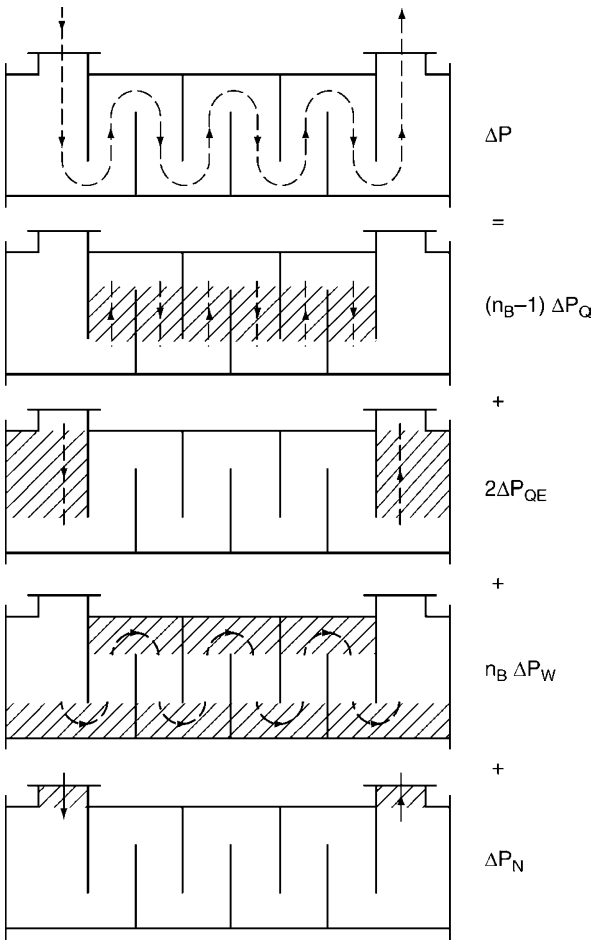

L1.5. Fig. 2. Components of the shell-side pressure drop as given by Eq. (1).

1.3 Shell-Side Pressure Drop

The pressure drop Δp in the heat exchanger shell – as seen in Fig. 2 – may be calculated from the following equation:

$$\Delta p = (n_B - 1)\Delta p_Q + 2\Delta p_{QE} + n_B \Delta p_W + \Delta p_N, \qquad (1)$$

where

Δp_Q = pressure drop in a central cross flow section
Δp_{QE} = pressure drop in an end cross flow section
Δp_W = pressure drop in a window section
Δp_N = pressure drop in both nozzles

In Eq. (1), n_B is the number of baffles.

The difference in the pressure drop between end window sections and central window sections – as a result of a possible difference in the baffle spacing S and S_E – is ignored in Eq. (1).

Equation (1) gives the irreversible pressure drop due to friction and flow separation in the wake region behind the individual tubes in the shell-side of the heat exchanger. Other reversible components of pressure change, which may or may not be present, due to change in momentum flow rate (in case of gases with relatively high density change between the inlet and outlet of the heat exchanger) or due to change in hydrostatic pressure (in case of liquids with relatively high level difference between the inlet and outlet nozzles) are treated in Subchap. L1.4.

1.3.1 Pressure Drop in a Central Cross Flow Section

A central cross flow section is that part of the heat exchanger shell, which lies between two adjacent baffles and is bounded from the top and the bottom by the planes that touch the upper and lower edges of the baffle cuts. A heat exchanger with n_B baffles has $(n_B - 1)$ central cross flow sections. According to K. J. Bell [1], the pressure drop in a central cross flow section may be calculated from the following equation:

$$\Delta p_Q = \Delta p_{Q,0} f_L f_B, \qquad (2)$$

where

$\Delta p_{Q,0}$ = pressure drop in a tube bundle with cross flow under real operating conditions in the absence of leakage and bypass streams
f_L = correction factor to take in consideration the influence of leakage streams through the gaps between the tubes and the holes in the baffles and through the gaps between the baffles and the heat exchanger shell

f_B = correction factor to take in consideration the influence of bypass streams through the gaps between the outermost tubes in the bundle and the inside surface of the heat exchanger shell.

According to E. S. Gaddis and V. Gnielinski [3] (see also Subchap. L1.4), the pressure drop $\Delta p_{Q,0}$ may be calculated from

$$\Delta p_{Q,0} = \xi n_{MR} \frac{\rho w_e^2}{2}, \tag{3}$$

where

ξ = drag coefficient for the tube bundle
n_{MR} = number of main resistances in the path of the main flow in a cross flow section
ρ = fluid density
w_e = characteristic velocity

The number of main resistances n_{MR} in the path of the main flow in a cross flow section is equal to the number of the shortest connection lengths between the tubes, which has to be crossed by the main flow during its motion in a cross flow section from one edge of the segmental baffles to the other. For an in-line tube arrangement and a staggered tube arrangement having the shortest connection between adjacent tubes present in the same row, the number of main resistances n_{MR} is equal to the number of the tube rows n_R in a central cross flow section. For a staggered tube arrangement having the shortest connection between adjacent tubes present in two neighboring rows, the number of main resistances n_{MR} is equal to $(n_R - 1)$. Further, a main resistance that lies on the baffle edge marking the boundary between a central cross flow section and a window section counts only as a half resistance. In general, the drawings of the heat exchanger should be used in evaluating the number of the main resistances. Figure 3 illustrates the rules for evaluating n_{MR}.

The characteristic velocity w_e is the mean fluid velocity in the narrowest cross section measured in the tube row on or near to the shell diameter parallel to the edge of the baffle cuts and is calculated from

$$w_e = \frac{\dot{V}}{A_E}, \tag{4}$$

with $\dot{V}$ the fluid volumetric flow rate through the heat exchanger shell. The flow area A_E in Eq. (4) is given by

$$A_E = SL_E. \tag{5}$$

L_E is the sum of the shortest connections connecting neighboring tubes and the shortest connections between the outermost tubes and the shell measured in the tube row on or near the shell diameter parallel to the edge of the baffle cuts ($L_E = 2e_1 + \Sigma e$). For an in-line tube arrangement and for a staggered tube arrangement with the narrowest cross section between adjacent tubes in the same row (i.e.,$b \geq 0.5\sqrt{2a+1}e$ is calculated from $e = (a-1)d_o$ and for a staggered tube arrangement with the narrowest cross section in the diagonal (i.e.,$b < 0.5\sqrt{2a+1}e$ is calculated from $e = (c-1)d_o$. Equations (17–19) define a,b, and c. Figure 4 illustrates the definition of L_E,e, and e_1. Tie rods connecting the baffles together and fixing the baffle spacing, which influence the length L_E (and thus reducing the area A_E), should be considered in evaluating L_E.

The drag coefficient ξ is given by the following equations:
For in-line tube arrangement

$$\xi = \xi_{lam} f_{z,l} + \xi_{turb} f_{z,t} \left[1 - \exp\left(-\frac{Re + 1000}{2000}\right)\right] \tag{6}$$

with

$$\xi_{lam} = \frac{f_{a,l,f}}{Re}, \tag{7}$$

$$f_{a,l,f} = \frac{280\pi[(b^{0.5} - 0.6)^2 + 0.75]}{(4ab - \pi)a^{1.6}}, \tag{8}$$

$$\xi_{turb} = \frac{f_{a,t,f}}{Re^{0.1(b/a)}}, \tag{9}$$

$$f_{a,t,f} = \left[0.22 + 1.2\frac{\left(1 - \frac{0.94}{b}\right)^{0.6}}{(a - 0.85)^{1.3}}\right] \times 10^{0.47((b/a)-1.5)} + [0.03(a-1)(b-1)]. \tag{10}$$

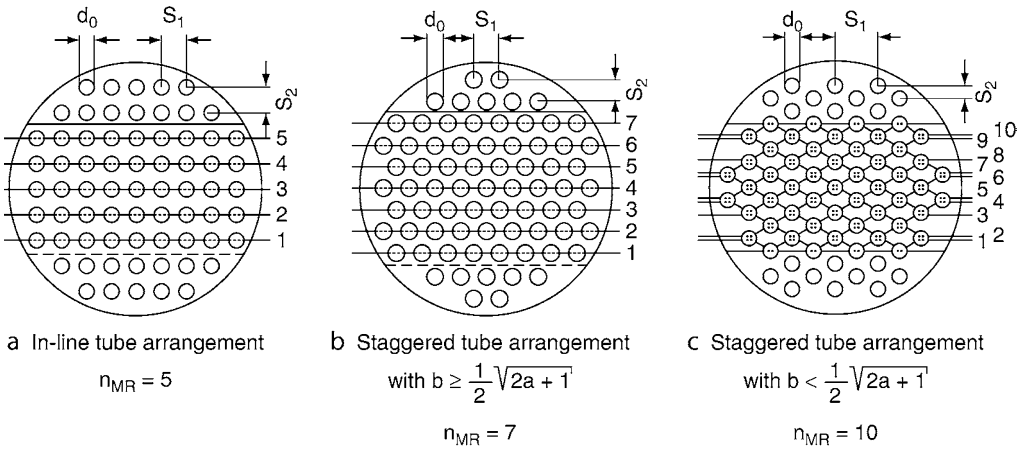

L1.5. Fig. 3. Determination of the number of main resistances n_{MR}.

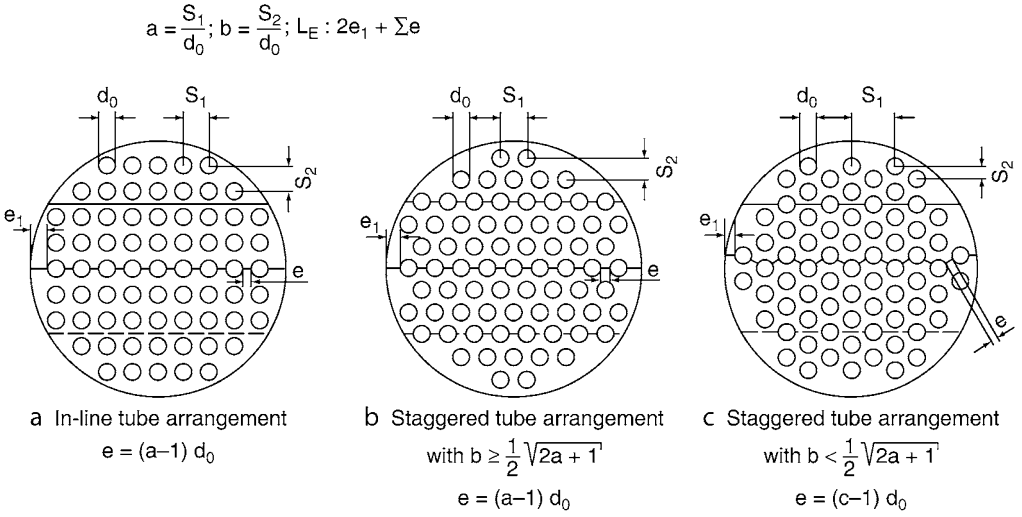

L1.5. Fig. 4. Definition of L_E,e and e_1.

For staggered tube arrangement:

$$\xi = \xi_{\text{lam}} f_{\text{z,l}} + \xi_{\text{turb}} f_{\text{z,t}} \left[1 - \exp\left(-\frac{\text{Re} + 200}{1000}\right)\right] \tag{11}$$

with

$$\xi_{\text{lam}} = \frac{f_{\text{a,l,v}}}{\text{Re}}, \tag{12}$$

$$f_{\text{a,l,v}} = \frac{280\pi\left[(b^{0.5} - 0.6)^2 + 0.75\right]}{(4ab - \pi)a^{1.6}} \quad \text{for } b \geq 0.5\sqrt{2a+1} \tag{13}$$

and

$$f_{\text{a,l,v}} = \frac{280\pi\left[(b^{0.5} - 0.6)^2 + 0.75\right]}{(4ab - \pi)c^{1.6}} \quad \text{for } b < 0.5\sqrt{2a+1}, \tag{14}$$

$$\xi_{\text{turb}} = \frac{f_{\text{a,t,v}}}{\text{Re}^{0.25}} \tag{15}$$

$$f_{\text{a,t,v}} = 2.5 + \left(\frac{1.2}{(a - 0.85)^{1.08}}\right) + 0.4\left(\frac{b}{a} - 1\right)^3 - 0.01\left(\frac{a}{b} - 1\right)^3, \tag{16}$$

$$a = \frac{s_1}{d_0} \text{ transverse pitch ratio}, \tag{17}$$

$$b = \frac{s_2}{d_0} \text{ longitudinal pitch ratio}, \tag{18}$$

$$c = \left((a/2)^2 + b^2\right)^{0.5} \text{ diagonal pitch ratio}. \tag{19}$$

The definition of the Reynolds number Re in the above equations is given by

$$\text{Re} = \frac{w_e d_o \rho}{\eta}. \tag{20}$$

The correction factors $f_{z,l}$ and $f_{z,t}$ for laminar and turbulent flow, respectively, take in consideration the influence of the change in the physical properties in the thermal layer adjacent to the tube surface due to heating or cooling of the shell-side fluid and are defined by

$$f_{\text{z,l}} = \left(\frac{\eta_w}{\eta}\right)^{\frac{0.57}{\left[\left(\frac{4ab}{\pi} - 1\right)\text{Re}\right]^{0.25}}}, \tag{21}$$

$$f_{\text{z,t}} = \left(\frac{\eta_w}{\eta}\right)^{0.14}. \tag{22}$$

A correction factor to take in consideration the influence of the number of tube rows on the pressure drop – as in the case of a tube bundle in a cross flow (see Subchap. L1.4) – is ignored because of the frequent change in the flow direction induced by the baffles. The dynamic viscosity η and the density ρ in the above equations are to be evaluated at the mean fluid temperature $\vartheta_m = (\vartheta_{in} + \vartheta_{out})/2$ and the dynamic viscosity η_w at the mean wall temperature ϑ_w. Moreover, for a gaseous medium with relatively high pressure drop, the gas density has to be evaluated at the mean gas pressure $p_m = (p_{in} + p_{out})/2$; since the gas pressure at the outlet of the heat exchanger is not known a priori, an iteration procedure is required.

The graphical presentations of the arrangement factors $f_{a,l,f}$, $f_{a,t,f}$, $f_{a,l,v}$, and $f_{a,t,v}$ in dependence on the transverse pitch ratio a and the longitudinal pitch ratio b, the dependence of the factors between square brackets in Eqs. (6) and (11) on the Reynolds number, the position of the shortest connections between tubes in tube bundles with staggered tube arrangement in dependence on a and b as well as the dependence of the drag coefficient ξ on the Reynolds number in case of isothermal flow for six customarily used tube bundles are given in Subchap. L1.4.

Leakage Correction Factor

According to J. Taborek [4], the leakage correction factor f_L may be calculated from

$$f_L = \exp\left[-1.33(1 + R_M)R_L^r\right] \tag{23}$$

with

$$r = [-0.15(1 + R_M) + 0.8], \tag{24}$$

$$R_M = \frac{A_{GSB}}{A_{SG}}, \tag{25}$$

$$R_L = \frac{A_{SG}}{A_E}. \tag{26}$$

A_{SG} is the sum of the areas of all gaps between the tubes and the holes in a baffle and between the shell and a baffle and is given by

$$A_{SG} = A_{GTB} + A_{GSB}. \tag{27}$$

The area A_{GTB} of all gaps between the tubes and the holes in a baffle is given by

$$A_{GTB} = \left(n_T - \frac{n_W}{2}\right)\frac{\pi\left(d_B^2 - d_o^2\right)}{4} \tag{28}$$

and the area A_{GSB} of the gap between the shell and a baffle is given by

$$A_{GSB} = \frac{\pi}{4}\left(D_i^2 - D_1^2\right)\frac{360 - \gamma}{360}, \tag{29}$$

where γ is the central angle of a baffle cut (see Fig. 10) measured in degrees and is given by

$$\gamma = 2\cos^{-1}\left(1 - \frac{2H}{D_1}\right). \tag{30}$$

In counting the number of tubes n_W in both upper and lower windows, the tubes that lie on the edge of the baffles and are thus partly in a cross flow section and partly in a window section count as half tubes. The leakage correction factor f_L in dependence on R_L with R_M as a parameter is shown in Fig. 5.

Sedimentation and corrosion – if present during operation of the heat exchanger – might reduce the area of the gaps between the tubes and the holes in the baffles and between the shell and the baffles and might thus lead to an increase in the shell-side pressure drop with elapse of time. Depending on the expected amount of deposits during operation, the leakage correction factor f_L, calculated from Eq. (23), should be correspondingly modified.

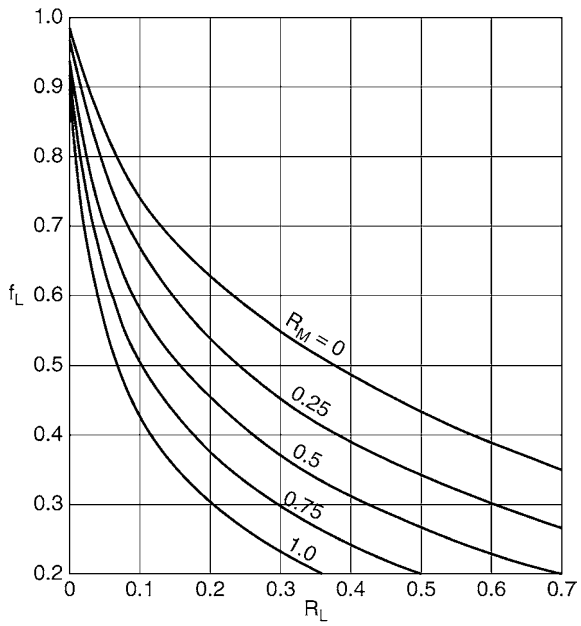

L1.5. Fig. 5. Leakage correction factor as a function of R_L and R_M as given by Eq. (23).

Bypass Correction Factor

The bypass correction factor f_B is calculated from

$$f_B = \exp\left[-\beta R_B\left(1 - \sqrt[3]{2R_S}\right)\right] \text{ for } R_S < \frac{1}{2} \tag{31}$$

and

$$f_B = 1 \text{ for } R_S \geq \frac{1}{2}, \tag{32}$$

where

$$\beta = 4.5 \text{ for laminar flow } (\mathrm{Re} < 100) \tag{33}$$

and

$$\beta = 3.7 \text{ for the transition region and turbulent flow } (\mathrm{Re} \geq 100). \tag{34}$$

The ratios R_B and R_S are given by

$$R_B = \frac{A_B}{A_E}, \tag{35}$$

$$R_S = \frac{n_S}{n_{MR}}. \tag{36}$$

n_S is the number of pairs of sealing strips (in Fig. 6, $n_S = 2$). The area A_E in Eq. (35) is calculated from Eq. (5) and the flow cross sectional area A_B, which is responsible for the bypass streams, is given by

$$A_B = S(D_i - D_B - e) \text{ for } e < (D_i - D_B) \tag{37}$$

and

$$A_B = 0 \text{ for } e \geq (D_i - D_B). \tag{38}$$

The bundle diameter D_B is the diameter of a circle, which touches the outermost tubes in the space between the upper and lower edges of adjacent baffles (see Fig. 10). Figure 7 shows the dependence of the bypass correction factor f_B on R_B and R_S.

1.3.2 Pressure Drop in an End Cross Flow Section

An end cross flow section is that part of the heat exchanger shell, which lies between one of the tube sheets and the adjacent baffle, and is bounded at its outlet (for the inlet end cross flow section) or at its inlet (for the outlet end cross flow section) by

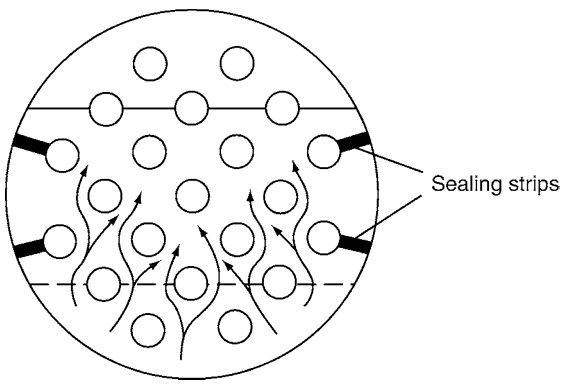

L1.5. Fig. 6. Arrangement for sealing strips n_S ($n_S = 2$ in the figure).

the plane that touches the edges of the baffle cuts. An inlet end cross flow section does not have leakage streams that flow in that section from a previous central cross flow section and an outlet end cross flow section does not have leakage streams that flow in a following central cross flow section. The influence of leakage on pressure drop in both end cross flow sections is thus ignored. Figure 8 shows the difference in the path of leakage streams between an end cross flow section and a central cross flow section.

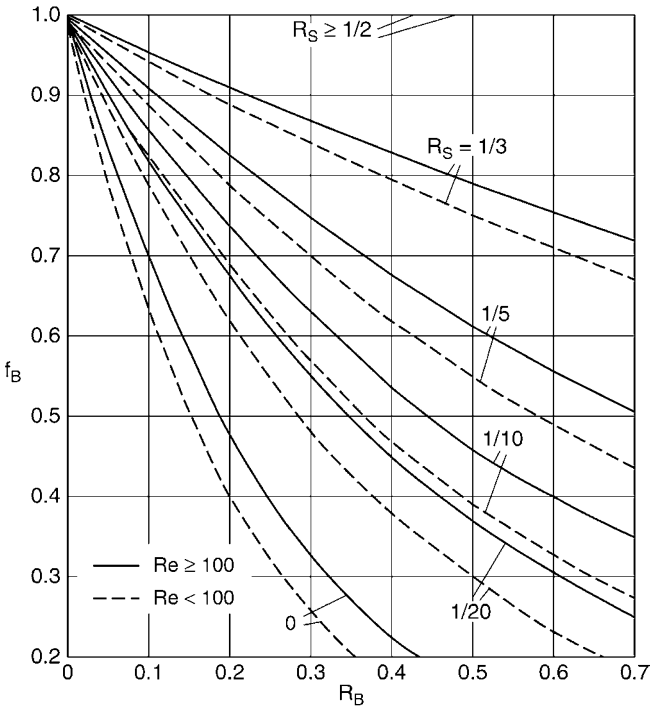

L1.5. Fig. 7. Bypass correction factor f_B as a function of R_B and R_S as given by Eq. (31).

The pressure drop Δp_{QE} in an end cross flow section may be calculated from the following equation:

$$\Delta p_{QE} = \Delta p_{QE,0} f_B. \tag{39}$$

$\Delta p_{QE,0}$ is the pressure drop in an end cross flow section in the absence of bypass streams.

If the baffle spacing in an end cross flow section S_E is equal to the baffle spacing S in a central cross flow section, then

$$\Delta p_{QE,0} = \Delta p_{Q,0} \left(\frac{n_{MRE}}{n_{MR}} \right) \tag{40}$$

with n_{MRE} the number of main resistances in an end cross flow section (in Fig. 3a $n_{MRE} = 7$, in Fig. 3b $n_{MRE} = 9$, and in Fig. 3c $n_{MRE} = 13$). A main resistance that lies on the baffle edge marking the boundary between an end cross flow section and a window section counts only as a half resistance (see Example 1).

If $S_E \neq S$ then

$$\Delta p_{QE,0} = \xi n_{MRE} \frac{\rho w_{e,E}^2}{2}. \tag{41}$$

The velocity $w_{e,E}$ is calculated from

$$w_{e,E} = \frac{\dot{V}}{A_{E,E}} = w_e \frac{S}{S_E} \tag{42}$$

and

$$A_{E,E} = S_E L_E. \tag{43}$$

The drag coefficient ξ in Eq. (41) for an end cross flow section is calculated from Eq. (6) or (11); The Reynolds number Re in Eqs. (6, 7, 9, 11, 12, 15, 21) should be replaced by the Reynolds number in an end cross flow section Re_E, which is defined by

$$Re_E = Re \frac{S}{S_E}. \tag{44}$$

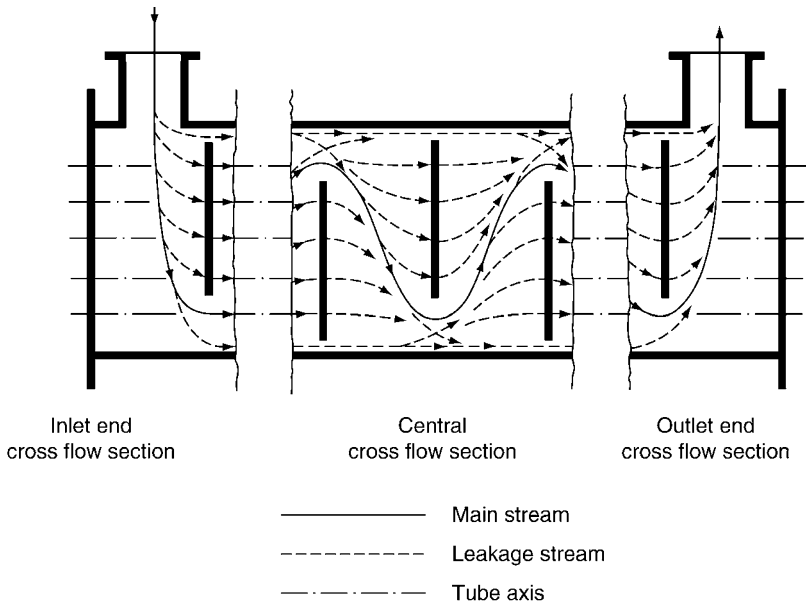

L1.5. Fig. 8. Difference in the path of leakage streams between an end cross flow section and a central cross flow section.

The bypass correction factor f_B is calculated from Eq. (31) or (32); the constant β in Eq. (31) is obtained from Eq. (33) or (34) depending on the numerical value of Re_E.

1.3.3 Pressure Drop in a Window Section

According to E. S. Gaddis and V. Gnielinski [2], the pressure drop Δp_W in a window section may be calculated from

$$\Delta p_W = \sqrt{\Delta p_{W,lam}^2 + \Delta p_{W,turb}^2} f_z f_L. \quad (45)$$

where

$$\Delta p_{W,lam} = \left[\frac{56}{\left(\frac{e w_z \rho}{\eta}\right)} n_{MRW} + \frac{52}{\left(\frac{d_g w_z \rho}{\eta}\right)} \left(\frac{S}{d_g}\right) + 2 \right] \left(\frac{\rho w_z^2}{2}\right) \quad (46)$$

and

$$\Delta p_{W,turb} = (0.6 n_{MRW} + 2) \left(\frac{\rho w_z^2}{2}\right). \quad (47)$$

n_{MRW} is the number of the effective main resistances in a window section. It is not essential that the numerical value of n_{MRW} is an integer; it can be calculated from

$$n_{MRW} = \frac{0.8H}{s_2}. \quad (48)$$

Equation (48) is valid when $n_{MRW} \le 2n_{RW}$, otherwise $n_{MRW} = 2n_{RW}$ (n_{RW} is the number of tube rows in a window section). d_g is the equivalent diameter of the flow area in a window section, which can be calculated from

$$d_g = \frac{4A_W}{U_W} \quad (49)$$

with A_W the cross-sectional flow area in a window section and U_W the wetted perimeter, calculated from the following equations:

$$A_W = A_{WT} - A_T \quad (50)$$

The cross-sectional area A_{WT} for a window section including the area of the window tubes is given by

$$A_{WT} = \frac{\pi}{4} D_i^2 \left(\frac{\gamma}{360}\right) - \frac{(D_1 - 2H) D_1}{4} \sin\left(\frac{\gamma}{2}\right) \quad (51)$$

and the area A_T of the window tubes is given by

$$A_T = \frac{\pi}{4} d_o^2 \left(\frac{n_W}{2}\right). \quad (52)$$

The wetted perimeter U_W is calculated from

$$U_W = \pi D_i \left(\frac{\gamma}{360}\right) + \pi d_o \left(\frac{n_W}{2}\right). \quad (53)$$

In evaluating the equivalent diameter d_g, the wetted area of the edge of the baffle has been ignored.

The characteristic velocity w_z in Eqs. (46) and (47) is evaluated from

$$w_z = (w_e w_p)^{1/2}. \quad (54)$$

w_e is given by Eq. (4) and w_p is calculated from

$$w_p = \frac{\dot{V}}{A_W}. \quad (55)$$

Equations for calculating the shortest connection e are given in Fig. (4). The correction factor f_z in Eq. (45) takes in consideration the dependence of the physical properties on temperature; it is given by

$$f_z = f_{z,l} \text{ for } Re < 100, \quad (56)$$

$$f_z = f_{z,t} \text{ for } Re \ge 100. \quad (57)$$

The correction factors $f_{z,l}$ and $f_{z,t}$ are calculated from Eqs. (21) and (22). The leakage correction factor f_L is given by Eq. (23). The influence of bypass streams in a window section has been ignored.

1.3.4 Pressure Drop in Inlet and Outlet Nozzles

The pressure drop Δp_N in both inlet and outlet nozzles may be calculated from

$$\Delta p_N = \xi_N \frac{\rho w_N^2}{2} \quad (58)$$

with ξ_N nozzle drag coefficient for both nozzles and w_N nozzle velocity given by

$$w_N = \frac{\dot{V}}{\frac{\pi}{4} d_N^2}. \quad (59)$$

It is assumed that both nozzles have the same nozzle diameter d_N and the same nozzle velocity w_N. According to V. Gnielinski [5], the drag coefficient ξ_N in the turbulent range, obtained from measurements with air and unbaffled shell-and-tube heat exchangers, may be correlated by

$$\xi_N = 5.79 \left(\frac{A_N}{A_F}\right)^{1.14} \left(\frac{d_N}{D_i}\right) \left(\frac{D_{BE}}{d_N}\right)^{2.4}. \quad (60)$$

The ratio of the cross-sectional area A_N of the nozzle to the free cross-sectional area A_F of the heat exchanger shell is given by

$$\frac{A_N}{A_F} = \frac{\frac{\pi}{4} d_N^2}{\frac{\pi}{4}\left(D_i^2 - n_T d_o^2\right)}. \quad (61)$$

The bundle diameter D_{BE} is the diameter of a circle, which touches the outermost tubes of all tubes in the shell of the heat exchanger (including the tubes in the window sections). In most heat exchanger layouts $D_{BE} \approx D_B$; however this is not essential in every case.

In some cases, the nozzle velocity w_N in the outlet nozzle differs from that in the inlet nozzle, for example, the case of a gas with a large density difference between the inlet and outlet of the heat exchanger. In such cases, it is recommended to use different drag coefficients $\xi_{N,in}$ and $\xi_{N,out}$ for inlet and outlet nozzles, respectively. According to V. Gnielinski [5]

$$\xi_{N,in} = 3.308 \left(\frac{A_N}{A_F}\right)^{1.14} \left(\frac{d_N}{D_i}\right) \left(\frac{D_{BE}}{d_N}\right)^{2.4}, \quad (62)$$

$$\xi_{N,out} = 2.482 \left(\frac{A_N}{A_F}\right)^{1.14} \left(\frac{d_N}{D_i}\right) \left(\frac{D_{BE}}{d_N}\right)^{2.4}. \quad (63)$$

Equation (58) can then be used to calculate the pressure drop in each nozzle separately using the corresponding drag coefficient and the corresponding nozzle velocity. In analogy, the same procedure may be used if (in seldom cases) the diameter of the outlet nozzle is different from that of the inlet nozzle. In such cases, different numerical values for the nozzle diameter d_N and the area ratio (A_N/A_F) have to be used.

According to V. Gnielinski [5], the nozzle drag coefficient is independent of the Reynolds number in the turbulent range. Previous estimation for the nozzle drag coefficient in the laminar and the turbulent ranges, based basically on sudden expansion of the flow at outlet of the inlet nozzle, was given by $\xi_N \approx 2$. Measurements made by V. Gnielinski [5] show that this value may be approached if the free cross-sectional area in the heat exchanger shell is relatively large (i.e., small ratio (A_N/A_F)). With decreasing free cross-sectional area in the shell (i.e., increasing number and diameter of the tubes in the shell), numerical values for ξ_N as high as 13 were measured experimentally. In the absence of a detailed experimental investigation in the laminar range similar to that made in the turbulent range [5], it may be safer to use Eq. (60) for both laminar and turbulent ranges provided that the calculated value $\xi_N \geq 2$; otherwise the value $\xi_N = 2$ should be used.

Mostly the nozzle pressure drop in a shell-and-tube heat exchanger with a large number of segmental baffles, compared with the total pressure drop, is small. However, the high negative exponent of the nozzle diameter in the equation for the nozzle pressure drop indicates that with decreasing nozzle diameter the nozzle pressure drop may contribute considerably to the total pressure drop (Eq. (58) gives $\Delta p_N \propto d_N^{-3.12}$ and the equation $\xi_N = 2$ gives $\Delta p_N \propto d_N^{-4}$).

Validity Ranges

The given equations for predicting the shell-side pressure drop may be used for heat exchangers having geometrical and operating parameters that lie within the following ranges:

$$1 < \mathrm{Re} < 5 \times 10^4$$

$$3 \leq \mathrm{Pr} \leq 10^3$$

$$0.2 \leq \frac{S}{D_i} \leq 1.0$$

$$0.15 \leq \frac{H}{D_i} \leq 0.4$$

$$R_B \leq 0.5$$

$$1.2 \leq \frac{t}{d_o} \leq 2.0$$

$$\frac{D_i}{d_o} > 10$$

$$f_L \geq 0.4$$

$$f_B \geq 0.4$$

The examined heat exchangers had tube bundles with equilateral triangular and staggered square tube arrangements [2]. The transverse pitch s_1 and the longitudinal pitch s_2 are related to the pitch t by the following relations:

For an equilateral triangular tube arrangement:

$$s_1 = t \tag{64a}$$

$$s_2 = 0.866t \tag{64b}$$

For a staggered square tube arrangement:

$$s_1 = 1.414t \tag{65a}$$

$$s_2 = 0.707t \tag{65b}$$

Measurements with in-line tube arrangement were not available. The fluids used were oil and water. The maximum deviations between measurements and predictions for the heat exchangers having geometrical and operating parameters within the ranges given above were about $\pm 35\%$. Heat exchangers with parameters highly outside the aforementioned ranges had much higher deviations. However, a small deviation from the mentioned geometrical and operating parameters did not lead immediately to much higher deviations.

It is worth mentioning that the validity ranges of the geometrical and operating parameters for the pressure drop equations given in this chapter are based on pressure drop measurements. On the other hand, the validity ranges of the same parameters for the heat transfer equations given in Chap. G8 are based on heat transfer measurements. It is not essential that the validity ranges of the parameters are the same in both cases. It is also important to emphasize that geometrical factors that lead to a reduction in the pressure drop have mostly a negative effect on the heat transfer performance of the heat exchanger; for example, increasing the area responsible for the bypass streams leads to a reduction in the pressure drop as well as in the heat transfer. This is also the case, when the gap area between the baffles and the exchanger shell is increased. On the other hand, increasing the gap area between the outer surface of the tubes and the holes in the baffles reduces the pressure drop but does not have the same adverse effect on the heat transfer as the gap area between the baffles and the shell, since leakage streams through the gap area between the tubes and the holes in the baffle contribute partly to heat transfer. All these factors have to be taken in consideration during dimensioning a shell-and-tube-heat exchanger with segmental baffles.

1.3.5 Simplified Equations for Certain Ranges of the Reynolds Numbers

The given equations for predicting the pressure drop in a central cross flow section, an end cross flow section, or a window section are formed by superimposing a laminar term and a turbulent term. Consequently, they cover a wide range of the Reynolds number. Equations of this form allow simple computer codes. However, if computations are made with a pocket calculator at very low or very high numerical values of the Reynolds number, the computational effort can be significantly reduced by eliminating some of the terms of the equations. The simplifications of the equations are as follows:

For calculating the pressure drop $\Delta p_{Q,0}$ in a central cross flow section:

Each of Eqs. (6) and (11) may be replaced by

For $Re \leq 10$:

$$\xi = \xi_{lam} f_{z,l}. \tag{66}$$

For $Re \geq 10^4$:

$$\xi = \xi_{turb} f_{z,t}. \tag{67}$$

The terms between square brackets in Eqs. (6) and (11) are effectively equal to unity in the range $Re \geq 10^4$.

For calculating the pressure drop $\Delta p_{QE,0}$ in an end cross flow section, when $S \neq S_E$:

Equation (41) may be replaced by

$$\Delta p_{QE,0} = \Delta p_{Q,0} \left(\frac{n_{MRE}}{n_{MR}}\right) \left(\frac{S}{S_E}\right)^{2-m}. \tag{68}$$

The exponent m is given by

For $Re \leq 10$ and $Re_E \leq 10$ simultaneously:

$$m = 1 \text{ for both in–line and staggered tube arrangements.} \tag{69}$$

For $Re \geq 10^4$ and $Re_E \geq 10^4$ simultaneously:

$$m = 0.1 \left(\frac{b}{a}\right) \text{ for in–line tube arrangement,} \tag{70}$$

$$m = 0.25 \text{ for staggered tube arrangement.} \tag{71}$$

In every case, m is the exponent of the Reynolds number in Eqs. (7), (9), (12), and (15).

For calculating the pressure drop Δp_W in a window section:

Equation (45) may be replaced by

For $Re \leq 10$:

$$\Delta p_W = \Delta p_{W,lam} f_{z,l} f_L. \tag{72}$$

For $Re \geq 10^4$:

$$\Delta p_W = \left[\sqrt{4 + (0.6 n_{MRW} + 2)^2} \left(\frac{\rho w_z^2}{2}\right)\right] f_{z,t} f_L. \tag{73}$$

Example 1

Figure 9 is a longitudinal and Fig. 10 is a transverse cross section of a shell-and-tube heat exchanger with two tube passes. Water at a flow rate of 60 $m^3\ h^{-1}$ is cooled in the heat exchanger shell from the inlet temperature $\vartheta_{in} = 68.5°C$ to the outlet temperature $\vartheta_{out} = 51.5\ °C$; the mean wall temperature amounts to 50°C. It is required to calculate the pressure drop through the heat exchanger shell due to friction and flow separation.

Given geometrical data:

Tube bundle diameter $D_B = 560$ mm

Inside shell diameter $D_i = 597$ mm

Baffle diameter $D_l = 590$ mm

Outer diameter of tubes $d_o = 25$ mm

Diameter of holes in baffles $d_B = 26$ mm

Nozzle diameter $d_N = 210$ mm

Height of baffle cut $H = 134.5$ mm

Total number of tubes in bundle $n_T = 258$

Number of tubes in both upper and lower windows $n_W = 82$

(Tubes that lie on the baffle edge, i.e., partly in a cross flow section and partly in a window section, count as half tubes (see Fig. 10).)

Number of tube rows in a window section $n_{RW} = 4.5$

(A tube row that lies on the baffle edge, i.e., partly in a cross flow section and partly in a window section, counts as a half row (see Fig. 10).)

Number of pairs of sealing strips $n_S = 0$

Number of baffles $n_B = 8$

Number of main resistances in a central cross flow section $n_{MR} = 11$

Number of main resistances in an end cross flow section $n_{MRE} = 15.5$

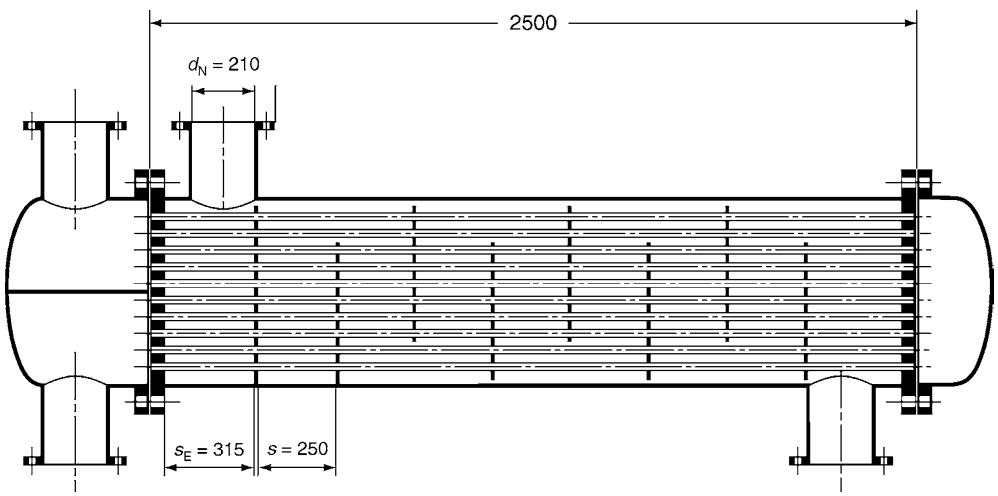

L1.5. Fig. 9. Longitudinal cross section in the heat exchanger of the example (dimensions in mm).

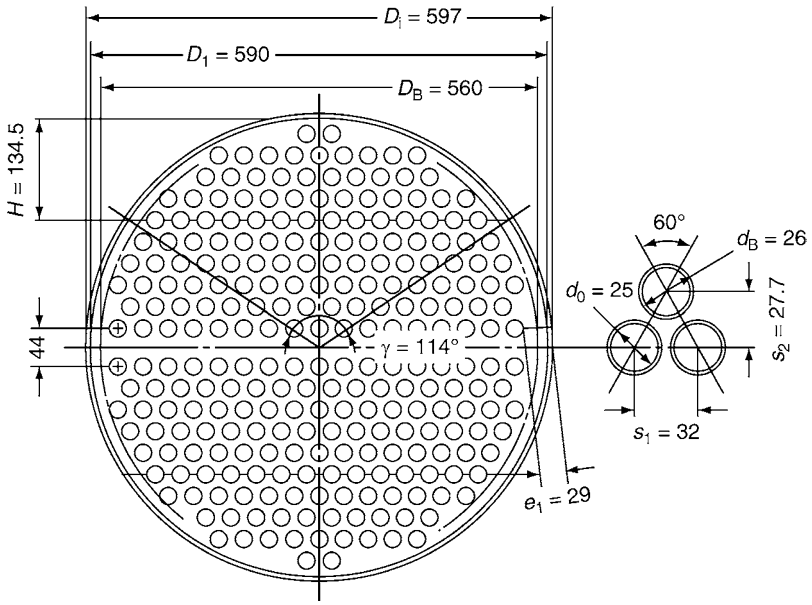

L1.5. Fig. 10. Transverse cross section in the heat exchanger of the example (dimensions in mm).

(A main resistance that lies on the baffle edge, i.e., partly in a cross flow section and partly in a window section, counts as a half main resistance in calculating n_{MR} and n_{MRE} (see Fig. 10).)

Baffle spacing between adjacent baffles $S = 250$ mm

Baffle spacing between the heat exchanger sheets and adjacent baffles $S_E = 315$ mm

Transverse pitch $s_1 = 32.0$ mm

Longitudinal pitch $s_2 = 27.7$ mm

Staggered tube arrangement

Further geometrical data are given in Figs. 9 and 10.

Physical properties of water:

$$\text{At a mean temperature } \vartheta_m = \frac{68.5 + 51.5}{2} = 60^\circ\text{C}$$

$$\text{Density } \rho = 983 \text{ kg m}^{-3}$$

$$\text{Dynamic viscosity } \eta = 467 \times 10^{-6} \text{ Pa s}$$

$$\text{At mean wall temperature } \vartheta_w = 50^\circ\text{C}$$

$$\text{Dynamic viscosity } \eta_w = 547 \times 10^{-6} \text{ Pa s}$$

Solution:

Calculation of the pressure drop Δp_Q in a central cross flow section:

$$a = \frac{s_1}{d_o} = \frac{32}{25} = 1.28$$

$$b = \frac{s_2}{d_o} = \frac{27.7}{25} = 1.11$$

Check: Is $b \geq \frac{1}{2}\sqrt{2a+1}$? (see Fig. 4) $\rightarrow 1.11\text{mm} \geq \frac{1}{2}\sqrt{2 \times 1.28 + 1} = 0.943\text{mm} \rightarrow$ yes

Thus, the shortest distance connecting adjacent tubes lies between tubes in the same row. Hence

$$e = (a-1)d_o = (1.28 - 1) \times 25 = 7 \text{ mm}$$

From Fig. 10 $\rightarrow e_1 = 29$ mm and the number of the shortest distances e is 16. Thus

$$L_E = 2e_1 + \Sigma e = 2 \times 29 + 16 \times 7 = 170 \text{ mm}$$

$$\text{Equation (5): } A_E = SL_E = 250 \times 170 = 42500 \text{ mm}^2$$

$$\text{Equation (4): } w_e = \frac{\dot{V}}{A_E} = \frac{\left(\frac{60}{3600}\right)}{42500 \times 10^{-6}} = 0.392 \text{ ms}^{-1}$$

$$\text{Equation (20): } \text{Re} = \frac{w_e d_o \rho}{\eta} = \frac{0.392 \times (25 \times 10^{-3}) \times 983}{467 \times 10^{-6}} = 2.06 \times 10^4$$

$$\text{Equation (16): } f_{a,t,v} = 2.5 + \left(\frac{1.2}{(a-0.85)^{1.08}}\right) + 0.4\left(\frac{b}{a} - 1\right)^3 - 0.01\left(\frac{a}{b} - 1\right)^3$$

$$= 2.5 + \left(\frac{1.2}{(1.28-0.85)^{1.08}}\right) + 0.4\left(\frac{1.11}{1.28} - 1\right)^3 - 0.01\left(\frac{1.28}{1.11} - 1\right)^3 = 5.48$$

The value of $f_{a,t,v}$ can also be obtained approximately from Fig. 9 in Subchap. L1.4.

$$\text{Equation (15): } \xi_{turb} = \frac{f_{a,t,v}}{\text{Re}^{0.25}} = \frac{5.48}{(2.06 \times 10^4)^{0.25}} = 0.457$$

$$\text{Equation (22): } f_{z,t} = \left(\frac{\eta_w}{\eta}\right)^{0.14} = \left(\frac{547 \times 10^{-6}}{467 \times 10^{-6}}\right)^{0.14} = 1.02 \text{ (turbulent flow)}$$

Since $\text{Re} > 10^4$, Eq. (67) can be used, or

$$\xi = \xi_{turb} f_{z,t} = 0.457 \times 1.02 = 0.466$$

If Eq. (11) is used instead of Eq. (67) to calculate ξ, a value $\xi = 0.477$ will be obtained.

$$\text{Equation (3): } \Delta p_{Q,0} = \xi n_{MR} \frac{\rho w_e^2}{2} = 0.466 \times 11 \times \left(\frac{983 \times 0.392^2}{2}\right) = 387 \text{ Pa}$$

Calculation of leakage correction factor f_L:

$$\text{Equation (28): } A_{GTB} = \left(n_T - \frac{n_W}{2}\right)\frac{\pi\left(d_B^2 - d_o^2\right)}{4} = \left(258 - \frac{82}{2}\right)\frac{\pi \times (26^2 - 25^2)}{4} = 8692\,\text{mm}^2$$

$$\text{Equation (30): } \gamma = 2\cos^{-1}\left(1 - \frac{2H}{D_1}\right) = 2\cos^{-1}\left(1 - \frac{2 \times 134.5}{590}\right) = 114^\circ$$

$$\text{Equation (29): } A_{GSB} = \frac{\pi}{4}\left(D_i^2 - D_1^2\right)\frac{360 - \gamma}{360} = \frac{\pi}{4}\left(597^2 - 590^2\right)\frac{360 - 114}{360} = 4459\,\text{mm}^2$$

$$\text{Equation (27): } A_{SG} = A_{GTB} + A_{GSB} = 8692 + 4459 = 13151\,\text{mm}^2$$

$$\text{Equation (25): } R_M = \frac{A_{GSB}}{A_{SG}} = \frac{4459}{13151} = 0.339$$

$$\text{Equation (26): } R_L = \frac{A_{SG}}{A_E} = \frac{13151}{42500} = 0.309$$

$$\text{Equation (24): } r = [-0.15(1 + R_M) + 0.8] = [-0.15 \times (1 + 0.339) + 0.8] = 0.599$$

$$\text{Equation (23): } f_L = \exp\left[-1.33(1 + R_M)R_L^r\right] = \exp[-1.33 \times (1 + 0.339) \times 0.309^{0.599}] = 0.414$$

Calculation of bypass correction factor f_B:

There are no sealing strips. Thus

$$\text{Equation (36): } R_S = \frac{n_S}{n_{MR}} = 0$$

$$\text{Equation (34): } \beta = 3.7 \text{ since Re} \geq 100$$

Check: $e = 7$ mm and $D_i - D_B = 597 - 560 = 37$ mm, i.e., $e < (D_i - D_B)$; thus Eq. (37) should be used.

$$\text{Equation (37): } A_B = S(D_i - D_B - e) = 250 \times (597 - 560 - 7) = 7500\,\text{mm}^2$$

$$\text{Equation (35): } R_B = \frac{A_B}{A_E} = \frac{7500}{42500} = 0.176$$

$$\text{Equation (31): } f_B = \exp\left[-\beta R_B\left(1 - \sqrt[3]{2R_S}\right)\right] = \exp\left[-3.7 \times 0.176 \times \left(1 - \sqrt[3]{2 \times 0}\right)\right] = 0.521 \text{ since } R_S = 0 \text{ (i.e., } < \frac{1}{2})$$

$$\text{Equation (2): } \Delta p_Q = \Delta p_{Q,0} f_L f_B = 387 \times 0.414 \times 0.521 = 83.5\,\text{Pa}$$

Calculation of the pressure drop Δp_{QE} in an end cross flow section:

$$\text{Equation (44): } \text{Re}_E = \text{Re}\frac{S}{S_E} = \left(2.06 \times 10^4\right) \times \frac{250}{315} = 1.63 \times 10^4$$

Since $S_E \neq S$, $\text{Re} > 10^4$ and $\text{Re}_E > 10^4$, Eq. (68) may be used with $m = 0.25$ (staggered tube arrangement, see Eq. (71)).

$$\text{Equation (68): } \Delta p_{QE,0} = \Delta p_{Q,0}\left(\frac{n_{MRE}}{n_{MR}}\right)\left(\frac{S}{S_E}\right)^{2-m} = 387 \times \left(\frac{15.5}{11}\right) \times \left(\frac{250}{315}\right)^{2-0.25} = 363.9\,\text{Pa}$$

If Eq. (41) and Eq. (11) are used instead of Eq. (68) to calculate $\Delta p_{QE,0}$, a value $\Delta p_{QE,0} = 374.7$ Pa will be obtained.

$$\text{Equation (39): } \Delta p_{QE} = \Delta p_{QE,0} f_B = 363.9 \times 0.521 = 189.6\,\text{Pa}$$

Calculation of the pressure drop Δp_W in a window section:

$$\text{Equation (51): } A_{WT} = \frac{\pi}{4}D_i^2\left(\frac{\gamma}{360}\right) - \frac{(D_1 - 2H)D_1}{4}\sin\left(\frac{\gamma}{2}\right) = \frac{\pi}{4} \times 597^2 \times \left(\frac{114}{360}\right) - \frac{(590 - 2 \times 134.5) \times 590}{4}\sin\left(\frac{114}{2}\right) = 48933\,\text{mm}^2$$

$$\text{Equation (52): } A_T = \frac{\pi}{4}d_o^2\left(\frac{n_W}{2}\right) = \frac{\pi}{4} \times 25^2 \times \left(\frac{82}{2}\right) = 20126\,\text{mm}^2$$

$$\text{Equation (50): } A_W = A_{WT} - A_T = 48933 - 20126 = 28807\,\text{mm}^2$$

$$\text{Equation (55): } w_p = \frac{\dot{V}}{A_W} = \frac{\left(\frac{60}{3600}\right)}{28807 \times 10^{-6}} = 0.579\,\text{ms}^{-1}$$

$$\text{Equation (54): } w_z = \left(w_e w_p\right)^{1/2} = (0.392 \times 0.579)^{1/2} = 0.476\,\text{ms}^{-1}$$

$$\text{Equation (48): } n_{MRW} = \frac{0.8H}{s_2} = \frac{0.8 \times 134.5}{27.7} = 3.88$$

The use of Eq. (48) is justified since $(n_{MRW} = 3.88) < (2n_{RW} = 2 \times 4.5 = 9)$.

Since $\text{Re} \geq 10^4$, Eq. (73) can be used

$$\text{Equation (73): } \Delta p_W = \left[\sqrt{4 + (0.6n_{MRW} + 2)^2}\left(\frac{\rho w_z^2}{2}\right)\right] f_{z,t} f_L = \left[\sqrt{4 + (0.6 \times 3.88 + 2)^2}\left(\frac{983 \times 0.476^2}{2}\right)\right] \times 1.02 \times 0.414 = 224.2\,\text{Pa}$$

If Eq. (45) is used instead of Eq. (73) to calculate Δp_W, a value $\Delta p_w = 225.1$ Pa will be obtained.

Calculation of the pressure drop Δp_N in inlet and outlet nozzles:

$$\text{Equation (59): } w_N = \frac{\dot{V}}{\frac{\pi}{4}d_N^2} = \frac{\left(\frac{60}{3600}\right)}{\frac{\pi}{4}\left(\frac{210}{1000}\right)^2} = 0.481\,\text{ms}^{-1}$$

$$\text{Equation (61): } \frac{A_N}{A_F} = \frac{\frac{\pi}{4}d_N^2}{\frac{\pi}{4}\left(D_i^2 - n_T d_o^2\right)} = \frac{\frac{\pi}{4}(210)^2}{\frac{\pi}{4}(597^2 - 258 \times 25^2)} = 0.226$$

$$\text{Equation (60): } \xi_N = 5.79\left(\frac{A_N}{A_F}\right)^{1.14}\left(\frac{d_N}{D_i}\right)\left(\frac{D_{BE}}{d_N}\right)^{2.4} = 5.79 \times (0.226)^{1.14} \times \left(\frac{210}{597}\right) \times \left(\frac{560}{210}\right)^{2.4} = 3.93$$

Equation (60) is used, since $\xi_N > 2$; it is assumed that $D_{BE} = D_B$.

$$\text{Equation (58): } \Delta p_N = \xi_N \frac{\rho w_N^2}{2} = 3.93 \times \frac{983 \times 0.481^2}{2} = 446.9\,\text{Pa}$$

Calculation of the shell-side pressure drop Δp:

$$\text{Equation (1): } \Delta p = (n_B - 1)\Delta p_Q + 2\Delta p_{QE} + n_B \Delta p_W + \Delta p_N = (8 - 1) \times 83.5 + 2 \times 189.6 + 8 \times 224.2 + 446.9 = 3204.2\,\text{Pa} = 3204.2 \times 10^{-5} = 0.032\,\text{bar}$$

2 Shell-and-Tube Heat Exchangers Without Baffles

Under otherwise identical operating conditions, the shell-side pressure drop in a shell-and-tube heat exchanger without baffles is much less than that in a baffled heat exchanger with a large number of baffles. For an approximate calculation of the total pressure drop Δp in a shell-and-tube heat exchangers without baffles, the concept of equivalent diameter may be used [6]:

$$\Delta p = \Delta p_p + \Delta p_N. \tag{74}$$

The pressure drop Δp_p in the shell for the flow parallel to the tubes is given by

$$\Delta p_p = \xi_p \left(\frac{L}{d_e}\right)\left(\frac{\rho w_{pa}^2}{2}\right), \tag{75}$$

the mean velocity w_{pa} in the shell is calculated from

$$w_{pa} = \frac{\dot{V}}{\frac{\pi}{4}\left(D_i^2 - n_T d_o^2\right)}, \tag{76}$$

and the equivalent diameter d_e is given by

$$d_e = \frac{D_i^2 - n_T d_o^2}{D_i + n_T d_o}. \tag{77}$$

The drag coefficient ξ_p may be calculated from

$$\xi_p = \frac{64}{Re_p} \text{ for } Re_p < 2300, \tag{78}$$

$$\xi_p = \frac{0.3164}{Re_p^{0.25}} \text{ for } 3 \times 10^3 \le Re_p \le 10^5. \tag{79}$$

The Reynolds number is defined by

$$Re_p = \frac{w_{pa} d_e \rho}{\eta}. \tag{80}$$

In Eq. (75), L is the length of the tubes between the heat exchanger sheets. Other notations are identical with those for baffled shell-and-tube heat exchangers. The nozzle pressure drop Δp_N is given by Eq. (58).

The use of Eq. (75) implies that the ratio $(L/D_i) > 10$ and that the tubes of the heat exchanger are uniformly distributed in the shell, such that no bypass currents exist in a part of the cross section where the fluid dynamic resistance to the flow is small in comparison with the rest of the free cross section.

3 Symbols

Latin letters

A_B cross-sectional area responsible for bypass stream defined by Eqs. (37) and (38) (m^2 (mm^2))

A_E flow area defined by Eq. (5) (m^2 (mm^2))

$A_{E,E}$ flow area defined by Eq. (43) (m^2 (mm^2))

A_F free cross-sectional area of heat exchanger shell (see Eq. (61)) (m^2 (mm^2))

A_{GSB} area of gap between the shell and a baffle (m^2 (mm^2))

A_{GTB} area of all gaps between the tubes and the holes in a baffle (m^2 (mm^2))

A_N cross-sectional area of a nozzle (see Eq. (61)) (m^2 (mm^2))

A_{SG} sum of the areas of all gaps between the tubes and the holes in a baffle and between the shell and a baffle (m^2 (mm^2))

A_T area of window tubes (see Eq. (52)) (m^2 (mm^2))

A_W cross-sectional flow area in a window section (see Eq. (50)) (m^2 (mm^2))

A_{WT} cross-sectional area for a window section including the area of the window tubes (see Eq. (51)) (m^2 (mm^2))

a transverse pitch ratio (1)

b longitudinal pitch ratio (1)

c diagonal pitch ratio (see Eq. (19)) (1)

D_1 baffle diameter (m (mm))

D_B diameter of a circle, which touches the outermost tubes in the space between the upper and lower edges of adjacent baffles (m (mm))

D_{BE} diameter of a circle, which touches the outermost tubes of all tubes in the shell of the heat exchanger (including the tubes in the window sections) (m (mm))

D_i inside shell diameter (m (mm))

d_B diameter of holes in baffles (m (mm))

d_e equivalent diameter for an unbaffled shell-and-tube heat exchanger (see Eq. (77)) (m (mm))

d_g equivalent diameter for a window section (see Eq. (49)) (m (mm))

d_N nozzle diameter (m (mm))

d_o outer diameter of tubes (m (mm))

e shortest connection between adjacent tubes in the same tube row or in neighboring tube rows (see Fig. (4)) (m (mm))

e_1 shortest connection between the outermost tube in the bundle and the shell measured in the tube row on or near the diameter of the shell that is parallel to the edge of the baffles (see Fig. (4)) (m (mm))

$f_{a,l,f}$ factor for in-line tube arrangement in the laminar range (see Eq. (8)) (1)

$f_{a,l,v}$ factor for staggered tube arrangement in the laminar range (see Eqs. (13) and (14)) (1)

$f_{a,t,f}$ factor for in-line tube arrangement in the turbulent range (see Eq. (10)) (1)

$f_{a,t,v}$ factor for staggered tube arrangement in the turbulent range (see Eq. (16)) (1)

f_B correction factor to take in consideration the influence of bypass currents through the gaps between the outermost tubes in the bundle and the inside surface of the heat exchanger shell (1)

f_L correction factor to take in consideration the influence of leakage streams through the gaps between the tubes and the holes in the baffles and through the gaps between the baffles and the heat exchanger shell (1)

f_z correction factor to take in consideration the change in physical properties with temperature in a window section (see Eq. (45)) (1)

$f_{z,l}$ correction factor to take in consideration the change in physical properties with temperature in the laminar rage (see Eq. (21)) (1)
$f_{z,t}$ correction factor to take in consideration the change in physical properties with temperature in the turbulent rage (see Eq. (22)) (1)
H height of baffle cut (m (mm))
L tube length in an unbaffled shell-and-tube heat exchanger (m (mm))
L_E sum of shortest connections e and e_1 ($L_E = 2e_1 + \Sigma e$, see Fig. (4)) (m (mm))
m exponent in Eq. (68) corresponding with the exponent of the Reynolds number in Eqs. (7), (9), (12) and (15) (1)
n_B number of baffles (1)
n_{MR} number of main resistances in the path of the main flow in a central cross flow section (1)
n_{MRE} number of main resistances in the path of the main flow in an end cross flow section (1)
n_{MRW} number of the effective main resistances in a window section (see Eq. (48)) (1)
n_R number of the tube rows in a central section (1)
n_{RW} number of tube rows in a window section (1)
n_S number of pairs of sealing strips (1)
n_T total number of tubes in heat exchanger including blind and support tubes (1)
n_W number of tubes in both upper and lower windows (baffle cuts) (1)
p_{in} inlet pressure (Pa)
p_m mean pressure (Pa)
p_{out} outlet pressure (Pa)
Δp shell-side pressure drop including nozzle pressure drop (Pa (bar))
Δp_N pressure drop in both inlet and outlet nozzles (Pa)
Δp_p shell-side pressure drop without nozzle pressure drop in an unbaffled shell-and-tube heat exchanger (see Eq. (75)) (Pa)
Δp_Q pressure drop in a central cross flow section between two adjacent baffles (Pa)
Δp_{QE} pressure drop in an end cross flow section (between a heat exchanger sheet and the adjacent baffle (Pa)
$\Delta p_{Q,0}$ pressure drop in a tube bundle with cross flow under real operating conditions in absence of leakage and bypass streams (corresponding to flow conditions in a central cross flow section) (Pa)
$\Delta p_{QE,0}$ pressure drop in a tube bundle with cross flow under real operating conditions in absence of leakage and bypass streams (corresponding to flow conditions in an end cross flow section) (Pa)
Δp_W pressure drop in a window section (Pa)
$\Delta p_{W,lam}$ pressure drop in a window section with laminar flow (see Eq. (46)) (Pa)
$\Delta p_{W,turb}$ pressure drop in a window section with turbulent flow (see Eq. (47)) (Pa)
R_B ratio A_B/A_E (see Eq. (35)) (1)
R_L ratio A_{SG}/A_E (see Eq. (26)) (1)
R_M ratio A_{GSB}/A_{SG} (see Eq. (25)) (1)
R_S ratio n_S/n_{MR} (see Eq. (36)) (1)
r exponent in Eq. (23) given by Eq. (24) (1)
Re Reynolds number in a central cross flow section (see Eq. (20)) (1)
Re_E Reynolds number in an end cross flow section (see Eq. (44)) (1)
Re_p Reynolds number for an unbaffled shell-and-tube heat exchanger (see Eq. (80)) (1)
S baffle spacing between adjacent baffles (m (mm))
S_B bypass stream
S_E baffle spacing between a heat exchanger sheet and the adjacent baffle (m (mm))
S_L leakage stream
S_M main stream
s_1 transverse pitch (m (mm))
s_2 longitudinal pitch (m (mm))
t pitch for an equilateral triangular or a staggered square tube arrangement (m (mm))
U_W wetted perimeter in a window section (see Eq. (53)) (m (mm))
$\dot{V}$ fluid volumetric flow rate through the heat exchanger shell ($m^3\ s^{-1}$ ($m^3\ h^{-1}$))
w_e velocity defined by Eq. (4) ($m\ s^{-1}$)
$w_{e,E}$ velocity defined by Eq. (42) ($m\ s^{-1}$)
w_N nozzle velocity (see Eq. (59)) ($m\ s^{-1}$)
w_p velocity in a window section defined by Eq. (55) ($m\ s^{-1}$)
w_{pa} velocity in the shell of an unbaffled shell-and-tube heat exchanger (see Eq. (76)) ($m\ s^{-1}$)
w_z velocity in a window section defined by Eq. (54) ($m\ s^{-1}$)

Greek Letters

β constant in Eq. (31) given by Eqs. (33) and (34) (1)
γ central angle of a baffle cut (∘)
η dynamic viscosity at mean fluid temperature (Pa s)
η_w dynamic viscosity at mean wall temperature (Pa s)
ϑ_{in} inlet fluid temperature (°C)
ϑ_m mean fluid temperature (°C)
ϑ_{out} outlet fluid temperature (°C)
ϑ_w mean wall temperature (°C)
ξ drag coefficient for the tube bundle (1)
ξ_{lam} drag coefficient for laminar flow (see Eq. (7)) (1)
ξ_{turb} drag coefficient for turbulent flow (see Eq. (9)) (1)
ξ_N nozzle drag coefficient for both inlet and outlet nozzles (see Eq. (60)) (1)
$\xi_{N,in}$ drag coefficient for inlet nozzle (see Eq. (62)) (1)
$\xi_{N,out}$ drag coefficient for outlet nozzle (see Eq. (63)) (1)
ξ_p drag coefficient for an unbaffled shell-and-tube heat exchanger (see Eq. (75)) (1)
ρ fluid density ($kg\ m^{-3}$)

The units between brackets (mm, bar and $m^3\ h^{-1}$) are not consistent with the M.K.S. units system; they are used in some places in the text and in the example for convenience.

4 Bibliography

1. Bell KJ (1963) Final report of the cooperative research program on shell and tube heat exchangers. University of Delaware, Engineering Experimental Station, Bulletin No. 5, Newark, Delaware
2. Gaddis ES, Gnielinski V (1977) Pressure drop on the shell side of shell-and-tube heat exchangers with segmental baffles. Chem Eng Processg 36(2):149–159
3. Gaddis ES, Gnielinski V (1983) Druckverlust in querdurchströmten Rohrbündeln, vt "verfahrenstechnik" 17(7):410–418
4. Taborek J (1992) Shell-and-tube heat exchangers: Single-phase-flow (Chap. 3.3), Handbook of Heat Exchanger Design. Begell House, Inc., New York/Wallingford, UK
5. Gnielinski V (2006) Widerstandsbeiwerte der mantelseitigen Ein- und Austrittsstutzen von Rohrbündelapparaten bei turbulenter Strömung, 90 Kurzmitteilungen. Chemie Ingenieur Technik 78(1–2):90–93
6. Slipcevic B (1966) Berechnung der Druckverluste in Rohrbündel-Wärmeaustauschern, Die Kälte, October: 556–564

L1.6 Pressure Drop in Fixed Beds

Karl-Ernst Wirth
Friedrich-Alexander-Universität Erlangen-Nürnberg, Erlangen, Germany

1 General

Fixed beds are solids accumulations consisting of single particles, which are passed through by a fluid (liquid, gas). They differ from packing materials, which normally are percolated by a two-phase mixture of liquids and gases. Unlike the single elements of a packing material, e.g., Raschig-rings and saddle body, which generally have a great surface per volume of the packed bed and low pressure drop, the particles in fixed beds are of compact shape and are often characterized as "spherical."

This chapter is about the pressure drop of fixed beds.

The pressure drop in fixed beds made of packing materials is described in Subchap. L2.6.

The pressure drop in fixed beds can be described by two different models:

- model of the hydraulic diameter,
- model of the flow around single particles.

The first model – the model of the hydraulic diameter – is older and leads to the relatively easy pressure drop equations like the Ergun equation [1]. The second model is newer and was firstly published by Molerus [2].

2 Pressure Drop Equation Based on the Model of the Hydraulic Diameter

The Ergun equation is based on the model that the real fixed bed can be replaced by parallel pipes for the flowing fluid and the pressure drop calculation is analog to the single-phase pipe flow, but with the hydraulic diameter of the fixed bed as a characteristic pipe dimension.

Evaluation of measurements yields the pressure drop equation for fixed beds using edged particles, the Ergun equation:

$$\frac{\Delta p}{\Delta L} = 150\frac{(1-\varepsilon)^2}{\varepsilon^3}\frac{\eta\nu}{\overline{d_\mathrm{p}}^2} + 1.75\frac{1-\varepsilon}{\varepsilon^3}\frac{\rho_\mathrm{f}\nu^2}{\overline{d_\mathrm{p}}}. \qquad (1)$$

The bulk material is characterized by the characteristic particle diameter, the Sauter-diameter $\overline{d}_\mathrm{p}$. It can be calculated from a measured particle size distribution:

$$\overline{d_\mathrm{p}} = \left[\sum_{i=1}^{n}\left(\frac{V_i}{V}\cdot\frac{1}{d_{\mathrm{p}i}}\right)\right]^{-1}. \qquad (2)$$

In Eq. (2), V_i/V is the volume of the ith-particle size fraction V_i referred to the total analyzed particle volume V and $d_{\mathrm{p}i}$ the average particle diameter of fraction i.

The constants in Eq. (1) depend on the shape and the porosity of the particles and thus has to be defined experimentally.

For the pressure drop in fixed beds, consisting of spherical particles, Brauer [3] found a correlation after analysis of measurements, which is similar to the Ergun equation:

$$\frac{\Delta p}{\Delta L} = 160\frac{(1-\varepsilon)^2}{\varepsilon^3}\frac{\eta\nu}{\overline{d_\mathrm{p}}^2} + 3.1\frac{1-\varepsilon}{\varepsilon^3}\frac{\rho_\mathrm{f}\nu^2}{\overline{d_\mathrm{p}}}\left[\frac{\eta\,(1-\varepsilon)}{\rho_\mathrm{f}\nu\overline{d_\mathrm{p}}}\right]^{0.1}. \qquad (3)$$

The Brauer equation is valid for fixed beds of monosized particles, i.e., consisting of equally sized spherical particles.

Using broad particle size distributions, the appropriate correction functions have to be considered in the pressure drop equations [3].

With pressure drop equations like the Ergun equation (1), the pressure drop in viscosity controlled ("laminar") flow is determined by the first part of the equation on the right side; the pressure drop in inertia-controlled ("turbulent") flow is determined by the second part of the equation on the right side.

In fact, there is a transition zone between both types of flow where the pressure drop is generated by the boundary layer formed by the fluid flow on the particle surface. The pressure drop caused by this flow pattern is not included in the fixed bed pressure drop equation of Ergun.

By modeling the void space in the fixed bed as parallel flow channels, the real flow paths are only insufficiently considered. This is shown among other things by the porosity dependence of the fixed bed pressure drop: it is not included correctly in the Ergun equation and hence both constants on the right side of Eqs. (1) and (3) are still functions of the fixed-bed porosity. This especially occurs for the broad particle size distributions of the fixed bed material.

The main disadvantage of the Ergun equation is that the model of the hydraulic diameter can only be applied to the

"turbulent" region, i.e., the inertia-controlled flow region, but it is not correct to use this model for the flow region where the flow is controlled by the fluid viscosity, thus on fixed beds consisting of fine grained solids (small particle Reynolds numbers) [2].

Up to now there have been no better pressure drop equations available for the technical important edged particles; the Ergun equation is wide spread. Hence, it is mentioned at this point.

The Carman–Kozeny equation is a special case of the Ergun equation. The Carman–Kozeny equation only applies to the Reynolds number region where the pressure drops are controlled by the fluid viscosity. With this, only the first part of the equation of the Ergun equation (1) is relevant.

Instead of the Sauter-diameter, the Carman–Kozeny equation contains as typical characteristic dimension of the particles the reciprocal value of the volume-related specific surface of the fixed-bed material.

Therewith, the Carman–Kozeny equation contains a changed proportional constant in comparison to the Ergun equation:

$$\frac{\Delta P}{\Delta L} = 4\frac{(1-\varepsilon)^2}{\varepsilon^3} S_v^2 \eta v. \tag{4}$$

Similar to the Ergun equation, the proportional constant in the Carman–Kozeny equation also depends on the particle shape, the width of the particle size distribution, and the fixed-bed porosity, and has to be determined experimentally. In general, the value 4 is used for the constant.

A generalized form of the Carman–Kozeny equation is the Darcy equation. In the Darcy equation, the properties of the fixed bed are summarized in a so-called permeability B:

$$\frac{\Delta P}{\Delta L} = \frac{1}{B}\eta v. \tag{5}$$

The permeability B has to be determined experimentally for each fixed bed.

3 Pressure Drop Equation Based on the Model of the Flow Around Single Particles

The pressure drop relation deduced by Molerus is based on the flow around single particles [2, 4]. During the flow around the particles, the fluid exerts a resistance W_1 on each particle. Depending on the number of particles z in the fixed bed, the resistance $z \cdot W_1$ is exerted on the fixed bed. This force is in equilibrium with the force caused by the pressure drop:

$$z \cdot W_1 = \Delta p \cdot F. \tag{6}$$

The number of particles in the fixed bed can be obtained from the solids mass balance. The number of particles equals to the ratio of solids volume in the fixed bed to the volume of a particle with the Sauter-diameter $\overline{d_p}$:

$$z = \frac{(1-\varepsilon)F\Delta L}{\overline{d_p^3}\frac{\pi}{6}}. \tag{7}$$

With Eqs. (6) and (7), the pressure drop can be described as

$$\frac{\Delta p}{\Delta L} \cdot \frac{\overline{d_p^3}\pi}{6} \cdot \frac{1}{1-\varepsilon} = W_1. \tag{8}$$

Referring Eq. (8) to the inertia force of the flowing fluid, the pressure drop is described in the dimensionless equation as

$$\mathrm{Eu} \equiv \frac{4}{3}\frac{\Delta p}{\rho_f v^2}\frac{\overline{d_p}}{\Delta L}\frac{\varepsilon^2}{1-\varepsilon} = \frac{W_1}{\frac{\rho_f}{2}\frac{\overline{d_p^2}\pi}{4}\left(\frac{v}{\varepsilon}\right)^2}. \tag{9}$$

With this, the Euler number Eu is defined similar to the drag coefficient of a single particle c_w. The Euler number is the dimensionless flow resistance W_1 of a single particle in the fixed bed, which is passed through with the average interstitial velocity v/ε.

The analysis of the flow around a single particle in a fixed bed with the help of the Navier–Stokes equation and evaluation of pressure drop measurements finally results in an equation for the Eu number. For spherical particles Molerus obtained:

$$\mathrm{Eu} \equiv \frac{24}{\mathrm{Re}}\left\{1 + 0.692\left[\frac{r_0}{\delta} + 0.5\left(\frac{r_0}{\delta}\right)^2\right]\right\} + \frac{4}{\sqrt{\mathrm{Re}}}\left[1 + 0.12\left(\frac{r_0}{\delta}\right)^{1.5}\right] + \left[0.4 + 0.891\frac{r_0}{\delta}\mathrm{Re}^{-0.1}\right], \tag{10}$$

with

$$\frac{r_0}{\delta} = \left[\frac{0.95}{\sqrt[3]{1-\varepsilon}} - 1\right]^{-1} \tag{11}$$

and the Reynolds number:

$$\mathrm{Re} \equiv \frac{\rho_f v \overline{d_p}}{\varepsilon\eta}. \tag{12}$$

Equation (11) describes the packing structure of the fixed bed and is valid for uniform random packing. For solid concentration $(1–\varepsilon) \to 0$, Eq. (10) turns into the equation for the drag coefficient of single particles, the Kaskas equation [3]

$$c_w = \frac{24}{\mathrm{Re}} + \frac{4}{\sqrt{\mathrm{Re}}} + 0.4. \tag{13}$$

This emphasizes the relevance of the Euler equation for the fixed bed percolation.

The first part of Eq. (10) describes the Stoke-flow around the particles. The middle part of the equation characterizes the flow resistance generated by the boundary layer of the fluid flow at the surface of the particles. The last part of the equation finally describes the separation characteristics of the fluid flow around the particles. A comparison of experimentally determined Euler-numbers and Euler-numbers calculated by Eqs. (10) and (11) is shown in Fig. 1.

In comparison to spherical particles there is a modified resistance in the fixed bed in the case of nonspherical particles. By introducing a pressure drop shape factor Φ_D, the resistance of nonspherical particles is related to that of spherical ones with the same Sauter diameter $\overline{d_p}$. In place of the Sauter diameter for spherical particles the equivalent diameter $\Phi_D\,\overline{d_p}$ of the nonspherical particles, i.e., the edged particles, is inserted in Eqs. (9) and (10).

According to evaluation of measurements, the following approximation function for the Euler number of nonspherical, edged particles Eu(Φ_D) results:

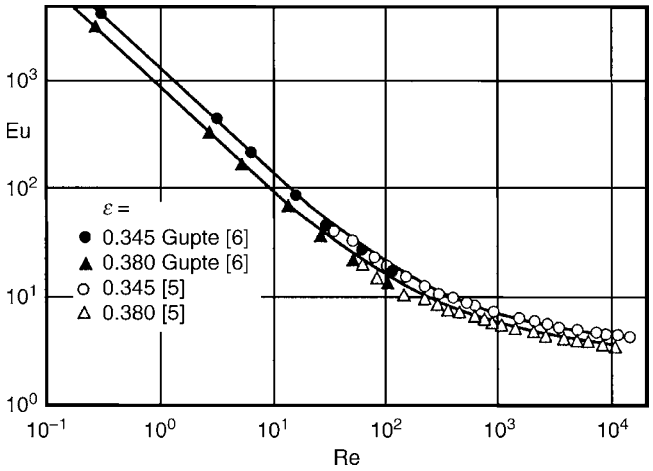

L1.6. Fig. 1. Comparison of experimental determined and calculated fixed-bed Euler number (plot calculated) for glass beads as test material.

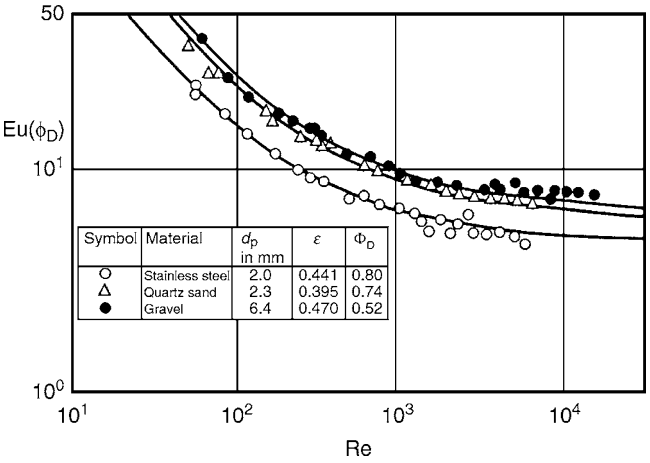

L1.6. Fig. 2. Comparison of experimentally determined and calculated fixed-bed Euler numbers for nonspherical particles with different pressure loss shape factors.

$$\mathrm{Eu}(\Phi_D) = \frac{24}{\mathrm{Re}\Phi_D^2}\left\{1 + 0.685\left[\frac{r_0}{\delta} + 0.5\left(\frac{r_0}{\delta}\right)^2\right]\right\} + \frac{4}{\sqrt{\mathrm{Re}\Phi_D^{1,5}}}\left[1 + 0.289\left(\frac{r_0}{\delta}\right)^{1,5}\right] + \frac{1}{\Phi_D}\left[0.4 + 0.514\frac{r_0}{\delta}\right], \quad (14)$$

with

$$\mathrm{Eu}(\Phi_D) = \frac{4}{3}\frac{\Delta p}{\rho_f v^2}\frac{\overline{d_p}}{\Delta L}\frac{\varepsilon^2}{1-\varepsilon} \quad (15)$$

and r_0/δ according to Eq. (11) and Re according to Eq. (12).

The Sauter diameter of nonspherical particles can in turn be calculated from a particle size analysis according to Eq. (2).

In Fig. 2 experimentally determined Euler numbers are compared with computed ones. The latter are depicted curvilinear.

The pressure drop shape factor for nonspherical, edged particles can be determined by *one* pressure drop measurement using Eqs. (11), (14), and (15). Insertion of the measured data and of the material properties of the fluid in Eqs. (11), (14), and (15) provides the only unknown, the pressure drop shape factor, after an iteration process. Alternatively to the described arithmetical calculation Φ_D can also be determined graphically (Fig. 2).

Using Eqs. (11), (14), and (15) and for the pressure drop shape factor $\Phi_D = 1$ the associated Euler numbers are depicted in Fig. 3 depending on the fixed-bed porosity ε. The ratio of the Euler number of nonspherical particles $\mathrm{Eu}(\Phi_D)$ to that of a nonspherical particle with a pressure loss shape factor $\Phi_D = 1$ is depicted in Fig. 4 depending on the Reynolds number and the pressure drop shape factor.

The ratio plotted on the ordinate is identical to the multiple of the pressure drop of irregular formed, nonspherical particles in a fixed bed in comparison to the pressure drop in a bulk consisting of "spherical particles with coarse surface ($\Phi_D = 1$)" with the same average particle diameter at/as the identical Reynolds number, and the same bed porosity.

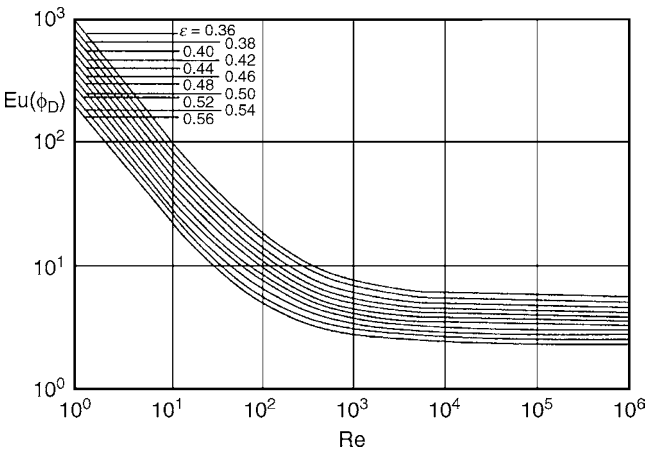

L1.6. Fig. 3. Diagram for determination of the Euler number for the "coarse" spheres ($\Phi_D = 1$) in fixed beds with different porosities (calculation of the curve according to Eq. (14)).

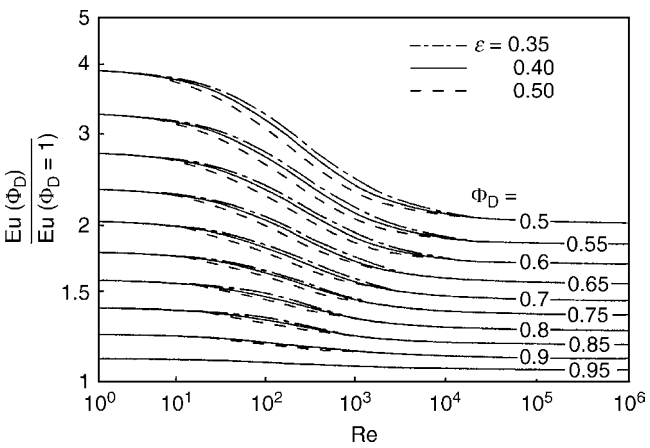

L1.6. Fig. 4. Diagram for determination of the pressure loss shape factor Φ_D from a measuring point (calculation of the curves according to Eq. (14)).

For a measuring point and using the operating parameter and the material properties, one can read off the Euler number for a "coarse sphere," $\mathrm{Eu}(\Phi_D = 1)$, from the ordinate of Fig. 3. With the measured pressure drop, the Euler number $\mathrm{Eu}(\Phi_D)$ can be calculated according to Eq. (15). The ratio of both Euler numbers has to be calculated and one has to read off from Fig. 4, the pressure drop shape factor of the applied bulk material Φ_D depending on the Reynolds number established, Eq. (12), and the fixed-bed porosity. Typical pressure drop shape factors are summarized in Table 1.

Example

A fixed bed reactor shall be operated at 150°C with spherical catalyst particles of a Sauter diameter of 3 mm and at a static pressure of 20 bar. As a reaction gas, a gas is applied which exhibits the same material data as air. The superficial gas velocity shall be 1 m/s. The fixed-bed porosity accounts for 0.4. To overcome the fluid pressure drop, there is a compressor available with a maximum pressure enhancement of 1 bar. Which length is the fixed bed reactor allowed to have?

At a static pressure of 20 bar, there is a pressure decrease of 1 bar. For practical purposes, the occurring density change can be neglected. For the material data of the fluid, one obtains therewith $\rho_f = 16.38\ \mathrm{kg/m^3}$ and $\nu = 14.8^{*}10^{-7}\ \mathrm{m^2/s}$.

For the Sauter diameter $\overline{d_p} = 3$ mm and the superficial gas velocity of 1 m/s, the particle Reynolds number results according to Eq. (12)

$$\mathrm{Re} = \frac{1\ \mathrm{m/s}^{*}3^{*}10^{-3}\ \mathrm{m}}{0.4^{*}14.8^{*}10^{-7}\ \mathrm{m^2/s}} = 5.07^{*}10^{3},$$

and for the aspect ratio r_0/δ one obtains with the porosity $\varepsilon = 0.4$ according to Eq. (11)

$$\frac{r_0}{\delta} = \left[\frac{0.95}{\sqrt[3]{0.6}} - 1\right]^{-1} = 7.91.$$

With $\mathrm{Re} = 5.07^{*}10^{3}$ and $r_0/\delta = 7.91$ the Euler number can at least be calculated according to Eq. (10) to $\mathrm{Eu} = 3.74$.

From the definition equation for the Euler number (Eq. (9)), one obtains for the length of the fixed bed

$$\begin{aligned}\Delta L &= \frac{4}{3}\frac{\Delta p}{\rho_f \nu^2}\overline{d_p}\frac{\varepsilon^2}{1-\varepsilon}\frac{1}{\mathrm{Eu}}\\ &= \frac{4}{3}\frac{10^5\ (\mathrm{kg/ms^2})}{16.38\ (\mathrm{kg/m^3})\ 1\ (\mathrm{m^2/s^2})}3^{*}10^{-3}\ \mathrm{m}\frac{0.4^2}{0.6}{*}\frac{1}{3.74}\\ &= 1.74\ \mathrm{m}.\end{aligned}$$

Which is the maximum length of the fixed bed if the spherical catalyst particles are replaced by coated quartz sand with the same Sauter diameter?

L1.6. Table 1. Pressure loss shape factors [5]

Material	Pressure loss shape factor Φ_D
Steel spheres (blasting material)	0.8
Clay granules	0.8
Quartz sand	0.74
Street chippings (broken edges)	0.63
Street chippings (sharp edged)	0.52

The Reynolds number as well as the aspect ratio has the same value for the coated nonspherical quartz sand as for the spherical catalyst. With both quantities and the pressure loss shape factor $\Phi_D = 0.74$ for quartz sand according to Table 1, one obtains the Euler number from the pressure drop equation for nonspherical particles (Eq. (14))

$$\mathrm{Eu}(\Phi_D) = 6.93.$$

With this a maximum length of the fixed bed for the nonspherical catalyst of

$$\begin{aligned}\Delta L &= \frac{4}{3}\frac{\Delta p}{\rho_f \nu^2}\overline{d_p}\frac{\varepsilon^2}{1-\varepsilon}\frac{1}{\mathrm{Eu}(\Phi_D)}\\ &= \frac{4}{3}\frac{10^5\ (\mathrm{kg/ms^2})}{16.38\ (\mathrm{kg/m^3})\ 1\ (\mathrm{m^2/s^2})}3^{*}10^{-3}\ \mathrm{m}\frac{0.4^2}{0.6}{*}\frac{1}{6.93}\\ &= 0.94\ \mathrm{m}\end{aligned}$$

can be calculated.

4 Symbols

c_w	drag coefficient of a single sphere (–)
B	permeability ($\mathrm{m^2}$)
$\overline{d_p}$	Sauter diameter (m)
d_{pi}	average particle diameter in the particle size interval i (m)
ΔL	length of the fixed bed (m)
Δp	pressure drop in the fixed bed ($\mathrm{kg\ m^{-1}\ s^{-2}}$)
F	cross-sectional area of the fixed bed ($\mathrm{m^2}$)
S_v	volume related specific surface ($\mathrm{m^{-1}}$)
v	superficial fluid velocity ($\mathrm{ms^{-1}}$)
V	total volume of the particles ($\mathrm{m^3}$)
V_i	volume of the solid particles in the particle size interval i ($\mathrm{m^3}$)
W_1	drag force per particle ($\mathrm{kg\ ms^{-2}}$)
z	number of particles (–)
ε	porosity (–)
ρ_f	fluid density ($\mathrm{kgm^{-3}}$)
η	dynamic viscosity ($\mathrm{kg\ m^{-1}\ s^{-1}}$)
Φ_D	pressure drop shape factor (–)

Dimensionless numbers

$\mathrm{Re} \equiv \frac{\rho_f \nu \overline{d_p}}{\varepsilon\eta}$	particle Reynolds number
$\mathrm{Eu} \equiv \frac{4}{3}\frac{\Delta p}{\rho_f \nu^2}\frac{\overline{d_p}}{\Delta L}\frac{\varepsilon^2}{1-\varepsilon}$	Euler number
$\frac{r_0}{\delta} \equiv \left[\frac{0.95}{\sqrt[3]{1-\varepsilon}} - 1\right]^{-1}$	aspect ratio

5 Bibliography

1. Ergun S (1952) Fluid flow through packed columns. Chem Eng Prog 48(2):S89–94

2. Molerus O (1982) Fluid–Feststoff–Strömungen. Strömungsverhalten feststoffbeladener Fluide und kohäsiver Schüttgüter. Springer-Verlag, Berlin
3. Brauer M (1971) Grundlagen der Einphasen- und Mehrphasenströmungen. Sauerländer Verl., Aarau u. Frankfurt
4. Molerus O (1993) Principles of flow in disperse systems. Chapman & Hall, London
5. Schweinzer J (1987) Druckverlust in und gaskonvektiver Wärmeübergang an Festbetten und Wirbelschichten. Diss., Univ. Erlangen, Nürnberg
6. Gupte AR (1970) Experimentelle Untersuchung der Einflüsse von Porosität und Korngrößenverteilung im Widerstandsgesetz der Porenströmung. Diss., Univ. Karlsruhe

L1.7 Pressure Drop in Orifices and Column Trays

Johann Stichlmair
Technische Universität München, Garching, Germany

1 Fundamentals

A gas (or vapor) flowing through a mass transfer column (e.g., absorption column and distillation column) suffers a significant pressure drop (better pressure loss). This chapter describes in detail the dry pressure loss of tray columns.

The basic equation for calculating the pressure loss Δp of a fluid flowing through a perforated plate is:

$$\Delta p = \zeta \cdot \frac{\rho}{2} \cdot u_h^2 \tag{1}$$

The symbol u_h denotes the mean velocity of the fluid in the holes of the plate. Equation (1) is, in essence, just a definition of the orifice coefficient ζ. Thus, the problem of pressure loss calculation is the prediction of the orifice coefficient.

1.1 Theoretical Approach

A perforated plate is a system of parallel holes with identical flow conditions. Thus, the significant mechanisms can be studied by considering a single hole in the plate. As shown in Fig. 1, two different situations have to be considered:

- Thin plate with a large hole, $s/d_h \to 0$
- Thick plate with a small hole, $s/d_h >> 0$

Flowing through a hole in a plate the fluid always undergoes a flow contraction that is followed by a flow expansion (see Fig. 1). During flow contraction the flow velocity increases and, in turn, the static pressure decreases (Bernoulli). Thus, the fluid moves in the direction of falling pressure. Here, the potential energy is transformed into kinetic energy without any significant energy losses. No permanent pressure loss arises during flow contraction.

During flow expansion after passing through the hole, the flow velocity decreases and, in turn, the static pressure increases. Fluid flow in the direction of increasing pressure always results in a significant pressure loss. The permanent pressure loss Δp during flow expansion can be calculated from the first principles of fluid mechanics.

Equation of impulse momentum:

$$(p^* - p) \cdot A = A \cdot \rho \cdot u \cdot (u - u^*) \tag{2}$$

Bernoulli equation:

$$\frac{\rho}{2} \cdot u^* + p^* = \frac{\rho}{2} \cdot u^2 + p + \Delta p \tag{3}$$

Eliminating the term $(p^* - p)$ yields:

$$\rho \cdot u \cdot (u - u^*) = \frac{\rho}{2} \cdot (u^2 - u^{*2}) + \Delta p \tag{4}$$

Rearranging Eq. (4) delivers the Borda-Carnot equation:

$$\Delta p = \frac{\rho}{2} \cdot (u^* - u)^2 \tag{5}$$

Thus, the permanent pressure loss is proportional to the square of the velocity difference before and after flow expansion.

However, it has to be noted that the velocity u^* in the vena contracta differs from the velocity u_h in the geometrical cross section of a hole. Equation (5) is rewritten to give:

$$\Delta p = \frac{\rho}{2} \cdot u_h^2 \cdot \left(\frac{u^*}{u_h} - \frac{u}{u_h} \right)^2 \tag{6}$$

A comparison of Eq. (6) with (1) gives a relation for the orifice coefficient:

$$\zeta = \left(\frac{u^*}{u_h} - \frac{u}{u_h} \right)^2 \tag{7}$$

The decisive velocity ratios are easily calculated from the continuity equation.

As shown in Fig. 1, the flow in the hole contracts to the vena contracta A^*, which is significantly smaller than the open area A_h of the hole. The ratio A^*/A_h defines the orifice discharge coefficient α, i.e., $\alpha \equiv A^*/A_h$. With the continuity equation follows:

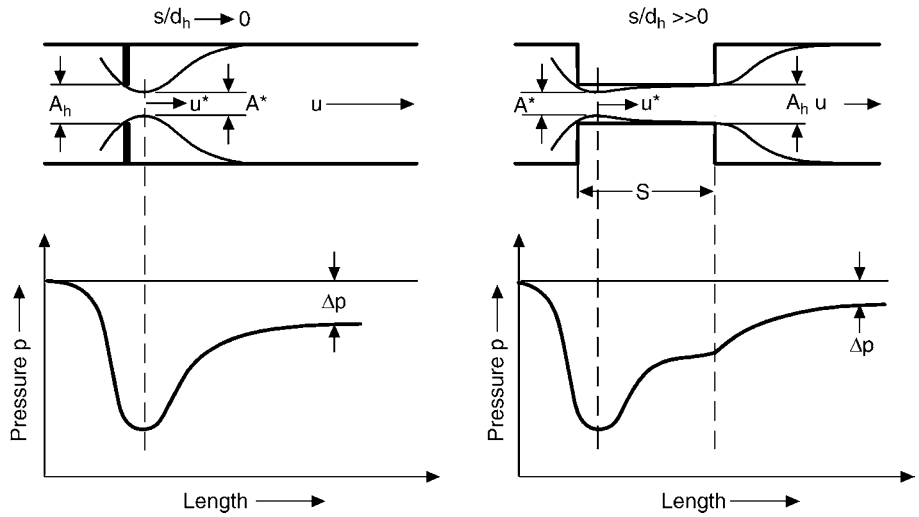

L1.7. Fig. 1. Fluid flow through a hole in a thin plate (*left*) and a thick plate (*right*).

$$\frac{u^*}{u_h} = \frac{1}{\alpha} \tag{8}$$

The ratio A_h/A is advantageously expressed by the relative free area φ, which is a geometrical quantity of the perforated plate, i.e., $\varphi \equiv A_h/A$. A combination with the continuity equation delivers:

$$\frac{u}{u_h} = \varphi \tag{9}$$

Equations (7)–(9) can be used for calculating the orifice coefficients of holes in thin and thick plates.

1.2 Orifice Coefficient of Holes in Thin Plates

In the special case of a large hole in a thin plate, the orifice coefficient results from Eqs. (7)–(9):

$$\zeta = (\frac{1}{\alpha} - \varphi)^2 \text{ for } s/d_h \to 0 \tag{10}$$

Equation (10) is the well-known orifice formula that describes the permanent pressure loss in nozzles used for flow rate measurements.

1.3 Orifice Coefficient of Holes in Thick Plates

In the special case of a small hole in a thick plate the flow expansion that causes the permanent pressure loss takes place in two steps. Firstly, from the vena contracta A^* to the hole area A_h and, secondly, from the hole area A_h to the column area A. The permanent pressure loss is the sum of the individual pressure losses of both expansions. The result is:

$$\zeta = \left(\frac{1}{\alpha} - 1\right)^2 + (1-\varphi)^2 \text{ for } s/d_h >> 0 \tag{11}$$

1.4 Orifice Discharge Coefficient

The evaluation of Eqs. (10) and (11) requires knowledge of the orifice discharge coefficient α. Generally, it depends on the Reynolds number in the hole and on the relative free area φ. However, at high Reynolds numbers and small values of the relative free area φ the following relation holds [1]:

$$\alpha = \frac{\pi}{\pi + 2} \approx 0.611 \tag{12}$$

For higher values of φ Eq. (13) is recommended:

$$\alpha = 0.6 + 0.4 \cdot \varphi^2 \tag{13}$$

1.5 Limiting Values of the Orifice Coefficient

The orifice coefficient of thin plates reaches its maximum value at large Reynolds numbers and low relative free areas. For $\varphi \to 0$ Eq. (10) becomes:

$$\zeta_o = \left(\frac{1}{0.611} - 0\right)^2 = 2.67 \text{ for } s/d_h \to 0 \text{ and } Re_h \geq Re_{crit} \tag{14}$$

The corresponding value of thick plates is:

$$\zeta_o = \left(\frac{1}{0.611} - 1\right)^2 + (1-0)^2 = 1.41 \quad \text{for } s/d_h >> 0 \text{ and } Re_h \geq Re_{crit} \tag{15}$$

It must be noted that thin plates have a higher pressure loss than thick plates since the flow expansion takes place in a single step. In thick plates, however, the expansion takes place in two smaller steps. In a diffuser, for instance, the expansion takes place in many very small steps that do not cause any significant pressure losses.

2 Dry Pressure Loss of Sieve Trays

Industrial sieve trays typically have values of s/d_h that are between the two special cases considered above. Additionally, the Reynolds number in the openings is often lower than the critical value Re_{crit} so that its influence on the orifice coefficient has to be considered also. The orifice coefficient cannot be rigorously modeled for these conditions. From a huge base of experimental data [2–9] an empirical correlation of the orifice coefficient ζ_o, for $\varphi \to 0$, has been developed [10, 11], which is shown in Fig. 2. As expected, the parameter lines of constant Reynolds numbers run between the theoretical limits of $\zeta_o = 2.67$ at $s/d_h \to 0$ and $\zeta_o = 1.41$ at $s/d_h >> 0$.

It must be noted that the influence of the Reynolds number on the orifice coefficient is opposite at thin and thick plates. In thin plates, the orifice coefficient ζ_o is inversely proportional to the orifice discharge coefficient α, which decreases with increasing Reynolds numbers. In thick plates, the friction of the fluid at the wall of the hole additionally contributes to the orifice coefficient. Wall friction decreases with increasing Reynolds numbers.

The correlation in Fig. 2 is valid for sharp-edged orifices with a very small relative free area, i.e., $\varphi \to 0$. In industrial columns the values of the relative free area are in the range $\varphi \leq 0.2$. The values $\zeta_o(\varphi \to 0)$ can be converted into the values $\zeta(\varphi > 0)$ by rewriting Eqs. (10) and (11), respectively:

$$\zeta(\varphi) = \zeta_o + \varphi^2 - 2 \cdot \varphi \cdot \sqrt{\zeta_o} \quad \text{for } s/d_h \to 0 \qquad (16)$$

And:

$$\zeta(\varphi) = \zeta_o + \varphi^2 - 2 \cdot \varphi \quad \text{for } s/d_h >> 0 \qquad (17)$$

In most cases the differences of the results of Eqs. (16) and (17) are very small for industrial sieve trays since the values of φ normally do not exceed 0.15 or 0.20.

3 Dry Pressure Loss of Bubble Cap and Valve Trays

Many different tray designs are used in industrial separation columns. Important examples are sieve trays, bubble cap trays, and valve trays. The dry pressure loss of sieve trays can be calculated from the correlation developed in Sect. 2.

For the calculation of the pressure loss of bubble cap trays and valve trays a slightly different approach is recommended [10, 11]. The orifice coefficient is not related to the velocity in the smallest geometrical area of the open area but to the whole active area of the tray. The reason for this different approach is that the quality of tray design depends not only on the pressure loss of a single element but also on the number of elements on a tray, i.e., the relative free area φ'. The following definition implies both quantities:

$$\Delta p = \zeta_t' \cdot \frac{\rho}{2} \cdot u^2 \qquad (18)$$

Thus, this relation between ζ and ζ_t' holds:

$$\zeta_t' = \zeta/\varphi^2 \qquad (19)$$

In Eq. (18) the symbol u denotes the superficial velocity of the fluid. More precisely, the volume flow of the fluid relates to the active area of the tray, i.e., the cross section of the column minus two times the area of the down comer. In a standard tray design

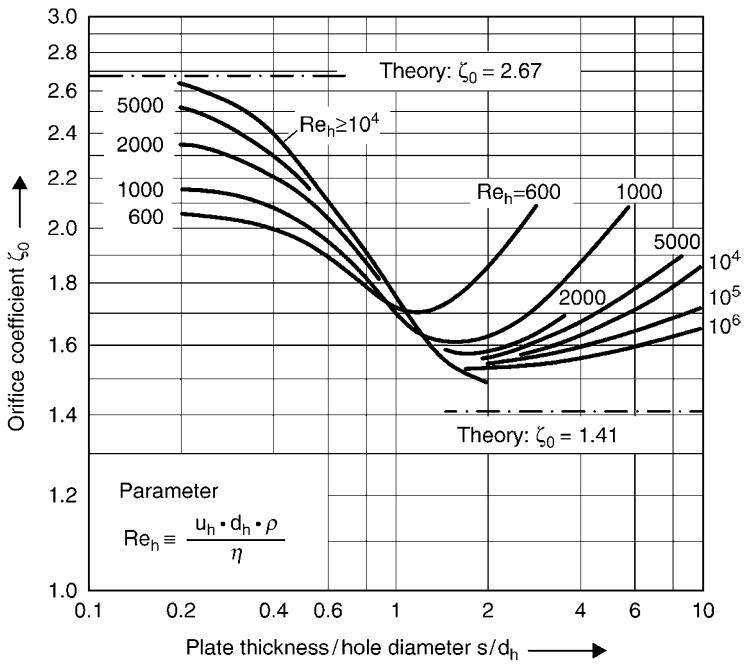

L1.7. Fig. 2. Correlation of the orifice coefficient ζ_o of sieve trays.

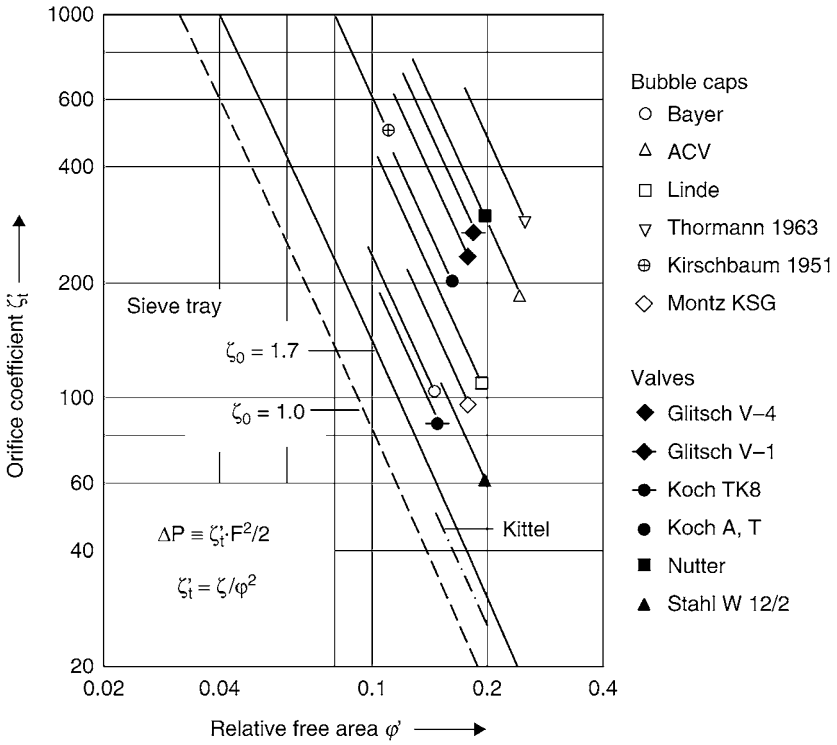

L1.7. Fig. 3. Correlation of the orifice coefficient ζ'_t of bubble cap and valve trays.

with a weir length of 70% of the column diameter, the active area of the tray is about 80% of the column cross section.

Bubble caps and valves are very complex elements with a multitude of geometrical parameters. Therefore, the pressure loss cannot be modeled rigorously. Since these elements are produced in large numbers it is advisable to determine the pressure drop experimentally. Most vendors provide such data of their products.

In Fig. 3a compilation of the orifice coefficients ζ'_t is presented for different tray designs. The symbols are plotted for the recommended number of elements per tray area. The parameter lines show the orifice coefficients ζ'_t when less elements are installed. Such a modification is often necessary for geometrical reasons.

The abscissa in Fig. 3 is the smallest relative free area φ' that is, for instance, either the slots or the chimney of a bubble cap. For comparisons sake, the orifice coefficient ζ'_t of a sieve tray with $\zeta_o = 1.7$ is also plotted in Fig. 3. The quality of a tray design is determined by the distance of the relevant parameter line from the line of a sieve tray with $\zeta_o = 1$, which is the theoretical minimum of a sieve tray with rounded edges.

4 Symbols

A area (m^2)
A^* area in the vena contracta (m^2)
A_{ac} active area of a column tray (m^2)
A_h area of the hole (m^2)
d_h hole diameter (m)
p pressure (N/m^2)
p^* pressure in the vena contracta (N/m^2)
s plate thickness (m)
u velocity of the fluid, superficial velocity in a column (m/s)
u^* velocity in the vena contracta (m/s)
u_h velocity in the hole (m/s)
α orifice discharge coefficient
Δp pressure loss (N/m^2)
φ relative free area of the plate
φ' relative free area of bubble cap and valve trays
ζ orifice coefficient, see Eq. (1)
ζ_o orifice coefficient for $\varphi \to 0$
ζ'_t orifice coefficient of a tray, see Eq. (18)
η dynamic viscosity of the fluid (kg/(m · s))
π circular constant, $\pi = 3.14159$
ρ density of the fluid (kg/m^3)
Re_h Reynolds number in the hole, $Re_h \equiv u_h \cdot d_h \cdot \rho/\eta$

5 Bibliography

1. Tietjens O (1960) Strömungslehre. Springer-Verlag, Berlin
2. Mayor CJ, Hertzog RR (1955) Flow capacities of sieve-plate liquid-extraction columns. Chem. Eng. Progr. 51(1):17-J–21-J
3. McAllister R, McGinnis P, Plank J (1958) Perforated-plate performance. Chem. Eng. Sci. 9:25–35
4. Smith P, van Winkle M (1958) Discharge coefficients through perforated plates at Reynolds numbers of 400 to 3000. AIChE J 3:266–268
5. Mersmann A (1962) Druckverlust und Schamuhöhen von gasdurchströmten Flüssigkeitsschichten auf siebböden. VDI Forschungsheft 491, VDI Verlag, Düsseldorf
6. Bene T (1964) Determination of local resistance coefficients for perforated plates. Int. Chem. Eng. 4:625–628

7. Zelfel E (1965) Versuche über den Widerstandsbeiwert von Einzelbohrungen. Chem.-Ing.-Tech. 37(12):1209–1214
8. Mühle J (1972) Berechnung des trockenen Druckverlustes von Lochböden. Chem.-Ing.-Tech. 44(1+2):72–79
9. Kutzer H (1972) Beeinflussbarkeit des Druckverlustes von Austauschböden durch die Formgebung der Austaucshelemente. Verfahrenstechnik 6(7): 243–250
10. Stichlmair J (1978) Grundlagen der Dimensionierung des Gas/Flüssigkeit-Kontaktapparates Bodenkolonne. Verlag Chemie, Weinheim
11. Stichlmair J, Fair JR (1998) Distillation - principles and practice. Wiley-VCH, New York

L2.1 Prediction of Void Fraction

Holger Schmidt
Areva NP GmbH, Erlangen, Germany

1 Introduction

The method by which the pressure drop of a gas–liquid flow is calculated differs significantly to that of a single-phase flow. This is primarily due to the interaction of the two phases, which can be accounted for by applying the void fraction to the equations of mass, momentum, and energy conservation. Fields in which this methodology is applied include the evaluation of pressure drops, the analysis of expansion characteristics, or the processes involving phase change. In the following section are described the definition of the void fraction and the difference in the procedure applicable to a single-phase flow by considering the void fraction in the conservation equations. As the void fraction is in relation to the single phase flow an additional parameter that depends upon the way, in which the phases are distributed, it is also described how these parameter can be calculated.

2 Flow Pattern

Because of the interaction between the phases, their cross-sectional distributions vary in accordance with the flow conditions. Furthermore, the cross-sectional distribution of the phases is also influenced by the orientation of the tube as illustrated by the flow patterns in Fig. 1. In the following, the characteristics of these typical types of adiabatic tube flows are named and described according to their labeling in Fig. 1 (A–E and a–e, respectively).

- For upwards flow through vertical tubes

(A) Bubble flow

Bubble flow is characterized by a large quantity of bubbles that appear to be mixed almost homogeneously throughout the liquid. The liquid phase nevertheless wets the tube wall.

(B) Slug flow

In slug flow, very large bubbles form and can be several times the tube diameter in length. There are also small bubbles.

(C) Chaotic flow or churn flow

In chaotic flow, there are large and small bubbles that appear to be randomly distributed.

(D) Wispy annular flow

In this type of flow, the liquid is predominantly distributed around the tube wall. The gas phase is present in the tube core, mixed with swarms of droplets that can form strands.

(E) Annular flow

The liquid is almost entirely distributed around the tube wall with few droplets suspended in the gas phase.

- For horizontal flow

(a) Bubble flow

The gas phase is present in the form of small bubbles that, under the influence of gravitation, are mainly distributed in the upper part of the tube.

(b) Stratified flow

The gas phase is above the liquid phase, with no waves at the phase boundary.

(c) Wavy flow

The gas phase lies above the liquid phase. In this case, there are waves present at the phase boundary.

(d) Slug flow (Intermittent flow)

The liquid and gas phases are separate. The waves are so intense that they occasionally occupy the whole cross section of the tube. In these areas, there is an increased occurrence of bubbles in the liquid phase and droplets in the gas phase.

(e) Annular flow

The gas flows in the middle of the tube. The tube wall is wetted by the liquid phase. There are droplets in the gas phase. Although the tube wall is completely wetted, the majority of the liquid flows at the bottom of the tube.

It can sometimes be of practical significance to predict the flow pattern that will occur. For instance, in slug flow, the differences between the liquid and gas phases can sometimes be so great that damages to the piping system can occur with changes in the flow direction. The flow pattern charts shown in Figs. 2 and 3 give an indication of the type of flow that will establish itself under certain undisturbed conditions.

For vertical upwards flow, the flow pattern map according to Hewitt and Roberts [1] is recommended. By means of the momentum fluxes $i_{g,0}$ and $i_{l,0}$, the types of flow to be expected can be determined. The momentum fluxes are:

VDI-GVC (ed.), *VDI Heat Atlas*, DOI 10.1007/978-3-540-77877-6_47,

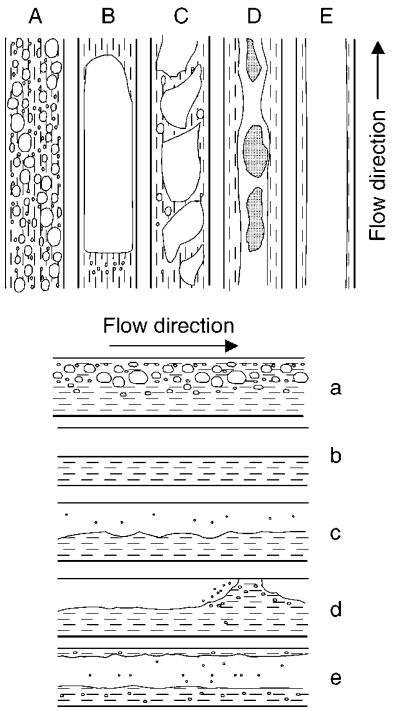

L2.1. Fig. 1. Types of flow pattern.

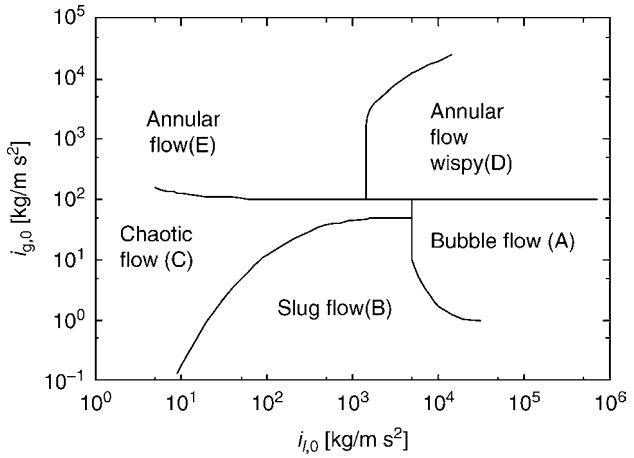

L2.1. Fig. 2. Flow pattern map according to Hewitt and Roberts [1] for vertically upwards flow in tubes.

$$i_{g,0} = (\dot{m} \cdot \dot{x})^2 / \rho_g \tag{1}$$

$$i_{l,0} = (\dot{m} \cdot (1 - \dot{x}))^2 / \rho_l \tag{2}$$

with the two relevant quantities for the description of gas–liquid flows, i.e., the steam quality $\dot{x}$ and the mass flux $\dot{m}$ given by:

$$\dot{x} = \dot{M}_g / (\dot{M}_l + \dot{M}_g) \tag{3}$$

$$\dot{m} = (\dot{M}_g + \dot{M}_l) / A \tag{4}$$

For horizontal flow, the flow pattern map developed by Taitel and Dukler [2] is recommended. In this case, various dimensionless quantities are used to estimate which type of flow pattern will occur. For the abscissa, the Lockhart-Martinelli parameter

$$X = \left(\left(\frac{\Delta p_R}{\Delta x} \right)_l \Big/ \left(\frac{\Delta p_R}{\Delta x} \right)_g \right)^{0,5} \tag{5}$$

must be evaluated. Here, the two frictional pressure losses are each equal to that which would occur if each phase occupies the entire cross section.

For the ordinate, three values are to be determined for the following boundary conditions:

- The boundary between bubble and slug flows

$$T_D = \left(\left(\frac{\Delta p_R}{\Delta x} \right)_l \Big/ \left(\left(\rho_l - \rho_g \right) \cdot g \right) \right)^{0,5} \tag{6}$$

- The boundary between annular and wavy flows and

$$F_D = \frac{\dot{m} \cdot \dot{x}}{\left(\left(\rho_l - \rho_g \right) \cdot \rho_g \cdot d \cdot g \right)^{0,5}} \tag{7}$$

- The boundary between wavy and stratified flows

$$K_D = \frac{\dot{m}^3 \cdot \dot{x}^2 \cdot (1 - \dot{x})}{\left(\rho_l - \rho_g \right) \cdot \rho_g \cdot g \cdot \eta_l} \tag{8}$$

3 Modeling

It becomes clear from the above-mentioned flow types that a gas–liquid flow is, in part, discontinuous. The flow conditions at a point, e.g., the density, can change abruptly. It is therefore usual in practical calculations to use simplified models of the complex and discontinuous flow behavior, treating the flow as if it is continuous. The most widely used modeling approaches are:

- The heterogeneous model
- The homogeneous model
- The drift flow model and
- The two-fluid model

Both the drift flow and the two-fluid models are so complex that they are only used in complex program systems such as RELAP [3], RETRAN [4], ATHLET [19], or for calculations involving phase separation processes. However, the heterogeneous and homogeneous models can be used with reasonable effort in practical calculations.

An important quantity that is used in nearly all modeling approaches to describe a gas–liquid flow is the void fraction ε. This is defined in Eq. (9) such that the discontinuities in the fluctuating flow may be treated as continuous by time-averaging over the interval $\Delta\tau$. To this end, the function R is introduced for which:

$R = 1$ if gas is present, and

$R = 0$ if liquid is present.

$$\varepsilon_{g,B} = \frac{\int_B \int_0^{\Delta\tau} R \; \mathrm{d}t \; \mathrm{d}B}{B \cdot \Delta\tau} \tag{9}$$

In the literature, there are various ranges of B over which the integration is carried out (e.g., point, line, surface, or volume). The most practically meaningful of these is that over the cross-sectional area. In the following, the quantity so defined will be referred to as the void fraction ε.

$$\varepsilon = \frac{\int_A \int_0^{\Delta\tau} R \; \mathrm{d}t \; \mathrm{d}A}{A \cdot \Delta\tau} \tag{10}$$

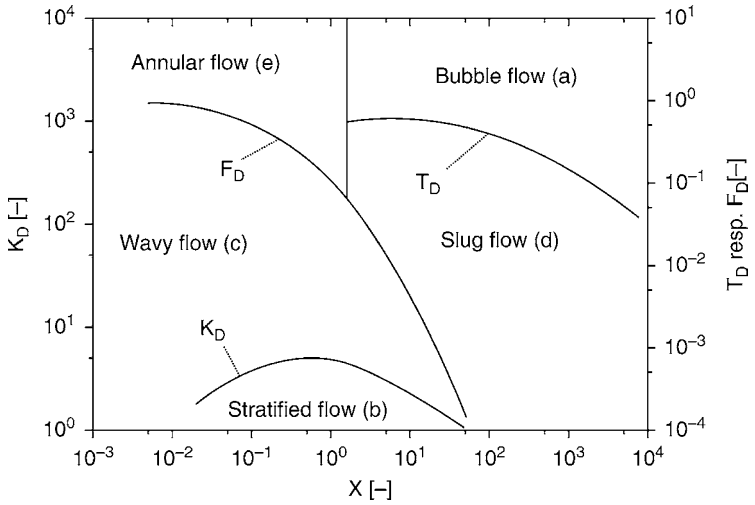

L2.1. Fig. 3. Flow pattern map according to Taitel and Dunkler [2] for horizontal flow in tubes.

In line with the general definition of the void fraction, a liquid fraction $\varepsilon_{l,B}$ can also be evaluated which denotes the fraction of the flow field occupied by the liquid phase:

$$\varepsilon_{l,B} = 1 - \varepsilon_{g,B} \tag{11}$$

3.1 Heterogeneous Model

In the heterogeneous model, the velocity of each phase is constant over the cross section and can be calculated using the void fraction according to Eq. (12) or (13).

$$u_g = \frac{\dot{M} \cdot \dot{x}}{\rho_g \cdot A \cdot \varepsilon} \tag{12}$$

$$u_l = \frac{\dot{M} \cdot (1 - \dot{x})}{\rho_l \cdot A \cdot (1 - \varepsilon)} \tag{13}$$

For the average density of a particular cross section, the following applies in accordance with the definition of the void fraction:

$$\bar{\rho} = \varepsilon \cdot \rho_g + (1 - \varepsilon) \cdot \rho_l \tag{14}$$

The slip ratio $s = u_g / u_l$, which is a frequently used quantity for the characterization of gas–liquid flows can be expressed in terms of the void fraction ε:

$$s = \frac{\dot{x}}{1 - \dot{x}} \cdot \frac{1 - \varepsilon}{\varepsilon} \cdot \frac{\rho_l}{\rho_g} \tag{15}$$

3.2 Homogeneous Model

The homogeneous model differs from the heterogeneous model in that the slip ratio, $s = 1$. This leads to a void fraction for the homogeneous model ε_{hom} of:

$$\varepsilon_{\text{hom}} = \frac{\rho_l \cdot \dot{x}}{\rho_l \cdot \dot{x} + \rho_g \cdot (1 - \dot{x})} \tag{16}$$

or the homogeneous density ρ_{hom} and the homogeneous velocity u_{hom}:

$$\rho_{\text{hom}} = \left(\frac{\dot{x}}{\rho_g} + \frac{1 - \dot{x}}{\rho_l} \right)^{-1} \tag{17}$$

$$u_{\text{hom}} = \frac{\dot{M}}{\rho_{\text{hom}} \cdot A} = u_g = u_l \tag{18}$$

Although the homogeneous model is very simple, it can nevertheless be used to construct very good descriptions of gas–liquid flows if:

- The phases are well mixed, as is for example the case downstream of fittings or
- The differences between the phases are small, as is the case at high pressures

3.3 Pressure Drop and Conservation Equations

The pressure drop along a piping system or vessel is determined through the evaluation of a momentum balance. This is viewed as one-dimensional in the direction of the flow path L. It is generally the case that the change in the momentum of a flow is equal to the sum of the intervening forces. In the steady state case, this means that the difference between the entry and exit momentum flows $\Delta \dot{I}$ is equal to the sum of the gravitational force F_G, the frictional force F_R, and the force resulting from the pressure difference F_p. For practical calculations, the forces or momentum flows are represented as pressure differences, where for constant flow cross sections:

$$\Delta p = \Delta p_A + \Delta p_G + \Delta p_R \tag{19}$$

with the total change in pressure Δp:

$$\Delta p = p_{\text{in}} - p_{\text{out}} = F_P / A \tag{20}$$

the frictional pressure drop Δp_R:

$$\Delta p_R = -F_R / A \tag{21}$$

the acceleration pressure drop Δp_A according to the heterogeneous model:

$$\Delta p_A = \Delta \dot{I}/A = \left(u_g^2 \cdot \rho_g \cdot \varepsilon + u_l^2 \cdot \rho_l \cdot (1-\varepsilon)\right)_{out} - \left(u_g^2 \cdot \rho_g \cdot \varepsilon + u_l^2 \cdot \rho_l \cdot (1-\varepsilon)\right)_{in} \quad (22)$$

and the geodetic pressure drop according to the heterogeneous model, where φ is the angle of inclination away from to the horizontal:

$$\Delta p_G = -F_G/A = \int_0^L (\varepsilon \cdot \rho_g + (1-\varepsilon) \cdot \rho_l) \cdot \sin(\varphi) \cdot g \; \mathrm{d}x \quad (23)$$

The contribution of the acceleration pressure drop term is equal to zero in the calculation of single-phase and incompressible pressure drops and does not influence the momentum balance. On the other hand, it is in precisely the case of evaporation processes that this contribution is to be accounted for, as the mass flow is accelerated from the slower moving liquid phase to the faster moving gas phase.

Unlike the calculation procedure for single-phase or incompressible geodetic pressure drops, in the case of a gas–liquid flow the integration must be carried out along the flow path insofar as the void fraction and the densities do not remain constant. In many practical applications, there is a phase change along the flow path and the void fraction changes. This phase change is caused by expansion evaporation (flashing) due to the pressure drop or the input or extraction of heat. For this reason, pressure drop calculations for a gas–liquid flow can often only be carried out in conjunction with an energy balance.

In line with the energy balance, the sum of the heat and power inputs, $\dot{Q}$ and P respectively, is equal to the sum of the changes in the kinetic energy of the flow $\dot{E}_T$, the flow enthalpy $\Delta \dot{H}$ and the power required to overcome the gravitational field $\dot{E}_G$ such that:

$$P + \dot{Q} = \Delta \dot{H} + \dot{E}_G + \dot{E}_T \quad (24)$$

with the change in enthalpy:

$$\Delta \dot{H} = \dot{M} \cdot (h_{out} - h_{in}) \quad (25)$$

the power required to overcome the gravitational field:

$$\dot{E}_G = \dot{M} \cdot g \cdot L \cdot \sin(\varphi) \quad (26)$$

and the change in the kinetic energy of the flow according to the heterogeneous model:

$$\dot{E}_T = \frac{1}{2} \cdot A \cdot \left(\left(u_g^3 \cdot \rho_g \cdot \varepsilon + u_l^3 \cdot \rho_l \cdot (1-\varepsilon)\right)_{out} - \left(u_g^3 \cdot \rho_g \cdot \varepsilon + u_l^3 \cdot \rho_l \cdot (1-\varepsilon)\right)_{in} \right) \quad (27)$$

For this reason, it is common practice to calculate the pressure drop in steps along the flow path L. It is assumed that the integrand in Eq. (23) and the frictional pressure drop are constant over a step of width Δx. The pressure and enthalpy after step Δx can then be determined using Eqs. (19–27) giving the input conditions for the next step.

The total mass of a gas–liquid mixture in a piping system according to the heterogeneous approach is given by integrating the product of the cross-sectional area and the average density along the flow path according to Eq. (14):

$$M = \int_0^L (\varepsilon \cdot \rho_g + (1-\varepsilon) \cdot \rho_l) \cdot A \; \mathrm{d}x \quad (28)$$

Knowledge of the total content of a vessel or piping system is of interest, for example, in determining the dimensions of expansion vessels.

4 Calculation of the Void Fraction

According to Eqs. (22), (23), (27), and (28), the void fraction is to be taken into account in all conservation equations for calculations involving gas–liquid flows. This quantity has therefore been intensively investigated. Many calculation algorithms for the void fraction are based upon the drift-flux model according to Zuber and Findly [5]. According to this model, the void fraction is given by:

$$\varepsilon = \left(\frac{C_0}{\varepsilon_{hom}} + \frac{\rho_g \cdot u_{gj}}{\dot{x} \cdot \dot{m}} \right)^{-1} \quad (29)$$

Here, the distribution factor C_0 and the weighted average drift velocity u_{gj} are to be determined from measured void fractions. Mayinger [6] and Chexal et al. [7] give an overview of a number measuring methods for determining the void fraction. These methods are based upon, for example:

- Gamma or neutron beam measurements, where the reduction of the beam intensity due to the fluid can be used to calculate the void fraction
- Traversable needle probes, which emit a signal that can be transferred to a time dependent signal of R, depending on the status at the end of the needle (according to Eq. (2))
- Impedance measurement, whereby more local or cross-section averaged void fractions can be measured depending of the positioning and geometry of the electrodes
- Weight or volume expansion measurements, which are volume averaged void fraction measurements over an entire system and
- Total pressure drop, where the void fraction can be calculated based upon correlations of the frictional pressure drop

A number of relationships for C_0 and u_{gj} are given in Table 1. There are other relationships for the calculation of the void factor in tubes or similar duct geometries than those according to Rouhani [8], such as those by Melber [9], Hughmark [10], or Nabizadeh [11]. Comparative studies by Friedel [12] or Woldesmayat and Ghajar [13] show that these models can be used with similar success. It must be pointed out that with small mass flow densities, downwards flow, counter-flow, or large flow

L2.1. Table 1. Values for C_0 and u_{gi}

Author		Application
Rouhani C. [8]	$C_0 = 1 + 0,2 \cdot (1 - \dot{x}) \cdot \frac{(g \cdot d_h)^{0.25} \cdot \rho_l^{0.5}}{\dot{m}^{0.5}}$ $u_{gj} = 1,18 \cdot \left(g \cdot \sigma \cdot \left(\rho_l - \rho_g\right)\right)^{0.25} \cdot (1 - \dot{x}) / \sqrt{\rho_l}$	Tubes and ducts for $\dot{m} > 250$ kg/m^2 s
Morooka S., T. Ishi-zuka, M. Iizuka, K. Yoshimura [14]	$C_0 = 1,08;\ u_{gj} = 3,04 \cdot \left[\frac{\sigma \cdot g \cdot (\rho_l - \rho_g)}{\rho_l^2}\right]^{0.25}$ $C_0 = 1,13;\ u_{gj} = 1,41 \cdot \left[\frac{\sigma \cdot g \cdot (\rho_l - \rho_g)}{\rho_l^2}\right]^{0.25}$	Longitudinal flow through a bundle of tubes or fuel element for $\dot{m}/\rho_{\text{hom}} > 5$ m/s and $\varepsilon < 0,9$ for $\dot{m}/\rho_{\text{hom}} < 5$ m/s and $\varepsilon < 0,9$
Schrage D.E., J.-T. Hsu, M. K. Jensen [15]	$C_0 = (1 + 0,36 \cdot \dot{m}^{-0,191} \cdot 1\text{n}(\dot{x}))^{-1};\ u_{gj} = 0$ $\dot{m}$ in kg/m^{2}s	Transverse flow through a bundle of tubes, guided flow, vertically upwards, medium R113 *Valid for $\dot{m}$ values from* 680 *to* 50
Margat, L, B. Thonon, L. Tadrist [16]	$C_0 = 0,9636;\ u_{gj} = 0,4275$ for $\dot{m} = 125$ kg/m^{2}s $C_0 = 0,8831;\ u_{gj} = 0,4296$ for $\dot{m} = 85$ kg/m^{2}s $C_0 = 0,7552;\ u_{gj} = 0,3453$ for $\dot{m} = 37$ kg/m^{2}s	Plate heat exchanger, medium R134a

cross sections it is advantageous to use the Chexal-Lellouche correlation [7] which is valid not only over a very wide range of parameters but also requires a great deal of programming.

If the flow channel differs significantly from a cylinder, various effects including separation or homogenization influence the results of these calculations. For this reason, specific values for C_0 and u_{gj} must be determined for such geometries. Some guideline values are given in Table 1.

An ideal homogenization, as can be assumed to occur downstream of a fitting is synonymous with $C_0 = 1$ and $u_{gj} = 0$. Figure 4 shows the difference between a homogenized and fully formed flow for which the void fractions were determined using the approach by Rouhani [8]. From Fig. 4, it is also clear that the difference between the homogeneous and heterogeneous calculations becomes smaller with increasing pressure and is particularly large for low steam qualities.

There is no relationship that accounts for the influence of the gravitational force on the void fraction. Results from Elkow and Rezkallah [17] indicate that the void fraction in a very small gravitational field can differ by up to 25% from that which would occur under comparable conditions on Earth. In this respect, a summary representation by Ohta [18] shows that the void fraction for small volumetric flow rates is greater, and for large volume flows less, than that present due to the gravitational field on Earth.

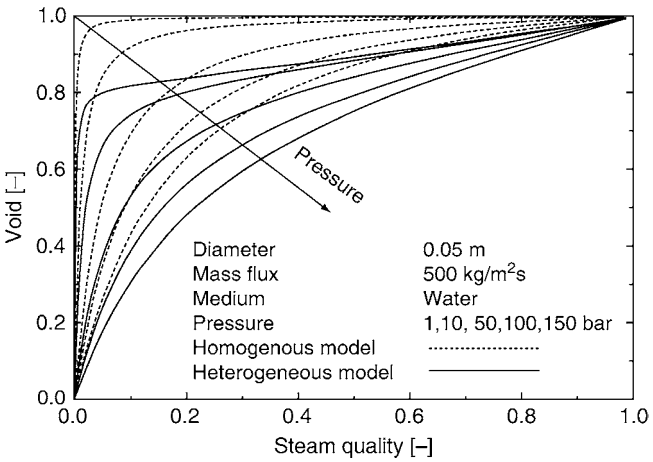

L2.1. Fig. 4. Void fraction ε as a function of the steam quality $\dot{x}$.

5 Examples

The following examples demonstrate the various ways in which the conservation equations can be solved. In each case, it is assumed that the frictional pressure drop is negligible, which at low mass fluxes is a plausible simplification by the model. The following chapters contain information concerning the prediction of the frictional pressure drop.

Example 1:

The pressure drop is to be determined in the vertical riser of a pool cleaner. The riser lifts water from the bottom of a pool to the top, carrying with it some mud. The pool cleaner is driven by blowing air into the riser. Given are:

The diameter $d = 0.02$ m, the lifting height $L = 0.5$ m, the water density $\rho_l = 998.21$ kg/m^3, the gas density $\rho_g = 1.188$ kg/m^3, the surface tension $\sigma = 0.01$ N/m, the air mass flow $\dot{M}_g = 0.001$ kg/s, and the water mass flow $\dot{M}_l = 0.1$ kg/s.
The values of the friction and acceleration pressure drops in the riser are neglected so that the total pressure drop is equal to the geodetic pressure drop given by Eq. (23). Since the properties of air and water can be considered constant, ε, ε_{hom}, C_0, and u_{gj} can be determined as follows using Eqs. (16) and (29) and Table 1 and with

$$\dot{x} = \dot{M}_g / (\dot{M}_g + \dot{M}_l) = 0.001/(0.001 + 0.1) = 0.0099$$

and

$$\dot{m} = \frac{(\dot{M}_g + M_l) \cdot 4}{\pi \cdot d^2} = \frac{(0.001 + 0.1) \cdot 4}{\pi \cdot 0.02^2} = 321.5 \frac{\text{kg}}{\text{m}^2\text{s}}$$

-:

$$\begin{aligned} u_{gj} &= 1.18 \cdot (g \cdot \sigma \cdot (\rho_l - \rho_g))^{0,25} \cdot (1 - \dot{x}) / \sqrt{\rho_l} \\ &= 1.18 \cdot (9.81 \cdot 0.01 \cdot (998.21 - 1.188))^{0,25} \cdot \\ &\quad (1 - 0.0099) / \sqrt{998.21} \\ &= 0.12 \ \text{m/s} \end{aligned}$$

$$C_0 = 1 + 0.2 \cdot (1 - \dot{x}) \cdot \frac{(g \cdot d_h)^{0.25} \cdot \rho_l^{0.5}}{\dot{m}^{0.5}}$$
$$= 1 + 0.2 \cdot (1 - 0.0099) \cdot \frac{(9.81 \cdot 0.02)^{0.25} \cdot 998.21^{0.5}}{321.5^{0,5}} = 1.23$$
$$\varepsilon_{\text{hom}} = \frac{\rho_l \cdot \dot{x}}{\rho_l \cdot \dot{x} + \rho_g \cdot (1 - \dot{x})}$$
$$= \frac{998.21 \cdot 0.0099}{998.21 \cdot 0,0099 + 1.188 \cdot (1 - 0.0099)} = 0.894$$
$$\varepsilon = \left(\frac{C_0}{\varepsilon_{\text{hom}}} + \frac{\rho_g \cdot u_{gj}}{\dot{x} \cdot \dot{m}} \right)^{-1} = \left(\frac{1.23}{0.894} + \frac{1.188 \cdot 0.12}{0.0099 \cdot 321.5} \right)^{-1} = 0.7.$$

Therefore, for the pressure drop:

$$\Delta p \approx \Delta p_{\text{G}} = \int_0^L (\varepsilon \cdot \rho_g + (1 - \varepsilon) \cdot \rho_l)_l \cdot \sin(\varphi) \cdot g \ \ \text{d}x$$
$$= (0.7 \cdot 1.188 + (1 - 0.7) \cdot 998.21) \cdot$$
$$\sin(90^\circ) \cdot 9.81 \cdot 0.5 = 1,473 \text{ Pa}$$

Example 2:
The pressure drop and the mass in a 10-m-long vertical evaporator of a natural circulation steam generator are to be determined. The inlet temperature of 360°C is equal to the saturation temperature. Due to the low mass flow density of 350 kg/m²/s, the frictional pressure drop can be neglected. The following values apply:

$$p_i = 528.3 \text{ kg/m}^3, \ p_g = 143.467 \text{ kg/m}^3.$$

Since the pressure of 186.7 bar is close to the critical pressure of 220.64 bar, the homogeneous model will be used as an approximation. The heat flow density is constant along the flow path and the steam quality at the outlet is 0.3. Consequently, the steam quality rises approximately linearly in the direction of flow. Thus, for the steam content at point x:

$$\dot{x} = x \cdot (\dot{x}_{\text{out}} - \dot{x}_{\text{in}})/L = x \cdot 0,3/10 \ \ \text{m}$$

and together with Eqs. (16) and (23), the following can be written for the geodetic pressure drop according to the homogeneous model:

$$\Delta p_{\text{G}} = \int_{\dot{x}_{\text{in}}}^{\dot{x}_{\text{out}}} \frac{\rho_l \cdot g \cdot L/(\dot{x}_{\text{out}} - \dot{x}_{\text{in}})}{\dot{x} \cdot (\rho_l - \rho_g)/\rho_g + 1} \cdot \sin(\varphi) \ \ \text{d}\dot{x}$$

or, after integrating:

$$\Delta p_{\text{G}} = \frac{\rho_l \cdot \rho_g \cdot g \cdot L \cdot \sin(\varphi)}{(\dot{x}_{\text{out}} - \dot{x}_{\text{in}}) \cdot (\rho_l - \rho_g)} \cdot \left[\ln \left(\frac{\dot{x} \cdot (\rho_l - \rho_g)}{\rho_g} + 1 \right) \right]_{\dot{x}_{\text{in}}}^{\dot{x}_{\text{out}}}$$

or, for $\dot{x}_{\text{in}} = 0$:

$$\Delta p_{\text{G}} = \frac{\rho_l \cdot \rho_g \cdot g \cdot L \cdot \sin(\varphi)}{x_{\text{out}} \cdot (\rho_l - \rho_g)} \cdot \ln \left(\frac{\dot{x}_{\text{out}} \cdot (\rho_l - \rho_g)}{\rho_g} + 1 \right)$$

and inserting the values:

$$\Delta p_{\text{G}} = \frac{528.3 \cdot 143.467 \cdot 9.81 \cdot 10 \cdot \sin(90^\circ)}{0.3 \cdot (528.3 - 143.467)} \cdot$$
$$\ln \left(\frac{0.3 \cdot (528.3 - 143.467)}{143.467} + 1 \right) = 38,024 \text{ Pa} = 0,38 \text{ bar}.$$

The acceleration pressure drop can be found using Eqs. (22) and (16) from the homogeneous model:

$$\Delta p_{\text{A}} = \dot{m}^2 \cdot \left(\rho_{\text{hom,out}}^{-1} - \rho_{\text{hom,in}}^{-1} \right)$$

or for $\dot{x}_{\text{in}} = 0$

$$\Delta p_A = \dot{m}^2 \cdot \dot{x}_{\text{out}} \left(\rho_g^{-1} - \rho_l^{-1} \right)$$

and inserting the values:

$$\Delta p_{\text{A}} = 350^2 \cdot 0,3 \cdot \left(143.467^{-1} - 528.3^{-1} \right)$$
$$= 187 \text{ Pa} = 0,00187 \text{ bar}.$$

For the total pressure drop, the approximation $\Delta p_{\text{R}} = 0$ is applied according to Eq. (19):

$$\Delta p = \Delta p_{\text{A}} + \Delta p_{\text{G}} + \Delta p_{\text{R}} = 187 + 38,024 + 0$$
$$= 38,211 \text{ Pa} = 0.38 \text{ bar}.$$

The mass of water within the evaporator tube is given by Eqs. (16) and (28). As for the calculation of the geodetic pressure drop, the integral is to be solved as follows:

$$M = \int_{\dot{x}_{\text{in}}}^{\dot{x}_{\text{out}}} \frac{\rho_l \cdot L/(\dot{x}_{\text{out}} - \dot{x}_{\text{in}}) \cdot A}{\dot{x} \cdot (\rho_l - \rho_g)/\rho_g + 1} \cdot \text{d}\dot{x}$$

or, after integrating:

$$M = \frac{\rho_l \cdot \rho_g \cdot L \cdot A}{(x_{\text{out}} - x_{\text{in}}) \cdot (\rho_l - \rho_g)} \cdot \left[\ln \left(\frac{\dot{x} \cdot (\rho_l - \rho_g)}{\rho_g} + 1 \right) \right]_{\dot{x}_{\text{in}}}^{\dot{x}_{\text{out}}}$$

and for $\dot{x}_{\text{in}} = 0$:

$$M = \frac{\rho_l \cdot \rho_g \cdot L \cdot A}{x_{\text{out}} \cdot (\rho_l - \rho_g)} \cdot \ln \left(\frac{\dot{x}_{\text{out}} \cdot (\rho_l - \rho_g)}{\rho_g} + 1 \right)$$

and inserting the values for an inner diameter of 0.05 m:

$$M = \frac{528.3 \cdot 143.467 \cdot 10 \cdot 0.05^2 \cdot 3.14}{0,3 \cdot (528.3 - 143.467) \cdot 4} \cdot$$
$$\ln \left(\frac{0.3 \cdot (528.3 - 143.467)}{143.467} + 1 \right) = 7,6 \text{ kg}.$$

Example 3:
The pressure drop along a vertically orientated evaporator tubes is to be calculated. In the calculation, variations in fluid properties due to changes in pressure are to be accounted for and the heterogeneous model has been applied. The conditions are as follows:

(a) As in Example 2, but with a heat flux of 93 kW/m² through the inner wall of the tube. The material parameters for water are determined by linear interpolation between the following values:

t	p	ρ_g	ρ_l	σ	h_g	h_l
°C	bar	kg/m³	kg/m³	10^{-3} N/m	kJ/kg	kJ/kg
360	186.7	143.5	528.3	1.89	2485.4	1764.2
350	165.4	113.4	574.5	3.68	2576.4	1671.9

(b) As in Example 3a, but with a heat flux of 21 kW/m^2 through the inner wall of the tube. Also, neon is used as the working fluid with an inlet temperature of 41 K. The material properties are determined by linear interpolation between the following values:

T	p	ρ_g	ρ_l	σ	h_g	h_l
K	bar	kg/m^3	kg/m^3	10^{-3} N/m	kJ/kg	kJ/kg
41	16.88	164.5	859	0.65	86.58	38.67
39	12.6	115.3	932	1.15	89.93	32.93

To account for the change in material properties and the flow of kinetic energy, the following steps are required:

1. Division of the flow path into elements with a step-length of Δx and with a heat flow of $\dot{Q}/\Delta x$ per element. Steps 2 to 11 are to be completed for each element as follows:
2. $\dot{E}_G$ according to Eq. (26).
3. $\dot{E}_T$ according to Eq. (27), $\dot{E}_T = 0$ for the first iteration.
4. $\Delta\dot{H}$ according to Eq. (24).
5. h_{out} according to Eq. (25) at the outlet of the element.
6. $\rho_{g,out}$, $\rho_{l,out}$, $h_{g,out}$, $h_{l,out}$, and σ_{out}at the outlet of the element in question as a function of the corresponding pressure p_{out}, $p_{out} = p_{in}$ for the first iteration.
7. $\dot{x}_{out}$ with $\dot{x}_{out} = (h_{out} - h_{g,out})/(h_{l,out} - h_{g,out})$.
8. ε_{out} according to Eq. (29) and Table 1.
9. Δp_A according to Eq. (22).
10. Δp_G by, for example, the following simplification of Eq.(23)
11. $$\Delta p_G = \left(\begin{matrix} \left(\varepsilon \cdot \rho_g + (1-\varepsilon)\cdot \rho_l\right)_{in} + \\ \left(\varepsilon \cdot \rho_g + (1-\varepsilon)\cdot \rho_l\right)_{out} \end{matrix} \right) \cdot 0,5 \cdot g \cdot \sin(\varphi) \cdot \Delta x\,.$$
12. Δp according to Eq. (19) and $p_{out} = p_{in} - \Delta p$.
13. Decision whether the repetition of steps 2 to 11 is necessary. At least one repetition must be completed in order to determine $\dot{E}_T$. As a criterion for stopping the iteration sequence, the change in the outlet pressure of an element is checked each time to see whether it is less than, say 1%. At the end of this iterative procedure, the outlet values become the inlet values for the next element.

Using this calculation procedure, Examples 3a and 3b were each calculated with 200 elements. The outlet values for the first and last elements are listed below.

	Example 3a		Example 3b	
Element	1	200	1	200
Δx [m]	0.05	0.05	0.05	0.05
$\dot{Q}$ [kW]	0.73	0.73	0.165	0.165
$\dot{E}_G$ [kW]	0.0003	0.0003	0.0003	0.0003
$\dot{E}_T$ [kW]	0.001	0.0018	0.0018	0.0136
$\Delta\dot{H}$ [kW]	0.729	0.727	0.1626	0.1508
h_{out} [kJ/kg]	1765.3	1976.3	38.90	84.47
$\rho_{g,out}$ [kg/m^3]	143.5	142.9	164.45	159.95
$\rho_{l,out}$ [kg/m^3]	528.3	529.2	859.07	865.75
$h_{g,out}$ [kJ/kg]	2485.4	2487.1	86.58	86.88
$h_{l,out}$ [kJ/kg]	1764.2	1762.4	38.66	38.14
σ_{out} [10^{-3} N/m]	1.89	1.92	0.65	0.70
$\dot{x}_{out}$ [-]	0.0014	0.295	0.005	0.95
ε_{out} [-]	0.0041	0.508	0.018	0.976
Δp_A [Pa]	0.72	0.79	2.23	3.89
Δp_G [Pa]	258.7	163.3	418.21	87.03
Δp [Pa]	259.5	164.13	420.44	90.93
i_{out} [bar]	186.74	186.33	16.87	16.48
$\sum_1^{200} \Delta p$ [bar]		0.408		0.397

6 Symbols

A	Cross-sectional area (m^2)
B	Range - point, line, surface, Volume according to Eq. (9) (-, m, m^2, m^3)
C_0	Distribution parameter
d	Diameter (m)
d_h	Hydraulic diameter (m)
$\dot{E}$	Energy flow (W)
F	Force (N)
F_D	Parameter according to Eq. (7)
g	Acceleration due to gravity (earth) (m/s^2)
h	Specific energy (kJ/kg)
$\dot{I}$	Momentum flow (kg m/ s^2)
i	Momentum flow density (flux) (kg/m s^2)
K_D	Parameter according to Eq. (8)
L	Length of flow path (m)
$\dot{M}$	Mass flow (kg/s)
$\dot{m}$	Mass flow density (flux) (kg/m^2 s)
P	Power (W)
$\dot{Q}$	Heat flow (W)
R	Function
s	Slip ratio
t	Time (s)
T_D	Parameter according to Eq. (6)
u	Velocity in the direction of flow (m/s)
u_{gj}	Weighted average drift velocity (m/s)
X	Lockhart-Martinelli parameter
x	Coordinate in the direction of flow (m)
$\dot{x}$	Steam quality
ε	Void fraction in relation to the cross-sectional area
$\varepsilon_{g,B}$	Void fraction in relation to the range B
$\varepsilon_{l,B}$	Liquid fraction in relation to the range B
$\Delta\dot{H}$	Enthalpy flow difference (W)
Δp	Pressure drop (Pa)
Δx	Step length in the direction of flow (m)
$\Delta\tau$	Time interval (s)
φ	Angle of inclination to the horizontal (°)
ρ	Density (kg/m^3)
η	Dynamic viscosity (N s/m^2)
σ	Surface tension (N/m)

Indices

A	Acceleration
out	At the outlet
B	Range - point, line, surface, volume according to Eq. (9)
G	Geodetic
in	At the inlet
g	Gaseous phase
g, 0	Exclusively gaseous phase
hom	Homogeneous
l	Liquid phase
l, 0	Exclusively liquid phase
P	Pressure
R	Friction
T	Exchange

7 Bibliography

1. Hewitt GF, Roberts DN (1969) Studies of two-phase flow pat-terns by simultaneous X-ray and flash photography, AERE-M, HMSO
2. Taitel Y, Dukler AE (1976) A model for predicting flow regime transitions in horizontal and near horizontal gas liquid flow. AIChE J 22(1):47–55
3. RELAP5/mod3 Code Manual, Volumes 1–7, NUREG/CR-5535, August 1995.
4. Paulsen MP et al. (October 1996) RETRAN-3D: A program for transient, thermal hydraulic analysis of complex fluid flow systems, volume 1: Theory and numerics. EPRI NP-7450
5. Zuber N, Findlay JA (November 1965) Average volumetric concentration in two-phase flow systems. J Heat Transfer 87:453–468
6. Mayinger F (1982) Strömung und Wärmeübergang in Gas-Flüssigkeits-Gemischen. Springer-Verlag, Vienna/New York. [*Flow and heat transfer in gas-liquid mixtures, Vienna/New York, Springer-Verlag, 1982*]
7. Chexal B et al. (March 1997) Void fraction technology for design and analysis. EPRI TR-106326
8. Rouhani C (1969) Modified correlations for void and two-phase pressure drop, AB Atomenergi. AE-RTV-841
9. Melber A (1989) Experimentelle und theoretische Untersuchungen über den Druckabfall von Zweiphasenströmungen in beliebig geneigten Rohren. Dissertation, TH Darmstadt. [*Experimental and theoretical investigations of the pressure drop in two-phase flows in arbitrarily inclined tubes, Dissertation, TU Darmstadt, 1989*]
10. Hughmark GA (1962) Holdup in gas-liquid flow. Chem Eng Prog 58(4):62–65
11. Nabizadeh-Araghi H (1977) Modellgesetze und Parameteruntersuchungen für den volumetrischen Dampfgehalt in einer Zweiphasenströmung. Dissertation, Universität Hannover. [*Modelling laws and parameter investigations for the volumetric steam content in a two-phase flow, Dissertation, University of Hanover, 1977*]
12. Friedel L (1978) Druckabfall bei der Strömung von Gas/Dampf-Flüssigkeitsgemischen in Rohren [*Pressure drops in the flow of gas/vapour-liquid mixes in tubes*]. Chem.-Ing.- Tech. 50(3):167–180
13. Woldesemayat MA, Ghajar AJ (2007) Comparison of void fraction correlations for different flow patterns in horizontal and upwards inclined pipes. Int J Multiphase Flow 33:347–370
14. Morooka S, Ishizuka T, Iizuka M, Yoshimura K (1989) Experimental study on void fraction in a simulated BWR fuel assembly (Evaluation of cross-sectional averaged void fraction). Nuclear Eng Design 114:91–98
15. Schrage DS, Hsu J.-T-, Jensen MK (1988) Two-phase pressure drop in vertical crossflow across a horizontal tube bundle. AIChE J 34(1):107–115
16. Margat L, Thonon B, Tadrist L (June 1997) Heat transfer and two-phase flow characteristics during convective boiling in a corrugated channel. Proc. of the Int. Conf. on Compact Heat Exchangers for the Process Industries, Snowbird, Utah, USA, pp. 323–330
17. Elkow KJ, Rezkallah KS (1997) Void fraction measurements in gas-liquid flows under 1-g and μ-g conditions using capacitance sensors. Int J Multiphase Flow 23(5):815–829
18. Ohta H (2003) Review of reduced gravity boiling heat transfer: Japanese research. J Jpn Soc Microgravity Appl 20(4):272–285
19. Steinhoff F, Graf, A *Wielenberg:* Validation of the Advanced Computer System ATHLET/ATHLET-CD. GRS Report GRS – A- 3348a, October 2006.

L2.2 Pressure Drop in Tubes, Valves, and Fittings

Anton Wellenhofer · Sebastian Muschelknautz
Linde AG, Pullach, Germany

1 Introduction

Two-phase flow (gas–liquid) in tubes, valves, and fittings is fundamentally different from single-phase flow. The pressure drop in single-phase flow is characterized by the level of turbulence and the wall roughness. The two-phase pressure drop, by contrast, is linked to the momentum exchange between the two phases and is characterized by the two-phase flow pattern.

This chapter is limited to adiabatic gas–liquid flow. Usually, adiabatic conditions are considered in process piping of chemical and petrochemical plants and cooling systems.

Two-phase flow under influence of an external heat source is characterized by phase transfer in the boundary layer. This task is described in Subchap. H3.2.

To evaluate the pressure drop in complex pipe systems, also taking fittings, valves, and other internals into account, the use of commercially available computer-based calculation tools may be considered. The software programs are mainly based on empirical or semi-empirical methods. Analytical, computer-based methods undergo a sharp development and gain more and more importance for specific tasks. For ubiquitous use, these methods are not fully matured.

The experimentally confirmed empirical and semi-empirical methods have not lost their value. These methods are further used for everyday sizing of tubes and equipment in two-phase service – by hand or as the base of the software tools used.

2 Pressure Drop in Straight Tubes

2.1 Introduction

As explained in Subchap. L2.1, the pressure drop in an adiabatic gas–liquid mixture Δp in straight tubes having the same diameter is composed of a pressure drop due to acceleration based on phase change of the mixture Δp_A, a hydrostatic part Δp_g due to level change, and pressure drop due to friction Δp_R:

$$\Delta p_{2ph} = \Delta p_A + \Delta p_g + \Delta p_R. \tag{1}$$

The frictional pressure drop Δp_A between the two locations (a) and (b) of a tube is calculated assuming momentum equilibrium (reference is made to Subchap. L2.1):

$$\Delta p_A = \frac{\dot{M}_G(b)\cdot u_G(b) + \dot{M}_f(b)\cdot u_f(b) - \dot{M}_g(a)\cdot u_g(a) - \dot{M}_f(a)\cdot u_f(a)}{(\pi/4)d^2} \tag{2}$$

Δp_A must be considered when a notable part of the mixture, e.g., a saturated mixture, is vaporized due to pressure loss in the tube. The increase of overall volume flow from (a) to (b) leads to an increased flow speed, resulting in an increased pressure drop.

The hydrostatic pressure drop is calculated as

$$\Delta p_g = \bar{\rho}\cdot g\cdot \Delta x, \tag{3}$$

where g is the acceleration of gravity, Δx is the vertical level difference, and $\bar{\rho}$ is the mean mixture density. The mean mixture density is defined as follows:

$$\bar{\rho} = (1 - \varepsilon) \cdot \rho_l + \varepsilon \cdot \rho_g. \tag{4}$$

To calculate the mean void fraction ε, reference is made to Subchap. L2.1.

2.2 Friction Pressure Drop

Two-phase flow in tubes results in different flow patterns. Considering the widely used flow pattern map by Hewitt and Roberts [1], for *vertical tubes* low gas flow results in either bubbly flow, bubbly slug flow, or churn turbulent flow, depending on the liquid volume flow. High gas flows lead either to n annular or a wispy annular flow pattern.

For *horizontal* two-phase flow, the flow pattern map by Taitel und Dukler [2] is commonly used. Dependent on the coefficients T_D, F_D, and K_D and the Lockhart–Martinelli parameter X, different flow types – bubbly flow, stratified flow, wavy flow, slug flow, and even annular flow – are predicted.

The two-phase pressure drop in straight tubes is the subject of numerous publications. The introduced methods to calculate the pressure drop are based on empirical correlations.

Most empirical methods are based on a two-phase multiplier which was introduced already in 1948 by Martinelli and Nelson [3]. The fundamental idea behind this is to calculate the pressure drop of one phase, either gas or liquid $\Delta p_{L,G}$, first. To evaluate the two-phase pressure drop Δp_R, the single-phase pressure drop is then multiplied with a two-phase multiplier $\Phi^2_{L,G}$ to consider the influence of the second phase

$$\Delta p_R = \Delta p_{L,G} \cdot \Phi^2_{L,G}. \tag{5}$$

Chisholm [4] used the liquid phase as the base phase:

$$\Delta p_R = \Delta p_L \cdot \Phi^2_L, \tag{6}$$

where

$$\Phi^2_L = 1 + (\Gamma^2 - 1)\left[\frac{21}{\Gamma} \cdot \dot{x}^{0.9}(1 - \dot{x})^{0.9} + \dot{x}^{1.8}\right], \tag{7}$$

$$\Gamma = \left(\frac{\rho_L}{\rho_G}\right)^{0.5} \cdot \left(\frac{\eta_G}{\eta_L}\right)^{0.1} \tag{8}$$

Δp_L is calculated assuming the liquid phase as the only phase in the tube, completely covering the tube cross section.

Friedel [5] developed a method which is valid for *horizontal and vertical upward flows*. The method is based on experimental data of freon-operated cooling cycles and gives acceptable predictions for ammonia, oil–gas mixtures, and liquid metals.

The single-phase pressure drop is calculated such that the overall mass flow is again considered liquid, covering the complete cross section of the tube.

$$\Phi^2_L = (1 - \dot{x})^2 + \dot{x}^2 \frac{\zeta_G}{\zeta_L} \cdot \frac{\rho_L}{\rho_G} + 3.43 \cdot \dot{x}^{0.69}(1 - \dot{x})^{0.24} \cdot \left(\frac{\rho_L}{\rho_G}\right)^{0.8} \cdot \left(\frac{\eta_G}{\eta_L}\right)^{0.22} \cdot \left(1 - \frac{\eta_G}{\eta_L}\right)^{0.89} \cdot \mathrm{Fr}_L^{-0.047} \cdot \mathrm{We}_L^{-0.033} \tag{9}$$

which is valid for viscosity ratios of $\eta_f/\eta_g \leq 1{,}500$ [5].

The friction factor for single-phase gas flow ζ_G and that for single-phase liquid flow ζ_L are calculated neglecting the wall friction (Techo [6]):

$$\zeta_{L,G} = \frac{64}{\mathrm{Re}} \tag{10}$$

and

$$\zeta_{L,G} = \left(0.86859 \cdot \ln\left[\frac{\mathrm{Re}_{L,G}}{1.964 \cdot \ln(\mathrm{Re}_{L,G}) - 3.825}\right]\right)^{-2}, \tag{11}$$

where $\mathrm{Re}_{G,L} > 1{,}055$.

For Eq. (9), Froude and Weber numbers are calculated as follows:

$$\mathrm{Fr}_L = \frac{16 \cdot \dot{M}^2_F}{g \cdot \rho^2_L \cdot \pi^2 \cdot d^5} \tag{12}$$

and

$$\mathrm{We}_L = \frac{16 \cdot \dot{M}^2_F}{\sigma \cdot \rho_L \cdot \pi^2 \cdot d^5}. \tag{13}$$

The pressure drop is then calculated as

$$\Delta p_R = \Delta p_L \cdot \Phi^2_L. \tag{14}$$

For horizontal tubes, Garcia et al. [6] derived an empirical equation based on a comprehensive set of measured data.

The influence of the tube roughness is neglected. For an unknown flow pattern, the following equation may be used:

$$f_m = 0.0925\mathrm{Re}^{-0.2534} + \frac{13.98\mathrm{Re}^{-0.9501} - 0.0925\mathrm{Re}^{-0.2534}}{\left(1 + \left(\frac{\mathrm{Re}}{293}\right)^{4.864}\right)^{0.1972}} \tag{15}$$

and

$$f_m = \frac{(\Delta p/x)D}{2\rho_m w^2_m}. \tag{16}$$

The pressure drop is calculated using Eqs. (15) and (16):

$$\Delta p = \frac{x \cdot 2\rho_m w^2_m}{D} \left(0.0925\mathrm{Re}^{-0.2534} + \frac{13.98\mathrm{Re}^{-0.9501} - 0.0925\mathrm{Re}^{-0.2534}}{\left(1 + \left(\frac{\mathrm{Re}}{293}\right)^{4.864}\right)^{0.1972}}\right), \tag{17}$$

where

$$\rho_m = \rho_L \lambda_L + \rho_G(1 - \lambda_L), \tag{18}$$

$$\lambda_L = \frac{\dot{V}_L}{\dot{V}_L + \dot{V}_G}, \tag{19}$$

$$w_M = w_G + w_L, \tag{20}$$

the superficial gas velocity

$$w_G = \frac{\dot{V}_G}{A} \tag{21}$$

the superficial liquid velocity

$$w_F = \frac{\dot{V}_L}{A} \tag{22}$$

and the mixture Reynolds number Re,

$$\mathrm{Re} = \frac{w_M \cdot D \cdot \rho_L}{\eta_L}. \tag{23}$$

The Reynolds number of the mixture is calculated using the viscosity of the liquid only. This definition acknowledges that the frictional resistance of the mixture is mainly due to the liquid phase.

The mean error for Eq. (15) has been calculated to 20.27%. A comparison of predicted versus calculated data is given in Fig. 1.

With known flow pattern, the following equation with a higher accuracy can be used:

$$f_M = F_2 + a_2 \cdot \mathrm{Re}^{b2} + \frac{\left(a_1 \cdot \mathrm{Re}^{b1} - a_2 \cdot \mathrm{Re}^{b2}\right)}{\left(1 + \left(\frac{\mathrm{Re}}{t}\right)^{c}\right)^{d}}. \tag{24}$$

The parameters for Eq. (23) are summed up in Table 1 [1].

Friedel [7] systematically compared the accuracy of different pressure drop calculation methods, and recommends the methods of Baroczy [8], Chisholm [4], and Lombardi and Pedrocchi [9] for practical use.

Current correlations to predict the pressure drop in horizontal tubes for diabatic and adiabatic flows were compared by Mauro et al. [10]. He compared the accuracy of the methods with experimental data of different refrigerants and different flow regimes. Highest accuracy is expected by the method by Quiben and Thome [11, 12] and Grönnerud [13]. Still the method by Friedel [5] yielded accurate results.

For vertical upward and horizontal flows, Storek et al. [14] developed an empirical model by systematically evaluating a comprehensive data base. He used the approach of a homogeneous equilibrium flow, extended by empirical correction functions. His model considered wall friction.

The pressure drop in inclining and declining tubes can be calculated with equations by Breggs and Brill [15], based on empirical data.

Kadambi [16] and Akai et al. [17, 18] measured the pressure drop in stratified flow pattern and horizontal tubes. The results can be confirmed using the two-phase multiplier by Lockart and Martinelli.

A model described in [19] can be utilized to calculate the pressure drop of water–steam mixtures in horizontal pipelines of geothermal plants.

Herrn-Stapelberg and Mewes [20] examined the slug flow in horizontal and slightly declined tubes. The developed model can be used to give information on the buildup and length of liquid slugs in offshore crude-oil pipelines.

A comprehensive overview is given by Friedel [7] and Mayinger [21].

Special attention shall be paid to the intersections from horizontal to vertical tubes as liquid may accumulate there. Considering sufficient gas velocity, the liquid may finally be entrained through the vertical tube. The increased liquid holdup in the horizontal tube shall be considered in calculating the (increased) pressure drop and the flow pattern.

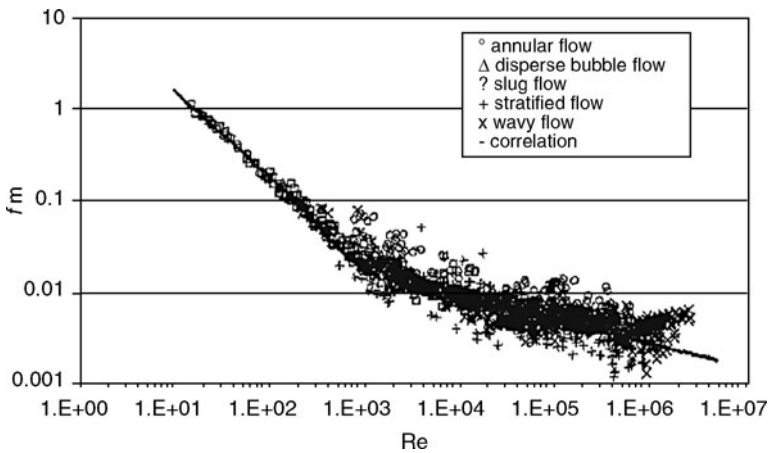

L2.2. Fig. 1. Correlation and measured data for different flow patterns [6].

L2.2. Table 1. Parameter of the gas–liquid friction factor correlations for different flow patterns [6]

Parameter	a_1	b_1	a_2	b_2	c	d	t
Slug flow	13.98	−0.9501	0.1067	−0.2629	3.577	0.2029	293
Disperse bubble flow	13.98	−0.9501	0.1067	−0.2629	2.948	0.2236	304
Stratified flow	13.98	−0.9501	0.0445	−0.1874	9.275	0.0324	300
Annular flow	3.671	0.6257	0.0270	−0.1225	2.191	0.2072	10,000

Example 1: Vertical tube

A cooling cycle is operated with freon 12. In a 10-m insulated tube DN150 located downstream of the expansion nozzle, a two-phase mixture flows under the following conditions:
$p = 1.5$ bar.a, $T = -20°C$

$$\dot{M}_F = 13 \text{ kg/s},\ \dot{m}_F = \frac{13 \text{ kg/s}}{\frac{\pi}{4} \cdot 0.15^2 \text{ m}^2} = 736 \text{ kg/m}^2\text{s},$$
$$\dot{x} = 0.02,$$
$$\dot{M}_L = 12.75 \text{ kg/s},\ \dot{M}_G = 0.25 \text{ kg/s},$$
$$\rho_L = 1{,}460 \text{ kg/m}^3,\ \rho_G = 9.1 \text{ kg/m}^3,$$
$$\eta_L = 0.3 \times 10^{-3} \text{ Pa} \cdot \text{s},\ \eta_G = 9.3 \times 10^{-6} \text{ Pa} \cdot \text{s},$$
$$c_{pf} = 0.94 \text{ kJ/kg K},\ \Delta H = 162 \text{ kJ/kg}.$$

The slip s, the void gas fraction ε, the phase velocities w_G and w_L of the gas and liquid, respectively, and the pressure drop $\Delta p_{2\text{ ph}}$ over the tube length shall be calculated.

According to Ahmad [22], the slip can be calculated by

$$s = \left(\frac{\rho_L}{\rho_G}\right)^{0.205} \cdot \left(\frac{\dot{m} \cdot d}{\eta_L}\right)^{-0.016} = \left(\frac{1{,}460}{9.1}\right)^{0.205} \cdot \left(\frac{736 \times 0.15}{0.3 \times 10^{-3}}\right)^{-0.016} = 2.3. \quad (25)$$

The void fraction is then calculated according to Subchap. L2.1:

$$\varepsilon = \frac{1}{1 + \frac{1 - 0.02}{0.02} \cdot 2.3 \cdot \frac{9.1}{1460}} = 0.59 \quad (26)$$

the gas velocity can then be calculated using the continuity equation:

$$w_G = \frac{\dot{M}_G}{\rho_G \cdot \varepsilon \cdot \frac{\pi}{4} \cdot d^2} = \frac{0.25}{9.1 \times 0.59 \cdot \frac{\pi}{4} \cdot 0.15^2} = 2.63 \text{ m/s} \quad (27)$$

and with the slip s the liquid velocity is calculated as

$$w_L = \frac{w_g}{s} = \frac{2.63}{2.3} = 1.14 \text{ m/s}. \quad (28)$$

Using the flow pattern map by Hewitt and Roberts [1], for vertical flow (reference is made to Subchap. L2.1) with the value for the abscissa

$$\frac{\dot{m}_F^2 \cdot (1 - x)^2}{\rho_L} = \frac{736^2 \cdot (1 - 0.02)^2}{1{,}460} = 356 \quad (29)$$

and the value for the ordinate

$$\frac{\dot{m}_F^2 \cdot x^2}{\rho_G} = \frac{736^2 \times 0.02^2}{9.1} = 2.4 \quad (30)$$

plug flow is expected. Accounting for the supervelocity of the bubbles compared to the liquid velocity in this flow regime, the calculated slip $s = 2.4$ seems reasonable.

The mixture mean density may be calculated with Eq. (4):

$$\bar{\rho} = (1 - 0.59) \cdot 1{,}460 + 0.59 \times 9.1 = 604 \text{ kg/m}^3 \quad (31)$$

the hydrostatic pressure drop is then calculated with Eq. (3) and a level difference of 10 m, the length of the vertical tube:

$$\Delta p_g = \bar{\rho} \cdot g \cdot \Delta x = 604 \times 9.81 \times 10 = 59{,}250 \text{ Pa}. \quad (32)$$

The two-phase friction pressure drop Δp_R is then calculated by Chisholm [4].

In the first step the superficial liquid velocity, assuming that the liquid fraction completely covers the tube cross section, is calculated as

$$w_L = \frac{\dot{M}_L}{\rho_L \cdot \frac{\pi}{4} \cdot d^2} = \frac{12.75}{1{,}460 \cdot \frac{\pi}{4} \cdot 0.15^2} = 0.5 \text{ m/s} \quad (33)$$

Δp_L is calculated (Subchap. L2.1) to be $\Delta p_L = 240$ Pa.

Next step is the calculation of the two-phase multiplier (according to [4]):

$$\Phi_L^2 = 1 + (\Gamma^2 - 1)\left[\frac{21}{\Gamma} \cdot \dot{x}^{0.9}(1 - \dot{x})^{0.9} + \dot{x}^{1.8}\right] = 1 + (\Gamma^2 - 1)\left[\frac{21}{\Gamma} \cdot 0.02^{0.9}(1 - 0.02)^{0.9} + 0.02^{1.8}\right] = 6.46, \quad (34)$$

where

$$\Gamma = \left(\frac{p_L}{p_G}\right)^{0.5} \cdot \left(\frac{\eta_G}{\eta_L}\right)^{0.1} = \left(\frac{1{,}460}{9.1}\right)^{0.5} \cdot \left(\frac{9.3 \times 10^{-6}}{0.3 \times 10^{-3}}\right)^{0.1} = 8.95, \quad (35)$$

$$\Delta p_R = 240 \times 6.46 = 1{,}550 \text{ Pa}.$$

The overall pressure drop is the sum of Δp_R and Δp_G: 59,250 + 1,550 = 60,800 Pa.

The pressure at the outlet of the vertical tube is now 1.5 bar.a – 0.608 bar.a = 0.892 bar.a.

The saturation temperature is reduced from −20 to approximately −30°C. Due to flashing of the liquid phase, an additional gas fraction is formed as follows:
Annotation: The heat transfer through the insulated tube is neglected.

$$\Delta \dot{M}_G = \frac{c_{p,L} \cdot \dot{M}_L \cdot \Delta T}{\Delta H} = \frac{0.94 \times 12.75 \times 10}{162} = 0.75 \text{ kg/s}. \quad (36)$$

The gas flow changes at the outlet of the tube to $M_G = 0.25 + 0.75 = 1$ kg/s and a liquid flow to $M_F = 12$ kg/s. With the new mass flow quality = 1/13 = 0.077, the void fraction is $\varepsilon = 0.85$.

The gas velocity at the outlet of the tube is now

$$w_G = \frac{1}{9.1 \cdot 0.85 \cdot \frac{\pi}{4} \cdot 0.15^2} = 7.3 \text{ m/s} \quad (37)$$

and the liquid velocity changes to $w_L = 7.3/2.4 = 3.0$ m/s.

With Eq. (1) the pressure drop by acceleration Δp_A is calculated as

$$\Delta p_A = \frac{1 \times 7.3 + 12 \times 3.2 - 0.25 \times 2.63 - 12.75 \times 1.14}{\frac{\pi}{4} 0.15^2} = 1{,}726 \text{ Pa}. \quad (38)$$

The overall pressure drop is summed to

$$\Delta p_{2ph} = \Delta p_A + \Delta p_g + \Delta p_R = 1{,}726 + 59{,}250 + 1{,}550 = 62{,}526 \text{ Pa}. \quad (39)$$

The hydrostatic pressure drop Δp_g is no pressure loss but a reversible pressure reduction by reducing height. The pressure drop due to acceleration Δp_A can be considered nonreversible because the liquid phase, in contrast to the gas phase, only marginally gains back pressure during deceleration of the gas–liquid mixture.

The accuracy of the calculation can be improved by using average property data between the inlet and outlet – in this case a more demanding iterative procedure is inevitable.

Example 2: Horizontal tube

The pressure drop in a horizontal tube DN150 of 10 m length shall be calculated:

$$p = 1.5\,\text{bar.a},\ T = -20^\circ\text{C},$$
$$\dot{x} = 0.02,$$
$$\dot{M}_L = 12.75\,\text{kg/s},\ \dot{M}_G = 0.25\,\text{kg/s},$$
$$\rho_L = 1{,}460\,\text{kg/m}^3,\ \rho_G = 9.1\,\text{kg/m}^3,$$
$$\eta_L = 0.3 \times 10^{-3}\,\text{Pa}\cdot\text{s},\ \eta_G = 9.3 \times 10^{-6}\,\text{Pa}\cdot\text{s},$$
$$\dot{M}_F = 13\,\text{kg/s},\ \dot{m} = \frac{13\,\text{kg/s}}{\frac{\pi}{4}\cdot 0.15^2\,\text{m}^2} = 736\,\text{kg/m}^2\text{s}. \quad (40)$$

The superficial gas velocity and the superficial liquid velocity are calculated as

$$w_{G,l} = \frac{\dot{V}_G}{A} = \frac{\dot{M}_G/\rho_G}{\pi\cdot\frac{D^2}{4}} = \frac{(0.25\,\text{kg/s})/(9.1\,\text{kg/m}^3)}{\frac{\pi}{4}\cdot 0.15^2\,\text{m}^2} = 1.55\,\text{m/s}, \quad (41)$$

$$w_{L,l} = \frac{\dot{V}_L}{A} = \frac{\dot{M}_L/\rho_L}{\pi\cdot\frac{D^2}{4}} = \frac{(12.75\,\text{kg/s})/(1{,}460\,\text{kg/m}^3)}{\frac{\pi}{4}\cdot 0.15^2\,\text{m}^2} = 0.49\,\text{m/s}, \quad (42)$$

The mean two-phase density is then calculated as

$$w_m = w_{G,l} + w_{F,l} = 1.55\ \text{m/s} + 0.49\ \text{m/s} = 2.04\ \text{m/s}, \quad (43)$$

where

$$\lambda_L = \frac{\dot{V}_L}{\dot{V}_L + \dot{V}_G} = \frac{\dot{M}_L/\rho_L}{\dot{M}_L/\rho_L + \dot{M}_G/\rho_G} = \frac{(12.75\ \text{kg/s})/(1{,}460\ \text{kg/m}^3)}{(12.75\ \text{kg/s})/(1{,}460\ \text{kg/m}^3) + (0.25\ \text{kg/s})/(9.1\ \text{kg/m}^3)} = 0.24. \quad (44)$$

Now the Reynolds number can be calculated as

$$\text{Re} = \frac{w_m\cdot D}{\eta_L/\rho_L} = \frac{2.04\ \text{m/s}\times 0.15\ \text{m}}{\frac{0.3\times 10^{-3}\text{Pa}\cdot\text{s}}{1{,}460\ \text{kg/m}^3}} = 1.48\times 10^6 \quad (45)$$

and without considering the flow pattern the pressure drop is calculated as

$$\Delta p_{2ph} = f_m\cdot\frac{2\rho_m w_m^2\cdot x}{D} = 0.00253\cdot\frac{2\times 357\ \text{kg/m}^3\cdot(2.04\ \text{m/s})^2\cdot 10\ \text{m}}{0.15\ \text{m}} = 501\ \text{Pa}, \quad (46)$$

where

$$f_m = 0.0925\text{Re}^{-0.2534} + \frac{13.98\text{Re}^{-0.9501} - 0.0925\text{Re}^{-0.2534}}{\left(1+\left(\frac{\text{Re}}{293}\right)^{4.864}\right)^{0.1972}} = 0.00253. \quad (47)$$

3 Pressure Drop in Bends

3.1 Introduction

When a fluid flows through a bend, the curvature causes a centrifugal force directed from the center of curvature to the outer wall. This force together with the adhesive forces at the wall (fluid adhesion, friction) is the reason for the formation of ideally two identical eddies in the bend. The eddies together with vortex generation and boundary layer detachment in the bend are responsible for the increased pressure drop through bends.

In Fig. 2 the gradient of the static pressure of the bended tube in flow direction is visualized for single-phase flow. The inlet of the bend is labeled "d" and the outlet, "e." The irreversible pressure drop Δp is the pressure drop between the labels "c" and "f." The dashed line expresses the pressure drop due to wall friction. The high pressure loss between "b" and "d" is denoted as the flow interruption in the inlet. The pressure gain between "e" and "g" is the result of the smoothening of the asymmetric velocity profile at the outlet of the bend.

The pressure loss of a two-phase mixture flowing through a bend is, in addition to the single-phase pressure loss, also

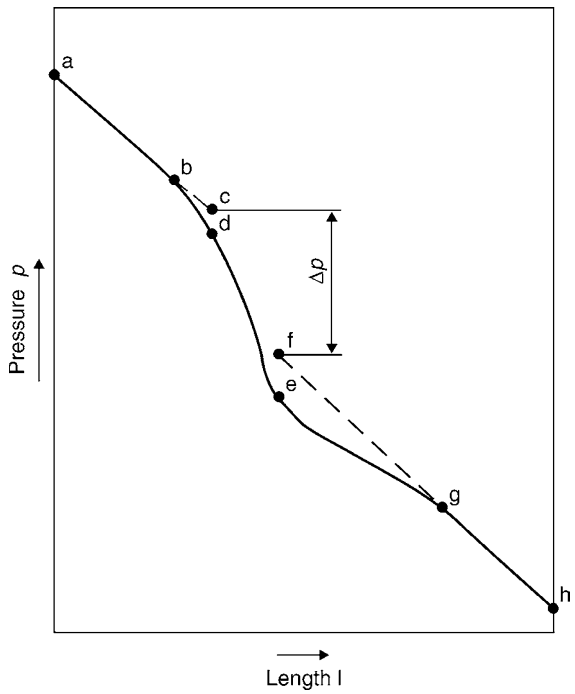

L2.2. Fig. 2. Schematic pressure drop in a 90° bend [23].

dependent on the plane and the outlet direction of the bend. An additional pressure loss occurs at the outlet of the bend, with ascending gas content. The lower velocity liquid fraction is accelerated by the gas flow and the gas looses its momentum.

Due to the vorticity of the fluid in the bend, a certain homogenization of the flow at the bend outlet is expected, which results in a homogenized flow pattern.

Two-phase flow studies for bends are not as numerous as for flow in straight tubes. The influence of the plane and outlet direction is considered, and correlations for the different planes and outlet directions are published. However, an elaborate and conclusive work is not available.

3.2 Pressure Drop for Single-Phase Flow

To calculate the two-phase pressure drop with the assistance of a two-phase multiplier, the single-phase pressure drop of the considered phase must be known.

One method to determine the single-phase pressure drop of the bend is to compare the bend with a straight tube of the same diameter with an equivalent length of x/d. According to Fig. 3, the equivalent length is dependent on the ratio bend radius and tube diameter, r/d. Figure 3 is valid for 90° bends.

The single-phase pressure drop is then calculated as given below:

$$\Delta p = \frac{\zeta}{2\rho} \cdot \frac{x}{d} \cdot \left(\frac{\dot{M}}{\frac{\pi}{4} \cdot d^2} \right)^2 . \tag{48}$$

The Darcy friction factor ζ may be evaluated as shown in Subchap. L1.1.

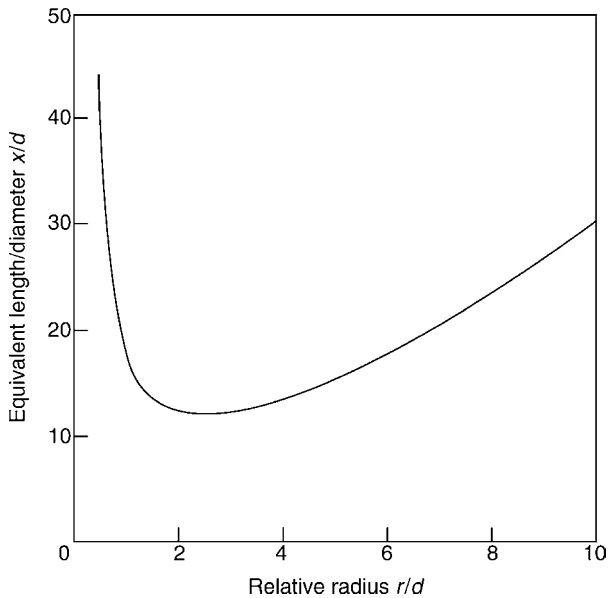

L2.2. Fig. 3. Ratio of the equivalent length and the tube diameter with the same pressure drop as that of a 90° bend [23].

3.3 Calculation of the Two-Phase Multiplier

A well-known correlation to calculate the two-phase multiplier for two-phase flow through 90° bends is presented by Chisholm [24] – the B-type equation. The two-phase multiplier Φ^2 is related to the liquid flow pressure drop Δp_f:

$$\Delta p_{2ph} = \Delta p_L \cdot \Phi_L^2 \tag{49}$$

Δp_{2ph}: two-phase pressure drop, where

$$\Delta p_L = \frac{\zeta}{2\rho_L} \cdot \frac{\dot{x}}{d} \cdot \left(\frac{\dot{M}_F}{\frac{\pi}{4} \cdot d^2} \right)^2 . \tag{50}$$

Assuming the friction factor ζ as independent of the Reynolds number, the two-phase multiplier Φ^2 is calculated as

$$\Phi_L^2 = 1 + \left(\frac{\rho_L}{\rho_G} - 1 \right) \left[B \cdot \dot{x} \cdot (1 - \dot{x}) + \dot{x}^2 \right], \tag{51}$$

where

$$B = 1 + \frac{2.2}{\zeta \cdot \frac{x}{d} \left(2 + \frac{r}{d} \right)} . \tag{52}$$

In Fig. 4 data measured by Fitzsimmons [25] is compared to the predictions calculated with Eq. (21).

In the area of a low void fraction, the calculated and measured data are consistent. At higher void fractions, a higher deviation is expected as the relation to the single-phase liquid

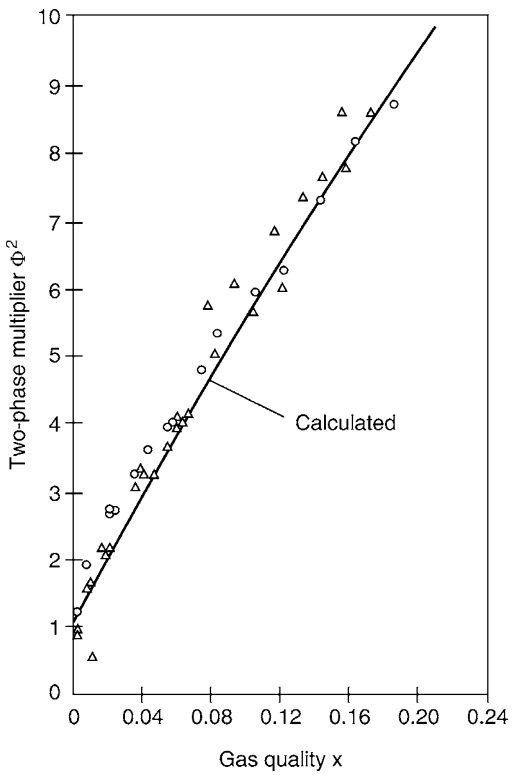

L2.2. Fig. 4. Measured and calculated [23] two-phase multiplier Φ^2 over gas quality.

pressure drop is not given any more. The two-phase pressure drop is expected to equalize to the vapor pressure drop under the influence of a rough surface. The rough surface is the result of the wavy liquid wall film. The free diameter is reduced accordingly by the liquid wall film thickness. Considering high gas velocities the pressure drop is further increased by the acceleration of the liquid by the gas stream.

For bends from 90° to 180° the coefficient B [24] is calculated as

$$B = 1 + \frac{2.2}{\zeta \cdot \frac{x_{90°}}{d}\left(2 + \frac{r}{d}\right)} \cdot \frac{x_{90°}}{x}. \tag{53}$$

Bends with $\alpha < 90°$ are conservatively considered 90° bends following Eq. (52).

Freeston et al. [26] studied water–steam mixtures in a 90° bend. He also studied the interaction of multiple bends attached in short distance between each other.

The influence of the wall friction in horizontal 180° bends was studied by Shimizu et al. [27], while Usui et al. [28] concentrated on upward and downward flows in vertical 180° bends.

Azzi et al. [29] evaluated different correlations and favored the Chisholm B-equation. For 90° upward bends, Azzi and Friedel [52] presented a more accurate correlation.

Example 3: Pressure drop in bends

A propene gas–liquid mixture flows through a bend ($d = 45$ mm, $a = 90°$, $r = 90$ mm) at a pressure of $p = 20$ bar ($\rho_L = 530$ kg/m^3, $\rho_G = 14.8$ kg/m^3, $\eta_L = 8 \times 10^{-5}$ Pa s), the total mass flow $\dot{M}_F = 0.6$ kg/s, and the vapor quality

$$\dot{x} = \frac{\dot{M}_g}{\dot{M}_g + \dot{M}_f} = 0.2. \tag{54}$$

The pressure drop shall be calculated.

Mass flow:

$$\dot{M}_G = \dot{x} \cdot \dot{M}_F = 0.2 \times 0.6 = 0.12 \text{ kg/s} \quad \text{(gas)}, \tag{55}$$

$$\dot{M}_L = (1 - x) \cdot \dot{M}_F = (1 - 0.2) \cdot 0.6 = 0.48 \text{ kg/s} \quad \text{(liquid)}. \tag{56}$$

The superficial liquid velocity is, therefore,

$$w_L = \frac{\dot{M}_L}{\rho_L \cdot \frac{\pi}{4} \cdot d^2} = \frac{0.48}{530 \cdot \frac{\pi}{4} \cdot 0.045^2} = 0.57 \text{ m/s} \tag{57}$$

and the Reynolds number $Re_{L,1}$ (for liquid at the superficial liquid velocity)

$$Re_L = \frac{w_L \cdot d \cdot \rho_L}{\eta_L} = \frac{0.57 \times 0.045}{8 \times 10^{-5}} = 170{,}000. \tag{58}$$

The Darcy friction factor of a hydraulic smooth tube at $Re_f = 170{,}000$ Reynolds–Zahl is considered with $\zeta = 0.017$ (reference is made to Subchap. L1.1).

With the relative radius r/d

$$\frac{r}{d} = \frac{90}{45} = 2 \qquad \text{(relative radius)}$$

the equivalent length can be determined by Fig. 3:

$$\frac{x}{d} = 12 \qquad \text{(equivalent length according to Fig. 3)}.$$

The equivalent pressure drop of the liquid phase is then calculated with Eq. (16):

$$\Delta p_L = \frac{\zeta}{2\rho_L} \cdot \frac{x}{d} \cdot \left(\frac{\dot{M}_F}{\frac{\pi}{4} \cdot d^2}\right)^2 = \frac{0.017 \times 12}{2 \times 530} \cdot \left(\frac{0.6}{\frac{\pi}{4} \cdot 0.045^2}\right)^2 \tag{59}$$

$$= 27 \text{ Pa},$$

where with Eq. (52)

$$B = 1 + \frac{2.2}{\zeta \cdot \frac{x}{d}\left(2 + \frac{r}{d}\right)} = 1 + \frac{2.2}{0.017 \times 12 \cdot \left(2 + \frac{90}{45}\right)} = 3.75 \tag{60}$$

and the two-phase multiplier with Eq. (51)

$$\Phi_L^2 = 1 + \left(\frac{\rho_{Lf}}{\rho_G} - 1\right)\left[B \cdot \dot{x} \cdot (1 - \dot{x}) + \dot{x}^2\right]$$

$$= 1 + \left(\frac{530}{14.8} - 1\right)\left[3.75 \times 0.2 \cdot (1 - 0.2) + 0.2^2\right] \tag{61}$$

$$= 23.3.$$

The two-phase pressure drop can be found with Eq. (49)

$$\Delta p_{2ph} = \Delta p_L \cdot \Phi_L^2 = 23.3 \times 27 = 629 \text{ Pa}. \tag{62}$$

4 Pressure Drop in Expansions, Reducers, and T-Pieces

4.1 Diffusers, Expansions, Reducers, and Contractions

The two-phase flow through reducers and expansions is fundamentally different from single-phase flow. The single-phase flow in a nozzle is considered a homogeneous acceleration without significant losses. The pressure drop in an expanding tube (diffuser) is dependent on the degree of boundary layer detachment due to pressure increase in the boundary layer by reduced velocity. In case of boundary layer detachment, the pressure drop as a result of dissipation (built up of vortices) is rather high. The overall pressure drop of a system without boundary layer detachment is reduced to the pressure drop due to wall friction.

If the flow pattern of a gas–liquid mixture consists of a liquid wall film and dispersed liquid droplets in the core gas, the momentum forces from the gas to the liquid determine the overall pressure drop.

In a nozzle the droplets are accelerated by the accelerating gas flow (momentum transfer from the gas to the liquid droplets). The loss of kinetic energy is considerable. This results in an exceptional high pressure drop, which significantly exceeds the pressure drop of a single-phase gas flow of a similar mean density as the two-phase mixture.

In the expansions the inertia of the dispersed liquid droplets leads to a supervelocity of the liquid droplets compared to the gas flow. This results in a momentum transfer from the liquid droplets to the gas, however, only a minor amount of kinetic energy is transferred to the gas. In addition, the supervelocity of the liquid promotes the detachment of the boundary layer.

In case of *bubbly flow* with small bubble size, the two-phase flow can be considered a homogenous mixture, with a behavior

L2.2. Table 2. Various models to calculate the density of a two-phase mixture [31]

Momentum density	$\frac{1}{\rho_{\mathrm{I}}} = \frac{\dot{x}^2}{\rho_{\mathrm{G}} \cdot \varepsilon} + \frac{(1-\dot{x})^2}{\rho_{\mathrm{L}} \cdot (1-\varepsilon)}$
Homogeneous density	$\frac{1}{\rho_{\mathrm{hom}}} = \frac{\dot{x}}{\rho_{\mathrm{G}}} + \frac{1-\dot{x}}{\rho_{\mathrm{L}} \cdot (1-\varepsilon)}$
Energy density	$\frac{1}{\rho_{\mathrm{E}}} = \left(\frac{\dot{x}}{\rho_{\mathrm{G}}} + \frac{1-\dot{x}}{\rho_{\mathrm{L}} \cdot (1-\varepsilon)}\right)^{-1} \cdot \left(\frac{\dot{x}^3}{\rho_{\mathrm{G}}^2 \cdot \varepsilon^2} + \frac{(1-\dot{x}^3)}{\rho_{\mathrm{L}}^2 \cdot (1-\varepsilon)^2}\right)$
Void density	$\frac{1}{\rho_{\mathrm{void}}} = \frac{\dot{x}^2}{\rho_{\mathrm{G}}} + \frac{(1-\dot{x})^2}{\rho_{\mathrm{L}}}$

comparable to a single-phase flow. Therefore, the predictions for single-phase flow may be used.

The pressure increase through a sudden expansion is often calculated with the model by Rouhani [30]. Best results are expected using the mean momentum mixture density (25% deviation, values calculated too low). The mean mixture density is essential for predicting the quality of the calculations. An overview of the different definitions based on mass, energy, or momentum conservation is given in Table 2.

The pressure drop in sudden contraction is preferably calculated using the mean density definition by mass [32, 33]. In every diameter a homogeneous mass distribution is considered. With this definition, the pressure drop can be calculated with an accuracy of ~20%.

In the throat area of a contraction, the gas is accelerated significantly faster than the liquid fraction, as long as there is a density difference between the gas and liquid phases. Based on this insight, Schmidt [31] developed a model to predict the pressure drop in horizontal and vertical expansions and contractions. The model differentiates between the liquid wall flow and the gas core flow with droplets. Momentum balance is then used to account for the change in diameter.

The prediction quality of the model is shown for air–water mixtures in Fig. 5 for expansions and in Fig. 6 for contractions.

The pressure increase in expansion is calculated as follows:

Indices

1. Fully developed flow upstream
2. Transient expansion or contraction
3. Fully developed flow downstream

$$\Delta p_{\mathrm{Erw}} = \frac{\dot{m}_2^2 \cdot \left[\frac{K_{1,2}\sigma_{2,3}}{\rho_{\mathrm{eff},2}} - \frac{K_{1,3}\sigma_{2,3}^2}{\rho_{\mathrm{eff},3}} - f^*_{\mathrm{Erw}} \cdot \rho_{\mathrm{eff},2}\left(\frac{\dot{x}}{\varepsilon_2 \rho_{\mathrm{g},2}} - \frac{(1-\dot{x})}{(1-\varepsilon_2)\rho_{\mathrm{fl}}}\right)^2 \left(1 - \sqrt{\frac{d_2^2}{d_3^2}}\right)^2\right]}{1 - \Gamma_{\mathrm{Erw}}\left(1 - \frac{d_2^2}{d_3^2}\right)} + \frac{\left(\frac{1}{2}\left(1 - \frac{d_2^2}{d_3^2}\right)(\rho_{\mathrm{eff},3} + \rho_{\mathrm{eff},2}) - \rho_{\mathrm{eff},3}\right) g \Delta z \sin\psi}{1 - \Gamma_{\mathrm{Erw}}\left(1 - \frac{d_2^2}{d_3^2}\right)} \tag{63}$$

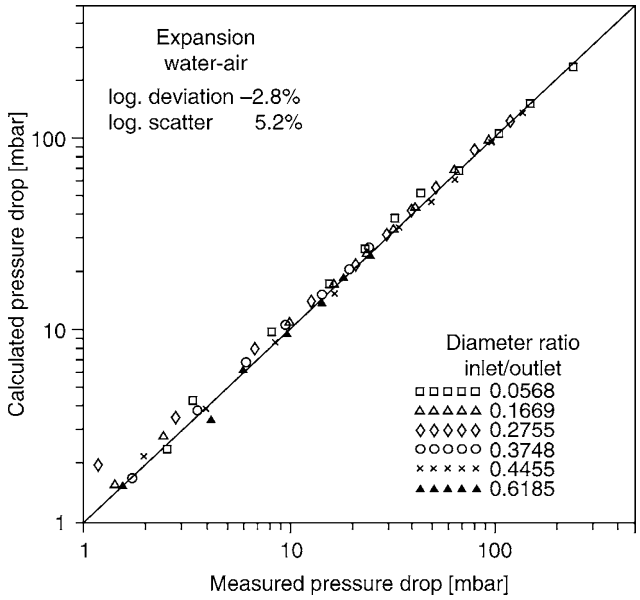

L2.2. Fig. 5. Comparison of the measured and predicted pressure increases of expansions with two-phase flow [31].

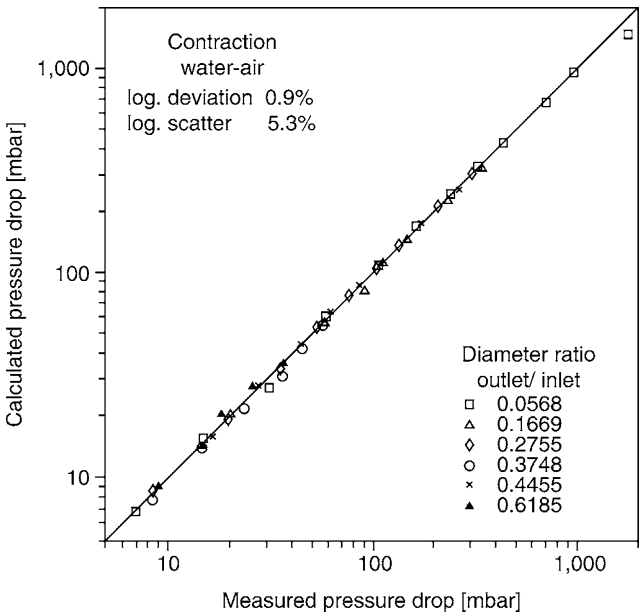

L2.2. Fig. 6. Comparison measured and predicted pressure drops of contractions with two-phase flow [31].

$K_1 \equiv 1$, turbulent flow (Re > 2,300), $K_1 \equiv 1.33$, laminar flow, ψ = angle: 0° = horizontal, 90° = vertical upward flow,

$$\varepsilon = 1 - \frac{(1-\dot{x})^2 \cdot 2}{1 - 2\dot{x} + \sqrt{1 + 4\dot{x}(1-\dot{x}) \cdot \left(\frac{\rho_{\mathrm{f}}}{\rho_{\mathrm{g}}} - 1\right)}}, \tag{64}$$

$$\frac{1}{\rho_{\text{eff}}} = \frac{\dot{x}^2}{\rho_G \varepsilon} + \frac{(1-\dot{x})^2}{\rho_L(1-\varepsilon)} + \rho_L(1-\varepsilon)\left(\frac{\varepsilon_K}{1-\varepsilon_K}\right)\left[\frac{\dot{x}}{\rho_G \varepsilon} - \frac{(1-\dot{x})}{(1-\varepsilon)\rho_L}\right]^2, \quad (65)$$

$$\varepsilon_K = \frac{1}{s}\left[1 - \frac{(1-\dot{x})}{1-\dot{x}+\dot{x}\cdot \text{We}^{0.27}\cdot \text{Re}^{0.05}}\right], \quad (66)$$

$$s = \frac{\dot{x}}{1-\dot{x}}\frac{1-\varepsilon}{\varepsilon}\frac{\rho_L}{\rho_G}, \quad (67)$$

$$\text{We} = \frac{\dot{m}^2\dot{x}^2}{\rho_G}\frac{d}{\sigma}\frac{(\rho_L-\rho_G)}{\rho_G}, \quad (68)$$

$$\text{Re} = \frac{\dot{m}^2(1-\dot{x})d}{\eta_L}, \quad (69)$$

where the friction factor:

$$f^*_{\text{Erw}} = 0.0049\dot{x}^2(1-\dot{x})^2\left(\frac{\eta_{L,2}}{\eta_{G,2}}\right)^{0.7}, \quad (70)$$

$$\Gamma_{\text{Erw}} = 1 - \left(\frac{d_2^2}{d_3^2}\right)^{0.25}. \quad (71)$$

The pressure loss in contraction is calculated as follows:

$$\Delta P_{\text{Kon}} = \frac{\dot{m}_3^2\left[\frac{K_{I,3}}{\rho_{\text{eff},3}} - \frac{K_{I,1}\sigma_{3,1}}{\rho_{\text{eff},1}} + f^*_{\text{Kon}}\cdot\rho_{\text{eff},3}\left(\frac{\dot{x}}{\varepsilon_3\rho_{G,3}} - \frac{1-\dot{x}}{(1-\varepsilon_3)\rho_L}\right)^2\left(1-\sqrt{\frac{d_3^2}{d_1^2}}\right)^2\right]}{1+\Gamma_{\text{Kon}}\left(\frac{\frac{1}{d_3^2}}{\frac{1}{d_1^2}}-1\right)}, \quad (72)$$

$$\varepsilon = 1 - \frac{(1-\dot{x})^2\cdot 2}{1-2\dot{x}+\sqrt{1+4\dot{x}(1-\dot{x})\cdot\left(\frac{\rho_L}{\rho_G}-1\right)}}, \quad (73)$$

$$\frac{1}{\rho_{\text{eff}}} = \frac{\dot{x}^2}{\rho_G\varepsilon} + \frac{(1-\dot{x})^2}{\rho_L(1-\varepsilon)} + \rho_L(1-\varepsilon)\left(\frac{\varepsilon_K}{1-\varepsilon_K}\right)\left[\frac{\dot{x}}{\rho_G\varepsilon} - \frac{(1-\dot{x})}{(1-\varepsilon)\cdot\rho_L}\right]^2, \quad (74)$$

$$\varepsilon_K = \frac{1}{s}\left[1 - \frac{(1-\dot{x})}{1-\dot{x}+\dot{x}0.18\text{We}^{0.12}\text{Re}^{0.50}}\right], \quad (75)$$

$$s = \frac{\dot{x}}{1-\dot{x}}\frac{1-\varepsilon}{\varepsilon}\frac{\rho_L}{\rho_G}, \quad (76)$$

$$\text{We} = \frac{\dot{m}^2\dot{x}^2}{\rho_G}\frac{d}{\sigma}\frac{(\rho_L-\rho_G)}{\rho_G}, \quad (77)$$

$$\text{Re} = \frac{\dot{m}(1-\dot{x})d}{\eta_L}, \quad (78)$$

$$f^*_{\text{Kon}} = 5.2\times 10^{-3}\dot{x}^{0.1}(1-\dot{x})\left(\left(\frac{d_3^2}{d_1^2}\right)\cdot\frac{\eta_L}{\eta_{G,3}}\right)^{0.8}, \quad (79)$$

$$\Gamma_{\text{Kon}} = 0.77\cdot\frac{d_3^2}{d_1^2}\cdot\left(1-\left(\frac{d_3^2}{d_1^2}\right)^{0.306}\right). \quad (80)$$

As the change of state of the two-phase media is essential to the calculation, an iterative approach is proposed.

In the first step, the media is considered incompressible. The density in the upstream, transient (2), and downstream areas (3) is considered the same.

In the ongoing iterative steps, the density in (3) is corrected considering the calculated pressured drop. A good accuracy can be expected after two calculation runs.

Example 4: Pressure increase through a sudden expansion

The pressure change of a water–air mixture flowing through a horizontal expansion shall be calculated.

The upstream pipe diameter is 0.0296 m (d_2), and the downstream pipe diameter is 0.0443 m (d_3).

p = 4.901 bar.a,

$$\dot{M}_F = 0.5692\ \text{kg/s},\ \dot{m} = \frac{0.5692\ /\text{s}}{\frac{\pi}{4}\cdot 0.0269^2\ \text{m}^2} = 1001.6\ \text{kg/m}^2\text{s}, \quad (81)$$

$$\dot{x} = 0.348,\ \rho_L = 997.41\ \text{kg/m}^3,\ \rho_{G,2} = 5.73\ \text{kg/m}^3,$$

$$\eta_L = 0.8961\times 10^{-3}\ \text{Pa}\cdot\text{s},\ \eta_G = 0.1825\times 10^{-4}\ \text{Pa}\cdot\text{s},$$

$$\sigma = 0.0719061\ \text{N/m},\ \psi = 0°.$$

The iterative approach is proposed, as the mixture is compressible:

Step 1: Incompressible flow through expansion considered

$$\rho_{G,2} = \rho_{G,3} = 5.73\,\text{kg/m}^3,$$

the mean volumetric void fraction in the upstream tube (1–2):

$$\varepsilon_2 = 1 - \frac{(1-\dot{x})^2\cdot 2}{1-2\dot{x}+\sqrt{1+4\dot{x}(1-\dot{x})\cdot\left(\frac{\rho_L}{\rho_G}-1\right)}} = 1 - \frac{(1-0.348)^2\cdot 2}{1-2\times 0.348+\sqrt{1+4\times 0.348(1-0.348)\cdot\left(\frac{997.41\,\text{kg/m}^3}{5.73\,\text{kg/m}^3}-1\right)}} = 0.934 \quad (82)$$

the dimensionless numbers:

$$\text{We}_2 = \frac{\dot{m}^2\dot{x}^2}{\rho_G}\frac{d}{\sigma*}\frac{(\rho_L-\rho_G)}{\rho_G} = \frac{(1001.6\,\text{kg/m}^3)^2\cdot 0.0348^2}{5.73\,\text{kg/m}^3}\frac{0.0296\,\text{m}}{0.0719\,\text{N/m}}\cdot\frac{(997.41\,\text{kg/m}^3 - 5.73\,\text{kg/m}^3)}{5.73\,\text{kg/m}^3} = 1.511\times 10^6, \quad (83)$$

$$\text{Re}_2 = \frac{\dot{m}^2(1-\dot{x})d}{\eta_L} = \frac{(1001.6\ \text{kg/m}^3)^2(1-0.348)\cdot 0.0269\ \text{m}}{0.8961\times 10^{-3}\text{Pa}\cdot\text{s}} = 2.157\times 10^4, \quad (84)$$

$$s_2 = \frac{\dot{x}}{1-\dot{x}}\frac{1-\varepsilon_2}{\varepsilon_2}\frac{\rho_L}{\rho_G} = \frac{x0.348}{1-\dot{x}}\frac{1-0.934}{0.934}\frac{997.41\ \text{kg/m}^3}{5.73\ \text{kg/m}^3} = 6.565, \quad (85)$$

$$\varepsilon_{K,2} = \frac{1}{s_2}\left[1 - \frac{(1-\dot{x})}{1-\dot{x}+\dot{x}\cdot \mathrm{We}_2^{0.27}\cdot \mathrm{Re}_2^{0.05}}\right]$$
$$= \frac{1}{6.565} \cdot \left[1 - \frac{(1-0.348)}{1-0.348+0.348\cdot(1.511\times10^6)^{0.27}\cdot(2.157\times10^4)^{0.05}}\right]$$
$$= 0.102. \quad (86)$$

With this result, the effective density of the two-phase mixture in the upstream tube can be calculated as

$$\frac{1}{\rho_{\mathrm{eff}}} = \frac{\dot{x}^2}{\rho_G\varepsilon_2} + \frac{(1-\dot{x})^2}{\rho_L(1-\varepsilon_2)} + \rho_L(1-\varepsilon_2)\left(\frac{\varepsilon_{K,2}}{1-\varepsilon_{K,2}}\right) \cdot \left[\frac{\dot{x}}{\rho_G\varepsilon_2} - \frac{(1-\dot{x})}{(1-\varepsilon)\cdot\rho_L}\right]^2$$
$$= \frac{0.348^2}{5.73\ \mathrm{kg/m^3}\times 0.934} + \frac{(1-0.348)^2}{997.41\ \mathrm{kg/m^3}\cdot(1-0.934)} + 997.41\ \mathrm{kg/m}\times(1-0.934)\cdot\left(\frac{0.102}{1-0.102_K}\right) \cdot \left[\frac{0.348}{5.73\ \mathrm{kg/m^3}\cdot 0.934} - \frac{(1-0.348)}{(1-0.934)\cdot 887.34\ \mathrm{kg/m^3}}\right]^2$$
$$= 0.0518\ \mathrm{m^3/kg}, \quad (87)$$

$$f^*_{\mathrm{Erw}} = 0.0049\cdot\dot{x}^2(1-\dot{x})^2\left(\frac{\eta_{L,2}}{\eta_{G,2}}\right)^{0.7}$$
$$= 0.0049\times 0.348^2(1-0.348)^2\left(\frac{0.8961\times10^{-3}\ \mathrm{Pa\cdot s}}{0.1825\times10^{-4}\ \mathrm{Pa\cdot s}}\right)^{0,7}$$
$$= 3.851\times10^{-3}, \quad (88)$$

$$\Gamma_{\mathrm{Erw}} = 1-\sigma_{2.3}^{0.25} = 1-0.4486^{0.25} = 0.1816. \quad (89)$$

The incompressible pressure drop is now calculated as

$$\Delta P_{\mathrm{Erw}} = 132.96\ \mathrm{mbar}. \quad (90)$$

Step 2: Calculation of a new density in the outlet tube (3)

Horizontal flow means no influence of gravitational forces. Also, the density changes of the water are neglected. The density change of the air is considered by the ideal gas law.

$$\rho_{G,3} = \frac{p_3}{R\cdot T_3} \rightarrow \rho_{G,3} = \rho_{G,2}\frac{p_2+\Delta P_{\mathrm{Erw}}}{p_3} = 5.89\ \mathrm{kg/m^3}. \quad (91)$$

With the new density the calculation steps are repeated

$$\varepsilon_3 = 0.934,$$
$$\varepsilon_{k,3} = 0.092,$$
$$\mathrm{We}_3 = 4.2835\times10^{56},$$
$$\mathrm{Re}_3 = 21.445\times10^4,$$
$$\rho_{\mathrm{eff}} = 21.1\ \mathrm{kg/m^3}.$$

The pressure drop is now calculated as

$$\Delta P_{\mathrm{Erw}} = 152.8\ \mathrm{mbar}. \quad (92)$$

An additional calculation step will not enhance the result significantly.

4.2 T-pieces

Upon dividing a gas–liquid flow in an asymmetric T-piece (straight tube with a branch), a new distribution of gas and liquid occurs. The void fractions of the resulting flows are not identical, as the inertia allocates the liquid in a straight direction.

Zetzmann [34] studied, using an air–water mixture, the phase distribution in vertically orientated T-pieces with the flow direction from bottom to top and with branch angles of 45° and 90°. He found a linear correlation between the inlet and outlet void fractions. The phase separation is amplified with a smaller branch diameter compared to the main tube diameter.

The results were basically supported by Honan et al. [35]. He detected in the normal case a substantial phase separation of the gas and liquid by the T-piece. Surprisingly, the phase separation was dependent neither on the angle of the branch nor on the inlet overall mass flow.

Whalley et al. [36] studied T-pieces with vertical and horizontal 90° branch. They concluded that the liquid routed to the branch is mainly the liquid of the wall film. The liquid in the gas core flow primarily follows the straight tube. The liquid mass flow was found proportional to the gas flow through the branch. For horizontal T-pieces with a small branch, Henry [37] developed a simple correlation, which is assured by air–water mixture experiments (deviation calculation and experiment: $<\pm20\%$) under atmospheric pressure and ambient temperature. Again the linear correlation of the gas and the liquid flows in the branch was confirmed.

With air–water mixtures Kubie et al. [38] modeled the behavior of steam–water mixtures in Y-branch pipes.

A model to calculate the fluid distribution in T-pieces, based on momentum equilibrium, was introduced by Skorek and Domanski [39]. The model accounts for most flow patterns and different angles of the branch.

5 Fittings and Valves

5.1 Pressure Release Valves and Pressure Safety Valves

Emergency release valves or pressure release valves for vessels are normally located in the gas area of the vessel in such a way that even under the transient conditions of a release action only the gas flows through the valve. While protecting a chemical reactor against excessive overpressure by a pressure safety valve, in many cases, two-phase flow release must be considered.

During pressure release, boil-up due to evaporation by pressure loss or the release of dissolved gases is expected. Also mixtures tending to build foam further assist the generation of a two-phase mixture in the system.

For this case the pressure release devices must be dimensioned, considering the two-phase release scenario.

A comprehensive presentation of the methods used to size pressure relief valves would exceed the framework of this compendium. An abstract of a set of well-known methods is given.

Different methods are used to calculate the two-phase mass flow through these valves. A well-known method is the ω

(Omega)-method by Leung [40]. This method considers the flow as homogeneous. An advantage of this method is the straightforward calculation without iterative steps and that only one set of property data at the release condition is required.

This method is recommended by the API, API 520 RP [41]. Herein, an elaborate explanation, guidelines, and examples for the ω-method are given.

Based on Leung's ω-method, the HNE-DS method was developed. This method is an extension of the ω-method by a nonequilibrium factor which characterizes the boiling delay of saturated mixtures flowing through the throat of the valve. This extension leads to a higher accuracy of this method. The ISO 4126-10, currently under standardization, proposes the HNE-DS method to size two-phase pressure safety valves. An explanation and a guideline are given by Schmidt [42] for initially subcooled flow and by Diener and Schmidt [43] for two-phase flow.

For sizing pressure safety valve for viscous media, the method by Wieczorek und Friedel (also based on the ω-method) may be used [44, 45]. For this method an overestimation of the pressure safety valve on an average by 29% is expected [44].

5.2 Valves and Orifices

The flow of a saturated two-phase mixture through a valve, if not considered properly, may lead to the failure of the internals by cavitations or vibration. Controlling a constant mass flow or a constant pressure drop by a two-phase operated valve is hardly possible. For that reason single-phase flow into the valve is preferred. Technically, the two-phase mixture is subcooled or pressurized by, e.g., level height.

In common the two-phase flow through tube internals with contraction–expansion characteristics cannot be neglected. Therefore, methods to calculate the pressure drop through such devices are presented herein.

To calculate the mass flow through *globe valves*, a method based on IEC 60534-2-1 seems reasonable. So all the methods are based on the coefficient of single-phase pressure drop. The pressure loss by wall friction is neglected as the flow length in the device is small compared to the length of the tube.

A physical consistent model was presented by Diener [46]. The mean logarithmic deviation for a measured data is given as <15% but the method is rather complicated. Therefore, Diener et al. modified the method customizing the well-known ω-method [40]. With this simplification the mean logarithmic deviation between measured and calculated values is 17% and therefore, getting close to the accuracy of the physical correct model [47, 48].

Fitzsimmons [25] compared the measured two-phase pressure drop also of *gate valves* to the homogeneous flow model and found the homogeneous model to be a conservative assumption.

Lex examined the fluid dynamics and the pressure drop of *ball valves* and presented a pressure drop, taking the valve dihedral angle into account [49].

McNeil developed a hybrid model, located between a homogeneous and two separate flow model, which is valid for two-phase compressible and incompressible media [50]. This iterative model was later simplified. The simplified model considers the gas as ideal and isentropic, the liquid as isothermal, and the slip as known [51].

It is evident that the two-phase pressure drop in *orifices* can also be calculated by modifying Leung's ω-method. Diener et al. proposed an approach in conjunction with their method to calculate the pressure drop of control valves [48].

6 Symbols

d	(inner) tube diameter (m)
f_m	Fannings friction factor (–)
f, f^*	Darcy friction factor = 4 * f_m (–)
ΔH	enthalpy of vaporization (kJ/kg)
K	friction coefficient, expansions, and contractions (–)
p	Pressure (Pa)
Δp	pressure drop (Pa)
s	slip
w	Velocity (m/s)
α	angle (°)
ψ	angle 0° = horizontal, 90° = vertical upwards (°)
$\dot{x}$	*vapor quality* ($\dot{x} = \dot{M}_g/(\dot{M}_f + \dot{M}_g)$) (–)
ε	volumetric void fraction (–)
ε_K	mean volumetric void fraction in the core flow (–)
Φ^2	two-phase multiplier (–)
ζ	Darcy friction factor (–)
Γ	pressure multiplier (–)

Indices

g	hydrostatic
2 ph	two-phase
m	mean
l	superficial
Erw	expansion
Kon	reduction
1	fully developed flow upstream
2	transient expansion or contraction
3	fully developed flow downstream

7 Bibliography

1. Hewitt GF, Roberts DN (1969) Studies of two phase flow patterns by simultaneous X-ray and flash photography. AERE-M 2159
2. Taitel Y, Dukler AE (1976) A model for predicting flow regime transitions in horizontal and near horizontal gas liquid flow. AIChE J 22(1):47–55
3. Martinelli RC, Nelson DB (1948) Prediction of pressure drop during forced – circulation boiling of water. Trans ASME 70:695
4. Chisholm D (1973) Int J Heat Mass Transfer 16(2):347–358 ff
5. Friedel L (1979) Improved friction pressure drop correlations for horizontal and vertical two phase pipe flow. 3R Int 18(7):485–492
6. Garcia F et al (2003) Power law and composite power law friction factor correlations for laminar and turbulent gas-liquid flow in horizontal pipes. Int J Multiphase Flow Issue 29:1605–1624
7. Friedel L (1983) Gas/Dampf-Flüssigkeitsströmung, Grundlagen der Verfahrenstechnik. VDI-Verlag, Düsseldorf
8. Baroczy CJ (1965) Chem Eng Prog Symp Ser 61(57):175
9. Lombardi D, Pedrocchi uE (1972) Energ Nucl 19:91 ff

10. Mauro AW et al (2007) Comparison of experimental pressure drop data for two phase flows to prediction methods using a general model. Int J Refrigeration 30:1358–1367
11. Quiben JM, Thome JR (2007) Flow pattern based two-phase frictional pressure drop model for horizontal tubes, part I: diabatic and adiabatic experimental study. Int J Heat Fluid Flow 28:1049–1059
12. Quiben JM, Thome JR (2007) Flow pattern based two-phase frictional pressure drop model for horizontal tubes, part II: new phenomenological model. Int J Heat Fluid Flow 28:1060–1072
13. Grönnerud R (1979) Investigation of liquid hold-up, flow-resistance and heat transfer in circulation type evaporators, part IV: two-phase flow resistance in boiling refrigerants, bull. De l'inst Du Froid, Annex 1972–1
14. Storek H et al (1980) Druckverlust der adiabatischen Gas/Flüssigkeitsströmung in kreisrunden Rohren. Chem-Ing-Tech Bd 52(6):S.531
15. Breggs HD, Brill JP (1973) A study of two-phase flow in inclined pipes. J Petrol Technol 25(5):607–617
16. Kadambi V (1981) Void fraction and pressure drop in two-phase stratified flow. Can J Chem Eng Bd 59(10):S.548/89
17. Akai M et al (1981) The prediction of stratified two-phase flow with a two-equation model of turbulence. Int J Multiphase Flow Bd 7(1):S.21/39
18. Akai M et al (1980) A co-current stratified air-mercury flow with wavy interface. Int J Multiphase Flow Bd 6(3):S.173/90
19. Freeston DH (1980) A comparison of experimental results of pressure drop for two-phase steam/water and air/water mixtures in a horizontal pipe. 7th Australasian hydraulics and fluid mechanics conf., Brisbane, S.424/26
20. Herrn-Stapelberg H, Mewes D (1998) Gesetzmässigkeiten der dreiphasigen Strömung von Öl, Wasser und Luft in horizontalen Rohrleitungen. VDI-Forschungsheft 668/91, VDI-Verlag
21. Mayinger F (1981) Strömung und Wärmeübertragung in Gas-Flüssigkeitsgemischen. Springer-Verlag, Wien/New York
22. Ahmad SY (1970) Axial distribution of bulk temperature and void fraction in a heated channel with inlet subcooling. Trans ASME J Heat Transfer 92:595–609
23. Chisholm D (1983) Two phase flow in pipelines and heat exchangers. George Godwin, London/New York
24. Chisholm D (1980) Two phase pressure drop in bends. Int J Multiphase Flow 6(4): S.363/67
25. Fitzsimmons DE (1964) Two phase pressure drop in piping components. HW-80970, Rev.1. General Electric Hanford Laboratories, Richland, Washington, DC
26. Freeston DH et al (1979) Two phase pressure drop measurements on a geothermal pipeline. Trans Geothermal Res Council Bd 9(9):S.233/36
27. Shimizu Y et al (1980) Hydraulic losses and flow patterns of swirling flow in U-bends. Bull JSME Bd 23(183):S.1443/50
28. Usui K et al (1981) Flow behaviour and pressure drop of two-phase flow through C-shaped bend in vertical plane, (I) upward flow (II) downward flow. J Nucl Sci Technol Bd 17(12), (1980) u. Bd. 18(3)
29. Azzi A, Friedel L, Belaadi S (2000) Two-phase gas/liquid flow pressure loss in bends. Forschung im Ingenieurwesen, Bd. 65:S.309–318
30. Rouhani SZ (1974) Modified correlations for void and two-phase pressure drop. Report AE-RTV-841, Atomenergi AB
31. Schmidt J (1993) Berechnung und Messung der Druckänderungen über scharfkantige plötzliche Rohrerweiterungen und -verengungen bei Gas/Dampf- Flüssigkeitsströmung, VDI Fortschr. ber. Nr. 236. Reihe 7
32. Guglielmini G et al (1986) Two phase flow pressure drops across sudden area contractions. Proceedings of the 8th international conference, San Francisco, 5, 2361/66
33. Harshe BL (1975) Two phase pressure loss across short abrupt contraction expansion geometries in horizontal flow. Dissertation, University of Cincinnati, Cincinnati
34. Zetzmann K (1982) Phasenseparation und Druckabfall in zweiphasig durchströmten vertikalen Rohrabzweigungen. Diss. Univ. Hannover
35. Honan TJ et al (1981) The measurement of phase separation in wyes and tees. Nucl Eng Design Bd 64:S.93/102
36. Whalley PB et al (1980) Two-phase flow in a T-junction. AERE-Report R 9699
37. Henry JA (1981) Dividing annular flow in a horizontal tee. Int J Multiphase Flow Bd 7(3):S.343/55
38. Kubie J et al (1979) Two-phase steam-water flow through Y-junctions. Int J Heat Fluid Flow Bd 1(4):S.161/67
39. Skorek T, Domanski, R (1995) Modelling of two-phase flow in dividing T-junctions with various branch orientations. Arch Thermodyn 16(1-2): 53–84
40. Leung JC (1996) Easily size relief devices and piping for two-phase flow. Chem Eng Prog Issue 92(12):28–50.
41. API Recommended Practice 520. American Petroleum Institute, 7th edn, Jan. 2000
42. Schmidt J (2007) Sizing of nozzles, venturis, orifices, control and safety valves for initially sub-cooled gas/liquid two-phase flow – The HNE-DS method. Forsch Ingenieurwes 71:47–58
43. Diener R, Schmidt J (2004) Sizing of throtteling device for gas/liquid two-phase flow. Part 1: safety valves. Proc Saf Prog 23(4):335–344
44. Wieczorek M, Friedel L (2003) Massendurchsatzkapazität von Vollhubsicherheitsventilen bei hochviskoser Flüssigkeitsströmung und Zweiphasenströmung Teil 1. TÜ Bd 44:S.22–28
45. Wieczorek M, Friedel L (2004) Verbesserte Bemessungsmethode für Vollhubsicherheitsventile bei nicht nachverdampfender Zweiphasenströmung. TÜ Nr. 6
46. Diener R (2000) Berechnung und Messung der Massendurchsatzkapazität von Stellventilen bei Zweiphasenströmung. Fortschritts-Berichten VDI-Reihe 7, Nr. 388
47. Diener R, Schmidt J, Kiesbauer J (2004) Einführung eines Expansionsfaktors zur Erweiterung der IEC 60534–2–1 für die Auslegung von Stellventilen bei Mehrphasenströmung, atp (46) Heft 6
48. Diener R, Schmidt J (2005) Sizing of Throtteling device for gas/liquid two-phase flow. Part 2: control valves, orifices and nozzles. Proc Saf Prog 24(1):29–35
49. Lex T (2004) Fluiddynamik von Gas-Flüssigkeitsgemischen in Kugelhähnen. Dissertation, ISBN 3-89963-081-5
50. McNeil DA (2000) Two-phase flow in orifice plates and valves. Proc Inst Mech Eng 214 (Part C):S.743–756
51. Mc Neil DA (1998) Two-phase momentum flux in pipes and its application to incompressible flow in nozzles. Proc Inst Mech Eng 212(Part C): S.631–641
52. Azzi A, Friedel L (2005) Two-phase upward flow 90° bend pressure loss model. Forsch Im Ingenieurwesen 69:120–130

L2.3 Sizing of Safety Devices for Heat Exchangers

Jürgen Schmidt
BASF SE, Ludwigshafen, Germany

1 Introduction

Heat exchangers are either constructed to be inherently safe or equipped with safety devices. These devices are rated such that on an abnormal plant operation neither the pressure nor the temperature in the appliance rises above the permissible values for the appliance. As a rule, burst discs or safety valves (mechanical safety devices) are used. Alternatively, the relevant operating parameters (e.g., pressure and temperature) can be reliably limited with safety-related process control systems. In addition to these primary safety devices, secondary safety measures are also established so as to mitigate the consequences of hazardous incidents.

For many standard heat exchangers with no use of hazardous substances, for example, in heating technology, the protection of heat exchanger is standardized. Hazard and risk analyses and the discussion of the effects of hazardous incidents should already be adequately covered in these standards. In the chemical and petrochemical industries, on the other hand, protection mostly requires case-by-case treatment. Details that should be taken into account in the selection and sizing of such appliances are given below. Tube bundle heat exchangers are considered here. However, most of the points and procedures can often be transferred to other types of heat exchangers.

2 Hazard and Risk Analysis

During a hazard analysis, first, all possible hazards, that arise inter alia from the hazardous properties of the substance, the operating conditions (system-inherent hazard potential), and the possible deviations from normal operation of the heat exchanger that may lead to impermissible process conditions (process maloperations and system failures) are identified. Second, the causes triggering these deviations must be determined, and their probability of occurrence must be estimated. For each deviation of normal operation of the heat exchanger, the possible effects must be discussed, and the level of damage must be estimated. At the beginning, safety measures are not taken into account, only operating and monitoring devices should be considered. The risk associated with a hazard is determined in terms of the probability of occurrence of a maloperation or system failure and the possible level of damage. The requirements for the reliability of safety measures (safety integrity) can, thus, be defined.

The hazard and risk analysis is carried out systematically by a team of experts with specialist knowledge and operating experience. Various methods are available for this [see ISSA 2008], for example, the risk graph as a qualitative method, see IEC 61511, Appendix E, or VDI/VDE 2180 [IEC 61511, VDI 2180]. Depending on the magnitude of the risk as a result of a deviation from normal operation, the Safety Integrity Level (SIL level 1–4) is obtained as the requirement for the safety measure. Often, for standard heat exchanger with no use of hazardous substances, no level or the SIL 1 level is specified. Particularly, in the chemical and petrochemical industries, SIL 2 and SIL 3 requirements are also common. Safety integrity of the level SIL 4 (catastrophic effects cannot be excluded) should be avoided. As a rule, it can no longer be achieved with safety-related PCS devices such as safety interlocks alone; here other, or additional, safety measures are necessary.

Alternatively, as well as the qualitative methods for risk estimation, quantitative, or semiquantitative methods can also

be used, for example, IEC 61511, Appendix A. The predictive value of such methods is often limited due to lack of data on the probability of failure of components or entire safety devices. Particularly in the chemical industry, the probability of a maloperation or a failure is also dependent on the operating conditions (substance, pressure, temperature, etc.) and, thus, cannot always be unambiguously determined.

In the case of a standard protection with mechanical safety devices (safety valves and burst discs), no quantitative data as to their reliability were demanded in the past – the fittings were classified as devices proven in operation. With correct sizing, installation, and regular testing of a certified safety device, the safety integrity of this component corresponds at least to the level SIL 3.

After the completion of the risk analysis, suitable countermeasures to protect the heat exchanger should be defined in accordance with the legal requirements and the plant safety policy of the particular organization. With such measures, the hazard risk is decreased below the tolerable risk level. As a rule, several, independent measures for risk reduction are taken (layers of protection concept). A priority here is to check whether a risk can be avoided by alternation of reaction or process conditions (material selection, reaction procedure, and process parameters such as pressure and temperature); if this is not entirely possible, then the cost for controlling the hazard should be kept as low as possible. This can be effected by means of a pressure-resistant design (inherent safe system) or through process control system measures with a monitoring function. In addition, it might be necessary – depending on the safety integrity of the countermeasure – to use a safety function (see IEC 61511). This, for example, includes the safe interlock of material and energy flows. Finally, as a rule, there remains the emergency discharge of the heat exchanger contents to protect against an impermissible pressure. If the discharged products are capable of further reaction, combustible, or toxic, then their safe removal, storage, and disposal must also be ensured.

3 Deviations from Normal Operation (Credible Scenarios)

With heat exchangers, various deviations from normal operation of the appliance (maloperations and system failures) are conceivable; typical examples are given in Table 1.

Each of these deviations can be the cause of an impermissible pressure or temperature in the heat exchanger. Essentially, in each case, one (independent) fault must be considered and assessed in the risk analysis (single-fault tolerance principle). In

L2.3. Table 1. Typical examples of deviations from normal operations in heat exchangers

Deviation from normal operation	Causes (examples)	Effects (examples)
Internal leakage/rupture of one or more heat exchanger tubes	• Oscillations (flow, machines) • Inadequate material strength • Corrosion and/or erosion • Exceeding of permissible temperature load cycle change, e.g., during start-up/shutdown • Pressure peaks, e.g., (rapid) valve closing • Flow-related heat exchanger asymmetries, e.g., due to partial tube blockages • Hot spots due to dry tubes as a result of vapor formation	Overflow/mixing of materials, sometimes with changes in pressure/temperature due to: • Material incompatibilities • Corrosion • Erosion • Mixture volume expansion during liquid mixing (alcohols, acids, etc.) • Evaporation/condensation • Heat release due to mixing or chemical reactions • Vacuum formation in freezers
External leakage of heat exchanger (shell-side)	• Material incompatibilities • Corrosion and/or erosion • Dynamic loads (pressure and temperature changes) • Mechanical action from outside	• Discharge of liquids, gases/vapors into the surroundings • Suction of air into the heat exchanger during underpressure (explosion risk) · Fire hazard/auto-ignition in the case of inflammable liquids in insulation
Blockage of liquids, gases/vapors	• External heating, e.g., fire, exposure to sunlight with consequent expansion of a liquid • Cooling failure • Vacuum formation due to failure of heating/cooling	• Discharge of liquids, gases/vapors into the surroundings • Leakage (see above)
Overpressures due to external pressure sources	• Impermissibly closed outlet	• Discharge of liquids, gases/vapors into the surroundings
	• Maximum pressure due to pumps, networks	• Leakage (see above)
	• Maloperations or failures in an adjacent plant part, e.g., with backflows	
Overheating at maximal operating pressure	• External heating, e.g., due to fire, exposure to sunlight	• Discharge of liquids, gases/vapors into the surroundings
	• Impermissible internal heating	• Leakage

individual cases and in particular for high risks, however, several independent faults should also be assumed simultaneously or directly consecutively (multi-jeopardy consideration). Essentially, however, the deviation from normal operation of the heat exchanger should not be specified unnecessarily on the supposedly safe side, since an oversized safety device also frequently leads to risks that are difficult to estimate during the discharge of the material flows. For example, account should be taken of dynamic forces on the emergency release system and the downstream appliances.

4 Assessment of Effects and Countermeasures

4.1 Leakage

With heat exchanger, it is necessary to check whether internal leakages or leakages on the shell can occur. Internal leakages can only seldom be completely ruled out. Such leakages are predominantly influenced inter alia by the material, the number, nominal width, and length of the tubes in the heat exchanger, the operating conditions, dynamic loads, and the fluids. Details on the estimation of the size of the leakage and the discharged mass flow rate are given in the later chapters. In principle, the main possible safety measures are inherent protection, safety-based PCS devices, or a mechanical safety device.

Internal leakages in heat exchangers with very large pressure differences on both sides can lead to violent pressure peaks in the apparatus if the low-pressure side is full of liquid and a large quantity of rapid gas flows from the high-pressure level through the leak. These pressure peaks spread very rapidly in the apparatus. In this case, a safety valve is unsuitable for protection, since it does not open sufficiently rapidly. Burst discs can be sufficiently rapid [IP Guideline, Thyer 2001]. The dynamic loads must be taken into account in the design strength of the heat exchanger.

Shell-side leakage in a heat exchanger is very rare when mechanical influences from the exterior are avoided, and can if necessary be ruled out with appropriate and timely inspections.

4.1.1 Leakage Sizes

At present, precise determination of leakage sizes is only possible in a few isolated cases. On the basis of values from experience with industrial heat exchangers and measurements on model appliances [Thyer 2001], the leakage size can in most cases at least be conservatively estimated.

Commonly, a full rupture of one heat exchanger tube below the manifold base is considered as a typical sizing case [API 520, ISO 23521]. Double the cross section of one tube is thus the release area. In the calculation of the mass flow rate, flow contraction at the manifold base and the pressure drop in the ruptured tube may be taken into account. Alternatively, in the case of compact heat exchangers, the cross section of one flow channel can be assumed as an appropriate leakage size [IP Guideline].

Tube rupture is very rare with ductile materials; however, it cannot be entirely ruled out. Experience shows that this rupture does not occur with double-shell tubes [see ISO 23521 §5.19.6]. On the other hand, in a large heat exchanger with a few thousand tubes and small nominal tube diameter, rupture of more than one tube is conceivable. The assessment must be made case by case.

In general, it is less probable that a tube with a large diameter will rupture completely than a tube of small diameter under identical installation conditions. With a decreasing number of tubes a complete rupture of a tube also becomes less probable.

In the chemical and petrochemical industries, cracks rather than complete tube rupture have been observed (leakage before breakage). It is, thus, a current practice under certain preconditions to permit leakage sizes smaller than twice the tube cross section:

1. Proper design of the heat exchanger, that is, all operation loads are taken into account (pressure, temperature, dead weight, additional stresses, thermal expansion, vibrations)
2. Appropriate manufacture and adequate testing (e.g., testing of tube weld points, determination of the corrosion resistance)
3. Minimum nominal diameter DN50 for long single-tube heat exchangers (tube coils in vessels)
4. Adequate strength of tube connections, for example, minimum nominal pipe diameter DN50 for very hazardous substances – for example, toxic – and DN25 for the other hazardous substances, and/or protection against tube tear off due to external force
5. Ductile material (e.g., austenitic steel such as 1.4571)
6. No corrosion or erosion stress loads (e.g., stress concentrations near welds, concentration of components with corrosive action, degassing of oxygen, unsuitable material pairings, excessive flow velocities)
7. No periodic oscillation close to the resonance frequency
8. No regular, large dynamic loads, for example, temperature load cycles during start-up/shutdown of the heat exchanger
9. No major external mechanical stresses
10. Regularly repeated inspection program
11. Reliable and timely leak detection before serious consequences (e.g., pressure, temperature, level, and concentration monitoring) and possibility of suitable countermeasures, e.g., number 12
12. Possibility of separating the heat exchanger off from other plant components during incidents

The leak size must be estimated case by case. On the basis of incident studies, leaks with an equivalent diameter of 5 mm ($\sim$20 mm^2 area) are commonly assessed as large enough in standard heat exchangers.

A shell-side leakage in heat exchangers is very rare and can in individual cases be ruled out if necessary with a suitable and timely inspection program. However, for the case where a leakage is assessed to be sufficiently probable, the leak areas must often be determined by experience based on current knowledge sources. This includes, for example, a leak with an equivalent diameter of 5 mm ($\sim$20 mm^2 area) under the preconditions stated above mainly based on experience by

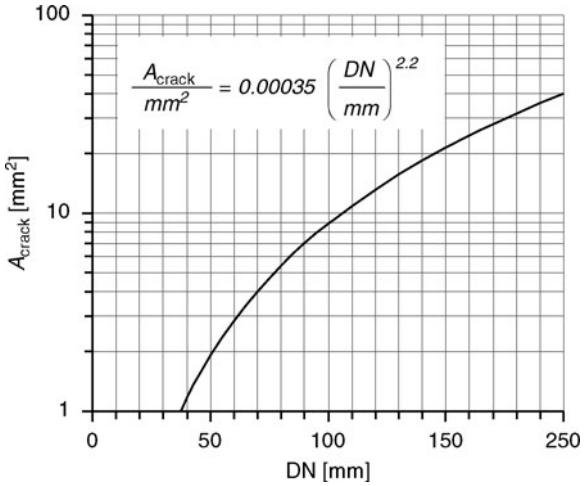

L2.3. Fig. 1. Crack size A_{crack} as a function of nominal diameter DN of the largest connection to a heat exchanger according to crack simulations of Strohmeier [Strohmeier 1990, 1993].

crack inspections. For installations with potentially water-contaminating subcooled liquids, hypothetical, and large leak areas are also described in the literature (about 11 mm diameter or 100 mm^2 area) [TAA1994, DVWK 131/1996]. On the other hand, the crack simulations of K. Strohmeier [Strohmeier 1990, Strohmeier 1993] gave leak areas of 4.4–7.9 mm^2 for cylindrical vessels with internal pressures up to 25 bar. For a vessel/flange joint with a pressure of 100 bar, 27 mm^2 was calculated. His simulations are fitted to a correlation and plotted in Fig. 1 [Ballast 2008].

For most chemical and petrochemical heat exchangers under moderate internal pressure the above-stated preconditions, an estimated leak area of 20 mm^2 appears to be sufficiently conservative.

4.1.2 Leak Mass Flow rate

For the precise calculation of the leak mass flow rate, the crack shape, the crack dimensions, and the wall roughness in the crack must be known. Detailed data on this subject and a model for the calculation of the leak mass flow rate with vaporizing two-phase flow are given by Westphal [1991].

When an approximate value – for example, the hole with a diameter of 5 mm – is taken as the basis for the leak area, the model of a frictionless flow through a nozzle with no heat transfer to the wall is adequate for the calculation of the leak mass flow rate. With vaporizing flow, homogeneously mixed phases are assumed to be in thermodynamic equilibrium. This is permissible for cracks, as Westphal has shown in his paper. Nozzle flow models are also the basis for other throttle devices such as control and safety valves. The leak mass flow rate can therefore be determined with the HNE-DS model [Diener and Schmidt 2004]. It applies for gases/vapors, liquids, and two-phase mixtures (see Sect. 6).

If a liquefied gas flows out of a leak, then in most cases only a part of the mass vaporises while flowing through the crack and the rest collects below the heat exchanger and forms a pool there. However, the liquid does not have to emerge in the direct vicinity of the leak if the heat exchanger is insulated. In addition to the vapor mass flow rate from the leak, which includes the flashing vapor, the mass flow rate as a result of the evaporation of liquid from the pool must then also be determined [Bosch 1997].

Example 1:

Exercise: How large is the leak mass flow rate through a leak area of 20 mm^2 (diameter 5 mm) for a highly subcooled methanol liquid with a temperature of 134.6°C under an initial pressure of 15 bar. The vapor pressure of the liquid at 134.6°C is 9.5 bar, and the density is 664.5 kg/m^3. The fluid discharges into the surroundings.

Solution: For a slightly subcooled liquid in front of the crack, which partially vaporises on flowing through the crack, the Bernoulli equation for non-vaporising, incompressible liquid flows may be used, see Table 3 ($F_F = 1$). Here, the vapor pressure of the liquid at inlet temperature may be used as the back pressure.

$$Q_m = 20 \cdot 10^{-6}\mathrm{m}^2 \cdot \sqrt{2 \cdot 664.5 \frac{\mathrm{kg}}{\mathrm{m}^3} \cdot 15 \cdot 10^5 \frac{\mathrm{N}}{\mathrm{m}^2} \cdot \left(1 - \frac{9.5}{15}\right)}$$
$$= 0.541 \frac{\mathrm{kg}}{\mathrm{s}}$$

4.1.3 Vapor Flash Fraction due to Shell-Side Leakages

Slightly subcooled or saturated liquids will partially vaporise while flowing through a crack. The vapor mass flow rate $Q_{m,g}$, based on the total mass flow rate, is defined as the flow mass quality:

$$\dot{x} = \frac{Q_{m,g}}{Q_{m,g} + Q_{m,l}} = \frac{Q_{m,g}}{Q_m}; \dot{x} \in [0..1] \quad (1)$$

For flows without appreciable heat loss to the wall, it can be approximately determined by an isenthalpic change of state between stagnation condition with the specific enthalpy $h(T_0)$, for example, in front of the crack, and the back pressure p of the surrounding.

$$\dot{x} = \frac{h(\mathrm{T}_0) - h'(\mathrm{T}''(p))}{h''(\mathrm{T}''(p)) - h'(\mathrm{T}''(p))} \quad (2)$$

Here, it was assumed that a homogeneous flow in thermodynamic equilibrium prevails in the crack and that therefore the boiling temperature adjusted itself to the local pressure p in each cross section under consideration (see Westphal 1991).

For the exact calculation of the mass flow quality, phase diagrams or equations of state are often used.

Example 2:

Exercise: How large are the mass flow quality at the exit from the crack and the vapor mass flow rate discharged, if the data from Example 1 are considered?

Solution: The specific enthalpy of methanol (liquid) at 134.6°C and 15 bar is 479 kJ/kg, and the specific enthalpies of boiling methanol at 1 bar (64°C) are 181 kJ/kg (liquid) and 1097 kJ/kg (vapor)

$$\dot{x} = \frac{479 - 181}{(1097 - 181)} = 0.272 = 27.2\%$$

The mass flow quality of the methanol after flowing through the crack is 27.2 wt.%. In the crack, the pressure at first decreases to the critical pressure and part of the liquid vaporises. Immediately upstream, there is a pressure jump to the ambient pressure with further vaporisation. Here the calculated vapor content is reached.

$$Q_{m,g} = \dot{x} \cdot Q_m = 0.272 \times 0.541 \frac{kg}{s} = 0.147 \frac{kg}{s}$$

The vapor mass flow rate due to flashing of methanol in the crack is 0.147 kg/s.

4.1.4 Dispersion Calculation

In those cases, where the release of hazardous substances, explosives, or flammable substances into the surroundings as a result of a shell-side leakage cannot be ruled out, dispersion calculation must be carried out to determine the time-dependent concentration distribution of the hazardous substances by means of the following steps:

1. Calculate the mass flow rate discharged due to a shell-side leakage as a function of time.
2. Estimate the pool size below the heat exchanger if liquid is discharged and not fully vaporized.
3. Calculate the released vapor mass flow rate. In case of flashing liquids it may consist of both the flow rate due to flashing in the crack and the flow rate vaporising from a pool below the heat exchanger. Special consideration must be taken if aerosols are created.
4. Near surrounding dispersion calculation for explosive substances: the area around the leakage where the concentrations of explosive substances may exceed the lower explosion limit must be estimated. An assessment of possible effects must be made (e.g. pressure wave propagation) and countermeasures should be discussed, for example, to avoid any ignition sources within this area and to keep a sufficient distance to neighbor plants and buildings. Typically, the dispersion of an explosive substance is estimated by means of a free jet calculation where the momentum of the released mass flow rate is taken into consideration [Schatzmann 1976, Bosch 1997]. If a gas or vapor is discharged with a molecular weight significant larger than that of air (heavy gas dispersion), the cloud will fall down and disperse around the heat exchanger. In this case the cloud size should be estimated by means of heavy gas dispersion calculations [VDI 3783Part2]
5. Dispersion calculation for hazardous substances: the concentration of the hazardous substances must not exceed the current exposure limits, for example, ERPG 2 value [TAAGS06]. In general, the maximum immission concentration is calculated and compared to the exposure limit. This concentration depends on several parameters like wind velocity and construction density in the surrounding of the leakage, which must be reasonably determined case by case. Far distance, immission calculations are generally done with simplified mixing models where the momentum of the free jet has almost no effect anymore and turbulent mixing of the hazardous substance with ambient air is dominant [VDI 3783Part1]. Special care must be taken if heavy case dispersion is considered [VDI 3783Part2].

In practice, there are a range of methods [e.g., Schatzmann 1976] containing the basic principles for corresponding computer programs [Witlox 1999] for carrying out dispersion calculations. The codes contain simplified models, which are, in most cases, conservative if they are physically meaningfully used. As long as the crack size can be conservatively estimated and the location and shape of a crack cannot be predicted, it seems not reasonable to use more precise computer codes for dispersion calculation.

In order to mitigate the consequences of such leakages, it is necessary to determine on a case-by-case basis whether concentration monitoring, segregation measures, the evacuation of areas with hazardous substances, or combustible substances and/or total containment concepts are suitable.

4.2 Blockage of Liquid and External Pressure Sources

If there is the possibility that liquid can be blocked in and heated in the heat exchanger, for example, by the following:

- Heat input from the surroundings (liquefied gases with a boiling point below the ambient temperature/supercritical liquids)
- Exposure to sunlight
- Internal heating
- In case of fire

then firstly it should be checked whether one of the valves cannot be locked open or mechanically blocked (organizational safety measure) to avoid an impermissible pressure build-up. If this is not the case or if this is not always possible, then the heat exchanger must be equipped with a mechanical safety device.

With very small liquid volumes blocked in, the risk to the surroundings as a result of a pressure build-up is mostly only slight. The tolerable discharge volume (minimum volume for protection) can be approximately estimated via a calculation of the dispersion of gases/vapors. Volumes between 5 l and 5000 l are typical, depending on the hazard potential of the fluid, the possible density change and the heating rate of the medium blocked in the appliance.

External pressure sources such as pumps or networks which are connected to a heat exchanger must not lead to a pressure or temperature larger than the permissible design values. If the permissible temperature or pressure of the heat exchanger is not sufficient, then it should first be checked whether the pressure source can be turned off by a safety interlock (see PCS safety device). If not, a mechanical safety device must be installed.

4.3 Overheating

The permissible design temperature of the heat exchanger must not be exceeded even in the event of a deviation from normal operation. Heating systems, for example, with saturated steam, must be adequately protected. This also applies for heat

exchangers in which exothermic chemical reactions, for example, as a result of an internal leakage or in a tubular reactor, cannot be ruled out. Heat exchangers should be protected against fire, if the risk of this breakdown scenario is assessed to be sufficiently high.

In the chemical industry, the risk due to heat input as a result of a fire is often decreased below the tolerable risk level by organizational and construction measures; such measures should be established in each individual case. They include, inter alia the following:

- Proper design, implementation, and installation of the appliance
- Regular inspection
- Timely and reliable leak and fire detection
- Construction of a tank pit with gradient for drainage of liquid into a separate area
- The possibility of segregating the appliance
- A fire service, which rapidly mitigates the consequences of a fire by effective countermeasures such as extinguishing the fire or cooling the appliance

Further safety measures are then, as a rule, not absolutely necessary.

According to the American regulation for petrochemical plant [API 520] a sufficiently great risk is always present when a combustible liquid or a combustible gas is present in the heat exchanger or in an adjacent part of the plant and a leakage cannot be ruled out. The protection of the appliance against an impermissible overpressure is then mostly ensured with a mechanical safety device. Depending on the material (e.g., aluminum), supplementary measures for minimization of the fire load and heat radiation (extinguishing and/or cooling) can also be necessary in order to prevent an impermissibly high temperature and thus, to ensure adequate strength and hermeticity of the appliance.

5 Sizing of Safety Devices

5.1 Inherently Safe Design of the Heat Exchanger

Safety devices on heat exchangers can be avoided if the appliances are inherently safely designed. For this, the permissible pressures of both sides of the heat exchanger are selected to withstand the maximum possible pressure resulting from the most credible maloperation or system failure, which has been determined during the risk analysis. Typically for standard tubular heat exchangers the permissible pressures of the inner-tube side and the shell-side are set equal to at least the maximum pressure that may occur during the worst case scenario. While in the case of larger heat exchangers, for economic reasons, the low-pressure side is designed at two thirds of the permissible pressure of the high-pressure side [API 521, p. 23]. Here, the material strength of the heat exchanger, which is tested at 150% of the permissible design pressure [see also ISO 23251 4.3.2], is exploited. Apart from the pressure resistance, essential care should also be taken that the permissible temperature of the appliance cannot be exceeded.

Essentially, a pressure- and temperature-resistant construction (inherently safe design) must include at least the connected pipes and appliances as far as the next possible shut-off point. All pipes connected to the heat exchanger must be installed such that the level of vibration (fluid induced and vibrations from rotating devices) is low, and should have adequate resistance to leakages and mechanical tube break-off. For larger plant heat exchangers, pipe nominal widths below DN25 should be avoided.

The heat exchanger must be made from a material with ductile properties under worst credible conditions (e.g., austenitic steel such as 1.4571), and which is technically resistant to the media under operating conditions. Shell-side leakages need not be assumed as a credible scenario if cracks can reliably be ruled out or the shell-side is regularly checked for cracks with critical crack lengths, so that firstly a crack is reliably and promptly detected before wall breakthrough and, secondly, effective countermeasures can be taken (leak-before break criterion).

Inherently safe design can be uneconomic for very large heat exchangers or appliances with very large pressure differences between tube interior and shell-side. In this case, mechanical safety devices are often used for the protection of the heat exchanger.

Inherent safety also includes both proper design and the suitable mode of operation and regular inspection and testing of the heat exchanger. In this way, incidents, for example, as a result of corrosion, can be prevented or – if necessary – promptly and reliably identified. Suitable countermeasures may be taken, so that the strength and hermeticity of the heat exchanger are maintained throughout the whole intended operating period. An efficient inspection and countermeasures policy can, for example, be drawn up analogously to the procedure, which is necessary for the regular extension of the inspection period for chemical plants [Hahn 2007].

Example 3:
Exercise: In a tubular heat exchanger, methanol at ambient pressure is heated with saturated steam from a 4 bar steam network. The safety device for the network activates at 4.5 bar. What design pressure should be selected for the heat exchanger in order to operate the appliance inherently safely?

Solution: At the maximum operating pressure (4.5 bar) in the steam network, the temperature of the steam is 147.7°C. This is the highest steam temperature that can be established in the heat exchanger (saturated steam) – the heat of mixing of the substances in case of an internal leakage is negligibly small. At this temperature, methanol has a vapor pressure of 13.2 bar. The permissible pressure of the heat exchanger must correspond to at least this pressure and the permissible temperature must be at least 150°C. Attached tubes and appliances are also designed for these permissible operating parameters.

5.2 Protection with Safety-Related PCS Devices

With process control systems, the causes and/or the effects of maloperations and system failures on heat exchangers can often be mitigated. Thus, for example, through emergency segregation of an appliance, the feed stream of material or

energy is stopped or the discharge is limited to a small partial volume. Such mitigation of consequence devices (secondary safety measures) are implemented with a reliability corresponding to the SIL requirement (SIL stage 1–3) depending on the hazard potential of a credible scenario.

Moreover, PCS devices can also be implemented as a primary safety device, when, for example, exceeding the permissible appliance pressure is reliably avoided by a safely interlock of a steam flow.

Essentially, the safety-related PCS devices should be simple and proven in operation [VDI 2180]. Pressure and temperature interlock systems are typical. In isolated cases, complex devices are also used, for example, concentration or conductivity measurements, when they satisfy the appropriate specification class for safety integrity.

A safety-related PCS device should be preferred to a mechanical pressure relief device if the cause of a deviation from normal operation of the heat exchanger can be prevented and if it ensures the safety of the appliance equivalently. In addition, it should be economically comparable to mechanical pressure relief devices and simply constructed.

A safety measure, which must satisfy the specification class SIL 4 should not correspond to a safety-related PCS device alone, but should also include further safety measures.

Example 4:
Exercise: In a tubular heat exchanger with a permissible pressure of 7 bar, methanol at ambient pressure is to be heated with saturated steam from a 5 bar steam network. The steam is throttled down to 1.5 bar in a pressure reducer. How must the heat exchanger be protected?

Solution: The pressure reducer is not a safety-related fitting, hence, it has no safety function and can fail. In practice, when such fittings are defective, they are often exchanged for other designs. Hence, on the steam side a temperature safety interlock must be installed, which safely blocks the steam flow at a temperature of maximum 123°C – this corresponds to the boiling temperature of methanol at the permissible design pressure of the heat exchanger (7 bar).

The level of reliability of the temperature interlock system is determined in accordance with the specification class (SIL level) from the risk analysis – in the present operating conditions with toxic methanol SIL 3. The safety function is realized with two independent channels (see VDI/VDE 2180). Here care must be taken that only two ball valves with one bleed device in-between (block-and-bleed system) are technically leak-proven. In the absence of a bleed device and above all with combinations of ball valve and control valve, residual leakages cannot be excluded. In practice, the leak volume flow rate can be conservatively estimated at, for example, 1–5% of the discharge coefficient k_{vs} of the control valve, provided the control valve is properly operated and regularly tested. The volume flow rate depends on the size and operating conditions of the heat exchanger. A mechanical safety device of small size can in addition be necessary, in order to remove residual leakages.

In general, the closure time of the temperature device should be selected such that no impermissible dynamic loads (pressure shocks) should be added on the heat exchanger.

5.3 Protection with Mechanical Safety Devices

The protection of a heat exchanger with a safety valve or burst disc is determined in five steps:

1. Hazard and risk analysis for the assessment of possible deviations from normal operation (see Sects. 2 and 3) and selection of a suitable type of the mechanical safety device
2. Calculation of the mass flow to be discharged through the safety device (inflow into the heat exchanger under worst case conditions)
3. Determination of the fluid state at the inlet to the safety device
4. Calculation of the mass flux through the safety device and hence the necessary size of the valve seat
5. Ensuring of safe operation under installation conditions

5.3.1 Calculation of the Mass Flow Rate to be Discharged

Inflow Due to Internal Leakage

As a rule, in tubular heat exchangers, the full rupture of a heat exchanger tube is assumed for the calculation of the mass flow rate [ISO 23251]. In individual cases, it can also be justified to assume the rupture of several tubes. On the other hand, for tube coils, double-mantle tubes and those heat exchangers, which are manufactured and operated subject to special quality requirements – for these, see the explanations in Sect. 3 – the assumption of leak-before-breakage behavior is permissible. In this case, the leak areas are smaller than for the full rupture of one tube. A typical leak area is 20 mm^2.

In case of a full rupture of a tube in a heat exchanger, this is assumed to be at the manifold base [IP Guideline], fluid flows through two tube cross sections into the shell-side of the heat exchanger and mixes with the medium which is there. The mass flow rate through these cross sections can be calculated with the nozzle flow model HNE-DS (see Sect. 6). The difference between the maximal (stagnation) pressure in the tube manifold and the opening pressure of the safety valve on the shell-side is as a rule assumed to be the driving pressure gradient. However, it is also permissible to calculate the mass flows through the two tube cross sections separately from one another: once with the maximal pressure in the tube manifold and next with a reduced pressure. The reduction corresponds to the pressure drop in the heat exchanger tube. Further, for example, for very long heat exchangers or with many baffles, a pressure drop in the shell-side of the heat exchanger can also be taken into account. The driving pressure gradient should be reduced by this pressure in order to calculate the mass flow rate.

With flashing fluids, the assumption of a homogeneous flow in thermodynamic equilibrium ($N \equiv 1$, see Sect. 6) can be justified when the flow time to the tube outlet is sufficiently great for the equilibrium to be established. This applies inter alia for the flow in the heat exchanger tube. For short tube ends, the boiling delay of the flow must also be taken into account ($N < 1$, see Sect. 6).

If a gas flows from the high-pressure side of the heat exchanger into a low-pressure part filled with liquid, then the gas displaces the liquid there. At the start of the incident, a liquid volume flow, which corresponds to the inflowing gas volume flow must be removed through the safety device. In the further course of the incident, the gas increasingly mixes with the liquid. The gas content before the safety valve changes continuously.

Inflow Due to Liquid Block-in

The minimum required mass flow rate to be discharged in the event of liquid block-in can be approximately calculated by the density change $d\rho/dT$ of the liquid at constant pressure and maximum heat input $\dot{Q}$, for example, maximum heating:

$$Q_{m,out} = V \cdot \frac{d\rho}{dT} \cdot \frac{dT}{dt} = \frac{\dot{Q}}{cp_l} \cdot \frac{1}{\rho} \cdot \frac{d\rho}{dT} \tag{3}$$

With very large heat exchangers or high-pressure heat exchangers with very large steel masses, it is permissible to additionally consider the changes in the heating temperature with time in Eq. (3) – for example, the daily change of the ambient temperature if the exposure to sunlight is assumed as worst credible scenario. The average temperature in the heat exchanger follows the ambient temperature with a time delay and damping.

Inflow from Pumps, Networks, and Other Pressure Sources

The minimum required mass flow rate to be discharged through the safety device $Q_{m,out}$ corresponds to the maximum feed into the heat exchanger $Q_{m,feed}$ with fully opened inlet valves and closed outlet valves.

$$Q_{m,out} = \sum Q_{m,feed} \tag{4}$$

In the case of an inflow via pumps or networks, the maximum operating pressure or (more conservative) the set pressure of the safety device in the network is taken as the basis. If the fluid flows into the heat exchanger through a control valve, then the minimum required mass flow rate to be discharged is determined by means of a nozzle flow model. The equivalent nozzle cross section A_{feed} can be calculated from the discharge coefficient of the control valve k_{vs}, which is determined experimentally with water at a temperature between 5°C and 50°C at a differential pressure of 1 bar [DIN EN 60534]:

$$A_{feed} \cong k_{vs} \sqrt{\frac{\rho_{H2O}}{2\Delta p_{H2O}}} = \frac{k_{vs}}{\sqrt{200}} \left[\frac{s}{m}\right] \tag{5}$$

$$\text{with} \sqrt{\frac{\rho_{H2O}}{2 \cdot \Delta p_{H2O}}} = \frac{1}{\sqrt{200}} \left[\frac{s}{m}\right] \tag{6}$$

The discharge coefficient is given by the control valve manufacturer in cubic meters per hour, it is dimensional. For the conversion from hours to seconds, the factor 1/3,600 must be taken into account.

The maximum inflow through the control valve can be calculated with the HNE-DS model (Sect. 6), wherein the pressure at the entrance of the control valve and the opening pressure of the safety valve represent the propulsive pressure difference. For longer tubes or other components with a significant pressure drop between the control valve and the heat exchanger, the pressure drop to the appliance may also be taken into account. The back pressure for the mass flow calculation then corresponds to the sum of the opening pressure of the valve and the pressure drop to the outlet of the control valve.

For gases/vapors or two-phase flows, it should be noted that a critical pressure condition can arise in the control valve. The back pressure in the nozzle flow model then corresponds to the critical pressure (see Sect. 6).

The calculation of the mass flow rate through control valves is also described in DIN EN 60534. However, the use of this standard is not recommended in the flow of two-phase mixtures. Mass flows, which are significantly too high or too low are calculated by DIN EN 60534, as has been shown by Diener [1999].

Control valves are components relevant to safety when the mass flow to be discharged through these fittings is specified for sizing the safety device. They must be correspondingly labeled and tested. In the event of an exchange, care must be taken that a fitting with a higher discharge coefficient k_{vs} is not installed. On the other hand, the control valve is no longer related to safety when a restriction orifice plate is connected upstream. In this case, the mass flow dischargeable through the plate without taking into account of the control valve is applied for the sizing of the safety device. It can also be calculated by means of the HNE-DS model [Diener 2005].

Example 5:

Exercise: Liquid methanol (density 671 kg/m^3) is cooled in a tubular heat exchanger. The heat exchanger is protected with a safety valve with a set pressure of 8.4 bar (abs). The liquid is fed by a pump, which can perform a pressure of 25 bar (abs). The feed is regulated with a control valve (k_{vs} = 6.4 m^3/h). The pressure drop between control valve and heat exchanger is 0.7 bar. How large is the mass flow rate to be discharged via the safety valve?

Solution: The maximum mass flow rate through the control valve is calculated with the nozzle flow model. The equivalent nozzle cross section is found to be:

$$A_{feed} = \frac{6.4 \frac{m^3}{h}}{3600 \frac{s}{h} \cdot \sqrt{200}} \left[\frac{s}{m}\right] = 1.26 \cdot 10^{-4} m^2$$

The pressure at the outlet of the control valve is calculated from the opening pressure of the safety valve, which corresponds to 1.1 times the set pressure (overpressure!) and the pressure drop in the tube:

$$p_{out} = (1.1 \cdot 7.4 \cdot bar + 1 \cdot bar) + 0.7 \cdot bar = 9.8 \cdot bar$$

Hence the maximum mass flow rate through the control valve with fully opened safety valve is as follows (see Table 3):

$$Q_{m,feed} = A_{feed} \cdot \sqrt{2 \cdot \rho \cdot p_{feed} \cdot (\eta_{feed} - \eta_{out})}$$

$$Q_{m,feed} = 1.26 \cdot 10^{-4} m^2 \cdot \sqrt{2 \cdot 671 \frac{kg}{m^3} \cdot 25 \cdot 10^5 \frac{N}{m^2} \cdot \left(1 - \frac{9.8}{25}\right)} = 5.68 kg/s$$

This mass flow rate must be discharged through the safety valve in order to avoid an impermissible overpressure in the heat exchanger.

Inflow in Case of Fire

According to the American legislation [ISO 23251] in the event of a fire about 108 kW/m^2 of heat is transferred into the heat exchanger through the surfaces wetted with liquid [Heller 1983]. This value may be decreased to 40.3 kW/m^2 if no flammable liquid can collect under the heat exchanger and a fire service can rapidly extinguish the fire. With very large heat exchangers or those installed high up, the heat input is only taken into account up to a height of 7.5 m. Furthermore, the value can be decreased by adequate fire protection insulation (see ISO 23251, Table 6). In the calculation of the wetted area, the feed and outlet tubes should also be included.

Essentially, the energy which is transferred into the heat exchanger through the fire must be removed with the mass flow rate through the fully opened valve. Thus, for vaporising liquids with pure vapor flow through the safety valve the following, for example, applies:

$$Q_{\mathrm{m,out}} = \frac{\dot{Q}}{\Delta h_{\mathrm{v},0}} \tag{7}$$

If, on the other hand, a gas/vapor–liquid mixture flows through the fitting, then a greater mass flow rate must be discharged (see, e.g., ISO 4126-10).

5.3.2 Fluid State at the Inlet of the Valve

The fluid state at the valve inlet results from the properties of the fluids involved on both sides of the heat exchanger, the possible operating conditions, and the deviation from normal operation of the heat exchanger assumed. For flashing liquids or when gases and liquids are mixed as a result of an internal leakage, large ranges of mass flow quality are often passed through, which must also be taken into account in the sizing procedure of a mechanical safety device. The change in the mass flow quality during significant pressure changes (flashes) can often be estimated on the basis of an isenthalpic change of state (see Sect. 4.1.3).

In general, the fluid state can only be established case by case.

5.3.3 Sizing of Safety Valves

The safety valve must be sized sufficiently large to safely discharge at least the maximum inflow into the heat exchanger:

$$Q_{\mathrm{m,SV}} = K_{\mathrm{dr}} \cdot Q_{\mathrm{m,nozzle}} \geq Q_{\mathrm{m,out}} \tag{8}$$

The dischargeable mass flow rate $Q_{\mathrm{m,SV}}$ is obtained from the mass flow rate through a frictionless nozzle with no heat transfer to the surroundings, corrected by the certified discharge coefficient of the valve K_{dr}. This discharge coefficient is published by the valve manufacturers for gases and liquids. For two-phase flow in a safety valve, an averaged discharge coefficient is recommended:

$$K_{\mathrm{dr,2ph}} = \varepsilon \cdot K_{\mathrm{dr,g}} + (1-\varepsilon) \cdot K_{\mathrm{dr,l}} \tag{9}$$

The weighting factor for averaging the discharge coefficient is the void fraction in the narrowest flow cross section of the valve:

$$\varepsilon = 1 - \frac{v_{\mathrm{l},0}}{v_0 \cdot \left[\omega \cdot \left(\frac{1}{\eta} - 1\right) + 1\right]} \tag{10}$$

The mass flow rate through the nozzle is determined using the HNE-DS model (Sect. 6).

The minimum necessary valve seat cross section is thus:

$$A \geq \frac{Q_{\mathrm{m,out}}}{K_{\mathrm{dr}} \cdot C \cdot \sqrt{2 \cdot \frac{p_0}{v_0}}} \tag{11}$$

5.3.4 Safe Operation under Installation Conditions

The size of the safety valve is initially carried out without taking into account the pipes in the valve inlet and exit. Such pipes in some cases affect the safe operation of the valve. For example, high frequency vibrations, so-called valve chatter, can be induced. For gases and liquids, the pressure loss in the inlet is therefore limited to 3% of the valve set pressure (overpressure) and the back pressure must not exceed 10% of the set pressure (overpressure). These values apply if the manufacturer does not specify more specific values.

For two-phase flow a physically meaningful criteria to ensure proper valve operation under installation conditions is not yet determined. As a consequence, an expansion bellow and a friction damper are recommended [ISO 4126-10].

6 The HNE-DS Model for the Calculation of Mass Flow Rates through Nozzles

The flow-through cracks, drill holes, nozzles, orifices, and control and safety valves is, as a rule, described by simple nozzle flow models. The differences in flow rate between the nozzle flow model and the mass flow rate through the actual geometry are taken into account by means of a correction factor, dependent on the particular geometry of the component. In addition, for flashing liquids, the thermodynamic nonequilibrium (boiling delay) and the mechanical nonequilibrium (slip) must be included in the model. The less the pressure in the fitting decreases and the longer the residence time of the flow, the sooner a thermodynamic equilibrium between the two phases will become established. Pipe flows and cracks of great depth are typical examples of this. On the other hand, in orifices and valves with very small or absolutely no gas content, a significant thermodynamic nonequilibrium is established, and has the effect that a markedly greater mass flow passes through these components than might be expected with equilibrium being assumed.

As the basis for the calculation of the mass flow rate through a nozzle, a one-dimensional, homogeneous, and frictionless flow with no heat transfer to the nozzle wall is assumed. The mass flow rate can be dimensionless defined as the flow coefficient:

$$C = \frac{Q_{\mathrm{m}}}{A \cdot \sqrt{2 \cdot \frac{p_0}{v_0}}}; A = \frac{\pi}{4} d^2; v_0 = \dot{x}_0 v_{g,0} + (1-\dot{x}_0) v_{l,0} \tag{12}$$

It can be derived from the momentum balance between the nozzle inlet and the narrowest cross section in the nozzle (nozzle throat):

$$C = \sqrt{\frac{-\int_{\eta_0}^{\eta} v^* d\eta}{(v^*)^2 - \beta^4}}; \eta = \frac{p}{p_0}; v^* = \frac{v}{v_0}; \beta = \frac{d}{d_0} \qquad (13)$$

The numerical solution of this equation gives the most exact results, irrespective of whether the flow in the nozzle is single-phase (gas or liquid), initially subcooled, or flashing (see Table 2).

The flow coefficient C reaches a maximum at the critical pressure ratio $\eta = \eta_{crit}$. This is the smallest physically possible pressure ratio between inlet and nozzle throat. It can be determined from the derivation of the flow coefficient (see Fig. 2):

$$\frac{dC}{d\eta} = 0 \rightarrow \max[C(\eta); \eta \in (\eta_b..1)] \qquad (14)$$

For the integration of Eq. (13), the specific volume of the two-phase fluid – it is based on the specific volume at the inlet – must be known. A suitable equation must be stated, depending on the type of flow, incompressible liquid, gas/vapor, two-phase flow, or initially subcooled liquid, which flashes in the nozzle. For two-phase flow, Leung [1986] derived an equation of state:

$$v^* = \dot{x} \cdot \frac{v_g}{v_0} + (1 - \dot{x}) \cdot \frac{v_l}{v_0} = \omega(N) \left(\frac{1}{\eta} - \frac{1}{\eta_0} \right) - 1 \qquad (15)$$

L2.3. Table 2. Characterization of flow parameters for different types of flow

Flow at inlet	Flow characteristics
Liquid	$\dot{x}_0 = 0; v^* = 1; \eta_0 = 1; \eta = \eta_b$
Gas/vapor	$\dot{x}_0 = 1; v^* = v_g/v_{g,0}; \eta_0 = 1; \eta \geq \eta_{crit}$ & $\eta \geq \eta_b$
Initially subcooled liquid	$\dot{x}_0 = 0; \eta_0 = \eta_S; \eta \geq \eta_{crit}$ & $\eta \geq \eta_b$
Vapor/flashing liquid	$\dot{x}_0 \geq 0; \eta_0 = 1; \eta \geq \eta_{crit}$ & $\eta \geq \eta_b$
Gas/non-flashing liquid	$\dot{x} = \dot{x}_0 = \text{const}; \eta_0 = 1; \eta \geq \eta_{crit}$ & $\eta \geq \eta_b; N \equiv 1$

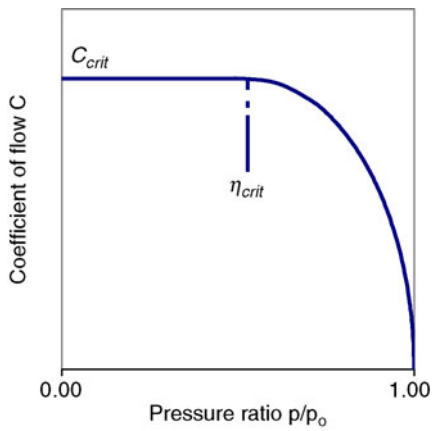

L2.3. Fig. 2. Flow coefficient as a function of the pressure ratio at subcritical and critical pressure ratio.

The thermodynamic nonequilibrium in the flow (boiling delay) must be allowed for by means of the compressibility factor $\omega(N)$. For this, Diener and Schmidt [Diener 2004] introduced a nonequilibrium factor N, which must be adapted to the measured data for the fitting considered:

$$\omega(N) = \frac{1}{\kappa} \frac{\dot{x}_0 \cdot v_{g0}}{v_0} + \frac{cp_{l0} \cdot T_0 \cdot p_0 \cdot \eta_0}{v_0} \cdot \left[\frac{v_{g0} - v_{l0}}{\Delta h_{v0}} \right]^2 \cdot N \qquad (16)$$

$$N = \left(\dot{x}_0 + cp_{l0} \cdot T_0 \cdot p_0 \cdot \eta_0 \cdot \left(\frac{v_{g0} - v_{l0}}{\Delta h_{v0}^2} \right) \cdot \ln\left(\frac{\eta_0}{\eta} \right) \right)^a \qquad (17)$$

Both factors are dependent only on the property data at the entrance of the nozzle, which are, as a rule, known or can be measured.

For the flow of a non-vaporising two-phase mixture, for example, air/water under ambient conditions, the mechanical nonequilibrium (slip) is important. Diener and Schmidt [Diener 2004] adopted a recommendation by Simpson et al. [Simpson 1983], who have intensively studied the flow-through control valves:

$$Q_{m,slip} = \phi \cdot C \cdot A \cdot \sqrt{2 \cdot \frac{p_0}{v_0}} \qquad (18)$$

$$\phi = \sqrt{\frac{v_0}{v_{eq,0}}} = \sqrt{\frac{v_0}{v_{l,0}}} \cdot \left\{ 1 + \dot{x}_0 \cdot \left[\left(\frac{v_{g,0}}{v_{l,0}} \right)^{1/6} - 1 \right] \cdot \left[1 + \dot{x}_0 \cdot \left[\left(\frac{v_{g,0}}{v_{l,0}} \right)^{5/6} - 1 \right] \right] \right\}^{-\frac{1}{2}}$$

The Eqs. (13–17) can be analytically solved for relevant special cases. For this, the different flow types in Fig. 3 are considered and corresponding density models enlisted for the integration. The results – the flow coefficients for different types of flow in integral form – are shown in Table 3. The accuracy of the analytical solution is inadequate only in the case of slightly

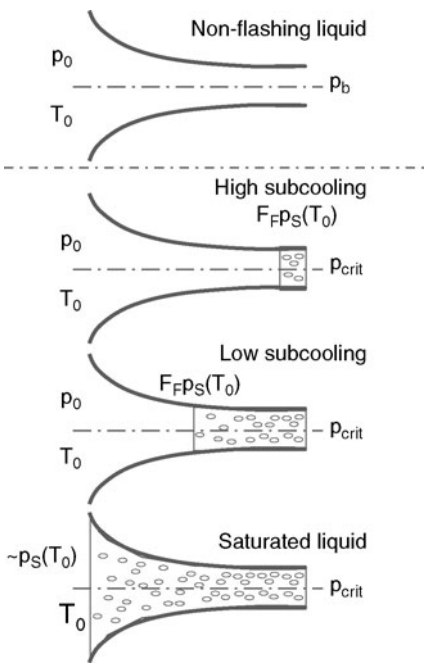

L2.3. Fig. 3. Flow types during flow-through nozzles.

L2.3. Table 3. Flow coefficients for different flow types

Flow coefficient for nozzles depending on flow type at the inlet ($\beta = 0$)	Subcritical flow: $\eta_b > \eta_{crit} \Rightarrow \eta = \eta_b$
	Critical flow: $\eta_b \le \eta_{crit} \Rightarrow \eta = \eta_{crit}$
	$\eta_{crit} = \frac{p_{crit}}{p_0}; \eta_b = \frac{p_b}{p_0}$
Strongly subcooled liquid ($\eta_b \ge \eta_{crit}$) (no vaporisation before the vena contracta) ($\dot{x}_0 = 0$): $C_l = \sqrt{1-\eta}$	$\eta_{crit} = F_F \cdot \eta_S = F_F \cdot \frac{p_S(T_0)}{p_0}$ $F_F = \left[0.96 - 0.28\sqrt{\frac{\eta_S \cdot p_0}{p_c}}\right]$ Orifice plates, control valves/safety valves
	$F_F \cong 1$ Cracks
Slightly subcooled liquid ($\eta_b < \eta_{crit}$) fashing in the nozzle ($\dot{x}_0 = 0$)	See Schmidt (2007)
Gases/vapors ($\dot{x}_0 = 1$): $C_g = \sqrt{\frac{\kappa}{\kappa-1}\left[(\eta)^{2/\kappa} - (\eta)^{\kappa+1/\kappa}\right]}$	$\eta_{crit} = \left(\frac{2}{\kappa+1}\right)^{\frac{\kappa}{\kappa-1}}$
Flashing two − phase flow ($\dot{x}_0 > 0$): $C_{2ph} = \frac{\sqrt{\omega(N)\cdot\ln\left(\frac{1}{\eta}\right) - (\omega(N)-1)(1-\eta)}}{\omega(N)\left(\frac{1}{\eta}-1\right)+1}$	η_{crit} as per Eq. (19) or (20) $\omega(N)$ as per Eqs. (16) and (17) $a = 3/5$: orifice plates, control valves
	$a = 2/5$ Safety valves, control valves (small travel)
	$a \cong 0$ Cracks, tubes

subcooled to boiling liquid at the valve inlet. Here reference is made to the solution by Schmidt [Schmidt 2007, 2009].

A discussion of real gas effects to be accounted for when sizing a safety valve for gas service is given in Schmidt (2009b).

For the determination of the flow coefficient, it is first necessary in each case to check whether the ratio between back pressure and pressure at the valve inlet η_b is lower than the critical pressure ratio η_{crit}. In this case, the flow coefficient is calculated with the critical pressure ratio, and critical flow prevails in the narrowest cross section. In the alternative case, with subcritical flow, the back pressure ratio is used.

The critical pressure ratio in two-phase flow is determined using the compressibility factor at thermodynamic equilibrium $\omega_{N=1}$. With a factor greater than 1, an analytical correlation is sufficiently accurate, while with small compressibility factors the iterative solution must be chosen:

$\omega_{N=1} \ge 1$:

$$\eta_{crit} = 0.55 + 0.217 \cdot \ln\omega_{N=1} - 0.046 \cdot (\ln\omega_{N=1})^2 + 0.004 \cdot (\ln\omega_{N=1})^3 \quad (19)$$

$\omega_{N=1} < 1$:

$$\eta_{crit}{}^2 + \left(\omega_{N=1}{}^2 - 2\cdot\omega_{N=1}\right)(1-\eta_{crit})^2 + \ldots\ldots + 2\cdot\omega_{N=1}{}^2 \cdot \ln(\eta_{crit}) + 2\cdot\omega_{N=1}{}^2\cdot(1-\eta_{crit}) = 0 \quad (20)$$

Styles (1971) investigated the start of liquid flashing in control valves and figured out that flashing begins markedly below the saturation pressure of the fluid. He takes into account the difference by means of the flashing factor F_F, which is also introduced in the equations in Table 3.

Example 6:

Exercise: How large must the safety valve be sized in order to discharge the flow of liquid methanol (see Example 5), if the set pressure of the safety valve is 8.4 bar (abs) and the temperature of the methanol at opening of the valve corresponds to the boiling temperature of 130°C. Property data of the boiling liquid are: $cp_{l0} = 3.50\text{kJ/(kg·K)}, \Delta h_{v0} = 922.7\text{kJ/kg}$; $v_{l0} = 1.49\cdot 10^{-3}\text{m}^3/\text{kg}$; $v_{g0} = 0.0418\cdot\text{m}^3/\text{kg}$

Solution:

(1) Calculation of the degree of subcooling and mass flow quality at the entrance of the valve: the vapor pressure of the boiling liquid corresponds to the set pressure of the safety valve, i.e., $\eta_0 = \eta_S = 1; \dot{x}_0 = 0$. This lead to: $v_0 = v_{l,0}$

(2) Mass flow through an ideal nozzle

$$N = \left(cp_{l0}\cdot T_0\cdot p_0\cdot\left(\frac{v_{g0}-v_{l0}}{\Delta h_{v0}{}^2}\right)\cdot\ln\left(\frac{1}{\eta}\right)\right)^{\eta_s^{-0.6}} = 0.169\cdot\ln\left(\frac{1}{\eta}\right)$$

$$\omega(N) = \frac{cp_{l0}\cdot T_0\cdot p_0}{v_0}\cdot\left[\frac{v_{g0}-v_{l0}}{\Delta h_{v0}}\right]^2\cdot N = 2.33\cdot\ln\left(\frac{1}{\eta}\right)$$

$$C_{2ph} = \frac{\sqrt{2.33\cdot\ln\left(\frac{1}{\eta}\right)\cdot\ln\left(\frac{1}{\eta}\right) - \left(\ln\left(\frac{1}{\eta}\right)-1\right)(1-\eta)}}{\ln\left(\frac{1}{\eta}\right)\cdot\left(\frac{1}{\eta}-1\right)+1}$$

The equation will be solved graphically, starting with a pressure ratio of $\eta = 1$ in steps of 0.01 until the maximum of the flow coefficient is reached (see Fig. 4).

Figure 4 leads to the unknown parameters: $C_{2ph} = 0.4345$, $\eta_{crit} = 0.706$; $N(\eta_{crit}) = 0.05878$; $\omega(N) = 0.81$

The mass flux of the nozzle is therefore:

$$\frac{Q_m}{A} = C\cdot\sqrt{2\cdot\frac{p_0}{v_0}} = 14590\cdot\frac{\text{kg}}{\text{m}^2\cdot\text{s}}$$

(3) Calculation of the necessary seat cross-sectional area A and the minimum required seat diameter d_0:

$$\varepsilon = 1 - \frac{v_{l0}}{v_0\cdot\left[\omega\cdot\left(\frac{1}{\eta}-1\right)+1\right]} = 0.252$$

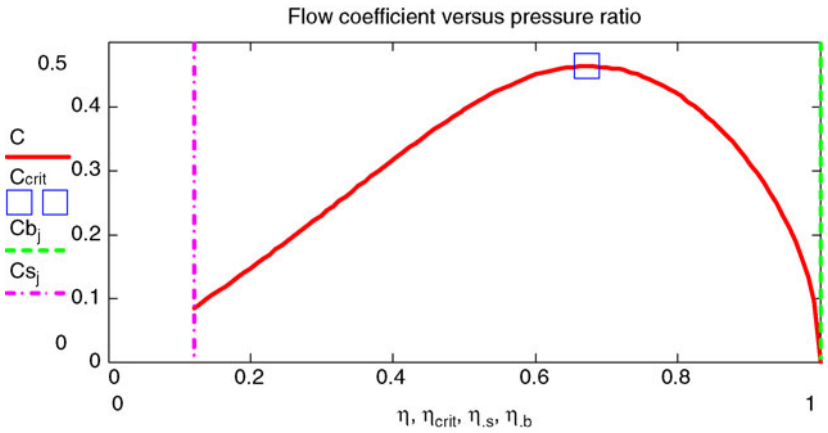

L2.3. Fig. 4. Graphical solution for the flow coefficient at the critical pressure ratio.

$$K_{\mathrm{dr,2ph}} = \varepsilon \cdot K_{\mathrm{dr,g}} + (1-\varepsilon) \cdot K_{\mathrm{dr,l}} = 0.568$$

$$A \geq \frac{Q_{\mathrm{m,out}}}{K_{\mathrm{dr,2ph}} \cdot C_{\mathrm{2ph}} \cdot \sqrt{2 \cdot \frac{p_0}{v_0}}} = 685 \cdot \mathrm{mm}^2$$

$$d \geq \frac{4}{\pi} \cdot \sqrt{A} = 29.5\,\mathrm{mm}$$

With a discharge coefficient of 0.568 for two-phase flow (based on the certified discharge coefficients for gas and liquid service of 0.5 and 0.77 taken from the valve manufacturer catalog), the minimum required seat diameter of the safety valve must be at least 29.5 mm. According to ISO 4126-10 it is recommended to install a bellow and friction damper in order to ensure safe operation of the safety valve.

In ISO 4126, Part 10, [ISO 4126], a further example of the sizing of a safety valve for two-phase flow is given.

7 Symbols

a	exponent of the non-equilibrium coefficient N	—
A	cross sectional area of the nozzle throat respectively the value seat area	m^2
C	flow coefficient	—
C_{crit}	flow coefficient at critical pressure ratio in the nozzle throat	—
cp_0	specific liquid heat capacity at inlet conditions	J/(kg K)
d	nozzle throat diameter	m
d_0	nozzle inlet diameter	m
F_F	flashing factor according to Styles	—
$K_{\mathrm{dr,2ph}}$	two-phase flow valve discharge coefficient	—
$h(T_0)$	specific enthalpy of the mixture at inlet temperature	J/kg
h'	specific enthalpy of the liquid	J/kg
h''	specific enthalpy of the vapor	J/kg
k_{vs}	discharge coefficient of the control valve	m^3/h
$K_{\mathrm{dr,g}}$	certified valve discharge coefficient for single-phase gar/vapour flow	—
$K_{\mathrm{dr,I}}$	certified valve discharge coefficient for single-phase liquid flow	—
N	non-equilibrium coefficient	—
p	pressure in the nozzle throat	Pa
p_{crit}	fluiddynamic critical pressure	Pa
p_0	nozzle inlet pressure	Pa
$p_{\mathrm{s}}(T_0)$	saturation pressure at inlet temperature	Pa
p_{b}	back pressure	Pa
p_{c}	thermodynamic critical pressure	Pa
Q_m	mass flow rate through the nozzle	Kg/s
T_0	nozzle inlet temperature	K
T_{c}	thermodynamic critical temperature	K
v	specific volume in the nozzle throat	m^3/kg
v_0	specific volume in the nozzle inlet	m^3/kg
v^*	dimensionless specific volume	—
$\dot{x}_0$	mass flow quality in the nozzle inlet	—
ε	void fraction in the nozzle throat	—
β	diameter ratio	—
η	ratio of local pressure to inlet pressure	—
η_{b}	ratio of back pressure to the inlet pressure	—
η_{crit}	ratio of critical pressure to inlet pressure	—
η_{S}	ratio of saturation pressure corresponding to nozzle inlet temperature (measure of liquid subcooling)	—
κ	isentropic coefficient	—
ω	compressibility coefficient	—
$\omega(N)$	compressibility coefficient depending on the non-equilibrium coefficient N	—
$\omega_{N=1}$	thermodynamic conditions, ω(N=1)	—
$\Delta h_{\mathrm{v,0}}$	latent heat of vaporization at inlet condition	J/kg

Index

0	sizing condition
c	thermodynamic critical property
crit	critical condition with respect to flow
feed	into the pressurized system
g	gas phase
l	liquid phase
out	dischargeable from the pressurized system
b	back
2ph	two-phase flow
s	subcooling
SV	through the safety valve

8 Bibliography

1. IVSS (Auflage 2008) Das PAAG Verfahren, Methodik Anwendung Beispiele. ISSA Prevention Series No. 2002 (G). 4
2. DIN EN 61511 (Mai 2005) Funktionale Sicherheit – Sicherheitstechnische Systeme für die Prozessindustrie, Teil 1 bis 3. Beuth Verlag, Berlin
3. VDI/VDE 2180 (April 2007) Sicherung von Anlagen der Verfahrenstechnikmit Mitteln der Prozessleittechnik (PCS). VDI-Verlag, Düsseldorf
4. Institute of Petroleum (August 2000) Guidelines for the design and safe operation of shell and tube heat exchangers to withstand the impact of tube failure. Institute of Petroleum, England
5. Thyer AM, Wilday AJ, Bankes G (November 2001) The experimental study and simulation of tube rupture in shell-and-tube heat exchangers. I ChemE, Hazards XVI
6. API 520 (January 2000) Sizing, selection, and installation of pressure-relieving devices in refineries, Part I sizing and selection, 7 edn. American Petroleum Institute
7. ISO 23521 (2006) Petroleum, petrochemical and natural gas industries – pressure-relieving and depressuring systems. DIN Deutsches Institute für Normung e.V., Beuth Verlag GmbH, Berlin
8. Technischer Ausschuss für Anlagensicherheit beim BMU, Abschlussbericht des Arbeitskreises Novellierung der 2. StörfallVwV (1994), Geschäftsstelle bei der Gesellschaft für Anlagen- und Reaktorsicherheit (GRS) mbH, Köln. TAA-GS-06
9. Deutscher Verband für Wasserwirtschaft und Kulturbau e.V. (DVWK), Regel zur Wasserwirtschaft 131/1996 (1996). Technische Regel wassergefährdender Stoffe (TRwS) – Bestimmung des Rückhaltevermögens. Kommissionsvertrieb Wirtwschafts- und Verlagsgesellschaft Gas und Wasser mbH, Bonn
10. VDI Richtlinie 3783 Ausbreitung von störfallbedingten Freisetzungen – Sicherheitsanalyse. Beuth Verlag GmbH, Berlin
11. Strohmeier K (1990) Leckanalyse bei Anwendung der Störfall-Verordnung. Chem-Ing-Technik 62(12)
12. Strohmeier K (1993) Abschätzung des Gefährdungspotentials druckverflüssigter Gase. Chem-Ing-Technik 65(4):S410–S414
13. Balast H (2008) Dispersion calculation. Presentation at the 66th meeting of the Dechema Working group "Safe Design of Chemical Plants". Frankfurt, 8 November
14. Westphal F (1991) Berechnungsmodell für die Leckraten aus Rissen in Wänden druckführender Apparate und Rohrleitungen. Dissertation Universität Dortmund
15. Diener R, Schmidt J (2004) Sizing of throttling devices for gas liquid two-phase flow, part 1: safety valves. Proc Saf Prog 23(4):335–344
16. Van den Bosch CJH, Weterings RAPM (eds) (1997) Methods for the calculation of physical effects – due to releases of hazardous materials. Yellow Book. Committee for the prevention of disasters
17. Schatzmann M (1976) Auftriebsstrahlen in natürlichen Strömungen – Entwicklung eines mathematischen Modells. Dissertation Universität Karlsruhe
18. VDI3783 Part 2 (1987) Environmental meteorology: dispersion of heavy gas emissions by accidental releases; safety study. Part 2. Beuth-Verlag, Berlin
19. VDI3783 Part 1 (1987) Dispersion of pollutants in the atmosphere: dispersion of emissions by accidental releases; safety study. Part 1. Beuth-Verlag, Berlin
20. Witlox HWM, Holt A (1999) A unified model for jet, heavy and passive dispersion including droplet rainout and re-evaporation. International Conference and Workshop on Modelling the Consequences of Accidental Releases of Hazardous Materials, CCPS, San Francisco, California, September 28–October 1, pp. 315–344
21. API 521: pressure-relieving and depressuring systems. American petroleum Institute, 5th Edition, 2008.
22. Hahn M, Reeh W, Wolff A, Röttger D (2007) Regelmäßige Prüffristverlängerungen für Druckgeräte nach BetrSichV: Gemeinsames Konzept von Betreiber, Eigenüberwachung und Aufsichtsbehörde. Chem-Ing-Technik 79(9):1443
23. DIN EN 60534 (2005) Stellventile für die Prozessregelung. Beuth-Verlag, Berlin
24. Diener R (1999) Berechnung und Massendurchsatzcharakteristik von Stellventilen bei Zweiphasenströmung. Fortschr. Berichte VDI, Reihe 7 Strömungstechnik Nr. 388. VDI Verlag, Düsseldorf
25. Diener R, Schmidt J (2005) Sizing of throttling devices for gas liquid two-phase flow, Part 2: control valves, orifices and nozzles. Proc Saf Prog 24(1):29–37
26. Heller FJ (1983) Safety relief valve sizing: API versus CGA requirements plus a new concept for tank cars. Proceedings – Refining Department, Vol. 62, API, Washington, DC, pp 123–135
27. ISO4126-10 (2007) Safety devices for protection against excessive pressure – sizing of safety valves and connected inlet and outlet lines for gas/liquid two-phase flow. DIN Deutsches Institute für Normung e.V., Beuth Verlag GmbH, Berlin
28. Leung JC (1986) A generalized correlation for one-component homogeneous equilibrium flashing choked flow. AichE J 32(10):1743–1746
29. Simpson HC, Rooney DH, Grattan E (1983) Two phase flow through gate valves and orifice plates. International Conference on the Physical Modelling of Multi-phase Flow, Coventry, 19–20 April
30. Schmidt J (2007) Sizing of nozzles, venturis, orifices, control and safety valves for initially sub-cooled gas/liquid two-phase flow – the HNE-DS method. Forsch Ing Wesen 71:47–54
31. Schmidt J, Egan S (February 2009) Case studies of sizing pressure relief valves for two-phase flow. Chem Engng Technol 32(2):263–272
32. Schmidt J, Peschel W, Beune A (February 2009) Experimental and theoretical studies on high pressure safety valves: sizing and design supported by numerical calculations (CFD). Chem Engng Technol 32(2):252–262
33. Styles GF (1971) Sizing control valves for choked conditions due to cavitation or flashing, Proc. 1 Symp. Flow, its measurement and control, Pittsburgh 1097–1109, Bd.1 3

L2.4 Calculating Critical Mass Flux

Florian Schmidt
Bayer Technology Services GmbH, Krefeld, Germany

1 Introduction

Keeping the pressure at the inlet cross section of a nozzle, an orifice, or any other duct constant and reducing step by step the pressure at the exit cross section results in an increased mass flux. If pressure falls below a certain value, no further increase in mass flux is observed (see Fig. 1). The resulting mass flux is called critical mass flux. It is dependent on the pressure at the inlet cross section p_0, the temperature T_0, the void fraction ε_0, the gas mass flow fraction $\dot{x}_0$, and the physical properties at the inlet cross section. At given inlet conditions the critical mass flux is the maximum possible mass flux through a valve (definitions of often used variables are to be found in Sect. 10).

For further explanation see Fig. 2. Also, in the following sections commonly used expressions and definitions are introduced. In Fig. 2, the pressure is plotted along the stream path from the inlet to outlet. Starting from the inlet pressure p_0 the pressure decreases along the pathway. The counterpressure in the exit cross section is called p_2. Due to the reduction of pressure the gas phase expands. The released potential energy and the pressure profile along the pathway lead to strong acceleration of the liquid and gas. This is why the pressure gradient increases along the pathway as shown in Fig. 2 and reaches its maximum in the so-called smallest cross section. This cross section (indexed 1) is to be found right upstream of the exit cross section (indexed 2).

For subcritical flow the pressure in the smallest cross section is

$$p_1 = p_2. \tag{1}$$

In the case of critical flow, a pressure jump occurs in the smallest cross section. It has been calculated (e.g., by Henry and Fauske [1]) that in the exit cross section a singularity can be found. The pressure in the smallest cross section is called critical pressure p_c and does not decease further even if the counterpressure p_2 is decreased.

$$p_1 = p_c \quad \text{(critical flow)}. \tag{2}$$

The ratio of the critical pressure p_2 and the pressure at the inlet p_0

$$\eta_c = \frac{p_c}{p_0} \tag{3}$$

is the critical pressure ratio.

The reason for critical flow, in general, is the strong expansion of gaseous phases. The potential energy contained in the pressurized gas phase at the inlet is transformed into kinetic energy of the two-phase flow. The critical mass flux $\dot{m}_c$ cannot be exceeded though otherwise the kinetic energy in the exit cross section due to the high velocity would exceed the released potential energy. Thus, the mass flux is limited to the critical mass flux.

This fact is taken into account in various methods for calculating the critical mass flux from the energy balance for a

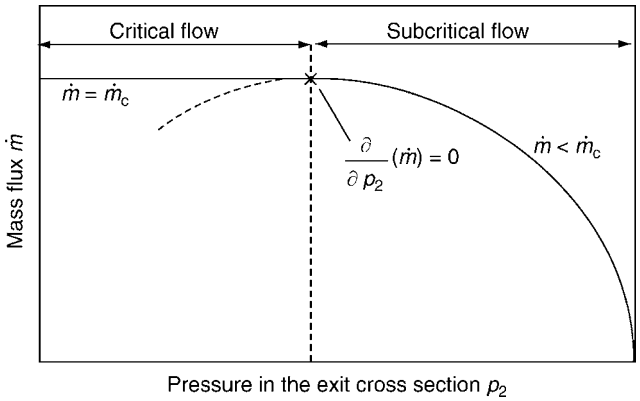

L2.4. Fig. 1. Mass flux depending on the pressure in the exit cross section for constant pressure, temperature, and void fraction at the inlet cross section.

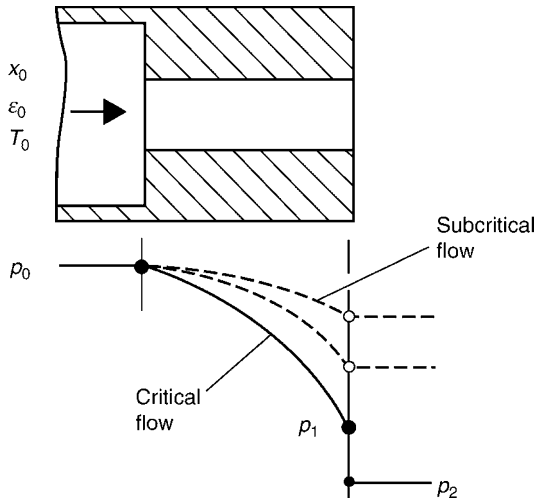

L2.4. Fig. 2. Pressure as a function of the flow path for various exit pressures.

two-phase flow (also in this chapter). Due to simplifying assumptions (e.g., no friction, no slip between the gas and liquid, and adiabatic change of conditions) the calculated mass flux is corrected by introducing the discharge coefficient C_d. It concludes

$$\dot{M} = C_d A_1 \dot{m}\,. \tag{4}$$

A_1 is the area of the smallest cross section. The discharge coefficient corrects also the contraction of the flow in case of high void fractions. Predicting the critical mass flux $\dot{m}_c$ and the critical pressure ratio η_c becomes more important when designing safety valves for the discharge of two-phase flow. In the following chapter methods for calculating the mass flux $\dot{m}$ and the discharge coefficient C_d are explained.

2 Selecting the Appropriate Calculation Method

The values of the critical mass flux and the critical pressure ratio depend on a variety of parameters. They are mainly influenced by

1. The physical properties of the system:
   - Evaporating flow (vapor–liquid flow, e.g., water–steam)
   - Nonevaporating flow (gas–liquid flow, e.g., water–air)
2. The geometry of the flow channel:
   - Design of the channel, e.g., nozzle, orifice, or pipe
   - Length-to-diameter ratio as a major parameter
3. The operating conditions:
   - Pressure p_0, temperature T_0, void fraction ε_0, gas mass flow fraction $\dot{x}_0$ at the inlet, and counterpressure in the exit cross section p_2.

2.1 Influence of the Physical Properties of the System

The major criteria for choosing the right calculation method are listed under (1) in the previous section. For further differentiation of the calculation method the criteria under (2) and (3) are to be taken into consideration.

In many cases, the system can be seen either as an evaporating system or a nonevaporating system (in some special cases vapor and liquid flow together with a noncondensable gas – e.g., nitrogen with water–steam. Details on such hybrid systems are to be found in Sect. 8.2). Considering an evaporating or nonevaporating system, especially the heat and mass transfer between liquid and gas shows large differences. Because of this, different assumptions for the calculation of the critical mass flux and the critical pressure ratio in evaporating or nonevaporating flow have to be made:

- Evaporating systems.
  - Intensive mass transfer between liquid and gas phases.
  - Because of evaporation, increasing gas mass flow fraction along the flow path $\frac{\partial \dot{x}}{\partial z} > 0$ and $\dot{x}_1 > \dot{x}_0$.
  - Phase changes occur mostly at thermodynamic equilibrium, e.g., $T_g = T_l = T$ and $p = p_s(T)$.
- Nonevaporating systems.
  - No mass transfer between liquid and gas phases.
  - Due to no mass transfer constant gas mass flow fraction along the flow path: $\frac{\partial \dot{x}}{\partial z} = 0$ and $\dot{x}_1 = \dot{x}_0 = \dot{x}$.
  - Circumstances permitting nonthermodynamic equilibrium phase change. Expansion leads to cooling of the gas phase while the temperature of the liquid phase stays nearly constant: $T_{g,1} < T_{l,1} \cong T_{l,0}$.

Nearly all, from the literature, available calculation methods are based on energy and mass balance for the two-phase mixture. They only differ in their assumption made for the heat and mass transfer and the kind of phase change between the inlet and outlet.

For evaporating flow assuming thermodynamic equilibrium is suitable. The most common calculation method is the Homogeneous Equilibrium Model (Sect. 4).

For nonevaporating flow calculation methods with constant gas mass flow fractions are to be used. These calculation methods are subdivided into those taking temperature

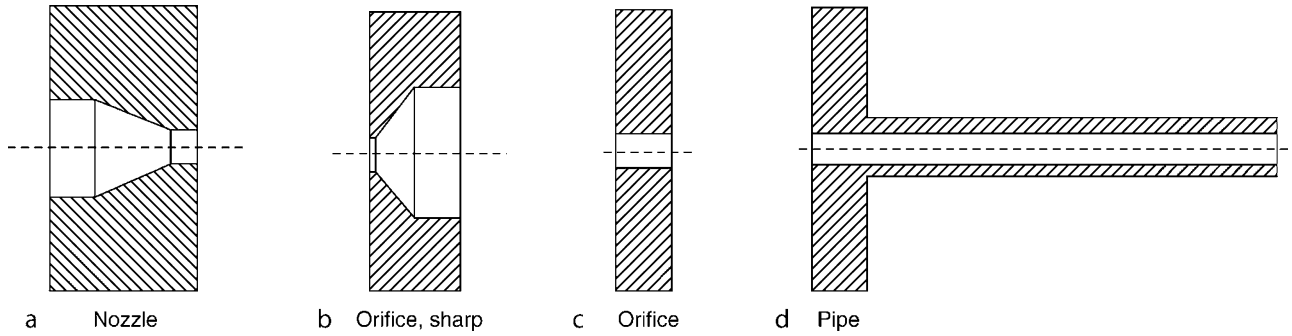

L2.4. Fig. 3. Considered geometries.

differences between the phases into account and those which do not. A calculation method that works for both cases is introduced in Sect. 6.

2.2 Geometry of the Duct

Hardekopf and Mewes [2] did an extended literature study on "critical flow of evaporating systems." In this study, especially, the geometry of the duct is of interest. The investigated geometries – nozzles, orifices, and pipes – are depicted in Fig. 3.

The intensity of the influence of the duct's geometry depends on the thermodynamic conditions in the inlet cross section:

Overheated vapor, vapor mass flow fraction: $\dot{x}_0 = 1$

For the calculation of shorter ducts, $L/D < 15$ the equations given in Sect. 3 are suitable. Orifices with sharp edges at the inlet are an exception. Friedrich and Vetter [3] observed in their experiments no critical flow when reducing the pressure in the exit cross section. The explanation for this phenomenon is the strong inner friction due to the sharp edges and the induced eddies. However, for these kinds of orifices the mass flow can be calculated with the equations given in Sect. 3 (when using the appropriate discharge coefficient C_D).

For long ducts, the influence of the friction at the wall of the duct cannot be neglected. Thus, the critical flow condition is not only dependent on the ratio η_c of the pressure at the exit and the inlet, but also on the absolute values of the pressure at the inlet p_0 and on the ratio of the length and diameter of the pipe. Using empirical equations to obtain the ratio of the critical pressure in the pipes is not advisable. Instead, the balance of energy, momentum, and mass along the axial coordinate should be solved numerically.

Two-phase mixture consisting of saturated vapor and liquid, vapor mass flow fraction: $0 < \dot{x}_0 < 1$

In this case, the mass flux and the critical pressure ratio can be calculated with the Homogeneous Equilibrium Model. The Homogeneous Equilibrium Model is explained in Sect. 4. For very long ducts, friction at the wall should be taken into account. For a rough estimation the simplified method from Sect. 4.2 can be applied. With very low vapor mass flow fractions at the inlet of short ducts, the liquid becomes overheated. This leads to not enough liquid evaporating to establish thermodynamic equilibrium. The reason for this is the short residence time inside very short fittings. A calculation procedure for the case of very low vapor mass flow fractions is proposed in Sect. 8.1.

Subcooled liquid

If the exit pressure p_2 is reduced, the liquid will first evaporate in the exit cross section not depending on the fitting's geometry. As explained in Sect. 5, in this case a flow very similar to the critical flow is observed, though the flow is a single-phase liquid flow. If the liquid is too subcooled to evaporate in the exit cross section, no critical flow will occur. In both cases, the mass flux can be calculated with the equations for single-phase liquid flow because no evaporation takes place inside the duct. The mass flux for a subcooled liquid at the inlet cross section can be calculated with the equations in Sect. 5.

The more complex case of an evaporating liquid along the duct or the possibility of a pure vapor flow exiting the duct is not covered in this publication. This can be the case for high values of the ratio of length to diameter L/D (especially for pipes). Mayinger [4] and Kolev [5] propose a calculation method for this case. Evaporation along the duct can be predicted by calculating the pressure drop for a single-phase liquid flow. Evaporation takes place if the pressure along the duct falls below the vapor pressure and enough nuclei are present. This is the case in most technical applications.

3 Mass Flux for a One Component Gas–Vapor Flow

The mass flux for a single-phase gas–vapor flow is calculated from the energy balance of the fluid. Mayinger [4] describes the following equation in his paper briefly. For the calculation of the mass flux the following assumptions are made:

- The kinetic energy of the gas is negligibly small.
- No friction at the walls.
- The change of condition from the inlet to the exit of the fitting is adiabatic.
- The change of condition is described by the ideal gas law.

By assuming no friction and an adiabatic change of conditions of the flow, the change of condition is necessarily also isentropic for the flowing gas or vapor between the inlet and the exit cross sections.

The mass flux is thus calculated as

$$\dot{m} = C_{d,g}\psi\sqrt{\frac{2p_0}{v_{g,0}}} \tag{5}$$

with

$$\psi \equiv \sqrt{\frac{\kappa}{\kappa-1}\left[\left(\frac{p_1}{p_0}\right)^{2/\kappa} - \left(\frac{p_1}{p_0}\right)^{(\kappa+1)/\kappa}\right]} \tag{6}$$

the discharge function and the discharge coefficient C_D of the single-phase gas flow. The discharge coefficient C_D corrects the error when calculating the mass flow, without taking friction and contraction in the smallest cross section into account. $v_{g,0}$ is the specific volume of the gas or vapor in the inlet cross section and κ the isentropic exponent for an ideal gas.

If the pressure p_1 in the exit cross section is reduced, the value of the discharge function ψ will increase and thus, also the mass flow according to Eq. (5), until the critical pressure p_c is reached. The discharge function has, according to Eq. (6), for the critical pressure ratio

$$\eta_c = \left(\frac{p_1}{p_0}\right)_c = \left(\frac{p_c}{p_0}\right) = \left(\frac{2}{\kappa+1}\right)^{\kappa/(\kappa-1)} \tag{7}$$

between the pressure in the exit cross section p_1 and the pressure at the inlet p_0, a maximum. That means the constraint (Fig. 1)

$$\frac{\partial}{\partial p_1}(\dot{m}) = 0 \text{ for } p_1 = p_0 \tag{8}$$

for critical flow conditions is fulfilled.

For calculating the critical mass flux, it is best first to calculate the critical pressure ratio η_c with Eq. (7) or the critical pressure p_c. The derived value is then to be compared with the pressure at the exit p_2. For this value of the pressure p_2 in Eq. (6) applies

$$\begin{aligned} p_1 &= p_2, \quad \text{if } p_2 > p_c\,, \\ p_1 &= p_c, \quad \text{if } p_2 < p_c. \end{aligned} \tag{9}$$

After the calculation of the discharge function according to Eq. (6) the mass flux is calculated from Eq. (5).

The manufacturer of orifices, nozzles, and valves or other fittings often give the discharge coefficient C_d as a table or as an empirical equation. These values are, most of the time, fitted to meet the experimental investigation concerning the critical mass flux. If the manufacturer delivers a discharge coefficient with his product, it is often best to use it as the value for C_d in Eq. (5). If not available, the discharge coefficient for orifices C_d can be calculated as described in Sect. 7 using Eq. (54), according to Morris [6]. For nozzles, the discharge coefficient can be derived from the empirical equation

$$C_{D,g} = C_{D,0} + C_{D,1}\left(\frac{p_2}{p_1}\right)^2 + (2C_{D,0} - C_{D,0})\left(\frac{p_2}{p_1}\right)^3 \tag{10}$$

introduced by Sallet [7]. $C_{D,0}$ and $C_{D,1}$ are the thresholds for the discharge coefficients at an exit pressure $p_2 = 0$. That means $C_{D,0} = 0.84$ for very low exit pressures and $C_{D,1} = 0.66$ in case of no pressure difference between the inlet and exit. These equations to calculate the discharge coefficient are solemnly of an empirical nature. Depending on the operating conditions and the physical properties of the liquids the calculated values can differ from reality.

4 Homogeneous Equilibrium Model

The equations for the Homogeneous Equilibrium Model are briefly explained by Mayinger [4]. The following assumptions apply:

- Liquid and gas are in thermodynamic equilibrium along the whole stream path.
- Slip between the two phases equals one (no slip).
- Friction at the wall is neglected.
- The change of conditions between the inlet and exit of the fitting is adiabatic.

From the two latter assumptions it is concluded that the change of conditions for the two-phase flow is also isentropic along the stream path. Following these assumptions the equation for the two-phase flow mass flux

$$\dot{m} = \sqrt{\frac{2(\bar{h}_0 - (1-\dot{x}_1)h_{l,1} - \dot{x}_1 - h_{g,1})}{(1-\dot{x}_1)v_l + \dot{x}_1 v_{g,1}}} \tag{11}$$

is derived from the energy and mass balance. In Eq. (11), v_l is the specific volume of the liquid and v_g the specific volume of the vapor in the inlet cross section. The liquid is assumed to be incompressible. Therefore,

$$v_l = v_{l,0} = v_{l,1.} \tag{12}$$

Herein, h_0 represents the mean enthalpy of the two-phase flow mixture in the inlet cross section. It is

$$\bar{h}_0 = \dot{x}_0 h_{g,0} + (1-\dot{x}_0)h_{l,0} \tag{13}$$

with the vapor mass flow fraction $\dot{x}_0$, the specific enthalpy of the vapor $h_{l,0}$, and the specific enthalpy of the liquid $h_{g,0}$ in the inlet cross section.

The vapor mass flow fraction in the inlet cross section is derived from the assumption of isentropic change of conditions from the equation

$$\bar{s}_0 = \bar{s}_1 = \dot{x}\,s_{g,1} + (1-\dot{x}_1)s_{l,1} = \dot{x}_0\,s_{g,0} + (1-\dot{x}_0)s_{l,0} \tag{14}$$

depending on the entropy of the gas and the liquid $\bar{s}_{g,0}$ and $\bar{s}_{l,0}$, respectively, and the vapor mass flow fraction $\dot{x}_0$ in the inlet cross section.

Equation (11) is capable of calculating the mass flux $\dot{m}$ either for a critical or a subcritical flow. Therefore, an addition equation is necessary to calculate the critical pressure p_c

$$\frac{\partial}{\partial p_1}(\dot{m}) = 0, \quad \text{if } p_1 = p_c. \tag{15}$$

The pressure in the smallest cross section is called p_1. In case of subcritical flow, the pressure in the smallest cross section p_1 equals the counterpressure p_2 and

$$\eta > \eta_c; \quad p_1 > p_2 \tag{16}$$

apply. All variables in Eq. (11) carrying the index 1 are to be calculated consequently for the counterpressure p_2. In the case of critical flow with

$$\eta > \eta_c; \quad p_1 > p_c \tag{17}$$

all variables in Eq. (11) carrying the index 1 are to be calculated for the critical pressure p_c.

Solving the Eqs. (11), (13), and (15) can be done iteratively. The pressure in the exit cross section p_1 is known in the first step, because it needs to be decided first whether the flow is critical or subcritical. The pressure p_1 is, therefore, stepwise reduced until the constraint according to Eq. (15) is met. As initial value for the pressure p_1 a high value should be chosen to ensure that the value is at the beginning not lower than the critical pressure. For each iteratively found value of the pressure p_1 another iteration needs to be done for the vapor mass flow fraction $\dot{x}_1$, before the mass flux $\dot{m}$ from Eq. (11) can be calculated.

The vapor mass flow fraction in the exit cross section $\dot{x}_1$ is then stepwise increased until the constraints according to the isentropic change of conditions in Eq. (14) are met. As initial value for the vapor mass follow fraction $\dot{x}_1$ the value at the inlet cross section $\dot{x}_0$ is likely to be chosen. The entropy can be derived from an equation of state or suitable tables. The procedure is illustrated in the temperature–entropy diagram in Fig. 4.

In this example the two-phase flow in the inlet cross section is in the state 0. The pressure in the exit cross section of the fitting equals the pressure p_1. p_1 is located in the T-s diagram on the isothermal curve, respectively, on the isochore curve. Starting at position 0, the orthographic line (isentropic change of condition $ds = 0$) leads to position 1, which represents the state of the two-phase flow in the exit cross section. The corresponding value of the vapor mass flow fraction in the exit cross section $\dot{x}_1$ can be read directly from the diagram. Using the T-s diagrams, one can avoid the stepwise iterative calculation of the vapor mass flow fraction $\dot{x}_2$. The iteration to obtain the critical pressure according to Eq. (15) needs to be carried out anyway. The above described method for solving the Homogeneous Equilibrium Model is rather complicated. Therefore, Leung [8] proposes a simplified calculation method. In his following publication various applications are featured (subcooled liquid in the inlet cross section [9], nonevaporating gas, or liquid flow [10]). A brief overview including some examples is then published by Leung in [11]. In the next section, the application of Leung's method for evaporating vapor or liquid flow is described.

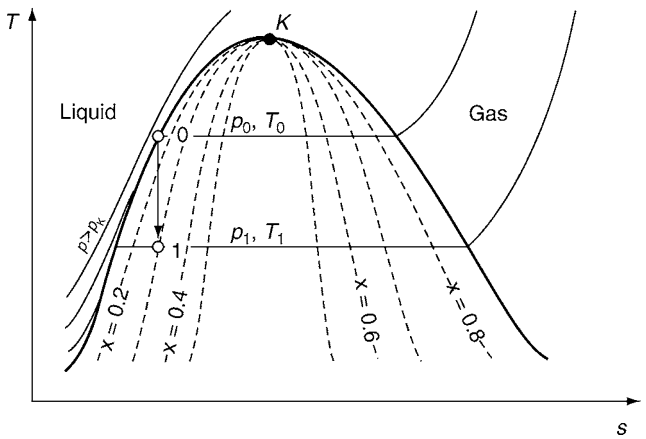

L2.4. Fig. 4. Isentropic change of conditions for the Homogeneous Equilibrium Model in a T-s diagram.

4.1 Simplified Solving of the Homogeneous Equilibrium Model Equations

This simplified method introduced by Leung [8] is suitable in case the two-phase flow in the inlet cross section is a saturated vapor–liquid mixture or a slightly subcooled liquid. The influence of wall friction on the pressure loss and thus, on the mass flux can be neglected for shorter ducts. For convenience the discharge function Ψ is introduced. The mass flux is, therefore, calculated as follows:

$$\dot{m} = \sqrt{\frac{2p_0}{v_0}}\Psi. \tag{18}$$

Leung [8] uses in his method a simplified thermodynamic equation of state for the two-phase flow,

$$\frac{v}{v_0} = \omega\left(\frac{p_0}{p} - 1\right) + 1, \tag{19}$$

which is calculated by the mean specific volume

$$v = \dot{x}\, v_g + (1 - \dot{x}) v_l \tag{20}$$

at a certain position along the stream path depending on the mean specific volume at the inlet cross section

$$v_0 = \dot{x}_0\, v_{g,0} + (1 - \dot{x}_0) v_{l,0} \tag{21}$$

and the ratio of the local pressure p and the inlet pressure p_0. In Eq. (19), ω is introduced as a variable which is mostly called "compressibility factor." For vapor–liquid systems, it is

$$\omega = \dot{x}_0 \frac{v_{g,0} - v_{l,0}}{v_0} + \frac{\eta_S\, c_{p,}\, p_{l,0}\, T_0}{v_0}\left(\frac{v_{g,0} - v_{l,0}}{h_{lg,0}}\right)^2. \tag{22}$$

Leung [8] solves Eq. (11) analytically. The enthalpy difference in Eq. (11) is derived by integrating the fundamental equation for isentropic change of conditions

$$\mathrm{d}h = \int_{p_0}^{p_1} -v\, \mathrm{d}p \tag{23}$$

from the inlet pressure p_0 to the exit pressure p_1, whereas v is calculated from Eqs. (19) and (22).

Leung [8] presents an equation which allows the explicit calculation of the mass flux $\dot{m}$, considering physical properties such as pressure and temperature at the inlet cross section. The discharge function is, therefore,

$$\psi = \frac{\sqrt{(1 - \eta_s) + \left[\omega\, \eta_S \ln\left(\frac{\eta_s}{\eta}\right) - (\omega - 1)(\eta_S - \eta)\right]}}{\omega\left(\frac{\eta_S}{\eta} - 1\right) + 1}. \tag{24}$$

It means

$$\eta_S = \frac{p_s(T_0)}{p_0} \tag{25}$$

the ratio of the vapor pressure at the inlet cross section $p_s(T_0)$ and the pressure at the inlet cross section p_0, and

$$\eta = \frac{p_1}{p_0} \tag{26}$$

the ratio of the pressure in the smallest cross section and the pressure at the inlet cross section p_0.

The pressure ratio η_s is a measure of the degree of subcooling of the liquid at the inlet cross section:

- Slightly subcooled liquid: $\eta_{S,min} \leq \eta_S < 1$.
- Saturated vapor–liquid mixture: $\eta_S = 1$.

$\eta_{S,min}$ is the smallest possible pressure ratio where some evaporation occurs between the inlet and exit of the fitting. According to Leung [8], smaller values of $\eta_{S,min}$ lead to nonphysical solutions of the introduced equation. It is, therefore,

$$\eta_{S,min} = \frac{2\,\omega}{1 + 2\,\omega}. \tag{27}$$

The calculation of the mass flux for a strongly subcooled liquid at the inlet cross section is described in Sect. 5.

The pressure at the smallest cross section p_1 equals, in case of a subcritical flow, the given counter pressure p_2 in the exit cross section, or in case of a critical flow, the critical pressure p_c. It is, therefore,

$$p_1 = \max(p_2, p_c). \tag{28}$$

The introduction of Eq. (24) in Eq. (18) and the derivation with respect to the pressure in the smallest cross section p_1 lead the critical conditions in Eq. (15) to

$$0 = \frac{\omega^2 - 2\,\omega + 1}{2\,\eta_S\,\omega}\eta_S^2 - 2\,(\omega - 1)\,\eta_c + \omega\,\eta_S \ln\left(\frac{\eta_c}{\eta_S}\right) + \frac{3}{2}\omega\,\eta_S - 1 \tag{29}$$

for calculating the pressure ratio η_c of the critical pressure p_c and the inlet pressure p_0

$$\eta_c = \frac{p_c}{p_0}, \tag{30}$$

which gives directly the critical pressure p_c. For obtaining the mass flux $\dot{m}$ first the compressibility factor ω from Eq. (22) is calculated. With ω the critical pressure ratio η_c is then calculated from Eq. (29) and the critical pressure is calculated according to Eq. (30). The pressure in the smallest cross section follows from the constraint of Eq. (28). From this pressure and the inlet pressure η according to Eq. (26) and the discharge function according to Eq. (24) is calculated. Finally, the mass flux is calculated from Eq. (18).

4.2 Influence of Friction

Calculating a two-phase vapor–liquid flow in a long pipe is complex, because in this case friction between the fluid and the wall cannot be neglected. The pressure drop due to friction and acceleration, the vapor mass flow fraction, and the velocity interact with each other. These variables often undergo an intense change along the stream path. Therefore, they are difficult to be described with integral equations, taking only the inlet and exit conditions into account.

A two-phase flow mixture can only be calculated by solving the balance of mass, energy, and momentum, depending on the spatial coordinate. For detailed information about this, one should refer to more specialized publications. A brief introduction and the calculation of vapor–liquid flows in the case of critical and subcritical flows are given by Kolev [5].

For short pipes with a small length to diameter ratio or if roughly calculating the method proposed by Leung [11] can be applied to pipes as well.

The compressibility factor ω is like done for shorter ducts, calculated from Eq. (22). For the discharge function Leung [11] proposes

$$\psi = \sqrt{\frac{\frac{1-\eta}{1-\omega} + \frac{\omega}{(1-\omega)^2}\ln[(1-\omega)\eta + \omega] - \ln\left[\frac{1}{\eta}((1-\omega)\eta + \omega)\right]}{4f\,\frac{L}{D}}}. \tag{31}$$

The ratio of the critical pressure and the pressure at the inlet η_c follows from

$$\psi_c = \frac{\eta_c}{\sqrt{2\omega}}. \tag{32}$$

For calculation of the critical pressure p_c or the pressure ratio η_c the system of equation from Eqs. (31) and (32) has to be solved taking

$$\psi_c = \psi \tag{33}$$

into account. The suitable pressure p_1 for calculating the pressure ratio η is given by the constraint in Eq. (28). In the case of a critical flow, the mass flux can be calculated from Eq. (18) for the given value of ψ_c. In the case of a subcritical flow the discharge function needs to be recalculated from Eq. (31), considering the pressure ratio η and the pressure in the exit cross section p_2.

In Eq. (31) L is the length and D the diameter of the duct. The friction coefficient f is set to a constant value

$$f \cong 0.005 \tag{34}$$

according to Leung [11].

5 Mass Flux for a Strongly Subcooled Liquid at the Inlet

If the temperature T_0 in the inlet cross section is below the vapor pressure T_s according to the pressure at the inlet cross section p_0, the liquid is called "sub cooled." Consequently, no vapor exists in the inlet cross section. If the ratio η_s of vapor pressure p_s and pressure at the inlet cross section p_0 defined by Eq. (25) does not fall below the value $\eta_{S,min}$ according to Eq. (27), no evaporation will take place along the fitting. In this case, the flow is single-phase and the equations introduced in Sect. 4 apply for calculating the critical mass flux for both critical and subcritical conditions.

Various authors (see [12, 13]) have calculated the mass flux from the Bernoulli's equation. The discharge function is

$$\psi = \sqrt{1 - \eta} \tag{35}$$

using the pressure ratio η of the pressure in the smallest cross section p_1 and the pressure at the inlet p_0 defined by Eq. (26). The mass flux $\dot{m}$ is calculated analogously using the method

described by Eq. (11) and the mass flow is, therefore,

$$\dot{m} = \sqrt{\frac{2p_0}{v_0}}\sqrt{1-\eta}. \tag{36}$$

Equation (36) is not capable of calculating the mass flux for critical conditions. This is because evaporation due to expansion of the vapor phase, which limits the mass flux, is not considered in Eq. (36). In reality, also for a subcooled liquid a maximum mass flux is observed, if the pressure in the exit cross section is reduced to a certain value. If the pressure in the exit cross section p_2 is reduced below the vapor pressure p_s, evaporation of the liquid will occur. If the pressure p_2 is reduced further, the pressure upstream the smallest cross section p_1 equals the vapor pressure p_s and will not fall below it. The critical pressure ratio is, therefore,

$$\eta_c = \eta_S = \frac{p_s(T_0)}{p_0}. \tag{37}$$

The liquid evaporates due to its high heat capacity at thermodynamic equilibrium and thus, at a constant temperature for the set vapor pressure p_s.

6 Homogeneous Nonequilibrium Model

Under certain conditions the mass transfer between the liquid and gas phases is negligible. This is the case if the gas phase consists of a noncondensable gas and the vapor pressure p_{lg} of the liquid is comparatively low to the pressure levels along the stream path. These conditions apply for the co-current flow of water and air.

For the Homogeneous Nonequilibrium Model the following assumptions are made:

- No mass transfer takes place between the gas and liquid. In many cases, a remarkable amount of gas can be dissolved in the liquid and due to pressure reduction along the stream path, desorption can occur. Mostly, the time of residence inside the fitting is so short that the amount of desorbed gas can be neglected. The diffusive resistance of the gaseous component inside the liquid is comparatively high to the evaporation rate of a single component liquid and therefore, desorption does not play an important role.
- The liquid and gas have the same velocity, and the slip is one.
- The wall friction is zero.
- The change of conditions of the two-phase flow mixture between the inlet and exit of the fitting is adiabatic.

On the way through the fitting the temperature of the gas phase is reduced due to expansion and a temperature difference between the gas and liquid is the consequence. Depending on the volumetric ratio of the gas and liquid, heat exchange takes place between the two phases. This reduces the temperature difference partly. For small void fractions at the inlet cross section (e.g., bubbly flow) the heat exchange takes place due to the high amount of heat stored in the liquid. In this case the assumption of equal temperatures for gas and liquid along the stream path is justified. A different situation is a high void fraction at the inlet cross section (e.g., droplet flow). In this case the stored heat of the liquid is not sufficient to avoid cooling of the gas. It can be assumed that the gas and liquid end up in a thermal nonequilibrium.

The existing calculation methods differ the way they deal with heat transfer between the gas and liquid. Tangren et al. [14] assume an isentropic change of conditions and equal temperatures for the two-phase flow mixture along the stream path. Starkmann et al. [15] investigated the two-phase flow mixtures with very high void fractions. They postulate no heat transfer between the two phases. Some authors (e.g., Starkmann et al. [15]) neglect the contribution of acceleration of the liquid due to the pressure difference in the energy balance. This is also valid for the widely used "Homogeneous Frozen Flow Model" (for explanations see e.g., Mayinger [4]). Henry and Fauske [1] consider acceleration of the liquid, but their equations contain some implicit terms which make the calculation unhandy. In addition, their method is only capable of calculating the critical mass flux. Subcritical flow is not featured in their work. This is why the method of Leung and Epstein [13] is recommended. It takes into account all the contributions to the energy balance of the mixture. In addition, it features the full thermal nonequilibrium ("Frozen Flow") as well as the heat transfer between the phases. Further assumptions are made by Leung and Epstein [13]:

- The gas is described as an ideal gas.
- The change of conditions for the two-phase flow mixture is isentropic (Comment: This assumption is explicitly made by the authors, but already follows from assuming a frictionless and adiabatic flow.).

For calculating the two-phase mass flux, Leung and Epstein [13] introduce the following method:

$$\dot{m} = \frac{\sqrt{2\dot{x}p_0 v_{g,0}\frac{\Gamma}{\Gamma-1}\left[1-\left(\frac{p_1}{p_0}\right)^{(\Gamma-1)/\Gamma}\right]+2(1-\dot{x})v_l(p_0-p_1)}}{\dot{x}v_{g,0}\left(\frac{p_1}{p_0}\right)^{-1/\Gamma}+(1-\dot{x})v_l}. \tag{38}$$

As no mass transfer occurs along the stream path the gas mass flow fraction is constant. It is, therefore,

$$\dot{x} = \dot{x}_0 = \dot{x}_1. \tag{39}$$

In Eq. (38) Γ is the isentropic exponent of the two-phase flow, which was already introduced by Tangren et al. [14]. The two-phase isentropic exponent is then calculated from

$$\Gamma = \frac{\dot{x}c_{p,g}+(1-\dot{x})c_{p,l}}{\dot{x}c_{v,g}+(1-\dot{x})c_{v,l}} \text{ for } T_g = T_l. \tag{40}$$

If the isentropic exponent Γ according to Eq. (40) is introduced to Eq. (38), this means that the temperatures between the gas and liquid along the stream path are equal. In case of very high void fractions, $\dot{x} \to 1$ the isentropic exponent of the two-phase flow merges into the isentropic exponent of the gas phase κ.

If the isentropic exponent of the two-phase flow Γ is not calculated according to Eq. (40), but set to the isentropic exponent of the gas phase κ,

$$\Gamma = \kappa = \frac{c_{p,g}}{c_{v,g}} \quad \text{for } T_g \neq T_l. \tag{41}$$

This corresponds to the maximum thermal nonequilibrium between the gas and liquid (Homogeneous Frozen Flow). If in Eq. (38), the second term under the radical $(2(1-\dot{x})\nu_l(p_0-p_l))$ is neglected and the isentropic exponent of the gas phase κ is used instead of the isentropic exponent of the two-phase flow Γ, an equation known as the "Homogeneous Nonequilibrium Model" as described by e.g., Mayinger [4] or Starkman et al. [15] is obtained. They neglect the contribution of acceleration due to the pressure gradient to the kinetic energy.

The critical mass flux $\dot{m}_c$ can be calculated analogously using the Homogeneous Equilibrium Model with Eq. (15) according to Leung and Epstein [13].

To avoid iterative calculation of the mass flux in Eq. (15), Leung and Epstein [13] introduce the empirical equation

$$\eta_c = \left[\left(\frac{\Gamma+1}{2}\right)^{(3/4)(\Gamma/(\Gamma-1))} + \left(\frac{\Gamma}{2}\frac{1-\varepsilon_0}{\varepsilon_0}\right)^{(3/4)(\Gamma/(\Gamma+1))}\right]^{-3/4} \tag{42}$$

to obtain the critical pressure ratio η_c. This equation is used by Churchill and Usagi [16] for nonlinear interpolation of the critical pressure ratio between the limit cases of a single-phase gas or liquid flow. According to Leung and Epstein [13], the difference between the empirically found critical pressure ratio (Eq. (42)) and the exact solution (Eq. (15)) is maximal 5%.

7 Calculating the Discharge Function for a Two-Phase Flow

For many calculation methods it is assumed that the mass flux of a two-phase flow can approximately be obtained with the equations of the ideal nozzle. In an ideal nozzle, the flow is frictionless and no heat transfer occurs between the two phases and the surrounding. This leads to an isentropic change of conditions from the inlet to the exit of the duct.

Depending on the geometry and the operating conditions of the fitting, in reality the mass flux is different from the one calculated for the ideal nozzle. The measured mass fluxes of a real system are lower than the predicted ones. The reasons are as follows:

- Friction between the fluids and the wall of the duct
- Heat transfer between the fluids and the surrounding through the wall of the duct
- Bend loss in the fittings (especially in safety valves the flow is often redirected many times)
- Reduction of free cross sections due to contraction of the flow at or behind the geometrically smallest cross section

The error due to neglecting friction and heat transfer to the surrounding is corrected by the discharge coefficient C_d. In case of a single-phase flow of liquid or gas, the discharge coefficient covers also the effects of the contraction of the flow at the smallest cross section. For two-phase flow contraction is observed only for operating conditions near a single-phase gas or liquid flow.

The calculation for the two-phase flow mass flux is done in two steps. First, the mass flux $\dot{m}_{id}$ is calculated for a frictionless adiabatic flow. A suitable calculation method for the ideal mass flux can be found in Parts 4 and 6. Second the mass flux is multiplied with the discharge coefficient C_d and thus, the correction is made. The methods for calculating the discharge coefficient C_d are explained next.

The manufacturer of safety valves, orifices, and such fittings often provide the single-phase discharge coefficient for liquid or gas i.e., the so-called α_w. In praxis, the discharge coefficient

$$C_{d,i} = k\alpha_{w,i} \tag{43}$$

is then calculated considering a safety margin k (commonly $k = 1.1$). In Eq. (43), the index i is g (gas) or l (liquid). Especially for safety valves and orifices, it is advisable to use the calculation instructions of the manufacturer. For two-phase flow the discharge coefficient is strongly dependent on the flow patterns and thus, on the operating conditions. Because of the extended experimental effort most manufacturers do not provide two-phase flow discharge coefficients. In praxis, the so-called "mean discharge coefficient" is often used. It is empirically calculated from discharge coefficients provided for the single-phase flow of the gas $C_{d,g}$ or the liquid $C_{d,l}$.

7.1 Discharge Coefficient for a Vapor–Liquid Flow

The discharge coefficient for a fitting that is in use for a two-phase flow mainly depends on the vapor or gas fraction. In the direction of the flow the pressure inside the fitting decreases strongly and some liquid is likely to evaporate. The vapor fraction can, therefore, change a lot along the stream path. In addition, the vapor fraction inside the fitting depends on the degree of subcooling, the vapor fraction at the inlet, the number of nuclei, the geometry of the duct, and the morphology of the wall. This is why the development of a general calculation method for the discharge coefficient for vapor–liquid flow is very difficult. In praxis commonly, the mean discharge coefficient

$$C_d = \varepsilon_g C_{d,g} + (1-\varepsilon_g) C_{d,l} \tag{44}$$

is in use. ε_g is the mean volumetric gas or vapor fraction of the flow. Some authors (e.g., Schmidt and Westphal [17, 18]) conducted experiments that revealed that the discharge coefficients calculated with Eq. (44) are overpredicted. This leads to an overprediction of the effective cross section and thus, of the mass flux. According to Schmidt and Westphal [17, 18], the effect of Eq. (44) is compensated when calculating the ideal mass flux $\dot{m}_{id}$ with the Homogeneous Equilibrium Model. The Homogeneous Equilibrium Model is explained in Sect. 4. Comparison to experimental data reveals (see [1, 2, 19]) that the mass fluxes calculated according to the Homogeneous Equilibrium Model are often underpredicted. Therefore, it is recommended to use Eq. (44) only in combination with the

Homogeneous Equilibrium Model when calculating the mass flux with Eq. (4).

7.2 Discharge Coefficients for Gas–Liquid Flow

Extensive experimental investigations on critical mass flux of a two-phase gas–liquid flow in orifices and nozzles have been carried out by Morris [20] and Lenzing and Friedel [21]. For nozzles he found an empirical equation to calculate the discharge coefficient depending on the slip between the gas and liquid. According to Morris [20] and Lenzing and Friedel [21], in the case of no slip between the phases,

$$S = \frac{w_g}{w_l} = 1, \tag{45}$$

the discharge coefficient is

$$\alpha_{nozzle} = 1. \tag{46}$$

The momentum transfer between the gas and liquid in nozzles or orifices is very intense due to the high velocity and the redirection of the flow. The relative velocity between the gas and liquid may be negligible compared to the high absolute values of the velocities $\bar{w} = w_g = w_l$. Because of many uncertainties, concerning the calculation of the slip for strongly accelerated flow, it is recommended to neglect the slip (i.e., Eq. (45)) for the calculation of discharge coefficients for gas–liquid flows in nozzles, i.e., the discharge coefficient is assumed to be one (Eq. (46)).

In case of the flow through orifices the situation is different. Contrary to the nozzle the orifice's geometry is not optimized for low pressure loss. Especially at the exit eddies lead to high pressure loss and thus, to reduced mass fluxes compared to a nozzle. For orifices, Morris [20] and Lenzing and Friedel [21] proposes the empirical equation

$$C_d = (1.26 - 0.26\beta)C_{d,l} \tag{47}$$

for calculation of the discharge coefficient. β is the ratio of the diameter of the orifice and the duct's diameter in front of the orifice

$$\beta = \frac{D_1}{D_0} \tag{48}$$

$C_{d,l}$ is the mean discharge coefficient

$$C_{d,l} = \varepsilon_{g,1} C_{d,g} + \left(1 - \varepsilon_{g,1}\right) C_{d,l} \tag{49}$$

in the smallest cross section of the orifice. The definition is according to the vapor–liquid flow (see Eq. (44)). The volumetric void fraction in the smallest cross section $\varepsilon_{g,1}$ is due to expansion and due to the pressure gradient higher than at the inlet cross section. The change of condition of the gas phase can be assumed to be isentropic. This leads to the void fraction in the smallest cross section

$$\varepsilon_{g,1} = \frac{1}{1 + \frac{1-\dot{x}}{\dot{x}} \frac{v_l}{v_{g,0}} \left(\frac{p_1}{p_0}\right)^{1/\kappa}}. \tag{50}$$

The liquid phase can be considered to be incompressible, and thus the specific volume of the liquid is

$$v_{l,1} = v_{l,0} = v_l. \tag{51}$$

The gas mass flow fraction of a gas–liquid flow is analogous to that given in Sect. 6

$$\dot{x} = \dot{x}_1 = \dot{x}_2. \tag{52}$$

In Eq. (49) $C_{d,g}$ and $C_{d,l}$ are the discharge coefficients of the single-phase gas or liquid flow. Morris [20] and Lenzing and Friedel [21] proposes the empirical equation

$$C_{d,l} = 0.61375 + 0.13318\left(\frac{D_1}{D_0}\right)^2 - 0.26095\left(\frac{D_1}{D_0}\right)^4 + 0.51146\left(\frac{D_1}{D_0}\right)^6 \tag{53}$$

for the single-phase liquid flow. For a single-phase gas flow, Eq. (53) is extended to feature also the compressible properties of the fluid. It is

$$C_{d,g=} \frac{1 - (1-w)^{0.5}}{2f\left(\frac{p_1}{p_0}\right)^{1/\kappa}}. \tag{54}$$

For convenience the variables

$$f = \frac{1}{C_{d,l}} - \frac{1}{2C_{d,l}^2}, \tag{55}$$

$$w = 4\left(\frac{p_1}{p_0}\right)^{2/\kappa}\left(1 - \frac{p_1}{p_0}\right)\frac{f}{K_N^2} \tag{56}$$

and

$$K_N = \sqrt{2\frac{\kappa}{\kappa - 1}\left(\frac{p_1}{p_0}\right)^{2/\kappa}\left(1 - \left(\frac{p_1}{p_0}\right)^{(\kappa-1)/\kappa}\right)} \tag{57}$$

are introduced.

8 Exceptions

The previously explained calculation methods cover many technically relevant setups. In some cases, e.g., the flow of an evaporating mixture in the presence of a noncondensable gas, the assumptions made are not valid. In the following parts some exceptions are covered.

8.1 Partly Evaporating Liquid

The Homogeneous Equilibrium Model as explained in Sect. 4 leads to good results for a vapor–liquid flow. In certain cases, only partial evaporation of the liquid takes place along the stream path. This is true for very short ducts and very low vapor mass flow fractions of even zero in the inlet cross section. During the short time of residence inside the fitting only a part of the liquid can evaporate. The reason is the limited evaporation rate due to the heat conduction inside the liquid bulk

L2.4. Table 1. Limitations for applying the Homogeneous Equilibrium Model according to Henry and Fauske [1]

Length/ diameter	Partial evaporation (=limitation for applying the Homogeneous Equilibrium Model)
$\frac{L}{D} \leq 12$	$\dot{x} < 14\%$
$\frac{L}{D} > 12$	$\dot{x} < 5\%$

phase. This leads to a certain amount of the dynamic nonequilibrium and consequently, the liquid becomes overheated along the stream path.

In such a case, neither the Homogeneous Equilibrium Model (Sect. 4) assuming thermodynamic equilibrium nor the Homogeneous Nonequilibrium Model (Sect. 6) assuming total thermodynamic nonequilibrium is suitable.

In cases where the degree of mass transfer is in between the total thermodynamic equilibrium and nonequilibrium, Henry and Fauske [1] propose a calculation method. A brief summary of this method can be found in the work by Lenzing and Friedel [21].

The limit of applying the Homogeneous Equilibrium Model is, according to Henry and Fauske [1], dependent on the vapor mass flow fraction at the inlet cross section $\dot{x}_0$ and the ratio of length and diameter of the duct. The authors recommend the following limits for the Homogeneous Equilibrium Model (Table 1).

Outside these limits the calculation method proposed by Henry and Fauske [1] is preferred compared to the Homogeneous Equilibrium Model (Sect. 4). The disadvantage of the method according to Henry and Fauske [1] is that only critical mass flux can be calculated, and subcritical flow is not covered.

8.2 Combined Gas–Vapor–Liquid Flow

If a liquid, its vapor, and a noncondensable gas are flowing together, the mass flux and the critical pressure ratio are different from the case of a two-phase gas–liquid or vapor–liquid flow due to the partial pressure of the gas in the gas phase. Mostly, this leads to higher values of the critical pressure ratio η_c due to the higher volume of the gas compared to an evaporating flow. Reducing the counter pressure at the exit cross section leads to critical conditions at higher pressures. Leung extends the calculation method ([11] in [22]) to consider the effect of a noncondensable gas. The resulting system of equation is relatively complex and can only be solved iteratively. An explanation of this method can be found in German in the work by Schmidt and Westphal [18].

8.3 Non-negligible Slip Between Gas and Liquid

In some cases, the velocity difference between gas and liquid is not to be neglected. Slip is mostly observed in longer ducts, if both phases – like for annular flow – flow separately. The appearing slip depends mainly on the flow pattern, the geometry of the duct, and the physical properties. Calculating the slip is, therefore, only possible with large uncertainties. For calculating the critical mass flux considering slip, Moody [23] proposes an extension to the Homogeneous Equilibrium Model (Sect. 4). The method of Morris [20] is suitable for nonevaporating gas–liquid systems.

9 Examples

9.1 Example 1: Discharge of an Evaporating Vapor–Liquid Mixture

The reactor is filled with Cyclohexane at saturated conditions and at a known temperature. In an emergency situation, the whole content of the reactor is to be discharged within a certain time period. For this purpose, a safety valve is mounted to the bottom of the reactor. The task is to calculate the diameter of the smallest cross section. It is assumed that the change of conditions takes place at thermodynamic equilibrium. The calculations are carried out using the Homogeneous Equilibrium Model. To minimize the effort the simplified method according to Leung [9] (see Sect. 4.1) is applied.

Given is

Volume of reactor	$V = 10\ \mathrm{m}^3$
Initial filling level	$\phi_0 = 85\%$
Temperature	$T_0 = 150°\mathrm{C}$
Counterpressure in discharge tank	$p_t = 0.12\ \mathrm{MPa}$
Required time period for discharge	$t_{ovr} = 5\ \mathrm{min}$
Discharge coefficient for liquid flow	$C_{d,l} = 0.6$
Discharge coefficient for gaseous flow	$C_{d,g} = 0.6$

In addition, the physical properties of Cyclohexane in the gaseous and liquid phases are known.
In the first step, the mass flow is calculated from the available

Vapor pressure at T_0	$p_0 = 0.55\ \mathrm{MPa}$
Density of the liquid at T_0	$\rho_{1,0} = 643.7\ \mathrm{kg/m}^3$
Density of the vapor at T_0, p_0	$\upsilon_{g,0} = 13.1\ \mathrm{kg/m}^3$
Evaporation enthalpy at T_0	$h_{v1,0} = 302.4\ \mathrm{kJ/kg}$

time period and the mass of Cyclohexane contained in the reactor. The mass of liquid Cyclohexane is

$$M_l = \phi V \rho_{l,0} = 5471.2\ \mathrm{kg},$$

and the mass contained as vaporous Cyclohexane is

$$M_g = (1 - \phi) V \rho_{g,0} = 19.7\ \mathrm{kg}.$$

Consequently, the mass flow during discharge is

$$\dot{M}_{ges} = \frac{M_{ovr}}{t_{ovr}} = \frac{M_g + M_l}{t_{ovr}} = 18.3\ \mathrm{kg/s}.$$

In the next step, the mass flux through the safety valve is calculated. It is yet not clear if the flow becomes critical or remains subcritical. Therefore, the critical pressure ratio η_c is calculated first.

The safety valve is mounted to the bottom of the reactor. This is why a single-phase liquid flow enters the valve and this leads to the vapor mass flow fraction

$$\dot{x}_0 = 0.$$

With these values the mean specific volume at the inlet cross section of the valve is calculated according to Eq. (21)

$$v_0 = 1.5536 \times 10^{-3}\ \mathrm{m^3/kg}.$$

From Eq. (22) the compressibility factor is obtained

$$\omega = 16.39.$$

The relatively high value for the compressibility factor is because of the low evaporation enthalpy $h_{v1,0}$ of Cyclohexane. This is evidence for a strong evaporation of Cyclohexane between the inlet and the exit of the valve.

The critical pressure ratio is calculated from Eq. (29)

$$\eta_c = 0.88$$

and with Eq. (30) the critical pressure

$$p_c = 0.484\ \mathrm{MPa}$$

is obtained. The given counterpressure $p_2 = p_t = 0.12$ MPa is below the critical pressure and thus, critical conditions are present in the smallest cross section. Therefore,

$$p_1 = p_c = 0.484\ \mathrm{MPa}$$

is set. From Eq. (24), the discharge function

$$\psi = 0.154$$

is calculated. So the mass flux

$$\dot{m} = \dot{m}_c = 4094.4\ \mathrm{kg/m^2 s}$$

can finally be calculated with Eq. (18). This calculation is carried out up to now for an ideal nozzle. Before the diameter of the valve can be calculated the discharge coefficient C_d has to be calculated first. As only liquid Cyclohexane enters the valve, from Eq. (44), it is found that the discharge coefficient for the single-phase liquid flow

$$C_d = 0.6$$

can be used. The diameter of the valve can now be calculated

$$D_1 = \sqrt{\frac{\dot{M}_{ges}}{C_d \dot{m} \frac{\pi}{4}}} = 97.4\ \mathrm{mm}.$$

When choosing the diameter of the safety valve one should pick the next bigger available size from the manufacturer. In praxis sometimes an additional safety margin has to be taken into account. It is in any case advisory to follow the calculation methods or recommendation of the manufacturer.

9.2 Example 2: Water–Air Flow through an Atomizer

(a) Water is to be atomized in very fine droplets by means of a twin-fluid atomizer. The atomization gas is air. Water and air are internally mixed inside the atomizer. It should be checked whether the chosen inlet pressure is sufficient to establish critical flow and thus create the pressure jump at the exit cross section. In the next step the diameter of the nozzle should be determined.

Given is

Pressure in the inlet of the nozzle	$p_0 = 0.5$ MPa
Pressure in the surrounding of the nozzle	$p_2 = 0.1$ MPa
Temperature at the inlet of the nozzle	$T_0 = 25°C$
Liquid mass flow	$\dot{M}_l = 1,000$ kg/h
Gas mass flow	$\dot{M}_g = 10$ kg/h

In addition, the physical properties of water and air are given:

Isentropic exponent	$k = 1.4$
Density of the liquid in the inlet of the nozzle	$\rho_1 = 997.05\ \mathrm{kg/m^3}$
Density of the gas in the inlet of the nozzle	$\rho_g = 5.858\ \mathrm{kg/m^3}$

For this nonevaporating system of water/air the calculation method for critical and subcritical mass fluxes proposed by Leung and Epstein [13] (Sect. 6) is suitable.

From the mass flow of water and air, the gas mass flow fraction $\dot{x}_0 = 0.9901$ % can be directly calculated (see Sect. 10).

To apply the method of Leung and Epstein [13] the slip must equal one. This assumption is justifiable due to the intense momentum transfer inside the mixing chamber of the atomizer. From the gas mass flow fraction and the densities of the two fluids, the volumetric gas fraction

$$\varepsilon_0 = 0.6299$$

at the inlet cross section is obtained. For the conversion between gas mass flow fraction and volumetric gas fraction, see Sect. 10. From the volumetric gas fraction ε_0 and the isentropic exponent κ of air according to Churchill and Usagi [16] and Eq. (42) follows the critical pressure ratio

$$\eta_c = 0.457.$$

From the definition of the critical pressure ration η_c in Eq.(3) the critical pressure

$$p_c = 0.2284\ \mathrm{MPa}.$$

is obtained. As $p_2 < p_c$ it can be concluded that – as for a reasonable operation of an atomizer necessary – the flow is critical. The pressure jump at the exit cross section is then

$$\Delta p = p_c = p_2 = 0.2284\ \mathrm{MPa} - 0.1\ \mathrm{MPa} = 0.1284\ \mathrm{MPa}.$$

To determine the diameter of the nozzle the mass flux needs to be calculated depending on pressure p_0, temperature T_0, and gas mass flow fraction $\dot{x}_0$ at the inlet cross section. According to Leung and Epstein [13], from Eq. (38) the mass flux

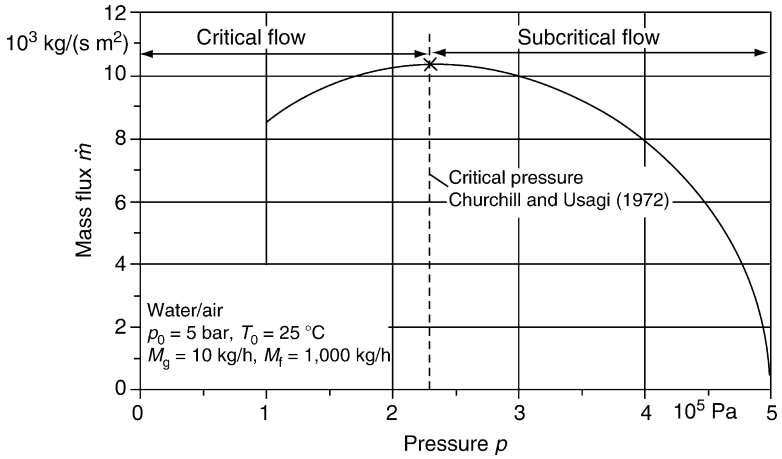

L2.4. Fig. 5. Mass flux according to Leung and Epstein [13], calculated from Eq. (38) as a function of the counterpressure p_1.

$$\dot{m} = 10.515 \times 10^3 \text{ kg/m}^2\text{s}$$

can be calculated. The diameter is obtained from the constraint

$$\dot{M} = C_d \dot{m} \frac{\pi}{4} D_1^4 \quad \text{with } \dot{M} = \dot{M}_g + \dot{M}_l.$$

The conditions inside the atomizer are more or less similar to the ones inside an ideal nozzle. According to Morris [6], in this case the discharge coefficient for the two-phase flow is

$$C_d \cong 1.$$

The diameter can now be calculated as follows:

$$D_1 \sqrt{\frac{\dot{M}}{\frac{\pi}{4}\dot{m}}} = 5.8 \text{ mm}.$$

(b) The critical pressure ratio according to Churchill and Usagi [16] as used in task (a) is only an approximation. It is now to be investigated how much the exact solution described by Leung and Epstein [13] differs from the approximation.

The mass flux is calculated depending on the counterpressure p_1 according to Eq. (38) with the given values for p_0, T_0 and the in (a) obtained value for $\dot{x}_0$. The calculated values for the mass flux are shown in Fig. 5 as a function of the counterpressure p_1. From the constraint that under critical conditions the derivative of the mass flux with respect to the counterpressure becomes zero (Eq. (15)), the critical pressure is

$$p_{c,\text{Leung u. Epstein}} = 0.23 \text{ MPa}.$$

For higher values of the counterpressure the flow becomes subcritical. The areas of critical and subcritical flows are marked in Fig. 5. For comparison, the approximation of the critical pressure p_c by Churchill and Usagi is also noted in Fig. 5 as a vertical dashed line. The graph by Leung and Epstein [13] is in good agreement with Churchill and Usagi's results. This is valid for the area where the derivative with respect to the pressure becomes zero. The difference between the exact and approximately found results is small

$$f_p = \frac{0.2284 \text{ MPa} - 0.23 \text{ MPa}}{0.23 \text{ MPa}} = 0.7\%$$

9.3 Calculation of the Discharge Coefficient of an Orifice for Two-Phase Flow

A pressurized tank should be discharged through a short pipe containing an orifice into the surrounding. The pipe is connected to the tank's head. Inside the tank water is provided with dissolved CO_2 in thermodynamic equilibrium. If the liquid is discharged, the dissolved CO_2 will leave the water and form bubbles, so that a bubbly flow enters the pipe through the orifice. The tank is relatively large compared to the discharging mass flow so that the discharge process can be considered to be stationary. The discharge coefficient should be calculated for the case of two-phase flow.

Given is

Pressure inside the tank	$p_0 = 0.5$ MPa
Pressure of the surrounding	$p_2 = 0.1$ MPa
Diameter of the pipe	$D_0 = 50$ mm
Diameter of the orifice	$D_0 = 5$ mm
Volumetric gas fraction in the pipe's inlet	$\varepsilon_0 = \varepsilon_{g,1} = 0.4$
Isentropic exponent of CO_2	$\kappa = 1.3$

In the first step the critical pressure ratio is calculated according to Leung and Epstein [13] with Eq. (42)

$$\eta_c = 0.4157.$$

From the definition of the critical pressure ratio in Eq. (3) the critical pressure

$$p_c = 0.2079 \text{ MPa}$$

is obtained. As $p_2 < p_c$, the pressure at the exit cross section is $p_1 = p_c$. This means that critical conditions for the flow exist.

For this case the discharge coefficient for the single-phase liquid flow is calculated according to Morris [20] and Henzing and Friedel [21] with Eq. (53)

$$C_{d,f} = 0.6151.$$

The value D_0 is only of importance for $(D_1/D_0) < 15$, because if $(D_1/D_0) < 15$ it has only minor influence on the discharge coefficient. The discharge coefficient for the single-phase gas flow is calculated according to Morris [20] and Henzing and Friedel

[21] with Eq. (54). To do so, the values for K_N, w, and f have to be calculated first using Eqs. (55–57). These values are

$$K_N = 0.6418$$
$$w = 0.4773, \text{and}$$
$$f = 0.3041.$$

Taking into account K_N, w, and f, the discharge coefficient for the single-phase gas flow becomes according to Eq. (54)

$$C_{d,g} = 0.8285.$$

It is always $C_{d,g} > C_{d,f}$. If the discharge coefficients for the single-phase gas and liquid flows are weighted with the volumetric gas fraction, the mean discharge coefficient for the two-phase flow is obtained according to Eq. (49)

$$C_{d,l} = 0.7004.$$

For orifices, in general, Morris [21] proposes in Eq. (47) a discharge coefficient of

$$C_{d,l} = 0.8643.$$

10 Symbols

A	area (m^2)
c_p	specific isochore heat capacity (J/kg K)
C_d	discharge coefficient for a two-phase flow (–)
D	diameter (m)
f	frictional coefficient for a two-phase flow (–)
h	specific enthalpy (J/kg)
$h_{f,g}$	evaporating enthalpy (J/kg K)
k	safety margin (–)
L	length (m)
M	mass (kg)
$\dot{M}$	mass flow (kg/s)
$\dot{m}$	mass flux (kg/s m^2)
p	pressure (Pa)
p_s	vapor pressure (Pa)
s	specific entropy (J/kg K)
$S \equiv \frac{w_g}{w_l}$	slip (–)
T	temperature (°C, K)
t	time (s)
v	specific volume (m^3/kg)
V	volume (m^3)
w	velocity (m/s)
$\dot{x} = \frac{\dot{M}_g}{\dot{M}_g + \dot{M}_l}$	vapor or gas mass flow fraction (–)
x,y,z	coordinates (m)
α_w	discharge coefficient provided by the manufacturer (–)
$\varepsilon \equiv \frac{V_g}{V_g + V_l}$	volumetric gas fraction (–)
$\eta \equiv \frac{p_1}{p_0}$	pressure ratio (–)
$\eta_c \equiv \frac{p_c}{p_0}$	critical pressure ratio (–)
Γ	isentropic exponent of the two-phase flow mixture (–)
κ	isentropic exponent of a singe-phase gas (–)
ω	compressibility factor (–)
ψ	discharge function (–)
ρ	density (kg/m^3)

Indices

0	quiescent condition, inlet cross section
1	smallest cross section
2	exit cross section
c	Critical
d	Discharge
g	gaseous, gas
l	Liquid
ovr	Overall
s	evaporating condition
t	Tank

Conversion of gas or vapor mass flow fraction to volumetric gas fraction:

$$\varepsilon = \frac{1}{1 + S\frac{\rho_g}{\rho_f}\frac{1-\dot{x}}{\dot{x}}}.$$

11 Bibliography

1. Henry RE, Fauske HK (1971) The two-phase critical flow of one-component mixtures in nozzles, orifices, and short tubes. J Heat Transfer 93(5):179–187
2. Hardekopf F, Mewes D (1988) Das kritische Druckverhältnis von Zweiphasenströmungen. VCH Verlagsgesellschaft Band 111: 177–197
3. Friedrich H, Vetter G (1962) Einfluß der Düsenform auf das Durchflußverhalten von Düsen für Wasser bei verschiedenen thermodynamischen Zuständen. Energie 14(1):3–9
4. Mayinger F (1982) Strömung und Wärmeübergang in Gas-Flüssigkeits-Gemischen. Springer-Verlag, Berlin
5. Kolev NI (1986) Transiente Zweiphasen-Strömung. Springer-Verlag, Berlin
6. Morris SD (1990) Discharge coefficients for choked gas-liquid flow through nozzles and orifices and applications to safety devices. J Loss Prev Process Ind 3:303–310
7. Sallet D (1983) Thermohydraulics of valves for nuclear application. 2nd Int. Tropical Meeting on Nuclear Thermohydraulics. St. Barbara, Cal. (USA) published by M. Merilo
8. Leung JC (1986) A generalized correlation for one-component homogeneous equilibrium flashing choked flow. AIChE J 32(10):1743–1746
9. Leung JC (1988) A generalized correlation for flashing chokes flow of initially subcooled liquid. AIChE J 34(4):688–691
10. Leung JC (1990) Similarity between flashing and nonflashing two-phase flows. AIChE J 36(5):797–800
11. Leung JC (1996) Easily size relief devices and piping for two-phase flow. Chem Eng Prog 28(12):28–50
12. AD-Merkblatt A2 (1993) Sicherheitseinrichtungen gegen Drucküberschreiten – Sicherheitsventile. Beuth-Verlag, Berlin
13. Leung JC, Epstein M (1990) A generalized correlation for two-phase nonflashing homogeneous choked flow. J Heat Transfer 112:528–530
14. Tangren RF, Dodge CH, Seifert HS (1949) Compressibility effects in two-phase flow. J Appl Phys 20(7):637–645
15. Starkman ES, Schrock VE, Neusen KF, Maneely DJ (1964) Expansion of a very low quality two-phase fluid through a convergent-divergent nozzle. J Basic Eng 86:247–256
16. Churchill SW, Usagi R (1972) A general expression for the correlation of rates of transfer and other phenomena. AIChE J 18(6):1121–1128
17. Schmidt J, Westphal F (1997) Praxisbezogenes Vorgehen bei der Auslegung von Sicherheitsventilen und deren Abblasleistungen für Durchströmung mit Dampf-Flüssigkeitsgemischen Teil 1. Chem Ing Tech 69(6):776–792
18. Schmidt J, Westphal F (1997) Praxisbezogenes Vorgehen bei der Auslegung von Sicherheitsventilen und deren Abblasleistungen für Durchströmung mit Dampf-Flüssigkeitsgemischen Teil 2. Chem Ing Tech 69(8):1074–1091

19. Friedel L (1986) Strömungswiderstand in Vollhubsicherheitsventilen bei Gas-Dampf-Flüssigkeitsströmungen. Techn Mitt 79:12
20. Morris SD (1991) Compressible gas-liquid flow through pipeline restrictions. Chem Eng Process 30:39–44
21. Lenzing T, Friedel D (1997) Über den Polytropenexponenten im Massenstromdichtemodell von Henry und Fauske. T. ü 38:3, 37–40
22. Leung JC (1991) Vent sizing for gassy and hybrid systems. Safety of chemical reactors and storage tanks 299–310, published by Benuzzi, A and Zapdivar, FM
23. Moody FJ (1965) Maximum flow rate of a single component, two-phase mixture. J Heat Transfer 87(1):134–142

L2.5 Flooding and Pressure Drop of Counter Current Gas-Liquid Flow in Vertical Pipes

Dieter Mewes
Leibniz Universität Hannover, Hannover, Germany

1 Introduction

The counter current flow of gases/vapors and liquids occur in so-called film columns, such as condensers with vertical tube bundles and film flow of the condensed liquid phases. Very often, the liquid phases are distributed by specially designed devices in the entrance section of the vertically positioned tubes in order to keep the films flowing downward along the inner surface of the tubes. Depending on the mass and heat flux governing of the concentration and temperature gradients, the contacting gaseous phase is either directed upward for counter current flow or downward for concurrent flow. The concurrent flow is described in Subsect. L2.2. Examples from technical applications are the condensation of vapors inside the vertically positioned tubes or tube bundles as well as the selective absorption of components from gaseous mixtures into liquid film flow. In both cases, the phase flows are counter currently directed to obtain maximum concentration or temperature gradients along the surface of the films.

In designing this type of equipment, besides the knowledge about heat and mass transfer, which is given in Chaps. J1 and M3, the engineer has to predict the pressure losses as well as the limits for counter current flow operation. Known methods are based on empirical equations, which are valid only for a limited field of experimentally varied parameters such as construction, material, and flow field.

Brauer [1] was the first who derived a model for counter currently directed gas and liquid flow in vertical tubes assuming laminar film flow and neglecting wavy surfaces. The theoretically derived results are confirmed experimentally by Feind [2]. Pressure drops and flooding points are given by equations using the following physics-based parameters:
The phase superficial velocities are given by

$$j_i \equiv \frac{4\dot{V}_i}{\pi D^2} \qquad (1)$$

$\dot{V}_i$ indicates the volume flows with i = g, f as subscripts for the gaseous or liquid phase respectively.

There are many published results on pressure drop and flooding point predictions available. Review articles are published by Bankoff and Lee [3], Hewitt and Wallis [4], McQuillan, Whalley and Hewitt [5, 6], Govan, Hewitt, and Richter and Scott [7] as well as the Ph.D. thesis by von Zhang [8] and Stephan [9].

j_g	-	Gas superficial velocity	m/s
j_f	-	Liquid superficial velocity	m/s
D	-	Inner tube diameter	m
g	-	Gravitational acceleration	m s^{-2}
η_f	-	Liquid viscosity	N m^{-2} s
η_g	-	Gas viscosity	N m^{-2} s
ρ_f	-	Liquid density	kg m^{-3}
ρ_g	-	Gas density	kg m^{-3}
Δp	-	Pressure drop of gaseous phase	N m^{-2}
σ	-	Surface tension	N m^{-1}

2 Counter Current Two-Phase Flow Phenomena

The possible flow patterns which can occur in adiabatic counter current gas–liquid flow in a single pipe are given in Fig. 1 schematically. At low liquid injection velocities and low superficial gas velocities, the liquid flow is directed downward as annular film with a relatively smooth surface (*a*). The disturbance waves at the film surface grow at higher gas velocities and medium liquid velocities until a critical wave amplitude is reached, beyond which liquid droplets are torn off from the wave crests. They are entrained into the gas stream (*b*), increasing the gas velocity further; part of the smooth falling film can reverse its flow direction from downward to upward, which results in a split film flow at the film entrance (*c*). At very high gas velocities, no more liquid can penetrate the tube and a liquid film hangs at a wall below the liquid entrance. This is the limiting case of counter current flow operation by increasing the gas velocity at a given liquid velocity (*d*). At sufficiently high gas velocities, the injected liquid flows upward concurrently with the gas flow above the liquid entrance, whereas a single-phase gas upward flow exists below the liquid entrance (*e*).

In Fig. 2 the vertically upward carried fraction of the injected liquid volume flow is given as a function of the gas

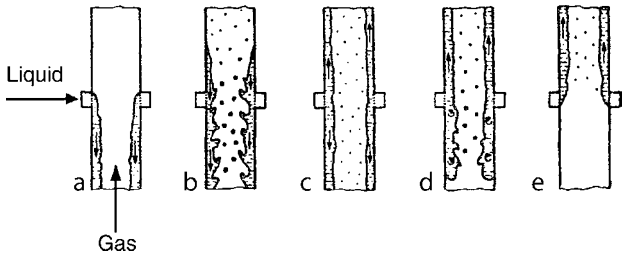

L2.5. Fig. 1. Flow patterns of gas–liquid flow in a vertical pipe at the transition between counter current and concurrent flow (**a**) counter current film flow; (**b**) onset of flooding indicated by counter current wavy film flow with dispersed droplets; (**c**) flooding indicated by counter current flow with a considerable fraction of liquid volume flow in upward direction; (**d** and **e**) flow reversal indicated by concurrent upward flow.

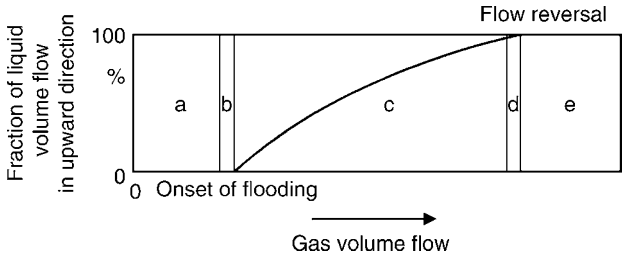

L2.5. Fig. 2. Fraction of upward directed liquid volume flow as function of gas volume flow.

volume flow. The liquid velocity is diminished to zero at the counter current flow limitation, marked by *d* in Fig. 2. In stationary operation flow patterns like *c* (Fig. 2), with liquid partly carried upward, are to be observed. The remaining downward carried liquid volume flow is a function of the gas volume flow, which is named as flooding curve and plotted in Fig. 3. The flooding curve divides the marked areas Ia and Ib for which counter current flow operations are either possible or not.

3 Flooding Point

The existing results from experiments on flooding are very sensitive to the construction of the entrance and outlet sections of the investigated tubes. Many results are summarized by Jeong and No [10] for different designed tubes. The mechanisms which cause flooding depend on the cross section designs, which are given in Fig. 4. The flooding mechanisms are extensively discussed by Stephan [9] and Zang [8].

They divide between

- Surface wave induced flooding: Large waves grow in amplitude that the waves meet each other in the tube cross section to form liquid bridges which disintegrate into liquid droplets or are carried upward by the gas flow.
- The increase of wave amplitude in the surrounding of the outlet, which starts as pressure induced up flow of the stationary hanging liquid torus dripping from the borderline of the tube outlet section.
- The dispersion of single droplets from the wavy film surface.

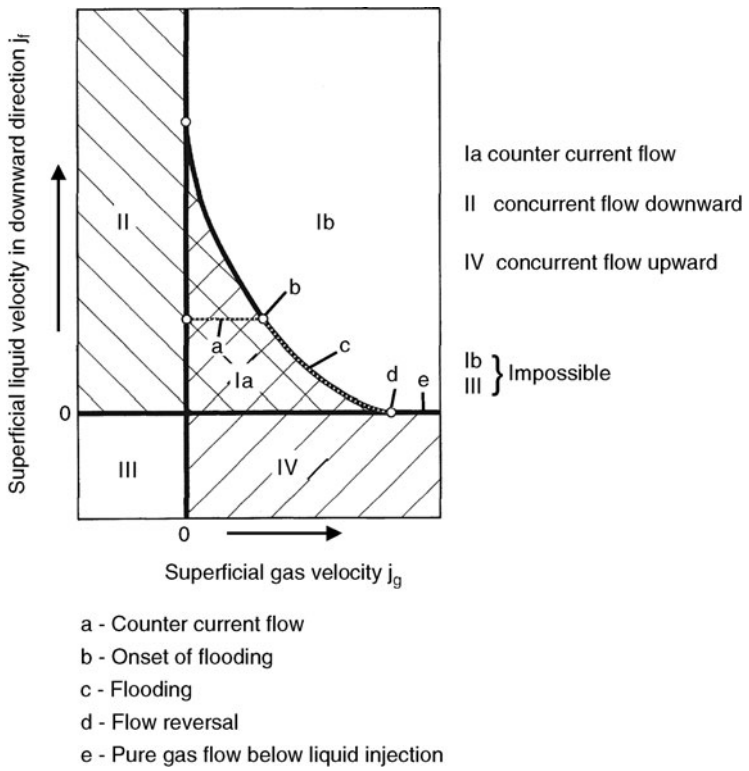

L2.5. Fig. 3. Flow pattern map and flooding function given by the liquid superficial velocity in downward direction in dependence of the superficial velocity of the gas/vapor flow.

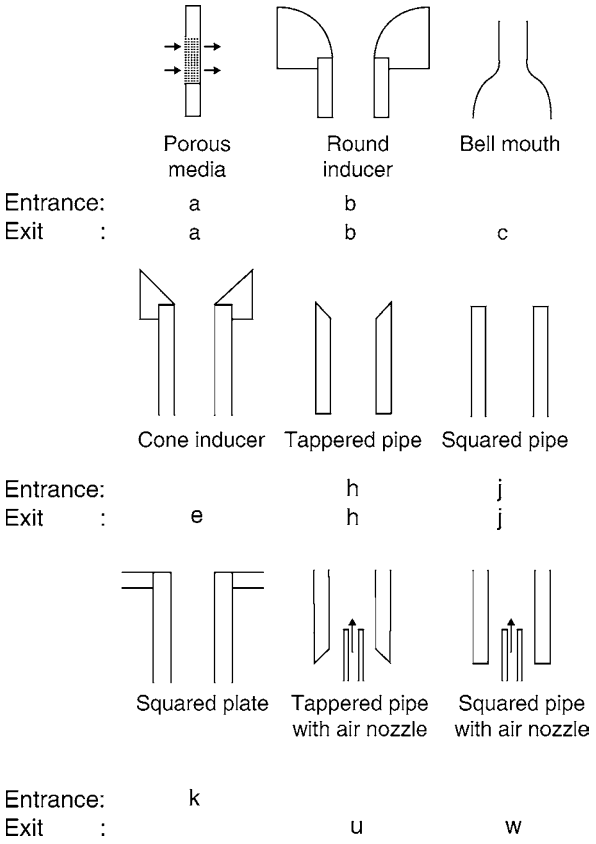

L2.5. Fig. 4. Description of the geometry identifiers for the inlet and outlet sections of experimentally tested pipes [10].

Experimental results give evidence that flooding is merely a result of instabilities caused by the design of the outlet section of the pipe. Flooding starts from there at much lower gas velocities than predictable from instabilities inside the tube. This explains the large deviations between the experimentally derived flooding curves according to Fig. 3. The construction of the tube entrance and outlet sections, the tube length and diameter, and the viscosity and surface tension of the investigated liquids are parameters.

Jeong and No [10] report from a survey of 2,500 data sets valid for liquids with similar viscosities like water the following empirically derived equation

$$j_g^{*1/2} = a\, j_f^{*} + b j_f^{*1/2} + c \qquad (2)$$

The superficial phase velocities are

$$j_i^{*} = j_i \left(\frac{\rho_i}{\left(\rho_f - \rho_g\right) D_g} \right)^{1/2} \qquad (3)$$

Subscripts i = g, f indicate the gaseous and the liquid phase.

Jeong and No [10] extracted 536 data points with the following experimental conditions: low upper head injection mode, air–water system, and vertical circular pipe test sections which are 0.7–1.5 m in pipe length and 2–5 cm in diameter. The best fit coefficients for the experimental results derived from selected data sets are

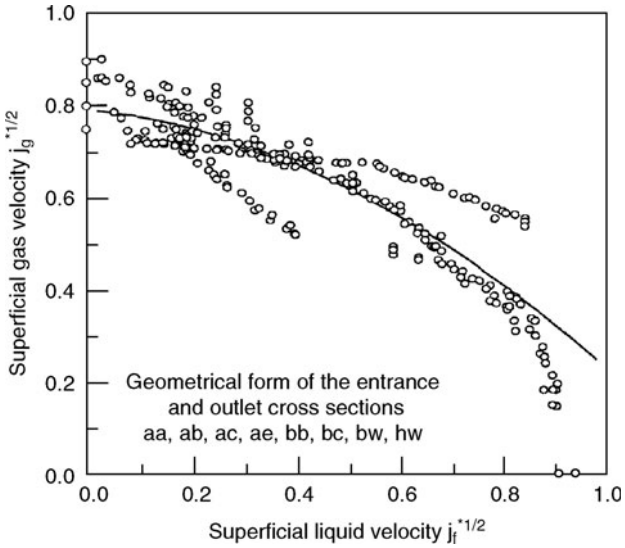

L2.5. Fig. 5. Comparison of flooding correlation Eq. (2) derived from data points having smooth exit geometry with experimental data [10].

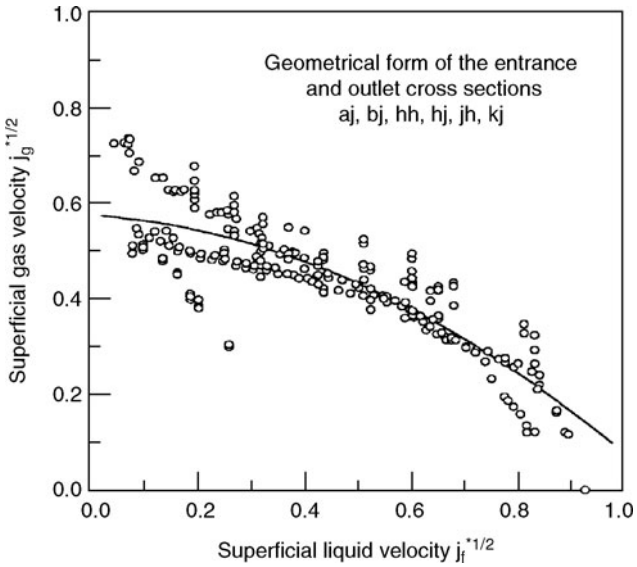

L2.5. Fig. 6. Comparison of flooding correlation Eq. (2) derived from data points having sharp exit geometry with experimental data [10].

$a = -0.439$, $b = -0.129$, $c = 0.791$

for smooth exit geometries: *aa ab ac ae bb bc bw hw* given in Fig. 5 and

$a = -0.418$, $b = -0.078$, $c = +0.576$

for sharp exit geometries: *aj bj hh hj jh jj kj* given in Fig. 6.

A comparison of results taken from Eq. (2) and measured flooding points is given in Figs. 5 and 6.

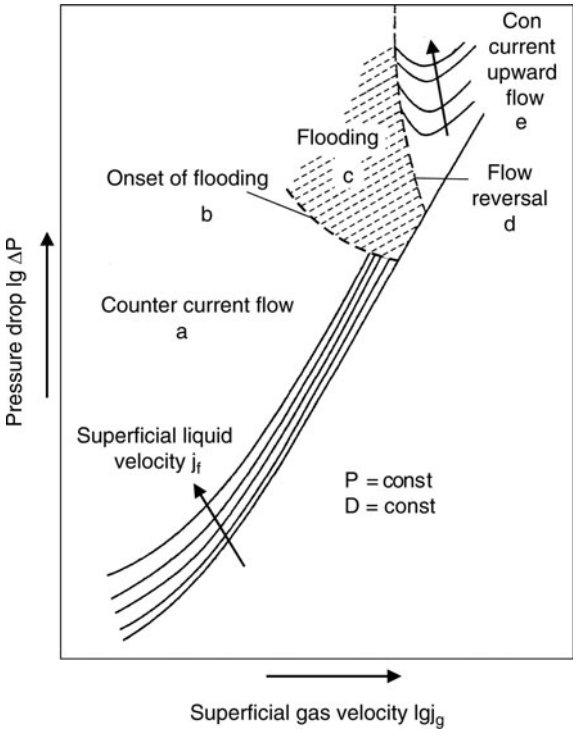

L2.5. Fig. 7. Flow transition and pressure drop in gas–liquid flow in vertical pipes.

4 Pressure Drop

The onset of flooding is connected with a strong increase of pressure loss in the gaseous phase flow. In Fig. 7 the measured pressure losses are plotted schematically as a function of the superficial gas velocities. The pressure losses increase already significantly below the flooding point.

The pressure losses are given by three fractions

- The hydrostatic pressure difference
- The friction pressure loss
- The acceleration pressure loss

The last term is omitted for nearly constant film thickness. The other two terms are of equal order as long as the film thickness is constant. If the superficial gas velocity exceeds the flooding point the friction losses become dominant. Slug flow occurs and results in large friction losses. A further increase of gas flow rate exceeding the counter current flow limitation *d*, leads to concurrent upward flow conditions with annular flow *e*, which causes a reduced pressure loss.

Methods for calculation of pressure losses are derived by Zhang [8] and Stephan [9]. They are based on the numerical solution of the momentum transport equations for both phase flows and rely on closure equations empirically derived from experiments. A similar approach is described by Guedes de Carvalho and Talaia [11] by assuming laminar flow in the liquid and turbulent flow in the gaseous phase.

In conclusion there are no methods available for the calculation of pressure losses below the flooding point that lead to more accurate results than those predicted by Feind [2]. This is due to the predominant effect of the exit geometry on flooding and the momentum transfer of dispersed liquid droplets from entrainment effects at the wavy film surface.

5 Example

The water volume flow of 0.14 m^3/h is fed as liquid film into a vertical pipe with 40 mm diameter. Which volume flow of gas marks the onset of flooding?

Densities: $\rho_F = 997\ kg/m^3$ and $\rho_g = 1.17\ kg/m^3$

Superficial liquid velocity	$j_f = \frac{4\dot{V}_l}{\pi D^2} = 0.03\ m/s$
Superficial gas velocity	$j_f^* = j_f \left(\frac{\rho_F}{(\rho_f - \rho_g) D_g}\right)^{1/2} = 0.048$
Superficial gas velocity at the onset of flooding	$j_g^{*1/2} = -0.418 j_f^* - 0.078 j_f^{*1/2} + 0.578 = 0.54$ $j_g^* = 0.29\ m/s$
Superficial gas velocity	$j_g = j_g^* \left(\frac{\rho_g}{(\rho_f - \rho_g) D_g}\right)^{-1/2} = 5.4\ m/s$
Gas volume flow	$\dot{V}_g = j_g \frac{\pi D^2}{4} = 24 m^3/h$

The experimental results give values about 18 m^s/h. The difference is due to the special inlet and outlet conditions of the pipe considered in the experiments.

6 Bibliography

1. Brauer H (1971) Grundlagen der Einphasen- und Mehrphasen-Strömungen. Vlg. Sauerländer, Aarau
2. Feind K (1960) Strömungsuntersuchungen bei Gegenstrom von Rieselfilmen und Gas in lotrechten Rohren; VDI-Forschungsheft 481. VDI-Vlg., Düsseldorf
3. Bankoff SG, Lee SC (1982) A critical review of the flooding literature; US Nuclear Regulatory Commission, Report No. NUREG/CR-3060
4. Hewitt GF, Whalley PB (1986) Vertical annular two phase flow. In: G (ed) Hetsroni Multiphase science and technology, vol 2. Hemisphere, Washington, DC
5. McQuillan KW, Whalley PB, Hewitt GF (1985) Flooding in vertical two-phase flow. Int J Multiphase Flow II (6):741–760
6. McQuillan KW, Whalley PB (1985) A comparison between flooding data for gas-liquid in vertical circular tubes. Chem. Engng Sci 40(8):1425–1440
7. Govan AH, Hewitt GF, Richter HJ, Scott A (1991) Flooding and churn flow in vertical pipes. Int J Multiphase Flow 17(1):27–44
8. Zhang J (1990) Flooding and associated phenomena in vertical adiabatic gas-liquid countercurrent flows, Ph.D. thesis, Department of Mechan. Thermodynamique, University of Catholique de Louvain

9. Stephan M (1990) Untersuchungen zur Gegenstrombegrenzung in vertikalen Gas-Flüssigkeitsströmungen, Diss. TU München, Thermodynamik
10. Jeong JH, H.C.NO (1995) Classification of flooding data according to the type of entrance and exit geomtries; Proc 2nd Int Conf Multiphase Flow, Kyoto, Japan
11. Guedes de Carvalho JRF, Talaia MAR (1998) Interfacial shear stress as a criterion for flooding in countercurrent film flow along vertical surfaces. Chem Engng Sci 53(11):2041–2051

L2.6 Pressure Drop and Flooding in Packed Towers

Alfons Mersmann
Technische Universität München, Munich, Germany

1 Application of Columns with Packings

Columns with packings are used as heat exchanger and mass transfer apparatus. Arranged-type packings (fabric, stacked packing elements) and dumped-type packing elements are the two types of packings used. In the case of separation processes like distillation and absorption, the gas or the vapor, and the liquid are moving in countercurrent flow. With respect to the design of such columns, it is necessary to calculate the pressure drop of the gas either in the absence or in the presence of a downward liquid flow and the maximum throughput. This chapter is restricted to the pressure drop and the flooding point of arranged-type packings and also of dumped-type packings in which the gas or the vapor is flowing upward in countercurrent to the liquid. The most known packing elements are Rasching rings and Pall rings, and also Berl, Intalox, Novolox, and Torus saddles. Their sizes are between 5 and 200 mm. The elements are made of stoneware, porcelain, glass, stainless steel, and plastic. Often, packing elements with a grill or lattice structures are used.

2 Scheme of a Column; Pressure Drop of Packed Columns

The packing is supported by a plate with holes. The percentage of the total hole area of this plate should approximately be the same as the voidage of the packing. With respect to the liquid flow to the wall, packings are subdivided into sections with heights between 1 and 3 m in order to redistribute the liquid. In the case of high-efficiency distributors and packing elements with a poor tendency of liquid flow to the wall the ratio 8 of the height to the diameter of the column can be chosen.

If the packed column is used as a mass transfer apparatus (rectification, stripping, absorption and desorption), the number of irrigation points should be approximately 250 openings/m^2 in the case of 50 mm packing elements [34]. The horizontal adjustment of trough distributors with holes is very important when the dripping flow is caused by gravity (see Fig. 1).

Distributors operated under pressure are less sensitive with respect to maldistribution; however, cleaning can be a problem.

Principally speaking, it is reasonable to distinguish between dry, wetted, and irrigated packings.

2.1 "Dry" Pressure Drop

When a gas or vapor is passing through a dry packing with the surface $a_t = 6(1 - \psi)\ d_p$ and the height H the so-called dry pressure Δp_t is given by

$$\Delta p_t = \xi \frac{\rho_G\ u_G^2}{2} \frac{(1-\psi)H}{\psi^3 d_p}$$

where ξ = friction factor of the packing

ψ = voidage or porosity of the packing
u_G = superficial gas velocity
ρ_G = density of the gas
d_P = particle diameter of an element according to

$$d_p = \frac{6 \text{ Volume of an element}}{\text{Surface of an element}}$$

Data of ψ and d_p are listed in Table 1. The exact voidage ψ is mostly a result of the filling procedure of the elements in the column. According to Eq. (1), the pressure drop is mainly dependent on the factor $(1 - \psi)/\psi^3$ or $(1 - \psi)/\psi^{4,65}$ [18]. Since the exact data of the voidage of a column under discussion are not known, it is understandable that "dry" pressure drops in columns with the same packing elements can be found in a certain range.

The friction factor ξ of different packing elements is plotted against the Reynolds number Re_G of the gas according to

$$Re_G = \frac{u_G d_p}{(1-\psi)\nu_G}$$

ν_G is the kinematic viscosity of the gas. The lines in Figs. 2 and 3 are valid for different types of elements shown in Figs. 4 and 5. Spheres, saddles, and cylinders are the basic types.

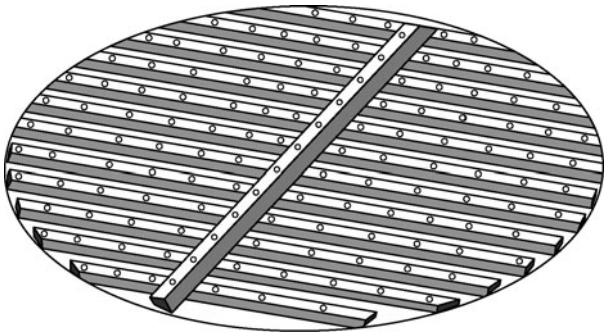

L2.6. Fig. 1. Trough distributor.

In Fig. 2, the friction factor ξ is plotted against the Reynolds number for the basic types: spheres and cylinders, and special corresponding forms. The friction factor decreases slightly with the Reynolds number and values can be found between 2 and 10 for $Re_G > 10^4$. In the case of saddle-type elements, it is reasonable to plot the friction factor ξ against a modified Reynolds number for which the hydraulic diameter $d_h = \psi\ d_P/(1-\psi)$ in Eqs. (1) and (2) is replaced by the diameter d_P of a sphere with the same volume as the element. In Fig. 2 friction factors for saddles can be found. The values in this modified plot are in the range between 3 and 10 for large Reynolds numbers. All these data are taken from the literature and there are fluctuations between ±25% and even 30% depending on the filling procedure. In the case of full elements, granules, long and very short cylinders and tablets the Ergun equation can be used:

$$\xi = \frac{300}{Re_G} + 3.5.$$

This equation can also be applied for elements with an inner voidage if the diameter d_P is replaced by the ring diameter multiplied by a factor which depends on the voidage ψ_R of the packing of Raschig rings. More information is available in several works [4–7, 9–11].

2.2 Pressure Drop in An Irrigated Packing

The hold-up of the liquid in an irrigated column increases with the superficial velocity or the liquid flow rate based on the unit of the cross-section area. As a consequence, the voidage of the dry packing is reduced with the result that the pressure drop is increased for a given gas flow rate. Even in the case where the packing is wetted only with some stagnant liquid, the pressure drop can be up to 20% higher in comparison with a completely dry packing.

In Figs. 6a and 6b, the pressure drop in an irrigated packing and the liquid hold-up, respectively, are plotted against the so-called F-factor with $F_V = u_G\ (\rho_G)^{1/2}$ for 50 mm Hiflow rings and three different superficial liquid velocities [19] (system air/water). The liquid hold-up is independent of the gas velocity below the loading range but increases with rising liquid velocities. In the gas velocity range above the so-called loading range the hold-up rises with the gas factor F_V. At the flooding point the downward liquid flow is blocked to a certain degree with the result that the hold-up is increased according to $h_L \rightarrow \psi$.

3 Operating Ranges of Packed Columns

3.1 Flooding Point

The higher the superficial liquid velocity the smaller is the superficial gas velocity at the flooding point. The diagram in Fig. 7 can be used for arbitrary gases, liquids, and packings in wide ranges of pressure and temperature in order to calculate the flooding limit. The accuracy of the lines in this diagram is approximately ±25%. This is understandable because the accuracy of the pressure drop of a gas flowing in a dry dumped-type packing is approximately the same as has been outlined already. According to Engel [33], the flooding limit can be calculated by the equation

$$\frac{\Delta\rho_t}{\rho_L g H} = \Delta\rho^*_{t,Fl} = C_{1,Fl} + C_{2,Fl}(B^*)^{C_{3,Fl}}$$
$$C_{1,Fl} = 2.92,\ C_{2,Fl} = -30.809$$
$$C_{3,Fl} = 0.01.$$

An even more accurate calculation of the flooding limit is difficult because the term flooding point is used for the description of two different physical phenomena:

In the case of small packing elements made of stoneware or ceramics with a high wettability and water (σ_L high) the voidage of the packing is filled with liquid for u_L = const but increasing u_G with the result that the downward flow of the liquid is hindered ($h_L \rightarrow \psi$).

Dealing with large elements made of plastics and with organic liquids (σ_L small) drops are formed and their number increases with the irrigation rate. Rising gas velocities lead to entrainment of the liquid. The importance of this phenomenon is increased by the following ratio:

$$\frac{\text{Drop diameter } d_T}{\text{Effective hydraulic diameter } d_{h,eff}} \text{ or}$$
$$\frac{d_T}{d_{h,eff}} = 0.61\ \frac{a_t}{\psi - h_L}\sqrt{\frac{\sigma_L}{(\rho_L - \rho_G)\times g}}$$
$$\text{with } h_L = \frac{\text{Liquid volume}}{\text{Total volume of the packing}}$$

The flooding limit is the result of numerous data published in the literature valid for elements within the following ranges:

$0.7 < \psi < 0.98$

$60\ m^{-1} < a_t < 300\ m^{-1}$

$0.01\ m < d_N < 0.09\ m.$

Reichelt [13] investigated the flooding limit of ceramic elements with the ratio of the column diameter based on the element diameter between 2 and 10. According to his recommendation the following hydraulic diameter should be used:

$$d_{hw} = \frac{\psi d_p}{\frac{3}{2}(1-\psi) + \frac{d_p}{D}}$$

This diameter takes into account the surface provided by the column wall. In addition, based on results obtained by Gieseler [14] and Billet [15] the flooding limit can be predicted with more accuracy in the case of viscous liquids when the dimensionless liquid velocity B^* is multiplied by the factor

L2.6. Table 1. Data of packings made of ceramics, metal and plastics

Dumped-type packings				
Element diameter d_N mm	Voidage ψ	Volume based surface a_t m^2/m^3	$d_p = \frac{6(1-\psi)}{a_t}$ mm	$d_N \cdot a_t$
Ceramic elements spheres				
2	0.4	1,800	2	3.6
4	0.4	900	4	3.6
6	0.4	600	6	3.6
8	0.4	450	8	3.6
10	0.4	360	10	3.6
20	0.44	180	20	3.6
30	0.48	105	30	3.1
Raschig rings				
5	0.55	1,000	2.5	5.0
10	0.65	440	4.8	4.4
15	0.70	330	5.5	4.9
20	0.72	240	7.0	4.8
25	0.73	195	8.3	4.8
35	0.76	140	10.3	4.9
50	0.78	98	13.5	4.9
100	0.81	44	26.0	4.4
Pall rings				
25	0.72	220	7.7	5.5
35	0.75	165	9.1	5.7
50 × 50 × 5	0.78	120	11.0	6.0
60 × 60 × 6	0.80	96	12.5	5.7
80 × 80 × 8	0.80	65	18.5	5.2
100 × 100 × 10	0.81	55	20.7	5.5
Berl saddles				
15	0.66	450	4.5	6.7
25	0.68	260	7.4	6.5
50	0.70	178	10.1	6.2
	0.73	120	13.5	6.0
Torus saddles				
12.5	0.71	622	2.8	7.7
20	0.72	335	5.0	6.7
25	0.74	255	6.2	6.3
35	0.76	178	8.7	6.2
50	0.79	120	10.5	6.0
75	0.80	92	13.0	6.9
Metal elements – Raschig rings				
5 × 5 × 0.3	0.87	1,000	0.8	5.0
10 × 10 × 0.5	0.89	500	1.3	5.0
15 × 15 × 0.5	0.92	350	1.4	5.2
25 × 25 × 0.6	0.93	220	1.9	5.5
35 × 35 × 0.8	0.94	150	2.4	5.2
50 × 50 × 1	0.95	48	2.7	5.5
100 × 100 × 1.5	0.96	110	5.6	4.8

L2.6. Table 1. (continued)

Dumped-type packings				
Element diameter d_N mm	Voidage ψ	Volume based surface a_t m^2/m^3	$d_p = \frac{6(1-\psi)}{a_t}$ mm	$d_N \cdot a_t$
Pall rings				
10 × 10 × 0.3	0.92	515	0.9	5.1
15 × 15 × 0.4	0.93	360	1.2	5.4
25 × 25 × 0.6	0.94	215	1.7	5.3
35 × 35 × 0.8	0.95	145	2.1	5.0
50 × 50 × 1.0	0.95	105	2.9	5.2
80 × 80 × 1.5	0.96	78	3.1	6.2
Raschig Super rings				
30	0.98	150	0.8	4.5
38	0.98	120	1.0	4.56
50	0.98	100	1.2	5.0
"Hiflow" rings				
25	0.965	185	1.1	4.6
50	0.98	93	1.3	4.6
"VSP" rings				
25	0.975	205	0.7	5.1
40	0.98	110	1.1	4.4
IMTP				
25	0.967	325	0.609	8.1
40	0.973	170	0.953	6.8
50	0.978	128	10.31	6.4
Plastic element Pall rings				
15	0.87	350	2.2	5.2
25	0.90	220	2.7	5.5
35	0.91	160	3.4	5.6
50	0.93	110	3.8	5.5
Torus-Sättel				
13	0.83	620	1.6	8.0
25	0.89	258	2.6	6.4
35	0.91	170	3.2	5.9
50	0.92	120	4.0	6.0
75	0.93	105	4.0	7.8
"Tellerette"				
25	0.87	180	4.3	4.5
50	0.93	110	3.8	5.5
"Nor-Pac"				
18 × 14	0.88	330	2.2	5.9
× 27	0.92	180	2.6	4.8
35 × 35	0.93	145	2.9	5.0
50 × 50	0.94	100	3.8	5.0
"Hiflow" rings				
15	0.91	313	1.73	4.7
25	0.92	218	2.2	5.4
38	0.94	125	2.88	4.75

L2.6. Table 1. (continued)

Dumped-type packings				
Element diameter d_N mm	Voidage ψ	Volume based surface a_t m^2/m^3	$d_p = \frac{6(1-\psi)}{a_t}$ mm	$d_N \cdot a_t$
50	0.93	114	3.7	5.7
90	0.96	59	4.1	5.3
"VSP"				
50	0.95	107	2.8	5.3
"Envipac"				
32	0.936	139	2.8	4.4
60	0.96	98	2.4	5.8
80	0.95	60	5.0	4.8

Arranged-type packings		
Voidage ψ	Volume-based surface a_t m^2/m^3	$d_P = \frac{6(1-\psi)}{a_t}$ mm
Stainless steel elements "Mellapak"		
0.975	250	0.6
0.975	500	0.3
Polypropylene elements "Mellapak"		
0.88	250	2.88

$(\nu_G/\nu_L)^{0.1}$. This means that the exponent of the liquid viscosity is only 0.233 instead of 0.333. Later, in Sect. 3.4, it will be shown that this exponent decreases with the liquid Reynolds number $u_L/(a_t\,\nu_L)$ and disappears for $\nu_L{}^2 a_t{}^3/g \to 0$.

Arranged-type packings are used for distillation and absorption columns in order to reduce the pressure drop of the vapor or the gas. According to Fig. 2, the pressure drop in such packings is approximately only 50% in comparison to the most favorable dumped-type elements. The flooding of arranged-type packings can be calculated as has been outlined earlier.

3.2 Loading Limit

The loading limit is defined as the superficial gas velocity at which the liquid hold-up increases for a given superficial liquid velocity. This limit can be taken from Fig. 7; however, this limit cannot be predicted very accurately because of the uncertainties of the voidage ψ caused by differences of the filling procedures of the elements. According to Engel [33] the loading limit can be calculated from

$$\Delta\rho^*_{t,\mathrm{Load}} = C_{1,\mathrm{Load}} + C_{2,\mathrm{Load}}(B^*)^{C_{3,\mathrm{Load}}}$$
$$C_{1,\mathrm{Load}} = 0.57576,\quad C_{2,\mathrm{Load}} = -0.63288$$
$$C_{3,\mathrm{Load}} = 0.017.$$

3.3 Other Operating Points

Figure 7 is a tool in order to calculate other operating points. Approximately, the simple relationship $u_G{}^0 = 0.65\ u_{G,Fl}$ is valid for the loading limit. According to Engel [32] the parameter in Fig. 7 can be described by the following equations:

$$\Delta p^*_t = C_1(\Delta p^*) + C_2(\Delta p^*)\cdot[C_3(\Delta p^*) + B^*]^{0.04}$$
$$C_1(\Delta p^*) = -4.3513\times10^{-6} + 8.6424\cdot\Delta p^* - 58.1789\cdot(\Delta p^*)^2 + 170.255\cdot(\Delta p^*)^3.$$
$$C_2(\Delta p^*) = -2.8884\times10^{-4} - 10.6464\cdot\Delta p^* + 71.4375\cdot(\Delta p^*)^2 - 210.7186\cdot(\Delta p^*)^3.$$
$$C_3(\Delta p^*) = +2.4758\times10^{-4} + 5.517\times10^{-3}\cdot\Delta p^* + 0.03503\cdot(\Delta p^*)^2 - 0.069512\cdot(\Delta p^*)^3.$$

3.4 Hold-Up

The total liquid hold-up is composed of the static hold-up and the dynamic hold-up which is important for mass transfer. In the case of large packing elements and low viscous irrigation liquids the dynamic contribution is dominant. Below the loading limit the liquid hold-up increases with the superficial liquid velocity and the superficial gas velocity plays no role. Experimental results of numerous authors [7, 18, 20, 27, 28, 31] are the basis of the following calculation procedure. In Fig. 8, the liquid hold-up $h_L{}^0$ below the loading point is plotted against the Froude number $(u_L{}^2 a_t/g\psi^4)^{1/3}$ with the expression $(\nu_L{}^2 a_t{}^3/g)$ as parameter. This diagram has been chosen because the most important equations valid for $h_L{}^0$ can be transformed into special equations with the possibility to compare them (see Table 2). According to Fig. 8, the liquid hold-up increases with rising values of the irrigation Froude number and the viscosity parameter. The higher the liquid viscosity and the larger the volume-based surface of a packing element, the smaller is the slope of the parameter in Fig. 8. Modern packing elements with outer sizes between 25 and 35 mm, voidages above 0.97 and small volume-based surfaces lead to viscosity parameters between 10^{-6} and 10^{-8} for low viscous liquids (distillation at normal and high pressure). The equations in Table 2 are developed for this case. In the equation of Stichlmair [18] there is no influence of the liquid viscosity, and the proportionality $h_L{}^0 \sim (u^{2/3}{}_L)$ is the steepest slope in Fig. 8. This can be expected for high Froude numbers. Billet, Mackowiak, and Kim [27] have derived an equation which takes into account the liquid viscosity. The relationship $h_L{}^0 \sim u_L{}^{0.5}$ can be expected for small and medium Froude numbers. Based on numerous experimental results, Bornhütter and Mersmann [20, 31] obtained the relationship $h_L{}^o \sim u_L{}^{0.5}$, which is reasonable for operating ranges applied in industrial columns. In the case that the viscosity parameter is above 10^{-4} the exponent of the superficial liquid velocity u_L is smaller $(u_L{}^{0.46})$. This corresponds to an equation published by Gelbe [18, 29] valid for very small packing elements. However, in this case the static hold-up can be dominant. The influence of the liquid surface tension σ_L is poor in packings with large elements; however, this liquid property plays an important role for the static hold-up and the liquid attached to the packing after stopping the irrigation. The hold-up at the flooding point can be described by the ratio $u_L/u_{G,Fl}$.

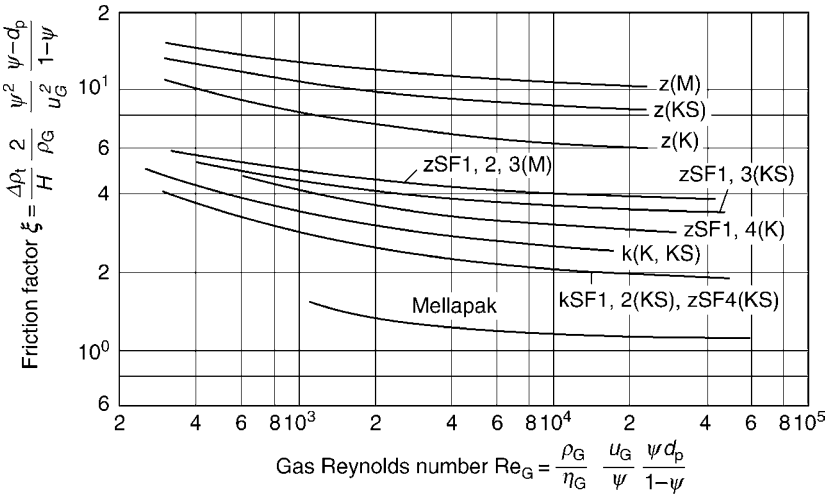

L2.6. Fig. 2. Friction factor of the basic type cylinder (z) and sphere (k) against the Reynolds number of the gas [16].

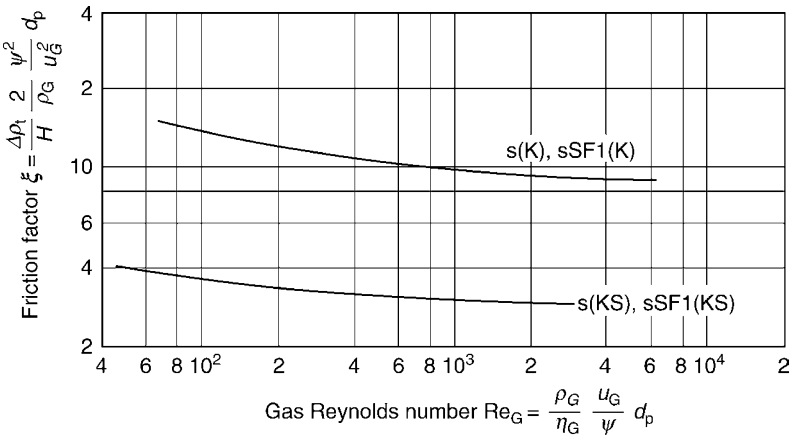

L2.6. Fig. 3. Friction factor of the basic type sphere (s) against the Reynolds number of the gas [16].

In the case of large packing elements ($\psi > 0.8$; $a_t < 200\ m^{-1}$) the authors recommend

$$\frac{h_{L,Fl}}{\psi} = 0.83 \cdot \left[\frac{u_L}{u_{G,Fl}} \cdot \left(\frac{\sigma_L}{\Delta\rho g}\right)^{1/2} \frac{a_t}{\psi}\right]^{1/3}$$

and for small elements ($\psi < 0.8$; $a_t > 200\ m^{-1}$)

$$\frac{h_{L,Fl}}{\psi} = 0.62 \cdot \left[\frac{u_L}{u_{G,Fl}} \cdot \left(\frac{\sigma_L}{\Delta\rho g}\right)^{1/2} \frac{a_t}{\psi}\right]^{1/4}$$

with an accuracy of ±20%. In the region between the loading and the flooding limit the hold-up is approximately

$$h_L = h_L^0 + (h_{L,Fl} - h_L^0) \cdot \left(\frac{u_G}{u_{G,Fl}}\right)^7.$$

Example

Calculate the pressure drop Δp of a gas which is flowing through a packing of 50 mm Hiflow rings with the height $H = 1$ m. The superficial velocities are

$$u_G = 2.36\ m/s \text{ and } u_L = 5.55\ 10^{-3} m^3/(m^2 s)$$

Data

Density of the gas $\rho_G = 1{,}2\ kg/m^3$
Density of the liquid $\rho_L = 1{,}000\ kg/m^3$
Kinematic viscosity of the gas $\nu_G = 13^*10^{-6}\ m^2/s$
Kinematic viscosity of the liquid $\nu_L = 10^{-6}\ m^2/s$
Voidage of the packing $\psi = 0.926$
Volume based surface $a_t = 90.7\ m^2/m^3$

1. Dimensionless irrigation rate

   $B^* = (\eta_L/(\rho_L g^2))^{1/3}(1-\psi)\ u_L/(\psi d_P) = 0.000198$
2. F-factor

   $F = u_G(\rho_G)^{1/2} = 2.59(Pa)^{1/2}$
3. Particle diameter

   $d_P = 6(1-\psi)/a_t = 0.00489\ m$
4. Friction factor at the operating point

   $Re_G = u_G d_P/((1-\psi)\nu_G) = 12,000;\ \xi = 2.0$

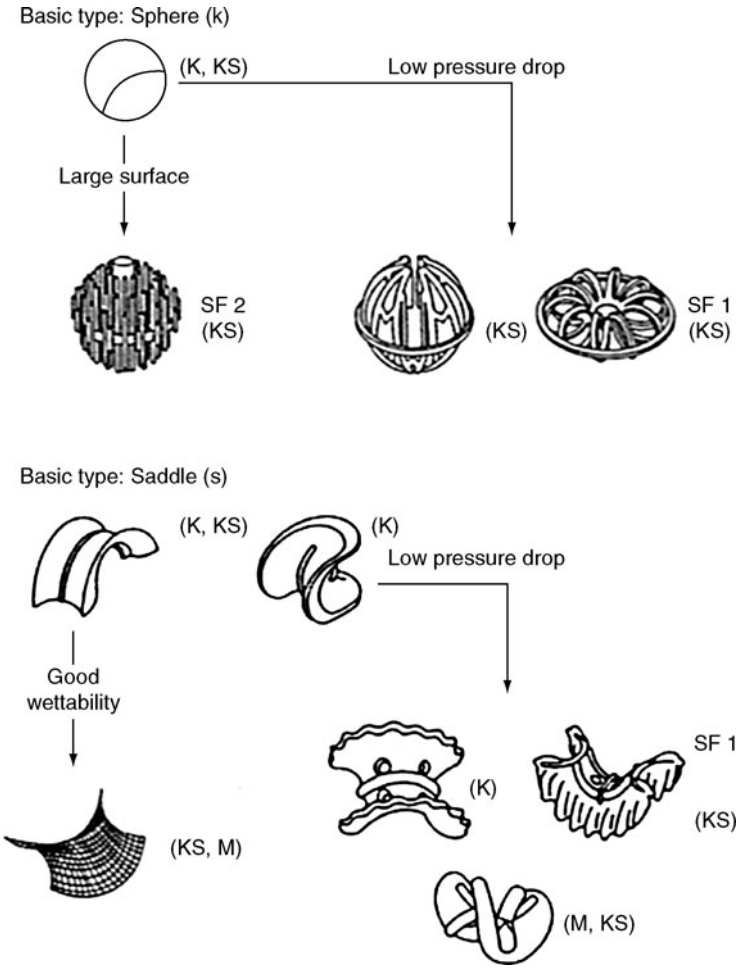

L2.6. Fig. 4. Elements of the basic type sphere (k), and saddle (s) with the information of the most common materials (K – ceramics, M – metals, KS – plastic, and SF – special forms).

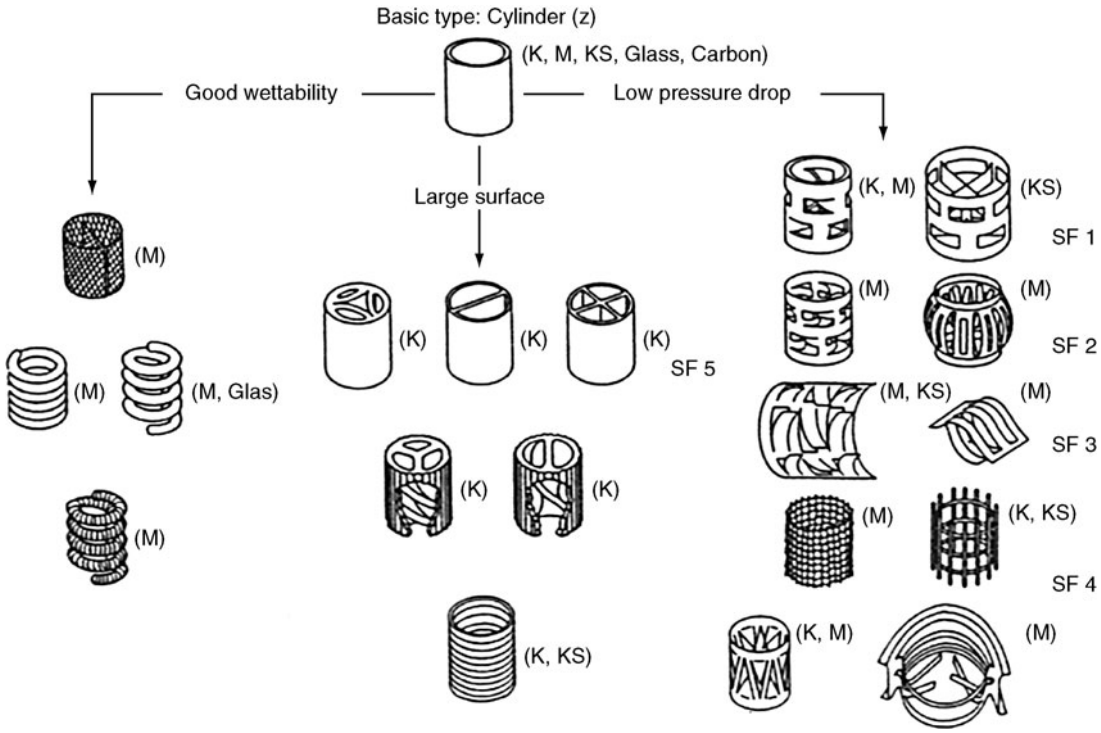

L2.6. Fig. 5. Elements of the basic type cylinder (z) [16], compare Fig. 3.

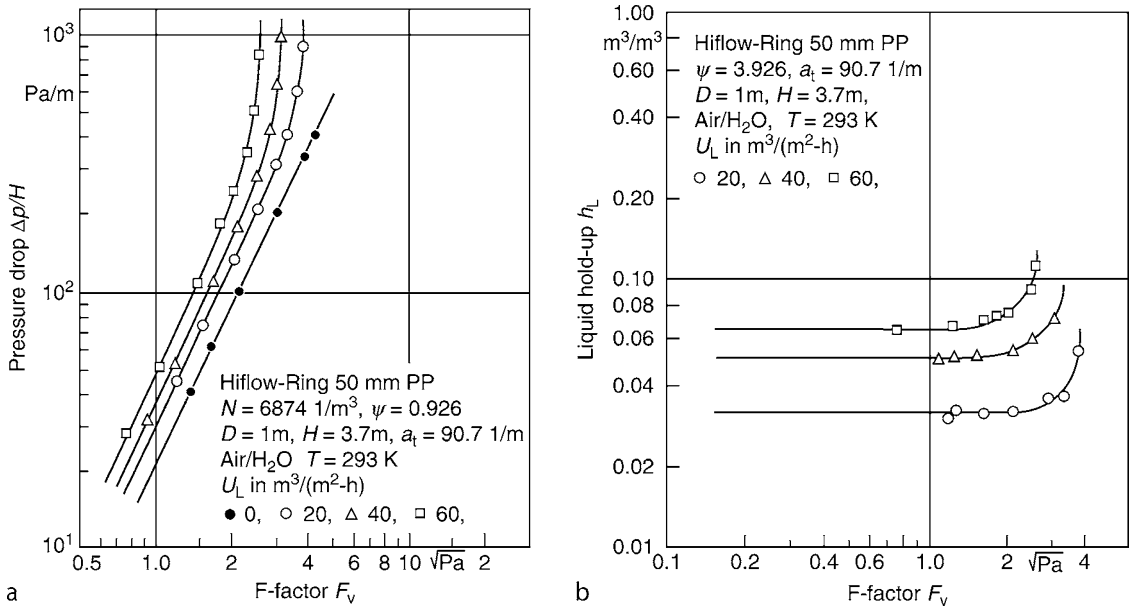

L2.6. Fig. 6. (a) Pressure drop of an irrigated packing against the F_v-factor [19]. Pressure drop based on H, $\Delta p/H$. (b) Liquid hold-up of an irrigated packing against the F-factor F_v.

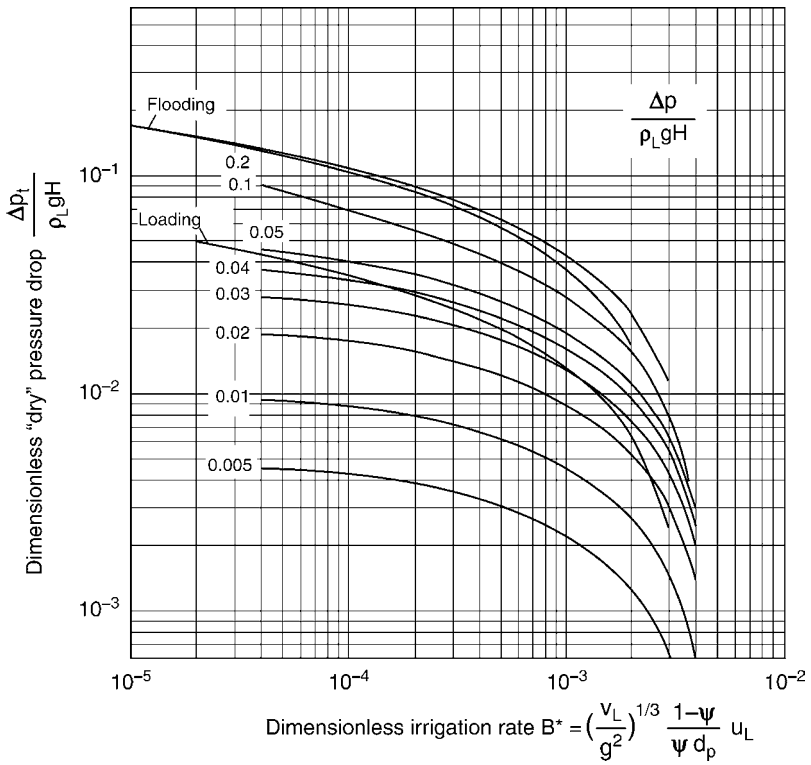

L2.6. Fig. 7. Dimensionless "dry" pressure drop against the dimensionless irrigation rate with the loading and the flooding limit.

5. Dimensionless "dry" pressure at the operating point

$$\Delta p_t/H = \xi \rho_G u_G^2 (1-\psi)/(2 d_p \psi^3) = 127.4\,\text{Pa/m}$$
$$\Delta p_t/(\rho_L g H) = 0.0130$$

6. Iteration of the dimensionless "dry" pressure drop at the operating point

$$\Delta p^* = \Delta p/(\rho_L g H) = 0.01675;\ \Delta p/H\ 164.3\,\text{Pa/m}$$

7. Flooding factor based on the "dry" pressure drop at the flooding point

$$\Delta p_{t,Fl}{}^* = C_{1,Fl} + C_{2,Fl} (B^*)^{*C3,Fl} = 0.0909$$

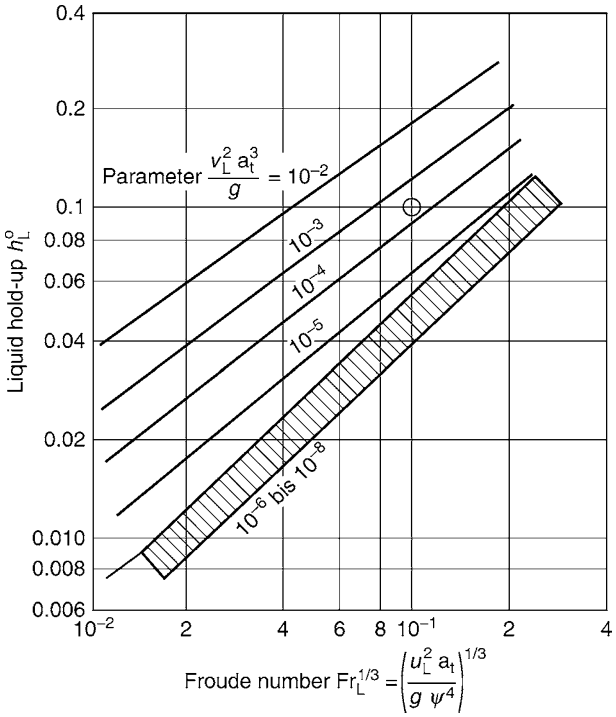

L2.6. Fig. 8. Liquid hold-up below the loading limit according to Bornhütter.

L2.6. Table 2. Hold-up

Author	Equation
Stichlmair [18] (no influence of v_L)	$h_L^0 = 0.555 \cdot \psi \cdot \left[\frac{u_L^2 a_1}{g\psi^{4,65}}\right]^{0,33}$
Billet, Mackowiak and Kim [27]	$h_L^0 = 2.5 \cdot \left[\left(\frac{v_L}{g^2}\right)^{1/3}\left(\frac{u_L}{\psi}\right)\left(\frac{1-\psi}{\psi d}\right)\right]^{0,5}$
	$h_L^0 = 1.07 \cdot \left(\frac{v^2 a_1^3}{g}\right)^{0,083} \cdot \left(\left[\frac{u_L^2 a_1}{g\psi^4}\right]^{1/3}\right)^{0,75}$
Bornhütter and Mersmann [20]	$h_L^0 = 4.34 \cdot \left[\left(\frac{v_L}{g^2}\right)^{1/3}\left(\frac{u_L}{\psi}\right)\left(\frac{1-\psi}{\psi d_p}\right)\right]^{0,57}$
	$h_L^0 = 1.56 \cdot \left(\frac{v^2 a_1^3}{g}\right)^{0,095} \cdot \left(\left[\frac{u_L^2 a_1}{g\psi^4}\right]^{1/3}\right)^{0,85}$
Engel [33]	$h_L^0 = 3.6 \cdot \left[\frac{u_L \cdot a_1^{0,5}}{g^{0,5}}\right]^{0,66}$
	$\left[\frac{v_L \cdot a_1^{3/2}}{g^{0,5}}\right]^{0,25} \cdot \left[\frac{\sigma_L \cdot a_t^2}{\rho_L \cdot g}\right]^{0,1}$

$$\text{Flooding factor} = (\Delta p_t^* / \Delta p_{t,Fl}^*)^{1/2} = 0.378 = 37.8\%$$

8. Comparison with experimental results

$\Delta p/H = 190\,\text{Pa/m}$

4 Bibliography

1. Hoppe K (1972) Entwicklungstendenzen und grenzparameter im gebiet der stoffaustauschapparate für den gas- bzw. Dampf-Flüssigkontakt. Chem Ing Techn 6:215–221
2. Barth W (1951) Der druckverlust bei der durchströmung von füllkörpersäulen und schüttgut mit und ohne berieselung; Chem Ing Techn 23:289–293
3. Wiggert K Druckverlust und flüssigkeitinhalt in berieselten schüttungen bei verschiedenen füllkörperarten; Mitt. Forschungsgruppe Wärme- und Kältetechnik, Max-Planck-Institut für, vol 92. Strömungsforschung, Göttingen, p 21
4. Kast W (1964) Gesetzmäßigkeiten des druckverlustesin füllkörperkolonnen; Chem Ing Techn 36: 464–468
5. Teutsch T (1964) Druckverluste in füllkörperschüttungen bei hohen berieselungsdichten. Chem Ing Techn 36:496–503
6. Brauer H (1957) Druckverlust in füllkörpersäulen bei einphasenströmung. Chem Ing Techn 29:785–790
7. Reichelt E, Blaß E (1971) Die berechnung von füllkörperapparaten bei gegenstrom von gas und flüssigkeit. Chem Ing Techn 43:949–956
8. Ergun S (1952) Fluid flow through packed columns. Chem Engng Progr 48:89–94
9. Schrader H (1958) Druckverlust, wärme- und stoffaustausch in berieselten Raschigringschüttungen. Kältetechnik 10:290–295
10. Glaser H (1955) Instationäre messung der wärmeübertragung, von raschigringschüttungen. Chem Ing Techn 27:637–643
11. Sonntag G (1957) Thesis TH dresden
12. Mersmann A (1965) Zur berechnung des flutpunktes in füllkörperschüttungen. Chem Ing Techn 37:218–226
13. Reichelt W (1974) Strömung in füllkörperapparaten bei gegenstrom einer gasförmigen phase. Verlag Chemie Weinheim
14. Gieseler M (1972) Durchströmungsverhalten von packungen und schüttungen aus koksen unterschiedlicher größe und gestalt in gegenwart einer flussigen phase hoher viskosität. Thesis TU, Clausthal
15. Billet R (1968) Rektifikation in kolonnen mit metallischen füllkörpern. Chem Ing Techn 40: 43–51
16. Mersmann A, Deixler A (1986) Packungskolonnen. Chem Ing Techn 58:19–31
17. Billet R (1989) Druckverlust in berieselten schüttungen. Chem Ing Techn 61:157–159
18. Stichlmair J (1988) Ullmanns encyclopedia of industrial chemistry, vol B3, VCH
19. Bornhütter K (1991) Stoffaustausch von füllkörperschüttungen unter berücksichtigung der strömungsform. Thesis TU München
20. Bornhütter K, Mersmann A (1990) Modifikation des flutpunktdiagramms nach mersmann hinsichtlich der anwendung auf moderne füllkörper größerer nennabmessungen. GVC fachausschuss "Thermische Zerlegung von Gas- und Flüssigkeitsgemischen" Berchtesgaden
21. Billet R, Mackowiak J (1985) Hiflow-Ring, ein hochleistungsfüllkörper für gas-flüssigsysteme; teil 3: Ausführung in Keramik; Chemie-Technik 14:195–206
22. Billet Mackowiak J (1985) Hochwirksame metallische packung für gas- und dampf-flüssigkeits-systeme; Chem Ing Techn 57: 976–978
23. Billet R, Mackowiak J (1984) How to use absorption data for design and scale-up of packed columns. Fette Seifen Anstrichmittel 86:349–358
24. Billet R, Mackowiak J (1984) Hiflow ring, ein hochlestungsfüllkörper für gas-flüssig-systeme. Teil 1: Ausführung in Kunststoff; Chemie-Technik 13:37–46
25. Billet R, Mackowiak J (1982) Wirksamkeit von kunststoff-füllkörpern bei der absorption, desorption und vakuumrektifikation; Verfahrensteechnik 16:67–74
26. Billet R, Mackowiak J (1988) Application of modern packings in thermal separation processes. Chem Ing Techn 11:213–227
27. Billet R, Mackowiak J (1989) Druckverlust in berieselten schüttungen. Chem Ing Techn 61: 157–159
28. Billet R, Mackowiak J (1980) Neuartige füllkörper aus kunststoffen für thermische stofftrennverfahren. Chemie-Technik 9:219–226

29. Gelbe H (1968) Der flüssigkeitsinhalt und die rektifizierwirkung beim vakuumbetrieb in füllkörperkolonnen. Fort.-Ber. VDI-Zeitschrift Reihe 3, No. 23
30. Blaß E, Kurtz R (1876) Der einfluss grenzflächenenergetischer größen auf den zweiphasen-gegenstrom durch raschigring-füllkörpersäulen. Verfahrenstechnik 10:721–724
31. Bornhütter K, Mersmann A (1992) Mass transfer in packed tower: the cylinder model. Chem Ing Techn 64:304–305
32. Engel V, Mersmann A (2000) Private communication
33. Engel V (1995) Fluiddynamik in packungskolonnen für gas-flüssig-systeme; VDI fortschr.-Ber. No. 605. Reihe 3, Verfahrenstechnik, Düsseldorf, VDI-Verlag
34. Kutzer S (1995) Zum abwasserstrippen mit füllkörperkolonnen; Thesis TU München

L2.7 Pressure Drop and Operating Limits of Trays

Johann Stichlmair
Technische Universität München, Garching, Germany

1 Fundamentals

The pressure loss of a gas (or vapor) flowing through a tray column results from the sum of the dry pressure loss Δp_d and the pressure loss Δp_L due to the hydraulic head of the tray:

$$\Delta p = \Delta p_d + \Delta p_L \tag{1}$$

The dry pressure loss can be predicted from the equations presented in Subchap. L1.7. The pressure loss Δp_L is primarily caused by the static head of the liquid in the froth on the tray. The influence of other mechanisms such as formation of bubbles, lateral mixing of liquid, and entrainment of drops can be neglected at normal operation conditions.

2 Two-Phase Flow on Trays

The theoretical prediction of the pressure loss of a tray requires detailed information about the two-phase flow on the tray. Of special importance are the height of the froth h_f and its liquid hold-up ε_L. The maximum gas load F_{max}, which can be modeled from first principles, is decisive for both quantities.

2.1 Maximum Gas Load of Trays

At high gas loads, there exists a so-called drop regime in the froth on the tray [1, 2]. Here, the gas (or vapor) constitutes the continuous phase, and the liquid constitutes the dispersed phase (droplet phase). The space above the plate consists of a zone of drop formation and a zone of drop entrainment. It is the velocity and not the direction of the gas jets emerging from the orifices (e.g., holes, bubble caps, valves) that determines the size of the droplets in the froth. The gas jets penetrate into the two-phase layer and act like a jet mill. The liquid drops are entrained into the jets, accelerated, and eventually deformed. After having lost their spherical shape, the drops are torn into pieces. Drop stability is described by the ratio of friction and surface forces that constitute the Weber number *We*:

$$\mathrm{We} \equiv \frac{\rho_G \cdot u_{Gh}^2 \cdot d}{\sigma} \tag{2}$$

The maximum size of drops is determined by a critical value of the Weber number We_{crit}.

The equation of continuity formulates a relationship between jet velocity u_{Gh} and superficial velocity u_G:

$$u_G = u_{Gh} \cdot \varphi \tag{3}$$

Here, φ denotes the relative free area of a tray. Combining Eqs. (2) and (3) allows the prediction of drop size in the drop formation zone:

$$d = \mathrm{We}_{crit} \cdot \frac{\sigma \cdot \varphi^2}{\rho_G \cdot u_G^2} \tag{4}$$

In the entrainment zone far above the plate, there exists a uniform gas velocity (i.e., superficial velocity) u_G. A balance of friction, weight, and buoyancy forces yields:

$$\frac{d^2 \cdot \pi}{4} \cdot \zeta_{sp} \cdot \frac{\rho_G}{2} \cdot u_G^2 = \frac{d^3 \cdot \pi}{6} \cdot (\rho_L - \rho_G) \cdot g \tag{5}$$

After rewriting:

$$d = \frac{3}{4} \cdot \frac{\zeta_{sp}}{(\rho_L - \rho_G) \cdot g} \cdot \rho_G \cdot u_G^2 \tag{6}$$

Eliminating the drop diameter from Eqs. (4) and (6) yields:

$$u_{G\,max} \cdot \sqrt{\rho_G} = \left(\frac{4 \cdot \mathrm{We}_{crit}}{3 \cdot \zeta_{sp}}\right)^{1/4} \cdot (\varphi^2 \cdot \sigma \cdot (\rho_L - \rho_G) \cdot g)^{1/4} \tag{7}$$

According to [3] the value of the critical Weber number is:

$$\mathrm{We}_{crit} = 12 \cdot \left(1 + \left(\frac{\eta_L^2}{d \cdot \sigma \cdot \rho_L}\right)^{0.36}\right) \approx 12 \tag{8}$$

For low viscous liquids normally processed in separation columns, Eq. (8) yields a value of 12.

The friction factor of spheres at high Reynolds numbers has a constant value:

$$\zeta_{sp} \approx 0.4 \tag{9}$$

In engineering literature, the gas load is often expressed by the so-called F-factor, which is defined by:

$$F \equiv u_G \cdot \sqrt{\rho_G} \tag{10}$$

Combining Eqs. (8), (9), and (10) delivers a very important relationship for the upper limit of the gas load on a tray [1, 2]:

$$F_{max} \approx 2.5 \cdot (\varphi^2 \cdot \sigma \cdot (\rho_L - \rho_G) \cdot g)^{1/4} \tag{11}$$

Equation (11) is valid for the so-called entrainment flooding. This theoretically derived equation corresponds very well with published experimental data and with the well-known empirical correlation of Fair [4]. It is important to note that the maximum gas load is proportional to $\sigma^{1/4}$ (σ surface tension) and $\varphi^{1/2}$ (φ relative free area). Both dependencies agree very well with experimental findings.

2.2 Liquid Hold-Up in the Froth

The mean liquid hold-up ε_L in the froth is defined as:

$$\varepsilon_L \equiv h_L/h_f \tag{12}$$

There exists a large database for both the clear liquid height h_L and the froth height h_f. All data are well correlated by [1, 2]:

$$\varepsilon_L = 1 - (F/F_{max})^{0.28} \tag{13}$$

This simple equation implies in the term F_{max} several system properties of the liquid and geometrical data of the tray.

2.3 Froth Height

The height of the froth on a tray is primarily determined by the conditions of the flow over the outlet weir. Firstly, the froth height h_f can, at normal operation, be not lower than the weir height h_w. Secondly, the volume flow over the weir contributes significantly to froth height. However, it has to be considered that the volume flow of the two phase mixture $\dot{V}_L/\varepsilon_L$ is the decisive quantity in the weir formula (Francis equation), and not the liquid flow $\dot{V}_L$ alone. Thirdly, the two-phase layer on the tray is additionally increased by elevation forces of the gas flowing upwards through the froth. All tree mechanisms lead to the following relationship [1, 2]:

$$h_f = h_w + \frac{1.45}{g^{1/3}} \cdot \left(\frac{\dot{V}_L/l_w}{\varepsilon_L}\right)^{2/3} + \frac{125}{(\rho_L - \rho_G) \cdot g} \cdot \left(\frac{F - 0.2 \cdot \sqrt{\rho_G}}{1 - \varepsilon_L}\right)^2 \tag{14}$$

At high liquid loads, the second term of Eq. (14) predominates the height of the froth. The third term is significant only at very high gas loads.

In column operation it has to be ensured that the froth height is lower than the tray spacing, which is typically in the rage from 0.3 to 0.6 m. Therefore, the feasible gas load F is in most cases lower than the maximum gas load F_{max}.

3 Pressure Loss of Tray Columns

The total pressure loss Δp of a tray can be easily predicted from Eq. (15):

$$\Delta p = \Delta p_d + h_f \cdot \varepsilon_L \cdot \rho_L \cdot g \tag{15}$$

The quantities in Eq. (15) are evaluated from Eqs. (13) and (14) and from the equations developed in Subchap. L1.7.

Typical values of the pressure loss of a tray are shown in Fig. 1. It should be noted that the general relation $\Delta p \propto \rho \cdot u^2$ holds for the dry pressure drop only. Normally, the pressure drop data are in the rage from 400 to 600 N/m^2 (i.e., 4–6 mbar). Assuming a mass transfer efficiency of a tray of 80% the pressure loss per equilibrium stage is as high as 5–8 mbar. This value is by a factor of 5 higher than the corresponding pressure drop of packed columns.

4 Example

Find the pressure loss of a sieve tray operated with air and water at ambient conditions.

Data: Tray design: $\varphi = 0.125$, $d_h = 5$ mm, $s/d_h = 1$, $h_w = 5$ cm
Tray operation: $u_G = 1.8$ m/s, $\dot{V}_L/l_w = 20$ m^3/(m · h)
System properties: $\rho_G = 1.2$ kg/m^3, $\eta_G = 18 \cdot 10^{-6}$ kg/(m · s), $\rho_L = 1{,}000$ kg/m^3, $\sigma = 0.072$ kg/s^2

4.1 Dry Pressure Loss

Evaluation of the orifice coefficient ζ from Fig. 2 in Subchap. L1.7.

$$Re_h = \frac{d_h \cdot u_h \cdot \rho_G}{\eta_G} = \frac{5 \cdot 10^{-3} \cdot 1.8/0.125 \cdot 1.2}{18 \cdot 10^{-6}} = 4.800$$

Reading from Fig. 2: $\zeta_o \approx 1.7$

Equation (16):

$$\zeta = \zeta_o + \varphi^2 - 2 \cdot \varphi \cdot \sqrt{\zeta_o} = 1.7 + 0.125^2 - 2 \cdot 0.125 \cdot \sqrt{1.7} = 1.39$$

Equation (1):

$$\Delta p = \zeta \cdot \frac{\rho_G}{2} \cdot u_{Gh}^2 = 1.39 \cdot \frac{1.2}{2} \cdot \left(\frac{1.8}{0.125}\right)^2 = 173 \text{ N/m}^2$$

4.2 Total Pressure Loss

Equation (13):

$$\varepsilon_L = 1 - (F/F_{max})^{0.28}$$

Equation (11):

$$F_{max} \approx 2.5 \cdot (\varphi^2 \cdot \sigma \cdot (\rho_L - \rho_G) \cdot g)^{1/4} =$$
$$2.5 \cdot (0.125^2 \cdot 0.072 \cdot (1.000 - 1.2) \cdot 9.81)^{1/4} = 4.55 \text{ Pa}^{1/2}$$

Equation (13):

$$\varepsilon_L = 1 - (1.8 \cdot \sqrt{1.2}/4.55)^{0.28} = 0.2087$$

Froth height h_f

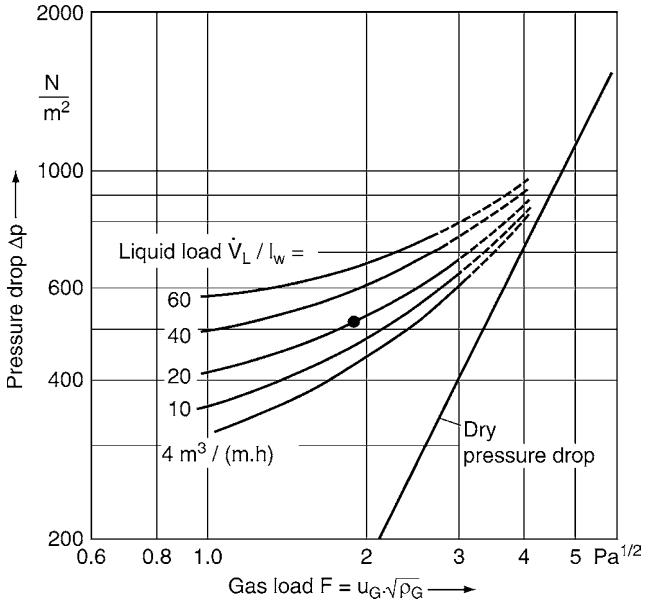

L2.7. Fig. 1. Pressure loss characteristics of a column tray.

Equation (14):

$$h_f = h_w + \frac{1.45}{g^{1/3}} \cdot \left(\frac{\dot{V}_L/l_w}{\varepsilon_L}\right)^{2/3} + \frac{125}{(\rho_L - \rho_G)\cdot g} \cdot \left(\frac{F - 0.2\cdot\sqrt{\rho_G}}{1-\varepsilon_L}\right)^2$$

$$= 0.5 + \frac{1.45}{9.81^{1/3}} \cdot \left(\frac{20/3,600}{0.2087}\right)^{2/3} + \frac{125}{(1,000 - 1.2)\cdot 9.81} \cdot \left(\frac{(1.8-0.2)\cdot\sqrt{1.2}}{1-0.2087}\right)^2$$

$$= 0.05 + 0.0604 + 0.0624 = 0.173\ \text{m}$$

Total pressure loss:

$$\Delta p = \Delta p_d + h_f \cdot \varepsilon_L \cdot \rho_L \cdot g = 173 + 0.173 \cdot 0.2087 \cdot 1.000 \cdot 9.81$$
$$= 173 + 354 = 527\ \text{N/m}^2$$

This value is marked in Fig. 1.

5 Symbols

d drop diameter (m)
F Gas load, $F \equiv u_G \cdot \sqrt{\rho_G}$ $(\text{Pa}^{1/2})$
F_h Gas load in the open area of the tray $(\text{Pa}^{1/2})$
g acceleration of gravity (m/s^2)
h_f froth height (m)
h_L clear liquid height (m)
h_w weir height (m)
l_w weir length (m)
$\dot{V}_L$ volume flow of the liquid (m^3/s)
u_G superficial gas velocity (m/s)
u_{Gh} gas velocity in the openings of a tray, velocity of the gas jets (m/s)
ε_L relative liquid hold-up in the froth
ζ_{sp} friction factor of a sphere
φ relative free area of a tray
ρ_G gas density (kg/m^3)
ρ_L liquid density (kg/m^3)
σ surface tension (kg/s^2)
We Weber number, We $\equiv \rho \cdot u \cdot d/\sigma$

6 Bibliography

1. Stichlmair J (1978) Grundlagen der Dimensionierung das Gas/Flüssigkeit-Kontaktapparates Bodenkolonne. Verlag Chemie, Weinheim
2. Stichlmair J, Fair JR (1998) Distillation - principles and practice. Wiley-VCH, New York
3. Wallis G (1960) One-dimensional two-phase-flow. McGraw-Hill, New York, p. 377
4. Fair JR (1961) How to predict sieve tray entrainment and flooding. Petro/Chem Eng 33(10):45/52

L3.1 Particle Motion in Fluids

Martin Sommerfeld
Martin-Luther-Universität Halle-Wittenberg, Halle (Saale), Germany

1 Introduction

The motion of particles (solids, droplets, and bubbles) in fluids is relevant for a number of processes in chemical engineering, biotechnology, process engineering, and energy conversion. The different forces acting on the particles constitute in many cases the basis for process layout and optimization. Examples of such processes are pneumatic conveying, fluidized beds, sedimentation, dispersion of particles in a stirred vessel, aerodynamic classification of powders, and particle separation in cyclones. Such kind of two-phase flows is termed as "dispersed flows" where individual particles are more or less homogeneously distributed in the continuous phase (i.e., gas or liquid). In dilute dispersed systems, the particle transport is governed mainly by fluid dynamic forces acting on the particle surface in addition to external field forces (e.g., gravity, buoyancy, and electrical forces). On the other hand one finds dense dispersed two-phase flows, e.g., fluidized beds, where additionally fluid dynamic interactions and collisions between particles are of great importance (see for example [1]). In a number of simple design strategies, a quasi-steady particle motion is assumed. Such approaches are for example used to determine the sedimentation velocity of particles, being the basis for determining the size of a sedimentation tank or a sedimentation centrifuge and to calculate the cut size of a cyclone based on a force balance. However, for the design of a number of processes, involving mostly turbulent flows, the full equation of motion for the particles has to be solved in order to obtain for example the particle residence time or better the residence time distribution. In such turbulent flows, the particle transport due to the turbulent eddies has to be accounted for, in addition to the relevant fluid dynamic and external forces. A residence time distribution of particles is for example important for finding the appropriate operational conditions of different multiphase chemical reactors, e.g., stirred vessel, bubble column, or loop reactor. In addition, the knowledge on particle motion and relevant forces is essential for the numerical calculation of dispersed multiphase flows. The two approaches mainly used for technical and industrial multiphase flows are the two-fluid (or Euler/Euler) method [2] and the Euler/Lagrange approach in combination with an appropriate turbulence model [3, 4]. More details about the numerical calculation of dispersed multiphase flow may be found in the publications [5–7].

2 Equation of Motion for Particles

The motion of particles in fluids may be described in a Lagrangian way by solving a set of ordinary differential equations along the trajectory in order to calculate the change of particle location and the linear as well as angular components of the particle velocity. This requires the consideration of all relevant forces acting on the particle. The equation of motion for small spherical particles in a viscous quiescent fluid (i.e., for small particle Reynolds numbers, which is also referred to as Stokes flow) goes back to the pioneering work of Basset, Boussinesq, and Oseen [8–10]. Therefore, the equation of motion is mostly referred to as BBO equation. Numerous publications deal with the extension of the BBO equation for turbulent flows. The thesis of Tchen [11] was probably the first study on particle motion in turbulent flows based on the BBO equation. A rigorous derivation of the equation of motion for small spherical particles in nonuniform flow has been performed by Maxey and Riley [12]. Neglecting the Faxen terms (for details see [3]), the equation proposed by Maxey and Riley [12] for small particle Reynolds numbers is as follows:

$$m_P \frac{d\vec{u}_P}{dt} = \frac{18\mu_F}{\rho_P D_P^2} m_P (\vec{u}_F - \vec{u}_P) - m_F \frac{D\vec{u}_F}{Dt} + 0.5 m_F \left(\frac{D\vec{u}_F}{Dt} - \frac{d\vec{u}_P}{dt} \right) + 9 \sqrt{\frac{\rho_F \mu_F}{\pi}} \frac{m_P}{\rho_P D_P} \int_{-\infty}^{t} \frac{\frac{D\vec{u}_F}{D\tau} - \frac{d\vec{u}_P}{d\tau}}{(t-\tau)^{1/2}} d\tau + (m_P - m_F)\vec{g}. \quad (1)$$

VDI-GVC (ed.), *VDI Heat Atlas*, DOI 10.1007/978-3-540-77877-6_48,

The forces on the right-hand side are the drag force, the fluid inertia (resulting from the pressure term), the added mass, the history force, and the gravity force reduced by the buoyancy. In the following sections, a possible extension of the BBO equation and the involved forces for higher particle Reynolds numbers will be introduced. In addition, other forces, which might be relevant for certain flow conditions, such as for example transverse lift forces, will be introduced and their relevance will be discussed. Neglecting heat and mass transfer phenomena, the calculation of particle trajectories requires the solution of three ordinary differential equations when particle rotation is accounted for. Hence, the differential equations for calculating the particle location and the linear and angular velocities in vector form are given by

$$\frac{\mathrm{d}\vec{x}_\mathrm{p}}{\mathrm{d}t} = \vec{u}_\mathrm{p}, \tag{2}$$

$$m_\mathrm{p}\frac{\mathrm{d}\vec{u}_\mathrm{p}}{\mathrm{d}t} = \sum \vec{F}_\mathrm{i}, \tag{3}$$

$$I_\mathrm{p}\frac{\mathrm{d}\vec{\omega}_\mathrm{p}}{\mathrm{d}t} = \vec{T}, \tag{4}$$

where $m_\mathrm{p} = \pi/6\rho_\mathrm{p}D_\mathrm{p}^3$ is the particle mass, $I_\mathrm{p} = 0.1 m_\mathrm{p} D_\mathrm{p}^2$ is the moment of inertia for a sphere, $\vec{F}_\mathrm{i}$ represents the different relevant forces acting on the particle, and $\vec{T}$ is the torque acting on a rotating particle due to the viscous interaction with the fluid.

Analytical solutions for the different forces and the torque only are available for small particle Reynolds numbers (i.e., Stokes regime). An extension to higher Reynolds numbers is generally based on introducing empirical correlations, which are derived from experiments or nowadays also from direct numerical simulations (DNS). The different forces relevant for particle motion [13] are introduced and discussed in the following sections.

3 Forces Relevant for Translational Motion of Particles

3.1 Drag Force

In most fluid–particle systems, the drag force is dominating the particle motion and consists of a friction and form drag. The extension of the drag force to higher particle Reynolds numbers is based on the introduction of a drag coefficient C_D, which is obtained from measurements of the drag force in a wind tunnel or a sedimentation experiment:

$$C_\mathrm{D} = \frac{F_\mathrm{D}}{\frac{\rho_\mathrm{F}}{2}(\vec{u}_\mathrm{F} - \vec{u}_\mathrm{P})^2 A_\mathrm{P}}, \tag{5}$$

where $A_\mathrm{P} = \pi/4 D_\mathrm{P}^2$ is the cross-section of a spherical particle. The drag force is then expressed by

$$\vec{F}_\mathrm{D} = \frac{3}{4}\frac{\rho_\mathrm{F} m_\mathrm{P}}{\rho_\mathrm{P} D_\mathrm{P}} c_\mathrm{D}(\vec{u}_\mathrm{F} - \vec{u}_\mathrm{P})|\vec{u}_\mathrm{F} - \vec{u}_\mathrm{P}|. \tag{6}$$

The drag coefficient is given as a function of the particle Reynolds number, defined as the ratio of inertial force to friction force:

$$\mathrm{Re}_\mathrm{P} = \frac{\rho_\mathrm{F} D_\mathrm{P}(\vec{u}_\mathrm{F} - \vec{u}_\mathrm{P})}{\mu_\mathrm{F}}. \tag{7}$$

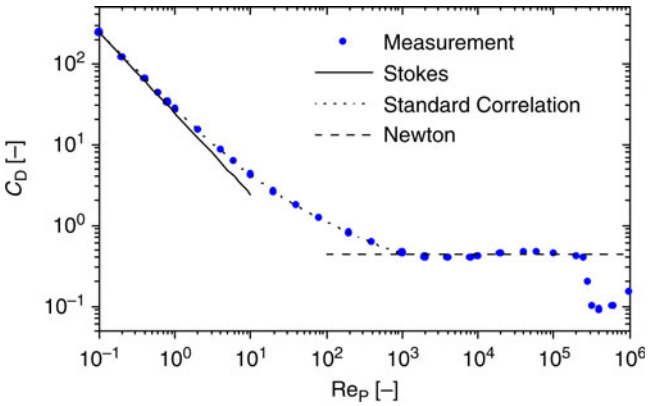

L3.1. Fig. 1. Drag coefficient as a function of particle Reynolds number, comparison of experimental data with correlations for the different regimes (the standard correlation corresponds to Eq. (9)).

The dependence of the drag coefficient of a sphere (spherical particle) on the Reynolds number is shown in Fig. 1 based on numerous experimental investigations (see for example [14]). From this dependence, one may identify several regimes which are associated with certain flow characteristics around the sphere.

- For small Reynolds numbers (i.e., $\mathrm{Re_P} < 0.5$), viscous effects are dominating and no separation of the flow around the particle is observed. Therefore, an analytical solution for the drag coefficient is possible as proposed by Stokes [15]:

$$C_\mathrm{D} = \frac{24}{\mathrm{Re_P}}. \tag{8}$$

This regime is referred to as the Stokes regime.

- In the transition region (i.e., $0.5 < \mathrm{Re_P} < 1{,}000$), inertial effects become of increasing importance. Above a Reynolds number of about 24, the flow around the particle begins to separate. Initially, this separation is symmetric [16]. It becomes unstable and periodic above $\mathrm{Re_P} \approx 130$. For this nonlinear regime, numerous correlations have been proposed [3, 16] which fit the experimental data more or less accurate. A frequently used correlation is that proposed by Schiller and Naumann [17], which fits the data up to $\mathrm{Re_P} = 1{,}000$ reasonably well (see Fig. 1):

$$C_\mathrm{D} = \frac{24}{\mathrm{Re_P}}(1 + 0.15\ \mathrm{Re_P^{0.687}}) = \frac{24}{\mathrm{Re_P}} f_\mathrm{D}. \tag{9}$$

- Above $\mathrm{Re_P} \approx 1{,}000$, the flow is fully turbulent and the drag coefficient remains almost constant up to the critical Reynolds number, since wake size and structure is not considerably changing. This regime is referred to as Newton regime with:

$$C_\mathrm{D} \approx 0.44. \tag{10}$$

- At the critical Reynolds number ($\mathrm{Re_{crit}} \approx 2.5 \cdot 10^5$), a drastic decrease of the drag coefficient is observed, being caused by the transition from a laminar to a turbulent boundary layer around the particle. This results in a decrease of the particle wake size.

- In the super-critical region (i.e., $Re_P > 4.0 \cdot 10^5$), the drag coefficient again increases continuously. For most practical particulate flows, however, this region is not relevant.

The drag coefficient may be altered by numerous other physical effects, such as turbulence of the surrounding flow, surface roughness of the particle, particle shape, wall effects, compressibility of the fluid, rarefaction effects, and particle concentration effects. All these effects can in general only be accounted for by empirical correction factors or functions being derived from detailed experiments.

The *turbulence level of the ambient flow* essentially causes a reduction in the critical Reynolds number as shown by Torobin and Gauvin [18]. With increasing turbulence intensity, the transition from laminar to turbulent boundary layer, i.e., the critical Reynolds number is shifted toward smaller particle Reynolds numbers.

A *surface roughness* on a spherical particle causes a reduction in the critical Reynolds number [19] since this is also associated with a modification of the boundary layer. The increasing effective surface area should however also yield an increase of the drag coefficient.

The *particle shape* has a strong influence on the drag force but also the transverse lift forces and the moment exerted on a particle. Additionally, a profile lift is acting on nonspherical particles. Naturally, the drag coefficient depends on the orientation of a nonspherical particle with respect to the instantaneous relative velocity vector. In order to account for the shape effect, this requires solving additionally for the particle rotational motion. For the Stokes regime, the hydrodynamic forces on ellipsoidal particles were analytically determined by Brenner [20] and the hydrodynamic torque by Jeffery [21]. The importance of considering particle shape effects also in technical processes, e.g., biomass burners, where the particle Reynolds number is mostly much larger than one was emphasized by Rosendahl [22]. However, in such a situation, data is required, which describes the drag coefficient (and the resistance coefficients of the transverse lift forces) as a function of the particle orientation. Such data for the drag coefficient are very rare. Regarding transverse lift forces almost no information is available on the particle shape effect. One attempt in creating such data was undertaken by Hölzer and Sommerfeld [23] by using the Lattice Boltzmann method for simulating the flow across differently shaped particles. Also, there is very little known about particle shape effects in the other forces, such as added mass and Basset force.

For most practical computations, where the particles are considered as point-particles anyway, the calculation of the change in particle orientation is not feasible. However, it is possible to approximately account for particle shape effects on the drag coefficient using a simplified approach on the basis of the correlations proposed by, e.g., Haider and Levenspiel [24], Thompson and Clark [25]. These correlations were evaluated on the basis of numerous experimental data obtained for particles fixed in a wind tunnel or from sedimenting particles. Hence, the drag coefficient is obtained for a given particle orientation. This is also the case in a sedimentation analysis since the particles will sediment in a more or less stable orientation for which the drag coefficient is maximized, i.e., discs will sediment horizontally aligned. The correlation proposed by Haider and Levenspiel [24] has the form:

$$C_D = \frac{24}{Re_P}\left(1 + A\ Re_P^B\right) + \frac{C}{1 + \frac{D}{Re_P}}. \tag{11}$$

The coefficients A–D are depending on the sphericity of the particle, which is defined as the ratio of the surface area of a volume equivalent sphere to the surface area of the considered nonspherical particle.

$$\phi = \frac{S_V}{S_{Particle}}. \tag{12}$$

The correlation coefficients A–D are

$$\begin{aligned} A &= \exp\left(2.3288 - 6.4581\phi + 2.4486\phi^2\right), \\ B &= 0.0964 + 0.5565\phi, \\ C &= \exp\left(4.905 - 13.8944\phi + 18.4222\phi^2 - 10.2599\phi^3\right), \\ D &= \exp\left(1.4681 + 12.2584\phi - 20.7322\phi^2 + 15.8855\phi^3\right). \end{aligned} \tag{13}$$

These correlations were obtained from experimental data for isometric nonspherical particles (i.e., cube octahedrons $\phi = 0.906$, octahedrons $\phi = 0.846$, cubes $\phi = 0.806$, and tetrahedrons $\phi = 0.67$) and disc-like particles with sphericities of $\phi = 0.026$, 0.043, 0.123, and 0.230. The drag coefficient according to Eq. (11) is plotted in Fig. 2 as a function of particle Reynolds number, defined with the volume equivalent diameter, with the sphericity as a parameter. This result reveals that the drag coefficient is increasing with decreasing sphericity. This increase is smaller in the Stokes regime compared to the Newton regime where the drag coefficient increases by several orders of magnitude. Moreover, the transition to the Newton regime (fully turbulent regime) is shifted to smaller particle Reynolds numbers with decreasing sphericity. Additionally, the width of the intermediate regime (i.e., between laminar and turbulent) is reduced. It should be noted that the sphericity is not the only possible parameter to characterize the particle shape. This parameter becomes meaningless when particles with rough surfaces

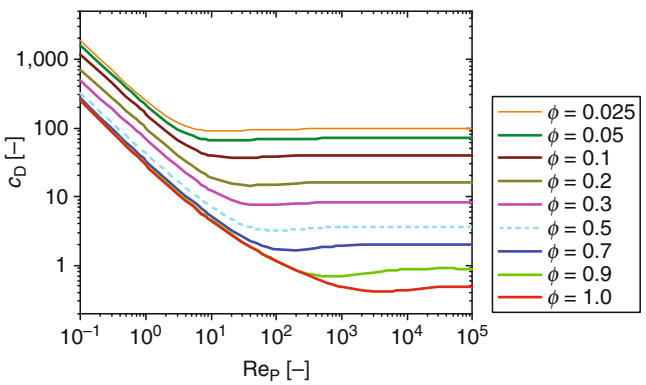

L3.1. Fig. 2. Drag coefficient of nonspherical particles as a function of particle Reynolds number with the sphericity as a parameter according to Eq. (11) [24].

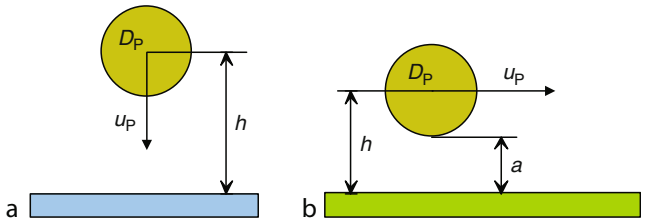

L3.1. Fig. 3. Illustration of wall effects: (**a**) motion normal to a wall; (**b**) motion parallel to a wall.

are considered whereby the sphericity approaches very small values. Therefore, also other parameters are used for shape characterization, such as aspect ratios, roundness, and a hydrodynamic shape descriptor called scruple [25].

The drag correlation proposed by Ganser [26] is based on using a Stokes- and Newton-shape factor, which are combined with the particle Reynolds number to give a generalized parameter $Re_P \cdot K_1 \cdot K_2$. Both shape descriptors are obtained as functions of the sphericity and the projected area in the direction of motion. Hence, this correlation includes the influence of particle orientation with respect to the relative flow.

The *motion of particles in the vicinity of a rigid wall* results in an increase of the drag coefficient and is additionally associated with a transverse lift force. Analytic solutions for the wall effect are again only available for very small particle Reynolds numbers. The particle motion normal to a wall (Fig. 3a) was for example considered by Brenner [27] and a wall-parallel motion (Fig. 3b) was analyzed by Goldman et al. [28, 29]. The first-order solution for a spherical particle moving toward a wall, which is valid for large distances from the wall, is given by [27]:

$$\frac{C_D}{C_{D,Stokes}} \cong 1 + \frac{9}{8}\frac{R_P}{h} + \left(\frac{9}{8}\frac{R_P}{h}\right)^2. \tag{14}$$

For a nonrotating spherical particle moving parallel to a wall in a quiescent fluid the increase of the drag is predicted by an asymptotic solution proposed by Faxen (see Goldman et al. [28]) for large distances from the wall:

$$\frac{C_D}{C_{D,Stokes}} = \left[1 - \frac{9}{16}\left(\frac{R_P}{h}\right) + \frac{1}{8}\left(\frac{R_P}{h}\right)^3 - \frac{45}{256}\left(\frac{R_P}{h}\right)^4 - \frac{1}{16}\left(\frac{R_P}{h}\right)^5\right]^{-1}. \tag{15}$$

The two results are shown in Fig. 4 as a function of the normalized gap between particle and wall (i.e., a/R_P). For large wall distance, the curves approach unity and a finite value is obtained for $a/R_P \to 0$. It should be noted that wall effects will be additionally influenced by particle rotation and a shear flow in the vicinity of the wall [28, 29].

Rarefaction effects become of importance in a low pressure environment or when the particles are very small (e.g., nanoparticles). In such a situation, the flow around the particle cannot be regarded as a continuum, instead the particle motion is induced by collisions of gas molecules with the particle surface. This implies that the no-slip condition at the particle surface is not anymore fulfilled. Rather, a partial or full slip is

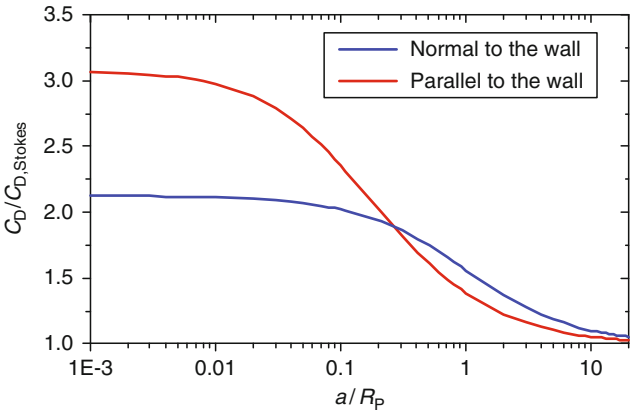

L3.1. Fig. 4. Modification of drag coefficient for a particle moving normal and parallel to a wall (Eqs. (14) and (15)).

found at the surface. This results in a reduction of the drag coefficient. The importance of rarefaction effects may be estimated based on the ratio of the mean free path of the gas molecules to the particle diameter, which is the particle Knudsen number:

$$Kn_p = \frac{\lambda}{D_p}. \tag{16}$$

The mean free path of the gas molecules λ can be calculated according to kinetic theory of gases from:

$$\lambda = \frac{\mu_F}{0.499\overline{c_{Mol}}\rho_F}, \tag{17}$$

where $\overline{c_{Mol}}$ is the standard deviation of the gas molecule velocity distribution (Maxwellian distribution) given by

$$\overline{c_{Mol}} = \left(\frac{8p}{\pi\rho_F}\right)^{1/2}. \tag{18}$$

Here ρ_F and p are the fluid density and the pressure, respectively. For atmospheric conditions (i.e., $p = 1.0$ bar, $T = 293$ K), the mean free path is about 0.06 µm. A classification of the different flow regimes in rarefied conditions or for very small particles may be based on the Knudsen number and is summarized in Table 1. In the Stokes regime which is generally valid for very small particles, the reduction of the drag coefficient may be accounted for by a correction function, the so-called Cunningham correlation [30]:

$$C_D = \frac{C_{D,Stokes}}{1 + Kn_P\left\{2.514 + 0.8\exp\left(-\frac{0.55}{Kn_P}\right)\right\}} = \frac{C_{D,Stokes}}{Cu}. \tag{19}$$

This correlation is valid for $0.1 < Kn_P < 1{,}000$ and $Re_P < 0.25$ and is only applicable for low particle Mach numbers. Therefore, it is often used in particle technology, as for example when considering the separation of fine particles from a gas stream.

The Cunningham correction, i.e., 1/Cu, is plotted in Fig. 5 as a function of the Knudsen number. It is obvious that a considerable reduction of the drag coefficient occurs for $Kn_P > 0.012$. At a Knudsen number of one (i.e., $\lambda = D_P$), the particle drag is already reduced by about 75% compared to the continuum regime.

L3.1. Table 1. Different regimes of rarefied flows with respect to particle motion

Flow regime	Range of Knudsen number
Continuum flow	$0 < \mathrm{Kn_P} < 0.015$
Slip flow	$0.015 < \mathrm{Kn_P} < 0.15$
Transition flow	$0.15 < \mathrm{Kn_P} < 4.5$
Free molecular flow	$4.5 < \mathrm{Kn_P} < \infty$

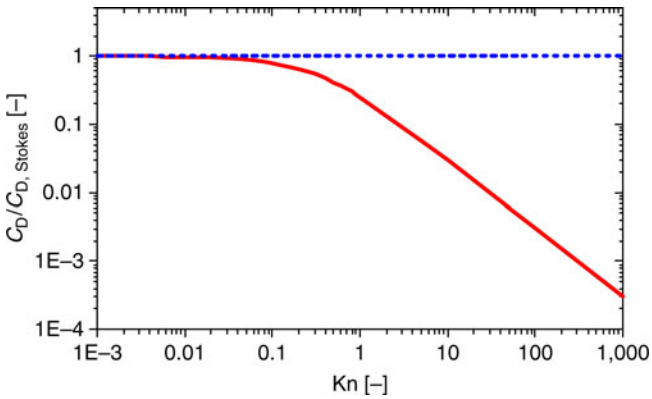

L3.1. Fig. 5. Modification of the drag coefficient due to rarefaction effects (Eq. (19)).

At *higher volume fraction* of the dispersed phase, a reduction of the sedimentation or rise velocity is observed in many technical multiphase flow processes. This phenomenon results mainly from the hydrodynamic interaction between the particles and is termed as hindered settling or rise, as well as swarm effect. A direct consideration of this phenomenon is only possible using DNS with resolving the flow around individual particles. For technical multiphase systems, this is however not feasible and therefore, mainly empirical correlations are being used in engineering computations. A well-known correlation obtained from the sedimentation of a concentrated suspension and the fluidization of a liquid–solid system (solids volume fraction between 1% and 20%) is that of [31]. They provided correlations for the decrease of the sedimentation velocity with increasing solids volume fraction on the basis of a power law with the exponent being dependent on the single-particle Reynolds number. This work was extended by Wen and Yu [32] who found a constant exponent for the entire relevant range of particle Reynolds numbers. The resulting modified drag coefficient for dispersed phase volume fractions up to $\alpha_P < 20\%$ or porosities larger than $\varepsilon > 80\%$ is given by

$$C_{D,sw} = C_D^* \cdot \varepsilon^{-1.65}. \tag{20}$$

Since the studies were performed using a fluidization experiment the single particle drag coefficient C_D^* is defined with the particle Reynolds number calculated on the basis of the superficial fluid velocity U_0, which can be replaced by the product of the relative (slip) velocity and the porosity:

$$C_D^* = \min\left\{\frac{24}{\mathrm{Re}_{P,S}}(1 + 0.15\ \mathrm{Re}_{P,S}^{0.687}), 0.44\right\}, \tag{21}$$

$$\mathrm{Re}_{P,s} = \frac{\rho_F D_P \varepsilon(\vec{u}_F - \vec{u}_P)}{\mu_F}. \tag{22}$$

Due to its simplicity, Eq. (20) is the most frequently applied correlation in the frame of a Lagrangian tracking approach. Other correlations are also provided in the book of Michaelides [7]. For higher dispersed phase volume fractions where mostly an Eulerian model is applied, drag correlations obtained for packed beds have to be used, e.g., the well-known correlation of Ergun [33].

3.2 Pressure Gradient and Buoyancy Force

The local pressure gradient in the flow gives rise to an additional force in the direction of the pressure gradient. Combining the pressure gradient in the fluid with the shear stress one obtains:

$$F_p = \frac{m_p}{\rho_p}(-\nabla p + \nabla\vec{\tau}). \tag{23}$$

From the Navier–Stokes equation of the fluid the pressure gradient and the shear stress can be related to the fluid acceleration and the gravity force:

$$-\nabla p + \nabla\vec{\tau} = \rho_F\left(\frac{\mathrm{D}\vec{u}_F}{\mathrm{D}t} - \vec{g}\right). \tag{24}$$

Hence, the total pressure force is obtained in the following form:

$$\vec{F}_p = m_p\frac{\rho_F}{\rho_p}\left(\frac{\mathrm{D}\vec{u}_F}{\mathrm{D}t} - \vec{g}\right). \tag{25}$$

The first term of Eq. (25) represents the fluid acceleration and the second one is the buoyancy force. It is obvious that in gas–solid flows, the pressure force may be neglected since $\rho_F/\rho_p << 1$. However, in liquid–solid or liquid–gas flows, this force is of importance.

3.3 Added Mass and Basset Force

The acceleration/deceleration of a particle in a fluid also requires accelerating/decelerating a certain fraction of fluid surrounding the particle, this is the so-called added mass. The Basset force is caused by the lagging of the boundary layer development on the particle surface with changing relative velocity (i.e., acceleration or deceleration of the particle and/or fluid) and is often referred to as "history" force. Analytic solutions for both forces are only available for small particle Reynolds numbers (see Eq. (1)). An extension to higher particle Reynolds numbers is only possible by introducing empirical coefficients C_A and C_B similar to the drag coefficient. Based on an experimental study of Odar and Hamilton [34], who examined the motion of a sphere in simple harmonic motion, the added mass and Basset force are expressed as

$$F_A = 0.5 C_A \rho_F \frac{m_P}{\rho_P}\frac{\mathrm{d}}{\mathrm{d}t}(\vec{u}_F - \vec{u}_P), \tag{26}$$

$$F_B = 9\sqrt{\frac{\rho_F\mu_F}{\pi}}\frac{m_P}{\rho_P D_P} \cdot C_B\left\{\int_0^t \frac{\frac{\mathrm{d}}{\mathrm{d}\tau}(\vec{u}_F - \vec{u}_P)}{(t-\tau)^{1/2}}\mathrm{d}\tau + \frac{(\vec{u}_F - \vec{u}_P)_0}{\sqrt{t}}\right\}. \tag{27}$$

The second term in the Basset force accounts for an initial slip velocity at $t = 0$ [35]. The coefficients C_A and C_B were obtained from the experiments of Odar and Hamilton [34] in the following form:

$$C_A = 2.1 - \frac{0.132}{A_C^2 + 0.12}, \tag{28}$$

$$C_B = 0.48 + \frac{0.52}{(A_C + 1)^3}. \tag{29}$$

The parameter A_C is called acceleration number and is defined by

$$A_C = \frac{|\vec{u}_F - \vec{u}_P|^2}{D_P \left| \frac{d|\vec{u}_F - \vec{u}_P|}{dt} \right|}. \tag{30}$$

It is obvious that the Basset force is quite time consuming to solve since it has to be integrated along the entire particle trajectory for each time step of the trajectory calculation. Therefore, this force is often neglected. An approximate solution procedure for the Basset force was introduced by Michaelides [36]. Numerical calculations of Sommerfeld [37] have shown that the consideration of the Basset force increases the computational time by a factor of about 10. An analysis of the importance of the different forces, especially added mass and Basset force, in an oscillatory flow field for different density ratios will be provided below.

3.4 Body Forces

Body or field forces are the gravity-buoyancy force, the Coulomb force, which arises when a particle moves in an electric field, as for example in an electrostatic precipitator or the thermophoretic force, which becomes of importance when a small particle moves in a flow with a high temperature gradient.

The gravity force is

$$\vec{F}_g = m_p \vec{g}. \tag{31}$$

The Coulomb force acting on a particle moving in an electric field with field strength $\vec{E}$ is given by

$$F_C = -q_p \vec{E}, \tag{32}$$

where q_p is the charge of the particle. In an electrostatic precipitator, for example, the particles are charged through an ion-bombardment created by a negative corona discharge in the vicinity of a charging wire. The charging of the particles is caused by two mechanisms, namely field charging and diffusion charging. The relevance of either of these mechanisms depends on the particle size. Field charging is dominant for particles larger than 2 μm while diffusion charging is prevailing for particles smaller than 0.2 μm [38]. In most cases, the temporal evolution of the charging process is not considered, rather the saturation charge or a portion of it is assumed. For the determination of the electrostatic force acting on the particle, additionally the electric field has to be calculated or a certain value may be assumed. More details about particle charging and their motion in an electric field may be found in the book of White [39].

3.5 Slip-Shear Lift Force

Particles moving in a shear layer experience a transverse lift force due to the nonuniform relative velocity over the particle and the resulting nonuniform pressure distribution. The lift force is acting toward the direction of higher slip velocity (Fig. 6). An expression for the slip-shear lift force for a freely rotating particle moving at constant velocity in a two-dimensional shear flow at low Reynolds number was derived from an asymptotic expansion by Saffman [40, 41]:

$$F^y_{LS,Saff} = 6.46 \frac{D_p^2}{4} (\rho_F \mu_F)^{0.5} \left| \frac{\partial u_F}{\partial y} \right| (u_F - u_p). \tag{33}$$

Extending this expression to a three-dimensional flow and introducing a correction function for higher particle Reynolds numbers yields:

$$\vec{F}_{LS} = 1.615 D_p^2 (\rho_F \mu_F)^{1/2} \left(\frac{1}{|\vec{\omega}_F|} \right)^{0.5} \cdot \{(\vec{u}_F - \vec{u}_P) \times \vec{\omega}_F\} f(\mathrm{Re}_P, \mathrm{Re}_S). \tag{34}$$

Here the fluid rotation is obtained from

$$\vec{\omega}_F = \mathrm{rot}\ \vec{u}_F = \nabla \times \vec{u}_F. \tag{35}$$

Introducing now a lift coefficient in Eq. (34) gives the following expression for the slip-shear lift force:

$$\vec{F}_{LS} = \frac{\rho_F}{2} \frac{\pi}{4} D_p^2 C_{LS} D_P ((\vec{u}_F - \vec{u}_p) \times \vec{\omega}_F), \tag{36}$$

with the lift coefficient given as

$$C_{LS} = \frac{2.90805}{\beta^{0.5} \mathrm{Re}_p^{0.5}} f(\mathrm{Re}_P, \mathrm{Re}_S). \tag{37}$$

The correction function $f(\mathrm{Re}_P, \mathrm{Re}_S)$ proposed by Mei [42] on the basis of calculations performed by Dandy and Dwyer [43] for a particle Reynolds number in the range $0.1 \le \mathrm{Re}_P \le 100$ is given by

$$f(\mathrm{Re}_P, \mathrm{Re}_S) = \frac{F_{LS}}{F_{LS,Saff}}, \tag{38}$$

$$f(\mathrm{Re}_P, \mathrm{Re}_S) = \left(1 - 0.3314\beta^{1/2}\right) \exp\left(-\frac{\mathrm{Re}_P}{10}\right) + 0.3314\beta^{1/2} \quad \text{for } \mathrm{Re}_P \le 40$$
$$= 0.0524(\beta\ \mathrm{Re}_P)^{1/2} \quad \text{for } \mathrm{Re}_P \ge 40, \tag{39}$$

with

$$\beta = 0.5 \frac{\mathrm{Re}_S}{\mathrm{Re}_P} \tag{40}$$

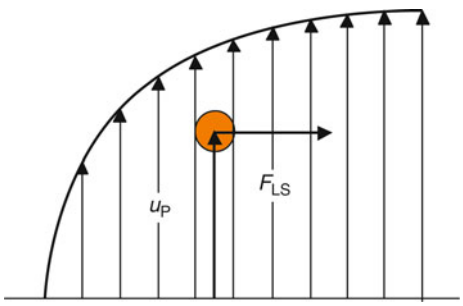

L3.1. Fig. 6. Illustration of the action of slip-shear lift force.

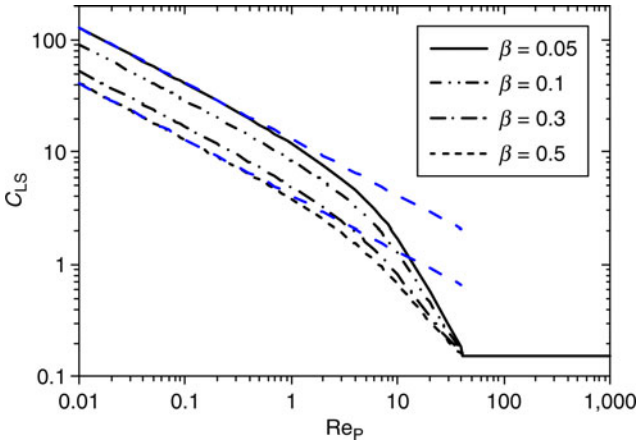

L3.1. Fig. 7. Lift coefficient as a function of particle Reynolds number with the nondimensional shear rate β as a parameter. The upper and lower straight lines indicate the lift coefficients according to the Saffman equation, i.e., Eq. (37) with $f(Re_P, Re_S) = 1.0$.

and the particle Reynolds number of the shear flow:

$$Re_S = \frac{\rho_F D_p^2 |\vec{\omega}_F|}{\mu_F}. \tag{41}$$

The dependence of the lift coefficient on the particle Reynolds number with the nondimensional shear rate β as a parameter is shown in Fig. 7. The lift coefficient continuously decreases within the first regime, i.e., from the Stokes limit up to $Re_P = 40$ (Eq. (39)), and then remains constant for higher particle Reynolds numbers. With increasing nondimensional shear rate the lift coefficient is decreasing in the first regime and independent of the shear rate in the second regime (see Eq. (39)). The upper and lower straight dashed lines indicate the result for the Saffman expression, which agree for the considered nondimensional shear rates only with the lift coefficient of Eq. (37) for particle Reynolds numbers up to 0.5. For the smallest shear rate considered a slight kink is found at the transition particle Reynolds number of 40.

3.6 Slip-Rotation Lift Force

Particles, which are not freely rotating in a flow, may also experience a lift force due to their rotation, the so-called Magnus force. High particle rotations may, for example, be induced by particle–wall collisions frequently occurring in confined flows, such as, pipe or channel flows [44, 45]. The rotation of the particle results in a displacement of the flow field around the particle, associated with a shift of the stagnation points and a transverse lift force (Fig. 8). An analytic expression for the slip-rotation lift force in the case of small particle Reynolds numbers was derived by Rubinow and Keller [46]:

$$\vec{F}_{LR} = \pi R_p^3 \rho_F \left\{ \vec{\Omega} \times \left(\vec{u}_F - \vec{u}_p \right) \right\}, \tag{42}$$

where $\vec{\Omega}$ is the relative rotation given by

$$\vec{\Omega} = \frac{1}{2} \nabla \times \vec{u}_F - \vec{\omega}_p. \tag{43}$$

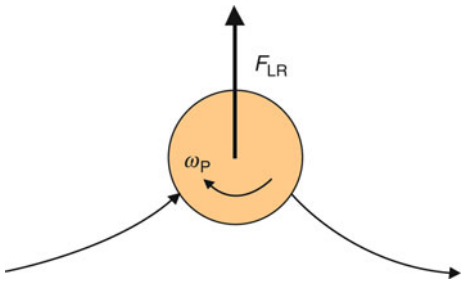

L3.1. Fig. 8. Illustration of the slip-rotation lift force acting on a stationary particle.

Also, the slip-rotation lift force may be extended for higher particle Reynolds numbers by introducing a lift coefficient [3]:

$$\vec{F}_{LR} = \frac{\rho_F}{2} \frac{\pi}{4} D_p^2 C_{LR} \left| \vec{u}_F - \vec{u}_p \right| \frac{\vec{\Omega} \times \left(\vec{u}_F - \vec{u}_p \right)}{\left| \vec{\Omega} \right|}. \tag{44}$$

For small particle Reynolds numbers, the lift coefficient is obtained according to Rubinow and Keller [46] in the form:

$$C_{LR} = 2\gamma = \frac{D_p \left| \vec{\Omega} \right|}{\left| \vec{u}_F - \vec{u}_p \right|} = \frac{Re_R}{Re_p}, \tag{45}$$

with

$$Re_R = \frac{\rho_F D_p^2 \left| \vec{\Omega} \right|}{\mu_F} \tag{46}$$

being the Reynolds number of particle rotation and γ the nondimensional relative rate of rotation. A lift coefficient for higher particle Reynolds numbers requires experimental information. Oesterlé and Bui Dinh [47] introduced the following correlation based on available literature data and additional own experiments for $Re_P < 140$:

$$C_{LR} = 0.45 + (2\gamma - 0.45) \cdot \exp(-0.075\gamma^{0.4} \cdot Re_p^{0.7}) \quad \text{for } Re_P < 140. \tag{47}$$

In the publication of Oesterlé and Bui Dinh [47], it is suggested that this correlation may be used up to particle Reynolds numbers of 2,000. The lift coefficient of particle rotation as a function of the particle Reynolds number with the nondimensional relative rate of rotation as a parameter is shown in Fig. 9. With increasing particle Reynolds number, the rotational lift coefficient continuously reduces up to about $Re_P = 500$ and then remains almost constant. In the first regime (i.e., up to $Re_P = 500$), the rotational lift coefficient increases with γ and in the second regime, it is independent of γ. This, however, does not agree with other high Reynolds number results provided in the literature; see for example Sawatzki [48]. Here the rotational lift coefficient increases linearly from $\gamma = 0$ to $\gamma = 1.3$ and then remains constant with a value of $C_{LR} = 0.47$. Hence, further studies are still necessary for obtaining the correct limits at higher particle Reynolds numbers of rotation. The horizontal lines between $0.1 < Re_P < 1.0$ correspond to the result of Rubinow and Keller [46] given by Eq. (45). It is obvious that this expression only holds for small particle Reynolds numbers of translation and rotation.

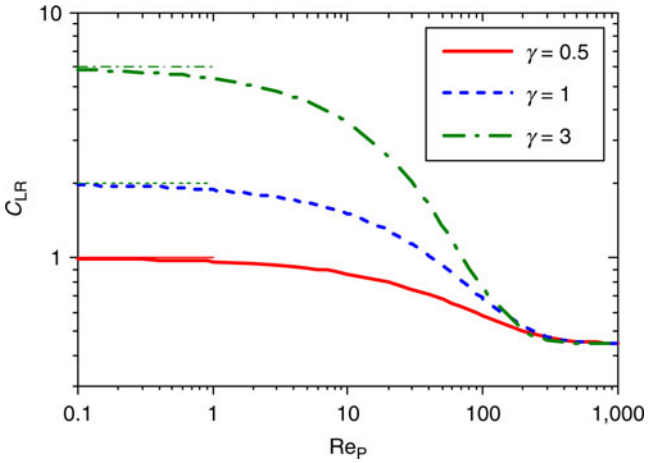

L3.1. Fig. 9. Lift coefficient of particle rotation as a function of particle Reynolds number with the nondimensional relative rate of rotation γ as a parameter. The horizontal lines correspond to the result of Rubinow and Keller [46] given by Eq. (45).

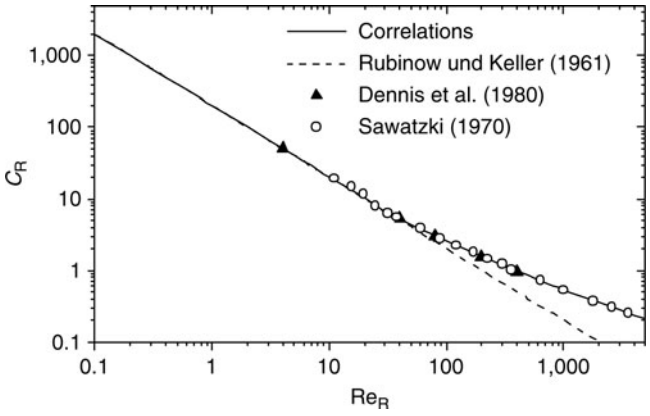

L3.1. Fig. 10. Coefficient of particle rotation as a function of particle rotational Reynolds number according to Eqs. (50) and (51) and comparison with experiments [50] and numerical calculations [49].

4 Torque on Rotating Particles

The torque acting on a rotating particle due to the interaction with the fluid was also derived by Rubinow and Keller [46] for a stagnant fluid and small particle Reynolds numbers:

$$\vec{T} = \pi \mu_F D_p^3 \vec{\omega}_p. \tag{48}$$

This expression may be extended for a three-dimensional flow and for higher Reynolds numbers by introducing a rotational coefficient:

$$\vec{T} = \frac{\rho_F}{2}\left(\frac{D_p}{2}\right)^5 C_R \left|\vec{\Omega}\right| \vec{\Omega}. \tag{49}$$

From the numerical simulations of Dennis et al. [49] and experimental data of Sawatzki [50], the rotational coefficient for higher particle Reynolds numbers is found to be

$$C_R = \frac{12.9}{Re_R^{0.5}} + \frac{128.4}{Re_R} \quad \text{for } 32 < Re_R < 1{,}000. \tag{50}$$

In the case of smaller particle, Reynolds numbers the result of Rubinow and Keller [46] yields:

$$C_R = \frac{64\pi}{Re_R} \quad \text{for } Re_R < 32. \tag{51}$$

The comparison of the above correlations (Eqs. (50) and (51)) with the simulations [49], and the experiments [50] yields a good agreement as shown in Fig. 10.

5 Particle Response Time and Stokes Number

The particle velocity or momentum response time may be used to characterize the capability of particles to follow a sudden velocity change in the flow, occurring, for example, in large scale vortex structures [51] or turbulent eddies. In order to derive the particle response time, the equation of motion is used by only considering the drag force:

$$m_p \frac{du_p}{dt} = \frac{\rho_F}{2}\frac{\pi}{4} D_p^2 C_D \left|u_F - u_p\right| (u_F - u_p). \tag{52}$$

Dividing by the particle mass and introducing the particle Reynolds number gives:

$$\frac{du_p}{dt} = \frac{18\mu_F}{\rho_p D_p^2}\frac{C_D\, Re_P}{24}(u_F - u_p). \tag{53}$$

The term $C_D\, Re_P/24$ corresponds to the nonlinear term in the drag coefficient f_D (Eq. (9)) and the reciprocal of the first term of Eq. (53) has the dimension of a time, the particle response time:

$$\tau_p = \frac{\rho_p D_p^2}{18\mu_F f_D}. \tag{54}$$

Hence the equation of motion becomes:

$$\frac{du_p}{dt} = \frac{1}{\tau_p}(u_F - u_p). \tag{55}$$

The solution of this equation for a simplified case, namely a jump of the fluid velocity from zero to u_F and an initial particle velocity of zero is

$$u_p = u_F\left(1 - \exp\left(-\frac{t}{\tau_p}\right)\right). \tag{56}$$

From this equation, it is obvious that τ_p is the time required for a particle, released with zero velocity into a flow with u_F, to reach 63.2% of the flow velocity as illustrated in Fig. 11.

In the Stokes regime, where f_D is unity, the particle response time becomes

$$\tau_p = \frac{\rho_p D_p^2}{18\mu}. \tag{57}$$

The Stokes number is the ratio of the particle response time to a characteristic time scale of the flow:

$$St = \frac{\tau_p}{\tau_F}. \tag{58}$$

Considering particle motion in a turbulence field, the fluid flow time scale corresponds to the time scale of the energetic eddies, i.e., the integral time scale of turbulence, $T_L \approx k/\varepsilon$. In the case of particle motion in large scale vortices (occurring, for example, in a shear layer), the eddy passage time across a fixed point in space is the relevant fluid time scale [51].

6 Forces Acting on Bubbles

The motion of bubbles in laminar or turbulent flows is much more complex than that of rigid solid particles. First of all, the interface between bubble and fluid is not rigid and hence an internal flow develops inside the bubbles. This implies that the no-slip condition does not apply at the interface. Thereby, the drag coefficient is reduced compared to a solid particle where the no-slip condition applies at the surface. This behavior of bubbles is depicted in the well-known diagram of Clift et al. [16], where the terminal velocity is plotted versus the volume equivalent diameter obtained from a number of experimental data (Fig. 12). Bubbles moving in clean liquid (fluid bubbles) rise considerably faster than those moving in contaminated liquid (rigid bubbles) for a wide range of bubble sizes. The second issue, which considerably complicates the modelling of bubble motion, is the temporal contamination of the bubble surface by surface active substances, e.g., surfactants. This yields eventually a rigid interface and the bubble behaves like a solid particle, whereby the drag coefficient increases (Fig. 14) and the rise velocity decreases (Fig. 12). The third phenomenon affecting bubble motion is bubble deformation and oscillation, which begins for volume equivalent bubble diameters around 1.5 mm for an air water system. Bubble oscillation is triggered by unsteady wake separation and causes the bubbles to rise in a zigzag or spiral manner.

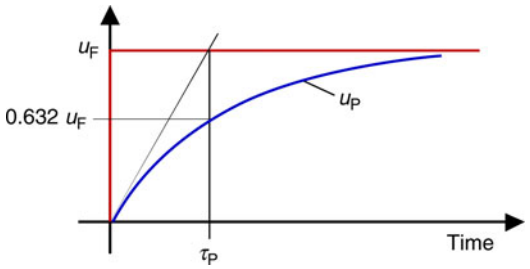

L3.1. Fig. 11. Graphical illustration of the particle response time.

The bubble shape is determined from the relative importance of the fluid dynamic force acting on the bubble to the force due to the surface tension. This ratio yields the Weber number given by

$$\mathrm{We_B} = \frac{|\rho_F - \rho_B| V_B^2 D_e}{\sigma}. \tag{59}$$

In case the Weber number becomes large, the spherical bubble shape cannot be maintained and bubbles become ellipsoidal, wobbling, or spherical-cap. The different bubble shapes can be

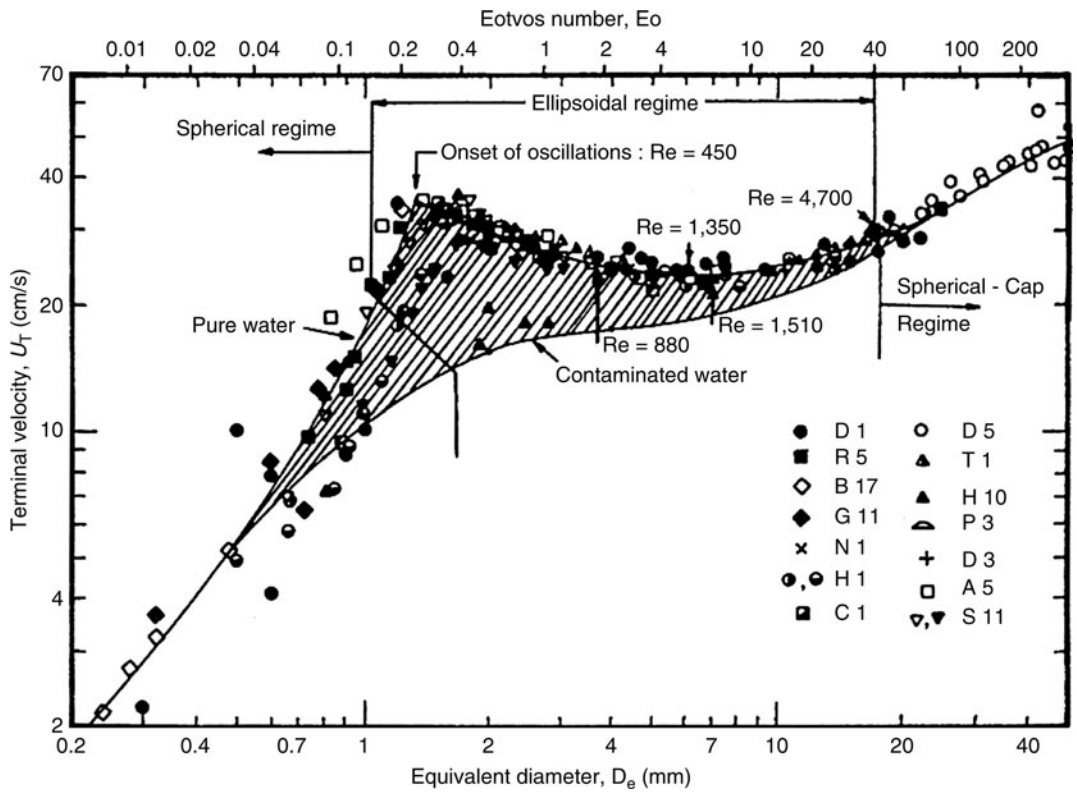

L3.1. Fig. 12. Collection of experimental data for the rise velocity of bubbles in different liquids by Clift et al. [16] together with fitting lines for pure and contaminated liquids.

characterized by introducing two additional nondimensional numbers, namely the Eötvös- and Morton-number:

$$\mathrm{Eo} = \frac{\mathrm{We_B}}{\mathrm{Fr_B}} = \frac{g|\rho_\mathrm{F} - \rho_\mathrm{B}|D_\mathrm{e}^2}{\sigma}, \tag{60}$$

$$\mathrm{Mo} = \frac{g\mu^4|\rho_\mathrm{F} - \rho_\mathrm{B}|}{\rho_\mathrm{F}^2\sigma^3}, \tag{61}$$

where

$$\mathrm{Fr_B} = \frac{V_\mathrm{B}^2}{gD_\mathrm{e}} \tag{62}$$

is the bubble Froude number. These nondimensional parameters are being used to obtain the well-known bubble shape diagram as shown in Fig. 13 [16]. For the numerical calculation of bubble motion, all forces have to be considered such as drag force, pressure force, added mass, Basset force, gravity force, and transverse lift force. The importance of these forces will be discussed below. Nevertheless, the Basset force is neglected in most computational studies due to the considerably increasing numerical effort, which is however not justified for all regimes of bubble size and oscillation frequency of the flow.

Numerous experimental studies are available for the determination of the drag coefficient for different sized bubbles rising in purified or contaminated liquids [52, 53], which were also summarized by Fan and Tsuchiya [54]. These data were obtained my measuring the bubble terminal velocity under

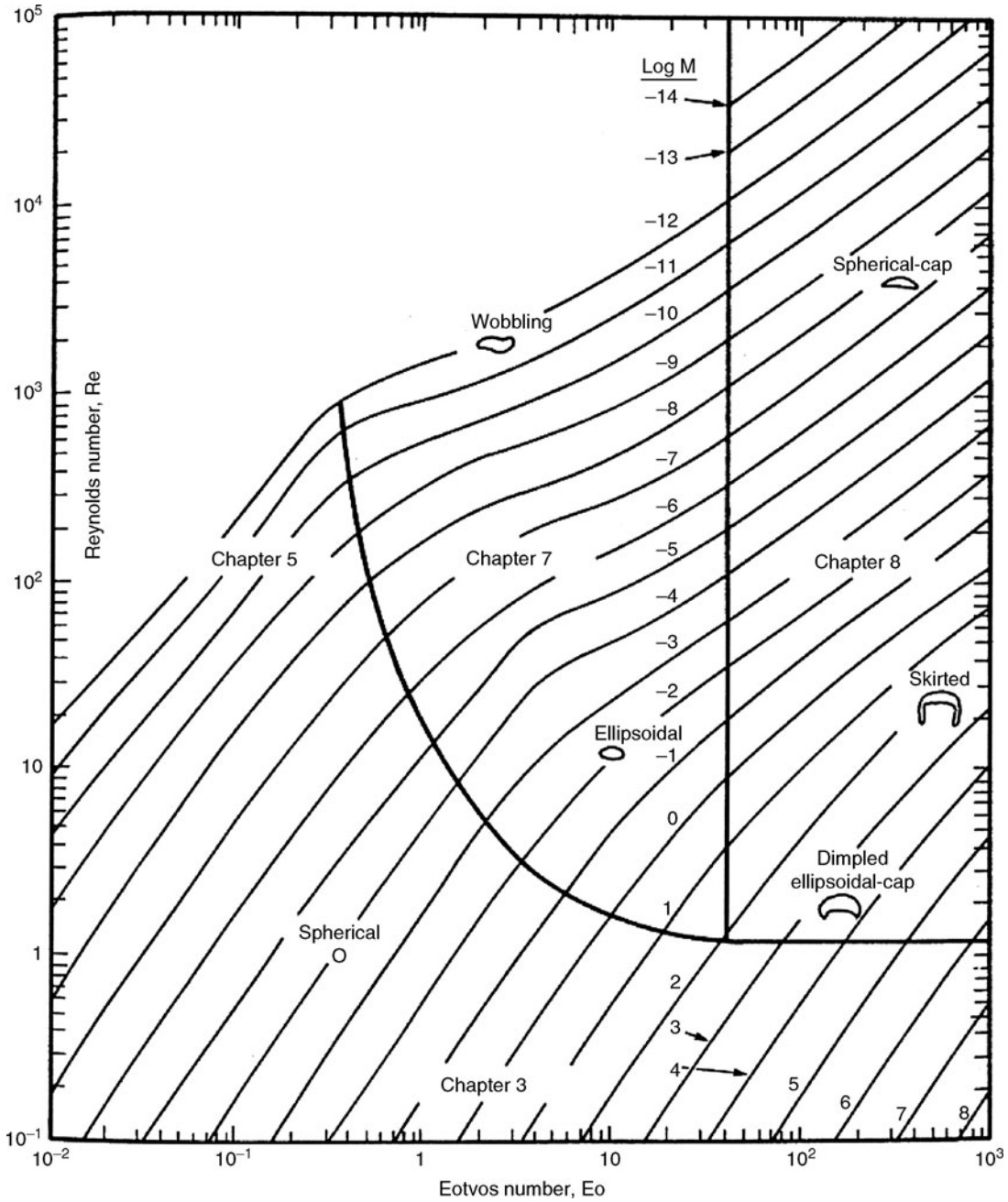

L3.1. Fig. 13. Bubble shape regimes as a function of Reynolds and Eötvös number with the Morton number as a parameter [16].

quasi-steady-state conditions neglecting added mass and Basset forces. In the low Reynolds number regime (including the laminar regime), a clear distinction between bubbles rising in purified and contaminated liquids can be made. In the Stokes regime (and in some cases up to bubble Reynolds numbers larger than 10), contaminated bubbles rise like rigid particles with a drag coefficient of

$$C_D = \frac{24}{Re_B}. \tag{63}$$

Whereas, in purified systems the drag coefficient is lower; namely

$$C_D = \frac{16}{Re_B}. \tag{64}$$

Most critical is the regime of ellipsoidal and wobbling bubbles where the transition of the drag coefficient is extremely affected by the type of liquid considered (see Fig. 14 for $Re_B > 400$). In a contaminated mixture of glycerine and water, for example, this transition is shifted to lower bubble Reynolds numbers if the glycerine content is increased [54].

When the bubble Reynolds number increases beyond about 1530 and the bubbles have a cap-like shape, the degree of contamination of the liquid does not play a role anymore and the drag coefficient approaches a constant value of about:

$$C_D \cong 2.61. \tag{65}$$

In the past, numerous correlations for the bubble drag coefficient as a function of bubble Reynolds number were proposed, mainly to match the transition region most closely for the different types of liquids. A discontinuous correlation for bubbles rising in purified liquid was, for example, proposed by Glaeser and Brauer [55]. Here the drag coefficient in the transition region depends on the Morton number and the bubble Reynolds number. The beginning and the end of the transition region are given by two Reynolds numbers both depending on the Morton number. The Morton number, as given above, is only dependent on the properties of the considered media, i.e., viscosity, density, and surface tension. Several correlations, which are rather easy to use were proposed by Tomiyama et al. [56] for different liquid qualities:

- purified fluids:

$$C_D = \max\left\{\min\left[\frac{16}{Re}\left(1 + 0.15\ Re^{0.687}\right), \frac{48}{Re}\right], \frac{8}{3}\frac{Eo}{Eo + 4}\right\}; \tag{66}$$

- slightly contaminated fluids:

$$C_D = \max\left\{\min\left[\frac{24}{Re}\left(1 + 0.15\ Re^{0.687}\right), \frac{72}{Re}\right], \frac{8}{3}\frac{Eo}{Eo + 4}\right\}; \tag{67}$$

- contaminated fluids:

$$C_D = \max\left[\frac{24}{Re}\left(1 + 0.15\ Re^{0.687}\right), \frac{8}{3}\frac{Eo}{Eo + 4}\right]. \tag{68}$$

As illustrated in Fig. 14, these correlations, however, do not properly describe the transition region in dependence on the degree of contamination and type of liquid considered as found in numerous experimental studies [54]. Especially in this region, with bubble sizes between 3 and 6 mm for an air/water system, a more accurate description is needed, since such bubble sizes are most important for industrial processes.

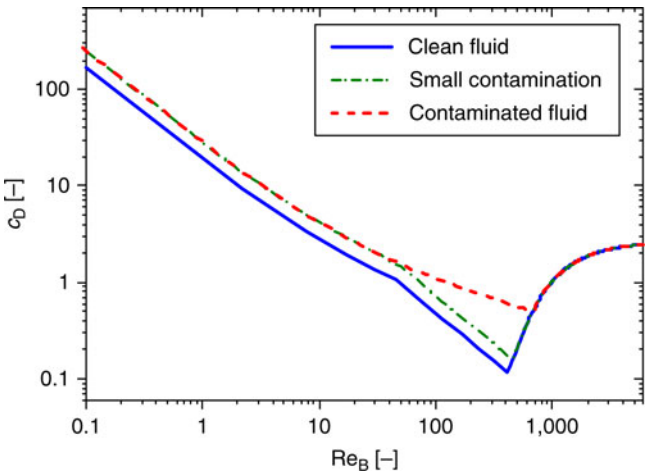

L3.1. Fig. 14. Bubble drag coefficient as a function of the bubble Reynolds number for clean and contaminated water according to the correlations of Tomiyama et al. [56] (see Eqs. (66) to (68)).

Hence, so far no generally applicable correlation for the drag coefficient of bubbles is available. Therefore, published results on the hydrodynamics in bubble columns or loop reactors have to be very critically assessed with regard to the drag correlation applied.

In bubbly flows, the added mass force is of great importance since especially wobbling bubbles never exhibit stationary rise behavior, rather they show zigzag or helical rising paths. Additionally, the density ratio ρ_L/ρ_B is considerably larger than one. For spherical bubbles in the Stokes regime the added mass coefficient is 0.5. In the case of ellipsoidal bubbles, the added mass coefficient is a tensor of the form [57]:

$$C_{A,ell} = \begin{Bmatrix} C_{A,h} & 0 & 0 \\ 0 & C_{A,h} & 0 \\ 0 & 0 & C_{A,v} \end{Bmatrix}. \tag{69}$$

For oblate bubbles, an analytic solution for the coefficients in horizontal (h) and vertical (v) direction was provided by Lamb [58] as a function of aspect ratio (i.e., minor axis to major axis, $E = h/b$):

$$C_{A,v} = \frac{E\cos^{-1}E - \sqrt{1-E^2}}{E^2\sqrt{1-E^2} - E\cos^{-1}E} \quad \text{for } E < 1, \tag{70}$$

$$C_{A,h} = \frac{\cos^{-1}E - E\sqrt{1-E^2}}{(2E^{-1} - E)\sqrt{1-E^2} - \cos^{-1}E} \quad \text{for } E < 1. \tag{71}$$

Moreover, transverse lift forces play an important role in the behavior of bubbles. For example, in bubble columns or pipe flows, the void fraction profile shows wall peaking for smaller bubbles (i.e., $D_B < 5.6$ mm in an air/water system under atmospheric conditions) and core peaking is observed for larger bubbles. The latter is also the responsible mechanism for yielding a heterogeneous flow regime in a bubble column as a result of bubble coalescence. The transverse lift force acting on bubbles

may be separated in two contributions, namely due to shear flow and bubble wake effects. Combining these two effects in one lift coefficient yields the following lift force [57]:

$$\vec{F}_L = C_{L,B}\rho_F \frac{\pi D_B^3}{6}(\vec{u}_F - \vec{u}_B) \times \text{rot}\ \vec{u}_F. \tag{72}$$

Here a positive value of $C_{L,B}$ yields a migration of the bubbles toward the wall. For spherical bubbles and for $Re_B >> 1$, the lift coefficient is 0.5 [59]. On the basis of experimental studies in a shear flow and simulations using the VOF (volume-of-fluid) method, Tomiyama et al. [60] suggest the following correlations for the lift coefficient:

$$C_{L,B} = \begin{Bmatrix} \min(0.288 \cdot \tan h(0.121\ Re_B)), f(Eo_h) & \text{for } Eo_h < 4 \\ f(Eo_h) & \text{for } 4 \le Eo_h \le 10.7 \end{Bmatrix}, \tag{73}$$

with

$$f(Eo_h) = 0.00105Eo_h^3 - 0.0159Eo_h^2 - 0.0204Eo_h + 0.474, \tag{74}$$

$$Eo_h = \frac{\rho \Delta\rho D_h^2}{\sigma}; \quad D_h = 2b. \tag{75}$$

For smaller bubbles, the lift coefficient correlates with the bubble Reynolds number (i.e., up to $Re_B \sim 60$) and has positive values (i.e., migration toward the wall of a pipe). If medium sized and large bubbles are considered, the lift coefficient correlates with the Eötvös number based on the volume equivalent bubble diameter [57]. The lift coefficient changes from positive to negative values at about Eo = 6, corresponding to a bubble diameter of 5.6 mm in an air/water system. In both regions (Eq. (73)), the lift coefficient was found to be almost independent of the Morton number. The theoretical studies of Legendre and Magnaudet [61] for a plane shear layer revealed that for bubble Reynolds numbers below about 3, the shear induced transverse lift is dominating and therefore, the lift coefficient will become dependent on the nondimensional shear rate:

$$S_r = \frac{\omega D_B}{|U_F - U_B|}; \quad \omega = \frac{dU_F}{dy}. \tag{76}$$

The correlation for the lift coefficient obtained from these simulations is given by

$$C_{L,B} = \sqrt{\left(\frac{6}{\pi^2}\frac{2.255}{(Re_B\ Sr)^{1/2}(1 + 0.2\ Re_B/Sr)^{3/2}}\right)^2 + \left(0.5\frac{1 + 16/Re_B}{1 + 29/Re_B}\right)^2} \tag{77}$$

and agrees with experiments of Tomiyama [57] up to a bubble Reynolds number of 2.0. For $Re_B > 5$, the influence of the shear rate on the lift coefficient becomes negligible and the correlation of Eq. (73) can be used. A proper transition between the two regimes has not yet been developed.

7 Importance of the Different Forces

In order to estimate the importance of the different forces, especially the importance of added mass and Basset force, acting on a particle in a turbulent flow, Hjelmfelt and Mockros [62] have performed an analysis for an oscillatory flow field. The starting point of their analysis was the Stokes form of the equation of motion given by

$$m_P\frac{du_P}{dt} = \frac{18\mu_F}{\rho_P D_P^2} m_P(u_F - u_P) - m_F\frac{du_F}{dt} + 0.5m_F\left(\frac{du_F}{dt} - \frac{du_P}{dt}\right) + 9\sqrt{\frac{\rho_F\mu_F}{\pi}}\frac{m_P}{\rho_P D_P}\int_{-\infty}^{t}\frac{\frac{du_F}{d\tau} - \frac{du_P}{d\tau}}{(t-\tau)^{1/2}}d\tau. \tag{78}$$

Rearranging this equation results in

$$\frac{du_P}{dt} + a u_P + c\int_{-\infty}^{t}\frac{du_P/d\tau}{(t-\tau)^{1/2}}d\tau = a u_F + b\frac{du_F}{dt} + c\int_{-\infty}^{t}\frac{du_F/d\tau}{(t-\tau)^{1/2}}d\tau, \tag{79}$$

with the coefficients a, b, and c defined by

$$a = \frac{18\mu_F/\rho_F}{(\rho_P/\rho_F + 0.5)D_P^2}, \quad b = \frac{3}{2(\rho_P/\rho_F + 0.5)}, \quad c = \frac{9}{(\rho_P/\rho_F + 0.5)}\sqrt{\frac{\mu_F}{\pi\rho_F}}. \tag{80}$$

The velocities of the particles and the fluid are expressed by Fourier integrals:

$$u_F = \int_0^\infty (\varsigma\cos\omega t + \lambda\sin\omega t)d\omega, \quad u_P = \int_0^\infty (\sigma\cos\omega t + \varphi\sin\omega t)d\omega \tag{81}$$

where ω is the frequency of oscillation. Introducing these Fourier integrals into the equation of motion of the particles (Eq. (79)) yields the amplitude ratio (i.e., amplitude of particle velocity over that of the fluid) and the phase angle (i.e., lag of particle response with respect to fluid) in the following form:

$$\eta = \sqrt{(1 + f_1)^2 + f_2^2}, \quad \beta = \tan^{-1}\left\{\frac{f_2}{1 + f_1}\right\}. \tag{82}$$

The functions f_1 and f_2 are obtained as

$$f_1 = \frac{\omega(\omega + c\sqrt{0.5\pi\omega})\ (b-1)}{(a + c\sqrt{0.5\pi\omega})^2 + (\omega + c\sqrt{0.5\pi\omega})^2}, \tag{83}$$

$$f_2 = \frac{\omega(a + c\sqrt{0.5\pi\omega})\ (b-1)}{(a + c\sqrt{0.5\pi\omega})^2 + (\omega + c\sqrt{0.5\pi\omega})^2}. \tag{84}$$

The parameter used to characterize the particle response is a modified Stokes number given by

$$N_s = \frac{\mu_F}{\rho_F\omega D_p^2}. \tag{85}$$

The result of this analysis is shown in Fig. 15 for three kinds of particles, namely copper and glass particles in air and air bubbles in water, by considering the different forces. For the three cases, the amplitude ratio and the phase angle is plotted versus the modified Stokes number. It is obvious that for copper particles and glass beads, the added mass, the pressure force, and the Basset term have almost no effect on the amplitude ratio.

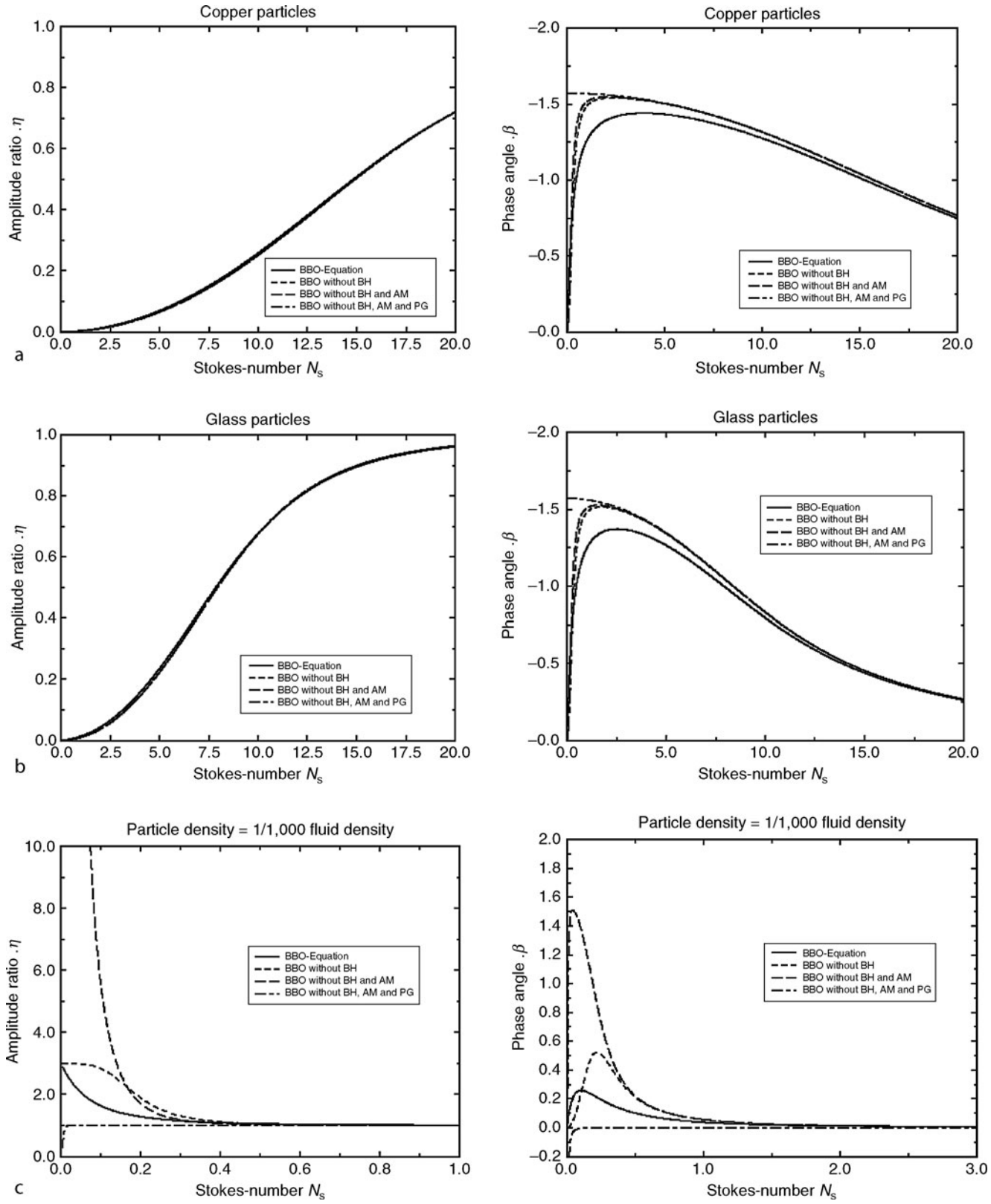

L3.1. Fig. 15. Particle response in an oscillatory flow field, influence of the different forces on the amplitude ratio (left column) and the phase angle (right column) for: (**a**) copper particles in air, (**b**) glass beads in air, and (**c**) air bubbles in water.

However, considerable differences are observed in the phase angle for $N_s < 5$, which means for large particles or high frequencies of the oscillatory fluid motion. Only, the added mass is not of great importance and may be neglected without considerable error. Considering a 100 μm particle, the pressure force and the Basset term become of importance for oscillation frequencies larger than about 310 Hz. For bubbly flows, large differences in the response arise for $N_s < 1.0$. However, for this case, the Basset

term may be neglected without introducing too large errors. The added mass and the pressure force on the other hand are of great importance in this region, i.e., for large bubbles and high frequencies of flow oscillation.

In particle-laden flows the drag force is of course the most important fluid dynamic force acting on the particles. The drag however may be affected by a number of physical effects as described above. Wall effects (i.e., particle motion toward or parallel to a wall) become generally only of importance for smaller particle Reynolds numbers. This is achieved for high viscous fluids where obviously the fluid between wall and particle has to be squeezed out. On the other hand, large and inertial particles (i.e., high particle Reynolds number) will not very strongly "feel" the wall before they collide with it and hence fluid dynamic wall effects may be neglected. Rarefaction effects will decrease the drag for very small particles, which is mostly accounted for by the Cunningham correction. Allowing for an error of 5%, rarefaction effects will become important already for particles smaller than about 3 μm for atmospheric conditions. Compressibility effects on the particle drag can be neglected if the particle Mach number is below about 0.5 [4].

The slip-shear lift force in particle-laden flows becomes important if the particles are large and the shear rate is high, as for example in boundary layers or other shear layers. However, this transverse lift force also depends on the slip velocity between particles and fluid. This implies that it might be neglected for smaller particles when the slip is small. For larger particles, the slip-shear lift force should be accounted for. An estimate introduced by Sommerfeld [37] showed that for particles in air, the lift force becomes important for particle sizes larger than about 80 μm and for water, as the continuous phase for sizes larger than about 20 μm. As the shear rate decreases, these sizes are of course shifted to larger values.

The slip-rotation lift force also depends on the slip between the phases and hence becomes less important with decreasing particle size where the slip velocity is also reduced. In addition, small particles will easily follow the rotation of the fluid (freely rotating particle) and therefore, the slip-rotation lift force might be neglected. However, in wall-bounded flows, the particle motion is strongly affected by wall collisions. Thereby, the particles can acquire extremely high angular velocities (e.g., a 100 μm-particle hitting the wall with about 10 m/s will have an angular velocity of $2{\cdot}10^5$ 1/s for a nonsliding wall collision). Therefore, this lift force will strongly affect the particle motion in the vicinity of the wall. With increasing particle size and hence particle inertia, their motion will be more and more affected by the slip-rotation lift force also in regions farther away from the wall. The region of importance may be estimated from the torque acting on the particle. The estimate introduced by Sommerfeld [37] gives, for a higher relative angular velocity, a limiting particle diameter above which the slip-rotation lift force becomes important of 30 μm in water and 90 μm in air.

The transverse lift force in bubbly flows is very important for a correct numerical prediction of the gas volume fraction distribution, such as bubbly pipe flows or in bubble columns. For small bubbles (i.e., $D_B < 5.6$ mm for air–water), this force is directed toward the wall. For larger bubbles, the sign of the lift force changes and thereby the bubbles are driven to the core of a pipe [57]. Therefore, this force is essential for predicting the transition from homogeneous to heterogeneous bubbly flow. The development of a heterogeneous bubbly flow is mainly the result of the transverse lift force, whereby the bubbles are driven to the core, where they will coalesce with other bubbles to form larger bubbles, which are rising in the core of the column. The effect of walls on the behavior of bubbles and the relevant forces is surely quite important. However, up to now, very little knowledge about the modification of forces acting on bubbles in the vicinity of walls and also the direct wall collision process is available.

8 Symbols

A_C	acceleration number (–)
A_P	particle cross-section (m^2)
C_A	coefficient of added mass force (–)
$C_{A,ell}$	added mass coefficient for ellipsoidal bubble (–)
C_B	coefficient of Basset force (–)
C_D	drag coefficient (–)
$C_{D,Stokes}$	stokes drag coefficient (–)
$C_{L,B}$	lift coefficient for bubbles (–)
C_{LS}	lift coefficient for slip-shear (–)
C_{LR}	lift coefficient for slip-rotation (–)
C_R	rotational coefficient (–)
$\overline{c_{Mol}}$	standard deviation of gas molecules velocity distribution (m/s)
Cu	Cunningham correction (–)
D_P	particle diameter (m)
$\vec{E}$	strength of electrical field (V/m)
Eo	Eötvös number (–)
$\vec{F}_A$	added mass force (N)
$\vec{F}_B$	Basset force (N)
$\vec{F}_C$	Coulomb force (N)
f_D	nonlinear term of drag coefficient (–)
$\vec{F}_D$	drag force (N)
$\vec{F}_e$	electrostatic force (N)
$\vec{F}_g$	gravity force (N)
$\vec{F}_i$	forces acting on a particle (N)
$\vec{F}_{LS}$	slip-shear lift force (N)
$\vec{F}_{LS,Saff}$	Saffman force (N)
$\vec{F}_{LR}$	slip-rotation lift force (N)
$\vec{F}_p$	pressure force (N)
Fr_B	Froude number (–)
$\vec{g}$	gravity vector (m/s^2)
h	wall distance (m)
I_P	moment of inertia (kg m^2)
k	turbulent kinetic energy (m^2/s^2)
Kn_P	particle Knudsen number (–)
m_F	fluid mass displaced by bubble (kg)
m_P	mass of a particle (kg)
Mo	Morton number (–)
N_s	modified Stokes number (–)
p	pressure (N/m^2)

q_P	particle charge (C)
R_P	particle radius (m)
Re_{crit}	critical Reynolds number (–)
Re_P	particle Reynolds number of translation (–)
Re_R	particle Reynolds number of rotation (–)
Re_S	particle Reynolds number of shear (–)
S	surface area of particle (m^2)
St	Stokes number (–)
$\vec{T}$	torque (N m)
t	time (s)
$\vec{u}_F$	instantaneous fluid velocity vector (m/s)
$\vec{u}_P$	instantaneous particle velocity vector (m/s)
$\dot{V}$	volume flow rate (m^3/s)
v_r	radial velocity (m/s)
v_φ	tangential velocity (m/s)
We_B	Weber number (–)
$\vec{x}_P$	particle position vector (m)

Greek symbols

β	nondimensional shear rate (–)
ε	porosity (–)
ε	dissipation of turbulent kinetic energy (m^2/s^3)
ϕ	sphericity (–)
γ	nondimensional relative rate of rotation (–)
λ	mean free path of the gas (m)
μ_F	dynamic viscosity (Pa s)
ρ_F	density of the fluid (kg/m^3)
ρ_P	density of particle material (kg/m^3)
σ	surface tension (N/m)
τ	time (s)
τ_F	characteristic time scale of fluid motion (s)
τ_P	particle response time (s)
ω	frequency (l/s)
$\vec{\omega}_F$	rotation of the fluid (l/s)
$\vec{\omega}_P$	angular velocity of the particle (l/s)
$\vec{\Omega}$	relative rotation between fluid and particle (l/s)

9 Bibliography

1. Sommerfeld M (2001) Validation of a stochastic Lagrangian modelling approach for inter-particle collisions in homogeneous isotropic turbulence. Int J Multiphase Flows 27:1828–1858
2. Simonin O (2000) Statistical and continuum modelling of turbulent reactive particulate flows. Part I: theoretical derivation of dispersed phase Eulerian modelling from probability density function kinetic equation. Theoretical and experimental modelling of particulate flow. VKI Lecture Series 2000–06, von Karman Institute for Fluid Dynamics, Belgium
3. Crowe CT, Sommerfeld M, Tsuji Y (1998) Fundamentals of gas–particle and gas–droplet flows. CRC Press, Boca Raton, FL
4. Sommerfeld M, van Wachem B, Oliemans R (2008) Best practice guidelines for computational fluid dynamics of dispersed multiphase flows. ERCOFTAC (European Research Community on Flow, Turbulence and Combustion, ISBN 978-91-633-3564-8
5. Gouesbet G, Berlemont A (1999) Eulerian and Lagrangian approaches for predicting the behaviour of discrete particles in turbulent flows. Prog Energy Combust Sci 25:133–159
6. Loth E (2000) Numerical approaches for motion of dispersed particles, droplets and bubbles. Prog Energy Combust Sci 26:161–223
7. Michaelides EE (2006) Particles, bubbles and drops: their motion, heat and mass transfer. World Scientific Publishing, Singapore
8. Basset AB (1888) On the motion of a sphere in a viscous liquid. Phil Trans R Soc A 179:43–69
9. Boussinesq JV (1885) Sur la resistance d'une sphere solide. CR Hebd Seanc Acad Sci Paris 100:935
10. Oseen CW (1927) Hydromechanik, Akademische Verlagsgem. Leipzig 132
11. Tchen C-M (1947) Mean value and correlation problems connected with the motion of small particles suspended in a turbulent fluid. Dissertation Technische Hochschule Delft, Martinus Nijhoff, The Hague
12. Maxey MR, Riley JJ (1983) Equation of motion for a small rigid sphere in a nonuniform flow. Phys Fluid 26:883–889
13. Sommerfeld M (2005) Bewegung fester Partikel in Gasen und Flüssigkeiten. In: VDI-Wärmeatlas (Herausgeber: VDI-Gesellschaft Verfahrenstechnik und Chemieingenieurwesen (GVC)), 10. Auflage, Springer-Verlag, Berlin, ISBN-10 3-540-25504-4, Kapitel Lca 1–9
14. Schlichting H (1965) Grenzschicht-Theorie. Verlag G. Braun, Karlsruhe
15. Stokes GG (1851) On the effect of the internal frictions of fluids on the motion of pendulums. Trans Camb Philos Soc 9:8–106
16. Clift R, Grace JR, Weber ME (1978) Bubbles, drops and particles. Academic Press, New York
17. Schiller L, Naumann A (1933) Über die grundlegende Berechnung bei der Schwerkraftaufbereitung. Ver Deut Ing 44:318–320
18. Torobin LB, Gauvin WH (1961) The drag coefficient of single spheres moving in steady and accelerated motion in a turbulent fluid. AIChE J 7:615–619
19. Sawatzki O (1960) Über den Einfluß der Rotation und der Wandstöße auf die Flugbahn kugeliger Teilchen im Luftstrom. Dissertation, Univ Karlsruhe
20. Brenner H (1964) The Stokes resistance of an arbitrary particle (IV) arbitrary fields of flow. Chem Eng Sci 19:703–727
21. Jeffery G (1922) The motion of ellipsoidal particles immersed in a viscous fluid. Proc R Soc 102A:161–179
22. Rosendahl L (2000) Using a multi-parameter particle shape description to predict the motion of non-spherical particle shapes in swirling flow. Appl Math Model 24:11–25
23. Hölzer A, Sommerfeld M (2009) Lattice-Boltzmann simulations to determine drag, lift and torque acting on non-spherical particles. Comput Fluids 38:572–589
24. Haider A, Levenspiel O (1989) Drag coefficient and terminal velocity of spherical and nonspherical particles. Powder Technol 58:63–70
25. Thompson TL, Clark NN (1991) A holistic approach to particle drag prediction. Powder Technol 67:57–66
26. Ganser GH (1993) A rational approach to drag prediction of spherical and nonspherical particles. Powder Technol 77:143–152
27. Brenner H (1961) The slow motion of a sphere through a viscous fluid towards a plane surface. Chem Eng Sci 16:242–251
28. Goldman AJ, Cox RG, Brenner H (1967a) Slow viscous motion of a sphere parallel to a plane wall-I motion through a quiescent fluid. Chem Eng Sci 22:637–651
29. Goldman AJ, Cox RG, Brenner H (1967b) Slow viscous motion of a sphere parallel to a plane wall-II Coette flow. Chem Eng Sci 22:653–660
30. Davies CN (1945) Definitive equation for the fluid resistance of spheres. Proc Phys Soc 57:1060–1065
31. Richardson JF, Zaki WN (1954) Sedimentation and fluidisation: Part I. Trans Inst Chem Eng 32:35–53
32. Wen CY, Yu YH (1966) Mechanics of fluidisation. AIChE J 62:100–111
33. Ergun S (1952) Fluid flow through packed columns. Chem Eng Sci 48:89–98
34. Odar F, Hamilton WS (1964) Forces on a sphere accelerating in a viscous fluid. J Fluid Mech 18:302–314
35. Reeks MW, McKee S (1984) The dispersive effect of Basset history forces on particle motion in turbulent flow. Phys Fluids 27:1573
36. Michaelides EE (1992) A novel way of computing the Basset term in unsteady multiphase flow computations. Phys Fluid A 4:1579–1582
37. Sommerfeld M (1996) Modellierung und numerische Berechnung von partikelbeladenen turbulenten Strömungen mit Hilfe des Euler/Lagrange-Verfahrens. Habilitaionsschrift, Universität Erlangen-Nürnberg, Shaker Verlag, Aachen
38. Löffler F (1988) Staubabscheidung. Georg Thieme Verlag, Stuttgart
39. White HJ (1963) Industrial electrostatic precipitation. Addison-Wesley, Reading, PA

40. Saffman PG (1965) The lift on a small sphere in a slow shear flow. J Fluid Mech 22:385–400
41. Saffman PG (1968) Corrigendum to: the lift on a small sphere in a slow shear flow. J Fluid Mech 31:624
42. Mei R (1992) An approximate expression for the shear lift force on a spherical particle at finite Reynolds number. Int J Multiphase Flow 18:145–147
43. Dandy DS, Dwyer HA (1990) A sphere in shear flow at finite Reynolds number: effect of shear on particle lift, drag, and heat transfer. J Fluid Mech 216:381–410
44. Sommerfeld M (2003) Analysis of collision effects for turbulent gas–particle flow in a horizontal channel: Part I. Particle transport. Int J Multiphase Flow 29:675–699
45. Sommerfeld M, Kussin J (2003) Analysis of collision effects for turbulent gas–particle flow in a horizontal channel: Part II. Integral properties and validation. Int J Multiphase Flow 29:701–718
46. Rubinow SI, Keller JB (1961) The transverse force on spinning sphere moving in a viscous fluid. J Fluid Mech 11:447–459
47. Oesterlé B, Bui Dinh T (1998) Experiments on the lift of a spinning sphere in a range of intermediate Reynolds numbers. Exp Fluids 25:16–22
48. Sawatzki O (1961) Über den Einfluß der Rotation und der Wandstöße auf die Flugbahn kugeliger Teilchen im Luftstrom. Dissertation, University Karlsruhe
49. Dennis SCR, Singh SN, Ingham DB (1980) The steady flow due to a rotating sphere at low and moderate Reynolds numbers. J Fluid Mech 101:257–279
50. Sawatzki O (1970) Strömungsfeld um eine rotierende Kugel. Acta Mech 9:159–214
51. Tang L, Wen F, Yang Y, Crowe CT, Chung JN, Troutt TR (1992) Self-organizing particle dispersion mechanism in free shear flows. Phys Fluids A 4:2244–2251
52. Haberman WL, Morton RK (1954) An experimental study of bubbles moving in liquids. Trans Am Soc Civil Eng Paper No. 2799, pp 227–250
53. Peebles FN, Garber HJ (1953) Studies on the motion of gas bubbles in liquids. Chem Eng Prog 49:88–97
54. Fan L-S, Tsuchiya K (1990) Bubble wake dynamics in liquids and liquid–solid suspensions. Butterworth-Heinemann, Oxford
55. Glaeser H, Brauer H (1977) Berechnung des Impuls- und Stofftransports durch die Grenzfläche einer formveränderlichen Blase. VDI-Forschungsheft 581, VDI-Verlag, Düsseldorf Germany
56. Tomiyama A, Kataoka I, Zun I, Sakaguchi T (1998) Drag coefficients of single bubbles under normal and micro gravity conditions. JSME Int J Ser B 41:472–479
57. Tomiyama A (2004) Drag, lift and virtual mass forces acting on a single bubble. Two-phase flow modelling and experimentation 2004. In: Celeta GP, Di Marco P, Mariani A, and Shah RK (eds) CD-ROM Proceedings of the 3rd international symposium on two-phase flow modelling and experimentation, Pisa, Italy, ISBN 88-467-1075-4.
58. Lamb H (1932) Hydrodynamics, 6th edn. Cambridge University Press, Cambridge
59. Auton TR (1987) The lift force on a spherical body in a rotational flow. J Fluid Mech 183:199–218
60. Tomiyama A, Celata GP, Hosokawa S, Yoshida S (2002) Terminal velocity of single bubbles in surface tension force dominant regime. Int J Multiphase Flow 28:1497–1519
61. Legendre D, Magnaudet J (1998) The lift force on a spherical bubble in a viscous linear shear flow. J Fluid Mech 369:81–126
62. Hjelmfelt AT, Mockros LF (1966) Motion of discrete particles in a turbulent fluid. Appl Sci Res 16:149–161

L3.2 Flow Patterns and Pressure Drop in Fluidized Beds

Karl-Ernst Wirth
Friedrich-Alexander-Universität Erlangen-Nürnberg, Erlangen, Germany

1 Conditions in Fluidized Beds

Fluidization is a technique in which a stream of a gas or liquid flows upward through a bed of particles at a velocity that suffices to loosen the particles and cause the mixture to behave as a liquid.

If the fluid flows at a low velocity, it percolates the bed through the voids without changing the structure of the packing, as is shown in Fig. 1a. The bed with this flow condition is called fixed bed and has a void fraction (porosity) of ψ_{sb} and a height of h_{sb}.

When the velocity is increased, the forces exerted by the fluid on the solid structure become greater. At first, some of the particles commence to move within a restricted range, but most of them remain in prolonged contact to form an expanded solid bed. On a further increase in velocity, all the particles reach a stage in which they are suspended in the fluid and there is no permanent contact with one another. In this state, the pressure drop in the fluid between two horizontal reference planes is in equilibrium with the combined weight of the solids and the fluid per unit area of the planes. This stage is referred to as the onset of fluidization or minimum fluidization and is illustrated in Fig. 1b. The void fraction (porosity) of the bed when it is thus loosened is ψ_L, and the height is h_L. The corresponding fluid velocity is called minimum fluidization velocity.

Beds fluidized by a liquid react toward a further increase in velocity by expanding uniformly. This is known as particulate fluidization, and is illustrated in Fig. 1c.

The behavior of beds fluidized by a gas is entirely different. In this case, the fraction of gas in excess of the flow rate required for minimum fluidization traverses the bed largely in the form of bubbles that are practically free from solids, as is illustrated in Fig. 1d. The void fraction of the bed is then $\psi > \psi_L$, and the height is $h > h_L$. Unless baffles are installed to disperse them, the gas bubbles become larger as they ascend, mainly as a result of coalescence. The fluidized bed is called bubbling fluidized bed.

If the reaction vessel is sufficiently high and narrow, the bubbles finally occupy the total area of the cross section and slugs of gas thus pulse through the fluidized bed, as is indicated by Fig. 1e. This kind of fluidized bed is called slugging fluidized bed.

As long as the bed has a definable upper surface, fluidization prevails in the dense (solid) phase. Once the upward velocity of the fluid becomes the same as the free-falling velocity of the particles, the entire bed will be carried over at the outlet. If the void fraction in gas–solids fluidized beds is large, bubbles will no longer be formed, and the upper surface of the bed will no longer be defined. However, since solid strands are formed, the fluidized bed may be circulated at a superficial gas velocity which is a multiple of the free-falling velocity of the single particles settle, as is shown in Fig. 1f.

2 Onset of Fluidization

The bed is in the most loosely packed state at the onset of fluidization, when the void fraction is ψ_L. It is evident from Table 1 that the numerical value of ψ_L increases with a reduction in the average particle size and a decrease in sphericity φ_s, which is defined by

$$\varphi_s = \frac{\text{Surface area of sphere of same volume as particle}}{\text{Surface area of particle}}.$$

The void fraction at the onset of fluidization also depends on the particle size distribution. This is evident from the figures for "rounded sand $\varphi_s = 0.86$" and "sand mixture (round particles)" in Table 1.

It is only under very restricted circumstances, i.e., a regular arrangement of ideal spheres with few size gradations, that the void fraction of a bed can be predicted [1]. Consequently, if the bed consists of particles of irregular shape and continuous size distribution, the void fraction ψ_L must be estimated from known examples (e.g., Table 1) or determined by experiment. In the following discussion, it is assumed that ψ_L is known. At the onset of fluidization, equilibrium is established between the force of resistance that acts between the fluid and the

solids and the force exerted by the weight of the solids less the buoyancy, i.e.,

$$\Delta pA = Ah_L(1-\psi_L)(\rho_s-\rho_f)g \tag{1a}$$

or

$$\frac{\Delta p}{h_L} = (1-\psi_L)(\rho_s-\rho_f)g, \tag{1b}$$

where Δp is the pressure drop in the fluid in overcoming the resistance of the bed, A is the cross-sectional area of the bed, h_L is the height of the bed at the onset of fluidization, ϱ_s and ϱ_f are the densities of the solid and the fluid, and g is the acceleration due to gravity.

The effect of the void fraction in the $\psi_{sb} \le \psi < 1$ range in predominantly laminar flow through beds of monodispersed spherical particles may be derived from the results of careful measurements [2] and from theoretical considerations [3]. However, the most convenient formulation currently adopted for the pressure drop in polydispersed beds of irregular particles of $\geq$5 µm size packed uniformly at random is that suggested by Ergun and Orning [4], which is valid for the entire range of Reynolds numbers, i.e.,

$$\frac{\Delta p}{h} = kS_v^2\frac{(1-\psi)^2}{\psi^3}\eta u + CS_v\frac{1-\psi}{\psi^3}\rho_f u^2, \tag{2a}$$

where S_v is the specific surface of the particles per unit volume, u is the superficial fluid velocity, η is the dynamic viscosity, and k and C are constants for fitting the experimental results. If it is assumed that the method adopted for the determination of particle size (generally screening) yields at least a rough value for the diameter d_p of spheres of equal volume, the specific surface can be expressed in terms of the mass distribution density $q_3(d_p)$ and the sphericity, which is derived from the particle size measurement and the sphericity which is assumed to be constant, i.e.,

$$S_v = \frac{6}{\varphi_s}\int_{d_{p\,min}}^{d_{p\,max}} d_p^{-1}q_3(d_p)\mathrm{d}(d_p).$$

This relationship defines the average particle size $\bar{d}_p$, which is referred to as the Sauter diameter of the particle size distribution, i.e.,

$$\bar{d}_p = \frac{6}{\varphi_s O_v} = \frac{1}{\int_{d_{p\,min}}^{d_{p\,max}} d_p^{-1}q_3(d_p)\mathrm{d}(d_p)}.$$

Equation (2a) can thus assume the form of

$$\frac{\Delta p}{h} = 36k\frac{(1-\psi)^2}{\psi^3}\frac{\eta u}{(\varphi_s\bar{d}_p)^2} + 6C\frac{1-\psi}{\psi^3}\frac{\rho_f u^2}{\varphi_s\bar{d}_p}.$$

Inserting the numerical values submitted by Ergun [5] for the constants k and C gives

$$\frac{\Delta p}{h} = 150\frac{(1-\psi)^2}{\psi^3}\frac{\eta u}{(\varphi_s\bar{d}_p)^2} + 1.75\frac{1-\psi}{\psi^3}\frac{\rho_f u^2}{\varphi_s\bar{d}_p}. \tag{2b}$$

If allowance is made for the kinematic viscosity $\nu = \eta/\varrho_f$, equating Eqs. (1b) and (2b) yields a correlation for the superficial velocity of the fluid at the onset of fluidization u_L and between the Reynolds number at the onset of fluidization and the Archimedes numbers. The Reynolds number at the onset of fluidization is $\mathrm{Re}_L = u_L\bar{d}_p/\nu$; and the Archimedes number,

$$\mathrm{Ar} = \frac{g(\bar{d}_p)^3}{\nu^2}\left(\frac{\rho_s}{\rho_f}-1\right).$$

Hence,

$$\mathrm{Re}_L = 42.9\frac{1-\psi_L}{\varphi_s}\left[\sqrt{1+3.1\cdot10^{-4}\frac{\varphi_s^3\psi_L^3}{(1-\psi_L)^2}\mathrm{Ar}}-1\right]. \tag{3}$$

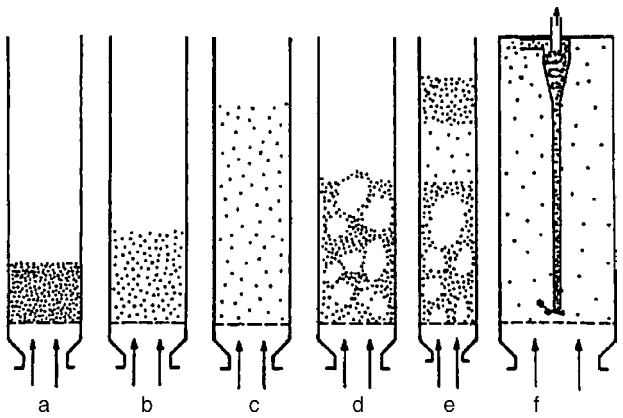

L3.2. Fig. 1. Conditions in fluidized beds.

L3.2. Table 1. Experimental values for the void fraction (porosity) at the onset of fluidization [11]

Particles	Average particle size						
	20	50	70	100	200	300	400
Angular sand (φ_s = 0.67)	–	0.60	0.59	0.58	0.54	0.50	0.49
Rounded sand (φ_s = 0.86)	–	0.56	0.52	0.48	0.44	0.42	–
Sand mixture (round particles)	–	–	0.42	0.42	0.41	–	–
Pulverized coal and glass	0.72	0.67	0.64	0.62	0.57	0.56	–
Anthracite (φ_s = 0.63)	–	0.62	0.61	0.60	0.56	0.53	0.51
Activated charcoal	0.74	0.72	0.71	0.69	–	–	–
Fischer–Tropsch catalyst (φ_s = 0.58)	–	–	–	0.58	0.56	0.55	–
Carborundum	–	0.61	0.59	0.56	0.48	–	–

If the data for the solids and the fluid are known, the superficial velocity of the fluid at the onset of fluidization can be determined. Thus if $Re_L \leq 1$, i.e., in the most frequently occurring case of creeping ("laminar") flow through a bed of fine particles, the following applies:

$$Re_L = \frac{1}{150}\frac{\varphi_s^2\psi_L^3}{1-\psi_L}Ar$$

and

$$u_L = \frac{1}{150}\frac{\varphi_s^2\psi_L^3}{1-\psi_L}\frac{g(\bar{d}_p)^2}{\nu}\left(\frac{\rho_s}{\rho_f}-1\right). \quad (4)$$

If $Re > 10^3$, i.e., for predominantly inertia determined ("turbulent") flow through a bed of coarse particles, the relationship is

$$Re_L = \sqrt{\frac{\varphi_s\psi_L^3 Ar}{1.75}}$$

and

$$u_L = \sqrt{\left(\frac{1}{1.75}\right)\varphi_s^2\psi_L^3 g\bar{d}_p\left(\frac{\rho_s}{\rho_f}-1\right)}. \quad (5)$$

The following simple empirical correlation for the determination of the velocity at the onset of fluidization has been submitted by Wen and Yu [6]:

$$Re_L = 33.7(\sqrt{1+3.6\cdot 10^{-5}Ar}-1).$$

The velocity at the onset of fluidization should be determined under actual operating conditions, which may differ considerably from those applicable to a freshly charged bed owing to carryover of fines, agglomeration, and increase or shrinkage in particle size as a consequence of chemical reactions.

3 Expansion of Fluidized Bed

3.1 Homogeneous Liquid–Solids Fluidized Bed

The expansion that ensues when the inlet velocity exceeds that at the onset of fluidization u_L can be very easily expressed in the form of an equation if the liquid–solids fluidized bed is homogeneous. Thus, if ψ is substituted for ψ_L and u for u_L, Eq. (4) could apply for $\psi \leq 0.8$ and Reynolds numbers derived from the particle size, i.e.,

$$Re_p = \frac{u\bar{d}_p}{\nu} \leq 1.$$

This implies that, if flow is "laminar", the structure of a liquid–solids fluidized bed does not differ very much from that of a fixed bed of the same porosity [3].

The simplest relationship for the expansion of these fluidized beds within the entire $\psi_L \leq \psi \leq 1$ range of void fractions and the entire range of Reynolds numbers is that submitted by Richardson and Zaki [7], i.e.,

$$\frac{u}{w_f} = \psi^n, \quad (6)$$

where w_f is the settling velocity of the individual particles in a medium of infinite extent. In practice, when the particle/fluidization vessel diameter ratio is « 1, the index n depends solely on $Re = w_f\bar{d}_p/\nu$. The following numerical values apply:

$n = 4.65$	for	$Re < 0.2$
$n = 4.35\ Re^{-0.03}$	for	$0.2 < Re < 1$
$n = 4.45\ Re^{-0.10}$	for	$1 < Re < 500$
$n = 2.39$	for	$Re > 500$

In particular, Eq. (6) states that if $u = w_f$, i.e., if the settling velocity is attained, the fluidized bed will be carried over.

3.2 Gas–Solids Fluidized Beds

3.2.1 Aggregative Fluidization

Gas bubbles cause the solids to move violently within the bed. Consequently, fluctuations occur in the height h and thus in the void fraction ψ. These two variables are connected as follows through the data for the system at the onset of fluidization:

$$\frac{h}{h_L} = \frac{1-\psi_L}{1-\psi}.$$

Hence, their numerical values represent averages with respect to time. The void fraction at all points within liquid–solids fluidized beds is practically the same as the porosity ψ, but a quantitative characterization of gas–solids fluidized beds is much more difficult. In a detailed description that has been published [8] on the flow mechanisms concerned, it was assumed that an element of volume within a gas–solids fluidized bed contains a time-averaged fraction ψ_B of gas bubbles and that the loosened bed enclosing the bubbles in the same element of volume has a void fraction ψ_S. As a rule, neither ψ_B nor ψ_S is constant for a given bed. In vessels that are symmetrical about an axis of rotation, they depend on the distance r from the axis and on the distance from the gas distributor, as has been demonstrated in studies with local sensors [8]. Local bubble volume fractions ψ_B measured in various cross sections at different distances from the gas distributor are presented as an example in Fig. 2a. It can be seen that the expansion of a gas–solids fluidized bed is governed in a complicated manner by local fluctuations.

An aggravating factor is that fluidization greatly depends on the diameter of the vessel. Figure 2b shows the local bubble volume fraction ψ_B measured at a distance of 15 cm from the gas distributor in fluidized beds of 100 and 200 mm diameter.

It is evident from these experimental results that no equation of general validity can be quoted for the relationship between the inlet velocity and the bed expansion. Likewise, empirical correlations derived by various authors from bed expansion measurements in laboratory apparatus are valid only for the layout concerned.

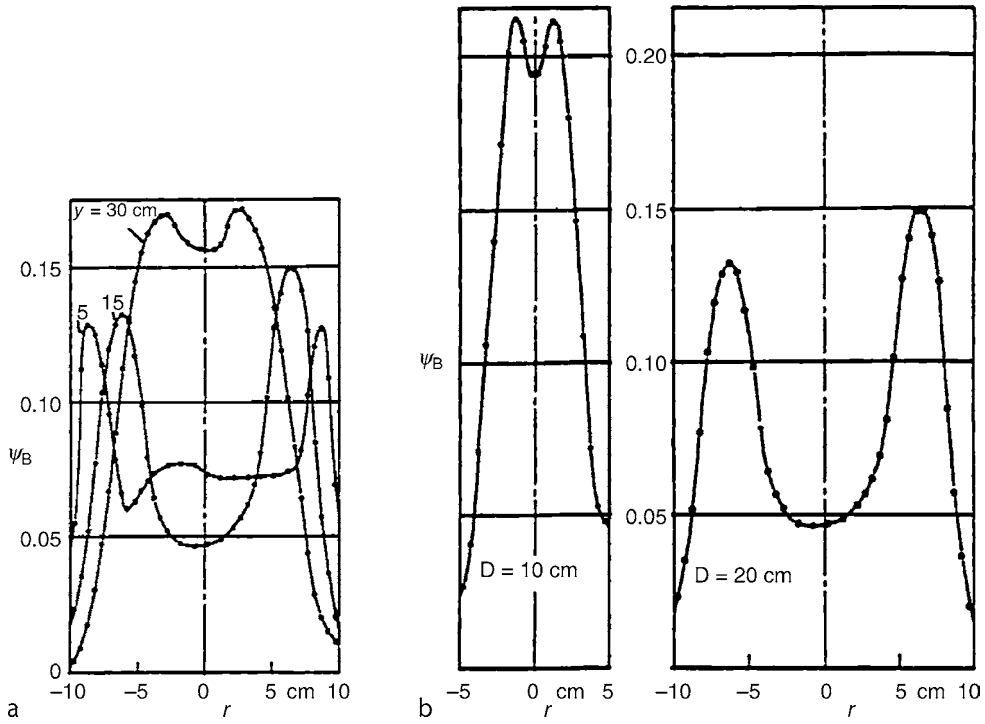

L3.2. Fig. 2. (**a**) Local bubble volume fraction ψ_B as a function of the distance r from the axis of a tubular bed for various spacings y from the gas distributor. Diameter of fluidized bed 20 cm; u = 8.94 cm/s. Sand (d_p = 85 μm, u_L = 1.8 cm/s); (**b**) local bubble volume fraction ψ_B as a function of the distance r from the axis of a tubular bed at a spacing of 15 cm from the gas distributor in fluidized beds of various diameters. Sand (d_p = 85 μm, u_L = 1.8 cm/s); u = 8.94 cm/s.

3.2.2 Circulating Fluidized Beds

The feature of circulating fluidized beds is that the superficial velocity are greater than the free-falling velocity of the individual particles, which are generally expressed in terms of $\bar{d}_p$. As a result, a stream of solids is carried over. In order to maintain steady-state conditions, the solids must be separated from the gas stream, e.g., in a cyclone, and returned to the bed.

State and pressure drop diagrams for these beds can be determined mathematically and graphically from simple force and mass balances [9]. Examples in dimensionless form are presented in Fig. 3. The ordinate axis represents the pressure gradient in the plant expressed in terms of that at minimum fluidization. The only values that this dimensionless form of pressure gradient can assume lie between zero and unity. In the former case, no solids are present in the pipe element; and in the latter case, the pipe element is completely filled with solids in a state of minimum fluidization. The axis of abscissae represents the superficial velocity expressed in dimensionless form as the particle Froude number, i.e.,

$$\mathrm{Fr}_p = \frac{u}{\sqrt{\frac{\rho_s - \rho_f}{\rho_f}\bar{d}_p g}}.$$

The parameter is a dimensionless form of the mass flow rate of circulated solids. It is expressed as the ratio of the volume flow rate of solids, as determined from the apparent density at minimum fluidization, to the volume flow rate of gas, i.e.,

$$\frac{\rho_f}{\rho_s(1-\psi_L)}\mu = \frac{\dot{M}_s}{\rho_s(1-\psi_L)}\frac{\rho_f}{\dot{M}_f},$$

where μ is the solids load in the gas stream, M_s is the mass flow rate of solids carried over, and M_f is the mass flow rate of gas through the bed.

The diagram also includes curves for constant relative velocity ratios, i.e., $(v_g - w)/w_f$, where v_g is the velocity of the gas phase with a low solids content and w is the velocity of the strands. This ratio indicates the factor by which the relative velocity between the gas and the solid aggregate, i.e., strands and clusters, exceeds the free-falling velocity of the individual particles.

A state and pressure drop diagram of this nature is valid only for a given gas–solids system that is characterized by the Archimedes number, which contains only the properties of the gas and the solids and the bed porosity at the onset of fluidization. All the operating points that are likely to occur in a circulating fluidized bed have been included in the diagram.

The solids separated by a cyclone from the gas stream are returned to a point immediately above the gas distributor in the circulating fluidized bed. The construction of the line through which they are returned is responsible for the differences in the

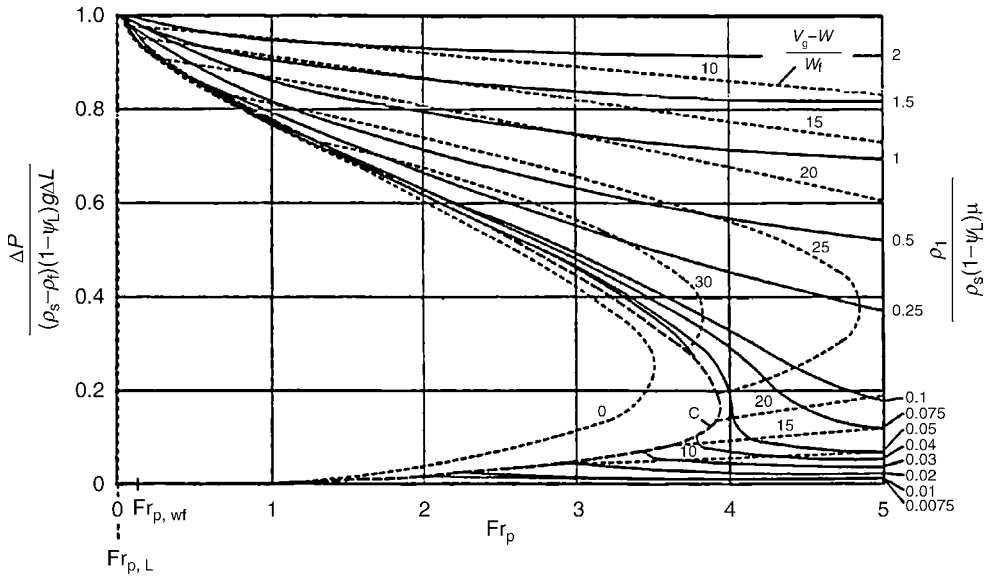

L3.2. Fig. 3. State and pressure diagram for the upward flow of demixed circulating gas–solids fluidized beds (Ar = 10; $\psi_L = 0.4$).

design of the beds, and the individual designs permit only very specific operating points [9]. There are three basic designs, i.e.,

1. Circulating fluidized beds with dosing devices and a pressure lock.
2. Circulating fluidized beds with dosing devices and a pressure feeder with a restricted differential pressure, e.g., a feeder-type fluidized bed and an L-valve.
3. Circulating fluidized beds with siphons.

The most widely adopted design in current practice is that with a siphon in the return line. The bed in this case is of given mass, i.e., the pressure drop in the bed is constant. At high gas velocities, the contents of the bed are uniformly distributed, apart from acceleration effects, over the entire height of the installation. A zone of steady-state conditions and a constant pressure gradient exists in the circulating fluidized bed. The pressure gradient can be calculated from the mass of the bed, i.e., the weight of the solids charged, by means of Eqs. (1a) and (1b). It is independent of the gas velocity as long as the solids remain uniformly distributed over the height of the installation. The corresponding curve in the dimensionless pressure drop diagram is parallel to the axis of abscissae. The relationships are shown schematically in Fig. 4.

If the volume of the solids return line is neglected and the solids are uniformly distributed, the maximum dimensionless pressure drop in circulating fluidized beds of constant cross-sectional area is equal to the ratio of the height h_L of the bed at the onset of fluidization to the total height of the installation, i.e., equal to the relative height to which the bed is filled with solids, i.e.,

$$\frac{\Delta P_{cb}}{(\rho_s - \rho_f)(1 - \psi_L)gH_{cb}} = \frac{h_L}{H_{cb}},$$

where H_{cb} is the height of the circulating bed.

If the Froude number Fr_p is reduced, the pressure drop curve corresponding to a charge of constant weight meets the boundary curve C at the point $Fr_{p,\,max}$. At values in the range between $Fr_{p,\,max}$ and the particle Froude number derived from the settling velocity of the individual particles $Fr_{p,\,wf}$, there are two pressure gradients in the circulating fluidized bed that correspond to the boundary curve C. Thus, there are two steady-state sections. One of them, with a pressure gradient corresponding to the upper branch of the boundary curve C, exists in the lower part of the circulating bed; and the other, with a pressure gradient corresponding to the lower branch of curve C, in the upper part. Nevertheless, the total pressure drop Δp_{cb} remains constant and continues to be governed by the weight of the charge and the height of the bed at the onset of fluidization. In practice, the transition at the point h_1 between two steady-state sections is not as abrupt as is indicated by the full-line theoretical curve in Fig. 4. It actually takes place gradually, and the height of the zone over which it proceeds is referred to as the transport disengaging height (TDH).

If the Froude number Fr_p is further reduced in the range between that derived from the velocity at the onset of fluidization $Fr_{p,\,L}$ and $Fr_{p,\,wf}$, two steady-state sections again exist in the circulating fluidized bed. Since Fr_p is smaller than $Fr_{p,\,wf}$, which is derived from the settling velocity of the individual particles, no solids can be carried over. Thus, there is a freeboard, and the pressure gradient is delineated by the axis of abscissae, i.e., it is zero. The pressure gradient in the lower part of the bed is fixed by the pressure drop curve for the volume flow rate ratio zero. In this range of Fr_p numbers, an aggregative or turbulent bed is formed – but only immediately above the gas distributor – and the total pressure drop in the circulating fluidized bed ΔP_{cb} again depends solely on the weight of the charge.

The solids concentration is a factor that affects heat transfer, and a knowledge of its axial distribution is therefore of great importance in thermal design. The average $(1 - \psi)$ over the

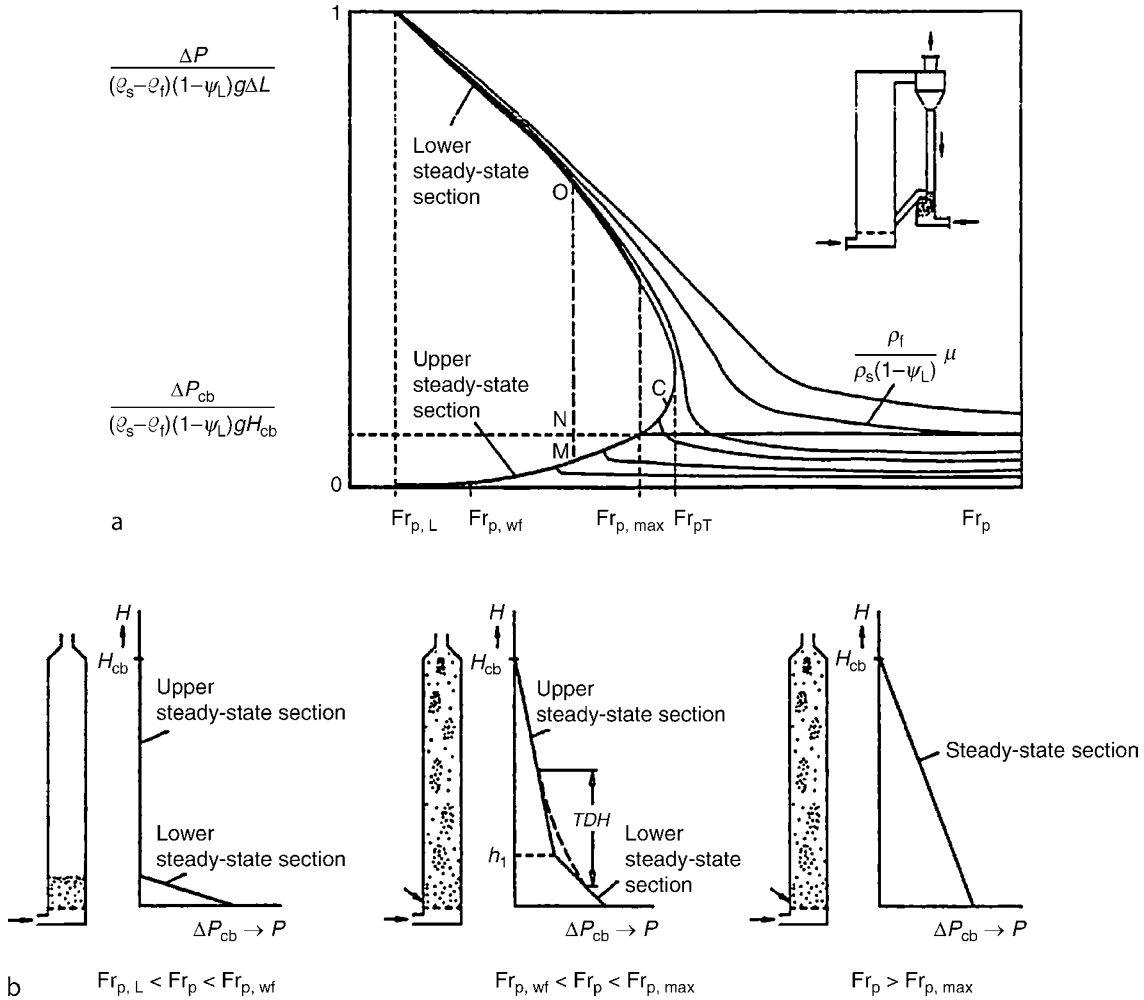

L3.2. Fig. 4. Diagram of state (**a**) and pressure profile (**b**) for a circulating fluidized bed with siphon.

cross section can be calculated from the dimensionless pressure drop, i.e.,

$$(1-\psi) = (1-\psi_L)\frac{\Delta P}{(\rho_s-\rho_f)(1-\psi_L)g\Delta L}.$$

Thus, the solids concentration in a circulating fluidized bed is proportional to the pressure gradient at a given height. It is constant in the axial direction if $Fr_p > Fr_{p,\,max}$, but depends on height if $Fr_p < Fr_{p,\,max}$. On a reduction of the Froude number Fr_p below $Fr_{p,\,max}$, the solids concentration decreases in the upper part of the bed and increases in the lower part. If $Fr_p < Fr_{p,\,wf}$, there will be a freeboard, i.e., the concentration in the upper part of the bed will be zero. In the lower part of the bed, even in this Fr_p range, the solids concentration continues to increase with a decrease in the Froude number. The maximum value is attained when the particle Froude number Fr_p is equal to that derived from the velocity at the onset of fluidization $Fr_{p,\,L}$, i.e., when fluidization in the circulating bed is a minimum.

The reason for the decrease in solids concentration in the upper part of the bed when Fr_p is reduced to below $Fr_{p,\,max}$ is that the stable solids load that the gas stream can carry is restricted by the boundary curve *C*. In this design of circulating fluidized bed, the mass of the bed remains constant if the Froude number Fr_p is reduced. The law of conservation of mass therefore entails that an axial concentration profile is formed if $Fr_p < Fr_{p,\,max}$. The relative length of the lower steady-state section h_1/H_{cb} is equal to the ratio of the sections NM and MO; and that of the upper steady-state section $(H_{cb} - h_1)/H_{cb}$, to the ratio NO/MO.

Accordingly, if $Fr_p < Fr_{p,\,max}$, the physics of gas flow is responsible for the solids concentration and the pressure gradients in the steady-state sections; and the weight of the charge, only for their relative length. Conversely, if $Fr_p > Fr_{p,\,max}$, the solids charge and thus the method of plant operation will govern the solids concentration and the pressure gradients in circulating fluidized beds with siphons.

If the superficial velocity is less than the settling velocity of the individual particles, expressed in terms of $\bar{d}_p$, the particle size distribution should be divided into as many intervals as possible, and the state and pressure drop diagrams for each should then be separately determined. Afterwards, the flow patterns in the circulating fluidized bed can be obtained from the mass fractions in each interval [9]. An example is given by circulating fluidized bed firing systems, in which the cross

section is usually widened. In this case, the height of the system should be divided into two parts, each of uniform cross-sectional area, and the associated diagrams of state should then be determined [9].

4 Operating Range of Inlet Velocities in Particulate and Aggregative Fluidized Beds

The range of inlet velocities in liquid–solids fluidized beds is restricted, on the one hand, by the velocity at the onset of fluidization u_L and, on the other hand, by the settling velocity of the particles, i.e., $u_L \leq u \leq w_f$. Pronounced inhomogeneities occur in gas–solids fluidized beds, i.e., gas bubbles at low and solid strands at high void fractions. As a consequence, a substantial fraction of the solids may be carried over and returned to the bed via a cyclone [10], as has been described in Sect. 3.2.2. A useful estimation of the operating range, even in aggregative gas–solids fluidized beds, can be obtained from the w_f/u_L ratio if the particles are spheres of the same diameter d_p. The Archimedes number and the Reynolds number derived from the settling velocity of the individual particles are related as follows:

$$\mathrm{Ar} = 3/4\mathrm{Re}_{wf}^2 c_w(\mathrm{Re}_{wf}),$$

in which $c_w(\mathrm{Re}_{wf})$ is the drag coefficient for the individual particles. The unique inverse function is

$$\mathrm{Re}_{wf} = \mathrm{Re}_{wf}(\mathrm{Ar}). \qquad (7)$$

Figure 5 has been derived from Eqs. (3) and (7) for $\varphi_s = 1$. It shows the Archimedes number as a function of the following ratio:

$$\frac{w_f}{u_L} = \frac{\mathrm{Re}_{wf}}{\mathrm{Re}_L} = f(\mathrm{Ar}, \psi_L).$$

The parameter is ψ_L, and the diagram is valid for spherical particles of uniform size.

The following simple expressions can be derived for the two limits – minimum fluidization and settling of the individual particles:

$$\left.\begin{aligned} \left(\frac{w_f}{u_L}\right)_{lam} &= \frac{25}{3}\frac{1-\psi_L}{\psi_L^3} = 78 \\ \left(\frac{w_f}{u_L}\right)_{turb} &= \sqrt{\frac{5.25}{\psi_L^3}} = 9 \end{aligned}\right\} \text{for } \psi_L = 0.4.$$

They apply if both limits are for purely "laminar" or for purely "turbulent" flow. The numerals 78 and 9 were obtained from the results of experiments. Particular attention should be paid to the fact that the operating range for fine particles is wider than that for coarse particles.

5 Pressure Drop

In a readily fluidizable bed of particles with low cohesion and of almost uniform size, a dimensionless expression for the pressure drop Δp can be obtained from the total weight G and the cross-sectional area A of the bed. It is shown in Fig. 6 as a function of the dimensionless superficial velocity, i.e., u expressed as a ratio of the velocity u_L at the onset of fluidization.

If the particles are sufficiently fine and the flow through the bed is thus "laminar", the slope of the curve is unity. Before the onset of fluidization, a value $\Delta p_{max}(G/A) > 1$ is attained as a result of compaction brought about by the bed's own weight. As fluidization progresses, the initial compaction is overcome, and the pressure drop within the bed falls to the equilibrium value $\Delta p/(G/F) = 1$. It is not until u/u_L » that the pressure drop commences to rise slightly again as a result of the additional losses brought about by the much more intense movement of the solids and the increase in the gas flow rate. If the inlet velocity falls below u_L, the pressure drop becomes less in the bed of loose solids. For this reason, it is advisable to define the onset of fluidization as the intersect of the decreasing inlet velocity branch of the curve for the fixed bed (extrapolated if necessary) and the horizontal curve for the fluidized bed. Whenever possible u_L determined direct by this means should be adopted for design purposes.

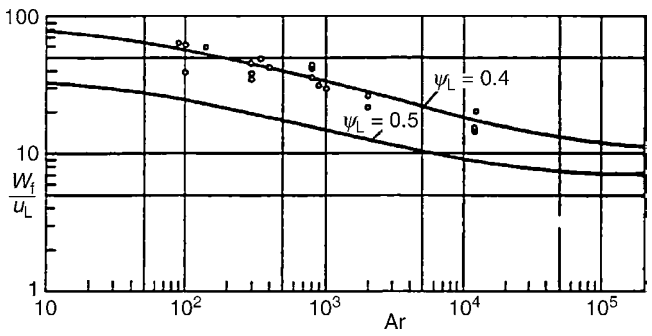

L3.2. Fig. 5. Operating range for particulate and aggregative fluidized beds: Archimedes number as a function of w_f/u_L with ψ_L as parameter. Measurements by [18].

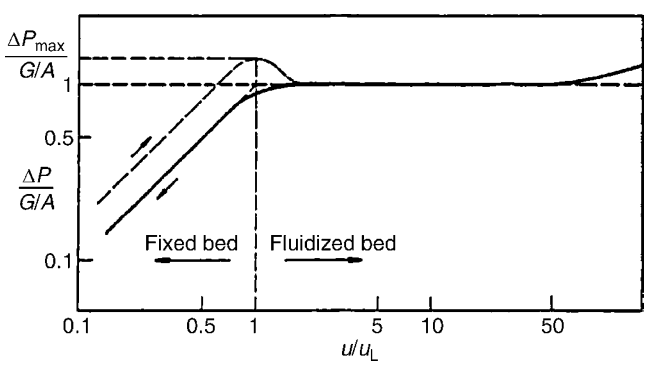

L3.2. Fig 6. Pressure drop curve for a readily fluidizable gas–solids bed.

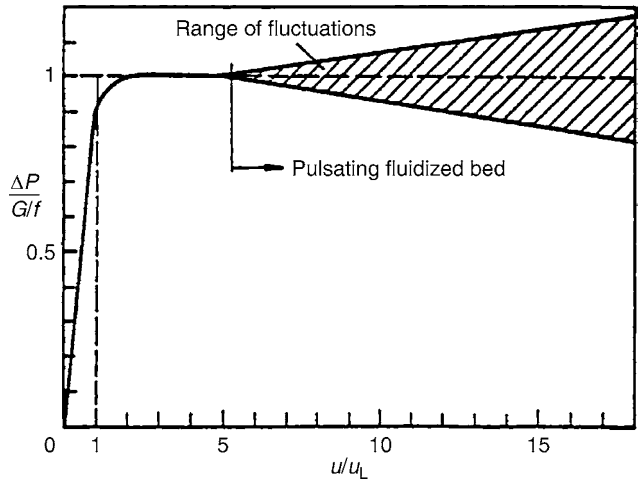

L3.2. Fig. 7. Fluctuations in pressure in a pulsating fluidized bed.

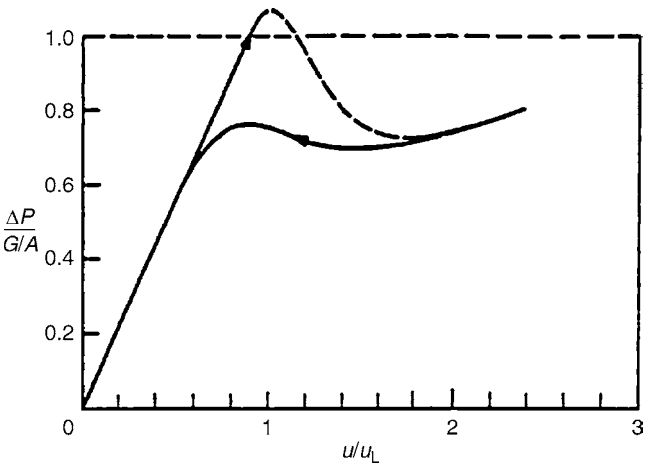

L3.2. Fig 8. Pressure drop in a channeling fluidized bed.

Pulsation and channeling in fluidized beds must be avoided in practice: pulsation entails undesirable mechanical stresses, and channeling indicates maldistribution. Both can be recognized by peculiarities in the pressure characteristic. Thus pronounced fluctuations in pressure, as is illustrated in Fig. 7, are a sign of pulsation.

Beds of fine particles are particularly cohesive and thus prone to channeling. The gas flows preferentially through the channels, and the surrounding sections of the bed remain largely unfluidized. The pressure drop in channels of comparatively large cross-sectional area is abnormally less than that in a well-fluidized bed, as can be seen in Fig. 8.

The gas distributor contributes substantially to the pressure drop in a bed. The design depends on the application – porous sintered metal, ceramics, plastics panels; fabrics stretched on a supporting grid; beds of material fixed between sheets of wire gauze; perforated sheet metal; or slotted or bubble-cap plates. Experience gained in operating fluidized beds has shown that the pressure drop over the gas distributor should be 10–20% of the pressure drop in the bed or at least about 3,000 N/m^2 if the bed is correspondingly low [11–13].

The void fraction in plates with perforations of a few millimeters diameter is $\varphi_{perf} < 10\%$. Their pressure drop can be determined by the Kneule and Zelfel diagram [14], which is reproduced in Fig. 9. The characteristic K on the axis of abscissae is given by

$$K = \mathrm{Re}_{perf}\left(\frac{d_{perf}}{b}\right)\left(\frac{b}{t}\right)^{0.7} N_{perf}^{0.25}, \tag{8}$$

where $\mathrm{Re}_{perf} = u_{perf} d_{perf}/\nu$ is the Reynolds number applicable to an average gas velocity u_{perf} in perforations of d_{perf} diameter, b is the thickness of the perforated plate, t is the spacing between perforations, and N_{perf} is the number of perforations.

The following relationships exist between φ_{perf}, d_{perf}, N_{perf}, t, and the bed diameter d:

$$\varphi_{perf} = \left(\frac{d_{perf}}{d}\right)^2 N_{perf} = \frac{\pi}{2\sqrt{3}}\frac{d_{perf}^2}{t^2}, \tag{9}$$

$$N_{perf} = \frac{2}{\sqrt{3}}\frac{A}{t^2}. \tag{10}$$

The thickness of the perforated plate is given by [14]

$$b \geq d_{perf}. \tag{11}$$

The measured dimensionless pressure drop ξ_{perf} on the axis of ordinates is defined by

$$\xi_{perf} = \frac{\Delta p_{perf}}{\frac{\rho_g}{2} u_{perf}^2}. \tag{12}$$

If the particles are fine and correspondingly cohesive, adequate fluidization may be ensured by designing the distributor so that the gas jets issuing from the perforations maintain the solids in sufficient motion. The conditions for this, as determined by experiment, are as follows:

$$\frac{\rho_g}{2} u_{perf}^2 = a\frac{G}{f},$$

where $0.5 < a < 0.75$ and

$$u_{perf} = b\sqrt{\frac{G}{f\rho_g}}, \tag{13}$$

where $1 < b < 1.2$.

The void fraction and the (generally higher) pressure drop in the gas distributor can be obtained from the superficial velocity required for fluidization and the diameter selected for the perforations.

Engineers engaged in practice can obtain more detailed information on specialized aspects of fluidization technology from standard works [15–17].

Example

Given

$$\varrho_s = 3\,\mathrm{g/cm^3},\ \bar{d}_p = 100\,\mu\mathrm{m},\ \text{and}\ \varrho_g = 10^{-3}\,\mathrm{g/cm^3}.$$

Fluidized bed diameter $d = 5$ m.

$$\varphi_s = 1, \nu = 15 \cdot 10^{-6}\,\mathrm{m^2/s},\ h_L = 3\,\mathrm{m}, \text{and}\ \psi_L = 0.4.$$

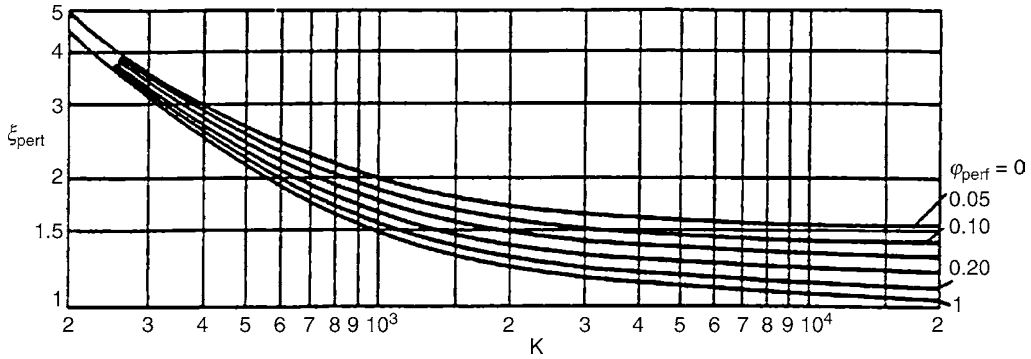

L3.2. Fig. 9. Resistance factor ξ_{perf} for a perforated-plate gas distributor as a function of the characteristic K with the void fraction φ_{perf} as parameter [14].

To be determined

1. Gas velocity $u = 10\,u_L$.
2. w_r/u_L.
3. Pressure drop in fluidized bed and design data for perforated-plate gas distributor.
   (1) If $Re \leq 1$ is assumed, it follows from Eq. (4) that

$$u_L = \frac{1}{150}\frac{1 \cdot 0.4^3}{0.6}\frac{9.81 \cdot 10^4 \cdot 10^{-12} \cdot 3}{15 \cdot 10^{-6} \cdot 10^{-3}} = 1.4 \cdot 10^{-2}\ \text{m/s},$$

$$u = 10 \cdot 1.4 \cdot 10^{-2} = 0.14\ \text{m/s}.$$

   Check

$$Re_L = \frac{1.4 \cdot 10^{-2} \cdot 10^2 \cdot 10^{-6}}{15 \cdot 10^{-6}} = 0.093 = 1.$$

   (2) $$Ar = \frac{9.81 \cdot 10^6 \cdot 10^{-18} \cdot 3}{225 \cdot 10^{-12} \cdot 10^{-3}} = 131.$$

   Reading off against $\psi_L = 0.4$ in Fig. 5 gives $w_f/u_L > 10$. In other words, the conditions lie within the operating range for the fluidized bed.
   (3) Pressure drop in fluidized bed as derived from Eq. (1a)

$$\Delta p = (1 - \psi_L)\left(\rho_s - \rho_g\right) g h_L$$

$$= 0.6 \cdot 3 \cdot 10^3 \cdot 9.81 \cdot 3 = 5.3 \cdot 10^4\ \text{N/m}^2.$$

$$\text{Estimation}: \quad 4\Delta p_{perf} = 0.1\Delta p_{bed} = 5.3 \cdot 10^3\ \text{N/m}^2.$$

Turbulent flow and thus very low void fractions φ_s represent the only means of obtaining high pressure drops of this order. In this case, it follows from Fig. 9 that $\xi_{perf} = 1.5$; and thus from Eq. (11),

$$u_{perf} = \sqrt{\frac{2 \cdot 5.3 \cdot 10^3}{1 \cdot 1.5}} = 84\ \text{m/s}.$$

The equation of continuity yields

$$\varphi_{perf} = \frac{u}{u_{perf}} = \frac{14 \cdot 10^{-2}}{84} = 1.67 \cdot 10^{-3}.$$

A point to observe in selecting the diameter d_{perf} of the perforations is that a large number of perforations N_{perf}, i.e., a narrow spacing t, improves gas distribution by preventing dead spots in the vicinity of the distributor but greatly increases the risk of fouling. Values of t and N_{perf} calculated from Eqs. (9) and (10) are listed against the corresponding values of d_{perf} in the following table. The value for K should be subsequently determined to verify the validity of the assumption $\xi = 1.5$.

d_{perf} (M)	t (m)	N_{perf} (–)	B (m)	K (–)	ξ_{perf}[a] (–)
0.001	0.023	$4.2 \cdot 10^4$	0.004	$5.8 \cdot 10^3$	1.6
0.002	0.047	$1.0 \cdot 10^4$	0.004	$1 \cdot 10^4$	1.5
0.005	0.147	$1.67 \cdot 10^3$	0.005	$2 \cdot 10^4$	1.5
0.010	0.233	418	0.010	$2.8 \cdot 10^4$	1.5

[a] From Fig. 9.

6 Bibliography

1. Jeschar R (1964) Druckverlust in Mehrkornschüttungen aus Kugeln. Arch Eisenhüttenwes 35(2):91–108
2. Rumpf H, Gupte AR (1971) Einfluss der Porosität und Korngrössenverteilung im Widerstandsgesetz der Porenströmung. Chem Ing Techn 43:367–375
3. Molerus O, Pahl MH, Rumpf H (1971) Die Porositätsfunktion in empirischen Gleichungen für den Durchströmungswiderstand Re<1. Chem Ing Techn 43:376–378
4. Ergun S, Orning AA (1949) Fluif flow through randomly packed columns and fluidized beds. Ind Eng Chem 41:1179–1184
5. Ergun S (1952) Fluid flow through packed columns. Chem Eng Prog 48:89–94
6. Wen CY, Yu YH (1966) A generalized method for predicting the minimum fluidization velocity. AIChE 12:610–612
7. Richardson JF, Zaki WF (1954) Sedimentation and fluidization: part 1. Trans Inst Chem Eng (London) 32:35–35
8. Molerus O (1982) Fluid-Feststoff-Strömungen. Springer-Verlag, Berlin
9. Wirth K-E (1990) Zirkulierende Wirbelschichten – Strömungs-mechanische Grundlagen, Anwendung in der Feuerungstechnik. Springer-Verlag, Berlin
10. Reh L (1968) Verbrennung in der Wirbelschicht. Chem Ing Tech 40:509–515
11. Kunii D, Levenspiel O (1969) Fluidization engineering. Wiley, London
12. Lehmann W, Müller F (1966) Mitt. Inst. Leichtbau u. ökonomische Verwendung von Werkstoffen, Dresden, vol 5, pp 227–238
13. Whitehead AB, Gartside G, Dent DC (1970) Flow and pressure maldistribution at the distributor level of a gas-solid fluidized bed. Chem Eng J 1:175–185

14. Kneule F, Zelfel E (1966) Der Druckverlust von Siebböden beim Betrieb ohne Flüssigkeiten. Chem Ing Techn 38:260–264
15. Geldart D (Hrsg.) (1986) Gas fluidization technology. Wiley, Chichester, NY
16. Davidson JF, Clift R, Harrison D (eds) (1985) Fluidization. Academic Press, London
17. Werther J Fluidized bed reactors. In Ertl G, Knözinger H, Schüth F, Weitkamp J (eds) Handbook of heterogeneous catalysis. Wiley-Verlag, Weinheim, pp. S.2106–S.2132
18. Bourgeois P, Grenier P (1968) The ratio of terminal velocity to minimum fluidising velocity od spherical particles. Canadian J Chem Eng 46:325–328

L3.3 Pressure Drop in Pneumatic Conveying Systems

Ulrich Muschelknautz
MK Engineering, Innsbruck, Austria

1 Types of Flow and Functional Diagram

The type of the two-phase flow, which develops in a pneumatic conveying system, depends crucially on the load ratio (solids-to-gas) μ . The load ratio is defined by

$$\mu = \dot{M}_s / \dot{M}_g. \tag{1}$$

Also the pressure drop of a pneumatic conveyor is strongly determined by the solids load. The transport of particles leads to a pressure drop in addition to that caused by the pure gas flow.

In thermal engineering applications, e.g., cooling, heating, drying, or incineration, the load ratio is typically $\mu = 0.05$–2, the gas velocities in the pipe are 15–30 m/s, and the average particle size d_{50} lies between ca. 50 µm and 2 mm. Under these operating conditions, the particles are usually uniformly distributed over the pipe cross section. This state of pneumatic conveying is referred to as fully suspended flow. The short routes which the particles have to traverse in pneumatic conveyor dryers of the type shown in Fig. 1 consist of frequent turns and changes in the cross section. In this case, the pressure drop is mainly caused by acceleration of the particles at the feeding point and behind the bends.

If the conveyor is intended solely for transportation, as is shown in Fig. 2, bends are avoided whenever possible. Under these circumstances, the weight and wall friction of the solids are primarily responsible for the additional pressure drop.

A fully suspended flow is feasible if the load ratio in a horizontal pipe remains less than the limited load ratio μ_{lim} [1–4]:

$$\mu_{lim} = (0.02...0.04) \cdot \left[\frac{\lambda_g v^3}{g D w_s} k + \frac{2}{\sqrt{\frac{a}{d_s}}} \frac{c^2}{gD} (1-k) \right]. \tag{2}$$

A load ratio μ, which is not more than about 10% greater than the limited load ratio μ_{lim}, does not create any problem for fully suspended flow. The smaller constant in Eq. (2) is valid for narrow particle size distributions and for approximately spherical particles, the larger constant has to be applied for broader particle size distributions and for particles with irregular but compact shape. Equation (2) is valid for conveying pipes with an inner diameter larger than 70 mm.

At higher solids load and/or lower gas velocity, a part of the product moves along the wall in the form of strands and the strand type conveying is achieved.

At high solids mass flow rates, direct transition from strand type conveying to plug flow occurs for solids with large particle sizes and, in the case of finely grained particles, blockage of the system develops. Plug flow conveying is frequently resorted in order to save energy in pure transportation tasks.

Typical data for the three types of conveyance are given in Fig. 3.

Plug flow conveyance may also be controlled. In this case, bypasses are usually installed by means of which the columns or plugs are restricted to given lengths [5, 6].

By itself, v is the superficial velocity, but in the term c/v it is the effective velocity.

The functional diagram in Fig. 4 shows on the right-hand side at the top the fully suspended flow at load ratios of

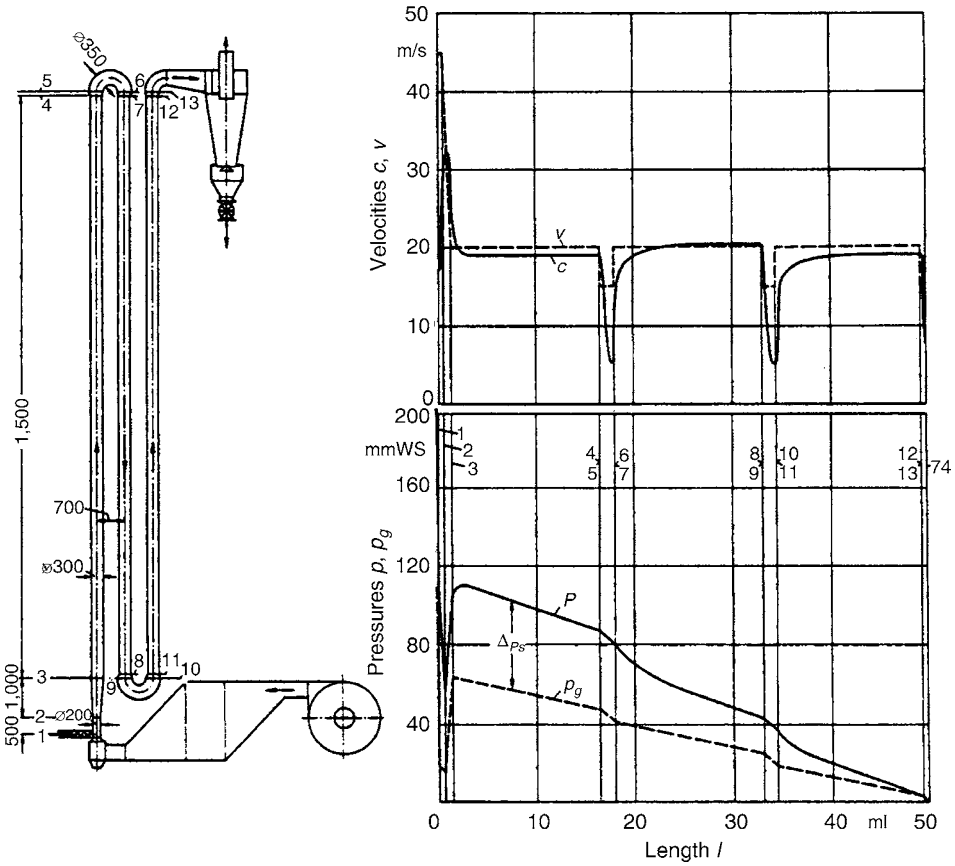

L3.3. Fig. 1. Schematic diagram of a pneumatic conveyor dryer with gas velocity v, average particle velocity c, pressure p_g of the pure gas, and pressure p of the loaded gas stream along the path through the pipe.

μ = 5–10. At higher load ratios and lower gas velocities, strands and plugs developed at weakly increasing pressure drop. If the solids mass flow rate $\dot{M}_s$ is further increased, there is a small velocity range in which dunes are conveyed. No stable pressure drop occurs; at leftmost in the diagram the conveyance is again regular at very high loadings and very small velocities. The pressure drop of this type of conveyance is again stable. The limit is achieved when an almost continuous, fluidized column of product is slowly pressed through the pipe. The flow power which has to be expended is for isothermal expansion

$$N = \dot{V}_1 \cdot p_1 \cdot \ln\frac{p_1}{p_2} = \dot{V}_2 \cdot p_2 \cdot \ln\frac{p_1}{p_2}. \qquad (3)$$

If before an adiabatic compression has been applied, the power of the fan has to be increased by a factor of about 1.33, including the efficiency factor.

2 Fully Suspended Flow

2.1 Particle Size Distribution

Measurements obtained e.g., by light scattering, laser diffraction, image analysis, screening, sedimentation or wind sifting are plotted in an RRSB net to determine the particle size distribution in the form of retained fraction $R(d)$ or a cumulative pass fraction $D(d) = 1 - R(d)$ curve [7], Fig. 5. They are described by

$$R(d) = \exp\left[-\left(\frac{d - d_{\min}}{d' - d_{\min}}\right)^{n}\right] \quad \text{for } d_{\min} < d < d', \qquad (4a)$$

$$R(d) = \exp\left[-\left(\frac{d_{\max} - d'}{d_{\max} - d}\right)^{0.1} \cdot \left(\frac{d}{d'}\right)^{n}\right] \quad \text{for } d' < d < d_{\max}, \qquad (4b)$$

where d' is the particle size corresponding to $R = 1/e = 0.36$, $d_{\min}$ is the minimum particle size, and $d_{\max}$ is the maximum particle size. The exponent n determines the slope of the distribution curve at d' and thus its width.

The courses of the velocities in Fig. 2 show that the velocity of coarser particles remains substantially below the gas velocity. Further preliminary estimates can be made from the velocity ratios $C = c/v$ in Fig. 3. If the entire particle size distribution at a given load ratio μ is expressed by the average diameter d_{50} at R = 0.5, the ratio of the mutual spacing a between the particles to the size of the particles d is given by

$$\frac{a}{d} = \left(\frac{\pi/6\rho_S/\rho_g \; c/v}{\mu}\right)^{1/3}. \qquad (5)$$

Spacings calculated according to Eq. (5) are listed in Table 1 for pulverized coal with the particle size distributions given in Fig. 5 at a load ratio of μ = 1. The first row of Table 1 shows the result

for the average particle size of the distribution. A spacing of 8.7 d_{50} = 244 µm characterizes the cloud of particles only very roughly. If, however, the distribution in Table 1 is divided into three classes, viz. 25% of fine, 50% of average, and 25% of coarse particles, quite different spacings are obtained: 1,100 µm for the coarse particles, 300 µm for the average particles, and 62 µm for the fine particles. Since the small particles move more rapidly than the large ones, frequent overtaking and collisions of particles occur. In the following discussion, these collisions are ignored. Research along these lines was recommenced in 1959 [6] and has since then been resumed. With respect to the pressure drop, collisions of particles with the wall are by far more important, because the associated velocity of impact is very much greater than that between the particles. At load ratios above $\mu = 2$ the mixture described earlier or a similar mixture behaves approximately like a collective of particles with the uniform particle size d_{50}, due to the numerous collisions between the particles. It is for this reason that the average particle size is resorted to for the analysis.

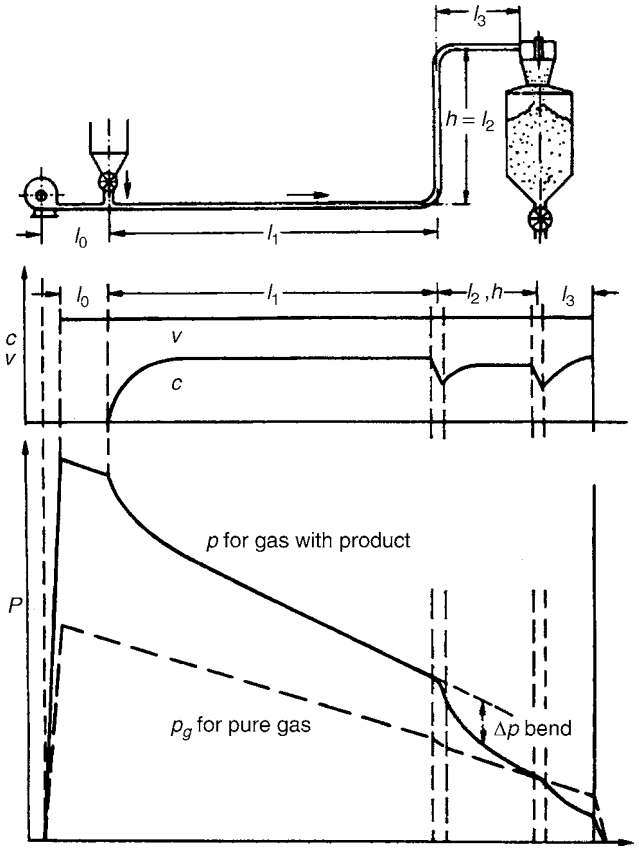

L3.3. Fig. 2. Conveying system with fully suspended flow. Shown are the gas velocity *v*, the mean particle velocity *c*, and the pressure of the pure gas flow as well as the pressure of the loaded gas flow along the path through the conveyor.

2.2 Equation of Motion and Velocity Ratio

In a fully suspended flow the forces acting on the particles of a cloud parallel to the direction of conveying are the drag force F_W, the component of weight parallel to the conveying direction F_G, the frictional force due to weight F_R, and the wall impact friction force due to particle impact at the wall F_S.

From the momentum balance it follows for the product mass M_S in a pipe section of length Δl

$$M_S c \frac{dc}{dl} = F_W + F_G + F_R + F_S. \quad (6)$$

2.2.1 Drag Force

According to [8, 9], the drag force of the product cloud is conveniently expressed in terms of its weight in a section of length Δl of the conveyor

$$M_S g = \dot{M}_s \frac{\Delta l}{c} g \quad (7)$$

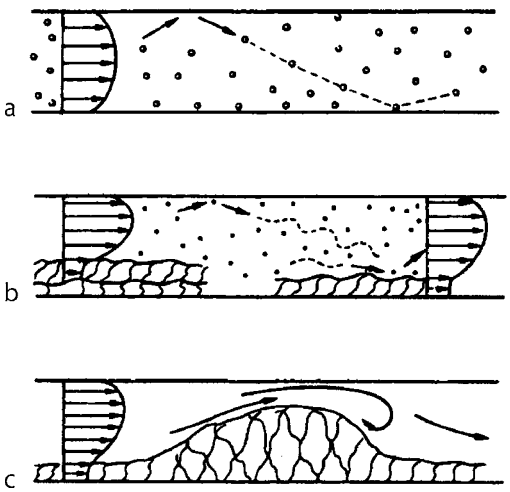

	μ	d_{50} mm	v m/s	c/v	Δp/100 m bar
a	1–10	0.1 1 10	20 30 40	0.8 0.65 0.5	0.15–0.5
b	10–50	0.01 0.1 0.5	20 25 30	1 0.3 0.4	0.75–2
c	20–50	0.01 0.1 1	15 20 25	1 0.3 0.5	0.4–0.8

L3.3. Fig. 3. Various conveyance states with typical data. (**a**) Fully suspended flow, (**b**) Strand type conveying, (**c**) Strand type conveying and plug flow.

L3.3. Table 1. Particle spacings a for pneumatic conveying of pulverized coal represented in Fig. 5, calculated according to Eq. (5)

		μ	d_{min} µm	d_{50} µm	d_{max} µm	a µm
I	One class	1	2	28	150	244
II	Three classes	0.25	2	4.5	17	62
		0.5	17	28	52	300
		0.25	52	80	150	1,100

I For the average particle size d_{50} and $\mu = 1$ for the total amount
II For three classes with different size fractions and solids loadings

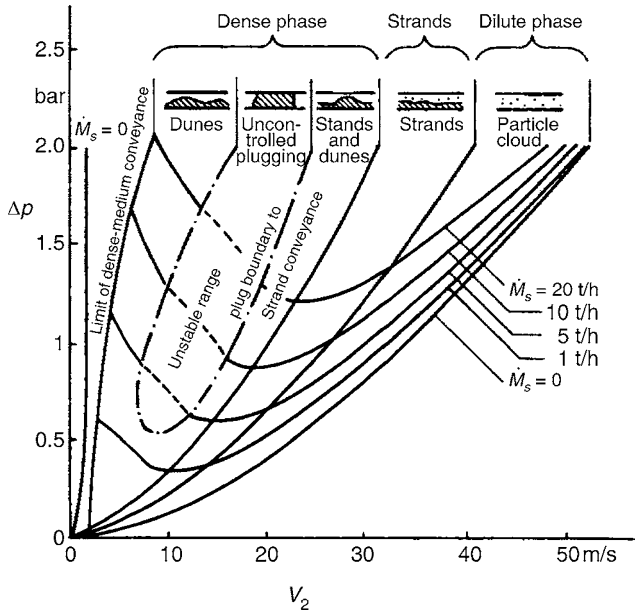

L3.3. Fig. 4. Functional diagram for pneumatic conveyance with typical operating data for a plant with $D = 150$ mm, air at 1.5 bar, and free-flowing product with particle sizes greater than 10 µm.

and the average settling velocity w_S of the solid particles [1]:

$$F_W = \mathrm{sgn}(v - c) M_S g \left(\frac{|v - c|}{w_S} \right)^{2-k}. \tag{8}$$

The drag force impels or retards if $v > c$ or $v < c$.

The settling velocity w_S in Eq. (8) has been adopted for practical reasons.

For a single particle with arbitrary shape the settling velocity depends on the drag coefficient c_w as follows:

$$w_{s0} = \left(\frac{(V_S/(d_S A_S)) \Delta\rho_{s,g} g d_s^{1+k}}{c_w \mathrm{Re}_S^k \eta_g \rho_g^{1-k}} \right)^{1/(2-k)}. \tag{9}$$

In Eq. (9) A_S and d_S denote the maximum cross section and the maximum particle diameter of the particle perpendicular to the direction of the flow onto the particle, respectively, V_S the particle volume, g the acceleration due to gravity, $\Delta\rho = \rho_s - \rho_g$ the density difference between particle and gas, η_g the gas viscosity, and

$$\mathrm{Re}_S = \frac{|v - c|\, d_S \rho_g}{\eta_g} \tag{10}$$

the Reynolds number for the flow around the particle.

The drag coefficient can be described for a wide range of particle Reynolds numbers ($0.5 < \mathrm{Re} < 1{,}000$) by a three-term approximation

$$c_w = \frac{A}{\mathrm{Re}_S} + \frac{B}{\mathrm{Re}_S^{0.5}} + C. \tag{11}$$

The values A, B, C depend on the particle shape and are listed in Table 2. The values given there are valid for the range $0.5 < \mathrm{Re}_S < \mathrm{Re}_G$. Values for Re_G vary depending on the particle shape, Table 2. For $\mathrm{Re}_S < \mathrm{Re}_G$ approaching Re_G the drag coefficient approaches the limit $c_{w,G}$, Table 2.

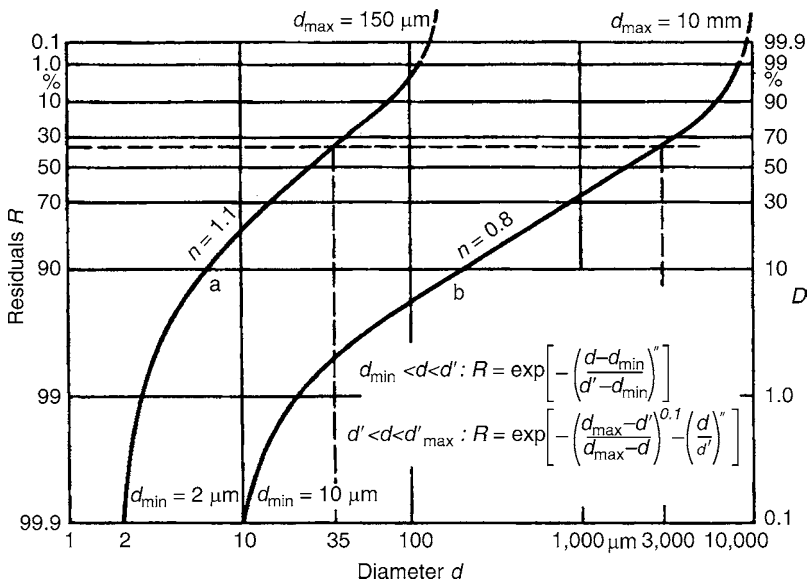

L3.3. Fig. 5. Size distribution curves plotted in a RRSB net with minimum and maximum particle sizes. (**a**) Pulverized black coal fed to burners, (**b**) Run-of-mine coal fed to roller mill.

L3.3. Table 2. Constants in Eq. (11) and values for limits c_{wG} for different particle shapes

	A	B	C	Re_{lim}	$c_{w,lim}$
Sphere	21.5	6.5	0.23	1,000	0.46
Compact angular	24	6	0.35	800	0.60
Cube	27	4.5	0.65	400	0.98
Cylinder	23	6	0.5	600	0.80
Elliptic grain	25	6	0.4	800	0.65
Elliptic lenses	28	6.5	0.7	150	1.4

For limited ranges of Reynolds numbers the settling velocity can be obtained by linearization in the c_w (Re_S) diagram:

$$c_w = \frac{K}{Re_S^k}. \tag{12}$$

The constants K and k are obtained by drawing the tangent to the c_w (Re_S) curve for any desired Re_S number.

From Eq. (11) it follows

$$k = \frac{A + 0.5B\sqrt{Re_S}}{A + B\sqrt{Re_S} + C\sqrt{Re_S}}, \tag{13}$$

$$K = \frac{A}{Re_S^{1-k}} + \frac{B}{Re_S^{0.5-k}} + C\,Re_S^k. \tag{14}$$

For the case of single particles with spherical shape, it is $V_S = (\pi/6)\,d_S^3$ and $A_S = (\pi/4)\,d_S^2$. Thus, it follows from Eqs. (9) and (12):

$$w_{S0} = \left(\frac{(4/3)\Delta\rho_{s,g} g d_S^{1+k}}{K \eta_g^k \rho_g^{1-k}}\right)^{1/(2-k)}. \tag{15}$$

Approximations for w_{S0}

The exponent k depends on the Re_S number. For laminar flow around the particle, it is $k = 1$. If the flow is in the transition region, it is $k = 0.5$ and if it is turbulent, it is $k = 0$. Should a first approximation suffice, Stokes' law may be applied for approximately spherical particles and Reynolds numbers up to $Re_S = 10$

$$w_{S0,Stokes} = \frac{\Delta\rho_{S,g} g d_S^2}{18\eta_g} \tag{16}$$

and in the transition region $Re_S = 10$–10^3 with the linearization according to Eq. (11)

$$w_{S0,Ü} = \frac{\left(\Delta\rho_{S,g} g\right)^{2/3} d_S}{4.3\left(\eta_g \rho_g\right)^{1/3}} \tag{17}$$

and in the turbulent region at $Re_S > 10^3$

$$w_{S0,N} = \sqrt{\frac{4}{3}\frac{\Delta\rho_{S,g} g}{\rho_g c_W} d_S} \tag{18}$$

with $c_w = 0.5$–0.7 depending on the particle shape.

Equation (15) or the approximations in Eqs. (16–18) give the settling velocities of single particles with spherical shape without allowance for the effects exerted by neighboring particles, agglomerates, or accumulations of small particles in the lee of the larger ones.

According to measurements of [10] for Re_S numbers between 50 and 1,000, the following dependence of the settling velocity on the solids load is obtained:

$$\frac{w_S}{w_{S0}} = 1 + (0.25 + k) \cdot \mu^{0.25}. \tag{19}$$

2.2.2 Weight and Friction due to Weight

It is

$$F_G + F_R = -M_S g(\sin\,\alpha + f\,\cos\,\alpha) \tag{20}$$

with the angle of slope of the conveying pipe α against the horizontal and with the coefficient of friction f, which is identical with the coefficient of sliding friction f_{sl}. Typical values are given in Table 3.

2.2.3 Force due to Wall Impact Friction

It is

$$F_S = -M_S g \frac{c^2}{Dg}\frac{\lambda_S^*}{2}. \tag{21}$$

The wall impact friction factor λ_S^* indicates the number of collisions on the wall per unit area, the intensity of impact, and the attendant loss in impetus of the particles. Comprehensive studies on actual and simulated weightlessness have revealed that, with respect to fluid dynamics, it depends on a modified Barth number,

$$Ba^* = \frac{\nu^k w_S^{2-k}}{Dg(1 - v_{Ba}^*/v)^{2-k}}, \tag{22}$$

and, with respect to mechanics, on the number of collisions S

$$S = \frac{d_S}{s}\frac{E_W}{E_S}\frac{\rho_S}{\rho_W} \tag{23}$$

and the load ratio μ [11–13]. In Eq. (23), s is the wall thickness of the conveyor. To calculate the Ba^* number, the velocity at the distance $y^* = d_S/2$ from the wall is used. It can be obtained quite accurately from the *Prandtl* one-seventh power law, i.e.,

$$v_{Ba}^* = 1.05\nu\left(\frac{d_S}{D}\right)^{1/7} \tag{24}$$

or from the general profile shown in Fig. 6 [14].

Guide values for the modulus of elasticity of the wall and the particle material E_W and E_S required to determine the expression for the number of collisions S are listed in Table 4.

The relationship between the impact friction factor λ_S^* and the load ratio μ is given by

$$\lambda_S^* = \frac{\lambda_S^*}{(1+\mu)^{0.25}} \tag{25}$$

The reference variable λ_{S0}^* for small load ratios μ which tends to zero can be obtained from the diagrams in Figs. 7 and 8 or from original works [11–13].

L3.3. Table 3. Coefficients of sliding friction *f* for various materials

Solid material	Particle size μm	Coefficient of sliding friction *f*		
		Against aluminum	Against stainless steel	Against steel
ABS powder (Butadiene)	30. . .50	0.51	0.44	0.57
Adipic acid	100	0.53	0.46	0.59
Bisphenol powder	50	0.55	0.51	0.64
Silicic acid	Micron range	0.67	0.67	0.84
Sodium perborate	150	0.44	0.42	0.54
PA granulate (Polyamide)	3,000. . .4,000 cubes	0.42	0.34	0.45
PE granulate (Polyethylene)	3,000 Lenticular pellets	0.23	0.19	0.28
Soot pellets	500. . .1,000 granulate pellets	0.78	0.72	0.90
PP granulate (Polypropylene)	3,000	0.27	0.23	0.32
PP powder (Polypropylene)	300	0.36	0.44	0.56
PS granulate (Polystyrol)	3,000. . .4,000 cubes	0.30	0.27	0.36
Soot powder	5. . .50	0.75	0.75	0.93
PVC powder	150	0.40	0.36	0.47
Alumina	40. . .100	0.58	0.53	0.66
TiO_2 pigment	1. . .20	0.90	0.90	1.11
TPA powder	100	0.34	0.40	0.52
Wheat flour	20. . .120	0.36	0.34	0.44

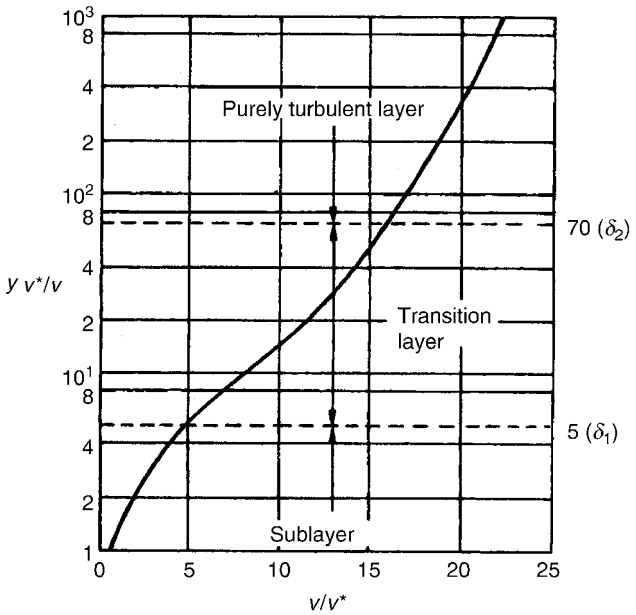

L3.3. Fig. 6. General velocity profile of a pure gas flow in a pipe ([14], p. 333).

2.2.4 Equation of Motion and Velocity Ratio

From the Eqs. (6), (8), (20), and (21) it follows:

$$M_S c\frac{dc}{dl} = M_S g\left[\operatorname{sgn}(v-c)\cdot\left\{\frac{|v-c|^2}{w_S}\right\}^{2-k} - (\sin\alpha + f\cos\alpha) - \frac{c^2}{Dg}\frac{\lambda_S^*}{2}\right]. \quad (26)$$

L3.3. Table 4. Moduli of elasticity and densities of various materials

Material	E 10^3 (N/mm^2)	ρ (kg/m^3)
Rubber hose, medium hard[a]	0.01	1,200
Polypropylene	1	910
Polyethylene	1.4	960
Rigid PVC	3	1,400
Glass	60	2,770
Al–Mg	70	2,700
Stainless steel	180	7,800
Normal steel	210	7,800
Rubber pellets medium hard[b]	0.005	1,300
ABS cubes 4mm	1.8	1,040
PP lenticular pellets 3.6 × 2.4 mm	1	870
PU cylindrical pellets 4 mm	1.2	1,100
PE cubes 3 mm	2	1,250
Nylon cylindrical pellets 4 mm	2.7	1,250
Wheat, barley, rice, etc., 2–4 mm	3	1,250
Glass beads C glass 1 mm	60	2,700
Aluminum cylindrical pellets 2 mm	70	2,700
Steel shot 1.4 mm	210	7,700

[a]Conduit
[b]Product conveyed

With the abbreviations

$$\beta = \sin\alpha + f\cos\alpha, \quad (27)$$

$$B = \left(\frac{w_S}{v}\right)^{2-k}, \quad (28)$$

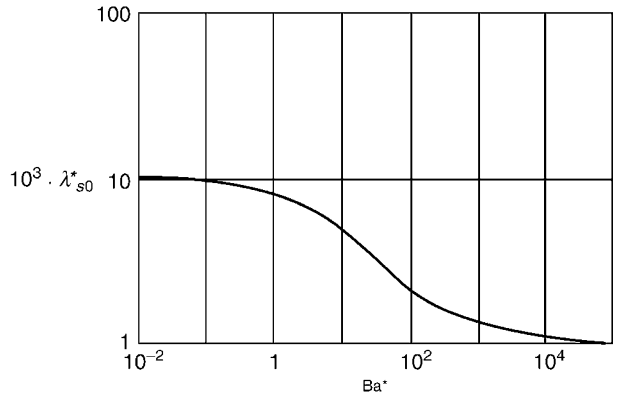

L3.3. Fig. 7. Minimum impact friction coefficient as a function of modified Barth number Ba* for a constant impact number $S = 5.5$ and a constant wall friction coefficient $\lambda_g = 0.015$ for the unladen flow, cf. Sect. 2.3.1.

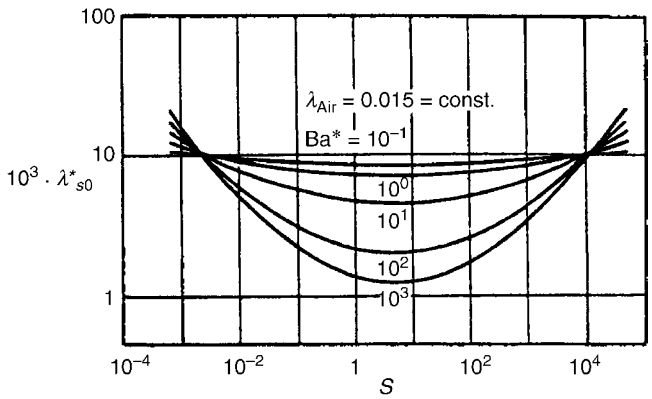

L3.3. Fig. 8. Impact friction coefficient as a function of the impact number S and the modified Barth number Ba* for a constant wall friction coefficient $\lambda_g = 0.015$ for the unladen flow, cf. Sect. 2.3.1.

the Barth number

$$\mathrm{Ba} = \frac{v^k w_S^{2-k}}{Dg}, \tag{29}$$

the dimensionless length

$$L = \frac{gl}{v^k w_S^{2-k}} \tag{30}$$

and the velocity ratio

$$C = \frac{c}{v} \tag{31}$$

the equation of motion can be expressed in a dimensionless form as [3, 8]

$$\frac{dC}{dL} = \mathrm{sgn}\,(1-C)\,\frac{(|1-C|)^{2-k}}{C} - \frac{B\cdot\beta}{C} - C\,\mathrm{Ba}\,\frac{\lambda_S^*}{2}. \tag{32}$$

By means of this equation the change in velocity during acceleration $C(L)$ or $c(l)$ and the velocity ratio obtained in steady-state operation C_e at $dc = 0$ can be determined for all states of fully suspended flow.

In Fig. 9a–c the terminal velocity ratio C_e has been plotted as a function of the following characteristic

$$\frac{v/w_S}{\beta^{1/(2-k)}} \tag{33}$$

according to Eq. (27) $\beta = 1$, if the conduit leads vertically upward. In this case no conveyance is possible if $v/w_S = 1$. The curves with the upward slope demonstrate that conveyance is feasible at velocity ratios of about 0.5, if $v/w_S = 3$ or higher. Below 0.5, a fully suspended flow conveyance in the classical sense is not possible. At high values of $\mathrm{Ba}\cdot\lambda_S^*/2$ (on the right-hand border of the diagram) the velocity ratio remains low; at low values ratios of almost unity are reached when the values on the axis of abscissa are increased. Cases of this nature arise if the diameter D of the pipe is large and the settling velocity w_S is low or if the wall impact friction factor λ_S^* is small.

If the conduit leads vertically downward, $\beta = -1$, the force of gravity acts downward together with the drag, and a final velocity equal, at the most, to twice the gas velocity is attained at an abscissa value of unity. However, if the wall impact friction factor λ_S^* is high and the conduit diameter is small, the velocity ratio may also fall below unity. If the values on the axis of abscissa are high, the curves which slope downward in Fig. 9 terminate in the curves for the pipes that lead vertically upward whenever the weight is no longer of any significance in conveying.

2.3 Pressure Drop

According to [8, 9] the general rule is applied that the total pressure drop Δp is the sum of the pressure drop Δp_g due to the wall friction of the gas, and the additional pressure drop due to the solids transport Δp_s:

$$\Delta p = \Delta p_g + \Delta p_Z. \tag{34}$$

2.3.1 Pressure Drop of the Pure Gas Flow

The component Δp_g is determined in the same way as that for pure gas. In the fully suspended flow, the total surface area of the particles of the pulverized coal represented in Fig. 5 is 10–20 times greater than the area of the wall in the tubular section in which the particles are conveyed. Under these conditions, the inertia of the solids slightly suppresses turbulence, and the velocity profile thus becomes flatter [15]. Figure 10 shows the profile of the pure gas flow and a sectional view of the conditions in the immediate vicinity of the wall. The general profile of the pipe flow can be seen in Fig. 6 in a dimensionless form. The shear stress acting between the wall and the pure gas flow is given by $\tau = \lambda_g/4\rho_g/2\overline{v}^2$, and the rate of shear by $v^* = \sqrt{\tau/\rho_g}$. The associated pressure drop is given by

$$\Delta\rho_g = -\left(\lambda_g\,\frac{\Delta l}{D} + \sum\xi\right)\,\frac{\rho_g}{2}\,v^2. \tag{35}$$

The coefficient of wall friction λ_g for a smooth pipe is

$$\lambda_g = 0.006 + \frac{0.55}{\mathrm{Re}_D^{1/3}}. \tag{36}$$

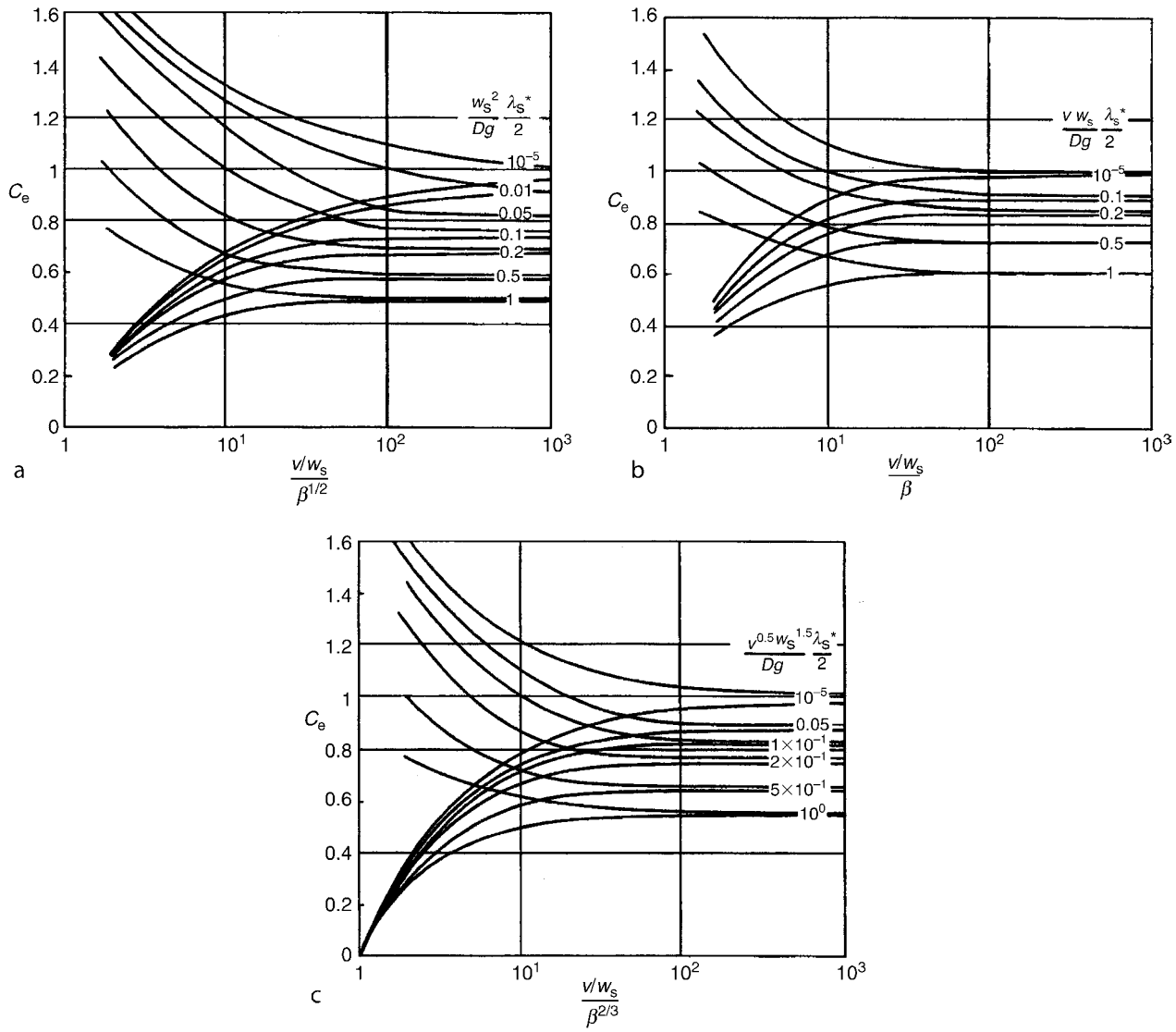

L3.3. Fig. 9. Terminal velocity ratio $C_e = c_e/v$: (**a**) $k = 0$, (**b**) $k = 1$, and (**c**) $k = 0.5$.

Thus, it depends solely on the Reynolds number for the pipe flow

$$\mathrm{Re_D} = \frac{vD\rho_g}{\eta_g}. \tag{37}$$

Pressure drop coefficients of bends are $\xi = 0.10$–0.15 if the radius of curvature has the usual value of $R = 10D$.

2.3.2 Additional Pressure Drop Caused by Conveying Solids

The additional pressure drop caused by conveying solids has two components:

$$\Delta p_Z = \Delta p_S + \Delta p_{SB}. \tag{38}$$

The pressure drop component caused by weight and impact friction Δp_S is determined by a relationship similar to Eq. (35) for Δp_g, i.e.,

$$\Delta p_S = -\lambda_S \frac{\Delta l}{D} \mu \frac{\rho_L}{2} v^2. \tag{39}$$

A more accurate breakdown [11, 12] yields

$$\lambda_S = \frac{2\beta}{C\,\mathrm{Fr}} + C\,\lambda_S^*, \tag{40}$$

where Fr is the Froude number in the 10^2–10^4 range, i.e.,

$$\mathrm{Fr} = \frac{v^2}{gD}. \tag{41}$$

The term β is defined by Eq. (27), which contains the coefficient of friction f. The first summand in Eq. (40) represents the additional pressure drop caused by the weight directly and by friction, and the second summand stands for friction by wall impact.

The additional pressure drop Δp_{SB} occurs during acceleration by Δc at the feeding point and behind the bends. It is obtained from the conservation of momentum, i.e.,

$$\Delta p_{SB} = -\mu\rho_g v \sum \Delta c. \tag{42}$$

This is the main component of the total additional pressure drop if the product is conveyed over short distances and through numerous bends. In this case, mostly the other components are

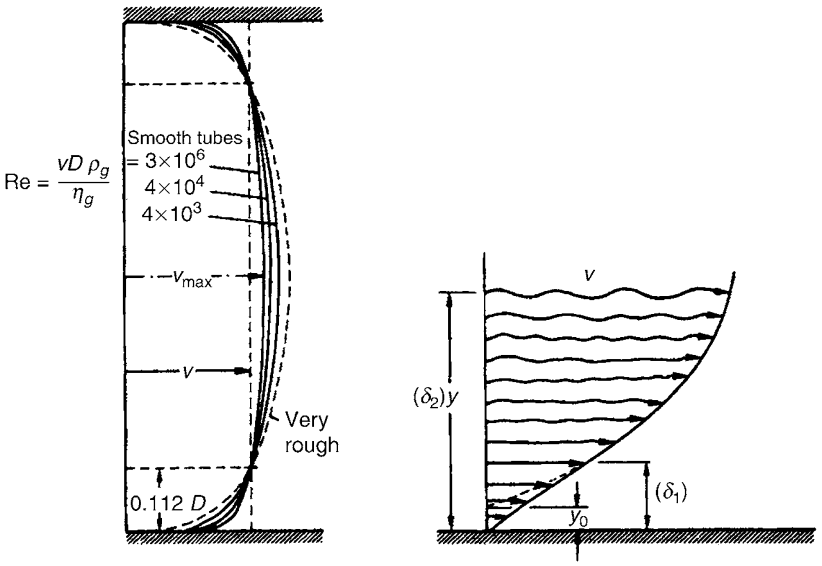

Re = $\frac{vD\rho_g}{\eta_g}$	2,320	10^4	10^5	10^6	10^7	10^8
λ Smooth tube	0.0472	0.0309	0.0180	0.0112	0.0081	0.0059
$\overline{v}/v_{max}$	0.776	0.811	0.849	0.877	0.893	0.908

L3.3. Fig. 10. Velocity profiles of a pure gas flow in a pipe.

not even taken into consideration. The subject is dealt with in the literature [16–21].

At the feeding point, it is $\Delta c = c_e$. Behind a bend, it is $\Delta c = c_e - c_2$. Here, c_e is the terminal particle velocity after the feeding point or after the bend and c_2 is the velocity, onto which the particles are decelerated within the bend. According to [20], it can be assumed in a first approximation that $c_2 = c_e/2$. A more accurate calculation allows for the dependency of the velocity c_2 on the angle at which the gas stream is diverted and for the length of section where a strand is accelerated until it is fully dissolved after the bend, cf. Sect. 2.3.3.

2.3.3 Deceleration in Bends and Reacceleration

Figure 11 shows the length of the path required for the particles to be accelerated or decelerated in relation to the terminal velocity. When the product is blown through bends, it immediately segregates owing to insufficient gas turbulence and slides in the form of almost motionless strands along the walls of the bend. As a rule, the weight of the strands and the motion imparted by the stream are neglected. Then the following relation can be applied on changes of direction through an angle ε (in radians) according to [23]

$$c_2 = c_1 \exp(-f\varepsilon). \tag{43}$$

The decrease of velocity from the value c_1 at the inlet to the bend to the value c_2 at the outlet of the bend is independent of the radius of curvature: The friction in a narrow bend is very high but does not last long, and the converse applies in wide bends.

Figure 12 shows how the product segregates in the bend to form strands. Some interval of time or length of path is required for a strand to disintegrate completely. The length of the path through which a strand has to be accelerated until it has entirely disintegrated is given by

$$l_{Str} = l_0\left[1 + K\left(\frac{\mu^{0.25} gD}{\nu^k w_S^{2-k}}\right)\right], \tag{44}$$

where l_0 is the length through which individual particles have to be accelerated. Numerical values for the extension factor K are listed in Table 5.

2.3.4 Calculation for High Pressure Drops

If the pressure drop Δp is more than 10% of the absolute pressure p, iteration must be resorted to and isothermal conditions are assumed. The gas density ρ_g and the gas velocity v are determined at the mean pressure, i.e.,

$$p_m = \frac{p_1 + p_2}{2}. \tag{45}$$

Parameters, which are independent of the pressure in the entire conduit, are the load ratio μ and, if the diameter of the pipe is constant, Re_D and λ_g as well. As a first approximation, the same applies to the second part of λ_S. The mean Froude number is taken for the first part, i.e.,

$$Fr_m = \frac{v_1 v_2}{Dg}. \tag{46}$$

If the pressure drops by more than 40%, the conduit must be divided from back to front into stages, in each of which the pressure ratio is 1:1.5–1:2. This can be achieved by reducing the pipe diameter in a ratio of approximately 1:0.9–1:0.85. In a fully suspended flow, the load ratio at the beginning of each stage

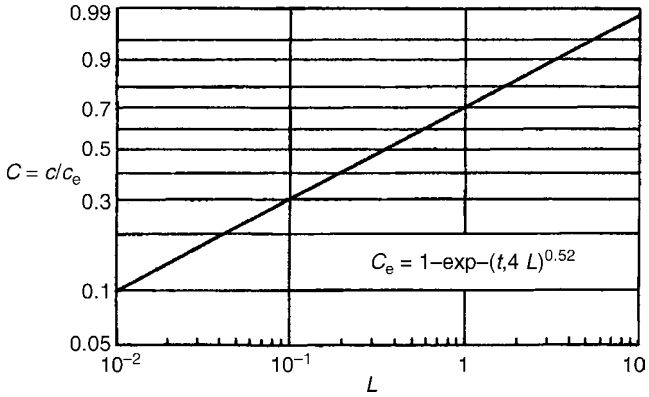

L3.3. Fig. 11. Velocity ratio C during acceleration as a function of the dimensionless length L (cf. Eq. (30)).

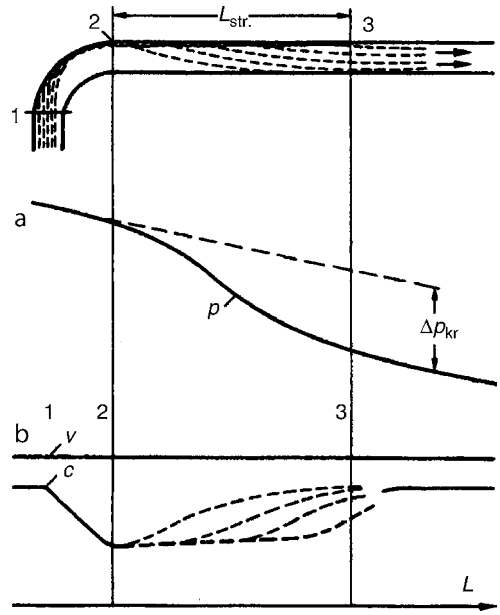

L3.3. Fig. 12. Schematic diagram of strand disintegration: (**a**) Pressure curve, (**b**) Velocity curve.

L3.3. Table 5. Factor K for the extension of the disintegration path through which strands have to be accelerated

	K
Behind a feeding point	1–3
Freely suspended strands	5
Strands at bends	
On the upper tube wall	10
On the vertical tube wall	15
On the lower tube wall	30

should be checked by means of Eqs. (1) and (2) to ensure that it does not lie below the limited load ratio.

Example 1 (Fully suspended flow)
The pneumatic conveying system shown in Fig. 13 conveys fine, medium, and coarse granules of polyester over a length of $l = 100\ \text{m} + 75\ \text{m} = 175\ \text{m}$ and through a height of $h = 25$ m.

The limited load ratio μ_{lim} for the fine particles is much higher than the value of 5 listed in Table 6. The limited load ratio for the particles of medium size is roughly the same as the design value; and that for the coarse particles is slightly less. Particles larger than 1 mm bounce mechanically at right angles to the pipe and do not require turbulence.

The Reynolds number Re_S and the settling velocity w_S of the fine particles lie at the lower limit of the transition range; and that for the coarse granules, at the upper limit. The increase in w_S effected through the load ratio is considerable in the former case, but slightly in the latter. A rough estimate in the light of the guide values listed in Fig. 3 suffices for determining the range of Reynolds numbers for w_S and k. The three particle sizes span the entire range of Barth numbers Ba^*, from the smallest to the largest, and correspond to velocity ratios of $C \approx 1$ to $C \approx 0.6$. In view of the great differences that exist in the relationships between the particles and the wall, the number of collisions S may be considerable greater or less than the figures quoted in the table of Fig. 3. The fine particles are mainly arrested aerodynamically in the layer next to the wall, against which the coarse particles impinge. The figures for λ_S^* and λ_S representing impact friction and additional pressure drop are correspondingly higher or lower. In all the cases the decrease in velocity at the bends is approximately the same. Coarse particles are conveyed more readily than fine particles, because they are comparatively slower and have very small λ_S^* values.

If the most that is required is a rough estimate it would suffice to take $\lambda_S^* \approx 0.0075$, $\beta \approx 0.6$, and $C_e \approx 0.8$ for all three cases in the example. They are responsible for a substantial part of the pressure drop if there are more than two bends. In this case it is expedient to determine only the terminal velocity ratio C_e or velocity c_e by setting $dC = 0$ in Eq. (32) and to determine the decrease in velocity in two bends by means of Eq. (42). Thus,

$$\begin{aligned}\sum \Delta c \approx c_e + 2c_e/(2\Delta p) &= -\left[\lambda_g + \mu\left(\frac{2 \cdot 0.6}{\text{Fr}} + 0.8 \cdot 0.0075\right)\right] \\ &\cdot \frac{l+h}{D} \cdot \frac{\rho_g}{2} v^2 - \mu\rho_g\, v\,(c_e + 2c_e/2) \\ &= (-34{,}000 - 7{,}000)\ \text{Pa} = -41{,}000\ \text{Pa}.\end{aligned}$$

The vertical section of the pipe is taken here as an example to illustrate the calculation of the length l_{Str} required for disintegration of the strands and reacceleration in case 2:

$$\begin{aligned}c_2 &= 22.5 \cdot \exp\left(-0.5 \cdot \frac{\pi}{2}\right) \\ &= 10.26\ \text{m/s}, \\ c_2/c_1 &= 10.26/21.5. \\ &= 0.47 \quad \text{at } L = 0.3.\end{aligned}$$

It can be derived from Fig. 11 that a dimensionless length of $\Delta L = 5.7$ is required up to a value of $c_3/c_e = 0.95$.

Example 2 (Fully suspended flow)
Plastic powder with a particle size of 150 µm and a particle density of $\rho_S = 1{,}000\ \text{kg/m}^3$ should be conveyed over a distance of 800 m with a gas mass flow rate of $M_g = 1{,}680$ kg/h at a load ratio of $\mu = 4.8$. Figure 13 shows the conduit. After one

L3.3. Table 6. Specimen calculation for the entrainment of polyester strands in an aluminum tube of 150 mm diameter and 5 mm thickness. E_{Tube} = 70,500 N/mm^2; E_S = 200 N/mm^2; f = 0.4. Varying quantities have been calculated for the fully accelerated particles. The index l denotes the horizontal stage of length l and the index h, the vertical stage of height h

d	10^{-6} m	30	300	3,000
μ		5	5	5
v_m	m/s	20	25	30
$\rho_{g,M}$	kg/m^3	1.4	1.45	1.4
Re_D	10^3	227	283	340
λ_g	10^{-3}	15	14.5	14
w	m/s	1	2.5	10
Re_S		2.3	57	2,270
k		0.81	0.50	0.15
K		29	13	1.8
w_{S0}	m/s	0.04	1.15	7.6
w_S	m/s	0.2	3.7	12.7
K_{lim}		1	2	4
μ_{lim}		42	5.2	3.1
v_w	m/s	0.9	10.3	22.6
Ba		0.4	9.3	83
Ba*		0.6	21	400
S		0.09	0.9	9
λ_S*	10^{-3}	9	7.5	1.7
f		0.05	0.2	0.4
C_l		0.995	0.89	0.72
$\lambda_{s,l}$	10^{-3}	9.5	7.7	3
C_h		0.99	0.86	0.63
λ_{Sh}	10^{-3}	9.4	7.5	3.1
c_1	m/s	19.9	22.3	21.8
c_2	m/s	9.1	10.2	9.9
c_3	m/s	19.8	21.5	18.9
c_4	m/s	9	9.8	8.6
c_5	m/s	19.9	22.3	21.8
$\sum \Delta c$	m/s	42	46	44
Δp_g	Pa	−4,917	−7,352	−10,220
Δp_{SB}	Pa	−5,809	−8,058	−9,210
Δp_{Sl}	Pa	−15,480	−19,620	−10,950
Δp_{Sh}	Pa	−2,201	−2,734	−1,617
$\sum \Delta p_S$	Pa	−23,490	−30,400	−21,770
Δp_{tot}	Pa	−28,410	−37,774	−32,000

iteration, two sections each with a length of 400 m are obtained. The data of the two sections are listed in the following table. The pressure drops from 3 bar to 1.7 bar at the end of Part A and to 1 bar at the end of Part B. The average densities ρ_g and the average velocities v are given in the table. The settling velocity w_{SO} is always calculated according to Eq. (17) at the average pressure. With λ_g, v, and w_S the limited load ratio is determined at the average pressure. The velocity ratio $C = c_e/v$ is 0.95. The calculation is performed with f = 0.5 and $\lambda_S^* = 0.005$. The

Pipe section			A		B	
D	m		0.1		0.125	
P	bar	3		1.73		1
$\bar{P}$	bar		2.36		1.36	
ρ_g	kg/m^3		2.83		1.63	
v	m/s		21		23.3	
w_{SO}	m/s		0.39		0.47	
w_S	m/s		0.68		0.82	
Re	$\cdot 10^5$		2.67		2.13	
λ_g			0.0145		0.015	
μ_{lim}			8.58		8.08	
Δp_g	Pa		36,193		21,237	
Δp_S	Pa		83,867		45,533	
$\Delta p_{S,B}$	Pa		11,410		3,992	
Δp_{Kr}	Pa		280		66	
Δp_{tot}	Pa		131,750		70,828	

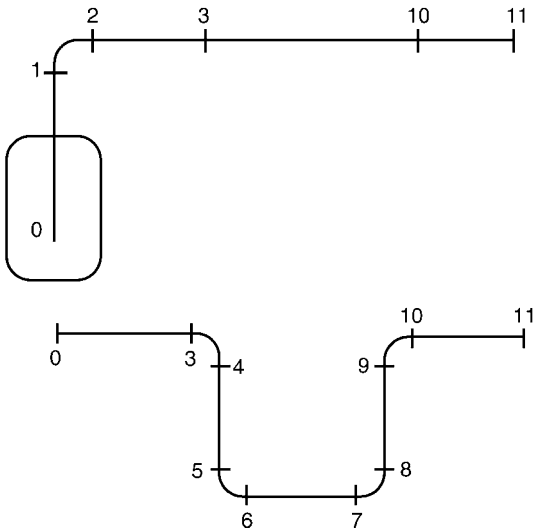

L3.3. Fig. 13. Conduit of example 2. Above: Side view. Below: Top view.

pressure drops Δp_g, Δp_S, Δp_{SB} and the pressure drops at the bends Δp_{Kr} are calculated according to Eqs. (35), (39), and (42).

In [2, 3, 8, 9], calculated data of numerous pneumatic conveying plants can be found.

3 Dense-Phase Conveying

If the throughput is larger than 5 ton/h and pressure drops as high as 1–6 bar are feasible, this method of conveyance is adopted to reduce gas requirements and to avoid wear of the conduit and abrasion of the product conveyed. The load ratio μ can be increased to 10–150. The superficial gas velocities are

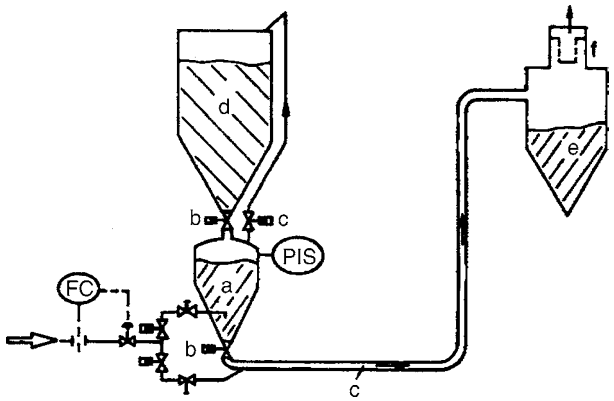

L3.3. Fig. 14. Dense-phase conveying. (**a**) Pressure vessel, (**b**) Valves and controllers, (**c**) Conduit, (**d**) Feed hopper, (**e**) Bunker, and (**f**) Bunker filter.

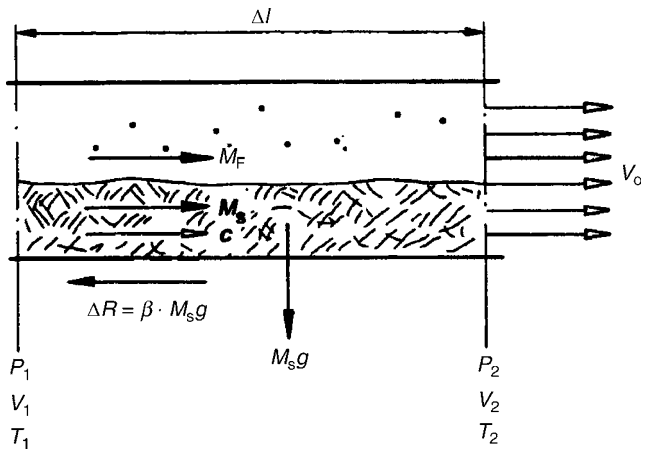

L3.3. Fig. 15. Pressure drop due to friction along a strand of bulk material.

merely 2–15 m/s and are often less than the settling velocity. The diameter of the pipe varies between 50 and 300 mm. Almost all products with particle sizes between 1 μm and 10 mm can be conveyed [24–26]. Figure 14 shows an installation for dense-phase conveying.

3.1 Movement of Particles in Pipes

If the gas velocity is not high enough, the particles are deposited on the lower surface of the conduit until the velocity in the remaining cross section is again sufficiently high to convey the increased load. Large differences in concentration thus occur in the cross section. The moving particles impart a large component of their momentum to the deposits on which they impinge. As a result, the growing deposits finally commence to move with the aid of the pressure gradient and pore flow. Conveyance of strands by moving particles and currents in this manner is often quite stable. However, if fluctuations occur, large plugs and conglomerates are formed and finally preponderate. The main resistance to conveyance is the force of friction caused by the weight of solids [2]

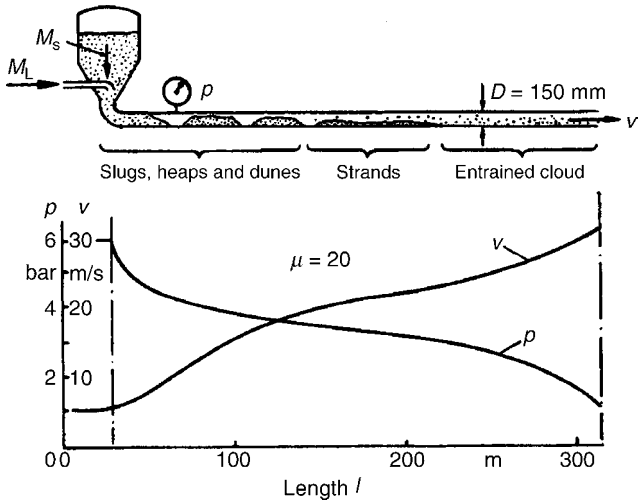

L3.3. Fig. 16. Gas velocity and pressure along the conveyor for dense-phase conveyance of 2-mm plastics granules.

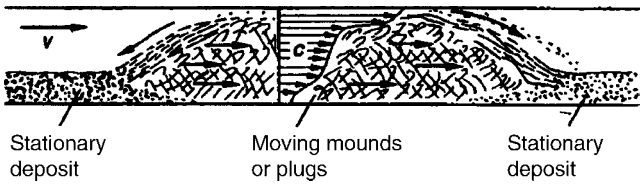

L3.3. Fig. 17. Movement of a plug of loose material (Drawing made from a photograph).

$$dR = \frac{\dot{M}_S g dl}{c}(\sin\alpha + f\cos\alpha) = \frac{\dot{M}_S g dl}{c}\beta \qquad (47)$$

The coefficient of friction is f = 0.3–0.8. The force of friction includes the wedging forces at right angles to the wall.

Figure 15 shows the conditions for a strand section.

At the inlet of long pipes of uniform diameter, there are high pressures, low velocities, high pressure drops, and large concentrations of conglomerates (Fig. 16). The mass flow rate of solids $\dot{M}_s$ and the load ratio μ remain constant over the entire length. As the pressure increases, the velocities c and v increase, the close succession of conglomerates loosen, and the pressure gradient becomes less. Toward the end of the pipe, strands and (frequently) individual particles are conveyed at higher velocities, with the result that the pressure drop increases again. In order to avoid this, the pipe is often widened in two to three stages.

3.2 Simplified Calculation

A heap of loose material is shown in Fig. 17. It pushes against a stationary deposit and bulldozes it ahead. The bulk of the air streams through the small free cross section above the mound and thus entrains the particles at a load ratio of about 5–10. As a result this bypass current flows against a high pressure gradient, and the heap of loose material is thus pushed forward. The pressure drop is also responsible for (usually laminar) pore flow in a heap of length Δl and void fraction ε.

In Eq. (47) the mass flow rate of solids is

$$\dot{M}_S = \mu \dot{M}_g = \mu A \rho_g v_0 \tag{48}$$

with the superficial velocity v_0. With $C = c/v_0$ and Eq. (47) it follows

$$dp_S = \frac{dR}{A} = \mu \rho_g g \; dl \frac{\beta}{C} \tag{49}$$

Even if the pressure drop in the dense-phase conveying is high, the pressure is released at almost constant temperature T. Hence [2]

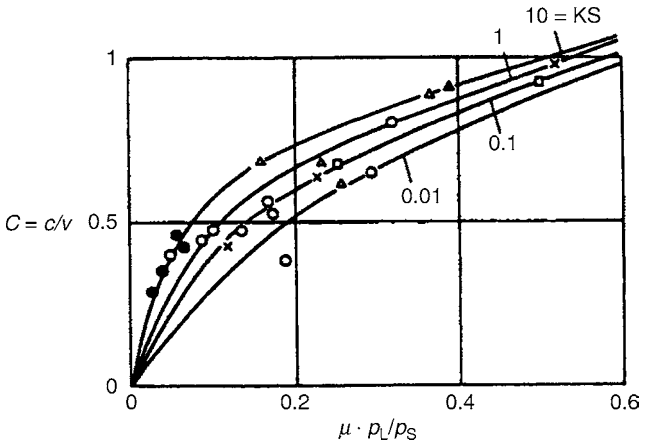

L3.3. Fig. 18. Comparison of measured and calculated velocity ratios C for the conveyance of strands of sand (25 μm) in a pipe of 50 mm diameter [2]. KS is the number of strands (cf. Eq. (30) in [2]).

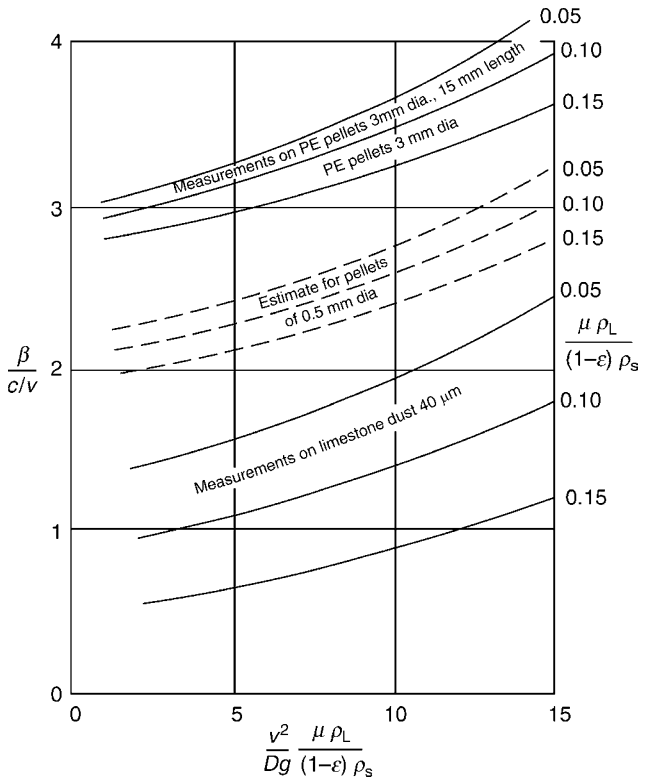

L3.3. Fig. 19. Empirical values for β/C.

$$\rho_g = \frac{p}{RT}. \tag{50}$$

The pressure at the inlet 1 and outlet 2 of a conduit is

$$p_1 = p_2 \exp\left(\frac{\mu g \Delta l}{RT} \frac{\beta}{C}\right). \tag{51}$$

The expression in brackets should not exceed 0.8. If it is higher, the conduit should be divided into a number of sections and the value of Δl of each section should be separately determined backward against the direction of conveyance. Figure 18 shows calculated and measured values of the velocity ratio C as functions of the modified density ratio $\mu\rho_g/((1-\varepsilon)\rho_S)$. In practice, the ratio β/C is usually obtained from tables, e.g., Table 7. If the velocity ratio is unknown, resort may be taken to empirical values such as those shown in Fig. 19.

The void fraction ε of the moving plug is 1.5–3 times greater than that of the stationary deposit. As can be seen from Fig. 20 the void fraction of fine dust depends considerably on the particle size.

The pressure drop along the plug is also responsible for (usually laminar) pore flow in the inner of the plug. The volume flow rate of that flow, however, is negligible compared to that of the main flow. For laminar pore flow through a heap of length Δl with the void fraction ε, the pressure loss along the heap is [28]

$$\Delta p = 165 K^2 \cdot \frac{(1-\varepsilon)^2}{\varepsilon^3} \cdot \frac{\eta_L \mu_0 \Delta l}{d_S^2} \tag{52}$$

where u_0 is the superficial velocity of the seepage flow.

If the Reynolds number for the seepage current is

$$\mathrm{Re} = \frac{u_0 \, d_S}{K(1-\varepsilon)\nu} > 20, \tag{53}$$

then

$$\Delta p = 80 K^{1.5} \frac{(1-\varepsilon)^{1.5}}{\varepsilon^2} \cdot \frac{\sqrt{\eta_g \, \rho_g \, u_0^{1.5} \, \Delta l}}{d_S^{1.5}}. \tag{54}$$

The shape factor for spheres is $K = 1$, for granules $K = 1.2$, and for very irregular particles $K = 2$.

4 Injectors for Solids Feeding

Instead of rotary feeders injectors are also used to feed solids into pneumatic conveyers with fully suspended flow. In dryers, the injectors split coarse blocks of wet product into small agglomerates with sizes between 100 and 500 μm. In jet mills, a pre-fragmentation takes place in the interior of the injector at motive gas velocities up to 500 m/s for air and up to 1,000 m/s for steam [29]. The following remarks bear on [10].

4.1 Pressure Buildup

Figure 21 shows an injector for solids feeding with the pressure and velocity profile along the injector. The motive gas in front of the nozzle has the pressure p_T and is expanded in the entrance

L3.3. Table 7. Examples of dense-phase conveying

Product	d_{50} µm	ρ_s kg/m³	f	l m	h m	D mm	$\dot{V}_g$ Sm³/h	$\bar{v}$ m/s	$\dot{M}_S$ t/h	µ	$\frac{\mu\rho_g}{\rho_{str}}$	Δp bar	C	β
Limestone dust	12	2,200	0.8	250	15	205	3,300	8.5	120	28	0.10	2.6	0.6	1
						215								
						230								
Flue gas dust	15	2,400	0.8	1,200	15	200	3,700	13	50	10	0.03	3.5	0.5	0.55
Alumina	45	2,500	0.7	130	15	100	280	5	8	22	0.12	2.5	0.15	0.55
PAN powder	75	1,200	0.6	150	—	36	17	4	1.2	53	0.20	1.4	0.6	0.55
Soda	100	2,100	0.7	200	30	100	950	18	35	28	0.08	2.5	0.3	0.6
Road salt	700	2,200	0.7	26	2	50	100	11	5.8	44	0.05	0.8	0.13	0.57
						211								
PP pellets	3,000	960	0.6	320	25	230	1,300	3.9	20	12	0.06	2.7	0.2	0.6
						250								
Coke	5,000	1,200	0.7	345	40	200	1,000	3.6	20	15	0.05	1.6	0.5	0.8
						210								
						235								

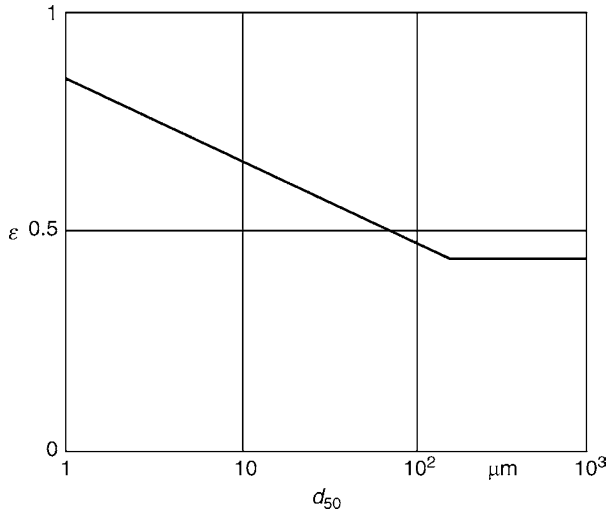

L3.3. Fig. 20. Void fraction of bulk ε of quartz according to measurements [27].

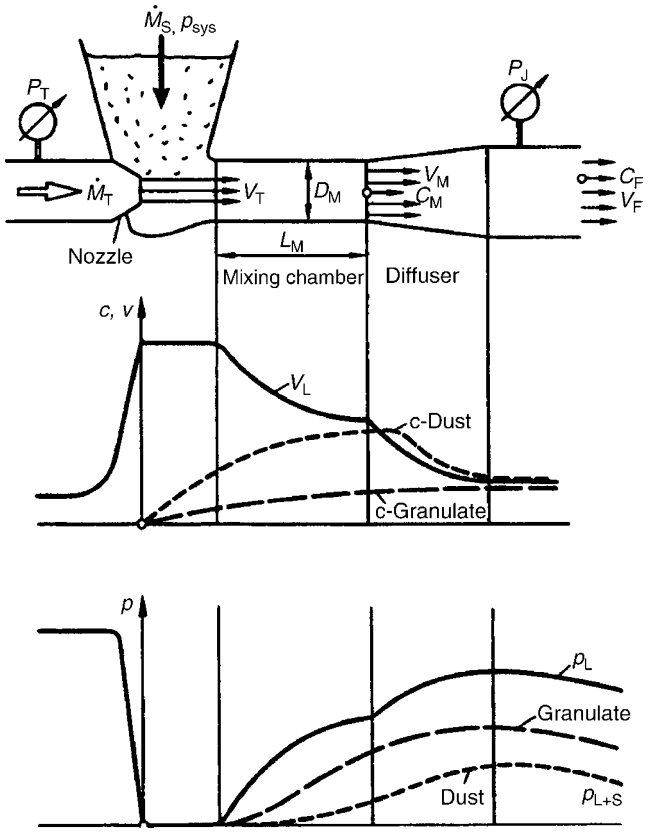

L3.3. Fig. 21. Injector for solids feeding with velocity and pressure profile.

zone of the feed onto the pressure p_{Sys}. In the zone of the free gas jet between the nozzle and the mixing chamber the velocity profile of the jet changes strongly due to momentum exchange. In the mixing chamber, the gas jet is decelerated on the mean velocity v_M, which is determined by the diameter D_M at the end of that section. This leads to an increase of the static pressure. When particles are fed in, an additional considerable momentum exchange with the solids occurs leading to a reduction of the pressure generation in the mixing chamber. The pressure reduction is stronger for fine particles than for coarser ones since the gas accelerates fine particles more strongly than coarser particles. In the following diffuser the static pressure is further increased due to the deceleration of the gas flow with the velocity v_F in the conveying pipe.

Depending on the pressure ratio of the nozzle, three types of injectors for solids feeding are differentiated according to Table 8.

At a pressure difference $\Delta p = p_T - p_{Sys} < 0.2$ bar the velocity of the motive gas can be calculated by assuming an incompressible gas. Up to a pressure of the motive gas of $p_T = 1.9 p_{Sys}$, the calculation can be performed by the average gas density

$$\bar{\rho}_{g,M} = \frac{(p_T + p_{Sys})/2}{RT}, \qquad (55)$$

L3.3. Table 8. Differentiation of injectors for solids feeding according to pressure ratios with guiding values for pressure generation at p_{Sys} = 1 bar, d_S = 100 µm, ρ_S = 2,650 kg/m^3, L_M/D_M = 4, η_{Diff} = 0.85

		Low pressure injector		Medium pressure injector		High pressure injector	
p_T/p_{Sys}		1.2		3		11	
v_T	m/s	175		400		500	
D_M/D_T		1.5	2	2	4	2.5	4
$\Delta p_{J,max}$ (μ = 0)	Pa	1,100	7,000	50,000	15,000	150,000	65,000
µ (for $\Delta p_J = 0.5 \times \Delta p_{J,max}$)		1.5	3	3	6	2	4

$$T = \sqrt{\frac{2\,(p_T - p_{Sys})}{\overline{\rho}_{g,M}}}. \tag{56}$$

For larger pressure differences the compressibility of the gas has to be taken into account. In practice, simple nozzles with no divergence after the minimal cross section are normally used, and thus the velocity of the motive gas can be calculated by the following equations:

In the final cross section of the nozzle the gas velocity is the Laval velocity

$$a_{Lav} = \sqrt{\frac{2\kappa}{\kappa + 1} RT}. \tag{57}$$

The subsequent expansion from $p_{Lav} = 0.53 p_T$ to the system pressure p_{Sys} leads to a acceleration in the free jet region within a distance of 0.5–1.5D_T by

$$\Delta v = \frac{p_{Lav} - p_{Sys}}{\rho_{Lav} a_{Lav}} \tag{58}$$

with $\rho_{Lav} = 0.63 \rho_{g,T}$. Thus, the effective velocity of the motive gas is

$$v_T = a_{Lav} + \Delta v. \tag{59}$$

For the design of the injector the velocity v_F in the pneumatic conveyor is given. A guiding value for the average gas velocity v_M in the mixing chamber is

$$v_M = \sqrt{v_T v_F}. \tag{60}$$

The real velocity can deviate from this value by ±30%. In the first step estimated mean density ρ_M in the mixing chamber the diameter of the mixing chamber is

$$D_M = \sqrt{\frac{M_T}{\frac{\pi}{4} v_M \rho_M}}. \tag{61}$$

A guiding value for the length of the mixing chamber is $L_M = 4D_M$. If the solids velocity is known, the pressure buildup can be calculated by taking into account momentum exchange and the pressure loss $\Delta p_{M,R}$ due to friction of the gas–solids flow in the mixing chamber:

$$\Delta p_M = \frac{M_T (v_T - v_M) - M_S \Delta c_M}{A_M} \eta_M + \Delta p_{M,R}. \tag{62}$$

The efficiency of the mixing in the mixing chamber has usually values between η_M = 0.7 and η_M = 0.9, reflecting that the momentum conversion of the gas and the solids can only be performed incompletely. Figure 22 shows the dependence of the mixing efficiency on the solids load μ.

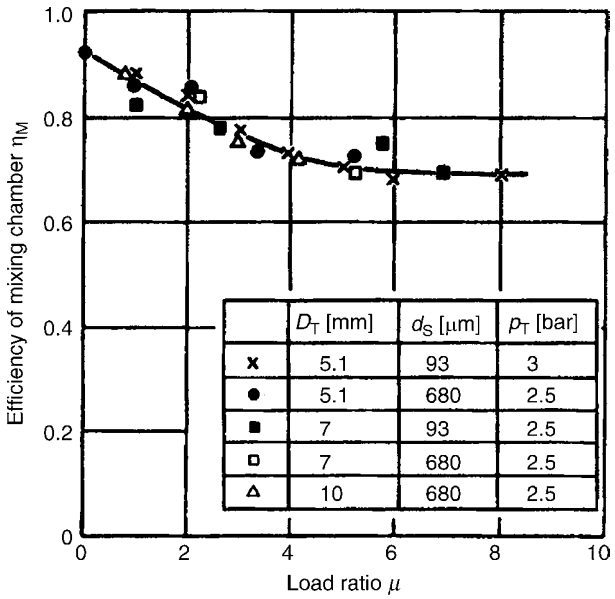

L3.3. Fig. 22. Measured efficiency η_M of the mixing chamber as a function of the load ratio μ [10].

The pressure loss due to friction $\Delta p_{M,R}$ is calculated according to Sects. 2.3.1 and 2.3.2:

$$\Delta p_{M,R} = \Delta p_g + \Delta p_S = -\left(\lambda_g + \lambda_S \mu\right) \frac{L_M}{D_M} \frac{\overline{\rho}_{L,M}}{2} v_M^2. \tag{63}$$

The pressure increase in the diffuser is calculated according to

$$\Delta p_{Diff} = \frac{\rho_{g,Diff}}{2} \left(v_M^2 - v_F^2\right) \eta_{Diff} - \mu \rho_{g,Diff} \sqrt{v_M v_R}\, \Delta c_{Diff}, \tag{64}$$

where the first part calculates the pressure buildup due to deceleration of the gas velocity and the second part calculates the pressure change due to the change of kinetic energy of the particles. Those diffusers have angles of aperture between 7° and 10° and efficiencies η_{Diff} between 0.85 and 0.9. The velocity change Δc_{Diff} of the solids is in most cases not very large. Therefore the second term in Eq. (64) can be neglected in the first estimations.

If at the end of the mixing chamber $c_M > v_F$, then for straight pipes sections of length $L_F > (5 \ldots 10)\, L_M$ behind the injector a small pressure buildup can be realized

$$\Delta p_F = -\mu \rho_{g,M} v_F \Delta c \tag{65}$$

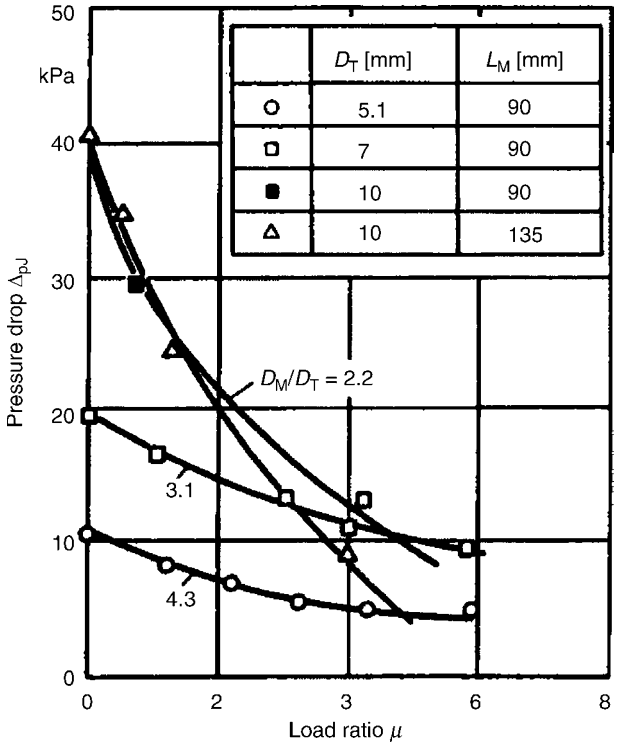

L3.3. Fig. 23. Measured characteristics of an injector for solid feeding as a function of the ratio D_M/D_T of the diameters of nozzle and mixing section and nozzle [10]; P_T = 2.5 bar; d_{50} = 93 µm; ρ_S = 2,650 kg/m^3; D_M = 22 mm.

with

$$\Delta c = c_M - c_F. \tag{66}$$

The terminate velocity c_F is obtained from Fig. 9a–c. The total pressure buildup of the injector for solids feeding is

$$\Delta p_J = \Delta p_M + \Delta p_{Diff} + \Delta p_F. \tag{67}$$

The given equations are valid for a neutral operation of the injector. If in addition the injector sucks off air, the pressure buildup diminishes by up to 15%. If a part of the motive gas is blown out of the solids feeding opening, then the attainable pressure increases by up to 15%.

4.2 Particle Velocity

The exact calculation is described in [10]. In a first approximation the maximal gas velocity between nozzle and mixing chamber is calculated as

$$v_{max} = 0.6 \cdot (v_T - v_M) + v_M \tag{68}$$

and the average gas velocity during the whole sequence of acceleration as

$$\bar{v} = \sqrt{v_{max} v_M}. \tag{69}$$

For the air drag of the particle cloud Eq. (8) is valid and for the particle acceleration

$$b = \bar{c}\frac{\Delta c}{\Delta l} = \mathrm{sgn}\,(v - c) \cdot g \left(\frac{|v - c|}{w_S} \right)^{2-k}. \tag{70}$$

The average particle velocity in the mixing chamber is

$$\bar{c}_M \approx \frac{2}{3}\Delta c_M. \tag{71}$$

Thus, it follows for the velocity change in the mixing chamber

$$\Delta c_M = \sqrt{\frac{\Delta l}{2/3} g \left(\frac{\sqrt{v_{max} v_M} - \bar{c}_M}{w_S} \right)^{2-k}}. \tag{72}$$

For the settling velocity w_S at the solids load μ Eq. (19) is valid. The result can be quickly obtained by iteration. The given equations allow for an estimation of the solids velocity at the end of the mixing chamber with an accuracy of 20%.

4.3 Characteristic Curve of an Injector for Solid Feeding

The characteristic curve of an injector for solid feeding i.e., the pressure buildup as a function of the solids load can be determined by Eqs. (55–72). At first one calculates the pressure buildup of the motive gas jet for $\mu = 0$, then for a medium and for a high solids load. As a rule the characteristics of the curve is fixed by these three points.

Figure 23 shows the measured characteristics of an injector for solids feeding as a function of the diameter ratio D_M/D_T.

For $D_M/D_T < 2$, a high pressure builds up at low solids loadings. However, only small solid loadings can be conveyed. For $D_M/D_T > 3$, the maximum possible pressure buildup is reduced by more than 50%, the maximum possible solids loading increases, however, considerably.

Example 3 (Injector for solids feeding)
In a pipe with diameter D_F = 90 mm, solid material with particle size d_S = 200 µm and particle density ρ_S = 2,650 kg/m^3 should be conveyed at a gas velocity of v_F = 20 m/s. The gas density in the pipe is 1.44 kg/m^3. The temperature of the gas is 293 K. The feeding of the solid material should be realized by an injector.

The mixing chamber of the injector is designed with L_M/D_M = 4.

$$M_T = \frac{\pi}{4} D_F^2 \rho_F v_F = \frac{\pi}{4} 0.09^2 \cdot 1.44 \cdot 20 = 0.183\,\mathrm{kg/s}.$$

It results in the Laval velocity

$$a_{Lav} = \sqrt{\frac{2\kappa}{\kappa + 1} RT} = \sqrt{\frac{2 \cdot 1.4}{1.4 + 1} \cdot 287 \cdot 293} = 313\,\mathrm{m/s}$$

and the Laval density

$$\rho_{Lav} = 0.63\, \rho_{g,T} = 0.63\, \frac{p_T}{R\,T} = 0.63 \cdot \frac{2.5 \cdot 10^5}{287 \cdot 293} = 1.87\ \mathrm{kg/m^3}$$

and a diameter of the nozzle of

$$D_T = \sqrt{\frac{\dot{M}_T}{\frac{\pi}{4} \rho_{Lav} a_{Lav}}} = \sqrt{\frac{0.183}{\frac{\pi}{4} \cdot 1.87 \cdot 313}} = 0.02\,\mathrm{m}.$$

Thus, the points of the characteristics according to Eqs. (57–59): v_T = 368 m/s.

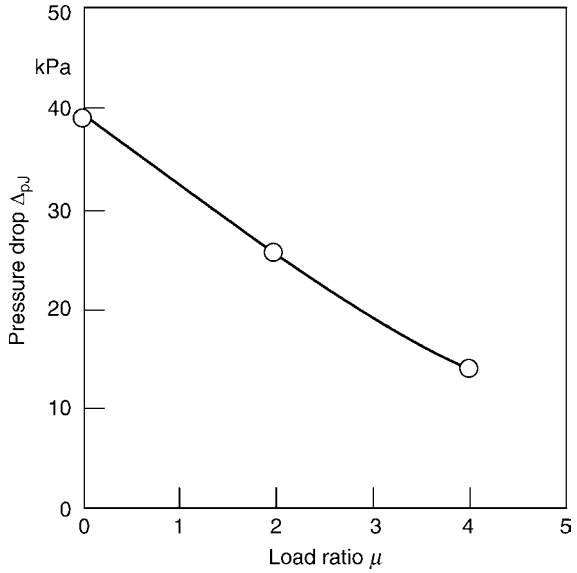

L3.3. Fig. 24. Calculated characteristics of the solids feeding injector in example 3.

Calculation for $\mu = 0$

According to Eq. (60): $v_M = \sqrt{v_T v_F} = \sqrt{368 \cdot 20} = 85\,\text{m/s}$, estimated pressure buildup until the end of the mixing chamber = 35,000 Pa.

Thus

$$\rho_M = \frac{p_M}{RT} = \frac{1.35 \cdot 10^5}{287 \cdot 293} = 1.6\,\text{kg/m}^3,$$

according to Eq. (61):

$$D_M = \sqrt{\frac{\dot{M}_T}{\frac{\pi}{4} v_M \rho_{L,M}}} = \sqrt{\frac{0.183}{\frac{\pi}{4} \cdot 85 \cdot 1.6}} = 0.041\,\text{m/s},$$

$$\mu = 0 \rightarrow M_S = 0; \quad \text{according to Fig. 22:} \quad \eta_M = 0.9,$$

and according to Eq. (62):

$$\Delta p_M = \frac{\dot{M}_T (v_T - v_M) - M_S \Delta c_M}{A_M} \eta_M + \Delta p_{M,R} = \frac{0.183(368 - 85) - 0}{\frac{\pi}{4} \cdot 0.041^2} 0.9 - 578 = 34{,}725\ \text{Pa},$$

Equation (64):

$$\Delta p_{Diff} = \frac{\rho_L}{2} (v_M^2 - v_F^2) \eta_{Diff} = \frac{1.6}{2} (85^2 - 20^2)\, 0.85 = 4{,}641\ \text{Pa},$$

Equation (67):

$$\Delta p_J = \Delta p_M + \Delta p_{Diff} = 34{,}725 + 4{,}641 = 39{,}366\ \text{Pa}.$$

Calculation for $\mu = 2$

Estimated pressure buildup until the end of the mixing section: 20,000 Pa. Accordingly, it is:

Density	$p_{L,M}$ = 1.4 kg/m^3
According to Eq. (60)	v_M = 99 m/s
According to Fig. 22	η_M = 0.83
Equation (68)	v_{max} = 0.6 (368−99) + 99 = 260 m/s
Equation (69)	$\bar{v} = \sqrt{v_{max} v_M} = \sqrt{260 \cdot 99} = 160\,\text{m/s}$

Estimated Re number according to Eq. (10):

$$\text{Re} = (160 - 50)\ \text{m/s} \cdot 200 \cdot 10^{-6} / 15 \cdot 10^{-16} = 1{,}466.$$

Thus, the Re number is in the Newton regime, therefore $k = 0$.

Equation (18)	w_{S0} = 3.14 m/s
Equation (19)	w_S = 5.00 m/s
Equation (72)	Δc = 40 m/s

Equation (62):

$$\Delta p_M = \frac{0.183(368 - 85) - 0.366 \cdot 40}{\frac{\pi}{4} \cdot 0.041^2} 0.83 - 1{,}125 = 20{,}618\ \text{Pa},$$

Equation (64):

$$\Delta p_{Diff} = \frac{\rho_L}{2} (v_M^2 - v_F^2)\ \eta_{Diff} = \frac{1.6}{2} (99^2 - 20^2)\ 0.85 = 5{,}594\ \text{Pa},$$

Equation (65):

$$\Delta p_F = -\mu \rho_L\, v_F \Delta c = -2 \cdot 1.4 \cdot 20 \cdot 20 = 1{,}120\,\text{Pa},$$

Equation (67):

$$\Delta p_J = \Delta p_M + \Delta p_{Diff} + \Delta p_F = 27{,}332\,\text{Pa}.$$

Calculation for $\mu = 4$: Δp_J = 14,500 Pa

Thus, it follows the characteristics for the solid feeding injector according to Fig. 24.

5 Symbols

A	cross-sectional area
a	spacing between particles
B	gravity parameter
Ba	Barth number
Ba*	modified Barth number
c	average particle velocity
Δc	particle velocity difference
c_w	drag coefficient for flow around a body
C	velocity ratio
d	particle size
d'	characteristic particle size of RRSB distribution
d_{50}	mean particle size of feed
D	pipe diameter
E	modulus of elasticity
f	coefficient of gliding friction
F	force
Fr	Froude number
g	acceleration due to gravity
h	height
K	elongation factor; parameter for calculating drag
k	exponent for calculating drag
L	dimensionless length
l, Δl	length, section length
M	mass
$\dot{M}$	mass flow
N	hydraulic power
n	exponent in RRSB particle size distribution
p	static pressure
Δp	pressure drop
R	size fraction retained on screen

dR	force due to wall friction of solids strand with length dl
Re	Reynolds number
s	wall thickness
S	impact coefficient; specific surface
T	temperature
$\dot{V}$	volume flow rate
V	volume
u_0	superficial velocity of gas in packed bed
v_0	average axial superficial velocity of gas
v	average axial velocity of gas
Δv	gas velocity difference
$v^\star$	shear stress velocity
v^*_{Ba}	air velocity close to the wall
w_{S}	settling velocity
W	air drag
$y^\star$	distance to wall
α	angle of inclination against the horizontal
β	coefficient for resistance caused by weight of product
ε	angle through which air stream is diverted; void fraction
η	dynamic viscosity; efficiency
λ_{g}	coefficient for pressure drop of pure gas flow
λ_{S}	coefficient for pressure drop of gas flow conveying solids
λ^*_{S}	coefficient for resistance due to collisions against wall
κ	adiabatic exponent
μ	load ratio
ρ	density
$\Delta\rho$	density difference between solids and gas
τ	shear stress at wall
φ	shape factor
ξ	pressure drop coefficient

Subscripts

B	acceleration
D	pipe
Diff	diffusor
e	at end of conduit
F	conveying pipe
g	gas
G	weight
J	injector
K	before nozzle for motive gas
Kr	bend
lav	laval state
lim	limiting
M	mixing chamber
m	mean
N	Newton regime
max	maximum
min	minimum
R	friction
S	solids; Impact friction
SB	solids acceleration
Stokes	stokes regime
Str	strand
Sys	system
T	motive gas
Ü	transition regime
V	related to volume
W	wall; drag
Z	addition
0	related on solids free cross section; single particle
1	beginning; inlet of bend
2	end; outlet of bend

6 Bibliography

1. Bohnet M (1965) Experimentelle und theoretische Untersuchungen über das Absetzen, das Aufwirbeln und den Transport feiner Staubteilchen in pneumatischen Förderleitungen. VDI-Forschungsheft 507
2. Muschelknautz E, Krambrock W (1969) Vereinfachte Berechnung horizontaler pneumatischer Förderleitungen bei hoher Gutbeladung mit feinkörnigen Produkten. Chem- Ing- Techn 41:1164–1172
3. Muschelknautz E, Wojahn H (1974) Auslegung pneumatischer Förderanlagen. Chem- Ing- Techn 46:223–235
4. Möller H (1964) Dissertation, Universität Karlsruhe
5. Flatt W, Allenspach W (1969) Erhöhen der Förderleistung und Verbessern des Wirkungsgrades pneumatischer Förderanlagen. Chem- Ing- Techn 41:1173–1176
6. Patent CH459060 (1968) Gebrüder Bühler AG, Rohrleitung für den pneumatischen oder hydraulischen Transport kurzer, gleichartiger Materialpfropfen
7. DIN 66145: 1976-4 (1976) Graphical representation of particle size distributions; RRSB-grid
8. Muschelknautz E (1959) Theoretische und experimentelle Untersuchungen über die Druckverluste pneumatischer Förderleitungen unter besonderer Berücksich-tigung des Einflusses von Gutreibung und Gutgewicht. VDI-Forschungsheft 476
9. Barth W (1958) Strömungsvorgänge beim Transport von Festteilchen und Flüssigkeitsteilchen in Gasen. Chem- Ing- Techn 30:171–181
10. Schlag H-P (1992) Experimentelle und theoretische Untersuchungen zur Berechnung der Kennlinien von gasbetriebenen Einphaseninjektoren und Gutaufgabeinjektoren. Dissertation, Universität Stuttgart. VDI-Fortschr. Berichte, VDI-Verlag, Düsseldorf, Reihe 3, No. 313
11. Muschelknautz E (1985) Reibungsverluste FRL 304. Research report for the BMFT-project SN/A-QV-543
12. Muschelknautz E (1985) Reibungsverluste FRL 304/a. Research report for the BMFT-project SN/A-QV-543
13. Muschelknautz E, Nemecek F, Reuter R (1986) Druckverlust der Flugförderung. Chem- Ing- Techn 598–599
14. Albring W (1978) Angewandte Strömungslehre, 5th edn. Akademie-Verlag, Berlin
15. Bohnet M, Triesch O (2003) Influence of particles on fluid turbulence in pipe and diffusor gas-solids flow. Chem- Ing- Techn 75:850–857
16. Vollheim R (1971) Pneumatischer transport. VEB, Leipzig
17. Welschof G (1962) Pneumatische Förderung bei grossen Fördergutkonzentrationen. VDI-Forschungsheft 492
18. Siegel W (1970) Experimentelle Untersuchungen zur pneumatischen Forderung körniger Stoffe in Rohren und Überprüfung der Ähnlichkeitsgesetze. VDI-Forschungsheft 538
19. Weber M (1974) Strömungsfördertechnik. Krauskopf-Verlag, Mainz
20. Molerus O (1982) Fluid- Feststoff- Strömungen. Springer-Verlag, Berlin
21. Krambrock W (1986) Technik der Gas- Feststoff- Strömung. GVC-December-Conference, Cologne, VDI-Verlag, Düsseldorf
22. Siegel W (1991) Pneumatische Förderung: Grundlagen, Auslegung, Anlagenbau, Betrieb. Vogel-Verlag, Würzburg
23. Weidner G (1955) Grundsätzliche Untersuchung über den pneumatischen Fördervorgang. Forsch Ing- Wesen 21(5):145–153
24. Krambrock W (1982) Aufbereitungstechnik 23:436–452

25. Möller H, Pust J (1985) Pneumatisches Fördern mit optimalem Energieverbrauch. Zement-Kalk-Gips ZKG Int 38(5):259–261
26. Hillgraf P (1987) Zement-Kalk-Gips ZKG Int 40:610–616
27. Wohlfarth A (1974) Internal report. Bayer AG, Leverkusen
28. Muschelknautz E (1990) Grundlagen der Mechanischen Verfahrenstechnik (Lecture notes), Universität Stuttgart
29. Muschelknautz E, Giersiepen G, Rink N (1970) Strömungsvorgänge bei der Zerkleinerung in Strahlmühlen. Chem- Ing- Techn 42:6–15

L3.4 Cyclones for the Precipitation of Solid Particles

Ulrich Muschelknautz
MK Engineering, Innsbruck, Austria

1 Flow Pattern

The pressure drop and the separation efficiency depend mainly on the tangential velocities in the cyclone. The tangential velocity u_a at the outer radius r_a depends on the inlet velocity v_e and on the design of the cyclone (cf. Fig. 1a–c).

1.1 Slotted Inlet

If the gas enters the cyclone through a tangential slot, the radial pressure field will force the gas stream against the wall. As a result, the jet is contracted and is thus accelerated. The effect is described by the contraction coefficient α (cf. Fig. 2), which primarily depends on the geometric ratio $\beta = b/r_a$ between the slot width b and the outer radius r_a. According to [1] α depends also on the load ratio of the particles in the inlet stream μ_e (Fig. 2):

$$\alpha = \frac{1 - \sqrt{1 + 4\left[\left(\frac{\beta}{2}\right)^2 - \left(\frac{\beta}{2}\right)\right]\sqrt{1 - \frac{1-\beta^2}{1+\mu_e}(2\beta - \beta^2)}}}{\beta}. \quad (1)$$

The outer tangential velocity is obtained from the momentum of the inlet jet expressed in terms of the outer radius, i.e.,

$$u_a = \frac{v_e r_e / r_a}{\alpha}. \quad (2)$$

The inlet velocity is given by

$$v_e = \frac{\dot{V}}{b h_e}. \quad (3)$$

It is referred to the central streamline of the entering flow (Figs. 2 and 3)

$$r_e = r_a - \frac{b}{2}. \quad (4)$$

1.2 Spiral Inlet

In the spiral inlet (Fig. 1b) the gas flow is decelerated due to wall friction. There is no contraction of the flow as in the case of a slotted inlet. The tangential outer velocity follows from the momentum balance with the force of friction

$$u_a = \frac{v_e \cdot r_e / r_a}{1 + \frac{\lambda_s}{2} \cdot \frac{A_{R,sp}}{\dot{V}} \cdot v_e \cdot \sqrt{r_e / r_a}}, \quad (5)$$

where λ_s is the coefficient of friction at the spiral wall according to [1] and $A_{R,sp}$ is the area in the spiral over which resistance is offered to friction

$$A_{R,sp} = \varepsilon\left[\frac{b + 2r_a}{2}(b + h_e)\right]. \quad (6)$$

The wall friction coefficient λ_0 for pure gas flowing within the spiral is approximately the double of that in the separation chamber, due to the small ratio between the area and volume in the spiral [1]. The wall friction coefficient for the gas carrying solids is higher and depends on the load ratio (cf. Sect. 1.2) according to

$$\lambda_s = \lambda_0\left(1 + 2\sqrt{\mu_e}\right). \quad (7)$$

1.3 Axial Guide Vanes

Axial guide vanes are mainly inserted in multicyclones at load ratios of $\mu_e < 0.1$. In most cases, simple plane vanes separated by a distance t with an overlap $ü$ of 25% (Fig. 1c) show sufficient performance. The guide vane angle δ is mostly between 15° and 30°.

The outer tangential velocity can be derived from this geometry (cf. Fig. 1c)

$$u_a = \frac{v_e \cos(\delta) r_e / r_a}{\alpha}, \quad (8)$$

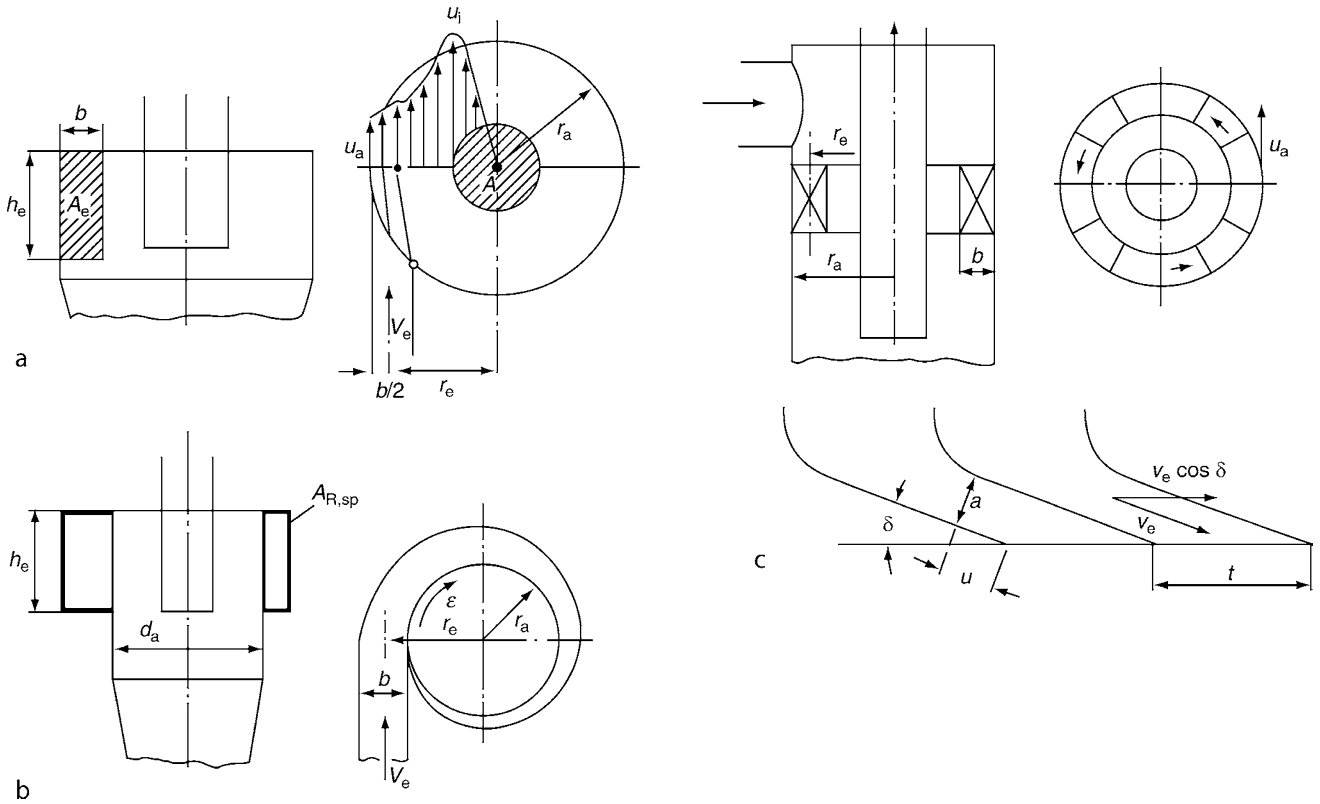

L3.4. Fig. 1. (**a**) Tangential slotted inlet. (**b**) Spiral inlet (full spiral: $\varepsilon = 2\pi$, half spiral: $\varepsilon = \pi$). (**c**) Guide vanes (axial inlet): elevation, plan, and development of the vane rig.

where the contraction coefficient has a value of $\alpha = 0.85$ for simple straight vanes, $\alpha = 0.95$ for bent vanes, and $\alpha = 1.05$ for bent and twisted vanes [1, 2].

1.4 Inner Tangential Velocity

The inner tangential velocity u_i at the radius r_i (Fig. 3) of the gas outlet pipe is calculated from the coefficient of friction λ_s and the total inner area A_R of the cyclone including the cover and the outer wall of the vortex tube [3–5], i.e.,

$$u_i = \frac{u_a \cdot r_a / r_i}{1 + \frac{\lambda_s}{2} \cdot \frac{A_R}{V} \cdot u_a \cdot \sqrt{r_a / r_i}}. \tag{9}$$

If the lower cone diameter is smaller than the vortex tube diameter, then the cone area, enclosed in A_R, is calculated down to the height, where the inner vortex touches the cone wall at the diameter $2r_i$.

The second term in the denominator of Eq. (9) may assume a value between 0.25 and 0.75 if the load ratio μ_e is small, and values up to 2, if the load ratio is high.

Depending on the load ratio, the coefficient of friction at the wall for the gas flow loaded with solids, λ_s, can be much higher than the coefficient of wall friction λ_0 for pure gas. In this case, the friction caused by the dust strands ($\mu_e = 0.01 \ldots 1.0$) or by a carpet ($\mu_e > 1.0$) is superimposed on the friction brought about by the roughness of the walls k_s/r_a [2]:

$$\lambda_s = \lambda_0 + 0.25\sqrt{\eta_g \mu_e \mathrm{Fr}_i \frac{\rho_g}{\rho_s(1-\varepsilon_{Str})}}\left(\frac{r_a}{r_i}\right)^{-5/8}. \tag{10}$$

The Froude number

$$\mathrm{Fr}_i = \frac{v_i}{\sqrt{2gr_i}} \tag{11}$$

allows for the cyclone dimensions. The void fraction ε_{Str} of the solid strands is roughly twice that of the loose particles [6].

Equation (10) has been confirmed by measurements [1] for conical and cylindrical cyclone models of 800 mm diameter and load ratios of 0.001 to 10. For cyclones of this size Eq. (10) is usually shortened as follows:

$$\lambda_s = \lambda_0\left(1 + 2\sqrt{\mu_e}\right). \tag{12}$$

In analogy to the flow through a pipe, the wall friction coefficient λ_0 for the unladen gas depends on the roughness parameter k_s/r_a and on the Reynolds number for the flow through the cyclone (Fig. 4)

$$\mathrm{Re}_R = \frac{2r_e v_{ax}/\nu_g}{2\frac{h}{r_m}\left(1 + \left(\frac{v_{ax}}{u_m}\right)^2\right)} \tag{13}$$

with

$$v_{ax} = \frac{0.9 \cdot \dot{V}}{\pi\left(r_a^2 - r_m^2\right)} \tag{14}$$

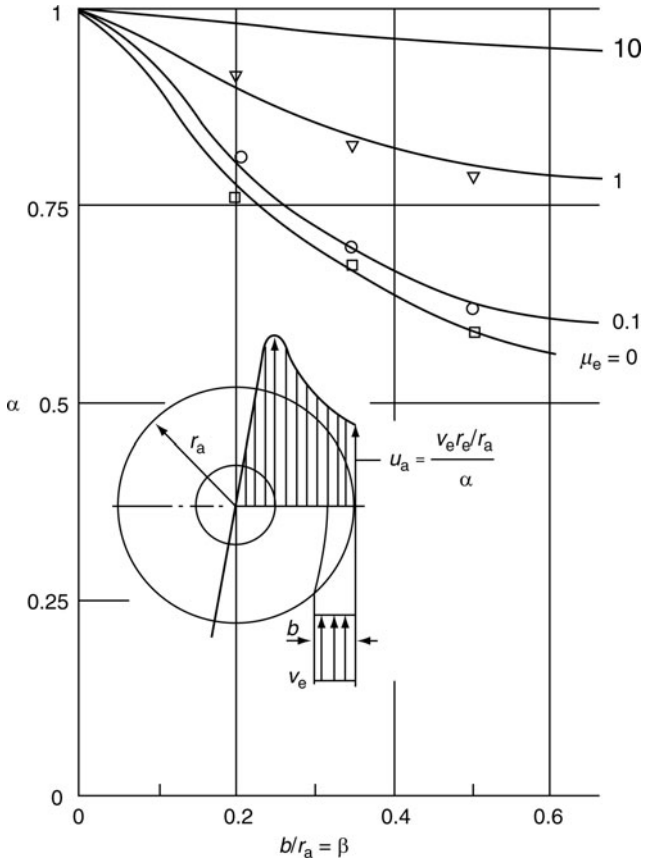

L3.4. Fig. 2. Coefficient of contraction α for tangential slotted inlet as a function of $\beta = b/r_a$, with the load ratio of particles at the inlet μ_e as a parameter.

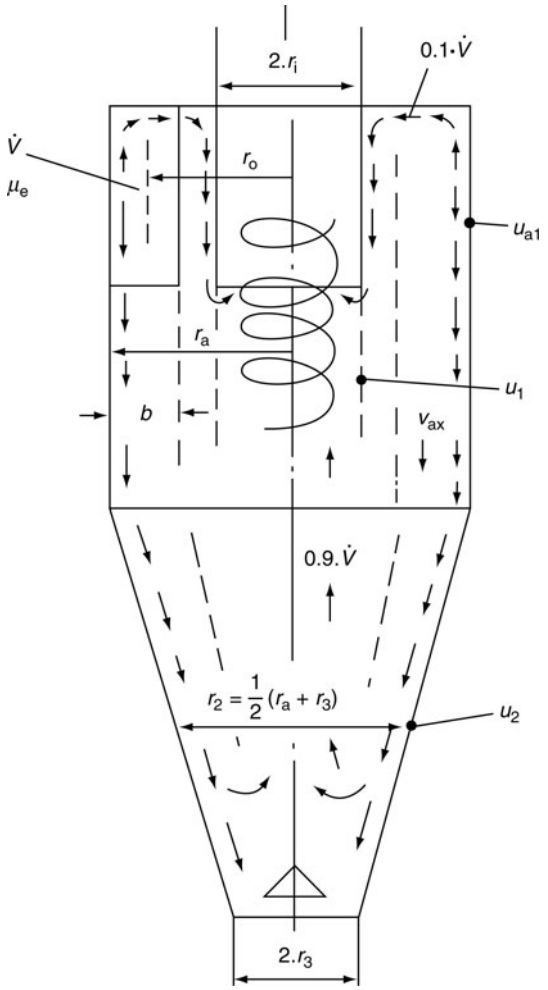

L3.4. Fig. 3. Flow pattern in a cyclone: About 90% of the entering gas flow streams as main flow along the cyclone wall downward and then as an inner vortex upward into the gas exit. About 10% of the entering gas streams as secondary flow along the top of the cyclone and then around the vortex tube into the gas exit.

and

$$r_m = \sqrt{r_a r_i}. \tag{15}$$

The wall friction coefficient is a function of temperature and pressure due to its dependency on the kinematic gas viscosity ν_g. If the temperature increases, then the kinematic viscosity ν_L increases as well and therefore, according to Eq. (13) and Fig. 4, also the wall friction coefficient rises. Thus, the inner tangential velocity (Eq. (9)) and the separation in the inner vortex (cf. Sect. 3.2) decrease when the temperature augments. This dependency has to be taken into account when the separation efficiency and the pressure drop of a cyclone are calculated. Hence, the model allows also for calculating the performance data of a cyclone at *high temperatures and/or high pressures* [8–10].

An alternative cyclone model for high temperatures and high pressures has been developed by [9–11]. Based on the approach of [12] this model divides the cyclone into four separation zones and calculates with particle flux balances. The tangential velocities of the main flow are calculated according to [13]. The wall friction coefficient is calculated as a function of the wall roughness and a Reynolds number, which is determined by the thickness and the tangential velocity of the boundary layer. Re-entrainment of particles, which are already separated from the gas stream, as well as the influence of the secondary flow on the cyclone separation efficiency are also taken into account.

The model allows also to calculate the separation effect, i.e., the width of the classification efficiency curve, cf. Sect. 3.2. Measurements in low loaded cyclones at temperatures up to 1,600°C and pressures up to 8 bar confirm the theory very well. All equations of the model are given in [9, 10].

2 Pressure Drop and Pressure Drop Reduction

The total pressure drop can be divided into three parts [4]:

$$\Delta p_{tot} = \Delta p_{inlet} + \Delta p_e + \Delta p_i. \tag{16}$$

Here the single pressure drops are calculated as differences of *total* pressures $p_{stat} + v^2\rho_g/2$ and $p_{stat} + u^2\rho_g/2$, since the main parts Δp_e and Δp_i are determined mainly by the tangential velocities in the cyclone.

At low and medium load ratios the pressure loss Δp_{inlet} in the inlet duct is much smaller than in the other parts p_e and p_i. It is [3]

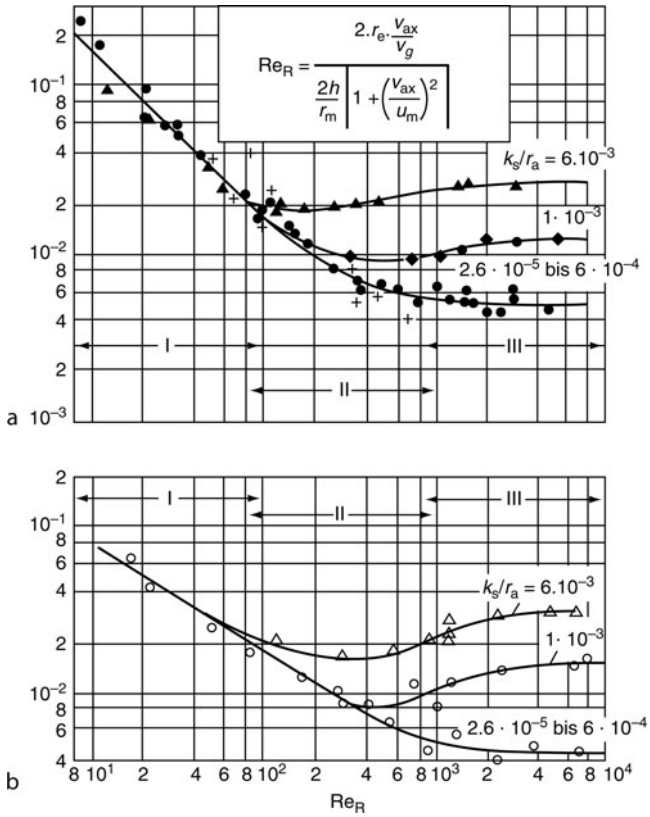

L3.4. Fig. 4. Coefficient of wall friction for pure gas as a function of the cyclone Reynolds number Re_R, Eq. (13), in a pure cylindrical (**a**) and a conical cyclone (**b**) [7].

$$\Delta p_{inlet} = 0 \text{ for slotted inlet}$$
$$\Delta p_{inlet} = -\frac{\pi \cdot r_i^2}{b \cdot h_e} \cdot \left(1 + \frac{\pi}{4}\left(\frac{r_i}{r_a}\right)^2\left(1 - \frac{1}{\alpha^2}\right)\right) \cdot \frac{\rho_g}{2} v_i^2 \quad \text{for spiral inlet,} \tag{17}$$
$$\Delta p_{inlet} = -(0.2 \ldots 0.5) \cdot \frac{\rho_g}{2} v_i^2 \text{ for axial inlet.}$$

In the equation for the pressure drop in a spiral inlet it is $\alpha = 1 + \frac{\lambda_s}{2}\frac{A_{R,sp}}{\dot{V}} v_e \sqrt{\frac{r_e}{r_a}}$ (cf. Eq. (5)).

The pressure drop Δp_e in the separation compartment depends on the outer tangential velocity, the area of the wall A_R, and the effective wall friction coefficient λ_s [14]:

$$\Delta p_e = -\lambda_s \frac{A_R}{0.9\dot{V}} \frac{\rho_g}{2} (u_a u_i)^{3/2}. \tag{18}$$

Allowance is thus made for the fact that the total gas flow rate $\dot{V}$ is split into a main flow of approximately $0.9\dot{V}$ and a secondary flow of approximately $0.1\dot{V}$ [15]. The main flow streams along the cyclone wall as an outer vortex downward and then, after reversing its axial direction, as an inner vortex upward into the gas outlet tube. The secondary flow streams in a short circuit through the boundary layer at the cover and at the outer wall of the gas outlet tube directly into the gas exit opening (Fig. 3).

The pressure drop in the gas outlet tube is for low and medium load ratios μ_e usually five to ten times larger than both other parts of the pressure drop in Eq. (16) together. At high load ratios the pressure drops in the separation compartment and in the gas outlet tube are of the same order.

The pressure drop in the gas outlet tube depends crucially on the ratio between the inner tangential velocity u_i and the mean axial velocity v_i in the gas outlet tube

$$v_i = \frac{\dot{V}}{\pi r_i^2} \tag{19}$$

i.e., [2]:

$$\Delta p_i = -\left[2 + 3\left(\frac{u_i}{v_i}\right)^{4/3} + \left(\frac{u_i}{v_i}\right)^2\right] \frac{\rho_g}{2} v_i^2. \tag{20}$$

The pressure drop, described by Eq. (20), arises between the imaginary cylinder area of the gas outlet pipe with radius r_i and a point in the gas outlet pipe far beyond the cyclone, where practically no more swirl exists in the gas flow. Thus, the calculated value allows also for the pressure drop, which emerges from the dissipation of the rotational energy due to wall friction in the pure gas pipe. In the model this additional pressure drop is counted along with the total cyclone pressure drop.

Often the pressure drop of a cyclone is measured between the cyclone inlet and a point in the pure gas pipe, which is very close to the cyclone cover. The pressure drop, resulting from this measurement, will be much lower than the value predicted by the theory.

Equation (20) yields the cyclone pressure drop in good agreement with measurements for those cases where the pure gas is blown into the atmosphere or where the pressure after the cyclone is measured at a point and where practically no swirl exists anymore (cf. [16]).

The pressure drop Δp_i in the gas outlet pipe can be reduced in a simple way by inserting a pressure plate, which acts as a radial diffusor. There the fast annular flow in the gas outlet pipe is guided in a small annular gap of height s between the cyclone cover and the pressure plate. The deflection of the flow is carried out with the deflection radius r_u. On its way outward the flow is decelerated, leading to an increase of the static pressure. The outlet spiral serves only as a collector. If the pressure plate is designed with the correct radius r_D, i.e., $r_D/r_i \geq 2$, $s/r_i = 0.2$, and $r_u/r_i \geq 0.1$, pressure recoveries between 40 and 50% can be achieved for swirl ratios u_i/v_i between 1.75 and 2.45, respectively. By inserting a simple outlet spiral without pressure plate the pressure recovery will be only about 15%, since in this case the spiral is not completely filled with the annular flow exiting the gas outlet pipe and thus, the flow is not sufficiently decelerated.

Pressure can be recovered more efficiently by installing swirl vane inserts in the gas outlet pipe. The device consists of a central, mostly cylindrical core with 6–12 curved guide vanes fixed on it. They deflect the annular flow with only small losses of kinetic energy into a pure axial flow and therefore, transform dynamical pressure into static pressure. Thus, the rotational energy stored in the annular flow is transformed into pressure instead of losing it due to dissipation, which would be the case, if no such measure is applied. At low to medium load ratios the

pressure drop can be reduced by 40–60%, depending on the swirl strength. For details see [14].

Cyclone with higher load ratios and short entrance ducts, where the solids feed has a low velocity at the beginning of the duct, exhibits a considerable pressure drop in the entrance duct and shows – compared to low loaded cyclones – modified influx conditions at the cyclone entrance [17, 18].

The differential pressure loss in a segment of such a cyclone entrance duct is the sum of the losses which result from gas and solids acceleration [19]

$$dp = dp_{gas} + dp_s = -\rho_g \cdot v \cdot dv - \mu_e \cdot \rho_g \cdot v \cdot dc. \qquad (21)$$

The total pressure drop in the entrance duct results from integrating Eq. (21) along the way through the duct. For high load ratios this pressure drop is of the same order as the pressure drops in the separation compartment and in the gas outlet pipe.

For high load ratios the mean solid velocity c_e at the end of the duct averaged over the duct cross section is often considerably smaller than the gas velocity v_e at that point. Then, in the succeeding entrance zone of the cyclone a rapid momentum exchange between solids and gas takes place. As is shown in [19] the solids velocity increases in this zone by the amount Δc and the gas velocity decreases by the amount

$$\Delta v = -\mu_e \cdot \Delta c. \qquad (22)$$

The velocities of solids and gas after the momentum exchange

$$c_{in} = v_{in} \qquad (23)$$

are generally considerably smaller than the gas velocity at the cyclone entrance v_e. In this case the cyclone calculation has to be performed by applying v_{in} instead of v_e as input quantity.

A more exact calculation allows for measured gas and solids flux pattern, whereupon with increasing height above the bottom of the duct the load ratio μ_e and the mean particle size d_{50} decrease and the gas and solids velocities v and c increase. For details see [20, 37].

3 Separation Efficiency

A factor to be taken into account in calculating the separation efficiency is that the restricted turbulence in the cyclone entails that only a certain solids fraction can be carried in the swirling flow [21]. If the load ratio in the inlet μ_e exceeds the limit μ_{lim} [2, 5], the excess mass fraction will be removed immediately after the gas jet enters the cyclone (Fig. 5), and only a small fraction that is restricted by the limit μ_{lim} will undergo the centrifugal separation process in the inner vortex of the cyclone. Accordingly, two separation mechanisms are distinguished:

- Separation due to exceeding the limiting load ratio, which is also called the wall separation
- Separation in the inner vortex

For load ratios in the inlet $\mu_e < \mu_{lim}$ only the second separation mechanism is active, and for load ratios $\mu_e \geq \mu_{lim}$, which is by far the more common case, both separation mechanisms are effective.

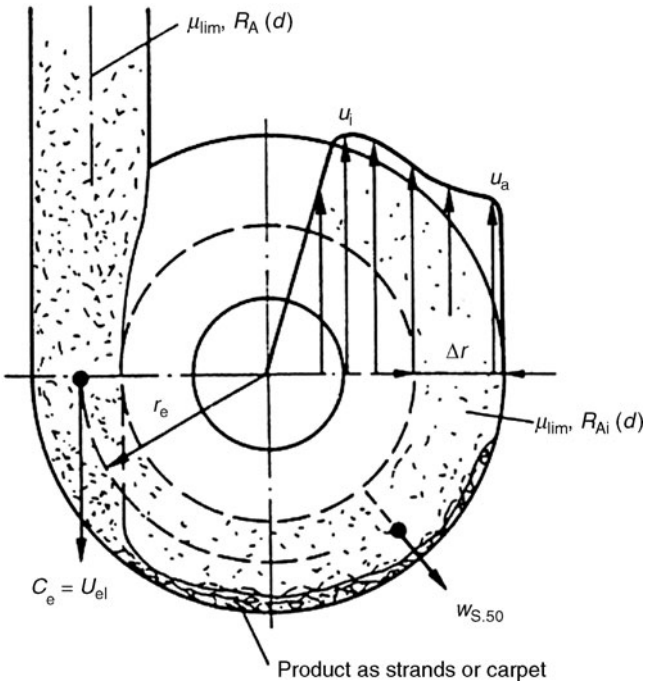

L3.4. Fig. 5. Separation due to exceeding the limited load ratio immediately after the cyclone entrance, cf. Eq. (33).

3.1 Separation at the Wall

If the load ratio in the inlet exceeds the limited load ratio, the excess mass is removed immediately after the cyclone inlet and forms strands or a continuous layer at the wall. Only a small fraction of finer particle size distribution remains in the gas flow and undergoes centrifugal separation in the vortex of the cyclone. This solids fraction is called the "inner feed." The wall separation thus leads to a classification of the solids feed [22]. The classification is characterized by the cut size for wall separation

$$d_e^* = \sqrt{w_{s,50} \frac{18\eta_g}{\Delta\rho \overline{z}_e}}, \qquad (24)$$

where $w_{s,50}$ is the settling velocity of a particle which is separated by 50% from the gas stream, while moving along the clarification area A_w in the zone of downward flow under the mean centrifugal acceleration $\overline{z}_e$ [23]. With a secondary flow of 10%, it is given as

$$w_{s,50} = \frac{0.5(0.9\dot{V})}{A_w}. \qquad (25)$$

The clarification area includes the cylindrical part of the cyclone and the upper part of the cone because of the reversing vortex, Fig. 3. For pure cylindrical cyclones A_w is the area of the total cylindrical wall.

Particles with the diameter d_e^* are separated by 50% from the gas stream moving along the clarification area A_w. Particles of sizes much larger than the cut size deposit immediately at the cyclone wall, whereas finer particles find their way into the inner area of the cyclone.

The mean centrifugal acceleration $\overline{z}_e$ along the streamline from the entrance of the radius $\overline{r}_e$ down to the lower end of the clarification area A_w of the radius r_2 (Fig. 3) is

$$\overline{z}_e = \frac{u_e u_2}{\overline{r}_z} \tag{26}$$

with the tangential velocities

$$u_e = \frac{u_a r_a/\overline{r}_e}{1 + \frac{\lambda_s}{2}\frac{A_{e1}}{0.9\dot{V}} u_a \sqrt{r_a/\overline{r}_e}} \tag{27}$$

of the radius $\overline{r}_e$ and

$$u_2 = \frac{u_a r_a/r_2}{1 + \frac{\lambda_s}{2}\frac{A_w}{0.9\dot{V}} u_a \sqrt{r_a/r_2}} \tag{28}$$

of the radius r_2. The area A_{e1}, over which the gas stream flows during its first turn, is approximately

$$A_{e1} = (2\pi r_a h_e)/2. \tag{29}$$

Allowing for contraction of the entering gas flow in the entrance zone (Fig. 5) the reference radius $\overline{r}_z$ is given by

$$\overline{r}_z = \sqrt{\overline{r}_e \cdot r_2} = \sqrt{\left(r_a - \frac{1}{2}\alpha b\right) r_2}. \tag{30}$$

The limited loading ratio μ_{lim} depends on the mean centrifugal acceleration for the separation and on the particle size distribution of the feed with the median diameter $d_{50,A}$ and further on the load ratio of the feed μ_e [2, 14, 22]:

$$\mu_{lim} = K_{lim} \cdot \left(\frac{d_e^*}{d_{50,A}}\right) \cdot (10\mu_e)^k. \tag{31}$$

The constant K_{lim} varies between 0.02 and 0.03. The minimum value was found for fine particles with large slope angles, and the maximum value for coarser particles with small slope angles. For a large number of dusts, it is $K_{lim} = 0.025$.

The exponent k has the value 0.81 for inlet loadings $\mu_e < 2.2 \times 10^{-5}$, is constant 0.15 for inlet loadings $\mu_e > 0.1$, and follows the curve

$$k = 0.15 + 0.66 \cdot \exp\left[-\left(\frac{\mu_e}{0.015}\right)^{0.6}\right] \tag{32}$$

in the region $2.2 \times 10^{-5} \le \mu_e \le 0.1$.

The efficiency for separation due to exceeding the limited load ratio is [2]

$$\eta_e = 1 - \frac{\mu_{lim}}{\mu_e}. \tag{33}$$

This separation mechanism takes place before the separation in the inner vortex and can, for feed loadings $\mu_e > 0.1$, easily exceed the latter (Fig. 9). With increasing feed loading μ_e the separation efficiency η_e rises, the separation efficiency of the inner vortex however, declines due to the decrease of the inner tangential velocity (Eqs. (9) and (10)).

The particle size distribution of the inner feed is determined by the characteristic particle size $d_{50,Ai}$ [22]. The complete residue curve of the inner feed may be approximated by an RRSB function as given in Eq. (34), i.e.,

$$R_{Ai}(d) = \exp\left[-\left(\frac{d}{d'_{Ai}}\right)^{n_{Ai}}\right] \tag{34}$$

with

$$d'_{Ai} = \frac{d_{50,Ai}}{0.7^{1/n_{Ai}}} \tag{35}$$

and

$$\begin{aligned} d_{50,Ai} &= d_{50,A} \quad \text{for } \mu_e < \mu_{lim} \\ d_{50,Ai} &= d_{50,A} - \left(d_{50,A} - d_e^*\right) \cdot \frac{(1 - \mu_{lim}/\mu_e)}{0.5} \\ &\text{for} \quad 0 \le \left(1 - \frac{\mu_{lim}}{\mu_e}\right) \le 0.5 \\ d_{50,Ai} &= d_e^* \quad \text{for } 0.5 < \left(1 - \frac{\mu_{lim}}{\mu_e}\right), \end{aligned} \tag{36}$$

where $d_{50,A}$ is the mean particle size of the feed.

The exponent n_{Ai} describes the width of the residue curve of the inner feed and depends on the loading of the feed according to

$$\begin{aligned} n_{Ai} &= \max(1.2; n_A) \quad \text{for } \mu_e \ge \mu_{lim}, \\ n_{Ai} &= n_A \quad \text{for } \mu_e < \mu_{lim}. \end{aligned} \tag{37}$$

Experiments have shown that for various particle size distributions of the feed and for various operating conditions the residue curve of the inner feed plotted over $d/d_{50,Ai}$ can be very well approximated by a single curve, which is shown in Fig. 6 [22].

3.2 Separation in the Inner Vortex

The separation in the inner vortex is characterized by the cut size d^* of the main stream [4]. It is given by the balance of the centrifugal force acting on the particles with a diameter of d^* and its drag at the radius r_i of the vortex tube. Assuming a secondary flow of 10% the cut size can be calculated from [5]

$$d^* = \sqrt{\frac{18\eta_g 0.9\dot{V}}{\Delta\rho u_i^2 2\pi h_i}}. \tag{38}$$

It depends mainly on the square of the inner tangential velocity and on the height h_i of the separation compartment (Fig. 7) below the vortex tube.

The cute size d^* characterizes the grade efficiency curve η_F for the separation in the inner vortex.

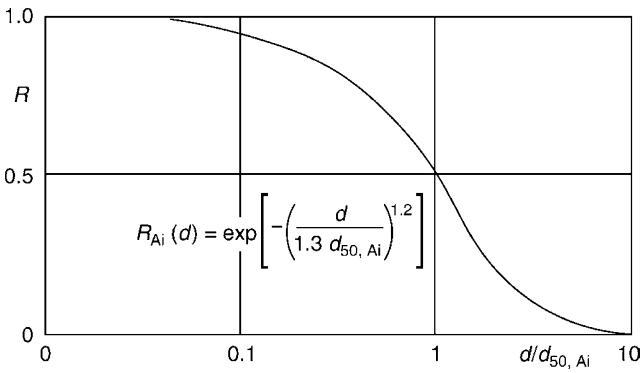

L3.4. Fig. 6. Residue curve of the inner feed for various feeds and operating conditions as a function of $d/d_{50,Ai}$, Eq. (34).

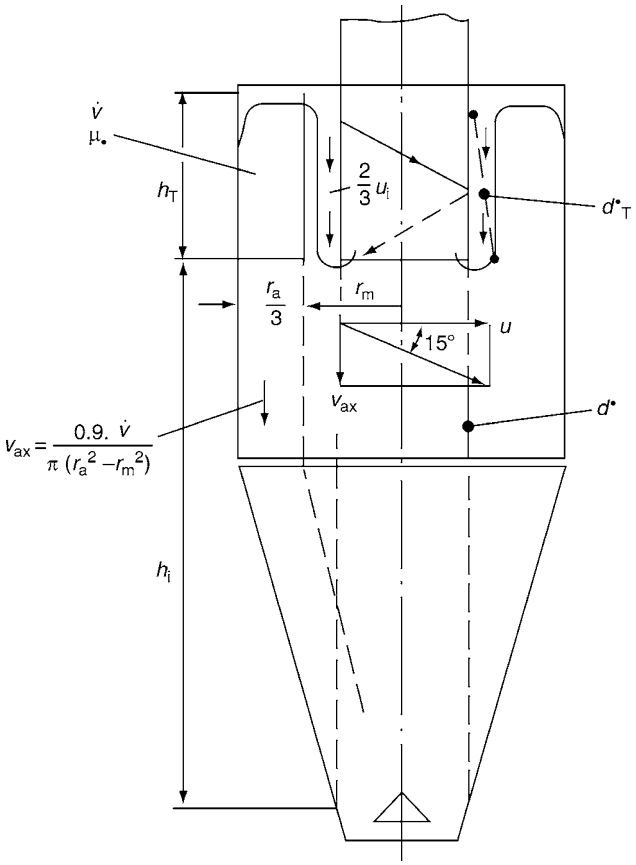

L3.4. Fig. 7. Calculation of the cut size d^* for the main gas stream, Eq. (38), and for the secondary gas stream (for details, see [15]).

Figure 8 shows experimental η_F- curves for various cyclone types [2]. The experimental value for the cut size is found to be the theoretical value multiplied by the factor ranging from 1.2 to 1.3, depending on the geometry and on the flow pattern in the cyclone. For the calculation the η_F- curve may be described in the region $D^{-1} \cdot d^* \le d \le D \cdot d^*$ by

$$\eta_F(d) = 0.5\left\{1 + \cos\left[\pi\left(1 - \frac{\log\left(\frac{d}{d^*}\right) + \log D}{2 \log D}\right)\right]\right\} \quad (39)$$

in the region $d < D^{-1} \cdot d^*$ by $\eta_F = 0$ and in the region $d > D \cdot d^*$ by $\eta_F = 1$; the shape of the curve is adapted to the cyclone type by the parameter [20]

$$D = \frac{d/d^*(\eta_F = 1)}{d/d^*(\eta_F = 0.5)}. \quad (40)$$

D may assume values between 2 and 4, and $D = 3$ for a typical cyclone.

The separation efficiency in the inner vortex is given by

$$\eta_i = \sum_{j=1}^{m} \eta_F(\bar{d}_j) \Delta R_{Ai}(\bar{d}_j). \quad (41)$$

In this equation, the residue curve of the inner feed is subdivided into m classes and it is calculated with the mean particle sizes in each particle size fraction. $\Delta R_{Ai}(d^*_j)$ is the mass fraction of the jth particle size fraction.

The grade efficiency in the inner vortex, $\eta_F(\bar{d}_j)$, is valid only if μ_e is less than μ_{lim}. A rough approximation of the grade efficiency can be obtained in one step from the cut size d^*, i.e.,

$$\eta_i \approx R_{Ai}(1.05 d^*). \quad (42)$$

3.3 Total Separation Efficiency

The total separation efficiency is the sum of two parts, according to the two separation mechanisms, i.e.,

$$\eta_{ges} = 1 - \frac{\mu_{lim}}{\mu_e} + \frac{\mu_{.lim}}{\mu_e} \cdot \eta_i. \quad (43)$$

The second part is calculated as in Sect. 3.2 by the grade efficiency curve $\eta_F(d)$, Eq. (39).

If the feed loading ratio is below the limited loading ratio, $\mu_e < \mu_{lim}$, only the separation in the inner vortex is valid and it is

$$\eta_{tot} = \eta_i. \quad (44)$$

The inner feed is, in this case, identical with the feed, i.e., $R_{Ai}(d) = R_A(d)$ (Fig. 9).

With increasing solids loading the inner tangential velocity decreases due to the increased wall friction. Therefore, the separation efficiency η_i in the inner vortex drops down, whereas the separation efficiency η_e at the wall increases and becomes dominant.

The amount of particle carryover is

$$S(\mathrm{kg/m^3}) = \left(1 - \eta_{ges}\right)\mu_e \rho_g \quad (45)$$

with η_{tot} calculated by Eqs. (43) and (44). The accuracy of S is approximately $\pm 20\%$ for a typical cyclone geometry.

The particle size distribution of the carryover, $R_F(d)$, can be determined in m size fractions by means of the total separation efficiency, the distribution of the inner feed, and the grade efficiency curve [22]:

$$\Delta R_F(d) = \frac{\mu_G}{\mu_e} \cdot \frac{(1 - \eta_{F,i}(d))}{1 - \eta_{ges}} \cdot \Delta R_{Ai}(d) \quad \text{for } \mu_e < \mu_G \quad (46)$$

$$\Delta R_F(d) = \frac{\mu_G}{\mu_e} \cdot \frac{(1 - \eta_{F,i}(d))}{1 - \eta_{ges}} \cdot \Delta R_A(d) \quad \text{for } \mu_e \ge \mu_G.$$

From Eq. (46) the total grade efficiency curve is obtained.

$$\eta_{F,tot}(\bar{d}) = 1 - \left(1 - \eta_{ges}\right)\frac{\Delta R_F(\bar{d})}{\Delta R_A(\bar{d})}. \quad (47)$$

Figure 10 shows the influence of the feed loading ratio on the total grade efficiency curve. For $\mu_e > \mu_{lim}$ the curves no more drop down to zero but increase with decreasing particle size. The reason for the intensified separation of fine particles with increasing solids loading is that the fine particles are overwhelmed in the solids strands immediately after entering the cyclone.

For $\mu_e < \mu_{lim}$ the fine particles are no more overwhelmed in the strands. Therefore, the grade efficiency curve decreases to zero with decreasing particle size (Fig. 8).

Curve	a	b	c
Design	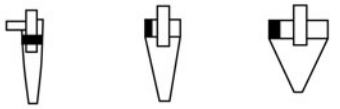		
Inlet	Axial	Tangential	Tangential
h/r_i	15.0	13.0	10.0
h_i/r_i	10.0	10.0	7.5
r_a/r_i	2.0	3.0	4.0
A_e/A_i	2.70	0.90	0.44
b/r_a	0.40	0.27	0.19

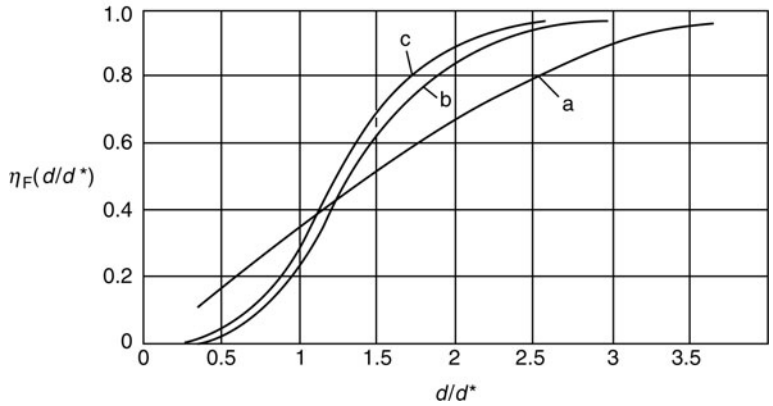

L3.4. Fig. 8. Grade efficiency curves for separation in the inner vortex for three different cyclone geometries [2].

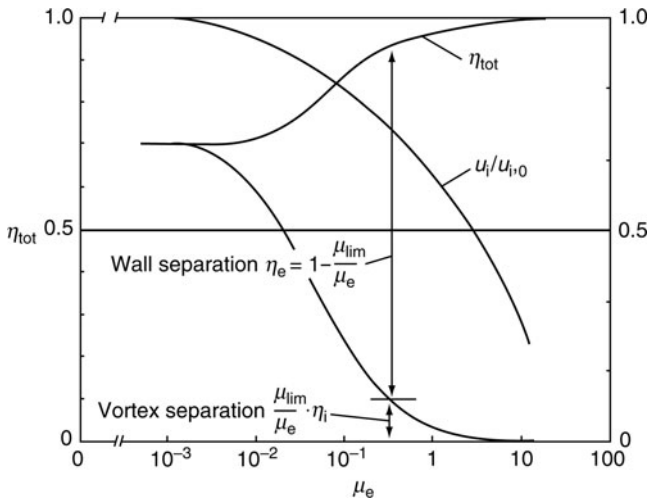

L3.4. Fig. 9. Separation efficiency and the inner tangential velocity u_i, related to the inner tangential velocity $u_{i,0}$ for pure gas, as a function of the feed loading ratio μ_e.

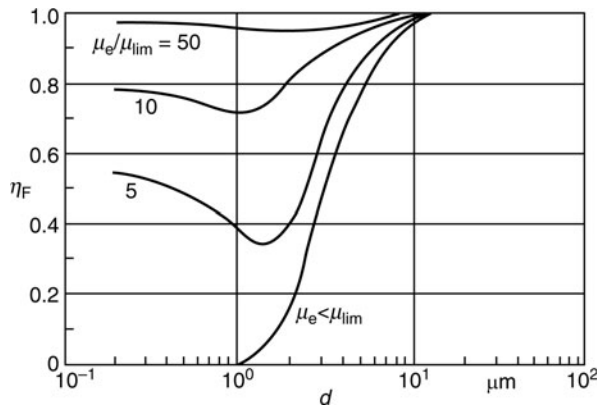

L3.4. Fig. 10. Influence of the load ratio of the feed μ_e on the total grade efficiency curve. For $\mu_e \leq \mu_{lim}$ only vortex separation is effective, for $\mu_e > \mu_{lim}$ wall separation also contributes to the separation.

An optimized calculation of the total separation efficiency, which takes also into account the secondary flow, is performed according to an approach of [22]:

$$\eta_{tot} = \left(1 - \frac{\dot{V}_{sec}}{\dot{V}}\right) \cdot \left[1 - \frac{\mu_{lim}}{\mu_e} + \frac{\mu_{lim}}{\mu_e} \cdot \eta_i\right] + \frac{\dot{V}_{sec}}{\dot{V}} \cdot \left[1 - \frac{\mu_D}{\mu_e} + \frac{\mu_D}{\mu_e} \cdot \eta_T\right]. \quad (48)$$

The first term describes the separation in the main flow and is calculated by means of Eqs. (24–44). The second term contains the separation in the secondary flow. The value of 10% for the fraction of the secondary flow, assumed in Eq. (38), is a mean value. The exact value depends essentially on the feed solids loading and is normally between 5% and 15%. According to [22] it is given by

$$\frac{\dot{V}_{sec}}{\dot{V}} = 0.0497 + 0.0684n + 0.0949n^2, \quad (49)$$

$$n = \frac{\ln(u_i/u_a)}{\ln(r_a/r_i)}. \quad (50)$$

An alternative approach for calculating $\dot{V}_{sec}$ is described in [24]. Both calculation methods are compared in [22].

The secondary flow can carry more solids than the main flow, due to its lower tangential velocity and therefore, reduced attenuation of the turbulence. Measurements [1, 22] have shown that the limited loading ratio in the boundary layer at the covering μ_D is much larger than the limited loading ratio μ_{lim} of the main flow. According to [22] μ_D is given by $\frac{\mu_D}{\mu_{lim}} = 6$ for $\mu_e \geq 6\mu_{lim}$ and $\mu_D = \mu_e$ for $\mu_e < 6\mu_{lim}$.

Cyclones with a vortex tube force the secondary flow to move in spirals around the tube down to the opening. On its way around the tube, the secondary flow rotates much slower than the surrounding main flow. The particles carried in the secondary flow need some time to be captured by the surrounding faster main flow. It results, analogous to the main flow, in a cut size d_T^* for the separation out of the vortex tube boundary layer (details, see [15]). The separation efficiency η_T for the removal of particles from the vortex tube boundary layer increases with increasing vortex tube length. Measurements for different feed loadings lead to the relation

$$\eta_T(h_T) = 0.0105 \cdot \arctan(35 \cdot h_T/h) \quad (51)$$

with [arctan $(35h_T/h)$] = Degree.

On the other hand, an elongation of the vortex tube, at constant total height of the cyclone, reduces the height h_i of the separation compartment below the vortex tube and thus degrades the separation efficiency η_i in the main flow, Eqs. (38)–(41). Therefore, there exists an optimum length of the vortex tube, which results in a maximum total separation efficiency and a minimum carryover of particles (Fig. 11). If the vortex tube is too short, the secondary flow transports a considerable mass of dust into the pure gas. The optimum vortex tube length

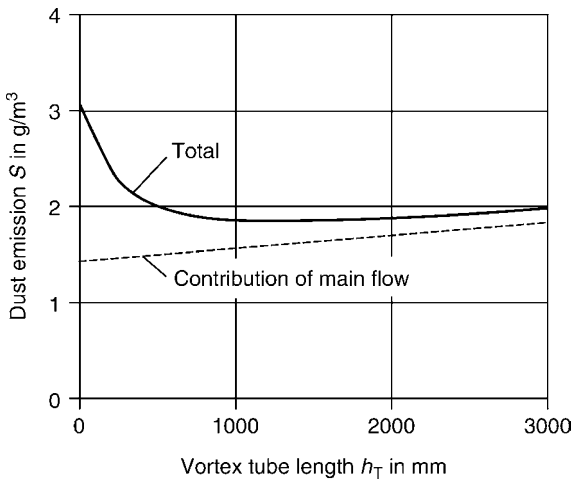

L3.4. Fig. 11. Dust emission S of the cyclone in example 1 as a function of the vortex tube length: total emission (solid curve) and contribution of the main flow (dashed curve) to the total emission.

calculated according to Eqs. (48)–(51) agrees very well with the experiments [22, 25, 26] for various cyclones.

The grade efficiency curve η_T for the vortex tube separation mechanism, described earlier, is calculated by Eq. (51). This curve has been measured for one cyclone. For other cyclones Eq. (51) is a rough approximation. By means of an improved calculation method η_T can be obtained as a function of the vortex tube cut size d_T^* and therefore, as a function of the geometry and of the flow pattern in the cyclone. For more details see [22].

For small solids loadings the dust removal from the secondary flow contributes up to 15% to the total separation efficiency [22].

For higher loadings its contribution to the total separation efficiency is considerably lower, since over 95% of the entering particles are separated due to exceeding the limited loading ratio. Nevertheless, also in this case it can be very useful to achieve an optimum separation efficiency of the vortex tube, as has been shown for example in reactor systems with circulating fluidized bed, where only small changes of the length and of the position of the vortex tube (eccentrically shifted) had a large influence on the mass flow and on the particle size distribution of the circulating particles [20].

Also the geometry of the product outlet has an influence on the separation efficiency and the pressure drop of a cyclone. Its influence on the separation efficiency is of the same order as that of the secondary flow. Recommendations for an optimum geometry of the product outlet are given in [1, 2, 19, 27–30].

3.3.1 Particle Size Distributions for Agglomerating Fine Dusts

Fine dusts <40 µm can constitute, depending on the preliminary conditions to which they were subjected, agglomerates of 10–100 particles. In cyclones of diameters >1 m and outer tangential velocities u_a of 10–15 m/s, these agglomerates are not or only partially dissolved in the boundary layer of the wall.

Figure 12 shows particle size distributions of cement dust collected in an electric precipitator. The curves 2 and 3 are shifted parallel with increasing exposure of the probe to a magnetic stirrer and ultrasound.

In cyclones it is for similar cases

$$d' = d'_0 \cdot \left(\frac{\dot{V}_0 \cdot \Delta p_{e,0}}{\dot{V} \cdot \Delta p_e}\right)^{0.78}. \quad (52)$$

The agglomerates are stressed mainly in the boundary layer at the wall of the separation compartment, where the power of the stream $N_{Str} = \dot{V} \cdot \Delta p_e$ is transformed. The parameter for the width of the RRSB particle size distribution n remains constant for the three different powers N (Fig. 12), the characteristic particle size d′ is converted according to Eq. (52). Experiments were performed for volume flow rates of 60,000–80,000 m^3/h at a flue gas temperature of 350°C and a dust concentration of 50 mg/Sm^3.

Example 1 (High loaded hot gas cyclone):
For the high loaded hot gas cyclone (gas temperature 870°C) shown in Fig. 13 the separation efficiency and the pressure drop

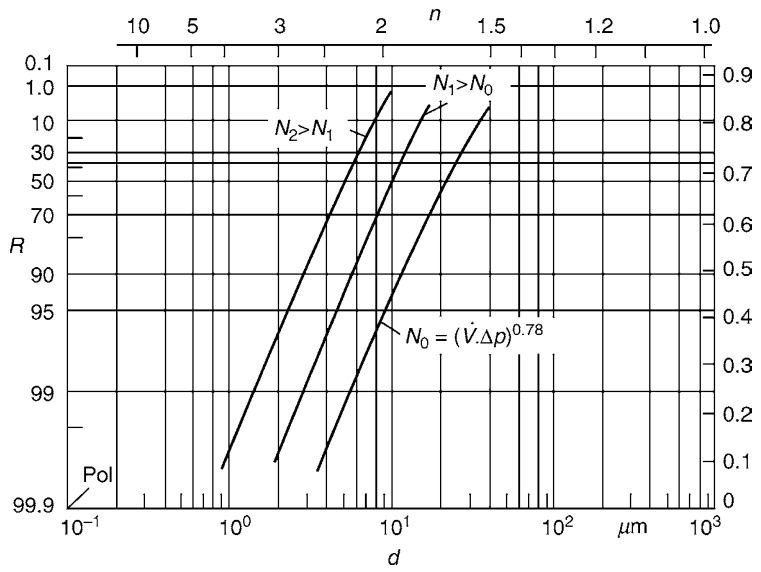

L3.4. Fig. 12. Residue curves of agglomerating dusts.

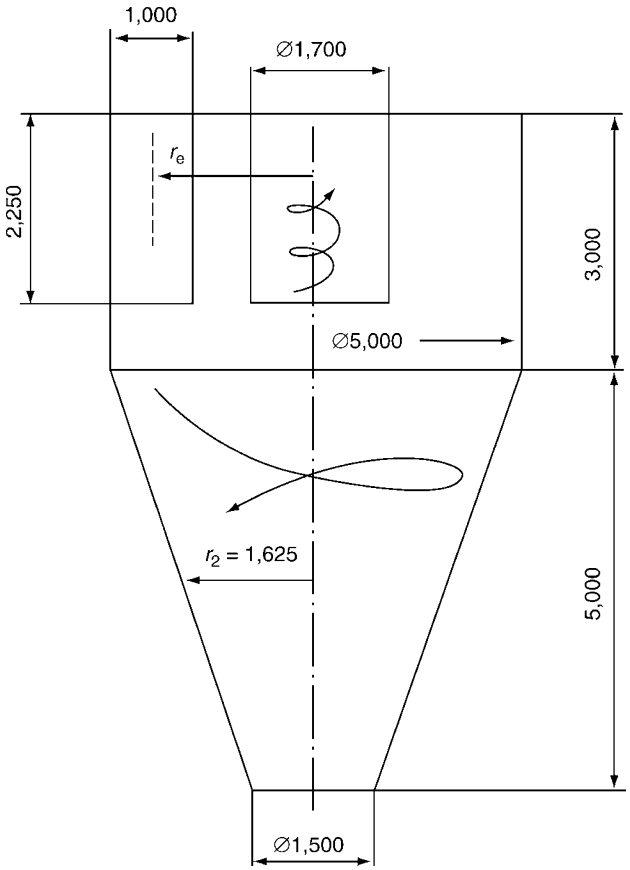

L3.4. Fig. 13. Geometry of the hot gas cyclone in Example 1.

are calculated. The feed has the particle size distribution $R_A(d)$ shown in Fig. 14.

The effective gas flow rate is 50 m^3/s, and the solids loading is μ_e = 5 kg/kg gas.

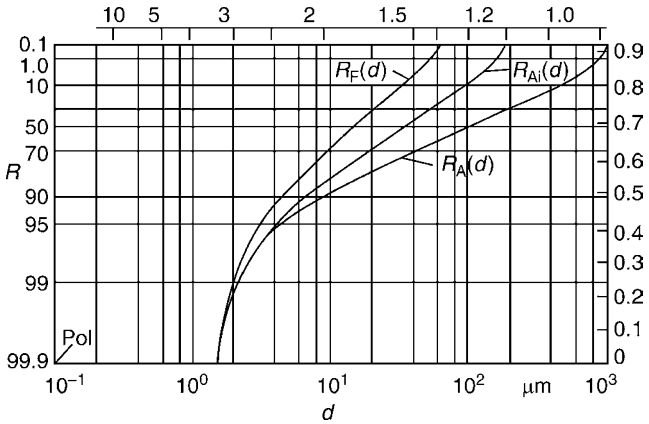

L3.4. Fig. 14. Residue curves of the feed $R_A(d)$, of the inner feed $R_{Ai}(d)$, and of the fines $R_F(d)$ for the Example 1, shown in an RRSB net.

Tangential velocities:

v_e = 22.2 m/s
β = b/r_a = 0.4 → α = 0.94 Eq. (1)
u_a = 18.9 m/s Eq. (2)

Operating data:

$\dot{V}$ = 50 m^3/s, T = 870°C
ρ_g = 0.305 kg/m^3, ρ_s = 2,000 kg/m^3
$\eta_g = 45 \cdot 10^{-6}$ Pa s, A_w = 81 m^2, A_R = 129 m^2

Coefficient of friction and tangential velocities:

λ_s = 0.0274 Eq. (12)
u_2 = 18.5 m/s Eq. (28)
u_i = 25.9 m/s Eq. (9)

Cut size and separation efficiency

d^*	= 29 μm	Eq. (38)
$w_{s,\,50}$	= 0.278 m/s	Eq. (25)
u_{e1}	= 20.2 m/s	Eq. (27)
$\overline{z}_e$	= 206 m/s^2	Eq. (26)
d_e^*	= 24 µm	Eq. (24)
μ_{lim}	= 0.0107	Eq. (31)
$\dot{V}_{sek}/\dot{V}$	= 0.078	Eqs. (49) and (50)
η_T	= 0.8841	Eq. (51)

Hence, the total separation efficiency including the separation at the vortex tube is

$$\eta_{tot} = (1 - 0.078) \cdot \left[1 - \frac{0.0107}{5} + \frac{0.0107}{5} \cdot 0.4256\right] + 0.078 \cdot \left[1 - \frac{0.0642}{5} + \frac{0.0642}{5} \cdot 0.8841\right] = 0.9987 \qquad \text{Eq. (48)}$$

and the emission is given by

$$S = \left(1 - \eta_{ges}\right) \cdot \mu_e \cdot \rho_g = 1,907\,\text{g/m}^3 \qquad \text{Eq. (45)}$$

The curve for the emission as a function of the vortex tube length has a broad minimum. Only for vortex tube lengths below 1,000 mm the emission increases considerably (see also measurements of [22, 25, 26]).

Pressure drops:

Δp_e = 127 Pa	Eq. (18)
Δp_i = 525 Pa	Eq. (20)

In Fig. 14 the particle size distributions of the feed $R_A(d)$, of the inner feed $R_{Ai}(d)$, and of the fines $R_F(d)$ are shown. Accordingly the dust, which arrives at the region of the inner vortex (R_{Ai}), is considerably finer than the feed. Each particle collective has a maximum particle size and a minimum particle size, d_{max} and d_{min}, respectively (see Subchap. L3.3). The parameter n_A for the width of the particle size distribution of the feed is readable at the upper scale.

3.3.2 Simplified Cyclone Design

If it has to be estimated in a short time whether a cyclone is appropriate for a dust removal problem, a simplified design according to the following scheme can be performed.
Example 2 (Rough design of a low loaded cyclone):

A cyclone for dust removal from air at environmental conditions is designed:

Gas flow rate	$\dot{V}$= 1 m^3/s
Solids loading of the feed	$\mu_e < 0.1$
Mean particle size of the feed	$d_{50,A}$ = 10 µm
Particle density	ρ_s = 2,600 kg/m^3
Allowed pressure drop	Δp_{tot} = 2,000 Pa

For a typical low loaded cyclone

It is approximately	$\Delta p_i \approx 0.9 \Delta p_{tot}$
Ratio of velocities	$u_i/v_i \approx 2$
Ratio of radii	$r_a/r_i \approx 3$
Ratio between height and radius	$h_i/r_a \approx 4$
Pressure drop coefficient of the vortex tube	$\xi_i \approx 15$

The pressure drop of the vortex tube is calculated approximately as that in a pipe flow:

$$\Delta p_i = \xi_i \cdot (\rho_g/2) \cdot v_i^2,$$
$$1,800 = 15 \cdot (1.189/2) \cdot v_i^2$$

Hence, it follows a mean axial velocity in the vortex tube of v_i = 14.2 m/s and an inner tangential velocity of $u_i = 2 \times 14.2 = 28.4$ m/s.

From v_i and the gas flow rate $\dot{V}$ the vortex tube radius is obtained:

$$n = \frac{\ln(u_i/u_a)}{\ln(r_a/r_i)} = 0.63.$$

The average axial velocity in the vortex tube and the gas flow rate determine the radius of the vortex tube

$$r_i = \sqrt{\frac{\dot{V}}{\pi \cdot v_i}} = 150\,\text{mm}.$$

With $r_a/r_i = 3$ it follows the cyclone radius r_a = 450 mm and with $h_i/r_a = 4$ the height of the separation compartment h_i = 1,800 mm.

From $h \approx h_i + 0.25 h_i$ (cf. [15]) the total height of the cyclone is obtained:

h = 2,250 mm.

Then the cut size d^* can be calculated according to Eq. (38) to d^* = 3.7 µm.

If for the feed an RRSB particle size distribution of medium width is assumed, i.e., n_A = 1, and further a sharp separation at the cut size d^* is assumed (cf. Eq. (42)), then a total separation efficiency of about 96% can be predicted. This estimation has for the given geometrical ratios and for low solids loadings an accuracy of a few percentages. However, for higher loadings the proper calculation procedure is recommended. Reviews [3, 19, 31–35] and short articles [21, 24, 36] about cyclones for the precipitation of solid particles are given in the literature.

4 Symbols

A_e	cross-sectional area of inlet (m^2)
A_i	cross-sectional area of gas outlet pipe (m^2)
A_R	area offering resistance to friction in cyclone (m^2)
$A_{R,Sp}$	area offering resistance to friction in spiral inlet (m^2)
A_W	area of cyclone wall (m^2)
b	width of inlet (m)

$\mathrm{Ba}(d)$	Barth number (–)
c_e	particle velocity at cyclone entrance (m/s)
c_{in}	particle velocity in entrance zone inside cyclone (m/s)
d	particle diameter (m)
d^*	cut size for separation in the cyclone vortex (m)
d_e^*	cut size for separation at wall (m)
d_T^*	cut size for separation in boundary layer around vortex tube (m)
$d_{50,A}$	median particle size of feed (m)
$d_{50,Ai}$	median particle size of inner feed (m)
d'	characteristic particle diameter of RRSB distribution (m)
D	parameter in η_F curve for separation in inner vortex (–)
$\mathrm{Fr_i}$	Froude number of cyclone flow (–)
h	total height of cyclone (m)
h_e	height of inlet (m)
h_i	height of separation compartment (m)
h_T	length of vortex tube (m)
k	exponent for calculating limited load ratio (–)
k_s/r_a	roughness parameter (–)
K_{lim}	constant for calculating limited load ratio (–)
m	number of size fractions (–)
$\dot{M}_{feed}$	mass flow of feed (kg/s)
$\dot{M}_{coarse}$	mass flow of collected coarse fraction (kg/s)
n	exponent for calculating tangential velocity (–)
n_A	slope parameter for residue curve of feed (–)
n_{Ai}	slope parameter for residue curve of inner feed (–)
Δp_{tot}	total pressure drop (Pa)
Δp_e	pressure drop in separation compartment (Pa)
Δp_{inlet}	pressure drop in inlet (Pa)
Δp_i	pressure drop in gas outlet pipe (Pa)
r_a	outer radius cyclone (m)
r_D	radius of pressure plate (m)
r_e	inlet radius (m)
r_i	radius of gas outlet pipe (m)
$r_m = \sqrt{r_a r_i}$	average radius (m)
r_u	radius of deflection at pressure plate (m)
r_2	average radius of cone (m)
r_3	radius of lower cone opening (m)
$\overline{r}_z$	reference radius for centrifugal acceleration (m)
$R(d)$	fraction retained on screen with mesh size d (Residue) (–)
$\Delta R(d)$	fraction retained in size interval around d (–)
$R_A(d)$	residue of feed (–)
$R_{Ai}(d)$	residue of inner feed (–)
$R_F(d)$	residue of fines (–)
$\mathrm{Re_R}$	Reynolds number of cyclone (–)
$\mathrm{Re_S}$	Reynolds number for flow around particles (–)
s	distance between pressure plate and cyclone cover (m)
S	particle emission (kg/m^3)
t	guide vane spacing (m)
$ü$	overlap guide vanes (m)
u	tangential velocity (m/s)
u_a	tangential velocity at radius r_a (m/s)
u_e	tangential velocity at radius r_e (m/s)
u_i	tangential velocity at radius r_i (m/s)
u_2	tangential velocity a t radius r_2 (m/s)
$u_m = \sqrt{u_a \cdot u_i}$	average tangential velocity (m/s)
v	axial velocity (m/s)
v_{ax}	average axial velocity in cyclone (m/s)
v_e	gas velocity at cyclone entrance (m/s)
v_i	average axial velocity in vortex tube (m/s)
v_{in}	gas velocity in entrance zone of cyclone (m/s)
$\dot{V}$	gas flow rate (m^3/s)
$\dot{V}_{sec}$	gas flow rate of secondary flow (m^3/s)
$w_{S,50}$	settling velocity of particles with size d_e^* (m/s)
$\overline{z}_e$	mean centrifugal acceleration at reference radius $\overline{r}_z$ (m/s^2)
α	coefficient of contraction (–)
$\beta = b/r_a$	relative width of inlet (–)
δ	guide vane angle (°)
ε	helix angle (°)
ε_{Str}	void fraction of strands (–)
η_g	dynamic viscosity of gas (Pa s)
η_{tot}	total separation efficiency (–)
η_e	separation efficiency at wall (–)
η_i	separation efficiency in cyclone vortex (–)
$\eta_F(d)$	grade efficiency (–)
λ_0	coefficient of friction for unladen gas (–)
λ_s	coefficient of friction for gas carrying solids (–)
μ_e	load ratio at inlet (–)
μ_{lim}	limited load ratio (–)
ν_g	kinematic viscosity of gas (m^2/s)
ρ_g	gas density (kg/m^3)
ρ_s	particle density (kg/m^3)
$\Delta\rho = \rho_s - \rho_g$	difference in density (kg/m^3)

5 Bibliography

1. Rentschler W (1991) Abscheidung und Druckverlust des Gaszyklons in Abhängigkeit von der Staubbeladung. VDI Fortschritt-Berichte, VDI-Verlag, Düsseldorf, Reihe 3, Nr. 242
2. Muschelknautz E (1970) Auslegung von Zyklonabscheidern in der technischen Praxis. Staub-Reinhaltung der Luft 30(5):187–195
3. Muschelknautz E vt- Hochschulkurs II: Mechanische Verfahrenstechnik 1972/74. Attachment to journal "Verfahrenstechnik"
4. Barth W (1956) Berechnung und Auslegung von Zyklonabscheidern aufgrund neuerer Untersuchungen. Brennstoff- Wärme- Kraft 8(1):1–9
5. Muschelknautz E, Trefz M Secondary flow and short circuit flow at the dust discharge end of cyclone separators. Calculation and design of multicyclones. 1. European Symposium Separation of Particles from Gases, Nürnberg, 19 to 21.4.1989, Preprints pp 345–362
6. Muschelknautz E, Brunner K (1967) Untersuchungen an Zyklonen. Chem-Ing- Techn 39(9/10):531–538
7. Muschelknautz E, Krambrock W (1970) Aerodynamische Beiwerte des Zyklonabscheiders aufgrund neuer und verbesserter Messungen. Chem-Ing- Techn 42(5):247–255
8. Muschelknautz E (1980) Theorie der Fliehkraftabscheider mit besonderer Berücksichtigung hoher Temperaturen und Drücke. VDI- Berichte, Nr. 363, pp 49–60
9. Lorenz T (1994) Heißgasentstaubung mit Zyklonen. VDI Fortschritt Berichte, VDI-Verlag, Düsseldorf, Reihe 3, Nr. 366

10. Morweiser M (1998) Einfluß von Druck und Temperatur auf Trenngrad und Druckverlust von Aerozyklonen. Dissertation TU Braunschweig
11. Bohnet M (1999) Zyklonabscheider für hohe Temperaturen und Drücke. VDI-Berichte, Nr. 1511, pp 81–97
12. Mothes H, Löffler F (1984) Zur Berechnung der Partikelabscheidung in Zyklonen. Chem Eng Proc 18:323–331
13. Meißner P (1978) Zur turbulenten Drehsenkenströmung in Zyklonabscheidern. Dissertation TH- Karlsruhe
14. Greif V (1996) Reduzierung des Druckverlustes von Zyklonabscheidern durch Rückgewinnung der Drallenergie und Erweiterung der Grenzbeladungstheorie auf kleine und kleinste Staubbeladungen. VDI- Fortschr.- Ber., VDI-Verlag, Düsseldorf, Reihe 3, Nr. 470
15. Muschelknautz E, Trefz M Design and calculation of higher and highest loaded gas-cyclones. 2. World Congress Particle Technology. Kyoto, Japan, 19. to 22.9.1990, Preprints
16. Weißker W-S, Borho K, Müller P, Sachweh B, Fritz W (1999) Auswirkung von Strömungsgleichrichter und Auswirbelrohr auf den Druckverlust eines Aerozyklons. VDI-Berichte, Nr. 1511, pp 65–80
17. Muschelknautz U, Muschelknautz E (1996) Special design of inserts and short entrance ducts to recirculating cyclones. Proceedings of CFB- V-Conference, Beijing
18. Hugi E, Reh L (1999) Design of cyclones with high solid entrance loads for circulating fluidized bed reactors. VGB PowerTech 4/99
19. Grace JR, Avidan AA, Knowlton TM (1997) Chap. 6: Cyclones and other gas solids separators. Circulating fluidized beds. Blackie Acad. & Profess, Weinheim
20. Muschelknautz U, Muschelknautz E (1999) Separation efficiency of recirculating cyclones in circulating fluidized bed combustions. VGB PowerTech 4/99
21. Albring W (1978) Angewandte Strömungslehre, 5th edn. Akademie-Verlag, Berlin, pp 313–318
22. Trefz M (1992) Die verschiedenen Abscheidevorgänge im höher und hoch beladenen Gaszyklon unter besonderer Berücksichtigung der Sekundärströmung. VDI- Fortschr.- Ber., VDI- Verlag, Düsseldorf, Reihe 3, Nr. 295
23. Eck B (1981) Technische Strömungslehre. Springer-Verlag, Berlin/Heidelberg, 8th edn. Vol II, pp 148–157
24. Ebert F (1967) Berechnung rotationssymmetrischer, turbulenter Grenzschichten mit Sekundärströmung. Deutsche Versuchsanstalt für Luft- und Raumfahrt, Forschungsbericht, Freiburg, pp 56–67
25. Kirch R (1988) Der Einfluß der Turbulenz auf die Partikelbewegung im Gaszyklon. VDI Fortschritt- Berichte, VDI-Verlag, Düsseldorf, Reihe 3, Nr. 145
26. Hoffmann D (1998) Sekundärströmungen im Tauchrohrbereich eines Zyklons und ihr Einfluß auf die Partikelabscheidung. Dissertation Technische Universität Graz
27. Obermair S, Woisetschläger J, Staudinger G (2003) Investigation of the flow pattern in different dust outlet geometries of a gas cyclone by laser Doppler anemometry. Powder Technol 138:239–251
28. Schmidt P (1996) Zyklonabscheider bei geringer Beladung – Funktion und Auslegung. VDI-Berichte, Nr. 1290, pp 23–43
29. Krambrock W (1971) Die Berechnung des Zyklonabscheiders und praktische Gesichtspunkte zur Auslegung. Teil 1, Aufbereit.- Tech 7:391–401
30. Krambrock W (1971) Die Berechnung des Zyklonabscheiders und praktische Gesichtspunkte zur Auslegung. Teil 2, Aufbereit.- Tech 10:643–649
31. Muschelknautz E (1972) Die Berechnung von Zyklonabscheidern für Gase. Chem- Ing- Techn 44(1/2):63–71
32. Hoffmann AC, Stein LE (2002) Gas cyclones and swirl tubes. Springer-Verlag, Berlin/Heidelberg
33. Löffler F (1988) Staubabscheiden. Georg Thieme Verlag, Stuttgart/New York
34. Mothes H (1982) Bewegung und Abscheidung der Partikeln im Zyklon. Dissertation Universität Karlsruhe
35. Bohnet M (1996) Behandlung von Abluft und Abgasen. Springer-Verlag, Berlin/Heidelberg,
36. Schmidt P (1990) Ungewöhnliche Zyklone. Chem- Ing- Techn 62(7):536–543
37. Muschelknautz S, Klug F (1990) Propellersonde zur Betriebsmessung von Gas- Feststoff- Strömungen bei hohen Temperaturen. Tagungsbericht zur VGB- Konferenz “Wirbelschichtsysteme,” Essen

L4.1 Formation and Movement of Bubbles and Drops

Norbert Räbiger[1] · *Michael Schlüter*[2]
[1]Universität Bremen, Bremen, Germany
[2]Technische Universität Hamburg-Harburg, Hamburg, Germany

1 Introduction

The heat and mass transfer between two immiscible fluid phases with different density is essential for many processes. Thereby usually one phase is dispersed into the other continuous phase to achieve preferably large interfacial areas and long contact times. Some examples are the distillation and rectification in petrochemical industry, the extraction out of fermentation brothes in biotechnology or the absorption of oxygen out of air in biological waste water treatment. The calculation of size and terminal velocity of fluid particles is the basis for the design and optimization of reactors and processes.

2 Formation and Movement of Bubbles and Drops at Orifices

The calculation of the particle size in multiphase flows is based on the equilibrium of forces acting on the particle surface. These forces are dominated by the hydrodynamic conditions above the dispersing system like orifices, nozzles, perforated plates, ceramics, or membranes. Due to the hydrodynamic conditions at the dispersing system a zone close and in more distance to the formation point has to be distinguished for the formation of drops and bubbles. For coalescing systems and/or under turbulent conditions, the particle size is dominated by coalescence and re-dispersion and therefore dependent on the local energy dissipation. For practical application the average particle size decisive for the calculation of the specific interfacial surface area a is often characterized by the Sauter-Diameter d_{32}

$$d_{32} = \frac{\sum n_i \cdot d_{Pi}^3}{\sum n_i \cdot d_{Pi}^2}. \quad (1)$$

In non-coalescing systems or low turbulence the particle diameter obtained by the dispersing system keeps almost constant.

At low flow rates the particle diameter is dominated by the force equilibrium at the dispersing system (primary diameter) and for higher throughput by the fragmentation above the dispersing system (secondary diameter). Whereas, the formation of bubbles and drops is very similar for low fluid throughput a significant difference in dispersion processes occurs for higher gas/liquid velocities (dynamic formation, Fig. 1).

The reason for the different behavior of bubbles and drops at high throughput is the different inertia and incompressibility. At low throughput the formation frequency is small enough to enable an undisturbed detachment of the particles and launch in almost the quiescent liquid. This range with periodically detaching of single particles is usually called "bubbly regime" or "periodic drop formation". At dynamic formation of fluid particles different formation mechanisms for drops and bubbles occur: Despite of high formation frequencies bubbles still detach as single particles but disintegrate into several secondary bubbles due to the dynamic of detachment [1, 2]. The slower formation of drops causes a deformation and aggregation to a liquid jet above a critical approaching velocity. The deformation energy and force of reaction (surface tension) causes a wavy shape of the jet and a disintegration at the tip (jet disintegration). The residual secondary droplets show similar to secondary bubbles a much smaller diameter with a wide size distribution [3].

This makes clear that the equilibrium of forces will also be affected significantly by the formation process of neighboring particles. Therefore, the distance between the orifices as well as the prechamber volume is of great importance for widely-used perforated plates and membranes in industry.

The following recommendations for the calculation of particle formation diameters at orifices are classified into the above mentioned sections of **periodical formation of primary particle** and **formation of secondary particle**.

2.1 Periodical Formation of Primary Particles

The distinction between periodical formation of primary particles and secondary dispersion by jet gassing or jet disintegration is of great practical importance. A small particle size

VDI-GVC (ed.), *VDI Heat Atlas*, DOI 10.1007/978-3-540-77877-6_49,

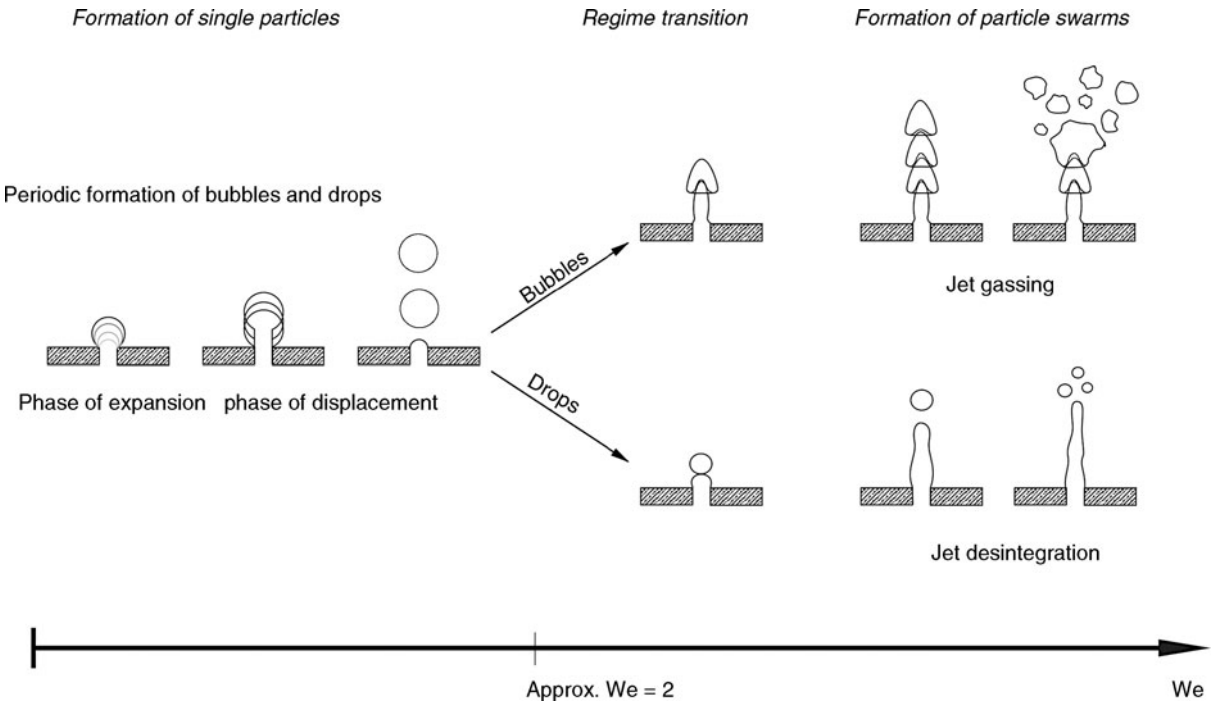

L4.1. Fig. 1. Schematic drawing of the particle formation at an orifice in dependency of the Weber number.

distribution can be reached in the regime of periodic particle formation whereas the Sauter-Diameter d_{32} increases with increasing throughput. The diameter of the generated particles is determined by the equilibrium of forces between buoyancy, surface tension, drag and inertia. Due to the balance of forces different models have to be taken into account (see Fig. 2).

For a very slow quasistatic formation process the formation of bubbles and drops follows the same mechanisms calculable with the analytical solution of the force balance by neglecting inertia. An overview is given by Chhabra [2], Räbiger [1], Blass [3], Tsuge [4] and Stölting [5].

For the periodic formation of fluid particles at nozzles and capillaries Voit [6] recommends a one step model that is applicable to Newtonian and to some extend also non-Newtonian liquids. Therefore, Voit simplifies the force balance by assuming a quasistatic equilibrium between buoyancy force

$$F_A = \frac{\pi}{6}\Delta\rho\, g\, d_p^3 \tag{2}$$

viscous force

$$F_\eta = 15\,\eta_K \frac{V_D}{d_P} \tag{3}$$

inertia force

$$F_T = 1.3\,\rho_K \left(\frac{V_D}{d_P}\right)^2 \tag{4}$$

and the force by surface tension

$$F_\sigma = \pi\, d_N\, \sigma \tag{5}$$

due to

$$d_P = \left[\left(\frac{F_\eta + F_T + F_\sigma}{\Delta\rho\, g}\right)\frac{6}{\pi}\right]^{1/3}. \tag{6}$$

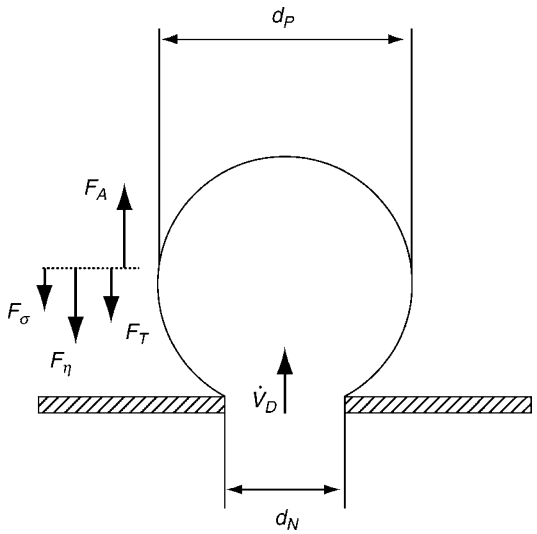

L4.1. Fig. 2. Equilibrium of forces for quasistatic formation of a particle.

For non-Newtonian liquids the effective viscosity is calculable by

$$\eta_{eff} = K^{\frac{1}{n}}\left[\frac{1}{6}\Delta\rho\, g\, d_P\right]^{\frac{n-1}{n}} \tag{7}$$

with the consistence factor K and the Ostwald de Waele index n for non-Newtonian behavior. K and n can be calculated by fitting the flow curve measured with a drag-torque viscometer to the power law

$$\eta_{eff} = K \cdot \dot{\gamma}^{n-1} \tag{8}$$

valid for most polysaccharide solutions, activated sludge, and fermentation brothes [7–10]. This method is applicable

for periodical formation of bubbles in Newtonian and non-Newtonian liquids and has been validated by Voit [6] for Carboxymethylcellulose (CMC: $K \leq 32$ mPas, $n \geq 0.4$), Polyacrylamid (PAA: $K \leq 7.1$ mPas, $n \geq 0.3$), Xanthan Gum (E 415: $K \leq 6.3$ mPas, $n \geq 0.2$), and water-based glucose solutions ($\eta_K \leq 5$ *Pas*) with a surface tension of $0.05\,\mathrm{N/m} \leq \sigma \leq 0.07\,\mathrm{N/m}$ a liquid density of $\rho_K = 1000\,\mathrm{kg/m^3}$, and a gas density of $\rho_D = 1.2\,\mathrm{kg/m^3}$. The orifice diameter was varied between $0.3\,\mathrm{mm} \leq d_N \leq 2.4\,\mathrm{mm}$. In accordance with Voit the deviation between calculated and measured diameter of primary bubbles is less than 10% and therefore in the order of measuring accuracy. The applicability of the model for periodical formation of droplets is due to Voit and also possible with an accuracy between experimental and calculated data in the range of the measuring accuracy [6].

Whereas the calculation of particle diameter according to equation 6 is quite complex due to the necessary iteration; the graphical solution given by Mersmann (1977) [11] gives a convenient possibility to estimate the primary particle diameter. Mersmann uses a normalized diagram with the simplified equilibrium of forces between viscous and buoyancy force ($d_{P\eta}$ according to eq. 6) as well as inertia and buoyancy force (d_{PT} according to eq. 6)

$$d_{P\eta} = C \cdot \left[\frac{K}{\Delta\rho g}\dot{V}_D^n\right]^{\frac{1}{3n+1}} \tag{9}$$

and

$$d_{PT} = 1.2 \cdot \left[\frac{\rho_K}{\Delta\rho}\frac{\dot{V}_D^2}{g}\right]^{0.2} \tag{10}$$

related to the smallest possible particle size, calculable with the force balance of surface tension and buoyancy according to

$$d_{P\sigma} = \sqrt[3]{\frac{6 d_N \sigma}{\Delta\rho g}}. \tag{11}$$

The constant C depends on the flowindex n calculabe by

$$C = 2.32^{\frac{4n}{3n+1}} \cdot \left(\frac{1}{6}\right)^{\frac{n-1}{3n+1}} \tag{12}$$

in accordance to Voit [8]. For the graphical analysis of the particle size the log–log scale diagram given by Mersmann [11] has been established (Fig. 3).

According to Mersmann [12] the diagrams is also valid for extreme conditions like bubbles and drops in highly viscous liquids ($\eta_K = 3$ Pas) and liquid metals ($\sigma = 0.5\,\mathrm{Nm^{-1}}$) as well as drops of liquid metals in vacuum or supercritical gases. As restriction the dynamic viscosity of the dispersed phase is limited to $\eta_D < 50$ mPas.

2.2 Formation of Secondary Bubbles and Drops by Jet Bubbling and Jet Breakup at Single Orifices and Perforated Plates

For industrial application it is necessary to reach high throughputs of the dispersed phase and small particle sizes to get huge specific interfacial areas (jet bubbling, jet breakup). In this case, the inertia forces a secondary fragmentation of the primary particles above the orifice. The range of secondary particle formation is often characterized by the dimensionless Weber- or Froude

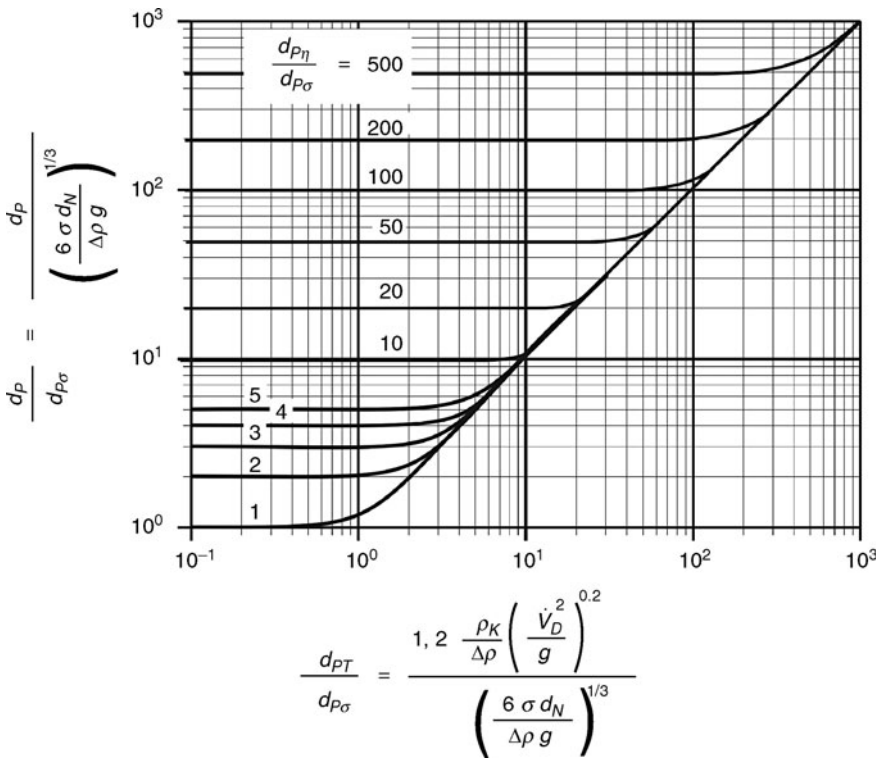

L4.1. Fig. 3. Normalized diagram to determine the primary particle diameter in Newton and Shear-Thinning liquids [11].

number. For small diameters of the orifice the buoyancy forces are neglectable and the surface tension dominates and vice versa for large orifices. Depending on the orifice diameter the dimensionless Weber- and modified Froude number

$$We_N = \frac{{w_N}^2 \cdot d_N \cdot \rho_D}{\sigma} \geq 2 \text{ for } d_N \sqrt{\frac{\rho_D \cdot g}{\sigma}} \left(\frac{\Delta\rho}{\rho_D}\right)^{5/8} \leq 2.32 \tag{13}$$

and

$$Fr_{N,\Delta\rho} = \frac{{w_N}^2}{d_N \cdot g} \left(\frac{\rho_D}{\Delta\rho}\right)^{5/4} \geq 0.37 \text{ for } d_N \sqrt{\frac{\rho_D \cdot g}{\sigma}} \left(\frac{\Delta\rho}{\rho_D}\right)^{5/8} > 2.32 \tag{14}$$

can be used as criteria for the formation of secondary particles [1, 13]. In this case the influences of an overlaid fluid flow w_K, the viscosity η_K, and the contact angle γ has been neglected. An overlaid fluid flow as well as an increased viscosity leads to an increased critical Weber number [1, 14, 15]. The contact angle γ depends on surface tension, wettability, and the geometry of the orifice [16, 17]. The critical Weber- and Froude numbers are important characteristic numbers for the performance of perforated plates, because if the throughput falls below this critical value a nonuniform fluid distribution occurs for gas as well as for liquid dispersion with the unwanted effect of a "raining" through the plate. For providing an uniform fluid distribution for every single orifice the critical Weber number $We_N \geq 2$ and Froude number $Fr_{N,\Delta\rho} \geq 0.37$ have to be reached. Although the upper limit for secondary particle formation can be described for bubbles and drops with the same laws the mechanism of secondary particle formation is totally different due to the deviation in density differences. This will be explained in the following section.

Bubble Formation in the Jet Bubbling Regime

At high gas throughput the particles are formed at the orifice that rapidly, that they follow each other directly and apparently forming a "gas jet". With high speed imaging Räbiger [18] was first able to show that single primary bubbles were created at the orifice even at very high gas throughputs. The diameter of this primary bubbles increases with increasing throughput (see Fig. 4, [1]). For higher critical Weber- and Froude numbers (see eq. 13 and eq. 14) the momentum of the liquid accelerated by the breaking bubble-tail leads to a fragmentation of primary bubbles above the orifice into multiple smaller secondary bubbles (see Fig. 4, [2]).

The primary as well as secondary bubble diameter increases with increasing gas throughput whereas the equation for calculating the primary bubble size (eq. 2.1) are still valid. In jet bubbling regimes the secondary bubble diameter at single orifices is calculable according to Brauer [19] by

$$d_{B,Sek} = d_N \cdot 0.72 \cdot {Fr_N}^{1/6}; \qquad \left(\frac{{We_{N,K}}^2}{Fr_N}\right)_{crit} \geq 675 \tag{15}$$

where Brauer distinguishes the transition between bubbling regime and jet bubbling regime with the critical relation between Weber number $We_{N,K}$ and Froude number Fr_N due to

$$\left(\frac{{We_{N,K}}^2}{Fr_N}\right)_{crit} = 675. \tag{16}$$

The Weber number

$$We_{N,K} = \frac{{w_N}^2 \cdot d_N \cdot \rho_K}{\sigma} \tag{17}$$

is calculated with the density ρ_K of the continuous phase.

When perforated plates are used for technical application the interactive forces between bubbles formed side-by-side induces a strong shear field above the plate. For approximately $We_N > 6$ this shear stress leads to a secondary bubble size that is independent of the Weber number but depends on the hole pitch t [14]. According to Klug, the liquid displaced by the rising bubbles flows back between the bubble chains and induces an increasing shear stress with decreasing distance between the chains. Therefore, the secondary bubble size of air bubbles formed in water decreases with decreasing hole pitch t. For higher viscosities the smaller hole pitch promotes coalescence

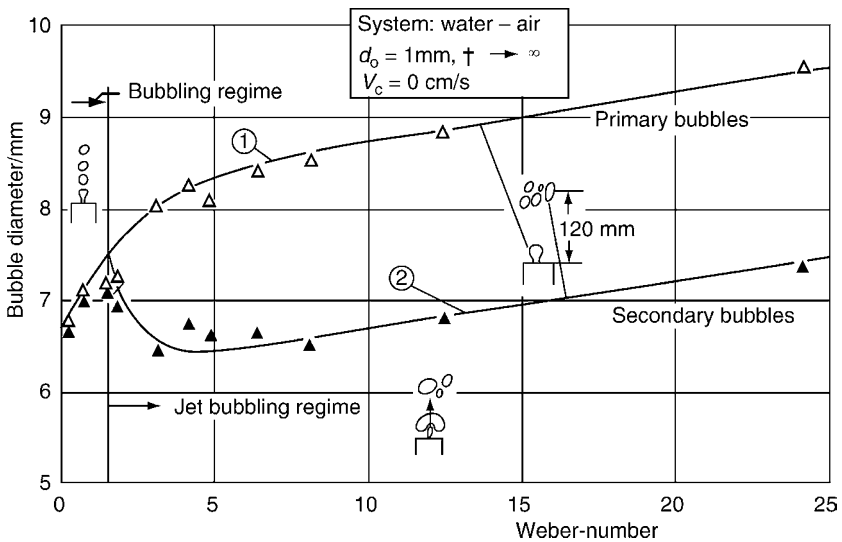

L4.1. Fig. 4. Diameter of primary and secondary bubbles at a single orifice [14].

and larger secondary bubble sizes [14]. Under the assumption of force balance between surface tension and shear stress

$$\frac{12}{c_{w,K}}\frac{\sigma}{\rho_K \cdot {w_R}^2 \cdot d_B} = \frac{12}{c_{W,K}}\frac{\tau_W}{\rho_K \cdot {w_r}^2} + 1 \qquad (18)$$

Klug is able to calculate the secondary bubble size for perforated plates. As Klug investigated also the influence of an overlaid liquid velocity, he used the relative velocity w_r between gas- and liquid phase $w_r = w_G - w_F$ as the reference parameter. For the determination of the shear stress Klug assumes that the bubble chains are raising in separated virtual channels with the distance of the hole pitch. Assuming wall attachment of the liquid at the channel walls the shear stress is calculable due to

$$\tau = C_{W,R} \cdot \rho_K \cdot \frac{{w_r}^2}{8} \qquad (19)$$

with the drag coefficient $C_{W,R}$ the laminar flow regime

$$C_{W,R} = \frac{64}{Re_R} \qquad (20)$$

as well as the turbulent flow regime

$$C_{W,R} = \frac{0.3164}{{Re_R}^{0}.25} \qquad (21)$$

is predictable. The Reynolds number inside the virtual channels is given by

$$Re_R = \frac{w_r \cdot d_h \cdot \rho_K}{\eta_K} \qquad (22)$$

with the hydraulic diameter of the virtual channels due to

$$d_h = \frac{\sqrt[3]{3} \cdot t^2 - \frac{\pi}{2} \cdot {d_B}^2}{3 \cdot (t - d_B) + \frac{\pi}{2} \cdot d_B}. \qquad (23)$$

For the drag coefficient of a sphere the equation according to Brauer [19]

$$C_{W,K} = \frac{24}{Re_D} + \frac{4}{{Re_D}^{0.5}} + 0.4 \qquad (24)$$

is applicable. Because the calculation of equation 18 is only possible by iteration, Fig. 5 and Fig. 6 gives a more convenient possibility to estimate the bubble diameter graphically.

The criteria for the flow regime is given by the coalescence of the primary bubbles directly above the orifice. According to Mersmann heterogeneous flow at perforated plates occurs if the hole pitch t becomes

$$t \leq 2.7 \cdot d_N \left(\frac{{w_N}^2}{g\, d_N}\right)^{1/6}. \qquad (25)$$

Additional to the hole pitch t the volume of the prechamber is important because at low gas throughput the pressure inside the prechamber is constant and defines the bubble size [7]. Whereas, for small gas throughput the particle size increases with increasing prechamber volume, particulary Tadaki and Maeda had shown with several experimental results that at a critical dimensionless gas throughput of $We_{N,K} \cdot {Fr_N}^{0.5} \geq 10$ the bubble size is independent of the prechamber volume [20].

Due to the wide distribution of particle diameters in the jet bubbling regime very different relative velocities occur that

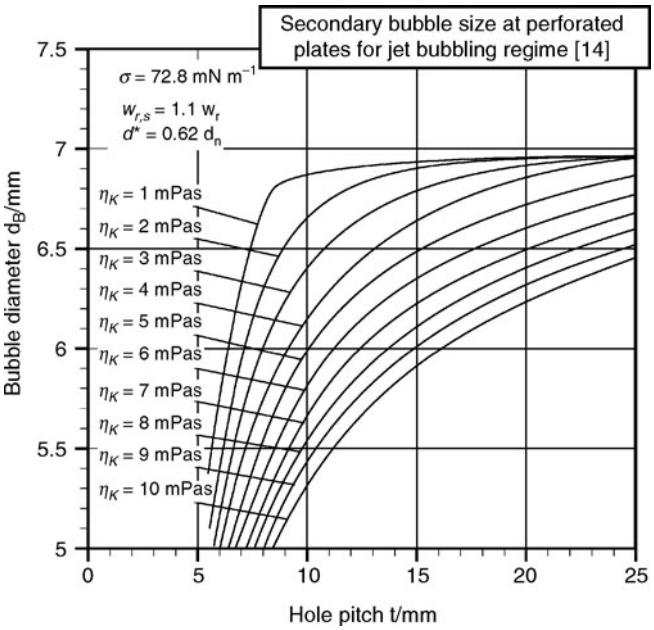

L4.1. Fig. 5. Size of secondary bubbles for perforated plates at high gas throughput ($We > 5$) for liquids with different viscosity.

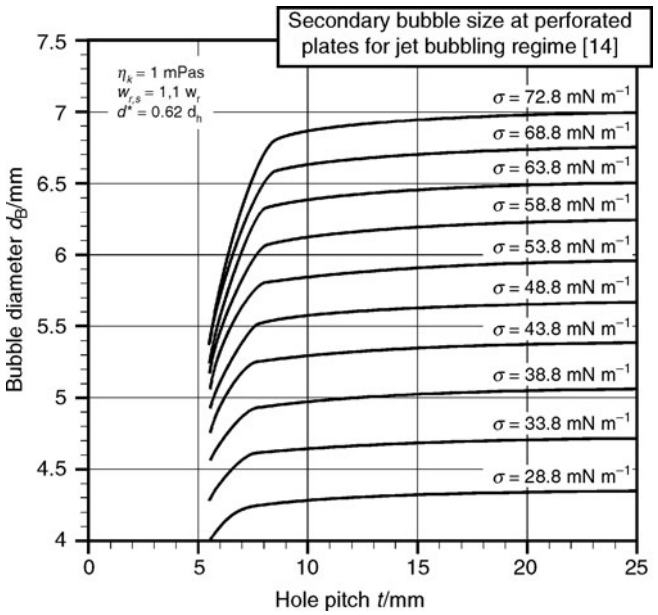

L4.1. Fig. 6. Size of secondary bubbles for perforated plates at high gastroughtput ($We > 5$) for liquids with different surface tension.

causes strong interactions of the particles. For coalescing systems this causes coalescence and redispersion during the rising of the bubbles with a wide bubble size distribution above the perforated plate. The diameter of a gas bubble that is just still stable without breakup is given by the force balance between buoyancy and surface tension according to Mersmann [11]

$$d_{P,max} = 3\sqrt{\frac{\sigma}{\Delta\rho \cdot g}}. \qquad (26)$$

For liquids with low viscosity up to $\eta_K = 3$ mPas the Sauter-diameter can be estimated roughly by

$$d_{S32} = 0.6 \cdot d_{P,max}. \tag{27}$$

For a more precise description of an apparatus operating in jet bubbling regime population balances have been developed that uses different classes of bubble sizes taking coalescence, redispersion, and convection into account. For a more detailed description of population balances the readers are referred to the work of Lehr [21].

Drop Formation by Jet Desintegration

Because drops detach slower from orifices than bubbles due to the smaller density deviation at higher throughputs, multiple drops merge to a single liquid jet. Thereby the periodically changing force balance during the particle formation process leads to a dynamic fluctuation of the jet shape and an instability at the tip of the jet where the jet disintegrates. The length of the jet increases with increasing throughput to a maximum until it decreases again due to the increasing forces of inertia. Whereas, for a liquid throughput too low for the maximum jet length all droplets show an uniform size for higher throughput with decreasing jet length the drop size distribution gets wider [22]. The drop size decreases with increasing length of the jet until the jet reaches its maximum length. This interesting case for industrial application with maximum specific surface area occurs for a liquid throughput of the perforated plate that is twice the critical liquid velocity w_{crit} according to equation 13 and 14

$$w_N = 2 \cdot w_{crit} = 2 \cdot \sqrt{\frac{2 \cdot \sigma}{\rho_D \cdot d_N}} \tag{28}$$

The minimum drop size for that velocity is given by Ruff [13] due to

$$d_{P,min} = d_N \left(2.3 - 0.73 \sqrt{\frac{\Delta\rho\, g\, {d_N}^2}{\sigma}} \right) \quad \text{for} \quad \sqrt{\frac{\Delta\rho\, g\, {d_N}^2}{\sigma}} < 2.2 \tag{29}$$

respectively.

$$d_{P,min} = d_N \left(\frac{2.3}{1 + \sqrt{\frac{\Delta\rho\, g\, {d_N}^2}{\sigma}}} \right) \quad \text{for} \quad \sqrt{\frac{\Delta\rho\, g\, {d_N}^2}{\sigma}} \geq 2.2. \tag{30}$$

For any liquid velocity w_N the Sauter-diameter d_{S32} is calculable by Ruff [13] with the empirical correlation

$$d_{S32} = d_{P,min} \cdot \left(2.319 - 1.669 \cdot \frac{w_N}{w_{crit}} + 0.709 \cdot \left(\frac{w_N}{w_{crit}} \right)^2 - 0.114 \cdot \left(\frac{w_N}{w_{crit}} \right)^3 + 0.00629 \cdot \left(\frac{w_N}{w_{crit}} \right)^4 \right) \tag{31}$$

whereas $d_{P,min}$ is given by the minimal particle diameter according to equation 29 and 30.

In technical processes usually the dispersion of liquids takes place with perforated plates in the jet disintegration regime, where the coalescence and redispersion should be calculable according to Mersmann with the Sauter-diameter d_{S32} due to equation 27. A higher reliability is only reachable by calculating a representative particle diameter for the apparatus with population models.

Example 1:

As solvent for the extraction of penicillin butyl acetate has to be fed into the fermentation broth via 50 glass capillaries with an inner diameter of $d_N = 2$ *mm* each. Therefore, a high throughput is necessary but the shear stress should be as low as possible to prevent any damage to the microorganism. What is the maximum throughput and what average drop diameter occurs?

Thermophysical Properties:

Fermentation broth (Penicillium chrysogenum) [7]: $\rho_K = 1000\ \mathrm{kgm^{-3}}$; $n = 0.29$; $K = 1.85$ Pas Solvent (Butylacetat) [22]: $\rho_D = 880\ \mathrm{kgm^3}$; $\eta_D = 0.74$ mPas; $\sigma = 0.0135\ \mathrm{Nm^{-1}}$

Answer:

To assure a defined but low shear stress the dispersion should take place in the regime of periodic drop formation. From the limiting load at the beginning jet decomposition $We_N = 2$ the maximum throughput of a single capillary is calculable by

$$v_{crit} = \sqrt{\frac{2 \cdot \sigma}{d_N \cdot \rho_D}} = 0.124\,\mathrm{ms^{-1}}. \tag{32}$$

The volumetric flow rate is given by the orifice diameter of a capillary due to

$$\dot{V}_{D,EK} = 3.89 \cdot 10^{-7}\mathrm{m^3 s^{-1}} \tag{33}$$

and the maximum acceptable volumetric flow rate inside the column is given by

$$\dot{V}_D = 70\ \mathrm{Lh^{-1}}. \tag{34}$$

The particle diameter at periodical drop formation is calculable according to Mersmann by eq. 6. The parameter for the graphical solution is given by eq. 9–11 due to

$$c = 3.33, \tag{35}$$

$$\frac{d_{P\eta}}{d_{P\sigma}} = 2.07 \quad \text{and} \tag{36}$$

$$\frac{d_{PT}}{d_{P\sigma}} = 0.61. \tag{37}$$

With this data the dimensionless diameter of

$$\frac{d_P}{d_{p\sigma}} \approx 2 \tag{38}$$

is metering from Fig. 3 which gives an particle diameter of

$$d_P = 10.32\ \mathrm{mm}. \tag{39}$$

The iterative calculation of the force balance due to eq. 6 gives a particle diameter of $d_P = 10.86$ mm.

Example 2:

For the biological treatment of process water an activated sludge tank is aerated through a static disperser (perforated plate with 1000 orifices, diameter of orifice $d_N = 0.7$ mm, hole pitch $t = 8$ mm) with pressurized air. The viscosity of the broth is rising with cell growth up to total solids $TS = 5g/L$. The coalescence of

bubbles in process water is inhibited. How does the bubble diameter change for a constant gas flow rate of $\dot{V}_D = 32\,\mathrm{m/h}$ if the static pressure is negligible? How does the secondary bubble size in process water without biomass change, if the surface tension is changing due to surface active agents from $\sigma = 72.8\,\mathrm{mN/m}$ to $\sigma = 40\,\mathrm{mN/m}$?

Thermophysical Properties:

Process water without biomass [9]:

$$\eta_{C1} = 1\,\mathrm{mPas}; \rho_{C1} = 998\,\mathrm{kg/m^3};$$
$$\rho_{D1} = 1\,\mathrm{kg/m^3}; \sigma_1 = 0.0728\,\mathrm{N/m}$$

Process water with biomass:

$$\eta_{C2} = 2\,\mathrm{mPas}; \rho_{C2} = 1003\,\mathrm{kg/m^3};$$
$$\rho_{D2} = 1\,\mathrm{kg/m^3}; \sigma_2 = 0.0728\,\mathrm{N/m}$$

Answer:

Because the velocity in each orifice is $w_N = 23\,\mathrm{m/s}$ and

$$d_N \sqrt{\frac{\rho_D \cdot g}{\sigma}} \left(\frac{\Delta\rho}{\rho_D}\right)^{5/8} = 0.61 \leq 2.32 \quad \text{and} \quad We_N = 5.1 \quad (40)$$

the perforated plate is operating in jet bubbling regime. According to Klug [14], the secondary bubble diameter in process water without biomass for a hole pitch of $t = 8$ mm can be estimated from Fig. 5 to $d_B \approx 6.7$ mm. Because of cell growth and increasing viscosity the bubble diameter is decreasing down to $d_B = 6.3$ mm. Figure 6 shows that a reduced surface tension causes for the hole pitch of $t = 8$ mm and $\sigma = 40$ mN/m a secondary bubble size of approximately $d_B = 5.1$ mm in comparison to $d_B = 6.7$ mm in process water without surface active agents added.

3 Movement of Bubbles and Drops

After the formation process of single particle at orifices the buoyancy or weight force leads to an acceleration of each particle until force balance between all forces acting on the particle is reached. Whereas the equations for calculating the force balance acting on solid particles are also applicable for fluid particles, the flexible, deformable surface induces some additional effects that have to be taken into account for moving particles. Because of the complex interaction between flow field and particle form, due to compressibility and density difference of the dispersed phase the drag coefficient is not predictable with a general law. In dependency of the particle diameter the terminal velocity of particles and drops may be either monotonic increasing or increasing with a distinct maximum.

This diversity of the dependency between drag coefficient and Reynolds number for single particles is shown in Fig. 7. Because the dependence is influenced by the ratio of viscosities and densities of both phases as well as the mobility of the interface, usually the calculation of the drag coefficient is carried out with empirical correlation for separated intervals of the Reynolds number. Whereas fluid particles behave like solid particles within the first Reynolds number interval (see Fig. 7, A), for particles with moving interface the internal circulation leads to a lower drag coefficient (Fig. 7, B). The viscosity of the dispersed phase determines the momentum transfer inside the particle and causes the difference between drops and bubbles. In this Reynolds number interval, the mobility of the interface is strongly effected by surface active agents as well as interfacial mass fluxes (due to Marangoni convection)

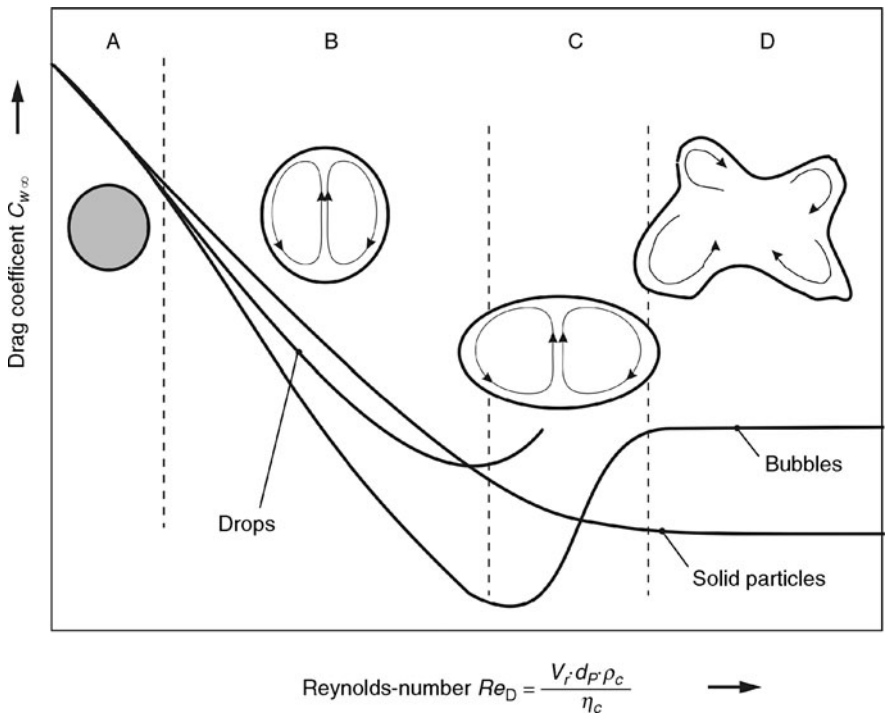

L4.1. Fig. 7. Schematic drawing of the drag coefficient in dependency of the Reynolds number for solid particles, drops and bubbles according to [23].

which may cause the same behavior for bubbles than that for drops and rigid spheres. The third interval (Fig. 7, C) is dominated by deformation and oscillation of drops and bubbles that causes a higher drag coefficient than for rigid spheres. This is caused mainly by the higher pressure drop of nonspherical shapes visible by the characteristic vortices in particle wakes. Dependening on the Reynolds number ring-vortices or periodically forming and detaching vortices occur that force the particles on zigzag, helical or irregular rising pathes. The change in the moving direction causes a reduction of the perpendicular part of the rising velocity, which leads to an increasing drag coefficient. Recent publication shows that the wake shedding is not only eminent for the ascending trajectory [24, 26], but also for mass transfer performance and selectivity of chemical reactions due to the influence of bubble wakes on the mixing efficiency [25–27]. Whereas drops in the Reynolds-interval (C) above a critical diameter disintegrate into several fragments, bubbles change first into an irregular shape and with further increase in the Reynolds number into a Taylor-Bubble shape (Fig. 7, C). In this regime the drag coefficient keeps almost constant at $C_D = 2.61$. Mersmann developed an overall description for a rough estimation of the terminal velocity of single bubbles and drops independent of the Reynolds-interval and applicable for Newtonian and partly for non-Newtonian liquids (Fig. 8).

The notation of the ordinate with the dimensionless velocity

$$v_r^* = v_r \cdot \sqrt[3]{\frac{\rho_c^2}{\eta_c \cdot g \cdot \Delta\rho}} = \sqrt[3]{Re_D \cdot Fr} = \sqrt[3]{Lj} \qquad (41)$$

in dependency of the dimensionless particle diameter

$$d_P^* = d_P \cdot \sqrt[3]{\frac{\rho_c \cdot g \cdot \Delta\rho}{\eta_c^2}} = \sqrt[3]{Ar} \qquad (42)$$

with the logarithm of the modified liquid-number (reciprocal to Morton-number)

$$log\left(K_{F,\Delta\rho}\right) = log\left(\frac{\rho_c \cdot \sigma^3}{g \cdot \eta_c^4}\right)\frac{\rho_c}{\Delta\rho} \qquad (43)$$

allows the convenient estimation of the terminal velocity of single drops and bubbles and is easily transferable to other usual forms of diagrams (compare for e.g., [28]). For a more detailed estimation it has to be emphasized that the transition regimes e.g., between drop oscillation and bubble deformation are depicted only very roughly in Fig. 8. Furthermore, there is no possibility to take into account separately the different influences of e.g., surface active agents on the particle movement in the different regimes. Because the consideration of the local phenomena acting on single particles becomes more important concerning the precise calculation and design in process engineering, the calculation of the terminal velocity for drops and particles will be discussed separately in more detail in the following Sect. 3.1.

3.1 Movement of Single Drops

Due to the above mentioned phenomenology of particle behavior at free ascending drops it is reasonable to describe the drop movement in the three regimes

- rigid interface
- internal circulation
- oscillation

more precisely. As useful dimensional number to describe this circumstances the Archimedes number

$$Ar = \frac{d_P^3 \cdot g \cdot \rho_c \cdot \Delta\rho}{\eta_c^2} \qquad (44)$$

has been established.

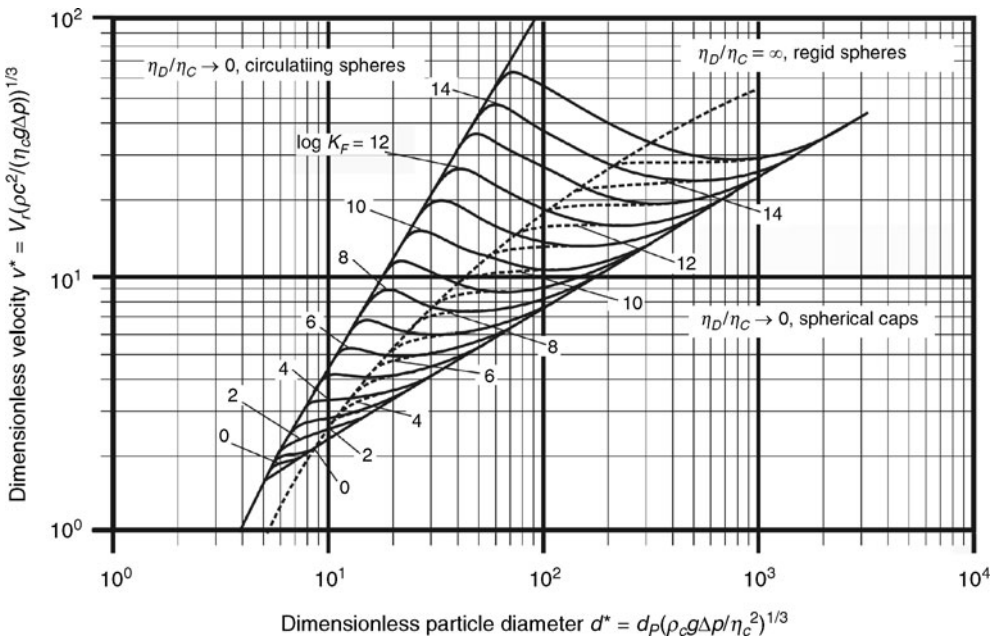

L4.1. Fig. 8. Dimensionless local relative velocity of bubbles and drops in dependency of the dimensionless particle diameter [8, 11].

Section A: $Ar \leq 1.83 \cdot K_{F,\Delta\rho}^{0.275}$

In this regime, valid for very small droplets, the interface of the particles is assumed to be rigid. Therefore, the laws for rigid spheres are applicable with the drag coefficient $C_{w\infty} = 24/Re_P$ to

$$Re_P = \frac{1}{18} \cdot Ar. \tag{45}$$

Section B: $1.83 \cdot K_{F,\Delta\rho}^{0.275} < Ar \leq 372.9 \cdot K_{F,\Delta\rho}^{0.275}$

Above a distinct drop size and therefore drop velocity, the increasing shear stress at the drop interface induces an internal circulation of the drop. Within this regime dominated by the friction force, the drag coefficient decreases in comparison to the rigid sphere down to $C_{w\infty} = 16/Re_P$ and is calculable with the Reynolds number due to the empirical correlation

$$Re_P = K_{F,\Delta\rho}^{0.15}\left(Ar^{0.523} \cdot K_{F,\Delta\rho}^{-0.1435} - 0.75\right). \tag{46}$$

according to Blass [29].

Section C: $Ar > 372.9 \cdot K_{F,\Delta\rho}^{0.275}$

With further increasing drop diameter, the flow around the drops forces a deformation and oscillation that leads to an increased drag coefficient. The relative velocity and Reynolds number increase slightly in this regime with increasing drop diameter until they decrease. As empirical correlation, Blass recommends the equation

$$Re_P = K_{F,\Delta\rho}^{0.15}\left(4.18 \cdot Ar^{0.281} \cdot K_{F,\Delta\rho}^{-0.0733} - 0.75\right). \tag{47}$$

for the calculation of the Reynolds number [29].

The upper limit in this regime of drop movement is determined by the stability of the particles, because from a distinct particle diameter the forces acting on the droplet causes the defragmentation into small droplets. According to Mersmann the probability for a sufficient stability of fluid particles decreases if

$$\frac{We_D}{Fr}\frac{\Delta\rho}{\rho_D} > 9. \tag{48}$$

As the drag coefficient shows a minimum at the beginning of drop oscillation, the calculation of the optimum particle diameter is eminent concerning the design of apparatus, reactors, and plants (e.g. for the calculation of the flooding point of a liquid–liquid column). This particle diameter with a maximum relative velocity is calculable with the intersection between the curves of equation 46 and 47 to

$$d_{P(v_{max})} = 7.186 \cdot \left(\frac{\eta_c^2}{\rho_c \cdot \Delta\rho \cdot g}\right)^{1/3} \cdot K_{F,\Delta\rho}^{0.0917} \tag{49}$$

The above mentioned equations 46 to 49 have been developed by Blass [29] for the design of extraction columns and are applicable for a viscosity of the continuous phase of $\eta_c < 5 \cdot 10^{-3}$Pas [29, 30].

For liquids with viscosities of $\eta_c > 5 \cdot 10^{-3} Pas$ and/or non-Newtonian rheological properties the empirical equation of Mersmann [31]

$$v_r = \frac{v_{r,d_{P,max}}}{1 + 15 \cdot \frac{2/3 + \eta_D/\eta_c}{1 + \eta_D/\eta_c}} \cdot v_{r,d_{P,max}} \cdot \sqrt[3]{\frac{\rho_c^2}{\eta_c \cdot \Delta\rho \cdot g}}\left(\frac{1}{d_P^*}\right)^{1.75} \tag{50}$$

with the velocity of the largest stable droplet of

$$w_{r,d_{P,max}} = 1.55 \cdot \sqrt[4]{\frac{\sigma \cdot \Delta\rho \cdot g}{\rho_c^2}} \quad \text{and} \quad d_P^* \equiv d_P \cdot \sqrt[3]{\frac{\rho_c \cdot \Delta\rho \cdot g}{\eta_c^2}} \tag{51}$$

gives an adequate solution [8, 12].

The equation by Mersmann is in good agreement with experimental data [32] because the drop oscillation that would not be satisfactorily predictable with equation 51 is damped down anyway to $\eta_c > 7 \cdot 10^{-3}$Pas [18]. Further description of the particle behavior in higher viscous and non-Newtonian liquids is given in [2]. Basically, all empirical equations have been derived out of measurements with more or less pure systems. Therefore, the equations are not taking into account specific impurities of the continuous phase such as surface active agents that accumulate at the interface, prevent surface agitation, and increase the drag coefficient. Furthermore, the nonequilibrium of forces may induce interfacial convection that can reach an eruptive character (Marangoni convection), and therefore, influences the drag coefficient of drops strongly [33].

Example 1:

In a spray column pentachlorethane is used as extracting solvent in water and dispersed with a perforated plate (orifices diameter d_N = 1.5 mm). What drop diameter is necessary to reach a maximum relative velocity between drops and surrounding liquid and how large is the reachable relative velocity with this drop size? Thermophysical Properties for Pentachlorethane/Water:

$$\eta_c = 0.95 \text{ mPas}; \rho_c = 998 \text{ kg/m}^3; \eta_D = 2.03 \text{ mPas};$$
$$\rho_D = 1674 \text{ kg/m}^3; \sigma = 0.0424 \text{ N/m}$$

Answer:

The drag coefficient of a single drop reaches a minimum with onset of oscillation. The associated drop diameter is calculable with equation 49 to

$$d_{P(w_{max})} = 7.186 \cdot \left(\frac{\eta_c^2}{\rho_c \cdot \Delta\rho \cdot g}\right)^{1/3} \cdot K_{F,\Delta\rho}^{0.0917} \tag{52}$$

with

$$K_{F,\Delta\rho} = \frac{\rho_c \cdot \sigma_c^3}{g \cdot \eta_c^4}\frac{\rho_c}{\Delta\rho} \tag{53}$$

follows $K_{F,\Delta\rho} = 1.41 \cdot 10^{10}$ and thus $d_{P(max)} = 3.15$ mm. This value is in good agreement with experimental data [29]. For the determination of the relative velocity the graphical or calculable solution is applicable.

a) Graphical solution:

For a drop diameter of d_P = 3.15 mm the dimensionless drop diameter d_P^* is calculable by using equation 42 due to

$$d_P^* = d_P \cdot \sqrt[3]{\frac{\rho_c \cdot g \cdot \Delta\rho}{\eta_c^2}} = 61.2 \tag{54}$$

as well as equation 43

$$log\left(K_{F,\Delta\rho}\right) = log\left(\frac{\rho_c \cdot \sigma^3}{g \cdot \eta_c^4}\frac{\rho_c}{\Delta\rho}\right) = 10.1. \tag{55}$$

Figure 8 shows a dimensionless velocity of $v^* \approx 11$ that enables the calculation of the terminal velocity of a pentachlorethane drop with equation 41 to

$$v_r = v_r^* \left(\frac{\rho^2}{\eta_c \cdot g \cdot \Delta\rho} \right)^{-1/3} = 0.203 \; ms^{-1}. \tag{56}$$

b) Calculated solution:
With the Archimedes number

$$Ar = \frac{g \cdot \Delta\rho \cdot d_P^3 \cdot \rho_c}{\eta_c^2} = 2.29 \cdot 10^5 \tag{57}$$

and the assumption

$$1.83 \cdot K_{F,\Delta\rho}^{0.275} < 2.29 \cdot 10^5 < 372.9 \cdot K_{F,\Delta\rho}^{0.275} \tag{58}$$

it becomes clear that the drop of pentachlorethane with a diameter of $d_P = 3.15 \; mm$ is just rising with internal circulation and without oscillation. Therefore, equation 46 is applicable due to

$$Re_P = K_{F,\Delta\rho}^{0.15} \left(Ar^{0.523} \cdot K_{F,\Delta\rho}^{-0.1435} - 0.75 \right) = 715.3. \tag{59}$$

With $Re_P = 715.3$ the terminal velocity of $v_r = 21.6 \; cm/s$ is in good agreement with the graphical solution considering the reading accuracy. Furthermore, a very good agreement with experimental data of Blass can be achieved [29].

3.2 Movement of Single Bubbles

Analogous to the behavior of moving single drops the relative velocity of single bubbles is dominated by the shape, whereas the influence of impurities and surface active agents is usually more important due to the larger difference in density and negligible inertia of the gas phase. For the characterization of bubble shapes the differentiation according to Peebles and Garber has been established [34] with four different general shapes (Fig. 9).

The change in bubble shape and flow field around the bubble occurs relatively sudden if a critical characteristic Reynolds number is passed. This depends on the properties of the continuous phase. With the dimensionless liquid number K_F as well as the Reynolds number of the bubble Re_D due to

$$k_F = \frac{\rho_c . \sigma^3}{g . \eta_c^4} \quad \mathrm{Re}_D = \frac{v_r \cdot d_B \cdot \rho_c}{\eta_c} \tag{60}$$

the calculation of drag force and terminal velocity is possible for different gas/liquid systems classified into four characteristic regimes (Fig. 9). For the graphical presentation of the results the normalized plot according to Mersmann [11] with the dimensionless velocity (equation 41) depending on the dimensionless particle diameter (equation 42) allows a clearly arranged differentiation between different gas/liquid systems by means of the dimensionless liquid number 43. Furthermore, the scope of validity of individual equations can be metered directly at the abscissa by using the Archimedes number because

$$d_P^* = \sqrt[3]{Ar}. \tag{61}$$

Section A: $Ar \leq 7$, $Re \leq 0.2$

Gas bubbles with an Archimedes number of $Ar \leq 7$ and a low rising velocities ($Re \leq 0.2$) are dominated by surface tension and therefore almost spherical. They are rising without internal circulation rectilinear (Regime A, not depicted in Fig. 9). Analogous to the sedimentation velocity of solid particles, the terminal bubble rising velocity for this range of diameter

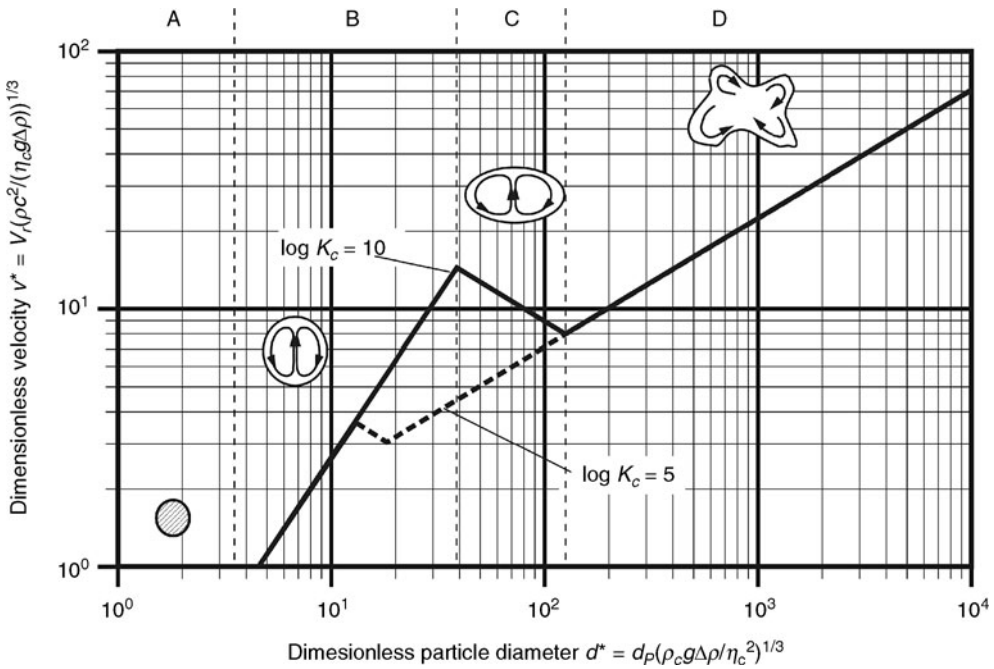

L4.1. Fig. 9. Dimensionless local relative velocity of gas bubbles in dependency of the dimensionless particle diameter [19, 34].

is calculable according to the drag law of Stokes with $C_{w\infty} = 24/Re_D$ due to

$$\sqrt[3]{Re_D \cdot Fr} = \frac{1}{18} \cdot Ar^{2/3} \tag{62}$$

[19].

Section A⁺: $Ar \leq 7.2$, $Re_D > 0.2$

For a distinct terminal rising velocity that strongly depends on impurities inside the gas/liquid system (e. g., $Re_D > 0.2$ [19]), the interface begins to move. Therefore, the drag coefficient decreases according to the correction factor of Hadamard–Rybczynski [35]

$$K_{HR} \equiv \frac{1 + \frac{\eta_D}{\eta_C}}{\frac{2}{3} + \frac{\eta_D}{\eta_C}} \tag{63}$$

for an air/water system and the ratio of $\frac{1}{K_{HR}} = \frac{1}{1.46}$ the corrected drag coefficient C_{W,A^+} is given by

$$C_{W,A^+} = \frac{24}{Re_D}\frac{1}{K_{HR}} \approx \frac{16}{Re_D} \tag{64}$$

respectively [36]. Therefore, the dimensionless terminal velocity of bubbles with moving interface is calculable by

$$\sqrt[3]{Re_D \cdot Fr} = \frac{1}{12} \cdot Ar^{2/3}. \tag{65}$$

For low Morton-numbers (e. g., for water) the minimum drag coefficient of a single bubble can be estimated to

$$C_{W,A,min} = 11.1 \cdot Re^{-0.71} \tag{66}$$

according to Maxworthy et al. [37].

Section B: $7.2 \leq Ar < 125 \cdot K_F^{0.25}$

With increasing Archimedes number, the forces of inertia become more dominant and the drag coefficient is calculable by the empirical equation

$$C_{W,B} = \frac{14.9}{Re_D^{0.078}} \tag{67}$$

due to [38] and [39] (see interval B in Fig. 9). The validity of this equation depends on the liquid properties and can be defined by the dimensionless liquid-number. The dimensionless terminal velocity is calculable by the empirical correlation

$$\sqrt[3]{Re_D \cdot Fr} = 0.136 \cdot Ar^{0.4266} \tag{68}$$

within this range of Archimedes numbers [19].

Section C: $125 \cdot K_F^{0.25} < Ar \leq K_F^{0.5}$

With further increasing Archimedes number (section C), the increasing forces induced by the flow around the particle cause a deformation of the bubble interface to a spheroid. This deformation depends strongly on the liquid properties. The increasing cross-section of the flattened bubble in the flow causes an increasing pressure drop that induces spacial and temporal fluctuating vortices at the rear side of the bubble (wake shedding). The vortex shedding causes a cyclic change in the orientation of the main bubble axis and induces a tumbling or helical rising trajectory. Because the terminal velocity is defined as the vertical part of the rising velocity vector, this tumbling or helical movement causes an decreasing terminal velocity with increasing tumbling or spiraling intensity despite the particle diameter increases. Peebles and Garber [34] used the empirical correlation

$$\sqrt[3]{Re_D \cdot Fr} = 1.91 \cdot K_F^{1/6} \cdot Ar^{-1/6} \tag{69}$$

for the description of their experimental results. The drag coefficient within this range is calculable by

$$C_{W,C} = \frac{1.332}{Fr} \tag{70}$$

Section D: $Ar > 22.6K_F^{0.5}$

For $Ar > 22.6K_F^{0.5}$ gas bubbles in water are rising with an irregular shape (Fig. 9, D) as "spherical cup bubbles" or "Taylor-Davis-Cup bubbles." The terminal velocity is calculable according to Brauer [19] with

$$\sqrt[3]{Re_D \cdot Fr} = 0.714 \cdot Ar^{1/6} \tag{71}$$

whereas, the drag coefficient within this range reaches the constant value of

$$C_{W,D} = 2.61. \tag{72}$$

For Newtonian liquids with low viscosity the helical rising trajectory leads to an decreasing terminal velocity, whereas, for increasing viscosities (approximately $\eta_C > 7$ *mPas*) the shape fluctuations are damped down and hence rectilineal trajectories occur [11, 18, 40, 41].

This dependency is considered with the dimensionless fluid number that decreases with increasing viscosity and diminishes the range of ellipsoidal bubbles. For dimensionless liquid numbers $K_F < 104$, the fluctuations of the bubble shape are fully damped by viscous forces [36].

Previous empirical correlations for a sectional calculation of the terminal velocity are well suitable to understand the physical interdependencies between bubble size, trajectory, and terminal velocity in pure systems. For the practical use their applicability is not convenient due to the dimensionless notation. Fan [42] published an empirical equation that uses a continuous function that is much more easy to use in process engineering. Fan connected the sections of different moving behavior in such a way, that for small bubble diameters Eq. 62 respectively Eq. 65 dominates, whereas for medium size and large bubbles the equation given by Mendelsohn [43]

$$v_r = \sqrt{\frac{2 \cdot \sigma}{\rho_C \cdot d_B} + \frac{g \cdot d_B}{2}} \tag{73}$$

gets an increasing influence [42].

Regarding the parameters k_1 which considers the dynamic surface tension, k_2 which takes into account impurities of the system, and k_3 which describes the mobility of the interface, Fan recommends the empirical equation

$$\sqrt[4]{We_C \cdot Fr} = \left[\left(\frac{K_C^{1/4}}{k_3}\frac{We_K}{Fr}\right)^{-k_2} + \left(\frac{2 \cdot k_1}{\sqrt{\frac{We_C}{Fr}}} + \frac{\sqrt{\frac{We_C}{Fr}}}{2}\right)^{-k_2/2}\right]^{-1/k_2}. \tag{74}$$

According to Fan the dynamic of the adsorption of surface active agents depends on whether it is used in a pure system ($k_1 = 1.2$) or a multicomponent system with impurities ($k_1 = 1.4$). Whereas, the parameter k_2 was experimental determined by Fan for several systems (table 1) the parameter k_3 is calculable due to

$$\text{for} \quad k_3 > 12 \quad k_3 = k_3^* \cdot K_F^{0.038} \tag{75}$$

$$\text{for} \quad k_3 \leq 12 \quad k_3 = 12 \tag{76}$$

with an acceptable reliability. The additional parameters are $k_3^* = 14.7$ for water and aqueous solutions and $k_3^* = 10.2$ for organic solvents. According to Fan, the scope of validity for the above mentioned equation is $10^{-5} < K_F < 10^{12}$ with an accuracy of −6% to +9% for 20 different Newtonian liquids. Despite the fact that Fan's equation is not able to fit the form transitions satisfactorily (section B → C, section C → D) its application is recommended especially for non pure systems, because the parameters have been adapted to a large variety of systems (Table 1).

For the detailed description of single bubbles rising in non-Newtonian liquids only a few investigations have been performed on shear thinning liquids like aqueous carboxylmethyl-cellulose (CMC-solutions) or viscous aqueous polyacrylamide (PAA-solutions) and aqueous glycerine solutions [18, 46, 47]. In highly concentrated CMC-solutions the terminal velocity increases with increasing bubble diameter due to a rectilinear trajectory, although strong fluctuations occur in the bubble shape. Therefore, highly concentrated CMC-solutions cause a more uniform movement of bubble swarms until no further coalescence occurs. Contrary to the uniform behavior of bubbles rising in CMC-solutions in viscoelastic PAA-solutions, an unsteady jump appears at a distinct bubble size [47, 48]. The reason for this sudden five to ten times increase in terminal velocity is mentioned by the higher mobility of the interface when surface active agents are sheared off or by the shear thinning effect of the PAA-solution. Furthermore, Starke has shown that the elastic properties of the liquid affect the bubble shape strongly and cause a significant reduction of the drag coefficient [47].

Hence, mainly the dimensionless plot of Mersmann is practically applicable for the calculation of the terminal velocity in non-Newtonian liquids (see Fig. 8).

L4.1. Table 1. Physical properties for different liquids and constants k_1, k_2, k_3 for the calculation of bubble terminal velocities by Eq. 74 [42]

liquid	ρ_C kg/m^3	η_C mPas	σ mN/m	Mo	d_P-range mm	k_3		k_1	k_2
						Exp.	Eq. (43)		
hot tap water	989	0.56	68.1	$3.09 \cdot 10^{-12}$	0.3...24	-	40.2	1.2	0.6
tap water	998	0.98	72.6	$2.37 \cdot 10^{-11}$	0.4...25	-	37.2	1.2	0.8
distilled water	998	1	72.7	$2.56 \cdot 10^{-11}$	0.3...63	37.6 ± 7.0	37.1	1.2	1.6
methanol	782	0.52	21.8	$8.84 \cdot 10^{-11}$	0.4...7	28.1	24.6	1.2	1.6
cold water (filtered)	999	1.47	74.8	$1.09 \cdot 10^{-10}$	0.5...18	33.9	35.1	1.2	1.6
0.42% glim in water	1000	1.03	32.8	$3.13 \cdot 10^{-10}$	0.2...6	-	33.8	1.2	0.8
varsol	782	0.85	24.5	$4.45 \cdot 10^{-10}$	0.2...16	23.2 ± 2.7	23.1	1.4	1.6
terpentine	864	1.46	27.8	$2.41 \cdot 10^{-9}$	0.3...6	20.7 ± 1.8	21.7	1.4	1.6
53% glycerine in water[1]	1135	6.86	70.3	$5.5 \cdot 10^{-8}$	1...10	-	27.7	1.4	1.1
56% glycerin in water	1143	9.15	69.9	$1.75 \cdot 10^{-7}$	1.2...4	–	26.6	1.4	1.1
66% glycerine in water[1]	1170	15.4	68.1	$1.49 \cdot 10^{-6}$	1...11	-	24.5	1.4	1.3
62% corn syrup in water	1262	55	79.2	$1.43 \cdot 10^{-4}$	0.4...5	20.3 ± 0.8	20.6	1.4	1.6
80% glycerine in water[1]	1206	52.9	65.9	$2.22 \cdot 10^{-4}$	1...12	-	20.2	1.4	1.5
68% corn syrup in water	1288	109	79.9	$2.11 \cdot 10^{-3}$	0.4...7	20.2 ± 0.6	18.6	1.4	1.6
mineral oil	866	58	20.7	$1.45 \cdot 10^{-2}$	0.5...30	12.0 ± 0.6	12	1.4	1.6
glycerine[2]	1260	157	63.2	$1.87 \cdot 10^{-2}$	3.5...14	15.9	17.1	1.4	1.6
Caster oil[2]	953	376	38.8	3.52	6...25	15.8	12	1.4	1.6
glycerine[2]	1270	1960	63.6	$4.43 \cdot 10^{2}$	7.5...29	13.7	12	1.4	1.6
corn syrup[2]	1380	4580	86	$4.91 \cdot 10^{3}$	4...26	13.4 ± 0.7	12	1.4	1.6
corn syrup[2]	1380	10380	95.6	$9.44 \cdot 10^{4}$	8...23	12.3 ± 0.5	12	1.4	1.6

[1] data from Kubota et al. [44]
[2] data from Kojima et al. [45]

L4.1. Table 2.

	η_C Pas	ρ_c kgm^{-3}	σ Nm^{-1}	K_F-	$lg(K_F)$	d_P^*	v^*	v_r ms^{-1}
dist. water/air	0.001	998	0.0727	$3.91 \cdot 10^{10}$	10.59	42.74	14.00	0.30
tap water/air	0.00098	998	0.0726	$4.22 \cdot 10^{10}$	10.63	43.32	14.00	0.30
aqueous glycerine/air	0.00915	1143	0.0699	$5.68 \cdot 10^{6}$	6.75	10.70	5.00	0.21

Example 4:
What is the terminal velocity of a gas bubble with a diameter of d_B = 2 mm in distilled water, tap water, and a 56% aqueous glycerine solution?
a) Graphical soluion:

The parameter for the graphical solution are given in (Table 2).

Due to the graphical solution it becomes clear that small differences in the viscosity and surface tension are difficult to read from the diagram. Therefore, similar values of the terminal velocity have to be used for distilled water and tap water despite of the fact that experimental data shows a significant difference between the terminal velocity of gas bubbles in distilled and tap water [42]. Furthermore, the terminal velocity in aqueous glycerine solutions is predicted much too high.
b) Calculated solution (in sections):

	Ar	$125 \cdot K_F^{0.25}$	$22.6 \cdot K_F^{0.5}$	$Re \cdot Fr$	v_r ms^{-1}
dist. water/air	$7.8 \cdot 10^4$	$5.6 \cdot 10^4$	$4.5 \cdot 10^6$	4932.39	0.36
tap water/air	$8.1 \cdot 10^4$	$5.7 \cdot 10^4$	$4.6 \cdot 10^6$	5022.67	0.36

The calculated solution considering the different sections of bubble movement shows a significant higher terminal velocity for distilled water and tap water. Furthermore, a distinction concerning the purity of the gas/liquid system is not possible. The terminal velocity of a single gas bubble rising in viscous liquids is calculable with a good accuracy.
c) Calculated solution (according to Fan):

	k_1	k_2	k_3	$We \cdot Fr^{-1}$	$(We \cdot Fr)^{0.25}$	v_r ms^{-1}
dist. water/air	1.2	1.6	37.14	0.54	1.75	0.287
tap water/air	1.2	0.8	37.25	0.54	1.28	0.210

Because the parameters for Eq. 74 have been adapted experimentally to a large variety of systems the consideration of surface active agents is possible with high accuracy. Therefore, the different terminal velocities in distilled water and tap water are well calculable. The comparison with experimental results shows a good agreement [42]. If the slope of the velocity curve in dependance of the particle diameter changes sharply like in the transition regimes (Fig. 9), the equation of Fan is less accurate. For higher viscous liquids in which the regimes for different moving behavior merge more smoothly the equation of Fan is a reliable approximation.

For the practical use of the above mentioned methods in process engineering it should always be considered whether surface active agents or higher viscosities are present. Whereas, for pure systems with low viscosity the calculation should be performed for each section of moving behavior, for contaminated systems and higher viscosities the method by Fan provides more accurate results.

4 Symbols

Phase

C	-	constant
$C_{W,K}$	–	drag coefficient of a single sphere
$C_{W,R}$	–	drag coefficient for an annular pipe flow
d_B	m	bubble diameter
d_h	m	hydraulic diameter
d_P	m	particle diameter
d_P^*	–	dimensionless diameter
$d_{P,min}$	m	minimal particle diameter
$d_{P,max}$	m	maximum particle diameter
d_N	m	diameter of nozzle/orifice
$d_{P\eta}$	m	bubble diameter with dominating viscous forces
d_{PT}	m	bubble diameter with dominating inertia forces
$d_{P\sigma}$	m	bubble diameter with dominating surface tension
d_{S32}	m	Sauter-diameter
F_A	N	buoyancy force
F_η	N	viscous force
F_T	N	force by inertia
F_σ	N	force by surface tension
g	ms^{-2}	gravitational force ($= 9.81\ ms^{-2}$)
K	$(Pas)^n$	consistency factor
n	–	exponent / flow-index
t	m	hole pitch
v_L	ms^{-1}	velocity of the liquid phase
v_G	ms^{-1}	velocity of the gaseous phase
v_{crit}	ms^{-1}	critical velocity before jet disintegration
v_N	ms^{-1}	velocity in the orifice
v_r	ms^{-1}	relative velocity
v_r^*	ms^{-1}	dimensionless relative velocity
$v_{r,dPma}$	ms^{-1}	relative velocity at maximum particle diameter
V_P	m^3	volume of particles
V_L	m^3	volume of liquid phase
$\dot{V}_D$	m^3s^{-1}	flow rate of the dispersed
$\dot{V}_{D,SC}$	m^3s^{-1}	flow rate of the dispersed phase through a single capillary
γ	^{o}	contact angle
$\dot{\gamma}$	s^{-1}	shear rate
ε_P		particle hold up
σ	Nm^{-1}	surface tension
$\Delta\rho$	kgm^{-3}	density difference ($\Delta\rho = \lvert\rho_C - \rho_D\rvert$)
ρ_C	kgm^{-3}	density of the continuous phase
ρ_D	kgm^{-3}	density of the dispersed phase

η_C	*Pass*	viscosity of the continuous phase
η_D	*Pass*	viscosity of the dispersed phase
η_{eff}	*Pass*	effective viscosity
τ_W	Nm^{-2}	shear stress inside the virtual channal

Dimensionless numbers:

Archimedes number

$$Ar = \frac{d_p^3 \cdot g \cdot \rho C \cdot \Delta\rho}{\eta_C^2} \tag{77}$$

Froude number

$$Fr = \frac{v_r^2}{dp \cdot g} \tag{78}$$

Froude number (particle formation)

$$Fr_N = \frac{v_N^2}{dN \cdot g} \tag{79}$$

Modified Froude number (particle formation)

$$Fr_{N,\Delta\rho} = \frac{v_r^2}{d_N \cdot g} \left(\frac{\rho_D}{\Delta\rho}\right)^{5/4} \tag{80}$$

Reynolds number of the dispersed phase

$$Re_D = \frac{v_r \cdot d \cdot \rho_C}{\eta_C} \tag{81}$$

Reynolds number in the virtual channel according to Klug [14]

$$Re_R = \frac{v_r \cdot d_h \cdot \rho_C}{\eta_C} \tag{82}$$

Dimensionless liquid number

$$K_L = \frac{\rho_C \cdot \sigma^3}{g \cdot \eta_C} \tag{83}$$

Modified dimensionless liquid number

$$K_{L,\Delta\rho} = \frac{\rho_C \cdot \sigma^3}{g \cdot \eta_C} \frac{\rho_C}{\Delta\rho} \tag{84}$$

Weber number of the dispersed phase

$$We_D = \frac{v_r^2 \cdot d_P \cdot \rho_D}{\sigma} \tag{85}$$

Weber number of the continuous phase

$$We_C = \frac{v_r^2 \cdot d_p \cdot \rho_C}{\sigma} \tag{86}$$

Weber number for particle formation

$$We_N = \frac{v_N^2 \cdot d_N \cdot \rho_D}{\sigma} \tag{87}$$

5 Bibliography

1. Räbiger N, Vogelpohl A (1986) Encyclopedia of fluid mechanics. Gulf Publishing, Houston
2. Chhabra RP (1993) Bubbles, drops, and particles in non-Newtonian fluids. CRC Press, Boca Raton, FL
3. Blass E (1988) Bildung und Koaleszenz von Blasen und Tropfen. Chem Ing Techn 12(60):937–947
4. Tsuge H (1986) Encyclopedia of Fluid Mechanics. Gulf Publishing, Houston
5. Stölting M (1980) Partikelbildung unterhalb des Strahlbereichs bei konstantem Volumenstrom. Chem Ing Techn 7(52):817–880
6. Voit H, Zeppenfeld R, Mersmann A (1987) Calculation of primary bubble volume in gravitational and centrifugal fields. Chem Eng Technol 10:99–103
7. Wittler R, Matthes R, Schügerl K (1983) Rheology of Penicillium chrysogenum Pellet Suspensions. Eur J Appl Microbiol Biotechnol 18:17–23
8. Voit H, Mersmann A (1889) Begasung strukturviskoser Flssigkeiten im Zentrifugalfeld, chap. Band 114. Dechema-Monographien. VCH Verlagsgesellschaft
9. Günder B (1999) Rheologische Eigenschaften von belebten Schlämmen und deren Einfluss auf die Sauerstoffzufuhr. Korrespondenz Abwasser 12(46): 1896–1904
10. Henzler HJ (2000) Particle stress in bioreactors. Adv Biochem Eng Biotechnol 67:38–82
11. Mersmann A (1977) Auslegung und Massstabsvergrösserung von Blasen und Tropfensäulen. Chem Ing Techn 9(49):679–691
12. Mersmann A, Beyer von Morgenstern I, Deixler A (1983) Deformation, Stabilität und Geschwindigkeit fluider Partikel. Chem Ing Techn 11(55): 865–867
13. Ruff K, Pilhofer T, Mersmann A (1976) Vollständige Durchströmung von Lochböden bei der Fluid-Dispergierung. Chem Ing Techn 48:3, S. 273
14. Klug P (1983) Der Blasenbildungsvorgang bei der Gasverteilung an Lochplatten. Ph.D. thesis, University of Clausthal
15. Zan W, Tan R (2003) A model for bubble formation and weeping at a submergedorifce with liquid cross-flow. Chem Eng Sci 58:287–295
16. Gaddis E, Vogelpohl A (1986) Bubble formation in quiescent liquids under constant flow conditions. Chem Eng Sci 1(41):97–105
17. Kyriakides N, Kastrinakis E, Nychas S (1997) Bubbling from nozzles submerged in water: Transition between bubbling regimes. Can J Chem Eng 75:684–690
18. Räbigner N (1984) Blasenbildung an Düsen sowie Blasenbewegung in ruhenden undströmenden Newtonschen und Nicht-Newtonschen Flüssigkeiten. VDI-Forschungsheft, VDI-Verlag, Düsseldorf
19. Brauer H (1971) Grundlagen der Einphasen- und Mehrphasenströmungen. Verlag Sauerländer, Aarau und Frankfurt am Main
20. Tadaki T, Maeda S (1963) On the shape and velocity of single air bubbles rising in various liquids. Kagaku Kogaku 25:254–264
21. Lehr F, Mewes D (2001) A transport equation for the interfacial area density applied to bubble columns. Chem Eng Sci 56:1159–1166
22. Pilhofer T, Mewes D (1979) Siebboden-Extraktionskolonnen. Verlag Chemie, Weinheim
23. Riquarts H (1989) Reaktionstechnik und Stoffaustauschtechnik in dispersen Zweiphasensystemen, *DECHEMA Monographien, Vol. 114, chap.* Strömungsmechanik disperser Zweiphasenströmungen. VCH, Weinheim
24. Brücker C (1999) Structure and dynamics of the wake of bubbles and its relevance for bubble interaction. Phys. Fluids 11:1781–1796
25. Bothe D, Koebe M, Wielage K, Prüss J, Warnecke HJ (2004) Bubbly Flows: Analysis, Modelling and Calculation, chap. Direct numerical simulation of mass transfer between rising gas bubbles and water, pp. 159–174. Heat and Mass Transfer. Springer
26. Schlüter M: (2006) Einfluss lokaler Phänomene auf den Stofftransport an Gasblasen in Zweiphasenströmungen. Shaker, Aachen
27. Koynov A, Tryggvason G, Schlüter M, Khinast J (2006) Mass transfer and chemical reactions in reactive deformable bubble swarms. Appl Phys Lett 88:134–102
28. Grassmann P (1983) Physikalische Grundlagen der Verfahrenstechnik. Verlag Sauerländer, Aarau
29. Blass E (1992) Direct numerical simulation of mass transfer between rising gas bubbles and water Principles and Practices of Solvent Extraktion. 159–174. New York, Marcel Dekker Inc.
30. Pilhofer T (1979) Grenzbelastungen verschiedener Gegenstrom-Extraktionskolonnen. Chem Ing Techn 51(3):231
31. Mersmann A (1980) Zum Flutpunkt in Flüssig/Flüssig-Gegenstromkolonnen. Chem Ing Techn 52(12):933–942

32. Dekee D, Carreau J, Mordarski J (1986) Bubble velocity and coalescence in viscoelastic liquids. Chem Eng Sci 49:2273–2283
33. Wolf S (1999) Phasengrenzkonvektion beim Stoffübergang in Flüssig-flüssig-Systemen, *Fortschr.-Ber. VDI*, vol. Reihe 3. VDI-Verlag, Düsseldorf
34. Peebles FN, Garber HJ (1953) Studies on the motion of gas bubbles in liquids. Chem Eng Progress 49(2):88–97
35. Sadhal SS, Ayyaswamy PS, Chung JN (1997) Transport Phenomena with Drops and Bubbles. Springer, Berlin
36. Hong WH, Brauer H. Stoffaustausch zwischen Gas und Flüssigkeit in Blasensäulen. VDI-Verlag (1984, volume = Reihe 3, number = Nr. 624, series = VDI-Forschungsheft, address = Düsseldorf,)
37. Maxworthy T, Gnann C, Kürten M, Durst F (1996) Experiments on the rise of air bubbles in clean viscous liquids. J. Fluid Mech 321:421–441
38. Clift R, Grace J, Weber M (1978) Bubbles, Drops and Particles. Academic Press, New York
39. Haas U, Schmidt-Traub H, Brauer H (1972) Umströmung kugelförmiger Blasen mit innerer Zirkulation. Chem Ing Techn 44(18):1060–1068
40. Siemes W (1954) Gasblasen in Flüssigkeiten. Teil II: Der Aufstieg von Gasblasen in Flüssigkeiten. Chem Ing Techn 26(11):614–630
41. Haberman WL, Morton RK (1954) An experimental study of bubbles moving in liquids. Trans Amer Soc Civil Engrs 2799:227/252
42. Fan L, Tsuchiya K (1990) Bubble Wake Dynamics in Liquids and Liquid-Solid Suspensions. Butterworth-Heinemann, Boston
43. Mendelson H (1967) The prediction of bubble terminal velocities from wave theory. AIChE J. 2(13):250–253
44. Kubota M, Akehata T, Shirai T (1967) The behaviour of single air bubbles in liquids of small viscosity. Kagaku Kogaku 31: 1074/1080
45. Kojima E, Akehata T, Shirai T (1968 Rising velocity and shape of single air bubbles in highly viscous liquids. Eng Japan 1:45–50
46. Miyahara T, Yamanaka S (1993 Mechanics of motion and deformation of a single bubble rising through quiescent highly viscous newtonian and non-newtonian media. J chem Eng Japan 3(26):297–302
47. Starke J (1998 Blasenbewegung in Blasenketten und viskoelastischen Flüssigkeiten, *VDI-Forschungsheft*, vol. Verfahrenstechnik,VDI-Verlag
48. Acharya A, Mashelkar RA, Ulbrecht J (1977 Mechanics of bubble motion and deformation in non-newtonian media. Chem Eng Sci 32:863–872

L4.2 Production and Mechanical Destruction of Foams

Alfons Mersmann
Technische Universität München, Munich, Germany

1 Introduction

Foams are produced when a gas is introduced or desorbed in a liquid which contains detergents. Pure liquids are non-foaming. The gas is dispersed into bubbles. A solution capable of foaming is a solvent – in most cases it is water with a high surface tension $\sigma = 72.4$ mJ/m^2 or 72.4 10^{-3} N/m at 25°C – with surface active agents which lead to a remarkable reduction of the surface tension. These detergents are more or less concentrated in the surface where an adsorption layer with the thickness of roughly one molecule diameter is formed.

The molar mass of strong surface active agents (detergents or tensides) is in the range of some hundreds of kilograms per kilomole (kg/kmol). The length of the hydrocarbon chain is between 1 and 5 nm with a hydrophilic functional group in the case of aqueous foams. When the molar mass of the detergent is too small, and the hydrophobic chain is too short, foams are not stable. However, if the molar mass assumes very high values with the consequence of low diffusivities of the surface active agents the detergent is only slowly enriched at the surface. This also leads to poor foam stabilities.

Gas can be introduced into the liquid by rotors (stirrers etc.) adjusted at the principal gas–liquid interface, falling drops, or spargers below the liquid surface. Bubbles can also be produced by depressurization and/or heating of a liquid which contains dissolved gas. The introduction of a gas leads to primary foams with bubbles in the diameter range of some millimeters. As a rule their liquid hold-up is small. Primary foams can be transformed to secondary foams by foam breakers. In secondary foams the liquid hold-up is high and the small bubbles are in the micrometer (μm) range. As a rule the objective of foam breaking is to form secondary foam with a high density and the ability of a certain flow in a gravitational field. This can be achieved if the mean bubble diameter is reduced to 50–100 μm by means of a power input. The specific energy in Joules per kilogram (J/kg) or square meters per square seconds (m^2/s^2) increases with the square w_u^2 of the tip speed w_u of a rotor. A minimum tip speed is necessary to start the mechanical destruction of primary foams. The density and the flow ability of secondary foams in a gravitational or centrifugal field increases with the tip speed of a rotor. The destruction of foams by the addition of chemicals (chemical destruction) is not considered here.

2 Detergents

According to [1] and [2] detergents can be

- Anionic
- Cationic
- Non-ionic and
- Amphoter

In Table 1 a survey of typical data and structures of the detergents CTAB, Mersolate, SDS, and Triton are given (see Table 1). These detergents have been investigated in research (see Fig. 1). All these substances can be characterized by their ability to reduce the surface tension of water in the concentration range between 10^{-4} and 10^{-3} mol/dm^3. In Fig. 2, the surface tension of aqueous solutions valid for 25°C is plotted against the concentration. Long-chained detergent molecules are adsorbed in a more flat structure (the chain is parallel to the surface) for low-concentrated solutions; however, with increasing concentration the hydrophilic groups are attracted by the water molecules at the surface whereas the hydrophobic tails form an adsoption layer.

In the case of a quick and strong stretching of this layer in combination with a remarkable reduction of the Gibbs surface concentration Γ according to

L4.2. Table 1. Properties and data of some tensides

Tenside	Type	molar mass kg/kmol	CMC kmol/m³	Surface concentration mol/m²	Area of a molecule nm²/molec
N-Cetyl-N, N, N-tnmethylammoniumbromide (CTAB)	cationic	346,46	$1 \cdot 10^{-3}$	$3.9 \cdot 10^{-6}$	0.4275
Pentadecan-sulfonacidsodium salt (Mersolat H 95)	anionic	314	$2 \cdot 10^{-3}$	$5.6 \cdot 10^{-6}$	0.2965
Dodecylsulfate (SDS)	anionic	288,38	$3 \cdot 10^{-3}$		
Octylphenolpolyglycolether (Triton X 100)	non-ionic	648,38	$4.4 \cdot 10^{-4}$	$4.4 \cdot 10^{-6}$	0.3773

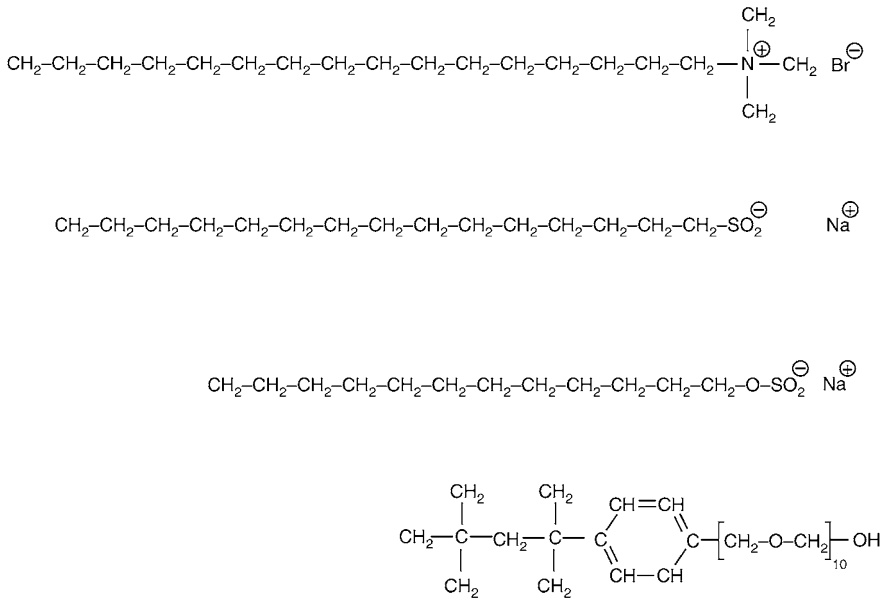

L4.2. Fig. 1. Structure of some tensides (see Table 1).

$$\Gamma = -\frac{a}{\Re T}\frac{\mathrm{d}\sigma}{\mathrm{d}a} \approx -\frac{c}{\Re T}\frac{\mathrm{d}\sigma}{\mathrm{d}c}$$

a transport of tenside molecules, or a so-called Marangoni flow to spots with high surface tension is started. This leads to a healing process of the adsorption layer with the result of a remarkable elasticity and stability of foam lamellae. The surface concentration Γ is proportional to the negative slope of the surface tension with respect to the activity, and decreases with the absolute temperature T. In diluted solutions the activity is often approximately the same as the concentration; however, in general there can be great differences. Above the Critical Micell Concentration (CMC) micells or molecule clusters are formed.

3 Properties of Primary Foams

Primary foams can be characterised by their

- Density ρ_S
- Volume fraction Ψ_L of the liquid or $\Psi_G = (1–\Psi_L)$ of the gas
- Density ρ_L and viscosity η_L of the lamella liquid
- The mean layer thickness s between bubbles in a gas in liquid dispersion
- The lamella thickness δ and the radius r_P of a Plateau channel of a polyhedric foam
- The volumetric interfacial area a and
- The Sauter diameter $d_{B,32} = \Sigma\, n_i d_i^3 / \Sigma\, n_i d_i^2$

Based on the definition

$$a = \frac{6(1-\psi_L)}{d_{B,32}} = \frac{6\psi_G}{d_{B,32}}$$

of the volumetric area and the definition of the mean layer thickness s according to

$$s = \frac{\psi_L}{a}$$

the relationship

$$\frac{\psi_L}{1-\psi_L} \approx \frac{\rho_S/\rho_L}{1-\rho_S/\rho_L} = 6\frac{s}{d_{B,32}} \text{ or } \psi_L = \frac{6s}{d_{B,32}+6s}$$

is obtained valid for $\rho_G << \rho_L$.

In Fig. 3, the mean Sauter diameter $d_{B,32}$ of foam bubbles is plotted against the volume fraction Ψ_L with the mean thickness s of the liquid between two bubbles as parameter [3]. Many experimental results have shown that the mean thickness s of aqueous primary foams is in the range between 10 and 20 µm and usually below 30 µm. In the case of primary foams

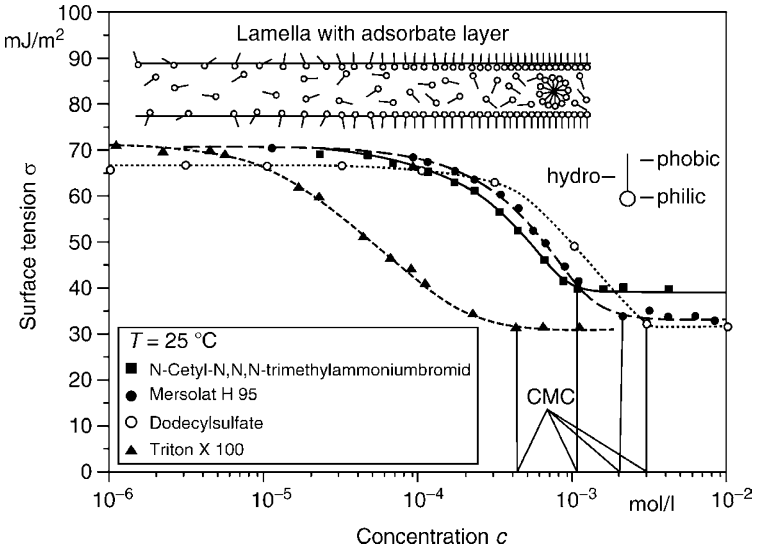

L4.2. Fig. 2. Surface tension of aqueous solutions.

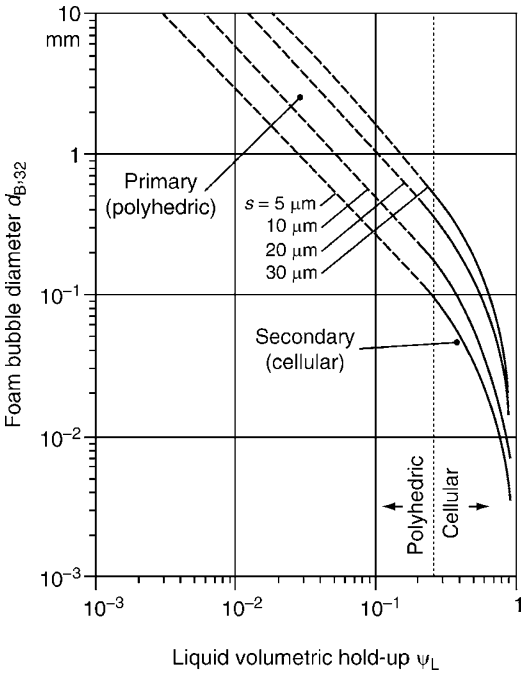

L4.2. Fig. 3. Mean bubble size $d_{B,32}$ against the liquid hold-up Ψ_L with the layer thickness s as parameter.

with large bubbles but a small liquid hold-up ($\Psi_L < 0.1$) and $6s << d_{B,32}$ one obtains $\psi_L d_{B,32} \approx 6s$. This means that the liquid hold-up increases approximately with a decreasing mean bubble diameter. Therefore, the objective of mechanical foam breaking is to reduce the bubble diameter to a higher degree or to release most of the gas into the bulk gas volume

The mean thickness s decreases with increasing foam age in a gravitational or centrifugal field because of the drainage of lamella liquid. In the beginning of drainage the bubble diameter remains constant; however, the foam density and the volumetric liquid hold-up are decreasing.

An apparatus is considered (e.g., a bubble column) with the cross section area f. Primary foam is continuously produced by a gas flow rate density $\dot{v}_G$ in $m^3/(m^2 s)$. The density of the foam decreases with the residence time τ of the foam in the apparatus:

$$\tau = \frac{V_S}{\dot{V}_S} = \frac{V_S(1-\psi_L)}{\dot{v}_G f}$$

In this equation V_S is the foam volume and $\dot{V}_S$ is the volumetric foam rate (see Fig. 4). With respect to the drainage effect the values of the foam density and of the hold-up increase from the top to the bottom of the foam in the column. A foam with a high liquid hold-up can be obtained when small bubbles are produced in the liquid. This can be done by means of a gas distributor with hole diameters below 0.5 mm and volumetric gas flow rates smaller than $\dot{v}_G = 0.05\ m^3/(m^2 s)$.

4 Structure of Primary Foams

The structure of a gas in liquid dispersion in a bubble-foam column is dependent on the ratio of the volumetric gas flow rate based on the rising velocity w_B of a single bubble in an extended quiescent liquid with a low viscosity [4]:

$$w_B \approx 1.55 \sqrt[4]{\frac{\sigma(\rho_L - \rho_G)g}{\rho_L^2}}$$

Here σ is the surface tension of the liquid and ρ_L its density. The structure can be predicted when a bubble/foam column is equipped with a perforated bottom plate with small holes (<0.5 mm) and the condition

$$\frac{\dot{v}_G}{w_B} < 0.2$$

is fullfilled. Above the distributor a gas/liquid dispersion is produced with the gas hold-up $\psi_G < 0.52$. Above this layer the hold-up of the gas is between 0.52 and 0.74 (cellular foam of bubbles with a maximum size $d_B^2(\rho_L - \rho_G)g/\sigma < 9$). At the top of the column polyhedric foam can be found with $\psi_G > 0.74$

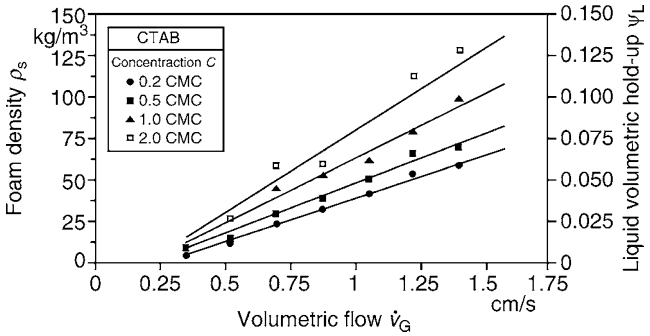

L4.2. Fig. 4. Density ρ_S of primary foams against the volumetric flow density $\dot{v}_G$.

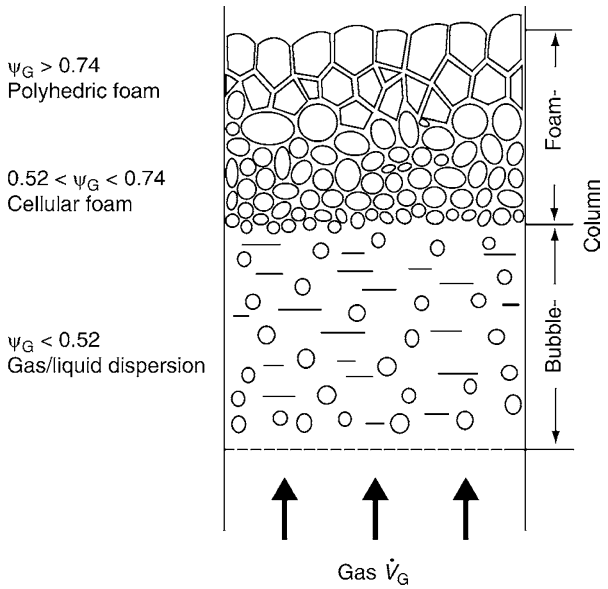

L4.2. Fig. 5. Structure of a gas in liquid dispersion (*below*) and of primary foam (*above*).

(see Fig. 5). The volumetric hold-up of the gas at the bottom of the column is approximately

$$\psi_G = \frac{\dot{v}_G/w_B}{1 + K\dot{v}_G/w_B}$$

with K ≈ 1.3 for low viscous liquids and K ≈ 2 for viscous liquids. The cellular foam in the bottom layer is transformed to polyhedric foam at the top due to drainage. In polyhedric foams the gas within the foam bubbles is surrounded by thin lamellae with the thickness δ (approximately 50 µm) and the Plateau channels with thicknesses $> \delta$. The basis of always three lamellae with opening angles of 120° is the Plateau channel with the radius r_P (see Fig. 6). The cross section area A_P of a Plateau channel for $r_P >> \delta$ is

$$A_P = 0.161 r_p^2,$$

and the radius r_P is approximately

$$r_P \approx \sqrt{0.84\psi_L} \cdot d_B$$

Since the liquid hold-up gets smaller with increasing height as a result of drainage this is also true for the radius r_P and the

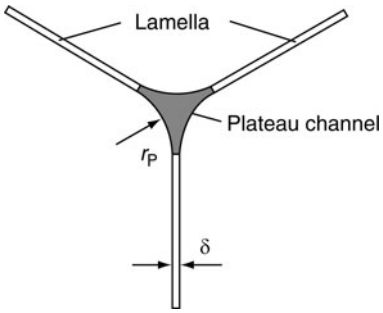

L4.2. Fig. 6. Cross section of a vertical Plateau channel.

area A_P. At the height h_K which is equal to the rising height in a capillary the radius r_P is

$$r_P = \frac{\sigma}{\rho_L g h_K}$$

and the radius in an arbitrary height h of a polyhedric foam layer with the total height h_{tot} and the mean liquid hold-up $\bar{\psi}_L$ is given by

$$r_P = \frac{\sigma}{\rho_L g\left(h - h_{tot}\bar{\psi}_L\right)}$$

As a rule the radius r_P is between 0.1 and 1 mm for aqueous foams.

Based on equations presented in the next section many authors have developed models for the prediction of drainage phenomena such as the reduction of the lamella thickness [7, 8], the liquid hold-up ψ_L [9] with increasing height, or the liquid overflow in the case of separations in foam columns. According to Hartland [7] the thickness of a lamella as a function of the height is given by

$$\delta = C_\delta \frac{(\eta_L \dot{v}_G)^{5/7} d_B^{9/7}}{(\rho_L g)^{1/7} (\sigma h)^{4/7}},$$

The number C_δ takes into account the flow condition at the surface of a lamella. $C_\delta = 0.71$ is valid for rigid surfaces which have an effect like solid walls; however, C_δ is smaller in the case of mobile surfaces. The lamella thickness δ is between 30 µm for "young" foams and 0.1 µm for foams after complete drainage. According to the last equation the thickness $\delta \to 0$ is expected for $h \to \infty$; however, in lamellae with thicknesses below 100 nm van der Waals forces as well as electrical and steric repulsion forces are important [13].

Besides the pressure difference Δp_{PL} between the Plateau channel and the lamella the pressure p_d according to

$$p_d = \frac{A_H}{6\pi\delta^3}$$

as a consequence of the van der Waals forces is effective for the thinning of a lamella. The Hamaker constant A_H is often in the range between 10^{-21} and 10^{-20} J for many liquids [14].

Contrary to these attracting forces electrical and steric repulsive forces are effective. If the lamella thickness is more than 1 nm and the electrical double layers are not interfering each

other the electrical repulsive force based on the unit area of a lamella is [15]

$$p_{el} = 64nkTe^{\kappa\delta}\left[\frac{e^{\frac{ze_0\psi_0}{2kT}} - 1}{e\left(\frac{ze_0\psi_0}{2kT} + 1\right)}\right]^2$$

with n as the number of ions per unit volume of the double layer, ψ_0 as the surface potential and $1/\kappa$ as the Debey-Hückel parameter according to

$$1/\kappa = (\varepsilon_r\varepsilon_0 kT/(\sum (ze_0)^2 n))^{1/2}.$$

In the case of large molecules the steric separation pressure is $p_{st} = p_{st}{}^0 \exp(-\delta/l_{st})$ with the reference pressure $p_{st}{}^0$ valid for $\delta = l_{st}$ as an empirical length which depends on the size and the structure of the detergent molecule under discussion.

The drainage of the lamella liquid into the Plateau channels is finished when the pressure in a lamella is the same as in the channel:

$$\Delta p_{PL} + p_d = p_{el} + p_{st}$$

Since the electrical and steric repulsion forces grow faster with the lamella thinning than the attracting forces (always based on the unit surface area) an equilibrium thickness δ^* will be obtained. This thickness is often in the range between 10 and 100 nm and is dependent on the kind and concentration of the detergent molecules. In the absence of any disturbance (evaporation, percussion, etc.) the lamella may stay stable for a very long time.

5 Drainage of Polyhedric Foams

A mechanical foam breaker can be applied in order to reduce the volume of primary foams to a higher degree; however, a complete separation into the two phases, gas and liquid, is nearly impossible. The decay of foams is started in a gravitational or centrifugal field by the drainage of the liquid present in the lamellae and in the Plateau channels. The drainage time $t_{Dr,L}$ of a lamella with the thickness δ_α at the beginning to the final thickness δ depends on the ratio of the surface force to the friction force within the liquid in the Plateau channels:

$$t_{Dr,L} = \frac{1}{c_L}\frac{r_P d_B^2 \eta_L}{2\sigma}\left(\frac{1}{\delta^2} - \frac{1}{\delta_\alpha^2}\right),$$

The quantity c_L depends on the kind of the detergent and is in the range $0.1 < c_L < 4$ [3]. After a certain drainage time the thickness δ is $\delta < 1/3\ \delta_\alpha$ with the result that the last equation can be simplified:

$$t_{Dr,L} \approx \frac{r_P \eta_L}{c_L 2\sigma}\left(\frac{d_B}{\delta}\right)^2.$$

Very thin lamellae are obtained after $t_{Dr,L} \to \infty$; however, evaporation and/or percussions may result in a breakage of a lamella. Contrary to the time $t_{Dr,L}$ of lamellae the drainage of Plateau channels is dependent on the ratio of gravitational or centrifugal forces and friction forces within the liquid. The flow velocity w_P of the liquid in a Plateau channel is given by

$$w_P = c_P \frac{r_P^2 \rho_L g}{\eta_L}.$$

The constant c_P is in the order of magnitude of 10^{-3} [3, 5]. Based on the very simple assumption that a Plateau channel with the length L_P is emptied by a liquid flow with the characteristic mean velocity w_P the order of magnitude of the drainage time of a Plateau channel is

$$t_{Dr,P} \approx \frac{L_P}{w_P} \approx \frac{L_P \eta_L}{c_P r_P^2 \rho_L g}$$

or with the equation derived for the liquid hold-up ψ_L

$$t_{Dr,P} \approx \frac{1.25 L_P \eta_L}{c_P \psi_L d_B^2 \rho_L g} \approx \frac{1.25}{c_P}\frac{L_P \eta_L}{6 s d_B \rho_L g}$$

In any case the qualitative result is: The higher the foam layer and the more viscous the liquid the longer is the decay time. This separation time can be reduced by the use of a centrifuge. In this case the gravitational acceleration must be replaced by the centrifugal acceleration $r\omega^2$ with ω as the angular speed and r as the effective radius of the foam layer in the centrifuge. This has been confirmed by experimental results [5].

6 Bubble Growth by Diffusion

Since the pressure in small bubbles is higher in comparison to adjacent large bubbles a diffusion of gas through the common liquid lamella takes place. As a result the diameter of small bubbles decreases with the tendency $d_B \to \infty$ for $t \to \infty$ and the size of large bubbles increases with time. This increase of large bubbles from the starting size $d_{B,\alpha}$ to the diameter d_B after the time t is given by [3]

$$d_B = \sqrt{d_{B,\alpha}^2 + c_B \frac{\sigma D_L}{\delta He_i} t}.$$

The quantity c_B depends of geometrical parameter (curvature, contacting area) of the bubbles and according to Gutwald [3] it is $c_B = 12$. D_L is the diffusion coefficient of the gas in the lamella liquid and the Henry coefficient He_i is defined by

$$He_i = \frac{p_i}{x_i}.$$

with the partial pressure p_i of the gas component i and x_i as its mole fraction. The diffusion time

$$t_{Dif} = \left(d_{B,\omega}^2 - d_{B,\alpha}^2\right)\frac{\delta He_i}{c_B \sigma D_L}$$

necessary to enlarge a bubble from the size $d_{B,\alpha}$ to the size $d_{B,\omega}$ is the time necessary in order to change a secondary foam into a coarse foam with the tendency of breakdown. This time is long for thick lamellae and high Henry coefficients and is reduced by strong diffusivities. Gas diffusion is decisive for the collapse of foams when the lamella thickness is below 1 µm. During diffusion a permanent breakdown of foam bubbles takes place, however, it is difficult to predict this breakage.

7 Bubble Size in Foams

It has been shown that the times necessary for the processes of drainage and diffusion are dependent on the bubble size and increase with the hold-up Ψ_L of the liquid. According to Fig. 3 the approximation $\Psi_L d_B \approx 6s$ is valid. In the following the

prediction of the mean bubble size is discussed. In the case of rising bubbles in a quiescent low-viscosity liquid in a gravitational field ($(\rho_L - \rho_G)\, g = \Delta\rho g$) the maximum stable bubble size is given by

$$\frac{d_{B,max}^2 \Delta\rho g}{\sigma} = C_B,$$

with $C_B \approx 9$ for the bubble Reynolds number [4]

$$\frac{w_B d_B \rho_C}{\eta_C} > 300.$$

The mean bubble size is $d_{B,50} \approx (0.5 \ldots 0.7)\, d_{B,max}$. In a turbulent flow field the bubble size decreases with increasing fluctuation velocities u',v', and w'. In the case of coalescing fluid particles (pure liquids, especially no detergents), the particle size depends of the local specific power input ε. With the macroscale of turbulence, Λ, this quantity is

$$\varepsilon = \frac{u'^3}{\Lambda}$$

valid for isotropic turbulence. The bubble size d_B is

$$d_B = C_\varepsilon \frac{\sigma^{0.6}}{\rho_c^{0.6} \varepsilon^{0.4}}$$

As a rule the mean specific power input ε is applied because the parameter Λ and C_δ are difficult to determine. In a system with a rotor with the diameter D (stirrer in a vessel, rotating foam breaker) in a cylindrical volume with the diameter T and the height H the mean specific power input is

$$\bar{\varepsilon} = \frac{4\mathrm{Ne}}{\pi^4} \left(\frac{D^3}{T^2 H}\right) \frac{w_u^3}{D}.$$

Ne is the Newton number ($0.5 < \mathrm{Ne} < 5$) and w_u is the tip speed $w_u = \pi$ and with n as the rate of rotation. The last equation can be transformed into

$$\frac{d_B}{D} = C_D \left(\frac{\sigma}{w_u^2 D \rho_L}\right)^{0.6} = \frac{C_D}{\pi^{1.2}} \left(\frac{\sigma}{n^2 D^3 \rho_L}\right)^{0.6} \text{ or}$$

$$d_B = C_D' \left(\frac{\sigma}{\rho_L}\right)^{0.6} \left(\frac{D}{w_u^3}\right)^{0.4} = C_D' D^{0.4} \left(\frac{\sigma}{\rho_L}\right)^{0.6} \left(\frac{1}{w_u^2}\right)^{0.6}$$

The quantities C_D and C_D' depend on the ratio $\varepsilon/\bar{\varepsilon}$, which is dependent of the geometry but difficult to predict or to determine.

This means that the bubble size decreases with the exponent 0.6 of the specific energy w_u^2 in $m^2/s^2 = J/kg$. For a given system, for example, geometry (geometry of the rotor and its diameter) and a given gas in liquid dispersion such an interdependency has been often confirmed experimentally.

In Fig. 7, the mean bubble size $d_{B,1}$ is plotted against the square of the rotor tip speed for different foams after a first destruction process realized by shear [3]. The experimental results are valid for a certain rotor-stator system (D = 300 mm; T = 634 mm; stator plate with 48 mm holes drilled on a radius of 130 mm). The rotor speed in the figure refers to the radius 130 mm because here the shear process of the foam bubbles takes place. This shearing results in a size reduction of the bubbles from 1 to 0.3 mm valid for $w_u^2 = 1{,}500\ m^2/s^2$ and an increase of the liquid hold-up ψ_L (see Fig. 3). The partially broken foam is further destructed by an impingement effect, for example, the foam is crashed into the side wall of the chamber. The mean bubble size is reduced from $d_{B,1}$ to $d_{B,2}$ (see Fig. 8). Now the square w_u^2 is calculated with the rotor diameter D according to $w_u = \pi n D$. In all cases the reduction of the bubble size depends of the square w_u^2. However, Triton foams can be continuously destructed at 100 m^2/s^2 whereas the foams of the other detergents need approximately 2,000 m^2/s^2 for the same size reduction. (In the literature many diagrams can be found in which the size of fluid [22] or solid [23] particles is plotted against volumetric or specific energy in the range from 10^2 up to 10^6 J/kg.)

In the case of a continuous destruction of a foam mass flow $\dot{V}_S \rho_L \psi_L$ the specific energy must be continuously added as specific power which can be provided by a rotor. The mean bubble size based on the rotor diameter D decreases with the exponent –0.6 of the Weber number. This has been experimentally confirmed for CTAB and Mersolat foams [3]. In the Fig. 9, the ratio d_B/D is plotted against the Weber number for coalescing fluid particles [16]. In addition, the size of non-coalescing bubbles in foams after the passage of a foam breaker is shown with $d_{B,1}$ obtained after only shearing and $d_{B,2}$ after an additional impingement effect [3, 5]. The different behavior of foams with the long-chained detergents CTAB and Mersolate on the one hand and Triton foams on the other hand indicates

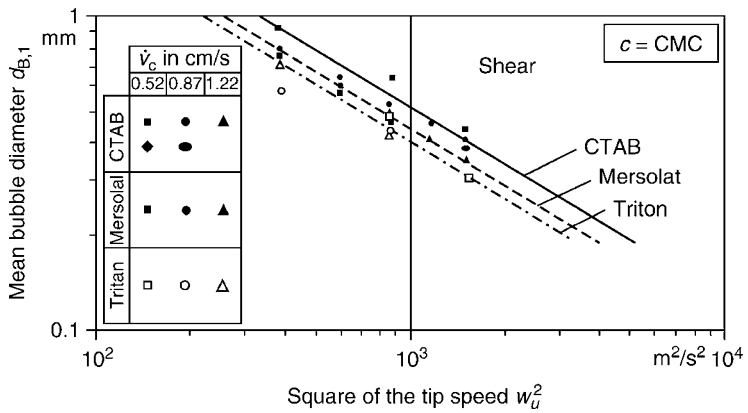

L4.2. Fig. 7. Mean bubble size $d_{B,1}$ after a shear process against the square of the tip speed.

that the property surface tension σ is not sufficient to describe the foam-breaking process.

8 Minimum Speed of Mechanical Defoamer

Many experiments carried out in industrial and scientific research have shown that the volume of primary foams can be remarkably reduced by rotors of different geometries. Sometimes the foam is passing channels in radial or radial/axial direction or contacting a rotor with blades. In all cases the foam is stressed by shear, stretch, and/or impingement forces (see Fig. 10). Blade stirrers applied in agitated vessels are easy to manufacture and can be very effective. The decisive mechanism of foam breaking is the repeated disruption or opening of gas bubbles with the result that a great deal of the gas is removed from the bubbles and transferred into the bulk gas without the formation of a new bubble. The shear, stretch, and/or impingement rate should be very high in order to avoid the healing effect of lamella holes by Marangoni flow. The spreading velocity w_L of a hole is

$$w_L = \sqrt{\frac{2\sigma}{\delta\rho_L}}$$

and increases inversely with the lamella thickness. The greater the difference $\Delta\sigma$ of a lamella spot with and without an adsorption layer the greater must be the tip speed in order to introduce the rupture of the lamella. According to these considerations the minimum tip speed $w_{u,min}$ can be derived [3]:

$$w_{u,min} = \sqrt{\frac{12K'\Delta\sigma(d_B - d_{B,X})}{d_B^2\psi_L\rho_L}}$$

with $K' = 1$ for non-ionic detergents and $K' = 2$ for ionic tensides. The diameter $d_{B,X}$ is the minimum size of a foam bubble deformed by shear, stretch, and/or impingement forces. The deformation degree $(d_B - d_{B,X})/d_B \approx 0.5$ has been experimentally determined.

With $K' = 2$ and $(d_B - d_{B,X})/d_B = 0.5$ the minimum tip speed is given by

$$w_{u,min} \approx 3.5\sqrt{\frac{\Delta\sigma}{d_B\psi_L\rho_L}}$$

By this way the velocity $w_{u,min} = 15.7$ m/s can be calculated for the data $\Delta\sigma = 40$ mJ/m^2, $\rho_L = 1{,}000$ kg/m^3, $\psi_L = 0.001$, and $d_B = 2$ mm for a "dry" aqueous primary foam.

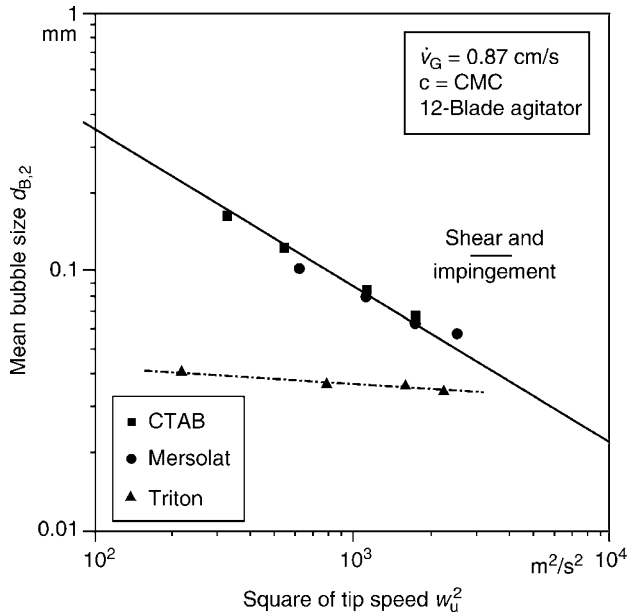

L4.2. Fig. 8. Mean bubble size $d_{B,2}$ after shear and impingement against the square of the tip speed.

9 Volume Reduction of Foams

As a rule the objective of foam breaking is the effective volume reduction of primary foams to such a degree that the secondary foam is flowing in a gravitational field. This requires high foam densities or liquid hold-up and, consequently, small bubbles in

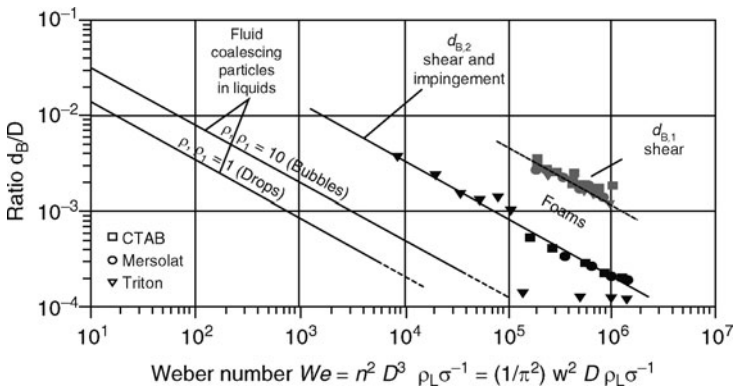

L4.2. Fig. 9. Ratio d_B/D against the Weber number for foams and coalescing fluid particles in liquids.

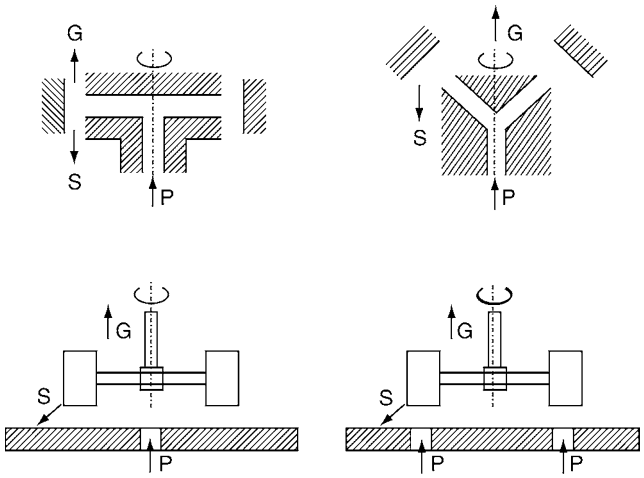

L4.2. Fig. 10. Rotating foam breakers; *P* Primary foam, *S* Secondary.

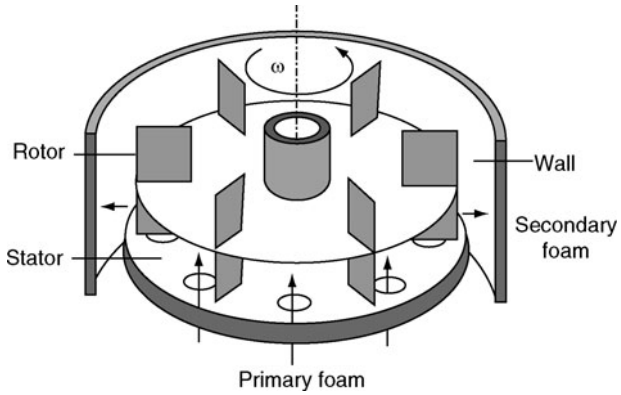

L4.2. Fig. 11. Mechanical foam breaker [3].

the secondary foam (see Fig. 3). This is the case when the size of the bubbles in low-viscous liquids is below 100 µm. In Fig. 11, a mechanical foam breaker with a triple effect is shown. At first the bubbles are stretched above the holes and then further deformed by the blades. This impingement effect is repeated on the chamber wall because the foam is accelerated in radial direction. By these effects the bubble size d_B of the entering primary foam is at first reduced to $d_{B,1}$ and then further to $d_{B,2}$. In the case of a tip speed of 40 m/s (34.7 m/s at the centers of the holes) and the properties $\rho_L = 1{,}000$ kg/m^3 and $\Delta\sigma = 40$ mJ/m^2 a liquid hold-up of $\Psi_L = 0.15$ and a bubble size of $d_{B,1} \approx 100$ µm has been obtained as a result of shear effects above the holes and stretching by the gas flow. Caused by the additional effect of impingement on the chamber wall a secondary foam with $\psi_L \approx 0.5$ and $d_{B,2} \approx 30$ µm has been produced. It is important to note that the thickness of the liquid film on the wall should be below 1 mm, otherwise drops can be introduced with the result that adhering gas penetrates into the secondary foam and its liquid hold-up is decreased.

In Fig. 12, the liquid hold-up ψ_L of secondary foams is plotted against the tip speed for CTAB foams of different detergent concentrations [3]. The lower the concentration of the lamella liquid (here as the manifold of the CMC) the higher is the density of the secondary foam. Above the tip speed of 30 up to 40 m/s it is difficult to reduce the bubble size and the liquid hold-up remains nearly constant. However, in the case of other detergents the hold-up can be quite different for the same geometry and operating parameter (see Fig. 13). The density of secondary Triton foams is much higher for the same tip speed and concentration because the stability of this foam is much lower than for the ionic long-chained detergents CTAB and Mersolate.

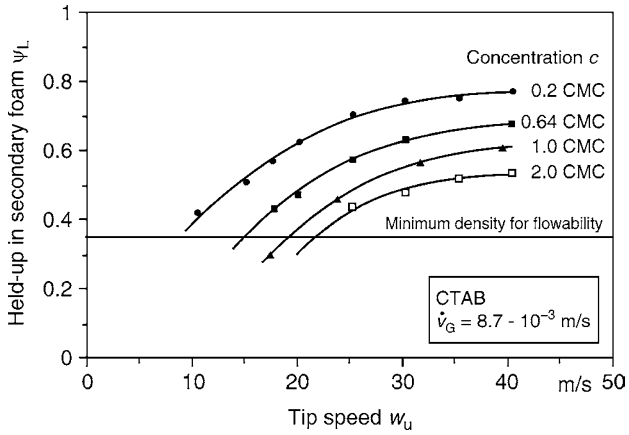

L4.2. Fig. 12. Liquid hold-up of secondary CTAB foams against the tip speed.

10 Collapse of Foams

The drainage of lamellae followed by gas diffusion from the small bubbles to the bigger ones and finally the coalescence of bubbles leads to the collapse of a stagnant foam layer. In Fig. 14 the bubble diameter is plotted against the time for CTAB foams with c = CMC. After approximately 200 s the drainage with $d_B \approx$ constant is finished. Then the diffusion accompanied by bubble collapse lead to an enlargement of large bubbles at the expense of smaller ones which finally disappear. After 10^4 s the final size of $d_B \approx 3$ mm is obtained regardless of how the foam has been produced. The polydisperse gas in liquid system breaks down and is finally separated in the gas and in liquid phase.

11 Irrigation of Foams

Principally speaking foams can be destroyed by falling or sprayed solvent drops. (The addition of a component with a low surface tension can be very effective) [18, 19]. A breaking of foam can be obtained if the degree of stretching and deformation of the bubbles within the foam is sufficient. A doubling of the surface of an originally spherical or polyhedric bubble in combination with a velocity of 5 m/s can be effective for foam breaking. The final falling velocity of 5 mm drops with

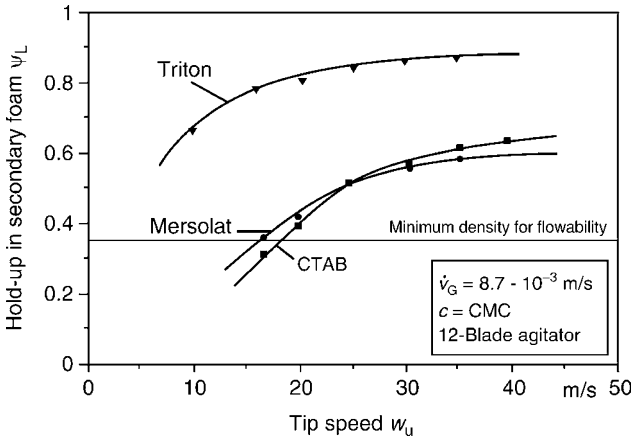

L4.2. Fig. 13. Liquid hold-up of secondary foams against the tip speed.

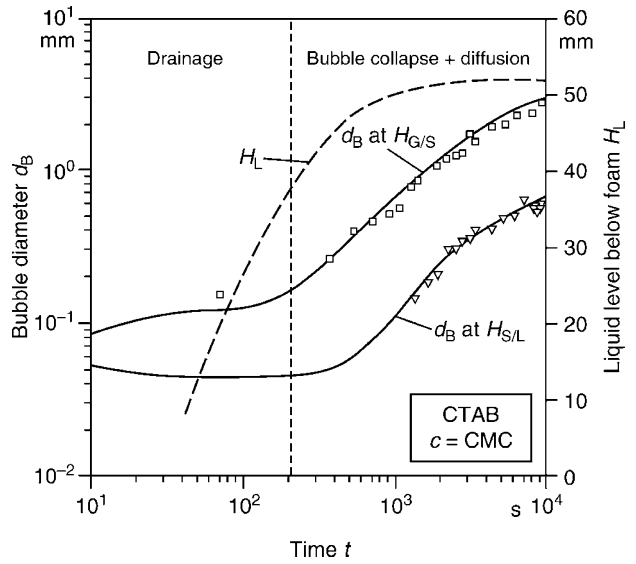

L4.2. Fig. 14. Bubble size d_B against the time.

ρ_L = 1,000 kg/m^3 is approximately 5 m/s. However, it can happen that gas is entrained by the drops with the result that the foam is stabilized. Therefore, irrigation can be problematic. Sometimes the foam breaking is achieved by impingement of horizontally moving jets.

12 Symbols

a	activity (mol/m^3)
a	volumetric interfacial area (m^2/m^3)
A_H	Hamaker constant (J)
A	cross sectional area (m^2)
c	concentration (mol/m^3)
c_B	constant according to Gutwald
c_D, C_D^I	Constant
c_P	constant according to Gutwald
C_B	constant according to Mersmann
C_δ	constant according to Hartland
C_ε	constant
d	diameter (m)
d_B	bubble diameter (m)
$d_{B,X}$	minimum diameter of a deformed bubble (m)
$d_{B,1}$	bubble size after shear (m)
$d_{B,2}$	bubble size after shear and impingement (m)
$d_{B,32}$	Sauter diameter (m)
$d_{B,50}$	mean bubble size (m)
D	diameter of a rotor (m)
D_L	diffusion coefficient (m^2/s)
e_0	elementary charge (A s)
f	cross section area of a column (m^2)
g	acceleration due to gravity (m/s^2)
h	height (m)
h_K	rising height in a capillary (m)
h_{tot}	total height (m)
H	height of a vessel (m)
He	Henry coefficient (Pa)
k	Boltzmann constant (J/K)
K, K'	constants
l_{st}	sterical length (m)
L	length (m)
n	number per volume (1/m^3)
n	rotating frequency (1/s)
Ne	Newton number
p	pressure (Pa)
r	radius (m)
$\Re$	gas constant (J/(mol K))
s	mean layer thickness (m)
t	time (s)
T	temperature (K)
T	diameter of a vessel (m)
u′	turbulent fluctuating velocity (m/s)
υ′	turbulent fluctuating velocity (m/s)
$\dot{\upsilon}$	volumetric flow density or mean velocity (m^3/(m^2 s))
V	volume (m^3)
$\dot{V}$	volumetrie flow (m^3/s)
w	flow velocity (m/s)
w′	turbulent fluctuating velocity (m/s)
w_B	rising velocity of a bubble (m/s)
w_u	tip speed (m/s)
We	Weber number
x	mole fraction (mol/mol)
z	valency
Γ	Gibbs surface concentration(mol/m^2)
δ	lamella thickness (m)
Δ	difference
ε	specific power input (W/kg)
$\bar{\varepsilon}$	mean specific power input (W/kg)
ε_0	permittivity (C/(Vm))
ε_r	relative permittivity
η	dynamic viscosity (Pa s)
κ	Debye-Hückel parameter (1/m)
Λ	macro scale of turbulence (m)
ρ	density (kg/m^3)
σ	surface tension (J/m^2)
τ	residence time (s)

ψ	volumetric hold-up (m^3/m^3)
$\bar{\psi}$	mean volumetric hold-up (m^3/m^3)
Ψ_0	surface potential (V)
ω	angular speed (1/s)

Indices

B	bubble
c	continuous phase
d	dispersion
Dr	drainage
Dif	diffusion
el	electrical
G	gas
i	component i
max	maximum
min	minimum
st	sterical
L	liquid, lamella
P	Plateau channel
S	foam
α	starting state
ω	final state
$*$	equilibrium

13 Bibliography

1. Fell B (1991) Tenside: Aktueller Stand - Absehbare Entwicklungen. Tenside Surf Det 28:S 6
2. Fabry B (1991) Eigenschaften, Rohstoffe, Produktion, Anwendungen. Chemie in unsererZeit 25(4):214–222
3. Gutwald S (1996) Uber die Wirkweise mechanischer Schaumzerstorer mit Praflverdichtung. Diss. TU Munchen
4. Mersmann A (1986) Stoffübertragung. Springer, Berlin
5. Furchner B (1989) Die Zerstorung wässriger Tensidschäume durch rotierende Einbauten. Diss. TU München
6. Lohmann T (1994) Mechanische Schaumzerstörung durch Beregnen Fortschr -Ber VDI, Reihe 3: Verfahrenstechnik. Nr. 356. VDI-Verl, Düsseldorf
7. Hartland S, Barber A D (1974) A model for a cellular foam. Trans Instn Chem Engrs 52:43–52
8. Steiner L, Hunkeler R, Hartland S (1977) Behaviour of dynamic cellular foams. Transl Chem E 55:153–163
9. Desai D, Kumar R (1983) Liquid holdup in semi-batch cellular foams. Chem Eng Sci 38(9):1525–1534
10. Shih F-S, Lemlich R (1967) A study of interstitial liquid flow in foam. Part III: Test of theory. AIChE J 13(4):751–754
11. Haas PA, Johnson HF (1976) A model and experimental results for drainage of solution between foam bubbles. I & EC Fundamentals 6(2):225–233
12. Desai D, Kumar R (1984) Liquid overflow from vertical co-current foam columns. Chem Eng Sci 39(11):1559–1570
13. Vrij A (1966) Possible mechanism for the spontaneous rupture of thin, free liquid films. Discussions Faraday Soc 42:23–33
14. Sonntag H (1977) Lehrbuch der Kolloidwissenschaft. VEB Deutscher verl. d. Wissensch. Berlin
15. Sonntag H, Strenge K (1970) Koagulation und Stabilität disperser Systeme. VEB Deutscher Verl. d. Wissensch, Berlin
16. Werner F (1997) Uber die Turbulenz in geruhrten newtonschen und nichtnewtonschen Fluiden. Herbert Utz Verl. Wissensch, Munchen
17. Zlokarnik M (1984) Auslegung und Dimensionierung eines mechanischen Schaumzerstörers. Chem Ing Tech 56(11):839–844
18. Meinecke H (1994) Tensidschaume. Charakterisierung und Zerstörung durch Beregnen mit arteigener Flussigkeit. Diss. Univ. GH Paderborn
19. Franke D (1966) Zur Mechanik tensidhaltiger Lamellen bei den Schaumzerstorung. Diss. Univ.-GH Paderborn
20. Furchner B, Mersmann A (1990) Foam breaking by high speed rotor. Chem Eng Technol 13:86–96
21. Gutwald S, Mersmann A (1997) Foam breaking: A physical model for impact effects with high speed rotors. Chem Eng Technol 20:76–84
22. Schubert H (2003) Neue Entwicklungen auf dem Gebiet der Emulgiertechnik, in: Mischen und Ruhren, Hrg. Wiley VCH, Kraume
23. Kirchner K, Leluschko J (1986): Untersuchungen zum Einfluss der Nassmahlung in Kugelmuhlen. Chem Ing Techn 58:5

L4.3 Droplet Separation

Hans Detlef Dahl
Marl, Germany

1 Introduction

1.1 Mechanisms of Droplet Formation

Mists or spray may be generated by a number of processes, such as condensation, chemical reaction, entrainment from column internals (trays, packings), spray nozzles, or the flashing of superheated liquids. The size distribution of the spray depends on the mechanism of droplet formation. The physical properties of gas and liquid influence the droplet size distribution as well. Liquids with lower surface tension or viscosity tend to produce rather smaller droplets. Typical ranges are shown in Table 1.

1.2 Key Factors for Separator Selection and Design

Before starting to select or to design a droplet separator it is essential to be aware of the following key factors:

- The amount of liquid and the size of the droplets, which shall be removed
- The type of flow in the separator' inlet (see Subchap. L2.1)
- The allowable amount of liquid in the gas stream leaving the separator
- The allowable pressure drop
- The presence of solids or salts, which may lead to plugging
- Tendency of the liquid to foam
- Material of construction

There is a great variety of different droplet separators. The most commonly used types are gravitational separators, often in combination with wire mesh elements, wave plate separators, and cyclones.

A comprehensive description of all kinds of droplet separators can be found in the work of Bürkholz [1]. For additional practical advice on the selection of mist eliminators, the works of Fabian et al. and Ziebold can be referred to [2, 3].

2 Gravitational Separators, Flash Drums

The maximum allowable axial vapor velocity in vertical flash drums equipped with wire mesh demisters can be estimated by using the Souders–Brown equation [4, 5]:

$$w = k\left(\frac{\rho_L - \rho_G}{\rho_G}\right)^{0.5}, \tag{1}$$

where the coefficient k is in the range of 0.05–0.11 m/s. For higher pressures it is proposed to reduce k according to the percentages given in Table 2.

Equation (1) is purely empirical. The resulting limit droplet diameter is often in the range of 200 µm (and 50 µm for separators without wire mesh).

To avoid surprises, it should be checked which limit droplet size will result. This can be done by using Newton's law for the limit droplet size:

$$d^* = \frac{3\rho_G c_W w^2}{4(\rho_L - \rho_G)g}, \tag{2}$$

whereas $c_W = 0.5$ for spherical droplets, if the Reynolds number

$$\mathrm{Re} = \frac{\rho_G d^* w}{\eta_G} \tag{3}$$

of this limit droplet is bigger than 1,000. If this should not be the case, Eqs. (22) and (24) can be applied if the centrifugal acceleration z is substituted by the gravitational acceleration g.

The pressure loss of the wire mesh pad is normally in the range below 250 Pa, the wires having diameters between 100 µm and 300 µm. This is sufficient to separate droplets 3–10 µm with an efficiency nearly 100%.

L4.3. Table 1. Typical ranges for droplet size distributions

Mechanism	Size (μm)
Condensation and chemical reaction	~0.1–25
Two-phase pneumatic nozzles	~1–200
Entrainment, flashing liquids, and single-phase pneumatic nozzles	~5–1,000

L4.3. Table 2. Adjustment of *k* [5]. Combine the single percentages in case more than one criterion applies, e.g., use 80% x 50% = 40% for a flash drum without wire mesh operating at 40 bar

		Adjustment of *k*, % of design value
Pressure	Atmospheric	100%
	10 bar	90%
	20 bar	85%
	40 bar	80%
	80 bar	75%
Glycol and amine solutions		60–80%
Separators without wire mesh demisters		50%
Compressor suction scrubbers		70–80%

If mists with droplet diameters lower than 3 μm are to be separated, fiber beds can be used. Their pressure loss ranges between 1,000 and 3,000 Pa (Fig. 1 shows a typical vertical separator).

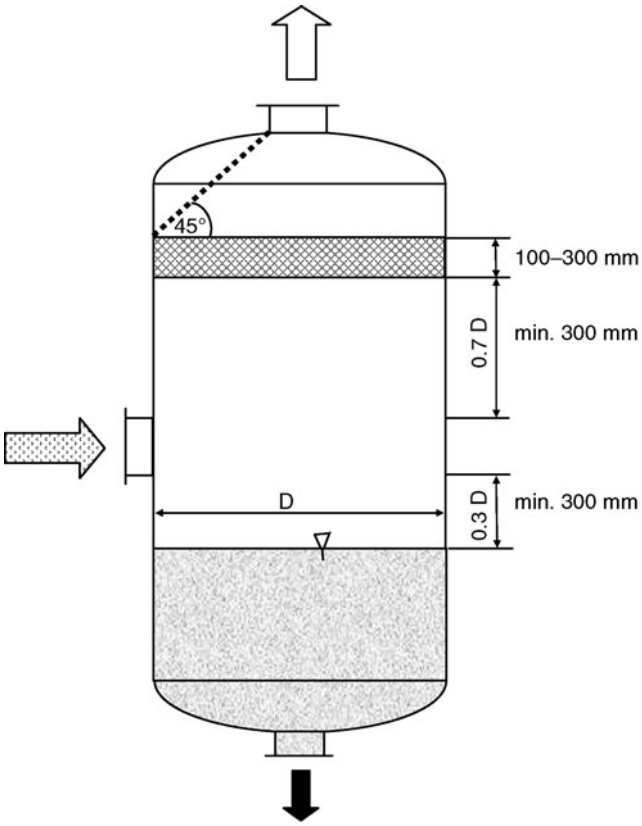

L4.3. Fig. 1. Vertical separator with wire mesh pad of typical dimensions.

3 Cyclones

The calculation of cyclones for droplet separation is similar to the calculation of cyclones for the separation of solid particles, which is described in detail in Subchap. L3.4. Therefore, this chapter deals only with those topics in which liquid and solid separators differ.

3.1 General Description

Figure 2 shows a cyclone for droplet separation. The liquid loaded gas stream is sent to the cyclone via a tangential pipe inlet. A part of the liquid flows as a film along the pipe wall into the cyclone, whereas the other part is distributed as droplets in the core.

The centrifugal forces caused by the rotational flow within the cyclone act on the droplets and force them toward the wall. There the liquid flows in the form a film or single threads toward the bottom of the separator. A cone prevents the already separated liquid from getting sucked back in the core of the rotational flow, which may happen due to the underpressure prevailing there.

Near the cyclone's upper shell a boundary layer is formed. As in this boundary layer the circumferential velocity is low, the gas and liquid in this layer are not subject to the centrifugal forces of rotational flow and can flow directly to the dip pipe in the center, where the static pressure is lower than on the outer diameter. In order to prevent the thin liquid from creeping in thin threads toward and into the dip pipe, it makes sense to install a collar, which redistributes the liquid in the form of large droplets to the main flow within the cyclone [6].

A very first check of the separation efficiency can be made using a simple empirical equation developed by Bürkholz [1] using experimental data obtained for cyclones with outer diameters of up to 100 mm:

$$d^*(\mu\mathrm{m}) = 1.7\left(\frac{r_\mathrm{i}(\mathrm{mm})}{\Delta p(\mathrm{mbar})}\right)^{1/3}. \qquad (4)$$

The results of this equation fit only for cyclones with $r_\mathrm{a}/h_\mathrm{i} < 0.25$ with the exact calculation. The influence of liquid load and its limit is not taken into account.

Applications of cyclones as liquid separators range from standardized units such as steam dryers to customized solutions such as separators in emergency relief systems [7].

Instead of the tangential inlet shown in Fig. 2 axial inlets can be applied as well. In this case the rotational flow is effected by means of guide vanes, which are arranged concentrically around the dip pipe.

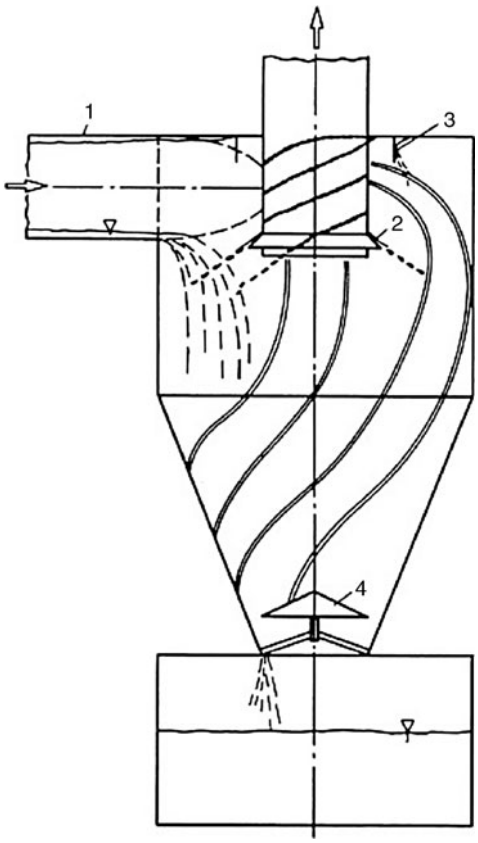

L4.3. Fig. 2. Cyclone for droplet separation, schematic: 1 – tangential pipe inlet, 2 – collar for liquid redistribution, 3 – additional collar for high liquid loads, 4 – cone.

With highly efficient internals in the dip pipe, which regain the angular momentum of the gas flow, it is possible to reduce the cyclone's pressure loss by a factor of 4. This closes the gap to wave plate separators, which when compared to cyclones have a lower pressure loss.

Cyclones are insensitive even against highest liquid loads. As their wall is increasingly wetted and rinsed from the inlet toward the liquid outlet, they are also well suited if solids with up to 30 g/l are present in the liquid. According to Muschelknautz and Herold [8], the inlet can be designed with sloped boxes in a way that all parts of the wall are completely wetted. The upper shell and the dip pipe, which tend to stay dry, can be cleaned with a few spray nozzles and clean or lightly contaminated liquid. The secondary flow along the upper shell drives the liquid with increasing film thickness toward the center and the dip pipe.

3.2 Calculation of the Flow

The flow, which enters the cyclone via the tangential inlet, is pressed to the wall by the radial pressure gradient, contracts, and accelerates. This is described by means of a contraction coefficient

$$\alpha = (u_e r_e)/(u_a r_a) \tag{5}$$

L4.3. Table 3. Contraction coefficient α for inlets with circular cross section and a ratio $d_{inlet}/r_a = 0.64$ as a function of the liquid load in the entrance μ_e

μ_e	0	0.1	1
α	0.69	0.7	0.8

which depends on the quotient of the inlet diameter d_{inlet} to the outer radius r_a and on the liquid load

$$\mu_e = \frac{\dot{M}_L}{\dot{M}_G} \tag{6}$$

of the flow entering the cyclone. The entrance radius r_e is

$$r_e = r_a - d_{inlet}/2 \tag{7}$$

Table 3 shows experimentally obtained values for the contraction coefficient.

By means of a balance of angular momentum the circumferential velocity along the radius of the dip pipe is calculated as [9, 10]:

$$u_i = \frac{u_a \frac{r_a}{r_i}}{1 + \frac{\lambda_L}{2}\frac{A_R u_a}{V}\sqrt{\frac{r_a}{r_i}}}. \tag{8}$$

By means of experimental tests with a cyclone model of 900 mm diameter and liquid loads up to 1 kg/kg, the dependence of the wall friction coefficient λ_L on the liquid load was determined. Due to liquid trickling along the wall, the wall friction coefficient increases compared to the friction coefficient for pure gas λ_0, as given in Subchap. L3.4:

$$\lambda_L = \lambda_0\left(1 + 0.4\mu_e^{0.1}\right). \tag{9}$$

Normally, cyclones are designed in a way that the pressure loss is in the range between 500 and 2,500 Pa. The calculation is carried out according to Subchap. L3.4. With highly efficient internals in the dip pipe, which recover the angular momentum of the flow, the pressure loss can be reduced to by a factor of 4.

3.3 Separation Efficiency

The turbulence of the gas flow in the cyclone does not suffice to carry unlimited amounts of liquid. Directly after entering the cyclone the amount of liquid exceeding the load limit separates from the gas and flows down along the cyclone's wall. This is the reason why the total separation efficiency increases for higher liquid loads (Barth [11]).

As it was shown by own experiments, the load limit of liquid separators lies only in the range of 10–35% of comparable dust cyclones, the reason being that droplets cannot re-enter the gas flow once they are separated as solid particles can do. As a liquid film, which was already formed in the pipe feeding the separator, does not influence the load limit mechanism, and the calculation is based not on the total liquid load in the cyclone' feed pipe but instead on the liquid load in the core of the flow $\mu_{e,k}$, which is the quotient of the droplet mass flow to the mass

flow of the gas. According to the experiments with mean droplet diameters in the range of 60–190 µm in the gas feed and liquid loads in the flow' core in the range of 0.01–0.5, the load limit μ_G can be calculated by means of the following empirical equation:

$$\mu_G = 0.0087\left(\frac{d_e^*}{d_{50}}\right)(10\mu_{e,k})^k \qquad (10)$$

with

$$k = 0.07 - 0.16\ln\mu_{e,k}. \qquad (11)$$

The limit droplet diameter d_e^* is calculated according to Subchap. L3.4. The same applies for the fractional separation efficiency curve and for the size distribution of the droplets entering the cyclones core flow. For liquid loads above the load limit the total separation efficiency is calculated as

$$\eta_{total} = \left(1 - \frac{\mu_G}{\mu_e}\right) + \frac{\mu_G}{\mu_e}\sum_{l=1}^{m}\eta_F(\bar{d}_l)\Delta R_{Ai,I}. \qquad (12)$$

When designing droplet separators it should be kept in mind that the droplets may shrink by evaporation.

Example

Total separation efficiency and pressure loss of the cyclone shown in Fig. 3 have to be calculated.

Operational and physical data: $V_G = 0.7\ m^3/s$; $\rho_G = 1.2\ kg/m^3$; $\eta_G = 18 \times 10^{-6}$ Pa s; $\rho_L = 1{,}000\ kg/m^3$; $d_{50} = 60$ µm; $A_w = 3.32\ m^2$; $A_R = 5.69\ m^2$.

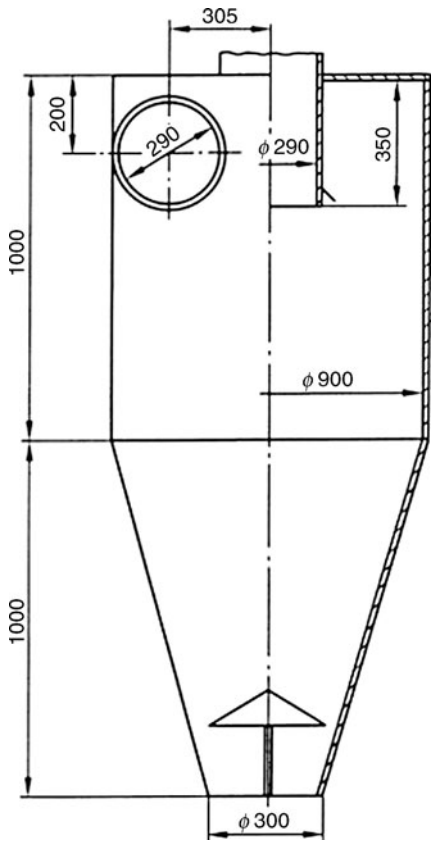

L4.3. Fig. 3. Example calculation: main dimensions of the droplet separation cyclone.

The feed' liquid load μ_e is 0.02, and the liquid load in the core of the flow is 0.01.

Angular velocities:

$$v_e = \frac{\dot{V}}{\pi/4 d_{inlet}^2} = 10.6\ m/s,$$

$\mu_e = 0.02$ and $d_{inlet}/r_a = 0.64 \rightarrow \alpha = 0.69$, Table 3

$u_a = 10.4$ m/s, Eq. (5)

$\lambda_L = \lambda_0(1 + 0.4\mu_e^{0.1}) = 0.0045(1 + 0.4 \cdot 0.02^{0.1})$ Eq. (9)
$= 0.0057$,

$u_i = 22.0$ m/s Eq. (8)

According to Subchap. L3.4:

$u_{e1} = 13.1$ m/s; $u_2 = 13.1$ m/s; $z_e = 530\ m/s^2$; $w_{s,50} = 0.095$ m/s, $d_c^* = 7.6$ µm; $d^* = 6.8$ µm,

$k = 0.81$, Eq. (11)

$\mu_G = 1.71 \times 10^{-4}$. Eq. (10)

Total separation efficiency

$$\eta_{total} = \left(1 - \frac{1.71 \times 10^{-4}}{0.02}\right) + \left(\frac{1.71 \times 10^{-4}}{0.02}0.57\right) = 0.9963 \quad \text{Eq. (12)}$$

The pressure loss according to Subchap. L3.4 is

$$\Delta p = \Delta p_i + \Delta p_e = 961\ Pa + 107\ Pa = 1{,}068\ Pa.$$

4 Wave Plate Separators

4.1 Working Principle and Comparison to Cyclones

Wave plate separators are packings of profiled plates which are arranged parallel to each other. The gas flow is perpendicular to the waves. Due to centrifugal forces droplets drift in the curved gas flow toward the plates where they separate from the gas (Fig. 4).

In wave plate separators with horizontal flow the separated liquid flows crosswise in vertical flutings downward. They are considerably smaller than cyclones and have a lower pressure loss (Fig. 5).

The plates at the inner side of the curve are more or less dry. In multistage packings the curve's outer side gets dry also toward the outlet. This causes, even with only lightly contaminated liquids, e.g., in the washing towers of desulphurization plants, crusting or fouling in the transition zone from the wet to the dry wall. Cleaning can be done periodically with the aid of high pressure spray nozzles.

4.2 Hydrodynamics

The already separated liquid can be forced back from the flutings into the gas flow by a combined overpressure/underpressure effect if the gas velocity is too high. For horizontal flow and vertical flutings the limit is at

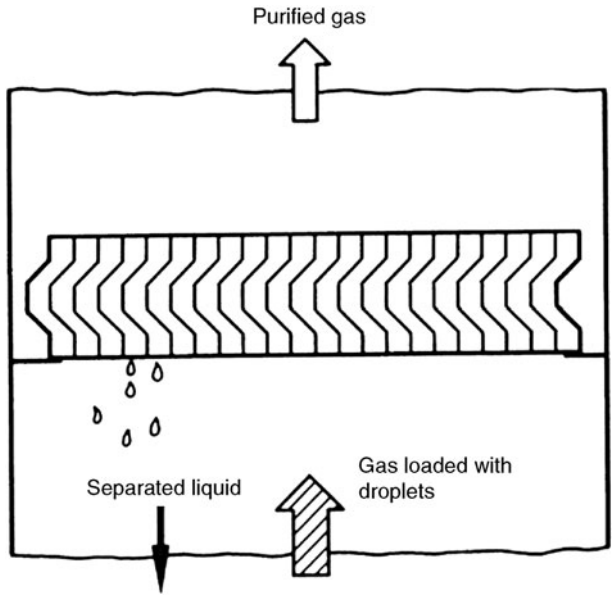

L4.3. Fig. 4. Schematic drawing of a vertically arranged wave plate separator.

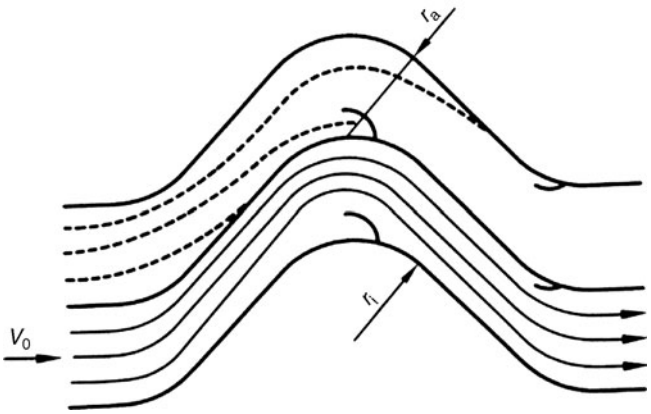

L4.3. Fig. 5. Path of droplets (- - -) and streamlines (—) in a wave plate separator.

$$\frac{\rho_G}{2} v_0^2 \approx 100 \text{ to } 150 \text{ Pa}. \tag{13}$$

With specially designed flutings in the lee, this limit moves up to 300 Pa (horizontal flow). Wave plates made out of thin metal sheets tend to vibrate crosswise to the flow.

For vertical flow in upward direction, as in washing towers of desulphurization units, the upper limit of the gas velocity is around 5–6 m/s (1 bar, $s = 20$ mm and $\rho_G = 1$ kg/m^3).

For other gas densities, the following formula may be used:

$$\left(\frac{\rho_G v_0^2}{\rho_L s g}\right)_{max} = 0.1 \text{ to } 0.15. \tag{14}$$

At larger velocities the entrainment of already separated liquid increases.

The gas flow constricts to 60% and 40% of the total cross section as its direction changes with angles 60° and 90°, respectively. This causes pressure loss.

As the width of the channels is much smaller than their length ($l/s >> 5$), it is not possible to recover pressure by decelerating the flow as in a diffusor. The pressure loss for every two direction changes or one packing element is roughly

$$\Delta\rho = (3 \text{ to } 6)\frac{\rho_G}{2} v_0^2 \tag{15}$$

for direction changes with $\alpha = 60°$–$90°$. For a number of packing elements n the pressure loss will increase roughly with a factor of $n^{1/4}$.

4.3 Separation Efficiency

Comparable to the cyclone, the separation limit is calculated approximately with the separation area:

$$A = 2\pi \frac{a}{360°} r_a l. \tag{16}$$

It is sufficient to take average contours according to Fig. 4. l is the height or length of the wave plate. The volume flow through one channel with the width s and the incoming gas velocity v_0 is

$$\dot{V} = l s v_0. \tag{17}$$

For a separation efficiency of 50%, the following equation applies for the settling velocity w_s^* of the limit droplet:

$$w_s^* = \frac{\dot{V}/2}{A}. \tag{18}$$

This droplet is subject to a mean centrifugal acceleration

$$\bar{z} = \frac{\bar{u}^2}{\bar{r}} \tag{19}$$

on its way with a radius of curvature

$$\bar{r} = \sqrt{r_a r_i}. \tag{20}$$

For direction changes of $\alpha = 45°$, $60°$, and $90°$ the flow constricts in average to 65%, 55%, and 45% of the channel width s, respectively. Therefore, the mean angular velocity

$$u = \frac{v_0}{0.65(0.55 \text{ or } 0.45 \text{ respectively})} \tag{21}$$

is much higher than the incoming velocity v_0.

The limit droplet diameter $d^* \sim d_e^*$ is calculated according to Stokes' law:

$$d_e^* = \sqrt{\frac{18\eta_G w_s^*}{\rho_L \bar{z}}}. \tag{22}$$

The Reynolds number of this limit droplet

$$\text{Re} = \frac{\rho_G w_s^* d_e^*}{\eta_G} \tag{23}$$

is normally in the range of 0.5 and 2. If this number is bigger than 10, which may be the case for a low viscosity or a high density of the gas, Stokes' law no longer applies. Then the following equation, which gives a good approximation for Reynolds numbers between 10 and 1,000, may be applied:

$$d_e^* = \frac{4.3(\rho_G \eta_G)^{1/3}}{(\rho_L \bar{z})^{2/3}} w_s^*. \tag{24}$$

The fractional separation efficiency curve is similar to that of the cyclone.

Normally, the liquid load of the gas entering the wave plate separator is 0.03 or below. However, if the separation efficiency of the first wave plate element is influenced by the limit load mechanism as in cyclones, it is possible to use cyclone theory for a rough estimate.

If the gas flow passes several packings subsequently, which are arranged with a larger distance between each other, the fractional efficiency for d_e^* is

$$\eta_F = 1 - 0.5e^{-0.7(i-1)} \tag{25}$$

whereas the total number of packings is i.

The number of 0.7 in the exponent of Eq. (25) is valid only for larger distances between the single packings and good mixing of the gas flow between these stages. In case of smaller distances and poor mixing, 0.7 has to be substituted by 0.25.

The modeling of wave plate separators with CFD simulation is described by Wang and Davies [12].

Example

Water droplets containing 2% lime shall separate in from a gas stream passing a wave plate separator in vertical direction. The gas stream has ambient pressure and a temperature of 75°C.

Physical data and dimensions:

$$\rho_G = 1\,\text{kg/m}^3;\ \eta_G = 21 \times 10^{-6}\,\text{Pa s};\ \rho_L = 1{,}025\,\text{kg/m}^3$$
$$r_i = s = 0.02\,\text{m};\ r_a = 2\,s = 0.04\,\text{m};\ \alpha = 90°;\ l = 0.5\,\text{m}.$$

Equation (14) shows in which flow range this separator can be operated:

$$v_0 = \sqrt{0.13 \cdot s \cdot g \cdot \frac{\rho_L}{\rho_G}} = 5.11\ \text{m/s} \approx 5\ \text{m/s},$$

$\dot{V} = 0.05\,\text{m}^3/\text{s}$,	Eq. (17)
$w_s^* = 0.8\,\text{m/s}$,	Eq. (18)
$r = 0.03\,\text{m}$,	Eq. (20)
$d_e^* = d^* = 8.5\,\mu\text{m}$,	Eq. (22)
$A = 0.031\,\text{m}^2$,	Eq. (16)
$\bar{u} = \frac{v_0}{0.45} = 11.1\,\text{m/s}$,	Eq. (21)
$\bar{z} = 4{,}100\,\text{m/s}^2$.	Eq. (19)

The calculation of the Reynolds number according Eq. (23) shows that Re = 0.32 < 1. Therefore, the application of Stokes' law has been correct.

The pressure loss according to Eq. (15) is

$$\Delta p = 6\frac{\rho_G}{2} v_0^2 = 75\,\text{Pa}.$$

5 Symbols

A	separation area (m^2)
A_R	friction area (m^2)
c_W	drag coefficient
d^*	limiting droplet diameter, defined as the diameter for which a separation efficiency of 50% is achieved (m)
d_e^*	limiting droplet diameter near the cyclone wall (m)
d_{50}	mean droplet diameter in the inlet (mass) (m)
d_{inlet}	cyclone inlet diameter (m)
g	gravity acceleration (m/s^2)
h_i	inner height (m)
i	number of subsequently arranged wave plate elements (–)
k	exponent (–)
l	length of settling path along the wave plate (m)
$\dot{M}$	mass flow (kg/s)
Δp	pressure drop (Pa)
r	radius (m)
$R_{A,i}$	cumulative weight oversize for droplets entering the cyclones core flow (–)
Re	Reynolds number (–)
s	channel width of wave plate separator (m)
u	circumferential velocity (m/s)
$\bar{u}$	mean circumferential velocity (m/s)
$\dot{V}_G$	gas volume flow (m^3/s)
v_0	velocity of the gas entering the wave plate separator (m/s)
w_s^*	settling velocity of d^* (m/s)
$w_{s,50}$	settling velocity of d_e^* (m/s)
$\bar{z}$	average centrifugal acceleration (m/s^2)
z_e	centrifugal acceleration (m/s^2)
α	angle (°)
α	contraction coefficient (–)
$\eta_F(d)$	fractional separation efficiency for droplet size d (–)
η_{total}	total separation efficiency (–)
η	dynamic viscosity (Pa s)
λ_0	friction coefficient for unloaded flow (–)
λ_L	friction coefficient for loaded flow (–)
μ_e	liquid load in inlet (–)
$\mu_{e,k}$	liquid load in cyclone center (core) (–)
ρ	density (kg/m^3)

Subscripts

a	on outer radius
G	gas phase
L	liquid phase
e	entrance
i	on inner radius

6 Bibliography

1. Bürkholz A (1989) Droplet separation. VCH Verlagsges. mbH, Weinheim
2. Fabian P et al (1993) Chem Eng 11:S.148–S.156 und (1993) 12:S.106–S.111
3. Ziebold S (2000) Chem Eng 5:S.94–S.100
4. Souders M, Brown GG (1934) Design of fractionating columns, entrainment and capacity. Ind Eng Chem 38(1):98–103
5. Gas Processing Suppliers Association (GPSA). Engineering data book, 11th edn. Gas Processing Suppliers Association, Tulsa
6. Linden AJ (1953) ter: Chem-Ing-Techn 25(6):S.328–S.330
7. Schmidt J, Giesbrecht uH (1997) Chem-Ing-Techn 69(3):S.312–S.319
8. Muschelknautz E, Herold uH (1975) Chem-Ing-Techn 47(7):S.267–S.273
9. Barth W (1956) Brennstoff-Wärme-Kraft 8:1–9
10. Muschelknautz E, Krambrock uW (1970) Chem-Ing-Techn 42(5): S.241–S.255
11. Barth W (1960) Allg Wärmetechn 9(11/12):S.252–S.256
12. Wang W, Davies uGA (1996) Chem Eng Res Des 74(A2):S.232–S.238

Specific Heat Transfer Problems

M1 Heat Transfer to Finned Tubes

Klaus Gerhard Schmidt
Institut für Energie- und Umwelttechnik (IUTA) e.V., Duisburg, Germany

Heat release and absorption from surfaces can be enhanced by fins. The fins are to be placed on the side of poorer heat transfer. Fins will be effective all the more as the ratio of the heat transfer coefficient from the side of better heat transfer to that of poorer increases.

Basic requirement for the following approach is an ideal contact between the fin base and tube or surface. The shown method has to be regarded as a first approach. It will not fit for abnormal dimensions or extremely high Reynolds numbers. Indispensable for such cases is the examination of appropriate literature and far reaching modeling related to experimental data.

A mean heat transfer coefficient has to be found and evaluated on the base of geometrically determined consideration. Therefore, the model cannot differentiate local changes in heat flux due to different temperatures over the fin caused by convection.

It is assumed that the direction of fluid flow corresponds to the orientation of the fins. Heat transfer by thermal radiation will not be considered as well as the heat transfer on the fin's tip which normally contributes less to the total surface.

Design, shape dimensions, and abbreviations of finned surfaces are shown in Fig. 1.

1 Heat Transfer for Finned Tube

The heat flow from a finned tube is

$$\dot{Q} = kA\Delta\theta_{LM}. \tag{1}$$

Related to the total surface and the temperature gradient between both fluids the heat transfer coefficient k is given by

$$\frac{1}{k} = \frac{1}{\alpha_v} + \frac{A}{A_i}\left(\frac{1}{\alpha_i} + \frac{d_0 - d_i}{2\lambda_t}\right). \tag{2}$$

Equation (2) does not include additional heat transfer resistances caused by

Fouling processes on the fin surface
Poor contact between the tube and fin base

α_v is a virtual heat transfer coefficient. Assuming uniform heat transfer coefficient α_m for bare tube and fin surface α_v is derived from the fin efficiency η_f.

The heat flow then is

$$\dot{Q} = \alpha_m(A_t + \eta_f A_f)(\Theta_t - \Theta_a). \tag{3}$$

The driving temperature gradient for this case is the difference between surface temperature of the tube and fluid. α_m may be calculated as shown in Chap. G6. The characteristic length of the circular fin tube is [1–4]

$$l = \frac{\pi}{2}\sqrt{d_0^2 + h_f^2}$$

Values calculated in this way are greater than those to get with the following method.

Experimentally based values for α_m can be derived from Eqs. (15), (16), and (18) for corresponding applications. Characteristic length has to be always the same for the whole calculation procedure. The velocity w_s in the smallest cross section is calculated from die velocity in the free flow w_0, the ratio from inflow cross sectional area A_0, and smallest sectional area between fins A_s.

$$w_s = w_0\frac{A_0}{A_s}. \tag{4}$$

This value can be fitted furthermore for the velocity change due to changing density with temperature of the fluid.

The fin efficiency is the ratio of the mean temperatures between the respective base of fin or tube and fluid.

$$\eta_f = \frac{\Theta_f - \Theta_a}{\Theta_t - \Theta_a}. \tag{5}$$

Together with this the virtual heat transfer coefficient becomes

$$\alpha_v = \alpha_m\left[\frac{A_t}{A} + \eta_f\frac{A_f}{A}\right] = \alpha_m\left[1 - (1 - \eta_f)\frac{A_f}{A}\right]. \tag{6}$$

The formal way to calculate fin efficiency is

$$\eta_f = \frac{\tanh X}{X} \tag{7}$$

with

$$X = \varphi\frac{d_0}{2}\sqrt{\frac{2\alpha_m}{\lambda_f\delta}}. \tag{8}$$

VDI-GVC (ed.), *VDI Heat Atlas*, DOI 10.1007/978-3-540-77877-6_50,

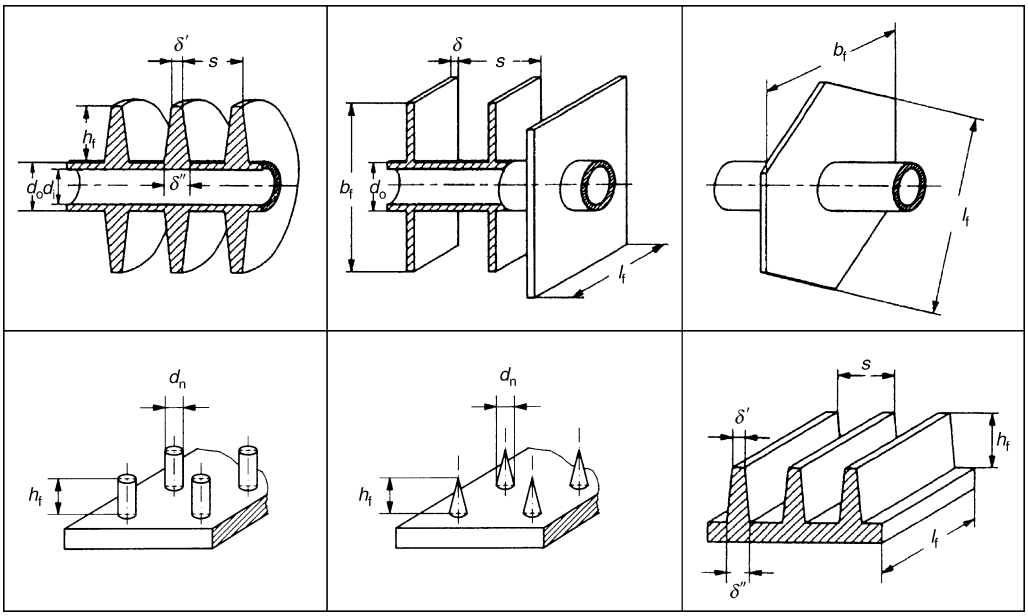

M1. Fig. 1. Different designs for finned surfaces.

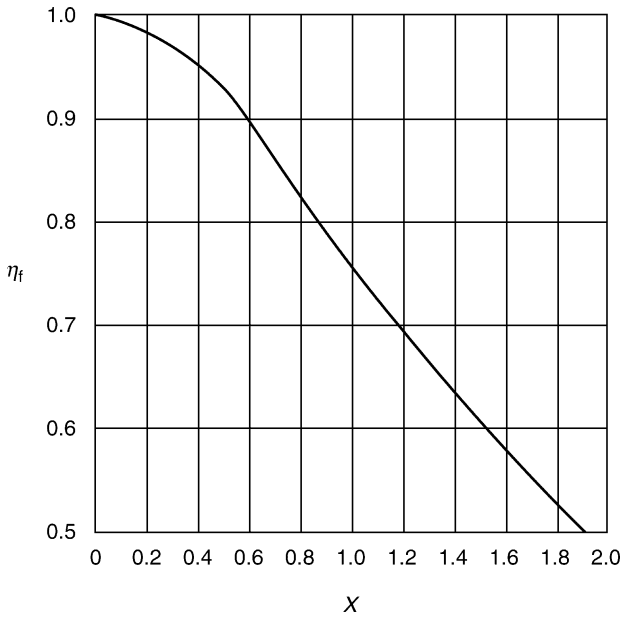

M1. Fig. 2. Efficiency factor of finned surfaces.

In Eq. (8) the product $\varphi d_0/2$ has the meaning of a weighted fin height which incorporates the design δ stays for the fin thickness. The function $\eta_f = f(X)$ is plotted in Fig. 2. The analytical calculation can be done by

$$\eta_f = \frac{\tanh X}{X} = \frac{1}{X}\frac{e^X - e^{-X}}{e^X + e^{-X}}. \tag{9}$$

Commonly used fins types are discussed next.

2 Examples for Fin Geometry

2.1 Circular Fins

$$\varphi = \left(\frac{D}{d_0} - 1\right)\left[1 + 0.35\ln\left(\frac{D}{d_0}\right)\right]. \tag{10}$$

For conic fins with thickness δ'' at the base and δ' at the tip, the mean δ is defined by

$$\delta = \frac{1}{2}(\delta'' + \delta'). \tag{11}$$

2.2 Rectangular Fins

$$\varphi = (\varphi' - 1)(1 + 0.35\ \ln\ \varphi'), \tag{12}$$

$$\varphi' = 1.28\frac{b_f}{d_0}\sqrt{\left(\frac{l_f}{b_f} - 0.2\right)}. \tag{13}$$

2.3 Adjacent Fins

For arrangements with in-line banks Eqs. (12) and (13) are valid.

For staggered banks a hexagon fin is to be defined for every tube with

$$\varphi' = 1.27\frac{b_f}{d_0}\sqrt{\left(\frac{l_f}{b_f} - 0.3\right)} \quad \text{with } l_f = \sqrt{s_1^2 + \frac{s_f^2}{4}}. \tag{14}$$

Along with the spacing two arrangements are to be distinguished according to Fig. 3 [5].

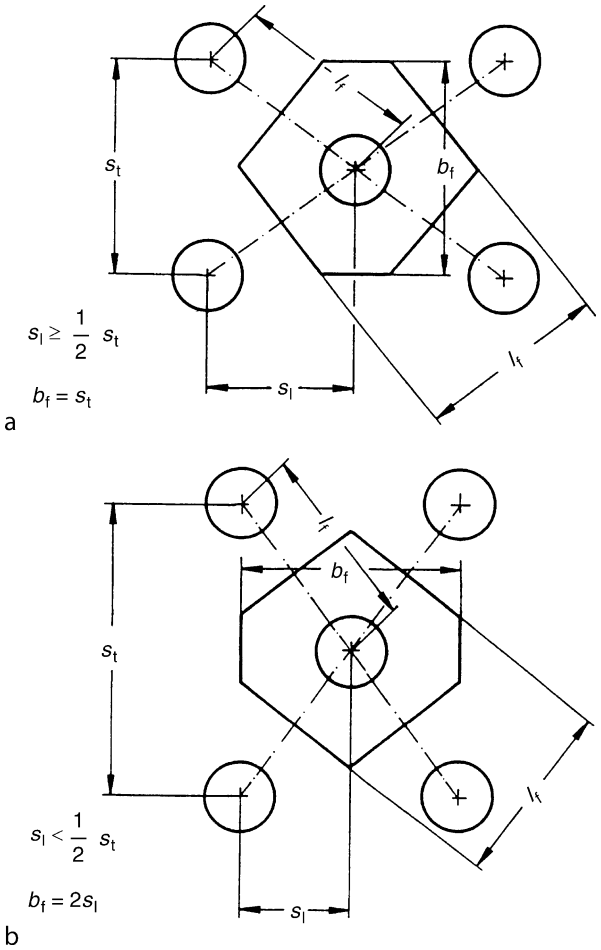

M1. Fig. 3. Schematic picture of different gaps in the hexagonally designed cross sections between parallel finned tubes in a bundle.

2.4 Straight Fins on Flat Plate

For this case in Eq. (8) the expression $\varphi d_0/2$ has to be substituted by the height of fin h_f and δ becomes

$$\delta = \frac{3}{4}\delta'' + \frac{1}{4}\delta'$$

2.5 Pin or Tip Needles on Flat Plate

Here the expression $\varphi d_0/2$ in Eq. (8) has to be substituted by the height of fin h_f and δ becomes

$$\delta = \frac{1}{2} d_n \quad \text{for pins}$$

$$\delta = \frac{9}{8} d_n \quad \text{for needles}$$

2.6 Heat Transfer in Banks of Finned Tubes in Cross Flow

Heat transfer in banks of finned tubes depends on geometric factors, physical properties, and the velocity of the fluid between the fins and the rows. Inflow pattern and the formation of microturbulences by surface roughness play an important role and are difficult to control. An all-in-one solution for a variety of applications and design cannot be given.

The advice to solve given problems of heat transfer in banks of finned tubes is to look for an empirical calculation formula on the base of experimental data [6–10]. The following equations are derived from industrial data [11] and the comparison with [12, 13].

This leads to more than four rows and

- Inline arrangement

$$\mathrm{Nu_d} = 0.22\mathrm{Re_d^{0.6}}\left(\frac{A}{A_{t0}}\right)^{-0.15}\mathrm{Pr}^{1/3}. \qquad (15)$$

- Staggered banks

$$\mathrm{Nu_d} = 0.38\mathrm{Re_d^{0.6}}\left(\frac{A}{A_{t0}}\right)^{-0.15}\mathrm{Pr}^{1/3}. \qquad (16)$$

The suffix d prompts to take as characteristic length the outer diameter d_0 of the tube. For circular fins, the ratio A/A_{t0} of the finned surface to the surface of the base tube becomes

$$\frac{A}{A_{t0}} = 1 + 2\frac{h_f(h_f + d_0 + \delta)}{s d_0}. \qquad (17)$$

The most important factors in this Eq. (17) are height h and spacing s (Fig. 1). They are essential for the formation of flow between fins and tubes and vary widely in industrial applications.

Calculations with the given Eqs. (15) and (16) were fitted within a range of ±10% to ±25% for $10^3 < \mathrm{Re_d} < 10^5$ and $5 \leq A/A_{t0} \leq 30$

For banks with one to three rows, it is recommended to modify the factor C of the Nusselt power equation

$$\mathrm{Nu_d} = C\mathrm{Re_d^{0.6}}\left(\frac{A}{A_{t0}}\right)^{-0.15}\mathrm{Pr}^{1/3}. \qquad (18)$$

For in-line arrangement $C = 0.20$, for staggered arrangement with two rows $C = 0.33$, and for three rows $C = 0.36$.

Example

Air has to be heated up from 90 to 120°C. Heating fluid is vapour condensing at 130°C. The mass flow of air is 1.92 kg/s.

The required power then is 59 kW.

Circular fin tubes	D = 56 mm, d_0 = 25.4 mm, δ = 0.4 mm	
	a = 2.42 mm, d_i = 21 mm	
Material	Aluminum with λ = 209 W/(m K)	
Arrangement	9 fins/in.	
	Spacing fins	s = 2.82 mm
	Spacing transversal	s_t = 60 mm
Inflow cross section	1 m^2	
Inflow velocity	2 m/s, calculated from mass flow and temperature	

Heat transfer coefficient	α_i = 10,454 W/(m^2 K)	
Width heat exchanger	17 tubes parallel -- >	17 s_t = 1.02 m
Height heat exchanger	1 m^2/1.02 m = 0.98 m	
Number fins single tube	0.98 m/0.00282 m = 348 fins	
A_f single fin	$A_f = 2\frac{\pi}{4}(D^2 - d_0^2)$ $= 2\frac{\pi}{4}(56^2 - 25.4^2)10^{-6}\,\text{m}^2$ $= 3.913 \cdot 10^{-3}\,\text{m}^2$	
A_f per tube	$A_f = 348 \cdot 3.913 \cdot 10^{-3}\,\text{m}^2$ $= 1.362\,\text{m}^2$	
A_t per tube	$A_t = (348+1)\pi d_0 a$ $= 349 \cdot \pi \cdot 25.4 \cdot 2.42 \cdot 10^{-6}\,\text{m}^2 = 0.067\,\text{m}^2$	
A_{t0} per tube	$A_{t0} = \pi \cdot d_0 \cdot 0.98m$ $= \pi \cdot 25.4 \cdot 10^{-3}\,\text{m} \cdot 0.98\,\text{m} = 0.078\,\text{m}^2$	
A per tube	$A = 1.362\,\text{m}^2 + 0.067\,\text{m}^2 = 1.429\,\text{m}^2$	
A_i per tube	$A_i = 0.98\,\text{m} \cdot \pi \cdot d_i$ $= 0.98\,\text{m} \cdot \pi \cdot 21 \cdot 10^{-3}\,\text{m} = 0.065\,\text{m}^2$	

We assume a heat exchanger with circular fins and in-line arrangement.

Straitened cross section of flow:

$$\frac{A_0}{A_s} = \frac{s_t(a+\delta)}{(s_t - d_0)a + (s_t - D)\delta} = \frac{60 \cdot 2.82}{(60 - 25.4) \cdot 2.42 \cdot (60 - 56) \cdot 0.4} = 1.984.$$

Flow velocity in the smallest cross section:

$$w_s = w_0 \frac{A_0}{A_s} = 2\text{m/s} \cdot 1.984 = 3.97\,\text{m/s}.$$

Influence of temperature:

$$w_{sT} = w_s \frac{273 + \frac{1}{2}(120+90)}{273+90} = 3.97\ \text{m/s} \cdot 1.04 = 4.13\ \text{m/s}.$$

Ratio of surfaces

$$\frac{A}{A_{t0}} = \frac{1.429\,\text{m}^2}{0.078\,\text{m}^2} = 18.321\ \text{(note : Eq.(17) will give 18.558)}.$$

Heat transfer air side

$$\text{Re}_d = \frac{d_0 w_{sT} \rho_{air}}{\eta_{air}} = \frac{0.0254\,\text{m} \cdot 4.13\,\text{m/s} \cdot 0.909\,\text{kg/m}^3}{22.37 \cdot 10^{-6}\,\text{kg/(ms)}} = 4,236,$$

$$\text{Nu}_d = 0.22\text{Re}_d^{0.6}\left(\frac{A}{A_{to}}\right)^{-0.15} \cdot \text{Pr}^{1/3} = 0.22 \cdot 4263^{0.6} \cdot 18.321^{-0.15} \cdot 0.706^{1/3} = 19.07,$$

$$\alpha_m = \frac{\text{Nu}_d \lambda_{air}}{d_0} = \frac{19.07 \cdot 0.0321\,\text{W/(m K)}}{0.0254\,\text{m}} = 24.10\,\text{W/(m}^2\text{K)}.$$

Fin efficiency: Circular fins in-line Eq. (10)

$$\varphi = \left(\frac{D}{d_0} - 1\right)\left[1 + 0.35\,\ln\left(\frac{D}{d_0}\right)\right] = 1.54,$$

$$X = \varphi \frac{d_0}{2}\sqrt{\frac{2\alpha_m}{\lambda_f \delta}} = 1.54\frac{0.0254\,\text{m}}{2}\sqrt{\frac{2 \cdot 24.14\,\text{W/(m}^2\text{K)}}{209\ \text{W/(mK)} \cdot 0.0004\,\text{m}}} = 0.47,$$

$$\eta_f = \frac{\tanh X}{X} = \frac{1}{X}\frac{e^X - e^{-X}}{e^X + e^{-X}} = \frac{1}{0.47}\frac{e^{0.47} - e^{-0.47}}{e^{0.47} + e^{-0.47}} = 0.93,$$

$$\alpha_v = \alpha_m\left[1 - (1 - \eta_f)\frac{A_f}{A}\right] = 24.10\left[1 - (1 - 0.93)\frac{1.362}{1.429}\right]\text{W/(m}^2\text{K)} = 22.49\,\text{W/(m}^2\text{K)}$$

$$\frac{1}{k} = \frac{1}{\alpha_v} + \frac{A}{A_i}\left(\frac{1}{\alpha_i} + \frac{d_0 - d_i}{2\lambda_t}\right) = \left[\frac{1}{22.49} + \frac{1.429}{0.065}\left(\frac{1}{10{,}454} + \frac{0.0254 - 0.021}{2 \cdot 209}\right)\right]\text{m}^2\text{K/W} = 0.0468\,\text{m}^2\text{K/W},$$

$$k = 21.37\,\text{W/m}^2\text{K}.$$

Logarithmic mean temperature difference

$$\Delta\Theta_{LM} = \frac{\Theta_{out} - \Theta_{in}}{\ln\frac{\Theta_{tube} - \Theta_{in}}{\Theta_{tube} - \Theta_{out}}} = \frac{30}{\ln\frac{40}{10}} = 21.64\,\text{K}.$$

Heat transfer surface necessary

$$A = \frac{\dot{Q}}{k\Delta\Theta_{LM}} = \frac{59{,}000}{21.37 \cdot 21.64}\,\text{m}^2 = 127.58\,\text{m}^2.$$

Number of rows

$$\text{NR} = \frac{127\,\text{m}^2}{17 \cdot 1.429\,\text{m}^2} = 5.25 \rightarrow 6\ \text{rows}.$$

Six rows are chosen.

A	total outer surface
A_s	smallest cross-sectional area
A_t	free outer surface of tube
A_{to}	surface of bare tube without fins
A_i	inside surface of tubes
A_f	fin surface
A_0	inflow cross-sectional area
X	operand Eq. (8)
a	free space between fins
b_f	width of angular fin
D	outer diameter of fin
d_o	outer diameter of tube
d_i	inner diameter of tube
d_n	diameter of needles
h_f	height of fin
k	overall heat transfer coefficient

l_f	length of angular fin
$\dot{Q}$	heat flow
δ	thickness of fin
s_l	spacing longitudinal
s_t	spacing transversal
w_s	velocity in the smallest cross section
w_0	inflow velocity
α_i	heat transfer coefficient in the inner tube
α_m	mean heat transfer coefficient for tube and fin
α_v	virtual heat transfer coefficient
$\Delta\Theta_{LM}$	logarithmic mean temperature difference
Θ_t	surface temperature tube
Θ_f	surface temperature fin
Θ_a	ambient temperature
η_f	fin efficiency
λ	thermal conductivity, uniform for fin f or tube t
ρ	density fluid
φ	operand Eq. (8)

3 Bibliography

1. Brandt F (1988) VDI-Wärmeatlas, Mb. 5. Auflage
2. Gnielinski V, Zukauskas A, Skrinska A (1983) Heat exchanger design handbook. Hemisphere Publishing Corporation, New York
3. Wehle F (1980) Forsch.i.d.Kraftwerkstechn. S. 165/169
4. Wehle F (1983) Theoretische und experimentelle Untersuchung der Wärmeübertragung bei Rippenrohrbündeln und Einfluss der Temperaturabhängigkeit der Stoffwerte auf den Wärmeübergang; Fortschr.Ber. VDI, Reihe 6, Nr. 121. VDI-Verlag, Düsseldorf
5. Ebeling N, Schmidt KG (1994) Waermeleistung von Rippenrohr-Waermeaustauschern mit zusammenhaengenden Rippen; Brennst.-Waerme-Kraft 46(10):437–438
6. Brauer H (1961) Spiralrippenrohre für Querstrom-Wärmeaustauscher. Z. Kältetechnik 13:S. 274/279
7. Briggs DE, Young u. EH (1963) Eng Prog Sym Ser 59(41):S. 1/9
8. Schmidt Th. E (1963) Z. Kältetechik 15:S. 98
9. Schmidt Th. E (1963) Z. Kältetechik 15:S. 370/378
10. Schmidt Th. E (1966) Verbesserte Methoden zur Bestimmung des Wärmeaustausches an berippten Flächen; Kaeltetech Klim 18(4):135–138
11. Confidential industrial data for evaluation of Eqs. (15) and (16)
12. Handbuch HTFS AM1, Aug 85, commercial edition
13. Report ESG-4 HTRI, June 72, confidential

M10 Heat Transfer and Momentum Flux in Rarefied Gases

Arnold Frohn · Norbert Roth · Klaus Anders†
Stuttgart, Germany

1 Introduction

Within the kinetic theory of gases heat transfer and flow processes of rarefied gases are described by the Boltzmann equation [1–14]. To this nonlinear integro-differential equation belong two characteristic lengths, namely the mean free path l of the molecules and a macroscopic length L characteristic for the body dimensions. The ratio of these quantities gives the Knudsen number

$$\mathrm{Kn} = l/L \tag{1}$$

as dimensionless parameter. At normal density, the mean free path is of the order of 10^{-7} m. In many technical applications, it can therefore be assumed that one has for the Knudsen number $\mathrm{Kn} \ll 1$. The term "rarefied gases" means that l is not negligibly small in comparison with L. This condition is often fulfilled at low density of the surrounding air, as for example in the higher layers of the earth's atmosphere. Similar conditions occur in vacuum or space technology. It should be mentioned that large values of the Knudsen number occur at normal density when very small particles are involved. Examples are aerosols in the atmosphere of the earth, fine powders in process engineering, or medical aerosols for inhalation.

For sufficiently small values of the Knudsen number fluid dynamic systems can be described with the Navier–Stokes equations of the continuum theory. These equations are obtained from macroscopic relations for conservation of mass, momentum, and energy. Viscous stress and heat conduction are described by empirical relations of the continuum theory, which depend linearly on the gradients of velocity and temperature. Within the continuum theory, the coefficients in these equations, heat conductivity λ, and viscosity η must be determined by experimental methods. In the kinetic theory of gases, the Navier–Stokes equations are obtained with the Chapman–Enskog method as solution of the Boltzmann equation for small values of the Knudsen number [5, 6]. With this method, the fluid properties λ and η can be determined theoretically from the law of the interaction force between the molecules. It follows from these calculations that λ and η for ideal gases are functions of the temperature, but do not depend on the gas density ρ. This result means that heat conduction in an ideal gas is independent of the density of the heat conducting gas. It is easy to see that this result can be valid only for a limited density range, since the heat conducting medium disappears when the density tends to zero and heat conduction is no longer possible. Similar considerations show that the viscous forces which are proportional to η must vanish when the density ρ tends to zero.

For large Knudsen numbers in the free-molecule regime, the number of molecular wall collisions becomes larger than the number of intermolecular collisions. Therefore, the influence

†Deceased

VDI-GVC (ed.), *VDI Heat Atlas*, DOI 10.1007/978-3-540-77877-6_59,

of collision processes can be neglected when solving the Boltzmann equation. In this regime, the molecules move independently from each other and transport energy and momentum directly from one wall to another. This means that the molecular transport of energy and momentum is proportional to the density. In vacuum technology manometers of the Pirani type take advantage of the density dependence of heat conduction at low densities. After calibration such instruments are used for pressure measurements in an approximate range from 10^{-3} to 1 mbar [15, 16].

Theoretical solutions of the Boltzmann equation are mathematically extremely difficult in the transition regime between the continuum and the free-molecule regime. Here, exact analytical solutions of the Boltzmann equation are available only in very idealized cases. Analytical approximate solutions have been presented for systems without flow or for simple geometrical configurations. The purpose of the present section is to describe the distinction between continuum theory and kinetic theory, i.e., between solutions of the Navier–Stokes equations and the Boltzmann equation. Some solutions of the Boltzmann equation for rarefied gases are discussed. Energy transfer by radiation is not taken into account, although its influence increases with decreasing density and becomes the only mechanism of energy transfer under high-vacuum conditions. Details of this energy transport by electromagnetic waves are discussed in Chaps. K1–K3.

2 Theory

2.1 Introduction

In the kinetic theory, the thermodynamic state of a gas is described with the molecular velocity distribution function. This central function which describes the statistical distribution of the molecular velocities has to be found as solution of the Boltzmann equation. The thermodynamic variables are then calculated as moments of the molecular velocity distribution function. For the special case of a gas in thermodynamic equilibrium one has the well-known Maxwellian distribution [7]. Using this distribution function, one obtains for the mean magnitude of the molecular velocity

$$\bar{c} = \sqrt{\frac{8kT}{m\pi}} = \sqrt{\frac{8RT}{\pi}} = \sqrt{\frac{8\,\tilde{R}T}{\pi\tilde{M}}}, \tag{2}$$

where k is the Boltzmann constant, m the mass of a molecule, T the temperature, $R = k/m$ the individual gas constant, $\tilde{R}$ the universal gas constant, and $\tilde{M}$ the mole mass. It should be mentioned that from the definition of mass density, pressure, and temperature as moments of the distribution function the thermal equation of state follows in the form

$$p = nkT = \rho RT \tag{3}$$

for arbitrary distribution functions, which means that Eq. (3) holds for arbitrary deviations from thermodynamic equilibrium. With the relation

$$\rho = mn \tag{4}$$

the mass density ρ can be determined from the number density n of the molecules and the mass of a molecule m.

In the continuum regime with small values of the Knudsen number, one has only small deviations from thermodynamic equilibrium, which also means small deviations from a locally Maxwellian distribution function. In this case, the Boltzmann equation can be linearized. Different mathematical methods and physical models for solving the resulting equations have been developed. The most important method for practical applications in fluid mechanics is the Chapman–Enskog method, which has been described comprehensively in the literature, for example in [5–7]. With this approach, one obtains the Navier–Stokes equations with the usual linear relations for macroscopic heat conduction and momentum flux processes.

The components of the heat flux vector are given by the well-known relation $\boldsymbol{q} = -\lambda \operatorname{grad} T$. Calculations of the heat conductivity coefficient λ using the intermolecular force law show that λ is a function of the temperature T, but it does not depend on the gas density ρ. Similarly, the viscosity η, which determines the components of the stress tensor, depends on the temperature but not on the density. The possibility to determine the temperature dependence of the transport coefficients theoretically is of practical importance when extrapolations of the transport coefficients λ and η for high temperatures are needed, for which experimental results are not available. According to Chapman and Cowling [5], the molecular model for elastic rigid spheres gives for the viscosity

$$\eta = \frac{5\pi}{32}\rho l\bar{c} \approx 0.5\rho l\bar{c}. \tag{5}$$

This relation can be used to determine the mean free path l from experimental results for the viscosity η. Figure 1 shows the mean free path for the gases helium and nitrogen at constant temperature as a function of pressure. The results have been obtained using Eqs. (2) and (5) with thermodynamic properties from

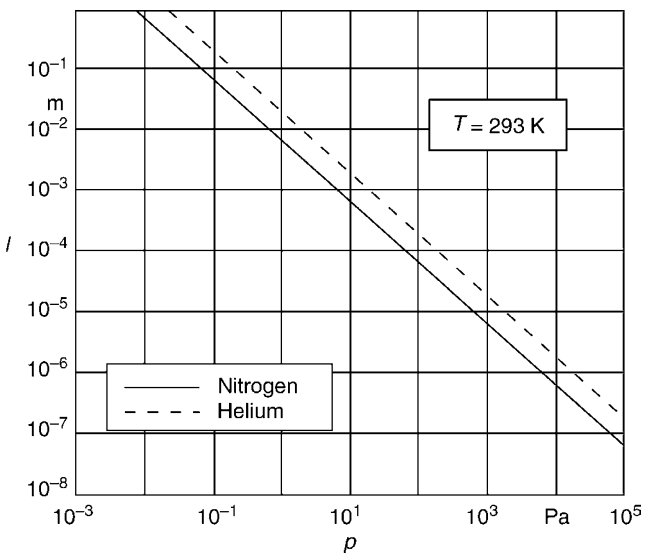

M10. Fig. 1. Mean free path for nitrogen and helium as a function of pressure according to Eqs. (2) and (5) with thermodynamic properties from Subchap. D3.1.

Subchap. D3.1 With the same molecular model one obtains for the heat conductivity coefficient

$$\lambda = \frac{25\pi}{64}\rho \bar{l} \bar{c} c_v, \tag{6}$$

where c_v is the specific heat capacity at constant volume [5]. For monatomic gases with the ratio of specific heats $\kappa = c_p/c_v = 5/3$ the Prandtl number is

$$\mathrm{Pr} = \frac{\eta\, c_p}{\lambda} = \frac{2}{3} \approx 0.67. \tag{7}$$

In the limit of a highly rarefied gas, i.e., at very large Knudsen numbers $\mathrm{Kn} \gg 1$, the molecular heat transport to a wall depends directly on the number of molecules incident on and reflected by the wall. For simple geometrical configurations of the walls, analytical expressions for the macroscopic heat transfer can be deduced. It has already been mentioned in the introduction that it is characteristic for the free-molecule regime that the heat flux is proportional to the density of the gas. In the transition regime, the heat flux has to be calculated as moment of the distribution function, which must be determined as solution of the Boltzmann equation.

Among the approaches used to solve the Boltzmann equation are expansions of the distribution function about absolute thermodynamic equilibrium or about local thermodynamic equilibrium, replacing the nonlinear collision term of the Boltzmann equation by a simpler mathematical model [14] or evaluation of momentum equations [17, 18]. In the past years, numerical calculations using Monte Carlo simulations or molecular gas dynamics have become more important [2, 19–21]. A critical discussion has been given by Bird [22]. Solutions of the Boltzmann equation have been presented mainly for problems with simple geometries, such as parallel plates, concentric cylinders, or concentric spheres. For technical applications, it would be important to have solutions for polyatomic gases. For this case, the Boltzmann equation becomes obviously too complicated. Available solutions are based on empirical assumptions. Usually, solutions for monatomic gases are modified by introducing macroscopic thermodynamic properties of polyatomic gases.

For convenience the following flow regimes may be defined:

$\mathrm{Kn} < 0.01$	continuum regime
$0.01 < \mathrm{Kn} < 0.1$	slip-flow and temperature-jump regime
$0.1 < \mathrm{Kn} < 10$	transitional regime

In the continuum regime, the Navier–Stokes equations with the usual expressions for heat flux and viscous stress are valid. This regime is a subject of the field of classical fluid mechanics and heat transfer [23–25]. In the slip-flow and temperature-jump regime the Navier–Stokes equations remain valid, but due to the rarefaction the gas adjacent to a wall no longer assumes the velocity or the temperature of the wall. The gas slips along the wall and a finite temperature jump between the gas and wall is observed. Temperature and velocity jumps can be taken into account by modified boundary conditions. In the transition regime, the Boltzmann equation has to be solved in its general form.

In the free-molecule regime it becomes easier to find solutions of the Boltzmann equation, since the effect of collisions vanishes and the collision term tends to zero. For this regime solutions exist for various special problems. Since it is extremely difficult to obtain solutions of the Boltzmann equation that cover the entire Knudsen number range, it has been tried to obtain approximate solutions by interpolation between solutions for the continuum regime and solutions for the free-molecule regime. It has been assumed that heat flow $\dot{Q}$ for arbitrary Knudsen numbers can be described by the heat transfer for the continuum regime $\dot{Q}_{\mathrm{Kont}}$ and the heat transfer for the free-molecule regime $\dot{Q}_{\mathrm{FM}}$ according to

$$\frac{1}{\dot{Q}} = \frac{1}{\dot{Q}_{\mathrm{Kont}}} + \frac{1}{\dot{Q}_{\mathrm{FM}}}. \tag{8}$$

It has been shown that this empirical rule can be useful for special cases, even for other quantities for example, the drag coefficient [26].

2.2 Boundary Conditions

In a problem, for the calculation of the heat transfer and the momentum flux at very small Knudsen numbers, i.e., in the continuum regime, knowledge of the boundary conditions is sufficient. In general, it is assumed that the heat conducting medium at the wall attains the wall temperature and velocity. With increasing Knudsen number, the gas temperature and velocity may show finite jumps at the wall. A theoretical description based on the kinetic theory needs as boundary condition the distribution function of the molecules reflected by the wall in dependence of the distribution function of the incident molecules [14]. This detailed description is usually too complicated for practical applications and is replaced by a simplified model based on the so-called accommodation coefficients. These coefficients describe the changes of certain moments of the distribution function by the interaction with the wall. The accommodation coefficient for the energy or temperature is defined, for example, by

$$\gamma = \frac{T_r - T_c}{T_w - T_c}. \tag{9}$$

In this equation, T_c represents the temperature of the molecules incident on the wall, T_w the wall temperature, and T_r the temperature of the molecules reflected by the wall. One has $T_r = T_e$ for $\gamma = 0$ and $T_r = T_w$ for $\gamma = 1$. In a similar way, accommodation coefficients can be defined for tangential and normal momentums of the molecules. The values of accommodation coefficients for technical surfaces are in a complicated way dependent on the state of the gas and the solid surface. An unambiguous prediction of these coefficients may be problematic. These questions have been discussed extensively in the literature [27, 28]. It has been mentioned that rarefied gases exhibit finite jumps of velocity and temperature at solid walls. The slip velocity at the wall for small but not negligible values of the Knudsen number can be expressed by

$$u(y=0) = \zeta \left(\frac{\partial u}{\partial y}\right)_{y=0}, \tag{10}$$

where y is a coordinate normal to the wall. A more detailed investigation gives for the molecular model of rigid spheres for the parameter of the slip velocity

$$\zeta = 2\,c\frac{2-\beta}{\beta}\,l \tag{11}$$

with $c = 0.4909 \approx 0.5$ and $0 < \beta < 1$, where β can be considered accommodation coefficient of the velocity tangential to the solid wall [11]. It can be seen that ζ is of the order of the mean free path. For the temperature of the gas adjacent to the solid wall, one assumes in a similar way

$$T\,(y=0) = T_{\mathrm{W}} + g\left(\frac{\partial T}{\partial y}\right)_{y=0}. \tag{12}$$

Here, the coefficient of the temperature jump g according to Kennard [11] is given by the relation

$$g = \frac{2-\gamma}{\gamma}\frac{15}{8}f\,l, \tag{13}$$

with

$$f = \frac{16}{15}\frac{\lambda}{\eta c_{\mathrm{v}}}\frac{1}{\kappa+1} = \frac{16}{15}\frac{1}{\mathrm{Pr}}\frac{\kappa}{\kappa+1}. \tag{14}$$

In problems containing the macroscopic length L, the ratio

$$\frac{g}{L} = \frac{2-\gamma}{\gamma}\frac{15}{8}f\,\mathrm{Kn} \tag{15}$$

plays an important role. Solutions presented in the literature are often for monatomic gases without inner degrees of freedom, therefore

$$\frac{\lambda}{\eta c_{\mathrm{v}}} = \frac{5}{2}, \quad c_{\mathrm{v}} = \frac{3}{2}R, \quad c_{\mathrm{p}} = \frac{5}{2}R, \quad \text{and} \quad \kappa = \frac{5}{3}. \tag{16}$$

In this case the correction factor is $f = 1$. Assuming additionally perfect accommodation, one has

$$g/l = \frac{15}{8}\mathrm{Kn}. \tag{17}$$

It can be seen that g is of the order of the mean free path l. It must be recognized that the coefficient g remains finite for perfect thermal accommodation. This means that temperature jumps also occur for $\gamma = 1$. For a stringent theory of polyatomic gases, one should introduce a proper molecular model, in practical applications the corresponding thermodynamic property values of polyatomic gases are introduced into Eq. (14). Under these conditions, one has in general $f \neq 1$ for the correction factor [29]. In the discussion of the solutions in Sects. 3 and 4 of this chapter, the changes caused by this approximate method are explained.

In the past years, more numerical solutions of the Boltzmann equation have been presented for special problems. This work deals with the numerical determination of the coefficients of the temperature jump and the slip velocity [30, 31], with the simulation of gas flow through pores and fine channels [32, 33] and with the heat transfer in rarefied gases including evaporation and condensation [34]. A few papers deal with mixtures of rarefied gases [35–39].

3 Solutions for Gases at Rest

3.1 Introduction

For small values of the Knudsen number $\mathrm{Kn} < 0.01$, the solution of the Boltzmann equation is in agreement with the results of the continuum theory, thus one has for the heat flux $\dot{q} = -\lambda$ grad T, which leads to the heat-conduction equation with the usual boundary conditions. Solutions for this Knudsen number range are not discussed here, as they are the same as those for solid bodies [23]. For the temperature-jump and slip-flow regime in the Knudsen number range $0.01 < \mathrm{Kn} < 0.1$ the heat-conduction equation of the continuum theory is still valid, but the temperature-jump boundary conditions of Eq. (12) must be introduced.

Using the temperature-jump boundary conditions, solutions of the heat-conduction equation are presented in the following for a few simple geometrical configurations, namely for parallel plates, for concentric cylinders, and for concentric spheres. As mentioned before, solutions of the continuum regime will be extended to the temperature-jump regime. The results obtained with this method, which generally are valid only for Knudsen numbers $\mathrm{Kn} < 0.1$, show characteristic features of the behavior of rarefied gases. In addition, approximate analytical solutions of the Boltzmann equation obtained from moment equations are discussed [7, 18]. The solutions of this approach are valid for an extended Knudsen number range.

By comparison with experiments, it can be shown that the heat flux obtained with the temperature-jump boundary condition for the case of plane parallel plates is valid for all Knudsen numbers. This result is probably due to the simple geometry. The solutions obtained with the temperature-jump boundary condition for concentric cylinders and concentric spheres are valid only for a limited Knudsen number range, which depends on the radii of the geometrical configuration. A discussion of the cylindrical case may be found in [7].

If not mentioned otherwise, the relations presented in the following are based on the assumptions of monatomic gases, perfect accommodation at the walls, and small temperature differences, i.e., for $|T_1/T_2 - 1| \ll 1$. Due to the assumption of small temperature differences, the calculations can often be performed with constant property values.

3.2 Plane Geometry

3.2.1 Steady Heat Conduction Between Parallel Planes for Knudsen Numbers Kn < 0.1

Solving the heat-conduction equation in a gas bounded by two plates for the steady case gives the linear temperature profile

$$T = b_1 y + b_0. \tag{18}$$

For plates with the distance s and the temperatures T_1 and T_2 one finds for the heat flux in the continuum regime

$$\dot{q}_{\mathrm{Kont}} = -\lambda\frac{\mathrm{d}T}{\mathrm{d}y} = \frac{\lambda}{s}(T_1 - T_2). \tag{19}$$

For the extension of this result to the temperature-jump regime $0.01 < \mathrm{Kn} < 0.1$ the boundary conditions of the temperature-jump regime Eq. (12) are introduced. One obtains the relations

$$\begin{aligned} T(y=0) &= b_0 = T_1 + g_1 b_1, \\ T(y=s) &= b_1 s + b_0 = T_2 - g_2 b_1, \end{aligned} \tag{20}$$

which allow to determine the constants b_0 and b_1. For the temperature distribution, it follows

$$\frac{T(y) - T_2}{T_1 - T_2} = \left(1 - \frac{y + g_1}{s + g_1 + g_2}\right) \tag{21}$$

and for the heat flux

$$\dot{q} = -\lambda \frac{\mathrm{d}T}{\mathrm{d}y} = \frac{\lambda}{s + g_1 + g_2}(T_1 - T_2). \tag{22}$$

Comparing this result with the classical solution for the continuum regime Eq. (19), one recognizes that the temperature-jump at the walls caused by the rarefaction of the gas reduces the heat flux and is equivalent to an increase of the plate distance from s to $s + g_1 + g_2$. The coefficient g is therefore often called temperature-jump distance. Figure 2 shows the temperature distribution between two parallel plates according to Eq. (21) schematically. Assuming small temperature differences and equal values of the accommodation coefficients at both walls, g_1 and g_2 have practically the same value. For monatomic gases, perfect accommodation, with $g_1 = g_2 = g$ and using Eq. (17), one gets for the temperature distribution between the plates

$$\frac{T(y^*) - T_2}{T_1 - T_2} = \left(1 - \frac{y^* + (15/8)\mathrm{Kn}}{1 + (15/4)\mathrm{Kn}}\right), \tag{23}$$

where $y^* = y/s$ and $\mathrm{Kn} = l/s$ have been introduced. This relation is represented in Fig. 3 for different values of the Knudsen number. The temperature distribution between the plates is still linear, and the temperature gradient is smaller in comparison with the continuum solution. For the ratio of the heat flux of a rarefied gas to the heat flux in the continuum, it follows

$$\frac{\dot{q}}{\dot{q}_{\mathrm{Kont}}} = \frac{\dot{Q}}{\dot{Q}_{\mathrm{Kont}}} = \frac{1}{1 + (15/4)\mathrm{Kn}}. \tag{24}$$

This means, for example, that for the plate distance of 1 cm the pressure of the heat conducting gas must be reduced by a factor of 100 in comparison with normal pressure, in order to reduce the heat flux by 0.25%.

In the following it is shown that Eq. (24), though it has been derived for the temperature-jump regime, is valid for the entire Knudsen number range.

Example 1

The space between two parallel plates with the distance $s = 1$ cm contains helium at the pressure $p = 1{,}000$ hPa. The temperatures of the plates are $T_1 = 273$ K and $T_2 = 278$ K, the accommodation coefficients of both plates are $\gamma = 1$. (a) Calculate the heat flux, (b) What is the heat flux when the pressure is reduced to 0.2 hPa? (c) What is the temperature-jump at the cold plate for case (b)?

Solution

(a) Mean free path and Knudsen number: From Eq. (5) it follows:

$$l = \frac{2\eta}{\rho \bar{c}}.$$

From Eq. (2) it follows for the mean molecular velocity at the cold plate:

$$\bar{c} = \sqrt{\frac{8 \cdot 2{,}080 \cdot 273}{3.1415}} = 1202.5 \ \mathrm{m/s}.$$

With Eqs. (3) and (4) one obtains $\rho = p/(RT_1) = 10^5/(2{,}080 \cdot 273) = 0.176\ \mathrm{kg/m^3}$.

With η from Subchap. D3.1 it follows

$$l_1 \approx \frac{2 \cdot 1.89 \cdot 10^{-5}}{0.176 \cdot 1202.5} = 1.79 \cdot 10^{-7}\mathrm{m}.$$

At the hot plate one obtains with the higher temperature

$$l_2 \approx \frac{2 \cdot 1.89 \cdot 10^{-5}}{0.173 \cdot 1213.5} = 1.80 \cdot 10^{-7}\mathrm{m},$$

where as an approximation, the value for the viscosity η at 273 K has been used. Since $l_1 \approx l_2$ one obtains for the Knudsen number

$$\mathrm{Kn} = \frac{l}{s} = \frac{1.8 \cdot 10^{-7}}{0.01} = 1.8 \cdot 10^{-5}.$$

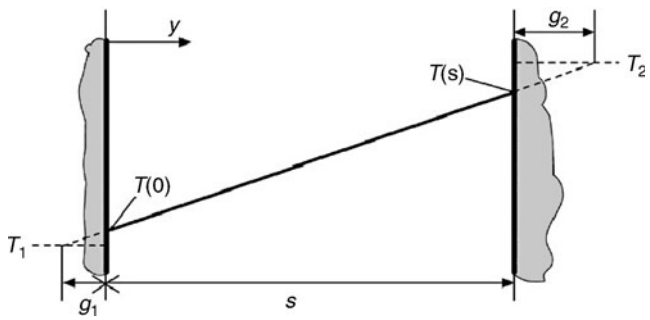

M10. Fig. 2. Schematic representation of temperature distribution for gas between two parallel flat plates in temperature-jump regime. The effect of the temperature-jump distances g_1 and g_2 is equivalent to an enlarged plate distance $s + g_1 + g_2$.

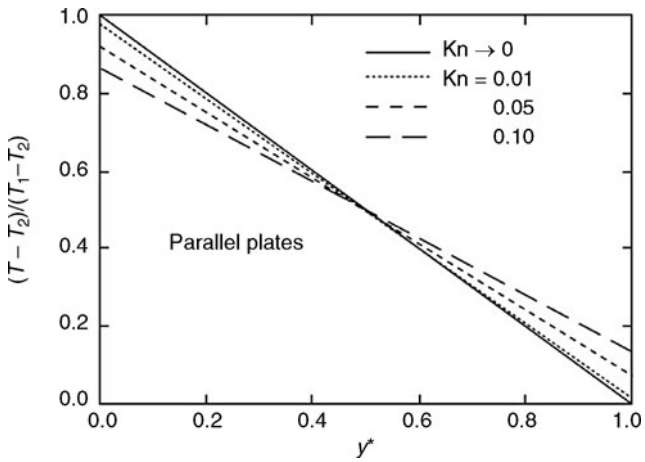

M10. Fig. 3. Temperature distribution for gas between two parallel plates with different values of the Knudsen number.

Since Kn < 0.01 the equations of the continuum theory apply, here Eq. (19) can be used. With the heat conductivity λ for the temperature 273 K from Subchap. D3.1 one has

$$\dot{q}_{\text{Kont}} = (0.143/0.01)\ (273 - 278) = -71.5\ \text{W/m}^2.$$

(b) The initial pressure p must be reduced by the factor 5,000 to reach the pressure 0.2 hPa. At constant temperature this means that the mean free path increases by the same factor. It follows $l = 9 \cdot 10^{-4}$ m and Kn = 0.09.

This means that Eq. (24) must be used to determine the heat flux. It follows

$$\dot{q} = \frac{\dot{q}_{\text{Kont}}}{1 + (15/4)\text{Kn}} = \frac{-71.5}{1 + 3.75 \cdot 0.09} = -53.46\ \text{W/m}^2.$$

(c) The temperature jump at the cold wall can be determined with Eq. (21). Since helium is a monatomic gas, Eq. (16) holds. With Eq. (13) and $\gamma = 1$, it follows

$$g = (15/8)l = 1.875 \cdot 9 \cdot 10^{-4} = 1.69 \cdot 10^{-3}\ \text{m}.$$

With Eq. (21) one obtains

$$\frac{T(0) - T_2}{T_1 - T_2} = \left(1 - \frac{1.69 \cdot 10^{-3}}{0.01 + 1.69 \cdot 10^{-3} + 1.69 \cdot 10^{-3}}\right) = 0.874$$

and

$$T(0) = 0.874 \cdot (273 - 278) + 278 = 273.63\ \text{K}.$$

For the temperature jump at the cold wall one has

$$T(0) - T_1 = 0.63\ \text{K}.$$

3.2.2 Unsteady Heat Conduction for Knudsen Numbers Kn < 0.1

In the following, a special solution of the unsteady heat-conduction equation is considered for a semi-infinite gas bounded by the plane $y = 0$ and extending in the direction of y positive. For $t \leq 0$, the temperature is T_0 everywhere. For $t > 0$, the temperature of the wall at $y = 0$ is T_1. It should be mentioned that no characteristic macroscopic length exists in this case, which could be used to define a Knudsen number. Using the temperature-jump boundary condition of Eq. (12) leads to the temperature distribution

$$\frac{T(y,t) - T_0}{T_1 - T_0} = \left[1 - \text{erf}\left(\frac{y}{g_1}\frac{g_1}{2\sqrt{at}}\right) - \exp\left(\frac{y}{g_1} + \frac{1}{4}\frac{4at}{g_1^2}\right) \cdot \text{erfc}\left(\frac{y}{g_1}\frac{g_1}{2\sqrt{at}} + \frac{2\sqrt{at}}{2g_1}\right)\right], \tag{25}$$

where

$$\text{erf}(\chi) = \frac{2}{\sqrt{\pi}}\int_0^{\chi} \exp(-\omega^2)\,\text{d}\omega \tag{26}$$

is the error function, and

$$\text{erfc}(X) = 1 - \text{erf}(X) \tag{27}$$

the complementary error function and a the thermal diffusivity [7]. The quantity $\sqrt{at}$ in Eq. (25) has the physical dimension of a length and may be considered a characteristic length of the problem. In the solution for the continuum regime, the gas assumes for $t > 0$ the temperature of the wall, without delay. It is characteristic for rarefied gases that the gas needs a finite time to attain the temperature of the wall. From Eq. (25) one obtains with $y = 0$ the temperature of the gas at the wall as a function of time:

$$\frac{T(0,t) - T_0}{T_1 - T_0} = 1 - \exp\left(\frac{at}{g_1^2}\right)\text{erfc}\left(\frac{\sqrt{at}}{g_1}\right). \tag{28}$$

Example 2

A plane wall with the temperature $T_1 = 303$ K comes suddenly in contact with a gas of the temperature 298 K. The pressure is 150 Pa. It is assumed that the wall temperature does not change with time and that the accommodation is perfect. What is the temperature at the wall after 0.05 ms? For an estimate of this temperature, use constant physical properties of air at $T_0 = 298$ K.

Solution

To determine the temperature at the wall as a function of time Eq. (28) is used. The quantity $\sqrt{at}$ can be considered a characteristic length of the problem.

From Eq. (3) one obtains

$$\rho = p/(RT_0) = 150/(287.2 \cdot 298) = 1.75 \cdot 10^{-3}\ \text{kg/m}^3.$$

Using the physical properties of air from Subchap. D2.2 one has for the heat diffusivity

$$a = \lambda/(\rho c_p) = 26.06 \cdot 10^{-3}/(1.75 \cdot 10^{-3} \cdot 1{,}007) = 1.479 \cdot 10^{-2}\ \text{m}^2/\text{s}.$$

Calculation of the mean free path: using Eq. (5) one obtains

$$l \approx \frac{2\eta}{\rho\bar{c}}.$$

From Eq. (2) it follows

$$\bar{c} = \sqrt{\frac{8 \cdot 287.22 \cdot 298}{3.1415}} = 466.9\ \text{m/s}.$$

With η from Subchap. D2.2 one finds

$$l \approx \frac{2 \cdot 18.48 \cdot 10^{-6}}{1.75 \cdot 10^{-3} \cdot 466.9} = 4.52 \cdot 10^{-5}\text{m}.$$

For the argument of the exponential function and the complementary error function in Eq. (28) one obtains with Eq. (13) the expression

$$\frac{\sqrt{at}}{g} = \frac{8\sqrt{at}}{15fl}.$$

The correction factor f differs from unity since air is a mixture of polyatomic gases. Using physical properties of air from Subchap. D2.2 with Eq. (14) gives

$$f = \frac{16}{15} \cdot \frac{1}{0.7141} \cdot \frac{1.4}{1+1.4} = 0.871.$$

It follows

$$\frac{\sqrt{at}}{g} = \frac{8\sqrt{1.479 \cdot 10^{-2} \cdot 0.05 \cdot 10^{-3}}}{15 \cdot 0.871 \cdot 4.52 \cdot 10^{-5}} = 11.65.$$

For large values of the argument, the complementary error function can be represented by a series expansion [7]. One has

$$\operatorname{erfc}(\chi) = \frac{\exp(-\chi^2)}{\sqrt{\pi}} \left(\frac{1}{\chi} - \frac{1}{2\chi^3} + \frac{1 \cdot 3}{2^2 \cdot \chi^5} - \cdots + \cdots \right).$$

For $\chi > 6$, the remainder after the first three terms can be neglected. Thus, one obtains for Eq. (28) the relation

$$\frac{T - T_0}{T_1 - T_0} = 1 - \exp(11.65^2) \cdot \frac{\exp(-11.65^2)}{\sqrt{\pi}} \cdot \left(\frac{1}{11.65} \cdot \frac{1}{2 \cdot 11.65^3} + \frac{1 \cdot 3}{2^2 \cdot 11.65^5} \right) = 0.952.$$

The temperature of the air at the wall is

$$T = 0.952\ (303 - 298) + 298 = 302.76\ \text{K}.$$

3.2.3 Extensions to Arbitrary Knudsen Numbers

The results presented in Sect. 3.2.1 have been derived for moderate rarefaction, i.e., for Knudsen numbers Kn < 0.1. Using moment equations, Lees and Liu derived an approximate analytical solution of the Boltzmann equation [17, 18, 40]. It has been shown by different experimental investigations that the theoretical results of Lees and Liu are in excellent agreement with experiments for all values of the Knudsen number [41–44]. The results which Lees and Liu derived for complete accommodation, $Y_1 = Y_2 = 1$, can be extended to include incomplete accommodation, i.e., accommodation coefficients less than unity. The result can be written as

$$\frac{\dot{q}}{\dot{q}_{\text{FM}}} = \frac{\dot{Q}}{\dot{Q}_{\text{FM}}} = \left[1 + \frac{4}{15\,\text{Kn}} \frac{\gamma_1 \gamma_2}{\gamma_1 + \gamma_2 - \gamma_1 \gamma_2} \right]^{-1}, \qquad (29)$$

where

$$\dot{Q}_{\text{FM}} = A \frac{\gamma_1 \gamma_2}{\gamma_1 + \gamma_2 - \gamma_1 \gamma_2} \frac{c_v + R/2}{\sqrt{2\pi RT}} p(T_1 - T_2) \qquad (30)$$

is the heat flow in the free-molecule regime [11]. In these equations, A represents the surface of a plate, while γ_1 and γ_2 are the accommodation coefficients of the plates. In the free-molecule regime, intermolecular collisions become negligible and the trajectories of the molecules are independent of each other. The molecules transport energy and momentum directly from one wall to another. Thus, the molecular transport of energy, i.e., the heat flow, is proportional to the number of molecules or to the density of the gas. The heat flow in the free-molecule regime does not depend on the distance between the plates. The ratio of the heat flux $\dot{q}$ to $\dot{q}_{\text{FM}}$ according to Eq. (29) is shown in Fig. 4 for different values of the accommodation coefficient. It is found that the empirical relation equation (8) proposed by Sherman [26] is valid in the present case of parallel flat plates. According to Sherman, the heat flow for arbitrary Knudsen numbers $\dot{Q}$ can be expressed by the heat flow of the limiting cases of the continuum $\dot{Q}_{\text{Kont}}$ and the free-molecule regime $\dot{Q}_{\text{FM}}$. One has

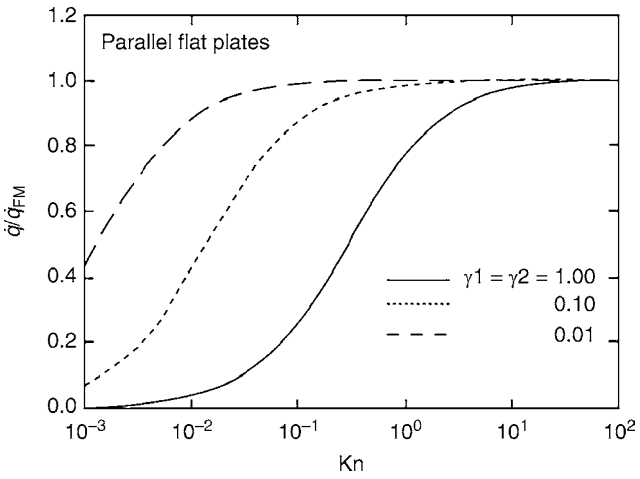

M10. Fig. 4. Dimensionless representation of heat flux between parallel flat plates according to Eq. (29) for different values of the accommodation coefficient.

$$\frac{\dot{Q}}{\dot{Q}_{\text{FM}}} = \frac{1}{1 + \dot{Q}_{\text{FM}}/\dot{Q}_{\text{Kont}}}. \qquad (31)$$

Using the thermal equation of state equations (3) and (5), the density ρ can be expressed as a function of the mean free path and the viscosity. With $\gamma_1 = \gamma_2 = 1$ and introducing Eqs. (22) and (30) one finds the relation

$$\frac{\dot{Q}_{\text{FM}}}{\dot{Q}_{\text{Kont}}} = \frac{1}{2} \frac{s}{l} (c_v + R/2) \frac{\eta}{\lambda}. \qquad (32)$$

For monatomic gases Eq. (16) holds, thus one has

$$Q_{\text{FM}}/Q_{\text{Kont}} = 4/(15\ \text{Kn}). \qquad (33)$$

Combining this result with Eq. (31) gives Eq. (29) for the special case of complete accommodation. It should be mentioned that the relations derived here are for monatomic gases and for small temperature differences. By multiplying the Knudsen number with the correction factor f of Eq. (14) in Sect. 2, one can derive equations for polyatomic gases.

The solutions presented so far make use of linearization based on the assumption of small temperature differences. Analytical solutions for large temperature differences are not available. To get an impression of the deviations from solutions obtained by linearization, Braun [42] studied numerical solutions of moment equations for parallel flat plates, without the assumption of small temperature differences. In Fig. 5, the difference between nonlinear and linear solutions is shown as a function of Knudsen number for different temperatures. At a temperature difference of 400 K deviations up to 40% are found.

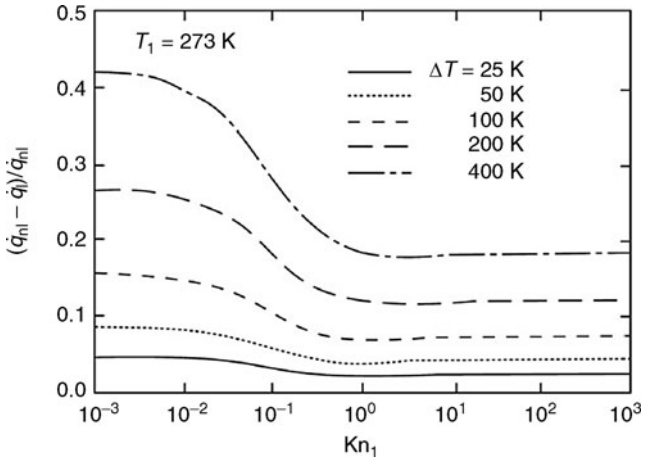

M10. Fig. 5. Difference between nonlinearized solution q_{nl} and linearized solution q_l for heat flux between flat plates as a function of Knudsen number according to Braun [42]. Here, $\Delta T = T_2 - T_1$ is the temperature difference between the plates. It should be mentioned that the Knudsen number has been evaluated for the state of the gas at the cold plate.

Example 3

For the measurement of the accommodation coefficient of argon in a new material, a heat transfer cell with parallel flat plates is used. The distance of the plates is s = 1 mm. It is assumed that the accommodation coefficients of the plates have the same value. In order to obtain clean conditions for the measurements, the pressure in the cell is reduced to 10^{-4} Pa at the beginning of an experiment. At this pressure one has free-molecule conditions. It can be assumed that the gas between the plates consists of water vapor which comes from the re-evaporation of water molecules formed at higher pressures as film on the walls. To determine the heat transferred by radiation, a measurement is made under vacuum conditions with the wall temperatures T_1 = 278 K and T_2 = 268 K. Under these conditions, a heat flux of 10 W/m^2 is measured.

(a) Determine the heat flux of water vapor under the assumption of complete accommodation.

(b) Argon is introduced into the cell until the pressure is 0.1 Pa. By adjusting the heating power the wall temperatures T_1 = 278 K and T_2 = 268 K are obtained. The measured heat flux is 10.4 W/m^2. What is the value of the accommodation coefficient for the investigated material?

Solution

(a) In the measurements under vacuum conditions, one has for the Knudsen number Kn $\gg$ 10. This can be shown by calculation in a similar way as in Examples 1 and 2. For the heat flux in the free-molecule regime Eq. (30) is used. With $c_v = c_p - R$ and c_p from Subchap. D3.1 it follows

$$\dot{q}_{FM} = \frac{\dot{Q}_{FM}}{A} = \frac{c_p - R/2}{\sqrt{2\pi RT}} p(T_1 - T_2)$$
$$= \frac{1864 - 461.4/2}{\sqrt{2 \cdot 3.1415 \cdot 461.4 \cdot 273}} 10^{-4} \cdot 10 = 1.84 \text{ mW/m}^2,$$

For T, the arithmetic mean value of the temperatures T_1 and T_2 has been introduced. This value of the heat is negligibly small in comparison with 10 W/m^2 obtained under vacuum conditions. It is therefore assumed that the heat flux of 10 W/m^2 is due to thermal radiation. This value has to be subtracted from the values measured at higher pressures.

(b) At the pressure 0.1 Pa one has the Knudsen number Kn $\gg$ 10. Thus, one has free-molecule conditions, and Eq. (30) can be used. With the relations for monatomic gases in Eq. (16) one obtains

$$\dot{q}_{FM} = \frac{\dot{Q}_{FM}}{A} = \frac{\gamma}{2-\gamma} \frac{2R}{\sqrt{2\pi RT}} p(T_1 - T_2),$$

$$10.4 - 10 = \frac{\gamma}{2-\gamma} \frac{2 \cdot 208.13}{\sqrt{2 \cdot 3.1415 \cdot 208.13 \cdot 273}} 0.1 \cdot 10$$
$$= \frac{\gamma}{2-\gamma} 0.697.$$

It follows γ = 0.729. It should be mentioned that under the described conditions thermal radiation gives an essential contribution to the heat transfer.

3.3 Concentric Cylinders

3.3.1 Steady Heat Conduction Between Concentric Cylinders for Knudsen Numbers Kn < 0.1

Using the temperature-jump boundary condition of Eq. (12), one obtains for concentric cylinders the heat flux

$$\dot{q} = \frac{\lambda}{r_1} \frac{(T_1 - T_2)}{\ln[(r_2 + g_2)/(r_1 - g_1)]}, \tag{34}$$

where r_1 is the radius of the inner cylinder and r_2 the radius of the outer cylinder. Since Kn < 0.1 one has $g_1 \ll r_1$ and $g_2 \ll r_2$, and the logarithm in Eq. (34) may be expanded in a series to give

$$\dot{q} = \frac{\lambda}{r_1} \frac{(T_1 - T_2)}{\ln(r_2/r_1) + g_1/r_1 + g_2/r_2}. \tag{35}$$

For $g_1 \to 0$ and $g_2 \to 0$ one obtains the special case of the continuum regime:

$$\dot{q}_{Kont} = \frac{\lambda}{r_1} \frac{T_1 - T_2}{\ln(r_2/r_1)}. \tag{36}$$

Combining Eqs. (35) and (36) and using Eq. (17) one has

$$\frac{\dot{q}}{\dot{q}_{Kont}} = \frac{\dot{Q}}{\dot{Q}_{Kont}} = \frac{\ln r_2^*}{\ln r_2^* + (15/8)\text{Kn}_1(1 + 1/r_2^*)} \tag{37}$$

with $r_2^* = r_2/r_1$, Kn = l/r_1, and $g_1 = g_2 = g$. This relation is valid only for Knudsen numbers Kn < 0.1 which in general holds true for all results based on temperature-jump boundary conditions. Some results for an extended Knudsen range are discussed in the next chapter. In the unsteady case solutions based on the temperature-jump boundary conditions lead to Bessel functions. Such solutions are important for the evaluation of experimental

results for the heat conductivity at higher densities as described in the literature [43].

3.3.2 Generalizations for Arbitrary Knudsen Numbers

Using momentum equations, Lees and Liu found an approximate analytical solution of the Boltzmann equation for the heat transfer between concentric cylinders. By comparison with experimental results it has been shown that the solution of Lees and Liu is in good agreement with experimental results for $0 < \mathrm{Kn} < \infty$, whereas Eq. (37) is wrong by a factor 2 in the free-molecule regime [40]. According to Lees and Liu, the relation

$$\frac{\dot{Q}}{\dot{Q}_{\mathrm{Kont}}} = \left(1 + \frac{15}{4}\frac{1}{\gamma_1}\frac{\mathrm{Kn}_1}{\ln r_2^*}\right)^{-1} \tag{38}$$

is valid for all Knudsen numbers. Here, γ_1 is the accommodation coefficient of the surface of the inner cylinder. It should be mentioned that the accommodation coefficient of the outer cylinder is irrelevant if $r_2^* \gg 1$. For the regime of free-molecule flow, Kennard [11] has derived

$$\dot{Q}_{\mathrm{FM}} = A_1\left[\frac{1}{\gamma_1}\frac{1}{r_2^*}\left(\frac{1}{\gamma_2} - 1\right)\right]^{-1}\frac{c_v + R/2}{\sqrt{2\pi RT}}p(T_1 - T_2), \tag{39}$$

where A_1 is the surface of the inner cylinder. According to Hurlbut [44] one has

$$\frac{\dot{Q}}{\dot{Q}_{\mathrm{FM}}} = \left(1 + \frac{4}{15}\gamma_1\frac{\ln r_2^*}{\mathrm{Kn}_1}\right)^{-1}. \tag{40}$$

From Eqs. (38) and (40) it follows $\dot{Q}/\dot{Q}_{\mathrm{Kont}} + \dot{Q}/\dot{Q}_{\mathrm{FM}} = 1$, which means that Sherman's empirical rule equation (8) is valid here. According to Lees and Liu [41], it follows for the steady temperature field in the gas between concentric cylinders

$$\frac{T(r) - T_2}{T_1 - T_2} = \left\{1 - \varphi\left[\frac{1}{2} + \frac{1}{\pi}\arccos(1/r^*)\right] - (1 - \varphi)\frac{\ln r^*}{\ln r_2^*}\right\}, \tag{41}$$

with

$$\varphi = \left(1 + \frac{4}{15}\frac{\ln r_2^*}{\mathrm{Kn}_1}\right)^{-1}. \tag{42}$$

The described relations have been obtained for monatomic gases. Using the correction factor introduced in Sect. 2 they can be applied to polyatomic gases. For this purpose, the Knudsen number has to be multiplied with the correction factor f of Eq. (14). It has been shown by Westerdorf [43] that calculations based on this method are in good agreement with experimental results for the polyatomic gases such as nitrogen and water vapor.

Example 4

Measurements of the heat conductivity λ are often performed by the so-called hot-wire method, which uses a cell consisting of a cylindrical tube that is kept at a fixed temperature. A fine wire is stretched along the axis of the tube. The wire is heated electrically, and the dissipated electrical power can be determined by measuring the electrical current and voltage. Consider a cylindrical cell of diameter 2 cm with an electrically heated platinum wire of diameter 0.1 mm. In order to minimize the end effects of the cell only the central length of the wire $L_D = 0.4$ m is used for the measurements. The dissipated electrical power $\dot{Q}_M = 32$ mW is determined. The cell contains nitrogen. The accommodation coefficient for nitrogen on platinum is $\gamma_1 = 0.53$. The temperature of the wire is 298 K, and the temperature of the cylinder is 293 K. From measurements at very low pressure, i.e., for $p \to 0$, it is found that the heat flow due to thermal radiation is $\dot{Q}_S = 2$ mW. Calculate the pressure in the heat transfer cell.

Solution

Using the heat conductivity of Subchap. D3.1, it follows for the heat flux in the continuum regime from Eq. (36)

$$\dot{Q}_{\mathrm{Kont}} = 2\pi r_1 L_D \dot{q}_{\mathrm{Kont}} = 2 \cdot 3.1415 \cdot 0.4 \cdot 0.026\ (298 - 293)/\ln(1 \cdot 10^{-2}/0.05 \cdot 10^{-3}) = 61.7\ \mathrm{mW}.$$

The conduction for arbitrary Knudsen numbers is given by Eq. (38). This equation has been derived for monatomic gases. It can be applied to nitrogen when the Knudsen number is multiplied with the correction factor f of Eq. (14). With property values for nitrogen at 298 K from Subchap. D3.1 one obtains $\mathrm{Pr} = 0.71$ and $\kappa = 1.4$. Thus, one finds for nitrogen

$$f = \frac{16}{15}\cdot\frac{1}{0.71}\cdot\frac{1.4}{1 + 1.4} = 0.876.$$

From the measurements, it follows

$$\dot{Q}/\dot{Q}_{\mathrm{Kont}} = (\dot{Q}_M - \dot{Q}_S)/\dot{Q}_{\mathrm{Kont}} = (32 - 2)/61.7 = 0.486.$$

With Eq. (38) one gets the Knudsen number

$$\mathrm{Kn}_1 = \frac{4}{15}\frac{\gamma_1 \ln r_2^*}{f}\left(\frac{\dot{Q}_{\mathrm{Kont}}}{\dot{Q}} - 1\right) = \frac{4}{15}\cdot\frac{0.53\ln 200}{0.876}\left(\frac{1}{0.486} - 1\right) = 0.904.$$

With Eqs. (1–5) and the viscosity value from Sect. 3.1, the Knudsen number can be used to evaluate the pressure. One has

$$p = \sqrt{\frac{\pi}{2}}\frac{\eta\sqrt{RT}}{\mathrm{Kn}_1 r_1} = 1.253\frac{1.78 \cdot 10^{-5}\sqrt{296.8 \cdot 298}}{0.904 \cdot 0.05 \cdot 10^{-3}} = 147\ \mathrm{Pa}.$$

3.4 Spherical Geometry

3.4.1 Steady Heat Conduction Between Concentric Spheres for Knudsen Numbers Kn < 0.1

With the temperature-jump boundary condition of Eq. (12) one obtains for the heat flux at the surface of the inner sphere of two concentric spheres

$$\dot{q} = \frac{\lambda}{r_1^2}\frac{T_1 - T_2}{g_1/r_1^2 + g_2/r_2^2 + 1/r_1 - 1/r_2}, \tag{43}$$

where r_1 is the radius of the inner sphere and r_2 the radius of the outer sphere. Introducing the known solution of the continuum regime,

$$\dot{q}_{\mathrm{Kont}} = \frac{\lambda}{r_1^2} \cdot \frac{T_1 - T_2}{1/r_1 - 1/r_2} \tag{44}$$

it follows for monatomic gases with Eq. (17) and with $g_1 = g_2 = g$ the equation

$$\frac{\dot{q}}{\dot{q}_{\mathrm{Kont}}} = \frac{\dot{Q}}{\dot{Q}_{\mathrm{Kont}}} = \frac{1 - 1/r_2^*}{(15/8)\mathrm{Kn}_1[1 + (1/r_2^*)^2] + 1 - 1/r_2^*}. \tag{45}$$

As in the case with cylindrical symmetry, the radius r_1 is used to define the dimensionless quantities $r_2^* = r_2/r_1$ and $\mathrm{Kn}_1 = l/r_1$. For the temperature distribution one obtains with $r^* = r/r_1$ the equation

$$\frac{T(r^*) - T_2}{T_1 - T_2} = \frac{(15/8)\mathrm{Kn}_1(1/r_2^*)^2 + 1/r^* - 1/r_2^*}{(15/8)\mathrm{Kn}_1[1 + (1/r_2^*)^2] + 1 - 1/r_2^*}. \tag{46}$$

From these equations follow of course with $r_2 \to \infty$ the results for a single sphere.

3.4.2 Unsteady Heat Conduction of Single Sphere for Knudsen Numbers Kn < 0.1

For a single sphere with constant wall temperature T_1 which suddenly comes in contact with a surrounding gas of the temperature T_0, the unsteady heat-conduction equation with the temperature-jump boundary condition gives for the temperature distribution in the gas:

$$\frac{T(r^*, t^*) - T_0}{T_1 - T_0} = \frac{8/(15\,\mathrm{Kn}_1)}{r^*[1 + 8/(15\,\mathrm{Kn}_1)]} \cdot \left\{1 - \mathrm{erf}\,\frac{r^* - 1}{2\sqrt{t^*}} - \left[1 - \mathrm{erf}\left(\frac{r^* - 1}{2\sqrt{t^*}} + \left(1 + 8/(15\mathrm{Kn}_1)\sqrt{t^*}\right)\right)\right] \cdot \exp[(1 + 8/(15\,\mathrm{Kn}_1)(r^* - 1) + \left(1 + 8/(15\,\mathrm{Kn}_1)^2 t^*\right))]\right\}, \tag{47}$$

where $t^* = t/t_{\mathrm{T}}$ with

$$t_{\mathrm{T}} = \frac{\rho C_p r_1^2}{\lambda} = \frac{r_1^2}{a}, \tag{48}$$

and a is the heat diffusivity. The characteristic time t_{T} for a spherical particle of radius 10 µm in air at standard conditions with property values from Subchap. D3.1 is approximately 5 µs. With $r^* = 1$ one finds for the temporal evolution of the gas temperature at the surface of the sphere

$$\frac{T(0, t^*) - T_0}{T_1 - T_0} = \frac{8/(15\,\mathrm{Kn}_1)}{1 + 8/(15\,\mathrm{Kn}_1)} \cdot \left\{1 - \left[1 - \mathrm{erf}(1 + 8/(15\,\mathrm{Kn}_1))\sqrt{t^*}\right] \cdot \exp\left[(1 + 8/(15\,\mathrm{Kn}_1))^2 t^*\right]\right\}. \tag{49}$$

As mentioned already in Sect. 3.1.2 for the plane case, a rarefied gas needs a finite time to assume the final gas temperature T_{G} at the wall according to the temperature-jump boundary conditions. Figure 6 shows the temperature at the surface as a function of t^* for different values of the Knudsen number according to Eq. (49). It can be seen that the gas temperature for large times, $t^* \to \infty$, tends to T_{G}. The temperature limit T_{G} is shown in Fig. 7 as a function of the Knudsen number.

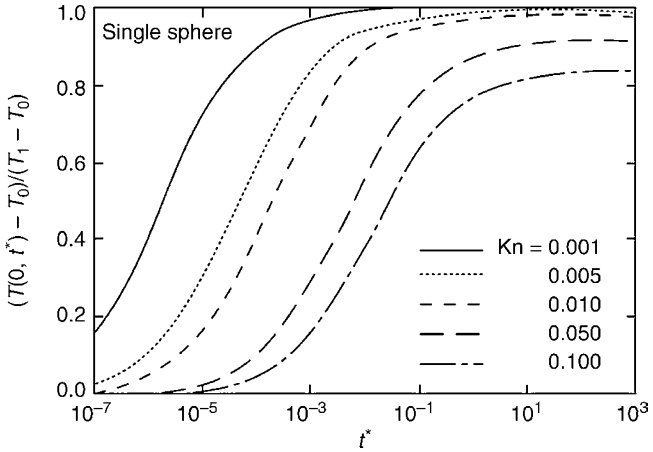

M10. Fig. 6. Gas temperature at the surface of a single sphere as a function of time for different values of the Knudsen number.

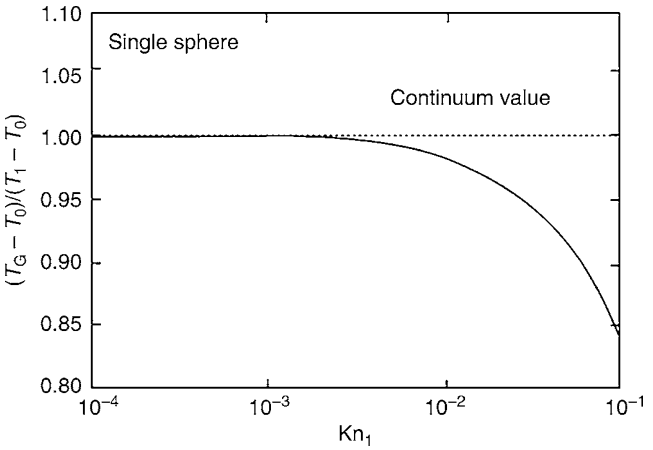

M10. Fig. 7. Temperature limit for large values of t^* at surface of single sphere as a function of Knudsen number.

3.4.3 Generalizations for Arbitrary Knudsen Numbers

For the steady heat conduction between concentric spheres, Lees has presented approximate analytical solutions of the Boltzmann equation, using the same method as described in the cases of plane and cylindrical geometry. The results are valid for all Knudsen numbers [18]. For the heat flux, Lees obtains

$$\frac{\dot{q}}{\dot{q}_{\mathrm{Kont}}} = \frac{\dot{Q}}{\dot{Q}_{\mathrm{Kont}}} = \frac{1}{1 + (15/4)\,\mathrm{Kn}_1 r_2^*/(r_2^* - 1)} \tag{50}$$

and for the temperature distribution

$$\frac{T(r^*) - T_2}{T_1 - T_2} = \left\{1 - \frac{\varphi}{2}\left[1 + \sin\left(\arccos\left(\frac{1}{r^*}\right)\right)\right] - (1 - \varphi)\frac{(r^* - 1)r_2^*}{(r_2^* - 1)r^*}\right\}, \tag{51}$$

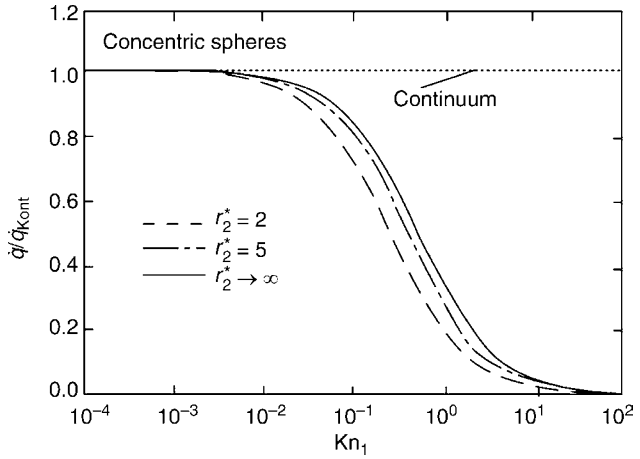

M10. Fig. 8. Heat flux $\dot{q}/\dot{q}_{cont}$ for concentric spheres as a function of Knudsen number with ratio of radii as parameter.

where

$$\varphi = \left(1 + \frac{4}{15}\frac{1}{\mathrm{Kn}_1}\frac{r_2^* - 1}{r_2^*}\right)^{-1}. \tag{52}$$

The heat flux according to Eq. (50) is shown in Fig. 8 for a wide range of the Knudsen numbers with the ratio of radii as parameter. For the free-molecule regime, Kennard has derived the formula

$$\dot{Q}_{FM} = A_1\left[\frac{1}{\gamma_1} + \left(\frac{1}{r_2^*}\right)^2\left(\frac{1}{\gamma_2} - 1\right)\right]^{-1} \cdot \frac{c_v + R/2}{\sqrt{2\pi RT}}p(T_1 - T_2), \tag{53}$$

where A_1 is the surface of the inner sphere, and γ_1 and γ_2 are the accommodation coefficients [11]. Springer and Wan [45] give the formula

$$\frac{\dot{q}}{\dot{q}_{kont}} = \frac{\dot{Q}}{\dot{Q}_{Kont}} = \left(1 + \frac{15}{4}\frac{\mathrm{Kn}_1}{\gamma_1}\frac{r_2^*}{r_2^* - 1}\right)^{-1}, \tag{54}$$

where γ_1 is the accommodation coefficient of the inner sphere. It should be mentioned that the accommodation coefficient of the outer cylinder is irrelevant if $r_2^* \gg 1$. Sherman's rule in Eq. (8) is valid here. The relations described in this section have been obtained for monatomic gases. The results can be extended to polyatomic gases by multiplying the Knudsen number with the correction factor f defined by Eq. (14).

4 Solutions for Gases in Motion

4.1 Introduction

In the previous chapters, heat conduction in rarefied gases at rest has been discussed. The Knudsen number $\mathrm{Kn} = l/L$ also plays, of course, an important role for rarefied gases in motion. With Eqs. (4) and (5), the Knudsen number can be expressed as a function of the viscosity as

$$\mathrm{Kn} = 2\eta/(\rho\bar{c}L). \tag{55}$$

Introducing a characteristic velocity u of the flow one obtains with Eq. (2) the relation

$$\mathrm{Kn} \approx \mathrm{Ma}/\mathrm{Re}, \tag{56}$$

where $\mathrm{Ma} = u/\sqrt{\kappa RT}$ is the Mach number and $\mathrm{Re} = (\rho\ u\ L)/\eta$, the Reynolds number. In the literature, results for rarefied gases in motion are therefore often represented as function of Re/Ma. At high Mach numbers the compressibility of the medium has to be taken into account. Studies of rarefied gases at high Mach numbers are of special importance for hypersonic flows [46–49]. In the following, a few examples of internal flows at low Mach numbers are discussed. Therefore, one has in this case $\mathrm{Ma}^2 \ll 1$. Due to the low Mach number, rarefaction effects play a role only when the Reynolds number does not become too large. For Mach numbers of 0.25 and Reynolds numbers up to approximately 40, the Knudsen number is of the order of 0.01. Compressible flows are discussed by Knobling [50].

4.2 Plane Couette Flow for Arbitrary Knudsen Numbers

The plane Couette flow deals with the viscous flow between parallel plane plates. It is assumed that the lower plate is at rest, whereas the upper plate moves with the velocity u_0. The distance of the plates is s. In general, the temperatures of the two plates may be different from each other. For the following it is assumed that the temperature is T_1 for the lower plate and T_2 for the upper plate. In the continuum regime with very small Knudsen numbers $\mathrm{Kn} < 0.01$, the gas does not slip over the walls and assumes the temperatures of the plates. This behavior corresponds to the classical boundary conditions of the continuum theory. It is well known that for $T_1 = T_2$ one has a linear velocity profile. With increasing Knudsen number temperature and velocity jumps are observed at the walls. As a consequence, the heat and momentum flux to the walls decrease when the gas becomes rarefied. Liu and Lees made use of a momentum method to obtain an approximate analytical solution of the Boltzmann equation for the problem of plane compressible Couette flow [51]. The results obtained are valid for all values of Knudsen number, Mach number, and temperature ratio T_2/T_1. For the representation of the results the Stanton number

$$\mathrm{St}_1 = \frac{\dot{q}y}{\rho_1\, c_{p,1}\, u_0\, (T_1 - T_2)} \tag{57}$$

and the drag coefficient

$$c_{D,1} = \frac{p_{xy}}{1/2\rho_1\, u_0^2} \tag{58}$$

are introduced. The quantity q_y represents the heat flux perpendicular to the plates and p_{xy} the shear stress. For the limit of small Mach numbers, i.e., for $\mathrm{Ma}^2 \ll 1$, Liu and Lees obtained analytical expressions for density, temperature, pressure, and velocity, which depend only on the temperature ratio T_2/T_1 and on the Knudsen number $\mathrm{Kn}_1 = l_1/s$. The same holds for the product of drag coefficient and Mach number $c_{D,1}\,\mathrm{Ma}_1$ and for the product of Stanton number and Mach number $\mathrm{St}_1\,\mathrm{Ma}_1$, where $\mathrm{Ma}_1 = u_0/\sqrt{\kappa RT_1}$. For higher Mach numbers, the equations in [51] have to be solved by iteration. Figure 9 shows the

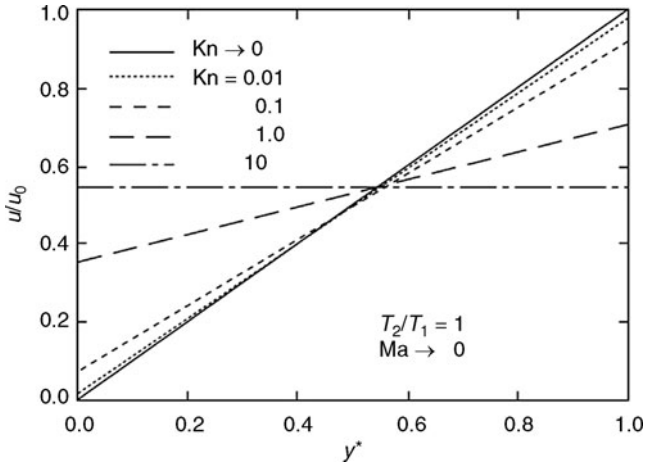

M10. Fig. 9. Velocity profile for plane Couette flow with $T_2 = T_1$ for various values of Knudsen number.

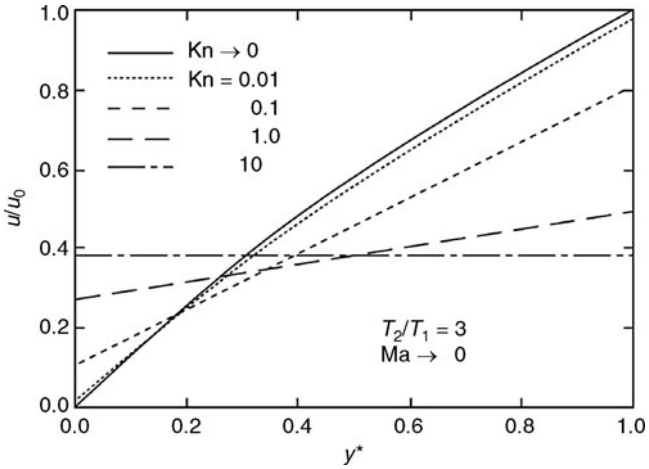

M10. Fig. 10. Velocity profile for plane Couette flow with $T_2/T_1 = 3$ for various values of Knudsen number.

results of the method for the velocity of monatomic gases between the plates as a function of $y^* = y/s$ for $T_1 = T_2$ and different values of the Knudsen number. All velocity profiles exhibit a constant slope. The velocity jump at the walls increases with increasing Knudsen number and has the same magnitude at both boundaries. The solid line for the continuum regime shows no temperature jump. Figure 10 shows velocity profiles for the temperature ratio $T_2/T_1 = 3$ and for different values of the Knudsen number. The profiles show a curvature, which decreases with increasing Knudsen number. The temperature jumps are in this case larger at the hot wall than at the cold wall. In Fig. 11, the influence of the temperature ratio on the velocity profile is visible for constant Knudsen number. With increasing temperature ratio the velocity jump at the wall increases. In Fig. 12, the quantity $St_1 \cdot Ma_1$ is shown as a function of the Knudsen number Kn_1 for different temperature ratios.

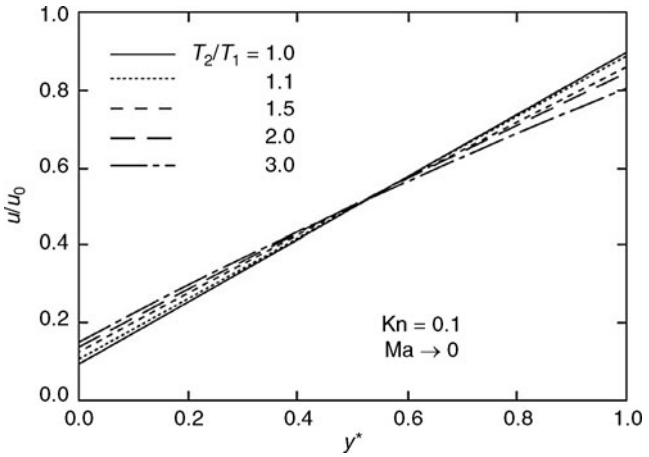

M10. Fig. 11. Velocity profile for plane Couette flow at Kn = 0.1 for various values of temperature ratio.

4.3 Cylindrical Poiseuille Flow at Constant Wall Temperature for a Wide Knudsen Number Range

The fully developed steady laminar viscous flow in a long tube of circular cross section is described by Poiseuille's formula. In the deduction, it is assumed that the pressure is constant over any cross section of the tube. In the continuum regime, the gas layer in contact with the wall adheres to it. It is well known that the resulting velocity profile is described by a parabola, whereas the flow rate is proportional to the pressure drop and to the fourth power of the tube radius. In the slip-flow regime, a Knudsen number effect is expected [11–13, 25]. The Knudsen number is defined by

$$\mathrm{Kn} = l/r_0, \tag{59}$$

where r_0 is the radius of the tube. In the literature, the so-called rarefaction parameter

$$\delta = \frac{\sqrt{\pi}}{2}\frac{r_0}{l} \sim \frac{1}{\mathrm{Kn}} \tag{60}$$

is often used instead of the Knudsen number [52]. Besides velocity jumps at the walls, a new phenomenon may be observed in flows through very long tubes, where the pressure drop along the tube may cause an increase of the mean free path so large that the Knudsen number changes by orders of magnitude. As a consequence different flow regimes may develop in the gas flow along the tube, in extreme situations from the continuum to the free-molecule regime. This is discussed later.

The problem of cylindrical tube flow in rarefied gases has been the subject of numerous investigations. In 1909, Knudsen described experiments in which he found a minimum of the mass flow for decreasing pressure [53]. In search for explanation of this minimum various methods for the solution of the linearized Boltzmann equation for Poiseuille flow in tubes have been developed [4, 54–58]. Many investigators made two assumptions. Entrance effects were neglected, which means that the length of the tube L is much larger than the tube radius r_0. In order to justify the linearization of the Boltzmann equation, it was assumed that the Mach number is small. For the pressure difference, it is assumed

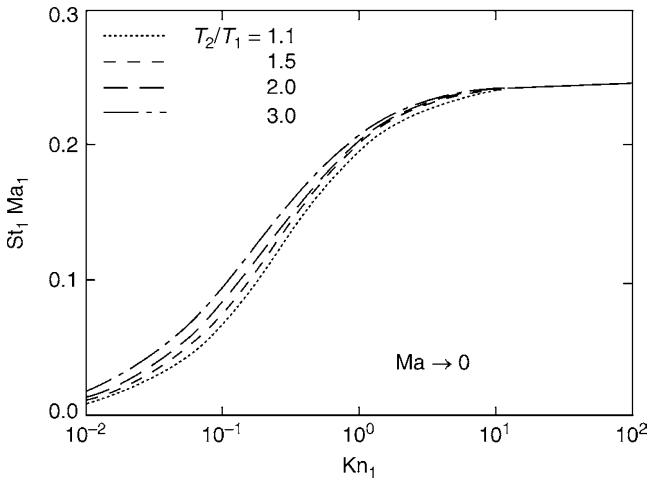

M10. Fig. 12. Product of Stanton number and Mach number for plane Couette flow as a function of Knudsen number with temperature ratio as parameter.

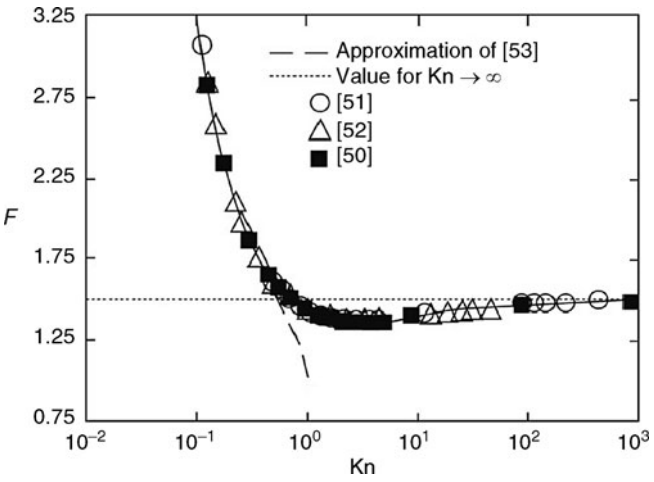

M10. Fig. 13. Mass flow according to Eq. (65) for isothermal cylindrical Poiseuille flow as a function of Knudsen number.

$$\frac{|p_1 - p_2|}{\bar{p}} \leq 1 \quad \text{with } \bar{p} = (p_1 + p_2)/2, \tag{61}$$

where $p_1 - p_2$ is the driving pressure difference. For technical applications, the paper by Sharipov and Seleznev is useful since it discusses the results for the flow of a rarefied gas through a tube with circular cross section for large pressure differences at constant temperature [52]. Sharipov and Seleznev show that linearization of the Boltzmann equation is allowed only for the general conditions

$$\frac{r_0}{L}\frac{|p_1 - p_2|}{\bar{p}} \ll 1 \quad \text{for } \overline{\text{Kn}} \geq 1 \tag{62}$$

or

$$\frac{1}{\overline{\text{Kn}}}\frac{r_0}{L}\frac{|p_1 - p_2|}{\bar{p}} \ll 1 \quad \text{for } \overline{\text{Kn}} \leq 1, \tag{63}$$

where the Knudsen number $\overline{\text{Kn}}$ is based on the mean free path

$$\bar{l} = (l_1 + l_2)/2 \tag{64}$$

as an average of states 1 and 2. At large pressure differences, a mixed flow with a transition from continuum conditions at the tube entrance to free-molecule conditions at the exit of the tube prevails. In the literature, the mass flow $\dot{M}$ is often described by the dimensionless quantity

$$F = \frac{-\dot{M}\sqrt{2RT}}{(\mathrm{d}p/\mathrm{d}x)\pi r_0^3}. \tag{65}$$

It should be mentioned that the quantity F changes its value in the case of the described mixed flow since it depends on the pressure gradient $\mathrm{d}p/\mathrm{d}x$. In Fig. 13, the quantity F is presented on the basis of a chart in [51]. In the same figure, the approximation

$$F = 0.2216\ \text{Kn}^{-1} + 1.0162 + 0.6194\ \text{Kn} - 0.7743\ \text{Kn}^2 \tag{66}$$

which according to Lo and Loyalka [58] is valid for small Knudsen numbers. The quantity F has a minimum in the transition regime, as can be seen in Fig. 13. It is interesting to mention that with Sherman's Eq. (8) this minimum is not obtained [58]. The mass flow $\dot{M}$ is of course constant. Sharipov and Seleznev therefore characterize the mass flow with the quantity

$$B = -\frac{L}{(p_1 - p_2)}\frac{M\sqrt{2RT}}{\pi r_0^3} \tag{67}$$

which is constant over the entire length of the tube. It can be shown that the value of this quantity can be obtained from F with the relation

$$B(\delta_1,\ \delta_2) = F((\delta_1 + \delta_2)/2) \tag{68}$$

for arbitrary pressure differences, if the conditions of Eqs. (62) and (63) are fulfilled. The values of B as a function of the rarefaction factor at the entrance and at the exit of the tube δ_1 and δ_2 may be found in [52].

Example 5

For determining the mass flow in a long tube the pressure is measured at two positions with the distance $L_1 = 1$ m. The measurements give the values $p_1 = 12$ Pa and $p_2 = 10$ Pa. The gas of the flow is nitrogen with the temperature 298 K. The radius of the tube is 5 mm.

(a) What is the mass flow?
(b) What is the mean flow velocity?

Solution

(a) Using Eqs. (1–5), the mean Knudsen number $\overline{\text{Kn}}$ is determined with the values of the dynamic viscosity from Subchap. D3.1:

$$\overline{\text{Kn}} = \sqrt{\frac{\pi}{2}}\frac{\eta\sqrt{RT}}{\bar{p}r_0} = 1.253\frac{1.78 \cdot 10^{-5}\sqrt{296.8 \cdot 298}}{11 \cdot 5 \cdot 10^{-3}} = 0.1206.$$

For the Knudsen numbers at the entrance and at the exit one finds $\text{Kn}_1 = 0.1206 \cdot 11/12 = 0.1106$ and $\text{Kn}_2 = 0.1206 \cdot 11/10 = 0.1327$. The gas is therefore in the slip-flow regime. For

determining the mass flow Eq. (65) is used. The quantity F can be taken from Fig. 13, or for the present case can be calculated with the approximation of Eq. (66) for $\overline{\mathrm{Kn}}$. One finds $F = 2.917$. With Eq. (65) it follows

$$\dot{M} = \frac{-F\mathrm{d}p/\mathrm{d}x\pi r_0^3}{\sqrt{2RT}} = \frac{(-2.917)\cdot(-2/1)\cdot 3.1415\cdot(5\cdot 10^{-3})^3}{\sqrt{2\cdot 296.8\cdot 298}} = 5.45\cdot 10^{-9}\ \mathrm{kg/s}.$$

(b) For the density one has $\bar{\rho} = \bar{p}/(\mathrm{RT}) = 11/(296.8\cdot 298) = 1.244\cdot 10^{-4}\ \mathrm{kg/m^3}$ and thus from the volume flow $\dot{M}/\rho$ the mean velocity

$$\bar{u} = \dot{M}/(\rho\pi r_0^2) = 5.45\cdot 10^{-9}\Big/\left(1.244\cdot 10^{-4}\cdot 3.1415\cdot(5\cdot 10^{-3})^2\right) = 0.56\ \mathrm{m/s}.$$

4.4 Cylindrical Poiseuille Flow with Constant Heat Flux at Wall for Knudsen Numbers Kn < 0.1

The relations described in the preceding chapter are for the isothermal case. Solutions for the temperature-jump and slip-flow regime have been described by Sparrow and Lin [59]. These authors deal with the case of constant wall temperature as well as with the case of constant heat flux at the wall. Velocity jumps as well as temperature jumps had to be taken into account. For constant heat flux at the wall the authors give for the Nusselt number the relation

$$\mathrm{Nu} = \frac{\frac{24}{11}}{1-\frac{6}{11}\frac{u(r_0)}{\bar{u}}+\frac{1}{11}\left(\frac{u(r_0)}{\bar{u}}\right)^2+\frac{24}{11}\frac{g}{r_0}}. \tag{69}$$

Here, the velocity ratio

$$\frac{u(r_0)}{\bar{u}} = \frac{1}{1+r_0/(4\zeta)} \tag{70}$$

and the coefficient g defined by Eqs. (13) and (14) have been used, and $\overline{u}$ is the velocity averaged over the cross section of the tube. The quantities $u(r_0)$ and ζ are defined in Eqs. (10) and (11), and the Nusselt number is given by

$$\mathrm{Nu} = \frac{\dot{q}}{(T_W-\bar{T})}\frac{r_0}{\lambda}, \tag{71}$$

where

$$\bar{T} = \frac{\int_0^{r_0} 2\pi r u(r)T(r)\mathrm{d}r}{\int_0^{r_0} 2\pi r u(r)\mathrm{d}r}. \tag{72}$$

Figure 14 shows a graphical represention of Nu according to Eq. (69) for monatomic gases as a function of Knudsen number for various values of the accommodation coefficient γ. The solution for the case of constant wall temperature cannot be given in closed form. It has, however, been shown that the Nusselt number for this case does not deviate much from the values in Fig. 14. They are approximately 5% higher [59].

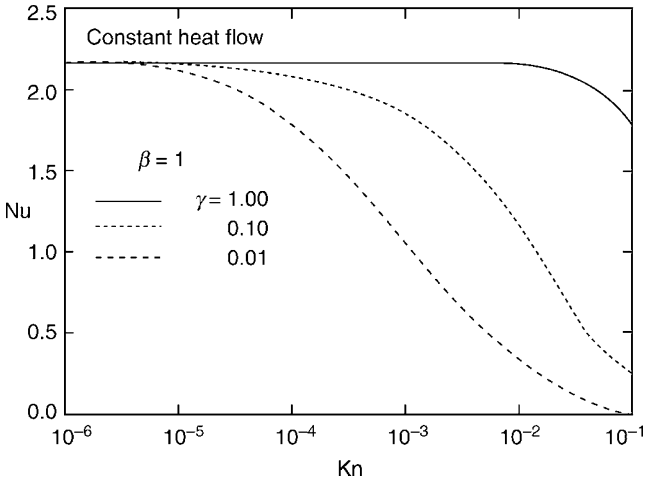

M10. Fig. 14. Nusselt number according to Eq. (69) for laminar tube flow with constant heat flux at the wall as a function of Knudsen number.

Example 6

Consider the laminar flow of air in a tube with radius 6 cm. The air is heated by a constant heat flow from the walls. The flow velocity averaged over a cross section is $\bar{u} = 10$ m/s. The average temperature in this cross section is 50°C, the wall temperature is 50.5°C, and the pressure is 7 Pa. The accommodation coefficient for the temperature has the value 0.5, and the accommodation coefficient for tangential momentum is 1. (a) What is the velocity at the wall? (b) What is the heat flow to the tube?

Solution

(a) By calculating the Knudsen number with Eqs. (1–5) and using the viscosity from Subchap. D2.2 one obtains

$$\mathrm{Kn} = \sqrt{\frac{\pi}{2}}\frac{\eta\sqrt{\mathrm{RT}}}{p r_0} = 1.253\frac{19.67\cdot 10^{-6}\sqrt{287.2\cdot 323}}{7\cdot 0.06} = 0.0179.$$

It follows that the flow is in the temperature-jump and slip-flow regime. This means that Eqs. (69–72) are valid. Using Eqs. (11) and (70) the velocity at the wall can be determined. With $\beta = 1$ Eq. (11) gives

$$\zeta = I = r_0\,\mathrm{Kn} = 1.07\,\mathrm{mm}$$

and thus

$$\frac{u(r_0)}{\bar{u}} = \frac{1}{1+r_0/(4\cdot\zeta)} = \frac{1}{1+0.06/(4\cdot 1.07\cdot 10^{-3})} = 6.66\cdot 10^{-2}.$$

It follows $u\,(r_0) = 0.66$ m/s.

(b) The Nusselt number can be determined with Eq. (69). The temperature-jump coefficient g follows from Eq. (13). With

$$f = \frac{16}{15}\cdot\frac{1}{0.711}\cdot\frac{1.4}{1+1.4} = 0.875.$$

Equation (14) gives

$$g = \frac{2-0.5}{0.5}\cdot\frac{15}{8}\cdot 0.875\cdot 1.07\cdot 10^{-3} = 5.26\cdot 10^{-3}\ \text{m} \quad \text{and} \quad g/r_0 = 0.088.$$

With Eq. (69) it follows for the Nusselt number

$$\text{Nu} = \frac{24/11}{1-\frac{6}{11}6.66\cdot 10^{-2}+\frac{1}{11}(6.66\cdot 10^{-2})^2+\frac{24}{11}0.088} = 1.89$$

With the value of the heat conductivity of air from Subchap. D2.2, it follows from the definition of the Nusselt number in Eq. (71) for the heat flux at the wall

$$\dot{q} = 1.89\cdot 27.88\cdot 10^{-3}\cdot(323.5-323)/0.06 = 0.44\ \text{W/m}^2.$$

5 Symbols

A	surface (m^2)
a	heat conductivity (m^2/s)
B	dimensionless mass flow (–)
b_0	auxiliary quantity (–)
b_1	auxiliary quantity (–)
$\bar{c}$	arithmetic mean of magnitude of molecular velocity (m/s)
c_D	drag coefficient (–)
c_v	specific heat capacity at constant volume (J/kg K)
c_p	specific heat capacity at constant pressure (J/kg K)
F	dimensionless mass flow (–)
f	correction factor for polyatomic gases (–)
g	temperature-jump coefficient (m)
Kn	Knudsen number (–)
L	characteristic length (m)
l	mean free path (m)
$\widetilde{M}$	mol mass (kg/kmol)
$\dot{M}$	Mass flow (kg/s)
Ma	Mach number (–)
m	mass of a molecule (kg)
Nu	Nusselt number (–)
N	number density (l/m^3)
$\dot{Q}$	heat flow (W)
$\dot{q}$	heat flux (W/m^2)
Pr	Prandtl number (–)
P	pressure (Pa)
p_{xy}	shear stress (Pa)
R	individual gas constant (J/kg K)
$\tilde{R}$	Universal gas constant (J/kmol K)
R	radial coordinate (m)
r_0	pipe radius (m)
Re	Reynolds number (–)
St	Stanton number (–)
S	distance between plates (m)
T	temperature (K)
t	time (s)
t_T	characteristic time in heat-conduction equation (s)
U	velocity in direction of x-coordinate (m/s)
X	coordinate in flow direction (m)
Y	coordinate vertical to direction of flow, coordinate vertical to wall (m)
β	accommodation coefficient for velocity (–)
γ	accommodation coefficient for temperature (–)
δ	rarefaction parameter (–)
ζ	coefficient of velocity slip (m)
η	dynamic viscosity (Pa s)
κ	ratio of specific heats (–)
λ	heat conductivity (W/m K)
ρ	density (kg/m^3)
φ	auxiliary variable (–)
χ	auxiliary variable (–)
ω	auxiliary variable (–)

Indices

0	initial value
1	plate 1, inner cylinder, inner sphere, entrance
2	plate 2, outer cylinder, outer sphere, exit
e	Incident
FM	free-molecule regime
G	Limit
Kont	continuum
l	linearized
nl	nonlinearized
r	reflected
T	belonging to temperature
W	Wall
y	y-direction

Constants

Boltzmann's constant

$$c = 5\cdot\pi/32 = 0.4909 \approx 0.5$$
$$k = 1.380658\cdot 10^{-23}\ \text{J/K}$$

6 Bibliography

1. Waldmann L (1958) Transporterscheinungen in Gasen von mittlerem Druck. In: Flügge S (ed) Handbuch der Physik Band XII. Springer-Verlag, Berlin
2. Bird GA (1994) Molecular gas dynamics and the direct simulation of gas flows. Clarendon Press, Oxford
3. Cercignani C (1969) Mathematical methods in kinetic theory. Plenum Press, New York
4. Cercignani C (1975) Theory and applications of the Boltzmann equation. Elsevier, New York
5. Chapman S, Cowling TG (1960) The mathematical theory of non-uniform gases, 2nd edn. University Press, Cambridge
6. Hirschfelder JO, Curtiss CF, Bird RB (1963) Molecular theory of gases and liquids, 2nd edn. John Wiley & Sons, New York
7. Frohn A (1988) Einführung in die Kinetische Gastheorie, AULA-Verl, Aufl. Wiesbaden
8. Grad H (1958) Principles of the kinetic theory of gases. In: Flügge S (ed) Handbuch der Physik Band XII. Springer-Verlag, Berlin
9. Jeans J (1954) The dynamical theory of gases, 4th edn. Dover Publications, New York
10. Jeans J (1962) An introduction to the kinetic theory of gases. University Press, Cambridge
11. Kennard EH (1938) Kinetic theory of gases, 1st edn. McGraw-Hill Book Company, New York

12. Loeb LB (1961) The kinetic theory of gases, 3rd edn. Dover Publications, New-York
13. Present RD (1958) Kinetic theory of gases, 1st edn. McGraw-Hill Book Company, New York
14. Smolderen JJ (1965) The evolution of the equations of gas flow at low density. In: Küchemann D, Sterne LHG (eds) Progress in aeronautical sciences, vol 6. Pergamon Press, Oxford
15. Dushman S, Lafferty JM (1962) Scientific foundation of vacuum technique. John Wiley & Sons Inc., New York
16. Wutz M, Adam H, Walcher W (1988) Theorie und Praxis der Vakuumtechnik, Vieweg-Verlag, Aufl. Braunschweig
17. Lavin ML, Haviland, JK (1962) Application of a moment method to heat transfer in rarefied gases. Phys Fluids 5:274–279
18. Lees L (1965) Kinetic theory description of rarefied gas flow. J Soc Ind Appl Math 13:278–311
19. Zhong X, Koura K (1995) Comparison of solutions of the Burnett equations, Navier-Stokes equations, and DSMC for Couette flow. In: Harvey J, Lord G (eds) Rarefied Gas Dynamics. Oxford University Press, Oxford, pp 354–360
20. Inamuro T, Sturtevant B (1991) Heat transfer in a discrete velocity gas. In: Beylich AE (ed) Rarefied gas dynamics. VCH Verlagsgesellschaft GmbH, Weinheim, pp 854–861
21. Usami M, Kyogoku H, Kato S (1991) Monte Carlo direct simulation of heat transfer through a rarefied gas. In: Beylich AE (ed) Rarefied gas dynamics. VCH Verlagsgesellschaft GmbH, Weinheim, pp 854–861
22. Bird GA (1995) The search for solutions in rarefied gas dynamics. In: Harvey J, Lord G (eds) Rarefied gas dynamics. Oxford University Press, Oxford, pp 753–772
23. Carslaw HS, Jaeger JC (1959) Conduction of heat in solids, 2nd edn. Clarendon Press, Oxford
24. Holman JP (1981) Heat transfer. MacGraw-Hill International Book Company, Auckland
25. Eckert ERG, Drake RM (1972) Analysis of heat and mass transfer. McGraw-Hill Book Company, NewYork
26. Sherman FS (1963) A survey of experimental results and methods for the transition regime of rarefied gas dynamics. In: Lauermann JA (ed) Rarefied gas dynamics, vol 2. Academic Press, New York, pp 228–260
27. Saxena SC, Joshi RK (1989) Thermal accommodation and adsorption coefficients of gases. In: Ho CY (ed) CINDAS data series on material properties, vols 2. Hemisphere Publishing Corp., New York
28. Wachmann HY (1962) The thermal accommodation coefficient: a critical survey. Am Rocket Soc J 32:2–12
29. Pazooki N, Loyalka SK (1985) Heat transfer in a rarefied polyatomic gas – I. Plane parallel plates. Int J Heat Mass Transfer 28:2019–2027
30. Siewert CE (2003) The linearized Boltzmann equation: a concise and accurate solution of the temperature-jump problem. J Quant Spectrosc Ra 77:417–433
31. Arya G, Hseueh-Chia C, Maginn EJ (2003) Molecular simulations of Knudsen wall-slip: effect of wall morphology. Mol Simulat 29:697−710
32. Shen C, Fan J, Xie C (2003) Statistical simulation of rarefied gas flows in micro-channels. J Comput Phys 189:512−527
33. Shinagawa H, Asai T, Sugiyama Y, Okuyama K (2002) An experimental and theoretical investigation of rarefied gas flows through circular tube of finite length. Chem Eng Sci 52:4027−4037
34. Siewert CE (2003) Heat transfer and evaporation/condensation problems based on the linearized Boltzmann equation. Eur J Mech B: Fluids 22: 391−409
35. Yeh BT, Frohn A (1973) Heat conduction in binary gas mixtures between concentric cylinders. Phys Fluids 16:801−805
36. Yeh BT, Frohn A (1973) Heat conduction between parallel flat plates in binary gas mixtures. Phys Fluids 16:330−332
37. Braun D, Frohn A (1976) Heat transfer in simple monatomic gases and in binary mixtures of monatomic gases. Int J Heat Mass Transfer 19: 1329−1335
38. Westerdorf M, Frohn A (1982) Measurements of conduction of heat in water vapour, nitrogen and mixtures of these gases in an extended temperature range. In: Grigull U (ed) Proceedings of the 17th international heat transfer Conference, Hemisphere Publ. Corp., vol 2, pp 99−104
39. Kosuge S, Aoki K, Takata S (2001) Heat transfer in a gas mixture between two parallel plates: finite-difference analysis of the Boltzmann equation. In: Bartel JJ, Gallis MA (ed) Rarefied gas dynamics. 22nd international symposium, American Institute of Physics. Sydney, Australia, pp 289–296
40. Lees L, Liu ChY (1962) Kinetic-theory description of conductive heat transfer from a fine wire. Phys Fluids 5:1137–1148
41. Yeh B-T (1971) Theoretische und experimentelle Untersuchung der Wärmeleitung in verdünnten binären Gasgemischen. Diss. RWTH Aachen
42. Braun D (1976) Wärmetransport in Gasen bei großen Temperaturdifferenzen und beliebigen Knudsenzahlen. Diss. RWTH Aachen
43. Westerdorf M (1985) Ein automatisiertes Messverfahren für die Untersuchung der Wärmeleitung in einem großen Knudsenzahlbereich. Diss. Univ. Stuttgart
44. Hurlbut FC (1964) Note on conductive heat transfer from a fine wire. Phys Fluids 7:904–906
45. Springer GS, Wan SF (1966) Note on the application of a moment method to heat conduction in rarefied gases between concentric spheres. AIAA J 4:441–1143
46. Springer GS (1971) Heat transfer in rarefied gases. Adv Heat Transfer 7:163–218
47. Dorrance WH (1962) Viscous hypersonic flow. McGraw-Hill Book Company, New York
48. Anderson JD Jr (1989) Hypersonic and high temperature gas dynamics. McGraw-Hill Book Company, New York
49. Park C (1990) Nonequilibrium hypersonic aerothermodynamics. John Wiley & Sons, New York
50. Knobling K (1972) Kenngrößen in der Gasdynamik. VDI-Z 114:1206–1210
51. Liu ChY Lees L (1961) Kinetic theory description of plane compressible Couette flow. Adv Appl Mech (Suppl 1), Rarefied Gas Dynamics. Academic Press, New York, pp 391–428
52. Sharipov FM, Seleznev VD (1994) Rarefied gas flow through a long tube at any pressure ratio. J Vac Sci Technol A 12:2933–2935
53. Knudsen M (1909) Die Gesetze der Molekularströmung und der inneren Reibungsströmung der Gase durch Röhren. Ann Phys 4:75–130
54. Lang H, Loyalka SK (1984) Some analytical results for thermal transpiration and the mechanocaloric effect in a cylindrical tube. Phys Fluids 27:1616–1619
55. Loyalka SK, Hamoodi SA (1990) Poiseuille flow of a rarefied gas in a cylindrical tube: solution of linearized Boltzmann equation. Phys Fluids A 2:2061–2065
56. Cercignani C, Sernagiotto F (1966) Cylindrical poiseuille flow of a rarefied gas. Phys Fluids 9:40–44
57. Lo SS, Loyalka SK, Storvik TS (1983) Rarefied gas flow in a cylindrical annulus. J Vac Sci Technol A 1:1539–1548
58. Lo SS, Loyalka SK (1982) An efficient computation of near-continuum rarefied gas flows. J Appl Math Phys (ZAMP) 33:419–424
59. Sparrow EM Lin SH (1962) Laminar heat transfer in tubes under slip-flow conditions. J Heat Transfer 84:363–369

M11 Spontaneous Condensation and Cavitation

Karlheinz Schaber[1] · *Günter H. Schnerr*[2]
[1]Karlsruher Institut für Technologie (KIT), Karlsruhe, Germany
[2]Technische Universität München, Garching, Germany

1 Introduction

A spontaneous phase transition can be defined as the formation of a disperse phase in a supersaturated – i.e., metastable – bulk liquid or gaseous phase. As a characteristic feature the phase transition enthalpy of the growing disperse phase is provided or absorbed by the bulk phase, resulting in a change of the bulk phase temperature.

In contrast to this, phase transitions in technical processes usually take place at cooled or heated surfaces, and the phase transition enthalpy is transferred as a heat flow through a heat exchange surface.

In general, suspensions of tiny droplets or solid particles formed by spontaneous phase transitions or other mechanisms in a bulk gas phase are called aerosols. Suspensions of liquid droplets are also termed as fog or mist [1, 2]. Typical aerosol droplet sizes are smaller than 10 µm (1 µm = 10^{-6} m). Aerosols possess a degree of stability with respect to settling in a gravitational field. This is due to the thermal or Brownian motion of molecules and its impact on the dynamics of tiny particles.

For suspensions of bubbles in a liquid bulk phase there exists no special term. In contrast to aerosols, bubble suspensions are highly dynamic systems because after formation a rapid phase separation in the presence of a gravitational field takes place.

Nevertheless, although the dynamic behavior of aerosols and bubble suspensions is rather different, their formation by spontaneous phase transitions is dominated by the same basic mechanisms: the phase transition is initiated by nucleation in a supersaturated phase. Afterward, the nuclei grow by diffusion, coagulation, and/or coalescence.

Supersaturation of a bulk gaseous or liquid phase is a necessary precondition for nucleation. In order to quantify supersaturation of a liquid or gaseous phase a saturation ratio S can be defined in various ways. Here, an isothermal definition which relates the actual state of the supersaturated phase to the equilibrium state at the same temperature and composition is used.

For a gaseous phase the dew point is used as a reference

$$S = p_{\mathrm{vap}}(T, y_1, \ldots, y_{K-1}) / p_{\mathrm{sat}}(T, y_1, \ldots, y_{K-1}). \qquad (1a)$$

For a liquid phase the bubble point is used as a reference

$$S = p_{\mathrm{vap}}(T, x_1, \ldots, x_{K-1}) / p_{\mathrm{sat}}(T, x_1, \ldots, x_{K-1}), \qquad (1b)$$

where p_{vap} is the actual total pressure of all condensable (vapor) components i ($i = 1, \ldots, K$). Inert components such as carrier

VDI-GVC (ed.), *VDI Heat Atlas*, DOI 10.1007/978-3-540-77877-6_60,

gases can be excluded, if they are not relevant for the phase equilibrium, i.e., if they are not soluble in the liquid phase.

Supersaturation ($S > 1$) may appear in various technical processes. Typical examples are

(1) Adiabatic mixing of gas–vapor mixtures with different temperatures.
(2) Simultaneous heat and mass transfer during absorption, evaporation, and condensation in the presence of inert gases can entail an intersection of the dew point line by the process trajectory, describing the change of state of the gas phase.
(3) Chemical reactions in the gas phase followed by desublimation of the generated substances.
(4) Due to the temperature and pressure drops during the adiabatic expansion of pure gases or mixtures the dew point may be exceeded.
(5) In rapid flows of liquids and in reflected shock waves the pressure can drop below the vapor pressure.

Supersaturation is a necessary but not a sufficient precondition for a spontaneous phase transition. The saturation must exceed a critical value S_{crit} before a phase transition is initiated either by heterogeneous or homogeneous nucleation. Heterogeneous nucleation requires foreign nuclei in the supersaturated bulk phase. If a sufficiently high concentration of nuclei is present, and if those are activated under the actual process conditions, nucleation usually takes place at values of S_{crit} close to 1.

In contrast to this, homogeneous nucleation requires a high degree of saturation because for the formation of critical molecule clusters (= homogeneous nuclei) a high activation energy barrier has to be surmounted.

The key parameter in nucleation is the nucleation rate J which is defined as the number of nuclei formed by homogeneous nucleation or activated in heterogeneous nucleation per unit volume and time. The dimension of J is usually given in $m^{-3}\ s^{-1}$ or $cm^{-3}\ s^{-1}$.

The critical saturation S_{crit} can be defined as the saturation S for which a spontaneous phase transition can be observed and measured, i.e., for which the nucleation rate is high enough

$$S_{crit} = S(J = 10^z\ \mathrm{cm^{-3}s^{-1}}). \tag{2}$$

The exponent z must be chosen according to the time scale of the considered process.

In Atmospheric Sciences it is convenient to choose $z = 0$.

In Process Technology where the flow residence time in an apparatus or in a machine is in the range of seconds usually z is chosen between 4 and 6 [3].

Gases or liquids under technical process conditions always contain a certain amount of small particles which can be activated as nuclei in supersaturated phases.

Consequently, in Process Technology heterogeneous and homogeneous nucleation often take place simultaneously.

Furthermore, there is no sharp transition between nucleation and growth. Both mechanisms overlap. During a nucleation event, even if the first formed nuclei would be growing, nucleation goes on until the saturation of the bulk phase drops to values lower than S_{crit}.

In this chapter of the Heat Atlas gas-to-liquid and liquid-to-gas spontaneous phase transitions in flowing media are considered.

2 Spontaneous Condensation

2.1 Nucleation

2.1.1 Homogeneous Nucleation of Pure Substances

The kinetics of a phase transition can be explained on a microscopic scale as a statistical phenomenon. Colliding molecules form clusters which decompose again at low supersaturations. Increasing supersaturation increases the probability that molecule clusters or the so-called embryos reach a critical size. Such critical molecule clusters are called nuclei. In the classical theory of homogeneous nucleation, the nucleation rate J, which is the number of emerging nuclei per unit volume and time, can be predicted by the basic equation for nucleation phenomena

$$J = K \exp\left(-\frac{\Delta G^*}{kT}\right), \tag{3}$$

where K is a frequency factor which indicates the number of collisions per unit volume and time, and the exponential term is the probability of the formation of critical clusters.

G^* is the Gibbs free energy required to form a nucleus of critical radius r^*, and k is the Boltzmann constant.

The nucleus is considered a small sphere of radius r^* forming an unstable thermodynamic equilibrium with the surrounding supersaturated gas phase which is determined by the Kelvin equation (capillarity approximation)

$$r^* = \frac{2\sigma v_L \widetilde{M}}{\Delta\mu}, \tag{4}$$

where σ is the surface tension, v_L is the specific liquid volume, and $\Delta\mu$ the difference of the pure component chemical potentials between the supersaturated gas phase and the liquid phase at bulk gas phase conditions (p_{vap}, T). For an incompressible nucleus

$$\begin{aligned}\Delta\mu &= \mu_{vap}(p_{vap}, T) - \mu_L(p_{vap}, T)\\ &= \tilde{R}T \ln\frac{\varphi p_{vap}}{\varphi_{sat} p_{sat}(T)} - \tilde{v}_L(p_{vap} - p_{sat}(T)).\end{aligned} \tag{5}$$

For pressures sufficiently far below the critical pressure the second term of Eq. (5) can be neglected. Furthermore, if the vapor behaves like an ideal gas the fugacity coefficients φ and φ_{sat} at bulk gas phase and at saturation conditions, respectively, can be set to 1, and Eq. (5) can be written

$$\Delta\mu^{id} = \tilde{R}T \ln S, \tag{6}$$

where $S = p_{vap}/p_{sat}(T)$ is the saturation ratio.

The Gibbs free energy for the formation of a nucleus is given by

$$\Delta G^* = (4/3)\pi\sigma r^{*2}. \tag{7}$$

Inserting Eq. (4) yields

$$\Delta G^* = \frac{16}{3}\pi\frac{\sigma^3 v_L^2 \widetilde{M}^2}{(\Delta\mu)^2}. \tag{8}$$

If the exponent of Eq. (3) is represented by Eqs. (6) and (8) one obtains

$$(\Delta G^*/kT)^{\mathrm{id}} = \frac{16\pi}{3\mathrm{k}}\left(\frac{\sigma}{T}\right)^3\left[\frac{\nu_\mathrm{L}\widetilde{M}}{\tilde{R}\ln S}\right]^2. \tag{9}$$

The characteristic feature of Eq. (9) is the strong dependence of the exponent on surface tension, temperature, and saturation degree.

The classical theory of homogeneous nucleation has been developed mainly by Volmer and Weber, Farkas, Becker and Döring, Zeldovich, and Frenkel [4]. Summaries on comprehensive treatments of nucleation are given in various publications [1, 5–7].

For the calculation of the frequency factor K, the Volmer–Frenkel approach modified by Feder et al. is used [8]

$$K = \Theta Z \alpha_\mathrm{c}\left(\frac{1}{4}n_1\bar{c}_1\mathrm{O}^*\right)n_1. \tag{10}$$

where n_1 is the number density of monomers, and $\bar{c}_1$ the mean monomer velocity

$$\bar{c}_1 = \left(\frac{8\tilde{R}T}{\pi\widetilde{M}}\right)^{1/2}. \tag{11}$$

The condensation coefficient α_c (sticking coefficient) multiplied by the collision rate ($n_1\ \bar{c}_1\ O^*/4$) describes the number of monomers impacting on the surface O^* ($= 4\pi r^{*2}$) of a critical cluster. For the condensation coefficient α_c usually values between 0.5 and 1 are assumed. The nonisothermal factor Θ

$$\begin{aligned}\Theta &= b^2/(b^2+q^2),\ b^2 = \tilde{R}T^2\\ &\left\{\left(\tilde{c}_{\mathrm{v,vap}}+\frac{\tilde{R}}{2}\right)+\frac{1-y_\mathrm{vap}}{y_\mathrm{vap}}\sqrt{\frac{\widetilde{M}_\mathrm{vap}}{\widetilde{M}_\mathrm{cg}}}\left(\tilde{c}_{\mathrm{v,cg}}+\frac{\tilde{R}}{2}\right)\right\},\\ q^2 &= \left\{\tilde{h}_\mathrm{vap}(T,p_\mathrm{vap})-\tilde{h}_{\mathrm{L,sat}}(T)-\frac{\tilde{R}}{2}T-\frac{2}{r^*}\frac{\sigma\widetilde{M}_\mathrm{vap}}{\rho_{\mathrm{L,sat}}}\right\}\end{aligned} \tag{12}$$

covers the deviation from the isothermal nucleation model. For gas–vapor mixtures with extreme low concentrations of the condensing vapor Θ tends toward 1.

The Zeldovich factor Z

$$Z = \left(\frac{\Delta G^*}{3\pi kT(i^*)^2}\right)^{1/2} \tag{13}$$

can be interpreted as a correction in order to guarantee a steady-state population of subcritical clusters during nucleation. Therefore, growing nuclei have to be replaced by new monomers. The number of monomers i^* on a critical cluster (nucleus) is given by a simple geometric approach

$$i^* = \frac{4}{3}\pi\frac{(r^*)^3}{m_1\nu_\mathrm{L}}, \tag{14}$$

where m_1 is the mass of a molecule, and ν_L the specific liquid volume.

The classical nucleation theory is a sufficiently good approach for a great variety of technical nucleation problems [9–19]. The isothermal dependence of the nucleation rate on saturation ratio is well predicted: experimental and theoretical slopes of J versus S are in good agreement. But the temperature dependence of the nucleation rate is often systematically different from that predicted by the classical theory. To overcome this problem Wölk et al. suggest empirical correction functions for the nucleation rate based on precise experimental data [20].

Some authors suggest introducing the factor $(1/S)$ in Eq. (10). It results from a correct treatment of the nucleation kinetics [6]. Nearly all comparisons of classical nucleation theory with experiment have omitted this factor, but it would be more correct to include it. Furthermore, one must be aware that in principle the surface tension of nuclei with typical diameters in the range of 1 nm is a function of the droplet radius [21]. But this fact is normally neglected in literature.

Finally, recent progress in applying molecular dynamic simulation to nucleation of pure substances should be mentioned. With this method it is possible to predict realistic nucleation rates if the intermolecular interactions of the substance can be described by simple but suitable molecular models [7, 22].

The following example should give an insight in the order of magnitude of the relevant nucleation parameters. Based on Eqs. (3), (9), (10–13) the values of Table 1 have been calculated for the nucleation of pure water vapor at $t = 20°\mathrm{C}$ (and 60°C) assuming $\alpha_\mathrm{C} = 1$. Water vapor is treated as an ideal gas.

Following properties have been used:

For 20°C: $p_\mathrm{sat}(T) = 23.37$ mbar; $\rho_\mathrm{vap} = 0.0173$ kg/m^3; $\sigma = 0.07274$ N/m; $\rho_\mathrm{L} = 988$ kg/m^3;

For 60°C: $p_\mathrm{sat}(\mathrm{T}) = 199.0$ mbar; $\rho_\mathrm{vap} = 0.1302$ kg/m^3; $\sigma = 0.06619$ N/m; $\rho_\mathrm{L} = 983$kg/m^3.

The values of Table 1 demonstrate the distinguishing feature of Eq. (3) which is the extremely sharp dependence of the nucleation rate on the saturation degree. But it is obvious that the frequency factor K is nearly independent of the saturation degree S.

With increasing temperature the nucleation rate increases at constant saturation. For a temperature of 60°C nucleation rates in the order of 10^6 cm^{-3} s^{-1} arise at $S = 2.8$.

Furthermore, in the presence of an inert gas the nonisothermal factor Θ and consequently, the nucleation rate would increase.

2.1.2 Homogeneous Nucleation of Binary Mixtures

The extension of the classical nucleation theory to binary mixtures was pioneered by Flood [23], Neumann und Döring [24],

M11. Table 1. Nucleation rate J of pure water vapor at 20°C dependent on the saturation S

S	r^*, 10^{-9} m	K, cm^{-3} s^{-1}	$\exp(-\Delta G^*/kT)$	J, cm^{-3} s^{-1}
2	1.55	6.0×10^{23}	2.2×10^{-79}	1.3×10^{-55}
3	0.98	1.4×10^{24}	4.9×10^{-32}	6.8×10^{-8}
3.5	0.86	1.9×10^{24}	8.3×10^{-25}	1.6×10^{0}
4	0.78	2.5×10^{24}	2.2×10^{-20}	5.4×10^{4}
4.2	0.75	2.8×10^{24}	4.5×10^{-19}	1.2×10^{6}
4.5	0.71	3.2×10^{24}	2.0×10^{-17}	6.3×10^{7}
5	0.67	3.9×10^{24}	2.6×10^{-15}	1.0×10^{10}
6	0.60	5.7×10^{24}	1.7×10^{-12}	9.6×10^{12}

and Reiss [25]. An actual survey on the state of the art is given, for instance, by Schmelzer [7] and Vehkamäki [26].

For condensing vapor mixtures the same basic Eqs. (3), (7), and (9) developed for pure vapors are applied. For pressures far below the component critical pressures, incompressible liquid droplets, and an ideal gas phase Eq. (9) can be written

$$(\Delta G^*/kT)^{\mathrm{id}} = \frac{16\pi}{3k}\left(\frac{\sigma(x^*)}{T}\right)^3\left[\frac{\nu_{\mathrm{L}}(x^*)\widetilde{M}(x^*)}{\tilde{R}\ln S}\right]^2. \tag{15}$$

The saturation ratio for a binary mixture of components A and B is defined according to Flood [23]

$$S = S_{\mathrm{A}}^{x^*} S_{\mathrm{B}}^{(1-x^*)}, \tag{16}$$

where S_{A} and S_{B} are the partial saturation degrees, and x^* is the mole fraction of component A in the critical cluster. The partial saturation ratios are defined in analogy to the pure component saturation ratio

$$S_i = p_i/p_{i,\mathrm{sat}}(x^*, T), \tag{17}$$

p_i is the partial pressure of component i in the supersaturated gas phase, and $p_{i,\mathrm{sat}}$ is the corresponding partial saturation pressure over a liquid solution with a flat surface and the composition x^* of the critical cluster. In order to calculate $p_{i,\mathrm{sat}}$ the extended Raoult's law can be applied

$$p_{i,\mathrm{sat}} = x_i^* \gamma_i \; p_{0i,\mathrm{sat}}(T), \tag{18}$$

where $p_{0i,\mathrm{sat}}$ is the pure component vapor pressure, and γ_i is the activity coefficient.

The composition of the critical nucleus can be determined using the generalized Kelvin equations (Gibbs–Thomson equations) for systems with an ideal gas phase

$$\tilde{R}T\ln S_i = \frac{2\sigma}{r^*}\tilde{v}_i(x^*), \tag{19}$$

where $\tilde{v}_i$ is the partial molar volume of the liquid mixture. Inserting A and B in Eq. (19) and division yields

$$\frac{\ln S_{\mathrm{A}}}{\ln S_{\mathrm{B}}} = \frac{\tilde{v}_{\mathrm{A}}(x^*)}{\tilde{v}_{\mathrm{B}}(x^*)}. \tag{20}$$

If the partial molar volumes as functions of the molar fractions x are known, the molar fraction x^* can be calculated by trial and error using Eq. (20) anticipating actual partial pressures of components A and B in the supersaturated gas phase. The partial molar volumes can be derived from the molar volume $\tilde{v}(T, p, x_i)$ of a binary mixture using the following equation:

$$\tilde{v}_i = \tilde{v} + (1 - x_i)\left(\frac{\partial\tilde{v}}{\partial x_i}\right)_{p,T}; \quad i = \mathrm{A}, \mathrm{B} \tag{21}$$

In order to estimate the frequency factor K, it has to be taken into account that in binary or multicomponent mixtures clusters of different composition exist. This leads to complex formulations which are described in the literature [26, 30].

For the rather frequent case, if one component (B) exists in great excess the frequency factor can be calculated with a simple equation [28]:

$$K = 4\pi r^{*2}\,\beta_{\mathrm{A}} n_{\mathrm{B}} \tag{22}$$

with

$$\beta_{\mathrm{A}} = n_{\mathrm{B}}\left(\frac{\tilde{R}T}{2\pi\widetilde{M}_{\mathrm{A}}}\right)^{1/2}, \tag{23}$$

where n_i are the number densities of molecules A and B.

The frequency factors for mixtures are in the same order of magnitude like those for pure components at similar conditions (T, p, S). That means, the nucleation rate or critical saturation according to Eq. (2) are dominated by the exponential factor in Eq. (3), too. Investigations of the binary systems HCl–H_2O [3] and HNO_3–H_2O [29] in the temperature range between 20°C and 60°C yield similar results for the critical saturation like those of water according to Table 1, if the excess component is water. In contrast to this, the H_2SO_4–H_2O system (with H_2O as excess component) shows different behavior [30]. Due to the extreme vapor pressure minimum at the azeotropic point the critical saturation for nucleation is higher than that for pure water ($S_{\mathrm{crit}} = 9$ at 25°C).

The saturation degree S^* of the classical nucleation theory defined by Eq. (16) is different from that defined by Eq. (1). By means of the latter it is possible to check quickly if a homogeneous gas phase is supersaturated or not. The calculation of S^* requires a heterogeneous system with nuclei of critical composition x^*.

Nevertheless, it has been shown for the HCl–H_2O system that S and S^* differ only in the range of 1% [3]. In contrast to this, for the H_2SO_4–H_2O system, which exhibits extreme phase behavior, the differences between S and S^* can be in the range of 5–30% [31].

2.1.3 Heterogeneous Nucleation

Heterogeneous nucleation requires foreign particles at which condensation or evaporation is already initiated in a slightly supersaturated gaseous or liquid phase.

If in a gaseous phase the foreign particles are insoluble in the condensing vapor, and if they are completely wettable (contact angle between liquid and solid equals to 180°), the critical saturation ratio can be estimated easily by the Kelvin equation which one obtains from Eqs. (4) and (6) for a pure component.

$$\tilde{R}T\,\ln\,S_{\mathrm{crit}} = \frac{2\sigma}{\mathrm{r}}\tilde{v}_{\mathrm{L}}. \tag{24}$$

Anticipating complete wettability of the foreign particle the first condensing thin liquid film has nearly the same curvature like that of a corresponding liquid droplet with the diameter of the particle. Consequently, Eq. (24) can be applied to estimate the critical saturation. For water at 20°C and a foreign particle diameter of 10 nm one gets $S_{\mathrm{crit}} = 1.237$, and for a particle with a diameter of 100 nm one obtains $S_{\mathrm{crit}} = 1.0215$. If the wettability of the particles is lower, the critical saturation ratio increases.

In the case of soluble particles, for example salt particles in condensing water, the Kelvin effect is compensated by the vapor pressure depression and thus the critical saturation ratio can drop slightly below $S_{\mathrm{crit}} = 1$ [2].

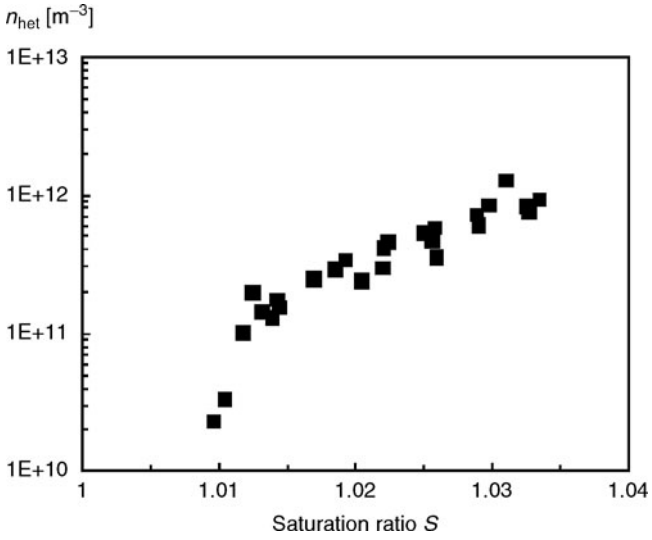

M11. Fig. 1. Formation of HCl aerosols initiated by heterogeneous nucleation in a flue gas quench cooler. Number concentration of activated particles versus (theoretical) saturation ratio (Gas inlet temperature: 200°C; adiabatic saturation temperature: 45°C; inlet gas concentration of HCl: 500–2,000 mg/m^3) [31].

In spontaneous condensation processes initiated by heterogeneous nucleation the concentration and the properties of foreign particles are decisive for the final concentration and sizes of the generated aerosol. Atmospheric air always contains sufficient particles as numerous investigations show [2, 5]. Typical concentrations of atmospheric particles are in the range of 10^4 cm^{-3} in rural and 10^6 cm^{-3} in urban regions. In industrial process gases high concentrations of tiny foreign particles can occur. Especially, in flue gases number concentrations of foreign particles between 10^6 and 10^8 cm^{-3} have been measured [27, 31, 32]. But usually size distributions as well as surface properties of foreign particles in process gases are unknown.

In general, for modeling and simulation of spontaneous condensation processes initiated by heterogeneous nucleation the key parameter is the number concentration of foreign nuclei which are activated under the special conditions of the considered process [33, 34]. This relevant number concentration can be detected only by experimental methods [32].

The activation (wettability) of foreign particles depends on the maximum saturation ratio which is reached in the considered process. As an example, experimental results of a flue gas scrubbing process are shown in Fig. 1. It can be seen that the number concentration of acid aerosol droplets increases with increasing maximum saturation ratio [31]. That means, the higher the saturation ratio, the more particles are activated as condensation sites. In this case the foreign nuclei are mainly soot particles from a gas burner.

In literature, the principles of heterogeneous nucleation are mostly described for condensation processes. But the fundamental features of heterogeneous nucleation, i.e., critical saturation is close to 1 if sufficient foreign nuclei can be activated, and phase transition at nearly equilibrium conditions are the same for evaporation processes.

2.2 Growth of Droplets

2.2.1 Growth by Condensation

Growth by condensation is the predominant mechanism of aerosol droplet enlargement after nucleation. The growth of droplets can be described by the transport equations for heat and mass transfer between the aerosol droplets and the supersaturated gas phase as well as by mass and energy balances. As the relative velocity between the growing small aerosol droplet and the surrounding flowing gas can be neglected, the mass transfer can be considered stationary diffusion, and the heat transfer can be considered stationary conductive heat transfer in the continuum regime. If the droplet radii are lower than the gas mean free path Λ the growth is governed by the kinetic theory [1].

Fuchs and Sutugin proposed the following approximate interpolation formula for the droplet growth rate of a condensing pure vapor in an inert gas which can be applied in the entire Knudsen number range [1]

$$\frac{\mathrm{d}r}{\mathrm{d}t} = \frac{\alpha_c D \tilde{v}_L}{r\tilde{R}T}\left(p_{vap} - p_{sat,r}(T,r)\right)\left[\frac{1+2\mathrm{Kn}}{1+3.42\mathrm{Kn}+5.32\mathrm{Kn}^2}\right]. \quad (25)$$

D is the Diffusion coefficient of the vapor in the gas phase, $\tilde{v}_L$ the molar volume of the liquid, Kn = Λ/d is the Knudsen number, and $p_{sat,r}$ is the saturation vapor pressure of the condensing component at the droplet surface, which can be calculated using the Kelvin equation

$$p_{sat,r} = p_{sat}(T)\exp\left\{\frac{2\sigma}{\mathrm{r}}\tilde{v}_L\right\}. \quad (26)$$

Equation (25) is valid for ideal gas conditions at low gradients of partial pressures and temperatures when the vapor phase mass fraction is low [35].

The accommodation coefficient α_C must be determined experimentally. Usually, α_C is assumed to be 1.

A more rigorous approach for higher vapor phase mass fractions including energy transfer has been presented by Gyarmathy [36].

$$\frac{\mathrm{d}r}{\mathrm{d}t} = \frac{1}{\rho_L}\frac{1-\frac{r^*}{r}}{r+1.59\Lambda}\frac{\ln S}{\frac{\Delta h_v^2}{\lambda R_{vap}T^2}+\frac{p-p_{vap}}{p}\frac{R_{vap}T}{p_{vap}D}}, \quad (27)$$

where Λ is the molecule mean free path, λ the thermal conductivity, Δh_v the evaporation enthalpy, p_{vap} the partial vapor pressure in the bulk phase, and R_{vap} the individual gas constant of the vapor.

It has to be emphasized that the bulk partial pressure p_{vap} and the equilibrium partial pressure at the droplet surface $p_{sat,r}$ as well as the temperatures change during droplet growth. The growth is finished if the saturation ratio in the bulk phase reaches $S = 1$.

In general, the growth of pure or multicomponent droplets has to be calculated by solving the mass and heat transfer equations simultaneously as shown in various publications [33, 34, 37].

In the pure vapor limit as the inert gas concentration tends to zero, transfer processes across the Knudsen layer may dominate and other transfer models have to be used [38–40].

2.2.2 Growth by Coagulation

Coagulation of particles or droplets decreases the number concentration of an aerosol. For particles with diameters $d < 1$ µm coagulation due to Brownian motion is the dominating coagulation mechanism [2]. For the estimation of collision rates, a theory based on Fickian Diffusion of particles has been developed by Smoluchowski [5]. According to this theory, the span $(t - t_0)$ in which an initial number concentration n_0 decreases to $n(t)$ can be calculated for a monodisperse aerosol using the following equations:

$$t - t_0 = -\int_{n_0}^{n(t)} \frac{\mathrm{d}n}{K_c(n)n^2} \tag{28}$$

with

$$K_c = \frac{4kTC_c}{3\eta}, \tag{29}$$

and the Cunningham correction for the Knudsen regime

$$C_c = 1 + \frac{\Lambda}{d}\left[2.514 + 0.8\,\exp\left(-0.55\frac{d}{\Lambda}\right)\right], \tag{30}$$

where Λ is the mean free path of molecules, and η is the viscosity of the carrier gas.

Assuming spherical particles, the diameter of the monodisperse particles increases with decreasing number concentration

$$d = d_0\left(\frac{n_0}{n}\right)^{1/3}. \tag{31}$$

The following example demonstrates that high initial number concentrations are reduced rapidly.

Example: Carrier gas: air at $t = 25°C$, and $p = 1$ bar

Initial diameter	d_0/µm	0.01	0.05	0.01
Initial number concentration	n_0/cm^{-3}	10^{12}	10^{12}	10^9
Final concentration	n/cm^{-3}	10^9	10^9	10^8
Span	$(t - t_0)$/s	0.91	2.24	2.25

3 Adiabatic Expansion of Pure Vapors and Gas–Vapor Mixtures

For demonstration and because of its practical importance, this chapter focuses on condensation of water vapor in nozzles of small or moderate size that are typical of many technical applications. Initially, the vapor phase is unsaturated and due to the fast time scale of the expansion phase transition is not established at thermodynamic equilibrium. Pure vapors or vapor/carrier gas mixtures supersaturate and start to nucleate either heterogeneously, homogeneously, or simultaneously both together. At maximum supersaturation S_{max}, the so-called Wilson point, substantial condensation with macroscopic latent heat release to the flow starts to grow and change local pressure, temperature, density, and flow velocity. The trend of all variations is toward choking conditions with Mach number $M = w/c = 1$. Therefore, initially subsonic flow accelerates toward $M = 1$, whereas supersonic flow decelerates to $M = 1$ [41]. As distinct from choking in adiabatic flow due to area variation, this is called thermal choking. If the average cooling rate $-\mathrm{d}T/\mathrm{d}t$ (K/µs) is of O(1), the Wilson point locates typically in the transonic regime with Mach numbers M_c = 1.1–1.3 at the Wilson point. Here, even a very small amount of heat addition to the flow of $q/c_pT_{01} < 0.1$ may cause thermal choking with $M = 1$ within the condensation zone. Then the flow pattern changes significantly and forms additional steady or high frequency moving shocks. Because of the strong coupling of flow and thermodynamics the sudden temperature increase across shocks decreases instantaneously the supersaturation, the driving potential for nucleation, and droplet growth. These instabilities driven by nonviscous interaction of local heat source distributions and compressibility of the fluid are of great practical importance.

Adiabatic expansions of pure vapors can be modeled as isentropic flow, whereas in vapor/carrier gas mixtures the components undergo individual isentropic expansions only, if the molar specific heats are equal [41]. Depending on the cooling rate heterogeneous and homogeneous condensations separate quantitatively. Oswatitsch showed in his pioneering work [42, 43] that simultaneous heterogeneous condensation growing at natural impurities in atmospheric air does not alter quantitatively the homogeneous nucleation and droplet growth. However, artificial seeding with high particle concentration is well known for flow control to minimize nonequilibrium losses in low-pressure steam turbines.

Typical thermodynamic and flow dynamic properties of high-speed condensing water vapor flows are

Vapor phase initially unsaturated	
	$\rho_{vap} \approx$ O(10^{-2}–1 bar), $T \approx$ 300–450 K
	$\rho_{vap} \approx$ O(10^{-2}–1 kg m^{-3})
	$\rho_{carrier\ gas} \approx$ O(1 kg m^{-3})
	$\rho_{liq} \approx$ O(10^3 kg m^{-3})
Speed of sound	$c \approx$ O($4{\cdot}10^2$ m s^{-1})
Typically high flow speed	$M \approx$ O(1) transonic flow
Cooling rate	$-\mathrm{d}T/\mathrm{d}t \approx$ O(1 K/µs), nonequilibrium phase transition
Homogeneous nucleation	$J \approx$ O(10^{25} m^{-3} s^{-1})
Heterogeneous nuclei concentration	$n_{het} \approx$ O(10^{10} m^{-3})
Condensate mass fraction/wetness	$g/g_{max} \approx$ O(1–5·10^{-2})

3.1 Steady-State Phenomena

Figure 2 shows the numerical simulation of a quasi 1-D Laval nozzle flow with a weak supersonic compression caused by heat release after homogeneous nucleation and droplet growth. The adiabatic expansion of the vapor/carrier gas mixture crosses the equilibrium limit at (2) and continues until the Wilson point (4). Intense droplet growth decreases the vapor pressure of the mixture from (4)→(5), but simultaneously the static pressure of

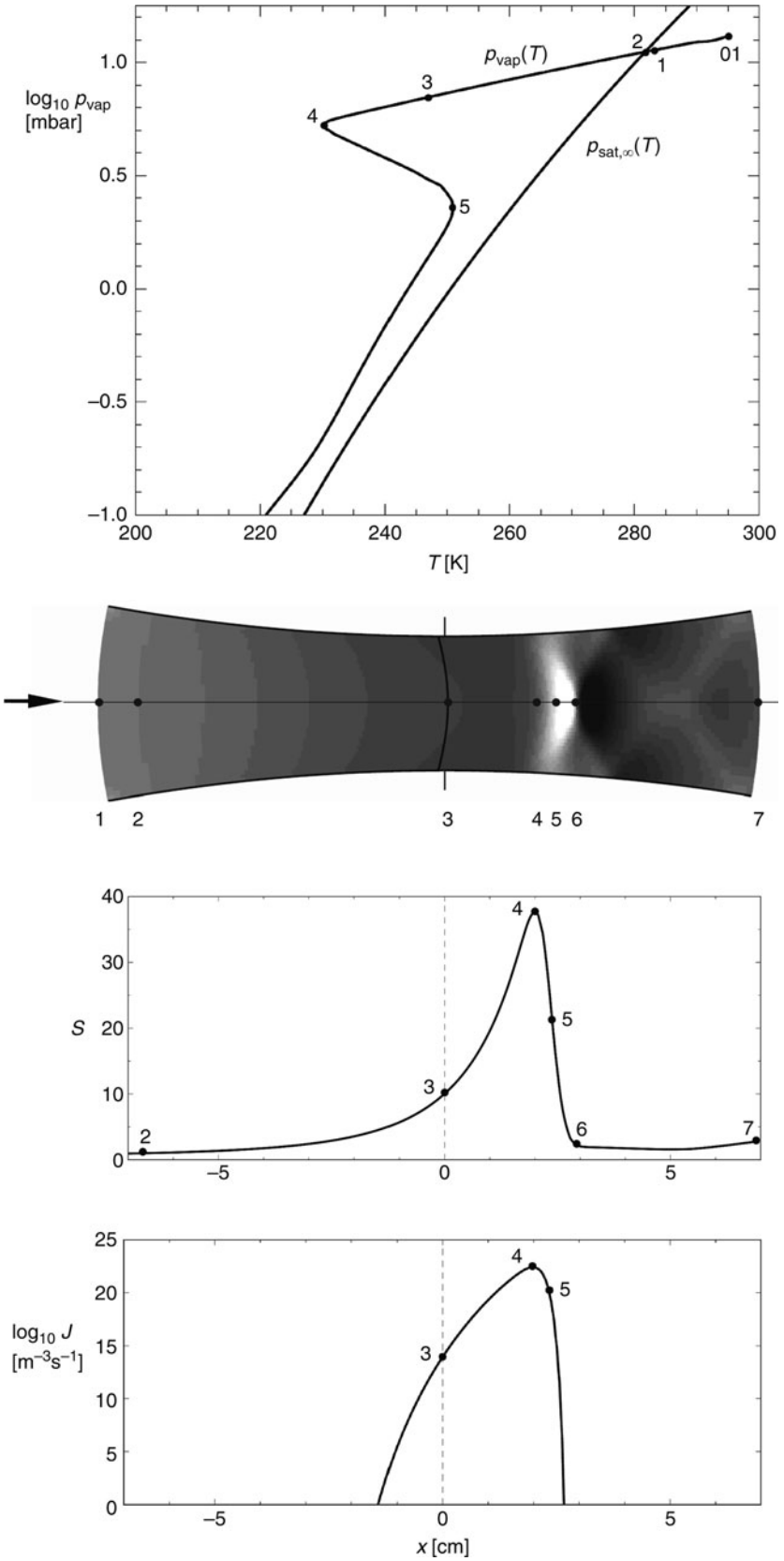

M11. Fig. 2. Continuous supersonic compression in steady Laval nozzle flow due to homogeneous condensation of the moderate water vapor content of atmospheric air; reservoir conditions: $\Phi_0 = 50.0\%$, $T_{01} = 295.0$ K, $p_{01} = 1.0$ bar, $x = 8.26\ g_{vapor}/kg_{dry\ air}$, numerical simulation, inviscid flow modeling.

From top: phase diagram; numerical Schlieren picture – visualization of density gradients in main flow direction, saturation ratio S at the nozzle axis; and homogeneous nucleation rate J at the nozzle axis.

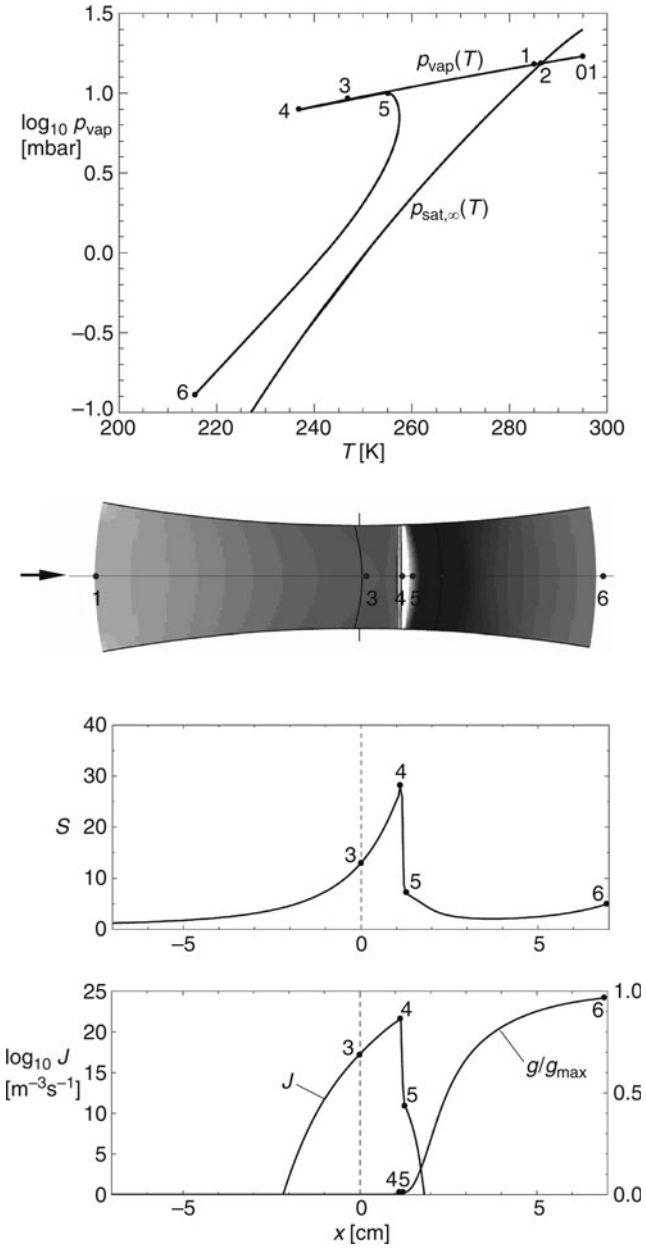

M11. Fig. 3. Shock in steady Laval nozzle flow due to homogeneous condensation of high relative humidity Φ_0 and high water vapor content of atmospheric air; reservoir conditions: Φ_0 = 65.0%, T_{01} = 295.0 K, p_{01} = 1.0 bar, x = 10.78 $g_{vapor}/kg_{dry\ air}$, numerical simulation, inviscid flow modeling.
From Top: phase diagram; numerical Schlieren picture – visualization of density gradients in main flow direction, saturation ratio S at the nozzle axis; and homogeneous nucleation rate J and growth of condensate mass fraction g/g_{max} at the nozzle axis.

the mixture increases. The remaining small supersaturation after (5) accounts for the fact that tiny droplets require a vapor pressure which is higher as that of a flat phase boundary. At (4) the supersaturation is $S \approx 40$ and the maximum nucleation rate is $J \approx 10^{22}$ m^{-3}s^{-1}. If the initial vapor pressure increases further a steady normal shock (4)→(5) forms (Fig. 3). At (5) after the shock, the flow remains still supersaturated and the complete latent heat addition happens downstream of the shock, starting in the local subsonic flow regime and reaccelerating to supersonic flow. Usually, the additional shock is called condensation shock, which is misleading to some extend, because the instantaneous temperature increase through this shock diminishes nucleation and further growth.

In practice it is important to know where condensation starts to grow in a nozzle with the given initial state. An empirical similarity law for the condensation onset defined by the Mach number M_c at the Wilson point was first published by Zierep and Lin [44, 45]. Here, thermodynamics of the problem is represented by a single parameter, the initial relative humidity Φ_0 at reservoir conditions, whereas flow dynamics, the time scale of the expansion, is represented by the exponent a. The time scale of the flow can be modeled either by the cooling rate $-dT/dt$ (K/μs) or by the temperature gradient $-dT/dx$ (K/cm). For slender plane nozzles, dT/dx depends on the wall curvature r^* and the height y^* at the throat

$$\left(-\frac{dT}{dx}\right)^* = 2 \cdot \frac{\gamma - 1}{\gamma + 1} \cdot T_{01} \cdot \sqrt{\frac{1}{\gamma + 1} \cdot \frac{1}{y^* r^*}} (\mathrm{K/cm}). \qquad (32)$$

Figure 4 shows equivalent nozzles with identical temperature gradients $-dT/dx$ (K/cm) at the axis.

Assuming isentropic expansion, the dependence of the Mach number M_c at the Wilson point can be formulated as

$$\Phi_0^a = \frac{\frac{\gamma+1}{2}}{1 + \frac{\gamma-1}{2} M_c^2} \quad 0 \le \Phi_0 \le 1. \qquad (33)$$

Increasing cooling rates at constant initial state result in higher onset Mach numbers M_c (Fig. 5). Equation (33) implies the limit of stability at $M_c = 1$. For condensation of water vapor in atmospheric air the parameter a was determined by Schnerr [46–48].

$$a = 0.0498 \cdot \left(-\frac{dT}{dx}(\mathrm{K/cm})\right)^{*0.3010}. \qquad (34)$$

If 2-D and 3-D flow pattern dominate, the previous slender nozzle approximation is no longer valid and the location of the condensation onset depends on the characteristic angle δ

$$\delta = \beta - \alpha, \qquad (35)$$

β is the angle between the isentropic iso-Mach line and the velocity vector at the onset, and α is the Mach angle (see Fig. 6).

If $\delta > 0$ close to local Wilson point conditions, weak wave interactions alter the flow structure only downstream of the condensation onset, as seen in Fig. 7. With increasing wall curvature the so-called X-shock becomes more distinct. It is caused by the intersection of characteristics of the same family. Obviously, the onset front of the parabolic white compression zone is not affected by these weak oblique shocks.

If $\delta < 0$ close to the local Wilson point, strong wave interaction alters the flow structure completely, including the location of the condensation onset. Close to the throat the condensation onset regime separates into parts (Fig. 8). In terms of gas dynamics, here the so-called subsonic heating fronts dominate.

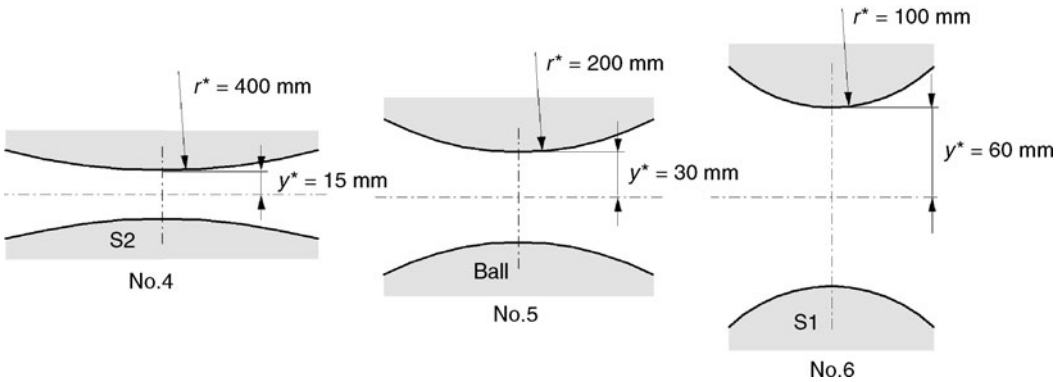

M11. Fig. 4. Equivalent 2-D plane circular arc Laval nozzles with constant characteristic length $l = (y^* r^*)^{1/2}$ – with constant temperature gradient $(-dT/dx)^*$ (K/cm) at the nozzle axis.

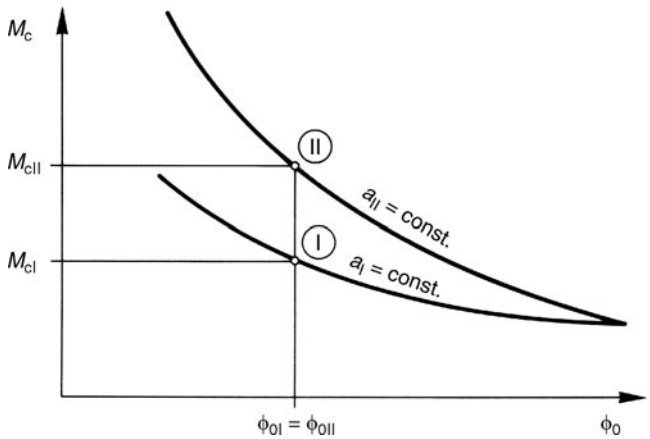

M11. Fig. 5. Condensation onset Mach number M_c according to Eq. (33) – effect of absolute temperature gradient $(-dT/dt)^*$ (K/cm) – nozzle geometry; T_{01} = const, p_{01} = const.

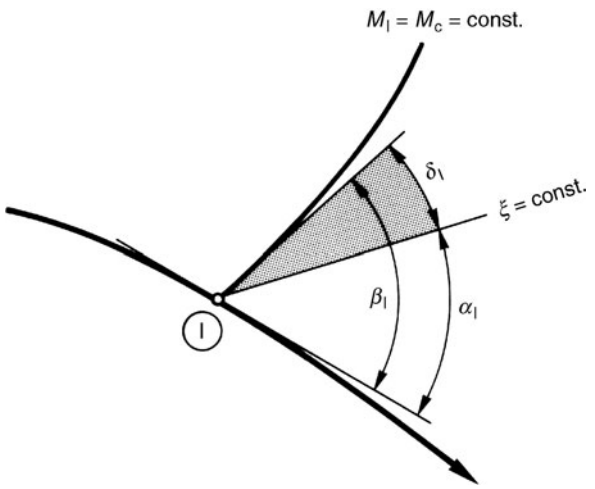

M11. Fig. 6. Characteristic angles at point I – Wilson point – of a streamline with iso-Mach line M_c = const. and isentropic characteristic ξ; α-Mach angle, β-angle between velocity vector at point I and Iso-Mach line M_c= const., δ-characteristic angle.

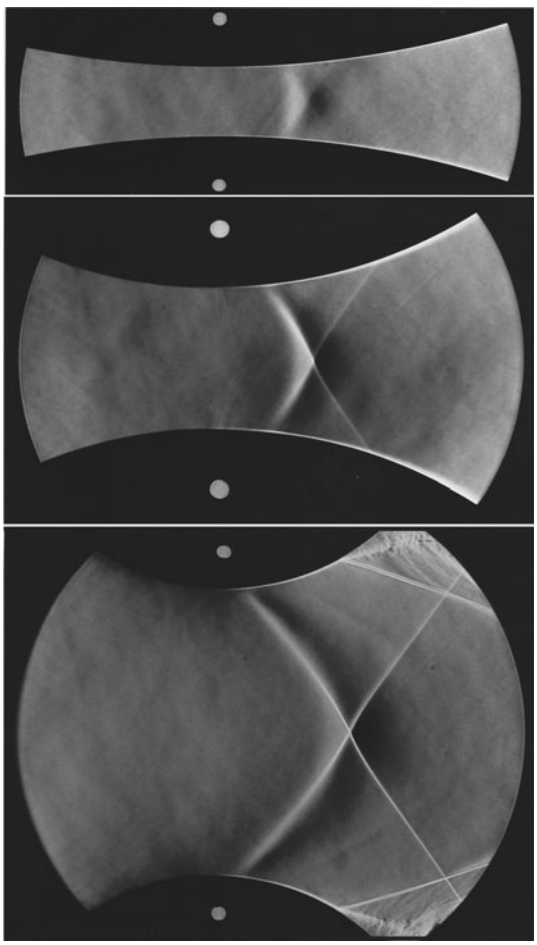

M11. Fig. 7. Effect of wall curvature on 2-D homogeneously condensing flow with evolution of X-shocks in equivalent nozzles according to Fig. 4 and at approximately constant reservoir conditions; experimental Schlieren picture, flow from left, humid atmospheric air.
From top: nozzle S2 y^* = 15 mm, r^* = 400 mm; Φ_0 = 36.4%, T_{01} = 296.6 K, x = 6.60 $g_{vapor}/kg_{dry\ air}$; nozzle BAll y^* = 30 mm, r^* = 200 mm; Φ_0 = 36.6%, T_{01} = 300.3 K, x = 8.30 $g_{vapor}/kg_{dry\ air}$; nozzle S1 y^* = 60 mm, r^* = 100 mm; Φ_0 = 37.2%, T_{01} = 295.0 K, x = 6.20 $g_{vapor}/kg_{dry\ air}$.

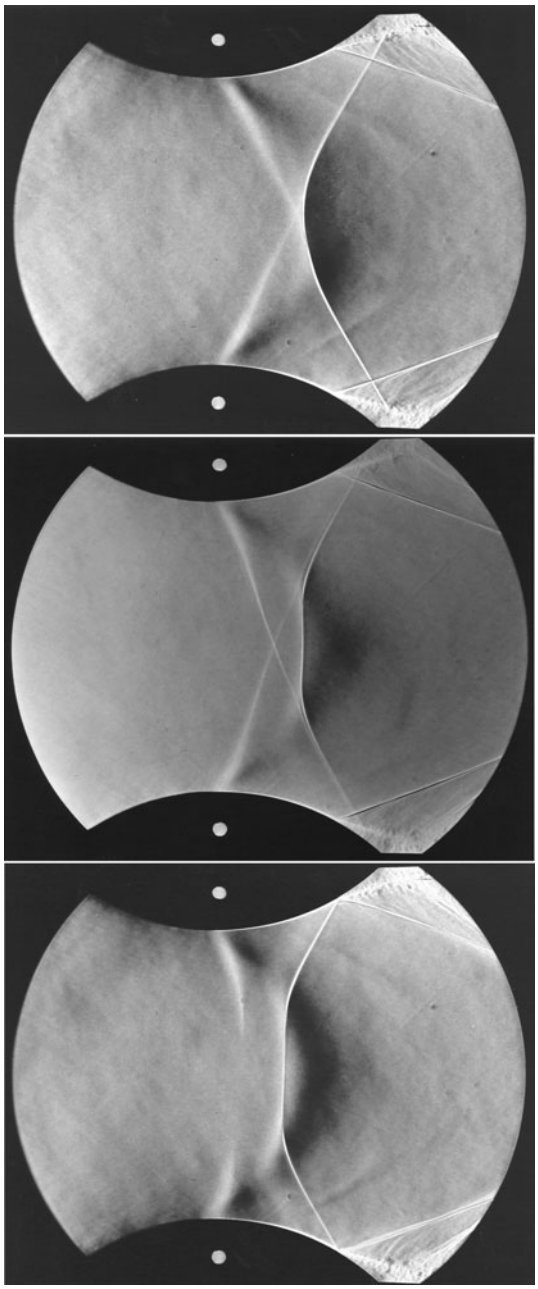

M11. Fig. 8. Complex interaction of pressure waves with homogeneous condensation in well curved circular arc nozzle S1; experimental Schlieren pictures, flow from left, relative humidity Φ_0 increases from top.
From top: Φ_0 = 62.2%, T_{01} = 288.8 K, x = 7.0 $g_{vapor}/kg_{dry\ air}$; Φ_0 = 63.2%, T_{01} = 293.0 K, x = 9.2 $g_{vapor}/kg_{dry\ air}$; Φ_0 = 71.3%, T_{01} = 286.8 K, x = 7.0 $g_{vapor}/kg_{dry\ air}$.

The limiting curve $\delta = 0$ separates these flow regimes. For $y^*/r^* < 0.3$ transonic condensation onset fronts predominate that remain undisturbed (Fig. 9).

If supersaturation in disperse two-phase flow mixtures increases again due to further expansion of the flow, a secondary nucleation zone establishes with quantitatively the same

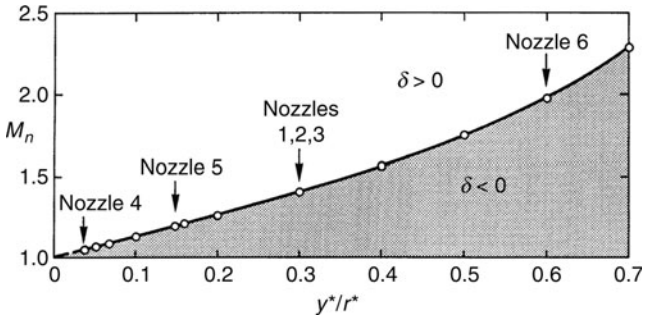

M11. Fig. 9. Limiting curve $\delta = 0$ dependent on wall curvature parameter y^*/r^* of circular arc nozzles – isentropic flow.

nucleation rate as in the primary zone [49]. Further grow of these additional nuclei to larger droplet size is not possible and the primary droplets dominate the condensate mass (Fig. 10).

In multistage turbomachinery multiple expansion and compression of the fluid are typical. If the fluid condenses in the flow through a first blade row and if it evaporates partially weakly or instantaneously through aerodynamic shocks, ahead of the following stage the fluid consists of vapor and preexisting very tiny droplets – fog, with high number concentrations typical for homogeneous nucleation, 5–8 orders higher as compared with natural heterogeneous particle concentrations. This high droplet concentration produces a much higher condensate mass fraction, even if the cooling rates of the primary and secondary expansion zones are equal. Figure 11 demonstrates this phenomenon by a simplified flow model over a wavy wall with homogeneous nucleation in two local supersaturated regimes [50]. The first aerodynamic shock weakens with increasing distance from the wall. Close to the wall the shock is strong and the condensate evaporates completely, and the pressure and temperature return to unsaturated state. In far distance the shock is very weak but the supersaturation ahead of the shock is not high enough for substantial homogeneous nucleation and condensate formation. In between there is a regime where tiny droplets survive passing through the shock. If this fogy layer enters the second expansion zone the droplet size increases instantaneously, and the droplet size and condensate mass fraction increase up to one order higher as in the primary zone. Another example of multiple condensation in a low-pressure steam turbine stage is shown in Fig. 16.

3.2 Unsteady Phenomena – Self-excited Flow Instabilities

High initial vapor contents and low cooling rates $-dT/dt$ (K/μs) shift the location of the Wilson point close to $M_c = 1$ with thermal choking, the limit of stability. Then self-excited high frequency oscillatory instabilities start [51–58]. The sequence of Schlieren pictures in Fig. 12 visualizes one cycle of the interaction of the moving shock with the nucleation zone. The shock enters the nucleation zone and reduces instantaneously the local peak value of the nucleation rate (Fig. 13). If the shock

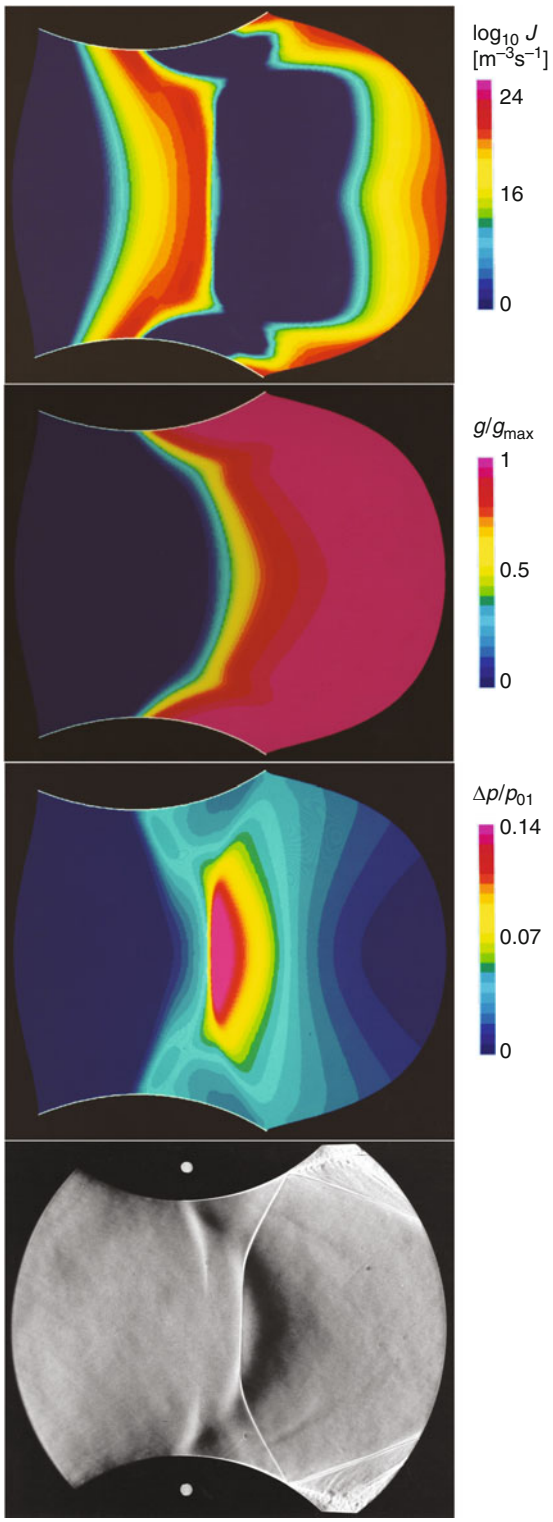

M11. Fig. 10. Homogeneous condensation in 2-D plane Laval nozzle S1 $y^* = 60$ mm, $r^* = 100$ mm, atmospheric moist air, flow from left; reservoir conditions: $\Phi_0 = 71.3\%$, $T_{01} = 286.8$ K, $p_{01} = 1.0$ bar, $x = 7.0\ g_{vapor}/kg_{dry\ air}$.
From top: homogeneous nucleation rate J within primary and secondary nucleation zone; condensate mass fraction g/g_{max}; diabatic compression ($p_{diabatic} - p_{adiabatic}/p_{01}$); experimental Schlieren picture, visualization of density gradients in main flow direction.

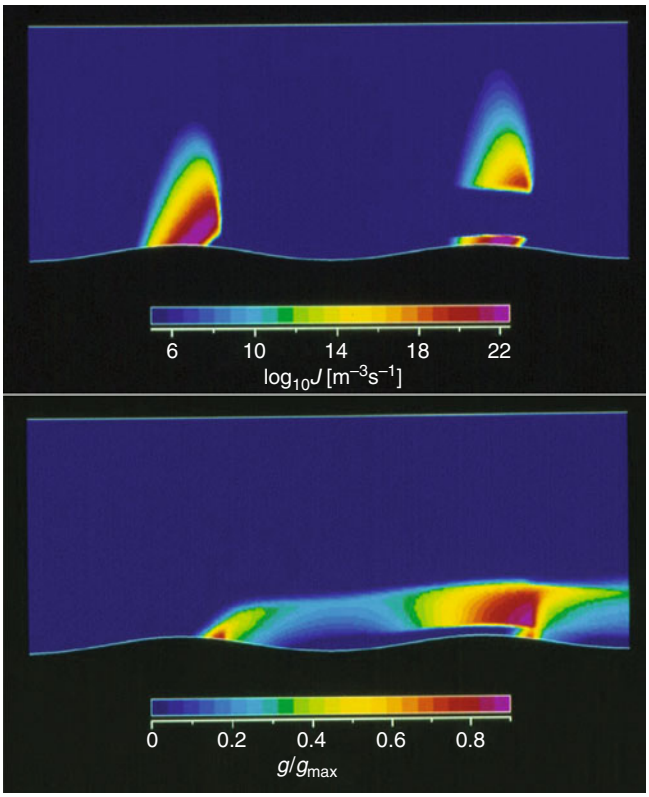

M11. Fig. 11. Periodic homogeneous condensation in transonic flow over a wavy wall with incomplete evaporation of condensate through the first shock; inviscid flow simulation, atmospheric moist air, flow from left with $M_{inlet} = 0.74$, thickness parameter of first bump $\tau_1 = 0.1096$ and of second bump $\tau_2 = 0.1$; reservoir conditions: $\Phi_0 = 50.0\%$, $T_{01} = 293.15$ K, $p_{01} = 1.0$ bar, $x = 7.36\ g_{vapor}/kg_{dry\ air}$.

approaches the throat region this interaction intensifies rapidly and is maximal exactly at the nozzle throat. Here, the nucleation rate decreases instantaneously 5 orders – lowermost picture of Fig. 12. In the next instant supersaturation and nucleation rate recover once again and a new shock of the following cycle builds up – first picture on top of Fig. 12.

Depending on the flow topology there exist different types of self-excited instabilities caused by homogeneous condensation. Figure 14 shows the frequency dependence of three different nozzle shapes on the relative humidity in the supply. Intuitively one would expect that the oscillation frequency increases monotonically with the vapor pressure content in the supply. As seen, this is not true for the quasi 1-D nozzle S2. At the limit of stability and with increasing vapor content the frequency decreases toward a sharp minimum and then it increases monotonically with the initial vapor pressure. Higher nozzle wall curvatures (nozzle S1) shift the limit of stability to higher values of Φ_0. If the scale of the temperature gradient varies substantially as for the nozzle A1 with parallel outflow with constant Mach number $M = 1.2$ at the nozzle exit, the topology of the frequency variation changes completely. Characteristic are two separated branches of low and high

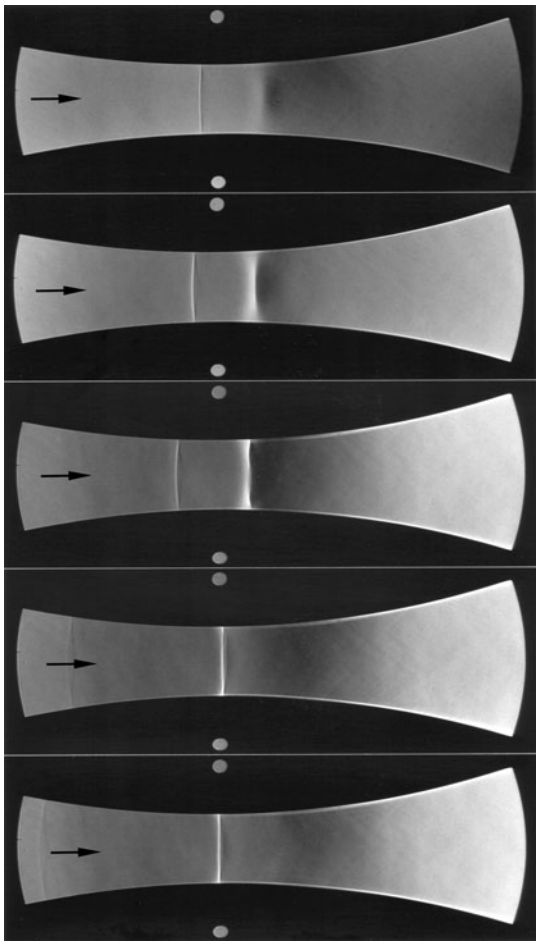

M11. Fig. 12. One cycle of self-excited oscillation with frequency f = 1145 Hz of homogeneously condensing flow in 2-D plane Laval nozzle S2 y^* = 15 mm, r^* = 400 mm; experimental Schlieren pictures, atmospheric moist air, flow from left, time increases from top; reservoir conditions: Φ_0 = 91.0%, T_{01} = 291.65 K, p_{01} = 1.0 bar, x = 9.5 $g_{vapor}/kg_{dry\ air}$.

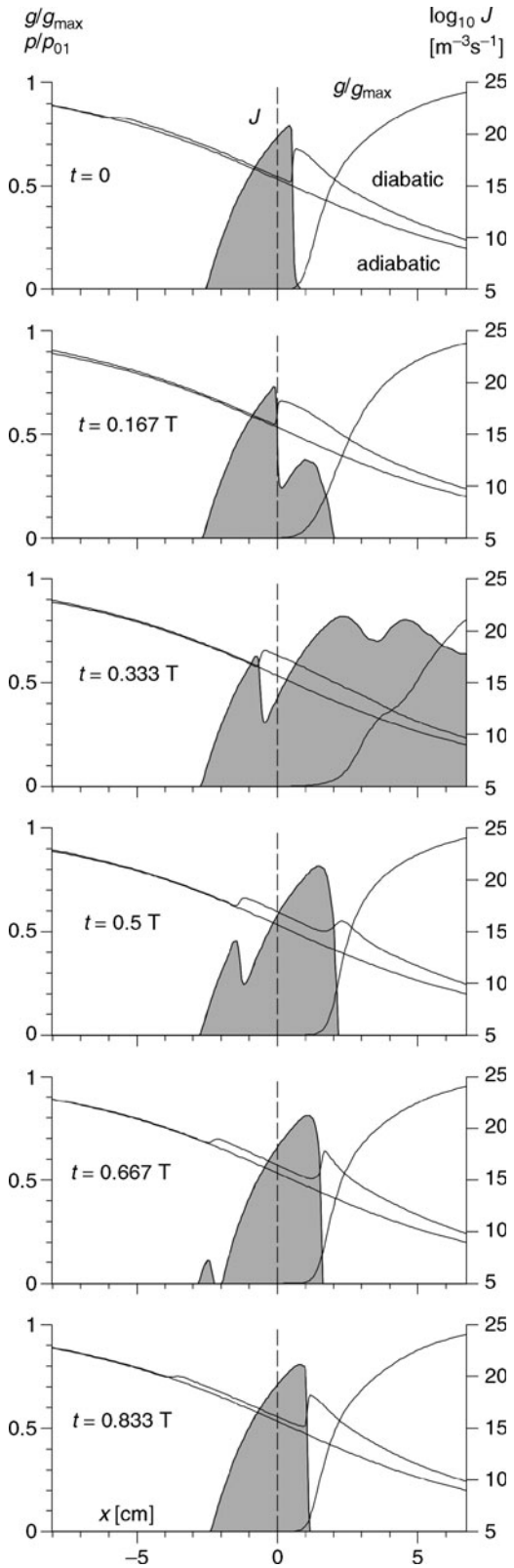

M11. Fig. 13. One cycle of self-excited oscillation in nozzle S2 according to Fig. 12, numerical simulation of static pressure ratio p/p_{01}, nucleation rate J (shaded area) and of condensate mass fraction g/g_{max} at the nozzle axis. The lower expansion curve starting at the ordinate at left depicts the steady-state adiabatic expansion.

frequencies and a hysteresis in between. Because of the sudden increase of the frequency by a factor of 2 or more, this higher order instability is of great practical importance. It was first detected by Adam and Schnerr [59–61] and its existence could be confirmed for a wide variety of nozzle shapes for flows of pure vapor [62] as well as for vapor/carrier gas mixtures [63].

The oscillation frequency f depends on the reservoir conditions, the time scale of the flow, defined by the geometry of the problem, and on fluid properties. In case of nozzle flows this results in

$$f = F_1\left(\underbrace{p_{01}, T_{01}, p_{vap,0}, p_{sat,\infty,0},}_{\text{reservoir state}}\ \underbrace{l, y^*,}_{\text{geometry}}\ \underbrace{c_p, c_{vap}, L, \tau_c}_{\text{fluid}}\right). \quad (36)$$

Using the Buckingham theorem and with the characteristic length $l = \sqrt{y^* r^*}$ this can be reduced to

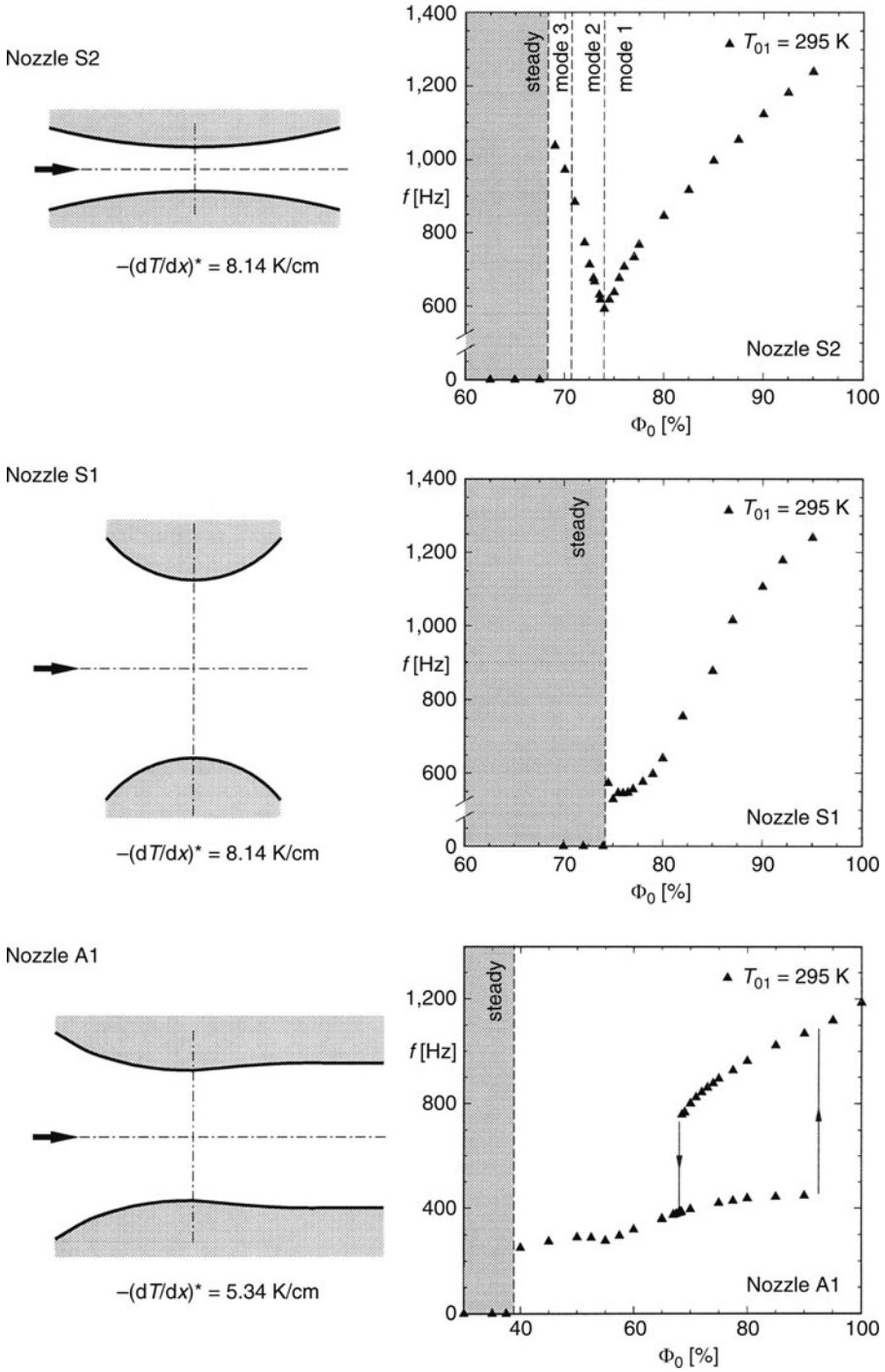

M11. Fig. 14. Dynamics of periodic shock formation and self-excited flow oscillations of homogeneously condensing flow in 2-D plane nozzles; inviscid numerical simulation, atmospheric moist air.
From top: circular arc nozzle S2 y^* = 15 mm, r^* = 400 mm; circular arc nozzle S1 y^* = 60 mm, r^* = 100 mm; nozzle A1 with parallel outflow $M_{\text{isentropic}}$ = 1.2, y^* = 45 mm, r^* = 300 mm.

$$\bar{f} = \frac{f \cdot l}{c^*} = F_2\left(\frac{p_{\text{vap},0}}{p_{\text{sat},\infty,0}}, \frac{p_{\text{vap},0}}{p_{01}}, \frac{L}{c_p T_{01}}, \frac{y^*}{l}, \frac{\tau_c c^*}{l}, \gamma\right). \quad (37)$$

If the fluid is the same and if the flow starts at constant reservoir conditions for pressure and temperature this yields

$$\bar{f} = \frac{f \cdot l}{c^*} = \mathrm{F}_3\left(\Phi_0, \frac{\tau_c}{\tau_f}\right), \quad (38)$$

where τ_c and τ_f are the characteristic time scale of phase transition and of the flow, respectively. For quasi 1-D nozzles with distinct frequency minimum the similarity law for the reduced frequency $\bar{f}$ dependent on the value of $\Phi_{0,\min}$ at the frequency minimum reads [59]

$$\bar{f} = \frac{f \cdot l}{c^*} = F_4\left(\Phi_0 - \Phi_{0,\min}\right). \quad (39)$$

In axial turbomachinery there exist additional excitation mechanisms such as periodic blade wake oscillations and rotor stator interactions [64]. The first mechanism is driven by shedding of shear layers from each blade trailing edge, whereas the second type concerns the convection of wakes with high dissipative losses and therefore with high temperature fluctuations from the stator into the rotating frame of reference. In contrast to the previously described self-excited instabilities both mechanisms are clearly driven by the fluid viscosity. If the origin of the shedding locates within the highly supersaturated regime with maximum nucleation rates, this source produces pressure and temperature fluctuations that interfere with nucleation dynamics within the blade-to-blade flow and triggers the instantaneous growth of the droplet size behind the blade row. This phenomenon is called wake chopping [65]. Figure 15 shows an example of turbulent vortex shedding behind a VKI 1 rotor blade. The strongest time-dependent variation of the nucleation rate happens just at the blade trailing edge and is of two orders of magnitude from $J = 10^{25}$ m^{-3} s^{-1} till 10^{27} m^{-3} s^{-1}. Close to the wake the droplet diameter increases periodically by a factor of 2 [63].

In case the nucleation and droplet growth had already begun in the stator, as seen in Fig. 16, the subsequent further growth of droplets in the disperse mixture in the rotor happens close to equilibrium $S \approx 1$. Despite the fact of the high cooling rate of the flow of O (1) nonequilibrium losses remain negligible, but the final maximum droplet size is much greater as without artificial seeding. Here, homogeneous and heterogeneous condensations are directly coupled, and due to the high concentration of seeding particles the phase transition process is dominated by heterogeneous condensation close to thermodynamic equilibrium [66].

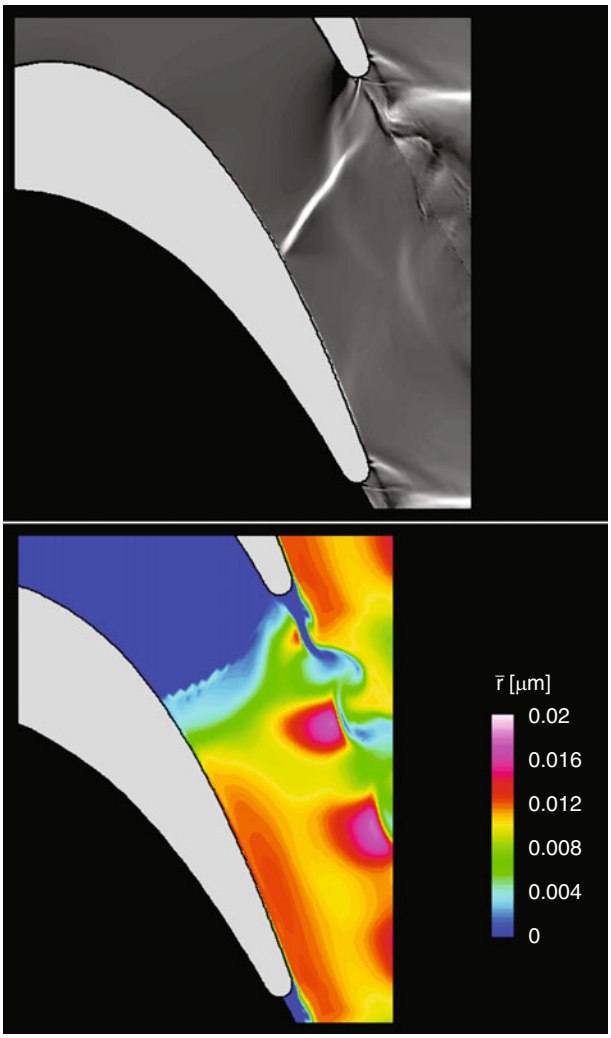

M11. Fig. 15. Vortex shedding from trailing edge of axial VKI-1 turbine cascade, homogeneously condensing turbulent flow of pure steam; flow data: $T_{01} = 357.5$ K, $p_{01} = 0.417$ bar, cascade inflow angle $\beta_1 = 120°$, rotor exit pressure $p_2 = 0.194$ bar, Re = $1.13 \cdot 10^6$, vortex shedding frequency $f_{vs} = 22.5$ kHz, Strouhal number St = 0.22. From top: instantaneous numerical Schieren picture; instantaneous droplet radii distribution triggered by unsteady wake flow.

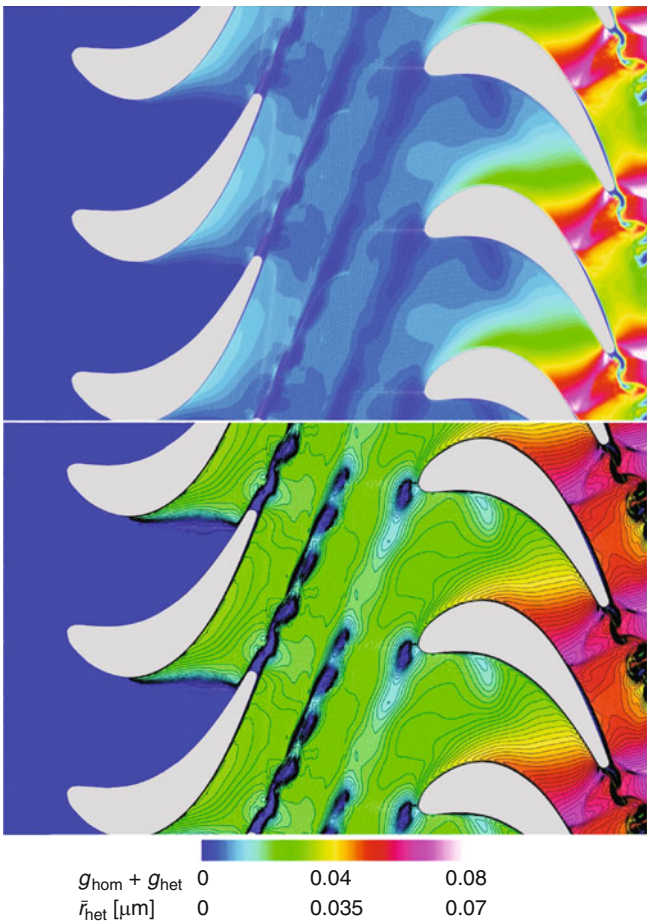

M11. Fig. 16. Rotor/stator interaction in condensing steam flow with artificial seeding through axial VKI-1 stage, numerical simulation of heterogeneously dominated condensing turbulent flow; flow data: $T_{01} = 357.5$ K, $p_{01} = 0.417$ bar, cascade inflow angle $\beta_1 = 120°$, rotor exit pressure $p_2 = 0.194$ bar, $M_{2,isentropic} = 1.13$, $Re_{rotor} = 1.13 \cdot 10^6$, vortex shedding frequency $f_{vs} = 22.5$ kHz, Strouhal number St = 0.22, initial particle number concentration $n_{het,0} = 10^{16}$ m^{-3}, seeding particle size $r_{het} = 10^{-8}$m. From top: total condensate mass fraction – dominated by heterogeneous growth; snapshot of heterogeneously controlled droplet size within stator and rotor.

3.3 CFD Modeling for Calculation of Condensing Flows

Numerical simulation of fluid mechanics requires the solution of the conservation laws for mass, momentum, and energy [63, 65]. If phase transition of the fluid takes place either by homogeneous or by heterogeneous condensation, closure of the set of conservation laws in differential form requires additional equations for modeling of nucleation, droplet growth, and for the transport of the condensate mass. In case of the classical nucleation theory coupled to appropriate droplet growth laws according to different Knudsen regimes $\mathrm{Kn} = \Lambda/d > 1$ or with $\mathrm{Kn} < 1$, the general form of the transport equation yields for any condensation process

$$\frac{\partial(\rho g)}{\partial t} + \nabla \cdot \left(\rho g \vec{v}\right) = \rho \cdot \frac{\mathrm{d}g}{\mathrm{d}t} = F_{\text{source term, condensation}}. \quad (40)$$

For homogeneous condensation this takes the form

$$\begin{aligned} &\frac{\partial}{\partial t}(\rho g_{\mathrm{hom}}) + \nabla \cdot (\rho g_{\mathrm{hom}} \vec{v}) \\ &\quad = \frac{4}{3}\pi \rho_{\mathrm{liq}} r_{\mathrm{hom}}^{*3} J_{\mathrm{hom}} + \rho_{\mathrm{liq}} \rho n_{\mathrm{hom}} \cdot \frac{\mathrm{d}}{\mathrm{d}t}\left(\frac{4}{3}\pi r_{\mathrm{hom}}^{3}\right), \\ &\frac{\partial}{\partial t}(\rho n_{\mathrm{hom}}) + \nabla \cdot (\rho n_{\mathrm{hom}} \vec{v}) = J_{\mathrm{hom}} \end{aligned} \quad (41)$$

with the homogeneous nucleation rate according to Volmer et al.

$$J_{\mathrm{hom}} = \left(\frac{p_{\mathrm{vap}}}{kT}\right)^2 \cdot \frac{1}{\rho_{\mathrm{liq}}} \cdot \sqrt{\frac{2k\sigma_\infty}{\pi R_{\mathrm{vap}}}} \cdot \exp\left(-\frac{4\pi r_{\mathrm{hom}}^{*2}\sigma_\infty}{3kT}\right). \quad (42)$$

For heterogeneous condensation [67–70] the transport equation reduces to

$$\frac{\partial}{\partial t}(\rho g_{\mathrm{het}}) + \nabla \cdot (\rho g_{\mathrm{het}} \vec{v}) = \rho_{\mathrm{liq}} n_{\mathrm{het}} \cdot \frac{\mathrm{d}}{\mathrm{d}t}\left(\frac{4}{3}\pi r_{\mathrm{het}}^{3}\right).$$

In case of $\mathrm{Kn} > 1$, if the mean free path Λ is larger as the droplet size d, for droplet growth the Hertz–Knudsen law [36] is appropriate

$$\frac{\mathrm{d}\bar{r}}{\mathrm{d}t} = \frac{\alpha}{\rho_{\mathrm{liq}}} \cdot \frac{p_{\mathrm{vap}} - p_{\mathrm{sat},r}}{\sqrt{2\pi R_{\mathrm{vap}} T}}, \quad (43)$$

whereas in case of $\mathrm{Kn} < 1$ and for pure vapor flows the modified growth law of Gyarmathy can be used

$$\begin{aligned} \frac{\mathrm{d}r_{\mathrm{hom}}}{\mathrm{d}t} = &\frac{1}{\rho_{\mathrm{liq}}} \cdot \frac{1 + 2\mathrm{Kn}}{r \cdot (1 + 3.42\mathrm{Kn} + 5.32\mathrm{Kn}^2)} \cdot \left(\frac{1 - r^*}{r}\right) \cdot \\ &\left(\frac{\Lambda_{\mathrm{vap}} R_{\mathrm{vap}} T^2}{(h_{\mathrm{vap}} - h_{\mathrm{liq}})^2}\right) \cdot \ln(S). \end{aligned} \quad (44)$$

4 Cavitation

For evaporation of liquids two limiting processes can be defined: boiling that means heat addition at constant pressure and cavitation as adiabatic depressurization of liquids (Fig. 17). Cavitation as dynamic phase transition from liquid to vapor state is the natural counterpart to flow-induced condensation processes as treated in Sect. 3. The temperature decrease during adiabatic expansion of liquids is very low. One reason is the exceptional great density difference of liquid and vapor phases, for water at 293 K $\rho_{\mathrm{liq}}/\rho_{\mathrm{vap}} \approx 50,000$. As first approximation cavitation can be regarded as isothermal process, especially if pure liquid and pure vapor phases are modeled as incompressible fluids. A significant difference concerns the existence of nonequilibrium during the expansion. As seen in Sect. 3, in expanding vapor flows homogeneous nucleation establishes immediately, if the cooling rate excites a certain threshold. Additional natural heterogeneous nuclei may be present but they cannot alter the dominating homogeneous kinetics. Heterogeneously controlled processes become dominant if the cooling rate is low enough and/or if artificial seeding provides so many foreign additional surfaces, that substantial supersaturation is prevented. The important quantity is the necessary work for formation of clusters and critical nuclei which is substantially larger for homogeneous nucleation in the single component liquid bulk phase, provided that the liquid is artificially purified, as compared to that for homogeneous nucleation in the pure vapor phase [71–77].

Moderate convective acceleration of liquids depressurizes immediately to vapor pressure and – in tendency – further toward the so-called negative pressures, more precisely toward tensile stress in the liquid. Except well-defined test configurations, the practical cavitation threshold coincides with the equilibrium vapor pressure at given temperature. Technical fluids contain sufficient number concentrations of impurities such as particles or microbubbles which act as heterogeneous nuclei, and the intermolecular binding energy at least of artificially purified single component liquids requires tensile stresses of the order of 10^3 bar for homogeneous formation of microbubbles which is far beyond any observation in real processes.

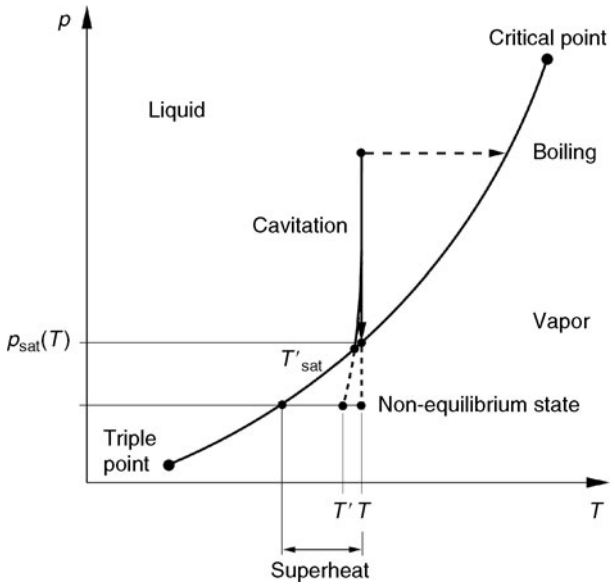

M11. Fig. 17. Phase diagram with path lines for evaporation by cavitation and boiling; comparison of isothermal and adiabatic depressurization with final equilibrium temperature T'_{sat}. T' is the theoretical final temperature in case of substantial nonequilibrium.

If expanding liquids contain dissolved gas, dispersion of the gas starts immediately above the vapor pressure threshold. This degassing process, usually called pseudocavitation, is continuous and smooth compared with the instantaneous vapor formation due to cavitation.

Cavitation plays an important role in turbomachinery – pumps, turbines, ship propellers, in injection systems of combustion engines, in chemical engineering, in medical applications, and many others [78–81]. Depending on the parameter range the two-phase mixture implies a wide variety of topologies. Most characteristic is the intense coupling of flow and cavitation dynamics. Because of the strong gradients caused by the collapse of the vapor-filled cavities these flows are always 3-D and unsteady.

Typical thermodynamic and fluid dynamic properties of cavitating flow are

Initially single-phase liquid fluid	$p_{liq} \approx O(1–10^3$ bar), $T \approx$ 300–400 K
	$p_{vap} \approx O(10^{-2}–1$ bar)
	$\rho_{liq} \approx O(10^3$ kg m^{-3})
	$\rho_{vap} \approx O(10^{-2}–1$ kg m^{-3})
Void fraction	$0 \le \alpha \le 1$
Speed of sound	$c \approx O(1–10^3$ m s^{-1})
Typically low or high flow speed	$M \approx O(0–10^1)$
Heterogeneous nuclei concentration	$n_{het} \approx O(10^8$ m^{-3})
Characteristic length scale	$L \approx O(10^{-4}–10^{-1}$ m)
Characteristic flow time scale	$t \approx O(10^{-5}–10^{-2}$ s)

4.1 Types of Cavitation

The Bernoulli equation demonstrates immediately that moderate acceleration of an initial flow with 1 bar and flow velocity up to 14.3 m/s decrease the pressure to the vapor pressure at 293 K with initiation of evaporation of the liquid fluid (Fig. 18).

The most important parameter to characterize such flows is the so-called cavitation number

$$\sigma_{ref} = \frac{p_{ref} - p_{vap}(T)}{\Delta p}. \tag{45}$$

For cascades this takes the form

$$\sigma_{ref} = \frac{p_{downstream} - p_{vap}(T)}{p_{upstream} - p_{downstream}}. \tag{46}$$

For a hydrofoil placed in an open water channel at distance h below the free surface with pressure $\tilde{p}$ above and with the inflow velocity w, this yields

$$\sigma_{ref} = \frac{\tilde{p} + \rho_{liq} g h - p_{vap}(T)}{\frac{1}{2}\rho_{liq} w^2} \tag{47}$$

and for pump flow

$$\sigma_{ref} = \frac{p_{inlet} - p_{vap}(T)}{\rho_{liq} w_{rot}^2} \tag{48}$$

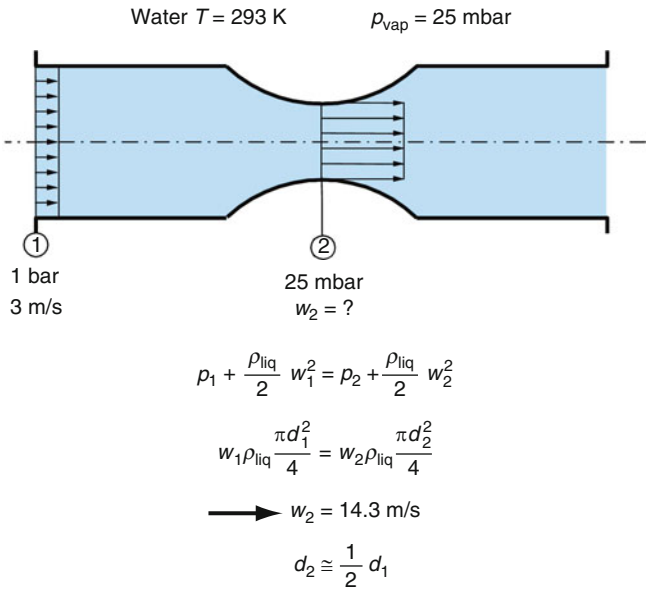

M11. Fig. 18. Estimation of cavitation onset at $p = p_{vap}$ (T_{sat}) in 1-D nozzle flow based on Bernoulli equation.

with u_{rot} as the rotational velocity at the outer diameter of the rotor. The definition of appropriate reference values, denoted by the subscript "ref," depends on the application under consideration and on the data that are available. Mostly, σ_{ref} is defined based on the inlet conditions. The vapor volume is characterized by the void fraction

$$\alpha = \frac{V_{vap}}{V_{vap} + V_{liq}} \tag{49}$$

and the vapor mass fraction x is defined by

$$x = \frac{m_{vap}}{m_{vap} + m_{liq}} = \frac{\alpha\rho_{vap}}{\alpha\rho_{vap} + (1-\alpha)\rho_{liq}}. \tag{50}$$

The Strouhal number is used for description of the shedding dynamics of sheets and clouds

$$St = \frac{f \cdot l}{w_{ref}}, \tag{51}$$

l is the typical length of the body or of the cavity itself. If viscosity plays a role, the dimensionless parameter is the Reynolds number

$$Re_{ref} = \frac{w_{ref} \cdot l}{\nu} \tag{52}$$

with ν as the kinematic liquid viscosity independent of the fact that in two-phase mixtures the viscosity decreases significantly. For characterization of pre-existing heterogeneous microbubbles the nuclei size r_0 and the number concentration n_0 (m^{-3}) are used.

Based on the topology of the distribution of liquid and vapor phases the cavitating types can be distinguished as follows [82, 83]:

Bubble cavitation: Typically, for fluids with larger dissolved air contents, consisting of a small number of large bubbles, that are convected with the main flow (Fig. 19, top).

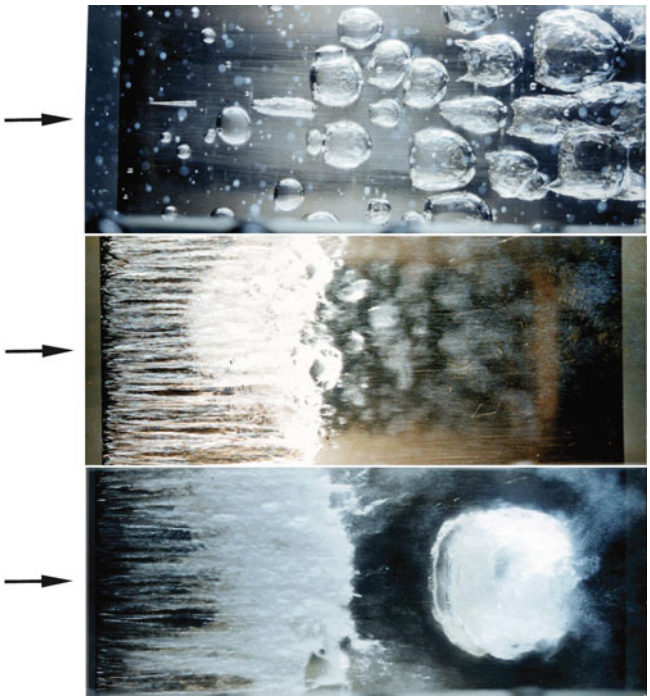

M11. Fig. 19. Evolution of cavitation topology at the suction side of a 2-D hydrofoil, flow from left, experiment Kuiper [110].
From top: traveling bubble cavitation; sheet cavitation; and cloud cavitation.

Sheet cavitation: Typically, at the leading edge of hydrofoils and propeller blades, a dispersed mixture of tiny vapor bubbles and liquid forms an attached sheet which becomes locally unstable in the collapse region (Fig. 19, middle).
Cloud cavitation: The entire cavitation regime consists of many small bubbles, large disperse two-phase mixtures grow up periodically, disperse clouds shed with high frequency from blade surfaces and collapse downstream – Fig. 19, bottom and Fig. 20, top. Concerning erosion, this is the most aggressive type.
Supercavitation: The vapor formation intensifies further, the blades or bodies are surrounded by large stable pure vapor pockets, and the solid bodies can become completely surrounded by vapor with significant reduction of viscous drag forces – Fig. 20, bottom.
Vortex cavitation: The characteristic pressure drop in vortex cores results in evaporation of the fluid in the core region, typically for ship propellers. Here, the collapse regions separate from solid walls and the erosion potential is less critical.
Based on the integral void fraction produced by cavitation the topology of these flows can be distinguished as
Incipient cavitation: Just the "onset" of cavitation with very low vapor formation, either as few single bubbles or as very thin attached sheets, not yet relevant for erosion. Modeling requires accurate parameter values of r_0, n_0, the Reynolds number Re_{ref}, and the degree of turbulence Tu.
Developed cavitation: Dominant is the strong unsteadiness of this type of flow, combined with chaotic cloud shedding and strong shock formation during collapse of the clouds. Concerning erosion, this is the most dangerous cavitation type, in technical applications such as turbines, pump flow,

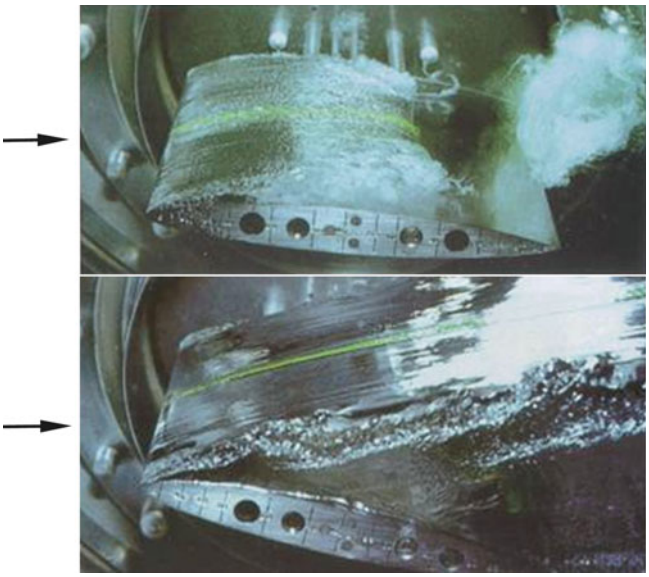

M11. Fig. 20. Cloud cavitation and supercavitation, 2-D NACA 16012 hydrofoil, chord = 0.1 m, $Re_{chord} = 6{\cdot}10^5$, experiment Franc and Michel [111]. Top cloud cavitation 6° angle of attack, $\sigma_{ref} = 0.81$; bottom supercavitation 15° angle of attack, $\sigma_{ref} = 0.13$.

this is the predominating mechanism, it is inertia controlled, viscosity effects are less important and can be neglected.
Supercavitation: Maximum void fraction with extended pure vapor regimes, liquid and vapor are separated by sharp interfaces, steady with exception of the closure region of the cavity.

4.2 Developed Cavitation

Because of its practical importance developed cavitation is in focus of this chapter. It is always 3-D, unsteady and dominantly driven by inertia-controlled nonviscous effects. At global scale the flow can be regarded as periodic or cyclic. However, small-scale dynamic phenomena are chaotic. Modeling requires the formation and growth of disperse sheets, break-off and fragmentation of macroscopic clouds from the sheets, and the accurate description of the collapse dynamics, starting from large cloudy structures down to the scale of single bubbles. If the erosion mechanism is in focus, it is necessary to resolve all time scales of the problem including shock dynamics based on the liquid speed of sound of the order of 1,500 m/s. Averaged quantities based on reduced time scales are sufficient for calculation of performance and efficiency of hydraulic machinery.

4.3 Modeling of Developed Cavitation

4.3.1 Modeling of Single-phase Basic Flow

Because of the intensive coupling of single-phase basic flow and cavitation dynamics accurate modeling of the basic flow is important. Incompressible assumption for pure liquid and pure vapor phases excludes the dynamics of shocks and

expansion waves emerging at the final stage of the bubble collapse. To account for these aspects the compressibility of liquid and vapor must be modeled and the time stepping of the simulation must account for all time scales in the collapse region, molecular viscosity and turbulence can be neglected.

4.3.2 Modeling of Two-phase Flow

Except the very last instant at the final stage of the collapse, the assumption of equilibrium thermodynamics is accurate and nonequilibrium effects can be neglected. Phase boundaries can be modeled as sharp interfaces by direct tracking of the interface or by approximate methods that capture interfaces (VOF – Volume of Fluid method) by the discrete distribution of the void fraction α [85]. If dealing with developed cavitation it is impossible to capture the interfaces of every single bubble of the disperse mixture. Instead of separate models for simulation of the liquid and vapor phases or of sheet and cloud cavitation with the need of an additional transition model in between, the homogeneous mixture model is more promising. This model requires only one set of conservation equations for mass momentum and energy, the density, void fraction etc., are modeled as mixture quantities. The transition from disperse two-phase regimes to pure vapor with $\alpha = 1$ establishes automatically by the void fraction variation (Fig. 21).

The growth and collapse of the vapor phase can be modeled according to equilibrium thermodynamics. This requires appropriate equations of state for all regimes, liquid, vapor, and of the two-phase mixture regime. The alternative is the use of well-known equations for bubble dynamics, e.g., the Rayleigh–Plesset equation [82, 84]

$$r\ddot{r} + \frac{3}{2}\dot{r}^2 = \frac{p_{sat} - p_\infty(t)}{\rho_{liq}} + \frac{p_{gas,0}}{\rho_{liq}} \cdot \left(\frac{r_0}{r}\right)^{3\gamma} - \frac{2\sigma_\infty}{\rho_{liq} r} - \frac{4\eta_{liq}}{\rho_{liq}} \frac{\dot{r}}{r}, \quad (53)$$

neglecting nonlinear terms, the gas content, surface tension and η_{liq} in Eq. (53) yields the Rayleigh equation

$$\dot{r} = \frac{dr}{dt} = \sqrt{\frac{2}{3} \cdot \frac{p_{sat} - p_\infty(t)}{\rho_{liq}}}. \quad (54)$$

Additional models are necessary to account for the interaction of bubbles in dispersed bubbly clouds [85]. As variants of Eq. (54) in the literature there exist many empirical modifications, typically in commercial CFD tools, to account for different time scales of evaporation and condensation. However, such corrections are only valid in a limited range of operating conditions and not generally valid.

4.3.3 Modeling of Phase Transition

Neglecting molecular transport by viscosity and heat conduction the latent heat exchange, necessary for evaporation, is provided within the liquid bulk. Therefore, if the flow is isentropic at the inlet it remains isentropic throughout the evaporation, only the shock-like collapse produces strong vorticity. In equilibrium thermodynamics isentropes terminate inside the two-phase regime at the triple line. Therefore, isentropic evaporation is always incomplete, but quantitative effects on the void fraction α are negligible (Fig. 22).

In two-phase regions the speed of sound decreases by several orders of magnitude. For two-phase mixtures without phase transition the well-known result of Wallis [84] is appropriate (Figs. 23 and 24)

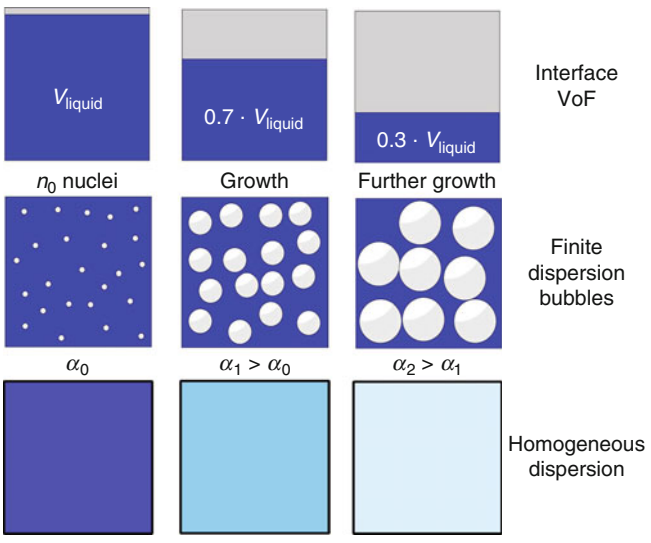

M11. Fig. 21. Alternative modeling of two-phase flow within a computational cell. *Rows*: top: stratified two-phase flow – interface Volume of Fluid (VoF); middle: bubbly two-phase flow – finite dispersed model; bottom: homogeneous mixture – small-scale structure excluded. *Columns*: left small void fraction $\alpha_0 \approx 0$; middle: mode void fraction $\alpha_1 \approx 0.3$; right: high void fraction $\alpha_2 \approx 0.7$.

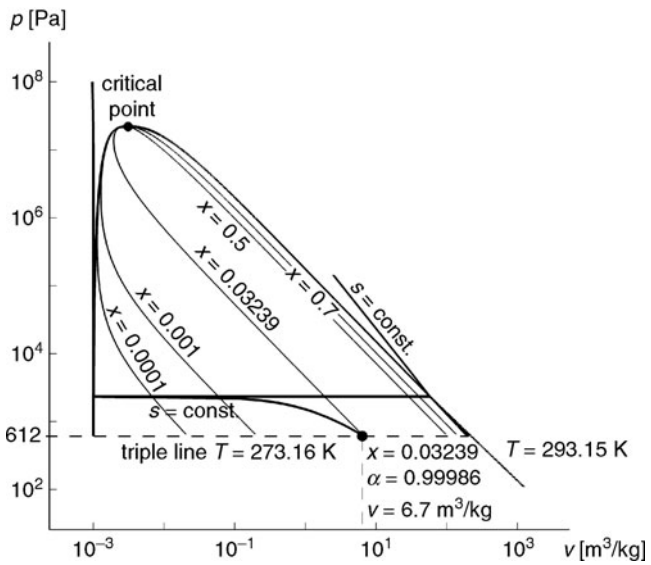

M11. Fig. 22. *p*, v-diagram with two-phase regime and isentropic depressurization from pure liquid phase till maximum liquid mass fraction $x = 0.03239$ and maximum void fraction $\alpha = 0.99986$ at triple line.

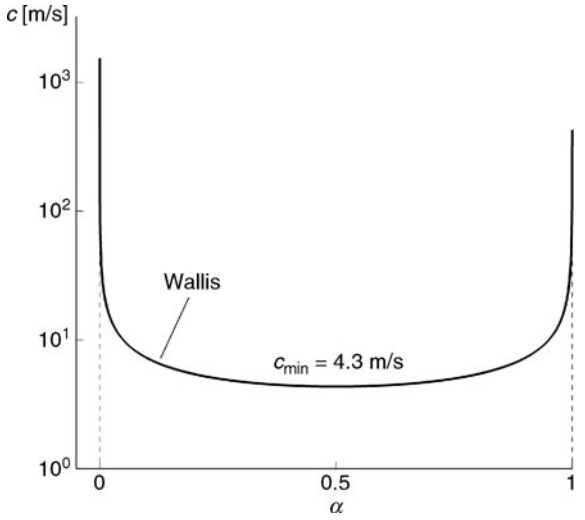

M11. Fig. 23. Equilibrium speed of sound *c* for two-phase mixtures without phase transition according to Wallis [84] – not valid for cavitating flows in thermodynamic equilibrium.

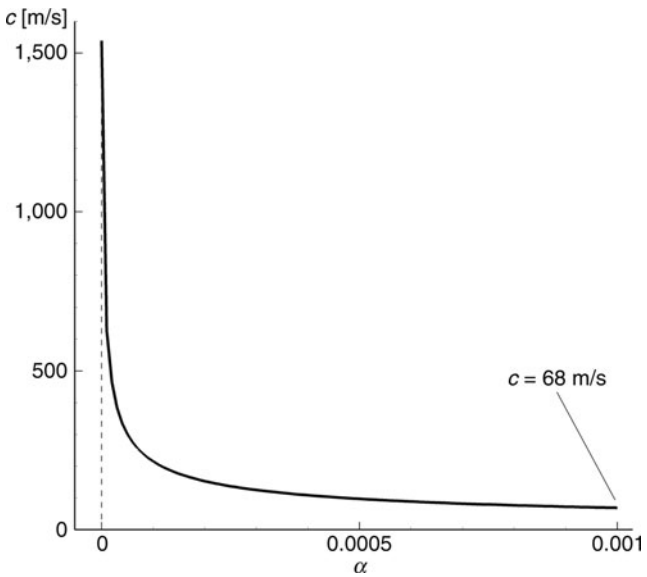

M11. Fig. 24. Strong decrease of equilibrium speed of sound c in two-phase mixtures without phase transition for small void fractions $\alpha < 10^{-3}$ – zoom of Fig. 23, not valid for cavitating flows in thermodynamic equilibrium.

$$\frac{1}{\rho c^2} = \frac{\alpha}{\rho_{vap} c_{vap}^2} + \frac{1-\alpha}{\rho_{liq} c_{liq}^2}. \tag{55}$$

In two-phase mixtures with phase transition, as in cavitating flows, the speed of sound decreases suddenly through a kink at the left-hand phase boundary, then it increases monotonically with increasing void fraction α [Eq. (56), Figs. 25 and 26 [82, 85]]. The extreme decrease of the speed of sound in disperse mixtures is important for the understanding of the propagation of waves and shocks in cavitating flows

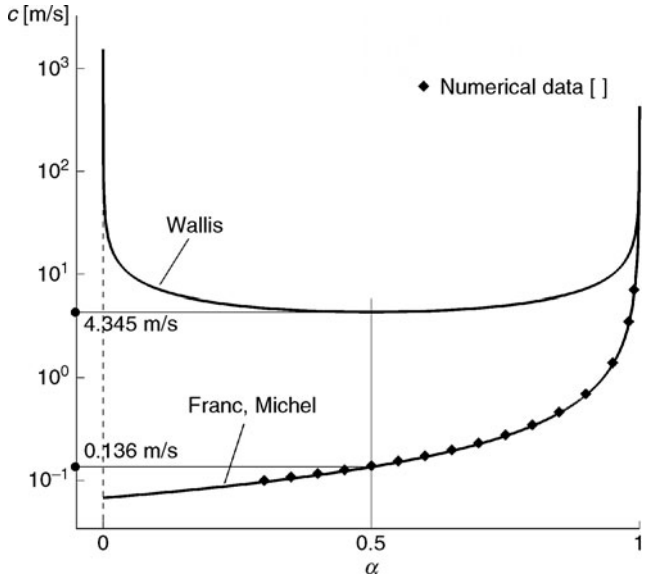

M11. Fig. 25. Equilibrium speed of sound c in two-phase mixtures with phase transition with a distinct kink at the left-hand phase boundary, sudden decrease of *c* below O (1 m/s), and monotonic increase with increasing void fractionα, appropriate modeling for cavitating flow in thermodynamic equilibrium. Comparison of theoretical prediction of Franc and Michel [82] with numerical data [90].

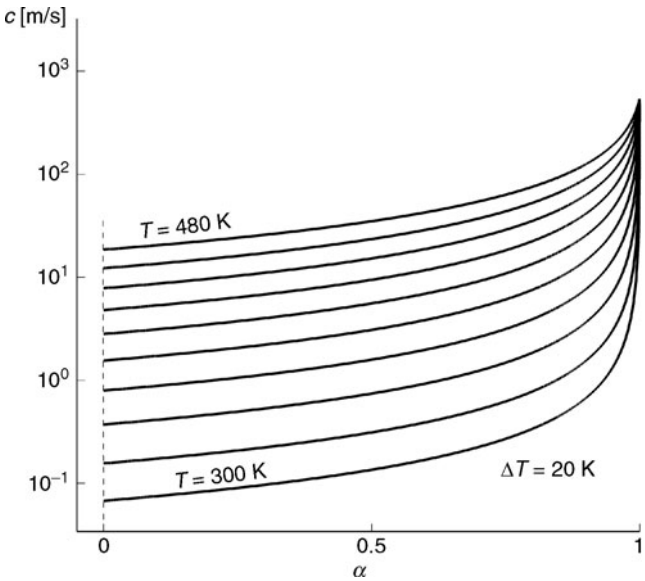

M11. Fig. 26. Temperature dependence of the equilibrium speed of sound *c* for cavitating flows according to Fig. 25

$$\frac{1}{\rho c^2} \cong \frac{\alpha}{\rho_{vap} c_{vap}^2} + \frac{1-\alpha}{\rho_{liq} c_{liq}^2} + \frac{(1-\alpha)\rho_{liq} c_{p,liq} T}{\left(\rho_{vap} L_{vap}\right)^2}. \tag{56}$$

Homogeneous nucleation

Homogeneous nucleation can be modeled based on molecular dynamics [72] or by applying the classical capillary theory as

known from condensation in vapor [73]. Assuming purified single component liquids yields necessary supersaturation ratios S, i.e., tensile stress in the liquid of the order of 10^3 bar. In practice such extreme conditions have never been observed. In nucleating vapor flow the quantitative contribution of homogeneous and heterogeneous growth depends directly on the time scale of the flow. In micronozzles of injection systems depressurization from O (10^3 bar) down to O (1 bar) establishes typically within a few microseconds. This raises the question of the nature cavitating kinetics under such conditions that is unknown until now.

Heterogeneous nucleation

Because of the uncertainties and also because most of the liquids used in technical applications consist of large concentrations of natural impurities, heterogeneous modeling is dominant. Substantial tensile stress is avoided by appropriate values of the parameters $r_0 \approx 10^{-7}$–10^{-8} m and the number concentration $n_0 \approx 10^6$–10^9 m^{-3}. Inclusion of the surface tension is important for nuclei radii $\leq 10^{-6}$ m, and it tends to decrease the cavitation threshold beyond the thermodynamic vapor pressure. Because pre-existing microbubbles are never monodispersed, this means that activation of nuclei begins at larger scales.

Equilibrium phase transition

The closure of disperse models requires quantitative values of all model parameters. Because these models approach equilibrium in most of the practical applications, it is reasonable to avoid uncertain details of these models completely and to assume thermodynamic equilibrium throughout. Physically, this means that real systems consist of sufficient high concentrations of foreign nuclei that initiate phase transition at $S \approx 1$. The great advantage of such a thermodynamic model is the fact that it avoids all additional free parameters that are usually used for "artificial" fitting of experiment and numerical data. The system of conservation equations is closed by the equations of state in the different regimes, and the accuracy of the equilibrium model depends only on thermodynamic data. For water, IAPWS [87] provides an exceptional detailed and accurate database.

4.4 Hydrodynamic and Wave Dynamic Phenomena

Unsteady compressible flows in thermodynamic equilibrium are controlled by two separate time scales. The first is determined by the convective transport of the fluid, the flow velocity w that is rather low in liquid flows, typically O (1 m)–O (10 m). The second is determined by the speed of sound c of the fluid that controls the propagation of shocks and expansion waves and varies in a wide range from O (10^3 m/s) to O(10^{-1} m/s), dependent on the local void fraction α. In high pressure injection systems, wave dynamics and convective transport control cavitation dynamics simultaneously. Understanding of the main driving mechanism for erosion without considering shock and wave dynamics is impossible. In hydraulics, the phenomenon of sudden pressure waves, e.g., caused by instantaneous closing of valves is known as *water hammer* or *Joukowski shock*.

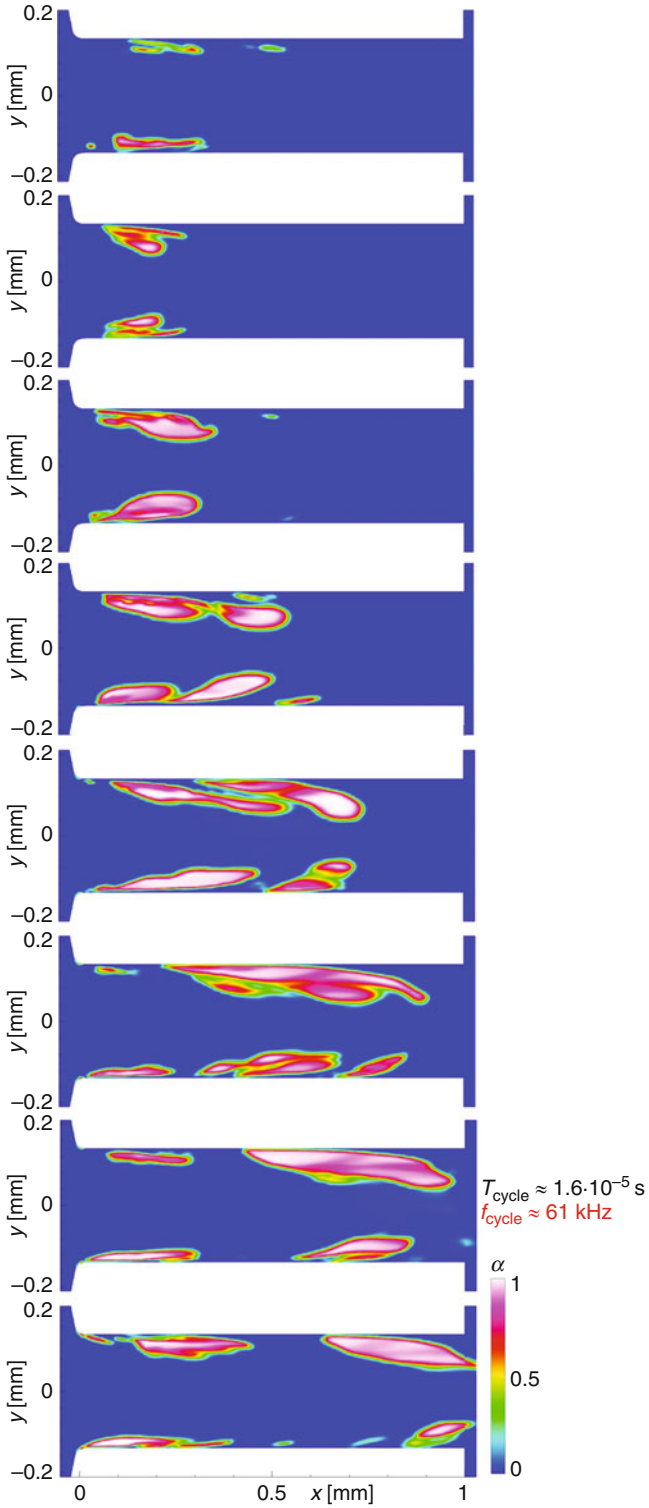

M11. Fig. 27. One cycle of unsteady and asymmetric high frequency void fraction formation in cavitating flow trough 2-D plane injection nozzle; inviscid flow modeling, numerical simulation, $T_{cycle} = 1.6 \cdot 10^{-5}$ s, $f_{cycle} = 61$ kHz; water as test fluid, $T_{inlet} = 293$ K, $p_{inlet} = 80$ bar, $p_{out,mix} = 26$ bar; $\Delta t_{CFD} = 10^{-9}$ s, second-order accurate discretization in space and time.

Phenomena such as sonoluminescence are essentially based on wave dynamics without convection. The amplitude of pressure waves Δp depends on the acoustic impedance ρc, whereas the convective pressure variation depends on ρw:

Waves $\Delta p \approx \rho c \cdot \Delta w$

Convective flow $\Delta p \approx \rho w \cdot \Delta w$

$\rho_{vap} = 0.02$ kg/m^3 $C_{vap} = 400$ m/s $T_{vap} = 293$ K } ρc { **8.0** kg/m^{2}s **vapor**

$\rho_{liq} = 10^3$ kg/m^3 $C_{liq} = 1500$ m/s $T_{liq} = 293$ K } ρc { **1.5·10^6** kg/m^{2}s **liquid**

	Δw [m/s]	Δp_{liq} [bar]	Δp_{vap} [bar]	
Waves	1	**15**	$8 \cdot 10^{-4}$	
	10	**150**	$8 \cdot 10^{-3}$	w = 15 m/s
Convective flow	1	$1.5 \cdot 10^{-1}$	$8 \cdot 10^{-6}$	
	10	1.5	$8 \cdot 10^{-5}$	

This comparison demonstrates the intensity of the wave impact on blade surfaces etc. in pure liquids even in case of low convective transport velocities of 1–10 m/s [88, 89, 91].

4.4.1 Collapse Dynamics and Erosion Mechanism

Figure 27 is an example of the unsteady void fraction evolution in a 2-D plane microchannel, scale and pressure difference are

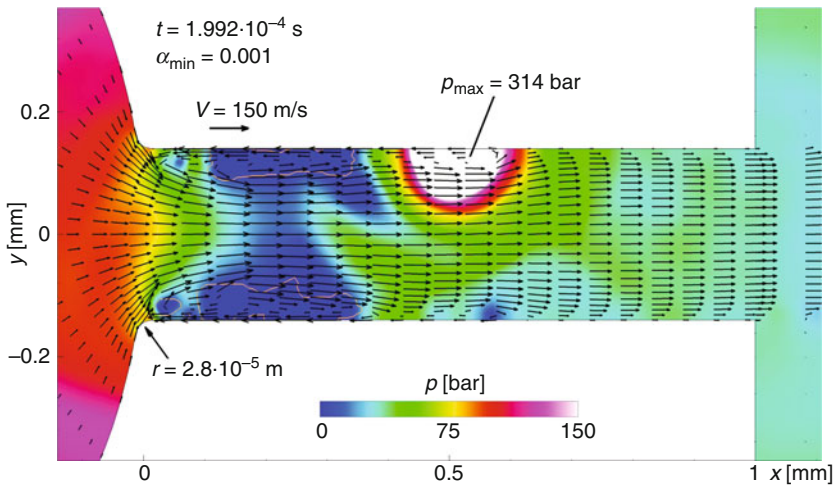

M11. Fig. 28. Instantaneous formation of a strong circular shock after violent vapor cloud collapse in the nozzle bore hole with maximum pressure $p_{max} = 314$ bar; $T_{inlet} = 293$ K, $p_{inlet} = 80$ bar, $p_{out,mix} = 26$ bar; $\Delta t_{CFD} = 10^{-9}$ s, second-order accurate discretization in space and time.

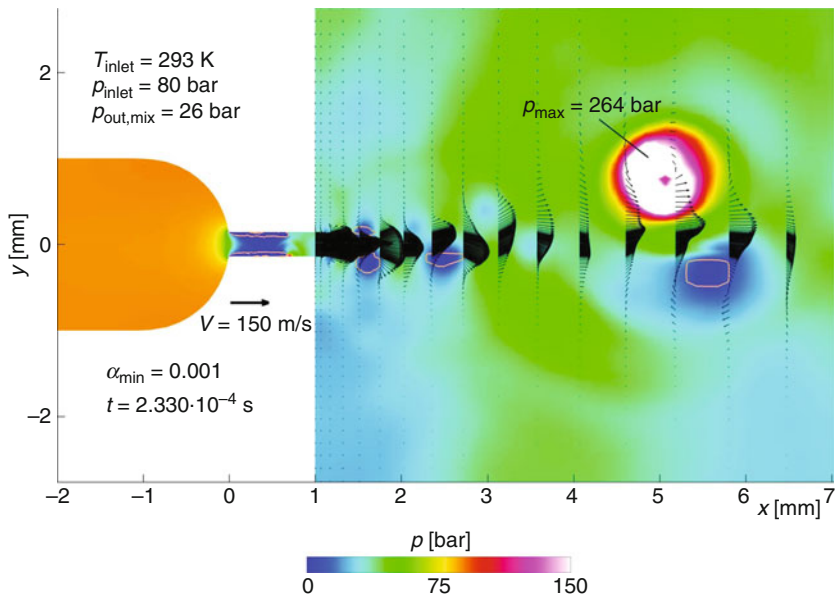

M11. Fig. 29. Instantaneous formation of a strong circular shock after violent cloud collapse in the cavitating shear layer of the outflow domain, maximum pressure $p_{max} = 264$ bar; $p_{in} = 80$ bar, $p_{out} = 26$ bar, $T_{in} = 293$ K; $\Delta t_{CFD} = 10^{-9}$ s, second-order accurate discretization in space and time.

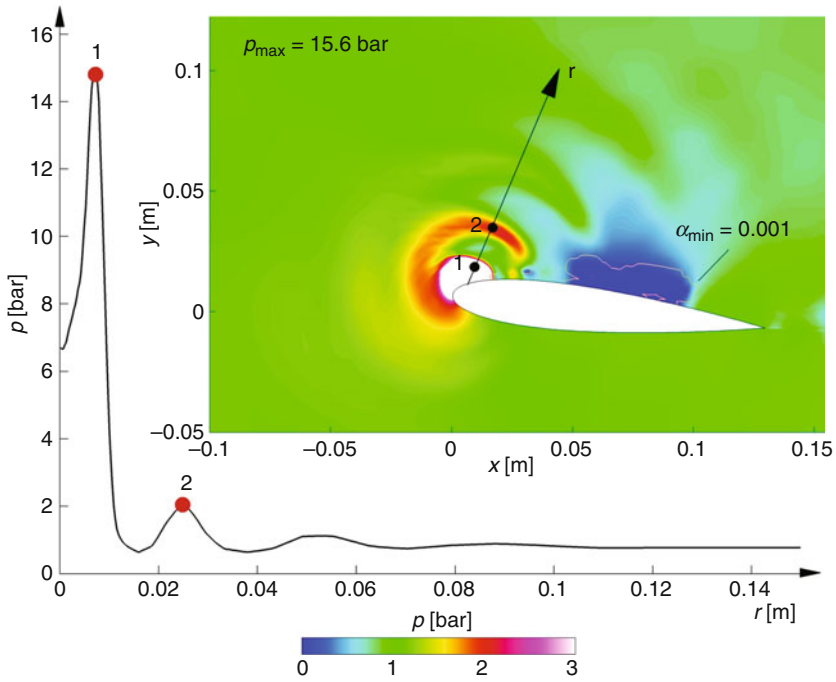

M11. Fig. 30. Radial pressure decay after collapse-induced shock formation at the leading edge of a 2-D hydrofoil 2-D plane NACA 0015 hydrofoil at 6° angle of attack; w_{inlet} = 12 m/s, T_{inlet} = 293 K, $p_{out,mix}$ = 0.74 bar, σ_{ref} = 1.0; $\Delta t_{CFD} = 10^{-7}$ s, second-order accurate discretization in space and time.

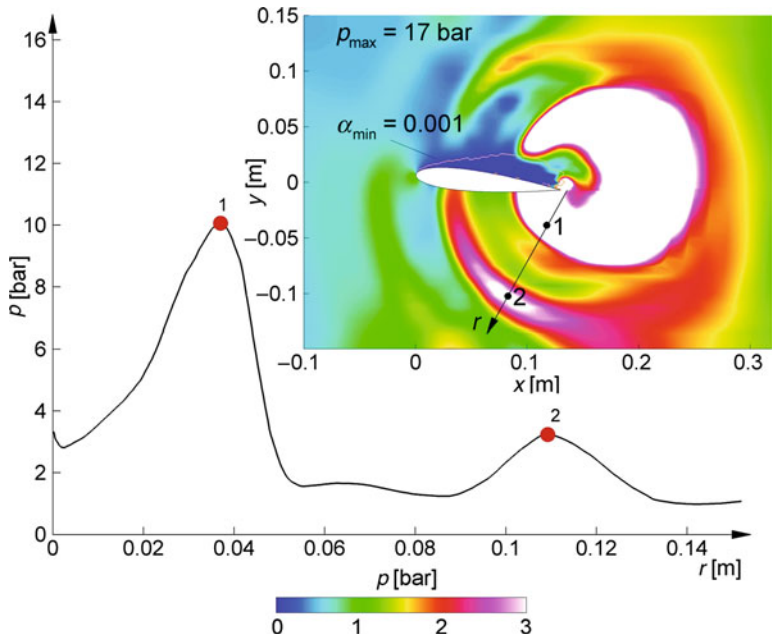

M11. Fig. 31. Radial pressure decay after collapse induced shock formation at the trailing edge of a 2-D hydrofoil 2-D plane NACA 0015 hydrofoil at 6° angle of attack; w_{inlet} = 12 m/s, T_{inlet} = 293 K, $p_{out,mix}$ = 0.74 bar, σ_{ref} = 1.0; $\Delta t_{CFD} = 10^{-7}$ s, second-order accurate discretization in space and time.

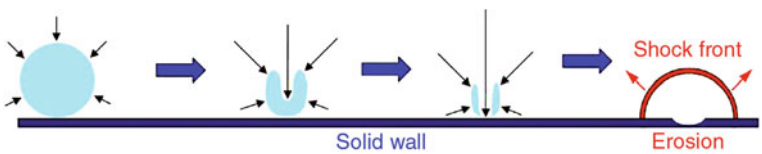

M11. Fig. 32. Sketch of the empirical idea of erosion mechanism driven by liquid jet impact during single vapor bubble collapse close to solid walls.

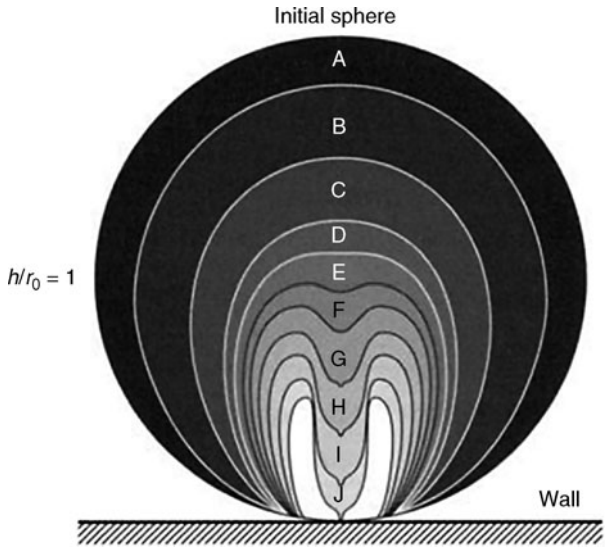

M11. Fig. 33. Asymmetric collapse of a liquid embedded vapor bubble close to solid surface, 10 instants in time; h/r_0 is the normalized distance of the bubble center from the wall, r_0 is the initial bubble radius, as given in the theory by Plesset and Chapman [112].

representative for injection nozzles. The strong expansion at the inlet initiates cavitation with local void fractions up to $\alpha \approx 1$. The instability of the flow is obvious, and the topology does not show any symmetry. Corresponding to the void formation, Figs. 28 and 29 show two instants with shocks inside the channel and outside. Both shocks evolve from local collapse events. The maximum intensity with 264 bar is about one order higher O (10^3 bar) as the average pressure outside of 26 bar. The real maximum intensity is at least one order higher, but the resolution of the numerical simulation is limited by the grid size. The interesting question in focus of this application is, how shocks interfere with the turbulence of the liquid jet, and can this interaction improve spray characteristics?

Figures 30 and 31 depict shocks emerging from the leading edge and from the trailing edge of a hydrofoil. In addition to their potential for erosion they produce instantaneous loads on the blade surface with strong variations of lift and drag [89–94].

The classical erosion model (Fig. 32) presumes the impact of a liquid jet during the bubble collapse as the main source of erosion. Fig. 33 shows the asymmetric deformation of an initially spherical bubble close to a wall, in detail [85]. The numerical simulation (Fig. 34) reproduces this analytical result accurately, and Fig. 35 demonstrates the exceptional strength of shocks emerging from the focus. In the violet region the pressure is about 4,000 bar. The last picture of Fig. 34 corresponds to the instantaneous shock evolution of Fig. 35.

4.5 CFD Techniques for Calculation of Cavitating Flows

Most of the CFD tools for simulation of cavitating flows are pressure based. Such methods are typical for incompressible flow

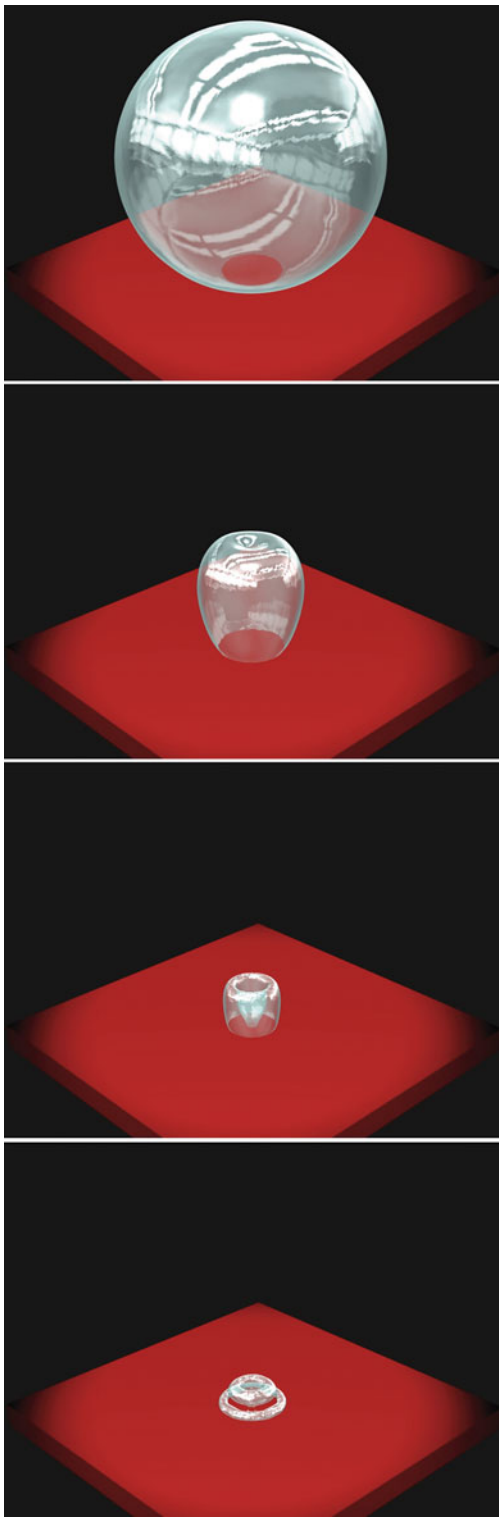

M11. Fig. 34. Numerical simulation of the asymmetric collapse of a liquid embedded vapor bubble close to solid surface, 4 instants in time, $t_0 = 0$ s, $t_1 = 1.59 \times 10^{-5}$ s, $t_2 = 1.71 \times 10^{-5}$ s, $t_3 = 1.76 \times 10^{-5}$ s, initial bubble radius $r_0 = 5 \times 10^{-4}$ m, collapse time $t_{collapse} = 1.74 \times 10^{-5}$ s, liquid pressure far from the bubble surface $p_{liq} = 10$ bar, pressure within the bubble $p_{vap} = 0.023$ bar; $\Delta t_{CFD} = 6{\cdot}10^{-9}$ s, second-order accurate discretization in space and time.

simulations. Extension to compressible flow applications is possible but not as effective and not as accurate as density-based methods that can resolve all scales of wave and shock dynamics effectively [95]. However, due to the physically determined small time steps CPU time requirements to perform such simulations are high and therefore not available in commercial codes.

It is interesting to note that the set of conservation equations for simulation of cavitating flows is quite similar to that for calculation of condensing flows [Eqs. (40–44)]. The transport equation for the mass fraction x reads

$$\frac{\partial(\rho x)}{\partial t} + \nabla \cdot (\rho x \vec{v}) = \rho \cdot \frac{\mathrm{d}x}{\mathrm{d}t} = F_{\text{source term, cavitation}}. \qquad (57)$$

Assuming homogeneous nucleation in cavitating flows, which is rather unclear – how to determine accurately the homogeneous nucleation rate J_{hom} – would result in

$$\begin{aligned} \frac{\partial}{\partial t}(\rho x_{\text{hom}}) + \nabla(\rho x_{\text{hom}} \vec{v}) &= \frac{4}{3}\pi \rho_{\text{vap}} r_{\text{hom}}^{*3} J_{\text{hom}} \\ &\quad + \rho_{\text{vap}} \rho n_{\text{hom}} \frac{\mathrm{d}}{\mathrm{d}t}\left(\frac{4}{3}\pi \bar{r}_{\text{hom}}^{3}\right), \\ \frac{\partial}{\partial t}(\rho n_{\text{hom}}) + \nabla(\rho n_{\text{hom}} \vec{v}) &= J_{\text{hom}}. \end{aligned} \qquad (58)$$

Application of the dispersed two-phase model for the determination of vapor contents leads to the following source term

$$\frac{\partial}{\partial t}(\rho x_{\text{het}}) + \nabla(\rho x_{\text{het}} \vec{v}) = \rho_{\text{vap}} \frac{n_0}{1 + n_0 \frac{4}{3}\pi r_{\text{het}}^3} \cdot \frac{\mathrm{d}}{\mathrm{d}t}\left(\frac{4}{3}\pi r_{\text{het}}^3\right). \qquad (59)$$

Assuming equilibrium phase transition reduces this set of conservation equation substantially. Then the transport equations can immediately be replaced by the algebraic equation of state of the pure phases and of the two-phase mixture region.

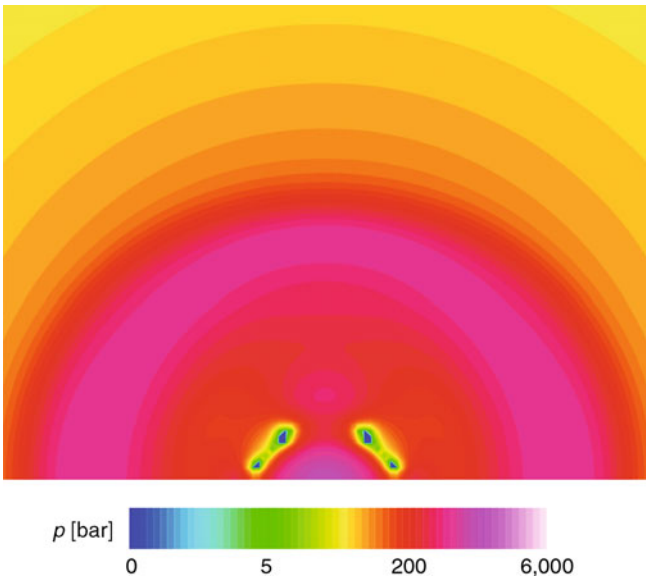

M11. Fig. 35. Visualization of instantaneous static pressure rise behind shock in the meridian plane according to the last picture of Fig. 34, maximum pressure p_{max} = 4,000 bar at time instant $t_3 = 1.76 \times 10^{-5}$ s; $\Delta t_{\text{CFD}} = 6 \times 10^{-9}$ s, second-order accurate discretization in space and time.

5 Aerosol Formation in Gas–Liquid Contact Devices

5.1 Phenomena and Scope

In gas–liquid contact devices such as absorbers, scrubbers, quench coolers, evaporators, and condensers, aerosols can be formed by spontaneous condensation or desublimation in supersaturated carrier gas–vapor flows. In contrast to the adiabatic expansion (Sect. 3) or cavitation (Sect. 4), supersaturation in gas–liquid contact devices may appear caused by a different mechanism: excluding chemical reactions in the gas phase, supersaturation can arise if the dew point line is intersected by the process trajectory, describing the change of state of the flowing gas due to simultaneous heat and mass transfer between both phases [3]. Figure 36 shows typical saturation curves along the interfacial area A of a gas–liquid contact device. Supersaturation in gas–liquid contact devices is a local phenomenon which vanishes again if the interfacial area tends versus infinite values. In this case, the thermodynamic equilibrium between both bulk phases is reached (S = 1). If nucleation and consequently, fog formation take place the saturation ratio of the gas phase decreases rapidly, and the growth of aerosol droplets is finished if values of S close to 1 are reached.

Supersaturation and fog formation especially may occur if high-strength inorganic acids such as HCl, HBr, HNO_3, and SO_3 (H_2SO_4) are absorbed in aqueous solutions, as well as if pure components or mixtures are condensed or evaporated in the presence of inert gases. The inert gas plays an important role: On the one hand, it causes a diffusion barrier which promotes supersaturation, and on the other hand, it serves as carrier medium for the aerosol droplets which are formed by nucleation and growth in the contact device.

The undesired aerosol formation in gas–liquid contact devices is a well-known phenomenon in the industry for more than 60 years. It has been described and explained in various publications [96, 97, 98], whereas the main emphasis

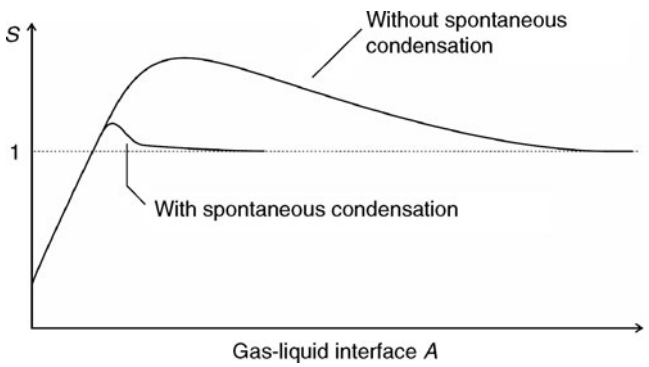

M11. Fig. 36. Typical curves of saturation versus interfacial area A of gas–liquid-contact devices for processes with and without nucleation.

is on condensation processes. Recent overviews on aerosol formation in absorption or wet scrubbing processes are given by Schaber [3, 34], Haep [99], Ulbrich et al. [100], Wix [31], and Brosig [101].

According to the scope of the VDI Heat Atlas, the following sections are focused to fog formation in condensation processes.

5.2 Modeling and Simulation of Aerosol Formation

Modeling of aerosol formation in an arbitrary contact device requires the description of the competing heat and mass transfer processes between gas and liquid phases on the one hand, and between gas and dispersed phases on the other hand. Both processes have rather different time scales, i.e., seconds for the first process and milliseconds for the latter process.

Since the physical situation in real industrial gas–liquid contact devices is far too complex for a detailed description including hydrodynamics, thermodynamics, and particle dynamics various simplified models have been described in the literature which are based on spatially one-dimensional flow of both phases in contact with one another. The interfacial area A has been chosen as an independent variable along which temperature and concentration profiles as well as saturation ratios of the bulk gas phase are calculated, using mainly a rigorous description of heat and mass transfer according to the film model. Homogeneous or heterogeneous nucleation and droplet growth are described by the methods discussed in Sect. 2. The simulation tools based on these models have been evaluated by experimental investigations, and it has been shown that the following basic assumptions are justified [31, 33, 99–102]:

(1) Spatially one-dimensional models including axial dispersion describe aerosol formation in packed columns sufficiently well. This is due to the fact that radial saturation profiles can be neglected in these devices.
(2) If heterogeneous nucleation takes place a monodisperse description of the growing aerosol droplets is a rather good approach for all contact devices.
(3) Processes with homogeneous nucleation require polydisperse modeling of the growing droplet fractions, especially in those cases when the nucleation event takes place within a larger interval of the saturation ratio S [31].

Aerosol formation may occur in a bulk gas phase as well as in a heat and mass transfer boundary layer. Concerning the total mass of aerosol droplets, the formation in a bulk gas phase is the dominating phenomenon. Nevertheless, some investigations show that aerosol formation in boundary layers may influence heat and mass transfer rates [103, 104].

Most of all investigations cited above are concerned with aerosol formation in absorption processes for the separation of hazardous gas components by means of packed columns. Although this topic is beyond the scope of the Heat Atlas, most of these findings can be transferred to condensation and evaporation processes discussed in the following section.

5.3 Fog Formation in Condensers and Evaporators

The essence of supersaturation and fog formation in condensation and evaporation in the presence of an inert gas can be demonstrated and explained with a simplified plug flow model suggested by Colburn and Edison [96] which allows to calculate the process path, i.e., the change of state of the gas phase during the process. A linear approach for heat and mass transfer together with a differential mass balance yields after integration and elimination of the interfacial area A the following equation:

$$p_{\mathrm{vap}} = \left(p_{\mathrm{vap},1} - p_{\mathrm{sat}}(T_{\mathrm{sf}})\right)\left[\frac{T - T_{\mathrm{sf}}}{T_1 - T_{\mathrm{sf}}}\right]^{L} + p_{\mathrm{sat}}(T_{\mathrm{sf}}) \qquad (60)$$

with

$$L = \frac{\alpha_{\mathrm{G}}}{\beta_{\mathrm{G}} c_{\mathrm{pG}} \rho_{\mathrm{G}}} = \mathrm{Le}^{0.6}. \qquad (61)$$

Le is the Lewis number $\mathrm{Le} = \lambda_{\mathrm{G}}/(\rho_{\mathrm{G}}\, c_{\mathrm{pG}}\, D)$, where D is the binary diffusion coefficient of the vapor component in the carrier gas.

Equation (60) is based on the following assumptions:

(1) The surface temperature of the condensing liquid film or the evaporating liquid can be considered constant along the gas–liquid interface.
(2) Heat and mass transfer can be described with simple linear transport equations, i.e., heat and mass transfer rates are low.
(3) The Lewis number is constant along the process path.

Figure 37 shows typical process paths according to Eq. (60). For infinite interfacial area A the process paths tend versus the film surface temperature T_{sf}. In this case, the thermodynamic equilibrium between gas and liquid phases is reached. For air–water mixtures the Lewis number is about 1, and the process paths are straight lines. If the Lewis number is >1 the process path is concave and higher saturation ratios are reached. For saturated gas–vapor mixtures, supersaturation arises directly after the condenser inlet. Supersaturation during condensation can be avoided if the gas–vapor mixture is superheated before it enters the condenser. It has also been established by experiments that supersaturation and aerosol formation initiated by heterogeneous nucleation can be avoided by superheating the gas–vapor mixture before condensation [27, 105].

Rigorous approaches for heat and mass transfer involving nonvanishing mass fluxes yield curved process paths as shown in Fig. 38 for condensation and evaporation processes [106].

If the Lewis numbers are smaller than or equal to 1, for instance for air–water mixtures, only low supersaturation can be expected in condensation. In contrast to that, high supersaturation arises if the liquid is evaporated in the presence of an inert gas. For Lewis numbers considerably >1 the opposite behavior can be observed.

Experimental investigations confirm this behavior [106].

As pointed out in Sect. 5.2 spatially one-dimensional modeling of process paths is a reliable method to predict

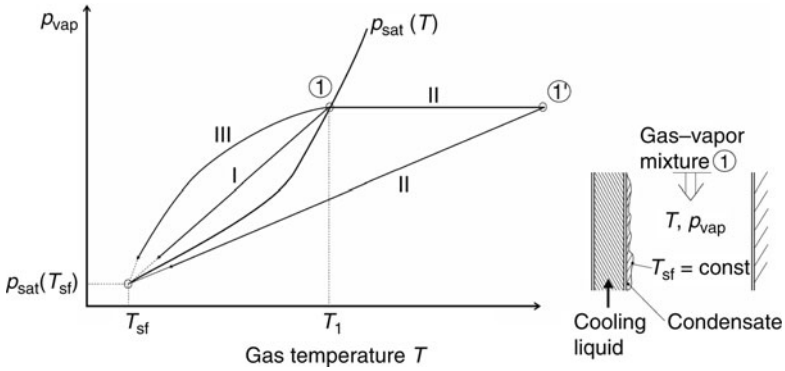

M11. Fig. 37. Process paths for the condensation of gas–vapor mixtures at constant film surface temperature T_{sf} and low vapor loading in comparison to a saturation curve $p_{sat}(T)$. Curves I and II: Le = 1; Curve III: Le > 1.

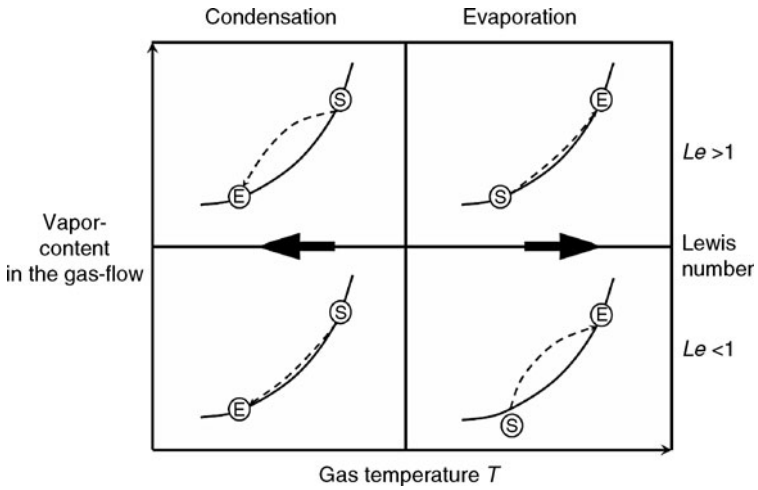

M11. Fig. 38. Process paths (dashed lines) for evaporation and condensation processes in the presence of inert gases (S = start; E = end) in comparison to saturation curves. The process paths are calculated based on a spatially one-dimensional model with rigorous equations for heat and mass transfer as well as temperature- and concentration-dependent Lewis numbers.

supersaturation and aerosol formation in condensation or evaporation processes if packed columns are used as contact devices where radial profiles of concentration and saturation can be neglected. But most of all condensation processes take place in surface condensers, for instance in tube bundle condensers. For these apparatuses two- or three-dimensional simulations of concentration, temperature, and saturation profiles yield strong radial gradients. But the crucial fact whether or not the gas flow becomes supersaturated ($S > 1$) and fog is formed initiated by heterogeneous nucleation can be predicted based on a one-dimensional model describing the process path along the axis of an apparatus [105, 107]. Investigations of saturation profiles in laminar tube flows underline this finding [108]. It has been demonstrated by Manthey that the theory and experiment match very well if the operation parameters for fog formation (fog limit) initiated by heterogeneous nucleation have to be determined for mixtures with Lewis numbers close to 1 [105]. Obviously, if in a certain cross section the saturation ratio is below 1 but there are local saturation peaks ($S > 1$), and aerosol formation takes place in a narrow section, small-scale transport of droplets in subsaturated sections ($S < 1$) leads to re-evaporation.

For mixtures with higher Lewis numbers saturation peaks may occur in a surface condenser which exceed the critical saturation for homogeneous nucleation, even if the mean saturation ratio in a cross section of an apparatus is far below the critical saturation S_{crit} for homogeneous nucleation [109]. For this case it has been shown by Mall-Gleißle that fog formation initiated by homogeneous nucleation already may occur if the saturation ratio predicted by a one-dimensional plug flow model exceeds $S = 1$ [106].

Summary of the findings describing the following recommendations to estimate the fog formation potential in condensation and evaporation in the presence of inert gases can be given:

(1) The Lewis number of the gas–vapor mixture is the decisive parameter governing the formation of a supersaturated gas phase.
(2) Spatially one-dimensional modeling of condensers and evaporators is sufficient for estimating the maximum saturation which is relevant to decide whether fog formation occurs.

(3) High temperature differences between gas phase and cooling medium favor fog formation.
(4) Superheating of gas–vapor mixtures before condensation decreases supersaturation and consequently, the tendency to fog formation.

6 Symbols

c	speed of sound (m/s)
d	diameter (m)
F_i	ith functional relation ($i = 1,\ldots, 4$)
f	frequency (s^{-1})
g	condensate mass (kg)
g/g_{max}	condensate mass fraction/wetness (–)
J	nucleation rate ($m^{-3}\ s^{-1}$)
$k = 1.380662 \times 10^{-23}$ J/K	Boltzmann constant
K	frequency factor ($m^{-3}\ s^{-1}$)
$\mathrm{Kn} = \Lambda/d$	Knudsen number (–)
L	latent heat (J kg^{-1})
m_1	mass of a molecule (monomer) (kg)
M	Mach number (–)
$N_A = 6.022045 \times 10^{23}\ mol^{-1}$	Avogadro constant
n	number concentration (m^{-3})
n_{het}	heterogeneous nuclei concentration (m^{-3})
n_{hom}	homogeneous nuclei concentration (kg^{-1})
O	surface of a cluster /nucleus (m^2)
p	pressure (bar)
$p_{i,sat}$	partial saturation vapor pressure of component i in a mixture (bar)
$p_{0i,sat}$	pure component saturation vapor pressure in a mixture (bar)
p_{sat}	total saturation vapor pressure (bar)
q	heat addition (J kg^{-1})
Re	Reynolds number (–)
r^*	critical nuclei radius, radius of curvature at the nozzle throat (m)
S	saturation ratio (–)
St	Strouhal number (–)
T_{cycle}	time interval of one cycle (s)
Tu	degree of turbulence (–)
w	velocity (m s^{-1})
$\vec{v}$	velocity vector (m s^{-1})
x	vapor mass fraction (–)
y^*	half nozzle height at the nozzle throat (m)
Z	Zeldovich factor (–)

Greek letters

α	Mach angle (°)
α	void fraction, vapor volume fraction (–)
α_C	accommodation coefficient (–)
β, δ	angle (°)
Λ	mean free path (m)
γ	heat capacity ratio (–)
Φ	relative humidity (–)
μ_i	chemical potential of a component i in a mixture (J/mol)
μ	chemical potential of a pure component (J/mol)
σ	surface tension (N m^{-1})
σ_{ref}	cavitation number at reference state (–)
Θ	nonisothermal factor (–)
τ_c, τ_f	characteristic time scales (s)

Subscripts

0	reservoir conditions
1, 2	conditions at position 1, 2
c	condensation onset
cycle	value of one cycle
G, gas	gaseous value
het	heterogeneous
hom	homogeneous
inlet	inlet value
L, liq	liquid value
max	maximum value
min	minimum value
out, mix	outlet value
r	curved surface with radius r
ref	reference value
rot	rotational velocity
sat	equilibrium saturation state
sf	liquid film surface property
vap	vapor value
∞	flat interface r = ∞, bulk value

Superscripts

a	exponent of similarity law
–	reduced value, averaged value
*	value of critical nucleus, value at $M = 1$

7 Bibliography

1. Friedlander SK (2000) Smoke, dust and haze. Oxford University Press, New York
2. Hinds WC (1982) Aerosol technology. John Wiley & Sons, New York
3. Schaber K (1995) Aerosol formation in absorption processes. Chem Eng Sci 50:1347–1360
4. Volmer M (1939) Kinetik der Phasenbildung. Theodor Steinkopff, Dresden u. Leipzig
5. Zettlemoyer AC (ed) (1969) Nucleation. Marcel Dekker Inc., New York
6. Oxtoby DW (1992) Homogeneous nucleation: theory and experiment. J Phys Condens Matter 4:7627–7650
7. Schmelzer JWP (2005) Nucleation theory and applications. Wiley-VCH, Weinheim
8. Feder J, Russell KC, Lothe J, Pound GM (1966) Homogeneous nucleation and growth of droplets in vapours. Adv Phys 15:111–178
9. Strey R, Wagner PE, Viisanen Y (1994) The problem of measuring homogeneous nucleation rates and the molecular contents of nuclei: progress in the form of nucleation pulse measurements. J Phys Chem 98:7748–7758
10. Hagen DE, Kassner JL (1984) Homogeneous nucleation rate for water. J Chem Phys 81:1416–1418
11. Schmitt JL, Adams GW, Zalabsky RA (1982) Homogeneous nucleation of ethanol. J Chem Phys 77:2089–2097
12. Sharaf MA, Dobbins RA (1982) A comparison of measured nucleation rates with the predictions of several theories of homogeneous nucleation. J Chem Phys 77:1517–1526
13. Peters F, Paikert B (1989) Nucleation and growth rates of homogeneously condensing water vapor in argon from shock tube experiments. Exp Fluids 7:521–530

14. Bier K, Ehrler F, Kissau G, Lippig V, Schorsch R (1977) Homogene Spontankondensation in expandierenden Dampfstrahlen des Kältemittels R 22 bei hohen normierten Drücken. Forsch IngWes 43:165–175
15. Gyarmathy G, Meyer H (1965) Spontane Kondensation. VDI-Forschungsheft 508. VDI-Verl. Düsseldorf
16. Hedbäck AJW (1982) Theorie der spontanen Kondensation in Düsen und Turbinen. Mitt. Inst. f. Therm. Turbomaschinen, ETH Zürich, Juris-Verl., Zürich
17. Bier K, Ehrler F, Theis G (1990) Spontaneous condensation in stationary nozzle flow of carbon dioxide in a wide range of density. In: Meier GEA, Thompson PA (eds) Proceedings of the IUTAM symposium Göttingen 1989: adiabatic waves in liquid-vapor systems, Springer-Verlag, Berlin, pp 129–141
18. Bier K, Ehrler F, Theis G (1984) Comparison of spontaneous condensation in supersaturated nozzle flow of different refrigerants. Proceedings of the international VDI-seminar ORC-HP-technology, Zürich. VDI-Berichte 539. VDI-Verl. Düsseldorf
19. Niekrawietz M (1989) Experimentelle Untersuchungen und Modellrechnungen zur spontanen Kondensation in Düsenströmungen übersättigter Kohlendioxid/Luft-Gemische. Diss., Univ. Karlsruhe (TH)
20. Wölk J, Strey R, Heath CH, Wyslouzil BE (2002) Empirical function for homogeneous water nucleation rates. J Chem Phys 117(10):4954–4960
21. Tolman RC (1949) The effect of droplet size on surface tension. J Chem Phys 17:333–337
22. Horsch M, Vrabec J et al. (2008) Homogeneous nucleation in supersaturated vapors of methane, ethane, and carbon dioxide predicted by brute force molecular dynamics. J Chem Phys 128:164510
23. Flood H (1934) Tröpfchenbildung in übersättigten Äthylalkohol-Wasserdampfgemischen. Z Phys Chem A 170:286–294
24. Neumann K, Döring W (1940) Tröpfchenbildung in übersättigten Dampfgemischen zweier vollständig mischbarer Flüssigkeiten. Z Phys Chem A 186:203–226
25. Reiss H (1950) The kinetics of phase transitions in binary systems. J Chem Phys 18:840–848
26. Vehkamäki H (2006) Classical nucleation theory in multicomponent systems. Springer-Verlag, Berlin
27. Steinmeyer DE (1972) Fog formation in partial condensers. Chem Eng Prog 68(7):64–68
28. Yue GK, Hamill P (1979) The homogeneous nucleation of H_2SO_4–H_2O aerosol particles in air. J Aerosol Sci 10:609–614
29. Mirabel P, Clavelin JL (1978) Experimental study of nucleation in binary mixtures: the nitric acid-water and the sulphuric-water systems. J Chem Phys 68:5020–5025
30. Mirabel P, Katz JL (1974) Binary homogeneous nucleation as a mechanism for the formation of aerosols. J Chem Phys 60:1138–1144
31. Wix A (2008) Theoretische und experimentelle Untersuchungen zur homogenen und heterogenen Nukleation bei der Säureabsorption in Gas-Flüssigkeits-Kontaktapparaten. Fortschritt-Berichte VDI 3, 894, VDI Verlag
32. Gretscher H, Schaber K (1999) Aerosol formation by heterogeneous nucleation in wet scrubbing processes. Chem Eng Process 38:541–548
33. Ehrig R, Ofenloch O, Schaber K, Deuflhard P (2002) Modelling and simulation of aerosol formation by heterogeneous nucleation in gas-liquid contact devices. Chem Eng Sci 57(7):1151–1163
34. Schaber K, Körber J, Ofenloch O, Ehrig R, Deuflhard P (2002) Aerosol formation in gas-liquid contact devices – nucleation, growth and particle dynamics. Chem Eng Sci 57:4345–4356
35. Young JB (1993) The condensation and evaporation of liquid droplets at arbitrary Knudsen number in the presence of an inert gas. Int J Heat Mass Transf 36:2941–2996
36. Gyarmathy G (1963) Zur Wachstumsgeschwindigkeit kleiner Flüssigkeitströpfchen in einer übersättigten Atmosphäre. ZAMP 14:280–293
37. Studzinski W, Zahoransky RA, Wittig SLK (1983) Zur Beschreibung homogener unärer und binärer Kondensationsvorgänge. Wärme und Stoffübertragung 17:241–250
38. Young JB (1991) The condensation and evaporation of liquid droplets in a pure vapour at arbitrary Knudsen number. Int J Heat Mass Transfer 34:1649–1661
39. Peters F, Meyer KAJ (1995) Measurement and interpretation of growth of monodispersed droplets suspended in pure vapour. Int J Heat Mass Transfer 38:3285–3293
40. Peters F, Paikert B (1994) Measurement and interpretation of monodispersed droplets in a shock tube. Int J Heat Mass Transfer 37:293–302
41. Wegener PP, Mack LM (1958) Condensation in supersonic and hypersonic wind tunnels. Adv Appl Mech 5:307–447
42. Oswatitsch K (1941) Die Nebelbildung in Windkanälen und ihr Einfluß auf Modellversuche. Jahrb Dtsch Luftfahrtforsch 1:692–703
43. Oswatitsch K (1942) Kondensationserscheinungen in Überschalldüsen. Z Angew Math Mech 22:1–14
44. Zierep J, Lin S (1967) Bestimmung des Kondensationsbeginns bei der Entspannung feuchter Luft in Überschalldüsen. Forsch Ingenieurwes 33:169–172
45. Zierep J (1971) Similarity laws and modeling. In: Wegener PP (ed) Gas dynamics series of monographs. Marcel Dekker, New York, pp 1–157
46. Schnerr G (1986) Homogene Kondensation in stationären transsonischen Strömungen durch Lavaldüsen und um Profile. Habil. Fakultät für Maschinenbau, Univ. (TH) Karlsruhe
47. Schnerr G (1988) Homogeneous condensation in transonic flow. Atmospheric aerosols and nucleation. In: Wagner PE, Vali G (eds) Proc. 12th Int. Conf. Atmospheric Aerosols and Nucleation, Wien, Austria (Lecture notes in physics), vol. 309. Springer, Berlin
48. Schnerr GH (1989) 2-D transonic flow with energy supply by homogeneous condensation: onset condition and 2-D structure of steady Laval nozzle flow. Exp Fluid 7:145–156
49. Schnerr GH (1993) Transonic aerodynamics including strong effects from heat addition. Comput Fluid 22(2):103–106
50. Li P (1992) Adiabate und kondensierende periodische transsonische Strömungen im ebenen Kanal. Dissertation Fakultät für Maschinenbau, Univ. (TH) Karlsruhe
51. Schmidt B (1962) Beobachtungen über das Verhalten der durch Wasserdampf-Kondensation ausgelösten Störung in einer Überschall-Windkanaldüse. Dissertation Fakultät für Maschinenbau, Univ. (TH) Karlsruhe
52. Barschdorff D (1967) Kurzzeitfeuchtemessung und ihre Anwendung bei Kondensationserscheinungen in Lavaldüsen. Strömungsmechanik und Strömungsmaschinen 6:18–39
53. Mosnier FP (1976) Unsteady supersonic flow with heat addition due to condensation. PhD Thesis, Graduate School of the Yale University, New Haven
54. Sichel M (1976) Unsteady transonic flow with heat addition. Department of Aerospace Engineering, The University of Michigan, Ann Arbor, MI
55. Wegener PP, Cagliostro DJ (1973) Periodic nozzle flow with heat addition. Combust Sci Technol 6:269–277
56. Deych ME, Filippov GA, Saltanov GA, Kurshakov AV, Kukushkin AN, Nozdrin GN (1974) Experimental study of unsteady phenomena in a flow of condensing vapor in nozzles. Fluid Mech – Soviet Res 3:151–157
57. Wegener PP, Mosnier FP (1981) Periodic transonic flows with heat addition: new results. Combust Sci Technol 24:179–189
58. Mundinger G (1994) Numerische Simulation instationärer Lavaldüsenströmungen mit Energiezufuhr durch homogene Kondensation. Dissertation Fakultät für Maschinenbau, Univ. (TH) Karlsruhe
59. Adam S (1996) Numerische und experimentelle Untersuchung instationärer Düsenströmungen mit Energiezufuhr durch homogene Kondensation. Dissertation Fakultät für Maschinenbau, Univ. (TH) Karlsruhe, Germany
60. Adam S, Schnerr GH (1997) Instabilities and bifurcation of non-equilibrium two-phase flows. J Fluid Mech 348:1–28
61. Schnerr GH, Adam S, Mundinger G (1994) New modes of periodic shock formation in compressible two-phase flows. In: Morioka S, van Wijngaarden L (eds) Proceedings of IUTAM symposium waves in gas/liquid and liquid/vapor two-phase systems, Kluwer Academic Publishers, Dordrecht, pp 377–386
62. Simpson DA, White AJ (2005) Viscous and unsteady flow calculations of condensing steam in nozzles. Int J Heat Fluid Flow 26(1):71–79
63. Heiler M (1999) Instationäre Phänomene in homogen/heterogen kondensierenden Düsen- und Turbinenströmungen. Dissertation Fakultät für Maschinenbau, Univ. (TH) Karlsruhe
64. Schnerr GH (2005) Unsteadiness in condensing flow: dynamics of internal flows with phase transition and application to turbomachinery. Proc. IMechE C: J Mech Eng 219:1369–1410

65. Bakhtar F, Heaton AV (1988) An examination of the effect of wake chopping on droplet sizes in steam turbines. Proceedings of the BNES conference technology on turbine plant operating with wet steam, London
66. Winkler G (2000) Laufrad-Leitrad-Wechselwirkung in homogen-heterogen kondensierenden Turbinenströmungen. Dissertation Fakultät für Maschinenbau, Univ. (TH) Karlsruhe
67. Kotake S, Glass II (1977) Condensation of water vapor and heterogeneous nuclei in a shock tube. UTIAS Report, No. 207, University of Toronto, Institute for Aerospace Studies
68. Kotake S, Glass II (1977) Condensation of water vapor in rarefraction waves: II. heterogeneous nucleation. AIAA J 15:215–221
69. Kotake S, Glass II (1981) Flows with nucleation and condensation. Prog Aerosp Sci 19:129–196
70. Fletcher NH (1958) Size effects in heterogeneous nucleation. J Chem Phys 29(3):572–576
71. Frenkel JI (1957) Kinetische Theorie der Flüssigkeiten. VEB Verlag der Wissenschaften, Berlin
72. Tokumasu T, Kamijo K, Oike M, Matsumoto Y (2001) Molecular dynamics study of the nucleation of bubble. In: Proceedings of the 4th international symposium on cavitation
73. Zima P, Maršík F, Sedlář M (2003) Cavitation rates in water with dissolved gas and other impurities. J Therm Sci 12(2):151–156
74. Bilicki Z (1996) Thermodynamic nonequilibrium in the two-phase system – a continuum with an internal structure. Arch Therm 17(1):109–134
75. Bilicki Z (1999) Mathematical model of rapid depressurisation with evaporation of a liquid. In: Proceedings of the 2nd international conference on heat transfer and transport phenomena in multiphase systems, pp 35–44
76. Bilicki Z (1999) Problems of modelling a rapid depressurisation of the liquid. In: Proc. 1st Conf. on recent developments in multiphase flow, pp 13–20
77. Kwak HY, Panton RL (1985) Tensile strength of simple liquids predicted by a model of molecular interactions. J Phys D: Appl Phys 18: 647–659
78. Michel JM, Kato H (eds) (1998) Proceedings of the 3rd international symposium on cavitation, Grenoble, France
79. Brennen CE (ed) (2001) Proceedings of the 4th international symposium on cavitation, Pasadena, USA
80. Matsumoto Y, Ikohagi T, Tsujimoto Y (eds) (2003). Proceedings of the 5th international symposium on cavitation, Osaka, Japan
81. Kuiper G (ed) (2003) Proceedings of the 6th international symposium on cavitation, Wageningen, Netherlands
82. Franc JP, Michel JM (2004) Fundamentals of cavitation. Kluwer Academic Publishers, Dordrecht
83. Lecoffre Y (1999) Cavitation bubble trackers. A.A. Balkema, Rotterdamm
84. Wallis GB (1969) One dimensional two-phase flow. McGraw-Hill, New York
85. Brennen CE (1995) Cavitation and bubble dynamics. Oxford University Press, New York
86. Sauer J (2000) Instationär kavitierende Strömungen – Ein neues Modell, basierend auf Front Capturing (VoF) und Blasendynamik. Dissertation Fakultät für Maschinenbau, Univ. (TH) Karlsruhe
87. IAPWS, International Association for the Properties of Water and Steam
88. Schmidt SJ, Sezal IH, Schnerr GH (2006) Compressible simulation of high speed hydrodynamics with phase change. In: Wesseling P, Onate E, Périaux J (eds) ECCOMAS CFD 2006 – European conference on computational fluid dynamics
89. Schnerr GH, Schmidt SJ, Sezal IH, Thalhamer M (2006) Shock and wave dynamics of compressible liquid flows with special emphasis on unsteady load on hydrofoils and on cavitation in injection nozzles. Invited Lecture. In: Proceedings of CAV2006 – sixth international symposium on cavitation, CD- ROM publication
90. Sezal IH (2009) Compressible dynamics of cavitating 3-d multi-phase flows. Dissertation Fakultät für Maschinenbau, TU München
91. Schmidt SJ, Sezal IH, Schnerr GH, Thalhamer M (2007) Shock waves as driving mechanism for cavitation erosion. In: Trebinjak I (ed) ISAIF – International symposium on experimental and computational aerothermodynamics of internal flows, CD-ROM publication
92. Sezal IH, Schmidt SJ, Schnerr GH, Thalhamer M, Förster M (2009) Shock and wave dynamics in cavitating compressible liquid flows in injection nozzles. Shock Waves. DOI 10.1007/s00193–008–0185–3
93. Sezal IH, Schmidt SJ (2008) Numerical investigation of three-dimensional cloud cavitation with special emphasis on collapse induced shock dynamics. Phys Fluids 20: 040703–040709
94. Schmidt SJ, Sezal IH, Schnerr GH, Thalhamer M (2008) Numerical analysis of shock dynamics for detection of erosion sensitive areas in complex 3-D flows. In: Proceedings of WIMRC cavitation forum 2008, Warwick, pp 107–120
95. Schmidt SJ, Sezal IH, Schnerr GH, Thalhamer M (2008) Riemann techniques for the simulation of compressible liquid flows with phase-transition at all Mach numbers – shock and wave dynamics in cavitating 3-D micro and macro systems. In: 46th AIAA aerospace sciences meeting and exhibit, January 7–10, 2008, Reno, AIAA Paper 2008–1238
96. Colburn AP, Edison AG (1941) Prevention of fog in cooler-condensers. Ind Eng Chem 33:457–458
97. Amelin AG (1967) Theory of fog condensation. Israel program for scientific translations. Jerusalem
98. Steinmeyer DE (1972) Fog formation in partial condensers. Chem Eng Prog 68(7):64–68
99. Haep S (2000) Bildung und Wachstum von Aerosolen unter Bedingungen der nassen Rauchgasreinigung. VDI Fortschritt-Berichte, Reihe 3, Nr. 641, VDI-Verlag. ISBN 3-18-364103-8
100. Ulbrich M, Sachweh B, Meckl S, Hölemann K (1999) Aerosolbildung in Absorptionsprozessen – Ursachen und Lösungsansätze. Chem Ing Techn 71:52–61
101. Brosig G (2009) Untersuchung von HCl-Nebeln in technischen Gasreinigungsanlagen. Fortschritt-Berichte VDI Reihe 3, Nr. 903, VDI-Verlag. ISBN 978-3-18-390303-0
102. Ofenloch O (2005) Entstehung und Verhalten von Aerosolen in Gaswaschanlagen. VDI Fortschritt-Berichte, Reihe 3, Nr. 832, VDI-Verlag. ISBN 3-18-383203-8
103. Browers HJH (1992) A film model for heat and mass transfer with fog formation. Chem Eng Sci 47(12):3023–3026
104. Rosner DE (1967) Enhancement of diffusion-limited vaporization rates by condensation within the boundary layer. Int J Heat Mass Trans 10 (13):1267–1279
105. Manthey A, Schaber K (2000) The formation and behavior of fog in a tube bundle condenser. Int J Therm Sci 39:1004–1014
106. Mall-Gleißle S (2008) Entstehung von Aerosolen durch homogene Keimbildung bei der Kondensation und Verdampfung. Fortschritt-Berichte VDI, Reihe 3, Nr. 891, VDI-Verlag. ISBN 978-3-18-389103-0
107. Manthey A Bildung und Verhalten von Nebel in einem Rohrbündelkondensator. http://ubka.uni-karlsruhe.de/dgi-bin/psview?document=2000/cheming/1
108. Housiadas Ch, Papanicolaou E, Drossinos Y (2002) Combined heat and mass transfer in laminar flow diffusion nucleation chambers. J Aerosol Sci 33:797–816
109. Mall-Gleißle S, Schaber K (2003) Aerosolbildung in Kondensatoren. Chem Ing Techn 75(11):1621–1624
110. Kuiper G (2006) Marin – Maritime research institute – The Netherlands, private communication
111. Franc JP, Michel JM (1985) Attached cavitation and the boundary layer: experimental and numerical treatment. J Fluid Mech 154:63–90
112. Plesset MS, Chapman RB (1971) Collapse of an initially spherical vapor cavity in the neighbourhood of a solid boundary. J Fluid Mech 47:283–290

M2 Heat Transfer to Walls with Welded Coils

Wolfgang Heidemann
Universität Stuttgart, Stuttgart, Germany

1 Introduction

In process and chemical engineering apparatuses like stirrer vessels, tanks, or autoclaves are often equipped with welded on coils at the outer surface. These coils are used for the heating and cooling of the respective vessel contents. For that purpose a heat carrier fluid flows through the pipes. Figure 1 shows the cross section of three typical stirrer vessel wall constructions. Compared to double-walled vessels, vessels with welded on coils allow smaller wall thicknesses and hence, are more economic. Furthermore, a good heat transfer inside of the coil is possible even though high viscous heating or cooling fluids are applied.

2 Theory

The calculation of the overall heat transfer from inside of the vessel to the heat carrier fluid requires – in case of known heat transfer coefficients α_t and α_w – the knowledge of the thermal resistance of the vessel wall. Komoßa [1] presented a method which implies the following simplifying assumptions:

- Since the wall thickness of the apparatuses to be observed is small compared to the diameter, a planar problem results.
- The heat transport is in steady state.
- Heat losses from the outer surface of the coil to the ambient are neglected.

Figures 3–5 show simple symmetrical subzones of the whole wall constructions depicted in Fig. 1. The symmetrical subzones according to Figs. 4 and 5 may be composed of three basic bodies with simple layout as follows:

- A part of the vessel wall
- The welded seam
- One half of the tube, stretched to a rectangular strip for simplicity

The thermal resistance of a vessel wall with welded on coils (see Fig. 1) results from adding up the single thermal resistances of the series-connected basic bodies.

2.1 Thermal Resistance of Rectangular Bodies

Considering a one-dimensional heat transfer, the thermal resistance of a rectangular body according to Fig. 2a can be calculated from $R_{th} = s/(\lambda \cdot A)$ with λ, s, A as thermal conductivity, thickness, and surface, respectively.

Since one half of the tube, stretched to a rectangular strip, as well as the part of the vessel wall (see Figs. 3–5) transfers heat only in a limited region X ($< l$), a two-dimensional heat flow results in reality. Using a numerical method presented by Heidemann [2], the thermal resistance for two-dimensional heat flow in a rectangular body according to Fig. 2b was numerically investigated for different boundary conditions. The variation from the thermal resistance R_{th} for the one-dimensional case is considered by introducing two correction factors ε and χ

$$R_{th} = \frac{1}{\varepsilon \cdot \chi} \cdot \frac{s}{\lambda \cdot A}. \tag{1}$$

The following polynomial functions are recommended for the calculation of the correction factors

$$\varepsilon = \sum_{i=0}^{3} \sum_{j=0}^{2} a_{ij} \cdot \left(\frac{s}{l}\right)^j \cdot \left(\frac{X}{l}\right)^i \tag{2a}$$

$$\chi = \sum_{i=0}^{2} \sum_{j=0}^{3} b_{ij} \cdot \left(\frac{s}{l}\right)^j \cdot \left(\frac{1}{1 + \frac{\lambda}{\alpha \cdot s}}\right)^i \tag{2b}$$

with a_{ij} and b_{ij} as polynomial coefficients, listed in Tables 1 and 3 as well as in Tables 2 and 4 for different wall constructions. Alternatively the correction factors can be taken out of the charts in Figs. 6 and 8 (for ε) and Figs. 7 and 9 (for χ), respectively.

2.2 Multilayered Vessel Walls

In practical applications vessel walls often consist of the basic wall material and an additional layer at the inside, for example,

- A protection layer made of tin, lead, or enamel
- A fouling layer resulting from pollutions of the vessel content

VDI-GVC (ed.), *VDI Heat Atlas*, DOI 10.1007/978-3-540-77877-6_51,

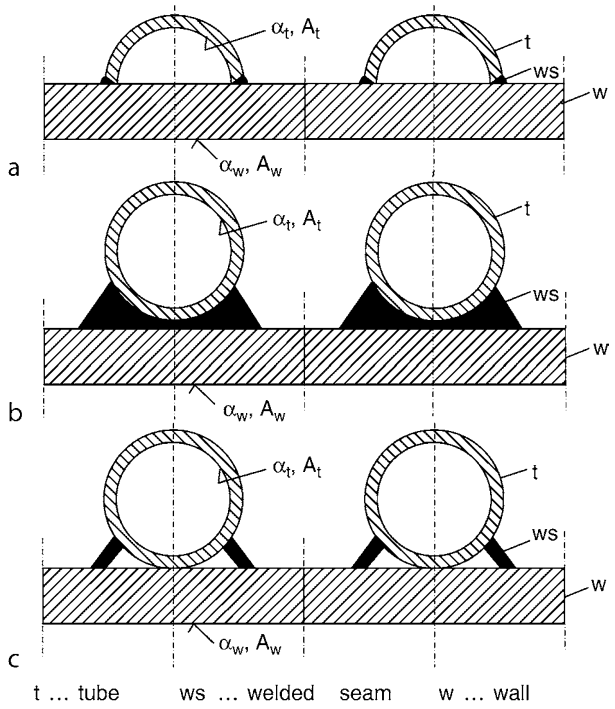

M2. Fig. 1. Cross section of vessel walls with welded on pipe coils at the outside. (**a**) Welded on half pipe, (**b**) welded on full pipe with intermediate layer, (**c**) welded on full pipe without intermediate layer.

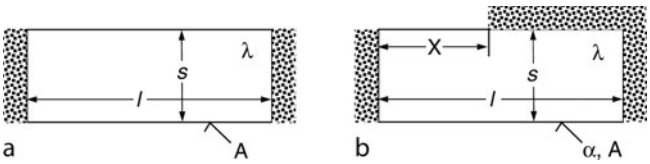

M2. Fig. 2. Heat conduction in rectangular bodies. (**a**) One-dimensional, (**b**) two-dimensional.

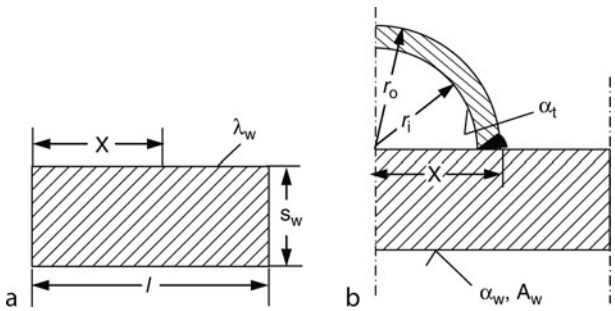

M2. Fig. 3. Cross section of welded on half pipe. (**a**) Part of the vessel wall, (**b**) symmetrical part.

In this case a fictitious wall layer thickness is introduced as follows

$$s_w = s'_w + s_{al}\frac{\lambda_w}{\lambda_{al}} \text{ with } \lambda_{al} < \lambda_w \qquad (3)$$

In Eq. (3) s'_w, λ_w, s_{al}, and λ_{al} denotes the wall thickness of the basic wall material, the thermal conductivity of the basic wall material, the thickness of the additional layer, and the thermal conductivity of the additional layer.

2.3 Thermal Conductivity of Weld Seams

If the welding material is similar to the basic wall material, the thermal conductivity of the basic wall material can approximately also be used for the weld seam.

3 Overall Heat Transfer Coefficient

3.1 Welded on Half Pipe

The overall heat transfer coefficient k related to the heat transfer area at the inside of the wall A_w (see Fig. 3) results from adding up the single thermal resistances

$$\frac{1}{k} = \frac{1}{\alpha_w} + \frac{1}{\varepsilon \cdot \chi}\cdot\frac{s_w}{\lambda_w} + \frac{1}{\alpha_t}\cdot\frac{1}{X} \qquad (4)$$

with $X = r_o$

$$\varepsilon = \varepsilon\left(\frac{X}{l}, \frac{s_w}{l}\right) \text{ from Fig. 6 or Eq. (2a) with Table 1}$$

$$\text{and } \chi = \chi\left(\frac{X}{l}, \frac{s_w}{l}, \frac{\lambda_w}{\alpha_w \cdot s_w}\right) \text{ from Fig. 7 or Eq. (2b) with Table 2}$$

Example 1

On a vessel wall made of stainless steel (λ_w = 15 W/(m K), s_w = 8 mm), a coiled half pipe (d_o = 32 mm, d_i = 28 mm) is welded with clearances of $2l$ = 100 mm. At the inside of the vessel wall a 0.1 mm thick fouling layer (λ_{al} = 0.75 W/(m K)) occurs. The heat transfer coefficients at the vessel wall and inside the coil are α_w = 1,300 W/(m^{2}K) and α_t = 2,000 W/(m^{2}K), respectively. Sought is the value of the overall heat transfer coefficient.

The fictitious wall thickness is obtained from Eq. (3)

$$s_w = 0.008\text{ m} + (0.0001 \cdot 15/0.75)\text{ m} = 0.01\text{ m}.$$

One receives

$$X = d_0/2 = 0.016\text{ m},\ l = 0.1\,\text{m}/2 = 0.05\,\text{m}$$

as well as

$$\frac{X}{l} = 0.016/0.05 = 0.32;\ \frac{s_w}{l} = 0.001/0.05 = 0.2;$$

$$\frac{\lambda_w}{\alpha_w \cdot s_w} = 15/(1,300 \cdot 0.01) = 1.154$$

Thus results in

ε = 0.39, for example, from Fig. 6 and χ = 0.76, for example, from Fig. 7.

From Eq. (4) follows

$$\frac{1}{k} = \left(\frac{1}{1,300} + \frac{1}{0.39 \cdot 0.76}\cdot\frac{0.01}{15} + \frac{1}{2,000}\cdot\frac{0.05}{0.016}\right)\frac{\text{m}^2\text{K}}{\text{W}}$$

$$= 0.0045809\frac{\text{m}^2\text{K}}{\text{W}}$$

$$k = 218.3 \frac{\mathrm{W}}{\mathrm{m^2 K}}$$

The comparison of the result with the exact (numerical) solution ($k_{num} = 229.2\,\mathrm{W/(m^2K)}$) shows an error of about 4.8% which is acceptable for most of the technical applications.

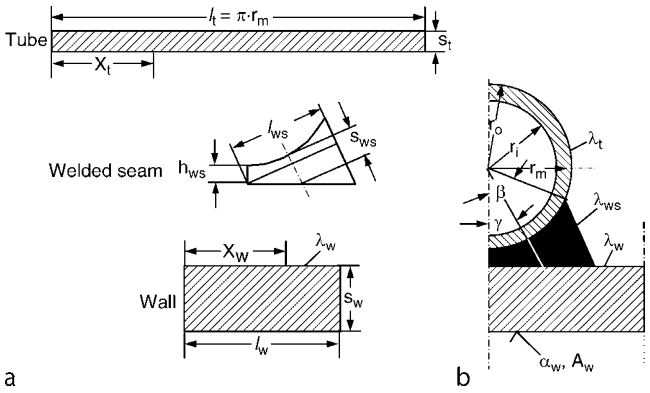

M2. Fig. 4. Cross section of welded on full pipe with intermediate layer. (**a**) Simplified parts, (**b**) Symmetrical geometry.

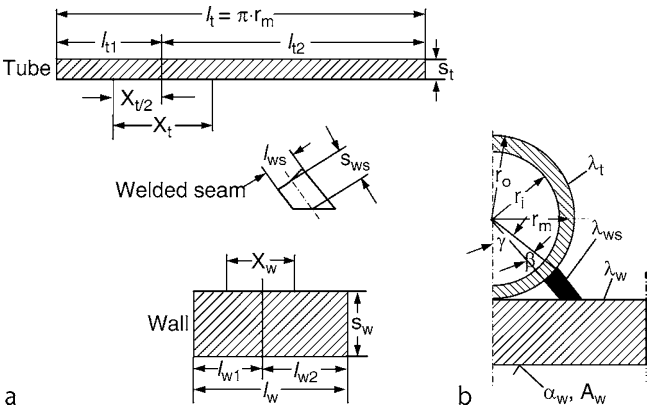

M2. Fig. 5. Cross section of welded on full pipe. (**a**) Simplified parts, (**b**) Symmetrical geometry.

3.2 Welded on Full Pipe with Intermediate Layer

$$\frac{1}{k} = \frac{1}{\alpha_w} + A_w(R_{th,w} + R_{th,ws} + R_{th,t}) + \frac{1}{\alpha_1} \cdot \frac{1_w}{\pi \cdot r_i} \tag{5}$$

In Eq. (5) is

- $R_{th,w} \cdot A_w = \dfrac{1}{\varepsilon \cdot \chi} \cdot \dfrac{s_w}{\lambda_w}$ (5a)

  with $\varepsilon = \varepsilon\left(\frac{X_w}{l_w}, \frac{s_w}{l_w}\right)$ from Fig. 8 or Eq. (2a) with Table 3

  $\chi = \chi\left(\frac{X_w}{l_w}, \frac{s_w}{l_w}, \frac{\lambda_w}{\alpha_w \cdot s_w}\right)$ from Fig. 9 or Eq. (2b) with Table 4,

- $R_{th,ws} \cdot A_w = \dfrac{s_{ws}}{\lambda_{ws}} \cdot \dfrac{l_w}{l_{ws}}$ (5b)

  with $s_{ws} = \frac{X_w}{2 \cdot \sin\gamma} - r_o$, $\gamma = \arctan\frac{X_w}{2 \cdot (r_o + h_{ws})}$, $l_{ws} \approx 2(r_0 + h_{ws})\,\sin\gamma$

- $R_{th,t} \cdot A_w = \dfrac{1}{\varepsilon \cdot \chi} \cdot \dfrac{s_t}{\lambda_t} \cdot \dfrac{l_w}{l_t}$ (5c)

  with $\varepsilon = \varepsilon\left(\frac{X_t}{l_t}, \frac{s_t}{l_t}\right)$ from Fig. 8 or Eq. (2a) with Table 3

  $\chi = \chi\left(\frac{X_t}{l_t}, \frac{s_t}{l_t}, \frac{\lambda_t}{\alpha_t \cdot s_t}\right)$ from Fig. 9 or Eq. (2b) with Table 4,

  and $\frac{X_t}{l_t} = \frac{\beta}{180°}$.

Example 2

A coiled full pipe with intermediate layer is welded on a vessel wall. At the inside of the vessel wall a 0.1 mm thick fouling layer ($\lambda_{al} = 0.75$ W/(m K)) occurs. The heat transfer coefficients at the vessel wall and inside the coil are $\alpha_w = \alpha_t = 500$ W/(m^{2}K), respectively. Sought is the value of the overall heat transfer coefficient. The following data are given:

Thermal conductivity of vessel material $\lambda_w = 15$ W/(m K)
Vessel wall thickness $s_w = 10$ mm
Breadth of welded seam $X_w = 24$ mm
Length of the symmetrical part of the vessel wall $l_w = 50$ mm
Thermal conductivity of welded seam $\lambda_{ws} = 14.6$ W/(m K)
Height of welded seam $h_{ws} = 6$ mm
Thermal conductivity of tube material $\lambda_t = 16.7$ W/(m K)
Outer radius of tube $r_o = 24$ mm

M2. Table 1. Coefficients a_{ij} for the calculation of the correction factor ε (Eq. (2a)) for welded on half pipes, scope $X/l \leq 1$

	$0.1 \leq s/l \leq 0.8$	$0.8 < s/l \leq 2.5$
a_{00}	0.0094	0.1789
a_{01}	0.3517	0.1748
a_{02}	0	0
a_{10}	0.9149	1.3656
a_{11}	0.3091	−0.1923
a_{12}	0	0
a_{20}	0.1376	−0.5110
a_{21}	−0.6724	−0.0051
a_{22}	0	0
a_{30}	0	0
a_{31}	0	0
a_{32}	0	0

M2. Table 2. Coefficients b_{ij} for the calculation of the correction factor χ (Eq. (2b)) for welded on half pipes, scope $s/l \leq 0.6$

	$0.13 \leq X/l \leq 0.425$	$0.425 < X/l \leq 0.55$
b_{00}	−0.0326	0.0464
b_{01}	3.4469	3.3813
b_{02}	−2.9828	−3.0581
b_{03}	0	0
b_{10}	1.0842	1.0312
b_{11}	−3.6929	−3.7555
b_{12}	3.2371	3.4597
b_{13}	0	0
b_{20}	0	0
b_{21}	0	0
b_{22}	0	0
b_{23}	0	0

M2. Table 3. Coefficients a_{ij} for the calculation of the correction factor ε (Eq. (2a)) for welded on full pipes, scope X/$l \leq 1$

	$0.1 \leq s/l \leq 0.8$	$0.8 < s/l \leq 2.5$
a_{00}	0	0.070
a_{01}	0.563	0.317
a_{02}	−0.253	−0.0476
a_{10}	0.973	0.909
a_{11}	−1.143	0.438
a_{12}	1.780	−0.136
a_{20}	0.058	0.950
a_{21}	3.547	−1.860
a_{22}	−5.034	0.419
a_{30}	−0.031	−0.930
a_{31}	−2.960	1.105
a_{32}	3.496	−0.235

M2. Table 4a. Coefficients b_{ij} for the calculation of the correction factor χ (Eq. (2b)) for welded on full pipes, scope $s/l \leq 0.6$

	$0.04 < X/l < 0.15$	$0.15 \leq X/l < 0.35$
b_{00}	−0.060	−0.116
b_{01}	4.029	3.867
b_{02}	−4.768	−3.707
b_{03}	1.518	0.474
b_{10}	1.414	1.536
b_{11}	−5.427	−5.742
b_{12}	5.116	5.275
b_{13}	0	0
b_{20}	−0.398	−0.436
b_{21}	1.900	2.043
b_{22}	−1.967	−2.085
b_{23}	0	0

M2. Table 4b. Coefficients b_{ij} for the calculation of the correction factor χ (Eq. (2b)) for welded on full pipes, scope $s/l \leq 0.6$

	$0.35 \leq X/l < 0.45$	$0.45 \leq X/l \leq 0.55$
b_{00}	−0.060	−0.049
b_{01}	4.029	4.425
b_{02}	−4.768	−5.757
b_{03}	1.518	2.133
b_{10}	1.414	1.583
b_{11}	−5.427	−6.518
b_{12}	5.116	6.374
b_{13}	0	0
b_{20}	−0.398	−0.589
b_{21}	1.900	2.761
b_{22}	−1.967	−2.849
b_{23}	0	0

Tube thickness $s_t = 4$ mm

Outline angle $\beta = 44°$

One calculates for the vessel wall

$$\frac{X_w}{l_w} = \frac{0.024}{0.05} = 0.48,\ \frac{s_w}{l_w} = \frac{0.01}{0.05} = 0.2,\ \frac{\lambda_w}{\alpha_w \cdot s_w} = \frac{15}{500 \cdot 0.01} = 3$$

Thus results in $\varepsilon = 0.571$, for example, from Eq. (2a) and Table 3 as well as $\chi = 0.747$ from Eq. (2b) and Table 4b. From Eq. (5a) follows

- For the vessel wall $R_{th,w} \cdot A_w = \frac{1}{0.571 \cdot 0.747} \cdot \frac{0.01}{15} \frac{m^2K}{W}$ $= 0.001561 \frac{m^2K}{W}$.
- For the welded seam $\gamma = \arctan\left(\frac{0.024}{2(0.024+0.006)}\right) = 21.8°$, $s_{ws} = \frac{0.024\,m}{2 \cdot \sin(21.8°)} - 0.024\,m = 0.0083\,m$ $l_{ws} = 2(0.024 + 0.006\,m) \cdot \sin(21.8°) = 0.0223\,m$

and from Eq. (5b) $R_{th,ws} \cdot A_w = \frac{0.0083}{14.6} \cdot \frac{0.05}{0.0223} \frac{m^2K}{W} = 0.001275 \frac{m^2K}{W}$.

One receives for the tube

$$\frac{X_t}{l_t} = \frac{44°}{180°} = 0.244,\ \frac{s_t}{l_t} = \frac{0.004}{\pi \cdot \left(0.024 - \frac{0.004}{2}\right)} = 0.0578,$$

$$\frac{\lambda_t}{\alpha_t \cdot s_t} = \frac{16.7}{500 \cdot 0.004} = 8.35.$$

With the values $\varepsilon = 0.266$ from Eq. (2a) with Table 3 and $\chi = 0.22$ from Eq. (2b) with Table 4a it follows for the tube

$$R_{th,t} \cdot A_w = \frac{1}{0.266 \cdot 0.22} \cdot \frac{0.004}{16.7} \cdot \frac{0.05}{\pi \cdot 0.022} \frac{m^2K}{W}$$

$$= 0.002961 \frac{m^2K}{W}.$$

From Eq. (5) it results

$$\frac{1}{k} = \left(\frac{1}{500} + 0.001563 + 0.001275 + 0.002961 + \frac{1}{500} \cdot \frac{0.05}{\pi \cdot 0.02}\right) \frac{m^2K}{W}$$

$$= 0.00939 \frac{m^2K}{W}$$

$$k = 106.5 \frac{W}{m^2K}.$$

3.3 Welded on Full Pipe

According to Fig. 5a the vessel wall as well as the stretched part of the tube is subdivided into two separate parts with individual lengths l_{w1}, l_{w2} and l_{t1}, l_{t2} respectively. The overall heat transfer coefficient results from the single serial and parallel connected thermal resistances

$$\frac{1}{k} = \sum_{i=1}^{2} \frac{1}{\alpha_w} \frac{l_w}{l_{w,i}} + A_w\left(R_{th,w,i} + R_{th,ws} + R_{th,t,i}\right) + \frac{1}{\alpha_t} \cdot \frac{l_w}{l_{t,i}}. \quad (6)$$

In Eq. (6) is

- $R_{th,w,i} \cdot A_w = \frac{1}{\varepsilon \cdot \chi} \cdot \frac{s_w}{\lambda_w} \cdot \frac{l_w}{l_{w,i}}$ $i = 1, 2$ (6a)

  with for $i = 1$

  $\varepsilon = \varepsilon\left(\frac{X_w}{2 \cdot l_{w,1}}, \frac{s_w}{l_{w1}}\right)$ from Fig. 8 or Eq. (2a) with Table 3

  $\chi = \chi\left(\frac{X_w}{2 \cdot l_{w,1}}, \frac{s_w}{l_{w,1}}, \frac{\lambda_w}{\alpha_w \cdot s_w}\right)$ from Fig. 9 or Eq. (2b) with Table 4, for $i = 2$

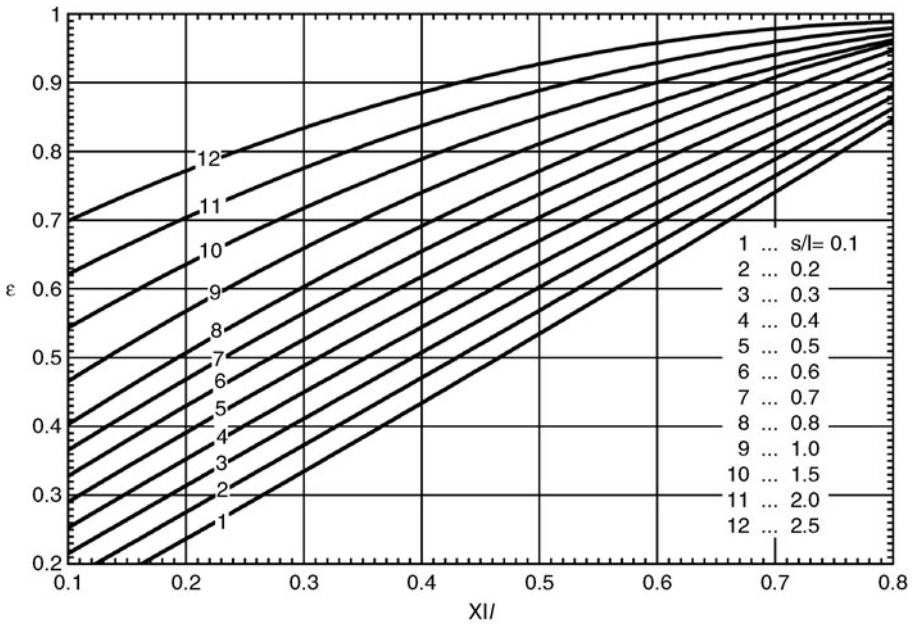

M2. Fig. 6. Correction factor ε for welded on half pipe (see Fig. 3).

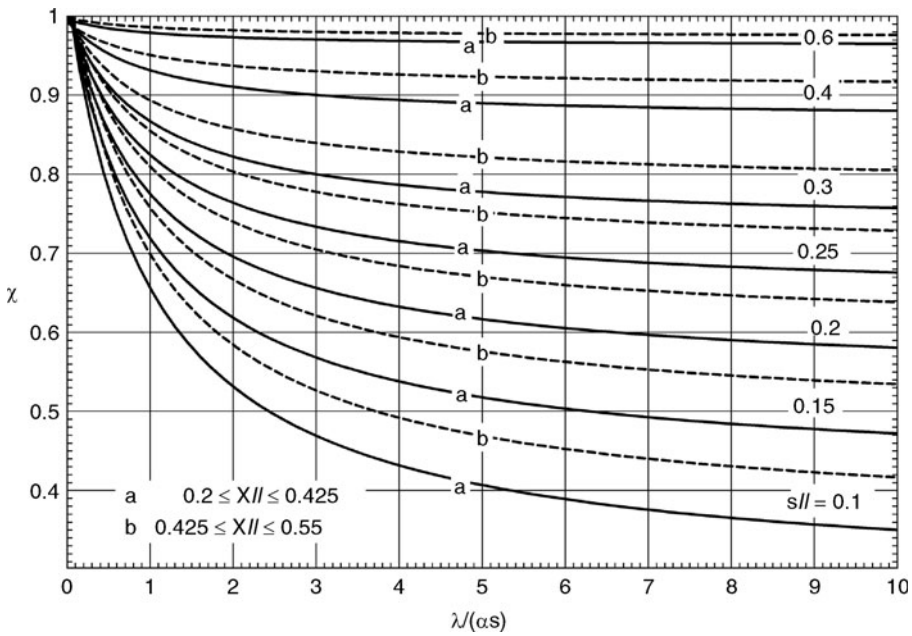

M2. Fig. 7. Correction factor χ for welded on half pipe (see Fig. 3).

$\varepsilon = \varepsilon\left(\frac{X_w}{2\cdot l_{w,2}}, \frac{s_w}{l_{w2}}\right)$ from Fig. 8 or Eq. (2a) with Table 3

$\chi = \chi\left(\frac{X_w}{2\cdot l_{w,2}}, \frac{s_w}{l_{w,2}}, \frac{\lambda_w}{\alpha_w \cdot s_w}\right)$ from Fig. 9 or Eq. (2b) with Table 4,

- $$R_{th,ws} \cdot A_w = \frac{s_{ws}}{\lambda_{ws}} \cdot \frac{2 \cdot l_w}{l_{ws}} \qquad (6b)$$
- $$R_{th,t,i} \cdot A_w = \frac{1}{\varepsilon \cdot \chi} \cdot \frac{s_t}{\lambda_t} \cdot \frac{l_w}{l_{t,i}} \; i = 1, 2 \qquad (6c)$$

with for $i = 1$

$\varepsilon = \varepsilon\left(\frac{X_t}{2\cdot l_{t,1}}, \frac{s_t}{l_{t,1}}\right)$ from Fig. 8 or Eq. (2a) with Table 3

$\chi = \chi\left(\frac{X_t}{2\cdot l_{t,1}}, \frac{s_t}{l_{t,1}}, \frac{\lambda_t}{\alpha_t \cdot s_t}\right)$ from Fig. 9 or Eq. (2b) with Table 4,

for $i = 2$

$\varepsilon = \varepsilon\left(\frac{X_t}{2\cdot l_{t,2}}, \frac{s_t}{l_{t,2}}\right)$ from Fig. 8 or Eq. (2a) with Table 3

$\chi = \chi\left(\frac{X_t}{2\cdot l_{t,2}}, \frac{s_t}{l_{t,2}}, \frac{\lambda_t}{\alpha_t \cdot s_t}\right)$ from Fig. 9 or Eq. (2b) with Table 4,

and $\frac{X_t}{l_t} = \frac{\beta}{180°}$, $\frac{l_{t,1}+0.5\cdot X_t}{l_t} = \frac{\gamma}{180°}$.

Example 3

On a 10-mm-thick vessel wall a coiled full pipe (d_o = 48 mm, s_t = 4 mm) is welded with clearances of $2l_w$ = 100 mm in such a way, that 75% of the outer tube surface is in contact with the ambience. The welded seam has a thickness of s_{ws} = 6 mm and a

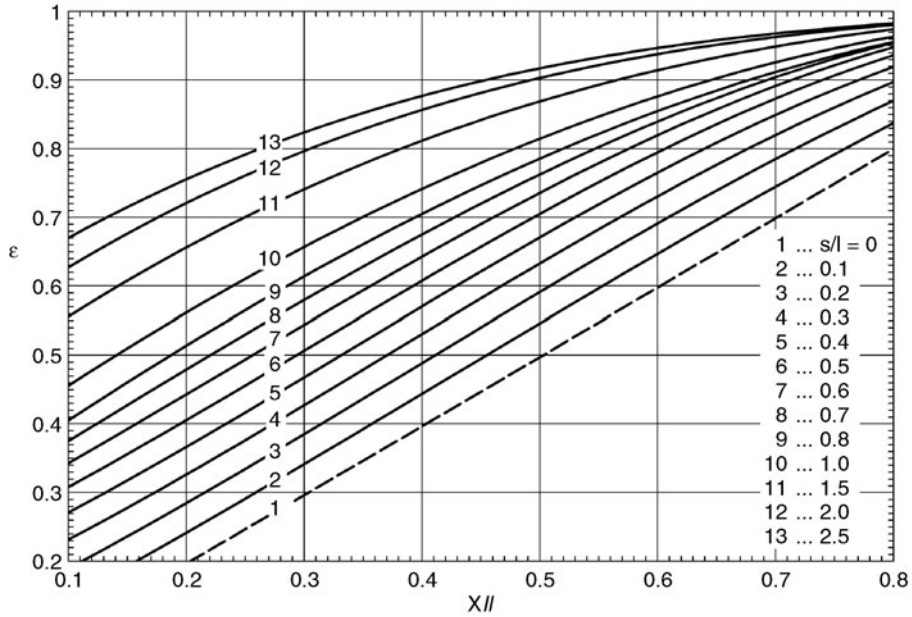

M2. Fig. 8. Correction factor ε for welded on full pipes (see Figs. 4 and 5).

length of $l_{ws} = 5$ mm. Furthermore, the following data are given: $l_{w,2} = 32.5$ mm, $X_w = 6$ mm, $\beta = 13°$. The heat transfer coefficients at the vessel wall and inside the coil are $\alpha_w = 1{,}000$ W/(m^{2}K) and $\alpha_t = 2{,}500$ W/(m^{2}K), respectively. The thermal conductivities of the tube, the welded seam, and the wall material correspond to example 2. Sought is the value of the overall heat transfer coefficient.

One calculates for the vessel wall

$$l_w = \frac{0.1\,\text{m}}{2} = 0.05\,\text{m},\ l_{w,1} = (0.05 - 0.0325)\,\text{m} = 0.0175\,\text{m},$$
$$\frac{\lambda_w}{\alpha_w \cdot s_w} = \frac{15}{1{,}000 \cdot 0.01} = 1.5$$

For part 1 of the wall ($i = 1$) one calculates

$$\frac{X_w}{2 \cdot l_{w,1}} = \frac{0.006}{2 \cdot 0.0175} = 0.171,\ \frac{s_w}{l_{w,1}} = \frac{0.01}{0.0175} = 0.571.$$

Thus results in $\varepsilon = 0.403$ from Eq. (2a) and Table 3 as well as $\chi = 0.971$ from Eq. (2b) and Table 4b.

Equation (6a) yields the thermal resistance

$$R_{th,w,1} \cdot A_w = \frac{1}{0.403 \cdot 0.971} \cdot \frac{0.01}{15}\frac{\text{m}^2\text{K}}{\text{W}} \cdot \frac{0.05}{0.0175} = 0.004867\,\frac{\text{m}^2\text{K}}{\text{W}}.$$

For part 2 of the wall ($i = 2$) one receives

$$\frac{X_w}{2 \cdot l_{w,2}} = \frac{0.006}{2 \cdot 0.0325} = 0.092,\ \frac{s_w}{l_{w,2}} = \frac{0.01}{0.0325} = 0.307$$

and calculates

$\varepsilon = 0.227$ from Eq. (2a) and Table 3

as well as $\chi = 0.863$ from Eq. (2b) and Table 4b.

From Eq. (6a) it results

$$R_{th,w,2} \cdot A_w = \frac{1}{0.227 \cdot 0.863} \cdot \frac{0.01}{15}\frac{\text{m}^2\text{K}}{\text{W}} \cdot \frac{0.05}{0.0325} = 0.005235\,\frac{\text{m}^2\text{K}}{\text{W}}.$$

One calculates for the welded seam from Eq. (6b)

$$R_{th,ws} \cdot A_w = \frac{0.006}{14.65} \cdot \frac{2 \cdot 0.05}{0.005}\frac{\text{m}^2\text{K}}{\text{W}} = 0.008191\,\frac{\text{m}^2\text{K}}{\text{W}}.$$

One receives for the tube

$$X_t = \frac{13°}{180°} \cdot \pi \cdot 0.022\,\text{m} = 0.005\,\text{m}, \gamma = \frac{(100 - 75)}{100} \cdot 180° = 45°$$
$$l_{t,1} = \frac{\gamma}{180°} \cdot l_t - \frac{X_t}{2} = 0.25 \cdot \pi \cdot 0.022 - 0.0025\,\text{m} = 0.0147\,\text{m},$$

$$l_{t,2} = \pi \cdot 0.022 - 0.0147\,\text{m} = 0.0544\,\text{m}, \frac{\lambda_t}{\alpha_t \cdot s_t} = \frac{16.74}{2{,}500 \cdot 0.004} = 1.674.$$

For part 1 of the tube ($i = 1$) one calculates

$$\frac{X_t}{2 \cdot l_{t,1}} = \frac{0.005}{2 \cdot 0.0147} = 0.17, \frac{s_t}{l_{t,1}} = \frac{0.004}{0.0147} = 0.272.$$

and obtains $\varepsilon = 0.285$ from Eq. (2a) and Table 3 as well as $\chi = 0.803$ from Eq. (2b) and Table 4b.

From Eq. (6a) it results

$$R_{th,t,1} \cdot A_w = \frac{1}{0.285 \cdot 0.803} \cdot \frac{0.004}{16.74} \cdot \frac{0.05}{0.0147}\frac{\text{m}^2\text{K}}{\text{W}} = 0.003551\,\frac{\text{m}^2\text{K}}{\text{W}}.$$

For part 2 of the tube ($i = 2$) one calculates

$$\frac{X_t}{2 \cdot l_{t,2}} = \frac{0.005}{2 \cdot 0.0544} = 0.046, \frac{s_t}{l_{t,2}} = \frac{0.004}{0.0544} = 0.0735.$$

and obtains $\varepsilon = 0.082$ from Eq. (2a) and Table 3, $\chi = 0.562$ from Eq. (2b) and Table 4b.

From Eq. (6a) it results

$$R_{th,t,2} \cdot A_w = \frac{1}{0.082 \cdot 0.562} \cdot \frac{0.004}{16.74} \cdot \frac{0.05}{0.0544}\frac{\text{m}^2\text{K}}{\text{W}} = 0.004765\,\frac{\text{m}^2\text{K}}{\text{W}}.$$

and from Eq. (6) one obtains

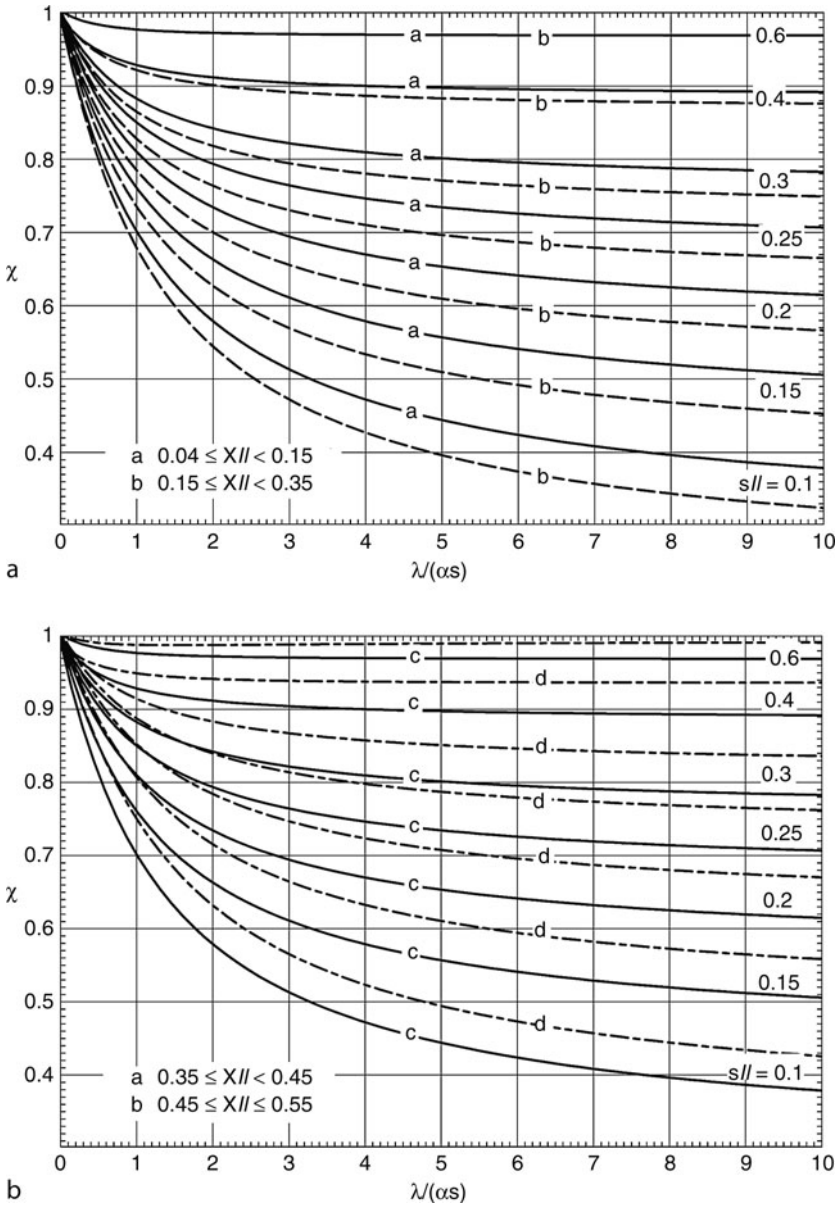

M2. Fig. 9. (**a**) Correction factor χ for welded on full pipes (see Figs. 4 and 5). (**b**) Correction factor χ for welded on full pipes (see Figs. 4 and 5).

$$k = \left[\frac{1}{\left(\frac{0.05}{1{,}000 \cdot 0.0175} + 0.004867 + 0.008191 + 0.003551 + \frac{1}{2{,}500} \cdot \frac{0.05}{0.0147}\right)}\right] \frac{\mathrm{W}}{\mathrm{m^2K}} + \left[\frac{1}{\left(\frac{0.05}{1{,}000 \cdot 0.0325} + 0.005235 + 0.008191 + 0.004765 + \frac{1}{2{,}500} \cdot \frac{0.05}{0.0544}\right)}\right] \frac{\mathrm{W}}{\mathrm{m^2K}}$$
$$= 97.8 \frac{\mathrm{W}}{\mathrm{m^2K}}$$

4 Symbols

A	surface (m^2)
R	thermal resistance ($K\ W^{-1}$)
X	section (m)
β, γ	angle (°)
ε, χ	correction factors (1)

Subscripts

al	additional layer
t	tube
th	thermal
w	wall
ws	welded seam
o	outer
i	inner

5 Bibliography

1. Komoßa H (1956) Zur Lösung stationärer Wärmeleitprobleme mit Hilfe von Analogieverfahren, Diss. TH Karlsruhe
2. Heidemann W (1995) Zur rechnerischen Ermittlung instationärer Temperaturfelder in geschlossener und diskreter Form, Diss. Universität Stuttgart

M3 Heat Transfer to Falling Films at Vertical Surfaces

Günter Schnabel
BIDECO GmbH, Biberach (Riss), Germany

1 General: Definitions

In falling-film equipment, a thin film of liquid generally flows downward under gravity on the inner surfaces of vertical tube bundles. Heat is transferred in order to

- raise the temperature of the liquid and/or
- evaporate some of the liquid.

The heating medium is mostly steam that condenses on the outer surfaces of the tubes. Occasionally, the falling film is cooled by heat removal. Features of falling-film equipment are

- high heat transfer coefficients
- short residence times
- short liquid holdup
- low pressure drops.

This chapter presents simple power-law equations for the determination of heat transfer during heating, cooling, and evaporation of falling films. They have been derived from verified compilations of measured values [1]. Three dimensionless numbers suffice for the description of heat transfer, viz.,

- the Nusselt number $\equiv \frac{\alpha}{\lambda}\left(\frac{\nu^2}{g}\right)^{1/3}$
- the Reynolds number $\mathrm{Re} \equiv \frac{\dot{m}}{\eta}$
- the Prandtl number $\mathrm{Pr} \equiv \frac{\nu}{a}$.

The term (ν^2/g) has the dimension of a length. It is used instead of the film thickness s, because s itself depends on Re. The wetting rate $\dot{m}$ is the mass flow rate of liquid per unit length of circumference, i.e., $\dot{m} = \dot{M}/\pi d$. Among the dimensionless numbers the following correlation exists:

$$\mathrm{Re} = \mathrm{Nu}^* \mathrm{Ph}^* \mathrm{Ga}^{1/3}/\mathrm{Pr}$$

with

$$\mathrm{Ph} = c_\mathrm{p}{}^* \Delta\vartheta/\Delta h_\mathrm{v}$$
$$\mathrm{Ga}^{1/3} = L/(\nu^2/g)^{1/3}$$

In nonboiling falling films, all the properties (λ, ν, η, and a) are determined at the average of the inlet and the outlet temperatures, i.e., at $\vartheta = (\vartheta_\mathrm{i} + \vartheta_\mathrm{o})/2$; and in boiling films, at the boiling point $\vartheta = \vartheta_\mathrm{sat}(p)$.

2 Film Thickness

A knowledge of the film thickness s is required for the determination of the liquid holdup. It can be obtained from the Nusselt theory [2] if the film is smooth and laminar, i.e.,

$$s_\mathrm{lam} = \left(\frac{3\,\nu^2}{g}\right)^{1/3} \mathrm{Re}^{1/3}; \quad \mathrm{Re} < 400. \tag{1}$$

Kapitza [3] recommended that allowance for surface waves in laminar falling films be made by inserting a numerical value of 2.4 instead of 3 in Eq. (1). Brauer [4] determined the following relationship for turbulent falling films from optical measurements:

$$s_\mathrm{turb} = 0.302\left(\frac{3\,\nu^2}{g}\right)^{1/3} \mathrm{Re}^{8/15}; \quad \mathrm{Re} > 400. \tag{2}$$

Equation (2) agrees well with the results obtained from semi-empirical correlations derived from general laws on velocity distribution [5–7].

3 Heat Transfer

Various boundary conditions apply to the free surfaces of nonboiling and boiling falling films. Thus, the temperature profile formed in the liquid film during heating or cooling differs from that formed during evaporation. Temperature fields in falling films that have been hydrodynamically developed at a constant wall temperature are shown graphically in Fig. 1. In a *nonboiling* falling film, the temperature profile $\vartheta(x, y)$ changes steadily,

VDI-GVC (ed.), *VDI Heat Atlas*, DOI 10.1007/978-3-540-77877-6_52,

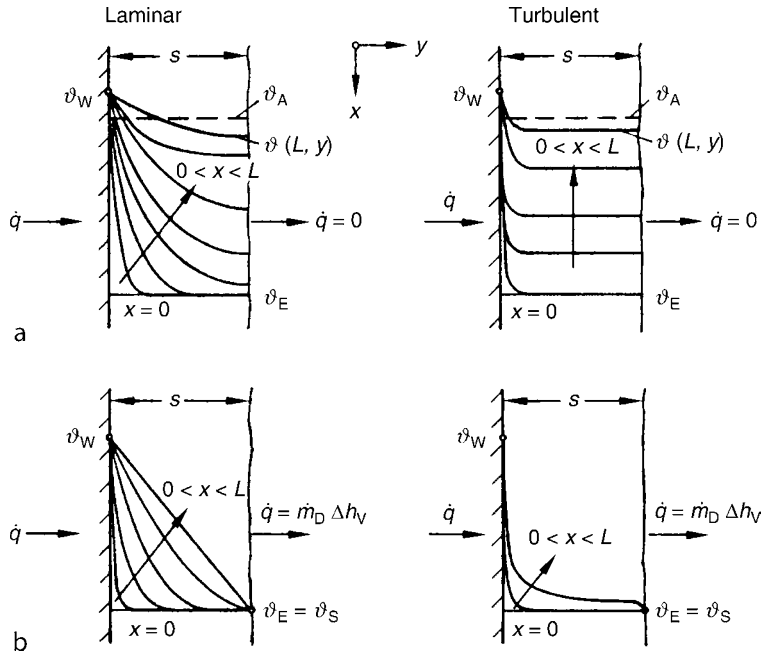

M3. Fig. 1. Temperature fields in hydrodynamically developed falling films. (**a**) Nonboiling, laminar, and turbulent falling films without evaporation at the free surface; (**b**) boiling, laminar, and turbulent falling films during evaporation at the free surface.

commencing at $x = 0$, from the inlet ϑ_i to the outlet ϑ_o temperature, as is illustrated in Fig. 1a. The outlet temperature is the calorific mean of the film temperature distribution, i.e.,

$$\vartheta_o = \frac{\int_0^s \varrho c u \vartheta \, dy}{\int_0^s \varrho c u \, dy}.$$

If the flow path x is short, the bulk of the liquid is not affected by the change in temperature. This length is referred to as the zone of thermal development. Initially, the temperature profile assumes the character of a boundary layer. It is parabolic at a point downstream, where flow is thermally developed. If heat is not removed, there is a horizontal tangent to the film at this point.

Temperature fields in *boiling* falling films are shown in Fig. 1b. If the wall temperature ϑ_w is not too high, no vapor bubbles are formed at the wall. When the flow path is short, the falling film is initially superheated near the wall, but evaporation does not occur. It is not until the flow path becomes longer and the temperature gradient penetrates to the surface that evaporation commences. Then, if flow is laminar, heat is transmitted, in accordance with the *Nusselt* condensation theory [2], by a linear temperature gradient to the surface where it is consumed in phase conversion. If film flow is turbulent, the temperature in the bulk is largely equalized. Steeper temperature gradients occur only in the immediate vicinity of the wall and at the surface. The boiling point at the phase boundary is that corresponding to the ambient pressure.

The definition of the heat transfer coefficient α in the heating or cooling of falling films differs from that in evaporation. Consequently, the two cases must be treated separately. A distinction must also be drawn between thermally developing and thermally developed flows. Another factor of some (minor) significance is the manner in which the heat is applied, i.e., whether $\dot{q}$ = constant or ϑ_w = constant.

3.1 Heat Transfer at Nonboiling Falling Films

The coefficient of local heat transfer is defined by

$$\alpha_x \equiv \frac{\dot{q}}{\vartheta_w - \vartheta_x}. \tag{3}$$

The rate of heat flow $\dot{Q}$ at a constant wall temperature over a path of length L is calculated from the average coefficient of surface heat transfer, which is defined by

$$\bar{\alpha} \equiv \frac{\dot{Q}}{A \Delta \vartheta_{log}} = \frac{\dot{m} c_p}{L} \ln \frac{\vartheta_w - \vartheta_i}{\vartheta_w - \vartheta_o}. \tag{4}$$

Conversely, if ϑ_w and α are known, Eq. (4) can be taken to determine the requisite length of tube L.

The average heat transfer coefficient in heating or cooling is obtained from the equations for $\overline{Nu}$, which are as follows in the $x = 0$ to $x = L$ range [1]:

- for laminar, hydrodynamically and thermally developed flow,

$$\overline{Nu} = C_\infty Re^{-1/3}, \tag{5}$$

  where $C_\infty = 1.30$ for ϑ_w = constant and $C_\infty = 1.43$ for $\dot{q}$ = constant;
- in the zone of thermally developing flow,

$$\overline{Nu} = \overline{C}_0 \sqrt[3]{Re^{1/3} \, Pr \left(\frac{\upsilon^2}{g}\right)^{1/3}} \Big/ L, \tag{6}$$

where $\overline{C}_0 = 0.912$ for ϑ_w = constant and $\overline{C}_0 = 1.10$ for $\dot{q}$ = constant;

- in the zone of transition to turbulent flow,

$$\overline{Nu} = 0.0425\,Re^{1/5}\,Pr^{0.344}; \tag{7}$$

- for turbulent flow,

$$\overline{Nu} = 0.0136\,Re^{2/5}\,Pr^{0.344}. \tag{8}$$

The highest value of $\overline{Nu}$ obtained from Eqs. (5–8) is taken to calculate the average heat transfer coefficient α.

The viscosity depends strongly on temperature, and its effect on heat transfer can be taken into account by multiplying the right-hand sides of Eqs. (5–8) by the Bays and McAdams [8] correction factor $(\eta/\eta_w)^{0.25}$, in which η is the dynamic viscosity at the average film temperature and η_w is that at the wall temperature. This factor is valid for both heating and cooling.

The average Nusselt number $\overline{Nu}$ has been plotted against the Reynolds number Re under the boundary condition of ϑ_w = constant in Fig. 2. The parameters are the Prandtl number Pr and the term $Pr(v^2/g)^{1/3}/L$ for the zone of thermal development, which is of significance only for very viscous materials. In the cases of this nature, however, high Reynolds numbers are hardly ever encountered. For this reason, the curves that characterize the zone of thermal development are shown in dashed lines for $Re > 10$ and are not continued beyond $Re > 100$. Again, the higher value should be applied.

Example 1

A predominantly aqueous liquid, e.g., milk or fruit juice, flows downward at a rate of 58.8 kg/h in a vertical, stainless steel tube (d_i = 23 mm; d_o = 25 mm). It is to be sterilized at elevated pressure by brief heating from $\vartheta_i = 25°C$ to $\vartheta_o = 125°C$. Steam condenses at a temperature of $\vartheta_s = 130°C$ on the outer surface of the tube. What is the length L of tube required?

If the area of the outer surface $A = \pi d_o L$ is taken as the reference, the following relationship can be obtained from Chap. C2:

$$\dot{Q} = kA\,\Delta\vartheta_m = k\pi d_o L\,\Delta\vartheta_m,$$

where

$$k = \left(\frac{1}{\bar{\alpha}_c} + \frac{d_o \ln\frac{d_o}{d_i}}{2\lambda} + \frac{d_o}{d_i\bar{\alpha}}\right)^{-1}.$$

The heat balance is

$$\dot{Q} = \dot{M}\,c_p(\vartheta_o - \vartheta_i).$$

It follows that

$$\frac{k\pi\,d_o\,L}{\dot{M}\,c_p} = \ln\frac{\vartheta_s - \vartheta_i}{\vartheta_s - \vartheta_o}.$$

(a) Determination of the heat transfer coefficient on the film side:

The reference temperature for the properties is $\vartheta_m = (25 + 125)/2°C = 75°C$. The values for the properties, which are approximately the same as those for water itself, are obtained by linear interpolation from Chap. D2. Thus,

$$\eta = 379.7 \cdot 10^{-6}\,kg/m; \quad \lambda = 663 \cdot 10^{-3}\,W/(m\,K);$$
$$v = 0.3895 \cdot 10^{-6}\,m^2/s; \quad Pr = 2.40.$$

The Reynolds number determined from these figures is

$$Re = \frac{58 \cdot 8}{3,600\pi \cdot 23 \cdot 10^{-3} \cdot 379.7 \cdot 10^{-6}} = 59.5.$$

The Nusselt number is derived from Eqs. (5–8) or from Fig. 2. Thus

$$\overline{Nu} = \begin{cases} 0.154 \text{ from Eq. (5)}, \\ 0.073 \text{ from Eq. (6)}, \\ 0.206 \text{ from Eq. (7)}, \\ 0.237 \text{ from Eq. (8)}. \end{cases}$$

$Nu_{max} = 0.237.$

Hence $\alpha = \overline{Nu}_{max}\,v \Big/ \left(v^2/g\right)^{1/3} = 6,299\,W/(m^2\,K).$

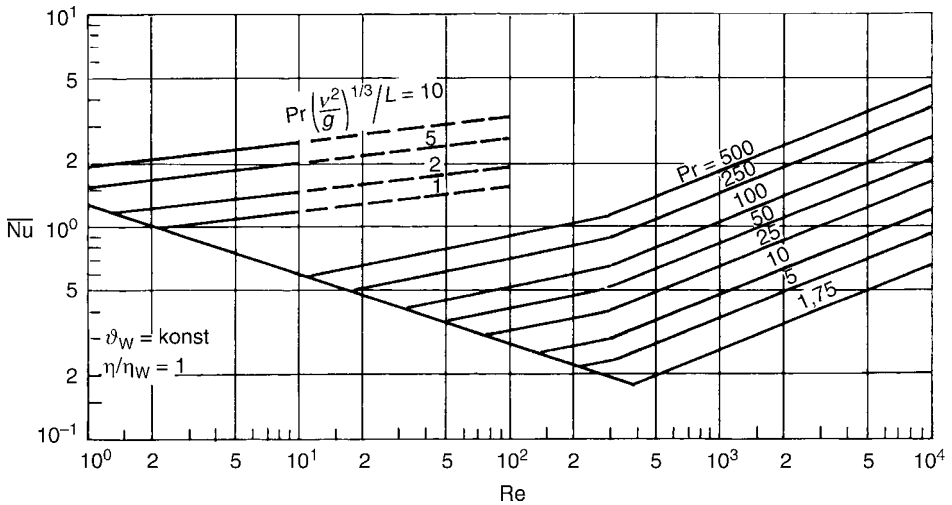

M3. Fig. 2. Average Nusselt number as a function of Re with Pr and $Pr(v^2/g)^{1/3}/L$ as parameters for nonboiling falling films.

In the determination of $\overline{\mathrm{Nu}}$ from Eq. (6), it was assumed that $L = 1$. Here, the calculation is performed in full for the sake of illustration, but it could have been dispensed with since $\mathrm{Re} \gg 10$ (see diagram).

(b) Determination of the heat transfer coefficient on the condensate side:

The heat balance is

$$\dot{M}_c \Delta h_v = \dot{M} c_p (\vartheta_o - \vartheta_i).$$

Hence the condensate flow rate at the lower end of the tube is

$$\dot{M}_c = \frac{\dot{M} c_p (\vartheta_o - \vartheta_i)}{\Delta h_{v,(130°C)}} = 0.00317\,\mathrm{kg/s}.$$

If the condensate temperature is assumed to be 125°C as an initial estimate, the Reynolds number for the condensate film will be

$$\mathrm{Re}_c = \frac{\dot{M}_c}{\pi d_o \eta_{125°C}} = \frac{0.00317}{25 \cdot 10^{-3} \pi \cdot 222.4 \cdot 10^{-6}} = 182.$$

Inserting $\mathrm{Re}_c = 182$ in Eqs. (24) and (25) in Chap. J1 gives the following value for the average Nusselt number:

$$\mathrm{Nu}_c = 0.9245 f_{waves} \mathrm{Re}_c^{-1/3} = 0.188.$$

Therefore, the average heat transfer coefficient on the condensate side is $\alpha_c = 6{,}752\ \mathrm{W/(m^2\,K)}$.

(c) Determination of L

Since $\lambda = 17\ \mathrm{W/(m\,K)}$ for stainless steel,

$$k = \left\{ \frac{1}{6{,}752} + \frac{25 \cdot 10^{-3} \ln 25/23}{2 \cdot 17} + \frac{25}{23 \cdot 6307} \right\}^{-1} = 2{,}619\,\mathrm{W/(m^2\,K)}.$$

Finally, $L = 1.0$ m. Therefore, the average wall temperature on the condensate side is

$$\bar{\vartheta}_{w,c} = \vartheta_s - \frac{\dot{M} c_p (\vartheta_o - \vartheta_i)}{\alpha_c \pi d_o L} = 117.3°C;$$

and the average condensate temperature is

$$\vartheta = \left(\vartheta_s - \bar{\vartheta}_{w,c}\right)/2 = 123.6°C.$$

This figure agrees quite well with the initial assumption.

A more accurate figure for the heat transfer coefficient on the condensate side and thus for the requisite length L involves a differential approach, because the wall temperature is not constant and the values for the properties also change considerably along the length of the path. If Eq. (37) in Chap. J1 is applied to the condensate side, the more accurate figure of $L = 1.16$ would be obtained.

Example 2

The kinematic viscosity at 50°C of an aqueous polymer solution is 500 times greater than that of water, but the other properties correspond to those of water at a temperature of 50°C. The solution flows downward in a tube of 1 m length at a mass flux of $\dot{m} = 0.544\ \mathrm{kg/(m\,s)}$. What is the average Nusselt number $\overline{\mathrm{Nu}}$?

The properties, as listed in Chap. D2, are

$$\mathrm{Pr} = 3.57 \cdot 500 = 1{,}785,$$
$$\nu = 0.554 \cdot 10^{-6} \cdot 500 = 2.770 \cdot 10^{-4}\,\mathrm{m^2/s},$$
$$\varrho = 988\,\mathrm{kg/m^3},$$
$$\eta = \nu\varrho = 0.2736\,\mathrm{kg/m\,s}.$$

Therefore, $\mathrm{Re} = 2$ and $\mathrm{Pr}(\nu^2/g)^{1/3}/L = 3.5$.

The following are obtained from Eqs. (5–8):

$$\overline{\mathrm{Nu}} = \begin{cases} 1.03 \text{ from Eq. (5)} \\ 1.50 \text{ from Eq. (6)} \\ 0.64 \text{ from Eq. (7)} \\ 0.24 \text{ from Eq. (8)} \end{cases} = 1.50 \text{ max},$$

$$\mathrm{Nu}_{max} = 1.50.$$

Hence heat transfer still takes place in the zone of thermal development. However, as the example demonstrates, this case arises only under extreme conditions. After all, the thickness of the film, as determined from Eq. (1), is $s = 3.6$ mm under the aforementioned conditions.

3.2 Heat Transfer During Falling-film Evaporation

The local heat transfer coefficient is defined by

$$\alpha_x = \frac{\dot{q}}{\vartheta_w - \vartheta_{sat}}. \tag{9}$$

In thermally developed flow, the entire amount of heat applied is consumed in vaporization. However, the evaporation rate in practice is usually small compared to the rate of downward liquid flow. Consequently, the film thickness and thus the heat transfer coefficient are practically constant, i.e., $\alpha \approx \alpha_x$. The heat transfer coefficient can be obtained from the evaporation rate, i.e.,

$$\alpha \approx \alpha_x = \frac{\dot{M}_v \Delta h_v}{A(\vartheta_w - \vartheta_{sat})}. \tag{10}$$

Conversely, the evaporation rate $\dot{M}_v$ can be calculated from Eq. (10) if the wall temperature ϑ_w is given and the heat transfer coefficient α is known.

If the heating rate is not too high, the liquid evaporates exclusively at the free surface of the falling film. Vapor bubbles are not yet formed on the heated surface at this stage. Since there have been comparatively few studies on nucleate boiling in falling films, the transition from convective to nucleate boiling cannot be uniquely defined. Nevertheless, as long as the difference $\Delta\vartheta$ between the temperature of the heated wall and the boiling point of the falling film does not exceed 6 K, the heating rate $\dot{q}$ has practically no effect on heat transfer to both water and refrigerants [9, 10], although nucleation does occur at smaller temperature differences.

3.2.1 Heat Transfer in Convective Boiling

The heat transfer equations for boiling at the surface of the film, i.e., convective boiling, are [1]

$$\mathrm{Nu} = \sqrt{\mathrm{Nu}_{\mathrm{lam}}^2 + \mathrm{Nu}_{\mathrm{turb}}^2}, \tag{11}$$

$$\mathrm{Nu}_{\mathrm{lam}} = 0.9\mathrm{Re}^{-1/3}, \tag{11a}$$

$$\mathrm{Nu}_{\mathrm{turb}} = 0.00622\mathrm{Re}^{0.4}\,\mathrm{Pr}^{0.65}; \quad \mathrm{Pr} < 50. \tag{11b}$$

Equation (11b) has not yet been verified by measurements for $\mathrm{Pr} > 7$, but has been found to agree well with measurements for turbulent film condensation [9]. This fact can be readily appreciated in view of the similarity that exists between the hydrodynamic relationships and the thermal boundary conditions. Consequently, a good approximation can be achieved by applying the effect of the Prandtl number on heat transfer during film condensation to that during falling-film evaporation. Thus, the validity of Eq. (11b) can be extended to $\mathrm{Pr} < 50$, as can be verified by comparing the results that it yields with those obtained from Eq. (39) in Chap. J1.

Equation (11) has also proved to be useful in the determination of heat transfer during the falling-film evaporation of water at pressures down to $p \approx 0.05$ bar ($\vartheta \approx 32°\mathrm{C}$) [9].

Equation (11) presupposes that the vapor produced exerts only a moderate shear stress on the falling film. The increase in heat transfer at higher vapor velocities has not yet been studied. A good approximation can undoubtedly be obtained by applying the effect of the gas velocity on heat transfer during condensation to that during evaporation, because – as has already been stated – falling-film evaporation and film condensation are subject to very similar laws. The following values serve as a guide in assessing the improvement in heat transfer that can be achieved in the evaporation of water:

Re_v	7,500	15,000	25,000
$\mathrm{Nu}_{\tau\varrho 0}/\mathrm{Nu}_{\tau=0}$	1.03	1.1	1.2

A more accurate calculation is presented in Chap. J1.

A thermal development zone in which the temperature profile is initially formed also exists in boiling falling films. Evaporation does not commence until the temperature field has reached the surface of the film. Aqueous films reach this stage after they have traversed a path of a few centimeters length. If the liquid is very viscous, a check should be made to determine whether the value for Nu calculated from the following form of Eq. (6) is higher than that obtained from Eq. (11):

$$\mathrm{Nu} = C_0 \sqrt[3]{\mathrm{Re}^{1/3}\,\mathrm{Pr}\left(\frac{\nu^2}{g}\right)^{1/3}} \Big/ L, \tag{6a}$$

where $C_0 = 0.608$ for ϑ_w = constant and $C_0 = 0.733$ for $\dot{q}$ = constant. If this is the case, evaporation will not be initiated along the path of length L.

Results obtained from Eqs. (11) and (6a) are presented graphically in Fig. 3, in which the parameters are the Prandtl number and $\mathrm{Pr}(\nu^2/g)^{1/3}/L$.

It has been demonstrated [9, 11] that heat transfer in falling-film evaporation can be greatly improved if tubes with longitudinal sinusoidal grooves are used instead of smooth tubes. The overall heat transfer coefficient has been increased by a factor as high as 2.5 in this case.

3.2.2 Heat Transfer in Nucleate Boiling

Significant factors in nucleate boiling are the heat flux $\dot{q}$, the roughness of the walls, the material from which the walls have been constructed, and the properties of the flowing medium itself. Heat transfer in all forms of boiling increases with the heat flux $\dot{q}$, but nucleate boiling is less desirable than the other forms, because it incurs the risk of fouling or damaged product. Fujita [12] measured heat transfer coefficients during nucleate boiling of water films on stainless steel tubes, and the value of α in $\mathrm{W/(m^2\,K)}$ that he thus determined at $\dot{q} > 1.6 \cdot 10^5\ \mathrm{W/m^2}$ was

$$\alpha = 1.24\,\dot{q}^{0.741}. \tag{12}$$

Hence α is independent of the Reynolds number for a falling film in pronounced nucleate boiling. Equation (12) yields results that are practically identical to those obtained by Bressler [13]. As opposed to this, Haase [14] determined a transition to nucleate boiling at smaller temperature differences. Therefore,

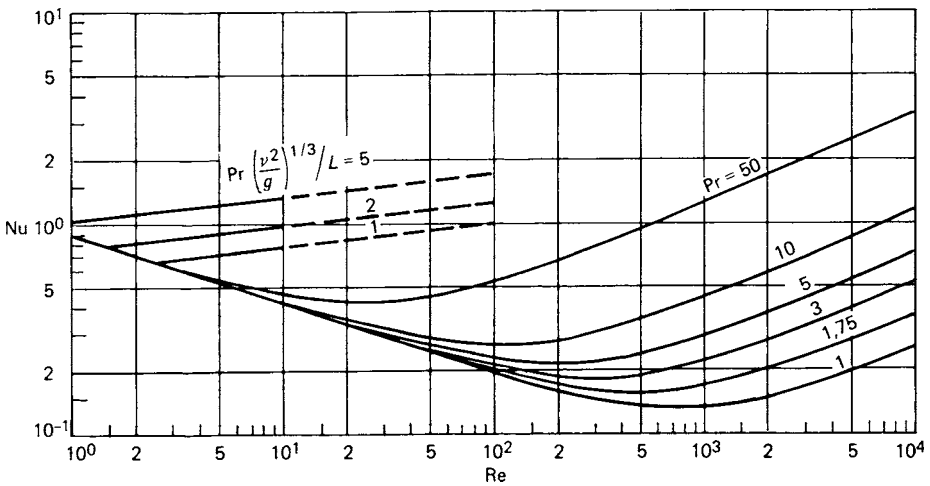

M3. Fig. 3. Nusselt number as a function of Re with Pr and $\mathrm{Pr}\,(\nu^2/g)^{1/3}/L$ as parameters in falling-film evaporation (convective boiling).

the application of Eq. (12) ought to ensure that the values of α are not overestimated in the nucleate boiling range if large temperature differences exist. Values of α calculated from Eqs. (11) and (12) are shown in Fig. 4 as a function of the heat flux $\dot{q}$ of a water film that evaporates at 100°C. A gradual transition from convective to nucleate boiling was assumed in compiling the diagram, because it was unknown whether more accurate studies exist.

In accordance with the definition, the curves for constant temperature difference $\Delta\vartheta$ in Fig. 4 are inclined at an angle of 45°. They can be adopted for the determination of the heat transfer coefficient. For instance, a value of α = 6,500 W/(m^2 K) can be read off against a temperature difference of $\Delta\vartheta$ = 15 K (between the heated wall and the falling film) and a Reynolds number of Re = 1,000 or 200; the associated heat flux is $\dot{q} = 9.5 \cdot 10^4$ W/m^2.

Struve drew up corresponding diagrams for the evaporation of Refrigerant R 11 falling films on brass tubes [10].

Example 3

An aqueous solution with a boiling point of 100°C is to be concentrated in a circulating falling-film evaporator. The film runs down the inner surfaces of the tubes, and the outer surfaces are heated by the condensation of saturated steam at a temperature of ϑ_c = 110°C. Fresh solution is fed to the evaporator at a rate of $\dot{M}_1$ = 2.0 kg/s. The tube bundle consists of 100 stainless steel tubes of 4 m length (λ = 17 W/(m K); d_i = 47 mm; d_o = 50 mm).

(a) The Reynolds number of the falling film must be Re $\geq$ 1,000 in order to ensure that all the tubes are thoroughly wetted. What must be the rate $\dot{M}_{rec}$ at which the liquid has to be recirculated in order to obtain Re = 1,000?

(b) To what extent can the solution be concentrated, i.e., at what rate $\dot{M}_2$ must the concentrate be continuously removed and what is the $\dot{M}_2/\dot{M}_1$ ratio?

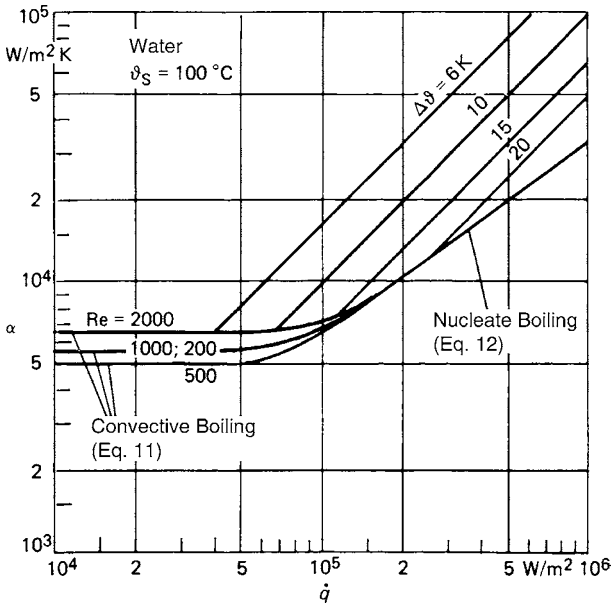

M3. Fig. 4. Heat transfer coefficient α as a function of $\dot{q}$, Re, and $\Delta\vartheta$ during nucleate and convective boiling of water films at 100°C.

The properties (for water as an approximation) can be obtained from Chap. D2. Thus,

$$\eta = 282.2 \cdot 10^{-6}\ \text{kg/m s}; \quad \text{Pr} = 1.756;$$
$$\nu = 0.294 \cdot 10^{-6}\ \text{m}^2/\text{s}; \quad \Delta h_v = 2257.3\ \text{kJ/kg};$$
$$\lambda = 0.677\ \text{W/(m K)}.$$

(a) Re $= \dot{m}/\eta = \dot{M}/z\pi d_i\eta =$ 1,000, where $\dot{M} = \dot{M}_1 + \dot{M}_{rec}$.

Hence the mass flow rate of recirculated liquid is

$$\dot{M}_{rec} = \text{Re}(z\pi d_i\eta) - \dot{M}_1$$
$$= 1{,}000(100\pi \cdot 47 \cdot 10^{-3} \cdot 282.2 \cdot 10^{-6}) - 2.0$$
$$= 2.17\ \text{kg/s}.$$

(b) The mass flow rate of liquid to be removed is

$\dot{M}_2 = \dot{M}_1 - \dot{M}_v$, where $\dot{M}_v = \dot{Q}/\Delta h_v$ and $\dot{Q} = kA(\vartheta_c - \vartheta_v)$. As in Example 1,

$$k = \left\{ \frac{1}{\bar{\alpha}_c} + \frac{d_o \ln \frac{d_o}{d_i}}{2\lambda} + \frac{d_o}{d_i \alpha_v} \right\}^{-1}. \tag{13}$$

Inserting Re = 1,000 and Pr = 1.756 in Eq. (11) gives a Nusselt number of Nu = 0.168. A value of α_v = 5,506 W/(m^2 K) is then obtained from the figures for the properties.

In order to determine the heat transfer coefficient on the condensate side, the corresponding temperature difference $\Delta\vartheta_c$ must be estimated and approximate calculations must be made as is indicated in Table 1.

Hence the temperature difference is obtained by the second approximation. Consequently,

$$\dot{Q} = 1.389 \cdot 10^6\ \text{W}; \quad \dot{M}_2 = 1.377\ \text{kg/s};$$
$$\dot{M}_v = 0.623\ \text{kg/s}; \quad \dot{M}_2/\dot{M}_1 = 0.6886.$$

Additional Check:
Since the temperature difference on the vaporization side is $\Delta\vartheta$ = 4 K, nucleate boiling does not occur. The Reynolds number for the vapor at the tube outlet is

$$\text{Re}_v = \frac{4\dot{M}_v}{z\varrho_v\pi d_i \nu_v} = \frac{4 \cdot 0.623}{100 \cdot 0.826\pi \cdot 47 \cdot 10^{-3} \cdot 15.28 \cdot 10^{-6}}$$
$$= 13{,}372.$$

Therefore, the heat transfer coefficient α_v ought to be, on an average, about 5% higher.

M3. Table 1. Determination of temperature on the condensate side

	First approximation	Second approximation
$\Delta\vartheta_c = \vartheta_c - \vartheta_{w,c}$	5 K	3.75 K
Thus ϑ_{cm} from Subchap. J1.1 and $(\text{Ph}^*\text{Ga}^{1/3}/\text{Pr})$	107.5°C	108°C
	1,179	884.6
$\text{Nu} = 0,9245^*\text{Re}^{-1/3}$ $= 0,9428(\text{Ph}^*\text{Ga}^{1/3}/\text{Pr})^{1/4}$	0.161	0.173
$\bar{\alpha}_c$	5,538 W/(m^2 K)	5,951 W/(m^2 K)
k from Eq. (13)	2,151.6 W/(m^2 K)	2,211 W/(m^2 K)
Check: $\Delta\vartheta_c = k/\alpha_c\Delta\vartheta_c$	3.88	3.72

4 Film Breakdown

Heated surfaces over which a falling film descends must be completely wetted. If the liquid film is interrupted, heat transfer will be greatly improved as a result of contact between the vapor and the wall. The following mechanisms lead to breakdown of the film.

(a) Dry spots may be formed as a consequence of inadequate supply of liquid. The governing factors are the wetting angle and the surface tension. A comprehensive review of the relevant mathematical models has been compiled by Ganić and Mastanaiah [15].
(b) Surface tension gradients caused by temperature and concentration gradients may give rise to channeling by the Marangoni effect, which is most likely to occur in mixtures.
(c) Vapor bubbles formed on the wall may cause the liquid to be entrained in the bulk of the vapor stream. As a consequence, the mass flux of liquid in the film is reduced, and dry spots may be formed.
(d) The wall temperature must always remain below a certain critical value in order to ensure that the surface is not covered by vapor as a result of the Leidenfrost effect. Normally, this effect is insignificant in falling-film evaporators, owing to their low temperature differences.

An experimental and theoretical study of these phenomena by Fujita and Ueda [16, 17] was restricted to water. Mechanisms (a) and (b) mainly occur in subcooled films that do not evaporate. They are difficult to describe, because the main parameters, i.e., the contact angle and the local surface tension gradients, do not permit easy measurement. Values relating to the breakdown of subcooled water films can be obtained from Fig. 5. Pure saturated liquids permit more effective wetting, because they do not allow significant surface tension gradients to occur in the film. Film breakdown is primarily caused by nucleation, i.e., mechanism (c).

In the experiments, permanently dry spots were formed at the lower end of the tube for $\dot{\Gamma} \leq 0.01 - 0.02\,\mathrm{kg/ms}$ (cf. Fig. 6) corresponding to a Reynolds number $\dot{\Gamma}/\mu$ of 140–180. A criterion for dryout is

$$B_F = \dot{\Gamma}\,\lambda/(\dot{q}\,L). \tag{14}$$

Dryout can be avoided in the evaporation of water if

$$B_F > 1.5. \tag{15}$$

Mixtures of ethylene or propylene glycol with water do not dry out unless B_F falls below a value of 5–35.

A simple equation for estimating the temperature difference required for the Leidenfrost effect has been derived from the measurements by Cichelli and Bonilla [19, 20], i.e.,

$$\begin{aligned}\Delta T_L &= T\mathrm{w}_L - T_{sat} \\ &= 0.555\left[52(1-p^*) + 0.04/p^{*2}\right],\end{aligned} \tag{16}$$

where $T\mathrm{w}_L$ is the wall temperature at which the Leidenfrost effect occurs and $p^* = p/p_c$.
For safety reasons, the actual wall temperature should be less than

$$\Delta T = T_w - T_{sat} = 0.6\Delta T_L \tag{17}$$

In the food and pharmaceutical industry, vessels are very often cleaned by rinsing the inner surface with caustic solution, e.g., 1 N NaOH, at 60–80°C. This process is called cleaning-in-place (CIP). It requires a completely wetted surface. A good practical number for that purpose is a specific flow rate of 0.5 l/(m s).

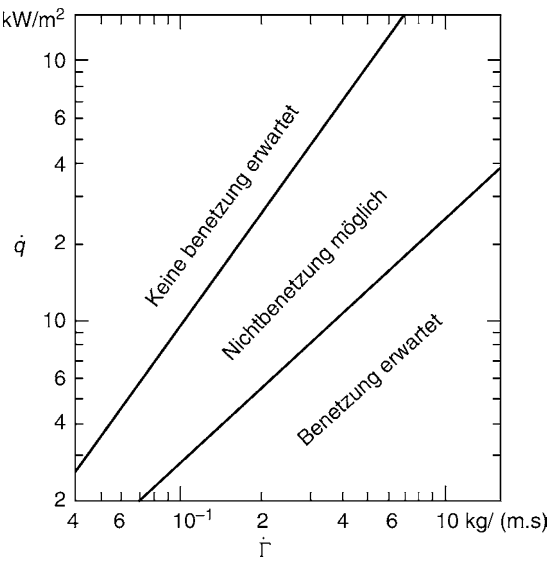

M3. Fig. 5. Breakdown on subcooled films in water; subcooling 20–50°C [17, 18].

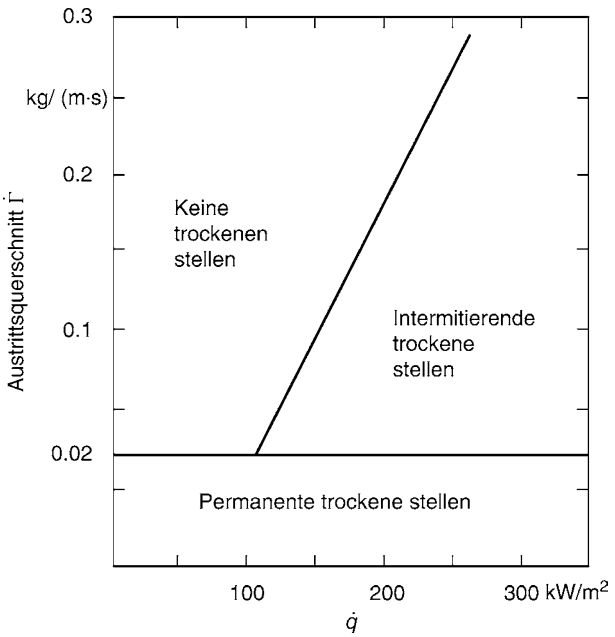

M3. Fig. 6. Breakdown of saturated water films at 99.5°C [17]; rising vapor current and downward falling film on a tube of 46-mm outer diameter and 1,000 mm length.

5 Bibliography

1. Schnabel G, Schlünder EU (1980) Wärmeübergang von senkrechten Wänden an nichtsiedende und siedende Rieselfilme. Verfahrenstechnik 14(2):79–83
2. Nußelt W (1916) Die Oberflächenkondensation des Wasserdampfes. VDI-Zeitschrift 60:542–575
3. Kapitza PL (1948, 1949) Wellenströmung der dünnen Schichten einer viskosen Flüssigkeit. J Exp Theoret Phys (UdSSR) 18(1):3–18; 19(2):105–120
4. Brauer H (1956) Strömung und Wärmeübergang bei Rieselfilmen. VDI-Forsch., Heft 457
5. Kosky P (1971) Thin liquid films under simultaneous shear and gravity forces. Int J Heat Mass Transfer 14:1220–1224
6. Kutadeladze S Fundamentals of heat transfer. Edward Arnold, London.
7. Portalsky S (1963) Studies of falling liquid film flow. Chem Eng Sci 18:787–804
8. Bays GS, McAdams WH (1937) Heat transfer coefficients in falling film heaters. Ind Eng Chem 29(11):1240–1246
9. Schnabel G (1980) Bestimmung des örtlichen Wärmeüberganges bei der Fallfilmverdampfung und Kondensation an gewellten Oberflächen zur Auslegung von Hochleistungsverdampfern. Diss. Univ. Karlsruhe
10. Struve H (1969) Der Wärmeübergang an einem verdampfenden Rieselfilm. VDI-Forsch.-Heft 534
11. Schnabel G, Gnielski V, Schlünder EU (1981) Örtliche Wärmeübergangskoeffizienten bei der Verdampfung von Rieselfilmen an senkrechten, profilierten Oberflächen. Chemie-Ing-Technik 53(3):187–190
12. Fujita T, Ueda T (1978) Heat transfer to falling liquid film and film breakdown. Int J Heat Mass Transfer 21:97–113
13. Bressler R (1958) Versuche über die Verdampfung von dünnen Flüssigkeitsfilmen. VDI-Z. 100:630–638
14. Haase B (1970) Der Wärmeübergang am siedenden Rieselfilm. Chem Technik 22(5):283–287.
15. Ganić EN, Mastanaiah K (1981) Hydrodynamics and heat transfer in falling film flow, low Reynolds number flow heat exchangers. Hemisphere Publ., pp 487–528
16. Fujita T, Ueda T (1978) Heat transfer to falling liquid films and film breakdown-I. Subcooled liquids films. Int J Heat Mass Transfer 21:97–108
17. Fujita T, Ueda T (1978) Heat transfer to falling liquid films and film breakdown-II. Saturated films with nucleate boiling. Int J Heat Mass Transfer 21:109–118
18. Ganić EN, Roppo MN (1980) A note on heat transfer to falling liquid films on vertical tubes. Lett Heat Mass Transfer 7(2):145–154
19. Cichelli MT, Bonilla CF (1945) Heat transfer to falling liquids under pressure. Trans. AIChE 41:755
20. Chen JC, Palen JW (1984) Two-phase flow and heat transfer in process equipment. AIChE-Today-Series. Am Inst Chem Eng

M4 Heat Transfer to Non-Newtonian Fluids

Manfred H. Wagner
Technische Universität Berlin, Berlin, Germany

1 Introduction

The flow of many liquids, for example, solutions, polymer melts, and concentrated dispersions, may differ considerably from Newtonian fluids. Knowledge of the rheology of non-Newtonian fluids is essential in the design of processing machinery and pipelines. However, the multiplicity of rheological systems and the complexity of the behavior of the fluids render it impossible to quote laws of general validity that describe the flow and rheological characteristics under any given condition. Recourse must therefore be taken to a description of the rheological behavior under the conditions that relate to those in practice. A case in question is the flow through pipes of non-Newtonian fluids, many of which are very viscous. It concerns hydrodynamically developed laminar flow and is the subject to which the analytical methods discussed here have been restricted.

The subjects dealt with are pressure drop (under nonisothermal conditions) and heat transfer during flow through circular tubes and rectilinear slits. Relationships for tubes of different geometries are considered in [1]. Heat transfer in turbulent flow is discussed in [2–4]. The following assumptions are made in deriving the relationships discussed in this contribution:

1. The flow is laminar and completely hydrodynamically developed.
2. The liquid adheres to the wall.
3. Thermal conductivity λ, specific heat c_p, and the density ρ of the liquid remain constant.
4. The temperature of the tube wall δ_w remains constant during heat transfer.
5. The rise in temperature due to viscous dissipation can be neglected. The maximum mean dissipative rise in temperature undser adiabatic boundary conditions $\Delta\delta_{ad}$ is

$$\Delta\delta_{ad} = \frac{\Delta p}{\rho c_P} \tag{1}$$

Dissipation can be ignored if $\beta\ \Delta\delta_{ad} < 0.1$, where β is the temperature coefficient for the liquid (cf. Eq. (13)). No reliable analytical correlations are known for heat transfer in a flow with considerable dissipation, particularly since the conventional definition of an average Nusselt number is pointless in this case [5]. A review on various studies of the subject is presented in [6].

2 Definition of Heat Transfer Coefficient

The average heat transfer coefficient α over a length l of tube is defined by

$$\dot{q} = \alpha\,\Delta\delta_{log} \tag{2}$$

$\Delta\delta_{log}$ is the logarithmic temperature difference and is given by

$$\Delta\delta_{log} = \frac{(\delta_w - \delta_i) - (\delta_w - \delta_o)}{\ln\left(\frac{(\delta_w-\delta_i)}{(\delta_w-\delta_o)}\right)} \tag{3}$$

where δ_i is the inlet temperature (which is constant over the entire cross-section at the inlet), δ_o is the average outlet temperature of the liquid, and δ_w is the constant wall temperature. The average Nusselt number is given by Eq. (4); and the Graetz number, by Eq. (5):

$$\mathrm{Nu} = \frac{\alpha d}{\lambda} \tag{4}$$

$$\mathrm{Gz} = \frac{wd^2}{al}\mathrm{Re.Pr}\frac{d}{l} = \mathrm{Pe}\frac{d}{l} \tag{5}$$

where w is the average flow velocity in the axial direction, d is the inner diameter of the tube or the slit width, and a is the diffusivity.

The average outlet temperature is obtained from a simple heat balance, that is,

$$\frac{\delta_w - \delta_o}{\delta_w - \delta_i} = e^{-4\frac{\mathrm{Nu}}{\mathrm{Gz}}} \tag{6}$$

3 Scalar Flow Rule for Steady-state Stratified Flow

The term "non-Newtonian fluids" embraces nonlinear/purely viscous and viscoelastic liquids. Quantitative rheological laws

VDI-GVC (ed.), *VDI Heat Atlas*, DOI 10.1007/978-3-540-77877-6_53,

generally define a functional relationship between the stress in the material and the complete prior history of strain. For steady-state stratified flow, for example, hydrodynamically developed duct flow, these laws can be reduced to a scalar flow rule, that is, to a (in general nonlinear) relationship between the velocity gradient, namely the shear rate $\dot{\gamma}$ and the shear stress τ.

The scalar flow rule can be determined by use of capillary, Couette, cone-and-plate, and other rheometers that allow realization of steady-state stratified flow [7]. The flow curve $\dot{\gamma}(\tau)$ and the viscosity function $\eta(\dot{\gamma}) = \tau(\dot{\gamma})/\dot{\gamma}$ for non-Newtonian liquids are nonlinear; but, if plotted on a log–log scale, sections of them can be described by the *Ostwald-de-Waele* power-law equations:

$$\dot{\gamma} = \Phi\tau^m \tag{7}$$

$$\eta = \frac{\tau}{\dot{\gamma}} = \Phi^{-\frac{1}{m}}\dot{\gamma}^{\frac{1}{m}-1} \tag{8}$$

The flow index $m = 1$ corresponds to Newtonian flow. Polymer solutions and melts display pseudo-plasticity, that is, the rate of shear increases over-proportionally with the shear stress, and the flow index is typically in a range of $1 < m < 5$. Shear thickening, that is, an index of $m < 1$, is observed in some dispersions. Equations. (7) and (8) may also be expressed in the following forms [5]:

$$\tau = K\dot{\gamma}^n \tag{9}$$

$$\eta = \frac{\tau}{\dot{\gamma}} = K\dot{\gamma}^{n-1} \tag{10}$$

The following relationship exists between the fluidity Φ and the consistency factor K:

$$K = \Phi^{-\frac{1}{m}} \tag{11}$$

The following applies for the flow index:

$$n = \frac{1}{m} \tag{12}$$

The index m is largely independent of temperature, but an exponential relationship exists for the fluidity Φ through the temperature shift factor a_T, which is given by

$$a_T = e^{-\beta(\delta-\delta_{ref})} \tag{13}$$

The exponential relationship concerned is

$$\Phi = \Phi(\delta) = \frac{\Phi(\delta_{ref})}{a_T} = \frac{\Phi_{ref}}{a_T} \tag{14}$$

Departure from isothermal conditions is described by a temperature weighting factor θ, which is defined by

$$\theta = \frac{\beta}{m}(\delta_w - \delta_i) \tag{15}$$

or, by use of Eqs. (13) and (14):

$$\theta = \frac{1}{m}\ln\left(\frac{\Phi_w}{\Phi_i}\right) \tag{16}$$

Alternatively, the dual relationship to Eq. (7) may be used, that is,

$$\tau = K(\delta_{ref})\dot{\gamma}^n = K_{ref}\dot{\gamma}^n \tag{17}$$

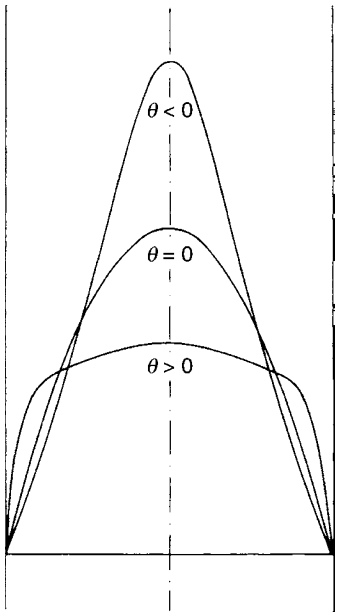

M4. Fig. 1. Velocity distribution during pipe flow: Temperature-independent viscosity ($\theta = 0$), heating ($\theta > 0$), and cooling ($\theta < 0$).

In this case, θ is given by

$$\theta = \ln\left(\frac{K_i}{K_w}\right) \tag{18}$$

A qualitative interpretation of the effect of θ on the pressure drop and heat transfer is presented in Fig. 1. If the viscosity of the liquid does not change with temperature ($\theta = 0$, since $\beta = 0$), the velocity and temperature fields are decoupled. The index m entails that the velocity field can be represented by a parabola of the order $m + 1$, and is independent of the direction of heat flow. If a real liquid is heated ($\theta > 0$), the viscosity decreases in the vicinity of the wall. As a result, the velocity gradient increases near the wall and decreases in the center of the duct, and the velocity field tends towards that for plug flow. By virtue of the higher shear rate at the wall, heat transfer is enhanced, and the pressure drop as compared to isothermal pipe flow at a temperature δ_i is reduced. As thermal development proceeds, the pressure gradient finally attains the value of isothermal flow at a temperature δ_w, and the velocity field again corresponds to a parabola of the order $m + 1$. The same applies *mutatis mutandis* to the cooling of a real liquid ($\theta < 0$). Since the viscosity is higher in the vicinity of the wall, the rate of shear at the wall decreases. As a consequence, the pressure drop as compared to isothermal pipe flow at a temperature δ_i, is increased, and heat transfer is reduced. In the light of these considerations, Kwant [8–11] made a detailed study of heat transfer to non-Newtonian liquids and presented his results in the form of simple regressions. The following discussion is largely in line with his ideas on the subject.

4 Pressure Drop and Heat Transfer for Fluids with Temperature-Independent Viscosity

Although Eq. (7) or Eq. (9) fits only certain sections of the experimentally determined flow curve, it allows the pressure

drop to be predicted with sufficient accuracy for engineering purposes, because the pressure drop largely depends on the rate of shear near the wall. The pressure drop in a length l of duct can be calculated from the Hagen-Poiseuille law, that is,

For the pipe with circular cross-section:

$$\frac{\Delta p}{l} = \frac{4}{d}\left[\frac{2(m+3)}{\Phi}\frac{w}{d}\right]^{\frac{1}{m}} \tag{19}$$

For the rectilinear slit:

$$\frac{\Delta p}{l} = \frac{2}{d}\left[\frac{2(m+2)}{\Phi}\frac{w}{d}\right]^{\frac{1}{m}} \tag{20}$$

If the viscosity does not change with temperature, the average Nusselt number for non-Newtonian liquids with flow indices of $1 \le m \le 10$ can be calculated from the following approximate relationships [9, 11]:

Pipe with circular cross-section

$$\mathrm{Gz} < 30\text{: } \mathrm{Nu}_0 = 3.66m^{0.13} + 0.050\,\mathrm{Gz}\,(\text{accuracy} \pm 2\%) \tag{21}$$

$$\mathrm{Gz} > 30\text{: } \mathrm{Nu}_0 = 1.018(m+3)^{1/3}\mathrm{Gz}^{1/3}\,(\text{accuracy} \pm 5\%); \tag{22}$$

Rectilinear slit

$$\mathrm{Gz} < 100\text{: } \mathrm{Nu}_0 = 3.77m^{0.13} + 0.0053\,\mathrm{Gz}\,(\text{accuracy} \pm 3\%), \tag{23}$$

$$\mathrm{Gz} > 100\text{: } \mathrm{Nu}_0 = 1.018(m+2)^{1/3} + \mathrm{Gz}^{1/3}\,(\text{accuracy} \pm 5\%). \tag{24}$$

More accurate Nusselt numbers derived by numerical analysis are given by Kwant [8].

5 Pressure Drop for Fluids with Temperature-Dependent Viscosity

The reference state that will be used in the case of temperature-dependent viscosity is isothermal pipe flow **after** complete thermal development, that is, at temperature δ_w. The relative pressure drop φ is defined as the ratio of the pressure drop in nonisothermal pipe flow Δp_θ to that in the corresponding isothermal pipe flow Δp_0 according to Eqs. (19) or (20) for a fluid characterized by fluidity $\Phi(\delta_w) = \Phi_w$, that is,

$$\varphi = \frac{\Delta p_\theta}{\Delta p_0} \tag{25}$$

Likewise, the relative shear rate at the wall Γ is the ratio of the shear rate in nonisothermal pipe flow $\dot{\gamma}_\theta$ to that in the corresponding isothermal pipe flow $\dot{\gamma}_0$ after complete thermal development, that is,

$$\Gamma = \frac{\dot{\gamma}_\theta}{\dot{\gamma}_0} \tag{26}$$

The following approximate relationships exist for φ [9, 11]:

Pipe with circular cross-section

$$\varphi = (0.6\mathrm{Gz})^{A'\theta}$$
$$(\text{limits of validity: } 2.5 < \mathrm{Gz} < 1,000; 1 \le m \le 5), \tag{27}$$

Heating ($\theta > 0$)

$$A' = \frac{2A}{m+1} \tag{28}$$

M4. Table 1. A (regression coefficient) for circular tubes as a function of θ and m

m \ θ	1	1.33	2	3	5
1	0.105	0.115	0.129	0.140	0.141
2	0.100	0.107	0.105	0.094	0.090
3	0.095	0.101	0.086	0.066	0.062

M4. Table 2. A (regression coefficient) for rectilinear gaps as a function of θ and m

m \ θ	1	1.33	2	3	5
1	0.105	0.109	0.123	0.134	0.132
2	0.100	0.102	0.100	0.088	0.070
3	0.095	0.096	0.082	0.061	0.049

A is a weak function of θ and m (cf. Table 1). As a first approximation, $A \approx 0.1$

Cooling ($\theta < 0$)

$$A' = 0.125 \quad \text{for } -2.5 < \theta < 0, \tag{29}$$

$$A' = 0.135 \quad \text{for } \theta < -2.5; \tag{30}$$

Rectilinear slit

$$\varphi = (1.8\mathrm{Gz})^{A'\theta} \tag{31}$$

(limits of validity: $1.1 > \mathrm{Gz} > 1,000; 1 \le m \le 5$),

Heating ($\theta > 0$):

$$A' = \frac{2A}{m+1} \tag{32}$$

A is a week function of θ and m (cf. Table 2). As a first approximation, $A \approx 0.1$.

Cooling ($\theta < 0$):

$$A' = 0.110 \quad \text{for } -2.0 < \theta < 0, \tag{33}$$

$$A' = 0.116 \quad \text{for } \theta < -2.0 \tag{34}$$

The relative shear rate Γ_o at the outlet is given by

$$\Gamma_o = [(1 - A'\theta)\varphi]^m \tag{35}$$

6 Heat Transfer for Fluids with Temperature-Dependent Viscosity

The following relationships exist between the Nusselt number Nu_θ and the relative shear rate Γ_o at the outlet, as defined by Eq. (35):

Pipe with circular cross-section

$$\frac{\mathrm{Nu}_\theta}{\mathrm{Nu}_0} = 1 + 0.271\,\ln\Gamma_o + 0.023(\ln\Gamma_o)^2 \tag{36}$$

Rectilinear gap

$$\frac{\mathrm{Nu}_\theta}{\mathrm{Nu}_0} = 1 + 0.238\,\ln\Gamma_o + 0.0224(\ln\Gamma_o)^2 \tag{37}$$

Example

An aqueous polymer solution flows through a circular tube with

Tube diameter	$d = 0.01$ m
Length of tube	$l = 10$ m
Average flow velocity	$w = 2$ m/s
Inlet temperature	$\delta_i = 20°C$
Pipe wall temperature	$\delta_w = 80°C$
Fluidity	$\Phi(\delta_i) = \Phi_i = 3{\cdot}10^{-2}$ Pa^{-m}s^{-1}
Fluidity	$\Phi(\delta_w) = \Phi_w = 1.5$ Pa^{-m}s^{-1}
Flow index	$m = 2.0$
Diffusivity	$a = 1.56{\cdot}10^{-7}$ m^2/s
Specific heat capacity	$c_p = 4.2{\cdot}10^3$ J/kgK
Density	$\rho = 10^3$ kg/m^3.

The first step is to calculate the pressure drop Δp_0 and the Nusselt number Nu_0 on the assumption of temperature-independent viscosity or fluidity $\Phi(\delta_w) = \Phi_w$ Applying Eq. (19) gives

$$\Delta p_0 = \frac{4l}{d}\left[\frac{2(m+3)}{\Phi_w}\frac{w}{d}\right]^{\frac{1}{m}} = \frac{4\cdot 10}{0.01}\left[\frac{2(2+3)}{1.5}\frac{2}{0.01}\right]^{\frac{1}{2}}$$
$$= 1.46\cdot 10^5 \mathrm{N/m^2} = 1.46\,\mathrm{bar}.$$

The Graetz number, as determined from Eq. (5), is

$$Gz = \frac{wd^2}{al} = \frac{2\cdot 0.01^2}{1.56\cdot 10^{-7}\cdot 10} = 128.2.$$

Applying Eq. (22) for the Nusselt number gives

$$Nu_0 = 1.018(2+3)^{1/3}Gz^{1/3} = 8.78.$$

The outlet temperature δ_o is obtained from Eq. (6), that is,

$$\delta_o = \delta_w - (\delta_w - \delta_i)\ exp(-4\frac{Nu_0}{Gz})$$
$$= 80°C - (60K)\exp\left(-4\frac{8.78}{128.2}\right) = 34.4°C$$

The next step is to determine the changes caused by a temperature-dependent viscosity or fluidity. The temperature weighing factor θ is obtained from Eq. (16), that is,

$$\theta = \frac{1}{m}\ln\left(\frac{\Phi_w}{\Phi_i}\right) = \frac{1}{2}\ln\left(\frac{1.5}{3\cdot 10^{-2}}\right) = 1.956.$$

Linear interpolation in Table 1 gives $A = 0.106$ for $\theta = 1.956$ and $m = 2$. Inserting in Eq. (27) for the relative pressure drop φ gives

$$\varphi = \frac{\Delta p_\theta}{\Delta p_0} = (0.6Gz)^{A'\theta} = (0.6Gz)^{\frac{2A}{m+1}\theta}$$
$$= (0.6\cdot 128.2)^{\frac{2\cdot 0.106}{2+1}1.956} = (0.6\cdot 128.2)^{0.138} = 1.823.$$

The actual pressure drop is therefore

$$\Delta p_\theta = \varphi\Delta p_0 = 1.823\cdot 1.46 = 2.66\,\mathrm{bar}.$$

The pressure drop Δp_θ is 82% higher than the pressure drop in isothermal pipe flow at temperature δ_w and fluidity Φ_w.

Obviously, the pressure drop Δp_θ is much less than the pressure drop Δp for isothermal pipe flow at temperature δ_i and fluidity Φ_i, which is obtained from Eq. (19) as

$$\Delta p = \frac{4l}{d}\left[\frac{2(m+3)}{\Phi_i}\frac{w}{d}\right]^{\frac{1}{m}} = \left[\frac{\Phi_w}{\Phi_i}\right]^{\frac{1}{m}}\Delta p_0 = e^\theta\Delta p_0$$
$$= 7.07\cdot 1.46\,\mathrm{bar} = 10.32\,\mathrm{bar}.$$

The relative shear rate Γ_o at the outlet is obtained from Eq. (35):

$$\Gamma_o = [(1 - A'\theta)\varphi]^m = [(1 - 0.138)1.823]^2 = 2.468.$$

The Nusselt number can then be calculated from Eq. (36), that is,

$$Nu_\theta = Nu_0[1 + 0.271\cdot\ln\Gamma_0 + 0.023(\ln\Gamma_0)^2]$$
$$= 8.78\left[1 + 0.271\cdot\ln 2.468 + 0.023(\ln 2.468)^2\right]$$
$$= 8.78\cdot 1.264 = 11.09$$

The actual Nusselt number Nu is therefore 26% higher than the value obtained on assuming that the viscosity does not depend on temperature. Accordingly, the actual temperature at the outlet, as determined from Eq. (6), is

$$\delta_{o,\theta} = \delta_w - (\delta_w - \delta_i)\ \exp\left(-4\frac{Nu_0}{Gz}\right)$$
$$= 80°C - (60K)\exp\left(-4\frac{11.09}{128.2}\right) = 37.6°C.$$

The effect of dissipation can be estimated from Eq. (1). Under adiabatic boundary conditions, the maximum rise in temperature caused by dissipation is

$$\Delta\delta_{ad} = \frac{\Delta p_0}{\rho c_p} = \frac{2.66\cdot 10^5}{10^3\cdot 4.2\cdot 10^3} = 0.06K.$$

Dissipation can therefore be neglected in this example.

7 Symbols

a	Diffusivity (m^2/s)
A	Regression coefficient (Tables 1 and 2)
A'	Regression coefficient (Eqs. 28–30) and (32–34))
a_T	Temperature shift factor
c_p	Specific heat capacity (J/kg K)
d	Inner pipe diameter; gap width (m)
Gz	Greatz number (Eq. (5))
K	Consistency factor (Pas^n)
K_i	Consistency factor at temperature δ_i(Pas^n)
K_w	Consistency factor at temperature δ_w (Pas^n)
K_{ref}	Consistency factor at reference temperature δ_{ref} (Pas^n)
l	Length of pipe (m)
m	Flow index
n	Flow index (Eq. (12))
Nu	Nusselt number
Nu_θ	Nusselt number that allows for the dependence of viscosity on temperature
Nu_0	Nusselt number based on the assumption that the viscosity does not change with temperature
Δp N/mm^2	Pressure drop
Δp_θ N/mm^2	Pressure drop that allows for the dependence of viscosity on temperature
Δp_0 N/mm^2	Pressure drop in isothermal pipe flow at temperature δ_w for a fluid characterized by fluidity $\Phi(\delta_w) = \Phi_w$

Pe	Péclet number ($\mathrm{Pe} = \frac{wd}{a}$)
Pr	Prandtl number ($\mathrm{Pr} = \eta_r c_p/\lambda$)
q	Heat flux ($\mathrm{W/m^2}$)
Re	Reynolds number ($\mathrm{Re} = \rho\ wd/\eta_r$)
w	Mean axial flow velocity (m/s)
α	Heat transfer coefficient ($\mathrm{W/m^2K}$)
β	Temperature coefficient ($\mathrm{K^{-1}}$)
$\dot{\gamma}$	Rate of shear ($\mathrm{s^{-1}}$)
$\dot{\gamma}_\theta$	Shear rate at wall with due allowance for the dependence of viscosity on temperature ($\mathrm{s^{-1}}$)
$\dot{\gamma}_0$	Shear rate at wall in isothermal pipe flow at temperature δ_w for a fluid characterized by fluidity $\Phi(\delta_w) = \Phi_w(\mathrm{s^{-1}})$
Γ	Relative shear rate
Γ_o	Relative shear rate at outlet
φ	Relative pressure drop
Φ	Fluidity ($\mathrm{Pa^{-m}s^{-1}}$)
Φ_i	Fluidity at temperature δ_i ($\mathrm{Pa^{-m}s^{-1}}$)
Φ_w	Fluidity at temperature δ_w($\mathrm{Pa^{-m}s^{-1}}$)
Φ_{ref}	Fluidity at the reference temperature δ_{ref} ($\mathrm{Pa^{-m}s^{-1}}$)
λ	Thermal conductivity (W/mK)
η_r	Representative kinematic viscosity ($\mathrm{Pas\ m^{-2}}$)
ρ	Density ($\mathrm{kg/m^3}$)
τ	Shear stress ($\mathrm{N/m^2}$)
θ	Temperature weighting factor (Eq. (15))
δ	Temperature (°C)
δ_i	Inlet temperature (°C)
δ_o	Mean outlet temperature (°C)
δ_w	Temperature of pipe wall (°C)
δ_{ref}	Reference temperature (°C)
$\Delta\delta_{ad}$	Rise in temperature due to dissipation under adiabatic boundary conditions (K)
$\Delta\delta_{log}$	Logarithmic temperature difference (Eq. (3)) (K)

8 Bibliography

1. Lawal A, Mujumdar AS (1989) Laminar duct flow and heat transfer to purely viscous non-Newtonian fluids. In: Mashelkar RA, Mujumdar AS, Kamal R (eds) Transport phenomena in polymeric systems. Ellis Horwood Lim, Chichester, pp. 352/443
2. Chmiel H (1971) Wärmeübertragung in der turbulenten Rohrströmung viskoleastischer Flüssigkeiten. Diss. Tech. Univ. of Aachen
3. Chmiel H, Rautenbach R, Schümmer P (1972) Zur Theorie des Wärmeübergangs in der turbulenten Rohrströmung viskoelastischer Flüssigkeiten. Chem Ing Techn 44:543/45
4. Dimant Y, Poreh M (1976) Heat transfer in flows with drag reduction. Adv Heat Transfer 12:77/113
5. Stephan K (1967) Wärmetransport in viskosen nicht-Newtonschen Flüssigkeiten. Chem Ing Techn. 39:243/50
6. Warren RC Viscous heating. In: Collyer AA and Clegg DW (eds) Rheological measurement. Elsevier Applied Science, London, pp. 119/149
7. Dealy JM (1982) Rheometers for molten plastics. Van Nostrand Reinhold, New York
8. Kwant PB (1971) Non-isothermal laminar flow. Diss. Tech. Univ. of Delft
9. Kwant PB, Zwaneveld A, Dijkstra FC (1973) Non-isothermal laminar pipe flow – I. Theoretical Chem Eng Sci 28:1303/16
10. Kwant PB, Fierens RHE, van der Lee A (1973) Non-isothermal laminar pipe flow – II. Experimental Chem Eng Sci 28:1317/30
11. Kwant PB, van Ravenstein Th.NM (1973) Non-isothermal laminar channel flow. Chem Eng Sci 28:1935/50

M5 Heat Transfer in Fluidized Beds

Holger Martin
Karlsruher Institute für Technologie (KIT), Karlsruhe, Germany

1 Range of Existence of Fluidization and Bed Expansion

In order to fluidize a particulate solid by an upward-flowing gas or liquid, the fluid velocity u (i.e., the volumetric flow-rate divided by the total cross-section) must be in the range between the minimum fluidization velocity, u_{mf}, and the terminal velocity, u_t:

$$u_{mf} < u < u_t. \tag{1}$$

The two limits in Eq. (1) define the range of existence of a fluidized bed. The limiting velocities are obtained from force (or momentum) balances as

$$\frac{u_{mf}\,d}{\nu} \equiv \mathrm{Re}_{mf} = \mathrm{Re}_{mf}(\mathrm{Ar}, \psi_{mf}), \tag{2}$$

$$\frac{u_t\,d}{\nu} \equiv \mathrm{Re}_t = \mathrm{Re}_t(\mathrm{Ar}), \tag{3}$$

where ψ_{mf} is the bed voidage at minimum fluidization (practically often between 0.4 and 0.7) and Ar is the Archimedes number $\mathrm{Ar} \equiv g d^3 \rho(\rho_P - \rho)/\eta^2$. For spherical monosized particles Eq. (2) becomes

$$\mathrm{Re}_{mf} = 42.9(1-\psi_{mf})\left(\sqrt{1 + \frac{\psi_{mf}^3}{(1-\psi_{mf})^2}\frac{\mathrm{Ar}}{3{,}214}} - 1\right), \tag{2a}$$

while (Eq. 3), for homogeneous fluidization, becomes

$$\mathrm{Re}_t = 18\left(\sqrt{1 + \frac{1}{9}\sqrt{\mathrm{Ar}}} - 1\right)^2, \quad \mathrm{Ar} < 2 \cdot 10^{10} \tag{3a}$$

equal to the terminal velocity of a single particle.

For heterogeneous, bubbling fluidization, the velocity may be greater than the single-particle values from Eq. (3a). According to Reh [1], this can be approximated by

$$\mathrm{Re}_{t(\mathrm{hetero})} \approx \sqrt{\frac{4}{3}\mathrm{Ar}} \quad \text{if } \mathrm{Re}_{t(\mathrm{hetero})} > \mathrm{Re}_t. \tag{3b}$$

Bed expansion, for homogeneous fluidization can be approximately calculated from

$$\frac{u}{u_t} = \frac{\mathrm{Re}}{\mathrm{Re}_t} = \psi^n \quad \text{with} \quad n = \frac{\ln\left(\frac{\mathrm{Re}_{mf}}{\mathrm{Re}_t}\right)}{\ln\ \psi_{mf}}. \tag{4}$$

By local measurements in fluidized beds, Bakker and Heertjes [2] have found that the gas volume fraction, ψ, within the range of the initial bed height ($z < L_{mf}$), is more or less independent of z for any given gas velocity, while it increases exponentially with z (up to 1) for $z > L_{mf}$. In the lower range ($z < L_{mf}$) the average gas volume fraction increases linearly with gas velocity. For this range a linear bed expansion equation, therefore, should approximately describe the otherwise quite complex situation.

$$\psi \approx \psi_{mf} + (1-\psi_{mf})\frac{u-u_{mf}}{u_t-u_{mf}}. \tag{4a}$$

2 Fluid-to-Particle Heat Transfer in Fluidized Beds

2.1 Definition of the Heat Transfer Coefficient

The heat transfer coefficient, α, between fluid and particles in a fluidized bed is defined as

$$\alpha \equiv \frac{\dot{Q}_{(f-P)}}{A(T_f - T_{P,O})_{av}}, \tag{5}$$

where $\dot{Q}_{(f-P)}$ is the total heat flow transmitted from the fluid to the particle surface, A. The average temperature difference, $(T_f - T_{P,O})_{av}$, between the fluid and the particle surface is the

VDI-GVC (ed.), *VDI Heat Atlas*, DOI 10.1007/978-3-540-77877-6_54,

logarithmic mean temperature difference if $T_{P,O}$ is constant and the fluid passes through the particles in plug flow (no backmixing)

$$(T_f - T_{P,O})_{av} = \frac{T_{f,in} - T_{f,out}}{\ln\left(\frac{T_{f,in} - T_{P,O}}{T_{f,out} - T_{P,O}}\right)} = \Delta T_{ln}, \tag{5a}$$

for total backmixing in the fluid flow ("ideal stirred tank") the average temperature difference becomes:

$$(T_f - T_{P,O})_{av} = T_{f,out} - T_{P,O} = \Delta T_{out}. \tag{5b}$$

2.2 Calculation of Heat Transfer Coefficients

Figure 1 shows Nusselt numbers $Nu = \alpha\, d/\lambda$ versus Reynolds number $Re = u\, d/\nu$ for a fixed bed with $\psi = 0.4$ (upper, dotted curve) and for a single sphere in cross flow (full, lower curve with $\psi = 1$), calculated for $Pr = \eta c_P/\lambda = 0.7$ from the equations given by Gnielinski [3]:

$$Nu_{\text{fixed bed}} = [1 + 1.5(1 - \psi)] \cdot Nu_{\text{single sphere}}(Re_\psi, Pr), \tag{6}$$

$$Nu_{\text{single sphere}}(Re_\psi, Pr) = 2 + \sqrt{Nu_{lam}^2 + Nu_{turb}^2}, \tag{6a}$$

$$Nu_{lam}(Re_\psi, Pr) = 0.664\sqrt[3]{Pr}\sqrt{Re_\psi}, \tag{6b}$$

$$Nu_{turb}(Re_\psi, Pr) = \frac{0.037 Re_\psi^{0.8}\, Pr}{1 + 2.443 Re_\psi^{-0.1}(Pr^{2/3} - 1)}, \tag{6c}$$

$$Re_\psi = \frac{Re}{\psi} = \frac{u\, d}{\psi \nu}. \tag{6d}$$

If the particles are fixed in space, as in a packed bed, the void fraction, ψ, can be varied independently from the fluid velocity (or the Reynolds number). In a fluidized bed, however, bed expansion and fluid flow rate are coupled by an expansion relationship, such as given by Eq. (4). Replacing the void fraction, ψ, in Eq. (6) by the function $\psi(Re, Ar, \psi_{mf})$, following from Eq. (4) with Eqs. (2) and (3), results in the slightly upward bent curves showing a flat maximum at intermediate Reynolds numbers, as shown in Fig. 1 for fixed values of Ar, or Re_t, from Eq. (3a).

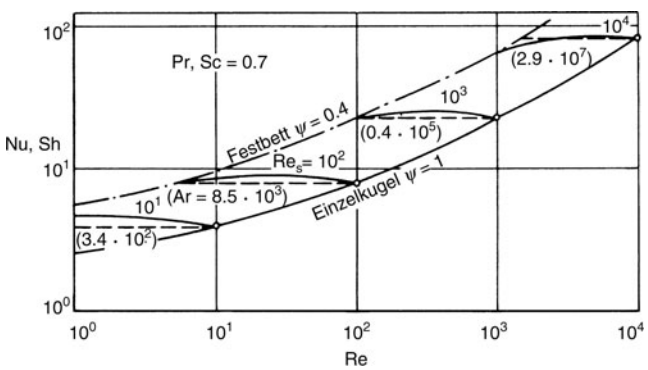

M5. Fig. 1. Nusselt number versus Reynolds number for Pr = 0.7 with Re_t (terminal-velocity Reynolds number) or Archimedes number, (Ar), respectively, as parameters.

For glass spheres or sand particles ($\rho_P \approx 2{,}500$ kg/m^3) fluidized by air at room temperature and normal pressure, the values of the terminal-velocity Reynolds number, Re_t, and the corresponding values of the Archimedes number, Ar, from Eq. (3a), as given in Fig. 1, belong to particle sizes of about 150 µm ($Re_t = 10$) up to about 7 mm ($Re_t = 10^4$).

Some of the known experimental results, especially those obtained from mass transfer experiments with liquid-fluidized beds [4, 5], in fact show a variation of Nu(Re) with a flat maximum, as resulting from the coupling of the fixed bed Eq. (6) with the bed expansion Eq. (4). Experimental uncertainty, however, is usually greater than the difference between these flatly curved and the straight, broken lines shown in Fig. 1, which are drawn through the end points of the curves, lying on the lower limiting curve for the single sphere.

It is therefore recommended to calculate the fluid-to-particle heat transfer coefficient within the range of existence of the fluidized bed from the simple relationship

$$Nu_{\text{fluidized bed}} \approx Nu_{\text{single sphere}}(Re_t, Pr). \tag{7}$$

That means, to use $\psi = 1$, and $Re_\psi = Re_t$ (Ar) from Eq. (3a) in Eq. (6).

Within the range of existence of the fluidized bed, $Re_{mf} < Re < Re_t$, the fluid-to particle heat transfer only depends on the acceleration of gravity, g, on the particle diameter, d, the particle density, ρ_P, and the physical properties of the fluid (ρ, c_P, η, λ), but not on the fluid velocity u.

2.3 Influence of Maldistribution and Backmixing

Many authors [6–10] have reported about heat (or mass) transfer coefficients which are lower than those for a single sphere in cross flow (lower curve in Fig. 1) for low Péclet numbers, Pe = RePr (or ReSc, respectively, for mass transfer).

These anomalously low heat (and mass) transfer coefficients, leading to Nusselt, or Sherwood numbers much lower than the theoretical Nu_{min} (= Sh_{min}) = 2 for a single sphere, today are usually regarded not as "true" heat transfer coefficients, but as "apparent" coefficients, which are not due to heat transfer alone, but contain effects which have not been taken into account in their evaluation from the experiments. Backmixing and maldistribution of flow lead to drastic reductions in the driving temperature difference as compared to the logarithmic mean in Eq. (5a), for example.

In the range of sufficiently large Péclet numbers (say Pe > 500) the corresponding numbers of transfer units, NTUs,

$$NTU = \frac{\alpha A}{c_P \dot{M}} = \frac{Nu}{Pe}\frac{A}{f}, \tag{8}$$

where A/f is the ratio of transfer surface area to cross-sectional area for the flow, are typically relatively small. Under these conditions, small maldistribution, or backmixing effects are nearly

negligible. For low Péclet numbers – and correspondingly high NTUs – even small maldistribution or backmixing effects suffice to shift the "apparent" heat (and mass) transfer coefficients by orders of magnitudes below the single-sphere values [10].

Various models have been developed to describe the effects of maldistribution and backmixing [6, 7, 9]. One of the simplest and practically most easily applicable of these models is the so-called "bypass model." In this model the total mass flow rate of fluid, $\dot{M}$, is subdivided in a main stream, free of backmixing, $(1-\upsilon)\dot{M}$, and a bypass flow, $\upsilon\dot{M}$. It is furthermore assumed that the bypass flow does not take part in heat transfer ($\mathrm{NTU}_{\mathrm{bypass}} \approx 0$, "model of the inactive bypass"). The outlet temperature of the fluid under these assumptions is the mixing value of the outlet temperature of the main stream and that of the bypass (which for inactive bypass remains equal to the inlet temperature):

$$\frac{T_{\mathrm{f,out}} - T_{\mathrm{P,O}}}{T_{\mathrm{f,in}} - T_{\mathrm{P,O}}} = (1-\upsilon)\exp(-\mathrm{NTU_m}) + \upsilon,$$
$$\upsilon = \dot{M}_{\mathrm{bypass}}/\dot{M}, \quad \mathrm{NTU_m} = \frac{\mathrm{Nu}}{(1-\upsilon)\mathrm{Re}\,\mathrm{Pr}}\frac{A}{f}. \tag{9}$$

Here, the ("true")Nusselt number is to be calculated from Eq. (7) or Eq. (6). Calculating the heat transfer coefficients from measured inlet and outlet temperatures under the assumption of plug flow (from Eqs. (5) and (5a)), "apparent" Nusselt numbers are obtained as

$$\mathrm{Nu_{app}} = -\mathrm{Re}\,\mathrm{Pr}\frac{f}{A}\cdot\ln[(1-\upsilon)\exp(-\mathrm{NTU_m}) + \upsilon]. \tag{10}$$

With $A/f = 6(1-\psi_{\mathrm{mf}})L_{\mathrm{mf}}/d$ and a bypass ratio of 5% ($\upsilon = 0.05$), $\psi_{\mathrm{mf}} = 0.5$, $L_{\mathrm{mf}}/d = 10$ (L_{mf} is the bed height at minimum fluidization), Pr = 0.7, and Re = $\mathrm{Re_t}$, Nu, and $\mathrm{Nu_{app}}$ are found as:

$\mathrm{Re_t}$	1	10	100	1,000	10,000
Nu	2.59	3.88	8.09	22.6	80.4
$\mathrm{Nu_{app}}$	0.07	0.699	6.06	21.8	79.6

Most experimental data in the low-Péclet-number range can be explained sufficiently well with the simple bypass model and an appropriate constant value of υ [11]. For a first approximation it is recommended to start with υ = 0.05.

Example 1

As an example the batchwise process of cooling roasted coffee beans in a fluid bed cooler is shown in Fig. 2. A batch of coffee beans is roasted for 150 s in a venturi-type fluidized bed apparatus. During this time the previous charge is to be cooled with ambient air in the cylindrical fluidized bed under the roaster. It is checked whether the 150 s would suffice to cool the coffee beans from their initial temperature $T_{\mathrm{P,I}} = 300°\mathrm{C}$ to a temperature below 35°C. The following data are given to solve this problem:

Particles (subscript "P"): coffee beans

Initial temperature	$T_{\mathrm{P,I}} = 300°\mathrm{C}$
Density	$\rho_{\mathrm{P}} = 630\ \mathrm{kg/m^3}$
Specific heat capacity	$c_{\mathrm{P}} = 1.70\ \mathrm{kJ/(kg\ K)}$
Conductivity	$\lambda_{\mathrm{P}} = 0.10\ \mathrm{W/(m\ K)}$
Solid mass per cross-section	$M_{\mathrm{P}}/f = m_{\mathrm{P}} = 60\ \mathrm{kg/m^2}$
Mean diameter	$d = 6\ \mathrm{mm}$

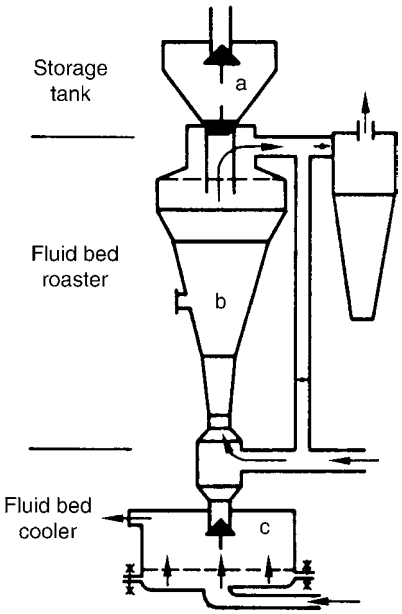

M5. Fig. 2. Roasting and cooling of coffee beans in a fluidized bed (Example 1).

Fluid (no subscript for properties): air at $p = 1$ bar

Temperature at the inlet	$T_{\mathrm{f,in}} = 20°\mathrm{C}$
Mass flux	$\dot{m} = 3\ \mathrm{kg/(m^2\ s)}$
Density	$\rho = 1\ \mathrm{kg/m^3}$
Specific heat capacity	$c = 1.0\ \mathrm{kJ/(kg\ K)}$
Conductivity	$\lambda = 0.029\ \mathrm{W/(m\ K)}$
Kinematic viscosity	$\nu = 20 \cdot 10^{-6}\ \mathrm{m^2/s}$

It can be assumed that the solid particles are well mixed, so that T_{P} only depends on time, but not on the position in the bed. If the local change of enthalpy of the gas is neglected against that of the solid, one gets

$$m_{\mathrm{P}} c_{\mathrm{P}} \frac{\mathrm{d}\bar{T}_{\mathrm{P}}}{\mathrm{d}t} = \dot{m}c\left(T_{\mathrm{f,in}} - T_{\mathrm{f,out}}(t)\right) \tag{11}$$

and from Eq. (9)

$$\varepsilon \equiv \frac{T_{\mathrm{f,in}} - T_{\mathrm{f,out}}}{T_{\mathrm{f,in}} - \bar{T}_{\mathrm{P}}} = (1-\upsilon)(1-e^{-\mathrm{NTU_m}}). \tag{12}$$

From these two equations, for the two unknowns $T_{\mathrm{P}}(t)$ and $T_{\mathrm{f,out}}(t)$, one obtains after elimination of $T_{\mathrm{f,out}}(t)$ and integration over t,

$$\Theta_{\mathrm{P}} = \frac{\bar{T}_{\mathrm{P}}(t) - T_{\mathrm{f,in}}}{T_{\mathrm{P,I}} - T_{\mathrm{f,in}}-} = \exp(-\varepsilon\tau^*) \tag{13}$$

with the efficiency of the fluid bed heat exchanger

$$\varepsilon = (1-\upsilon)(1-e^{-\mathrm{NTU_m}}), \tag{14}$$

the dimensionless time

$$\tau^* \equiv \frac{\dot{m}c}{m_{\mathrm{P}} c_{\mathrm{P}}} t, \tag{15}$$

and the NTUs

$$\mathrm{NTU_m} = \frac{6k\,m_\mathrm{P}}{\rho_\mathrm{P} d(1-\upsilon)(\dot{m}c)_\mathrm{f}} \cdot t. \qquad (16)$$

The outside heat transfer coefficient in Eq. (9) had to be replaced here by an overall heat transfer coefficient k, because the surface temperature of the particles $T_{\mathrm{P,O}}$ is not known, but only the caloric average temperature $\bar{T}_\mathrm{P}$. This overall coefficient, k, also includes the internal conduction resistance (see Chap. E2):

$$\frac{1}{k} = \frac{1}{\alpha_\mathrm{o}} + \frac{1}{\alpha_\mathrm{i}} \qquad (17)$$

The outside heat transfer coefficient is calculated from Eqs. (7) and (6).

The Archimedes number is

$$\mathrm{Ar} = \frac{gd^3}{\nu^2}\frac{\rho_\mathrm{P}-\rho}{\rho} = 3.34 \cdot 10^6.$$

From this, Eq. (2a), with $\psi_\mathrm{mf} = 0.4$, gives $\mathrm{Re_{mf}} = 326$, and Eq. (3a) yields $\mathrm{Re_t} = 3{,}180$.

From the actual flow rate, Re is found: $\mathrm{Re} = \dot{m}d/(\rho\nu) = 900$ (so the velocity is actually within the range of fluidization), and $\mathrm{Pr} = 0.69$; $\mathrm{Nu_{lam}} = 33.1$; $\mathrm{Nu_{turb}} = 21.3$; $\mathrm{Nu} = 41.32$ and $\alpha_\mathrm{o} = \lambda/d$, $\mathrm{Nu} = 200\ \mathrm{W/(K\,m^2)}$.

Calculation of the internal heat transfer coefficient from Chap. E2–Sect. 3.1.1.

With the dimensionless time $\tau = \kappa t/(d/2)^2 = 1.56$; $\mathrm{Nu_i} = 3.41$; $\alpha_\mathrm{i} = \lambda/(d/2)$, $\mathrm{Nu_i} = 114\ \mathrm{W/(K\,m^2)}$.

From this one finds $k = 72.6\ \mathrm{W/(m^2\,K)}$; $\tau^* = 4.41$ (Eq. (15)); $\mathrm{NTU_m} = 2.305/(1-\upsilon)$ and with varying values of the bypass ratio υ:

υ	0.00	0.05	0.10	0.20	0.30
ε	0.900	0.866	0.831	0.755	0.674
$\bar{T}_\mathrm{P}/°\mathrm{C}$	25.3	26.1	27.2	30.0	34.3

From this calculation one can find out that the time of 150 s probably suffices to cool the coffee beans to a temperature below 35°C, even if the bypass ratio is chosen to be as high as 30%.

Alternatively total backmixing of the air in the fluidized bed can be assumed, see Eq. (5b). In this case the efficiency is $\varepsilon = \mathrm{NTU}/(1+\mathrm{NTU}) = 2.305/3.305 = 0.697$, and the particle temperature after 150 s turns out to be $\bar{T}_\mathrm{P} = 32.9°\mathrm{C}$ (so total backmixing has roughly the same effect as an inactive bypass of about 25% in this case).

3 Heat Transfer from Immersed Surfaces to Gas-Fluidized Beds of Solid Particles

3.1 Definition of the Heat Transfer Coefficient

The heat transfer coefficient, α, between gas-fluidized beds of solid particles and the surfaces of immersed heating or cooling equipment (such as plates, tubes, or tube bundles) is defined as

$$\alpha \equiv \frac{\dot{Q}_{(\mathrm{O-B})}}{A_\mathrm{O}(T_\mathrm{O} - T_\mathrm{B})}, \qquad (18)$$

where $\dot{Q}_{(\mathrm{O-B})}$ is the heat flow transmitted from the surface area A (subscript: O) of the heat exchanger elements immersed in the fluidized bed (subscript: B). T_O is the surface temperature of these immersed elements, and T_B is the bed temperature, which may be assumed to be more or less uniformly distributed sufficiently far away from the exchanger elements.

Because of the great surface area of the solid particles and the intensive mixing in fluidized beds one usually does not have to distinguish between gas and solid temperatures. In most cases one can also assume that the bed temperature T_B in a fluidized bed is independent of the position ("ideal stirred tank").

3.2 Calculation of Heat Transfer Coefficients

Figure 3 shows the heat transfer coefficients, α, between a vertical cylindrical heater and an air-fluidized bed of glass spheres (of 400 µm diameter) as a function of fluid velocity, u, as measured by Wunder [12].

In contrast to the monotonous increase of heat transfer coefficients with gas velocity for a single-phase gas flow (without the particles), shown as the dotted curve in Fig. 3, in the fluidized bed a steep rise of heat transfer coefficients is observed immediately after the minimum fluidization. The values increase up to a maximum, α_max, at a certain gas velocity, u_opt (and a corresponding gas volume fraction, ψ_opt), while they decrease with even higher gas velocities (and correspondingly increasing bed height). The very steep increase immediately following the minimum fluidization conditions obviously is caused by the free motion of particles and the "particle-convective" net energy transport from the heater surface to the bulk of the bed.

Apart from this particle convective transport, heat is also transferred directly to the gas ("gas convection"), and – especially so for higher temperatures – also by radiation between the heater surface and the particles. Treating these mechanisms approximatively as independent and parallel, the total heat transfer coefficient can be written as the sum of three parts [13].

$$\alpha = \underbrace{\alpha_\mathrm{P}}_{\text{particle convection}} + \underbrace{\alpha_\mathrm{G}}_{\text{gas convection}} + \underbrace{\alpha_\mathrm{R}}_{\text{radiation}}. \qquad (19)$$

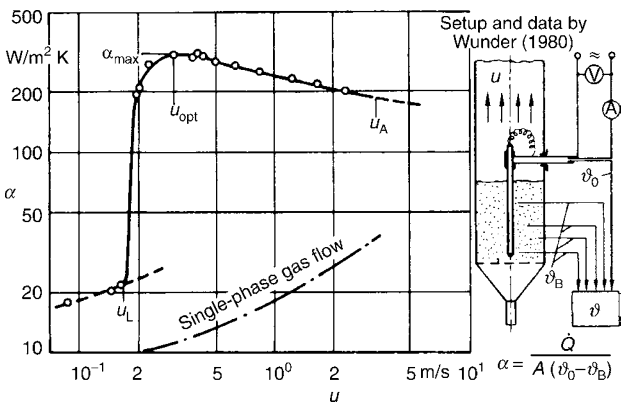

M5. Fig. 3. Heat transfer coefficient between immersed surface and fluidized bed versus gas velocity.

With $Nu_P = \alpha_P\, d/\lambda$, $Nu_G = \alpha_G\, d/\lambda$, and $Nu_R = \alpha_R\, d/\lambda$ (the conductivity, λ, is that of the gas in all cases!) the particle convective part, Nu_P, is obtained first, from:

$$Nu_P = (1-\psi)\, Z\, (1-\exp(-N)) \tag{20}$$

with Z and N from:

$$Z = \frac{1}{6}\frac{(\rho c)_P}{\lambda}\sqrt{\frac{g d^3(\psi-\psi_{mf})}{5(1-\psi_{mf})(1-\psi)}},\quad N = Nu_{WP}/(C_K Z), \tag{21}$$

$$\frac{1}{Nu_{WP}} = \frac{1}{Nu_{WP,max}} + \frac{\lambda/\lambda_P}{4\left(1+\sqrt{\frac{3C_K}{2\pi}\frac{\lambda}{\lambda_P}Z}\right)}, \tag{21a}$$

$$Nu_{WP,max} = 4\left(\left(1+\frac{2\ell}{d}\right)\ln\left(1+\frac{d}{2\ell}\right)-1\right), \tag{21b}$$

$$\ell = 2\Lambda\left(\frac{2}{\gamma}-1\right), \tag{21c}$$

$$\Lambda = \sqrt{\frac{2\pi\tilde{R}T}{\tilde{M}}}\frac{\lambda}{p(2c_p-\tilde{R}/\tilde{M})}, \tag{22}$$

$$\lg\left(\frac{1}{\gamma}-1\right) = 0.6 - \left(\frac{1{,}000\,K}{T}+1\right)\Big/ C_A. \tag{23}$$

The value of constant C_K from the comparison with experimental data is

$$C_K = 2.6. \tag{24}$$

$Nu_{WP,max}$ is the Nusselt number containing the maximum heat transfer coefficient between wall and particle according to Schlünder [14]. It results from the limiting heat transfer resistance by conduction through the gaseous gap between a plane wall and a spherical particle at short contact times, and only depends on the ratio $2\ell/d$, of the modified mean free path of the gas molecules and the particle radius $d/2$. This is also called a Knudsen number in the literature. This modified mean free path is defined by Eq. (21c), where Λ is the effective mean free path, and γ is the accommodation coefficient. The mean free path, Λ, is calculated as a function of gas properties from Eq. (22), based on the kinetic theory of gases.

The accommodation coefficient, γ, a measure of the incompleteness of energy transfer during a molecule–wall collision, depends, primarily, upon the kind of gas, and on temperature. According to Reiter et al. [15] the temperature dependence of γ can be approximated empirically by Eq. (23). The constant C_A can be calculated from a measured value $\gamma_0 = \gamma(T_0)$. For the noble gases the following values are found

Gas	He	Ne	Ar	Kr	Xe
C_A	50	6	3	2.5	2.25
γ(25°C)	0.235	0.573	0.876	0.933	0.956

For some other gases the following values are recommended (see also [16]):

Gas	H_2	H_2O	Air	CO_2
C_A	∞	3.62	2.8	2.8
γ(25°C)	0.20	0.80	0.90	0.90

The gas convective part, Nu_G, is calculated according to Baskakov [17] from the empirical Eq. (25)

$$Nu_G = 0.009\ Pr^{1/3}\ Ar^{1/2} \tag{25}$$

while the radiative part follows from a linearized form of the Stefan–Boltzmann equation:

$$Nu_R \cong 4\varepsilon\sigma\, T_m^3\, (d/\lambda). \tag{26}$$

In Eq. (26), ε is an effective emissivity ($0 < \varepsilon < 1$), which primarily depends on the surface properties of the immersed surfaces (the surface of the particles in a fluidized bed is very close to a black body). The Stefan–Boltzmann constant has the value: $\sigma = 5.67 \cdot 10^{-8}$ W/(m^{2}K^4). The maximum heat transfer coefficient α_{max} can be found from Eqs. (19–26), for the gas volume fraction $\psi = \psi_{opt}$. This value can be obtained from Eq. (20) with $\partial Nu_P/\partial\psi = 0$:

$$\frac{\psi_{opt}-\psi_{mf}}{1-\psi_{mf}} = \frac{1}{2}\left(1-\frac{N(\psi_{opt})}{e^{N(\psi_{opt})}-1}\right). \tag{27}$$

This equation has to be solved iteratively. For large particles, that is, small values of N, ψ_{opt} is close to the minimum fluidization voidage, ψ_{mf}. For small particles, and correspondingly large values of N, the optimal bed voidage comes closer to the center of the range of existence of the fluidized bed:

$$\lim_{N\to 0}\ \psi_{opt} = \psi_{mf}, \tag{27a}$$

$$\lim_{N\to\infty}\ \psi_{opt} = \frac{1}{2}(1-\psi_{mf}). \tag{27b}$$

Figure 4 shows a contour line plot of the heat transfer coefficient for glass or sand particles fluidized by air at 25°C and 1 bar over

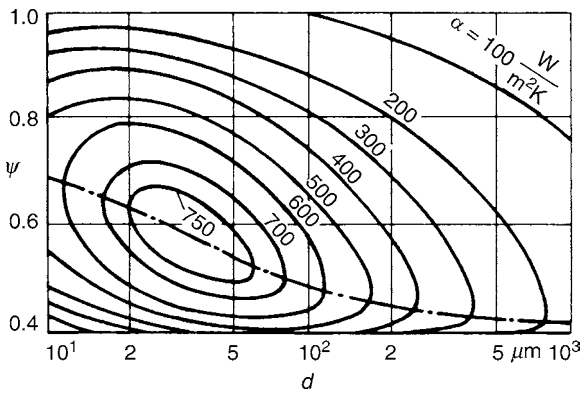

M5. Fig. 4. Heat transfer coefficient between immersed surface and fluidized bed: Influence of particle diameter, d, and gas volume fraction, ψ (bed expansion, voidage). Air, 25°C, 1 bar; sand or glass particles. Dotted line: $\psi = \psi_{opt}$.

a particle diameter, d, and bed voidage, ψ, plane, as calculated from Eqs. (19–26).

3.3 Influence of Particle Properties, Gas Properties, and Operation Parameters

Following Eqs. (19–26), the heat transfer coefficient between gas-fluidized beds of solid particles and immersed surfaces depends upon a number of quantities, which may be classified into the three groups: particle properties, gas properties, and operation parameters.

3.3.1 Particle Properties

Five quantities, the diameter, d, the void fraction at minimum fluidization, ψ_{mf}, the volumetric heat capacity, $(\rho c)_P$, the density, ρ_P, and the conductivity, λ_P, of the particles play some role in the model Eqs. (19–26). Mainly three of them, d, ψ_{mf}, $(\rho c)_P$, are primary parameters in the particle convective part Eqs. (20–24). The conductivity of the particles, λ_P, only plays a part in the particle convective heat transfer, if the conductivities of the solid and the gas are in the same order of magnitude, as for example for polystyrene foam particles and air. In most practical cases, the transient internal conductive resistance in the particles (the second term on the right-hand side of Eq. (21a)) can be neglected against the first one. The particle density, ρ_P, additionally plays a role for the gas convective part, Eq. (25), in the Archimedes number.

Figure 5 shows the variation of the maximum heat transfer coefficient, α_{max}, as a function of the particle diameter, d. The curve is calculated with the properties of air at $p = 1$ bar, $T = 25°C$, and glass (or sand) particles ($\rho_P = 2{,}500$ kg/m^3, $c_P = 750$ J/(kg K)) with a void fraction at minimum fluidization of $\psi_{mf} = 0.4$. The radiative part was neglected.

It can be seen from Figs. 4 and 5 that there is an absolute maximum of the heat transfer coefficient at a certain particle size, in this case at $d = 38$ µm. For smaller particles the finite heat capacity of the solids is a limiting factor; the fine particles in contact with the heater wall rapidly reach the surface temperature. For larger particles the conductive resistance in the gaseous gap plays a limiting role, α_{max} decreases up to a minimum at $d = 3$ mm. The increase for even greater diameters is due to the gas convective part α_G from Eq. (25) ($\alpha_G \propto \sqrt{d}$).

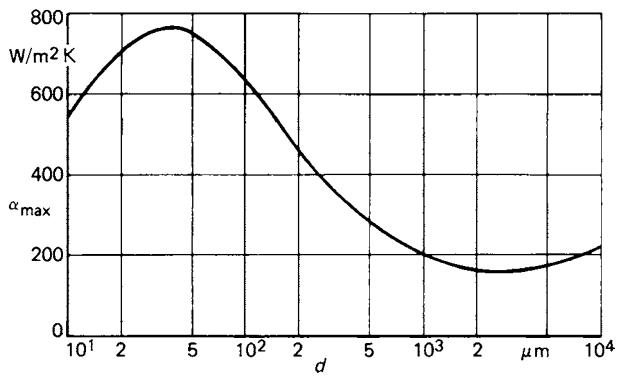

M5. Fig. 5. Maximum heat transfer coefficient between immersed surface and fluidized bed versus particle diameter. Air, 25°C, 1 bar; sand or glass particles.

With decreasing solids fraction, $(1 - \psi_{mf})$, the particle convective part becomes smaller. The volumetric heat capacity of the particles $(\rho c)_P$ affects the particle convective heat transfer especially for smaller particles; in the limiting case $N \to \infty$ from Eqs. (20) and (27) one gets

$$\lim_{N\to\infty} \alpha_{P,max} = \frac{1}{6}(\rho c)_P \sqrt{\frac{gd(1-\psi_{mf})}{20}} \tag{28}$$

that is, $\alpha_{P,max}$ is directly proportional to the volumetric heat capacity and to the square root of the solid fraction at minimum fluidization. For sufficiently large particles, however, the heat capacity plays a vanishing role. For $N \to 0$ from Eqs. (20) and (27) one finds

$$\lim_{N\to 0} \alpha_{P,max} = \frac{\lambda}{d}(1-\psi_{mf})\frac{Nu_{WP}}{C_K}. \tag{29}$$

The conductivity of the particles, λ_P, only plays a role if the internal conduction resistance in (Eq. 21a), the second term on the right side, comes in the order of magnitude of the first one:

$$\frac{\alpha_{WP,max}}{\alpha_{WP}} = 1 + \frac{\lambda}{\lambda_P}\cdot\frac{Nu_{WP,max}/4}{1+\sqrt{\frac{3C_K}{2\pi}\frac{\lambda}{\lambda_P}Z}}. \tag{30}$$

In many practical cases, the ratio (λ/λ_P) is very small, even for relatively poor conductors, such as sand, fluidized with air it is typically about (0.03/2), that is only 1.5%.

The internal resistance of the particles, however, is not negligible if the particles are porous solids, such as polystyrene foam, with conductivities in the same order of magnitude as that of gases.

3.3.2 Gas Properties

The relevant properties of the fluidizing gas are the conductivity, λ, and the modified mean free path of the molecules, ℓ (or its ratio to the particle radius, $2\ell/d$). Only these two gas properties affect the particle convective component. From an empirical equation the maximum heat transfer coefficients are found to be roughly proportional to $\lambda^{0.6}$, which is better explained by the model Eqs. (19–24) with the two properties, λ and ℓ.

Density, ρ, heat capacity (at constant pressure), c_P, and viscosity, η, play an additional role in the gas convective component only.

3.3.3 Operation Parameters

The operation parameters are gas flow rate, pressure, temperature, and shape, size and arrangement of the heater (or cooler) surfaces. The gas flow rate is coupled to particle size and density by the range of existence of fluidization ($u_{mf} < u < u_t$). Within this range the bed voidage, ψ, changes from ψ_{mf} to 1. At a certain gas velocity, u_{opt}, the maximum heat transfer

coefficient, α_{max}, is reached. From Eqs. (19–27) the function $\alpha(\psi)$ can be obtained for the whole range ($\psi_{mf} < \psi < 1$), so $\alpha_{max} = \alpha(\psi_{opt})$ can be calculated without any knowledge of the actual bed expansion behavior. These maximum values are in reasonable agreement with many experimental values [13, 18].

The question what is the value of the average gas velocity required to reach the bed voidage in the zone of the bed, where the heater (or cooler) elements are positioned, however, can only be answered, if the bed expansion behavior of the actual equipment is known, from experiments [19].

For a first approximation it is recommended to use the simple linear expansion relationship from Eq. (4a), combined with $\alpha(\psi)$ from Eqs. (19–27), to obtain heat transfer coefficients as a function of gas velocity (as long as the heater surfaces are placed within the range $z < L_{mf}$ of the initial bed height L_{mf}. In Eq. (4a) u_{mf} is to be calculated from Eq. (2a), and u_t from Eq. (3a) or from Eq. (3b) if the latter gives greater values. Figure 6 shows the curves for $\alpha(u)$ as calculated in this way for four different particle sizes, from $d = 47$–$1{,}400$ µm (=1.4 mm), as compared with experimental data by Wunder [12].

The pressure has some effects on α_P via the mean free path ($\ell \propto 1/p$), and has much stronger effects, on α_G via the gas density ($\rho \propto p$). The gas convective part increases approximatively proportional to the square root of the pressure $\alpha_G \propto \sqrt{p}$, while the effect on the particle convective part is much smaller. Higher pressure can improve the heat transfer primarily for larger particles.

Higher temperatures also have an effect via the physical properties. Conductivity, viscosity, and mean free path increase with temperature, while the density decreases with increasing temperature. The contribution of radiation, see Eq. (26), increases with the third power of the average absolute temperature. For $T_m = 1{,}000$ K (= 727°C) one already obtains $\alpha_R = \varepsilon\ 227$ W/(K m^2).

The shape, size, and position of the heater (or cooler) surfaces are not required for the calculation from Eqs. (19–26). The comparison with experimental data [20] has shown that these equations are applicable for single cylindrical heaters or coolers, immersed vertically or horizontally [21] in the bed center. Even experiments with spherical probes, with coils of tubes, or tube bundles have been found to agree relatively well with the model predictions.

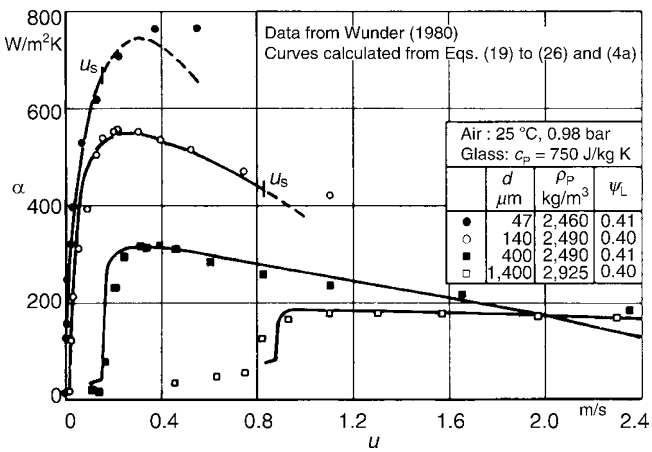

M5. Fig. 6. Heat transfer coefficient immersed surface-to-fluidized bed versus gas velocity.

Example 2

To determine the size of the heater surfaces for an allothermal fluid-bed coal gasification process the heat transfer coefficient between these surfaces (tubes, tube bundles) and the pressurized-steam-fluidized bed of coal particles is needed. The steam enters the bed at 800°C at a pressure of 40 bars.

Particle properties: coal:

$\rho_P = 1{,}400$ kg/m^3, $c_P = 1{,}500$ J/(kg K), $d = 50$–500 µm, $\psi_{mf} = 0.5$.

Gas properties: steam (water) at 800°C and 40 bar:

$\eta = 40.5 \cdot 10^{-6}$ Pa s	$\widetilde{M} = 18$ kg/kmol
$c_P = 2.38 \cdot 10^3$ J/(kg K)	$C_A = 3.62$; $\gamma = 0.462$ (Gl. (23))
$\lambda = 0.110$ W/(m K)	$\Lambda = 11.29$ nm (Gl. (22))
$\rho = 8.14$ kg/m^3	$\ell = 75.20$ nm (Gl. (21))

The effective emissivity of the heater surface and the fluid-bed is assumed to be $\varepsilon = 0.9$.

Eq. (26) thus gives a radiative heat transfer coefficient of $\alpha_R = 247$ W/(m^2 K).

From Eqs. (19–27) one finds:

d	50	100	200	500	µm	Eq.
α_G	54.9	77.6	109.8	173.6	W/(m^2 K)	(25)
ψ_{opt}	0.726	0.667	0.607	0.552	–	(27)
$\alpha_{P,max}$	1,189	1,390	1,289	866.1	W/(m^2 K)	(20)
α_{max}	1,491	1,715	1,646	1,287	W/(m^2 K)	(19)

Under the conditions used here, a heat transfer coefficient of $\alpha_{max} \approx 1{,}670$ W/(m^2 K) was found experimentally for a particle size fraction of $d < 500$ µm in a pilot plant [22].

The absolute maximum, appearing at a particle size of about 40 µm for air (25°C, 1 bar) (see Fig. 5), in this case is shifted to a particle size of about 150 µm. This is confirmed by the results of [22]: For a smaller size fraction, $d < 100$ µm, lower maximum heat transfer coefficients of $\alpha_{max} \approx 1{,}390$ W/(m^2 K) have been observed.

3.4 Limits of Application

The set of Eqs. (19–27) to calculate the heat transfer coefficients between immersed surfaces and gas-fluidized beds of granular solids have been compared within wide ranges of all the relevant parameters with experimental data from a number of different sources, see [13, 18, 20, 23]. In the range of very fine powders ($d < 40$ µm), where these equations predict lower heat transfer coefficients with decreasing particle size (see Fig. 5), very few experimental data are available, which do not allow a definitely clear conclusion. Other calculation methods from the literature [7, 8, 24, 25], which in other ranges lead to more or less similar results, predict a different behavior in this fine powder range, for example, a further increase of heat transfer with decreasing particle size [7, 8], or constant limiting maximum value [24, 25], which agrees more or less with the absolute maximum

obtained from our equations (about 750 W/(m^2 K) for air-fluidized beds of sand or glass particles at normal conditions). In this fine-powder range experiments are difficult, as fine powders are not easily fluidized, because the adhesion forces between the particles are in the same order of magnitude as the fluid-particle forces.

The equations given in Sect. 3 from Chap. M5 are not applicable to liquid-fluidized beds. For these cases, some purely empirical equations, based on an evaluation of a great amount of data are given in the next subchapter.

4 Heat Transfer from Immersed Surfaces or Container Walls to Liquid-fluidized Beds

4.1 Calculation of Heat Transfer Coefficients

For liquid-fluidized beds of solid particles the heat transfer coefficient between immersed surfaces and the bed – as defined for gas-fluidized beds in Eq. (18) – can be calculated, according to Haid et al. [26], from:

$$\mathrm{Nu} = c\mathrm{Re}^{a}\ \mathrm{Pr}^{b}(1-\psi)^{1-a}\psi^{-1}, \qquad c = 0.0734, \quad a = 0.75, \quad b = 0.63. \tag{31}$$

The three constants have been fitted by non-linear regression to all available data [27] for heat transfer to liquid fluidized beds. The exponents of the terms $(1-\psi)^{1-a}$ and ψ^{-1} have been found by assuming the validity of an equation $\mathrm{Nu_h} = c\mathrm{Re}_h^{a}\ \mathrm{Pr}^{b}$ with a hydraulic diameter in $\mathrm{Nu_h}$ and $\mathrm{Re_h}$, which is proportional to the particle diameter, d, and to the ratio $\psi/(1-\psi)$ [26].

The experimentally verified range of validity is given as:

$0.02 < \mathrm{Re} < 9{,}400$	$1.65 < \mathrm{Pr} < 7{,}700$
$3.85 < \mathrm{Ar} < 6.7 \cdot 10^7$	$\psi_{mf} < \psi < 1$

The relationship between bed expansion (or the liquid volume fraction ψ) and the flowrate (or the Reynolds number, Re) for the liquid-fluidized bed is given by Eq. (4) with Eqs. (2a) and (3a) for $\mathrm{Re_{mf}}$ and $\mathrm{Re_t}$ respectively. With these, Eq. (31) can also be written as

$$\mathrm{Nu} = c\mathrm{Re}_{t}^{a}\ \mathrm{Pr}^{b}(1-\psi)^{1-a}\psi^{na-1} \tag{32}$$

with n, as already given in Eq. (4),

$$n = \frac{\ln(\mathrm{Re_{mf}}/\mathrm{Re_t})}{\ln \psi_{mf}}, \tag{33}$$

as a function of (ψ_{mf}, Ar, Pr, ψ) in place of (Re, Pr, ψ).

The maximum heat transfer coefficient can be found from Eq. (32) as

$$\mathrm{Nu} = c\mathrm{Re}_{t}^{a}\ \mathrm{Pr}^{b}(1-\psi_{opt})^{1-a}\psi_{opt}^{na-1} \tag{34}$$

at a liquid volume fraction ψ_{opt}, which can be obtained from

$$\psi_{opt} = \frac{n-1/a}{n-1}. \tag{35}$$

4.2 Limits of Application

At $\psi = \psi_{mf}$ the lower limit of the range of existence of fluidization is reached. Below that, for $\psi < \psi_{mf}$ there is the range of fixed beds, where heat transfer is to be calculated from Chap. M7. For $\psi \to 1$ Eqs. (31) and (32) give $\mathrm{Nu} \to 0$. It is recommended to check for $\psi > 0.95$ whether the heat transfer coefficients for fluidized beds from these equations are already lower than the corresponding value for single-phase liquid flow according to Chap. G1. If so, the heat transfer coefficient ought to be calculated from Chap. G1 for single-phase liquid flow.

Example 3

In a vertical shell-and-tube heat exchanger the fouling of the surface by crystallizing salt should be avoided by fluidized solid particles (see Chap. C4). In the tubes, glass beads of a diameter of d = 3 mm should therefore be fluidized by the upward flowing aqueous solution at an average temperature of 20°C.

What are the values of heat transfer coefficients that can be expected at the inner walls of the tubes within the range of existence of the liquid-fluidized bed of these glass beads?

Tube length	l = 2,100 mm
Inner diameter of the tubes	d_{it} = 21 mm
Glass beads	
Diameter	d = 3 mm
Void fraction	ψ_{mf} = 0.4
Density	ρ_P = 2,500 kg/m^3
Aqueous solution	
Density	ρ = 1,183 kg/m^3
Specific heat capacity	c_P = 3,081 J/(kg K)
Conductivity	λ = 0.545 W/(K m)
Viscosity	$\eta = 2.41 \cdot 10^{-3}$ Pa·s
Archimedes number	$\mathrm{Ar} = g\,d^{3}(\rho_P - \rho)\rho/\eta^2$

Ar = $9.81 \cdot 3^3 \cdot 10^{-9}$ (2,500 − 1,183) 1,183/$(2.41 \cdot 10^{-3})^2$ = 71,051.

Equation (2a): Reynolds number at minimum fluidization

$\mathrm{Re_{mf}} = 42.9\ (1 - 0.4)\ (1 + 0.4^3 \cdot 71{,}051/(0.6^2 \cdot 3{,}214))^{0.5} - 1 = 31.4$.

$u_{mf} = \eta\ \mathrm{Re_{mf}}/(\rho\ d)$, u_{mf} = 0.0213 m/s.

Equation (3a): terminal Reynolds number

$\mathrm{Re_t} = 18\ ((1 + (71{,}051)^{0.5}/9)^{0.5} - 1)^2$; $\mathrm{Re_t}$ = 369.9; u_t = 0.251 m/s.

Equation (33): exponent of the bed expansion equation

n = ln (31.4/369.9)/ln (0.4) = 2.691.

Equation (35): optimum void fraction

$\psi_{opt} = (2.691 - 1/0.75)/(2.291 - 1) = 0.803$.

Corresponding Reynolds number: $\mathrm{Re} = \mathrm{Re_t}\ \psi^n$

$\mathrm{Re_{opt}} = 369.90.803^{2.691} = 205$.

Equation (34): maximum Nusselt number

$\mathrm{Pr} = \eta c_P/\lambda = 13.62$;

$\mathrm{Nu_{max}} = 0.0734\mathrm{Re}_t^{0.75}\ \mathrm{Pr}^{0.63}(1-\psi)^{0.25}\psi^{0.75n-1} = 17.1$; α_{max} = 3,106 W/(m^2 K)

at minimum fluidization, with $\mathrm{Re_{mf}}$ = 31.4 and ψ_{mf} = 0.4, Nu, and α, are found

$Nu = 0.0734 \cdot 31.4^{0.75} \cdot 13.62^{0.63} \cdot 0.6^{0.25} \cdot 0.4^{-1}$; $Nu_{mf} = 11.1$; $\alpha_{mf} = 2{,}017\ W/(m^2\ K)$

at terminal velocity, with $Re_t = 369.9$ and $u_t = 0.251$ m/s, that is, at $\psi \to 1$, Eqs. (31) and (32) give $Nu \to 0$. Here the *Reynolds* number of the tube flow

$Re = (d_{it}/d)\ Re_t = (21/3)\ 369.9 = 2589.3$,

and one finds from Chap. G1 for tube-flow $Nu = 15.60$

$\alpha = (\lambda/d_{it})\ Nu = 0.545 \cdot 15.6/(21 \cdot 10^{-3})\ W/(m^2\ K) = 405\ W/(m^2\ K)$.

5 Bibliography

1. Reh L (1977) Trends in research and industrial application of fluidization. Verfahrenstechnik 11(6):381–384 and 7, 425–428
2. Bakker PJ, Heertjes PM (1960) Porosity distributions in a fluidized bed. Chem Eng Sci 12:260–271
3. Gnielinski V (1978) Gleichungen zur Berechnung des Wärme- und Stoffaustausches in durchströmten ruhenden Kugelschüttungen bei mittleren und großen Péclet-Zahlen. Verfahrenstechnik 12(6):363–366
4. Donnadieu G (1961) Transmission de la chaleur dans les milieux granulaires. Etude du lit fixe et du lit fluidise. Rev Inst Franç Petrole 16:1330 ff
5. Damronglerd S (1973) Transfert de matière en fluidisation homogène. These, Université Paul Sabatier de Toulouse
6. Zabrodsky SS (1966) Hydrodynamics and heat transfer in fluidized beds. The M.I.T. Press, Cambridge, MA (Chap. 8, Figs. 8–11)
7. Kunii D, Levenspiel O (1969) Fluidization engineering. John Wiley & Sons, Inc., New York
8. Xavier AM, Davidson JF (1985) Heat transfer in fluidized beds. In: JF Davidson et al. (eds) Fluidization, 2nd edn. Academic Press, London
9. Schlünder EU (1977) On the mechanism of mass transfer in heterogeneous systems. Chem Eng Sci 32:845–851
10. Martin H (1978) Low Péclet number particle-to-fluid heat and mass transfer in packed beds. Chem Eng Sci 33:913–919
11. Subramanian D, Martin H, Schlünder EU (1977) Stoffübertragung zwischen Gas und Feststoff in Wirbelschichten. Verfahrenstechnik 11(12):748–750
12. Wunder R (1980) Wärmeübergang an vertikalen Wärmetauscherflächen in Gaswirbelschichten. Diss. T.U. München
13. Martin H (1980) Wärme- und Stoffübertragung in der Wirbelschicht. Chemie-Ing-Techn 52(3):199–209
14. Schlünder EU (1971) Wärmeübergang an bewegte Kugelschüttungen bei kurzfristigem Kontakt. Chemie-Ing-Techn 43(11):651–654
15. Reiter TW, Camposilvan J, Nehren R (1972) Akkommodationskoeffizienten von Edelgasen an Pt im Temperaturbereich von 80 bis 450 K. Wärme- und Stoffübertragung 5(2):116–120
16. Heyde M, Klocke HJ (1979) Wärmeübergang zwischen Wirbelschicht und Einbauten – ein Problem des Wärmeübergangs bei kurzfristigem Kontakt. Chemie-Ing-Techn 51(4):318–319
17. Baskakov AP, et al. (1973) Heat transfer to objects immersed in fluidized beds. Powder Technol 8:273–282
18. Martin H Fluid Bed Heat Exchangers. Proceedings of the 1981 international seminar advancements in heat exchangers, Dubrovnik, Sept. 1981
19. Bock HJ (1980) Experimentelle und theoretische Untersuchungen zum Einfluss der lokalen Hydrodynamik auf den lokalen Wärmeübergang in Gas-Feststoff-Wirbelschichten. Diss. U. Erlangen
20. Martin H (1984) Heat transfer between gas fluidized beds of solid particles and the surfaces of immersed heat exchanger elements. Chem Eng Process 18:157–169 and 199–233
21. Janssen K (1973) Beitrag zur Berechnung von Wärmeübergangszahlen zwischen Fluidatbetten und darin eintauchenden Wärmetauschflächen in Abhängigkeit von den Strömungsbedingun-gen inhomogener Fluidisierungszustände. Diss. RWTH Aachen
22. Jüntgen H, van Heek KH (1977) A technical scale gas generator for steam gasification of coal using nuclear heat. Nuclear Technol 35:581–590
23. Grewal NS, Saxena SC (1983) Experimental studies of heat transfer between a bundle of horizontal tubes and a gas solid fluidized bed of small particles. Ind Eng Chem Process Des Dev 22(3):367–376
24. Molerus O, Mattmann W (1992) Heat transfer mechanisms in gas fluidized beds. Chem Eng Technol 15:139–150, 240–244 and 291–294
25. Dietz S (1994) Wärmeübergang in blasenbildenden Wirbelschichten. Diss. Univ. Erlangen-Nürnberg
26. Haid M (1997) Correlations for the prediction of heat transfer to liquid–solid fluidized beds. Chem Eng Process 36:143–147
27. Haid M, Martin H, Müller-Steinhagen H (1994) Heat transfer to liquid–solid fluidized beds. Chem Eng Process 33:211–225

M6 Heat Transfer from a Wall to Stagnant and Mechanically Agitated Beds

Evangelos Tsotsas
Otto-von-Guericke-Universität Magdeburg, Magdeburg, Germany

1 Introduction

Granular and powdery products are often treated in contact equipment of various geometrical configurations (tray, paddle, drum, etc.). Heat transfer from the wall of the apparatus to the bed, or vice versa, is essential for this kind of processing and will, therefore, be discussed in the present chapter. Immersed surfaces such as the shaft of stirring devices may be used additionally to the apparatus wall for heating or cooling. Modelling of heat transfer will be presented in Sects. 2–5 on the basis of a model that considers the bed of particles as one continuous phase. This is usually called the penetration model. The heat exchanged between the wall and the bed may be used to just change bed temperature. Alternatively, a part of the supplied heat may be consumed for phase change or chemical reaction in the interior of the bed. These two cases will be distinguished, describing the former as heat transfer to beds without latent sinks (Sect. 2) and the latter as heat transfer to beds with latent heat sinks (Sect. 3). In case of merely heating or cooling, further distinction will be made between stagnant (static) and mechanically agitated beds (Sects. 2.1 and 2.2, respectively). Mechanical agitation can be provided by the rotation of the equipment (e.g., rotary drum) or by embedded, rotating stirrers. Modelling with heat sinks will be discussed for drying, distinguishing between drying in pure vapor atmosphere (vacuum contact drying, Sect. 3.1) and drying in the presence of inert gas (atmospheric contact drying, Sect. 3.2). Only mechanically agitated beds will be treated explicitly in Sect. 3. Parameters, which are necessary in order to conduct calculations with the penetration model, will be presented in Sect. 4. Extensions and some recent applications will be briefly outlined in Sect. 5, with reference to the relevant literature. Subsequently, a short introduction to emerging new modelling approaches that consider every particle of the bed individually (discrete models) will be given in Sect. 6. At the end, four examples that document and further illustrate calculations according to Sects. 2–4 will be provided.

2 Heat Transfer to Beds Without Latent Sinks

Figure 1 gives a qualitative impression of the temperature profile between a heating wall and an adjoining bed, which is free of latent sinks. There is a steep temperature drop in the immediate vicinity of the wall, $\vartheta_W - \vartheta_0$, followed by a further decrease toward the interior of the bed, $\vartheta_0 - \vartheta_{bed}$ (ϑ_{bed}: average caloric bed temperature). The temperature jump $\vartheta_W - \vartheta_0$ and the temperature difference $\vartheta_0 - \vartheta_{bed}$ are assigned to a contact heat resistance, $1/\alpha_{WS}$, and to a penetration resistance, $1/\alpha_{bed}$, respectively. Therefore, it is

$$\alpha_{WS} = \dot{q}/(\vartheta_W - \vartheta_0), \quad (1)$$

$$\alpha_{bed} = \dot{q}/(\vartheta_0 - \vartheta_{bed}). \quad (2)$$

The overall heat transfer coefficient

$$\alpha = \dot{q}/(\vartheta_W - \vartheta_{bed}) \quad (3)$$

is obtained to

$$\frac{1}{\alpha} = \frac{1}{\alpha_{WS}} + \frac{1}{\alpha_{bed}}. \quad (4)$$

Equations for the calculation of α_{WS} are given in Sect. 4.1. To derive α_{bed}, the bed is considered as a quasi-continuum with effective properties. These are the density $\rho_{bed,dry}$, the specific heat capacity $c_{bed,dry}$, and the thermal conductivity $\lambda_{bed,dry}$, where the subscript "dry" indicates the absence of latent sinks (in many cases moisture). In this way, Fourier's theory of

VDI-GVC (ed.), *VDI Heat Atlas*, DOI 10.1007/978-3-540-77877-6_55,

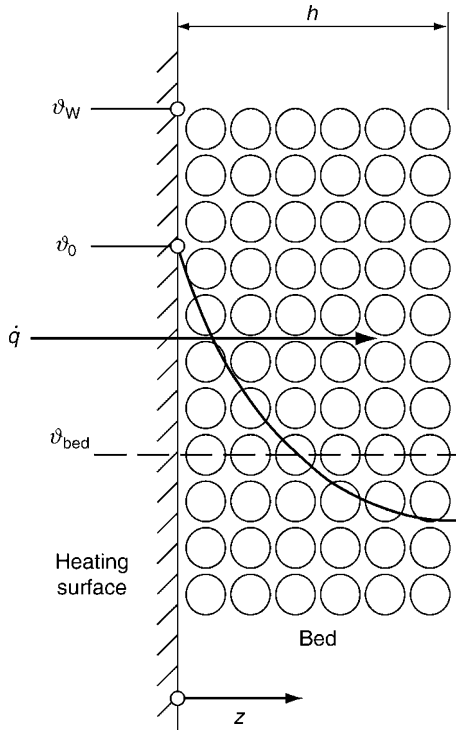

M6. Fig. 1. Scheme of heat transfer from a wall to an adjoining bed of particles.

conduction can be applied. Applying Fourier's theory, stagnant and mechanically agitated beds will be distinguished in the following.

2.1 Stagnant Beds

Using the standard boundary condition of constant temperature ϑ_0, the time-averaged heat penetration coefficient of the stagnant bed is obtained to

$$\alpha_{\mathrm{bed,dry}} = \frac{2}{\sqrt{\pi}} \frac{\sqrt{(\rho\lambda c)_{\mathrm{bed,dry}}}}{\sqrt{t}}. \tag{5}$$

Here, t is the residence time of the bed on the heating surface. The thermal conductivity of the bed $\lambda_{\mathrm{bed,dry}}$ can be calculated according to Subchap. D6.3.

Equations (5) and (4) yield an overall heat transfer coefficient of

$$\frac{\alpha}{\alpha_{\mathrm{WS}}} = \frac{1}{1+\sqrt{\pi\tau}/2}, \tag{6}$$

with

$$\tau = \frac{\alpha_{\mathrm{WS}}^2}{(\rho\lambda c)_{\mathrm{bed,dry}}} t. \tag{7}$$

A critical residence time

$$t_c = \frac{4}{\pi} \frac{(\rho\lambda c)_{\mathrm{bed,dry}}}{\alpha_{\mathrm{WS}}^2} \tag{8}$$

for the heating process can be derived from the condition $\alpha_{\mathrm{WS}} = \alpha_{\mathrm{bed}}$. Thus, it is

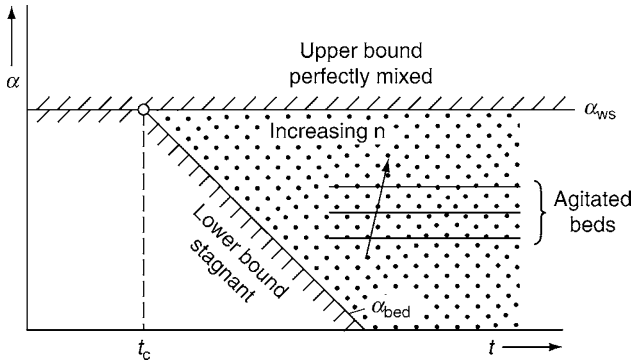

M6. Fig. 2. Wall-to-bed heat transfer coefficient α as a function of time t. Under the critical time t_c, it is approximately $\alpha = \alpha_{\mathrm{WS}}$. Above the critical time t_c, the heat transfer coefficient α decreases with the square root of time for stagnant beds. In case of mechanically agitated beds, α reaches some constant final value, which depends on the quality of mixing, but cannot overcome α_{WS}.

$$t << t_c \rightarrow \alpha \approx \alpha_{\mathrm{WS}}, \tag{9a}$$

$$t >> t_c \rightarrow \alpha \approx \alpha_{\mathrm{bed}}. \tag{9b}$$

Consequently, the contact resistance $1/\alpha_{\mathrm{WS}}$ is rate controlling at short times, whereas the penetration resistance $1/\alpha_{\mathrm{bed}}$ dominates at long times, as illustrated in Fig. 2.

The critical time t_c depends, among others, on particle diameter d and pressure p. At normal pressure, it usually counts seconds; in vacuum, it may reach several minutes. This behavior has been verified experimentally by Wunschmann [1], as Fig. 3 – where momentaneous overall heat transfer coefficients are plotted against time – shows. At high pressures, it is $t >> t_c$, and the measurements agree with Eq. (5). On contrary, at low pressures, it is $t << t_c$, so that the overall heat transfer coefficient equals the contact heat transfer coefficient α_{WS}. Details about the experiments and their evaluation can be found in [1], along with further data from the literature.

Equations (5–9) can also be applied to beds gliding as a rigid body along a heating surface. In this case, the residence time results from the velocity u of bed movement (assumed constant) and from the length L of the heating surface to

$$t = L/u. \tag{10}$$

2.2 Mechanically Agitated Beds

Heat transfer to mechanically agitated beds can be described in a similar way as for stagnant beds by the so-called penetration model that replaces continuous mixing by a sequence of stagnant periods. Every fictitious static period is of duration t_{R}, which inserted in Eq. (5) results to a coefficient for heat penetration of

$$\alpha_{\mathrm{bed}} = \frac{2}{\sqrt{\pi}} \frac{\sqrt{(\rho\lambda c)_{\mathrm{bed,dry}}}}{\sqrt{t_{\mathrm{R}}}}. \tag{11}$$

Stagnant periods are assumed to end with instantaneous and perfect mixing. Their duration t_{R} can be correlated in the form

$$t_{\mathrm{R}} = t_{\mathrm{mix}} N_{\mathrm{mix}}, \tag{12}$$

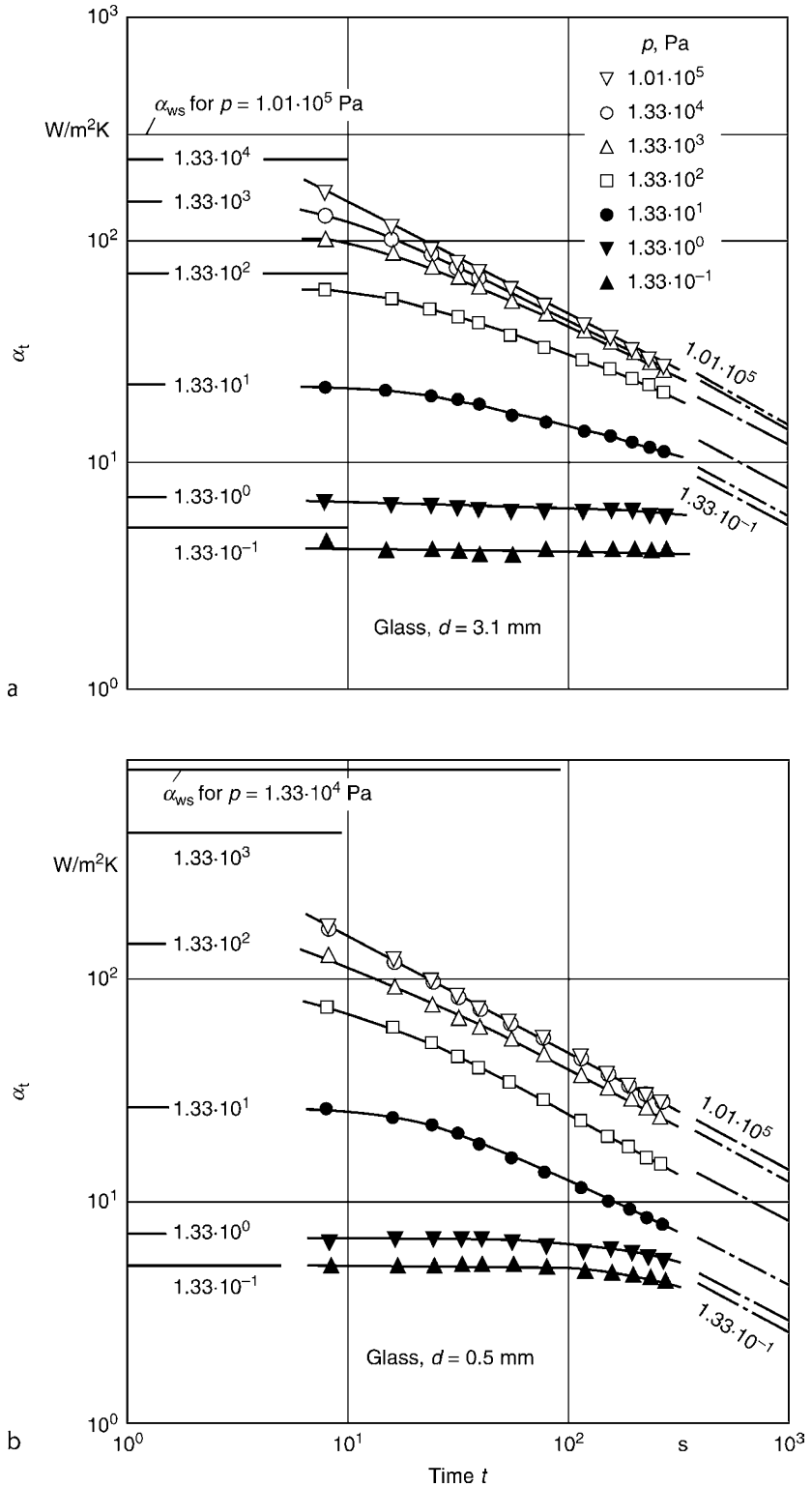

M6. Fig. 3. Evolution of the momentaneous heat transfer coefficient α_t between wall and stagnant bed: measurements by Wunschmann [1] for glass spheres ($\rho_{bed,\,dry} = 1{,}800$ kg m^{-3}, $c_{bed,\,dry} = 633$ J kg^{-1} K^{-1}, $\lambda_p = 0.93$ W m^{-1} K^{-1}) in air at various pressures p and particle diameters d.

with the time constant of the stirring device

$$t_{mix} = 1/n, \tag{13}$$

where n is the rotational frequency of the shaft of the stirrer and N_{mix} is a mixing number. The mixing number depends on the mechanical properties of the system (apparatus, stirrer, particles) and on n. It denotes how often the shaft of the stirrer must turn around, before perfect mixing of the bed can be achieved once. The determination of N_{mix} is discussed in Sect. 4.3.

The overall heat transfer coefficient α is still obtained by the series combination of resistances according to Eq. (4). By

improving mechanical mixing (small t_R), it is possible to increase the penetration coefficient α_{bed} and, therefore, also the overall coefficient α. However, the latter can never overcome the upper bound set by the contact coefficient α_{WS}. This is shown in Fig. 4 by means of measured data from [1]. After some transient, constant values of the overall heat transfer coefficient are reached. Depending on stirrer frequency, these values lie between α_{WS} and the heat transfer coefficient to the stagnant bed according to Eq. (5) (compare with Fig. 2).

From Eqs. (4), (11), and (12), it follows

$$\frac{\alpha}{\alpha_{WS}} = \frac{1}{1 + \sqrt{\pi N_{therm} N_{mix}/2}}, \tag{14}$$

with

$$N_{therm} = \frac{\alpha_{WS}^2}{(\rho\lambda c)_{bed,dry}} t_{mix}. \tag{15}$$

All nonmechanical properties of the system are summarized in the parameter N_{therm}.

A common presentation of Eqs. (6), (7), (14), and (15) is given in Fig. 5 [2] – in comparison with, again, data from [1] for glass spheres with d = 1.0 mm. The values of N_{mix} for agitated beds have been fitted to the measurements. This resulted to N_{mix} = 23 for a blade and to N_{mix} = 3 for a broom stirrer. Better performance of the broom stirrer is due to the fact that the bristles efficiently sweep the heating surface clean of already

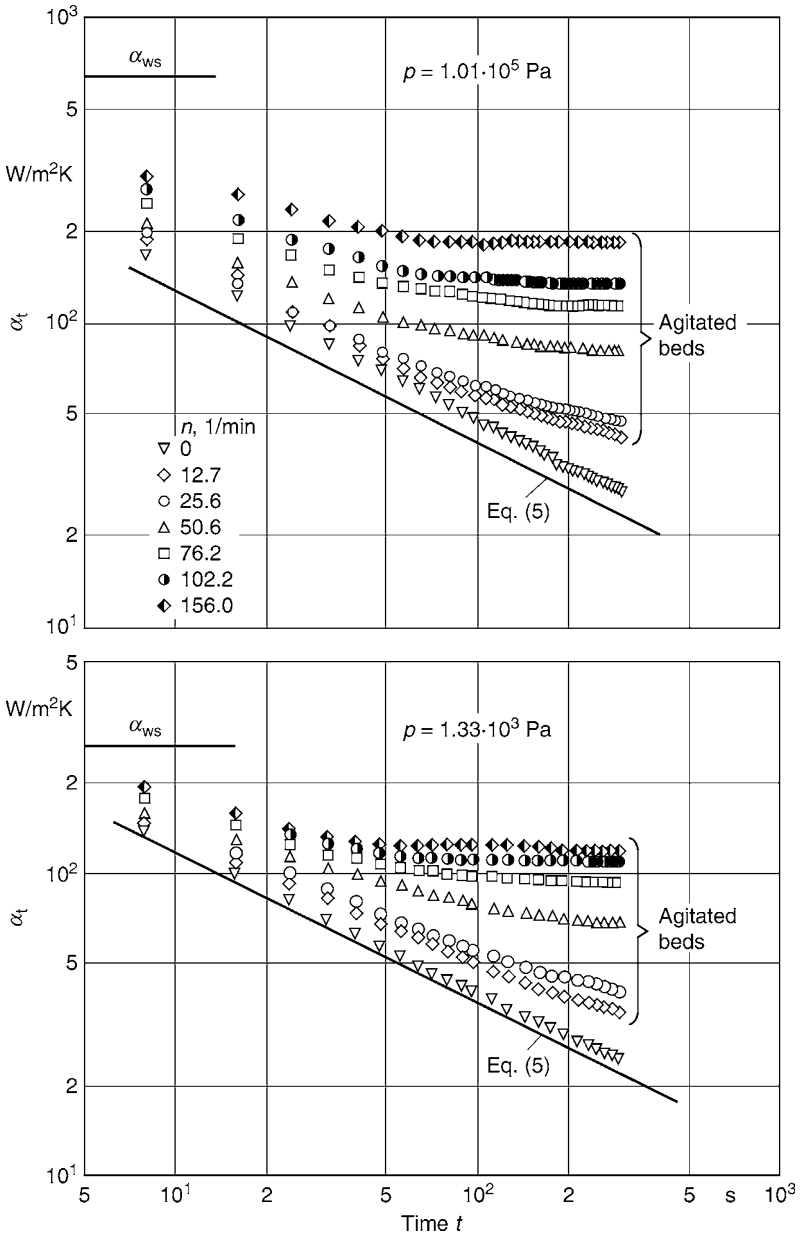

M6. Fig. 4. Momentaneous heat transfer coefficients α_t to mechanically agitated beds over time: measurements by Wunschmann [1] for glass spheres (d = 1 mm) at different pressures p and various stirrer frequencies n. The limiting case of the stagnant bed (n = 0) is included.

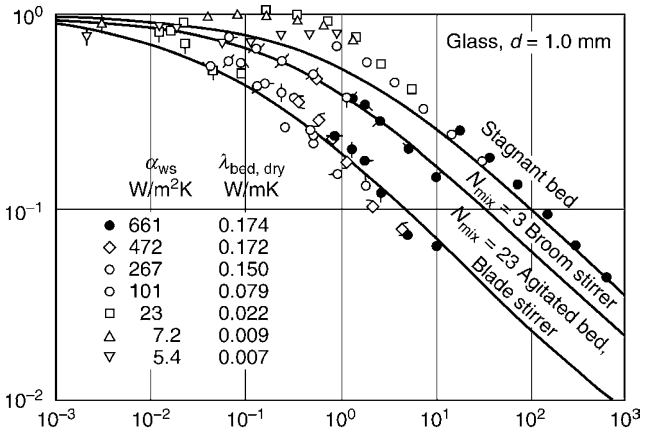

n, 1/min	0	12.7	25.6	50.6	76.3	102	157
p, Pa	α_t/α_{ws}	α/α_{ws}, Blade stirrer					
$1.01\cdot10^5$	●	●	●	●	●	●	●
$1.33\cdot10^4$	◇	◇	◇	◇	◇	◇	◇
$1.33\cdot10^3$	○	○	○	○	○	○	○
$1.33\cdot10^2$	○	○	○	○	○	○	
$1.33\cdot10^1$	□	□	□	□	□	□	□
$1.33\cdot10^0$	△		△			△	
$1.33\cdot10^{-1}$	▽		▽			▽	

n, 1/min	0	12.7	25.6	50.6	76.3	102	157
p, Pa	α_t/α_{ws}	α/α_{ws}, Broom stirrer					
$1.01\cdot10^5$	●	●	●	●	●	●	●
$1.33\cdot10^4$	◇			◇		◇	
$1.33\cdot10^3$	○			○		○	
$1.33\cdot10^2$	○			○		○	
$1.33\cdot10^1$	□			■		■	
$1.33\cdot10^0$	△						
$1.33\cdot10^{-1}$	▽						

M6. Fig. 5. Common presentation of heat transfer to stagnant and agitated beds (data from [1], evaluation from [2]). *Stagnant beds*: Reduced momentaneous heat transfer coefficients α_t/α_{WS} versus dimensionless time τ, solid line according to Eq. (6). *Agitated beds*: Reduced steady-state values of the heat transfer coefficient α/α_{WS} versus N_{therm}. Solid lines according to Eq. (14).

heated particles. The dependence of N_{mix} on n has been neglected in this presentation.

3 Heat Transfer to Mechanically Agitated Beds with Latent Sinks

As mentioned in the Introduction, drying (the removal of bed moisture by evaporation) will be used in order to explain the calculation of heat transfer from the wall when heat consumption by phase change or chemical reaction takes places in the bed. Distinction is made between two different modes of operation, namely processing in pure vapor atmosphere (vacuum contact drying) and processing in inert gas atmosphere (atmospheric contact drying), because the presence or not of inert gas has a significant influence on the mechanisms of heat transfer. The discussion will be restricted to mechanically agitated beds.

It is assumed that all the liquid phase is present in the interior of porous particles, not in the voids of the bed.

3.1 Pure Vapor Atmosphere

The penetration model has been extended to vacuum contact drying by Schlünder and Mollekopf [3], who assumed that a steep drying front propagates into the bed during every fictitious stagnant period. Not only temperature, but also moisture profiles are levelled out at the end of every such period (Fig. 6). Profiles within a stagnant period are illustrated in more detail in Fig. 7. Here, X is the moisture content of the bed (in kg moisture per kg dry solids), which is evenly distributed above the drying front; ϑ_{bed} is the respective bed temperature, z_T is the position of the drying front at the considered point of time.

Heat transfer kinetics can, again, be expressed in the form

$$\alpha_{WS} = \dot{q}_0/(\vartheta_W - \vartheta_0), \tag{16}$$

$$\alpha_{bed} = \dot{q}_0/(\vartheta_0 - \vartheta_{bed}). \tag{17}$$

The contact heat transfer coefficient α_{WS} does not change in principle and can be calculated according to Sect. 4.1 for pure vapor atmosphere. On contrary, the consumption of heat by evaporation in the interior of the bed (the latent heat sink) has a significant influence on the penetration coefficient, which is in this case obtained to

$$\alpha_{bed} = \frac{2}{\sqrt{\pi}} \frac{\sqrt{(\rho\lambda c)_{bed,dry}}}{\sqrt{t_R}} \frac{1}{\operatorname{erf}\zeta} = \frac{\alpha_{bed,dry}}{\operatorname{erf}\zeta}. \tag{18}$$

For the sake of distinction, the penetration coefficient of the dry bed according to Eq. (11) is denoted by $\alpha_{bed,dry}$ in Eq. (18). Similarly, α_{dry} is the overall heat transfer coefficient to the dry bed. The serial combination of resistances (Eq. (4)) remains valid and leads for the overall heat transfer coefficient of the wet bed to the relationship

$$\alpha = \frac{\alpha_{WS}}{1 + (\alpha_{WS}/\alpha_{dry} - 1)\operatorname{erf}\zeta}. \tag{19}$$

As the equations show, material properties of the dry bed are sufficient for the calculation of vacuum contact drying. The influence of the latent sink appears only in the dimensionless position of the drying front

$$\zeta = \frac{z_T}{2\sqrt{\kappa_{bed,dry}\, t}}, \tag{20}$$

with

$$\kappa_{bed,dry} = \frac{\lambda_{bed,dry}}{(\rho c)_{bed,dry}}. \tag{21}$$

According to [3] (Neumann's solution) ζ is determined by the relationship

$$\sqrt{\pi}\zeta \exp(\zeta^2)\left[\left(\frac{\alpha_{WS}}{\alpha_{dry}} - 1\right)\operatorname{erf}\zeta + 1\right] = \frac{1}{Ph}\left(\frac{\alpha_{WS}}{\alpha_{dry}} - 1\right), \tag{22}$$

with

$$Ph = \frac{X\Delta h_v}{c_{bed,dry}(\vartheta_W - \vartheta_{bed})}. \tag{23}$$

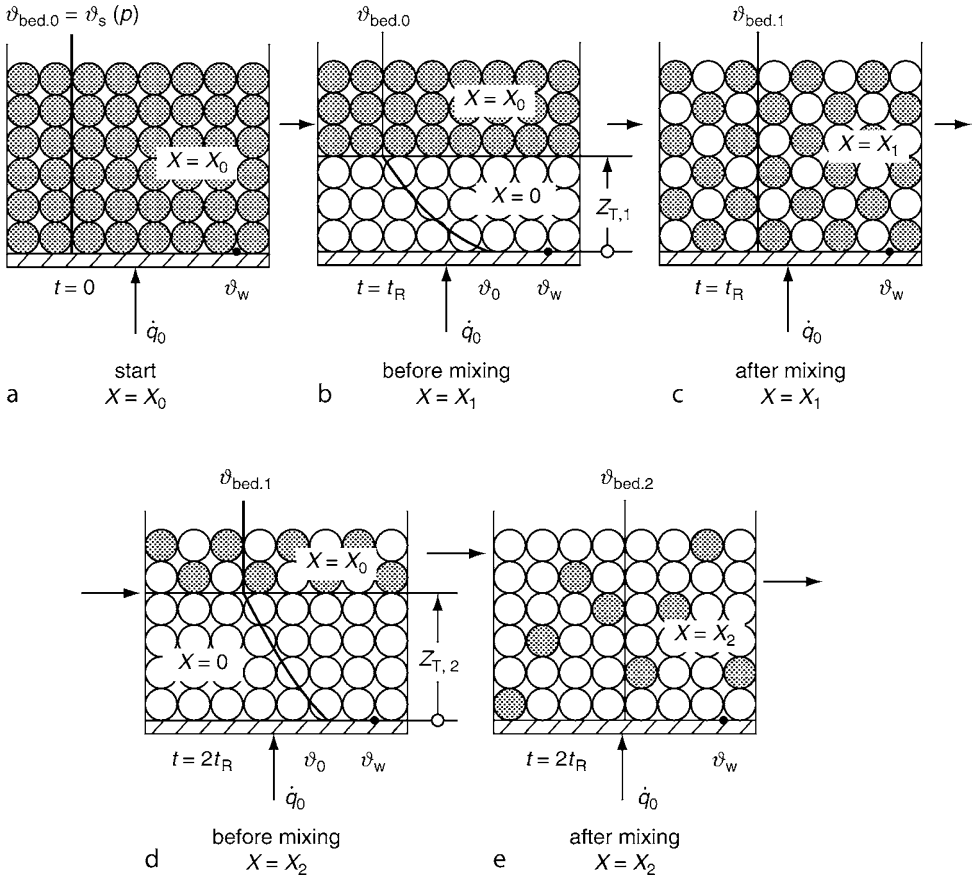

M6. Fig. 6. Scheme of the penetration model for vacuum contact drying.

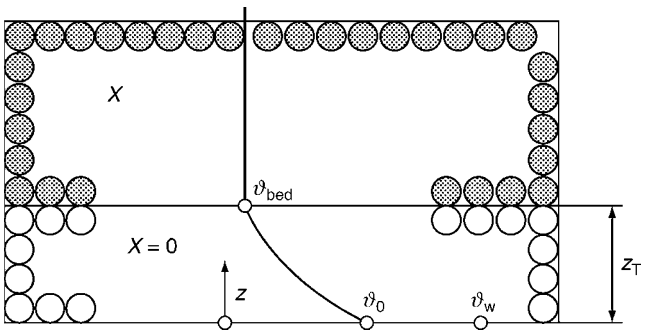

M6. Fig. 7. Temperature and moisture profiles during a fictitious stagnant period.

With decreasing moisture content X, the phase change number Ph decreases, the penetration depth of the drying front increases, and the penetration heat transfer coefficient α_{bed} (Eq. (18)) decreases. At the limit of $X \to 0$, one obtains $\zeta \to \infty$, $\mathrm{erf}\,\zeta \to 1$ and $\alpha_{bed} \to \alpha_{bed,dry}$. The increase of z_T with progressing drying is indicated in an exaggerated way in Fig. 6.

According to [4], accurate values of the error function can be obtained from

$$\mathrm{erf}\,\zeta = 1 - (a_1 t + a_2 t^2 + a_3 t^3)\exp(-\zeta^2), \tag{24a}$$

with

$$t = 1/(1 + p\zeta) \tag{24b}$$

and $a_1 = 0.3480242$, $a_2 = -0.0958798$, $a_3 = 0.7478556$, and $p = 0.47047$.

Heat fluxes at the wall, $\dot{q}_0$, and at the phase change front, $\dot{q}_{lat}$, are calculated by

$$\dot{q}_0 = \alpha(\vartheta_W - \vartheta_{bed}), \tag{25}$$

$$\dot{q}_{lat} = \alpha(\vartheta_W - \vartheta_{bed})\exp(-\zeta^2). \tag{26}$$

The comparison with measured data shows a good agreement when using the heat flux at the phase change front $\dot{q}_{lat}$ in order to calculate the drying rate $\dot{m}$:

$$\dot{m} = \dot{q}_{lat}/\Delta h_v. \tag{27}$$

The remaining heat input is used to increase the temperature of the bed [3]. Consequently, the changes of moisture content and average caloric bed temperature within a stagnant period are obtained to

$$\Delta X = \frac{\dot{m} t_R A}{M_{dry}} \tag{28}$$

and

$$\Delta\vartheta_{bed} = \Delta X \frac{\Delta h_v}{c_{bed,dry} + c_1 X}[\exp(\zeta^2) - 1]. \tag{29}$$

Here, A is the covered area of the heating wall and M_{dry} is the dry mass of the product. The term $c_1 X$ accounts for still existing liquid moisture. Moisture content and bed temperature at the beginning of the $(i + 1)$th stagnant period result from the respective values of the foregoing period to

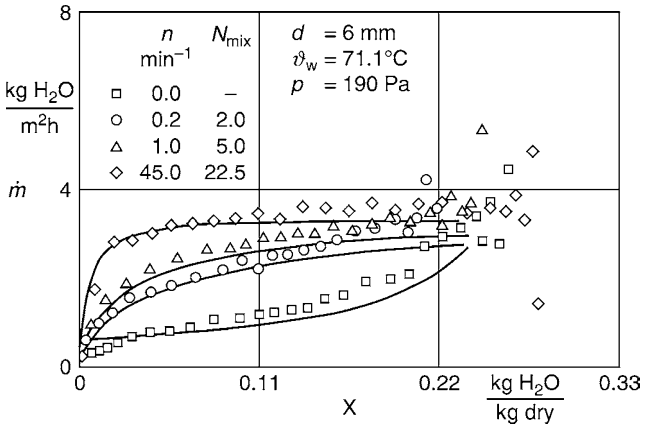

M6. Fig. 8. Influence of stirrer frequency n on vacuum contact drying of coarse-grained, water-loaded material (magnesium silicate, d = 6.0 mm) in a tray dryer (D = 240 mm) according to [5] ($\rho_{bed,dry}$ = 980 kg m^{-3}, $c_{bed,dry}$ = 800 J kg^{-1} K^{-1}, $\lambda_{bed,dry}$ = 0.151 W m^{-1} K^{-1}, δ = 20 µm, α_{WS} = 32 W m^{-2} K^{-1}, ϑ_W = 71°C, p = 190 Pa).

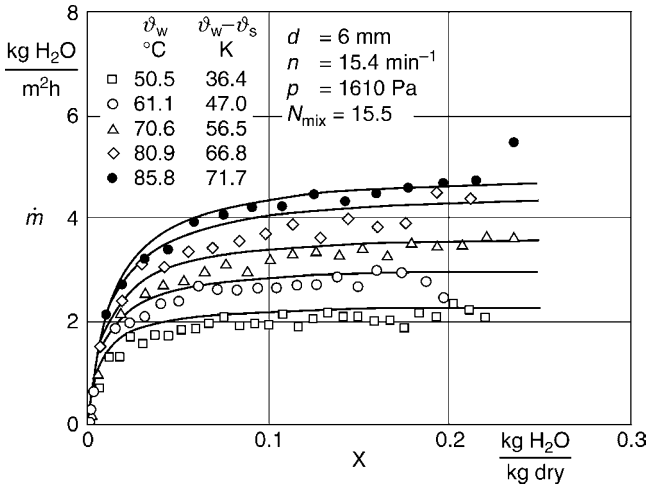

M6. Fig. 9. Influence of heating plate temperature ϑ_W on vacuum contact drying of coarse-grained, water-loaded material (magnesium silicate, d = 6.0 mm) in a tray dryer (D = 240 mm) according to [5] ($\rho_{bed,dry}$ = 980 kg m^{-3}, $c_{bed,dry}$ = 800 J kg^{-1} K^{-1}, $\lambda_{bed,dry} \approx$ 0.175 W m^{-1} K^{-1}, δ = 20 µm, α_{WS} = 46 W m^{-2} K^{-1}, p = 1,610 Pa (ϑ_S = 14.1°C), n = 15.4 min^{-1}, N_{mix} = 15.5).

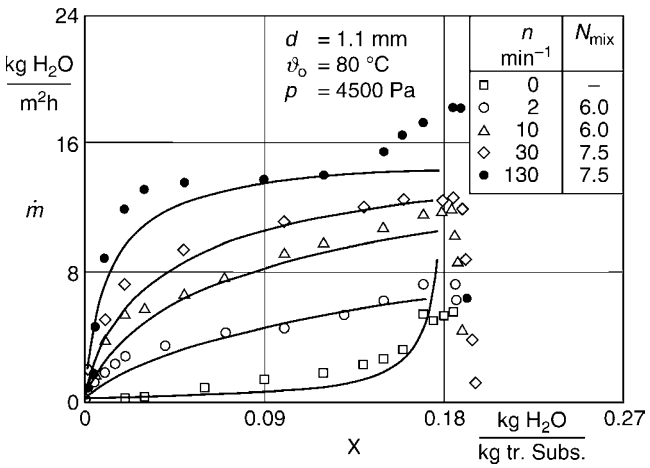

M6. Fig. 10. Influence of stirrer frequency n on vacuum contact drying of fine-grained, water-loaded material (aliminum silicate, d = 1.1 mm) in a paddle dryer (D = 134 mm) according to [5] ($\rho_{bed,dry}$ = 1,020 kg m^{-3}, $c_{bed,dry}$ = 800 J kg^{-1} K^{-1}, $\lambda_{bed,dry}$ = 0.153 W m^{-1} K^{-1}, δ = 2.5 µm, α_{WS} = 226 W m^{-2} K^{-1}, ϑ_o = 80°C, p = 4,500 Pa).

$$X_{i+1} = X_i - \Delta X_i, \tag{30}$$

$$\vartheta_{bed,i+1} = \vartheta_{bed,i} + \Delta\vartheta_{bed,i}. \tag{31}$$

For $i = 0$, it is $X = X_0$ (initial moisture content) and $\vartheta_{bed} = \vartheta_S$ (saturation temperature at the imposed pressure). Consequently, the drying curve, $\dot{m}(X)$, and the temperature curve, $\vartheta_{bed}(X)$, can be calculated step-by-step.

Equation (4) yields simple limiting cases for vacuum contact drying:

1. $\alpha_{WS} << \alpha_{bed} \rightarrow \alpha \approx \alpha_{WS}$ and $\dot{m}(X_0) \sim (\vartheta_W - \vartheta_S)^n$ with $n \approx 1$.
2. $\alpha_{WS} >> \alpha_{bed} \rightarrow \alpha \approx \alpha_{bed}$ and $\dot{m}(X_0) \sim (\vartheta_W - \vartheta_S)^n$ with $n < 1$.

The condition $\alpha_{WS} << \alpha_{bed}$ is fulfilled with big particles. Then, the contact resistance is rate controlling. Heat transfer and drying rate can hardly be increased by better mixing (Fig. 8). Drying rate at the beginning of the process $\dot{m}(X_0)$ is almost directly proportional to the driving temperature difference $\vartheta_W - \vartheta_S$ (Fig. 9).

The condition $\alpha_{WS} >> \alpha_{bed}$ is approximated with fine-grained materials. Then, the penetration resistance of the bed is rate controlling. This resistance can be reduced significantly by intensifying the mechanical agitation, as Fig. 10 shows. Since the coefficient α_{bed} decreases with increasing difference between heating surface temperature and bed temperature – due to deeper penetration of the drying front – the dependence of initial drying rate $\dot{m}(X_0)$ from $\vartheta_W - \vartheta_S$ is weaker than linear (Fig. 11).

3.2 Inert Gas Atmosphere

Atmospheric conditions (the presence of inert gas) do not change the calculation of either the contact coefficient α_{WS} or the parameters of the penetration model (t_R or N_{mix}). However, they do modify essentially the processes taking place in the interior of the bed, because emerging vapor must – instead of leaving the bed – recondense at the next cold position along the temperature profile. Consequently, net evaporation occurs only at the free surface of the bed. These effects are taken into account in the scheme of Fig. 12, which was proposed by Tsotsas and Schlünder [6] for heat transfer. According to it, both the bed temperature ϑ_{bed} and the moisture content X are known and evenly distributed at the beginning of the considered fictitious stagnant period. During this period, heat comes from the wall into the bed with a time-averaged flux of $\dot{q}_0$. By analogy to the previous paragraphs, it is

$$\dot{q}_0 = \alpha_{WS}(\vartheta_W - \vartheta_0), \tag{32}$$

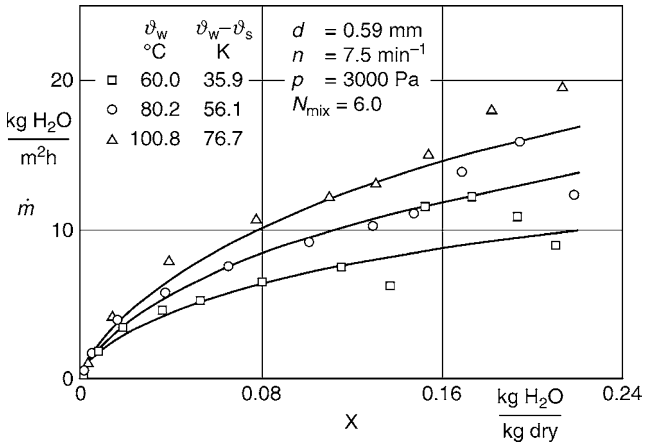

M6. Fig. 11. Influence of heating plate temperature ϑ_W on vacuum contact drying of fine-grained, water-loaded material (aluminum silicate, d = 0.59 mm) in a tray dryer (D = 240 mm) according to [5] ($\rho_{bed,dry}$ = 1,030 kg m^{-3}, $c_{bed,dry}$ = 800 J kg^{-1} K^{-1}, $\lambda_{bed,dry} \approx$ 0.140 W m^{-1} K^{-1}, δ = 2.5 µm, $\alpha_{WS} \approx$ 318 W m^{-2} K^{-1}, p = 3,000 Pa (ϑ_S = 24.1°C), n = 7.5 min^{-1}, N_{mix} = 6.0).

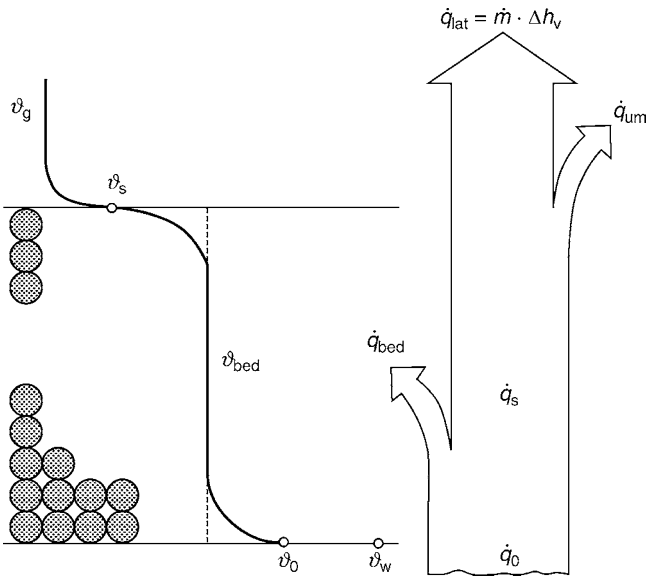

M6. Fig. 12. Temperature profiles and heat fluxes during one fictitious stagnant period for contact drying in inert gas atmosphere. At the beginning of the stagnant period, temperature (dashed line) and moisture content are evenly distributed. Moisture is assumed to remain equally distributed throughout the stagnant period.

$$\dot{q}_0 = \alpha_{bed}(\vartheta_0 - \vartheta_{bed}), \alpha_{bed} \text{ at } (\vartheta_0 + \vartheta_{bed})/2. \quad (33)$$

Assuming t_R as short enough for the formation of a drying front to be avoided, leads to the conclusion that the heat penetration coefficient can be calculated under atmospheric conditions by Eq. (11), replacing however the properties of the dry bed with those of the wet bed (subscript: wet):

$$\alpha_{bed} = \frac{2}{\sqrt{\pi}} \frac{\sqrt{(\rho\lambda c)_{bed,wet}}}{\sqrt{t_R}}. \quad (34)$$

Whereas the capacity

$$(\rho c)_{bed,wet} = (c_{bed,dry} + X c_l)\rho_{bed,dry} \quad (35)$$

is nearly temperature-independent, the thermal conductivity $\lambda_{bed,wet}$ is a strong function of temperature (calculation in Sect. 4.2). Therefore, the unknown temperature ϑ_0 cannot be simply eliminated (as in Sects. 2 and 3.1), but must be determined by iterative solution of Eqs. (32) and (33). The value of $\dot{q}_0$ also results from this iteration.

Simultaneously with the heat transfer from the wall to the bulk of the bed, heat is also transferred from the bulk of the bed to the free bed surface. There, this heat is used to evaporate moisture or it gets lost to the environment (Fig. 12). In the time average, one can write

$$\dot{q}_s = \alpha_{bed}(\vartheta_{bed} - \vartheta_s), \alpha_{bed} \text{ at } (\vartheta_{bed} + \vartheta_s)/2, \quad (36)$$

$$\dot{q}_s = \dot{q}_{lat} + \dot{q}_{um}, \quad (37)$$

$$\dot{q}_{lat} = \dot{n}\Delta\tilde{h}_v, \quad (38)$$

$$\dot{n} = n_g\beta_g \ln\frac{p - p_g}{p - p_S(\vartheta_s)} \quad (39)$$

and

$$\dot{q}_{um} = (\alpha_g + \alpha_{rad})\ (\vartheta_s - \vartheta_g). \quad (40)$$

The heat transfer coefficient α_{bed} can, again, be calculated with the help of Eq. (34).

Equation (39) is the usual expression for one-side diffusion kinetics in case of convective drying, with the partial pressure of the evaporating component in the bulk of the gas phase p_g and the saturation pressure at the free surface of the bed $p_S(\vartheta_s)$. By means of the analogy between heat and mass transfer, the gas-side mass transfer coefficient β_g can be eliminated. For the combination of water and air with a Lewis number close to unity, one obtains in mass units

$$\dot{q}_{lat} = \dot{m}\Delta h_v, \quad (41)$$

$$\dot{m} = \frac{\alpha_g}{c_{p,g}} \frac{\tilde{M}_{H_2O}}{\tilde{M}_{air}} \ln\frac{p - p_g}{p - p_S(\vartheta_s)} \quad (42)$$

instead of Eqs. (38) and (39).

Should the surrounding gas be hotter than the free surface of the bed ($\vartheta_g > \vartheta_s$), then the heat flux $\dot{q}_{um}$ would change direction. This case is usually denoted by combined contact and convective drying. Heat transfer coefficients to or from the gas by convection (α_g) or radiation (α_{rad}) can be estimated with the help of respective chapters of Heat Atlas.

Due to the temperature dependence of α_{bed} and the coupling between heat and mass transfer at the free surface of the bed, the bed surface temperature ϑ_s must be calculated iteratively from Eqs. (36–40), or Eqs. (36), (37), (40–42). At the end of the iteration values for the heat fluxes and the drying rate $\dot{m}$ are also obtained.

The change of average bed temperature during the considered stagnant period is

$$\Delta\vartheta_{bed} = \frac{\dot{q}_{bed}\, t_R}{(\rho c)_{bed,wet} h}, \quad (43)$$

with the bed height h and

$$\dot{q}_{bed} = \dot{q}_0 - \dot{q}_s. \quad (44)$$

The change of moisture content is obtained from Eq. (28). Similarly to vacuum contact drying, the calculation is conducted from one to the next fictitious stagnant period with the help of Eqs. (30) and (31). The initial values $X = X_0$ and $\vartheta_{bed} = \vartheta_{bed,0}$ are not subjected to any restrain.

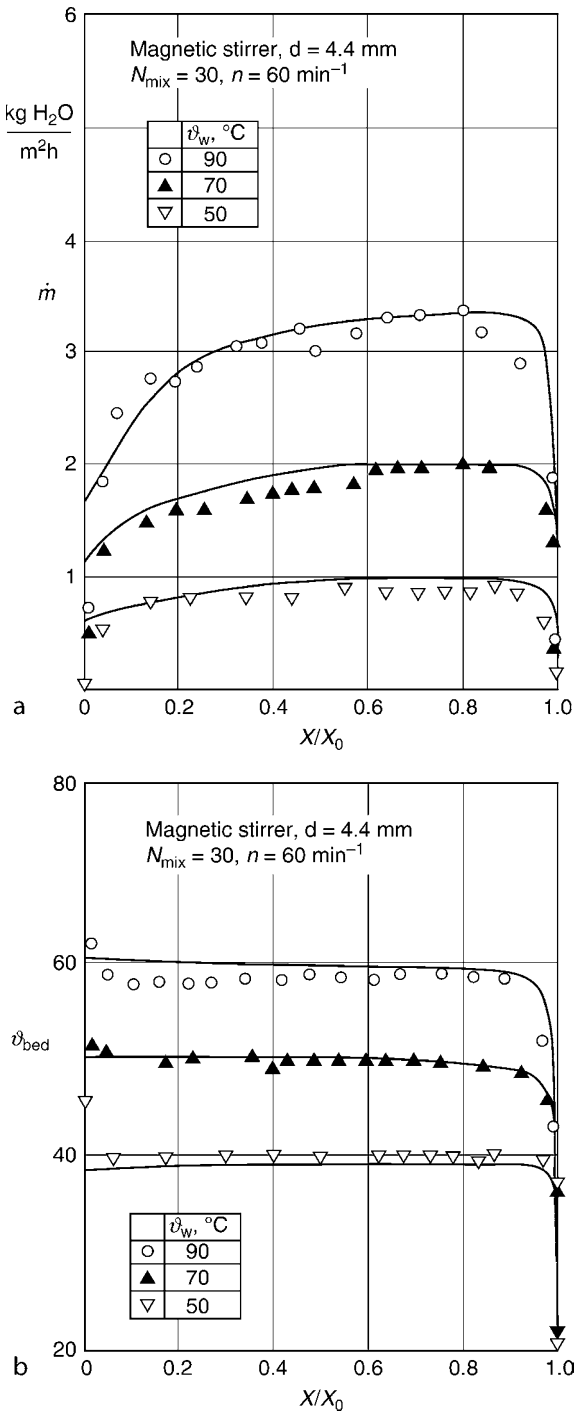

M6. Fig. 13. (a) Drying curves and (b) bed temperature curves during atmospheric contact drying of water-loaded aluminum silicate (d = 4.4 mm) in a mini-plant tray equipment (D = 100 mm) according to [6] ($p = 10^5$ Pa, $n \cong 60$ min^{-1}, $N_{mix} = 30$, $X_0 = 0.24$, $\vartheta_{bed,0} \cong 20$°C, free convection to ambient air at the upper surface of the bed).

The foregoing discussion and Sect. 4.2 indicate that the wet bed works in a similar way like a heat pipe, transporting heat from the wall to the free surface of the bed, where it is consumed by evaporation. The transportation of moisture back to the hot side, which is achieved by capillarity in classical heat pipes, takes place by mechanical agitation of the particle system.

Typical drying and temperature curves for water-loaded aluminum silicate in an open, mini-plant tray dryer are shown in Fig. 13. The bed temperature ϑ_{bed} attains a nearly constant value over a broad range of moisture content. The described calculation (solid lines, see also Sect. 4.2) is in good agreement with the experimental results, can, however, not predict the decrease of drying rate to zero and the increase of bed temperature at the end of the process. This can be repaired by multiplying the right-hand side of Eq. (42) with an empirical correction factor, which should change value from unity to zero as a function of X/X_0 at small moisture contents. Reduction of the surface area available for evaporation by successive drying out of particles is the physical background of this behavior.

By closing the mini-plant dryer and imposing water-jet vacuum on it, the drying curves of Fig. 14 are obtained. All other conditions are identical to those of Fig. 13. One can see that change from the atmospheric to the vacuum mode of operation increases the drying rates by a factor of approximately two. This result may be due to additional mass transfer resistances in the presence of inert gas, but should not be generalized. It should be noticed that the value of the mixing number N_{mix} does not change with the operational mode. Similar results have been obtained with larger dryers and with smaller particles.

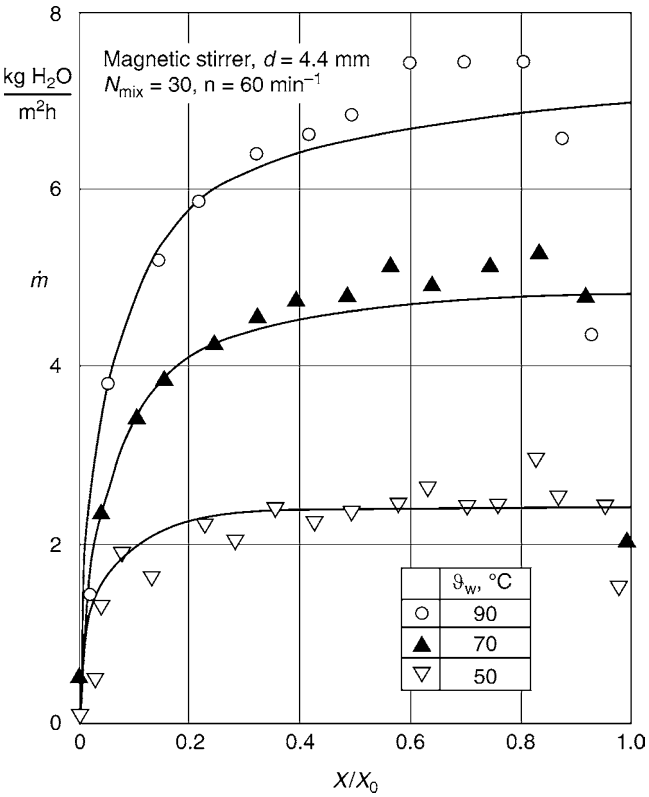

M6. Fig. 14. Drying curves measured under water-jet vacuum for the same material, equipment and operating conditions as in Fig. 13.

4 Calculation of Relevant Quantities

4.1 Contact Heat Transfer Coefficient

According to Schlünder [2], it is

$$\alpha_{WS} = \varphi\alpha_{WP} + \alpha_{rad}, \tag{45a}$$

$$\alpha_{WP} = \frac{4\lambda_g}{d}\left[\left(1+\frac{2\,(l+\delta)}{d}\right)\ln\left(1+\frac{d}{2\,(l+\delta)}\right)-1\right], \tag{45b}$$

$$\alpha_{rad} = 4\,C_{W,bed}\,T^3, \tag{45c}$$

$$C_{W,bed} = \sigma/(1/\varepsilon_W + 1/\varepsilon_{bed} - 1). \tag{45d}$$

The symbols mean:

α_{WP}	wall–particle heat transfer coefficient,
φ	surface coverage factor ($\varphi \approx 0.8$ for mono-dispersed beds of spheres),
α_{rad}	heat transfer coefficient by radiation,
σ	radiation coefficient of the black body ($\sigma = 5.67 \cdot 10^{-8}$ W m^{-2} K^{-4}),
ε_W, ε_{bed}	emission coefficients of wall and bed, respectively,
λ_g	thermal conductivity of the gas,
d	particle diameter,
δ	surface roughness of particles.

l is the modified mean free path of gas molecules:

$$l = 2\frac{2-\gamma}{\gamma}\sqrt{\frac{2\pi\tilde{R}T}{\tilde{M}}}\frac{\lambda_g}{p(2\,c_{p,g}-\tilde{R}/\tilde{M})}, \tag{46}$$

with

p	pressure,
$c_{p,g}$	specific heat capacity of the gas,
$\tilde{M}$	molar mass of the gas,
$\tilde{R}$	universal gas constant ($\tilde{R}$ = 8.314 J mol^{-1} K^{-1}),
γ	accommodation coefficient.

The accommodation coefficient γ can be calculated according to [7] by means of the correlation:

$$\log\left(\frac{1}{\gamma}-1\right) = 0.6 - \frac{(1000\ \mathrm{K}/T)+1}{C}. \tag{47}$$

Here, T is the absolute temperature. The quantity C depends on the molar mass of the gas (He: $C = 50$, H_2O: $C = 3.6$, air: $C = 2.8$).

The surface roughness of the particles can be estimated with the help of, e.g., REM-pictures. Schlünder [2] uses $\delta = 0$ for glass, polymeric, and metallic particles, whereas Mollekopf [5] applies a value of $\delta = 2.5$ µm for particles made of aluminum silicate.

4.2 Thermal Conductivity of Wet Packed Beds in Inert Gas Atmosphere

Based on Krischer [8], see also ◉ Subchap. D6.3, Tsotsas and Schlünder [6] have proposed to calculate the thermal conductivity λ_p of partially wet porous particles in the presence of inert gas by series and parallel combination of the resistances of all possible paths of heat transfer according to the equations:

$$\lambda_l = (1-\psi_p)\lambda_s + \psi_l\lambda_l + b\,(\psi_p-\psi_l)\,(\lambda_g+\lambda_{diff}) + (1-b)\,(\psi_p-\psi_l)\,\lambda_g, \tag{48a}$$

$$\lambda_{ll} = \left[\frac{1-\psi_p}{\lambda_s}+\frac{\psi_l}{\lambda_l}+\frac{b\,(\psi_p-\psi_l)}{\lambda_g+\lambda_{diff}}+\frac{(1-b)\,(\psi_p-\psi_l)}{\lambda_g}\right]^{-1}, \tag{48b}$$

$$\lambda_p = \left(\frac{1-a_p}{\lambda_l}+\frac{a_p}{\lambda_{ll}}\right)^{-1}, \tag{48c}$$

$$b = 1-\left(1-\frac{X}{X_S}\right)^9, \tag{49}$$

$$\psi_l = (\rho_p/\rho_l)X. \tag{50}$$

The symbols mean:

λ_s	thermal conductivity of the solid phase,
λ_l	thermal conductivity of the liquid,
λ_g	thermal conductivity of the gas,
λ_{diff}	thermal conductivity by evaporation, diffusion, recondensation (heat pipe effect),
ψ_p	particle porosity,
ψ_l	volumetric fraction of liquid in particles,
X_S	saturation moisture content (can be different from X_0),
ρ_p	particle density,
ρ_l	liquid density.

The parameter b in Eq. (49) defines empirically the ratio of pore volume contained between wet pore walls to the total pore volume. The proportion of series combination in the overall resistance scheme is denoted by a_p. A value of a_p = 0.075 can be recommended for capillary porous particles with ψ_p = 0.30–0.40.

No liquid or solid are present in the voids of the bed, but the mechanism of evaporation, diffusion, and recondensation can still work transporting heat from wet to dry patches of the surfaces of adjoining particles. Therefore, the thermal conductivity in the voids of the bed can be approximated by

$$\lambda_H = \left(\frac{1-a_H}{\lambda_l}+\frac{a_H}{\lambda_{ll}}\right)^{-1}, \tag{51a}$$

with

$$\lambda_l = b\,(\lambda_g+\lambda_{diff})+(1-b)\,\lambda_g, \tag{51b}$$

$$\lambda_{ll} = \left(\frac{b}{\lambda_g+\lambda_{diff}}+\frac{1-b}{\lambda_g}\right)^{-1}. \tag{51c}$$

For packed beds, a value of a_H = 0.20 can be used (◉ Subchap. D6.3).

The thermal conductivity of the wet bed in inert gas atmosphere $\lambda_{bed,wet}$ is calculated by combining λ_p and λ_H according to the model of Zehner, Bauer, and Schlünder, as described in ◉ Subchap. D6.3. Doing so, λ_H should be put in place of fluid thermal conductivity λ_f.

For the thermal conductivity λ_{diff}, it holds

$$\lambda_{diff} = \frac{\delta}{\tilde{R}^2 T^3} \frac{p_S}{[1-(p_s/p)]} \Delta\tilde{h}_v^2, \tag{52}$$

where p is the total pressure and $\Delta\tilde{h}_v$ is the molar evaporation enthalpy. In case of water and air, the Antoine equation

$$p_S(\text{Pa}) = \exp\left[23.462 - \frac{3,978.205}{233.349 + \vartheta(^\circ\text{C})}\right] \tag{53}$$

and the correlation

$$\delta(\text{m}^2\,\text{s}^{-1}) = \frac{2.252}{p\,(\text{Pa})} \left(\frac{T(\text{K})}{273}\right)^{1.81} \tag{54}$$

can be used in order to calculate the saturation pressure p_S and the binary diffusion coefficient in the gas phase δ, respectively. The mechanism of evaporation, diffusion, and recondensation, which is expressed in the thermal conductivity λ_{diff}, depends strongly on temperature, so that very large (at the limit infinite) values of λ_{diff} are obtained when the boiling point of the liquid at the prevailing total pressure is approached (see Eq. (52)). Consequently, λ_p, λ_H, and $\lambda_{bed,wet}$ are also strong functions of temperature [9]. The same quantities depend additionally on moisture content X. For $X > 0$, it is always $\lambda_{bed,wet} > \lambda_{bed,dry}$, whereas the thermal conductivity of the dry bed $\lambda_{bed,dry}$ results at $X = 0$.

One further method for calculating $\lambda_{bed,wet}$ has been reported in [10]. In case of particles much different from the capillary porous structure with $\psi_p = 0.30$–0.40, $\lambda_{bed,wet}$ should be measured. The apparatus described in [10] can be used to this purpose.

4.3 Mixing Number

The mixing number N_{mix} must be gained by fitting to experimental data. Mollekopf [5] recommends for free-flowing products the empirical correlation

$$N_{mix} = C\text{Fr}^x, \tag{55a}$$

with

$$\text{Fr} = \frac{(2\pi n)^2 D}{2g}. \tag{55b}$$

Here, n is the revolution frequency of the shaft of the stirrer or of the drum, D is the diameter of the apparatus, and g is the acceleration of gravity. The quantities C and x depend on the type of apparatus used. Mollekopf [5] evaluated vacuum contact drying experiments in two tray dryers (D = 240 and 400 mm), two paddle dryers (D = 134 and 506 mm), and one rotary drum dryer (D = 340 mm), obtaining the following results:

Tray dryer	$C = 25$, $x = 0.2$,
Paddle dryer	$C = 9$, $x = 0.05$,
Rotary drum dryer	$C = 16$, $x = 0.2$.

Only experiments in the tray dryer with D = 240 mm stem from Mollekopf himself, the other results originating from less well-documented industrial data. Therefore, the use of these correlations should be precautious. Another reason for precaution is that N_{mix} may additionally depend on moisture content or temperature in case of cohesive or agglomerating materials. Consequently, values of N_{mix} should be controlled by comparison of a few full-scale experiments with the model whenever possible. A scheme that may be used in order to derive N_{mix} for new products on the basis of lab-scale experiments, when data with a reference product are available at both the laboratory and the production scale, is described in [11]. Coarse first estimates for processing of free-flowing particulate material in contact equipment may be obtained with a value of $N_{mix} = 10$.

5 Extensions and Applications

In case of equipment heated by steam or oil, an additional resistance, $1/\alpha_o$, exists at the heating medium side. This resistance can be accounted for by serial combination with the contact resistance $1/\alpha_{WS}$:

$$1/\alpha'_{WS} = 1/\alpha_o + 1/\alpha_{WS}. \tag{56}$$

Heat conduction in the wall has been neglected in Eq. (56). The value of α'_{WS} should replace α_{WS} in all calculations. Additionally, the driving temperature difference should be set to $\vartheta_o - \vartheta_{bed}$ (instead of $\vartheta_W - \vartheta_{bed}$), where ϑ_o is the temperature of the heating medium.

In some applications, dry, fine-grained particles glide across bundles of heating tubes at relatively small filling grades of the apparatus. Modifications of the models from Sect. 2 for such applications have been proposed in [12].

An application of the vacuum contact drying model to pasty material has been discussed in [13]. The same model has been extended in order to take hygroscopic interactions between moisture and the solids into account [14, 15]. In this case, the bed depicted schematically in Fig. 8 contains both free and bound moisture with the contents X_f and X_h, respectively. Whereas the invading drying front removes the free moisture completely, temperature increase behind the front will cause some part of bound moisture to evaporate. This can be considered by an effective specific heat capacity of the bed according to the definition

$$c_{bed,h} = c_{bed,dry} + c_l X_h - \Delta h_{v,h} (\partial X_h / \partial \vartheta)_p. \tag{57}$$

Here, $\Delta h_{v,h}$ is the evaporation enthalpy of bound moisture and $(\partial X_h/\partial\vartheta)_p$ is the slope of the sorption isobar. All equations of Sect. 3.1 can still be applied by using $c_{bed,h}$ in place of $c_{bed,dry}$ and X_f in place of X. The decrease of free moisture content and the change of bed temperature during a certain stagnant period are calculated by Eqs. (28) and (29), respectively. The decrease of bound moisture content is then obtained from the change of bed temperature and the isobar slope. Beds without free moisture can be treated by putting $c_{bed,h}$ instead of $c_{bed,dry}$ in the equations of Sect. 2.

Michaud et al. [16, 17] investigate vacuum contact drying of crystalline materials in both stagnant and mechanically agitated beds, where the agitation may be either continuous or intermittent. In this application, which is important for the treatment of

active pharmaceutical ingredients, the particles are compact, so that the liquid phase is located in the voids of the bed and possesses some mobility. The respective extension of the penetration model [16, 17] is especially important for stagnant beds (compare with [18]). The absence of stirring prolongs the drying process significantly, but may be necessary in case of fragile crystals. Notice that the equations of Sect. 3.1 can be immediately applied to stagnant beds when the moisture is immobile, the entire process being just one stagnant period. Calculated curves of this kind are included in Figs. 8 and 10. Quasi-stationary approximations, which are simpler than the exactly solved penetration model, are presented in [16, 17], but also in [15].

Vacuum contact drying of beds composed of two or more size fractions is discussed in [15, 19]. Should the different size fractions be evenly distributed in space, then the equations of Sects. 2 and 3 of this chapter may be applied. Concerning properties, the thermal conductivity of the bed should be calculated with the (lower) porosity of the poly-dispersed packing (Subchap. D6.3). The only information available about the contact resistance under such circumstances is based on simulation results which indicate that the overall value of $1/\alpha_{WS}$ might be close to the value for the finest size fraction [15]. However, stochastically homogeneous multi-component beds are rare in practice, especially when mechanical agitation is applied. In such cases, segregation upon particle size is usually observed. Since the segregation patterns depend on apparatus geometry, modelling must also be specific to certain types of equipment. Such a model has been developed in [19] for vacuum contact drying of binary mixtures in tray dryers, assuming complete segregation with the fine fraction at the bottom and the coarse fraction at the top.

The evaluation of atmospheric contact drying in [6] is based on heat transfer coefficients α_g (Eqs. (40) and (42)) for free convection between the surface of the bed and the ambient gas between 9 and 11.5 W m^{-2} K^{-1}. These values are higher than from a flat plate, due to the rough surface of particle beds. The same effect is discussed in [20], where equations for α_g in aerated rotary drums with and without lifters are given. A further application of the penetration model to atmospheric contact drying can be found in [21].

Rate and selectivity during contact drying of particles loaded with binary liquid mixtures have been discussed extensively in [20, 22–24] for both vacuum and atmospheric conditions. A favorable selectivity is necessary for, e.g., the retention of desired volatiles in foods. It may be reached either by manipulation of operating parameters, such as the composition of inlet gas in the atmospheric case [23], or by combination with membranes [24]. Upgrades of the penetration model describe the contact drying process properly [20, 22].

Finally, it should be noticed that intra-particle mass transport kinetics do not appear in the presented contact drying models, the drying process being considered as either exclusively (vacuum mode) or mainly (atmospheric mode) controlled by heat transfer to the bed. This contrasts the usual treatment of convective drying, which is an upscale of single-particle drying curves to industrial equipment. In spite of ample evidence for validity of the contact drying modelling approach, exceptions are possible in case of either very large particles or of products with very high internal diffusion resistances. Another case of significance of mass transport is freeze drying, where the permeability for vapor flow through the still wet part of the packing may be important and even lead to inverse propagation of the drying front. The drying front always moves from top to bottom (against the direction of heat supply) during contact drying of frozen solutions of pharmaceuticals in vials [25], because the emerging vapor would, otherwise, not be able to escape.

6 Remarks on Discrete Models

The entire previous discussion has been based on the penetration model, which is – in spite of correction by the contact heat transfer coefficient (compare with Sect. 5 of Subchap. D6.3) – a continuous approach. A clear disadvantage of the penetration model is that the motion of particles in agitated beds is not described on first principles, but lumped in the mixing number. Therefore, first efforts toward discrete modelling by the thermal discrete element method (thermal DEM) have been undertaken recently [11, 26, 27]. The results show that the mechanical part of the problem (mixing of identical, but virtually segregated particles in a rotary drum) can be described realistically [26]. As to the thermal part (heat transfer from the wall of the drum to the bed without sinks), the behavior of thermal DEM results is similar to the behavior of the data of Fig. 3 in case of a stagnant bed, and similar to the behavior of the data of Fig. 4 in case of mechanical agitation. However, the penetration of heat to mechanically agitated beds was found to be quantitatively much better than expected [11, 27]. This finding may have various reasons [11] and shows – along with still very high computational times – that thermal DEM is not yet mature for practical use. However, a fast further development can be expected, due to the potential of the method to couple the mechanical with the thermal part of the problem and to provide distributions of significant product properties.

7 Examples

Example 1

The contact, wall-to-bed heat transfer coefficient α_{WS} shall be calculated as a function of pressure for the following cases:
(a) Air, $d = 0.1$ mm, $\delta = 0$; (b) air, $d = 1$ mm, $\delta = 0$; (c) air, $d = 1$ mm, $\delta = 2.5$ µm; (d) helium, $d = 1$ mm, $\delta = 0$.
Given values: $\varphi = 0.8$, $\varepsilon_W = \varepsilon_{bed} = 0.9$, $\vartheta = 60°C$.
Constants: $\sigma = 5.67 \cdot 10^{-8}$ W m^{-2} K^{-4}, $\tilde{R} = 8.314$ J mol^{-1} K^{-1}.
Gas properties: Air: $\tilde{M} = 28.96$ kg kmol^{-1}, $c_{P,g} = 1{,}009$ J kg^{-1} K^{-1}, $\lambda_g = 0.02894$ W m^{-1} K^{-1};
Equation (47) → $\gamma = 0.871$, Eq. (46) → $l = 0.03359/p$ (p in Pa, l in m).
Helium: $\tilde{M} = 4.00$ kg kmol^{-1}, $c_{P,g} = 5{,}200$ J kg^{-1} K^{-1}, $\lambda_g = 0.161$ W m^{-1} K^{-1};
Equation (47) → $\gamma = 0.232$, Eq. (46) → $l = 0.61503/p$ (p in Pa, l in m).

From Eqs. (45a–d), it follows:

α_{WS} in W m^{-2} K^{-1}				
p in Pa	A	B	C	D
10^5	3751.3	591.3	396.4	1791.8
10^4	1813.8	381.3	332.0	771.2
10^3	492.3	187.5	182.2	175.2
10^2	72.6	55.4	55.1	27.2
10^1	13.7	13.4	13.4	8.9

Example 2

Wheat shall be preheated in the first stage of a dryer for cereals. To this purpose, the wheat is gliding along a bank of heating elements (140 heating elements in four rows, Fig. 15). Calculate the outlet temperature of the wheat bed $\vartheta_{bed,out}$.

Inlet temperature of wheat: $\vartheta_{bed,in} = 15°C$.

Material properties of the bed of wheat particles: $\rho_{bed} = 800$ kg m^{-3}, $\lambda_{bed} = 0.2$ W m^{-1} K^{-1}, $c_{bed} = 1{,}800$ J kg^{-1} K^{-1}.

Throughput: $\dot{M} = 30{,}000$ kg wheat per hour.

Total residence time: $t_{total} = 500$ s.

Surface temperature of the heating elements: $\vartheta_W = 100°C$.

Heat transfer surface area per heating element: $A = 0.5$ m^2.

Assumptions

- Mass flow (plug flow of the solids) with a constant gliding velocity.
- No drying during preheating.
- The pre-heater may be subdivided to contact zones and thermal equilibration zones (Fig. 15). Temperature profiles are completely levelled out in the equilibration zones.
- The wheat particles can be approximated by spheres with $d = 2$ mm and $\delta = 0$ for calculating α_{WS}.

The contact heat transfer coefficient α_{WS} is calculated at approximately $(\vartheta_W + \vartheta_{bed,in})/2 \approx 60°C$. From Example 1 with $p = 10^5$ Pa $\rightarrow l = 3.36 \cdot 10^{-7}$ m.

Equations (45c, d) with $\varepsilon_W = \varepsilon_{bed} = 0.9$, $T = 333$ K $\rightarrow \alpha_{rad} = 6.9$ W m^{-2} K^{-1}.

Equation (45b) $\rightarrow \alpha_{WP} = 405.3$ W m^{-2} K^{-1}.

Equation (45a) with $\varphi = 0.8 \rightarrow \alpha_{WS} = 331.1$ W m^{-2} K^{-1}.

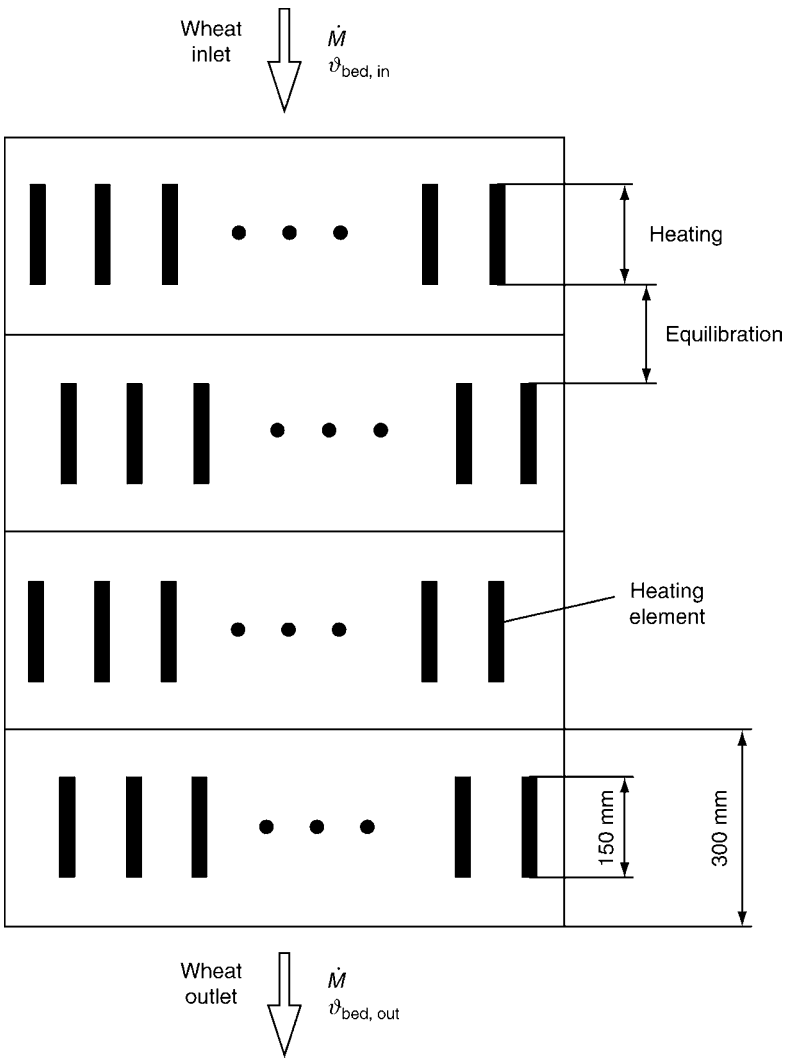

M6. Fig. 15. Schematic representation of the preheating stage of the cereal dryer of Example 2; the apparatus is completely filled with product.

Residence time per heating element: $t = t_{total}/8 \rightarrow t = 62.5$ s.
Equation (5) $\rightarrow \alpha_{bed} = 76.6$ W m^{-2} K^{-1}.
Equation (4) $\rightarrow \alpha = 62.2$ W m^{-2} K^{-1}.
Heat balance for the wheat bed per row of heating elements (subscript $i = 1$–4):

$$\Delta T_{bed,i} = \frac{\alpha(\vartheta_W - \vartheta_{bed,i})A_i}{\dot{M} c_{bed}}.$$

With $A_i = 35$ $A \rightarrow A_i = 17.5$ m^2, it follows: $\Delta\vartheta_{bed,1} = 6.2$ K, $\Delta\vartheta_{bed,2} = 5.7$ K, $\Delta\vartheta_{bed,3} = 5.3$ K, $\Delta\vartheta_{bed,4} = 4.9$ K, and $\vartheta_{bed,out} = 37.1$°C.

Example 3

Free-flowing particulate material shall be contact-dried in pure vapor atmosphere (vacuum).
Apparatus: Batch tray dryer with $D = 240$ mm, $\varepsilon_W = 0.9$.
Particles: Ceramic spheres, $d = 1$ mm, $\delta = 2.5$ µm, $\varepsilon_{bed} = 0.9$, $\rho_{bed,dry} = 1{,}000$ kg m^{-3}, $c_{bed,dry} = 800$ J kg^{-1} K^{-1}, $\lambda_{bed,dry} = 0.140$ W m^{-1} K^{-1} (calculated according to Subchap. D6.3 with $\lambda_p = 1$ W m^{-1} K^{-1} and $\vartheta = 50$°C).
Moisture: Water, $X_0 = 0.20$, $\gamma = 0.80$.
Operating parameters: $p = 2{,}000$ Pa ($\vartheta_S = 17.5$°C), $\vartheta_W = 90$°C, $n = 15$ min^{-1}, $M_{dry} = 1$ kg.
The product is initially at boiling temperature.
Calculate the drying rate for the first fictitious contact period of the penetration model.
The contact heat transfer coefficient α_{WS} is calculated at approximately $\vartheta = 50$°C.
Gas properties: $\tilde{M} = 18.01$ kg kmol^{-1}, $c_{P,g} = 1{,}907$ J kg^{-1} K^{-1}, $\lambda_g = 0.0212$ W m^{-1} K^{-1}.
Equation (46) $\rightarrow l = 9.18 \cdot 10^{-6}$ m.
Equation (45) $\rightarrow \alpha_{WS} = 200.8$ W m^{-2} K^{-1}.
Equation (55b) $\rightarrow$ Fr $= 0.0302$.
Equation (55a) with $C = 25$ and $x = 0.2 \rightarrow N_{mix} = 12.4$.
Equation (12) $\rightarrow t_R = 49.6$ s.
Equation (11) $\rightarrow \alpha_{bed,dry} = 53.6$ W m^{-2} K^{-1}.
Equation (4) $\rightarrow \alpha_{dry} = 42.3$ W m^{-2} K^{-1}.
Equation (23) with Δh_v (17.5°C) $= 2{,}460{,}000$ J kg^{-1} $\rightarrow$ Ph $= 8.483$.
Eq.(22) $\rightarrow f(\zeta) = 0.4417 - \sqrt{\pi}\zeta \exp(\zeta^2)(1 + 3.7472\, erf\, \zeta)$.
Solution: $\zeta = 0.1497 \rightarrow$ erf $\zeta = 0.1677$.
Equation (19) $\rightarrow \alpha = 123.3$ W m^{-2} K^{-1}.
Equations (26) and (27) $\rightarrow \dot{m} = 12.79$ kg m^{-2} h^{-1}.
Equation (28) with $A = \pi D^2/4 \rightarrow \Delta X = 0.00798$.
Equation (29) with $c_l = 4{,}190$ J kg^{-1} K^{-1} $\rightarrow \Delta\vartheta_{bed} = 0.27$ K.
Equation (30) $\rightarrow X_1 = 0.1920$.
Equation (31) $\rightarrow \vartheta_{bed,1} = 17.77$°C.
X_1 and $\vartheta_{bed,1}$ are input values for the second stagnant period. The entire drying curve can be calculated step-by-step on a PC.

Example 4

Free-flowing particulate material is processed in a batch tray dryer which is open to the ambient atmosphere. After some time (at $X = 0.11$), a nearly constant bed temperature is obtained. Calculate the drying rate for these quasi-steady-state conditions.

Operating parameters: $\vartheta_W = 90$°C, $n = 60$ min^{-1}, $N_{mix} = 30$, $\vartheta_g = 20$°C, $p = 10^5$ Pa, ambient relative humidity: 40%, $\alpha_g = 11.5$ W m^{-2} K^{-1} (free convection), radiation heat transfer coefficient from the free surface of the bed to the environment: $\alpha_{rad} = 5$ W m^{-2} K^{-1}.

Product: Ceramic spheres, capillary porous, loaded with water; $d = 4.4$ mm, bed porosity $\psi = 0.40$, particle porosity $\psi_p = 0.375$, $\rho_{bed,dry} = 1{,}000$ kg m^{-3}, $c_{bed,dry} = 800$ J kg^{-1} K^{-1}, solid phase thermal conductivity $\lambda_s = 10$ W m^{-1} K^{-1}, particle roughness $\delta = 2.5$ µm, emission coefficients of particles, wall and bed $\varepsilon = 0.9$.

The temperature dependence of the thermal conductivity of the partially wet bed arising from λ_{diff} (Eqs. (52), (53), and (54)) shall be taken into account. Otherwise, 60°C may be used. For the sake of simplicity, properties of dry air may be used in the gas phase.

Calculation of α_{WS}
Equation (47) with $C = 2.8$, $T = 333.15$ K $\rightarrow \gamma = 0.871$.
Equation (46) with $\tilde{M} = 28.96$ kg kmol^{-1}, $\tilde{R} = 8{,}314$ J kmol^{-1} K^{-1}, $c_{P,g} = 1{,}009$ J kg^{-1} K^{-1}, $\lambda_g = 0.0286$ W m^{-1} K^{-1} (dry air at 60°C) $\rightarrow l = 3.321 \cdot 10^{-7}$ m.
Equation (45b) $\rightarrow \alpha_{WP} = 147.291$ W m^{-2} K^{-1}.
Equations (45c, d) (60°C, $\varepsilon = 0.9$) $\rightarrow \alpha_{rad} = 6.861$ W m^{-2} K^{-1}.
Equation (45a) with $\varphi = 0.8$ (packed bed of spheres) $\rightarrow \alpha_{WS} = 124.694$ W m^{-2} K^{-1}.
The bed temperature ϑ_{bed}, which has been assumed to be constant, must be calculated iteratively. Additionally, two smaller iteration loops are necessary in order to determine the temperatures ϑ_0 and ϑ_s, because of the temperature dependence of λ_{diff}. The iterations can be carried out easily by means of, e.g., the half-step algorithm. It follows: $\vartheta_0 = 68.01$°C, $\vartheta_{bed} = 60.21$°C, and $\vartheta_s = 51.43$°C.
Here, calculations shall be presented only for the last step of the iteration.
Calculation for the free-surface side of the bed
$(\vartheta_{bed} + \vartheta_s)/2 = 55.82$°C. At this temperature, one obtains from
Equation (54) $\rightarrow \delta = 3.156 \cdot 10^{-5}$ m^2 s^{-1}.
Equation (53) $\rightarrow p_S = 16{,}393$ Pa.
Equation (52) $\rightarrow \lambda_{diff} = 0.4547$ W m^{-1} K^{-1}.
A value of $\Delta\tilde{h}_v = 42{,}521{,}610$ J kmol^{-1} ($\Delta h_v = 2{,}361{,}000$ J kg^{-1}) was used in Eq. (52), corresponding to a temperature of 60°C. From

$$\rho_p = \rho_{bed,dry}/(1 - \psi) \tag{58}$$

it follows: $\rho_p = 1666.7$ kg m^{-3}. Equation (50) must yield at $X = X_S$ (saturation) the particle porosity ψ_p. Thus, it is

$$X_S = \psi_p \rho_l \big/ \rho_p. \tag{59}$$

With $\rho_l = 983.2$ kg m^{-3} (60°C), it follows $X_S = 0.221$ and from Eq. (49), $b = 0.99795$.
Equations (51b) and (51c) for bed voids $\rightarrow \lambda_I = 0.4824$ W m^{-1} K^{-1}, $\lambda_{II} = 0.4680$ W m^{-1} K^{-1}.
Equation (51a) with $a_H = 0.20 \rightarrow \lambda_H = 0.4794$ W m^{-1} K^{-1}.
Equation (50) $\rightarrow \psi_l = 0.18647$.
Equations (48a) and (48b) with $\lambda_l = 0.6544$ W m^{-1} K^{-1} (60°C) for particles $\rightarrow \lambda_I = 6.4630$ W m^{-1} K^{-1}, $\lambda_{II} = 1.3329$ W m^{-1} K^{-1}.
Equation (48c) $\rightarrow \lambda_p = 5.0153$ W m^{-1} K^{-1}.
Equations (7a–f) from Subchap. D6.3 with $k_p = \lambda_p/\lambda_H = 10.461$, $k_{rad} = \alpha_{rad} d/\lambda_H = 0.0630$ (α_{rad} approximately at 60°C,

same value as in α_{WS}), $k_G = 1$ (Knudsen effect can be neglected), $C_f = 1.25$ (spheres), $\psi = 0.40$, flattening coefficient: 0.0077 (ceramic) $\rightarrow \lambda_{bed,wet} = 1.8245\ W\ m^{-1}\ K^{-1}$.
Equation (35) with $c_l = 4{,}184\ J\ kg^{-1}\ K^{-1}$ (60°C) $\rightarrow (\rho c)_{bed,wet} = 1{,}260{,}240\ J\ m^{-3}\ K^{-1}$.
Equation (13) $\rightarrow t_{mix} = 1$ s.
Equation (12) $\rightarrow t_R = 30$ s.
Equation (34) $\rightarrow \alpha_{bed} = 312.386\ W\ m^{-2}\ K^{-1}$.
Equation(53) for $\vartheta_S \rightarrow p_S = 13{,}261$ Pa.
From Eq. (53) at 20°C and from the given relative humidity of the ambient air (40%), it follows: $p_g = 938$ Pa.
Equation (42) with $\alpha_g = 11.5\ W\ m^{-2}\ K^{-1}$, $\tilde{M}_{H_2O} = 18.01\ kg\ kmol^{-1}$, $\tilde{M}_{air} = 28.96\ kg\ kmol^{-1}$, $c_{p,g} = 1{,}009\ J\ kg^{-1}\ K^{-1}$ (60°C) $\rightarrow \dot{m} = 0.0009416\ kg\ m^{-2}\ s^{-1} = 3.39\ kg\ m^{-2}\ h^{-1}$.
This is the requested drying rate.
Equation (40) with $\alpha_{rad} = 5\ W\ m^{-2}\ K^{-1}$ to the environment (given value) $\rightarrow \dot{q}_{um} = (11.5 + 5)\ (51.43 - 20)\ W\ m^{-2} = 518.60\ W\ m^{-2}$.
Equation (36) $\rightarrow \dot{q}_s = 312.386\ (60.21 - 51.43)\ W\ m^{-2} = 2742.75\ W\ m^{-2}$.
Equation (41) $\rightarrow \dot{q}_{lat} = 0.0009416 \cdot 2{,}361{,}000\ W\ m^{-2} = 2223.12\ W\ m^{-2}$.
Control by means of Eq. (37): $\dot{q}_s - \dot{q}_{um} - \dot{q}_{lat} = 1.03\ W\ m^{-2}$.
The fact that this value is close to zero verifies the results of the iteration loop around ϑ_s.
Calculation for the heating-plate side of the bed
$(\vartheta_0 + \vartheta_{bed})/2 = 64.11$°C. In a similar way as before one obtains $\delta = 3.302 \cdot 10^{-5}\ m^2\ s^{-1}$, $p_S = 24{,}054$ Pa, $\lambda_{diff} = 0.7130\ W\ m^{-1}\ K^{-1}$, $\lambda_H = 0.7330\ W\ m^{-1}\ K^{-1}$, $\lambda_p = 5.3148\ W\ m^{-1}\ K^{-1}$, $\lambda_{bed,wet} = 2.3115\ W\ m^{-1}\ K^{-1}$, $\alpha_{bed} = 351.612\ W\ m^{-2}\ K^{-1}$.
Control
Equation (32) $\rightarrow \dot{q}_0 = 124.694\ (90 - 68.01) = 2742.03\ W\ m^{-2}\ K^{-1}$.
Equation (33) $\rightarrow \dot{q}_0 = 351.612\ (68.01 - 60.21) = 2742.58\ W\ m^{-2}\ K^{-1}$.
Proximity between these two values verifies the closure of the lower iteration loop (around ϑ_0).
With $\vartheta_{bed} = \text{const.}$ (quasi-steady-state assumption), it is $\dot{q}_{bed} = 0$, so that it must be $\dot{q}_0 = \dot{q}_s$. This equality is fulfilled with sufficient accuracy (verification of the large iteration loop around ϑ_{bed}).
The results correspond approximately to the upper experiment of Fig. 13 (empty circles). In practice, a computer program would be used to follow the evolution of bed temperature ϑ_{bed} stepwise. The temperature dependence of material properties can easily be accounted for in such software. The properties of the gas phase should be calculated for air saturated with vapor and not for dry air, as approximately done in this example.

8 Symbols

a	proportion of series combination in the calculation of λ_p and λ_H (–)
A	area (m^2)
b	proportion of voids located between wet walls (Eq. (49)) (–)
c	specific heat capacity ($J\ kg^{-1}\ K^{-1}$)
d	particle diameter (m)
D	apparatus diameter (m)
g	gravitational acceleration ($m\ s^{-2}$)
h	bed height (m)
Δh_v	phase change enthalpy ($J\ kg^{-1}$)
l	modified mean free path of gas molecules (m)
L	length (m)
$\dot{m}$	drying rate ($kg\ m^{-2}\ s^{-1}$)
M	mass (kg)
$\dot{M}$	mass flow rate ($kg\ s^{-1}$)
$\tilde{M}$	molar mass ($kg\ kmol^{-1}$)
n	revolution frequency (s^{-1})
n	molar density ($mol\ m^{-3}$)
$\dot{n}$	molar flux ($mol\ m^{-2}\ s^{-1}$)
N_{mix}	mixing number (–)
p	pressure (Pa)
$\dot{q}$	heat flux ($W\ m^{-2}$)
$\tilde{R}$	universal gas constant ($J\ mol^{-1}\ K^{-1}$)
t	time (s)
T	thermodynamic temperature (K)
u	flow velocity ($m\ s^{-1}$)
X	moisture content (–)
z	distance from the heating surface (m)
α	heat transfer coefficient ($W\ m^{-2}\ K^{-1}$)
β	mass transfer coefficient ($m\ s^{-1}$)
γ	accommodation coefficient (–)
δ	particle roughness (m)
ε	emissivity (–)
ζ	dimensionless position of phase change front (Eq. (20)) (–)
ϑ	temperature (°C)
κ	thermal diffusivity (Eq. (21)) ($m^2\ s^{-1}$)
λ	thermal conductivity ($W\ m^{-1}\ K^{-1}$)
ρ	density ($kg\ m^{-3}$)
σ	radiation coefficient of the black body ($W\ m^{-2}\ K^{-4}$)
τ	dimensionless time (Eq. (7)) (–)
φ	surface coverage factor (–)
ψ	porosity (–)
ψ_l	volumetric liquid fraction (Eq. (50)) (–)
Subscripts	
bed	bed
c	critical
diff	by evaporation, diffusion, and recondensation
dry	dry
f	free moisture
f	fluid
g	gas
h	hygroscopic
H	void
i	ith stagnant period
in	at the inlet
l	liquid
lat	latent, at the location of phase change
mix	mixing
o	outer, at the heating medium side
out	at the outlet
p	particle

P	at constant pressure
R	stagnant period
rad	radiation
s	solid
s	at the free surface of the bed
S	saturated vapor, saturation with liquid
t	momentaneous value
T	at the phase change front
um	to the environment
wet	wet
W	wall
WP	wall to particle
WS	wall to bed
0	first particle layer
0	initial

9 Bibliography

1. Wunschmann J (1974) Wärmeübertragung von beheizten Flächen an bewegte Schüttungen bei Normaldruck und im Vakuum. Diss., Univ. Karlsruhe
2. Schlünder E-U (1984) Heat transfer to packed and stirred beds from the surface of immersed bodies. Chem Eng Process 18:31–53
3. Schlünder E-U, Mollekopf N (1984) Vacuum contact drying of free flowing mechanically agitated particulate material. Chem Eng Process 18:93–111
4. Abramowitz M (ed) (1965) Handbook of mathematical functions. Dover Publications, New York
5. Mollekopf N (1983) Wärmeübergang an mechanisch durchmischtes Schüttgut mit Wärmesenken in Kontaktapparaten. Diss., Univ. Karlsruhe
6. Tsotsas E, Schlünder E-U (1986) Contact drying of mechanically agitated particulate material in the presence of inert gas. Chem Eng Process 20:277–285
7. Martin H (1980) Wärme- und Stoffübertragung in der Wirbelschicht. Chem Ing Tech 52:199–209
8. Krischer O (1956) Die wissenschaftlichen Grundlagen der Trocknungstechnik, 1st edn. Springer, Berlin
9. Schlünder E-U, Tsotsas E (1988) Wärmeübertragung in Festbetten, durchmischten Schüttgütern und Wirbelschichten, 1st edn. Thieme, Stuttgart
10. Blumberg W, Schlünder E-U (1995) Thermal conductivity of packed beds consisting of porous particles wetted with binary mixtures. Chem Eng Process 34:339–346
11. Tsotsas E (2007) Modeling of contact dryers. Drying Technol J 25:1377–1391
12. Guderian J, Köneke D, Weinsprach P-M (1991) Heat transfer to trickling granular materials. Chem Eng Process 30:157–174
13. Dittler A, Bamberger T, Gehrmann D, Schlünder E-U (1997) Measurement and simulation of the vacuum contact drying of pastes in a LIST-type kneader dryer. Chem Eng Process 36:301–307
14. Tsotsas E, Schlünder E-U (1987) Vacuum contact drying of mechanically agitated beds: the influence of hygroscopic behaviour on the drying rate curve. Chem Eng Process 21:199–208
15. Tsotsas E (1985) Über den Einfluß der Dispersität und der Hygroskopizität auf den Trocknungsverlauf bei der Vakuum- Kontakttrocknung rieselfähiger Trocknungsgüter. Diss., Univ. Karlsruhe.
16. Michaud A, Peczalski R, Andrieu J (2008) Modeling of vacuum contact drying of crystalline powders packed beds. Chem Eng Process 47:722–730
17. Michaud A, Peczalski R, Andrieu J (2007) Experimental study and modelling of crystalline powders vacuum contact drying with intermittent stirring. Drying Technol J 25:1163–1173
18. Kohout M, Collier AP, Stepanek F (2006) Mathematical modelling of solvent drying from a static particle bed. Chem Eng Sci 61:3647–3685
19. Tsotsas E, Schlünder E-U (1986) Vacuum contact drying of free flowing mechanically agitated multigranular packings. Chem Eng Process 20:339–349
20. Blumberg W (1995) Selektive Konvektionstrocknung im Drehrohr. Fortschr Ber VDI, Ser. 3, No. 384. VDI-Verlag, Düsseldorf (Diss., Univ. Karlsruhe)
21. Gevaudan A, Andrieu J (1991) Contact drying modelling of agitated porous media beads. Chem Eng Process 30:31–37
22. Heimann F (1988) Über die Vakuumkontakttrocknung von mechanisch durchmischtem, rieselfähigem Schüttgut, das mit einem binären Gemisch befeuchtet ist. Fortschr Ber VDI, Ser. 3, No. 152. VDI-Verlag, Düsseldorf (Diss., Univ. Karlsruhe)
23. Riede T, Schlünder E-U (1990) Selective evaporation of a binary mixture into dry or humidified air. Chem Eng Process 27:83–93
24. Knebel T, Schlünder E-U (1995) Retention of volatiles in contact drying combined with membrane separation. Chem Eng Process 34:219–227
25. Barresi AA, Pisano R, Fissore D, Rasetto V, Velardi SA, Vallan A, Parvis M, Galan M (2009) Monitoring of the primary drying of a lyophilization process in vials. Chem Eng Process 48:408–423
26. Kwapinska M, Saage G, Tsotsas E (2006) Mixing of particles in rotary drums: a comparison of discrete element simulations with experimental results and penetration models for thermal processes. Powder Technol 161:69–78
27. Kwapinska M, Saage G, Tsotsas E (2008) Continuous versus discrete modelling of heat transfer to agitated beds. Powder Technol 181:331–342

M7 Heat and Mass Transfer in Packed Beds with Fluid Flow

Evangelos Tsotsas
Otto-von-Guericke-Universität Magdeburg, Magdeburg, Germany

1 Introduction

A complete description of heat and mass transfer in packed beds with fluid flow means computation of velocity, concentration, and temperature fields in three dimensions (3D) with full local resolution. For this purpose, the positions and surface contours of every particle in the bed must be precisely known. Subsequent computation of the flow field is not an easy task, and the computational demand increases if mass transfer has also to be considered. Most demanding is the consideration of heat transfer in coupled heat and mass transfer problems. Treating the thermal conductivity of packings with a stagnant fluid phase in Subchap. D6.3, we have pointed out that a dilemma exists between the number of particles that can be considered and the resolution that can be attained in regions with high heat fluxes, such as the regions around particle contact points. The same dilemma applies to flow and mass transfer.

Nevertheless, fully resolved 3D computations are nowadays possible with methods of computational fluid dynamics (CFD). The classical CFD approach, which can be implemented with the help of commercially available codes, is to solve discretized forms of the conservation equations (e.g., Navier–Stokes equations for momentum transfer). Careful and critical computations have been presented for particle-to-fluid heat and mass transfer [1] and for heat transfer in the vicinity of the wall of a packed bed reactor [2]. Alternatively, the Lattice-Boltzmann (LB) method can be used. This is a cellular automata technique comparable to a certain extent with direct numerical simulation in fluid mechanics. Recent applications to isothermal packed bed reactors [3, 4], packed membrane reactors [5], and adsorbers [6] indicate advantages in computational speed. However, nonisothermal conditions pose serious challenges of conceptual, calibration, and computational nature, so that thermal LB techniques are still in the state of development [7].

Some hundreds of particles can be treated by the LB method with a resolution of some tens of voxels per particle diameter when only flow and mass transfer are taken into account. From the practical point of view, this is of interest only for narrow packed tubes with a very small ratio between tube diameter D and particle diameter d. Even if CFD develops toward significantly larger particle ensembles, other simpler models will be necessary for organizing and understanding the enormous amount of produced computational data. Such models are obtained by refraining from a precise description of local topology. Voxels are, instead, grouped together by allocating them either to the particle or to the fluid phase, whereby the volumetric fraction of the fluid phase is described by local porosity. In a packed tube, this kind of smoothening is conducted in a natural way by averaging over the circumferential coordinate, which gives rise to two-dimensional (2D) models. However, loss of microscale features means that transport phenomena cannot be treated on first principles. They have to be approximated by introducing transport coefficients in analogy to Fickian or Fourier kinetics. Dispersion coefficients and effective thermal conductivities are transport coefficients of this kind. Their task is to capture, . . . , at least in the fluid phase – both molecular and flow-dependent transport mechanisms. If the distinction between the phases is preserved, we talk about two-phase models. However, this distinction can also be abandoned by regarding state variables as local averages between the phases. Respective models are called quasi-homogeneous.

Quasi-homogeneous models are most common in practical use and well supported by comparison with experimental data. Therefore, after some discussion on porosity and flow in

VDI-GVC (ed.), *VDI Heat Atlas*, DOI 10.1007/978-3-540-77877-6_56,

the following subsections, two models of this kind – the $\Lambda_r(r)$-model and the α_w-model – are treated in detail.

2 Bed Porosity

It is known from the extrapolation of experimental results that infinitely extended, random packed beds made of equally sized spheres have porosities (void fractions) between $\psi_\infty = 0.36$ and 0.42. The range from $\psi_\infty = 0.36$ to 0.38 is occupied by the relatively dense packed beds that can be obtained by shaking the respective container. Without this kind of compaction, the packed beds remain rather loose – with porosities of $\psi_\infty =$ 0.40–0.42. For comparison, regular (ordered) packings of equally sized spheres have porosities between $\psi_\infty = 0.259$ (cubic face-centered or densest hexagonal arrangement) and $\psi_\infty = 0.476$ (simple cubical packing). For dense, random beds of cylinders with $d \approx l$ (d: diameter, l: length) it is $\psi_\infty = 0.25$–0.35. Loose beds of this kind have approximately the same porosity as the beds of spherical particles. Porosity decreases moderately at $d/l > 1$, and increases significantly at $d/l < 1$ [8]. Packings of Raschig rings have approximately the same "external porosity" as packings of full cylinders of equal size. By taking additionally the inner porosity of the rings into account, the total porosity of the bed can be calculated. Increased void fractions are observed with fine powders ($d < 100$ µm) because of repelling interparticle forces.

Packed beds made of particles with a broad size distribution are always less porous than monodispersed packed beds. In case of spherical particles, approximate calculations can be performed with the empirical equation [9]

$$\psi_{pd}/\psi_\infty = -0.112\ \zeta^3 + 0.017\ \zeta^2 - 0.259\ \zeta + 1. \qquad (1)$$

Here, ψ_{pd} is the porosity of the random polydispersed packing of spheres; ψ_∞ is the porosity of the respective monodispersed packing, as previously explained. The parameter ζ can be calculated from the particle size distribution according to Eq. (8) of Subchap. D6.3.

Apart from experiments, various packing algorithms can also be used in order to investigate phase distribution and porosity [10–12]. Both the real and the simulated packed beds show that the presence of a rigid wall disturbs seriously the randomness of the packing. This gives rise to porosity profiles such as those depicted exemplarily in Figs. 1 and 2. Consequently, the porosity of packed beds made of equally sized, smooth spheres decreases steeply with increasing distance from the wall to reach a pronounced minimum after approximately half of a particle diameter. Periodic oscillations are observed at longer distances. These oscillations are damped and vanish after some particle diameters. The precise position of the first minimum, the wavelength, and the decline of amplitude depend for $D/d > 5$ only weakly on the ratio between the tube and particle diameters (Fig. 1).

Oscillations are not very pronounced in case of the relatively rough, not perfectly spherical and not exactly monodispersed particles which are typical in practice. For such particles, the porosity decreases almost monotonously, approaching ψ_∞ after a rather short distance. Particles of irregular shape and polydispersed packings of spheres show the same behavior (Fig. 2).

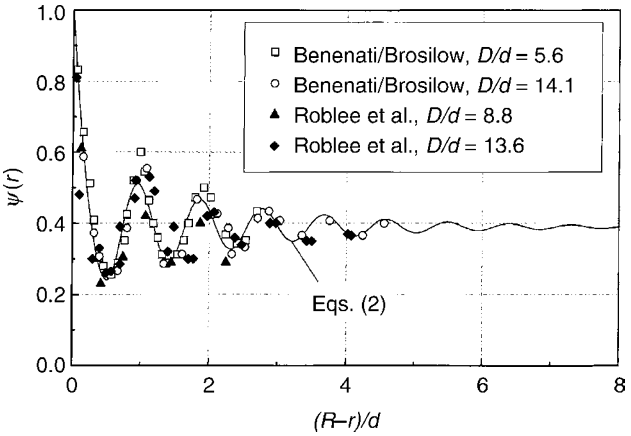

M7. Fig. 1. Radial porosity profiles in tubes packed with almost perfect spheres; Measurements from [65, 66], calculation after Eq. (2) [13] for $D/d = 16$, $\psi_\infty = 0.39$.

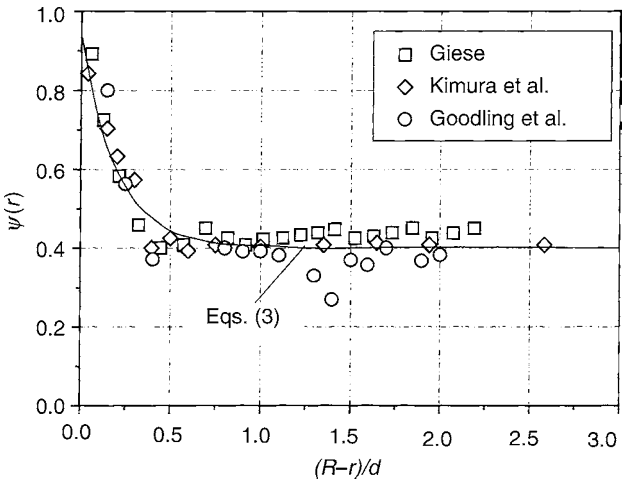

M7. Fig. 2. Radial porosity profiles in tubes packed with imperfect spheres or irregular particles. Measurements from [14] (rough, slightly nonspherical catalyst particles with $d = 6 \pm 1$ mm), from [67] (crashed material), and from [68] (polydispersed spheres); calculations after Eqs. (3) [14].

Similarly, only weak oscillations of bed porosity are observed with Berl saddles or Raschig rings.

The porosity profile in circular tubes filled with smooth spheres of equal size can be calculated by the semiempirical equations proposed by Bey and Eigenberger [13] as follows:

$$r^* < 0 \Rightarrow \psi(r) = \psi_{min} + (1 - \psi_{min})\, r^{*2}, \qquad (2a)$$

$$r^* \geq 0 \Rightarrow \psi(r) = \psi_\infty + (\psi_{min} - \psi_\infty) \exp(-r^*/a_1) \cos(\pi r^*/b_1) \qquad (2b)$$

with

$$r^* = [(R - r)/x_{min}] - 1, \qquad (2c)$$

$$x_{min} = 0.5d\left(\frac{D}{d} - \sqrt{\left(\frac{D}{d} - 1\right)^2 - 1}\right) \qquad (2d)$$

and

$$\psi_{\min} = 0.24, \tag{2e}$$

$$a_1 = 4, \tag{2f}$$

$$b_1 = 0.876 \tag{2g}$$

($R = D/2$: tube radius).

While Eq. (2) considers the mentioned oscillation, simpler relationships are also capable of capturing the main feature of any porosity profile, namely the increase of void fraction in the immediate vicinity of the wall. Giese [14] proposed for this purpose the exponential function

$$\psi(r) = \psi_\infty \left(1 + a_2 \exp\left[-b_2 \frac{R - r}{d}\right]\right) \tag{3a}$$

with

$$a_2 = 1.36, \tag{3b}$$

$$b_2 = 5 \tag{3c}$$

and

$$\psi_\infty = 0.40. \tag{3d}$$

This function agrees well with the data of Fig. 2 and is a good choice for practical calculations with spherical particles in general. The porosity at the wall is $\psi(r = R) = 0.94$ and $\psi(r = R) = 1$ according to Eqs. (3a, b) and (2a, c), respectively. The latter value corresponds to ideal point-contacts.

From the foregoing discussion it is evident that average porosity in a packed tube depends on the ratio D/d. The function $\psi(D/d)$ can be predicted for equally sized spheres and $D/d < 1.86$ from geometrical considerations. In the range $1.86 < D/d < 2$ different packing arrangements are possible, so that only an upper bound and a lower bound of bed porosity can be derived deterministically [15, 16]. As a consequence, significant scattering is obtained in practice upon repacking. Such scattering is typical for diameter ratios up to $D/d \approx 4$ and is enhanced additionally by differences in particle size. Irrespective of this effect, quite reliable values of $\psi(D/d)$ can be calculated at $D/d > 2$ by integration of the porosity profiles according to Eqs. (2a, b) and (3a) from $r = 0$ to $r = R$. Similar results are obtained for monodispersed packings of spheres from the empirical relationship

$$\psi = \psi_\infty + (1 - \psi_\infty)\frac{0.526}{D/d}, \tag{4}$$

which has been derived by Sonntag [17]. Sonntag proposes for cylinders and Raschig rings,

$$\psi = \psi_\infty + (1 - \psi_\infty)\frac{0.480}{D/d}. \tag{5}$$

Here, d is the diameter of a sphere of equal volume to the particle. The average porosity ψ – and not the porosity ψ_∞ of an infinitely extended bed – should be used when calculating the pressure drop in packed beds.

3 Flow

Because of very short inlet and outlet transition regions, flow in a circular packed tube can usually be considered one-dimensional. It can be calculated with the help of the extended Brinkman equation

$$\frac{\partial p}{\partial z} = -f_1 u_0(r) - f_2[u_0(r)]^2 + \frac{\eta_{\text{eff}}}{r}\frac{\partial}{\partial r}\left(r\frac{\partial u_0(r)}{\partial r}\right). \tag{6}$$

The first two terms on the right-hand side of this equation account for pressure drop due to the particles. The third right-hand side term expresses the influence of friction in the vicinity of the wall by means of an effective viscosity η_{eff}.

For imperfect spheres – typical of many practical applications – the equations of Ergun

$$f_1 = 150\frac{[1 - \psi(r)]^2}{[\psi(r)]^3}\frac{\eta_f}{d^2}, \tag{7a}$$

$$f_2 = 1.75\frac{[1 - \psi(r)]}{[\psi(r)]^3}\frac{\rho_f}{d}, \tag{7b}$$

can be applied in combination with local values of porosity $\psi(r)$ from Eq. (3). Viscosity and density of the fluid are denoted by η_f and ρ_f, respectively. The effective viscosity can be calculated according to Giese et al. [18] as

$$\eta_{\text{eff}}/\eta_f = a_3 \exp(b_3 \text{Re}_o), \tag{8}$$

with

$$a_3 = 2.0, \tag{9a}$$

$$b_3 = 2.0 \cdot 10^{-3}. \tag{9b}$$

Herein, the Reynolds number

$$\text{Re}_o = u_0 d/\nu_f \tag{10}$$

is defined with the average value of superficial velocity over the entire cross section of the tube, u_0; (ν_f: kinematic viscosity, $\nu_f = \eta_f/\rho_f$). Giese et al. [18] derived for perfect spheres,

$$a_3 = 2.0, \tag{11a}$$

$$b_3 = 3.5 \cdot 10^{-3}. \tag{11b}$$

In this case, the still applicable Eq. (7) must be combined with porosity profiles from Eq. (2). Equation (6) can be solved numerically with the boundary conditions

$$r = 0 \;\Rightarrow\; \partial u_0/\partial r = 0, \tag{12a}$$

$$r = R \;\Rightarrow\; u_0 = 0, \tag{12b}$$

at the axis and the wall of the tube.

Pressure drop for particles of other than spherical shape or for annular packed beds is discussed in [11, 19, 20]. Though the use of alternative correlations from Subchap. L1.6 for f_1, f_2 is in principle possible, their usage is still rare. Alternative concepts for the pressure drop calculation can be found in [21, 22]. A computational comparison between the influence of increased porosity in the vicinity of the wall and the influence of wall friction on pressure drop has been presented in [23].

Neglecting both wall friction and the dependence of local porosity on the radial coordinate [i.e., setting $\psi(r) = \psi$ for every r], leads to the limiting case of constant superficial velocity over the entire cross section of the tube [$u_0(r) = u_0$ for every r]. The mistake inherent in this popular approximation of "plug flow" is illustrated in Fig. 3, with velocity profiles calculated by Eqs. (6)–(10), and (12). The profiles show that the through

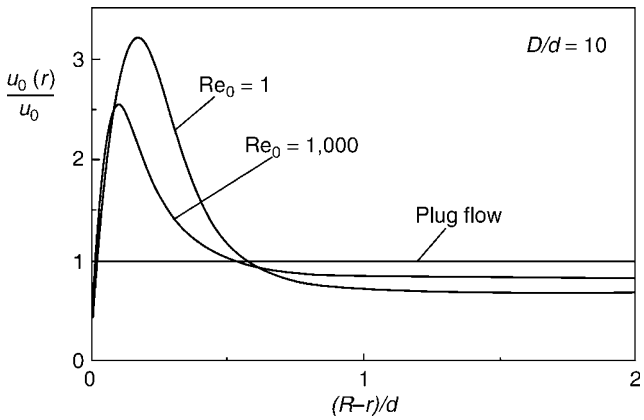

M7. Fig. 3. Macroscopic flow maldistribution in packed tubes; profiles calculated with Eqs. (6), (7)–(10), (12) for $D/d = 10$.

put at the margin of the bed is larger and in the middle of the tube, smaller than in case of plug flow. The nonslip boundary condition is fulfilled at the wall. This behavior, which is more pronounced at small Reynolds numbers, can be described as macroscopic flow maldistribution [24]. One modern possibility to prove the existence of macroscopic flow maldistribution and to measure radial velocity profiles is laser Doppler anemometry (LDA) [14, 18], the other is nuclear magnetic resonance (NMR) or magnetic resonance imaging (MRI) [25, 26]. Both methods are applicable only in liquid phase. Transparent particles and an adaptation of the refraction index of the liquid to that of the particles are additionally necessary for LDA. LDA measurements from [14, 18] are the origin of the presented equations.

Flow fields, which are two- or three-dimensional at the macroscopic level, may occur in packed beds because of changing cross section of the conduit, obstacles, fluid feed from the side, strong change of fluid properties with temperature, etc. Respective calculations can be conducted with extended (vectorial) versions of Eq. (6) [6].

Apart from macroscopic flow maldistribution, the terms of microscopic and mesoscopic flow maldistributions have also been introduced in [24]. Microscopic flow maldistribution refers to individual voids, and is caused by changing void contour and the nonslip boundary condition at the surface of particles. Mesoscopic flow maldistribution appears due to the formation of relatively dense clusters in the interior of beds packed with small particles. With such particles, ranging in diameter from about 0.5 mm down to some µm, inhomogeneities can occur even over the entire tube cross section. Therefore, good and reproducible packing is an important issue for, e.g., chromatographic columns [27]. Unfortunately, there are hardly any methods for modeling such effects till now.

4 Equations of Quasi-Homogeneous Models

As already mentioned in the Introduction, two quasi-homogeneous models, which are supported by comprehensive comparison with experimental data and frequently used in practice, are treated in more detail. These are the $\Lambda_r(r)$-model and the α_w-model.

According to the $\Lambda_r(r)$-model, heat transport and mass transport in a packed circular tube are described by the relationships

$$\left\{[1-\psi(r)]\,\rho_p c_p + \psi(r)\rho_f c_f\right\}\frac{\partial \vartheta}{\partial t} = \frac{1}{r}\frac{\partial}{\partial r}\left[\Lambda_r(r) r \frac{\partial \vartheta}{\partial r}\right] + \Lambda_{ax}(r)\frac{\partial^2 \vartheta}{\partial z^2} - u_o(r)\rho_f c_f \frac{\partial \vartheta}{\partial z} \tag{13a}$$

and

$$\psi(r)\frac{\partial y}{\partial r} = \frac{1}{r}\frac{\partial}{\partial r}\left[D_r(r) r \frac{\partial y}{\partial r}\right] + D_{ax}(r)\frac{\partial^2 y}{\partial z^2} - u_0(r)\frac{\partial y}{\partial z}, \tag{13b}$$

respectively. Here, ϑ is the temperature, y is the mass fraction or some other measure of composition, t is the time, r is the radial coordinate, and z is the axial coordinate. The subscripts p and f denote the particles and the fluid, respectively. Not only porosity and flow velocity are considered to depend on the radial coordinate [$\psi(r)$, $u_0(r)$, as previously explained] but also the effective thermal conductivities [$\Lambda_r(r)$ and $\Lambda_{ax}(r)$] and the dispersion coefficients [$D_r(r)$ and $D_{ax}(r)$]. Because the dependence of the radial effective thermal conductivity on the radial coordinate, $\Lambda_r(r)$, can be quite important, it gives the model its name. It should be noted that packed beds with fluid flow are anisotropic with respect to heat and mass transport. In the presence of, e.g., adsorption or catalytic reaction, appropriate source or sink terms must be added to the equations. Such terms couple the two equations with each other in case of significant heat release or consumption. Reaction or other kinetics should be determined separately by measurements in gradient-free ("differential") reactors or on single particles.

Apart from the trivial boundary condition at the axis of the tube, initial conditions, boundary conditions at the wall, and boundary conditions at the inlet and outlet of the bed are necessary for the numerical solution of Eqs. (13a, b). These should be selected and defined in a problem-specific way. Concerning the important thermal boundary condition at the wall, one should write in case of, e.g., a constant wall temperature ϑ_w

$$r = R \;\rightarrow\; \vartheta = \vartheta_w. \tag{14}$$

At the end of the bed (outlet) good results can be obtained either by the simple expression

$$z = L \;\rightarrow\; \partial\vartheta/\partial z = 0, \tag{15a}$$

$$\partial y/\partial z = 0 \tag{15b}$$

or, for chemical reactors, by the "softer" boundary condition

$$z = L \;\rightarrow\; \partial^2\vartheta/\partial z^2 = 0, \tag{16a}$$

$$\partial^2 y/\partial z^2 = 0. \tag{16b}$$

Sometimes it will be reasonable to account for heat fluxes by radiation or packed transitional zones at the inlet or outlet.

By assuming uniform distribution of porosity, axial velocity ("plug flow"), and effective transport coefficients over the cross section, Eqs. (13) are transformed to the equations of the α_w-model, which are

$$\left\{(1-\psi)\rho_p c_p + \psi\rho_f c_f\right\}\frac{\partial\vartheta}{\partial t} = \Lambda_r\left[\frac{\partial^2\vartheta}{\partial r^2}+\frac{1}{r}\frac{\partial\vartheta}{\partial r}\right]+\Lambda_{ax}\frac{\partial^2\vartheta}{\partial z^2}-u_0\rho_f c_f\frac{\partial\vartheta}{\partial z} \quad (17a)$$

for the heat transport and

$$\psi\frac{\partial y}{\partial t} = D_r\left[\frac{\partial^2 y}{\partial r^2}+\frac{1}{r}\frac{\partial y}{\partial r}\right]+D_{ax}\frac{\partial^2 y}{\partial z^2}-u_0\frac{\partial y}{\partial z} \quad (17b)$$

for the mass transport. Simultaneously, an artificial thermal boundary condition of the third kind is imposed at the wall:

$$r = R \quad -\Lambda_r(\partial\vartheta/\partial r) = \alpha_w(\vartheta-\vartheta_w). \quad (18)$$

This boundary condition introduces the wall heat transfer coefficient α_w that appears in the name of the model. It is the price to be paid as compensation for the simplification attained in Eqs. (17a, b) in comparison to Eqs. (13a, b). A wall mass transfer coefficient β_w can be defined, if necessary, in analogy to Eq. (18). The remaining boundary conditions, source terms and sink terms, are set in the same way as for the $\Lambda_r(r)$-model.

Both models can be expressed for nonaxisymmetric geometries by appropriate coordinate transformations. The accumulation terms may be eliminated in case of steady-state problems. However, it should be noted that certain solvers approach the steady state from transient numerical computations so that the complete equations have to be implemented. The terms for axial heat transfer and axial dispersion can be eliminated without significant loss of accuracy in many cases, but not always, because e.g., axial conduction plays an important role at small flow velocities. The same is true for reactors operated in the region of multiple reaction states.

The subsequent Sect. 5 of this chapter treats axial dispersion of heat and mass in common for both models. Important differences in the radial transport coefficients between the two models are worked out in Sects. 6 and 7. Some remarks about the validity of quasi-homogeneous approaches appear in Sect. 5 and are discussed further in Sect. 8, together with some hints about more complex models.

5 Axial Dispersion of Heat and Mass

The coefficient D_{ax} for axial dispersion of mass in Eq. (17b) can be calculated for random beds made of equally large spheres according to the equation

$$\frac{D_{ax}}{\delta} = \frac{\delta_{bed}}{\delta}+\frac{Pe_0}{K_{ax}}, \quad (19a)$$

with

$$K_{ax} = 2. \quad (19b)$$

Here,

$$Pe_0 = u_0\, d/\delta \quad (20)$$

is the so-called molecular Péclet number, u_0, and D_{ax} are averages that do not depend upon the radial position. With the help of the "effective" Péclet number

$$PE_{ax} = u_0\, d/D_{ax} \quad (21)$$

Eq. (19a) can be transformed to

$$\frac{1}{PE_{ax}} = \frac{\delta_{bed}/\delta}{Pe_0}+\frac{1}{K_{ax}}. \quad (22)$$

For $Pe_0 \to 0$, $D_{ax} = \delta_{bed}$ is obtained, which means that axial dispersion is due to diffusion. The ratio δ_{bed}/δ (δ: diffusion coefficient in the solids-free fluid phase) depends on porosity and can be calculated according to Eq. (6) from Subchap. D6.3. On the contrary, $PE_{ax} = K_{ax} = 2$ is obtained for $Pe_0 \to \infty$. At this limit the bed behaves as a cascade of ideally mixed compartments [28], and axial dispersion is caused by mixing of the fluid in the voids of the packing.

Results of respective measurements by several authors are plotted in Fig. 4 in the form of fitting curves and data regions over the Reynolds number. The latter is by definition equal to $Re_0 = Pe_0/Sc$, where $Sc = \nu_f/\delta$ is the Schmidt number. Detailed information can be found in [24]. All measurements were carried out by the transient tracer method. Particles were compact and inert with respect to the tracer. Data acquired with gases ("ER," "GP") agree well with Eqs. (22) and (19b), except for the weak maximum that the data of Fig. 4 show in the region of medium Reynolds numbers.

On the contrary, experiments conducted with liquids ("MK," "EW," "CP") show much smaller effective Péclet numbers, that means much more dispersion. It is evident that, in this case, some additional mechanism that creates axial dispersion must exist apart from diffusion and the cascade effect. According to [24], this could be a combination of microscopic flow maldistribution with lateral mass transport. The resulting axial dispersion is usually called Taylor dispersion [29]. Recent MRI measurements [30] clearly indicate the existence of significant regions with nearly stagnant liquid in packed beds, supporting the mentioned theory. Increased axial dispersion during the flow of aqueous solutions through packed beds can be of considerable

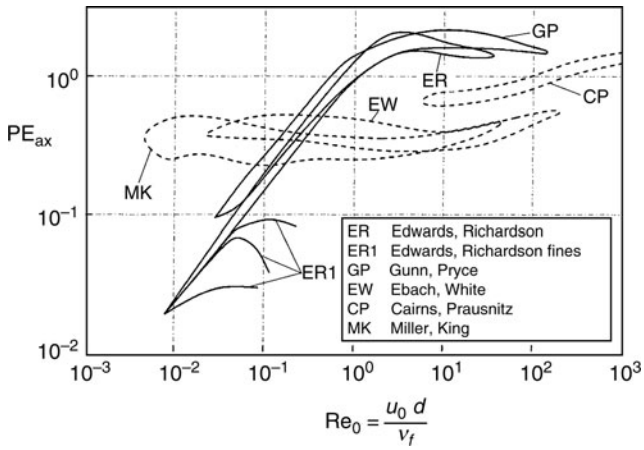

M7. Fig. 4. Axial dispersion of mass according to transient tracer experiments conducted by various authors in randomly packed beds of equally sized spheres. Full lines: Measurements with gases; Broken lines: Measurements with liquids.

importance for the design of bioseparation processes. Correlations that distinguish between liquids and gases on an empirical basis and account for the mentioned weak maximum have been presented in [31, 32].

The behavior of data gained with fine particles (data group "ER 1"with d = 0.1 to 0.2 mm in Fig. 4) can also be assigned to Taylor dispersion, though in this case to Taylor dispersion driven by mesoscopic flow maldistribution (cluster formation) [24]. On the contrary, the macroscopic velocity profiles discussed in Sect. 3 do not appear to be significantly reflected in the results of tracer experiments for axial dispersion.

Since Taylor dispersion is not genuine back-mixing, it can be observed only under transient conditions. At steady state, Eq. (19a) or Eq. (22) can be used. These equations give good results also in case of cylindrical particles, by calculating d as the diameter of a sphere of equal volume. The situation is less clear with Raschig rings, because some authors propose to still use K_{ax} = 2, whereas some others recommend values smaller by up to 50%.

Equations (19)–(22) can be applied locally – that means with the local values of porosity and flow velocity – in order to approximately calculate the function $D_{ax}(r)$ for Eq. (13b). More precise results about radial profiles of the axial dispersion coefficients are not available till now.

Heat transfer in the direction of flow can be treated similarly to mass transfer, calculating Λ_{ax} for Eq. (17a) from

$$\frac{\Lambda_{ax}}{\lambda_f} = \frac{\lambda_{bed}}{\lambda_f} + \frac{Pe_0}{K_{ax}} \tag{23a}$$

or

$$\frac{1}{PE_{ax}} = \frac{\lambda_{bed}/\lambda_f}{Pe_0} + \frac{1}{K_{ax}} \tag{23b}$$

with

$$K_{ax} = 2 \tag{23c}$$

and

$$Pe_0 = u_0 \rho_f c_f d/\lambda_f, \tag{24}$$

$$PE_{ax} = u_0 \rho_f c_f d/\Lambda_{ax}. \tag{25}$$

Similar to the calculation of $D_{ax}(r)$, Eqs. (23)–(25) can be applied locally to obtain $\Lambda_{ax}(r)$ for Eq. (13a). Equations providing the thermal conductivity of the packed bed without flow λ_{bed} have been presented in Subchap. D6.3. Remarks about the local application of such equations are given in Sect. 6.

However, axial dispersion of heat in packed tubes with fluid flow is not due to the effective thermal conductivity Λ_{ax} alone, but to a combination of heat transport in the direction of flow, heat transfer between particle surface and the fluid, and heat conduction in the particles. As several investigations show [33–35], linear combination of these three effects (expressed in the following by the quantity A) provides a good approximation for the axial dispersion of heat according to the equations:

$$A = A_1 + A_2 + A_3, \tag{26}$$

$$A_1 = \frac{(1 + K^*)^2}{Pe_0} \frac{\Lambda_{ax}}{\lambda_f}, \tag{27a}$$

$$A_2 = \frac{K^{*2} Pe_0}{Nu A_v d}, \tag{27b}$$

$$A_3 = \frac{K^{*2} Pe_o}{60\,(1-\psi)\,\lambda_p/\lambda_f}. \tag{27c}$$

In Eqs. (27)

$$K^* = \left[(1-\psi)\,\rho_p c_p\right] \Big/ \left[\psi\,\rho_f c_f\right] \tag{28}$$

is the thermal capacity ratio and

$$Nu = \alpha d/\lambda_f \tag{29}$$

is the Nusselt number for heat transfer between the particulate (subscript: p) and the fluid (subscript: f) phase. The surface area of the packing per unit volume is denoted by A_v; (for spheres: $A_v d = 6\,(1-\psi)$).

The relative importance of the three terms of Eq. (26) changes with the molecular Péclet number Pe_0, as shown in Fig. 5, with calculations carried out at ψ = 0.40, Pr = 1, and $K^* >> 1$ (solids/gas). The ratio λ_{bed}/λ_f was obtained from Eq. (5) in Subchap. D6.3, and the Nusselt number was calculated according to Chap. G9. The intersection points of the curves define in Fig. 5 two critical Péclet numbers and three regions. For $Pe_0 < Pe_{0,cr,1}$ axial dispersion of heat is mainly due to the effective thermal conductivity Λ_{ax}. The difference between particle and fluid temperature is small, and application of the quasi-homogeneous model is well justified. On the contrary, fluid-to-particle heat transfer takes over the dominant role at $Pe_{0,cr,1} < Pe_0 < Pe_{0,cr,2}$. Temperature differences between the phases, which should be accounted for by a heterogeneous model, become significant. The same is true for $Pe_0 > Pe_{0,cr,2}$, where heat conduction in the interior of the particles prevails.

The discrimination of mechanisms according to Fig. 5 is crucial for the proper design of thermal storage equipment (regenerators) as well as for the correct identification of transport parameters from transient thermal response experiments. Derivation of Nusselt numbers from such experiments leads in the region $Pe_0 < Pe_{0,cr,1}$ to biased results. Such "apparent" Nusselt numbers deviate from the correlation of Gnielinski (Chap. G9) to lower values and tend even to zero

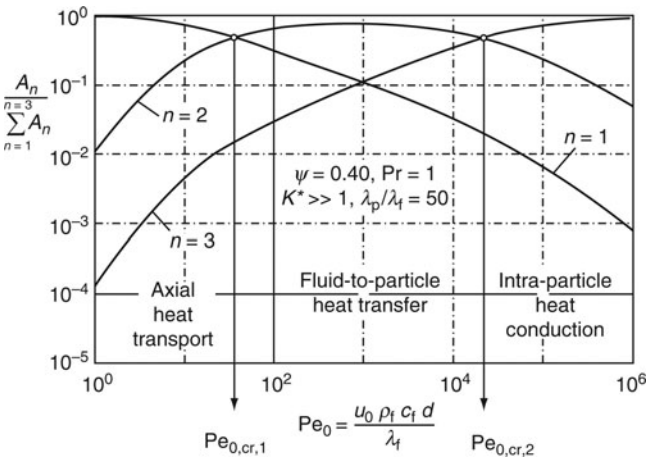

M7. Fig. 5. Relative contributions of axial heat transport (n = 1), fluid-to-particle heat transfer (n = 2), and intraparticle heat conduction (n = 3) to the experimentally observable axial dispersion.

at $Pe_0 \to 0$. On the contrary, reasonable results, which are in good agreement with Eq. (23a), are obtained when deriving the effective thermal conductivity Λ_{ax} from measured data in this region. An alternative, steady-state method for measuring Λ_{ax} ("back-conduction method") has been discussed in [36], among others.

6 Radial Transport Parameters of the $\Lambda_r(r)$-model

Local values of the radial (or, more general, lateral) effective thermal conductivity $\Lambda_r(r)$ (see Eq. (13a)) can be calculated for (nearly) spherical particles and gases according to Winterberg et al. [37] by means of the following equations:

$$\Lambda_r(r) = \lambda_{bed}(r) + K_1 Pe_0 \frac{u_{0,c}}{u_0} f(R-r)\,\lambda_f, \tag{30}$$

$$0 < R - r \le K_2 d \;\Rightarrow\; f(R-r) = \left(\frac{R-r}{K_2 d}\right)^n, \tag{31a}$$

$$K_2 d < R - r \le R \;\Rightarrow\; f(R-r) = 1\,, \tag{31b}$$

$$K_1 = 1/8, \tag{32a}$$

$$K_2 = 0.44 + 4\exp(-Re_0/70), \tag{32b}$$

$$n = 2. \tag{32c}$$

Here, Re_0 and Pe_0 are the Reynolds and the molecular Péclet numbers – defined with the average superficial flow velocity u_0 by Eqs. (10) and (24), respectively. The superficial velocity in the center of the bed, $u_{0,c} = u_0(r = 0)$, is obtained from Eqs. (6) to (10) and Eq. (12), in combination with Eq. (3). The thermal conductivity of the bed without flow is also considered to be a function of radial position $\lambda_{bed}(r)$. In order to derive this function, local values of porosity $\psi(r)$ from Eq. (3) are inserted in Eqs. (5a)–(5e) from Subchap. D6.3, so that the ratio $k_{bed}(r) = \lambda_{bed}(r)/\lambda_f$ is obtained. This ratio, which is denoted by $k_{bed,0}(r)$ for the sake of distinction, is then expanded by additive consideration of thermal radiation according to Zehner and Schlünder [38] to obtain

$$k_{bed}(r) = k_{bed,0}(r) + \left(1 - \sqrt{1-\psi(r)}\right) k_{rad} + \sqrt{1-\psi(r)}\left(\frac{1}{k_{rad}} + \frac{1}{k_p}\right)^{-1}. \tag{33}$$

The quantities k_{rad} and k_p are defined in Eqs. (7e) and (3b), respectively, of Subchap. D6.3. The described procedure neglects in comparison to the application of Eqs. (7) from Subchap. D6.3 flattened contacts and the Knudsen effect ($\varphi = 0$ and $k_G = 1$ in Eq. (7a) and (7f) of Subchap. D6.3, respectively). Additionally, there is a difference in the consideration of radiation, which is very small at $\psi = 0.4$, but significant at the very high values of porosity that prevail in the vicinity of the wall. In case of $\varphi > 0$ or $k_G > 1$, Eq. (7) of Subchap. D6.3 should be applied with $k_{rad} = 0$. Then, the result should be inserted as $k_{bed,0}$ in Eq. (33), accounting for radiation with the value of k_{rad} from Eq. (7e), Subchap. D6.3. Data that might support a more accurate calculation of local thermal conductivity without flow in the vicinity of the wall, especially of the contribution of radiation, are not available till now.

Figure 6 illustrates the influence of the parameters K_1, K_2, and n on the profile of thermal conductivity $\Lambda_r(r)$ according to Eqs. (30) and (31). All three parameters have in common that they do not change the basis value of $\lambda_{bed}(r)$, but merely the flow dependent part of the effective thermal conductivity. The increase of this part with increasing flow velocity is defined by the "slope parameter" K_1. Onset and local extent of the inhibition caused by the wall are described by the "damping parameter" K_2 and the exponent n.

Slope parameters derived from thermal injection experiments are compared in Fig. 7 with the recommended value of $K_1 = 1/8$ (Eq. (32a), more details in [37]). In such experiments, a gas stream that has a somewhat higher temperature than the main flow is injected steadily at the axis of the packed tube. Radial profiles of temperature are measured at some position downstream. Because the wall is not reached by the thermal perturbation, such profiles are not influenced by the parameters K_2 and n. Consequently, they can be used for the separate determination of K_1. Figure 7 shows good agreement with the

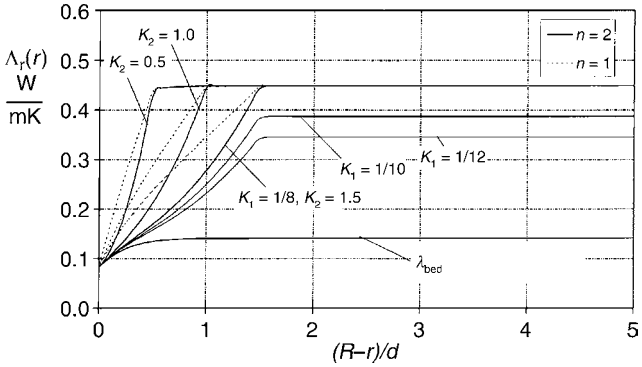

M7. Fig. 6. Influence of the parameters K_1, K_2, and n on the profile of radial effective thermal conductivity according to Eqs. (30) and (31); (spherical ceramic particles in air, ambient conditions, $Pe_0 u_{0,c}/u_0 = 86$, $D/d = 10$).

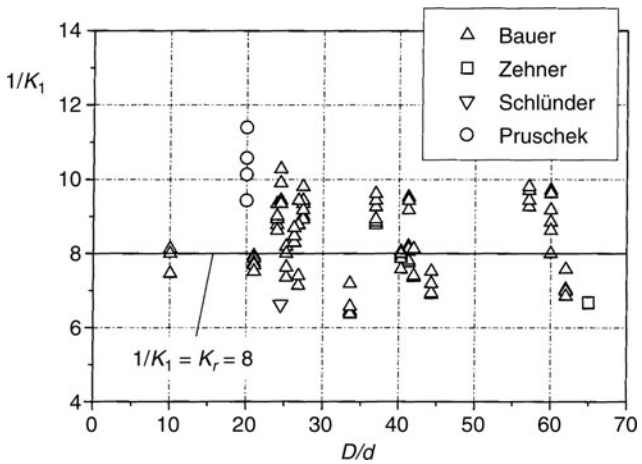

M7. Fig. 7. Inverse of the recommended value of the slope parameter K_1 (Eq. (32a)) in comparison with values derived by means of the $\Lambda_r(r)$-model from data measured by various authors (thermal injection experiments, see in [37] for more details).

value $K_1 = 1/8$ or with $1/K_1 = 8$, which is denoted in the literature by K_r. The value of $1/K_1 = K_r = 8$ can be derived on first principles, by flow pattern (stream line deflection and cross-mixing due to the particles [39]) or by random walk [41] considerations. Due to this fundamental agreement, no fine-tuning of K_1 has been conducted in [37]. Independence of the slope parameter from the diameter ratio D/d (Fig. 7) is a merit of the $\Lambda_r(r)$-model. It results from the explicit consideration of porosity and flow profiles, especially of the values prevailing in the center of the tube.

The additive combination between quiescent and flow-dependent thermal conductivities becomes obvious in the limiting case of an unconfined bed. Without wall effects, Eq. (30) reduces to

$$\frac{\Lambda_r}{\lambda_f} = \frac{\lambda_{bed}}{\lambda_f} + \frac{Pe_0}{K_r} \tag{34a}$$

or

$$\frac{1}{Pe_r} = \frac{\lambda_{bed}/\lambda_f}{Pe_0} + \frac{1}{K_r} \tag{34b}$$

with

$$K_r = 1/K_1 = 8, \tag{34c}$$

$$PE_r = u_0 \rho_f c_f d/\Lambda_r \tag{35}$$

and Pe_0 according to Eq. (24). The analogy to Eq. (23) for axial dispersion of heat or Eqs. (19)–(22) for axial dispersion of mass is evident in this form – up to the different values of K_r and K_{ax}. By setting the two right-hand side terms of Eq. (34a) or (34b) equal to each other, a critical molecular Péclet number

$$Pe_{0,cr} = (\lambda_{bed}/\lambda_f) K_r, \tag{36}$$

can be derived. The conduction term prevails at $Pe_0 < Pe_{0,cr}$, whereas the flow-dependent (cross-mixing) term is more important at $Pe_0 > Pe_{0,cr}$. For example, with the typical value of $\lambda_{bed}/\lambda_f = 6.25$ and $K_r = 8$, $Pe_{0,cr} = 50$ is obtained for gas-filled packed beds. However, it should be stressed that $Pe_{0,cr}$ is an orientation help, not a stability criterion.

In case of heating or cooling at constant wall temperature (Nusselt–Graetz problem), the result depends on all three model parameters K_1, K_2, and n (Eq. (32)). An exponent of $n = 2$ was found to properly describe respective data in [37]. However, this was rather a choice than an optimization, with other values having also been proposed in the literature (e.g., $n = 1$, that means a linear profile, in [42]). With fixed values for K_1 and n (Eq. (32a, c)), the damping parameter K_2 can be derived from Nusselt–Graetz data by uniparametric fitting. This provides results such as those of Fig. 8, where every point represents the evaluation of one measured temperature profile. As the plot shows, agreement with Eq. (32b) is good, and there is again no explicit dependence on the diameter ratio D/d. Equation (32b) means that the region of inhibited cross-mixing extends at high flow rates over 44% of one particle diameter, which looks like a reasonable value.

For heat transfer in liquid–particle systems a slight modification of Eq. (32b) to

$$K_2 = 0.44 + 4\exp(-Pe_0/50) \tag{37}$$

has been proposed [43].

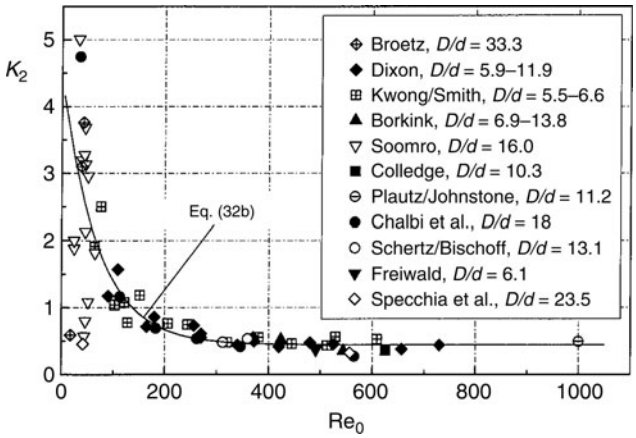

M7. Fig. 8. Recommended values (Eq. (32b)) of the damping parameter in comparison with values derived by means of the $\Lambda_r(r)$-model from data measured by various authors (heating or cooling at constant wall temperature, more details in [37]).

Furthermore,

$$K_1 = 1/6.25, \tag{38a}$$

$$K_2 = 0.40 + 0.6\exp(-Re_0/230), \tag{38b}$$

can be recommended according to [44] for heat transfer in packed beds made of cylinders with an aspect ratio not too far from unity. As before, the diameter of a sphere of equal volume to the cylindrical particle should be used for d in this case. Equation (3a) should be applied with the parameters

$$a_2 = (0.65/\psi_\infty) - 1, \tag{39a}$$

$$b_2 = 6.0. \tag{39b}$$

Profiles of the radial mass dispersion coefficient appearing in Eq. (13b) are similar to the profiles of $\Lambda_r(r)$. They can be calculated with the help of the relationship

$$D_r(r) = \delta_{bed}(r) + K_1 Pe_0 \frac{u_{0,c}}{u_0} f(R - r)\,\delta, \tag{40}$$

where Pe_0 is the molecular Péclet number according to Eq. (20). Equations (31a) and (31b) remain the same. For imperfect spheres it still holds $n = 2$, whereas the slope parameter is obtained [37] as

$$K_1 = \frac{1}{8}\left[1 + \frac{3}{Pe_{0,c}^{0.5}}\right]^{-1}. \tag{41a}$$

Only the constant part is considered in the damping parameter, so that it is

$$K_2 = 0.44. \tag{41b}$$

Superficial velocity in the core of the bed $u_{0,c}$ is still calculated by means of Eqs. (6)–(10), combined with Eq. (3). The respective molecular Péclet number is denoted by $Pe_{0,c}$. Local application of Eq. (6) from Subchap. D6.3 provides the ratio between effective diffusion coefficient of the packed bed $\delta_{bed}(r)$ and diffusivity δ.

The equations for radial dispersion of mass have been developed in [37] on the basis of experiments with steady-state

tracer injection at the axis of the bed. Unlike the previously discussed thermal injection, downstream profiles reach the wall, in many experiments of this kind, so that they depend not only on K_1 but also on K_2 and n. Nevertheless, the results can be presented in a similar way as in Fig. 4 – compared with Eq. (22) and (23b) – by considering the middle of the tube ($r = 0$, subscript: c) and defining correspondingly the molecular and the effective Péclet number ($Pe_{0,c} = u_{0,c}\, d/\delta$, $PE_{r,c} = u_{0,c}\, d/D_{r,c}$). In this way, Fig. 9 is obtained. This figure shows, apart from diffusion at small values and cross-mixing at large values of the molecular Péclet number, a weak transitional maximum. In absence of a satisfactory theoretical explanation, this nonlinearity has been approximated empirically in the second right-hand side term of Eq. (40a). Without such secondary considerations, the main mechanisms are the same as already discussed in connection with Eq. (34). Because δ_{bed}/δ is much smaller than the ratio λ_{bed}/λ_f, critical Péclet numbers that can be defined similarly to Eq. (36) have also relatively small values of, e.g., $Pe_{0,cr} = (\delta_{bed}/\delta)\, K_r \approx 2$ ($K_r = 1/8$ and $K_1 = 8$). Taylor dispersion is not an issue at steady state. All the same, increased radial dispersion can be occasionally observed with fine particles ($d <$ 0.5 mm, data not shown here), probably due to cluster formation (the previously discussed mesoscopic maldistribution of flow).

In total, the recommended correlations have been validated by comparison with a large database consisting of more than 600 experiments in the range of $Re_0 = 1.5$–4181, $D/d = 4.1$–101.3, and $d = 0.6$–30 mm [37, 43, 44]. Besides isothermal wall boundary conditions, temperature distributions, adiabatic operation, and constant heat flux have been investigated by appropriate modification of Eq. (14). Different geometries of the cross section of the containment are included in the database, namely circular, annular, or rectangular. Annular or planar geometries can be easily treated by appropriate modification of the spatial coordinates [43].

Restrictions result from the relatively small amount of data with liquids and from steady-state conditions in all experiments

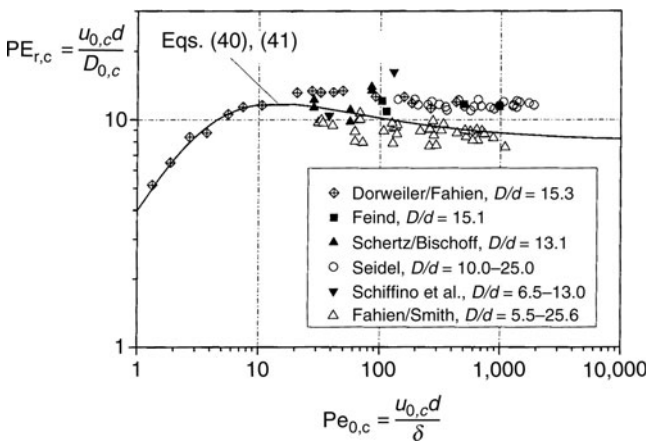

M7. Fig. 9. Radial dispersion of mass, presented on the basis of steady-state injection experiments. Every data point has been obtained from the evaluation of one measured radial profile of tracer concentration (more details in [37]).

of the database. Furthermore, parameters of the $\Lambda_r(r)$-model are missing for particle shapes other than spherical or cylindrical. A possible procedure for such cases would be to use the diameter of the sphere of equal volume (without consideration of internal voids) in place of d, in combination with the correlations for spherical particles for all parameters except λ_{bed} and K_1. The quiescent thermal conductivity λ_{bed} can be calculated according to Eq. (7) from Subchap. D6.3 without the influence of radiation, which should be added subsequently according to Eq. (33). To set the slope parameter K_1 (or $1/K_1 = K_r$) for Raschig rings or for irregular (broken) material, the recommendations by Bauer [8], which are summarized in Table 1, may be used. The constant at the right-hand side of Eq. (38a) should be changed correspondingly. However, it should be stressed that Bauer has evaluated with the α_w-model, so that certain deviations occur for spherical and cylindrical particles between the present recommendations and Table 1 ($1/K_1 = 7$ according to Table 1 instead of $1/K_1 = 8$ according to Eq. (32a) for spheres, $1/K_1 = 4.6$ according to Table 1 instead of $1/K_1 = 6.25$ according to Eq. (38a) for full cylinders). A value of $1/K_1 = 6.7$ has been suggested in [45] for full cylinders. According to [46], $1/K_1$ should be somewhat larger for full cylinders than for Raschig rings, the latter having half the value of $1/K_1$ for spheres. In case of broader than usual particle size distributions, the diameter

$$d = \left(\sum Q_i/d_i\right)^{-1} \tag{42}$$

can be used (Q_i: volume fraction of ith constituent, compared with Eq. (10) in Subchap. D6.3).

In case of strongly exothermic catalytic reaction, mass transport and heat transport are coupled to each other, but heat transport is more important for overall performance. Respective packed bed reactor experiments with spherical particles from [47–51] have been evaluated in [52] (with separately determined reaction data and the recommended values for all other transport parameters of the $\Lambda_r(r)$-model) for the heat transport damping parameter K_2. Somewhat different results are obtained when fitting K_2 to measured concentration or temperature profiles. Despite this effect, which is indicated by beams, K_2-values from reactor data agree reasonably in Fig. 10 with values from experiments without reaction (compare with Fig. 8). Fine adjustment of Eq. (32b) in the region of small

M7. Table 1. Inverse value of the slope parameter, $1/K_1$, for different particle shapes, as recommended by Bauer [8] for beds with large D/d; (d_i: inner diameter, d_o: outer diameter, l: length)

Particle shape	$1/K_1$ (= K_r)
Sphere	7.0
Full cylinder	4.6
Raschig ring	$K_r = 8/[1.75\ \Delta\psi_1 + 3.46\ (1-\Delta\psi_1)\ (l/d)^{2/3}]$ $\Delta\psi_1 = \left[1 + \frac{1-\psi_1}{\psi_1}\left(\frac{d_i}{d_o}\right)^2\right]^{-1}$ $\psi_1 = 0.39 + 0.02\ [\lvert(l/d_o)-0.85\rvert]^{4/3}$
Irregular (broken)	5.7

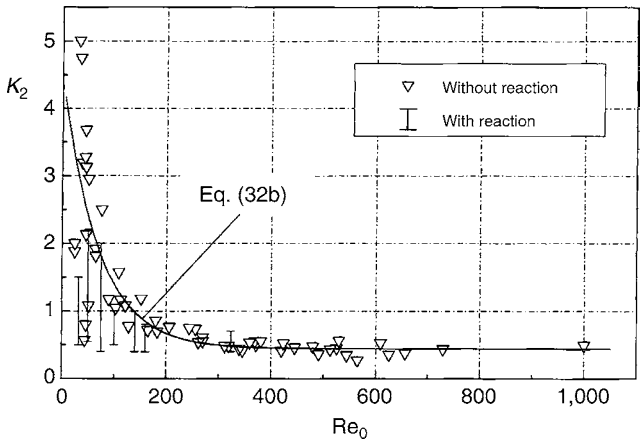

M7. Fig. 10. Damping parameters for heat transport gained from purely thermal experiments (compare with Fig. 8) as well from experiments with chemical reaction [52].

Reynolds numbers would not make great sense, because the sensitivity of the model upon K_2, K_1, and n decreases, and λ_{bed} becomes the controlling parameter at low flow velocities.

7 Radial Transport Parameters of the α_w-model

Application of the α_w-model (Eq. (17)) requires values for Λ_r and D_r, which are both considered to be constant over the entire cross section. The radial (or lateral) effective thermal conductivity Λ_r can be calculated according to Eq. (34a). The same equation can be used for the dispersion coefficient D_r – by replacing fluid and bed thermal conductivities (λ_f, λ_{bed}) with diffusion coefficients (δ, δ_{bed}) and calculating the molecular Péclet number from Eq. (20) (instead from Eq. (24)). The heat transfer coefficient at the wall α_w (Eq. (18)) is usually expressed in a Nusselt number

$$Nu_W = \alpha_W d/\lambda_f \tag{43}$$

and correlated with the Reynolds number Re_0 (Eq. (10)) and the Prandtl number Pr in the form

$$Nu_W = N_{W0} + a\ Re_0^{m_1} Pr^{m_2}. \tag{44}$$

The Sherwood number, $Sh_w = \beta_w d/\delta$, would replace Nu_W, and the Schmidt number, $Sc = \nu_f/\delta$, would replace Pr in case of mass transport.

The plethora of proposals that specify the above mentioned relationships in the literature is difficult to evaluate, because parameters are typically fitted by different methods to different but usually small sets of measured data. One of the most comprehensive and reliable evaluations is that by Nilles and Martin [52, 53]. These authors calculate the quantity K_r (Eq. (34c), similar to the inverse of the slope parameter, $1/K_1$) according to [8] as

$$K_r = K_{r,\infty}\left[2 - \left(1 - \frac{2}{D/d}\right)^2\right]. \tag{45}$$

The limiting value $K_{r,\infty}$, which is valid for the unconfined bed ($D/d \to \infty$), should be set according to Table 1, and the Nusselt number at the wall should be calculated from

$$Nu_W = \left(1.3 + \frac{5}{D/d}\right)\frac{\lambda_{bed}}{\lambda_f} + 0.19 Re_0^{0.75} Pr^{1/3} \tag{46}$$

(λ_{bed}/λ_f from Eq. (7), Subchap. D6.3, with the average bed porosity). Nilles and Martin indicate a validity range from Pe_0 = 1 to 10^4 ($Pe_0 = Re_0\ Pr$) and from D/d = 1.2 to 51 for heat transfer; (mass transfer was not investigated systematically). The correlations can be applied to particles of other than spherical shape by using the diameter of the sphere of equal volume.

The explicit dependence on the diameter ratio D/d, especially in Eq. (45), is mainly caused by the fact that macroscopic flow maldistribution has been neglected in Eq. (17). From a physical point of view, a boundary condition of the third kind (Eq. (18)) is justified only in the presence of a thin unmixed fluid layer at the wall. This can be assumed at high Péclet numbers ($Pe > Pe_{0,cr}$, see Eq. (36)), but not in the region $Pe_0 < Pe_{0,cr}$ [55]. The necessary correction is implemented by Nu_{w0} on the right-hand side of Eq. (46). As systematic comparisons show [37, 43, 44], the model of Martin/Nilles is usually in good agreement with the $\Lambda_r(r)$-model for thermal experiments. However, significant deviations may arise in the presence of exothermic reaction in relatively thin tubes, because of a tentative overestimation of temperature and reaction rate near the wall by the α_w-model. In general, chemical reaction magnifies the effect of even small temperature differences [49].

8 Complementary Remarks

Use of two separate heat and mass balances for the fluid and the solid phases instead of Eqs. (13a) and (17a) leads to heterogeneous or two-phase models (see, e.g., [56]). The solids can be considered either a second continuum or discrete inclusions, using reactor coordinates or spherical, intraparticle coordinates, respectively. Interface fluxes, which can be expressed in terms of a Nusselt number (Eq. (29)) or a Sherwood number ($Sh = \beta d/\delta$) for fluid-to-particle transfer, couple the phase balance equations with each other.

One-dimensional heterogeneous models are relatively easy to apply. In fact, the treatment of axial dispersion of heat in Sect. 5 of this chapter stems from such models. On the contrary, the application of two-dimensional heterogeneous models has the difficulty of additional transport parameters (e.g., separate effective thermal conductivities for the two phases), which are – in spite of some progress in this direction [47] – not accurately known. Thorough investigations about conditions of equivalence between heterogeneous and quasi-homogeneous models [57, 58] have not yet provided generally accepted and validated criteria. Qualitatively, it can be stated that heterogeneous models should be used when large differences in temperature or concentration can be expected between the solid and the fluid phases. Such steep gradients may occur in the course of fast dynamic processes (e.g., in regenerators with high throughput, during start-up, in the presence of moving reaction fronts, during reactor runaway). At steady state, steep gradients require

chemical (e.g., catalysis) or physical (e.g., drying) transformations which are both fast and accompanied by high release or consumption of thermal energy. Hein [46] measured under the steady-state conditions discussed in [48] temperature differences of maximum 10 K between the particles and the gas in catalytic packed bed reactors.

A further issue is the interconnection between momentum and heat balance because of temperature-dependent fluid properties (density, viscosity). In exothermic packed bed reactors, this can lead to the so-called thermal channeling (bypassing of the central, hot part of the bed). To model thermal channeling, the momentum equation must be expressed in two dimensions and solved iteratively with the heat balance [47].

Recent applications of quasi-homogeneous models include hydrogen storage [59] and membrane reactors [5, 60]. An application of the $\Lambda_r(r)$-model for the design of industrial packed bed reactors is discussed in detail in [61].

9 Examples

Example 1

The results of one experiment by Dixon [45] are calculated. In the experiment, air enters, at a temperature of $\vartheta_{in} = 21.5°C$ and with a mass flow rate of $\dot{M} = 9.1$ kg/h, a steam-heated tube ($D = 75.4$ mm, $L = 203.2$ mm), which has a wall temperature of $\vartheta_w = 100°C$. The tube is filled with spherical ceramic particles of diameter $d = 6.4$ mm ($\lambda_p = 1.2$ W/mK, $c_p = 774.51$ J/kgK and $\rho_p = 3000$ kg/m^3). Without wall influence, the porosity of the bed would be $\psi_\infty = 0.40$. Calculate the radial temperature profile at the outlet of the bed with the help of the α_w-model.

Material properties from Subchap. D2.2 at, approximately, $\vartheta = (\vartheta_{in} + \vartheta_w)/2 \approx 60°C \rightarrow \rho_f = 1.045$ kg/m^3, $c_f = 1009$ J/kgK, $\lambda_f = 0.0286$ W/mK, $\nu_f = 19.27\ 10^{-6}$ m^2/s, Pr = 0.71.

Cross-sectional area of the tube: $F = \pi\ D^2/4 \rightarrow F = 4.465\ 10^{-3}$ m^2.

Average superficial flow velocity: $u_0 = \dot{M}/(F\ \rho_f) \rightarrow u_0 = 0.542$ m/s.

Eq. (10) $\rightarrow Re_0 = 180.0$.

Eq. (24) $\rightarrow Pe_0 = 127.8$.

Calculation of quiescent thermal conductivity λ_{bed} according to Subchap. D6.3:

$\psi_\infty = 0.40$, $D/d = 11.78$, Eq. (4) $\rightarrow \psi = 0.427$.

$k_p = \lambda_p/\lambda_f = 41.958$.

Subchap. D6.3, Table 1 $\rightarrow C_f = 1.25$ (shape factor), $\varphi = 0.0077$.

Subchap. D6.3, Eq. (7f) $\rightarrow k_G \approx 1$.

Subchap. D6.3, Eq. (7e) $\rightarrow k_{rad} = 1.535$;
(with $\varepsilon = 0.9$ (estimated value) and $T = 333.15$ K).

Subchap. D6.3, Eq. (7c) $\rightarrow N = 0.995$.

Subchap. D6.3, Eq. (7b) $\rightarrow k_c = 9.681$.

Subchap. D6.3, Eq. (7a) $\rightarrow k_{bed} = \lambda_{bed}/\lambda_f = 7.919$
$\rightarrow \lambda_{bed} = 0.226$ W/mK.

Calculation of the (constant) radial effective thermal conductivity Λ_r:

Table 1, spherical particles: $\rightarrow K_{r,\infty} = 7$.

Eq. (45) with $D/d = 11.78 \rightarrow K_r = 9.177$.

Eq. (34a) $\rightarrow \Lambda_r/\lambda_f = 21.845 \rightarrow \Lambda_r = 0.625$ W/mK.
(corresponding to $Pe_r = 5.850$)

Calculation of the Nusselt number at the wall Nu_w:

Eq. (46) $\rightarrow Nu_w = 21.986$.

To calculate the required temperature profile, Eqs. (17a) and (18) are applied for the steady state without axial dispersion. The boundary condition at the entrance of the tube is

$$z = 0 \rightarrow \vartheta = \vartheta_{in} = 21.5°C.$$

According to [56] (see also [62]) it is

$$\frac{\vartheta(r) - \vartheta_w}{\vartheta_{in} - \vartheta_w} = D_1 \sum \frac{4J_0(\beta_n r/R)}{(D_1^2 + 4\beta_n^2)J_0(\beta_n)} \exp(-4\beta_n^2/D_2)$$

with

$$D_1 = Nu_w \frac{D/d}{\Lambda_r/\lambda_f} = 11.856 \text{ and } D_2 = Pe_r \frac{D/d}{L/D} = 25.571.$$

The eigenvalues β_n are obtained from the equation

$$f(\beta_n) = [D_1\ J_0(\beta_n)/2]\ -\ \beta_n\ J_1(\beta_n) = 0,$$

where J_0 and J_1 are Bessel functions of 0th and 1st order, respectively.

By linear interpolation in the tables of [62], the first two eigenvalues (higher terms of the series can, in this case, be neglected without significant loss of accuracy) are calculated to

$\beta_1 = 2.0444$ and $\beta_2 = 4.7964$.

The respective values of the Bessel functions can also be obtained from mathematical tables by interpolation [63]. Alternatively, equations that approximate the Bessel functions with a high accuracy may be used. Results based on equations from [63] are summarized in Table 2.

In this way, the radial temperature profile at the outlet of the tube can be calculated. Results are also included in Table 2. Figure 11 shows the comparison with the data measured by Dixon [45].

M7. Table 2. Intermediate and final results of the calculations of Example 1, based on the α_w-model

r/R (–)	$\beta_1\ r/R$ (–)	$J_0(\beta_1\ r/R)$ (–)	$\beta_2\ r/R$ (–)	$J_0(\beta_2\ r/R)$ (–)	ϑ_{out} (°C)
0.0	0.0000	1.0000	0.0000	1.0000	39.75
0.1	0.2044	0.9896	0.4796	0.9433	40.30
0.2	0.4089	0.9586	0.9593	0.7828	41.93
0.3	0.6133	0.9081	1.4389	0.5456	44.63
0.4	0.8178	0.8397	1.9186	0.2710	48.38
0.5	1.0222	0.7553	2.3982	0.0034	53.13
0.6	1.2266	0.6578	2.8778	−0.2159	58.79
0.7	1.4311	0.5499	3.3575	−0.3563	65.23
0.8	1.6355	0.4351	3.8371	−0.4028	72.27
0.9	1.8400	0.3167	4.3168	−0.3581	79.69
1.0	2.0444	0.1984	4.7964	−0.2415	87.25

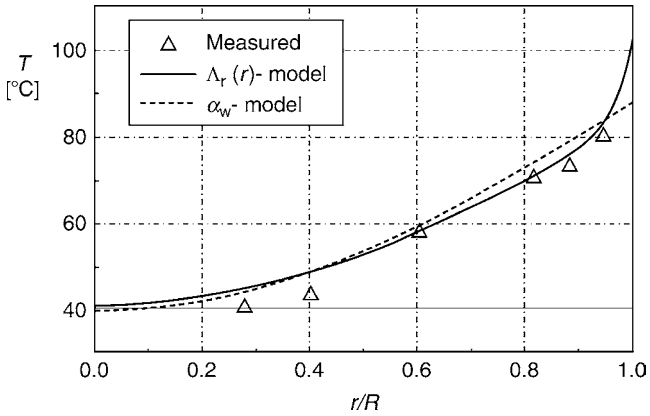

M7. Fig. 11. Calculation of data measured by Dixon [45] with the α_w-model (Example 1) and the $\Lambda_r(r)$-model (Example 2).

M7. Table 3. Calculated porosity and velocity profiles for Example 2

r/R (–)	$\psi(r)$ (–)	$u_0(r)/u_0$ (–)
0.00	0.400	0.833
0.10	0.400	0.833
0.20	0.400	0.833
0.30	0.400	0.833
0.40	0.400	0.833
0.50	0.400	0.833
0.60	0.400	0.833
0.70	0.400	0.834
0.75	0.400	0.835
0.80	0.402	0.841
0.85	0.406	0.863
0.90	0.428	0.970
0.91	0.438	1.020
0.92	0.451	1.090
0.93	0.469	1.188
0.94	0.492	1.330
0.95	0.524	1.540
0.96	0.566	1.856
0.97	0.626	2.329
0.98	0.701	2.793
0.981	0.707	2.813
0.982	0.721	2.848
0.983	0.730	2.859
0.984	0.739	2.860
0.985	0.749	2.850
0.986	0.762	2.817
0.987	0.767	2.801
0.988	0.785	2.704
0.989	0.790	2.671
0.990	0.800	2.594
1.000	0.944	0.000

Example 2

The results of the same experiment as in Example 1 are now calculated with the help of the $\Lambda_r(r)$-model.

Material properties as in Example 1

Calculation of the velocity profile $u_0(r)$:

Equation (8) with $a_3 = 2.0$, $b_3 = 2.0 \cdot 10^{-3}$ from Eq. (9) $\rightarrow \eta_{eff}/\eta_f = 2.8667 \rightarrow \eta_{eff} = 57.74\ 10^{-6}$ Pa s.

Equations (3a)–(3d) $\rightarrow \psi(r)$ as shown in Table 3.

To obtain the velocity profile $u_0(r)$, Eqs. (6), (7), and (12) must be solved with the computed profile of bed porosity. Since this is not possible analytically, a solver, which works with a Newton iteration and adaptive mesh, is used. The results are summarized in Table 3.

Calculation of quiescent thermal conductivity λ_{bed}:

Calculation at the axis of the tube ($r = 0$) with $\psi(r = 0) = 0.40$ (see also the remarks in Sect. 6 of this chapter):

Subchap. D6.3, Eq. (5c): $\rightarrow N = 0.953$.

Subchap. D6.3, Eq. (5b): $\rightarrow k_c = 8.317$.

Subchap. D6.3, Eq. (5a): $\rightarrow k_{bed,0} = 6.667$.

Subchap. D6.3, Eq. (7e): $\rightarrow k_{rad} = 1.535$ (with an estimated value of $\varepsilon = 0.9$ and $T = 333.15$ K).

M7. Table 4. Calculated thermal conductivities and temperature profile at the outlet of the bed for Example 2, based on the $\Lambda_r(r)$-model

r/R (–)	$\lambda_{bed}(r)/\lambda_f$ (–)	$\Lambda_r(r)/\lambda_f$ (–)	$\Lambda_{ax}(r)/\lambda_f$ (–)	ϑ_{out} (°C)
0.00	8.162	21.473	72.105	41.10
0.10	8.162	21.473	72.105	41.53
0.20	8.162	21.473	72.105	42.92
0.30	8.162	21.473	72.105	45.25
0.40	8.162	21.473	72.105	48.49
0.50	8.162	21.473	72.105	52.61
0.60	8.162	21.473	72.105	57.55
0.70	8.160	21.471	72.103	63.22
0.72	8.159	21.470	72.102	64.43
0.74	8.157	21.467	72.099	65.67
0.76	8.153	21.463	72.095	66.93
0.78	8.145	21.456	72.088	68.21
0.80	8.131	21.442	72.074	69.50
0.82	8.107	21.418	72.050	70.82
0.84	8.063	21.374	72.006	72.16
0.86	7.985	21.296	71.928	73.51
0.88	7.847	19.809	71.790	74.89
0.90	7.606	15.912	71.548	76.55
0.92	7.194	12.511	71.137	78.66
0.94	6.521	9.512	70.464	81.41
0.96	5.495	6.824	69.437	85.17
0.98	4.100	4.432	68.042	90.74
1.00	2.653	2.653	66.596	100.00

Eq. (33): → $k_{bed} = 8.162$ → $\lambda_{bed} = 0.233$ W/mK

Values calculated at other positions are presented in the form of $k_{bed}(r) = \lambda_{bed}(r)/\lambda_f$ in Table 4.

Calculation of the axial effective thermal conductivity $\Lambda_{ax}(r)$*:*

Λ_{ax} is calculated according to Eqs. (23) and (24) by using local values of the quiescent thermal conductivity (that means: $\lambda_{bed}(r)$) and, approximately, the average superficial flow velocity u_0. Results (normalized by means of λ_f) are tabulated in Table 4.

Calculation of the radial effective thermal conductivity $\Lambda_r(r)$:

Calculation in the middle of the bed ($r = 0$):

Eq. (32a) → $K_1 = 0.125$.
Eq. (32b) → $K_2 = 0.7457$.
Eq. (32c) → $n = 2$.
Eq. (31b) → $f(R-r) = 1$.
Table 3 → $u_{0,c}/u_0 = 0.833$.
Equation (30) → $\Lambda_r(r = 0)/\lambda_f = 21.47$ → $\Lambda_r(r = 0) = 0.614$ W/mK.

More values of $\Lambda_r(r)/\lambda_f$ are presented in Table 4.

With this input, it is possible to calculate the radial profile of temperature at the outlet of the packed tube by solving Eq. (13a) together with the boundary conditions according to Eqs. (14) and (15a). Additionally, temperature at the entrance of the reactor is set to a constant value:

$$z = 0 \rightarrow \vartheta = \vartheta_{in} = 21.5^{\circ}\text{C}.$$

For reasons of symmetry, the temperature profile must be flat in the middle of the tube:

$$r = 0 \rightarrow \partial\vartheta/\partial r = 0.$$

Computations have been carried out by using a solver for transient, two-dimensional, nonlinear partial differential equations from [64]. This solver implements an implicit method of lines, decomposing the partial differential equation to a system of ordinary differential equations and applying a robust integrator to the latter. The transient converges to the required steady-state solution, which is documented in Table 4 by means of selected results.

Figure 11 compares calculations with the experimental results from [45], also allowing for a comparison with the predictions of the α_w-model from Example 1. The results of both models do not differ significantly in the core of the bed. However, the different boundary conditions become remarkable in the vicinity of the wall. In fact, the $\Lambda_r(r)$-model works with a boundary condition of the first kind according to Eq. (14), that means with the real wall temperature ϑ_w, whereas the α_w-model uses a boundary condition of the third kind at $r = R$, thus calculating a temperature jump. Such differences can be significant in the presence of a chemical reaction. Without reaction, the deviations between the two models are small, with just a slight advantage for the $\Lambda_r(r)$-model, as the evaluation of numerous measured data shows.

10 Symbols

A_v	volumetric surface area (1/m)
c	specific heat capacity (J/kg K)
d	particle diameter (diameter of equal volume sphere) (m)
D	tube diameter (m)
D	dispersion coefficient (m^2/s)
F	cross-sectional area (m^2)
K	constant in flow-dependent part of effective thermal conductivities or dispersion coefficients (–)
K^*	thermal capacity ratio (–)
K_1	slope parameter (–)
K_2	damping parameter (–)
l	length of cylindrical particle (m)
L	bed length (m)
n	exponent of damping function (–)
$\dot{M}$	mass flow rate (kg/s)
p	pressure (Pa)
Q	volume fraction (–)
r	radial coordinate (m)
r^*	reduced distance from the wall, Eq. (2c) (–)
R	tube radius (m)
t	time (s)
T	absolute temperature (K)
u_0	superficial flow velocity (m/s)
y	distance from the wall (m)
y	mass fraction (–)
z	axial coordinate
k_{bed}, k_G, k_{rad}, C_f, φ, ε	see Subchap. D6.3
α	heat transfer coefficient (W/m^2K)
β	mass transfer coefficient (m/s)
β_n	eigenvalue (–)
δ	diffusivity (m^2/s)
η	dynamic viscosity (kg/ms)
ζ	distribution parameter (Subchap. D6.3, Eq. (8)) (–)
ϑ	temperature (°C)
λ	thermal conductivity (W/mK)
Λ	effective thermal conductivity (W/mK)
ν	kinematic viscosity (m^2/s)
ρ	density (kg/m^3)
ψ	porosity (–)

Subscripts

ax	axial
bed	bed
c	core of the bed
cr	critical
eff	effective
f	fluid
i	inner
in	inlet
min	minimal
o	outer
out	outlet
p	particle
p	at constant pressure
pd	polydispersed
r	radial
w	at the wall
∞	unconfined (infinitely extended) bed

11 Bibliography

1. Romkes SJP, Dautzenberg FM, van den Bleek CM, Calis HPA (2003) CFD modelling and experimental validation of particle-to-fluid mass and heat transfer in a packed bed at very low channel to particle diameter ratio. Chem Eng J 96:3–13
2. Dixon AG, Nijemeisland M, Stitt H (2003) CFD simulation of reaction and heat transfer near the wall of a fixed bed. Int J Chem Reactor Eng 1: Article A22
3. Freund H, Zeiser T, Huber F, Klemm E, Brenner G, Durst F, Emig G (2003) Numerical simulations of single phase reacting flows in randomly packed fixed-bed reactors and experimental validation. Chem Eng Sci 58:903–910
4. Sullivan SP, Sani FM, Jones ML, Gladden LF (2005) Simulation of packed bed reactors using lattice Boltzmann methods. Chem Eng Sci 60:3405–3418
5. Tota A, Hlushkou D, Tsotsas E, Seidel-Morgenstern A (2007) Packed-bed membrane reactors. In FH Keil Modeling of process intensification, 1st edn. Wiley-VCH, Weinheim, pp 99–148
6. Manjhi N, Verma N, Salem K, Mewes D (2006) Lattice Boltzmann modelling of unsteady-state 2D concentration profiles in adsorption bed. Chem Eng Sci 61:2510–2521
7. Verma N, Mewes D (2008) Simulation of temperature fields in a narrow tubular adsorber by thermal lattice Boltzmann methods. Chem Eng Sci 63:4269–4279
8. Bauer R (1977) Effektive radiale Wärmeleitfähigkeit gasdurchströmter Schüttungen mit Partikeln unterschiedlicher Form und Größenverteilung. VDI-Forschungsh. 582. VDI-Verl, Düsseldorf
9. Tsotsas E (1991) Eine einfache empirische Gleichung zur Vorausberechnung der Porosität polydisperser Kugelschüttungen. Chem Ing Tech 63:495–496
10. Cheng YF, Guo SJ, Lai HY (2000) Dynamic simulation of random packing of spherical particles. Powder Technol 107:123–130
11. Mueller GE (1999) Radial void fraction correlation for annular packed beds. AIChE J 45:2458–2460
12. Nandakumar K, Shu Y, Chuang KT (1999) Predicting geometrical properties of random packed beds from computer simulation. AIChE J 45:2286–2297
13. Bey O, Eigenberger G (1997) Fluid flow through catalyst filled tubes. Chem Eng Sci 52:1365–1376
14. Giese M (1998) Strömung in porösen Medien unter Berücksichtigung effektiver Viskositäten. Diss. TU München
15. Tsotsas E, Schlünder E-U (1990) Measurement of mass transfer between particles and gas in packed tubes at very low tube to particle diameter ratios. Wärme- u. Stoffübertr. 25:245–256
16. De Klerk A (2003) Voidage variation in packed beds at small column to particle diameter ratio. AIChE J 49:2022–2029
17. Sonntag G (1960) Einfluß des Lückenvolumens auf den Druckverlust in gasdurchströmten Füllkörpersäulen. Chem Ing Tech 32:317–329
18. Giese M, Rottschäfer K, Vortmeyer D (1998) Measured and modelled superficial flow profiles in packed beds with liquid flow. AIChE J 44:484–491
19. Nemec D, Levec J (2005) Flow through packed bed reactors, Part 1: single-phase flow. Chem Eng Sci 60:6947–6957
20. Sodré JR, Parise JAR (1998) Fluid flow pressure drop through an annular bed of spheres with wall effects. Exper Therm Fluid Sci 17:265–275
21. Eisfeld B, Schnitzlein K (2001) The influence of confining walls on the pressure drop in packed beds. Chem Eng Sci 56:4321–4329
22. Eisfeld B, Schnitzlein K (2005) A new pseudo-continuous model for the fluid flow in packed beds. Chem Eng Sci 60:4105–4117
23. Winterberg M, Tsotsas E (2000) Impact of tube-to-particle diameter ratio on pressure drop in packed beds. AIChE J 46:1084–1088
24. Tsotsas E, Schlünder E-U (1988) On axial dispersion in packed beds with fluid flow. Chem Eng Process 24:15–31
25. Gladden LF (2003) Magnetic resonance: ongoing and future role in chemical engineering. AIChE J 29:2–9
26. Tang D, Jess A, Ren X, Bluemich B, Stapf S (2004) Axial dispersion and wall effects in narrow fixed bed reactors: a comparative study based on RTD and NMR measurements. Chem Eng Technol 27:866–873
27. Park J, Gibbs SJ (1999) Mapping flow and dispersion in a packed column by MRI. AIChE J 45:655–660
28. Aris R, Amundson NR (1957) Some remarks on longitudinal mixing or diffusion in fixed beds. AIChE J 3:280–282
29. Taylor G (1953) Dispersion of soluble matter in solvent flowing slowly through a tube. Proc R Soc Lond Ser A 219:186–203
30. Johns ML, Sederman AJ, Bramley AS, Gladden LF, Alexander P (2000) Local transitions in flow phenomena through packed beds identified by MRI. AIChE J 46:2151–2161
31. Cavalho JRF, Delgado JMPQ (2003) Effect of fluid properties on dispersion in flow through packed beds. AIChE J 49:1980–1985
32. Delgado JMPQ (2007) Longitudinal and transverse dispersion in porous media. Chem Eng Res Des 85:1245–1252
33. Vortmeyer D, Schaefer RJ (1974) Equivalence of one- and two-phase models for heat transfer in packed beds: one dimensional theory. Chem Eng Sci 29:485–491
34. Vortmeyer D (1989) Packed bed thermal dispersion models and consistent sets of coefficients. Chem Eng Process 26:263–268
35. Tsotsas E (1990) Über die Wärme- und Stoffübertragung in durchströmten Festbetten: Experimente, Modelle, Theorien. Fortschritt-Berichte VDI, Reihe 3, Nr. 223, VDI-Verl, Düsseldorf
36. Vortmeyer D, Adam W (1984) Steady-state measurement and analytical correlations of axial effective thermal conductivities in packed beds at low gas flow rates. Int J Heat Mass Transfer 27:1465–1472
37. Winterberg M, Tsotsas E, Krischke A, Vortmeyer D (2000) A simple and coherent set of coefficients for modelling of heat and mass transport in packed tubes with and without chemical reaction. Chem Eng Sci 55:967–979
38. Zehner P, Schlünder E-U (1970) Wärmeleitfähigkeit von Schüttungen bei mäßigen Temperaturen. Chem Ing Tech 42:933–941
39. Schlünder E-U (1966) Wärme- und Stoffübertragung zwischen durchströmten Schüttungen und darin eingebetteten Einzelkörpern. Chem Ing Tech 38:967–979
40. Baron T (1952) Generalized graphical method for the design of fixed bed catalytic reactors. Chem Eng Prog 48:118–124
41. Cheng P, Vortmeyer D (1988) Transverse thermal dispersion and wall channelling in a packed bed with forced convective flow. Chem Eng Sci 43:2523–2532
42. Winterberg M, Tsotsas E (2000) Modelling of heat transport in beds packed with spherical particles for various bed geometries and/or thermal boundary conditions. Int J Therm Sci 39:556–570
43. Winterberg M, Tsotsas E (2000) Correlations for effective transport coefficients in beds packed with cylindrical particles. Chem Eng Sci 55:5937–5943
44. Gunn DJ, Ahmad MM, Sabri MN (1987) Radial heat transfer to fixed beds of particles. Chem Eng Sci 42:2163–2171
45. Dixon AG (1988) Wall and particle-shape effects on heat transfer in packed beds. Chem Eng Commun 71:217–237
46. Hein S (1998) Modellierung wandgekühlter katalytischer Festbettreaktoren mit Ein- und Zweiphasenmodellen. Diss. TU München
47. Haidegger E (1990) Der radiale Wärmetransport in wandgekühlten Festbettreaktoren mit exothermer chemischer Reaktion. Diss. TU München
48. Vortmeyer D, Haidegger E (1991) Discrimination of three approaches to evaluate heat fluxes for wall-cooled fixed bed chemical reactors. Chem Eng Sci 46:2651–2660
49. Daszkowski T (1991) Stoff- und Wärmetransport in schüttungsgefüllten Rohrreaktoren. Diss. Universität Stuttgart
50. Daszkowski T, Eigenberger G (1990) Zum Einfluß einer genaueren Strömungsmodellierung auf die Beschreibung von Festbettreaktoren. Chem Ing Tech 62:852–855
51. Winterberg M, Tsotsas E, Krischke A, Vortmeyer D (1999) On the invariability of transport parameters in packed beds upon catalytic reaction. Récents Progrès en Génie des Procédés 13:65, 205–212
52. Nilles M (1991) Wärmeübertragung an der Wand durchströmter Schüttungsrohre. Fortschr.-Ber. VDI, Ser. 3, No. 264, VDI-Eds, Düsseldorf
53. Martin H, Nilles M (1993) Radiale Wärmeleitung in durchströmten Schüttungsrohren – Eine vergleichende Auswertung neuer experimenteller Befunde. Chem Ing Tech 65:1468–1477
54. Tsotsas E, Schlünder E-U (1990) Heat transfer in packed beds with fluid flow. Chem Eng Sci 45:819–837
55. Schlünder E-U, Tsotsas E (1988) Wärmeübertragung in Festbetten, durchmischten Schüttgütern und Wirbelschichten. Thieme, Stuttgart
56. Dixon AG, Cresswell DL (1979) Theoretical prediction of effective heat transfer parameters in packed beds. AIChE J 25:663–676

57. Dommeti SMS, Balakotaiah V, West DH (1999) Analytical criteria for validity of pseudohomogeneous models of packed bed catalytic reactors. Ind Eng Chem Res 38:767–777
58. Momen G, Hermozilla G, Michau A, Pons M, Marty P, Hassouni K (2009) Experimental and numerical investigation of the thermal effects during hydrogen charging in packed bed storage tank. Int J Heat Mass Transfer 52:1495–1503
59. Kuerten U, van Sint Annaland M, Kuipers JAM (2004) Oxygen distribution in packed bed membrane reactors for partial oxidations: effect of the radial porosity profiles on the product selectivity. Int Eng Chem Res 43:4753–4760
60. Brandstädter WM, Kraushaar-Czarnetzki B (2007) Maleic anhydride from mixtures of n-butenes and n-butane: simulation of a production-scale non-isothermal fixed-bed reactor. Ind Eng Chem Res 46:1475–1484
61. Carslaw H-S, Jaeger JC (1959) Conduction of heat in solids, 2nd edn. Oxford University Press, Oxford
62. Bronstein IN, Semendjajew KA (1987) Taschenbuch der Mathematik, 23rd edn. Harri Deutsch, Thun and Frankfurt/Main
63. Press WH, Teukolsky SA, Vetterling WT, Flannery BP (1992) Numerical recipes in FORTRAN, 2nd edn. Cambridge University Press, Cambridge
64. Melgaard DK, Sincovec RF (1981) General software for two-dimensional non-linear partial differential equations. ACM T Math Software 7:126–135
65. Benenati RF, Brosilow CB (1962) Void fraction distribution in beds of spheres. AIChE J 8:359–361
66. Roblee LKS, Baird RM, Tierny JW (1958) Radial porosity variations in packed beds. AIChE J 4:460–464
67. Kimura M, Nono K, Kaneda T (1955) Distribution of void in a packed tube. Chem Eng Japan 14:387–400
68. Goodling JS, Vachon RI, Stelpflug WS, Ying SJ (1983) Radial porosity distribution in cylindrical beds packed with spheres. Powder Technol 35:23–29

M8 Humidifying and Drying of Air

Manfred Zeller[1] · *Ulrich Busweiler*[2]
[1]RWTH Aachen, Aachen, Germany
[2]Sachverständigenbüro, Darmstadt, Germany

1 Moist Air; Properties and Mollier *h,Y*-Diagram

Moist air is a mixture consisting of dry air and water vapor. The formation of freezing fog shall be neglected. In the majority of practical applications, it is valid to assume the gas phase to be an ideal gas mixture. As the mass of dry air does not change during most processes, state variables are specific to the mass of dry air.

Composition of moist air

The humidity ratio is defined as

$$Y = \frac{M_W}{M_L}. \tag{1}$$

Relative humidity is defined as the ratio of the actual partial pressure of water vapor in moist air to the partial saturation pressure at a stated temperature.

$$\varphi = \frac{p_D}{p_{DS}}; 0 \le \varphi \le 1. \tag{2}$$

Both values are interrelated by the following equation

$$Y = \frac{R_L}{R_D} \cdot \frac{p_D}{p - p_D} = 0.622 \frac{\varphi\, p_{DS}}{p - \varphi\, p_{DS}} \tag{3}$$

where R_L = 287 J/kg K, gas constant of air, and R_D = 461 J/kg K, gas constant of water vapor.

The saturation vapor pressure $p_{DS}(\vartheta)$ can be taken from water steam tables. A sufficiently exact approximation for the temperature range $0 \le \vartheta \le 70°C$ can be found in Sect. 3.1 from Chap. N4, Eq. (14), and for the range $0 \le \vartheta \le 60°C$ can be found in Eq. (39) of Chap. M8, respectively.

Density

For moist air with a humidity ratio Y the following equation, specific to the volume of moist air, applies

$$\rho_{wet} = \frac{M_L + M_W}{V} = \frac{p}{R_L T} \cdot \frac{1 + Y}{1 + \frac{R_D}{R_L} Y} \tag{4}$$

while for dry air, specific to the volume of humid air,

$$\rho_{dry} = \frac{M_L}{V} = \frac{\rho_{wet}}{1 + Y} = \frac{p}{R_L T} \cdot \frac{1}{1 + \frac{R_D}{R_L} Y} \tag{5}$$

is valid.

Specific Enthalpy

The term "specific" is used here to describe the reference of a value to the mass of gas (dry air) contained in the gas/vapor mixture (humid air) – in contrast to the common definition, which relates the value to the mixture's total mass. In case of unsaturated moist air, utilizing the usual point of reference at 0°C, the specific enthalpy of moist air with the humidity ratio Y *is*

$$\begin{aligned} &H = c_{pL}\vartheta + Y(\Delta h_{Vo} + c_{pD}.\vartheta), \\ &\text{whereas } c_{pL} = 1\text{kJ/kg K}, c_{pD} = 1.86\text{kJ/kg K} \\ &\text{and } \Delta h_{Vo} = 2,500 \text{ kJ/kg}. \end{aligned} \tag{6}$$

In the so-called fog area, the air is oversaturated, i.e., it contains liquid water droplets as well. The specific enthalpy is then calculated as

$$h = h_S + (Y - Y_S) c_W \vartheta \tag{7}$$

where h_S is the enthalpy, Y_S the humidity ratio at saturation, and c_W = 4.19 kJ/kg K.

h,Y-*diagram according to Mollier.*

In order to graph state changes of humid air, the *h, Y*-diagram as proposed by *Mollier* (Fig. 1) is commonly used. The isotherms are according to Eqs. (8) and (9)

$$\left(\frac{\partial h}{\partial Y}\right)_{\vartheta\,=\,\text{konst}} = \Delta h_{Vo} + c_{pD}\vartheta \tag{8}$$

for unsaturated air and

$$\left(\frac{\partial h}{\partial Y}\right)_{\vartheta\,=\,\text{konst}} = c_W \vartheta \tag{9}$$

in fog domain.

To expand the most important part, i.e., the region of unsaturated air, for practical applications, a tilted coordinate system with the isotherm at 0°C running horizontally is applied. This results in the *Y*-axis being rotated downwards by an angle corresponding to $\tan \alpha = \Delta h / \Delta Y = \Delta h_{Vo}$ while taking into account the correct scaling of the axes. The lines of constant Y thus remain vertical, whereas the lines of constant h run parallel to the rotated *Y*-axis. Differences in enthalpy are still represented by vertical distances. The isotherms' gradient in the unsaturated region increases

VDI-GVC (ed.), *VDI Heat Atlas*, DOI 10.1007/978-3-540-77877-6_57,

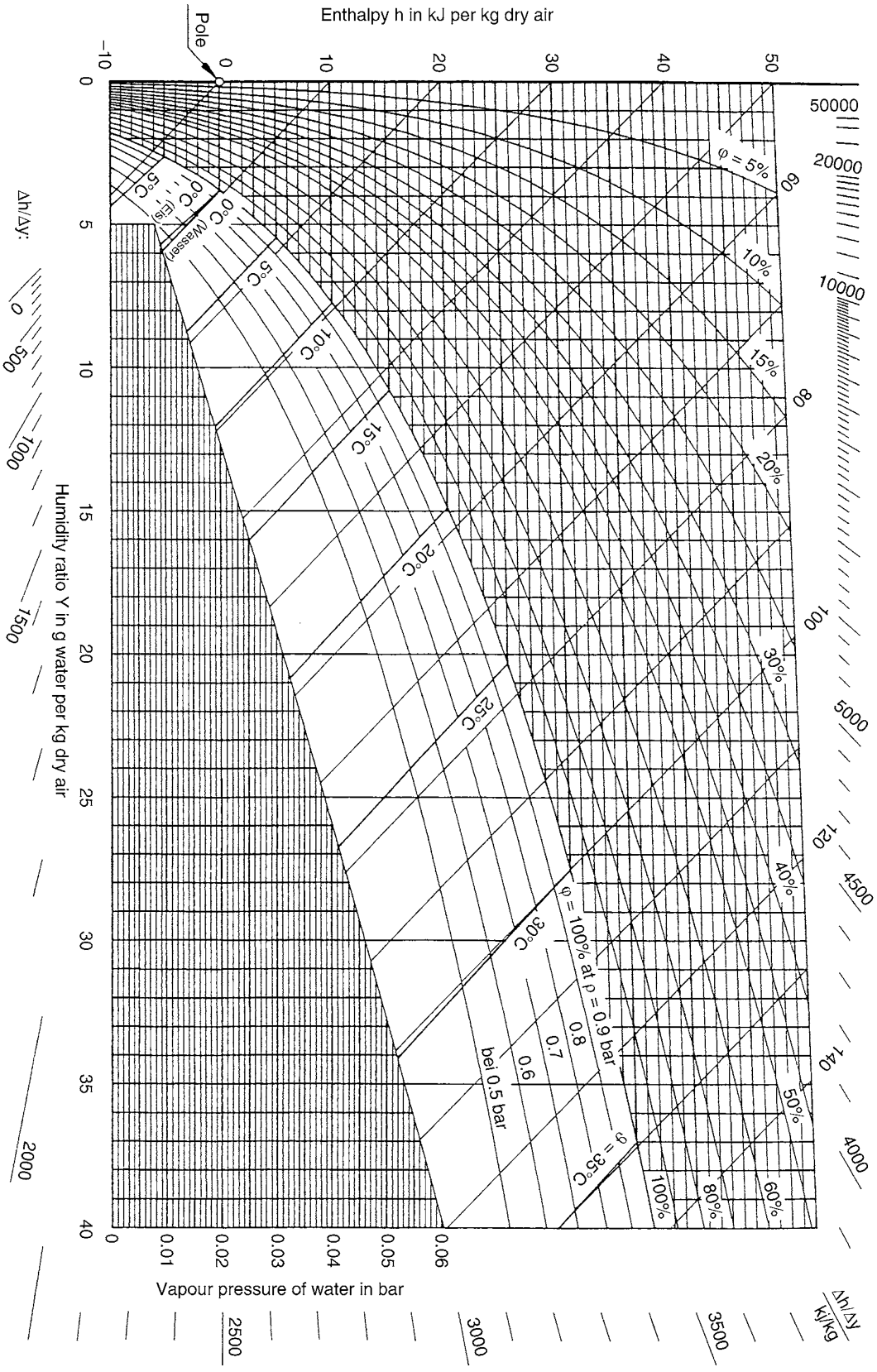

M8. Fig. 1. Mollier *h,Y*-diagram.

slightly by $\Delta h/\Delta Y = c_{pD}\vartheta$. At the saturation line, the isotherms bend. As evident from Eq. (9), the fog isotherm at 0°C coincides with a line of constant enthalpy (h = constant), while at higher temperatures, the fog isotherms run with a minor gradient than the lines of constant enthalpy cutting the saturation line at the inflection points of the isotherms.
Annotation: The so-called fog isotherms are in accordance with the wet bulb temperature lines.

In principle, a *h,Y*-diagram is only valid for a certain total pressure *p*. As long as humid air can be considered an ideal gas ($p < 10$ bar), it is possible to apply a diagram, valid for a certain total pressure *p*, at other total pressures as well as just by using the relation

$$\frac{\varphi_2}{\varphi_1} = \frac{p_2}{p_1}. \tag{10}$$

Only the labels at the lines of constant φ change according to Eq. (10). The isotherms in the unsaturated region remain the same up to the new saturation line, and the corresponding fog isotherms have to be shifted parallel to the new inflexion points. A pressure change from 1 bar to 2 bar would, for example, turn the line of φ = 50% into the new saturation line, and all previous lines with $\varphi < 50\%$ would have their labels multiplied by 2. In the same way, a reduction of the total pressure, for example, from 1 bar to 0.8 bar would imply extending the isotherms of the unsaturated region to the corresponding line of $\varphi = 100\%$ at 0.8 bar and multiplying the labels at the lines for φ = constant with a factor of 0.8.

A useful value for displaying changes of state is the measure of gradient $\Delta h/\Delta Y$ (slope "enthalpy to humidity ratio"). It is therefore included at the outline of the *h,Y*-diagram as sections of a pencil of lines originating from a pole ($Y = 0$, $h = 0$).

2 Humidification

Depending on the type of process that is applied to increase the content of water or water vapor in air, two methods can be distinguished:

- Humidifying by mixing with steam
- Humidifying by evaporation

When humidifying air with steam, water is added to air as steam that has been produced beforehand. Humidification using evaporation employs various devices to mix air with water, which then evaporates totally or partially while extracting heat from the surrounding air. Therefore, humidification of air by evaporation always leads to a decrease in air temperature in contrast to humidification by steam mixing.

2.1 Humidification by Steam Injection

If a dry air flow $\dot{M}_L$ is mixed with a steam flow $\dot{M}_D$, an energy and mass balance yield the direction of the change of state given by

$$\frac{\Delta h}{\Delta Y} = \frac{h_{LA} - h_{LE}}{Y_A - Y_E} = h_D \tag{11}$$

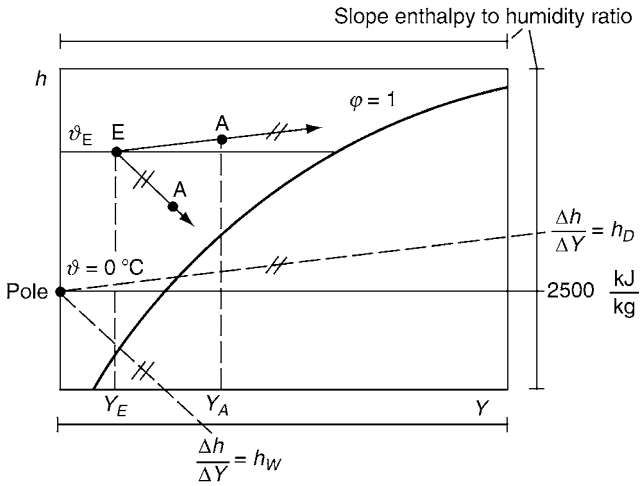

M8. Fig. 2. Change of state of moist air humidified with steam or liquid water.

which can be easily graphed in the *h,Y*-diagram according to Fig. 2 utilizing the slope scales on the diagram perimeter. For this, the slope corresponding to the calculated gradient is connected with its origin (pole) and the resulting line is shifted parallel to the point of state E at the air entry. The change of state of air then runs along the obtained straight line. The change in humidity ratio and the state of air at the outlet A are derived from the mass balance:

$$\Delta Y = Y_A - Y_E = \frac{\dot{M}_D}{\dot{M}_L} \tag{12}$$

Because of $c_{pD} \cdot \vartheta_D \ll \Delta h_{Vo}$, only a minor change in air temperature occurs (about 1–4 K).

For a proper operation of steam humidifiers, it is crucial to achieve a good mixing of the injected steam through steam lances or distributor pipes in order to avoid condensation at duct walls or successive units. Additional measures, e.g., superheating of the steam by heating the jacket tube or condensing separators have to be installed to prevent condensate dripping from distributor pipes. Only few publications exist about the necessary length of the mixing path. It is determined empirically and can usually be obtained from manufacturer's data. Finer steam spreading and lower steam flow per manifold length yield shorter mixing paths. Additionally, air velocity, humidity levels at the inlet and outlet, exit air temperature, as well as the characteristics of successive installations have a major influence. Irrespective of the really installed system, applicable guide values, which have been determined empirically [1], can be taken from Fig. 3.

These diagrams are based upon the recommended steam pipe arrangement in Fig. 4. They are valid for specific increases in air humidity. Deviations can be accounted for by applying the following adjustment

$$L_B(\Delta Y \pm \Delta(\Delta Y)) = (1 \pm 0.25) \cdot L_B(\Delta Y)_{\text{diagram}}$$

with $|\Delta(\Delta Y)| = 2\,g/kg$.

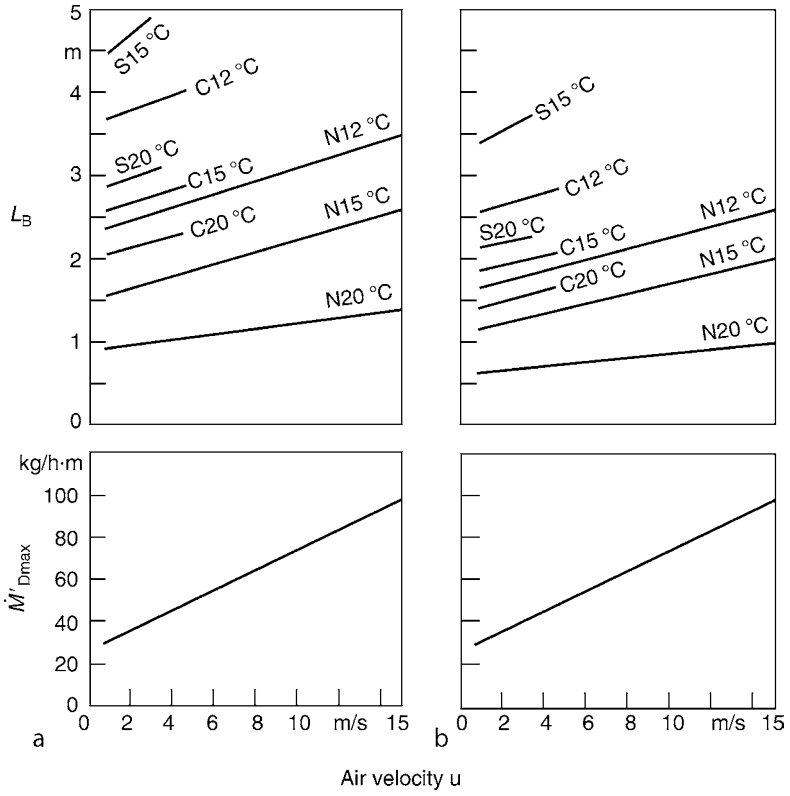

M8. Fig. 3. Humidification paths L_B in steam humidifiers for different operation modes and boundary conditions according to [1]. Parameters: Air temperature behind the humidifier (°C) and type of obstacles: S filter for suspended matter, C fine filter, N common obstacles (e.g., pipe elbow, blowing fan): (a) Full outside air operation with $Y_E \approx 1$ g/kg and $\Delta Y \approx 7$ g/kg (b) Operation with partially recirculated air with $Y_E \approx 4$ g/kg and $\Delta Y \approx 4$ g/kg.

Another 25% reduction of the humidifier path can also be realized if the steam flow to distribution pipe length ratio is decreased to the half of the maximum value from the diagram.

Behind the mixing path L_B, the humidity distribution will normally not have reached uniformity. Without further measures, this might require a multiple of L_B about the magnitude of 5 L_B.

Example 1

Given:

Geometry of humidifier duct (height $H = 1$ m, width $B = 1.5$ m)
Humidifier path (provided by customer $L_B = 2$ m)
Complete outside air supply
Inlet air conditions: $\vartheta_{LE} = 15°C$, $Y_E = 1$ g/kg
Humidity ratio at exit: $Y_A = 8$ g/kg
Air velocity in front of the humidifier: $u_{LE} = 3$ m/s
Fine filter C behind humidifier
Steam inlet temperature: $\vartheta_D = 102°C$

Find:

Required steam flow $\dot{M}_D$ as well as the number of steam distribution pipes n_R.

Using the dry air density according to Eq. (5)

$$\rho_{trE} = \frac{10^5}{287 \cdot 288} \cdot \frac{1}{1 + 0.001 \cdot 461/288} = 1.2\,\text{kg/m}^3$$

the mass flow of dry air results as

$$\dot{M}_L = \rho_{trE} u_{LE} HB = 1.2 \cdot 3 \cdot 1 \cdot 1.5\ \text{kg/s} = 5.44\ \text{kg/s}.$$

According to Eq. (12) the required steam supply is

$$\dot{M}_D = \dot{M}_L (Y_A - Y_E) = 5.44 \cdot 0.007\,\text{kg/s} = 0.038\,\text{kg/s} = 137\ \text{kg/s}.$$

After rearrangement of Eq. (11) with $h_D = \Delta h_{Vo} + c_{pD}\vartheta_D$ the exit temperature of dry air can be calculated as

$$\vartheta_{LA} = \frac{(Y_A - Y_E)c_{pD}\ \vartheta_D + (c_{pL} + Y_E c_{pD})\vartheta_{LE}}{c_{pL} + c_{pD} Y_A} = \frac{0.007\ \cdot\ 1.86 \cdot 102 + (1 + 0.001 \cdot 1.86) \cdot 15}{1 + 1.86 \cdot 0.008}\ °C = 16.1°C.$$

The permissible steam flow per distributor tube length at $u = 3$ m/s is taken from Fig. 3 (complete outside air operation) as

$$\dot{M}'_{D\,max} = 40\,\text{kg/hm}$$

and in the case of a fine filter behind the humidifier and an air temperature of 16.1°C, which has been interpolated linearly between C 15°C und C 20°C, the necessary humidifier path length is read off:

$$L_{B\,max} = 2.6\ m.$$

Applying the condition $\dot{M}'_D \le \dot{M}'_{D\,max}$ and the recommendations according to Fig. 4 for the arrangement of steam distribution pipes, the resulting length of one steam distribution pipe is

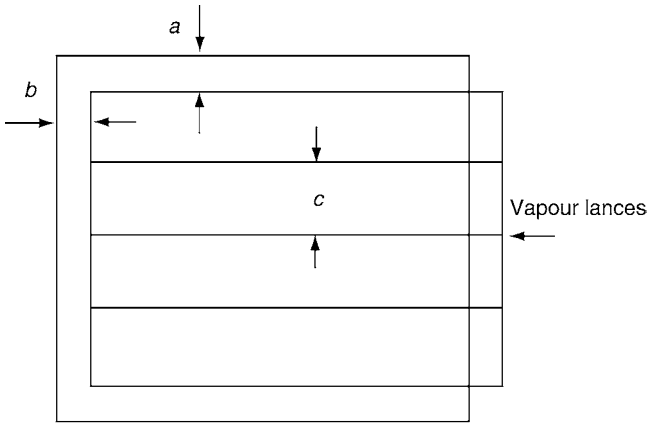

u m/s	a mm	b mm	C_{max} mm	$\dot{M}'_{Dmax}$ kg/h je per m tube length
1	300	150	450	30
2	250	150	450	35
3	200	150	400	40
5	150	150	350	50
10	100	150	350	70

M8. Fig. 4. Recommended maximum distance of steam distribution pipes at specified maximum steam flow per meter of tube length according to [1]. *u* = air velocity, *a*, *b* = distances from walls, $\dot{M}_{Dmax}$ = maximum steam flow per meter tube length, and *c* = distance between pipes.

$$L_R = B - b = 1.5\,\text{m} - 0.15\,\text{m} = 1.35\,\text{m}$$

and the number of distribution pipes n_R

$$n_R \geq \frac{\dot{M}_D}{L_R \dot{M}'_{D\,max}} = \frac{137}{1.35 \cdot 40} = 2.54 \text{ Rohre.}$$

Then the number of pipes is chosen as $n_R = 3$ and so the steam mass flow to pipe length ratio can be calculated as

$$\dot{M}'_D = \frac{137}{1.35 \cdot 3}\text{kg/hm} = 33\,\text{kg/hm.}$$

As identified before in Fig. 3, $\dot{M}'_{D\,max} = 40$ kg/h m requires a humidifier path length of 2.6 m. Due to the fact that only a path length $L_B = 2$ m is provided by customer, which is about 25% shorter, the steam flow per pipe length according to [1] (see Sect. 2.2) has to be reduced to $\dot{M}'_{Dmax}/2 = 20$ kg/h m. The number of distribution pipes then increases to

$$n_R = \frac{\dot{M}_D}{L_R \dot{M}'_{D\,max}/2} = \frac{1.37}{1.35 \cdot 20} = 5\,\text{pipes.}$$

2.2 Humidification by Evaporation

Evaporation occurs if water has not yet reached the boiling temperature at the current pressure while the partial pressure of water vapor at the phase interface, i.e., the water surface, is greater than the partial pressure of water vapor in the ambient air. Numerous types of evaporation humidifiers exist. A general difference concerns the supplied water flow rate. It either equals exactly to the amount of steam picked up by the air flow or it is greater than the water vapor retained in air while the none-vaporated fraction is recirculated.

Complete evaporation of supplied water

Main embodiments of these humidifiers comprise spray humidifiers, e.g., rotating centrifugal discs or nozzles, ultrasonic humidifiers and sprinkled mats. Humidification performance can be calculated according to Sect. 2.1. Only h_D and $\dot{M}_D$ have to be replaced by h_W and $\dot{M}_W$. In contrast to steam injection, humidification with water results in a considerable cooling of the air stream as the air has to provide the vaporization heat of water (Fig. 2, case $\Delta h/\Delta Y = h_W$).

Partial evaporation and recirculation of the humidification water

Humidification water is pumped in a cycle with only the evaporated fraction being compensated. Essentially, two constructions can be distinguished: sprinkling humidifiers and spray chamber humidifiers (which in literature are usually denominated "air washers").

Within sprinkling humidifiers the air passes through water-sprinkled installations which consist of packing material or surfaces with various geometries. Basis of calculation is the knowledge of the empirically determined heat and mass transfer characteristics of the installations. If these data are available, e.g., as number of transfer units (NTUs) – characteristic, the installation's dimensions as well as state changes of air can be determined by the method described in Chap. N4. Commonly, however, these data are not available. In most cases, only device specific humidification characteristics equal to those describing the operating behaviour of air washers, as discussed later on, are utilized as the basis for calculations.

Spray chamber humidifiers or rather air washers are employed predominantly. Inside these devices, the humidification water is atomized by nozzles while the air to be humidified is moved in or against the spray direction. If humidification is the primary task, the air washer is operated adiabatically, i.e., no heat is transferred to the recirculated humidifying water except for the normally negligible pumping energy, the enthalpy of the added water, and heat transfer through the walls of the device. The humidification performance of an adiabatic air washer can be characterized with the humidifying efficiency

$$\eta_B = \frac{Y_A - Y_E}{Y_K - Y_E} \approx \frac{\vartheta_{LA} - \vartheta_{LE}}{\vartheta_K - \vartheta_{LE}} \qquad (13)$$

which describes the ratio of the real to the maximal achievable change in air humidity and which approximately, i.e., as long as the isotherms can be assumed to be running nearly parallel ($c_{pD} \cdot \vartheta \ll \Delta h_{Vo}$), corresponds to the ratio of temperature change. The achievable maximum humidity is the saturation humidity ratio at the so-called cooling limit temperature (respectively, adiabatic saturation temperature) ϑ_K corresponding to the entry state of the air. It can be obtained by extending the fog isotherm (line of constant wet bulb temperature) running

through the entry state of the air. As a precondition of this, the *Lewis* factor has to be equal to

$$\frac{\alpha}{\beta_Y c_{p_{1+Y}}} = 1 \tag{14}$$

whereas $c_{p_{1+Y}} = c_{pL} + Y c_{pD}$, which is sufficiently exact for mixtures of water vapor and air in the range of usual air humidification processes [2]. The cooling limit state (Y_K, ϑ_K) can be calculated by iterating equation

$$\frac{h_{LE} - h_{LK}}{Y_E - Y_K} = c_W \vartheta_K \tag{15}$$

using the vapor pressure curve $p_{DS} = f(\vartheta_S)$ (e.g., Eq. (39)) or $Y_S = f(\vartheta_S)$ with $\vartheta_S = \vartheta_K$ and h according to Eq. (6), respectively. From Eq. (15) also follows that the state of air inside the humidifier changes along the extended fog isotherm (wet bulb temperature line) ϑ_K, as shown in Fig. 5.

The humidifying efficiency η_B is influenced by many parameters. The most important are the droplet-size distribution of the spray and the resulting overall droplet surface, respectively, the relative velocity between droplets and air as well as the residence time of the droplets. These parameters are determined by the flow rates of water and air, by the type, number, and arrangement of nozzles, by the nozzle inlet pressure, and the dimensions of the spray chamber.

Numerous efforts have been made to precalculate the change of state of air in spray chambers, e.g., [3, 4]. They comprise dividing the droplets into classes and solving numerically the transport equations for the particular droplet classes and the air flow while taking into account the interactions at the phase interface. The shortcoming of these numerical methods is the insufficient knowledge of the droplet-size spectrum. Available are only spectra of single nozzles injecting into free space. Within installations, these spectra change significantly due to the number and arrangement of nozzles, the chamber design, and air flow velocity. This results in unsatisfying agreement between experimental and numerical data. Furthermore, a considerable part of the mass transfer obviously takes place at the water-sprinkled chamber walls. Because of these effects, numerical calculations indeed allow for parametric studies and a deeper understanding of the physical processes, but they do not suffice for quantitative predictions. Hence practical applications still rely on the use of experimentally acquired characteristics hardly suitable for generalization.

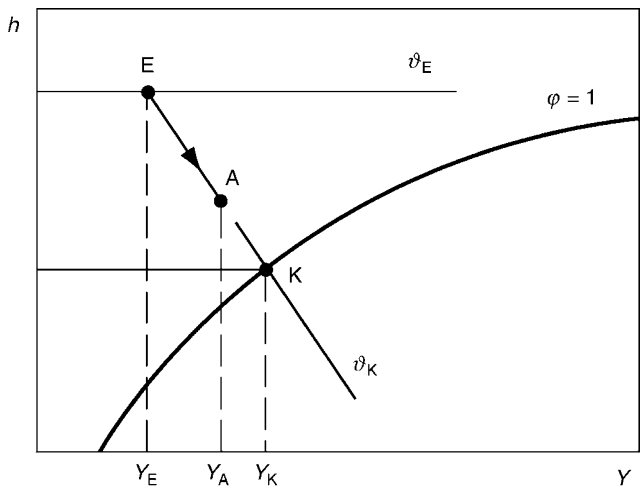

M8. Fig. 5. State change of moist air inside an adiabatic spray chamber.

Various approaches exist to describe experimentally determined humidifying efficiencies with equations. The integration of a simple mass balance for an air washer element yields

$$\eta_B = 1 - e^{-K_Y \dot{M}_W / \dot{M}_L}. \tag{16}$$

This equation assumes that the characteristic humidifier number K_Y remains constant along the humidifier and is independent of the ratio of water and air flow rate $\dot{M}_W/\dot{M}_L$. The quantity K_Y contains the droplet surface area relating to the water flow rate. Constancy of K_Y is only valid if the water flow rate is controlled by switching on and off single nozzles and not by alternating the nozzle inlet pressure as it is done usually. Furthermore, Eq. (16) does not take into account the chamber walls therefore not reproducing satisfactorily existing experiments.

Extended approaches, which included, e.g., the humidifier length and the air velocity into the calculation of K_Y [3, 5], did not lead to substantial improvements.

Based on the depicted circumstances, some authors [6, 7] are acting on the assumption of no further physically founded, in terms of dimension theory inconsistent power approach to evaluate experimental data:

$$\eta_B = C(u_L)^n \left(\dot{M}_W/\dot{M}_L\right)^m. \tag{17}$$

Depending on experimental procedures as well as data analysis methods, the authors obtained different algebraic signs for the exponent n. If the mass flow ratio of water and air is varied at constant air mass flow by means of the nozzle inlet pressure [6, 7], the resulting exponent is positive, because the spectrum of droplet sizes simultaneously shifts toward smaller droplets. However, if the variation of the water mass flow is achieved with the change of number of nozzles at a constant nozzle inlet pressure, the residence time becomes dominant leading to a negative exponent n [8].

The variety of influencing parameters explains why the proposed equation and diagrams for η_B are closely restricted to the underlying experimental boundary conditions and why the humidifier characteristic

$$\eta_B = f\left(\dot{M}_W/\dot{M}_L\right) \tag{18}$$

has to be determined for every humidifier separately. Previous attempts to generalize the empirical findings with respect to the controlling geometrical and process factors have not proved successful. Corresponding to the numerous influencing parameters a large number of characteristic curves based on Eq. (18) is required for designing humidifiers. Parameters of noticeable influence are the type of nozzle, nozzle i.d., nozzle arrangement, number of nozzle banks, nozzle inlet pressure, spray direction related to air flow (upstream or downstream) as well as opposing banks in double-row nozzle banks, fan arrangement (situated ahead or behind the chamber), in case of the fan located ahead also the forming of the downstream diffuser,

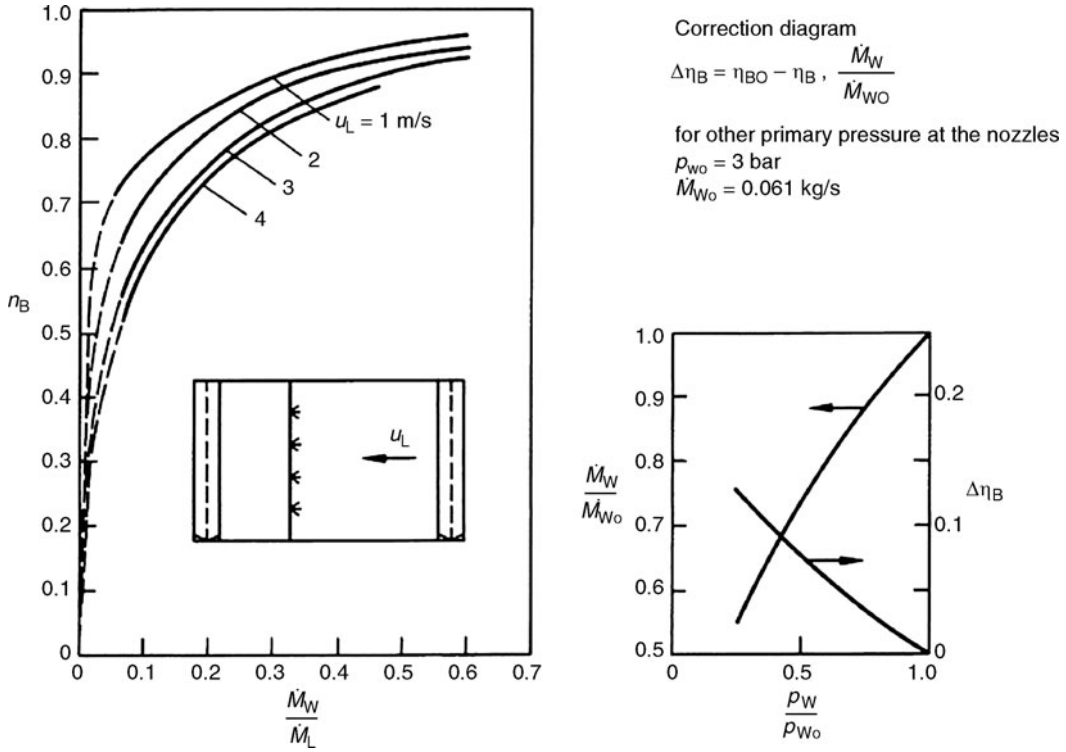

M8. Fig. 6. Humidifying efficiency $\eta_B = f(\dot{M}_W/\dot{M}_L, u_L)$ for swirl nozzles with diameter d = 3 mm, nozzle inlet pressure p_{Wo} = 3 bar, fixed chamber geometry and suction fan; correction diagram for differing nozzle inlet pressures [8].

chamber length, air velocity. Figure 6 gives an example of a humidifier characteristic. The correction factor $\Delta\eta_B$ mainly includes the influence of variations in the droplet-size spectrum due to changes of the nozzle inlet pressure.

In general the following applies: Water sprays discharging in opposed direction to the air flow (upstream) yield higher humidifying efficiencies than downstream discharging [8, 9]. In double-row nozzle banks, downstream bank designs are preferable to upstream or opposing designs as well. Furthermore, higher humidifying efficiencies can be achieved with fans situated behind the chamber [8]. If the fan is placed ahead the chamber, the forming of the downstream diffusor and further installations play an important role.

The necessary length of the humidification path depends primarily on the air velocity and the water/air flow ratio. A length of 1–1.5 m is usually sufficient.

Example 2

Given:

Humidifier geometry, nozzle type and arrangement corresponding to Fig. 6.

Furthermore, the following values are known:

$$u_L = 3 \text{ m/s}, \left(\dot{M}_W/\dot{M}_L\right)_o = 0.4 \text{ at } p_{wo} = 3\text{bar},$$

state of air at inlet : $\vartheta_{LE} = 22°\text{C}, Y_E = 7$ g/kg, $p = 1$ bar.

Find:

Humidifying efficiency η_B at p_{Wo} = 3 bar and p_W = 1.5 bar, state of air at outlet ϑ_{LA}, Y_A at p_W = 1.5 bar.

Figure 6 gives at $\dot{M}_W/\dot{M}_L = 0.4$, u_L = 3 m/s and p_{Wo} = 3 bar a humidifying efficiency η_B = 0.88. The water/air flow ratio corresponding to a change in nozzle inlet pressure and as the case may be in air velocity can be calculated from

$$\frac{\dot{M}_W}{\dot{M}_L} = \frac{\dot{M}_W/\dot{M}_{Wo}}{u_L/u_{Lo}} \left(\frac{\dot{M}_W}{\dot{M}_L}\right)_o .$$

In the given case the air velocity remains unchanged, that means that $u_L/u_{Lo} = 1$ applies. The ratio $\dot{M}_W/\dot{M}_L$ amounts to 0.705 according to the correction diagram in Fig. 6 at p_W/p_{Wo} = 0.5. This yields

$$\frac{\dot{M}_W}{\dot{M}_L} = \frac{0.705}{1} \cdot 0.4 = 0.28.$$

At this water/air flow ratio and an inlet pressure p_{Wo} = 3 bar, a humidifying efficiency of η_B = 0.825 would result according to Fig. 6. At the same water/air flow ratio, yet with a lower nozzle inlet pressure p_W, the humidifying efficiency decreases along with the correction diagram in Fig. 6 by $\Delta\eta_B(p_W/p_{Wo} = 0.5)$ to η_B = 0.74.

Calculation of the state of air at the outlet requires knowledge of the adiabatic saturation state (ϑ_K, Y_K) corresponding to (ϑ_{LE}, Y_E). It can be obtained iteratively: The adiabatic saturation temperature is guessed to be $\vartheta_K^* = 14°\text{C}$. Equation (39) then yields

$$p_{DS} = 10^{-3} \cdot 10^{8.3246} - \frac{1799.73}{14 + 238.734} \text{ bar} = 0.016 \text{ bar}$$

and Eq. (3)

$$Y_K = 0.622 \cdot \frac{0.016}{1 - 0.016} = 0.0101\,\text{kg/kg}.$$

Solving Eq. (15) for ϑ_K using Eq. (6) results in

$$\vartheta_K = \frac{(c_{pL} + Y_E c_{pD})\vartheta_{LE} - (Y_K - Y_E)\Delta h_{Vo}}{c_{pL} + Y_K c_{pD} - (Y_K - Y_E)c_W}$$
$$= \frac{(1 + 0.007 \cdot 1.86) \cdot 22 - (0.0101 - 0.007) \cdot 2500}{1 + 0.0101 \cdot 1.86 - (0.0101 - 0.007) \cdot 4.19}$$
$$= 14.5^\circ\text{C} \neq \vartheta_K^*.$$

The new approximation $\vartheta_K^* = 14.2^\circ$C leads to

$$p_{DS} = 0.0162\,\text{bar} \rightarrow Y_K = 0.0102\,kg/kg \rightarrow \vartheta_K = 14.1^\circ\text{C} \approx \vartheta_K^*.$$

Then, the final result is $\vartheta_K = 14.2^\circ$C and $Y_K = 0.0102$ kg/kg.

(Hint: The iteration method which uses the calculated result as new starting value is computationally unstable, therefore relaxation is applied.)

Eqs. (13), (15), and (6) finally yield

$$Y_A = 7 + 0.74 \cdot (10.2 - 7) = 9.37\ \text{g/kg}\ (\text{Eq.}(13))$$
$$h_{LA} = h_{LE} + c_W \vartheta_K (Y_A - Y_E)$$
$$= 39.37 + 4.19 \cdot 14.2 \cdot 0.00237 = 39.93\ \text{kJ/kg}\ (\text{Eq.}(15))$$
$$\vartheta_{LA} = \frac{h_{LA} - Y_A \Delta h_{Vo}}{c_{pL} + Y_A c_{pD}} = 16.2^\circ\text{C}\ (\text{Eq.}(6)).$$

The state at the outlet can be obtained directly from the h,Y-chart by marking off a segment from point LE with the length $0.74.\overline{LE, K}$ on the line of constant wet bulb temperature passing through inlet state point (ϑ_{LE}, Y_E) of the air.

3 Dehumidification

Two in principle different methods exist:

- Dehumidification by absorption or adsorption
- Dehumidification by cooling and condensation

3.1 Dehumidification by Sorption Processes

These processes utilize the ability of sorbents to bind water molecules and therefore to lower the vapour pressure below the saturation water pressure level.

Different types of sorption processes can be distinguished:

- "Liquid sorption" employs liquid sorbents which create a homogenous phase with the absorbed water vapour (absorption).
- "Solid sorption" occurs at the inner surfaces of a solid sorbent where water vapour deposits due to surface forces and creates a separate phase (adsorption).

The binding mechanisms of absorption and adsorption processes can be of chemical or physical nature. Common liquid sorbents for air dehumidification are aqueous solutions of hygroscopic salts like LiCl, LiBr and $CaCl_2$ or mixtures of these. For adsorptive air dehumidification silica gel or synthetic zeolites are used.

Adsorptive processes with silica gel or molecular sieve (zeolite) are applied preferably because of their favourable operational properties. Therefore, only air dehumidification by solid sorption is discussed in the following. Applied techniques are either packed beds of sorbent granulates (fixed bed adsorption) or rotatory adsorbers (desiccant wheels).

During fixed bed adsorption, the humid air has to pass the granulate. As the sorption capacity of the adsorbent is limited, the humidity ratio of the exhausting air flow increases after a certain time (breakdown) and dehumidification has to be stopped. The adsorbent is then regenerated by a hot air reversely flowing through the packed bed.

Desiccant wheels allow for a continuous dehumidification. For that purpose, the wheel is divided in two sectors one with a flow of humid process air and the other with a counterflow of hot regeneration air. Crucual parameters for the dehumidification performance of an adsorption device are

- The sorption equilibrium of sorbent and processed humid air. It defines the theoretically achievable humidity ratio and is a major basis for the dimensioning of the device.
- The sorption kinetics, i.e., the velocity of water vapour deposition inside the adsorbent. This comprises a variety of series-connected heat and mass transfer processes which prohibit deriving a simple calculation method for adsorption devices [10]. Therefore dimensioning is based on empirical data or complex numerical calculations [11, 12].

In Chap. N2, a mathematical model for the coupled heat and moisture transfer is accomplished as well. It enables predicting the process in desiccant wheels, if sorption equilibrium and the heat and mass transfer relations for the flow in the wheel matrix are known.

The sorption equilibrium is usually described by sorption isotherms. They represent the equilibrium moisture content related to the weight of unloaded sorbent in dependency on water vapour concentration or air humidity ratio. Figure 7 shows sorption isotherms of different adsorbents at a consistent temperature of 25°C. For different temperatures and a customary silica gel, the sorption isotherms are displayed in Fig. 8.

In order to calculate adsorptive dehumidification of air, plotting the equilibrium as "isosteres" (W = constant), i.e., lines of constant moisture content, proves to be helpful. Figure 9 contains exemplary isosteres of the same silica gel as in Fig. 8 for $W = 0.02$, 0.05 and 0.2 $\text{kg}_{H_2O}/\text{kg}_{adsorbent}$ in a h,Y-diagram. Using the isosteres, it is possible to determine the reachable moisture contents in case that the entry states of process air and regeneration air are known. For example, if the adsorbent is regenerated with hot air at 80°C and 15 $\text{g}_{H_2O}/\text{kg}_{adsorbent}$ the resulting equilibrium moisture content is 0.02 kg/kg. Therefore, the flow of humid process air can reach in ideal conditions an exit state that is in equilibrium with 0.02 kg/kg, thus being on the 0.02 kg/kg isostere as well.

Adsorption and desorption both occur with changes in the temperature of the air flow. The heat released during adsorption includes the binding energy in addition to the heat of condensation. It depends on the loading and amounts to, e.g., 10% of the heat of condensation in case of water vapour adsorption on silica gel. Heat releases from condensation and binding energy

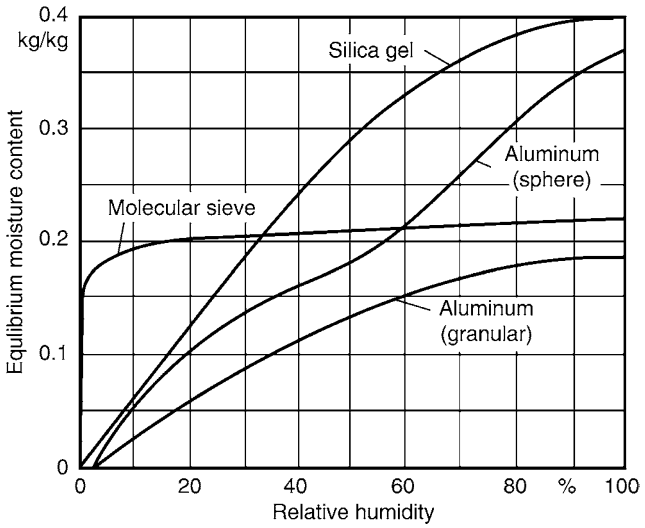

M8. Fig. 7. Sorption isotherms of different sorbents at 25°C [10, 13].

are summarized as sorption heat and cause the temperature of the humid process air to increase. Additionally, the adsorbent is heated up during regeneration and this heat is subsequently transferred to the process air flow. Analogous to the adsorption process, the desorption involves a decrease in regeneration air temperature.

In cases of technical interest (humidity ratio at inlet $Y = 5, \ldots, 15$ g/kg), the specific temperature increase due to adsorption is

$$\frac{\Delta\vartheta}{\Delta Y} = \text{from } 3 \text{ to } -6\,\frac{K}{g/kg}.$$

Low inlet humidity ratios result in higher specific temperature increases.

Because of sorption kinetics with finite heat and mass transfer coefficients, technical adsorption devices cannot reach the state of equilibrium between air flow and sorbent. In order to estimate the influence of kinetics, *Van den Bulck* et al. [14] defined a

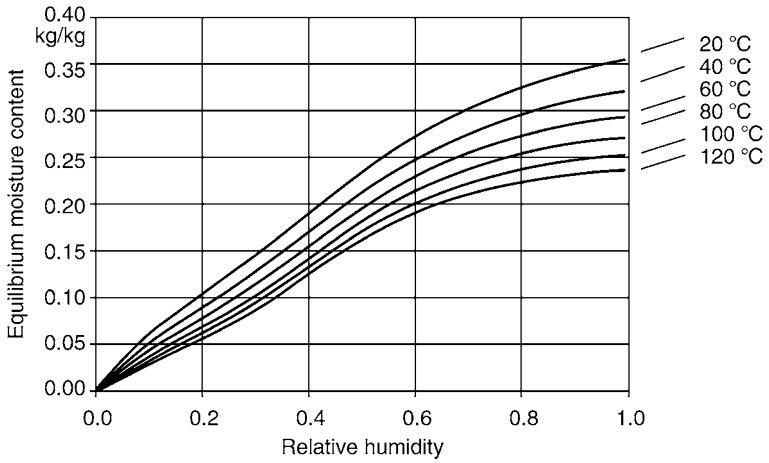

M8. Fig. 8. Sorption isotherms of a commercially available granular silica gel [8].

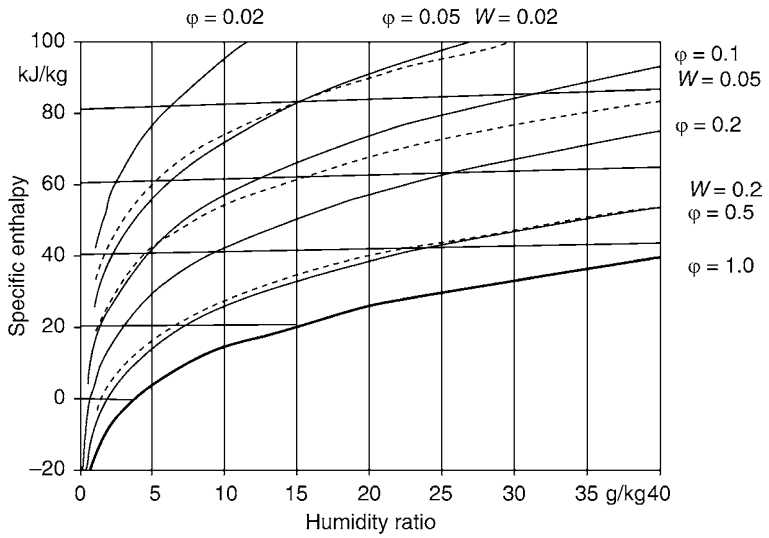

M8. Fig. 9. *h,Y*-diagram with sorption isosteres for a commercially available granular silica gel.

dehumidifying efficiency for desiccant wheels in analogy to the humidifying efficiency (Eq. 13), which relates the change in humidity ratio of a real adsorption device to the ideal case

$$\eta_E = \frac{\Delta Y_{real}}{\Delta Y_{ideal}}. \qquad (13a)$$

Figure 10 shows the interrelation between ideal dehumidification, determined by sorption equilibrium, and real dehumidification, additionally influenced by sorption kinetics. The dehumidifying efficiency at common operating conditions is about $\eta_E = 0.7–0.9$.

The dehumidification performance of an adsorption device and the achievable outlet humidity ratio depend on more than 20 parameters [15]. Hence, the interrelation between humidity ratio at air inlet and air outlet can only be graphed for one particular adsorption device and certain operation conditions. Figure 11 displays as an example the performance diagram of a customary desiccant wheel. For differing operating conditions, the dehumidification performance has to be determined either experimentally or numerically.

Applying the previously defined characteristic values, "dehumidifying efficiency" and "specific temperature increase," the operating behaviour of a desiccant wheel can be described in a simplified way. They provide an approximate conversion for differing air entry states. As a simplification for this, it is assumed that these values do not change over the considered ranges of temperature and humidity.

If no data about the sorption equilibrium are available, as a further approximation it can be assumed, that the isosteres in the h,Y-diagram are running in parallel to the lines of constant relative humidity.

Example 3a

Given:

The performance diagram according to Fig. 11 (manufacturer information) and the inlet state of process air (ϑ_E = 25°C; Y_E = 10 g/kg). Total pressure P = 1 bar.

Find:

The exit state of dehumidified air (ϑ_A, Y_A).

The outlet temperature ϑ_A and the outlet humidity ratio Y_A can be taken from the diagram in Fig. 11 as: ϑ_A = 53.4°C; Y_A = 3.2 g/kg.

If the humidity ratio at the exit is higher than required, it is possible to lower the value of Y_A e.g., through a larger wheel. This can be only done until the limit of the "ideal" dehumidifier is reached. In order to estimate the potential of improvements, it is necessary to determine the humidity ratio at the exit for the ideal case.

As for this example, no data about the sorption equilibrium are available, except the performance diagram, the simplifying assumption is made, that the isosteres in a h,Y-diagram are running in parallel to the lines of constant relative humidity.

The dehumidification path with air inlet state (ϑ_E = 25°C; Y_E = 10 g/kg) and air outlet state (ϑ_A = 53.4°C; Y_A = 3.2 g/kg) is plotted in the h,Y-diagram. The relative humidity for the inlet

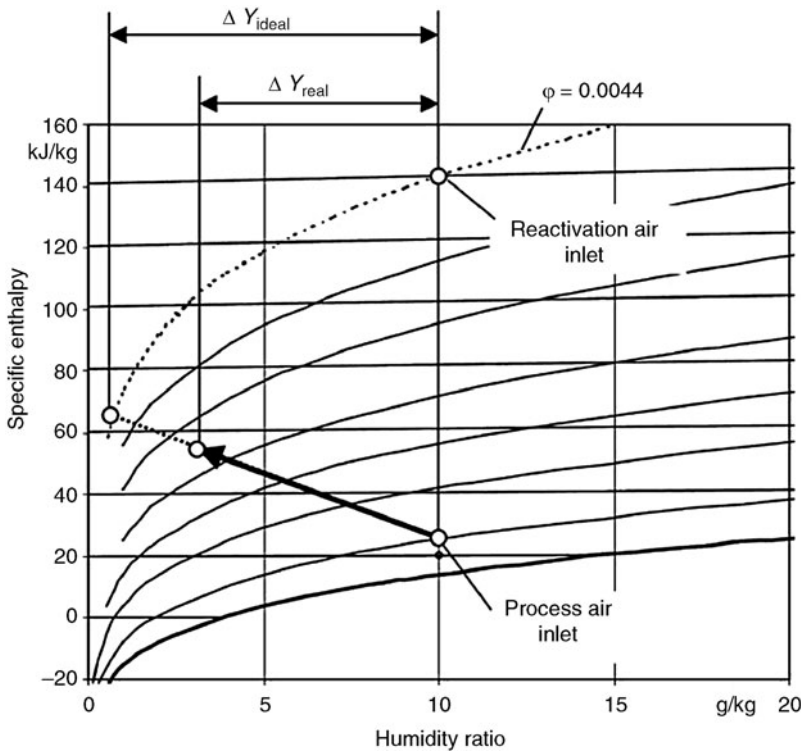

M8. Fig. 10. State change in a desiccant wheel and dehumidifying efficiency.

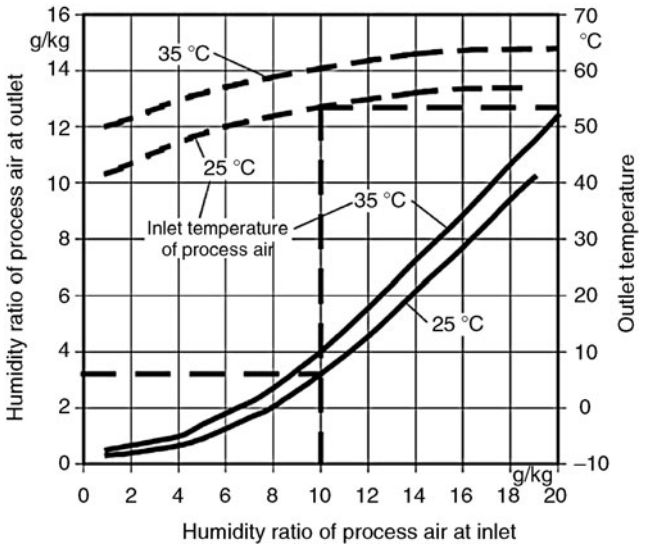

M8. Fig. 11. Performance diagram of a commercially available desiccant silica gel wheel for the following conditions: inlet temperature of regeneration air: 140°C, inlet humidity ratio of regeneration air = inlet humidity ratio of process air, relation of sectors regeneration air/process air t = 1:3, face velocity in front of the wheel: 3 m/s, depth of the wheel: 200 mm, wheel revolution per hour: 10 h^{-1}.

state of regeneration air (ϑ = 140°C; Y = 10 g/kg) is then determined. (Notice: The performance diagram in Fig. 11 is based on a regeneration air temperature of 140°C and the premise: humidity ratio of regeneration air = humidity ratio of process air.)

It can be taken from a corresponding h,Y- diagram or calculated from Eqs. (2) and (3) as well as a steam pressure table.

$$\varphi = \frac{P_D(Y = 10\,\text{g/kg},\ P = 1.0\ \text{bar})}{P_{DS}(\vartheta = 140°\text{C})} = \frac{P}{P_{DS}} \cdot \frac{Y}{0.622 + Y}$$
$$= \frac{1\,\text{bar}}{3.61\,\text{bar}} \cdot \frac{0.01}{0.622 + 0.01} = 0.0044.$$

If the dehumidification path is extended from state (ϑ_E; Y_E) to state (ϑ_A; Y_A) to the left, it intersects with the φ = 0.44% line at the unknown exit state of an ideal dehumidifier:

$$Y_{A\,ideal} = 0.7\,\text{g/kg};\ \vartheta_{A\,ideal} = 65°\text{C}.$$

Lines for $\varphi < 0.1$ are normally not included in the h, Y-diagrams. But they can be derived from known lines of the same relative humidity. For a given temperature ϑ = 40°C, the conversion is

$$\frac{Y_1}{Y_2} = \frac{\varphi_1}{\varphi_2} \cdot \frac{1 - \frac{\varphi_2 \cdot P_{DS}}{P}}{\frac{\varphi_1 \cdot P_{DS}}{P}}.$$

If $\varphi P_{DS} \ll P$:

$$Y_1 = Y_2 \cdot \frac{\varphi_1}{\varphi_2}$$

applies.

In the considered case, this is φ_1 = 0.1; φ_2 = 0.0044 und $Y_1 = Y(\varphi = 0.1; \vartheta = 40°\text{C})$ = 4.6 g/kg (according to Eq. (3)). Y_2 results as

$$Y_2 = 4.6\,\text{g/kg} \cdot \frac{0.0044}{0.1} = 0.2\,\text{g/kg}.$$

Converting this for several temperatures and connecting the calculated points yields a curve for φ = constant = 0.0044.

The exit state of an ideal dehumidifier can be computationally assessed only with an iterative approach. The values for $Y_{A\,ideal}$ and $\vartheta_{A\,ideal}$ have to fulfil the following conditions:

$$\vartheta_{A\,ideal} = \vartheta_E + \frac{\vartheta_A - \vartheta_E}{Y_A - Y_E} \cdot (Y_{A\,ideal} - Y_E)$$

and

$$\varphi = \frac{P_D(Y_{A\,ideal}, P_{ges} = 1.0\ \text{bar})}{P_{DS}(\vartheta_{A\,ideal})} = 0.0044.$$

Starting at an estimated value $Y^*_{A\,ideal}$<1.0 g/kg yields

$$\vartheta^*_{A\,ideal} = 25° + \frac{(53.4 - 25)\text{K}}{(2.3 - 10.0)\text{g/kg}} \cdot (1.0 - 10.0)\,\text{g/kg} = 63.7°\text{C}$$

and

$$\varphi^* = \frac{P_D(1.0\,\text{g/kg}_1, P_{gcs} = 1.0\,\text{bar})}{P_{DS}(63.7°\text{C})} = \frac{0.16\,\text{kPa}}{23.6\,\text{kPa}} = 0.0068.$$

Because of $\varphi^* > 0.0044$, *a value* $Y^*_{A\,ideal}$<1.0 g/kg has to be chosen for the next iterative step.

Example 3b

Approximated determination of the exit air humidity ratio at another entry state of regeneration air.

Given:

- Entry state of process air same as in Example 3a (ϑ_E = 25°C; Y_E = 10 g/kg)
- Entry state of regeneration air ϑ = 90°C; Y = 12 g/kg instead of ϑ = 140°C; Y = 10 g/kg as in Example 3a
- Performance diagram according to Fig. 11

Find:

Humidity ratio of process air at the exit for the changed entry state of regeneration air. Approximation based on Fig. 11.

A precise determination of the exit air humidity ratio requires a corresponding performance diagram by the manufacturer for the intended state of regeneration air.

As an approximation, the diagram in Fig. 11 can be converted for the changed state of regeneration air.

For the regeneration air state ϑ = 140°C; Y = 10 g/kg, the following values are known:

- Exit state of process air ϑ_A = 53.4°C; Y_A = 3.2 g/kg
- Dehumidifying efficiency $\eta_E = \frac{10.0 - 3.4}{10.0 - 0.7} = 0.71$
- The specific temperature increase
  $\frac{\Delta\vartheta}{\Delta Y} = \frac{53.4 - 25.0}{3.4 - 10.0} \frac{\text{K}}{\text{g/kg}} = -4.3 \frac{\text{K}}{\text{g/kg}}$

(see Example 3a). Using the simplifying assumption that the specific temperature increase and the dehumidifying efficiency

remain constant, the exit state of process air for the new state of regeneration air can be determined.

As in Example 3a, the relative humidity of the new entry state of regeneration air is calculated first:

$$\varphi = \frac{P_D(Y = 12\,\text{g/kg},\ P = 1.0\ \text{bar})}{P_{DS}(\vartheta = 90°\text{C})} = \frac{P}{P_{DS}} \cdot \frac{Y}{0.622 + Y}$$
$$= \frac{1\,\text{bar}}{0.702\ \text{bar}} \cdot \frac{0.012}{0.622 + 0.012} = 0.027.$$

The exit state of process air in an ideal dehumidifier can be obtained as in Example 3a either graphically from the h, Y-diagram or numerically. The values of $Y_{A\ ideal}$ and $\vartheta_{A\ ideal}$ have to fulfil the following conditions:

$$\vartheta_{A\,ideal} = 25°\text{C} - 4.3\frac{\text{K}}{\text{g/kg}} \cdot (Y_{A\,ideal} - Y_E)$$

and

$$\varphi = \frac{P_D(Y_{A\,ideal}, P_{ges} = 1.0\,\text{bar})}{P_{DS}(\vartheta_{A\,ideal})} = 0.027.$$

The outlet state of process air in ideal dehumidification conditions is determined as

$$Y_{A\,ideal} = 2.8\ \text{g/kg};\ \vartheta_{A\,ideal} = 56°\text{C}.$$

The dehumidifying efficiency then yields the outlet air humidity ratio of the real dehumidifier:

$$Y_{A\,real} = Y_E - \eta_E(Y_E - Y_{A\,ideal})$$
$$= 10.0 - 0.71(10.0 - 2.8)\ \text{g/kg} = 4.9\ \text{g/kg}.$$

The real outlet air temperature of the process air results as

$$\vartheta_{A\,real} = \vartheta_E + \frac{\Delta\vartheta}{\Delta Y} \cdot (Y_{A\,real} - Y_E)$$
$$= 25°\text{C} - 4.3\frac{\text{K}}{\text{g/kg}} \cdot (4.9 - 10.0)\,\text{g/kg} = 46.9°\text{C}.$$

3.2 Dehumidification by Cooling

Air drying is usually carried out in surface coolers, which have their surface temperature decreased below the dew point by a coolant (water, brine) or an evaporating refrigerant. Coolers are usually constructed as extended surface heat exchangers with the process air on the outside of the finned pipes. The circular or continuous plate finned pipes have to be arranged in a way that allows the condensate to drain off easily. If the heat exchanger surface is cooled below 0°C, water vapour precipitates as ice or frost. Thus, lower humidity ratios are achievable; however, the cooler has to be defrosted in regular time intervals when the flow resistance has to become high. Such operating conditions will not be considered in this chapter.

Dimensioning air coolers can be accomplished with two methods: either using computer-based numerical simulations of the air flow along the single pipe rows [16, 17] or integral calculations which divide the cooler into a "dry" section, where only sensible heat is transferred and a "wet" section, which includes simultaneous water vapour condensation as well [18]. Comparisons with comprehensive experimental results realized on serial-production coolers show that the differences between the dimensioning methods are in the range of general uncertainties [17]. Therefore, the integral method, which offers easier handling and is based on the American ARI-Standard 410–8, is described in the following:

The substantial assumptions being the basis of this method are:

- The Lewis factor (Eq. (14)) equals to one.
- The heat transfer coefficient for the sensible heat flux on the air side, abbreviated "dry" heat transfer coefficient α_{dry} in the following, is not changing due to retained water. Condensed water causes opposing effects which more or less compensate each other or only cause effects in the range of measurement and numeric inaccuracy [17, 19].

  The precision of the air cooler calculation crucially depends on the dry heat transfer characteristic. The multitude of existing geometric variations regarding finned tube systems makes it necessary to thoroughly examine the conformity with the ascertained system when using literature sources. Differences between systems can result in considerable errors. If possible, an experimentally determined heat transfer correlation tailored to the particular system should be applied and only, if not available, another adequate formula from literature, e.g., Chap. M1, should be used.

- Although the heat transfer coefficient α_{dry} is changing along the fins as well as from one transverse tube row to another, it is assumed constant and equal to the average heat transfer coefficient. The error thus introduced is justifiable [16, 17, 19].
- The logarithmic averaged mean temperature difference is used as a driving force. This has proven feasible for operating conditions being used for air dehumidification even if the flow arrangement differs from pure countercurrent or parallel flow conditions, such as cross-current flow or co-cross flow setups [17].

Assuming the validity of $\alpha/(\beta_Y c_{p_{1+Y}}) = 1$ as well as constant temperature at the surface of the cooler, an energy and mass balance yields the state change of the air as

$$\frac{dh}{dY} = \frac{h - h_{So}}{Y - Y_{So}} \tag{19}$$

i.e., it runs linearly in the h,Y-diagram pointing towards the state of saturation at the surface temperature of the cooler ϑ_{So}. In reality, the surface temperature changes due to the limited coolant flow rate. This results in a curved progression of the state of the air according to Fig. 12.

At this point, two tasks arise:

1. Presetting the air mass flow $\dot{M}_L$ together with the state at entry and exit, (Y_E, ϑ_{LE}) and (Y_A, ϑ_{LA}), coolant flow rate $\dot{M}_K$, the inlet temperature of coolant ϑ_{KE}, the cross-section of the coil $B{\cdot}H$ and the type of the heat exchanging system. Then, the surface area of the coil A_{WT}, respectively, the number of pipe rows n_l in the air flow direction is to be determined.

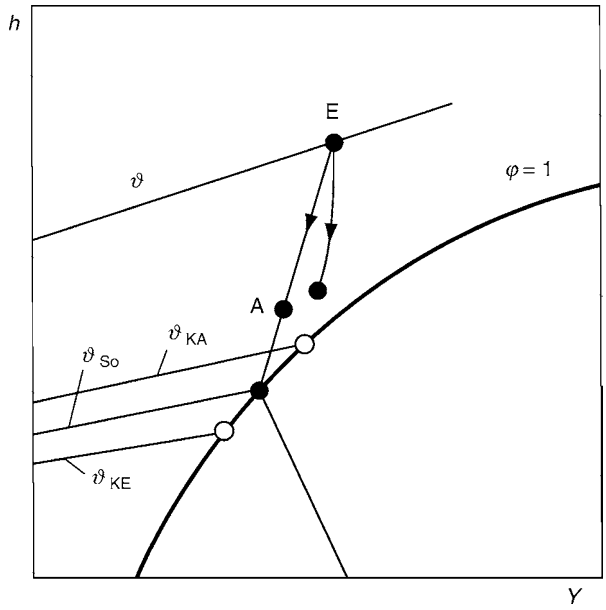

M8. Fig. 12. Air cooling process inside a cooler at constant and at variable surface temperature.

2. Presetting $\dot{M}_L$, Y_E, ϑ_{LE}, $\dot{M}_K$, ϑ_{KE} and the complete dimensions of the cooling coil, consecutively calculating the air exit state (Y_A, ϑ_A) and the exit temperature of the coolant ϑ_{KA}.

As the first mentioned task specifies fixed exit states, the calculation requires less iteration. Therefore it is utilized to illustrate the necessary steps.

Determining the total heat flux and the exit temperature of the coolant

$$\dot{Q} = \dot{Q}_{dry} + \dot{Q}_{wet} = \dot{M}_L \cdot (h_{LE} - h_{LA}) \tag{20}$$

$$\vartheta_{KA} = \frac{\dot{Q}}{\dot{M}_K \cdot c_K} + \vartheta_{KE}. \tag{21}$$

Boundary conditions between dry and wet section

The boundary between the dry and the wet surface region is defined by the constraint that at this point the average surface temperature of the coil ϑ_{SmG} equals the dew point temperature corresponding to the air entry state in case of counterflow or equals the dew point temperature corresponding to the air exit state in case of parallel flow:

$$\begin{aligned} &\vartheta_{SmG} = \vartheta_{LE} \text{ and } h_{SmG} = h\{\vartheta_{LE_\tau}, \varphi = 1\} \text{ at counter flow} \\ &\vartheta_{SmG} = \vartheta_{LA} \text{ and } h_{SmG} = h\{\vartheta_{LA_\tau}, \varphi = 1\} \text{ at parallel flow.} \end{aligned} \tag{22}$$

Local balances yield enthalpy and temperature of the air, h_{LG} und ϑ_{LG}, the temperature of the coolant ϑ_{KG} as well as the pipe surface temperature ϑ_{SoG} at this point:

$$\begin{aligned} h_{LG} &= \frac{\vartheta_{LE_\tau} - \vartheta_{KA} + K \cdot h_{LE} + C \cdot h_{SmG}}{C + K} \text{ counter flow} \\ h_{LG} &= \frac{\vartheta_{LA_\tau} - \vartheta_{KA} + K \cdot h_{LA} + C \cdot h_{SmG}}{C - K} \text{ parallel flow} \end{aligned} \tag{23}$$

$$\vartheta_{LG} = \vartheta_{LE} - \frac{h_{LE} - h_{LG}}{c_{pL} + Y_E \cdot c_{pD}} \text{ counter flow}$$

$$\vartheta_{LG} = \vartheta_{LA} - \frac{h_{LA} - h_{LG}}{c_{pL} + Y_A \cdot c_{pD}} \text{ parallel flow} \tag{24}$$

$$\vartheta_{KG} = \vartheta_{LE_\tau} - C \cdot (h_{LG} - h_{SmG}) \text{ counter flow}$$

$$\vartheta_{KG} = \vartheta_{LA_\tau} - C \cdot (h_{LG} - h_{SmG}) \text{ parallel flow} \tag{25}$$

$$\vartheta_{SoG} = \vartheta_{KG} + \frac{W_K + W_W}{W_K + W_W + W_R}(\vartheta_{LE_\tau} - \vartheta_{KG}) \text{ counter flow}$$

$$\vartheta_{SoG} = \vartheta_{KG} + \frac{W_K + W_W}{W_K + W_W + W_R}(\vartheta_{LA_\tau} - \vartheta_{KG}) \text{ parallel flow} \tag{26}$$

$$with\ K = \frac{\dot{M}_L}{\dot{M}_K \cdot c_K} \text{ and } C = \frac{W_R + W_W + W_K}{c_{p_{1+Y}} W_L}. \tag{27}$$

Applied herein are the following values, which are all related to the total surface area on the air side of the heat exchanger A_{WT}:

	$W_L = 1/\alpha_{dry}$	"Dry" heat transfer resistance on the air side
	$W_R = W_L \frac{1-\psi}{\psi} \frac{c_{p_{1+Y}}}{b}$ (28)	Fin thermal resistance
	$W_W = \frac{A_{WT} \ln \frac{d_a}{d_i}}{2\pi\lambda_W L} \approx \frac{A_{WT}\delta_W}{\pi d_i L \lambda_W}$	Thermal resistance of the prime tube wall
	$W_K = \frac{A_{WT}}{\alpha_K A_K}$	Heat transfer resistance on coolant side
Where		
	$b = \frac{\partial h_S}{\partial \vartheta_S}$	Slope of saturation line $h\{\vartheta_\tau, \varphi = 1\}$ at the mean coil surface temperature $(\vartheta_{Sm} + \vartheta_{So})/2$ Eq. (43)
	$\psi = \frac{A_B + \eta_R A_R}{A_{WT}}$	Total surface effectiveness
	$\eta_R = \frac{\tanh(mH_{R,eq})}{mH_{R,eq}}$ (29)	Fin efficiency
	$m = \sqrt{\frac{2\alpha_{dry}}{\delta_R \lambda_R} \cdot \frac{b}{c_{p_{1+Y}}}}$ (30)	Fin parameter
	$H_{R,\,eq}$	Equivalent fin heigth (see Chap. M1, Eq. (8)).

For the dry section of the cooler

$$W_{R_{dry}} = W_L \cdot \frac{1 - \psi}{\psi}$$

and

$$m = \sqrt{\frac{2\alpha_{dry}}{\lambda_R \delta_R}} \tag{31}$$

apply.

Heat transfer rate and total surface area for heat transfer in the dry surface region

$$\begin{aligned} \dot{Q}_{dry} &= \dot{M}_L \cdot (h_{LE} - h_{LG}) \text{ counter flow} \\ \dot{Q}_{dry} &= \dot{M}_L \cdot (h_{LG} - h_{LA}) \text{ parallel flow} \end{aligned} \tag{32}$$

$$A_{dry} = \frac{\dot{Q}_{tr}(W_L + W_{R_{dry}} + W_W + W_K)}{\Delta\vartheta_{In}} \tag{33}$$

where

$$\Delta\vartheta_{In} = \frac{(\vartheta_{LE} - \vartheta_{KA}) - (\vartheta_{LG} - \vartheta_{KG})}{\ln\frac{\vartheta_{LE}-\vartheta_{KA}}{\vartheta_{LG}-\vartheta_{KG}}} \text{ counter flow}$$

and

$$\Delta\vartheta_{In} = \frac{(\vartheta_{LG} - \vartheta_{KG}) - (\vartheta_{LA} - \vartheta_{KA})}{\ln\frac{\vartheta_{LG}-\vartheta_{KG}}{\vartheta_{LA}-\vartheta_{KA}}} \text{ parallel flow.} \tag{34}$$

Surface area for heat transfer in the wet surface region as well as total surface area of the coil and the required number of cooling tube rows respectively

$$\dot{Q}_{wet} = \dot{Q} - \dot{Q}_{dry} \tag{35}$$

$$A_{wet} = \frac{\dot{Q}_{wet} \cdot W_L c_{p_{1+Y}}}{\Delta h_{In}} \tag{36}$$

where

$$\Delta h_{In} = \frac{(h_{LG} - h_{SmG}) - (h_{LA} - h_{SmA})}{\ln\frac{h_{LG}-h_{SmG}}{h_{LA}-h_{SmA}}} \text{ counter flow}$$

$$\Delta h_{In} = \frac{(h_{LE} - h_{SmE}) - (h_{LG} - h_{SmG})}{\ln\frac{h_{LE}-h_{SmE}}{h_{LG}-h_{SmG}}} \text{ parallel flow} \tag{37}$$

and

$$c_{P1+Y} = c_{pL} + \frac{1}{2}(Y_E + Y_A)c_{pD}.$$

Determination of the saturation enthalpy at mean coil surface temperature

In order to evaluate Eq. (37), the saturation enthalpy corresponding to the average surface temperature either at the exit or entry of the coil is required. It results from a local balance at the appropriate position Z, that is, the air exit in the case of counter flow and the air entry in the case of parallel flow, according to Fig. 13:

$$h_{SmZ} = h_{LZ} + \frac{\vartheta_{KZ} - \vartheta_{SmZ}}{C} \tag{38}$$

with C from Eq. (27) in connection with the saturation enthalpy $h_{SmZ} = h\{\vartheta_{SmZ}, Y_{SZ}\}$.

With the following approximation for the vapour pressure curve which has an accuracy of 0.1% throughout the range $0 \le \vartheta_S \le 60°C$

$$\frac{p_{DS}}{\text{bar}} = 10^{-3} \cdot 10^{8.3246 - \frac{1799.73}{\frac{\vartheta_S}{°C} + 238.734}} \tag{39}$$

and

$$h_S = c_{pL}\vartheta_S + Y_S(\Delta h_{Vo} + c_{pD}\vartheta_S)$$

as well as

$$Y_S = 0.622\frac{p_{DS}}{p - p_{DS}}$$

it is possible to determine h_{SmZ} iteratively when setting $\vartheta_S = \vartheta_{SmZ}$ and $Y_S = Y_{SZ}$. Into the value C of Eq. (38) defined in Eq. (27), the slope b enters according to Eq. (28). Strictly speaking, the determination of the slope b would have been established at point Z. But on the other hand Eq. (36) and Eq. (37) are coming off Eq. (38) assuming a constant gradient averaged between points G and Z, this value is applied as well when calculating h_{SmZ}. In practice, the real impact of the variation in slope b is not important. As a consequence, the following is valid:

$$b = \frac{h_{SmG} - h_{SmZ}}{\vartheta_{SmG} - \vartheta_{SmZ}}. \tag{40}$$

The calculation becomes a little simpler yet sufficiently precise, if the line of saturation is linearized around ϑ_{SmZ}:

$$h_{SmZ} = a + b\,\vartheta_{SmZ}. \tag{41}$$

Thus, using Eq. (38) h_{SmZ} can be obtained from

$$h_{SmZ} = \frac{\vartheta_{KZ} + Ch_{LZ} + \frac{a}{b}}{C + \frac{1}{b}}. \tag{42}$$

With a given type of cooling coil, i.e., known heat exchanger surface per pipe row A_{WT}/n_l, the required number of pipe rows n_l results from

$$n_l = \frac{A_{WT}}{A_{WT}/n_l}$$

with

$$A_{WT} = A_{dry} + A_{wet}.$$

In general, the resulting number of tube rows will not be an integer making it necessary to round the value up or down. The consecutive calculation then equals the second task where the surface of the cooling coil is known and the air exit state has to be determined. This requires the iteration over the whole procedure in case of counterflow because the exit temperature of

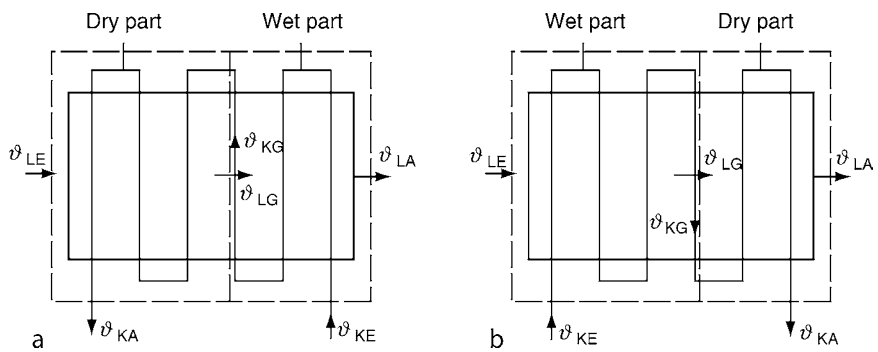

M8. Fig. 13. Temperature distribution: (**a**) cross-counterflow, (**b**) co-cross flow.

the coolant has to be estimated at first. If the altered coil surface shall still achieve the initially given air exit state, an additional adjustment, e.g., by changing the coolant's entry temperature is possible; however, this implies a further iterative step.

Slope b, included in resistance W_R, Eq. (28), and fin parameter m, Eq. (30), of the wet section of the coil, can be likewise expressed by linearizing the saturation line around temperature ϑ_{Sm} or by using the following correlation together with Eqs. (3) and (39):

$$b = c_{pL} + Y_S c_{pD} + 3.7 Y_S (0.622 + Y_S) \times \frac{1799.7}{\left(\frac{\vartheta_S}{°C} + 238.7\right)^2} \left(\Delta h_{vo} + c_{pD} \vartheta_s\right). \quad (43)$$

If solely the humidity ratio at the coil exit Y_A is given and the air exit temperature can adjust freely, the whole coil is conveniently operated below the air dew point. In this case, the calculation is considerably simplified. The states at the surface of the cooler are then known both at air entry and air exit. An integral balance around the cooler and a local balance at either entry or exit yield the initially unknown air exit enthalpy

$$h_{LA} = \frac{\vartheta_{LE} + (K + C) \cdot h_{LE_\tau} - C \cdot h_{SmE}}{K} \text{ counter flow}$$
$$h_{LA} = \frac{-\vartheta_{KE} - (K \cdot h_{LE} + \vartheta_{LA_\tau} + C \cdot h_{SmA}}{C - K} \text{ parallel flow.} \quad (44)$$

Herewith and using Eqs. (38) and (39), the mean driving force is determined according to Eq. (37):

$$\Delta h_{ln} = \frac{(h_{LE} - h_{SmE}) - (h_{LA} - h_{SmA})}{\ln \frac{h_{LE} - h_{SmE}}{h_{LA} - h_{SmA}}}. \quad (45)$$

The necessary cooling surface $A_{WT} = A_{wet}$ then results from Eq. (36).

Determining the air exit temperature

This problem occurs when solving the second task. The calculation procedure provides at first only the air enthalpy at the exit h_{LA}. Using this value in a total balance on the air side yields the average effective saturation enthalpy at the coil surface

$$h_{Sm} = h_{LE} - \frac{h_{LE} - h_{LA}}{1 - e^{-\kappa}}$$
$$\kappa = \frac{A_{WT}}{\dot{M}_L c_{p_{1+Y}} W_L}. \quad (46)$$

The corresponding effective surface temperature of the coil can then be determined iteratively from Eq. (39). Consecutively, the temperature at the air exit is given in an analogous manner as Eq. (46):

$$\vartheta_{LA} = \vartheta_{Sm} + (\vartheta_L - \vartheta_{Sm}) e^{-\kappa}. \quad (47)$$

Figure 14 depicts a flow chart of the calculation procedure for both tasks.

Example 4

Given:

Plate-fin-tube cooling coil in a cross counterflow setup as illustrated in Fig. 15.

Inside diameter of tube d_i = 12.4 mm

Outside diameter of tube d_a = 13.2 mm

Thermal conductivity of the tubes λ_W = 372 W/m K

Longitudinal tube spacing s_l = 27.8 mm

Transverse tube spacing s_q = 31.6 mm

Fin thickness δ_R = 0.15 mm

Fin pitch t_R = 2.4 mm

Thermal conductivity of the fins λ_R = 190 W/m K

Number of transverse tubes n_q = 22

Coil cross section B · H = 0.92 · 0.7 m^2

Heat transfer law on air side: As justified at the beginning of this subchapter, the calculation utilizes an empirical correlation for the considered system of finned tubes [17].

$$\frac{Nu}{Re\,Pr} = \frac{\alpha_L}{c_p u_{max}} = 0.2 Re^{-0.306}$$

where $Re = \frac{u_{max} l_{fcl}}{\nu}$, l_{fcl} as contact length in flow direction (see Chap. M1) and u_{max} being the face velocity at the minimum flow area.

Mass flow rates and thermodynamic states:

$$\dot{M}_L = 2.2 kg/s; \vartheta_{LE} = 32°C; Y_E = 0.015 kg/kg;$$
$$h_{LE} = 70.39 kJ/kg; \vartheta_{LA} = 17°C;$$
$$Y_A = 0.012 kg/kg; h_{LA} = 47.38 kJ/kg.$$

Coolant water: $\dot{M}_K$ = 1.6 kg/s; ϑ_{KE} = 7°C.

Total pressure: p = 1.013 bar.

Calculate:

Heat transfer area A_{WT}, number of transverse tube rows n_l.

Total heat transfer rate, Eq. (20): $\dot{Q}_K = 2.2 \cdot 23 = 50.62$ kW

Temperature of coolant at exit, Eq. (21):

$$\vartheta_{KA} = \frac{50.62}{1.6 \cdot 4.19} + 7 = 14.55°C$$

State at dry-wet boundary, Eq. (22): ϑ_{SmG} = 20.3°C; h_{SmG} = 58.37 kJ/kg.

Air side heat transfer coefficient:

Contact length in flow direction according to Chap. M1:

$$l_{fcl} = \frac{\pi}{2} \sqrt{d_a^2 + \left(s_q \cdot \sqrt{\frac{1}{\pi} \cdot \frac{s_l}{s_q}} - \frac{d_a}{2}\right)^2} = 0.026 m$$

average density, Eq. (4):

$$\rho_L = \frac{101300}{287 \cdot 297.5} \cdot \frac{1 + 0.0135}{1 + 461/287 \cdot 0.0135} = 1.18 kg/m^3$$

air velocity:

$$u_L = \frac{\dot{M}_L (1 + Y_E)}{B \cdot H \rho_L} = \frac{2.2 \cdot 1.015}{0.92 \cdot 0.7 \cdot 1.18} = 2.95 m/s$$

face velocity at the minimum flow area:

$$u_{L,max} = \frac{u_L}{1 - \frac{d_a}{s_q} - \left(1 - \frac{d_a}{s_q}\right) \frac{\delta_R}{t_R}} = 5.4 m/s$$
$$Re = \frac{u_{L,max} l_{fcl} \rho_L}{\eta_L} = \frac{5.4 \cdot 0.026 \cdot 1.18}{18.45 \cdot 10^{-6}} = 8980$$
$$\alpha_L = \alpha_{dry} = 0.2 \cdot Re^{-0.306} \cdot \rho_L c_{p_{1+Y_m}} \cdot u_{L,max}$$
$$= 0.012 \cdot 1.18 \cdot 1025 \cdot 5.4 = 80 W/m^2 K$$

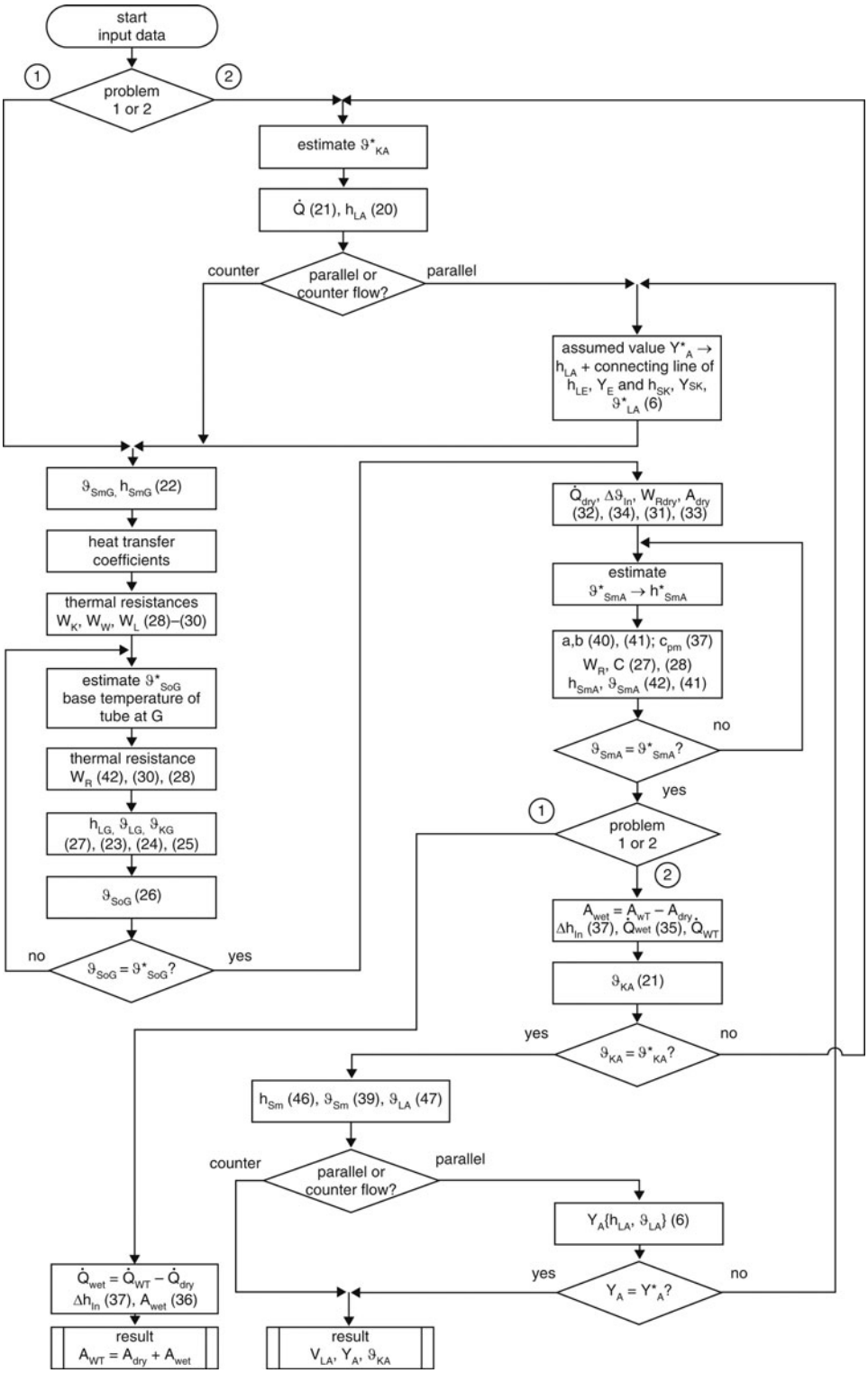

M8. Fig. 14. Flow sheet of the calculating procedure for an air cooler (brackets contain equation numbers).

Water side heat transfer coefficient:

$$\mathrm{Re_K} = \frac{4\dot{M}_K}{\pi d_i n_q \eta_K} = \frac{4 \cdot 1.6}{\pi \cdot 0.0124 \cdot 22 \cdot 0.00128} = 5834.$$

According to ◉ Chap. G1, Eq. (39), applies

$$Nu_K = 0.012(\mathrm{Re}^{0.87} - 280) \cdot \mathrm{Pr}^{0.4}(1 + (d_i/L)^{2/3})$$
$$= 0.012(5834^{0.87} - 280) \cdot 9.3^{0.4}(1 + (0.0124/0.92)^{2/3}) = 49.8$$
$$\alpha_K = \frac{\lambda_K Nu_K}{d_i} = \frac{0.58 \cdot 49.8}{0.00124} = 2335\ \mathrm{W/m^2K}$$

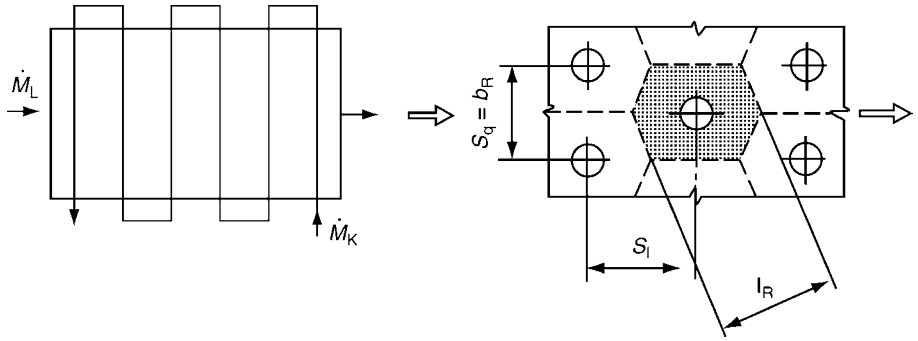

M8. Fig. 15. Schematic flow arrangement and piping layout (staggered tubes).

Heat transfer resistances Eqs. (27–29):

$$\frac{A_R}{n_l} = 2.\frac{B}{t_R}.\left(s_l H - n_q \frac{\pi d_a^2}{4}\right)$$
$$= 2.\frac{0.92}{0.0024}.\left(0.0278\cdot 0.7 - 22\frac{\pi\cdot 0.0132^2}{4}\right)$$
$$= 12.61\,\mathrm{m^2/transverse\ tube\ row}$$

$$\frac{A_{WT}}{n_l} = \frac{A_R + A_B}{n_l} = 13.4\,\mathrm{m^2/transverse\ tube\ row}$$

$$\frac{A_B}{n_l} = n_q.\pi d_a.B.\left(1 - \frac{\delta_R}{t_R}\right) = 0.79\ \mathrm{m^2/transverse\ tube\ row}$$

$$\frac{A_K}{n_l} = n_q.\pi d_i.B = 0.79\ \mathrm{m^2/transverse\ tube\ row}$$

$$W_K = \frac{1}{2335}.\frac{13.4}{0.79} = 0.0073\ \mathrm{m^2K/W}$$

$$W_L = \frac{1}{\alpha_L} = 0.0125\ \mathrm{m^2K/W}$$

$$W_W = \frac{A_{WT}\delta_W}{n_l n_q \pi d_i B \lambda_W} = \frac{13.4\cdot 0.0004}{22\cdot\pi\cdot 0.0124\cdot 0.92\cdot 372}$$
$$= 0\cdot 000018\ \mathrm{m^2K/W}.$$

Equivalent fin height: According to Chap. M1, Eq. (14), the initial result using

$$b_R = s_q \text{ and } l_R = \sqrt{s_l^2 + \left(\frac{s_q}{2}\right)^2}$$

is corresponding to Fig. (15)

$$\varphi' = 1.27\frac{b_R}{d}\sqrt{\frac{l_R}{b_R} - 0.3} = 1.27.\frac{s_q}{d_a}.\sqrt{\sqrt{\left(\frac{s_l}{s_q}\right)^2 + 0.25} - 0.3} = 2.57.$$

The equivalent fin height then equals according to Chap. M1, Eq. (12), together with Chap. M1, Eq. (8),

$$H_{R.eq} = \frac{d_a}{2}.(\varphi' - 1).(1 + 0.35.\ln\varphi') = 0.0137\,\mathrm{m}.$$

Now, the slope of the saturation line

$$b\left\{\frac{\vartheta_{SmG} + \vartheta_{SoG}}{2}\right\}$$

as well as c_p at the dry-wet boundary G is calculated.

As the temperature ϑ_{SoG} is unknown up to this point, it has to be estimated at first. A value $\vartheta_{SoG} < 20.3°C$ is expected. To shorten the process of calculation, the example continues using the iteration result $\vartheta^*_{SoG} = 18.3°C$ as initial value.
Then, from Eqs. (39) and (3) follows $Y_{SoG} = 0.0132$ kg/kg and hence using Eq. (43)

$$b = 1 + 1.86\cdot 0.0141 + 3.7\cdot 0.0141(0.622 + 0.0141)\cdot$$
$$\frac{1799.7}{(19.3 + 238.7)^2}(2500 + 1.86\cdot 19.3) = 3.3\,\mathrm{kJ/kg\ K}.$$

The specific heat capacity of humid air at the dry-wet boundary G is:

$$c_{p_{1+Y}} = c_{pL} + Y_G\cdot c_{pD} = 1 + 0.015\cdot 1.86 = 1.028\,\mathrm{kJ/kg\ K}.$$

Fin efficiency according to Eqs. (30) and (29):

$$m_{wet} = \sqrt{\frac{2\cdot 80\cdot 3.3}{0.00015\cdot 190\cdot 1.028}} = 134.2\mathrm{m^{-1}}$$

$$\eta_{Rwet} = \frac{\tanh(134.2\cdot 0.0137)}{134.2\cdot 0.0137} = 0.52.$$

Fin thermal resistance according to Eq. (28):

$$\psi_{wet} = \frac{0.79 + 0.52\cdot 12.61}{13.4} = 0.545$$

$$W_{Rwet} = 0.0125\cdot\frac{1 - 0.545}{0.545}\cdot\frac{1.028}{3.32} = 0.0032\,\mathrm{m^2K/W}.$$

State variables at the dry-wet boundary G:
Eq. (27) gives

$$K = \frac{2.2}{1.6\cdot 4.19} = 0.328\,\mathrm{kg\ K/kJ}$$

and

$$C = \frac{0.0032 + 0.000018 + 0.0073}{1.028\cdot 0.0125} = 0.82\ \mathrm{kg\ K/kJ}.$$

Eq. (23) yields:

$$h_{LG} = \frac{20.3 - 14.55 + 0.328\cdot 70.39 + 0.82\cdot 58.37}{0.82 + 0.328} = 66.81\,\mathrm{kJ/kg}$$

Temperature results are $\vartheta_{LG} = 28.5°C$ from Eq. (24) and $\vartheta_{KG} = 13.4°C$ from Eq. (25).

Recomputing of the initially estimated tube base temperature at the dry-wet boundary yields, using Eq. (26),

$$\vartheta_{SoG} = \frac{W_W + W_K}{W_W + W_K + W_{Rwet}} (\vartheta_{LE_\tau} - \vartheta_{KG}) + \vartheta_{KG} = 18.2°C.$$

The result agrees well with the estimated value.

Heat transfer rate and heat transfer area of the dry section:
Eq. (32) provides

$$\dot{Q}_{dry} = 2.2(70.39 - 66.81) = 7.88\,kW$$

and according to Eq. (34) is

$$\Delta\vartheta_{ln} = \frac{32 - 14.55 - (28.5 - 13.4)}{\ln\frac{32-14.55}{28.5-13.4}} = 16.25\,K.$$

From Eq. (31) follows:

$$m_{dry} = 74.93 m^{-1};\ m_{dry} H_{Req} = 1.019;\ \eta_{Rdry} = 0.76;$$
$$\psi = 0.77 \text{ and } W_{Rdry} = 0.0037 m^2 K/W.$$

Eq. (33) results in

$$A_{dry} = \frac{7880 \cdot (0.0125 + 0.0037 + 0.000018 + 0.0073)}{16.25} = 11.4\ m^2$$

and consecutively

$$n_{ldry} = \frac{A_{dry}}{A_{WT}/n_l} = 0.85.$$

The cooler thus comprises one pipe row which remains dry.

Saturation enthalpy at the exit:
The calculation of h_{SmA} has to be done iteratively as well. The corresponding saturation temperature ϑ_{SmA} will be between ϑ_{KE} = 7°C and ϑ_{LA} = 17°C, tending towards ϑ_{LA} because of the thermal resistance relationships. Again, an initial estimate, that equals the iterative result within an acceptable tolerance, is used for brevity.

With ϑ^*_{SmA} = 13.8°C, Eq. (39) gives h^*_{SmA} = 38.65 kJ/kg. The constants a and b, which linearize the saturation line between ϑ_{SmG} and ϑ_{SmA} according to Eqs. (40) and (41), then result in $a = -3.22$ and $b = 3.03$.

The value of C from Eq. (27) remains virtually unaltered. In the expression of C, slope b merely enters as a parameter of the thermal resistance W_R. The latter changes to W_{Rwet} = 0.0033 m^2K/W according to Eq. (28), using m_{wet} = 128.6 m^{-1} from Eq. (30), η_{Rwet} = 0.54 from Eq. (29) and Ψ_{wet} = 0.56 from Eq. (28). Hence C = 0.826 kg K/kJ.
Eq. (42) gives

$$h_{SmA=} \frac{7 + 0.826 \cdot 47.38 - 3.22/3.03}{0.826 + 1/3.03} = 39\,kJ/kg$$

and Eq. (41) results in

$$\vartheta_{SmA} = \frac{39 + 3.22}{3.03} = 13.9°C \approx \vartheta^*_{SmA}.$$

Total heat exchanger area and number of transverse pipes rows respectively:

From Eq. (35) results

$$\dot{Q}_{wet} = \dot{Q} - \dot{Q}_{dry} = 42.7\,kW$$

and using Eq. (37)

$$\Delta h_{ln} = \frac{(66.81 - 58.37) - (47.38 - 39)}{\ln\frac{66.81-58.37}{47.38-39}} = 8.41\,kJ/kg.$$

From Eq. (36) then it is obtained

$$A_{wet} = \frac{42700 \cdot 0.0125 \cdot 1.025}{8.41} = 65.1\ m^2.$$

This concludes in

$$n_{lwet} = \frac{A_{wet}}{A_{WT}/n_l} = 4.9.$$

The total heat exchanger area then becomes

$$A_{WT} = 11.4 + 65.1 = 76.5\ m^2$$

and the total number of transverse tube rows

$$n_l = \frac{A_{WT}}{A_{WT}/n_l} = \frac{76.5}{13.4} = 5.7, \text{ i.e., } 6 \textit{ tube rows}$$

4 Symbols

A	m^2	Heat transfer area
C	kg K/J	Operand according to Eq. (27)
$H_{R,eq}$	m	Fin height, equivalent fin height
K	kg K/J	Operand according to Eq. (27)
K_Y	–	Characteristic humidifier number
L	m	Pipe, duct and path length respectively
M	kg	Mass
$\dot{M}$	kg/s	Mass rate of flow
R	J/kg K	Gas constant
W	m^2K/W	Thermal resistance referred to total external area
W	kg/kg	Specific moisture content of adsorbent
b	J/kg K	Slope of saturation line h_S (ϑ, φ = 1)
c	J/kg K	Specific heat
$c_{P_{1+Y}}$	J/kg K	Specific heat of humid air per unit mass of dry air
h	J/kg	Specific enthalpy of air per unit mass of dry air
Δh_V	J/kg	Specific heat of evaporation at 0°C
m	m^{-1}	Fin parameter
p	bar	Total pressure or barometric pressure
p_i	bar	Partial pressure
Y	kg/kg, g/kg	Humidity ratio referred to dry air
α	W/m^2K	Heat transfer coefficient
β_Y	kg/m^2s	Mass transfer coefficient referred to ΔY
δ	m	Thickness
η	–	Humidifying efficiency, dehumidifying efficiency, fin efficiency
ϑ	°C, K	Temperature
ρ	kg/m^3	Density
φ	–	Relative humidity

5 Indices

A	Outlet, exit
B	Humidifying, tube base
D	Vapour
E	Inlet, entry, dehumidifying
G	Dry-wet boundary
K	Cooling limit or adiabatic saturation state or wet bulb state, coolant
L	Air, dry air
R	Fin
S	Saturation
W	Water, tube wall
WT	Heat exchanger
Z	Identification marking of an ascertained position
a	Outside
dry	Dry
i	Inside
m	Averaged over coil surface
o	Refers to $\vartheta = 0°C$ or tube base surface
wet	Wet
τ	Dew point

6 Bibliography

1. Hofmann WM (1976) Befeuchtungsstrecken nach Dampfluftbefeuchtern. HLH 27(1):17–18.
2. Amonn W (1977) Betriebsverhalten eines nichtadiabaten Gleichstrom-Sprühdüsenluftwäschers. Diss. Aachen.
3. Wittorf H (1968) Der Wärme- und Stoffaustausch im Luftwäscher. Diss. Aachen.
4. Demirdzic I, Kaludjercic P, Peric M (1984) Analyse und Berechnung des Wärme- und Stoffaustausches im Luftwäscher. HLH 35(12):575–584.
5. Seng G (1972) Luftbefeuchtung im adiabat betriebenen Luftwäscher. HLH 23(5):143–146.
6. Fekete I (1968) Untersuchung von Klimaanlagen mit Luftwäschern. HLH 19 (4):142–144.
7. Karpis EE (1967) Untersuchungen des Wärme-und Stoffaustausches in waagerechten und senkrechten Düsenkammern von Klimaanlagen. Luft- und Kältetechnik 3(5):223–226.
8. Weck F (1980–1984) E- Berichte Nr. 3363, 3394, 3510, 3545 der Fa. Krantz-Lufttechnik, Aachen. Persönliche Mitteilung.
9. Moog W (1976) Analyse der physikalischen Vorgänge im Düsenkammer-Luftbefeuchter. HLH 27(8):294–298.
10. Kast W (1988) Adsorption aus der Gasphase, Verlag Chemie, Weinheim.
11. Gutermuth W (1980) Untersuchung der gekoppelten Wärme- und Stoffübertragung in Sorptionsregeneratoren. Diss. TU Darmstadt.
12. Busweiler U (1984) Nichtisotherme Ad- und Desorption an Einzelkörnern technischer Adsorbentien am Beispiel der Wasserdampfadsorption an Silicagel und Molekularsieb. Diss. TH Darmstadt.
13. Steiner R (1988) Luftentfeuchtung – Lufttrocknung. Technik am Bau 7:529–532.
14. Van den Bulck E, Mitchell JW, Klein SA (1984) The design of dehumidifiers for use in desiccant cooling and dehumdification systems ASME paper 84- HAT- 32, ASME- AICHE National Heat Transfer Conference, Niagara Falls, NY.
15. ASHRAE (1996) Handbook HVAC systems and equipment, Atlanta, GA.
16. Paikert P (1971) Erfahrungen bei der Projektierung von Feuchtluftkühlern mit digitalen Rechnern. Kältetechnik – Klimatisierung 23(1):8–14.
17. Verweyen N, Zeller M (1989) Wärmetechnische Untersuchung von Feuchtluftkühlern. FLT- Bericht 3/1/70/89 (Forschungsvereinigung für Luft- und Trocknungstechnik, Frankfurt)
18. ARI- Standard 410- 81 Standard for forced circulation air- cooling and air-heating coils (1981) Air-Conditioning and Refrigeration Institute, Arlington, VA.
19. Fornasieri, E., Mattarolo L (1991) Air- side heat transfer and pressure loss in finned tube heat exchangers: state of art. Proc. of the European Conference on Finned Tube Heat Exchangers, ITT of Stuttgart University, Stuttgart, Germany.

M9 Convective Heat Transfer at High Velocities

Bernhard Weigand[1] · *Nimai-Kumar Mitra*[2,†]
[1]Universität Stuttgart, Stuttgart, Germany
[2]Bochum, Germany

1 Introduction

High-velocity effects on the heat transfer play an important role in a lot of technical applications, like in re-entry problems for space applications, for heat transfer at high velocities around gas turbine blades or in rocket engines. High-velocity convection involves essentially two different phenomena:

- Conversion of mechanical energy into thermal energy, resulting in strong temperature variations in the fluid
- Variation of fluid properties as a result of temperature variations.

The Mach number is the characteristic dimensionless group which characterizes the compressibility of the fluid ($\mathrm{Ma} = w/w_\mathrm{s}$). For small Mach numbers ($\mathrm{Ma} < 0.3$), the above mentioned phenomena are rather unimportant and the flow can be considered as incompressible. The speed of sound w_s is defined by

$$w_\mathrm{s} = \sqrt{(\partial p/\partial \rho)_\mathrm{s}}, \tag{1}$$

which simplifies for ideal gases to

$$w_\mathrm{s} = \sqrt{\kappa R T} = \sqrt{\kappa(\widetilde{R}/\widetilde{M})T}. \tag{2}$$

Flows with Mach numbers larger than 0.3 are normally considered to be compressible. However, also for very small Mach numbers there might be substantially changes in fluid properties. For such cases, these effects can be treated by using temperature-dependent fluid properties for the incompressible flow [1, 2]. These types of flows will not be considered in this section. In the following, the flows will be subdivided into incompressible flows ($\mathrm{Ma} < 0.3$), subsonic flows ($0.3 \leq \mathrm{Ma} < 0.7$), transonic flows ($0.7 \leq \mathrm{Ma} < 1.3$), supersonic flows ($1.3 \leq \mathrm{Ma} < 6$), and hypersonic flows ($\mathrm{Ma} \geq 6$). An important feature of flows with Mach numbers larger than one is that shock waves can form in the flow. These shock waves result in a strong increase in pressure and temperature in the area behind the shock wave. Figure 1 visualizes a typical shock wave formed around a body and the resulting velocity and temperature profiles [3]. At the stagnation point of the body, the whole kinetic energy will be converted into thermal energy. The stagnation temperature is given by

$$T_0 = T_\infty + w^2/2c_p = T_\infty + \Delta T. \tag{3}$$

For an ideal gas with constant c_p this equation can be rewritten to

$$T_0 = T_\infty\big(1 + \mathrm{Ma}^2(\kappa - 1)/2\big). \tag{4}$$

The highest temperature is normally obtained at the stagnation point of the body. These temperatures can exceed by far the melting temperature of the material. However, when a viscous high-speed boundary-layer flow is decelerated to zero velocity at an insulated wall, it approaches, depending on the Prandtl number, an adiabatic wall temperature T_aw which differs from the stagnation temperature T_0 (due to the disequilibrium between viscous dissipation and heat conduction). The adiabatic

†Deceased

VDI-GVC (ed.), *VDI Heat Atlas*, DOI 10.1007/978-3-540-77877-6_58,

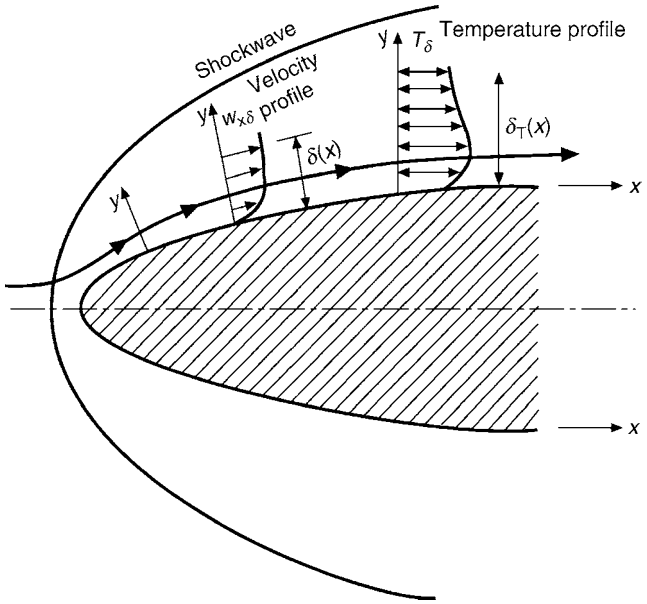

M9. Fig. 1. Supersonic flow ($Ma_\infty > 1$) around a blunt body. For $Ma_\infty >> 1$ the shock wave follows nearly the body geometry [3].

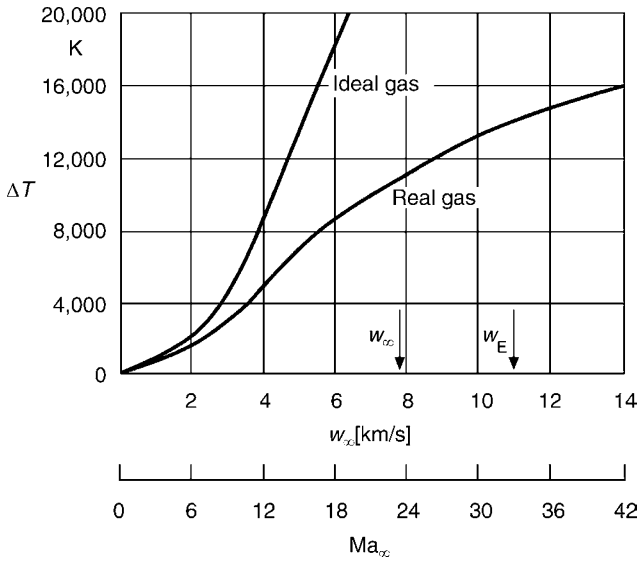

M9. Fig. 2. Temperature increase ΔT (Eq. (3)) as a function of the flight speed ($w_\infty = 7.9$ km/s is the speed of a geostationary satellite, $w_\infty = 11.2$ km/s is the escape velocity [6]).

wall temperature can be calculated from the dimensionless recovery factor r, defined by

$$r = \frac{T_{aw} - T_\infty}{T_0 - T_\infty}. \tag{5}$$

From measurements and analytical calculations it is known that the recovery factor can be calculated approximately by

- Laminar flows ($0.6 < Pr < 15$): $r \approx Pr^{1/2}$ and
- Turbulent flows ($0.25 < Pr < 10$): $r \approx Pr^{1/3}$

The recovery factor is not only a temperature ratio but also gives the percentage of the free-stream kinetic energy, which is converted into thermal energy during deceleration of the flow on an adiabatic wall. For turbulent flows, the recovery factor is also strictly speaking a function of the turbulence structure. Rotta [4] provides an equation, relating the recovery factor for turbulent flows as a function of the friction coefficient and the turbulent Prandtl number.

The heat flux at the wall is given for high-speed flows by

$$\dot{q}_w = -\lambda\left(\frac{\partial T}{\partial n}\right)_w = \alpha(T_{aw} - T_w), \tag{6}$$

where n denotes the normal direction from the wall. It is of major importance that one notices in high-speed flows the correct driving temperature potential for heat transfer is $(T_{aw} - T_w)$. This means whether the heat is transferred to or from the body will depend on whether the surface temperature is above or below the adiabatic wall temperature [5–8].

Beside the Nusselt number, it is convenient to express the heat transfer to or from a body at high velocities in terms of the Stanton number, St, defined by

$$St = \frac{Nu}{Re\ Pr} = \frac{\dot{q}_w}{\rho_\infty w_\infty c_p (T_{aw} - T_w)} = \frac{\alpha}{\rho_\infty w_\infty c_p} \tag{7}$$

The Stanton number is the ratio of the actual to maximum possible heat flow per area. For $St \to 1$, the free-stream energy flux arriving within the frontal area is completely transferred to the body in case of $r = 1$, $T_w = 0$.

For high Mach number flows (hypersonic flows), additional thermodynamic effects can be present like ionization and dissociation, recombination, and excitation of the vibrational energy modes of the molecules [6]. These effects can be observed for example for reentry bodies and hypersonic flows in rocket nozzles. For every body, moving with hypersonic speed, shock structures evolve which cause very high temperatures behind the shock wave. Here, non-equilibrium effects, dissociation, and chemical reaction might be present. The equation of state for dissociating gases differs from the ideal gas law. The excitation of the vibrational energy modes of the molecules and dissociation of the molecules into atoms reduces the stagnation temperature due to the necessary energy consumption for these reactions. This is depicted in Fig. 2 [6, 9], where ΔT from Eq. (1) is shown for different flow speeds for ideal and real gases. The dissociated gas can recombine at the body surface and might result in an enormous heat release at the surface. Here the catalytic character of the surface is of importance [9, 10]. Since heat transfer characteristics depend strongly upon the nature of the non-equilibrium effects, it would by far exceed the scope of the present note to go into details on these effects and their influence on heat transfer. The reader is referred to [9–11] for more details on these effects.

For hypersonic flows, which might be of interest for astronautic applications, the heat transfer can be calculated by assuming rarified gases. These effects are not considered in this section. The reader is referred to Chap. M10 of the present book for more details.

The following discussion of convective heat transfer at high velocities will be based on the Navier–Stokes equations and the energy equation. These equations have to be solved together with an equation of state and are strongly coupled for

compressible flows. As mentioned before, temperature dependent fluid properties need normally to be considered for compressible flows. Here especially the dynamic viscosity varies strongly with temperature. The viscosity for gases can be approximated for a wide variety of gases by the Sutherland law [6]

$$\frac{\eta}{\eta_{\mathrm{ref}}} = \left(\frac{T}{T_{\mathrm{ref}}}\right)^{3/2} \frac{T_{\mathrm{ref}} + T_1}{T + T_1} \tag{8}$$

In this equation, η_{ref} is a reference quantity taken at the reference temperature $T_{\mathrm{ref}} = 288\,\mathrm{K}$. T_1 is a constant and equal to 110 K for air. The Sutherland law has been approximated (especially for analytical solutions) by the simpler expression

$$\frac{\eta}{\eta_{\mathrm{ref}}} = \left(\frac{T}{T_{\mathrm{ref}}}\right)^{\omega}, 0.5 \le \omega \le 1 \tag{9}$$

The other fluid properties (c_p, Pr) can be obtained from Part. D of the Heat Atlas for the gas under consideration. If non-equilibrium effects are absent, c_p and Pr might be considered as constant, depending on the temperature range under consideration. The thermal conductivity λ can then be calculated as follows: $\lambda = \eta c_p / \mathrm{Pr}$.

2 Heat Transfer for External Flows

In contrast to the vast body of correlations existing for heat transfer in incompressible flows, the number of correlations for heat transfer at high velocities is limited. If the fluid properties can be considered to be constant, all so far developed correlations in the Heat Atlas can be used with the only restriction that the heat transfer coefficient need to be based on the correct driving temperature difference given by Eq. (6) [5, 7]. However, normally this assumption can not be made.

In the following, some solutions are given for simple cases. For more complicated cases, one needs normally to solve the problem numerically. For boundary layer problems, this can be done by using available boundary layer codes [5, 8]. If this simplification is not allowed, 3D CFD methods can be used today [12].

2.1 Laminar Flow Along a Flat Plate

2.1.1 Flow Without Shock-Boundary Layer Interaction

Figure 3 depicts the temperature distribution in a boundary layer at a flat plate [3]. As it can be seen from Fig. 3, the temperature profile depends strongly on the conversion of mechanical energy into thermal energy inside the boundary layer. If the Prandtl number $\mathrm{Pr} = \eta c_p/\lambda$ can be considered to be one (which is an acceptable assumption for a lot of gases), an exact relationship between temperature and velocity profile can be established (see Schlichting [6]). For an adiabatic wall one obtains for the temperature distribution

$$T = T_\infty + \left(w_\infty^2 - w_x^2\right)/\left(2c_p\right) \tag{10}$$

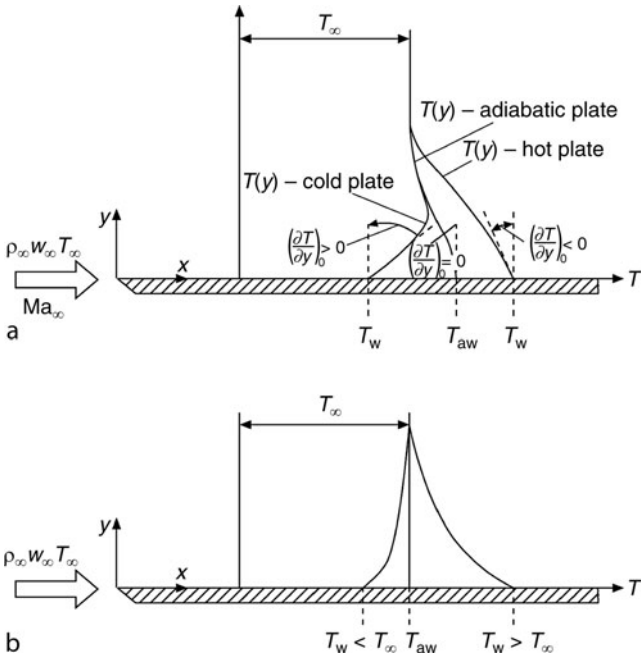

M9. Fig. 3. Flow along a flat plate with typical temperature profile in the boundary layer (**a**) with and (**b**) without dissipative heating [3].

The adiabatic wall temperature is given by Eq. (10) by setting $w_x = 0$ at the wall and one obtains for an ideal gas

$$T_{\mathrm{aw}} = T_\infty + w_\infty^2/\left(2c_p\right) = T_\infty\left(1 + \mathrm{Ma}_\infty^2(\kappa - 1)/2\right) \tag{11}$$

where $T_\infty, w_\infty,$ and Ma_∞ are the temperature, velocity, and Mach number of the free-stream.

For a constant surface temperature of the plate, the exact solution for Pr = 1 is

$$\frac{T}{T_\infty} = 1 + \frac{1}{2}\mathrm{Ma}_\infty^2(\kappa - 1)\left(1 - \left(\frac{w_x}{w_\infty}\right)^2\right) + \frac{T_w - T_{\mathrm{aw}}}{T_\infty}\left(1 - \frac{w_x}{w_\infty}\right) \tag{12}$$

For $\mathrm{Pr} \neq 1$, Eqs. (11–12) can be modified to a first approximation by introducing the recovery factor. Thus,

$$T_{\mathrm{aw}} = T_\infty\left(1 + r\mathrm{Ma}_\infty^2(\kappa - 1)/2\right), \tag{13}$$

$$T/T_\infty = 1 + r\left(\mathrm{Ma}_\infty^2\left(1 - (w_x/w_\infty)^2\right)(\kappa - 1)/2\right) + (T_w - T_{\mathrm{aw}})/T_\infty(1 - w_x/w_\infty) \tag{14}$$

Equations (12) and (14) are independent of the viscosity law and consider the conversion of mechanical energy into thermal energy within the boundary layer [6].

From Eq. (12) one sees that for $(T_w - T_\infty)/T_\infty > \mathrm{Ma}_\infty^2(\kappa - 1)/2$ heat transfer takes place from the fluid to the surface and for $(T_w - T_\infty)/T_\infty = \mathrm{Ma}_\infty^2(\kappa - 1)/2$ no heat transfer takes place, thus the wall is adiabatic. This is shown in Fig. 4 [6]. If the Mach number tends to zero, a linear relationship between the temperature and the velocity is obtained from Eq. (12).

The heat transfer coefficient, defined by Eq. (6), can be obtained from Eq. (12). This results in the following equation for the Nusselt number:

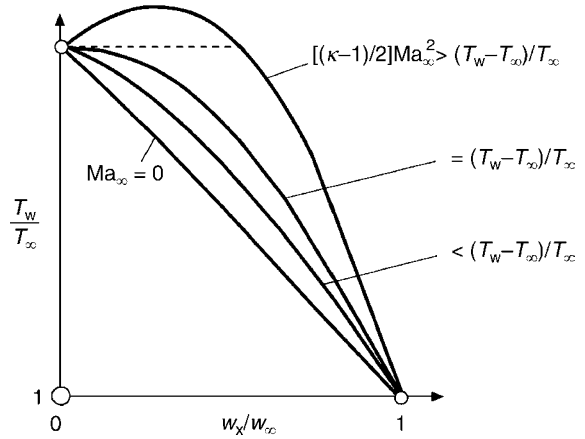

M9. Fig. 4. Temperature distribution T_w/T_∞ as a function of the velocity ratio w_x/w_∞ for a compressible laminar flow along a flat plate with Pr = 1 [6].

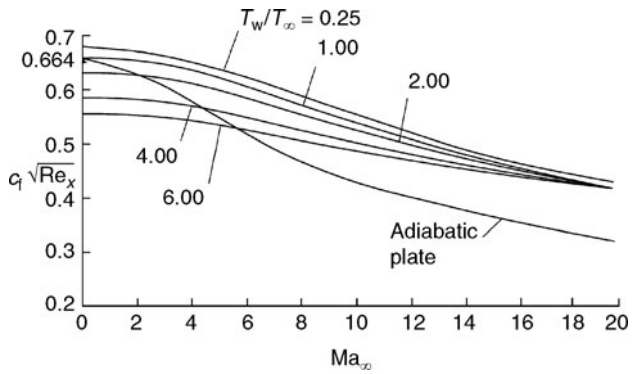

M9. Fig. 5. Average value of the friction factor c_f for a flat plate [10].

$$\frac{\mathrm{Nu}_x}{\mathrm{Re}_x} = \frac{c_{fx}}{2} \tag{15}$$

In Eq. (15) the following definitions have been used

$$\begin{aligned} \mathrm{Nu}_x &= \frac{\alpha x}{\lambda}, \mathrm{Re}_x = \frac{w_\infty \rho_\infty x}{\eta_w}, \\ \alpha &= -\lambda_w \left(\frac{\partial T}{\partial y}\right)_w / (T_{aw} - T_w), \\ c_{fx} &= \eta_w \left(\frac{\partial w_x}{\partial y}\right)_w / (\rho_\infty w_\infty^2/2) \end{aligned} \tag{16}$$

Introducing the Stanton number into Eq. (15), one obtains for Pr = 1

$$\mathrm{St} = \frac{\mathrm{Nu}}{\mathrm{Re}\,\mathrm{Pr}} = \frac{c_{fx}}{2\,\mathrm{Pr}} \tag{17}$$

Equation (17) is strictly valid only for Pr = 1. In the case of arbitrary Prandtl numbers, Eq. (17) might be modified to

$$\mathrm{St} = \frac{c_{fx}}{2\,\mathrm{Pr}^{2/3}} \tag{18}$$

Figures 5 and 6 show the distribution of the mean friction factor and the Stanton number for Pr = 0.75 as a function of the approach Mach number Ma_∞ for different temperature ratios of the wall temperature to free-stream temperature T_w/T_∞.

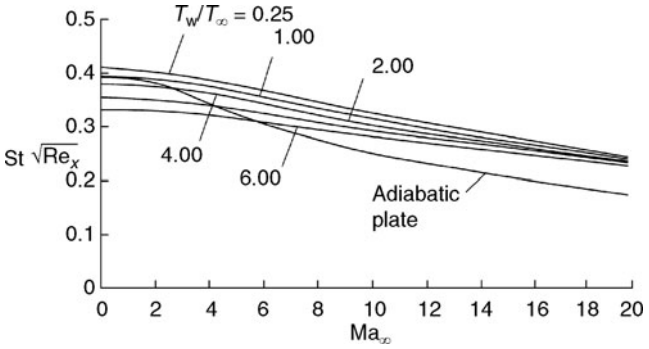

M9. Fig. 6. Average value of the Stanton number St for a flat plate [10].

The calculations have been obtained by van Driest [10]. It is clearly visible that for a constant temperature ratio T_w/T_∞ the friction factor and the Stanton number decrease with growing Mach numbers.

2.1.2 Flow with Viscous Interaction with the External Flow

The boundary layer development at the plate normally introduces a pressure gradient in the flow. This can cause shock interactions in hypersonic flows. The boundary layer displaces the external flow and this deflection causes a shock wave, or may change the shape of the shock wave in case of a contoured body. The pressure gradient can be characterized by the interaction parameter K defined by [9, 10]

$$K = \mathrm{Ma}_\infty \mathrm{d}\delta_1(x)/\mathrm{d}x \tag{19}$$

where δ_1 denotes the displacement thickness.

Strong interaction: For this case the parameter $K >> 1$ and one obtains a strong shock. Here the following relations can be used [13]

$$\begin{aligned} p_\delta/p_\infty &\approx ((\kappa+1)/2)\kappa K^2 \\ p(x)/p_\infty &= p_0(T_w/T_0)\sqrt{C}\mathrm{Ma}_\infty^3/\sqrt{\mathrm{Re}_{x\infty}} \end{aligned} \tag{20}$$

where p_δ denotes the pressure at the outer edge of the boundary layer and p_∞ is the pressure at approach conditions. In addition, the Chapman-Rubesin parameter C [6] has been introduced. This important dimensionless quantity for compressible flows is defined by

$$C = \frac{\rho\eta}{\rho_\delta \eta_\delta} \tag{21}$$

where ρ_δ and η_δ are the density and the dynamic viscosity at the outer edge of the boundary layer. The friction coefficient and the Stanton number are given by

$$\begin{aligned} c_{fx} &= c_{f0}(T_w/T_\infty)C^{3/4}\left(\mathrm{Ma}_\infty/\sqrt{\mathrm{Re}_{x\infty}}\right)^{3/2} \\ \mathrm{St} &\approx 0.37 c_{fx} \end{aligned} \tag{22}$$

In Eqs. (20, 22), c_{f0} denotes the friction factor for a flat plate without viscous interaction, p_0, T_0 are the stagnation values of pressure and temperature, $p(x)$ is the local pressure along the

plate and $Re_{x\infty}$ is the Reynolds number based on the approach velocity and the fluid properties taken at approach conditions.
Weak interaction: This case relates to $K << 1$ and a weak shock is obtained. For this case the following equations can be used:

$$\begin{aligned} p_\delta/p_\infty &= 1 + \kappa K \\ p(x)/p_\infty &= 1 + KF\sqrt{C}Ma_\infty^3/\sqrt{Re_{x\infty}} \\ F &= 0.968/Ma_\infty^2\, T_w/T_\infty + 0.145(\kappa - 1) \end{aligned} \tag{23}$$

$$(c_{fx} - c_{f0})\sqrt{Re_{x\infty}} = 2CF^2 Ma_\infty^3/\sqrt{Re_{x\infty}} \tag{24}$$

The Stanton number can be calculated approximately from the Reynolds analogy. The position of the strong interaction is located directly after the leading edge of the plate. For a weak interaction, the position is directly after the location for the strong interaction. Figure 7 shows the pressure distribution for strong and weak interactions on a flat plate [13].

2.2 Turbulent Flow Along a Flat Plate

For turbulent flow along a flat plate, the flow and heat transfer can be calculated numerically by using boundary layer codes [5, 8]. The results agree favorable with measurements. Here, a semi-empirical equation for c_f from van Driest [8] will be reported which shows nicely the influencing parameters for the solution. The equation from van Driest is based on a mixing length approach for modelling the turbulent flow and assumes a simplified viscosity law by Eq. (9). The friction coefficient is given by

$$\begin{aligned} &\frac{0.242\left(\sin^{-1}\varepsilon_1 + \sin^{-1}\varepsilon_2\right)}{A\sqrt{c_{fx}(T_w/T_\delta)}} \\ &\quad = 0.41 + \log(Re_x\ c_{fx}) - \omega\log(T_w/T_\delta) \end{aligned} \tag{25}$$

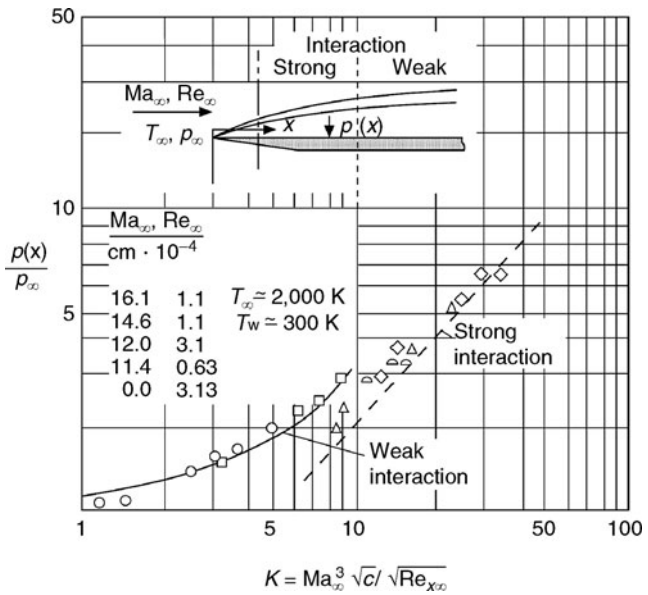

M9. Fig. 7. Pressure distribution for viscous interaction on a flat plate [13].

with the following quantities

$$\begin{aligned} &\varepsilon_1 = \frac{2A^2 - B^2}{Z}, \varepsilon_2 = \frac{B}{Z}, Z = \left(B^2 + 4A^2\right)^{1/2} \\ &B = \frac{T_\delta}{T_w}\left(1 + r\frac{\kappa - 1}{2}Ma_\delta^2\right) - 1, A = \left[r\frac{\kappa - 1}{2}Ma_\delta^2\frac{T_\delta}{T_w}\right]^{1/2} \end{aligned} \tag{26}$$

where the subscript "δ" refers again to the conditions at the edge of the boundary layer. For obtaining the heat transfer, the Reynolds analogy can be used as a first approximation if the Prandtl number Pr = 1 and in addition also the turbulent Prandtl number Pr_t = 1. One obtains

$$St = \frac{c_{fx}}{2} \tag{27}$$

If the molecular Prandtl number is not equal to one, one can use the following equation developed by von Karman, if Pr_t = 1 [6]

$$St = \frac{c_{fx}/2}{1 + 5\sqrt{c_{fx}/2}\left((Pr - 1) + \ln\left(1 + \frac{5}{6}(Pr - 1)\right)\right)} \tag{28}$$

If in addition, also $Pr_t \neq 1$, the following equation developed by Reichardt can be used [6]

$$St = \frac{c_{fx}/2}{Pr_t + \sqrt{c_{fx}/2}((Pr - Pr_t)a + A_1)} \tag{29}$$

The quantity a depends on the ratio of Pr / Pr_t, the turbulence structure and the friction coefficient. Table 1 gives values of a, for different ratios of Pr / Pr_t [6]. The quantity A_1 in Eq. (29) can be approximated by $A_1 \approx 4(1 - Pr_t)$.

2.3 The Use of Reference Properties for Heat Transfer Calculations

The Nusselt number, the Stanton number, and the friction coefficient for compressible flows can be obtained from the related incompressible flow relationships, if the fluid properties are taken at a reference temperature T_{ref} [5, 7, 14]. On the basis of examinations of a number of exact laminar boundary-layer solutions for constant w_∞, T_∞, T_w, Eckert [7] concluded that if the specific heat may be treated as constant, the following reference temperature correlates the available solutions within a few percent for Mach numbers up to 20 and over a wide range of free-stream and surface temperatures:

$$T_{ref} = T_\infty + 0.5(T_w - T_\infty) + 0.22(T_{aw} - T_\infty) \tag{30}$$

For very large temperature differences through the boundary layer, the assumption of constant specific heat, which has been made, is no longer valid. Eckert's reference property method is again applicable if reference enthalpy values are used in Eq. (30) resulting in

$$h_{ref} = h_\infty + 0.5(h_w - h_\infty) + 0.22(h_{aw} - h_\infty) \tag{31}$$

M9. Table 1. Dependence of the quantity a on Pr/Pr_t.

Pr/Pr_t	0.5	0.72	1.44	2.0	5.0	10.0
a	10.22	9.55	8.25	7.66	6.04	5.05

In this case, the heat flux at the wall has of course to be based on the enthalpy difference instead of a temperature difference, resulting in

$$\dot{q}_w = \hat{\alpha}(h_{aw} - h_w)$$
$$\mathrm{St} = \frac{\hat{\alpha}}{\rho w_\infty} \tag{32}$$

where again all fluid properties are evaluated at the reference conditions, given by Eq. (31).

A different concept to evaluate the reference conditions has been followed by Herwig [15]. He derived a reference temperature from an asymptotic theory for a flow along a flat plate with zero pressure gradient. The reader is referred to [15] for more details. In addition, there are several other empirical equations for the reference temperature [12, 16].

2.4 Boundary Layer Flows with External Pressure Gradients

For laminar flows over a flat plate with a superimposed pressure gradient, the density variations can have a large effect on the flow and heat transfer. As a consequence of the external pressure gradient, the temperature distribution on the edge of the boundary layer is no longer constant. Similarity solutions can be found under a number of restrictive conditions [5, 6, 14, 15, 17–19, 37]. One is that the free-stream velocity distribution has to follow the equation

$$w_{x\infty} = C_1 \tilde{x}^m \tag{33}$$

For $m = 0$, one obtains the flow along a flat plate without pressure gradient. If $m > 0$ the flow is accelerated, while for $m < 0$, the flow is decelerated. Cohen and Reshotko [20] reported self- similar solutions for various values of $\beta = 2m/(1 + m)$ and different wall temperatures. They assumed Pr = 1 and a linear viscosity dependence from temperature according to $\eta/\eta_{ref} = bT/T_{ref}$. Figure 8 shows some velocity distributions inside the boundary layer for different acceleration parameters β and the corresponding enthalpy profiles. The profiles are plotted versus a modified y-coordinate, defined by

$$Y = \sqrt{((m+1)/2(U_\delta v_0 \tilde{x})(T_\delta/T_0))} \int_0^y (\rho/\rho_0)\mathrm{d}\bar{y}$$
$$U_\delta = w_{x\delta}\sqrt{(T_0/T_\delta)}, \tilde{x} = \int_0^x b p_\delta/p_0 \sqrt{(T_\delta/T_0)}\mathrm{d}\bar{x} \tag{34}$$

In Fig. 8, the following expressions are used

$$S = \frac{c_p T + w_x^2/2}{c_p T_0} - 1, \; f' = \frac{w_x}{w_{x\delta}} \tag{35}$$

For the friction coefficient and for the Stanton number one obtains from the analytical solution of the compressible boundary layer equations

$$c_f = 2\tau_w/(\rho_w w_{x\delta}^2) = f_w'' \left[2b(1 + S_w)\sqrt{((m+1)/2(v_{\infty 0}/U_\delta \tilde{x}))}\right]$$
$$S_w = T_w/T_0 - 1, \mathrm{Re}_w = w_{x\delta}\tilde{x}/v_w \tag{36}$$
$$\mathrm{St}/c_f = \mathrm{Nu}/(\mathrm{Re}_w \; c_f) = -S_w''/(S_w 2 f_w'')$$

Table 2 summarizes some values for the temperature and velocity gradients at the wall, which have been reported by Cohen and Reshotko [20]. More data can be found in [20].

Eckert [7] gives an empirical equation for the heat flux at the wall for a laminar flow with pressure gradient

$$\dot{q}_{wx} = \left(0.35/\mathrm{Pr}^{2/3}\right)\left(\rho_{ref}\eta_{ref} w_{x\delta} r_0^n c_p (T_w - T_{aw})/\sqrt{x_{ref}}\right)$$
$$x_{ref} = \int_0^x \rho_{ref}\eta_{ref} w_{x\delta} r_0^{2n}\mathrm{d}\bar{x} \tag{37}$$

In Eq. (37) the index "ref" indicates that the fluid properties have to be taken at the reference value T_{ref} and r_0 is the radius of the body ($n = 0$ denotes a planar surface, whereas $n = 1$ denotes a rotational symmetric body). The Stanton number is given by

$$\mathrm{St}_x = \alpha/(w_{x\delta}\rho_{ref} c_p) = 0.35\eta_{ref} r_0^n/\sqrt{x_{ref}} \tag{38}$$

2.4.1 Stagnation Point Flow

From the self-similar solution of the stagnation point flow Fay and Riddle [21] developed a correlation for the heat flux. They considered dissociation and recombination. The equation from Fay and Riddle for the heat flux (without dissociation) at the stagnation points reads

$$\dot{q}_w = B c_p \mathrm{Pr}^{-0.6}\sqrt{\rho_\delta \eta_\delta}\sqrt{\mathrm{d}w_{x\delta}/\mathrm{d}x}(T_{aw} - T_w) \tag{39}$$

where $B = 0.57$ for a two-dimensional stagnation line on a cylinder and $B = 0.763$ for the axis-symmetric stagnation point on a sphere. The velocity gradient of the free-stream is given by the pressure distribution

$$\mathrm{d}w_{x\delta}/\mathrm{d}x = 1/r_0\sqrt{2(p_\delta - p_\infty)/\rho_\delta} \tag{40}$$

Combining Eqs. (39) and (40) one sees that the heat flux is proportional to $1/\sqrt{r_0}$, where r_0 denotes the radius of the body in the stagnation area. From Eq. (39) one can derive the following equation for the Stanton number

$$\mathrm{St} = \dot{q}_w/\left[(T_{aw} - T_w)\rho_\delta w_{x\delta} c_p\right] = B\,\mathrm{Pr}^{-0.6}\sqrt{\tilde{w}'_{x\delta}/\mathrm{Re}_{2r_0}}$$
$$\tilde{w}'_{x\delta} = (2r_0/w_{x\delta})\mathrm{d}w_{x\delta}/\mathrm{d}x \tag{41}$$

The Stanton number, which has been derived by Lees [13] from the laminar boundary layer theory for the stagnation point heat transfer is

$$\mathrm{St} = B_1\,\mathrm{Pr}^{-2/3}\sqrt{\tilde{w}'_{x\delta}/\mathrm{Re}_{2r_0}} \tag{42}$$

where $B_1 = 0.354$ for a cylinder and $B_1 = 0.5$ for a sphere. One sees from Eqs. (41) and (42) that in Lees equation the Stanton number depends on the Prandtl number by the exponent (−2/3), while in Fay and Riddle's equation this dependence is (−0.6).

Comparing the Stanton number for a sphere with a cylinder, one obtains that

$$\frac{\mathrm{St}_{Sphere}}{\mathrm{St}_{Cylinder}} \approx \sqrt{2} \tag{43}$$

Figure 9 shows the Stanton number as a function of the Reynolds number Re_{2r_0} [13]. The measurements, which have

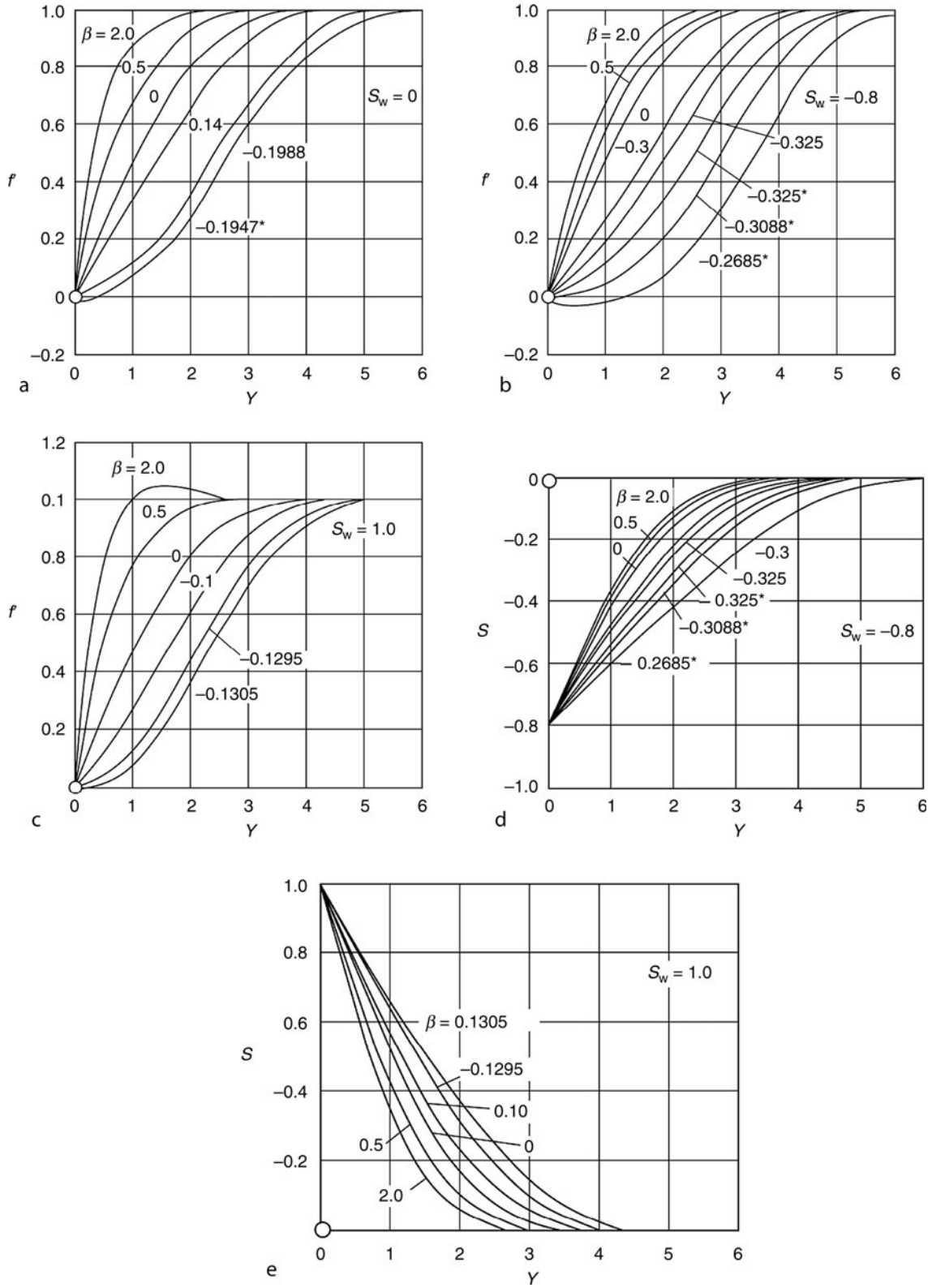

M9. Fig. 8. Velocity and enthalpy profiles for laminar compressible flows with different pressure gradients [6].

been taken at different values of the Mach number, ranging from 8 to 21, show a nearly linear behavior in the logarithmic diagram. Eckert [7] provides an empirical equation for the Stanton number, which is based on reference conditions

$$\mathrm{St} = B_2 / \left(\mathrm{Pr}_{\mathrm{ref}}^{2/3} \sqrt{\mathrm{Re}_{x,\mathrm{ref}}} \right) \tag{44}$$

In Eq. (44), the constant $B_2 = 0.5$ for the planar stagnation point and $B_2 = 0.7$ for the axis-symmetric stagnation point.

M9. Table 2. Velocity and temperature gradients at the wall for self-similar solutions with a pressure gradient.

S_w	β	f''_w	S'_w	$c_f \mathrm{Re}_w/\mathrm{Nu}$
−1.0	−0.3000	0.3182	0.4262	1.4930
	−0.1400	0.4166	0.4554	1.8300
	0	0.4696	0.4696	2.0000
	0.5	0.5806	0.4948	2.3470
	2.0	0.7381	0.5203	2.8370
−0.8	−0.30	0.2086	0.3155	1.0580
	−0.14	0.3841	0.3590	1.7120
	0	0.4696	0.3757	2.0000
	0.5	0.6547	0.4030	2.5990
	1.5	0.8689	0.4261	3.2630
	2.0	0.9480	0.4331	3.5020
−0.4	−0.20	0.2183	0.1626	1.0740
	0	0.4696	0.1878	2.0000
	0.50	0.7947	0.209	3.0420
	2.0	1.3329	0.2304	4.6280
0	0	0.4696	0	2.000
	0.5	0.9277	0	3.436
	2.00	1.6870	0	5.565
1.0	−0.1295	0	−0.3388	0
	0	0.4696	−0.4696	2.0000
	0.50	1.2351	−0.5725	4.3150
	2.00	2.4878	−0.6613	7.5270

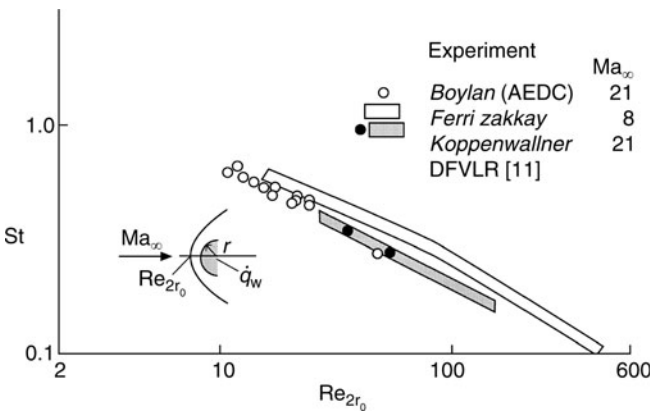

M9. Fig. 9. Stanton number as a function of the Reynolds number for a stagnation flow [13].

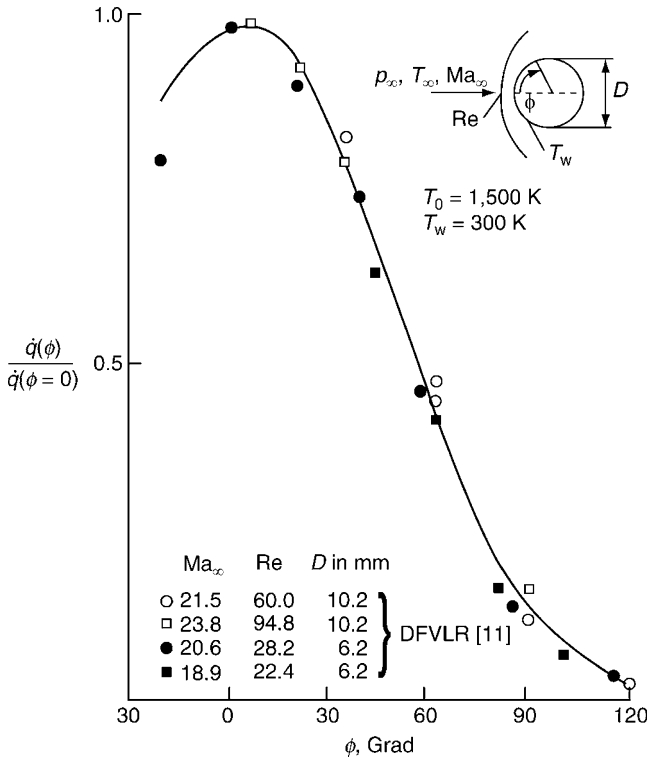

M9. Fig. 10. Heat flux ratio for the heat transfer around a cylinder [13].

2.4.2 Flow Around a Cylinder

Figure 10 shows measurement data for the heat flux ratio around a cylinder [13]. As indicated in Fig. 10, ϕ denotes the circumferential coordinate. For $\phi = 0$, the heat flux $\dot{q}(\phi = 0)$ at the stagnation point is obtained. The Reynolds number is

based on the diameter D of the cylinder and the flow conditions in front of the shock wave. Beckwith and Gallagher [22] provide an empirical correlation for the Stanton number distribution around the cylinder. The equation is based on experimental data and is given by

$$\mathrm{St}/\mathrm{St_S} = 0.7(\cos\phi)^{2/3} + 0.3 \tag{45}$$

In the equation, $\mathrm{St_S}$ is the value of the Stanton number at the stagnation point.

2.4.3 Flow Around a Cone

For the supersonic flow around a cone with an attached shock, a conical flow exists outside the boundary layer. The boundary layer flow can be transformed into a flow along a flat plate by using the Mangler transformation [6]. Friction coefficient and Stanton number for the flat plate solution simply have to be multiplied by a factor of $\sqrt{3}$ in order to obtain the values for the cone [7].

3 Heat Transfer for Internal Flows

Flow and heat transfer for internal flows in ducts play an important role e.g., in rocket engine and Ram and Scramjet design [23, 24]. The heat addition to duct flows can be analyzed approximately by 1D models. From the first law of Thermodynamics for an open system (shown in Fig. 11) with the assumption of a constant c_p and the assumption of one incoming and one outgoing mass flow, one obtains [3]

$$\dot{M}c_pT_{02} = \dot{M}c_pT_{01} + \dot{Q}_\mathrm{w},\ \dot{Q}_\mathrm{w} = \int_{\text{Surface}} \dot{q}_w \mathrm{d}S \tag{46}$$

In this equation $\dot{Q}_\mathrm{w}$ is the heat flux from the wall into the fluid. This quantity can be obtained by integrating the heat flux density $\dot{q}_w$ over the whole surface which is in contact with the fluid. For an ideal, caloric perfect gas the conditions at pipe exit can be calculated from the following Eq. [18]

$$\begin{aligned} T_{01}/T_{02} &= \mathrm{Ma}_2^2\left(1+\kappa\mathrm{Ma}_1^2\right)^2/\left(\mathrm{Ma}_1^2\left(1+\kappa\mathrm{Ma}_2^2\right)^2\right) \\ &\quad\cdot\left(1+((\kappa-1)/2)\mathrm{Ma}_2^2\right)^2/\left(1+((\kappa-1)/2)\mathrm{Ma}_1^2\right)^2 \\ T_2/T_1 &= \mathrm{Ma}_2^2/\mathrm{Ma}_1^2\left(1+\kappa\mathrm{Ma}_1^2\right)^2/\left(1+\kappa\mathrm{Ma}_2^2\right)^2 \end{aligned} \tag{47}$$

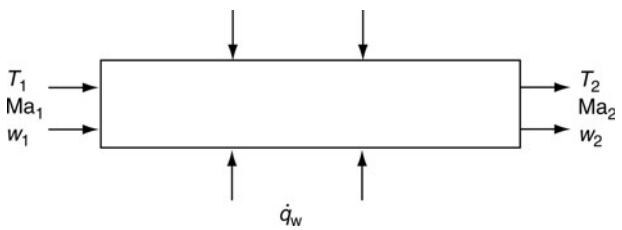

M9. Fig. 11. Duct with heat addition from the wall [3].

If the flow enters the channel with subsonic speed, $\mathrm{Ma}_1 < 1$, the Mach number in the flow increases in case of heat addition, so that $\mathrm{Ma}_2 > \mathrm{Ma}_1$. For a constant area duct, the Mach number can reach in case of heat addition in steady state the maximum value of $\mathrm{Ma}_2 = 1$ at the exit of the duct and the duct is chocked. Further heat addition to the flow is only possible unsteadily with strong variations in the inlet conditions. For an adiabatic flow, the Mach number at exit will also increase, because of the friction effects in the pipe and the resulting heat dissipation within the flow. For an isothermal wall, the flow will approach a value of the Mach number of $1/\sqrt{\kappa}$ at the exit of long pipes [25]. If the incoming flow into the pipe has a Mach number larger than one, $\mathrm{Ma}_1 > 1$, heat addition will decrease the outlet Mach number of the flow, so that $\mathrm{Ma}_2 < \mathrm{Ma}_1$.

Equation (47) assumes a one-dimensional, compressible, inviscid flow with heat addition. For 1D viscous, nonisothermal flows, there are no simple equations, which enable to calculate the flow conditions at the exit of the duct. Shapiro [25, 26] provides differential equations for the 1D viscous duct flow with heat addition, area changes in flow direction and mass addition. These equations can only be solved numerically. However, most of the commercial flow-net solver available today have these equations implemented (e.g., Miller [27]).

For the simple case of a pipe with constant area and a constant mass flow and by assuming the validity of the Reynolds analogy and further that $T_\mathrm{aw} \approx T_0$ (which is correct if Pr = 1 or for arbitrary Pr if the Mach number is small) Shapiro [25, 26] gives the following equations

$$\mathrm{d}T_0/\mathrm{d}x = 2c_\mathrm{f}(T_\mathrm{w} - T_0)/D, \tag{48}$$

$$\begin{aligned} &\mathrm{dMa}^2/\mathrm{d}x = (F_{T0}/T_0)\mathrm{d}T_0/\mathrm{d}x + 4F_\mathrm{f}c_\mathrm{f}/D, \\ &F_{T0} = \mathrm{Ma}^2\left(1+\kappa\mathrm{Ma}^2\right)\left[1+((\kappa-1)/2)\mathrm{Ma}^2\right]/\left(1-\mathrm{Ma}^2\right), \\ &F_\mathrm{f} = \kappa\mathrm{Ma}^4\left[1+((\kappa-1)/2)\mathrm{Ma}^2\right]/\left(1-\mathrm{Ma}^2\right). \end{aligned} \tag{49}$$

If the wall temperature $T_\mathrm{w} = \text{const.}$, Eq. (48) can be integrated analytically between the inlet (x_1) and exit (x_2) of the pipe. This results in

$$\frac{4c_\mathrm{f}(x_2 - x_1)}{2D} = \ln\left[\frac{T_\mathrm{w} - T_{01}}{T_\mathrm{w} - T_{02}}\right] \tag{50}$$

Unfortunately, Eq. (49) has to be solved numerically, because of the strong nonlinear nature of this equation. In the excellent book of Shapiro [25, 26] the reader can find a lot of other calculated cases and also several approximation solutions for 1D compressible flows.

3.1 Pipe Flow

The analysis of the flow field and the heat transfer in a pipe for compressible flows at high velocities requires the solution of the Navier–Stokes equations or the boundary layer equations. In literature a lot of these calculations can be found for laminar flows. A lot of these cases can be treated by solving the boundary layer equations. The reader is referred to Cebeci and Bradshaw [8] and Kays et al. [5] for more details.

For turbulent, subsonic flows in a pipe, the friction coefficient can be calculated, as for incompressible flow, by using the Karman-Nikuradse equation

$$1/\sqrt{4c_f} = -0.8 + 2\log\left(\mathrm{Re}\sqrt{4c_f}\right) \tag{51}$$

For a viscous turbulent subsonic flow with heat transfer, Shapiro [26] recommends the following equation for the friction factor in the pipe

$$c_f = 0.079\mathrm{Re}^{-0.25} \tag{52}$$

Assuming the Reynolds analogy, an empirical equation for the Nusselt number can be derived, which agrees well with measurements for air for values of the Reynolds number up to 10^5 and for Mach numbers between zero and one [26]:

$$\mathrm{Nu} = 0.0364(\mathrm{Re}\,\mathrm{Pr})^{0.75} \tag{53}$$

3.2 Laval Nozzle

In a Laval nozzle a compressible internal flow is obtained, which has a lot of different applications in aerospace as well as in wind tunnel testing. The flows in such nozzles are basically characterized by the fact that the Mach number can range from subsonic to hypersonic speeds. The flow acceleration, characterized by the pressure gradient, increases from the entrance to the throat area and decreases from there on. The axial distribution of the heat transfer coefficient is qualitatively similar to the axial distribution of the pressure gradient. Figure 12 shows schematically the geometry and typical distributions of the Mach number, the temperature and the heat transfer coefficient in the Laval nozzle [3].

The flow in the Laval nozzle can be predicted by using the Navier–Stokes equations or the boundary layer equations. Because of the strong acceleration of the core flow, interactions between boundary layer and core flow need to be taken into account. Back [28] analyzed the laminar flow in a Laval nozzle with local similarity methods. Carden [29] gives a simple method for determining the local heat transfer coefficients.

For the turbulent flow in a Laval nozzle, Bartz [30] provides the following empirical equation

$$\alpha = \left[\left(0.026/D^{*0.2}\right)\left(\eta_0^{0.2}c_p/\mathrm{Pr}^{0.6}\right)\left(p_0c^*\right)^{0.8}\right] \cdot \left(D^*/r_e\right)^{0.1}\left(A/A^*\right)^{0.9}\sigma \tag{54}$$

In this equation $c^* = p_0A^*/\dot{M}$ is a characteristic velocity, D^* is the throat diameter and $\sigma = (\rho_{\mathrm{ref}}/\rho_\delta)^{0.8}(\eta_{\mathrm{ref}}/\eta_0)^{0.2}$ considers the influence of changing fluid properties. The fluid properties $\rho_{\mathrm{ref}}, \eta_{\mathrm{ref}}$ should be taken at the reference temperature

$$T_{\mathrm{ref}} = 0.5(T_0 + T_w) + 0.22\,\mathrm{Pr}^{1/3}(T_0 - T_w) \tag{55}$$

The density ρ_δ can be calculated from a 1D isentropic nozzle flow analysis and r_e is the radius of curvature of the throat. Bartz [30] also provides a modified expression for σ

$$\sigma = \left[\left(0.5T_w/T_0\left(1 + \mathrm{Ma}^2(\kappa-1)/2\right) + 0.5\right]^{0.8-\omega/5} \cdot \left[1 + \mathrm{Ma}^2(\kappa-1)/2\right)^{\omega/5}\right]^{-1} \tag{56}$$

The local Mach number in Eq. (56) can be calculated from a 1D isentropic flow analysis of the nozzle. Another equation, which has been recommended by Back et al. [31], shows better agreement with measurements as Eq. (54). This equation is given by

$$\mathrm{St} = \frac{c_f/2}{\sqrt{c_f/2}(5\ln(5\,\mathrm{Pr}+1) - 14 + \sqrt{2c_f})} \tag{57}$$

The friction coefficient c_f can be taken from the flat plate solution. Equation (57) can be further improved by using a correction method given in Back et al. [31].

A simple calculation method for the skin-friction and the heat transfer in rocket nozzles has been given by Mastanaiah [32]. The method is based on the simultaneous solution of the integral form of momentum and energy equations. The turbulent flow has been modelled via the mixing length approach. The numerical results presented have been compared with experimental data in 10°–10° and 30°–15° convergent-divergent nozzles, and N_2H_4–N_2O_4 rocket nozzle with an 15° half-angle of divergence.

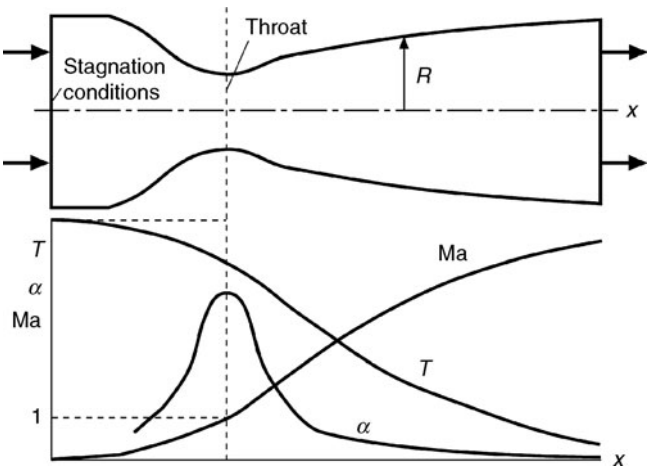

M9. Fig. 12. Schematic distributions of Mach number, temperature, and heat transfer coefficient in a Laval nozzle [3].

4 Related Aspects

4.1 Flow Separation

Flow separation can be caused by an increase in pressure in flow direction or sudden changes in geometry. With this, density differences are associated, which might cause shocks in supersonic or hypersonic flows. Typical examples are the heat transfer on blunt bodies and cones, flat surface with a step in geometry, concave surface elements or shock impingement regions. Vortices and reattachment induces at the body surface locally extremely high heat transfer coefficients, whose positions and values are still a challenge for numerical methods. Many experimental and numerical investigations of flow separation for high speed flows have been done in the past. A nice summary, including

several correlations for the heat transfer, are given by Merzkirch et al. [33]. The reader is also referred to Holden [34, 35] concerning further detailed information on this topic.

4.2 Transition

The equations, which have been provided above, are only valid if the flow is either laminar or turbulent. However, in a lot of applications, the flow (either external or internal) will undergo flow transition from a laminar to a turbulent state. This effect can change dramatically the heat transfer on the surface under consideration. The reader is referred to White [16] and Hirschel [12] who give two quite comprehensive overviews on this effect.

4.3 Roughness

Surface roughness for a turbulent flow will increase the friction factor and to a smaller extend also the heat transfer. Roughness can also strongly influence the position for which laminar to turbulent transition takes place. The reader is referred to Schlichting [6] and Schneider [36] for some literature on roughness effects in compressible flows.

5 Symbols

A, b	constants (–)
A	area (m^2)
$A^* = \pi D^{*2}/4$	throat area (m^2)
$c^* = p_0 A^* \dot{M}$	characteristic velocity (ms^{-1})
D	diameter (m)
D^*	throat diameter (m)
f	dimensionless stream-function (–)
K	Viscous interaction parameter, Eq. (19) (–)
r	recovery factor, Eq. (5) (–)
r_0	radius (m)
S	dimensionless enthalpy function, Eq. (35) (–)
T	temperature (K)
T_0	stagnation temperature (K)
T_{aw}	adiabatic wall temperature (K)
w_s	sonic velocity (ms^{-1})
w	velocity (ms^{-1})
δ	boundary layer thickness (m)
δ_1	boundary- layer displacement thickness (m)
ω	exponent of the viscosity law (–)
Indices	
δ	outer edge of the boundary layer
∞	approach conditions
0	stagnation condition
aw	adiabatic wall
w	at the wall
ref	reference condition
Dimensionless numbers	
C	Chapman-Rubesin parameter $= \rho\eta/(\rho_\delta \eta_\delta)$
Ma	Mach number $= w_\infty / w_s$
Pr	Prandtl number $= \eta c_p/\lambda$
Re_x	Reynolds number $= w_x x/\nu$
Ec	Eckert number $= w_\infty^2/(2c_p T_\infty) = [(\kappa-1)/2]Ma_\infty^2$
Nu_x	Nusselt number $= \alpha x/\lambda$
$c_f = \xi/4$	Skin friction coefficient $= \tau_w/(\rho_\infty w_\infty^2/2)$
St	Stanton number = Nu/(Re Pr)

6 Bibliography

1. Gersten K, Herwig H (1992) Strömungsmechanik. Vieweg, Braunschweig
2. Herwig H (1985) Asymptotische Theorie zur Erfassung des Einflusses variabler Stoffwerte auf Impuls- und Wärmeübertragung. Fortschr.- Ber. VDI, R. 7, Nr. 93, VDI, Düsseldorf
3. Mitra NK (2006) Wärmeübertragung bei schallnahen Strömungen, VDI Wärmeatlas, Abschnitt Mn. Springer, New York
4. Rotta JC (1964) Temperaturverteilungen in der turbulenten Grenzschicht an der ebenen Platte. Int J Heat Mass Trans 7:215–228
5. Kays W, Crawford M, Weigand B (2004) Convective heat and mass transfer. Mc Graw-Hill, New York
6. Schlichting H (1982) Grenzschicht- Theorie. Karlsruhe, G. Braun
7. Eckert ERG, Drake RM Jr (1972) Analysis of heat and mass transfer. McGraw-Hill, New York
8. Cebeci T, Bradshaw P (1984) Physical and computational aspects of convective heat transfer. Springer, New York
9. Dorrance WH (1962) Viscous hypersonic flow. McGraw-Hill, New York
10. Anderson JD (1989) Hypersonic and high temperature gas dynamics. McGraw-Hill, New York
11. Truitt WR (1960) Fundamentals of aerodynamic heating. The Ronald Press Co., New York
12. Hirschel EH (2005) Basics of aerothermodynamics. Springer, New York
13. Koppenwallner G (1984) Hypersonic aerothermodynamics and heat transfer. Lecture Series 1984, VKI, Brussels
14. Jischa M (1982) Konvektiver Impuls-, Wärme- und Stoffaustausch. Vieweg, Braunschweig
15. Herwig H (1987) An asymptotic approach to compressible boundary layer flow. Int J Heat Mass Trans 30:59–68
16. White, F (1974) Viscous fluid flow. McGraw-Hill, New York
17. Stewartson K (1964) The theory of laminar boundary layers in compressible fluids. oxford mathematical monographs. Clarendon Press, Oxford
18. Levy S (1954) Effect of large temperature changes (including viscous heating) upon laminar boundary layers with variable free stream velocity. J Aero Sci 21(7):459–474
19. Li TY, Nagamatsu HT (1955) Similar solutions of compressible boundary layer equations. J Aero Sci 22(9):607–616
20. Cohen C, Reshotko E (1956) Similar solutions for the compressible laminar boundary layer with heat transfer and pressure gradient. NACA Rep 1293
21. Fay JA, Riddel FR (1958) Theory of stagnation point heat transfer in dissociated air. J Aero Space Sci 25(2):73–85
22. Beckwith JE, Gallagher JJ (1962) Local heat transfer and recovery temperatures on a yawed cylinder at a mach number of 4.15 and high Reynolds numbers. NASA TR-R- 104
23. Sutton GP, Biblarz O (2001) Rocket propulsion elements. John Wiley&Sons, New York
24. Curran ET, Murthy SNB (2000) Scramjet propulsion. Progress in astronautics and aeronautics 189 AIAA, Reston, Virginia, USA
25. Shapiro AH (1954) The dynamics and thermodynamics of compressible flows, vol 1. Ronald Press Co, New York
26. Shapiro AH (1954) The dynamics and thermodynamics of compressible flows, vol 2. Ronald Press Co, New York
27. Miller DS (1990) Internal flow systems. Design and performance predictions. Gulf publishing company book division, UK
28. Back LH (1970) Acceleration and cooling effects in laminar boundary layers- subsonic, transonic and supersonic speeds. AIAA J 8(4):794–802
29. Carden WH (1965) Local heat transfer coefficients in a nozzle with high-speed laminar flow. AIAA J 3(12):2183–2188

30. Bartz DR (1957) A simple equation for rapid estimation of rocket nozzle convective heat-transfer coefficients. Jet Propul 27:49–51
31. Back LH, Massier PF, Gier HL (1964) Convective heat transfer in a convergent- divergent nozzle. Int J Heat Mass Trans 7:549–568
32. Mastanaiah K (1978) Prediction of skin-friction and heat transfer from compressible turbulent boundary layers in rocket nozzles. Int J Heat Mass Trans 21:1403–1409
33. Merzkirch W, Page R, Fletcher LS (1988) A survey of heat transfer in compressible separated and reattached flows. AIAA J 26(2):144–150
34. Holden MS (1977) Shock wave-turbulent boundary layer interaction in hypersonic flow. AIAA-77–45, 15th Aerospace Science Meeting, Los Angeles, 24.-26. January
35. Holden MS (1986) A review of aerothermal problems associated with hypersonic flight. AIAA-86–0267, 24th Aerospace Science Meeting, Reno, 6.-9. January
36. Schneider SP (2007) Effects of Roughness on Hypersonic Boundary-Layer Transition. AIAA-2007–0305, 45th Aerospace Sciences Meeting, Reno, 8–11. January
37. Weigand B (2004) Analytical methods for heat transfer and fluid flow problems. Springer, New York

Specific Heat Transfer Devices

N1 Heat Transfer in Regenerators

Helmuth Hausen[2,†] (*Revised by Wolfgang Bender*)[1]
[1]VDEh-Betriebsforschungsinstitut GmbH, Düsseldorf, Germany
[2]Hannover, Germany

1 Operating Principle of Regenerators

The term "regenerator" denotes a heat transfer device which comprises a packing through which two different gases are alternately passed. The amount of heat to be transferred is temporarily stored in this heat-storing packing through which the gas stream is directed, and which is also variously referred to as the regenerator's checker (work), matrix, grating, bed, heat store, or storage mass. The regenerative heat transfer involves locally non-steady-state subprocesses which are generally referred to as "heating" or "cooling." Depending on the viewpoint, these terms apply either to the storage mass or to the different gas flows.

The function of a regenerator is illustrated in Fig. 1 which, by way of example, shows a regenerator pair as used in cryogenic applications. The cylindrical tanks contain heat-storing masses which may be porous, interspersed with passages, or of a checkerwork structure. The two different gases are alternately routed through these storage masses in opposite directions to obtain a gas counterflow offset in time. As a result of this cyclic reversal, the temperature of the storage mass varies upward and downward periodically, i.e., the packing temporarily absorbs a certain amount of heat during the "hot cycle" before releasing it to the colder gas again during the "cold cycle." The regenerative heat transfer process is characterized by a locally alternating non-steady-state heat transfer, which takes place initially between the gas stream 1 and the storage mass and, subsequently, between the storage mass and the gas stream 2. In the course of this process, the two gas streams pass over the same heating surface of the storage mass in succession. The function of a regenerator pair as used in hot industrial furnace applications is shown in Fig. 2, the so-called regenerator burner system. The regenerative heat transfer process follows the same proceedings as with the cryogenic application.

2 Regenerator Design and Application

In terms of apparatus engineering, regenerators can be classified into two groups:

- Fixed-matrix regenerator system (Siemens/Cowper patent): A regenerator of this type is cycled discontinuously between heating and cooling. Thus, to achieve a continuous heat transfer, at least two separate regenerators (i.e., a regenerator pair) are required so that the first gas stream can be cooled while the other is being heated at the same time, as shown in Figs. 1 and 2. The temperature of the exiting gas streams is not constant with this design.
- Moving-matrix regenerator system (Ljungström patent): In this regenerator design, a continuous changeover between heating and cooling takes place. Only a single packing is used to ensure an uninterrupted heat transfer from one gas stream to the other. This packing may either be a rotating storage mass which is exposed, in turn, to one or the other gas stream, or a stationary storage mass onto which the incoming gas streams are directed via rotating vaned hoods. Here again, hot or cold gas can be passed alternately through one and the same section of the storage mass. The temperature of the outlet gas flows can be kept constant in this case.

In terms of functional engineering, regenerators can also be classified in two groups:

- Central regenerator system: Two or more fixed-matrix regenerators work together to heat or cool one gas stream to the required conditions. To achieve a gas stream of constant temperature a special control system is necessary, as described next.
- Decentralised regenerator system: Normally, this system is used for heat recovery at high temperature plants. Many regenerators e.g., 10 – 40 are installed at the plant, and each sucks a part of the waste gas. The temperature of the heated gas stream is not constant, and the control system controls the energy balance of the whole plant.

Examples of classic central high-temperature regenerator applications include the hot-blast stoves (Cowper) associated with blast furnaces and the regenerative chambers on glass melting furnaces. Examples of decentral applications include the

†Deceased

VDI-GVC (ed.), *VDI Heat Atlas*, DOI 10.1007/978-3-540-77877-6_61,

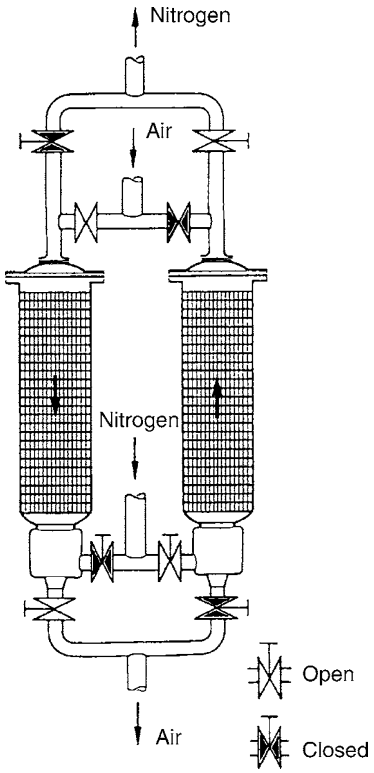

N1. Fig. 1. Operating principle of a regenerator for cryogenic application.

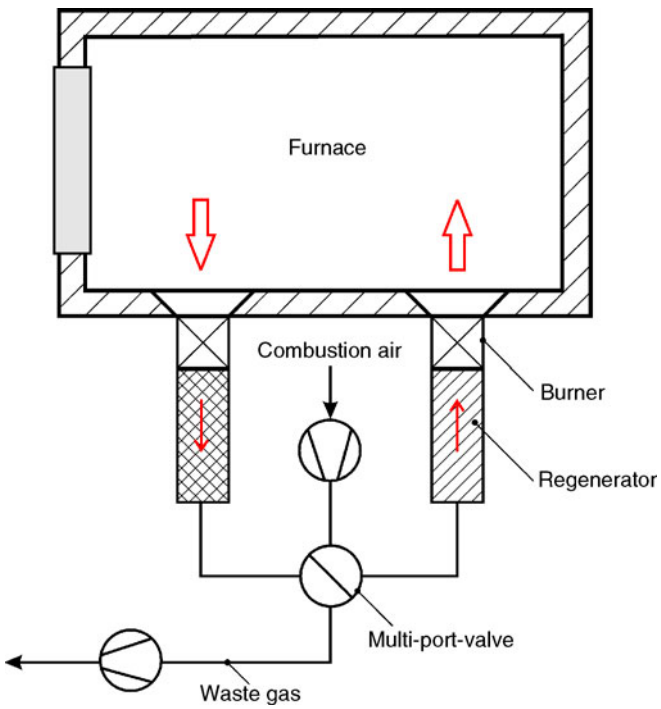

N1. Fig. 2. Operating principle of a regenerator burner for industrial furnaces.

regenerative chambers on coke ovens, and in recent years this regenerator principle has also been used in the so-called regenerator burners on industrial heating furnaces.

In the hot-blast stove (Cowper) according to Fig. 3, most of the interior space is filled by the heat-storing packing referred to

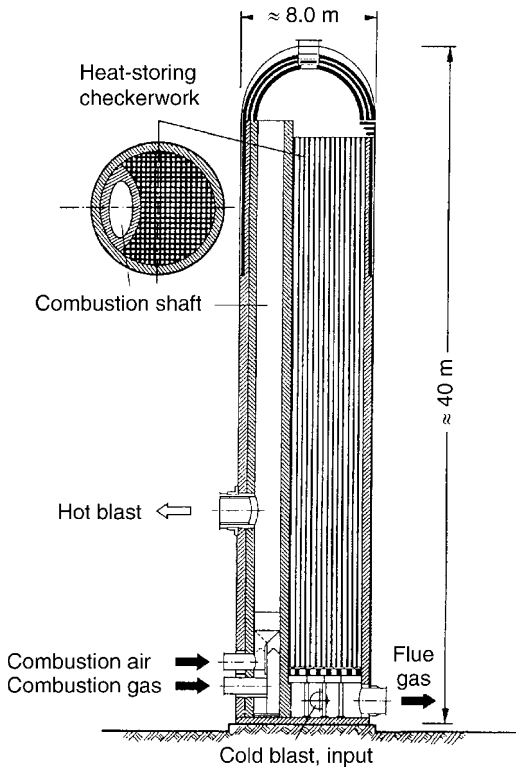

N1. Fig. 3. Hot-blast stove as Cowper.

as checkerwork, which consists of refractory bricks. In addition, each Cowper possesses a combustion shaft (Fig. 3, left-hand side) in which, e.g., the blast furnace gas is burnt to produce a hot flue gas. This flue gas is then blown through the checkerwork from the top downward, transferring its heat to the storage mass (i.e., the checkerwork). After flow reversal, air (referred to as "blast" in metallurgical terminology) is passed through the checkerwork from the bottom up and is thereby heated to a high temperature. The resulting "hot blast" is then injected into the blast furnace.

The hot blast is often required to exhibit not only a high temperature, but also one that remains as constant as possible. This can be achieved by ducting a progressively decreasing portion of the total airflow, which in itself remains unchanged, past the Cowper stove via a bypass line during the blast heating period, then mixing it with the hot air as it exits the stove. Therefore, the airflow through the Cowper stove must be heated to the point where its (decreasing) outlet temperature, at the end of the hot period, is still as high as, or slightly higher than, the required constant temperature of the mixed blast. Methods for calculating this process have been developed by Hausen [1, p. 387–392; 2], Willmott [3], and Razelos and Benjamin [4]. Another approach for producing a hot blast of maximum temperature constancy is to run four or more Cowpers simultaneously, on a regime which ensures that two of them deliver hot air at any given time. In an arrangement of this type, one Cowper has always been "on blast" for longer than the other. As a result, two gas flows of different temperatures are always available for mixing, and the mixed blast temperature can be maintained as constant as possible. Calculation equations for this technique can be found in the work by Schmidt and Willmott [5].

Nowadays one main application of regenerators is the heat recovery and preheating of combustion media at high

temperature heating plants (e.g., heating and melting furnaces in the metal, ceramic, chemical, and glass industry) and waste gas past combustion plants [6, 7]. The thermal power of these regenerators is less than the well-known hot-blast stoves or coke over regenerative chambers. They also must fulfill the actual demands:

- handling of gas temperature above 1,300°C,
- high load of dust and aggressive components,
- media preheating up to more than 1,000°C,
- longer operating time with low maintenance effort.

These requirements lead to some general principles of smaller regenerator design, especially for the application as regenerator burner:

- the regenerator and the burner(s) are connected with a short piping to avoid heat losses and the operation of valves at the hot side,
- the entire regenerator inside walls and packages must be made of ceramic materials,
- the flow direction should be vertical to avoid dust congregation,
- uncontrolled flow must be tied up.

Figure 4 shows an example of a switching regenerator unit, with a fixed storage mass, installed at a reheating furnace in a forging plant. The hot gas, about 1,200°C, from the furnace is sucked through the burner and the regenerator unit. The heat is stored in the ceramic mass and after reversing the flow the combustion air is heated up to 1,000°C. The function of burning – cooling the regenerator – and sucking – heating the regenerator – changes periodically. The usual time period is about 10 s up to 90 s. For the energy and temperature control of the whole furnace exist several methods, which have different impact on the single regenerator and burner unit.

Another regenerator system has a rotating heat storage mass (Fig. 5). The hot gas from the furnace streams through the right area and heats the storage mass. By continuous rotation the hot mass is transported to the combustion air side (left), where the air is preheated. The average temperature of the whole air stream is nearly constant. The disadvantage of this system is a permanent leakage flow about 5–15% between air and gas. The problems of tightening systems for moving elements at high temperature are not solved yet.

In both cases – switching and rotating regenerators – the heat recovery works well and a decrease in gas consumption at industrial furnaces to about 30% is reached.

3 Geometry and Material of Storage Masses

The heat storage masses employed in high-temperature sections of big regenerators, e.g., of a Cowper, consist of refractory bricks measuring approx. 200 mm in original thickness. The time between two flow reversals is about 1–2 h in a unit of this type. Brick thickness has been progressively reduced to about 40 mm or less, especially in regenerators for the chemical industry. This has permitted a decrease in reversal times to less than a quarter hour. As shown in Fig. 6a, rectangular bricks can be arranged into a packing, providing smooth shafts, or into a more checkerwork-type configuration. It is also possible to build the packing of molded bricks, Fig. 6b–d. The previously employed method of changing the cross section of vertical passages over their linear length by installing filler bricks of varying size and shape is no longer common.

The time between the flow reversals in regenerator systems for heat recovery at industrial furnaces is shorter, less than 180 s. According to this, the thickness of the storage mass is smaller, about 1–5 mm. Figure 7 shows pictures of a storage mass for a hot-blast stove and three different masses for small regenerators: honeycombs, balls, and RASCHIG rings. Honeycombs are less sensitive to dust and they have little pressure drop. Balls and rings have a higher heat transfer coefficient, but they are sensitive to blocking by dust and the pressure drop is very high.

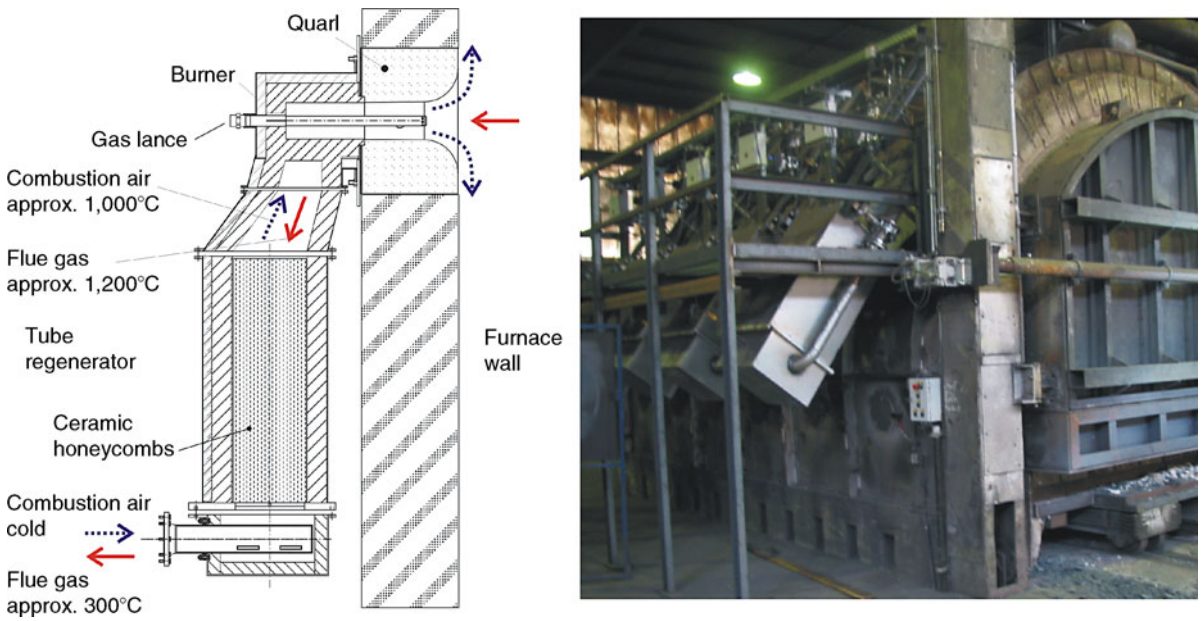

N1. Fig. 4. Fixed-matrix regenerator system at a forging furnace.

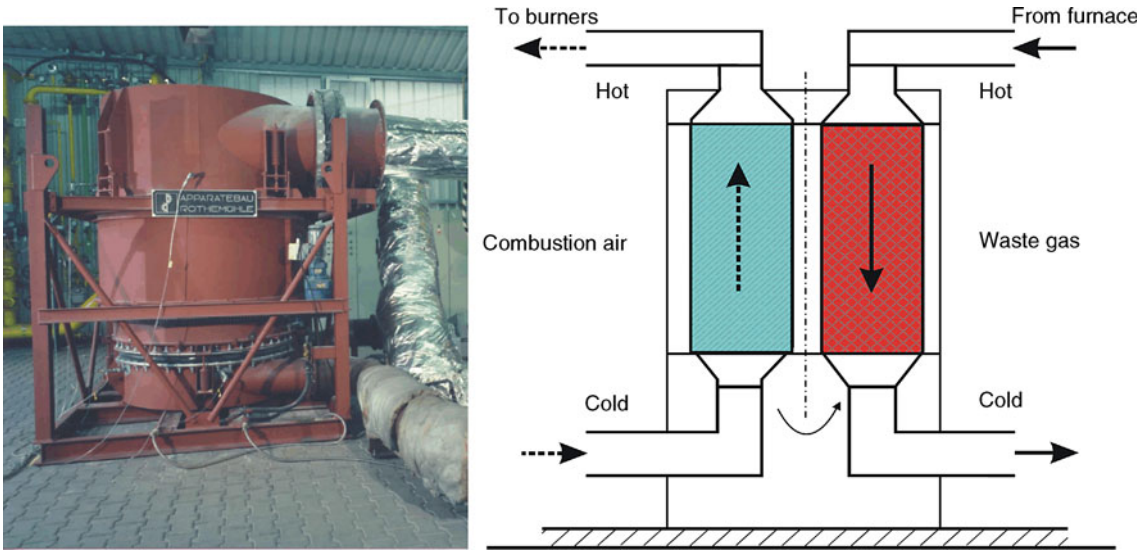

N1. Fig. 5. Moving-matrix regenerator system.

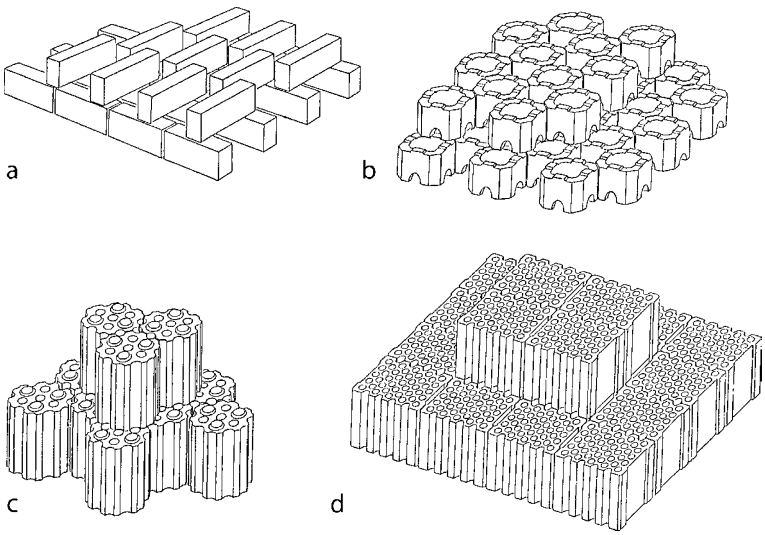

N1. Fig. 6. Bricks for large regenerators.

In the case of low or only moderately high temperature, the heat storage mass can be made of metal, e.g., steel or aluminum, so that narrower gas flow passages are obtained (Fig. 8). In cryogenics, obliquely corrugated strips of sheet aluminum were originally used. These were placed on top of each other with their corrugation directions alternating, so that a system of fine criss-crossing passages was produced. This costly packing design was later replaced successfully with gravel or stone chippings. Metal panel-type heating elements as shown in Fig. 8 are today used mainly in regenerators based on the Ljungström in Fig. 8 patent which operate as combustion air preheaters or flue gas heaters in boiler installations. The thickness of the sheet metal is about 0.5–1 mm. The hydraulic diameter of the gas passages amounts to between 4 and 9 mm. Extremely small dimensions were adopted for the regenerators in the Philips cryocooler developed for cryogenic applications; their packing consists of thin, wound copper wire.

The geometrical properties of a checkerwork packing can be described in terms of the following four parameters:

- hydraulic diameter of the flow passage d_h,
- portion of free cross section of flow φ,
- specific heating surface area of checkerwork f_v,
- equivalent wall thickness δ_{gl} of a storage mass assembled from plates.

It has been shown by Heiligenstaedt [8] that the interrelationships between these four variables are such that selecting of any two of them will suffice to determine the two others. The following equations apply:

$$f_v = \frac{4\varphi}{d_h} \tag{1}$$

$$\delta_{gl} = \frac{d_h \cdot (1-\varphi)}{2\varphi} \tag{2}$$

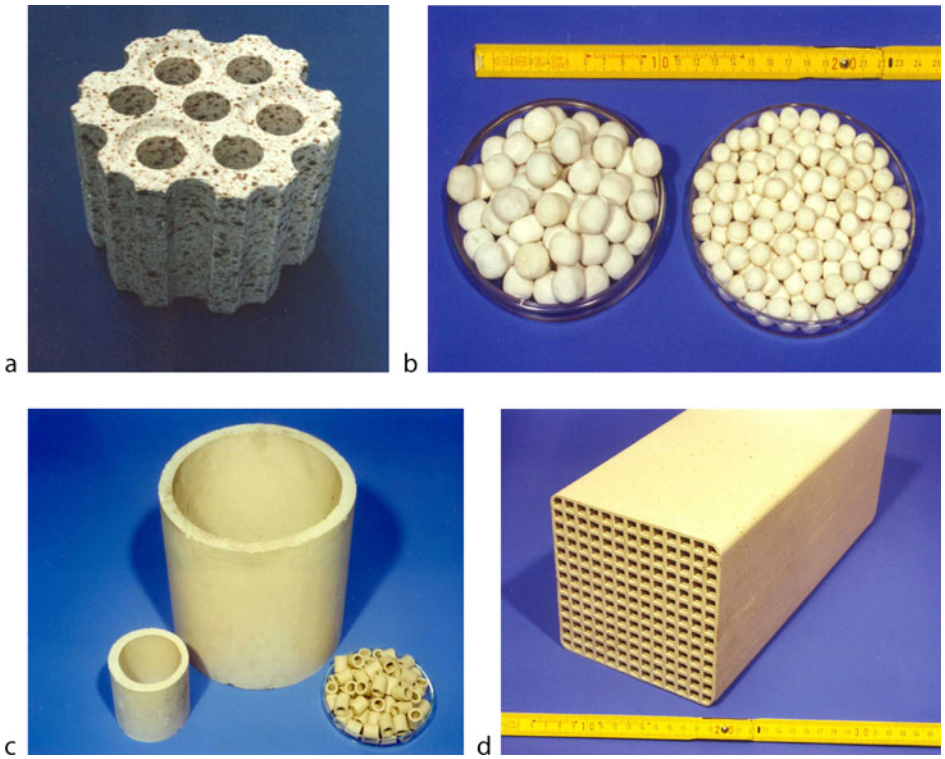

N1. Fig. 7. Ceramic storage mass for smaller regenerators.

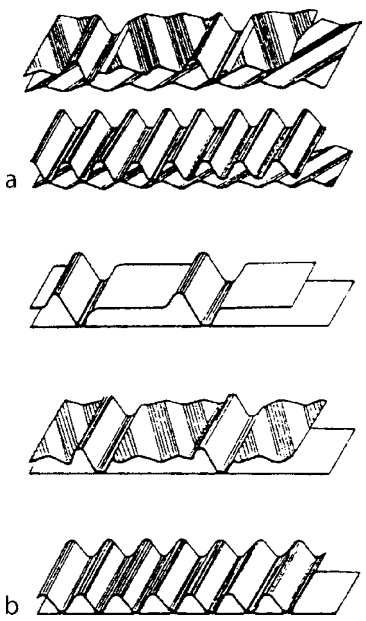

N1. Fig. 8. Metallic profiles for low-temperature regenerators.

The two diagrams in Fig. 9 plot common packing data for a variety of regenerators. It emerges that the checkerworks employed differ quite substantially in terms of their geometry, according to the different operating conditions of the individual regenerator units.

4 Temperature Distribution and Heat Storage in Regenerators

In regenerators with cycling function, the temperature of gas and storage mass changes periodically. Figure 10 shows the calculated temperature distribution of a regenerator during heating and cooling periods in three plains top, middle, and bottom.

The hot gas enters the regenerator with constant temperature of 1,200°C, the average temperature of the storage mass in this plain rises from 950°C up to nearly 1,200°C at the end of the heating period. In the middle plain the temperature curves of gas and storage mass are nearly parallel and they rise from about 550–600°C up to 900–950°C. At the bottom the gas outlet temperature rises up to 450°C at the end of the heating period. In the cooling period the cold air enters the regenerator in the bottom with a temperature of 20°C, the hot air leaves the regenerator at 1,200°C at the beginning and about 900°C after 180 s.

The gas outlet temperature in the heating period has a great impact on the construction of the waste gas system. Due to high temperature the material of piping and valves is expensive. The maximum temperature can be reduced by shortening the heating periods. Also the gas outlet temperature in the cooling period is important to the connected process, especially, a great temperature decrease can be avoided by shortening the time period, too. On the other side, the shortening of the time period reduces the regenerator efficiency by raising the leakage losses and decreasing the overall working time. Therefore, the integration of the regenerator system in the whole plant has a great influence on the layout and construction of the regenerator itself.

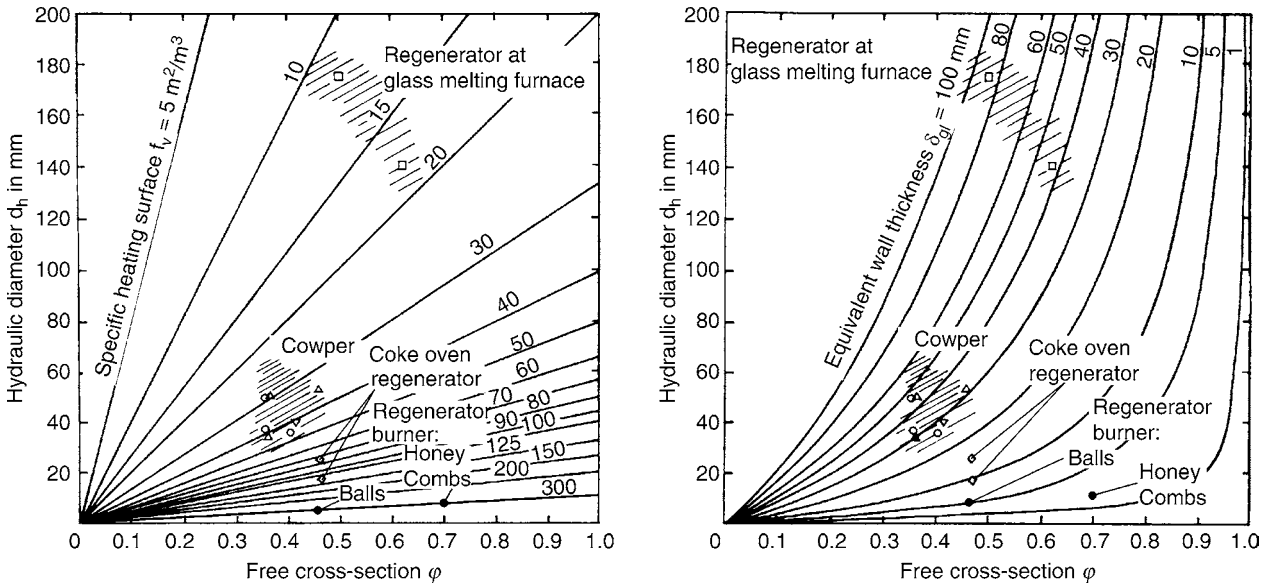

N1. Fig. 9. Comparison of geometric parameters of different storage masses.

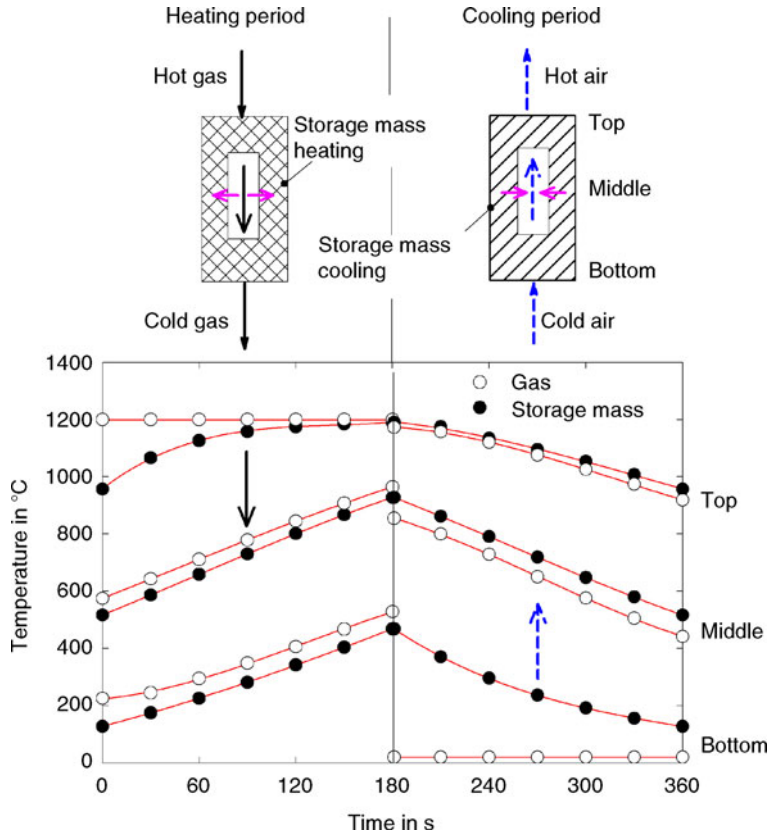

N1. Fig. 10. Temperature distribution in a regenerator storage mass.

5 Calculation of Regenerators

For the general layout and the construction of a regenerator, usually it is not necessary to possess an accurate knowledge of local and time-dependent temperature distributions. For this task, it is normally sufficient to determine the heat transfer coefficient by the method of Hausen [1].

5.1 Calculation by Heat Transfer Coefficient

The heat transfer coefficient k for steady regenerators can be calculated with the equation:

$$k = \frac{Q_{Per}}{A \cdot (t_1 + t_2) \cdot \Delta T_m}; \qquad (3)$$

Q_{Per} is the heat amount, which is stored in the storage mass, A is the transfer area, t_1 and t_2 are lengths of time of heating and cooling periods, respectively, and ΔT_m is the average temperature difference between the two gas streams.

Further on the stored heat amount is transferred from the gas stream 1 to the gas stream 2

$$Q_{Per} = \dot{M}_1 \cdot \bar{c}_{p1} \cdot t_1 \cdot \Delta T, \tag{4a}$$

$$Q_{Per} = \dot{M}_2 \cdot \bar{c}_{p2} \cdot t_2 \cdot \Delta T_2, \tag{4b}$$

$\dot{M}$ is the mass flow, $\bar{c}_p$ the average heat capacity, t the period time, and ΔT the difference between entry and exit temperatures. With the assumption that the values of heat capacity are not temperature dependent, this is the logarithmic average value of the temperature differences at both ends of the regenerator. This heat transfer coefficient includes the heat transfer on the surface and the heat conduction inside the storage mass. It is calculated in two steps, first is the calculation of k_0:

$$\frac{1}{k_0} = (t_1 + t_2) \cdot \left[\frac{1}{\alpha_1 \cdot t_1} + \frac{1}{\alpha_2 \cdot t_2} + \left(\frac{1}{t_1} + \frac{1}{t_2} \right) \frac{\delta}{\lambda_s} \Phi \right]. \tag{5}$$

Hereby Φ is a function of $\frac{\delta^2}{2a}\left(\frac{1}{t_1} + \frac{1}{t_2}\right)$ which can be taken from Fig. 11, with δ as thickness of the storage material.

A normally sufficient approximation value δ_{gl} for thickness can be calculated by

$$\delta_{gl} = \frac{\delta}{2} + \frac{V_s}{A}. \tag{6}$$

To obtain the real heat transfer coefficient k of the regenerator, one has to calculate the relation of k/k_0. In this way one has to calculate the reduced regenerator length Λ and the reduced regenerator time Π:

$$\Lambda = 2 \cdot \frac{k_0 \cdot (t_1 + t_2) \cdot A}{C_{Per}} \tag{7}$$

$$\Pi = 2 \cdot \frac{k_0 \cdot (t_1 + t_2) \cdot A}{C_s} = \frac{C_{Per}}{C_s} \cdot \Lambda. \tag{8}$$

with $C_{Per} = \frac{1}{2}\left(\dot{M}_1 \cdot \bar{c}_{p1} \cdot t_1 + \dot{M}_2 \cdot \bar{c}_{p2} \cdot t_2\right)$ and C_s as the heat capacity of the storage mass. With these values for Λ and Π, we can determine the relation k/k_0 from Figs. 12 and 13. With the value for the heat transfer coefficient k, a regenerator can be calculated as well as a recuperator. Note that the temperature dependence of the heat capacity of gas and storage mass is not included.

5.2 Step-based Method

Nevertheless, some notes are included here for the event that a precise determination of the temperature distribution is desired. The former calculations are performed using the local mean brick temperature T_{sm} in the given regenerator cross section considered. The heat transfer coefficient, too, should then preferably be related to the difference between the gas temperature and the mean brick temperature T_{sm}. This heat transfer coefficient α_m is calculated from the true heat transfer coefficient α, the thickness δ, and the heat conductance λ_s of the brick material using the equation

$$\frac{1}{\alpha_m} = \frac{1}{\alpha} + \frac{\delta}{\lambda_s} \Phi, \tag{9}$$

where Φ is the function determined from Fig. 11.

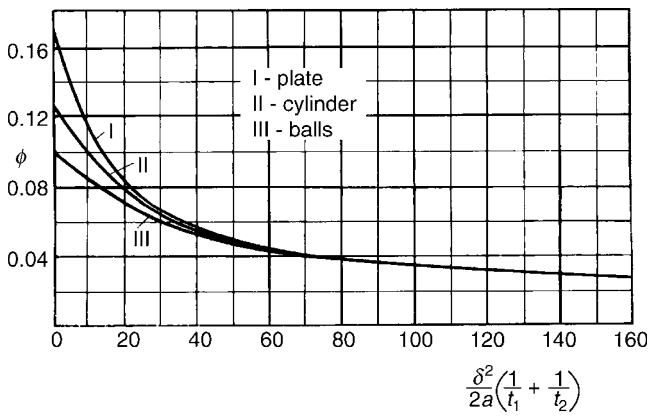

N1. Fig. 11. Function Φ for the calculation of the heat transfer coefficient.

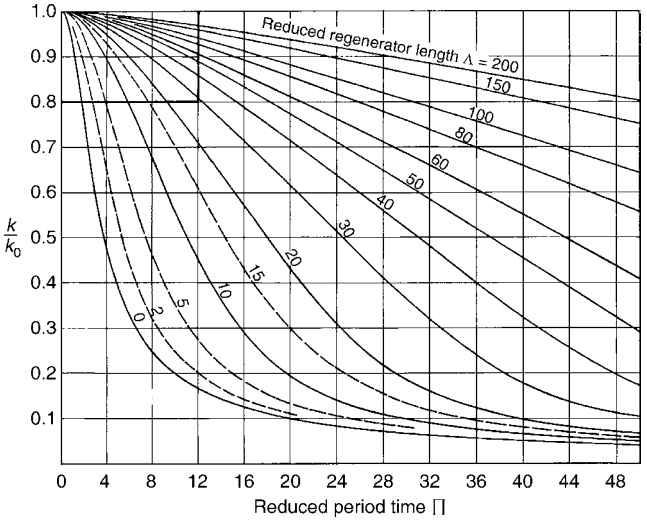

N1. Fig. 12. Relation k/k_0 depending on Λ and Π.

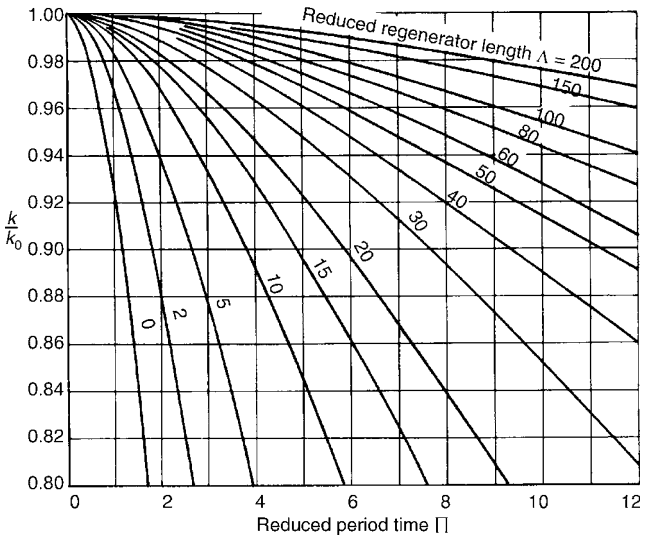

N1. Fig. 13. Enlarged part of Fig. 12.

For calculating the temperature distribution in the longitudinal regenerator direction as a function of time, several approaches are known. Emphasis is placed here on those using the finite difference method, i.e., which proceed in steps and are therefore particularly suitable for computer-based execution as described, e.g., by Kuhn and Sucker [9, 10].

Two methods are explained, both of which are based on a transformation of the original graphic technique developed by Hausen [1, 11] into an all-numerical equation system. According to method I, which was given its numerical form by Willmott [12], the storage mass and the gas temperature are alternately determined at each step. Method II, on the other hand, which lent itself to numerical use virtually unchanged from the outset, initially involves calculation of the storage mass temperature only.

First, the space–time mesh on which the calculation process is based is explained with reference to Fig. 14. The longitudinal coordinate in the flow direction is assumed to be the heat-transferring surface area f of that portion of the heat storage mass which extends between the gas inlet point and the given regenerator point considered. It is further assumed, considering the example of a cold period in Fig. 14, that the temperatures T_{s1} and T_{s2} of the storage mass at points f and $f + \Delta f$ are known for time t, and that the temperature T_{s3} at point f is known for time $t + \Delta t$. The data sought is the storage mass temperature T_{s4} at point $f + \Delta f$ at time $t + \Delta t$. All storage mass temperature values represent local mean temperatures. For clarity's sake, the index m for the storage mass temperature has been omitted in the following equations. The corresponding gas temperature values T_{g1}, T_{g2}, T_{g3}, and T_{g4} are not shown in Fig. 14.

Step-based method I: Using the step-based method I according to Willmott [12], the desired temperatures T_{s4} of the storage mass and T_{g4} of the gas can be obtained by means of the following equations:

$$T_{s4} = \frac{\left(\frac{2\dot{W}}{\alpha_m \cdot \Delta f} + 1\right) \cdot \left[T_{g2} + \left(\frac{2}{\alpha_m \cdot \Delta t} \frac{dC_s}{df} - 1\right) T_{s2}\right] + \left(\frac{2\dot{W}}{\alpha_m \cdot \Delta f} - 1\right) \cdot T_{g3} + T_{s3}}{\left(\frac{2\dot{W}}{\alpha_m \cdot \Delta f} + 1\right) \cdot \left(\frac{2}{\alpha_m \cdot \Delta t} \frac{dC_s}{df} + 1\right) - 1}, \quad (10)$$

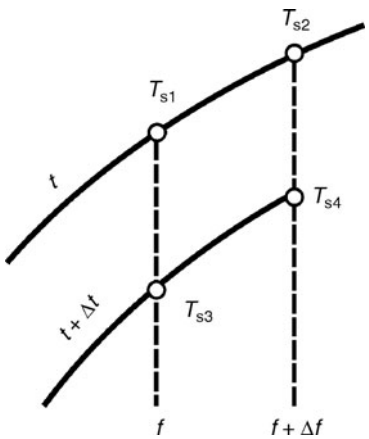

N1. Fig. 14. Calculation steps to investigate the storage mass temperature.

$$T_{g4} = T_{g3} + \frac{T_{s3} + T_{s4} - 2T_{g3}}{\frac{2\dot{W}}{\alpha_m \cdot \Delta f} + 1}. \quad (11)$$

In the foregoing Eqs. (10) and (11), $\dot{W}$ is the heat flow capacity of the flowing gas volume, C_s is the heat capacity of the storage mass, and dC_s denotes that part of the latter which corresponds to a very small portion df of its surface area. The value of α_m is determined by Eq. (9). For very thin or metal heat-storing elements, $\alpha_m = \alpha$. The iterative application of this step-based method I is best performed by means of computing software.

(This is discussed in more detail in the calculation in Example 3 at the end of Part N. The resulting temperature curves of the gas and packing are also presented for hot and cold periods.)

Step-based method II: In the method proposed by Hausen [11], which is also referred to as the step-based method II, only the temperature of the storage mass is determined initially.

$$T_{s4} = T_{s1} + \frac{(T_{s2} + T_{s3} - 2T_{s1}) + \frac{\alpha_m}{2}\left[\frac{\Delta f}{\dot{W}} - \frac{df}{dC_s}\Delta t\right] \cdot (T_{s2} - T_{s3})}{1 + \frac{\alpha_m}{2}\left[\frac{\Delta f}{\dot{W}} + \frac{df}{dC_s}\Delta t\right]}. \quad (12)$$

The symbols used are the same as in Eqs. (10) and (11). A simplification of Eqs. (10) and (12) is obtained if the position and time value at each step are selected such that $\frac{1}{\dot{W}}\Delta f = \frac{df}{dC_s}\Delta t$. This is particularly true for Eq. (12), which can then be expressed in the following simplified form:

$$T_{s4} = T_{s1} + \frac{T_{s2} + T_{s3} - 2T_{s1}}{1 + \frac{\alpha_m \Delta f}{\dot{W}}}. \quad (13)$$

In the step-based method II, the gas temperature associated with the calculated packing temperature curve is usually determined at the end of the computing process only, e.g., once the system has reached its equilibrium state. For calculating the gas temperature, Eq. (11) can be used in the same way as in step-based method I.

Evaluation notes on the two step-based methods I and II: The two step-based methods permit a calculation of the entire temperature curve at time $t + \Delta t$ (and, accordingly, for other increments) via Eqs. (10), (11), and Eq. (12) or (13), by iterating from f to $f + \Delta f$, $f + 2\Delta f$, etc. Both step-based methods can also be used with variable – and in particular, time-dependent – values of α_m, $\dot{W}$, and C_s by inserting slightly different values for these variables at each step. It is recommended to work with the α_m, $\dot{W}$, and C_s values applicable in each case to the temperature T_{s1} or $1/2\,(T_{s2} + T_{s3})$. With constant values of α_m, $\dot{W}$, and C_s one additionally obtains the required storage mass temperature T'_s at the gas inlet point, using the equation

$$T'_s = T'_g + \left(T'_{s0} - T'_g\right) \cdot e^{-\frac{\alpha_m \cdot df}{dC_s} t}. \quad (14)$$

Further to the known variables in Eq. (14), T'_g denotes the constant gas inlet temperature and T'_{s0} is the storage mass temperature at time $t = 0$. If one intends to compute the temperature values for multiple successive periods, it should be noted that the local temperature distribution of the storage mass determined at the end of one period will be equal to the

initial distribution at the start of the next period. To obtain the periodic equilibrium condition of the regenerator, the step-based methods must be applied for as many successive periods as are necessary until the temperature distributions remain unchanged at the end of the full period.

Both step-based methods yield a rather accurate determination of the changes in mean brick temperature over time. Time-related changes in gas temperature, however, are accurately rendered on a time-average basis only. This is due to the use of α_m according to Eq. (9). As a result, the rapid changes over time to which the gas temperature (and similarly the brick surface temperature) are subject immediately after the reversal are not taken into account. If a good numerical approximation of these rapid transients is desired, reference should be made to the publications by Willmott [3] and Hausen [1, p. 312].

The accuracy of the step-based methods I and II can be evaluated as follows, according to Hausen [13]. If identical lengths in space and time are adopted for the computing steps in both methods, then step-based method I will be more accurate than method II for the region near the regenerator's gas inlet point. However, the same accuracy in this region can also be achieved with step-based method II if the space and time steps are each set to one-half of the value used in method I. Slightly further away from the inlet, but at least starting from the position coordinate $(\alpha_m/\dot{W})f = 5$, both step-based methods yield the same very high accuracy with identical step sizes, and the calculation may therefore be based on large steps, e.g., $(\alpha_m/\dot{W})\Delta f = 3$. Step-based method II has one advantage here, in that it permits calculation of the storage mass temperature only, without any loss of accuracy. This reduces the computing time significantly, because only the simple Eq. (13) needs to be solved in this case.

5.3 Notes on Additional Calculation Methods

Besides the step-based methods, which are particularly suitable for implementation in computer software, other authors have attempted to give more analytical descriptions of the temperature distribution inside a regenerator. Thus, Anzelius [14] expressed the cooling and heating behavior of a storage mass of constant initial temperature by means of Bessel functions. Nußelt [15, 16], Schneidler [17], and Ackermann [18] proposed analytical approaches which also address quick temperature changes in the heat-storing material. However, any attempt to evaluate these analytical approaches leads back to numerical difference methods. The calculation method developed by Schack [19, 20] derives the calculation of regenerators from that of recuperators by introducing empirical elements for the checkerwork temperature distribution into the computing equations. Relying on Laplace transformation, Nahavandi and Weinstein [21] as well as Sandner [22] arrive at calculation equations which essentially coincide with Nußelt's integral equations. A more easily manageable approximation method for solving the integral equations was published by Iliffe [23]. Another approach to solve the regenerator equations has been presented by Vortmeyer and Le Mong [24, 25]. These authors use an equivalence relation between single- and two-phase fixed bed models. This method yields a quasi-homogeneous equivalence equation for the two-phase gas/brick system which, following mathematical transformation, becomes a partial differential equation analogous to the non-steady-state heat conduction equation and can thereupon be solved analytically. This interesting calculation variant abandons the concept of gas/brick heat transfer and instead considers the fictitious heat conductance merely in a brick phase. Willmott [26] and Schellmann [27] have disclosed implicit difference methods which make it possible to calculate not only the local mean brick temperature T_{sm}, but also local temperature differences within a brick cross section. The two methods are based on three-dimensional mathematical models. Especially, the calculation of smaller regenerators requires the operation of three-dimensional models, hence the influence of the transient effects is very high. The analytical solutions give just an approach of the real state.

Example 1

The first example shows the calculation of the true heat transfer coefficient with the equations in Sect. 5.1 of this chapter, to determine the average exit temperature values $\bar{T}_1''$ and $\bar{T}_2''$ by given entry temperature values.

A group of hot-blast stoves with two equal regenerators is used for the preheating of hot blast for the blast furnace. During the heating period hot combustion gas flows through the checkerwork, and during the cooling period cold air flows. The checkerwork consists of bricks with a thickness of $\delta = 0.03$m. The values of the storage material are $\rho_s = 1.800\ \mathrm{kg/m^3}$, $c_s = 1.200\ \mathrm{J/(kg \cdot K)}$, and $\lambda_s = 1\mathrm{W/(m \cdot K)}$. The temperature conductivity is

$$a = \frac{\lambda_s}{\rho_s \cdot c_s} = \frac{1}{1{,}800 \cdot 1{,}200}\ \mathrm{m^2/s} = 0.463 \cdot 10^{-6}\ \mathrm{m^2/s}.$$

The heat transporting surface of the storage mass is $A = 40.000\ \mathrm{m^2}$ and the volume of the solid mass is $V_s = 900\ \mathrm{m^3}$. The resulting heat capacity of the storage mass is

$$C_s = V_s \cdot \rho_s \cdot c_s = 900 \cdot 1.800 \cdot 1.200\ \mathrm{J/K} = 1.944 \cdot 10^9\ \mathrm{J/K}.$$

The mass flow through the regenerator in the course of the heating period is $\dot{M}_1 = 31\ \mathrm{kg/s}$ with an average specific capacity of $\bar{c}_{p1} = 1.000\ \mathrm{J/(kg \cdot K)}$, an air stream of $\dot{M}_2 = 28\ \mathrm{kg/s}$ and $\bar{c}_{p2} = 1.040\ \mathrm{J/(kg \cdot K)}$ flows in the cooling period. The heat capacity streams are

$$\dot{W}_1 = \dot{M}_1 \cdot \bar{c}_{p1} = 31 \cdot 1.000\ \mathrm{J/(s \cdot K)} = 31.000\ \mathrm{J/(s \cdot K)},$$
$$\dot{W}_2 = \dot{M}_2 \cdot \bar{c}_{p2} = 28 \cdot 1.040\ \mathrm{J/(s \cdot K)} = 29.120\ \mathrm{J/(s \cdot K)}.$$

The time of heating and cooling periods are equal, $t_1 = t_2 = 1\ \mathrm{h} = 3.600\ \mathrm{s}$. Thereby results the average heat capacity of both gas streams:

$$C_{Per} = \frac{1}{2} \cdot \left(\dot{W}_1 \cdot t_1 + \dot{W}_2 \cdot t_2\right)$$
$$= \frac{1}{2} \cdot (31.000 \cdot 3.600 + 29.120 \cdot 3.600)\ \mathrm{J/K} = 108.2 \cdot 10^6\ \mathrm{J/K}.$$

The hot combustion gas enters the regenerator with the temperature $T_1' = 1{,}250°\mathrm{C}$, and the cold blast with the temperature $T_2' = 100°\mathrm{C}$. The heat transfer coefficients are $\alpha_1 = 31\ \mathrm{W/(m^2 \cdot K)}$ and $\alpha_2 = 22\ \mathrm{W/(m^2 \cdot K)}$.

The true heat transfer coefficient k and the average exit temperature values $\overline{T}_1''$ and $\overline{T}_2''$ shall be calculated.

$$\frac{\delta^2}{2a}\cdot\left(\frac{1}{t_1}+\frac{1}{t_2}\right)=\frac{0.03^2}{2\cdot 0.463\cdot 10^{-6}}\cdot\frac{2}{3.600}=0.54.$$

By using Fig. 11 you get

$$\Phi=\frac{1}{6}-0.00556\cdot 0.54=0.1636.$$

Furthermore is

$$\frac{\delta}{\lambda_s}\Phi=\frac{0.03}{1}\cdot 0.1636\ \mathrm{m^2\cdot K/W}=0.00491\ \mathrm{m^2\cdot K/W}.$$

Set in Eq. (5) delivers

$$\frac{1}{k_0}=(3.600+3.600)\cdot\left[\frac{1}{31\cdot 3.600}+\frac{1}{22\cdot 3.600}+\frac{2}{3.600}\cdot 0.00491\right]\mathrm{m^2\cdot K/W}$$
$$=0.175\ \mathrm{m^2\cdot K/W},$$
$$k_0=5.71\ \mathrm{W\cdot(m^2\cdot K)}.$$

This delivers with Eqs. (7) and (8):

$$\Lambda=2\cdot\frac{5.71\cdot(3.600+3.600)\cdot 40.000}{108.2\cdot 10^6}=30.4,$$
$$\Pi=2\cdot\frac{5.71\cdot(3.600+3.600)\cdot 40.000}{1.944\cdot 10^9}=1.69.$$

With these values one get by using Fig. 12:

$$\frac{k}{k_0}=0.99$$

and finally the true heat transfer coefficient:

$$k=0.99\cdot 5.71\ \mathrm{W/(m^2\cdot K)}=5.65\ \mathrm{W/(m^2\cdot K)}.$$

The required values of exit temperatures $\overline{T}_1''$ and $\overline{T}_2''$ can be estimated by the combination of Eqs. (3) and (4).

$$Q_{\mathrm{Per}}=k\cdot A\cdot(t_1+t_2)\cdot\Delta T_m=\dot{W}_1 t_1\left(T_1'-\overline{T}_2''\right)=\dot{W}_2 t_2\left(T_2''-T_2'\right)$$
$$=5.65\cdot 40.000\cdot 2\cdot\Delta T_m=31.000\cdot 1\cdot\left(1.250-\overline{T}_1''\right)$$
$$=29.120\cdot 1\cdot\left(T_2''-100\right).$$

This means for ΔT_m when the specific heat capacity of the gas does not depend on the temperature:

$$\Delta T_m=\frac{\left(T_1'-\overline{T}_2''\right)-\left(\overline{T}_1''-T_2'\right)}{\ln\dfrac{\left(T_1'-\overline{T}_2''\right)}{\left(\overline{T}_1''-T_2'\right)}}=\frac{\left(1.250-\overline{T}_2''\right)-\left(\overline{T}_1''-100\right)}{\ln\dfrac{1.200-\overline{T}_2''}{\overline{T}_1''-100}}$$

By "testing" one will get from the last two equations:

$$\overline{T}_1''=210^\circ\mathrm{C}\quad\text{and}\quad\overline{T}_2''=1.207^\circ\mathrm{C}.$$

This means that the hot combustion gas is cooled in the regenerator down to 210°C and the cold blast is heated up to 1,207°C as average values.

Example 2

Reversal of the equation of Example 1: Which heat transfer surface do you need for heating the hot blast up to $\overline{T}_2''=900^\circ\mathrm{C}$? The other conditions and values remain constant as in Example 1. With these conditions the heat balance follows as:

$$T_1'-\overline{T}_1''=\frac{\dot{W}_2 t_2}{\dot{W}_1 t_1}\cdot\left(\overline{T}_2''-T_2'\right)=\frac{29.120}{31.000}\cdot(900-100)^\circ\mathrm{C}$$
$$=751.5^\circ\mathrm{C}$$

and the average exit temperature $\overline{T}_1''$ of combustion gas:

$$\overline{T}_1''=(1.250-751.5)^\circ\mathrm{C}=498.5^\circ\mathrm{C}.$$

With these values you can calculate the average temperature difference:

$$\Delta T_m=346.9^\circ\mathrm{C}$$

Out of the heat balance

$$k\cdot A\cdot(t_1+t_2)\cdot\Delta T_m=\dot{W}_1 t_1\left(T_1'-\overline{T}_1''\right)$$

follows with $t_1=t_2$

$$k\cdot A=\frac{31.000\cdot 751.5}{2\cdot 346.9}\ \mathrm{W/K}=33.578\ \mathrm{W/K}.$$

By using the approach value for $k=5.65\ \mathrm{W/(m^2\cdot K)}$ – as in example 1 – you get

$$A=\frac{33.578}{5.65}\mathrm{m^2}=5.943\,\mathrm{m^2}.$$

With this approach value of A, a constant relation of A/V_s, a reduced heat capacity $C_s=0.149\cdot 1.944\cdot 10^9$ and $k_0=5.71$ you get the following preliminary values:

$$\Lambda=2\cdot\frac{5.71\cdot(3.600+3.600)\cdot 5.943}{108.2\cdot 10^6}=4.52,$$
$$\Pi=2\cdot\frac{5.71\cdot(3.600+3.600)\cdot 5.943}{0.149\cdot 1,944\cdot 10^9}=1.69.$$

Furthermore you get out of Fig. 13 the relation k/k_0=0.95, which is used to obtain more exactly:

$$k=5.71\cdot 0.95\ \mathrm{W/(m^2\cdot K)}=5.42\ \mathrm{W/(m^2\cdot K)}$$

and following the required heat transfer surface:

$$A=6.195\ \mathrm{m^2}.$$

With this more exact value of A normally Λ and Π must be calculated again: The results would be $\Lambda=4.71$ and $\Pi=1.69$. With these values the relation of $k/k_0=0.95$ would remain constant, therefore a repetition of the calculation is not necessary.

Remark: The calculations as in Examples 1 and 2 give sufficient and usable results. For more detailed information e.g., about the time-dependent and local temperature profiles you must use the step-based method or another extensive calculation method, see following Example 3.

Example 3

The temperature profile of the checkerwork can be calculated with e.g., the step-based method (Sect. 5.2 in this chapter). To execute the parameter studies the use of a computational model is helpful. Kuhn and Sucker [9, 10] presented this for selected

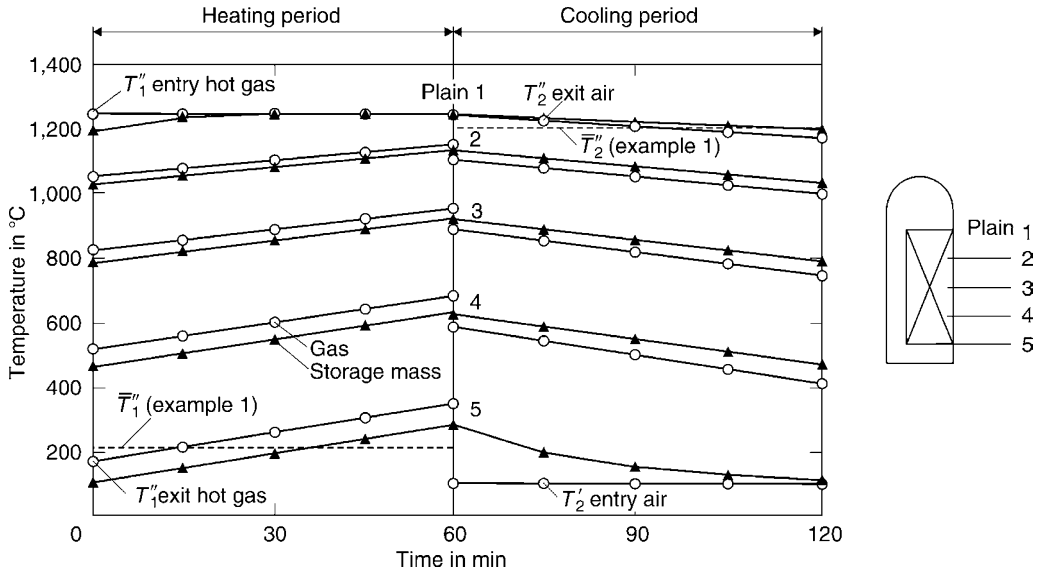

N1. Fig. 15. Calculated storage mass and gas temperature profiles.

cases. The following results are discussed in the example of Fig. 15. The used computational model involves temperature-dependent material values. Figure 15 shows the respective temperatures of hot combustion gas and air as well as the average temperature of storage mass, depending on the time of the heating and cooling periods, at five selected plains in the storage mass. The filled triangles characterize the storage mass temperature. The temperature profile is continuous in all plains, which can be recognized at the switching point. The gas temperature – open circles – has a jump at this point. In Fig. 15 the calculated average exit temperature values $\overline{T}_1''$ and $\overline{T}_2''$ are also drawn. The comparison shows the differences between the results of Examples 1 and 3 as well as the used calculation methods. For simple layout calculations the method described in Sect. 5.1 in this chapter gives quickly a sufficient result. To get more information about local and time-dependent temperature profiles in the regenerator, one must use a more detailed step-based method.

6 Symbols

A	temperature conduction (m^2/s)
A	surface (m^2)
c	specific heat capacity (J/(kg K))
d_h	hydraulic diameter (m)
f	heat transporting surface in a regenerator (m^2)
Δf	local step for step-based calculation method (m^2)
f_v	specific heat surface (m^2/m^3)
k	true heat transfer coefficient ($W/(m^2 K)$)
$\dot{M}$	mass flow (kg/s)
Q_{Per}	transferred heat amount in a whole period (J)
t	time (s)
Δt	time step for step-based calculation method (s)
T	temperature (°C)
T_g	temperature of gas (°C)
T_s	temperature of storage mass (°C)
V_s	volume of storage mass (m^3)
$\dot{W}$	heat capacity stream (W/K)
α	heat transfer coefficient ($W/(m^2 K)$)
δ	wall thickness (m)
δ_{gl}	equivalent wall thickness (m)
λ	heat conductivity (W/(m K))
ρ	density (kg/m^3)
Λ	reduced regenerator length (–)
Π	reduced regenerator time (–)
Φ	function in accordance with Fig. 11 (–)
ϕ	free flow profile (–)
1	heating period
2	cooling period
$'$	entry
$''$	exit
g	gas
s	storage mass
m	average
V	based on volume
Per	period
–	average, based on time
0	basic value

7 Bibliography

1. Hausen H (1976) Wärmeübertragung im Gegenstrom, Gleichstrom und Kreuzstrom. 2. Aufl. Springer-Verl, Berlin
2. Hausen H (1970) Berechnung der Wärmeübertragung in Regeneratoren bei zeitlich veränderlichem Mengenstrom. Int J Heat Mass Transfer 13:S. 1753–S. 1766
3. Willmott AJ (1968) Simulation of a thermal regenerator under conditions of variable mass flow. Int J Heat Mass Transfer 11:S. 1105–S. 1116
4. Razelos P, Benjamin MK (1979) Computer model of thermal regenerators with variable mass flow rates. Int J Heat Mass Transfer 21:S. 735–S. 743
5. Schmidt FW, Willmott AJ (1981) Thermal energy storage and regeneration. McGraw-Hill Book Company, New York s. bes. S. 159–S. 164
6. Adler W, Bender W, Sucker D, Wahlbrink J, Liere-Netheler W (2005) Neues Beheizungssystem mit Rohrregenerator und Flachflammenbrenner. VDI-Berichte 1888 p. 513/518. 22. Deutscher Flammentag
7. Marion M et al. (2008) Steigerung der Energieeffizienz bei Schmiedeöfen. Stahl und Eisen 128(7):29–34

8. Heiligenstaedt W (1966) Wärmetechnische Rechnungen für Industrieöfen. 4. Aufl. Verl. Stahleisen, Düsseldorf
9. Kuhn P, Sucker D (1984) Anwendung eines neuen mathematischen Modells zur Ermittlung der energetisch günstigsten Betriebsweise von Winderhitzern. Stahl u Eisen 104(11):S. 545–S. 550
10. Kuhn P, Sucker D (1986) Improvement of process control in hot-blast stoves. Proc. Eur. Ironmaking Congr., vol. 3. Aachen. p IV/6
11. Hausen H (1931) Näherungsverfahen zur Berechnung des Wärmeaustausches in Regeneratoren. Z Angew Math Mech 11(2):S. 105–S. 114
12. Willmott AJ (1964) Digital computer simulation of a thermal regenerator. Int J Heat Mass Transfer 7:S. 1291–S. 1303
13. Hausen H (1980) Genauigkeit von Differenzverfahren zur Berechnung des Temperaturverlaufs in Regeneratoren. Wärme- und Stoffübertragung 14(1): S. 1–S. 6
14. Anzelius A (1926) Über Erwärmung vermittels durchströmender Medien. Z Angew Math Mech 6(4):S. 291–S. 294
15. Nußelt W (1927) Die Theorie des Winderhitzers. VDI-Z 71:S. 85–S. 91
16. Nußelt W (1928) Der Beharrungszustand im Winderhitzer. VDI-Z 72:S. 1052–S. 1054
17. Schneidler W (1928) Mathematische Theorie der Wärmespeicher. Z Angew Math Mech 8(5):S. 385–S. 393
18. Ackermann G (1931) Die Theorie der Wärmeaustauscher mit Wärmespeicherung. Z Angew Math Mech 11(3):S. 192–S. 205
19. Schack A (1943/44) Die Berechnung der Regeneratoren. Arch Eisen-Hüttenwesen 17(5/6):S. 101–S. 118
20. Schack A (1983) Der industrielle Wärmeübergang. 8. Aufl. Verl. Stahleisen, Düsseldorf; s. bes. S. 188–S. 198
21. Nahavandi AN, Weinstein AS (1961) A solution to the periodic flow regenerative heat exchanger problem. Appl Sci Res A, 10:S.335–S. 348
22. Sandner H (1971) Beitrag zur linearen Theorie des Regenerators. Diss. TU München
23. Iliffe CE (1948) Thermal analysis of control-flow regenerative heat exchanger. Proc Inst Mech Eng 159:S. 363–S. 372
24. Vortmeyer D, Le Mong S (1976) Anwendung des Äquivalenzprinzipes zwischen Ein- und Zweiphasenmodellen auf die Lösung der Regeneratorgleichungen. Wärme- und Stoffübertragung 9:S. 29–S. 37
25. Vortmeyer D (1989) Packed bed thermal dispersion models and consistent sets of coefficients. Chem Eng Process 26:S. 263–S. 268
26. Willmott AJ (1969) The regenerative heat exchanger computer representation. Int J Heat Mass Transfer 12:S. 997–S. 1014
27. Schellmann E (1970) Näherungsverfahren zur Berechnung der Wärmeübertragung in Regeneratoren unter Berücksichtigung der Wärmeverluste. Chem Ing Techn 42(22):S. 1358–S. 1363

N2 Combined Heat and Mass Transfer in Rotating Regenerators

Gerd Gaiser
Reutlingen, Germany

1 Setup of Rotating Regenerator Systems

The previous section dealt with regenerators with non-moving heat storage media, where hot and cold gas alternately flow through the static regenerator. The outlet temperatures of both media vary during the operation (during the heating and cooling phases). For a continuous operation, two parallel devices are required. Each of the devices is passed through by the hot and the cold gas flux alternately.

The regenerators with moving heat storage medium, considered in this section, show a relative movement of the heat storage medium in relation to the gas fluxes. The first type of these regenerators consists of a rotating heat storage medium, while the inlet of the hot and cold gas is static (Ljungström system, see Fig. 1). The second type consists of a static heat storage medium while the gas inlet and outlet distributors rotate synchronously (Rothemühle system).

Figure 2 shows a Ljungström regenerator for a power plant application. The Rothemühle system for a comparable application is shown in Fig. 3.

With both systems the continuous rotation results in an alternating flow of the hot and cold gas through the heat storage medium. Each virtual segment of the storage medium of a rotating regenerator (shown as hatched segment in Fig. 1) undergoes a continuous heating-up on the warm gas side and a continuous cooling-down on the cold gas side during one rotation. During the warm gas phase the hot gas enters the segment with a constant temperature. The volume element undergoes a continuous heating-up. The changeover of the volume element to the cold gas side corresponds to the switching of the gas fluxes in a static regenerator. This analogy is valid under the assumption that no heat flux occurs in circumferential direction from one segment to an adjacent one. This condition will apply for most of the storage media used in these applications. So, a regenerator with one moving heat storage medium in its functionality performs like a pair of interconnected regenerators with static heat storage media.

With static regenerators the outlet temperatures vary with time but are locally constant. In contrast, rotating regenerators show locally different outlet temperatures in circumferential direction. In case of constant inlet conditions and a constant rotational speed, the local outlet temperatures are constant with time. Therefore in this case the average value of the outlet temperatures is constant with time. In order to homogenize the local temperature differences in practical applications, a mixing of the outlet gas fluxes should be aimed at, especially in the case of regenerators with large diameters. In air conditioning applications, this is often done by arranging the fan behind the regenerator.

The benefits of rotating regenerators consist in the uniform and continuous operation without interruption of the gas fluxes, as well as in the temporally constant average outlet temperatures, and in the shorter cycle times which allow a more compact installation size. These benefits have led to a broad application of rotating regenerators in the power plant technology as well as in the ventilation and air conditioning technology and for air conditioning in the process technology. An additional benefit for applications in ventilation and air conditioning technology

VDI-GVC (ed.), *VDI Heat Atlas*, DOI 10.1007/978-3-540-77877-6_62,

consists in the continuously adjustable efficiency by varying the rotational speed of the rotating regenerator.

In contrast to recuperative heat exchangers, regenerative heat exchangers show the following additional benefits: as already shown by Hausen [1], using regenerative heat exchangers the same amount of heat can be transferred at a three-times smaller temperature difference as in the case of recuperative heat exchangers. Also regenerative heat exchangers are less sensitive to fouling, especially in the case of straight flow channels as used in applications for ventilation and air conditioning technology. This is supported by a certain self-cleaning effect by the alternating flow direction. In addition, potential deposits have significantly less effects on the thermal efficiency in the case of regenerators than in the case of recuperators: the heat transfer and subsequently the thermal efficiency are affected only to a minor extent by deposits since deposits also act as heat storage medium. In contrast, in the case of recuperative heat exchangers deposits significantly reduce the overall heat transfer. Furthermore, regenerators can be more easily cleaned as the heat transferring surfaces are better accessible for cleaning.

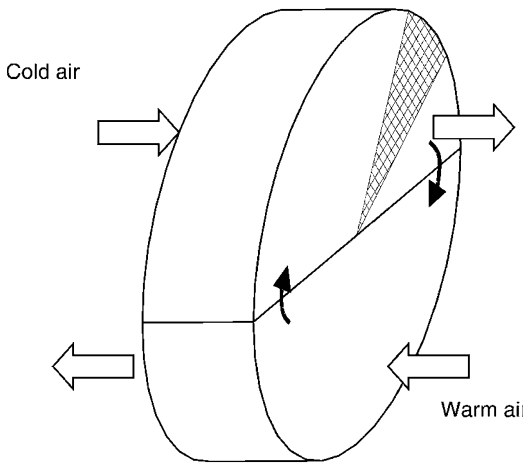

N2. Fig. 1. Scheme of a regenerator with rotating heat storage medium.

2 Rotating Regenerator Systems in Power Plant Applications

The preheating of the combustion air in the power plant technology is a common application for rotating regenerators. The warm-up of the combustion air is done using heat from the hot flue gas. On the flue gas side, the inlet temperatures are in the range of 320–350°C; the outlet temperatures are about 120°C. The preheating of the combustion air happens from an inlet temperature of 50°C to an outlet temperature of 300°C. Typical flow velocities are in the range of 12–15 m/s in the single channels of the storage medium. When calculating the design it has to be considered that the mass fluxes of air and exhaust gas are different and the proportions depend on the type of fuel. Regenerators for these applications are designed for volume fluxes up to 1.5 Mio Nm^3/h and for diameters up to 20 m. The rotating mass is up to 1,000 tons [2, 3]. For these applications, the heat storage medium is divided into several segments. The rotational speed for these applications is about 0.5–2 rotations per minute.

Besides the preheating of the combustion air, rotating regenerators in the power plant technology are also used for cooling and reheating of the exhaust gas in connection with wet desulphurization systems and with DENOx Systems. A further field of application is their use with gas turbines. The technique of sealing leakage and leakage reduction as well as the preheating of different gas fluxes in the same apparatus is reported by Allgäuer and Dietrich [2].

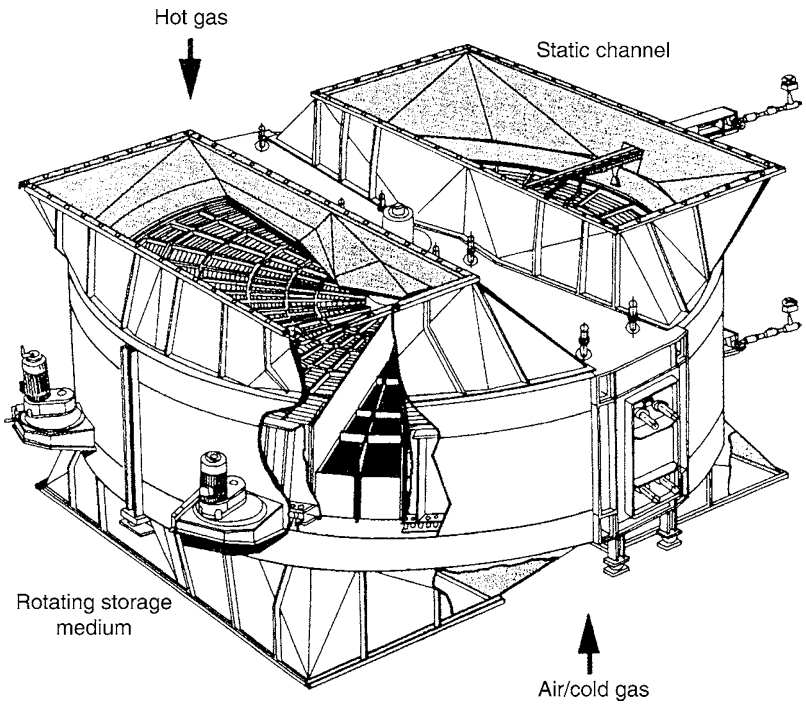

N2. Fig. 2. Regenerator with continuously rotating storage medium (Ljungström system).

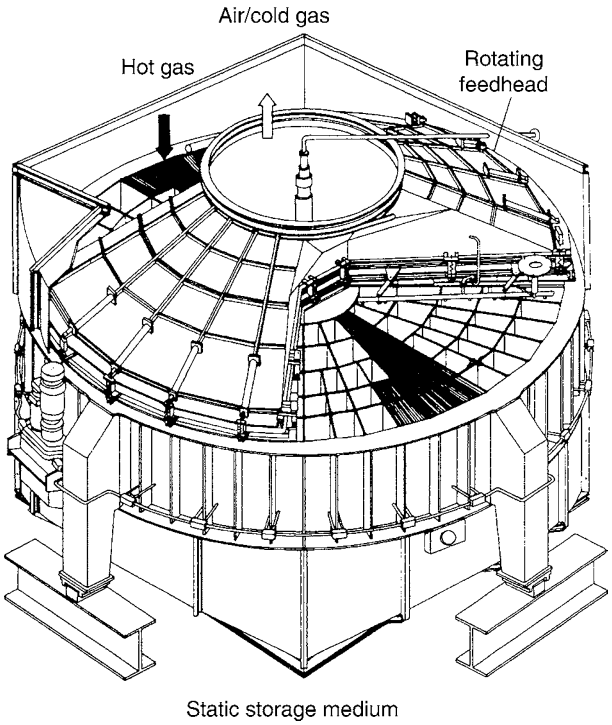

N2. Fig. 3. Regenerator with static storage medium and continuously rotating gas distribution system (Rothemühle system).

2.1 Design of the Storage Medium

For power plant applications storage media formed of rolled sheet metal plates are commonly used. Figure 4 shows some characteristic sheet designs. The sheet thickness usually is in between 0.5 and 1 mm. The average channel height for these applications in exhaust technology is in the range of 5 and 15 mm. In flow direction, different sheet designs can be arranged consecutively to achieve desired temperature profiles.

Requirements for the design of the storage medium are a low pressure drop and a low sensitivity toward fouling effects. Therefore, the heat storage plates commonly used show fluid channels oriented in main flow direction, where these channels may be formed of various cross sections. The dust in the exhaust gases may result in deposits on the heat storage plates which are periodically cleaned during operation using steam or pressurized air. To avoid a stream expansion in these cases usually "closed" profiles (as shown in Fig. 4b) are used. These closed profiles consist of alternating layers of flat plates and profiled plates. For applications with little risk of deposits "open" profiles (as shown in Fig. 4a) are used. The profile of both adjacent plates results in a lateral permeability and as a consequence of this to thinner boundary layers and to a higher heat transfer. For applications with gas turbines ceramic storage media are used. Recent designs consist of adjacent layers of each a flat and a corrugated ceramic foil in a rolled setup. This kind of setup

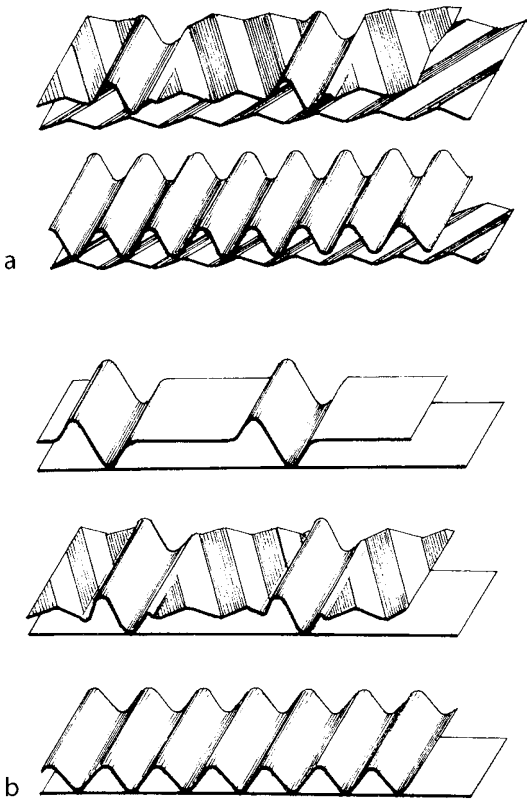

N2. Fig. 4. Metallic plate profiles for regenerators for power plant applications: (**a**) open profiles for high heat transfer and (**b**) closed profiles for good cleaning efficiency.

allows the setup of channels with extra small width, resulting in a high heat transfer and a high heat transferring surface. Thereby the required very high thermal efficiencies can be achieved.

For most of the power plant applications the major part of the storage medium consists of steel plates. In cases where a passing below the dew point at the cold end cannot be excluded, enameled plates are used in this zone to avoid the risk of corrosion. For difficult applications storage media made of plastic material, e.g., fluoride-based plastics, are used [4]. The storage plates are consecutively exposed to air and exhaust gases and thereby are exposed to a perpetual temperature cycling. Therefore, the calculation of the passing below the dew point must not be performed with the average temperature at the cold end of the regenerator, but must be performed considering the minimum storage medium temperature occurring in one cycle.

Due to the small thickness of the heat storage plates a uniform temperature distribution across the plate thickness may be assumed [4], as also has been proved by Kumpf [5] in simulation studies.

3 Rotating Regenerator Systems for Air Conditioning Applications and Process Applications

Regenerators with rotating storage medium are state of the art for heat recovery in ventilation and air conditioning technology. In the most common air ventilation application in winter, the fresh air is preheated by the exhaust air, while in summer the fresh air is precooled by the exhaust air which helps in reducing cooling power. Particularly for treatment of high air fluxes, regenerators with rotating storage medium have become state of the art for a long time. Examples for applications are ventilation and air conditioning devices for office buildings, department stores, production facilities, etc.

For the application in ventilation and air conditioning two different designs are used: the first one without systematic moisture recovery and the second one with systematic moisture recovery. With the first application sensible heat is transferred by the storage medium. Only after the exhaust air in the rotor has been cooled below the dew point, a humidity transfer occurs by condensation on the exhaust gas side (winter operation) and evaporation on the fresh gas side. The humidity transfer thereby varies depending on the temperatures and the humidity of both the fresh air and the exhaust air. A disadvantage is the formation of condensate on the heat transferring surfaces since this on the one hand promotes fouling on humid surfaces and on the other hand may result in icing of the channels during cold inlet temperatures.

In summer, the fresh air often is warmer and more humid than the exhaust air. In this case an uncoated regenerator reduces only the temperature of the incoming air while their water content remains constant. In this case, the incoming air achieves even a higher relative humidity.

For a systematic humidity transfer in ventilation and air conditioning technology regenerators are commonly designed with a water-vapor-adsorbing coating of the heat storage medium. Thereby, in the warm-cycle during the cooling of the exhaust air, an adsorption of the water vapor occurs at the sorptive surface. During the preheating of the incoming air in the cold-cycle, a desorption of the water vapor occurs and the incoming air is humidified thereby. This configuration can transfer both sensible and latent heat throughout the year. In winter besides the heat recovery an additional humidity recovery is achieved. In summer, both a precooling and a dehumidification of the incoming air is achieved. This assembly is also called sorption regenerator. By the simultaneous transfer of humidity a passing of the dew point and thereby the formation of condensate on the heat transferring surfaces can be effectively avoided. The recovery of humidity is also of economic benefit as in winter the latent heat fraction linked to the air humidity may achieve values of up to 40% of the entire enthalpy of the exhaust air.

Regenerators with rotating storage medium also find a wide field of applications in heat recovery in industrial equipment as well as in process technology. In cases where a conditioning of the incoming air is desired in addition to the heat recovery (e.g., with paint finishing systems) sorption regenerators with simultaneous humidity transfer are used. Regenerators for ventilation and air conditioning applications are designed in diameters from 0.5 up to 5 m for air fluxes between 1,500 and 150,000 m^3/h. For air conditioning in paint spray lines, air fluxes up to 10^6 m^3/h are treated in parallel regenerators.

Figure 5 shows the scheme of a regenerator for ventilation applications [6]. At the intersection of the exhaust air segment to the fresh air segment a part of the air contained in the channels of the storage medium is moved to the fresh air side by the rotation of the storage medium. Depending on the rotational speed the amount of this leaking air may be 1.3–3% [7, 8]. To avoid this leaking air a purge segment can be arranged between the exhaust air segment and the fresh air segment. By the arrangement of such a purge segment as shown in Fig. 6, the amount of leakage air can be reduced to values of less than 0.05% [7]. Details on the hygienic rating of this measure have been composed by Beckert and Dehli [7].

3.1 Design of the Storage Medium

The storage medium of regenerators for ventilation and air conditioning applications commonly shows a rolled setup by a pair of each a flat and a corrugated layer of thin material. Thereby, straight, sinusoidally shaped channels oriented parallel to the main flow direction are formed. The height of the layers are designed in between 1.5 and 4 mm, resulting in a laminar flow. In ventilation applications, the storage medium usually consists of a corrosion-resistive aluminum alloy. In process applications for the transfer of latent heat in the condensation range often plastic-coated aluminum alloy sheets are used. The thickness of the sheets used varies between 60 and 120 μm depending on the height of the corrugation. Therefore, a uniform temperature distribution across the layer thickness may be assumed in these cases. Figure 7 shows the typical setup of such a rolled storage medium for applications in ventilation and air conditioning.

For simultaneous transfer of humidity with sorption regenerators the storage medium is coated with a water-vapor-adsorbing material. While former regenerators usually had a

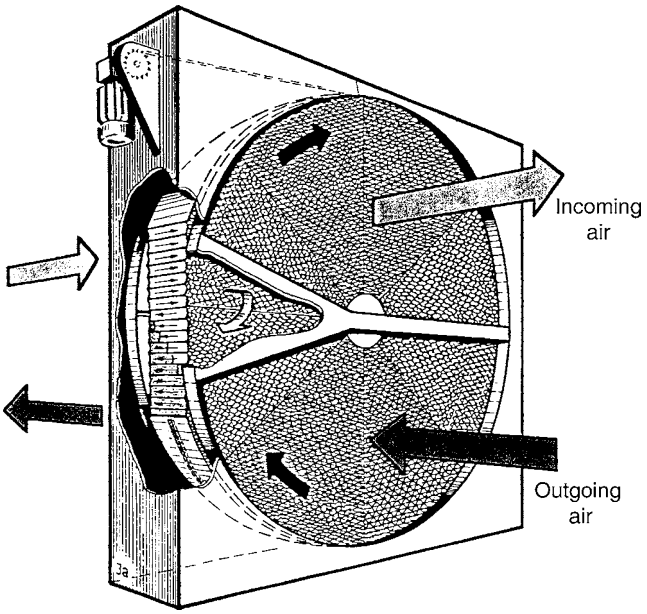

N2. Fig. 5. Regenerator with rotating storage medium for ventilation and air conditioning applications (from [6]).

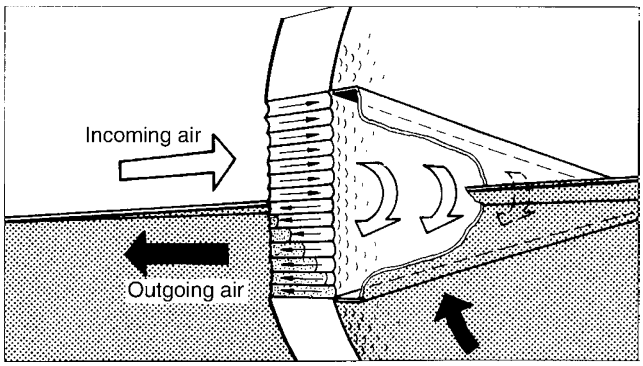

N2. Fig. 6. Purge segment to avoid exhaust air leakage from the exhaust air segment into the fresh air segment (from [6]).

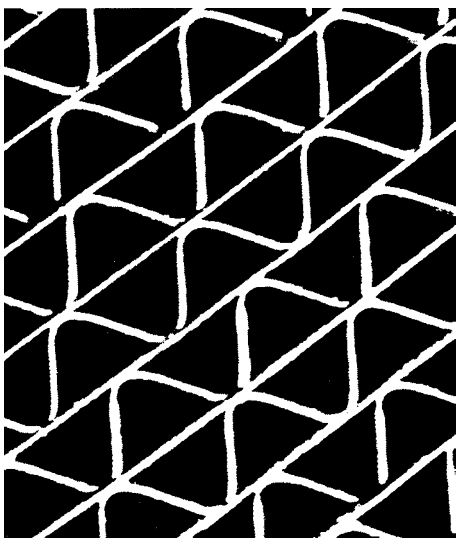

N2. Fig. 7. Storage medium for regenerators in ventilation and air conditioning applications.

coating of lithium chloride, nowadays silicagel or in case of the process technology zeolithes are increasingly used as the sorptive layer. For applications in ventilation and air conditioning only thin layers are needed with respect to the high rotational speeds.

3.2 Air Dehumidification with Sorption Regenerators

Sorption regenerators can be used for systematic dehumidification of process air (see also Chap. M8). Thereby, the major part of the coated storage medium is flown through by the process air to be dried (Fig. 8). The humidity is adsorbed at the coated surface. In a smaller segment of the rotor the adsorbed humidity is desorbed with hot air. The rotating storage medium results in a continuous dehumidification of the process gas flux. For this application low rotational speeds in between 5 and 10 revolutions per hour are used. In addition for this application, the storage medium consists of a higher specific adsorptive mass of the coating.

For coating of the storage medium different adsorbents are used. The coating with silicagel as often used is insensitive to surface humidity and therefore can be used even into the dew point range. The coating with lithium chloride allows a high loading capacity due to the different bonding mechanisms. In addition, coatings of lithium chloride show a bacteriostatic behavior [7]. Thereby, even during elongated standstill of the regenerator a reproduction of bacteria on the rotor can be excluded. Coatings with zeolithes are used when especially low air humidities are aimed at.

3.3 Cooling with Sorption Regenerators

A sorptive cooling system [9], in the literature also known as "Desiccant Evaporative Cooling" (DEC), consists of a sorption regenerator in combination with a non-sorption regenerator and two moistening devices. Figure 9 shows the scheme of such a system. The corresponding constitutional changes of the air are shown in the h,Y diagram in Fig. 10. The function is as follows: outside air (A) enters the sorption regenerator, which adsorbs a part of the humidity from the air. Due to the

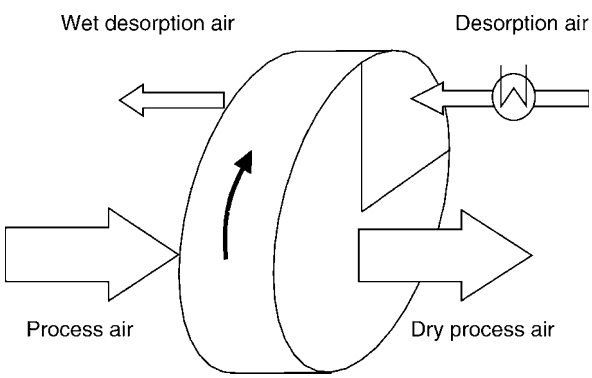

N2. Fig. 8. Air dehumidification with a sorption regenerator.

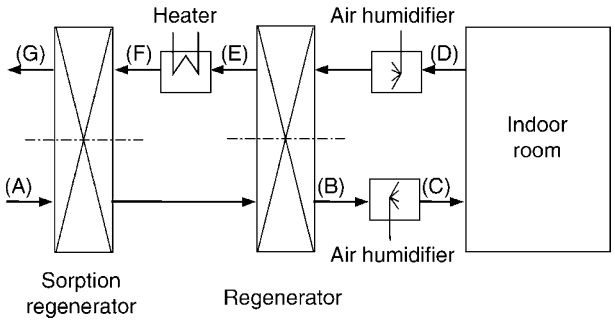

N2. Fig. 9. Scheme of an adsorptive cooling system with a sorption regenerator and a non-sorption regenerator.

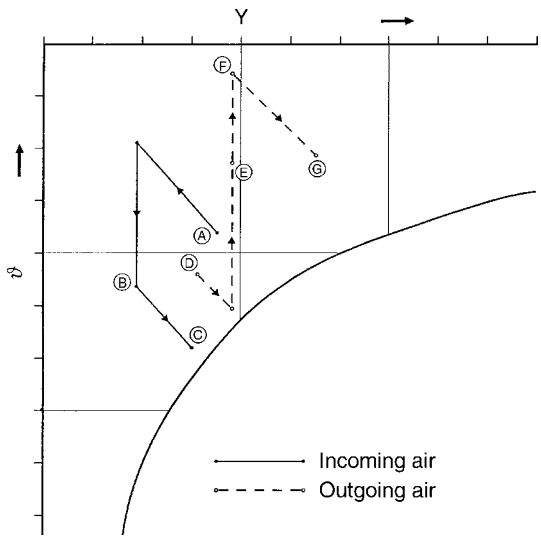

N2. Fig. 10. Constitutional changes of the incoming air and the outgoing air in an adsorptive cooling system.

sorption the temperature of the dehumidified air rises. In the subsequent non-sorption regenerator, the air is cooled down to the state (B). In the subsequent moisturizer, the air is humidified and its temperature decreases further to the state (C). The air, conditioned to that target state (C) is then released into the room. The air in the room is warmed up to state (D). The outgoing air from the room (D) flows through a moisturizer in which it is cooled down due to the humidification. The outgoing air then enters the non-sorption regenerator in which it is warmed up to the state (E). In the subsequent heater, the outgoing air is heated up to desorption temperature (F) and then enters the sorption regenerator as desorption air. After the desorption of the sorption regenerator the outgoing air leaves the system with the state (G). Alternatively, only a part of the outgoing air may be used as desorption air.

For a high cooling power of the system a high efficiency of the regenerators is required as well as a sufficient desorption of the sorption regenerator. This leads to the required desorption temperature. If waste heat with sufficient temperature, e.g., from a production process, is available it may be used for the heater. The system in the cooling operation works with 100% fresh air and therefore is especially suitable for cases where a high air change ratio is required besides the cooling. In winter, the system acts as a sorption regenerator. In this case, heat recovery and humidity recovery can be controlled separately by the independent control of the two regenerators.

4 Calculation of Heat and Mass Transfer

4.1 Calculation Methods

The calculation of the heat transfer in regenerators traces back to Nußelt [10, 11] and Hausen [12–14]. The calculation of the heat transfer and the temperature profile according to the step method I of Hausen or step method II of Willmott [15, 16] have been described in detail in the previous Chap. N1. Vortmeyer and Le Mong [17] have reduced the separate calculation of air temperature and storage medium temperature to a single-phase model by means of an equivalence model. Hausen [18, 19] has also considered the effects of temperature-dependent properties as well as time-dependent mass fluxes. Kuhn and Sucker [20] used a mathematical model for their calculation of regenerators. Bahnke and Howard [21] considered the effect of longitudinal heat conduction on the performance of regenerators. Further calculation procedures have been described in the previous section.

At the beginning the analogy between regenerators with rotating storage medium and regenerators with static storage medium has been discussed. So the calculation methods described in the previous section can also be applied for calculation of the pure heat transfer.

For applications in ventilation and air conditioning as well as in the process technology, however, a simultaneous mass transfer occurs due to the moisture in the air. As described in Sect. 3, at non-adsorbing storage media the moisture transfer happens by condensation and evaporation of the moisture. Hausen [22] has already examined the condensation and evaporation of moisture in regenerators. Kruse and Vauth [23] as well as Vauth [24] have experimentally investigated the condensation of the moisture and the problem of the icing of the regenerator at cold outside temperatures. Vauth [24] has calculated the coupled mass transfer using a finite difference method. Further, calculation models and numerical solving procedures for the combined heat and mass transfer by condensation and evaporation have been published by Holmberg [25], van Leersum and Banks [26], Klein [27], and Frauhammer et al. [28]. All authors use numerical methods for the solving of the resulting system of differential equations.

The operation behavior of regenerators with adsorbing storage media has been investigated experimentally by Spahn and Gnielinski [29]. Maclaine-Cross and Banks [30] have calculated the heat transfer and the mass transfer separately but using a single film transfer coefficient. The simultaneous heat and mass transfer in regenerators with adsorptive storage medium have been calculated by Holmberg [31], Klein [27], and Gutermuth [32] by using a finite difference method.

A simple handmade calculation procedure is described in Chap. M8 (Humidifying and Drying of Air). This procedure

however requires additional empirical data on the operation behavior of the sorption regenerator.

4.2 Balance Model for the Heat Transfer in Regenerators

The design of regenerators may be done according to the step calculation procedures mentioned above and described in Chap. M8. However, considering todays PCs and the widespread use of established mathematical software (e.g., Maple™, Mathcad™, Matlab™, Mathematica™, or similar) the calculation by numerical solution of the system of differential equations resulting from the model suggests itself. By that, additional parameters like different storage media designs in axial direction can be considered easily. In particular, this modeling can easily be extended to the calculation of the combined heat and mass transfer in sorption regenerators for the ventilation and air conditioning technology.

The following paragraph will at first consider the pure heat transfer model. Later on, the model will be extended to the simultaneous heat and mass transfer in air conditioning applications.

Thereby, the following assumptions are made: the temperature is considered to be constant in radial direction (from the center to the outer diameter). With regard to the thin metal sheets and the channels oriented straight in main flow direction the heat transport in tangential direction is neglected. In addition, heat losses to the ambience are not considered here. In view of the thin metal sheets being >0.1 mm thick, the temperature across the sheet thickness is considered to be uniform. Kumpf [5] has shown that this is valid even for the thicker plates as used for power plant applications. The heat conduction of the heat storage medium in axial direction however has to be considered.

Thereby, the equation for the energy balance of the streaming air results as follows:

$$A \cdot \rho_L \cdot \varepsilon \cdot c_{p_L} \cdot \frac{\partial \vartheta}{\partial t} = \mp \dot{m}_L \cdot c_{p_L} \cdot \frac{\partial \vartheta}{\partial z} + A \cdot \lambda_L \cdot \varepsilon \cdot \frac{\partial^2 \vartheta}{\partial z^2} + \alpha \cdot A \cdot a_v \cdot (\vartheta_{Sp} - \vartheta). \quad (1)$$

The negative sign is valid for the warm-air cycle, the positive sign is valid for the cold-air cycle.

The corresponding energy balance for the storage medium results as follows:

$$A \cdot (1-\varepsilon) \cdot \rho_{sp} \cdot c_{sp} \cdot \frac{\partial \vartheta_{sp}}{\partial t} = A \cdot (1-\varepsilon) \cdot \lambda_{sp} \cdot \frac{\partial^2 \vartheta_{sp}}{\partial z^2} + \alpha \cdot A \cdot a_v \cdot (\vartheta - \vartheta_{sp}). \quad (2)$$

Thereby z means the flow direction, ϑ is the temperature of the gas flux, and ϑ_{Sp} is the temperature of the heat storing medium in the particular cycle. The values for the flow cross section A, the heat transfer coefficient α, and the mass flux also refer to the actual cycle. They may be different for the warm-air cycle and the cold-air cycle. The temperature-dependence of the thermophysical properties is accounted for.

The resulting system of differential equations is solved according to the finite volume discretization method. A variable local step size may be considered. For calculation of the steady-state profiles, the equation systems for the cold-air cycle and those for the warm-air cycle are solved alternately. The calculation of the alternating cycles is repeated until the quasi-steady-state (cyclic-steady-state) is achieved. Thereby, the initial condition for the heat storing medium in each cycle results from the corresponding temperature of the heat storing medium at the end of the previous cycle. For the cold-air cycle, the boundary condition results from the temperature of the incoming air at the cold rotor inlet side.

$$z = 0 : \vartheta = \vartheta_2'.$$

For the heat storing medium, the boundary condition

$$z = 0 : \partial \vartheta_{Sp} / \partial z = 0$$

is used.

For the warm-air cycle, the boundary condition results from the temperature of the outgoing room air at the warm rotor inlet side:

$$z = L : \vartheta = \vartheta_1'.$$

For the heat storing medium, the boundary condition

$$z = L : \partial \vartheta_{Sp} / \partial z = 0$$

is used accordingly.

As mentioned in the beginning, the calculated chronological profiles of the temperatures in one cycle correspond to the temperature profiles across the circumferential angle ψ of the corresponding regenerator segment. Results of the calculations will be discussed in Sect. 5. Figure 11 illustrates the terms for the individual air streams. The relation between the circumferential rotor angle ψ and the time is

$$\psi = 360^\circ \cdot n \cdot t. \quad (3)$$

In regenerators with rotating heat storing medium the air streams flow in countercurrent flow direction. However, the heat storing mass moves transverse to the corresponding air stream. Therefore, the heat storing medium at any circumferential location sees the same air inlet temperature. This results in a cross-countercurrent flow as already has been descriptively shown by Martin [33].

As already shown by Hausen [1], a theoretical cycle duration of 0, in the case of the rotating regenerator corresponding to an infinite high rotational speed would correspond to the characteristics of a countercurrent heat exchanger. So, with increasing rotational speed the temperature profile averaged over one

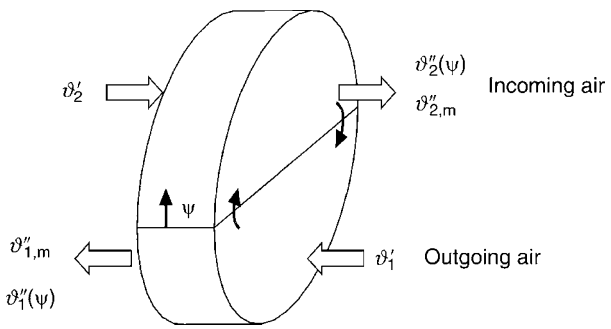

N2. Fig. 11. Denomination of the air streams in the regenerator model.

period approaches the profile of the countercurrent heat exchanger. The explanations in Sect. 5 show that this is already valid in good approximation for higher rotational speeds as used in some technical applications.

For these applications the simplified solution as a countercurrent heat exchanger may be used, which gives a significant saving in calculation time. The balance equations for this simplified consideration are described in Sect. 4.3. The terms are shown in Fig. 12. Results with this model will be described in Sect. 5.

4.3 Balance Model for the Combined Heat and Mass Transfer in Sorption Regenerators

For applications in ventilation and air conditioning the calculation of the simultaneous transfer of heat and moisture is of significant importance. With regard to the widespread use of sorption regenerators in ventilation, air conditioning, and process industry applications, the simultaneous heat and mass transfer in these apparatus will be considered. The following additional assumptions are made for the moisture transfer: the sorptive coating of the heat transferring medium is considered to be thin, so that pore diffusion effects within the sorptive coating layer can be neglected compared to the laminar mass transfer. With regard to the thin coating layers typically used this assumption is considered to be valid.

As shown by Frauhammer et al. [28] and Holmberg [31], the assumption can be made that the moisture of the air passes the phase boundary with the state of the streaming air and the sorption enthalpy only contributes to the energy balance of the heat storing medium. By that the energy balance of the streaming air results as follows:

$$A \cdot \rho_L \cdot \varepsilon \cdot c_{p_L} \cdot \frac{\partial \vartheta}{\partial t} = \mp \dot{m}_L \cdot c_{p_L} \cdot \frac{\partial \vartheta}{\partial z} + A \cdot \lambda_L \cdot \varepsilon \cdot \frac{\partial^2 \vartheta}{\partial z^2} + \alpha \cdot A \cdot a_v \cdot (\vartheta_{Sp} - \vartheta). \quad (4)$$

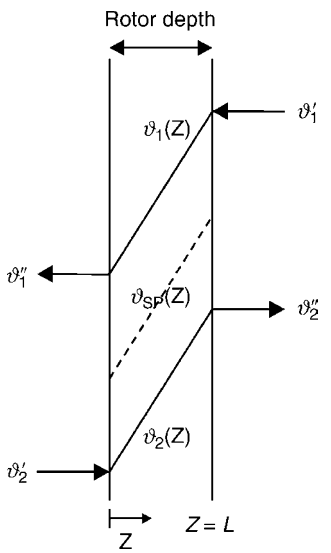

N2. Fig. 12. Approximated case of high rotational speeds. Approximation toward the solution of the countercurrent heat exchanger.

With regard to the high flow velocities in these applications the axial diffusion of the water vapor in the air has been neglected. With the discretization method of finite volumes used here this assumption has no negative effects on the convergence.

The energy balance of the storing medium results as follows:

$$A \cdot (1-\varepsilon) \cdot \rho_{sp} \cdot c_{sp} \cdot \frac{\partial \vartheta_{sp}}{\partial t} = A \cdot (1-\varepsilon) \cdot \lambda_{sp} \cdot \frac{\partial^2 \vartheta_{sp}}{\partial z^2} + \alpha \cdot A \cdot a_v \cdot (\vartheta - \vartheta_{sp}) + \beta \cdot A \cdot a_v \cdot \Delta h_{ads} \cdot \rho_L \cdot (Y - Y^*). \quad (5)$$

The mass balance of the moisture in the air in this case results in:

$$A \cdot \rho_L \cdot \varepsilon \cdot \frac{\partial Y}{\partial t} = \mp \dot{m}_L \cdot \frac{\partial Y}{\partial z} + \beta \cdot A \cdot a_v \cdot \rho_L \cdot (Y^* - Y). \quad (6)$$

The mass balance for the moisture loading of the adsorbent on the heat storing medium in this case results in:

$$A \cdot (1-\varepsilon) \cdot \rho_{sp} \cdot f_s \cdot \frac{\partial X}{\partial t} = \beta \cdot A \cdot a_v \cdot \rho_L \cdot (Y - Y^*). \quad (7)$$

The diffusion of the moisture within the adsorbent coating layer has been neglected as mentioned before.

For the moisture of the entering air fluxes, the following additional boundary conditions are valid:

$$z = 0 : Y = Y_2', \quad z = L : Y = Y_1'.$$

Analogue to the case of the pure heat transfer, the calculation of the steady state is done by calculating the systems of equations for the warm-air cycle and those for the cold-air cycle alternately. The calculation of the alternating cycles is repeated until the quasi-steady-state (cyclic-steady-state) is achieved. The initial condition for the moisture load of the sorptive layer in each cycle results from the moisture load of the sorptive layer at the end of the previous cycle. For the sorption of the moisture a sorption isotherm described by Holmberg [31] for silicagel-coated sorption regenerators is used. Likewise the sorption enthalpy is used according to Holmberg [31].

For the case of very high rotational speeds also in the case of combined heat and mass transfer an approximative modeling may be done according to the model of a (hypothetical) countercurrent heat and mass exchanger. This simplified modeling implies that the heat transferring walls show an unlimited high permeability for the moisture.

For this case the energy balance for the outgoing air is as follows:

$$A_1 \cdot \rho_L \cdot \varepsilon \cdot c_{p_L} \cdot \frac{\partial \vartheta_1}{\partial t} = -\dot{m}_{L1} \cdot c_{p_L} \cdot \frac{\partial \vartheta_1}{\partial z} + A_1 \cdot \lambda_L \cdot \varepsilon \cdot \frac{\partial^2 \vartheta_1}{\partial z^2} + \alpha_1 \cdot A_1 \cdot a_v \cdot (\vartheta_{Sp} - \vartheta_1). \quad (8)$$

In analogy the energy balance for the incoming air is given by

$$A_2 \cdot \rho_L \cdot \varepsilon \cdot c_{p_L} \cdot \frac{\partial \vartheta_2}{\partial t} = \dot{m}_{L2} \cdot c_{p_L} \cdot \frac{\partial \vartheta_2}{\partial z} + A_2 \cdot \lambda_L \cdot \varepsilon \cdot \frac{\partial^2 \vartheta_2}{\partial z^2} + \alpha_2 \cdot A_2 \cdot a_v \cdot (\vartheta_{Sp} - \vartheta_2). \quad (9)$$

According to the regenerator model for the thin metal sheets the assumption is made that the wall temperature is uniform across the thickness of the metal sheets. In the simplified

countercurrent model, the wall is in contact with both air streams. Thereby, the energy balance of the wall results in

$$\begin{aligned} A_{ges}\cdot(1-\varepsilon)\cdot\rho_{sp}\cdot c_{sp}\cdot\frac{\partial\vartheta_{sp}}{\partial t} &= A_{ges}\cdot(1-\varepsilon)\cdot\lambda_{sp}\cdot\frac{\partial^2\vartheta_{sp}}{\partial z^2} \\ &+\alpha_1\cdot A_1\cdot a_v\cdot(\vartheta_1-\vartheta_{sp}) \\ &+\alpha_2\cdot A_2\cdot a_v\cdot(\vartheta_2-\vartheta_{sp}) \\ &+\beta_1\cdot A_1\cdot a_v\cdot\Delta h_{ads}\cdot\rho_L\cdot(Y_1-Y^*) \\ &+\beta_2\cdot A_2\cdot a_v\cdot\Delta h_{ads}\cdot\rho_L\cdot(Y_2-Y^*). \end{aligned} \tag{10}$$

The moisture balance of the outgoing air is

$$A_1\cdot\rho_L\cdot\varepsilon\cdot\frac{\partial Y_1}{\partial t}=-\dot{m}_{L1}\cdot\frac{\partial Y_1}{\partial z}+\beta_1\cdot A_1\cdot a_v\cdot\rho_L\cdot(Y^*-Y_1). \tag{11}$$

The moisture balance of the incoming air correspondingly results in

$$A_2\cdot\rho_L\cdot\varepsilon\cdot\frac{\partial Y_2}{\partial t}=\dot{m}_{L2}\cdot\frac{\partial Y_2}{\partial z}+\beta_2\cdot A_2\cdot a_v\cdot\rho_L\cdot(Y^*-Y_2). \tag{12}$$

The mass balance of the adsorbent moisture load correspondingly results in

$$\begin{aligned} A_{ges}\cdot(1-\varepsilon)\cdot\rho_{sp}\cdot f_s\cdot\frac{\partial X}{\partial t} &= \beta_1\cdot A_1\cdot a_v\cdot\rho_L\cdot(Y_1-Y^*) \\ &+\beta_2\cdot A_2\cdot a_v\cdot\rho_L\cdot(Y_2-Y^*). \end{aligned} \tag{13}$$

For the inlet temperatures of incoming air and outgoing air as well as for the storage medium the same assumptions are made as in the case of the dynamic regenerator model. The outlet temperatures of the air streams correspond to the averaged outlet temperatures in the dynamic regenerator model. The terms are shown in Fig. 12. Results obtained by this model will be discussed in Sect. 5.

In ventilation and air conditioning applications the effects of the rotational speed are of major importance. Therefore, the calculation of the dynamic model with the alternating cycles is discussed in the following. The system of differential equations is discretized according to the method of finite volumes and is solved with an implicit solver using the software tool Mathcad™. (Note: The calculation files, as used here, can be provided by the author.)

5 Calculation Examples for the Transfer of Heat and Moisture in Sorption Regenerators for Ventilation and Air Conditioning Technology

The operation behavior of sorption regenerators with simultaneous heat and mass transfer will be regarded in the following using the simulation model as described above. Experimental investigations for this application have been performed by Spahn and Gnielinski [29]. Simulation studies using a finite difference method have been performed by Gutermuth [32]. Both articles have considered a storage medium setup of undulated asbestos with a sorptive coating of lithium chloride.

In the following, a regenerator consisting of a rolled setup of pairs of each a corrugated and a flat thin metal sheets as shown in Fig. 7 is considered. Values for the heat transfer in sinusoidally shaped channels have been published by Shah and London [34] as a function of the channel geometry. A ratio λ/a of the wavelength λ of the corrugated sheet in relation to its amplitude a of $\lambda/a = 3.5$ results in a Nu number of Nu = 3.3. The heat conduction of the aluminum alloy of the heat storage sheets considered here is $\lambda_{Sp} = 209$ W/m K. Void fraction ε, hydraulic diameter d_h, and specific surface area a_V of the storage medium are calculated according to the corrugation shape, corrugation height, and thickness of the layers.

The effects of the sorption of the moisture on the temperature profile in the sorptive regenerator become evident already at the heat-up of the sorption regenerator. Figure 13 shows the local and time-dependent temperatures of air and storage medium during the warm-up of the sorption regenerator in the first warm-air cycle. At the beginning the storage medium has the temperature of the cold ambient. The outgoing air has a temperature of $\vartheta_1' = 22°C$. The outgoing air enters the regenerator with a velocity of $w_1' = 3.5$ m/s. Figure 13 thereby shows the (hypothetic) case of dry air. The flow direction is from right to left. The storage medium is heated up from the indoor side. Figure 14 shows the warm-up in the case of real humid outgoing air with a relative moisture of $\varphi_1' = 40\%$ when entering the regenerator. Comparing the figures demonstrates explicitly the effects of the moisture transfer on the temperature profiles of air and storage medium. During the sorption of the moisture at the adsorbing surface of the storage medium, the sorption enthalpy is set free at the surface. This contributes additionally to the warm-up of the storage material. Thereby in the range where the moisture is adsorbed, higher temperatures of both storage medium and air occur.

In the following example the effects of different rotational speeds on the quasi-steady-state temperature profiles in the regenerator will be considered. The following conditions are considered in the simulation according to a winter operation in the ventilation technology: the outgoing air has a temperature of $\vartheta_1' = 22°C$, the incoming air has a temperature of $\vartheta_2' = -10°C$. The outgoing air enters the regenerator with a velocity of $w_1' = 3.5$ m/s. The mass flux of the outgoing air and the mass flux of the incoming air are the same. The flow cross section of the warm-air segment and the cold-air segment are the same in the case considered here so that both streams show the same mass flux density. The length of the regenerator is $L = 200$ mm. The corrugation height of the sheets is 2 mm which corresponds to an amplitude of the corrugation of $a = 1$ mm.

The outgoing air has a relative humidity of $\varphi_1' = 40\%$, the incoming air has a relative humidity of $\varphi_2' = 90\%$. Figure 15 shows the temperature profiles in the quasi-steady-state for a rotational speed of $n = 10$ revolutions per minute.

The profile of the air temperature in the cold-air cycle is shown on top in Fig. 15a. Below that the temperature profile of the storage medium in the cold-air cycle is shown (Fig. 15b). The profile of the air in the warm-air cycle is shown in Fig. 15c, while Fig. 15d shows the temperature profile in the storage medium in the warm-air cycle. At the high rotational speed of 10 rpm a relative moderate change in temperature occurs during the cycle. The temperature profiles at a low rotational speed of 3 rpm are shown in Fig. 16. All other conditions are kept the same.

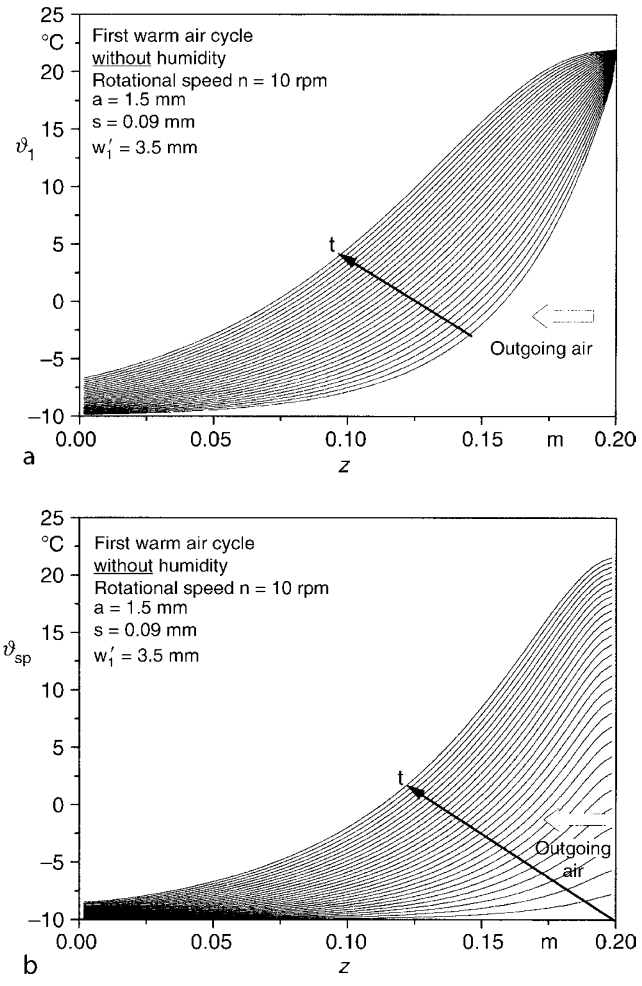

N2. Fig. 13. Temperature profiles during the warm-up of the regenerator during the first warm-air cycle in the case of dry air. (**a**) outgoing air (**b**) storage medium.

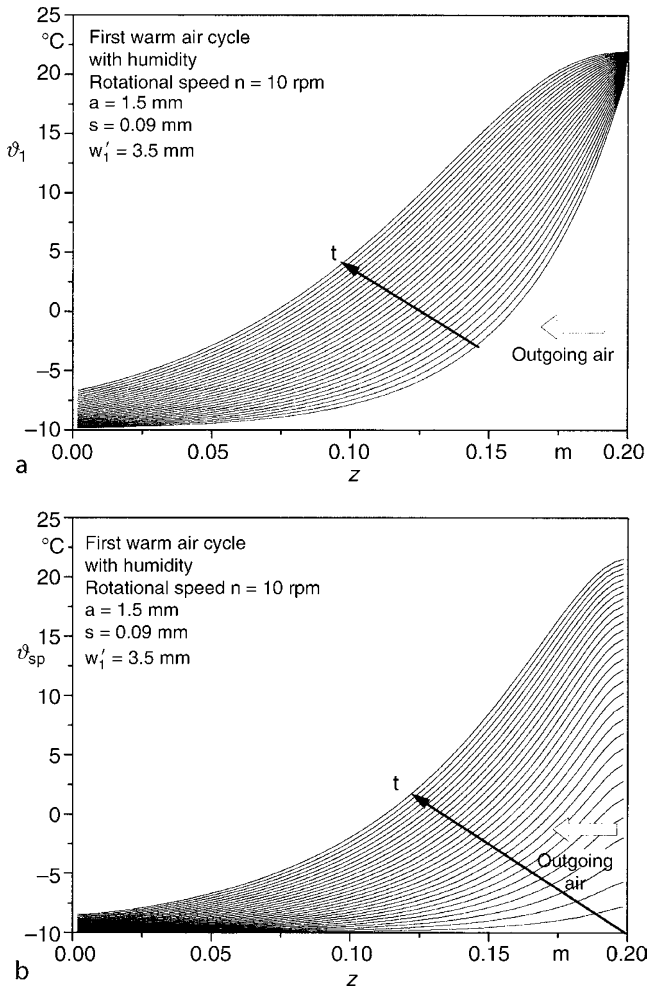

N2. Fig. 14. Temperature profiles during the warm-up of the regenerator during the first warm-air cycle in the case of humid air. (**a**) outgoing air (**b**) storage medium.

As shown in Fig. 15 in this case the outlet temperatures of the incoming air vary between $\vartheta''_{2,a} = 19°C$ at the beginning of the cycle and $\vartheta''_{2,e} = 12.5°C$ at the end of the cycle. Based on the circumferential angle of the regenerator on the one side ($\psi = 0$) an outlet temperature of $\vartheta''_{2,a} = 19°C$ results. With an increasing angle ψ, the outlet temperature decreases to $\vartheta''_{2,e} = 12.5°C$. In the application in the ventilation technology the air flux is fed into the air-guiding channel resulting in an average air temperature $\vartheta''_{2,m}$. This average air temperature results from the area-based average of the individual air temperatures over the segment. In the case considered here the averaged temperature of the incoming air results in $\vartheta''_{2,m} = 16.2°C$.

The outgoing air in the warm-air cycle behaves analogous. Here at the beginning of the cycle the outgoing air is cooled down to a temperature of $\vartheta''_{1,a} = -0.3°C$. At the end of the cycle this outlet temperature moves down to $\vartheta''_{1,e} = -7.5°C$.

At the low rotational speed of 3 rpm as shown in Fig. 16, the differences in temperature are much bigger. At the beginning of the cold-air cycle the incoming air is warmed up to a temperature of $\vartheta''_{2,a} = 20.4°C$. At the end of the cold-air cycle this temperature sinks to $\vartheta''_{2,e} = 6.8°C$. As a consequence the averaged temperature of the incoming air is $\vartheta''_{2,m} = 12.4°C$. This is significantly lower than in the case of the higher rotational speed.

The corresponding moisture profiles of the incoming air and the outgoing air as shown in Figs. 17 and 18 also show considerably bigger differences at the low rotational speed. At the higher rotational speed of 10 rpm a higher recovered humidity of $Y''_{2,m} = 5.96$ g/kg is achieved, compared to a recovered humidity of $Y''_{2,m} = 4.68$ g/kg in the case of the low rotational speed of 3 rpm. The results illustrate how the efficiency of the sorption regenerator depends on the variation of the rotational speed.

Figure 19 shows the thermal efficiency η_{Th}

$$\eta_{\vartheta,1} = \frac{\vartheta'_1 - \vartheta''_1}{\vartheta'_1 - \vartheta'_2} \tag{14}$$

as a function of the regenerators rotational speed. In a similar way an efficiency for the humidity recovery can be defined.

$$\eta_{Y,1} = \frac{Y'_1 - Y''_1}{Y'_1 - Y'_2} \tag{15}$$

Figure 19 shows that the thermal efficiency increases with increasing rotational speed. For high rotational speeds it approaches the limiting value of the hypothetical counter current heat and moisture exchanger, which is shown as a dashed line in Fig. 19. Higher efficiencies can be achieved in the case of higher

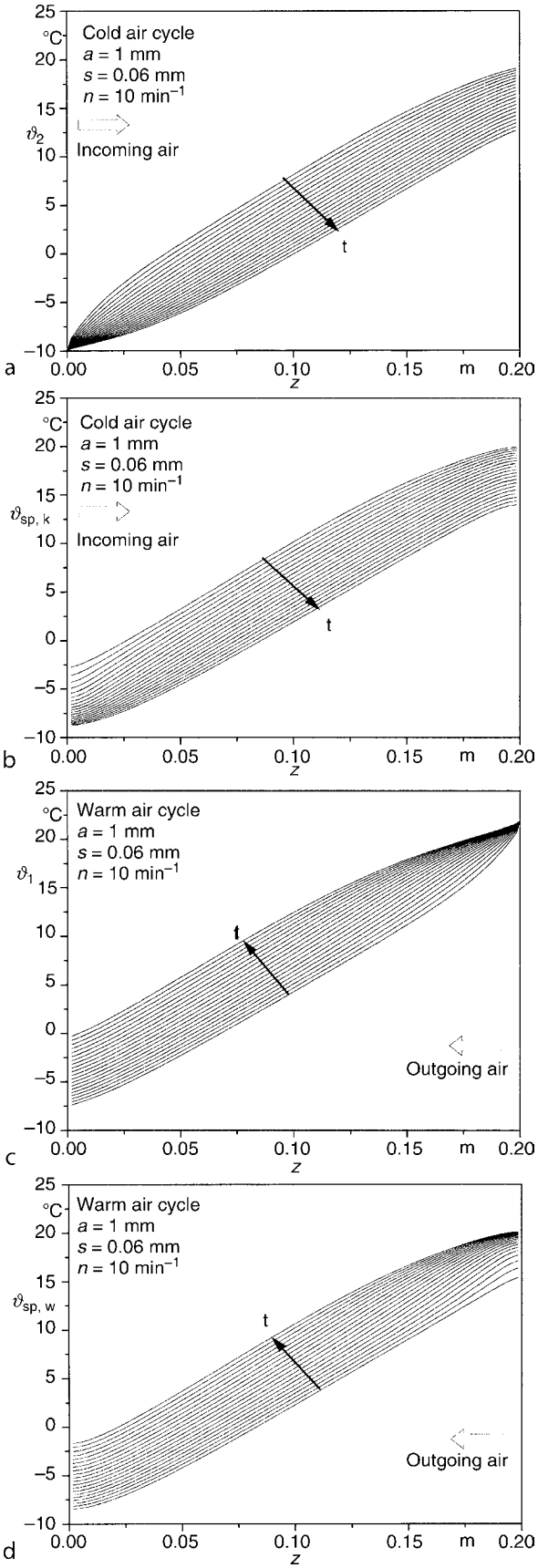

N2. Fig. 15. Temperature profiles in the quasi-steady-state for a rotational speed of n = 10 rpm. (**a**) incoming air (**b**) storage medium in cold air cycle (**c**) outgoing air (**d**) storage medium in warm air cycle.

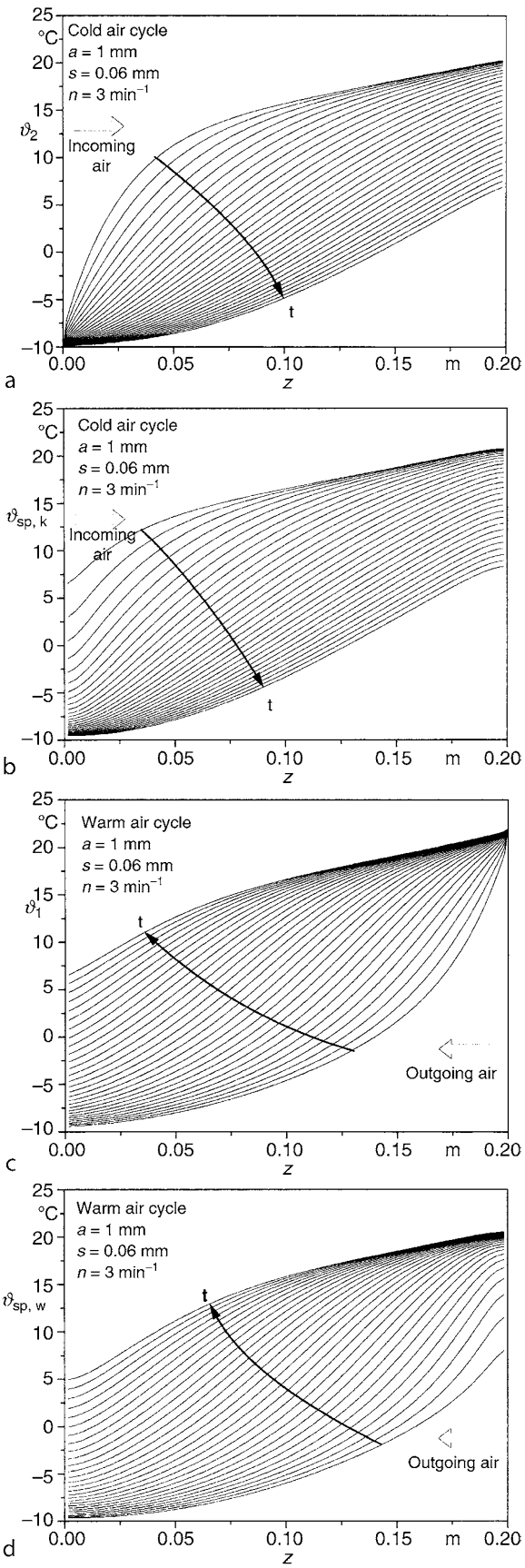

N2. Fig. 16. Temperature profiles in the quasi-steady-state for a rotational speed of n = 3 rpm. (**a**) incoming air (**b**) storage medium in cold air cycle (**c**) outgoing air (**d**) storage medium in warm air cycle.

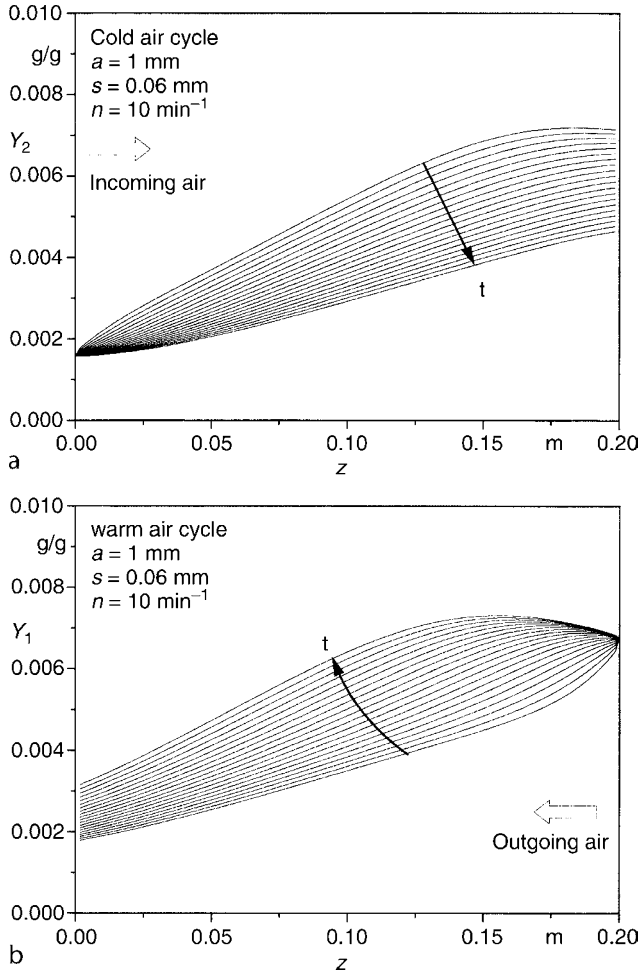

N2. Fig. 17. Moisture profiles in the quasi-steady-state at a rotational speed of n = 10 rpm. (**a**) incoming air (**b**) outgoing air.

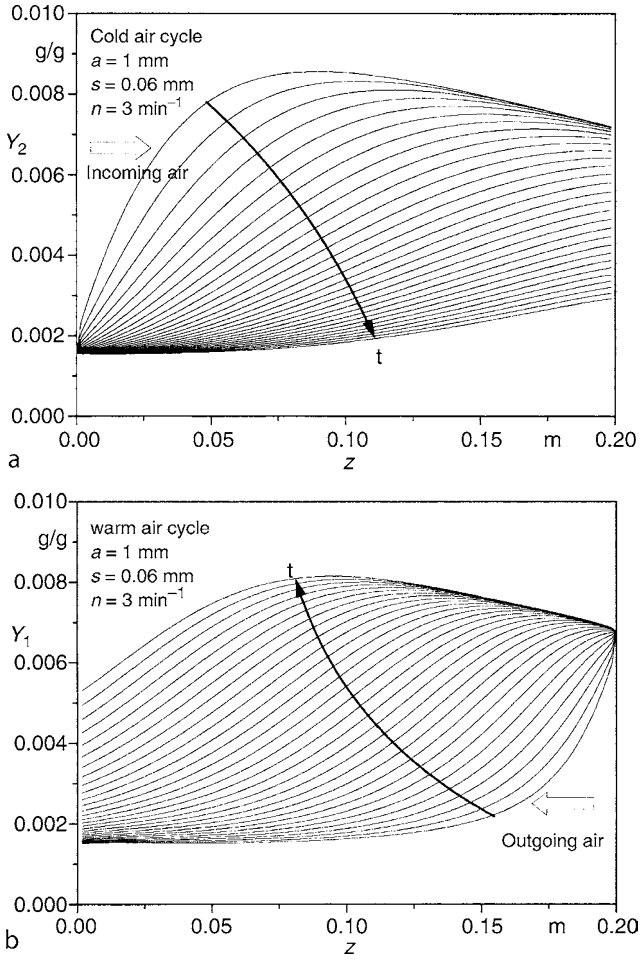

N2. Fig. 18. Moisture profiles in the quasi-steady-state at a rotational speed of n = 3 rpm. (**a**) incoming air (**b**) outgoing air.

rotational speeds. In the case of high rotational speeds of 10 rpm, as commonly used in air conditioning applications, the efficiency closely approaches the efficiency of the hypothetical counter current heat and moisture exchanger. Therefore, such applications may also be calculated approximately using the simplified model described by Eqs. (7)–(12).

The effect of the rotational speed on the efficiency for humidity recovery of the regenerator is shown in Fig. 20. This efficiency also increases with increasing rotational speed. Comparing Figs. 19 and 20 shows that at low rotational speeds the efficiency of moisture recovery is lower than the thermal efficiency. The operation characteristics at low rotational speeds below 0.5 rpm will be discussed in Sect. 6 where the sorption regenerator is used for air-dehumidification.

In the case of high rotational speeds the efficiency can be increased by the use of corrugated sheets with a small corrugation height resulting in a higher heat transfer. Figure 21 shows a comparison between sheets with amplitudes of 1 and 1.5 mm. Low rotational speeds result in similar efficiencies. This is due to the high cycle duration where the temperatures of air and storage medium approach each other. In this case a higher heat transfer does not benefit the efficiency. In the case of higher rotational speeds, however, a clear benefit of the higher heat

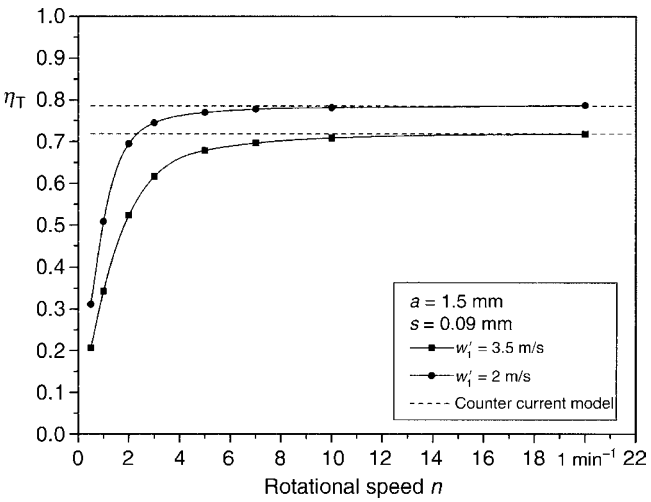

N2. Fig. 19. Effects of the rotational speed on the thermal efficiency of the regenerator.

transfer in the case of the smaller channel height is clearly visible from Fig. 21.

For technical applications, it has to be considered that the outlet temperature of the air significantly varies across the

circumferential rotor angle ψ, especially in the case of low rotational speeds. Figure 22 shows the outlet temperatures of the incoming air at the warm side of the regenerator as a function of the circumferential rotor angle ψ for different rotational speeds.

6 Calculation Examples for the Heat and Mass Transfer in Sorption Regenerators for Air Dehumidification

The balance model shown in Sect. 4 can be used in the same way for calculation of sorption regenerators for air dehumidification. As an example, process air having a temperature of $\vartheta_2' = 22°C$ and a relative humidity of $\varphi_2' = 70\%$ shall be dehumidified in a sorption regenerator. The storage medium of the regenerator is considered to consist of corrugated metal sheets having a layer height of 3 mm corresponding to an amplitude of $a = 1.5$ mm and a sheet thickness of 0.09 mm. The sorptive coating consists of silicagel. Sorption enthalpy and sorption isotherm are used according to Holmberg [31]. The segment for the process air comprises 75% of the rotor cross section; the segment for the desorption air comprises 25% of the rotor cross section. The flow velocity of the process air is $w_2' = 1$ m/s. The desorption is done with ambient air, which is preheated to a temperature of $\vartheta_1' = 115°C$ before entering the desorption segment. The amount of desorption air is designed to have the same mass flux density g_z as the process air. The rotational speed of the rotor is $n = 7.5$ revolutions per hour.

Figure 23 shows the temperature profiles for the dehumidification cycle in the quasi-steady-state. The storage medium has been warmed up in the previous desorption cycle and is now being cooled by the process air during the dehumidification cycle. Accordingly at the beginning of the cycle the process air is being warmed up by the storage medium being still warm from the previous desorption cycle. Due to the higher temperatures of storage medium and process air and the unfavorable sorption equilibrium resulting therefrom, a minor dehumidification of the process air occurs at the beginning of the cycle. During the cycle the water content $Y_2''(t)$ of the process air decreases at first. In the further part of the cycle the water content $Y_2''(t)$ of the process air increases continuously due to the increasing moisture load of the storage medium. This results in the moisture profile of the outgoing process air as shown in Fig. 24 as a function of the circumferential rotor angle ψ. In the case of higher rotational speeds the moisture of the outgoing process air increases at the beginning of the cycle (corresponding to a small circumferential rotor angle ψ). At higher rotational speeds the moisture of the outgoing process air increases toward the end of the cycle (Fig. 24). The high moistures of the process air at the beginning of the cycle could be avoided if the storage medium would be cooled in a separate purge segment after the desorption segment.

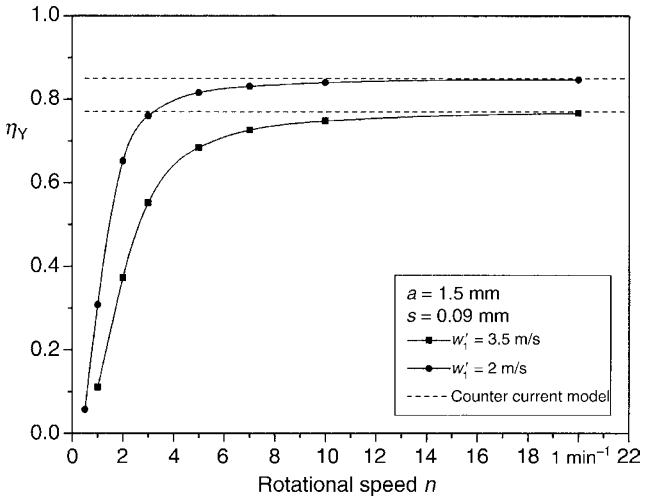

N2. Fig. 20. Effects of the rotational speed on the efficiency for humidity recovery of the regenerator.

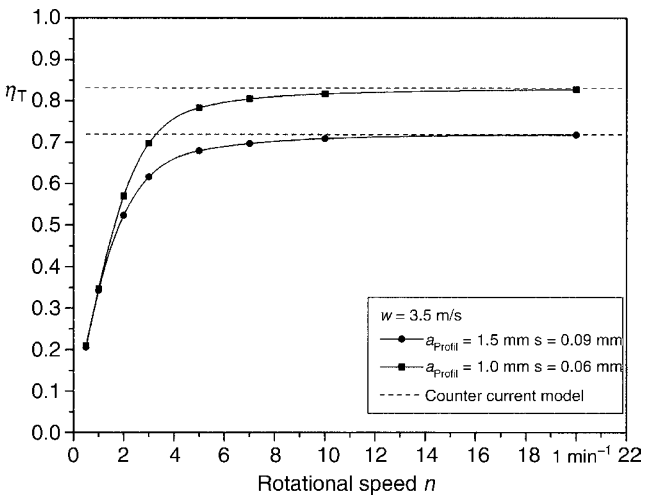

N2. Fig. 21. Thermal efficiency of the regenerator at different channel sizes of the storage medium.

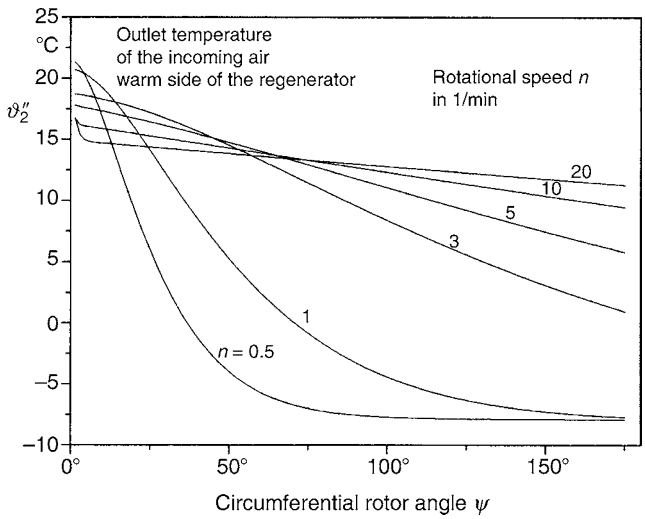

N2. Fig. 22. Outlet temperatures of the incoming air at the warm side of the regenerator as a function of the circumferential rotor angle ψ.

The sorption enthalpy released during the dehumidification warms up the storage medium. As a consequence this results in a warming of the process air in flow direction. During the desorption cycle the moisture desorbs from the storage medium and is carried away by the desorption air. The storage medium is warmed up by the hot desorption air. Figure 25 shows the profile of the moisture load of the storage medium during the desorption cycle. At first the moisture desorbs at the side where the desorption air enters the regenerator. Then the desorption air in flow direction passes the colder parts of the storage medium and cools down there. Therefore, a part of the moisture having been desorbed upstream is then adsorbed again downstream (smaller z-coordinate in Fig. 25). By that the moisture load increases there initially (as can be seen by the intersecting lines in Figs. 25 and 27). In the further desorption process the temperature profiles move in flow direction and the downstream zones also warm up. The desorption proceeds.

At the conditions (concerning segment partitioning, flow velocity, and rotational speed) considered in Fig. 25 the desorption takes place only to a certain extent of the rotor depth z. Figure 26 shows the moisture load of the sorptive layer in the case of a lower rotational speed of $n = 5$ rph with the rest of the conditions being the same. The profiles show that by a longer period a complete desorption occurs across the entire rotor depth. However, during the longer period the storage medium is heated up by the hot desorption air to high temperatures almost across the entire rotor depth. These high temperatures of the storage medium result in a worse sorption equilibrium in the beginning of the following dehumidification cycle and thereby to a minor dehumidification of the process air.

The profiles of the moisture load during the desorption cycle in the case of a higher rotational speed of $n = 10$ rph is shown in Fig. 27. At this short duration of the desorption cycle,

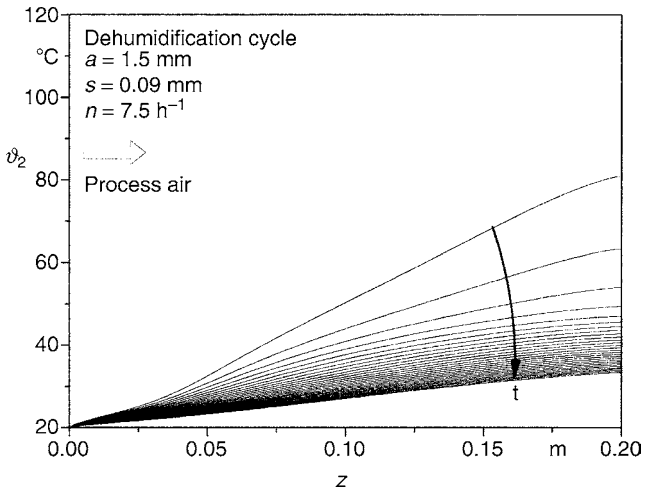

N2. Fig. 23. Temperature profiles during the dehumidification cycle (rotational speed n = 7.5 revolutions per hour).

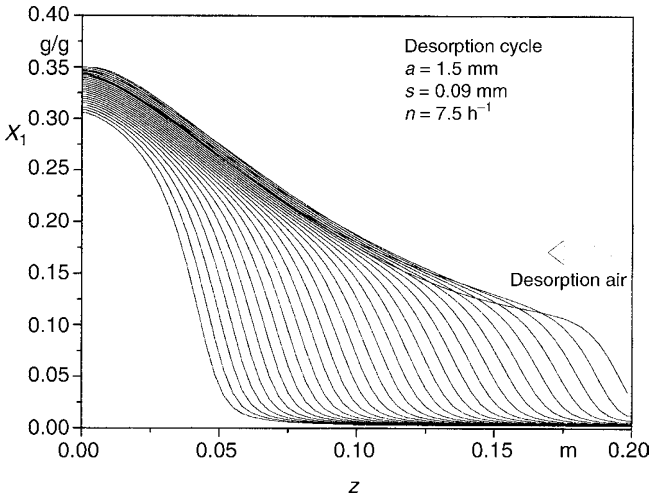

N2. Fig. 25. Moisture load of the sorptive layer during the desorption cycle at a rotational speed of n = 7.5 revolutions per hour.

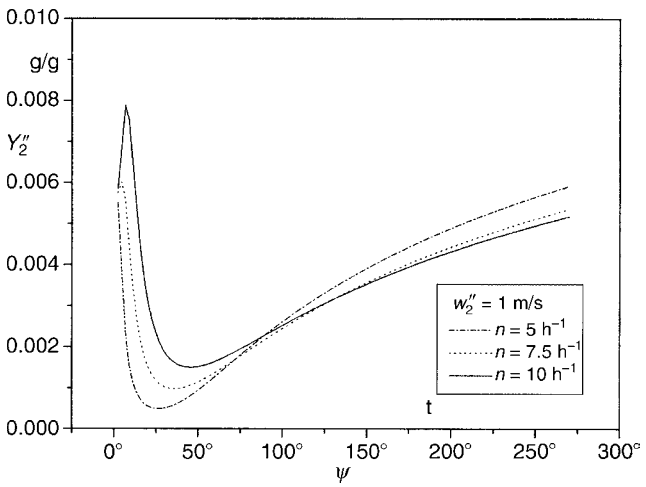

N2. Fig. 24. Water content of the process air at the outlet of the regenerator as a function of the circumferential rotor angle ψ.

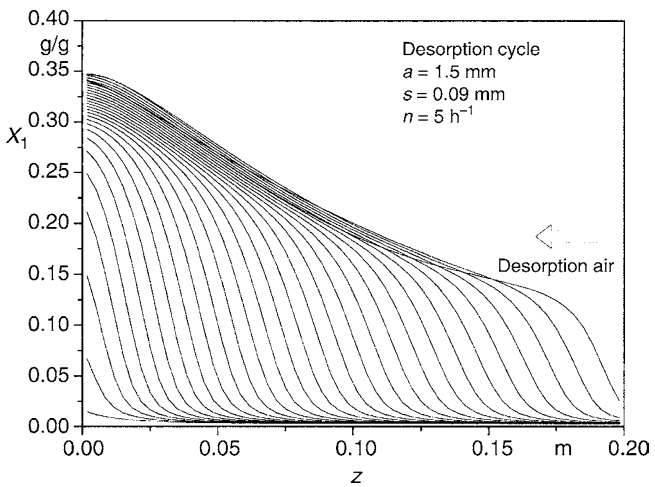

N2. Fig. 26. Moisture load of the sorptive layer during the desorption cycle at a rotational speed of n = 5 revolutions per hour.

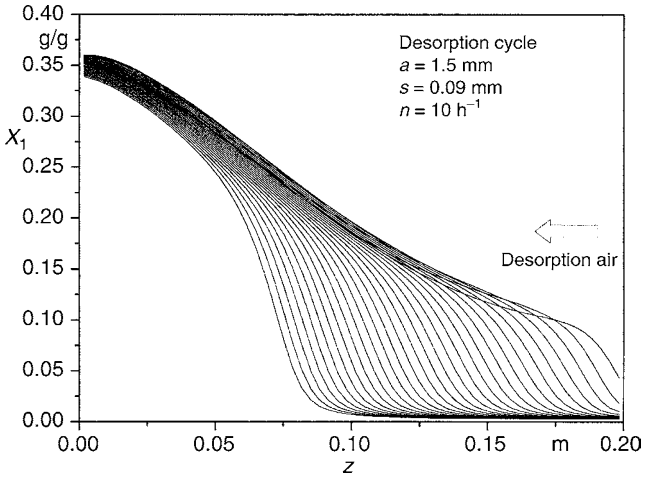

N2. Fig. 27. Moisture load of the sorptive layer during the desorption cycle at a rotational speed of $n = 10$ revolutions per hour.

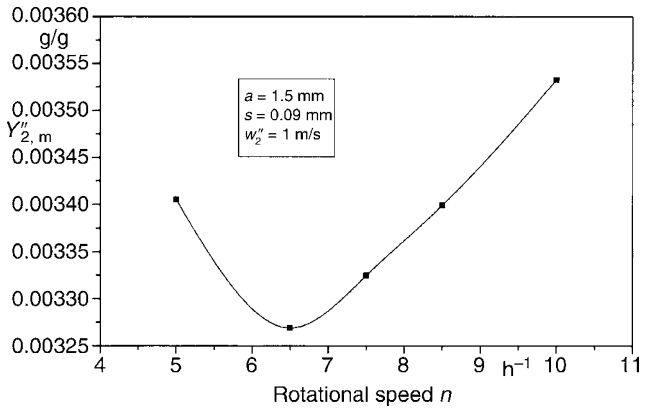

N2. Fig. 28. Effects of the rotational speed on the residual moisture of the dehumidified process air.

however, only half of the storage medium (in depth) is desorbed completely. The remaining high moisture loads at small z-coordinates on the one hand side and the high temperatures after the desorption at high z-coordinates on the other hand side result in a lower desorption of the process air during the following dehumidification cycle.

Due to the effects described there is an optimum of the rotational speed with regard to the residual moisture load of the dehumidified process air as shown in Fig. 28. At the flow velocity considered in this example the optimum for the rotational speed is 6.5 rph. In the case of higher flow velocities this optimum moves toward higher rotational speeds. Analogue results obtained with a regenerator coated with lithium chloride have been reported by Gutermuth [32]. Gutermuth also has investigated different partition ratios of the dehumidification segment and the desorption segment.

The results prove that the operating characteristics in the technical application of sorption regenerators can only be calculated by simultaneously considering heat and mass transfer. The calculation files as used here can be provided by the author.

7 Symbols

A	flow cross section (m^2)
A_1	flow cross section outgoing air (m^2)
A_2	flow cross section incoming air (m^2)
a	amplitude of the corrugation of the storage medium (mm)
a_V	volumetric specific surface of the storage medium (m^2/m^3)
c_{Sp}	specific heat capacity of the storage medium (J/kg K)
c_{P_L}	specific heat capacity of air (J/kg K)
d_h	hydraulic diameter (m)
f_S	mass fraction of the adsorbent (silicagel) in relation to the entire storage medium (g/g)
g_z	mass flux density in flow direction (kg/m^2 s)
Δh_{ads}	adsorption enthalpy (kJ/kg)
L	length of the regenerator (also called depth of the rotor) (m)
m_L	mass flux of the dry air (kg/s)
n	rotational speed of thr sorption regenerator (application "heat recovery") (1/min)
n	rotational speed of thr sorption regenerator (application "air dehumidification") (1/h)
s	sheet thickness (mm)
t	time (s)
w	flow velocity (m/s)
w'_1	flow velocity of the outgoing air at the inlet of the regenerator (m/s)
w'_2	flow velocity of the incoming air at the inlet of the regenerator (m/s)
Y	moisture load of the air (g/g)
Y_1, Y_2	moisture load of the air fluxes 1 and 2 (g/g)
Y'_1, Y'_2	moisture load of the air fluxes 1 and 2 at the inlet (g/g)
Y''_1, Y''_2	moisture load of the air fluxes 1 and 2 at the outlet (g/g)
$Y_{1,m}$, $Y_{2,m}$	average moisture load of the air fluxes 1 and 2 (g/g)
Y^*	equilibrium moisture load of the air at the adsorbing surface (g/g)
X	moisture load of the adsorbent layer on the storage medium (g/g)
z	coordinate in flow direction (m)
α	heat transfer coefficient (W/m^2 K)
α_1	heat transfer coefficient outgoing air (W/m^2 K)
α_1	heat transfer coefficient incoming air (W/m^2 K)
β	mass transfer coefficient (m/s)
β_1	mass transfer coefficient outgoing air (m/s)
β_2	mass transfer coefficient incoming air (m/s)
ϑ	temperature (°C)
ϑ_1	temperature air flux 1 (outgoing air) (°C)
ϑ_2	temperature air flux 2 (incoming air) (°C)
ϑ_{Sp}	temperature of the storage medium (°C)
$\vartheta_{Sp,W}$	temperature of the storage medium in the warm air cycle (°C)
$\vartheta_{Sp,K}$	temperature of the storage medium in the cold air cycle (°C)

$\vartheta_{Sp,m}$	chronological average of the temperature of the storage medium (°C)
$\vartheta_{1,m}$, $\vartheta_{2,m}$	chronological average of the air temperatures 1 and 2 (°C)
$\vartheta_{1,a}$, $\vartheta_{2,a}$	air temperatures 1 and 2 at the beginning of the particular cycle (°C)
$\vartheta_{1,e}$, $\vartheta_{2,e}$	air temperatures 1 and 2 at the end of the particular cycle (°C)
ϑ_1', ϑ_2'	air temperatures 1 and 2 at the inlet (°C)
ϑ_1'', ϑ_2''	air temperatures 1 and 2 at the outlet (°C)
ε	void fraction of the storage medium
λ_{Sp}	heat conductivity of the storage medium (W/m K)
λ_L	heat conductivity of air (W/m K)
λ	wavelength of the corrugation of the storage medium (mm)
ρ_{Sp}	density of the material of the storage medium (kg/m^3)
ρ_L	density of air (kg/m^3)
φ	relative humidity of air
ψ	circumferential rotor angle coordinate (°)

8 Bibliography

1. Hausen H (1976) Wärmeübertragung im Gegenstrom, Gleichstrom und Kreuzstrom. 2. Aufl. Springer-Verlag, Berlin
2. Allgäuer G, Dietrich K (2000) Regenerative Wärmetauscher zur Luftvorwärmung und zur Wiederaufheizung von Abgasen: Luvo, REA- und DENOX-Gavo. In: Podhorky M, Krips H (eds) Vulkan-Verlag, Wärmetauscher, pp 436–451
3. Company Brochure ABB Abgastechnik
4. Company Brochure Kraftanlagen Heidelberg, now ABB-Abgastechnik
5. Kumpf T (1992) Untersuchung von Wärme-/ Stoffübergang, Druckverlust und Strömungsvorgänge in Regeneratorstrukturen, Diplomarbeit. Institut für Chemische Verfahrenstechnik, Universität Stuttgart
6. Company Brochure GEA-Rototherm
7. Beckert J, Dehli F (1973) Hygienische Beurteilung regenerativer Wärmeaustauscher. HLH 24(2):55–58
8. Dehli F (1970) Übertragungsrate zwischen Fortluft und Außenluft bei Regenerativ-Wärmeaustauschern zur Wärmerückgewinnung. HLH 21(7):235–238
9. Desicool-Adsorptionskühlung, Company Brochure Fa. Munters
10. Nußelt W (1927) Die Theorie des Winderhitzers. VDI-Z 71:85–91
11. Nußelt W (1928) Der Beharrungszustand des Winderhitzers. VDI-Z 72:1052–1054
12. Hausen H (1929) Über die Theorie des Wärmeaustausches in Regeneratoren. Z Angew Math Mechan 9:173–200
13. Hausen H (1931) Näherungsverfahren zur Berechnung des Wärmeaustausches in Regeneratoren. Z Angew Math Mechan 11(2):105–114
14. Hausen H (1942) Vervollständigte Berechnung des Wärmeaustausches in Regeneratoren. VDI-Beiheft "Verfahrenstechnik" 2:31–43
15. Willmott AJ (1964) Digital computer simulation of a thermal regenerator. Int J Heat Mass Trans 7:1291–1303
16. Willmott AJ (1968) Simulation of a thermal regenerator under conditions of variable mass flow. Int J Heat Mass Trans 11:1105–1116
17. Vortmeyer D, Le Mong S (1976) Anwendung des Äquivalenzprinzipes zwischen Ein- und Zweiphasenmodellen auf die Lösung der Regeneratorgleichungen. Wärme und Stoffübertragung 9:29–37
18. Hausen H (1964) Berechnung der Wärmeübertragung in Regeneratoren bei temperaturabhängigen Stoffwerten und Wärmeübergangszahlen. Int J Heat Mass Trans 7:112–123
19. Hausen H (1970) Berechnung der Wärmeübertragung bei zeitlich veränderlichem Mengenstrom. Int J Heat Mass Trans 7:1753–1766
20. Kuhn P, Sucker D (1984) Anwendung eines neuen mathematischen Modells zur Ermittlung der energetisch günstigsten Betriebsweise von Winderhitzern. Stahl und Eisen 104(11):545–550
21. Bahnke GD, Howard CP (1964) The effect of longitudinal heat conduction on periodic flow heat exchanger perfomance. Trans ASME, J Engng Pwr 86:105–120
22. Hausen H (1937) Feuchtigkeitsablagerungen in Regeneratoren. Z VDI-Beiheft Verfahrenstechnik 2:62–67
23. Kruse H, Vauth R (1976) Betriebsgrenzen und Übertragungsverhalten im Winter von Regenerativ-Wärmetauschern mit metallischer Speichermasse. HLH 27(4):114–121
24. Vauth D (1979) Wärme- und Stoffaustausch in Regenerativ-Wärmeaustauschern mit nicht-absorbierenden Speichermassen. Dissertation, Universität Hannover
25. Holmberg RB (1977) Heat and mass transfer in rotary heat exchangers with nonhygroscopic rotor materials. Trans ASME 99:196–202
26. van Leersum JG, Banks PJ (1977) Equilibrium heat and mass transfer in regenerators in which condensation occurs. Int J Heat Mass Trans 20:927–934
27. Klein H (1988) Heat and mass transfer in regenerative enthalpy exchangers. MSc thesis, University of Wisconsin, Madison
28. Frauhammer J, Klein H, Eigenberger G, Nowak U (1998) Solving moving boundary problems with an adaptive moving grid method: rotary heat exchangers with condensation and evaporation. Chem Eng Sci 53 (19):3393–3411
29. Spahn H, Gnielinski V (1971) Wärme- und Stoffaustausch in einem Sorptionsregenerator. Verfahrenstechnik 5(4):143–149
30. Maclaine-Cross IL, Banks PJ (1972) Coupled heat and mass transfer in regenerators – prediction using an analogy with heat transfer. Int J Heat Mass Trans 15:1225–1242
31. Holmberg RB (1979) Heat and mass transfer in rotary heat exchangers with hygroscopic rotor materials. Trans ASME 101(5):205–210
32. Gutermuth W (1980) Untersuchung der gekoppelten Wärme- und Stoffübertragung in Sorptionsregeneratoren. Dissertation, Technische Hochschule Darmstadt
33. Martin H (1988) Thieme Verlag, Wärmeübertrager
34. Shah RK, London AL (1978) Laminar flow forced convection in ducts. Academic Press, New York.

N3 Heat Transfer and Power Consumption in Stirred Vessels

Edward S. Gaddis
Technische Universität Clausthal, Clausthal-Zellerfeld, Germany

1 Introduction

Stirred vessels are important equipments in process engineering, particularly in batch processes. They are used in

- Heating or cooling of liquids
- Mixing and temperature equalization in solutions and mixtures
- Intensifying mass transfer and carrying out chemical reactions in liquid mixtures and suspensions
- Aerating liquids and suspensions
- Dispersing and emulsifying processes
- Suspending of solids

In stirred vessels, various mechanisms take place either simultaneously or successively. Usually, the vessels are fitted from outside with jackets or welded coils of semicircular or circular cross section to heat or cool the contents of the vessels; if the heat transfer area is not sufficient, additional coils or plates may be inserted from inside (see Fig. 1). A stirred vessel is equipped from inside with an impeller, which can have – according to the requirements of the process – different shapes. Figure 2 shows some types of the impellers commonly used in the industry. Flat-blade turbines (Fig. 2a), pitched-blade impellers (Fig. 2b), and propellers (Fig. 2c) are high-speed impellers, which are generally used with low-viscosity liquids ($\eta \leq 1$ Pa s). While flat-blade turbines induce mainly a radial flow, pitched-blade impellers and propellers generate basically an axial flow. Paddles (Fig. 2d) belong to the low-speed impellers and are usually used with high viscous liquids ($\eta \leq 10$ Pa s). Other low-speed impellers such as anchor impellers (Fig. 2e, 1 Pa s $\leq \eta \leq 10^2$ Pa s) and helical impellers (Fig. 2f, 10 Pa s $\leq \eta \leq 10^3$ Pa s) operate usually with a close clearance to the inner surface of the vessel and are used basically to intensify heat transfer in high viscous liquids. Scraped-surface heat exchangers are double-tube heat exchangers that are used for heating, cooling, or freezing of highly viscous liquids and pastes; the heating or cooling medium flows through the external annular space, and the internal cylindrical space has a shaft fitted with a number of scraper blades that wipe the wall of the inner tube (see Fig. 8). High-speed impellers are fitted usually with baffles to suppress vortex formation (Fig. 3).

2 Heat Transfer

2.1 Heat Transfer in a Stirred Vessel

2.1.1 Single-Phase Systems

Newtonian Liquids

Heat Transfer from the Inner Surface of a Stirred Vessel Numerous studies [1] have revealed that heat transfer from the inner wall surface of a stirred vessel, for example, the type shown in Fig. 1, and a liquid inside the vessel can be described by dimensionless equations of the following form:

$$\mathrm{Nu} = C\mathrm{Re}^{a}\mathrm{Pr}^{b}\left(\frac{\eta}{\eta_{\mathrm{w}}}\right)^{e}, \qquad (1)$$

VDI-GVC (ed.), *VDI Heat Atlas*, DOI 10.1007/978-3-540-77877-6_63,

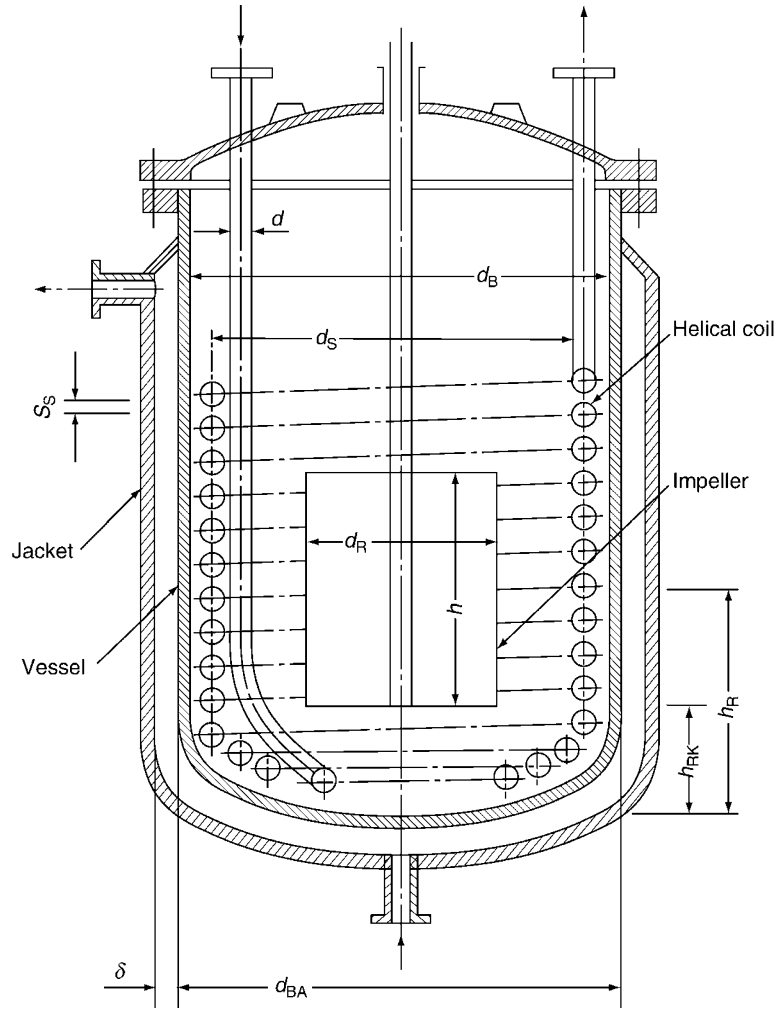

N3. Fig. 1. A stirred vessel with a jacket, a coil, and a paddle.

with

Nusselt number $\mathrm{Nu} = \frac{\alpha d_B}{\lambda}$,

Reynolds number $\mathrm{Re} = \frac{n d_R^2 \rho}{\eta}$,

Prandtl number $\mathrm{Pr} = \frac{\nu}{a}$.

In analogy with the flow through tubes, the exponents of the Reynolds number, the Prandtl number, and the viscosity ratio in Eq. (1) have in the turbulent range approximately the following numerical values:

- Exponent of the Reynolds number $a \approx \frac{2}{3}$,
- Exponent of the Prandtl number $b \approx \frac{1}{3}$,
- Exponent of the viscosity ratio $e \approx 0.14$.

The constant C in Eq. (1) takes into account all the geometrical effects. Unless otherwise stated, the physical properties (a, η, υ, λ, *and* ρ) are to be evaluated at mean liquid temperature and η_w at mean wall temperature. The empirical correlations for heat transfer prediction are derived from experimental measurements carried out with stirred vessels having, in many cases, a standard geometry. Customarily, the standard geometry is defined as follows:

- Ratio of impeller diameter to vessel diameter $\frac{d_R}{d_B} = \frac{1}{3}$
- Ratio of liquid height to vessel diameter $\frac{h_L}{d_B} = 1$
- Ratio of height of impeller above bottom to height of liquid $\frac{h_R}{h_L} = \frac{1}{3}$
- Ratio of baffle width to vessel diameter $\frac{b_S}{d_B} = \frac{1}{10}$
- Number of baffles (if present) $n_S = 4$

The standard geometrical parameters mentioned above are valid for high-speed impellers; they do not apply for close-clearance impellers (e.g., anchor impellers and helical impellers) and for other low-speed impellers.

Many authors examined the influence of the individual geometrical parameters of the stirred vessel and the impeller on heat transfer and included these effects in their correlations through dimensionless parameters in the form

$$C = C^* \pi_1^f \pi_2^p \cdots \tag{2}$$

$\pi_1, \pi_2, \ldots$ are geometrical ratios and C^* is a constant. A list of a large number of published correlations is found in the work of R. Poggemann et al. [2]. The Nusselt numbers calculated by means of the correlations presented in this chapter are mean values and are based, in many cases, on measurements carried

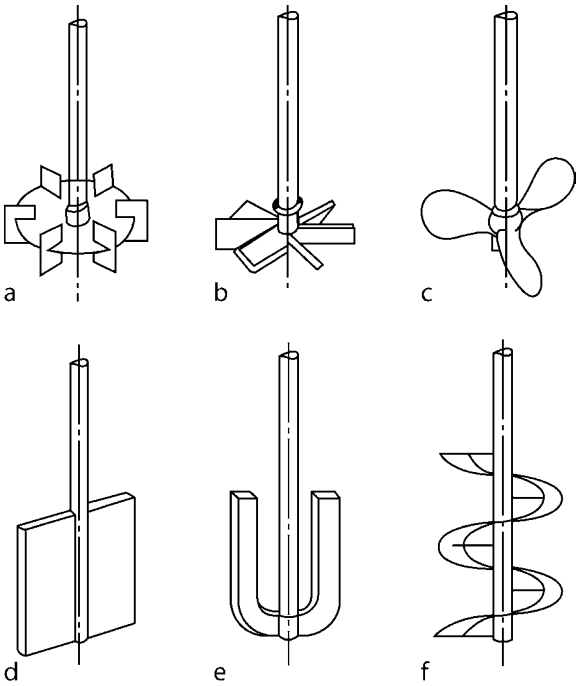

N3. Fig. 2. Some commonly used impellers: (**a**) flat-blade turbine, (**b**) pitched-blade impeller, (**c**) marine-type propeller, (**d**) paddle, (**e**) anchor impeller, (**f**) helical impeller.

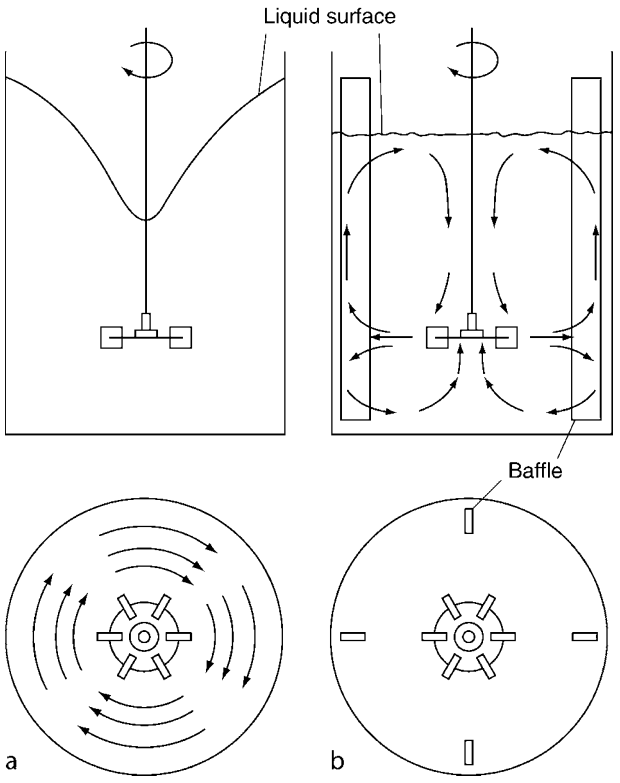

N3. Fig. 3. Stirred vessels: (**a**) unbaffled (vortex formation), (**b**) baffled (vortex formation suppressed).

out under steady state conditions. In batch operation, heat transfer is primarily transient, at least in the early operation period. However, in the turbulent range, the heat transfer in batch operation can be regarded as quasi-steady state, and the equations developed under steady state conditions may still be used. In the laminar range, to reach steady state conditions, a fairly long operation period is required. Thus, heat transfer is transient during an appreciable part of the process or during the entire process with pronounced temperature gradients. This chapter is primarily devoted to heat transfer in the transition and the turbulent ranges ($\mathrm{Re} > 10$). Investigations related to heat transfer with laminar flow in stirred vessels are presented in various works [3–5]. The validity ranges given for the empirical correlations presented in this chapter are the ranges of the Reynolds number, the Prandtl number, and the important geometrical parameters $\pi_1, \pi_2, \ldots$ examined by the investigators presenting the correlations. Strictly speaking, the correlations should only be used within the given ranges. However, it might be reasonable to assume that small deviations from the examined ranges will not lead immediately to much higher deviations between actual measurements and predictions.

Flat-blade turbine or pitched-blade impeller

According to Nagata et al. [6], the following equations give the Nusselt number for a stirred vessel fitted with a flat-blade turbine or a pitched-blade impeller (Fig. 2a and b, respectively):
For an unbaffled vessel:

$$\mathrm{Nu} = 0.54\left(\frac{d_\mathrm{R}}{d_\mathrm{B}}\right)^{-0.25}\left(\frac{h}{d_\mathrm{B}}\right)^{0.15}\left(\frac{h_\mathrm{R}}{h_\mathrm{L}}\right)^{0.15} (\sin\gamma)^{0.5} Z^{0.15}\mathrm{Re}^{2/3}\mathrm{Pr}^{1/3}\left(\frac{\eta}{\eta_\mathrm{w}}\right)^{0.14} \tag{3}$$

For a baffled vessel:

$$\mathrm{Nu} = 1.4\left(\frac{d_\mathrm{R}}{d_\mathrm{B}}\right)^{-0.3}\left(\frac{h}{d_\mathrm{B}}\right)^{0.45}\left(\frac{h_\mathrm{R}}{h_\mathrm{L}}\right)^{0.2}\left(\frac{h_\mathrm{L}}{d_\mathrm{B}}\right)^{-0.6} (\sin\gamma)^{0.5} Z^{0.2}\mathrm{Re}^{2/3}\mathrm{Pr}^{1/3}\left(\frac{\eta}{\eta_\mathrm{w}}\right)^{0.14} \tag{4}$$

Validity ranges:

$$10^2 \le \mathrm{Re} \le 4\times 10^5,$$
$$2 \le \mathrm{Pr} \le 2\times 10^3,$$
$$0.035 \le \frac{h}{d_\mathrm{B}} \le 0.2,$$
$$0.15 \le \frac{h_\mathrm{R}}{h_\mathrm{L}} \le 0.5,$$
$$2 \le Z \le 16,$$
$$45^\circ \le \gamma \le 90^\circ.$$

Additional for an unbaffled vessel

$$0.3 \le \frac{d_\mathrm{R}}{d_\mathrm{B}} \le 0.6,$$
$$\frac{h_\mathrm{L}}{d_\mathrm{B}} \approx 1.0$$

and for a baffled vessel

$$0.3 \le \frac{d_\mathrm{R}}{d_\mathrm{B}} \le 0.4,$$
$$0.67 \le \frac{h_\mathrm{L}}{d_\mathrm{B}} \le 1.0.$$

For a multistage impeller, that is, a system with more than one impeller mounted on the shaft (with $\Delta h < 1.5 d_\mathrm{R}$), h and h_R in

Eqs. (3) and (4) should be replaced by $n_R h$ and $\sum_{i=1}^{n_R} \left(h_{R,i}/n_R\right)$, respectively. Equations (3) and (4) yield for the standard geometry of the stirred vessel and the impeller (i.e., $d_R/d_B = 1/3$, $h_R/h_L = 1/3$, $h_L/d_B = 1$, $h/d_R = 1/5$ and $Z = 6$) the following equations:

For an unbaffled vessel:

$$\mathrm{Nu} = 0.53(\sin\gamma)^{0.5}\mathrm{Re}^{2/3}\mathrm{Pr}^{1/3}\left(\frac{\eta}{\eta_w}\right)^{0.14} \quad (5)$$

For a baffled vessel:

$$\mathrm{Nu} = 0.66(\sin\gamma)^{0.5}\mathrm{Re}^{2/3}\mathrm{Pr}^{1/3}\left(\frac{\eta}{\eta_w}\right)^{0.14} \quad (6)$$

The width of a blade b_R (in axial direction) of a flat-blade turbine with a standard geometry amounts to one quarter of the impeller diameter. Flat-blade turbines create high shear forces; therefore, they are very suitable for dispersing processes. In the literature, different names are given for this type of impeller (e.g., "bladed-disc turbine," "disc impeller," and "Rushton turbine"). High-speed impellers are customarily denoted as turbines.

Propeller

Strek and Masiuk [7] proposed the following correlation for a propeller (Fig. 2c) in a stirred vessel with four baffles:

$$\mathrm{Nu} = 0.505\psi_p\mathrm{Re}^{2/3}\mathrm{Pr}^{1/3}\left(\frac{\eta}{\eta_w}\right)^{0.14} \quad (7)$$

In Eq. (7), ψ_P is a function of the number Z of propeller blades and the pitch ratio (S/d_R), and can be calculated from Eq. (8) or from Fig. 4,

$$\psi_p = \exp(0.3\ln Z - 0.0144Z)\left\{\frac{0.278\exp[0.0469\exp(0.923\ln Z)]}{\frac{S}{d_R}} + 1\right\}^{-1} \quad (8)$$

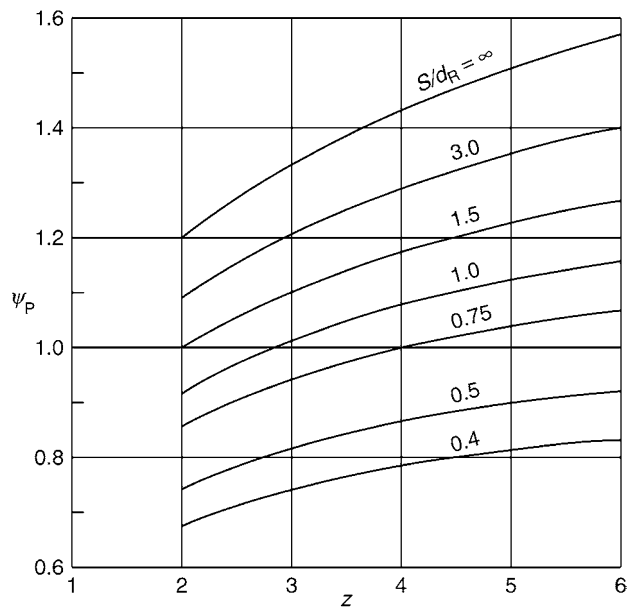

N3. Fig. 4. ψ_p as a function of the number of propeller blades with the pitch ratio S/d_R as a parameter according to Eq. (8).

Validity ranges:

$$1.7 \times 10^4 \le \mathrm{Re} \le 9 \times 10^5,$$

$$1.9 \le \mathrm{Pr} \le 2.4,$$

$$0.4 \le \frac{S}{d_R} \le \infty \text{ commonly } 0.5 \le \frac{S}{d_R} \le 1.5,$$

$$1 \le Z \le 45 \text{ commonly } 2 \le Z \le 5.$$

Equation (7) was derived with water as a working medium in a narrow range of temperature. Generally, the axial flow of a propeller is directed toward the bottom of the vessel. The power consumption for propellers is lower than that for radial impellers (e.g., flat-blade turbines) with the same impeller diameter and the same speed of rotation. Propellers generate a high circulation rate and, therefore, are suitable for temperature equalization as well as for mixing.

Pfaudler impeller

Post [8] gives for a "Pfaudler" impeller, shown in Fig. 5a and b, the following equations:

For an unbaffled vessel

$$\mathrm{Nu} = 0.354\mathrm{Re}^{0.714}\mathrm{Pr}^{0.260}. \quad (9)$$

For a baffled vessel with one baffle according to Fig. 5b

$$\mathrm{Nu} = 0.349\mathrm{Re}^{0.719}\mathrm{Pr}^{0.264}. \quad (10)$$

For a baffled vessel with two baffles according to Fig. 5b

$$\mathrm{Nu} = 0.365\mathrm{Re}^{0.720}\mathrm{Pr}^{0.262}. \quad (11)$$

For a baffled vessel with four standard baffles as described previously

$$\mathrm{Nu} = 0.339\mathrm{Re}^{0.716}\mathrm{Pr}^{0.293}. \quad (12)$$

Validity ranges:

$$4.5 \times 10^3 \le \mathrm{Re} \le 5.7 \times 10^4,$$

$$8.4 \times 10^2 \le \mathrm{Pr} \le 6.3 \times 10^3$$

$$\frac{d_R}{d_B} = 0.575,$$

$$\frac{h_L}{d_B} = 1$$

$$\frac{h}{d_B} = 0.15,$$

$$\frac{h_i}{d_B} = 0.092,$$

$$\frac{R}{d_B} = 0.4,$$

$$\beta = 15^\circ.$$

The difference in heat transfer between heating and cooling can be taken into consideration in Eqs. (9–12) by means of the correction factor $(\eta/\eta_w)^{0.14}$.

Paddle

Lichtenberg [9] gives the following equation for a baffled vessel with a paddle and four baffles (Fig. 2d):

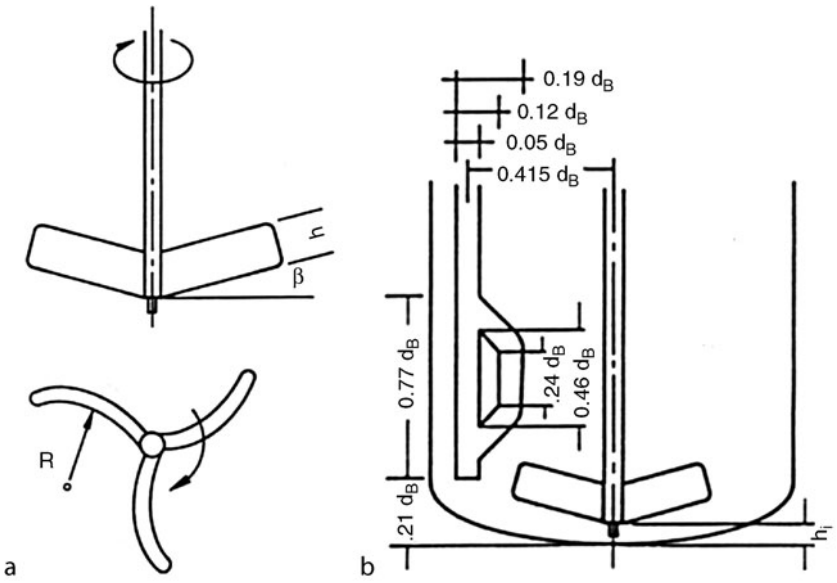

N3. Fig. 5. Pfaudler impeller with dimensions considered in [8].

$$\mathrm{Nu} = 1.31\left(\frac{d_R}{d_B}\right)^{0.39}\left(\frac{h}{d_B}\right)^{0.34}\mathrm{Re}^{2/3}\mathrm{Pr}^{1/3}\left(\frac{\eta}{\eta_w}\right)^{0.14}. \quad (13)$$

Validity ranges:

$$270 \le \mathrm{Re} \le 4.8 \times 10^5,$$
$$2.4 \le \mathrm{Pr} \le 1.1 \times 10^3,$$
$$0.25 \le \frac{d_R}{d_B} \le 0.6,$$
$$0.1 \le \frac{h}{d_B} \le 0.6,$$
$$\frac{h_L}{d_B} = 1.13,$$
$$0.22 \le \frac{h_R}{d_B} \le 0.47,$$
$$\frac{h_{RK}}{d_B} = 1/6,$$
$$\frac{b_S}{d_B} = 0.067.$$

According to Lichtenberg, the following limiting criterion must be observed for the geometrical ratios:

$$\left(\frac{d_R}{d_B}\right)^{0.39}\left(\frac{h}{d_B}\right)^{0.34} > 0.35 \rightarrow 0.4,$$

with the constant 0.35 valid for $(h/d_B) \approx 0.1$ and the constant 0.4 for $(d_R/d_B) \approx 0.25$.

Stein and Müller [10] examined a paddle in a stirred vessel with four baffles and the following geometrical ratios:

$$\frac{d_R}{d_B} = 0.471,$$
$$\frac{h}{d_B} = 0.471,$$
$$\frac{h_L}{d_B} = 1.263,$$
$$\frac{h_R}{d_B} = 0.690,$$
$$b_S/d_B = 0.1.$$

The ratios h_L/d_B, h_R/d_B, and b_S/d_B differ from those examined by Lichtenberg. Substituting $d_R/d_B = 0.471$ and $h/d_B = 0.471$, examined by Stein and Müller, in Eq. (13) gives the following equation:

$$\mathrm{Nu} = 0.76\mathrm{Re}^{2/3}\mathrm{Pr}^{1/3}\left(\frac{\eta}{\eta_w}\right)^{0.14}. \quad (14)$$

The constant in Eq. (14) determined by Stein and Müller was 0.74 (deviation about 2.7%).

Anchor impeller

Zlokarnik [11] recommends the following equations for an Anchor impeller (Fig. 2e):
For cooling:

$$\mathrm{Nu} = 0.242\left(\mathrm{RePr}^{1/2} + 4000\right)^{2/3}\left(\frac{\nu}{\nu_w}\right)^{m}. \quad (15)$$

For heating:

$$\mathrm{Nu} = 0.358\left(\mathrm{RePr}^{1/2} + 4000\right)^{2/3}\left(\frac{\nu}{\nu_w}\right)^{-m}. \quad (16)$$

Validity ranges:

$$1 \le \mathrm{Re} \le 10^5,$$
$$3 \le \mathrm{Pr} \le 3.6 \times 10^4,$$
$$1.02 \le \frac{d_B}{d_R} \le 1.1.$$

The numerical value of m, which depends on the ratio d_B/d_R, can be determined from Fig. 6. The dependence of m on d_B/d_R during heating given in Fig. 6 can be equally calculated from the following equation:

$$m = 2.2 \times 10^{-3}\left[\frac{d_B}{d_R} - 0.99\right]^{-1}. \quad (17)$$

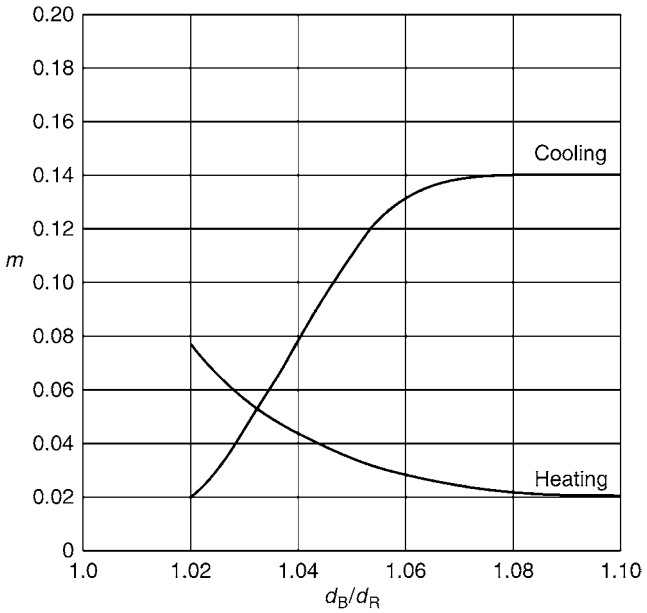

N3. Fig. 6. The dependence of m in Eqs. (15) and (16) on d_B/d_R during heating or cooling.

For very small numerical values of the Reynolds number (Re < 10), the comments given at the beginning of Sect. 2.1.1 about laminar flow in stirred vessels have to be observed.

Helical impeller

Blasinski and Kuncewicz [12] recommend the following equations for a helical impeller (Fig. 2f):

$$\mathrm{Nu} = 0.248\left(\frac{S_B}{d_R}\right)^{-0.22}\left(\frac{S}{d_R}\right)^{-0.28}\mathrm{Re}^{0.5}\mathrm{Pr}^{0.33}\left(\frac{\eta}{\eta_w}\right)^{0.14} \quad (18)$$

$$\text{for } 34 \le \mathrm{Re} \le 130$$

and

$$\mathrm{Nu} = 0.238\left(\frac{S}{d_R}\right)^{-0.25}\mathrm{Re}^{0.67}\mathrm{Pr}^{0.33}\left(\frac{\eta}{\eta_w}\right)^{0.14} \quad (19)$$

$$\text{for } 130 \le \mathrm{Re} \le 6.89 \times 10^3.$$

In Eq. (18), $s_B = (d_B - d_R)/2$.
Validity ranges:

$$81 \le \mathrm{Pr} \le 1.1 \times 10^4,$$
$$0.0172 \le \frac{S_B}{d_R} \le 0.0556,$$
$$0.357 \le \frac{S}{d_R} \le 0.894,$$
$$0.0715 \le \frac{b_{WR}}{d_R} \le 0.143.$$

According to Blasinski and Kuncewicz, the width of the helical impeller b_{WR} has no effect on the Nusselt number in the examined range. The experimental measurements were made during unsteady heat transfer with a pseudoplastic fluid.

Stein [13] determined the heat transfer on the inner surface of a stirred vessel equipped with a helical impeller composed of an external helical ribbon, an internal screw, and a bottom blade as shown in Fig. 7a. The experimental results were correlated with the following equation:

$$\mathrm{Nu} = C_{WR}\mathrm{Re}^{2/3}\mathrm{Pr}^{1/3}\left(\frac{\eta}{\eta_w}\right)^{0.14}. \quad (20)$$

Validity ranges:

$$20 \le \mathrm{Re} \le 2 \times 10^5.$$

The examined range of the Prandtl number is not given [13].

According to Stein, Eq. (20) can be equally used for other helical impellers with special forms shown in Fig. 7 (b: Paravisc impeller "Ekato," c: Alfa impeller "Stelzer," and d: MUT impeller "Dieder"). All impellers were equipped with bottom blades of different shapes. The experimentally determined constant C_{WR} for each impeller is given in Table 1. Because of uncertainties in the experimental measurements of about 10%, Stein recommends to use a constant value $C_{WR} = 0.48$ for all impellers and for both directions of rotation. The geometrical parameters of the impellers are given in Table 2. More details can be found in [13].

Scraped-surface heat exchanger

According to Weisser, heating or cooling a liquid without phase change in a scraped-surface heat exchanger (Fig. 8) may be calculated from the following equation [14]:

$$\mathrm{Nu} = 1.2Z^{0.26}\mathrm{Re}^{0.5}\mathrm{Pr}^{0.33}. \quad (21)$$

In Eq. (21), the characteristic length in the formation of the Reynolds number is the internal diameter of the inner tube of the heat exchanger (either no clearance or very small clearance exists between the edge of scraper blade and the internal tube surface), or

$$\mathrm{Re} = \frac{nd_B\rho}{\eta}.$$

Validity ranges:

$$150 \le \mathrm{Re} \le 1.8 \times 10^4,$$
$$7 \le \mathrm{Pr} \le 200,$$
$$Z = 2 \text{ or } 4.$$

In case of phase change during cooling, Weisser and Vogelpohl [14] and Weisser [15] suggest the following equation:

$$\mathrm{Nu} = 1.41Z^{0.5}\mathrm{Re}^{0.5}\mathrm{Pr}^{0.45}. \quad (22)$$

The above equation was derived using sugar solutions with a maximum ice volumetric fraction of 10%. The higher Nusselt number achieved with phase change compared with that without phase change is due to the transport of ice crystals from the cooled surface to the liquid core; this enhances heat transfer [14].

Theoretical approach for predicting the Nusselt number with a rectangular pitched-blade impeller

For approximate heat transfer calculations from the inner surface of a stirred vessel equipped with a rectangular pitched-blade impeller, Stein [16] developed the following equation for the Nusselt number in analogy to heat transfer on a plate using simplified assumptions:

$$\mathrm{Nu} = 0.4K_{ko}\mathrm{Re}^{2/3}\mathrm{Pr}^{1/3}\left(\frac{\eta}{\eta_w}\right)^{0.14}. \quad (23)$$

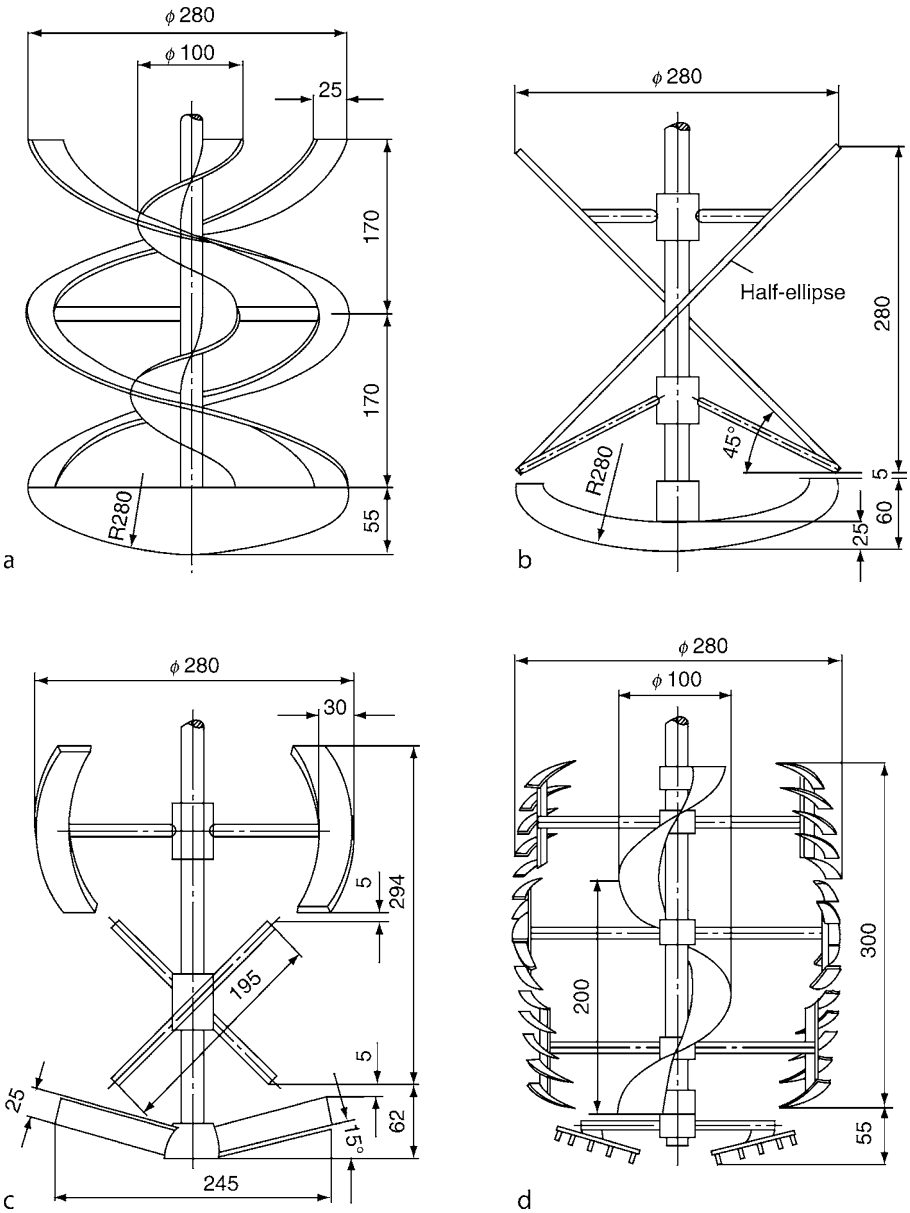

N3. Fig. 7. Different impeller forms for which Eqs. (20) and (119) are valid according to [13].
(**a**) Helical impeller with an external helical ribbon and an internal screw
(**b**) Paravisc impeller "Ekato"
(**c**) Alfa impeller "Stelzer"
(**d**) MUT impeller "Dieder"

N3. Table 1. Numerical values of the constant C_{WR} in Eq. (20) for the impellers examined in [13]

	Helical impeller with an external helical ribbon and an internal screw	Paravisc impeller	Alfa impeller	MUT impeller
C_{WR}[a]	0.43	0.49	0.54	0.47
C_{WR}[b]	0.48	–	–	–

[a]Impeller induces an outside downward flow
[b]Impeller induces an outside upward flow

N3. Table 2. Geometrical parameters of the impellers examined in [13]

	Helical impeller with an external helical ribbon and an internal screw	Paravisc impeller	Alfa impeller	MTU impeller
h_{WR}/d_R	1.214	1.0	1.05	1.071
b_{WR}/d_R	0.089	0.107	0.107	0.036
s_B/d_R	0.03	0.03	0.03	0.03
s/d_R	1.214	2.0	3.142	0.842
n_{WR}	2	2	2	5

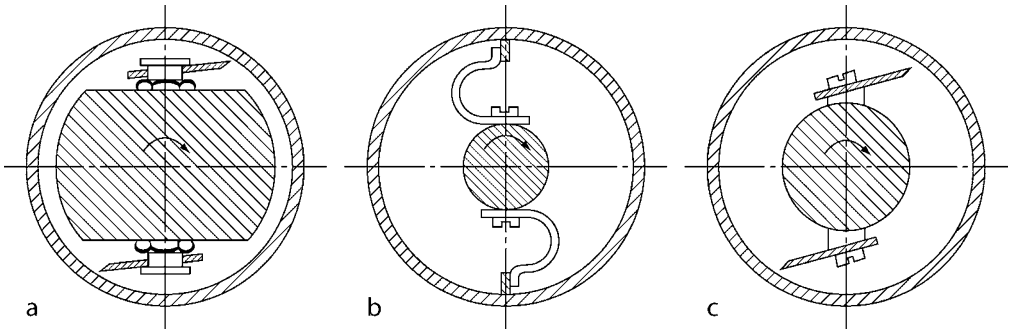

N3. Fig. 8. Possible arrangements of scraper blades on the shaft of a scraped-surface heat exchanger.
(**a**) Movable scraper blades
(**b**) Spring loaded scraper blades
(**c**) Fixed scraper blades

K_{Ko} is a dimensionless number, which takes into account the constructional and geometrical features of the stirred vessel and the impeller, and is defined by

$$K_{Ko} = \left[10.47 n_R Z \left(\frac{b_R}{d_R}\right)\left(\frac{h}{d_R}\right)\sin^3\gamma\left(\frac{d_R}{d_B}\right)\left(\frac{h_L}{d_B}\right)^{-1}\right]^{1/3}. \quad (24)$$

The following assumptions, which correspond to the geometrical parameters of the baffles mounted in the experimental equipment, were used for the derivation of Eq. (23):

$$n_S = 4,$$
$$\frac{b_S}{d_B} = 0.1,$$
$$\frac{l_S}{h_L} = 0.73,$$
$$\frac{x_S}{d_B} = 0.03.$$

The case $\gamma = 90°$ represents an impeller with vertical rectangular blades. Equation (23) is valid for stirred vessels with baffles and dished bottom in the transition region; according to Stein, the equation can still be used approximately for laminar or turbulent flow.

With the help of a theoretical equation for the power consumption of the impeller (see Sect. 3), Stein derived the following equation, which relates the Nusselt number to the power consumption:

$$\mathrm{Nu} = 0.38\mathrm{Ne}_t^{1/9}\left(\frac{d_R}{d_B}\right)^{5/9}\left(\frac{h_L}{d_B}\right)^{-1/9} Pr^{1/3}\left[\frac{P_t d_B^4 \rho^2}{V_L \eta^3}\right]^{2/9}\left(\frac{\eta}{\eta_w}\right)^{0.14}. \quad (25)$$

In Eq. (25), Ne_t is the Newton number, P_t is the power consumption with turbulent flow, and V_L is the liquid volume. The expression in the square brackets is the dimensionless power consumption per unit liquid volume. Equation (25) shows that for the same power consumption, the same vessel diameter, the same liquid height, and the same physical properties, an impeller with the largest possible diameter with respect to heat transfer is advantageous. The influence of the Newton number – because of the small exponent in Eq. (25) – is negligible.

Example 1:
It is required to calculate the heat transfer coefficient on the heated inner surface of a stirred vessel fitted with four baffles. The vessel is filled with an aqueous solution agitated by a propeller. The physical properties of the aqueous solution may be assumed to be identical with those of pure water. The following geometrical and operational data are available:

Internal vessel diameter $d_B = 1$ m
Propeller diameter $d_R = 0.35$ m
Speed of rotation of propeller $n = 2.4\mathrm{s}^{-1}$
Number of propeller blades $Z = 3$
Propeller pitch $S = 0.35$ m
Mean liquid temperature $\vartheta = 88°C$
Mean wall temperature $\vartheta_w = 95°C$

Physical properties of water:
At mean liquid temperature $\vartheta = 88°C$:
Prandtl number $\mathrm{Pr} = 2.02$
Thermal conductivity $\lambda = 0.672\ \mathrm{W\,m^{-1}\,K^{-1}}$
Density $\rho = 966\ \mathrm{kg\,m^{-3}}$
Dynamic viscosity $\eta = 323 \times 10^{-6}$ Pa s
At mean wall temperature $\vartheta_w = 95°C$:
Dynamic viscosity $\eta_w = 299 \times 10^{-6}$ Pa s
Solution:
Reynolds number $\mathrm{Re} = \frac{nd_R^2\rho}{\eta} = \frac{2.4\times0.35^2\times966}{323\times10^{-6}} = 8.8\times10^5$,

Equation (8): $\psi_p = \exp(0.3\ln Z - 0.0144Z)\left\{\frac{0.278\exp[0.0469\exp(0.923\ln Z)]}{\frac{S}{d_R}} + 1\right\}^{-1}$
$= \exp(0.3\times\ln 3 - 0.0144\times 3)\left\{\frac{0.278\exp[0.0469\exp(0.923\ln 3)]}{\frac{0.35}{0.35}} + 1\right\}^{-1}$
$= 1.01$

The value of ψ_P can also be obtained directly from Fig. 4.

Equation (7): $\mathrm{Nu} = 0.505\psi_p \mathrm{Re}^{2/3}\mathrm{Pr}^{1/3}\left(\frac{\eta}{\eta_w}\right)^{0.14}$
$= 0.505\times1.01\times\left(8.8\times10^5\right)^{2/3}(2.02)^{1/3}\left(\frac{323\times10^{-6}}{299\times10^{-6}}\right)^{0.14} = 5985$

The heat transfer coefficient α can be calculated from the Nusselt number, or

$$\alpha = \frac{\mathrm{Nu}\lambda}{d_B} = \frac{5985 \times 0.672}{1} = 4022\ \mathrm{Wm^{-2}K^{-1}}$$

Heat transfer from the outer surface of a coil

Figure 9 shows two different forms of coils, which are used to heat or cool a liquid inside a stirred vessel. In case of a helical coil (Fig. 9a), the baffles can be inserted inside or outside the coil. Mostly, the plates for fixing the coil in the vessel are constructed to function as baffles. A meander coil (Fig. 9b) reduces vortex formation; thus, additional baffles may not be needed. Consequently, such systems are referred to as vertical tube baffles (see also Figs. 10 and 11).

Flat-blade turbine

Mahlfeldt [17] gives the following equation for calculating the Nusselt number in a baffled stirred vessel fitted with a spiral coil (Fig. 9a):

$$\mathrm{Nu_R} = 0.225 \left(\frac{d_R}{d_B}\right)^{0.18} \left(\frac{d}{d_B}\right)^{0.52} \left(\frac{d_S}{d_B}\right)^{-0.27} \left(\frac{h_R}{d_B}\right)^{0.14} \left(\frac{Z}{4}\right)^{0.28} \mathrm{Re}^{2/3}\mathrm{Pr}^{1/3} \left(\frac{\eta}{\eta_w}\right)^{0.14}, \quad (26)$$

with

$$\text{Nusselt number } \mathrm{Nu_R} = \frac{\alpha d}{\lambda}.$$

Validity ranges:

$$1.5 \times 10^3 \le \mathrm{Re} \le 7.7 \times 10^5,$$
$$2 \le \mathrm{Pr} \le 1190,$$
$$0.2 \le \frac{d_R}{d_B} \le 0.4,$$
$$0.023 \le \frac{d}{d_B} \le 0.054,$$
$$0.5 \le \frac{d_S}{d_B} \le 0.7,$$
$$0.27 \le \frac{h_R}{d_B} \le 0.63,$$
$$4 \le Z \le 6,$$

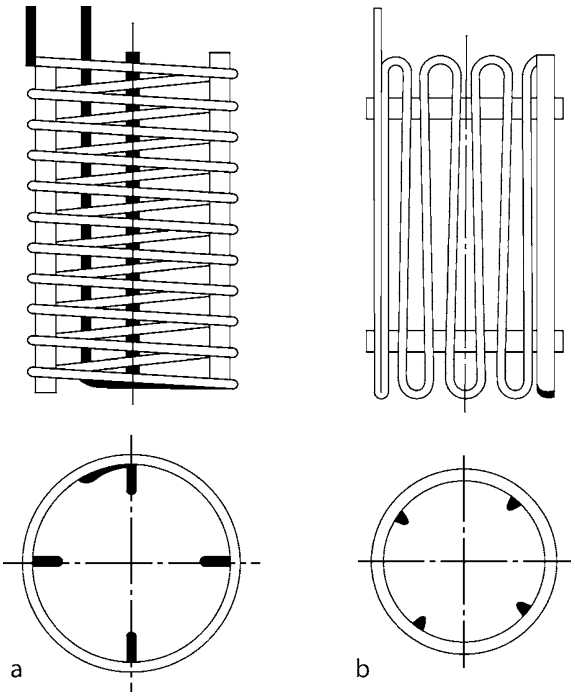

N3. Fig. 9. Coils: (**a**) helical coil, (**b**) meander coil.

According to Dunlap and Rushton [18], the Nusselt number for a stirred vessel equipped with vertical tube baffles (Fig. 10) may be calculated from

$$\mathrm{Nu_R} = 0.09 \left(\frac{d_R}{d_B}\right)^{0.33} \left(\frac{2}{n_S}\right)^{0.2} \mathrm{Re}^{0.65}\mathrm{Pr}^{0.3} \left(\frac{\eta}{\eta_{GS}}\right)^{0.4}. \quad (27)$$

Validity ranges:

$$10^3 \le \mathrm{Re} \le 2 \times 10^6,$$
$$2 \le \mathrm{Pr} \le 10^3,$$
$$\frac{1}{6} \le \frac{d_R}{d_B} \le \frac{1}{2},$$
$$2 \le n_S \le 8,$$

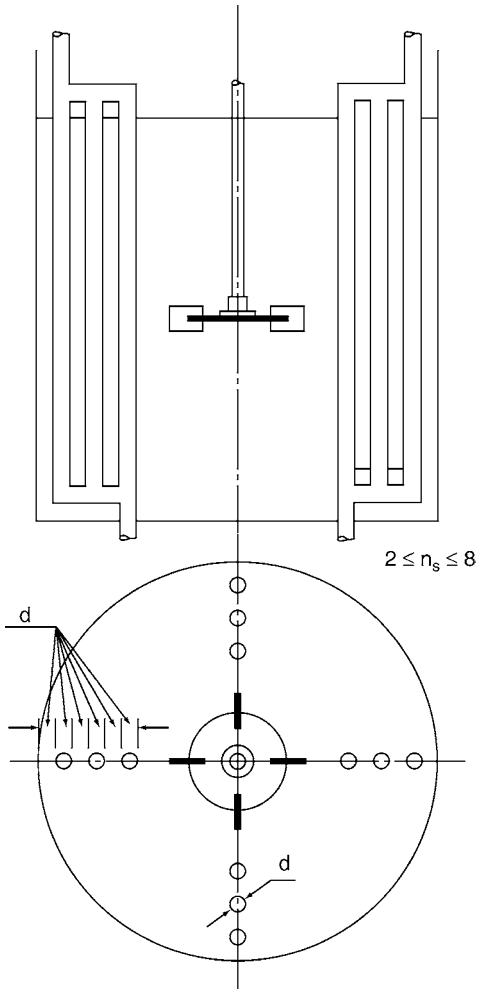

N3. Fig. 10. Stirred vessel with vertical tube baffles, for which Eq. (27) is valid.

$$0.035 \le \frac{d}{d_B} \le 0.040,$$
$$\frac{h_R}{h_L} = 0.5,$$
$$Z = 4,$$
$$n_{RS} = 3.$$

The dynamic viscosity η_{GS} in Eq. (27) is calculated at the mean temperature $(\vartheta + \vartheta_w)/2$ of the thermal boundary layer.

Havas et al. [19, 20] suggest the following equation for a stirred vessel equipped with tube baffles with the construction shown in Fig. 11:

$$Nu_R = 0.291\left(\frac{d_R}{d_B}\right)^{0.89}\left(\frac{d}{d_R}\right)^{0.667} Re^{0.667} Pr^{0.4}\left(\frac{\eta}{\eta_w}\right)^{0.16}. \quad (28)$$

Validity ranges:

$$3 \times 10^3 \le Re \le 5 \times 10^5,$$
$$4 \le Pr \le 240,$$
$$0.3 \le \frac{\eta}{\eta_w} \le 4,$$
$$0.25 \le \frac{d_R}{d_B} \le 0.5,$$
$$0.01 \le \frac{d}{d_B} \le 0.02,$$
$$\frac{h_R}{h_L} = 0.5,$$
$$n_S = 5,$$
$$\beta = +50^\circ \text{ or } -50^\circ,$$
$$Z = 6,$$
$$8 \le n_{RS} \le 18.$$

Other geometrical parameters examined by Havas et al. are given in Fig. 11.

Correlations for predicting the heat transfer from vertical plate coils in a stirred vessel equipped with two flat-blade turbines can also be presented [21].

Propeller

Skelland et al. [22] give the following equation for a baffled stirred vessel fitted with a helical coil:

$$Nu_R = 0.0573\left(\frac{h_R}{d_B}\right)^{-0.254}\left(\frac{S}{d_R}\right)^{2.33}\left(\frac{d}{d_B}\right)^{0.572}\left(\frac{s_S}{d}\right)^{-0.018} (n_S)^{-0.077}\left(\frac{b_S}{d_B}\right)^{-0.058} Re^{0.67} Pr^{0.41}\left(\frac{\eta}{\eta_w}\right)^{0.034}. \quad (29)$$

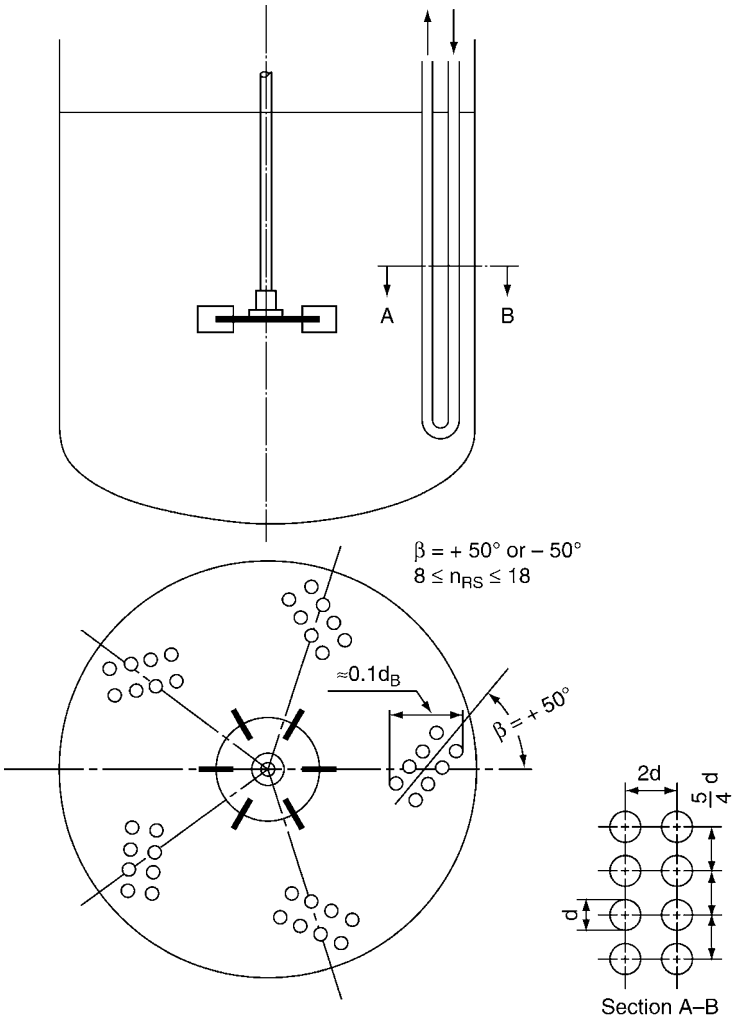

N3. Fig. 11. Stirred vessel with vertical tube baffles, for which Eq. (28) is valid.

Validity ranges:

$$1.3 \times 10^4 \le \mathrm{Re} \le 1.1 \times 10^6,$$
$$3 \le \mathrm{Pr} \le 300,$$
$$0.16 \le \frac{h_R}{d_B} \le 0.82,$$
$$1.0 \le \frac{S}{d_R} \le 1.33,$$
$$0.014 \le \frac{d}{d_B} \le 0.042,$$
$$1.2 \le \frac{s_S}{d} \le 8.0,$$
$$2 \le n_S \le 6,$$
$$0.06 \le \frac{b_S}{d_B} \le 0.17,$$
$$0.16 \le \frac{d_R}{d_B} \le 0.5,$$
$$1.4 \le \frac{d_S}{d_R} \le 4.1,$$
$$0.5 \le \frac{d_S}{d_B} \le 0.7,$$
$$\frac{h_L}{d_B} \approx 1.1.$$

Paddle

According to Chilton et al. [23], the following equation can be used for an unbaffled stirred vessel equipped with a helical coil:

$$\mathrm{Nu_R} = 0.87\left(\frac{d}{d_B}\right)\mathrm{Re}^{0.62}\mathrm{Pr}^{1/3}\left(\frac{\eta}{\eta_w}\right)^{0.14}. \quad (30)$$

Validity ranges:

$$300 \le \mathrm{Re} \le 4 \times 10^5,$$
$$3 \le \mathrm{Pr} \le 2 \times 10^3,$$
$$\frac{d_R}{d_B} = 0.6,$$
$$\frac{h}{d_B} = 0.1,$$
$$\frac{d}{d_B} = 0.042,$$
$$\frac{d_S}{d_B} = 0.8,$$
$$\frac{h_L}{d_B} = 0.83,$$
$$\frac{h_{RK}}{d_B} = 0.15,$$

Anchor impeller

Balsinski et al. [24] examined heat transfer in a stirred vessel equipped with an anchor impeller and a helical coil fixed inside the impeller and recommend the following equation:

$$\mathrm{Nu_R} = 0.084\left(\frac{d_S}{d_B}\right)^{0.74}\mathrm{Re}^{0.55}\mathrm{Pr}^{0.33}\left(\frac{\eta}{\eta_w}\right)^{0.14}. \quad (31)$$

Validity ranges:

$$31 \le \mathrm{Re} \le 2.8 \times 10^4,$$
$$19 \le \mathrm{Pr} \le 8.3 \times 10^3,$$
$$\frac{d_R}{d_B} = 0.95,$$
$$\frac{d}{d_B} = 0.04,$$
$$0.4 \le \frac{d_S}{d_B} \le 0.73.$$

Example 2:

It is required to calculate the heat transfer coefficient α at the outer surface of a helical coil in a stirred vessel. The liquid in the vessel is agitated by means of a flat-blade turbine with six blades and the outer diameter d of the tube of the coil is 0.022 m. The following operating conditions and geometrical parameters are given:

$$n = 1.5\,\mathrm{s}^{-1},$$
$$\frac{d_R}{d_B} = \frac{1}{3},$$
$$\frac{h_R}{d_B} = \frac{1}{3},$$
$$\frac{d_S}{d_B} = 0.7.$$

Furthermore, the data given in Example 1 related to the vessel diameter and physical properties should be used in this example.

Solution:

$$d_R = \frac{d_B}{3} = \frac{1}{3}\ \mathrm{m},$$
$$\mathrm{Re} = \frac{n d_R^2 \rho}{\eta} = \frac{1.5 \times \left(\frac{1}{3}\right)^2 \times 966}{323 \times 10^{-6}} = 4.98 \times 10^5,$$

Equation (26):

$$\mathrm{Nu_R} = 0.225\left(\frac{d_R}{d_B}\right)^{0.18}\left(\frac{d}{d_B}\right)^{0.52}\left(\frac{d_S}{d_B}\right)^{-0.27}\left(\frac{h_R}{d_B}\right)^{0.14}\left(\frac{Z}{4}\right)^{0.28}$$
$$\mathrm{Re}^{2/3}\mathrm{Pr}^{1/3}\left(\frac{\eta}{\eta_w}\right)^{0.14}$$
$$= 0.225\left(\frac{1}{3}\right)^{0.18}\left(\frac{0.022}{1}\right)^{0.52}(0.7)^{-0.27}\left(\frac{1}{3}\right)^{0.14}\left(\frac{6}{4}\right)^{0.28}$$
$$\left(4.98 \times 10^5\right)^{2/3}(2.02)^{1/3}\left(\frac{323}{299}\right)^{0.14}$$
$$= 215.4$$

Hence

$$\alpha = \frac{\mathrm{Nu_R}\lambda}{d} = \frac{215.4 \times 0.672}{0.022} = 6579\ \mathrm{W\,m^{-2}K^{-1}}.$$

Non-Newtonian liquids

Numerous experimental data gained with non-Newtonian liquids were examined by Edwards and Wilkinson [25]. It was demonstrated that heat transfer correlations developed for Newtonian liquids can still be used for non-Newtonian liquids, if the viscosity η of the Newtonian liquids in the Reynolds number, the Prandtl number, and the viscosity ratio is replaced

by the apparent viscosity η_{app} of the non-Newtonian liquids as defined by

$$\eta_{app} = \frac{\tau}{\dot{\gamma}}, \tag{32}$$

with τ the shear stress associated with the shear rate $\dot{\gamma}$. Different to Newtonian liquids, the relation between τ and $\dot{\gamma}$ for non-Newtonian liquids is nonlinear; the flow curve relating τ and $\dot{\gamma}$ can be determined experimentally for the considered non-Newtonian liquid. The apparent viscosity η_{app} decreases with increasing shear rate $\dot{\gamma}$ for pseudoplastics and increases for dilatants. It is assumed [25] that a linear relationship exists between the shear rate $\dot{\gamma}$ in a stirred vessel and the speed of rotation n of the impeller, or

$$\dot{\gamma} = k_S n. \tag{33}$$

The proportionality constant k_S may be approximated as follows:

For pseudoplastics:

Paddles, flat-blade turbines, propellers, and other high-speed impellers [25]:

$$k_S \approx 11. \tag{34}$$

Typical values available in the literature for k_S vary between 9 and 15 [25].

Anchor impellers:

$$k_S \approx 9.5 + \frac{9s^2}{s^2 - 1}. \tag{35}$$

Helical impellers [12]:

$$k_S = 4\pi. \tag{36}$$

For dilatants:

High-speed impellers with standard geometry [25]:

$$k_S \approx \frac{22s^2}{s^2 - 1}. \tag{37}$$

In Eqs. (35) and (37), $s = \frac{d_B}{d_R}$.

Since the Nusselt number is roughly proportional to the viscosity raised to the power $(-1/3)$, the uncertainty in evaluating the apparent viscosity is largely reduced.

Example 3:

In Example 1, instead of using an aqueous solution, the stirred vessel is filled with a pseudoplastic liquid with flow characteristics given by the flow curve shown in Fig. 12. It is required to calculate the heat transfer coefficient α for the case in which the propeller in the stirred vessel is replaced by an anchor impeller with a diameter $d_R = 0.91$ m and a speed of rotation $n = 0.8\,s^{-1}$. Other physical properties of the pseudoplastic liquid are similar to that of pure water and are given in Example 1.

Solution:

The constant k_s in Eq. (33) for an anchor impeller is given by Eq. (35), or

$$k_S = 9.5 + \frac{9s^2}{s^2 - 1} = 9.5 + \frac{9\left(\frac{1.0}{0.91}\right)^2}{\left(\frac{1.0}{0.91}\right)^2 - 1} = 61.9.$$

Equation (33): $\dot{\gamma} = k_S n = 61.9 \times 0.8 = 49.5\ s^{-1}$.

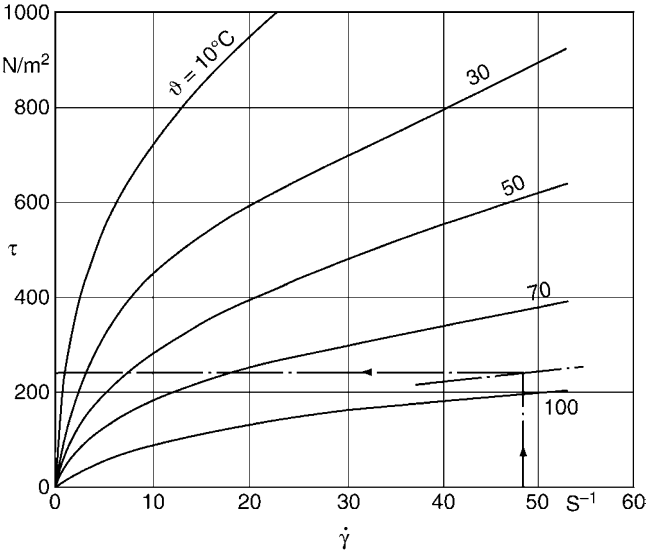

N3. Fig. 12. Flow curve for a 6% aqueous solution of carboxymethyl cellulose (CMC).

The shear stress τ at $\dot{\gamma} = 49.5\,s^{-1}$ and $\vartheta = 88°$ C can be estimated from Fig. 12, or

$$\tau = 247\,N\,m^{-2}.$$

Equation (32): $\eta_{app} = \frac{\tau}{\dot{\gamma}} = \frac{247}{49.5} = 4.99$ Pa s.

At liquid temperature $\vartheta = 88°$ C:

$$\rho = 966\,kg\,m^{-3}.$$

Thus,

$$Re = \frac{nd_R^2\rho}{\eta_{app}} = \frac{0.8 \times 0.91^2 \times 966}{4.99} = 128.2$$

and

$$Pr = \left(\frac{Pr}{\eta}\right)_{(\text{in Example 1})} \times \eta_{app} = \left(\frac{2.02}{323 \times 10^{-6}}\right) \times 4.99 = 31207.$$

In Eq. (16), $\nu = \eta/\rho$ should be replaced by $\nu_{app} = \eta_{app}/\rho$ and $\nu_w = \eta_w/\rho_w$ should be replaced by $\nu_{w,app} = \eta_{w,app}/\rho_w$, where ν_{app} is the apparent kinematic viscosity corresponding to the apparent dynamic viscosity η_{app} at liquid temperature ϑ, $\nu_{w,app}$ the apparent kinematic viscosity corresponding to the apparent dynamic viscosity $\eta_{w,app}$ at wall temperature ϑ_w and ρ_w the liquid density at wall temperature ϑ_w.

Now

$$\frac{\nu_{app}}{\nu_{w,app}} = \left(\frac{\left(\frac{\eta_{app}}{\rho}\right)}{\left(\frac{\eta_{w,app}}{\rho_w}\right)}\right) = \left(\frac{\eta_{app}}{\eta_{w,app}}\right) \times \left(\frac{\rho_w}{\rho}\right)$$

$$= \cdot\left(\frac{\left(\tau/\dot{\gamma}\right)_\vartheta}{\left(\tau/\dot{\gamma}\right)_{\vartheta_w}}\right) \times \left(\frac{\rho_w}{\rho}\right) = \left(\frac{(\tau)_\vartheta}{(\tau)_{\vartheta_w}}\right) \times \left(\frac{\rho_w}{\rho}\right).$$

At wall temperature $\vartheta_w = 95°$ C:

$$\rho_w = 962\,kg\,m^{-3}$$

and

$\tau = 205\,\mathrm{N\,m^{-2}}$ (estimated from Fig. 12 at $\dot{\gamma} = 49.5\,\mathrm{s^{-1}}$ and $\vartheta_w = 95°\,\mathrm{C}$).

Thus,

$$\frac{\nu_{app}}{\nu_{w,app}} = \left(\frac{247}{205}\right) \times \left(\frac{962}{966}\right) = 1.2.$$

Equation (17):

$$m = 2.2 \times 10^{-3}\left[\frac{d_B}{d_R} - 0.99\right]^{-1} = 2.2 \times 10^{-3}\left[\frac{1.0}{0.91} - 0.99\right]^{-1} = 0.02,$$

Equation (16): $\mathrm{Nu} = 0.358\left(\mathrm{RePr}^{1/2} + 4000\right)^{2/3}\left(\frac{\nu}{\nu_w}\right)^{-m}$

$$= 0.358\left(128.2 \times 31207^{0.5} + 4000\right)^{2/3}(1.2)^{-0.02}$$
$$= 318.$$

Hence

$$\alpha = \frac{\mathrm{Nu}\lambda}{d_B} = \frac{318 \times 0.672}{1} = 214\,\mathrm{W\,m^{-2}K^{-1}}.$$

2.1.2 Multiphase Systems

There are only a few publications available about heat transfer for multiphase systems in stirred vessels. A review is made by Steiff et al. and Kurpiers et al. [26–31].

Gas–Liquid Mixtures

Heat transfer studies on stirred gas–liquid mixtures show that in the case of a homogenous bubble flow, substantial enhancement of the heat transfer with increasing superficial gas velocity u_{GO} $\left(u_{GO} = \dot{V}_G/\left((\pi/4)d_B^2\right)\right)$ occurs only at low impeller speed. At high speed of rotation, the enhancement of heat transfer achieved by increasing the superficial gas velocity is relatively small; the heat transfer may even be impaired if the superficial gas velocity is increased at very high speed of rotation [26]. In the range of heterogeneous bubble flow, that is, above a superficial gas velocity of about 0.05–0.15 m $\mathrm{s^{-1}}$, heat transfer is independent of the speed of rotation or the superficial gas velocity [26]. The gas phase is often introduced in the liquid by means of a gas distributor, for example, a ring underneath the impeller. In case of a flat-blade turbine, the gas is guided through the disc of the impeller into the zone of high shear rate; there it is dispersed in the form of fine bubbles. For this reason, flat-blade turbines are eminently suitable for gas dispersion. On the other hand, impellers generating an axial flow (e. g., propellers) are less suitable for gas dispersion; the buoyancy-induced upward motion of the bubbles near the impeller shaft at high gas flow rates has a negative effect on the downward axial flow induced by the impeller. Another method of gas dispersion is aeration induced by hollow impellers. According to [28, 30, 31], the Nusselt number at the inner surface of a stirred vessel with four baffles, a standard flat-blade turbine, and a ring gas distributor may be calculated from the following equation:

$$\mathrm{Nu} = 0.1\left\{\xi\left(\frac{d_B}{d_R}\right)\left(\frac{d_B^3}{V_L}\right)\mathrm{Ne_B Re}^3 + \mathrm{GaRe_G}\left[1 - 2\left(\frac{d_R}{d_B}\right)\left(\frac{d_R}{h_{LO} - h_{BR}}\right)\mathrm{Ne_B^{0.5}Fr}\right]\right\}^{0.25}\mathrm{Pr}^{0.4}\left(\frac{\eta}{\eta_w}\right)^{0.23}. \quad (38)$$

The constant ξ depends on the ratio $\left(d_B/d_R\right)$ as follows:

$$\xi = 0.2 \text{ for } \left(\frac{d_B}{d_R}\right) = 3,$$

$$\xi = 0.37 \text{ for } \left(\frac{d_B}{d_R}\right) = 1.93.$$

The dimensionless numbers present in Eq. (38), are defined as follows:

$\mathrm{Ne_B} = \dfrac{P_B}{\rho n^3 d_R^5}$. Newton number for gas−liquid mixture,

$\mathrm{Fr} = \dfrac{n^2 d_R}{g}$. Froude number,

$\mathrm{Ga} = \dfrac{d_B^3 g}{\nu^2}$. Galileo number,

$\mathrm{Re_G} = \dfrac{u_{GO} d_B}{\nu}$. Reynolds number (characteristic velocity is the superficial gas velocity);

thus,

$$\mathrm{GaRe_G} = \frac{d_B^4 g u_{GO}}{\nu^3}.$$

V_L in Eq. (38) is the volume of the unaerated liquid, P_B is the power consumption of the impeller for the gas–liquid mixture. Equations for calculating the Newton number Ne_B for gas–liquid mixtures are presented in Sect. 3; other equations can also be found in [32]. Differences in calculating the Newton number from the different equations are – because of the small exponent of the Newton number – largely suppressed

According to [28], Eq. (38) is valid also for the following limiting cases:

Unagitated gas–liquid system (bubble column):

$$\mathrm{Ne_B} = 0,\ \mathrm{Re} = 0.$$

Unaerated agitated liquid:

$$GaRe_G = 0.$$

Validity ranges:

Equation (38) was derived from measurements obtained with different liquids and air in a vessel with the following dimensions and geometrical ratios:

$$d_B = 0.45\,\mathrm{m},$$
$$\frac{d_B}{d_R} = 1.93,\ 3,$$
$$\frac{h_R}{d_R} = 0.5,$$

$$\frac{h_{LO}}{d_B} = 1.35,$$
$$\frac{h_{BR}}{d_B} = 0.083.$$

The dimensionless numbers were changed in the following ranges:

$$4.3 \le \mathrm{Pr} \le 630,$$
$$0.024 \le \frac{\eta}{\eta_w} \le 3.6,$$
$$2.47 \times 10^8 \le \mathrm{Ga} \le 2.16 \times 10^{12},$$
$$0.65 \le \mathrm{Ne_B} \le 4.65,$$
$$1.26 \times 10^3 \le \mathrm{Re} \le 4.15 \times 10^5,$$
$$0.127 \le \mathrm{Fr} \le 2.19,$$
$$5.47 \le \mathrm{Re_G} \le 7.83 \times 10^4.$$

Example 4:

It is required to calculate the heat transfer coefficient α at the inner surface of a heated stirred vessel filled with an aqueous solution. The liquid is agitated by means of a flat-blade turbine having six blades and is aerated by means of a ring underneath the impeller. The gas flow rate $\dot{V}_G$ amounts to 6 $m^3\ h^{-1}$. The physical properties of the aqueous solution may be assumed to be similar to those of pure water. The stirred vessel has four baffles and the following dimensions and operating parameters:

Vessel diameter $d_B = 0.5\,m$
Geometrical ratios: $d_R = \frac{d_B}{3}$,
$h_R = 0.5 d_R$
$h_{LO} = 1.35 d_B$
$h_{BR} = 0.083 d_B$
Speed of rotation of impeller $n = 7\ s^{-1}$
Power consumption of impeller $P_B = 106\,W$
Mean liquid temperature $\vartheta = 20°\,C$
Mean wall temperature $\vartheta_w = 30°\,C$

Physical properties of water:

At mean liquid temperature $\vartheta = 20°\,C$:
Prandtl number Pr = 6.99,
Thermal conductivity $\lambda = 599.6 \times 10^{-3}\,W\,m^{-1}\,K^{-1}$
Density $\rho = 998.3\,kg\,m^{-3}$
Dynamic viscosity $\eta = 1002.6 \times 10^{-6}\,pa\,s$
Kinematic viscosity $\nu = 1.004 \times 10^{-6}\,m\,s^{-2}$

At mean wall temperature $\vartheta_w = 30°\,C$:

Dynamic viscosity $\eta_w = 797.7 \times 10^{-6}\,pa\,s$

Solution:

$$\mathrm{Re} = \frac{n d_R^2 \rho}{\eta} = \frac{7 \times \left(\frac{0.5}{3}\right)^2 \times 998.3}{1002.6 \times 10^{-6}} = 1.94 \times 10^5,$$
$$u_{GO} = \frac{\dot{V}_G}{\left(\frac{\pi d_B^2}{4}\right)} = \frac{\left(\frac{6}{3600}\right)}{\left(\frac{\pi \times 0.5^2}{4}\right)} = 0.00849\,m\,s^{-1},$$
$$\mathrm{Re_G} = \frac{u_{GO} d_B}{\nu} = \frac{0.00849 \times 0.5}{1.004 \times 10^{-6}} = 4228,$$
$$\mathrm{Ga} = \frac{d_B^3 g}{\nu^2} = \frac{0.5^3 \times 9.81}{(1.004 \times 10^{-6})^2} = 1.22 \times 10^{12},$$
$$\mathrm{Fr} = \frac{n^2 d_R}{g} = \frac{7^2 \times \left(\frac{0.5}{3}\right)}{9.81} = 0.832,$$
$$\mathrm{Ne_B} = \frac{P_B}{\rho n^3 d_R^5} = \frac{106}{998.3 \times 7^3 \times \left(\frac{0.5}{3}\right)^5} = 2.41,$$
$$V_L = \left(\frac{\pi d_B^2}{4}\right) h_{LO} = \left(\frac{\pi d_B^2}{4}\right)(1.35 d_B) = 1.06 d_B^3,$$
$$\xi = 0.2 \ (\text{since } (d_B/d_R) = 3).$$

Hence

$$\mathrm{Nu} = 0.1\left\{\xi\left(\frac{d_B}{d_R}\right)\left(\frac{d_B^3}{V_L}\right)\mathrm{Ne_B Re}^3 + \mathrm{GaRe_G}\left[1 - 2\left(\frac{d_R}{d_B}\right)\left(\frac{d_R}{h_{LO} - h_{BR}}\right)\mathrm{Ne_B}^{0.5}\mathrm{Fr}\right]\right\}^{0.25} \mathrm{Pr}^{0.4}\left(\frac{\eta}{\eta_w}\right)^{0.23}$$
$$= 0.1\left\{0.2 \times (3) \times \left(\frac{1}{1.06}\right) \times 2.41 \times \left(1.94 \times 10^5\right)^3 + \left(1.22 \times 10^{12}\right) \times 4228 \times \left[1 - 2 \times \left(\frac{1}{3}\right) \times \left(\frac{\frac{1}{3}}{1.35 - 0.083}\right) \times 2.41^{0.5} \times 0.832\right]\right\}^{0.25} \times 6.99^{0.4} \times \left(\frac{1002.6}{797.7}\right)^{0.23}$$
$$= 2493.$$

The heat transfer coefficient is thus given by

$$\alpha = \frac{\mathrm{Nu}\lambda}{d_B} = \frac{2493 \times (599.6 \times 10^{-3})}{0.5} = 2990\,W\,m^{-2}K.$$

Immiscible Liquids

Heat transfer to a mixture of two immiscible liquids is a complex process. It depends not only on the heat transfer parameters of the single-phase "liquid", but also on additional parameters of the two-phase "liquid–liquid," which include the fractions of each component, the local form and distribution of each phase in the stirred vessel, the interfacial tension, as well as the concentration of impurities. At high impeller speed and correspondingly a uniform distribution of the dispersed phase, it can be assumed that a quasi-homogeneous mixture is present in the stirred vessel. The equations derived for the single-phase liquid can be used for the two-phase mixture, when the physical properties of the single-phase liquid are replaced by the mean physical properties of the quasi-homogeneous two-phase mixture. Mostly, the equation derived by Olney and Carlson [33] for the dynamic viscosity

$$\eta_m = \eta_d^{\varphi} \eta_c^{(1-\varphi)} \tag{39}$$

and the equation derived by Maxwell [26, 34] for the thermal conductivity

$$\lambda_m = \lambda_c \left[\frac{2\lambda_c + \lambda_d - 2\varphi(\lambda_c - \lambda_d)}{2\lambda_c + \lambda_d + \varphi(\lambda_c - \lambda_d)}\right] \tag{40}$$

are used for the two-phase mixture. The density and the specific heat are determined usually from the arithmetic mean

$$\rho_m = \varphi\rho_d + (1 - \varphi)\rho_c, \tag{41}$$
$$c_m = \varphi c_d + (1 - \varphi)c_c. \tag{42}$$

In Eqs. (39–42), the subscripts *m*, *d*, and *c* are for the quasi-homogenous two-phase mixture, the dispersed phase, and the continuous phase respectively; φ is the volumetric fraction of the dispersed phase. The influence of phase separation in the vicinity of the wall on heat transfer in agitated emulsions has

been reported in [26, 34]. Both radial flow and axial flow impellers are used to disperse a liquid. However, preference is given to radial flow impellers, especially flat-blade turbines, for dispersion purposes owing to the high shear rates, high turbulence, and the associated good dispersion characteristics.

Suspensions

If the suspended solids are uniformly distributed (i.e., turbulent flow, high impeller speed, small fraction of solid particles, and small particle diameter), it may be assumed that a quasi-homogenous phase is present inside the stirred vessel. The heat transfer equations for the single-phase liquid can be used for the suspension provided that the physical properties for the single-phase liquid are replaced by the mean physical properties of the suspension. There are different equations present in the literature to determine the mean dynamic viscosity of the suspension. According to Eilers (as reported [31]), the following equation may be used:

$$\eta_m = \eta_c \left[1 + \frac{2.5\varphi}{2\left(1 - \frac{\varphi}{\varphi_{max}}\right)}\right]^2, \tag{43}$$

where φ is volumetric fraction of the dispersed phase, φ_{max} the maximal volumetric fraction in the batch, η_m the mean dynamic viscosity of the quasi-homogenous suspension, and η_c the dynamic viscosity of the continuous phase (liquid phase). For a batch of spherical particles, $\varphi_{max} = 0.74$. Other equations are reported in [26]. The other physical properties of the suspension can be determined as described in the section titled "*Immiscible liquids*." According to Kwasniak [34], the mentioned procedure of calculation should be applied only if the density of the solid particles is substantially higher than that of the liquid ($\rho_d > 2.2\rho_c$). Under such conditions, the boundary layer near the heat transfer surface of the stirred vessel will not be free of solid particles and the mean values of the physical properties of the suspension can be used in all parameters of the heat transfer equations. If the density of the solid particles differs only insignificantly from that of the liquid ($\rho_d \approx \rho_c$), phase separation will occur in the boundary layer. In such cases, the physical properties of the continuous liquid phase should be used in the parameters relevant to heat transfer in the vicinity of the wall (i.e., λ in Nu, a in Pr, and η_w in the viscosity ratio (η/η_w)); the mean physical properties of the suspension should be inserted in the other parameters (i.e., ν in Re and Pr as well as η in the viscosity ratio (η/η_w)). Axial flow impellers (e.g., propellers) are usually used for suspending solid particles in a liquid, because their power consumption is lower than that for radial-flow impellers.

Gas–Suspension Mixtures

Although axial-flow impellers are preferred for suspending solids, they are not suitable for mixing suspensions with gases owing to the adverse effect exerted by the movement of the gas bubbles on the axial-flow induced by the impeller. Flat-blade turbines are predominantly used for this task. Studies on gas–suspension mixtures have revealed that heat transfer in the three-phase system "gas–solid–liquid" can be determined from equations of the two-phase systems "gas–liquid" and "solid–liquid" [31]. Thus, Eq. (38) for gas–liquid mixtures can also be used for gas–suspension mixtures provided that the physical properties of the liquid in Eq. (38) are replaced by the mean physical properties of the solid–liquid mixture as given in the section titled "Suspensions." The validity of Eq. (38) for gas–suspensions was checked by experiments in which the solid particles were glass beads: the diameter of the beads was varied between 15 and 1800 μm and the volumetric fraction between 0.01 and 0.1.

The distribution of the solid particles can be improved in multistage systems by mounting a number of agitators on the same shaft. According to [30, 31], the following equation may be used for gas–suspensions in a stirred vessel equipped with a two-stage system having two flat-blade turbines:

$$Nu = 0.1\left[11.58\left(\frac{d_B}{d_R}\right)\left(\frac{d_B^3}{V_L}\right)Ne_B Re^3 + GaRe_G\right]^{0.238} Pr^{0.362}\left(\frac{\eta}{\eta_w}\right)^{0.23}. \tag{44}$$

The dimensionless numbers in Eq. (44) are formed with the mean physical properties of the solid–liquid suspension according to the equations given in the section titled "Suspensions."
Validity ranges:
Geometrical ratios:

$$\frac{d_B}{d_R} = 3,$$
$$\frac{h_{R1}}{d_R} = 0.5,$$
$$\frac{h_{R2}}{d_R} = 2.58,$$
$$\frac{h_{LO}}{d_B} = 1.35,$$

Operating dimensionless parameters:

$$4.2 \le Pr \le 632,$$
$$0.033 \le \frac{\eta}{\eta_w} \le 3.02,$$
$$2.69 \times 10^8 \le Ga \le 2.16 \times 10^{12},$$
$$1.94 \le Ne_B \le 10.2,$$
$$6.51 \times 10^2 \le Re \le 4.05 \times 10^5,$$
$$0.021 \le Fr \le 2.15,$$
$$0 \le Re_G \le 7.07 \times 10^4.$$

h_{R1} and h_{R2} in Eq. (44) are the height of the lower and the upper agitators from the bottom of the vessel respectively. According to [31], Eq. (44) is also valid for the single-phase system "liquid" and for the two-phase systems "gas–liquid" and "solid–liquid." For the single-phase system "liquid" and for the two-phase-system "gas–liquid," the physical properties of the liquid and for the two-phase system "solid–liquid" the mean physical properties of the suspension have to be used.

2.2 Heat Transfer from a Jacket or from a Coil

2.2.1 Heat Transfer from a Jacket

A limited number of publications are available about heat transfer on the jacket side of a stirred vessel. The relatively

simple flow geometry in the annular space between the outer surface of the stirred vessel and the inner surface of the jacket encouraged workers to develop equations for predicting the jacket-side heat transfer on semitheoretical basis using different analogies. Known methods are due to Lehrer [35] and Stein and Schmidt [36–38]. The last method presented by Stein and Schmidt [38] is a modification and hence a replacement of earlier methods. Heat transfer coefficients on the jacket side calculated by means of these methods differ significantly. For that reason, both the method of Lehrer [35] and the modified method of Stein and Schmidt [38] are described hereafter; a numerical example using both methods and some comments are also presented.

Method of Lehrer

Lehrer [35] used the Prandtl analogy between momentum and heat transfer and derived the following equation:

$$\mathrm{Nu}_{S,L} = \left[\frac{0.03\mathrm{Re}_S^{0.75}\mathrm{Pr}}{1+\frac{1.74(Pr-1)}{\mathrm{Re}_S^{0.125}}}\right]\left(\frac{\eta}{\eta_w}\right)^{0.14} \tag{45}$$

with

Nusselt number $\mathrm{Nu}_{S,L} = \frac{\alpha d_g}{\lambda}$,

Reynolds number $\mathrm{Re}_S = \frac{u_h d_g \rho}{\eta}$.

The physical properties in Eq. (45) (λ, ρ, η, Pr) are evaluated at the mean jacket-side liquid temperature ϑ_J and the dynamic viscosity η_W at the mean jacket wall temperature $\vartheta_{J,w}$. The characteristic length d_g in the Nusselt number and in the Reynolds number and the characteristic velocity u_h in the Reynolds number are given by

$$d_g = \left(\frac{8}{3}\right)^{1/2}\delta, \tag{46}$$

$$u_h = (u_S u_O)^{1/2} + u_A. \tag{47}$$

δ in Eq. (46) is the width of the annular space and u_O in Eq. (47) is the velocity through the inlet tube of the jacket given by

$$u_O = \frac{\dot{V}_J}{\left(\frac{\pi}{4}\right)d_O^2} \tag{48}$$

with $\dot{V}_J$ the volumetric flow rate in the jacket and d_O the inside diameter of the inlet tube. u_S in Eq. (47) is the velocity in the annular space of the jacket; its magnitude depends on the type of flow in the annular space as dictated by the layout of the inlet tube (radial or tangential). $(u_S u_O)^{1/2}$ is the geometric mean velocity in the jacket and u_A is an additional velocity component introduced by Lehrer to take into account the influence of buoyancy.

For radial inlet:

$$u_S = \frac{\dot{V}_J}{\left(\frac{\pi}{4}\right)\left(d_J^2 - d_{BA}^2\right)}, \tag{49}$$

$$u_A = 0.5(2gh_S\beta\Delta\vartheta_J)^{1/2} \tag{50}$$

with d_{BA} the outer vessel diameter, d_J the inner diameter of the jacket ($d_J = d_{BA} + 2\delta$), g the acceleration due to gravity, h_S the jacket height, β the volumetric expansion coefficient, and $\Delta\vartheta_J$ the temperature rise or temperature drop of the jacket-side liquid ($\Delta\vartheta_J = |(\vartheta_{J,i} - \vartheta_{J,o})|$). In Eq. (47), the velocity u_A due to buoyancy is added to the geometric mean velocity $(u_S u_O)^{1/2}$, since an upward jacket-side flow and cooling the contents of the stirred vessel with a temperature rise $\Delta\vartheta_J$ are assumed; in that case u_A and $(u_S u_O)^{1/2}$ have the same direction. This applies also for a downward jacket-side flow and heating the contents of the stirred vessel (temperature drop $\Delta\vartheta_J$). If the velocity component u_A opposes the geometric mean velocity $(u_S u_O)^{1/2}$ (i.e., an upward jacket-side flow and heating the contents of the stirred vessel or a downward jacket-side flow and cooling the contents of the stirred vessel) u_A should be subtracted from $(u_S u_O)^{1/2}$.

For tangential inlet:

$$u_S = \frac{\dot{V}_J}{h_S\delta}, \tag{51}$$

$$u_A = 0. \tag{52}$$

The velocity component u_A due to buoyancy has also a nonzero value with tangential inlet. However, since u_A and $(u_S u_O)^{1/2}$ are perpendicular to each other in this case, vector addition is required; for simplicity Lehrer ignored u_A.

Equation (45) was examined using a jacketed stirred vessel equipped with four baffles and different paddles [35]. The tests were carried out with cooling the contents of the vessel. Other parameters are given below:

$$d_B = 610\,\mathrm{mm}$$
$$\delta = 25.4\,\mathrm{mm}$$
$$\frac{h_L}{d_B} = 1,$$
$$d_O = 19.1\,\mathrm{mm}\ \text{(for radial inlet)}$$
$$d_O = 12.7\ \text{(for tangential inlet)}$$
$$5 < \mathrm{Pr} < 7\ \text{(cooling medium: water)}$$
$$9\times10^3 \le \mathrm{Re}_S \le 4\times10^4\ \text{(for radial inlet)}$$
$$2.2\times10^4 \le \mathrm{Re}_S \le 8\times10^4\ \text{(for tangential inlet)}$$

The ratio of the calculated Nusselt number to the Nusselt number derived experimentally for radial inlet varied between 0.794 and 1.258 with an average of 1.014 and for tangential inlet from 0.759 to 1.293 with an average of 1.037 [35].

Method of Stein and Schmidt

Stein and Schmidt [38] presented different models and carried out own experimental measurements. The measurements were used to compare the different models discussed in the paper including the model of Lehrer. Finally, Stein and Schmidt [38] recommended the following procedure to determine the jacket-side heat transfer coefficient:

A characteristic length l_{ch} is calculated from

$$l_{ch} = \left(\left(\frac{\pi}{2}\right)^2 d_{BA}^2 + h_S^2\right)^{0.5}. \tag{53}$$

A characteristic diameter d_{ch} is calculated from

$$d_{ch} = d_h = 2\delta. \tag{54}$$

A characteristic velocity u_{ch} is calculated as follows:

For radial inlet tubes:

$$u_{ch} = u_{Mit}\left(\frac{\ln\left(\frac{b_{Mit}}{b_{Ein}}\right)}{1-\left(\frac{b_{Ein}}{b_{Mit}}\right)}\right) \tag{55}$$

with

$$b_{\mathrm{Ein}} = \left(\frac{\pi}{8}\right)\left(\frac{d_{\mathrm{O}}^2}{\delta}\right), \tag{56}$$

$$b_{\mathrm{Mit}} = \left(\frac{\pi}{2}\right) d_{\mathrm{BA}} \left(1 + \left(\frac{\pi}{2}\right)^2 \left(\frac{d_{\mathrm{BA}}}{h_{\mathrm{S}}}\right)^2\right)^{0.5}, \tag{57}$$

$$u_{\mathrm{Mit}} = \frac{\dot{V}_{\mathrm{J}}}{2\delta b_{\mathrm{Mit}}}. \tag{58}$$

For tangential inlet tubes and tangential inlet nozzles with diameter d_{O}:

$$u_{\mathrm{ch}} = \left(u_{\mathrm{x}}^2 + u_{\mathrm{z}}^2\right)^{0.5}, \tag{59}$$

$$u_{\mathrm{x}} = u_{\mathrm{O}} \left(\frac{\ln\left[1 + \left(\frac{\xi_{\mathrm{J}} d_{\mathrm{BA}} h_{\mathrm{S}}}{d_{\mathrm{O}}^2}\right)\left(\frac{u_{\mathrm{x}}(0)}{u_{\mathrm{O}}}\right)\right]}{\left(\frac{\xi_{\mathrm{J}} d_{\mathrm{BA}} h_{\mathrm{S}}}{d_{\mathrm{O}}^2}\right)}\right), \tag{60}$$

$$u_{\mathrm{x}}(0) = K_3 + \left(K_3^2 + K_4\right)^{0.5}, \tag{61}$$

$$K_3 = \left(\frac{u_{\mathrm{O}}}{4}\right) - \left(\frac{d_{\mathrm{O}}^2 u_{\mathrm{O}}}{4\xi_{\mathrm{J}} d_{\mathrm{BA}} h_{\mathrm{S}}}\right), \tag{62}$$

$$K_4 = \frac{d_{\mathrm{O}}^2 u_{\mathrm{O}}^2}{2\xi_{\mathrm{J}} d_{\mathrm{BA}} h_{\mathrm{S}}}, \tag{63}$$

$$u_{\mathrm{z}} = \frac{\dot{V}_{\mathrm{J}}}{\pi d_{\mathrm{BA}} \delta}, \tag{64}$$

$$u_{\mathrm{O}} = \frac{\dot{V}_{\mathrm{J}}}{\left(\frac{\pi}{4}\right) d_{\mathrm{O}}^2}. \tag{65}$$

The friction factor ξ_{J} in the above equations is calculated as follows:

For laminar flow through a rectangular gap or an annulus the following equation applies

$$\xi_{\mathrm{J}} = \frac{96}{\mathrm{Re_J}} \tag{66}$$

with the Reynolds number $\mathrm{Re_J}$ given by

$$\mathrm{Re_J} = \frac{u_{\mathrm{ch}} d_{\mathrm{ch}} \rho}{\eta}. \tag{67}$$

For turbulent flow through a noncircular conduit, the friction factor ξ_{J} is equivalent to the friction factor for a circular conduit with the same equivalent diameter. For technically smooth tubes, the friction factor due to Blasius may be used, or

$$\xi_{\mathrm{J}} = \frac{0.3164}{\mathrm{Re_J^{0.25}}} \quad \text{for } 3 \times 10^3 \leq \mathrm{Re_J} \leq 10^5. \tag{68}$$

The characteristic velocity u_{ch} for tangential inlet tubes and tangential nozzles has to be determined iteratively.

Other required dimensionless parameters are:

Grashof number $\mathrm{Gr_J}$ defined by

$$\mathrm{Gr_J} = \frac{g\rho(\rho - \rho_{\mathrm{w}}) d_{\mathrm{ch}}^3}{\eta^2} \text{ (can be either positive or negative, depending on } \rho \text{ and } \rho_{\mathrm{w}}) \tag{69}$$

and the equivalent Reynolds number $\mathrm{Re_{J,eq}}$ defined by

$$\mathrm{Re_{J,eq}} = \left[\mathrm{Re_J^2} \pm \left(\frac{|\mathrm{Gr_J}| \times \left(\frac{h_{\mathrm{S}}}{d_{\mathrm{ch}}}\right)}{50}\right)\right]^{1/2}. \tag{70}$$

The physical properties ρ and η have to be evaluated at the mean jacket-side liquid temperature ϑ_{J} and the density ρ_{w} has to be evaluated at the mean jacket wall temperature $\vartheta_{\mathrm{J,w}}$. The positive sign in Eq. (70) has to be used, when natural convection assists forced convection and vice versa.

The last step embraces the computation of the Nusselt number $\mathrm{Nu_J}$ from the following equation:

$$\mathrm{Nu_J} = \left(\mathrm{Nu_A^3} + \mathrm{Nu_B^3} + \mathrm{Nu_C^3} + \mathrm{Nu_D^3}\right)^{1/3} \left(\frac{\eta}{\eta_{\mathrm{w}}}\right)^{0.14}, \tag{71}$$

where

$$\mathrm{Nu_J} = \frac{\alpha d_{\mathrm{ch}}}{\lambda}, \tag{72}$$

$$\mathrm{Nu_A^3} = 3.66^3, \tag{73}$$

$$\mathrm{Nu_B^3} = 1.62^3 \mathrm{Pr Re_{J,eq}} \left(\frac{d_{\mathrm{ch}}}{l_{\mathrm{ch}}}\right), \tag{74}$$

$$\mathrm{Nu_C^3} = 0.664^3 \mathrm{Pr}\left(\mathrm{Re_{J,eq}}\left(\frac{d_{\mathrm{ch}}}{l_{\mathrm{ch}}}\right)\right)^{1.5}, \tag{75}$$

$$\mathrm{Nu_D^3} = 0 \text{ for } \mathrm{Re_{J,eq}} < 2300, \tag{76}$$

$$\mathrm{Nu_D^3} = 0.0115^3 \mathrm{Pr Re_{J,eq}^{2.7}} \left(1 - \left(\frac{2300}{\mathrm{Re_{J,eq}}}\right)^{2.5}\right)^3 \times \left(1 + \left(\frac{d_{\mathrm{ch}}}{l_{\mathrm{ch}}}\right)^{2/3}\right)^3 \text{ for } \mathrm{Re_{J,eq}} > 2300. \tag{77}$$

The thermal conductivity λ has to be evaluated at the mean jacket-side liquid temperature ϑ_{J} and the dynamic viscosity η_{w} at the mean jacket wall temperature $\vartheta_{\mathrm{J,w}}$. Details about the basis of the different equations are found in [38]. Equation (71) was examined using a jacketed unbaffled stirred vessel with an internal diameter of 544 mm, a flat bottom, and a variable height. The liquid in the vessel was agitated by means of a paddle. The three different inlet arrangements to the jacket (radial inlet tube, tangential inlet tube, and tangential nozzle) were examined. The tests were carried out with an upward flow for the case in which, the contents of the vessel were cooled. Other geometrical and operating parameters are given below:

$$58 \leq \mathrm{Re_{J,eq}} \leq 1.1 \times 10^4,$$

$$3 \leq \mathrm{Pr} \leq 830,$$

$$1.2 \leq \frac{\eta}{\eta_{\mathrm{w}}} \leq 3.5,$$

$$0.035 \leq \frac{d_{\mathrm{ch}}}{l_{\mathrm{ch}}} \leq 0.054.$$

The own measurements show for some experimental points deviations up to about ±50% between predictions and measurements. The mean relative errors for all measurements amount to 28.6% for radial inlet tubes, 26.4% for tangential inlet tubes, and 27.7% for tangential nozzles and are lower than those obtained from the model of Lehrer (43.7%, 44.0%, and 58.9%, respectively) [38].

Example 5:

It is required to calculate the heat transfer coefficient α on the jacket-side of a stirred vessel. The jacket is equipped with a tangential inlet tube placed at the bottom of the jacket. The contents of the stirred vessel are cooled by means of water

flowing through the annular space of the jacket. The data given below are available:

Outside vessel diameter	$d_{BA} = 0.6\,m$
Width of annular space	$\delta = 0.025\,m$
Height of jacket	$h_S = 0.6\,m$
Inlet diameter of tangential inlet tube	$d_O = 0.025\,m$
Jacket-side mass flow rate	$\dot{M}_J = 2.5\,kg\,s^{-1}$
Inlet water temperature	$\vartheta_{J,i} = 20°C$
Outlet water temperature	$\vartheta_{J,o} = 40°C$
Mean jacket wall temperature	$\vartheta_{J,w} = 80°C$

Physical properties:

At mean water temperature in jacket $\vartheta_J = \frac{20+40}{2} = 30°C$:

Prandtl number	$Pr = 5.42$
Thermal conductivity	$\lambda = 0.615\,W\,m^{-1}\,K^{-1}$
Density	$\rho = 995.7\,kg\,m^{-3}$
Dynamic viscosity	$\eta = 798 \times 10^{-6}\,Pa\,s$

At inlet water temperature $\vartheta_{J,i} = 20°C$:

Density	$\rho = 998.3\,kg\,m^{-3}$

At mean jacket wall temperature $\vartheta_{J,w} = 80°C$:

Density	$\rho_w = 971.8\,kg\,m^{-3}$
Dynamic viscosity	$\eta_w = 355 \times 10^{-6}\,Pa\,s$

Solution:

Method of Lehrer:

$$\dot{V}_J = \frac{\dot{M}_J}{\rho_{(at\,\vartheta_J=30°C)}} = \frac{2.5}{995.7} = 2.51 \times 10^{-3}\,m^3\,s^{-1},$$

Equation (51): $u_S = \frac{\dot{V}_J}{h_S \delta} = \frac{2.51\times10^{-3}}{0.6\times0.025} = 0.167\,m\,s^{-1}$,

Equation (48): $u_O = \frac{\dot{V}_J}{\left(\frac{\pi}{4}\right)d_O^2} = \frac{2.51\times10^{-3}}{\left(\frac{\pi}{4}\right)\times0.025^2} = 5.1\,m\,s^{-1}$,

Equation (52): $u_A = 0\ m\,s^{-1}$,

Equation (47): $u_h = (u_S u_O)^{1/2} + u_A = (0.167 \times 5.1)^{1/2} + 0 = 0.923\,m\,s^{-1}$,

Equation (46): $d_g = \left(\frac{8}{3}\right)^{1/2}\delta = \left(\frac{8}{3}\right)^{1/2}\times0.025 = 0.0408\ m$,

$$Re_S = \frac{u_h d_g \rho}{\eta} = \frac{0.923 \times 0.0408 \times 995.7}{798 \times 10^{-6}} = 4.7 \times 10^4,$$

Equation (45):

$$Nu_{S,L} = \left[\frac{0.03 Re_S^{0.75} Pr}{1 + \frac{1.74(Pr-1)}{Re_S^{0.125}}}\right]\left(\frac{\eta}{\eta_w}\right)^{0.14} = \left[\frac{0.03 \times (4.7\times10^4)^{0.75} \times 5.42}{1 + \frac{1.74(5.42-1)}{(4.7\times10^4)^{0.125}}}\right]\left(\frac{798\times10^{-6}}{355\times10^{-6}}\right)^{0.14} = 193.5.$$

The heat transfer coefficient is given by

$$\alpha = \frac{Nu_{S,L}\lambda}{d_g} = \frac{193.5 \times 0.615}{0.0408} = 2917\ W\,m^{-2}K^{-1}.$$

Method of Stein and Schmidt:

Equation (53):

$$l_{ch} = \left(\left(\frac{\pi}{2}\right)^2 d_{BA}^2 + h_S^2\right)^{0.5} = \left(\left(\frac{\pi}{2}\right)^2 \times 0.6^2 + 0.6^2\right)^{0.5} = 1.12\,m,$$

Equation (54): $d_{ch} = 2\delta = 2 \times 0.025 = 0.05\,m$,

The iterative solution of Eqs. (59–63) gives with the help of Eqs. (67) and (68) the following numerical value for the velocity u_{ch}:

$$u_{ch} = 0.855\,m\,s^{-1}.$$

Check:

Equation (67): $Re_J = \frac{u_{ch} d_{ch} \rho}{\eta} = \frac{0.855\times0.05\times995.7}{798\times10^{-6}} = 53341$.

Equation (68): $\xi_J = \frac{0.3164}{Re_J^{0.25}} = \frac{0.3164}{53341^{0.25}} = 0.02081$ (since $3 \times 10^3 \le Re_J \le 10^5$; assumption: smooth tube),

$u_O = 5.1\,m\,s^{-1}$ (s. solution: method of Lehrer),

Equation (62): $K_3 = \left(\frac{u_O}{4}\right) - \left(\frac{d_O^2 u_O}{4\xi_J d_{BA} h_S}\right) = \left(\frac{5.1}{4}\right) - \left(\frac{0.025^2 \times 5.1}{4 \times 0.02081 \times 0.6 \times 0.6}\right) = 1.169\,m\,s^{-1}$,

Equation (63): $K_4 = \frac{d_O^2 u_O^2}{2\xi_J d_{BA} h_S} = \frac{0.025^2 \times 5.1^2}{2 \times 0.02081 \times 0.6 \times 0.6} = 1.085\,m^2\,s^{-2}$,

Equation (61): $u_x(0) = K_3 + \left(K_3^2 + K_4\right)^{0.5} = 1.169 + (1.169^2 + 1.085)^{0.5} = 2.735\,m\,s^{-1}$,

Equation (60):

$$u_x = u_O\left(\frac{\ln\left[1 + \left(\frac{\xi_J d_{BA} h_S}{d_O^2}\right)\left(\frac{u_x(0)}{u_O}\right)\right]}{\left(\frac{\xi_J d_{BA} h_S}{d_O^2}\right)}\right) = 5.1\left(\frac{\ln\left[1 + \left(\frac{0.02081\times0.6\times0.6}{0.025^2}\right)\left(\frac{2.735}{5.1}\right)\right]}{\left(\frac{0.02081\times0.6\times0.6}{0.025^2}\right)}\right) = 0.853\,m\,s^{-1},$$

Equation (64): $u_z = \frac{\dot{V}_J}{\pi d_{BA}\delta} = \frac{2.51\times10^{-3}}{\pi\times0.6\times0.025} = 0.0532\,m\,s^{-1}$,

Equation (59): $u_{ch} = \left(u_x^2 + u_z^2\right)^{0.5} = (0.853^2 + 0.0532^2)^{0.5} = 0.855\,m\,s^{-1}$.

Thus, the numerical value $u_{ch} = 0.855\,m\,s^{-1}$ fulfills Eqs. (59–63).

Equation (69):

$$Gr_J = \frac{g\rho(\rho - \rho_w)d_{ch}^3}{\eta^2} = \frac{9.81 \times 995.7 \times (995.7 - 971.8) \times 0.05^3}{(798\times10^{-6})^2} = 4.58 \times 10^7,$$

Equation (70):

$$Re_{J,eq} = \left[Re_J^2 + \left(\frac{|Gr_J| \times \left(\frac{h_S}{d_{ch}}\right)}{50}\right)\right]^{1/2} = \left[(53341)^2 + \left(\frac{(4.58\times10^7)\times\left(\frac{0.6}{0.05}\right)}{50}\right)\right]^{1/2} = 53444.$$

The positive sign in Eq. (70) is considered, since natural convection assists forced convection. Comparing the numerical values of Re_J and $Re_{J,eq}$ indicates that natural convection in the considered case is insignificant.

Equation (73): $Nu_A^3 = 3.66^3 = 49.03$,

Equation (74): $Nu_B^3 = 1.62^3 PrRe_{J,eq}\left(\frac{d_{ch}}{l_{ch}}\right) = 1.62^3 \times 5.42 \times 53444 \times \left(\frac{0.05}{1.12}\right) = 5.5 \times 10^4$,

Equation (75): $Nu_C^3 = 0.664^3 Pr\left(Re_{J,eq}\left(\frac{d_{ch}}{l_{ch}}\right)\right)^{1.5} = 0.664^3 \times 5.42 \times \left(53444 \times \left(\frac{0.05}{1.12}\right)\right)^{1.5} = 1.85 \times 10^5$,

Equation (77):

$$Nu_D^3 = 0.0115^3 PrRe_{J,eq}^{2.7}\left(1 - \left(\frac{2300}{Re_{J,eq}}\right)^{2.5}\right)^3\left(1 + \left(\frac{d_{ch}}{l_{ch}}\right)^{2/3}\right)^3 = 0.0115^3 \times 5.42 \times 53444^{2.7} \times \left(1 - \left(\frac{2300}{53444}\right)^{2.5}\right)^3\left(1 + \left(\frac{0.05}{1.12}\right)^{2/3}\right)^3 = 6.84 \times 10^7.$$

Equation (71): $$\mathrm{Nu_J} = \left(\mathrm{Nu_A^3} + \mathrm{Nu_B^3} + \mathrm{Nu_C^3} + \mathrm{Nu_D^3}\right)^{1/3} \left(\frac{\eta}{\eta_w}\right)^{0.14}$$
$$= \left(49.03 + \left(5.5 \times 10^4\right) + \left(1.85 \times 10^5\right) + \left(6.84 \times 10^7\right)\right)^{1/3} \left(\frac{798 \times 10^{-6}}{355 \times 10^{-6}}\right)^{0.14}$$
$$= 458.6\,.$$

The heat transfer coefficient α is given by

$$\alpha = \frac{\mathrm{Nu_J}\lambda}{d_{ch}} = \frac{458.6 \times 0.615}{0.05} = 5641\,\mathrm{W\,m^{-2}K^{-1}}.$$

The example shows that high uncertainty exists in evaluating the jacket-side heat transfer coefficient. This might lead in certain cases to underestimating the heat transfer surface required for a particular heat transfer rate during dimensioning a newly designed stirred vessel for a particular process. It is also not clear a priori, which method predicts the more conservative heat transfer coefficient under all possible design conditions. In many cases this can be compensated during operation by changing the flow rate and/or the temperature of the jacket-side liquid. If this facility is not available, it might be advantageous – particularly in cases, in which underestimating the heat transfer rate has an adverse effect on the process – to calculate the heat transfer coefficient from both methods and use in dimensioning the stirred vessel the more conservative value. However, in many cases the heat transfer coefficient on the inner surface of the stirred vessel, especially with high viscous liquids, is much smaller than the jacket-side heat transfer coefficient; in such cases the high uncertainty in evaluating the jacket-side heat transfer coefficient is largely suppressed in calculating the overall heat transfer coefficient.

2.2.2 Heat Transfer from the Inside Surface of a Helical Coil

Helical Coil of Circular Tubes Inside the Stirred Vessel

Secondary effects in the flow through a helical coil of circular tubes are responsible for a better heat transfer than that in straight tubes. Equations for the determination of the heat transfer coefficient in such cases are presented in Chap. G3.

Helical Coil of Semicircular Tubes Welded at the Outside Surface of the Stirred Vessel

According to Stein and Schmidt [37], the equations given in Chap. G3 for heat transfer from a helical coil of circular tubes can be used also for a helical coil of semicircular tubes welded at the outer surface of a stirred vessel. The inside tube diameter in the Reynolds number and in the Nusselt number in the equations in Chap. G3 should be replaced now by the thermal diameter $d_{th,H}$ of the semicircular tubes given by $d_{th,H} = (\pi/2)d_i$ with d_i the internal diameter of the semicircular tubes. The critical Reynolds number for a helical coil of semicircular tubes can be calculated from the equation in Chap. G3 for a helical coil of circular tubes by replacing the curvature ratio in that equation by the ratio $(d_i/(2d_{BA}))$.

2.3 Methods of Heating or Cooling of a Stirred Vessel

In batch operation, the temperature of the contents of the stirred vessel, at least during the early period of the process, is time dependent. The change of temperature of the vessel contents with time depends on the method used to heat (or cool) the contents of the stirred vessel. Usually, one of the following methods is used:

1. Heat added at a constant heat flow rate $\dot{Q}$ (e.g., electrical heating); heat removal at a constant heat flow rate is difficult to achieve technically.
2. Heat added or removed at a spatially constant and time-independent temperature ϑ_J of the heating or cooling medium (e.g., condensation of a saturated vapor or boiling of a saturated liquid in the jacket).
3. Heat added or removed by means of a thermal fluid (mostly liquid) flowing in the jacket or through the coil. The temperature of the thermal fluid changes from the constant inlet temperature $\vartheta_{J,i}$ to the time-dependent outlet temperature $\vartheta_{J,o}(t)$.

Equations (78)–(80), given hereafter to calculate the change of temperature of the vessel contents with time are valid under the following assumptions:

- Heat capacity of the stirred vessel is small compared with heat capacity of the vessel contents.
- Heat losses to or heat gains from the surroundings are negligible.
- Heat added or removed by means of a continuous gas flow during aerating the contents of the stirred vessel in a two-phase system "gas–liquid" or a multiphase system "gas–liquid–solid" is negligible.
- Physical properties (specific heats) of the jacket-side fluid and the vessel contents are independent of temperature.
- Overall heat transfer coefficient is independent of temperature.
- Mechanical power required by an impeller (dissipated in the vessel contents as heat) is negligible.
- Heat added to the vessel contents due to a chemical reaction is negligible.

For constant heat flow rate $\dot{Q}$:

$$\vartheta(t) = \vartheta_0 + \frac{\dot{Q}}{Mc}t. \tag{78}$$

For spatially constant time-independent temperature ϑ_J of the thermal fluid:

$$\frac{\vartheta_J - \vartheta(t)}{\vartheta_J - \vartheta_0} = \exp\left(-\frac{UA}{Mc}t\right). \tag{79}$$

For constant inlet temperature $\vartheta_{J,i}$ and time-dependent exit temperature $\vartheta_{J,o(t)}$ of the thermal fluid:

$$\frac{\vartheta_{J,i} - \vartheta(t)}{\vartheta_{J,i} - \vartheta_0} = \exp\left[-\frac{\dot{M}_J c_J}{Mc}\left\{1 - \exp\left(-\frac{UA}{\dot{M}_J c_J}\right)\right\}t\right]. \tag{80}$$

Wolf [39] included the mechanical power P_{Ad} required by the impeller and any additional periphery equipment (e.g., pumps

and compressors, which consume mechanical power and lead to heat dissipation in the contents of the vessel) and obtained the following equations:
For constant heat flow rate $\dot{Q}$:

$$\vartheta(t) = \vartheta_0 + \frac{\dot{Q} + P_{Ad}}{Mc}\, t. \tag{81}$$

For spatially constant time-independent temperature ϑ_J of the thermal fluid:

$$\frac{\vartheta_J + \left(\frac{P_{Ad}}{UA}\right) - \vartheta(t)}{\vartheta_J + \left(\frac{P_{Ad}}{UA}\right) - \vartheta_0} = \exp\left(-\frac{UA}{Mc}t\right). \tag{82}$$

For constant inlet temperature $\vartheta_{J,i}$ and time-dependent exit temperature $\vartheta_{J,o}(t)$ of the thermal fluid:

$$\frac{\vartheta_{J,i} + \left(\frac{K_1}{K_2}\right) - \vartheta(t)}{\vartheta_{J,i} + \left(\frac{K_1}{K_2}\right) - \vartheta_0} = \exp\left[-\frac{\dot{M}_J c_J}{Mc}\left\{1 - \exp\left(-\frac{UA}{\dot{M}_J c_J}\right)\right\}t\right], \tag{83}$$

where

$$K_1 = \frac{P_{Ad}}{Mc}, \tag{84}$$

$$K_2 = \frac{\dot{M}_J c_J}{Mc}\left\{1 - \exp\left(-\frac{UA}{\dot{M}_J c_J}\right)\right\}. \tag{85}$$

Equations (78)–(83) give the temperature $\vartheta(t)$ of the vessel contents as a function of the elapsed time t. Rearranging the equations gives the required time t to reach a certain temperature $\vartheta(t)$.

The specific heat capacity c in Eqs. (78–85) for the contents of the stirred vessel (single-phase liquid or quasi-homogeneous-phase in two-phase or multiphase systems) and the specific heat capacity c_J for the jacket (or coil) fluid are to be evaluated at the mean temperatures; bearing in mind that the temperatures are time- and space-dependent. The thermal resistance of the vessel wall and any possible fouling have to be considered in evaluating the overall heat transfer coefficient. In case of enameled stirred vessels, the thermal resistance of the enamel may be larger than that of the thermal boundary layers of the fluids on both sides of the vessel wall, as well as that of the vessel wall itself. If the overall heat transfer coefficient U changes with time due to change in the physical properties, the time-dependent overall heat transfer coefficient $U(t)$ has to be replaced by a mean value U. Another procedure, which might be more appropriate (but time-consuming) in case of a significant change in $U(t)$ with time (due to a possible significant change in the viscosity of the vessel contents with time) is to apply the given equations for small time intervals (or small temperature intervals) with a mean overall heat transfer coefficient in each interval.

2.4 Remarks on Maximal Heat Removal

Increasing the speed of rotation of the impeller during cooling the contents of a stirred vessel leads to an increase in the vessel-side heat transfer coefficient and hence to an increase in the heat removed by the cooling medium in a jacket or in a coil; at the same time, the power consumption of the impeller increases with the increase in the impeller speed. During exothermal reactions, not only the heat of reaction, but also the mechanical energy dissipated as heat should be removed from the vessel contents. Since the power consumption of the impeller increases much faster with the impeller speed than the overall heat transfer coefficient, the net heat removal – i.e., heat of reaction less heat dissipated by the impeller – from the vessel contents with increasing impeller speed under otherwise same operating conditions passes through a maximum. Increasing the impeller speed beyond the optimal speed based on maximal net heat removal during dimensioning a newly designed stirred vessel leads to an increase in both investment and operating costs. Thus, the optimal impeller speed based on economical considerations is either less than or equal to the optimal impeller speed based on maximal net heat removal. Methods as well as examples for the determination of the optimal impeller speed for maximal net heat removal can be presented [40, 41].

3 Power Consumption

In this section, diagrams and equations are presented for the determination of the power consumption of different impellers in single-phase and multiphase systems; they are valid for stirred vessels without internal coils. The remarks made in Sect. 2 about the validity ranges of the empirical correlations apply also in this section. The predicted power consumption of the impellers does not include the additional power required to cover the demand of other components of the stirred vessel (e.g., gearbox and shaft bearings); the power consumption of these components has to be added to the power consumption of the impeller in determining the total power consumption of the system.

3.1 Single-Phase Systems

3.1.1 Newtonian Liquids

The power consumption of an impeller to agitate a single-phase Newtonian liquid in a vessel can be determined from dimensionless equations of the following form [42]:

$$\mathrm{Ne} = f(\mathrm{Re}, \mathrm{Fr}, \pi_1, \pi_2, \ldots), \tag{86}$$

with

$$\text{Newton number Ne} = \frac{P}{\rho n^3 d_R^5},$$

$$\text{Reynolds number Re} = \frac{d_R^2 n \rho}{\eta},$$

$$\text{Froude number Fr} = \frac{n^2 d_R}{g}.$$

π_1, π_2,...are geometrical parameters. The Froude number takes into account the fluid dynamic effects at the free surface of the liquid such as vortex formation. If vortex formation is suppressed (e.g., through the use of baffles), the Froude number

in Eq. (86) can be ignored. Thus, in the case of suppressing vortex formation the Newton number for systems having same geometrical ratios but different sizes may be determined from the simpler equation

$$\mathrm{Ne} = f(\mathrm{Re}). \tag{87}$$

According to measurements made by a number of investigators, the Newton number in the laminar range can be expressed by

$$\mathrm{Ne} = \frac{C_{\mathrm{N,lam}}}{\mathrm{Re}} \tag{88}$$

and in the turbulent range by

$$\mathrm{Ne} = \frac{C_{\mathrm{N,turb}}}{\mathrm{Re}^{m}} \; (m << 1). \tag{89}$$

$C_{\mathrm{N,lam}}$ and $C_{\mathrm{N,turb}}$ are constants. If the stirred vessel is equipped with baffles, the Newton number in the turbulent range is nearly constant at high Reynolds numbers. The range of the Reynolds number, in which Eqs. (88) and (89) are valid, depends on the type of the impeller. In a number of publications, the dependence of the Newton number on the Reynolds number in a wide range covering laminar, transition, and turbulent ranges is presented graphically. A comprehensive review can be found in [43, 44].

Flat-blade turbine or pitched-blade impeller

Figure 13 gives the dependence of the Newton number on the Reynolds number and the Froude number for a flat-blade turbine (see Fig. 2a) from measurements made by Rushton et al. [45, 46] on stirred baffled and unbaffled vessels with a flat bottom and an inner vessel diameter of 457 mm. The equipment used has the following standard geometrical parameters:

$$\frac{d_{\mathrm{R}}}{d_{\mathrm{B}}} = \frac{1}{3},$$
$$\frac{h_{\mathrm{R}}}{d_{\mathrm{B}}} = \frac{1}{3},$$
$$\frac{h_{\mathrm{L}}}{d_{\mathrm{B}}} = 1,$$
$$Z = 6$$
$$\frac{h}{d_{\mathrm{R}}} = \frac{1}{5},$$
$$\frac{b_{\mathrm{R}}}{d_{\mathrm{R}}} = \frac{1}{4},$$
$$n_{\mathrm{S}} = 4 \text{ (for baffled vessel)}.$$

The exponent r of the Froude number in Fig. 13 is also given [45, 46]:
For unbaffled vessels:

$$r = 0 \quad \text{for Re} \leq 300, \tag{90}$$
$$r = \frac{a - \log \mathrm{Re}}{b} \quad \text{for Re} > 300. \tag{91}$$

For baffled vessels:

$$r = 0 \text{ (Newton number independent of the Froude number)}. \tag{92}$$

According to Rushton et al. [45, 46], the constants a and b in Eq. (91) have the following values in the examined ranges:

$$a = 1.0, \tag{93}$$
$$b = 40.0. \tag{94}$$

The baffle width b_s was changed in three steps as follows:

$$\frac{b_{\mathrm{S}}}{d_{\mathrm{B}}} = 0.04, 0.10, 0.17.$$

Figure 13 shows that the baffles have no influence on the Newton number in the laminar range (Re $\leq$ 10), but they lead to a higher Newton number in the transient and turbulent ranges; the increase in the Newton number is larger when the width of the baffles is increased. The Newton number for baffled vessels has a minimum at a Reynolds number of about 200 and is independent of the Reynolds number at very high Reynolds numbers (Re $\geq 10^4$).

Figure 14 shows the dependence of the Newton number on the Reynolds number from experimental measurements made

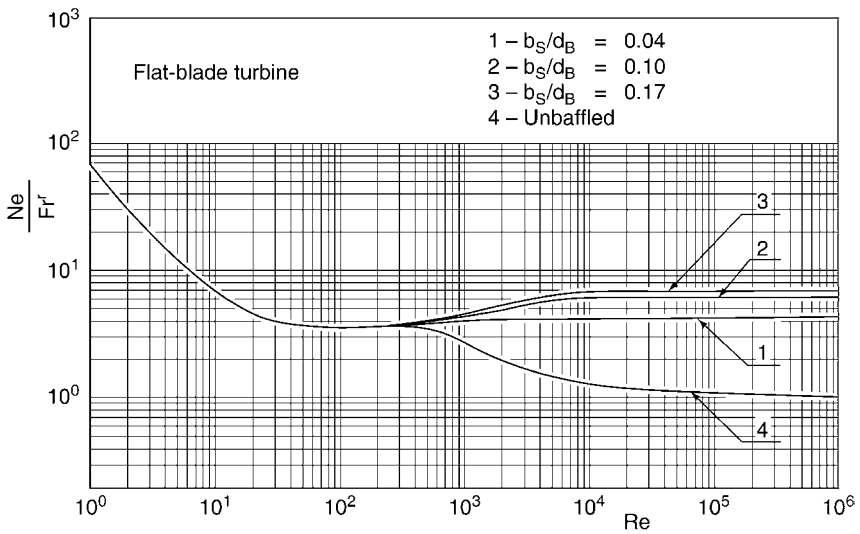

N3. Fig. 13. Dependence of the Newton number on the Reynolds number and the Froude number for a flat-blade turbine according to Rushton et al. [45, 46]. (With permission of the American Institute of Chemical Engineers.)

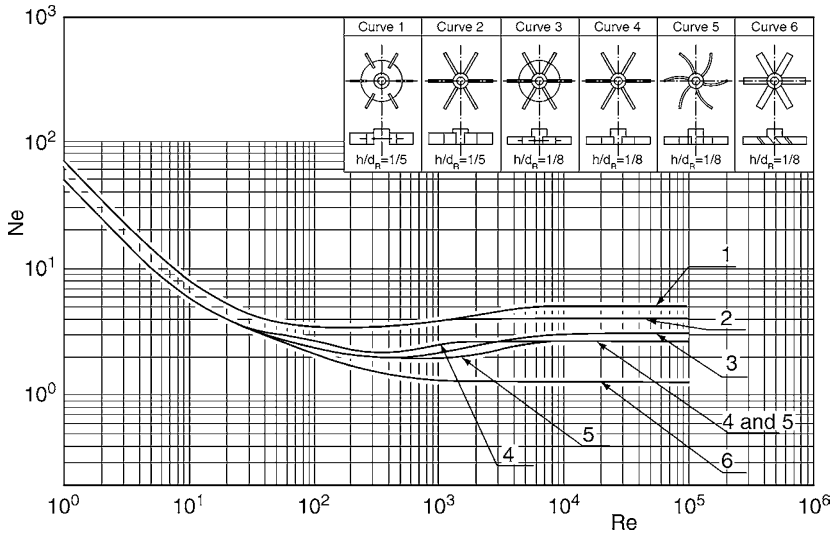

N3. Fig. 14. Dependence of the Newton number on the Reynolds number for different impellers according to Bates et al. [47]. (With permission of the Ind Chem Process Des Dev – American Chemical Society.)

by Bates et al. [47] for six different impellers. The examined stirred vessels shown in Fig. 14 had internal vessel diameters between 152 and 610 mm and were equipped with four baffles with a ratio $(b_S/d_B) = 1/12$; the other geometrical parameters (d_R/d_B), (h_R/d_B), and (h_L/d_B) were similar to the standard parameters in the investigation of Rushton et al. [45, 46]. Curves 1 and 3 are for two different flat-blade turbines, curves 2 and 4 for two different flat-blade impellers with the blades having full length originating at the hub, curve 5 for an impeller with curved blades, and curve 6 for a pitched-blade impeller. The impellers shown in curves 1 and 3 or 2 and 4 differ from one another in the ratio (h/d_R). According to Bates et al. [47], the experimentally determined Newton number in their investigation for the standard flat-blade turbine (curve 1) was in the turbulent range less than that determined by Rushton et al. [45, 46] under similar operating conditions. At a Reynolds number $Re = 10^5$, Bates et al. measured with two stirred vessels equipped with baffles having slightly different baffle width ratios ($b_S/d_B = 1/12$ and $1/10$) Newton numbers of 4.8 and 5.0, respectively; Rushton et al. measured for the same Reynolds number and a baffle width ratio $b_S/d_B = 1/10$ a Newton number of 6.3.

Hirschberg [43] recommends the following equations to predict approximately the Newton number for standard impellers:

For an unbaffled stirred vessel:

Flat-blade turbine or pitched-blade impeller:

$$Ne = \frac{50}{Re} \text{ for } 1 < Re < 3.1, \tag{95}$$

$$Ne = \frac{4}{(\log Re)^2} \text{ for } 3.1 < Re < 553, \tag{96}$$

$$Ne = \frac{1}{Re^{0.1}} \text{ for } 553 < Re < 10^5. \tag{97}$$

For a baffled stirred vessel:

Flat-blade turbine:

$$Ne = \frac{80}{Re} \text{ for } 1 < Re < 16, \tag{98}$$

$$Ne = 5 \text{ for } 16 < Re < 10^5. \tag{99}$$

Pitched-blade impeller:

$$Ne = \frac{80}{Re} \text{ for } 1 < Re < 40, \tag{100}$$

$$Ne = 2 \text{ for } 40 < Re < 10^5. \tag{101}$$

The higher power consumption of a flat-blade turbine at low Reynolds numbers in the laminar range $(1 \le Re \le 3.1)$ as a result of using baffles (compare Eqs. (95) and (98)) was not noticed by Rushton et al. [45, 46] (see Fig. 13).

Propeller

The power consumption for a propeller (see Fig. 2c) may be predicted according to Rushton et al. [45, 46] for different geometrical parameters from Fig. 15. The measurements were made with stirred vessels (flat bottom) having different vessel diameters varying from 330 to 1372 mm. Curves 1–5 in Fig. 15 are for unbaffled stirred vessels and curve 6 is for a baffled vessel with four baffles and a geometrical ratio $b_S/d_B = 0.1$. The geometrical parameters of the examined propellers are given in Fig. 15.

Equations (90)–(92) giving the exponent r of the Froude number are also valid for a propeller. The constants a and b in Eq. (91), which depend on the geometrical ratio d_R/d_B, are given in Table 3.

Hirschberg [43] recommends the following equations for an approximate evaluation of the Newton number for propellers with standard geometries:

For an unbaffled stirred vessel:

$$Ne = \frac{50}{Re} \text{ for } 1 < Re < 3.1, \tag{102}$$

$$Ne = \frac{4}{(\log Re)^2} \text{ for } 3.1 < Re < 2 \times 10^4. \tag{103}$$

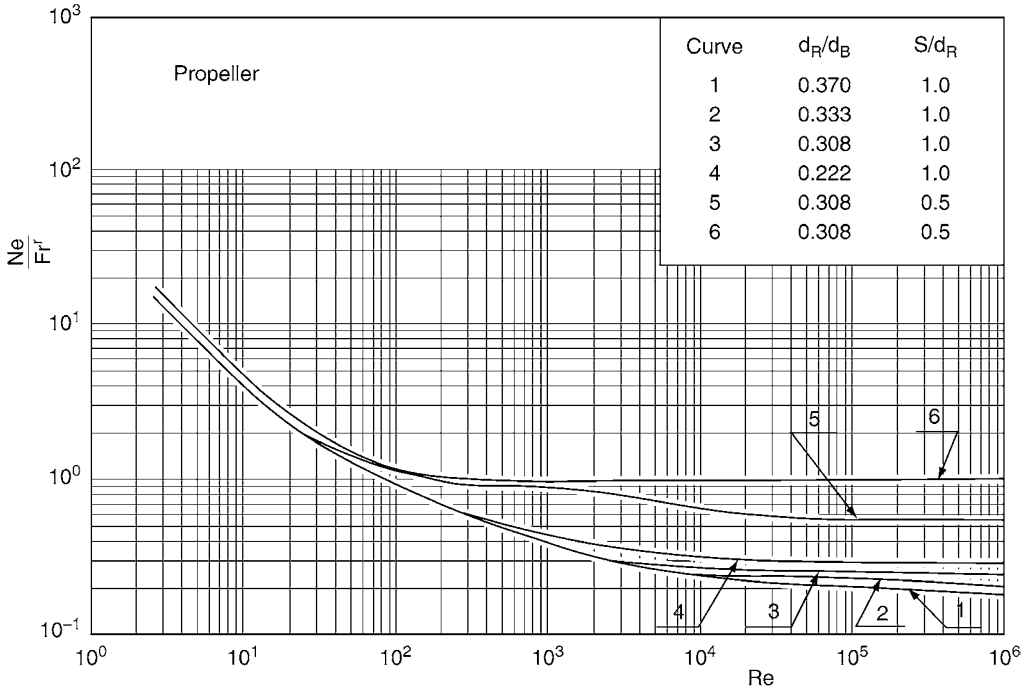

N3. Fig. 15. Dependence of the Newton number on the Reynolds number and the Froude number for a Propeller according to Rushton et al. [45, 46]. (With permission of the American Institute of Chemical Engineers.)

N3. Table 3. Values of the constants a and b in Eq. (91) for propellers with different ratios d_R/d_B

d_R/d_B	a	b
0.471	2.6	18.0
0.370	2.3	18.0
0.333	2.1	18.0
0.308	1.7	18.0
0.222	0	18.0

For a baffled stirred vessel:

$$\mathrm{Ne} = \frac{50}{\mathrm{Re}} \text{ for } 1 < \mathrm{Re} < 3.1, \tag{104}$$

$$\mathrm{Ne} = \frac{4}{(\log \mathrm{Re})^2} \text{ for } 3.1 < \mathrm{Re} < 635. \tag{105}$$

$$\mathrm{Ne} = 0.8\mathrm{Re}^{-0.07} \text{ for } 635 < \mathrm{Re} < 2 \times 10^5. \tag{106}$$

Pfaudler *impeller*

According to Post [8], the Newton number for a Pfaudler impeller (see Fig. 5) is given by:
For an unbaffled stirred vessel:

$$\mathrm{Ne} \approx 0.32 \text{ for } 6 \times 10^3 < \mathrm{Re} < 5 \times 10^4. \tag{107}$$

For a baffled stirred vessel with four standard baffles:

$$\mathrm{Ne} \approx 1.2 \text{ for } 2 \times 10^4 < \mathrm{Re} < 5 \times 10^4. \tag{108}$$

Validity ranges:

$$\frac{d_R}{d_B} = 0.513,$$
$$\frac{h_L}{d_B} = 1.0.$$

Paddle

Figure 16 shows the dependence of the Newton number on the Reynolds number for a paddle (see Fig. 2d) according to measurements carried out by Zlokarnik [48] in an unbaffled stirred vessel with a flat bottom and internal diameters of 200, 400, and 600 mm.
Validity ranges:

$$\frac{d_R}{d_B} = 0.5,$$
$$\frac{h_L}{d_B} = 1,$$
$$\frac{h}{d_R} = 1,$$
$$\frac{h_{RK}}{d_R} = 0.4.$$

Hirschberg [43] recommends for an approximate evaluation of the Newton number for a paddle ($h/d_R < 0.25$) the following equations:
For an unbaffled stirred vessel:

$$\mathrm{Ne} = \frac{50}{\mathrm{Re}} \text{ for } 1 < \mathrm{Re} < 3.1, \tag{109}$$

$$\mathrm{Ne} = \frac{4}{(\log \mathrm{Re})^2} \text{ for } 3.1 < \mathrm{Re} < 553, \tag{110}$$

$$\mathrm{Ne} = \frac{1}{\mathrm{Re}^{0.1}} \quad \text{for } 553 < \mathrm{Re} < 10^5. \tag{111}$$

For a baffled stirred vessel:

$$\mathrm{Ne} = \frac{80}{\mathrm{Re}} \quad \text{for } 1 < \mathrm{Re} < 24, \tag{112}$$

$$\mathrm{Ne} = \frac{10}{3} \quad \text{for } 24 < \mathrm{Re} < 10^5 \text{ and } \frac{d_R}{d_B} = \frac{1}{3}. \tag{113}$$

Anchor Impeller

The dependence of the Newton number on the Reynolds number for an anchor impeller (see Fig. 2e) according to measurements made by Zlokarnik [48] is shown in Fig. 17; the examined stirred vessels with flat bottom had internal diameters of 190 and 290 mm.

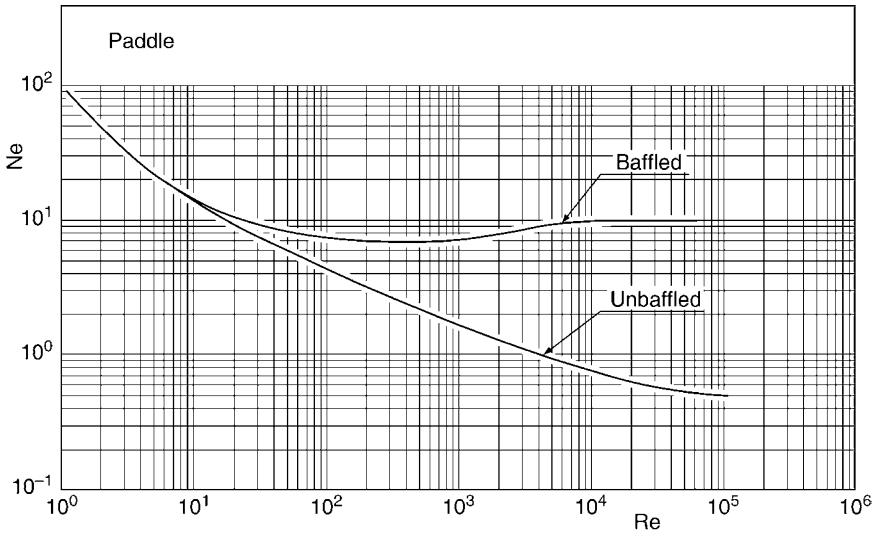

N3. Fig. 16. Dependence of the Newton number on the Reynolds number for a paddle according to Zlokarnik [48] (With permission of "VCH-Verlag.")

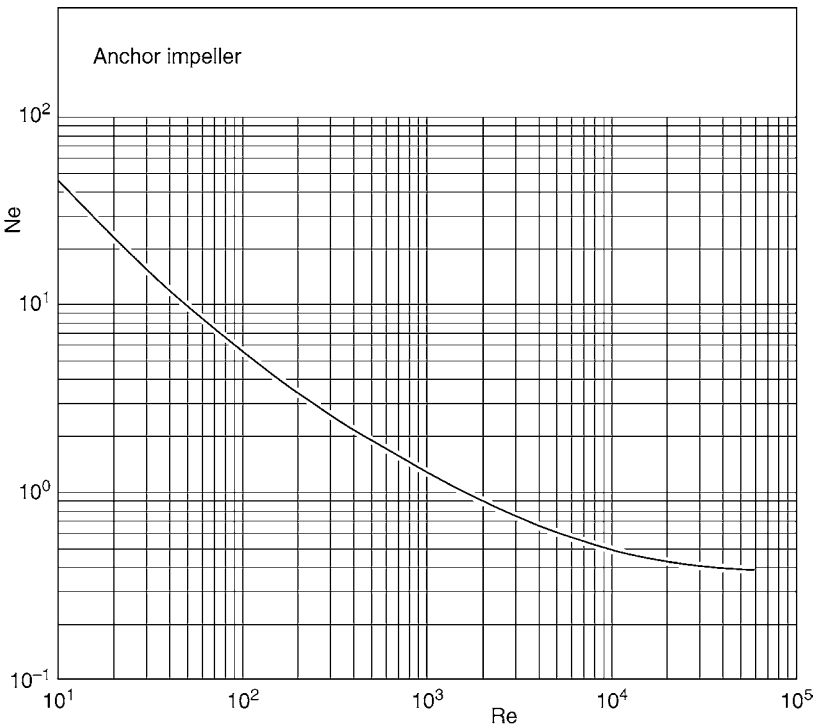

N3. Fig. 17. Dependence of the Newton number on the Reynolds number for an anchor impeller according to Zlokarnik [48]. (With permission of "VCH-Verlag.")

Validity ranges:

$$\frac{h}{d_B} = 1.0,$$
$$\frac{b_{SR}}{d_R} = 0.1,$$
$$\frac{d_B}{d_R} = 1.02,$$
$$\frac{h_{RK}}{d_R} = 0.01,$$
$$\frac{h_L}{d_B} = 1.0.$$

The examined anchor impellers had two or four arms; the measurements show that the Newton number is independent of the number of arms.

Uhl and Voznik [49] examined the influence of the clearance between the anchor impeller and the inside surface of the vessel on the power consumption of an anchor impeller. The experimental measurements were presented graphically. According to their measurements, the power consumption of the impeller increases with decreasing clearance. However, the influence of the clearance on the Newton number diminishes at high Reynolds numbers ($Re > 10^3$); this is attributed to the decreasing influence of viscosity with increasing Reynolds number.

For an approximate determination of the Newton number for anchor impellers, Hirshberg [43] recommends the following equations:

For an unbaffled stirred vessel:

$$Ne = \frac{180}{Re} \quad \text{for } 1 < Re < 167, \tag{114}$$

$$Ne = \frac{3}{Re^{0.2}} \quad \text{for } 167 < Re < 5 \times 10^4. \tag{115}$$

For a baffled stirred vessel:

$$Ne = \frac{180}{Re} \quad \text{for } 1 < Re < 30, \tag{116}$$

$$Ne = 6 \text{ for } 30 < Re < 10^5. \tag{117}$$

Helical impeller

Figure 18 shows the dependence of the Newton number on the Reynolds number based on measurements carried out by Zlokanik [48] with helical impellers having two ribbons and a pitch ratio $(S/d_R) = 0.5$. Other geometrical parameters are

$$\frac{h_L}{d_B} = 1.0,$$
$$\frac{h}{d_B} = 1.0$$
$$\frac{d_B}{d_R} = 1.02,$$
$$\frac{h_{RK}}{d_R} = 0.01,$$
$$\frac{b_{WR}}{d_R} = 0.1.$$

Additional measurements presented in [48] with geometrically different helical impellers having one or two ribbons and pitch ratios $(S/d_R) = 0.5$ or 1.0 show that the influence of the number of the ribbons and the pitch ratio can be accounted for by means of the geometrical ratio (F_W/d_R^2) with F_W the area of the helical ribbons. Accordingly, the Newton number for the examined helical impellers (different number of ribbons and different pitch ratios) can be predicted from

$$Ne = 10^3 Re^{-1} \left(\frac{Fw}{d_R^2}\right)^{0.187}. \tag{118}$$

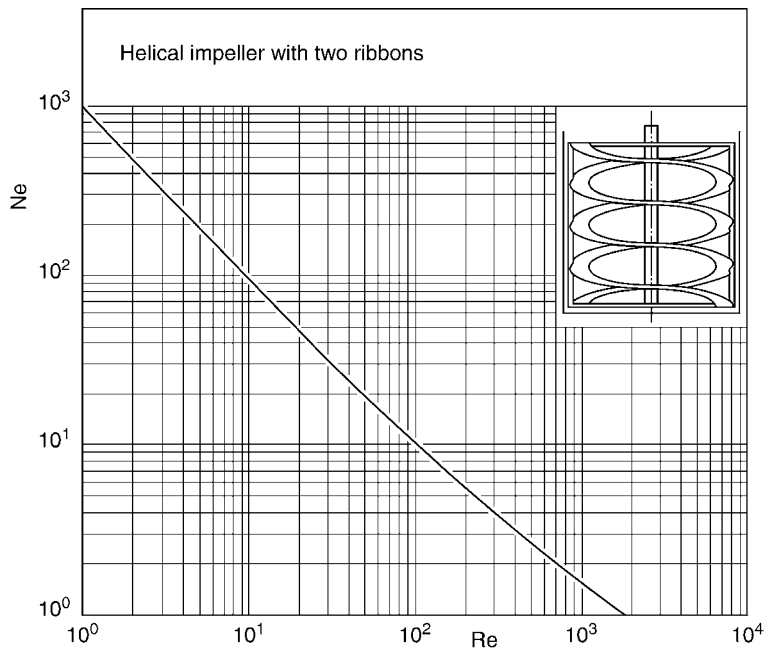

N3. Fig. 18. Dependence of the Newton number on the Reynolds number for a helical impeller with two ribbons and a pitch ratio $(S/d_R) = 0.5$ according to Zlokarnik [48] (With permission of "VCH-Verlag.")

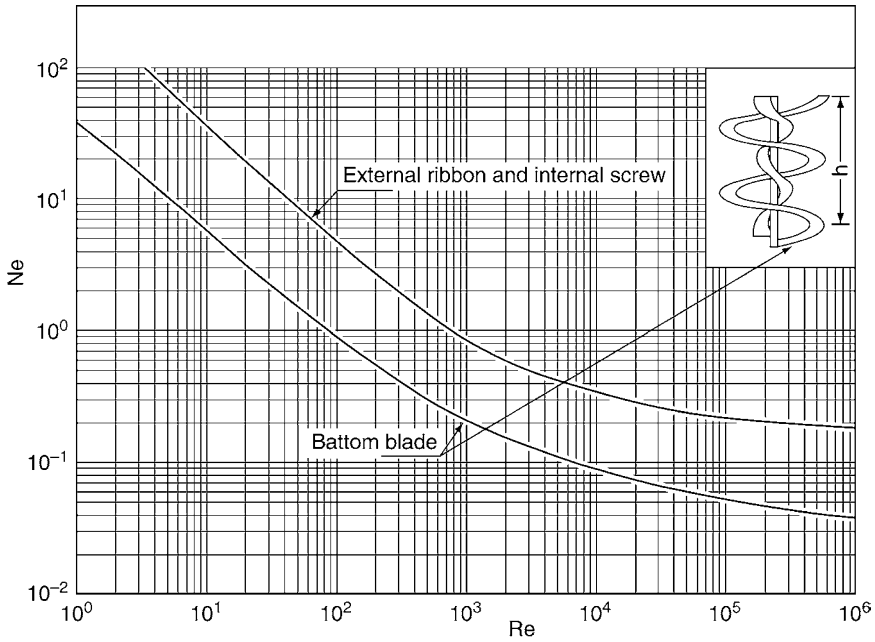

N3. Fig. 19. Dependence of the Newton number on the Reynolds number for a helical impeller equipped with an external helical ribbon and an internal screw as well as a bottom blade according to Oldshue [50]. (With permission of "McGraw-Hill Publications Co.")

Oldshue [50] presents Fig. 19 for the evaluation of the Newton number for a stirred vessel equipped with a helical impeller especially designed for very viscous materials. The impeller is constructed with an outer helical ribbon and an inner screw fixed to the shaft of the impeller. The inner screw pumps the viscous material downwards and the outer helical ribbon pumps it upwards. Figure 19 shows also the additional power consumption, when the stirred vessel is provided with a bottom blade.

Validity ranges:

$$\frac{d_{R,S}}{d_{R,W}} = \frac{1}{3},$$

$$\frac{h}{d_{R,W}} = 1.0$$

$$\frac{s_B}{d_{R,W}} = 0.0375,$$

$$\frac{b_{WR}}{d_{R,W}} = \frac{1}{6}.$$

A smaller ratio $(s_B/d_{R,W})$ or a higher ratio $(h/d_{R,W})$ leads to higher energy consumption [50]. According to Oldshue, this impeller type has been installed with diameters in the range of 0.5–3 m with rotational speed in the range of 5.5–45 min^{-1}.

Stein [13] examined also a helical impeller constructed from an outer helical ribbon, an inner screw, and a bottom blade (see Fig. 7) and recommends the following equation:

$$Ne = \left[\left(\frac{C_{S,lam}}{Re}\right)^2 + \left(\frac{C_{S,turb}}{(10+Re)^{1/4}}\right)^2\right]^{1/2}. \quad (119)$$

Equation (119) is also valid for the other impellers with special forms shown in Fig. 7 (b: Paravisc impeller "Ekato," c: Alfa impeller "Stelzer," and d: MUT impeller "Dieder;" all impellers are equipped with bottom blades). The numerical values for the constants $C_{S,lam}$ and $C_{S,turb}$ are given in Table 4.

N3. Table 4. Values of the constants $C_{S,lam}$ and $C_{S,turb}$ in Eq. (119) for the different impellers

	Helical impeller with an outer helical ribbon and an inner screw	Paravisc-impeller "Exato"	Alfa-impeller "Stelzer"	MUT impeller "Dieder"
$C_{s,lam}$	315	290	190	430
$C_{s,turb}$	4.3	4.3	4.3	4.3

The constant $C_{S,lam}$ can be calculated in dependence on the geometrical parameters from an empirical correlation given by Shamlou and Edwards [51] (As quoted in [13]), or

$$C_{S,lam} = 150\left(\frac{h_{WR}}{d_R}\right) n_{WR}^{0.5} \left(\frac{b_{WR}}{d_R}\right)^{0.335} \left[0.5\left\{\left(\frac{d_B}{d_R}\right) - 1\right\}\right]^{-0.335} \left(\frac{S}{d_R}\right)^{-0.5}. \quad (120)$$

Scraped-surface heat exchanger

Skelland and Leung [52] recommend for a scraped-surface heat exchanger (see Fig. 8) the following equation:

$$Ne = 77500 Re^{-1.27} Z^{0.59}. \quad (121)$$

Validity ranges:

$$90 \le Re \le 242,$$

$$\frac{d_R}{d_B} = 1.0,$$

$$2 \le Z \le 5,$$
$$\frac{h}{d_R} = 6.0.$$

Other correlations for predicting the power consumption of a scraped-surface heat exchanger can be found in [14, 53].

Theoretical approach for predicting the Newton number with a rectangular pitched-blade impeller

For approximate power consumption calculations in a stirred vessel equipped with a rectangular pitched-blade impeller, Stein [16] developed the following equation for the Newton number using simplified assumptions:

$$\mathrm{Ne} = 10.47 n_R Z \left(\frac{b_R}{d_R}\right)\left(\frac{h}{d_R}\right)\sin^3\gamma. \qquad (122)$$

The case $\gamma = 90°$ represents an impeller with vertical rectangular blades. Equation (122) is valid for a baffled stirred vessel with four baffles in the turbulent range.

Example 6:

Calculate the power consumption of a flat-blade turbine with standard dimensions in a stirred vessel with four baffles; the vessel is filled with an aqueous solution with physical properties similar to those of pure water. The following geometrical and operating parameters are valid:

Vessel diameter $d_B = 0.5\,\mathrm{m}$

Geometrical ratios $\frac{d_R}{d_B} = \frac{1}{3}$,

$$\frac{h_R}{d_B} = \frac{1}{3},$$
$$\frac{h_L}{d_B} = 1.0,$$
$$\frac{b_S}{d_B} = \frac{1}{10},$$

Speed of rotation $n = 3\,\mathrm{s}^{-1}$

Mean liquid temperature $\vartheta = 20°\mathrm{C}$

Physical properties of water at mean temperature $\vartheta = 20°\mathrm{C}$

Density $\rho = 998.3\,\mathrm{kg\,m}^{-3}$

Dynamic viscosity $\eta = 1002.6 \times 10^{-6}\,\mathrm{pa\,s}$

Solution:

Reynolds number $\mathrm{Re} = \frac{n d_R^2 \rho}{\eta} = \frac{3 \times \left(\frac{0.5}{3}\right)^2 \times 998.3}{1002.6 \times 10^{-6}} = 8.3 \times 10^4$,

Equation (99): Ne = 5.

Hence,

$$P = \mathrm{Ne}\rho n^3 d_R^5 = 5 \times 998.3 \times 3^3 \times \left(\frac{0.5}{3}\right)^5 = 17.3\,\mathrm{W}.$$

3.1.2 Non-Newtonian Liquids

Correlations derived to predict the Newton number from the Reynolds number during the agitation of a Newtonian liquid can also be used to predict the Newton number for a non-Newtonian liquid, if the Newtonian dynamic viscosity η in the Reynolds number is replaced by the apparent dynamic viscosity η_{app} of the non-Newtonian liquid. Equations for calculating the apparent viscosity of a non-Newtonian liquid are presented in Sect. 2.1.1.

3.2 Multiphase Systems

3.2.1 Gas-Liquid Mixtures

The power required in the turbulent range to agitate a gas–liquid mixture in a stirred vessel is lower than that required for a single-phase liquid. Zlokarnik [54] recommends for predicting the Newton number during aerating a liquid in a baffled stirred vessel by means of a standard flat-blade turbine the following equation:

$$\mathrm{Ne}_B = \frac{\left[1.5 + \left(0.5A^{0.075} + 1600A^{2.6}\right)^{-1}\right]}{F}, \qquad (123)$$

where

$$\mathrm{Ne}_B = \frac{P_B}{\rho n^3 d_R^5} \qquad (124)$$

with P_B the power consumption of the impeller for agitating a gas–liquid mixture,

$$A = Q\left[1 + 38\left(\frac{d_B}{d_R}\right)^{-5}\right], \qquad (125)$$

$$Q = \frac{\dot{V}_G}{n d_R^3}, \qquad (126)$$

$$F = 1 + \left[\left(3.9\mathrm{Re}^{0.12} + 6 \times 10^{-12}\mathrm{Re}^{3.45}\right)\left(0.22Q^{0.1} + 6.25Q^3\right)\right]^{-1}$$
$$\text{for } 10^3 < \mathrm{Re} < 10^4, \qquad (127)$$

$$F = 1 \quad \text{for Re} > 10^4. \qquad (128)$$

Three dished stirred vessels with internal diameters 200, 300, and 450 mm were used for the derivation of Eq. (123). The gas used was air; it was fed under the flat-blade turbine through an aerating tube.

Validity ranges:

$$0.2 \le \frac{d_R}{d_B} \le 0.45,$$
$$\frac{h_L}{d_B} = 1.0,$$
$$\frac{h_R}{d_R} = 1.0,$$
$$\frac{h_{OBR}}{d_R} = \frac{1}{9},$$
$$\frac{b_S}{d_B} = 0.1,$$
$$n_S = 4.$$

Further restrictions for the use of Eq. (123) are given below:

- The Froude number should exceed a certain level given by $\mathrm{Fr} \ge 0.65$.
- The gas flow rate should not exceed the limit that can be dispersed by the impeller; otherwise the stirred vessel will be flooded.

According to Zlokarnik and Judat [55], the gas flow rate that will lead to flooding the stirred vessel is given for a flat-blade turbine by the following equation:

$$Q_{\text{flooding}} = 0.194\text{Fr}^{0.75} \text{ for } 0.1 < \text{Fr} < 2. \quad (129)$$

Equation (129) was derived empirically for the following geometrical ratios:

$$\frac{d_R}{d_B} = 0.3,$$
$$\frac{d_R}{h_L} = 0.43,$$
$$\frac{h_R}{d_R} = 1.0.$$

Equation (123) shows an increasing Newton number with decreasing gas flow rate. At a gas flow rate $\dot{V}_G = 0$ (i.e., $Q = 0$ and $A = 0$) and a Reynolds number $\text{Re} > 10^4$, Eq. (123) leads to $\text{Ne}_B = \infty$. Since the Newton number Ne_B with decreasing gas flow rate approaches the Newton number *Ne* for an unaerated single-phase liquid, Eq. (123) should only be used in the range $\text{Ne}_B \leq \text{Ne}$. For a low gas flow rate, for which Eq. (123) leads to $\text{Ne}_B > \text{Ne}$, the Newton number Ne_B for the gas–liquid mixture should be replaced by the Newton number Ne for the single-phase liquid. Equation (123) shows also that the Froude number has no influence on the Newton number in the range $\text{Fr} \geq 0.65$. It has, however, some influence in the range $\text{Fr} < 0.65$; according to Zlokarnik [54], this is insignificant.

For a multistage impeller with n_R flat-blade turbines mounted on the same shaft, Henzler [56] recommends the following equation to calculate the Newton number Ne_B:

$$\text{Ne}_B = n_R \left[\frac{\text{Ne} + 187Q\text{Fr}^{-0.32}\left(\frac{d_R}{d_B}\right)^{1.53} - 4.6Q^{1.25}}{1 + 136Q\left(\frac{d_R}{d_B}\right)^{1.14}} \right] \quad (130)$$

with

$$\text{Ne} \approx 4.9.$$

Validity ranges:

$$\text{Fr} \leq 0.07\left(\frac{d_B}{d_R}\right)^3,$$
$$0.2 \leq \frac{d_R}{d_B} \leq 0.42,$$
$$\frac{\Delta h_R}{d_B} > 0.75,$$
$$\text{Re} \geq 10^4.$$

In the range $800 < \text{Re} < 10^4$ and $Q < 0.05$, the Newton number may be approximately calculated [56]

$$\text{Ne}_B = \frac{(\text{Ne}_B)_{\text{at } Re = 10^4}}{F}. \quad (131)$$

The function F in Eq. (131) is given by Eq. (127).

According to Henzler [56], the n_R flat-blade turbines operate independently if the distance Δh_R between adjacent impellers fulfills the condition $\Delta h_R > 0.75 d_B$.

Example 7:

Calculate the power consumption of the flat-blade turbine in Example 6 for the case in which the liquid is aerated by means of a tube placed under the impeller and the speed of rotation of the impeller is increased to 7 s^{-1}. The gas flow rate amounts to 6 $m^3\,h^{-1}$. Otherwise, the data given in Example 6 are valid.

Solution:

$$\text{Re} = \frac{nd_R^2\rho}{\eta} = \frac{7 \times \left(\frac{0.5}{3}\right)^2 \times 998.3}{1002.6 \times 10^{-6}} = 1.94 \times 10^5,$$

Equation (126): $Q = \frac{\dot{V}_G}{nd_R^3} = \frac{\left(\frac{6}{3600}\right)}{7 \times \left(\frac{0.5}{3}\right)^3} = 0.0514,$

Equation (128): $F = 1$ (since $\text{Re} > 10^4$),

Equation (125):

$$A = Q\left[1 + 38\left(\frac{d_B}{d_R}\right)^{-5}\right] = 0.0514\left[1 + 38 \times (3)^{-5}\right] = 0.0595,$$

Equation (123):

$$\text{Ne}_B = \frac{\left[1.5 + \left(0.5A^{0.075} + 1600A^{2.6}\right)^{-1}\right]}{F} = \frac{\left[1.5 + \left(0.5 \times 0.0595^{0.075} + 1600 \times 0.0595^{2.6}\right)^{-1}\right]}{1} = 2.19.$$

Hence,

$$P_B = \text{Ne}_B \rho n^3 d_R^5 = 2.19 \times 998.3 \times 7^3 \times \left(\frac{0.5}{3}\right)^5 = 96.4\,\text{W}.$$

3.2.2 Immiscible Liquids

At a high impeller speed and correspondingly a uniform distribution of the dispersed phase in a stirred vessel, it is reasonable to assume that a quasi-homogeneous liquid is present in the stirred vessel. The empirical equations and the diagrams developed for predicting the Newton number for the single-phase system can be used for the two-phase system provided that the physical properties of the single-phase liquid are replaced by the mean physical properties of the quasi-homogenous liquid of the two-phase system. Equations for calculating the physical properties ρ_m and η_m in a two-phase system are given in Sect. 2.1.2.

3.2.3 Suspensions

If the suspended solids are uniformly distributed (i.e., turbulent flow, high impeller speed, small fraction of solid particles, and small particle diameter), it may be assumed that a quasi-homogenous phase is present inside the stirred vessel. The empirical equations and the diagrams developed for predicting the Newton number for the single-phase liquid can be used for the suspension provided that the physical properties of the single-phase liquid are replaced by the mean physical properties of the suspension. Equations to calculate the mean physical properties of a suspension (ρ_m, η_m) are given in Sect. 2.1.2.

3.2.4 Gas–Suspension Mixtures

In analogy to the presentation made in Sect. 2.1.2 about heat transfer in gas–suspension mixtures, Eq. (123) can be used also for predicting the Newton number in gas–suspension mixtures provided that the mean physical properties of the suspension (ρ_m, η_m) according to the equations given in Sect. 2.1.2 are used instead of the physical properties of the single-phase liquid.

The use of a multistage impeller with a number of flat-blade turbines mounted on the same shaft improves the distribution of the solid particles in comparison with a single flat-blade turbine. Equations (130) and (131) can thus be used for gas–suspension mixtures with the appropriate physical properties ρ_m and η_m.

4 Vortex Depth in Stirred Vessels Without Baffles

The depth of the vortex h_V for a single-phase liquid in an unbaffled stirred vessel increases with increasing impeller speed. The maximum power consumption is reached, when the lowest point of the vortex reaches the upper edge of the impeller. A further increase in the impeller speed leads to sucking gas from the surroundings and dispersing the gas in the single-phase liquid. The depth of the vortex $h_{V,crit}$ ($h_{V,crit} = h_{LC}$, see Fig. 20) and the corresponding Reynolds number Re_{crit}, when the lowest point of the vortex just reaches the upper edge of the impeller, are usually referred to as the critical vortex depth and the critical Reynolds number. If the Reynolds number is increased beyond the critical value, a decrease in the power consumption of the impeller occurs. Operating the impeller in the range $Re \geq Re_{crit}$ is not advisable; since it leads to mechanical vibrations.

Zlokarnik [57] recommends the following equations to calculate the vortex depth:
For a flat-blade turbine:

$$\frac{h_V}{d_R} = 62.0\,Fr\left(0.1 - Ga_R^{-0.18}\right)\left(\frac{h_{LC}}{d_R}\right)^{-0.16}. \quad (132)$$

For a propeller:

$$\frac{h_V}{d_R} = 13.8\,Fr\left(0.25 - Ga_R^{-0.10}\right)\left(\frac{h_{LC}}{d_R}\right)^{-0.33}. \quad (133)$$

For a grid impeller:

$$\frac{h_V}{d_R} = 20.0\,Fr\left(0.25 - Ga_R^{-0.19}\right). \quad (134)$$

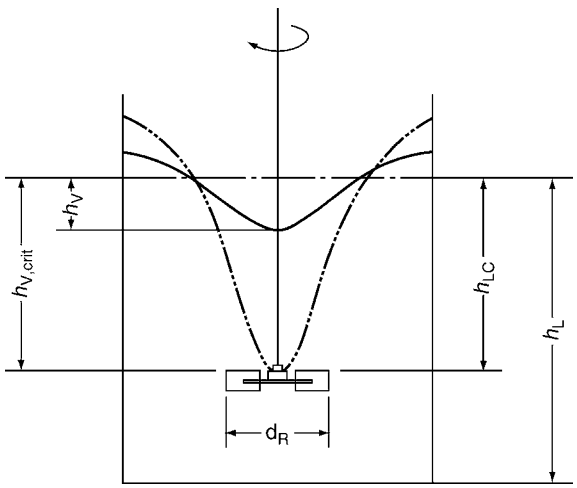

N3. Fig. 20. Critical vortex depth.

(A grid impeller is an impeller in the form of a frame with two horizontal and two vertical bars; mostly [examined case] an additional horizontal bar of equal length to the upper and lower bars midway between is present. This type of impeller is considered a representative for other low-speed impellers, which create essentially a tangential flow.)

The Froude number Fr and the Galileo number Ga_R in Eqs. (132–134) are defined by

$$Fr = \frac{n^2 d_R}{g},$$

$$Ga_R = \frac{Re^2}{Fr} = \frac{d_R^3 \rho^2 g}{\eta^2}.$$

Validity ranges:
For a flat-blade turbine:

$$2.7 \times 10^6 \leq Ga_R \leq 1.7 \times 10^{10},$$
$$5 \times 10^{-2} \leq Fr \leq 1,$$
$$1.0 \leq \frac{h_L}{d_B} \leq 1.75.$$

For a propeller:

$$1.1 \times 10^8 \leq Ga_R \leq 1.7 \times 10^{10},$$
$$2 \times 10^{-1} \leq Fr \leq 3,$$
$$1.0 \leq \frac{h_L}{d_B} \leq 1.75.$$

For a grid impeller:

$$2.9 \times 10^5 \leq Ga_R \leq 2.7 \times 10^{11},$$
$$1.1 \times 10^{-2} \leq Fr \leq 4 \times 10^{-1},$$
$$0.5 \leq \frac{h_L}{d_B} \leq 1.75.$$

The investigation was carried out with three stirred vessels having flat bottoms and internal diameters 300, 400, and 600 mm. The important geometrical parameters are given in Table 5.

Substituting in Eq. (132), Eq. (133) or Eq. (134) $h_V = h_{V,crit} = h_{LC}$ gives the critical Froude number Fr_{crit} from

N3. Table 5. Examined geometrical parameters in the investigation in [58]

	Flat-blade turbine	Propeller	Grid impeller
$\frac{d_R}{d_B}$	$\frac{1}{3}$	$\frac{1}{3}$	$\frac{1}{2}$
$\frac{h_R}{d_R}$	1	1	–
$\frac{h_{RK}}{d_R}$	–	–	$\frac{1}{5}$
$\frac{h}{d_R}$	$\frac{1}{5}$	–	$\frac{3}{2}$
$\frac{b_R}{d_R}$	$\frac{1}{4}$	–	–
$\frac{b_{SR}}{d_R}$	–	–	$\frac{1}{10}$

which the critical impeller speed n_{crit} and hence the critical Reynolds number Re_{crit} can be calculated. The Galileo number Ga_R does not depend on the speed of rotation. Further equations for predicting the vortex depth are also given [58].

5 Symbols

Latin Letters

A	heat transfer area between contents of a stirred vessel and thermal fluid in a jacket or a coil (m^2)
A	parameter in Eq. (123) given by Eq. (125) (1)
a	exponent of the Reynolds number in Eq. (1) (1)
a	liquid thermal diffusivity at mean liquid temperature ϑ or ϑ_J ($a = \lambda/\rho c$) ($m^2\ s^{-1}$)
a	constant in Eq. (91) given by Eq. (93) and Table 3 (1)
b	exponent of the Prandtl number in Eq. (1) (1)
b	constant in Eq. (91) given by Eq. (94) (1)
b_{Ein}	length given by Eq. (56) (m)
b_{Mit}	length given by Eq. (57) (m)
b_R	width of a blade of an impeller (in axial direction) (m)
b_S	baffle width (m)
b_{SR}	width of arm of an anchor impeller or vertical bar of a grid impeller (m)
b_{WR}	width of helical impeller or outer helical ribbon in Fig. 19 (m)
C	constant in Eq. (1) (1)
C^*	constant in Eq. (2) (1)
$C_{N,lam}$	constant in Eq. (88) (1)
$C_{N,turb}$	constant in Eq. (89) (1)
$C_{S,lam}$	constant in Eq. (119) (see Table 4) (1)
$C_{s,turb}$	constant in Eq. (119) (see Table 4) (1)
C_{WR}	constant in Eq. (20) given in Table 1 (1)
c	specific heat of liquid or quasi-homogeneous phase in two-phase and multiphase systems at mean liquid temperature ϑ ($J\ kg^{-1}\ K^{-1}$)
c_J	specific heat of liquid in a jacket or inside a coil at mean liquid temperature ϑ_J($J\ kg^{-1}\ K^{-1}$)
d	external diameter of a tube of a coil (m (mm))
d_B	internal vessel diameter or internal diameter of the inner tube of a scraped-surface heat exchanger (m (mm))
d_{BA}	external vessel diameter (m (mm))
d_{ch}	characteristic length given by Eq. (54) (m)
d_g	equivalent diameter given by Eq. (46) (m)
d_h	equivalent diameter (see Eq. (54)) (m)
d_i	internal diameter of a circular tube or a semicircular tube (m)
d_J	internal diameter of jacket ($d_J = d_{BA} + 2\delta$) (m)
d_O	inside diameter of jacket inlet tube (radial or tangential) or nozzle diameter (m (mm))
d_R	impeller diameter or diameter of scraper blades (m (mm))
$d_{R,S}$	diameter of the inner screw for the helical impeller in Fig. 19 (m)
$d_{R,W}$	diameter of the outer helical ribbon for the helical impeller in Fig. 19 (m)
d_S	mean diameter of a spiral coil (m)
$d_{th,H}$	thermal diameter of a semicircular tube welded at the outside surface of a stirred vessel ($d_{th,H} = (\pi/2)d_i$) (m)
e	exponent of viscosity ratio in Eq. (1) (1)
F	parameter in Eq. (123) given by Eqs. (127) and (128) (1)
F_W	area of helical ribbons (m^2)
Fr	Froude number ($Fr = n^2 d_R/g$) (1)
Fr_{crit}	critical Froude number ($Fr_{crit} = n_{crit}^2 d_R/g$) (1)
f	exponent in Eq. (2) (1)
Ga	Galileo number ($Ga = d_B^3 g/\nu^2$) (1)
Ga_R	Galileo number ($Ga_R = Re^2/Fr = d_R^3 \rho g/\eta^2$) (1)
Gr_J	Grashof number for jacket-side liquid ($Gr_J = g\rho(\rho - \rho_w)d_{ch}^3/\eta^2$) (1)
g	gravity acceleration ($m\ s^{-2}$)
h	height of impeller blade (see Figs. 1 and 5a) or length of a scraped-surface heat exchanger (m)
h_{BR}	height of gas distribution ring from bottom of a stirred vessel (m)
h_i	distance between the lower point of the impeller and the bottom of stirred vessel (see Fig. 5b) (m)
h_L	liquid height in a stirred vessel (m)
h_{LC}	height of liquid above upper edge of an impeller (m)
h_{LO}	liquid height of unaerated liquid or unaerated suspension in a three-phase system "gas–liquid–solid" (m)
h_{OBR}	distance between the opening of the aerating tube and the impeller (m)
h_R	height of impeller above vessel bottom (see Fig. 1) (m)
h_{R1}	height of lower impeller above vessel bottom (case of a two-stage impeller) (m)
h_{R2}	height of higher impeller above vessel bottom (case of a two-stage impeller) (m)
$h_{R,i}$	height of impeller i on a shaft equipped with n_R impellers above vessel bottom (m)
h_{RK}	distance between the lower edge of an impeller and the bottom of a stirred vessel (see Fig. 1) (m)
Δh_R	spacing between impellers mounted on a common shaft (m)
h_s	height of jacket (m (mm))
h_V	vortex depth (m)
$h_{V,crit}$	critical vortex depth (m)
h_{WR}	height of a helical impeller (m)
K_1	quantity in Eq. (83) defined by Eq. (84) ($K\ s^{-1}$)
K_2	quantity in Eq. (83) defined by Eq. (85) (s^{-1})
K_3	quantity with the dimension of velocity (see Eq. (62)) ($m\ s^{-1}$)
K_4	quantity with the dimension of square of velocity (see Eq. (63)) ($m^2\ s^{-2}$)
K_{Ko}	dimensionless number given by Eq. (24) (1)
k_S	constant in Eq. (33) (1)
l_{ch}	characteristic length given by Eq. (53) (m)
l_s	immersed height of baffles (m)
M	mass of liquid or quasi-homogenous mixture in a stirred vessel (kg)

$\dot{M}_J$ mass flow rate of fluid in the jacket or through the inside of a coil (kg s^{-1})
m exponent of the kinematic viscosity ratio in Eqs. (15) and (16) (1)
m exponent of Reynolds number in Eq. (89) (1)
Ne Newton number ($Ne = P/(\rho n^3 d_R^5)$) (1)
Ne_B Newton number for a gas–liquid mixture ($Ne = P_B/(\rho n^3 d_R^5)$) (1)
Ne_t Newton number in a single-phase turbulent flow ($Ne_t = P_t/(\rho n^3 d_R^5)$) (1)
Nu Nusselt number for heat transfer from the inside surface of a stirred vessel ($Nu = \alpha d_B/\lambda$)) (1)
Nu_A Nusselt number given by Eq. (73) (1)
Nu_B Nusselt number given by Eq. (74) (1)
Nu_C Nusselt number given by Eq. (75) (1)
Nu_D Nusselt number given by Eqs. (76) and (77) (1)
Nu_J jacket-side Nusselt number given by Eq. (71) (($Nu_J = \alpha d_{ch}/\lambda$) (1)
Nu_R Nusselt number for heat transfer from the outside surface of an immersed coil ($Nu_R = \alpha d/\lambda$) (1)
$Nu_{S,L}$ jacket-side Nusselt number given by Eq. (45) ($Nu_{S,L} = \alpha d_g/\lambda$) (1)
n speed of rotation of an Impeller (s^{-1})
n_{crit} critical speed of rotation of an Impeller (s^{-1})
n_R number of impellers mounted on a shaft (1)
n_{RS} number of tubes in a vertical tube baffle (1)
n_s baffle number (1)
n_{WR} number of ribbons of a helical impeller (1)
P power consumption of an impeller (W)
P_{Ad} total power dissipated in the contents of a stirred vessel as heat due to power consumption of the impeller and any additional periphery equipment (W)
P_B power consumption of an impeller for a gas–liquid mixture (W)
P_t power consumption in a single-phase turbulent flow (W)
Pr Prandtl number at mean liquid temperature ϑ or ϑ_J($Pr = \upsilon/a$) (1)
p exponent in Eq. (2) (1)
Q parameter in Eq. (125) given by Eq. (126) (1)
$Q_{flooding}$ critical value of the parameter Q, which if exceeded the stirred vessel will be flooded (see Eq. (129)) (1)
$\dot{Q}$ heat flow rate (W)
R radius of curvature of an impeller blade (see Fig. 5a) (m)
Re Reynolds number in Eq. (1) ($Re = nd_R^2\rho/\eta$), in case of a scraped-surface heat exchanger ($Re = nd_B^2\rho/\eta$) (1)
Re_{crit} critical Reynolds number ($Re_{crit} = n_{crit}d_R^2\rho/\eta$) (1)
Re_G Reynolds number ($Re_G = u_{GO}d_B/\upsilon$) (1)
Re_J jacket-side Reynolds number ($Re_J = u_{ch}d_{ch}\rho/\eta$) (1)
$Re_{J,eq}$ jacket-side equivalent Reynolds number given by Eq. (70) (1)
Re_S jacket-side Reynolds number ($Re_S = u_h d_g \rho/\eta$) (1)
r exponent of the Froude number in Figs. 13 and 15 (1)
S pitch of a propeller or a helical impeller ($S = \pi d_R \tan\gamma$) (m (mm))
s ratio (d_B/d_R) (1)
S_B clearance between vessel and helical impeller ($s_B = (d_B - d_R)/2$) or between vessel and outer helical ribbon in Fig. 19($s_B = (d_B - d_{R,W})/2$) (m)
S_S space between tubes in a coil (see Fig. 1) (m)
t time (s)
U overall heat transfer coefficient (constant or mean value) (W m^{-2} K^{-1})
$U(t)$ overall heat transfer coefficient (time dependent) (W m^{-2} K^{-1})
u_A velocity due to buoyancy given by Eqs. (50) and (52) (m s^{-1})
u_{ch} velocity given by Eq. (55) (m s^{-1})
u_{GO} superficial gas velocity ($u_{GO} = \dot{V}_G/((\pi/4)d_B^2)$)) (m s^{-1})
u_h characteristic velocity in annular space of a jacket given by Eq. (47) (m s^{-1})
u_{Mit} velocity given by Eq. (58) (m s^{-1})
u_O velocity in inlet tube of a jacket given by Eq. (48) (m s^{-1})
u_S velocity in annular space of a jacket given by Eqs. (49) and (51) (m s^{-1})
u_x velocity given by Eq. (60) (m s^{-1})
$u_x(0)$ velocity given by Eq. (61) (m s^{-1})
u_z velocity given by Eq. (64) (m s^{-1})
V_L volume of unaerated liquid or unaerated suspension (m^3)
$\dot{V}_G$ volumetric gas flow rate (m^3 s^{-1} (m^3 h^{-1}))
$\dot{V}_J$ jacket-side volumetric flow rate (m^3 s^{-1} (m^3 h^{-1}))
x_s gap between a baffle and the inside surface of a stirred vessel (m)
Z number of blades of an impeller or number of scraper blades in a scraped-surface heat exchanger (1)

Greek Letters

α heat transfer coefficient (W m^{-2} K^{-1})
β angle of an impeller blade (see Fig. 5a) (°)
β angle between vertical tube baffle and radius (see Fig. 11) (°)
β volumetric coefficient of expansion (K^{-1})
γ blade angle of a propeller or ribbon angle for a helical impeller (°)
$\dot{\gamma}$ shear rate (s^{-1})
δ thickness of annular space of a jacket (($\delta = (d_J - d_{BA})/2$) (m (mm))
η dynamic viscosity of liquid at mean liquid temperature ϑ or ϑ_J (Pa s)
η_{app} apparent dynamic viscosity of non-Newtonian liquid at mean temperature ϑ (Pa s)
η_{GS} dynamic viscosity of liquid at mean temperature $(\vartheta + \vartheta_w)/2$ of the thermal boundary layer in a stirred vessel (Pa s)
η_w dynamic viscosity of liquid at mean wall temperature ϑ_w or $\vartheta_{J,w}$ (Pa s)

$\eta_{w,app}$ apparent dynamic viscosity of a non-Newtonian liquid at mean wall temperature ϑ_w (Pa s)
ϑ mean temperature of liquid or homogeneous mixture in a stirred vessel (°C)
$\vartheta_{(t)}$ temperature of liquid or homogeneous mixture in a stirred vessel (at time t during transient operation) (°C)
ϑ_0 initial temperature of liquid or homogeneous mixture in a stirred vessel (at time $t = 0$ during transient operation) (°C)
ϑ_J mean liquid temperature in a jacket or spatially constant and time independent fluid temperature in a jacket (see Eq. (79)) (°C)
$\vartheta_{J,i}$ inlet liquid temperature in a jacket (°C)
$\vartheta_{J,o}$ outlet liquid temperature in a jacket (°C)
$\vartheta_{J,o(t)}$ outlet liquid temperature in a jacket (time dependent) (°C)
$\vartheta_{J,w}$ mean jacket wall temperature (°C)
$\Delta\vartheta_J$ temperature rise or temperature drop of jacket-side liquid (K)
ϑ_w mean wall temperature in a stirred vessel (°C)
λ thermal conductivity of liquid at mean liquid temperature ϑ or ϑ_j (W m^{-1} K^{-1})
ν kinematic viscosity of liquid at mean liquid temperature ϑ or ϑ_j (m^2 s^{-1})
ν_{app} apparent kinematic viscosity of non-Newtonian liquid at mean liquid temperature ϑ (m^2 s^{-1})
ν_w kinematic viscosity of liquid at mean wall temperature ϑ_w (m^2 s^{-1})
$\nu_{w,app}$ apparent kinematic viscosity of non-Newtonian liquid at mean wall temperature ϑ_w (m^2 s^{-1})
ξ constant in Eq. (38) (1)
ξ_j jacket-side friction factor given by Eqs. (66) and (68) (1)
π_1 geometric ratio in Eqs. (2) and (86) (1)
π_2 geometric ratio in Eqs. (2) and (86) (1)
ρ liquid density at mean liquid temperature ϑ or ϑ_j (kg m^{-3})
ρ_w liquid density at mean wall temperature ϑ_w or mean jacket wall temperature $\vartheta_{J,w}$ (kg m^{-3})
τ shear stress (Pa)
ϕ volumetric fraction of the dispersed phase (1)
ϕ_{max} maximal volumetric fraction of solid material in a batch (1)
ψ_p parameter in Eq. (7), defined by Eq. (8) (1)

Subscripts

c physical property for the continuous phase in a mixture (-)
d physical property for the dispersed phase in a mixture (-)
m mean physical property for a mixture (-)

Note: The units between brackets (mm, m^3h^{-1}) are not consistent with the MKS units system; they are used in some places in the text and in the examples for convenience.

6 Bibliography

1. Edwards MF, Wilkinson WL (1972) Heat transfer in agitated vessels – Part 1: Newtonian fluids. Chem Eng August, 310–319
2. Poggemann R, Steiff A, Weinspach P-M (1979) Wärmeübergang in Rührkesseln mit einphasigen Flüssigkeiten. Chem-Ing-Tech 51(10):948–959
3. Brauer H, Thiele H (1971) Leistungsbedarf und Wärmeübertragung beim Rühren im laminaren Strömungsbereich, verfahrenstechnik, 1. Part: 5 (10), pp. 420–428, 2. Part: 5 (11), pp. 448–452
4. Rautenbach R, Bollenrath FM (1978) Zum Wärmeübergang in Rührgefäßen an hochzähe Newtonsche und nichtnewtonsche Substanzen. Chem-Ing-Tech 50(4):314–315
5. Kuriyama M, Ohta M, Yanagawa K, Arai K, Saito S (1981) Heat transfer and temperature distribution in an agitated tank equipped with helical ribbon impeller. J Chem Eng Jpn 14(4):323–330
6. Nagata S, Nishikawa M, Takimoto T, Kida F, Kayama T (1972) Turbulent heat transfer from the wall of a jacketed tank. Heat Transfer-Jpn Res 1(1):66–74
7. Strek F, Masiuk S (1970) Heat transfer in mixing vessels with propeller agitators. verfahrenstechnik 4(6):238–241
8. Post TA (1983) Geometrical influences on local and total mass and heat transfer in an agitated tank, Diss. ETH No. 7249. Swiss Federal Institute of Technology, Zürich
9. Lichtenberg G (1966) Untersuchung des Einflusses der Abmessungsverhältnisse von Blattrührern auf die Wärmeübertragung in Rührgefäßen. Wissenschaftliche Zeitschrift der Technischen Hochschule. Magdeburg 10(3):259–267
10. Stein WA, Müller W (1992) Wärmeübergang auf der Innenseite eines Rührbehälters – Part 1. Forschung im Ingenieurwesen 58(4):87–95
11. Zlokarnik M (1969) Wärmeübergang an der Wand eines Rührbehälters beim Kühlen und Heizen im Bereich $10^0<Re<10^5$. Chem-Ing-Tech 41 (22):1195–1202
12. Blasinski H, Kuncewicz C (1981) Heat transfer during the mixing of pseudoplastic fluids with ribbon agitators. Int Chem Eng 21(4):679–683
13. Stein WA (1993) Rührleistung und Wärmeübergang auf der Innenseite eines Rührbehälters mit verschiedenen Wendel-Rühren. Forschung im Ingenieurwesen 59(9):165–172
14. Weisser H, Vogelpohl A (1975) Rührleistung und Wärmeübergang von Kratzkühlern beim Erwärmen und Kühlen. Maschinenmarkt 81 (44):796–798
15. Weisser H (1975) Der Wärmeübergang im Kratzkühler bei teilweiser Phasenänderung. Chem-Ing-Tech 47(2):73
16. Stein WA (1992) Wärmeübergang auf der Innenseite eines Rührbehälters – Part 2. Forschung im Ingenieurwesen 58(5):119–127
17. Mahlfeldt U (1974) Wärmeübergang in Rührkesseln, Diplomarbeit, Institut für Thermische Verfahrenstechnik, Universität Karlsruhe
18. Dunlap IR, Rushton JH (1953) Heat-transfer coefficients in liquid mixing using vertical-tube baffles. Chem Engng Prog Symp Ser 5(49): 137–151
19. Havas G, Deak A, Sawinsky J (1982) Heat transfer coefficients in an agitated vessel using vertical tube baffles. Chem Eng J 23:161–165
20. Havas G, Deak A, Sawinsky J (1983) The effect of the impeller diameter on the heat transfer in agitated vessels provided with vertical tube baffles. Chem Eng J 27:197–198
21. Petree DK, Small WM (1978) Heat transfer and power consumption for agitated vessels with vertical plate coils. AICHE Symp Ser 174(74): 53–59
22. Skelland AHP, Blake WK, Dabrowski JW, Ulrich JA, Mach TF (1965) Heat transfer to coils in propeller-agitated vessels. AICHE J 11(5):951–954
23. Chilton JH, Drew JB, Jebens RH (1944) Heat transfer coefficients in agitated vessels. Indus Eng Chem 36(6):510–516
24. Blasinski H, Heim A, Kuncewicz C (1977) Heat transfer to a spiral coil during the mixing of a non-Newtonian liquid by anchor mixers. Int Chem Eng 17(3):548–553
25. Edwards MF, Wilkinson WL (1972) Heat transfer in agitated vessels – Part 2: Non-Newtonian fluids. Chem Eng 328–335
26. Steiff A, Poggemann R, Weinspach P-M (1980) Wärmeübergang in Rührkesseln mit mehrphasigen Systemen. Chem-Ing-Tech 52(6):492–503

27. Steiff A, Weinspach P-M (1982) Zur Fluiddynamik und zum Wärme- und Stoffübergang in gerührten begasten Suspensionsreaktoren. Chem-Ing-Tech 54(5):526–527
28. Kurpiers P, Steiff A, Weinspach P-M (1984) Zum Wärmeübergang in gerührten Mehrphasensystemen. Chem-Ing-Tech 56(3):234–235
29. Kurpiers P, Steiff A, Weinspach P-M (1985) Zum Wärmeübergang und zur Maßstabsübertragung in gerührten Ein- und Mehrphasenreaktoren mit eingebauten Heizelementen. Chem-Ing-Tech 57(7):632–633
30. Kurpiers P, Steiff A, Weinspach P-M (1985) Zum Wärmeübergang "Reaktorwand/-Fluid" in einem gerührten Ein- und Mehrphasenreaktor beim Einsatz ein- und zweistufiger Scheibenrührer. Chem-Ing-Tech 57(8):700–701
31. Kurpiers P (1985) Wärmeübergang in Ein- und Mehrphasenreaktoren mit ein- und zweistufigen Rührern, Diss. Universität Dortmund 1984. VCH Verlagsgesellschaft, Weinheim
32. Midoux N, Charpentier J-C (1984) Mechanically agitated gas-liquid reactors – Part 1: hydrodynamics. Int Chem Eng 24(2):249–287
33. Olney RB, Carlson GJ (1947) Chem. Eng. Prog. 43:473–80 (as reported in [26])
34. Kwasniak J (1973) Wärmeübergang beim Rühren von Suspensionen und Emulsionen. verfahrenstechnik 7(10):287–292
35. Lehrer IH (1970) Jacket-side Nusselt number. Ind Eng Chem Process Des Dev 9(4):553–558
36. Stein WA, Schmidt W (1986) Wärmeübergang im flüssigkeitsdurchströmten Mantel eines Rührbehälters. Chem-Ing-Tech 58(2):162–163 (MS 1455/86)
37. Stein WA, Schmidt W (1986) Heat transfer in agitated tank jackets with liquid media. Ger Chem Eng 9:362–371
38. Stein WA, Schmidt W (1993) Wärmübergang auf der Wärmeträgerseite eines Rührbehälters mit einem einfachen Mantel. Forschung im Ingenieurwesen 59(5):73–90
39. Wolf K-H (1997) Aufheizzeit und Abkühldauer des Fermenterinhaltes unter Berücksichtigung eingetragener Leistungen und Einfluß auf den Wärme-Sterilisationseffekt. Bioscope 5(4/5):57–63
40. Pawlowski J, Zlokarnik M (1972) Optimieren von Rührern für eine maximale Ableitung von Reaktionswärme. Chem-Ing-Tech 44(16):982–986
41. Penny WR, Koopman RN (1972) Prediction of net heat removal capabilities for agitated vessels (and pumped- through heat exchangers). AICHE Symp Ser 68(118):62–73
42. Brauer H (1971) Grundlagen der Einphasen- und Mehrphasenströmungen, Aarau and Frankfurt/Main. Verlag Sauerländer, Chap. 19, p 879
43. Hirschberg HG (1988) Handbuch der Kältetechnik, 6. Volume/Part B, Wärmeaustauscher. Springer-Verlag, Berlin, Chap. 15, Rührkessel, pp 555–589
44. Ulrich H (1971) Leistungsbeiwerte verschiedener Rührer. Aufbereitungs-Technik 1:7–18
45. Rushton JH, Costich EW, Everett HJ (1950) Power characteristics of mixing impellers – Part 1. Chem Eng Prog 46(8):395–404
46. Rushton JH, Costich EW, Everett HJ (1950) Power characteristics of mixing impellers – Part 2. Chem Eng Prog 46(9):467–476
47. Bates RL, Fondy PL, Corpstein RR (1963) An examination of some geometric parameters of impeller power. Ind Eng Chem Process Des Dev 2(4):310–314
48. Zlokarnik M (1967) Einigung von Rühren zum Homogenisieren von Flüssigkeitsgemischen. Chem-Ing-Tech 39(9/10):539–548
49. Uhl VW, Voznik HP (1960) The anchor agitator. Chem Eng Prog 56(3):72–77
50. Oldshue JY (1983) Fluid mixing technology, chemical engineering. McGraw-Hill, New York, Chap. 3, p. 64
51. Shamlou PA, Edwards MF (1985) Power consumption of helical ribbon mixers in viscous Newtonian and Non-Newtonian fluids. Chem Engng Sci 40(9):1773–81 (quoted in [13])
52. Skelland AHP, Leung LS (1962) Power consumption in a scraped-surface heat exchanger. Br Chem Eng 7(4):264–267
53. Weisser H (1972) Untersuchungen zum Wärmeübergang im Kratzkühler. Diss. Universität Karlsruhe
54. Zlokarnik M (1973) Rührleistung in begasten Flüssigkeiten. Chem-Ing-Tech 45(10a):689–692
55. Zlokarnik M, Judat H (1967) Rohr- und Scheibenrührer – zwei leistungsfähige Rührer zur Flüssigkeitsbegasung. Chem-Ing-Tech 39(20): 1163–1168
56. Henzler H-J (1982) Verfahrenstechnische Auslegungsunterlagen für Rührbehälter als Fermenter. Chem-Ing-Tech 54(5):461–476
57. Zlokarnik M (1971) Trombentiefe beim Rühren in unbewehrten Behältern. Chem-Ing-Tech 43(18):1028–1030
58. Rieger F, Ditl P, Novak V (1979) Vortex depth in mixed unbaffled vessels. Chem Eng Sci 34:397–403

N4 Cooling Towers

Paul J. Erens
Private Consulting Engineer, Stellenbosch, Republic of South Africa

1 Introduction

The words cooling and tower come from early model evaporative cooling towers which were used for cooling water by evaporation and were substantial in height to gain a natural draught effect. However, the means of achieving airflow was in some cases replaced by forced or induced draught fan systems, without the need for tall towers but the name cooling tower has stuck. The term in general includes wet as well as dry cooling systems, but as the subject of dry heat exchangers is adequately covered in other sections of this publication this section is dedicated to wet systems using evaporative cooling where the water being cooled is in direct contact with the air flowing through the cooling tower.

Evaporative cooling towers are devices which are used to remove heat from various types of machinery or industrial process equipment either directly or through intermediate heat exchangers by making use of evaporative cooling. By implication, when using this principle, some water, usually 1–2% of the water flow rate, is sacrificed in order to get rid of the heat.

In any closed thermodynamic cycles there is always a heat source and heat sink e.g., in a steam cycle the steam has to be condensed by transferring heat to the surroundings or in a refrigeration cycle heat is absorbed in the evaporator and released in the condenser also giving off heat to the surroundings. This process of transferring heat to the surroundings takes place through various types of heat exchanger which are either air cooled or water cooled. Simple thermodynamics tells us that to obtain maximum efficiency in the cycle it is desirable to give off heat at the lowest possible temperature.

An evaporative cooling tower is a device which can theoretically cool water near to the wet-bulb temperature which is usually considerably lower than the dry-bulb temperature. This is one reason that a cooling tower or other evaporative cooling device is often favored over a dry cooling system when getting rid of heat at temperatures slightly above the atmospheric temperature. A further reason for using evaporative cooling is the increased ability of the air to absorb heat when taking up moisture. For example, air at a dry-bulb temperature of 25°C and a wet-bulb temperature of 20°C when heated up to 35°C by dry heating is able to absorb only 10.3 kJ/kg, whereas with heating combined with evaporation i.e., saturation of the air, this is increased to 71.9 kJ/kg of dry air representing a sevenfold increase. This leads to greatly reduced airflow rates and fan power consumption when compared to dry cooling.

When heat in a fluid is being disposed of at temperatures considerably higher than that of the surroundings the advantage

VDI-GVC (ed.), *VDI Heat Atlas*, DOI 10.1007/978-3-540-77877-6_64,

of evaporative cooling is somewhat diminished and dry heat exchangers are often regarded as suitable equipment. However, when cooling solids such as steel billets, direct cooling with water is often preferred and a cooling tower can be efficiently used to re-cool the water.

The need for cooling at around atmospheric temperatures is not restricted to thermodynamic cycles but also to numerous manufacturing processes such as the cooling of food products after cooking in cans or in the operation of machinery such as air compressors, rolling mills, and hydraulic and electrical equipment. In fact, there are far more evaporative cooling towers used in manufacturing and industrial processes than in thermodynamic cycles. In general, cooling towers are used to cool water between 85°C and wet-bulb temperature, but most cooling towers operate with a water temperature below 55°C and down to about 20°C.

In some systems where closed circuit cooling is required, *closed circuit evaporative coolers* are employed where any fluid or condensable gas is passed through a closed circuit tube bundle placed inside a cooling tower with water recirculating over the outside.

2 Types of Cooling Towers and Evaporative Coolers/Condensers

Evaporative cooling towers can be grouped into various categories as follows:

	Mechanical draught cooling tower (MDCTs)	Natural draught cooling tower (NDCTs)
Open circuit	Forced draught	Counterflow
	Induced draught	Crossflow
	Counterflow	
	Crossflow	
Closed circuit	Evaporative coolers	
	Evaporative condensers	

Some examples of cooling towers are shown in Figs. 1–4.

In a few cases mechanically assisted natural draught cooling towers may be encountered. Many different variations are also shown in Singham [1], Stoecker and Jones [2] and Burger [3], and Kröger[4].

3 Cooling Tower Construction and Materials

3.1 Basic Elements

All cooling towers, no matter what the configuration is, have certain basic elements viz:

(1) A casing or shell;
(2) Fill or packing material;
(3) A water distribution system;
(4) An air-moving system, fan or natural draught;
(5) A drift elimination system;
(6) Makeup supply;
(7) Blowdown system;
(8) Basin;
(9) Inlet louvres, wind louvers, and wind barriers.

3.1.1 Structure

The main structure of the cooling towers is usually made of one or more of the following materials:

(1) Wood
(2) FRP (fiber reinforced plastic) or molded plastics
(3) Steel or other metals
(4) Reinforced concrete

3.1.2 Fill Materials, Packing, or Wet-deck

Most fill materials are made from plastics, metals, or wood, with the greater majority in molded or vacuum formed plastics. The preferred plastics are PVC, polyethylene, polypropylene, and ABS. Many fills today are also made of steel particularly where high temperature water is being cooled. Although wood is still sometimes used, this is usually only for particular applications such as in phosphoric acid towers or when wood is in free supply.

Fill materials are discussed in detail in Sect. 5.

3.1.3 Nozzles and Water Distribution

Even distribution of water in cooling towers is very important to achieve maximum cooling effect and efficient cooling tower operation. The water distribution system is required to spread the water evenly over the fill material and can consist of closed water ducts with a number of nozzles in plastic or metal, open overflow ducts or open ducts with low pressure nozzles.

In small towers it is important to use well-designed square-pattern sprayers or multiple small nozzles to achieve the desired distribution usually operating in the pressure range of 2–5 m of water, see Fig. 5a. In very large towers, low pressure nozzles (0.5–1.5 m water) with less ideal distribution characteristics may be used provided there is sufficient overlap between the adjacent nozzles. Some examples are shown in Fig. 5b with two upward spraying nozzles shown in Fig. 5c. It has been proved that nozzles which give a radial distribution with maximum water loading at the center decreasing linearly with radius produce excellent distribution when their spray patterns are overlapped. Some small towers also use rotating spreaders, similar to a lawn sprinkler, but these can only be used in circular towers. The size and number of nozzles and distribution ducts depend on the required flow density required for a particular application.

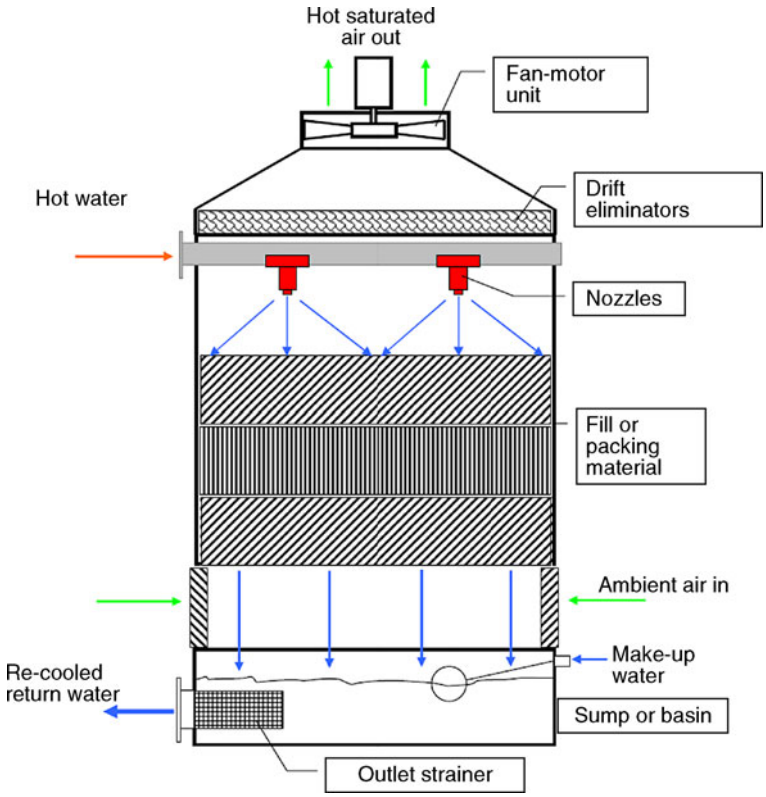

N4. Fig. 1. Induced draught counterflow cooling tower.

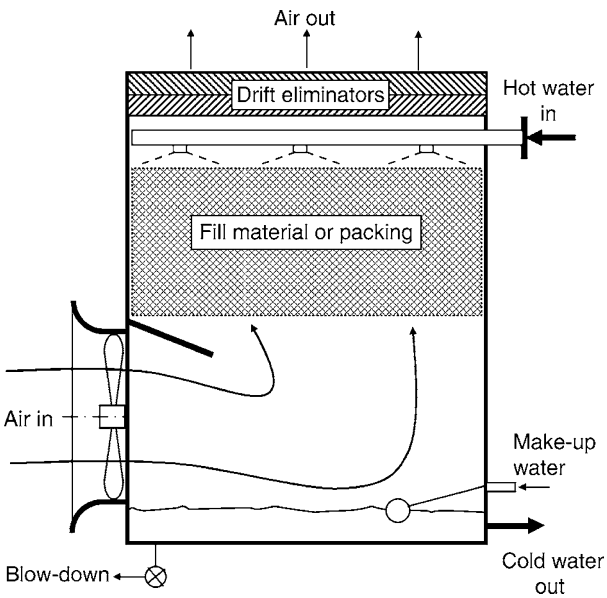

N4. Fig. 2. Forced draught, axial fan, and counterflow cooling tower.

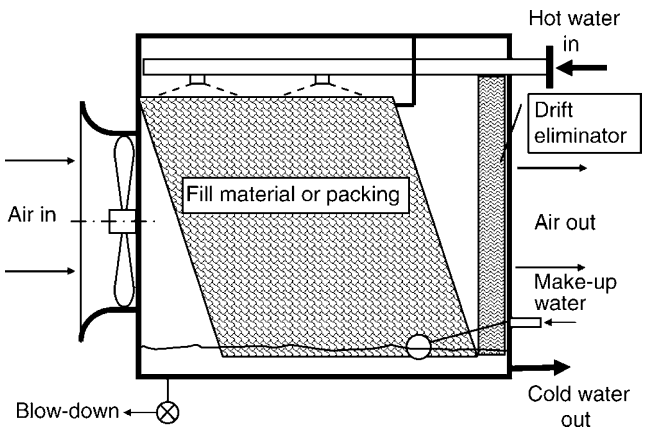

N4. Fig. 3. Forced draught, axial fan, and crossflow cooling tower.

High pressure sprayers are seldom, if ever, used in view of the severe pumping power requirements and their tendency to produce small droplets leading to high drift loss.

Water distribution piping can be in plastics or metals, depending on temperature and corrosion considerations. In general they are low pressure systems and only require thin-walled piping. Low pressure nozzles are often fixed beneath open distribution duct systems fed from a main header channel or pipe.

3.1.4 Drift Eliminators

Monjoie and Lauraine [5] have discussed a method of measuring drift as well as three classes of drift eliminators with classification according to separation efficiency. The separation efficiency defined as a percentage of water flow rate in the tower is strongly related to drop-size distribution as well as air velocity through the tower. Foster et al. [6] have discussed two types of drift eliminators and their separation efficiency having measure droplet distributions upstream and downstream of them, while Chan and Golay [7] have compared three different wave forms for drift elimination. Golay et al. [8] have discussed a number of methods to measure drift.

N4. Fig. 4. A site-built counterflow induced draught cooling tower (Picture supplied by Industrial Water Cooling, South Africa).

Drift eliminators are required to retain spray droplets which move upward with the air within the cooling tower. They generally consist of devices which are designed to induce a number of sudden directional changes of the air in order to deflect the entrained droplets onto solid surfaces so that the water runs back into the tower. There are various patents using PVC-film, composites or S-shaped louvres in plastic or metal. In general, a separation efficiency of roughly 0.01–0.0005% of cooling tower water flow rate is attainable without special arrangements such as double rows of drift eliminator to reduce this further.

In practice, separation efficiency of 0.0002% can be achieved but at much greater cost and care should be taken not to unnecessarily overspecify this requirement. The 0.01% figure is usually adequate for most industrial applications although in recent times there has been a demand for high efficiency drift eliminators of the 0.0002% class due to environmental considerations.

The % figures quoted above usually apply to a maximum velocity of 3 m/s using medium or low pressure sprayers and these will not be achieved should the velocity go above this figure or where the sprayers form fine water droplets.

Some examples of drift eliminators are shown in Fig. 6.

3.1.5 Air-moving System

The air-moving system in MDCTs is usually chosen to give air velocities of 2.5–3.5 m/s in the tower. This velocity is limited to <3.5 m/s to avoid upward transfer of water through the fill and also the drift eliminators. Probably, the most common air-moving system is the axial fan in either forced- or induced-draught towers, with some forced draught towers using centrifugal fans.

Both types of fan can be direct-driven (up to about 2 m diameter in axial fans) and above this through belts or gearboxes with drive shafts. It is becoming more and more common to find variable frequency fan-speed controls (VFDs) as a means of controlling the temperature of the cooled water.

Fan pressures are generally low in the order of 150–300 Pa so that single-stage axial fans can be used although some towers use two-stage low-speed axial fans to achieve low noise output.

In natural draught cooling towers the difference in air densities inside and outside the tower is the driving force and generally much lower fill air velocities below about 1.5 m/s are experienced.

3.1.6 Makeup and Blowdown Equipment

Obviously, when water is continually being evaporated and bled off it is necessary to add water to the system to make up the evaporation and blowdown loss. This amount is usually in the order of 1–2% of the flow rate through the cooling tower. Makeup is usually controlled by means of a level control in the pond, but can also be controlled from elsewhere in the system. It is usually controlled by monitoring the level in the pond.

3.1.7 The Basin

The basin of a cooling tower is used to catch the re-cooled water and often also to act as a reservoir for the system although

N4. Fig. 5. (**a**) A Selection of medium-pressure square-pattern nozzles (nozzles shown inverted). (**b**) A selection of low-pressure down-spraying nozzles. (**c**) Two up-spraying nozzles.

separate reservoirs are often used. The size and volume of the basin are usually determined from practical considerations regarding the particular application.

In small molded FRP and sheet metal cooling towers, the basin is often an integral part, whereas in large towers these can be built of FRP, steel, or concrete.

It is not unusual to find even medium-sized molded FRP towers mounted on concrete basins with the water falling directly into the basin.

Basins often also incorporate deflectors, protruding inlets, and inward-sloping catchment ledges to prevent water from leaving the tower via the air inlets.

Some cooling towers are produced without basins using inclined water collection ducts between which the air flows upward into the tower. The advantage of such systems is the virtual elimination of light from the tower which helps to reduce algae formation.

3.1.8 Inlet Louvres, Wind Louvres, and Wind Barriers

Loss of water from a cooling tower through splashing or wind transport needs to be avoided as it represents an

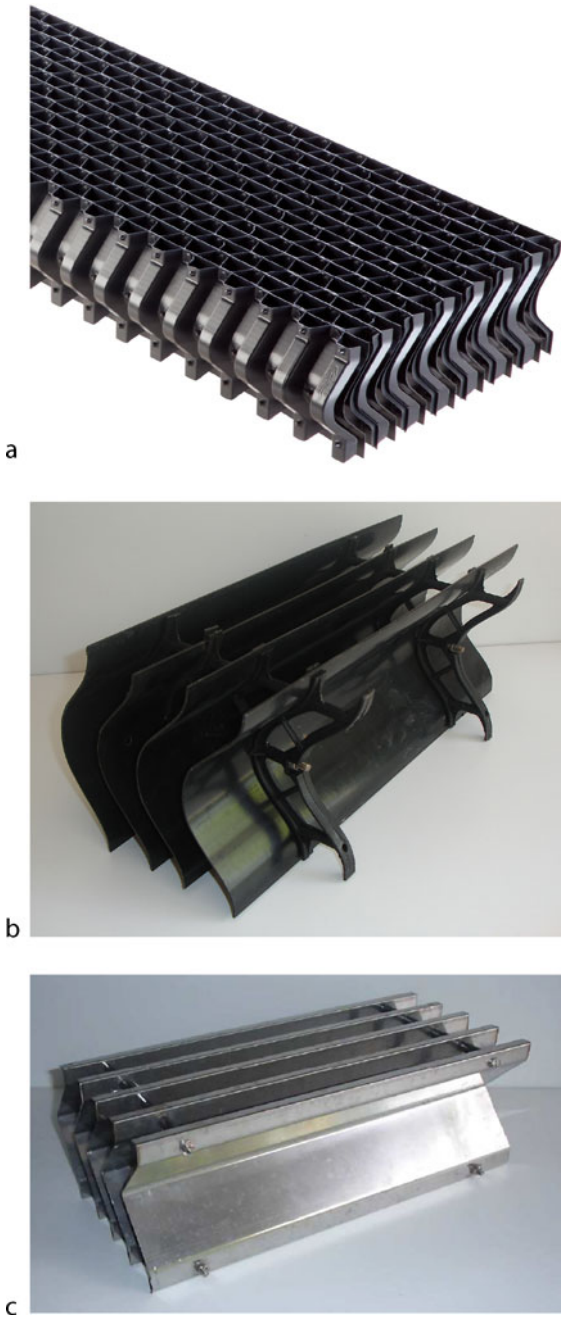

N4. Fig. 6. (**a**) Vacuum-formed drift eliminator (Picture supplied by Brentwood Industries Inc., USA). (**b**) PVC-wave drift eliminator (Picture supplied by Industrial Water Cooling, South Africa). (**c**) Stainless steel drift eliminator (Picture supplied by Industrial Water Cooling, South Africa).

environmental problem as well as a potential source of chemical loss from the tower. This type of loss is prevented by judicious design of tower inlets as well as inlet louvres, wind barriers, and wind louvres.

Inlet louvres are sometimes but not always used to catch water droplets splashed from beneath the tower. They are sloped inward so that any water impinging on them runs back toward the basin. Louvres are manufactured from plastics, FRPs, fiber cement, and galvanized or stainless steel. They are often quite

widely spaced and their effectiveness in preventing water from being blown out of the tower is often limited.

Wind louvres are usually vertically mounted and they are generally much more closely spaced. While their main purpose is to prevent water from being blown out of the tower, they also serve as splashguards.

An additional and often the only means of preventing wind loss is to place dividing walls beneath the fill in the center of the tower, often in both directions. These are fairly effective in preventing wind flow through the tower at right angles to it but they do not prevent the wind almost parallel or at an acute angle to the tower air inlets from entering at one end and leaving at the other, carrying substantial amounts of water with it.

4 Basic Evaporative Cooling Theory

4.1 Properties of Moist Air (Psychrometric Theory)

The properties of moist air are determined by considering the air and water vapor as perfect gasses, the basics of which are summarized next according to Bosnjakovic [9] and numerous first-course texts on thermodynamics.

The mass ratio of water to air in terms of partial pressures is given by

$$X = \frac{M_W}{M_A} = \frac{R_A \cdot p_W}{R_W \cdot p_A} = 0.622 \frac{p_W}{p_{\text{atm}} - p_W} \tag{1}$$

The relative humidity which is the ratio of the partial pressure of water vapor in an air mixture to the saturated value at the same temperature is given as

$$\phi = \frac{p_W}{p''_W(\vartheta)} = \frac{X}{0.622 + X} \cdot \frac{p_{\text{atm}}}{p''_W(\vartheta)} \tag{2}$$

The maximum concentration of water on a mass basis is therefore given as the value of X at the saturated condition in terms of the partial pressure of water vapor at atmospheric temperature $[\vartheta_{\text{atm}}]$:

$$X = X''(\vartheta_{\text{atm}}) = 0.622 \frac{p''_W(\vartheta_{\text{atm}})}{p_{\text{atm}} - p''_W(\vartheta_{\text{atm}})} \tag{3}$$

Practical measurement of the moisture content of water is achieved using measurements of wet-bulb and dry-bulb temperatures, using a sling psychrometer or similar device in conjunction with the following Eq.:

$$p_W = p''_W(\vartheta_{AF}) - \frac{0.5}{755} \cdot p \cdot (\vartheta_{db} - \vartheta_{wb}) \tag{4}$$

where, the saturation pressure of water vapor $[p''_w]$ as a function of temperature is approximated between 0°C and 70°C using

$$\ln p''_W = -5143.12 \left[\frac{1}{273.15 + \vartheta} - \frac{1}{373.16} - 5.471 \ln \left(\frac{373.16}{273.15 + \vartheta} \right) + 0.01656[373.16 - (273.15 + \vartheta)] \right] \tag{5}$$

It follows from partial pressure law that the density of moist air at atmospheric pressure is given by

$$\rho_A = \frac{M_A + M_W}{V} = \frac{1 + X}{R_A + X \cdot R_W} \cdot \frac{p_{\text{atm}}}{T} = \frac{1 + X}{(1 + X/0.622)} \cdot \frac{p_{\text{atm}}}{R_L T} \tag{6}$$

The enthalpy of a moisture–air mixture can be calculated by summing the enthalpies of the air and moisture components to give

$$h_A = (c_{pA} + c_{pv} X) \cdot \vartheta_A + X \cdot \Delta h_{V0} \tag{7}$$

where Δh_{V0} is the enthalpy of evaporation of water at 0°C.

The enthalpy of saturated air is in turn given by

$$h''_A(\vartheta) = (c_{pA} + c_{pv} \cdot X'')\vartheta_A + X'' \cdot \Delta h_{V0} \tag{8}$$

since $h_v = \Delta h_{V0} + c_{pv}\vartheta_v$ and the enthalpy of liquid water can be calculated from

$$h_W = c_{pw} \cdot \vartheta_W \tag{9}$$

The following average values for specific heat of air, water vapor, and water can be used:

$$c_{pA} = 1.006\,\text{kJ/kg K}, \qquad c_{pv} = 1.861\,\text{kJ/kg K}$$
$$c_{pW} = 4.18\,\text{kJ/kg K}$$

While the enthalpy of evaporation at 0°C is $\Delta h_{v0} = 2500$ kJ/kg K.

4.2 Counterflow Theory

The derivation of counterflow cooling tower theory is given in numerous texts including Fujita and Tazuka [10], Kröger [4], Poppe and Rögener [11], Singham [1], Stoecker and Jones [2], Sutherland [12], Baker and Shryock [13], and is summarized next.

A film of water running down the surface of a duct with upward flowing air as shown in Fig. 7a is considered. The following basic assumptions are made:

(1) The system is adiabatic with no heat transfer through the sides of the duct.
(2) The temperature throughout the water film is constant and there is no diffusion resistance between the air and water surfaces so that the temperature of the air at the surface is equal to the water temperature. In other words, $\vartheta_A = \vartheta_w$ at the surface.
(3) The areas for both heat and mass transfer are equal.
(4) The air leaves in a saturated condition.

The energy balance (Fig. 7b) is given by

$$\dot{M}_A \cdot dh_A - \dot{M}_W \cdot dh_W - h_W \cdot \dot{M}_W = 0 \tag{10}$$

and the mass balance (Fig. 7c) by

$$\dot{M}_A \cdot dX + d\dot{M}_W = 0 \tag{11}$$

The energy transfer at the water–air interface is also given as the sum of heat transfer and mass transfer:

$$\dot{M}_A \cdot dh_A = h_v \cdot d\dot{M}_W + \alpha \cdot (\vartheta_W - \vartheta_A) \cdot dA \tag{12}$$

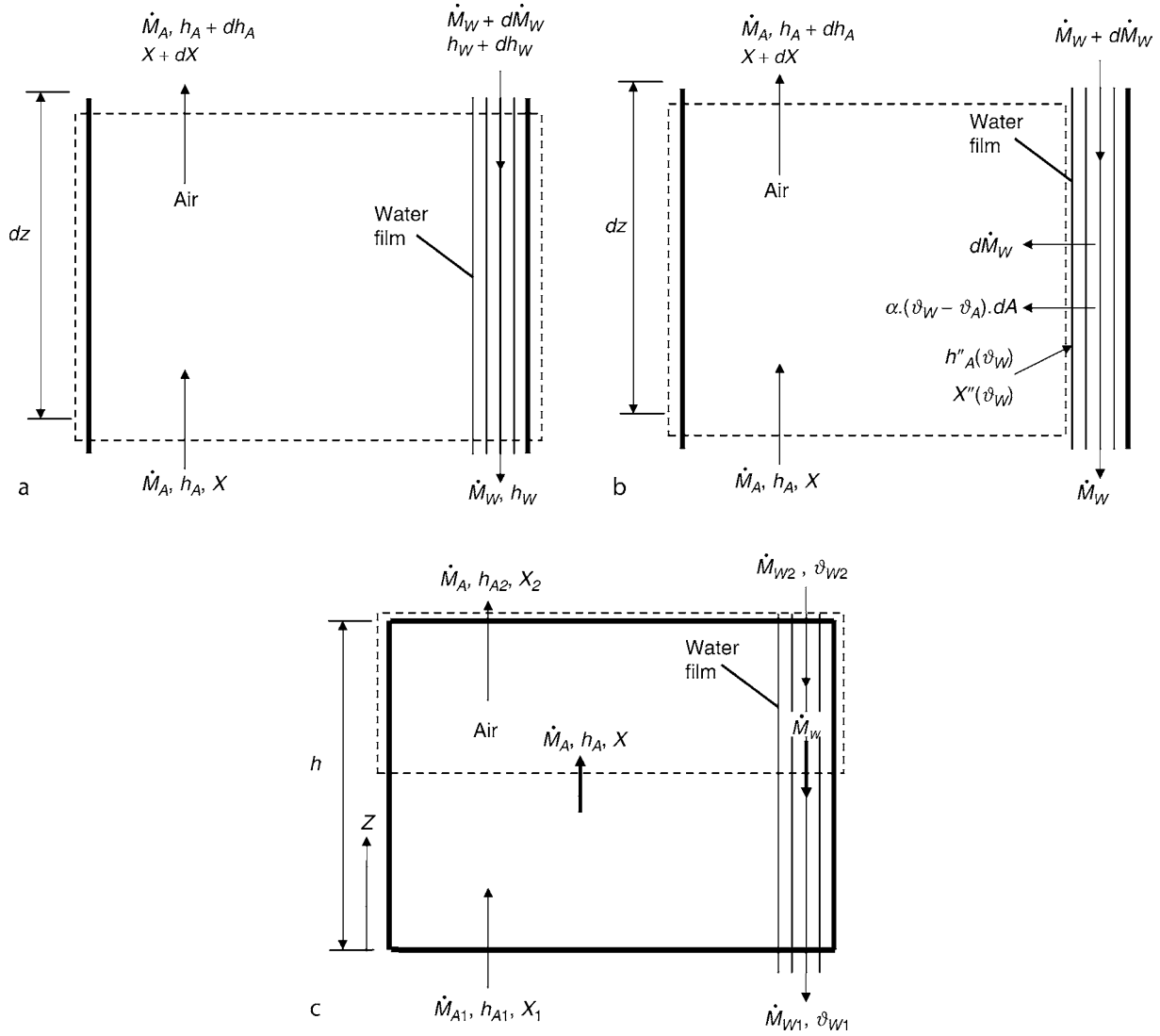

N4. Fig. 7. (**a**) Counterflow element model. (**b**) Counterflow energy balance (heat and mass transfer). (**c**) Energy and mass balance for a counterflow system.

The mass transfer rate expressed in terms of concentration difference is given by

$$d\dot{M}_A = \beta_x \cdot \left[X'' \cdot (\vartheta_W) - X\right] \cdot dA \tag{13}$$

Combining the aforementioned equations with the specific heat of the mixture given as

$$c_{pm} = c_{pA} + c_{pv} \cdot X$$

The following equation is obtained:

$$\begin{aligned}\dot{M}_W \cdot dh_W = \beta_x \cdot dA \cdot \Bigg\{ & h''_A(\vartheta_w) - h_A + \left(\frac{\alpha}{\beta_X . c_{pm}} - 1\right) \\ & \times \left[h''_A \cdot (\vartheta_W) - h_A - (X'' \cdot (\vartheta_W) - X) \right. \\ & \left. \cdot \left(\Delta h_{V0} + c_{pv} \cdot \vartheta_W\right)\right] \\ & - \left(X'' \cdot (\vartheta_W) - X\right) \cdot c_{pW} \cdot \vartheta_W \Bigg\}\end{aligned} \tag{14}$$

Merkel [14] simplified the aforementioned equations by applying the following approximations:

(1) Lewis number $\dfrac{\alpha}{\beta_X \cdot c_{pm}} \approx 1$

(2) $\left(X'' - X\right) \cdot c_{pW} \cdot \vartheta_W << h''_A - h''$

Also assuming the evaporation rate relative to the flow is negligible, Merkel's energy transfer equation in terms of enthalpy potential is

$$\dot{M}_W \cdot c_{pW} \cdot d\vartheta_W = \beta_X \cdot dA \cdot (h''_A - h_A) \tag{15}$$

with h''_A = Enthalpy of saturated air at the water surface temperature and h_A = Enthalpy of the air–water mixture flowing past the water and by integrating the Merkel number is obtained as

$$Me = \int \frac{\beta_h \cdot dA}{\dot{M}_w} = \int \frac{c_{pW} \cdot d\vartheta_W}{h''_A - h_A} \tag{16}$$

The energy balance between air and water is

$$\dot{M}_A \cdot (h_{A2} - h_{A1}) = \dot{M}_W \cdot c_{pW} \cdot (\vartheta_{W2} - \vartheta_{W1}) \tag{17}$$

Equations (16) and (17) connect the cooling of the water to the mass transfer rate of the water, considerably simplifying the

calculations. Merkel's assumptions (1 and 2 earlier) have very little influence on results obtained for mechanical draught towers, but they do not result in a correct prediction of air outlet conditions which is problematic in natural draught calculations.

The complete energy balance then becomes

$$\dot{M}_A\left[h_{A2} - h_{A1} - c_{pW}\cdot\vartheta_{W1}\cdot(X_2 - X_1)\right] = \dot{M}_{W2}\cdot c_{pW}\cdot(\vartheta_{W2} - \vartheta_{W1}) \tag{18}$$

4.3 Numerical Calculation Methods

4.3.1 Poppe Method

From Eqs. (10), (13), and (14) it can be shown that

$$\dot{M}_A\cdot dh_A = \beta_x\cdot dA\cdot\left\{h_A'' - h_A + \left(\frac{\alpha}{\beta_X\cdot c_{pm}} - 1\right)\cdot\left[h_A'' - h_A - (X'' - X)\cdot(\Delta h_{V0} + c_{pv}\cdot\vartheta_W)\right]\right\} \tag{19}$$

Using Eqs. (13), (14), and (19) the water temperature can be expressed as independent variable giving

$$\frac{dX}{d\vartheta_W} = c_{pW}\cdot\frac{\dot{M}_W}{\dot{M}_A}\cdot\left\{\frac{X'' - X}{h_A'' - h_A + (\alpha/\beta_X\cdot c_{pm} - 1)\cdot[h_A'' - h_A - (X'' - X)\cdot(\Delta h_{V0} + c_{pv}\cdot\vartheta_W)] - (X'' - X)\cdot c_{pW}\cdot\vartheta_W}\right\} \tag{20}$$

and

$$\frac{dh_A}{d\vartheta_W} = c_{pW}\cdot\frac{\dot{M}_W}{\dot{M}_A}\cdot\left\{1 + \frac{(X'' - X)\cdot c_{pW}\cdot\vartheta_W}{h_A'' - h_A + (\alpha/\beta_X\cdot c_{pm} - 1)\cdot[h_A'' - h_A - (X'' - X)\cdot(\Delta h_{V0} + c_{pv}\cdot\vartheta_W)] - (X'' - X)\cdot c_{pW}\cdot\vartheta_W}\right\} \tag{21}$$

Applying Eqs. (11) and (13) the number of transfer units are given as

$$\mathrm{NTU} = \int\frac{\beta_X\cdot dA}{\dot{M}_W} = \int\frac{dX/d\vartheta_W}{X'' - X}\cdot d\vartheta_W \tag{22}$$

From which it can be seen that

$$\mathrm{NTU} = \frac{\dot{M}_W}{\dot{M}_A}\cdot Me \tag{23}$$

Considering Fig. 7c a simple mass balance gives

$$\dot{M}_{W2} = \dot{M}_W + \dot{M}_A\cdot(X_2 - X)$$

so that

$$\frac{\dot{M}_A}{\dot{M}_W} = \frac{\dot{M}_A}{\dot{M}_{W2}}\cdot\left[1 - \frac{\dot{M}_A}{\dot{M}_{W2}}\cdot(X_2 - X)\right]^{-1} \tag{24}$$

Bosnjakovic [9] derived the following equation giving Lewis number in terms of the air–water content, avoiding the need to approximate it:

$$\frac{\alpha}{\beta_X\cdot c_{pm}} = 0.865^{2/3}\cdot\frac{\frac{0.622 + X''}{0.622 + X} - 1}{\ln\left(\frac{0.622 + X''}{0.622 + X}\right)} \tag{25}$$

Equations (20) and (21) together with Eqs. (22), (24), and (25) can be numerically integrated between the inlet and outlet conditions for given water and airflow ratio, water inlet and outlet temperatures, air inlet wet- and dry-bulb temperatures, and atmospheric pressure, using Runge–Kutta procedure. Since the outlet moisture concentration X_2 is unknown an iterative solution is required. The NTU for the given duty is then calculated by integrating Eq. (22) numerically using Simpson's rule. When the NTU is known for a particular transfer medium from measurements this procedure can be used iteratively to calculate the water outlet temperature for given air and water inlet conditions and flow rates.

In addition, the outlet air state as well as the rate of evaporation can be determined. Kloppers and Kröger [15–17] have shown how the method can be expanded to include supersaturated conditions.

4.3.2 Merkel's Method

Excellent results are obtained using Merkel's Eq. (16) and either a stepwise numerical integration procedure or four-step Chebychev integral to calculate the Merkel number. An example of such a calculation is given by Kröger [4, p. 263].

Yadigaroglu and Pastor [19] and Kloppers and Kröger [15–17, 20] have discussed differences between the more rigorous Poppe method and Merkel's approximate method of calculation. Kloppers and Kröger [21] have also investigated the influence of the Lewis factor assumption on performance predictions. While the Poppe method gives excellent results allowing the determination of the precise air exit conditions as well as accurate predictions of evaporation rates, the Merkel method is most frequently used because of its simplicity. However, according to Kloppers and Kröger [15, 16], as the Merkel method assumes saturated conditions at the exit the value of X is not exact and the evaporation rate calculation is less accurate although the prediction of outlet water temperature is excellent in spite of the deviation of Lewis number from unity. They also found that the Merkel method is considerably improved when the change of water flow rate is taken into account in the numerical integration procedure.

Various methods of integrating Merkel's equation theoretically have been developed in the past by approximating the saturation curve with a parabolic or exponential equation but this is no longer necessary in view of the availability of computer solutions.

4.3.3 NTU Method

Jaber and Webb [22] have shown how the NTU method as applied to heat exchangers can be used for cooling tower calculations, making the same assumptions that Merkel did and approximating the saturated air enthalpy as a linear function of temperature over the range of cooling. (See also Webb [23], Webb and Villacres [24, 25], and Webb and Jaber [26].) A numerical example of such a calculation is also given in Kröger [4, p. 274], who also states that the accuracy of this method is much improved by dividing the calculation into a number of steps.

4.4 Crossflow Theory

Differential equations for a crossflow situation can be derived considering the element in Fig. 8 where the vertical water flow is at right angles to the horizontal airflow. This leads to a set of partial differential equations in the vertical and horizontal directions.

The change of moisture concentration in the horizontal direction is given by

$$\frac{\partial X}{\partial x} = \frac{\beta_X \cdot a \cdot V}{\dot{M}_A} \cdot (X''(\vartheta_W) - X) \tag{26}$$

and the accompanying change of air enthalpy by

$$\frac{\partial h_A}{\partial x} = \frac{\beta_X \cdot a \cdot V}{\dot{M}_A} \cdot \left\{ h_A''(\vartheta_W) - h_A + \left(\frac{\alpha}{\beta_x \cdot c_{pm}} - 1\right) \cdot [h_A''(\vartheta_W) - h_A - (X''(\vartheta_W) - X) \cdot (\Delta h_{V0} + c_{pv} \cdot \vartheta_{W0}] \right\} \tag{27}$$

While the temperature change of the water is

$$\frac{\partial \vartheta_W}{\partial y} = \frac{\dot{M}_A}{\dot{M}_W} \cdot \left[\vartheta_W \cdot \frac{\partial X}{\partial x} - \frac{1}{c_{pW}} \cdot \frac{\partial h_A}{\partial x} \right] \tag{28}$$

The Merkel approximation of these equations can be shown to be

$$\frac{\partial h_A}{\partial x} = \frac{\beta_X \cdot a \cdot V}{\dot{M}_A} \cdot (h_A''(\vartheta_W) - h_A) \tag{29}$$

$$\frac{\partial \vartheta_W}{\partial y} = -\frac{\dot{M}_A}{c_{pW} \cdot \dot{M}_W} \cdot \frac{\partial h_A}{\partial x} \tag{30}$$

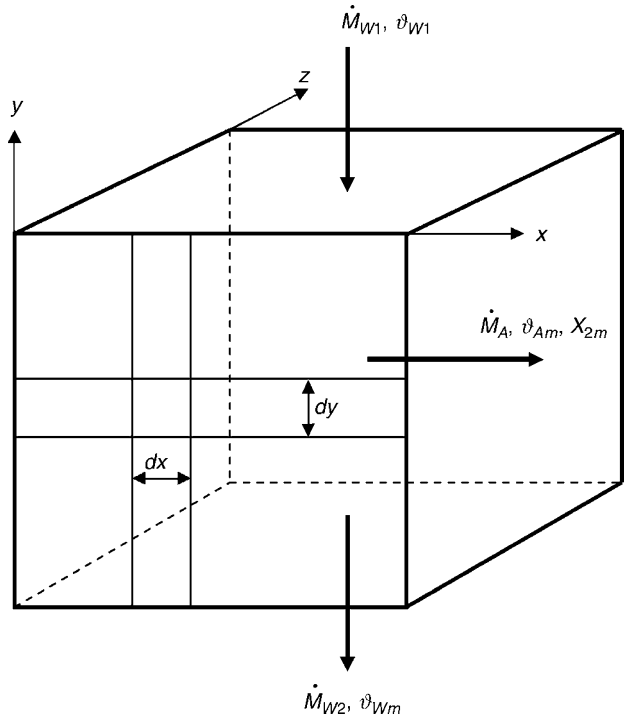

N4. Fig. 8. Crossflow element model.

The above partial differential equations can be integrated numerically and they have to satisfy the overall energy balance given by

$$\dot{M}_A \cdot [h_{A2} - h_{A1} - c_{pW} \cdot \vartheta_{W2m} \cdot (X_{2m} - X_1)] = \dot{M}_{W1} \cdot c_{pW} \cdot (\vartheta_{W1} - \vartheta_{W2m}) \tag{31}$$

where ϑ_{W2m} and X_{2m} refer to mixing temperature and water content of the outlet water and air streams, respectively. Kloppers and Kröger [27] present a critical analysis of crossflow calculation methods.

5 Fill Materials, Transfer Coefficients, and Pressure Drops

5.1 Fill Transfer and Pressure Drop Coefficients

Theoretical derivations have been done to obtain values for the transfer coefficient β_X but this can only be done for fairly simple geometries e.g., in the work by Poppe and Rogener [11]. Dreyer [28] developed a program to predict the transfer coefficients of splash packs using a complex computer simulation involving dripping, splashing, and film formation and the associated heat and mass transfer with a view to optimizing film design. However, the transfer coefficients used for cooling tower design are invariably determined from experimental test rigs and used in programs employing either Poppe's or Merkel's method of integration. These measurements are usually expressed in equations containing the air and water mass flow rates per unit area or their ratio.

The most common one giving the dimensionless Merkel number as

$$\frac{K \cdot a \cdot V}{\dot{M}_W} = K \cdot \left(\frac{\dot{M}_W}{\dot{M}_A}\right)^{-n} \tag{32}$$

where K (kg/m^2–s/m^3) is a mass transfer coefficient per unit volume. This is usually published as a value per m of h/m^2 of area so that

$$\frac{K \cdot a}{\dot{M}_W} = K_1 \cdot \left(\frac{\dot{M}_W}{\dot{M}_A}\right)^{-n} \Big/ \mathrm{m} \tag{33}$$

Other forms of correlating equations are given below and it is emphasized that these are all dimensional equations so the units used for $\dot{M}_A^a$ and $\dot{M}_w^b$ are of major importance.

$$\frac{\mathrm{NTU}}{h[m]} = K_1 \cdot \dot{M}_A^a \cdot \dot{M}_w^b \tag{34}$$

$$\frac{\mathrm{NTU}}{h[m]} = K_2 \cdot \dot{M}_A^a \cdot \dot{M}_w^b \cdot \vartheta_{Wi}^c \cdot \mathrm{ATD}^d \tag{35}$$

Equally important in the design of cooling towers is the pressure drop (often also referred to as the pressure loss coefficient) as in mechanical draught towers the airflow has to be matched to a chosen fan or in natural draught towers with the difference in densities inside and outside the tower.

The pressure drop coefficient is defined as

$$K_p = \frac{\Delta P}{\rho_m \cdot V^2/2} \tag{36}$$

Next are some commonly encountered correlating equations for pressure drop coefficients as given by Kloppers and Kroger [29]:

$$K_p = K_3 \cdot \dot{M}_A^e \cdot \dot{M}_w^f + K_4 \tag{37}$$

$$K_p = K_5 \cdot \dot{M}_A^g \cdot \dot{M}_W^h \cdot ATD^j \tag{38}$$

It should be noted that these coefficients are usually a weak function of airflow rate and quite strongly dependent on water flow rate.

Typical transfer and pressure drop correlations are shown in Fig. 9a and b.

G_w = Water loading kg/m^2/s; G_A = Airflow rate kg/m^2/s. (L_{fi} = 1.0 m), the form of the second type of equation is proposed by Kloppers and Kröger [29].

5.2 Types of Fill Material

Cooling towers used in the industry contain numerous different kinds of fill material depending on operating conditions. To achieve a high thermal efficiency a high surface transfer area is required and packings with up to 400 m^2/m^3 have been produced. However, high surface densities go hand in hand with high pressure drops and they clog more easily so a compromise is often made.

In high surface density packings, the water is usually spread out over vertical closely packed sheets of plastic material, mostly PVC, and are referred to as film-packs. At the other extreme splashing rather than a water film is used to produce multiple free-falling droplets with high surface area. This is done by using splash bars, wood lattice, or grids of steel or plastic spaced at intervals ranging from 100 to 750 mm. The surface densities thus achieved are considerably lower than that achieved with film-pack, but so are the pressure drops. However, using splashpack a far deeper pack than with film-pack is required to achieve the same amount of cooling leading to greater required pumping heads.

As a compromise trickle-packs are used giving water surface areas somewhere in between film-packs and splash-packs. These packs use a combination of film surface and droplet surface areas and are usually constructed of steel or plastic meshes in various configurations spaced more densely than the splash-packs. They are particularly suitable when nonclogging or easily cleanable fill materials are required for small- and medium-sized cooling towers.

The choice of material from which a pack is made usually depends on the cost, durability, operating temperature, and corrosion resistance. Therefore, stainless steel mesh packs are often used where temperature and durability are strong considerations. Where severe corrosion is a concern, plastics and wood are often used as even stainless steel is sometimes subject to corrosion problems.

Various types of packings are described and their transfer and pressure drop characteristics are given by Cale [30], Kröger [4], and Singham [1].

Some examples of film-, trickle-, and splash-fill are shown in Fig. 10 a–c.

6 Design of Cooling Towers

6.1 Design Conditions for Cooling Towers

To correctly design a cooling tower a number of parameters need to be known including altitude, wet- and dry-bulb temperatures, required water inlet and outlet temperatures, cooling rate, and water flow rate.

In addition to this information on operating conditions including water conditions or dust concentrations in the air, type of operation e.g., continuous or intermittent, as well as supply voltage and frequency is required.

In NDCTs variations of temperature and pressure with altitude as well as temperature inversions can also affect the results.

In selecting design conditions it is important to take the particular application into account. For instance, in air conditioning and chiller applications it is common practice to use a wet bulb which does not extend for more than ten days of the year. It is then accepted that for short periods the system may not cope adequately. Care should also be taken when using published weather data which gives average mean daily values for various periods over numbers of years, as these can often lead to under-design in abnormally long wet-bulb periods. When performance is absolutely critical the maximum expected wet- and dry-bulb conditions should be used.

When designing a cooling tower the total Me transfer units have to be determined and pressure drops have to be accounted for and balanced against either fan pressure in a mechanical draught tower or draught pressure in a natural draught tower.

6.2 Total Transfer Coefficient

The total transfer units include

(1) Fill transfer coefficient;
(2) Spray zone transfer coefficient;
(3) Rain zone coefficient.

The above values must be calculated for the given height of each section and added so that

$$\frac{K \cdot a \cdot V}{\dot{M}_W} = \frac{K \cdot a \cdot ATD_{\text{fill}}}{\dot{M}_W} + \frac{K \cdot a \cdot ATD_{\text{spray}}}{\dot{M}_W} + \frac{K \cdot a \cdot ATD_{\text{rain}}}{\dot{M}_W} \tag{39}$$

In MDCTs using high density film-fills the spray and rain zone transfer coefficients are usually insignificant compared to the fill transfer coefficient. However, in large MDCTs and NDCTs using trickle- or splash-fills the rain zone especially can make a significant contribution to the overall cooling and pressure drops and need to be taken into account.

The rain zone transfer can be determined using correlations derived by De Villiers and Kröger [31] in terms of tower

Analysis	Empirical relation	Correlation coefficient
Merkel	$Me_M/L_{fi} = 4.299\ G_w^{-0.657}\ G_a^{0.711}\ T_{wi}^{-0.476}$	0.986

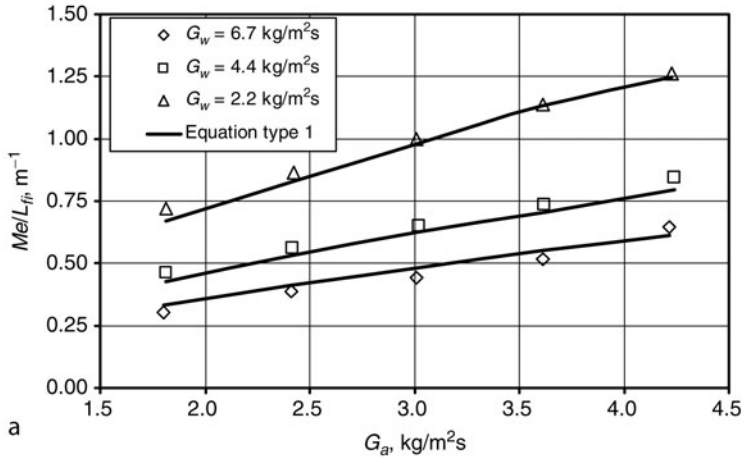

Empirical relations for the loss coefficient (L_{fi} = 1.0 m).

Approach	Eq. type	Empirical relation	Correlation coefficient
Merkel	1	$K_{fdm}/L_{fi} = 12.498\ G_w^{0.209}\ G_a^{-0.267}$	0.874
	2	$K_{fdm}/L_{fi} = 8.829\ G_w^{0.416}\ G_a^{-1.390} + 5.104\ G_w^{0.134}\ G_a^{0.320}$	0.939

Equation types 1 and 2 for the loss coefficient are plotted below.

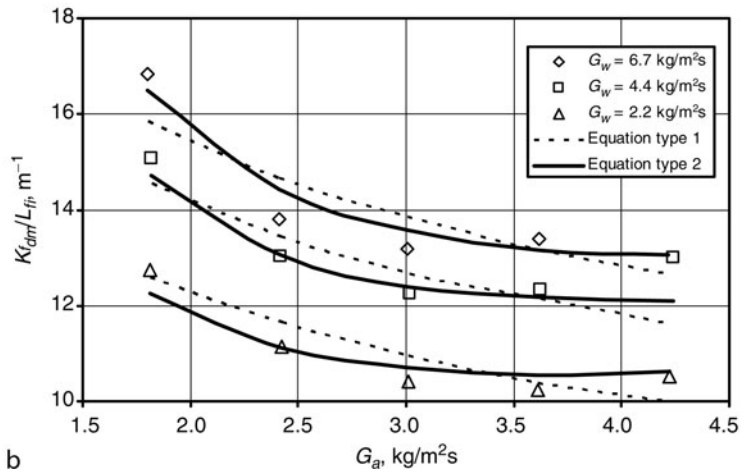

N4. Fig. 9. (**a**) Example of empirical relation for the Merkel number according to the Merkel analyses. (L_{fi} = 1.0 m). (**b**) Example of empirical relations for the fill pressure loss coefficient.

geometry, rain zone height, and droplet size. However, this requires a representative drop diameter. Pearce [32], using the FLUENT CFD program to model rain zones, has shown that the Sauter mean diameter is the representative drop diameter. Terblanche et al. [33] measured drop size distributions beneath film-fills, trickle-fills, and two types of splash-fill. Spray zone transfer can be calculated in a similar way but the Sauter mean needs to be determined for the type of nozzle used.

6.3 Total Pressure Drop

The total pressure drop consists of the following:

(1) Inlet to tower including inlet louvres and support columns;
(2) Rain zone pressure drop;
(3) Fill support system;
(4) Fill;

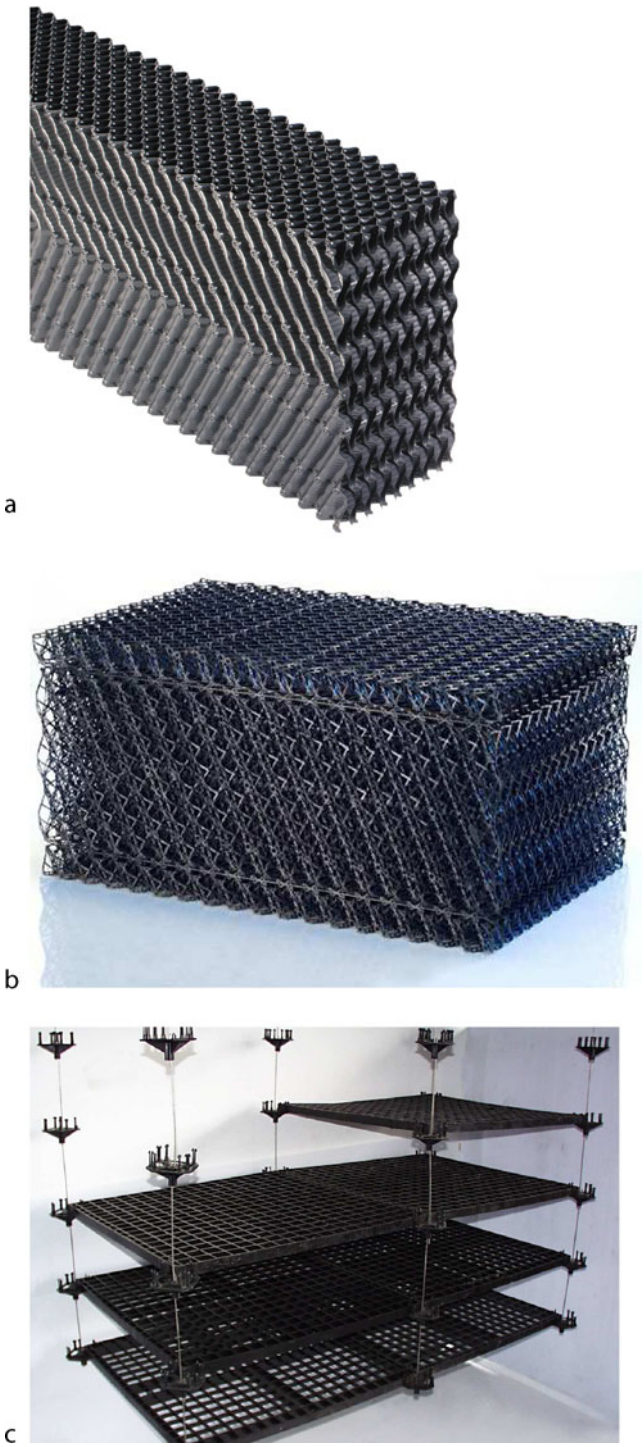

N4. Fig. 10. (**a**) Film-fill (Picture supplied by Brentwood Industries Inc.). (**b**) Trickle-fill (Picture supplied by GEA Aircooled Systems, South Africa). (**c**) Splash-fill (Picture supplied by GEA Aircooled Systems, South Africa).

(5) Water distribution system and supports;
(6) Drift eliminator support system;
(7) Drift eliminators;
(8) Outlet duct system;
(9) Dynamic pressure of exhaust air.

Each loss coefficient is usually expressed in terms of the mean velocity of the air in the fill so that they can be added together. In the case of the inlet air, the coefficient based on inlet air velocity has to be converted to one based on velocity through the fill so that

$$K_{P1} = K_{p\text{Inlet}} \cdot \frac{V_{\text{Inlet}}^2}{V_{\text{Fill}}^2}$$

And the total pressure loss coefficient is given by

$$K_{\text{Total}} = K_{P1} + K_{P2} + K_{P3} + K_{P4} + K_{P5} + K_{P6} + K_{P7} + K_{P8} + K_{P9} \quad (40)$$

6.4 MDCTs

In a MDCT the fan static pressure is balanced by the pressure drops.

$$\text{Fan static pressure} = K_{\text{Total}} \cdot \rho_{\text{Fill}} \cdot V_{\text{Fill}}^2/2 \quad (41)$$

The static pressure losses together with fan diameter and volume flow rate are used to select a suitable fan.

Whatever type of mechanical draught tower is used computer programs for fan selection are usually employed to select a suitable fan. These could be directly driven fans up to about 1.8 m diameter or fans driven through a gear box or belt transmission system. With large towers the motors are nearly always mounted external to the tower with the fan driven through a transmission system and drive shaft.

Forced draught towers very often use belt-driven centrifugal or axial fans mounted on the side of the tower although certain makes have single or double-impeller axial fans either directly or indirectly driven. As centrifugal fans tend to run more quietly than axial fans of the same capacity, there is often a preference for these in air-conditioning applications. However, in industrial and process applications axial fans tend to dominate.

6.5 NDCTs

In a NDCT, the thermal calculation procedure is identical to that for MDCTs. However, the velocity of the air through the fill has to be assumed and then checked using a draught equation which balances all the flow resistances with the buoyancy of the hot moist air inside the tower against the exterior cold air. This requires multiple iterative procedures which can only be followed using computer routines as hand calculations are an order of magnitude more time consuming than for mechanical draught towers. The relevant draught equations for NDCTs are given in very concise form by Kröger [4] and Singham [1]. In practice even in very tall NDCTs, the air velocities through the fill are much lower than mechanical draught towers, in the order of 0.5–1.5 m/s.

The hyperbolic shape of NDCTs has little to do with the fluid dynamics of the towers and is mainly there for structural reasons. However, the increased exit velocity does help to prevent recirculation of hot outlet air back into the cooling tower.

On the other hand, the higher exit velocity represents a higher flow resistance due to the resulting increase in dynamic loss at the exit.

In a natural draught cooling tower flow of air is achieved due to a difference in the densities of the air inside and outside the tower. A balance is reached when the pressure losses as calculated in Sect. 4.3 are balanced by the pressure difference inside and outside the tower. As the fill height can be quite considerable in large natural draught towers an average height rather than fill exit is used. Referring to Fig. 11.

$$-g \cdot [H_{\text{Exit}} - (H_{\text{Fillin}} + H_{\text{Fillout}})/2] \cdot (\rho_{A2} - \rho_{A1}) = K_{\text{Total}} \cdot \frac{\rho_{Ai} \cdot V_{A1}^2}{2} \tag{42}$$

where, the total loss coefficient is calculated as in Eq. (40).

Equation (42) together with the transfer equations has to be solved iteratively to find the steady-state operating condition of the tower. This is usually done in the following steps:

(1) assume a fill velocity (usually between 0.5 and 1.5 m/s);
(2) calculate the cooling rate and outlet condition of the air from the fill;
(3) calculate the total pressure drop;
(4) compare calculated pressure drop to pressure difference due to temperature difference;
(5) adjust velocity until Eq. (42) is balanced.

As natural draught cooling towers are often very high (up to 200 m) this can have a significant influence on the calculated results. Kröger [4] has shown how both pressure and temperature gradients in the atmosphere can be taken into account. As natural draught cooling towers are also very large, the aforementioned one-dimensional approach is essentially an approximation and more accurate results are achieved using axisymmetric two-dimensional computational fluid dynamic procedures as such as those proposed by Majumdar et al. [34, 35]. If wind effects need to be included this would require a three-dimensional numerical approach due to the absence of symmetry.

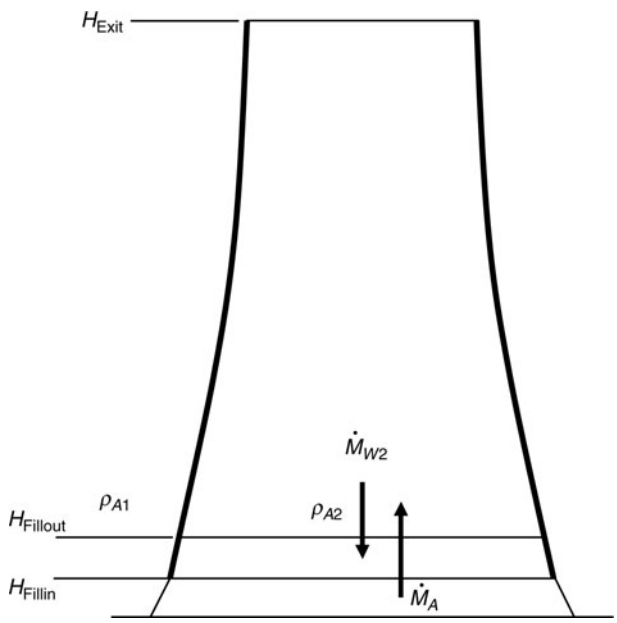

N4. Fig. 11. Natural draught model.

The air mass flow through the fill is given by

$$\dot{M}_A = A_f \cdot \rho_{A1} \cdot V_{A1} \tag{43}$$

and the inlet air density by

$$\rho_{A1} = \frac{p_A}{R_A \cdot T_A} = \frac{p_{\text{atm}} - p_w}{R_A \cdot T_A} \tag{44}$$

Combining Eqs. (42–44) it can be shown that the mass flow through the tower is given by

$$\dot{M}_A = A_f \cdot \sqrt{\frac{2 \cdot \rho_{A1}^2}{K_{\text{Total}} \cdot \rho_{A1}} \cdot g \cdot [H_{\text{Exit}} - (H_{\text{Fillin}} + H_{\text{Fillout}})/2] \cdot (\rho_{A1} - \rho_{A2})} \tag{45}$$

7 Plume Formation

In built-up areas and near highways where low winter temperatures occur, a problem created by the use of evaporative cooling is that of plume formation which people consider unsightly, often leading to mist or drizzle as well as poor visibility on highways. In recent years this subject has enjoyed a considerable amount of attention leading to the use of hybrid systems where dry heat exchangers or stack gases are used to re-evaporate the droplets, thus eliminating visible plumes. When air at saturated or near-saturated conditions is mixed with outside air at low temperatures a supersaturated condition outside the saturation curve is created leading to plume formation as shown in Fig. 12. It has been shown that the degree of plume formation is a function of the area enclosed between the mixing line and the saturation line which should be as small as possible, preferably zero. Kröger [4] gives the theory describing plume formation and discusses several ways of dealing with it by using combinations of wet and dry cooling.

8 Closed Circuit Evaporative Coolers and Condensers

In many instances, it is required that the machine being cooled should not be exposed to open circuit cooling tower water to avoid maintenance problems in the machinery being cooled. This is often the case in compressor cooling in very dusty environments, e.g., cement factories, or where machinery has very small channels through which the water is pumped. Often the fluid being cooled may be another substance such as alcohol, paint, oil or a condensing refrigerant or product in which case a closed circuit is essential. The closed circuit evaporative cooler is nothing more than a heat exchanger inside a cooling tower and is equivalent to a cooling tower with water pumped through an external heat exchanger. Figure 13 shows the arrangement for a closed circuit evaporative cooler/condenser.

In both these devices a multi-tube coil in the tower serves as fill as well as heat exchanger, and sometimes the cooling

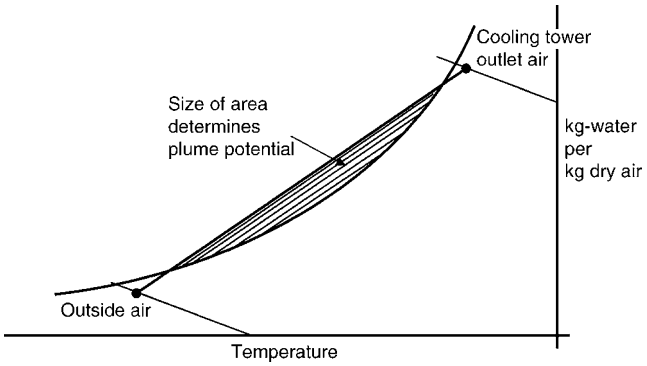

N4. Fig. 12. Psychrometric chart illustrating potential for plume formation.

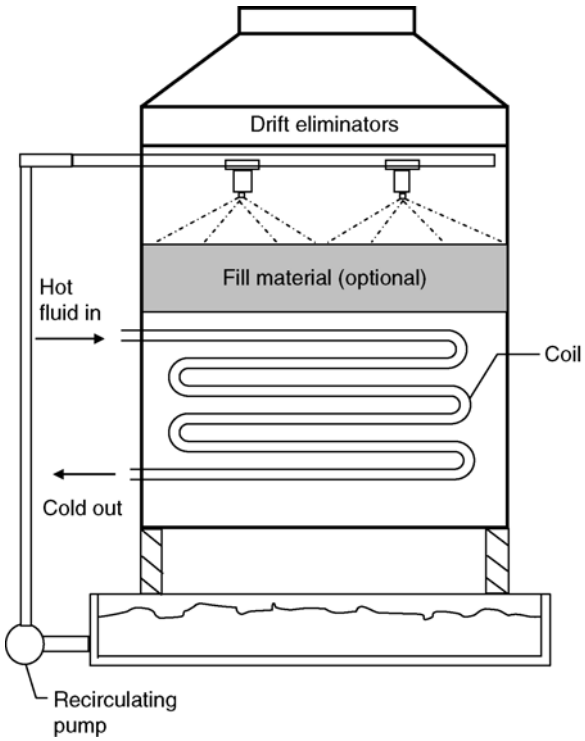

N4. Fig. 13. Closed circuit evaporative cooler or condenser.

capability can be enhanced by the addition of normal cooling tower fill material above or below the coil which increases the evaporative cooling surface area.

These closed circuit evaporative coolers are often referred to as deluged coolers meaning the coil is entirely covered with water at a high flow rate where the evaporation rate is similar to that of a normal cooling tower. Spray cooled heat exchangers which are essentially dry coolers are sometimes sprayed to enhance cooling during high temperature periods where all or most of the water evaporates are also encountered but are beyond the scope of this article.

Probably, the most commonly found closed circuit evaporative cooling device is the evaporative condenser used for condensing refrigerants such as ammonia and HFCLs where, due to the high pressure requirements, they are very competitive against shell-and-tube condensers combined with cooling towers. However, where high pressure is not a consideration a normal plate heat exchanger external to the cooling tower is often price-wise more competitive and the system is easier to maintain.

Evaporative coolers and condensers are very much the same in external appearance to cooling towers and they can usually be identified by the separate closed circuit inlet and outlet headers.

The theory of evaporative coolers/condensers is more complicated than direct evaporative cooling as it incorporates three sets of differential equations for the air, water, and internal fluid which have to be solved simultaneously and a numerical solution of the problem is essential. This theory is covered by Erens [36–39], Finlay and Grant [40], Kröger [4], Leidenfrost and Korenic [41], Mizushina [18] and Webb [42, 43], Parker and Treybal [44]. The combination of coil with fill material has been discussed by Erens [37].

The governing equations for a counterflow closed circuit evaporative cooler are derived next. Similar equations can be derived for evaporative condensers as well as crossflow evaporative coolers and condensers. It is assumed that the airflow is upward and the water flows vertically downward. The fluid inside the tubes moves at right angles to the air and water and can flow in a serpentined arrangement from top to bottom or bottom to top. Obviously, in condensers the tubes are usually slightly inclined and because of condensate flow the general direction is downward i.e., top to bottom.

Considering the element in Fig. 14 and applying Merkel's approximations on the air side:

$$\dot{m}_A \cdot dh_A = \beta_X \cdot dA \cdot (h''_A - h_A) \tag{46}$$

The energy balance between air, water, and process fluid inside the tubes gives

$$\dot{m}_W \cdot c_{pW} \cdot d\vartheta_W = \dot{m}_A \cdot dh_A + \dot{m}_p \cdot c_{pp} \cdot d\vartheta_p \tag{47}$$

and for the heat transfer inside the tubes:

$$\dot{m}_p \cdot c_{pp} \cdot d\vartheta_p = -U_t \cdot (\vartheta_p - \vartheta_W) \cdot dA \tag{48}$$

where U_t is the total heat transfer coefficient between the process fluid and the deluge water so that

$$U_t = \left[\frac{1}{\alpha_W} + \frac{A_e}{A_i \cdot \alpha_p} + \sum \frac{A_e}{A_n} \cdot R_n\right]^{-1} \tag{49}$$

where α_w is the heat transfer coefficient between the water film and tube wall, α_p is the process fluid heat transfer coefficient and the Rn includes all other resistances such as fouling both internal and external as well as the tube wall resistance.

Equations (46–48) have to be integrated numerically over the height, width, and length of the cooler to obtain a solution. By making the simple assumption that the recirculating water has a constant average temperature, Parker and Treybal [44] and Webb [43] have obtained fairly accurate solutions mathematically. The value of β_x has to be determined experimentally in a similar way to that for a conventional fill material.

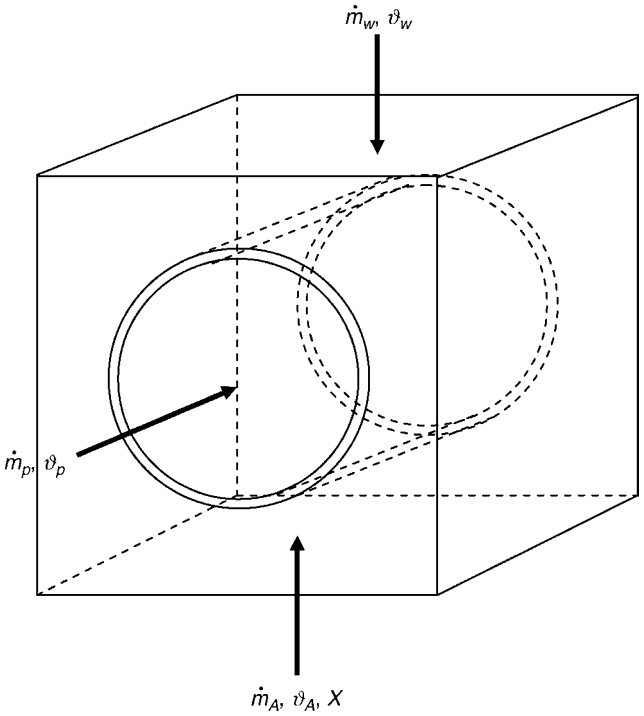

N4. Fig. 14. Closed circuit evaporative cooler element model.

9 Acceptance Testing

It would be most unusual for a cooling tower to be installed and that the situation arises where the design load occurs at the same time as the design ambient conditions. For this reason, acceptance testing codes have been established, whereby the tower can be tested at a certain condition and the performance predicted for the specified design conditions. The various codes require accurate measurements of water flow rate, inlet and outlet water temperatures, ambient air wet- and dry-bulb temperature and pressure, fan shaft power, wind velocity, and direction.

The cost of an independent cooling tower acceptance test is usually quite high and acceptance testing is therefore not justified in the case of small- and medium-sized towers where the acceptance test cost is a considerable portion of the total cost. Tests are therefore usually carried out only on very large towers. In the USA, the CTI has a system of certifying small tower performance based on standard tests, thus avoiding the expense of testing individual small towers.

Generally, drift-loss measurements are not included in an acceptance test, as this can often prove more difficult and costly than the thermal acceptance test.

The various acceptance test codes are given in British Standard 4485 [45, 46], Cooling Tower Institute [47–50] and Deutsche Normen 1947 [51]. The CTI [52] also publishes a code for testing of closed circuit cooling towers.

10 Water Conditioning

Proper treatment of cooling tower water is essential not only to keep the fill from clogging but also to control corrosion, deposition of solids (scaling) in equipment and to prevent the growth of dangerous bacteria such as *Legionella*.

Burger [3] and Nestor and Cappeline [53] discuss the various factors determining blowdown as well as algae and bacterial control in cooling towers.

When cooling tower water is evaporated the concentrations of chemical substances usually referred to as total dissolved solids (TDS) and total suspended solids (TSS) increase in value. Incoming water from a municipal source usually has a TDS of 50 to 100 ppm, and concentration due to evaporation should not exceed 800 to 900 ppm. This is to prevent precipitation of salts in the fill material. The number of cycles is therefore given by

$$\text{Cycles\_of\_concentration } (C) = \frac{\text{Maximum\_TDS}}{\text{Feedwater\_TDS}} \qquad (50)$$

Blowdown is usually controlled by monitoring the TDS level in the water.

The blowdown can be calculated as

$$\text{Blowdown} = \text{Evaporation\_Rate}/(C-1) - \text{Drift\_loss} \qquad (51)$$

In some cases, the level of the TSS, where feedwater has high levels of silica or high calcium sulfate concentration, can determine the cycles of concentration and also the blowdown rate. In such cases scaling, not just in the fill but in expensive heat exchanger equipment, is the main concern and usually requires more sophisticated monitoring methods for control of blowdown.

Suspended solids entering with the feedwater or ingested at the air intakes can be removed using sidestream filtering depending on the size of the particles involved. A flow rate of 5–10% of cooling tower rate is usually employed. This type of cleaning also assists in removing biological contamination as biological formations often cling to small particles in the water.

In small towers blowdown is often done manually, while in larger units a blowdown solenoid valve is controlled from a TDS sensor. Wirth and Westbrook [54] discuss a method of controlling salinity. The various factors influencing blowdown control are discussed more in detail by Burger [3].

Algae and biological growth are both problematic in cooling tower water, whereas algae requires sunlight to develop and many other biological growths can occur without light forming slimes under any conditions. The latter formations create problems in that they form coatings on the fill and in equipment to which solid particles are attached, clogging the fill and insulating the heat transfer surfaces. These substances have to be prevented from forming by use of biocides, ozone, and chlorine dosing or UV irradiation. All of these methods have their own advantages and disadvantages as corrosion and their influence on precipitation also have to be considered.

Most large installations make use of combinations of filtering and dosing using sophisticated monitoring methods to control water condition, thus maintaining a high cooling efficiency.

11 Symbols

a	area per unit volume (m^2/m^3)
c_p	specific heat at constant pressure (J/kg °C)

p	pressure (Pa)
h	enthalpy (J/kg °C)
Δh_{V0}	enthalpy of evaporation at 0°C (J/kg)
ATD	air travel distance (m)
C	cycles of concentration (–)
K	transfer coefficient (kg/s m^2)
$K_{1,2,3,4,5}$	constants
K_p	pressure loss coefficient (–)
$\dot{M}$	mass flow rate (kg/s)
M	molecular mass (kg/kmol)
Me	Merkel number (–)
R	gas constant (J/kg K)
T	temperature (Kelvin)
V	volume (m^3)
V	velocity (m/s)
X	mass of water per mass air (kg/kg)
α	heat transfer coefficient (W/m^2 °C)
β_X	mass transfer coefficient (kg/m^2 s]
θ	temperature (°C)
ρ	density (kg/m^3)
φ	relative humidity(–)

Subscripts

A	air
atm	atmospheric
db	dry bulb
m	mean value
wb	wet bulb
v	vapor
W	water or water vapor

Superscripts

$''$	saturated condition

Indice constants

a, b, c, d, e, f, g, h, i, j

12 Bibliography

1. Singham JR (1983) Chapter 3.12 Cooling towers. Heat exchanger design handbook. Hemisphere Corp.
2. Stoecker WF, Jones JW (1982) Refrigeration and air conditioning. McGraw Hill, 40–57, 365–379
3. Burger R (1990) Cooling tower technology, 2nd edn, Burger
4. Kröger DG (2004) Air-cooled heat exchangers and cooling towers, Penwell Corporation, OK
5. Monjoie M, Lauraine H (1985) Cooling tower drift losses. Hamon Sobelco Internal Publication, p 1–8
6. Foster PM, Williams MI, Winter RJ (1974) Droplet behaviour and collection by counterflow cooling tower eliminators. Environment 8:349–360
7. Chan J, Golay W (1977) Comparative performance evaluation of current design evaporative cooling tower drift eliminators. Environment 11:775–781
8. Golay MW, Glantschnig WJ, Best FR (1986) Comparison of methods for measurement of cooling tower drift. Atmos Environ 20(2):269–291
9. Bosnjakovic F (1965) Technical thermodynamics (English version). Holt, Rinehart and Winston
10. Fujita T, Tezuka S (1986) Calculations on thermal performance of mechanical draft cooling towers. ASHRAE Trans 92: 274–287
11. Poppe M, Rögener H (2006) Berechnung von Rückkühlwerken. VDI-Wärmeatlas 10.Auflage
12. Sutherland JW (1983) Analysis of mechanical draught counterflow air/water cooling towers. J Heat Transfer 105:576–583
13. Baker DR, Shryock HA (1961) A comprehensive approach to the analysis of cooling tower performance. J Heat Transfer 83: 339–350
14. Merkel F (1926) Verddunstungskühlung. VDI-Zeitschrift 70(4):123–128
15. Kloppers JC, Kröger DG (2005) Cooling tower performance evaluation – Merkel, Poppe, and e-NTU methods of analysis. J Eng Gas Turb Power 127(1):1–7
16. Kloppers JC, Kröger DG (2005) A critical investigation into the heat and mass transfer analysis of counterflow wet cooling towers. Int J Heat Mass Transfer 48, 3–4:765–777
17. Kloppers JC, Kröger DG (2005) Refinement of the transfer coefficient correlation of wet cooling tower fills. Heat Transfer Eng 26(4):35–41
18. Mizushina T Design of coolers, condensers and evaporative coolers. Heat transfer design sourcebook, Afghan and Schlunderer, pp 419–440
19. Yadigaroglu G, Pastor EJ (1974) An investigation of the accuracy of the Merkel Equation for evaporative cooling tower calculations. ASME paper no. 74-HT-59, Boston, MA, July 15–17
20. Kloppers JC, Kröger DG (2003) Cooling tower performance, a critical evaluation of Merkel assumptions. R&D J SAIMechE 20(1):6–10
21. Kloppers JC, Kröger DG (2005) The Lewis factor and it's influence on the performance predicition of wet cooling towers. Int J Therm Sci 44:879–884
22. Jaber H, Webb RL (1989) Design of cooling towers by the effectiveness-NTU method. J Heat Transfer 111:837–843
23. Webb RL (1988) A critical evaluation of cooling tower design methodology. Heat transfer equipment design. Hemisphere Pub. Co., Washington, DC
24. Webb RL, Villacres A (1984) Cooling tower performance. ASHRAE J 5: 34–40
25. Webb RL, Villacres A (1984) Algorithms for performance simulation of cooling towers, evaporative condensers and fluid coolers. ASHRAE Trans 90: 416–458
26. Webb RL, Jaber H (1989) Design of cooling towers by the effectiveness-NTU method. J Heat Transfer 111: 837–843
27. Kloppers JC, Kröger DG A critical investigation into the heat and mass transfer analysis of crossflow wet cooling towers. Numer Heat Transfer: Part A: Appl 46(8):785–806
28. Dreyer AA (1994) Modelling of cooling tower splashpack, PhD thesis, University of Stellenbosch, Stellenbosch, Repubilc of South Africa
29. Kloppers JC, Kröger DG (2003) Loss coefficient correlation for wet cooling tower fills. Appl Therm Eng 23(17):2201–2211
30. Cale SA (1982) Development of evaporative cooling packing. Commission of the European Communities, Report EUR 7709 EN
31. De Villiers E, Kröger DG (1999) Analysis of heat, mass and momentum transfer in the rain zone of counterflow cooling towers. J Eng Gas Turb Power-Trans ASME 121(4):751–755
32. Pearce DJ (2007) Evaluation and performance prediction of cooling tower rain zones. M.Sc. (Eng) Thesis, University of Stellenbosch
33. Terblanche R, Reuter HCR, Kröger DG (2008) Drop size distribution below different wet-cooling tower fills. Appl Therm Eng. doi:10.1016/j.applthermaleng. 2008.07.013
34. Majumdar AK, Singhal AK, Mukerjee (1985) VERA2D-84. A computer program for two-dimensional analysis of flow, heat and mass transfer in evaporative cooling towers. Report CS-4073, Vols. 1 & 2, Electric Power Research Institute
35. Majumdar AK, Singhal AK, Spalding DB (1983) Numerical modelling of wet cooling towers. Trans ASME, J Heat Transfer 105:728–743
36. Erens PJ (1987) A procedure for the design or rating of counterflow evaporative cooler cores. SAIMechE R&D J, 3(1):18–25
37. Erens PJ (1988) Comparison of some design choices for evaporative cooler cores. Heat Transfer Eng, 9(2):29–35
38. Erens PJ, Dreyer AA (1988) An improved procedure for calculating the performance of evaporative closed circuit coolers. 25th national heat transfer conference, AIChE Symposium Series No 263, Vol. 84, Houston, TX
39. Erens PJ, Dreyer AA (1989) A general approach for the rating of evaporative closed circuit coolers. R & D J, SAIMechE R&D J 5(1):1–10
40. Finlay IC, Grant WD (1972) Thermal design of evaporative coolers. Natl Eng Lab 15–46
41. Leidenfrost W, Korenic B (1982) Evaporative cooling and heat transfer augmentation related to reduced condenser temperature. Heat Transfer Eng 3:38–59

42. Webb RL (1984) A unified theoretical treatment for thermal analysis of cooling towers, evaporative condensers and fluid coolers. ASHRAE Trans 90:398–415
43. Webb RL, Villacres A (1985) Performance simulations of evaporative heat exchangers (cooling towers, fluid coolers and condensers). Heat Transfer Eng 6:31–38
44. Parker RO, Treybal RE (1961) The heat, mass transfer characteristics of evaporative coolers. Chemical Engineering Progress Symposium Series. Heat Transfer 57(32):138–149
45. British Standard 4485: Part 2, 1969, 2–24
46. Cooling Tower Institute (1996) Acceptance test code for closed circuit cooling towers, 1–19
47. Cooling Tower Institute (1990) Acceptance test code for water cooling towers, 1–50
48. Cooling Tower Institute (1994) Recommended practice for airflow testing of cooling towers, 1–6
49. Cooling Tower Institute (1995) Standard for water flow measurement, Part 1 and 2, 1–16
50. Cooling Tower Institute (1997) Acceptance test code for water cooling towers, 1–15
51. Deutsche N (1947) Performance test on cooling towers, June 1959, 2–28
52. Cooling Tower Institute (1996) Acceptance test code for closed circuit cooling towers, 1–19
53. Nestor GJ, Cappeline M (1979) Water related problems of evaporative cooling systems and control methods. Ind Water Eng 16:14–25
54. Wirth JR, Westbrook G (1977) Cooling water salinity and brine disposal optimized with electrodialysis water recovery/brine concentration system. Combustion 33–37

N5 Heat Pipes

Peter Stephan
Technische Universität Darmstadt, Darmstadt, Germany

1 Introduction

Heat transfer devices with a very high heat flux density at low temperature differences are typically based on closed two-phase (liquid–vapor) systems. The latent heat of vaporization of the fluid is transferred from the location of the evaporator near the heat source to the location of the condenser near the heat sink. Heat pipes are such heat transfer devices with the particularity that the liquid transport is caused by capillary forces.

Figure 1 shows the principle design of a heat pipe. A closed fluid container, typically a closed pipe or a hollow plate, is internally lined with a capillary structure which is saturated with the liquid phase of the heat transfer fluid. Upon heating one end of the container the liquid evaporates at this location and partially retracts into the capillary structure. The generated vapor flows toward the cold end of the container where it condenses and fills the capillary structure. The difference in the liquid filling height in the structure causes a capillary force that sucks the condensed liquid back to the evaporator. The two-phase loop is thereby closed and the latent heat transferred from the heat source to the heat sink. In between the evaporator and condenser zones an adiabatic transport zone can be located.
Specific features of a heat pipe are

- High heat transport capability at low temperature differences between heat source and sink; e.g., the effective thermal conductivity can be more than two orders of magnitude higher than the thermal conductivity of pure copper.
- Fluid transport without any mechanically moving parts. Therefore, a heat pipe typically shows no wear-out and needs no maintenance.
- The condensate can be transported in a nongravitational environment (e.g., in satellites) or even against gravity.
- Local temperature differences in space or time tend to equalize fast and automatically without control.
- A compact and low-mass architecture of the heat exchanger is possible.
- Complex structural shapes of the heat exchanger can be realized.

Due to these features heat pipes are applied in particular in the following areas:

- Thermal control in space applications, e.g., in satellites.
- Cooling of electronic components, e.g., CPUs.
- Heat recovery in industrial processes and in buildings.

The spectrum of applications hereby spreads over a huge range of operation temperatures from about 5 to 2,200 K.

2 Selection of Fluid, Wall Material, and Capillary Structure

The fluid should have the following properties: high latent heat of vaporization, high thermal conductivity, low viscosity, high surface tension, low wetting contact angle, and neither extremely low nor extremely high vapor pressure at the given operating temperature. Some of these properties are expressed in the so-called merit number M [1],

$$M = \frac{\sigma \Delta h_v}{v_l}, \tag{1}$$

which is not a dimensionless number but has a unit W/m^2 or kW/cm^2. Figure 2 shows the merit number for some fluids that are used in heat pipes. For a given application and its fixed operating temperature range the selection of a fluid with a high merit number is highly desirable. Figure 3 shows further qualified fluids for different temperature ranges.

The selection of the solid material for the container wall and the capillary structure depends not only on its thermal conductivity, which should be rather high, but sometimes even more important on its compatibility with the fluid. Here compatibility comprises (i) good wetting characteristics and (ii) chemical stability to avoid corrosion and the generation of

VDI-GVC (ed.), *VDI Heat Atlas*, DOI 10.1007/978-3-540-77877-6_65,

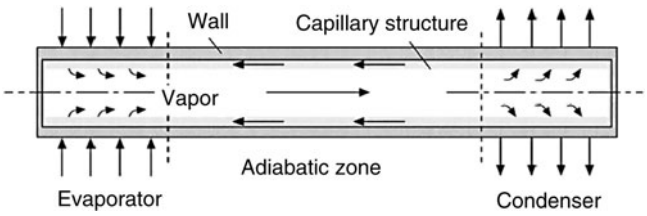

N5. Fig. 1. Principle design of a heat pipe.

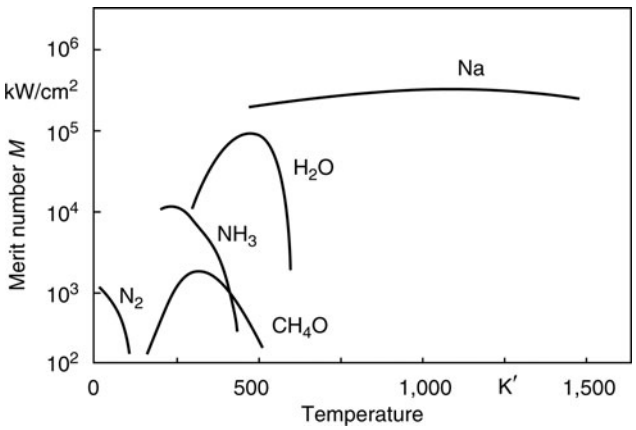

N5. Fig. 2. Merit number for some fluids.

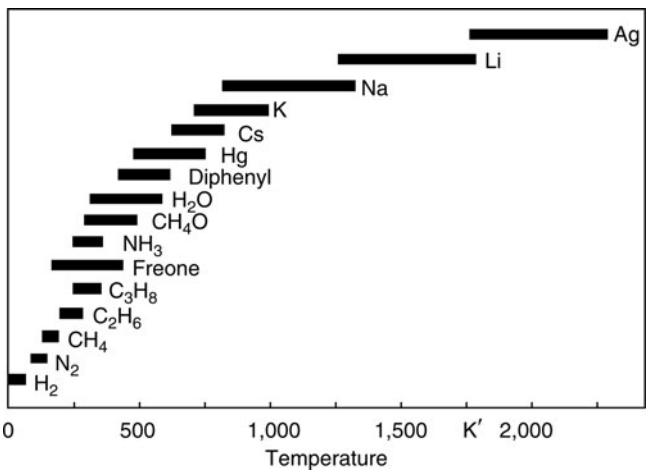

N5. Fig. 3. Qualified fluids for different operating temperature ranges.

noncondensable gases that might block the condenser zone. Long-term tests showed that the following solid–fluid combinations are compatible:

- Freons with aluminum and stainless steel. (However, it should be noted that the use of such chlorofluorocarbons and hydrochlorofluorocarbons is forbidden in many applications today due to their negative effect on the ozone layer of the earth.)
- Ammonia with aluminum, construction steel, stainless steel, and nickel.
- Acetone with copper.
- Methanol with copper.

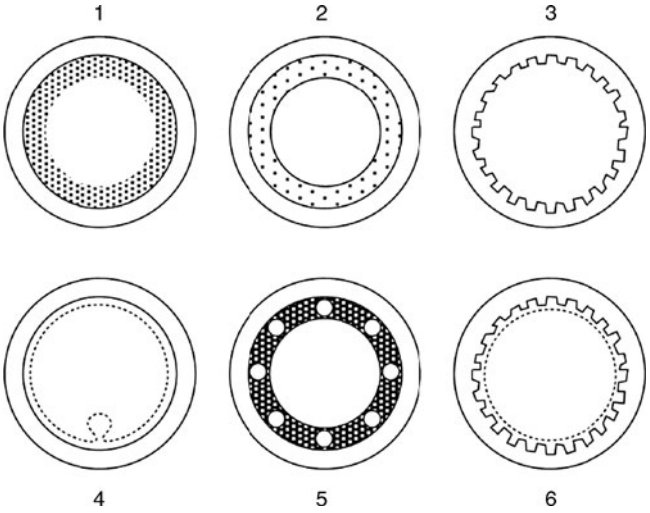

N5. Fig. 4. Different capillary structures: (1) wick or mesh structure, (2) sinter structure, (3) open axial grooves, (4)–(6) combined structures.

- Water with copper.
- Potassium with copper.
- Sodium with stainless steel, nickel, and inconel.
- Lithium with niobium, tantalum, tungsten, and molybdenum.
- Silver with tantalum and tungsten.

The compatibility also depends on the production and post-cleaning methods which might explain the partly different compatibility observations from different authors using the same material combinations [1–5]. Reay and Kew [1] as well as Brost and Groll [5] have given details about specific production and cleaning methods.

Additionally to the aforementioned compatibility issues, the capillary structure should have the following features:

- Generation of a high capillary pressure in the evaporator region which means it should be a fine structure.
- Low liquid flow resistance or pressure drop along main flow direction which means it should be a gorse structure.
- Insensitivity against vapor bubble generation and growth to avoid a blockage of the capillary structure.
- Large storage capability for the liquid phase.

As can be seen these features are partly controversial and therefore require a compromise for the selection of the capillary structure. In any case the selection of the combination fluid/wall material/capillary structure has to be proved finally by a computation of the performance limits of the selected design and its comparison with the performance requirements (for details see Sect. 4 of this chapter).

Figure 4 schematically shows the cross section of a heat pipe with different capillary structures that were proven in the past. Wick or mesh structures (1) and sinter structures (2) allow a high capillary pressure, but typically generate a high liquid flow resistance and are sensitive to vapor bubble formation. Open axial grooves (3) have a relatively small flow resistance, and bubbles that might be generated can vent to the vapor core, but they allow only low to moderate capillary pressures. Some more

sophisticated structures (4, 5, 6) partly combine positive features of the aforementioned structures (1) to (3).

3 Theory and Design for Steady-State Operation

The heat transfer characteristics are determined by the hydrodynamic flow resistances and the heat resistances. The theoretical background and the equations for a basic thermohydraulic design for the steady-state operation mode are given in the following subsections.

3.1 Pressure Profiles

Figure 5 shows a typical pressure profile in the vapor/gas phase and the liquid phase along the heat pipe. As the fluid circulates in a closed circuit the sum of all pressure drops and differences along a single loop must be zero:

$$0 = \Delta p_c + \Delta p_g + \Delta p_l. \tag{2}$$

Herein, Δp_g is the total pressure drop along the vapor flow, Δp_l the total pressure drop along the liquid flow, and Δp_c the capillary pressure difference that has to equalize these two pressure drops and thereby drive the fluid flow. Equation (2) is the basic equation for the hydraulic design.

As can be seen in Fig. 5, the pressure difference between liquid and gas phases typically is highest at the evaporator end and lowest at the condenser end. Thus, the capillary structure is saturated with liquid at the condenser end and the liquid–vapor interface is almost flat, and the liquid recedes more and more into the capillary structure toward the evaporator end. Both situations are schematically indicated at the bottom of the figure. The location where the capillary structure is flooded is also called "wet-point." Due to the possible pressure recovery along the vapor flow in the condenser the wet-point can also be located in the condenser entrance region. The location where the capillary structure tends to dry out first at the capillary limit is also called "dry-point."

3.1.1 Capillary Pressure Difference

In a steady-state operation mode the curvature of the liquid–vapor menisci at each location along the heat pipe attune to local pressures of the vapor and liquid phases. This means, according to

$$p_c = p_g - p_l = \sigma\left(\frac{1}{R_1} + \frac{1}{R_2}\right), \tag{3}$$

a meniscus will have a curvature K, which in a general 3D case can be expressed by two main radii R_1 and R_2.

Chi [3] instead defined an effective radius of curvature R_{eff} that characterizes the capillary structure. His definition is based on the assumption of a spherical liquid–vapor phase interface and takes into account the wetting angle of the liquid at the solid structure. It follows

$$p_c = \frac{2\sigma}{R_{eff}} \cos\vartheta. \tag{4a}$$

The maximum capillary pressure that can be generated by a capillary structure for given surface tension σ and wetting angle ϑ depends only on the geometry of the capillary structure or the minimum effective radius of curvature $R_{eff,min}$. It follows

$$p_{c,max} = \frac{2\sigma}{R_{eff,min}} \cos\vartheta. \tag{4b}$$

$R_{eff,min}$ can be derived theoretically, e.g., for open grooves from their geometry or alternatively experimentally for any kind of

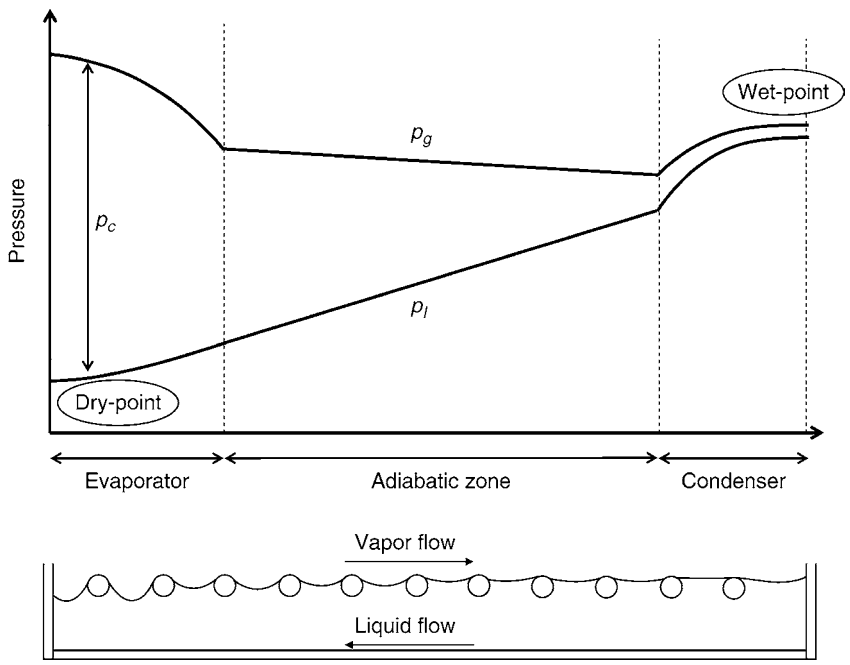

N5. Fig. 5. Pressure profiles along a heat pipe.

structures including those with statistical pore size distributions, e.g., sintered metals [4]. Table 1 shows minimum effective radii of curvature $R_{\text{eff,min}}$ for different types of structures.

The capillary pressure difference Δp_c in Eq. (2) equals the difference of the capillary pressure $p_{c,evap}$ at the evaporator end and the capillary pressure $p_{c,cond}$ at the condenser end:

$$\Delta p_c = p_{c,evap} - p_{c,cond.} \tag{5a}$$

Thus, the capillary pressure difference becomes maximal if

(a) $p_{c,evap}$ becomes maximal and
(b) $p_{c,cond}$ becomes minimal.

These conditions are fulfilled if

(a) the liquid is receded as far as possible into the capillary structure at the evaporator end (i.e., $R_{\text{eff,evap}} = R_{\text{eff,min}}$) and
(b) the capillary structure is completely flooded with liquid at the condenser end (i.e., $R_{\text{eff,cond}} \rightarrow \infty$). (Note that the amount of fluid filled into the heat pipe should always be chosen such that there is little excess liquid. This excess liquid accumulates at the condenser end, and therefore, this condition is fulfilled under standard operating conditions.)

It follows

$$\Delta p_{c,max} = \frac{2\sigma}{R_{\text{eff,min}}} \cos\vartheta. \tag{5b}$$

The wetting angle ϑ is the macroscopically apparent contact angle, and it depends on the pairing fluid/capillary material, the surface roughness, the surface state (e.g., oxidation state), and the local heat flux. Typically, the apparent contact angle is measured under isothermal conditions with standardized methods, see e.g., [4]. Here, the influence of the local heat flux in the contact line area is neglected. Wayner [6], Stephan [7], and Khrustalev and Faghri [8] developed numerical methods to compute the apparent contact angle under evaporating conditions. These values are little higher than those under isothermal conditions and increase with the evaporative heat flux, but general correlation still do not exist. If accurate and reliable data for ϑ are not available (e.g., from measurements) the values listed in Table 2 are used for heat pipe design. In case a range of wetting angles is given in the literature the upper value should be chosen for the design to be on the safer side when calculating $\Delta p_{c,max}$.

N5. Table 1. Minimum effective radii of curvature [3]

Capillary structure	$R_{\text{eff,min}}$	Geometric parameter	
Circular artery	R	R	Radius of artery
Rectangular groove	w	w	Groove width
Triangular groove	$w/\cos\beta$	w	Groove width
		β	Opening angle
Screen wicks/ meshes	$(w + d)/2$	w	Mesh width
		d	Wire diameter
	$1/(2N)$	N	Mesh number per unit length
Sintered powders	$0.41R$	R	Particle radius

3.1.2 Liquid Pressure Drop

The pressure drop along the liquid flow comprises the pressure loss due to friction $\Delta p_{l,fric}$ and the hydrostatic pressure difference $\Delta p_{l,stat}$, thus

$$\Delta p_l = \Delta p_{l,fric} - \Delta p_{l,stat.} \tag{6}$$

Since the friction pressure loss is proportional to the mass flow and the mass flow varies in both the evaporator and the condenser zone, an effective length of the heat pipe is defined and used for pressure loss calculation instead of the overall geometrical length. The effective length is defined by

$$l_{\text{eff}} = \frac{1}{\dot{Q}} \int_0^l \dot{Q}(z)\,\mathrm{d}z, \tag{7}$$

where l is the length in axial flow direction z, $\dot{Q}(z)$ is the axial heat flow along the heat pipe at a position z, and $\dot{Q}$ is the total or maximum axial flow. Assuming constant radial heat flux in the evaporator and condenser zone $\dot{Q}(z)$ will rise linearly from the evaporator end toward the adiabatic zone, it will be constant along the adiabatic zone, and it will decrease linearly from the adiabatic zone to the condenser end. With this, Eq. (7) results in

$$l_{\text{eff}} = \frac{1}{2} l_{evap} + l_{ad} + \frac{1}{2} l_{cond}. \tag{8}$$

The liquid flow in a capillary structure is typically laminar; however, the specific flow characteristics in specific capillary structures require specific approaches for the pressure loss calculation.

- The Hagen–Poiseuille equation can be used for open or covered capillary grooves and artery structures:

$$\Delta p_{l,\,fric} = -\frac{32 \nu_l}{A_l \Delta h_v d_{c,h}^2} \dot{Q} l_{\text{eff}}. \tag{9}$$

  Herein, $d_{c,h}$ is the hydraulic diameter of the flow channel and A_l is cross-sectional area of the channel. For heat pipes with N axial grooves with a cross section A_{groove} each, it follows $A_l = N A_{\text{groove}}$.

- For sinter structures or wicks the pressure loss according to Darcy's law is applied:

$$\Delta p_{l,\,fric} = -\frac{\nu_l}{K A_l \Delta h_v} \dot{Q} l_{\text{eff}}. \tag{10}$$

  Herein, K is the permeability of the capillary structure. For homogeneous meshes, it is according to Marcus [10]

$$K = \frac{d^2 \varepsilon^3}{122(1-\varepsilon)^2} \tag{11}$$

  with the porosity ε and the wire diameter d.

N5. Table 2. Wetting angles for various fluids

Fluid	Wetting angle ϑ
Water [9]	40°–45°
Hydrocarbons [9]	35°
Ammonia [6]	20°–25°

For homogeneous sinter metals it is according to Chi [3]

$$K = \frac{r^2 \varepsilon^3}{37.5(1-\varepsilon)^2} \tag{12}$$

with the radius r of the sintered particles.

For nonhomogeneous structures the permeability can be measured [4].

The hydrostatic pressure difference along the liquid flow is calculated by

$$\Delta p_{l,stat} = -\rho_l g\ h, \tag{13}$$

with the height h against the gravitational axis. Figure 6 shows a tilted heat pipe with a tilt angle α against the horizontal line.

Assuming that the geometry of the capillary structure does not allow circumferential liquid flow (e.g., axial grooves), the height is given by

$$h = \pm l \sin\alpha, \tag{14}$$

with the total length l of the heat pipe. The negative algebraic sign is valid if the evaporator is located below the condenser. In this case the hydrostatic pressure difference assists the liquid flow ($\Delta p_{l,stat} > 0$). If the evaporator is located above the condenser, the positive sign is valid, and the gravity opposes the flow ($\Delta p_{l,stat} < 0$).

In case the geometry of the capillary structure also allows circumferential liquid flow (e.g., wicks) the height is given by

$$h = \pm l \sin\alpha + d_i \cos\alpha, \tag{15}$$

with the inner diameter d_i of the pipe.

3.1.3 Vapor Pressure Drop

The hydrostatic pressure difference along the vapor channel can be neglected. The hydrodynamic pressure drop along the vapor flow consists of the friction part along the entire vapor channel and an additional inertia part in the evaporator and condenser zone due to the acceleration and deceleration of the vapor flow in these two zones. Many authors have developed analytical or numerical, one- or two-dimensional solutions for the Navier–Stokes equations for several different heat pipe configurations (e.g., [3, 4, 11, 12]). Typically, the Mach number in the vapor flow will be small enough (Ma < 0.3) to assume incompressible flow characteristics. However, some special heat pipes (e.g., high temperature liquid metal heat pipes) or special operating situations (e.g., some start-up procedures) require the consideration of compressible flow characteristics. These special cases are, e.g., described by Faghri [4]. Assuming incompressible flow the following approach for calculating the pressure drop is applied.

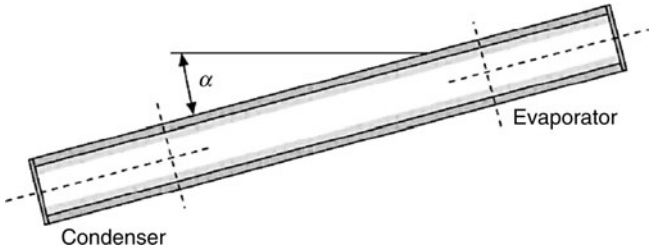

N5. Fig. 6. Tilted heat pipe.

The pressure drops in the evaporator zone, the adiabatic zone, and the condenser zone are treated separately. It yields

$$\Delta p_g = \Delta p_{g,evap} + \Delta p_{g,cond} + \Delta p_{g,ad}. \tag{16}$$

The pressure drop in the adiabatic transport zone is governed by friction only. The axial Reynolds number is

$$\mathrm{Re}_a = \frac{\dot{Q} d_{g,h}}{\nu_g \rho_g A_{g,a} \Delta h_v}, \tag{17}$$

with the hydraulic diameter $d_{g,h}$ of the axial cross section $A_{g,a}$.

The flow is laminar for $\mathrm{Re}_a < 2{,}300$. In this case the pressure drop $\Delta p_{g,ad}$ is calculated according to the Hagen–Poiseuille law

$$\Delta \rho_{g,ad} = -\frac{32 \nu_g}{A_{g,a} \Delta h_v d_{g,h}^2} \dot{Q} l_{ad}. \tag{18}$$

For $\mathrm{Re}_a > 2{,}300$ the flow is considered to be turbulent, which means that the transition region between laminar and turbulent flows is omitted. Following the Blasius approach, it is

$$\Delta \rho_{g,ad} = -\frac{0.3164}{\sqrt[4]{\mathrm{Re}_a}} \frac{\dot{Q}^2 l_{ad}}{2 \rho_g A_{g,a}^2 \Delta h_v^2 d_{g,h}}. \tag{19}$$

In the evaporator and condenser zone the vapor velocity has also a radial component. The deformation of the flow profile compared to a purely axial flow is described by the radial Reynolds numbers in the evaporator and condenser. It is defined by

$$\mathrm{Re}_r = \frac{\dot{Q} r_g}{\nu_g \rho_g A_{g,r} \Delta h_v}. \tag{20}$$

Here, r_g is the radius of the vapor channel in the axial cross section and $A_{g,r}$ the surface area where evaporation or condensation takes place. The radial added vapor mass in the evaporator zone has a stabilizing effect to the axial vapor flow for Reynolds numbers $|\mathrm{Re}_r| >> 1$, i.e., the transition from laminar to turbulent flow is shifted to higher axial Reynolds numbers. In the condenser zone, vapor mass is subtracted and a Reynolds number $|\mathrm{Re}_r| >> 1$ has a destabilizing effect to the axial vapor flow. The laminar–turbulent transition is shifted to lower axial Reynolds numbers.

For $|\mathrm{Re}_r| << 1$ the inertia effects originating from the radial velocity components are negligible compared to the friction effects and for $|\mathrm{Re}_r| >> 1$, vice versa.

- For $|\mathrm{Re}_r| << 1$ and $\mathrm{Re}_a < 2{,}300$, i.e., laminar friction dominated flow, the Hagen–Poiseuille law yields

$$\Delta p_{g,evap} = -\frac{32 \nu_g}{A_{g,a} \Delta h_v d_{g,h}^2} \dot{Q} \frac{l_{evap}}{2}. \tag{21}$$

and

$$\Delta p_{g,cond} = -\frac{32 \nu_g}{A_{g,a} \Delta h_v d_{g,h}^2} \dot{Q} \frac{l_{cond}}{2}. \tag{22}$$

- For $|\mathrm{Re}_r| << 1$ and $\mathrm{Re}_a > 2{,}300$, i.e., turbulent friction dominated flow, it is

$$\Delta p_{g,evap} = -\frac{0.3164}{\sqrt[4]{Re_a}} \frac{\dot{Q}^2 l_{evap}}{4\rho_g A_{g,a}^2 \Delta h_v^2 d_{g,h}} \tag{23}$$

and

$$\Delta p_{g,cond} = -\frac{0.3164}{\sqrt[4]{Re_a}} \frac{\dot{Q}^2 l_{cond}}{4\rho_g A_{g,a}^2 \Delta h_v^2 d_{g,h}}. \tag{24}$$

- For $|Re_r| \geq 1$ the inertia effects have to be taken into account. In the evaporator zone and the condenser zone the inertia forces act in contrary direction, i.e., a pressure recovery can be observed in the condenser. According to the model of Cotter [11] the pressure recovery in the condenser is approximately 40% of the pressure drop in the evaporator. The models of Busse [12] and Faghri [4] predict almost 100% pressure recovery which is in accordance with the experimental investigations of Haug [13]. Assuming 100% pressure recovery it follows

$$\langle \Delta p_{g,evap} + \Delta p_{g,cond} \rangle_{|Re_r|\geq 1} = \langle \Delta p_{g,evap} + \Delta p_{g,cond} \rangle_{|Re_r|<<1}, \tag{25}$$

and the aggregated pressure drops in the evaporator and condenser can be calculated using Eqs. (21–24).

Example 1

A heat pipe is used for electronics cooling in a satellite. The required heat flux is 50 W and the operating temperature ϑ_{sat} = 10°C. The heat pipe is made of an aluminum tube with 32 rectangular axial open grooves (w = 0.5 mm, h = 0.8 mm). The grooves are equally distributed around the circumference of the tube (d_i = 9 mm, d_a = 14 mm). The lengths of the evaporator and condenser zone are 100 mm each. The length of the adiabatic transport zone is 780 mm. Ammonia is used as the working fluid. The heat is supplied and rejected homogeneously to the evaporator and from the condenser, respectively (constant heat flux density can be assumed). The questions are:

(a) What is the maximal capillary pressure difference $\Delta p_{c,\,max}$ that the capillary structure can withstand?
(b) What is the capillary pressure difference Δp_c under the given operating conditions?

The required properties of NH_3 at 10°C are

ρ_l = 624.6 kg/m^3,	ν_g = 19.08 · 10^{-7} m^2/s,
ρ_g = 4.865 kg/m^3,	σ = 23.88 · 10^{-3} N/m,
λ_l = 499.6 · 10^{-3} W/(m K),	Δh_v = 1225.5 kJ/kg,
ν_l = 2.490 · 10^{-7} m^2/s.	

Solution

(a) According to Eq. (5b) the maximal pressure difference is

$$\Delta p_{c,max} = \frac{2\sigma}{R_{eff,min}} \cos\vartheta.$$

The minimal effective radius of curvature is taken from Table 1. For rectangular open grooves, we find

$$R_{eff,min} = w = 0.5 \text{ mm}.$$

According to Table 2 the apparent wetting angle ϑ is in the range from 20° to 25°. For a conservative calculation of the maximal capillary pressure difference the upper value has to be considered. With ϑ = 25° it follows

$$\Delta p_{c,max} = \frac{2 \cdot 23.88 \cdot 10^{-3}}{0.5 \cdot 10^{-3}} (\text{N/m}^2) \cos 25° = 86.6 \text{ Pa}.$$

(b) The capillary pressure difference for given operating conditions is calculated using Eq. (2):

$$\Delta p_c = -(\Delta p_g + \Delta p_l).$$

The pressure drop along the liquid flow is given by Eq. (6). For a satellite application (zero gravity) the hydrostatic pressure difference yields $\Delta p_{l,stat}$ = 0. With Eqs. (6) and (9), it follows

$$\Delta p_l = \Delta p_{l,stat} = -\frac{32\nu_l}{A_l \Delta h_v d_{c,h}^2} \dot{Q} l_{eff}.$$

The effective length of the heat pipe is (see Eq. (8))

$$l_{eff} = \frac{1}{2} l_{evap} + l_{ad} + \frac{1}{2} l_{cond} = \left(\frac{100}{2} + 780 + \frac{100}{2}\right) \text{mm} = 880 \text{ mm}.$$

The cross-sectional area of a single groove is

$$A_{groove} = w \cdot h = 0.5 \cdot 0.8 \text{ mm}^2 = 0.4 \text{ mm}^2.$$

Thus, the entire liquid flow cross section is

$$A_l = N \cdot A_{groove} = 32 \cdot 0.4 \text{ mm}^2 = 12.8 \text{ mm}^2.$$

The hydraulic diameter is

$$d_{c,h} = \frac{4 \cdot A_{groove}}{2h + w} = \frac{4 \cdot 0.4}{2 \cdot 0.8 + 0.5} \text{ mm} = 0.762 \text{ mm}.$$

As a result one gets

$$\Delta p_l = \frac{-32 \cdot 2.49 \cdot 10^{-7} \cdot 50 \cdot 880 \cdot 10^{-3}}{12.8 \cdot 10^{-6} \cdot 1225.5 \cdot 10^3 \cdot (0.762 \cdot 10^{-3})^2} \text{ Pa} = -38.5 \text{ Pa}.$$

The pressure drop along the vapor flow is calculated according to Eq. (16):

$$\Delta p_g = \Delta p_{g,evap} + \Delta p_{g,cond} + \Delta p_{g,ad}.$$

First, one has to check whether the axial flow in the adiabatic zone is laminar or turbulent. Equation (17) yields

$$Re_a = \frac{\dot{Q} d_{g,h}}{\nu_g \rho_g A_{g,a} \Delta h_v} = \frac{50 \cdot 9 \cdot 10^{-3}}{19.08 \cdot 10^{-7} \cdot 4{,}865 \cdot 63.62 \cdot 10^{-6} \cdot 1225.5 \cdot 10^3} = 621.8,$$

wherein the hydraulic diameter of the vapor channel is $d_{g,h}$ = d_i = 9 mm and its cross section $A_{g,a} = \pi d_i^2/4$ = 63.62 mm^2.

Thus, the vapor flow is laminar, and the pressure drop in the adiabatic zone follows from Eq. (18):

$$\Delta p_{g,ad} = -\frac{32\nu_g}{A_{g,a}\Delta h_v d_{g,h}^2}\dot{Q}l_{ad} = \frac{-32\cdot 19.08\cdot 10^{-7}\cdot 50\cdot 780\cdot 10^{-3}}{63.62\cdot 10^{-6}\cdot 1225.5\cdot 10^{3}\cdot (9\cdot 10^{-3})^2}\ \text{Pa} = -377\ \text{mPa}.$$

To calculate the pressure drops in the evaporator and condenser zone we have to specify the possible influence of the radial flow components first. As the geometries of the evaporator and condenser are equal, their radial *Reynolds* numbers are – apart from the sign – equal too. It follows from Eq. (20)

$$|\text{Re}_r| = \frac{\dot{Q}r_g}{\nu_g\rho_g A_{g,r}\Delta h_v} = \frac{50\cdot 4.5\cdot 10^{-3}}{19.08\cdot 10^{-7}\cdot 4{,}865\cdot 2{,}827\cdot 10^{-6}\cdot 1225.5\cdot 10^{3}} = 7.0,$$

with the radius of the vapor channel $r_g = d_i/2 = 4.5$ mm and the surface area of the evaporator and condenser zone, $A_{g,r} = \pi d_i \cdot l_{evap/cond} = 2{,}827\ \text{mm}^2$. For $\text{Re}_r = 7$ the inertia effects are not negligible and the pressure drops are calculated according to Eq. (25),

$$\langle \Delta p_{g,evap} + \Delta p_{g,cond}\rangle_{|\text{Re}_r|\geq 1} = \langle \Delta p_{g,evap} + \Delta p_{g,cond}\rangle_{|\text{Re}_r|<<1},$$

and Eqs. (21) and (22)

$$\Delta p_{g,evap} + \Delta p_{g,cond} = -\frac{32\nu_g\dot{Q}}{A_{g,a}\Delta h_v d_{g,h}^2}\left(\frac{l_{evap}}{2}+\frac{l_{cond}}{2}\right) = \frac{-32\cdot 19.08\cdot 10^{-7}\cdot 50\cdot 100\cdot 10^{-3}}{63.62\cdot 10^{-6}\cdot 1225.5\cdot 10^{3}\cdot (9\cdot 10^{-3})^2}\ \text{Pa} = -48.3\ \text{mPa}.$$

The pressure drop along the vapor flow accumulates to

$$\Delta p_g = -(377 + 48.3)\ \text{mPa} = -425.3\ \text{mPa}$$

and the capillary pressure difference under the given operation conditions is

$$\Delta p_c = (0.4253 + 38.5)\ \text{Pa} = 38.93\ \text{Pa}.$$

3.2 Heat Transport

From the point of view of an external observer a heat pipe can be regarded as a thermal conductor with very low heat resistance. With that the temperature difference ΔT between heat source and heat sink simply follows the resistance law

$$\Delta T = \dot{Q}R_{total} \tag{26}$$

with the total heat resistance R_{tot} of the entire heat pipe. This heat resistance includes all single heat resistances that are relevant to the heat pipe system. The single heat resistances are shown in Fig. 7. Some act as parallel resistances and the others as serial resistances in the overall circuit.

The single resistances are:

$R_{e,evap}$	Radial heat resistance between external heat source and outer evaporator wall
$R_{w,evap}$	Radial heat resistance of the evaporator wall
$R_{c,evap}$	Radial heat resistance of the capillary structure in the evaporator zone
$R_{ph,evap}$	Radial heat resistance of the liquid–vapor phase interface in the evaporator zone
R_g	Axial heat resistance along the vapor flow
$R_{ph,cond}$	Radial heat resistance of the liquid–vapor phase interface in the condenser zone
$R_{c,cond}$	Radial heat resistance of the capillary structure in the condenser zone
$R_{w,cond}$	Radial heat resistance of the condenser wall
$R_{e,cond}$	Radial heat resistance between outer condenser wall and external heat sink
R_l	Axial heat resistance along the liquid flow in the capillary structure
R_w	Axial heat resistance in the wall

The heat from the external heat source and the heat to the external heat sink can be transferred by conduction, convection, or radiation. The related heat resistances are typically as high as

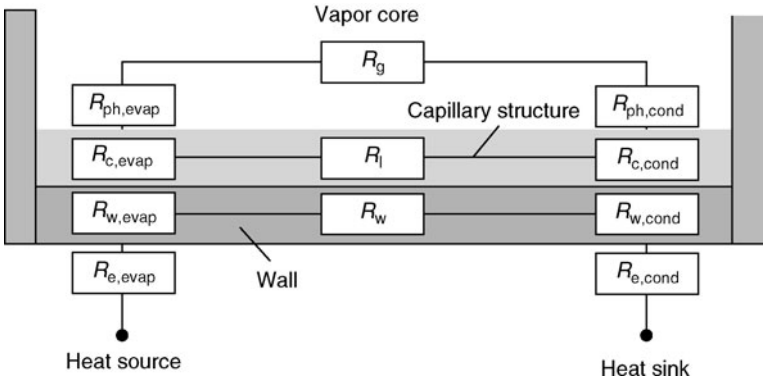

N5. Fig. 7. Heat resistances in a heat pipe.

or even higher than the overall internal heat resistance of a heat pipe. If this internal heat resistance is R_{HP} it follows

$$R_{total} = R_{e,evap} + R_{e,cond} + R_{HP}. \quad (27)$$

To calculate the external resistances $R_{e,evap}$ and $R_{e,cond}$ the reader is referred to Parts F (natural convection), G (forced convection), and K (radiation) because no specific heat pipe problems have to be considered here.

Table 3 shows the orders of magnitude of the individual heat resistances that can be observed typically in heat pipes.

Comparing these orders of magnitude it becomes obvious that some of the parallel or serial heat resistances in the circuit can be neglected compared to others. The negligible resistances are R_l and R_w compared to R_g and R_g, $R_{ph,evap}$, $R_{ph,cond}$ compared to $R_{w,evap}$, $R_{w,cond}$, $R_{c,evap}$, and $R_{c,cond}$. Therefore, the overall internal heat resistance of a heat pipe can be approximated by

$$R_{HP} = R_{w,evap} + R_{c,evap} + R_{w,cond} + R_{c,cond}. \quad (28)$$

For circular heat pipes the radial heat resistance of the evaporator wall $R_{w,evap}$ follows from *Fourier*'s law:

$$R_{w,evap} = \frac{\ln(d_{w,o}/d_{w,i})}{2\pi l_{evap}\lambda_w} \quad (29)$$

with the outer wall diameter $d_{w,o}$, the inner wall diameter $d_{w,i}$, and the thermal conductivity λ_w of the wall material.

For planar heat pipes one obtains

$$R_{w,evap} = \frac{s_w}{A_{evap}\lambda_w}, \quad (30)$$

where s_w is the thickness of the wall and A_{evap} the evaporator surface area.

The solid capillary structure is assumed to be saturated with liquid, and the evaporation takes place at the free surface of the liquid. Pool or flow boiling has to be avoided because vapor bubbles might block the capillary action. The radial heat transfer in the capillary structure is dominated by thermal conduction. The heat resistance $R_{c,evap}$ is calculated in analogy to Eqs. (29) and (30). It follows

$$R_{c,evap} = \frac{\ln(d_{k,o}/d_{k,i})}{2\pi l_{evap}\lambda_{eff}} \quad (31)$$

or

$$R_{c,evap} = \frac{s_k}{A_{evap}\lambda_{eff}}. \quad (32)$$

N5. Table 3. Orders of magnitude of individual heat resistances according to Asselman and Green [14]

Heat resistance	K/W
$R_{w,evap}$, $R_{w,cond}$	10^{-1}
$R_{c,evap}$, $R_{c,cond}$	10^{+1}
$R_{ph,evap}$, $R_{ph,cond}$	10^{-5}
R_g	10^{-8}
R_l	10^{+4}
R_w	10^{+2}

Herein, λ_{eff} is the effective thermal conductivity of the capillary structure (composite of solid structure and liquid). According to Chi [3] and Faghri [4] the following equations can be used to calculate λ_{eff} for different capillary structures.

Porous structures:

(a) Considering solid and liquid resistances separately and assuming them in a serial circuit one yields

$$\lambda_{eff} = \frac{\lambda_l\lambda_w}{\varepsilon\lambda_w + \lambda_l(1-\varepsilon)}. \quad (33)$$

(b) Considering solid and liquid resistances separately and assuming them in a parallel circuit one yields

$$\lambda_{eff} = \varepsilon\lambda_l + \lambda_w(1-\varepsilon). \quad (34)$$

In practice the values λ_{eff} for porous structures will be somewhere in between these values given by Eqs. (33) and (34). Thus,

$$\frac{\lambda_l\lambda_w}{\varepsilon\lambda_w + \lambda_l(1-\varepsilon)} \le \lambda_{eff} \le \varepsilon\lambda_l + \lambda_w(1-\varepsilon).$$

Rectangular axial grooves:

$$\lambda_{eff} = \frac{(bh\lambda_l\lambda_w) + w\lambda_l(0.185b\lambda_w + h\lambda_l)}{(b+w)(0.185b\lambda_w + h\lambda_l)}, \quad (35)$$

with the groove width w, the distance b between the individual grooves, and the groove height h.

Triangular axial grooves:

$$\lambda_{eff} = 0.85\left(\frac{\lambda_l}{\lambda_w}\sin\beta\right)^{0.63} \quad (36)$$

with the opening angle β.

Screen meshes:

$$\lambda_{eff} = \frac{\lambda_l[(\lambda_l+\lambda_w) - (1-\varepsilon)(\lambda_l-\lambda_w)]}{(\lambda_l+\lambda_w) + (1-\varepsilon)(\lambda_l-\lambda_w)}. \quad (37)$$

Sintered structures:

$$\lambda_{eff} = \frac{\lambda_l[(2\lambda_l+\lambda_w) - 2(1-\varepsilon)(\lambda_l-\lambda_w)]}{(2\lambda_l+\lambda_w) + (1-\varepsilon)(\lambda_l-\lambda_w)}. \quad (38)$$

Equations (35) and (36) for open grooves are used in engineering practice to calculate the radial heat transfer. However, it should be noted here that the underlying assumptions of one-dimensional heat conduction and a fully saturated structure are not fulfilled in many cases. In the evaporator the liquid is most often receded into the capillary structure to a certain extent. In case that $\lambda_l << \lambda_w$ (which is basically always the case except for liquid metal heat pipes) the heat flux distribution in the capillary structure is nonuniform and strongly two- or even three-dimensional. Stephan [7] developed a numerical method to compute the radial heat resistance for the two-dimensional case. The resulting values for λ_{eff} were higher than those calculated with Eqs. (35) and (36).

The radial heat resistance at the liquid–vapor phase interface $R_{ph,evap}$ describes the molecular interaction at the interface. It is

$$R_{ph,evap} = \frac{2-f}{2f}\frac{T_g\sqrt{2\pi RT_g}}{\rho_g\Delta h_v^2} \quad (39)$$

with the saturation temperature in the gas phase T_g, the individual gas constant R of the fluid, and the accommodation

coefficient f. However, as stated before, this resistance can be neglected in the overall heat resistance analysis.

The axial heat resistance along the vapor flow, R_g, follows from the Clausius–Clapeyron equation and yields

$$R_g = \frac{T_g \Delta\rho_g}{\dot{Q}\rho_g \Delta h_v}. \tag{40}$$

This resistance is directly proportional to the temperature drop along the vapor flow which might be of special interest. However, for the overall heat resistance analysis, it can be neglected too.

The heat resistances in the condenser zone are calculated exactly in the same way than those in the evaporator zone. Equations (29)–(39) therefore hold also for the condenser, with the difference that the geometric data of the condenser section has to be inserted. Another difference is that the capillary structure is typically slightly flooded or at least saturated in the condenser zone, thus the accuracy of Eqs. (33)–(38) is higher in the condenser zone than in the evaporator zone.

Example 2

(a) What is the heat resistance of the heat pipe described in Example 1?

(b) How big is the temperature difference between the outside evaporator surface and the outside condenser surface?

The thermal conductivity of the wall material ammonia is given by $\lambda_w = 221$ W/(m K).

Solution

(a) According to Eq. (28) the heat resistance is

$$R_{HP} = R_{w,evap} + R_{c,evap} + R_{w,cond} + R_{c,cond}.$$

The radial heat resistance in the solid evaporator wall follows from Eq. (29)

$$R_{w,evap} = \frac{\ln(d_{w,o}/d_{w,i})}{2\pi l_{evap}\lambda_w} = \frac{\ln(14/10.6)}{2\pi \cdot 100 \cdot 10^{-3} \cdot 221}\,\mathrm{K/W} = 2.0 \cdot 10^{-3}\,\mathrm{K/W},$$

with the inner diameter of the relevant circumference

$$d_{w,i} = d_i + 2 \cdot h = (9 + 2 \cdot 0.8)\ \mathrm{mm} = 10.6\,\mathrm{mm}.$$

The heat resistance of the capillary structure in the evaporator is calculated according to Eq. (31). The effective thermal conductivity is approximated using Eq. (35) for rectangular grooves

$$\lambda_{eff} = \frac{(bh\lambda_1\lambda_w) + w\lambda_1(0.185b\lambda_w + h\lambda_1)}{(b+w)(0.185b\lambda_w + h\lambda_1)}.$$

It follows

$$\lambda_{eff} = \frac{(0.384 \cdot 0.8 \cdot 0.4996 \cdot 221)\ \mathrm{W/K\,m}}{(0.384 + 0.5) \cdot (0.185 \cdot 0.384 \cdot 221 + 0.8 \cdot 0.4996)} + \frac{0.5 \cdot 0.4996\ \mathrm{W/K\,m}}{(0.384 + 0.5)} = 2.67\ \mathrm{W/mK}$$

with the distance b between the grooves, which is $b = (\pi d_i/N) - w = (\pi\ 9\ \mathrm{mm}/32) - 0.5\ \mathrm{mm} = 0.384$ mm. With the relevant outer diameter for the capillary structure, $d_{c,o} = d_{w,i}$, Eq. (31) gives

$$R_{c,evap} = \frac{\ln(d_{c,o}/d_{c,i})}{2\pi l_{evap}\lambda_{eff}} = \frac{\ln(10.6/9)}{2\pi \cdot 100 \cdot 10^{-3} \cdot 2.67}\,\mathrm{K/W} = 97.6 \cdot 10^{-3}\,\mathrm{K/W}.$$

As the geometry of the condenser zone is equal to that of the evaporator zone, the heat resistances in the condenser are equal too. Thus,

$$R_{w,cond} = R_{w,evap} = 2.0 \cdot 10^{-3}\,\mathrm{K/W}$$

and

$$R_{c,cond} = R_{c,evap} = 97.6 \cdot 10^{-3}\,\mathrm{K/W}.$$

With that, the overall heat resistance of the heat pipe yields

$$R_{HP} = 2 \cdot (2.0 + 97.6) \cdot 10^{-3}\,\mathrm{K/W} = 0.2\,\mathrm{K/W}.$$

(b) The temperature difference between the outer evaporator and the outer condenser surface is calculated according to Eq. (26). With the heating power of 50 W, it follows

$$\Delta T = \dot{Q}R_{WR} = 50 \cdot 0.2\ \mathrm{K} = 10\ \mathrm{K}.$$

4 Heat Transport Limits

The considerations in Sect. 3 of this chapter are valid for the steady-state operation of a heat pipe. In the design phase, it is important to check additionally if a heat pipe can reach such a steady-state operation, or, in other words, if the required heat flux is not too high for a specific design and the heat pipe will fail because a performance limit is reached. Figure 8 shows the performance limits. Generally, the operating temperature must be in the range between the melting temperature and the critical temperature. In this range the maximum heat transport capability $\dot{Q}_{max}$ is limited by different phenomena, indicated by the different curves in Fig. 8. A steady-state operating mode $(\dot{Q}, T)$ can only be reached in the area below these curves. In the following subsections of this chapter the different limits are briefly discussed and calculation procedures are given.

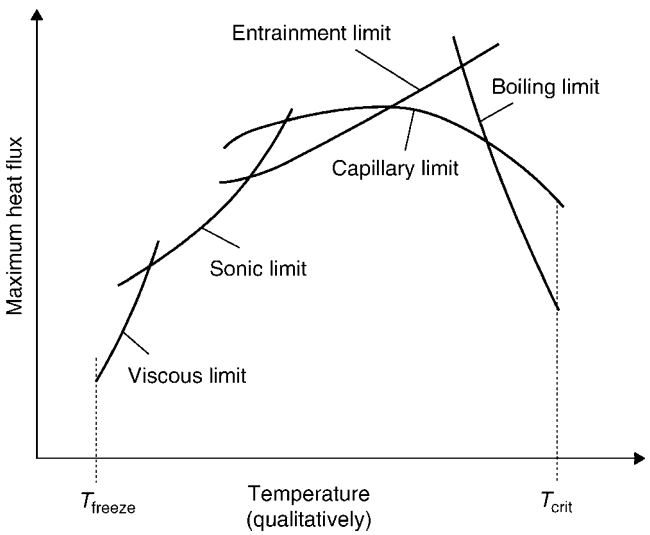

N5. Fig. 8. Heat transport limits.

4.1 Capillary Limit

To keep the fluid circulating, the capillary pressure difference Δp_c must, according to Eq. (2), overcome the sum of all pressure drops in the 2-phase loop. This is only possible if Δp_c is smaller or equal to the maximal pressure difference $\Delta p_{c,max}$ that can be provided by the capillary structure (see Eq. (5b)). Thus, in any steady-state operating mode $(\dot{Q}, T)$ the inequality

$$\Delta p_{c,max} \geq \Delta p_c = -(\Delta p_l + \Delta p_g) \tag{41}$$

must be fulfilled. If an analysis shows that this is not the case the heat pipe design has to be changed (i.e., fluid, capillary structure, geometry, etc.) or the operating mode has to be shifted.

4.2 Viscous Limit

For operating temperatures little above the melting point of the fluid the vapor pressure and vapor density are very low and viscous forces dominate the flow behavior. The vapor pressure drop cannot be higher than the absolute pressure near the evaporator end. In the limiting case, the vapor pressure at the condenser end becomes zero. Busse [15] analyzed this case for heat pipes with circular cross section and the assumption of an isothermal flow of a perfect gas. He derived the maximum axial heat flux

$$\dot{q}_{vis} = \frac{d_g^2 \Delta h_v}{64 \eta_g l_{eff}} \rho_{g,evap} p_{g,evap} \tag{42}$$

with the vapor density $\rho_{g,evap}$ and the vapor pressure $p_{g,evap}$ at the evaporator end. Operating modes $(\dot{Q}, T)$ must be chosen such that the axial heat flux is lower than this value.

4.3 Sonic Limit

The sonic limit might be relevant specifically for high temperature heat pipes with metallic fluids. If one decreases the temperature and thus the pressure in the condenser at a constant evaporator temperature a rising heat flow and rising fluid flow velocities will be the result. Inertia forces dominate the flow. The sonic limit is reached when the vapor velocity at the evaporator exit reaches the sonic velocity. In this case, the heat flow cannot be further increased by a pressure or temperature reduction in the condenser. According to Busse [15] the related maximum axial heat flux is

$$\dot{q}_s = 0.474 \, \Delta h_v \sqrt{\rho_{g,evap} p_{g,evap}}. \tag{43}$$

4.4 Entrainment Limit

In heat pipes with open capillary structures the vapor and countercurrent liquid flow generate a shear force at the fluid interface. With increasing heat flux, the vapor and liquid velocities rise until the shear forces might destabilize the interface and surface waves are generated. As a result, the condensate flow toward the evaporator is partly dammed up and liquid droplets are entrained. Entrainment occurs if the shear forces exceed the surface tension forces. Based on this force balance the maximum axial heat flux follows

$$\dot{q}_e = \Delta h_v \sqrt{\frac{\sigma \rho_g}{2 R_{h,c}}} \tag{44}$$

according to [4] with the hydraulic radius $R_{h,c}$ of the capillary structure:

$R_{h,c} = w$	For axial grooves with the groove width w,
$R_{h,c} = 0.5w$	For screen wicks or meshes with the mesh width w, and
$R_{h,c} = 0.41r$	For sinter structures with the particle radius r.

4.5 Boiling Limit

At high heat fluxes the wall superheat in the evaporator zone might be high enough to activate potential nucleation sites at the solid–liquid interface and as a result vapor bubbles might be generated inside the capillary structure. Bubbles can escape into the vapor space from open capillary grooves, and the boiling limit is typically not critical for open capillary structures. However, covered grooves, sintered structures, or meshes are very sensitive to growing vapor bubbles as they might interrupt the capillary driven condensate flow or even cause a local dry-out. The critical wall superheat is calculated based on the consideration of the thermodynamic equilibrium of a vapor nucleus. It follows

$$\Delta T_{crit} = T_w - T_g = \frac{2 \sigma T_g}{\Delta h_v \rho_g} \left(\frac{1}{R_b} - \frac{1}{R_{eff}} \right). \tag{45}$$

Herein, R_b is the radius of the vapor nucleus, R_{eff} the effective radius of curvature of the capillary structure (Table 1), T_g the vapor temperature which is assumed to be the saturation temperature, and T_w the temperature of the wall next to the vapor nucleus. A vapor nucleus will generate a bubble if the critical wall superheat ΔT_{crit} is exceeded. According to Bergles and Rohsenow [16] the radius R_b can be approximated by

$$R_b = \sqrt{\frac{2 \sigma T_g \lambda_l}{\dot{q}_{evap} \Delta h_v \rho_g}} \tag{46}$$

for a given radial heat flux $\dot{q}_{evap}$ in the evaporator zone. Typical values of R_b range from about 0.1 to 10 µm, and thus lie in the order of magnitude of surface roughness values. The maximum radial heat flux related to the boiling limit is calculated by

$$\dot{q}_b = \frac{\Delta T_{crit}}{A_{evap} R_{c,evap}} \tag{47}$$

with the heat resistance $R_{c,evap}$ of the capillary structure in the evaporator zone according to Eqs. (31) or (32).

Example 3

What is the maximum performance (heating power) that the heat pipe specified in Example 1 can transfer at an operating temperature of ϑ_{sat} = 10°C (referring to p_g = 6.149 bar)? To

answer this question, determine the individual performance limits first.

Solution

(a) *Capillary limit*: The capillary limit follows from Eq. (41)

$$\Delta p_{c,max} \geq \Delta p_c = -(\Delta p_l + \Delta p_g),$$

where the equal sign is relevant in the limiting case. The maximum capillary pressure difference was already calculated in Example 1: $\Delta p_{c,max}$ = 86.6 Pa. Gravitational forces are not relevant in this example (satellite application). Therefore, the liquid pressure drop follows from Eqs. (6) and (9):

$$\Delta p_l = \Delta p_{l,stat} = -\frac{32 v_l}{A_l \Delta h_v d_{c,h}^2} \dot{Q} l_{eff}$$

which yields

$$\begin{aligned}\Delta \rho_l &= \frac{-32 \cdot 2.49 \cdot 10^{-7} \cdot 880 \cdot 10^{-3} \cdot \dot{Q}}{12.8 \cdot 10^{-6} \cdot 1225.5 \cdot 10^3 \cdot (0.762 \cdot 10^{-3})^2} \text{(Pa/W)} \\ &= -0.770 \cdot \dot{Q} \text{ (Pa/W)}.\end{aligned}$$

The pressure drop along the vapor flow follows from Eq. (16):

$$\Delta p_g = \Delta p_{g,evap} + \Delta p_{g,cond} + \Delta p_{g,ad}.$$

As the Reynolds number cannot be calculated a priori without a given heating power, an assumption has to be made first. A useful assumption for a standard heat pipe is $Re_a < 2{,}300$ and $Re_r > 1$. With this, Eq. (19) gives

$$\begin{aligned}\Delta \rho_{g,ad} &= -\frac{32 v_g}{A_{g,a} \Delta h_v d_{g,h}^2{}^2} \dot{Q} l_{ad} \\ &= \frac{-32 \cdot 19.08 \cdot 10^{-7} \cdot 780 \cdot 10^{-3} \cdot \dot{Q}}{63.62 \cdot 10^{-6} \cdot 1225.5 \cdot 10^3 \cdot (9 \cdot 10^{-3})^2} \text{ (Pa/W)} \\ &= -7.54 \cdot 10^{-3} \cdot \dot{Q} \text{ (Pa/W)}.\end{aligned}$$

In analogy to Example 1 the pressure drops in the evaporator and condenser now can be calculated using Eqs. (21), (22), and (25). This yields

$$\begin{aligned}\Delta p_{g,evap} + \Delta p_{g,cond} &= -\frac{32 v_g}{A_{g,a} \Delta h_v d_{g,h}^2} \dot{Q} \left(\frac{l_{evap}}{2} + \frac{l_{cond}}{2} \right) \\ &= \frac{-32 \cdot 19.08 \cdot 10^{-7} \cdot 100 \cdot 10^{-3}}{63.62 \cdot 10^{-6} \cdot 1225.5 \cdot 10^3 \cdot (9 \cdot 10^{-3})^2} \dot{Q} \text{ (Pa/W)} \\ &= -0.967 \cdot 10^{-3} \dot{Q} \text{ (Pa/W)}.\end{aligned}$$

It follows

$$\begin{aligned}\Delta p_g &= -(0.967 + 7.54) \cdot 10^{-3} \cdot \dot{Q} \text{ (Pa/W)} \\ &= -8.51 \cdot 10^{-3} \cdot \dot{Q} \text{ (Pa/W)}\end{aligned}$$

and the capillary pressure difference

$$\Delta p_c = (8.51 + 770) \cdot 10^{-3} \dot{Q} \text{ (Pa/W)} = 778.51 \cdot 10^{-3} \dot{Q} \text{ (Pa/W)}$$

Thus, the capillary limit will be reached at a heating power

$$\begin{aligned}\dot{Q} &= \frac{\Delta p_c}{778.51 \cdot 10^{-3}} \text{ (W/Pa)} = \frac{\Delta p_{c,max}}{778.51 \cdot 10^{-3}} \text{ (W/Pa)} \\ &= \frac{86.6 \text{ Pa}}{778.51 \cdot 10^{-3}} \text{ (W/Pa)} = 111.2 \text{ W}.\end{aligned}$$

Finally the underlying assumptions $Re_a < 2{,}300$ and $Re_r > 1$ have to be validated:

$$\begin{aligned}Re_r &= \frac{\dot{Q} d_{g,h}}{v_g \rho_g A_{g,a} \Delta h_v} \\ &= \frac{111.2 \cdot 9 \cdot 10^{-3}}{19.08 \cdot 10^{-7} \cdot 4{,}865 \cdot 63.62 \cdot 10^{-6} \cdot 1225.5 \cdot 10^3} = 1382.9\end{aligned}$$

and

$$\begin{aligned}|Re_r| &= \frac{\dot{Q} r_g}{v_g \rho_g A_{g,r} \Delta h_v} \\ &= \frac{111.2 \cdot 4.5 \cdot 10^{-3}}{19.08 \cdot 10^{-7} \cdot 4{,}865 \cdot 2{,}827 \cdot 10^{-6} \cdot 1225.5 \cdot 10^3} = 15.6.\end{aligned}$$

Thus, the assumptions were justified.

(b) *Viscous limit*: According to Eq. (42) the maximum axial heat flux related to the viscous limit is

$$\begin{aligned}\dot{q}_{vis} &= \frac{d_g^2 \Delta h_v}{64 v_g l_{eff}} p_{g,evap} \\ &= \frac{(9 \cdot 10^{-3})^2 \cdot 1225.5 \cdot 10^3}{64 \cdot 19.08 \cdot 10^{-7} \cdot 880 \cdot 10^{-3}} 6.149 \cdot 10^5 \text{ (W/m}^2\text{)} \\ &= 5.68 \cdot 10^{11} \text{ (W/m}^2\text{)}.\end{aligned}$$

The performance limit yields

$$\dot{Q} = \dot{q}_{vis} \cdot A_{g,a} = 5.68 \cdot 10^{11} \cdot 63.62 \cdot 10^{-6} \text{ W} = 36.1 \text{ MW}.$$

(Comment: The calculation proves what one could have expected. The viscous limit is extremely high, because the pressure drop along the vapor flow is very small compared to the pressure drop along the liquid flow. Here, the viscous limit will not be relevant.)

(c) *Sonic limit*: The axial heat flux reaching the sonic limit is given by Eq. (43)

$$\begin{aligned}\dot{q}_s &= 0.474 \Delta h_v \sqrt{\rho_{g,evap} \, p_{g,evap}} \\ &= 0.474 \cdot 1225.5 \cdot 10^3 \sqrt{4.865 \cdot 6.148 \cdot 10^5} \text{ (W/m}^2\text{)} \\ &= 1.0 \cdot 10^9 \text{ (W/m}^2\text{)}.\end{aligned}$$

The related performance limit is

$$\dot{Q} = \dot{q}_s \cdot A_{g,a} = 1.0 \cdot 10^9 \cdot 63.62 \cdot 10^{-6} \text{ W} = 63.6 \text{ kW}.$$

(Comment: The sonic limit is very high, because the pressure drop along the vapor flow is quite low for realistic heat fluxes as can be seen, e.g., in Example 1.)

(d) *Entrainment limit*: The entrainment limit follows from Eq. (44) with $R_{h,c} = w$.

$$\begin{aligned}\dot{q}_e &= \Delta h_v \sqrt{\frac{\sigma \rho_g}{2 R_{h,c}}} \\ &= 1225.5 \cdot 10^3 \sqrt{\frac{23.88 \cdot 10^{-3} \cdot 4.865}{2 \cdot 0.5 \cdot 10^{-3}}} \text{ (W/m}^2\text{)} \\ &= 1.32 \cdot 10^7 \text{ (W/m}^2\text{)}\end{aligned}$$

and the performance limit is

$$\dot{Q} = \dot{q}_e \cdot A_{g,a} = 1.32 \cdot 10^7 \cdot 63.62 \cdot 10^{-6} \text{ W} = 840 \text{ W}.$$

(e) *Boiling limit*: The boiling limit is not relevant for the given heat pipe design with open capillary grooves.

With the solutions a) to e) one can summarize the theoretical-limits:

(a) Capillary limit	111.2 W
(b) Viscous limit	36.1 MW
(c) Sonic limit	63.6 kW
(d) Entrainment limit	840 W

Comparing these values one recognizes that the capillary limit is critical at the given operating temperature because the theoretical value is by far the lowest. Thus, the maximum performance (heating power) is

$$\dot{Q} = 111.2 \text{ W}.$$

Above this value the heat pipe will fail because the capillary forces are not high enough to return the condensate to the evaporator.

5 Bibliography

1. Reay DA, Kew PA (2006) Heat pipes, 5th edn. Elsevier, Boston
2. Peterson GP (1994) An introduction to heat pipes: Modeling, testing and applications. Wiley & Sons, New York
3. Chi SW (1976) Heat pipe theory and practice. McGraw-Hill, New York
4. Faghri A (1995) Heat pipe science and technology. Taylor & Francis, Washington, DC
5. Brost O, Groll M (1986) Wärmerohre – Auslegung, Betrieb, Anwendungsbeispiele, Wärme, No. 3, pp 36–40, and No. 4, pp 71–74
6. Wayner PC (1995) Effect of thin film heat transfer on the apparent contact angle and capillary suction. Proceedings of the 9th international heat pipe conference, paper A1, Albuquerque
7. Stephan P (1992) Wärmedurchgang bei Verdampfung aus Kapillarrillen in Wärmerohren. PhD Thesis, Fortschrittberichte VDI, Reihe 19, No. 59, VDI, Düsseldorf
8. Khrustalev D, Faghri A (1995) Heat transfer during evaporation on capillary grooved structures of heat pipes. Trans ASME 117:740–747
9. Fritz W (1935) Berechnung des Maximalvolumens von Dampfblasen. Phys Z 36:379–384
10. Marcus BD (1972) Theory and design of variable conductance heat pipes. Report No. CR 2018, NASA, Washington, DC
11. Cotter TP (1965) Theory of heat pipes. Scientific Laboratory Report No. LA-3246-MS, Los Alamos
12. Busse CA (1967) Pressure drop in the vapor phase of long heat pipes. Proceedings of the IEEE conference of thermionic conversion specialists, Palo Alto, pp 391–398
13. Haug F (1984) Druckrückgewinn in einem zylindrischen Wärmerohr bei hohen radialen Reynolds- Zahlen und hohen Mach- Zahlen. PhD Thesis, University of Stuttgart
14. Asselman GAA, Green DB (1973) Heat pipes. Philips Techn Rev 33:104–113
15. Busse CA (1973) Theory of the ultimate heat transfer limit of cylindrical heat pipes. Int J Heat Mass Transfer 16:169–186
16. Bergles AE, Rohsenow WM (1964) The determination of forced-convection surface boiling heat transfer. ASME J Heat Transfer 86:365–372

N6 Pressure Drop and Heat Transfer in Plate Heat Exchangers

Holger Martin
Karlsruher Institut für Technologie (KIT), Karlsruhe, Germany

1 Introduction: Description of the Apparatus

Plate heat exchangers of the type shown in Fig. 1 are presently offered by many manufacturers worldwide as a standard series production apparatus. They consist of a number of gasketed metal plates clamped between a stationary head and a follower plate by tie bolts. A wavy surface of a special design is stamped on the thin-walled plates (see Fig. 2). The plates are typically rectangular with circular ports at the four corners through which the two heat exchanging fluids may enter and leave. The gaskets are so arranged as to direct the two fluids through alternate flow channels formed by the space between the plates. The corrugated surface pattern of the plates subdivides the flow cross section into a number of interconnected parallel flow channels with multiple changes in direction as well as cross-sectional area. The corrugations on adjacent plates crisscross, providing multiple points of contact and offering mechanical support against pressure differences across the plates. Descriptions of this type of heat exchanger can be found in relevant text and handbooks [1–3], in Chap. O2, or on the websites of manufacturers. The main application area of this type of apparatus is liquid–liquid heat transfer in the lower pressure range (usually below 1.6 MPa) because the construction and the long gaskets are unfavorable for high pressures in general. Due to the small interplate spacing and the high vorticity of the flow, high heat transfer coefficients can be attained. Ease of cleaning, simple adjustment to changed operating conditions by replacement or addition of plates, and the compactness and, correspondingly, a small liquid hold-up are usually cited as the most important advantages of plate heat exchangers.

2 Plates with Chevron-type Corrugations

The most commonly offered shape of the plates is the chevron-type corrugation as shown in Fig. 2. It is characterized by a sinusoidal corrugation pattern with an amplitude $\hat{a}$ and a wavelength Λ. The crests and troughs of this pattern are oriented in an angle φ against the main flow direction (the vertical in Fig. 2) in one, or in several strips of a width B on the plate. The plates in a pack are so arranged (rotation of each second plate around its surface normal by 180°) that the crests of the corrugations of adjacent plates have a regular rhombic pattern of contact points. Manufacturers usually offer series of plates in various sizes with the same chevron pattern in two or more inclination angles, φ (caution: angles given by various manufacturers are partly measured against the horizontal (i.e. $90° - \varphi$), or they give the chevron angle 2φ). The plates with small angles ($0° < \varphi < 45°$) are called "soft" plates (they have lower pressure drop), those with greater angles ($45° < \varphi < 90°$) with correspondingly higher pressure drop are called "hard" plates.

3 Pressure Drop and Heat Transfer

3.1 Definitions

The friction factor, ξ, the Reynolds number, Re, and the Nusselt number, Nu, are defined as

$$\xi = \frac{2\Delta p d_h}{\rho w^2 L_p}, \tag{1}$$

$$\mathrm{Re} = \frac{\rho w d_h}{\eta}, \tag{2}$$

VDI-GVC (ed.), *VDI Heat Atlas*, DOI 10.1007/978-3-540-77877-6_66,

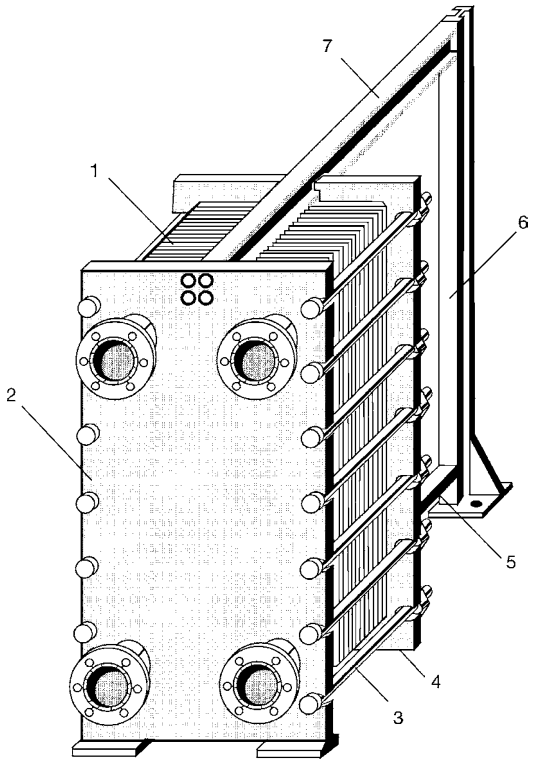

N6. Fig. 1. Plate heat exchanger [2]
1: plate pack, 2: stationary head, 3: tie bolt, 4: follower plate, 5: bottom bar, 6: end support, 7: top bar

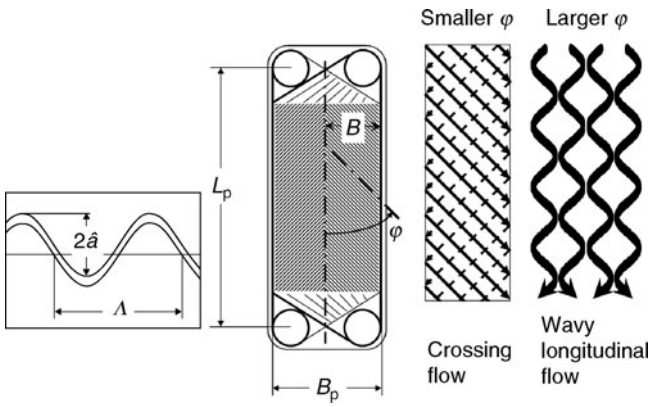

N6. Fig. 2. Chevron-type plate. Inclination angle, φ, and the two flow patterns observed

$$\mathrm{Nu} = \frac{\alpha d_h}{\lambda} \tag{3}$$

($\xi = 4f$, if f denotes the Fanning friction factor, which is also often used in the literature) with the pressure drop, Δp, for the (vertical) flow through a gap between two plates over the length, L_p, of a plate (see Fig. 2) (the pressure drop in the distributor and collector channels has to be accounted for separately) and the hydraulic diameter, d_h, defined as

$$d_h = 4\hat{a}/\Phi, \tag{4}$$

where $\hat{a}$ is the amplitude of the sinusoidal corrugation pattern, and Φ is the ratio of the wavy plate surface to its plane projection. The ratio Φ depends on the ratio of amplitude to wavelength, or simpler on the wave number:

$$X = 2\pi\hat{a}/\Lambda. \tag{5}$$

For a sinusoidal corrugation it can be approximately calculated from the formula

$$\Phi(X) \approx \frac{1}{6}\left(1 + \sqrt{1+X^2} + 4\sqrt{1+X^2/2}\right) \tag{6}$$

obtained from a three-point integration over the length of the sine-curve (integration error < 2%).

For $\Lambda/\hat{a} = 2\pi$, that is $X = 1$, the surface enhancement factor becomes $\Phi = 1.22$. Twenty-two percent of surface enhancement is a typical value for technical plates. The fluid velocity, w, in Eqs. (1) and (2) is to be calculated as the volumetric flow rate through the gap between two plates, divided by the average cross section of the gap:

$$w = \frac{\dot{V}_{\mathrm{gap}}}{2\hat{a} \cdot B_p}. \tag{7}$$

The plate width B_p is a certain multiple (mostly an integer multiple) of the width B of the pattern. For the plate shown in Fig. 2, $B_p = 2B$.

As the reference area A_p for the heat transfer coefficients the enlarged surface inside the gaskets is chosen (the plane surface, A_0, is nearly equal to $A_0 \approx B_p L_p$):

$$A_p = \Phi \cdot A_0. \tag{8}$$

There are other definitions used in the literature, so in comparing data from different sources it is always advisable to carefully check the definitions.

The heat transfer coefficient is defined here as

$$\alpha = \frac{\dot{Q}}{A_p \cdot \Delta T_m} \tag{9}$$

that is with the mean difference between fluid and plate surface temperature averaged over the whole surface, A_p (see Chaps. C1 and C2 for the correct mean temperature differences). The physical properties are to be taken at the arithmetic mean of fluid inlet and outlet temperatures:

$$T_m = \frac{1}{2}(T_{\mathrm{in}} + T_{\mathrm{out}}). \tag{10}$$

3.2 Influence of Inclination Angle and Flow Rate

The influence of inclination angle and flow rate on pressure drop and on heat transfer can be approximately found from the following simple flow model, based on available experimental data for pressure drop and heat (or mass) transfer [3–10] and equations for heat transfer based on the Lévêque equation [11, 12] for thermally developing flow [13].

3.2.1 Pressure Drop

Limiting case 0: $\varphi = 0°$, smooth longitudinal flow

Re < 2,000 (laminar),

$$\xi_0 = \frac{B_0}{\mathrm{Re}} \tag{11}$$

Re ≥ 2,000 (turbulent),

$$\xi_0 = (1.8 \lg \mathrm{Re} - 1.5)^{-2}. \tag{12}$$

The constant $B_0 = \xi_0 \mathrm{Re}$ depends on the cross-sectional shape of the channel; for a circular duct, one would get $B_0 = 64$. For sinusoidally shaped ducts B_0 can be calculated numerically [14]. Practically, it may often suffice to use as an average value also

$$B_0 \approx 64. \tag{13}$$

Limiting case 1: ($\sin\varphi = 1$) $\varphi = 90°$, wavy longitudinal flow: The pressure drop in this limit quite sensitively depends on the relative position of the adjacent wave patterns. If the wave patterns are in phase, the wavy longitudinal flow has a friction factor $\xi_{1,0}$, that is much higher than for the smooth longitudinal flow ($\varphi = 0°$).

According to Focke et al. [6] one finds

$$\xi_{1,0} = \frac{B_1}{\mathrm{Re}} + C_1, \quad \mathrm{Re} < 2{,}000, \tag{14}$$

$$\xi_{1,0} = \frac{K_1}{\mathrm{Re}^n}, \quad \mathrm{Re} \geq 2{,}000 \tag{15}$$

with the constants (only determined for $\Lambda/\hat{a} = 4$) $B_1 = 597$, $C_1 = 3.85$, $K_1 = 39$, and $n = 0.289$.

Were the wave patterns, however, phase-shifted by π (= 180°), the wave crests would contact each other, and the flow would be completely blocked:

$$\xi_{1,\pi} \to \infty. \tag{16}$$

The pressure drop for wavy longitudinal flow is therefore approximated by

$$\xi_1(\mathrm{Re}) = a \cdot \xi_{1,0}(\mathrm{Re}) \tag{17}$$

with an empirical factor a ($1 \leq a < \infty$).

Crossed corrugation patterns ($0° < \varphi < 90°$): Two flow patterns have been observed in the gaps between two plates, the wave patterns of which are in pointwise contact with each other [4, 5] (see Fig. 2): For small angles, φ (low pressure drop), the crossing flow along the valleys of the corrugation of the two plates over the whole width of the chevron pattern is mainly observed. For greater angles, φ (high pressure drop), the wavy longitudinal flow between vertically adjacent contact points additionally becomes more important. The combined effects of the longer flow path (by a factor $1/\cos\varphi$) along the furrows, of the flow reversals at the edges of the corrugation pattern ($b \tan\varphi$), the crossing of the streamlets ($c \sin\varphi$), and the smooth change of the crossing flow to the longitudinal wavy flow were taken into account to develop an equation for the friction factor, ξ, as a function of the inclination angle, φ, and the Reynolds number [13]: $\xi = f(\varphi, \mathrm{Re})$

$$\frac{1}{\sqrt{\xi}} = \frac{\cos\varphi}{\sqrt{b\tan\varphi + c\sin\varphi + \xi_0(\mathrm{Re})/\cos\varphi}} + \frac{1-\cos\varphi}{\sqrt{\xi_1(\mathrm{Re})}} \tag{18}$$

with $\xi_0(\mathrm{Re})$ and $\xi_1(\mathrm{Re})$ from the equations for the limiting cases of the smooth ($\varphi = 0°$) and the wavy longitudinal ($\varphi = 90°$) flow, respectively (Eqs. (11–17)).

The empirical constants, a, b, and c, will certainly depend on the geometrical parameters of the corrugation ($\hat{a}$, Λ). From a comparison of published pressure drop data ($\Lambda/\hat{a} \approx 4$–8) with the model Eq. (18), in the form $\xi(\varphi, \mathrm{Re} = 2{,}000)$, as shown in Fig. 3, the approximate values $a = 3.8$, $b = 0.18$, and $c = 0.36$ have been found. These values may be used for an estimation of the pressure drop to be expected in typical chevron-type plate heat exchangers. In case that pressure drop data for a certain plate-type are available as a function of Re for one or several inclination angle, the parameters (a, b, c) can be fitted to these data and used in Eq. (18) to interpolate between the data and even extrapolate into adjacent ranges of inclination angle and Reynolds number. This was done for the data of Heavner et al. [10], as shown in Fig. 4.

3.2.2 Heat (and Mass) Transfer

Because of the periodic structure of the individual flow channels, the heat (and mass) transfer can be determined approximately from the generalized Lévêque equation [13]:

$$\mathrm{Nu} = 1.615\,[(\xi\,\mathrm{Re}/64)\mathrm{Re}\,\mathrm{Pr}\,d_h/L]^{1/3}. \tag{19}$$

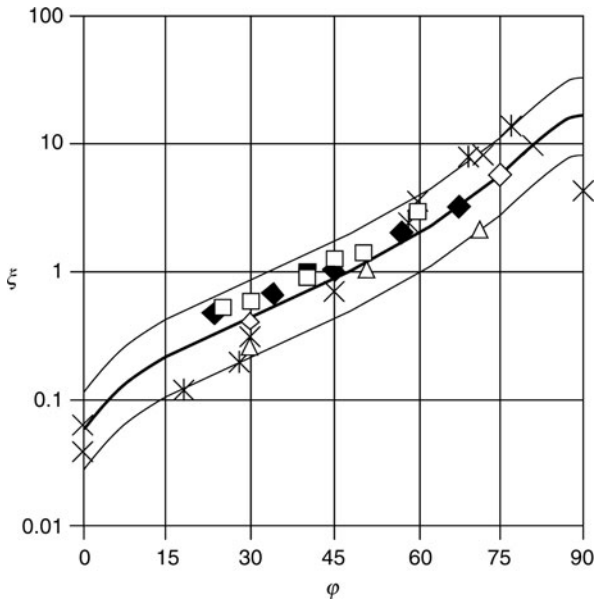

N6. Fig. 3. Friction factor versus inclination angle of chevron-type plate heat exchangers: ξ (φ, Re = 2,000) versus φ
◇: Okada et al. [4], model plates: φ = 30°, 45°, 60°, 75°
✕: Focke et al. [6], model plates: φ = 0°, 30°, 45°, 60°, 72°, 80°, 90°
✱: Gaiser [7], model plates: φ = 18°, 28°, 45°, 58°, 69°, 77°
△: Bassiouny [9], technical p. (*Schmidt, Bretten*): φ = 29.75°, (29.75 and 71°), 71°
□: Bond [8]: diagram for technical plates, and HEDH [8]: diagram for technical plates: φ = 30°, 40°, 50°, 60°
◆: Heavner et al. [10], technical plates (*APV*): φ = 23°, (23 a. 45)°, 45°, (23 a. 90)°, (45 a. 90)°
Curves: Eq. (18) for ξ (φ, Re) with the parameters (a, b, and c) = (3.8, 0.18, and 0.36); upper curve: 2ξ, lower curve 0.5ξ

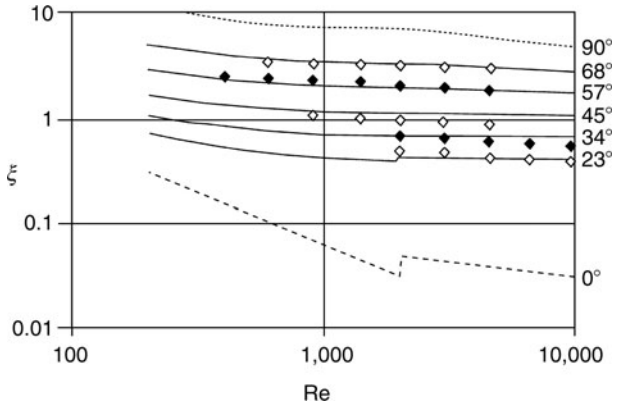

N6. Fig. 4. Friction factor, ξ, versus Reynolds number, Re, of chevron-type plate heat exchangers, with the inclination angle, φ, as a parameter
Curves: Eq. (18) with (a, b, c) = (1.6, 0.40, 0.36). *Symbols*: empirical correlations of Heavner et al. (1993), representing their data for technical plates (for Re = 2,000) their data are also shown in Fig. 3 (compared with the other set (a, b, c) = (3.8, 0.18, 0.36))

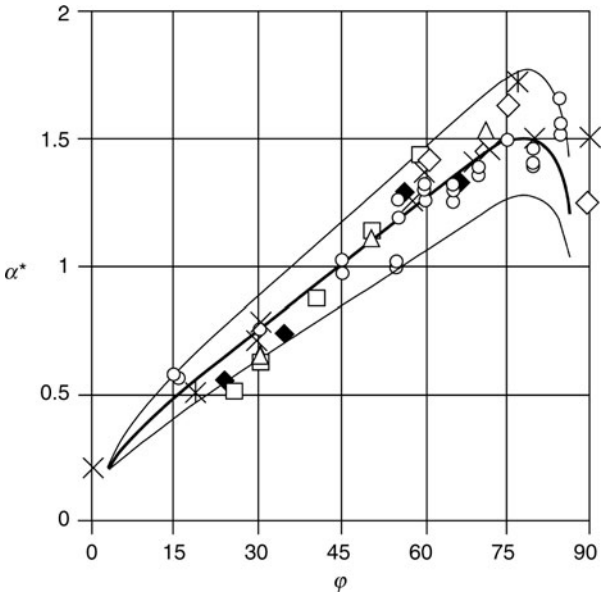

N6. Fig. 5. Influence of the inclination angle, φ, on heat transfer in plate heat exchangers.
Normalized heat transfer coefficient, $\alpha^* = \alpha(\varphi)/\alpha(45°)$, versus φ for Re = 2,000
Symbols as in Fig. 3 and ○: Rosenblad and Kullendorff [5] (mass transfer, small model plate, Re = 1,880), φ = 15°, 30°, 45°, 55°, 60°, 70°, 75°, 80°, 85°
Curves: Eqs. (19–22) ± 20% with ξ from Eq. (18), parameters as in Fig. 3

For the fully developed laminar tube flow, according to the Hagen–Poiseuille law the term (ξ Re/64) is equal to 1, and Re Prd_h/L is called a Graetz number. Rewritten, and analogously applied to mass transfer as well, Eq. (19) becomes:

$$\mathrm{Nu}/\mathrm{Pr}^{1/3} = \mathrm{Sh}/\mathrm{Sc}^{1/3} = 0.4038\,[\xi\,\mathrm{Re}^2 d_h/L]^{1/3}. \qquad (20)$$

For the length, L, the distance between two crossing points of the corrugation pattern has to be used:

$$d_h/L = (d_h/\Lambda)\sin(2\varphi), \quad 0° < \varphi < 90°. \qquad (21)$$

This generalized form of the Lévêque equation is also applicable to thermally developing boundary layers of short lengths, L, in a turbulent flow (see also [12]).

Is the heat (or mass) transfer coefficient known for one kind of plate, say for an inclination angle of φ = 45° (that is, sin(2φ) = 1), the dependency on the inclination angle can be obtained with a sufficient degree of approximation. A relative heat (or mass) transfer coefficient

$$\alpha^* = \frac{\alpha(\varphi)}{\alpha(45°)} = \frac{\beta(\varphi)}{\beta(45°)} \qquad (22)$$

is plotted in Fig. 5 for Re = 2,000 as a curve obtained from Eqs. (20) and (21) together with Eq. (18) for $\xi(\varphi, \mathrm{Re})$ in comparison with the corresponding values obtained from published experimental data for heat (and mass) transfer in chevron-type plate channels. The parameters(a, b, c) have been used as fitted to the pressure drop data (3.8, 0.18, and 0.36) from Fig. 3. For the limiting cases of an uncrossing longitudinal flow, φ = 0° and φ = 90°, the Lévêque equation is not applicable because of $L \to \infty$ (from Eq. (21)). These limits, however, are less important for technical plate heat exchangers, since without the crossing points no mechanically stable plate packs can be formed (at least not without added distance keepers).

Equation (20) describes a special form of analogy between momentum, heat, and mass transfer, which predicts that heat or mass transfer coefficients under these conditions (that is, for short, periodically repeated, thermal, or diffusional boundary layers in laminar, or in turbulent flow) are proportional to the cubic root of the frictional pressure drop. The product

$$\xi\,\mathrm{Re}^2 = 2\frac{\rho \Delta p d_h^3}{\eta^2 L_p} = 2\mathrm{Hg} \qquad (23)$$

is proportional to the Hagen number, Hg, which is directly proportional to the pressure gradient, $\Delta p/L_p$. A check of the validity of the Lévêque analogy for chevron-type plates is shown by comparing the empirical equations based on the experimental data of Focke et al. [6] with the calculations from Eq. (20).

The pressure drop, and mass transfer data, correlated in the work of Focke et al. [6] in the form of friction factors f(Re) and Colburn factors j(Re) are plotted in Fig. 6 as $\mathrm{Sh}^* = \mathrm{Sh}/\mathrm{Sc}^{1/3} = j\,\mathrm{Re}/\Phi^2$ versus [$\xi \mathrm{Re}^2 d_h/L$] with d_h/L from Eq. (21). The values for $\mathrm{Sh}/\mathrm{Sc}^{1/3}$ and [$\xi \mathrm{Re}^2 (d_h/\Lambda)\sin(2\varphi)$] were evaluated for the lowest, the highest, and three intermediate Reynolds numbers for the measurements with inclination angles of φ = 30°, 45°, 60°, 72°, and 80°, respectively. The data for φ = 0° and φ = 90°, because of $L \to \infty$, as mentioned earlier, cannot be compared with the Lévêque equation. The range of Reynolds numbers investigated is about 60 < Re < 30,000. The geometric parameters of the plates used by Focke et al. [6] are Λ = 10 mm, $\Lambda/\hat{a}$ = 4, d_h/Λ = 0.683, and Φ = 1.464. The upper line in Fig. 6 shows the theoretical relationship

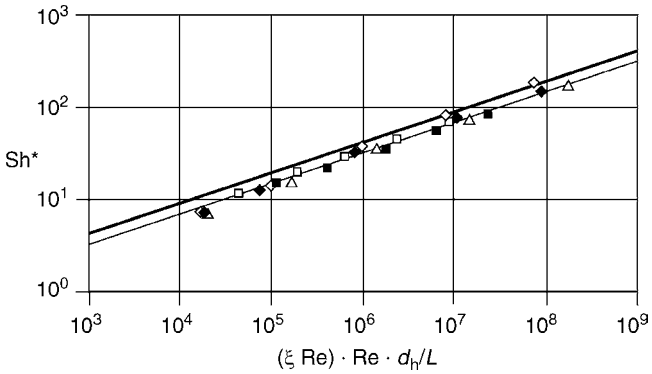

N6. Fig. 6. Test of the validity of the Lévêque analogy for chevron-type plates *Symbols*: Sh* = Sh/$Sc^{1/3}$ measured and empirically correlated by Focke et al. [6] versus (ξ Re)Re d_h/L, with $L = \Lambda/\sin(2\varphi)$ (= distance between two crossing points) Calculated from the empirical correlations as given in [6] (Table 3) for the lowest, the highest, and three intermediate Reynolds numbers for the experiments with inclination angles of $\varphi = 30°$(diamond), 45° (full diamond), 60°(triangle), 72°(full square), and 80°(square), with the friction factors measured in the same equipment and also empirically correlated by the authors [6] (Table 2). *Lines*: Sh* = Sh/$Sc^{1/3}$, calculated from Eq. (20), and $\Lambda/\hat{a} = 4$, $\Phi = 1.464$, as given by Focke et al. [6]. *Lower line*: Sh* (theoretical) – 20.6% (fitting curve)

$$(\alpha, \beta) \propto [\Delta p \cdot \sin(2\varphi)]^{1/3}. \tag{24}$$

The lower line is a parallel to this (in a distance of –20.6%) and corresponds to an average curve through the data of Focke et al.

A more detailed comparison with other published data (especially with heat transfer data for technical plates) shows that the dependency of Nusselt numbers on Reynolds numbers can be better represented by a slightly modified form of the Lévêque equation. The exponent 1/3 0 0.333. . . is replaced by a slightly larger value q (present recommendation: $q = 0.374$). The geometric parameter (d_h/Λ), for practical reasons, is included into the modified factor ($c_q = 0.122$), since most of the manufacturers do not publish the geometric details of their corrugation patterns [13]:

$$\mathrm{Nu} = c_q \mathrm{Pr}^{1/3} (\eta/\eta_w)^{1/6} [2\mathrm{Hg}\ \sin(2\varphi)]^q. \tag{25}$$

The constants, c_q and q, can be recommended from the comparison with the data of Heavner et al. [10] to be $c_q = 0.122$ and $q = 0.374$. Equation (25) also contains a correction $(\eta/\eta_w)^{1/6}$, to account for the temperature dependency of the viscosity of the liquid.

Since the product $\xi\ \mathrm{Re}^2$ is directly proportional to the pressure gradient, $\Delta p/L_p$, see Eq. (23), one will get the same heat transfer coefficient for the same pressure gradient with hard plates, $\varphi = (45 + x)°$, and soft plates, $\varphi = (45 - x)°$, $(0 < x < 45)$: The function $\sin(2\varphi)$ is symmetric around its maximum of 1 at $\varphi = 45°$. For $x = 15$, for example, $\sin(2{\cdot}30°) = \sin(2{\cdot}60°) = 0.866$. The flow rates, however, differ by more than a factor of 2 in this case. For the same pressure drop, hard plates, with angles above 45° therefore lead to higher residence times of the fluid (higher NTU) and correspondingly higher changes in fluid temperature.

3.3 Channels between Plates of Different Inclination Angle

Plates of equal size and corrugation parameters, but different inclination angles, φ_1, and φ_2, can be alternately used in one plate pack, in order to meet a certain thermal duty with an economically optimal usage of a given pressure gradient. It was shown that it is simply allowed to calculate, in these cases, with the arithmetic mean of the two angles:

$$\varphi = \frac{1}{2}(\varphi_1 + \varphi_2). \tag{26}$$

3.4 Other Variables of Influence

The sets of parameters determined from the comparison with the relatively few available data in the pressure drop equation, (a, b, c), Eq. (18), and in the heat transfer equation, (c_q, q), Eq. (25) depend on the characteristic length of the corrugation pattern ($\hat{a}$, Λ, B, . . .), which are usually not given by the plate manufacturers. An application of these sets of parameters on ratios of wavelength to amplitude far outside the range of the data used here $4 \leq \Lambda/\hat{a} \leq 8$ is therefore not recommended.

4 Comments on Other Types of Plates and on Multiphase Flow in Plate Heat Exchangers

A plate type apart from the chevron-type, which is still offered by some manufacturers, is the washboard, or intermating trough plate [3], which may be described as a corrugation (not necessarily sinusoidal) with an inclination angle of $\varphi = 90°$, that is with the crests and troughs perpendicularly oriented against the flow direction. The plate spacing that is smaller than twice the amplitude of the corrugation is kept constant by dimples pressed into the crests and troughs to provide contact with those on adjacent plates. The shape of the corrugation waves is usually a multistep trapezoidal one. For this type of plate some empirical equations for pressure drop and heat transfer can be found in the literature [3, 15].

For multiphase flow, evaporation and condensation in plate heat exchangers there are not many published data to be found in the literature. The experimental results of Kreissig and Müller-Steinhagen [16] for the pressure drop in two-phase flow through plate heat exchangers show that a linear interpolation between the two single-phase pressure drops might be a reasonable approximation in this case, while in two-phase tube flow the two-phase pressure drop shows a characteristic maximum between the two single phase pressure drops at gas to massflow ratios of around 90%.

5 Numerical Example

The complete hydrodynamic and thermal design of a heat exchanger requires the determination of an economically optimal flow velocity. Methods to determine such an optimal velocity are found in the relevant textbooks [1, 2]. For low-viscosity liquids (water) this velocity in the tubes of a shell-and-tube heat exchanger is typically in the order of magnitude of 1–3 m/s. For chevron-type plate heat exchangers, because of the higher flow resistance lower velocities of 0.2–0.8 m/s are economically reasonable. The mean temperature difference must also be determined for the kind of flow configuration that is chosen for the apparatus. The logarithmic mean temperature difference is only correct if pure co-current, or countercurrent flow is taking place in the apparatus (see Chap. C1, or [2, 9]).

For technical plate heat exchangers with chevron plates, made of stainless steel, the possible overall heat transfer coefficients, k, and the flow velocities, w, of a water-to-water application (average temperature 40°C) are to be calculated for a given pressure gradient of $\Delta p/L_p = 0.1$ bar/m, if there are plates available with inclination angles of $\varphi = 30°$, and 60°.

Plate data (stainless steel):

Wall thickness	$s_w = 0.75$ mm
Heat conductivity	$\lambda_w = 15$ W/(K m)
Amplitude	$\hat{a} = 2$ mm
Wavelength	$\Lambda = 12.6$ mm

The hydraulic diameter d_h is

with $X = 2\pi\hat{a}/\Lambda$ (Eq. (5))	$X = 0.9973$
with Φ (0.9973) (Eq. (6))	$\Phi = 1.218$
from $d_h = 4\hat{a}/\Phi$ (Eq. (4))	$d_h = 6.568$ mm

The Hagen number $\rho(\Delta p/L_p)\ d_h^3/\eta^2 = (\xi/2)\mathrm{Re}^2$ (Eq. 23) is found with the physical properties of water at 40°C:

$\rho = 992$ kg/m^3	$c_p = 4.179$ kJ/(K kg)
$\eta = 653\ 10^{-6}$ Pa s	$\lambda = 629\ 10^{-6}$ mW/(K m)
	Pr = 4.341

to be Hg = $6.592 \cdot 10^6$.

From this with Eq. (25) with $(\eta/\eta_w) \approx 1$, for $\varphi = 30°$ and 60°, one gets (with $c_q = 0.122$, $q = 0.374$) Nu = 86.76 and from Eq. (3) $\alpha = 8{,}309$ W/(K m^2). From $1/k = (2/\alpha) + (s_w/\lambda_w)$ one gets

$$k(30°) = k(60°) = 3{,}440\,\mathrm{W/(K\,m^2)}.$$

For the mixed channel from two plates with 30° and 60°, that is, from Eq. (26) $\varphi = (30° + 60°)/2 = 45°$, the heat transfer coefficient would be greater by a factor $(1/\sin(2 \cdot 30°))^{0.374} = 1.055$, and the overall heat transfer coefficient is about 4.5% greater:

$$k(45°) = 3{,}596\,\mathrm{W/(K\,m^2)}$$

The flow velocities to be expected are calculated from Reynolds numbers iteratively obtained from Eq. (18):

$$\mathrm{Re}(\mathrm{Hg}, \varphi) = \sqrt{2\mathrm{Hg}}\,\frac{1}{\sqrt{\xi(\mathrm{Re}, \varphi)}}$$

with Eqs. (11–17) and the constants $(a, b, c) = (3.8, 0.18, 0.36)$ one finds with Hg = $6.592 \cdot 10^6$:

Re (60°) = 2,610	$w(60°) = 0.262$ m/s
Re (45°) = 3,951	$w(45°) = 0.396$ m/s
Re (30°) = 5,649	$w(30°) = 0.566$ m/s

The pressure drop in the distributor and collector channels of the plate heat exchanger has to be accounted for separately, which may be a nonnegligible contribution especially for the soft plates ($\varphi < 45°$).

6 Symbols

$\hat{a}$	amplitude of the corrugation (see Fig. 2) (m)
A_0	plane projection of the plate surface (m^2)
A_p	actual plate surface, $A_p = \Phi A_0$ (m^2)
B	width of the corrugation pattern (see Fig. 2) (m)
B_p	plate width (see Fig. 2) (m)
c_q	factor in modified Lévêque analogy (Eq. (25)) (1)
d_h	hydraulic diameter, $d_h = 4\hat{a}/\Lambda$ (m)
j	Colburn factor, $j = \mathrm{Nu}\,\mathrm{Re}^{-1}\,\mathrm{Pr}^{-1/3} = \mathrm{Sh}\,\mathrm{Re}^{-1}\,\mathrm{Sc}^{-1/3}$ (1)
L	length between two crossing points (Eq. (21)) (m)
L_p	plate length (see Fig. 2) (m)
q	exponent in modified Lévêque analogy (Eq. (25)) (1)
X	wave number = $2\pi\hat{a}/\Lambda$ (l)
α^*	normalized heat transfer coefficient $\alpha^* = \alpha(\varphi)/\alpha(45°)$ (Eq. (22)) (l)
φ	inclination angle of the corrugation (see Fig. 2) (1)
Φ	surface enhancement factor = A_p/A_0 (1)
Λ	wavelength (see Fig. 2) (m)
ξ	friction factor (Eq. (1)) (1)

7 Bibliography

1. Gregorig R (1973) Wärmeaustausch und Wärmeaustauscher. Aarau, Frankfurt/Main: Sauerländer
2. Martin H (1992) Heat exchangers. Hemisphere Publ. Corp., Washington
3. Cooper A, Usher JD (1989) Plate heat exchangers. In: Schlünder EU (ed in Chief) Heat exchanger design handbook, vol. 3, Section 3.7, 1983 (supplement). Hemisphere Publ. Corp., Washington
4. Okada K et al. (1972) Design and heat transfer characteristics of new plate heat exchanger. Heat Transfer Japn Res 1:90–95
5. Rosenblad G, Kullendorff A (1975) Estimating heat transfer rates from mass transfer studies on plate heat exchanger surfaces. Wärme und Stoffübertragung 8:187–191
6. Focke WW, Zachariades J, Olivier I (1985) The effect of the corrugation angle on the thermohydraulic performance of plate heat exchangers. Int J Heat Mass Transfer 28:1469–1479
7. Gaiser G (1990) Strömungs- und Transportvorgänge in gewellten Strukturen. Diss. Univ. Stuttgart

8. Bond MP (1981) Plate heat exchangers for effective heat transfer. Chem Eng 162–167
9. Bassiouny MK (1985) Experimentelle und theoretische Untersuchungen über Mengenstromverteilung. Druckverlust und Wärmeübergang in Plattenwärmeaustauschern. Fortschr. Ber. VDI R. 6, Nr. 181. VDI- Verl, Düsseldorf
10. Heavner RL, Kumar H, Wanniarachchi AS (1993) Performance of an industrial plate heat exchanger: effect of chevron angle. AIChE symposium series, no. 295, vol. 89. Heat Transfer Atlanta, pp 262–267
11. Lévêque A (1928) Les lois de la transmission de chaleur par convection. Ann Mines Ser 12(13):201–415
12. Schlünder EU (1971) Die wissenschaftliche Theorie der Wärmeübertragung – geschichtliche Entwicklung und heutiger Stand. DECHEMA Monographien, Band 65:1–18
13. Martin H (1996) A theoretical approach to predict the performance of chevron- type plate heat exchangers. Chem Eng Process Lausanne 35:301–310
14. Fischer L, Martin H (1997) Friction factors for fully developed laminar flow in ducts confined by corrugated parallel walls. Int J Heat Mass Transfer 40:635–639
15. Böhm J (1955) Wärmeübergang an Plattenwärmetauschern. Kältetechnik 7(12):358–362
16. Kreissig G, Müller-Steinhagen H (1992) Frictional pressure drop for gas/liquid two- phase flow in plate heat exchangers. Heat Transfer Eng 13:42–52

O2 Vibration of Tube Bundles in Heat Exchangers

Horst Gelbe[1] · *Samir Ziada*[2]
[1]Technische Universität Berlin, Berlin, Germany
[2]McMaster University, Hamilton, ON, Canada

1 Introduction

Flow-induced vibrations are examined for tube bundles with gas, liquid, or gas–liquid mixture cross-flows. The effect of the axial flow or the flow inside the tubes is generally negligible, except in the case of tubes with a long length between the supports and small stiffness, such as thin-walled plastic tubes (of which the procedure to evaluate the vibration is given in [1]). The guidelines in the Sect. 5 deal with the design requirements for standard heat exchangers in chemical and process industries, but not, however, with the additional requirements to ensure long service lives for equipments such as those used in nuclear and conventional power plants.

1.1 Tube Vibration Response and Critical Parameters

Even at relatively low flow velocities, the tube arrays in heat exchangers exhibit turbulent buffeting vibrations due to cross flow. The vibration amplitude increases as fluid density increases. If the amplitude exceeds a critical level A_k, *long-term*

VDI-GVC (ed.), *VDI Heat Atlas*, DOI 10.1007/978-3-540-77877-6_68,

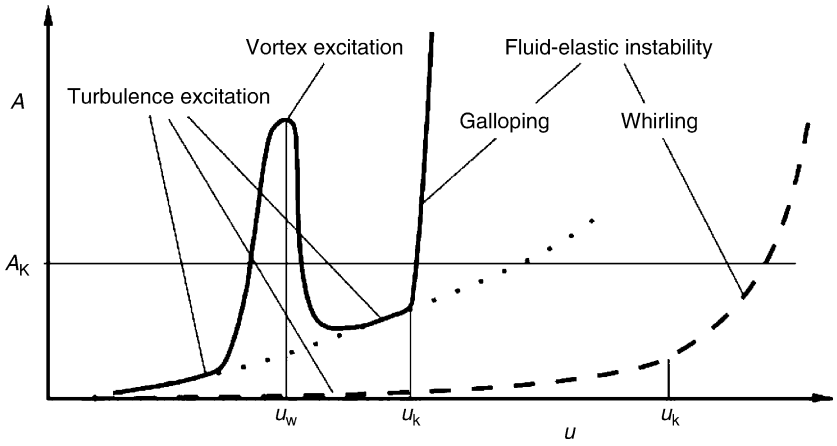

O2. Fig. 1. Schematic of the vibration response of a tube as a function of cross-flow velocity, ——— liquid flow, – – – gas flow.

damage can arise, such as material fatigue and/or fretting wear failures due to friction and impact between the tubes and the support baffles. If the flow velocity exceeds a critical value u_k, then the amplitude increases either rapidly or more slowly, depending on the excitation mechanism of fluid-elastic instability, and results in *short-term damage*, such as tearing the tubes from the tube sheets, or causing the tubes to impact against each other. Figure 1 shows two examples of typical tube vibration response as a function of the cross-flow velocity. The causal excitation mechanisms are also highlighted.

1.2 Excitation Mechanisms

The most important design calculation serves to determine the critical flow velocity u_k ($u < u_k$) at which the *fluid-elastic instability* is initiated (Sects. 3 and 5). This instability can produce very fast damage, e.g., within hours of its onset. Fluid-elastic instability is caused by a self-generated fluid force, which is proportional to either the tube vibration displacement (whirling) or vibration velocity (galloping). This force acts against and therefore reduces either the spring stiffness or the damping of the system, respectively [2]. Both excitation types can occur separately or simultaneously.

The second design calculation is for the vibration amplitude A ($A < A_k$), resulting from *turbulence excitation* (Sect. 4.2) at the operating flow velocity $u < u_k$, to avoid long-term damage, especially for liquid and two-phase flows.

Vortex shedding excitation (Sect. 4.3.1) is important only in tube bundles exposed to liquid flows, when the spacing rations are industry relevant, i.e., normally small. This type of excitation can cause either short or long-term failure. It is therefore important to ensure that the vibration amplitude A at the vortex resonance velocity u_w does not exceed the critical amplitude A_k or alternatively, the maximum flow velocity of the equipment can be selected to be less than the vortex resonance velocity, i.e., $u < u_w$.

Acoustic resonance (Sect. 4.3.2) is excited only in tube bundles exposed to gas flows. Standing acoustic waves, normal to the flow and to the tube axis, can be excited by vortex shedding or turbulent fluctuations, leading to loud noise emissions and to an increase in the pressure drop of the shell side flow.

During the design phase, heat exchangers must be checked at the least for possible short-term damage that may be caused by fluid-elastic instability, and in the case of liquid flows, vortex shedding excitation must be assessed as well.

Tube vibrations due to turbulent excitation and whirling cause the tubes to vibrate in the flow direction as well as perpendicular to it, i.e., in the streamwise and transverse directions. However, vortex shedding and galloping vibrations occur predominantly normal to the flow direction. The co-ordinate systems for the tube vibrations and the flow velocities are defined in the following:

- in flow direction and normal to the tube axis — x or u,
- normal to the flow direction and to the tube axis — y or v,
- in tube axis direction — z or w.

1.3 Tube Bundle Geometries

The characteristics and the effects of all four excitation mechanisms are influenced by the layout geometry and spacing ratio of the tubes. Equations to calculate the maximum gap velocity u_s as well as the solidity ratio ε_R in symmetrical staggered and in-line arrays with a constant layout angle α (the four standard tube layouts) are presented in Fig. 2 as functions of the spacing ratio $\tau = t/d_a$. Based on its geometrical characteristics, the 60° layout seems to belong to the staggered arrays, but from the fluid mechanics point of view, it should be treated in a way similar to that used for in-line arrays.

It is noteworthy that in many publications, the tube bundle velocity is calculated using $u_\tau = u_\infty \frac{\tau}{\tau-1}$, which for the 45° und 60° layouts leads to the following deviations from the gap velocity u_s:

For the 45° layout and $\tau \leq 1.7$: $u_s = 0.707\,u_\tau$,

For the 60° layout and $\tau \leq 3.7$: $u_s = 0.866\,u_\tau$.

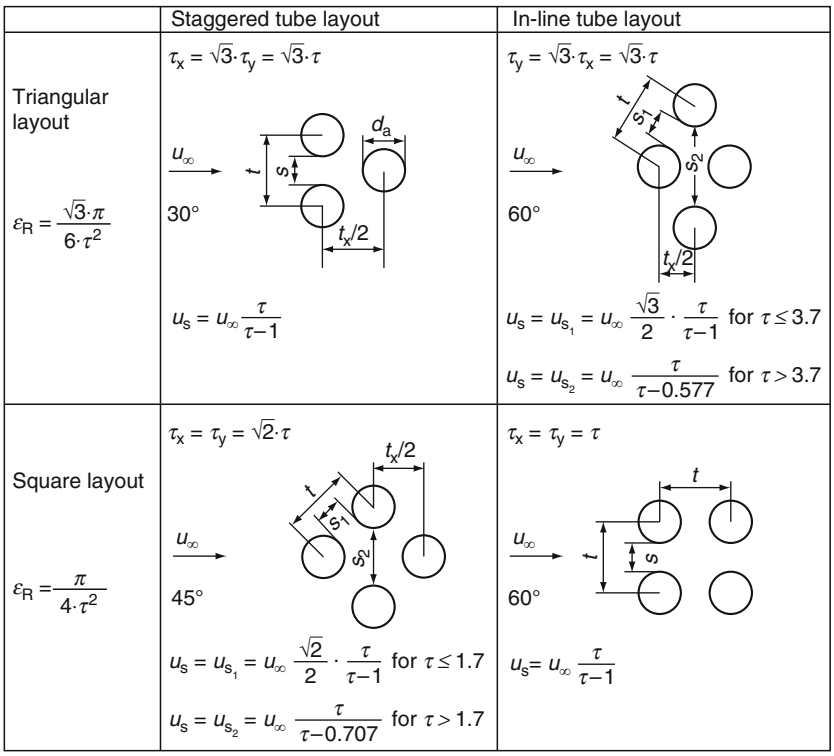

O2. Fig. 2. Standard tube layouts with gap velocity u_s and solidity ratio ε_R.

The calculations in the Sects. 3 and 5 are based on u_s, whereas those presented in Sect. 4 are based on u_τ.

2 Structural Parameters

2.1 Definitions

The structural parameters needed to perform the calculations are the total mass per unit length m, the tube natural frequency of mode i f_i, and the logarithmic decrement of damping Λ_i. The vibration of a tube with mass M, damping constant r, and spring stiffness c is described by the linear differential Eq. (1), in which F is a time-dependent force acting on the mass. This force, which is generated by the flow, may include components dependent upon the tube vibration displacement x and vibration velocity $\dot{x}$:

$$M \cdot \ddot{x} + r \cdot \dot{x} + c \cdot x = F(t, x, \dot{x} \ldots). \tag{1}$$

The natural frequency and damping of the tube can be found from the homogeneous differential Eq. (2):

$$\ddot{x} + 2 \cdot \zeta \cdot \omega_0 \cdot \dot{x} + \omega_0^2 \cdot x = 0 \tag{2}$$

with the system undamped circular frequency $\omega_0 = (c/M)^{0.5}$ and the damping coefficient $\zeta = r/(2\,M\,\omega_0)$. The circular frequency of the damped system is

$$\omega = \omega_0 \cdot \sqrt{1 - \zeta^2} \tag{3}$$

and the natural frequency

$$f = \frac{\omega}{2 \cdot \pi}\,(\mathrm{Hz}). \tag{4}$$

The logarithmic decrement Λ of damping is defined by:

$$\Lambda = \frac{1}{n}\ln\left(\frac{\hat{x}(t)}{\hat{x}(t + n \cdot T)}\right) = 2 \cdot \pi \cdot \frac{\zeta}{\sqrt{1 - \zeta^2}}, \tag{5}$$

where $\hat{x}$ represents the maximum mass displacement at the initial time t and after n cycles $(t + nT)$ with period $T = 1/f$. For small damping ratios, $\zeta \ll 1$,

$$\Lambda \approx 2\pi\zeta \tag{6}$$

2.2 Tube Mass

The mass per unit length m is the effective vibrating mass normalized by the length of the tube. It is comprised of the mass of the tube, including the fluid inside it m_R and the hydrodynamic mass m_h:

$$m = m_R + m_h, \tag{7}$$

with

$$m_R = \frac{\pi}{4} \cdot \left[\rho_R \cdot \left(d_a^2 - d_i^2\right) + \rho_i \cdot d_i^2\right] \tag{8a}$$

and

$$m_h = c_h \cdot \rho_f \cdot \frac{\pi}{4} \cdot d_a^2. \tag{8b}$$

The hydrodynamic mass coefficient c_h is depicted as a function of the spacing ratio in Fig. 3 [2]. In square tube layouts (45° und 90°), the value of c_h is about 10% lower. The value of m_h is negligible when the density of the fluid medium is small, such as in air.

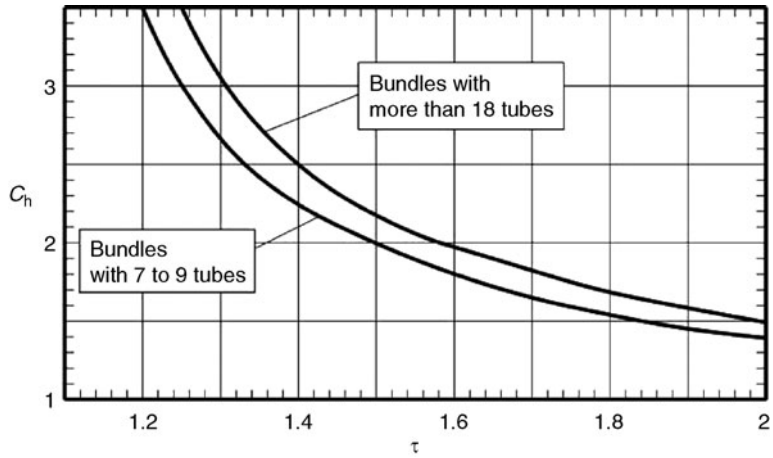

O2. Fig. 3. Hydrodynamic mass coefficient c_h for triangular arrays (30° and 60°) as a function of tube pitch ratio [2].

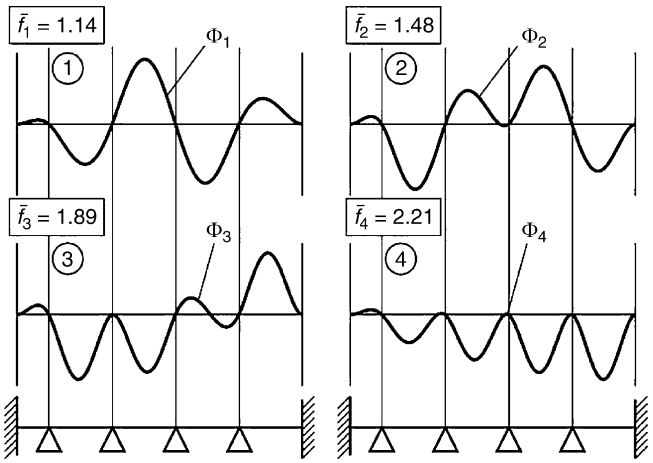

O2. Fig. 4. The first four mode shapes and their relative natural frequencies of a multi-supported tube with $N = 5$ and $X = l/2$ (see Table 2 for more details).

2.3 Tube Natural Frequencies and Mode Shapes

2.3.1 Straight Tubes

In tube bundles, many different resonance modes may be excited. Typical examples of these modes, for a tube with five spans, are illustrated in Fig. 4, which shows the first four mode shapes and their relative natural frequencies. To determine the critical conditions for vibration in heat exchangers, it is often sufficient to know the first natural frequency; however, a higher frequency may be the critical one in situations involving uneven flows (e.g., tubes, which are heavily loaded near support plates but elsewhere more lightly impinged by the flow, or in axial flow over U-shaped bundles). Knowledge of the mode shapes is also essential when vortex shedding or turbulence excitations (see Sects. 4 and 6) or when unevenly distributed fluid forces (Sect. 5) have to be taken into consideration.

The natural frequency f_i of a flexible tube is determined from the ratio between the bending stiffness and the mass per unit length. Important tube characteristics, which influence the natural frequencies are the nature of the support at the tube ends, the number of tube spans N, and the span length l. Tables 2 and 3 for $N > 1$ give the relative natural frequency for the first mode shape, Table 1 for $N = 1$ includes also the relative values of the second mode frequency:

$$\bar{f}_1 = \frac{f_1}{f^*} \quad \text{and} \quad \bar{f}_2 = \frac{f_2}{f^*}, \tag{9a, b}$$

whereby f^* represents the first natural frequency of a tube with a length l, simply supported at both ends as reference value:

$$f^* = \frac{\pi}{2 \cdot l^2}\sqrt{\frac{E \cdot I}{m}} \quad \text{and} \quad I = \frac{\pi}{64}\left(d_a^4 - d_i^4\right). \tag{10a, b}$$

Table 1 shows the relative natural frequencies $\bar{f}_1$, $\bar{f}_2$ and the equivalent length for buckling $\bar{l}_k$ (for considering the influence of axial forces), for the standard cases of a tube without intermediate supports along its length. Table 1 also shows the integral average displacement of the mode shape $\bar{\Phi}$ normalized by the maximum displacement for this mode [see comments to Eq. (38)], as well as the corresponding quadratic average $\bar{\Phi}^2$.

When the cross flow velocity is not uniformly distributed along the tube axis (partial admission, see Fig. 24), the flow excitation force can be weighted by means of the partial energy ratio for a tube section of length l_r:

O2. Table 1. Relative natural frequencies, equivalent length for buckling and integral average displacement of the first mode shape for some beams (or tubes) with different types of end supports, and without intermediate supports

Relative values	Support types for $N = 1$			
	l = L, EI, m	l = L, EI, m	l = L, EI, m	l = L, EI, m
$\bar{f}_1$	1.00	1.56	2.27	0.356
$\bar{f}_2$	4.00	5.06	6.25	2.23
$\bar{l}_k$	1.00	0.7	0.5	2.00
$\bar{\Phi}$	0.637	0.565	0.522	0.392
$\bar{\Phi}^2$	0.500	0.438	0.394	0.250

$$\Delta S_r = \frac{\int_{l_r} \Phi^2(z)\, dz}{\int_0^L \Phi^2(z)\, dz}, \qquad (11)$$

l_r sectional length of a tube with length L (Fig. 24),
$\Phi(z)$ normalized mode shape.

Figure 5 shows the partial energy ratio ΔS_r for the first mode of tubes without intermediate supports as a function of the normalized length, z/l. Depending on the location of the considered tube section, ΔS_r can be determined from the figure.

Table 2 relates to the first mode of a tube with multiple intermediate loose supports and fixed supports at both ends, which gives rise to N spans along the tube. The table gives the relative natural frequency $\bar{f}_1$ and the partial energy ratios ΔS_1 and ΔS_N for the first and last spans. This is relevant to tubes which are welded or riveted to the tube sheets and have a constant span length between the tube support baffles but a different span length X at one end near the tube sheets. Each tube has one natural frequency for the entire tube geometry, meaning that individual spans cannot be treated as independent tubes with their local length and support type.

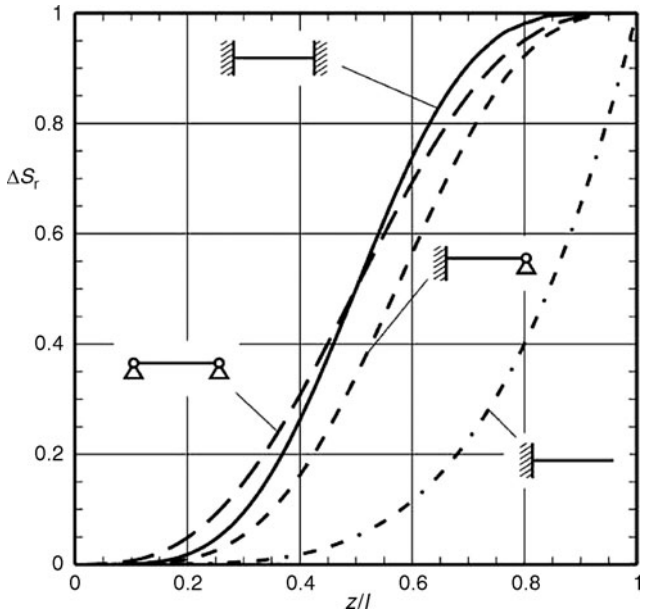

O2. Fig. 5. Partial energy ratio of a tube with $N = 1$ for the first mode shape as a function of z/l.

Since the sum of all $\Delta S_n = 1$, Table 2 can be used to approximately estimate the partial admission energy ratio for each of the intermediate spans:

$$\Delta S_n = \frac{1 - \Delta S_1 - \Delta S_N}{N - 2}. \qquad (12)$$

These middle span calculations are accurate if the intermediate spans have the same length l_n, as well as same structural and fluid properties and the same flow velocity over all the spans.

Table 3 provides similar information for tubes, which have loose (or pin) supports at both ends. For higher order resonance modes or for other configurations (e.g., elastic boundary at supports, in-active intermediate supports, variable span lengths or other geometries with mixed boundary conditions), the tube resonance modes can be calculated by other means such as standard finite element programs, or other design codes, e.g., the program GOOD VIBRATION [3].

All the values in the tables relate to a single tube in ideal supports. Experience shows that with the assumption of zero moment at the tube supports (i.e., assuming the clearance $\Delta d_B = 0$ und the support thickness $b = 0$), the actual frequency will be within ±5% of the estimated value, given that the value of Δd_B remains within 0.3–0.6 mm and b/d_a is smaller than 0.4. Note that Δd_B and b have opposite effects on the natural frequency, which increases with b and decreases with Δd_B. Small values of Δd_B and larger values of b can increase the damping, esp. for the first mode, and thereby reduce the long-term damage. Too large manufacturing clearances or tolerances at tube supports can eventually cause several supports to become inactive, resulting in a substantial reduction in the natural frequency [4, 5].

In tube bundles, the system natural frequencies can be slightly influenced by the mutual interaction of vibrating tubes. Where tube bundles have multiple supports, the system frequencies lie within frequency bands close to the natural frequencies of the individual tubes [2].

O2. Table 2. Relative natural frequencies and partial energy ratios for the first mode shape of a multi-supported tube, which is *fixed* at both ends. N is the number of spans, X is a variable span length at one side, ΔS_1 is for the first span with length X, and ΔS_N is for the last span with length l

	Relative natural frequencies and partial energy ratios, both ends fixed 																
	$X = 0.4 \cdot l$			$X = 0.8 \cdot l$			$X = l$		$X = 1.2 \cdot l$			$X = 1.4 \cdot l$			$X = 1.8 \cdot l$		
N	$\bar{f}_1$	ΔS_1	ΔS_N	$\bar{f}_1$	ΔS_1	ΔS_N	$\bar{f}_1$	$\Delta S_1 \Delta S_N$	$\bar{f}_1$	ΔS_1	ΔS_N	$\bar{f}_1$	ΔS_1	ΔS_N	$\bar{f}_1$	ΔS_1	ΔS_N
2	1.98	4E-3	1.0	1.79	0.13	0.88	1.56	0.50	1.22	0.84	0.16	0.94	0.94	0.06	0.59	0.98	0.02
3	1.44	1E-3	0.34	1.35	0.04	0.25	1.28	0.17	1.12	0.57	0.06	0.90	0.85	0.01	0.58	0.97	2E-3
4	1.24	5E-4	0.13	1.2	0.02	0.10	1.17	0.08	1.08	0.40	0.03	0.89	0.81	4E-3	0.58	0.96	2E-4
5	1.15	2E-4	0.06	1.13	9E-3	0.05	1.11	0.04	1.06	0.29	0.02	0.89	0.79	1E-3	0.58	0.96	0
6	1.09	1E-4	0.04	1.09	5E-3	0.03	1.08	0.02	1.04	0.21	0.01	0.89	0.78	3E-4	0.58	0.96	0
11	1.03	0	5E-3	1.03	7E-4	4E-3	1.02	4E-3	1.02	0.07	2E-3	0.89	0.78	8E-7	0.58	0.96	0

O2. Table 3. Relative natural frequencies and partial energy ratios for the first mode shape of a multi-supported tube, which is *loosely* supported at both ends. N is the number of spans, X is a variable span length at one side, ΔS_1 is for the first span with length X, and ΔS_N is for the last span with length l

	Relative natural frequencies and partial energy ratios, both ends loose 																
	$X = 0.4 \cdot l$			$X = 0.8 \cdot l$			$X = l$		$X = 1.2 \cdot l$			$X = 1.4 \cdot l$			$X = 1.8 \cdot l$		
N	$\bar{f}_1$	ΔS_1	ΔS_N	$\bar{f}_1$	ΔS_1	ΔS_N	$\bar{f}_1$	$\Delta S_1 \Delta S_N$	$\bar{f}_1$	ΔS_1	ΔS_N	$\bar{f}_1$	ΔS_1	ΔS_N	$\bar{f}_1$	ΔS_1	ΔS_N
2	1.32	6E-3	0.99	1.16	0.15	0.85	1.00	0.50	0.79	0.81	0.19	0.61	0.92	0.08	0.39	0.98	0.02
3	1.12	1E-3	0.74	1.07	0.05	0.61	1.00	0.33	0.81	0.81	0.05	0.63	0.93	0.01	0.40	0.98	2E-3
4	1.06	5E-4	0.56	1.04	0.02	0.47	1.00	0.25	0.81	0.83	0.01	0.63	0.94	2E-3	0.40	0.98	2E-4
5	1.04	2E-4	0.44	1.03	0.01	0.38	1.00	0.2	0.82	0.84	3E-3	0.63	0.94	2E-4	0.40	0.98	0
6	1.02	1E-4	0.36	1.02	7E-3	0.32	1.00	0.17	0.82	0.84	6E-4	0.63	0.94	0	0.40	0.98	0
11	1.01	0	0.19	1.01	1E-3	0.18	1.00	0.09	0.82	0.84	0	0.63	0.94	0	0.40	0.98	0

2.3.2 U-tubes

It is possible to compute accurate values of the natural frequencies and the corresponding mode shapes of U-bend tubes either analytically [6] or with Finite Element programs. For estimation purposes, the supported straight tube sections and the unsupported U-bend sections can be regarded separately. In the event that only the straight tube sections have cross-flows, then only these are to be taken into consideration. The computation for the supported straight tube sections can be performed with the help of Tables 2 and 3. For the mixed support case, i.e., fixed at one end and pinned at the other, the values from the two appropriate tables should be averaged. When the unsupported U-bend tubes have also cross-flows, then the calculation of the first natural frequency of the U-bend tubes is given in [7].

2.3.3 Effect of Axial Forces on the Natural Frequencies

Axial compressive forces cause a reduction while tensile forces cause a rise in the natural frequencies. The frequency of a tube f_i with an axial force F_R changes according to Eq. (13), whereby the sign of compressive forces is negative and of tensile forces is positive [8]:

$$f_i(F_R) = f_i \cdot \sqrt{1 + \frac{F_R}{F_{R,k}}} \tag{13}$$

and

$$F_{R,k} = \frac{\pi^2 \cdot E \cdot I}{\left(\bar{l}_k \cdot l\right)^2}. \tag{14}$$

$F_{R,\,k}$ is the critical force necessary for the buckling of the tube. The equivalent length (for buckling failure) $\bar{l}_k = l_k/l_n$ depends on the type of the supports, and its value for each span n can be found in Table 1 [9]. The largest value of $l_k = \bar{l}_k \cdot l_n$ should be selected. For firmly fixed tubes, the axial force F_R is calculated from the difference in thermal expansions between the tubes and the shell, as well as from the pressures p_i inside the tube and p_a in the shell side, which, depending upon the construction can cause axial tensile or compressive forces.

O2. Table 4. Recommended plate stiffness X for different types of tube sheets

	X_A	X_I		
Shell diameter in m		<0.6	0.6–1.2	>1.2
Stiff tube sheet, p_a, $p_i \geq 30$ bar	1	0.9	0.8	0.7
Flexible tube sheet, p_a, $p_i < 30$ bar	1	0.7	0.6	0.5
Membrane tube sheet	0.8	0.4	0.3	0.2

The plate stiffness of the tube sheets has a strong effect. Further influences can be attributed to the nature of the tube sheet boundary conditions, the density (or the spacing ratio) of the tube holes, and to an unequal distribution of the tubes. Bundle interior tubes (Index I) are less stressed due to thermal expansions than exterior tubes (Index A), which are positioned in the proximity of the shell at the edge of the plate.

Therefore, the rigidity of the tube sheet is calculated via an empirical rigidity factor X, with $X = 1$ for a rigid plate and $X = 0$ for a flexible membrane. If the bundles exterior tubes (A) are connected rigidly to the tube sheet, then $X_A = 1$, whereas for the tubes in the center of the tube sheet (I), the rigidity factor can be substantially smaller, $X_I < 1$, depending on the tube sheet thickness and the shell diameter. Recommended values can be found in Table 4.

The following equations and recommendations are valid for tubes, which are uniformly distributed at the center of the tube sheet. They are appropriate for the calculations of the compressive stresses (frequency reduction), as well as erring on the safe side for interior tubes with assumed values of X_I, which are too small. For the case of tensile stresses, some lower values may result. But in the vibration analysis, the possible frequency increases from such tensile stresses should not be taken into consideration.

In equipments without stress relief the axial tube force F_R is expressed as:

$$F_R = F_{R\vartheta,v} + F_{Rp}. \tag{15}$$

(a) Axial tube force due to prevention of thermal expansion and lateral contraction:

$$F_{R\vartheta,v} = \frac{A_R \cdot E_R}{1 + \dfrac{n_R^* \cdot A_R \cdot E_R}{X \cdot A_M \cdot E_M}} \cdot \left[\gamma_M \cdot \Delta\vartheta_M - \gamma_R \cdot \Delta\vartheta_R - \frac{\pi}{2} p_a \left(\frac{\nu_R \cdot d_a^2}{A_R \cdot E_R} + \frac{\nu_M \cdot d_i^2}{A_M \cdot E_M}\right)\right]. \quad (16a)$$

The greatest stress occurs at the exterior tubes:
Exterior tubes:

$$X = X_A; \qquad n_R^* = n_{RA}^* = n_{RA0} + (n_R - n_{RA0}) \cdot X_I^3 \quad (16b)$$

Interior tubes:

$$X = X_I; \qquad n_R^* = n_{RI}^* = n_R - n_{RA0}(1 - X_I^3). \quad (16c)$$

For cylindrical shells, the minimal number of load bearing exterior tubes ($X_A = 1$, $X_I = 0$) is:

$$n_{RA0} = \left[e + \frac{d_i - d_H}{3 \cdot \tau \cdot d_a}\right] \cdot \mathrm{NRR} \le n_R. \quad (16d)$$

For tube layout angle α: 60° 45° 30° 90°
Constant e in Eq. (16d): 1.0 1.3 1.6 1.8

(b) Axial tube force due to external forces:

$$F_{Rp} = \frac{\pi}{4 \cdot \left(n_R + X \cdot \dfrac{A_M \cdot E_M}{A_R \cdot E_R}\right)} \cdot \left[\begin{array}{l} p_a \cdot \left(d_i^2 - n_R d_a^2\right) \\ +X \cdot p_i \cdot n_R \cdot d_i^2 - (1 - X)^2 \cdot p_i \cdot \left(d_H^2 - n_R d_i^2\right) \end{array}\right], \quad (16e)$$

X should be given separately for interior and exterior tubes according to Table 4.

For comparatively rigid shell compensators, Eqs. (15), (16a), and (16e) are valid with appropriately reduced values of E_M.

The principal effects of the pressures p_i, p_a, and X_I on the axial tube force $F_{Rp,v}$ for equipments without stress release are described in ([10], Fig. 8). The forces cancel out with equal inner and outer pressures. Considerable axial compressive forces will develop only in the following cases:

- In the exterior tubes for $p_a - p_i > 5$ bar,
- In the interior tubes for $p_i - p_a > 5$ bar and $X_I < 0.5$.(16f).

In equipments with full stress relief $F_{R\vartheta,v}$ is zero and F_{Rp} can be calculated according to Eq. (16e) with $E_M = 0$ and using the parameters cited in Table 5, which shows the critical pressures at which axial compressive forces are to be expected, and the maximally loaded tubes, which are normally the interior tubes (I).

O2. Table 5. Critical pressure values and parameters to be used in Eq. (16e) for equipments with stress relief

Equipment with	Axial pressure force for		X	d_1
Shell compensator	$p_i - p_a > 5$ bar and $X_I < 0.5$	I	X_I	$d_K > d_1$
U-bend tubes	$p_a - p_i > 5$ bar	I ≡ A	1	0
Floating head	$p_a - p_i > 5$ bar, $p_i - p_a > 5$ bar, and $X_I < 0.5$	I	X_I	0
Stuffing box	$p_i - p_a > 5$ bar	I ≡ A	0	d_1

2.4 Acoustic Natural Frequencies of the Shell-side Volume

Gas flows across tube bundles can excite the acoustic resonance modes, which consist of standing waves of the gas column inside the shell-side volume. These standing waves are in a direction perpendicular to the flow and tube axis. The frequencies of these acoustic modes are:

In a rectangular duct

$$f_{ai} = \frac{i \cdot a_{ge}}{2 \cdot W_y}, \quad i = 1, 2, 3 \ldots \quad (17a)$$

and in a cylindrical container

$$f_{ai} = \frac{\lambda_{ij} \cdot a_{ge}}{\pi \cdot d_i}, \quad i, j = 1, 2, 3 \ldots, \quad (17b)$$

where W_y is the duct dimension in the y-direction, λ_{ij} the eigen values of the Bessel function (Table 6), and a_{ge} the effective speed of sound in the bundle. The effective speed of sound in a bank of tubes a_{ge} according to [11] is:

$$a_g > a_{ge} > \frac{a_g}{\sqrt{1 + \varepsilon_R}}, \quad (18)$$

with ε_R is the solidity ratio (percentage by volume of the tubes relative to the total volume of the shell), which is given in Fig. 2 for various tube layouts. The lower value resulting from Eq. (18) seems to give reliable frequency estimates for large size bundles, i.e., bundles with large depth W_x in the direction of the flow. If one assumes $W_x = W_y$ for cylindrical ducts, then measured values for rectangular ducts ([12], Fig. 9) suggest that a_{ge} lies mid-way between the two limit values of Eq. (18).

2.5 Damping

Predicting the damping of vibrating systems is subject to considerable uncertainty. Different levels of damping, up to a factor of 2, can be observed within the very same tube bundle, as a result of manufacturing tolerances. Correlations from published data [13] suggest deviations of about a factor 4. The following guidelines deliver a lower bound of damping, which leads to conservative designs.

In the literature, the damping values are often represented as the Lehr's damping coefficient ζ (given either as an absolute or a percentage). In the following, the logarithmic decrement Λ in absolute value will be used. Some damping types are amplitude dependent and also a function of the natural modes [4], e.g., the higher modes have reduced damping. All the equations presented below are valid for small amplitudes at the critical conditions, e.g., at the initial phase of instability.

O2. Table 6. Eigen values λ_{ij} of the Bessel function [71]

	i				
j	0	1	2	3	4
0	0	1.841	3.054	4.201	5.318
1	3.832	5.331	6.706		

System damping is an additive effect composed of three basic parts:

(a) *Material- and support damping* of tubes without any effect from intermediate supports. The material damping is negligible. The damping of fixed, or rigid, supports at the tube ends depends on the support design and the tube length, e.g., $\Lambda_M = 0.01 \ldots 0.04$. Without intermediate supports, the lower value applies to long tubes ($L > 2$ m), and a higher value is more appropriate for shorter tubes. Supports with O-rings or clamps produce higher damping, which is also amplitude dependent [4]. For loose end supports structural damping is dominant [1] [see (c)] and $\Lambda_M = 0$.

When the tube has intermediate supports, the importance of material and end-support damping decreases as the number of intermediate supports increases, so that, for $N > 2$, it can be ignored relative to the other damping components. For $N = 2$, then 50% of the values for $N = 1$ should be taken into consideration.

(b) *Viscous damping* due to the fluid surrounding the vibrating tube. In the case of gas flow with low density, this can be neglected. The damping formula given in [14] has been adjusted such that even for small Stokes number, the estimated damping values are on the safe side:

$$\Lambda_v = \pi \cdot \frac{\rho_f \cdot d_a^2}{m \cdot \mathrm{ST}^{0.42}} \cdot \frac{1 + \left(\frac{1}{\tau'}\right)^3}{\left(1 - \left(\frac{1}{\tau'}\right)^2\right)^2} \tag{19}$$

with the Stokes number $\mathrm{ST} = \dfrac{\pi \cdot f_i \cdot d_a^2}{2 \cdot \nu_f} > 30$,

$\tau' = 1.7\tau > 2$ for a standard triangular layout,
$\tau' = 1.9\tau > 2$ for a standard square layout.

(c) *Structural damping*. In multiple support tube bundles ($N > 2$), most of the total damping comes from this source; practically 100% in gases and from 70 to 90% in liquids (the remainder being viscous damping). The sources of structural damping are Coulomb friction as well as impact and squeeze film processes in the gaps between tubes and support plates. For loose or pinned supports at both tube ends, the value N in Eqs. (20) and (21) should be increased to $N^1 = N + 2$.

When tube bundles are exposed to gas flow, friction and impact processes are dominant. From the work of Pettigrew et al. [13], the following equations can be derived:

$$\Lambda_{Sg} = \frac{\pi}{10} \cdot \frac{N-1}{N} \cdot \sqrt{\frac{b}{0.8\,[\mathrm{m}]}} \quad \text{for } l_{am} < 0.8 \text{ m}, \tag{20a}$$

$$\Lambda_{Sg} = \frac{\pi}{10} \cdot \frac{N-1}{N} \cdot \sqrt{\frac{b}{l_{am}}} \quad \text{for } l_{am} \geq 0.8 \text{ m}, \tag{20b}$$

with b thickness of support plate, l_{am} the arithmetic mean of the three longest tube sections. At boring clearances Δd_B = 0.4–0.7 mm, the effect of Δd_B is small. With further reductions in the support clearance, the damping increases – so for this and other reasons, the value of Δd_B should be kept as small as possible.

When tube bundles are exposed to liquid flow, the impact damping processes in combination with squeeze film damping are dominant. According to [14]:

$$\Lambda_{Sl} = 44 \cdot \pi \cdot \frac{N-1}{N} \cdot \frac{1}{f_i} \cdot \left[\frac{\rho_l \cdot d_a^2}{m}\right] \cdot \left[\frac{b}{l_{am}}\right]^{0.6}. \tag{21}$$

(d) Total damping values are the sum of the three basic parts:

Gases (at low pressures):

$$\left.\begin{array}{ll} N = 1 & \Lambda_g = \Lambda_M \\ N = 2 & \Lambda_g = \Lambda_M/2 + \Lambda_{Sg} \\ N \geq 3 & \Lambda_g = \Lambda_{Sg} \geq 0.03/i^{0,2} \end{array}\right\} \tag{22}$$

Liquids :

$$\left.\begin{array}{ll} N = 1 & \Lambda_l = \Lambda_M + \Lambda_V \\ N = 2 & \Lambda_l = \Lambda_M/2 + \Lambda_V + \Lambda_{Sl} \\ N \geq 3 & \Lambda_l = \Lambda_V + \Lambda_{Sl} \geq 0.04/i^{0,2} \end{array}\right\} \tag{23}$$

3 Fluid-elastic Instability

3.1 Introduction

The phenomen of fluid-elastic instability is described in [1, 2, 15, 16]. It can be seen from Fig. 1 that there are some differences between whirling and galloping. According to [1, 17], the following stability equation for the dimensionless critical gap velocity u_k^* for whirling can be derived:

$$u_k^* = \frac{u_{sk}}{f_i \cdot d_a} = K \cdot \sqrt{\Delta} \tag{24}$$

with u_{sk} as the critical gap velocity, $K(\tau)$ the stability constant, and $\Delta = \frac{m \cdot \Lambda}{\rho_f \cdot d_a^2}$ the mass-damping parameter.

Whirling is caused by a soft self-excitation mechanism [15], in which all the tubes of the bundle participate. These vibrate on elliptical trajectories in both the x and y directions. The coupling effect weakens as the spacing ratio becomes larger. For gas flows ($\Delta > 2$) across staggered tube bundles (30° und 45° layouts), the fluid-elastic instability is initiated by whirling. In such cases, Eq. (24) as well as the exponent 0.5 of the mass-damping parameter Δ are confirmed (Fig. 6).

Galloping is caused by a hard self-excitation mechanism [15] involving single tubes or individual tube rows, which vibrate exclusively in y-direction and independently of the movements of the remaining tubes. Galloping leads to steep amplitude increases and arises particularly in in-line tube bundles (60° and 90° layouts) with free flow lanes and in liquids. In these cases, galloping can occur before the onset of whirling, which then leads to low K-constants, to smaller exponents of the mass-damping parameter and to weak dependence on the spacing ratio.

Since the stability equation ought to be valid for both excitation types, its general form is:

$$u_k^* = K(\tau) \cdot \Delta^P. \tag{25}$$

$K(\tau)$ as well as P are functions of the tube layout, the spacing ratio, and of the fluid flow across the array.

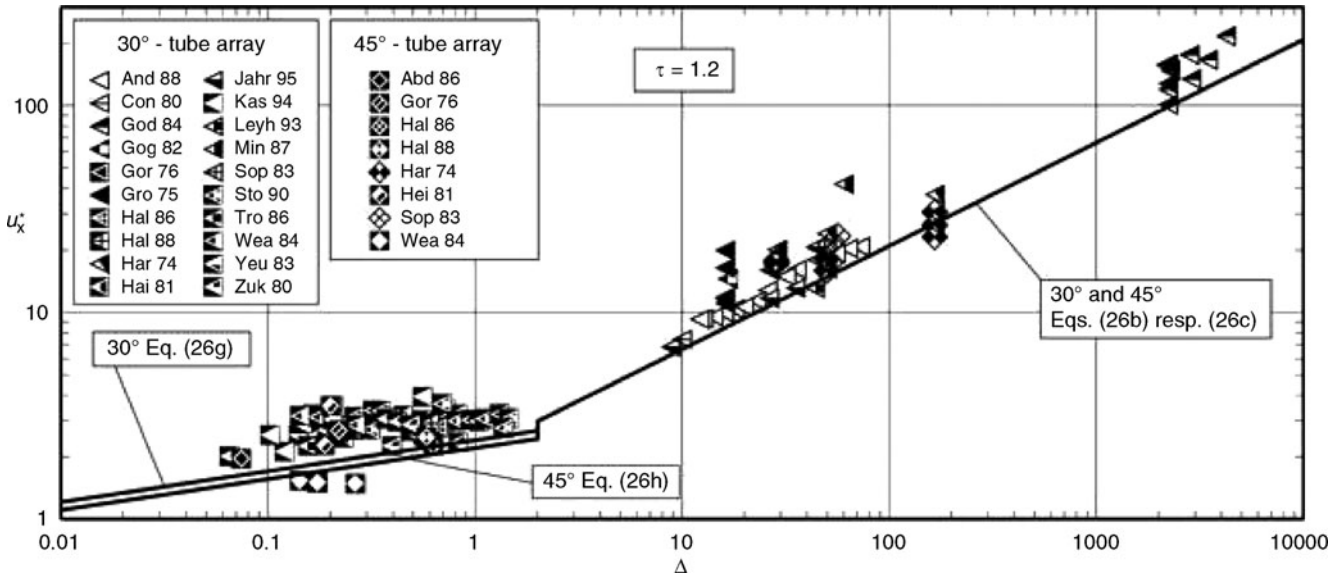

O2. Fig. 6. Stability diagram: dimensionless critical gap velocity as a function of the mass-damping parameter for tube layout geometries of 30° and 45° with the stability constants for $\tau = 1.20$ [21].

The suggested equations described in Sect. 3.2 for single-phase flows are based on a re-valuation of the data reported in the original works of Chen and Jendrzejczek [2, 18], Weaver and Fitzpatrick [19], and Pettigrew and Taylor [20], as well as in more recent publications. They reproduce the lower limits of the scatter in all measured data points. In comparison with previous guidelines, the recommended equations show smaller deviations and reduce the scatter of the measured data points for all tube layout geometries and all fluid flow conditions [21].

3.2 Single-phase Flow

The stability equation is

$$u_k^* = \frac{u_{sk}}{f_i \cdot d_a} = K(\tau) \cdot \left[\frac{m \cdot \Lambda}{\rho_f \cdot d_a^2}\right]^P \qquad (26)$$

with $P = 0.5$ for gas flow across 30° and 45° layouts as well as for single rows,
$P = 0.4$ for gas flow across 60° and 90° layouts,
$P = 0.15$ for liquid flow and all layouts.

The stability constant $K(\tau)$ for *ideal tube bundle situations* can be taken from Figs. 8 and 9 or Tables 7 and 8. It is clear from these figures that the 30° layout is the least susceptible to instability, and the 60° layout has the smallest critical flow velocity without any influence of the pitch ratio. The second and third tube rows, relative to the other rows, are at greater risk to vibrate; however, in [22], the last tube row of square bundles (90° layout) exposed to liquid flows was most susceptible to instability.

Figures 6 and 7 show the stability diagrams for $\tau = 1.20$, i.e., at the practically smallest values of τ, with all experimental data. Reference [23] gives further information and [21] offers all data sources, additional correlations and comparisons with previous guidelines. The demarcation between gases and liquids is approximately at $\Delta = 2$.

In the liquid range, the coincidence of different excitation mechanisms (whirling, galloping, vortex excitation) is possible.

O2. Table 7. Stability constants for standard tube layout geometries subjected to *gas flow* [21]

Tube layout geometry	K_{min}	$K(\tau)$	P	Δ	Eqs.
Tube row [2]	4.4	6.0 (τ − 0.375)	0.5	3 . . . 300	(26a)
30°[a]	2.1	7.0 (τ − 0.9)	0.5	2 . . . 4000	(26b)
45°[a]	2.1	5.3 (τ − 0.8)	0.5	2 . . . 300	(26c)
60°[a]	3.1	3.1	0.4	2 . . . 200	(26d)
90°[a]	4.1	2.9·τ	0.4	2 . . . 200	(26e)

[a]Smaller values are realistic in real heat exchangers due to variations in the approach flow angle [see Sect. 5.2, Eq. (46) and Table 9]

O2. Table 8. Stability constants for standard-tube layout geometries subjected to *liquid flow* [21], $P = 0.15$

	K_{min}	$K(\tau)$	Δ	Eqs.
Tube row [18]	2.2	3.1 (τ − 0.375)	0.05 . . . 3	(26f)
30°[a]	2.4	1.5 (τ + 0.5)	0.05 . . . 2	(26g)
45°[a]	2.2	1.2 (τ + 0.6)	0.05 . . . 2	(26h)
60°	1.8	1.8	0.05 . . . 2	(26i)
90°	1.9	1.0 (τ + 0.7)	0.05 . . . 2	(26k)

[a]Smaller values are realistic in real heat exchangers due to variations in the approach flow angle [see Sect. 5.2, Eq. (46) and Table 9]

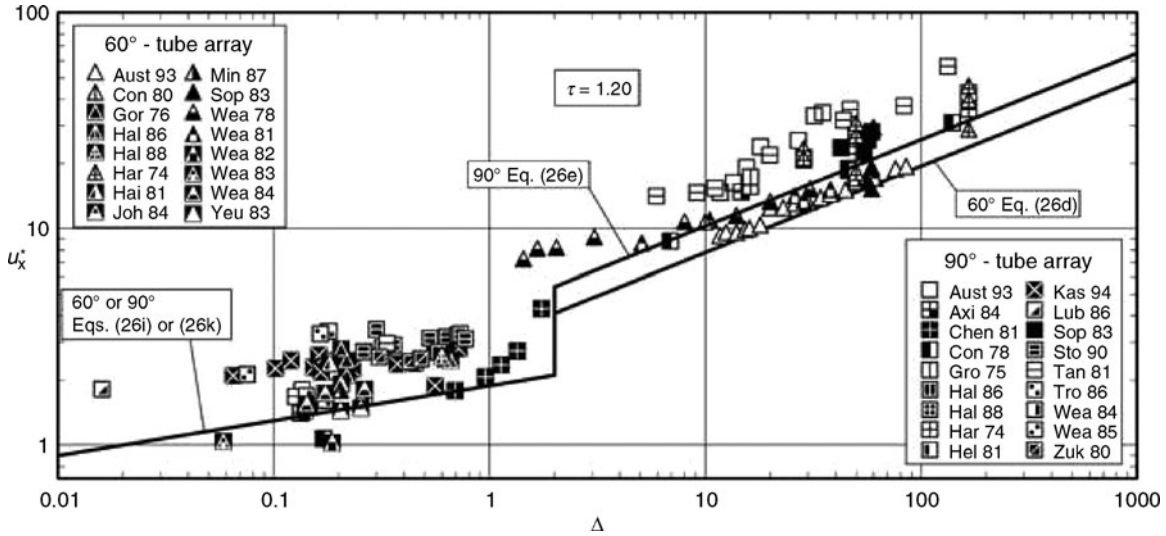

O2. Fig. 7. Stability diagram: dimensionless critical gap velocity as a function of the mass-damping parameter for tube layout geometries of 60° and 90° with the stability constants for $\tau = 1.20$ [21].

Therefore, it is essential for liquid flows that the selected operating velocity does not coincide with that for tube resonance by vortex shedding (Sect. 4.3). This is because vortex resonance can hasten the onset of fluid-elastic instability. This was the case in some test measurements by Weaver et. al., reported in Figs. 6 and 7, which though they lie below the stability boundary, are included as a helpful warning.

The stability diagrams are valid under the following major boundary conditions:

1. For tubes starting from the second tube row, in bundles with *ideal conditions,* i.e.,
   - for homogeneous bundles with constant cross section, uniform distribution of the tubes without free channels or boundary gaps,
   - for tubes with evenly distributed flow along the entire length and in the *y*–direction.
2. The structural parameters m, Λ_i, and f_i are determined from tube tests in quiescent fluid with density ρ_f.

For more details and conditions see [10, 21]. The effects of various deviating boundary conditions, which normally arise in real (circular) heat exchangers, are described in Sect. 5. For *nonideal flow conditions* (i.e., with nonuniform flow), the appropriate *equivalent gap velocities* (Sect. 5.3) should not exceed the critical values.

Figure 8 and Table 7 give the stability constants $K(\tau)$ and the exponents P for gas and steam flow, and Fig. 9 and Table 8 for liquid flow across *standard tube layout geometries.*

In *nonstandard tube layouts*, i.e., with deviations in the layout angle α, which is no more than $\pm 5°$, the equations for the standard situation can be used [24].

Should the deviations be greater than $\pm 5°$, then the stability constants for staggered arrays can be obtained from interpolations between the values for 60°, 45°, and 30° as well as from the limiting instability curve for a tube row ($\tau_x = \infty$). Suitable diagrams can be found in [10], for gas flow also in [21].

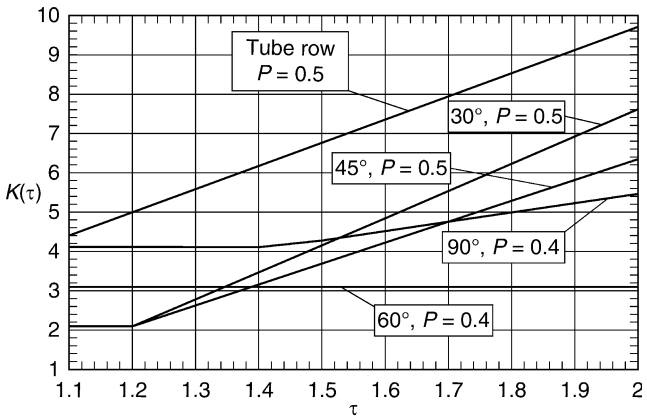

O2. Fig. 8. Stability constants for gas flow and standard tube layout geometries as a function of the pitch ratio.

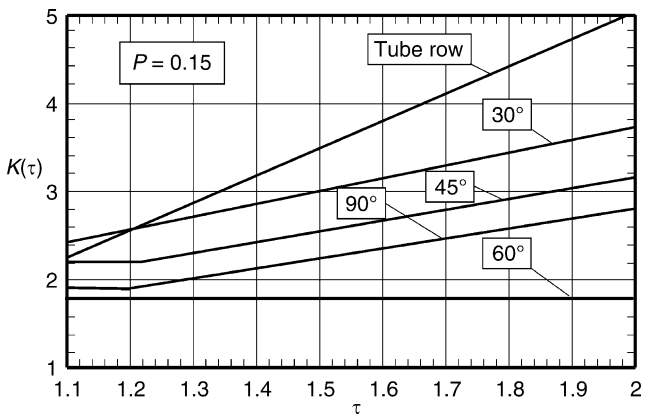

O2. Fig. 9. Stability constants for liquid flow and standard tube layout geometries as a function of the pitch ratio.

The 30° layout bundles react very sensitively to *changes in the approach flow angle* when these are larger than ±8° [25]. Then the stability constant declines and the value for the 60° layout bundle can be attained already at deviations of ±12° [26, 27]. Because of the prevalence of changes in the approach flow direction in real heat exchangers with 30° and 45° tube layouts, it is recommended to select smaller values of u_{sk} for tubes in the endangered regions (Sect. 5.2, Table 9). The 45° layout is less sensitive than the 30° layout, because the angle deviations can be larger (approximately ±15°) before an influence has been observed and the changes of the stability constants are smaller.

3.3 Two-phase Flow

At present, compulsory design guidelines for two-phase flows of gases and liquids do not exist. The addition of another fluid phase changes the nature of the interaction mechanism between the tubes and the fluid. Therefore, the stability equations developed for single-phase flows cannot be used without taking further parameters into consideration.

In Figs. 10 and 11, some results are presented for measurements of the 30° as well as the 60° and 90° tube layouts, which can help in estimating the critical velocities. For the sake of comparison, the corresponding stability equations for the single-phase flow case with $\tau = 1.20$ are also included. In order to make comprehensive rough estimates possible, the measured data were normalized using the structural data corresponding to pure liquid phase instead of the locally measured two-phase parameters. Therefore:

- Mass per unit length m, frequency f, and damping Λ are the values *in pure liquid*.
- The fluid density ρ_{gl} results from the linear average of ρ_g and ρ_l:

$$\rho_{gl} = \dot{\varepsilon}_g \cdot \rho_g + (1 - \dot{\varepsilon}_g) \cdot \rho_l \quad \text{and} \quad \dot{\varepsilon}_g = \frac{\dot{V}_g}{\dot{V}_g + \dot{V}_l}. \quad (27a, b)$$

- $\dot{\varepsilon}_g$ is the gas volume flow fraction, which, if available, is printed next to the data points.
- The effect of the pitch ratio has not been considered in the shown data points [28, 29]. However, the pitch ratio is indicated in the figures.
- The velocity parameter is determined from the gap velocity u_s, which is based on the average two-phase flow density ρ_{gl}.

Several publications [28–37] show that u_k^* is dependent on the two-phase flow regime. For bubbly flows, the dimensionless critical gap velocity increases with $\Delta^{0.5}$. For higher values of $\dot{\varepsilon}_g$, for which dispersed flow predominates, the value of u_k^* seems to be independent of Δ in air–water flows [31, 35, 36]. If refrigerant flow is used [31, 36], the value of u_k^* for $\dot{\varepsilon}_g > 0.6$ decreases with increasing $\dot{\varepsilon}_g$.

The locally measured two-phase flow data for $\dot{\varepsilon}_g = 40 \ldots 70\%$ show that viscous damping Λ_V reaches a maximum value of about 5 times higher than the corresponding single-phase value [35, 37]. This is obviously the reason that the measured critical velocities for two-phase flows, as shown in Figs. 10 and 11, are higher than those obtained from the equations for single-phase flows. Formulas to determine the hydrodynamic mass coefficient and the fluid damping from the local void fraction can be found in references [34, 37].

References [28, 29, 37] give additional information regarding the effect of the tube layout geometry and the spacing ratio as well as the influence of the two-phase flow regime on the dimensionless critical gap velocity u_k^*.

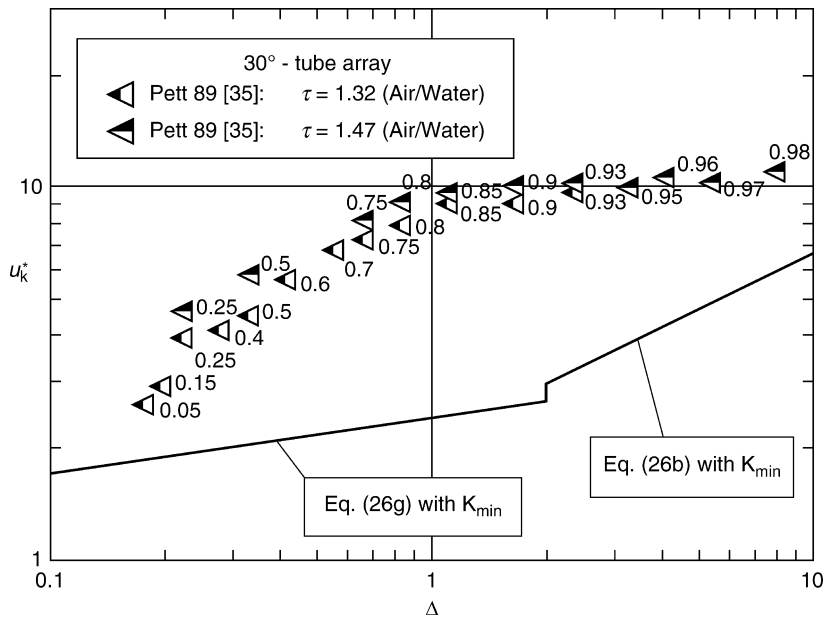

O2. Fig. 10. Dimensionless critical gap velocity as a function of the mass-damping parameter for the 30° tube layout geometry. The stability lines shown are for the single- phase flow with the lowest stability constant.

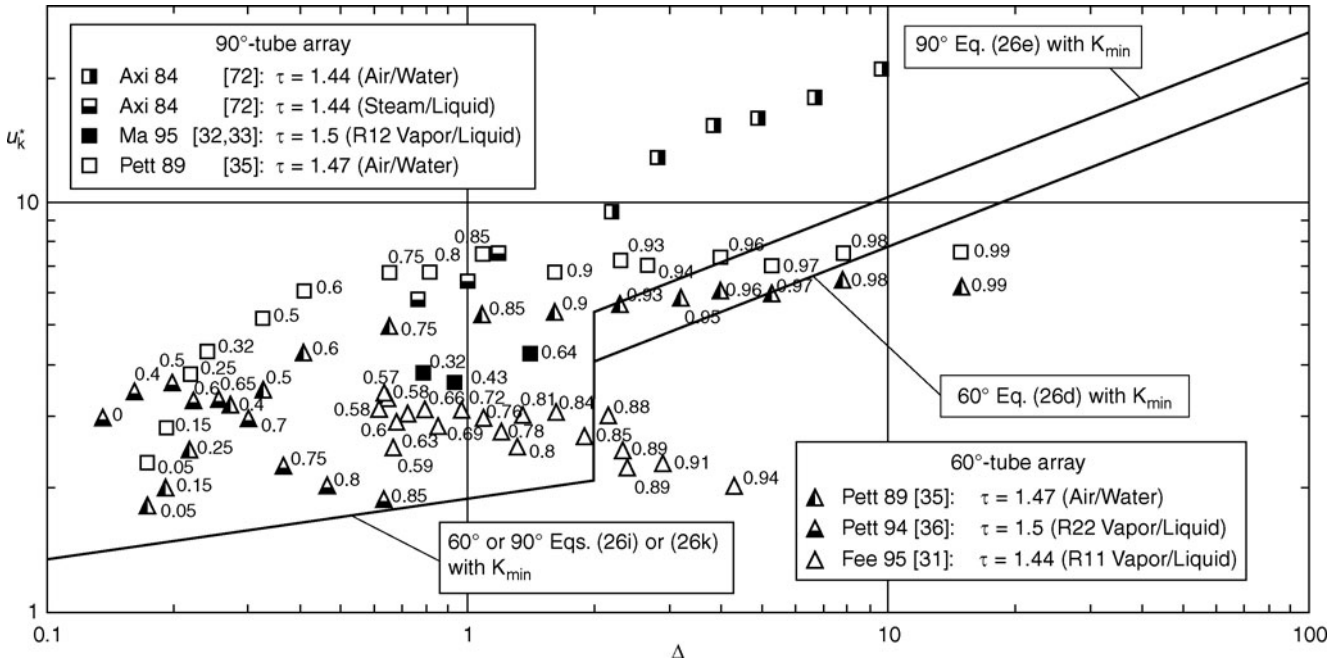

O2. Fig. 11. Dimensionless critical gap velocity as a function of the mass-damping parameter for the 60° and 90° tube layout geometries. The stability lines shown are for the single-phase flow with the lowest stability constant.

4 Turbulence and Vortex Shedding Excitations

4.1 Introduction

The tubes of heat exchangers are inherently exposed to turbulence excitation at all flow velocities. In addition, periodic excitations due to vortex shedding also exist and must be assessed at critical ranges of flow velocity. Small amplitude vibrations excited by flow turbulence, also called turbulent buffeting, are often the cause of fretting wear damage of the tubes. This mechanism should therefore be carefully considered for power plant heat exchangers, e.g., steam generators, because of their long service life expectation.

The nature of these two flow excitations is depicted in Fig. 12, which shows the normalized power spectral density of the fluid force S_F [see Eq. (28)] acting on the tubes of an in-line tube bundle with a relatively large tube spacing ratio (τ = 3.0). The turbulent excitation extends over a wide frequency range and is represented by the two straight lines, which approximate the bound spectrum of turbulent forces, i.e., the spectrum enveloping the highest turbulent forces. On the other hand, the spectral peak near a Strouhal number of 0.2 is caused by vortex shedding excitation. The presence of this excitation and the amplitude of its spectral peak depend on the spacing ratio of the tube layout. For example, this vortex shedding excitation does not exist in tube bundles with small spacing ratios, $\tau \leq 1.5$ [38, 39].

Turbulent flow excitation will be dealt with in Sect. 4.2 without any considerations to the vortex shedding excitation. The latter will be separately addressed in Sect. 4.3. The flow parameters in these two sections are based on the bundle velocity $u_\tau = u_\infty \cdot \tau / (\tau - 1)$, which is different from the gap velocity u_s used in Sect. 3. Conversion to u_s for tube layouts with 45° and 60° can be easily derived with the aid of Fig. 2 or Eq. (66b).

4.2 Turbulent Buffeting

4.2.1 Power Spectral Density of Turbulence Excitation

The bound spectrum shown in Fig. 12 is used to estimate the maximum amplitude of turbulent buffeting vibration. Introductory material on this topic can be found in [1], whereas recent measurements and a brief review can be found in [40] and [41], respectively. The normalized form of power spectral density of the fluid force is given by [39, 42]:

$$S_F = S_y \cdot \frac{4 \cdot u_\tau}{d_a \cdot \left(\rho \cdot u_\tau^2 \cdot l \cdot d_a\right)^2}, \qquad (28)$$

where S_y is the measured power spectral density of the fluid force in y-direction, which is substantially higher than that measured in x-direction. The normalization procedure shown in Eq. (28) collapses the values of S_F for different Reynolds numbers on a single curve when plotted against the dimensionless frequency of turbulence excitation $f \cdot d_a / u_\tau$.

Design bound spectra of S_F for different tube layouts are given as functions of Sr_i in Fig. 13a for staggered (30°, 45° and 60°) and in Fig. 13b for in-line (90°) tube arrangements. The normalized power spectral densities S_F given in Fig. 13 are valid for single-phase flows, whether gas or liquid. The tube with natural frequency f_i will be excited by the turbulence fluid

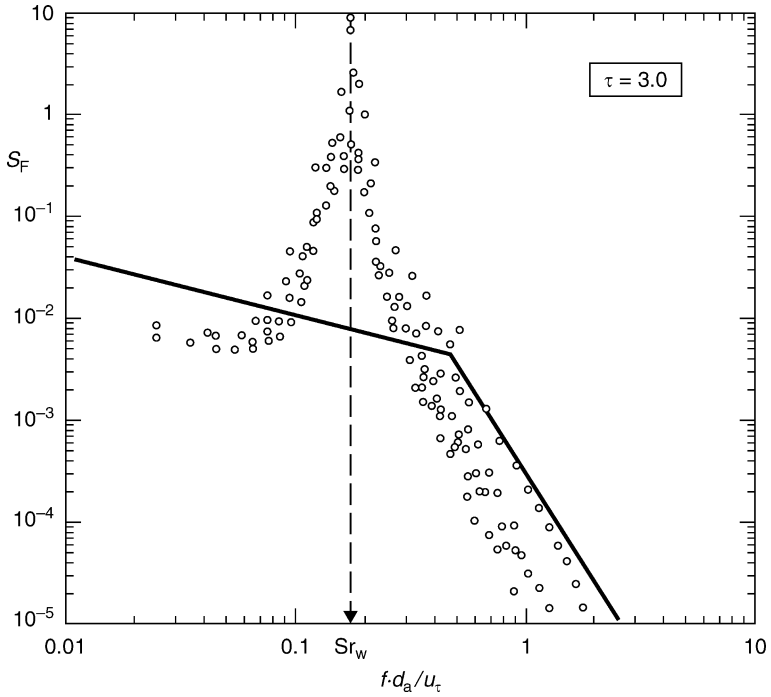

O2. Fig. 12. Normalized power spectral density of the fluid force as a function of the dimensionless frequency for an in-line tube bundle, $\tau = 3.0$; Re = 10^4– $5 \cdot 10^4$; data for tube rows 1–6 [38]; Sr_w Strouhal number of vortex resonance frequency.

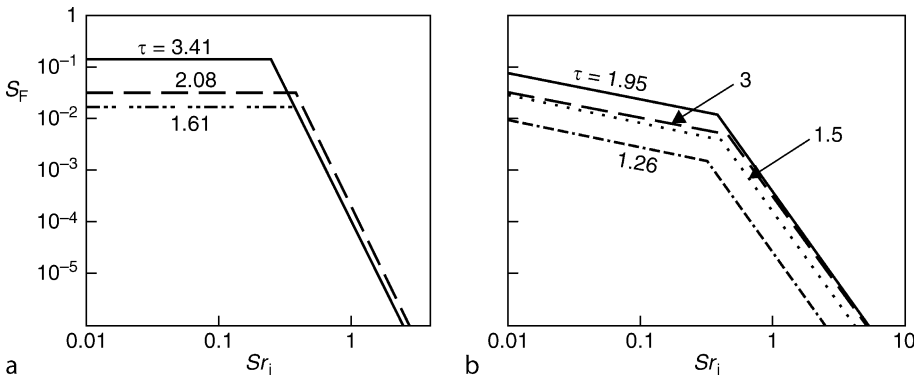

O2. Fig. 13. Bound spectra of normalized power spectral densities of turbulence excitation force as functions of the dimensionless turbulence resonance frequency [39, 42], (a) for staggered tube layouts (30°, 45°, and 60°), (b) for in-line tube layouts (90°).

force at the frequency $f = f_i$. Therefore, the *dimensionless turbulence resonance frequency* is defined by:

$$\mathrm{Sr}_i = \frac{f_i \cdot d_a}{u_\tau}. \tag{29}$$

The bound spectra of Fig. 13 can also be expressed by the following equations, which are given for staggered and in-line bundles separately:

Staggered tube layouts:

For $1.25 \le \tau \le 2.1$

$$0.01 \le \mathrm{Sr}_i < 0.36 : S_F = 4.2 \cdot \tau^{2.8} \cdot 10^{-3}, \tag{30a}$$

$$0.36 \le \mathrm{Sr}_i \le 3.0 \ : S_F = 2.7 \cdot \tau^{2.8} \cdot 10^{-5} \cdot \mathrm{Sr}_i^{-5}, \tag{30b}$$

and for $2.1 \le \tau \le 3.5$

$$0.01 \le \mathrm{Sr}_i < 0.65\,\tau^{-0.8} : S_F = 4.2 \cdot \tau^{2.8} \cdot 10^{-3}, \tag{30c}$$

$$0.65\,\tau^{-0.8} \le \mathrm{Sr}_i \le 3.0 \ : S_F = 5 \cdot \tau^{-1.2} \cdot 10^{-4} \cdot \mathrm{Sr}_i^{-5}. \tag{30d}$$

In-line tube layouts:

For $1.25 \le \tau \le 2.1$

$$0.01 \le \mathrm{Sr}_i < 0.36 : S_F = \left(2.4 \cdot \tau^{2.3} - 3\right) \cdot 10^{-3} \cdot \mathrm{Sr}_i^{-0.5}, \tag{31a}$$

$$0.36 \le \mathrm{Sr}_i \le 3.0 : \ S_F = \left(1.2 \cdot \tau^{2.3} - 1.8\right) \cdot 10^{-4} \cdot \mathrm{Sr}_i^{-3.5}, \tag{31b}$$

and for $2.1 \le \tau \le 3.5$

$$0.01 \le \mathrm{Sr}_i < 0.23\,\tau^{0.6} : S_F = \tau^{-3.1} \cdot 10^{-1} \cdot \mathrm{Sr}_i^{-0.5}, \tag{31c}$$

$$0.23\,\tau^{0.6} \le \mathrm{Sr}_i \le 3.0 \ : S_F = 1.4 \cdot \tau^{-1.4} \cdot 10^{-3} \cdot \mathrm{Sr}_i^{-3.5}. \tag{31d}$$

4.2.2 Turbulence Vibration Response for Single Phase Flow

The amplitude of turbulent buffeting is determined by means of random vibration theory. The Root Mean Square (RMS) amplitude, or the effective amplitude, of the tube turbulent buffeting can be calculated from the formula given by Blevins [1]. This formula gives the effective amplitude A_{RMS} of a simply supported beam of length l and excited by homogenous turbulence at its resonance frequency f_i:

$$\frac{A_{RMS}(z)}{d_a} = \sum_i \Phi_i(z) J_i \cdot \frac{\sqrt{2}}{16 \cdot \pi} \left(\frac{1}{Sr_i}\right)^{1.5} \frac{\rho \cdot d_a^2}{m} \left(\frac{S_F}{\Lambda_i}\right)^{0.5}. \quad (32)$$

$\Phi_i(z)$ is the normalized mode shape of vibration, for which the maximum vibration amplitude is $\Phi_i = 1$.
$J_i = (2 \cdot l_c/l)^{0.5}$ is the joint acceptance coefficient, which is given by Eq. (49). The maximum value of J_i for vibration mode i is $J_i = 1/\sqrt{i}$. More information on the joint acceptance coefficient and on the effect of l_c/l can be found in [43].
l_c is the correlation length: $l_c = 6\ d_a$ [1, 40] up to $8\ d_a$ [44, 45] for the first two tube rows. In the inlet flow region, the correlation length can be taken as $l_c = (11 - 2N_{RR})\ d_a \geq 3\ d_a$ (where N_{RR} is the row number of the bundle), and in other flow regions, $l_c = 3\ d_a$.

If the approach flow is highly turbulent, the turbulence power spectral density S_F for the first tube row could be up to 5 times higher [41, 46]. The average peak vibration amplitude A can be calculated from the RMS amplitude as follows:

$$A = \sqrt{2} \cdot A_{RMS}. \quad (33)$$

The *weighted amplitude* $\tilde{A}$ (or $\tilde{A}_{RMS}$) for nonuniform flow distribution and multiple support situations can be calculated at the operating velocity $u_\tau < u_{\tau k}$ from the Eqs. (62) and (63) and the maximum amplitude $\hat{A}_t$ from Eq. (64) in Sect. 5.3.3. It should then be compared with the critical amplitude A_k, which is based on the expected life span and the fretting wear properties of the tube material. More information on estimating A_k can be found in [46, 47]. If A_k is unknown, an upper limit for $\hat{A}_{t,RMS}/d_a$ of 1% is recommended.

4.2.3 Turbulence Excitation in Two-phase Flow

Estimation of the vibration amplitude for two-phase flows is described in [28, 29, 37, 44–46]. Accordingly, for gas volume flow fraction of $\dot{\varepsilon}_g < 25\%$, the liquid flow data can be used. In the ranges of $\dot{\varepsilon}_g = 25$–90% and 90–100%, the power spectral density of the fluid force at constant mass flow rates increases steeply.

4.3 Vortex Shedding

Vortex shedding in the interstitial space between the tubes of bundles constitutes a narrow band excitation and is treated in the literature as a periodic excitation at the vortex resonance frequency $f_w = f_i$. The vortex shedding frequency f_w changes linearly with the flow velocity and its dimensionless form is called the Strouhal number Sr_w:

$$Sr_w = \frac{f_w \cdot d_a}{u_\tau}. \quad (34)$$

For the Reynolds number range, which is relevant to industrial applications, Sr_w is independent of the Reynolds number. The flow velocity u_τ is the velocity component perpendicular to the tube axis [48]. For tube bundles exposed to dense fluid flow (small mass-damping parameter), vortex shedding excitation can cause mechanical resonance of the tubes, and for those exposed to gas flow, vortex shedding can cause acoustic resonance in the shell-side volume, see Fig. 14.

Recent studies showed that periodic vortex formation in tube bundles is generated and controlled by the hydrodynamic instability mechanism of one or more of the following inherently unstable flows: (a) the wakes of the tubes; (b) the jets issuing between adjacent tubes; and (c) the shear layers separating from the tube shoulders. Therefore, the Strouhal number of vortex shedding is a function of the tube layout pattern, the spacing ratio between the tubes, and the location of the tubes within the bundle (i.e., front or middle tube row). A recent review of this topic can be found in [49].

As can be seen in Fig. 14, tube or acoustic resonance occurs when the vortex shedding frequency f_w becomes close to either the tube natural frequency f_i or the acoustic natural frequency f_{ai}, respectively. When the tube vibration amplitude of any mode exceeds 2% of the tube diameter, i.e., when

$$A \geq 0.02\ d_a, \quad (35)$$

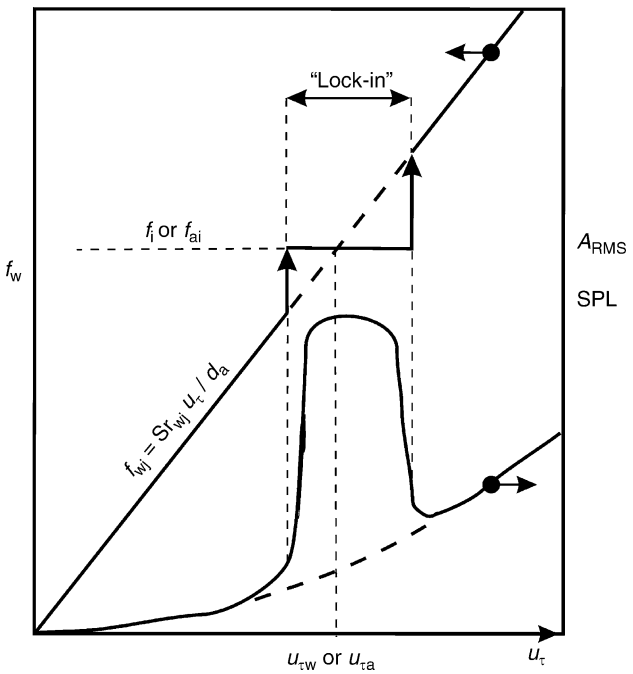

O2. Fig. 14. Illustration of the excitation mechanism of tube and acoustic resonances as the flow velocity is increased. f_{wj} is the vortex shedding frequency, A_{RMS} is the tube vibration amplitude, *SPL* is the sound pressure level.

the tube response to flow excitation becomes substantially stronger due to the mutual interaction and enhancement mechanism between the vortex shedding process and the tube vibration [1]. Under these conditions, the vortex shedding frequency jumps to the tube resonance frequency and remains constant (i.e., $f_w = f_i$) within a velocity range, which is known as "*the lock-in range*." Short-term failures are expected to occur if this lock-in mechanism takes place.

The most recently developed design charts of Strouhal numbers [39, 50, 51] are given in Figs. 15–17. It is noteworthy that up to three vortex shedding frequencies f_{wj} (or Strouhal numbers Sr_{wj}) can appear simultaneously in some tube bundles. In general, the Strouhal numbers Sr_{w2} und Sr_{w3} appear at the front rows at low Reynolds numbers, especially for closely packed tube bundles. Periodic flow excitations at these higher Strouhal numbers are capable of exciting acoustic resonances, but seem relatively weak to excite strong tube resonances. On the other hand, the lower Strouhal number Sr_{w1} is the strongest and can cause intense acoustic resonances and/or large amplitude tube vibrations. It also becomes dominant over the whole tube bundle at high Reynolds numbers and in bundles with large spacing ratios.

In addition, this lower Strouhal number can negatively affect the fluid-elastic instability because its vortex resonance flow velocity $u_{\tau w}$ is often close to the critical velocity, $u_{\tau k}$ or u_{sk}, for fluid-elastic instability (see Sect. 3.1).

Recent work showed that tube and acoustic resonances are caused by the same excitation mechanism in staggered tube bundles (30°, 45°, and 60° layouts). Therefore, the same Strouhal number charts Sr_w can be used for either excitation mechanism, i.e., for acoustic or tube resonance. However, for in-line tube bundles with 90° tube layout, acoustic resonances are not caused by the vortex shedding excitation f_w. Therefore, two different Strouhal number charts ($Sr_w \neq Sr_{wa}$) must be developed; one for the tube resonance Sr_w and the other for the acoustic resonance Sr_{wa}. Note that there is only one dominant Strouhal number Sr_w for in-line tube bundles, which is given in Fig. 18 as a function of τ_x and τ_y [38, 52, 53]. The Strouhal numbers Sr_w and Sr_{wa} are shown together in Fig. 19 for the 90° standard tube layout bundles.

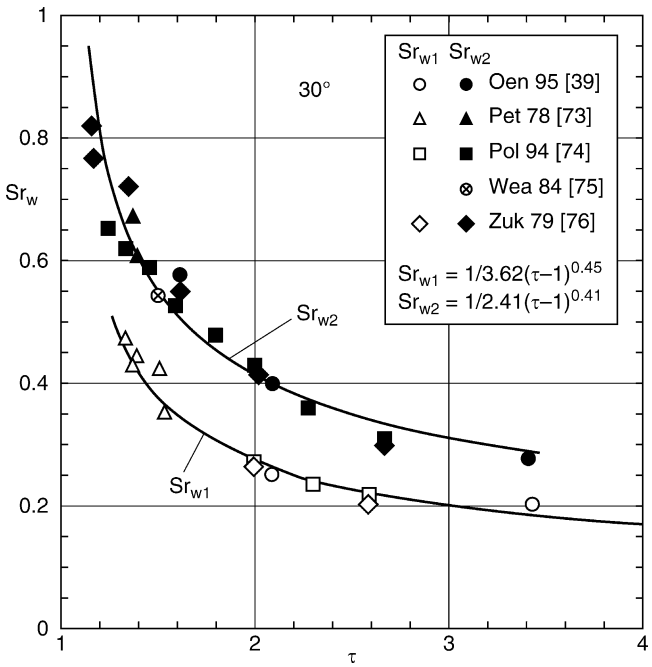

O2. Fig. 15. Strouhal numbers of vortex shedding as a function of the pitch ratio for tube bundles with 30° tube array [39].

4.3.1 Tube Vibration Response

Tube resonance due to vortex shedding excitation is only significant for single-phase flows of dense fluids, and especially within the inlet region of heat exchangers. In gas flows, vortex shedding excitation is too weak to cause excessive tube vibration.

In general, vibration amplitudes less than 1% of the tube diameter are considered acceptable (see also [47]). This amplitude, which can be calculated from Eq. (38), is normally, i.e.,

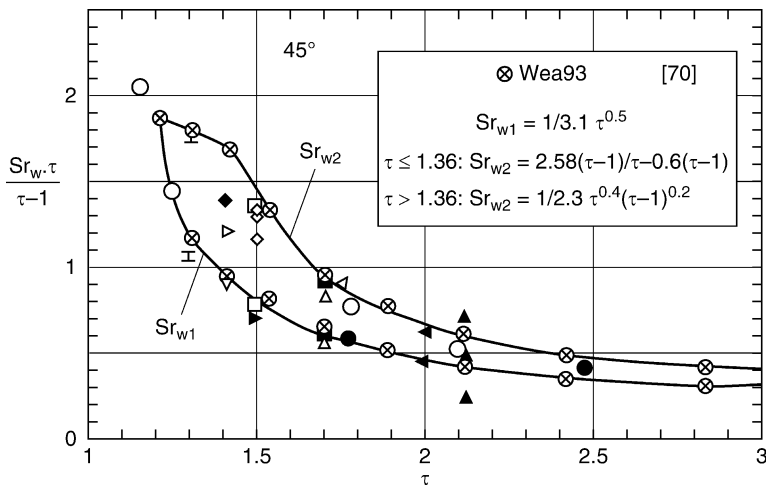

O2. Fig. 16. Strouhal numbers of vortex shedding as a function of the pitch ratio for tube bundles with 45° tube array [70].

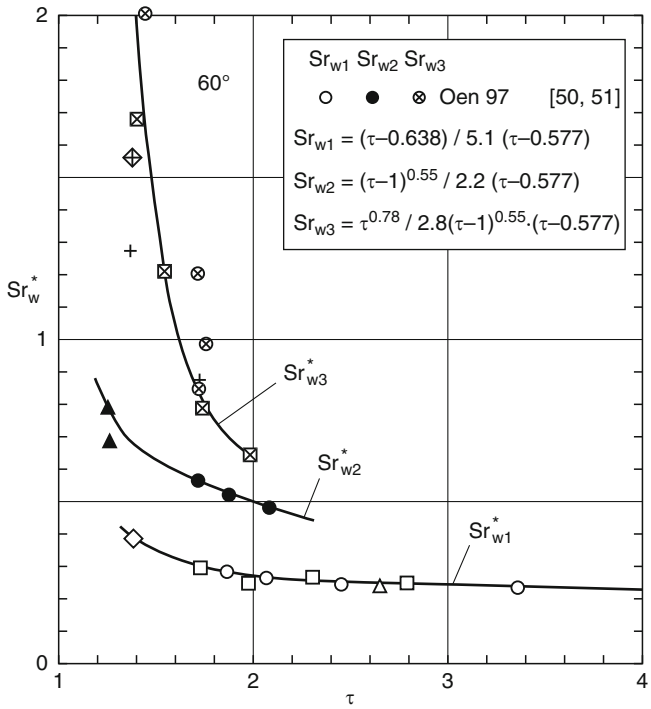

O2. Fig. 17. Strouhal numbers of vortex shedding $Sr_w^* = Sr_w \cdot (\tau - 0.577)/(\tau - 1)$ as a function of the pitch ratio for tube bundles with 60° tube array [50, 51].

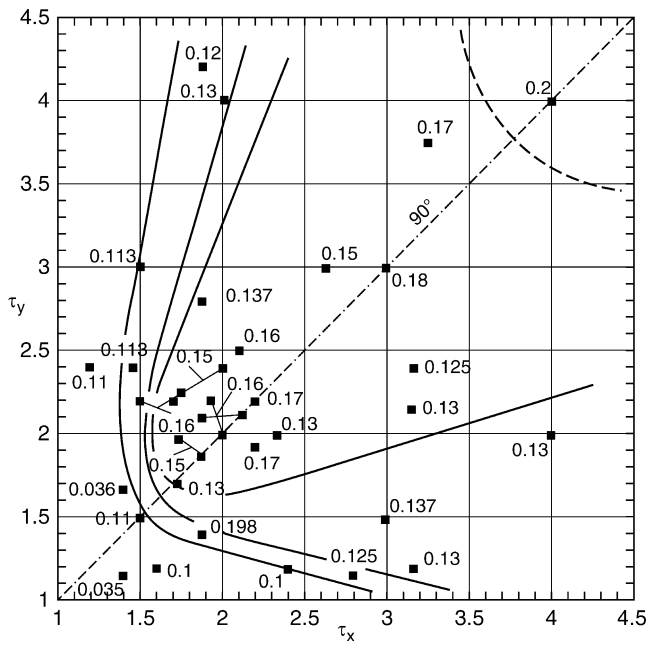

O2. Fig. 18. Strouhal numbers of vortex shedding in in-line tube bundles with 90° tube layout arrangement as a function of the transverse and streamwise pitch ratios [38].

when complying with the recommendations in Sect. 5.5 and observing a stability ratio $K^* < 0.9$, below the value of 1%, if the following parameter limits for the 30° and 60° tube layouts are not exceeded (limits of Δ for 45° and 90° layouts are given in brackets):

	$N = 1$ or 2	$N \geq 3$
in gas flow	$\tau \leq 1.7$ and $\Delta > 6$ (10/20)	$\tau \leq 1.8$
in liquid flow	$\tau \leq 1.3$ and $\Delta > 0.35$ (0.8/10)	$\tau \leq 1.4$

In two-phase flows, vortex shedding excitation has not been observed for $\dot{\varepsilon}_g > 20\%$ [28, 29, 43].

If the above-mentioned conditions are not met, the critical flow velocities $u_{\tau wji}$ must be estimated. At these critical velocities, i.e., when $f_{wj} = f_i$, tube resonance and lock-in with vortex shedding can occur. From Eq. (34), the following equation is obtained for the critical velocities:

$$u_{\tau wji} = \frac{f_i \cdot d_a}{Sr_{wj}}. \tag{36}$$

In estimating the critical velocity, u_τ must be divided by k_α (Eq. (46)) to obtain the gap velocity u_s.The values of Sr_{wj} can be obtained from Figs. 15 to 19.

Based on the data of single cylinder in cross flow, it is advisable to maintain a 30% margin below the critical flow velocity, i.e.,

$$u \leq 0.7\, u_w. \tag{37}$$

But this margin leads to overly conservative design in tube bundles, because the operating velocity is often above u_w and variable along the full length of the tubes. Therefore, a more useful and accurate approach to assess vortex-induced vibration is to calculate first the maximum tube vibration amplitude A at the critical flow velocity u_w and hence the amplitude A for the operating velocity $u(z)$.

The following equation can be used to estimate the vibration amplitude of a tube with length l and simply supported at both ends with baffle plates at the critical flow velocity [54]:

$$\frac{A(z)}{d_a} = \sum\nolimits_i \Phi_i(z) c_y \cdot \frac{\bar{\Phi}}{8 \cdot \pi} \cdot \frac{\sqrt{2}}{Sr_{wj}^2 \cdot \Delta_i} \tag{38}$$

c_y is the dynamic lift coefficient, which is shown in Figs. 20 and 21. These are the maximum values for row 2 in Fig. 20 and for row 3 in Fig. 21.

$\Delta_i = m \cdot \Lambda_i / \rho_f \cdot d_a^2$ is the mass-damping parameter,

$\Phi_i(z)$ is the normalized vibration mode shape with $\Phi_i = 1$ corresponding to the maximum vibration amplitude,

$\bar{\Phi} = \frac{\int_0^l |\Phi_i(z)| dz}{l}$ considers the support conditions on the mode shape and is obtained from Table 1.

Equation (38) is valid for tube vibration amplitude ratios A/d_a less than 10%. Additional models to calculate the correlated lift coefficient ($c_y \cdot \sqrt{2} \cdot \bar{\Phi}$) can be found in [1].

The lift coefficient c_y depends on the tube layout geometry, the tube row within the bundle, the spacing ratio, and the Reynolds number, which is based on the gap velocity u_s. Note that the maximum lift coefficient for staggered bundles is at approximately $\tau = 2$ and also that the effect of Reynolds number for staggered bundles (Fig. 20) is opposite to that for in-line bundles (Fig. 21). For staggered bundles, the lift coefficient becomes smaller after the third row [55]; after the sixth row c_y is only 30% of the values from Fig. 20. The lift coefficient for small spacing ratios, $\tau \leq 1.5$, is very small, approximatly $c_y = 0.1 \cdot (\tau - 1.1)$.

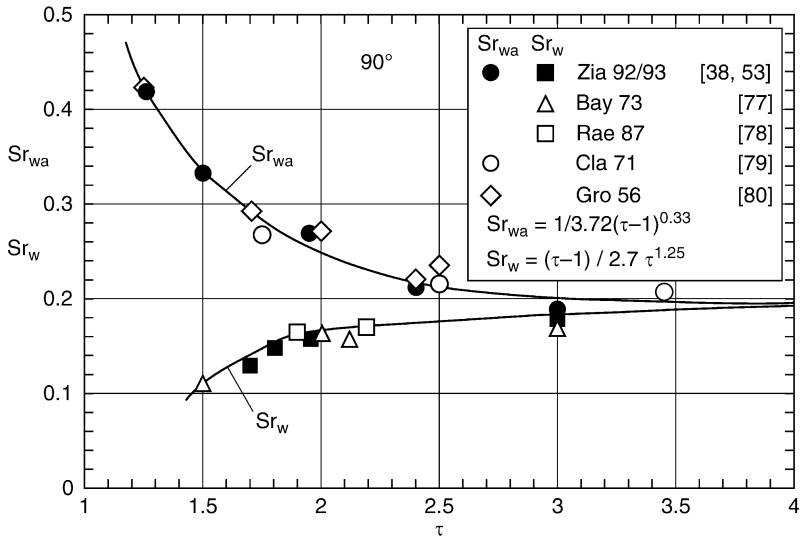

O2. Fig. 19. Acoustic and vortex shedding Strouhal numbers as functions of the pitch ratio for square bundles (90° tube layout).

The proximity to the condition of maximum tube resonance can be assessed by considering the frequency ratio from Eqs. (34) and (38):

$$\eta_{i,j} = \frac{f_{w,j}}{f_i} = \frac{u}{u_{w,i,j}}. \tag{39}$$

If the velocity u and therefore the value of $\eta(z)$ changes between η_u and η_o along the length or a sectional length l_r of a tube (see Fig. 24), then the *amplitude weighting factor*

$$k_{A,i,j} = \frac{1}{\eta_o - \eta_u} \cdot \int_{\eta_u}^{\eta_o} f_{VA}(\eta)\, d\eta \tag{40}$$

can be used to estimate the reduction in the amplitude from that maximum, which would occur at the frequency coincidence ($\eta = 1$). $f_{VA}(\eta)$ is the dynamic response amplification function which, for example, can be approximated for tube bundles by the following linear triangle function:

$$\begin{aligned} f_{VA} &= 0 && \text{for } \eta < 0.78 \text{ and } \eta > 1.22, \\ f_{VA} &= 4.54 \cdot \eta - 3.54 && \text{for } 0.78 \le \eta \le 1, \\ f_{VA} &= 5.54 - 4.54\,\eta && \text{for } 1 < \eta \le 1.22. \end{aligned} \tag{41}$$

For tubes with different levels of flow excitation along sectional tube spans, the vibration amplitude can be calculated by taking into account the tube vibration mode shape Φ_i, according to Eqs. (62) or (63), which give the weighted vibration amplitude $\tilde{A}_i$ (see Sect. 5.3.3).

If the estimated maximum amplitude for any mode is less than 2% of the tube diameter, then the lock-in phenomenon is not expected to occur [56], see also [1, p 55]. In addition, lock-in normally does not occur in bundles ($N \ge 3$) exposed to liquid flows if $\tau \le 1.5$, in bundles exposed to gas flows if $\tau \le 2.0$, nor in bundles subjected to two-phase flows if $\dot{\varepsilon}_g > 15\%$.

The estimated maximum vibration amplitude $\hat{A}_w$ according to Eq. (64) should be less than the acceptable value A_k based on fretting wear considerations and the expected life span of the equipment [46, 47]. This value should be less than 2% of the tube diameter to avoid short-term damages. If A_k is unknown, an upper limit for $\hat{A}_w/d_a$ of 1% is recommended. If the

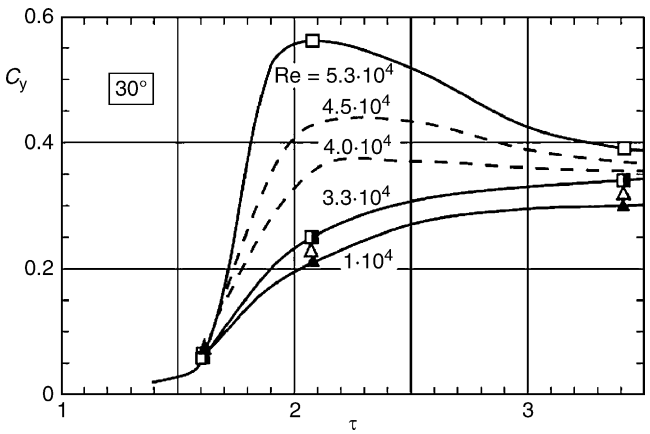

O2. Fig. 20. Dynamic lift coefficient for the first two tube rows in staggered tube bundles (30° tube array) as a function of the pitch ratio. The data are also valid for the 45° and 60° tube arrays [39], Re = $u_s\, d_a/\nu$.

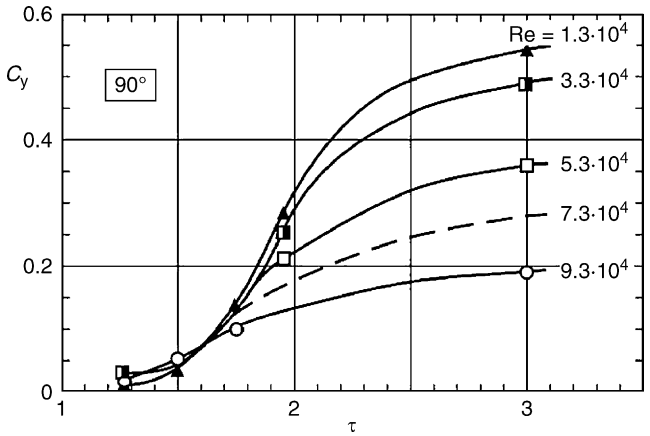

O2. Fig. 21. Dynamic lift coefficient for the 90° tube array as a function of the pitch ratio. The data are for tube rows $N_{RR} \ge 3$ [42], Re = $u_s\, d_a/\nu$.

amplitude $\hat{A}_w$ is too large, structural modifications should be considered (see Sects. 5.5 and 6.3), or otherwise the operating flow velocity of the equipment must be reduced.

4.3.2 Acoustic Resonance

The mechanism of acoustic resonance of tube bundles is similar to the mechanism of tube resonance, which is addressed in the previous section (Fig. 14). For in-line bundles, the Strouhal numbers at which acoustic resonances occur, Sr_{wa}, differ from the Strouhal numbers for tube resonance Sr_w [52, 57, 58].

Therefore, acoustic Strouhal numbers for in-line bundles are provided in Fig. 22, which give the value of $\tau_x \cdot Sr_{wa}$ as a function of the streamwise and transverse spacing ratios, τ_x and τ_y, respectively. The difference between Sr_{wa} und Sr_w is highlighted in Fig. 19, which shows both values against the pitch ratio for the case of 90° tube layout geometry.

For staggered tube bundles, acoustic resonances occur at the Strouhal numbers of vortex shedding, i.e., $Sr_{wa} = Sr_w$, and therefore Figs. 15–17 can be used to determine the critical flow velocity for acoustic resonance excitation. This critical velocity can be obtained from the following equation:

$$u_{\tau aji} = \frac{f_{ai} \cdot d_a}{Sr_{waj}}. \tag{42}$$

As in the case of tube resonance, coincidence between the frequency of vortex shedding and that of acoustic resonance, i.e., when $f_{ai} = f_{wj}$ or $f_{ai} = f_{wa}$, does not necessary mean that lock-in will actually occur. Whether lock-in will occur, or not, depends on the acoustic attenuation (damping) relative to the excitation energy provided by vortex shedding.

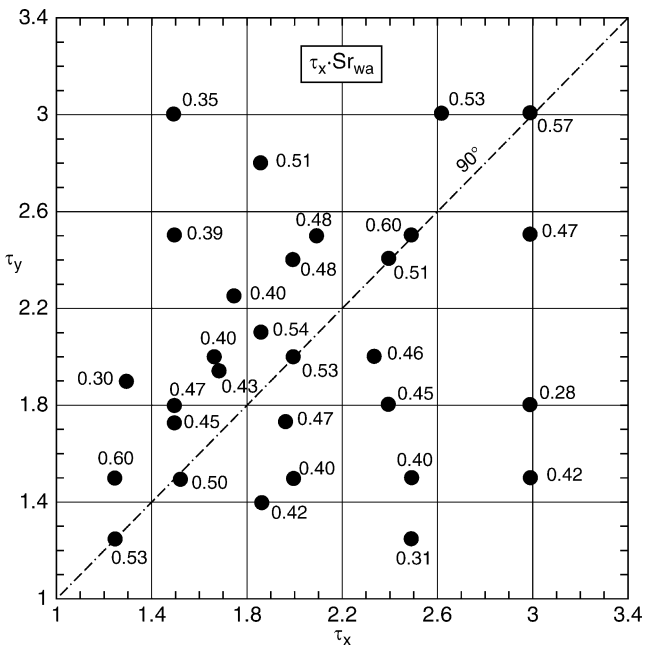

O2. Fig. 22. Acoustic Strouhal number multiplied by the streamwise pitch ratio for in-line tube bundles with 90° tube layout arrangement. τ_x and τ_y are the streamwise and the transverse pitch ratios [38].

Several damping criteria exist in the literature that can be used to predict whether acoustic resonance will, or will not, occur [59–61]. According to Blevins [1], acoustic resonance will occur if $u_\tau / (f_{ai} \cdot d_a) > 2$. Chen and Young [59, 62] developed a damping parameter, G, for in-line tube bundles:

$$G = \frac{\mathrm{Re}}{\mathrm{Sr}_{wa}} \cdot \frac{1}{\tau_y} \left(1 - \frac{1}{\tau_x}\right)^2 \leq 2000 \tag{43}$$

with $\mathrm{Re} = u_\tau \cdot d_a / \nu$. Chen states that resonance will occur if $G > 2000$.

Eisinger et al. [63] reported that this criterion is suitable for large size bundles and for both in-line and staggered tube layout geometries. However, he recommended the following limits:

$G > 2700$: Always resonance,
$G < 1300$: Always no resonance.

A reliable general criterion for the range $1300 < G < 2700$ does not exist, and must await further studies. The criteria of Fitzpatrick [60] and Ziada et al. [61] are based on small scale model tests and appear to be less reliable for large size industrial applications. Additional information and other criteria based on Chen's method can be found in [55, 64].

To avoid acoustic resonance, it is recommended to maintain the maximum flow velocity in the equipment below 80% of the critical velocity for acoustic resonance, i.e.,

$$u_\tau \leq 0.8\, u_{\tau a} \tag{44}$$

where $u_{\tau a}$ is the lowest possible acoustic resonance velocity. However, if u_τ is found to be larger than the critical velocity $u_{\tau a}$, then the damping parameter, G, must be calculated to assess the liability of the heat exchanger to acoustic resonance. If several critical velocities for acoustic resonances are found to be within the operating velocity range, i.e., if

$$u_{\tau aji} < 1.25\, u_\tau, \tag{45}$$

then the value of G must be based on the highest critical velocity. Resonance is not expected to occur if $G < 1300$. If this is not the case, countermeasures must be implemented. For example, acoustic baffle plates can be added in the shell side between the tubes such that the lowest critical velocity for acoustic resonance is increased to at least 20% higher than the maximum flow velocity of the equipment.

5 Design of Heat Exchangers against Vibration Excitation

5.1 Introduction

The design equations presented in Sects. 3 and 4 are based on *ideal conditions*, as they normally exist in wind tunnel experiments. Real conditions in heat exchangers require additional considerations:

- Altering of the critical velocity for fluid-elastic instability (Sect. 5.2), e.g., regarding a change of the radial velocity distribution, which generates a variable approach flow direction in the bundle or possibly higher velocities in the gaps between the exterior tubes and the shell.

- Calculation of equivalent velocities and amplitudes (Sect. 5.3), e.g., for tubes with a varying cross flow velocity and with variable fluid or structural properties along the entire length.
- Estimation of the velocity distribution in critical sections of the heat exchanger bundle (Sect. 5.4), e.g., in the inlet, the outlet, or in the window region.

Guidelines for appropriate engineering design to avoid vibration damages are given in Sect. 5.5.

5.2 Adjusted Critical Velocities for Fluid-elastic Instability

It is not possible to calculate the risk of vibration excitation for an individual tube in the bundle, only the risk for a tube row can be determined with the assumption that the radial velocity distribution is constant. If this is not the case, the most endangered tube in the tube row, i.e., for the inlet or outlet flow region the tube at the center of the nozzle, should be considered.

Three factors influence the critical velocity in heat exchangers:

$$u_{sk} = u_{sk,min} \cdot k_{IF} \cdot k_{RS}. \tag{46}$$

$u_{sk,min}$ is the *reduced critical velocity* due to varying approach flow directions, as shown in Table 9 [26, 27]. It has to be used in all sections of heat exchangers with cylindrical shells.
k_{IF} is the *inlet flow factor* for the first two tube rows in the inlet section, which can be taken from Table 9. This factor accounts for the lower approach flow velocity and excitation force for the first tube row [4, 15, 16]. For the second tube row, it includes an adjustment to the velocity distribution model of Mohr [26], as described in Sect. 5.4.2.
k_{RS} is the *boundary stream factor*, which considers the higher risk of outer tubes because of the smaller gaps between them and the shell and the higher velocity in comparison to the mean velocity of the considered tube row. k_{RS} is relevant in heat exchanger sections with an accelerated flow, e.g., in the inlet flow region of windows and in the exit region of cylindrical shells. In the following, k_{RS} is described briefly.

CFD-simulations of the velocities in boundary gaps show a marked increase of the approach flow velocity of the outer tubes. This is especially the case when the distance between shell and tube is small and the boundary gaps of the upstream tubes are greater. In addition, the flow must accelerate due to the reduction in the flow area as the chord of the circular boundary becomes smaller [26].

This situation can be seen for gap A in (Fig. 23). The outer tube in tube row i with the smallest boundary gap width $s_{RS,i}$ is exposed to higher flow velocity and therefore higher level of vibration excitation. The approach flow velocity is taken to be the RMS-value of the two velocities in the boundary gap and in the gap adjacent to the next tube in row i. The boundary stream factor for tube row i in sections with accelerated flow is:

$$k_{RS,i} = \sqrt{\frac{2}{1 + \left(\frac{s_{RS,i-1}}{s_{RS,i}}\right)^n}} \le 1, \tag{47}$$

where $s_{RS} = 0.5(d_1 - d_a) - \sqrt{x_{RR}^2 + y_{Ra}^2}$, index $i-1$ refers to the upstream tube row and the exponent n is:

$$n = 10/(10 + d_1/d_a)^{0.5} \ge 1.4 \tag{47a}$$

Equation (47) is valid for

$$\frac{s_{RS,i}}{d_a \cdot (\tau - 1)} \ge 0.4 \text{ and } 1 < \frac{s_{RS,i-1}}{s_{RS,i}} \le 4.0, \tag{47b}$$

otherwise the boundary stream factor becomes $k_{RS} = 1$. Some more details and limitations are described in [10, 26].

It is assumed in Eq. (46) that the vibration risk for the outer tube is proportional to the gap flow velocity, which is the usual assumption for inner tubes of the bundle. Whether an influence of the adjacent wall exists or not has not yet been proven by experiments. Nevertheless, if a tube row becomes critical due to the high approach flow velocity of its outer tube, which may happen for the first tube rows in the window, then this tube should be removed.

For the decelerated flow sections, the boundary stream factor can be assumed $k_{RS} = 1$. Since only every second section has an accelerated flow, the correction for the whole tube length is about 50% smaller than the calculated correction from Eq. (47).

O2. Table 9. Reduced critical velocities and inlet flow factors for all fluids in heat exchangers

Tube array	Reduced critical velocity $u_{sk,min}$	Eqs.	Inlet flow factor k_{IF}	
			Tube row one	two[a]
30°	$1.3 \cdot u_{sk60} \le u_{sk30}$	(46a)	$(1 + 0.4\tau)/\tau$	1.0
45°	$u_{sk90} \le u_{sk45}$	(46b)		0.9
60°	$u_{sk60} \le u_{sk30}$	(46c)		1.0
90°	u_{sk90}	(46d)		0.8

[a]In conjunction with the use of Eqs. (69–73)

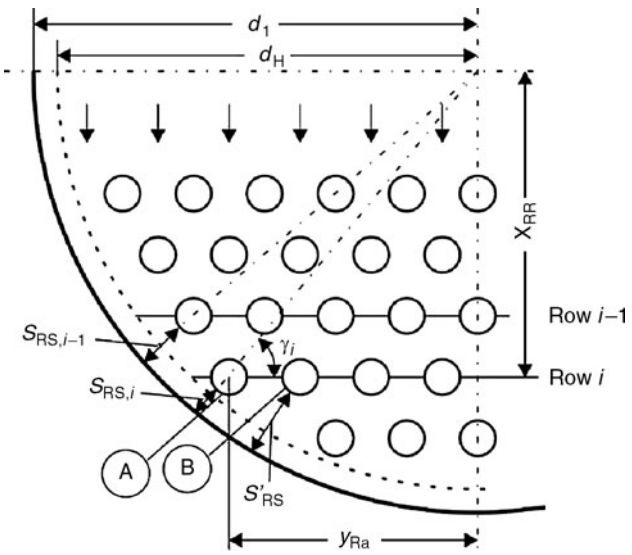

O2. Fig. 23. Influence of the boundary gap velocities at accelerated flow conditions on endangered outer tubes.

If the curvature of the shell is small, i.e., if the shell diameter is large, the tube row is located in the center of the shell or if there are "no tubes in the window," then k_{RS} increases to the limit case:

$$k'_{RS} = 0.3 + 0.7\, k_{RS} \tag{48}$$

5.3 Influence of Partial Fluid Force Admission

The correlation of the unevenly distributed lateral forces $F(z)$ with the mode shape of the tube is usually described by the joint acceptance coefficient J_i, e.g., [1, Eqs. (7–44)]:

$$J_i = \frac{\int_0^L F'(z) \cdot \Phi_i(z)\, \mathrm{d}z}{\int_0^L \Phi_i^2(z)\, \mathrm{d}z}, \tag{49}$$

with J_i being a correlation factor and $F'(z) \leq 1$ is the normalized distribution function of the lateral forces. The basic approach to calculate the fluid forces acting on tube arrays was presented by Connors [65] for Whirling and by Blevins [1] for vortex shedding with lock-in:

$$F(z) \sim \hat{u}^2 \cdot \Psi^2(z) \cdot \Phi_i(z), \tag{50}$$

where $\hat{u}$ is the maximum velocity as shown in Fig. 24, $\Psi(z) \leq 1$ is the normalized distribution function of the velocity and $\Phi_i(z) \leq 1$ is the normalized mode shape function of the i^{th} mode.

The *energy ratio* S_i results from Eqs. (49) and (50) and is used to correlate the forcing function when the flow distribution is not uniform along the tube:

$$S_i = \frac{\int_0^L \psi^2(z) \cdot \Phi_i^2(z) dz}{\int_0^L \Phi_i^2(z) dz} \leq 1. \tag{51}$$

5.3.1 Equivalent Velocity and Energy Ratio

Equations (49–51) yield the *equivalent velocity* $\tilde{u}_i$ for the whole tube length, which can be compared with the critical velocity $u_{k,i}$:

$$\tilde{u}_i = \hat{u} \cdot \sqrt{S_i}. \tag{52}$$

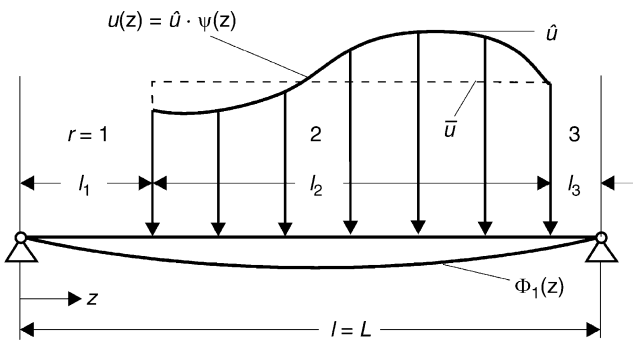

O2. Fig. 24. Partial admission of a tube with variable velocities.

For bundles with homogeneous fluid flow ($S_i = 1$ for $\Psi = 1$), i.e., for tubes with approximately constant forces along the entire length, it is always the first mode (with the lowest frequency), which becomes critical. However, in the majority of cases the detailed velocity distribution is not known. Therefore, it is normally sufficient to divide the tube length into sections with average constant velocities. If the velocity (or amplitude) in the section r for a simply supported tube with the length l_r is constant (see Fig. 24), then the energy ratio from Eq. (51) becomes:

$$S_i = \sum_{r=1}^{R} \psi_r^2 \cdot \Delta S_{i,r}, \tag{53}$$

where Ψ_r is constant. $\Delta S_{i,r}$ is the partial energy ratio for the section r due to Eq. (11) and can be obtained from Fig. 5 for the first mode.

In heat exchangers with multi-supported tubes, the excitation forces in the sections with the greatest spans (or partial energy ratios) in conjunction with maximum fluid velocities are dominant, but the sections with lower or no force admission contribute to an energy dissipation of the vibrating tube. Therefore, it would be too conservative to consider only the section with maximum velocity (e.g., the inlet flow region), because the *equivalent*, i.e., the *weighted velocity* is the true indicator of the excitation level of the whole tube.

The tube shown in Fig. 25 is a window tube with four flow paths and three tube spans ($M = 4$, $N = 3$). It is advantageous to perform the calculation according to various sections, either per flow path (m, r) or per tube span (n, r). Beside variable velocities, other fluid or structural data, e.g., mass, density, damping, or changing of the fluid state and the mass flow, which depend on the tube length, can be included too. These values are assumed constant per flow path m [66]. Values for partial

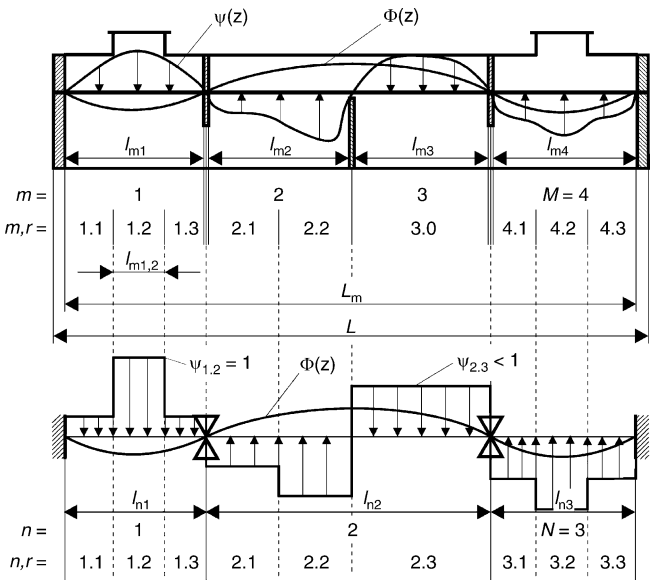

O2. Fig. 25. Subdividing the tube length in sections of constant velocities. m, r is the numeration of the flow paths and n, r the numeration of the tube spans.

energy ratios can be taken from Tables 2 or 3 or by means of computer programs [3].

For a constant velocity in the whole section m, the energy ratio is similar to Eq. (53):

$$S = \sum_{m=1}^{M} \psi_m^2 \cdot \Delta S_m. \tag{54}$$

Here in Eq. (54) and in the following, the subscript i referring to the mode shape has been omitted. ΔS_m is the partial energy ratio for the flow path length l_m, as defined by Eq. (11).

When the velocity in the section m is subdivided, then

$$S = \sum_{m,r=1,1}^{M,R} S_{m,r} = \sum_{m,r=1,1}^{M,R} \psi_{m,r}^2 \cdot \Delta S_{m,r}, \tag{55}$$

$$\Delta S_{m,r} = \int_{l_{m,r}} \Phi^2(z)\mathrm{d}z \Big/ \int_0^L \Phi^2(z)dz \text{ and } \sum_{m,r=1,1}^{M,R} \Delta S_{m,r} = 1. \tag{55a}$$

An approximate calculation – without the use of a computer program – is only possible for the first mode, by means of Eq. (12), Fig. 5 and Tables 2 and 3 in Sect. 2.3. For this purpose $\Delta S_{m,r}$ can be split up into two parts:

$$\Delta S_{m,r} = \Delta S_m \cdot \Delta S'_{m,r} \quad \text{and} \quad \sum_{r=1}^{R} \Delta S'_{m,r} = 1, \tag{55b}$$

where $\Delta S'_{m,r}$ or $\Delta S'_{n,r}$ are, contrary to Eq. (55a), not related to the tube length L, but to the flow path length l_m or span length l_n. The values of $\Delta S'_{m,r}$ or $\Delta S'_{n,r}$ can be taken from Fig. 5, the values of ΔS_m or ΔS_n from Tables 2 or 3 and from Eq. (12).

The calculation should be executed practically in table form for the partial sections m,r (see Table 11 in Sect. 6.2).

5.3.2 Stability Ratio for Fluid Elastic Instability

The stability equation (25) can be written as:

$$u_k^* = \frac{u_{sk}}{f \cdot d_a} = \frac{\hat{u}_{sk} \cdot \sqrt{S}}{f \cdot d_a} = K(\tau) \cdot \Delta^P. \tag{56}$$

The resultant maximum critical velocity in the case of constant fluid and structural data is:

$$\hat{u}_{sk} = u_{sk} \Big/ \sqrt{S}. \tag{57}$$

The stability ratio K^* defines the risk of the vibration excitation by fluid-elastic instability. It is the ratio of the equivalent velocity divided by the critical velocity:

$$K^* = \frac{\tilde{u}_s}{u_{sk}} = \frac{\hat{u}_s \cdot \sqrt{S}}{u_{sk}}. \tag{58}$$

Variable fluid properties or structural data:

Based on the knowledge of the different sectional critical velocities u_{skm}:

$$u_{km}^* = \frac{u_{skm}}{f \cdot d_a} = K_m(\tau) \cdot \left[\frac{m_m \cdot \Delta_m}{\rho_m \cdot d_a^2}\right]^{P_m} \tag{59}$$

it is possible to obtain the general equation for the maximum critical veöocity ($K^* = 1$), which is analogous to Eq. (57):

$$\hat{u}_{sk} = \frac{1}{\sqrt{\sum_{m=1}^{M} \frac{S_m}{u_{skm}^2}}} \tag{60}$$

with S_m from Eq. (55). It should be mentioned that the accuracy of these calculations depends on the knowledge of Φ_i. So in most cases, computer programs [3] are necessary for the design.

The critical volume flow in section m can be calculated from the following equation, which uses the notation indicated in Fig. 25:

$$\dot{V}_{k,m} = \hat{u}_{sk} \cdot \sum_{r}^{R} \frac{\psi_{m,r} \cdot A_{qsm,r}}{k_{LF} \cdot k_{PF}}, \tag{61}$$

where m may be any flow path and $A_{qsm,r}$ is the cross sectional area corresponding to $\Psi_{m,r}$. The two factors in the denominator k_{LF} for leakage flow and k_{PF} for partial flow will be explained in Sect. 5.4.1, Eqs. (67) and (68). The critical inlet volume flow $\dot{V}_{k,IF}$ can be obtained by multiplying Eq. (61) by ρ_m/ρ_{IF}.

5.3.3 Weighted Turbulence and Vortex Amplitudes

The maximum amplitudes A_i resulting from Eqs. (38–41) for vortex shedding [or $A_{i,RMS}$ from Eq. (32) for turbulent buffeting] in the partial sections r have to be weighted by the partial energy ratio $\Delta S_{i,r}$. For the simply supported tube in Fig. 24, the weighted maximum amplitude is approximately [1, 43]:

$$\tilde{A}_i = \sqrt{\sum_{r=1}^{R} A_{i,r}^2 \cdot \Delta S_{i,r}}. \tag{62}$$

In heat exchangers with multi-supported tubes and constant fluid properties and structural data, the weighted maximum amplitude for the mode i is:

$$\tilde{A}_i = \sqrt{\sum_{n=1}^{N} \Delta S_{i,n} \cdot A_{i,n}^2 \cdot J_{w,i,n}^2}. \tag{63}$$

$A_{i,n}$ must be weighted by means of Eq. (62), when the velocity in span n is subdivided. $J_{w,i,n}$ is a correlation factor and is $J_{w,i,n} \leq 1$ for vortex shedding and $J_{w,i,n} = 1$ for turbulent buffeting.

In the case of *vortex excitation*, $J_{w,i,n}$ considers the forces, which act out of phase or opposing directions at different tube spans l_n. In the following, it is recommended to consider – in the normal case – only the two spans n with the maximum loadings in Eq. (63) for every mode:

$J_{w,i,,n} = 1$ for the most severely loaded span, i.e., when $\Delta S_{i,n} \cdot A_{i,n}{}^2$ is maximal for a span n or "for all spans and all modes where lock-in cannot be avoided" [1, p. 458],

$J_{w,i,,n} = 0.5$ for the span with the second highest value of $\Delta S_{i,n} \cdot A_{i,n}{}^2$,

$J_{w,i,,n} = 0$ for all other spans.

This recommendation will lead to conservative results.

For the case, in which the fluid or structural data vary over the length of the tube, which leads to changing values of $A_{i,n}$ as well as $\Delta S_{i,n}$, the weighting of the amplitudes is described in [1, 43].

From the summation of the mode shapes $A_i(z)$ [resp. $A_{i,\mathrm{RMS}}(z)$], the course of the Amplitude $A(z)$ can be obtained as:

$$A_i(z) = \tilde{A}_i \cdot \Phi_i(z) \quad \text{and} \quad A(z) = \sum_i A_i(z). \tag{64}$$

From Eq. (64), the maximum value of the vortex shedding amplitude $\hat{A}_w$ or of the turbulent buffeting amplitude $\hat{A}_t = \sqrt{2} \cdot \hat{A}_{t,\mathrm{RMS}}$ can be identified for a tube.

5.4 Approximation of the Axial Velocity Distribution

With the aid of CFD simulations [26, 27, 67, 68], the influence of the bundle geometry on the velocity distribution could be determined and thereby the energy ratio and the instability ratio K^* for the most endangered tube rows could be quantified. The following tube rows are particularly endangered and should be always analyzed:

- The first and the second tube rows of the bundle approached by the inlet flow, because of the nozzle jet flow and possible turbulent buffeting and vortex excitation,
- the first and the second tube rows in the windows, because they are exposed to the maximum cross flow velocity in all sections over the whole tube length.

Furthermore, some tubes adjacent to vertical free flow lanes or to impinging plates may have a much greater excitation risk in those cases, when the design recommendation in Sect. 5.5 have not been followed.

The following equations provide *equivalent* axial distributions of flow velocity with sectional constant values, primarily derived to assess the influence of fluid-elastic instability. Their application to calculate the amplitudes caused by vortex shedding and turbulent excitations is described in Sect. 6.3.

5.4.1 Volume Flow and Distribution Function

The total volume flow in any flow path m is given by Eq. (61):

$$\dot{V}_m = \dot{V}_{\mathrm{IF}} \cdot \rho_{\mathrm{IF}}/\rho_m = \hat{u}_s \cdot \sum_{r=1}^{R} \frac{\psi_{m,r} \cdot A_{\mathrm{qsm},r}}{k_{\mathrm{LF}} \cdot k_{\mathrm{PF}}}. \tag{65}$$

$\dot{V}_{\mathrm{IF}}$ is the inlet volume flow. The gap of cross-sectional area $A_{\mathrm{qsm},r}$ should be calculated according to Eq. (66a), without consideration of possible small free flow lanes, i.e., as if the cross-section area were to be completely filled with tubes within the inner diameter of the shell. This leads to a conservative design for tubes in the bundle. Tubes adjacent to free flow lanes have to be considered separately.

$$A_{\mathrm{qsm},r} = s' \cdot l_{m,r} \cdot \frac{\tau - 1}{\tau} \cdot k_\alpha, \tag{66a}$$

s' is the chord length of the tube row in the shell cross section, $l_{m,r}$ the length of the flow path and k_α considers the gap flow velocity dependence on the tube layout according to Fig. 2:

$$\begin{aligned}
&30^\circ\text{- and } 90^\circ\text{-tube layout}: && k_\alpha = 1 \\
&45^\circ\text{-tube layout}: && k_a = 1.414 \text{ for } \tau \le 1.7; \\
& && k_\alpha = \frac{\tau - 0.707}{\tau - 1} \text{ for } \tau > 1.7; \\
&60^\circ\text{-tube layout}: && k_a = 1.155 \text{ for } \tau \le 3.7; \\
& && k_\alpha = \frac{\tau - 0.577}{\tau - 1} \text{ for } \tau > 3.7.
\end{aligned} \tag{66b}$$

The values of the correction factors k_{LF} and k_{PF} in Eq. (65) depend on the considered flow path m and on the tube row:

- $k_{\mathrm{LF}} \le 1$ considers the axial leakage flow through the gaps between support plates and tubes and between the plates and the shell in all sections m, except the inlet and outlet regions.

$$k_{\mathrm{LF}} \approx \left(1.1 - \frac{0.1 \cdot \Delta d_{\mathrm{B}}}{[\mathrm{mm}]}\right) \cdot \sqrt{f_{\mathrm{L}}} \text{ for } \Delta d_{\mathrm{B}} \le 1.0 \text{ mm}. \tag{67}$$

  When the boring clearance is $\Delta d_{\mathrm{B}} > 1$ mm, then the bracket value becomes 1.0. The factor f_{L} will be calculated from Subchap. L1.5 [Fig. 5 or Eqs. (23) and (24), as well as Eq. (5), also for bundles with gaps]. The radial bypass flow between bundle and shell should not be considered here. When fouling is possible, k_{LF} will approach to 1.0.
- $k_{\mathrm{PF},\,i} \le 1$ considers the partial flow, which approaches the window tube row in cross flow:

$$k_{\mathrm{PF},i} = 1.1 \cdot A_{\mathrm{qF},i}/A_{\mathrm{qF\,max}}, \tag{68}$$

  $A_{\mathrm{qF},i}$ is the partial free axial cross section of the window, downstream of tube row i (see Fig. 30), A_{qFmax} is the whole free axial cross section of the window [see Subchap. L1.5, Eqs. (50)–(53)].

The correction factors k_{LF} and k_{PF} can also be used to consider added or reduced mass flow, e.g., in conjunction with condensation or vaporization.

5.4.2 Inlet and Outlet Regions with Nozzles

Basically, the velocity distribution at tube rows near the inlet and outlet nozzles is influenced by the geometric data of the heat exchanger, the pitch ratio of the bundle, the nozzle diameter, and the distance bundle/nozzle. A velocity peak normally appears at the nozzle center line and decays within the first tube rows due to the large pressure drop in the bundle. In staggered tube arrays, this peak decays after three to four tube rows and in in-line tube arrays after five to six tube rows.

The model of Mohr [26] describes the equivalent velocity distribution at the second tube row of 30° – and at the third tube row of 60° – arrangements. The approximate calculation

for the other tube layouts are also feasible, when the inlet flow factors k_{IF} in Table 9 are taken into consideration.

The basis of the model is the worst case scenario, in which the maxima of the velocity and of the mode shape are coincident, as shown in Fig. 26. A further criterion is the equivalence of the energy ratios in the model and in the corresponding CFD-simulation for every partial flow path. An unsymmetrical position of the nozzle can also be considered, which would shift the velocity profile by the eccentricity of the nozzle position Δl_S [3, 26].

The velocity distribution for the tube in the center line of the nozzle will be divided into five flow path lengths with three flow areas, as shown in Fig. 26:

(I) Flow path with maximum velocity: $\psi_1 = 1$ (for one tube span)

$$l_1 = d_S \cdot Y \cdot \frac{l}{s'} - \left| l_S - \frac{l}{2} \right|, \quad d_S \le l_1 \le l_2, \quad \text{and} \quad \frac{l}{s'} \ge 1. \tag{69a}$$

$$s_1 = d_S \cdot Y \cdot f\left(\tau, \frac{d_1}{d_S}, \frac{l}{d_1}\right), \quad 0.5 d_S \le s_1 \le s_2, \tag{69b}$$

$$A_{qs1} = \frac{\tau - 1}{\tau} \cdot (l_1 \cdot s_1 - 0.215 \cdot s_1^2) \cdot k_\alpha \text{ for } s_1 \le l_1. \tag{69c}$$

The jet expansion factor Y is a function of h/d_a:

$$Y = 1.1 \cdot \left(\frac{h}{d_a}\right)^{0.25} \ge 0.9. \tag{70}$$

The geometry function reads as follows:

$$f\left(\tau, \frac{d_1}{d_S}, \frac{l}{d_1}\right) = 0.4 \cdot \frac{\tau}{\tau - 0.95} \cdot \frac{1 - 0.09 \cdot (d_1/d_S)}{(l/d_1)^{0..3}}. \tag{71}$$

(II) Flow path with reduced velocity:

$$l_2^* = 0.9 \cdot l \cdot \frac{\tau}{\tau - 0.5} \cdot \left(\frac{d_S}{l} + 0.2\right)^{0.7}, \tag{72a}$$

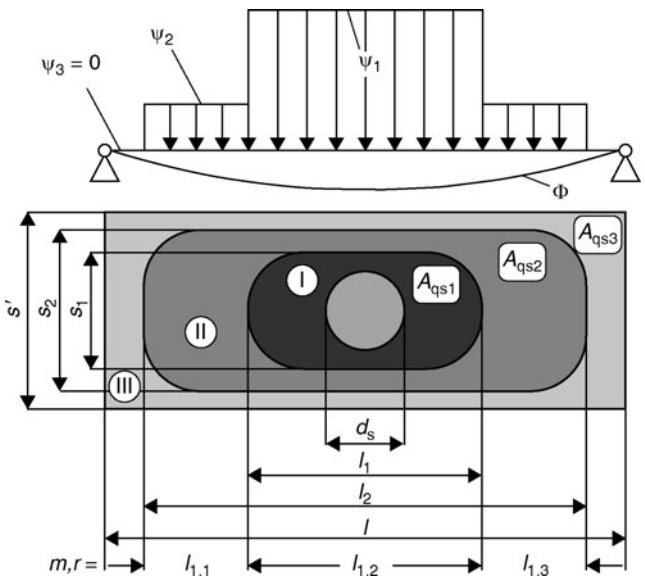

O2. Fig. 26. Model of the inlet velocity distribution by Mohr and Gelbe [26, 67, 68].

$$l_2 = l_2^* \le l, \tag{72b}$$

$$s_2 = 1.35 \cdot s' \cdot f\left(\tau, \frac{d_1}{d_S}, \frac{l}{d_1}\right) \cdot \left(\frac{d_S}{s'} + 0.2\right)^{0.7} \le s' \tag{72c}$$

$$A_{qs2} = \frac{\tau - 1}{\tau} \cdot (l_2 \cdot s_2 - l_1 \cdot s_1) \cdot k_\alpha, \tag{72d}$$

$$\psi_2 = 1.2 \cdot \frac{l_2^* - l_1}{l}. \tag{72e}$$

(III) Flow path with reverse flow: $\psi_3 = 0$

$$A_{qs3} = \frac{\tau - 1}{\tau} \cdot k_\alpha \cdot s' \cdot l - A_{qs1} - A_{qs2}. \tag{73}$$

The scope of application for this model has been validated for:

$$\frac{h}{d_a} > 0.5; \frac{d_1}{d_S} \le 7.5; \frac{l}{d_1} \le 3; \frac{d_S}{l} \ge 0.1; \tau \le 2.$$

The critical volume flows determined by the model with Eq. (61) are on the safe side in the range of 80–100% from the real values [26].

For a *quick and rough estimate*, it is recommended to use the *jet flow model* given in Eqs. (74a) and (b) to check the second tube row and primarily the first tube row, when considering the inlet flow factor k_{IF} in Table 9. This model is for $\frac{h}{d_a} > 0.5$ more accurate than a model using the projected area of the nozzle cross-section, which should be used for $\frac{h}{d_a} < 0.5$.

$$l_1 = s_1 = 1.20 \cdot d_S \cdot \left(\frac{h}{d_a}\right)^{0.25} \ge 0.9 \cdot d_S; \; l_1 \le l; \; s_1 \le s', \tag{74a}$$

$$A_{qs1} = l_1 \cdot s_1 \cdot \frac{\tau - 1}{\tau} \cdot k_\alpha \quad \text{and} \quad \Psi_2 = \Psi_3 = 0. \tag{74b}$$

When the *jet flow model* is used to calculate the vibration amplitude caused by vortex shedding or turbulent excitation, then the length l_1 from Eq. (74a) should be divided into three sections and the flow path length l into five sections as shown in Fig. 26. An example is given in Sect. 6.3.

In the *outlet flow region*, the last tube row, which is directly facing the nozzle, can be calculated with the model by Mohr [Eqs. (69–73)]; for the penultimate tube row, a similar approach can be used, with the exception, that a value $\psi_2 = 0.8$ should be used instead of ψ_2 from Eq. (72e). For all other tube rows, the velocity is usually considered uniform [10].

5.4.3 Window Region with Tubes

If the span length between the support plates is small compared with the shell diameter, i.e., for

$$l_m < d_1 \cdot 0.3/(\tau - 1), \tag{75a}$$

then it is acceptable to assume u = constant for the section m. If in contrast

$$l_m > d_1 \cdot 0.3/(\tau - 1), \tag{75b}$$

then velocity peaks appear in regions with *accelerated flow* at the edge of the support plate, i.e., at the peak of the mode shape of the window tube (see Fig. 25, Sect 2.2), which increase the level of vibration excitation [26]. The flow path length for the

first three tube rows in the window should be divided into two parts:

$$l_{m,2} = l_{m,1} = l_{m/2}. \tag{76}$$

The ratio of the two velocities is:

$$\Psi_{m,2}/\Psi_{m,1} = 1 + \frac{1.6 \cdot m^{1.6}}{d_1^{1.6}} - \frac{0.46 \cdot m^{1.6}}{d_1^{1.6}} \cdot \frac{d_1}{l_m \cdot (\tau - 1)}, \tag{77a}$$

and

$$1 \le \Psi_{m,2}/\Psi_{m,1} \le 2. \tag{77b}$$

If $l_m > 1.5\ d_1$, which occurs in some rare cases, then the length approached by flow l'_m is smaller than l_m:

$$l'_m = 0.2 \cdot l_m + 1.2 \cdot d_1 \le l_m. \tag{78}$$

Then l_m is divided into three partial sections and Eq. (76) can be used: $l_{m,3} = l_{m,2} = l'_m/2$. The value of $\Psi_{m,3}/\Psi_{m,2}$ can be calculated from Eqs. (77a) and (b) with l'_m instead of l_m; $\Psi_{m,1} = 0$.

The velocity can be assumed constant, u = constant, in sections with a decelerated flow (e.g., outlet flow region of a window) and for window tube rows after the third row.

5.5 Engineering Design Recommendations

Special attention for an effective engineering design is necessary in heat exchangers working near the critical velocity (stability ratio $K^* > 0.8$) or whose capacity is to be enlarged. The designer's goal should be to avoid peaks of velocity, especially in sections with maximum mode shapes or to reduce the mode shape maxima by the installation of additional support plates. A detailed vibration analyses should provide hints to the necessary measures.

5.5.1 General Remarks

The influence of the geometric and structural data on the critical velocity for fluid-elastic instability is described by the stability equation (26):

For gases:

$$u_{sk} \sim K(\tau) \cdot \frac{d_m^{1.5}}{l^2} \cdot E^{0.5} \cdot \left(\frac{s_R}{\rho_f}\right)^{0.5} \cdot \Lambda^{0.5}, \tag{79a}$$

for liquids:

$$u_{sk} \sim K(\tau) \cdot \frac{d_m^{1.5}}{l^2} \cdot E^{0.5} \cdot \left(\frac{s_R}{\rho_f}\right)^{\approx 0.35} \cdot \Lambda^{0.15}, \tag{79b}$$

with $d_m = 0.5 \cdot (d_a + d_i)$ average tube diameter,
$s_R = 0.5 \cdot (d_a - d_i)$ tube wall thickness.

Effective measures therefore include the reduction of the span length l or increase of d_m or s_R. A span length reduction normally leads only to an approximate linear increase of the critical volume flow $\dot{V}_k$. Raising Λ is also feasible, e.g., by reducing the boring clearances and increasing the thickness of the support plates, but this measure is only effective when the first or second modes (with large span lengths) are critical. If possible, the boring clearance at the tube supports should be $\Delta d_B \le 0.3$ mm [4]. But also in uncritical exchangers, Δd_B should be smaller than 0.6 mm, since otherwise tube supports tend to become inactive; this may result in fretting wear failures [5].

The proposed measures also provide a risk prevention of turbulence or vortex shedding excitations. Tie rods outside the bundle may be endangered by vortex shedding excitation and should be checked. They should not be installed at the center line of the nozzles.

5.5.2 Nozzle Inlet and Outlet Flow Region

The inlet flow should be as equally distributed as possible, especially when this section is critical, e.g., for flow paths $N \le 3$. This basically holds also for the outlet flow region, where the flow conditions are somewhat better. Some general recommendations are listed in the following:

- The distance between the bundle and nozzle h (see Fig. 27, point A) should be sufficiently large. Increasing this distance up to $h = 2.5 \cdot d_a$ leads to a substantial increase in the critical volume flow, whereas for $h > 2.5 \cdot d_a$ this influence becomes smaller [67, 68]. The model by Mohr describes the influence of h/d_a [see Sect. 5.4.2 and Eq. (70)]. For critical inlet flow regions without a partial support plate, this value is recommended:

$$\frac{h}{d_a} \ge 2. \tag{80}$$

- If a bundle shall include the maximum number of tube rows (i.e., fully packed with tubes), some tube rows with a chord length $s' < d_S$, resp. $h/d_a < (\tau - 0.5) \le 1$, should be removed.
- A louvre distributor can be installed under the nozzle (see Chap. O1, Fig. 21d), which divides the flow in axial or radial direction, depending on the geometric parameters [69]. It additionally provides a protection from the impingement of liquid droplets and is therefore a much better vibration design, than an impingement plate.
- The nozzles can be enlarged to reduce the inlet velocity and their minimum diameter can be chosen to avoid recirculation at the baffle plates. For example Eq. (72) gives:

$$\begin{aligned} \tau = 1.28 &: \ d_S \ge 0.37 \cdot l_m, \\ \tau = 1.40 &: \ d_S \ge 0.42 \cdot l_m, \\ \tau = 2.0 &: \ d_S \ge 0.57 \cdot l_m. \end{aligned} \tag{81}$$

If the above-mentioned measures are not feasible or not effective, it will be necessary to implement additional supports for the endangered tube rows:

- A partial support plate can be installed at the center of the nozzle, e.g., with the height H_1 and an overlap with the baffle plate as shown in Fig. 27. This is also advisable, when the baffle plate edge is positioned normal to the nozzle cross-section (point C in Fig. 27). In this case, the partial support plate protects the exterior tubes in the first tube rows (point B in Fig. 27) against the intensified diagonal flow.

5.5.3 Impingement Plates

Impingement plates protect the bundle from the impingement of liquid droplets (Chap. O1, Sect. 2.4), but normally they increase the risk of vibration excitation [69]. Therefore circular impingment plates should have a diameter of $d_P > 1.2 \cdot d_S$ and holes like a perforated plate. High local velocities arise at the radial edge of the plate (point A in Fig. 28), which coincides with the maximum amplitude of the mode shape. This endangers the exterior tubes in the first tube rows (point B in Fig. 28). In this case also, a partial support plate can provide additional support to these tube rows (point E in Fig. 28).

Additional measures are described below:

- The impingement plates with rectangular shape should be brought close to the shell wall (point C in Fig. 28) to avoid high radial velocities. Instead, high axial velocities arise at the supports, which can be beneficial for the reduction of the vibration excitation.
- Strengthened tubes or solid rods can be used in the first two or three tube rows. This solution is more advantageous with regard to vibration prevention than impingement plates.
- The above-mentioned louvre distributor is suitable for impingement prevention as well as for flow distribution.

5.5.4 Endangered Window Tubes

If window tubes are critical, then the following measures are feasible:

- Partial support plates bearing three or more of the first window tube rows and optionally overlapping with the baffle plate.
- Supporting grids (see Chap. O1, Fig. 22) to increase the damping and avoid high vibration amplitudes. They are

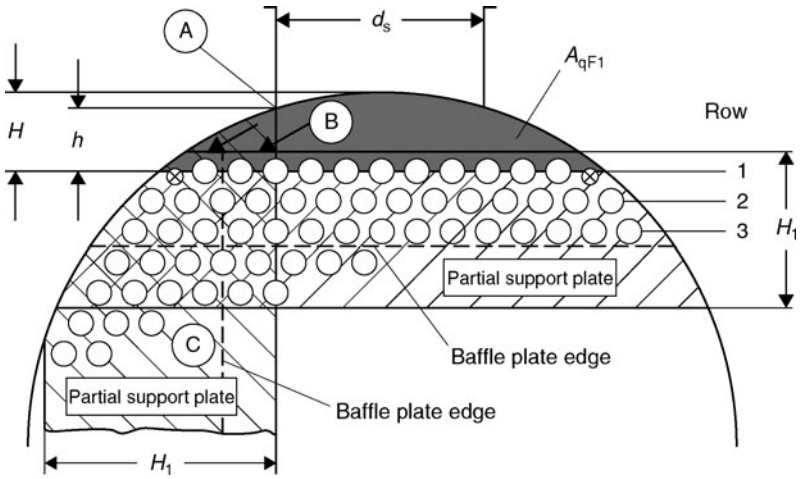

O2. Fig. 27. Partional tube support plates in the inlet and outlet flow region.

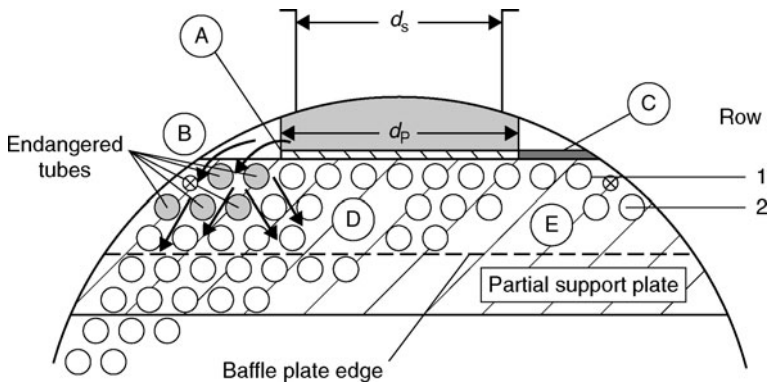

O2. Fig. 28. Impingement and partial support plates.

often installed in heat exchangers bundles with axial flow and large tube spans. The contraction of the cross-section area can be kept low by an axial offset of the grids. But greater clearances and the risk of inactive supports have to be considered.

- In especially critical cases, window tubes should be avoided altogether (see Chap. O1, Figs. 12 and 13).
- To prevent fretting wear, the distance between baffle plate and the first window tube row should be about $0.05 \cdot d_a$ and when the baffle plate overlaps the first tube row, the boring diameter of the half-round holes should be $d_B \geq 1.1 \cdot d_a$.

5.5.5 Bypass Flow through Open Flow Lanes

Open flow lanes in the center part or between bundle and shell wall (see Chap. O1, Fig. 16) cause a directional change of the flow; owing to the high flow resistance of the bundle, the flow velocity in these gaps can be substantially higher than within the bundle. Tubes adjacent to these gaps are therefore exposed to a higher vibration risk, especially the tubes at the end of the gaps, where a constriction leads to local high velocities.

- Boundary gaps can be considered by the boundary stream factor k_{RS} (see Sect. 5.2). In rectangular plane channels, the maximum loads of the exterior tubes have been measured at a gap width of $d_a(\tau - 1)/2$; these tube loads are found to be approximately 25% higher than the average of the considered tube row [26]. Therefore, the following difference between the shell and the outer tube limit d_H is recommended:

$$d_1 - d_H > 2d_a \frac{\tau - 1}{\sqrt{\tau}}. \qquad (82)$$

  The influence of the boundary gap width on the critical load of the outer tubes will be smaller with an increase in the difference $d_1 - d_H$, but the by pass flow will also increase.
- Vertical gaps should be avoided or closed by dummy tubes. The velocity in open flow lanes can be approximately estimated using the equation of continuity.
- Sealing strips or dummy tubes should be placed at the beginning of the open flow lanes and consecutively at distances of two or three tube rows (as described in Chap. O1 with regard to Fig. 16).
- In particular critical cases, endangered outer tubes with small gap widths (see point A in Fig. 23) should be removed.

6 Example Calculation

The critical shell-side volume flow of water has to be calculated for a heat exchanger, sketched in Figs. 29 and 30. The cold water on the shellside has an overpressure of $p_a = 10$ bar, the hot medium in the tubes $p_i = 5$ bar. The medium tube temperature is $\vartheta_R = 64°C$, i.e., $\Delta\vartheta_R = 44$ K higher than 20°C (stress free fitting condition), $\Delta\vartheta_M = 0$. The tubes are fixed in the tube sheets.

6.1 Fluid and Structural Data

Geometric data:

Inner diameter of the shell	$d_1 = 700$ mm
Outer diameter of the shell	$d_2 = 720$ mm
Cross-sectional area of shell wall	$A_M = 22\,305$ mm^2
Outer diameter of the tubes	$d_a = 25$ mm
Inner diameter of the tubes	$d_i = 21$ mm
Cross-sectional area of the tube wall	$A_R = 144.5$ mm^2
Tube layout angle	$\alpha = 30°$
Pitch ratio	$\tau = 1.4$
Tube support width	$b = 10$ mm
Boring diameter of holes in tube support plates	$d_B = 25.6$ mm
Window cutout height: baffle edge to shell	$H_u = 244$ mm
Distance: bundle to nozzle	$h = 60.9$ mm
Diameter of the baffle plates	$d_u = 695$ mm
Outer tube limit	$d_H = 690$ mm
Nozzle diameter	$d_S = 211$ mm
Distance: tube sheet to nozzle center	$l_S = 297.5$ mm
Cross-sectional flow area of the nozzle	$A_{qS} = 34\,967$ mm^2
Number of tube rows	$NRR = 18$
Number of tubes in the bundle	$n_R = 294$
Material and fluid data	
Tube sheet stiffness, interior tubes	$X_I = 0.5$
Tube sheet stiffness, exterior tubes	$X_A = 1.0$
Density of tube material	$\rho_R = 7850$ kg/m^3
Modulus of elasticity for tubes and shell	$E = 210{,}000$ N/mm^2
Poisson's ratio	$\nu = 0.3$
Thermal expansion coefficient	$\gamma_R = 1.18 \cdot 10^{-5}$ 1/K
Density of fluid in the tubes	$\rho_i = 900$ kg/m^3
Density of fluid in the shell	$\rho_f = 1000$ kg/m^3
Viscosity of water	$\nu_f = 1.0 \cdot 10^{-6}$ m^2/s

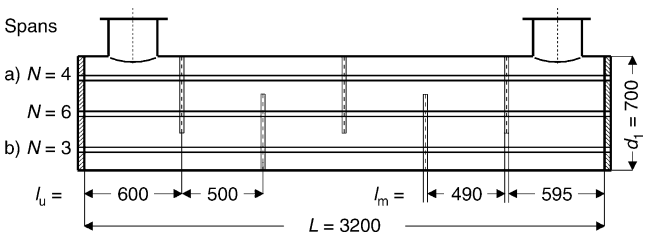

O2. Fig. 29. Sketch of the heat exchanger; dimensions are in mm.

Structural data:

Tube mass per unit length	Eq. (8a)	m_R = 1.446 kg/m
Hydrodynamic mass coefficient	Fig. 3	c_h = 2.5
Hydrodynamic mass per unit length	Eq. (8b)	m_h = 1.227 kg/m
Mass per unit length	Eq. (7)	m = 2.673 kg/m
Thermal expansion		$\gamma_R \cdot \Delta\vartheta_R = 51.92 \cdot 10^{-5}$
The exterior tubes are critical	Eq. (16f)	
Load bearing exterior tubes	Eq. (16b)	$n^*_{RA} = 63$
Minimal number of load bearing tubes	Eq. (16d)	$n_{RA0} = 30$
Axial force due to thermal expansion	Eq. (16a)	$F_{R\vartheta v} = -12\,434$ N
Axial force due to external forces	Eq. (16e)	$F_{Rp} = 650$ N
Total axial force	Eq. (15)	$F_R = -11\,784$ N

O2. Table 10. Influence of the support conditions on the fluid and structural data

Support conditions (see Fig. 29)	Support type:	a	b
Number of flow paths	M	6	6
Number of spans	N	4	3
Related span length	l (m)	1	1
End span length	X (m)	0.6	1.1
Mean span length, Eq. (20)	l_{am} (m)	0.867	1.067
Relative natural frequency, Table 2	$\bar{f}_1$	1.30	1.17
Equivalent length of buckling, Table 1	$\bar{l}_k$	1	1
Reference natural frequency, Eq. (10)	f^* (Hz)	43.2	43.2
First natural frequency, Eq. (9) without axial forces	f_1 (Hz)	56.2	50.5
Critical buckling force, Eq. (14)	$F_{R,k}$ (N)	19,959	19,959
Corrected natural frequency, Eq. (13)	$f_1(F_R)$ (Hz)	36.0	32.3
Viscous damping, Eq. (19)	$\Lambda_{v,1}$	0.0143	0.0150
Structural damping, Eq. (21)	$\Lambda_{Sl,1}$	0.0463	0.0405
Total damping, Eq. (22)	Λ_1	0.0606	0.0555
Mass-damping parameter, Eq. (24)	Δ_1	0.259	0.237
Critical velocity for fluid-elastic instability and i =1:			
30°-layout, Table 8, Eq. (26g)	u_{sk} (m/s)	2.09	1.85
60°-layout, Table 8, Eq. (26i)	u_{sk} (m/s)	1.32	1.17
Reduced critical velocity for 30°-layout, Table 9, Eq. (46a)	u_{sk} (m/s)	1.72	1.53

6.2 Fluid-elastic Instability

Endangered tube rows are RR 1 and RR2 due to the high inlet velocity and RR 13 due to the lowest frequency and with approximately constant loads in all flow paths (i.e., $\Delta S \approx 1$). Therefore, a first estimate of the critical volume flow is possible when analyzing tube row 13:

Tube row 13 *for the first mode, support type (b)*

Lowest cross-section flow area, Fig. 30	$A_{qs} = 0.092$ m^2
Reduced critical velocity, Table 10	$u_{sk} = 1.53$ m/s
Leakage flow factor, Eq. (67)	$k_{LF} = 0.85$
Partial flow factor, Eq. (68)	$k_{PF} = 1$
Boundary stream factor, Eq. (46)	$k_{RS} = 1$
Critical volume flow $\dot{V}_k \approx (1.53 \cdot 0.092)/0.85$, Table 10	$\dot{V}_k = 0.166$ m^3/s
A more accurate computation with the program [3] gives	$\dot{V}_k = \dot{V}_{k,IF} = 0.175$ m^3/s

Tube row 14 is unproblematic in relation to row 13, since $k_{PF} < 1$ and $k_{RS} = 1$ (no narrow boundary gap).

Tube row 2 *for the first mode, support type (a)*:
Tube row 2 is endangered by fluid-elastic instability, first by the inlet jet flow and secondly by the smallness of the boundary gap width of the outer tubes in rows 2 and 17 (see Fig. 30). In Fig. 31, the velocity distribution, due to the equations described in Sect. 5.4, are shown. In the following, the use of these equations will be demonstrated, but more details can be found in [10].

Inlet flow region, section $m = n = 1$ (see results in Table 11)

Eq. (70)	Y = 1.374
Eq. (69a)	$l_{1Mo} = l_{1,2} = 341.7$ mm
Eq. (71)	$f = 0.9165$
Eq. (69b)	$s_{1Mo} = s_{1,2} = 265.7$ mm
Eq. (69c)	$A_{qs1Mo} = A_{qs1,2} = 21603$ mm^2
Eq. (72a) and Fig. 26	$l_{2\,Mo} = 551.4$ mm $< l_1 = 595$ mm
	$l_{1,1} = l_{1,3} = 104.9$ mm
Eq. (72c)	$s_{2Mo} = 445.9$ mm $< s' = 504.8$ mm
Eq. (72d)	$A_{qs2Mo} = 44308$ mm^2
	$A_{qs1,1} = A_{qs1,3} = 22154$ mm^2
Eq. (72e)	$\psi_{1,1} = \psi_{1,3} = 0.423$
Eqs. (67), (68), and Table 9	$k_{LF} = k_{PF} = k_{IF} = 1$
Table 10	$u_{sk} = 1.72$ m/s

Mean sections n = 2–3 (or m = 2–5)

Due to the symmetry of modes and velocities, the four flow paths can be combined into two groups, as shown in Table 11:
first group n, r = 2,1/3,1 with accelerated flow,
second group n, r = 2,2/3,2 with decelerated flow.
The window cross-sectional areas A_{qF} and the gap cross-sectional areas A_{qs} can be taken from Fig. 30.

Eq. (67)	$k_{LF} = 1.04 \cdot \sqrt{0.668} = 0.85$
Eq. (68) and Fig. 30	$k_{PF} = 0.42$
Eq. (65) and Fig. 30	$\psi_{2,1} = 0.20$
Eq. (47)	$s_{RS,2} = 5.0$ mm
Eq. (47)	$s_{RS,3} = 13.4$ mm
Eq. (47a)	$n = 1.62$
Eq. (47)	$k_{RS,2} = 0.58$
Eqs. (46, 46a), Table 10 (Accelerated flow)	$u_{sk} = 1.72 \cdot 0.58 = 1.0$ m/s

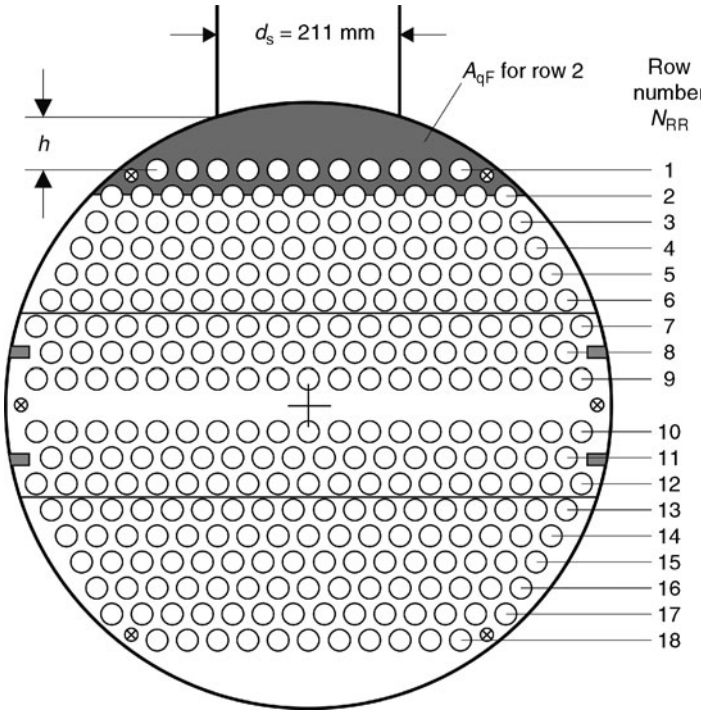

Row number N_{RR}	Window cross-section $A_{qF,i}$	Chord length s'	Tube gap cross-section A_{qs} for l_m = 490	Tube gap cross-section A_{qs} for l_m = 595
1	20419	438.5	61397	74553
2	28623	504.8	70669	85812
3	37626	550.7	77939	94641
4	47542	598.1	83731	101674
5	58088	631.0	88336	107265
6	69036	656.7	91932	111632
7	80159	676.0	94635	114914
8	A_{qFmax}			
9	74700			

O2. Fig. 30. Bundle cross-section view with window cross-sections A_{qF} [from Subchap. L1.5, Eqs. (50) to (52)], chord lengths s' and tube gap cross-sections A_{qs}; dimensions are in mm or mm^2.

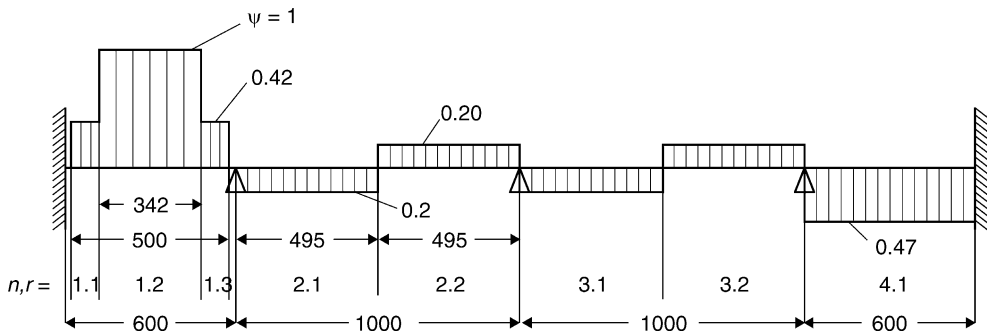

O2. Fig. 31. Axial distribution of flow velocity for tube row two; dimensions are in mm.

O2. Table 11. Sectional calculation of fluid-elastic instability for tube row 2

Sections		$l_{m,r}$	u_{sk}	$A_{qsm,r}$					$\Delta S_{m,r}$	$\frac{S_{m,r}}{u_{sk}^2} \cdot 10^3$	$\Psi \cdot \hat{u}_{sk}$ m/s
M, r	*n, r*	mm	m/s	m^2	k_{LF}	k_{PF}	k_{RS}	$\psi_{m,r}$	Mode 1		
Column		1	2	3	4	5	6	7	8	9	10
1,1	1,1	105	1.72	0.0221	1	1	1	0.42	0.0001	0.006	2.44
1,2	1,2	342	1.72	0.0216	1	1	1	1	0.0050	1.690	5.82
1,3	1,3	105	1.72	0.0221	1	1	1	0.42	0.0009	0.054	2.44
2,1/4,1	2,1/3,1	495	1.00	0.0714	0.85	0.42	0.58	0.20	0.4940	19.760	1.16
3,1/5,1	2,2/3,2	495	1.72	0.0714	0.85	0.42	1	0.20	0.4940	6.679	1.16
6,1	4,1	595	1.00	0.0858	1	1	0.58	0.47	0.0060	1.325	2.74
								$\sum$ =	1.00	29.514	

Equations (55) and (60): Spalte 9 $\sum_{m=1}^{M} \sum_{r=1}^{R} \frac{S_{m,r}}{u_{skm}^2} = 29.514 \cdot 10^{-3}$; $\frac{1}{\hat{u}_{skm}} = \sqrt{0.029514} = 0.1718$; $\hat{u}_{sk} = 1/0.1718 = 5.82$ m/s

Outlet flow region, section n = 4 (or m = 6)

$k_{LF} = k_{PF} = 1$; $\Psi_{4,1} = 0.470$; $u_{sk} = 1.0$ m/s

The results are summarized in Table 11. Values of $\Delta S_{m,r}$ for the first mode in column eight were roughly estimated by using Eq. (55b), Table 2, Eq. (12), and Fig. 5. The partial sections, which have the greatest influence on the excitation, are given in column 9 of the table:

The inlet flow region is uncritical, but the window regions with accelerated flow, *m*, *r* = 2,1/4,1, have the greatest influence, caused by the maximum mode shape in these regions and by the endangered outer tubes in the tube rows two and 17. But removing these tubes, i.e., $k_{RS} = 1$, is not necessary in this case, because the tube row 13 is the critical one and not tube row two.

From Eqs. (60) and (61), the maximum critical velocity and the critical volume flow of tube row two for the first mode are:

$$\hat{u}_{sk} = 1/0.1718 = 5.82 \text{ m/s},$$
$$\dot{V}_k = \dot{V}_{k,IF} = 0.234 \text{ m}^3/\text{s}.$$

Due to the low energy ratio S_1 it should be examined, whether higher modes could be critical for tube row two. A more accurate computation with a computer program [3] shows that the first mode is critical.

Tube row 1:

Tube row 1 is not endangered by fluid-elastic instability, due to the relative large distance of the bundle from the nozzle, h/d_a = 2.44 [Eq. (80)], and the inlet flow factor k_{IF} = 1.114 (from Table 9). But the influence of turbulent buffeting and vortex shedding has to be examined at the critical and the operating volume flows, as shown in Table 12, because the nozzle diameter d_S = 211 mm is smaller than the recommended value by Eq. (81): $d_S \geq 0.42 \cdot l_m$ = 250 mm.

Summing up of the results:

The operating volume flow should be about 85% of the critical volume flow: $\dot{V}_k = 0.175$ m^3/s, i.e., $\dot{V}_B = 0.15$ m^3/s. The stability ratios K^* [Eq. (58)] for the tube rows one, two, and 13 are shown in Table 12 at the volume flows of 0.15 and 0.17 m^3/s. The maximum amplitudes for turbulent buffeting $\hat{A}_t = \sqrt{2} \cdot \hat{A}_{tRMS}$ and vortex shedding $\hat{A}_w$ (computed by [3]) are also inserted in this table. The critical values have been grey shaded.

When using a heat exchanger with a shell compensator or a floating head, i.e., with a tube frequency of 50.5 instead of 32.3 Hz for tube row 13, then the capacity could be increased by a factor 50.5/32.3 = 1.56 to $\dot{V}_k = 0.26$ m^3/s and $\dot{V}_B = 0.22$ m^3/s. A similar effect could be achieved by swapping the working fluids, i.e., the cold water inside the tubes and the hot fluid in the shellside.

O2. Table 12. Stability ratios and amplitudes for the tube rows 1, 2, and 13 [3]

Operating volume flow			$\dot{V}_B = 0.15$ m^3/s			$\dot{V}_B = 0.17$ m^3/s		
RR	d_S (mm)	$\dot{V}_k$ (m^3/s)	K^* (%)	$\hat{A}_t/d_a$ (%)	$\hat{A}_w/d_a$ (%)	K^* (%)	$\hat{A}_t/d_a$ (%)	$\hat{A}_w/d_a$ (%)
1	211	0.254	59	0.70	1.00	67	0.90	2.40
1	240	0.294	51	0.46	0.07	58	0.60	0.42
2	211	0.234	64	0.25	0.21	73	0.31	0.13
13	211	0.175	86	0.09	0.01	97	0.15	0.06

6.3 Vibration Amplitudes Caused by Vortex and Turbulence Excitations

With a pitch ratio τ = 1.4 and the number of spans $N \geq 3$, the vibration amplitudes should be lower than 1% of the tube diameter (Sect. 4.3.1). Table 12 shows the vibration amplitudes excited by vortex shedding and turbulent buffeting: For the small nozzle diameter d_S = 211 mm, the amplitudes in the first tube row approach the danger limit for lock-in when the volume flow comes up to the critical flow rate of 0.17 m^3/s. At this flow rate, both tubes, row one by vortex shedding ($\hat{A}_w/d_a$ = 2.4%) and tube row 13 by fluid-elastic instability (K^* = 97%) are endangered.

As shown in Fig. 32, the third and the fourth modes are dominant for vortex shedding in this case. The amplitudes are too high to avoid long term and possibly also short term damages. Therefore, d_S has to be enlarged to a minimum of 240 mm, as recommended by Eq. (81). Then the amplitudes become lower than 0.60% of d_a as shown in Table 12.

***Tube row 1**, inlet flow region, third mode*:

To demonstrate the calculation procedures, the amplitude of the first tube row shall be determined for ***vortex shedding excitation*** of the third mode of vibration ($\tilde{A}_{w3}/d_a$ = 1.37) as shown in Fig. 32. First the Strouhal numbers are obtained from Fig. 15 and the resulting critical vortex excitation velocities according to Eq. (36) are shown in Table 13.

The Strouhal number Sr_{w2} in the 30° layouts and at τ = 1.4 is active only for Reynolds numbers <75,000 and then only in the first three tube rows [39]. The Reynolds number for the third

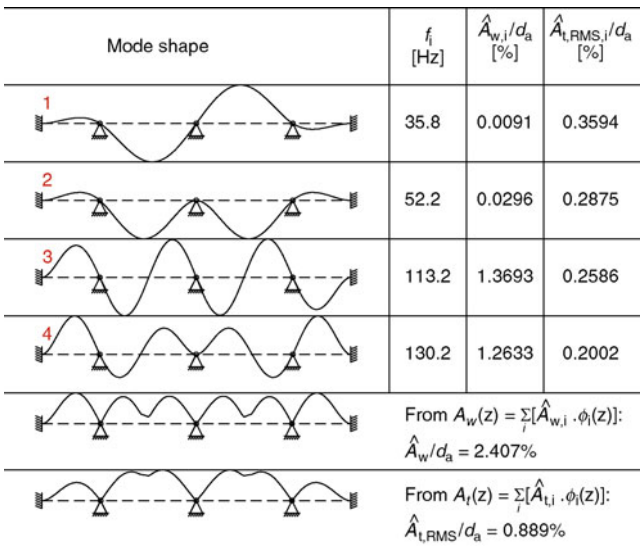

O2. Fig. 32. Mode shapes and related amplitudes for vortex shedding and turbulent buffeting of the first tube row at $\dot{V}_B = 0.17$ m^3/s [3].

mode is $Re_{w2} = 4.68 \cdot 0.025/1 \cdot 10^{-6} = 117{,}000$ and therefrom 70% due to Eq. (37) gives a limiting value of Re = 82,000, which is larger than 75,000. Therefore, the only critical resonance velocity in the third mode is 6.78 m/s. Such a high velocity can only be reached in the inlet flow region. To determine the velocity distribution in the inlet region, the *jet flow model* Eq. (74) is used:

Eq. (74a)	$l_{1Mo} = 298$ mm
Eq. (74b)	$A_{qs1Mo} = 0.0254$ m^2
	$u_{s1Mo} = 6.70$ m/s
Eq. (39)	$\eta = 0.988$
Eqs. (40) and (41)	$k_A(\eta) = f_{VA} = 0.946$
Eq. (55b), Table 14, and Fig. 5	$\Delta S = 0.13 \cdot 0.85 = 0.11$
Eqs. (19), (21), and (22)	$\Lambda_3 = 0.0241$
Eq. (38)	$\Delta_3 = 0.104$
Fig. 20	$c_y = 0.03$
Table 1	$\bar{\Phi} = 0.565$
Eq. (38) : resonance value	$A_{w3}/d_a = 0.0522$
Corrected value	$k_A \cdot A_{w3}/d_a = 0.0494$
Eq. (63)	$J_{w3} = 1$
Eq. (63) Weighted value	$\tilde{A}_{w3}/d_a = 1.64\%$

The so calculated amplitude is higher than the value from Fig. 32. The reason is the assumption of a constant equivalent velocity with the length of 298 mm, which was derived considering the fluid-dynamic instability. In reality, the peak velocity exists along the length of the nozzle diameter, approximately 211 mm, and starts to decrease gradually outside the nozzle cross-section. For analyzing the vortex shedding excitation caused by a variety of critical velocities, it is necessary to know the real velocity distribution and its gradients in the relevant sections, in order to have a reasonable estimate of the resonance flow velocities and their excitation levels. This can be achieved by means of the amplitude weighting factor $k_{A,i,j}$ according to the Eqs. (39) and (40).

O2. Table 13. Critical velocities for vortex shedding u_{swji}, m/s

	Sr_{wj} | Mode i	1	2	3	4
RR 1	$Sr_{w1} = 0.417$	2.14	3.13	6.78	7.80
	$Sr_{w2} = 0.604$	1.48	2.16	–	–

It is possible to reconstruct an approximate representation of the velocity distribution. For example, the inlet and outlet flow sections can be divided into five sections, and for every section a linear velocity gradient between a lower u_{szu} and an upper velocity u_{szo} is defined: these will be calculated by means of u_{sB} in the adjacent sections. So it is possible to estimate *amplitude weighting factors* (Eqs. 39 and 40), as shown in Table 14.

In the present case, the calculated approach length (l_{1Mo} = 298 mm) is divided into three parts (1,1–1,3) with $l_{1,1} = l_{1,3} = 0.2 \cdot l_{1Mo} = 60$ mm, $\Psi_{1,1} = \Psi_{1,3} = 0.88$, and $\Psi_{1,2} = 1$. Other details can be obtained from Table 14. The resulting amplitude for vortex excitation in the third mode (see column 9) is $\tilde{A}_{w3}/d_a = \sqrt{0.000177} = 0.0133$ or *1.33%*, which is in good agreement with the result of 1.37% in Fig. 32.

As an example, the calculation of the amplitude for ***turbulent buffeting*** in the third mode: $\tilde{A}_{t,RMS,3}/d_a = 0.26\%$ from Fig. 32, will be illustrated for the inlet flow section with values from columns three and eight in Table 14. The excitation in the inlet flow section is dominant, whereas the other sections contribute only a small amount of energy.

Eq. (29)	$Sr_{i1,2} = 0.4026$
Eq. (29)	$Sr_{i1,1+1,3} = 0.4572$
Eq. (30b)	$S_{F1,2} = 0.00655$
Eq. (30b)	$S_{F1,1+1,3} = 0.00346$
Eq. (32)	$(A_{t,RMS,3}/d_a)_{1,2} = 0.00770$
Eq. (32)	$(A_{t,RMS,3}/d_a)_{1,1+1,3} = 0.00463$
Table 14	$\Delta S_{1,2} = 0.076$
Table 14	$\Delta S_{1,1+1,3} = 0.034$
Eq. (63)	$\Delta S_{1,2} \{(A_{t,RMS,3}/d_a)_{1,2}\}^2 = 4.506 \cdot 10^{-6}$
Eq. (63)	$\Delta S_{1,1+1,3} \{(A_{t,RMS,3}/d_a)_{1,1+1,3}\}^2 = 0.729 \cdot 10^{-6}$
	$\sum = 5.235 \cdot 10^{-6}$
Eq. (63)	$\tilde{A}_{t,RMS,3}/d_a = 0.23\%$

The difference between this value and the value of 0.26 from Table 12 results from the flow excitation in the outlet flow region, which has not been considered in this calculation. The computation for all relevant tube rows, spans, modes and for variable design parameters is rather complex, and therefore the use of a computer program, such as [3], is recommended, which is anyway necessary for the estimation of the partial energy ratios ΔS.

O2. Table 14. Detailed calculation of the vortex-induced vibration amplitude in the third mode for tube row one at the inlet flow section, $u_{sw3} = 6.78$ m/s

	$l_{m,r}$ (mm)	$A_{qs}(10^3 \cdot m^2)$	u_{sB} (m/s)	u_{su}/u_{so} (m/s)	η_u/η_o(–)	$\Delta\eta$ (–)	k_A (–)	ΔS (–)	$\Delta S \cdot k_A^2 \cdot (A_{w3}/d_a)^2$
m,r	1	2	3	4	5	6	7	8	9
1,1	60	5.08	6.19	3.10/6.61	0.46/0.97	0.51	0.161	0.010	$0.007 \cdot 10^{-4}$
1,2	178	15.24	7.03	6.61/7.03	0.97/1.04	0.07	0.919	0.076	$1.746 \cdot 10^{-4}$
1,3	60	5.08	6.19	3.10/6.61	0.46/0.97	0.51	0.161	0.024	$0.017 \cdot 10^{-4}$
$\sum$	298	25.40						0.110	$1.770 \cdot 10^{-4}$
1	595	74.56						0.130	

7 Symbols

Symbol	Description (unit)
A	amplitude (m)
A	area (m^2)
$A_M = \left(d_2^2 - d_1^2\right) \cdot \pi/4$	cross-sectional area of shell wall (m^2)
A_q	flow cross-sectional area (m^2)
$A_R = \left(d_a^2 - d_i^2\right) \cdot \pi/4$	cross-sectional area of tube wall (m^2)
a	speed of sound (m/s)
b	tube-support width (m)
c	spring stiffness (N/m)
c_h	hydrodynamic mass coefficient (−)
c_y	dynamic lift coefficient (−)
d	diameter (m)
d_1	inner diameter of exchanger shell (m)
d_2	outer diameter of exchanger shell (m)
d_H	outer tube limit (m)
E	modulus of elasticity (N/m^2)
F	force (N)
FRR	tube row in window (−)
f	frequency, function (Hz, −)
$\bar{f}_i$	relative natural frequency (−)
H	height of a window cutout (m)
h	lowest distance between bundle and nozzle (m)
I	area moment of inertia (m^4)
J	joint-acceptance coefficient, correlation factor (−)
$K(\tau)$	stability constant (−)
K^*	stability ratio (−)
k	correction factor (−)
L	total length of tube (m)
l	partial length of tube, span length between supports (m)
l_c	correlation length (m)
l_m	length of a flow path (m)
$\bar{l}_k$	relative equivalent length of tube for buckling (−)
l_S	distance tube sheet and nozzle centre (m)
l_u	distance of baffle plates (m)
M	mass (kg)
M	number of flow paths (−)
m	mass/unit length (kg/m)
m_h	hydrodynamic added mass/unit length (kg/m)
N	number of tube spans (−)
NRR	number of tube rows (−)
N_{RR}	tube row number (−)
n	exponent (−)
n_R	number of tubes in the bundle (−)
n_R^*	number of load bearing tubes (−)
P	exponent of the mass-damping parameter (−)
p	gauge pressure (N/m^2)
R	number of partial sections in a tube span or flow path (−)
r	damping constant (N · s/m)
Re	Reynolds number (−)
RR	tube row (−)
S	energy ratio (−)
s	gap width, wall thickness, width of flow area (m)
s'	chord length of a tube row in the shell cross section (m)
S_F	normalized power spectral density of fluid force (−)
Sr	Strouhal number (−)
Sr_i	dimensionless turbulence resonance frequency (−)
ST	Stokes number (−)
t	tube spacing (m)
u_∞	upstream flow velocity in x-direction (m/s)
$u^\star$	dimensionless gap velocity = $u_s/(f \cdot d_a)$ (−)
u_s	gap velocity in x-direction (m/s)
$\hat{u}_s$	maximum value of gap velocity $u_s(z)$ (m/s)
$\tilde{u}_s$	equivalent gap velocity (m/s)
u_τ	bundle velocity = $u_\infty \cdot \tau / (\tau - 1)$ (m/s)
$\dot{V}$	volumetric flow rate (m^3/s)
v	velocity in y-direction (m/s)
w	velocity in z-direction (m/s)
X	span length at tube ends (m)
X	dimensionless plate stiffness (–)
x	co-ordinate of tube position (m)
Y	jet expansion factor under the nozzle (–)
y	co-ordinate of tube position (m)
α	tube layout angle (°)
γ	linear thermal expansion coefficient (1/K)
Δ	mass-damping parameter (–)
$\Delta d_B = d_B - d_a$	boring clearance at the tube supports (m)
$\Delta l_S = l_S - 0.5\, l_m$	eccentricity of the nozzle position (m)
ΔS	partial energy ratio (–)
ϑ	temperature (K)
$\Delta\vartheta = \vartheta - \vartheta_0$	difference in average wall temperature during operating conditions ϑ from that corresponding to stress free conditions ϑ_0 (K)
$\eta = f_w/f_i$	frequency ratio (–)
ε	volume fraction (–)
$\dot{\varepsilon}_g$	volume fraction of gas flow (–)
ζ	damping coefficient (–)
Λ	logarithmic decrement of damping (–)
ν	kinematic viscosity m^2/s
ν	Poisson's ratio (–)
ρ	density (kg/m^3)
τ	pitch ratio (–)
Φ_i	normalized ith vibration mode shape (–)
Ψ	normalized distribution function of flow velocity (–)

Indices

A	exterior tubes of the bundle, amplitude
a	outer side of tubes, acoustic
B	holes in tube support plates, operating conditions
F	window
f	fluid in shell side
g	gas phase
gl	gas/liquid (two-phase)
H	outer tube limit
i	mode i
I	interior bundle tubes
IF	inlet flow region
j	integer referring to vortex Strouhal number
K	shell compensator
k	critical value for instability
LF	leakage flow
l	liquid phase
M	material damping, shell
Mo	model
m	average, flow section number, integer
n	tube span number, integer
o	upper value
P	impingement plate
PF	partial flow
q	cross-section
R	tube
Ra	border
RMS	root mean square
RR	tube row
RS	boundary flow
r	sectional number of a flow path or a tube span, integer
S	structural damping, nozzle
s	gap between the tubes
t	turbulent buffeting
u	flow dividing baffle plate, lower value
V	viscous damping
VA	dynamic response amplification
w	vortex shedding, critical value for vortex shedding
x	co-ordinate in flow direction, normal to the tube axis
y	co-ordinate normal to the flow direction and the tube axis
z	co-ordinate along the tube axis
α	tube layout
τ	bundle
Φ	mode

8 Bibliography

1. Blevins RD (1990) Flow-induced vibration, 2nd edn. Van Nostrand Reinhold, New York
2. Chen SS (1987) Flow-induced vibration of circular cylindrical structures. Hemisphere Publishing, Washington, DC
3. Gelbe H, Mohr U, Schröder K (2002) Schwingungen in Wärmeübertrager-Rohrbündeln. Computerprogramm "GOOD VIBRATION"nach VDI-Wärmeatlas, Kap. Oc., TU Berlin
4. Jahr M (1995) Einflüsse von Strukturparametern und Strömungsverteilung auf das Schwingverhalten mit Luft angeströmter Rohrbündel. Dissertation, Technical University of Berlin, Berlin, D83
5. Yeh YS, Chen SS (1990) Vibration of component cooling water heat exchangers. ASME PVP Conference, Nashville, TN, vol 189, pp 153–164
6. Gorman DJ (1988) Exact analytical solutions for free vibration of steam generator U-tubes. J Press Vess Technol 110(11):422–429
7. TEMA-Standards of Tubular Exchanger Manufactures Association (1987) 7th edn. New York
8. Gasch R, Knothe K (1989) Strukturdynamik. Bd. 2: Kontinua und ihre Diskretisierung. Springer-Verlag, Berlin
9. AD-Merkblatt B5 (1991) Ebene Böden und Platten nebst Verankerungen. Beuth Verlag, Berlin
10. Gelbe H, Schröder K, Ziada S (2006) Schwingungen in Wärmeübertrager-Rohrbündeln. VDI-Wärmeatlas 10. Aufl. Springer-Verlag, Berlin, Oc, pp 1–36
11. Parker R (1978) Acoustic resonances in passages containing banks of heat exchanger tubes. J Sound Vib 57:245–260
12. Ziada S, Oengören A, Bühlmann ET (1989) On acoustical resonance in tube arrays. Part I: experiments. J Fluid Struct 3:293–314
13. Pettigrew MJ, Goyder HGD et al (1986) Damping of multi-span heat exchanger tubes. Part I: in gases. ASME PVP Conference, III, Chicago, IL, vol 104, pp 81–87
14. Pettigrew MJ, Rogers RJ, Axisa F (1986) Damping of multi-span heat exchanger tubes. Part II: in liquids. ASME PVP Conference, III, Chicago, vol 104, pp 89–98
15. Andjelić M (1988) Stabilitätsverhalten querangeströmter Rohrbündel mit versetzter Dreiecksteilung. Dissertation, University of Hannover, Hannover
16. Andjelić M, Popp K (1989) Stability effects in a normal triangular cylinder array. J Fluid Struct 3:165–185
17. ConnorsHJ (1970) An experimental investigation of the flow-induced vibration of tube arrays in cross-flow. Ph.D. Thesis, University of Pittsburgh, PA
18. Chen SS, Jendrzejczek JA (1982) Stability of tube arrays in cross- flow. Nuclear Eng Design 75:351–373
19. Weaver DS, Fitzpatrick JA (1987) A review of flow-induced vibration in heat exchangers. Proceedings of International Conference on Flow-induced Vibrations, Bowness-on-Windermere, vol A1, pp 1–17
20. Pettigrew MJ, Taylor CE (1991) Fluid-elastic instability of heat exchanger tube bundles. Review and design recommendations. Proceedings of International Conference Institution of Mechanical Engineers on Flow-induced Vibration, Brighton, vol C 416/015, pp 349–368
21. Schröder K, Gelbe H (1999) New design recommendations for fluid-elastic instability in heat exchanger tube bundles. J Fluid Struct 13(3): 361–379
22. Troidl H (1986) Strömungsinduzierte Schwingungen querangeströmter Rohrbündel bei versetzter und fluchtender Rohranordnung. Dissertation, Technical University, München
23. Gelbe H, Schröder K (1998) Bestimmung der fluidelastischen Instabilität in querangeströmten Rohrbündeln. Chem Ing Techn 70(1/2):80–88
24. Chen SS, Jendrzejczyk JA (1981) Experiments on fluid instability in tube banks subjected to liquid cross-flow. J Sound Vib 78(3):355–381
25. Yeung HC, Weaver DC (1983) The effect of approach flow direction on the flow-induced vibrations of a triangular tube array. ASME J Mech Design 105:76–82
26. Mohr U (2001) Einfluß von Geometrie und Geschwindigkeitsverteilung auf die Schwingungsanregung von Rohrbündel-Wärmeübertragern. Fortschr.-Ber. VDI, Reihe 11, Nr. 304, VDI-Verlag, Düsseldorf
27. Mohr U, Schröder K, Gelbe H (2000) The effect of approach flow direction on the fluid-elastic instability of tubes in triangular tube arrays. Proceedings of 7th International Conference on Flow-induced Vibration, Luzern (Switzerland). Balkema, Rotterdam, pp 481–488
28. Pettigrew MJ, Taylor CE, Kim BS (2000) The effect of tube bundle geometry on vibration in two-phase cross-flow. Proceedings of 7th International Conference on Flow-induced Vibration, Luzern (Switzerland). Balkema, Rotterdam, pp 561–568
29. Pettigrew MJ et al (2001) The effect of tube bundle geometry on vibration in two-phase cross-flow. J Press Vess Technol 123:414–420
30. Ulbrich R, Mewes D (1994) Vertical, upward gas-liquid two-phase flow across a tube bundle. Int J Multiphas Flow 20(2):249–272
31. Feenstra P, Judd RL, Weaver DS (1995) Fluid-elastic instability in a tube array subjected to two-phase R-11 cross-flow. ASME PVP Conference on Flow-induced Vibration, Hawaii, vol 298, pp 13–27
32. Mann W, Mayinger F (1995) Flow-induced vibration of tube bundles subjected to single- and two-phase cross-flow. Proceedings of 2nd International Conference on Multiphase Flow, Kyoto, vol 4, pp 9–15

33. Mann W (1997) Schwingungsanregungen in Rohrbündeln durch Dichteschwankungen in Dampf-Flüssigkeits-Strömungen. Fortschritts - Ber. VDI, Reihe 6, Nr. 359. VDI-Verlag, Düsseldorf
34. Feenstra P, Weaver DS, Judd RL (2000) Modelling two-phase flow-excited fluid-elastic instability in tube arrays. Proceedings of 7th International Conference on Flow-induced Vibration, Luzern (Switzerland). Balkema, Rotterdam, pp 545–554
35. Pettigrew MJ, Tromp JH et al (1989) Vibration of tube bundles in two-phase cross-flow. Part 1: hydrodynamic mass and damping. Part 2: fluid-elastic instability. Trans ASME J Press Vess Technol 111:466–487
36. Pettigrew MJ, Taylor CE et al (1994) Vibration of tube bundles in two-phase Freon cross-flow. ASME PVP Conference on Flow-induced Vibration, Minneapolis, MN, vol 273, pp 211–226
37. Pettigrew MJ, Taylor CE (2003) Vibration analysis of shell-and-tube heat exchangers: an overview – Part 1: flow, damping, fluidelastic instability. J Fluid Struct 18(5):469–483
38. Ziada S, Oengören A (1992) Acoustic and tube resonances in tube bundles. Bericht Nr. SAK/TB92–63. Sulzer Innotec, Wintherthur
39. Oengören A, Ziada S (1995) Vortex shedding, acoustic resonance and turbulent buffeting in normal triangular tube arrays. 6th International Conference on Flow-induced Vibration, London, Balkema, Rotterdam, pp 295–313
40. Romberg O (1998) Zum Turbulenzeinfluß auf das Schwingungsverhalten querangeströmter Rohrbündel. Fortschr.- Bericht VDI, Reihe 11, Nr. 267. VDI- Verlag, Düsseldorf
41. Taylor CE, Pettigrew MJ (1999) Random excitation forces in heat exchanger tube bundles. ASME PVP Conference on Flow-induced Vibration, Boston, MA, vol 389, pp 35–42
42. Oengören A, Ziada S (1992) Unsteady fluid forces acting on a square tube bundle in air cross-flow. ASME International Symposium on Flow-induced Vibration and Noise, Anaheim, CA, vol 1, pp 55–74
43. Au-Yang MK (1999) Joint and cross acceptances for cross flow-induced vibration. Part I and II. ASME PVP Conference on Flow-induced Vibration, Boston, MA , vol 389, pp 17–33
44. Axisa F, Antunes J et al (1988) Random excitation of heat exchanger tubes by cross-flow. Flow-induced vibration of cylinder arrays in cross-flow. ASME Publ Nr G 442:23–46
45. Axisa F (1992) Random excitation of heat exchanger tubes by two-phase cross-flow. Proceedings of International Symposium on Flow-induced Vibration, Anaheim, CA, vol 1, pp 119–140
46. Pettigrew MJ, Taylor CE (2003) Vibration analysis of shell-and-tube heat exchangers: an overview – Part 2: vibration response, fretting-wear, guidelines. J Fluid Struct 18(5):485–500
47. Pettigrew MJ, Yetisir M et al (1999) Prediction of vibration and fretting-wear damage: an energy approach.ASME PVP Conference on Flow-induced Vibration, Boston, MA, vol 389, pp 283–290 (see also pp 273–282)
48. Ziada S, Bolleter U, Chen YN (1984) Vortex shedding and acoustic resonance in a staggered-yawed array of tubes. ASME Symposium on Flow-induced Vibrations, New York, vol 2, pp 227–242
49. Ziada S (2006) Vortex shedding and acoustic resonance in heat exchanger tube bundles. J Braz Soc Mech Sci Eng 28:186–199
50. Oengören A, Ziada S (1997) Flow periodicity and acoustic resonance in parallel triangular tube bundles. 4th International Symposium on Fluid-structure Interactions, Aeroelasticity, Flow-induced Vibration and Noise. Dallas, TX. ASME AD 53–2, II (1997) pp 183–192
51. Ziada S, Oengören A (2000) Flow periodicity and acoustic resonance in parallel triangular tube bundles. J Fluids Struct 14: 197–219
52. Ziada S, Oengören A (1992) Vorticity shedding and acoustic resonance in an in-line tube bundle. Part I: vorticity shedding. J Fluid Struct 6(3):271–292
53. Ziada S, Oengören A (1993) Vortex shedding in an in-line tube bundle with large tube spacings. J Fluid Struct 7:661–687
54. Pettigrew MJ, Gorman DJ (1981) Vibration of heat exchanger tube bundles in liquid and two-phase cross-flow. Flow-induced vibration design guidelines. ASME PVP 52:89–110
55. Weaver DS (1993) Vortex shedding and acoustic resonance in heat exchanger tube arrays. Technology for the 90s, Chapter 6. ASME Publication, New York, pp 776–810
56. Pettigrew MJ (1981) Flow-induced vibration phenomena in nuclear power station components. Power Ind Res 1:97–133
57. Ziada S, Oengören A, Bühlmann ET (1989) On acoustical resonance in tube arrays. Part I: experiments. J Fluid Struct 3(3):293–314
58. Oengören A, Ziada S (1992) Vorticity shedding and acoustic resonance in an in-line tube bundle. Part II: acoustic resonance. J Fluid Struct 6(3): 293–309
59. Chen YN (1968) Flow-induced vibration and noise in tube bank heat exchangers due to von Karman streets. ASME J Eng Ind 90:134–146
60. Fitzpatrick JA (1986) A design guide proposal for avoidance of acoustic resonances in in-line heat exchangers. ASME J Vib Acoust Stress Reliab Des 108:296–300
61. Ziada S, Oengören A, Bühlmann ET (1989) On acoustical resonance in tube arrays. Part II: damping criteria. J Fluid Struct 3(3):315–324
62. Chen YN, Young WC (1974) Damping capability of tube banks against vortex-excited sonic vibration. ASME J Eng Ind 96:1072–1075
63. Eisinger FL, Sullivan RE, Francis JT (1992) A review of acoustic vibration criteria compared to inservice experience with steam generator in-line tube banks. ASME International Symposium on Flow-induced Vibration and Noise, Anaheim, CA, vol 4, pp 81–95
64. Eisinger FL, Francis JT, Sullivan RE (1994) Prediction of acoustic vibration in steam generator and heat exchanger tube banks. ASME PVP Conference on Flow-induced Vibration, Minneapolis, MN, vol 273, pp 67–83
65. Connors HJ (1978) Fluidelastic vibration of heat exchanger tube arrays. ASME J Mech Design 100:347–353
66. Goyder HGD (1992) A practical method for assessing tube vibration in heat exchangers. ASME International Sympoisum on Flow-induced Vibration and Noise, Anaheim, CA, vol 1 (HTD-Vol 230/NE-Vol 9), pp 237–260
67. Mohr U, Gelbe H (1999) Influence of the geometry in tube bundle heat exchangers on the velocity distribution and the vibration excitation. ASME PVP Conference on Flow-induced Vibration, Boston, MA, vol 389, pp 1–8
68. Mohr U, Gelbe H (2000) Velocity distribution and vibration excitation in tube bundle heat exchangers. Int J Thermal Sci 39:414–421
69. Leyh T (1993) Strömungsinduzierte Rohrbündelschwingungen in einem gasdurchströmten realen Wärmeübertrager. Dissertation, Technical University of Berlin, Berlin
70. Weaver DS, Lian HY, Huang XY (1993) Vortex shedding in rotated square tube arrays. J Fluid Struct 7:107–121
71. Blevins RD (1979) Formulas for natural frequency and mode shape. Van Nostrand Reinhold, New York
72. Axisa F, Villard B et al (1984) Vibration of tube bundles subjected to air-water and steam-water cross-flow. Preliminary results on fluid-elastic instability. Proceedings of ASME Symposium on Flow-induced Vibrations, New Orleans, LA, vol 2, pp 269–284
73. Pettigrew MJ, Gorman DJ (1978) Vibration of heat exchange components in liquid and two-phase cross-flow. Proceedings of BNES, International Conference on Vibration of Nuclear Plants, Keswick. Proceedings of BNES Paper 2.3
74. Polak DR, Weaver DS (1994) Vortex shedding in normal triangular tube arrays. ASME PVP Conference on Flow-induced Vibration, Minneapolis, MN, vol 273, pp 145–156
75. Weaver DS, Yeung HC (1984) The effect of tube mass on the flow-induced response of various tube arrays in water. J Sound Vib 93:409–425
76. Zukauskas A, Katinas V (1980) Flow-induced vibrations in heat exchanger tube banks. IUTAM Symposium on Practical Experiences with Flow-induced vibrations, Karlsruhe(Germany) 1979. Springer-Verlag, Berlin
77. Baylac G, Bai B, Gregoire JP (1973) Study of flow and acoustic phenomena in a tube bank. International Symposium on Vibration Problems in Industry, Keswick, Proceedings of UKAEA/NPL Paper, vol 219, pp 1–36
78. Rae GJ, Wharmby JS (1987) Strouhal numbers for in-line tube arrays. Int. Conf. on Flow Induced Vibrations. Bowness-on-Windermere (Great Britain) 1987. Proc. BHRA Pap. E4, pp. 233–242
79. Clasen P, Gregorig R (1971) Eín Schwingungskriterium eines querangeströmten Rohres. Teil 4: Schwingversuche in einem fluchtenden Rohrbündel. Chem Ing Tech 43:982–985
80. Grotz BJ, Arnold FR (1956) Flow-induced vibrations in heat exchangers. Department of Mechanical Engineering, Stanford University, Ca (USA). Report. No. 31, AD 104568

Construction of Heat Exchangers

O1 Hints on the Construction of Heat Exchangers

Günther Kirchner
BASF SE, Ludwigshafen, Germany

1 Heat Exchangers

The following factors are important in selecting the most suitable heat exchanger for any of the numerous applications that may arise in chemical and process engineering:

- the operating temperature and pressure,
- differences in product temperatures,
- corrosion,
- leakage and safety aspects,
- phase conversion,
- economy,
- space requirements.

Particular attention has been devoted to these aspects in the following description of the various types of heat exchangers.

VDI-GVC (ed.), *VDI Heat Atlas*, DOI 10.1007/978-3-540-77877-6_67,

1.1 Construction Codes and Operation

In Germany, the construction of heat exchangers is subject to the provisions of the national boiler and pressure vessel code [1]. The legal requirements for their inspection and their performance as pressure vessels are considered to be met if the corresponding specifications in the relevant design codes (in Germany: *Druckgeräterichtlinie 97/23/EG* [2], *AD 2000-Regelwerk* [3]) are satisfied. The regulations also refer to the pertinent (*DIN*) standards.

Acceptance and routine performance tests that are specified in the regulations [4] are supervised by specialized bodies [in Germany: e.g., *Technischer Überwachungsverein* (*TÜV*)]. They are analogous to the performance tests described in the *Standard Testing Procedure for Heat Exchangers* compiled by the *American Institute of Chemical Engineers* (*AIChE*).

2 Shell-and-Tube Heat Exchangers

Shell-and-tube heat exchangers are comparatively easy to construct and are very versatile. They can be used for gases and liquids over a wide range of temperatures and pressures and in phase conversion, i.e., condensation and evaporation. Consequently, they are widely accepted in many branches of industry, particularly in the chemical industry and power stations.

2.1 Nomenclature and Standards

Guides to the nomenclature used in various national codes and standards (i.e., DIN 28 183) are given in the form of drawings, an example of which is presented below (Fig. 1). This drawing lists the main components of a shell-and-tube heat exchanger with two stationary heads.

Currently available English translations of some German (*DIN*-) standards, that relate to shell-and-tube heat exchangers, are listed in the appendix. In common with other national codes, they can be supplemented by *TEMA* standards [5], although these are specifically related to *American Society of Mechanical Engineers* (*ASME*).

2.2 Types

2.2.1 Shell-and-Tube Heat Exchangers with Two Fixed Tube Sheets

In this design, the two tube sheets are welded onto the shell (Fig. 2). As a result of this inflexible connection, the stresses caused by differences between the shell-side and tube-side temperatures cannot be relaxed. If the differences are big and the stresses are thus excessively high, an expansion joint may be fitted into the shell.

Under these circumstances, the tube sheets are no longer supported by the shell and must therefore be of a more robust design. An example is shown in Fig. 3.

2.2.2 Shell-and-Tube Heat Exchangers with Floating Head

Only one tube sheet in a floating head shell-and-tube heat exchanger is fixed to the shell and the other is free to move within the shell. Thus, differential expansion between the shell and the tubes does not present any problems. The sole purpose served by the movable tube sheet and its dished head is to baffle flow on the tube side. Since the tube bundle can be withdrawn from the shell, floating-head heat exchangers are mainly used in applications where the outsides of the tubes have to be frequently cleaned. In this case, square tube pitch is an advantage. If fouling of the inner surfaces of the tubes is anticipated, the fixed dished end can be flanged instead of welded (Fig. 4).

2.2.3 U-Tube Shell-and-Tube Heat Exchangers

As can be seen from Fig. 5, the U-tube heat exchanger has only one tube sheet, into which both ends of the tubes are inserted. The only means available for cleaning the inner surfaces of the tubes is by chemicals. The outer surfaces,

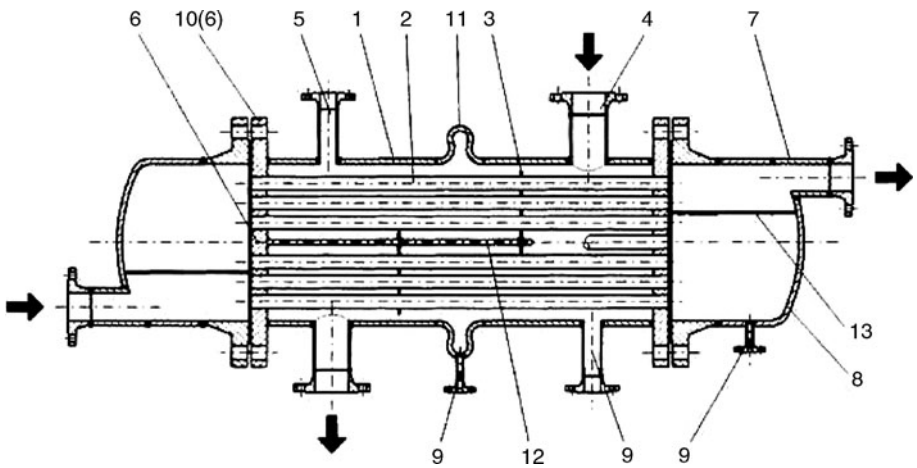

O1. Fig. 1. Parts of a shell-and-tube heat exchanger with two tube sheets and an expansion joint in the shell. (1) Shell, (2) inner tube, (3) segmental baffle; support plate, (4) shell nozzle, (5) vent connection, (6) tube sheet, (7) dished head nozzle, (8) dished head, (9) drain connection, (10) stationary head flange, (11) expansion joint, (12) tie rods, (13) pass partition.

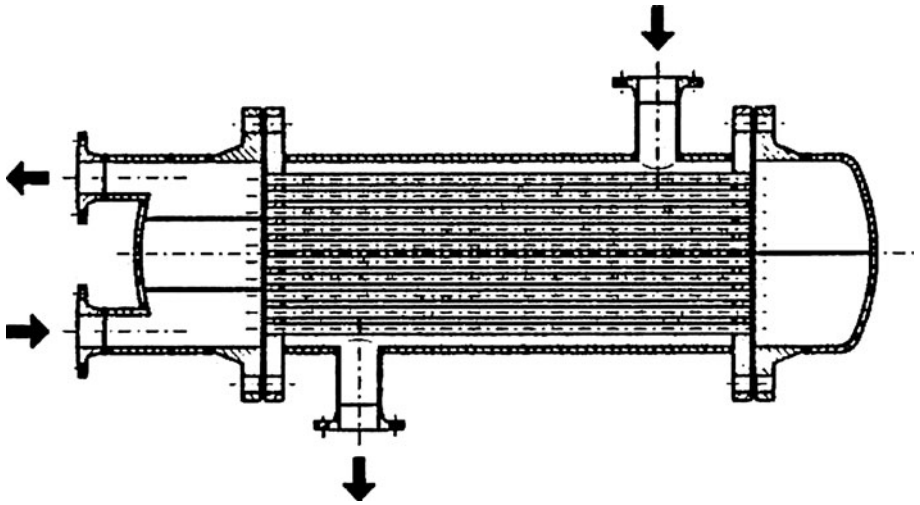

O1. Fig. 2. Four-pass shell-and-tube heat exchanger with two fixed tube sheets.

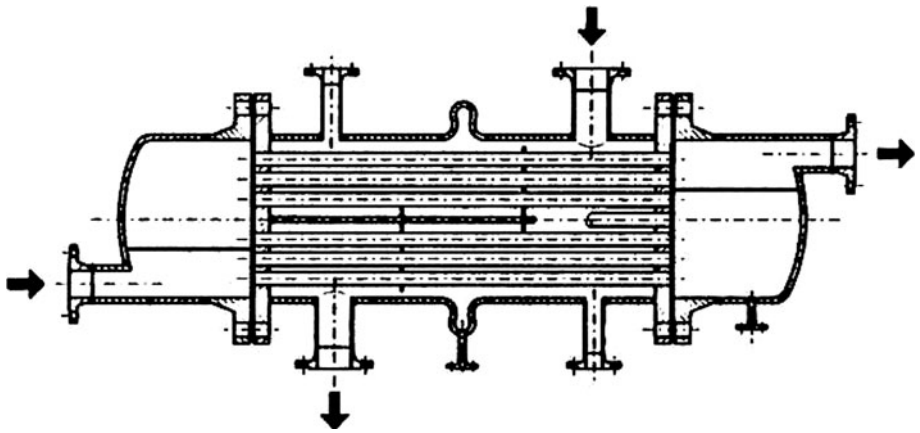

O1. Fig. 3. Shell-and-tube heat exchanger with expansion joint.

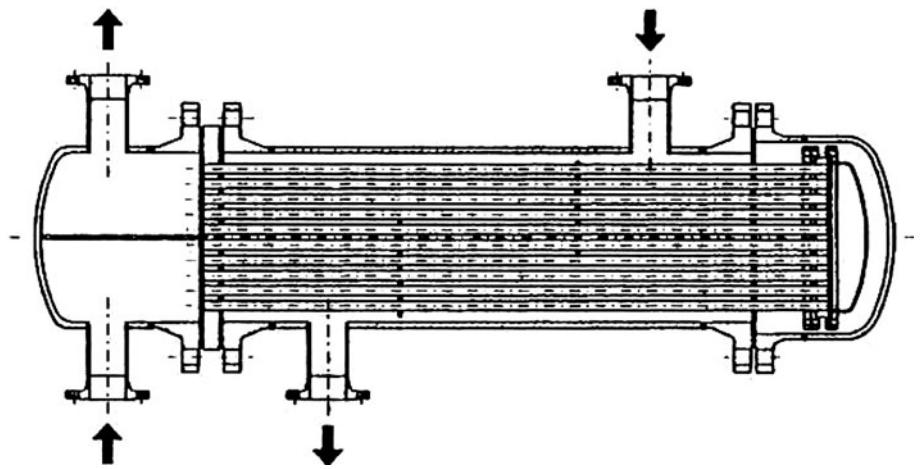

O1. Fig. 4. Shell-and-tube heat exchanger with floating head.

however, can be cleaned mechanically, because the tube bundle can be removed from the exchanger. The tubes with the smallest bending radius are those closest to the center line of the heat exchanger. If this radius is less than a given minimum, the first row of tubes must be arranged cross-wise (cf. Fig. 6). The smallest bending radius is determined by wall thickness, diameter, and material of the tube. Table 1 gives minimal bending radii for various tube diameters for carbon steel and for

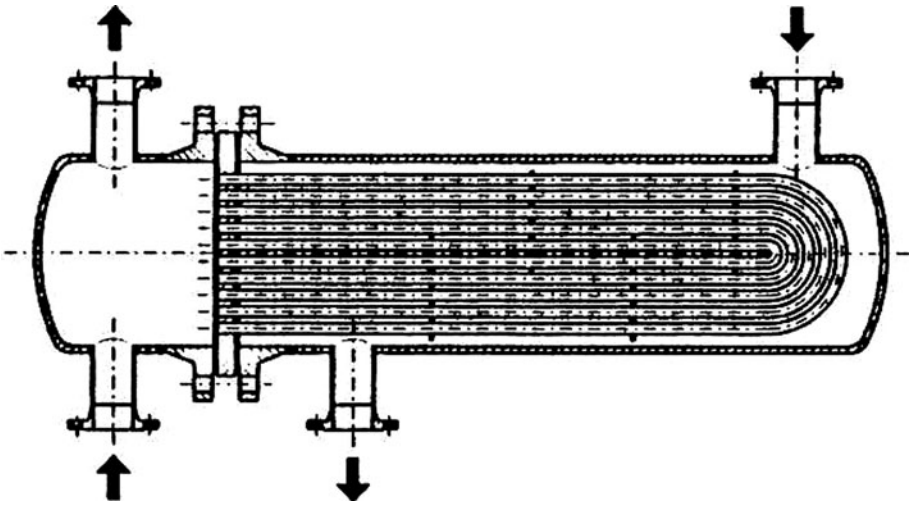

O1. Fig. 5. Shell-and-tube heat exchanger with U-tubes.

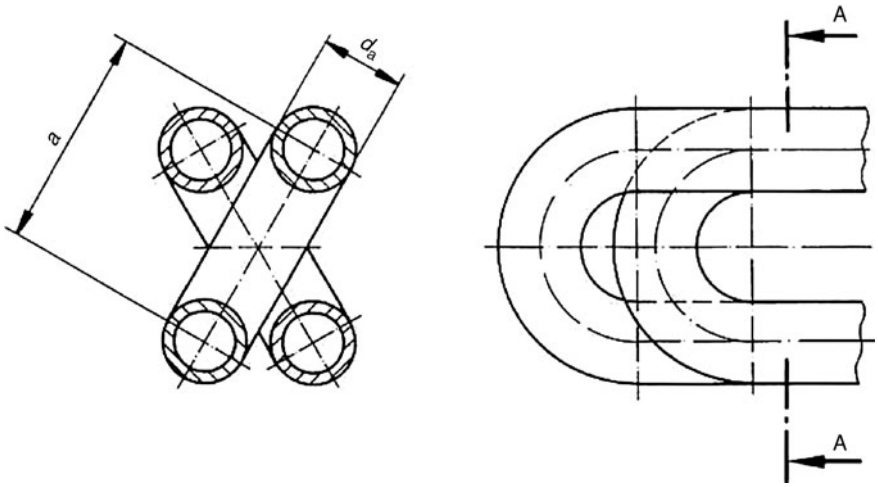

O1. Fig. 6. Arrangement of U-tubes.

O1. Table 1. Minimal radii of curvature for U-tubes with wall thickness *s*, in mm

Outer diameter d_o in mm	Smallest radius of curvature for U-tubes with wall thickness *s* in mm				
	s = 1.2	1.6	2.0	2.6	3.2
16	30	24	20	–	–
20	47	34	26	23	–
25	–	51	37	35	27
30	–	62	42	38	35
38	–	–	52	47	42

CrNi-steel. Examples of specifications for steel U-tubes are those given in DIN 28 178.

Tube bundles with floating head or U-tubes can be fitted in vessels or large tanks of any given design, as is illustrated in Fig. 7. They can be used to heat or evaporate the liquid within the vessel.

2.3 Design Considerations

2.3.1 Flow Patterns in Shell-and-Tube Heat Exchangers

The first step in designing a shell-and-tube heat exchanger is to decide which fluid is to flow inside the tubes and which outside, i.e., on the shell side. The flow pattern depends primarily on thermodynamic and fluid dynamic aspects and on the permissible pressure drop. The choice is also affected by design criteria. Thus, the fluid selected for tube-side flow would be that at the higher pressure, tends towards higher fouling, or necessitates an expensive material of construction because of its very corrosive effect. Fluids whose physical properties entail low heat transfer coefficients should flow on the shell side.

2.3.2 Geometric Considerations

The geometry of a shell-and-tube heat exchanger should be designed to permit optimum flow velocities on both the tube and shell side. This aim is usually realized by computer programs. The input data and the data to be optimized include the properties of the fluids, the length and other dimensions of the tubes, the tube spacing, the maximum allowable pressure drop, and the most economic flow rate.

2.3.3 Flow Velocities

Heat transfer coefficients can generally be enhanced by raising the flow velocity, but this necessarily entails a higher pressure drop. An improvement in heat transfer and the associated reduction in transfer area, i.e., low equipment costs, are obtained at the expense of higher pump or compressor outputs. Consequently, costs optimization is required to determine the economic optimum flow velocity.

Another consideration is the reduction of fouling by ensuring that the flow velocity is not less than a given minimum, which depends on the specific properties of the fluid. Thus, if river water flows on the tube side, the velocity should not be <1 m/s, and values of 1.5–2.5 m/s should be aimed at. The average velocities on the shell side should be about 0.8 m/s for liquid fluids. An upper limit is imposed on the flow velocity by vibration, cavitation, and erosion.

The maximum velocity in gas streams should not exceed 20 m/s at atmospheric pressure and 70 m/s in vacuo. In the case of wet steam, lower velocities are recommended. In these cases, the tubes should be protected against direct impingement of the vapor flow. Dependent on the pressure in the condenser, steam velocities in the vapor channels should be between 30 and 70 m/s [6].

2.3.4 Multiple-Pass Operation

The velocity can be increased and/or the flow path can be lengthened if the tube bundle is divided into two or more groups by

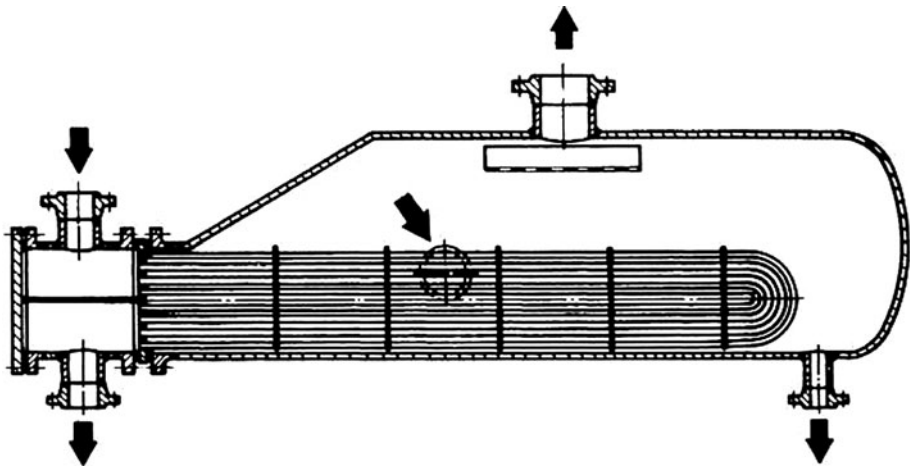

O1. Fig. 7. Shell-and-tube heat exchanger, kettle-type reboiler.

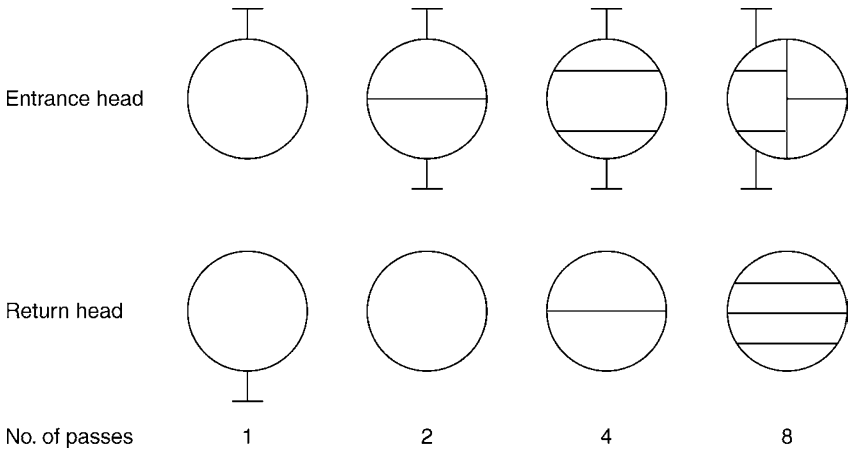

O1. Fig. 8. Typical pass layouts in multiple-pass heat exchangers.

inserting pass partitions in the dished head and thus diverting the stream of fluid on the tube side. The number of passes in standard designs is one, two, four, or eight.

Figure 8 shows the pass layouts of the partitions in the dished heads of multiple-pass shell-and-tube heat exchangers. The partitions should be arranged so that the number of tubes is roughly the same in each pass.

2.3.5 Inner Tubes, Length, and Wall Thickness of Tubes

The outer diameters specified in the German standard on seamless alloy and carbon steel tubes for use in shell-and-tube heat exchangers (DIN 28180) are 16, 20, 25, 30, and 38 mm.

The chemical industry favors the tubes of 25 mm outer diameter, which have a wall thickness of 2 mm.

Tubes of smaller diameter are mainly used in mechanical engineering for coolers and radiators.

The wall thickness depends on the design value (obtained from engineering codes, e.g., *AD Merkblätter*), the material to be used (i.e., on costs considerations), and the operating conditions (erosion, corrosion, and vibration). It usually lies between 1.2 and 3.2 mm. Reference values for the number of tubes, the heat transfer area, and the outer tube limit (OTL) are listed against the shell diameter in Tables 2–4.

2.3.6 Tube Pitch

The tube spacing largely influences the fluid velocity on the shell side and thus the pressure drop and heat transfer. The figures specified in German standards (DIN 28182) are listed in Table 5. It can be seen that they depend on the tube outer diameter d_o and the means adopted for expanding the tubes into the tube sheets. The minimum feasible pitch depends on the method of tube end attachment, the material of construction or the tube/tube sheet pairing, the tube wall thickness, and the tolerances for machining.

O1. Table 2. Number of tubes and number of passes, heat transfer area, and outer tube limit (OTL) of shell-and-tube heat exchangers with two fixed tube sheets (dimensions in mm)

		Nominal shell diameter													
		150	200	250	300	350	400	500	600	700	800	900	1000	1100	1200
Tube outer diameter: 25 Triangular pitch: 32 DIN 28 184, Part 1	No. of tubes	14	26	44	66	76	106	180	258	364	484	622	776	934	1124
	No. of passes	2	2	2	2	2	2	2	2	2	2	2	2	2	2
	Heat transfer area in m^2/m	1.1	2.0	3.5	5.2	6.0	8.3	14.1	20.3	28.6	38.0	48.9	61.0	73.4	88.3
	OTL	143.2	191	247.7	298	316.3	372.5	478.3	575.5	672	771	868	966	1058	1159
	No. of tubes	–	–	–	–	68	88	164	232	324	432	556	712	860	1048
	No. of passes	–	–	–	–	4	4	4	8	8	8	8	8	8	8
	Heat transfer area in m^2/m	–	–	–	–	5.3	6.9	12.9	18.2	25.4	33.9	43.7	55.9	67.5	82.3
	OTL	–	–	–	–	325	368.6	481.4	573	666	772	866	966	1055	1160

O1. Table 3. Number of tubes and number of tube-side passes, heat transfer area and outer tube limit (OTL) of shell-and-tube heat exchangers with two fixed tube sheets (dimensions in mm)

		Nominal shell diameter													
		150	200	250	300	350	400	500	600	700	800	900	1000	1100	1200
Tube outer diameter: 20 Triangular pitch: 25 DIN 28 184, part 4	No. of tubes	26	48	76	92	100	140	256	376	532	724	936	1196	1436	1736
	No. of passes	2	2	2	4	8	8	8	8	8	8	8	8	8	8
	Heat transfer area in m^2/m	1.6	3.0	4.7	5.7	6.2	8.7	1.6	23.6	33.4	45.4	58.8	75.1	90.2	109
	OTL	151	199.3	248.4	297.8	328.8	373.3	485.5	573.7	671.2	769.6	868.5	969.9	1059.7	1162.9
Tube outer diameter: 16 Triangular pitch: 20	No. of tubes	36	60	96	128	164	228	404	–	–	–	–	–	–	–
	No. of passes	2	4	4	8	8	8	8	–	–	–	–	–	–	–
	Heat transfer area in m^2/m	1.8	3.0	4.8	6.4	8.2	11.4	20.3	–	–	–	–	–	–	–
	OTL	147.4	198	252.6	299.6	330.8	377.5	485	–	–	–	–	–	–	–

O1. Table 4. Number of tubes and number of tube-side passes, heat transfer area, and outer tube limit (OTL) of shell-and-tube heat exchangers with welded or flanged floating heads (dimensions in mm)

		Nominal shell diameter													
		150	200	250	300	350	400	500	600	700	800	900	1000	1100	1200
Tube outer diameter: 25 Triangular pitch: 32 DIN 28 190 (welded floating heads)	No. of tubes	–	18	28	40	52	70	128	–	–	–	–	–	–	–
	No. of passes	–	2	2	2	2	2	2	–	–	–	–	–	–	–
	Heat transfer area in m^2/m	–	1.41	2.2	3.14	4.08	5.5	10.1	–	–	–	–	–	–	–
	OTL	–	167.7	211.3	255.5	288.2	328	434.7	–	–	–	–	–	–	–
Tube outer diameter: 25 Square pitch: 32 DIN 28 191 (flanged floating heads)	No. of tubes	10	18	32	46	42	70	122	172	248	344	432	560	688	840
	No. of passes	2	2	2	2	4	4	4	8	8	8	8	8	8	8
	Heat transfer area in m^2/m	0.785	1.41	2.51	3.61	3.3	5.5	9.58	13.5	19.5	27.0	33.9	44.0	54.0	66.0
	OTL	125.6	167.7	226.8	268.2	292.8	349.3	450	539.4	639.0	738.9	827.4	931.8	1025.2	1125.4

O1. Table 5. Tube pitch specified in DIN 28 182 (dimensions in mm)

Outer diameter of inner tube *d*	Tube pitch *t* for attaching tubes to tube sheet	
	by welding, expanding or combinations with welding (usual case)	by welding
16	21	20
20	26	25
25	32	30
30	38	36
38	47	45

2.3.7 Estimation of the OTL and the Tube Spacing Plan

The tubes in shell-and-tube heat exchangers with fixed tube sheets are mostly spaced in a triangular pattern. The number that can thus be accommodated within a given circumscribed circle (OTL) is greater than that achieved with a square pitch. The tube pitch patterns that can be obtained are shown, together with the relevant pitch angle, in Fig. 9. Both triangular and square patterns can be arranged either through or around the center point of shell-and-tube heat exchangers that are completely filled with tubes and without cleaning lanes. Each case must be considered on its own merits in deciding to which arrangement preference should be given, i.e., how the space within the shell can be best utilized.

The OTL for a given tube count z and pitch t in the geometry shown in Fig. 10 can be obtained from the following relationship:

$$\mathrm{OTL} = \sqrt{f_1 z t^2 + f_2 z^{1/2} t + d_o}. \quad (1)$$

The numerical value for the constant f_1 is 1.1 for triangular and 1.3 for square tube pattern and that for f_2 can be obtained from Table 6. Equation (1) is valid for shells completely filled with tubes. The number of tubes corresponding to empty sections of the shell must be added to the given number z. The constant f_2 applies to lanes for pass partitions with seals of uniform width, viz. 10 mm, but not for U-tube heat exchangers. Equation (1) is sufficiently accurate if $z/t > 10\ \mathrm{mm}^{-1}$.

2.3.8 Baffles on Shell side

Segmental baffles are usually fitted within the shell to guide the stream of fluid. Designs of baffles for shells completely filled with tubes are shown in Figs. 11 and 14. The streams flow alternately in the axial and transverse directions over the outer surfaces of the tubes.

The value selected for the average velocity between the cross-current segmental baffles should be roughly the same as that in the window for the axial stream.

Figures 12 and 13 show segmental baffles in shells incompletely filled with tubes ("no tubes in window" design). The doughnut and disc baffles illustrated in Fig. 14 allow a tubeless central and peripheral zone, with the result that axial flow over the outer surfaces of the tubes can be avoided, as is evident from Fig. 15. Oblique flow over the tubes can be reduced if baffle plates are arranged between the segmental baffles, as is illustrated in Fig. 13.

In order to minimize leakage flows, the baffle pitch e between segment baffles in Figs. 12 and 14 should not be <20%, and the baffle cut (window opening segment height) f not <15% of the

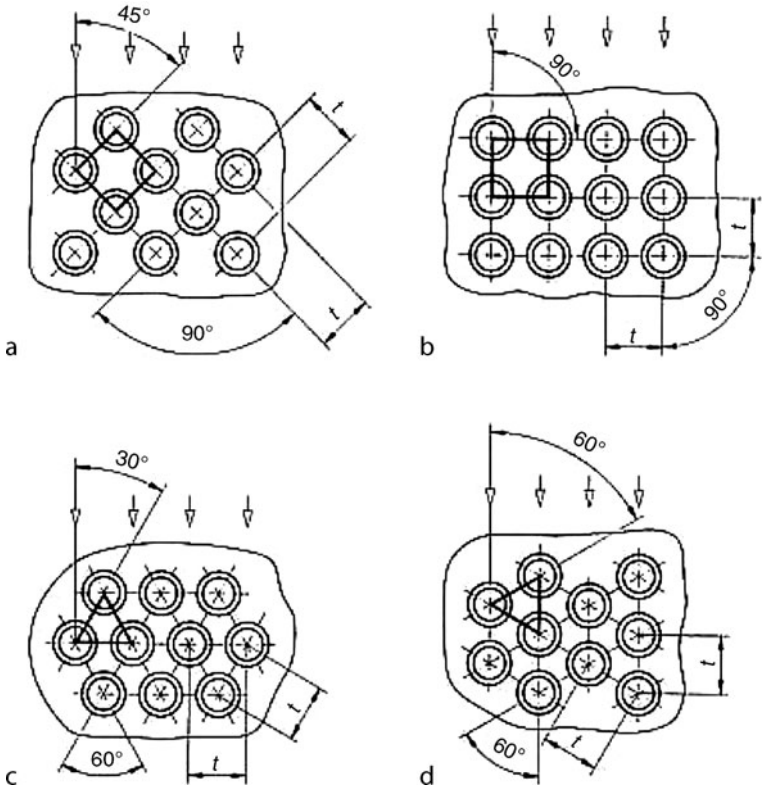

O1. Fig. 9. Square (**a**, **b**) and triangular (**c**, **d**) tube pitch patterns. The inflow angle is shown in each case.

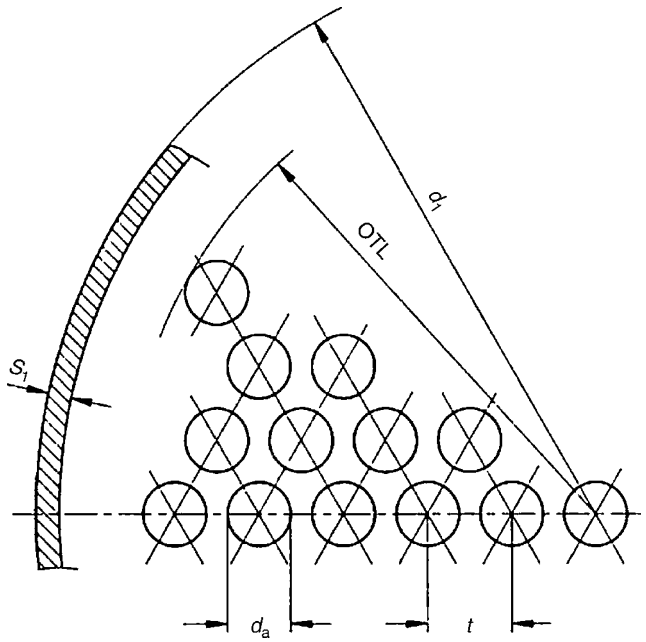

O1. Fig. 10. Estimation of outer tube limit (*OTL*).

O1. Table 6. Constant f_2 for the estimation of the outer tube limit (dimensions in mm)

No. of passes	1	2	4	8
f_2 in mm	0	22	70	105

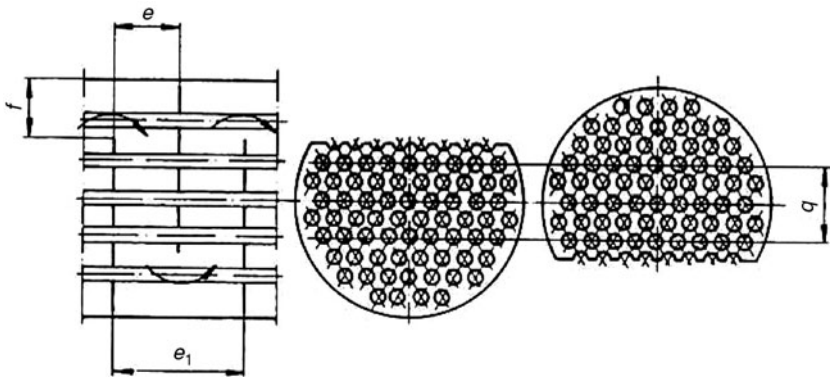

O1. Fig. 11. Segmental baffle in heat exchanger completely filled with tubes.

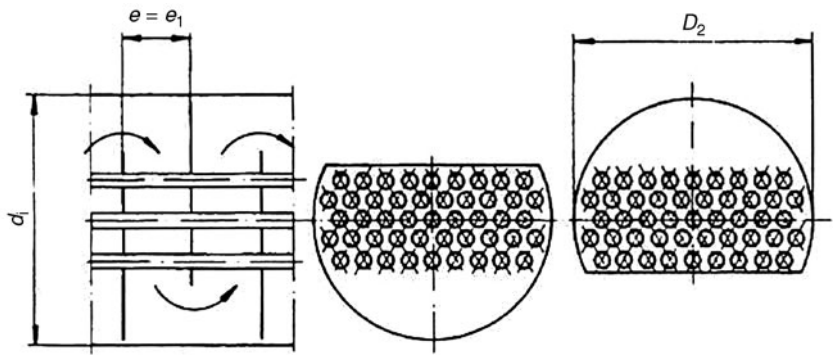

O1. Fig. 12. Segmental baffle in heat exchanger partly filled with tubes.

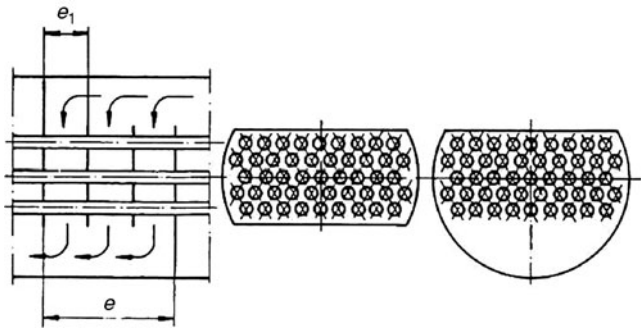

O1. Fig. 13. Segmental baffle with sheet-metal deflector.

shell inner diameter d_i. The baffle cut f should not exceed 45% of the shell inner diameter.

The openings in the doughnut baffle shown in Fig. 14 should account for at least 20% of the cross-sectional area of the shell.

In certain cases, the flow cross-section in the shell has to be split in the axial direction in order to – for example – induce a countercurrent in a U-tube heat exchanger. Under these circumstances, the shell is divided by a longitudinal baffle.

2.3.9 Support Plates

At very high volume flow rates, crossflow is no longer feasible, because cross-flow velocities become too high and vibration and/or erosion occurs. Shell-side flow in heat exchangers will then be in the axial direction, and the shell-side fluid will flow parallel to the tubes. In this case, the tubes are supported in grids built up of flat sections.

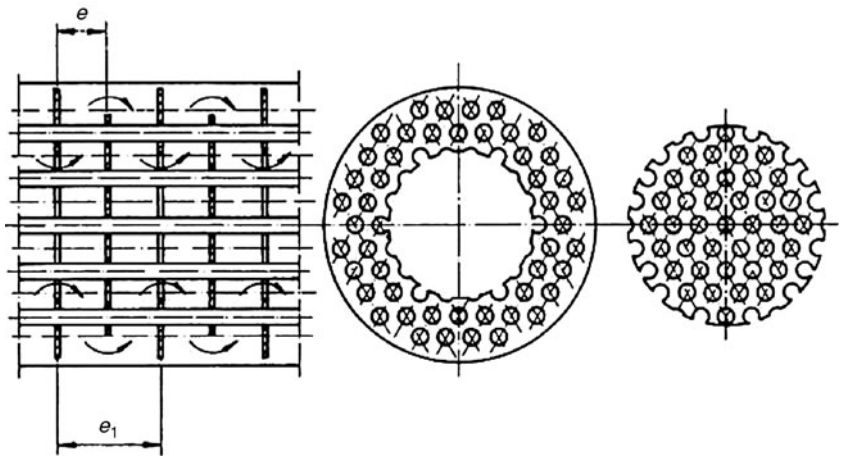

O1. Fig. 14. Disc and doughnut baffles in heat exchanger completely filled with tubes.

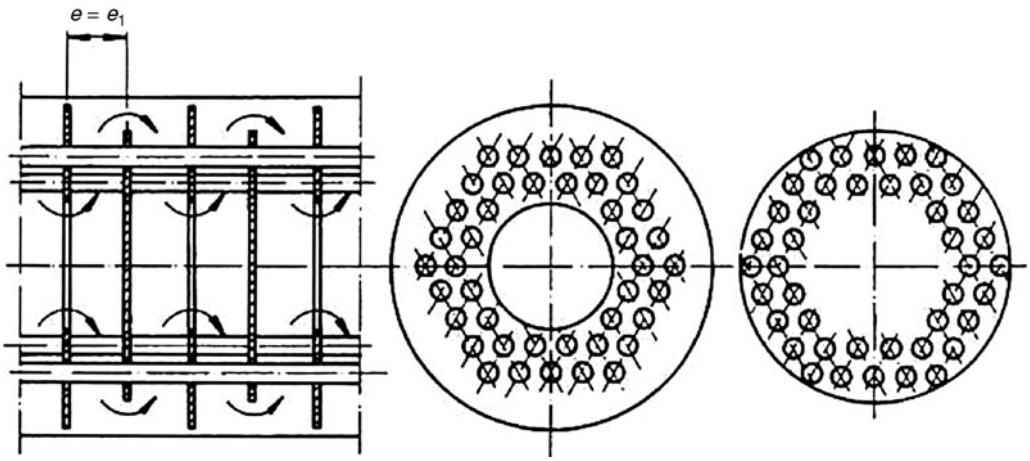

O1. Fig. 15. Disc and doughnut baffles in heat exchangers with no tubes in window.

2.3.10 Sealing Strips and Dummy Tubes

Dummy tubes, sealing strips, spacers, and segmental baffles can be seen in Fig. 16, which shows the arrangement of tubes in an eight-pass shell-and-tube heat exchanger. A measure that is generally adopted to reduce bypass streams is to insert dummy tubes in the pass partition lanes that lie in the direction of flow; and to insert a pair of sealing strips behind every fifth tube bank in the cross-flow zones. The design of floating head shell-and-tube heat exchangers entails that an annular zone of up to 40 mm width may be free of tubes within the shell. In this case, special attention should be given to the fact that maldistribution can be avoided by sealing strips.

2.3.11 Clearances Between the Inner Diameter of the Shell and the Outer Diameter of Segmental Baffles

Dimensions and tolerances for shell-and-tube heat exchangers are laid down in DIN 28008. Figures for the diametric clearance between the shell inner diameter d_i and the outer diameter D_2 of segmental baffles are listed in Table 7. Owing to the conditions of manufacture, these clearances are inevitable, and the only means of reducing them is to machine the inner surfaces of the shell.

2.4 Design Details

2.4.1 Tube-to-Tube Sheet Joint

Figure 17a–c, e, and f are examples of standardized tube end weldings in tube sheets, as given in DIN 8558 part 2, tag C 10.1–10.4. Other feasible means of attaching the tubes to the tube sheet are rolling (Fig. 17d and g), and hydraulic or explosive expansion. Welding and roller expansion can also be combined, see DIN 28 187. Crevice-free welding (Fig. 17f) is preferred, if there is the risk of crevice corrosion on the shell side due to the presence of chlorine.

Roller-expanded connections are suitable only for low temperatures and pressures or for slight fluctuations in temperature and pressure. Consequently, preference is usually given to welded joints in the chemical industry and in boiler construction.

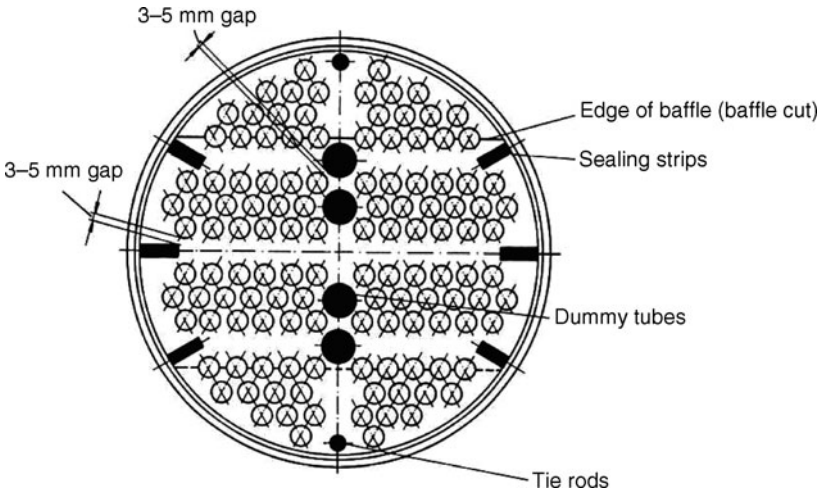

O1. Fig. 16. Tube pitch plan with dummy tubes, sealing strips, spacers, and segmental baffles.

O1. Table 7. Diametric Clearances between the shell inner diameter and the segmental baffle outer diameter (dimensions in mm)

Shell diameter d_i	Diametric Clearance
≤400	3
450–1000	4
>1000	6

The tubes are usually welded in two staggered layers. In all cases, the thickness of the stressed welded should be at least the same as that of the tube wall.

If the inner tubes are to be coated, resort is mostly taken to the connections illustrated in Fig. 17a, c, and e.

2.4.2 Tube Sheet

Design calculations, e.g., that recommended in *AD-Merkblatt B5* [3], for shell-and-tube heat exchangers completely filled with tubes and without an expansion joint in the shell usually reveal that the tube sheet need be very thick. For manufacturing reasons, the choice generally falls on tube sheets of 12–20 mm thickness, the actual value depending on the diameter of the heat exchanger. The design of a "thin" tube sheet welded to the shell flange is illustrated in Fig. 18. "Thick" plates (Fig. 19) may be necessitated by strength considerations, e.g., if the shell not completely filled by the tubes or if an expansion joint has been fitted. In this case, the tube sheet may also be designed as a flange.

Differential thermal expansion between the shell and the tubes may impose additional stresses in heat exchangers with fixed tube sheets, i.e., without expansion joints. Instructions on how allowance can be made for the additional forces thus induced in the walls of pressure vessels are given in the *S*3 series of *AD-Merkblätter* [3]. However, these instructions do not apply to other additional forces, e.g., those induced by increases in weight or irregular temperature distribution. Under these circumstances, the stresses can be determined by the method

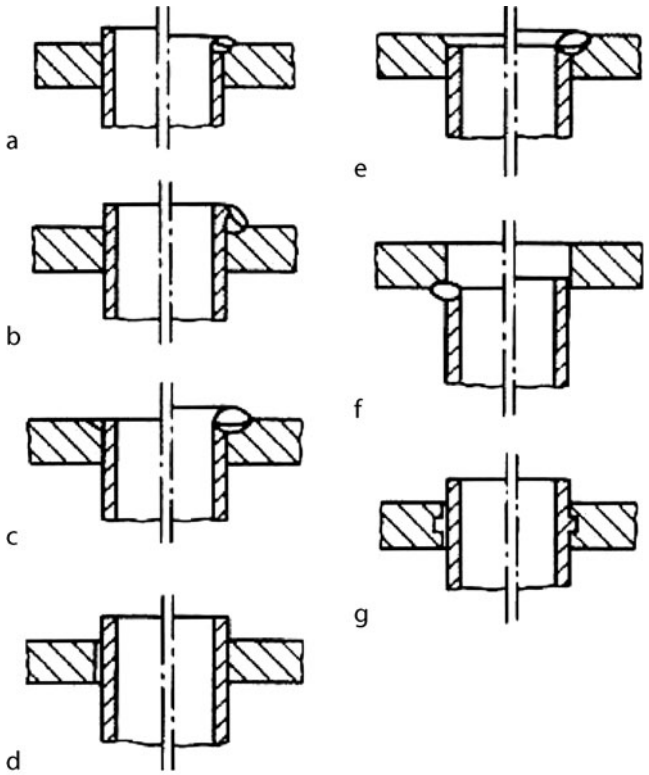

O1. Fig. 17. Means of securing tubes in the tube sheet (Methods **a**–**d** are described in DIN 8558, methods **e**–**g** are described in Sect. 2.4.1).

suggested by Sterr [7], in which case the relationships to temperature and pressure must be known at startup, during taking on stream, during operation, and at breakdowns.

2.4.3 Impingement Protection

As a result of the high inflow velocities, the innermost bank of tubes immediately below the shell inlet may suffer damage by

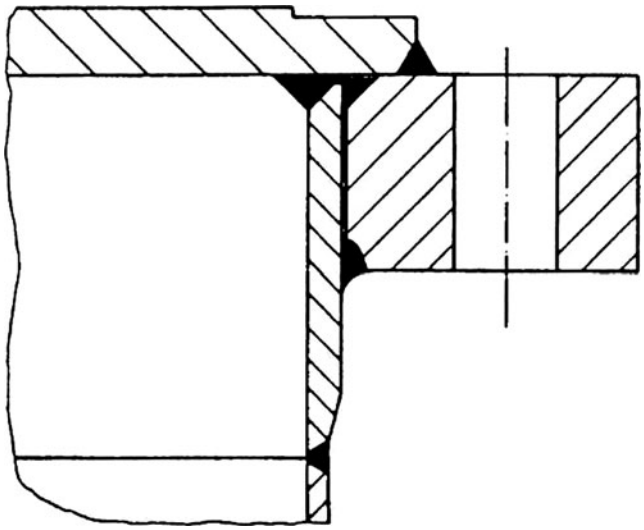

O1. Fig. 18. Thin tube sheet.

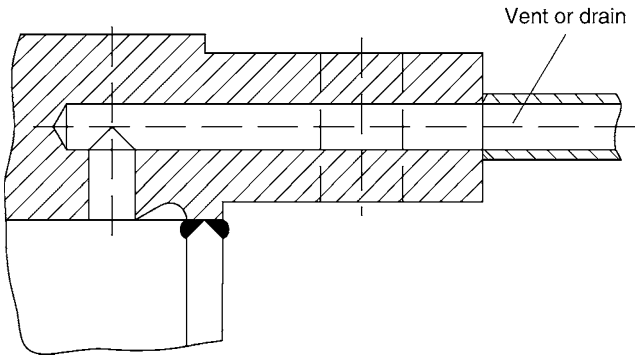

O1. Fig. 19. Thick tube sheet.

erosion or cavitation. It should thus be protected by an impingement plate or louver under the following circumstances.

- If the inner tubes are exposed to condensing vapor.
- If ρv^2 for single-phase flow of noncorrosive or non-erosive liquids exceeds 2300 kg/ms^2.
- If ρv^2 for all other liquids up to the boiling point exceeds 750 kg/ms^2.

Another condition that must apply is that $\rho {v_1}^2 < 6000$ kg/ms^2 [7], where v is the average flow velocity at the inlet and ρ is the effective flow velocity between the tubes in the first row, as is illustrated in Fig. 20.

In shell-and-tube heat exchangers with fixed tube sheets, the impingement baffles are secured in the form of plates or louvers and are secured to the shell as is shown in Figs. 21 and 22. According to Fig. 22, the impingement plate should be designed somewhat wider than the cross-section of the incoming flow [8].

2.4.4 Design of Segmental Baffles and Support Plates

Apart from directing flow, segmental baffles serve to protect the tubes from damage by vibration and to prevent them

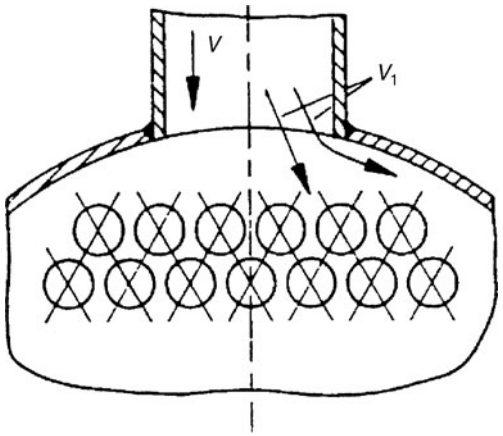

O1. Fig. 20. Flow velocities v_1 and v_2 at shell-side inlet and between the tubes.

from buckling. The requisite thicknesses of segmental baffles and support plates are listed as functions of the rated shell diameter and the distance between supports e_1 (Figs. 11–15) in Table 8.

Thicker segmental baffles are required if pulsating flow is anticipated (An example of a heavy-duty design is given in DIN 28185). If the volume flow rate is high, segmental baffles must be more widely spaced. In this case, the conditions for the prevention of buckling and damage by vibration no longer apply, and additional support plates must therefore also be installed (Fig. 23).

Very often, the design entails a large spacing between the first or last segmental baffle and the tube sheet. The ensuing dead spot can be made smaller by installing a baffle under the shell nozzle, as is shown in Fig. 24.

2.4.5 Nozzles

The head and shell nozzles must be designed to avoid the formation of gas or vapor cushions that could impede heat transfer or promote the concentration of contaminants at the vapor/liquid phase boundary and thus lead to corrosion of the inner tubes, shell, or dished ends.

Provision must also be made for vents and drains in the event that the shell-side and tube-side spaces cannot be completely drained or vented. They may assume the form of separate connections or holes drilled in the tube sheets (cf. Fig. 19). Vents and drains should also be drilled in the pass partitions (Fig. 25).

2.4.6 Pass Partition Seals

A type of seal that is frequently used for a dished-end partition is shown in Fig. 25a. Its breadth b is usually 8–10 mm. A flexible partition seal is illustrated in Fig. 25b. Partitions upon which a seal has been mounted, as is demonstrated in Fig. 25c, are often encountered in coolers that operate at low temperatures and pressures ($p = 6$ bar and $t < 150$°C).

The pass partitions must be reinforced or supported if pressure surges are likely, the difference in pressure between the baffles is high, or the vessel is cleaned by flushing under pressure.

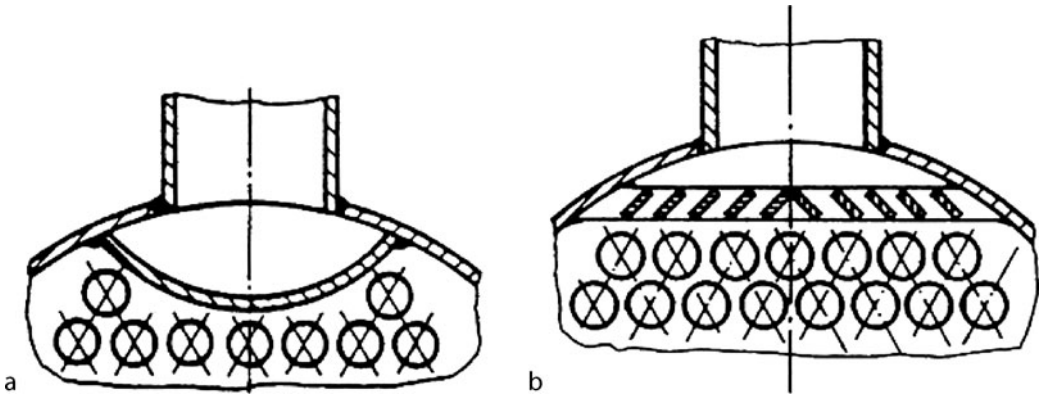

O1. Fig. 21. Designs of impingement protection: **a**) plate **b**) louver.

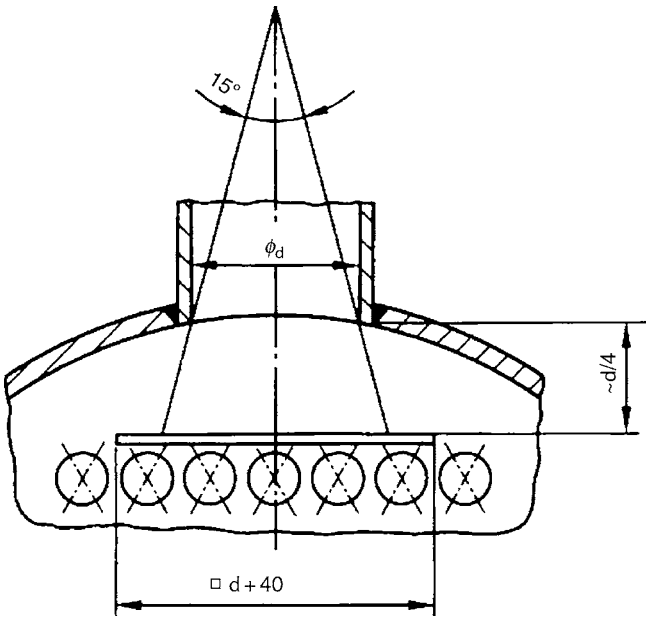

O1. Fig. 22. Arrangement of impingement plates.

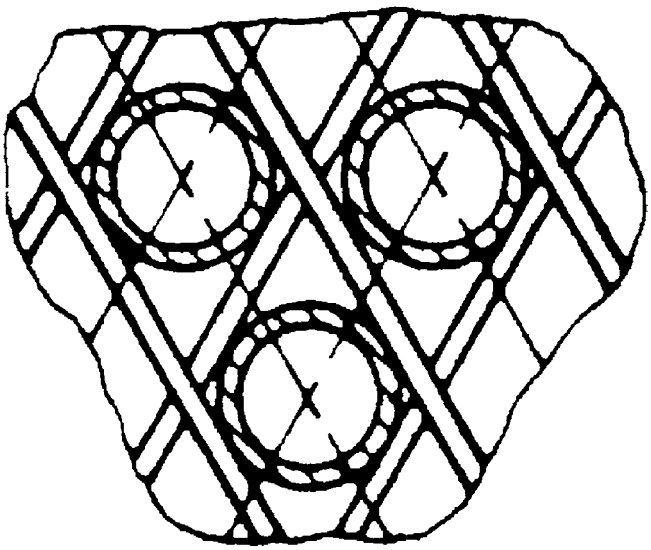

O1. Fig. 23. Supporting grid.

O1. Table 8. Thickness of segmental baffles and support plates in relation to the pitch e_1 (DIN 18 185) (dimensions in mm).

Nominal diameter	Pitch e_1					
	≤150	151–300	301–450	451–600	601–750	>750
	Thickness s					
150–350	4	4	4	4	5	6
400–700	4	4	5	5	6	8
800–1000	–	6	6	8	8	10
1100–2000	–	6	8	8	10	10

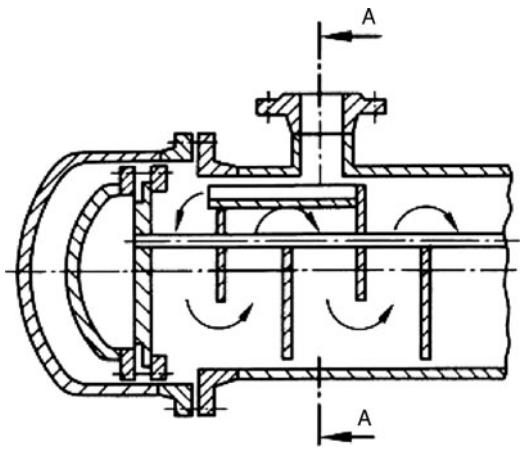

O1. Fig. 24. Baffle to reduce dead space.

If the partition is thicker than the width of the seal, it must be chamfered at the surface of contact to ensure a snug fit. Whenever the inner surfaces of the dished heads and tubes have to be coated with a baking finish, the partition should be beveled to a width of about 5 mm. Otherwise, the coating may be damaged at the edges of the groove that forms the seal in the tube sheet (cf. Fig. 25a) when the dished head is assembled or the partition vibrated during operation. Figures for the minimum thickness of pass partitions are submitted in Table 9.

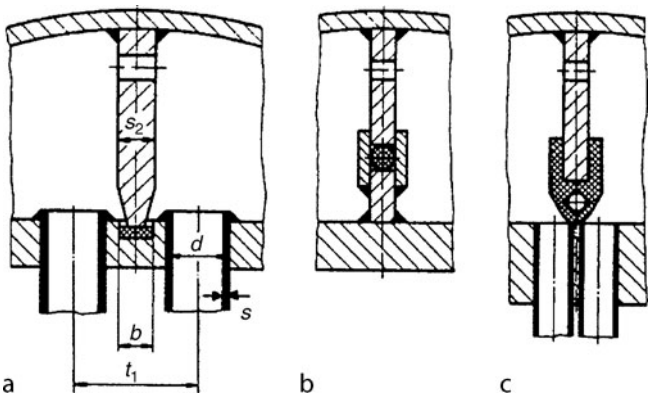

O1. Fig. 25. Seals for pass partition plates in dished head (Methods **a**–**c** are described in Sect. 2.4.6).

O1. Table 9. Thickness of partitions (dimensions in mm)

Dished head diameter	Carbon steel	Alloy steel
≤600	8	6
>600	12	10
>1400	16	14

2.4.7 Seals on Longitudinal Baffles

Figure 26 shows how a longitudinal baffle is sealed against the shell wall in a shell-and-tube heat exchanger with removable tube bundles and two shell-side passes. The thickness of the sheet-metal partition is about 8 mm for shells of up to 700-mm diameter; and about 12 mm, for larger exchangers. The leaf springs on the assembly should be designed so that the seal is pressed against the shell wall under the excess pressure that acts on the inlet side during operation.

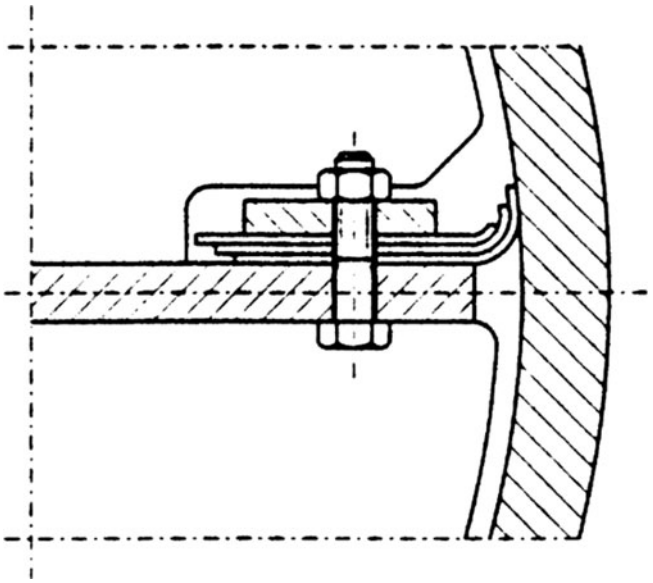

O1. Fig. 26. Seal on longitudinal partition plate.

2.4.8 Tie Rods

Two designs of tie rods are shown in Fig. 27. Their purpose is to secure the baffles in their intended position. Since the baffles (whether segments, discs or doughnuts) may not vibrate during operation, the tie rods should mainly be fitted close to the edges of the baffles. The tie rod arrangement described in DIN 28184 Parts 1–3, DIN 28190, and DIN 28191 apply only to certain sections between segmental baffles.

Sealing strips and dummy tubes can also serve as tie rods. The number and diameter of tie rods required in shells of various diameters can be obtained from Table 10.

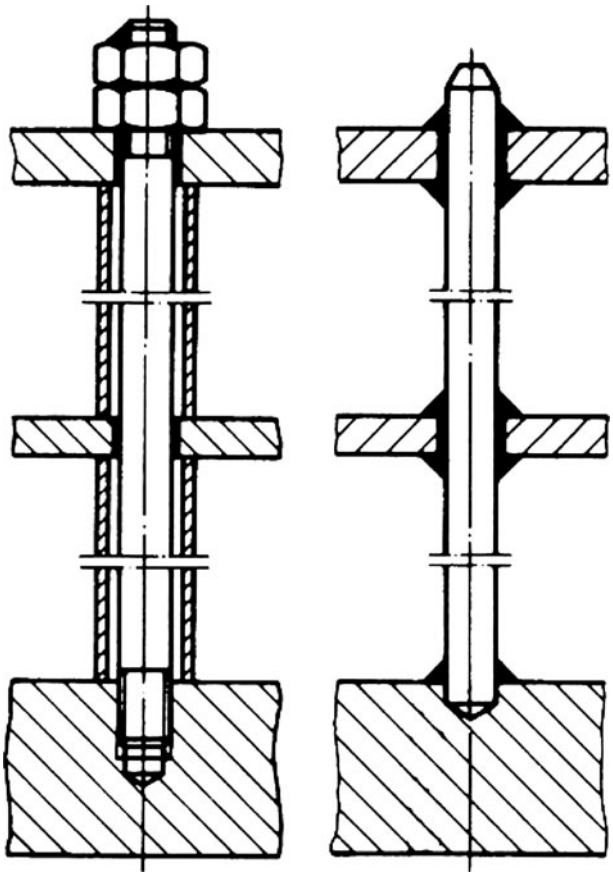

O1. Fig. 27. Tie rods for segmental or support baffles.

2.4.9 Surface Coatings

Parts of shell-and-tube heat exchangers can be coated with a baking finish if the medium, e.g., river water, is likely to cause encrustation or corrosion.

Some coatings are impermeable to water vapor, and others are not. They ought to be impermeable if the aqueous medium with which they are in contact is at a temperature higher than that at the opposite side, as otherwise the coating will peel off when the water diffuses through it and condenses on its underside at the metal interface. Dished heads are always coated with impermeable finishes, because the outside temperature is often

O1. Table 10. Number and diameter of tie rods (dimensions in mm)

Rated shell diameter	Tie rod diameter	Minimum number
150–200	10	4
250–500	12	6
600–1200	12	8
1400–2000	16	12

lower than that on the inside. (The maximum sustained temperature that a baking finish can with stand is about 150°C.)

The thickness of the coating required depends on the surface of the tubes. It should be approximately 200 µm to ensure the absence of pores. Allowance must be made for the associated reduction in the surface heat transfer coefficient. The thermal conductivity of the coatings is about 0.7 W/mK. Instructions on substrate preparation are given in DIN 28051.

2.5 Evaporators

2.5.1 Vertical Evaporators with Tube-side Evaporation

These evaporators are usually of the natural-circulation type (thermosyphon reboiler, Fig. 28). The pressure drop in the circulating product must be kept low, because flow is caused solely by differences in density between the liquid and the two-phase stream formed by evaporation. The cross-sectional area of the vapor tube should be at least equal to the sum of the cross-sectional areas of the evaporation tubes, and the cross-sectional area of the lower inlet tube should be at least one-half of that of the vapor tube. Only one tube-side pass is feasible, and there are usually two fixed tube sheets.

If the tubes are short and the shell side is heated by condensing steam, baffles can be dispensed with. The number of passes is defined by the ratio of the mass flow Tate of inlet liquid to that of the outlet vapor and normally lies between 6 and 14.

Natural-circulation evaporators are useful for concentrating liquids and as reboilers in columns. Forced circulation is necessary if the pressure drop becomes too high for natural circulation. In this case, a pump must be installed in the inlet pipe, and an attempt should be made to attain as many as 40 circulation passes.

A special design of the natural-circulation type is the Robert evaporator, which is integrated at the bottom of the column and extends over the entire column cross-section (Fig. 29). The circulating fluid flows upward through the heat exchanger tubes and is returned through the central downcomer.

The tubes are usually very short. For large Robert evaporators, at least one of the two tube sheets must be thick enough to bear the load exerted by the correspondingly heavier tube bundle without appreciably sagging.

2.5.2 Falling-Film Evaporators

Falling-film evaporators (Fig. 30a, b) are vertical shell-and-tube heat exchangers that are usually steam-heated on the shell side.

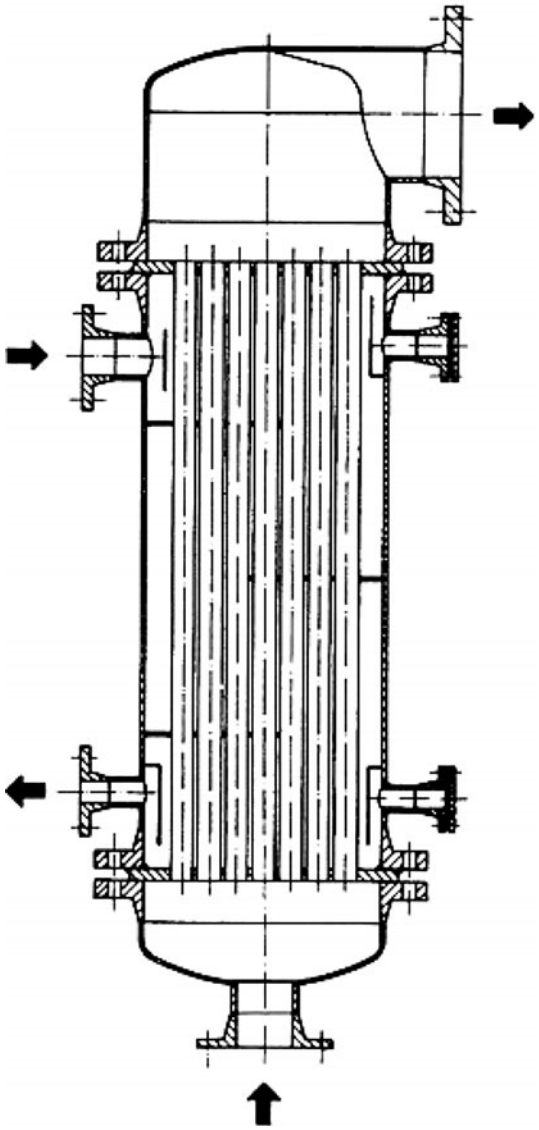

O1. Fig. 28. Thermosyphon Reboiler.

The liquid flows downwards along the inner walls of the tubes and is thus partially evaporated.

Ideal operation entails that all the tubes are uniformly wetted by a continuous film of liquid. As a consequence, the liquid flow rate should not be less than 1 m^3/h/m of circumference of all the tubes.

The liquid distributors in large evaporators are mostly plates, in which the perforations (Fig. 31) have been designed such, that the liquid jets impinge on the interstices between the evaporator tubes and then flow towards the next bank.

It must be ensured that the liquid flows uniformly into the distributor. If, for instance, it were introduced at the center of the evaporator, a cone located underneath the inlet pipe would allow it to spread evenly outwards. Maldistribution caused by departures from the horizontal or currents within the distributor can be avoided if the bead of liquid on the perforated plate is not allowed to fall below 50 mm, even under minimum load. An annular gap must be located between the distributor and the dished end in order to permit pressure equalization between the space above and the space below the perforated plate.

If some of the liquid evaporates on entering the distributor, tubes of larger diameter should be selected to ensure that the flow of vapor does not disturb the falling film on the tube walls.

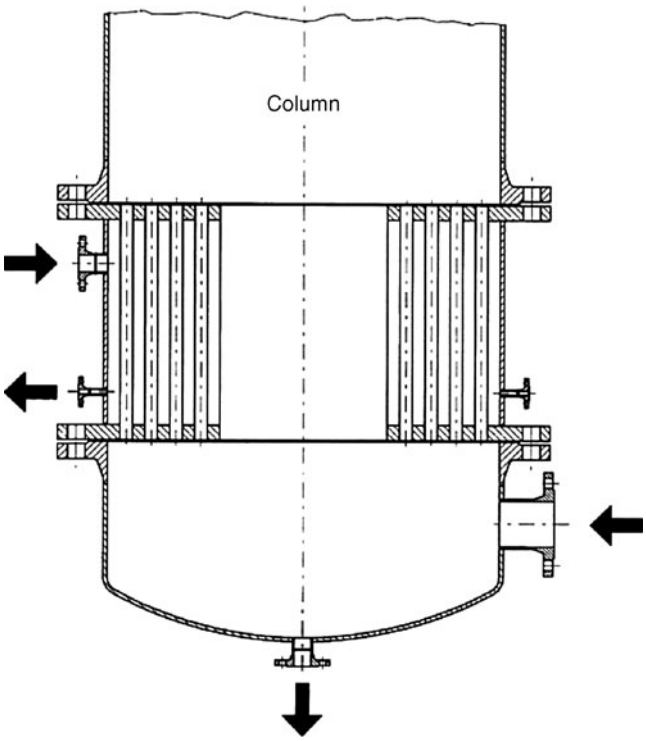

O1. Fig. 29. Robert evaporator.

The design shown in Fig. 32 can be adopted in special cases in which the face-milled vertical tubes project above the upper tube sheet. The projections may be expanded into a tulip shape or be tangentially slotted or perforated. Another possibility is to insert shaped inserts into the tubes. If expansion into a tulip shape is selected, the tube spacing must be wider than that recommended in DIN 28182. In this case, the liquid should be introduced through an annular distributor or over a cowl.

In order to ensure that the liquid is uniformly distributed, the overflow or inlet edges of all the tubes must be smooth and even, i.e., without beads or burrs. The upper tube sheet in evaporators with tulip shaped tube inlets must be resistant to bending.

2.5.3 Vertical Evaporators with Shell-side Evaporation

This design is mainly encountered in steam generation, and the heating medium (within the tubes) may be a contaminated product.

The water enters underneath the shell, and the vapor–liquid mixture is withdrawn at the top. Problems arising from thermally induced stresses in the shell and the upper support plate can be avoided by ensuring that the tube-side heating medium is not admitted at the upper end, as otherwise it will be at its maximum temperature when it comes into contact with the hottest part of the shell. The ensuing superheating of the steam may then give rise to impermissibly high thermally induced stresses. Particular care must be devoted to ensuring that the steam is completely and uniformly withdrawn and does not

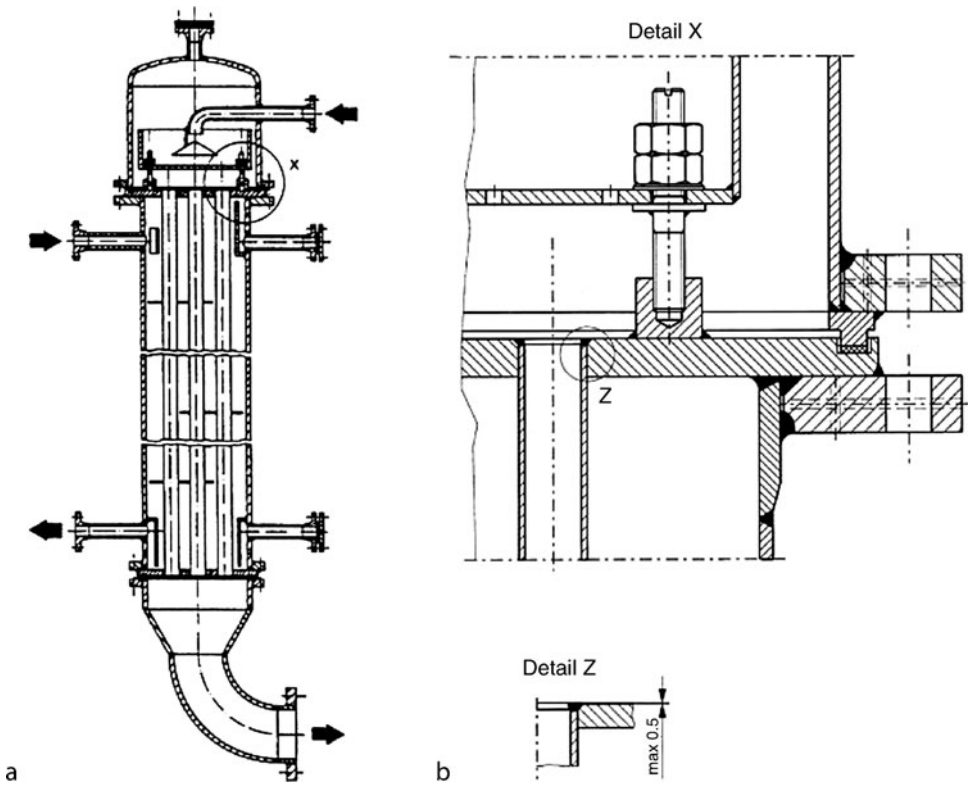

O1. Fig. 30. (**a**) Falling-film evaporator and (**b**) detailed sections through a falling-film evaporator.

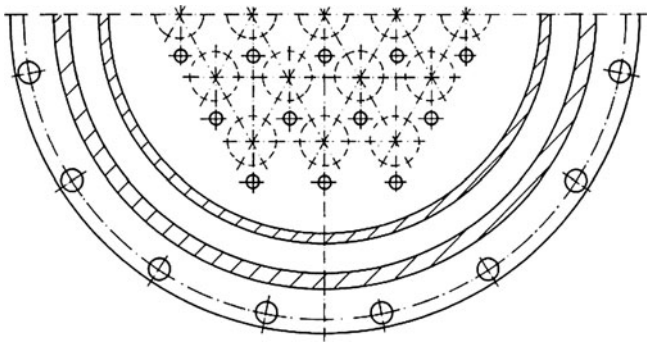

O1. Fig. 31. Perforated-plate distributor.

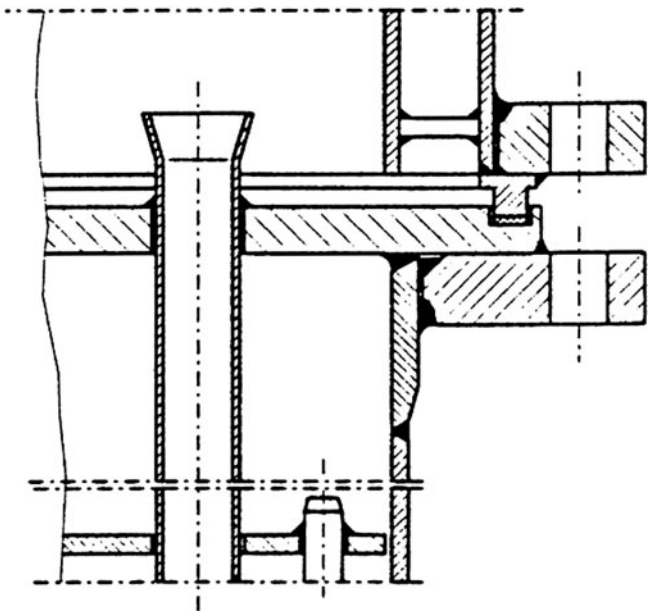

O1. Fig. 32. Tulip-shaped evaporator tube inlet.

accumulate to form a stationary cushion. Several outlets distributed over the circumference or internal siphons are generally required for this purpose. Another point to ensure is effective and complete venting underneath the upper support plate.

The shell side is frequently designed as a recirculating evaporator, and a steam dryer is required to separate the liquid from the vapor.

A multiple-effect design may also be adopted for the tube side. The installation of a floating head or V-tube bundle gives rise to a variant that is frequently resorted to in high-pressure techniques. In this design, the fixed support plate is underneath. The shell extends well above the tubes and is used as a vapor space, in which case an external steam dryer is not required.

2.5.4 Horizontal Evaporator with Shell-side Evaporation

Pool boiling occurs in this type of evaporator, i.e., there is no defined flow pattern. The design is therefore recommended whenever the product need not or cannot be circulated or only retardation of boiling is aimed at. As a rule, the tubes should be flooded on the shell side. Consequently, if the evaporator is completely filled with tubes, an external vapor space (steam dryer) is required, usually together with several outlets. If the evaporator is not completely filled with tubes, the free space above the tube bundle can be utilized as the vapor space.

Some of the many variants that this permits are described below.

If the first tube bank in a bundle lies within a large shell-side vapor space formed above the bundle in an evaporator only partially filled with tubes, it will serve as a mist extractor and steam superheater.

A second variant consists of a U-tube or floating head bundle inserted on the shell side. Its best-known representative is a kettle reboiler (cf. Fig. 7). The tubes are expanded mechanically into full-bore support plates, which are spaced in accordance with the heat flux in the bundle. For instance, the spacing in kettle reboilers is between 500 and 700 mm.

2.6 Condensers

This section concerns surface condensers for total and partial condensation with a liquid, e.g., water, as the cooling medium. Since the vapor has a higher volume flow rate than that of the liquid – or at least at the commencement of condensation – it is usually designed to pass through the shell.

If inert, i.e., incondensable, gases are contained in the vapor, they must be allowed to escape through a separate outlet, the location of which depends on the gas/vapor density ratio (Fig. 33). Thus it must be fitted on the downside of the condenser if the density of the inert gas is higher than that of the vapor; and on the upper side, if the density is less. The flow of cooling liquid through the tubes should be arranged so that the inert gases pass over the coldest tube before they are removed.

The tube wall on the condensation side should be as "dry" as possible. In other words, the condensate should run off the surface of the tube by the shortest possible path in order to improve heat transfer. It is for this reason that horizontal condensers are generally superior to vertical.

2.6.1 Vertical Condensers with Shell-side Condensation

The design can be recommended for moderate condensation rates at pressures above atmospheric. It is most frequently adopted for heating recirculation and falling-film evaporators, in which case the shell-side condensation of steam or vapor causes the product to evaporate within the tubes.

At high condensation rates, the condensate film that flows along the tubes becomes thicker and thus impairs heat transfer. The design gives rise to difficulties if the vapor contains inert gases with a density lower than its own. In this case, the two outlets for the inlet and the inert gas would be located at the upper end of the evaporator. Hence design measures must be

adopted to ensure that the vapor is not short-circuited through the inert gas outlet.

2.6.2 Vertical Condensers with Tube-side Condensation

The point to observe in this design is that the vapor should flow downwards through the tubes and thus not hinder the descending condensate film. If this is not feasible or cannot be realized in all the tubes, e.g., in multiple tube-side passes, the cross-section of the tube must be large enough to ensure that the rising vapor does not hold up or even break down the descending condensate film.

2.6.3 Horizontal Condensers with Tube-side Condensation

Heat transfer is favored somewhat more by this design than it is in vertical condensers, because the upper part of the tubes always remains unwetted. If the condenser has been designed with only one tube-side pass, it should be slightly inclined at a slope of at least of 1% so that the condensate can flow more rapidly out of the tubes.

2.6.4 Horizontal Condensers with Shell-side Condensation

This is the most common and most effective design of condenser. If the pressure is above atmospheric or if only partial condensation occurs, the condenser may be almost completely filled with tubes provided that the maximum vapor inlet velocity is not exceeded. If vapors are condensed at subatmospheric pressures, their initial volume will be so great that the flow velocities between the first tube banks will be very high. In this case, some unfilled, i.e., tubeless, space must be left in the inlet zone. In vacuum condensation, additional wedge-shaped tubeless vapor channels frequently have to be formed and/or the spacing in the first few tube banks has to be increased (cf. Fig. 33).

At any rate, positive condensate removal must be ascertained, as otherwise the lower tubes may be flooded. This aim is generally achieved by cutouts or slots on the lower side of the support plate or segment baffles. A single crossflow pass of vapor over the tube bundle is standard practice in vacuum condensation with the consequence that the condensers are fitted with full-bore support plates and not with baffles.

If the inlet vapor is wet, it is absolutely essential to protect the first tubes from erosion by means of impingement baffles.

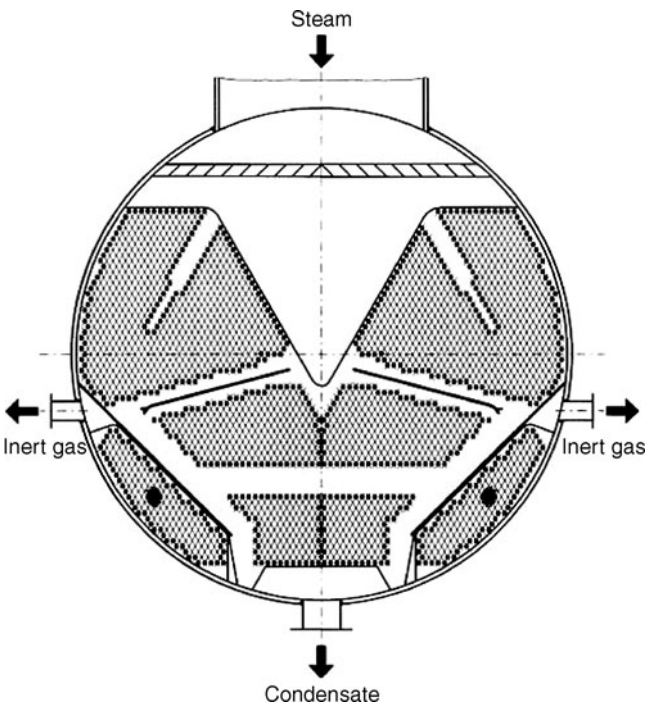

O1. Fig. 33. Pattern of tubes in a vacuum condenser.

3 Compact Heat Exchangers

3.1 Plate Heat Exchangers

Plate heat exchangers consist of an assembly of several profiled sheet-metal panels (Fig. 34), each of 0.4–0.8 mm thickness (Fig. 35). The assemblies are mounted in frames and bolted together. The compressive forces thus induced are absorbed by spacers, which are often very thick and are also bolted in the frame together with the assembly.

The heat transfer media are fed through four openings, one at each corner of a panel. Two openings at a time are alternately shut off from the remainder of the flow compartment so that the two media flow alternately in the spaces between the panels. Individual openings can be closed to allow all the panels or certain assemblies to be connected *in tandem* and a multiple-pass arrangement can thus be achieved (Fig. 36).

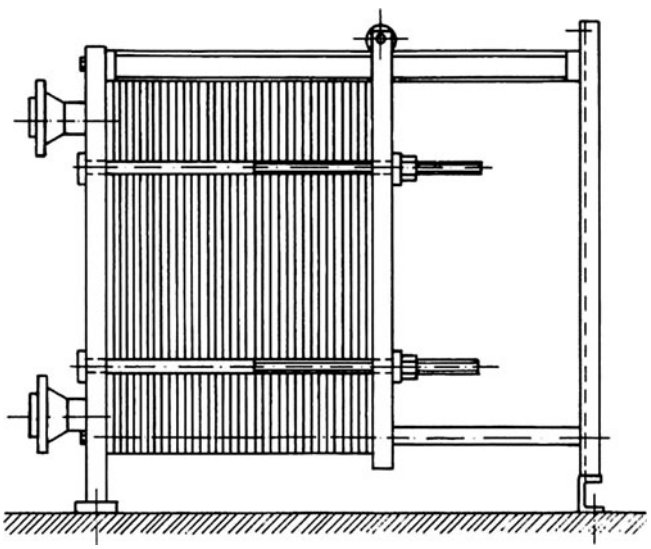

O1. Fig. 34. Assembled plate heat exchanger.

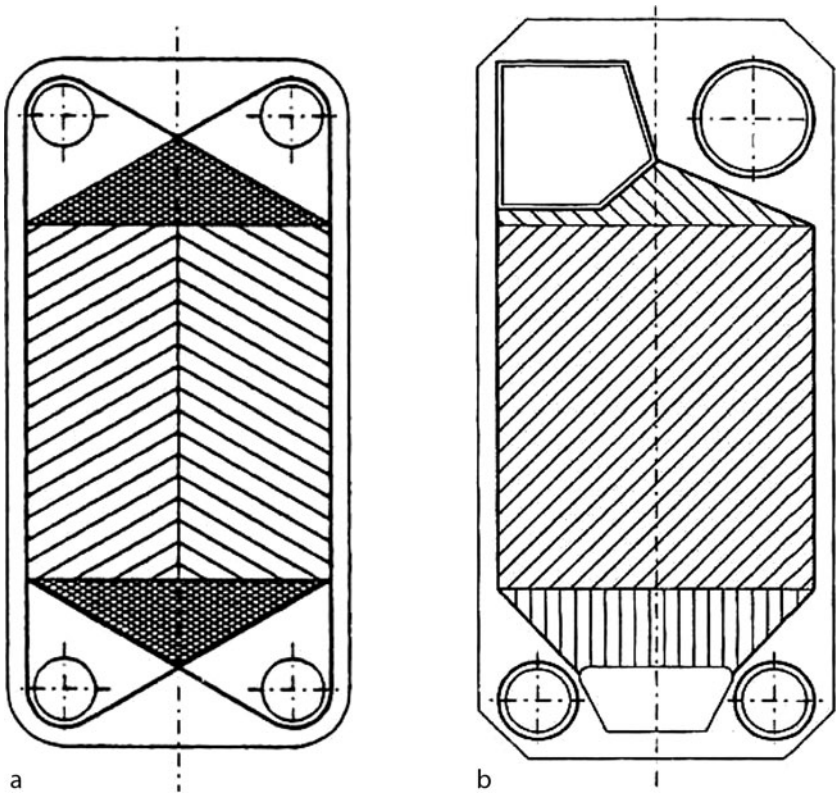

O1. Fig. 35. Individual plates for (**a**) heater and (**b**) evaporator.

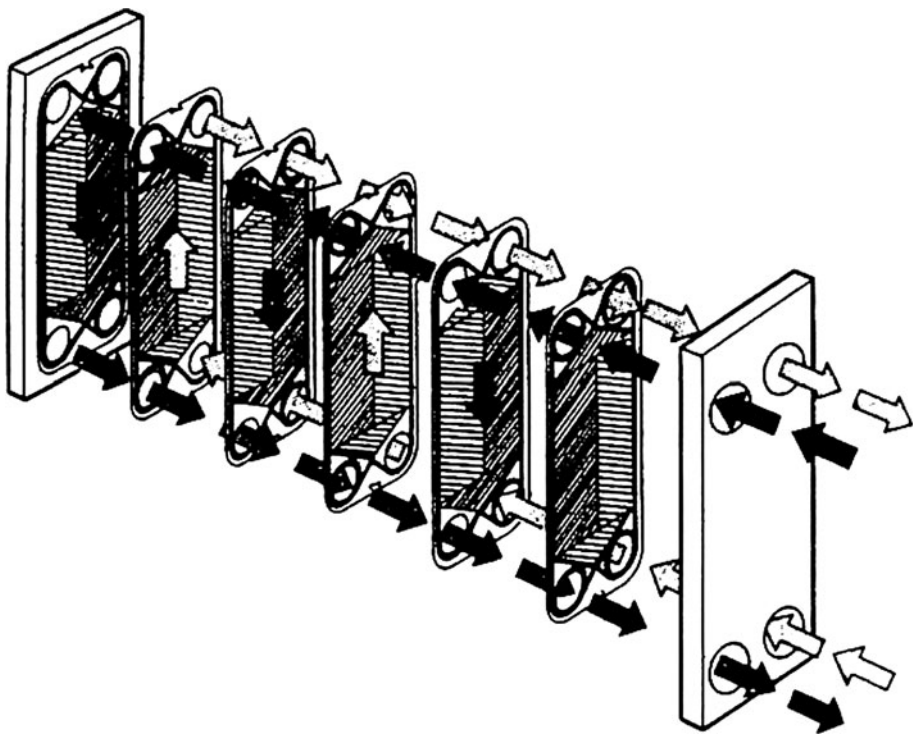

O1. Fig. 36. Flow pattern in plate heat exchanger.

The operational limits of plate heat exchangers are primarily set by the compressive strength of the plates and the heat resistance of the seals. As a general rule, operation is feasible at pressures of up to 25 bar and maximum temperatures of 170°C. The materials of construction are predominantly chromium–nickel steels; but titanium, nickel alloys, and other specialties are also encountered.

The profiles on the individual panels can be varied to allow optimum operation under given conditions. For instance, they permit allowance to be made for solids fractions, high viscosities, or a permissible pressure drop. They can also ensure that flow is always turbulent, with the consequence that extremely high heat transfer coefficients can be achieved. Thus if the panels are tightly packed, high heat transfer rates can be attained within a small space.

Great turbulence is responsible for comparatively high pressure drops but reduces fouling. In fact, the tendency to fouling in plate heat exchangers is four times less than that in shell-and-tube types.

The individual panels are separated from one another by elastomer seals that are of complicated shape and are often assembled by adhesives, which serve no other function, i.e., do not act as seals. There is a growing trend towards panels that allow seals to be secured mechanically. The great advantage of this is that the seals can be easily removed for cleaning.

Heat exchangers in which the plates are welded full-face together, see Fig. 37, are becoming widely accepted and allow a wide variety of designs. The advantage over conventional plate heat exchangers is that no sealing problems arise. A disadvantage is encountered in cleaning welded versions, because the individual plates can no longer be dismantled.

3.2 Spiral Heat Exchangers

Spiral heat exchangers consist of two steel strips of the same width that are wound in the form of equi-spaced spirals around a central body. Usually, a number of steel pegs are welded to the strips in order to ensure that the spacing remains constant. The widened ends of the spirals accommodate the inlet and the outlet and also serve as distributors for the respective flow compartments. The channels thus formed are alternately caulk-welded. After it has been faced, the entire structure is sealed at the one end and covered with a flat lid at the other (Fig. 38). An advantage that is thus obtained is that both flow paths can be mechanically cleaned. Two different methods apply for operating spiral heat exchangers.

(1) *Countercurrent*: In this case, the one product flows spirally inwards towards an axial outlet, and the other product flows outwards.
(2) *Crossflow*: Here, the one product is led through a spiral flow channel caulk-welded at both sides. The other product flows axially through the other cross-section, which is open at both sides.

A special design is the reflux condenser shown in Fig. 39. The vapors rise upwards through a central pipe and condense on the spiral windings. The condensate is trapped in an annular vessel, from which it is run off.

Spiral-plate heat exchangers have diameters of up to 2 m and are constructed from strips of 2 m maximum width. Any material that can be welded and cold-worked may be used for the construction. As a rule, the operating pressure is restricted to 20 bar. The maximum operating temperature is governed by the heat resistance of the lid seal. The width of the flow channels can be varied within wide limits, with the result that the spiral

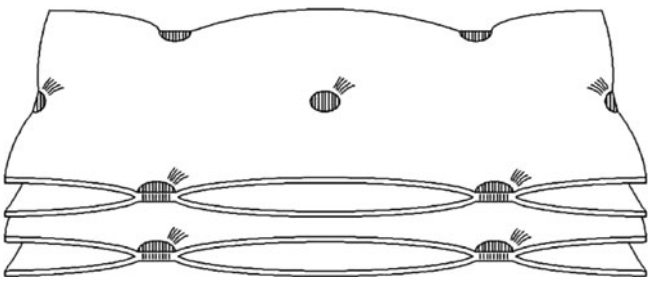

O1. Fig. 37. Profile of welded plates.

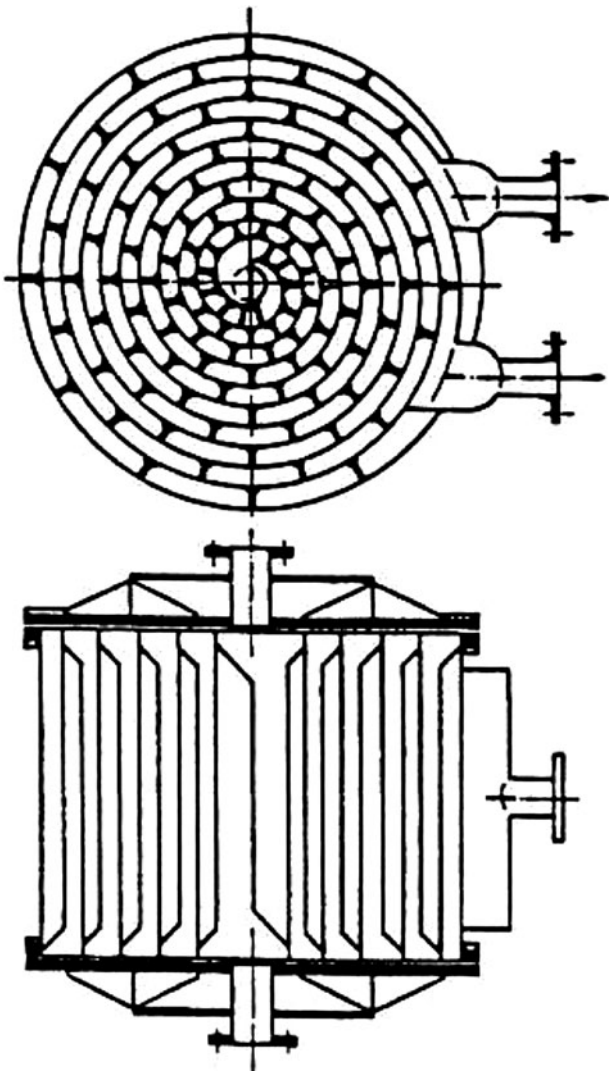

O1. Fig. 38. Spiral heat exchanger.

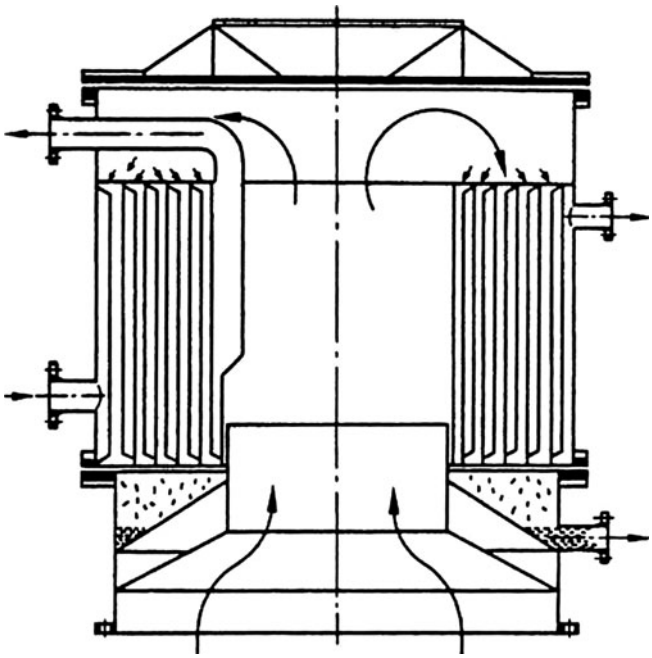

O1. Fig. 39. Spiral-plate heat exchanger used as condenser.

heat exchanger can be readily adapted to allow optimum conditions for a given process.

4 Other Designs

4.1 Helical Coil Heat Exchanger

A helical coil heat exchanger is particularly easy to construct: a tube is spirally wound around a cylinder and inserted in a cylindrical vessel provided with an inlet and an outlet for the heating or cooling medium. The capacity of the vessel can be fully exploited by inserting several coils, the one within the other, and connecting them in parallel. The coil inlets and outlets may be located at the top or bottom, depending on requirements and the means for installation (Fig. 40).

A disadvantage of this design is that it can be mechanically cleaned on the outside but not on the inside. The flow velocity of the medium on the outside is low, and the specific heat transfer is thus poor.

4.2 Double-Tube Heat Exchangers

This heat exchanger consists of an outer tube and a concentric inner tube. It is generally in the form of straight sections connected by 180° bends (Fig. 41). The mass flow rates and thus the flow velocities are usually low. Consequently, heat transfer is poor, and very long tube lengths are therefore required. Double-tube heat exchangers are mainly used in high pressure techniques, because the thick tubes allow very high temperatures and pressures to be controlled. If the straight lengths are connected by large bends (of at least 3D), the inner tube may be cleaned by a go-devil. However, the only means of cleaning the outer tube is by chemicals.

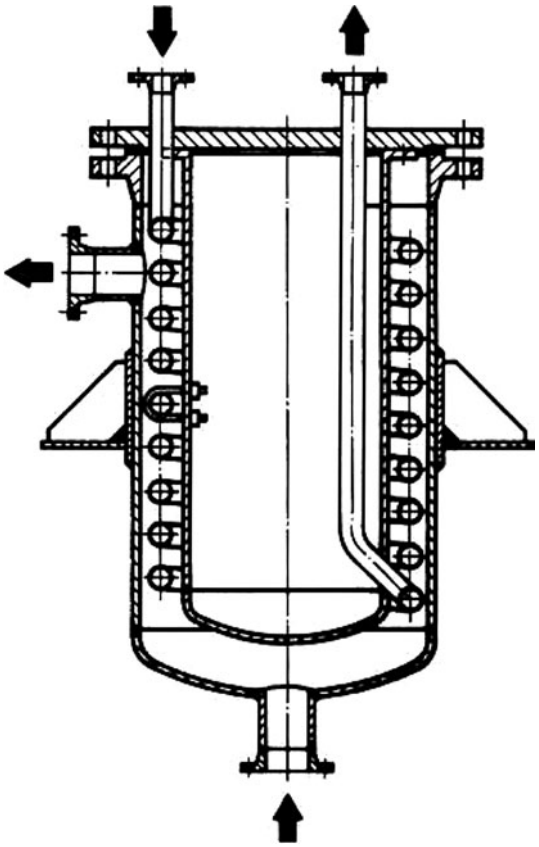

O1. Fig. 40. Helical-tube heat exchanger.

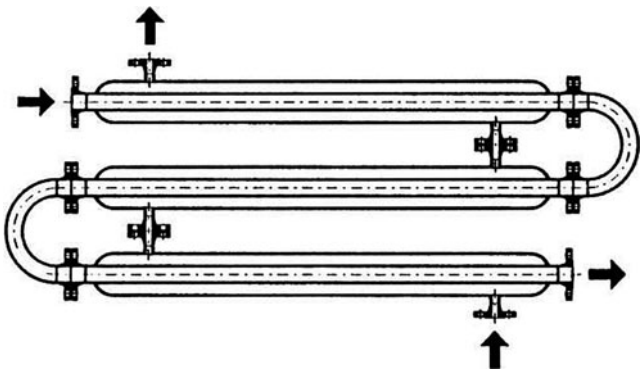

O1. Fig. 41. Double-tube heat exchanger.

4.3 Safety Heat Exchangers

This term is generally applied to heat exchangers that are designed to prevent the product streams from mixing in the event of leakage. In most cases, they are shell-and-tube heat exchangers with concentric double tubes instead of single tubes. If any leakage occurs, the product enters the annulus and is led outside. A monitor allows any leaks to be immediately detected, and there is no likelihood that the product streams will mix (Fig. 42).

Heat transfer between the double tubes can be improved by two fundamentally different designs.

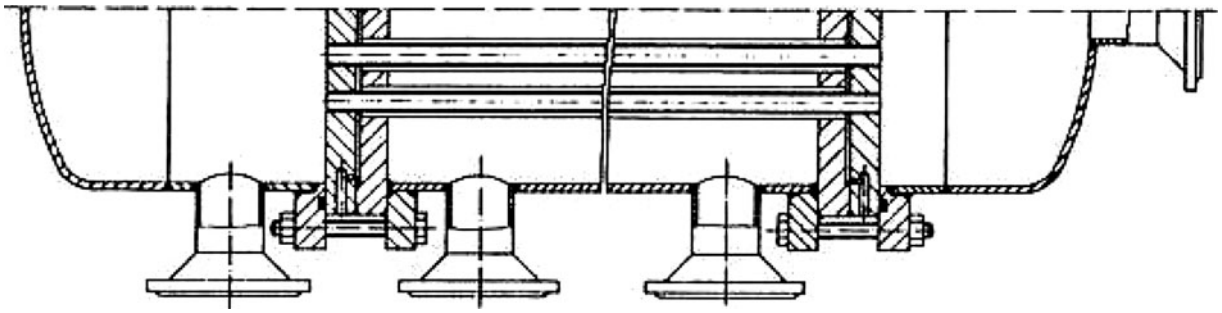

O1. Fig. 42. Safety heat exchanger.

(1) The annulus between the concentric tubes is filled with a medium that is compatible with both products and has a comparatively high thermal conductivity.
(2) One of the two tubes has spiral fins – either the outer tube with internal fins or the inner tube with internal fins. The inner tube is then widened to form a metallic contact with the outer.

An advantage of the first variant is that the pressure of the intervening medium can be set to a value that allows rapid detection when it is reduced by leakage. However, problems may arise in finding a medium that is compatible with both products.

The same effect can be achieved in plate heat exchangers by means of double plates. If a leak occurs, the product concerned passes outside through the gap between the double plates.

4.4 Graphite Heat Exchangers

By virtue of its resistance to heat and chemicals, graphite is attracting increasing attention in the design of heat exchangers. It possesses the good thermal conductivity of metals and the very good corrosion resistance of nonmetals. Since it is porous in the original state, it is impregnated with phenol-formaldehyde or furan resins. Under these circumstances, its range of service temperatures is –60°C to 200°C. Impregnation increases its strength by a factor of about 2–3.

Graphite heat exchangers can be operated at pressures ranging from 1 bar to about 15 bar. Pressure surges, e.g., water hammer or the rapid opening and closing of valves, may damage graphite and must therefore be avoided. The physical properties of graphite that affect the design of heat exchangers are listed in Table 11.

Graphite is resistant to the large majority of all known chemicals with the exception of free bromine and chlorine, free fluoride ions, sulfuric acid/potassium dichromate, and concentrated nitric acid.

Graphite heat exchangers can be used in almost all heat transfer processes, e.g., cooling or heating of corrosive media and condensation or evaporation in natural-circulation or falling-film evaporators. Different designs exist to cope with the various operating conditions and applications. Shell-and-tube and block heat exchangers are the most common.

O1. Table 11. Physical properties of graphite [9]

Property	Unit	Graphite impregnated with synthetic resin[a]
Tensile strength	N/mm^2	28 bis 33
Flexural strength (axial)	N/mm^2	50 bis 60
Compressive strength	N/mm^2	75 bis 85
Modulus of elasticity	N/mm^2	$(20 \text{ bis } 30) \cdot 10^3$
Poisson ratio	–	0.2 bis 0.25
Elongation at break	%	0.15 bis 0.3
Density	kg/m^3	2.0 bis 2.1
Thermal conductivity	W/m K	80[b]
Specific heat capacity	kJ/kg K	1.0
Thermal coefficient of linear expansion	1/K	$3.5 \cdot 10^{-6}$
Temperature limit	°C	200

[a]Measured in the axial direction of tubes
[b]Measured in the radial direction of tubes

The shell-and-tube types, see Fig. 43, consist of a graphite tube bundle and a steel shell that may be clad, enamelled or coated if corrosion protection is required on both sides. The design of the heat exchanger is governed by the properties of graphite that are similar to those of ceramics. Features are the thick support plate and the adjustable spring bolts for tensioning. The only means of securing the tubes in the support plates are those applicable to all other unbreakable graphite joints, viz. bonding with adhesives. The capacities of graphite heat exchangers normally range up to 1000 m^2 and a pressure of 6 bar.

Block heat exchangers consist of cylindrical blocks through which lateral holes have been drilled at several levels. A standard layout is illustrated in Fig. 44. The stack of graphite blocks is housed in a steel shell. The dished ends are frequently constructed from graphite or PTFE-coated steel and are tensioned together with the blocks by means of adjustable spring bolts. The diameter of the drilled holes can be brought into line with the processing conditions and lies between 8 and 16 mm. The codes for the design, construction, and testing of pressure vessels, e.g., *AD-Merkblätter* [3], also apply to graphite shell-and-tube heat exchangers.

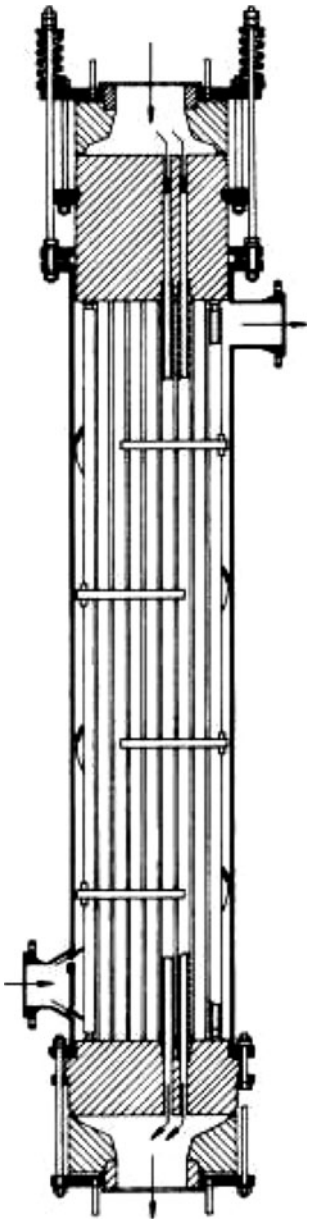

O1. Fig. 43. Graphite shell-and-tube heat exchanger.

Special graphite designs are annular and plate heat exchangers. The flow pattern in an annular type is comparable to that in a spiral heat exchanger. A system of circular channels is milled into graphite discs of 40–110 mm thickness and about 400–600 mm diameter. The number and size of the channels can be engineered to ensure effective heat transfer for given media under given process conditions. Annular heat exchangers are eminently suitable as reflux and vacuum condensers.

With the exception of the sealing system, graphite plate heat exchangers correspond to their metal counterparts. Since graphite can be shaped, the edges of the heat transfer plates can be formed to effect a seal. The sealant is an elastomer. The maximum design temperatures and pressures for graphite plate heat exchangers are 140°C and 6 bar.

Points to observe in graphite heat exchangers are that no forces or moments must be allowed to act at the graphite supports and that preference should be given to expansion joints in individual cases.

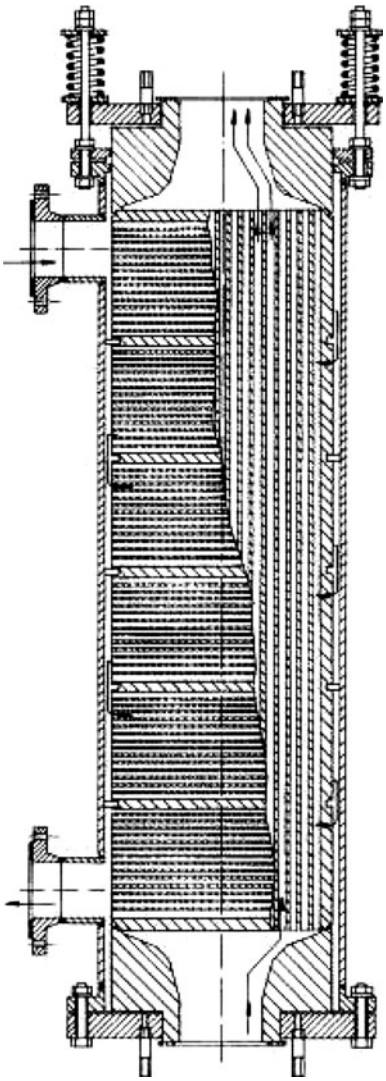

O1. Fig. 44. Graphite block heat exchanger.

4.5 Thin-Film Heat Exchangers

Thin-film heat exchangers are resorted to far highly viscous and heat-sensitive products. They feature high heat transfer coefficients, good part-load performance, and short residence times and are most frequently designed as evaporators.

A thin-film evaporator consists of a heated cylindrical or conical section fitted with a rotor (Fig. 45) and an upper dome for the removal of the entrained droplets. The product is fed above the jacket heater, spread over the circumference by a distributor ring, and whirled by the rotor blades against the heated wall in the form of a thin film, which descends in a spiral path. The vapor formed rises upwards in countercurrent flow and passes through the separator. The unevaporated fraction reaches the lower end and is removed from the evaporator.

Depending on the demands imposed, the rotor is fitted with fixed or movable wiper blades (Fig. 46).

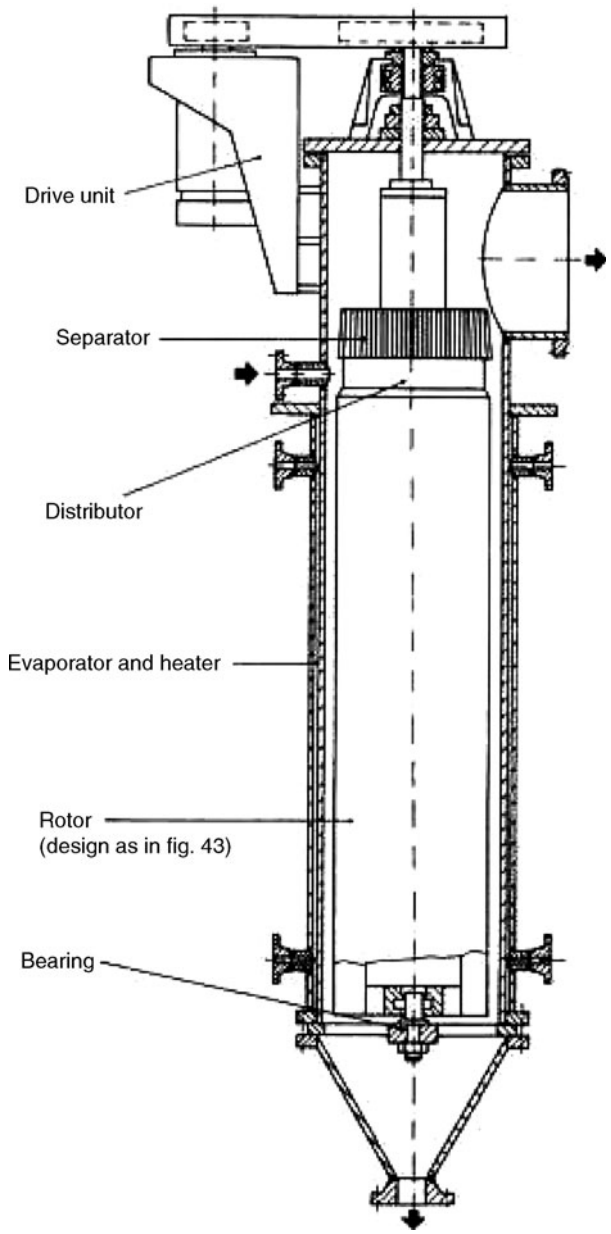

O1. Fig. 45. Thin-film heat exchanger.

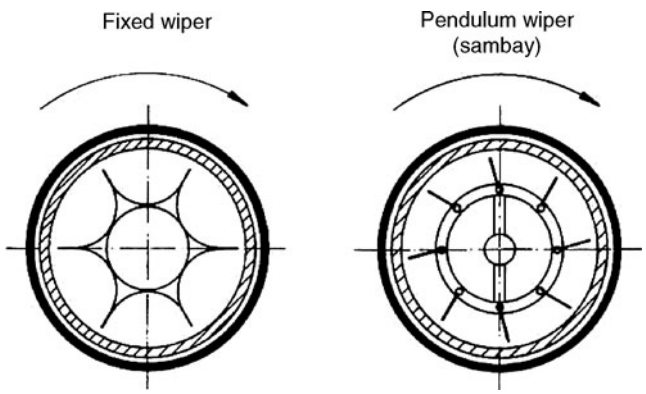

O1. Fig. 46. Rotors in thin-film heat exchanger.

Thin-film evaporators are designed in lengths of up to 15 m and outer diameters of up to 2 m.

4.6 Air-Cooled Heat Exchangers

Air-cooled heat exchangers are frequently used in chemical production plant, refineries, steelworks, foundries, and power stations. The basic requirement is an adequate difference throughout the whole year between the temperature of the ambient air and that of the product to be cooled.

From the physical aspect, air is a poor coolant, but it has many properties that render it superior to water for cooling purposes. Examples are that

- it is available in unlimited amounts;
- it is cleaner;
- it presents less corrosion and cleaning problems.

Various designs of air-cooled heat exchangers are described in DIN 45635 (Fig. 44).

The position of the tube bundle in relation to that of the fan decides whether an induced-draught or other forced-draught system is adopted. In induced-draught systems (Fig. 47, upper row), the fan is located in the current of hot air, and the greater volume of heated cooling air necessitates higher power requirements.

The position of the tube bundle is another factor to observe in the design of air-cooled heat exchangers. Those with horizontal bundles occupy the most floor space, but are the most frequently encountered, because they incur the lowest capital investment costs. As a rule, air-cooled heat exchangers in the form of a roof require two-thirds of the floor space occupied by the corresponding horizontal version. The inclined cooling elements may present technical advantages in condensation processes. Preference is given to the V-roof in countercurrent condensation, because of the simplicity that it allows in intake and discharge. Cooling elements may be arranged vertically if the floor space is very restricted, but the static loads imposed limit their application to small heat exchangers.

The tubes are generally finned, and the heat transfer area can thus be increased by a factor of 5–30, depending on the application. The geometry of the core tube and the fin and the means of attachment can be varied, and the entire design must be optimized from the economic, material, and manufacturing aspects. The main types of tubes are as follows.

- The oval or circular tubes shown in Fig. 48 are usually of unalloyed or stainless steel. The fins are rectangular sheet-metal strips that are forced mechanically onto the tube or steel tapes that are helically wound around the tubes. A metallic bond between the tube and the fins, as illustrated in Fig. 49a, is effected by dip-galvanizing.
- The G-type finned tube shown in Fig. 49b consists of a circular tube with a helical groove into which aluminum tape has been wound under tension and compressed. The strength of the tube wall is reduced to an extent that depends on the depth of the groove.

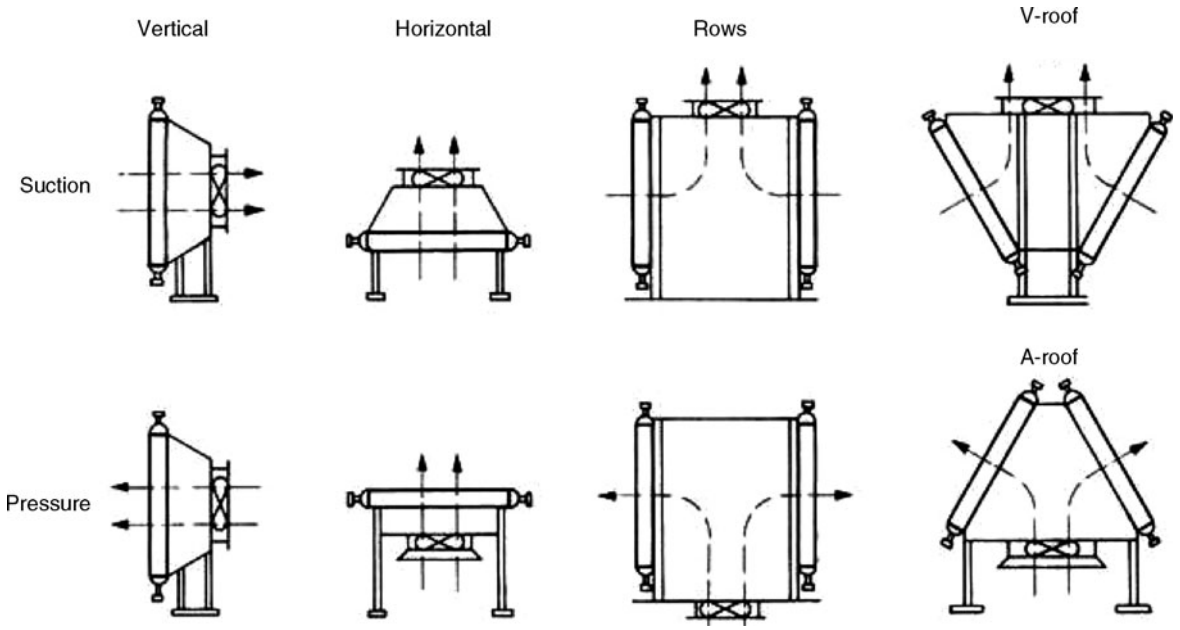

O1. Fig. 47. Air-cooled heat exchangers.

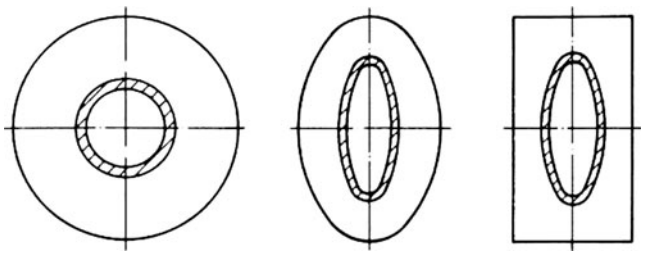

O1. Fig. 48. Circular and oval finned tubes.

- The L-type finned tube illustrated in Fig. 49c is produced by spirally winding an aluminum L-tape under tension around a circular tube so that the bases of the fins, which are of about 3 mm width, lie close together.
- The bimetal tube with cold-impact press-formed fins shown in Fig. 49d is obtained by inserting a circular core tube in an aluminum tube. The fins are then formed mechanically, and the outer tube is pressed onto the core tube.

The choice of the material selected for the tube primarily depends on the properties of the product to be cooled or condensed. Allowance must be made for its physical properties, including the resistance to corrosion by the ambient air, the processing characteristics, the compatibility with the core tube, and the means of securing the base of the fins to the tube. The most common pairings are steel tubes and fins formed into a block by galvanizing and copper tubes with aluminum fins.

The finned tube assemblies may be up to 15 m in length and 3 m in width and usually consist of 3–7 staggered or in-line banks. They are stiffened by side walls and tube supports and are self-supporting. In-line tubes give rise to a lower pressure drop but to poorer heat transfer than staggered tubes.

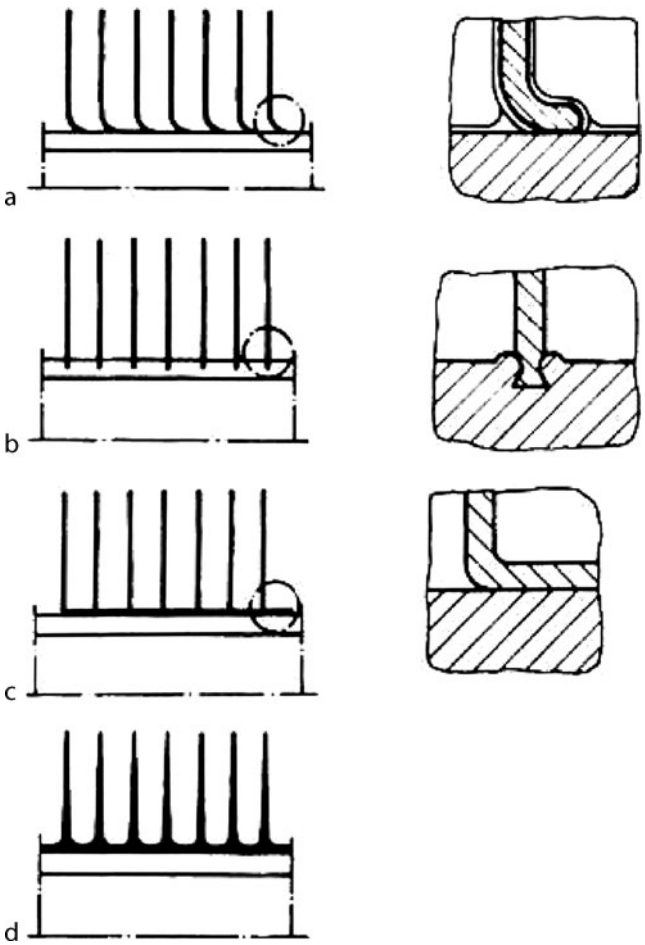

O1. Fig. 49. Various types of fins (Methods **a**–**d** are described in Sect. 4.6).

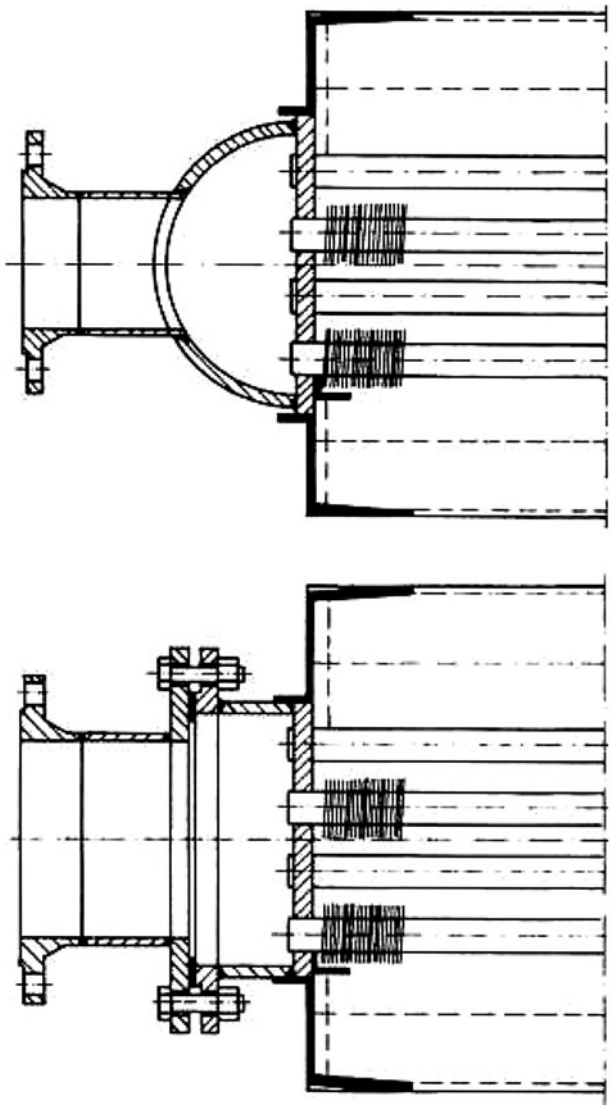

O1. Fig. 50. Designs for dished ends on air-cooled heat exchangers.

The ends of rectangular bundles of straight tubes are welded or milled into the support plates. The product is distributed and collected by means of the support plate and the dished end, which may be welded or – if the inner surfaces of the tubes have to be cleaned – flanged to the support plate (Fig. 50).

The current of cooling air is set in motion by axial flow fans with glass-reinforced-plastic or aluminum rotors that are installed in ducts connected to the tube bundles. The air velocity in the heat exchanger is about 2–3 m/s. If it is low, screens may have to be installed in order to ensure smooth and continuous operation.

The fans are usually driven by V-belts or, if the air flow rate is high, by gear transmission systems. In certain cases, power may be supplied by directly coupled, low-speed multipole motors.

The air flow rate in the heat exchanger can be controlled if necessary, e.g., if the temperature of the medium is to be kept constant or if the installation has to be protected from frost.

Fluctuations in outdoor temperature can be compensated by varying the flow rate of cooling air continuously or in stages. The following means are thus adopted:

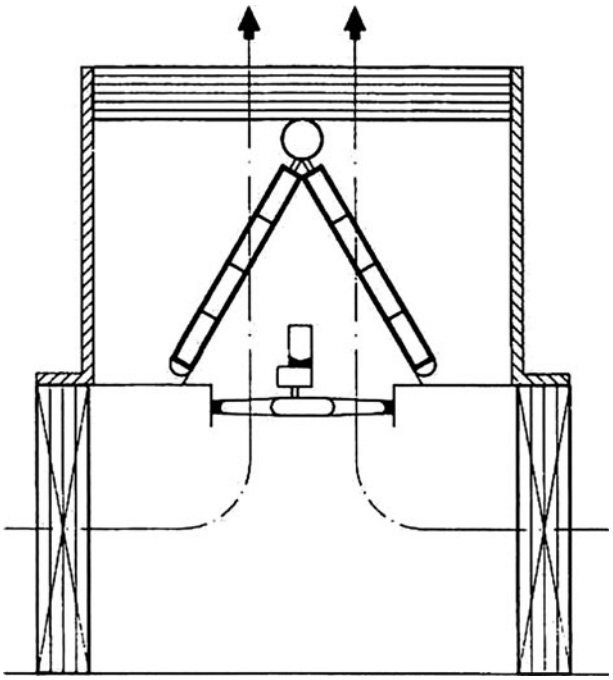

O1. Fig. 51. Air-cooled heat exchanger with silencer.

- switching individual fans on or off,
- electric motors with pole-changing switches,
- fan blades that can be adjusted while the fan is running,
- regulating the fan motors by frequency converters,
- louvres e.g., heat transfer by free convection in winter with the fans switched off.

The operation of fans and their motors is the subject of legislation on noise suppression, and permissible values in decibels are laid down for sound pressure levels. Guidelines also exist on the measurement of sound emission from air-cooled installations, e.g., DIN 45635. Recently, more recourse is being taken to silencers, as illustrated in Fig. 48, to restrict the sound pressure level to below the permissible limit.

5 Appendix

Selection of DIN standards (English translations) in the construction of heat exchangers. Currently available from Beuth Verlag GmbH, Berlin

DIN

2391 Part 1 Seamless precision steel tubes; dimensions

2391 Part 2 Seamless precision steel tubes; technical delivery conditions

2393 Part 1 Welded precision steel tubes; dimensions

2393 Part 2 Welded precision steel tubes; technical conditions of delivery

2401 Part 1 Components subject to internal or external pressure; pressure and temperature data; terminology; nominal pressure ratings

2448 Seamless steel pipes and tubes; dimensions, conventional masses per unit length

2458 Welded steel pipes and tubes; dimensions, conventional masses per unit length
2462 Part 1 Seamless.stainless steel tubes; masses per unit length
2463 Part 1 Welded austenitic stainless steel; pipes and tubes; dimensions, conventional masses per unit length
8558 Part 2 Design and workmanship of welded joints; steel vessels and apparatus used in the chemical industry
17173 Seamless circular tubes made from steels with low temperature toughness; technical delivery conditions
17174 Welded circular tubes made from steels with low temperature toughness; technical delivery conditions
17175 Seamless tubes of heat-resistant steels; technical conditions of delivery
17177 Electric pressure-welded steel tubes for elevated temperatures; technical conditions of delivery
17455 General purpose welded circular stainless steel tubes; technical delivery conditions
17456 General purpose seamless circular stainless steel tubes; technical delivery conditions
17457 Welded circular austenitic stainless tubes subject to special requirements; technical delivery conditions
17458 Seamless circular austenitic stainless steel tubes subject to special requirements; technical delivery conditions
28180 Seamless steel tubes for tubular heat exchangers; dimensions, dimensional deviations and materials
28181 Welded steel tubes for tubular heat exchangers; dimensions, dimensional deviations and materials
28182 Tubular heat exchangers – tube pitches, diameter of bores in tube sheets, baffles and support plates
28 184 – tubular heat exchangers with two fixed heads
28 185 – components for tubular heat exchangers
28 190 – floating head heat exchanger with welded floating head – examples of design
28 191 – floating head heat exchanger with flanged floating head – examples of design
28 008 – tolerances for construction of tubular heat exchangers
EN 10220 Seamless and welded steel tubes – general tables of dimensions and masses per unit length

6 Bibliography

1. GPSG - Geräte- und Produktsicherheitsgesetz, Gesetz über technische Arbeitsmittel und Verbraucherprodukte (German law about safety of equipment and products, issued January 6, 2004)
2. Pressure Equipment Directive 97/23/EC of the EU which sets out the standards for the design and manufacture of pressure equipment
3. AD 2000-Regelwerk, issued by *Verband der Technischen Überwachungs-Vereine e. V.*, Essen (German regulation), see http://www.ad-2000-online.de
4. Betriebssicherheitsverordnung – BetrSichV (German safety regulation for manufacturing sites with the need of operational supervision), see www.druckgeraete-online.de
5. TEMA, Standards of Tubular Exchanger Manufacturers Association, see www.tema.org
6. Podhorsky M, Krips H (1990) Wärmetauscher, Aktuelle Probleme der Konstruktion und Berechnung. FDBR-Fachbuchreihe, Band 5, Vulkan-Verlag Essen
7. Sterr G (1975) Die festigkeitsmäßige Berechnung von Wärmeaustauschern mit geraden Rohren. TÜV 8
8. A working guide to shell-and-tube heat exchangers. Stanley Yokell, McGraw-Hill. 1. Aufl. 1990
9. Würmseher H, Swozil A, Künzel J (1983) Kohlenstoff und Graphit als Werkstoff für hohe Korrosionsbeanspruchung im Druckbehälter- und Apparatebau. Swiss Chem 5(10a)